Materials Science and Engineering Technology

Edited by
Zhang Mei

TRANS TECH PUBLICATIONS

Materials Science and Engineering Technology

Edited by
Zhang Mei

Materials Science and Engineering Technology

Selected, peer reviewed papers from the
2014 International Conference on
Materials Science and Engineering Technology
(MSET 2014),
June 28-29, 2014, Shanghai, China

Edited by

Zhang Mei



Copyright © 2014 Trans Tech Publications Ltd, Switzerland

All rights reserved. No part of the contents of this publication may be reproduced or transmitted in any form or by any means without the written permission of the publisher.

Trans Tech Publications Ltd
Kreuzstrasse 10
CH-8635 Durnten-Zurich
Switzerland
http://www.ttp.net

Volume 936 of
Advanced Materials Research
ISSN print 1022-6680
ISSN cd 1022-6680
ISSN web 1662-8985

Full text available online at *http://www.scientific.net*

***Distributed** worldwide by*

Trans Tech Publications Ltd
Kreuzstrasse 10
CH-8635 Durnten-Zurich
Switzerland

Fax: +41 (44) 922 10 33
e-mail: sales@ttp.net

and in the Americas by

Trans Tech Publications Inc.
PO Box 699, May Street
Enfield, NH 03748
USA

Phone: +1 (603) 632-7377
Fax: +1 (603) 632-5611
e-mail: sales-usa@ttp.net

Preface

Nowadays many developed countries are in recession and their consumption of natural resources like energy, minerals and other raw materials is lower than usual. At the same time the global prices of those materials stay at a high level because the BRICS-countries (short for Brazil, Russia, India, China and South Africa) have developed their economy to a higher level. Consequently, their consumption of those materials has been reaching a higher level as well. Considering the total population of the BRICS, their need will be increasing and the prices for raw materials are obviously to remain stable or go up in the future. Prices at such high levels remind us of the fact that the available resources of refinery or processing facilities and the natural reserves of those discovered materials on earth hardly cover the increasing demand.

The reasons to promote the subjects of science are extraordinarily the same as those for Materials Science and Engineering Technology, and we won't to repeat them in the foreword for MSET2014.

When we were collecting the papers for the Conference on Materials Science and Engineering Technology, the interesting things were that a number of authors were quite keen to look for the same chance to make public the theoretical works of intellectual creativity or formal results of scientific research or practice, written by those who are their former class mates, campus fellows, friends, relatives, colleagues and cooperators. It is really a chance for us to organize a chance for our smart intellectuals to expose, exchange and confidently approve each other the value of their arduous work. In six months, we have collected 758 copies of papers in the scope the mentioned subjects and their close-related subjects, and 420 copies selected after peer-view. 232 copies are in the research of materials science while 61 copies of materials properties, measuring methods and applications, 61 copies of methodology of research and analysis and modeling and 66 copies are on the subjects of close –related to materials manufacturing and processing.

Material science is one of the most important matters of our life and with us as ever we have existed, unlike computer or information technology but unfortunately we have never known all materials we have used or around us. Nevertheless, we have been working very hard to discover new sources of materials we are in need of and striving non-stop for new synthetic stuffs or man-made matters. High demand has pushed our scholars, experts and professionals to continue the mission, not only for the materials themselves but non-perilous to the life and environment as well, causing the least hazard to the world. We appreciate our authors consciously to involve into that mission.

Engineering technology appeared in the antient time in human life. All tools we found or created beside we can simply use as part of our body such as our hands and feet, eyes and teeth, are mechanics, but modern mechanical has extended its concept since steam and gasoline engine, electric motor were found. It has spread to all corners of life, without what, we can not survive in contemporary days. Consequently, there are countless subjects for our learned people to work at. As the organizer of the conference MSET2014,we have selected 232 copies of papers in materials science which are comparatively at a high level of each research.

Conference on Materials Science and Engineering Technology is scheduled to hold in Shanghai from June 28 to 29, 2014, experts and scholars, a group of the authors and other related people will attend the conference with apparent interest, we are expecting a full success of the conference.

We appreciate those who responded to our proposal and submitted their papers, especially those whose papers have been selected for the conference MSET2014, the sponsors who have provided their valuable and professional suggestions and instructions and the scholars and professors who have spent their efforts as peer reviewers. We expect the conference to be successful and we hope that our proposal

'China Made jumping to China Create' will result in many more conferences on various other scopes and subjects, nation-wide, encouraging more professionals, scholars and students to contribute their talents to improving our life.

Thank you!

Zhang Mei

March 25, 2014

Program Committee

General Chair:
Dr. R.K. Kotnala, Editorial Board Member of J. Nanoparticle Research, Indian

Technological Committees

Prof. Xiaokui Yue, Northwestern Polytechnical University, China
Prof. Zhanglian Hong, Zhejiang University, China
Dr. Yinong Wang, Dalian University of Technology, China
Prof. Qudong Wang, Shanghai Jiaotong University, China
Dr. Jianguo Lv, Zhejiang University, China
Prof. Jian Weng, Xiamen University, China
Dr. Honggang Dong, Dalian University of Technology, China
Dr. Di Zhang, Shanghai Jiaotong University, China
Dr. Xuegong Yu, Zhejiang University, China
Dr. Pingwu Du, University of Science and Technology of China, China
Dr. WeiFeng Liu, China University of Petroleum, China
Dr. Yi Cao, School of Electrical Engineering, Henan University of Technology, China
Dr. Zhijun Zhang, School of Mechanical Engineering and Automation northeastern University, China
Prof. Yongsheng Zhao, Yanshan University, China
Prof. Fuzhen Xuan, East China University of Science and Technology, China
Prof. Fushuan Wen, South China University of Technology, China
Prof. Zhaojun Yang, Jilin University, China
Prof. Lizhong Xu, Yanshan University, China
Prof. Xuemin Tian, China University of Petroleum, China
Prof. Haisheng Yu, Qingdao University, China
Prof. Yibin Song, Yantai University, China
Prof. Yong Zhang, Jinan University, China
Prof. Yuqiang Wu, Qufu Normal University, China
Prof. Yumei Wang, Weifang University, China
Prof. Yanbin Qu, Harbin Institute of Technology, China
Prof. Xiaohua Liu, Ludong University, China
Li Guo, College of Mechanical and Vehicle Engineering, Hunan University, China
Prof. Mei Su, Central South University, China
Dr. Mahmoud Ibrahim Mahmoud Moussa, Benha University, Egypt

SPONSORED BY

Shanghai JiaoTong University
East China University of Science and Technology
Shanghai University of Engineering Science)
Engineering and Industry Technology Institute

Table of Contents

Preface and Program Committee

Chapter 1: Polymers and Composites

Mechanical and Thermal Properties of Siloxane Reinforced Biphenyldiol Formaldehyde Resin Curing Epoxy Resin Composites
S.H. Chen, J.G. Gao, H.Z. Han and C. Wang 3

Polymer Blend through Inclusion Complexation
C.Y. Liu, W.I. Lin and J.B. Wang 8

Fabrication and Properties of Composites of Linear Polyacrylamide and Functionalized Carbon Nanotubes
R.M. Yang, Y.H. Liu, G.X. Dong and D.J. Zhao 12

Thermal Degradation Behavior of Polypropylene and Ethylene Vinyl Acetate Copolymer Treated with Intumescent Flame Retardants Containing Caged Bicyclic Phosphates
X. Li and Y.X. Ou 17

Effect of Pr Modification Treatment on the Microstructure and Mechanical Properties of Cast Al-Mg_2Si Metal Matrix Composite
S. Yi 23

Curing Kinetics of Silicone Epoxy Resin Containing Fluorene
W.X. Deng, Y.W. Zhong, J. Qin, X.B. Huang and J.W. Peng 28

Synthesis of Core @ Shell Composite Particles with a Tunable Shell Containing Natural Urushiol
L.H. Zheng, B.L. Chen, H.B. Huang, Q.H. Chen and J.H. Lin 34

Preparation and Properties of Polypropylene-Graft-Cardanol by Reactive Extrusion
Q.H. Chen and J.H. Lin 39

Analysis and Experiment of Compressive Residual Strength of Composite Laminates with Holes
X.H. Kong and Z.J. Wang 43

Microstructures of Poly (9'9-Dihexylfluorene) Grown in the Non-Solvent Vapor
X.Q. Xiao, W.B. Bai and J.H. Lin 53

Synthesis and Properties of Polypropylene Carbonate Polyol-Based Waterborne Polyurethane
C.S. Xu, C.C. Tian, W.D. Zhang, J.W. Xing, Z.S. Cai, Y. Ren, W.Z. Xu and H.Y. Liu 58

Curing Process of Epoxy Resin Using Low Molecular Polyamide 651 as Curing Agent
C.H. Han, L. Wang and D.Y. Zhao 63

Synthesis of Bis(*p*-aminophenoxy)Dimethylsilane(*p*-APDS) and its Process Optimization
L.X. Chen, F. Yang and J. Yun 67

Structure and Mechanical Properties of Starch/Styrene-Butadiene Latex Composites
G. Chen, Z.J. Zhu, P. Salminen and M. Toivakka 74

Experimental Advances in Effect of Waviness on Properties of Fibre Reinforced Composite Materials
J. Zhu and J.H. Wang 82

Effect of Crosslinker Type on the Properties of Surface-Crosslinked Poly(sodium acrylate) Superabsorbents
Y. Xiong, X. Zhang and M.Z. Liu 89

Phase Separation in Thermosetting Blends of Epoxy Resin with PS-*b*-PCL and PI-Si Block Copolymers
J.D. Ding, W.Z. Li, T.Q. Jiang, Z.L. Xia and W.J. Gan 95

Chapter 2: Ceramics and Functional Materials

Effect of PZN Addition on Piezoelectric and Ferroelectric Properties of Pb ($Zr_{1/2}Ti_{1/2}$)O_3 Ceramics
T. Promjun, S. Sukprasong, L. Chumprasert and A. Ngamjarurojana 101

Effect of External Magnetic Field on Dielectric Spectroscopy of Modified PZT Ceramics
A. Ngamjarurojana, T. Promjun and A. Limpichaipanit 105

Optical Interferometric Technique for Induced Strain Ferroelectric Loop Study at Low Frequency
S. Somwan, K. Chirapatpimol, A. Limpichaipanit, K. Chokethawai and A. Ngamjarurojana 110

Effect of Dielectric Properties and Elastic Strain Behavior on x/65/35 PLZT Ceramics in Lanthanum (x) Ions Contents
L. Chumprasert, P. Larwongsa, A. Limpichaipanit and A. Ngamjarurojana 115

Dielectric and Ferroelectric Behavior in 8/40/60 PLZT Ceramics
L. Chumprasert, K. Chirapatpimol, A. Limpichaipanit, K. Chokethawai and A. Ngamjarurojana 119

Preparation and Optoelectronic Properties of In_2O_3 Microtubes
S. Chen, Y.Z. Long, H.D. Zhang, S.L. Liu, L.Z. Liu, J.C. Zhang, G.X. Liu and F.K. Shan 123

The Anti-Plane Shear Problem of Two Symmetric Cracks Originating from an Elliptical Hole in 1D Hexagonal Piezoelectric QCs
J. Yang and X. Li 127

CdS-Bentonite Sulfide Ion Sensor: pH Effect and Selectivity
K. Udomphan, A. Wongchaisuwat and L. Meesuk 136

Relationship between Annealing and Shape Memory Effect of Shape Memory Polyurethane
J. Ying, M. Nishikawa and M. Hojo 140

Preparation of Uniform α-Alumina Microspheres by Catalytic Precipitation and Calcination Process
Z. Wang, X.Q. Shen, M.X. Jing, L. Yan and Z. Luo 145

Phase Structure and Piezoelectric Properties of $(K_{0.5}Nb_{0.5})NbO_3$ - $CaZrO_3$ Ceramics
P.C. Myoung 149

A Novel Model for Predicting the Thermal Conductivity of Fiber Reinforced Ceramic Materials
R. Xu, J.K. Mao, J.Y. Zhang, D.C. Lou and W. Guo 154

Nucleation, Crystallization and Characterization of Mica-Based Glass-Ceramics with Fluorapatite
J. Bai and D. Chayasuwan 164

Preparation of C@$ZrSiO_4$ Inclusion Pigment Using Compound Colorants via Non-Hydrolytic Sol-Gel Method
X.Y. Xu, W.H. Jiang, T. Chen, J.M. Liu, L.F. Miao and X.J. Zhang 170

Fabrication and Characterization of SiC-Coated Multi-Walled Carbon Nanotubes Reinforced Reaction Bonded SiC Composite
N. Song, H. Liu, Y.T. Yuan and J.Z. Fang 176

Carbonization Effect on Phase Structures of Zirconium Oxides with 2-3 Percent Yttrium
Z.Q. Xue and Y.Q. Guo 181

Numerical Research of the Beryllia Ceramics Formation Process
U.K. Zhapbasbayev, G.I. Ramazanova and Z.K. Sattinova 187

Chapter 3: Films and Membranes

Cu(In,Ga)Se_2 Films Deposited by Sputtering with Single Cu(In,Ga)Se_2 and Cu-Ga-In_2Se_3 Targets and a Subsequent Selenization Procedure
D.H. Kuo, Y.C. Tu and W.L. Chen 197

Effect of Hydrogen Dilution Ratio and Substrate Roughness on the Microstructure of Intrinsic Microcrystalline Silicon Thin Films
B.J. Yan, S.L. Liu, X.W. Liu and T.T. Jiang 202

The Photoluminescence from (Eu, Yb) Co-Doped Silicon-Rich Si Oxides
C.L. Heng, W.Y. Su, Q.W. Zhang, X.Q. Ren, P.G. Yin, H.P. Pan, S.D. Yao and T.G. Finstad 207

Compatibility of Polyvinylidene Difluorid/Polyurethane and Preparation of Composite Tubular Membrane
D.Y. Zuo, H.J. Li, C.H. Yi and H.L. Gan 212

Preparation and Properties of Two-Dimensional Braid Heterogeneous-Reinforced Polyvinylidene Fluoride Hollow Fiber Membrane
Q. Quan, C.F. Xiao, H.L. Liu, W. Zhao, X.Y. Hu and G.L. Huan 218

Effect of Ethanol Composition in Water Coagulation Bath on Structure and Performance of Homogeneous-Reinforced Polyvinyl Chloride Hollow Fiber Membranes
H.L. Liu, C.F. Xiao, Q.L. Huang, Z.L. Fan, X.Y. Hu, W. Shu and G.L. Huan 226

Fabrication and Characterization of CuO Micro-Dimensional Structures for Superhydrophobic Surface
Y.H. Fan, Z.J. Chen, L.Y. Deng and H. Chen 233

Low Temperature Preparation of Aluminum Titanate Film via Sol-Gel Method
Y. Bao, W.H. Jiang, G. Feng, J.M. Liu and Q. Wu 238

Multilayer Film through Inclusion Complexation
C.Y. Liu and W.I. Lin 243

Preparation and Characterization of Bipolar Membranes Modified by Adding Multi-Carboxylic Metallophthalocyanine Derivatives into the Cation Layer
M. Lu, Y.Y. Hu and R.Y. Chen 248

Highly Strained Silicon Nitride Thin Film Deposited by PECVD with Double Frequencies in Strained Silicon Technologies
B. Shu, J.M. Chen, H.M. Zhang, F. Zhu, P.L. Quan, J.Y. Gu, R.X. Xuan, H.Y. Hu and J.J. Song 255

Layer Formation of SAPO-34 Zeotype Material by EPD Seeding Method Followed by Hydrothermal Secondary Growth
S.M.H. Davarani, S. Fatemi and Z. Jabbari 259

Substrate Dependence of Microcrystalline Silicon Growth with SiH_4 Diluted by Ar
H. Cheng, Y.C. Qian and J. Xue 264

Study on the Polarization Reversal Characteristics of a Ferroelectric Thin Film with Surface Transition Layers
L. Cui, Z.Y. Qiu, Z.Y. Han, R.Y. Li and J.X. Che 269

Fabrication of Diamond Films on Cu Metal Substrates with Buffers (SiC or $MoSi_2$) by Hot Filament Chemical Vapor Deposition
Q. Zhao, M.J. Dai, D. Tan, C.B. Wei, W.Q. Qiu and H.J. Hou 276

Epitaxial Pd-Doped $LaFeO_3$ Films Grown on (100) $SrTiO_3$ by Pulsed Laser Deposition
Y.W. Duan 282

The Preparation of the Highly Preferred Orientation of Wurtzite Structure Zinc Oxide Films
L.L. Lan, D. Zhou, G.R. Gu, B.J. Wu and L.H. Tian 287

Chapter 4: Nanomaterials and Applied Nanotechnologies

A Facile Method to Preparation of Amphiphilic Perylene Tetracarboxylic Diimide/ZnS Hybrid Nanocomposites and Improved Semiconducting Property
J.G. Song, H.Y. Wang, N.S. An and Y.L. Chen 295

Pt-TiO_2 Nanocomposites in Alginate for Enhancing Photocatalytic Activity
Y.R. Wang 300

Preparation of Carboxymethyl Chitosan Magnetic Nanoparticles and Separation of Chinese Medicines Components
Y.H. Xie, Y.T. Zhang, X.Z. Huang, Y.H. Ding and L.P. Huang 304

Comparison of Hydrogen Sulfide Sensing Properties between Multiple-Walled Carbon Nanotubes (MWNTs) and MWNTs-$HAuCl_4$ Materials
S.X. He, G.Z. Xie, Y.D. Jiang, G.D. Zhang and Y. Zhou 310

Effect of Cu,Cr Co-Doped on Structure and Magnetic Properties of Sm_2Co_{17} Alloy Films
C. Wang, Q.Q. Fang, D.D. Wang, J.J. Yang and J.G. Li 315

Hyaluronic Acid Functionalized Porous Silica Nanoparticles for Drug Delivery and Release
L.Y. Cui, Y.H. Li, W. Zhang, J.P. Zhang and Q. Duan 322

Preparation and Characterization of Fibrillated Nanofibrous Filter Material
T. Yu, Y.B. Jiang and J. Hu 327

The Improvement of Pd Nanoclusters Electro-Catalytic Properties for FAO by the Addition of Co Element
M. Lei, L.S. Wang, X.L. Liu, J.B. Wang, R. Xu, C.X. Lei, G.H. Yue, Y. Chen and D.L. Peng 332

Synthesis and Characterization of Emulsion Coating of Fluorinated Polymethacrylate Modified by POSS
B.J. Tian, J.G. Gao and C. Wang 337

The Performance of Gold Nanoparticles Supported on Mesoporous Zirconia for the Synthesis of Azoxybenzene
M.L. Jia, M.J. Feng, X. Li and Z.R.G.T. Bao 343

The Facile Hydrothermal Preparation of WO_3 and its Photocatalytic Performance under Visible-Light Irradiation
F.F. Li, H.T. Gao and G.J. Liu 347

Hydrothermal Synthesis and Characterization of Cerium-Based Oxides
R. Dangerfield, S. Sharp and R.G. Wang 352

Controlled Synthesis of Core-Shell Structure SiO_2 /$NaGdF_4$:Eu^{3+} Magnetic and Optical Bifunctional Composite
Y.L. Wu, M. Liao, H.X. Ding, R.C. Yang, D.D. Xiong and Q. Xiao 359

Electrochemical Properties of Graphene Nanosheet/Polyaniline Nanocomposite as Electrode for Supercapacitors
R.R. Yao, N.N. Yao, D.L. Zhao and L. Xu 364

Graphene/Sulfur Nanocomposite for High Performance Lithium-Sulfur Batteries
S.W. Ma, D.L. Zhao, N.N. Yao and L. Xu 369

Preparation and Characterization of Magnesium Oxide Aerogels
J.W. Wu, L.F. Yao, J. Shen, G.Q. Zu and F. Wang 374

Enhanced Field Emission Characteristics of ZnS Dentalation Nanostructures
J.J. Qi, Z.Q. Deng, Z. Wu and Y. Zhang 379

Enhancement of Titania Photocatalytic Properties by Fabrication of MWCNT-TiO_2 Nanocomposites
E. Soroodan Miandoab and S. Fatemi 384

Study on Tensile and Impact Performance for the MWCNTs/EP Composite
F. Yan, J.W. Fu and D.Y. Zhao 390

The Natural Rubber/Zinc Oxide Nanocomposites: Its Morphology, Mechanical and Thermal Decomposing Properties
M.Z. Lv, L. Fang, P.W. Li and C.L. Yang 394

Effect of Grain Size on the Fracture Toughness of Bimodal Nanocrystalline Materials
Y.G. Liu, X.D. Mi and S.F. Tian 400

Numerical Simulation of Synthetic Heat Transfer in Laminar Nanofluid in a Horizontal Pipe
M. Mirzaei, M.J. Gishin and M. Abbaspour 409

Particle Swarm Optimization Technique for DNA Sensor Model Based Nanostructured Graphene
V. Popov 415

Preparation of Ethanol-Sensing Gas Sensor Based on PECH/Multi-Wall Carbon Nanotubes Sensitive Films
W. Yao, G.Z. Xie, H.L. Tai, Y.D. Jiang and Y. Zhou 419

Preparation and Characterization of Polyacetylene/Expanded Graphite Composites
M.M. Hu, L.H. Song and B.L. Tao 424

Preparation and Mechanics Properties of the EP/SiO_2 Nanocomposites
W.F. Zeng, Y. Jiang, S.F. Bu, Y.H. Ding and J.R. Yin 429

Effects on Characteristics of the SiO_2-to-Na_2O Ratio on Nano-SiO_2 Metakaolin-Based Geopolymers
K.L. Lin, K. Gao, D.Y. Wang, K.W. Luo, W.H. Chang, D.Y. Huang, H. Cheng and R. Cui 434

Microstructures of ZnO Electrospun Nanofibers on AZO Glass
X.Z. Lu, Y.Y. Chang, M.T. Xu and B. Peng 439

Chapter 5: Materials for Energy Sources and Energy Supply

Research of Properties on Li-Ion Batteries Based on a Polypyrrole Derivative Bearing TEMPO as a Cathode Material
L.H. Xu, F. Yang, C. Su and C. Zhang 447

Nanostructured Morphology of Spinel $LiMn_2O_4$ Oxide under Microwave Heating
D. Huo 452

Effect of SnO_2 Particle Size on Properties of Ag-SnO_2 Electrical Contact Materials Prepared by the Reductive Precipitation Method
Z.J. Lin, X.D. Sun, S.H. Liu, J.L. Chen, M. Xie, J.G. Li, X.D. Li, D. Huo, M. Zhang and Q. Zhu 459

Electrochemical Investigation of $La_{0.2}Sr_{0.8}TiO_{3+\delta}$-$Ce_{0.8}Sm_{0.2}O_{2-\delta}$ Composite Cathode for the Direct High Temperature Steam Electrolysis
G.J. Wu, K. Xie and Y.C. Wu 464

Highly Hydroxylated Graphite Felts Used as Electrodes for a Vanadium Redox Flow Battery
W.W. Li, Y.Q. Chu and C.A. Ma 471

A Novel Route to Prepare Titanium Doped Mesoporous Carbon
H. Tian, Y. Zhang and Y.J. Liu 476

Enhanced Electrochemical Performances of $LiFePO_4$/C Cathode Materials by Deposited with Ge Film
Y.D. Huang, Y.B. Lin and Z.G. Huang 480

Study on Ag/SnO_2/TiO_2 Electrical Contact Materials Prepared by Liquid Phase *In Situ* Chemical Route
Y.C. Zhu, J.Q. Wang, L.Q. An and H.T. Wang 486

A Novel Synthesis of Nanometer Spherical β-$Ni(OH)_2$ Cathode Materials with High Electrochemical Performances
L. Chen, Y.M. Wang, J. Liu and X.Y. Wang 491

A High Rate, High Capacity and Long Life ($LiFePO_4$+AC)/$Li_4Ti_5O_{12}$ Hybrid Battery-Supercapacitor
X.B. Hu, Z.J. Lin and Y.L. Zhang 496

Chapter 6: Chemical Physics

Modeling of Recrystallization Texture of Rolled Polycrystalline Aluminium
K. Wierzbanowski, M. Kotra, M. Wroński and K. Sztwiertnia 505

Numerical Analysis on Decay Heat Power of Weapon-Grade Uranium and Depleted Uranium
Y.L. Wang, W.L. Yu, T. Wang and S.Q. Dong 509

Hydrogen Storage Mechanism of Fe_3O_4: A First-Principles Study
H. Zhang, N.P. Cheng, Z.Q. Chen and Q. Hui 515

Phase Field Crystal Study for the Effect of Heating Rate on the Premelting of Grain Boundary
Y.L. Lu, T.T. Hu and H. Mu 523

A First-Principles Study on Electronic Properties of Ce/N Codoped Anatase TiO_2
S.Y. Yang, L.F. Yao and H. Chen 529

Effective Nuclear Field Measurement in a Single Quantum Well via Time-Resolved Kerr Rotation Technique
L.P. Yan, R. Kaji and S. Adachi 534

Theoretical Investigation on Rearrangement Mechanism of Fluoroalkylsilane
Y.F. Zhou and Q.Y. Ma 540

Assessments of Impurity Diffusion Coefficients of Selected Pure Metals in Fcc Fe
X.X. Hu, X.G. Lu and Y.L. He 545

The Properties of a Novel Green Long Afterglow Phosphor Zn_2GeO_4:$Mn^{2+}_{0.01}$, $Pr^{3+}_{0.01}$
M.H. Wan, Y.H. Wang, X.S. Wang, H. Zhao, Z.F. Hu and C. Wang 552

Dy^{3+} Doping Blue-Green $Sr_4Al_{14}O_{25}$:Eu^{2+} Phosphor for Enhancing Luminescent Properties and the Mechanism Study
Z. Kong, H.B. Wang, E.P. Zhang, T. Qiu, J. Zhang and Z.G. Ji 562

Magnetic and Electrical Property in Mg^{2+} Deficient $La_{1.4}Sr_{1.6}Mn_2O_7$ Perovskite
Y. Zong, X. Zhao and W. Chen 571

The Ideal "Defects" of the Crystal Structure of GaAs
K. Iskakova, R. Akhmaltdinov and A. Amaonova 577

Cooperative Energy Transfer of Er-Gd-Tb System in Tb^{3+}, Er^{3+} Co-Doped $K_2GdZr(PO_4)_3$ as a Potential Visible Quantum Cutting Phosphor
L.F. Niu, W. Liang, C.Z. Wu and Y.H. Wang 585

First-Principles Investigations of Electronic, Dynamic and Thermodynamic Properties of α-MnO_2
A.M. Hao and N.Q. Wang 591

Chapter 7: Materials and Technologies in Microelectronics

Ultra-Multilevel-Storage Phase Change Memory
Y. Yin and S. Hosaka 599

Surface Passivation of Crystalline Silicon by a-Si:H Thin Films
Y. Wang, W. Li, A.R. Guo, F. Yu, J. He and Y.D. Jiang 603

Microwave-Assisted Synthesis of Graphene Oxide-MnO_2 Composites for Supercapacitors
Y.W. Duan, X. Sun, H.Y. Zhao and Z.B. Liu 607

Te Inclusions in CdMnTe Crystal Grown by the Traveling Heater Method and their Effects on the Electrical Properties
P. Shen, J.J. Zhang, L.J. Wang, J.H. Min, J. Huang, X.Y. Liang, K. Tang, M. Shen, L. Wang and Y.B. Xia 613

The Effect of the Cu Source on Optical Properties of Cu-Doped ZnO Films
L.C. Chen, X.Y. Zhang and K.L. Lee 618

The Model of Nano-Scale Cu-Particle Removal in CO_2-Based Micelle Solutions with Different Surfactants
Y.R. Wang 624

Failure Analysis of the Solder Joints in Flip-Chip BGA Packages under Free-Drop Test
G.Z. Yuan, X. Chen and X.F. Shu 628

The Advantages of Ga-Graded Obtained by Growth Profile Modification and Na Incorporation on Cu(In,Ga)Se_2 Solar Cells
R. Sakdanuphab, S. Chatraphorn and K. Yoodee 633

Near-Field Broadband Light Transparency via Tunneling and Cavity Effects
X.N. Zhang, G.Q. Liu, Z.Q. Liu and Y.H. Chen 639

Modification of Epoxy Resin with Silicone for Electronic Encapsulation Application
L.X. Chen, L.Y. Fan and L.S. Gao 643

Effect of Annealing Oxygen Flow Rate on the Properties of Vanadium Oxide Films Deposited by Reactive Magnetron Sputtering
H.F. Zhang, Z.M. Wu, X.F. Wu and Y.D. Jiang 651

TEM Study of AlGaN/GaN on Hexagonal SiC Substrates
A. Gkanatsiou, C.B. Lioutas, N. Frangis, N. Chandraraj, E.K. Polychroniadis, P. Prystawko and M. Leszczynski 656

Chapter 8: Biomaterials, Biotechnologies and Pharmaceutics

Protein Adsorption on Titanium Surface Functionalized with Bioactive Gelatin Methacrylate Hydrogel Coating
G.X. Tan, Y. Tan, C.Y. Ning, L. Zhang, L. Zhou and H. Wang 663

Extraction and Antifungal Activity of a Lipopeptide Biosurfactant
F.R. Fang, S. Zhong, Y. Dong and L.J. Gong 669

Immobilized Recombinant Chitinase and its Inhibition Effect on Botrytis Cinerea
N. Zhang, R.X. Yan and W.Q. Guan 674

Electrospinning Synthesis of PLA Fiber Film Containing Antimicrobial Silver Nanorods
J.Q. Bai, Y.H. Li, Q. Duan and J.J. Chang 681

Characterization of Three Calcium Phosphate Microporous Granulated Bioceramics
N.H.A. Camargo, P.F. Franczak, E. Gemelli, B.D. da Costa and A.N. de Moraes 687

Characterization of Different Nanostructured Bone Substitute Biomaterials
N. Levandowski, N.H.A. Camargo, D.F. Silva, G.M.L. Dalmônico and P.F. Franczak 695

Sintering and Characterization of Calcium Phosphate Biomaterials Elaborated from Fossilized Calcareous Shell
D.F. Silva, N.H.A. Camargo, N. Levandowski, P.F. Franczak and M.S. Schneider 701

The Content of Physiologically Active Substances in Several Medicinal Mushrooms with Various Doses of γ-Irradiation
S.J. Huang, Y.L. Liu, J.L. Mau and S.Y. Tsai 707

Synthesis and Characterization of Three Hydrated Calcium Phosphates Used as Biocement Precursors
P.F. Franczak, N.H.A. Camargo, N. Levandowski and D.F. da Silva 712

Preparation and Release Profiles of a Solid Oleoylchitosan Coated Poly(lactic-co-glycolic acid) Nanoparticles
Y.Y. Li and F.S. Liu 717

Polymer-Tethered pH-Sensitive Magnetic Nanoparticles for Targeted Delivery of Anti-Cancer Drug
Y.Q. Shen, M.L. Pu and W. Jiang 723

Preparation and Anti-Tumor Activity of Polysaccharides from *Phellinus pini* Mycelia
A.J. Liu, H.C. Sun, Y. Chen, W.H. Wang, C.H. Liu and Y.M. Wang 728

A Facile Method to Synthesize Responsive Magnetic Polymer Composite Nanoparticles with Multifunctional Groups
M.L. Pu, W. Jiang and Y.Q. Shen 734

The Effects of Immobilization Conditions and Materials on the Desulfurization Performance of Immobilized UP-3
N. Guo, Y.F. Hou, Y.Y. Gu and C.H. Li 740

The Release Characteristics of Different Model Drugs from Medicated PLGA Microspheres
T. Chen, Y.Y. Liang, Y.G. Zhao, X.Y. Zhang, T.S. Qi and Q. Shang 746

Synthesis and Performance of pH-Sensitive Hydrogel Microspheres and *In Vitro* Evaluation as Potential Drug Carriers
Y.Y. Liang, T. Chen, Y.Q. Cui, R.Q. Tian, T.S. Qi and Q. Shang 751

Study on Structure Analysis and Cell Toxicity of Okra Polysaccharide
L.J. Min 757

Resveratrol Loaded Self-Microemulsifying Drug Delivery System (SMEDDS): Development and Optimization
G.Q. Liu, H.F. Zhou, J. Zhang, Z.M. Yan, M.X. Duan, Y.F. Long and Q. Xia 763

Stress Analysis of the Hip Joint Endoprosthesis Ceramic Head for Different Values of Shape Deviations
V. Fuis and P. Janicek 770

Synthesis and Characterization of Amphiphilic Copolymer Poly[2-(dimethylamino)ethyl methacrylate-co-methyl methacrylate]
F.P. Wang, T. Yuan, W.X. Li, J.Y. Zhang and Q.Z. Wang 776

Assessment Antibacterial Activities on Essential Oil of Plant Extract
C.C. Shiao, C.M. Ma, B.Y. Chen and H.W. Chen 780

Preparation, Characterization of Cellulose Fibers Grafting by β-Cyclodextrin and their Application for Antibacterial Products
C. Dong, Y. Ye, L.Y. Qian, B.H. He and H.N. Xiao 784

Detoxification Capabilities of Adsorbents for Artificial Liver Support Devices: A Comparison
W.P. Ding, L.L. Zou, Y.Y. Pei, S.J. Sun and D.Y. Gao 789

Prediction of the Tertiary Structure and the Dimerization Interface of FNR Protein in *Klebsiella pneumoniae*
Q.R. Zhang and X. Li 795

Potassium Dichromate Surface Modification of Poly-Lactic Acid (PLA) and Poly-Lactide-Co-Glycolide (PGLA) Fibers
B.Q. Wang, P.H. Zhang and M.H. Fang 801

Chapter 9: Materials and Technologies in Environmental Engineering

Preparation and Photocatalytic Performance Study of La-WO_3 Co-Doping TiO_2
X.Z. Diao and D. Zhou 809

Preparation and Photocatalytic Performances of F-Doped TiO_2
X.Z. Diao and X.L. Zhang 814

Preparation of Doped TiO_2 Responded to Visible Light
Y.H. Zhou, X.H. Wang, J. Chen and R. Pu 819

Development and Comparative Analysis of Aluminosilicate Based Ceramic Filters for Ground Water Defluoridation
J.K. Efavi, A. Yaya, S. Adeborna and J. Fobil 822

Adsorption of Ni (II) from Aqueous Solution Based on Porous Magnetic/Chitosan Resin
H. Song, X.H. Yu, X.Q. Zhang, G.F. Yan and Y.Z. Zhen 829

Highly Efficient Adsorption of Eriochrome Black T in Wastewater on Mesoporous Alumina Sphere
H. Liu, N. Tian, Y.Y. Tian, C. Dai and Y.X. Wang 834

Construction and Application of Molecularly Imprinted Film Sensor on Determination of Chlorpyrifos in Water
G.F. Lin, Y.H. Wang, G.C. Li, W. Bai, H. Zhang and S.C. Wang 843

An Investigation of some Factors Affecting the Dispersant NNO Adsorption on Imidacloprid Particle
H. Hao, J.G. Feng, X.Y. Guo, W.J. Liu and X.M. Wu 850

Adsorption Studies of Methacrylic Acid-Styrene-Acrylic Polyethers Copolymer on Imidacloprid Particles
H. Hao, J.G. Feng, T.F. Fan, W.J. Liu and X.M. Wu 854

Adsorption Characteristics of Methacrylic Acid-Styrene Copolymer onto Azoxystrobin Particles Surfaces
H. Hao, J.G. Feng, W.T. Chen, W.J. Liu and X.M. Wu 859

Preparation of 5-Sulfosalicylic Acid Modified Silica Gel and its Adsorption Performances for Lead
X.Z. Wu, J. Meng, F.P. Li and L.L. Luo 864

Preparation and Characterization of Mesoporous Activated Carbon from Alligator Weed with H_3PO_4
H.M. Xu, G.F. He, M.T. Shi, J. Tu, W. Liu and W.N. Xiang 868

Silica Gel as an Adsorbent in the Removal of Cationic Blue X-Bl from Aqueous Solutions and its Regeneration by UV-Fenton Oxidation
Q.Y. Xiong 875

Optimization and Evaluation of Preparation Process of Activated Carbon Loaded ZrO_2 Catalyst for Oxidative Desulfurization
C. Yang, Y.F. Hou, M. Liu, N. Guo and J.H. Zhang 881

Research on the Quicklime Treatment Dewatered Sludge Technology and Mechanical
J.L. Chen, Z. Deng, R.L. Zhang, P.L. Zhu and W.W. Ding 887

Simultaneous Reduction and Immobilization of $Cr_2O_7^{2-}$ in Metakaolinite-Based Geopolymer Complexed Reductant
J.Y. Chen, X.R. Lei and S. Tao 892

Chapter 10: Materials and Technologies of Chemical Industry

Construction of a Novel 3D Indium Phosphate–Phosphite with Extra-Large 16-MRs Channels: Synthesis, Structure and Fluorescence Property
H.D. Li 901

The Effect of Polyvinyl Pyrrolidone and Nickel Acetylacetonate on the Fabrication of Polyacrylonitrile Precursor Fiber
Z.H. Wang, H.Q. Rong, A.Y. Xu, H.M. Lin and S.H. Zhao 905

Morphology and Conductivity of Self-Assembled Pyrene-Perylenetetracarboxylic Diimide Dyad
Y. Shi and X.Y. Li 911

Synthesis, Structure and Characterization of a Novel 3D Zinc Organophosphonate
H.D. Li 915

Hydrothermal Synthesis and Characterization of Hexagonal $Mg(OH)_2$ Flame Retardant with Bischofite and NH_3
X.X. Song, L.J. Li and Z.Q. Liu 919

Effect of Solvent Properties on the Swelling Assisted with Protrusion of PS@TiO_2
B.L. Chen, L.H. Zheng, J.H. He, Q.H. Chen and J.H. Lin 929

Non-Isothermal Crystallization Kinetics of Semi-Aromatic Polyamide and the Preparation of its Fiber
Y.J. Chen, P.T. Wu, H.J. Xu, D. Wang, Y.M. Wang and Y.P. Wang 933

Recycled Paper Cellulose Aerogel Synthesis and Water Absorption Properties
J.D. Feng, S.T. Nguyen and H.M. Duong 938

Preparation of P(GMA-co-EGDMA) Monolithic Columns with Adjustable Porous Properties
H.T. Zhang, Q.Y. Zhang, B.L. Zhang and C.M. Li 942

The Synthesis and Electro-Optical Properties of Perylene Dicarboximide Dimer with Electron Withdrawing Groups
H.M. Wei, N. Zhao, N. Jiang, W.F. Duan and B.X. Gao 950

Effect of Aniline Oligomer on the Electrosynthesis of Polyaniline Fibres
B.S. Li, L. Zhang, W.W. Zhang and Y. Yu 955

Preparation and Properties of Electroactive PANI by Electrodeposition
B.S. Li, Y. Yu, W.W. Zhang and L. Zhang 960

Electrocatalytic Hydrogenation of Oxalic Acid to Glyoxylic Acid on a Self-Organized TiO_2 Nanotube Electrode
Y. Qian, F.M. Zhao, Q.Q. Qiu and C.A. Ma 965

Preparation of Zircon Whiskers via Non-Hydrolytic Sol-Gel Process Combined with Molten Salt Method
H.D. Wang, W.H. Jiang, G. Feng, J.M. Liu, Q. Wu and L.F. Miao 970

Low Temperature Preparation of Mullite Whisker via Non-Hydrolytic Sol-Gel Process Combined with Molten Salt Method
K.L. Fu, W.H. Jiang, G. Feng, J.M. Liu, Q. Wu, L.F. Miao, T. Chen, Q. Zhang, H.D. Wang and J.R. Zha 975

Co-Ni Bimetallic Catalysts Coated on Cordierite Monoliths for Hydrazine Decomposition
S.G. Pakdehi, M. Salimi and M. Rasoolzadeh 981

Low-Cost Synthesis and Morphology Control of Magnesium Oxysulfate Hydrate Whiskers
C.H. Gao, L. Ding, Y.M. Wu, C.X. Wang and J. Xu 986

The Preparation of Starch Sodium Octenyl Succinate and its Application as Surface Sizing Agent
C.W. Tang, Z.L. Liu, Y.F. Cao, F.Z. Tan and Y. Li 992

Structure and Property Development of Polyacrylonitrile Fiber with Ionic Liquid as Solvent during Spinning Process
H.M. Cheng, E.J. Zhang, X.M. Yin, Y.M. Zhang and H.P. Wang 997

Plasticization of Cellulose Diacetate by Ionic Liquid
N. Liu, J.W. Zhang and H.P. Wang 1002

Studies of Vapor-Liquid Equilibrium of Meta-Xylylenediamine-Aniline System
X.H. Wang 1007

Experimental Studies of Catalytic Hydrogenation of Isophthalonitrile for Meta-Xylenediamine Preparation
Y.G. Li 1012

Orthogonal Investigation of Influencing Factors on the Modification of Montmorillonite by THPC in Acid Conditions
P. Chen and J.C. Wang 1017

Chapter 11: Corrosion and Surface of Materials, Technologies of Coatings

The Effects of PTFE Content on Microstructures and Properties of Composite Brushing Plating Coating
Y. Wang, X.F. Cui, G. Jin, H.P. Li, W. Zheng and X.M. Zhang 1025

Novel Infrared Stealth Properties of Cotton Fabric with ZnO: (Al, In) Coating
X.L. Yu, L.P. Zhang, Y. Zhong, H. Xu and Z.P. Mao 1031

Research on Influencing Factors of Adiabatic Coating Performance
G.Y. Cao, H.J. Guo, L. Li, Y.Q. Li and J. Peng 1035

One-Step Processing to Fabricate Highly Transparent Superhydrophobic Surface via Granuliform Silica Aerogels
B. Xu, J.J. Ge and Z.S. Cai 1042

Deep Cryogenic Treatment and CrN Coating Effects on Micro-Scale Abrasion of Aluminum Alloy AA 6101-T4
E.S. Ashiuchi, V.F. Steier, C.R.M. Silva, T.D. Barbosa, T.F.O. Melo and J.A. Araújo 1047

Wear Resistance of Ti-40Zr Alloy with TiN and ZrN Multilayer Coatings
F.C. Dias, C.R.M. Silva, P.V. Muterlle, V.A.R. Henriques and J.A. Araújo 1056

Preparation and Tribological Property of Novel Self-Assembled Composite Films on Silicon
S.H. Teng and H. Pan 1066

Study on the BTSPS Silane Film Prepared on the Surface of the 2A12 Aluminum Alloy
L.J. Peng, S.H. Chen, Y.N. Feng and T.Y. Li 1071

Hydrophobicity of Beeswax-Chitosan Latex Coated Paper
W.W. Zhang, L.Y. Qian and H.N. Xiao 1077

Research on Cerium Conversion Coating on ZM5 Magnesium Alloy
R.X. Zhu, G.M. Gao and Z. Miao 1082

Microstructure and Properties of Laser Surface Carburized Titanium and Titanium Alloys
J.J. Dai, C.Z. Chen, S.Y. Li and L. Zhuang 1086

The Application Research of Ship Metal Corrosion in Marine Environment
C.Y. Hu, S.W. Kou and J.J. Guo 1091

Corrosion Resistance of Three 316 Stainless Steels
J.S. Lu, Q.S. Lu and J. Xue 1097

The Corrosion Behavior of Cu-Ni-Si Alloy in Sea Water with Deep-Sea Bacteria
Y.Y. Shen, L. Zhang, L.H. Dong, T. Liu, Q. Lei and Z. Li 1102

Corrosion Performance of Medical Titanium Alloy with Different Surface Morphology
J. Zhang, S.Y. Zhang, B. Liu, M.X. Li, Q.Q. Lin and J.Q. Wang 1106

Analyzing the Corrosion of "Hai Yang Shi You 931" Jack-Up Drilling Unit
W. Hong and X. Zhi 1112

Effects of Soil Type of Shanghai and Electrode Potential on Near-Neutral pH Stress Corrosion Cracking of Pipeline Steel X60
G.F. Li and D.F. Yan 1116

The Effects of Hydrogen on Properties of Surface Films Formed on Iron in Sulfate Solutions
A. Ejaz, Z.P. Lu, J.J. Chen, X.F. Xia, Q. Xiao and B. Lu 1120

Corrosion Inhibition of Gemini Surfactant for Copper in 3.5% NaCl
K. Cao, H.Y. Sun and B.R. Hou 1125

A Study of the Corrosion Resistance of M50NiL Bearing Steel by Ion Implantation
J. Jin, Y.B. Chen, K.W. Gao and X.l. Huang 1132

Chapter 12: Alloys and Steels, Metallurgical Technologies

Microstructure Evolution Characterization of Multi-Pass Hot Rolling Simulation of Nb-Ti Microalloyed Steel
B. Shen, S.H. Zhu and H.H. Zhang 1141

Grade E550 Heavy Steel Plate by TMCP for Offshore Energy Exploration
W.H. Sun and Z.C. Bi 1146

Preparation of Crystalline Hematite from Bauxite
J. Liu, Q.Q. Jiang, J. Wang, L. Chen and X.Y. Wang 1153

The Effect of Heat Treatment of Gray and Nodular Cast Iron with Ferrite Matrix on Mechanical Properties and Corrosion Rate Compared with Medium Carbon Steel
M.A. Gebril, M.S. Aldlemey and F.I. Haider 1158

Microstructure and Tensile Behavior of Ti-Rich Ti-Ni-Cu Melt-Spun Ribbon
W.J. He, G.H. Min and O. Tolochko 1163

The Oxide Defect of C70250 Alloy
Z.P. Chen, C.J. Xiang and H.Q. Li 1168

A Study on Austenite Catalytic Cryogenic Treatment of Cr-W-Mo-V High Alloy Medium-Upper Carbon Steel
Y.Q. Ma, X.J. Zhang, Y.F. Liang and G.F. Liu 1173

Effect of Forging Process on V-Nb-Ti Microalloyed Non-Quenched and Tempered Steels
T.H. Man, P. Gao, Y.G. He, Z.L. Zhan, L. Tan and Y.Z. Bao 1179

Experimental Study and Calculation of the Precipitation Behavior of Carbides in Fe-5.78Cr-0.35C Alloy during High-Temperature Aging
M.Y. Wang, J.J. Wang, Y.L. He, X.G. Lu and L. Li 1184

Effect of Temperature on the Ti-Fe Alloy Prepared by Molten Salt Electrolysis
R.M. Shi, L.F. Bao and B. Zhang 1189

Preparation of Ti-Fe Alloy from Titanium Concentrate by Electro-Deoxidization in $CaCl_2$
R.M. Shi, L.F. Bao and B. Zhang 1195

Study on Atomic Mobility and Molar Volume for FCC Fe-Co Phase
X.M. Gong, X.G. Lu and Y.L. He 1201

Molar Volume of Fcc Phase in the Ni-Cr-Mo System
J.C. Li, X.G. Lu and Y.L. He 1209

Effect of Aging Treatment on Phase Transformation of a Pseudoelastic NiTi Alloy
P.V. Muterlle, E.B. Villamarin, P. Herrera and E.P. da Silva 1216

Improvement of Paint Hardening Response of a Novel Al-Mg-Si Alloy for Automotive Panel by Adding Zn and Pre-Ageing Matching
Z.H. Li, L.Z. Yan, Y.A. Zhang, X.W. Li, F. Wang, H.W. Liu, S.H. Huang and B.Q. Xiong 1224

Effect of Mn and Si on the Microstructure and Mechanical Properties of Bearing Steel
M. Wang, G. Xu, Z.L. Xue, T. Xiong and M.X. Zhou 1229

Influence of Nitrogen Atmosphere Annealing on Structural and Transport Properties of $Fe_{1.125}Te$
Y.J. Li, Z.P. Wu, Y.H. An, G.F. Wang, C.L. Sun, Y.T. Huang, P.G. Li, L.H. Li and W.H. Tang 1234

Interface Reaction Thermodynamics of AgCuTi Brazing Filler Metal and Alumina Ceramic
H.L. Ning, L.F. Lan, L. Wang, J.B. Peng, Z.J. Peng and J.S. Ma 1239

Influence of Deformation on Aging Precipitation Behavior of an Al-Cu-Mg-Si Alloy
X.W. Li, B.Q. Xiong, Y.A. Zhang, Y.Q. Zeng, F. Wang, Z.H. Li, H.W. Liu and S.H. Huang 1247

Workpiece Surface Integrity of GH4169 Nickel-Based Superalloy when Employing Abrasive Belt Grinding Method
G.J. Xiao, Y. Huang, Y.H. Yang and H. Yi 1252

Studies on Refining Effect and Process Optimization about LF
S.L. Cheng, X.X. Qi and Q. Jia 1258

Influence of RE Addition on Ferro-Matrix Friction Material by *In Situ* Carbothermal Reduction from Vanadium-Bearing Titanomagnetite
Y. Li, K.Q. Feng, W.L. Deng, G.M. Zhang and Y. Zhou 1262

Influence of the Mo and V Contents on Microstructure and Secondary Hardening of 6Cr6W2MoV Steel
X.J. Zhang, Y.Q. Ma, Y.F. Liang and G.F. Liu 1267

Study on Wear Behaviors of Ni_3Al/Cr-Carbides Cladding Layer on High Strength Steel Substrate
K.R. Gong, T.B. An, Z.F. Zhou, Z.L. Tian and C.H. Li 1273

Study on the Mechanical Stability of Retained Austenite in Cold-Rolled Medium-Mn Steel
J. Hu, W.Q. Cao, J. Shi and H. Dong 1283

Influence of Heat Treatment on Fatigue Resistance of Sintered Ti 35Nb 7Zr 5Ta β Alloy
A.H. Franco, C.R.M. Silva, P.V. Muterlle, J.L.A. Ferreira and J.A. Araújo 1290

Effect of Hydrogen on the Micro- and Macro-Strain near the Surface of Austenitic Stainless Steel
O. Takakuwa, Y. Mano and H. Soyama 1298

Thermographic and Microstructural Analysis of Martensitic Stainless Steel ASTM A743 CA6NM Arising out of Layered GMA Welding Process Using AWS 410 NiMo Welding Wire
M.T. Santos, P.V. Muterlle and G.C. de Carvalho 1303

Two High Strength Low Alloy Steels for Offshore Application
T.C. Yang, C.Y. Huang, T.C. Cheng, C. Yu and R.K. Shiue 1312

Numerical Simulation on Influence of Water-Cooled Stool in the Process of Unidirectional Solidification
X.D. Li, M.G. Shen and C. Wu 1317

Application of Calcium Treatment to Sulfur Gear Steel 20CrMo
X.D. Wu, D.X. Zhang and R.L. Chen 1323

Chapter 13: Building Materials and Technologies in Construction

Nonlinear Dynamic Finite Analysis of BFRP-Strengthened Masonry Structure Based on ABAQUS
Z. Lei, Y. Wang and J.T. Qu 1331

Crystal Structure and Hydration Characteristics of Tricalcium Silicate Doped with Magnesium Oxide
L. Chen, X. Wang, X.D. Shen, S.H. Ma and W.Q. Zhou 1336

Mechanical Damage Model of Concrete Subject to Freeze-Thaw Cycles Coupled with Bending Stress and Chloride Attack
P. Du, Y. Yao, L. Wang and Y. Cao 1342

Numerical Investigation on Fatigue Problem of Cable Net Structure of Five-Hundred-Meter Aperture Spherical Radio Telescope
P. Jiang 1351

Study on Compressive Performances of Fiber Reinforced Mortar with the Application of Jute and PP
J.F. Yin, Y. Zhang, T.T. Yan and H. Qiu 1356

Study on Low-Cycle Fatigue Life of Base Metal of the Shock Absorber
A.L. Li, R. Gao, M.D. Sun and X. Meng 1361

Corrosion Behavior of F30S30 Concrete under Wet-Dry Cycles in Simulated Seawater with Magnesium Salt and Sulfate
G.G. Liu, A.B. Ma, C.M. Pang, P. Zhang, H.G. Qin and L. Wang 1366

Different Salt Solution on the Deterioration of Marine Engineering Concrete under the Action of Chemical-Mechanical Coupling
H.G. Qin, J.J. Deng, P. Zhang, C.M. Pang and Y.K. Hou 1373

Polymer Modified Cementitious Waterproofing Coatings: Application and Problems
W. Yao, Q.Q. Hu, Y. Mu, J.B. Chen and F.Q. Zhao 1378

Analysis of Curing Agent on the Strength of Lightweight Soil Using Recycled Sludge
G.C. Wang, L.C. Yu and L. Sha 1382

Study on Engineering Characteristics of Coarse-Grained Soil Based on Large-Scale Triaxial Test
F.Y. Chu 1387

Copolymerization Kinetics of Polyetyhylenglycol Allylether Type Polycarboxylate Superplasticizer
Y.F. Tian, X.P. Zhu, Y.T. Deng and K. Wang 1393

Improving the Volume Stability of Steel Slag for Construction and Building Materials
P.G. Li, F.Q. Zhao and Z. Ma 1399

Effect of Grinding Aids on the Particles Characteristics of Cement and Analysis of Action Mechanism
J.H. Zhao, D.M. Wang, X.G. Wang, S.C. Liao and H. Lin 1404

Effect of Mineral Admixtures on Rheological Properties of Cement Paste
L.C. Zhang and A.L. Zhang 1409

Theoretical Study on Seismic Behavior of LYTAG Concrete
L.C. Zhang 1414

The Frost Resistance of LYTAG Concrete
A.L. Zhang and L.C. Zhang 1419

Recombinant Materials and Contemporary Energy Efficient Architecture
M. Mahdavinejad, S. Ghanavati, N. Elmi, A.N. Larki and A. Zia 1423

Effect of the Composite of Fly Ash and Slag on Alkali-Silica Reaction
T.C. Liu, B. Xiao, G.H. Li, N.H. Luo and L.S. Zhang 1428

Analysis of the Influence of Clay Dosage and Curing Age on the Strength of Plastic Concrete
L.M. Hu, X.L. Lv, D.Y. Gao, K.B. Yan and S.Q. Song 1433

The Experimental Study on Bearing Capacity of Reinforced Concrete Structure with Different Reinforce Methods
Q.Y. Liu and X.M. Liu 1438

Mechanical Properties of Crumb Rubber Concrete
J. Cai 1442

Research on Improving Shrinkage Performance of Cement Stabilized Gravel with Waste Rubber Particles
Q.Y. Liu, M. He and J. Wang 1446

Bending Properties of Laser Welded Web-Core Steel Sandwich Plates
X.X. Jiang, L. Zhu, J.S. Qiao, Y.X. Wu, Z.G. Li and J.H. Chen 1451

Effect of Rubber Particles on Properties of Pseudo-Ductile Cementitious Composites
C.M. Pang, C.K.Y. Leung and W. Sun 1456

Back Analysis of Thermal Parameters of Mass Concrete and its Application Based on Micro-Genetic Algorithm
G.R. Chen and B. Yang 1463

A Effective Solution Method Based on Bayesian Rule for Prediction of Long-Term Tensile Strength of GFRP Bars in Concrete Beams
L. Dai, X.J. He and F. Shen 1468

Seismic Fragility Analysis of RC Isolated Continuous Girder Bridge Using Radial Basis Function Neural Network
B.L. Chen, X.H. Long and J.J. Li 1473

Robust Design of Structures with Uncertain Parameters and Frequency Constraints Using Non-Probabilistic Methods
J.Y. Chen, Y. Luo and D.H. Liu 1479

Research Based on Scanning Electron Microscopy to Determine Original Water-Cement Ratio of Hardened Concrete
Y. Li, H. Tong, J.B. Yang and W.G. Dong 1485

Numerical Simulation for the Damping Effect of Empty Holes on Blasting Vibration
K.F. Bian, H.B. Li and Y.Q. Liu 1490

Analysis on the Effect of External-Wall Insulation on Energy Consumption of Residential Building in Lanzhou
C.N. Li, G. Wang and Y.J. Wang 1496

Energy Consumption for Heating Residential Building from Implementing Deferent Energy-Saving Standard
C.N. Li, Y.J. Wang and Y. Cai 1502

The Scheme Comparison of Integral Structure after Adding Steel Storey to Concrete Frame
N. Sun, G.P. Shu and Z.M. Wang 1506

Finite Element Analysis of Rainfall Infiltration in a Compacted Loess Embankment
Q.F. Lv, P.F. Liu and Y.X. Zhao 1511

Numerical Analysis on Synergetic Behaviors of AE in Concrete Failure Process
L.H. Wei 1518

Simulation and Analysis of Energy Consumption Transformation in Office Buildings' Envelopes of Lanzhou
X.L. Han, H.M. Wang and C.N. Li 1522

Study on the Key Technology of Hot Regeneration of Plant-Mixed Asphalt Material
Q. Jin, X.Z. Cui, J.J. Lou, W.Z. Tang, W. Sui and Z.J. Gao 1527

Analyses of the Protective Effect of Polyethylene-Triethoxysilane and Triethoxysilane Emulsion Coatings on Concrete Substrate
X.Y. Zhang, S.C. Li, T.J. Zhao and Z.Q. Jin 1531

Chapter 14: Technologies and Materials in Oil Industry

Research Progress of Thickening Agents for Supercritical CO_2
W.C. Sun, B.J. Sun and Z. Fan 1541

Study on the Crosslinkers Used in Gelling Agents
Q.R. Sun and R.W. Liu 1549

Oil, Water, Slag Three Phases Separation Technology of Heavy Aging Oil
M. Zheng 1553

Research on Chemical Degradation of PAM in Oil Recovery Application
R.W. Liu 1556

The Application of Based on Case-Based Reasoning for Drilling Parameter Optimization in HaiTa Oilfield
L. Chang, T. Yan, S. Li and H.M. Fei 1560

Chapter 15: Methods and Devices of Measurements in Materials Engineering

Evaluation of Uncertainty of Hydrogen's Consistency in Transformer Oil by Gas Chromatography
H.L. Shen and H.Y. Luo 1567

Dissolution of Zirconium Power and Detection of Zirconium Powder Content by ICP-AES Method
X.L. Zhang, W.H. Zhu, X. Zheng and H.X. Liu 1571

Application of Magnetic Barkhausen Noise in the Evaluation of Heat Treatment Process
H.C. Yin, L. Zhou, Z.S. Wang and C.B. Cai 1576

Stress-Stain Response of PVC Geomembrane under Uniaxial Tension Test
H.M. Wu and Y.M. Shu 1582

Design of the EMF-PF and Error Correction
K.X. Wei 1587

TURBISCAN: History, Development, Application to Colloids and Dispersions
Z.Q. Liu, X. Yang and Q. Zhang 1592

A Progress in Development and Application of Size Exclusion Chromatograph/Multi-Angle Laser Light Scattering
X. Yang, Z.Q. Liu and Q. Zhang 1597

Chapter 16: Technologies and Equipment for Manufacturing and Processing of Materials

Application of Polycarboxylic Acid Anti-Crease Finishing Agent for Silk
L. Xu 1605

A Same Area Method Used to Calculate the Strain in Forming for an Axisymmetric Workpiece
Z.R. Han, Q. Xu and Z.B. Yuan 1609

Applying BP Neural Network Model to Forecast the Largest Coiling Torque of down Coilers
K. Zhao, Z.G. Wang and C.M. Liu 1614

Brazing Incoloy 800 Using the MBF-51 Filler Foil
W.S. Chen and R.K. Shiue 1620

Activating of Nickel Slag and Preparing of Cementitious Materials for Backfilling
K.Q. Li, Y.Y. Zhang, P. Zhao and L. Feng 1624

Preparation and Characterization of Plasma Treated Melt-Blown Polypropylene Nonwovens Grafted with Acrylic Acid
D. Wang, Q.Y. Xu, Y.J. Chen, H.J. Xu, Y.M. Wang and Y.P. Wang 1630

Microstructure and Mechanical Properties of High-Entropy Alloys CoCrFeNiAl by Welding
L. Cui, B. Ma, S.Q. Feng and X.L. Wang 1635

Microstructure Refinement and Crack Initiation in the Forging Process
W.L. Zhao and Q.X. Ma 1641

Effect of Aging on Microstructure and Performance after Superplastic Deformation of Fine Grained 1420 Al-Li Alloy
Y.L. Zhang, H.L. Hou and Y.Q. Wang 1647

Numerical Simulation of One Pulse Power Laser Shock Peening
L. Chen 1653

Analysis of Hydraulic Prop High Frequency Induction Cladding Temperature Field
F.D. Zhu, B.Y. Zhu and B. Liu 1657

CFD Simulation on Hydrodynamics of Liquid-Liquid Slug Flow in Microchannel
Y. Wang 1662

Characterization of Local Cavity Pressures in Squeeze Casting of Magnesium Alloy AM50
X.Z. Zhang, A. Yu and H. Hu 1666

Microstructure and Mechanical Properties of Brazed Joints Used in Electronic Devices
X.R. Wu, W.Q. Qu and H.T. Li 1671

Structure and Performance of Chemical Duplex Plating Ti Metal Layer on Diamond Surface by Hydrothermal Method
D. Xiang, L.Q. Jia and K.G. Liu 1676

Numerical Simulation and Optimization Technology of Lost Foam Casting
H.Z. Chen, H.Z. Dong and Z.D. Shan 1681

A Research on Optimization of Cutting Parameters Based on NSGA-II
X.Z. Liang, G.R. Yan and H.Z. Chu 1687

Behavior of Microwave Heating of 316 Stainless Steel Green Body
Z.W. Li, K.Y. Jiang, F. Wang and J.L. Zhang 1694

Effects of Environment Temperatures on the Microstructures and Mechanical Properties for Welding Joints of A5083-H111 Alloy
C.G. Wang, Y. Liu, X.M. Wang, G.Q. Gou and H. Chen 1701

Experimental Research on Grinding Surface Layer Behavior and Process Parameter Optimization of Spiral Bevel Gears
X.Z. Ming, Z.G. Li, X.W. Xiong and J. Zhou 1707

Development of Permanent Magnet Generator Used for Magnetic Field Assisted Micro Electroforming Technology
H.J. Li, P.M. Ming, X.H. Bao, X.D. Zhang and X.Y. Bi 1716

Spray Cooling Unit for Heat Treatment of Stainless Steel Sheets
M. Hnizdil, M. Chabicovsky, M. Raudensky, E. Magadoux and F. Code 1720

Research on Forming Accuracy of Two Point Incremental Forming for Aluminum 1060
Q.C. Wang, H.H. Hu, J.H. Wu and J. Cao 1725

A Servo Control System Based on Fuzzy PI Method for Transverse Flux Machine in Mechanical Press
J. Xie, A.L. Gao, Y.X. Wu and Z.Y. Gao 1730

Effect of Traverse Speed on the Microstructure and Mechanical Properties in Friction Stir Welded Dissimilar Barrier Butt Joints of AA2024 to AA6061/SiC/55p Composite
X.C. Song, L.J. Guo, X.S. Feng, Y.H. Yin and F. Cui 1735

Deformation Behavior of Aluminum Alloy Tube in Semi-Dieless Metal Bellows Forming Process with Local Heating Technique
Z.C. Zhang, K. Manabe, T. Furushima, K. Tada and O. Sasaki 1742

Properties of X80 Pipeline Girth Welds for Different Welding Procedures
X.D. He, K. Tong, M.H. Liang, L.X. Zhu and W.P. Lin 1747

Investigation of Porous Defects in Spray Formed 7XXX Aluminum Alloy
Y.B. Yin, Y.A. Zhang, B.Q. Xiong, F. Wang, H.W. Liu, Z.H. Li and X.W. Li 1754

A Study on Development of the Optimal Neural Network in GMA Welding Process
Q.Q. Wu, J.H. Lee, J.P. Lee, M.H. Park, Y.S. Kim and I.S. Kim 1759

Potential Spark Erosion Approaches to Silicon Nanoparticles Production
A. Farooq and W. Wang 1764

Study on CMT Welding of Stainless Steel Railway Vehicle Body
W.Q. Wang, Q.L. Meng and L.Y. Niu 1769

Energy Consumption Discussions of Porcelain Produce with Operating Conditions in a Simplified Model
J.L. Yu 1775

Microstructure and Mechanical Properties of Submerged Arc Welding Filled with Ni Wire Dissimilar Joints Comprising SUS304 and Q245R
P.X. Zhang, P. Zhao and Y.Q. Cui 1780

The Behavior of Second Phase Particles in a Ti-Nb Microalloyed Steel during Welding Thermal Cycle
M.A. Chen and C.S. Wu 1786

Study on the Technology and Defects in Low-Pressure Semi-Solid Die Casting of Aluminum Alloy Wheel Hub
R. Wang, H. Zhu and H.H. Zhang 1791

Influence of Heat-Treatment on Properties, Microstructure and Corrosion Resistant of Zirconium Sheet
P. Dang, X.W. Zhang, Y. Wang, Q. Zhang and C.L. Li 1796

Multi Response Optimization of Carbon-Carbon (C/C) Drilling Parameters by Using Grey Theory Technique
K.V. Krishna Sastry and V.S. Rao 1801

Study on Optimal Condition of Activated Carbon Prepared by Microwave Heating from Shot Coke
Y.F. Hou, Y.Y. Gu, Q.P. Mou, G. Yao and J.H. Zhang 1809

Adhesive Systems for the Production of Multi-Layer Bonded Fabrics for Composite Applications
I. Käppler, A. Younes, G. Bardl and C. Cherif 1816

Development of a Novel Technology for New Generation of Non-Crimp Fabrics – Manufacturing and Simulation
P. Matthäi, O. Döbrich and C. Cherif 1821

Optimization of Drafting Conditions in the Break Drafting Zone Additional Pressure Bar on INA-V Spinning Frame
Q.G. Feng, J.Z. Ren and Y.F. Zhang 1825

Non-Isothermal Resistance Heating for Hot-Stamped Parts with Tailored Properties and Tempering Treatment on Directly Hot-Stamped Parts
C.N. Sun and H.H. Zhang 1830

Comparisons of Explicit and Implicit Finite Element Methods for Sheet Metal Forming
L. Chen 1836

Numerical Simulation Study of the Influence of Turning Depth on the Bending Vibration Mode of Work-Piece
M.M. Wu, S.C. Li and Q. Zhang 1840

Application of Multidisciplinary Design Optimization in the Casting Process Optimization
M.Z. Wang, G. Chen and Z. Zhou 1845

Analysis of the Common Causes of Papermaking Cast Iron Dryer's Defects and the Study of Test On-Line
W.W. Li, Q. Du and W.Z. Li 1851

Reserch on a NO_x Emission Forecasting Method Based on Naïve Bayesian
Z. Lin, W. Xin and Z. Qi 1857

Analysis of Grinding Roller Stress Distribution of Vertical Roller Mill
X.H. Jiang, P. Ye and Z.K. Li 1862

Establish the Load Distribution Model for Vertical Mill Grinding Roller in Width Direction
P. Ye and S. Ye 1868

The Optimal Levenberg-Marquardt Algorithm to Predict Welding Quality Using Mahalanobis Distance Theory
I.S. Kim, Q.Q. Wu, J.H. Lee, J.P. Lee, M.H. Park and Y.S. Kim 1873

Research on the Ni-Cr Alloy Coatings on the Hydraulic Prop by High-Frequency Induction Cladding
F.D. Zhu, B.Y. Zhu and J. Liu 1878

Research on Material Structure, Appearance and Color Design and Application of Humidifiers - With Student Consumers as Research Objects
X.L. Nie, C.Y. Ouyang and L. Ning 1882

260t Ladle Stress and Deformation Finite Element Analysis
Y.P. Sun, D.C. Zhang, M. Yang and Y. Li 1886

1450 Cold Rolling Mill Rack Finite Element Modal Analysis
D.C. Zhang, C.W. Dong, M. Yang and Y.P. Sun 1890

Set-Up and Application of Thermal Fatigue Knowledge Ontology
C.F. Guo, Z. Dong, H.X. Ning and C.D. Wan 1894

Void Formation and Growth at Solder-Bonded Interfaces in HP LEDs
W. Liu and P. Jin 1900

Evaluation of Thermal Fatigue Crack States of Super-Hard Cutting Tools Based on the Extension Theory
C.F. Guo, Z. Dong, C.D. Wan and Y.K. Zhang 1905

Relationship between the Textures and the Elastic Moduli of Electron Beam Welded Joint in Ti-6Al-4V Titanium Alloy
X.Z. Li and S.B. Hu 1910

Investigation of the Influence of Geometric and Technological Factors on the Stress-Strain State of Metal in the Implementation of the Combined Rolling-Pressing Process
S. Lezhnev and E. Panin 1918

Chapter 17: Research in Area of Applied Materials

Influences of Material Parameters on Terminal Effect of PELE with Tungsten Fiber Composite Jacket
J.S. Zhu, Z. Fan and B. Gao 1927

Analysis and Optimization of Segregators' Structures on Separation Efficiency
C.F. Guo, S.K. Li and C.D. Wan 1933

Manufacturing and Analysis of Non-Asbestos Sealing Gasket
M. Zhang, M.H. Liu and Y.X. Li 1937

The Swelling Properties of Nitrile Rubber with Different Acrylonitrile Contents in Cyclohexane Medium Research
H.M. Wang, X.R. Lv and S.J. Wang 1942

Effect of Reserved Texture on Mechanical Properties of Cold Drawn Pearlitic Steel Wire
L.C. Zhou, Y.F. Zhao and F. Fang 1948

Microstructural and Mechanical Properties of 9%Ni Steels Used for the Construction of LNG Storage Tanks
S. Hany, B. Duponchel, C. Poupin, A.A. Kais, D. Dewael, J.B. Vogt, J. Bouquerel, H. Kacem, A. Mouftiez, S. Hariri, M. Milochova, E. Bychkov and E.A. Aad 1953

Influence of Moisture and Temperature on Relaxation Function of Oil-Paper Insulation in Traction Transformers
H.L. Shen and H.Y. Luo 1958

Influence of Si Content on the Characteristics of Al-Zn-In-Mg-Ti Sacrificial Anode
S.S. Wang, C.H. Liang and N.B. Huang 1963

The Application of Green Materials in Product Packaging Design
C.Y. Ouyang, L. Li, Y.J. Xiong and X.L. Nie 1969

The Hand Making of Radius Fillers and the Establishment of its Evaluative Requirements
H.L. Wang, M.R. Xiong, Y.X. Duan, J. Yang, D.X. Yan and S.C. Xu 1973

Comparative Study of High-Power White LED's Lifetime Based on Temperature Accelerated Test
S. Wei, N.Y. Zou, Y.C. Zhang and D.S. Li 1985

Study of Surface-Enhanced Raman Spectroscopy of Crystal Violet in Acid Aqueous
X. Jia and L.L. Dong 1989

Evaluation of Sound Absorption Capability from PET Mesh to PET/PU Composite Board
Y.C. Liu, J.H. Huang, C.H. Huang, M.H. Tsai and Y.C. Chuang 1994

Mode I Crack Problem for a Functionally Graded Orthotropic COATING-Substrate Structure
L.F. Guo, X. Li and Y.Z. Yang 1999

Investigation of the Fluorescence Spectra of the Fluorescent Dyes
S. Sukprasong, T. Promjun, K. Chokethawai and A. Ngamjarurojana 2007

X-Ray Analysis of Residual Stress in Weld Region of X70 Pipeline Steel
Z. Boumerzoug, K. Digheche and V. Ji 2011

Static Tensile Properties Simulation of Plane Woven-Reinforced Laminates with Hole Damage
W.G. Wei 2017

A Review of Numerical Study on Explosion and Shock Wave Resistance of Metal Foam Material
J.K. Yi, H. Shen, K.B. Yan and B. Gao 2024

Modelling Method for Preventing Thermal Runaway Reaction Accident of Thermal Reactive Material
I.T. Chu, S.Y. Tsai, W.T. Huang, J.M. Tseng, J.S. Li and C.P. Lin 2030

Thermal Structure Coupling Research and Thermal Fatigue Life Prediction of the Large Mining Machinery Brake
Z.L. Liu, M.M. Zhao and M.L. Li 2035

Study on the Response of Composite Material Cylinder with Metal Liner under Thermal Mechanical Impact
Y.D. Xu, G.S. Chen and J. Ma 2041

Porous Glass Composite as Diesel Particulate Filter and the Microwave Regeneration
C.C. Lee, N. Yoshikawa and S. Taniguchi 2050

The Fracture Properties of Sandwich Structures Based on a Metal Foam Core
Y. Shen, Y. Li, W. Cantwell and Y.Y. Zhao 2054

Research on Tribological Properties of Cast Iron at High-Speed Dry Sliding Condition
C. Yue, S.G. Bao and Y.Y. Huang 2063

Chapter 18: General Mechanical Engineering

A Semi-Analytical and Semi-Numerical Method for Acoustics Radiation Characteristics of Rotational Shells
J. Lu 2071

Validation of a Novel Method for Thermal Performance Evaluation of Parabolic Trough Receivers
Y.X. Xiong, Y.T. Wu, C.F. Ma, P. Xu and D.Y. Li 2075

Analysis of Penetration-Explosion Warhead Fragments Distribution and Damage Efficiency
P.F. Zhang and J.P. Zhou 2082

MR Based Brake-by-Wire System with Self-Energizing Capability
X.H. Liu, L.Y. Yu and L.X. Ma 2087

Design and Optimization of the Bridge Expansion Joints Cleaning Machine
J.P. Jiang, B.X. Zhang, J.B. Wang, D.Y. Zhang, L. Wang, X.F. Cheng and C.G. Wu 2094

Research on Tracked Vehicle Suspension Parameter Optimization Based on Surrogate Model Method
H.Y. Wang, Q.L. Wang, Q. Rui and W.B. Ma 2098

The Simulation of Heat Transfer and Flow Performance for Supercharged Boiler Superheater
H.Y. Zhang, H.T. Xie and X.D. Jin 2103

The Resistance Performance Influences from Hull Line Variation of V-Shaped Non-Ballast Ship (NoBS)
H. El Kady, D.F. Han and L.G. Gao 2109

A Computational Fluid Dynamics Method for Resistance Prediction of the Floating Hull of Wave Glider
A. Elhadad, W.Y. Duan and R. Deng 2114

Bifurcation and Chaos in Couplings with Clearance
M. Houfek and L. Houfek 2120

Material Selection and Finite Element Analysis for the Enclosure of Mine Exploration Robot
Z.Y. Song, J.Y. Zhao and R.Q. Jia 2125

Initial Pressure Influence on Explosion Pressures of Methane-Air Deflagrations in Linked Vessels
Y.H. Cui, J.C. Jiang, Y. Yu and Q.W. Zhang 2130

Optimization Design of Transverse Flux Permanent Generator Based on Response Surface Method
Z.Y. Gao, J. Xie and S.M. Wang 2135

Application of the Lumped-Parameter Model in Concept Design Phase of Side Impact Safety Development
C. Tao and P. Yun 2140

Chapter 19: Mechatronics, Control and Automation

Improved Dynamic Bayesian Networks in Sea-Battlefield Situation Assessment
Y.T. Yu and Y. Ding 2149

Energy Control of HEV Based on Fuzzy Controller Optimized by Particle Swarm Optimization
L.Y. Zhao and N.N. Zhang 2155

Non-Ideal Excitation Approach for Piezoelectric Vibration Based Energy Harvesting
D. da Costa Ferreira, F.R. Chavarette, C. Henrique Cerqueira Costa Basquerotto and N.J. Peruzzi 2160

The Study of Water Level Fuzzy Control for Supercharged Boiler Drum
H.Y. Zhang, X.D. Jin and H.T. Xie 2165

The Application of HPWM in Improving Vehicle Lateral Stability
A.J. Zhang, Y.H. Xu and X. Lv 2171

Chapter 20: Power Engineering

Photovoltaic Power Generation Data Preprocessing Using Wavelet Thresholding
K. Bai, H.D. Qu, J. Zong, Z. Li, H.X. Zhai and Z. Zhao 2179

Transmission Line Insulators Detection Based on KAZE Algorithm
D. Li, M. Zhang and Z.B. Tong 2184

Identification of Lightning Strikes on Transmission Lines Based on Integral Method and Wavelet Analysis
H.W. Yan, Y.L. Zhu, G.C. Fan and X. Xiong 2190

Research of Power-On Detection in POE Topology
Z. Han, J. Wu, Q.Y. Dong, K. Ren and J. Dong 2196

The Research of Photovoltaic Array Intelligent Fault Diagnosis Based on the BP Neural Network
W.J. Zhang, Q. Ge and C.Y. Huang 2201

Chapter 21: Electronic Engineering

Application of AM-OLED Micro-Display in Stereo Display System
Y.H. Tai, J.S. Shi, Z.Q. Chen, Q. Li and B. Zhuo 2209

The Design of Wide-Stopband HTS Bandpass Filter
H. Yang and Y. Zhou 2214

Design of a Reader Antenna for UHF RFID
H. Yang and L. Guo 2220

An Effective Model for Wire Medium Based on the 4th Order Dispersion Equation
Z. Yang, W. Song and X.Q. Sheng 2225

Design of a Sine Sweeping Constant Current Source Based FPGA and DDS
Y.P. Yu, H. Zhao, Y. Liu, R.J. Yang, G.M. Dong and Y.S. Xing 2230

Chapter 22: Measurements, Data and Signal Processing, Computational Methods and Algorithms

The Effect of Measurers' View Angle Deviation on Measurement Data
S.L. Jia, Y.N. Tian, J.H. Ji and X.M. Shang 2237

The Engine Fault Diagnosis Based on Time Domain and Frequency Domain
Z.T. Yao and H.X. Pan 2243

The Application of Improved Dynamic Decision Tree Based on Particle Swarm Optimization during Transportation Process
X.H. Li, L. Li and X. Fu 2247

Modeling and Simulation Method of Component Based Petri Net
Y.H. Zhang and X.F. Zhang 2254

On the Hybrid Mean Value of the Square Residue
Q. Lan 2259

Feature Extraction Method Based on Moment Invariants
W.B. Li, H.W. Quan and X.F. Huang 2263

Numerical Movement Tracking of Mitral Valve Annulus
W. Zhang, R. Yin, Y.X. Deng, J.Y. Zeng, L. Ding and Y.P. Li 2267

Simulation of Ising Model by Monte Carlo Method
C.Y. Song and C.D. Li 2271

On Infinite Lower Order of Vector Valued Dirichlet Series
W.C. Lu 2276

An Improved Mean Filter Algorithm for Impulse Noise Elimination
W. Tang and J. Tang 2281

Background Extraction by Fast Independent Component Analysis in Video Surveillance
D. Rui, T. Jin and W. Wei 2286

Chapter 23: Communication and Information Technologies

The Design of Multi-Protocol Network Based on Point-to-Point Protocol and Frame Relay
W.T. Gong 2293

Construction and Sharing of Library Digital Resources in China and Southeast Asia
D.T.T. Thuy 2298

A Model Integration Framework Based Portability for GNSS Simulation
H.W. Zhou, H.T. Hou, W.X. Zhang, Q. Li and Q. Chang 2302

A Fast Fault-Identification Algorithm Tailored for Optical Interconnection Networks in High-Performance Computers
H. Li 2307

Research on Agent-Based Mobile Database Structure
Q.Y. Tian, L. Fei and W. Tian 2313

A New Cache-Based Network Coding Retransmission Scheme in Wireless Communication Networks
L. Wang and M. Liu 2318

Chapter 24: Product Design and Engineering Management

The Shapes of Products and the Lifestyle with Slow Rhythm
L.S. Guo 2325

Application of Traditional Chinese Decorative Patterns in Ceramics Design
C.Y. Ouyang, Y.J. Xiong and L. Li 2329

Packaging Material Barriers Faced by Foods and Agricultural Products Export of China and Countermeasures
H.L. Shao, H.X. Cui and J. Lu 2335

Safeguard System on the Quality of Excellent Engineers Training
C.M. Liu 2339

Design Methodologies of Ship General Arrangements - A Review
D.F. Han, H. Abdelkhalek and M. Chen 2344

The Design and Simulation of Collision Avoidance System Based on Dual-Mode Collaborative
S. Chen, J.M. Yu and Y. Liu 2352

Quantitative Risk Assessment and Early Warning for pH Value of Disqualified Imported Textile
M.Y. Wei, X.Y. Hu, C. Jiang, J.X. Zang and W.L. Xue 2358

Discussions of Resource Utilization of Coal Gangue
H.M. Li 2364

Research on Modes of Recycling and Remanufacturing with Considering the Carbon Footprint
Y. Jiang 2368

Chapter 25: Geophysical Research and Resources

Spatiotemporal Distribution of Rainfall Erosivity in the Bailong River Basin, Gansu Province
P. Zhang, G. Wang, L.M. Tian and Y.L. Zhang 2377

The Mineral Characteristics and Occurrence of Gold in Nali Gold Deposit, Guangxi
Z.W. Li, C.D. Liu, X.Q. Zhao, J.H. Lu and G.L. Guo 2383
Effect of Deficit Irrigation on Root-Shoot Development and Grain Yield of Winter Wheat
B. Hu and M. Zhang 2389

CHAPTER 1:

Polymers and Composites

Advanced Materials Research Vol. 936 (2014) pp 3-7
© (2014) Trans Tech Publications, Switzerland
doi:10.4028/www.scientific.net/AMR.936.3

Mechanical and Thermal Properties of Siloxane Reinforced Biphenyldiol Formaldehyde Resin Curing Epoxy Resin Composites

Shihui Chen[a], Jungang Gao[*b], Hongzhe Han[c], Chao Wang[d]

[1]College of Chemistry and Environmental Science, Hebei University, Baoding 071002, China

[a] csh19900001@163.com, [b]gaojg@hbu.cn, [c]hanhongzhe2012@163.com, [c]tony_purple@qq.com

Keywords: biphenyldiol; epoxy resin; siloxane; mechanical property; thermal degradation

Abstract. In order to modify the properties of the epoxy composites, an alkali catalyzed biphenyldiol formaldehyde resin (BPFR) was synthesized and used to cure epoxy resin (ER). γ-Glycidoxypropyl trimethoxysilane (KH-560) was used as a reinforcer of the composites. Laminates of the BPFR/ER fiberglass reinforced composites with different (KH-560) contents were prepared. The influence of the KH-560 content on the glass transition temperature (T_g) and thermal degradation properties of the composites was researched by dynamic mechanical analyzer (DMA) and thermogravimetric analysis (TG). The mechanical, electrical properties of the composites were determined. The results showed that the interfacial bonding strength between resin matrix and fiberglass can be efficiently improved with the presence of KH-560. When the ratio of BPFR and ER is 3 : 7, the content of KH-560 is 5 ~7 wt%, the impact resistance of the fiberglass reinforced composites is 61.35~78.59 kJ/m^2, the tensile resistance is 150.37~162.54 MPa, which are all 30 % higher than that of no added; The dielectric constant ε and dielectric loss tanδ of the composites is between 0.50~0.68 and between 0.008~0.01, respectively.

Introduction

Phenol-formaldehyde resin (PFR) is an excellent thermosetting resin, having good mechanical, flame retardancy and heat resistance properties; it has been used in preparing fiberglass-reinforced laminate, molding compounds, insulation materials and adhesives, especially in the high-technology fields, such as spaceflight, rocketry, etc [1]. PFR can also be used as curing agent of epoxy resin, which has better thermal properties than the phthalic anhydride-cured epoxy, with a higher glass transition temperature (T_g) and a higher thermal decomposition temperature [2]. Because of the more intensive aromatic ring in biphenyldiol, the biphenyldiol formaldehyde resin (BPFR) will have higher heat resistance and residual rate at high temperature. Epoxy resins (ER) are high-performance thermosetting polymers, which has excellent adhesion, corrosion resistance, insulation, high mechanical strength, good electrical insulation and compatibility with a great number of materials. It is widely used in adhesives, coatings, electrical insulating materials and composites, and is an indispensable basis for industrial materials. But epoxy resin after curing is usually more brittle, and its fatigue resistance, heat resistance, impact strength are relatively poor, and it is also difficult to meet the requirements of the development of modern engineering technology and application. In this work, a novel biphenyldiol formadehyde resin (BPFR) was synthesized. The BPFR was used to cure epoxy resin, KH-560 was used as modified reagent, and the fiberglass reinforced composites were prepared. The dynamic mechanical properties, thermal degradation behavior, mechanical and electrical properties were determined.

Experimental Section

Materials. Formaldehyde, ethanol, toluene, sodium hydroxide, N, N'-dimethylformamide (DMF), analytical reagents and supplied by Tianjin Kermel Chemical Reagent Co., Ltd; bisphenol A epoxy resin, 0.44 mol epoxy group/100g, Wuxi Resin Factory, China; N, N-dimethyl benzylamine, chemical reagent, Shanghai yuanfan additives factory, China; biphenyldiol, chemical reagent, recrystallization at 70 ^{o}C in 30 % aqueous solution of DMF, T_m 284 ^{o}C; γ-glycidoxypropyl trimethoxysilane (KH-560), chemical reagent, Shengda fine chemical Co. China.

Biphenyldiol formaldehyde resin was prepared by the condensation of biphenyldiol and formaldehyde in a molar ratio of 1 : 2.5, and with the slow addition of sodium hydroxide (2.5% of the total mass of the system), the reaction system was heated to 85 ^{o}C and held about 120 min, followed by dehydration under vacuum, finally a transparent viscous liquid was obtained. Then synthesized resin was dissolved by ethanol and obtained 60 % content of ethanol solution.

Sample Preparation and Characterization. Samples were prepared as follows: for samples of pure BPFR/ER, with the mass ratio of BPFR/ER and glass fiber all 1 : 1, and BPFR : ER = 3 : 7, 4 : 6, 5 : 5 , 6 : 4, 7 : 3, 10 : 0, labeled as 1, 2, 3, 4, 5, 6 respectively. For samples of BPFR/ER/KH-560, the mass ratio of BPFR/ER/KH-560 and glass fiber cloth were all 1 : 1, and with the mass ratio of BPFR : ER =3 : 7, the KH-560 content for resin was 0, 3, 5, 7, 9, 11 wt% and labeled as No. 0, No. 3, No. 5, No. 7, No. 9, No. 11, respectively. The resin which contains 1 wt% N,N'-dimethyl benzylamine was dissolved by small amount of acetone and coated onto the heat-cleaned glass cloth, after that the solvent were removed and pre-cured at 120 ^{o}C for 20min.. Laminated strips of 20×5×1 mm were prepared by hot pressing and curing at 180 ^{o}C for 30 min. The dynamic mechanical behavior of the materials was characterized by a dynamic mechanical analyzer (DMA, Q8000, Perkin-Elmer Co. USA) at a heating rate of 2 ^{o}C/min, under the frequency of 2 Hz.

The 3 mm thickness laminates of fiberglass reinforced composites with different KH-560 content were prepared with the same method and conditions. The tensile strength, impact strength and electrical properties were determined according to ASTM D638 and D256, Tensile strength test was performed using an electronic tensile tester (WSM-20kN, Changchun Equipment Co., Ltd. China). The notch impact test was carried out on an XCJ-40 impact tester (Hebei Chengde pilot plant, China). The electronic properties were determined with high impedance meter (ZC36 type) and high-frequency Q, (QBG-3D type, Shanghai Ai Yi Electronic Equipment Co., Ltd.).The thermogravimetric analysis (TG, Pyris-6, Perkin-Elmer Co. USA) was performed at a heating rate of 10 ^{o}C/min from 25 to 800 ^{o}C in static air.

Results and Discussions

DMA analysis of the Curing Samples. The DMA spectra of BPFR/ER composites are shown in Fig. 1. As seen in Fig. 1, the mechanical loss (tanδ) α peak temperature T_p increases with the increasing epoxy resin content correspondingly, and the peak width increases gradually. Normally, there is a corresponding relationship between the glass transition temperature (T_g) and the mechanical loss α peak temperature (T_p) of the material, and the T_p is often designated as T_g [3]. It can be seen that the addition of ER can increase the crosslingking density of the system, which preventing the relaxtion of chain segments and with a result of higher T_g as well as a wider peak, relevantly. This reflects the dispersion of the chain segments motion, and the high crosslinking density leads to a long process for the relaxation movement of molecular segments, thus the corresponding temperature T_p increases [4]. The mechanical loss peaks of the pure BPFR system tend to reduce with the increase of temperature, indicating a high crosslinking density and no

apparent molecular chain segments motion. Comprehensively, the performance of the composites is appropriate with the BPFR/ER mass ratio 3 : 7.

The properties of composites not only depend on the reinforcing agents, property of resin matrix and content, it also depends on the interfacial bonding strength between fiber glass and resin matrix. Generally, it is necessary to process the fiber glass in order to enhance the interfacial bonding strength. A significant way is using siloxane as a coupling agent [5]. The siloxane coupling agent on the surface of glass fiber may ensure the effective stress transfer, and substantially raise the comprehensive performance of composites. In this work, KH-560 was used to improve the interfacial bonding strength. Meanwhile, the reaction between epoxy group in the siloxane and biphenoldiol formaldehyde resin may promote the performance of the BPFR/ER composites further. The influence of different contents of KH-560 on the dynamic mechanical property of the BPFR/ER composite is shown in Fig. 2.

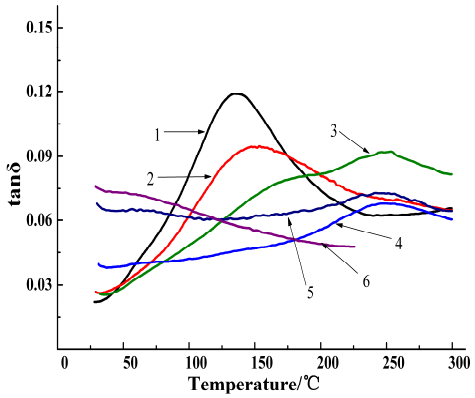


Fig.1 DMA spectra of BPFR/ER with different proportions

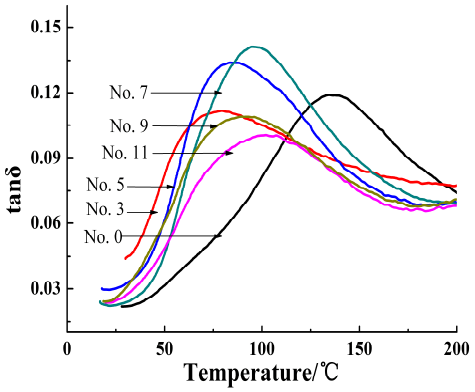


Fig. 2 DMA spectra of BPFR-ER composites with different KH-560 contents

Mechanical and Electrical Properties of Composites. The mechanical properties of the composites with different contents of KH-560 are listed in Table 1, all data are average values of 5 samples. It can be seen from Table 1, the tensile and impact strength is enhanced with increasing KH-560 content, when the content of KH-560 is 5, 7 wt%, the tensile strength can be 150 ~162 MPa, the impact strength 61~78 kJ·m^{-2}, which are all increased by over 30 % than that of no added(No.0). However, the mechanical properties decrease when more KH-560 is added in the composites. When the content of KH-560 is 11 wt%, the tensile strength and impact strength decrease to 52.98 MPa and 32.73 kJ/m^2, respectively. This indicates the mechanical properties of the material can be improved with an appropriate proportion of KH-560. It is consistent to the previous analysis both of the influence on resin matrix, glass fiber and danymic mechanical property. The reason is proper amount KH-560 siloxane can not only improve the compatibility but also form chemical bonds with hydroxyl both on the surface of glass fiber and resin matrix. It promotes to the interfacial strength between glass fiber and resin, and changes the stress of fiber glass transfer from resin. Consequently, when external force is act on to the materials, it plays an effective function of stress dispersion.

Table 2 shows the change of electrical properties of the composites along with the addition of KH-560. These data show that after adding KH-560, the volume resistivity ρ_v and surface resistivity ρ_s of materials display an increasing trend, while the dielectric loss tanδ and dielectric constant ε decrease. The increase of ρ_v and ρ_s arouse from high polarity of coupler. It is provble that the addition of silane coupler optimize the electrical properties of the composites.

Tab. 1 Tensile and impact resistance of BPFR/ER/KH-560 laminates

Samples	Tensile strength /MPa	Standard deviation	Impact strength /kJ·m^{-2}	Standard deviation
No.0	107.52	7.74	40.32	3.26
No.3	114.11	6.43	48.07	5.31
No.5	162.54	5.35	61.35	4.39
No.7	150.37	6.62	78.59	1.82
No.9	146.35	3.58	46.32	2.29
No.11	52.98	4.03	32.73	6.48

Tab. 2 Electrical properties of BPFR/ER/KH-560 laminates

Samples.	ρ_v	ρ_s	tanδ	ε
No.0	1.30×10^{13}	4.57×10^{12}	0.0086	0.6656
No.3	4.22×10^{13}	5.22×10^{13}	0.0113	0.5092
No.5	1.33×10^{12}	2.67×10^{12}	0.0062	0.6797
No.7	2.45×10^{13}	1.60×10^{13}	0.0156	0.5012
No.9	1.20×10^{13}	1.57×10^{12}	0.012	0.5917
No.11	1.02×10^{12}	4.48×10^{11}	0.0103	0.5546

Thermal Degradation Behavior. Thermogravimetric analysis of the BPFR/ER with different content of KH-560 was determined at a heating rate of 10 °C/min. Figure 3 is thermogravimetric curves of the 6 samples. As seen from Fig. 3, under the same weight loss rate of pyrolysis, the corresponding temperatures of samples increase with the adding KH-560 amount at same heating rate, it suggests that the thermal properties of the BPFR/ER composites has been effected by siloxane. Because of the increased content of inorganic –Si-O-, and the limitation to small molecule from diffusing caused by increasing crosslinking center, the weight loss rate decrease gradually. It should be noted that, when the content of KH-560 is 11 wt%, the pyrolysis temperature of the composites decline contrarily. This is because excess coupling agent cannot participate crosslinking reaction and small molecule has a low thermal stability.

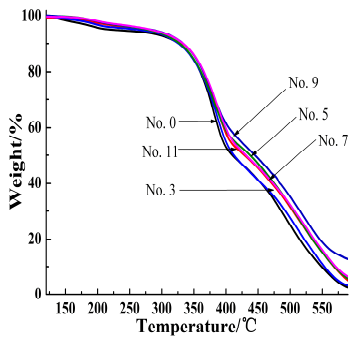


Fig. 3 TG curves of BPFR/ER with different KH-560 contents

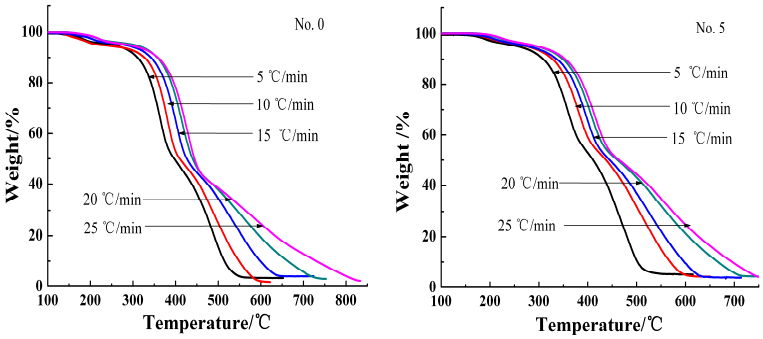


Fig. 4 TG curves for No.0 and No.5 at different heating rates

In order to investigate the activation energy and reaction order of thermal degradation process, samples No. 0 and No.5 were taken as examples for analysis. Thermal degradation was determined at different heating rates 5, 10, 15, 20 and 25 °C/min, respectively. The TG curves for No. 0 and No. 5 are shown in Figure 4.

As the figures displayed above, it shows that the thermal degradation process of the composites can be roughly divided into three stages: the first stage is between 150~300 °C, weight loss for

about 5 wt%, which is the volatilization of moisture and other small molecule. The second stage is between 300 ~ 450 ^{o}C, weight loss in this stage is mainly caused by oxidative cleavage of ether bond, carbonyl group and C-H. In this stage, the weight loss of the resin is nearly 60 wt%, which shows thermal degradation in the second stage is substantially dominated. The third stage is between 465 ~ 650 ^{o}C, which is the degradation and oxidation of metheylene, aromatic ring and the carbonization of the resin [6].

In this work, the thermal degradation kinetics of the two stages are all investigated by the Friedman method with dynamic treatment [7], respectively.

$$\ln(\frac{\mathrm{d}\alpha}{\mathrm{d}t}) = \ln(\beta\frac{\mathrm{d}\alpha}{\mathrm{d}T}) = \ln A + n\ln(1-\alpha) - \frac{E_a}{RT} \quad (1)$$

According Eq. 1, the average activation energy E_a at the different heating rates and α for each sample can be calculated from the using plot of the $\ln(\mathrm{d}\alpha/\mathrm{d}t)$ ~ $1/T$, the reaction order n can be obtained from plot of the $\ln(1-\alpha)$ ~ $1/T$, respectively. The average E_a and n for No.0 and No.5 are listed in Table 3, the linear relative coefficients of E_a and n are all between 0.9816 and 0.9957.

Tab. 3 Thermal degradation kinetic parameters calculated by Friedman method

Samples	β (^{o}C·min^{-1})	E_a/kJ·mol	r_1	n	r_2
No.0	Mean	59.287	0.9911	1.67	0.9895
No.5	Mean	54.547	0.9932	2.01	0.9942

Summary

Biphenyldiol formaldehyde resin (BPFR) can be synthesized from biphenoldiol and formaldehyde in the presence of sodium hydroxide. The interfacial bonding strength between resin matrix and glass fiber can be efficiently improved by siloxane KH-560. When the mass ratio of BPFR/ER is 3 : 7, and with a 5~7 wt% KH-560, the impact strength and tensile strength can be 61.35~78.59 kJ/m^2 and 150.37~162.54 MPa, respectively, which are all increased by over 30 %. The dielectrical properties also can be improved. The addition of siloxane coupling agent can enhance the thermal properties of BPFR/ER composites.

References

[1] K Hirano, M. Asami Phenolic resins-100 years of progress and their future. Reactive & Functional Polymer, 73 (2013) 256-269.

[2] C. S Tyberg, K. Bergeron, M. Sankarapandian Structure-property relationships of void-free phenolic-epoxy matrix materials. Polymer, 41 (2000) 5053-5062.

[3] J. K. Gillham The TBA torsion pendulum: a technique for characterizing the cure and properties of thermosetting systems. Polym. Int., 44 (1997), 262-276.

[4] M. Ogata, N. Kinjo, T. Kawata, Effects of crosslinking on physical properties of phenol-formaldehyde novolac cured epoxy resins. J. Appl. Polym. Sci. 48(1993): 583-601.

[5] Y. Liu, S. Shen, L. Li, et al. Research progress on the treatment of glass fiber surface by coupling agent. Insulating Materials, 43 (2010), 34-39.

[6] Y. Chen, Z. Chen, H. Liu. Effect of methylene substituents on the thermal degradation of phenolic resin. Acta Polymerica Sinica, (5) (2008), 399-404.

[7] H. L. Friedman, Kinetics of thermal degradation of char-forming plastics from thermogravimetry. Application to a phenolic plastic. J. Polym. Sci. C, 6 (1964), 183-195.

Advanced Materials Research Vol. 936 (2014) pp 8-11
© (2014) Trans Tech Publications, Switzerland
doi:10.4028/www.scientific.net/AMR.936.8

Polymer Blend through Inclusion Complexation

Chun-Yuan Liu[a*], Wei-In Lin[b], Jenshi B. Wang[c]

Department of Chemical Engineering, I-Shou University, No.1, Sec. 1, Syuecheng Rd., Dashu District, Kaohsiung City 84001,Taiwan

[a]email: cyliu@isu.edu.tw, [c]email: jbwang@isu.edu.tw

Keywords： polymer blend , inclusion chemistry

Abstract: A new method is proposed to improve blend compatability through inclusion complexation. The host polymer and the guest polymer are synthesized respectively and blended to form a film. The transparency of blend film increases and, at some composition, a third T_g is obsereved, indicating the inclusion complex between these two polymers

Introduction

Nowadays, there is no denying the fact that polymer blends[1-3] are ubiquitous among all high performance polymer materials. A lot ot research work is intensely motivated for tailored properties, reduced product cost, and processability. Compared with small molecules, most polymers are not compatible to each other in that the entropy gain of mixing is too small to form a homogeneous mixture. To improve the blend compatibility, introduction of some interacting groups onto polymer chains is very effective methods. Among them, hydrogen-bonding[4,-6] and Coulombic forces[7] between cation and anion are most popular techniques.

In addition to these two methods above, here, we present another alternative, inclusion complex(IC), to improve blend compatibility. Forming inclusion complexes with guest molecules selectively, Cyclodextrins(CD's)[8-12], the macrocyclic and water-soluble oligosaccharides, are widely used in many areas, particularly in drug research and biochemistry. CD's have a hydrophobic cavity where various guest molecules can be inserted to form IC's, while the hydrophilic nature of their outer surfaces render CD's somewhat water soluble. It is said that CD's are all purpose molecular containers for organic, inorganic, organometallic compounds which may be neutral, ionic or even radical. The host polymer, poly(acrylic acid) containing ß–Cyclodextrin(ß–CD), and the guest polymer, poly(methacrylic acid) containing adamantane groups, were synthesized respectively. Even a small contents of IC groups would improve significantly the blend compatibility.

Experimental

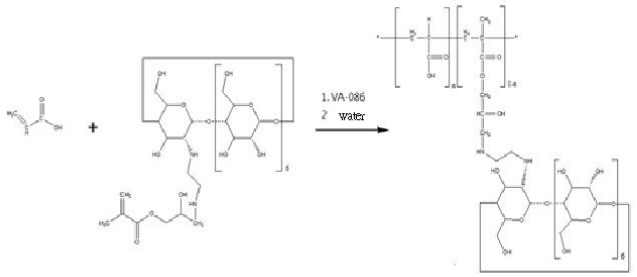
Synthesis of monomer containing ß –CD

In dry pyridine ß –CD was reacted p-TsCl overnight and after evaporation to dryness, the residue was dissolved in water and precipitated in acetone. The white crystal(ß–CD-6-O-TsCl) from twice recrystallization, was reacted with excess amount of ethylene diamine(EDA) for 4 hr at 60°C to

obtain a white solid(EDA-6-ß–CD). Then, the ß–CD containing monomer was synthesized by reaction between EDA-6-ß–CD and glycidyl methacrylate with a small amount of 1, 4 dihydroxyl benzene as inhibitor in DMF for 8 hr. After reaction, the monomer((GMA-EDA-6-ß–CD) was obtained by precipitation the solution into acetone and vacuum drying.

Preparation of host polymers:

PAA-based host polymers(PAA-co-GMA-EDA-EDA-6-ß-CD) were prepared by free radical copolymerization of acrylic acid and GMA-EDA-6-ß–CD , as showm in Scheme 1. Preparation of host polymer



Preparation of guest polymers

As shown in Scheme 2 , PMA-based guest polymers(PMA-g-3AD) were prepared by labelling adamantane group onto of PMA chain. The guest polymer obtained was purified by reprecipitation and dialysis.

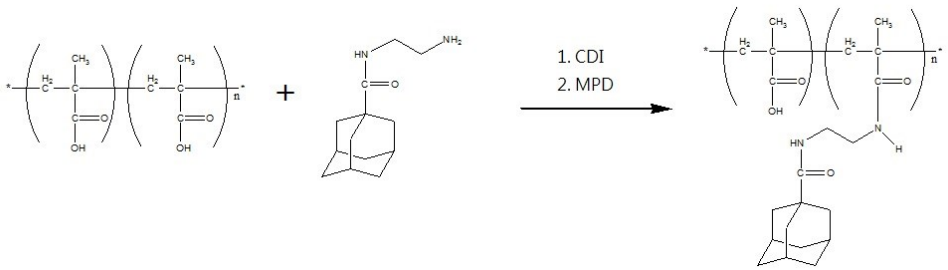


Fig 2. Preparation of guest polymer

Preparation of blend film:

PAA-based host polymer and PMA-based guest polymer were dissolved in water, which were then casted on Teflon plate for one week and vacuum dried until no decrease in weight before DSC measurement.

Results and discussion:

The characterization of polymers is listed in Table 1., where the molecular weights were measured by GPC and contents of ß-CD and adamantane moiety were obtained from **^{1}H** NMR.

Table 1. Characterization of host and guest polymers

Polymers M.W. (x10^5)		β-CD content (mole %)	adamantane content (mole %)
PAA-co- GMA-EDA-6-β-CD	3.8	3.9	0
PMA-g-3AD	3.7	0	9.8

As shown in Table 2., the T_g of host polymer(PAA-co- GMA-EDA-6-β-CD) is higher than that of PAA by ca. 12 ^oC, while the T_g's of guest polymer(PMA-g-3AD) and PMA are almost the same. Compared with PAA/PMA blend, the transparency of host polymer/guest polymer blend increases and, at some compositions, a third T_g appears, ranging from 128.4 to 137.8 ^oC, indicating the inclusion complex between the host polymer and the guest polymer. It is strongly suggested that a various of blend compatibility can be obtained by changing the contents of inclusion groups.

Table 2. Compositions and DSC results of blend films

Sample	Weight ratio	molar ratio of β-CD/adamantane	Tg_1 (^oC)	Tg_2 (^oC)	Tg_3 (^oC)
1. A	--	--	98.5	--	--
2. A / B blend	1/1	--	97.2	--	210.2
3. C	--	--	110.5	--	--
4. D	--	--	--	--	210.5
5. C / D blend	1/1	1/1.97	--	137.3	208.3
6. C / D blend	1.71/1	1/1.16	--	131.0	207.5
7. C / D blend	2.40/1	1/0.82	113.5	137.8	203.8
8. C / D blend	2.71/1	1/0.73	112.5	128.4	--
9. C / D blend	0.91/1	1/2.17	--	--	207.1
10. C / D blend	0.78/1	1/2.53	--	--	204.1

A： PAA (MW=3.8×10^5) ， B： PMA(MW=3.7×10^5)

C： PAA-co-GMA-EDA-6-β-CD (β-CD content: 3.9 mole%，MW=3.8×10^5)

D： PMA-g-adamantane (adamantane content: 9.8 mole%， MW=3.7×10^5)

Summary

A new method is proposed and demonstrated to improve blend compatibility through inclusion complexation. PAA-based host polymer and PMA-based guest polymer are synthesized and blended to form a film. The transparency of blend film increases and, at some composition, a third T_g is obsereved, indicating the inclusion complex between these two polymers

References

[1] Sionkowski, Progress in Polymer Science, 36(2011), 1254-1276 Olabishi, L.M. Robeson, M.T. Shaw, Polymer-Polymer Miscibility; Academic Press, New York, 1979

[2] D.R. Paul, S. Newman(Eds), Polymer Blend, Academic Press New York, 1978

[3] M. M. Coleman, J.F. Graf, P.C. Painter, Specific Interactions and the Miscibility of Polymer Blend, Teconomic Publishing Company: Lancaster, Pennsylvania, USA, 1991

[4] M.M. Coleman, P.C. Painter, Progress in Polymer Science, 20(1995), 1-59

[5] Y. He, B. Zhu, and Y. Inoue, Progress in Polymer Science, 29(2004), 1021-1051

[6] K. Shinoda, T. Hayashi, T. Yoshida, K. Sakai, and A. Nakajima, Polymer J., 8(1976), 202-207

[7] X.Y. Ling. et al,, Chem. Commun., 37(2009), 5521-5523

[8] X.Y. Ling et al., Angew. Chem.Int. Edit., 46(2009), 983-987

[9] F. Van de Manakker et al., Biomacromolecules, 10(2009), 3157-3175

[10] D. Tauva. et al., Macromolecules, 41(2008), 3640-3645 Tomatsu., A. Hashidzume, and A. Harada, J. Am. Chem. Soc., 128(2000), 2226-2227

Advanced Materials Research Vol. 936 (2014) pp 12-16
© (2014) Trans Tech Publications, Switzerland
doi:10.4028/www.scientific.net/AMR.936.12

Fabrication and Properties of Composites of Linear Polyacrylamide and Functionalized Carbon Nanotubes

Runmiao Yang*, Yuhai Liu, Guanxiu Dong, Dejian Zhao

Jiangsu University of Technology, Changzhou 213001, China;

E-mail: yangrunmiao@jsut.edu.cn

Keywords: atom transfer radical polymerization, carbon nanotubes, graft, transmission electron microscopy

Abstract: Polyacrylamide (PAM) was chemically anchored to the surface of multi-walled carbon nanotubes (MWCNTs) by atom transfer radical polymerization (ATRP) of acrylamide (AM). It started from the functional groups such as –COOH on the sidewall of MWCNTs, which derived from the oxidation of carbon nanotubes. FT-IR and ^{1}H NMR results shown that the multi-walled carbon nanotubes grafted PAM (MWCNT-g-PAM) have been successfully carried out. The MWCNT-g-PAM showed different relative weight loss kinetics with PAM determined by thermal gravimetric analysis (TGA). The transmission electron microscopy (TEM) shown that the PAM grafted polymer was wrapped on the surface of carbon nanotubes.

Introduction

Carbon nanotubes (CNTs) have emerged as a miracle material that will have significant impact on the 21st century due to their unique structure. However, since the crude multi-walled carbon nanotubes (MWCNTs) are large molecules with thousands of carbon atoms in an aromatic delocalized system, they are practically insoluble in most solvents and incompatible with chemical and biological systems [1-4]. Several papers about the application of acid treated MWCNTs (MWCNT-COOH) in LPA have been reported, but the solubility and compatibility of MWCNT-COOH are still not so good [5]. In order to make polymer/CNT composites, chemical modification of carbon nanotubes is necessary. Several approaches including side-wall functionalization, polymer encapsulation, and polymer grafting have been tried to overcome these problems [6-7]. At present, the strategies for grafting appropriate polymers onto the surface of the CNTs include "grafting from" method, "grafting to" method, via efficient radical coupling reaction and γ-ray irradiation methods. Among these approaches, living radical polymerization, especially atom transfer radical polymerization (ATRP) "grafting from" technique, is the method used most to graft polymer chains with controlled MW from substrates [8-9]. In general, there are two obvious benefits to the chemical treatment of nanotube surfaces: (1) improved compatibility of the filler with the polymer and/or (2) further reaction with the matrix to accomplish covalent bonding between the nanocomposite components. In both cases, the final functionality of the nanotube surface should, in principle, match the chemistry of the matrix [10].

In this work, surface-modified MWCNTs (MWCNT-g-PAM) were synthesized based on the hydroxyl functionalized MWCNTs through ATRP of acrylamide (AM). FT-IR and ^{1}H NMR results shown the PAM-functionalized multi-walled carbon nanotubes have been successfully carried out. The PAM-functionalized MWCNT showed unusual relative weight loss kinetics determined by TGA. The grafted MWCNTs have a better reinforcing effect on the mechanical properties of the matrices compared to the raw carbon nanotubes.

Experimental section

Materials

All water used in this experiment was deionized water. The MWCNTs (diameter 10-30 nm, Length 5-15 μm, Sun Nanotech Co Ltd in Nanchang) were used without further purification.

2-bromoisobutyryl bromide (98%) was used as received from Aldrich. CuBr (Sinopharm Chemical Reagent Co., Ltd) was purified by stirring in acetic acid, washing with ethanol, and then drying under vacuum. AM (Sinopharm Chemical Reagent Co., Ltd, 99%)was recrystallized from chloroform and stored in a refrigerator prior to use. 2-dimethylaminoprydine (DMAP), triethylamine (TEA) and $CuBr_2$ (Sinopharm Chemical Reagent Co., Ltd)were purified before used. Me_6[14]aneN_4 was synthesized according to our previous works [11]. Other organic reagents purchased from Shanghai Reagent Company were of analytical grade and were used as received.

General procedure for polymerization from MWCNT

The general strategy for preparing initiator (bromoisobutyrate group-functionalized MWCNT, MWCNT-Br) used for ATRP of AM according to literature [12], as shown in Fig. 1: the crude MWCNT was firstly oxidated by 60% HNO_3 to obtaining carboxyl-contained MWCNT (MWCNT-COOH), which was then reacted with $SOCl_2$, glycol, and α-bromoisobutyryl bromide in sequence to generating MWCNT-Br. The in situ ATRP approach to polymer-functionalization of MWCNT is described as follows: 50 mg of MWCNT-Br initiator, 15 mg of CuBr/$CuBr_2$ (10/1, molar rate) catalyst, 80 mg of Me_6[14]aneN_4 ligand, a certain amount of AM monomer and DMF solvent were placed in a dried tube and degassed by freeze-pump-thaw cycles three times. Then the tube was sealed under vacuum, immersed in a thermostated oil bath at 40 ^oC immediately and kept stirring for 24 h. After polymerization, the mixture was diluted with a large amount of H_2O and filtrated through a 0.45 μm polytetrafluoroethylene (PTFE) membrane three times to ensure that no any possible un-grafted polymer and free reagents were mixed in the product [13]. The resulting solid was then redispersed in 5 mL of DMF and precipitated in 100 mL of ether. The MWCNT-g-PAM was obtained by filtration and drying. The synthesis route is displayed in Fig. 1.

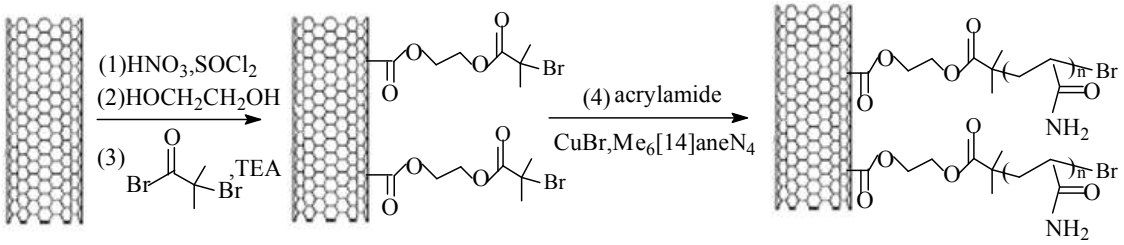


Fig. 1. Formation of MWCNT-*g*-PAM.

Characterization

^{1}H NMR spectra were performed in an AV-300 NMR spectrometer (BRUKER BIOSPIN AG, Switzerland), using D_2O as solvents. The IR spectra were recorded in solid state using KBr pellet. A MAGNA-IR 750 (Nicolet Instrument Co. U.S.A) was used to record the spectra in the range of 400–4000 cm^{-1}. The morphologies of the MWCNT-g-PAM was studied by transmission electron microscopy (TEM) performed on a JEOL – 2010 (JEOL, Japan). Thermal gravimetric analysis (TGA) was carried out on a PE TGA-7 instrument at a heating rate of 10 ^oC /min under nitrogen.

Results and Discussion

Fig. 2 reveals the representative FT-IR spectra of crude MWCNTs and the MWCNT-*g*-PAM. The crude MWCNTs reveal that the characteristic stretching vibration signal is hardly detected, but clearly observed for the MWCNT-*g*-PAM. The–NH stretching which appeared as a shoulder band around, 3200 cm^{-1} of the graft copolymer, has overlapped with a broad peak 3420 cm^{-1} of the hydroxyl group. The characteristic absorption peaks C-H at 2926 cm^{-1} can be found in FT-IR spectra of MWCNT-*g*-PAM. The band at 1656 cm^{-1} is due to the carbonyl group of amide moiety of the grafted AM chain, the presence of the above bands in the graft copolymer gives strong evidence of grafting.

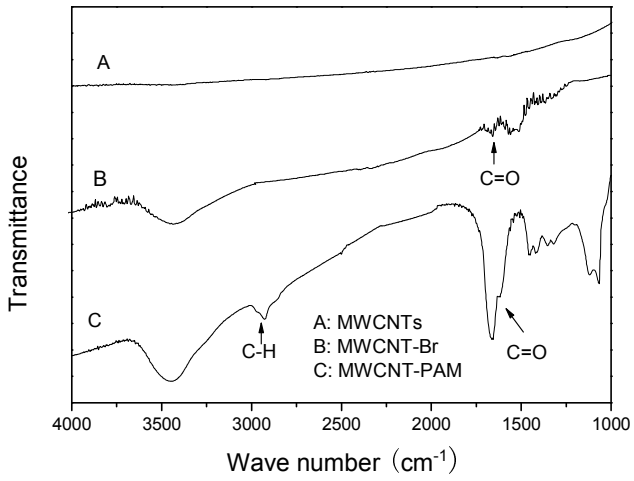


Fig. 2. FT-IR spectra of (A) MWCNTs, (B) MWCNT–Br and (C) MWCNT-*g*-PAM.

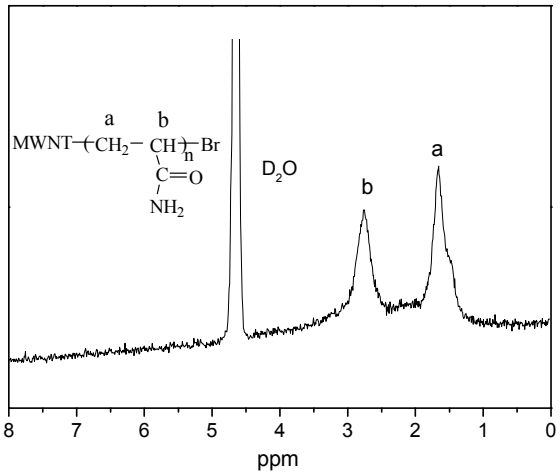


Fig. 3. ^{1}H NMR spectra of MWCNT-*g*-PAM.

The formation of MWCNT-*g*-PAM can be verified by its ^{1}H NMR spectrum shown in Fig.3. The integration ratio of peaks d=1.5–1.9 (a) and d=2.5–3.1 (b), which are the peaks of methene and methine protons in the main chain of PAM, is 2:1, indicating the formation of PAM.

The TGA results were shown in Fig. 4. For MWCNT, there is only a very slight decomposition before 450 °C and a weak thermal decomposition peak appeared nearby 110 °C, which is related to the hydroxyl part on the carbon nanotubes. After grafting, the weight loss before 450 °C increased. A thermal decomposition peak appeared between 245 and 345 °C. This peak should be attributed to the decomposition of the grafted polymer part. The loss-weight fractions (fwt) of the polymer layers for the MWCNT-*g*-PAM ranging from about 20 % to 30 % were determined from TGA data and increased with an increase in the weight ratio (Rwt) of AM monomer to MWCNT-Br initiator, indicating that the contents of the polymer side chains on the functionalized MWCNTs can be controlled by Rwt. The average Mw of grafted PAM side chains on MWNT-*g*-PAM calculated from TGA data. $Mw= fwt/[(1-fwt)\times 0.71\times 10^{-3}]$. herein, 0.71 represents the concentration of ATRP initiator sites per gram of neat MWCNTs (mmol/g). In order to compare conveniently, we assume that every ATRP initiator site participates in the polymerization reaction. so the calculated Mw of the grafted PAM is 1500. The major decomposition temperature corresponding to surface grown PAM on MWCNTs is higher and wider than that of pure PAM. All these results indicate that the PAM was covalently linked to MWCNTs.

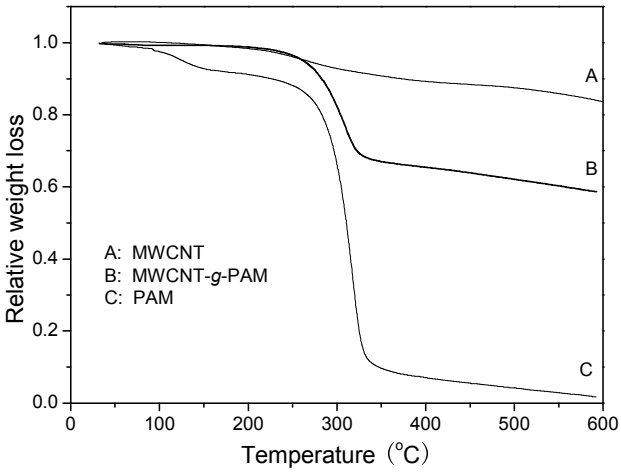


Fig. 4. TGA curves of (A) MWCNTs, (B) MWCNT-*g*-PAM, (C) PAM

MWCNTs and the MWCNT-*g*-PAM were mixed in water by sonication for 30 min at room temperature. MWCNTs were deposited to the bottom in water within seconds (Fig. 5A), a very stable solution of MWCNT-*g*-PAM in wate was observed (Fig. 5B)

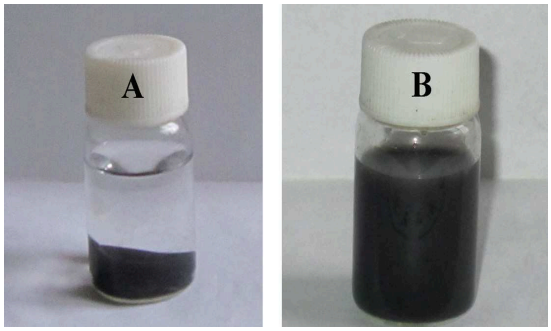


Fig. 5. Solubility of the (A)MWCNTs and (B)MWCNT-g-PAM in water.

A few drops of MWCNT-*g*-PAM composites dispersion in water was deposited onto carbon-coated grids, TEM images were observed after the solvent was evaporated. Fig.6 shows the TEM images of the pristine MWCNTs and the MWCNT-*g*-PAM composites. Very well separated MWCNTs are observed in Fig 6B, while the pristine MWCNTs are densely entangled as shown in Fig. 6A. After coated with PAM, a thin layer and several protuberances of the polymers were accreted on the surface of the MWCNTs. This reveals that the PAM chains grafted onto the surface of MWCNTs.

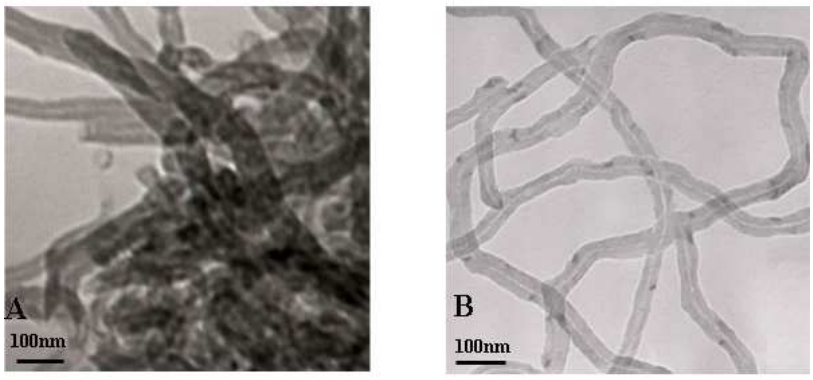


Fig. 6. TEM micrograph of (A) MWCNTs and (B) MWCNT-*g*-PAM in water.

Summary

A novel approach to the functionalization of pristine MWCNTs has been successfully carried out. FT-IR and NMR were used to verify the success of the graft polymer formation. Both debundling of MWCNT ropes and polymer attachment are achieved in a single step. Detailed research by TGA and TEM demonstrates that PAM were probably strongly anchored on the side walls of the nanotubes. This convenient noncovalent method can be employed to graft other functional polymer chains onto MWCNTs, and may be useful for the preparation of MWCNT- polymer hybrid nanomaterials without risking the destruction of the intrinsic graphitic structure of the pristine MWCNTs.

Acknowledgements

The authors acknowledge the support of this work by the National Natural Science Foundation of China (Grant No. 21204032) and Excellent Young Teacher Training Project of Jiangsu Province.

References

[1] C.A. Dyke, J.M. Tour, Solvent-free functionalization of carbon nanotubes, J. Am. Chem. Soc. 125, (2003) 1156-1157.

[2] Y. Jeong, J. Kim, G.W. Lee, Optimizing functionalization of multiwalled carbon nanotubes using sodium lignosulfonate. Colloid Polymer Science 288 (2010) 1-6.

[3] C.Ma, W. Zhang, Y. Zhu, L.Ji, R. Zhang, N. Koratkar, J. Liang, Alignment and dispersion of functionalized carbon nanotubes in polymer composites induced by an electric field. Carbon 46 (2008) 706-720.

[4] S. Ravindran, S. Chaudhary, B. Colburn, M. Ozkan, C.S. Ozkan, Covalent Coupling of Quantum Dots to Multiwalled Carbon Nanotubes for Electronic Device Applications, Nano Lett. 3 (2003) 447-453.

[5] Z. Wang, G. Luo, J. Chen, et al. Carbon nanotubes as separation carrier in capillary electrophoresis, Electrophoresis. 24, (2003), 4181-4188.

[6] C. Gao, YZ. Jin, H. Kong, RLD. Whitby, SFA. Acquah, GY. Chen, Polyurea-functionalized multiwalled carbon nanotubes: synthesis, morphology, and Raman spectroscopy, J. Phys. Chem. B. 109 (2005), 11925-11932.

[7] H Tsuji, M Ogiwara, SK Saha, T Sakaki, Enzymatic, alkaline, and autocatalytic degradation of poly(L-lactic acid): effects of biaxial orientation, Biomacromolecules. 7, (2006), 380-387.

[8] S Banerjee, SS.Wong, Structural characterization, optical properties, and improved solubility of carbon nanotubes functionalized with wilkinson's catalyst, J. Am. Chem. Soc.124 (2002), p. 8940.

[9] D. Zhou, LP. Yang, RM. Yang, WH. Song, SH. Peng, YM. Wang. Novel quasi-interpenetrating network/functionalized multi-walled carbon nanotubes double-network composite matrices for DNA sequencing by CE, Electrophoresis. 29, (2008), p. 4637-4645.

[10] S. Qin, D. Qin, WT. Ford, et al. Polymer Brushes on Single-Walled Carbon Nanotubes by Atom Transfer Radical Polymerization of n-Butyl Methacrylate, J. Am. Chem. Soc.126, (2004), 170-176.

[11] RM. Yang, YM. Wang, XG. Wang, et al. Synthesis of poly(4-vinylpyridine) and block copoly (4-vinyipyridine-b-styrene) by atom transfer radical polymerization using 5,5,7,12,12, 14-hexamethyl-1,4,8,11-tetraazamacrocycoltetradecane as ligand, Eur. Polym. J. 39, (2003), 2029-2033.

[12] H. Kong, C. Gao, D. Yan, Controlled Functionalization of multiwalled carbon nanotubes by in situ atom transfer radical polymerization, J. Am. Chem. Soc. 126, (2004), 412-413

[13] X. L. Wu, P. Liu, Poly(vinyl chloride)-grafted multi-walled carbon nanotubes via Friedel-Crafts alkylation, eXPRESS Polymer Letters, 4, (2010) 723-728

Advanced Materials Research Vol. 936 (2014) pp 17-22
© (2014) Trans Tech Publications, Switzerland
doi:10.4028/www.scientific.net/AMR.936.17

Thermal degradation behavior of polypropylene and ethylene vinyl acetate copolymer treated with intumescent flame retardants containing caged bicyclic phosphates

Xin Li[1, a] and Yuxiang Ou[2,b]

[1] Beijing Key Laboratory of Clothing Materials R&D and Assessment, School of Materials Science & Engineering, Beijing Institute of Fashion Technology, Beijing 100029, China

[2] National Laboratory of Flame-Retarded Materials, Beijing Institute of Technology, Beijing 100081, PR China

[a]clylx@bift.edu.cn, [b]yuxiangou@263.com

Keywords: PP; EVA; Intumescent flame retardant; Caged bicyclic phosphate; Thermal degradation

Abstract: Polypropylene (PP) and ethylene vinyl acetate copolymer (EVA) were treated with intumescent flame retardants containing caged bicyclic phosphates. The behavior of thermal degradation of the flame-retarded PP and EVA were studied by TG, DSC, and the FTIR spectra of PP's residues at different temperature were recorded. In addition, the possible thermal degradation and char formation mechanisms were analyzed and discussed.

Introduction

Polyolefinic polymers and copolymers are widely used in many industrial and agriculture fields. Due to their chemical constitution, these polymers are easily flammable, and so flame retarding is required for a great number of applications of polyolefins. There exist several ways to impart them flame retardancy. One of the solutions is to corporate additives into the base polymers. Up to now, the most effective flame retardant additives in polyolefines are halogen-antimony systems. But the corrosiveness, the toxicity of their combustion products and the smoke production have limited the applications of these systems. At the present time, certain sections of industry, notably those concerned with aerospace, electronics, cable and wire manufacture, are particularly interested in halogen-free flame retardants, such as phosphorus-nitrogen systems which are known as intumescent flame retardants. They do not present serious corrosive and toxic gases problems and produce much less smoke in comparison with halogen-antimony formulations [1].

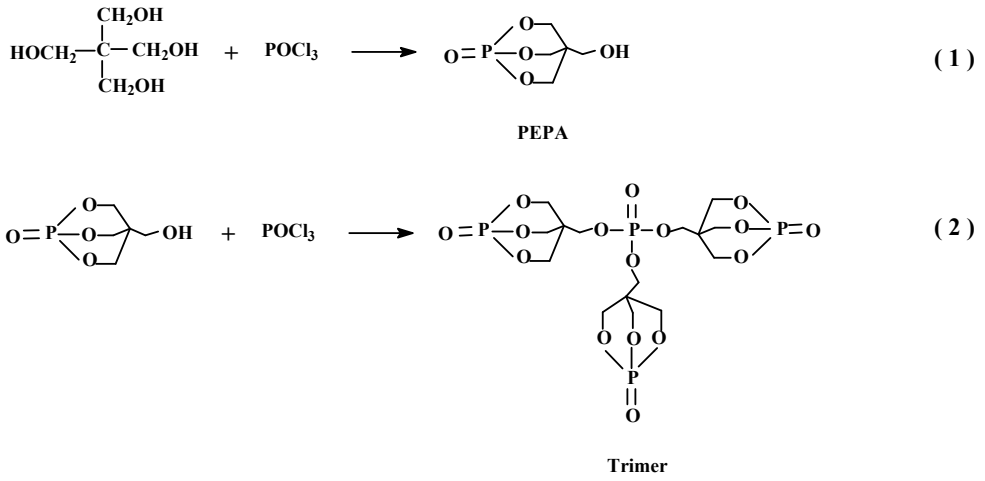
In this work, we have studied the thermal degradation behaviour of PP and EVA treated with halogen-free intumescent flame retardants containing caged bicyclic phosphate. The aim of our work is to study the effects of the intumescent flame retardants based on caged bicyclic phosphate on the thermal degradation process and mechanism of flame-retarded PP and EVA. In addition, the authors want to examine the char formation performance of the flame retardants studied.

Experimental

Materials. PP(J300, MFI 1.5), EVA(EVA18-3, MFI 2~3; EVA45,MFI 40~60) and APP(A.R. grade) were kindly supplied by Beijing Yanshan Petrochemical Works and Beijing Organic Chemical Works respectively. Both ammonium polyphosphate (APP, Beijing Haotian Additive Works, n~20, N≥12%, P_2O_5≥65%) and melamine(MA) is commercial sample. Both 1-oxo-4-hydeoxymethyl -2,6,7-trioxa-1-phosphabicyclo [2.2.2] octane (PEPA) and tri(1-oxo-2,6,7-trioxa-1-phosphabicyclo [2.2.2] octane-methyl) phosphate (Trimer) are synthesized at the authors' laboratory via the following reactions [2] (Fig.1). All of the reagents and solvents are of analytical grade and were purchased from Beijing Reagent Corporation.

The used flame retardants are two ternary mixtures which are composed of a phosphate, MA and APP. The phosphate Trimer is for the first mixture(IFR-T), and PEPA for the second mixture(IFR-P).

The composition of the two mixtures is as follows: Trimer:APP:MA=100:32:49 (mass ratio) for IFR-T, and PEPA:APP:MA=100:54:54 (mass ratio) for IFR-P.



(1)

(2)

Fig.1. Reaction routes for PEPA and Trimer

Sample Preparation. Ternary mixed flame retardants(IFR-T and IFR-P) were prepared by manual mixing in a mortor and by grinding at room temperature for 3h in a ball crusher.

The flame-retarded PP and EVA samples for testing were prepared by mixing PP(EVA) and IFR-T(IFR-P) in a double roller mixer at 170~175℃, and then pressed on a flat vulcanizer at 160~165℃ for 3~5 min. All of the raw materials were dried at 60℃ under pressure until weight constant before use.

The formulation of tested samples are shown in Table 1.

Table 1. The formulations (wt%) of the tested samples

Samples	PP/IFR-T	PP/IFR-P	EVA18/IFR-T	EVA18/IFR-P	EVA45/IFR-T	EVA45/IFR-P
PP	80	80				
EVA18			80	80		
EVA45					80	80
IFR-T	20		20		20	
IFR-P		20		20		20

Measurement and Testing. The TG measurement was done using a Du Pont TGA-2950 thermogravimetric analyzer at a heating rate of 10℃/min in nitrogen with a flow rate of 40mL/min, heating from 50℃ to 600℃.

Powder polymers were thermal degraded at 200℃, 300℃, 350℃, 400℃ and 500℃ respectively for 5 min in a muffle furnace. The obtained residues in KBr discs were recorded on A MAGNA 560 FTIR spectrophotometer.

Results and Discussion

TG Analysis of PP Series. The thermal analysis results of the samples are summarized in Table 2. Fig.2 shows their TG and DTG curves.

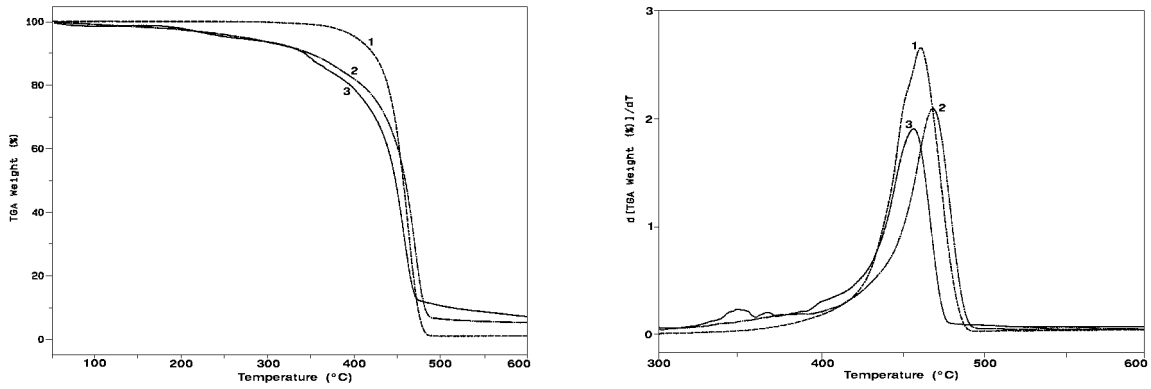
It can be seen from Table 2 and Fig.2 that the weight loss of flame-retarded PP occurs at much lower temperature in comparison with pure PP, for example about 130℃ lower for $T_{5\%}$ and 25℃ lower for $T_{10\%}$. This is mainly due to the release of NH_3 and H_2O from MA at relative lower temperature [3]. Among the three samples listed in Table 2, the pure PP has the largest R_{max} and the highest rate of thermal degradation, and PP/IFR-P in the next place, PP/IFR-T the third. Three of them have the weight loss peak on their TG curves in the range of 450~470℃. When vigorous thermal-oxidation takes place to pure PP, it losses its weight rapidly, and the carbon sketch of PP is

destroyed quickly. In the mean time, water vapor, CO, CO_2, hydeocarbons with low molecular mass and aldehydes are produced [4]. The thermal-oxidation reaction proceeds rather thoroughly for pure PP, and it is completely oxidized without any residue left at about 500℃. On the other hand, the intumescent flame retardants (IFR) based on Trimer or PEPA can decrease the weight loss rate, and R_{max} of flame-retarded PP is 0.7%·min^{-1} lower than that of pure PP on the average. When IFR decomposes at high temperature, viscous phosphoramides are formed. The surface of the base polymer is covered by these compounds. As a result, the pyrolysis rate of carbon skeleton of base polymer and the volatility of the pyrolytic products with lower molecular mass can be retarded. Besides, the carbon skeleton can be catalyzed to produce stable network char layer by cross-linking due to the formation of the additional covalent carbon chains. It has been demonstrated that P-O-C bond could provide a link between pyrolytic polymer and alkyl group, and promote the formation of char containing phosphorus. Moreover, P-N bond is also helpful to the formation of corss-linking network structure [5,6]. As was stated above, it can be seen that both IFR-T and IFR-P have the ability to stabilize the carbon skeleton structure of base polymers and to increase the char yield due to cross-linking. IFR-T shows better char formation than IFR-P for PP.

Table 2. TG data of PP series

samples	T5% a / ℃	T10%a / ℃	R maxb / %·min-1	T maxc / ℃	CHRd / %
PP	404.4	422.3	2.688	462.1	0
PP/IFR-T	268.5	344.3	1.903	458.7	10.1
PP/IFR-P	272.6	350.0	2.086	469.5	7.7

[a] $T_{5\%}$ and $T_{10\%}$ represent the temperatures at which the weight loss corresponds 5% or 10% respectively.
[b] T_{max} is the temperature at which the peak of weight loss on the TG curves appears.
[c] R_{max} represents the maximum rate of weight loss.
[d] CHR represents the char yield at 600℃.

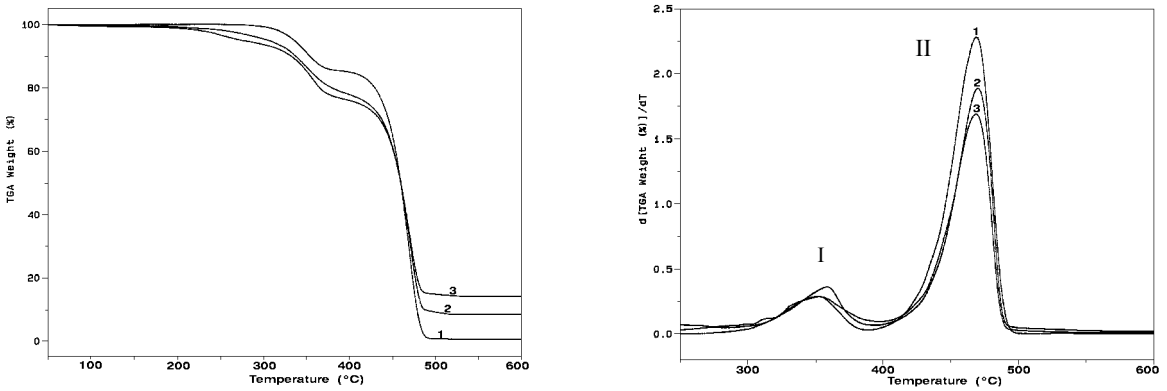


(a) TG curves (b) DTG curves

Fig.2. TG(a) and DTG (b) curves of PP system
1: PP; 2: PP/IFR-P; 3: PP/IFR-T

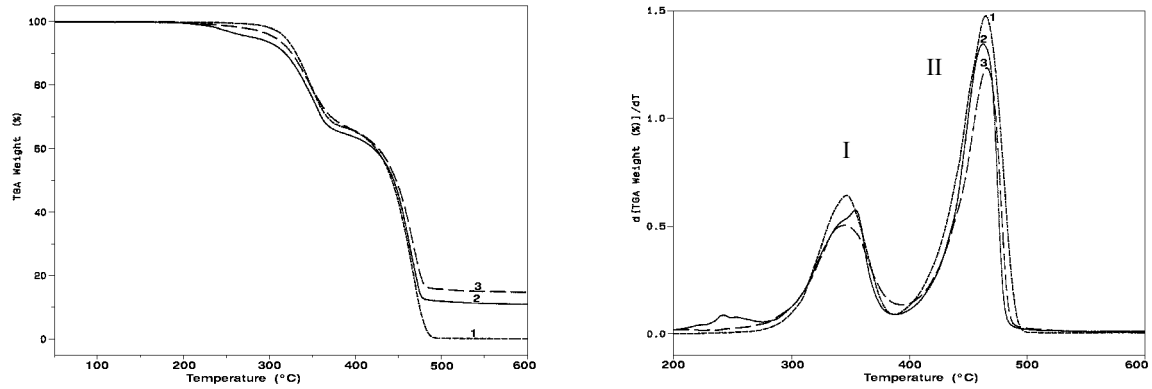
TG Analysis of EVA Series. EVA shows two weight loss peaks on the TG curves within pyrolysis process (see Fig. 3, Fig. 4 and Table 3). The first peak appears at the range of 300~380℃ due to the release of acetic acid from EVA. The height of the first peak increases with the increase of VA, but smaller than that of the second peak which occurs at the range of 410~490℃ corresponding the thermal degradation of EVA's carbon skeleton. There exist short chains in EVA which is formed by the linking of polar acetate group into the ethylene branch chain. Therefore, the thermal degradation of EVA is characterized by the cleavage of side chains and the release of acetic acid, and belongs to the type of chain-stripping degradation. During the pyrolysis of EVA, many reactive centres in the molecular chains are formed, and so char layer will be produced because of the cross-linking between molecular chains. The char formation can be promoted with the increase of VA in EVA [7]. In comparison with flame-retarded PP, IFR retards the degradation of EVA in the second weight loss stage more effectively. Consequently, the char yield of flame-retarded EVA is enhanced. Besides, the

char formation of IFR for EVA45 is better than for the EVA18. In contrary with PP, the char yield of IFR-P is quite higher than that of IFR-T for EVA systems. This indicates that PEPA based IFR is more effective for EVA's char formation from the cross-linking reaction than Trimer based IFR. This is probably due to the fact that PEPA possesses hydroxyl group which reacts with oxygen containing polymers and catalyzes the char formation.



(a) TG curves (b) DTG curves

Fig.3. TG (a) and DTG (b) curves of EVA18 series
1:EVA18; 2:EVA18/IFR-T; 3.EVA18/IFR-P



(a) TG curves (b) DTG curves

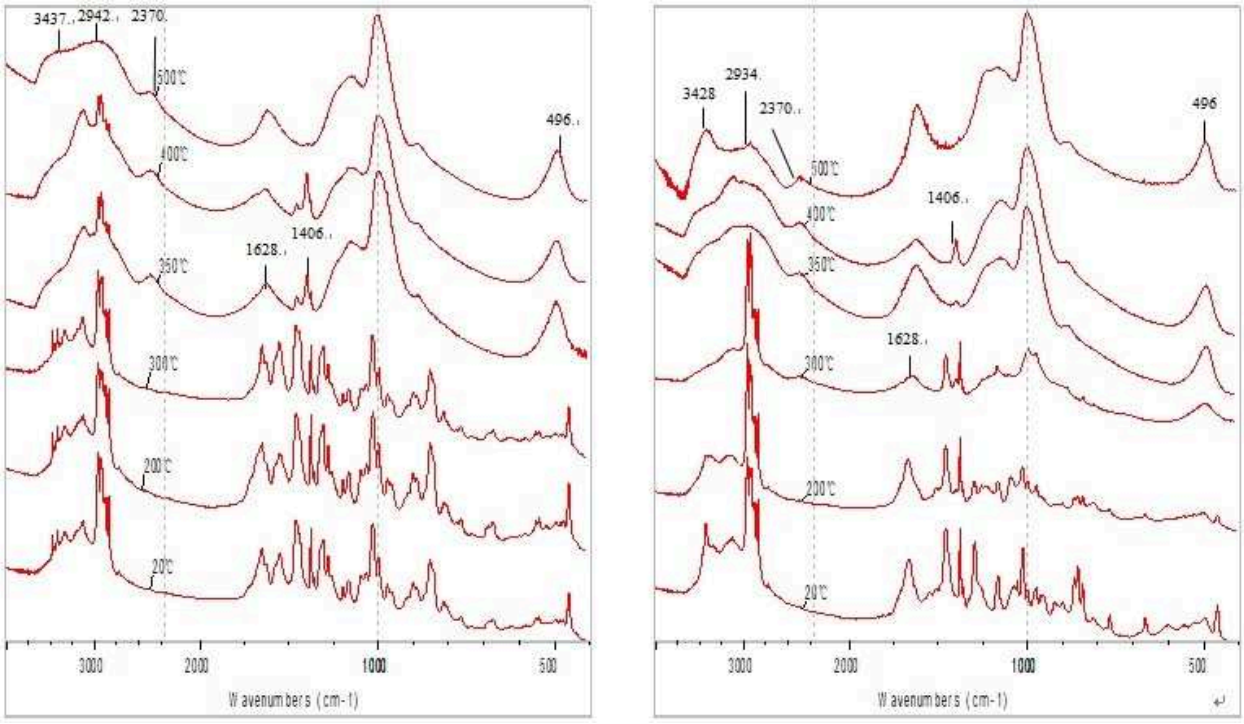
Fig.4. TG (a) and DTG (b) curves of EVA45 series
1:EVA45; 2:EVA45/IFR-T; 3.EVA45/IFR-P

Table 3. TG data of EVA series

sample	$T_{5\%}$ / ℃	$T_{10\%}$ / ℃	R_I [a] / %·min^{-1}	R_{II} [a] / %·min^{-1}	CHR / %
EVA18	334.9	351.7	0.300（351.7℃）	2.314（469.5℃）	0
EVA18/IFR-T	276.9	331.7	0.369（357.7℃）	1.905（470.2℃）	11.3
EVA18/IFR-P	302.9	336.5	0.298（351.7℃）	1.702（469.5℃）	14.6
EVA45	317.2	329.8	0.655（346.6℃）	1.488（464.4℃）	0
EVA45/IFR-T	276.0	318.0	0.576（353.4℃）	1.348（462.7℃）	15.4
EVA45/IFR-P	304.3	326.0	0.510（344.7℃）	1.243（465.9℃）	18.7

[a] R_I and R_{II} represent the first and the second weight loss peak respectively, and the figures in the parenthesis are the corresponding temperatures.

FTIR spectra of PP series. In order to study the chemical reaction taken place in the process of thermal oxidation-degradation and the resulting char's composition, the FTIR spectra of the residues of flame-retarded PP were recorded. These residues were obtained by the heating PP at different temperature(200~500℃) for 5 min. The FTIR spectra are shown in Fig.5.



(a) PP/IFR-T (b) PP/IFR-P

Fig.5. FTIR spectra of residues of PP series

The FTIR spectra of residues obtained by heating both PP/IFR-T and PP/IFR-P at 500℃ have the similar patterns. This demonstrates that the compositions of these two residues might be nearly the same. In these two spectra, there exist absorption peaks due to P-O-C bonds (at 1000cm^{-1}) [5], polyaromatics (at 1628cm^{-1}), C=N bonds (at 2370cm^{-1}), carbon skeleton of PP (at 2930~2950cm^{-1}) and OH group from phosphoric acid and polyphosphoric acid (at 3400cm^{-1}). The last two peaks from PP/IFR-T are broader than those from PP/IFR-P. It may be considered that the residues formed by heating flame-retarded PP contain polyaromactics, incompletely burned carbon-carbon chains, phosphoric acid or polyphosphoric acid and species containing C=N bonds [8]. The absorption peak due to polyaromatic appears in the FTIR spectrum of residue obtained from heating flame-retarded PP at 350℃ for PP/IFR-T system, while at 300℃ for PP/IFR-P system. In addition, the FTIR spectrum at PP/IFR-P system at 300℃ has already got much changes. This proves that the carbon-carbon skeleton of PP/IFR-P thermally degrades at lower temperature than that of PP/IFR-T. For both systems, the absorption peak due to P-N bond [9] at 1406cm^{-1} appears at 350℃, and this peak has strengthened significantly at 400℃ but disappeared at 500℃. It is thought that P-N bond is formed at relatively low temperature, and involved in the cross-linking reactions. At higher temperature, P-N bond is not likely to form. Therefore, it is probably impossible to find $(PN)_x$ structure in the residue formed at high temperature.

It is evident from the FTIR spectra and TG curves of the flame retardant systems that the heat resistance of PP/IFR-T is better than that of PP/IFR-P in air. The carbon skeleton of the former has not been completely destroyed at 400℃ in air. But in nitrogen, PP/IFR-T has lost 5% of its weight at 268.5℃, and 10% at 344.3℃, while the corresponding temperatures of PP/IFR-P are 272.6℃ and 350.0℃ respectively, about 5~6℃ higher than those of PP/IFR-T. The possible explanation for this might be the difference of pyrolysis model and pyrolytic rate for these two flame retardant systems.

Summary

1. In comparison with pure PP, the initial weight loss temperature and the 5% weight loss temperature of PP/IFR-T and PP/IFR-P are lowered about 130℃ and about 75℃ respectively. The

rate of thermal pyrolysis and weight loss rate have been notably decreased, and the char yield and the stability of char layer increased for the flame-retarded PP.

2. The pyrolysis of flame-retarded EVA with IFR-T or IFR-P proceeds in two stages. The weight loss of the first stage is smaller than that of the second stage. The intumescent flame retardants used can effectively retard EVA's pyrolysis in the second stage, and can promote the char formation via cross-linking reactions. PEPA is better than Trimer for EVA's char formation because of the existence of hydroxyl group in PEPA's molecule.

3. The ability of char formation of IFR-T for PP is better than that of IFR-P, and the thermal oxidation-resistance of the char layer produced from PP/IFR-T is higher than that from PP/IFR-P.

4. Both PP/IFR-T and PP/IFR-P produce P-N bond at relatively low temperature, and this bond may be involved in the cross-linking reaction. But it might be impossible to find $(PN)_x$ structure in the residues fromed at higher temperatures.

References

[1] J. Green, An overview of the fire retaradant chemicals industry, past-present-future, Fire and Materials 19 (1995) 197-204.

[2] X. Li, Y. X. Ou, Y. H. Zhang, D. J. Lian, Synthesis and Structure of A Novel Caged Bicyclic Phosphate Flame Retardant, Chinese Chemical Letter, 11 (2000) 887-890.

[3] G. Camino, M. P. Luda, L. Costa, Developments in intumescent fire-retardant systems: Ammomium polyphosphate-poly(ethyleneurea formaldehyde) mixtures, In: Fire and polymers II, G. L. Nelson (Eds.), Washington D C, 1995, 77-90.

[4] G. Camino, L. Costa, L. Trossarelli, Study of the mechanism of intumescence in fire retardant polymers, part II: Mechanism of action in polypropylene-ammonium polyphosphate-pentaerythritol mixtures, Polym Deg Stab, 7 (1984) 25-31.

[5] I. S. Reshetnikov, M. Y. Yablokova, N. A. Khalturiskij, Intumescent chars. In: Fire retardancy of polymers: the use of intumescence, M. Le Bras, G. Camino, S. Bourbigot et al (Eds.), Cambridge, 1998.

[6] R.Delobel, M. Le Bras, N. Ouassou, Thermal behaviors of ammonium polyphosphate-pentaerythritol and ammonium pyrophosphate-pentaerythritol intumescent additives in polypropylene formulations, J Fire Science, 8 (1990) 85-99.

[7] S. Q. Han. The application of high temperature LOI in flame-retarded polymer [doctor degree thesis], Beijing: Beijing Institute of Technology, 2000.

[8] N. Grassie, R. Mcguchan, Pyrolysis of polyacrylonitrile and related polymers—VI: acrylonitrile copolymers containing carboxylic acid and amide structures, European Polym J, 8 (1972) 257-269

[9] Q. L. Li, Synthesis, application and mechanism investigation of novel phosphorus-nitrogen system flame retardants [doctor degree thesis], Beijing: Beijing Institute of Technology, 1999.

Advanced Materials Research Vol. 936 (2014) pp 23-27
© (2014) Trans Tech Publications, Switzerland
doi:10.4028/www.scientific.net/AMR.936.23

Effect of Pr modification treatment on the microstructure and mechanical properties of cast Al-Mg_2Si metal matrix composite

SI Yi [1,a *]

[1]Department of Applied Chemistry, Liaoning Petrochemical Vocational and Technology College, China

[a]siyi9555@126.com

Keywords: Al/Mg_2Si composites; casting; Pr addition; microstructure; tensile properties

Abstract: The effect of different concentrations of Pr on the microstructure and tensile properties of cast Al-18 wt.%Mg_2Si in situ metal matrix composite was investigated. The results show that the addition of proper amount of Pr has significant modification effect on primary Mg_2Si in the Al-18 wt.% Mg_2Si composite. With the increase of Pr content from 0.1 to 0.7%, the morphology of primary Mg_2Si is changed from irregular or dendritic to polyhedral shape, and its average particle size is significantly decreased from 65 to 17 μm. When the Pr content exceeds 1.0%, the primary Mg_2Si become coarse again. Tensile tests reveal that the Pr addition improves the tensile strength and ductility of the material. Comparing with those of unmodified composite, the ultimate tensile strength and percentage elongation with 0.7% Pr are increased by 36.5% and 161.6%, respectively.

Introduction

Al-based composites reinforced by in-situ Mg_2Si particles have been lately introduced as a new group of particulate metal matrix composites (PMMCs) with attractive advantages such as low specific gravity, high strength at elevated temperature, excellent wear resistance, and low coefficient of thermal expansion, since the intermetallic compound Mg_2Si formed on solidification exhibits a high melting temperature, low density, high hardness, low thermal expansion coefficient and reasonably high elastic modulus [1]. Thus, the Al-Mg_2Si in-situ metal matrix composites have high potential as candidates to replace Al-Si alloys used in aerospace and automotive applications, in particular in the applications where the alloys are a substitute for cast iron when the engineering advantage of light weight and wear resistance in service are considerations such as for the production of engine blocks, air compressor cylinders and cylinder heads. However, conventional casting process usually produces coarse primary or eutectic Mg_2Si phases, and the Mg_2Si particles themselves are hard and brittle, which causes the serious disseverance to the matrix and stress concentration at the tips or edges of the Mg_2Si particles, leading to the cracking at the grain boundary or in Mg_2Si particles oneself, thereby, mechanical properties, especially elongation are significantly reduced.

Chemical modification is a simple and effective technique for improving the morphology and size of Si particles in Al-Si alloys, which was usually used in the industrial field. Recently, several investigations have been carried out for the modification of primary and eutectic Mg_2Si crystals in Al-Mg_2Si, Al-Si-Mg_2Si and Mg-Si-Mg_2Si composites by the additions of P [2], Sr [3], RE elements such as Y[4], Nd [5] and Ce [6], Li [7] and Na [8] to the melts.

Past investigation concentrated on RE modification on Mg_2Si phase, but the influence of RE on the mechanical properties of Al/Mg_2Si composites was rarely reported. The present study first investigates the modification effect of RE element Pr on the Mg_2Si phase in Al/Mg_2Si composite, and then an attempt was made to reveal the tensile properties of the composite with different amounts of Pr additions. The relationship between tensile properties and microstructures was also discussed.

Experimental procedure

Commercially pure aluminum (ingot, 99.1% purity), magnesium (ingot, 98.5 % purity), silicon (block, 98.4 % purity) and Al-10Pr master alloy were used as precursor materials to prepare Al–18

wt.% Mg_2Si composite. Aluminum ingot and silicon blocks were charged into a graphite crucible and heated in an electric resistance furnace, and then the different amounts of Pr were introduced into the melt by adding Al-10Pr master alloy at 800℃. The Pr level, ranging from 0.1 to 1.3 wt% in step of per 0.1 wt%, was added into the melt. After that, magnesium blocks were added into the melt when temperature dropped to about 720℃. Then the melt was degassed with C_2Cl_6. After gently stirred, the melt is cast into a steel mold preheated at 200℃ to produce 30 mm diameter rods.

All the specimens for microstructure characterization were cut from the same positions of the ingots at 10 mm from the bottom of the castings. The specimens were mechanically ground, and then polished through standard routines. Each cross section was etched using 0.5vol% hydrofluoric acid (HF) water solution. The microstructures of the composites were investigated by a optical microscope (OM). The average grain size was measured by linear intercept method.

Tensile properties at room temperature were conducted using a computer controlled universal tensile testing machine. For each group, four tensile test specimens were used. Each value of tensile properties was the average value of four tensile specimens.

Results

Microstructure

Fig. 1 show the optical microstructures of the composites containing different amounts of Pr. From Fig. 1, the dark particles are primary Mg_2Si, the gray matrix is (α-Al+Mg_2Si) binary eutectic, and the white phase surrounding the primary Mg_2Si or in the eutectic matrix is primary α-Al. As can is seen from Fig. 1a, the morphology of the primary Mg_2Si particles of the unmodified composite shows a mixture of coarse dendritic and polyhedral shape. The average diameter of the Mg_2Si particles reaches 64.7 μm and the size distribution is far from uniform, the maximum is near 92 μm and the minimum only is 27 μm. The addition of Pr produces modification effect on primary Mg_2Si and efficiency depends on the addition level of Pr. With 0.1 and 0.4%Pr addition, the morphology of

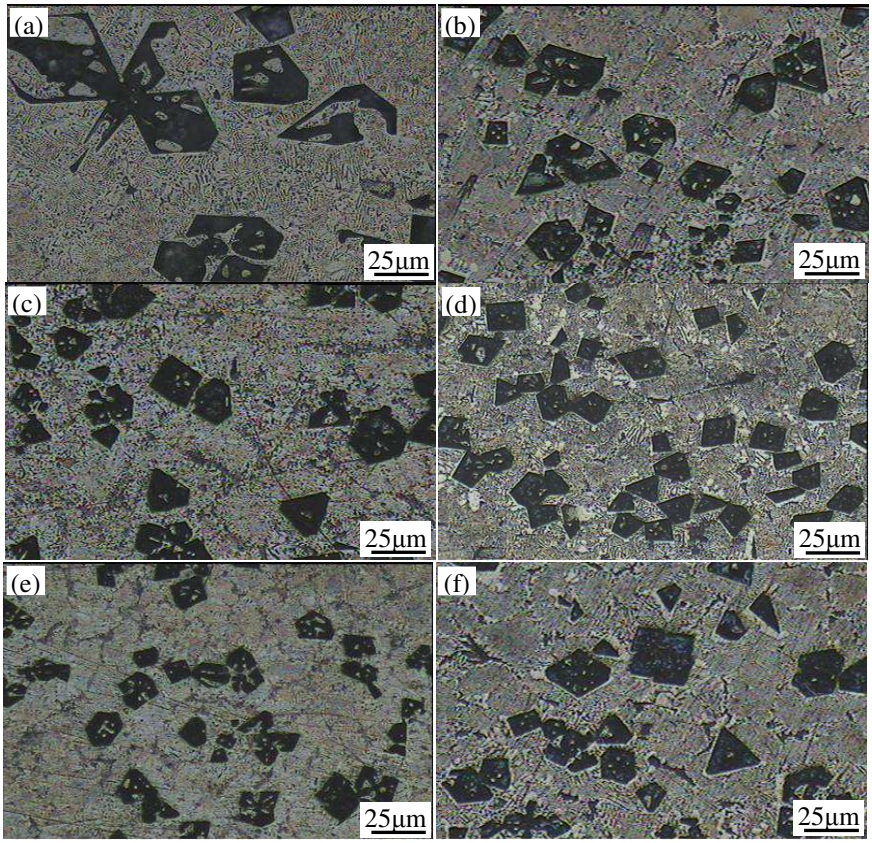


Fig. 1 Optical microstructures of the Al-18wt.%Mg_2Si composites containing different amounts of Pr (wt.%): (a) 0, (b) 0.1, (c) 0.4, (d) 0.7, (e) 1.0 and (f) 1.3.

primary Mg_2Si do not be changed significantly, but their sizes are decreased to 35.2 and 28.6 μm, respectively (Fig. 1b and 1c). As the addition level of Pr increases to 0.7%, the size of primary Mg_2Si further is reduced to 17.3 μm or less, and its morphology transforms into fully polyhedral morphology (Fig.1d). The addition of 1.0%Pr done not obviously change the morphology and size of primary Mg_2Si, and its morphology still keeps the irregular and polyhedral modified morphology (Fig. 1e). However, when the addition level of Pr is further increased to 1.3%, it is found that some coarse Mg_2Si particles are formed again, but smaller than that in the unmodified composite. As compared to those in Fig. 1(d) and 1(e), its sizes increases to about 31.4 μm, although there is no obvious change in the modified morphology of primary Mg_2Si (Fig. 1f). It should be noticed that the additions of 0.7%Pr of the particles more uniform, as shown in Fig. 1(d). Based on the experimental results, it can be concluded that minor Pr (less more 0.4 %) results in partial modification on primary Mg_2Si, while more Pr additive (0.7–1.0 wt%), produces full modification. But, excess Pr (1.3%) leads to the appearance of over-modification phenomenon. The variation of primary Mg_2Si grain size with different Pr is shown in Fig. 2.

Tensile properties

The influence of Pr addition level on the tensile properties of the composites is shown in Fig. 3. It is seen that the trend of variations in the ultimate tensile strength (UTS) and percentage elongation (EL) of the composites with Pr content was similar, i. e. the UTS and EL of the composites increased firstly with an increase in Pr content and then decreased. The unmodified composite had an UTS of 191 MPa with an elongation of 0.73%, while the UTS of 0.7%Pr-modified composite was 262 MPa with an elongation of 1.90%. The tensile strength and elongation of modified composites increased 36.5% and 161.6%, respectively. However, excess Pr (1.3%) decreases UTS and EL to 245 MPa and 1.22%, respectively.

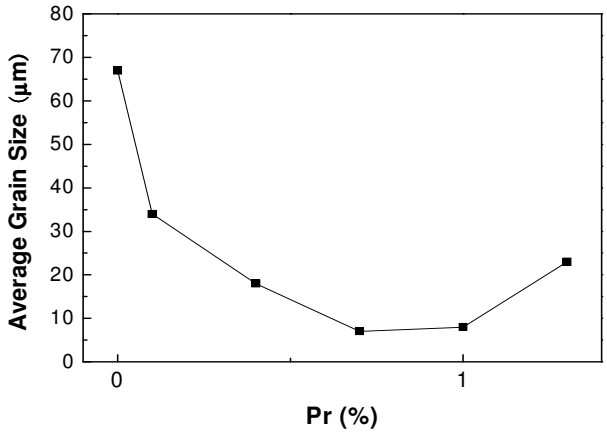


Fig. 2 The variation of primary Mg_2Si grain size with different Pr contents

The reason for the refinement of Mg_2Si crystals by the addition of Pr might be related to the composition supercooling caused by the segregation of Pr at the front of the solid/liquid interface of Mg_2Si during solidification. It can be considered that because of the extremely low solidity of Pr in the Al matrix, the Pr element is easy to congregate at the growing interface of Mg_2Si, resulting in a local composition supercooling in the alloy melt. With the concentration increase of Pr, the composition supercooling is further increased. When the concentration of Pr reaches a certain extent, the growth of Mg_2Si phase can be suppressed and thus its crystals become fine. Another refining reason might be because Pr addition may create some distortion in the Mg_2Si lattice due to a high solidity limit of Pr in Mg_2Si and the larger radius size of Pr atom, and thus change the surface energy of the Mg_2Si crystals. Therefore, Pr addition may arrest and suppress the anisotropic growth of the Mg_2Si dendritic morphology. With regards to the detailed modifying mechanism, there is still a need for further research to be carried out. Variations in the tensile properties for Al-18 wt.%Mg_2Si in situ metal matrix composites are mainly be due to the change in the average sizes of primary Mg_2Si particles. Above studies have revealed that the variation tendency of the UTS and EL with Pr content

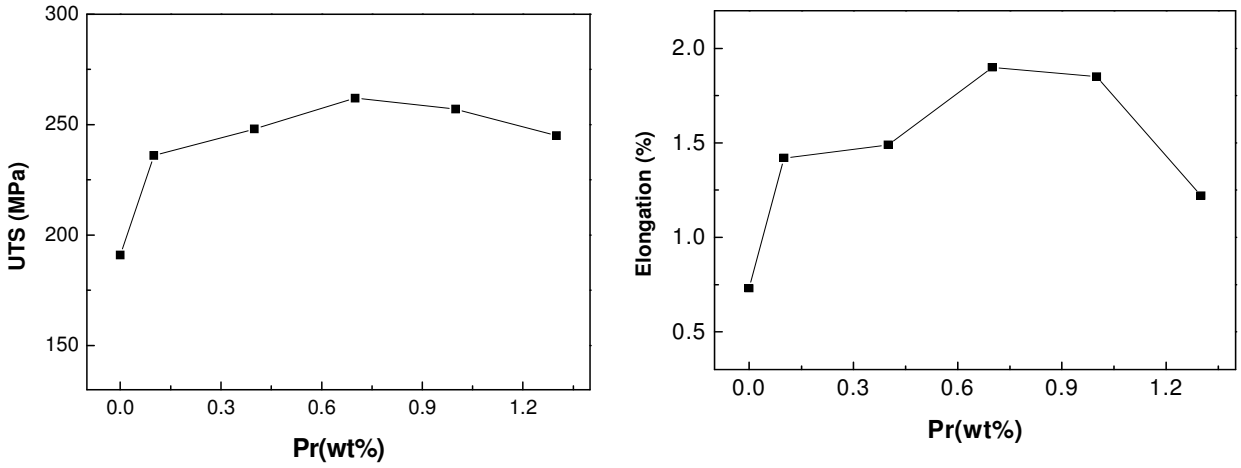


Fig. 3. The curves of tensile properties vary with the contents of Pr

for the composites basically is similar to that of primary Mg_2Si with Pr content. For particulate metal matrix composite, the matrix receiving load plastically deforms and stress transfers to the particles via interface during stretching process. The primary Mg_2Si particles in the unmodified composite are coarse and prone to crack because coarse particles permits larger defects to be presented in the particle, which cause it to have a lower fracture stress [9]. When small uniaxial tensile loading exerts on the sample of the material, the primary Mg_2Si particles first cracks. Consequently, the stress intensity in the matrix bounded on the tip of the cracks of the broken Mg_2Si crystallites increases, rapid crack propagation takes place, resulting in the premature failure and the low fracture strength of the whole composite (Fig. 3), which is similar to the embrittlement in the unmodified hypereutectic Al-Si alloy [10] and an angular particulate-reinforced 6061-Al composite containing 20 pct vol Al_2O_3. On the contrary, the modified composite has fine primary Mg_2Si particles. These particles do not crack prematurely after yielding large loading, then retard the crack formation and propagation in the matrix during stretching process, and therefore, the modified composite possessed better plasticity and strength (Fig. 3). On the other hand, the uniformity distribution of the primary Mg_2Si particles in the modified composite (Fig. 1d) could also enhance the strength and ductibility, which has also been demonstrated in many PMMCs such as aluminum 6092/B4C composite.

The decrease of tensile properties for 1.0 and 1.3%Pr-modified composite might be attributed to the existence of Pr-containing brittle intermetallic compounds. And as the Pr additive increases, the relative amount of Pr-containing intermetallic compounds increases. So, the tensile properties in the Pr-modified composite are influenced. It was also confirmed that the formation of MM-containing intermetallic compounds decreases the tensile properties of A356 alloy [13]. In the present study, the addition of Pr increases UTS and EL until the amount of Pr reaches 1.0%. This probable is because the temperature of melting Al-MM master alloy is low (725℃), MM-containing intermetallic compounds such as Al_4La, AlCe, Al_2Ce, $A_{11}Ce_3$ and $A_{11}La_3$ existing in Al-MM master alloy are not melted and remained in the microstructure of materials, which deteriorates tensile properties. While the temperature of melting Al-Pr master alloy in our experiment reaches 800 ℃, so Pr-containing intermetallic compounds are melted and then Pr solubilizes in Al matrix when amount of Pr is small, and Pr-containing intermetallic compounds precipitate when amount of Pr is large in subsequent solidification process. Only the latter lowers tensile properties of the composite.

Conclusions

The influences of different Pr contents on the microstructures and tensile properties of in situ Al-18 wt,% Mg_2Si composites were investigated. The following conclusions can be drawn:

(1) The addition of proper amount of Pr is found to be modifying the primary Mg_2Si in the composites.

(2) With the increase of Pr content, primary Mg_2Si particle morphology is changed from dendritic to polygonal, and its size decreases from 65 to 17 μm. When the Pr exceeds 1.0 wt.%, the size of the primary Si becomes larger furthe.

(3) The tensile properties of the modified composite are improved by adding suitable amount of Pr. After modification with 0.7 % Pr, the ultimate tensile strength (UTS) increased about 36.5% from 191 to 262 MPa and percentage elongation (EL) increased about 161.6% from 0.73 to 1.90%. The refined primary Mg_2Si particles have a higher fracture stress and resistance of crack, which leads to the enhancement of tensile properties.

References

[1] Zhang J, Fan Z and Wang Y Q, et al. Microstructural refinement in Al-Mg_2Si in-situ composites. *J Mater Sci Lett*, 1999, 18 (10): 783-784.

[2] Qin Q D, Zhao Y G and Zhou W, et al. Effect of phosphorus on microstructure and growth manner of primary Mg_2Si crystal in Mg_2Si/Al composite. *Mater Sci Eng A*, 2007, 447 (1-2): 186-191.

[3] Qin Q D, Zhao Y G and Cong P J. Strontium modification and formation of cubic primary Mg_2Si crystals in Mg_2Si/Al composite. *J Alloy Compd*, 2008, 454 (1-2): 142-146.

[4] Jiang QC, Wang H Y and Wang Y, et al. Modification of Mg_2Si in Mg-Si alloys with yttrium. *Mater Sci Eng A*, 2005, 392 (1-2): 130-135.

[5] Chen J， Li Q A, Li J H, et al. Microstructure and mechanical properties of Mg-6Al magnesium alloy with yttrium and neodymium. *China Foundry*, 2009, 6 (2):124-128.

[6] Zhou Y G, Qin Q D and Zhou W, et al. Microstructure of the Ce-modified in situ Mg_2Si/Al-Si-Cu composite. *J Alloys Compd*, 2005, 389 (1-2): L1–L4.

[7] Hadian R, Emamy M and Varahram N, et al. The effect of Li on the tensile properties of cast Al-Mg_2Si metal matrix composite. *Mater Sci Eng A*, 2008, 490 (1-2): 250-257.

[8] Emamy M, Khorshidi R, Honarbakhsh Raouf A. The influence of pure Na on the microstructure and tensile properties of Al-Mg_2Si metal matrix composite. *Mater Sci Eng A*, 2011, 528 (13-14): 4337–4342.

[9] Kiser M T, Zok F W, Wilkinson D S. Plastic flow and fracture of a particulate metal matrix composite. *Acta Mater*, 1996, 44 (9): 3465–3476.

[10] Wang R Y, Lu W H, Hogan L M. Growth morphology of primary silicon in cast Al-Si alloys and the mechanism of concentric growth. *Journal of Crystal Growth*, 1999, 207 (1): 43.

Advanced Materials Research Vol. 936 (2014) pp 28-33
© (2014) Trans Tech Publications, Switzerland
doi:10.4028/www.scientific.net/AMR.936.28

Curing Kinetics of silicone epoxy resin containing fluorene

Deng Weixing, Zhong Yuanwei, Qin Jie, Huang Xuebing, Peng Jinwen*

Key Laboratory of New Processing Technology for Nonferrous Metals and Materials, Ministry of Education, School of Material Science and Engineering, Guilin University of Technology, 12 Jiangan Road, Guilin 541004, Guangxi, China

*Corresponding author, e-mail: jwpengd@163.com;

Keywords: 9,9-bis(4-hydroxyphenyl)fluorene; organic silicon-modified epoxy resin; curing kinetics

Abstract: A new epoxy resin based on dichlorosilane and 9,9-bis(4-hydroxyphenyl)fluorene was synthesized to produce a highly heat-resistant network. The chemical structure was characterized with FTIR spectroscopy and 1H-NMR. 4-4′-Diaminodiphenylsulfone (DDS) was used as the curing agent. The curing kinetics of different epoxy/DDS systems were investigated using non-isothermal differential scanning calorimetry (DSC). The results showed that the values of activation energy (E) were affected by the chemical structure of epoxy resin, and BPEBF exhibited lower curing reactivity towards DDS compared to E-51.

Introduction

Epoxy resins have been widely applied in polymer industry fields as structural adhesives, coatings, encapsulation material, insulating materials and composite matrices due to their superior electrical and mechanical properties, low shrinkage, good cohesiveness, excellent moisture and chemical resistance in comparison with many materials[1-5]. However, the conventional epoxy resins do not posses adequate thermal and mechanical properties to meet the requirements of high performance structural products [3, 6, 7]. Thus, designing novel high-performance epoxy resins have been the trends of recent studies [8-10].

Introducing siloxane (Si-O bond) into the epoxy skeleton is considered to be an effective way to improve thermal properties of epoxy resins, owing to its superior thermo-oxidative stability. In the past few years, many researchers have synthesized various kinds of siloxane-modified epoxy resins. It has been confirmed that the incorporation of siloxane into epoxy can noticeably enhance the thermal stability of siloxane-modified epoxy resins [11-16].

In this work, a novel organic silicone epoxy resin containing fluorene (BPEBF) was synthesized and characterized with FTIR spectroscopy and ^{1}H-NMR. The epoxy resin was cured with 4-4′-Diaminodiphenylsulfone (DDS). The curing kinetics were studied with dynamic differential scanning calorimetry (DSC) and simulated with both Kissinger and Ozawa methods.

Experimental

Materials

9,9-Bis(4-hydroxyphenyl)fluorene, Dichlorodiphenylsilane, Tetrabutyl ammonium bromide (TBAB) and Epichlorohydrin were obtained from Sigma-Aldrich. 4,4'-Diaminodiphenylsulfone (DDS) and bisphenol A epoxy resin E51 were provided by Sinopharm Chemical Reagent Co., Ltd. All chemical agents were used without further purification.

Synthesis of BPEBF

9,9-Bis-(4-hydroxyphenyl)-fluorene and anhydrous 1,4-dioxane were added into a round bottom flask and heated to 40 °C. Dichlorodiphenylsilane was added dropwisely to the solution. Hydrogen chloride was expelled by bubbling dry nitrogen. The reaction was stirred at 40 °C for 4 hours and heated to 70 °C followed by addition of ECH, TBAB and aqueous NaOH solution (50 wt %). The reaction was stirred for another 4 hours and cooled to room temperature. Excess ECH and solvent were removed and the residue was washed with water and ethanol leading to a white precipitation. Pure silicone epoxy resin containing fluorene was obtained by recrystallization from acetone/ethanol (5:1, v/v) in 65% yield.

Result and discussion

Synthesis and characterization

Scheme 1 presents the chemical structure and the procedure for the synthesis of silicone epoxy resin containing fluorene, which is denoted as BPEBF. Pure BPEBF was obtained by recrystallization from acetone/ethanol as white podwer. The melt point of BPEBF is 180 °C determined by DSC.

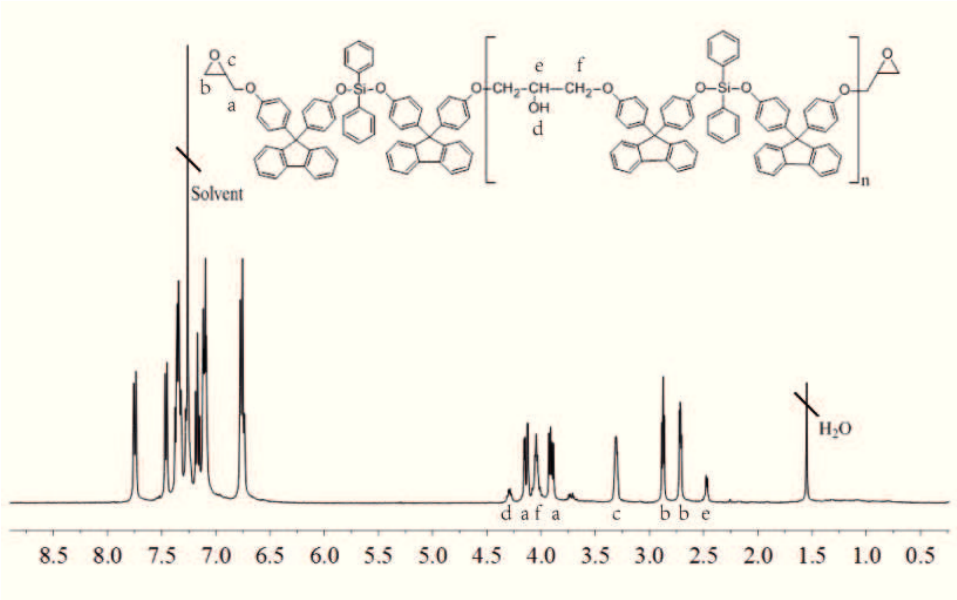


Fig. 1. 1H NMR spectrum of silicone epoxy containing fluorene (BPEBF) in CDCl3.

Fig. 1 shows the ^{1}H NMR spectrum of BPEBF in $CDCl_3$. The chemical shifts at 7.34 – 7.76 are attributed to the protons on fluorene and peaks at 6.75-7.19 are attributed to the protons on phenyl groups. The characteristic chemical shifts of oxirane can be clearly read at 4.12, 3.91, 3.30 2.87 and 2.71. FTIR was also used to characterize the structure of BPEBF. The characteristic absorption peaks of phenyl-oxide-silicone at 1245 cm^{-1} and absorption peak of oxirane at 913 cm^{-1}, 1243 and 1034 cm^{-1} are attributed to the stretching vibrations of C-O-C, 1119 and 1111 cm^{-1} indicate the phenyl-silicone-phenyl stretching vibration. Epoxy equivalent weight titration results showed the EEW of BPEBF is 500 g / eq.

Curing kinetics of epoxy resin-DDS systems

The curing behavior and kinetics of a novel silicon-modified epoxy resin containing fluorene (BPEBF) was studied by DSC technique together with E-51 epoxy. Figure 2 shows the DSC thermograms of different epoxy/diamine systems at heating rates of 5, 10,15 and 25 °C/min. From Figure 2, information about the nature of the curing reaction such as initial curing temperature (T_i), peak temperature (T_p), final curing temperature (T_f) and the curing range at different heating rates

could be derived. The peak temperatures of different systems obtained are summarized in Table 1. Meanwhile, as can be seen from the thermograms that the exothermic peak shifts to a higher temperature with higher heating rate.

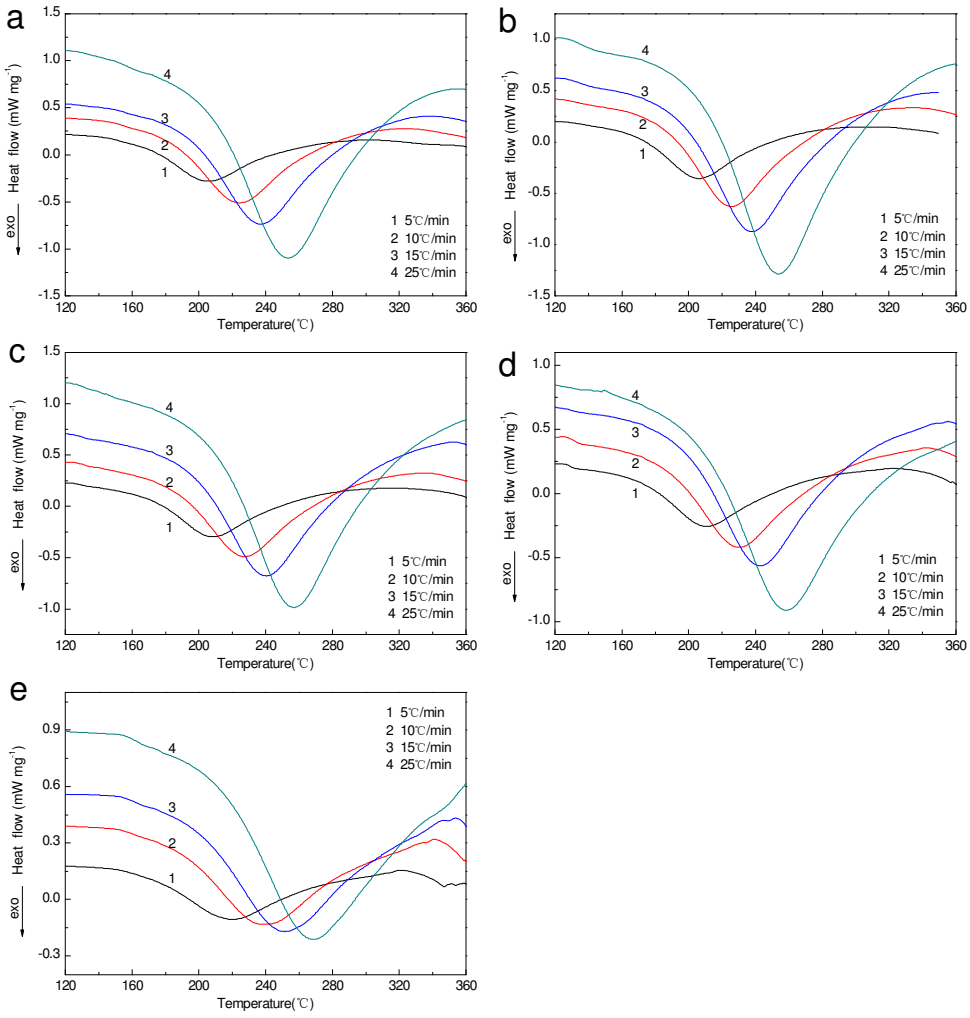


Figure 2 Dynamic DSC thermograms for different epoxy/DDS systems at heating rates of 5, 10, 15 and 20 oC/min under nitrogen atmosphere. (a) E-51/DDS; (b) B0.1E0.9/DDS; (c) B0.2E0.8/DDS; (d) B0.3E0.7/DDS ; (e) BPEBF/DDS.

To evaluate the kinetic parameters of the epoxy/diamine systems, the well-known Kissinger and Ozawa methods were applied to calculated the activation energy (E) and the pre-exponential factor (A) because of their simple ways to deal with the dynamic curing process. Kissinger method is based on the fact that T_p varies with the heating rates, and it assumes that the maximum reaction rate occurs at the peak temperature. The Kissinger's equation can be expressed as Eq. (1):

$$\ln\frac{\beta}{T_p^2} = \ln\left(\frac{AR}{E_k}\right) - \frac{E_k}{RT_p} \tag{1}$$

where β is the heating rate and R is the ideal gas constant. The E_k values of curing can be derived from the slope of $\ln(\beta/T_p^2)$ versus $1/T_p$ plot. Figure 3 shows the plots of $\ln(\beta/T_p^2)$ versus $1/T_p$ for

different cured systems. For Ozawa's method, it's on the assumption that the degree of conversion at peak temperature for different heating rates is constant. Ozawa's equation can be expressed as follows:

$$\ln \beta = -5.331 - 1.052\left(\frac{E_o}{RT_p}\right) + \ln\left(\frac{AE_o}{R}\right) - \ln f(\alpha) \tag{2}$$

Thus, E_o could be obtained by plotting lnβ versus $1/T_p$, as shown in Figure 4. According to the Kissinger method, the pre-exponential factor A can be calculated with Eq.(3):

$$A \approx \frac{\beta E \exp\left[E / RT_p\right]}{RT_p} \tag{3}$$

In addition, when the value of E_k was introduced into the Crane's equation[17], as shown in Eq.(4), the curing reaction order (n) could be obtained from the slope of lnβ versus $1/T_p$ plot when E_k/nR is much higher than $2T_p$. All the results obtained are summarized in Table 2.

$$\frac{d(\ln \beta)}{d(1/T_p)} = -\left[\frac{E_k}{nR} + 2T_p\right] \tag{4}$$

As can be seen from Table 2, the E values calculated from Ozawa method were slightly higher than that of the Kissinger method. The differences may be caused by their different assumptions, but the trend of E values determined by both of methods was consistent with each other. Table 1 and Table 2 showed that the T_p and E values of BPEBF/DDS system were higher than that of E-51/DDS system, respectively. And they increased with increasing the content of BPEBF in mixture resins. This results mean that BPEBF exhibited lower curing reactivity compared to E-51 and would require a higher curing temperature. The decreased reactivity of BPEBF can be obviously attributed to the steric hindrance based on the fluorene structure, which may reduce the molecular mobility and depress the reactivity of reactive group. In addition, the reaction orders of these five epoxy/diamine cured systems were very close to each other and all less than 1, which mean that the reaction type of these systems was all the same but the cure reaction may proceed complicatedly.

TABLE 1 PEAK TEMPERATURE (TP, OC) OF CURE EXOTHERMS FORTHE EPOXY/ DDS systems at different DSC heating rates (β)

samples	β (°C/min)			
	5	10	15	25
E-51/DDS	205.8	224.5	236.8	253.5
$B_{0.1}E_{0.9}$/DDS	206.1	225.6	237.9	253.8
$B_{0.2}E_{0.8}$/DDS	208.4	227.7	240.6	256.8
$B_{0.3}E_{0.7}$/DDS	211.0	230.3	243.0	258.7
BPEBF/DDS	219.5	238.7	251.6	268.6

TABLE 2 CURING KINETIC PARAMETERS FOR THE EPOXY/DDS SYSTEMS DERIVED FROM THE MULTI-TEMPERATURE SCAN METHOD

samples	Kissinger method			Ozawa method	
	E_k(KJ·mol^{-1})	A(s^{-1})	n	E_o (KJ·mol^{-1})	A(s^{-1})
E-51/DDS	61.836	8.231×10^5	0.881	66.683	2.812×10^6
$B_{0.1}E_{0.9}$/DDS	62.392	1.031×10^6	0.882	67.238	3.539×10^6
$B_{0.2}E_{0.8}$/DDS	62.487	1.081×10^6	0.882	67.336	3.721×10^6
$B_{0.3}E_{0.7}$/DDS	63.644	1.201×10^6	0.883	68.518	4.101×10^6
BPEBF/DDS	64.065	9.962×10^5	0.882	69.055	3.430×10^6

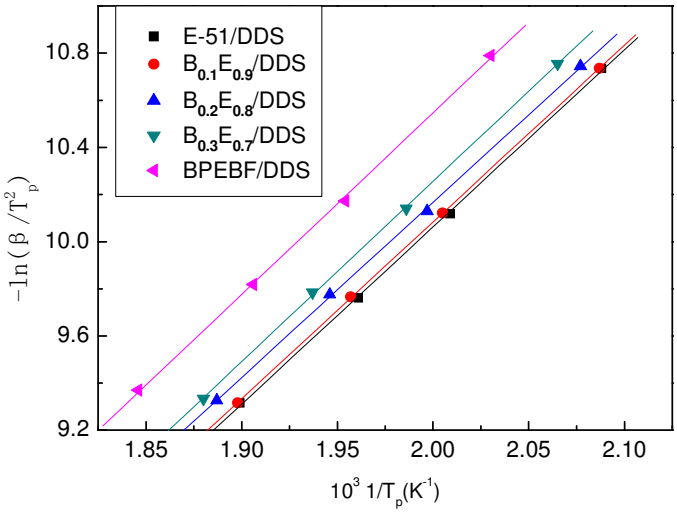


Figure 3 Plots for determination of the E and A by Kissinger method of different epoxy/DDS systems

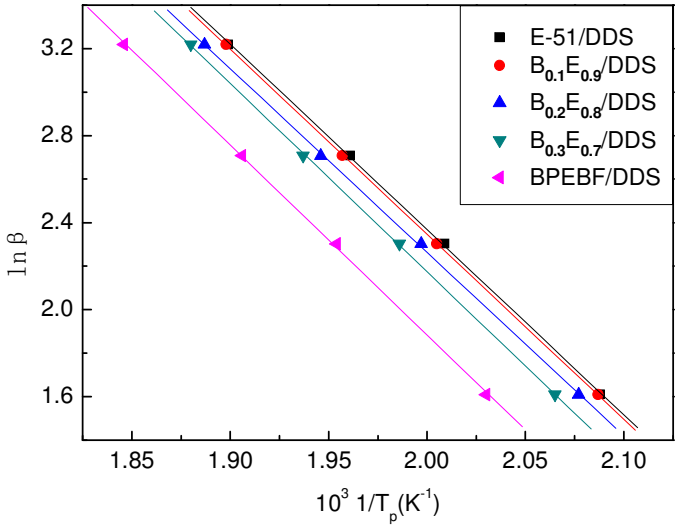


Figure 4 Plots for determination of the E and A by Ozawa method of different epoxy/DDS systems

Conclusions

A novel organic silicon-modified epoxy resin containing fluorene (BPEBF) was successfully synthesized and characterized. The DSC analysis indicated that BPEBF exhibited lower curing reactivity towards DDS compared to E-51 and would require a higher curing temperature. BPEBF might become an attractive candidate for electronic encapsulation materials, laminate materials and high performance composite materials.

Acknowledgements

This work was financially supported by the National Natural Science Foundation of China (No. 51363004), the Guangxi Natural Science Foundation (2012GXNSFAA053212), Funds from Key Laboratory of New Processing Technology for Nonferrous Metals and Materials (2KF-12), Guangxi Small Highland Innovation Team of Talents in Colleges and Universities, and Guangxi Funds for Specially-appointed Expert.

References

[1] Lee, K. Neville, Handbook of epoxy resins, NK. McGraw-Hill. 1967.
[2] G. Lubin, Handbook of composites, NK. Nostrand Reinhold. 1982.
[3] P. Chen, D.Z. Wang, Applications of epoxy resins, Beijing. Academic. 2001.
[4] P. Khurana, S. Aggarwal, A.K. Narula, V. Choudhary, Studies on the curing and thermal behaviour of DGEBA in the presence of bis(4-carboxyphenyl) dimethyl silane. Polym. Int. 52(2003) 908-917.
[5] E.Sharmin, L.Imo, S.M.Ashraif, S.Ahmad, Acrylic-melamine modified DGEBA-epoxy coatings and their anticorrosive behavior, Prog. Org. Coat. 50(2004) 47-54.
[6] M.Zhiguang, G.Jungnag, Curing Kinetics of o-Cresol Formaldehyde Epoxy Resin and Succinic Anhydride System Catalyzed by Tertiary Amine, J. Phys.Chem.B. 110(2006) 12380-12383.
[7] I. Blanco, G. Cicala, M. Costa, A. Recca, Development of an epoxy system characterized by low water absorption and high thermomechanical performances. J. Appl.Polym. Sci. 100(2006) 4880-4887.
[8] X. Meiran, W.Zhonggang, Z. Yunfeng, Synthesis and properties of a novel, liquid, trifunctional, cycloaliphatic epoxide. J. Polym. Sci. Part A: Polym. Chem. 39(2001) 2799-2804.
[9] L.Yanfang, D. Zhongjie, Z. Chen, L. Congju, L. Hangquan, Curing behavior and thermal properties of multifunctional epoxy resin with methylhexahydrophthalic anhydride. J. Appli.Polym. Sci. 103(2007) 2041-2048.
[10] P. Guoyuan, D. Zhongjie, Z. Chen, L. Congju, Y. Xiaoping, L. Hangquan, Synthesis, characterization, and properties of novel novolac epoxy resin containing naphthalene moiety. Polym. 48(2007) 3686-3693.
[11] R.Mikami, Siloxane-Modified Epoxy Resin Composition, Toray Silicone Company, Ltd., Tokyo, Japan: USA. 1981.
[12] S.T. Lin, S.K. Huang, Synthesis and characterization of siloxane-modified epoxy resin. J. Polym. Res. 1(1994) 151-162.
[13] S.D.Smith, T.E. Long, J.E. McGrath, Thermogravimetric analysis of poly(alkyl methacrylates) and poly(methylmethacrylate-g-dimethyl siloxane) graft copolymers. J.Polym. Sci. Part A: Polym. Chem. 32(1994) 1747-1753.
[14] W.J. Wang, L.H. Peng, G.H. Hsiue, FC.Chang, Characterization and properties of new silicone-containing epoxy resin. Polym. 41(2000) 6113-6122.
[15] S. Ananda Kumar, T.S.N. Sankara Narayanan, Thermal properties of siliconized epoxy interpenetrating coatings. Prog. Org. Coat. 45(2002) 323-330.
[16] S. Ahmad, A.P. Gupta, E. Sharmin, M. Alam, Synthesis, characterization and development of high performance siloxane-modified epoxy paints. Prog. Org.Coat. 54(2005) 248-255.
[17] L.W. Crane, P.J. Dynes, D.H. Kaelble, Analysis of curing kinetics in polymer composites. J.Polym. Sci: Polym.Letters Edition. 11(1973) 533-540.

Advanced Materials Research Vol. 936 (2014) pp 34-38
© (2014) Trans Tech Publications, Switzerland
doi:10.4028/www.scientific.net/AMR.936.34

Synthesis of Core @ Shell Composite Particles with a Tunable Shell Containing Natural Urushiol

Longhui Zheng[1, a], Baoling Chen[1, b], Haibin Huang[1, c], Qinhui Chen [1, 2, d*] and Jinhuo Lin [1, 2, e]

[1] College of Material Science and Engineering, Fujian Normal University, Fuzhou 350007, China

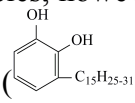
[2] Fujian Key Laboratory of Polymer Materials, Fuzhou 350007, China

[a]lhzheng88@163.com, [b]chenbaoling1989@163.com, [c]hbhuang90@163.com, [d]chenqh@fjnu.edu.cn, [e]jhlin@fjnu.edu.cn

Keywords: urushiol; polystyrene; renewable resources; core @ shell composite particles

Abstract: The core @ shell composite particles of polystyrene @ urushiol-titanium chelate polymer (PS @ UTi) was prepared through in-situ reaction between sulfonated polystyrene microspheres coated tetrabutyl titanate and urushiol. The resultant PS @ UTi was characterized by scanning electron microscope and transmission electron microscope. Results indicated that the PS @ UTi with the excellent properties of raw lacquer was synthesized. The shell thickness of UTi coated on PS was tunable by changing the sulfonation time.

Introduction

The core @ shell composite particles has increasingly attracted interest because of their unique electronic, optical and catalytic properties [1,2]. They show broad potential applications in photovoltaic [3] and biological [4] applications, catalysis [5], Janus materials [6,7], etc. There are various core @ shell types, including inorganic/inorganic, inorganic/organic, organic/inorganic, and organic/organic materials. Some synthesis approaches have been proposed including lithographic techniques, laser-beam processing, laser-induced assembly and colloidal aggregation, etc [8]. In core @ shell composite particles, however, existing core and shell parts of them mainly come from synthetic material. Urushiol (

) is a natural resource, which can be extracted from raw lacquer, thus becomes more and more important in the situation of resource scarcity. Urushiol is the main component of raw lacquer, for their excellent performance, outstanding characteristic and widespread application prospect, receiving a widespread attention of research workers [9-11]. Thus, it is very interesting to introduce the urushiol-metal polymers into core @ shell composite particles.

Two adjacent phenolic hydroxyls of urushiol can react easily with metal compounds and generated urushiol-metal chelate polymer [12,13]. Herein, we report a simple approach to synthesize the core @ shell composite particles of polystyrene @ urushiol-titanium chelate polymer (PS @ UTi) by using sulfonated polystyrene particles as templates. Then, tetrabutyl titanate is absorbed on the surface of sulfonated polystyrene sufficiently and reacts with urushiol.

Experimental

Materials

Chinese lacquer purchased from the Institute of Lacquer, Xi'an, China. Urushiol was obtained after extraction with ethanol from Chinese lacquer. Styrene (St), tetrabutyl titanate and ethanol were purchased from Sinopharm Medicine Holding Co., Ltd. Sulfuric acid was purchased from Tianjin Fuchen Chemical Reagent Factory. St was used after purification by alkaline Al_2O_3 to remove the inhibitor.

Characterization

The morphology and the composition of the samples were characterized by a JSM-7500F scanning electron microscope (SEM) with operation voltage of 5 kV. Transmission electron microscope (TEM) images were obtained with a JEM-2010 electron microscope.

Synthesis of the core @ shell composite particles of PS @ UTi

The sulfonated polystyrene (SPS) microspheres with different sulfonation time were synthesized according to the literature of [14,15]. 1 g of SPS particles were dispersed in 100 mL of ethanol, and then 100 mL of tetrabutyl titanate (TBT) was added into the ethanol dispersion under stirring for 8 h to allow a complete adsorption. The mixture was centrifugated and washed with ethanol to remove redundant tetrabutyl titanate. And then, 5 g of urushiol in ethanol was added into the mixture. The reaction was maintained for 4 h under stirring. The core @ shell composite particles of PS @ UTi were purified by centrifugation and washed with ethanol for several times.

Results and Discussion

After sulfonation of polystyrene particles with concentrated sulfuric acid, sulfone groups were simultaneously derived in the gel shell. When tetrabutyl titanate was adsorbed in the gel shell, two adjacent phenolic hydroxyls of urushiol reacted easily with tetrabutyl titanate and generated core @ shell composite particles of PS @ UTi [13].

The images of Fig.1 exhibited the TEM image of PS @ UTi. It was clearly that the particles were divided into two parts, including inner core and outer shell. Fig.2 was SEM images of PS @ UTi with different sulfonation time. As shown in Fig.2, the as-synthesized sample was well dispersed. While increasing the sulfonation time from 1 h to 6 h, the average diameter of PS @ UTi became larger and larger from 256 nm (Fig. 2a, at the sulfonation time of 1 h) to 295 nm (Fig. 2g, at the sulfonation time of 6 h). The sulfonated layer was thicker and thicker and the amount of butyl titanate adsorbed on sulfonated polystyrene increased with extension of sulfonation time. Thus, the shell thickness was larger and larger. In addition, the particles of PS @ UTi with a rougher surface could be obtained after reacting to urushiol. In order to explore the thickness of the shell further, the particles of PS @ UTi were calcined to remove the polystyrene core in 450 ^{o}C for 1 h at the atmosphere of nitrogen. It was found that the sulfonation time was a key role to affect the shell layer of PS @ UTi (Fig.3). When the sulfonation time of PS @ UTi was less than 2 h, the particles collapsed completely (Fig.3a and Fig.3b). When the sulfonation time of PS @ UTi was 4 h, the particles collapsed partly (Fig.3c). With prolonging sulfonation time to 6 h, the particles became intact (Fig.3d). It demonstrated that we can obtain monodisperse core @ shell particles with tunable shell thickness by varying the sulfonation time.

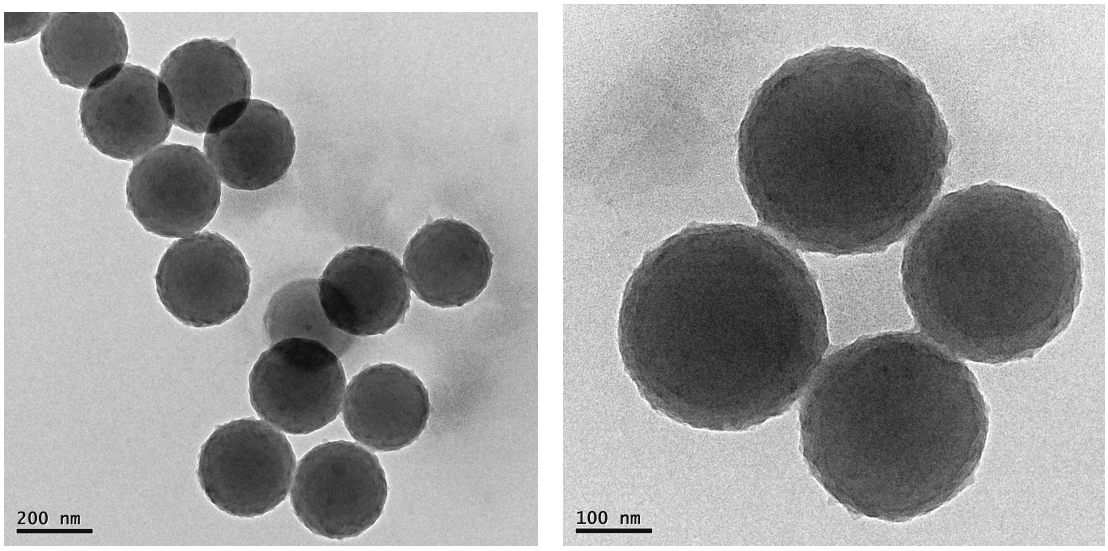


Fig.1 TEM images of PS @ UTi with sulfonation time of polystyrene particles for 1 h.

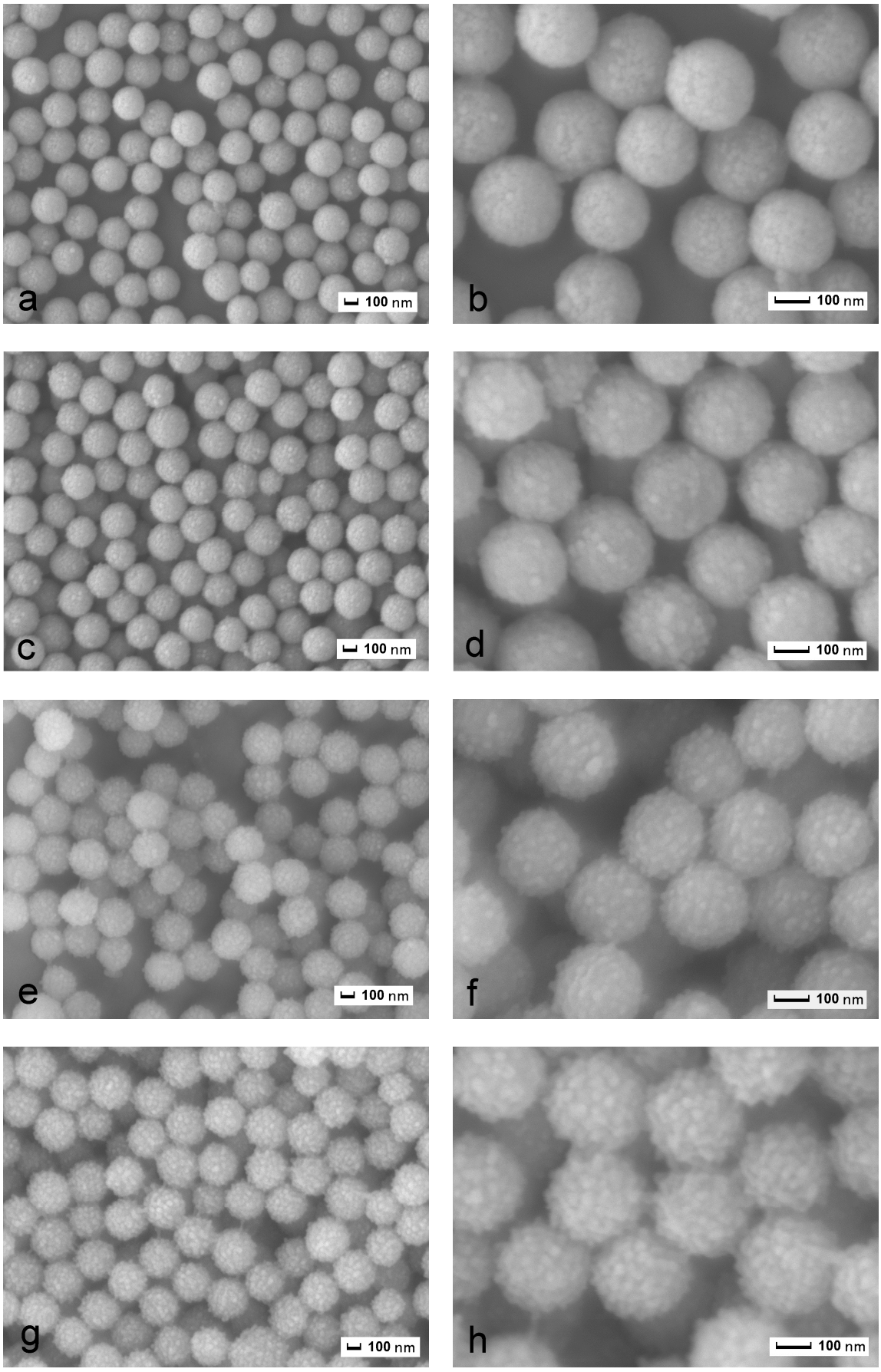


Fig.2 SEM images of PS @ UTi with different sulfonation time of polystyrene particles. (a) (b) 1h, (c) (d) 2 h, (e) (f) 4 h and (g) (h) 6 h.

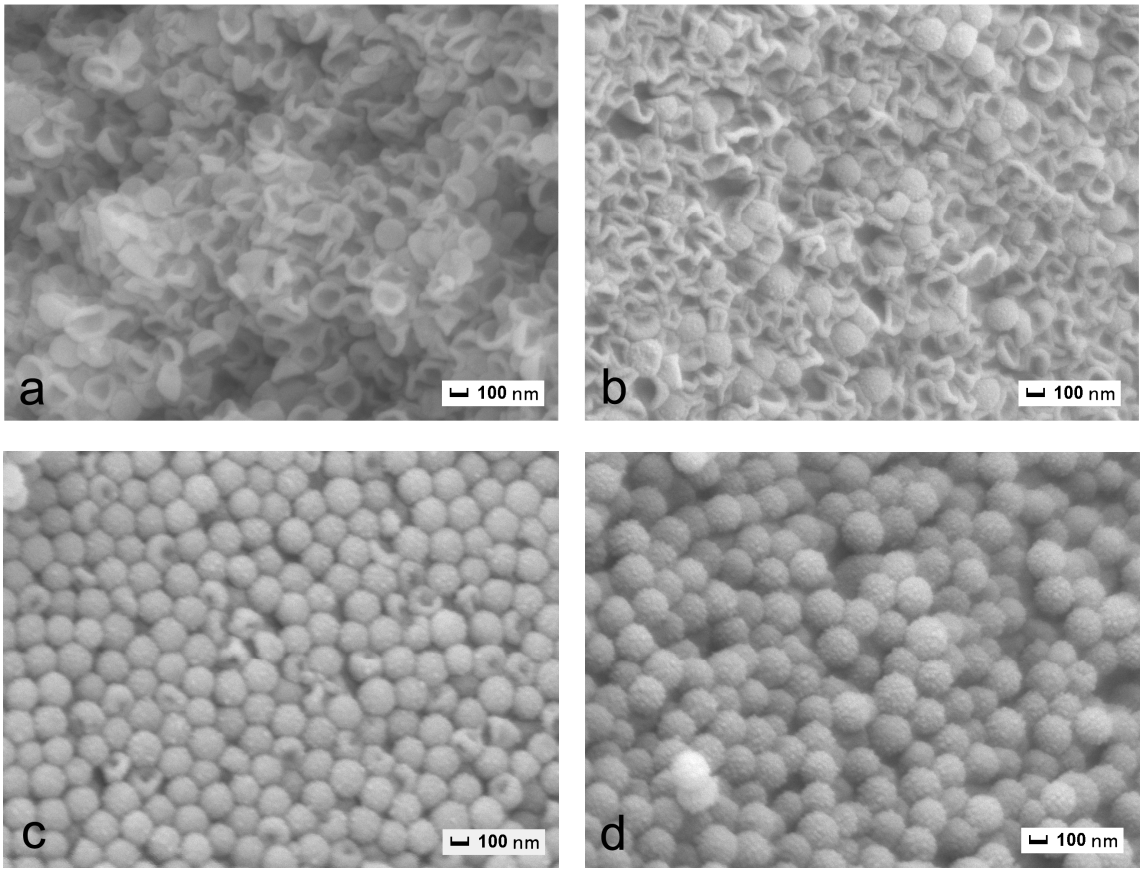


Fig.3 SEM images of PS @ UTi after calcined with different sulfonation time of polystyrene particles. (a) 1 h, (b) 2 h, (c) 4 h and (d) 6 h.

Conclusions

The core @ shell composite particles of PS @ UTi was successfully prepared through in-situ reaction between tetrabutyl titanate coated on the surface of sulfonated polystyrene microspheres and urushiol. The thickness of UTi shell of PS @ UTi core @ shell composite particles was tunable by changing the sulfonation time. Further investigations on the application of PS @ UTi are underway in our laboratory.

Acknowledgments

This work was supported by the National Natural Science Foundation of China (No. 51103024) and Fujian Normal University Foundation for Excellent Young Teachers (No. fjsdky2012004).

References

[1] C.J. Serpell, J. Cookson, D. Ozkaya, P.D. Beer, Core @ shell bimetallic nanoparticle synthesis via anion coordination, Nat. Chem. 3 (2011) 478-483.

[2] K. Zhang, Y. Xiang, X. Wu, L. Feng, W. He, J. Liu, W. Zhou, S. Xie, Enhanced Optical Responses of Au @ Pd Core/Shell Nanobars, Langmuir. 25 (2008) 1162-1168.

[3] J.A. Czaban, D.A. Thompson, R.R. LaPierre, GaAs Core−Shell Nanowires for Photovoltaic Applications, Nano. Lett. 9 (2008) 148-154.

[4] V. Salgueiriño-Maceira, M.A. Correa-Duarte, Increasing the Complexity of Magnetic Core/Shell Structured Nanocomposites for Biological Applications, Adv. Mater. 19 (2007) 4131-4144.

[5] M. Zhu, C. Wang, D. Meng, G. Diao, In situ synthesis of silver nanostructures on magnetic Fe_3O_4 @ C core–shell nanocomposites and their application in catalytic reduction reactions, J. Mater. Chem. A. 1 (2013) 2118-2125.

[6] Q.H. Chen, L.H. Zheng, B.L. Chen, J.H. Lin, Scalable synthesis of TiO_2–Ag Janus composite particles, Eur. Polym. J. 49 (2013) 2610-2616.

[7] Q.H. Chen, B.L. Chen, L.H. Zheng, J.H. Lin, Preparation of Polyaniline/Polystyrene Janus Composite Particles, Chem. J. Chinese Univ. 34 (2013) 1788-1793.

[8] R. Ghosh Chaudhuri, S. Paria, Core/shell nanoparticles: classes, properties, synthesis mechanisms, characterization, and applications, Chem. Rev. 112 (2012) 2373-2433.

[9] J.R. Xia, J.H. Lin, Y.L. Xu, Q.H. Chen, On the UV-induced polymeric behavior of Chinese lacquer, ACS Appl. Mater. Interfaces. 3 (2011) 482-489.

[10] J.R. Xia, Y.L. Xu, J.H. Lin, B.H. Hu, A facile approach to imbed PbS nanocrystal in UV cured polyurushiol matrix, Mater. Lett. 63 (2009) 1499-1501.

[11] X.L. Zheng, J.B. Weng, B.H. Hu, X.Z. Lv, D.L. Meng, A.S.C. Chan, Fabrication of a stable superhydrophobic film constructed by poly(vinylpyrrolidone)/poly(urushiol)-CuS through layer-by-layer assembly, Mater. Chem. Phys. 130 (2011) 1054-1060.

[12] Q.H. Chen, J.H. Lin, Characterization and Properties of Urushiol-praseodymium Polymer, Chemistry and Industry of forest products. 26 (2006) 19-22.

[13] B.H. Hu, W.D. Chen, J.H. Lin, The synthesis of urushiol titanium chelate polymers and their structural characteristics, Chinese journal of polymer science. 11 (1993) 198-203.

[14] Z.Z. Yang, D. Li, J.H. Rong, W.D. Yan, Z.W. Niu, Opal Hydrogels Derived by Sulfonation of Polystyrene Colloidal Crystals, Macromol. Mater. Eng. 287 (2002) 627-633.

[15] Z.Z. Yang, Z.W. Niu, Y.F. Lu, Z.B. Hu, C.C. Han, Templated Synthesis of Inorganic Hollow Spheres with a Tunable Cavity Size onto Core–Shell Gel Particles, Angew. Chem. Int. Ed. 42(2003) 1943-1945.

Advanced Materials Research Vol. 936 (2014) pp 39-42
© (2014) Trans Tech Publications, Switzerland
doi:10.4028/www.scientific.net/AMR.936.39

Preparation and Properties of Polypropylene-graft-cardanol by Reactive Extrusion

Qinhui Chen [1, 2, a] and Jinhuo Lin [1, 2, b]

[1] College of Material Science and Engineering, Fujian Normal University, Fuzhou 350007, China

[2] Fujian Key Laboratory of Polymer Materials, Fuzhou 350007, China

[a]chenqh@fjnu.edu.cn, [b]jhlin@fjnu.edu.cn

Keywords: poly (propylene) (PP); reactive extrusion; cardanol; renewable resources; compabilization; anti-aging

Abstract: The polypropylene-graft-cardanol (CAPP) was prepared by reactive extrusion with polypropylene (PP) and natural renewable cardanol which could improve the inherent defects of PP such as chemical inertness and hydrophobicity. Moreover, the cardanol grafted onto PP could resolve the degradation of PP during the process of reactive extrusion. In this paper, CAPP was prepared in the presence of three different kinds initiator. The compatibilization and the anti-aging performance of cardanol grafted onto PP were studied. Results showed that the initiator dicumyl peroxide (DCP) exhibited the optimum initiated efficiency. Cardanol grafted onto PP was benificial for the composite of bamboo powder and PP.The initiator of DCP caused the degradation of PP chains during the aging processing. After aged for 24 h, the yield strength decreased from 28 MPa to 15 MPa and the elongation at break reduced by 795 %. The CAPP possessed outstanding anti-aging performance owing to the cross-linking and entanglement of the side chains of cardanol grafted onto PP. The yield strength, tensile strength and the elongation at break of CAPP-DCP changed lightly even when it was in long-term irradiation for 480 h.

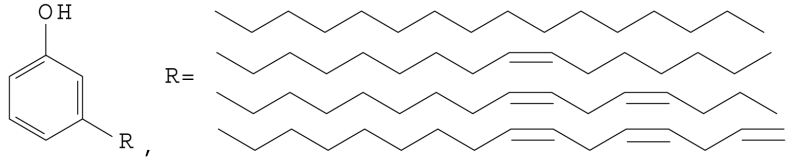
Introduction

Polypropylene (PP) is a kind of non-polar crystal polymer. In order to improve the surface energy of PP, researchers have done their best in many modifications[1-6]. In particular, the graft modification of reactive extrusion, which has advantages due to its solvent-free properties, continuity in producing process and ease in reaction time manipulation, has shown remarkable results and thus aroused widespread interest[7-10]. However, the tertiary carbon atom in the PP structure is prone to cause molecular chain's β rupture and severe degradation during the reactive extrusion process[11-13]. Natural cardanol (a liquid extracted from cashew nutshell) is a phenolic compound containing long unsaturated alkyl side chain [9] (Scheme 1). In this study, the polypropylene-graft-cardanol (CAPP) was prepared by reactive extrusion in order to improve the surface activity. The compatibilization and the anti-aging performance of cardanol grafted onto PP were also investigated.

Experimental

A certain proportion of PP, cardanol and intiator (dissolved in ether) (Table 1) was mixed evenly in a high-speed mixer (2600 r/min). The mixture was then extruded at 180 °C, 50 r/min using the co-rotating twin-screw extruder (HAAKE, Polylab Rheomix PTW24/28, Germany), and pressed into a CAPP sheet with 0.6 mm thickness using the tri-roll calendar. The rolled sheets were cut into 130 mm × 10 mm rectangular samples and placed in the accelerated aging chamber with mercury lamp for aging experiments. The content of CAPP was quantified by UV-vis spectrometer (TU-1900, Beijing Purkinge General Instrument Co., Ltd, China). CAPP was dissolved in boiling n-octane and then kept in 90 ^{o}C of water bath. The grafting ratio of CAPP was measured at the temperature of 90 ^{o}C. Standard curve was decided by a series of cardanol standard solution at 273 nm and 90 °C after dissolved in 1-octane. Using the LR5K universal testing machine of LLOYD British Company, the

yield strength, elongation at break and tensile strength of the material were tested with tensile rate of 5 cm/min and preload of 5 N. Each kind of sample was tested in parallel five or more times, and the average was obtained.



Scheme 1 Chemical structure of cardanol

Results and Discussion

Effect of Initiator on Grafting Ratio

The effect of initiator type on grafting ratio was investigated in order to select the optimum initiator (Table 1). Results showed that grafting reaction couldn't carry out during reactive extrusion in the absence of initiator, e.g. CAPPm. In the presence of 0.2 % DCP, the grafting ratio reached the value of 5.20 %. The grafting ratio initiated by benzoyl peroxide **(**BPO) and ditert-butyl peroxide (dTBP) is lower than that by DCP. The reactive materials would remain in extruder for 1 min at a screw speed of 50 rpm and at the temperature of 180 ^{o}C. According to the literature of[14], the decomposition temperature of BPO and dTBP is 133 ^{o}C and 190 ^{o}C when the calculated value of half-life ($t_{1/2}$) was 1 min, whereas that of DCP is 171 ^{o}C. The reactive temperature of PP-graft-cardanol was too high for BPO. BPO decomposed rapidly at the selected temperature, when all kinds of components in extruder didn't mix completely. Therefore, the number of reactive sites decreased. However, the processing temperature was too low for dTBP. Most of dTBP had left the extruder before it decomposed, so the initiated efficiency wasn't good. In a word, DCP exhibited better initiated efficiency than the other two kinds of initiator.

TABLE1 FORMULA AND GRAFTING RATIO OF PP-GRAFT-CARDANOL AND ITS MIXTURE

Samples	PP	Cardanol	Initiator	Mass of initiator	Grafting ratio
PP	100	0	DCP	0	0
CAPPm	100	5			0
CAPP0	100	0	DCP	0.2	0
CAPP-DCP	100	5	DCP	0.2	4.45
CAPP-BPO	100	5	BPO	0.2	0.92
CAPP-dTBP	100	5	dTBP	0.2	1.01

Compatibilization of Cardanol Grafted onto PP on the Composite Materials of Bamboo Power and PP

Fig. 1 was the polarization microphotos at the magnification of 50 of bamboo plastic composite materials. It could be found that the compatibility of bamboo power and PP was bad. Bamboo powder aggregated at the matrix of PP and the interface between bamboo powder and PP was very distinct. Bamboo powder couldn't be pregnant into PP because of the different polarity between them. The chemical structures of the hydroxyl groups and phenyl groups in cardanol which was grafted onto polypropylene were the same as that of lignin in bamboo powder. Grafting reaction increased the compatibility between bamboo powder and PP, so bamboo powder dispersed in the matrix of PP uniformly.

Effect of Anti-aging Performance of Cardanol Grafted onto PP

To investigate the improvement of grafting reaction during the destruction of PP materials, the destruction of PP and 5 % cardanol blend (CAPPm) was studied as reference (Figure 2). Cardanol in CAPPm reduced the crystallinity of PP, which decreased the intermolecular forces among PP. The yield strength of CAPPm was lower than that of pure PP. However, cardanol played the role of plasticizer in the blend of PP and cardanol, thus shifting the deformation of CAPPm from brittle one

to plastic one. The tensile strength and elongation at break of CAPPm showed an increase. As compared with CAPP-DCP, no chemical bonds existed between cardanol and PP chains; instead cardanol was just dispersed in PP molecular gaps. The elongation at break for such blends of CAPPm was smaller than that of CAPP-DCP with intermolecular interactions. Secondly, when CAPP-DCP was in long-term irradiation under high-pressure mercury lamp (480h), the cardanol side chains underwent cross-linking reactions to form sequential interpenetrating polymer networks with PP. Because of the combined results of the degradation of PP chains in CAPP-DCP and the polymerization of cardanol side chains, the tensile strength and elongation at break of CAPP-DCP changed lightly during the aging process. Overall, the melted graft-modified products of CAPP-DCP with intermolecular forces had better anti-aging properties than the blend products of CAPPm.

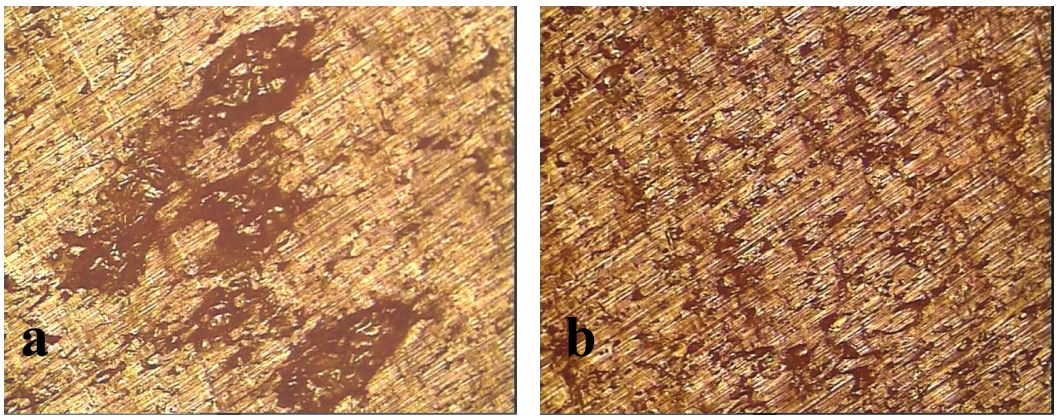


Fig. 1 Polarization Microphotos at The Magnifications of 50 of Bamboo Plastic Composites (a: Bamboo Powder/PP; b: Bamboo Powder/CAPP-DCP)

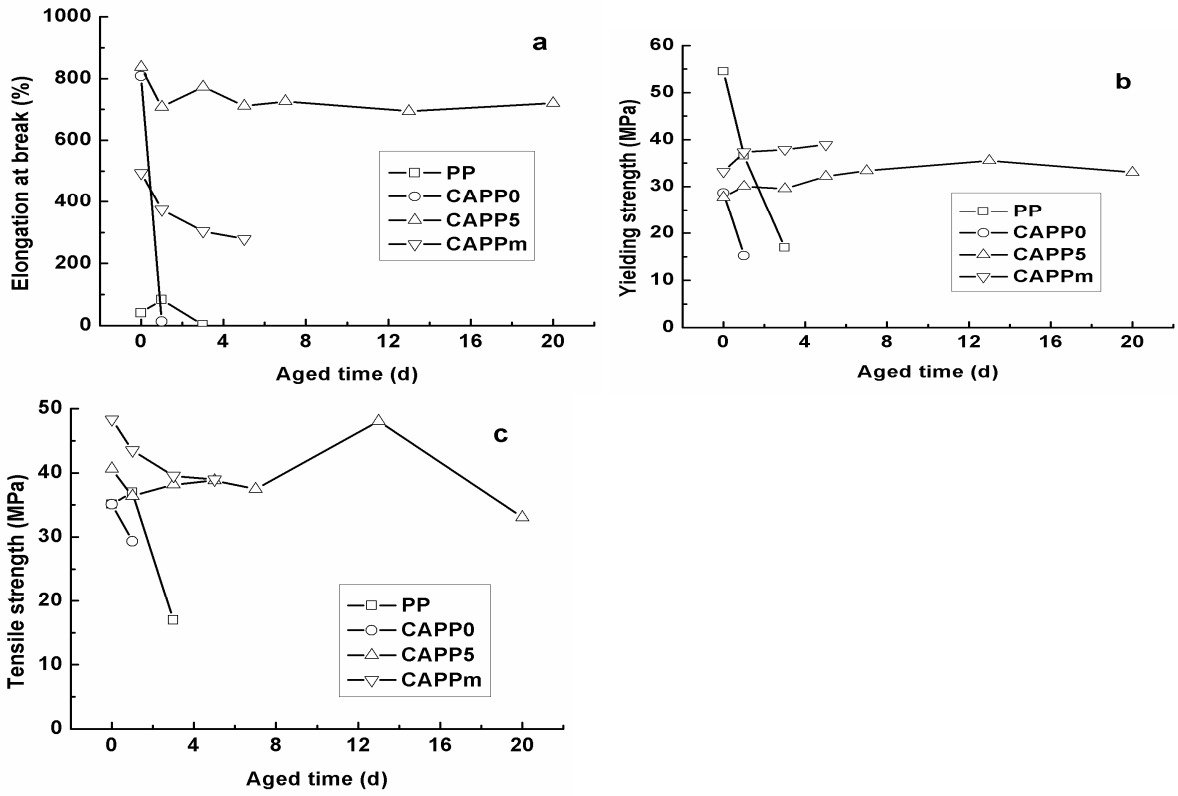


Figure 2 Mechanical Properties of Unmodified and Modified pp vs. Aged Time

Conclusions

The initiator of DCP exhibited the optimum initiated efficiency. Cardanol grafted onto PP was benificial for the composite of bamboo powder and PP.The initiator of DCP caused the degradation of PP chains during the aging processing. After aged for 24 h, the yield strength decreased from 28 MPa to 15 MPa and the elongation at break reduced by 795 %. The CAPP possessed outstanding anti-aging performance owing to the cross-linking and entanglement of the side chains of cardanol grafted onto PP. The yield strength, tensile strength and the elongation at break of CAPP-DCP changed lightly even when it was in long-term irradiation for 480 h.

Acknowledgments

This work is supported by the National Natural Science Foundation of China (No. 51103024) and Fujian Normal University Foundation for Excellent Young Teachers (fjsdky2012004).

References

[1] H. Li, H. Zhao, X. Zhang, Y. Lu, Y. Hu, A novel route to the synthesis of PP-g-PMMA copolymer via ATRP reaction initiated by Si–Cl bond, European Polymer Journal. 43 (2007) 109-118.

[2] K.E. Russell, Free radical graft polymerization and copolymerization at higher temperatures, Progress in Polymer Science. 27 (2002) 1007-1038.

[3] W. Qiu, T. Endo, T. Hirotsu, A novel technique for preparing of maleic anhydride grafted polyolefins, European Polymer Journal. 41 (2005) 1979-1984.

[4] C. Cai, Q. Shi, L. Li, L. Zhu, J. Yin, Grafting acrylic acid onto polypropylene by reactive extrusion with pre-irradiated PP as initiator, Radiation Physics and Chemistry. 77 (2008) 370-372.

[5] Q. Chen, F. Yin, L. Zheng, X. Xiao, J. Lin, Crystallization Behavior of Polypropylene-graft-cardanol Prepared by Reactive Extrusion, INTERNATIONAL POLYMER PROCESSING. 28 (2013) 43-48.

[6] S. Kumar, B.S. Butola, M. Joshi, POSS/polypropylene hybrid nanocomposite monofilaments by reactive extrusion, Fibers Polym. 14 (2013) 428-435.

[7] M.R. Badrossamay, G. Sun, Preparation of rechargeable biocidal polypropylene by reactive extrusion with diallylamino triazine, European Polymer Journal. 44 (2008) 733-742.

[8] T.G. Zhu L, Shi Q, Yin J, Rare earth compounds assisted melt grafting of maleic anhydride onto isotactic by reactive extrusion, Chemical J of Chinese University. 27 (2006) 970-974.

[9] Q. Chen, H. Xue, J. Lin, Preparation of polypropylene-graft-cardanol by reactive extrusion and its composite material with bamboo powder, Journal of Applied Polymer Science. 115 (2010) 1160-1167.

[10] M. Rätzsch, M. Arnold, E. Borsig, H. Bucka, N. Reichelt, Radical reactions on polypropylene in the solid state, Progress in Polymer Science. 27 (2002) 1195-1282.

[11] H. Azizi, I. Ghasemi, M. Karrabi, Controlled-peroxide degradation of polypropylene: Rheological properties and prediction of MWD from rheological data, Polymer Testing. 27 (2008) 548-554.

[12] B.-R. Sheng, B. Li, B.-H. Xie, W. Yang, J.-M. Feng, M.-B. Yang, Influences of molecular weight and crystalline structure on fracture behavior of controlled-rheology-polypropylene prepared by reactive extrusion, Polymer Degradation and Stability. 93 (2008) 225-232.

[13] L. Zhu, G. Tang, Q. Shi, C. Cai, J. Yin, Neodymium oxide co-catalyzed melt free radical grafting of maleic anhydride onto co-polypropylene by reactive extrusion, Reactive and Functional Polymers. 66 (2006) 984-992.

[14] D. Munteanu. Metal Containing Polymers Systems [M]. New York: Hanser, 1985: 479-509.

Advanced Materials Research Vol. 936 (2014) pp 43-52
© (2014) Trans Tech Publications, Switzerland
doi:10.4028/www.scientific.net/AMR.936.43

Analysis and Experiment of Compressive Residual Strength of Composite Laminates with Holes

Xianghong Kong[1,a], Zhijin Wang[1,b]

[1] College of Aerospace Engineering, Nanjing University of Aeronautics and Astronautics, Nanjing 210016, China

[a]kxh86@126.com, [b]zhijin@nuaa.edu.cn

Keywords: finite element; composite laminates; compressive residual strength; progressive damage analysis; stiffness degradation

Abstract: Experiment and Finite element analysis were used to study the strengths of composite laminates with and without holes. Finite element progressive damage analysis with Tsai-Wu criteria was applied to calculate the compressive residual strength of composite laminate. Abaqus and its user subroutine USDFLD were used for the finite element analysis. Tsai-Wu criteria as the failure criteria was realized in USDFLD as a Fortran program segment, and the stiffness degradation for the damaged elements was also realized by USDFLD. Analytic results gotten by progressive damage method were very close to the experimental results.

Introduction

Composite materials are wildly used in many industries, especially in aviation and aerospace industries because of their fantastic mechanical property. Composite laminates and sandwich structures are used to manufacture more and more components of aircraft. In some structures of aircraft, one or more holes need to be opened on them. And the strength of the main or secondary bearing structures containing holes should meet design requirements. Thus, analyses and experiments of these structures are used to assess their strengths. The major challenge in design and analysis of composite structures containing stress concentrators is the size effect on the strength of composite structures[1]. Many studies on tensile and compressive residual strength of composite laminate were done in recent years, especially studies on laminates with holes. And there also be many studies on residual strength of composite after impact. Chun H. Wang et al have researched the residual strength of composite laminates containing scarfed holes and straight-sided holes, and they found that scarfed holes produce a significant increase in the strain concentration and substantial reduction in the residual strength[1]. The residual strength of glass fibre reinforced vinyl-ester laminates with multiple holes was investigated by S. Kazemahvazi et al[2]. The quasi-static tensile strength of the laminates with different amount of holes and different hole arrangements was investigated, and three different failure modes were found by S. Kazemahvazi et al[2]. The tensile residual strength of repaired CFRP composite plates were assessed by R. D. S. G. Campilho et al using a two-dimensional numerical analysis[3]. Jun-Jiang Xiong[4], S. Sánchez-Sáez[5], F. Cesari[6], Shi-Xun Wang[7] et al have studied the compressive and tensile residual strength of composite after impact . Jun-Jiang Xiong[4],T.P. Philippidis[8] et al also studied fatigue residual strength of composite. The second rank expression of Tsai-Wu criteria was used to calculate the strength of 3D braided composite beam by Zuo Weiwei et al[9]. Engineering evaluation and FEM prediction were used to study the compressive residual strength of composite laminates after the impact by Jia Jiandong et al[10]. The 3D progressive damage theory was applied in residual strength calculation of composite[11, 12].

Finite element analysis (FEA) and experiment were used to study the compressive residual strength of composite laminates containing holes, and the second rank expression of Tsai-Wu criteria as used by Zuo Weiwei et al[9] was applied as strength criteria in this paper. USDFLD, a Fortran program of Abaqus user subroutine, was used to realize the progressive damage process of composite laminates. Stiffness degradation method used in this paper is the same as that used by Kong Xianghong et al[12]. Nine kinds of experimental samples of composite laminates with different geometrical dimensions were manufactured for experiment research, and there were six samples for each kind in order to exclude the effect of uncertainties of the samples. There also be nine kinds of finite element (FE) models of composite laminates created with Abaqus for FEA. In order to compare the results of FEA, three different load increments were applied on each kind of FE models respectively for FEA with progressive damage.

Experimental samples and FE models

Material of composite laminates.

The UD-composite layer material of laminates used in experiment and FEA is T700/BA9916, and the thickness of a composite layer is 0.15mm. The composite laminates of experimental samples have the same ply number, ply stacking sequence and thickness. There are 25 plies with the total thickness of 3.75mm for each laminate, and the ply stacking sequence of each composite laminate is $(0°/45°/-45°/45°/90°/-45°/0°/0°/-45°/0°/0°/45°/\overline{90°})_s$. The mechanical property and strength of UD-composite layer are shown in Table 1.

Table 1. Mechanical property of T700/BA9916

Elastic properties	E_{11} [GPa]	E_{22} [GPa]	E_{33} [GPa]	μ_{12}	μ_{13}	μ_{23}	G_{12} [GPa]	G_{13} [GPa]	G_{23} [GPa]
	114	8.61	8.61	0.3	0.3	0.45	4.16	4.16	3
Strength [MPa]	X_t	X_c	Y_t	Y_c	Z_t	Z_c	S_{xy}	S_{xz}	S_{yz}
	2688	1458	69.5	236	55.5	175	136	136	95.6

Geometrical shape of experimental samples and FE models.

The geometrical shape of composite laminate with a hole for experiment and FEA is shown in Fig. 1. There are four parameters for a composite laminate containing a hole: diameter (D) of the hole, length (L), width (W) and thickness (T) of the composite laminate. The hole center is at the geometrical center of the composite laminate.

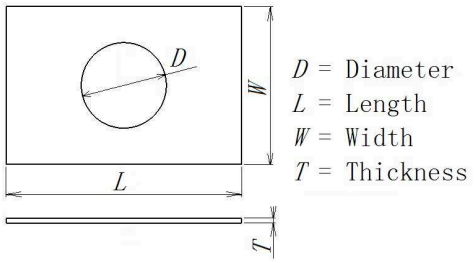


Fig. 1. Geometrical shape of composite laminate

The FE models of composite laminates with holes for compressive strength analyses are similar to those shown in Fig.2 and Fig. 3. Three-Dimension stress elements are used in the FE models. The ply's orientation of 0° is along the X-axis, and the 90° along the Y-axis in Fig. 2.The degree of

freedoms (DOF) of the nodes on the left side of the FE model are constrained, and the compressive loads are loaded on the nodes of the right side as shown in Fig. 2. There are 25 plies of elements of each FE model as shown in Fig. 3. The thickness of the elements along Z-axis is 0.15mm, and the total thickness of a FE model is 3.75mm. That is one layer of elements for one layer of composite laminates. The red elements named “Elem-0” belong to the plies of which the orientation is 0°, the other elements named “Elem-45N”, “Elem-45P” and “Elem-90” belong to -45°, 45° and 90° plies respectively.

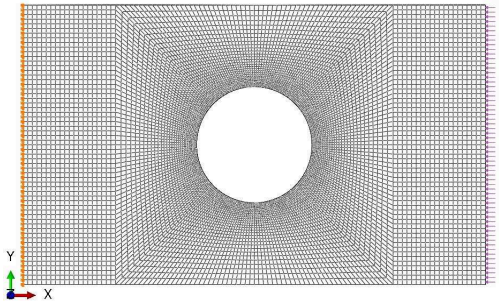


Fig. 2. FE model of composite laminate with hole

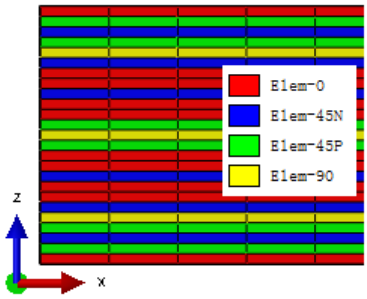


Fig. 3. FE model along thickness direction

Geometrical parameters of experimental samples and FE models.

There are nine groups of experimental samples with different parameters shown in Table 2. The first group named “NoHole” in Table 2 contains six composite laminates without holes, and these composite laminates are used to study the mechanical property for comparison with those composite laminates containing holes. The rest groups contains the composite laminates with holes, and the “W” & “D” in the group names mean the width and hole diameter of the composite laminates of each group. FE models have the same geometrical parameters as the experimental samples have.

Table 2. Geometrical parameters of composite laminates

No.	Group	*D* [mm]	*W* [mm]	*L* [mm]	*T* [mm]	*Q*
1	NoHole	0	12	140	3.75	6
2	W36D6	6	36	250	3.75	6
3	W60D10	10	60	250	3.75	6
4	W60D20	20	60	250	3.75	6
5	W60D25	25	60	250	3.75	6
6	W60D30	30	60	250	3.75	6
7	W60D40	40	60	250	3.75	6
8	W120D65	65	120	180	3.75	6
9	W200D100	100	200	180	3.75	6

D = Diameter, *W* = Width, *L* = Length, *T* = Thickness, *Q* = Quantity

Experimental results

Experiments were done according to Standard Test Mehod for Compressive Properties of Polymer Matrix Composite Materials Using a Combined Loading Compression (CLC) Test Fixture, ASTM D 6641. The manufacture of composite laminates for compressive experiment, measuring and testing technique and data processing method for these compressive experiments were directed by ASTM D 6641.

The compressive loads are loaded on experimental samples along the length direction of composite laminates, and the ends of the samples were fixed by fixtures as ASTM D 6641 requires.

Experiment of composite laminates without hole.

Experimental data of composite laminates without hole are giver in Table 3. The data are gotten by compressive experiment of six samples. The area (A) is the area of transverse section of each sample, and it is calculated by Eq. 1. W and T in Eq. 1 are measured.

$$A = W \times T \tag{1}$$

Theoretically, A is equal to 45mm^2, but because of the manufacturing technique, there are some differences between the sample's area and theoretical area. The max loads (F_{max}) are the damage loads of samples during experiment, and they are measured values for experimental data. The strength (S) is calculated with Eq. 2 for each sample, and this strength is UD-compressive strength along the length direction of composite laminate.

$$S = 1000 \times F_{max}/A \tag{2}$$

Table 3. Experimental data of composite laminates without holes

No.	A [mm^2]	F_{max} [kN]	S [MPa]
1	46.3	30.36	656
2	46.6	28.92	620
3	45.4	27.39	604
4	46.0	28.47	619
5	46.3	28.59	617
6	46.2	29.28	637
A = Area, F_{max} = Max Load, S = Strength			

Experiment of composite laminates with holes.

There are eight groups of composite laminates containing holes used in compressive experiment, and each group has six samples. The experimental data of damage loads of composite laminates with holes are shown in Table 4, and the data of residual strength are given in Table 5.

Table 4. The damage loads of composite laminates with holes

Group	F_{max} [kN]					
	1	2	3	4	5	6
W36D6	56.92	54.39	57.22	55.87	61.04	54.19
W60D10	81.51	84.11	83.17	81.79	83.47	81.23
W60D20	67.38	65.89	69.88	67.62	67.99	66.15
W60D25	57.76	60.28	57.49	60.89	63.93	60.17
W60D30	48.32	55.95	58.07	54.49	41.66	50.23
W60D40	34.23	35.54	36.67	35.1	34.1	37.72
W120D65	70.55	84.08	78.77	79.95	80.18	77.84
W200D100	123.23	112.34	96.62	102.66	101.24	115.84

Table 5. The compressive residual strengths of composite laminates with holes

Group	S [MPa]					
	1	2	3	4	5	6
W36D6	421.63	402.89	423.85	413.85	452.15	401.41
W60D10	360.93	373.82	369.64	363.51	370.98	361.02

W60D20	299.47	292.84	310.58	300.53	302.18	294.0
W60D25	256.71	267.91	255.51	270.62	284.13	267.42
W60D30	214.75	248.67	258.09	242.18	185.16	223.24
W60D40	152.13	157.96	162.98	156.0	151.56	167.64
W120D65	156.78	186.84	175.04	177.67	178.18	172.98
W200D100	164.31	149.79	128.83	136.88	134.99	154.48

Experimental data analysis.

Experimental data of nine groups of composite laminates given in Table 3, Table 4 and Table 5 illustrate the relationship between the mechanical properties and geometrical parameters of composite laminates. The samples of W36D6 and W60D30 have the same area of the minimum bearing transverse section, and the damage loads of them are similar as Fig. 4 shows.

There is the same phenomenon between the samples of W60D10 and W120D65, though the minimum bearing transverse section areas of the two groups have a little difference. The area (Amin) of the minimum bearing transverse section is calculated with Eq. 3.

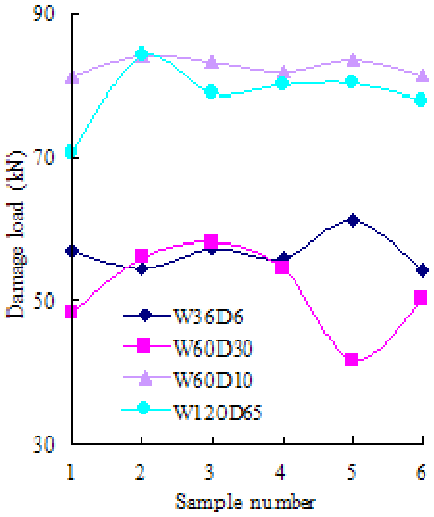


Fig. 4. Damage loads of the samples with similar A_{min}

$$A_{min} = (W - D) \times T \quad (3)$$

Hole diameter has an important effect on compressive residual strength of composite laminate as Fig. 5 shows. The residual strength of samples of NoHole group is much bigger than the other samples with holes, even the hole is small. From the data of the five groups of samples with the same width and different holes, it is proved that the bigger the hole diameter is, the smaller the compressive residual strength is. The compressive residual strengths of samples with the same relative minimum transverse section area (A_r) and different hole diameters are also different. The relative minimum transverse section area (A_r) is calculated by Eq. 4. There are two pairs of samples with the same A_r respectively shown in Fig. 6.

$$A_r = A_{min}/A \times 100\% \quad (4)$$

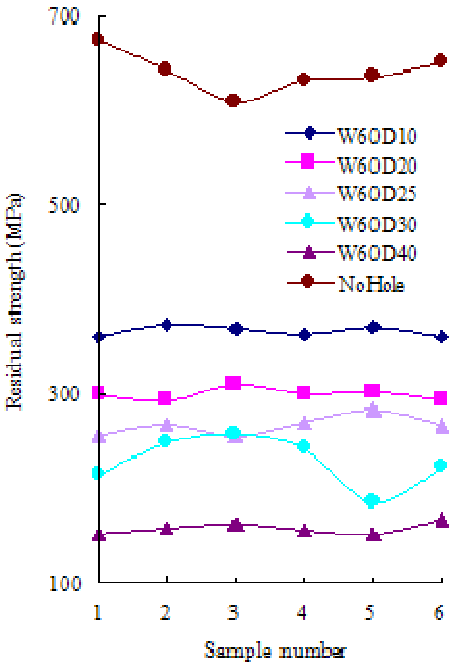


Fig. 5. Residual strength of samples with different D

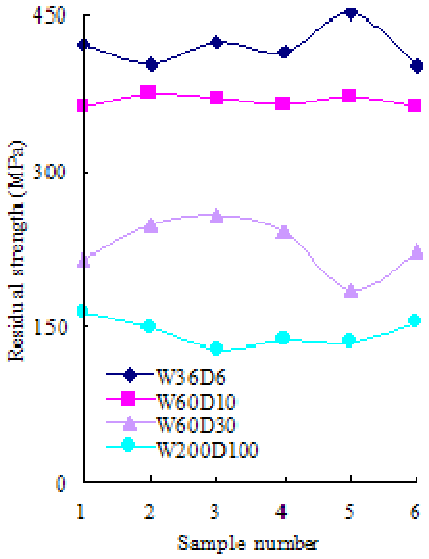


Fig. 6. Residual strengths of samples with the same A_r

The A_r of the groups of W36D6 and W60D10 is 83.33%, and for the other pair it is 50%. It is obvious that the bigger the hole diameter is, the smaller the compressive residual strength is for the samples with the same A_r, and the bigger the A_r is, the bigger the compressive residual strength is.

Finite element analysis

Composite laminate FEA process.

Compressive residual strength analysis of composite laminate using FE method contains two main processes: the stress analysis and the strength analysis. The stress analysis is a common static analysis, and the strength analysis is realized by an Abaqus user subroutine USDFLD. USDFLD is a Fortran subroutine, and it can be used to introduce solution-dependent material properties since such properties can easily be defined as functions of field variables[13]. The whole analysis process is shown in Fig. 7. There are one loop and two select statements in an iteration of the loop. Compressive displacement load is loaded on FE model for static analysis, and the displacement load increases in each iteration of the analysis loop. And the reference load (RF) can be given by Abaqus. The RF increases while the displacement load increases before there is no failure element. When there are failure elements, the stiffness of these failure elements will be degraded by USDFLD, and then the RF will decreases. The composite laminate is considered damaged and loses bearing capacity when the current RF is much smaller than the maximum value of RF as it appeared during analysis.

Tsai-Wu criteria is applied in USDFLD for strength analysis, and it will be used for every element using the current stress of a element in every iteration of the loop. The workflow of USDFLD in an iteration is as Fig. 8 shows. As a Fortran subroutine, in order to pass some values and calculate some coefficients, some parameters are defined in USDFLD. State varieties are used to mark field values which decide the material property type assigned to each element. And field values of next iteration are decided by the element stress of last iteration, they also reflect the current failure type of the element.

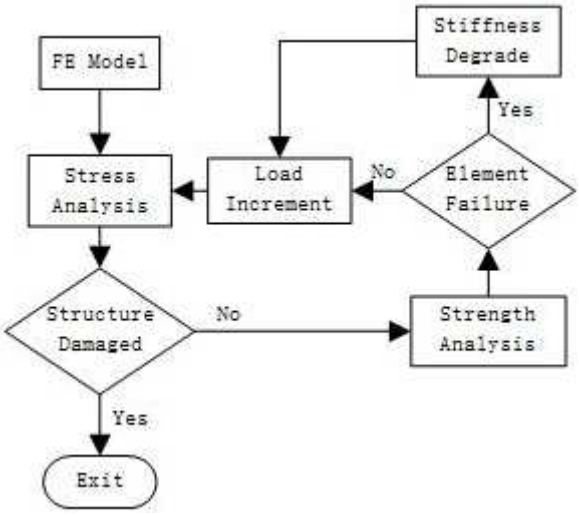


Fig. 7. FE strength analysis process

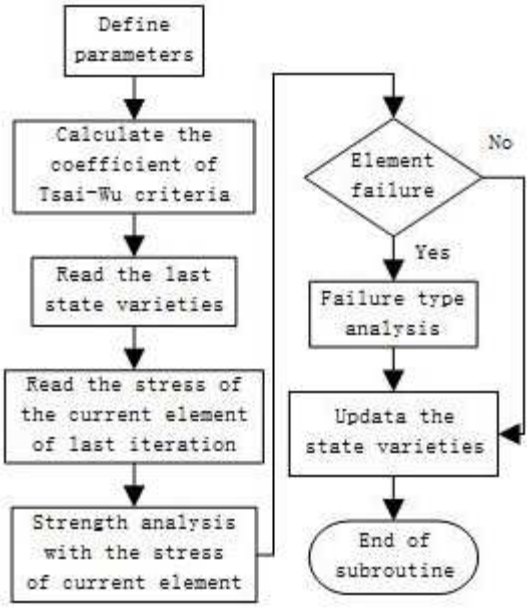


Fig. 8. Workflow of USDFLD

Composite laminate damage process.

Composite laminate damage process can be shown in two methods: use Load-Equivalent strain curves and use element progressive damage figures. The max load (F_{max}) appeared during compressive process can be found easily by Load-Equivalent strain curves. The max load is the damage load of corresponding composite laminate. And the compressive residual strength (S) of composite laminate can be calculated with Eq. 2. From element progressive damage figures, the initial damage position and progressive damage process can be easily illustrated.

There are three curves in Fig.9. These curves are the Load-Equivalent strain curves of composite laminate without hole. The data of three curves are gotten by FEA using different displacement load increment (ΔU). In Fig.9, the three curves have different equivalent strain increment ($\Delta\varepsilon$). The equivalent strain increment is calculated by Eq. 5.

$$\Delta\varepsilon = \Delta U/L \tag{5}$$

Where, L is the length of the FE model of the composite laminate. While the equivalent strain (ε_L) can be calculated by Eq. 6.

$$\varepsilon L = U/L \tag{6}$$

Where, U is the displacement load along the length direction of the composite laminate. The equivalent strain increments of the three curves with the number of 1, 2 and 3 in Fig. 9 are 0.0002, 0.0004 and 0.0006 respectively. It illustrates that the smaller the $\Delta\varepsilon$ is, the smaller the Fmax is.

During the process of compressing of the composite laminate without hole, the elements of "Elem-0" of which plies the orientation is 0° were first damaged. When the 0° plies of the composite laminate were completely damaged, the composite laminate lose its bearing capacity, thus the composite laminate was treated as damaged. The progressive damage process of the elements of "Elem-0" is shown in Fig. 10. The load condition of Fig. 10 is the same as that of No. 2 in Fig. 9. The red elements in Fig. 10 are damaged elements, and the FE model in Fig. 10 is part of the FE model of the composite laminate without hole. The X-axis direction is the length direction of composite laminate, and that is the 0° direction.

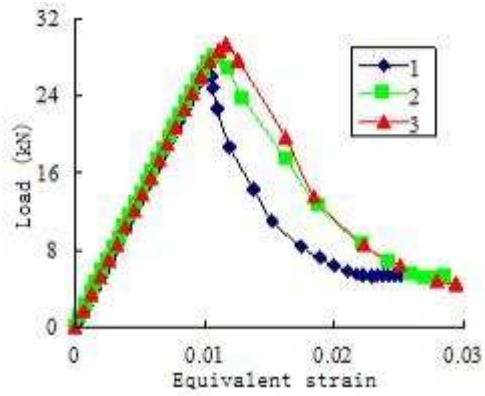


Fig. 9. Load-equivalent strain curve of composite laminate without hole

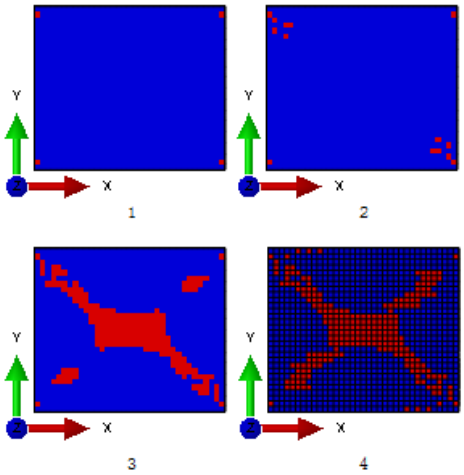


Fig. 10. Progressive damage process of composite laminate without hole

FEA data of composite laminate without hole is shown in Table 6. There are three groups of FEA data numbered with 1, 2 and 3. The three groups of data correspond to the three curves in Fig. 9 by their number. Comparing with the data of Table 3, it is obvious that the FEA data are similar to the experimental data. It proves that progressive damage analysis with FE method can get the relative accurate compressive strength value of composite laminate.

Table 6. FEA data of laminate without hole

No.	F_{max} [kN]	S [MPa]
1	26.31	584.67
2	27.91	620.22
3	29.35	652.22

FEA results of composite laminates with holes.

The damage loads and compressive residual strengths of composite laminates with holes are shown in Tables 7. The strength (S) is calculated using the max load (F_{max}) by Eq. 1 and Eq. 2. The data with different column number in Tables 7 were gotten by different equivalent strain increments. The data with column number 1, 2 and 3 were gotten by FEA with the equivalent strain increments of 0.0002, 0.0004 and 0.0006 respectively. The comparisons of experimental results and FEA results are shown in Fig. 11 and Fig. 12.

Table 7. FEA data of laminates with holes

Group	F_{max} [kN]			S [MPa]		
	1	2	3	1	2	3
W36D6	49.94	54.77	60.24	369.93	405.70	446.22
W60D10	81.71	93.90	100.69	363.16	417.33	447.51
W60D20	60.06	68.43	74.53	266.93	304.13	331.24
W60D25	51.33	57.85	63.60	228.13	257.11	282.67
W60D30	44.02	49.88	53.71	195.64	221.69	238.71
W60D40	29.70	32.59	35.23	132.0	144.84	156.58
W120D65	80.58	89.84	96.94	179.07	199.64	215.42
W200D100	145.34	164.99	179.17	193.79	219.99	238.89

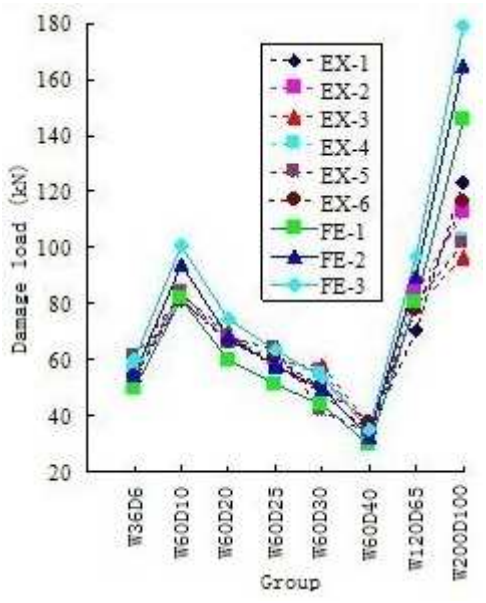


Fig. 11. Damage loads of composite laminates with holes

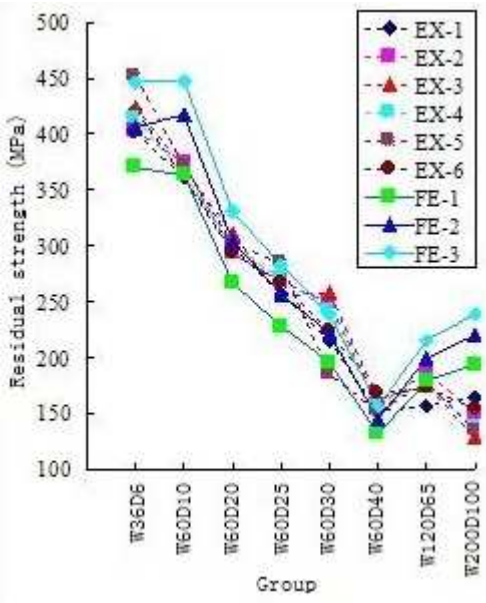


Fig. 12. Residual strength of composite laminates with holes

The damage loads of composite laminates with holes gotten by experiment and FEA are shown in Fig. 11. "EX-" and "FE-" in Fig. 11 are experimental data and FEA data respectively. And the number after them is the sample number, for instance, the data of "EX-1" are the damage loads with the column number of 1 in Table 4, and the data of "FE-1" are the damage loads with the column number of 1 in Table 7. From the curves shown in Fig. 11, it can be proved that most of the FEA data are similar to the experimental data, but there is obvious difference between the data of "W200D100" gotten by experiment and FEA.

The compressive residual strengths of composite laminates with holes shown in Fig. 12 illustrate that the data calculated with FE progressive damage analysis are much close to the experimental results except the data of W200D100. It is because that the element size and load increment size can affect the FEA result. More study need to be done for composite laminates with big holes to make clear the relationship between the FEA result and the sizes of element and load increment.

During the process of compressing of the composite laminates with holes, the elements at the hole side along the transverse direction were first damaged, and then the damage elements extend to both sides of laminates. For the layers of Elem-0, fiber compressive failure is the main damage type; for the layers of Elem-45P and Elem-45N, fiber-matrix in-plane shear failure is the main damage type; and for the layers of Elem-90, matrix compressive failure is the main damage type.

Conclusions

1) Compressive experiments of composite laminates with holes illustrate that holes can decrease the compressive strengths of composite laminates greatly.

2) The damage loads of the composite laminates with the same minimum bearing transverse section (A_{min}, Eq. 3) are approximately equal.

3) For the composite laminates with the same width and different hole diameters, the bigger the hole diameter is, the smaller the compressive residual strength is.

4) For the composite laminates with the same relative minimum transverse section area (A_r, Eq. 4), the bigger the hole diameter and the width are, the smaller the compressive residual strength is.

5) The FEA results gotten by progressive damage analysis with Tsai-Wu criteria are much close to the experimental results.

6) There are three main failure modes for laminates:
fiber compressvie failure for 0° layers;
matrix compressive failure for 90° layers;
fiber-matrix in-plane shear failure for 45° and -45° layers.

Reference

[1] Chun H. Wang, Andrew J. Gunnion, Adrian C. Orifici, Andrew Rider.Residual strength of composite laminates containing scarfed and straight-sided holes[J]. Composites Part A, 2011, 42: 1951–1961.

[2] S. Kazemahvazi, J. Kiele, D. Zenkert.Tensile strength of UD-composite laminates with multiple holes[J]. Composites Science and Technology, 2010, 70: 1280–1287.

[3] R.D.S.G. Campilho, M.F.S.F. de Moura, J.J.M.S. Domingues. Numerical prediction on the tensile residual strength of repaired CFRP under different geometric changes[J]. International Journal of Adhesion & Adhesives, 2009, 29: 195– 205.

[4] Jun-Jiang Xiong, Hong-Yun Li, Ben-Yin Zeng. A strain-based residual strength model of carbon fibre/epoxy composites based on CAI and fatigue residual strength concepts[J]. Composite Structures, 2008, 85: 29–42.

[5] S. Sánchez-Sáez, E. Barbero, C. Navarro.Compressive residual strength at low temperatures of composite laminates subjected to low-velocity impacts[J]. Composite Structures, 2008, 85: 226–232.

[6] F. Cesari, V. Dal Re, G. Minak, A. Zucchelli.Damage and residual strength of laminated carbon–epoxy composite circular plates loaded at the centre[J]. Composites: Part A, 2007, 38: 1163–1173.

[7] Shi-Xun Wang,Lin-Zhi Wu, Li Ma.Low-velocity impact and residual tensile strength analysis to carbon fiber composite laminates[J]. Materials and Design, 2010, 31: 118–125.

[8] T.P. Philippidis, V.A. Passipoularidis.Residual strength after fatigue in composites: Theory vs. experiment[J]. International Journal of Fatigue, 2007, 29: 2104–2116.

[9] Zuo Weiwei, Xiao laiyuan, Liao Daoxun. Calculating the strength of 3D-braided composite rectangle beam by using Tsai-Wu criteria[J]. J. Huazhong Univ. of Sci. & Tech. (Natrue Science Edition),2006, 34(12):74-76.

[10]Jia Jiandong, Ding Yunliang, Liu Xiaoming. Engineering and FEM methods for evaluating compressive strength after impact for composite laminates[J]. Journal of Nanjing University of Aeronautics & Astronautics[J], 2010, 42(3): 335-339.

[11]Cui Haipo, Wen Weidong, Cui Haitao. Research on low velocity impact damage and residual strength of composites[J]. ACTA Mechanica Solida Sinica, 2006, 27(3): 237-242.

[12]Kong Xianghong, Wang Zhijin. Finite element incremental damage strength analysis based on abaqus[J]. Computer Applications and Software, 2012, 29(10): 236-240.

[13]Abaqus User Subroutines Reference Manual, 1.1.49.

Advanced Materials Research Vol. 936 (2014) pp 53-57
© (2014) Trans Tech Publications, Switzerland
doi:10.4028/www.scientific.net/AMR.936.53

Microstructures of Poly (9'9-dihexylfluorene) Grown in the Non-solvent Vapor

Xueqing Xiao[1, 2, 3,a], Weibin Bai[1,b] and Jinhuo Lin[1, 2,c *]

[1]College of Material Science and Engineering, Fujian Normal University, Fuzhou 350007, China

[2]Fujian Key Laboratory of Polymer Materials, Fuzhou 350007, China

[3]School of Material Science and Engineering, Fujian University of Technology, Fuzhou 350108, China

[a]xxqqxxq@163.com, [b]bai-wb@163.com, [c]jhlin@fjnu.edu.cn

Keywords: self-assembly, conjugated polymer, microsphere

Abstract. In this research, the microspheres of poly (9'9-dihexylfluorene) were fabricated with dichloromethane as a good solvent by self assembly methods. The effects of poor solvent vapor, polymer concentration, and the temperature of environment on the formation of the sphere patterns were investigated. It was found that the microsphere could be easily prepared in the ethanol non-solvent vapor atmosphere. Besides, increasing the environment temperatures was advantageous to fabricate microspheres. Furthermore, the property of non-solvent vapor was a key role to the formation of the sphere.

Introduction

In recent years, conjugated polymers have attracted much attention due to their widespread applications. They can be used in displays, sensors, photovoltaic cells, thin-film transistors, nonlinear optics, and solar cells because of their low-cost, large-area electronics [1, 2]. For instance, a series of the conjugated polymers have been synthesized and their properties have been investigated. There have two main ways to prepare conjugated polymers, namely, via a reduction oxidation process or via a metal-catalyzed coupling method [3].

It is noteworthy that the optoelectronic properties of conjugated polymers in the solid state are highly affected by their structure of the molecules chains and the decree of order [4]. In addition, the optical and transport properties of conjugated polymers are intimately related to their nanometer scale morphology [5]. Therefore, it is necessary to control the degree of order when obtaining thin conjugated deposits from solution. At the same time, nanostructures conjugated polymers have potential applications in separation, drug delivery, photonic band gap, electronic, catalysis, and lithography [6]. As a result, polymer nanostructures, such as nanotubes, nanofibers, nanowires, nanorods, and other arrays are prepared by various methods.

Several methods like dispersion polymerization miniemulsion polymerization, solution synthesis, template methods, electrospinning technology, and self-assembly have been used to fabricate the nanostructure conjugated polymers. [7-10]. Among the above methods, self-assembly of conjugated polymers into nanostructures and microstructures is importance. However, the design and self-assembly nanostructures conjugated polymer remains a challenging and attractive target in nanoscience and nanotechnology [11]. Herein, we attempted to fabricate microspheres of conjugated polymers by non-solvent vapor self-assembly.

Experimental

Materials

N-bromohexane, fluorene， anhydrous ferric chloride ($FeCl_3$), Dichloromethane (CH_2Cl_2), methylbenzene, acetone, ethanol, and ethyl acetate were all A. R. and purchased from Sinopharm Chemical Reagent Co., Ltd. The poly(9,9-dihexylfluorene) used in this work was synthesized by solid-state oxidative coupling polymerization using our previous reported avenue [14].

Self-assemble of the Poly(9,9-dihexylfluorene)

The glass substrates (1×1 cm^2) were cleaned by detergents, demineralized water, ethanol, and acetone successively, and then dried in air before positioning them in a glass vessel. The atmosphere of ethanol nonsolvent was obtained by adding 3 mL of nonsolvent into a hermetic glass bottle and then the bottle would be full of saturated vapor after 2 h. The poly(9,9-dihexylfluorene) was dissolved in good solvent. Then, its solution was dropped onto a clean glass substrate in the nonsolvent vapor After the solvent evaporated completely, a thin layer was obtained on the substrate.

Characterization

The morphologies of the poly(9,9-dihexylfluorene) by the non-solvent vapor method were performed on a JSM-7500F scanning electron microscope (SEM) at an accelerating voltage of 5 kV.

Results and Discussion

Influence of Concentration on Microspheres Formation

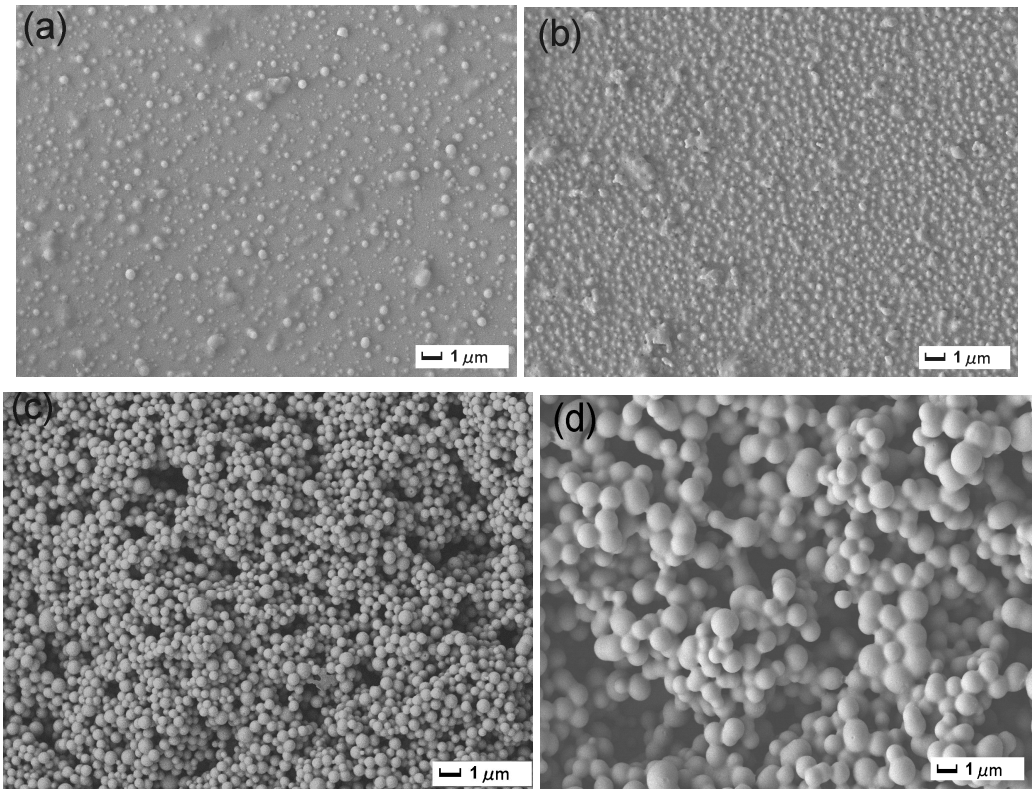


Fig. 1. SEM images of the poly(9,9-dihexylfluorene) microsphere patterns prepared from CH_2Cl_2 in the ethanol vapor atmosphere under the following concentration: (a) 0.1 mg/mL, (b) 0.5 mg/mL, (c) 1.0 mg/mL, (d) 2.5 mg/mL.

The influence of the polymer concentration on the morphologies of poly (9'9-dihexylfluorene) was shown in Fig.1. Some microsphere pattern could be obtained when the poly (9'9-dihexylfluorene)/CH_2Cl_2 concentration was 0.1 mg/mL and 0.5 mg/mL.When the concentration was 1 mg/mL, it was found that discrete and quite well-shaped spheres could be formed. As the concentration further increases to 2.5 mg/mL, the spheres patterns still could be obtained as shown in Fig. 1 (d). But, the spheres size increased and heavily fused with one another.

Why do spherical assemblies in the non-solvent ethanol vapor atmosphere? It could be explained by two parts: the decrease of temperature and crystallinity of polymers [12]. When the poly (9'9-dihexylfluorene)/CH_2Cl_2 solution was drop into the glass surface, the good solvent of CH_2Cl_2 would evaporate quickly. So, the temperature gradient between the solution surface and the surrounding would form. Because of the existence of temperature gradient, ethanol non-solvent vapor

could be condensed onto the solution. As a result, the good solvent would be turned to non-solvent for the poly (9'9-dihexylfluorene) and the molecular of the poly (9'9-dihexylfluorene) was precipitation. On the other hand, crystallinity of polymers was another important factor. The poly (9'9-dihexylfluorene) was a random regularity structure, which was synthesized by the solid-state oxidative coupling polymerization. It was advantageous to the assembly of spherical geometry. With the increase of the concentration of polymer, the much molecular and the higher solution viscosity make condensation so slow that the ethanol vapor droplet infused into solution more slow, indirectly causing the sphere growth, as shown in Fig.1.

Influence of Temperature on Microspheres Formation

As discussed above, microspheres could be self-assembled by casted the poly(9,9-dihexylfluorene)/CH_2Cl_2 solution into ethanol vapor. In order to study the impact of the environmental temperatures on the pattern formation, -18°C, 5°C, and 25°C was investigated, as shown in Fig. 2. It was found that the temperature was a key role to controlling the formation of the sphere pattern. When the temperature was -18°C, the sphere patterns could not be formed. When the temperature was 5°C, some sphere patterns was observed. When the temperature was 25°C, the regular spheres were formed. With the increase of temperature, the good solvent of the solution was evaporated quickly, and then the non-solvent vapor ethanol would condensate fast. The good solvent would turn to a poor solvent for the infusing of the ethanol vapor. So, the poly(9,9-dihexylfluorene) ould be precititate to sphere.

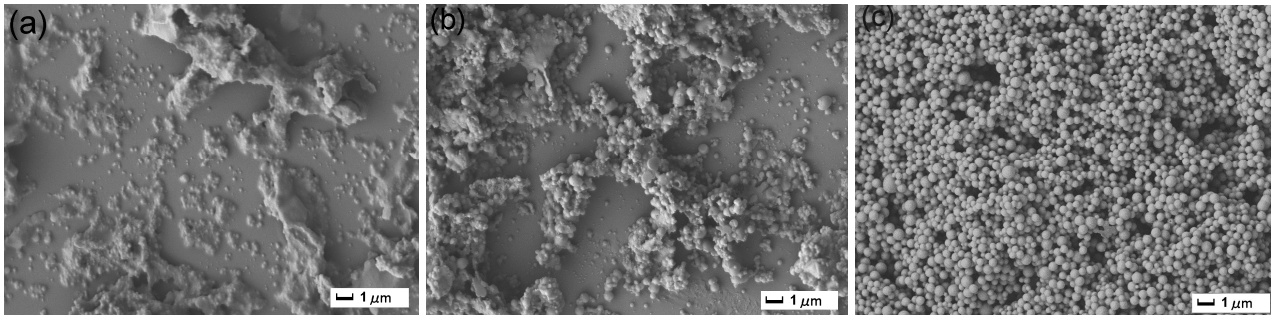
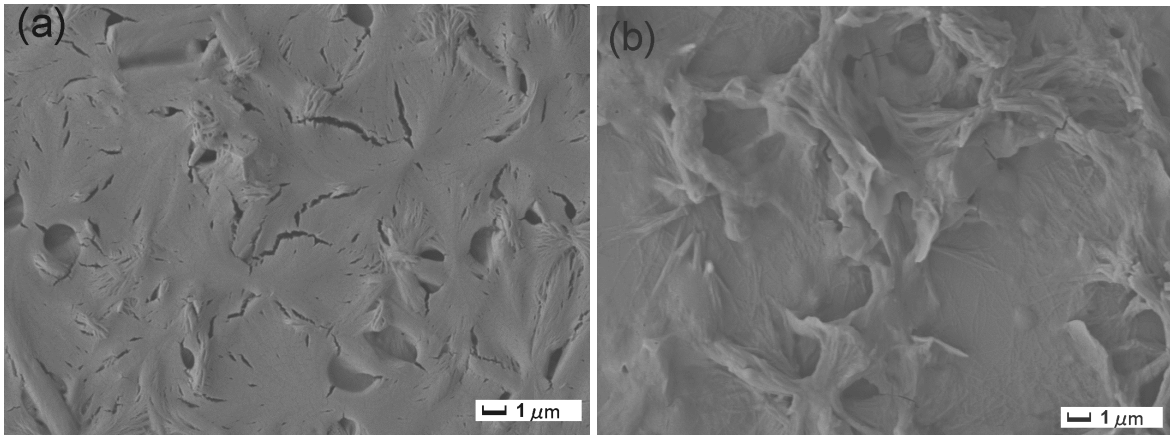


Fig. 2. SEM Images of the Poly(9,9-dihexylfluorene) Microsphere Patterns Prepared from CH2Cl2 in the Ethanol Vapor Atmosphere under the Following Temperatures: (a) -18, (b) 5, and (c) 25 °C.

Influence of Non-solvent Vapor on Microspheres Formation

Fig.3 illustrates the mogphologies of poly (9'9-dihexylfluorene)/CH_2Cl_2 with a concentration of 1 mg/mL under different nonsolvent vapors. Fig.3(a), Fig. 3(b), and Fig. 3(d) showed that the spheres could not be fabricated in the methylbenzene, ethanol, and ethyl acetate vapor. However, it was easily formed in the ethanol non-solvent vapor atmosphere, as shown in Fig.3 (c). The result showed that the spheres formation had affinity with the property of the non-solvent.



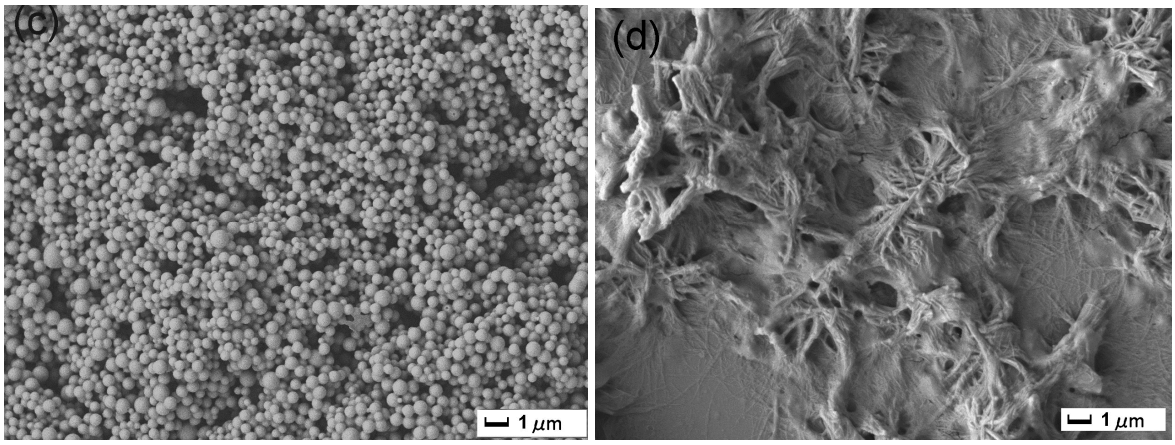


Fig.3. SEM Images of the Self-assembly of Poly(9,9-dihexylfluorene)/CH2Cl2 Solution in the Different Vapors: (a) Methylbenzene, (b) Acetone, (c) Ethanol, and (d) Ethyl Acetate.

Conclusion

The well-ordered spheres poly(9,9-dihexylfluorene) were successfully obtained by the self assembly method of non-solvent vapor with good solvent CH_2Cl_2. The experiments demonstrated that non-solvent vapor atmosphere played a key role on the morphology of the poly(9,9-dihexylfluorene) microspheres film during the formation. From SEM, the sizes and the dispersion of the sphere of poly(9,9-dihexylfluorene) increased with increasing of concentration. The relativity uniform sphere patterns could be easily formed with 1 mg/mL in the ethanol vapor at 25^{o}C.

References

[1] D. Nyström, P. Antoni, S. Holdcroft, A. Hult, E. Malmström Jonsson, G. Vamvounis, Solution-processed superhydrophobic conjugated polymer films, Soft Matter. 21 (2012) 5753-5755.

[2] H. Liu, J. Xu, Y. Li, Aggregate nanostructure of organic molecular materials, Accounts Chem. Res. 43 (2010) 1496-1508.

[3] C. Yuan, Q. Fang, A new procedure for the synthesis of π-conjugated polymers via ligand-free iron(iii)-catalyzed oxidative homocoupling reaction of grignard reagents, RSC Adv. 21 (2012), 8055-8060.

[4] W. Lei, Z. Yan, Y. Yan, W. Jian, P. Jian, C. Yong, Organic supernanostructures self-assembled via solution process for explore detection, Langmuir. 25 (2009) 1306-1310.

[5] S.-J. Park, A.-G. Kang, M. Fryd, G. Saven, S.-J. Park, Highly tunable photoluminescent properties of amphilic conjugated block copolymers, J. Am. Chem. Soc. 132 (2010) 9931-9933.

[6] G. Lu, Y. Chen, Y. Zhang. M. Bao, Y. Bian, J. Jiang, Morphology controlled self-assembled nanostructures of sandwich mixed (phthalocyaninato) (porphyrinato) europium triple- deckers. Effect of hydrogen bonding on tuning the intermolecular interaction, J. Am. Chem. Soc. 130 (2008) 11623-11630.

[7] T. Kietzke, D. Neher, K. Landfester, R. Montenegro, R. Guntner, U. Scherf, Novel approaches to polymer blends based on polymer nanoparticles, Nat. Mater. 6 (2003) 408–412.

[8] A. J. C. Kuehne, M. C. Gather, J. Sprakel, Monodisperse conjugated polymer particles by Suzuki–Miyaura dispersion polymerization, Nat. Commun. 3 (2012) 1088.

[9] L. Pan, H. Qiu, C. Dou, Y. Li, L. Pu, J. Xu, Y. Shi, Conducting polymer nanostructures: template synthesis and applications in energy storage, Int. J. Mol. Sci. 11 (2010) 2636-2657.

[10] A. J. C. Kuehne, D. A. Weitz, Highly monodisperse conjugated polymer particles synthesized with drop-based microfluidics, Chem. Comm. 47 (2011) 12379–12381.

[11] S. Cui, H. Liu, L. Gan, Y. Li, D Zhu, Fabrication of low-dimension nanostructures based on organic conjugated molecules, Adv. Mater. 20 (2008) 2918-2925.

[12] T. Adachi, L. Tong, J. Kuwabara, T. Kanbara, A. Saeki, S. Seki, Y. Yamamoto, Spherical assemblies from pi-conjugated alternating copolymers: toward optoelectronic colloidal crystals. J. Am. Chem. Soc. 135 (2013) 870-876.

Advanced Materials Research Vol. 936 (2014) pp 58-62
© (2014) Trans Tech Publications, Switzerland
doi:10.4028/www.scientific.net/AMR.936.58

Synthesis And Properties Of Polypropylene Carbonate Polyol-based Waterborne Polyurethane

Cheng Shu Xu[1,2a], Cheng Cheng Tian[2a],Wei Dong Zhang[2b], Jian Wei Xing[2a], Zai Sheng Cai[1], Yan Ren[2a],Wei Zhu Xu[2a], Hai Yan Liu[2a]

[1.]Key Laboratory of Science & Technology of Eco-Textile, Ministry of Education, Donghua University , Shanghai 201620,China;

[2a.] School of Textile and Material, Xi'an Polytechnic University,

[2b.] Office of personnel, Xi'an Polytechnic University, Xi'an 710048, China

Emails: Cheng Shu Xu xcs7910@163.com, Cheng Cheng Tian tiancheng246@163.com, Wei Dong Zhang zhangwd@xpu.edu.cn, Jian Wei Xing xjw1123@sina.com, Zai Sheng Cai zshc@dhu.edu.cn, Yan Ren 55245431@qq.com, Wei Zhu Xu 652283004@qq.com, Hai Yan Liu 604473118@qq.com.
Author for correspondence: Zai Sheng Cai

Keywords: waterborne polyurethane; polypropylene carbonate polyols; polyethylene-1,4-buthylene adipate glycol；Polytetramethyleneether glycol

Abstract: Different kinds of anionic polyhydric alcohols water-borne polyurethane(WPU) emulsion and films were prepared by separately taking polypropylene carbonate polyol(PPC), polyethylene-1,4-buthylene adipate glycol (PBA) and polytetramethylene ether glycol(PTMG) with the same molecular weight as soft segment. Their structure and properties were characterized with Fourier transform infrared spectrometry(FT-IR), X-ray diffraction(XRD), rigidity, adhesive power, contact angle and water absorption. Comparing their properties, it was found that the rigidity, adhesive power and water resistance of PPC WPU were similar to those of PBA WPU.

Introduction

PPC is a kind of aliphatic polycarbonate polyols copolymerized by carbonate dioxide and epoxy. Since PPC was firstly synthesized by Shohei Inoue at the end of 1960s, it had drawn a lot of attention to the investigation of its synthesis and properties as a type of eco-friendly materials[1-3]. Compared with polyester polyurethane, the better water-resistance ability, inoxidizability and barrier property of WPU prepared by taking PPC as soft segment were reported[4-6]. But, there leaves a blank area about the research report of PPC WPU[7]. In this presentation, different kinds of anionic polyhydric alcohols WPU emulsion and films were prepared by separately taking PPC, PBA and PTMG as soft segment and adopting dimethylolpropionic acid (DMPA) as the hydrophilic chain extender agent. The structure of WPUs were characterized by FT-IR. The properties' difference between PPC WPU and the typical polyether WPU, PPC WPU and the typical polyester WPU were characterized by XRD, adhesive strength, rigidity, water contact angle and water absorption.

Experimental

Materials employed**.** PPC (Mn=2000g/mol, hydroxyl value=56.1mgKOH/g) was obtained from Jiangsu Zhongkejinlong Chemical Co., Ltd. (China). PBA (Mn=2000g/mol) and PTMG (Mn=2000g/mol) were bought from Jininghuakai resin Co., Ltd. (China). Isophorone diisocyanate(IPDI)was obtained from Bayer (Germany). DMPA, 1, 4-butanediol (BDO), triethanolamine (TEA) were supplied by Sinopharm Chemical Reagent Co., Limited (China).

Preparation of WPU. In the preparation of the WPU emulsions running in bulk, dehydrated polyol and IPDI were placed in a 500mL 3-neck flask equipped with a stirring apparatus, a thermometer and a condenser and the reaction was last for 2h at 70℃. DMPA and BDO were added subsequently as the chain extender and the reaction was continued for 2h at 70℃. When the amount of NCO reached a certain value, the PPC WPU polymer emulsion was obtained after neutralizing the system with a certain amount of TEA in 30min and emulsifing it for 50min with deionized water under vigrous stirring. The compositions for the preparation of polyurethane were shown in Table 1.

TABLE 1 COMPOSITION FOR THE PREPARATION OF POLYURETHANE

Code	Compositions (g)	Polyolscontent (%)	DMPA content (%)
WPU1	IPDI/PPC/DMPA/BDO(10.00/37.95/1.00/0.52)	79.5	2.0
WPU2	IPDI/PPC/DMPA/BDO(10.00/31.60/1.54/0.44)	72.5	3.5
WPU3	IPDI/PPC/DMPA/BDO (10.00/26.54/1.96 /0.38)	68.3	5.0
WPU4	IPDI/PBA/DMPA/BDO(10.00/31.60/1.54/0.44)	72.5	3.5
WPU5	IPDI/PTMG/DMPA/BDO(10.00/31.60/1.54/0.44)	72.5	3.5

The certain amount of WPU emulsions were coated onto a teflon plate which was stored for 96h under room temperature and then dried for 24h at 60℃to prepare WPU films.

Testing and Characterization. The WPU films were tailored into samples sizing 2cm×2cm with a weight M_1. The samples were dried with filter paper and weighed M_2 after being immersed into water for 24h under room temperature. The water absorption was calculated according to the following formula [8]:

$$\text{water absorption}=\frac{M_2-M_1}{M_1}\times 100\%$$

To determine the water contact angles a drop of deionized water was placed on the film surface and after 1min. The test was conducted using a G-1 contact angle meter (Kyowa Corporation, Japan). Each sample was tested 3 times and the average of the three data was taken as the water contact angle.

The rigidity and adhesive strength of WPU films were tested separately according to GB/T6739-2006 and GB/T9286-1998.

In the determination of FT-IR spectrometry the FT-IR spectra of the films were obtained by using a Nicolet 5700 Fourier transform infrared spectrometer (Nicolet Instrument Inc., USA) in the transmission mode. The films were evenly grinded with potassium bromide (KBr) to perform the testing.

The crystallinity of WPU films were tested by a D/Max-2550 PC X-ray diffraction instrument (RIGAKU., Japan).

Results and Discussion

Infrared Spectroscopic Analysis.Fig.1 showed the FT-IR curves of different kinds of polyols WPU. In Figure 1, the absorption peaks around 3330cm^{-1} represented the N-H stretching vibration peaks of carbamido and the absorption peaks around 1540cm^{-1} characterized the N-H deformation vibration peaks of carbamido in WPU2， WPU4 and WPU5. The vibration peak at 1750cm^{-1}~1620cm^{-1} of WPU2 referred to the overlapping of C=O stretching vibration peak of carbamate and C=O stretching vibration peak of the ester group in PPC WPU soft segment, while to WPU4, the vibration peak at 1750cm^{-1}~1620cm^{-1}represented the overlapping of C=O stretching peak in carbamate and C=O stretching vibration peak of the ester group in PBA WPU soft segment. The absorption peak in WPU5 at 1720cm^{-1}~1620cm^{-1} characterized the C=O stretching vibration peak of carbamate. The attribution analysis and the qualitative analysis of FT-IR spectra indicated that the polymers were characterized as kinds of polyurethane.

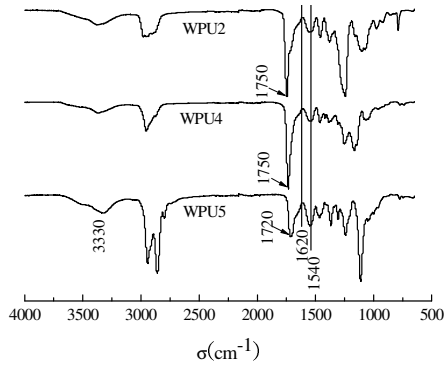


Fig.1 FT-IR Spectra of WPU Films

X-ray diffraction analysis. The XRD curves of different kinds of polyhydric alcohols WPU films were shown in Fig. 2. It could be seen from Fig. 2 that the X-ray diffraction of all the WPUS belonged to dispersion diffraction and had diffraction peaks around 20°.It was concluded there didn't existed an obvious crystallinity in the PPC WPU, PBA WPU and PTMG WPU, and the structure regularity of WPU5, WPU4 and WPU2 declined by order as the diffraction peaks of these WPUs declined by order. The crystallinity of WPU was generally considered to be caused by the gathering and the ordering arrangement of the soft segment, while the hard segment dispersing in the soft segment could weaken the crystallinity of polyurethane[9]. The structure regularity of WPU2 and WPU4 was lower than that of WPU5 as the polarity of PPC and PBA was stronger than PTMG and the stronger inter-force between the hard segment and the soft segment compelled the hard segment disperse evenly into the soft segment to decrease the order arrangement and restrained the micro-phase separation between the hard segment and the soft segment.

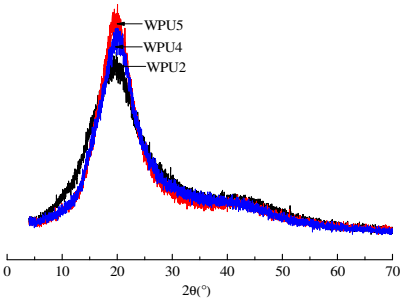


Fig.2 XRD Patterns of WPU Films

Rigidity and adhesive strength analysis of WPU films. From the results of rigidity and adhesive strength tests for WPU films shown in Table 2, it was found the rigidity of PPC WPU film was promoted from 4H to 5H and its adhesive strength was promoted from 1 level to 0 level when the DMPA amount of WPU was improved from 2.0 percent to 5.0 percent. The improvement of rigidity and adhesive strength was accounted for the increase of ester-group amount and hard segment when promoting the DMPA amount. It was concluded that the carbonic ester group in PPC could provide WPU with a better adhesive strength and rigidity. It was found when the DMPA amount of WPUs were the same, the rigidity and adhesive strength of PPC WPU film was similar to the counterparts of PTMG WPU and PBA WPU.

TABLE 2 HARDNESS AND ADHESION OF WPU FILMS

Sample code	Hardness	Adhesion
WPU1	4H	1 level
WPU2	5H	0 level
WPU3	5H	0 level
WPU4	5H	0 level
WPU5	4H	0 level

Water absorption and water contact angles of WPU films. The water absorption and water contact angles of WPUs were shown in Tab. 3. From Table 3 it was found that the water absorption of PPC WPU film was improve from 30.8 percent to 69.8 percent while its water contact angle declined from 80.1°to 63.7°when the DMPA amount of WPU was improved from 2.0 percent to 5.0 percent as the increase of DMPA amount improve the hydrophily of PPC WPU film. When the DMPA amount of WPUs were the same, the water absorptions of PPC WPU film, PBA WPU film and PTMG WPU film were 55.4 percent, 51.6 percent and 28.3 percent separately, and their water contact angles were 74.5°, 78.2° and 77.8° separately. From the phenomena mentioned above it was concluded that the water resistance of PTMG WPU was significantly better than that of PPC WPU and PBA WPU, while the water resistance ability of PPC WPU was a little poorer than that of PBA WPU, as the water resistance ability of the ether group in PTMG was better than that of the ester group in PPC and PBA, and the water resistance ability of the carbonic ester group in PPC was poorer than that of the ester group in PBA.

TABLE 3 WATER ABSORPTION AND WATER CONTACT ANGLES OF WPU FILMS

Sample code	Water absorption(%)	Contact angle(°)
WPU1	30.8	80.1
WPU2	55.4	74.5
WPU3	69.8	63.7
WPU4	51.6	78.2
WPU5	28.3	77.8

Conclusions

PPC, PBA and PTMG with the same molecular weight were chosen as soft segment to prepare different kinds of polyols WPU emulsion and their films. It was found that the adhesive strength, rigidity and water resistance ability of PPC WPU film were similar to the counterparts of PBA WPU film.

The soft segment gathering and ordering arrangement of PPC WPU was poor and there didn’t existed a significant crystallinity.

Reference

[1] Y.H. Huang, X.H. Yang, S.L. Zhao, Studies on the blends of carbon dioxide copolymer. Ⅲ.NBR/PPC systems, J. Appli. Polym. Sci. 61 (1996) 1479-1486.

[2] B.H. Liu, L.B. Chen, M. Zhang, A.F. Yu, Degradation and stabilization of Poly(propylene carbonate), Macromol. Rapid Commun, 23 (2002) 881-884.

[3] S. Inoue，H. Konuma, T. Tsuruta, Copolymerization of carbon dioxide and epoxide, J. Polym. Sci., Part B: Polym. Phys., 7 (1969) 287-292.

[4] R.F. Harris, M.D. Joseph, C. Davidson, Polyurethane elastomers based on molecular weight advanced poly(ethylene ether carbonate) diols, J. Appli. Polym. Sci., 41 (1990) 487-507.

[5] D.S. Wang, A.F. Yu, S.J. He, S.Y. Yang, Synthesis and properties of Poly(propylene carbonate) polyurethane, Acta Polymerica Sinica, 2 (1999) 162-166.

[6] D.S. Wang, A.F. Yu, S.J. He, S.Y. Yang, L.B. Chen, Studies on Poly(propylene carbonate) polyurethane/ Poly(methyl methacraylate) IPNs, Polymer Material Science & Engineering, 16 (2000) 135-138.

[7] C.S. Xu, Z.S. Zai, W.J. Xing, Synthesis and Characterizations of Polypropylene Carbonate Polyol Waterborne Polyurethane Grafted with Amino silicone oil, Polymer Material Science And Engineering, 29 (2013) 9-12.

[8] J. Zong, Q. Zhang, H. Sun, Characterization of polydimethylsiloxane-polyurethanes synthesized by graft or block copolymerizations, Polym. Bull., 65 (2010) 477-493.

[9] K. Kojio, Y. Nonaka, T. Masubuchi, M. Furukawa, Effect of the composition ratio of copolymerized poly(carbonate) glycol on the microphase-separated structures and the mechanical properties of polyurethane elastomers, J. Polym. Sci. Part B: Polym.Physi., 42 (2004) 4448-4458.

Advanced Materials Research Vol. 936 (2014) pp 63-66
© (2014) Trans Tech Publications, Switzerland
doi:10.4028/www.scientific.net/AMR.936.63

Curing Process of epoxy Resin Using Low Molecular Polyamide 651 as Curing Agent

Chunhua Han[2, a], Lin Wang[2, b], Dongyu Zhao[1, 2,C,*]

[1] Key Laboratory of Chemical Engineering Process & Technology for High-efficiency Conversion, College of Heilongjiang Province, Harbin, China

[2] School of Chemistry and Materials Science, Heilongjiang University, Harbin, China

[a]hanchunhua11@163.com, [b]973196253@qq.com, [c]zhaodyu@aliyun.com

Keywords: Epoxy resin; Low molecular polyamide 651 (PA651); Curing time; Curing agent content; Dynamic mechanical behavior

Abstract. In this paper low molecular polyamide 651(PA651) is used as the curing agent of epoxy resin. The optimum curing conditions and dosage of the curing agent are obtained by DMA and FT-IR analysis. Based on the dynamic mechanical temperature spectra of samples test, the best curing conditions are room temperature 2 hours, 70℃ 2 hours, 125℃ 2.5 hours and 150℃ 1 hours (RT / 2 h + 70 ℃ / 2 h +125℃ / 2.5 h + 150 ℃ / 1 h). The best dosage of curing agent PA651 is 50 wt %. Since the analysis of Fourier Infrared spectral verified that epoxy groups react completely, the curing conditions are the best curing process.

Introduction

Epoxy resin is a thermoplastic oligomer, the molecular weight between 300-2000 and performance is very bad. Epoxy resin can form three-dimensional network structure when adds the second component (curing agent), and become insoluble and infusible high polymer, and it appears excellent electrical insulation, chemical resistance, adhesion and a series of excellent performances. Epoxy resin is widely used in coatings, adhesives and engineering materials, EP adhesives have good adhesion to most all kinds of metals and nonmetal materials. With the improved performance of modified epoxy resin and new epoxy resin which have unique properties continue to be synthesized, the application fields of epoxy resin are further expanded in biology, medicine, environmental protection and the other fields such as: Protein fixed [1], Enzyme load [2], Ion recognition [3], Tooth filling agent [4], The fabric finishing agent [5] and the other new fields.

Curing agent is indispensable in application of the epoxy resin. There are many kinds of epoxy resin curing agents, however the modified amine curing agents account for 71% of the amount of curing agents. In this paper curing agent is low molecular polyamide resin 651(PA651). The structure of epoxy resin cured by PA651 contains long carbon chain fatty acid and amino，and allows the cured product having high elasticity and adhesive strength and water resistance.

Experiment

Different cure conditions

Epoxy 51 (E-51) and low molecular polyamide 651 (PA651) heat for two hours at the temperature of 60℃. Then the E-51 and PA651 are mixed in the ratio of 2:1 and stired evenly. Put the mixture into the heating PTFE mold which is covered with mold release agent. Set three kinds of curing conditions, RT/7 d+60 ℃/2 h， RT/2 h+70 ℃/2 h+125 ℃/2.5 h, RT/2 h+70 ℃/2 h +125 ℃/2.5 h+150 ℃/1 h。

Different content of curing agent

Taking 50g E-51 and a certain amount of PA651 (30 wt%, 35 wt%, 40 wt%, 45 wt%, 50 wt%, 55 wt%, 60 wt%) respectively heats at 60℃ for 2h. Putting the mixture into the heating PTEF mold which is covered with mold release agent in the certain curing condition of RT/2 h+70 ℃/2 h+125 ℃/2.5 h+150 ℃/1 h.

Results and discussion

DMA detection of epoxy resins which in the different curing conditions

Fig.1 shows tanδ-T curves of epoxy resin in different curing conditions. In Fig.1 line a, line b, and line c respectively represents the curing condition is RT/7 d+60 ℃/2 h，RT/2 h+70 ℃/2 h+125 ℃/2.5 h，RT/2 h+70 ℃/2 h +125 ℃/2.5 h+150 ℃/1 h. Tanδ is known as the loss factor, used to indicate the size of the internal friction. Tanδ maximum corresponding temperature is the glass transition temperature (T_g). Fig.1 shows with the increase of temperature internal friction curve line a, line b, and line c are complete and symmetrical peak shapes. This proved epoxy resin can be cured completely in these three kinds of curing conditions, epoxide groups almost completely react. Line a, line b and line c corresponding T_g gradually increased and the internal friction peak is gradually reduced, this shows in the process of thermal curing and post-curing treatment that there are chemical reactions resulting thermosetting compound three-dimensional network structure has changed and a small amount of residual epoxy groups react with the curing agent. Comparing with line a, line b and line c can conclude that the best cure condition is RT/2 h+70 ℃/2 h +125 ℃/2.5 h+150 ℃/1 h.

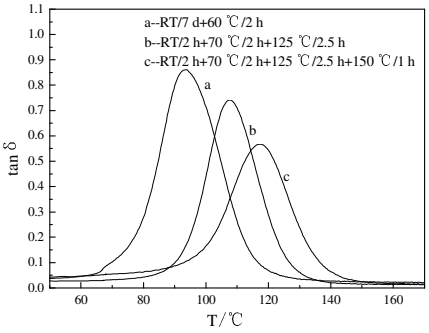


Fig.1 tanδ-T curves of epoxy resin in different curing conditions.

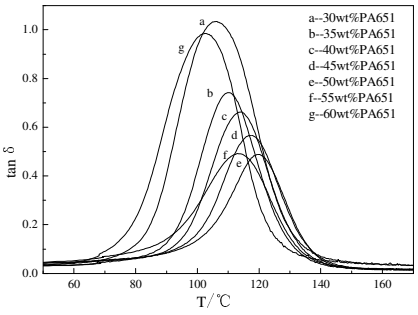


Fig.2 tanδ-T curves of the epoxy resin which in different amount of curing agent,

DMA detection of epoxy resins which under the condition of different curing agent percentage

PA651 dosage range widely, epoxy resins of different curing agent percentage are prepared at the best curing condition in order to determine the optimal dosage of PA651.

In Fig.2 line a, line b, line c, line d, line e, line f and line g are epoxy resin friction curves which curing agent amount respectively is 30w%, 35w%, 40w%, 45w%, 50w%, 55w% and 60w%. In the picture it shows that when the content of curing agent below 50%, the cured epoxy resin of T_g increase with the increasing content of PA651. The reason of this phenomenon is the dosage of PA651 increasing makes epoxy resin crosslink density increase. However T_g of cured epoxy resin decreases with the increase of PA651 dosage when the amount of PA651 above 50w%. The reason is epoxy groups almost completely react when the PA651 dosage at around 50w%, and the excess curing agents play the role of plasticizer makes the T_g lower if continue to increase the amount of PA651. Therefore, the optimum amount of curing agent PA651 is 50w%.

Infrared spectrum analysis of cured epoxy resin

Epoxy resin sample cured in the condition of RT / 2 h + 70 ℃, 2 h + 2.5 h + 125 ℃ / 125 ℃ / 1 h and dosage of curing agent is 50w%.

Fig.3 shows the full FTIR spectrum of cured epoxy resin. The strong absorption at 3379.09 cm^{-1} is assigned as stretching vibration peak of N-H from amide and O-H from alcohol. The absorption peak at1648.3 cm^{-1} is stretching vibration peak of C=O from amide. The vibration stretching peak of carbon skeleton of benzene appears at1608.14 cm^{-1} and 1509.94 cm^{-1}, besides that the characteristic absorption band of benzene ring surface of the inner and outer deformation vibration is found at 1106.48 cm^{-1} and 828.14 cm^{-1} . Absorption peak at 1460.74 cm^{-1} is C-H deformation vibration peak. Absorption peak at 1296.95 cm^{-1} is C-N deformation vibration peak and absorption peak at 1248.19 cm^{-1} is aromatic ether deformation vibration peak. The absorption peaks at 1036.02 cm^{-1} and 1181.95 cm^{-1} are caused by fatty ether deformation vibration peak. Compared with standard spectra of pure epoxy resin, absorption peak of epoxy groups at 910-920 cm^{-1} disappeared. It proves that the epoxy groups completely react.

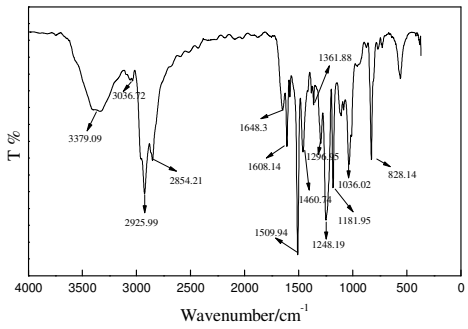


Fig.3 FTIR spectrum of cured epoxy resin

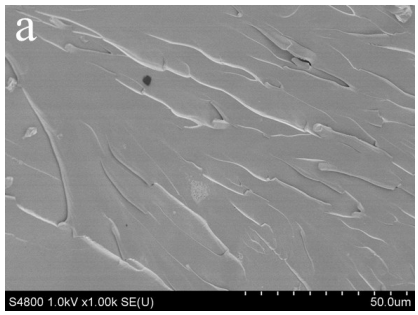


Fig.4 SEM test result of cured epoxy resin

Scanning electron microscopy images of cured epoxy resin

Fig.4 shows the SEM test result of cured epoxy resin. In the picture the section of cured epoxy resin is neat and crack distribution is uniform, so it proves that epoxy resin is a typical brittle fracture. This shows cured epoxy resin itself is very brittle.

Conclusion

In this work the best curing conditions and optimum amount of curing agent is found. The best curing condition is RT/2 h+70℃/ 2h+125℃/ 2.5 h+150℃/1 h and the optimum amount of curing agent is 50w%.

Acknowledgments

The work was supported by Harbin Scientific and Technological Special Fund for Innovative Talents (Grant Num 2012RFXXG093).

Reference

[1] M.L Sun, Epoxy resin application theory and technology, Beijing: Mechanical press, 2002.5-9.
[2] P Torres, F Batista-Viera, Immobilization of β-galactosidase from bacillus circulars onto epoxy-activated acrylic supports, molecular catalysis: Enzymatic, 2012, 74(3-4): 230-235.
[3] M Juan, Bolivara, C Mateoa, V Grazua, Heterofunctional supports for the one-step purification, immobilization and stabilization of large multimeric enzymes: amino-glyoxyl versus amino-epoxy supports, process biochemistry, 2010, 45(10):1692-1698.

[4] R.K Puri, V Kumar, M.P Mahajan, Mercury(II) ion recognition by newly synthesized oxadiazaphosphepine based receptors: coated graphite and polymeric membrane electrodes, inclusion phenomena and macrocyclic chemistry, 2011, 69(1-2):263-271.
[5] M. A. Ameer, A. A. Ghoneim, F. Heakal, Interface analysis of pure Sn, pure Ag and - Sn Ag binary alloys in H_2SO_4: surface and interface analysis, 2010, 42(2): 95-101.
[6] F Franco, P Monica, Ultraviolet curing for surface modification of textile fabrics: nanoscience and nanotechnology, 2011, 11(10):8663-8669.

Advanced Materials Research Vol. 936 (2014) pp 67-73
© (2014) Trans Tech Publications, Switzerland
doi:10.4028/www.scientific.net/AMR.936.67

Synthesis of Bis(*p*-aminophenoxy)dimethylsilane(*p*-APDS) and Its Process Optimization

Lixin Chen[1,a*],Fei Yang[2,b], Jin Yun[3,c]

(Department of Applied Chemistry, Northwestern Polytechnical University , Xi′an , 710072 , China)
[a]lixin@nwpu.edu.cn,[b]yangfei19880304@mail.nwpu.edu.cn, [c]949702303@qq.com

Keyword: *p*-aminophenol; dimethyldichlorosilane; silicone-containing diamine; optimum synthesis process; bis(*p*-aminophenoxy)dimethylsilane(*p*-APDS)

Abstract: Bis(*p*-aminophenoxy)dimethylsilane(*p*-APDS) was prepared by the reaction of *p*-aminophenol or 4-acetamidophenol with dimethyldichlorosilane in the presence of triethylamine or pyridine through four different means. The structure of diamines was examined by melting point apparatus, FT-IR and nuclear magnetic resonance apparatus ^{1}H-NMR. The productivity, process and cost of four means were compared. The results showed that benzene as a solvent, triethylamine as acid, *p*-aminophenol and dimethyl dichlorosilane at 40℃ for 4h is the most economical and reasonable process for synthesis of bis(*p*-aminophenoxy)dimethylsilane (*p*-APDS).

Introduction

As a kind of resin system which is derived from polyimide, bismaleimides(BMI) is more important because of its relatively low cost, high thermal stability, non-volatility and non-flammability among the addition type polymides[1,2,3]. Such kind of resin can supply higher operating temperature than that of the epoxy resin, simultaneously still can maintain epoxy-like processing property. Thus, they are widely used as high heat-resistance materials in the aerospace industry, in multilayer printed-circuit boards and in surface mounting devices, as well as high-temperature adhesive agents and in many other applications[4]. However, the cured resins are brittle due to the aromatic nature and the high crosslinking density of the network. At present, many methods have been employed to overcome the inherent brittleness of bismaleimide resin[5]. For example, the linear chain extension reaction of the constituent prior to crosslinking with aromatic diamines via Michael addition reaction, the incorporation of engineering thermo-plastics such as polyimide, polyethersulfone or polyether-ketone, polyhydantoin etc [6-8], or natural rubber[9].

Using diamine to modify BMI is an earlier method and also a convinent way to improve its toughness. The modifying mechanism is based on BMI and diamine Michael addition reaction. The linear polymer was synthesized by double bond in BMI reacting with primary amine in diamine which elongated the space of cross-linked points[10,11]. The application of diamines, for example, DDS, extends the backbone of BMI, but reduces the heat resistance. In recent years, using diamine containing siloxane attracted researchers' attention due to the physical and chemical characteristics of the Si-O bond. The siloxane unit is characterized by a lower intermolecular force, ease of retation and the relatively long Si-O bond, and these characteristics enable the siloxane to be flexible and to display properties which are fairly constant over a wide temperature range[12]. Consequently, a series of silicone-containing BMI had been prepared as a thermal stable resin[13]. Thus, we take attention to explore a kind of diamine-bis-(*p*-aminophenoxy)dimethyl silane, which can provide a higher thoughness, while still maintaining heat resistance because of the existance of Si-O bond and benzene rings at the same time.

We explored four processes to synthesize (*p*-APDS). The main objection of this research was to optimize a synthetic route of (*p*-APDS) based on compromising yield, cost and purify. The structure of the resultant was characterized by FT-IR, ^{1}H-NMR, melting point.

Experimental

Materials and Reagents.

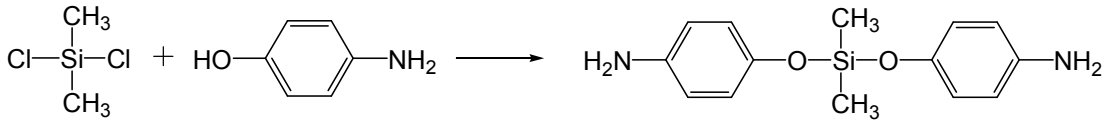
All chemicals were used after removal of water and were dried. *P*-aminophenol (Aladdin Industrial Co.), 4-acetamidophenol (HWRK Chem Co.,Beijing), dimethyldichlorosilane (Alfa Aesar Chem. Co., Tianjin). Triethylamine (TEA), tetrahydrofurane and dichloromethane were purchased from Guanghua Science and Technology Co., Ltd. Guangdong. Benzene and pyridine were purchased from Tianjin Fu Chen Chemical Reagents Factory. N,N-Dimethylformamide (DMF) and petroleum ether were purchased from Tianjin Fuyu Fine Chemical Co., Ltd.. Diethylamine and toluene were purchased from Tianjin Tianli Chemical Reagent Co., Ltd.. Hydrochloric acid (Beijing Chemical Plant). Sodium hydroxide (Paini, Zhenzhou).

Instruments.

Infrared measurements were performed on a Nicolet Avatar 360 FT-IR spectrometer (America). The ^{1}H NMR spectra were recorded in $CDCl_3$ solution using a Bruker Avance 400 MHz (Germany). The melting point was performed by a X-5 micro melting point apparatus (China).

Experiments

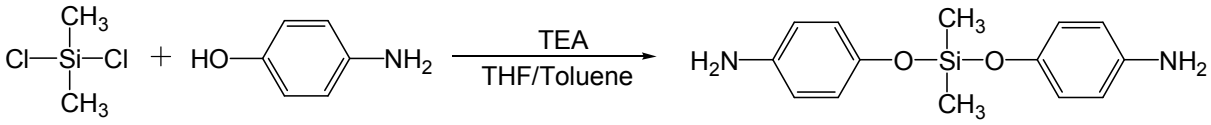
Method A



Scheme 1 The Principle of method A

A mixture of 10.9g (0.1mol) of *p*-aminophenol, 10.12g (0.1mol) triethylamine, and 100ml anhydrous benzene were introduced into a three-necked flask to which 6.966g (0.054mol) of dichlorodiphenylsilane was added drop-wise in 2h at 40℃. When the addition was completed, the reaction was continued at 60℃ for another 4h. The mixture was then filtered to remove salt. The filtrate was purified by water-washing and got the lower liquid. The liquid was then concentrated on a rotary evaporator. The residue was dissolved in the mixture of petroleum ether and benzene (1:1 of Volume ratio) at heating condition and filtrated. The product was crystallized from the mixture at 2~5℃ to yield brown-yellow crystals and dried under reduced pressure -0.01MPa at 50℃ for 24h or more. The yield was 41.25%.

Method B

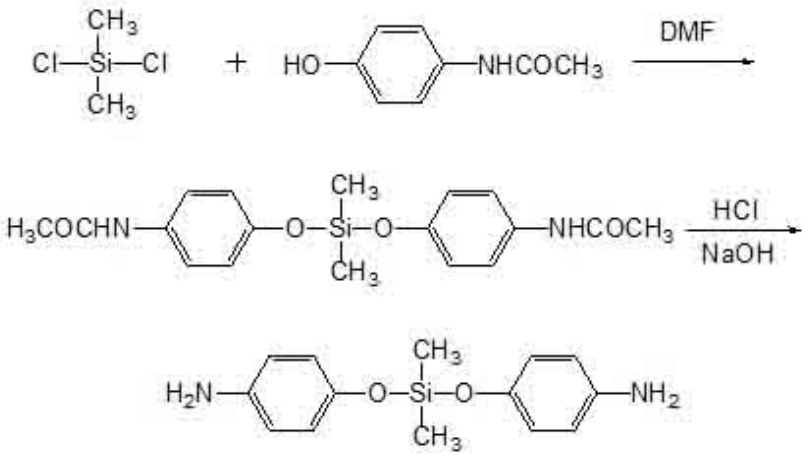


Scheme 2 The Principle of Method B

Into a three-necked flask, mixture of *p*-aminophenol (10.9g, 0.1mol), triethylamine (10.12g, 0.1mol), 25ml of tetrahydrofurane and 5ml of toluene were introduced. A solution of dichlorodimethylsilane (6.45g, 0.05mol) was added into the mixture drop wise over a period of 2h at 60℃. The reaction mixture was refluxed at 70℃ for 6h. Then formed salt was removed from the mixture by filtration and the filtrate was concentrated by a rotary evaporator. The residue was dissolved in ether and the insolubles were isolated by filtration. The product was crystallized from

ether at 0℃ to yield brown-yellow crystals and dried under reduced pressure -0.01MPa at 50℃ for 24h or more. The yield was 36.8%.

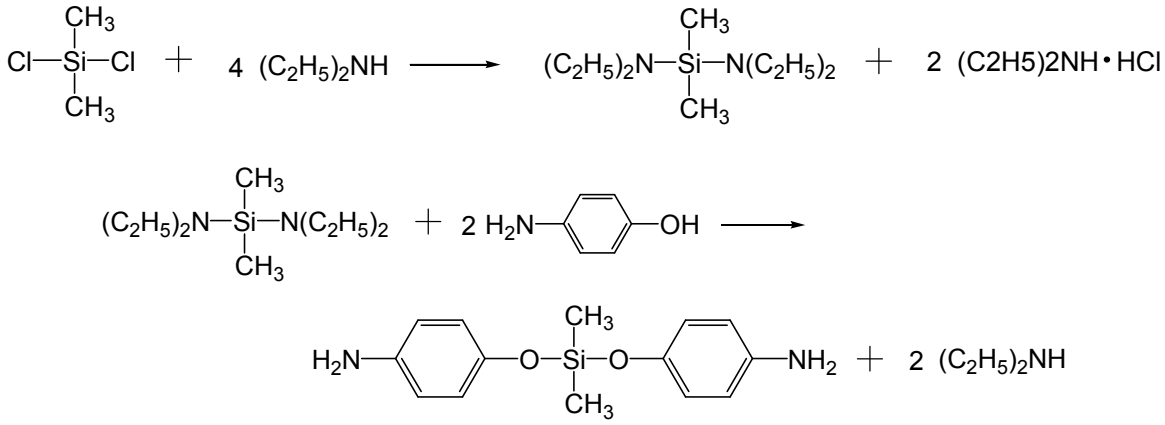
Method C



Scheme 3 The Principle of Method C

To a solution of 4-Acetamidophenol (15.1g, 0.1mol) in DMF(60ml) and pyridine(7.91g, 0.1mol), dichlorodimethylsilane (6.45g, 0.05mol) was added by drop wise at -10℃~-6℃ in 2h. Then the reaction mixture was proceeded 2h at room temperature, and heated at 40℃ for 4h. After cooling at temperature, the reaction mixture was filtrated and the filtrate was added into hydrochloric acid of 5 mol/L. The mixture was refluxed a period of time and then evacuated under reduced pressure. The crude product was crystallized from cold water and filtrated. After regulating pH to 10 with a solution of NaOH of 5 mol/L, the liquid was refluxed for 1h. The brown products was crystallized when cooling down and was dissolved at heated temperature in ethanol. The products was crystallized after decolored with active carbon. The yield was 32.67%.

Method D



Scheme 4 The Principle of Method D

Into a three-necked round bottom flask equipped with a magnetic stirrer and a dropping funnel, 29.2g (0.4mol) of diethylamine and 50ml of anhydrous dichloromethane were placed. The mixture reaction was vigorously stirred at -17℃~-20℃. Dichlorodimethylsilane (12.9g, 0.1mol) was added dropwise for 2h. The reaction was kept at this temperature for 2h. The white suspension was filtered to obtain a transparent solution that was concentrated at normal pressure, then collected fraction of 17mm Hg under 81~82℃. The viscous liquid was bis (N,N-diethyl amine) dimethylsilane.

10.9g (0.1mol) of *p*-aminophenol dissolved in 80 ml of anhydrous benzene were introduced into a 250 ml three-necked flask containing a magnetic stirrer and a reflux condenser. 10.1g (0.05mol) of

bis(N,N-diethylamine)dimethylsilane was introduced into reaction flask via a dropping funnel for 60min. The reaction mixture was kept 2h at this temperature. The mixture was filtered and the filtrate was concentrated by a rotary evaporator. The residue was dissolved in the mixture of petroleum ether and benzene (4:6 of volume ratio). The yellow product was crystallized from the liquid at 2~5℃. The yield was 29.58%.

Results and discussion

In the present work, four types of synthesis process of a kind of silicone-containing diamine—bis-(*p*-aminophenoxy) dimethylsilane(*p*-APDS) are used, and a better synthesis method is decided by comparising the productivity, the cost, and the structure-property of their products.

Confirm of structures.

Common spectroscopic methods including FT-IR (Fig 1), ^{1}H-NMR (Fig 2) were used to confirm the structures of (*p*-APDS) and the results were collected in Table 1. From the figure 1 and figure 2, it can be determined that the resultants of four methods are the same. In the FT-IR spectra of diamine, peaks at about 1239cm^{-1}(Si-O asymmetrical stretching), 1093 cm^{-1}(Si-O symmetrical stretching), and 973 cm^{-1}(Si-O asymmetrical stretching) approved the Si-O bonds formation. Additionally, band at 3650-3590 cm^{-1} that was related to the O-H bond of hydroxyl group in the *p*-aminophenol was disappeared. Furthermore, the evident presence of absorption bands at 3275-3345 cm^{-1}(N-H stretching) and no peaks at 1650 cm^{-1}(C=O stretching of acylamino) demonstrated structure of target product. ^{1}H-NMR spectra of bis(*p*-aminophenoxy)dimethylsilane (Fig 2) exhibited the chemical shifts characteristic for Si-CH_3 signal at 0.21-0.23 ppm, amine protons at 3.36-3.52 ppm, aromatic protons appearing as doublet at 6.51 ppm and 6.68 ppm. The amino peaks existed in the diamine spectrum shifted to higher fields as a result of appearing of electrondonating oxygen groups. From the above, we can determine the resultant of four methods is bis(*p*-aminophenoxy)dimethylsilane.

Table 1 Characterization of bis(p-aminophenoxy)dimethylsilane

spectroscopic methods	A	B	C	D
^{1}H-NMR ($CDCl_3$,δ)	0.21(s, 6H, Methyl) 3.36(s, 4H, NH) 6.51(d, 4H, Phenyl) 6.68(d, 4H, Phenyl)	0.21(s, 6H, Methyl) 3.52 (s, 4H, NH) 6.51(d, 4H, Phenyl) 6.63(d, 4H, Phenyl)	0.23(s, 6H, Methyl) 3.40 (s, 4H, NH) 6.51(d, 4H, Phenyl) 6.68(d, 4H, Phenyl)	0.23(s, 6H, Methyl) 3.40 (s, 4H, NH) 6.51(d, 4H, Phenyl) 6.68(d, 4H, Phenyl)
FT-IR(KBr), cm^{-1}	3275-3340(NH_2) 3037(CH, Aromatic) 2958-2818 (CH, Methyl) 1614(C-N, N-H) 1517 (C=C, Aromatic) 1482(Si-Ph) 1256(Si-CH_3) 1087(Si-O)	3284-3345(NH_2) 3028(CH, Aromatic) 2958-2818 (CH, Methyl) 1614(C-N, N-H) 1508 (C=C, Aromatic) 1482(Si-Ph) 1256(Si-CH_3) 1095(Si-O)	3275-3345(NH_2) 3028(CH, Aromatic) 2962-2814 (CH, Methyl) 1614(C-N, N-H) 1508 (C=C, Aromatic) 1473(Si-Ph) 1256(Si-CH_3) 1087(Si-O)	3284-3345(NH_2) 3028(CH, Aromatic) 2962-2814 (CH, Methyl) 1614(C-N, N-H) 1508 (C=C, Aromatic) 1473(Si-Ph) 1256(Si-CH_3) 1087(Si-O)

Melting point measurement.

The synthetic resultant of the above four processes are the (p-APDS) crystals. Generally speaking, the narrower the melting temperature range is, the higher purity the resultant has. It is convenient to obtain the melting point of the products with melting point detector. The results are listed in table 2. According to the references, the melting point of the (p-APDS) crystals is 64℃, and the melting points of the resultants listed in table 2 are all close to this figure. Thus, the resultants are (*p*-APDS).

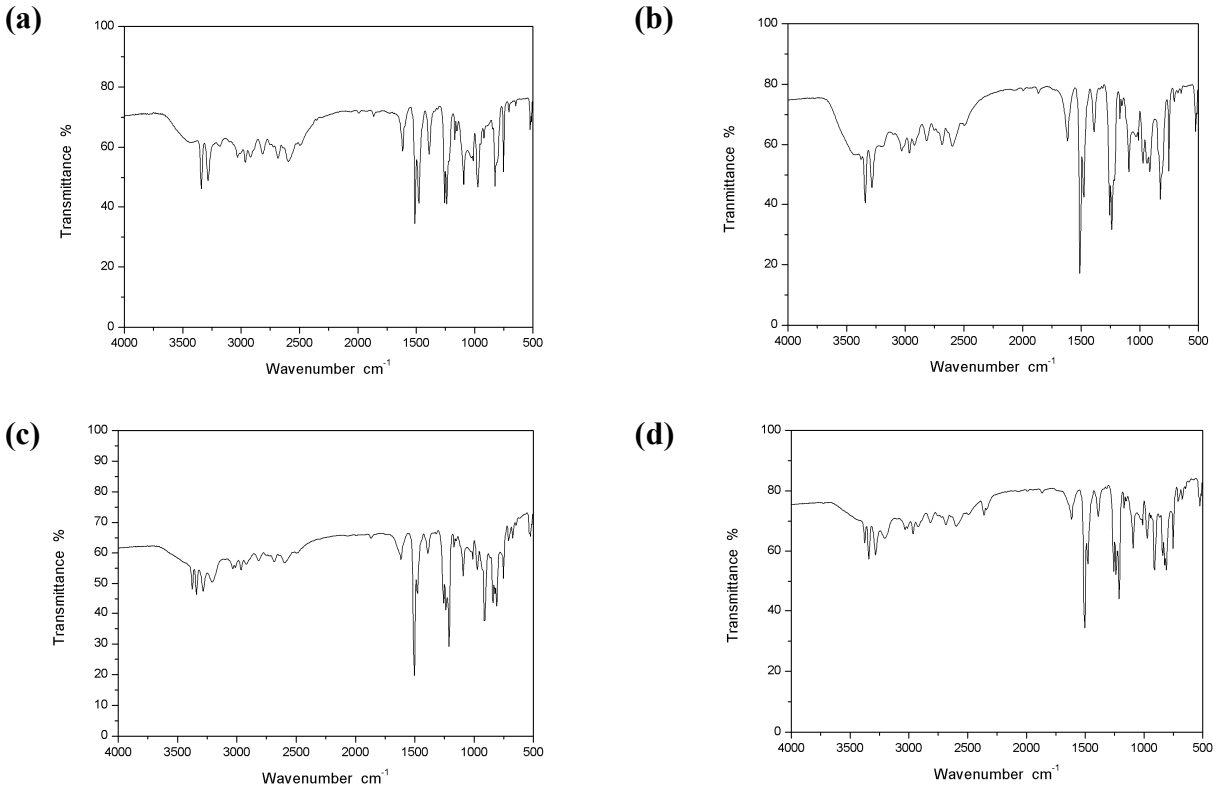


Fig 1 FT-IR of Four Methods of bis-(p-aminophenoxy)dimethyl silane

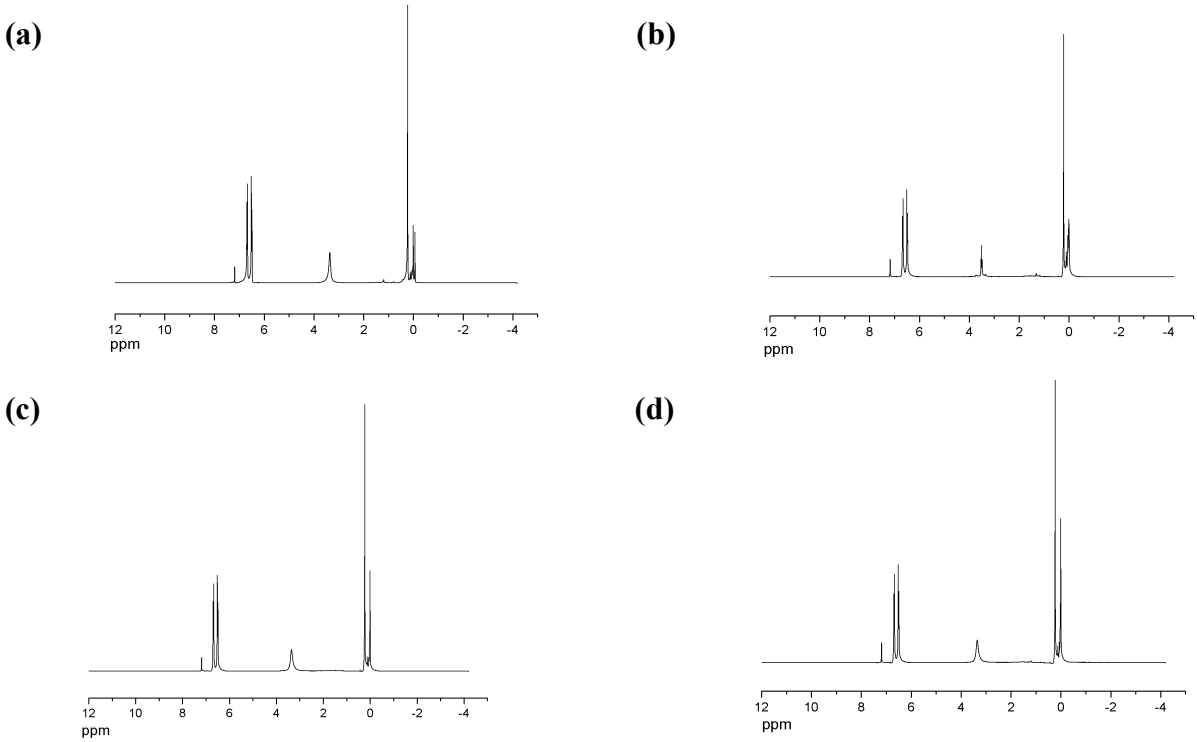


Fig 2 H-NMR of Four Methods of bis-(p-aminophenoxy)dimethyl silane

Table 2 The melting point of bis(p-aminophenoxy)dimethylsilane

	A	B	C	D
Melting Point/℃	58.5~63.8	59.7~64.6	62~64	62.5

Yield of product.

Since four synthetic methods of (*p*-APDS) were used in this paper, the optimal synthesizing technology was determined by optimizing the synthetic conditions of four synthetic ways and we obtain the optimum yield ultimately. Four synthesis processes are listed in table 3.

Table 3 Synthetic processes of four methods

	Solvent	T/℃	Ratio(A:B)	Time/h	Yield/%
A	Benzene	40	1:2.05	4	41.25
B	THF+Toluene	70	1:2.05	6	36.8
C	DMF	Room temperature+40	1:1.7	6	32.67
D	Dichloromethane+Benzene	-20+80	1:2.4	2	29.58

Note: A in the table is dimethyldichlorosilane, and B is *p*-aminophenol.

We studied the influence of different factors on the process of each method, and ultimately determined their optimal synthesis before. In this paper, method A, B and C are one-step synthetic processes and the product of method D is synthesized by a two-step method. Method A in yield is greater than method B, on account of the differences in their solvent, the reaction temperature and the time. We had taken the same conditions as process A during process B, such as in the proportion of 1:2.05(A:B) at 40℃ for 4 hours, however, the yield is lower than 36.8%. This may be present by-products because of reaction degree is not enough, which is caused by lower temperature and shorter reaction time. In addition, we applied a mixed solvent of benzene and petroleum ether when recrystallization in method B that is same as method A, the result showed us the yield is only 11.36% and there are more by-products than when using ether as a recrystallization solvent. The yield of method C which use acetaminophen as raw material and reactive at room temperature and 40℃ for 2 hours respectively is only 32.67%. In this reaction, we gave protection of amino group in *p*-aminophenol and ensured that hydroxyl group was priority to react with dimethyldichoride and this made it easier for the reaction. However, this process is too complicated due to it includes too many procedures and the conditions of reaction are hard to control, so the yield is lower relatively.

The reaction product of dimethyldichlorosilane and diethylamine was reacted with the *p*-aminophenol in Method D, leading Si-Cl bond into Si-N bond, which decreased its activity and reacted with hydroxyl group. This process is easy to achieved, however the course of reaction is more miscellaneous than others at the same time and get lower yield at last.

From the above, the reactive process and yield of one-step method are much better than two-step one, and method A is a desired synthetic process of bis(*p*-aminophenoxy) dimethylsilane.

Costs of four methods.

Silicon-containing diamine is very expensive in the past, for example, bis(3-aminopropyl) tetramethyl disioxane, which is currently commercialized in the United States, is worth more than $ 500 per 100g. Therefore, the emphasis of the synthetic work is to improve the yield and to reduce the cost. According to the upper analysis of yield and structure, we calculate the cost of per gram of each method. The data is listed in table 4. We can conclude method A is the lowest cost of them from the table.

Table 4 The cost of four methods

	A	B	C	D
cost/¥	1.76	5.48	4.09	3.83

Conclusion

With dimethyldichlorosilane and *p*-aminophenol as the main raw materials, bis(*p*-aminophenoxy)dimethylsilane was synthetized through four kinds of methods. The discussion about structure, the melting point, the process and the costs make us to determine the optimal synthetic method of the product. With benzene as solvent, bis(*p*-aminophenoxy) dimethylsilane(*p*-APDS) was prepared by the reactions of *p*-aminophenol and dimethyldichlorosilane(1:2.05) in the presence of triethylamine at 40℃ for 4h, at last using a mixed of benzene and petroleum ether as recrystallization solvent, recrystallizing to obtain the product. The melting point of product is 58.5~63.8℃.

References

[1] D.J. Gong, J Yu, S.H.Jin, etal. Bismaleimide Research progress of toughening. Insulating material. 44(2011)41-46

[2] Chandra R, Rajabi L. Recent advances in bismaleimides andepoxy-imide/bismaleimide formulations and composites. Macromol Sci Rev Macromol Chem Phys.37(1997)61– 96

[3] Anton Airinei, Nicusor Fifere, Mihaela Homocianu, etc. Optical properties of some new azo photoisomerizable bismaleimide derivatives. Int.J.Mol.Sci. 12(2011)6176-6193

[4] Wei-Jye Shu, Ruey-Shi Tsai. Studies of Silicon-Containing Bismaleimide Resins. Part I: Synthesis and Characteristics of Model Compounds and Polyaspartimides. Designed Monomers and Polymers. 13(2010) 33–49.

[5] Stenzenberger HD. Addition polyimides. Adv Polym Sci. 117(1994)165– 220

[6] Zhu S, Gu A, Liang G, Yuan L. Dielectric properties and their dependence of polyetherimide/ bismaleimide blends for high performance copper clad laminates. Pol Res. 18(2011):1467–1549

[7] Luo Y, Yu X, Cai X, Li S. Polyesterimide-modified bismaleimide resins. I. Effect of polyesterimide content. Macromol Sci Pure Appl Chem. 39(2002)825 –836

[8] Kurdi J, Kumar A. Synthesis and characterization of modified bismaleimide/polysulfone semi-interpenetrating polymer net-works. Appl Polym Sci. 102(2006)369–379.

[9] Du M, Guo B, Jia D. Effects of thermal and UV-inducedgrafting of bismaleimide on mechanical performance of reclaimed rubber/natural rubber blends. Pol Res. 2005, 12(2005)473–482

[10] Dix LR, Ebdon JR, Flint NJ, Hodge P, O'Dell R. Eur Polym J.31(1995)647.

[11] Zhao J. Bismaleimide toughened Research. China adhensive. 18(2009)48-52.

[12] Wang C. S., Leu T. S., Hsu K.R. Novel bismaleimide with naphthalene side group. 1, From 1-naphthalene and 2,6-dimethylaniline. Polymer. 39(1998)2921-2927.

[13] Cao H. W., Xu R.W., Yu D.S. Thermal and Dielectric Properties of Bismaleimide-Triazine Resins Containing Octa(maleimidophenyl)silsesquioxane. Journal of Applied Polymer Science. 109(2008)3114-3121.

Advanced Materials Research Vol. 936 (2014) pp 74-81
© (2014) Trans Tech Publications, Switzerland
doi:10.4028/www.scientific.net/AMR.936.74

Structure and mechanical properties of starch/ styrene-butadiene latex composites

Gang Chen[1,a*], Zhengjun Zhu[1,b], Pekka Salminen[1,2,c] and Martti Toivakka[3,d]

[1]State Key Laboratory of Pulp and Paper Engineering, Guangzhou 510640, China
[2]Styron LLC, Samstagern 138833, Switzerland

[3]Laboratory of Paper Coating and Converting, Abo Akademi University, Turku FI20500, Finland

[a*] Corresponding author：papercg@scut.edu.cn, [b]zzhu@styron.com, [c]psalminen@styron.com, [d]mtoivakka@abo.fi

Keywords: Starch, Migration, Phase separation, Co-continuity, Mechanical properties, Perera approach

Abstract: The structure of the starch/styrene-butadiene latex composites was characterized using Scanning Electron Microscopy (SEM). In order to get a better contrast between starch and latex, OsO_4 were used to stain latex. Ion-beam cutting and liquid nitrogen cracking were employed to fabricate qualified cross-sections for SEM characterization. During drying, starch and latex migrate, creating non-uniform structure with latex dominated in the lower surface (next to the substrate) and starch in the upper surface (open to the air). The film formation of latex is slower than the starch/latex film forming. Phase separation occurs with starch granules embedded in the latex-starch matrix, reinforcing the composites. The analysis of composite structure and use of Perera approach indicate that good adhesion is present between latex phase and starch phase, starch granules and latex-starch matrix. When the latex is substituted by starch, the elastic modulus and tensile strength increase whilst the elongation at break decreases. When the volume fraction of starch is higher than 41.7 %, increasing starch content, the increase of ultimate tensile strength and elastic modulus accelerate, whereas the elongation at break decreases slower, which may arise from the phase co-continuity of starch.

Introduction

Since styrene-butadiene (SB) latex was emulsion polymerized in the World War II [1], SB latex is widely used as a binder. However, the fluctuations of crude oil raw materials and the increasing environmental concerns put stress on SB latex industry. Starch is an eco-friendly, sustainable, low-cost natural polymer, which can partly substitute SB latex in synthesized rubber and paper coatings [2].

The blends of starch and SB latex need to form a film to execute the binding power. The migration of starch and SB latex during the film formation in the paper coating is acknowledged [3]. However, there are some contradict conclusions on the effect of starch on the latex migration. Ikeda et al. [4] and Hamada et al. [5] found that starch induced the latex migration in the starch-latex dual binder system, while the opposite result was achieved by Du et al. [6] and Zang et al. [7]. This contradiction has not been addressed due to the lack of study on the interactions between latex and starch. Meanwhile, the inclusion of more starch in the paper coating can give rise to various mechanical failures, such as picking and cracking [8]. Therefore, it is advantageous to investigate the interactions between the latex and starch and their contributions to the mechanical properties.

In this study, morphologies of the surfaces and cross-sections of the starch/ SB latex composites were investigated by using Scanning Electron Microscopy (SEM). Together with mechanical tests and the use of Perera approach [9], interactions between SB latex and starch were qualified. This study can be further used to analyze and understand the problems caused by using more starch as mentioned in the context.

Experimental

Materials.

The latex is a low Tg (2 °C) styrene-butadiene latex with a density of 1.0 g/cm^3, produced by Styron. The starch is a thermo modified starch from Cargill, the density of which is 1.4 g/cm^3.

Sample Preparation.

Starch was dispersed into distilled water at 20 % solid concentration in a beaker. The dispersion was put into a preheated (93 °C) water bath and cooked for 60 minutes with continuous stirring at 450 rpm. Pre-calculated amount of starch and latex were mixed by stirring at 450 rpm for 30 minutes. The mass ratios between starch and latex are 0/100, 10/90, 20/80, 30/70, 40/60, 50/50, 60/40, 70/30. A vibration mesh with the mesh diameter of 38 μm was used to remove the air bubbles in the blends. The filtered blends were drawn onto a Mylar film using a laboratory-made applicator driven by a rod coater. The thickness of wet coating films was adjusted by using different applicator slots to obtain dry films with the thickness of 100-150 μm. The wet films were dried in a conditioned room at 23 °C and 50% relative humidity (RH) for 24 hours. The dried films were carefully peeled off from the Mylar substrate. The films for the mechanical tests were annealed in a hot air oven at 70 °C for 1 hour. The annealed films were kept in the condition room for at least 2 days before measuring the mechanical properties.

Scanning Electron Microscopy.

The selected un-annealed samples were stained with 1 g osmium tetroxide crystals in a fume hood for 48 hours, referring to Chinga et al. [10]. In order to get a satisfactory cross-section for SEM imaging, liquid nitrogen cracking (refer to Landreau [11]) and ion-beam cutting were employed. The surfaces and the cross-sections of the stained samples were then imaged with Zeiss Leo 1530 Gemini SEM. In-lens, secondary electron imaging (SEI) and back-scattered electron imaging (BSI) modes were used.

Mechanical Tests. S

amples were punched out from the annealed film using a steel barbell cutting die with a total length of 75 mm, the gauge length of 25 mm and the central width of 4 mm. The mechanical measuring was performed on an Instron 8872 with a deformation rate at 10 mm/min.

Results and Discussion

Surface Topography.

The morphology of the upper surface (open to air) and lower surfaces (next to the Mylar substrate) of the composites was shown in Figure 1. The white dots in Fig. 1 are the OsO_4 stained SB latex particles. There are clear differences between the lower surfaces and upper surfaces. The Mylar surfaces have a monolayer of latex particles whilst the air surfaces are dominated by starch with only a few latex particles. This difference indicates that starch and latex particles migrate in the starch/SB latex composite and that the migration ability and directions are different. Because that Mylar film is a non-absorbent substrate of water, water can only be evaporated at the upper surface during the drying. Starch is a water soluble polymer, therefore larger migration tendency to the upper surface compared to latex particles [12, 13], dominating the upper surface. The latex particles may migrate to the lower surface induced by the attraction between the Mylar substrate and latex particles, accumulating at the lower surface. The different migration abilities may result in the non-uniform distributions of latex and starch, which may further affect the properties of the composites.

As the addition level of starch increases from 40 wt% to 70 wt%, the latex amount in the upper surfaces increases, while the opposite result is observed at the lower surface. Furthermore, the latex amount in the upper surface (Fig. 1(b) and 1(d)) is always smaller than its fraction in the formula. This may imply that starch can hinder the migration of latex to the lower surface when the starch addition is high enough. This may attribute to the increased viscosity of the blends induced by starch, which can restrict the movement of latex particles.

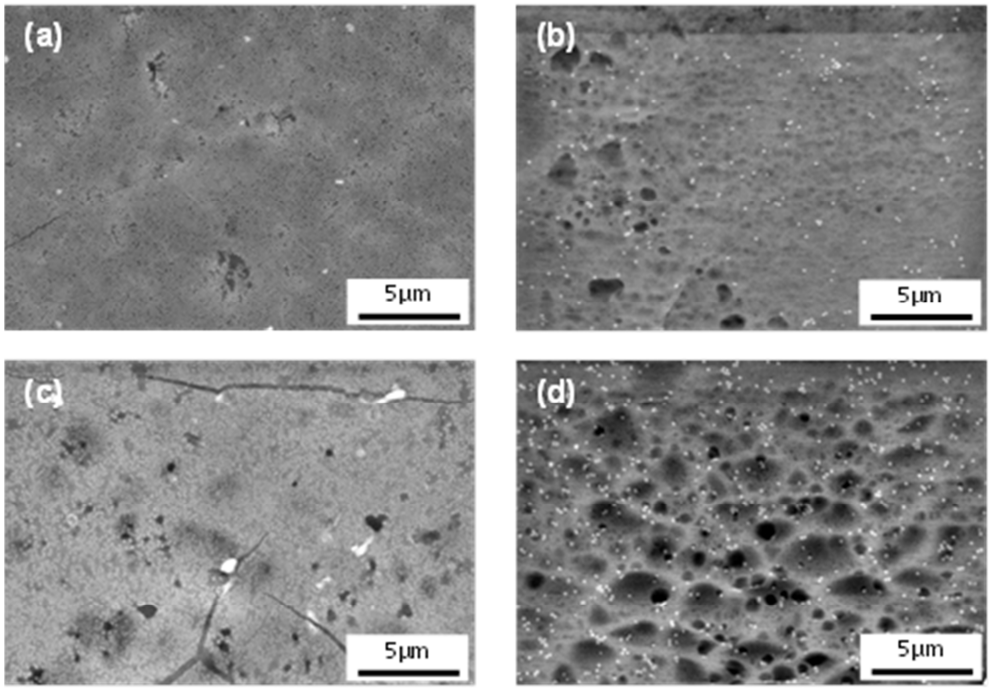


Fig. 1 BSI-SEM images of OsO_4 stained surfaces of starch/latex composites. a, b: lower and upper surface, 40 wt% starch; c,d: lower and upper surface, 70 wt% starch.

As shown in Fig. 2, these latex particles are in the shape of dodecahedron and separated from each other with clear gaps. In the current drying condition (23 ^{0}C), the film formation of late stops at the deformation of the latex particles and that the molecules inter-diffusion and entanglement have not yet taken place [14]. This may also indicate that the film formation of latex is slower than that of the composite.

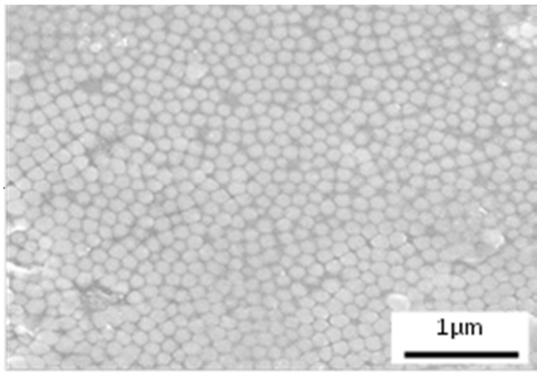


Fig. 2 In-lens field emission SEM images of Fig. 1(a)

Cross-section Morphology of the Composites.

The ion-beam cutting cross-sections were characterized using the BSI mode of SEM, as shown in Fig. 3. Grey scale particles can be clearly identified in Fig. 3(a) and 3(c). These grey particles seem to be the starch granules, due to the following reasons. Firstly, both the shape (round or oval) and the diameter (1-10 µm) of the grey particles are approximate to that of starch granules. Secondly, the amount of the grey particles increases with increasing the starch content from 40wt% to 70wt%, by comparison 3(a) with 3(c). Furthermore, the grey particles are more easily damaged (burnt out) by the electron beam during SEM imaging than the remaining matrix and more damaged areas are present when the starch content increases from 40wt% to 70wt%, as shown in Fig. 3(b) and 3(d). However, it is still unclear where these granules come from. It is improbable that all the granules are undispersed granules left during the cooking, since the starch was cooked long enough (60 minutes at 93 °C). Some of the granules may come from retrogradation due to the drying at low temperature (23 °C) [15]. Additionally, starch and latex are incompatible. The presence of

incompatible phase can accelerate the formation and growth of the starch crystals, therefore increasing the retrogradation of starch [16].

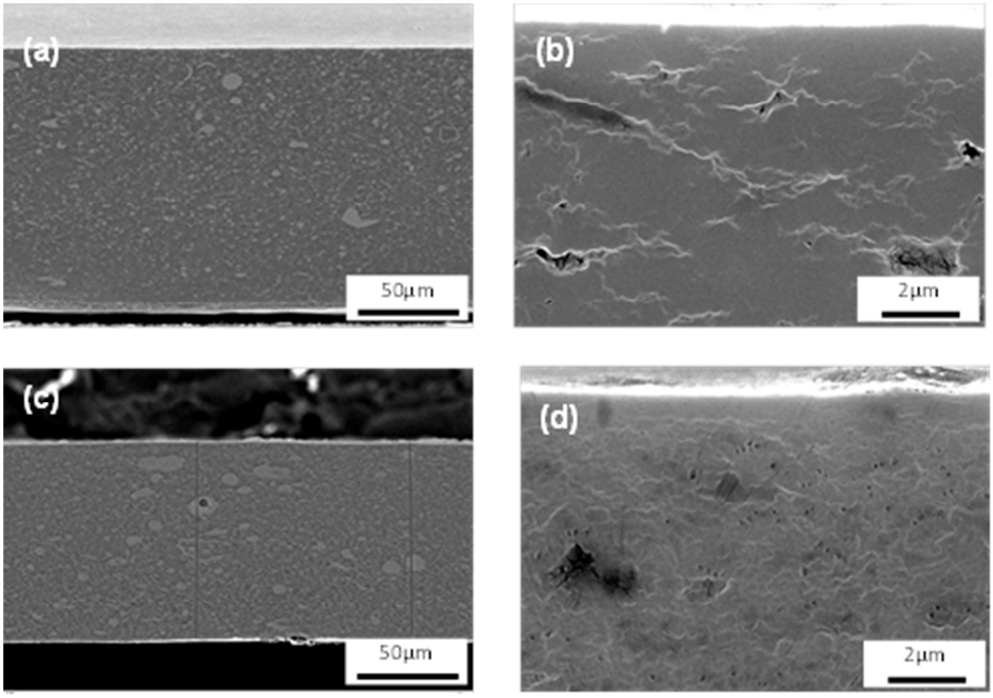


Fig. 3 Ion-beam cut cross-section images captured by BSI-SEM. a: 40 wt% starch; b: Partial magnification of (a); c: 70 wt% starch; d: Partial magnification of (c).

These gray scale particles imply the possibility of phase separation of latex and starch. Phase separation is commonly present in the starch-polymer composites, resulting from the incompatibility of hydrophilic starch and hydrophobic polymer [17, 18]. The phase separation can be clearly seen in Fig. 4. The gray particles are embedded in the matrix without clear gap between the two (as shown by the arrows in Fig. 4), which may indicate that good adhesion is present between the particles and the surrounding matrix [17]. This good adhesion may result from the hydrogen bonds between the particles and the starch in the surrounding matrix. In addition, the remaining surfactants in the latex may also improve the adhesion at the interphase. The area of starch particles in the Fig. 3 is smaller than the starch volume fraction in the formulas, which may indicate that only part of the starch is present as particles reinforced in the composites and the remaining starch, together with latex, is working as matrix.

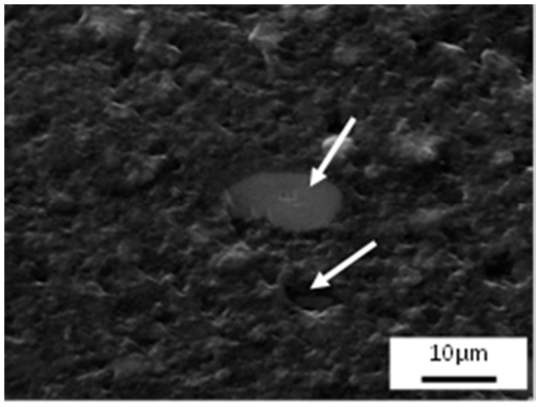


Fig. 4 SEI-SEM image of the cross-section created by liquid nitrogen cracking (starch content: 40 wt%)

Mechanical Properties of the Composites.

The stress-strain curves of the composites containing various starch mass ratios are shown in Fig. 5. The mechanical properties of the composites change a lot with the increasing substitution of latex by starch. The ultimate tensile strength and elastic modulus increase, whereas the elongation at break decreases. However, it should be noted that samples containing 0-20 wt% starch did not break when the Instron machine reached its maximum extensional strain. Therefore, the elongation at beak and ultimate tensile strength should be bigger than the test results.

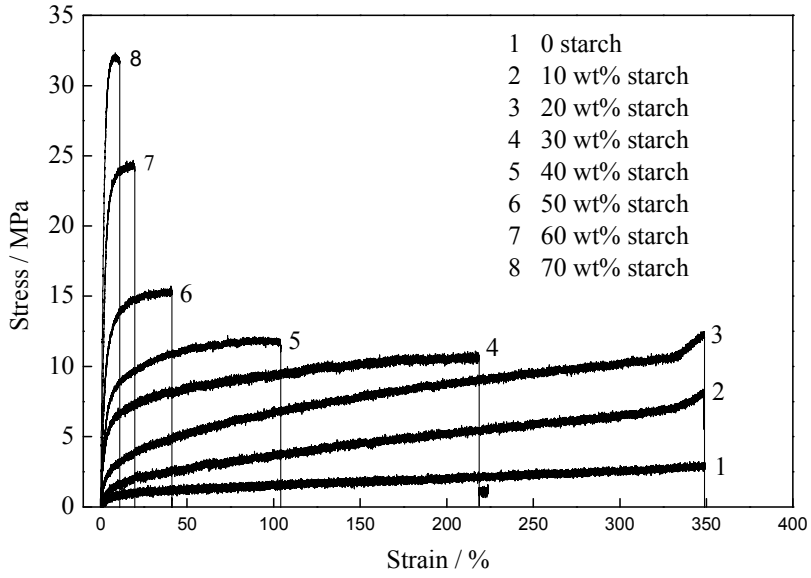


Fig. 5 Stress-strain curves of starch/ latex composites

The effects of starch content on the ultimate tensile strength, elastic modulus and elongation at break are shown in Fig.6. As illustrated in Fig.6(a), the ultimate tensile strength increases with more starch inclusion in the composites. The exception point (30 wt% starch) may result from the restriction of current test method, as stated above. The reinforcing function of starch in the composites can attribute to the following two reasons. Firstly, the starch molecules in the matrix can form hydrogen bonds, which can further develop into dense networks of starch in the composites, improving the tensile strength. Secondly, the starch granules (as shown in Fig. 3 and Fig. 4) can transfer the stress of the starch-latex matrix, reinforcing the composites [19].

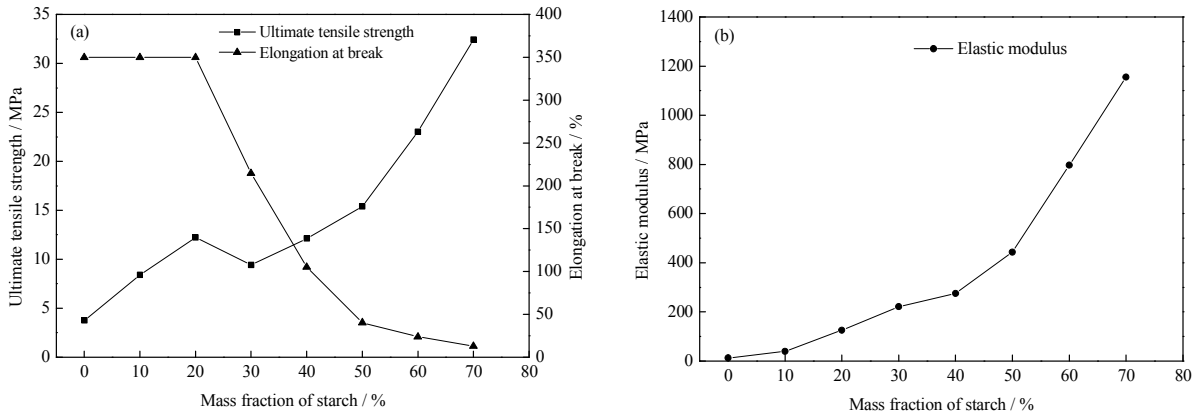


Fig. 6 Effect of starch content on the ultimate tensile strength (a■), elongation at break (a▲) and elastic modulus (b)

As shown in Fig. 6(a), increasing the starch content can decrease the elongation at break sharply. The reason for the exception points (0-20 wt% starch content) has already been mentioned in the context. The elongation of the film is related to the mobility of the molecule chains under stress [20]. The hydrogen bonds between the starch restrict the movement of the starch molecule chains, therefore lowering the elongation of the composites. Additionally, the presence of starch molecules

and starch granules may reduce the mobility of latex molecules, which can furthermore decrease the elongation at break of the composites.

The elastic modulus increases with the addition of starch, as shown in Fig. 6(b). This may attribute to the much higher elastic modulus of starch (2.3 GPa [21]) than that of latex (0.012 GPa).

It seems that the effect of starch content on the mechanical properties strengthens when the starch addition is higher than 50 wt%, as illustrated by the accelerated increasing tendency of the ultimate tensile strength and elastic modulus, and the slower decreasing tendency of elongation at break. This cannot be explained by the dominant phase because the volume fraction of starch is 41.7 % at this point and latex is still the dominant phase. Therefore, the concept of co-continuity [11,22] is introduced. Although the starch has not become the dominant phase, the starch molecule chains in the composite are networking, forming the co-continuous phase. After that, the effect of starch on the mechanical properties becomes more prominent.

Perera Approach.

Perera approach was adopted to evaluate the adhesion force between the starch phase and latex phase. Perera approach was initially used in the pigment/ latex composites, using the ratio between the ultimate tensile strength of the pigmented film (σ) over that of the unpigmented film (σ_0) as an indicator for the adhesion between the pigment and latex [9, 23]. If the ratio, σ/σ_0, is bigger than 1 and increases with increasing pigment volume, good adhesion is present between the two phases. Therefore, the pigment can reinforce the composites, and vice versa.

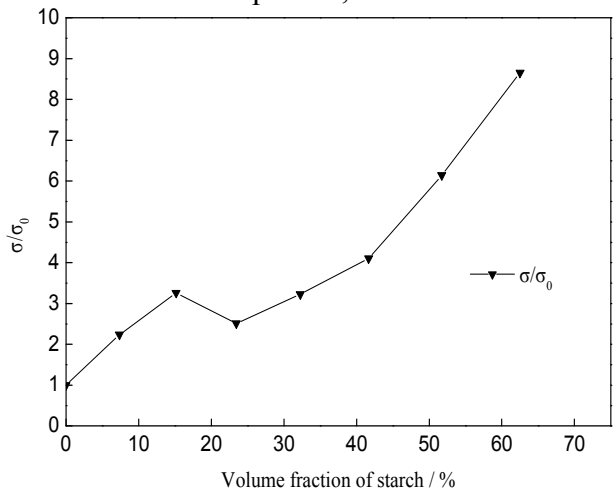


Fig. 7 Effect of volume percentage of starch on σ/ σ0

The ratios between the ultimate tensile strength of starch/ latex composites (σ) and that of latex film (σ_0) are plotted against the starch volume fractions, as shown in Fig. 7. The σ/σ_0 of composites is bigger than 1 and increases with the addition of starch. This indicates that there is good adhesion between starch phase and latex phase. This conclusion develops the conclusion from Fig. 4. Therefore, it may conclude that good adhesion is present between starch granules and starch-latex matrix, and between starch phase and latex phase.

Conclusions

(1) In the experiment condition (drying at 23 ^{0}C), the starch/ SB latex can form a cohesive film, but the film formation of the latex particles are uncompleted.

(2) During drying, the relative migration of starch and latex takes place in the starch/ SB latex composites. Starch dominates the upper surface and a monolayer of latex particles is accumulated at the lower surface. The use of abundant starch may hinder the migration of latex particles to the lower surface.

(3) Phase separation of starch and latex is present in the dried composites. Part of the starch is in the form of granules, reinforcing the starch-latex matrix. Good adhesion is observed between starch granules and starch-latex matrix, and between starch phase and latex phase.
(4) Increasing the starch content, the ultimate tensile strength and the elastic modulus increase, whilst the elongation at break decreases.
(5) Starch may become co-continuous phase when the starch content is 50 wt% (e.g. 41.7 % in volume fraction). After that, the effect of starch content on the mechanical properties of the composites becomes more prominent.

Acknowledgement

The research was sponsored by the High End Foreign Expert Program of China (Project NO. GDW20134400139) and New Century Talents Support Program of Chinese Ministry of Education (Project NO. D08001III). Abo Akademi University and Stryron LLC are highly appreciated for the great support of this work.

References

[1] S. Humphreys, Emulsion polymerisation and latex applications, Rapra Technology Limited, Shropshire UK, 2003, pp. 3-12.

[2] H.W. Maurer, Starch and Starch Products in Surface Sizing and Paper Coating, Tappi Press, Atlanta GA, 2001, pp. 1-5.

[3] M.J. Whalen-Shaw, Binder migration in paper and paperboard coatings, Tappi Press, Atlanta GA, 1993, pp. 19-36.

[4] A. Ikeda, T. Enomae, F. Onabe, Interaction between latex and starch in coatings during drying, Japan TAPPI Journal, 55(2) (2001) 82-89.

[5] H. Hamada, T. Enomae, I. Shibata, A. Isogai, F. Onabe, Effects of water-soluble cellulosic polymers on coating development and quality, Proceedings of Pita Coating Conference, Edinburgh, 2003, pp. 4-5.

[6] Y. Du, Y. Zang, J. Du, Effects of starch on latex migration and on paper coating properties, Ind Eng Chem Res, 50(16) (2011) 9781-9786.

[7] Y. Zang, J. Du, Y. Du, Z. Wu, S. Cheng, Y. Liu, The migration of styrene butadiene latex during the drying of coating suspensions: when and how does migration of colloidal particles occur?, Langmuir, 26(23) (2010) 18331-18339.

[8] P. Rättö, J. Hornatowska, The influence of coating colour composition on the crack area after creasing, Nordic Pulp and Paper Research Journal, 25(4) (2010) 448-494.

[9] D.Y. Perera, Effect of pigmentation on organic coating characteristics, Progress in organic coatings, 50(4) (2004) 247-262.

[10] G. Chinga, T. Helle, Staining with OsO_4 as a means to explore paper coating structure, Paperi ja Puu, 85(1) (2003) 1-5.

[11] E. Landreau, L. Tighzert, C. Bliard, F. Berzinet, C. Lacoste, Morphologies and properties of plasticized starch/polyamide compatibilized blends, European Polymer Journal, 45(2009) 2609–2618.

[12] F. Dobler, M. Plass, G. Welsch, M. MeKelvy, D. Poncelet, J. Marbaix, Considerations for the selection of binder in double and triple coated systems-effect of under layer starch migration on end use performance, PaperCon. Tappi Press, Atlanta GA, 2010, pp.1-3.

[13] K. Yamazaki, T. Nishioka, Y. Hattori, K. Fujita, Print mottle effect of binder migration and latex film formation during coating consolidation, Tappi J, 76(5) (1993) 79-84.

[14] J. Keddie, A.F. Routh., Fundamentals of latex film formation: processes and properties, Springer-Verlag, New York, 2010 pp.8-10.

[15] S.E. Bruun, Starch, in: Lehtinen E. Pigment Coating and Surface Sizing of Paper, Paperi ja puu, Helsinki, 2000, pp. 142-144.

[16] L.M. Robeson. Polymer blends: a comprehensive review, Hanser Gardener Publications Inc., Munich, 2007, pp. 26-27.

[17] A. Rashid, M.A. Misman, H.I. Ahmad, Mechanical and biodegradation properties of sago starch natural rubber latex Composites, 7th Asian Australian Conference on Composite Materials, Taibei 2010.

[18] E. Schwach, L. Averous. Starch-based biodegradable blends: morphology and interface properties, Polym Int, 53(12) (2004) 2115–24.

[19] S.Y. Fu, S.Q. Feng, B. Lauke, Y. Mai, Effects of particle size, particle/matrix interface adhesion and particle loading on mechanical properties of particulate–polymer composites, Composites: Part B, 39 (2009) 933-934.

[20] S. Mali, M. V. E. Grossmann, M. A. Garcia, M. M. Martino, N. E. Zaritzky, Microstructural characterization of yam starch films. Carbohydrate Polymers, 50(4) (2002) 379-386.

[21] J.A. Radley, Industrial Uses of Starch and its Derivatives, Applied Science Pulisher, London, 1976, pp. 153-157.

[22] S. Joseph, S.Thomas, Morphology, morphology development and mechanical properties of polystyrene/polybutadiene blends, European Polymer Journal, 39 (2003) 115–125.

[23] E. Lazarus, P. Salminen, P. Alam, M. Toivakka, On the mechanisms of wet and dry Strength of paper coatings: part 1 - experimental studies, Tappi PaperCon, New Orleans LA, 2012.

Advanced Materials Research Vol. 936 (2014) pp 82-88
© (2014) Trans Tech Publications, Switzerland
doi:10.4028/www.scientific.net/AMR.936.82

Experimental advances in effect of waviness on properties of fibre reinforced composite materials

ZHU Jun[1, a], WANG Jihui[2, b *]

[1]Department of Engineering Structure and Mechanics, Wuhan University of Technology, No. 122, Luoshi Road, Wuhan, 430070, P. R. China

[2]School of Materials Science and Engineering, Wuhan University of Technology, No. 122, Luoshi Road, Wuhan, 430070, P. R. China

[a]zhuj1109@163.com, [b]jhwang@whut.edu.cn

Keywords: waviness; composite materials; fabrication technique; characterization; failure mode

Abstract: Categories, fabrication techniques, characterization techniques, and effect of waviness on properties of fibre reinforced composite materials and structures are reviewed. Waviness exerts a great affluence on properties of composite materials and structures, which leads to a significant degradation or reduction of mechanical performances, such as static compressive/tensile strength, compressive fatigue life, and so on. Various factors related to waviness nested into the composite materials and structures, including wave geometry, thickness position of the wavy layer, percentages of layers with waviness, are considered and stated in detail. Failure mode of laminate containing waviness and the reasons for their failure initiation are analytically stated. At last, some prospects about this study are presented.

Introduction

In recent decades, composite materials are commonly and widely used in all walks of life due to their high specific strength and stiffness coupled with low cost. No matter that it is intentional or unintentional, defects are inevitably introduced in the process of manufacture and service. Waviness is one of the most frequently encountered flaws in large and thick composite structures. It results from manufacturing processes or from local buckling of prepreg or from wet hoop-wound filament strands under the pressure exerted by the overwrapped layers during the filament winding process or from the lamination residual thermal stresses [1] which are induced by the different thermal expansion rates between fibre and matrix materials during curing. Waviness has little effect on thin composite materials while greatly affects properties of the large and thick composite structures [2, 3, 4, 5, 6, 7, 8, 9, 10, 11, 12]. So it is gradually received attention and becomes a research focus in composites research field.

Only one review upon effect of fibre waviness on the mechanical properties of unidirectional fibre composites has been finished by Piggott since 1995 [12]. Additionally, in a review literature by Chou in 1989 [13], the effect of waviness on the linear and nonlinear elastic behavior of flexible composites is also considered. This paper mainly presents the experimental advances in effect of waviness on fibre reinforced composite materials after 1995.

Category and Characterization

A variety of defects are frequently produced in manufacture and service of composite materials and structures. However, only the flaw with fibre waviness induced by infusion processes and inherent in fabric architectures is focused here, including in-plane waviness, out-of-plane waviness and a particular waviness which is entirely different from in-plane waviness and out-of-plane waviness [3, 4, 11, 14, 15]. In-plane waviness, or fibre waviness, describes the fibre deviations from straight 0° in the plane of the fabric sheet. Out-of-plane waviness, or layer waviness, involves the entire layer of a multidirectional laminate undulating in the through-thickness direction. The through-thickness waviness in woven fabric such as A130 woven fabric, which is inevitably caused

by the woven architecture, is a typical unintentionally induced or inherent waviness [9, 14, 16]. It is neither in-plane waviness, nor the case of entire layer undulating in the through-thickness direction. In nature, the woven architecture it uses causes the fibre strand distortion in the thickness direction of layer.

Most researchers usually idealize the waviness geometry with a sinusoidal curve along one spatial coordinate direction of composite laminate (x axis is commonly chosen) and adopt the following four factors to characterize the waviness geometry in literatures [4, 9, 11, 14], the wavelength, amplitude, wave severity (the ratio of wave amplitude to wavelength) and the maximum angle of fibre rotation (the angle of wavy fibres inclined to the nominal fibre direction). It is noted that there is a so close relationship between wave severity and the maximum angle of fibre rotation for all cases throughout most literatures that they are deemed the equivalent waviness parameter.

The methods to measure the geometric parameters of waviness nested into composite materials and structures are developed, for example, the direct measuring technique by means of a protractor on micrographs or an angular reticule in a microscope [10, 17], the Yurgartis sectioning technique [18], the Clarke CLSM (i. e. Confocal Laser Scanning Microscope) technique [19], Digital image analysis (such as a multiple field image analysis method and a Fourier transform misalignment analysis method) [20, 21], and so on. Before measuring, the waviness geometric profile must be obtained by NDT (i. e. non-destructive testing) technique. To date, there have been a number of studies on characterizing the waviness geometry using NDT, such as ultrasonic testing [22, 23, 24, 25], radiographic testing [22, 26], electromagnetic testing [27], thermography [22], and shearography [28]. However, both the measuring methods and the NDT techniques mentioned above are not universal. Direct measurement is no doubt the simplest and the most convenient method to measure amplitude, wavelength and the maximum off-axis fibre angle, while the ultrasonic technique developed by Smith et al. was the most successful one in obtaining a high-resolution waviness profile. Multi-method is combined together to measure the object in actual experimental operation.

Fabrication Techniques

In order to simulate the realistic conditions of laminate with waviness, various fabrication techniques are developed to product representative artificial in-plane and out-of-plane waviness in a laboratory specimen. First of all, the basic criteria for a fabrication technique to generate waviness are flatness of the laminate, ease of fabrication, controllable waviness parameters, ease of varying the maximum misalignment angle and its location, controllable volume of fibre waviness (fraction of wavy fibres relative to straight ones), uniformity of laminate thickness, and symmetry. In fact, these factors related with both waviness geometry and attribute are challenging for any manufacture method, seen in the following section.

Adams and Hyer [3] developed a three-step fabrication method of making a flat laminate with one 0˚ wavy layer in the mid-plane, using a thermoplastic prepreg. Based on this, a single-step method was then established by Adams and Bell [4] to manufacture both single-layer and multiple-layer out-of-plane waviness into a wave-free thermoset crossply composite laminates. Their results indicated that producing a high wave severity (greater amplitude and shorter wavelength) was proved difficult as the applied consolidation pressure tended to flatten the wave, decreasing the amplitude while increasing the wavelength. Hsiao and Daniel [5] developed a prepreg-winding method for fabrication of thick specimens with controlled waviness, which the prepreg was wound a rectangular mandrel with rounded ends. The unidirectional composites with plies of sine-wave shape of uniform amplitude waviness across thickness were obtained. By using a three-step method differing from the previous one [3], they manufactured flat unidirectional composite laminates which the amplitude of sine-wave changed gradually from maximum to zero on the outer layers. Wang et al. [11] developed three methods (i. e. transverse-strip method, ply-drop method and constant-thickness ply-drop method) to produce waviness of various parameters at a mesoscale or a ply level. Different parametric waviness specimens according to the

requirements of a variety of tests were made by these techniques. It demonstrated that the most remarkable advantages are ease of fabrication with basic manufacturing knowledge and simplicity of experimental setup with no delicate or sophisticated equipment. However, voids or porosities even cavities were formed in the wavy regions due to lack of resin flow into gap between the base and the wavy layers, and warpage was caused by residual stress induced during cool down. Wang [14] chose a hand-made process to induce in-plane waviness into the 0˚ reinforcing fabrics which were then fabricated into [0/±45/0]s laminates. Composite specimens with various wave geometries, thickness position of the wavy layer, and percentage of 0˚ wavy layers were made and tested. Nelson et al. [10, 17] designed a process to product of layer panels containing waviness, which were infused under vacuum with one layer of peel-ply on the top and bottom surfaces and one layer of flow medium on the top surface of the laminate. In-plane waves were introduced by pulling the fibres manually for a one entire wavelength. Out-of-plane wave forms, also for one entire wavelength, were created by casting resin into a CNC machined mold and placing the castings under the laminate. On the basis of this, they improved their design and fabrication process to ensure flaw with waviness was as similar as possible to those found in composite structures (wind turbine blades) [15]. Then, the two kinds of waves were manufactured by the novel methods improved.

Furthermore, fabrication methods of waviness appeared in some analytical literatures in order to validate their numerical predictions. Chun et al. [8] used several sets of two half molds with curved surfaces to produce thick composites with controlled fibre waviness with various wave severities, which was similar in principle to Kuo's method [29] where a sinusoidal matching mold was used. The prepreg tapes were cut and layered on top of a half mold. After the lay up, the other half mold was place on top of it. The sandwiched prepregs together with the molds as one piece were then placed inside the curing mold. The sandwiched prepregs and integrated molds were cured in an autoclave following a curing cycle developed for thick composites [30]. Wisnom and Atkinson [31] manufactured a unidirectional composite panel with a transverse out-of-plane wave using a unidirectional prepreg strip as a kink former. Khan et al. [32] fabricated laminates with transverse out-of-plane waves using similar ideas to the kink former, matching mold and Chun et al.'s methods.

Review the fabrication techniques stated in the previous section, it was found that only two techniques to manufacture fibre reinforced plastics composite materials and structures containing in-plane waviness were developed, respectively by Wang [14] and by Nelson et al [15, 17].. The other ones were primarily aimed to introduce out-of-plane waviness into composite laminates. Most fabrication methods are not enough accurate to fabricate wave expected due to absolutely hand lay-up and may be introduce other defects such as porosity, inclusion, etc. Moreover, some manufacture methods are suitable for thermoplastic experimental materials of prepreg, others are appropriate for thermoset prepreg, only Wang and Nelson' methods could be applicable to dry fabrics. Further efforts are required to develop innovative fabrication methods for wavy laminates based on dry fabrics. More attention should be also paid to the third inherent waviness mentioned previously which was formed in the productive procedure.

Effect of Waviness on Properties of Composite Materials

Effect of Waviness on Mechanical Performances

Effect of waviness on mechanical performances was performed by many researchers [1, 3, 4, 5, 7, 8, 9, 12, 14, 15, 33]. Adams and Hyer [3] fabricated flat specimens of 0°/90° carbon fibre/polysulphone thermoplastic containing isolated layer waves. A central zero degree wavy layer in a 22-layer bidirectional laminate produced reduction of between 1 and 36% in quasi-static IITRI compression fixture tests, although the wavy 0˚ layers accounted for only 20% of the load carrying capacity of the laminate. For moderate layer wave geometries ($\delta/\lambda < 6\%$, the Greek letters δ and λ denote amplitude and wavelength respectively), failure approximately occurred at 88% of the strength of control specimens either in the tabs or within the wavy layer, while for $\delta/\lambda > 6\%$ (more

severe waviness), failure occurred at an average 63% of control strength. Thereafter, Adams and Bell [4] produced multiple-nested wavy 0˚ layers into other wave-free thermoset crossply laminates, which both the ratio of 0˚ wavy layers to 0˚ normal layers and wave severity were constant. The tests were performed by the same fixture as before, which determined the effect of multiply-layer wavy regions on compression strength. Results demonstrated if the volume fraction of 0˚ layers containing waviness to all 0˚ layers was 33% and larger, the strength decreased by 35% and kept relatively constant. And, the percentage reduction in compression strength was approximately equal to the percentage of 0˚ wavy layers when not more than 33%. Hsiao and Daniel [5] employed a new test method/fixture (i. e. NU fixture) based on a modified IITRI compression fixture to conduct on unidirectional laminates with uniform and graded waviness. It was shown that in unidirectional composites both major Young's modulus and compressive strength were degraded seriously with increasing waviness. To be specific, it caused serious degradation of compressive strength and appreciable reduction of 42% in modulus for specimens with uniform fibre waviness, while it leaded to a significant 30% reduction in compressive strength and only a slight reduction of 6% in modulus for specimens with graded fibre waviness.

Compared with out-of-plane, experimental and analytical investigations about effect of in-plane waviness on composite materials are fewer. Static compressive test, compressive fatigue test and static tensile test were all performed on an Instron 8501 servo hydraulic testing machine with a load capacity of 100 kN in Wang's research [14]. For waviness in one surface ply of the specimen, compressive strength converged to a single decreasing trend with the increase of wave severity, but it was little loss in compressive strength when wave severities was below 0.062. For specimens with undulating fibre fraction ranged from 0 to 1, a larger fraction of 0˚ layers with waviness resulted in a greater reduction in compressive strength for each specific wave severity, and greater wave severity produced a greater reduction in compressive strength for each in-plane waviness layer fraction. In-plane waviness showed a roughly proportional effect on the compressive strength over the entire range to 100%, which was quite different from the results of out-of-plane waviness cases in reference [4]. For specimens embedded with in-plane waviness, a considerable reduction in the compressive fatigue life occurred. When results of compressive fatigue tests were normalized by the static compressive strength, the changing trend was similar for most specimens. Additionally, from the testing results, it can be concluded that very moderate in-plane waviness does not influence the tensile strength significantly while severe in-plane waviness remarkably reduces the tensile strength. Besides, similar results are obtained by others [16, 34, 35, 36, 37].

Nelson et al. [15, 17] investigated the influence of both in-plane and out-of-plane waviness on static tensile and compressive properties. Ultimate stress values for the each of the 0˚ in-plane wave groups tested in tension were found to have a significant decrease in ultimate stress and the modulus of elasticity accounted for 85% to 106% of the control, while the same trend happened in compression. Nevertheless, for the ±45˚ groups with in-plane wave, ultimate stress values slightly decreased by 2% to 4% and the modulus of elasticity increased by 3% to 16% in comparison with the control group for tension, while the ultimate compressive stress was significantly higher compared with control groups, reaching to 112% to 133%. For the out-of-plane cases, ultimate failure stress for 0˚ and ±45˚ tension groups were decreased compared with the control, but were still increased compared with the in-plane waves results [15], while compressive strength was significant decreases in ultimate strength.

It is concluded that the fabrication techniques of in-plane and out-of-plane developed by different researchers have some shortcomings and limitations in simulating the realistic composite materials and structures with waviness as these manufacture methods are completely hand-made and easily induce new defects. So exploring innovative and novel techniques is very necessary for furthering the investigation of composite with waviness.

Failure Modes

Failure mode is relatively single for the laminate with the same waviness type. Adams and Hyer [3], and Adams and Bell [4] pointed out brooming was the common and pronounced failure mode,

which was characterized by through the thickness direction splaying of layers and numerous delamination near the waviness. An angled fracture plane through the specimen thickness was evident, suggesting the presence of shear failure mode. The wavy 0° layers commonly were fractured at or near an inflection point of the layer wave, midway between the crest and trough of the wave. Hsiao and Daniel [5] proved that the dominant failure mode of out-of-plane wavy laminate under axial compression was interlaminar shear failure. Interlaminar shear stress concentrated in the local region at first, delamination and layer buckling ensued. In Wang's research [14], it was proved that an angled fracture across the specimen width was observed in most of the failed specimens by a shear failure mode. It was very interesting that the angled fracture planes through the width were found to pass through the inflection point of the in-plane wave, being consistent with Adams and Hyer's [3] and Adams and Bell's conclusions [4]. The majority of compressive fatigue specimens had the same failure mode, but one failure plane was oriented at an angle through the specimen width which was similar to static compression failure, while others were perpendicular to the load direction near the grip position. Failure in tensile specimens, whether with or without in-plane waviness, were characterized by numerous fibres fracture and delamination through the gauge length of the specimen. Nelson et al.' results [15] manifested that initial failure occurred at low loading levels in areas where fibres were not continuous through the length of the in-plane sample. As strain levels increased, cracks initiated in the resin at the end of the wave before delaminating and grew through the entire wave section resulting ultimately in fibre failure. For specimens embedded into out-of-plane wavy layer, cracks also initiated in the resin at the end of the wave before delaminating in the first stage. However, after delamination the failure area was concentrated at the peak area of the wave.

In a word, these results indicate whether in-plane or out-of-plane waviness, delamination is bound to occur near the wavy region in the course of failure and the fibre fracture incline to initiate at or near the inflection point of the wave in the form of shear mode. These failure modes and observations of fibre reinforced composites with flaw of waviness were commonly found in current investigations.

Obviously, fibre waviness has been shown to play an important role in static compressive/tensile strength and fatigue endurance. Of course, these results listed above are only a small part of all researches in this field, and deviate from real situations, but it indicates that the degradation of strength and modulus are more or less occurred due to waviness exiting in the composite materials and structures.

Summary

The effect of both in-plane and out-of-plane waviness on the fibre reinforced composite materials and structures are reviewed. Also, the various fabrication techniques and the failure modes of composite laminate containing waviness are stated in detail. Although the failure mechanism of composite materials containing waviness is not very clearly by now, and there are some disadvantages among the different fabrication techniques, the works are most significant. In fact, they could provide experience for further study and inspire new ideas and innovative methods for other researchers who are interesting in this field.

Many new works are not done and not mentioned in this research. For example, the influence of wet and hot conditions on the laminate with waviness is not taken into account. Moreover, the new manufacturing methods improved are worth exploring for further studies, such as a deeper investigation of the effect of waviness on mechanical performance of composites, validation of theoretical models, and application for improvement of thick low cost structures quality like wind turbine blades.

References

[1] K.D. Potter and P.M. Weaver, A concept for the generation of out-of-plane distortion from tailored FRP laminates, Composites Part A: Applied Science and Manufacturing 35 (2004) 1353-1361.

[2] T.A. Bogetti, J.W. Gillespie and M.A. Lamontia, Influence of ply waviness on the stiffness and strength reduction on composite laminates, J. Thermoplast. Compos. Mater. 5 (1992) 344-369.

[3] D.O.H. Adams and M. Hyer, Effects of layer waviness on the compression strength of thermoplastic composite laminates, J. Reinf. Plast. Compos. 12 (1993) 414-429.

[4] D.O.H. Adams and S.J. Bell, Compression strength reductions in composite laminates due to multiple-layer waviness, Compos. Sci. Technol. 53 (1995) 207-212.

[5] H. Hsiao and I. Daniel, Effect of fiber waviness on stiffness and strength reduction of unidirectional composites under compressive loading, Compos. Sci. Technol. 56 (1996) 581-593.

[6] H. Hsiao and I. Daniel, Elastic properties of composites with fiber waviness, Compos Part A–Appl. Sci. Manuf. 27 (1996) 931-941.

[7] I. Daniel and H. Hsiao, Effects of strain rate and fiber waviness on the compressive behaviour of composite laminates, ICCM-12, Paris, France, July 5-9, 1999.

[8] H.-J. Chun, J.-Y. Shin and I.M. Daniel, Effects of material and geometric nonlinearities on the tensile and compressive behavior of composite materials with fiber waviness, Composites Science and Technology 61 (2001) 125-134.

[9] J. Mandell, D. Samborsky and L. Wang, Effects of fiber waviness on composites for wind turbine blades, International Sampe Symposium and Exhibition, SAMPE 2003, 2653-2666.

[10] T.W. Riddle, D.S. Cairns and J.W. Nelson, Characterization of Manufacturing Defects Common to Composite Wind Turbine Blades: Flaw Characterization, AIAA SDM Conference, Denver, Colorado, 2011.

[11] J. Wang, K. Potter, K. Hazra and M. Wisnom, Experimental fabrication and characterization of out-of-plane fiber waviness in continuous fiber-reinforced composites, J. Compos. Mater. 46 (2012) 2041-2053.

[12] M.R. Piggott, The effect of fibre waviness on the mechanical properties of unidirectional fibre composites: a review, Compos. Sci. Technol. 53 (1995) 201-205.

[13] T.-W. Chou, Flexible composites, Journal of Materials Science 24 (1989) 761-783.

[14] L. Wang, Effects of In-plane Fiber Waviness on the Properties of Composite Materials, M. S. Thesis, Montana State University, Bozeman, Montana, 2001.

[15] J.W. Nelson, T.W. Riddle and D.S. Cairns, Effects of defects in composite wind turbine blades: Round 2, Sandia National Laboratories, September, 2012.

[16] J.S. Lightfoot, M.R. Wisnom and K. Potter, Defects in woven preforms: formation mechanisms and the effects of laminate design and layup protocol, Compos Part A–Appl. Sci. Manuf. 51 (2013) 99-107.

[17] J.W. Nelson, D.S. Cairns and T.W. Riddle, Manufacturing Defects Common to Composite Wind Turbine Blades: Effects of Defects, Proceedings AIAA Aerospace Science Meeting, Wind Energy Symposium, 2011.

[18] S. Yurgartis, Measurement of small angle fiber misalignments in continuous fiber composites, Compos. Sci. Technol. 30 (1987) 279-293.

[19] A. Clarke, G. Archenhold and N. Davidson, A novel technique for determining the 3D spatial distribution of glass fibres in polymer composites, Compos. Sci. Technol. 55 (1995) 75-91.

[20] C. Creighton, M. Sutcliffe and T. Clyne, A multiple field image analysis procedure for characterisation of fibre alignment in composites, Compos Part A–Appl. Sci. Manuf. 32 (2001) 221-229.

[21] K.K. Kratmann, M. Sutcliffe, L. Lilleheden, R. Pyrz and O.T. Thomsen, A novel image analysis procedure for measuring fibre misalignment in unidirectional fibre composites, Composites Science and Technology 69 (2009) 228-238.

[22] R. Adams and P. Cawley, A review of defect types and nondestructive testing techniques for composites and bonded joints, NDT international 21 (1988) 208-222.

[23] R. Smith and B. Clarke, Ultrasonic C-scan determination of ply stacking sequence in carbon-fibre composites, Insight 36 (1994) 741-747.

[24] R.A. Smith, L.J. Nelson, M.J. Mienczakowski and R.E. Challis, Automated analysis and advanced defect characterisation from ultrasonic scans of composites, Insight-Non-Destructive Testing and Condition Monitoring 51 (2009) 82-87.

[25] A. Jüngert, Damage Detection in wind turbine blades using two different acoustic techniques, 7th fib PhD Symposium, Stuttgart, Germany, September 11-13, The NDT Database & Journal (NDT) 2008.

[26] J. Martín-Herrero and C. Germain, Microstructure reconstruction of fibrous C/C composites from X-ray microtomography, Carbon 45 (2007) 1242-1253.

[27] R.F. Anastasi, Investigation of fiber waviness in a thick glass composite beam using THz NDE, The 15th International Symposium on: Smart Structures and Materials & Nondestructive Evaluation and Health Monitoring, San Diego, California, March 09, International Society for Optics and Photonics 2008, 69340K-69348K.

[28] D. Francis, R. Tatam and R. Groves, Shearography technology and applications: a review, Measurement Science and Technology 21 (2010) 102001.

[29] C.-M. Kuo, K. Takahashi and T.-W. Chou, Effect of fiber waviness on the nonlinear elastic behavior of flexible composites, Journal of Composite Materials 22 (1988) 1004-1025.

[30] H. Hsiao, S. Wooh and I. Daniel, Fabrication methods for unidirectional and crossply composites with fiber waviness, Journal of advanced materials 26 (1995) 19-26.

[31] M.R. Wisnom and J.W. Atkinson, Compressive failure due to shear instability: experimental investigation of waviness and correlation with analysis, J. Reinf. Plast. Compos. 15 (1996) 420-439.

[32] B. Khan, K.D. Potter and M.R. Wisnom, Simulation of process induced defects in resin transfer moulded woven carbon fibre laminates and their effect on mechanical behaviour, The 8th International Conference on Flow Processes in Composite Materials (FPCM8), Douai, France, 2006.

[33] P. Davidson, A.M. Waas, C.S. Yerramalli, K. Chandraseker and W. Faidi, Effect of Fiber Waviness on the Compressive Strength of Unidirectional Carbon Fiber Composites, 53rd AIAA/ASME/ASCE/AHS/ASC Structures, Structural Dynamics and Materials Conference, Honolulu, Hawaii, April, 2012, 23-26.

[34] A. Mrse and M. Piggott, Compressive properties of unidirectional carbon fibre laminates: II. The effects of unintentional and intentional fibre misalignments, Composites Science and Technology 46 (1993) 219-227.

[35] M.R. Wisnom and J. Atkinson, Fibre waviness generation and measurement and its effect on compressive strength, J. Reinf. Plast. Compos. 19 (2000) 96-110.

[36] D.P. Avery, D.D. Samborsky, J.F. Mandell and D.S. Cairns, Compression strength of carbon fiber laminates containing flaws with fiber waviness, ASME Wind Energy Symposium, ASME/AIAA, AIAA, Nashville, 2004, 54-63.

[37] P. Duangmuan, Layer Waviness Effects on Compression Strength of Composite Laminates: Progressive Failure Analysis and Experimental Validation, PhD thesis, The University of Utah, Salt Lake City, 2012.

Advanced Materials Research Vol. 936 (2014) pp 89-94
© (2014) Trans Tech Publications, Switzerland
doi:10.4028/www.scientific.net/AMR.936.89

Effect of Crosslinker Type on the Properties of Surface-crosslinked Poly(sodium acrylate) Superabsorbents

Yun Xiong[1,2, a], Xu Zhang[2,b] and Mingzhu Liu[2,c*]

[1] School of Chemical Engineering and Pharmacy, Wuhan Institute of Technology, Wuhan 430073, China

[2] College of Chemistry and Chemical Engineering, Lanzhou University, Lanzhou 730000, China

[a]xiongy@lzu.edu.cn, [b] 0505zhangxu@163.com, [c]mzliu@lzu.edu.cn

Keywords: superabsorbent, crosslinker type, acrylic acid, compressive strength, salt sensitivity.

Abstract. A series of poly(sodium acrylate) superabsorbents hydrogels were synthesized through aqueous solution using *N*,*N*-methylenebisacrylamide (NNMBA), pentaerythritol triacrylate (PETA), ethylene glycol dimethacrylate (EGDMA) and dimethyl diallyl ammonium chloride (DMDAAC) as crosslink agents separately to investigate the effect of crosslinker type on the properties of acrylic-based superabsorbents. Furthermore, the polymers were surface-crosslinked using trimethylolpropane triglycidyl ether to improve the properties of swollen hydrogel. The morphology of the samples was characterized by scanning electron microscope (SEM). The swelling behaviors in 0.9 wt% NaCl aqueous solution and synthetic urine were investigated, and the compressive strength, salt sensitivity and water retention ability were also investigated. The results showed that the superabsorbent crosslinked by PETA which was a three-functional agent had the most water absorbency under load and the highest compressive strength compared with others, while the superabsorbent crosslinked by DMDAAC which was a cationic crosslinker had the best salt resistance and the most water absorbency under atmospheric pressure.

Introduction

Superabsorbent polymers (SAPs), which can absorb and retain large amounts of aqueous fluids even under some pressure due to the exist of hydrophilic groups in their three-dimensional networks, are well known materials with everyday applications such as personal hygiene products, soil and water conservation, drug-delivery systems and so on [1,2]. Among them, poly(acrylic acid) (PAA) has long been the most important part of the absorbent resin because of its low costs, relatively simple technology and the stable quality in use. However, the poor salt-resisting, as well as the low gel strength, resilience, dispersion and surface-drying, turns out to be ubiquitous in the traditional preparation of PAA SAPs, which seriously affects the quality of products and restricts their wide application.

For the past few years, a number of effective methods have been taken out to improve overall performance of poly(acrylic acid) SAPs such as being copolymerized with other monomers [3], grafted to the natural macromolecules [4], and composited with inorganic substance [5]. Besides that, some researchers focused on the change of crosslinkers because the structure and amount of crosslinking agent also played an important role in the properties of SAPs [6,7,8]. In this work, three kinds of crosslinkers with different structures and functional groups (shown in Fig. 1), which have never or seldom been used in the preparation of SAPs, were used compared with the most common crosslinker NNMBA to investigate the effect of crosslinker structure on the properties of poly(sodium acrylate) superabsorbents. Among which, pentaerythritol triacrylate (PETA) is a three-functional agent while the others are two-functional agents, ethylene glycol dimethacrylate (EGDMA) has hydrophilic ester group, and dimethyl diallyl ammonium chloride (DMDAAC) is a cationic crosslinker. We hope to find out excellent crosslinking agents to improve the performance of acrylic-based superabsorbents.

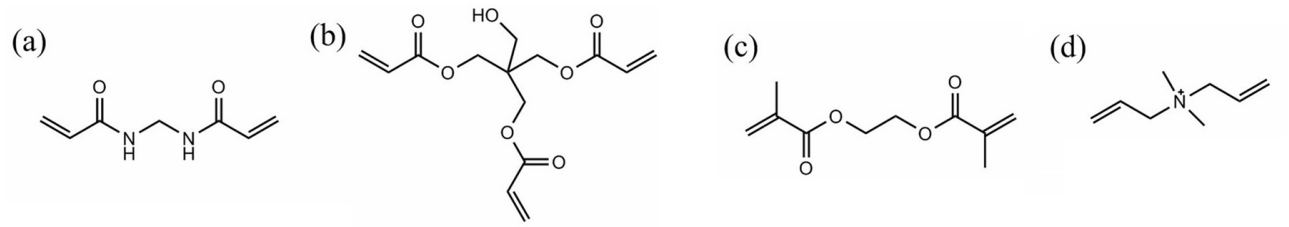


Fig. 1 Chemical structure of crosslinkers: (a) NNMBA, (b) PETA, (c) EGDMA, (d) DMDAAC.

Experimental

Materials

Acrylic acid (AA, CP, Beijing Eastern Chemical Works, Beijing, China) was distilled under reduced pressure before use. *N*,*N*-methylenebisacrylamide (NNMBA, CP, Shanghai Chemical Reagent Co., Shanghai, China) was recrystallized with 95% ethanol before use. Pentaerythritol triacrylate (PETA, AR, Guangzhou Sunlake Trading Co., Ltd., Guangzhou, China), ethylene glycol dimethacrylate (EGDMA, AR, Afaaisuo Chemical Co., Ltd., Tianjin, China), dimethyl diallyl ammonium chloride (DMDAAC, 60% solution, Aladdin reagents Co., Ltd., Shanghai, China), trimethylolpropane triglycidyl ether (TMPTGE, industrial grade, Taizhou Whaley Synthetic Materials Co., Ltd., Jiangsu, China) and ammonium persulfate (APS, AR, Xi'an Chemical Reagent Factory, Xi'an, China) were used directly. Other reagents were of analytical grade and used without purification. All the solutions were prepared with distilled water.

Preparation of superabsorbent polymers (SAPs)

NaOH aqueous solution with the concentration of 6 mol/L was added slowly to 5mL acrylic acid (AA) for neutralization in a four-necked flask with ice-bath. Then, adding exact amounts of NNMBA and APS as well as distilled water to the flask and stirring until the materials dissolved completely. After being purged with nitrogen for half an hour, the reactor was heated to 75ºC and kept for 3 hours. The shredded products were dried at 80ºC in an oven to a constant weight and then milled through 26-60 mesh screens, which was noted as SAP01. The synthesis process of SAP02, SAP03 and SAP04 is similar to that of SAP01 just using PETA, EGDMA and DMDAAC as crosslinker instead of NNMBA respectively. All of the four SAPs were confirmed by FTIR. In order to improve the overall performances of superabsorbents, the samples were surface crosslinked with TMPTGE, and the final product was noted as SAP1, SAP2, SAP3 and SAP4, respectively.

Water Absorbency under Atmospheric Pressure

The accurately weighed 0.200g sample was immersed in 0.9 wt% NaCl aqueous solution or synthetic urine [9] and allowed to swell at the temperature of 20ºC under atmospheric pressure for 1 hour. The swollen hydrogel was filtrated through an 80-mesh nylon screen for 10 minutes to remove the excess water and weighed. Each sample was measured three times and the average value was selected as the final result. The water absorbency (WA) was calculated by the following equation:

$$WA = (M - M_0) / M_0 \quad (1)$$

Where, M is the weight of swollen hydrogel and M_0 is the weight of dry sample.

Water Absorbency under Load (WA_p)

Accurately weighed 0.400g sample was evenly spread in the bottom of a plastic tube with the diameter of 25.9mm and the height of 35.0mm, which sealed by a 240-mesh polyester fabric at one end. And then a polytetrafluoroethylene cylinder with the diameter of 25.3mm and the mass of 106.4g was loaded on the sample and placed in a hollow porous support which in a beaker. Afterwards, 0.9 wt% NaCl aqueous solution or synthetic urine was added into the beaker making sure the liquid level high enough to immerse the sample but below the top edge of the plastic tube about 0.5cm. Non-absorbed liquid was removed and the plastic tube with the swollen hydrogel was weighed after 1 h.

Each sample was measured three times and the average value was selected as the final result. The water absorbency of sample in 0.9 wt% NaCl aqueous solution or synthetic urine (WA_p) was calculated using the following equation:

$$WA_p = (M_2 - M_1 - M_0) / M_0 \quad (2)$$

Where, M_2 is the weight of plastic tube with swollen hydrogel, M_1 is the weight of plastic tube and M_0 is the weight of dry sample.

Measurements of the Compressive Strength of the Hydrogels

Uniaxial compression measurements [10] were performed on the hydrogels swollen in synthetic urine to determine the compressive strength, and the apparatus used were showed in Fig. 2. Briefly, 1.000 g of the swollen hydrogel was placed in a sample cell, while a polytetrafluoroethylene rod was put on the hydrogel. The initial height h_0 was recorded after the sample was compressed with the initial load for 5 min. Then the pressure was increased to m_i and the corresponding height h_i was noted after compressing for 5 min. Each sample was measured three times and the average value was selected as the final result. The modulus E was determined from the slope of the plot of m_ig/A versus h_i/h_0. A was cross-sectional area of the sample cell.

Water Retention Test

A piece of swollen gel (noted as M_0) was spreaded in the bottom of a 200 mL beaker and placed in an oven at 37℃. The gel was weighed every 30 minutes (noted as M_i) and the water retention rate (WR) was calculated by the following equation (M_d is the weight of xerogel):

$$WR = (M_0 — M_i) / (M_0 — M_d) \quad (3)$$

Results and Discussion

Water Absorbency in NaCl aqueous solution and synthetic urine

Fig. 2 shows the water absorbency in NaCl aqueous solution and synthetic urine with various amounts of crosslinkers under atmospheric pressure. Water absorbency of polymer shows a relation to the crosslinking density, ionic osmotic pressure, and affinity of the hydrogel with water. The crosslinker content which influence the crosslinking density also plays an important role in the formation of a three-dimensional network and significantly affects the water absorbency of the SAPs. When the crosslinker content was lower, the swollen hydrogel was poorly crosslinked and became slimy gel without good dimensional stability, for the soluble noncrosslinked polymer dissolved in water and the network was insufficiently formed. As the crosslinker content increased, more crosslinked points in polymeric chains occurred, causing a higher crosslinking density and more insoluble polymers to hold the water, and the swelling capacity increased up to a certain level. However, when the crosslinker content increased high enough, the excessive crosslinker would result in a decrease in the space between the polymer chains and would lead to a highly crosslinked rigid structure that could not be expanded to hold a large quantity of water [11,12].

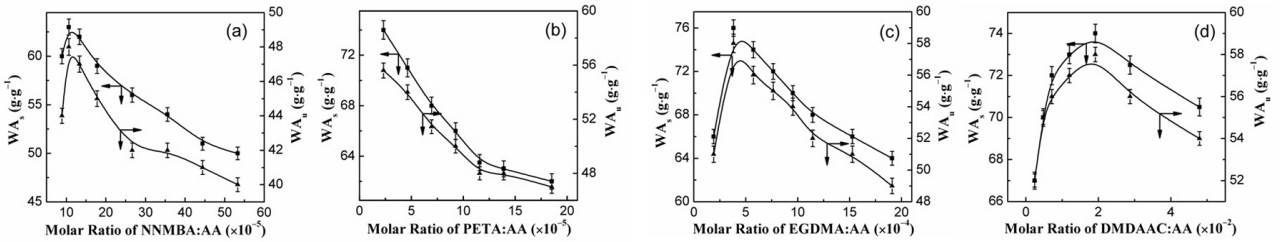


Fig. 2 Effect of the crosslinker amount on the water absorbency of superabsorbents. (a) NNMBA as crosslinker, (b) PETA as crosslinker, (c) EGDMA as crosslinker, (d) DMDAAC as crosslinker.

Surface morphology analysis of superabsorbents

Fig. 3 shows the surface structures of dried hydrogels. The cross-sections of the samples exhibited pores architecture, which was the typical structure of hydrophilic polymer. Compared with the photographs of other samples, the pore size of SAP2 appeared more uniformly, and the porous structure was well-distributed and more difficult to collapse. This was because there were three reactive functional groups in the PETA molecule, and the distance between double bonds was large

enough, leading to the small steric effect and high reactivity, which was usually used to synthetize multibranched polymers. The pore size of SAP1 was small and fragile, while the pore size of SAP2 was big and with uneven distribution. That was attributed to the steric effect of methyl in the EGDMA molecule, which influenced the crosslinking effect. The morphology of SAP4 had more linear structure, it could be speculated the crosslinking effect of DMDAAC was not good as others. These were verified subsequently in the water absorbency and mechanical strength experiments.

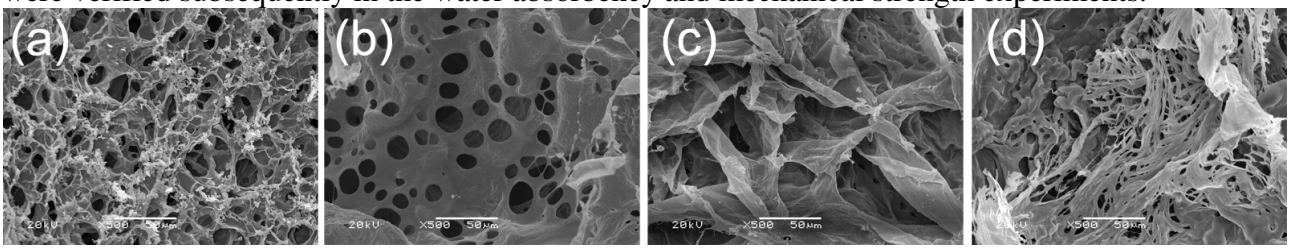


Fig. 3 SEM photographs of dried superabsorbents: (a) SAP1, (b) SAP2, (c) SAP3, (d) SAP4.

Swelling kinetics in synthetic urine

Fig. 4(a) displays the swelling kinetic behaviors of the optimized final products synthesized using NNMBA, PETA, EGDMA and DMDAAC separately as crosslinker in synthetic urine. The swelling increased with time and reached a limiting value which is the swelling equilibrium in 20 minutes, which sugguested it was suitable to allow the samples swollen more than 30 minutes to determine the swelling ratio in each experiment. The absorption rate of superabsorbent was mainly influenced by swelling ability, surface area, particle size and density of the polymer [13]. It can be seen from figure 8 that the water absorption and swelling rate of the four samples are close. That's because the amount of crosslinkers is relatively less than that of structural units in the polymer, and the different type of crosslinkers just change the crosslinking density but not the hydrophily of network. Plus, it is noteworthy that the equilibrium water absorption of the four samples in synthetic urine are all less than 60 g g^{-1}, which indicates the change of crosslinker can not improve the salt resistance of superabsorbents fundamentally.

Salt sensitivity

In order to further study the salt sensitivity of superbasorbents prepared using different crosslinkers, the effect ionic strength on the water absorbency of samples in saline solution has been investigated and the results are shown by the water-absorbing curves presented in fig. 4(b). The trends of the water-absorbing curve of superabsorbents crosslinked by different crosslingers are similar, and decrease as the ionic strength of the saline solution increases. Generally, the swelling ability of anionic hydrogels in various salt solutions is appreciably decreased in comparison with the swelling values in distilled water [14]. This well-known undesired swelling loss is often attributed to a charge-screening effect of the additional cations causing a nonperfect anion–anion electrostatic repulsion. Therefore, according to the Donnan membrane equilibrium theory, the osmotic pressure resulting from the mobile ion concentration difference between the gel and aqueous phases decreased, and consequently, the absorbency decreased. In addition, SAP4 had the best salt resistance among all of the samples as shown in fig. 4(b). That is maybe attributed to the nitrogen cationic in DMDAAC crosslinker.

Water Retention Capacity of Superabsorbents

It is important to investigate the water retention capacity of SAPs in view of practical applications. In this work, water retention (WR) of superabsorbent swollen in synthetic urine was determined at 37°C which closes to the body temperature. Fig. 4(c) shows that the water retention curves of the four samples all decreases with time, which is due to the evaporation of water in the swollen hydrogel. The water in the hydrogel can be classified into bound water, half-bound water and free water, and the free water has high mobility and can easy be lost. The percentages of bound water and half-bound water are related to the number of hydrophilic groups in a unit volume in the SAPs [15]. In our work, although the type of crosslinker used in the preparation of SAPs is different, monomer and monomer amount in all four samples is the same, which leads to the water retention capacity of the four samples

is similar to each other. This sugguests that the type of crosslinker has little effect on the water retention capacity. By the figure it also can be seen that even dried at 37°C for 7 hours, the water retention is still up to 80%, which is expected to be used in personal care materials and agriculture.

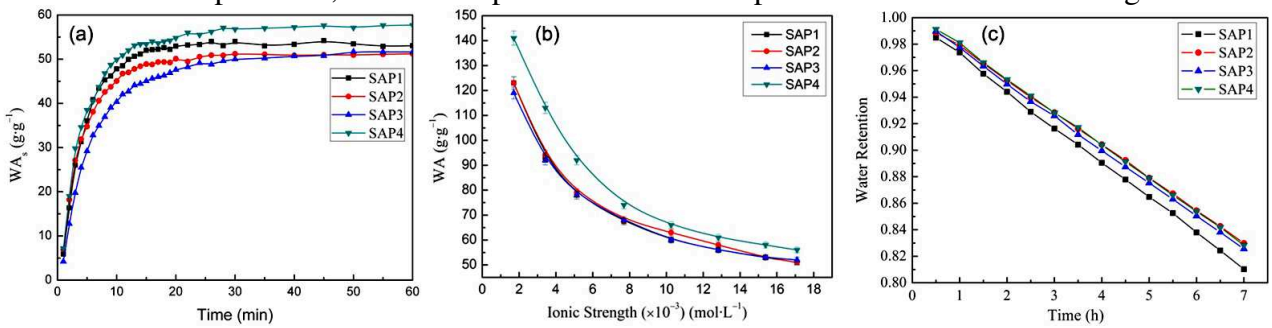


Fig. 4 (a) Swelling kinetic behaviors of the optimized final products in synthetic urine, (b) Effect of the ionic strength of the NaCl solution on the water absorbency of superabsorbents, (c) Water retention capacity of superabsorbents at 37°C.

Mechanical properties of the SAPs

Mechanical strength is an extremely important property for the application of hydrogels, usually given in the patent literature and technical data sheets offered by industrial SAP manufacturers[16,17]. The water absorbency under load (WA_{ps} and WA_{pu}) and compressive strength (compressive modulus E) is measured to denote mechanical strength of hydrogels, and the data of different samples are listed in Table 1. The influences types of crosslinker on compressive strength of the hydrogels have been studied. The results showed that SAP2 which was crosslinker by PETA maintains the highest WA_p and E among the four kinds of samples. This could be attributed to the increasing of the cross-linking points. There are three reactively double bonds in one PETA molecule, but only two in others.

Table 1 The water absorbency under load (WAps and WApu) and compressive strength (E) of superabsorbent hydrogels using different crosslinkers.

Parameters \ Sample code	SAP1	SAP2	SAP3	SAP4
WA_{ps} ($g \cdot g^{-1}$)	11	12	8	6
WA_{pu} ($g \cdot g^{-1}$)	10	11	7	6
E ($\times 10^4$) (Pa)	11.49	12.06	5.92	4.77

Summary

In this work, effect of crosslinkers types on the superabsorbent performance has been studied, and four kinds of crosslinkers, NNMBA, PETA, EGDMA and DMDAAC have been used to synthesize poly(sodium acrylate) superabsorbent polymers. SEM photograghs showed the samples crosslinked by PETA which was a three-functional agent had the uniform pore size, and the porous structure was well-distributed and more difficult to collapse, which led to the most water absorbency under load and the highest compressive strength compared with others. And at the meanwhile, due to the nitrogen cationic in DMDAAC crosslinker, the superabsorbent crosslinked by DMDAAC had the best salt resistance and the most water absorbency under atmospheric pressure.

Acknowledgement

This work is supported by the National Natural Science Foundation of China (No. 21202076), Special Doctorial Funds of the Ministry of Education of China (No. 20110211120015) and the Fundamental Research Funds for the Central Universities (No. lzujbky-2013-197).

References

[1] K. Kabiri, H. Omidian, M.J. Zohuriaan-Mehr, S. Doroudiani, Superabsorbent Hydrogel Composites and Nanocomposites: A Review, Polym. Composite. 32 (2011) 277-289.

[2] M. J. Zohuriaan-Mehr, H. Omidian, S. Doroudiani, K. Kabiri. Advances in non-hygienic applications of superabsorbent hydrogel materials. J. Mater. Sci. 45 (2010) 5711-5735.

[3] Y.H. Zhang, L.M. Wang, X.H. Li, Salt-resistant superabsorbents from inverse-suspension polymerization of PEG methacrylate acryamide and partially neutralized acrylic acid, J. Polym. Res., 18 (2011) 157-161.

[4] G.B. Marandi, S. Hariri, G.R. Mahdavinia, Effect of hydrophobic monomer on the synthesis and swelling behaviour of a collagen-graft-poly[(acrylic acid)-co-(sodium acrylate)] hydrogel. Polym. Int. 58 (2009) 227-235.

[5] P.S. Liu, L. Li, N.L. Zhou, et al., Synthesis and properties of a poly(acrylic acid)/montmorillonite superabsorbent nanocomposite. J. Appl. Polym. Sci. 102 (2006) 5725-5730.

[6] H. Omidian, S.A. Hashemi, P.G. Sammes, I.Meldrum, A model for the swelling of superabsorbent polymers, Polymer 39 (1998), 6697-6704.

[7] K. Kabiri, H. Omidian, S.A. Hashemi, et al., Synthesis of fast-swelling superabsorbent hydrogels: effect of crosslinker type and concentration on porosity and absorption rate. Eur. Polym. J. 39 (2003) 1341-1348.

[8] M. Sun, J. Zhang, Y. Gao, X. Xie. The effect of crosslinkers on superabsorbents. Acta Polym. Sin. (2004) 595-599.

[9] C. Chang, B. Duan, J. Cai, L. Zhang, Superabsorbent hydrogels based on cellulose for smart swelling and controllable delivery, Eur. Polym. J. 46 (2010) 92–100.

[10] H.L. Liu, M.Z. Liu, L.J. Zhang, L.W. Ma, J. Chen, Y.J. Wang. Dual-stimuli sensitive composites based on multi-walled carbon nanotubes and poly(N,N-diethylacrylamide-co-acrylic acid) hydrogels. React. Funct. Polym. 70 (2010) 294–300.

[11] L. Zhao, Y. Xiong, M.Z. Liu, X.H. Qi, Study on superabsorbent of maleic anhydride/acrylamide semi-interpenetrated with poly(vinyl alcohol), Polym. Adv. Technol. 21 (2010) 483–489.

[12] Y.H. Zhang, L.M. Wang, X.H. Li, P.X. He, Salt-resistant superabsorbents from inverse-suspension polymerization of PEG methacrylate, acryamide and partially neutralized acrylic acid, J. Polym. Res. 18 (2011) 157–161.

[13] J.E. Elliott, M. Macdonald, J. Nie, C.N. Bowman, Structure and swelling of poly(acrylic acid) hydrogels: effect of pH, ionic strength, and dilution on the crosslinked polymer structure. Polymer, 45 (2004) 1503-1510.

[14] G.B. Marandi, N. Sharifnia, H. Hosseinzadeh, Synthesis of an alginate–poly(sodium acrylate-coacrylamide) superabsorbent hydrogel with Low salt sensitivity and high pH sensitivity, J. Appl. Polym. Sci. 101 (2006) 2927-2937.

[15] G.B. Marandi, S. Hariri, G.R. Mahdavinia, Effect of hydrophobic monomer on the synthesis and swelling behaviour of a collagen-graft-poly[(acrylic acid)-co-(sodium acrylate)] hydrogel, Polym. Int., 58 (2009) 227-235.

[16] M.R.Moura, F.A.Aouada, S.L.Favaro, E. Radovanovic, A.F. Rubira, E.C. Muniz, Release of BSA from porous matrices constituted of alginate-Ca^{2+} and PNIPAAm-interpenetrated networks, Mater. Sci. Eng. C 29 (2009) 2319-2325.

[17] A. Pourjavadi, M. Ayyari, M.S. Amini-Fazl, Taguchi optimized synthesis of collagen-g-poly (acrylic acid)/kaolin composite superabsorbent hydrogel, Eur. Polym. J. 44 (2008) 1209-1216.

Advanced Materials Research Vol. 936 (2014) pp 95-98
© (2014) Trans Tech Publications, Switzerland
doi:10.4028/www.scientific.net/AMR.936.95

Phase separation in thermosetting blends of epoxy resin with PS-*b*-PCL and PI-Si block copolymers

Jindian Ding[a] , Weizhen Li[b*], Tianqi Jiang[c], Zonglian Xia[d],

Wenjun Gan[e*]

School of Chemistry and Chemical Engineering, Shanghai University of Engineering Science

Shang hai, 201620, China

[a]dingjindian@163.com , [b]liweizhen@sues.edu.cn, [c]943296107@qq.com,[d]838900107@qq.com

[e]wjgan@sues.edu.cn

Keyword: atomic transfer radical polymerization; amphiphilic diblock polymer; polystyrene; poly(ε-caprolactone)

Abstract: Amphiphilic diblock copolymer poly(styrene-*b*-ε-caprolactone) were synthesized. Firstly, polystyrene was synthesized via sequential atomic transfer radical polymerization (ATRP), and then the tetra hydro lithium aluminum (LiAlH4) was used as a reducing agent in tetra hydro (THF) to reduce polystyrene to the pre-polymer monohydroxy-terminated polystyrene (PS-OH). As following, amphiphilic diblock were obtained by ring opening polymerization. And the structure of diblock polymer was investigated by FTIR. Furthermore, the block copolymers were added into the mixture of epoxy and Me-THPA. And the optical microscopy(OM) shows that the microphase separation occured in this system and the PS-*b*-PCL can promote the phase separation in the system.

Introduction

Well-defined compositions, architectures, and functionalities copolymers were usually synthesized by ionic polymerization, free radical polymerization and living/controlled free radical polymerization[1,2]. Typically living/controlled free radical polymerization are employed because the ability of controlling the copolymer architectures of the free radical polymerization are weak and the monomers of ionic polymerization are usually limited [3,4].

Poly(styrene-b-ε-caprolactone) is one of the amphiphilic copolymer with well-defined composition and architecture[5,6]. One of the main method is to synthesize PCL macroinitiator and use click chemistry to obtain the block copolymer[7]. Another method is to synthesize PS through free radical polymerization or azide reaction to get the hydroxyl terminated polystyrene, which react with ε-caprolactone as followed[8].

Roderic P. Quirk[9] prepared hydroxy-terminated styrene (HO-PS-OH) by anionic polymerization，which used propylene oxide , sodium naphthalene and THF as initiator.

Z.Yin[10] synthesized hydroxy-terminated initiator by 2-bromoisobutyryl bromide and ethylene glycol, then atom transfer radical polymerization was used to obtain hydroxy-terminated PS.

Wenchun Fan[11] synthesized star-shaped macroinitiators(PS) through pentaerythritol tetrakis(2-bromoisobutyrate). They obtained well-defined architecture copolymers through synthesis of well-defined initiator. After mixing with diglycidyl ether of bisphenol A (DGEBA), reaction-induced phase separation occurred in the thermosetting blends of epoxy.

In this paper, PS-b-PCL was synthesized. At frist, polystyrene was synthesized via sequential atomic transfer radical polymerization (ATRP). A simple reduction reaction with LiALH4 was used to obtain monohydroxyl terminated polystyrene(PS-OH). As followed, amphiphilic diblock were

obtained by ring opening polymerization. And the block copolymer was mixed with DGEBA and polyimide-siloxane(PI-siloxane). It was found that the block copolymer is able to promote the system's phase separation of the thermosetting blends of epoxy resin with PI-Si block copolymers.

Materials

Diglycidyl ether of bisphenol A (DGEBA) with epoxide equivalent weight of 182-192 was purchased from DOW Chemical Company. The curing agent is methyl tetrahydrophthalic anhydride (Me-THPA), which is supplied by Shanghai Reagent Co.,China. Polyimide-siloxane(20%) (Siltem STM1500) was supplied by Sabic innovative plastics.

Styrene (St), ε-caprolactone and LiAlH4 were purchased from Shanghai Reagent Co.,China as analytically pure grade.

Synthesis of the Block Copolymer PS-b-PCL

For the synthesis of PS-b-PCL, a 200ml round-bottom flask, mono-functional initiators, ethyl bromoacetate, CuBr, Bpy, styrene were charged. The system was connected to a standard Schlenk line system. The reactive mixture was degassed via three pump-freeze-thaw cycles and then immersed in a thermostated oil bath at 110 ºC. After the polymerization, the Br-PS-COOC2H5(Mn = 4000 g /mol, PS-Br) was obtained. Then the LiAlH4 was used as a reducing agent in THF to reduce polystyrene to the pre-polymer monohydroxy-terminated polystyrene (PS-OH). By using PS-OH as an initiator and Sn(OEt)2 as a catalyst, the mediate controlled ring-opening polymerization of ε-caprolactone(ε-CL) (ROP) leaded to the block copolymer polystyrene-b-poly(ε-caprolactone) (PS-b-PCL, Mn= 9600 g /mol).

FTIR of the Synthesized Copolymers

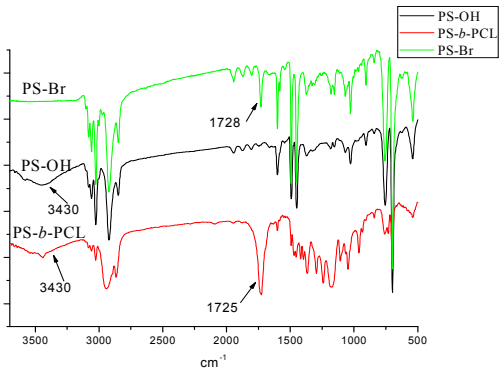


Fig.1. FTIR of Polymers Synthesized

Fig.1 shows the FTIR spectra of the macroinitiators and the block copolymer. The peaks at 700 cm-1 and 750 cm-1 in the PS-Br spectrum are consistent with stretching vibration of benzene and at 1450 cm-1,1490 cm-1are consistent with bending vibration. And the peak at 1728 cm-1 is consistent with the stretching vibration of C=O. In the spectrum of PS-OH, the peak at 1728 cm-1 disappeared. And meanwhile, the peak at 3430 cm-1 appeared, which means monohydroxy-terminated polystyrene was obtained. These spectra indicate that PS-b-PCL was successfully synthesized

Effect on the Phase Separation

DGEBA, Me-THPA, PS-b-PCLand PI-siloxane were mixedand investigated using OM. It shows that the PS-b-PCL can promote phase separation in the system(Fig.2).

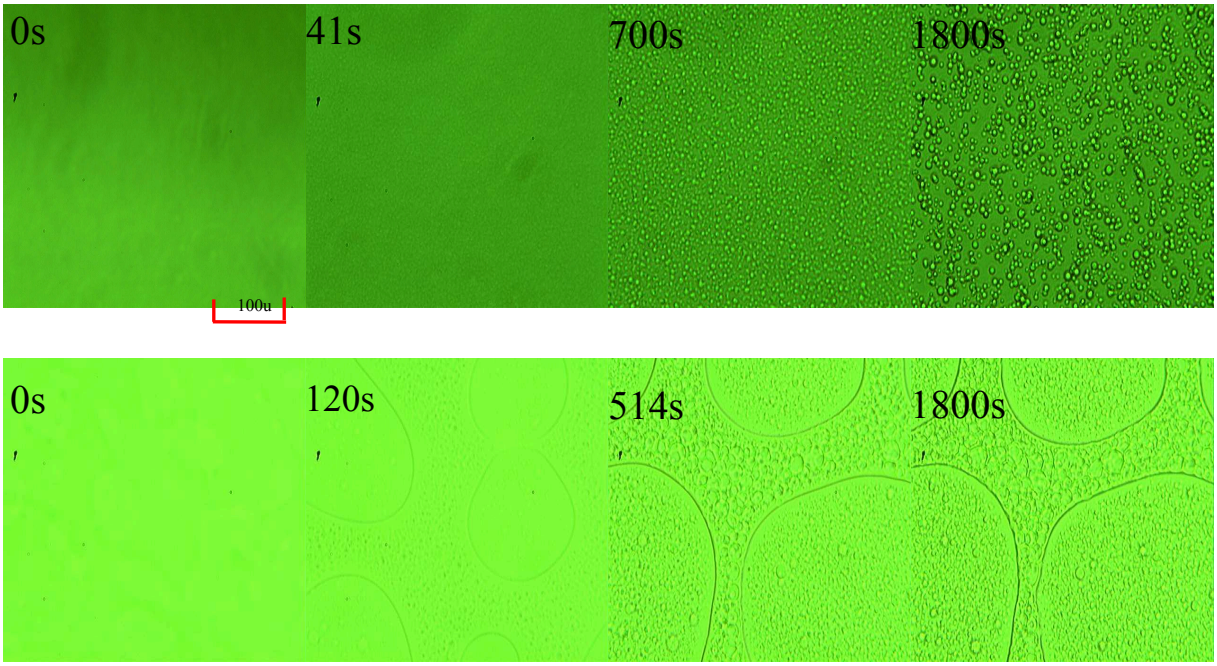


Fig.2 OM images of the phase morphology development of DM-AS1020 system cured at 150℃;the frist group of pictures are PI-siloxane 20 phr and the other group of pictures are PI-siloxane 20 phr and PS-b-PCL 10 phr.

Those images cleared showed that reaction-induced separation occurred in the system, and with the block copolymer PS-b-PCL added, phase separation changed significantly. The dispersed phase alter to reverse phase.

Conclusion

Monohydroxy-terminated polystyrene (PS-OH) was obtained through a simple reduction reaction by using LiAlH4 as a reducing agent in THF. The phase separation of the blend of epoxy with PS-b-PCLand PI-siloxane were investigated. It was found that PS-b-PCL can promote the phase separation in the system.

Acknowledgment

This work is supported by the foundation of Shanghai University of Engineering Science innovation project of post-graduate (2012yjs23) and innovation project of graduate (A-0523-12-01K176).

References

[1] J.S. Wang.K. Matyjaszewski. "Living" /controlled radical polymerization transition-metal catelyzed atom transfer radical polymerization in the presence of a conventional radical initiator. Macromolecule. 28(1995)7572- 7575.

[2] M. Kamigaito, T. Ando, M. Sawamoto. Metal-Catalyzed Living Radical Polymerization. Chemical Reviews.101(2001)3689-3746.

[3] D. Han,X. Tong,Y. Zhao. Block copolymer micelles with a dual-stimuli-responsive core for fast or slow degradation. Langmuir.28 (2012)2327-2331.

[4] F.S. Bates, M.A. Hillmyer, T.P. Lodge,C.M. Bates,K.T. Delaney,G.H. Fredrickson. Multiblock Polymers: Panacea or Pandora's Box. Science . 336(2012)434-440.

[5] F.L. Meng,Z.G. Xu,S.X. Zheng.Microphase Separation in Thermosetting Blends of Epoxy Resin and Poly(ε-caprolactone)-block-Polystyrene Block Copolymers. Macromolecules. 41(2008) 1411-1420.

[6] Y. Hu , Z.P. Jiang , R. Chen , W.Wu; X.Q. Jiang.Degradation and Degradation—Induced Re-Assembly of PVP-PCL Micelles.Biomaeromolecules.11(2010)481488.

[7] G.K. Such, A.P.R. Johnston, K. Liang,F. Caruso. Synthesis and functionalization of nanoengineered materials using click chemistry.Progress in Polymer Science.37 (2012)985-1003.

[8] R.P. Quirk, G.M. Liza´rraga.Investigation of the Reaction of Poly(styryl)lithium with Propylene Oxide. Macromolecules. 31(1998)3424-3430.

[9] W.C. Fan,S.X. Zheng.Reaction-induced microphase separation in thermosetting blends of epoxy resin with poly(methyl methacrylate)-block-polystyrene block copolymers: Effect of topologies of block copolymers on morphological structures.Polymer. 49(2008)3157–3167.

[10] Z. Yin, C. Koulic, C. Pagnoulle,R. Jerome. Reactive Blending of Functional PS and PMMA: Interfacial Behavior of in situ Formed Graft Copolymers. Macromolecules.34(2001)5132-5139.

[11] W.C. Fan, L. Wang, S.X. Zheng. Double Reaction-induced Microphase Separation in Epoxy Resin Containing Polystyrene-block-poly(ε-caprolactone)-block-poly(n-butyl acrylate) ABC Triblock Copolymer. Macromolecules.43(2010)10600-10611.

CHAPTER 2:

Ceramics and Functional Materials

Advanced Materials Research Vol. 936 (2014) pp 101-104
© (2014) Trans Tech Publications, Switzerland
doi:10.4028/www.scientific.net/AMR.936.101

Effect of PZN Addition on Piezoelectric and Ferroelectric Properties of $Pb(Zr_{1/2}Ti_{1/2})O_3$ Ceramics

Tanabat Promjun [1,a] ,Saksit Sukprasong [1,b] , Ladapak Chumprasert [2,c] , and Athipong Ngamjarurojana[3,d]

[1]Faculty of Science at Si Racha, Kasetsart University Si Racha Campus, Chon Buri

[2]Departments of Visual Design, Faculty of Fine Arts, Srinakharinwirot University, Bangkok

[3]Department of Physics and Materials Science, Faculty of Science, Chiang Mai University

[a] tanabat-promjun.cmu@hotmail.com, [b] saksitsukprasong@yahoo.com,

[c] deerdaow@gmail.com, [d] ngamjarurojana@yahoo.com

Keywords: PZN–PZT, Dielectric properties, Piezoelectric properties and Ferroelectric properties

Abstract: Ceramics in the $xPb(Zn_{1/3}Nb_{2/3})O_3$–$(1-x)Pb(Zr_{1/2}Ti_{1/2})O_3$ [xPZN–(1-x)PZT] solid solution system are expected to display excellent dielectric, piezoelectric, and ferroelectric properties in compositions close to the morphotropic phase boundary (MPB). The dielectric behavior of ceramics with $x = 0.1 - 0.5$ has been characterized in order to identify the MPB compositions in this system. Combined with x-ray diffraction analysis, dielectric, piezoelectric and ferroelectric measurements, it was consistently shown that an MPB exists around x = 0.3 in this binary system. When $x \leq 0.2$, the tetragonal phase dominates at ambient temperatures. In the range of $x \geq 0.4$, the rhombohedral phase dominates.

Introduction

Lead zirconate titanate, $Pb(Zr,Ti)O_3$ or PZT, is a well known piezoelectric that has been widely employed in a large number of sensing and actuating devices. PZT ceramics have very high Curie temperature (~ 390 ^oC). Lead zinc niobate, $Pb(Zn_{1/3}Nb_{2/3})O_3$ or PZN, which exhibits a perovskite structure and a Curie temperature of ~140 ^oC, is one of the most important relaxor ferroelectric materials with a high dielectric constant and large electrostrictive coefficient. They have excellent dielectric, piezoelectric and elastic properties suitable for wide range of practical applications [1-3]. Though the PZN-PZT based ceramics have excellent electrical properties, poor mechanical properties such as fracture strength and toughness have been reported [4].

Lead zirconate titanate, $Pb(Zr,Ti)O_3$ or PZT, is a well known piezoelectric that has been widely employed in a large number of sensing and actuating devices. PZT ceramics have very high Curie temperature (~ 390 ^oC). They have excellent dielectric, piezoelectric and elastic properties suitable for wide range of practical applications [1-3]. Lead zinc niobate, $Pb(Zn_{1/3}Nb_{2/3})O_3$ or PZN, which exhibits a perovskite structure and a Curie temperature ~ 140 ^oC, is one of the most important relaxor ferroelectric materials with a high dielectric constant and large electrostrictive coefficient [4-5].

Recent work by Fan and Kim [5-6] has shown that the perovskite phase of $Pb(Zn_{1/3}Nb_{2/3})O_3$ (PZN) ceramics was stabilized by adding a Ti-rich side tetragonal phase of $Pb(Zr_{0.47}Ti_{0.53})O_3$ (PZT) located across the morphotropic phase boundary (MPB). When 40% PZT was added, a rhombohedral perovskite phase was formed without any trace of the pyrochlore phase. The rhombohedral phase fraction decreased markedly with increasing PZT concentration. This work has shown promise in producing pure perovskite phase PZN–PZT ceramics with the conventional mixed-oxide method make the perovskite phase structure stable and give the significantly improved piezoelectric properties.

Vittayakorn et al. [7-8] has shown processing conditions on phase-pure perovskite PZN–PZT ceramics with the conventional mixed-oxide method and B-site precursor. The resulting ceramics were are expected to display excellent dielectric, piezoelectric, and ferroelectric properties in

compositions close to the morphotropic phase boundary (MPB). It was consistently shown that an MPB exists around x = 0.25 in this binary system. Excellent piezoelectric properties were found in 0.3PZN–0.7PZT, the composition closest to the MPB with a rhombohedral structure.

The aim of this work was to study the influence of vibro-milling methods (conventional mixed oxide) at synthesizing pyrochlore-free lead zinc niobate – lead zirconate titanate ceramics PZN-PZT ceramics, and to correlate the presence of pure perovskite phases with the dielectric, piezoelectric, and ferroelectric properties.

Experimental Procedure

The specimens studied in this research were fabricated according to the formula: $xPb(Zn_{1/3}Nb_{2/3})O_3$-$(1-x)Pb(Zr_{1/2}Ti_{1/2})O_3$, where x= 0.1-0.5 . Raw materials of PbO, ZrO_2, TiO_2, ZnO and Nb_2O_5 with >99% purity were used to prepare samples by a conventional mixed oxide process. The obtained mixture was used zirconia ball media with isopropanal as a medium in a polyethylene jar for 30 min via vibro-milling technique. The mixed slurry was dried and calcined at 900°C for 2h. The calcined powders were ball-milled again with additives and consolidated into disks of 12.5 mm diameter using isostatic pressing about 150 MPa. PbO-rich atmosphere sintering of the ceramics was performed in a high-purity alumina crucible at varied sintering temperature between 1150 to 1250 °C depending upon the compositions. The crystal structure and symmetry of the sintered bodies were examined by X-ray diffraction (XRD) and sintered densities were measured by the Archimedes method.

For electrical properties characterizations, Electrode (Dupont, QS 171) was printed on the lapped surfaces for electrode. The electrode was fired by infrared furnace at 850°C for 45 min. The specimens were poled in silicone oil at 150°C by applying a DC field of 3kV/mm for 30min. The dielectric properties of the sintered ceramics are studied as functions of both temperature and frequency with an automated dielectric measurement system. The computer-controlled dielectric measurement system consists of a precision LCR-meter (Hewlett Packard, model 4284A), a temperature chamber, and a computer system. The capacitance and the dielectric loss tangent are determined over the temperature range of 50 and 450 °C with the frequency ranging from 100 Hz to 100 kHz. The piezoelectric constant (d33) was measured using a quasi-static piezoelectric d33 meter (Model ZJ-3d, Institute of Acoustics Academic Sinica, China). The planar coupling coefficient (kp) and the mechanical quality factor (Qm) were determined by the resonance and anti-resonance technique using an impedance analyzer (Model HP4294A, Hewlett-Packard, CA). Ferroelectric switching measurements were made using a modified Sawyer-Tower circuit4 with a linear variable differential transducer (LVDT) for strain measurement, DSP lock-in amplifier (SR830, Stanford Research), high voltage power supply (TREK 609C-6, Trek), and computerized control and data acquisition.

Results and Discussion

The XRD patterns of $xPb(Zn_{1/3}Nb_{2/3})O_3$-$(1-x)Pb(Zr_{1/2}Ti_{1/2})O_3$, where x= 0.1-0.5 specimens with perovskite structure for all compositions are shown in Fig.1a. Perovskite phase formation, crystal structure and lattice parameter was determined by XRD at room temperature as a function of x. The pyrochlore phase was not observed in this system at all. The crystal symmetry for $Pb(Zn_{1/3}Nb2/3)O_3$ at room temperature is rhombohedral R3m with a lattice parameter a = 5.742 Å (JCPDS No. 22-0663) [9]. The crystal structure of $Pb(Zr_{1/2}Ti_{1/2})O_3$ at room temperature is tetragonal P4mm with a lattice parameter a = 4.031 Å and c = 4.145 Å (JCPDS No. 70-4057) [10]. Therefore, crystal symmetry should change from tetragonal to rhombohedral due to the effects of the increased PZN fraction. In these patterns, the crystal structure of the specimens are revealed by the claimed (002) and (200) peak are change to (202) peak. The perovskite structure appears to change from tetragonal to rhombohedral across the MPB with the increasing amount of PZN content around 0.3 mol%.

Fig.1b., XRD peak profiles of the (200) and (002) peaks at x = 0.1 and 0.2 were shown tetragonal phase. At the x = 0.3 composition, (202) peak is observed, indicating the co-existence of the rhombohedral and tetragonal phase. The (202) peak in compositions x = 0.4 and 0.5 was clearly observed, indicating that the crystal transformed into rhombohedral phase.

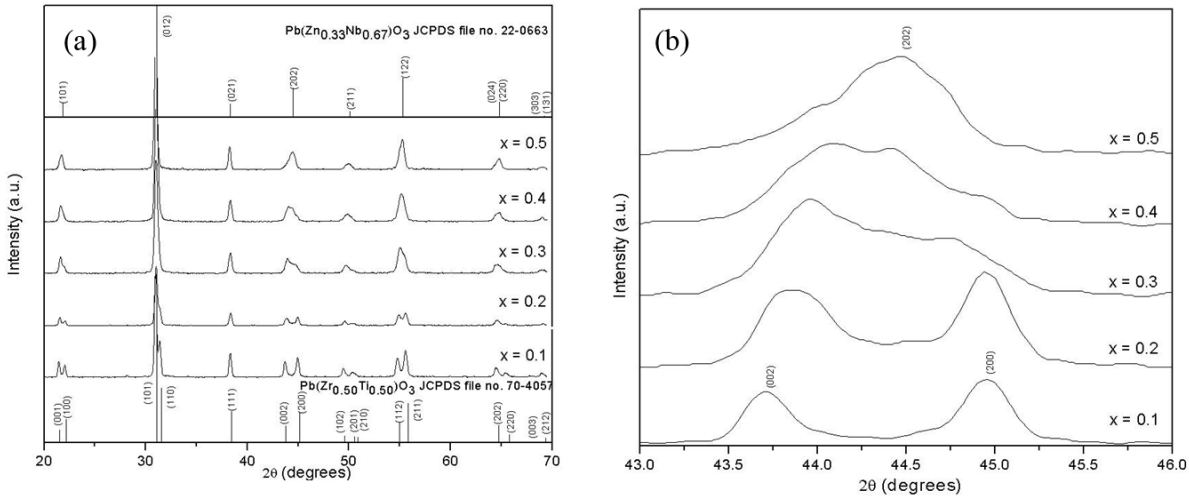


Fig.1. (a) XRD diffraction patterns of sintered *x*PZN-(1 − *x*)PZT ceramics.
(b) selected region of the diffraction patterns.

Density, dielectric constant (ε_r), electromechanical coupling factor (k_p), mechanical quality factor and piezoelectric constant (d_{33}) were plotted as a function of the amount of PZN content in Fig 2. The density was increased with the increase of PZN contents approximately from 7.7 to 7.9 g/cm3. Therefore, the improved piezoelectric and dielectric properties, which were observed, might be due to the increased density. In addition, this softening effect that could be confirmed by the increasing of ε_r , k_p and d_{33} value and decreasing of Q_m as shown in Fig 2.

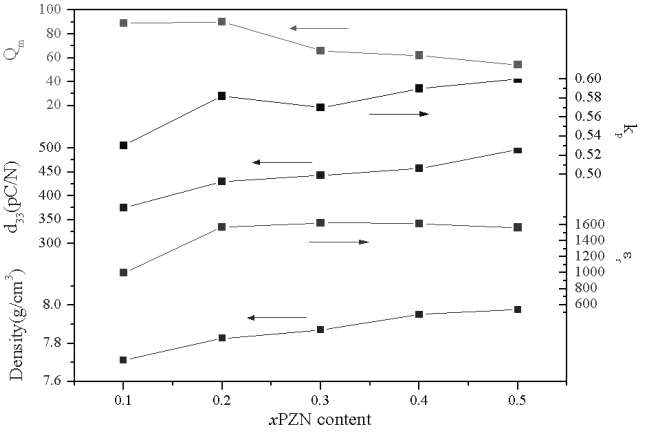


Fig.2. Density, dielectric constant (ε_r), piezoelectric constant (d_{33}), electromechanical coupling factor (k_p), and mechanical quality factor (Q_m) of xPZN-(1 −x)PZT ceramics

Table 1. P-E and s-E properties of xPZN-(1 − x)PZT ceramics

x	Ferroelectric properties (at 25 °C)					Loop squareness (R_{sq})	Strain % @ 4MV/m
	P_r (C/m^2)	P_s (C/m^2)	E_C (MV/m)	P_r/P_s	E_c/E_{max}		
0.1	0.196	0.211	2.35	0.929	0.575	1.648	0.189
0.2	0.287	0.300	1.97	0.957	0.482	1.483	0.278
0.3	0.321	0.337	1.31	0.953	0.320	1.607	0.397
0.4	0.375	0.393	1.19	0.954	0.291	1.736	0.432
0.5	0.403	0.420	0.99	0.960	0.242	1.719	0.508

The polarization-field (P–E) hysteresis loops of xPZN-(1 - x)PZT ceramics are shown in Fig. 3. To further assess ferroelectric characteristics in PZN-modified PZT ceramics, the ferroelectric

parameters. Strain of specimens as function of the electric filed was shown in Fig. 4. It was shown increasing strain and decreasing coercive field. As listed in Table 1, the strain level increased from 0.1589 in 0.1PZN–0.8PZT to reach the maximum value of 0.508 in 0.5PZN–0.5PZT at 4MV/m on applied field.

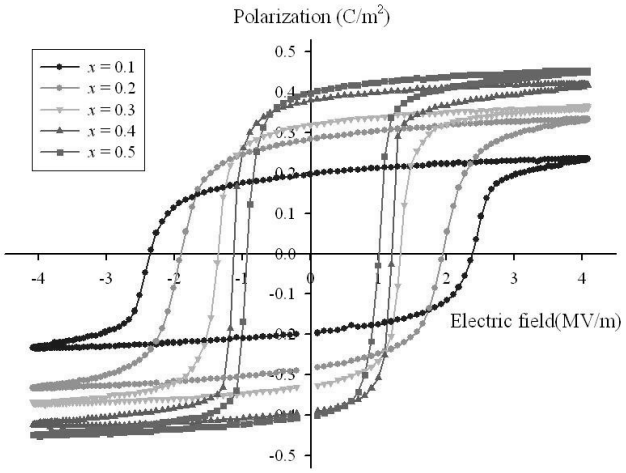


Fig.3. Polarization and electric filed of xPZN-(1 - x)PZT ceramics whereas x = 0.1- 0.5

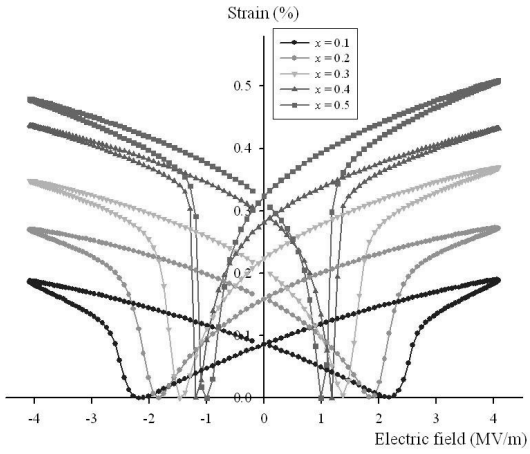


Fig.4 Strain and electric filed of xPZN–(1 − x)PZT ceramics whereas x = 0.1- 0.5

Conclusions

In this study, ceramics in the $xPb(Zn_{1/3}Nb_{2/3})O_3$–$(1 - x)Pb(Zr_{1/2}Ti_{1/2})O_3$ system (when x = 0.1, 0.2, 0.3, 0.4 and 0.5) were successfully prepared by a solid-state mixed-oxide technique. PZT ceramic was identified by XRD as a single-phase material with a perovskite structure having tetragonal symmetry, while the mixed compositions showed a gradual change from tetragonal to rhombohedral symmetry, with a possible morphotropic phase boundary (MPB) between the two phases near the 0.3PZN–0.7PZT composition. Most importantly, this study showed that the addition of PZN could improve the dielectric, piezoelectric and ferroelectric behavior in PZT ceramics.

Acknowledgments

This work was supported by the Thailand Research Fund (TRF), Commission on Higher Education (CHE) and Chiang Mai University. The authors are thankful to Laser and Applied Optics Research Laboratory for facility supports, Faculty of Science, Chiang Mai University for financial support. We also acknowledge Assoc. Prof. Dr. Supon Ananta and Assoc. Prof. Dr. Rattikorn Yimnirun for discussion and advised support.

References

[1] Y. Xu, Ferroelectric Materials and Their Applications, Elsevier Science Publishers, Amsterdam, The Netherlands (1991).
[2] K. Uchino and. J. R. Giniewicz, Micromechatronics, Marcel Dekker, New York, (2003).
[3] A.J. Moulson and J.M. Herbert, Electroceramics (2nd ed.), Wiley, New York (2003).
[4] K. Tajima, H. Hwang, M. Sando, K. Niihara, J. Eur. Ceram. Soc., , 19, (1999) 1179-1182.
[5] IEEE Standard on Piezoelectricity, IEEE Standard 176–1978. Institute of Electrical and Electronic Engineers, New York, (1978).
[6] Shannon R. D., Acta Crystal.A , 32, (1976), 751-767.
[7] J.X. Fang and Z. W. Yin, Physics of Dielectric, Science Press, Beijing, (1989).
[8] R. B. Atkin, and R. M. Fularath, J. Am. Ceram. Soc., 54, (1971), 265-270.
[9] Powder Diffraction File No. 22-0663. International Centre for Diffraction Data, Newton Square, PA, 2004.
[10] Powder Diffraction File No. 70-4057. International Centre for Diffraction Data, Newton Square, PA, 2004.

Advanced Materials Research Vol. 936 (2014) pp 105-109
© (2014) Trans Tech Publications, Switzerland
doi:10.4028/www.scientific.net/AMR.936.105

Effect of External Magnetic field on Dielectric Spectroscopy of Modified PZT Ceramics

Athipong Ngamjarurojana[1,a] Tanabat Promjun[2,b] and Apichart Limpichaipanit[1,c]

[1]Department of Physics and Materials Science, Faculty of Science, Chiang Mai University, Chiang Mai 50200

[2]Faculty of Science at Si Racha, Kasetsart University Si Racha Campus, Chon Buri 20230

[a]ngamjarurojana@yahoo.com, [b]tanabat-promjun.cmu@hotmail.com, [c]apichart_limpichaipanit@hotmail.com

Keywords: Dielectric spectroscopy, magnetoelectric, multiferroic

Abstract: This work involves the fabrication of high purity $Pb(Zr,Ti)O_3$ ferroelectric based in ceramic forms, and a study of the correlation between their compositions and electrical properties. In order to enhance multiferroic characteristics of $Pb(Zr,Ti)O_3$ ferroelectric based ceramics compound ferrites additives were added and the dielectric property as a function of magnetic field strength. Those are expected to explain multiferroic characteristics (ferroelectric-ferromagnetic coupling interaction) by quantitative evaluation which is the key to understand physical mechanism in coupling interaction to enhance multiferroic characteristics in materials.

Introduction

Multiferroics are materials in which magnetic and electric orders are strongly coupled, and have attracted increasing attention. Recent experimental research on multiferroics has shown that ferroelectricity and magnetism not only coexist in the same material but also couple so strongly that the magnetic degree of freedom can be manipulated by an electric field and the electric degree of freedom can be manipulated by a magnetic field. This property promises important technological applications in the future. Multiferroic magnetoelectric (ME) materials not only exhibit ferroelectricity and ferromagnetism simultaneously, but also the magnetoelectric coupling effect, which is defined as induced electric polarization under applied external magnetic field or induced magnetization by the external electric field [1,2]. Recently, multiferroic magnetoelectric materials have stimulated increasing interest due to the extensive and potential applications in sensors, memories, actuators and transducers [3]. The room-temperature single-phase multiferroic compounds are very scarce due to the fact that the ferroelectricity and ferromagnetism are incompatible.[1,4,5] However, the multiferroic magnetoelectric materials consisting of the alternating ferroelectric and ferromagnetic phases were proposed in the form of bulk or film. Recently, due to the incorporation into microelectronic technical applications, nanocomposite films on substrates have stimulated increasing interest.

Thus, in this study $Pb(Zr_{1/2}Ti_{1/2})O_3$ based ceramics were prepared and the influences of compound ferrites, such as Fe_2O_3 , $CoFe_2O_4$ and $Pb(Fe_{1/2}Nb_{1/2})O_3$ (PFN), addition on structure and dielectric properties of the ceramics were investigated, which are especially important from the viewpoint of the development of practical magnetoelectric materials.

Experimental Procedure

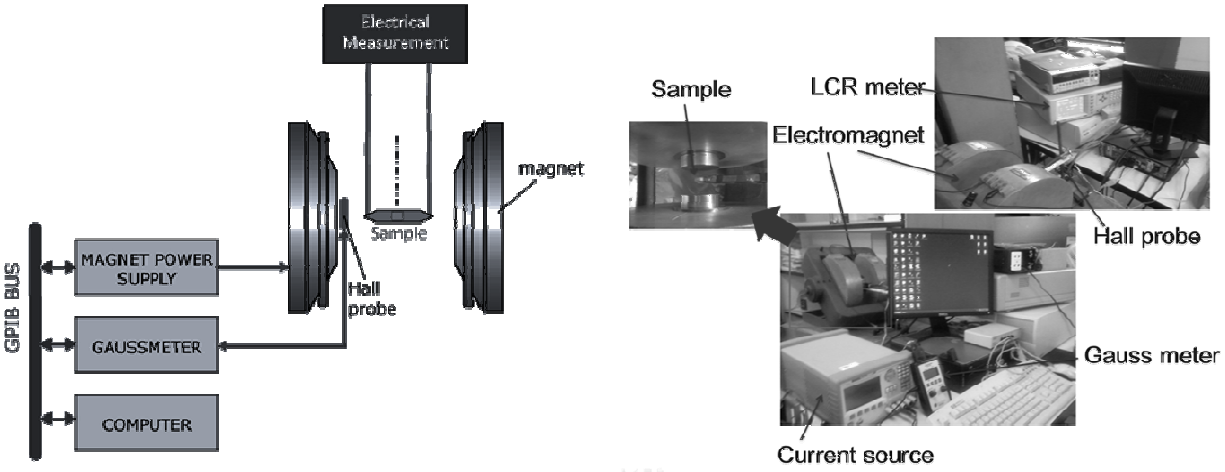
Raw materials of PbO, ZrO_2, TiO_2, ZnO, Nb_2O_5, Fe_2O_3 and CoO with >99% purity were used to prepare samples by a conventional mixed oxide process. The starting powders were mixed by zirconia ball media with isopropanal as a medium in a polyethylene jar for 30 min via vibro-milling technique. The mixed slurry was dried and calcined at 900 ^oC for 2 h. The calcined powders were vibro -milled again with additives and consolidated into disks of 12.5 mm diameter using uniaxial pressing about 150 MPa. PbO-rich atmosphere sintering of the ceramics was performed in a high-

purity alumina crucible at 1200 °C for 2 h. The crystal structure and symmetry of the sintered bodies were examined by X-ray diffraction Rigaku model Miniflex II.

For electrical properties characterizations, silver electrode was printed on the lapped surfaces. The electrode was fired at 600 ^{o}C for 30 min. The dielectric properties of the sintered ceramics were studied as functions of both magnetic field strength and frequency with an automated dielectric measurement system. The computer-controlled dielectric measurement system consisted of a high precision LCR-meter (Tonghui, model TH2819A), and a computer system. The capacitance and the dielectric loss tangent were determined with the frequency ranging from 100 Hz to 100 kHz as shown as Figure 1 (a-b).

The specimens studies were fabricated according to the formula:

- $Pb(Zr_{1/2}Ti_{1/2})O_3$-$Pb(Zn_{1/3}Nb_{2/3})O_3$ (PZNZT) + 0.5 wt% Fe_2O_3 (composite route)
- $Pb(Zr_{1/2}Ti_{1/2})O_3$-$Pb(Zn_{1/3}Nb_{2/3})O_3$ (PZNZT) + 0.5 wt% $CoFe_2O_4$ (composite route)
- $Pb(Zr_{1/2}Ti_{1/2})O_3$- $Pb(Fe_{1/2}Nb_{1/2})O_3$ ceramics (conventional mixed oxide route)



(a) (b)

Figure 1 (a) Diagram of measuring system (b) sample holder with measuring system

Results and Discussion

Figure 2 shows the XRD patterns of all sintered samples. PZNZT ceramics with Fe_2O_3 and $CoFe_2O_4$ had rhombodral crystal structure with pure perovskite phase When the PFN addition on PZT (0.5PZT-0.5PFN), the main phase is tetragonal where peak splitting of crystal planes in the same crystal family can be seen. When 70% PFN by molar fraction was added, the main phase was tetragonal where peak splitting were decreasing. When 50% PFN by molar fraction was added, the main phase was rhombohedral. Some major peaks (e.g. 20-45° and 58°) appear to be broader than that of pure PFN, which results from the overlapping between PFN and PZT peaks. It is interesting to note from XRD pattern that the phase present at 30% PZT by molar fraction addition are both rhombohedral and tetragonal and this composition is generally called morphotropic phase boundary(MPB).

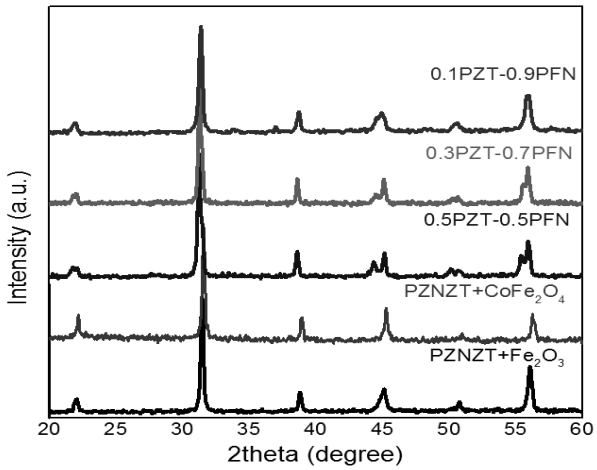


Figure 2 XRD diffraction patterns of modified PZT based ceramics.

Figure 3-7 shows the relationship between dielectric constant, dielectric loss and frequency. All of samples were shown clearly decreasing of dielectric constant with increasing applied magnetic field at low frequency. Again, it can be seen that different sample phase (i.e. rhombohedral versus tetragonal) results in different dielectric behavior. In the ceramics containing rhombohedral phase, dielectric constant slightly linear gradually decreased behavior. Tetragonal phase ceramics did not exhibit the transition; dielectric constant continually decreased like decay behavior.

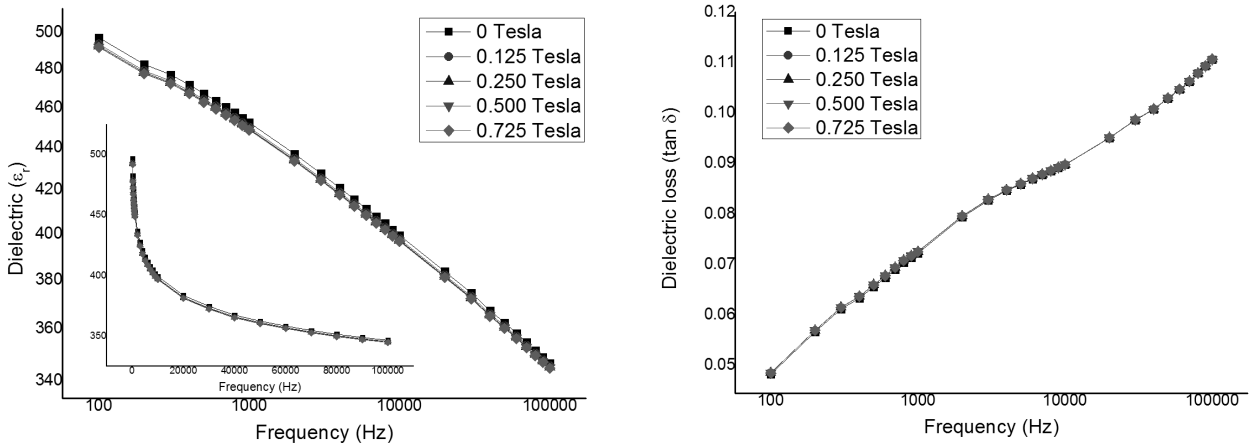


Figure 3. Frequency dependence of the dielectric constant and dielectric loss of PZNZT+ 0.5 wt% Fe_2O_3 the ceramic

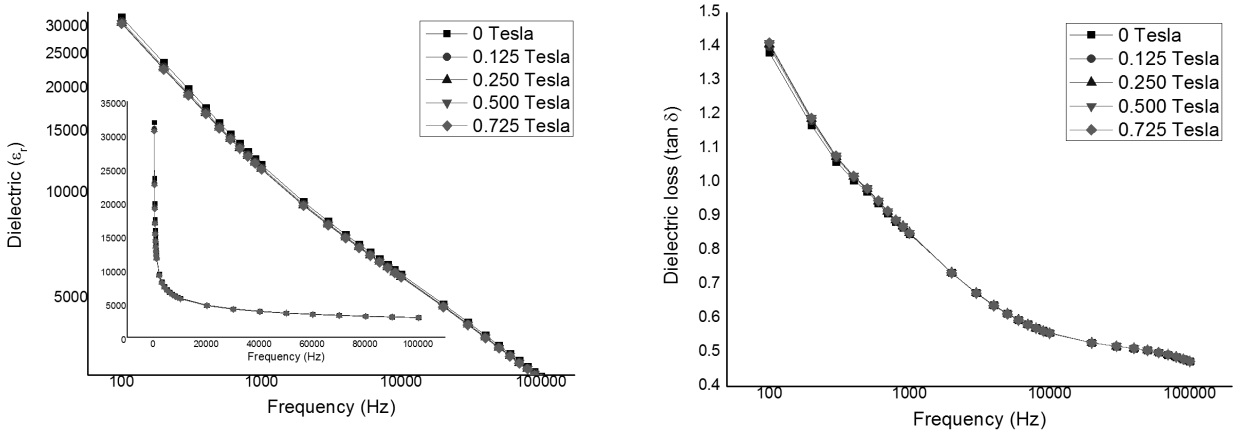


Figure4. Frequency dependence of the dielectric constant and dielectric loss of PZT + $CoFe_2O_3$ the ceramic

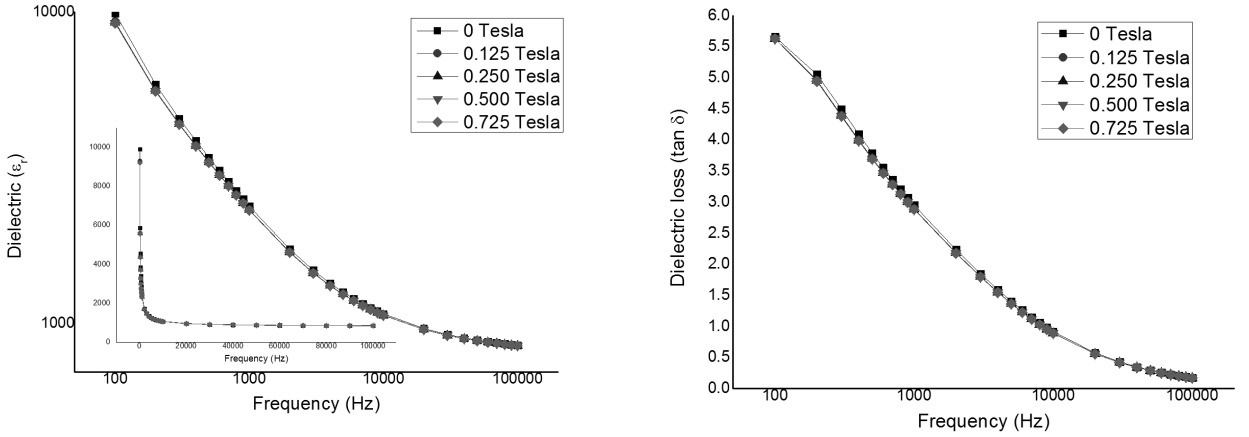


Figure 5. Frequency dependence of the dielectric constant of the 0.5PZT-0.5PFN ceramic

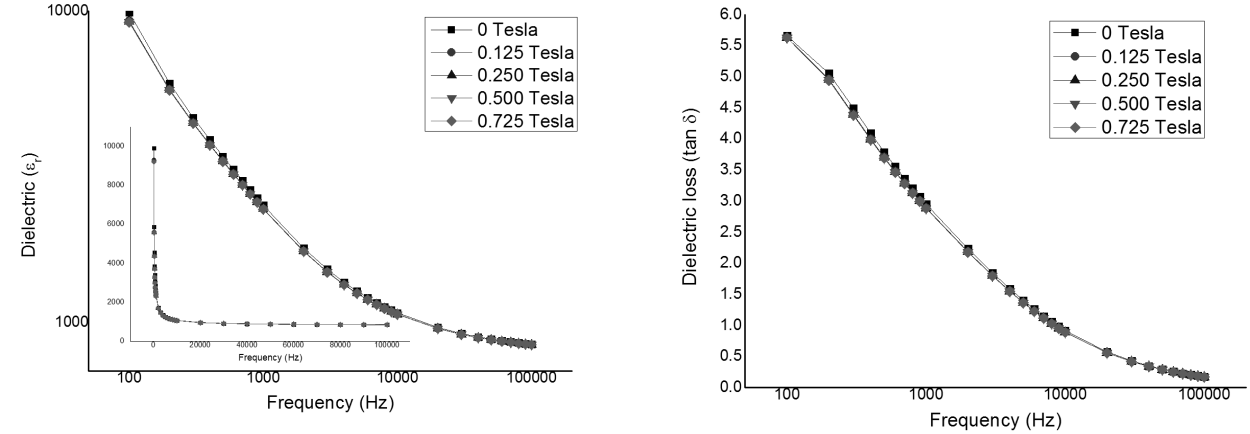


Figure 6. Frequency dependence of the dielectric constant of the 0.3PZT-0.7PFN ceramic

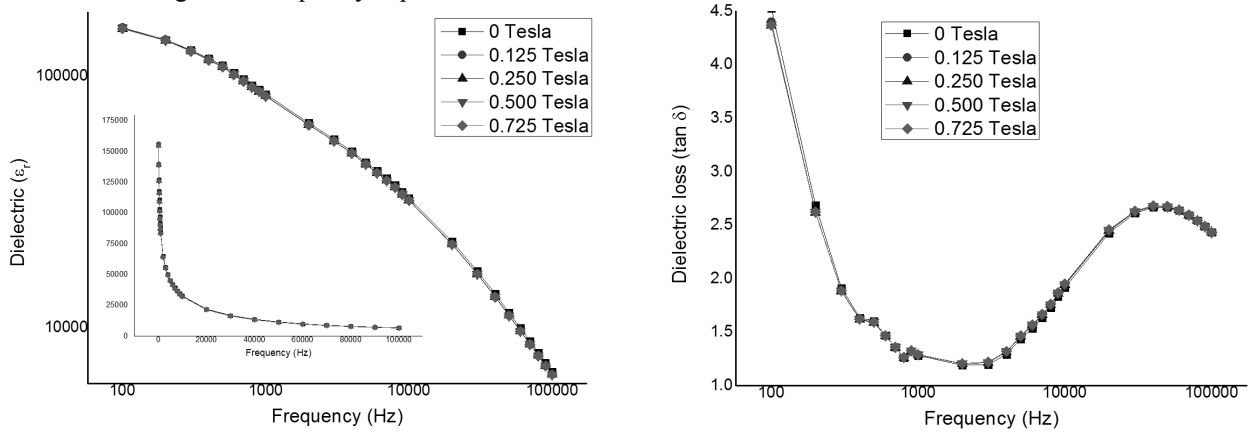


Figure 7. Frequency dependence of the dielectric constant of the 0.1PZT-0.9PFN ceramic

Conclusions

The magnetic-field-dependent dielectric properties were successfully investigated for modifed PZT by compound ferrites additives. The structural properties were found to have a significant effect on the magnetic, dielectric and magneto-dielectric properties of the composite samples. Changes in the positions of the transitional-metal ions in the magnetic phases led to variations in the magnetic properties. The decrease in dielectric constant with increasing applied magnetic field was attributed to a relaxation of the ferroelectric phase due contractive deformations occurring in the magnetic phase of the investigated particulate composite due to an magnetostriction of the magnetic phase in the presence of an external magnetic field that it was shown structure –property relation in this research.

Acknowledgments

This work was supported by the Thailand Research Fund (TRF), Commission on Higher Education (CHE) and Chiang Mai University. The authors are thankful to Laser and Applied Optics Research Laboratory for facility supports, Faculty of Science, Chiang Mai University for financial support. We also acknowledge Assoc. Prof. Dr. Apinpus Rujiwatra for discussion and advised support.

References

[1] M. Fiebig, Revival of the magnetoelectric effect, J. Phys. D: Appl. Phys. 38 R123 (2005)
[2] N. A. Spaldin and M. Fiebig, The Renaissance of Magnetoelectric Multiferroics, Science 309 391 (2005)
[3] W. Eerenstein, N. D. Mathur and J. F. Scott Nature 442 759 (2006)
[4] R. Ramesh and N. A. Spaldin, Multiferroics: progress and prospects in thin films,Nat. Mater. 6 21 (2007)
[5] C. Galassi, Advances in Processing of Bulk Ferroelectric Materials, Springer Series in Materials Science, (2011).

Advanced Materials Research Vol. 936 (2014) pp 110-114
© (2014) Trans Tech Publications, Switzerland
doi:10.4028/www.scientific.net/AMR.936.110

Optical Interferometric Technique for Induced Strain Ferroelectric Loop Study at Low Frequency

Siripong Somwan[1,2,a], Khem Chirapatpimol[1,b] , Apichart Limpichaipanit[1,c], Komsanti Chokethawai[1,d] and Athipong Ngamjarurojana[1,e]

[1]Department of Physics and Materials Science, Faculty of Science, Chiang Mai University, Chiang Mai 50200, Thailand

[2] Division of Physics, Faculty of Science and Agricultural Technology, Rajamangala University of Technology Lanna Changmai (RMUTL), Chiang Mai 50200, Thailand

[a] ppoonngg4@hotmail.com, [b] kchirapatpimol@gmail.com, [c] apichart_limpichaipanit@hotmail.com, [d] komsanti@gmail.com, [e] ngamjarurojana@yahoo.com

Keywords: Ferroelectric; Optical interferometry, Piezoelectric, Electrostrictive

Abstract: Michelson interferometric technique was modified in the setup and used to measure very small changes in optical path length for electric field induced-strain phenomena. Induced-strain is established in the sample when the beam of light propagating through the sample surface undergoes a shift in phase, which in turn leads to a change in the intensity of the interference pattern formed where the reference and probing beams recombine. In this work the electric field induced-strain was measured as a function of electric field (s-E loop) and polarization (s-P loop) of $PbMg_{1/3}Nb_{2/3}O_3$ (PMN) and $0.7PbMg_{1/3}Nb_{2/3}O_3$-$0.3PbZr_{0.52}Ti_{0.48}O_3$ (0.7PMN-0.3PZT) ceramics, which showed electrostrictive (quadratic shape curve) and piezoelectric (butterfly shape curve) behavior at various frequency (0.01-1Hz).

Introduction

The piezoelectric or electrostrictive materials are the most used functional materials as sensors and actuators. Piezoelectric/electrostrictive sensor converts a mechanical variable into a measurable electrical quantity. Alternately, the actuator converts an electrical signal into a mechanical strain the s-E loop. The polarization is related to the strain the s-P loop can provide a means of investigating displacement or strain behavior because it can be used to drive the induced-strain with a nonlinear field to give a linear displacement. The solid state theory that describes the deformation of piezoelectric/electrostrictive ceramic is subjected to an electrical field is shown in Equations (1) and (2);

$$x_{ij} = d_{mij}E_m + M_{ijmn}E_mE_n \quad (1)$$

$$x_{ij} = g_{mij}P_m + Q_{ijmn}P_mP_n \quad (2)$$

where x_{ij} is the component of elastic strain, E_m and E_n are the components of electric field, P_m and P_n are the components of polarization, d_{mij} and g_{mij} are the piezoelectric tensor components, and M_{ijmn} and Q_{ijmn} are the electrostriction tensor components [1-3].

Induced-strain properties of piezoelectric and electrostrictive materials can be investigated by various experimental techniques. Four methods that have been used generally are fibre optic probe, linear variable differential transformers (LVDT), capacitance probe and strain gauges and laser interferometry. The highest resolution method for investigate of electric-field induced strain is the laser interferometry which is based on the Michelson interferometer. The Michelson interferometer technique is a simple and low cost measurement of the electric field-induced displacement. When two laser beams of the same wavelength (λ) interfere, the light intensity varies periodically (λ/2 period) corresponding to the change of optical path length between the two beams.

The intensity of the point of detection changes relative to the displacement can be written as Equation (3);

$$I = I_p + I_r + 2(I_p I_r)^{1/2}\cos(\frac{4\pi\Delta d}{\lambda}) \quad (3)$$

where I_p is the light intensity of the probing beam, I_r is the light intensity of the reference beam and Δd is optical path difference [1].

Experimental

In this research, the modified Michelson interferometric technique was used to measure strain in PMN and 0.7PMN-0.3PZT ceramics as a function of various electric field strengths to obtain a full understanding of the field induced-strain with various frequency of piezoelectric/electrostrictive materials. Preliminary characterization of dielectric behavior was carried out by measuring dielectric constant of the samples at the frequency of 1-100 kHz and the temperatures between 25 and 250^{o}C using LCR meter. A schematic diagram of the system is shown in Figure 1. A modified Michelson interferometer was constructed. It was the system with rigid optical component mounted on a vibration freed optical table to reduce the noise signal of ambient vibrations. The sample under investigation was placed in spring load sample holder which was subjected to an electric high extension field and a polarized beam from a Helium-Neon laser (monochromatic source, λ = 632.8 nm). The frequency used in this work was in the range of 0.01-1 Hz. When the sample was subjected to the applied electric field, the reflected laser beam from the sample (M_2) underwent interference with the reflected laser beam from the reference mirror (M_1) as shown in Figure 1. The resultant interfering intensity variations were detected by a photodiode. Then the amplified signal was captured on a digital oscilloscope along with P-E hysteresis loop measured by a modified Sawyer-Tower circuit which had all interfaces with PC.

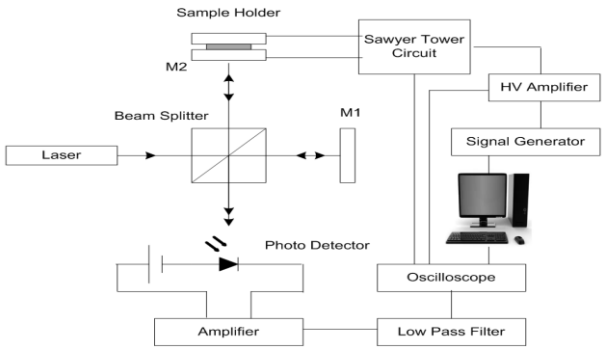


Figure 1. Modified Michelson interferometer

Results and Discussion

Figure 2 shows dielectric constant of PMN and 0.7PMN-0.3PZT as a function of temperature. It can be seen that dielectric property of the two samples is completely different where PMN was paraelectric and 0.7PMN-0.3PZT was ferroelectric (and piezoelectric) which was agreed with the previous result [4]. It should be noted that the difference in dielectric behavior would also result in the difference in response to electric field (i.e. electrostrictive strain and polarization) as discussed further in the next paragraphs.

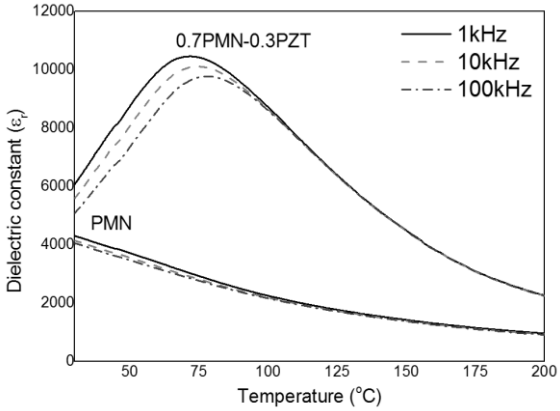


Figure 2. The temperature dependences of the dielectric constant (ε_r) of PMN and 0.7PMN-0.3PZT

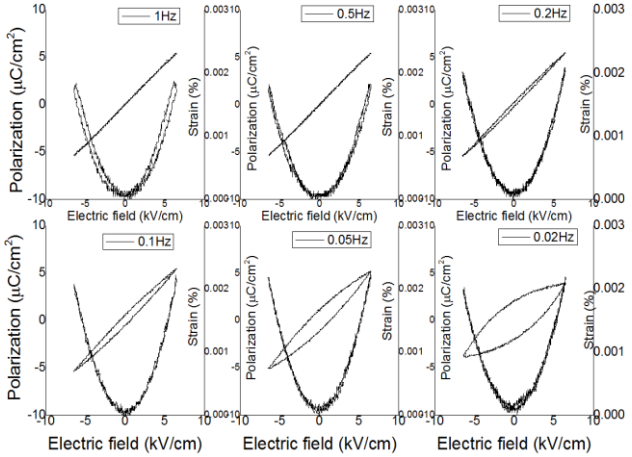


Figure 3. The s-P-E loop curve of PMN, strain proportional to the square of the electric field

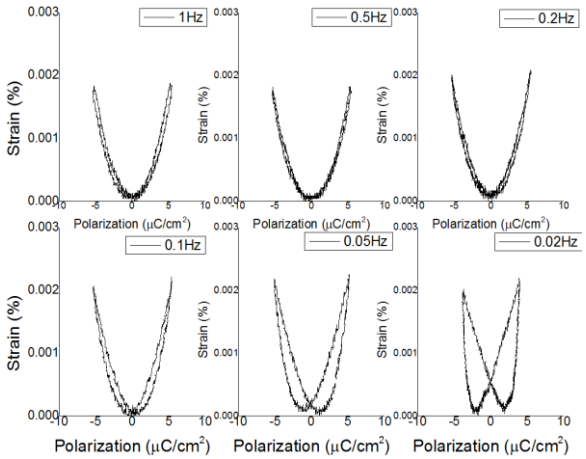


Figure 4. The s-P curve of PMN at various frequencies

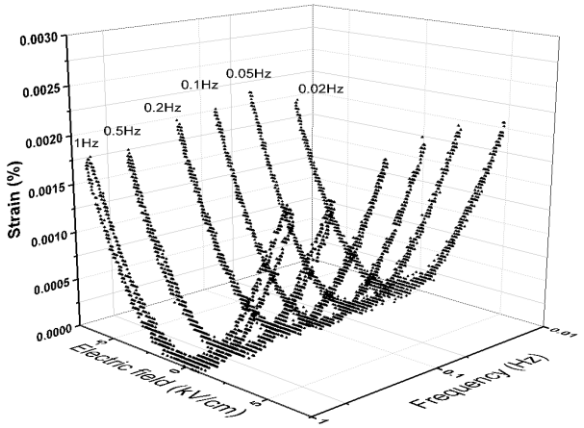


Figure 5. The field induced-strain (s-E) of PMN at various frequencies

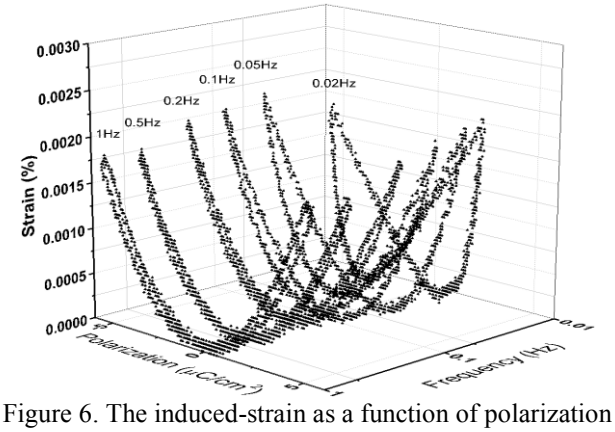


Figure 6. The induced-strain as a function of polarization (s-P) curve of PMN at various frequencies

In Figure 3 and 4, the results of optical interferometry are summarized in these two Figures to further explain the dielectric properties of PMN. Considering the s-P-E graph in Figure 3, the hysteresis polarization occurred at low frequency (clearly seen at 0.05 and 0.02 Hz). The strain behavior was quadratic in relation to electric field and proportional to the square of polarization at high frequency (≥ 0.2 Hz) as shown in Figure 4. When the frequency was less than 0.2 Hz, the response of strain to polarization was no longer quadratic where the characteristic strain loop can be seen. Figure 5 and 6 conclude the induced strain behavior at various frequencies. It can be seen clearly that frequency affected the change in the strain behavior in terms of the change of polarization.

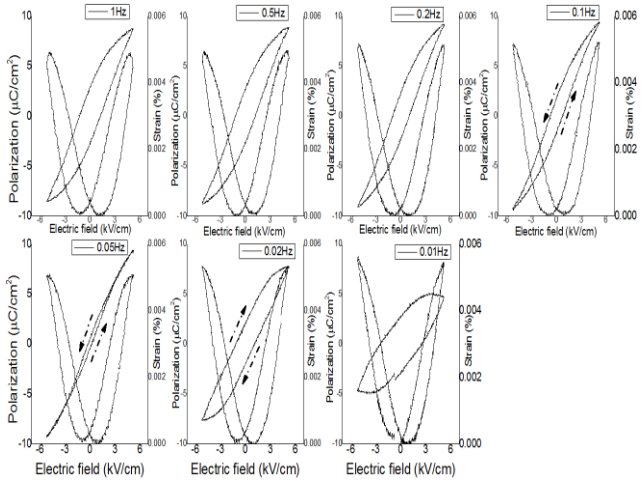


Figure 7. The s-P-E loop curve of 0.7PMN-0.3PZT, induced-strain exhibiting a butterfly loop

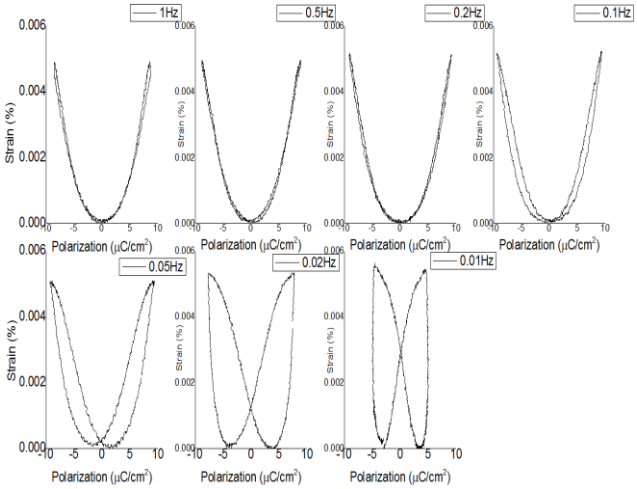


Figure 8. The s-P curve of 0.7PMN-0.3PZT at various frequencies

In Figures 7 and 8, the results of optical interferometry are summarized in these two Figures to further explain the dielectric properties of 0.7PMN-0.3PZT. Considering the s-P-E graph in Figure 7, graph had butterfly shape curve with electric field at all frequency. The strain behavior was proportional to the square of polarization at high frequency (≥ 0.2 Hz), which demonstrated 90^{o} rotation dominant as shown in Figure 8 [3]. When the frequency was less than 0.2 Hz, the response of strain to polarization was no longer quadratic where the characteristic strain loop can be seen and polarization changed from anti clockwise (0.1 Hz) to absence (0.05 Hz) and anti-clockwise (0.02 Hz) hysteresis [5]. Figures 9 and 10 conclude the increasing of strain with decreased frequencies. It can be seen clearly that frequency affected the change in the strain behavior in terms of the change of polarization.

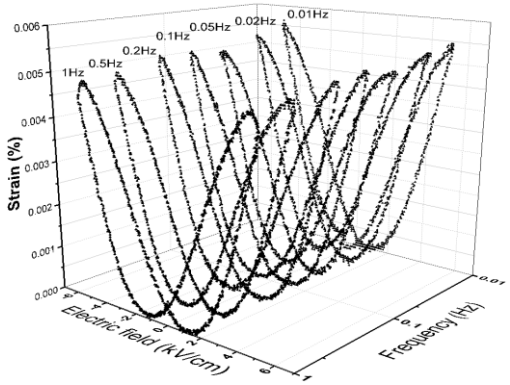


Figure 9. The field induced-strain (s-E) of 0.7PMN-0.3PZT at varies frequency

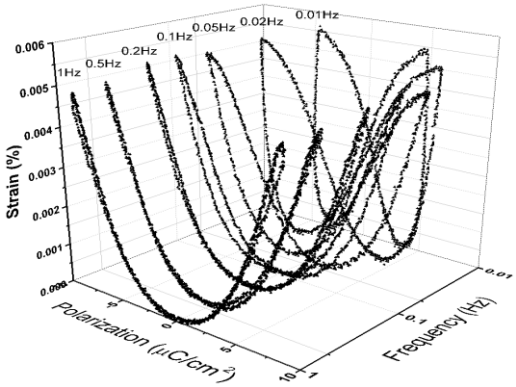


Figure 10. The induced-strain as a function of polarization (s-P) curve of 0.7PMN-0.3PZT at varies frequency

Conclusion

The dielectric characteristic of the two samples was completely different where PMN was paraelectric and 0.7PMN-0.3PZT was ferroelectric (and piezoelectric). The strain and polarization of both samples showed frequency dependence. Induced-strain of PMN was proportional to square of electric field at all frequency and showed electrical loss when the frequency was less than 0.2 Hz. For 0.7PMN-0.3PZT, butterfly shape curve of s-E was observed at all frequency, but showed quadratic shape curve with polarization at 0.2-1 Hz that related to 90^{o} domain rotation and when the frequency was lower than 0.1 Hz, polarization changed from anti clockwise to anti-clockwise hysteresis. The induced strain of 0.7PMN-0.3PZT increased with decreasing frequency.

Acknowledgments

This work was supported by the Thailand Research Fund (TRF), Commission on Higher Education (CHE) and Chiang Mai University. The authors are thankful to Laser and Applied Optics Research Laboratory for facility supports and Graduate School and Faculty of Science, Chiang Mai University for financial support.

References

[1] R. Yimnirun, S. Eury, V. Sunda, P.J. Moses, S.J. Jang and R.E. Newnham, Electrostriction Measurements on Low Permittivity Dielectric Materials, Journal of the European Ceramic Society, 19 (1999) 1269-1273.

[2] L.E. Cross, Ferroelectric materials for electromechanical transducer applications, Materials Chemistry and Physics, 43 (1996) 108-115.

[3] K. Uchino, J.R. Giniewicz, Micromechatronics, Marcel Dekker, Inc., New York, 2003, pp. 37-98.

[4] R. Yimnirun, S. Ananta, P. Laoratakul, Dielectric and ferroelectric properties of lead magnesium niobate –lead zirconate titanate ceramics prepared by mixed-oxide method, Journal of European Ceramic Society, 25 (2005) 3235-3242.

[5] D. Damjanovic, Hysteresis in piezoelectric and ferroelectric materials, Science of Hysteresis, 3 (2006) 337-465.

Advanced Materials Research Vol. 936 (2014) pp 115-118
© (2014) Trans Tech Publications, Switzerland
doi:10.4028/www.scientific.net/AMR.936.115

Effect of Dielectric Properties and Elastic Strain Behavior on x/65/35 PLZT Ceramics in Lanthanum (x) ions Contents

Ladapak Chumprasert[1,2,a], Pranod Larwongsa[1,b] , Apichart Limpichaipanit[1,c], and Athipong Ngamjarurojana[1,d]

[1]Department of Physics and Materials Science, Faculty of Science,

Chiang Mai University, Chiang Mai, Thailand

[2]Department of Visual Design, Faculty of Fine Arts,

Srinakharinwirot University, Bangkok, Thailand

[a] deerdaow@gmail.com, [b] sohryuken@hotmail.com, [c] apichart_limpichaipanit@hotmail.com, [d] ngamjarurojana@yahoo.com

Keywords: Elastic Strain Behavior, PLZT, Ferroelectric, Dielectric

Abstract. In this paper the effect of lanthanum addition on the phase formation, dielectric and ferroelectric characteristics of x/65/35 PLZT. This ceramics were prepared using mixed-oxide synthetic route via a rapid vibro-milling method. All samples were sintered at 1200°C for 12 h. X-ray diffraction was used to observe the crystal structure. It was found that when increasing lanthanum content, the structure remained rhombohedral. It can be seen that the change of behavior to ferroelectric relaxor with the increasing of lanthanum content resulted in the change of elastic strain

Introduction

Lanthanum modified lead zirconate titanate (PLZT) ferroelectric materials have many excellent functional properties, such as piezoelectricity, dielectricity, pyroelectricity and electroopticity. Therefore, they have been widely used in various electronic devices such as sound element, memory and light modification [1] the phase diagram of PLZT system at room temperature, the actual solubility of La in the solid solution depends on the ratio of the two compounds ($PbZrO_3$ and $PbTiO_3$). At 65/35 ratio of $PbZrO_3$ to $PbTiO_3$, a concentration of 9 mol% lanthanum (La) or PLZT 9/65/35 is sufficient to reduce the temperature of the stable ferroelectric rhombohedral phase (FE_{Rh}) to below room temperature [2] varying the amount of La in this region (65/35) could result in the change of crystal structure (from ferroelectric rhombohedral phase (FE_{Rh}) to paraelectric cubic phase (PE) passing through morphotropic phase boundary (MPB) or the boundary region between ferroelectric tetragonal phase (FE_{Tet}) and ferroelectric rhombohedral phase (FE_{Rh}) and also dielectric behaviour (from normal ferroelectric to relaxor ferroelectric) [2, 3].

Research work by Zhang et. Al. [4] revealed that the amount of La added to PZT 40/60 affected the microstructure, ferroelectric and dielectric properties significantly. They pointed out that the particular reason is the change of tetragonality in samples. There has been development of x/65/35 PLZT ceramics with different amount of La (x) ranging from 5 mol% up to the limit of solubility.

This work would serve as a revision to summarize the effect of La content to the electrical properties of x/65/35 PLZT ceramics. In this work x/65/35 PLZT ceramics (where x = 6, 8, 9, 10 and 12 mol% La) was fabricated and the relationship between composition and electrical properties was investigated.

Experimental Procedure

Stoichiometric amount of starting oxides La_2O_3 (Sigma-Aldrich), PbO (Fluka), ZrO_2 (Riedel-de Haën) and TiO_2 (Sigma-Aldrich) was calculated to fabricated x/65/35 PLZT where x is the amount of lanthanum (x = 6, 8, 9, 10 and 12 mol%) . All powders were weighed, mixed and further milled

by vibro milling (McCrone Micronizing Mill) for 30 minutes with a corundum cylindrical media in ethanol. After drying at 120°C for 24 h, the mixture of oxides was calcined at 900°C for 3 h in air. Green pellets of 12.5 mm diameter were prepared using uniaxial-pressure of 200 MPa. The pellets were then placed in a high purity alumina crucible in air and sintered at 1200°C for 12 h.

XRD patterns at room temperature were recorded with X-ray diffraction (Rigaku model MiniFlex II). The CuKα radiation was used as X-ray source. The relative amounts of perovskite phases and were determined from XRD patterns of the samples by measuring the major peak intensities. The sintered samples were polished, cleaned and screen printed with silver electrodes. The dielectric properties of the sintered ceramics were studied as functions of both temperature and frequency with an automated dielectric measurement system. The computer-controlled dielectric measurement system consisted of a high precision LCR-meter, a temperature chamber and a computer system. The capacitance and the dielectric loss tangent were determined over the temperature range of 30-250°C with the frequency of 1-100 kHz. Induced-strain measurements in the terms of strain were made using a modified Michelson interferometric technique as a function of various electric field strengths at the frequency of 0.2 Hz.

Results and Discussion

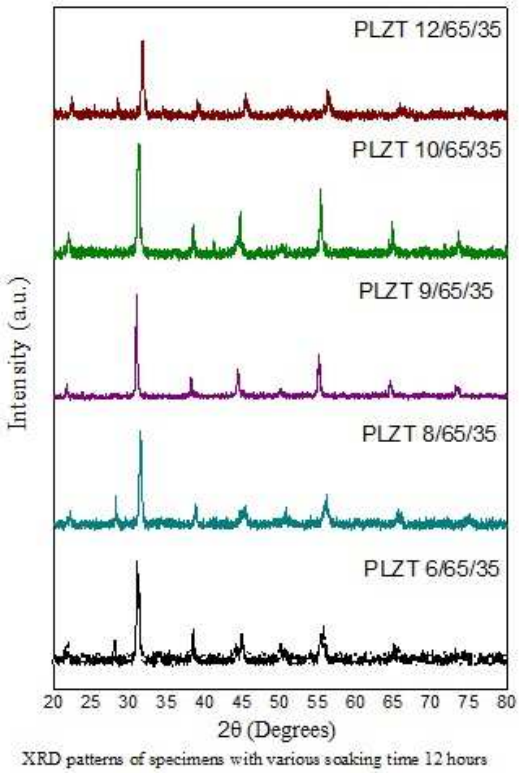


Fig. 1 XRD Patterns of x/65/35 PLZT

Fig.1 shows the XRD patterns of PLZT with different amount of lanthanum sintered at 1200°C for 12 h. It can be seen that all PLZT ceramic samples exhibit perovskite with rhombohedral crystal structure. There was no presence of ZrO_2 in the samples, which was different from the previous study that reported XRD patterns with the peaks of ZrO_2 from either incomplete calcination or PbO evaporation during sintering [5, 6].

The graphs in Fig. 2 show that dielectric behavior of x/65/35 PLZT ceramics changes toward relaxor ferroelectric behavior when the amount of La is increased. It can also be seen that the temperature of maximum dielectric constant is significantly decreased from 219°C in 6/65/35 PLZT

to 34°C in 12/65/35 PLZT. The values of T_m and dielectric properties (at T_m) are summarized in Table 1.

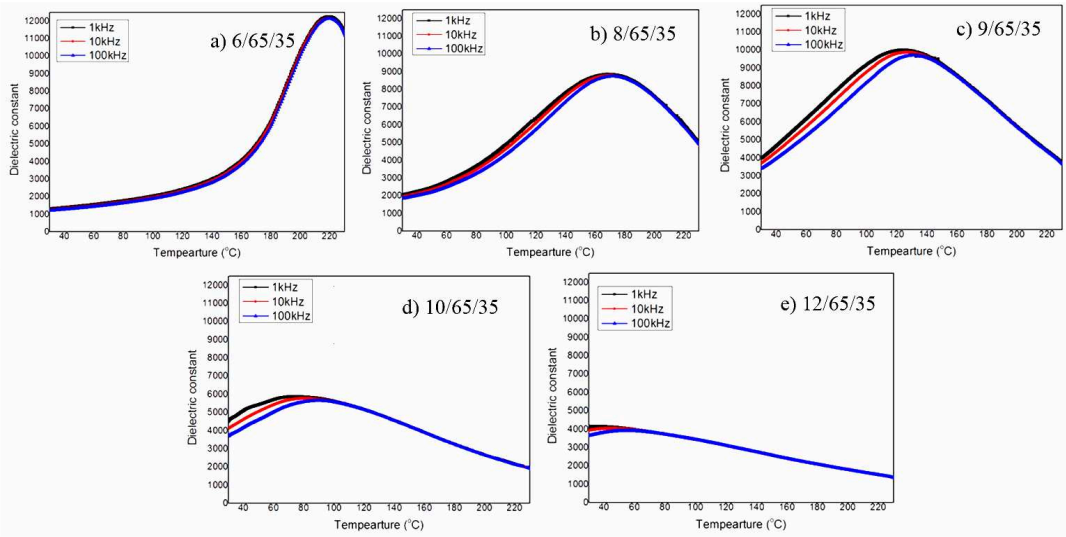


Fig. 2 Dielectric Constant of x/65/35 PLZT

The graphs of strain versus electric field (Fig. 3) imply the relationship between dielectric properties and ability to switch domain during polarization when an electric field is applied. At the content of 6 and 8 mol% La, the resulting strian from the applied field shows a bigger loop when the electric field was increased. The strain behaviour is in the region of "memory" when the La content was increased, the ferroelectric behavior of x/65/35 PLZT ceramics was changed to slimmer hysteresis loop or relaxor ferroelectric [7] hence the remanant polarization was greatly decreased, resulting in a slimmer butterfly loop with less strain at zero electric field (Fig. 3(d)). Moreover, the saturated electric field increased, resulting in an increase in maximum strain (Table 1). When the La content is 12 mol% (Fig. 3(e)), the strain behavior is changed from "quadratic" to a less degree where the S-E curve appears to be flatter (lower maximum strain) [8] .

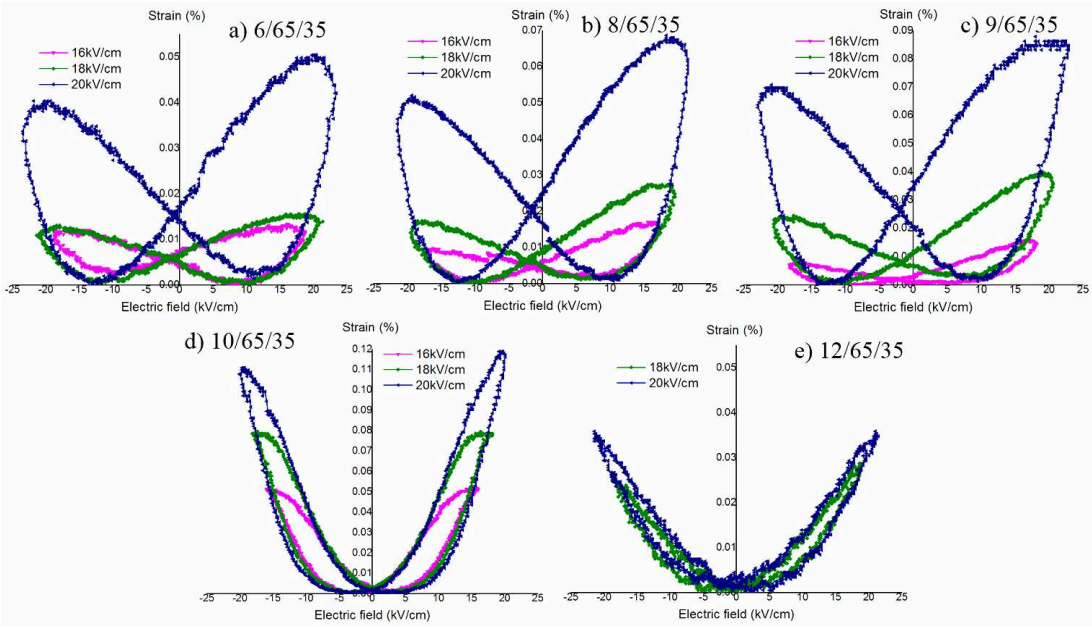


Fig. 3 S-E Characteristics of x/65/35 PLZT Based Ceramic

TABLE 1 FERROELECTRIC PROPERTIES OF X/65/35 PLZT

La content x/65/35	T_m (°C) @ 1kHz	Dielectric properties (at T_m)		Strain % @ 20 kV/cm
		ε_r	tanδ	
x =6 (6/65/35)	219.1	12277	0.0070	0.05
x =8 (8/65/35)	162.5	10443	0.0274	0.07
x =9 (9/65/35)	124.4	10024	0.0080	0.07
x =10 (10/65/35)	76.6	8004	0.0002	0.12
x =12 (12/65/35)	33.6	4175	0.0190	0.035

Conclusion

It can be concluded from the resulted that elastic strain behavior was directly associated with dielectric properties. The amout of La significantly affected the electrical behaviors. When the La content was increased, x/65/35 PLZT ceramics were ferroelectric relaxors and the strain behavior tended to be quadratic. However, there was no change of crystal structure (i.e. rhombohedral) when the La content varied.

Acknowledgement

This work was supported by the Thailand Research Fund (TRF), Commission on Higher Education (CHE) and Chiang Mai University. The authors are thankful to Laser and Applied Optics Research Laboratory for facility supports, and Faculty of Science, Chiang Mai University and Jewelry Design Center, Faculty of Fine Arts, Srinakharinwirot University for financial support.

References

[1] G.H. Heartling, Hot pressed (Pb,La)(Zr,Ti)O_3 ferroelectric ceramics for electro-optic application, J. Am. Ceram. Soc. (1971) 1-11.

[2] K.H. Härdtl, and D. Hennings, J. Am. Ceram. Soc. 55 (1972), 230.

[3] A. Pelaiz Barranco, A. Huanosta Tera, R. Valenzuela Monjaras, J. Antonio Eiras, D. Garcia, F. Calderon Pinar, O. Perez ^{Martinez}, Influence of synthesis process on the AC response of PLZT (8/65/35) ferroelectric ceramics, J. Eur. Ceram Soc. 23 (2003) 1337-1343.

[4] G.H. Heartling, Ferroelectric Ceramic: History and Technology, J. Am. Ceram. Soc., (1999) 797-816.

[5] E. Breval, M. Klimkiewicz, C. Wang and J.P. Dougherty, Annealing of sintered Pb0.9175La0.055Zr0.775Ti0.025O3 in air, J. Am. Ceram. Soc. 90 (2007) 2664-2666.

[6] L. Chumprasert, A. Limpichaipanit, K. Chokethawai, S. Ananta and A. Ngamjarurojana, Effect of soaking time on phase formation and electrical properties of PLZT based ceramics, Ferroelectrics 208-209 (2013) 16-32.

[7] M. Cerqueira, R.S. Nasar, E.R. Leite, E. Longo, and J.A. Varela, Synthesis and characterization of PLZT (9/65/35) by the Pechini method and partial oxalate, Mater. Lett. 35 (1998) 166-171.

[8] V. Priyadarsini, P.V. salija, A.S. Divya and V. Kumar, Influence of strontium substitution on ferroelectric-relaxor transition in PLZT (7/60/40), J. Am. Ceram. Soc. 93 (2010) 3854-3586.

Advanced Materials Research Vol. 936 (2014) pp 119-122
© (2014) Trans Tech Publications, Switzerland
doi:10.4028/www.scientific.net/AMR.936.119

Dielectric and Ferroelectric Behavior in 8/40/60 PLZT Ceramics

Ladapak Chumprasert[1,2,a], Khem chirapatpimol[1,b] , Apichart Limpichaipanit[1,c], Komsanti Chokethawai[1,d] and Athipong Ngamjarurojana[1,e]

[1]Departments of Physics and Materials Science, Faculty of Science,

Chiang Mai University, Chiang Mai, Thailand

[2]Departments of Visual Design, Faculty of Fine Arts,

Srinakharinwirot University, Bangkok, Thailand

[a] deerdaow@gmail.com, [b] kchirapatpimol@gmail.com, [c] apichart_limpichaipanit@hotmail.com, [d] komsanti@gmail.com, [e] ngamjarurojana@yahoo.com

Keywords: Tetragonality, PLZT, Ferroelectric, Dielectric

Abstract. This paper describes the relationship between sintering time conditons, tetragonality from phase formation, dielectric and ferroelectric characteristics of tetragonal PLZT (lanthanum modified lead zirconate titanate) ceramics with the pressureless sintering conditions. Ferroelectric compounds of $Pb_{0.92}La_{0.08}(Zr_{0.4},Ti_{0.6})_{0.98})O_3$, PLZT 8/40/60, were prepared using mixed-oxide synthetic route via a rapid vibro-milling method. X-ray diffraction, is used to observe the tetragonality characteristic and the presence of pyrochlore. When sintering time was increased (≥ 8 hours), pyrochlore was developed. It can be observed that with the increased sintering time, it were changed the structure and ferroelectric behavior of the PLZT ceramics.

Introduction

PLZT ferroelectric materials have many excellent functional properties, such as piezoelectricity, dielectricity, pyroelectricity and electroopticity. Therefore, they have been widely used in various electronic devices such as sound element, memory and light modification [1]. The PLZT ferroelectric system has been studied intensively for technological applications. These compound crystallize in the ABO_3 perovskite structure type, where the A and B sites are occupied by Pb^{2+} and (Zr^{4+}, Ti^{4+}) ions, respectively [2].

Lanthanum modified lead zirconate titanate (PLZT) ceramics, with variable dopant concentration and ratio of Zr/Ti, have shown to exhibit a variety of phases such as ferroelectric (FE), antiferroelectric (AFE) and paraelectric (PE) phases. Due to these advantages, PLZT ceramics have received much attention for the researcher all over the world [3-5]. The tetragonal ferroelectric phase of PLZT 8/40/60 shows a change of lattice parameter a and c indicated by the change of XRD peak. The ratio of c/a is called tetragonality which relates to the change of unit cell dimension and can be seen from x-ray diffraction from XRD patterns.

PLZT powders were traditionally prepared by a solid state reaction process using oxides as the starting materials [6-7]. Many wet chemistry based routes were also developed to prepare ultra-fine powders for PLZT ceramics, which include chemical co-precipitation, sol-gel process and hydrothermal reaction [3,8-9]. Every method has its own advantages and disadvantages. For example, the conventional solid state reaction method requires a calcination, which will lead to formation of PLZT powders.

Microstructure, phase transition from x-ray pattern of PLZT 8/40/60 ceramics were studied recently. And there is no such research involving lattice parameter that indicate the tetragonality of PLZT in the tetragonal phase of formula 8/40/60 ceramics. The purpose of this study is to investigate the tetragonality from various sintering time on properties of PLZT ceramics were investigated in lattice parameter from tetragonal phase formation.

Experimental procedure

Stoichiometric amounts of starting oxides La_2O_3 (Sigma-Aldrich), PbO (Fluka), ZrO_2 (Riedel-de Haën) and TiO_2 (Sigma-Aldrich) of PLZT ceramics having composition $Pb_{0.92}La_{0.08}(Zr_{0.4}Ti_{0.6})O_3$ were weighed, mixed and further milled by vibro milling (McCrone Micronizing Mill) for 30 minutes with a corundum cylindrical media in ethanol. After drying at 120°C for 24 hours, the mixture of oxides was calcined at 900°C for 4 hours in air. Green pellets of 6 mm diameter and 15 mm length were prepared using isostatic-pressure of 150 MPa. The pellets were then placed in a high purity alumina crucible in air. The pellets were then sintered at 1200°C various of sintering time from 2-12 hours.

XRD pattern at room temperature was recorded with X-ray diffraction (Philips PW 1729 diffractometer). The CuKα radiation was used as X-ray source. The relative amounts of perovskite phases and were determined from XRD patterns of the samples by measuring the major peak intensities tetragonality.

The sintered samples were polished, cleaned and screen printed with silver electrodes. The dielectric properties of the sintered ceramics were studied as functions of both temperature and frequency with an automated dielectric measurement system. The computer-controlled dielectric measurement system consisted of a precision LCR-meter, a temperature chamber and a computer system. The capacitance and the dielectric loss tangent were determined over the temperature range of 50-450°C with the frequency ranging between 1-100 kHz. Ferroelectric switching measurements were made using a modified Sawyer-Tower circuit.

Results and discussion

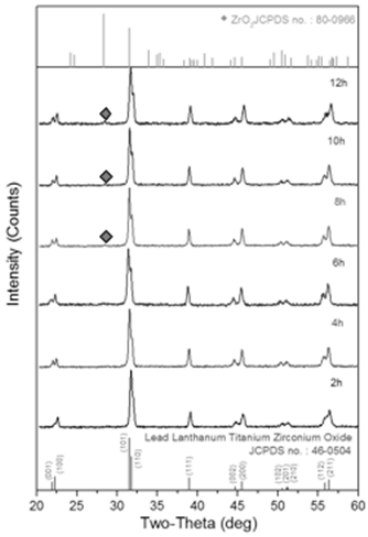


Fig. 1 XRD patterns of $Pb_{0.92}La_{0.08}(Zr_{0.4}Ti_{0.6})_{0.98}O_3$ ceramics

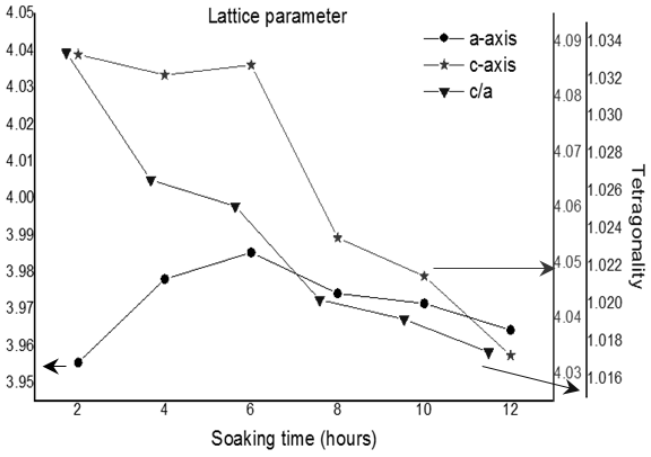


Fig. 2 Lattice parameter and tetragonality of $Pb_{0.92}La_{0.08}(Zr_{0.4}Ti_{0.6})_{0.98}O_3$ ceramics

Fig.1 shows the XRD patterns of $Pb_{0.92}La_{0.08}(Zr_{0.4}Ti_{0.6})_{0.98}O_3$ ceramics sintered at 1200°C with various sintering time of 2, 4, 6, 8, 10 and 12 h. In these patterns pure perovskite tetragonal phase transition of the samples at soaking times of 2-6 hours, as revealed by the evolution of (101) and (110), which could be matched with JCPDF no. 46-0504, confirmed the tetragonal phase of all samples. In general, only a perovskite phase was observed at a low soaking time of PLZT 8/40/60, in which is agreement with other workers [7]. The perovskite stucture of appear a small pyrochlore dovelopment with soaking time of 8-12 hours with a further increase in soaking times. the peak of the diffraction pattern where 2θ is 28.13 degrees, which could be matched with JCPDF no. 80-0966 in Fig.1. Pyrochlore phase generally affects the electrical property. Pyrochlore phase at higher sinter temperature of PLZT is shown, which resulted in a decrease of the dielectric constant.

Fig.2 the tetragonal lattice parameter of a and c were determined at various of soaking times. The results given in Fig. 2 revealed that the tetragonal cell parameters of PLZT 8/40/60 ceramics had a change of dimensions and it can be seen that the tetragonality or c/a decreased with soaking time 2-12 h.

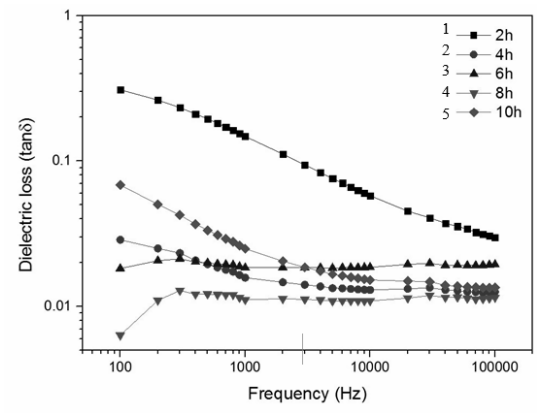


Fig. 3 Dielectric constant (ε_r) of $Pb_{0.92}La_{0.08}(Zr_{0.4}Ti_{0.6})_{0.98}O_3$ ceramics

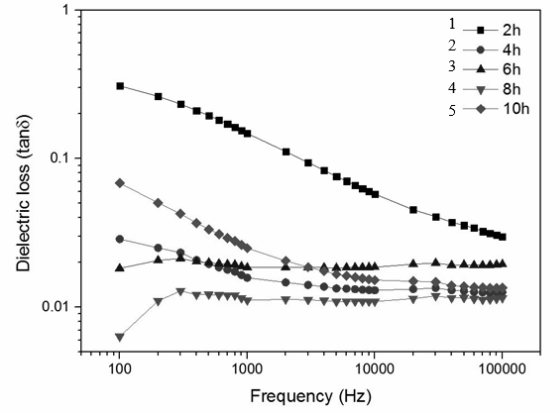


Fig. 4 Dielectric loss (tanδ) of $Pb_{0.92}La_{0.08}(Zr_{0.4}Ti_{0.6})_{0.98}O_3$ ceramics

As shown in Figs. 3-4, the dielectric constant (ε_r) and loss (tanδ) as a function of frequency are plotted. Curves 1-5 represent different soaking time of the function, (1) 1200-2h; (2) 1200-4h; (3) 1200-6h; (4) 1200-8h; (5) 1200-10h. The dielectric constant in soaking time is 12 h was not measured because of the development of pyrochlore phase. The dielectric constant and loss is decreased with the increasing of frequency.

The temperature dependences of the dielectric constant in Fig. 5 at 1 kHz for PLZT 8/40/60 PLZT ceramics. The change of the dielectric peaks may be caused from the different of soaking time at sintered temperature. The Curie temperature (T_c) as a function of all condition is displayed, which was constant at 251°C. Maximum dielectric constant at a lower soaking time of 2-6 h is 2851, 4829 and 7539. When increasing soaking times from 8 to 10 h, the dielectric constant decreased. It decreased from 6687 to 5980 which could be due to the development of pyrochlore phase at higher soaking time of 8 and 10 h. The dielectric properties at T_c, which are report in Table 1 are comparable with other results reported in literature for ceramic 8/40/60 PLZT with ferroelectric tetragonal phase [7].

The polarization-field (P-E) hysteresis loop of PLZT 8/40/60 ceramics is shown in Fig. 6 with variation of sintering time from 2-12 hours. The well developed ferroelectric characteristics in PLZT 8/40/60 ceramics, the ferroelectric parameters, i.e. P_r, P_s and E_c, have been extracted from the experimental data and given in Table 1. The PLZT 8/40/60 exhibits a memory polarization hysteresis loop, which is a switching characteristic of restrained ferroelectric domains. However,

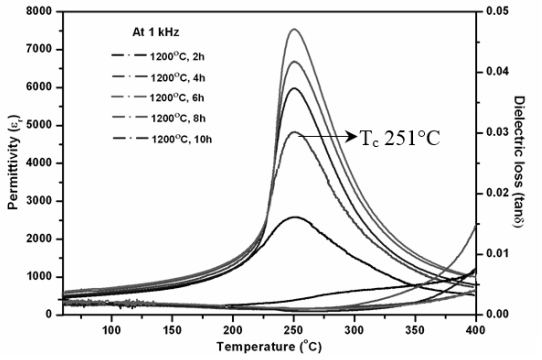


Fig. 5 Temperature dependences of the dielectric constant (ε_r) at 1 kHz

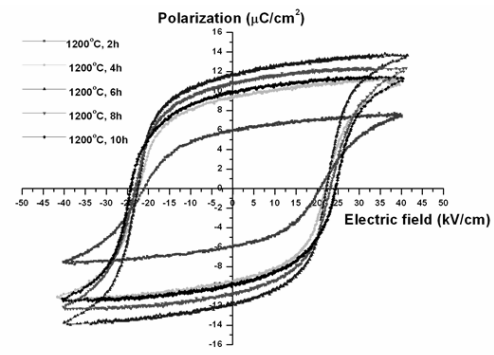


Fig. 6 P-E hysteresis loops of PLZT 8/40/60 with variation of soaking times

the polarization curve of all sintering time was increased from 2-6 h, values of remnanent polarization (P_r) increased. However, when the soaking time was 8-10 h, it was decreased in remnanent polarization (P_r). The observation of the electrical properties of PLZT 8/40/60 could be

attributed to the tetragonal ferroelectric phase when the sintering time increases, which could be matched with x-ray diffraction pattern as shown in Fig. 1.

Table 1 Dielectric and ferroelectric properties of $[Pb_{0.92}, La_{0.08}][Zr_{0.4}Ti_{0.6}]_{0.98}O_3$ ceramics (at 1 kHz)

Sintering (°C) /time (h)	Dielectric properties (at T_c)		Ferroelectric properties		
	ε_r	tanδ	P_r ($\mu C/cm^2$)	P_s ($\mu C/cm^2$)	E_c (kV/cm)
1200°C, 2h	2851	0.0234	5.9	6.2	20.4
1200°C, 4h	4829	0.0097	9.4	9.7	21.7
1200°C, 6h	7539	0.0103	11.7	12.0	22.3
1200°C, 8h	6687	0.0109	10.8	11.1	23.4
1200°C, 10h	5980	0.0061	9.9	10.0	24.4

Conclusion

Lanthanum modified lead zirconate titanate ceramics were obtained by employing mixed-oxide synthetic route sintered at 1200°C with variation of soaking times from 2-12 hours. XRD analysis indicated a small amount of pyrochlore at 8-12 hours, which made a decreasing not only dielectric constant but also remnanent polarization. The tetragonality was decreased when the pyrochlore phase is developed. The structures of tetragonal PLZT 8/40/60 ceramics was realated with the electrical properties such as dielectric constant and ferroelectric from hysteresis loop. It can be concluded that a lattice parameter (a and c) existed in PLZT (8/40/60) system, the tetragonality (c/a) increased with the soaking time increasing and associated with the structure and electrical properties

Acknowledgement

This work was supported by the Thailand Research Fund (TRF), Commission on Higher Education (CHE) and Chiang Mai University. The authors are thankful to Laser and Applied Optics Research Laboratory for facility supports, Graduate School and Faculty of Science, Chiang Mai University and Jewelry Design Center, Faculty of Fine Arts, Srinakharinwirot University for financial support.

References

[1] Y.T. Chen, S.C. Lin, S.Y. Cheng, Temperature dependence of dielectric and piezoelectric properties of PLZT-PZN ceramic tapes, J. Alloy Compd. 449 (2008) 101-104.

[2] A. Pelaiz Barranco, A. Huanosta Tera, R. Valenzuela Monjaras, J. Antonio Eiras, D. Garcia, F. Calderon Pinar, O. Perez Martinez, Influence of synthesis process on the AC response of PLZT (8/65/35) ferroelectric ceramics, J. Eur. Ceram Soc. 23 (2003) 1337-1343.

[3] L.B. Kong, J. Ma, W. Zhu, O.K. Tan, Preparation and characterization of PLZT (8/65/35) ceramics via reaction sintering from ball milled powders, Mater. Lett. 52 (2002) 378-387.

[4] G.H. Heartling, C.E. Land, Recent improvements in the optical and electrooptic properties of PLZT ceramics, Ferroelectrics 3 (1972) 269-280.

[5] G.S. Snow, Improvements in atmosphere sintering of transparent PLZT ceramics, J. Am. Ceram. Soc. 56 (9) (1973) 479-480.

[6] B. Vodopivec, Z. Kutnjak, J. Holc, M. Kosec, Ferroelectric behavior in 5/65/35 hot-pressed PLZT ceramics, J. Eur. Ceram. Soc. 27 (2007) 1093-1096.

[7] J. Zhang, S. Mo, H. Wang, Shanxue Zhen, Hongwei, Chen, C. Yang, Microstructure and electrical properties of PLZT ceramics from Pb_3O_4 as the lead source, J. Alloy Compd. 509 (2011) 2838-2841.

[8] K. Kitaoka, H. Kozuka, T. Yoko, Preparation of lead lanthanum zirconate titanate fibers by sol-gel method, J. Am. Ceram. Soc. 81 (5) (1998) 1189-1196.

[9] M. Cerqueira, R.S. Nasar E. Leite, R.E. Longo, J.A. Varela, Synthesis and characterization of PLZT (9/65/35) by the Pechini method and partial oxalate, Mater. Lett. 35 (1998) 166-171.

Advanced Materials Research Vol. 936 (2014) pp 123-126
© (2014) Trans Tech Publications, Switzerland
doi:10.4028/www.scientific.net/AMR.936.123

Preparation and Optoelectronic Properties of In_2O_3 Microtubes

Shuai Chen[1,a], Yun-Ze Long[1, 2, 3, 4,b, *], Hong-Di Zhang[1, 2,c],
Shu-Liang Liu[1,d], Ling-Zhi Liu[1,e], Jun-Cheng Zhang[1, 2,f],
Guo-Xia Liu[1, 3,g], Fu-Kai Shan[1, 3,h, *]

[1]College of Physics, Qingdao University, Qingdao 266071, P. R. China

[2]Key Laboratory of Photonics Materials & Technology in Universities of Shandong (Qingdao University), Qingdao 266071, P. R. China

[3]State Key Laboratory Cultivation Base of New Fiber Materials & Modern Textile, Qingdao University, Qingdao 266071, P. R. China

[4]Collaborative Innovation Center for Marine Biomass Fibers, Materials and Textiles of Shandong Province, Qingdao 266071, P. R. China

[a]chenshuai2008com@163.com, [b]yunze.long@163.com, [c]hongdi_zhang@163.com,

[d]jiandanweisui@163.com, [e]liulingzhi0811@126.com, [f]jc-zhang@qdu.edu.cn,

[g]gxliucn@gmail.com, [h]fkshan@gmail.com

Keywords: Indium oxide; Microtubes; Electrospinning; UV light sensing

Abstract: Ultrathin indium oxide (In_2O_3) microtubes were successfully fabricated by electrospinning, magnetron sputtering and followed calcination. The hollow In_2O_3 tubes were characterized by scanning electron microscopy (SEM), X-ray diffraction (XRD) and UV-visible spectroscopy. Outer diameter of the microtubes was in the range of 700-900 nm, and inner diameter was about 400-600 nm. Optoelectronic properties of the In_2O_3 tubes were investigated by irradiation of UV light with different wavelengths (254, 308 and 365 nm). It was found that the In_2O_3 microtubes had a fast and strong response to UV irradiation.

Introduction

Electrospinning has been recognized as a convenient and efficient technique to produce ultrathin fibers. A wide variety of materials including bio-macromolecules, organic polymers, semiconductor ceramics and even metals have been fabricated by electrospinning [1-2]. Besides polymer fibers, electrospinning can also be used to fabricate inorganic oxide nanofibers from polymer solution containing inorganic/organic composite ingredients [3]. Hollow nanofibers have a broad application prospect in many fields such as gas storage, drug sustained release and sensing devices [4-6]. Up to date, many methods have been reported to produce various kinds of fibers with hollow structure [7,8].

In_2O_3 is known to be a representative n-type semiconductor material. It has exhibited promising applications in microelectronic fields, such as semiconductor sensors, flat panel display and solar energy conversion [9]. Studies have demonstrated that In_2O_3 semiconductor device has an excellent sensitivity in detecting low concentration of gas such as gasoline, alcohol, ammonia, butane gas and so on. Meanwhile, In_2O_3 also has a very high sensitivity for UV detection, which can be used to protect human body from ultraviolet irradiation. In_2O_3 nanofibers can improve sensitivity and decrease response time due to their higher surface-to-volume ratio.

In this work, In_2O_3 microtubes have been successfully prepared by a new method combining electrospinning, magnetron sputtering and calcination. The In_2O_3 microtubes fabricated by this approach have a smaller outer diameter (700-900 nm) and a thinner wall thickness (50-200 nm). Particularly, the In_2O_3 microtubes show fast and strong response to UV irradiation.

Experimental details

Firstly, poly(vinylidene fluoride) (PVDF) precursor solution was prepared for electrospinning. 2.0 g PVDF was added into 8.0 g of the mixed solvent, containing N,N-dimethyl formamide and acetone with the weight ratio of 1:1 and stirred for 3 h at 60 ^oC in water bath. The solution was loaded into a 5 ml plastic syringe with stainless steel needle connected to a high-voltage power supply (Tianjin Dongwen, China). By electrospinning with a voltage of 13 kV and distance of 10 cm, the PVDF nanofibers were deposited on the collector.

Taking advantage of FJL-560 Ultrahigh Vacuum Magnetron Sputtering Deposition System, a thin layer of In_2O_3 was deposited on the electrospun PVDF nanofibers, which acted as a hard template. The sputtering parameters were controlled as following: In_2O_3 target, sputtering power (90 W), distance between target and substrate (10 cm), sputtering time (1 h), volume ratio of Ar and O_2 (10 : 0.1), room temperature and 1 atm.

In order to get hollow tube structure, the In_2O_3/PVDF composite fibers have been calcined for 2 h under 600 ^oC in a muffle furnace to remove the PVDF fiber template. Then, the furnace was naturally cooled down to room temperature.

The tubes were characterized by a scanning electron microscope (SEM, FEI DB235 Dual-Beam System), an X-ray diffraction (XRD, Rigaku D/max-2400) diffractometer, and a TU-1901 Dual-beam UV-visible Spectrophotometer. The UV photo-detection property of In_2O_3 microtubes was tested by three kinds of UV lamps: PLS-LAM365 (365 nm UV light), PLS-LAM300 (308 nm UV light), PLS-LAM254 (254 nm UV light). The photo-response measurements of the device were carried out under following conditions: applied bias voltage 5 V; room temperature and in air.

Results and discussion

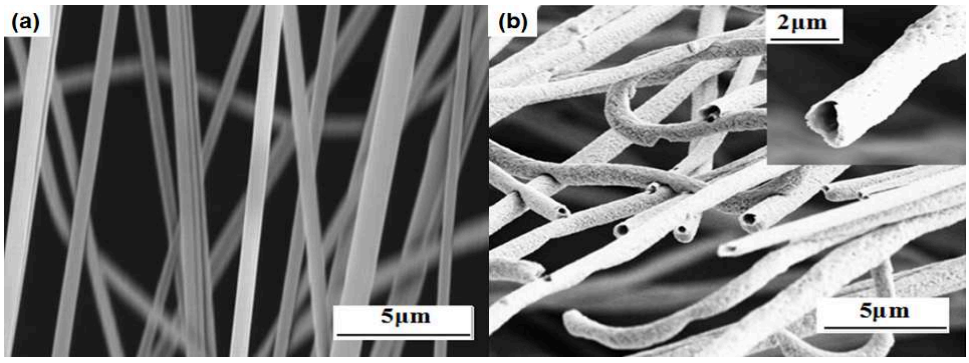


Fig. 1 SEM images of the In_2O_3 microtubes.

Fig. 1 shows the SEM images of the In_2O_3 hollow nanofibers. It is obvious that the pure PVDF nanofibers are very smooth as shown in Fig. 1a. From Fig. 1b, we can see that the PVDF fiber template has been burned out and In_2O_3 microtubes have been formed after calcination under 600^oC. Outer diameter of the tubes is broadly distributed in the range of 700-900 nm, and inner diameter is 400-600 nm. The wall thickness of the microtubes is approximately 50-200 nm. After calcining, the deposited In_2O_3 particles become more compacted.

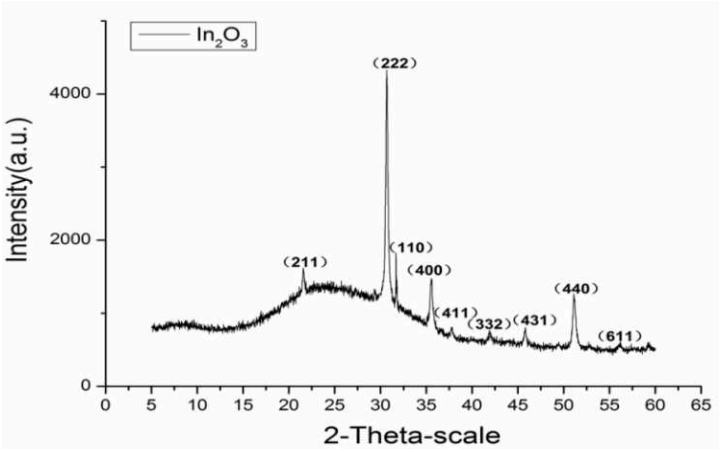


Fig. 2 XRD patterns of the In_2O_3 microtubes.

The crystal structure of the In_2O_3 microtubes after calcining at 600°C was examined by XRD. The XRD patterns prove that the In_2O_3 microtubes have cubic structure with diffraction peaks of (222), (400) and (440). All the diffraction peaks of the sample in Fig. 2 could be indexed to In_2O_3 (JCPDS No. 06-0416). There are no impurity peaks obviously in the XRD patterns, so the sample is In_2O_3 of cubic structure in high purity.

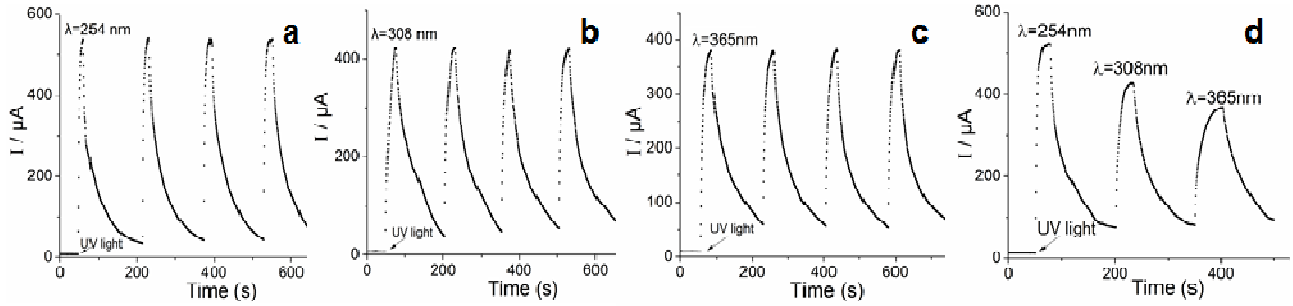


Fig. 3 Photoresponse of the In_2O_3 microtubes under UV illumination with different wavelengths of 254 nm, 308 nm, and 365 nm.

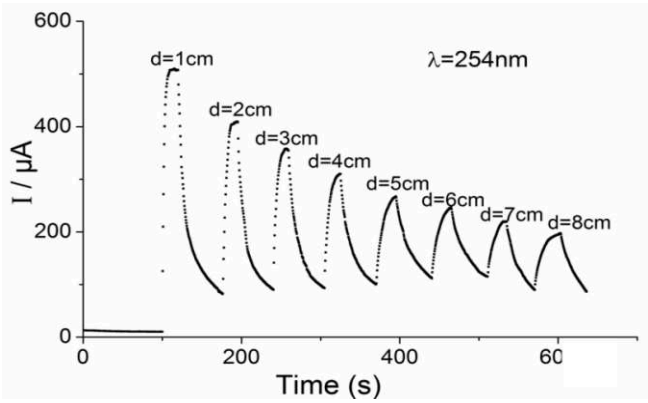


Fig. 4 Photoresponse of the microtubes at different distances from the UV lamp to In_2O_3 tubes.

Figs. 3a-c show the time-dependent photocurrent curves. When the UV light was turned on and turned off periodically and a total of four cycles of data were recorded under UV illumination with different wavelengths when the distance is 1.0 cm. The conductance of the sample was observed to increase rapidly when the UV light was turned on, and it decreased gradually when the UV light was turned off. The sensitivity defined as I_{max}/I_0 is as high as 10^2 and the response time was obtained to be less than 10 s. Fig. 3d shows the photoresponse and *I-V* characteristic curves of the

microtubes exposed to sequential UV illumination with different wavelengths of 254, 308 and 365 nm. The photocurrents increase from initial current (background current under bias of 5.0 V) 5.2 μA to 523 μA, 427 μA and 367 μA under UV illumination with wavelengths of 254 nm, 308 nm and 365 nm, respectively.

Fig. 4 shows the response of the In_2O_3 microtubes at different distances from the UV lamp to electrode under the same UV light of 254 nm. From this figure, we can observe that the sensitivity is decreased with the distance increasing. Furthermore, the decrease trend slows down with increasing distance. While the distance was 1.0 cm, the current could be brought to 508 μA from background current of 5.2 μA. But while the distance was 8 cm, the current only could be brought to 196 μA with the reason that the number of photon which can excite electrons directly from the valence band to the conduction band is less, leading to the lower sensitivity. But compared with the initial current without UV irradiation, the photocurrent has increased greatly.

Conclusion

In_2O_3 microtubes were successfully synthesized by a new method combined electrospinning with magnetron sputtering and calcination. From the SEM images, we could observe the hollow structures clearly. We have investigated photoresponse of the In_2O_3 tubes under UV illumination with different wavelengths and found that the In_2O_3 microtube device could enhance the conduction significantly when exposed to UV light. We also studied the relationship between the distance and sensitivity. Further study on gas sensing property of these electrospun In_2O_3 microtubes is now in progress.

Acknowledgments

This work was supported by National Natural Science Foundation of China (51373082, 11074138 and 11004114), Natural Science Foundation of Shandong Province (China) for Distinguished Young Scholars (JQ201103), Taishan Scholars Program of Shandong Province (ts20120528), National Key Basic Research Development Program of China (973 special preliminary study plan, 2012CB722705), and Program for Scientific Research Innovation Team in Colleges and Universities of Shandong Province, China.

References

[1] D.H. Reneker, A.L. Yarin, H. Fong and S. Koombhongse: J. Appl. Phys. Vol. 87 (2000), p. 4531.
[2] K.H. Lee, Y.H. Kim, M.S. Khil, Y.M. La and D.R. Lee: Polymer. Vol. 44 (2003), p. 1287.
[3] C. Shao, H.Y. Kim, J. Gong, B. Ding, D.R. Lee and S.J. Park: Mater. Lett. Vol. 57 (2003), p. 1579.
[4] N.F. Attia, M.M. Menemparabath, S. Arepalli and K.E. Geckeler: Int. J. Hydrogen Energ. Vol. 38 (2013), p. 9251.
[5] C.M. Hangarter, N. Chartuprayoon, S.C. Hernandez, Y. Choa and N.V. Myung: Nano Today. Vol. 8 (2013), p. 39.
[6] S. Chakraborty, I.C. Liao, A. Adler, K.W. Leong: Adv. Drug Deliv. Rev. Vol. 61 (2009), p. 1043.
[7] A.R. Boccaccini, U. Schindler and H.G. Kruger: Mater. Lett. Vol. 51(3) (2001), p. 225.
[8] R.M. Patel, J.H. Bheda and J.E. Spruiell: J. Appl. Polym. Sci. Vol. 42 (1991), p. 1671.
[9] Z.W. Pan, Z.R. Dai and Z.L. Wang: Science. Vol. 291(5510) (2001), p. 1947.

Advanced Materials Research Vol. 936 (2014) pp 127-135
© (2014) Trans Tech Publications, Switzerland
doi:10.4028/www.scientific.net/AMR.936.127

The Anti-plane Shear Problem of two Symmetric Cracks Originating from an Elliptical Hole in 1D Hexagonal Piezoelectric QCs

Yang Juan[1,2,a] and Li Xing[1,b]

[1]Institute of Mathematics and Computer Science, Ningxia University, Yinchuan 750021, China

[2]Institute of ethnic preparatory education, Ningxia University, Yinchuan 750002, China

[a]yj8024548@163.com,[b]li_x@nxu.edu.cn

Keywords: One-dimensional hexagonal piezoelectric quasicrystals, Crack, Elliptical hole, SIFs, EDIFs, Complex variable function method, Conformal mapping

Abstract. Using the complex variable function method and the technique of conformal mapping, the fracture mechanics of two symmetric collinear cracks originating from an elliptical hole in a one-dimensional (1D) hexagonal piezoelectric quasicrystals (QCs) are investigated under anti-plane sh-ear loading and electric loading. The crack is assumed to be either electrical impermeable or perme-able. The exact solutions in closed-form of the stress intensity factors (SIFs) of the phonon field andthe phason field, and the electric displacement intensity factors (EDIFs) are obtained. In the limiting cases, the new results such as Griffith crack, a circular hole with equal two edge cracks and cross crack can be obtained from the present solutions. In the absence of the phason field, the obtainable results in this paper match with the classical results.

Introduction

Piezoelectric materials generate an electric field when subjected to strain fields and undergo deformation when an electric field is applied. This inherent electromechanical coupling is widely exploited in the design of many devices like transducers, sensors and actuators[1,2].

D.Shechtman was awarded the Nobel Prize of Chemistry 2011 due to the discovery of QCs in 1984, which has aroused the great interest on the structure and material again[3]. The theoretical frame of QCs comes from physical research which has been done by some researchers[4]. Experim-ents have shown that QCs are quite brittle[5] and the defects of quasicrystalline materials have been observed[6]. It is well known that the presence of defects such as holes and cracks, greatly affects the physical and mechanical properties of solid materials including QCs. Therefore, the study of crack problem of quasicrystalline materials is meaningful both in theoretical and practical applications. Fan[7] presented the mathematical theory of quasicrystalline elasticity. Using this theory, a straight dislocation and a moving screw dislocation in (1D) hexagonal QCs were addressed by Li and his coauthors[8,9]. It is well known that the complex variable method initially developed by Muskh elishvili is an effective method for solving elasticity and defect problems[10]. Therefore, some workers developed the complex variable method to solve defect problems of quasicrystals. For 1D hexagonal QCs many efforts have been made in the fields of the mechanic involving the elasticity and defects by the complex variable method[11-15]. The collinear periodic cracks and/or rigid line inclusions of antiplane mode in 1D hexagonal QCs have been studied[16].

But the paper mentioned before discussed various elasticity and defect problems of QCs. To our knowledge, the study of QCs functional aspects is very little, especially the study of QCs piezo-electric properties. Therefore, the present paper is devoted to investigating the elastic problem

of an elliptical hole with two symmetric collinear cracks in a 1D hexagonal piezoelectric QCs by means of complex variable function method with conformal mapping. Two kinds of crack surface conditions, i.e. electrical impermeable and electrical permeable are adopted. The exact solutions of SIFs for the phonon field and the phason field, and the EDIFs are obtained respectively, which are useful in practice.

Basic Theory

The generalized Hooke's law of 1D hexagonal piezoelectric quasicrystal, whose period plane is the (x_1, x_2) -plane and whose quasiperiodic direction is the x_3 -axis, is given by[13]

$$\begin{aligned}
&\sigma_{11} = C_{11}\varepsilon_{11} + C_{12}\varepsilon_{22} + C_{13}\varepsilon_{33} + R_1\omega_3 - e_{31}^1 E_3,\\
&\sigma_{22} = C_{12}\varepsilon_{11} + C_{22}\varepsilon_{22} + C_{13}\varepsilon_{33} + R_1\omega_3 - e_{31}^1 E_3,\\
&\sigma_{33} = C_{13}\varepsilon_{11} + C_{13}\varepsilon_{22} + C_{33}\varepsilon_{33} + R_2\omega_3 - e_{33}^1 E_3,\\
&\sigma_{23} = \sigma_{32} = 2C_{44}\varepsilon_{31} + R_3\omega_2 - e_{15}^1 E_2,\\
&\sigma_{13} = \sigma_{31} = 2C_{44}\varepsilon_{31} + R_3\omega_1 - e_{15}^1 E_1, \sigma_{12} = \sigma_{21} = 2C_{66}\varepsilon_{12},\\
&H_3 = R_1(\varepsilon_{11} + \varepsilon_{22}) + R_2\varepsilon_{33} + k_1\omega_3 - e_{33}^2 E_3,\\
&H_1 = 2R_3\varepsilon_{31} + k_2\omega_1 - e_{15}^2 E_1, H_2 = 2R_3\varepsilon_{32} + k_2\omega_2 - e_{15}^2 E_2,\\
&D_3 = e_{31}^1(\varepsilon_{11} + \varepsilon_{22}) + e_{33}^1\varepsilon_{33} + e_{33}^2\omega_3 + \in_{33} E_3,\\
&D_1 = 2e_{15}^1\varepsilon_{31} + e_{15}^2\omega_1 + \in_{11} E_1, D_2 = 2e_{15}^1\varepsilon_{32} + e_{15}^2\omega_2 + \in_{11} E_2.
\end{aligned} \tag{1}$$

where $\sigma_{ij}, H_j (i, j = 1,2,3)$ are the phonon and phason stress components; $E_j, D_j (j = 1,2,3)$ are the electric fields and the electric misplacement; $\varepsilon_{ij}, \omega_j (i, j = 1,2,3)$ are the phonon and phason strains; k_1, k_2 are two elastic constants in the phason field; $R_i (i = 1,2,3)$ are three phonon-phason coupling elastic constants; $C_{11}, C_{12}, C_{13}, C_{33}, C_{44}, C_{66}$ are six elastic constants in the phonon field and $C_{66} = \dfrac{C_{11} - C_{12}}{2}$; $e_{ij}^1, e_{ij}^2 (i = 1,3,\ j = 1,3,5)$ are piezoelectric coefficients; $\in_{11}, \in_{33}$ are two dielectric coefficients.

The strain–displacement and electric field–electric potential relations are given by

$$\varepsilon_{ij} = \frac{1}{2}(\partial_j u_i + \partial_i u_j), \omega_j = \partial_j \omega, E_j = -\partial_j \phi, (i, j = 1,2,3) \tag{2}$$

Where $u_i (i = 1,2,3)$ are phonon displacement components, ω_3 is the phason displacement, ϕ is the electric potential. we have used the tensor notation and $\partial_j u_i = \dfrac{\partial u_i}{\partial u_j}$, the same hereafter.

In the absence of body force and electric charge density, the equilibrium equations are

$$\begin{aligned}
&\partial_1\sigma_{11} + \partial_2\sigma_{12} + \partial_3\sigma_{13} = 0, \partial_1\sigma_{21} + \partial_2\sigma_{22} + \partial_3\sigma_{23} = 0,\\
&\partial_1\sigma_{31} + \partial_2\sigma_{32} + \partial_3\sigma_{33} = 0, \partial_1 H_1 + \partial_2 H_2 + \partial_3 H_3 = 0,\\
&\partial_1 D_1 + \partial_2 D_2 + \partial_3 D_3 = 0.
\end{aligned} \tag{3}$$

For the anti-plane shear problem in which all field variables are independent of x_3. In this case, we have the following deformation geometrical equations

$$\partial_3 u_i = 0, \partial_3 \omega = 0, \partial_3 \sigma_{ij} = 0, \partial_3 H_i = 0, \partial_3 D_i = 0. \tag{4}$$

Substitution of Eq. (4) into Eqs. (1)-(3) leads to one is a plane elasticity problem of general crystals, which can be solved by the route of linear elastic theory[10]. We do not discuss it here. And the other is an anti-plane phonon-phason coupling elasticity problem as follows

$$\begin{aligned}
&\sigma_{23} = \sigma_{32} = 2C_{44}\varepsilon_{31} + R_3\omega_2 - e_{15}^1 E_2, \sigma_{13} = \sigma_{31} = 2C_{44}\varepsilon_{31} + R_3\omega_1 - e_{15}^1 E_1,\\
&H_1 = 2R_3\varepsilon_{31} + k_2\omega_1 - e_{15}^2 E_1, H_2 = 2R_3\varepsilon_{32} + k_2\omega_2 - e_{15}^2 E_2,\\
&D_1 = 2e_{15}^1\varepsilon_{31} + e_{15}^2\omega_1 + \in_{11} E_1, D_2 = 2e_{15}^1\varepsilon_{32} + e_{15}^2\omega_2 + \in_{11} E_2,\\
&\partial_1\sigma_{31} + \partial_2\sigma_{32} = 0, \partial_1 H_1 + \partial_2 H_2 = 0, \partial_1 D_1 + \partial_2 D_2 = 0,\\
&\varepsilon_{3j} = \varepsilon_{j3} = \frac{1}{2}\partial_j u_3, \omega_j = \partial_j\omega, E_j = -\partial_j\phi. (j = 1,2)
\end{aligned} \tag{5}$$

From Eq. (5), one obtains

$$\begin{aligned}
&C_{44}\nabla^2 u_3 + R_3\nabla^2\omega + e_{15}^1\nabla^2\phi = 0, R_3\nabla^2 u_3 + K_2\nabla^2\omega + e_{15}^2\nabla^2\phi = 0,\\
&e_{15}^1\nabla^2 u_3 + e_{15}^2\nabla^2\omega - \in_{11}\nabla^2\phi = 0.
\end{aligned} \tag{6}$$

where $\nabla^2 = \frac{\partial^2}{\partial x_1^2} + \frac{\partial^2}{\partial x_2^2}$ is the two dimensional Laplace operator, under the condition of $\begin{vmatrix} C_{44} & R_3 & e_{15}^1 \\ R_3 & K_2 & e_{15}^2 \\ e_{15}^1 & e_{15}^2 & -\in_{11} \end{vmatrix} \neq 0$, Eq. (6) can be written as

$$\nabla^2 u_3 = 0, \nabla^2\omega = 0, \nabla^2\phi = 0. \tag{7}$$

According to the theory of complex variable function, u_3, ω and ϕ can be represented as the real part and the imaginary part of one analytic function, respectively. We assume that

$$u_3 = \mathrm{Re}\,\varphi_1(z), \omega = \mathrm{Re}\,\varphi_2(z), \phi = \mathrm{Re}\,\varphi_3(z). \tag{8}$$

where $z = x_1 + ix_2, i = \sqrt{-1}$, $\varphi_i(z)(i = 1,2,3)$ are arbitrary analytic functions.

Solution of Elastic Field

Considering a problem about an elliptical hole with two symmetric cracks in a 1D hexagonal piezoelectric QCs. It is assumed that the quasi-periodic direction of 1D hexagonal piezoelectric QCs is along the positive direction of x_3 axis. a and b are the long semi-axes and short semi-axes respectively, $c - a$ is crack length. The solid is subjected to uniform remote anti-plane shear loadings of the phonon field and the phason field, and electric loading at infinity as shown in Fig. 1.

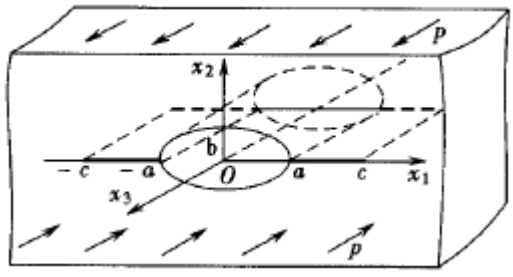


Fig. 1. An elliptical hole with two cracks embedded in 1D hexagonal piezoelectric QCs

Electric Impermeable Problem

By the linear elastic theory, the above problem is equivalent to the surface of cracks is subjected to the shear stress and electric displacement $\sigma_{32} = -p, H_2 = -q, D_2 = -T$, the problem of the electric impermeable boundary condition can be expressed as

$$\begin{aligned}
&\sqrt{x+y} \to \infty : \sigma_{32} = 0, H_2 = 0, D_2 = 0,\\
&(x,y) \in L : \sigma_{32} = -p, H_2 = -q, D_2 = -T.
\end{aligned} \tag{9}$$

where L denotes the boundary of the elliptical hole with four straight cracks.

For electric impermeable problem, we solve the boundary value problems (7) and (9) by using the complex variable function method .

By Eqs. (5) and (8), the stresses and the electric displacements can be written as

$$\begin{aligned}
\sigma_{23} &= \sigma_{32} = -\frac{1}{2i}\Big[C_{44}(\varphi_1' - \overline{\varphi_1'}) + R_3(\varphi_2' - \overline{\varphi_2'}) + e_{15}^1(\varphi_3' - \overline{\varphi_3'})\Big],\\
H_2 &= -\frac{1}{2i}\Big[R_3(\varphi_1' - \overline{\varphi_1'}) + k_2(\varphi_2' - \overline{\varphi_2'}) + e_{15}^2(\varphi_3' - \overline{\varphi_3'})\Big],\\
D_2 &= -\frac{1}{2i}\Big[e_{15}^1(\varphi_1' - \overline{\varphi_1'}) + e_{15}^2(\varphi_2' - \overline{\varphi_2'}) - \in_{11}(\varphi_3' - \overline{\varphi_3'})\Big].
\end{aligned} \tag{10}$$

Substituting Eq. (10) into Eq. (9), we obtain

$$\begin{aligned}
&C_{44}(\varphi_1' - \overline{\varphi_1'}) + R_3(\varphi_2' - \overline{\varphi_2'}) + e_{15}^1(\varphi_3' - \overline{\varphi_3'}) = 2pi,\\
&R_3(\varphi_1' - \overline{\varphi_1'}) + k_2(\varphi_2' - \overline{\varphi_2'}) + e_{15}^2(\varphi_3' - \overline{\varphi_3'}) = 2qi,\\
&e_{15}^1(\varphi_1' - \overline{\varphi_1'}) + e_{15}^2(\varphi_2' - \overline{\varphi_2'}) - \in_{11}(\varphi_3' - \overline{\varphi_3'}) = 2Ti.
\end{aligned} \tag{11}$$

We propose the following conformal mapping

$$\begin{aligned}
z = \omega(\zeta) = \frac{a+b}{2}\frac{2(d^2+1)(1+\zeta^2) + (d^2-1)\sqrt{(1+\zeta)^4 + 2k(1-\zeta^2)^2 + (1-\zeta)^4}}{8d\zeta}\\
+ \frac{a-b}{2}\frac{8d\zeta}{2(d^2+1)(1+\zeta^2) + (d^2-1)\sqrt{(1+\zeta)^4 + 2k(1-\zeta^2)^2 + (1-\zeta)^4}}
\end{aligned} \tag{12}$$

to transform the region at the z plane onto the interior of the unit circle at the ζ plane, where

$$d = \frac{c + \sqrt{c^2 - a^2 + b^2}}{a+b}, \quad k = \frac{d^4 + 6d^2 + 1}{(d^2-1)^2}.$$

Eq. (12) maps the upper edge of a onto A_2, the lower edge of a onto A_1, and $\omega^{-1}(c) \to 1$, $\omega^{-1}(-c) \to -1$, $\omega^{-1}(bi) \to i$, $\omega^{-1}(-bi) \to -i$, as shown in Fig.2.

By means of Eqs. (8) and (12), one has

$$\psi_i(\zeta) = \varphi_i(z) = \varphi_i(w(\zeta)), (i = 1,2,3),\ \varphi_i'(z) = \frac{\psi_i'(\zeta)}{w'(\zeta)}. \tag{13}$$

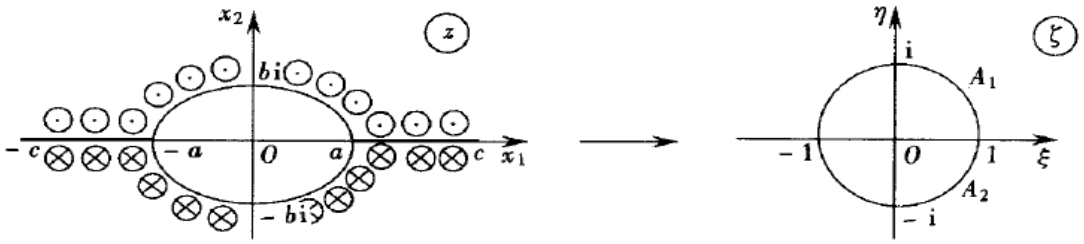


Fig. 2. Conformal mapping from exterior of an elliptical hole with two cracks onto unit disk

Substituting Eq. (13) into Eq. (11), noting that $\zeta = \sigma = e^{i\theta}$, we have

$$\begin{aligned}
&\psi_1'(\sigma) - \frac{w'(\sigma)}{\overline{w}'(\sigma)}\overline{\psi_1'}(\sigma) + \frac{R_3}{C_{44}}\left[\psi_2'(\sigma) - \frac{w'(\sigma)}{\overline{w'}(\sigma)}\overline{\psi_2'}(\sigma)\right] + \frac{e_{15}^1}{C_{44}}\left[\psi_3'(\sigma) - \frac{w'(\sigma)}{\overline{w'}(\sigma)}\overline{\psi_3'}(\sigma)\right] = \frac{2pi}{C_{44}}w'(\sigma),\\
&\frac{R_3}{k_2}\left[\psi_1'(\sigma) - \frac{w'(\sigma)}{\overline{w}'(\sigma)}\overline{\psi_1'}(\sigma)\right] + \left[\psi_2'(\sigma) - \frac{w'(\sigma)}{\overline{w'}(\sigma)}\overline{\psi_2'}(\sigma)\right] + \frac{e_{15}^2}{k_2}\left[\psi_3'(\sigma) - \frac{w'(\sigma)}{\overline{w'}(\sigma)}\overline{\psi_3'}(\sigma)\right] = \frac{2qi}{k_2}w'(\sigma),\\
&\frac{e_{15}^1}{\in_{11}}\left[\psi_1'(\sigma) - \frac{w'(\sigma)}{\overline{w'}(\sigma)}\overline{\psi_1'}(\sigma)\right] + \frac{e_{15}^2}{\in_{11}}\left[\psi_2'(\sigma) - \frac{w'(\sigma)}{\overline{w'}(\sigma)}\overline{\psi_2'}(\sigma)\right] - \left[\psi_3'(\sigma) - \frac{w'(\sigma)}{\overline{w'}(\sigma)}\overline{\psi_3'}(\sigma)\right] = \frac{2Ti}{\in_{11}}w'(\sigma).
\end{aligned} \tag{14}$$

Multiplying both sides of two equations of Eq. (14) by $\frac{1}{2\pi i}\frac{d\sigma}{\sigma - \zeta}$, where ζ is an arbitrary point in $|\zeta| < 1$, and integrating around the unit circle ℓ, we have

$$\begin{aligned}
&\frac{1}{2\pi i}\int_\ell \frac{\psi_1'(\sigma)}{\sigma-\zeta}d\sigma-\frac{1}{2\pi i}\int_\ell \frac{w'(\sigma)}{\overline{w'(\sigma)}}\frac{\overline{\psi_1'}(\sigma)}{\sigma-\zeta}d\sigma+\frac{R_3}{C_{44}}\left[\frac{1}{2\pi i}\int_\ell \frac{\psi_2'(\sigma)}{\sigma-\zeta}d\sigma-\frac{1}{2\pi i}\int_\ell \frac{w'(\sigma)}{\overline{w'(\sigma)}}\frac{\overline{\psi_2'}(\sigma)}{\sigma-\zeta}d\sigma\right]\\
&+\frac{e_{15}^1}{C_{44}}\left[\frac{1}{2\pi i}\int_\ell \frac{\psi_3'(\sigma)}{\sigma-\zeta}d\sigma-\frac{1}{2\pi i}\int_\ell \frac{w'(\sigma)}{\overline{w'(\sigma)}}\frac{\overline{\psi_3'}(\sigma)}{\sigma-\zeta}d\sigma\right]=\frac{2pi}{C_{44}}\frac{1}{2\pi i}\int_\ell \frac{w'(\sigma)}{\sigma-\zeta}d\sigma,\\
&\frac{R_3}{k_2}\left[\frac{1}{2\pi i}\int_\ell \frac{\psi_1'(\sigma)}{\sigma-\zeta}d\sigma-\frac{1}{2\pi i}\int_\ell \frac{w'(\sigma)}{\overline{w'(\sigma)}}\frac{\overline{\psi_1'}(\sigma)}{\sigma-\zeta}d\sigma\right]+\left[\frac{1}{2\pi i}\int_\ell \frac{\psi_2'(\sigma)}{\sigma-\zeta}d\sigma-\frac{1}{2\pi i}\int_\ell \frac{w'(\sigma)}{\overline{w'(\sigma)}}\frac{\overline{\psi_2'}(\sigma)}{\sigma-\zeta}d\sigma\right]\\
&+\frac{e_{15}^2}{k_2}\left[\frac{1}{2\pi i}\int_\ell \frac{\psi_3'(\sigma)}{\sigma-\zeta}d\sigma-\frac{1}{2\pi i}\int_\ell \frac{w'(\sigma)}{\overline{w'(\sigma)}}\frac{\overline{\psi_3'}(\sigma)}{\sigma-\zeta}d\sigma\right]=\frac{2qi}{k_2}\frac{1}{2\pi i}\int_\ell \frac{w'(\sigma)}{\sigma-\zeta}d\sigma,\\
&\frac{e_{15}^1}{\in_{11}}\left[\frac{1}{2\pi i}\int_\ell \frac{\psi_1'(\sigma)}{\sigma-\zeta}d\sigma-\frac{1}{2\pi i}\int_\ell \frac{w'(\sigma)}{\overline{w'(\sigma)}}\frac{\overline{\psi_1'}(\sigma)}{\sigma-\zeta}d\sigma\right]+\frac{e_{15}^2}{\in_{11}}\left[\frac{1}{2\pi i}\int_\ell \frac{\psi_2'(\sigma)}{\sigma-\zeta}d\sigma-\frac{1}{2\pi i}\int_\ell \frac{w'(\sigma)}{\overline{w'(\sigma)}}\frac{\overline{\psi_2'}(\sigma)}{\sigma-\zeta}d\sigma\right]\\
&-\left[\frac{1}{2\pi i}\int_\ell \frac{\psi_3'(\sigma)}{\sigma-\zeta}d\sigma-\frac{1}{2\pi i}\int_\ell \frac{w'(\sigma)}{\overline{w'(\sigma)}}\frac{\overline{\psi_3'}(\sigma)}{\sigma-\zeta}d\sigma\right]=\frac{2Ti}{\in_{11}}\frac{1}{2\pi i}\int_\ell \frac{w'(\sigma)}{\sigma-\zeta}d\sigma.
\end{aligned}\tag{15}$$

We notice that $\psi_i'(\zeta)$ are analytic in $|\zeta|<1$ and continuous in $|\zeta|\le 1$. It follows from the Cauchy's integral formula in complex functions that

$$\frac{1}{2\pi i}\int_\ell \frac{\psi_i'(\sigma)}{\sigma-\zeta}d\sigma=\psi_i'(\zeta),|\zeta|<1 \tag{16}$$

Through derivation of Eq. (12), we have

$$\begin{aligned}
\omega'(\zeta)=(1-\zeta^2)[(d^2+1)+&\frac{(d^2-1)(1+k)(1+\zeta^2)}{\sqrt{(1+\zeta)^4+2k(1-\zeta^2)^2+(1-\zeta)^4}}]\times\{-\frac{a+b}{8d\zeta^2}\\
+&\frac{8d(a-b)}{[2(d^2+1)(1+\zeta^2)+(d^2-1)\sqrt{(1+\zeta)^4+2k(1-\zeta^2)^2+(1-\zeta)^4}]^2}\}
\end{aligned}\tag{17}$$

From Eq. (17), it is not difficult to find that $\omega'(\zeta)$ is analytic in $|\zeta|>1$ and continuous in $|\zeta|\ge 1$. According to the Cauchy's integral formula of infinite region, one finds

$$\frac{1}{2\pi i}\int_\ell \frac{\omega'(\sigma)}{\sigma-\zeta}d\sigma=\omega'(\infty)=\frac{(d^2+1)(a+b)}{4d}\overset{def}{=}F(\zeta) \tag{18}$$

By Eq. (17), one has $\frac{\omega'(\sigma)}{\overline{\omega'(\sigma)}}=-\frac{1}{\sigma^2}$. Since $\psi_i'(\zeta)$ are analytic in $|\zeta|<1$, we can assume that $\psi_i'(\zeta)$ have Taylor series: $\psi_1'(\zeta)=\sum_{n=0}^{\infty}a_n\zeta^n,\psi_2'(\zeta)=\sum_{n=0}^{\infty}b_n\zeta^n,\psi_3'(\zeta)=\sum_{n=0}^{\infty}c_n\zeta^n$.

We notice that $\overline{\psi_i'(\sigma)}$ are regarded as the boundary values (the values on the unit circle ℓ) of $\overline{\psi_1'}(\frac{1}{\zeta})=\sum_{n=0}^{\infty}\overline{a_n}(\frac{1}{\zeta})^n,\overline{\psi_2'}(\frac{1}{\zeta})=\sum_{n=0}^{\infty}\overline{b_n}(\frac{1}{\zeta})^n,\overline{\psi_3'}(\frac{1}{\zeta})=\sum_{n=0}^{\infty}\overline{c_n}(\frac{1}{\zeta})^n$ respectively. Thus, $\frac{\omega'(\sigma)}{\overline{\omega'(\sigma)}}\overline{\psi_i'}(\sigma)$ in Eq. (15) areregarded as the boundary values of $-\frac{1}{\zeta^2}\overline{\psi_i'}(\frac{1}{\zeta})$, which are analytic functions in $|\zeta|>1$. According to the Cauchy's integral formula of infinite region, for $|\zeta|<1$, we have

$$\frac{1}{2\pi i}\int_\ell \frac{w'(\sigma)}{\overline{w'(\sigma)}}\cdot\frac{\overline{\psi_i'}(\sigma)}{\sigma-\zeta}d\sigma=0 \tag{19}$$

Substituting Eqs. (16) and (18)-(19) into Eq. (15), yields

$$\begin{aligned}
&\psi_1'(\zeta)+\frac{R_3}{C_{44}}\psi_2'(\zeta)+\frac{e_{15}^1}{C_{44}}\psi_3'(\zeta)=\frac{2pi}{C_{44}}F(\zeta),\\
&\frac{R_3}{k_2}\psi_1'(\zeta)+\psi_2'(\zeta)+\frac{e_{15}^2}{k_2}\psi_3'(\zeta)=\frac{2qi}{k_2}F(\zeta),\\
&\frac{e_{15}^1}{\in_{11}}\psi_1'(\zeta)+\frac{e_{15}^2}{\in_{11}}\psi_2'(\zeta)-\psi_3'(\zeta)=\frac{2Ti}{\in_{11}}F(\zeta).
\end{aligned} \tag{20}$$

From Eq. (20), one obtains

$$\begin{aligned}
\psi_1'(\zeta)=&2\mathrm{i}\frac{e_{15}^1k_2T+(e_{15}^2)^2p+\in_{11}k_2p-R_3\in_{11}q-R_3e_{15}^2T-e_{15}^1e_{15}^2q}{C_{44}(e_{15}^2)^2-2e_{15}^1e_{15}^2R_3+k_2(e_{15}^1)^2-R_3{}^2\in_{11}+C_{44}\in_{11}k_2}F(\zeta),\\
\psi_2'(\zeta)=&2\mathrm{i}\frac{(e_{15}^1)^2q+C_{44}\in_{11}q-R_3\in_{11}p+C_{44}e_{15}^2T-e_{15}^1e_{15}^2p-e_{15}^1R_3T}{C_{44}(e_{15}^2)^2-2e_{15}^1e_{15}^2R_3+k_2(e_{15}^1)^2-R_3{}^2\in_{11}+C_{44}\in_{11}k_2}F(\zeta),\\
\psi_3'(\zeta)=&2\mathrm{i}\frac{R_3{}^2T+e_{15}^1k_2p-R_3e_{15}^1q-R_3e_{15}^2p+C_{44}e_{15}^2q-C_{44}k_2T}{C_{44}(e_{15}^2)^2-2e_{15}^1e_{15}^2R_3+k_2(e_{15}^1)^2-R_3{}^2\in_{11}+C_{44}\in_{11}k_2}F(\zeta).
\end{aligned} \tag{21}$$

Substituting Eq. (21) into Eq. (13), one has

$$\begin{aligned}
\varphi_1'(z)=&2\mathrm{i}\frac{e_{15}^1k_2T+(e_{15}^2)^2p+\in_{11}k_2p-R_3\in_{11}q-R_3e_{15}^2T-e_{15}^1e_{15}^2q}{C_{44}(e_{15}^2)^2-2e_{15}^1e_{15}^2R_3+k_2(e_{15}^1)^2-R_3{}^2\in_{11}+C_{44}\in_{11}k_2}\frac{F(\zeta)}{\omega'(\zeta)},\\
\varphi_2'(z)=&2\mathrm{i}\frac{(e_{15}^1)^2q+C_{44}\in_{11}q-R_3\in_{11}p+C_{44}e_{15}^2T-e_{15}^1e_{15}^2p-e_{15}^1R_3T}{C_{44}(e_{15}^2)^2-2e_{15}^1e_{15}^2R_3+k_2(e_{15}^1)^2-R_3{}^2\in_{11}+C_{44}\in_{11}k_2}\frac{F(\zeta)}{\omega'(\zeta)},\\
\varphi_3'(z)=&2\mathrm{i}\frac{R_3{}^2T+e_{15}^1k_2p-R_3e_{15}^1q-R_3e_{15}^2p+C_{44}e_{15}^2q-C_{44}k_2T}{C_{44}(e_{15}^2)^2-2e_{15}^1e_{15}^2R_3+k_2(e_{15}^1)^2-R_3{}^2\in_{11}+C_{44}\in_{11}k_2}\frac{F(\zeta)}{\omega'(\zeta)}.
\end{aligned} \tag{22}$$

Substituting Eq. (22) into Eq. (9), we have

$$\sigma_{31}-i\sigma_{32}=2pi\frac{F(\zeta)}{\omega'(\zeta)},H_1-iH_2=2qi\frac{F(\zeta)}{\omega'(\zeta)},D_1-iD_2=2\mathrm{T}i\frac{F(\zeta)}{\omega'(\zeta)}. \tag{23}$$

From Eq. (23), the stresses fields and displacements fields can be determined, we omit them since the complexity of the expressions.

The intensity factors at the crack tip are very useful in practice, the vector of the SIFs of the phonon field and the phason field, and the EDIFs in z plane can be defined as

$$\sigma_{31}-i\sigma_{32}=-\frac{K_{III}^{II}}{\sqrt{2\pi(z-z_1)}},H_1-iH_2=-\frac{K_{III}^{\perp}}{\sqrt{2\pi(z-z_1)}},D_1-iD_2=-\frac{K_{III}^{D}}{\sqrt{2\pi(z-z_1)}}. \tag{24}$$

where $z=re^{i\theta}$, K_{III}^{II}, $K_{III}^{\perp}$ and K_{III}^{D} denote the SIFs of the phonon field and the phason field, and the EDIFs respectively.

Utilizing the conformal mapping $z=\omega(\zeta)$, from Eq. (24), the computational formulae of the SIFs and the EDIFs in ζ plane are obtained as follows

$$K_{III}^{II}=\lim_{\zeta\to1}2\sqrt{\pi}p\frac{F(\zeta)}{\sqrt{\omega''(\zeta)}},K_{III}^{\perp}=\lim_{\zeta\to1}2\sqrt{\pi}q\frac{F(\zeta)}{\sqrt{w''(\zeta)}},K_{III}^{D}=\lim_{\zeta\to1}2\sqrt{\pi}T\frac{F(\zeta)}{\sqrt{\omega''(\zeta)}}. \tag{25}$$

where $\zeta=1$ is the corresponding point of the crack tip $z=c$.

From Eqs. (17) and (18), we have

$$\frac{1}{\sqrt{\omega''(1)}}\to\frac{\sqrt{2d(d^2-1)}}{\sqrt{(d^2+1)[(d^2-1)a+(d^2+1)b]}},\zeta\to1(z\to c) \tag{26}$$

$$F(1)\to\frac{(d^2+1)(a+b)}{4d},\zeta\to1(z\to c) \tag{27}$$

Substituting Eqs. (26) and (27) into Eq. (25), we obtain the SIFs of the phonon and the phason, and the EDIFs for electric impermeable in ζ plane as following, respectively,

$$
\begin{aligned}
K_{III}^{II} &= \lim_{\zeta\to 1} 2\sqrt{\pi}p\frac{F(\zeta)}{\sqrt{\omega''(\zeta)}} = \frac{p(a+b)\sqrt{\pi(d^4-1)}}{\sqrt{2d[(d^2-1)a+(d^2+1)b]}},\\
K_{III}^{\perp} &= \lim_{\zeta\to 1} 2\sqrt{\pi}q\frac{F(\zeta)}{\sqrt{w''(\zeta)}} = \frac{q(a+b)\sqrt{\pi(d^4-1)}}{\sqrt{2d[(d^2-1)a+(d^2+1)b]}},\\
K_{III}^{D} &= \lim_{\zeta\to 1} 2\sqrt{\pi}T\frac{F(\zeta)}{\sqrt{\omega''(\zeta)}} = \frac{T(a+b)\sqrt{\pi(d^4-1)}}{\sqrt{2d[(d^2-1)a+(d^2+1)b]}}.
\end{aligned}
\tag{28}
$$

Electric Permeable Problem

the electric permeable boundary condition can be expressed as

$$
\begin{aligned}
&\sqrt{x_1+x_2}\to\infty : \sigma_{32}=0, H_2=0, D_2=0,\\
&(x_1,x_2)\in L : \sigma_{32}=-p, H_{32}=-q, \phi=\lambda(\text{const ant}).
\end{aligned}
\tag{29}
$$

Similarly, for electric permeable problem, we solve the boundary value problems (7) and (29). Substituting $\phi=\lambda$ into Eqs. (1)-(3), and through derivation, we have

$$
\begin{aligned}
\sigma_{23} &= \sigma_{32} = -\frac{1}{2i}\Big[C_{44}(\varphi_1'-\overline{\varphi_1'})+R_3(\varphi_2'-\overline{\varphi_2'})\Big],\\
H_2 &= -\frac{1}{2i}\Big[R_3(\varphi_1'-\overline{\varphi_1'})+k_2(\varphi_2'-\overline{\varphi_2'})\Big],\\
D_2 &= -\frac{1}{2i}\Big[e_{15}^1(\varphi_1'-\overline{\varphi_1'})+e_{15}^2(\varphi_2'-\overline{\varphi_2'})\Big].
\end{aligned}
\tag{30}
$$

Substituting Eq. (30) into Eq. (29), we obtain

$$
\begin{aligned}
&C_{44}(\varphi_1'-\overline{\varphi_1'})+R_3(\varphi_2'-\overline{\varphi_2'})=2pi,\\
&R_3(\varphi_1'-\overline{\varphi_1'})+k_2(\varphi_2'-\overline{\varphi_2'})=2qi,\\
&e_{15}^1(\varphi_1'-\overline{\varphi_1'})+e_{15}^2(\varphi_2'-\overline{\varphi_2'})=-\frac{(e_{15}^1k_2-e_{15}^2R_3)p+(e_{15}^2C_{44}-e_{15}^1R_3)q}{C_{44}k_2-{R_3}^2}.
\end{aligned}
\tag{31}
$$

Similar to the electric permeable derivation process, we have

$$
\psi_1'(\zeta)=2\mathrm{i}\frac{k_2p-R_3q}{C_{44}k_2-{R_3}^2}F(\zeta), \psi_2'(\zeta)=2\mathrm{i}\frac{C_{44}q-R_3p}{C_{44}k_2-{R_3}^2}F(\zeta).
\tag{32}
$$

According to Eqs. (13), (30) and (32), the expression of the SIFs and the EDIFs can be determined in z plane.

The SIFs of phonon and phason fields, and the EDIFs for electric permeable can be obtained in ζ plane as follows

$$
\begin{aligned}
K_{III}^{II} &= \lim_{\zeta\to 1} 2\sqrt{\pi}p\frac{F(\zeta)}{\sqrt{\omega''(\zeta)}} = \frac{p(a+b)\sqrt{\pi(d^4-1)}}{\sqrt{2d[(d^2-1)a+(d^2+1)b]}},\\
K_{III}^{\perp} &= \lim_{\zeta\to 1} 2\sqrt{\pi}q\frac{F(\zeta)}{\sqrt{w''(\zeta)}} = \frac{q(a+b)\sqrt{\pi(d^4-1)}}{\sqrt{2d[(d^2-1)a+(d^2+1)b]}},\\
K_{III}^{D} &= \lim_{\zeta\to 1} 2\sqrt{\pi}\frac{(e_{15}^1k_2-e_{15}^2R_3)p+(e_{15}^2C_{44}-e_{15}^1R_3)q}{C_{44}k_2-{R_3}^2}\frac{F(\zeta)}{\sqrt{\omega''(\zeta)}}\\
&= \frac{(e_{15}^1k_2-e_{15}^2R_3)p+(e_{15}^2C_{44}-e_{15}^1R_3)q}{C_{44}k_2-{R_3}^2}\frac{T(a+b)\sqrt{\pi(d^4-1)}}{\sqrt{2d[(d^2-1)a+(d^2+1)b]}}.
\end{aligned}
\tag{33}
$$

Discussion and Results

We have obtained the SIFs and the EDIFs of an elliptic hole with two straight cracks in 1D hexagonal piezoelectric QCs above. These results are discussed further as follows

If the long semi-axes b tends to zero, i.e., $b\to 0$, Eq. (28), we obtain

$$
K_{III}^{II} = p\sqrt{\pi c}, K_{III}^{\perp} = q\sqrt{\pi c}, K_{III}^{D} = T\sqrt{\pi c}.
\tag{34}
$$

These are the exact analytic solutions of the SIFs and the EDIFs at the crack tip $(c,0,0)$ of Griffith crack in a 1D hexagonal piezoelectric QCs. In the absence of the EDIFs, the obtainable results are identical to the results in Ref[7].

If the short semi-axes a tends to zero, i.e., $a \to 0$, Eq. (28) leads to

$$K_{III}^{II} = p\sqrt{\pi c}, K_{III}^{\perp} = q\sqrt{\pi c}, K_{III}^{D} = T\sqrt{\pi c}. \tag{35}$$

Eq. (35) gives the exact analytic solutions of the SIFs and the EDIFs at the crack tip $(c,0,0)$ of cross crack in a 1D hexagonal piezoelectric QCs(shown in Fig.3). The results show that if the solid is shear loading and electric loading along the quasiperiodic direction (x_3 direction) at infinity, the SIFs and the EDIFs at the crack tip of the crack parallel to x_1 axis are not affected by the crack parallel to x_2 axis. Because of its symmetry, the results are the same as the state of Griffith crack.

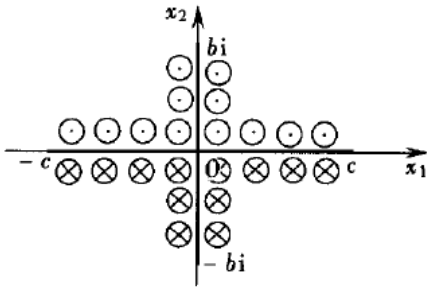


Fig. 3. Asymmetric cross crack.

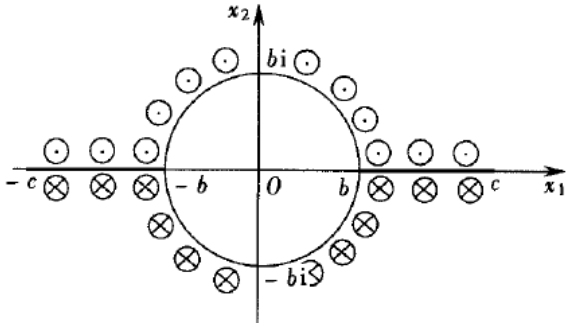


Fig. 4. Circular hole with equal two edge cracks

If $a \to b$, from Eq. (28), we have

$$K_{III}^{II} = p\sqrt{\pi c(1-\frac{b^4}{c^4})}, K_{III}^{\perp} = q\sqrt{\pi c(1-\frac{b^4}{c^4})}, K_{III}^{D} = T\sqrt{\pi c(1-\frac{b^4}{c^4})}. \tag{36}$$

These are the exact analytic solutions of the SIFs and the EDIFs of a circular hole with equal two edge cracks in a 1D hexagonal piezoelectric QCs. Seen from the result, when the circular hole with two straight cracks is the shear loading and electric loading, the SIFs and the EDIFs at the crack tip are not only related to the radius of a circle, but also the crack length.

As far as electric permeable problem, it can make similar discussions.

Conclusions

Under two kinds of the electric impermeable and electrical permeable boundary conditions, the anti-plane shear problem of an elliptical hole with two symmetric collinear cracks in 1D hexagonal pizoelectric QCs is solved by means of complex variable function method with conformal mapping in this paper. The exact solutions of the SIFs for the phonon field and the phason field, and the EDIFs are obtained in closed-form.These solutions are found for the first time in a 1D hexagonal piezoelectric QCs and have significance to the theory of brittle fracture of solids including QCs. As far as the phonon field and the phason field are concerned, these analytic solutions match with the result given in Ref[17]. About the effect of electric load on defect, there are the following two aspects: about the electric impermeable problem, from Eq. (28), it can seen the SIFs and the EDIFs does not occur coupling, and they are affected by crack size, and they have singularity at the crack tip. Electric load did not change the stress field of QCs, the EDIFs is only related to the size of the electrical load, but for strain field, it will change; about the electric permeable problem, from Eq. (33), it can seen the effect of stress and crack size on the SIFs and the EDIFs. The SIFs for the phonon field and the phason field has nothing to do with the material itself. But the EDIFs not only depends on shear loadings of the phonon field and the phason field, but also depends on the properties of the materials, and has no singularity at the crack tip. So, influence of the electric load on defects cannot be ignored, electric load has played an accelerating role in materials fracture. Therefore, this research is necessary.

With the variation of the hole-size and the crack lengths, the present results can be applied to sti-mulate many new crack configurations in practice, such as Griffith crack, cross crack, and circular hole with equal two edge cracks, which are new and useful to theoretical researchers, in particular for the study of QCs. As far as the phonon field is concerned, the special cases of the present results such as Griffith crack and a circular hole with two edge cracks agree well with the classical results[18–19]. In the absence of the phason field, the obtainable results in this paper match with the classical ones[20-21]. By using the conformal mapping technique developed in this paper and the complex variable function method, the complicated defect problem is solved electively, which can analyse similar fracture problems of this kind.

Acknowledgements

This work is supported by the National Natural Science Foundation of China (51061015,11362018), Specialized Research Fund for the Doctoral Program of Higher Education of China(20116401110002).

References

[1] S. S. Rao, M. Sunar, Applied Mechanics Review, 47 (1994) 113–123.
[2] K. Uchino, Acta Materialia, 46 (1998) 3745–3753.
[3] D. Shechtman, I. Blech, D. Gratias, J. W. Cahn, Phys. Rev. Lett, 53 (1984) 1951-1953
[4] S. B. Rochal, V. L. Lorman, Phys. Rev. B, 66 (2002) 144-204.
[5] X. M. Meng, B. Y. Tong, Y. K. Wu, Acta.Mech.Sin, 30 (1994) 60–64. (in Chinese)
[6] Z. Zhang, K. Urban, Phil. Mag. Lett., 60 (1989) 97–102.
[7] T. Y. Fan, The Mathematical Theory of Elasticity of Quasicrystals and its Applications, Beijing Science Press, Beijing , 2010.(in Chinese)
[8] X. F. Li, T. Y. Fan, Phys. Stat. B, 212 (1999) 19–26.
[9] T. Y. Fan, X. F. Li, Y. F. Sun, Phys. Sin. Overseas Edition, 8 (1999) 288–295.
[10] N. I. Muskhelishvili, Some basic problem of the mathematical theory of elasticity, Groningen, Noordhoff, 1963.
[11] Y. Gao, S. P. Xu, B. S. Zhao, J Elast, 86 (2007) 221-233.
[12] L. H. Li , T. Y. Fan, Appl. Math. Comput, 196 (2008) 1-5.
[13] X. Wang, E. Pan, J Phys, 70 (2008) 911-933.
[14] J. H. Guo, Z. X. Lu, Appl. Math. Comput, 217 (2011) 9397-9403.
[15] Y. F. Wu, W. Q. Chen, X. Y. Li, Philosophical Magazine, 93 (2013) 858–882.
[16] W. C. Shi, Appl. Math. Comput, 215 (2009) 1062–1067.
[17] J. H. Guo, G.T. Liu, Applied Mathematics and Mechanics(English Edition), 29 (2008) 439-446
[18] G. C. Sih, ASME J. Appl. Mech, 32 (1965) 51.
[19] H. Tada, P. C. Paris, The Stress Analysis of Cracks Handbook, Del Research Corporation, Hellertown, Pennsylvania, 1973.
[20] B. L. Wang, Piezoelectric material and fracture mechanics of its structure, National defence industry press, Beijing, 2002. (in Chinese)
[21] C. F. Gao, Mechanics Research Communications, 26 (1999) 427-432.

Advanced Materials Research Vol. 936 (2014) pp 136-139
© (2014) Trans Tech Publications, Switzerland
doi:10.4028/www.scientific.net/AMR.936.136

CdS -bentonite Sulfide ion Sensor: pH Effect and Selectivity

Kemawadee Udomphan [a] , Atchana Wongchaisuwat [b] and Ladda Meesuk[c*]

Department of Chemistry, Faculty of Science, Kasetsart University, Chatuchak, Bangkok 10900, Thailand.

[a]mikichan_af_tamp@hotmail.com; [b]fsciatw@ku.ac.th; [c]fscildm@ku.ac.th

Keywords: CdS, potentiometric electrode, bentonite, sulfide ion, fixed interference method

Abstract: CdS-bentonite was prepared by an *in situ* solid-solid reaction and used as a sulfide ion potentiometric sensor. The electrode responded constant potential in the pH range of 5-10. Selectivity of the electrode was primarily estimated in terms of Nernstian slope. It was found that the electrode could be used to measure sulfide ion in water samples without interfering from Co^{2+}, Mn^{2+}, Zn^{2+}, Hg^{2+}, Cl^{-}, F^{-} or PO_4^{3-}ions. A selectivity coefficient of sulfate over sulfide was determined by using mixed solution method (fixed interference method) which indicated that SO_4^{2-} would be an interfering ion while measuring S^{2-}**,** but could be prevented by conventional precipitation method.

Introduction

Bentonite is a commercial name of a clay mineral which consists of montmorillonite as main composition. Montmorillonite is a layered silicate clay mineral in which an alumina octahedral arrangement situated between two tetrahedral of silica sheet. Substitutions of Al^{3+} within the lattice structure of Si^{4+} in tetrahedral sheet and Mg^{2+} for Al^{3+} in octahedral sheet resulted unbalanced charge in the structural units of bentonite. The charge imbalanced is compensated by exchangeable cation such as Na^{+}, Ca^{2+} and Mg^{2+} in the interlayer spaces. Bentonite has several advantages such as ion exchange property, adsorptive property, swelling behavior and large surface area. [1]

CdS is a bright yellow, sparingly soluble precipitate with a solubility product constant (K_{sp}) about $1x10^{-29}$. It exists in nature in three different crystal forms, hexagonal wurtzite, cubic zinc blend and high pressure rock-salt phase. There are many applications of cadmium sulfide, for examples; semiconductor, solar cell, photodetectors, field effect transistors and electrically driven lasers [2].

A number of bentonite-modified electrodes and electrochemical sensors have been reported [3-7]. In this work, we studied the effect of pH to the activity of CdS- bentonite electrode as well as its selectivity.

Experimental

Chemicals and apparatus

Ca-bentonite from Lopburi province, central Thailand, was provided by Klong Yang Co. Ltd. All other chemicals were analytical grade. Carboxymethyl cellulose (CMC, 3%), polytetrafluoroethylene (PTFE, 60%, DuPont), artificial graphite (Thai carbon and graphite), sodium sulfide flakes (ion free extra pure, Na_2S, loba chemie) cadmium chloride ($CdCl_2$, Univar), hydrochloric acid (6M HCl, Carlo Erba), silver nitrate ($AgNO_3$, Carlo Erba), mercuric nitrate, ($Hg(NO_3)_2.H_2O$ Carlo Erba), cobalt chloride, ($CoCl_2.6H_2O$, Univar) manganese chloride, ($MnCl_2.4H_2O$, Univar), zinc sulphate, ($ZnSO_4.7H_2O$, Univar), potassium fluoride, (KF, Unilab), potassium chloride, (KCl, Univar). Ion meter (ORION, 420A) was used to measure potential of the solution. Silver-silver chloride electrode was used as a reference electrode. The amount of Ca(II) and Cd(II) in bentonite was determined by atomic absorption spectrometer (Perkin Elmer, Analyst 800). Preparation of CdS- bentonite and construction of CdS- bentonite potentiometric electrode have been reported in our previous article [8].

The study of pH effect to the activity of CdS-bentonite potentiometric sensor

In order to investigate the appropriate pH range for CdS-bentonite potentiometric sensor, sulfide solutions of 0.001 and 0.01 M were prepared and adjusted to pH 2-12 with HNO_3 and NaOH (0.001-1 M). Potential of each sulfide solution was measured by using CdS-bentonite electrode. Then, the measured potentials of each sulfide solution *vs* pH were plotted.

Selectivity of CdS-bentonite potentiometric sensor

Selectivity of the sensor was verified by means of Nernstian slope and a selectivity coefficient was determined by using the mixed solution method or fixed interference method[16]. Selectivity coefficient was determined by the use of Nicolsky equation:

$$E_{AB} = k_A + \frac{S}{Z_A}\log\left(a_A + K_{AB}a_B^{Z_A/Z_B}\right) \quad (1)$$

Where K_{AB} is the selectivity coefficient of the electrode for B over A, k_A is a constant coresponds to that in Nernst Equation for primary ion A, a_B is the fixed concentration of interfering ion B added to each solution of A, S is slope of the calibration curve of primary ion, z_A and z_B are charges of ions A and B, a_A is the activity of the primary ion (used in terms of concentration) at which the electrode responded equally to both ions, which can be estimated by the point at the intercept of extrapolation of linear portion of calibration curve as in Fig.1.

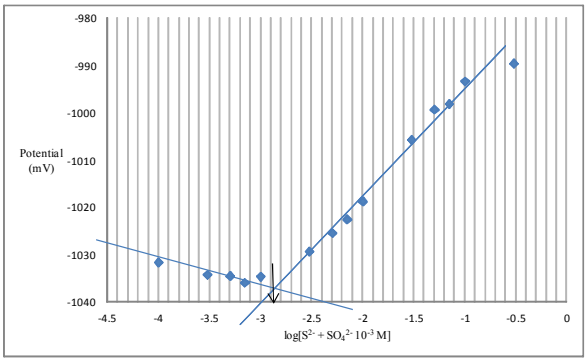


Fig.1 Potential and log $[S^{2-}]$ in the presence of fixed $[SO_4^{2-}]$, showing a_A at the intercept

At the intercept, each ion contributes equally to the potential, then in equation (1), $a_A = K_{AB}.(a_B^{z_A/z_B})$.The selectivity coefficient of the electrode for B over A, is calculated by equation (2):

$$K_{AB} = \frac{a_A}{a_B^{Z_A/Z_B}} \quad (2)$$

Results and discussion

Effect of pH to the activity of CdS-Bentonite potentiometric sensor.

At two sulfide ion concentrations (0.001 and 0.01 M), it was found that, the potential were constant at pH range 5–10, beyond which a potential change was observed as shown in Fig.2. This pH range can be taken as the appropriate working pH of the sensor.

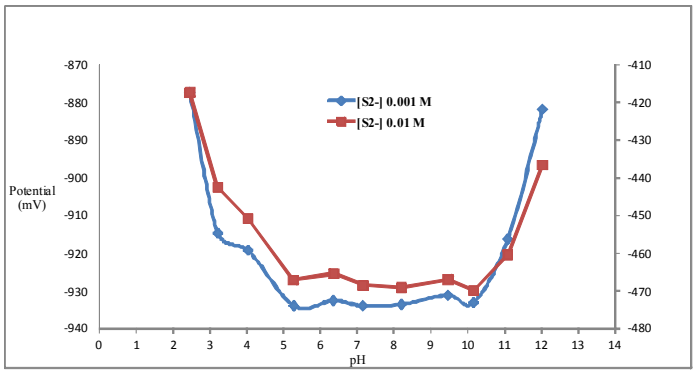


Fig.2. Plot of potential of sulfide ion at different pH

Selectivity of CdS-bentonite potentiometric sensor

When the electrode was used to measure potential of several ions such as Co^{2+}, Mn^{2+}, Zn^{2+}, Cl^{-}, F^{-} PO_4^{3-} and S^{2-}, the electrode gave best response to S^{2-}, in terms of Nernstian slope, as shown in Table 1. Calibration curve of S^{2-} gave good straight line with slope 29.3, closed to theoretical value. While slope of other ions did not fit to Nernstian slope. However, in solutions of Hg^{2+} and $SO_4^{2-}$the slopes were 28.17 and 30.65, respectively.These were only 4.5% and 3.84% far from theoretical value, which indicated that, Hg^{2+} and SO_4^{2-} could be interfering ions when the electrode is used to measure sulfide ion in real water samples.

TABLE 1. SLOPE OF S^{2-} COMPARED WITH OTHER IONS

Ion	S^{2-}	Co^{2+}	Mn^{2+}	Hg^{2+}	Zn^{2+}	Cl^{-}	F^{-}	SO_4^{2-}	PO_4^{3-}
Slope	*29.3*	21.09	20.48	*28.17*	22.17	31.82	30.07	30.65	13.14
Theoretical	29.5	29.5	29.5	29.5	29.5	59	59	29.5	19.65

To verify the interference of Hg^{2+} and SO_4^{2-}over S^{2-}, the selectivity coefficient of electrode was performed by using the mixed solution method (fixed interference method) described above. However, it was found that, the selectivity coefficient of Hg^{2+} over S^{2-} ($K_{S^{2-}Hg^{2+}}$) could not be determined by this method, the solubility of HgS is very low (Solubility Product Constant , K_{sp} = $1.6x10^{-54}$), even at low concentration of Hg^{2+} (about $1x10^{-5}$M) added to S^{2-} solution, precipitate of HgS was formed. The selectivity coefficient of SO_4^{2-}over S^{2-}($K_{AB,}$ A= S^{2-}, B= SO_4^{2-}) was calculated by using equation (2) where a_A at the intercept was $1.26x10^{-3}$M (Fig.1) and the SO_4^{2-} concentration added to S^{2-} (a_B) was $1x10^{-3}$M, and $z_A = z_B = 2$, the calculated K_{AB} was 1.26. In other word, the selectivity coefficient of S^{2-}over SO_4^{2-} (K_{BA}) would be about 0.79. This indicated that SO_4^{2-} ion will interfere the measurement of S^{2-} when the electrode is used to measure S^{2-} ion in real water samples. The selectivity coefficient of SO_4^{2-} is consistent with the measured slope in Table 1. When the electrode is used to measure S^{2-} ion in water samples, interference of SO_4^{2-} ion could be simply prevented by adding $BaCl_2$ to the solution to form white precipitate, $BaSO_4$.

CONCLUSIONS

CdS-bentonite was used to construct a potentiometric electrode to measure S^{2-} in solution. The concentration of response linear range was around $1x\ 10^{-4}$ - 0.3 M of sulfide ion. The appropriate working pH of the electrode was 5-10. Selectivity studies from Nernstian slope

indicated that Co^{2+}, Mn^{2+}, Zn^{2+}, Cl^{-}, F^{-} and PO_4^{3-} would not interfere the measurement of S^{2-}, while Hg^{2+} and SO_4^{2-}could be an interfering ions in terms of Nernstian slope. Nevertheless, since the solubility product constant (K_{sp}) of HgS is very low, in solution containing Hg^{2+} and S^{2-}, the HgS precipitae will be observed and can be filtered off, before performing S^{2-} measurement. The selectivity coefficient of SO_4^{2-}over S^{2-} was 1.26, agreed well with the slope of SO_4^{2-} in the calibration graph of SO_4^{2-} solution which was found closed to that of S^{2-}, which indicates that SO_4^{2-} ion will be an interference while measuring S^{2-} ion in water sample, however this could be simply prevented by adding $BaCl_2$ to precipitate $BaSO_4$ prior to S^{2-} measurement.

Acknowledgement

This work was supported by Kasetsart University Research and Development Institute (KURDI). A partly financial support from Center for Advanced Studies in Tropical Natural Resources, National Research University-Kasetsart University (CASTNAR, NRU-KU) is also appreciated.

References

[1] D.A.C. Manning, Introduction to industrial minerals. Chapman & Hall, London, 1995.

[2] [V. Singh, P.K. Sharma, P.Chauha, Synthesis of CdS nanoparticles with enhanced optical properties. Mater. Charact. 62 (2011) 43-52.

[3] K. Itayat, A.J. Bard, Clay-modified electrodes. 5. Preparation and electrochemical characterization of pillared clay-modified electrodes and membranes, J. Phys. Chem. 89 (1985) 5565-5568.

[4] M. Darder, M. Colilla, E. Ruiz-Hitzky, Biopolymer-clay nanocomposites based on chitosan intercalated in montmorillonite, Chem. Mater., 15 (2003) 3774-3780.

[5] N.L. Dias Filho, G.L. Okajima, G.Pires, R.M. Costa, D.R. do Carmo, A.H. Rosa, Voltammetry of mercury(II) based on an organo-clay modified graphite electrode, Port. Electrochim. Acta. 26 (2008) 163-179.

[6] A. Abdulla, A. Issa, Y. Salim Al-Degs, N. A. A. Al-Rabady, Selective electrochemical detection of toxic heavy metals at ultra trace levels using natural clay-modified- electrode, Eurasian J. Anal. Chem. 4(3), (2009) 245-256.

[7] M. Darder, M. Colilla, E. Ruiz-Hitzky, Chitosan-clay nanocomposites: application as electrochemical sensors, Appl. Clay. Sci. 28 (2005) 199-208.

[8] K. Udomphan, A. Wongchaisuwat, L.Meesuk, CdS-intercalated Bentonite: A novel sulfide ion selective electrode, Applied Mechanics and Materials. 110-116 (2012) 472-477.

[9] G.D.Christian, Potentiometric electrodes and potentiometry, Chapter 13th in Analytical Chemistry, 6th Edition, John-Wiley&Sons, Inc., New York, 2004, pp 369-407.

Advanced Materials Research Vol. 936 (2014) pp 140-144
© (2014) Trans Tech Publications, Switzerland
doi:10.4028/www.scientific.net/AMR.936.140

Relationship between Annealing and Shape Memory Effect of Shape Memory Polyurethane

Jia YING[1,a], Masaaki NISHIKAWA[1,b], Masaki HOJO[1,c]

[1] Department of Mechanical Engineering and Science, Kyoto University
C3, Kyoto Daigaku-Katsura, Nishikyo-ku, Kyoto, 615-8540, Japan

[a] ying.jia.85c@st.kyoto-u.ac.jp, [b] nishikawa@me.kyoto-u.ac.jp, [c] hojo_cm@me.kyoto-u.ac.jp

Keywords: Shape memory polyurethane, Annealing, Shape memory effect

Abstract: The relationship of annealing and shape memory effect of uniaxially oriented shape memory polyurethane was studied; meanwhile a new method of adjusting shape recovery ratio by annealing was proposed for further consideration. Experiments were designed to compare the influence on length change from annealing and shape memory effect with shape memory polyurethane film at 65°C. We found that for shape memory polyurethane which had residual strain from material processing procedure, annealing and shape memory effect have the same effect on its length change if they are both carried out at the same temperature. It is because annealing and shape memory effect have the same mechanism, which is the change of state from low conformational entropy states to the recovery of a stable high entropy state in the polymer. Moreover, it is proved by experiment that shape recovery ratio of shape memory polyurethane can be adjusted by annealing.

Introduction

Shape memory polymers (SMPs) are polymers with the ability to store and recover strains on the order of several hundred percent when subjected to a particular thermomechanical cycle [1]. Polyurethane (PU) is one of the most important materials in the SMP family. Shape recovery is one of the indexes that people are concerned about for evaluating shape memory effect. In general, SMPs are considered to consist of 'netpoints' and molecular switches. Netpoints are hard segments acting as a fixed phase under a certain thermomechanical cycle, which are assumed as crystalline, glassy domains, chain entanglements or chemical cross-links. The soft segments work as a reversible phase, which actively move as the thermal energy is inputted [2].

Meanwhile, annealing of polymer is a kind of second process wherein the polymer is brought to a certain temperature, kept for a certain time and then cooled to room temperature [3]. Annealing is also one of the ways to modify the material properties of thin films to the preferred properties [4, 5]. For example, the crystallinity of the polymer can be adjusted from annealing, as degree of crystallinity is determined by structural regularity of the polymer. Annealing can decrease the regularity if the polymer has a regular structure, which is obtained from external forces. In contrast, it also could increase the regularity if the initial structure is disordered. There are also some other researchers doing investigation on effects of annealing and thin film thickness [6] or effects of annealing with morphology change [3]. Thus, annealing treatment of shape memory polyurethane (SMPU) and the influence of annealing on shape memory recovery are quite important.

In this study, thermal annealing experiment of SMPU film was carried out to see how annealing affects film length by time. After that, annealing and thermal cycle experiments with different time combination were conducted to discover the relationship between annealing and shape recovery effect of this film. Finally, experiments with precisely controlled annealing time and thermal recovery time from calculation were carried out in order to validate our finding.

Experiments

Uniaxially oriented SMPU film with approximately 50μm thickness was prepared. Raw materials which were thermoplastic polyurethane with glass transition temperature of 55°C (MM5520) were provided by SMP Technologies Inc. For annealing, water bath was used to control the temperature. For thermal cycle, a tensile test machine with heating system imbedded was used and a microscopy was used for recording the length change of the film as seen in Fig.1. Annealing was carried out at 60°C, 65°C and 70°C, for each temperature, 3 repetitions were done to see if the results had good repeatability. Length change of the film was recorded. Curve fitting was done.

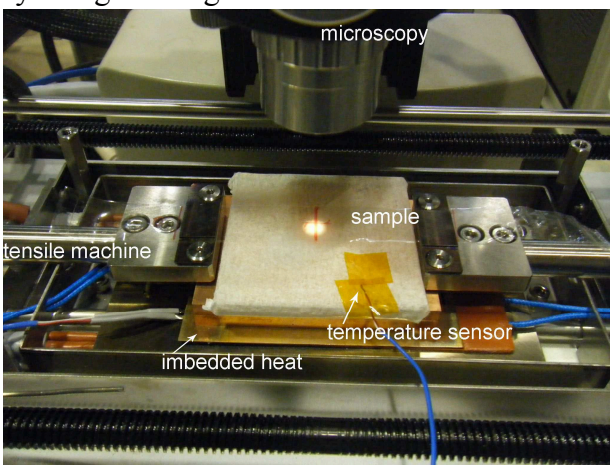


Fig.1 Device for shape memory thermal cycles. The line marked on SMPU film sample is for the ease of measuring the length change by microscopy.

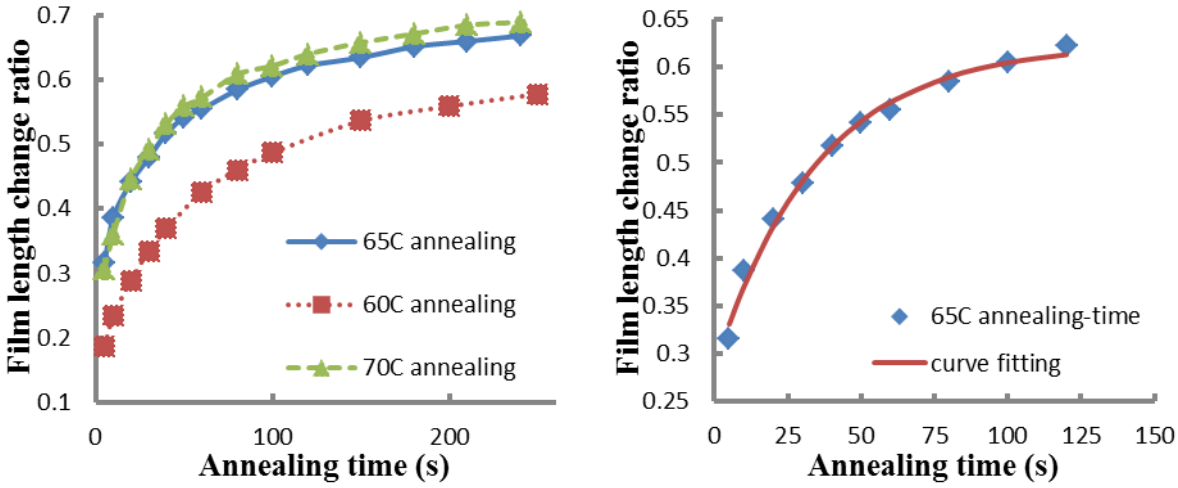
Thermal cycles were done by fixing the film in the tensile machine, followed by increasing temperature to 65°C and keeping there by the imbedded heat. After that, approx. 15(±1) % of elongation was applied to the film. Then temperature was cooled down to room temperature at 27°C within 10min. Shape recovery was carried out at 65°C water bath. 4 samples with different annealing time and shape recovery time were prepared. Table 1 shows annealing time and shape recovery time of these 4 samples. For example, sample No.2 went through a 10s of annealing followed by a thermal cycle with recovery time of 20s. This experiment was repeated three times. After that the relationship of annealing and shape recovery was revealed.

TABLE 1, ANNEALING TIME AND SHAPE RECOVERY TIME OF 4 SAMPLES

Sample number	Annealing time [s]	Elongation ratio in thermal cycle	Shape recovery time [s]
1	/	15%	30
2	10	15%	20
3	20	15%	10
4	30	15%	/

From the curving fitting equation and the relationship of annealing and shape recovery, the time which is needed for a desired length change ratio can be calculated. Annealing and thermal cycle experiments with controlled time that calculated from equation were conducted and results were analyzed.

Results and Discussion



(a) Figure of film length change ratio with respect to annealing time

(b) Curve fitting to length change ratio-annealing curve by least square

Fig. 2 (a) Relationship of film length change ratio and annealing time at 60°C, 65°C, and 70°C. (b) Least square fitting to the curve at 65°C.

Fig.2 (a) shows the relationship of length change ratio and annealing time at three different temperatures. 3 repetitions were done for each temperature. Only the intermediate curve for each temperature is shown here. From this figure, it can be seen that with the increasing of time, length change ratio caused by annealing becomes stable. It is because with the time increasing, residual strain from material manufacturing process decreases. Also it shows that length change ratio differs at different temperatures. Equation from curve fitting for 65°C is as following:

$$y = -0.3379*e^{(-0.0287*t)} + 0.6237 \quad (1)$$

where y is length change ratio, and t is annealing time.

From this equation, length change ratio at any annealing time can be calculated.

Fig.3 shows a total length change ratio of 4 samples described in Table 1. Here length change ratio is defined by the difference between lengths before annealing and after thermal cycle divided by the original length before annealing. From this figure, we can see that no matter it was pure annealing or pure shape memory thermal cycle, or different time combination of annealing and shape recovery, as long as they are the same in total time, the length change ratio is almost the same. This means, for this SMPU, length change from annealing and shape memory effect at the same temperature is the same. This can be understood as follows: annealing is a process that by heating up material, polymer chains relax from the low entropy state created by the stretch from manufacturing, follows by returning to stable high entropy state if annealing time is long enough. Meanwhile, the mechanism of shape memory effect is similar, by stretching at relatively high temperature above the glass transition temperature and cooling down, it temporarily stores energy of low conformational entropy state in molecular chains between crosslinking nodes, when heating above the glass transition temperature, stored strain recovers via an increase in the network free volume, chain rearrangement, and finally the recovery of a stable high entropy state in polymer.

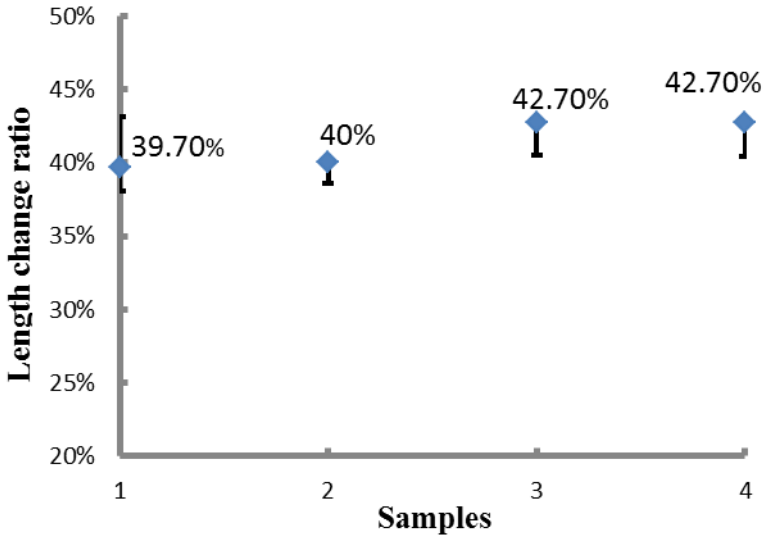


Fig.3 Total length change ratio of 4 samples. The figure shows results from 3 replications of experiment.

From these results, we can assume, it is a feasible and easy way to control the shape recovery ratio of SMP by controlling the annealing level, which is of interest in various parts of fields where SMP is used. Here is an example of controlling shape recovery ratio at 45% by annealing time. 45% shape recovery ratio is equivalent to (1-45%) / (1+15%) length change ratio by pure annealing. With the equation from curving fitting, the time which is needed to have this length change ratio by pure annealing is 41.7s. We performed experiments of 3 samples with a total processing time of 41.7s and length change during the experiments was measured. We can see all 3 samples closely reached to a length change ratio of 45%. This proves that shape recovery ratio of shape memory polyurethane can be designed by annealing.

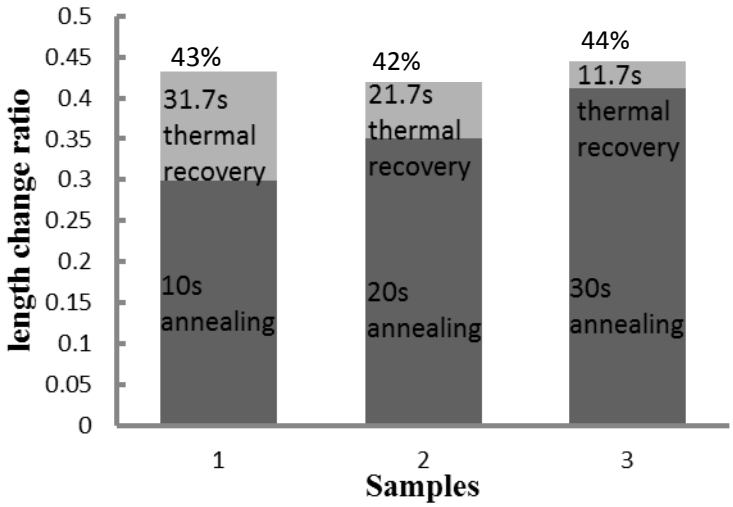


Fig. 4, All three samples with same total annealing time and thermal recovery time reach the designated shape recovery ratio.

Conclusions

(1) We studied length change of SMPU film under annealing at 3 different temperatures. From the results it can be seen that different temperatures lead to different length change ratio at same time interval.

(2) By comparing the length change ratio from annealing and thermal effect of SMPU, we concluded that annealing and shape memory effect had same effect on length change of SMPU.

(3) We also demonstrated that for obtaining a certain length change ratio of SMPU, result is same if the total processing time of annealing and thermal recovery is same as the pure annealing time which is needed for the equivalent effect. Therefore, we conclude that we can control shape recovery ratio of SMPU by adjusting annealing time.

References

[1] K. Otsuka, C. M. Wayman (Eds.), Shape Memory Materials, Cambridge University Press, New York, 1998.

[2] J. Leng, X. Lan, Y. Liu, S. Du, Shape-memory polymers and their composites: Stimulus methods and applications, Prog. Mater, Sci. 56 (2011) 1077-1135.

[3] M. Talukdar, Effect of annealing on morphology of thermotropic liquid crystalline polyesters, Int. J. Res. Rev. Appl. Sci. 4, 4 (2010) 405- 410.

[4] Y. Fu and J. R. Lakowicz, Spectroscopy, A closer look at polymer annealing, Nature, 472 (2011) 178-179.

[5] J. Petermann, M. Miles, H. Gleiter, Growth of polymer crystals during annealing, J. Macromol. Sci. B. 12, 3 (1976) 393-404.

[6] G. Li, V. Shrotriya, Y. Yao, Y. Yang, Investigation of annealing effects and film thickness dependence of polymer solar cells based on poly(3-hexylthiophene), J. Appl. Phys. 98 (2005) 043704

Advanced Materials Research Vol. 936 (2014) pp 145-148
© (2014) Trans Tech Publications, Switzerland
doi:10.4028/www.scientific.net/AMR.936.145

Preparation Of Uniform A-Alumina Microspheres By Catalytic Precipitation And Calcination Process

Wang Zhou[1,a], Shen Xiangqian[2,b]*, Jing Maoxiang[3,c],

Yan Liang[4,d] and Luo Zhou[5,e]

Institute for advanced materials, Jiangsu University, Zhenjiang, 212013, China

[a]wangqi-07@163.com,[b]shenxq@mail.ujs.edu.cn, [c]mxjing2004@mail.ujs.edu.cn,
[d]2460134180@qq.com and [e]1113428443@qq.com

Keywords: α-alumina, precipitation, microspheres, urea, catalyst

Abstract. Uniform α-alumina microspheres with mean partice size about 5-6 μm were prepared by the catalytic precipitation and calcination process. The spherical hydrated alumina precursor was first synthesized by the precipitation using ammonium aluminum sulfate and urea. During the reaction process, the urea can be decomposed to the mediator urease, which acts as the catalyst to influence the precipitate formation. The as-prepared α-alumina microspheres exhibit a very good shaping ability and the green body shaped by the dry-press process has a low linear shrinkage rate 5.8% at the sintering process.

Introduction

Alumina ceramics are widely used for various applications due to their excellent physical and chemical properties [1]. As spherical alumina powders have a high fluidity, low surface energy, leading a high compact density, therefore the preparative process for alumina microspheres has been demanded for technologically.

So far, there are three ways to prepare spherical alumina, such as chemical [2], physical [3,4], and physical-chemical processes [5]. Aman et al [6] employed the aerosol decomposition process at a low temperature to obtain ultrafine spherical alumina powder. Li et al. [2] developed the crystallization-precipitation process and prepared the high purity alumina. The spray-dry process [7,8] could produce spherical alumina on a large scale, but the impurities were difficult to control. In the present work, the uniform α-alumina microspheres were prepared by calcination of the precursor which was synthesized by the precipitation process using urease as the catalyst from starting reagents of ammonium aluminum sulfate and urea.

Experimental

The ammonium aluminum sulfate (AA) was provided by Zhengzhou research institute of CHALCO, and different concentrations of AA solutions (0.8, 1.1 and 1.4 $molL^{-1}$) were prepared by dissolving appropriate amount of AA salts in 800 mL deionized water, under a vigorous magnetic stirring at 75℃, with addition of about 40 g urea into the AA solution. After addition of urea, the white precipitation was observed, and continued to stir the solution for another 0.5 h. Then the suspension was separated with vacuum filtration, and the white precipitate was washed three times by deionized water. The as-prepared precursor was dried at 100℃ for 25 h in a vacuum oven. Finally, the dried precursor was calcined in an electric muffle furnace at 1230℃ for 2 h to form α-phase alumina.

The crystallinity and fraction of α-phase alumina were examined by X-ray diffraction (XRD, Rigaku D/Mmax2500PC diffractometer with Cu-Kα radiation). The particle morphology was investigated by scanning electron microscopy (SEM, JEOL, JSM-6460LV). The particle size distribution was charactized by laser particle analyser (Helos BF, German). The density was examined by powder integrated analyser (BT-1000, Dandong Bettersize Instruments, China).

Results and discussion

Catalytic precipitation

In the catalytic precipitation, there are generally three reactions (eqs(1)- (3)). By this precipitation the amorphous hydrated alumina should be formed, which is confirmed by the XRD analysis showed in Fig.1(a). Similar results were reported by Kara [9].

$$CO(NH_2)_2 + 3H_2O \rightarrow 2NH_3 \cdot H_2O + CO_2 \quad (1)$$

$$NH_3 \cdot H_2O + H_2O \rightarrow NH_4^+ + OH^- \cdot H_2O \quad (2)$$

$$Al^{+3} + 3OH^- \rightarrow Al(OH)_3 \quad (3)$$

According to the above three reactions, the precipitation process is largely influenced by the contents of AA and urease. As observed on SEM morphologies (Fig. 2) of the precursor obtained at different AA concentrations, when the AA solution concentration increasing from 0.8 to 1.1 molL^{-1} the mean particle size reduces from about 6.8 μm to 5.8 μm. With increasing AA concentration, more NH_4^+ ions and less OH^- ions in the solution, resulting in a longer time to form the precipitate. As the value of Al^{3+} and HO^- ions solubility production is possibly lower than *Ksp* at 80℃. The precipitation is a crystallization grown-controlled process. That is to say that increasing AA concentration at a constant urea content will bring about more nuclei and the precipitated particles will be much smaller.

TAB.1 INFLUENCE OF UREASE DOSAGE ON PRECIPITATION

Dosage/mg	0	0.25	0.5	0.75	1.0
Time/h	8	6	5.5	2.5	2.4

It was found out that the observed precipitation time was affacted by the content of urea, which was the resultant product of urea decomposed over 80℃. As observed in Table 1, the effect of urea dosage on the precipitation, with increasing urea concentration the time requirement for the precipitate occurring decreases. It takes about 8 h without using urea and 3.5 h with 1 mg of urea to observe the precipitate occurring respectively. Hence the mediator urease would act as the catalyst, which can in some degree control the precipitation process.

Calcination and characteristics of α-alumina microspheres

When the amorphous hydrated alumina is calcined over 1200℃, the phase can be changed from the amorphous precipitate to γ-phase and α-phase alumina, and this process consists of water removal and phase transformation [10]. To achieve a high α-phase transformation percentage, the calcination temperature is determined to at 1230℃. Fig.1 (b) showes the XRD pattern of the crystalline structure of the resultant alumina calcined at 1230℃ for 2 h. From Fig.1 (b), it can be seen that the diffraction peaks are basically indexed to the α-phase alumina (JCPDS 10-0173) and the estimated the phase transformation percentage is over 95.

Figure 3 showes the α-alumina microspheres morphologies and the corresponding particle size distributions, which are prepared by calcination of the precursors precipitated at different AA concentrations. It can be observed from Fig. 3, these microspheres are uniform, with a standard normal particles size distribution. The mean particle size is 5.6 μm for the specimen obtained at AA concentration of 0.8 molL^{-1} and 5.2 μm for another obtained at 1.1 molL^{-1}, respectively.

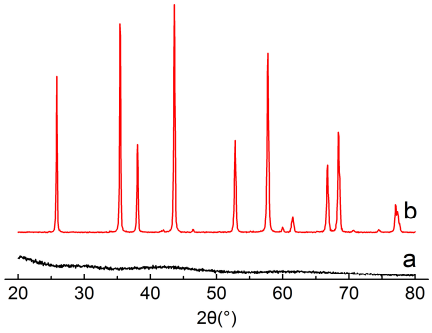


Fig.1 XRD patterns of amorphous precursor (a) and resultant α- Al_2O_3 (b) calcined at 1230℃for 2 h

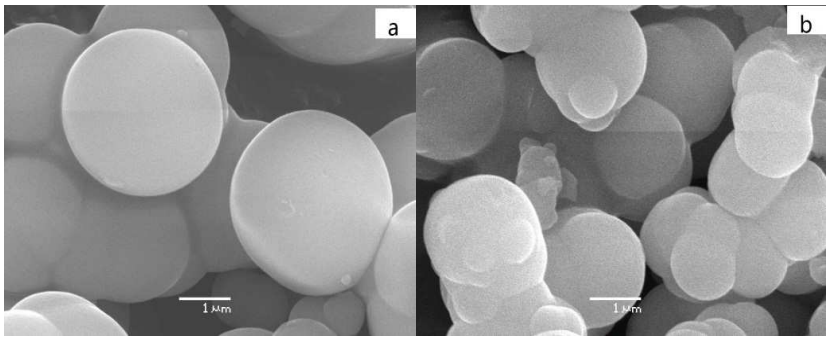


Fig.2 SEM morphologies of precursors prepared at different AA concentrations: （a）0.8 molL^{-1}（b）1.1 molL^{-1}

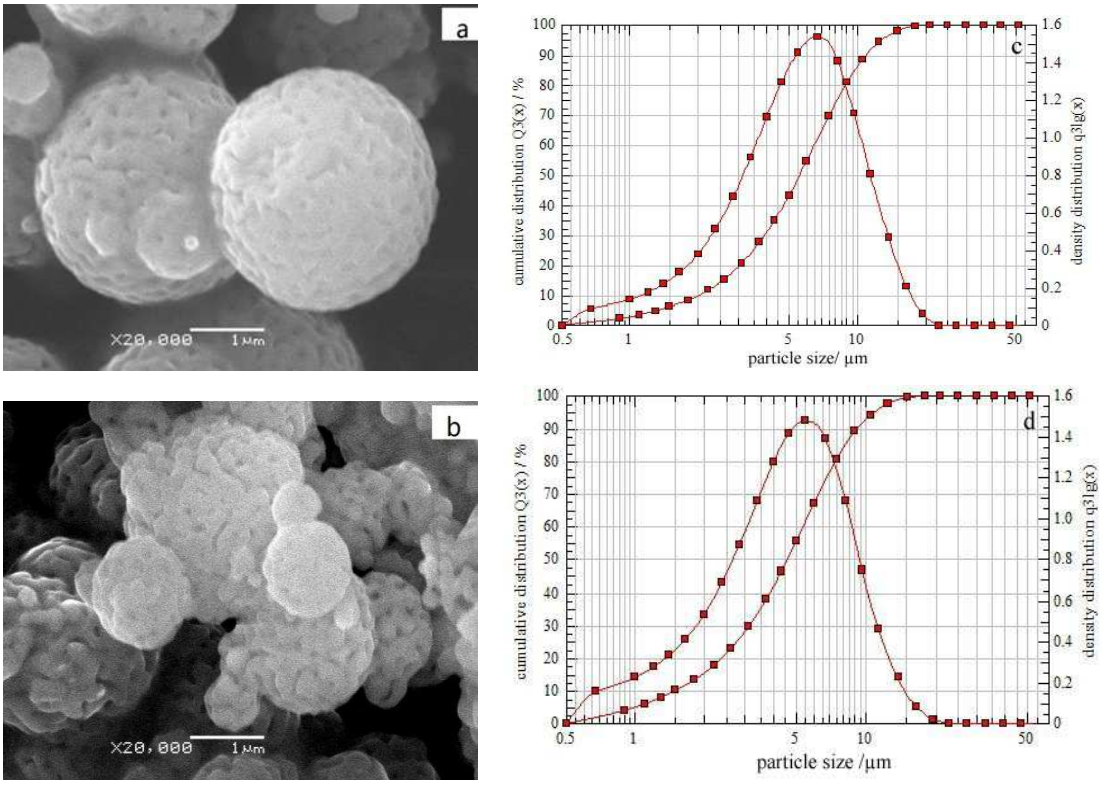


Fig.3 SEM morphologies and particle size distribution of α- Al_2O_3 microspheres by calcination of the precursor obtained at different AA concentrations:（a）and (c) 0.8 molL^{-1},（b）and (d) 1.1 molL^{-1}

In order to evaluate the as-prepared α-Al_2O_3 microspheres sintering property, the as-prepared α-Al_2O_3 microspheres is compared to the powder derived from the process using ammonium aluminum carbonate hydroxide(AACH) as the starting reagent [11]. These two kind of powders are shaped by the dry-press with 5 MPa force. It was found the powder derived from the process with AACH could not be shaped, while for the as-prepared α-Al_2O_3 microspheres the green body exhibits a high strength. Subsequenty, the green body is sintered in an electric muffle furnace at 1500℃for 2 h and the linear shrinkage rate is 5.8%, with a bulk density of 3.0 g/cm^3.

Conclusion

The uniform α-Al_2O_3 microspheres with mean particle size about 5-6 μm have been successfully prepared by calcination of the amorphous hydrated alumina precursor, which was obtained by the precipitation process using aluminum ammonium sulfate and urea as the starting reagents. The precipitation process is largely influenced by the AA concentration and the urease, which is the mediator from the decomposition of urea and act as the catalyst. The as-prepared α-Al_2O_3 microspheres have a very good shaping ability and the resultant green body shaped by the dry-press process has a lower shrinkage at the sintering process, with a ceramic bulk density of 3.0 g/cm^3.

Acknowledgements

This work was supported by the Science and Technology Support Program of Jiangsu Province (grant No. BE2012143), the Jiangsu Provincial Postgraduate Cultivation and Innovation Project (grant No.CXZZ13_0662).

References

[1] A. Krell, P. Blank, H.W. Ma, T. Hutzler and M. Nebelung, Processing of high-density submicrometer Al_2O_3 for new applications, J. Am. Ceram. Soc. 86 (2003) 122-124.

[2] D.H. Li, X.Q. Shen, Z. Wang, Preparation of High Purity Spherical Alumina. Rare Metal Mat. Eng. 37 (2008) 252-255.

[3] T. Hirayama, High-temperature characteristics of transition powder with ultrafine spherical particles, J. Am. Ceram. Soc. 70 (1987) 122-124.

[4] T. I. Barry, P. K. Bayliss, L. A. Lay, Mixed oxides prepared with an induction plasma Torch, J. Mater. Sci. 3 (1968) 229-238.

[5] S.G.Deng, Y.S. Lin, Granulation of sol-gel derived nanostructured alumina, AIChE J. 43 (1997) 505-514.

[6] Y. Aman, C. Rossignol, V. Garnier, E. Djurado, Low temperature synthesis of ultrafine non vermicular α–alumina from aerosol decomposition of aluminum nitrates salts, J. Eur. Ceram. Soc. 33 (2013) 1917-1928.

[7] A. Islam, Y.H. Taufiq-Yap, C.M. Chu, E.S. Chan, P. Ravindra, Synthesis and characterization of millimetric gamma alumina spherical particles by oil drop granulation method, J. Pour. Mater. 19 (2012) 807-817.

[8] Z.R. Ismagilov, R.A. Shkrabina, N.A. Koryaba, New techology for production of spherical alumina supports for fluidized bed combustion, Catal. Today 47 (1999) 51-57.

[9] F. Kara, G. Sahin, Hydrated aluminum sulfate precipitation by enzyme-catalysed urea decomposition, J. Eur. Ceram. Soc. 20 (2000) 689-695.

[10] M. Nguefack, A.F. Popa, S. Rossignol, C. Kappenstein, Preparation of alumina through a sol-gel process. Synthesis, characterization, thermal evolution and model of intermediate bohmite, Phys. Chem. Chem. Phys. 5 (2003) 4279-4289.

[11] K. Morinaga, T. Torikai, K. Nakagawa, S. Fujino, Fabrication of fine α-Al_2O_3 powders by thermal decomposition of ammonium aluminum carbonate hydroxide (AACH), Acta Mater. 48 (2000) 4735-4741.

Advanced Materials Research Vol. 936 (2014) pp 149-153
© (2014) Trans Tech Publications, Switzerland
doi:10.4028/www.scientific.net/AMR.936.149

Phase Structure and Piezoelectric Properties of $(K_{0.5}Nb_{0.5})NbO_3$ - $CaZrO_3$ Ceramics

Myoung Pyo Chun

[1]Korea Institute of Ceramic Engineering and Technology (KICET), Seoul 153-801, Korea

myoungpyo@kicet.re.kr

Keywords: KNN, $CaZrO_3$, Phase transition, Lattice parameter, Piezoelectric constant.

Abstract. Lead-free piezoelectric ceramics of $(1-x)(K_{0.5}Na_{0.5})NbO_3$ - $xCaZrO_3$ (abbreviated as KNN-CZ, x = 0 ~ 0.04) were synthesized by the conventional solid state method. Their phase structures and piezoelectric properties were investigated with x-ray diffraction (XRD), Scanning Electron Microscope (SEM), d_{33} meter and Impedance Analyzer. KNN-CZ samples exhibit only pure perovskite phases with a small monoclinic distortion. It was observed that the lattice parameter b has a maximum at x = 0.02 but the monoclinic distortion angle β shows a minimum at the same composition. From the dependence of the lattice parameters (a, b, c, β) and cell volume on the content of CZ, it is considered that the intermediate phase transition exists near at x = 0.02. Piezoelectric properties show the maximum value of d33 = 121 pC/N and kp = 0.35 for the sample with x = 0.02, which seems to be due to the co-existence of the two different phases.

Introduction

A variety of piezoelectric elements are increasingly used in electronic apparatuses as electronic technology is being developed. The most widely used piezoelectric ceramics are lead-oxide-based ferroelectrics (PZT) [1-3]. However, the toxicity of lead oxide and its high vapor pressure during processing have led to a demand for alternative lead-free piezoelectric materials. The search for alternative piezoelectric materials is now focused on alkali niobates (KNN) [4-5] and modified bismuth titanates (BNT) [6-7] based on the perovskite structure. It is well known that the highest piezoelectric performances are obtained for the composition of morphotropic phase boundary (MPB). Two different phases coexisting around MPB can generate more polarization directions and make the polarization switching much easier, which contributes to the highest piezoelectric property. Therefore, searching for new MPB compositions is a promising way to develop lead-free piezoelectric ceramics with highly electrical performances. There are some previous studies on the formation of the phase boundary using various ABO_3 compounds [8-9]. In order to obtain a phase boundary in KNN ceramics, their rhombohedral to orthorhombic transition temperature should be shifted to near room temperature by substituting them with other components [10]. Even though it was reported that the addition of $CaZrO_3$ could shift the TR–O to above room temperature [11], there are few reports on the effect of $CaZrO_3$ on the phase structure and electrical properties of KNN ceramics.

In this work, lead-free piezoelectric ceramics of $(1-x)(K_{0.5}Na_{0.5})NbO_3$ - $xCaZrO_3$ (KNN-CZ, x = 0 ~ 0.04) were fabricated by the conventional solid state method, their phase structures and piezoelectric properties were investigated with X-ray diffraction (XRD), Scanning electron microscopy (SEM). In particular, the possibility of phase boundary in this composition system was studied by analyzing the lattice parameters (a, b, c) and the monoclinic angle (β) as a function of the content of $CaZrO_3$.

Experimental

$(1-x)(K_{0.5}Na_{0.5})NbO_3$ - $xCaZrO_3$ (x = 0 ~ 0.04) powders were synthesized by using the conventional solid state method. The raw materials such as K_2CO_3 (Kojundo Chemical, 99.99%), Na_2CO_3 (Wako Pure Chemical, >99.5%), TiO_2 (Wako Pure Chemical, 99.7%), Nb_2O_5 (Kojundo Chemical, 99.9%), and ZrO_2 (Kojundo Chemical, 99.99%, 99.9%) were weighed and were mixed

for 24 h in ethanol with Zirconia balls of 5φ by wet ball milling. The mixed powders were dried and then calcined at 900°C for 5 h. The calcined powders were uniaxially pressed at 800 kgf/cm^2 using 10 wt. % poly vinyl alcohol (PVA) as a binder to form discs of 10 mm in diameter and 1 mm in thickness. These discs were sintered at 1160°C for 3 h in air. Silver external electrodes were formed by screen printing a silver paste on both sides of a sample and firing at 700°C for 10 minutes. After that, the poling of samples was performed by applying a dc voltage of 2.5 kV/mm to both sides of a sample at 120°C for 30 minutes. Piezolectric constant of d_{33} was measured with d_{33} meter [Piezotest, PM100]. The crystal structures were determined by using X-ray Diffractometer [Mac Science, KFX-987228-SE] with Cu-K_α radiation and the lattice parameters were calculated from the X-ray patterns. The surfaces of the sintered samples were etched thermally and their microstructures were observed with SEM [Topcon, Sm-300]. Raman spectra of samples were measured with Micro Raman spectrophotometer [Jasco, NRS-3100].

Raw Materials	K_2CO_3, Na_2CO_3, Nb_2O_5, $CaCO_3$, ZrO_2
Mixing	Ball milling for 24h at 180 rpm, ZrO_2 ball Φ5, Solvent ethanol
Calcination	900℃x5hour
Binder Mixing	PVA (15% in D.I water) 10wt%
Forming	Disk, Thickness 1mm, Dia. 10mm, 800 kgf/cm^2
Sintering	1160℃, 2hr in air
Termination	Ag-paste, 700℃ x 10 min.
Poling	2.5kV/mm, 30min., 120°C
Aging	24h
Measurement	Microstructure (SEM), Phase Analysis (XRD) Raman Spectroscopy, Piezoelectric Properties(d33)

Fig.1. A Schematic Diagram of Experimental Procedure.

Result and Discussion

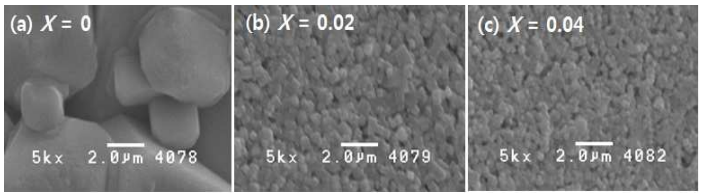


Fig.2. SEM Micrographs of (1- x)KNN - xCZ Samples
Sintered at 1160oC for 3h in Air.

Fig. 2 (a)-(c) show SEM micrographs of (1-x)KNN - xCZ (x = 0 ~ 0.04) samples sintered at 1160°C for 3h in air. Pure KNN reveals a bimodally and abnormally grown microstructure consisting of spherical shaped grains ranging from 2 up to 8um as shown in Fig. 2(a) but samples including small amount of CZ do not exhibit any grain growth except that their microstructures, consisting of uniform sub-micron grains, become more densified with increasing the content of CZ as shown in Fig. 2(b) and (C). The addition of a small of amount of CZ is very effective on inhibiting the grain growth of KNN, which is likely to be because some of CaO and/or ZrO_2 exist in the grain boundary region due to a solubility limit of KNN and hinder the grain growth of KNN. There are many studies that the dopants located near the grain boundary inhibit the grain growth of

$BaTiO_3$ [12-13] and KNN [14]. It was reported in a study of KNN-ZrO_2 ceramics that ZrO_2 inclusions of around 50 nm in size exist at the junctions of the matrix grains and Zirconia is enriched in the grain boundary region in comparison to the grain interior by TEM/EDAX.

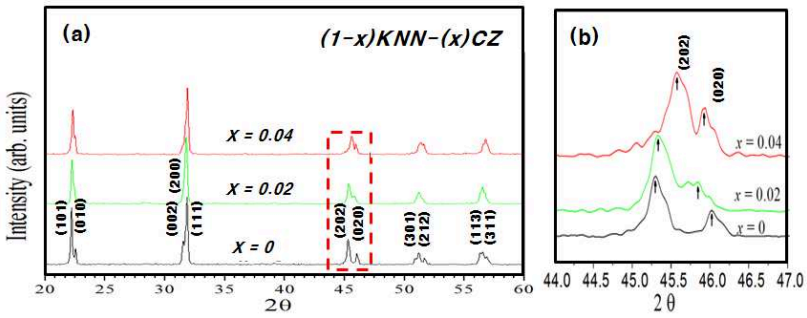


Fig. 3. X-ray Diffraction Patterns of (1-x)KNN - xCZ Samples Sintered at 1160oC in the Range of 2θ (a) from 20o to 60o and 44o to 47o.

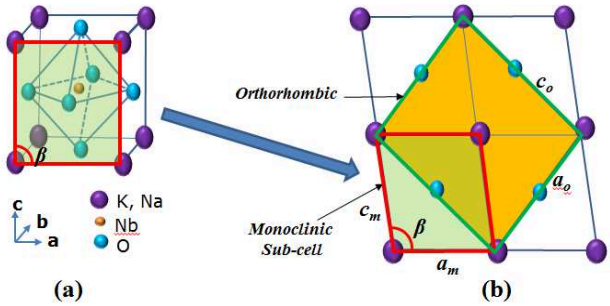


Fig. 4. Schematic Diagram of the KNN Structure at Room Temperature: (a) Perovskite ABO3 Subcell, and (b) Relationship Between the Orthorhombic (ao, co) and the Monoclinic (am, cm, β) Unit Cells.

Fig. 3 (a) and (b) show the XRD patterns of (1-*x*)KNN - *x*CZ samples sintered at 1160°C and are completely in accord with the standard card (JCPDS No. 71-2171) of orthorhombic $KNbO_3$. All the samples exhibit only pure perovskite phases, suggests that Ca^{+2} and Zr^{+4} have diffused into the KNN lattice, with Ca^{+2} entering the $(Na0.5K0.5)^{+1}$ site and Zr^{+4} occupying the B site, to form a homogeneous solid solution. Fig. 1(b) is the magnification of XRD pattern (a) in the 2θ range of 44–47°, which clearly exhibits the peak splitting of (202) and (020) diffraction lines with a separation distance between them decreased with increasing the content of CZ. The crystal structure of samples can be considered as an orthorhombic phase because the intensity of (202) diffraction line is greater than that of (020). The orthorhombic structure can be expressed with the monoclinic one according to the orientation relationship between them as shown in Fig. 4 (a) and (b). The lattice constants (a_m, b_m, c_m, β) of monoclinic unit cell can be calculated by the following equations:

Where the lattice constants a_o, b_o, c_o and β were calculated from the (101), (010), (002), (200), (111), (202), and (020) diffraction lines of Fig. 3(a) and (b).

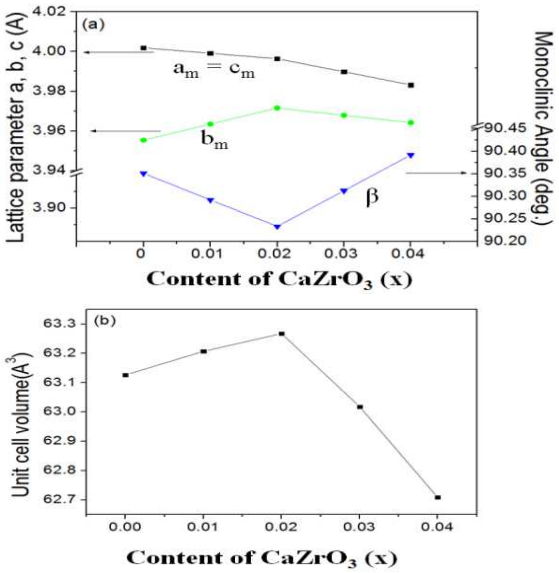


Figure 5(a) and (b) Show the Variations of the Lattice Constants (a, b, c, β) and Monoclinic Sub-cell Volume of (1-x) KNN - x CZ Samples.

Figure 5(a) shows the variations of the lattice constants a_m, b_m, c_m and the monoclinic angles β of (1-x)KNN - xCZ samples. As x increases, the lattice parameters a_m and c_m decrease monotonically but b_m increases at first and has the maximum value at x = 0.02 and then decreases again over x = 0.02. In contrast to b_m, the monoclinic angles β decreases at first and has the minimum value at x = 0.02 and then increases again over x = 0.02. In considering the ionic radius, it is likely that Ca^{+2} (1.34 A) ions incorporate A-site of the ABO_3 perovskite structure consisted of Na^+ (1.39 A) and K^+ (1.64 A) ions and contract its monoclinic sub-cell isotropically to result in a monotonic decrease of the lattice parameters b_m, while Zr^{+4} (0.72 A) ions seem to occupy B-site consisted of Nb^{+5} (0.64 A) ions and expand its sub-cell anisotropically.

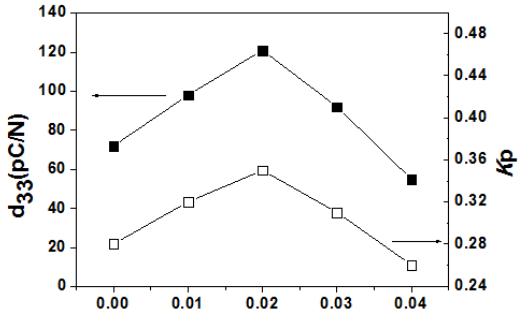


Figure 6 The Composition Dependence of d33 and kp for (1-x) KNN - x CZ Samples.

Figure 5(b) shows the variations of the monoclinic sub-cell volume. As x increases, the sub-cell volume increases at first and has the maximum value at x = 0.02 and then decreases again over x = 0.02. The combined effects between Ca^{+2} (1.34 A) ions contracting the sub-cell and Zr^{+4} (0.72 A) ions expanding its sub-cell seem to give rise to both a maximum b_m and a minium β at x = 0.02.

Fig. 6 Fig. 5 shows the piezoelectric coefficient (d_{33}) and coupling factor (k_p) of all compositions. Both d_{33} and k_p increase firstly with increasing CZ content and reach maximum at x = 0.02, but then decrease rapidly when the CZ content is larger than 0.02. The maximum d_{33} and k_p in x = 0.02 composition are 121 pC/N and 0.35, respectively. These values are comparable with other KNN-based piezoelectric ceramics. The composition dependence of d_{33} and k_p may be attributed to the existence of the intermediate phase transition region near at the composition rage of x = 0.02, which can make the polarization switch more easily and have the highest ferroelectric and piezoelectric

properties as similar results were shown in previous reports [15-16]. It is considered that this study may be contributed to the formation of the phase boundary and enhancing the piezoelectric properties of KNN-based ceramics.

Summary

Lead-free piezoelectric ceramics of (1- x)($K_{0.5}Na_{0.5}$)NbO_3 - $x$$CaZrO_3$ (KNN-CZ, x = 0 ~ 0.04) were fabricated by the conventional solid state method, their phase structures and piezoelectric properties were investigated. The introduction of a small of amount of $CaZrO_3$ is very effective on inhibiting the grain growth of KNN and enhancing its densification. The ceramic with x = 0.02 has the maximum piezoelectric constants of d33 = 121 pC/N and kp = 0.35, which seems to be attributed to the existence of the intermediate phase transition region near at this composition. Our results might be helpful for developing KNN-based piezoelectric ceramics.

References

[1] Y. Tsur, T. D. Dunbar, and C. A. Randall: J. Electroceram. Vol. 7 (2001), p. 25.

[2] G. V. Lewis, and C. R. A: J. Phys. Chem. Sol. Vol. 47 (1986), p. 89.

[3] R. D. Shannon: Acta Crystallogr. A32 (1976), p. 751.

[4] D. Makovec, Z. Smardzija, and M. Drofenik: J. Am. Ceram. Soc. Vol. 87 (2004), p. 1324.

[5] K. J. Park, C. H. Kim, Y. J. Yoon, S. M. Song, Y. T. Kim, and K. H. Hur: J. Eur. Ceram. Soc. Vol. 29 (2009), p. 1735.

[6] Lee J. K., Hong K. S. and Jang J. W. J. Am. Ceram. Soc. 84, (2006), p. 2001.

[7] Lu H. Y. and Lin M. H: Ceram. Int. Vol. 31 (2005), p. 989.

[8] J.G.Wu, Y.Y.Wang, D.Q.Xiao, J.G.Zhu, P.Yu, L.Wu, and W.J.Wu: Japanese Journal of Applied Physics 46 (2007), p. 7375.

[9] Y.Guo,K.Kakimoto,H.Ohsato: Applied PhysicsLetters 85 (2004), p. 4121.

[10] R.P.Wang, H.Bando, T.Katsumata, Y.Inaguma, H.Taniguchi, M. Itoh: Physica Status Solidi RRL3 (2009), p. 142.

[11] W.Liang, W.Wu, D.Xiao, J.Zhu: Journal of the American Ceramic Society 94 (2011), p. 4317.

[12] Buessem, W. R. and Kahn, M: J. Am. Ceram. Soc. 54 (1971), p. 458.

[13] Park, Y. and Kim, H. G: Ceram. Int. 23 (1997), p. 329.

[14] Barbara Malic, Janez Bernard, Andreja Bencan, Marija Kosec, Journal of the European Ceramic Society 28 (2008), p.1191.

[15] Chong Zhanga, Zhong Chena, Wei-jing Ji a, Lei Wanga, Y.B. Chenb, Shu-Hua Yaoa, Shan-Tao Zhanga, Yan-Feng Chena, Journal of Alloys and Compounds 509 (2011), p.2425.

[16] Tao Huang, Dingquan Xiao, Chao Liu, Fangxu Li, BoWu, Jiagang Wu, JianguoZhu, Ceramics International 40 (2014), p. 2731.

Advanced Materials Research Vol. 936 (2014) pp 154-163
© (2014) Trans Tech Publications, Switzerland
doi:10.4028/www.scientific.net/AMR.936.154

A Novel Model for Predicting the Thermal Conductivity of Fiber Reinforced Ceramic Materials

XU Rui[1, a *], MAO Jun-kui[1], ZHANG Jing-yu[1], LOU De-cang[2], GUO Wen[2]

College of Energy and Power Engineering, Nanjing University of Aeronautics and Astronautics, Nanjing 210016, China;

China Gas Turbine Establishment, Chengdu 610500, China

[a.] xurui112358@gmail.com

Keywords: fiber reinforced ceramic; composite material; thermal conductivity; prediction model

Abstract. The prediction of fiber reinforced ceramic is one of the most important procedure when investigating the application of ceramic composite. Numerical simulations were applied and a novel model was brought out in this paper. Firstly, four different models for predicting thermal conductivities of unidirectional fiber reinforced materials were compared, which include the Rayleigh，LN，ST and TE model,. It shows that Rayleigh model and LN model have good precision only in low fiber volume content cases. There existed big differences between the experimental and numerical results if predicted the high fiber volume content with either these four models. Then a novel model based on LN model was studied with the correction of the representative volume element method. Further comparison results indicate that the error can be reduced as 55.6% with this novel model. At the same time, the longitudinal (k_{11}) and transverse (k_{22}) thermal conductivities predicted by the novel model were also analyzed. It was found that k_{11} had a linear relationship with fiber volume fraction and thermal conductivity ratio (p). But k_{22} had a nonlinear relationship with fiber volume fraction, which increased much greatly when fiber volume fraction increasing at high fiber volume fraction and p>1.

Introduction

There is always a stable need to develop new materials to fulfill requirements of different power equipments, which is more urgent for aero turbine engine because of the high operation temperature. Now the firing temperature in combustion and the inlet temperature of turbine are far beyond the melting point of current single crystal superalloy. A lot of air is extruded from compressor to cool the hot section components such as combustor, guide vane and turbine blade, which may result in distinguished power loss.

The ceramic matrix composites (CMCs) have been studied extensively since the 1960s as one of the most exciting candidate materials for structural gas turbine hot section components. They are well known for the high-temperature resistant, high specific strength and low density. Higher fuel efficiency will be achieved by replacing those metallic hot section components with CMCs due to the reduced coolant demands and increased firing temperature. In the 1980s, SNECMA made nozzles flaps using nD-Cf /SiC(n=2,3) composites named “Sepcarbinox”, which was tested on M53-2 and M88-2 engine. GE and P&W had applied SiCf /SiC composite in combustor liner which can be operating more than 10000h at 1200℃ condition. NASA Glenn Research Center also developed SiCf /SiC turbine blades to decrease the coolant by 15% to 25%. In most cases above, the CMCs were used as insulator to prevent too much heat flux transferred inside and endure the extreme high temperature. It is obvious that the performance of structures with CMCs depends on the thermophysical properties, especially the thermal conductivity. In this paper, thermal conductivity of unidirectional composite which can also be found as element in multi-dimensional composite materials will be discussed.

As for unidirectional fibers composite materials, it can be assumed that fibers are arranged in the microstructure periodically shown in figure 1. So it can be treated as periodically piled structural

unit, which is named RVE (Representative Volume Element) shown in figure 2. The primary important thermal conductivities of composite are in the two principal directions, namely in the directions parallel (k11) and normal (k22) to the fibers. Once these conductivities are known, the conductivities in other directions can be calculated using the transformation matrix [7].

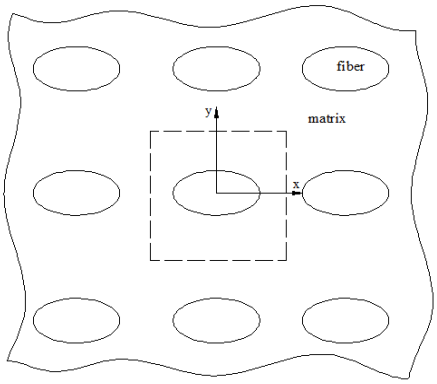


Fig.1 Fiber Arrange Structure

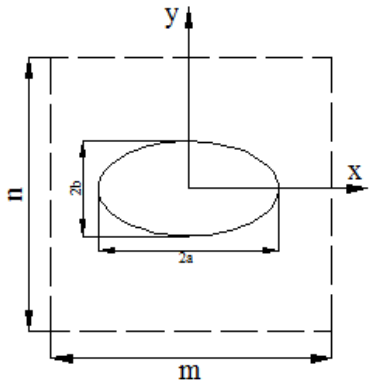


Fig.2 RVE

With reinforcing phases, CMCs form heterogeneous systems with distinct micro-structural geometries. Considering the different thermal conductivities of the constituents and various micro-structural arrangements, it makes predicting effective thermal conductivities (ETC) of composites much more complicated. The effective longitudinal thermal conductivity k11 of a 2D array follows the rule of mixtures exactly [2-4], thus k11 is not the interest of this work. From here on, the discussed effective thermal conductivity is focused on the transverse one.

A number of theoretical, empirical and semi-empirical models have been published in the literatures to describe the transverse thermal conductivity, which include those proposed by Rayleigh, Springer and Tsai [8], Behrens [9], Halpin-Tsai [10], Lewis and Nielsen [11]. The semi-theoretical model developed by Springer and Tsai assumes a square distribution of cylindrical fibers in the matrix material. The estimation of the thermal conductivity in the direction normal to the fibers is based on the analogy between the response of the composite to shear loading and heat transfer. Halpin-Tsai derived a theoretical model for the transverse thermal conductivity using the analogy between in-plane field equation and boundary conditions to the transverse transport coefficients. Lewis and Nielsen modified and adapted the Halpin-Tsai equation for elastic modulus of composite materials to thermal conductivity of particulate-filled composites, which can also be used in unidirectional fiber thermal conductivity prediction by adjusting the parameters. Zou derived analytical expressions based on the thermal-electrical analogy technique for transverse thermal conductivities of unidirectional composites[12].

In recent years more attention has been given to determine properties by using the FEM(Finite Element Method)[6-7]. Islam and Pramila [13] used FEM method to predict the effective transverse thermal conductivity of fiber reinforced composites systematically. Four different boundary conditions representing the periodicity of the temperature field were employed and ideal perfect contact between fiber and matrix was assumed. Lu[18] investigated 2D arrays using FEM, which included the square arrays of long circular/square cylinders and hexagonal arrays of long circular cylinder. Klett [33] used a finite-element model to predict the thermal conductivities of parallel and transverse to the fiber axis C/C composites.. Xia and Guo [20] also investigated the thermal conductivity of composite which had high-conductivity component with a given fraction. Some researchers also brought out some multi-scale methods including the asymptotic expansion homogenization (AEH) scheme, sub-structuring method, and multi-level homogenization scheme. Chung [34] used the AEH method to predict heat conduction in unidirectional FRP composites with temperature dependent thermal conductivity. The equations that govern the heat conductions at the macro and micro scales were solved concurrently. Rodrigo[35] developed a numerical procedure to calculate the effective conductivity of unidirectional fibrous composites with an interfacial thermal resistance between the constituent phases.

Experimental tests have also been conducted to measure the ETC (effective thermal conductivity) of fiber reinforced composites. Pilling et al. [30] measured ETC of unidirectional carbon fiber-

reinforced plastic (FRP) composites in the axial and transverse fiber directions. The tests were conducted between 80 and 270 K. The ETC of the tested composites and the thermal conductivities of the carbon and epoxy constituents are strongly dependent on temperature. Manocha [36] tested unidirectional C/C composites using high-pressure impregnation/carbonization technique with PAN.

Compared with the theoretical, empirical and semi-empirical models, more detailed and micro information can be caught with FEM method based on RVE. More accurate results will be achieved due to these information. But it requires that the microstructure of the composite material has a periodicity distribution and a detailed node description for each micro characteristic, which leads to generate mesh difficultly and a long calculate time. At the same time it is more difficult to define the size and internal geometry characteristics of RVE, especially in the real inhomogeneous composite. Although the theoretical, empirical and semi-empirical models are simple and easy to use, the low accuracy is the fatal disadvantage.

In response to these difficulties in thermal simulation, this paper compared accuracy and applied range of typical theoretical models. Correction was applied to improve accuracy and expand of semi-empirical model with the results concluded from the FEM simulations. Further comparisons were carried out and the improvement of accuracy was demonstrated. Then the novel model was used to estimate thermal conductivity of unidirectional fiber reinforced composite to study the effective thermal conductivity transformation rule with fiber volume fraction and fiber-to-matrix thermal conductivity.

Validation of Theoretical and Empirical Model

For unidirectional fiber composite materials, Prediction of the longitudinal thermal conductivity k11 can be assumed fibers and matrix in parallel and bond together well.

$$k_{11} / k_m = V_f k_f / k_m + V_m \quad . \tag{1}$$

Where k is the thermal conductivity, V is the volume fraction. Subscript f and m represent the fiber and matrix respectively.

Rayleigh equation:

$$\frac{k_{22}}{k_m} = \frac{(p+1)+(p-1)V_f}{(p+1)-(p-1)V_f} \quad . \tag{2}$$

Dimensionless parameter is defined as p=kf /km.

G. S. Springer and S. W. Tsai (ST model) [8] used parallel model method and shear loads comparable method to establish expression for predicting thermal conductivity of unidirectional fiber-reinforced composite.

$$\frac{k_{22}}{k_m} = (1-2\sqrt{V_f/\pi}) + \frac{1}{B}(\pi + \frac{4}{\sqrt{1-\left(B^2 V_f/\pi\right)}}(\tan^{-1}\frac{B\sqrt{V_f/\pi}}{\sqrt{1-B^2 V_f/\pi}} - \tan^{-1}\frac{1+B\sqrt{V_f/\pi}}{\sqrt{1-B^2 V_f/\pi}})) \quad . \tag{3}$$

Here $B = 2\left(k_m / k_f - 1\right)$.

Behrens[9] assumed composite structure is orthogonal symmetric and established the thermal conductivity formula for elliptical fiber reinforced composite in a square arrangement:

$$\frac{k_{22a}}{k_m} = 1 + (p-1)V_f - (p-1)^2 \frac{\sigma - \varepsilon^2/2}{1-\varepsilon^2} \frac{\left(1-\varepsilon^2\right)V_f - \left(\sigma - \varepsilon^2/2\right)}{(p+1)\varepsilon^2/2 - (p-1)\left(V_f - \sigma\right)} \quad . \tag{4a}$$

$$\frac{k_{22b}}{k_m} = 1 + \frac{(p-1)V_f \varepsilon^2}{(p+1)\varepsilon^2/2 - (p-1)\left(V_f - \sigma\right)} \quad . \tag{4b}$$

Here $\sigma = \sqrt{\varepsilon^4/4 + (1-\varepsilon^2)V_f^2}$, parameter ε is the ellipse eccentricity. When ε increases to be 0, the shape of fiber will become circle and the above equation will become fundamental Rayleigh equation.

Halpin-Tsai (HT model) [10] equation:

$$k_{22} = \frac{1+\zeta\eta V_f}{1-\eta V_f} \quad . \tag{5}$$

Here $\eta = (k_f/k_m - 1)/(k_f/k_m + \zeta)$ .For circular and square fiber, $\zeta = 1.0$ and the equation also becomes Rayleigh equation.

Lewis and Nielsen (LN model) [11] added correction term ψ:

$$\frac{k_{22}}{k_m} = \frac{1+ABV_f}{1-B\psi V_f} \quad . \tag{6}$$

Here $B = (k_f/k_m - 1)/(k_f/k_m + A)$, constant A is related to the materials of sharp and orientation. Correction term $\psi = 1 + \left((1-\phi_m)/\phi_m^2\right)V_f$, ϕ_m represent the largest filling fraction, for hexagonal array, quadrilateral array and random array, ϕ_m = 0.907, 0.785, 0.82 respectively.

Zou gave a thermal conductivity expression (TE model) by the thermal-electrical analogy method for elliptical fiber reinforced composite.

$$for \quad |c| > |d| \qquad \frac{k_{22}}{k_m} = 1 - \frac{1}{c} + \frac{\pi}{2d} - \frac{c}{d\sqrt{c^2-d^2}}\cos^{-1}\frac{d}{c} \quad . \tag{7a}$$

$$for \quad |c| < |d| \qquad \frac{k_{22}}{k_m} = 1 - \frac{1}{c} + \frac{\pi}{2d} - \frac{c}{d\sqrt{d^2-c^2}}\ln\left|\frac{d+\sqrt{d^2-c^2}}{c}\right| \quad . \tag{7b}$$

Here $\rho = a/b$, $c = \sqrt{\pi\rho/V_f}/2$, $d = \rho(1/p - 1)$。

In order to compare the accuracy of various theoretical models and indicate the occasion application, this paper selected unidirectional glass fiber reinforced plastic composites as a study target. We assumed that fibers were circular and were arranged in square. According the constituent material properties given in the literature 14, effective thermal conductivities were calculated at kf /km equals to 4.4 and 666 respectively. Rayleigh model, ST model, LN model, TE model and FEM simulation were compared with the experimental values in Figure 3 and figure 4. FEM simulation was performed according to the literature 1.

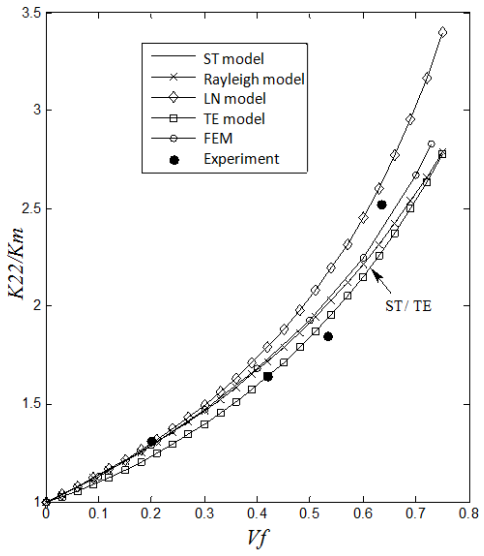


Fig.3 Relationship between Thermal Conductivity and Fiber Volume Fraction(kf /km =4.4)

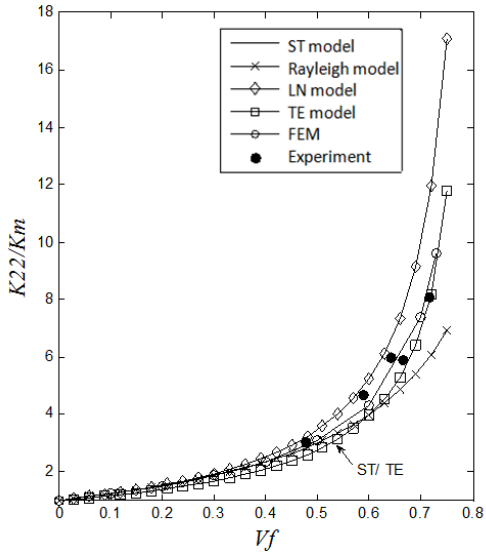


Fig.4 Relationship between Thermal Conductivity and Fiber Volume Fraction(k_f/k_m =666)

Table 1 TABLE OF ERROR

error	ST/ TE	Rayleigh	LN	FEM
kf /km =4.4	0.019	0.018	0.034	0.015
kf /km =666	0.570	1.648	2.796	0.156

The calculation results from four models are more or less in agreement with the experimental values. The effective thermal conductivity increases with the fiber volume fraction increasing, and this growth trend also accelerates when volume fraction is high. Rayleigh model nearly coincides with the NS results, and it is in good agreement with the experimental values at relatively low volume fraction (Vf <0.4). But at high volume fraction, Rayleigh model become less than NS model gradually due to the Rayleigh model ignores the interaction between the fibers. Throughout the whole range of the volume percentage, ST model and TE model thermal coefficient curve is overlapping, but the results are lower than experiment data. TE model consider heat flux flow parallel to the boundary and only calculate the thermal resistance in direction parallel to heat conduction, but in fact there is a small amount of heat flux flowed in a large angle with mainstream (showed in figure 5). It results in thermal resistance is sometimes too large and the equivalent thermal conductivity will be relatively too small. LN model based on the Kerner formula had been improved for particulate reinforced composites at low volume fraction. It also gave A and ϕ_m values to predict the thermal conductivity of unidirectional fiber composites, but from the figures it was found that the calculation results are gradually larger when the volume fraction is relatively high (Vf >0.6)。 Comparatively speaking FEM results are more accurate than the prediction model and more close to the experimental value.

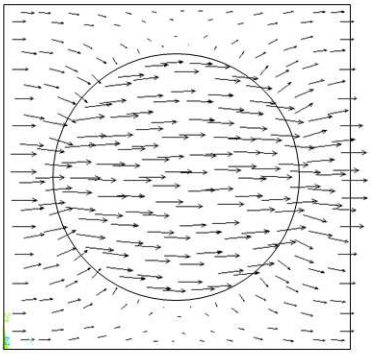


Fig.5 The direction of heat flow in the RVE

Correction Model

LN model increases the prediction accuracy at low fiber volume fraction after introducing the correction term. While at high volume fraction, the predicted data is still too large. Literature 11 proposed three boundary conditions for the correction term ψ to be met.

(1)when $V_f=0$, $\psi V_f=0$;

(2)when $V_f=0$, $\frac{d(\psi V_f)}{dV_f}=1$;

(3)when $V_f=V_m$, $\psi V_f \approx 1$。

The general formula of correction term ψ was considered like this:

$$\psi=1+\left(\frac{1-\phi_m}{\phi_m^{n+1}}\right)V_f^n \quad (8)$$

As the accuracy of numerical simulation is the best, this paper used the results of the numerical simulation at kf /km=10 to obtain the parameter n=4.38.

Besides the literature 14, this article further selected test data from literature 21 to verify accuracy of the proposed LN modified model (LNM model). Figure 6 and Figure 7 show LN model and LN modified model in comparison with the experimental values from literature 14 and 21. These experiment data was tested in one condition that the thermal conductivity of fiber kf is greater than the matrix thermal conductivity km. As it can be seen from figures and table, the revised LN model results are in better agreement with the experimental value and have a small error, the error is reduced by 55.6%.

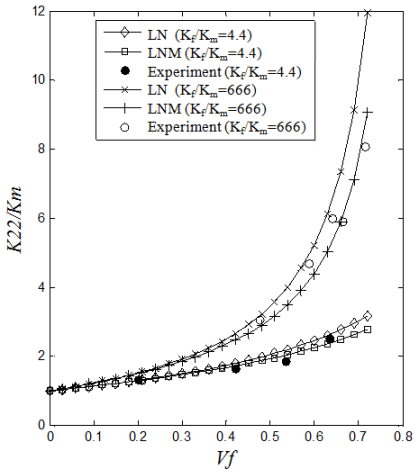


Fig.6 Comparison between LN model and LN correction model with experiment data from literature 14

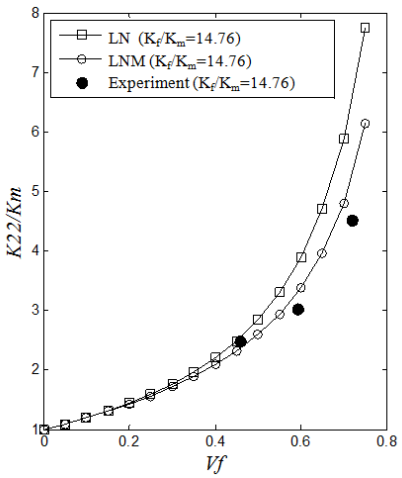


Fig.7 Comparison between LN model and LN correction model with experiment data from literature 21

Table 2 TABLE OF ERROR

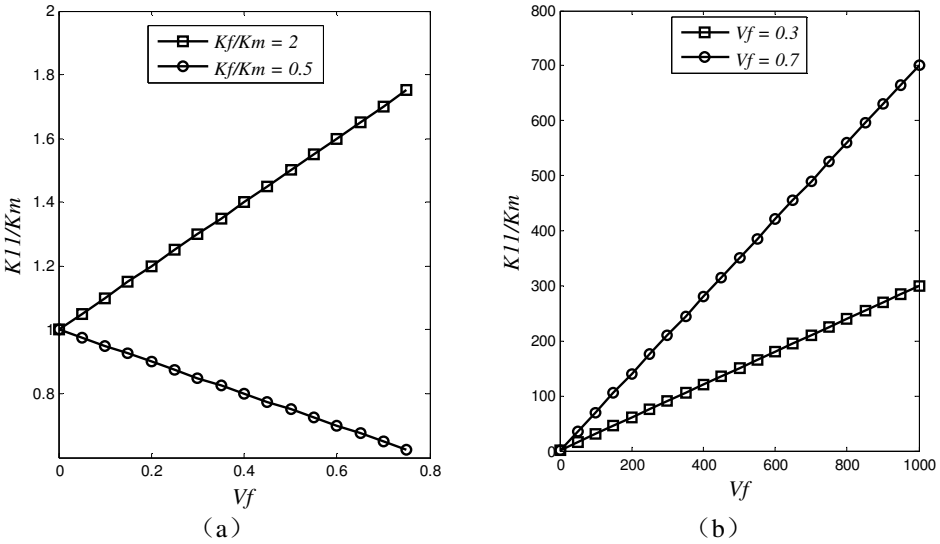
error	LN	LNM	Error reduction
kf /km =4.4	0.034	0.0151	55.6%
kf /km =666	2.796	0.230	91.7%
kf /km =14.76	1.470	0.203	86.2%

Thermal Conductivity Prediction for Unidirectional Composite

C/C and C/SiC composites are two kinds of typical unidirectional fiber reinforced ceramic matrix composites. C fibers are obviously anisotropic, fiber axis thermal conductivity is about several times or even dozens of times than radial thermal conductivity, C fiber axial thermal conductivity is about 4.7~600. Matrix material can be considered isotropic, as the C matrix microstructure have different effects on thermal properties of the material, the thermal conductivity is about 25~134. The cold isostatic SiC material thermal conductivity was determined between 0.1~0.35 using flash method by Wu QingRen.

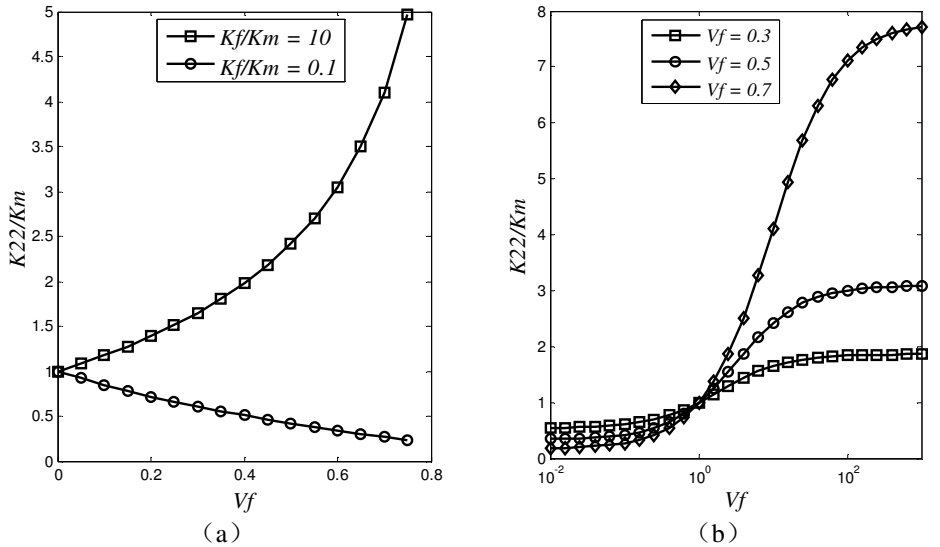
On the basis of the LNM model was validated, we further carried out computational analysis on C fiber reinforced composite materials thermal conductivity. Figure 8 and Figure 9 show thermal conductivity variation predicted by modified LN model.

The longitudinal thermal coefficient varied with fiber volume fraction and the thermal conductivity ratio was showed in figure 8. The unidirectional fiber reinforced composite longitudinal thermal conductivity is predicted by the parallel model. From figure 8, it can be seen that the longitudinal thermal conductivity shows a linear relationship with fiber volume fraction and the thermal conductivity ratio, the slopes are kf /km -1 and Vf respectively.



（a） （b）

Fig.8 Relationship between Longitudinal Thermal Conductivity with Vf (a) and kf /km (b)



（a） （b）

Fig.9 Relationship between Transverse Thermal Conductivity with V_f (a) and k_f/k_m (b)

Figure 9 shows the transverse thermal conductivity varied with Vf and kf /km. When kf /km>1, relation curve between transverse thermal conductivity and fiber volume fraction is bullish, that is to say increasing volume fraction at high volume fraction can significantly improve the transverse thermal conductivity. When kf /km <1, transverse thermal conductivity decreases with fiber volume fraction increasing, but the slope changes are not dramatic. From figure 9(b), it can be seen that the transverse thermal conductivity is proportional to the thermal conductivity ratio. But it has limited effect on transverse thermal conductivity, when the thermal conductivity ratio increases (or decreased) to a certain extent, the effective thermal conductivity coefficient tends to be constant.

Summary

The unidirectional fiber reinforced composites transverse thermal conductivity was studied in this paper, ST model, Rayleigh model, TE model, LN model and numerical simulation results were compared with the experimental values. It is found that the calculated effective thermal conductivity from ST model and TE model which ignore smaller portions thermal process is small; LN model prediction results are fit at low volume fraction but larger than experiment data at high volume fraction; Rayleigh model agrees well with the experimental values at low volume fraction while at high volume fraction it has low accuracy.

As for low accuracy of LN model, it was amended based on the numerical simulation results. Amended LN model fits the experimental values well, the error is reduced by 55.6%.

Relationship between longitudinal thermal conductivity and the fiber volume fraction or thermal conductivity ratio was discovered by the parallel model, it is found that the linear slope is kf /km-1 and Vf respectively. Transverse thermal conductivity was predicted by LN modified model, it is shown when kf /km >1 and volume faction is relatively high, increasing the volume fraction can significantly improve the transverse thermal conductivity; the thermal conductivity ratio has limited influence on k22, when the thermal conductivity ratio increases or decreases to a certain extent, the effective thermal conductivity coefficient tends to be constant.

References

[1] Liang C.H. Application of fiber reinforced ceramic matrix composite in foreign aviation engine [J]. Aeronautical Manufacturing Technology.2006, 3: 40~45

[2] J.C. Maxwell, A Treatise on Electricity and Magnetism[M], third ed., Dover Publications Inc., New York, reprinted 1954(Chapter 9)

[3] Da Yu Tzou. A Universal Model for the Overall Thermal Conductivity of Porous Media[J]. Journal of Composite Materials. 1991, 25(8):1064~1084

[4] Zhang H.F., Ge X.S. Ye H. Resistance network for predicting the thermal conductivity of composite materials [J]. Journal of Functional Materials. 2005, 36(5):757~759

[5] Nie R.H., Jiao G.B., Wang B. Prediction on coefficient of thermal conductivity for 2D braided C/SiC composites [J]. Acta Materiae Composite Sinica. 2009,26(3):169~174

[6] Song W.D., Wang J, Liu H.Y., Finite Element Model of Real Structure for Particle Reinforced Composites [J]. Transactions of Beijing Institute of Technology. 2009, 29(6):501~505

[7] Wang J.P., Wang L., Huang W., Thermal Conductivity Coefficient Transformation of Anisotropic Material on the Non-main Direction [J]. Journal of WuHan University of Technology, 1997,19(1):109~111

[8] G. Springer and S. Tai. Thermal Conductivities of Unidirectional Materials[J]. J. Composite Materials. 1967, Vol.1:166~173

[9] E. Behrens. Thermal Conductivities of Composite Materials. J. Composite Materials[J]. 1968, Vol. 2(1):2~17

[10] J. Ashton, J. Halpin, and P. Petit. Primer on composite materials: Analysis[M]. Technomic Pub.Co., Stamford,Conn. 1969

[11] T. Lewis and L. Nielsen. Dynamic Mechanical Properties of Particulate-Filled Composites[J]. Journal of Applied Polymer Science, 1970, Vol.17(6): 1449~1471

[12] Mingqing Zou, BoMing Yu, DuanMing Zhang, YongTing MA. Study on optimization of transverse thermal conductivities of unidirectional composites[J]. Journal of heat transfer. 2003, Vol.125(6):980~987

[13] Md.R. Islam, A. Pramila. Thermal conductivity of Fiber Reinforced Composites by the FEM[J]. Journal of Composite Materials. 1999,33(18):1699~1715

[14] J. D. Thornburg, C. D. Pears. Prediction of the thermal conductivity of filled and reinforced plastics[J]. ASME Paper 65-WA/HT-4.1965

[15] Jianfeng Wang, James K. Carson, Mike F. North, Donald J. Cleland. A new approach to modeling the effective thermal conductivity of heterogeneous materials[J]. International Journal of Heat and Mass Transfer. 2006, 49(17-18): 3075~3083

[16] D. P. H. Hasselman, K.Y. Donaldson, J.R. Thomas Jr. Effective Thermal Conductivity of Uniaxial Composite with Cylindrically Orthotropic Carbon Fibers and Interfacial Thermal Barrier[J]. Journal of Composite Materials. 1993, 27(6):637~644

[17] John A. Charles, Dale W. Wilson. A model of passive thermal nondestructive evaluation of composite laminates[J]. Polymer Composites. 1981, 2(3):105~111

[18] Cheng G.D., Liu S.T., Prediction of Thermal Conductivity of Unidirectional Fiber Reinforced Composites [J]. ACTA MATERIAE COMPOSITAE SINICA. 1996,13(1):78~85

[19] Yibin Xu, Koichi Yagi. Automati FEM model generation for evaluating thermal conductivity of composite with random materials arrangement[J]. Computational Materials Science. 2004,30(3):242~250

[20] R. C. Progelhof, J. L. Throne, R. R. Ruetsch. Methods for predicting the thermal conductivity of composite systems: A review[J]. Polymer Engineering & Science. 1976, Vol. 16(9):615~625

[21] M. W. Pilling, B. Yates, M. A. Black. The thermal conductivity of carbon fibre-reinforced composites[J]. Journal of Materials Science. 1979, 14(6):1326~1338

[22] J Koráb, P Štefánik, ŠKavecký. Thermal conductivity of unidirectional copper matrix carbon fiber composites[J]. Composites Part A: Applied Science and Manufacturing. 2002,33(4):577~581

[23] A. Bensoussan, J. L. Lions, G. Papanicolou. Asymtotic Analysis of Periodic Structures[M]. North-Holland. Amsterdan, 1978

[24] A.Pramila. Thermal Conductivity of Fiber Reinforced Composites by the FEM[J]. Journal of Composite Materials. 1999,33(18):1699~1715

[25] Cheng W., Zhao S.G., Liu Z.G., Thermal Property of 3DBraided Fiber Composites: Experimental and Numerical Results [J]. Acta Aeronautica Et Astronautica Sinica， 2002,23(2):102~105

[26] He F., Carbon fiber and Graphite fiber[M]. Beijing：Chemical Industry Press, 2010.7

[27] Hugh O. Pierson, David A. Northrop. Carbon-Felt, Cabon-Matrix Composites: Dependence of Thermal and Mechanical Properties on Fiber Precursor and Matrix Structure[J], Journal of Composite Materials, 1975,9:118:137

[28] Wu Q.R, Wen B.X., Studies on Temperature Dependence of Thermal Conductivity and Linear Expansion for SiC Material [J]. JOURNAL OF SOUTH CHINA UNIVERSITY OF TECHNOLOGY, 1996,24(3):11~15

[29] Pilling, M.W., Yates, B., Black, M.A.: The thermal conductivity of carbon fiber-reinforced composites. J. Mater.Sci.14, 1326–1338 (1979)

[30] Xia, Z. Z., and Guo, Z. Y., 2001, Simulations on Optimization of Thermal Conduction by Life Evolvement Processes, Advances on Natural Science, 11, pp. 845– 852.

[31] Shih-Yuan Lu, The effective thermal conductivities of composites with 2-D arrays of circular and square cylinders, Journal of composite materials, March 1995 vol. 29 no.4: 483-506

[32] J.W. Klett, V.J. Ervin, D.D. Edie, Finite-element modeling of heat transfer in carbon/carbon composites, Composites Science and Technology, March 1999, vol. 59, Issue 4:593-607

[33] Chung, P.W., Tamma, K.K., Namburu, R.R.: Homogenization of temperature-dependent thermal conductivity in composite materials. J. Thermophys. Heat Transf. 2001 vol. 15 no.1, 10-17

[34] Rodrigo P. A. Rocha and Manuel E. Cruz. Computation of the effective conductivity of unidirectional fibrous composites with an interfacial thermal resistance. International Journal of Computation and Methodology, 2001, vol. 39, Issue 2:179-203

[35] L.M. Manocha, Ashish Warrier, S. Manocha, D. Sathiyamoorthy, et al. Thermophysical properties of densified pitch based carbon/carbon materials—I. Unidirectional composites. Carbon, Volume 44, Issue 3, March 2006, Pages 480–487

Advanced Materials Research Vol. 936 (2014) pp 164-169
© (2014) Trans Tech Publications, Switzerland
doi:10.4028/www.scientific.net/AMR.936.164

Nucleation, Crystallization and Characterization of Mica-Based Glass-Ceramics with Fluorapatite

BAI Jia[1, a *] and CHAYSUWAN Duangrudee[2, b]

[1]Huadian Electric Power Research Institute, Hangzhou 310030, China

[2]Department of Materials Engineering, Faculty of Engineering, Kasetsart University, Bangkok 10900, Thailand

[a]jia-bai@chder.com, [b]fengddc@ku.ac.th

Keywords: mica; fluorapatite; glass-ceramic; crystallization; microstructure

Abstract: The glass system of SiO_2-Al_2O_3-MgO-MgF_2-$SrCO_3$-$CaCO_3$-CaF_2-P_2O_5 was used to prepare machinable glass-ceramics for restorative dental applications. The aim of this study was to apply various heat treatments to produce mica-based glass-ceramics. Differential Thermal Analysis (DTA) was used to determine the optimal heat treatment conditions for nucleation and growth of the crystalline phases in the quenched glass. It was found that the optimum nucleation temperatures for the first and the second crystallization temperatures (T_{p1} and T_{p2}) were 642°C and 635°C, respectively, and the optimum nucleation times were between 2 and 4 hours. X-Ray Diffraction (XRD) showed the phases developed were anorthite, calcium-mica, fluorapatite, strontium apatite, forsterite, fluorite and stishovite phases. The microstructures of glass-ceramics were observed by Scanning electron microscope (SEM), found to exhibit plate-like mica crystals with high interlocking and randomly oriented with a higher soaking temperature and prolongation of the soaking time for crystallization.

Introduction

Ceramics used for implants and for the repair and reconstruction of diseased or damaged body parts are called 'bioceramics', and are used mainly to repair hard tissue such as bones, joints or teeth. Glass-ceramics have the advantage of good control of mechanical properties by heat treatment and are widely used and accepted today in dental applications to meet the patient's need of new, durable and aesthetic materials [1].

As we know, ceramics are brittle, and the quality of the final product is very fabrication technique-sensitive, in terms of strength. Attention has focused on the development of machinable mica-based glass-ceramics because they possess many good properties necessary for restorative dental applications. Mica has excellent machinability. Consequently, mica glass-ceramics can be machined using conventional metallic tools and their machining precision is high. In addition, it is easier to process mica-based glass-ceramics into surgical parts with various complex shapes [2,3]. Fluorapatite improves the biocompatibility for both medical and dental application, since apatite is the mineral phase of tooth and bone. According to the research of Keawsupsak et al., the introduction of not more than 4 mol% fluorapatite into the glass-ceramic system increases both the strength and fracture toughness [4].

Materials and Method

Glass Preparation

The glass system of SiO_2-Al_2O_3-MgO-MgF_2-$SrCO_3$-$CaCO_3$-CaF_2-P_2O_5 was developed [4]. The reagents were mixed and melted in a high density alumina crucible in a furnace (Nabertherm, HT 16/18, Lilienthal, Germany, max. 1,800°C) at 1,400°C for 1 hour. Batch size was approximately 100 g.

The resulting melts were rapidly quenched by pouring directly into water at room temperature to prevent phase separation and crystallization. The glass frit produced was then dried in an industrial

oven (ESPEC, PH-101, Japan). They were then ground and size separated by sieving (Endecotts, England) into fine (smaller than 45μm, powder) and coarse (between 45μm and 2mm) particles. The glass powder was used in the subsequent analysis to determine the optimum nucleation temperature and time. The coarse particles were re-melted at 1400°C. The melt was poured into a carbon mould, preheated to 50°C below their glass transition temperature for 1 hour in order to decrease the stress concentration, and formed transparent glass cylinders approximately 150 mm long by 25 mm diameter. The obtained glass rods were then immediately placed in a purpose-designed furnace (Linn High Therm, LM 512, Eschenfelden, Germany, max. 1,200°C) to anneal for 1 hour and, consequently, to heat-treat for the nucleation and crystallization of the glass-ceramic which was more opaque.

Glass-ceramics Synthesis

Mica-based glass-ceramics are formed by melting and recrystallizing. The recrystallization process must be carefully controlled to create a multiphase solid with crystalline phases dispersed in a glassy matrix. Heat treatment processes were applied in order to transform either glass frit or glass rod to glass-ceramics, according to the following regime [5]: firstly, the temperature was raised from room temperature up to the optimum nucleating temperature and held for the optimum nucleating time (determined from DTA runs). The temperature was then increased to the crystallization temperature plus 20°C (T_p+20°C) and held for different length of time as 1, 3, 6 and 10 hours, respectively. The resultant glass-ceramic was then cooled in the furnace to room temperature (Fig. 1). This process was called the recrystallization process and includes two individual processes, nucleation and crystal growth.

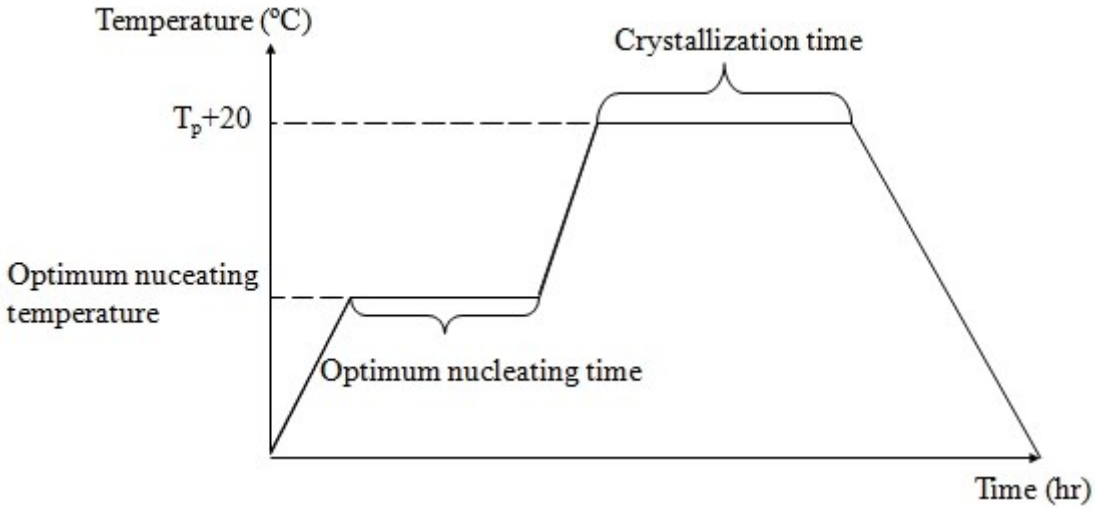


Fig. 1 Schematic of heat treatment process

Characterization Techniques

The differential thermal analysis (DTA) was performed using a Perkin Elmer TAC7/DX (Perkin Elmer, DTA7, Massachusetts, USA) with alumina as the reference material. Both alumina and our glass powder were filled in the platinum crucibles and their weight is 67mg±0.25mg. The program was performed in dry nitrogen at a heating rate of 10°C/min.

X-ray powder diffraction (XRD) analysis was used on both glass and glass-ceramic samples at room temperature. A Philips powder diffractometer (Philips, X'pert PW 3040/00, Eindhoven, The Netherlands) was used with Cu Kα X-rays between 5° and 80°.

The samples were coated by gold sputtering with a vacuum evaporation/deposition method. The microstructures were observed with a scanning electron microscope (Philips, XL30&EDX, The Netherlands).

Results and Discussion

Glass Characterization

The DTA curve of the as-quenched glass powder was 400°C to 1200°C to determine the glass transition (T_g), crystallization (T_p) and melting (T_m) temperatures, as shown in Fig.2. The optimum nucleation temperature and time were determined according to the method of Marotta A. et al. [5].

The glass transition temperature (T_g) was denoted by an endothermic peak at approximately 630℃. The two exothermic peaks, corresponding to T_{p1} and T_{p2} (representing the first crystallization and the second crystallization temperatures), were at 772°C and 878°C respectively. The endothermic peaks above 1,000°C are due to the decomposition, softening and probably melting processes of the different crystalline phases.

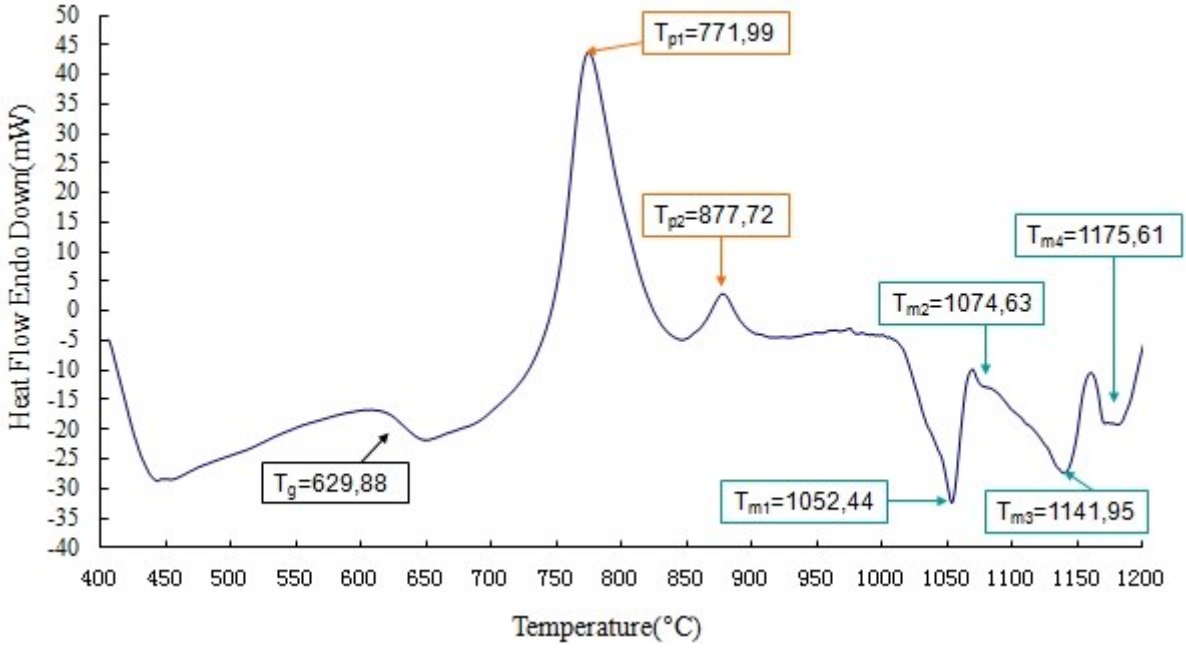


Fig. 2 DTA curve of glass powder

Determination of the optimum nucleation temperature and time of heat treatment

From DTA thermographs, the new crystallization temperatures, T_{p1}*, were determined. T_{p1}*-T_{p1} were plotted against temperatures of heat treatment, namely T_g, T_g-15°C, T_g-30°C, T_g+15°C and T_g+30°C. The point of intersection of tangent lines was 642°C, considered as the optimum nucleating temperature.

The optimum nucleating time was selected by a similar process. The samples were heated from 400°C to the optimum nucleating temperature, namely 642°C and held for 0.5, 1, 3, 4, 8 and 10 hours, respectively. T_{p1}*-T_{p1} were plotted against holding times. The optimum length of time was 2 hours.

The same method done for T_{p1} was used for T_{p2}. Accordingly, the optimum nucleating temperature and time for T_{p2} was 635°C and 2 hours, respectively.

The glass-ceramics were heat treated with different experimental conditions. Table 1 gives the glass codes, heat treatment condition and crystallization time for each sample.

Table 1 Glass codes, heat treatment conditions and crystallization time for subsequent analysis

Sample codes	Heat treatment	Nucleation [^{o}C/ h]	Crystallization [^{o}C/ h]
GCF4_1_1	T_{p1}	642/ 2	792/ 1
GCF4_1_3	T_{p1}	642/ 2	792/ 3
GCF4_1_6	T_{p1}	642/ 2	792/ 6
GCF4_1_10	T_{p1}	642/ 2	792/ 10
GCF4_2_3	T_{p2}	635/ 2	898/ 3
GCF4_2_6	T_{p2}	635/ 2	898/ 6
GCF4_2_10	T_{p2}	635/ 2	898/ 10

X-ray diffraction analysis (XRD)

Calcium-mica ($CaMg_6Al_2Si_6O_{20}F_4$), fluorapatite ($Ca_5(PO_4)_3F$), strontium apatite ($Sr_6Ca_4(PO_4)_6F_2$), forsterite (Mg_2SiO_4), anorthite ($CaAl_2Si_2O_8$), fluorite (CaF_2) and stishovite (SiO_2) phases were found in all heat-treated glass-ceramics. Fig. 3 presents a typical phase evolution for the glass-ceramic powder heat-treated at T_{p1} and held for different soaking time for crystallization. The diffraction peaks became more intensive with increasing crystallization time.

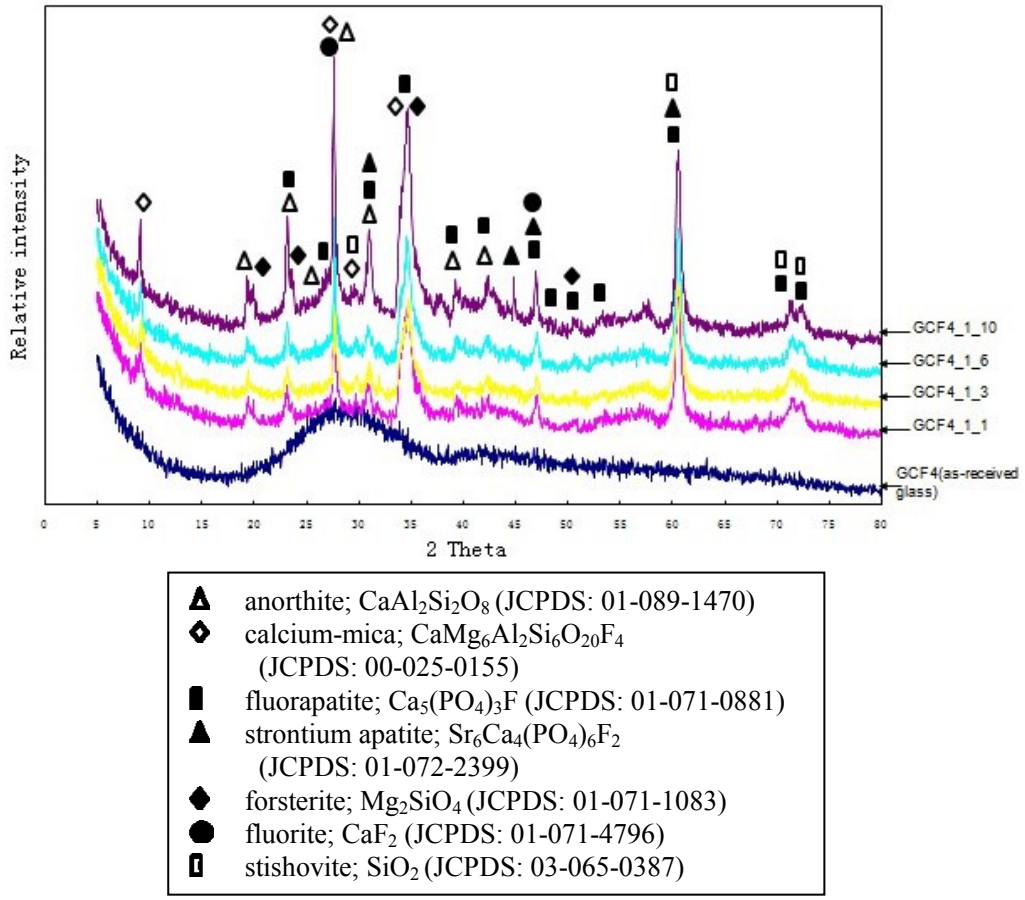


Fig. 3 XRD patterns of as-received glass and T_{p1}-heat-treated glass-ceramics with crystallization time of 1, 3, 6 and 10 hrs.

The change in peak intensity for the glass-ceramics crystallized at T_{p1}+20°C (792°C), GCF4_1_6, and T_{p2}+20°C (898°C), GCF4_2_6, both for 6 hours, are shown in Fig. 4.The main peaks of T_{p2} were more intensive than those of T_{p1} because temperature of T_{p2} was higher than that of T_{p1}. In this case, the bioactivity of glass-ceramics has been developed.

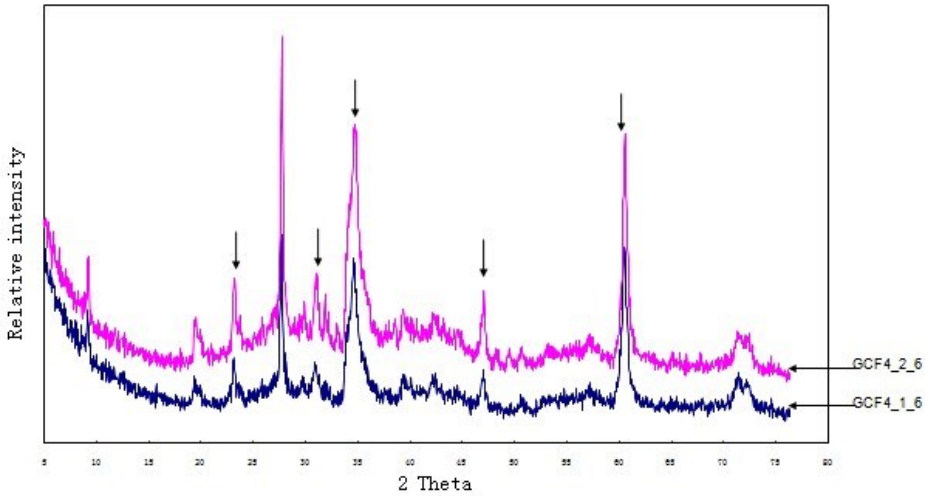


Fig. 4 XRD patterns for glass-ceramics at T_{p1} and T_{p2} for 6 hours crystallization time.

Microstructure analysis

The different heat treatments result in difference in microstructure. Fig. 5 (a) and (b) show the microstructure on fracture surfaces for the specimens heat treated at T_{p1} for 1 and 3 hours. The crystals can hardly be observed when the crystallization time is short. With prolongation of the soaking time for crystallization, the crystals occur and the equiaxed grains increased. Finally, the bulk microstructures consist of plate-like structures, as shown in Fig. 5(c) and Fig. 5(d). The plate-like morphologies indicate to be mica crystals.

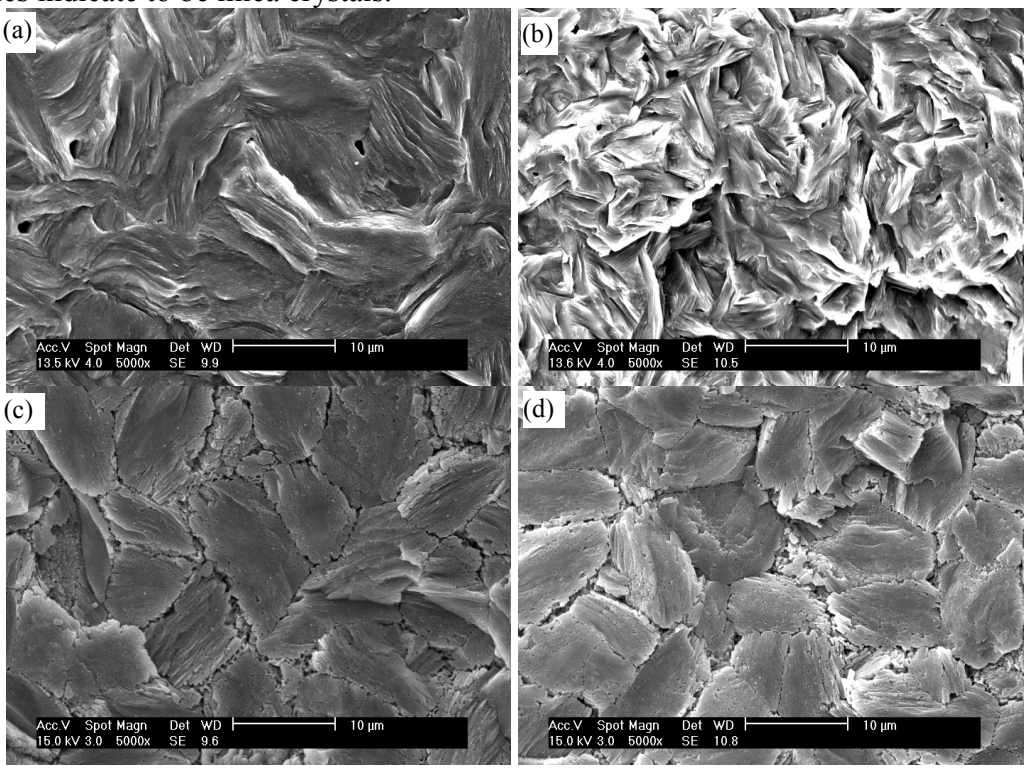


Fig. 5 SEM micrographs of fracture surface
(a) GCF4_1_1, no etching (b) GCF4_1_3, no etching
(c) GCF4_1_6, etched by HF (d) GCF4_2_6, etched by HF

The plane of the mica crystals will be the preferred direction of cleavage when the glass-ceramics are machined. The machinability of mica glass-ceramics is determined by their microstructure such as plate-like mica, which is a highly interlocked array of 2D sheet crystals embedded in a glassy matrix. A great number of interlocking mica crystals in the glass-ceramics prevents macroscopic fracture of these materials during continuous machining [6]. The machinability increases simultaneously with increasing of the crystallinity of mica [7].

Conclusion

Mica-based glass-ceramics with fluorapatite can be successfully prepared with various heat treatments conditions following recrystallization process including two individual processes, nucleation and crystal growth. The optimum nucleation temperature and time have been determined for the first crystallization temperature (T_{p1}) and the second crystallization temperature (T_{p2}).

From XRD patterns, it can be concluded that there is no significant difference in crystalline phases formed for different crystallization times for heat-treatments at either T_{p1} or T_{p2}. The crystals peaks became more intensive with prolongation of the crystallization time or with a higher crystallization temperature.

The bulk microstructure consists of plate-like structures indicate to be mica crystals, which are highly interlocked. With prolongation of the soaking time for crystallization, the grain size of interlock mica increases. Plate-like calcium-mica and fluorapatite crystal are considered as dominant crystalline phases.

References

[1] J.M. Powers, R.L. Sakaguchi, Craig's restorative dental materials, twelfth ed., Mosby Elsevier, 2006.

[2] X.F. Chen, L.L. Hench, D. Greenspan et al., Investigation on phase separation, nucleation and crystallization in bioactive glass-ceramics containing fluorophlogopite and fluorapatite, Ceramics international 24 (1998) 401-410.

[3] S. Taruta, K. Mukoyama, S.S. Suzuki et al., Crystallization process and some properties of calcium mica-apatite glass-ceramics, Journal of Non-Crystalline Solids 296(3) (2001) 201-211.

[4] D. Chaysuwan, K. Sirinukunwattana, K. Kanchanatawewat et al., Machinable glass-ceramics forming as a restorative dental material, Deantal Materials Journal 30(3) (2011) 358-367.

[5] A. Marotta, F. Buri, F. Branda, Nucleation in glass and differential thermal analysis, Journal of Materials Science 16 (1981) 341-344.

[6] S.H. Kilcoyne, P.M. Bentley et al., A small angle neutron scattering study of mica based glass-ceramics with applications in dentistry. Physica B: Condensed Matter 350(1-3) (2004) 529-531.

[7] A. Mallik, A. Basumajumdar, P. Kundu et al., Some studies on nucleation, crystallization, microstructure and mechanical properties of mica glass-ceramics in the system $0.2BaO{\cdot}0.8K_2O{\cdot}4MgO{\cdot}Al_2O_3{\cdot}6SiO_2{\cdot}2MgF_2$, Ceramic International 39 (2013) 2551-2559.

Advanced Materials Research Vol. 936 (2014) pp 170-175
© (2014) Trans Tech Publications, Switzerland
doi:10.4028/www.scientific.net/AMR.936.170

Preparation of C@$ZrSiO_4$ Inclusion Pigment using Compound Colorants via Non-hydrolytic Sol-gel Method

Xia yi XU[1,a], Wei hui JIANG[1,2,b *], Ting CHEN[1,c], Jian min LIU[1],

Li feng MIAO[1], and Xiao jun ZHANG[1]

[1] School of Material Science and Engineering, Jingdezhen Ceramic Institute, Jingdezhen 333001, Jiangxi, China

[2]Jiangxi Key Laboratory of Advanced Materials, Jingdezhen 333001, Jiangxi, China

[a]xuxiayi6085@163.com, [b]jwhjiang@163.com, [c]chenting12@gmail.com

Keywords: C@$ZrSiO_4$ inclusion pigment, compound colorants, non-hydrolytic sol-gel process.

Abstract: C@$ZrSiO_4$ inclusion pigment was prepared by using commercial carbon black RX8002C and phenolic resin (PF) as compound carbon source via non-hydrolytic sol-gel (NHSG) process. The RX8002C carbon could well disperse in phenolic resin solution, which developed a compound carbon source after calcination. Dense $ZrSiO_4$ layer was coated on the carbon surface as a protector. The structure and morphology of samples were characterized by X-ray diffraction (XRD) and transmission electron microscopy (TEM). The chromatic value of the pigments was measured by the CIE color system. The results show that the compound colorants can be well coated by $ZrSiO_4$ dense layer to develop a black inclusion pigment. When the compound proportion is 1:4 and the compound colorants amount is 4wt.%, the chromatic value of the C@$ZrSiO_4$ inclusion pigment is 27.54.

Introduction

The black ceramic pigment is an important decorating material in ceramic industry. Most black pigments are got from two main crystalline structures, spinel crystals and hematite, which can resist high temperature but easily be influenced by the basic glaze and firing conditions [1]. Therefore, the development of the inclusion pigment takes a great interest owing to its properties, such as good thermal and chemical stability at elevated temperature [2]. Over the past few years, kinds of methods have been used to prepare zirconium silicate based inclusion pigments, such as solid state synthesis [3], hydrothermal method [4], precipitation method [5], hydrolytic sol-gel method [6] and so on. Non-hydrolytic sol-gel process (NHSG) was firstly proposed by R Corriu *et al.* [7] in the early 1990s, which did not go through metal alkoxide hydrolysis but directly turned into gel by polycondensation of reactants. This method makes the sol homogeneous at the atomic level during the sol-gel process. In addition, the $ZrSiO_4$-based inclusion pigments still have many problems, such as low encapsulation rate, poor chromophoric performance and high synthesis temperature. The preparation of $ZrSiO_4$-based inclusion pigments with NHSG method could greatly reduce the synthesis temperature of $ZrSiO_4$ by adding appropriate mineralizer [8], which greatly resolved these above problems. Carbon black was reported as a promising colorant for black ceramic pigment application [9-10]. However, its homogenous dispersion is a great problem for the coating process. In this study, C@$ZrSiO_4$ inclusion pigment was synthesized via non-hydrolytic sol-gel process. Compound colorants, commercial carbon and in-situ carbon were used as colorants. The in-situ carbon was carbonized by phenolic resin (PF), which could disperse the commercial carbon and enhance the color value simultaneously. The morphology and structure of the pigment were investigated. The influence of the compound proportion and the addition amount of compound colorants on L* value was studied.

Experimental procedures

Tetraethoxysilane (TEOS, AR) and zirconium tetrachloride ($ZrCl_4$, CP) were selected as precursors, and LiF (AR) was used as mineralizer at the molar ratio of TEOS:$ZrCl_4$:LiF=1.2:1:0.36. All the reagents were completely dissolved in isopropyl alcohol with the $ZrSiO_4$ concentration of 1 mol/L. The precursors were continuously heated reflux at 110 ^oC for 24 h to get the $ZrSiO_4$ sol via non-hydrolytic sol-gel process. Meanwhile, the commercial carbon black (RX8002C, particle size about 28nm) and phenolic resin (PF) were added into isopropyl alcohol with constantly stirring for 24 h to get a well dispersed suspension. The obtained suspension was added into the $ZrSiO_4$ sol, and then the mixture was dried at 110 ^oC to get a xerogel. Finally, the xerogel was calcined at 1000 ^oC in N_2 atmosphere for 2 h at a heating rate of 3 ^oC min^{-1} to obtain C@$ZrSiO_4$ inclusion pigment, and then recalcined at 900 ^oC in the air at a heating rate of 5 ^oC min^{-1} to remove the uncoated carbon black.

The phase compositions of samples were characterized by using the Bruker D8 Advance X-ray diffraction with Cu Kα radiation in the angle range from 10 to 80^o with a step of 0.02 ^{o} and a scan speed of 9 ^{o} min^{-1}. Infrared spectroscopy (IR) studies were determined by Nicolet 5700 infrared spectrometer in the wavenumber range of 4000-400 cm^{-1}. Microstructures of the pigment samples were observed by using JEM-2010 transmission electron microscope. The chromatic parameters CIE-L*a*b* of samples were measured by the Automatic WSD-3C color system.

Results and Discussion

Fig. 1 shows the FT-IR spectrum of the colorants/$ZrSiO_4$ dry xerogel prepared via NHSG method. It exhibits bands at around 1610.1 and 3440.0 cm^{-1}, which is belong to the C=O [11] and -OH [12] band occluded in phenolic resin, respectively. The peak splitting appears at 1373.8 and 1461.9 cm^{-1} due to the isopropyl group in isopropyl alcohol. The 1037.5 cm^{-1} band is attributed to the vibration of Si-O-Zr band [13], which indicates that the sol is homogeneous mixed at the atomic level via the non-hydrolytic sol-gel process. This result leads to the low-temperature synthesis of $ZrSiO_4$ with mineralizer LiF, resulting in accelerating the inclusion process at lower temperature [9].

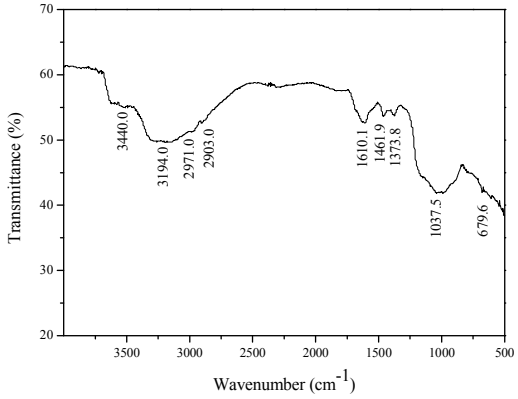


Fig. 1 FT-IR spectrum of the colorants/$ZrSiO_4$ xerogel prepared via NHSG method

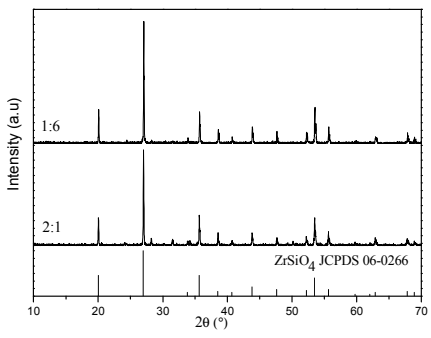


Fig. 2 XRD patterns of the C@$ZrSiO_4$ inclusion pigment with different compound proportion

Fig. 2 shows the XRD patterns of the C@$ZrSiO_4$ inclusion pigments under different compound proportions heated at 1000 ^oC for 2 h. The pure $ZrSiO_4$ phase is formed when the compound proportion of phenolic resin and carbon black is from 1:6 to 2:1, which indicates that the compound proportion has no influence on the synthesis of $ZrSiO_4$ in this range.

Fig. 3 shows the L* values of C@$ZrSiO_4$ inclusion pigments with the different weight ratios of PF to C, including 0:1, 1:6, 1:5, 1:4, 1:3, 1:2, 1:1, 2:1 and 1:0. The L* value of the C@$ZrSiO_4$ pigments firstly decreases with increasing the compound proportion and then increase. All of them exhibit better chromophoric performance than individual carbon black or phenolic resin (1:0 and 0:1). The carbon black can well disperse in phenolic resin solution, which makes the compound colorants easier to be wrapped by $ZrSiO_4$ [14]. At lower compound proportion, the phenolic resin solution is not enough to disperse carbon black, while too much phenolic resin affect the chromophoric performance due to its long polymer chain molecular structure hindering the package of carbon black. When the compound proportion is 1:4, the L* value of C@$ZrSiO_4$ inclusion pigment is 37.09.

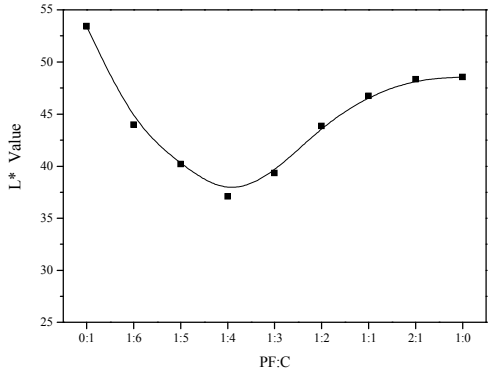


Fig. 3 L* values of the C@$ZrSiO_4$ inclusion pigment with different compound proportion

On the base of 1:4 compound proportion, Fig. 4 shows the XRD patterns of the C@$ZrSiO_4$ inclusion pigment with different addition amounts of compound colorants heated at 1000 ^oC for 2 h. When the total colorants range from 2-12 wt.%, there is no effect on the preparation of $ZrSiO_4$.

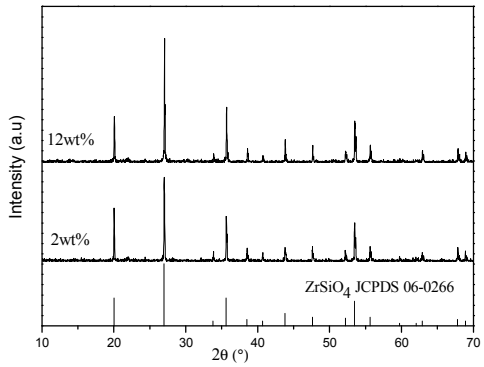


Fig. 4 XRD patterns of the C@$ZrSiO_4$ inclusion pigment with different compound colorants addition

Fig. 5 shows the L* values of C@$ZrSiO_4$ inclusion pigments with different addition amounts of compound colorants (PF:C=1:4), such as 2 wt.%, 4 wt.%, 6 wt.%, 8 wt.%, 10 wt.% and 12 wt.% for $ZrSiO_4$. The corresponding L* value was 40.28, 27.54, 37.09, 38.44, 44.72 and 49.14, respectively. The more compound colorants amounts, the better chromophoric performances are achieved. However, increasing the compound colorants amount constantly, over colorants impacted the mass transfer process during the synthesis of $ZrSiO_4$, which leads to the low encapsulation rate and high L* value.

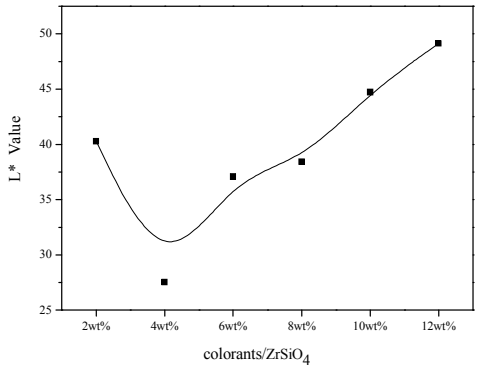


Fig. 5 L* values of the C@$ZrSiO_4$ inclusion pigment with different compound colorants addition

TEM micrographs of carbon black, in-situ carbon got from PF and @$ZrSiO_4$ inclusion pigment are shown in Fig. 6. The morphological features revealed that the size of carbon black particles is range of 25-30 nm (Fig. 6(a)), and the in-situ carbon got from PF is 10-15 nm size (Fig. 6(b)). The phenolic resin can be carbonized to in-situ carbon and coated by $ZrSiO_4$ together with carbon black at elevated temperature (Fig. 6(c)). The result indicates that C@$ZrSiO_4$ inclusion pigment can be synthesized by using PF and carbon black as compound colorants.

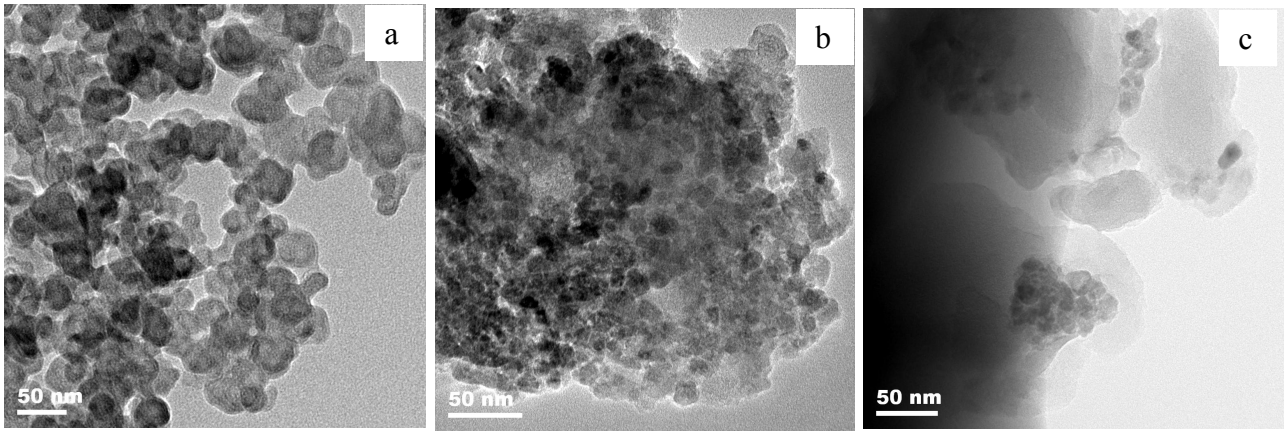


Fig. 6 TEM micrographs of RX8002C (a), in-situ carbon got from PF (b) and @$ZrSiO_4$ inclusion pigment prepared with compound colorants (c)

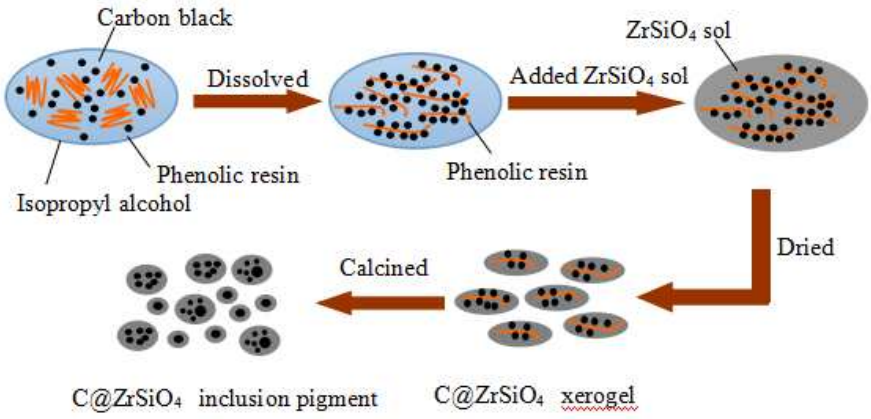


Fig. 7 Schematic of the C@$ZrSiO_4$ inclusion process

Fig. 7 shows the schematic of $ZrSiO_4$ coating carbon process. Firstly, the PF and commercial carbon black compound colorants were dissolved in the isopropyl alcohol to get a suspension due to the well dispersing effect of phenolic resin, and then the $ZrSiO_4$ gel was added into the suspension with stirring. After drying the C@$ZrSiO_4$ xerogel was obtained. Finally, the commercial carbon

black and in-situ carbon black got from PF were coated by $ZrSiO_4$ dense layer through calcined at 1000 ^oC for 2 h in N_2 atmosphere and recalcined at 900 ^oC for 1 h in the air to remove the redundant carbon black. Therefore, the $C@ZrSiO_4$ black inclusion pigment is achieved, which has excellent chromophoric performance and is a promising candidate for ceramic pigment applications.

Conclusions

The $C@ZrSiO_4$ inclusion pigment was prepared via non-hydrolytic sol-gel (NHSG) method by using phenolic resin and carbon black as compound colorants. The results indicate that the compound proportion and addition amount have no influence on the synthesis of $ZrSiO_4$. When the compound proportion is 1:4 and the compound colorants amount is 4wt.%, the best chromatic value of the $C@ZrSiO_4$ inclusion pigment is 27.54, which indicates that it is an excellent black ceramic pigment for ceramic pigment applications.

Acknowledgements

The work was financially supported by National Natural Science Foundation of China (NO.50962006, NO.51162013), Science and Technology Supporting Plan Project of Jiangxi Province (NO.20111BBE50018), major discipline academic and technical leader training plan project of Jiangxi province (NO.20113BCB22009), Natural Science Foundation of Jiangxi Province (NO.2010GZC0103, NO.20114BAB206024).

References

[1] J. Calbo, S. Sorlí, M. Llusar, Minimization of toxicity in nickel ferrite black pigment, Bri. Ceram. Trans. 103(2004) 3-9.

[2] E. Ozel, S. Turan, Production of colored zirconium silicate pigments from zirconium silicate, J. Eur. Ceram. Soc. 27(2007) 1751-1757.

[3] K.R. Pyon, B.H. Lee, The influence of firing conditions on the color properties of $Pr\text{-}ZrSiO_4$ pigments synthesized using rice husk ash, J. Korean. Ceram. Soc. 46(2009) 397-404.

[4] Y. Zhang, D.Z. Zeng, P.G. Rao, Hydrothermal synthesis of cadmium sulfoselenide inclusion pigment, J. Sol-Gel. Sci. Technol. 48(2008) 289-293.

[5] M. Hosseini-Zori, F. Bondioli, T. Manfredini, Effect of synthesize parameters on a hematite-silica red pigment obtained using a coprecipitation route, Dyes. Pigments. 77(2008) 53-58.

[6] F. Zhao, Y.F. Gao, H.G. Luo, Reactive formation of zirconium silicate inclusion pigments by deposition and subsequent annealing of a zirconium silicateia and silica double shell, Am. Chem. Soc. 23(2009) 13295-13297.

[7] R. Corriu, P.H. Mutin, D. Leclercq, Preparation of monolithic metal oxide gels by a non-hydrolytic sol-gel process, J. Mater. Chem. 2(1992) 673-674.

[8] W.H. Jiang, Y.H. Yang, Q.X. Zhu, Iron-zirconium silicate pigments prepared by non-hydrolytic sol-gel method at low temperature, Adv. Mater. Res. 412(2012) 223-226.

[9] W.H. Jiang, Y. Feng, J.M. Liu, Preparation of $ZrSiO_4$/C Inclusion pigments by non-hydrolytic sol-gel method combined with the process of carbon black modification, Mater. Sci. Forum. 745(2013) 545-550.

[10] F. Zhao, W.D. Li, H.J. Luo, Sol-gel modified method for obtention of gray and pink ceramic pigments in zircon matrix, J. Sol-Gel Sci. Technol. 49 (2009) 247-252.

[11] Z.Y. Jiang, S.Q. Li, J.M. Zeng, Preparation and characterization of self-dispersal nanometer carbon black pigment, Adv. Mater. Res. 189*(*2011) 3836-3839.

[12] H Zhao, M Deng, Effects of the synthetic ways of sulfonated-phenol-formaldehyde (SPF) polymers on application properties of cementitious materials, Polym-Plast. Technol. 50(2011) 916-922.

[13] S Kongwudthiti, P Praserthdam, W Tanakulrrungsank, M Inoue, The influence of Si–O–Zr bonds on the crystal-growth inhibition of zirconium silicateia prepared by the glycothermal method, J. Mater. Process. Technol. 136(2003) 186-189.

[14] XJ Yang, MZ Qiu, LQ Hu, B Wu, Effects of nanometer carbon powder on the ablative and heat protection properties of phenolic resin (In Chinese), Journal of solid rocket technology. 27(2004) 2.

Advanced Materials Research Vol. 936 (2014) pp 176-180
© (2014) Trans Tech Publications, Switzerland
doi:10.4028/www.scientific.net/AMR.936.176

Fabrication and Characterization of SiC-coated Multi-Walled Carbon Nanotubes Reinforced Reaction Bonded SiC Composite

Ning SONG[1,a,*], Hong LIU[1,b,], Yong-tao YUAN[1,c] and Jing-zhong FANG[1,d]

[1]Optical and Electronic Institute, Chinese Academy of Sciences, Chengdu 610209, China

[a]03073114@163.com, [b]hongliu@126.com, [c]yongtyuan@163.com, [c]fjzh@ioe.ac.cn

*Ning SONG

Keywords: Multi-walled carbon nanotubues, Coating, Reaction bonded silicon carbide.

Abstract: SiC-coated multi-walled carbon nanotubes (SiC-coated MWNTs) made by RF magnetron sputtering were introduced into the SiC suspensions to enhance the mechanical behaviors of reaction bonded silicon carbide ceramics. The composites were prepared by the epoxy resin curing and liquid silicon infiltration at 1550℃for 60min. The distribution, morphology, and reinforcing behaviors of MWNTs were investigated. X-ray diffraction (XRD) reveals that the MWNTs were reserved during the reaction sintering. The flexural strength and fracture toughness increase with MWNTs ranging from 0wt% to 0.5wt%, reaching the peaks value of 347MPa and 4.3MPam$^{1/2}$ respectively at the MWNTs fraction of 0.5 wt%. This improvement derives from the MWNTs pullout. The consequent decline at MWNTs fraction of 1wt% is resulted from the corrosion of agglomerated MWNTs and the increase of residual silicon.

Introduction

Reaction bonded silicon carbide (RBSC) ceramic is an attractive structural material since the development in the 1950s. In general, the RBSC is prepared by reaction sintering of SiC/C mixtures or porous carbon with liquid silicon [1, 2]. The main advantages of the RBSC are: (a) low sintering temperature as compared to pressure-less or hot pressing densification; (b) short sintering time; (c) full densification; (d) near-net shaping compared with the conventional sintered SiC. Additionally, in the view of the low coefficient of thermal expansion (CTE) and high thermal conductivity, the RBSC is believed to be a promising candidate for the large scale, complex shaped and ultra-light weight structural components [3, 4]. However, due to the presence of the residual silicon the mechanical properties, such as flexural strength, Young's modulus, fracture toughness and hardness, were lower than normal sintered SiC. To improve the mechanical property, many works have been made by fabricating RBSC composites using the starting SiC particles with an appropriate multimodal particle size distribution, boron carbide (B_4C) as an alternative source of carbon, and silicon alloy infiltration [5-7]. In summary, the current attempts have focused on the elimination of residual silicon and the particulate reinforcing.

An alternative is to add carbon nanotubes which represent a promising candidate to substitute the carbon fibers as reinforcing element in composites due to their tremendous mechanical properties. Theoretical and experimental studies have shown that CNTs with very high aspect ratios have excellent mechanical properties: the Young's modulus of MWNTs has been calculated to be up to 1.4 times that of graphite whiskers and the extraordinary flexibility under large strains and resist failure under repeated bending [8]. Thus, MWNTs can effectively toughen the ceramic matrix composites via various toughening mechanisms, such as MWNTs pull out, MWNTs bridging, MWNTs debonding and crack deflection [9-11]. However, using carbon nanotubes as reinforcing additives in the RBSC, there are two major obstacles to be overcome. Firstly, the more critical issues are MWNTs dispersion and MWNTs/SiC interaction-factors, which influence mechanical and electrical properties of the resulting composite material. Secondly, theses MWNTs will be corroded with the liquid silicon during the sintering [12, 13].

In this study, to avoid the degradation and aggregation of the MWNTs during the sintering, MWNTs was coated with SiC by RF magnetron sputtering firstly. Then, SiC-coated MWNTs were introduced into SiC/C suspension. Epoxy resin curing and liquid silicon infiltration (LSI) were combined to prepare composites. The MWNTs fraction ranged from 0 to 1.5wt%. The effects of SiC-coated MWNTs on microstructure and mechanical properties were investigated. Morphology changes of MWNTs after LSI were evaluated.

Experimental

Raw materials and fabrication

MWNTs (supplied by Shenzhen NANO tech. Port Co., Ltd., China) have dimensions of 60–100 nm in diameter and 5–15 μm in length. SiC powders (Jiechuang New Material Technology Co., Ltd, Xuzhou, China) with size of 3.5μm were chosen. Carbon black was introduced as carbon resource in LSI.

The silicon carbide and carbon black powders combined with epoxy resin and dispersant were ball-milled in n-butyl alcohol. After 24h of ball milling, a uniform SiC/C suspension was obtained. The MWNTs were first purified with nitric acid to remove the catalyst such as Fe and then coated with SiC by RF magnetron sputtering. With this treatment, the SiC-coated MWNTs were used as "raw". Before adding to the suspension, the SiC-coated MWNTs were pre-dispersed by ultrasonication and mechanical homogenization. Subsequently, the curing agent for epoxy resin and dispersed SiC-coated MWNTs were ball milled with the obtained SiC suspension for 45min. After mixing, the slurry was vacuumed and then poured into the mold to obtain the green body. The resulting green body was dried at 80℃, carbonized at 1000℃ and then sintered via LSI in vacuum at 1550 ℃ for 60 min.

Characterization

Fracture toughness and the flexural strength of the composites were measured in air at room temperature. Flexural strength measurements were performed on bar specimens (3mm×4mm×40mm) using a three-point bend fixture with a span of 30 mm. Fracture toughness was evaluated using a single edge notched beam (SENB) test in the dimension of 2mm×4mm×26 mm with a span of 20 mm , a notch of 2mm in depth and 0.02mm in width. Crystalline phases of the produced MWNT/SiC composites were characterized by X-ray diffraction (XRD, Philips X' Pert Pro MPD DY1219). Microstructure of the fracture surfaces were examined by scanning electron microscopy (SEM, FEI INSPECT-F). The densities of the samples were measured using Archimedes' method in distilled water at 20℃.

Results and discussion

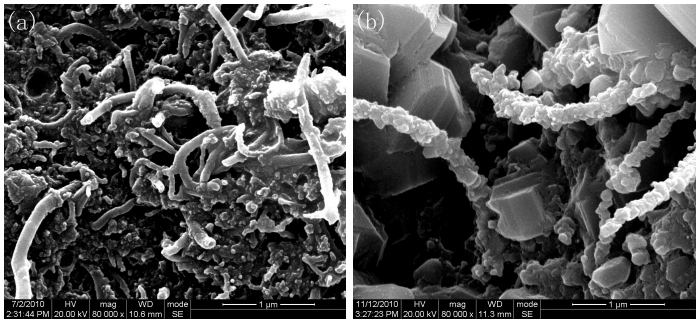


Fig. 1 SEM Images of the MWNTs: (a) Purified MWNTs, (b) SiC-coated MWNTs.

Fig. 1 shows SEM photographs of the MWNTs before (Fig. 1(a)) and after coating with SiC by RF magnetron sputtering (Fig. 1(b)). As shown in Fig. 1 (a), after the purification by nitric acid the surface of MWNTs became smooth and the randomly entangled pristine MWNTs could be separated into single tubes. After coating with SiC by RF magnetron sputtering, the surface of MWNTs became rough coated with polycrystalline SiC particles which could protect the MWNTs from siliconization during reaction sintering.

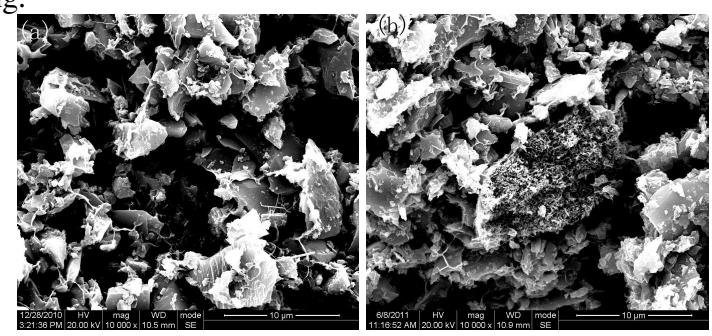


Fig. 2 SEM Images of the Fracture Surfaces of the Green Body After Carbonization with Different MWNTs Fractions: (a) 0.5wt%, (b) 1.5wt%.

Fig. 2 exhibits the microstructures of the fracture surfaces of green body after carbonization with MWNTs fraction of 0.5wt% (Fig.2 (a)) and 1.5wt% (Fig.2 (b)). From Fig.2 (a), no agglomerated SiC-coated MWNTs are observed in the image, implying the homogeneous dispersion of the SiC-coated MWNTs in the matrix. This homogeneous dispersion is ascribed to a series of treatments, including acid purification, coating with SiC, ultrasound vibration and ball milling. With the increasing of the fraction of the SiC-coated MWNTs, the agglomeration in the matrix could avoid formidably as seen in Fig.2 (b).

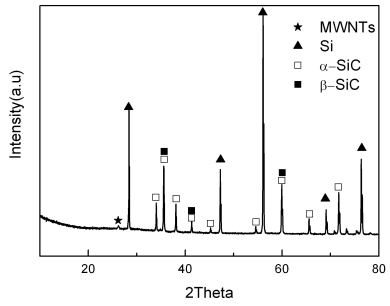


Fig. 3 XRD Pattern of Sample with the MWNTs Fraction of 0.5wt%.

Fig. 3 shows the XRD pattern of the sample with 0.5wt% SiC-coated MWNTs. The composite consist of α-SiC, β-SiC, silicon and MWNTs. The diffraction peak around 2θ=26° with lower relative intensity is attributed to the MWNTs, which indicates the MWNTs are partly preserved in the structure after the reaction sintering.

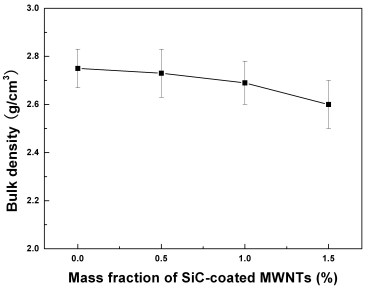


Fig. 4 Bulk Density of the SiC-coated MWNTs Reinforced RBSC Composite as a Function of MWNTs Fraction.

The bulk density as a function of SiC-coated MWNTs is illustrated in Fig. 4. Compared with the monolithic RBSC, the bulk density is decreased by the SiC-coated MWNTs, resulting from the increase of agglomeration of the MWNTs and residual silicon of low density. Due to the low residual carbon of epoxy resin and high porosity of the green body after the carbonization at 1000℃, the bulk

density of the monolithic RBSC is only 2.75g/cm^3 with high proportion of the residual silicon. From Fig. 3, the MWNTs were preserved in the composites, which indicate that the SiC coating can protect the MWNTs from silicification in high fraction of silicon. With the increasing of the fraction of MWNTs, the agglomeration of the MWNTs leads to higher porosity than the monolithic RBSC in the structure as seen in Fig. 2. At the MWNTs fraction of 1.5wt%, the bulk density declines to 2.6g/cm^3.

Variations of the flexural strength and fracture toughness are shown in Fig. 5 with the SiC-coated MWNTs fraction in the range from 0 to 1.5wt%. The flexural strength increases in the initial stage, reaching the peak value of 347MPa at the MWNTs fraction of 0.5wt%. Because of the silicification of the MWNTs and the increase of residual silicon, the flexural strength is reduced when the SiC-coated MWNTs is further increased. The fracture toughness increases from 2.7MPa·m$^{1/2}$ (monolithic RBSC) to 4.3MPa·m$^{1/2}$ (SiC-coated MWNTs fraction of 0.5 wt%). The enhancement is result from the preserved MWNTs in the composites after the infiltration. Owing to the increase of the fraction of SiC-coated MWNTs, the agglomeration which leads to the porosity and defects become form smoke into smother and the residual silicon with high brittleness increases more and more. Due to the damage of the MWNTs, the fracture toughness is degraded at a MWNTs fraction of 1.5 wt%.

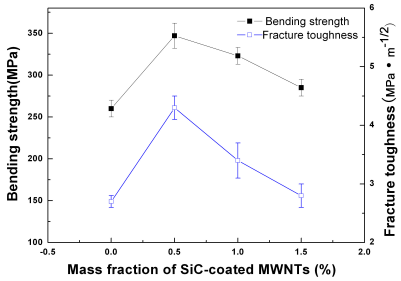


Fig. 5 Flexural Strength and Fracture Toughness as a Function of SiC-coated MWNTs Content (wt %).

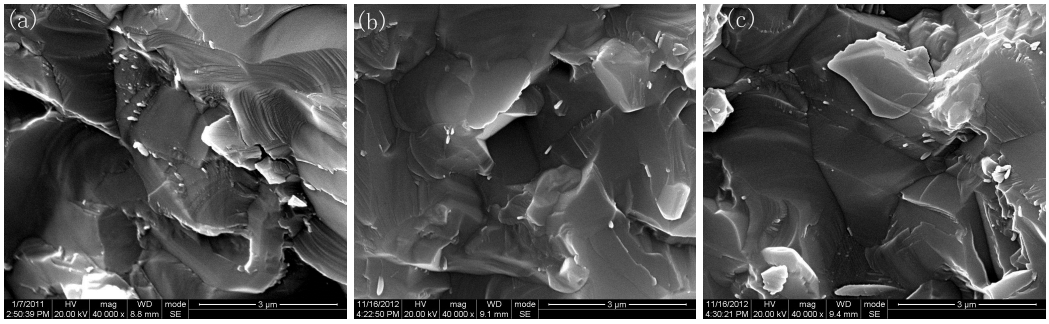


Fig. 6 SEM Images of the Fracture Surfaces of the MWNTs Reinforced RBSC with Different MWNTs Fractions: (a) 0.5wt%, (b) 1wt%, (c) 1.5wt%.

The improvement of fracture toughness derives from MWNTs pullout as seen in the fracture surfaces of the different fraction SiC-coated MWNTs reinforced RBSC of Fig. 6. Owing to the high strength and high elastic modulus of MWNTs, the MWNTs pull out is believed to consume extensive fracture energy. The maximum MWNTs pull out is at the MWNTs fraction of 0.5 wt%, which is in agreement with the variations of the flexural strength and fracture toughness. So, MWNTs pullout is considered the most effective mechanism of MWNTs toughening. No agglomeration of the MWNTs appears on fracture surface of composites, which indicates that the agglomerate MWNTs were silicified absolutely. In general, the shorter fiber pull-out, the stronger bond, the length of fiber pull-out reflects the bond strength between the fiber and matrix in the fiber reinforced composites [14]. Because of the SiC coating, the bond strength between the MWNTs and RBSC become stronger, which can be seen from the shorter and thin MWNTs pull-out compared with the purified MWNTs.

Summary

SiC-coated MWNTs reinforced RBSC composite was prepared by a combination of epoxy resin curing and reaction sintering. The MWNTs can be preserved with the SiC coating made by RF

magnetron sputtering at the MWNTs fraction of 0.5 wt%. At the MWNTs fraction of 1.5 wt%, the agglomerations of MWNTs are siliconized by the liquid silicon due to the increase of porosity and defects. Also, the bulk density declines to 2.6 g/cm^3.

Compared with the monolithic RBSC, the flexural strength and fracture toughness are improved by the MWNTs incorporation. However, the increment is small due to the silicification of MWNTs and the increase of residual silicon. The pull-out of MWNTs is great importance for the improvement of fracture toughness of the composites. To further develop the reinforcing RBSC with the MWNTs, it is necessary to reduce the agglomerations of MWNTs and residual silicon in the sintered body. So, further investigation should focus on distribution of the modified MWNTs and the porosity reduction of the green body.

Acknowledgement

This work was financially supported by the Light of Western (A09K009).

References

[1] Q. W. Huang, L. H. Zhu, High-temperature strength and toughness behaviors for reaction-bonded SiC ceramics below1400 ℃, Mater. Lett. 59 (2005) 1732–1735.
[2] M. Wilhelm, M. Kornfeld, W. Wruss, Development of SiC-Si composites with fine grained SiC microstructures, J. Eur. Ceram. Soc. 19 (1999) 2155-2163.
[3] G. I. Babayants, A.G. Lanin, Thermal stress resistance and heat-induced damage of silicon carbide materials for laser mirrors, J. Eur. Ceram. Soc. 20 (2000) 1515–1520.
[4] G. Amirthan, A.Udaya kumar, M. Balasubramanian, Thermal conductivity studies on Si/SiC ceramic composites, Ceram. Int. 37 (2011) 423–426.
[5] S. Suyama, T. Kameda, Y. Itoh, Development of high-strength reaction-sintered silicon carbide, Diam. Relat. Mater. 12 (2003) 1201–1204.
[6] S. Aroati, M. Cafri, H. Dilman, M.P. Dariel, N. Frage, Preparation of reaction bonded silicon carbide (RBSC) using boron carbide, J. Eur. Ceram. Soc. 31 (2011) 841–845.
[7] R. Voytovych, V. Bougiouri, N.R. Calderon, J. Narciso, N. Eustathopoulos, Reactive infiltration of porous graphite by NiSi alloys, Acta Mater. 56 (2008) 2237–2246.
[8] A. Peigney , Ch. Laurent, E. Flahaut, A. Rousset, Carbon nanotubes in novel ceramic matrix nanocomposites, Ceram. Int. 26 (2000) 677-683.
[9] Z. Xia, L.Riester, W. A. Curtin, Direct observation of toughening mechanisms on carbon nanotubes ceramic matrix composites, Acta Mater. 52 (2004) 931–944.
[10] A.R. Boccaccini, D.R. Acevedo, G. Brusatin, P. Colombo, Borosilicate glass matrix composites containing, J. Eur. Ceram. Soc. 25 (2005) 1515–1523.
[11] J.L. Li , G.Z. Bai, J.W. Feng, W. Jiang, Microstructure and mechanical properties of hot-pressed carbon nanotubes compacted by spark plasma sintering, Carbon 43 (2005) 2649–2653.
[12] K. Hernadi, E. Ljubovic, J.W. Seo, L. Forro, Synthesis of MWNT-based composite materials with inorganic coating, Acta Mater. 51(2003) 1447-1452.
[13] N Song, H Liu, Y. T. Yuan, X Li, J. Z. Fang, Fabrication and corrosion resistance of SiC-coated multi-walled carbon nanotubes, J. Mater. Sci. Thechol. 29 (2013) 1146-1150.
[14] X. H. Zhang, C. Q. Hong, J. C. Han, H. X. Zhang, S. H. Meng, W. Qu, Preparation and properties of titanium diboride ceramic matrix reinforced by carbon nanotubes, J. Inor. Mater. 21 (2006) 899-904.

Advanced Materials Research Vol. 936 (2014) pp 181-186
© (2014) Trans Tech Publications, Switzerland
doi:10.4028/www.scientific.net/AMR.936.181

Carbonization Effect on Phase Structures of Zirconium Oxides with 2-3 Percent Yttrium

Zhiqin Xue [a], Yongquan Guo[b,*]

North China Electric Power University, School of Energy Power and Mechanical Engineering, Beijing China

[a]xuezhiqin@ncepu.edu.cn, [b]yqguo@ncepu.edu.cn, *corresponding author

Keywords: ZrO_2, Y_2O_3 doping, carbonization, phase structure, toughness strengthen

Abstract. Phase evolutions and structures of zirconium oxides with 2 percent yttrium before and after carbonization have been systemically studied with X-ray diffraction and Rietveld structural refinement. The carbonization decreases the structural stability of original ZrO_2. According to the X-ray diffraction patterns, three phases with monoclinic, tetragonal and cubic structure coexist after carbonization. With increasing carbonizing temperature, the content of tetragonal phase in ZrO_2 with 2% mol Y_2O_3 doped increases，however, the phase content of monoclinic phase decreases. The content of tetragonal phase in ZrO_2 with 3% mol Y_2O_3 doped increases greatly after carbonization. It implies that carbonization is beneficial for the formation of ZrO_2 tetragonal phase.

Introduction

As being a fundamental material, zirconia has been widely used in manufacturing due to its attractive mechanical, thermal, electrical and optical properties [1,2]. In order to keep the advanced performance of ZrO_2 in various fields and temperatures, many methods have been proposed for improving its strength and toughness, which are various in physical and chemical methods, e.g. second-phase strengthening and whisker strengthening, *etc* [3,4]. ZrO_2 has three kinds of polymorphs generally, they are corresponding to cubic, tetragonal and monoclinic structures, which are stabilized in different temperature regions, in the temperature ranges from 2953 to 2643 K for cubic, 2643 to1223 K for tetragonal, below 1223 K for monoclinic, respectively [5]. The existence of hexagonal phase is identified by slowly cooling from high temperature to room temperature under high pressure, however，the followed studies are very limited [6].

The spontaneous stress-induced martensitic transformation from the tetragonal to the monoclinic phase plays an important role on ZrO_2-toughened ceramics [5]. The phase transition induces the increase of cell volume and presses on the substrate gradually. Thereby the stress-induced compressive strain can effectively prevent the extension of cracks [7]. Usually, t-ZrO_2 could be stabilized at room temperature by doping cations such as Y^{3+}, Ce^{2+}*etc* [8]. The cost is lower than that of other methods such as nano-crystalline stabilized ZrO_2 at intermediate temperature under ambient conditions [9-14]. Based on the previous reports on the phase transformation mechanism and stability for ZrO_2, the Y_2O_3 doping in Zirconia, which has formed fully stabilized ZrO_2 (FSZ) or partially stabilized ZrO_2(PSZ) or other multiphase case, exhibit excellent performance in strength and fracture toughness caused by the stress-induced martensitic transformation from t→m [15]. In this study, the carbonization technology was used to synthesize the ZrO_2 with 2% and 3% molY_2O_3 for investigating the effects of carbonation temperature on the content of tetragonal phase. The phase structure of samples was checked by X-ray diffraction and their crystal structures were determined using Rietveld refinement technology. It reveals that the content of tetragonal phase in

ZrO_2 with 2% mol Y_2O_3 is going up with increasing the carbonization temperature. The carbonization causes the formation of the t-ZrO2 for the samples with 3% mol Y_2O_3 doping in ZrO_2.

Experiment

The starting materials ZrO_2 with 2% - 3% mol Y_2O_3 were mixed, ground and pelletized with diameter of Φ 20 mm and thickness of 4- 6 mm, followed by sintering in SX-8-16-type silicon molybdenum rod resistance furnace at 1600 ℃ for 4h under an atmosphere of oxygen.

The sintered samples were carburized in a ceramic crucible buried with graphite powder in various temperatures and periods. In order to enhance the activity of the carbon, the graphite powder was mixed uniformly with a small amount of $BaCo_3$ powder, and the crucible was sealed with cement for preventing oxidation.

The phases in samples were checked using a Rigaku diffractometer with rotating anode and an 18-kW X-ray generator $CuK_{\alpha 1}$ radiation (λ = 1.54056 Å), and a graphic monochromator for diffracted beams were used. A step-scanning mode was adopted with a scanning step of 0.02° / *s* (2θ) for determining structure with a Rietveld method. .

Analysis and Discussion

The diffraction data were analyzed by using Rietveld's powder diffraction profile-fitting [16]. For the carburized samples with 2% mol Y_2O_3, the XRD patterns exhibit that the monoclinic, tetragonal and cubic phases coexist in all samples under various sintering temperatures and periods, as shown in Fig 1. It is significant that the content of tetragonal phase is going up with increasing carbonizing temperature. The lattice parameters and unit cell volumes for the monoclinic phase are listed in Table 1.

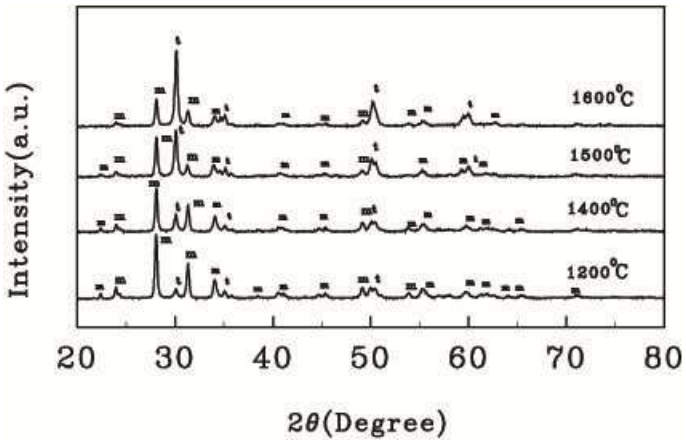


Fig 1. XRD patterns of carbonized zirconia with 2% mol Y_2O_3 under various temperatures

Table 1. Analysis of monoclinic phase in carbon doped zirconia with 2% mol Y_2O_3

Monoclinic phase: S.G.: $P2_1/c$; Z=4				
Carbonization temperature (℃)	1200	1400	1500	1600
Parameters a (Å)	5.169（7）	5.169（6）	5.164（8）	5.166（5）
b (Å)	5.220（9）	5.221（6）	5.223（7）	5.213（6）
c (Å)	5.325（1）	5.325（6）	5.325（9）	5.330（4）
β (°)	99.24	99.26	99.18	98.97
Cell volume V ($Å^3$)	141.8（6）	141.8（8）	141.8（5）	141.8（2）

For these carburized samples with 3% mol Y_2O_3, XRD analysis shows that the tetragonal phase is obtained, and small amount of cubic and monoclinic phase exist as impurity. The space group of tetragonal phase is also $P4_2/nmc$, Z = 2. The refined lattice parameters are a = 3.609(1) Å, and c = 5.184(3)Å. The experimental and calculated XRD patterns of multiphase are given in Fig 2. The residual factor is R*p* = 3.19%, the weighted residual factor is R*wp* = 4.22% and the good fit factor s = 2.08, which indicate that the refinement can be accepted. The lattice parameters and unit cell volume of tetragonal phase are listed in Table 2. The refined structural parameters and ionic positions of multiphase are listed in Table 3. The nearest bond lengths and neighbors of the ions and the O-Zr bond angles in tetragonal phase have been listed in Table 4. The refined results reveal that carbon prefers to occupy Zr position, i.e. 2b crystal position.

Based on the structural refinement, the contents of multiphase can be determined by the reported formula [17]:

$$w_i = \frac{Z_i M_i V_i S_i}{\sum (Z_i M_i V_i S_i)} \tag{1}$$

Where Z_i, M_i, V_i, S_i are presented the numbers of the molecular in a unit cell, the relative molecular mass, the *i*th cell volume, and the scale factor, respectively. The calculated weight percent of tetragonal, cubic and monoclinic phases are 91.14%, 3.73% and 5.13%, respectively. It is noted that the content of dopant of carbon is very lower than that in ZrO_2 – WC composites, where the dopant of WC is as high as 30 vol.% reported by Ref [18] . The more content of dopant is, the more stress induced by doping secondary phase is. It implies that the carbonization technology is beneficial for strengthen toughness by stabilizing more tetragonal zirconia since its content of 3.5 wt%.

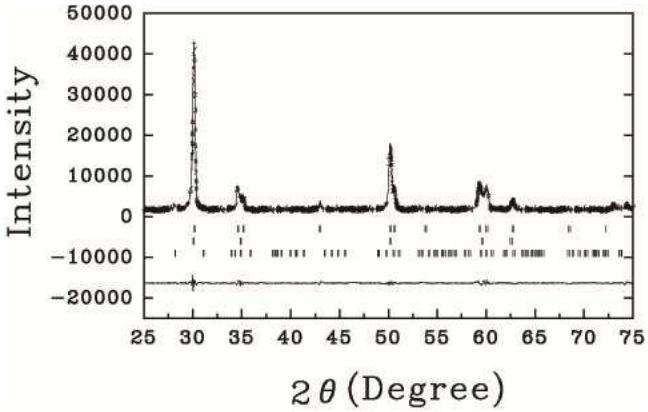


Fig 2. The refined XRD pattern of carbon doped zirconia with 3% mol Y_2O_3

The relationship among the three polymorphs of zirconia in crystallography has been discussed in Ref [1], the reconstructive transformation could be used to explain the transition from tetragonal to monoclinic, *i.e.* two unit cells with tetragonal symmetry combine to one monoclinic cell resulting in volume changes. The oxygen vacancies tend to increase with increasing the doping content of Y_2O_3 [9]. And the structural stability of tetragonal ZrO_2 phase is attributed to the small crystallite size and great oxygen deficiency in phase-pure tetragonal ZrO_2. Y^{3+} substitution for Zr^{4+} cause the increase of ionic radius ratio between the cation and nation (r_+/r_-) since the ionic radius of Y^{3+} is larger that that of Zr^{4+}, which is beneficial for the stability of the tetragonal structure.

Table 2. Analysis of tetragonal phase in carbon doped zirconia with 3% mol Y_2O_3

Tetragonal phase: S.G.: $P4_2/nmc$; Z=2				
Carbonization temperature (℃)	1200*	1400	1500	1600
Parameters a (Å)	3.065(7)	3.065(6)	3.065(4)	3.613(6)
c (Å)	5.180(3)	5.181(2)	5.180(5)	5.168(2)
Cell volume V ($Å^3$)	67.3(5)	67.3(6)	67.3(4)	67.4(9)

*: Calculated results of phase unrefined

Table 3. Analysis of multiphase in carbon doped zirconia with 3% mol Y_2O_3 (Carbonization at 1200 ℃)

Tetragonal phase: S.G.: $P4_2/nmc$; Z=2						
Parameters: a=3.609(1) (Å), c =5.184(3) (Å)						
Atomic position	Atom	x	y	z	B	N
2b	Zr	3/4	1/4	1/4	0.24	1.43
2b	Y	3/4	1/4	1/4	0.10	0.06
2b	C	3/4	1/4	1/4	0.16	0.51
4d	O	1/4	1/4	0.863(6)	1.56	4
Cubic phase: S.G.: Fm3m ; Z=4						
Parameters: a=5.145(8) (Å)						
Atomic position	Atom	x	y	z	B	N
4a	Zr	0	0	0	0.76	4
8c	O	1/4	1/4	1/4	0.13	8
Monoclinic phase: S.G.: $P2_1/c$; Z=4						
Parameters: a=5.195(9) (Å), b =5.225(4) (Å), c =5.342(8) (Å), β=98.17°						
Atomic position	Atom	x	y	z	B	N
4e	Zr	0.2718(6)	0.0324(8)	0.2106(3)	0.68	4
4e	O^I	0.0725(4)	0.3427(3)	0.2996(9)	0.19	4
4e	O^{II}	0.4468(2)	0.7612(5)	0.4564(4)	0.57	4

B: factor of temperature; N: numbers of atom in a cell

Table 4. Ionic coordination number, bond length and bond angle of tetragonal phase in carbon doped zirconia 3% mol Y_2O_3

Ion	Coordination number	Bond	Bond length (Å)
(Zr^{4+}, Y^{3+}, C^{4+})	8	(Zr, Y, C) -- 4O	1.994
		4O	2.509
O^{2-}	10	O -- 2(Zr, Y,C)	1.994
		2(Zr, Y,C)	2.509
		2O	2.592
		4O	2.705
O -- (Zr, Y, C) -- O bond angle		O -- (Zr, Y, C) -- O bond angle	
100.45		118.93	

Summary

The crystal structures and structural phase transitions of carbon doped ZrO_2 have been investigated by means of the X-ray powder diffraction and Rietveld refinement technique. The carbonization is beneficial for the stability of tetragonal phase, which is identified in 3% mol Y_2O_3 doped ZrO_2 after carbonization. The space group of tetragonal phase is $P4_2/nmc$, with Z=2. The content of tetragonal phase in 2% mol Y_2O_3 doped ZrO_2 is going up with increasing carbonization temperature. Large ionic radius ratio (r_+/r_-) is beneficial for the stability of the tetragonal structure.

References

[1] D.N. Wang, Y.Q. Guo, K.M. Liang, K. Tao, crystal structure of zirconia by Rietveld refinement, Science in China, 42 (1999) 80-86.

[2] J.P. Singh, Narottam P.Bansal, Takashi Goto, Jacques Lamon, Sung R.Choi, Morsi M.Mahmoud, Guido Link, Processing and Properties of Advanced Ceramics and composites IV, John Wiley & Sons, Inc., Hoboken, New Jersey, 2012, pp.175-181.

[3] Diletta Sciti, Laura Pienti, Daniele Dalle Fabbriche, Stefano Guicciardi, Laura Silvestroni, Combined effect of SiC chopped fibers and SiC whiskers on the toughening of ZrB_2, Ceram. Int. 40 (2014) 4819-4826.

[4] T. Zhu, L. Xu, X. Zhang, W. Han, et al, Densification microstructure and mechanical properties of ZrB_2-SiC ceramic composites, J. Eur. Ceram. Soc. 29 (2009) 2893–2901.

[5] C.H. Wang, M.C. Wang, J.K. Du, Y.Y. Sie, C.S. Hsi, H.Er Lee, Phase transformation and nanocrystallite growth behavior of 2 mol% yttria-partially stabilized zirconia (2Y-PSZ) powders, Ceram. Int., 39 (2013) 5165–5174

[6] J. OuYang, X.Y. Li, J. Jin, Y. Zhang, H.M. Ynag, Research Progress in the Structural， Mechanical Properties of ZrO_2 and Their Applications, Materials Review (A), 27 (2013) 13-18.

[7] H. Yan, M.M. Dou, H.P. Li, Transformation toughening mechanisms and application of ZrO2 ceramics, J. Ceram., 21 (2000) 46-50.

[8] Y.W. Hsu, K.H. Yang, K.M.Chang, Synthesis and crystallization behavior of 3 mol% yttria stabilized tetragonal zirconia polycrystals (3Y-TZP) nanosized powders prepared using a simple co-precipitation process, J Alloys Compd, 509 (2011) 6864–6870.

[9] Q. Mahmood, A. Afzal, H.M. Siddiqi, A. Habib, Sol-gel synthesis of tetragonal ZrO_2 nanoparticles stabilized by crystallite size and oxygen vacancies, J. Sol-Gel Sci. Technol.; 67 (2013) 670-674.

[10] I.G. Tredici, F. Maglia, M. Dapiaggi et al, Synthesis of bulk tetragonal zirconia without stabilizer: the role of precursor nanopowders, J. Eur. Ceram., 32 (2012) 343–352.

[11] O. Vasylkiv, Y. Sakka, Synthesis and colloidal processing of zirconia nanopowder, J. Am. Ceram. Soc., 84 (2001) 2489–2494.

[12] X. Li, Y. Shimizu, A. Pyatenko et al, Tetragonal zirconia spheres fabricated by carbon-assisted selective laser heating in a liquid medium, Nanotechnology, 23 (2012) 115602-115614.

[13] J.C. Heather,W.J. Seong, J.P. Igor,Current ceramic materials and systems with clinical recommendations: A systematic review, J. Pros. Dent., 98 (2007) 389–404.

[14] P.F. Manicone, P.R. Iommetti, L. Raffaelli, An overview of zirconia ceramics: Basic properties and clinical applications, J. Dent., 35 (2007) 819–826.

[15] A.H. Heuer; Transformation toughening in ZrO_2-containing ceramics;J. Am. Ceram. Soc., 70 (1987) 689–698.

[16] R.A. Young, Introduction to the Rietveld method “In” The Rietveld Method, Oxford University Press, Oxford, 1995.

[17] D.B. Wiles, and R.A. Young, A new computer program for Rietveld analysis of X-ray powder diffraction patterns, J.Appl.Cryst., 14 (1981) 149-151.

[18] G. Anné,S. Put, V. Kim, D.T. Jiang, J. Vleugels, O.V. Biest, Hard,Tough and Strong ZrO_2-WC Composites from Nanosized Powders, J. Eur. Ceram. Soc., 25 (2005) 55–63

Advanced Materials Research Vol. 936 (2014) pp 187-194
© (2014) Trans Tech Publications, Switzerland
doi:10.4028/www.scientific.net/AMR.936.187

Numerical Research of the Beryllia Ceramics Formation Process

U.K. Zhapbasbayev[1], G.I. Ramazanova[1], Z.K. Sattinova[2]

[1]Kazakh-British Technical University, Almaty, Kazakhstan

[2]L.N. Gumilyev Eurasian National University, Astana, Kazakhstan

e-mail: Satkzamir@yandex.ru

Keywords: Thermoplastic slurry; Formation process; Solidification; Viscous–plastic state; Solid–plastic state

Abstract: Simulation results of the formation process of the ceramic fabrications by a hot molding method are presented. Mathematical model describes motion and heat exchange of the liquid thermoplastic slurry of beryllia including the aggregate state change. Velocity and temperature fields during the formation process in the bushings with flat cavity are obtained. Heat flow distribution at the wall of the form-building cavity is demonstrated. The increase of the slurry density during the transition from the liquid state into the viscous–plastic and solid–plastic states is defined.

Introduction

The method of hot molding includes motion and heat exchange of the slurry in the liquid state, as a solid–liquid mixture and as a solid–plastic mixture [1,2]. At stages of filling the form-building cavity and holding under pressure, it is very important to ensure a most structure destruction for obtaining the homogeneous slurry [2]. It is achieved by ultrasonic (US) exposure [2,3]. Minimal friction upon walls of the form-building cavity and maximal plasticity must be reached during the solidification process, to avoid the destruction of the newly formed structure of the molding.

Hydrodynamics of thermoplastic slurry during molding relates to the class of the physical processes of flow and deformation. Slurry flow maintains its configuration after leaving the feeder. It was found during experiments, that for considered molding velocities, the flow of the thermoplastic slurry in the casting mould is laminar [2]. The slurry arrives in the mold at the temperature of $75℃$ and cools down up to $45℃$, at which the molding can be extracted from the mold without buckling [2].

Development and realization of the hot molding method mainly have an empirical nature [5,6], and carrying out of the detailed analysis of the motion and heat exchange will allow to more soundly study the ceramics formation process. Below, the modeling of the ceramics formation process of beryllia by hot molding method is presented.

Rheological Model of the Thermoplastic Slurry

Thermoplastic slurry (high-viscous suspension) is a two phase dispersed system, where solid mineral phase is beryllia powder, and liquid phase is an organic binder. Organic binder consists of 3 components: paraffin, beeswax and oleic acid in the ratio of $0.82: 0.15: 0.03$.

Thermoplastic slurry with thixotropic nature of flow can be related to viscous–plastic fluids of Shvedov–Bingham within the range of shear rate of $0.005 - 1200s^{-1}$ [2,4]:

$$\tau = \tau_0 + \mu \frac{\partial u}{\partial y} \tag{1}$$

where τ is the shear stress; τ_0 is yield point; μ is plastic viscosity coefficient, $\partial u/\partial y$ is the change of the longitudinal velocity along y coordinate.

Ultrasonic exposure influences on the rheological properties of the slurry. Plastic viscosity coefficient, μ, and yield point, τ_0, of the slurry depend on temperature, T, and mass fraction of the binder, ω. The experimental data of μ and τ_0 before ultrasonic exposure for the binder mass fraction $\omega = 0.117$ are described by empirical dependences according to the experimental data of [2,5,6]:

$$\mu(T) = 293.6259 \cdot exp(-0.05816 \cdot T) \quad (2)$$

$$\tau_0(T) = 11.4 + 11.41 \cdot exp\left(-\frac{T-70.05}{5.47}\right) \quad (3)$$

and after ultrasonic exposure:

$$\mu(T) = 629.544 \cdot exp(-0.0709 \cdot T) \quad (4)$$

$$\tau_0(T) = 18.1 + 8.3 \cdot exp\left(-\frac{T-69}{4.8}\right) \quad (5)$$

The temperature is defined in Celsius's ºC in empirical dependences (Eqs. (2)–(5)).

Density of the thermoplastic slurry is defined by the concentration of the binder and densities of the beryllia powder and the binder:

$$\rho = \frac{\rho_{ber} \cdot \rho_{bin}}{(1-\omega)\rho_{bin} + \omega\rho_{ber}} \quad (6)$$

where ρ_{ber} is the density of the beryllia, ρ_{bin} is the density of the binder, ω is relative mass content of the binder normalized to unity.

Density of the binder depends on the temperature and is determined from empirical equation according the experimental data [6]:

$$\rho_{bin}(T) = 0.852 + 0.0725 \cdot cos[\pi(0.01786 \cdot T - 5.3274)] \quad (7)$$

The density of the beryllia is $\rho_{ber} = 3.02\ g/cm^3$. The density of the binder ρ_{bin} in the range of temperature between 75 ºC and 45 ºC is changed within $0.7840\ g/cm^3$ and $0.8845\ g/cm^3$ and the density of the thermoplastic slurry during solidification increases from $2.2643\ g/cm^3$ to $2.3548\ g/cm^3$.

As it was determined experimentally in [1,4,5], ultrasonic exposure has almost no influence on either thermal conductivity or thermal capacity. Both the thermal conductivity, λ, and thermal capacity, c_p, depend on the temperature in accordance with (8) and (9):

$$\lambda(T) = 1.6 + 4.8 \cdot exp(-0.017 \cdot T) \quad (8)$$

$$c_p(T) = 70 + 1070 \cdot exp(0.0027 \cdot T) \quad (9)$$

Thus, rheological properties of the beryllia thermoplastic slurry are functions of temperature, and an aggregate transformation of liquid suspension into solid–plastic state during the forming process is occurred.

Mathematical Model

A flow and a heat exchange of thermoplastic slurry in a bushing are considered. The bushing has a form-building flat cavity (Fig.1). Heat exchange with the coolant occurs on the outer surface of the bushing.

The flat cavity has a thickness of $2y_1 = 0.0015\ m$, a width of $B = 0.03\ m$ and a length of $L = 0.071\ m$. The cooling contour of the bushing is divided into 3 parts. Temperature of the cooling water in the first part is $\theta_1 = 73$℃, in the second part is $\theta_2 = 59$ ℃, in the third part is $\theta_3 = 45$℃.

The liquid slurry flows in the cavity with the initial temperature of $\theta_0 = 75$ ℃. The mass of slurry is cooled and solidified during the movement. At the exit of the cavity, it becomes a structural form. Motion of the thermoplastic slurry is a laminar flow. The feature of the beryllia slurry is its high thermal conductivity: however Prandtl number $Pr = \mu c_p/\lambda$ is much higher than unity due to high viscosity of the thermoplastic slurry. Density of the slurry is variable and increases with solidification.

The problem is studied in Cartesian axes of z and y. OZ axis coincides with the cavity axis direction, and OY axis is radially directed to the cavity axis. Molding velocity is directed vertically downward along the axis OZ. Radial component of the velocity along the axis OY originates from the cooling of the liquid slurry on the side of the wall. An intensive circulation of water occurs in the cooling contours. Therefore wall temperature of each part of the cavity is believed to be equal to the temperature of the cooling fluid.

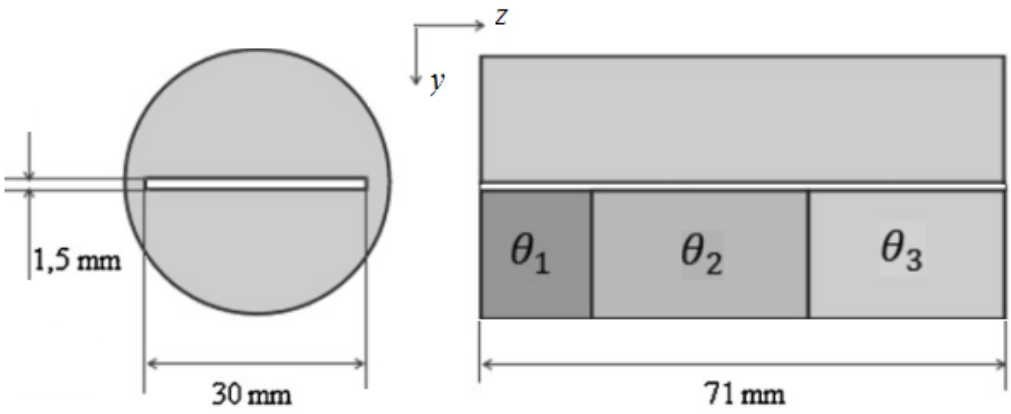


Fig. 1. Bushing diagram of a flat cavity

Rheological properties of the liquid slurry are changed as a result of solidification, and the heat of phase transition is released on the surface of the aggregate transition. Cooling of the slurry may lead to the irregularity of the temperature profile and rheological properties of the pressed out slurry. Solidification begins on the side of the wall, while the slurry may be in liquid state in the center of the cavity. As a result, replenishment by the liquid slurry for the compensation of internal volume shrinkage in the cooling zone of the cavity may occur.

The motion of the slurry is considered to be steady-state along the direction of the molding velocity and for is investigation a set of motion equations of non-Newtonian fluids involving the Shvedov-Bingham model for expression of τ according to Eq. (1) is used [9,10]:

$$\rho u\frac{\partial u}{\partial z}+\rho v\frac{\partial u}{\partial y}=-\frac{dp}{dz}+\frac{\partial}{\partial y}\left(\mu\frac{\partial u}{\partial y}\right)+\frac{\partial \tau_0}{\partial y}+\rho g \tag{10}$$

$$\frac{\partial \rho u}{\partial z}+\frac{\partial \rho v}{\partial y}=0 \tag{11}$$

$$\rho u c_p\frac{\partial T}{\partial z}+\rho v c_p\frac{\partial T}{\partial y}=\frac{\partial}{\partial y}\left(\lambda\frac{\partial T}{\partial y}\right)+H_k\left(u\frac{\partial \rho}{\partial z}+v\frac{\partial \rho}{\partial y}\right)+\mu\left(\frac{\partial u}{\partial y}\right)^2 \tag{12}$$

The following notations are here used: z, y – axial and radial coordinates; u, v –components of the velocity vector; $p, \rho, T, \tau_0,\ c_p,\ \mu,\ \lambda$ –pressure, density, temperature, shear stress, coefficients of thermal capacity, viscosity and heat conductivity of the slurry, respectively.

The heat of aggregate transition of the beryllia slurry is found by experimental data and is equal to $H_k = 7800\, J/kg$ [4]. Rheological properties of the slurry are expressed according to the previously mentioned empiric equations $(2)-(9)$.

Condition of conservation of the mass flow rate permits to define a pressure gradient for pressing out thermoplastic slurry from the molding mold [9]:

$$\int_S \rho u\, dS = \rho_0\, u_0 S \tag{13}$$

where S is cross-section area of the cavity.

Both velocity and temperature distributions at the inlet are considered to be constant along the cross-section of the cavity and all the thermo-physical properties of the slurry are constant:

$$\text{if } z=0: \quad u=u_0,\quad v=0,\quad T=\theta_0 \tag{14}$$

Symmetry conditions are assumed at the cavity axis:

$$\text{if } z>0,\ y=0: \quad \frac{\partial u}{\partial y}=\frac{\partial T}{\partial y}=v=0 \tag{15}$$

For the longitudinal velocity, the conditions of sticking and sliding are set at the wall, depending on the aggregate state of the slurry. It is assumed that the temperature of the cavity wall at each zone is maintained to be constant and equal to the temperature of the cooling fluid. Marking the water temperature in the first, second and third contours as $\theta_1, \theta_2, \theta_3$, respectively, the boundary conditions for the temperature at the wall are achieved [12]:

$$T = \theta_1,\ \mathrm{u} = 0 \tag{16}$$

if $0 \le z < l_1,\ y = y_1$.

$$T = \theta_2, -\frac{\mathrm{dp}}{\mathrm{dz}} = \frac{1}{\mathrm{y_1}}\left[\tau_{0\mathrm{w}} + \left(\mu\frac{\partial \mathrm{u}}{\partial \mathrm{y}}\right)_{\mathrm{w}}\right] \tag{17}$$

if $l_1 \le z < l_2,\ y = y_1$.

$$T = \theta_3, -\frac{\mathrm{dp}}{\mathrm{dz}} = \frac{1}{\mathrm{y_1}}\left[\tau_{0\mathrm{w}} + \left(\mu\frac{\partial \mathrm{u}}{\partial \mathrm{y}}\right)_{\mathrm{w}}\right] \tag{18}$$

if $l_2 \le z < l_3,\ y = y_1$.

Eqs. (10)–(18) can be presented in the dimensionless form for the convenience. Coordinates z, y are divided by the half thickness y_1, velocity components u and v – by v_0, pressure – by the value of dynamic head $\rho_0 u_0^2$, temperature T – by θ_0, density, yield point, coefficients of thermal capacity, viscosity, thermal conductivity – by their values at the temperature θ_0. The equations in the dimensionless form include Reynolds number Re, Prandtl number Pr and Eckert number Ec.

The system of Eqs. $(2) - (13)$ is solved numerically at boundary conditions of Eqs. (14)-(18) [7,9]. The considered zone is broken down into elementary cells with sides $\Delta z_i, \Delta y_j$. Difference analogues of the motion equation (10) and energy equation (12) were obtained by the Crank-Nicolson method of the second order precision, and difference analogue of Eq. (11) – by two-layer scheme of the second order precision. Pressure gradient is defined by the splitting method [7,8] from the condition of flow rate conservation (Eq.(13)).

Discussion of the Calculated Data

Calculations were carried out for the slurry with account of rheological properties before and after ultrasonic exposure. In Fig.2. the distributions of the temperature and the longitudinal component of the velocity in three thermal contours of the flat bushing at the thickness of the cavity of $2y_1 = 0.0015\,m$ and molding velocity of $u_0 = 0.2\,m/min$ without and with ultrasonic exposure, are demonstrated. The longitudinal component of the velocity and the temperature of the slurry at the inlet, of the channel are constant along the cross-section, and are equal to $u = u_0, T = T_0$. The profile of the longitudinal component of the velocity attains the shape of shear flow of the fluid near the inlet section due to high viscosity of the thermoplastic slurry (Fig.2).

Sliding velocity at the wall is almost zero. Wall temperature in the first cooling contour is $\theta_1 =$ 73℃ and the temperature field is changed from 75℃ to 73 ℃ in this zone. Temperature isolines (isotherms) show the zones of the constant temperature and internal structure of the slurry being in liquid state.

Wall temperature is $\theta_1 = 59$℃ in the second cooling contour. Dynamic viscosity, $\mu(T)$, density, $\rho(T)$, and yield point, $\tau_0(T)$, increase with temperature decrease, and viscous-plastic property of the slurry begins to be evident. The slurry slides along the cavity wall, and sliding velocity increases along the length of the second contour during motion down. It resulted in that profile of the longitudinal component of the velocity down the flow will level with constant center in the near-axial zone (Fig.2).

A growth of heat extraction of wall in the second cooling contour leads to a reduction of the temperature field (Fig.2). There is a transition zone in the beginning of the second contour, where the temperature field is variable and expresses the transition of the slurry from the liquid state into the viscous-plastic state. The temperature of the slurry is changed from 73 ℃ to 59 ℃ and defines upper boundary of the zone with constant temperature 59 ℃. The slurry is in viscous-plastic state near the wall due to the heat extraction, while the slurry in the central part of the cavity is in a liquid state. The presence of different structural states along the cross-section results in the change of the rheological and thermo-physical properties of the slurry.

The wall temperature in the third cooling contours is equal to $\theta_3 = 45$℃, which leads to the further cooling of the slurry and reduces the temperature from 59 ℃ to 45 ℃ in the transition zone. According to the experimental data, change in aggregate state takes place at the temperature of $\theta_f = 55$℃. In Eq. (12) for energy, the heat release during the change of aggregate state occurs due to solidification of the viscous-plastic slurry. Solidification leads to a density change of the slurry.

There are density gradients $\frac{\partial \rho}{\partial z}, \frac{\partial \rho}{\partial y}$ in the transition zone, and the heat of change of the aggregate state influences on the distribution of the temperature field.

Further growth of sliding velocity is observed in the third contour. This results in leveling of the longitudinal component of the velocity u along the cross section of the cavity and there is almost piston-like distribution of u at the outlet of the bushing (Fig.2). The transition from viscous-plastic state (green zone in Fig.2) into solid-plastic state (blue zone in Fig.2) takes place in this zone, where rheological and thermo-physical properties of the slurry are homogeneous.

Comparing the temperature field of the slurry in the cavity without ultrasonic (Fig.2a) and with ultrasonic exposure (Fig.2b) one may notice the difference in isotherm distributions. Structural change of the slurry occupies more area in the case of ultrasonic exposure (Fig.2b), than without ultrasonic exposure. It is explained by the increase of the slurry fluidness during ultrasonic exposure due to the change of rheological properties.

Calculation data confirm the experimental fact that, ultrasonic exposure, raising the fluidness of the slurry, reduces the molding velocity during the formation process to get ceramic fabrications.

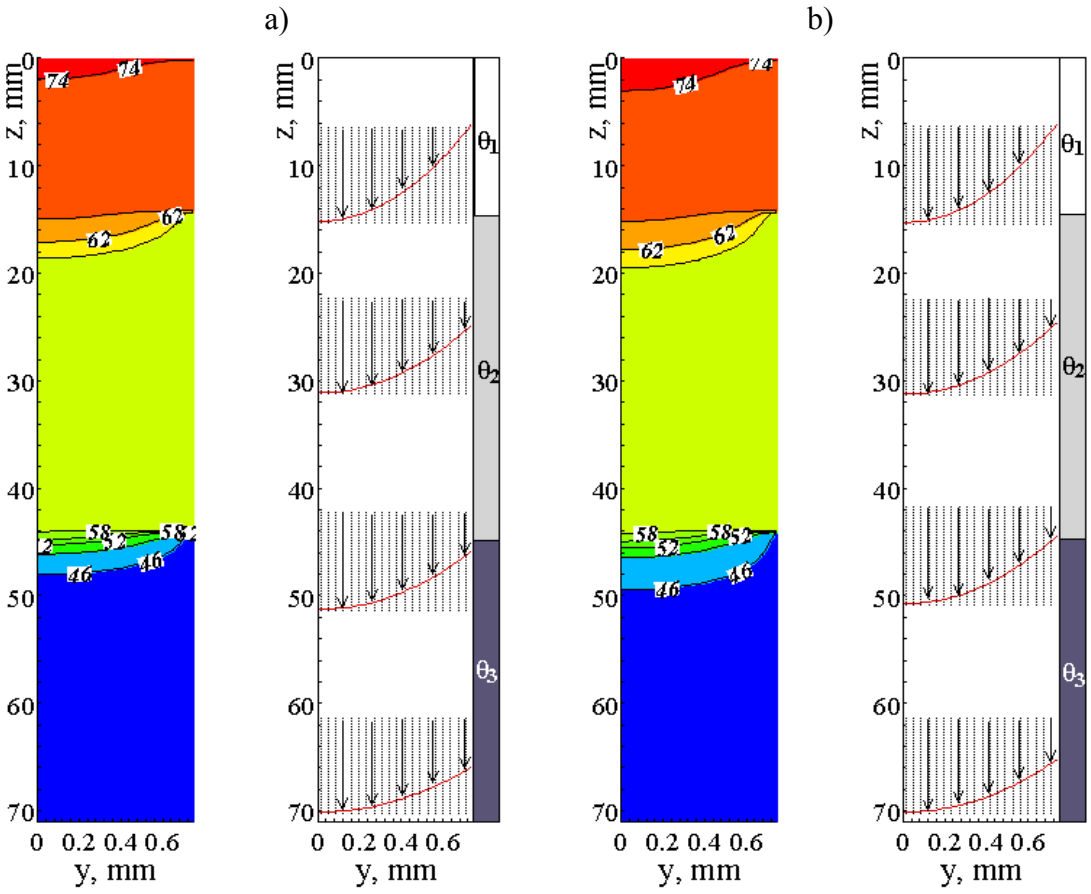


Fig. 2. Distribution of the temperature and longitudinal velocity in the cavity without (a) and with (b) ultrasonic exposure: $h = 0.00075\ m,\ u_0 = 0.2\ m/min$

Increase of molding velocity $u_0 = 0.4\ m/min$ by twice, while the other parameters stay the same, influences on the structural change of the slurry (Fig.3). Calculation data for without ultrasonic exposure (Fig.3a) and with ultrasonic exposure (Fig.3.b) here are also shown. In contrast to the previous regime of formation, the increase of molding velocity leads to the extension of the

transition zone of structural changes from one state into another. It is evident from the temperature distribution (Fig.3): the transition zone from liquid state (red) to viscous-plastic state (green) and the transition zone from viscous-plastic state (green) to solid-plastic state (blue).

Transition zones are expanded in the case with ultrasonic exposure and this is explained by a change in rheological properties of slurry and increase of slurry fluidity (Fig.3).

It can be seen from Figs.2 and 3 that transition zones have curvilinear convex surfaces with different areas. It can lead to uneven shrinkage of the slurry along the section of the form-building cavity.

The density of thermal flow at the wall describes a heat exchange between the slurry and the wall of cavity and can be expressed as:

$$q_w = -\lambda \left(\frac{\partial T}{\partial y}\right)_w$$

Variation of the density of thermal flow by the length of the cavity of flat bushing is shown in Fig.4. The wall temperature in the first cooling contour is $\theta_1 = 73$℃, a small change of thermal flow density q_w at wall is observed and this is due to minor difference between the initial temperature of the hot slurry θ_0 and the wall temperature θ_1. The reduction of wall temperature till $\theta_2 = 59$ ℃ in the second cooling contour leads to a sharp increase of thermal flow density q_w in the narrow area of transition zone due to uneven reduction of the wall temperature from $\theta_1 = 73$ ℃ to $\theta_2 = 59$ ℃. Downwards by the direction of the motion, thermal flow density, q_w, steadily approaches zero due to leveling of the slurry temperature field.

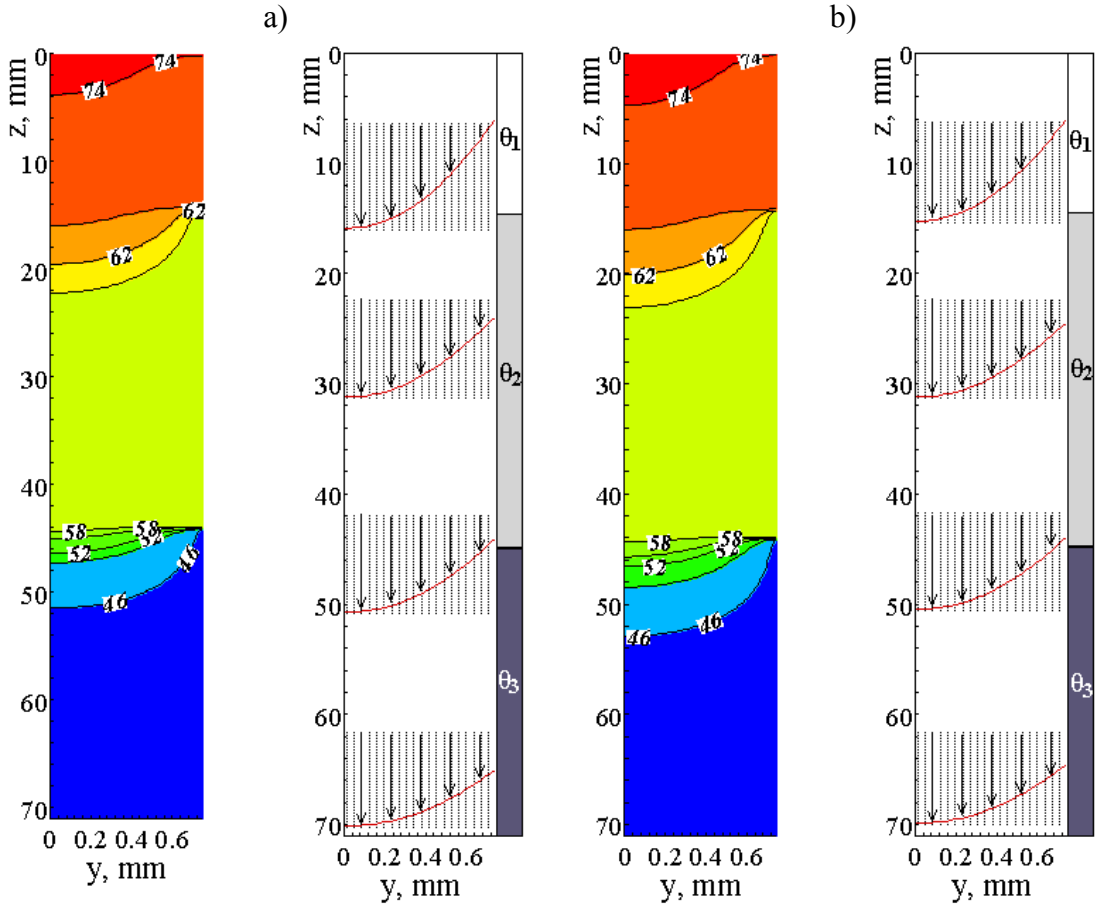


Fig. 3. Distribution of the temperature and longitudinal velocity in the cavity without (a) and with (b) ultrasonic exposure: $h = 0.00075\ m,\ u_0 = 0.4\ m/min$

Thermal flow density, q_w, in the third cooling contour changes similarly due to abrupt reduction of the wall temperature from $\theta_2 = 59$ ℃ to $\theta_3 = 45$ ℃ with a monotonic decrease by leveling of temperature field.

Process of transition of the slurry from one structural state into another in the cavity can be also analyzed through the change of the density. Change of the slurry density along the length of the axial plane of the cavity is demonstrated in the Fig.5.

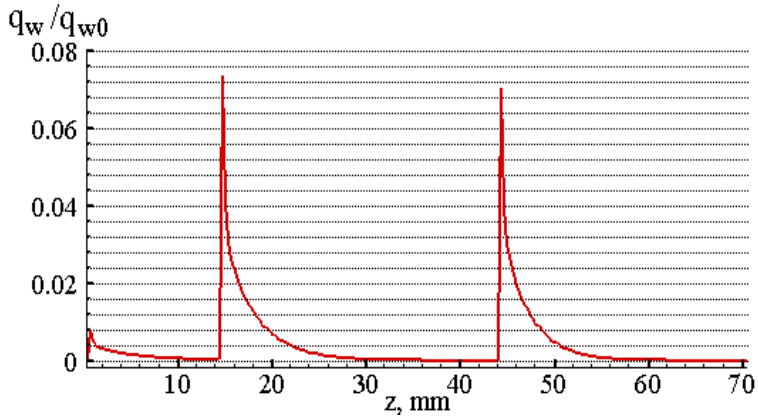


Fig. 4. Change of the thermal flow density at the wall along the length of the cavity: $h = 0.00075\ m,\ u_0 = 0.2\ m/min$

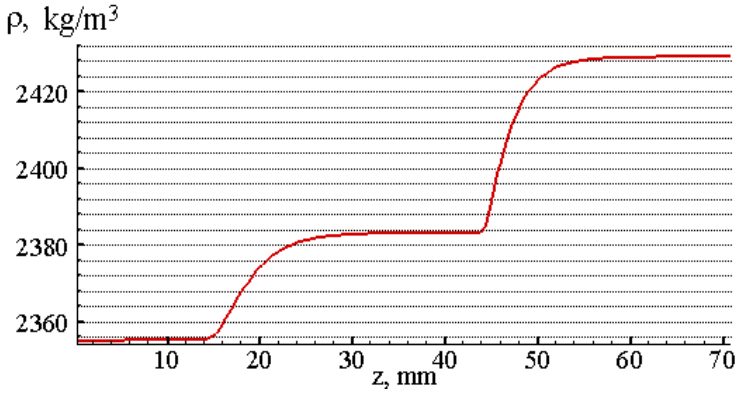


Fig. 5. Change of the density of the slurry along the length of the cavity: $h = 0.00075\ m,\ u_0 = 0.2\ m/min$

A change of density along the first cooling contour is small, i.e. the slurry maintains the initial liquid state. In the second contour, density of the slurry increases from 2355 to 2383 and is stable all the way of this part, i.e. a transition of the slurry from liquid state into viscous-plastic state is taken place. Density of the slurry increases from 2383 to 2429 in the third contour, the slurry is hardened and turns from viscous-plastic state into solid plastic state [5].

Conclusion

Investigation results show that the mathematical model describes all the stages of the ceramic molding including the changes of aggregate state. Ultrasonic exposure enhances the rheological properties and increases the fluidity of the thermoplastic slurry in the form-building cavity. All the stages of the hot molding method of the thermoplastic slurry (liquid state, viscous-plastic state, solid-plastic state) can be presented by the changes of the longitudinal velocity and temperature along the length of the cavity. Density of heat flow at the wall of the form-building cavity is changed in accordance with the boundary conditions and expresses heat extraction at the wall. The slurry density increases during the transition from the liquid state into viscous plastic and solid-plastic states. Such a density distribution expresses balancing mechanism of volumetric changes of the slurry and is in a satisfactory compliance with the experiment [2,6].

Optimum conditions of the ceramic molding process by the hot molding method can be found with calculations, which will allow obtain the hardened fabrication with homogeneous structure of beryllia at the outlet.

References

[1] Akishin, G.P., Turnaev, S.K., Vaispapir, V.Ya., Gorbunova, M.A., Makurin, Yu. N., Kiiko, V.S., Ivanovskii, A.L. Thermal conductivity of beryllium oxide ceramic. *Refractories and Industrial Ceramics,* 2009; 50: 465-468.

[2] Akishin, G. P., Turnaev, S. K., Vaispapir, V. Ya., Kiiko, V. S., Shein I. R., Pletneva E. D., Timofeeva M. N., Iva A. L. Composition of beryllium oxide ceramics. *Refractories and Industrial Ceramics,* 2011; 11: 377-381.

[3] Dobrovol'skii, A.G. Slurry Casting. Moscow: Metallurgiya, 1977. [in Russian]

[4] Dvinskikh, Yu.V., Popil'skii, R.Ya., Kostin, L.I., Kulagin, V.V. Thermophysical properties of thermoplastic casting slips of some high-refractory oxides. *Ogneupory,* 1979; 12: 37–40. [in Russian]

[5] Shakhov, S.A. Use of ultrasound in order to intensify molding of high-temperature thermocouple sheaths. *Refractories & Industrial Ceramics,* 2008; 49: 261-263.

[6] Shakhov, S.A., Gagarin, A.E. Rheological characteristics of thermoplastic disperse systems treated with ultrasound. *Glass and Ceramics*; 2008; 65:122–124.

[7] Anderson, J.D., Tannehill, J.C., and Pletcher, R.H. Computational Fluid Mechanics and Heat Transfer. Moscow: Mir, 1990. [Russian transl.]

[8] Shakhov, S.A. Controlling the deformation behavior of thermoplastic slips with ultrasound. *Glass and Ceramics*, 2007; 64:354-356.

[9] Zhapbasbayev, U.K., Ramazanova, G.I., Sattinova, Z.K. Mathematical model of hot-cast molding of ceramic. *Glass and Ceramics,* 2011, 68: 216-220.

[10] Zhapbasbayev U.K., Kaltayev A., Bitsoyev G.D., Turnayev S.K. Hydrodynamics of moulding of ceramic articles from beryllium oxide with ultrasonic activation. Proceedings ASME International Mechanical Engineering Congress and Exposition, Orlando, Florida, 2005.

CHAPTER 3:

Films and Membranes

Advanced Materials Research Vol. 936 (2014) pp 197-201
© (2014) Trans Tech Publications, Switzerland
doi:10.4028/www.scientific.net/AMR.936.197

$Cu(In,Ga)Se_2$ Films Deposited by Sputtering with Single $Cu(In,Ga)Se_2$ and Cu-Ga-In_2Se_3 Targets and a Subsequent Selenization Procedure

Dong-Hau Kuo[a], Yung-Chin Tu[b] and Wei-Liang Chen[c]

Department of Materials Science and Engineering, National Taiwan University of Science and Technology, Taipei 10607, Taiwan

[a]dhkuo@mail.ntust.edu.tw, [b]m9904302@mail.ntust.edu.tw, [c]d10004016@mail.ntust.edu.tw

Keywords: $Cu(In,Ga)Se_2$; Thin-Film Solar Cells; Sputtering; Selenization

Abstract: $Cu(In,Ga)Se_2$ (CIGSe) thin films were prepared by sputtering with single CIGSe or Cu-Ga-In_2Se_3 target and subsequent selenization at 550-700°C. The one- and two-step selenization procedures and the ceramic and cermet targets were used for process comparisons. Microstructure, film growth and film composition were used to evaluate the growth performance. CIGSe films sputtered from the CIGSe target had a low Cu content. CIGSe films prepared with single Cu-Ga-In_2Se_3 target had shown different performance after the one- and two-step selenization procedures. The two-step process did not grow the dense films due to the vaporization of Se-containing species from the incomplete reaction. The high-temperature requirement is the major disadvantage for the post-selenization approach.

Introduction

$Cu(In_{1-x}Ga_x)Se_2$ solar cell devices with efficiencies above 20% have become a leading material for thin film solar cell applications [1,2]. These quaternary compounds semiconductors have a direct band gap, high efficiency, high absorption coefficient, and long term stability [3]. The most efficient solar cells are obtained from absorber layers with a Cu/(In+Ga) ratio of 0.8-0.92 [1,4].

CIGSe films have been successful made by vacuum-type co-evaporation and non-vacuum-type hydrazine methods below 600°C. Their advantage is the incorporation of Se together during film formation. Post-annealing instead of post-selenization is needed. If the CIGSe films are made by stacking the metallic or alloy layers, these films need a post-selenization procedure to form compounds [5,6]. For the quaternary compound, the multiple precursor sources or targets have been used for the composition control. Single $Cu(In,Ga)Se_2$ target [7] and single cermet target containing metallic Cu and Ga and ceramic In_2Se_3 are less been adapted for CIGSe thin films.

Here, CIGSe films are prepared by sputtering with single CIGSe or Cu-Ga-In_2Se_3 target followed by post-annealing at 550-700°C. Film growth, microstructure and film composition are investigated.

Experimental Procedure

$Cu(In,Ga)Se_2$ (CIGSe) thin films grown on Mo-coated soda-lime glass plates were prepared by the post-selenization of the precursor films deposited by dc-magnetron sputtering with a CIGSe or Cu-Ga-In_2Se_3 target. The CIGSe target was formed at 800°C for 1 h by hot pressing the powder mixture of Cu_2Se, In_2Se_3 and Ga_2Se_3. The Cu-Ga-In_2Se_3 cermet target was hot pressed the powder mixture of Cu, Ga and In_2Se_3 at 550°C for 1 h. The target compositions were based upon the $Cu_{0.9}(In_{0.7}Ga_{0.3})Se_2$ formula. The substrate temperature and growth time were 400°C and 8 h for using the CIGSe target, but they were 150°C and 3 h for the cermet target. The sputtering power was 80 watt. Our post-selenization was executed with one-step and two-step heating procedures in a tube furnace. For the one-step method, the film was heated to 550-700°C with a holding time of 1 h. The two-step method was heated to 300°C with a holding time of 0.5 h and followed by heating to 550-700°C for 1 h. During selenization, the precursor films were loaded in a lid-covered ceramic crucible with a Se or ($SnSe_2$+Se) pellet together for atmospheric control.

Phase identification of CIGSe layer was analyzed by X-ray diffractometry (XRD, Rigaku D/Max-RC). A field-emission scanning electron microscope (SEM, JEOL JSM 6500F) equipped with energy dispersive spectroscopy (EDS) was used for composition analysis and microstructural characterization.

Results and Discussion

Fig. 1(a) shows the SEM image for the as-deposited CIGSe film from a CIGSe target. It had nanometer-sized grains. After selenization, grains were bigger but the surface was rough (Fig. 1(b)). The problems for this approach were a prolonged deposition time of 8 h, the small grain size and a severe deficiency of Cu in CIGSe with the Cu/(In+Ga) ratio of 0.6. The rough surface on the annealed sample is related to the condensation of Se vapor on CIGSe films, the dissolution of Se with CIGSe, and the vaporization of the Se-rich phase. To make a modification, the cermet Cu-Ga-In_2Se_3 target for CIGSe was used. To avoid the preferential formation of $CuInSe_2$ and phase separation, In_2Se_3 ceramic instead of metallic indium was used.

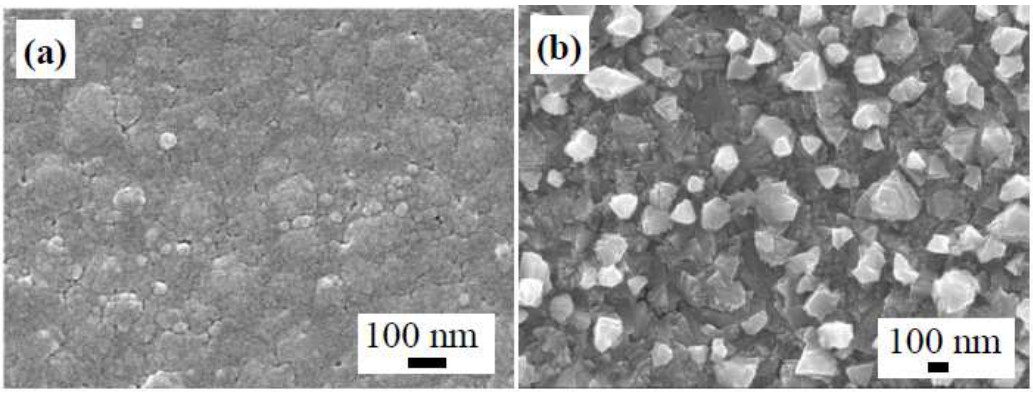


Fig. 1 Surface SEM images of CIGSe films (a) after deposition at 400°C with a CIGSe target followed by (b) selenization at 550°C with a one-step heating procedure.

Fig. 2 Surface SEM images of CIGSe films after deposition with a cermet target at 150°C followed by selenization at different temperatures with a one-step heating procedure. After selenization at 550°C, there were small and white particles on surface. These particles existed before and after selenization and were related to the formation of $CuInSe_2$ from the metallic Cu-In phase. With increasing the selenization temperatures to 600 and 650°C, the grain sizes remained smaller than 0.8 μm. The CIGSe film was difficult in grain growth. Until selenization at 700°C, the fast grain growth led to a non-uniform distribution in grain size ranging from 1 to 6 μm. The CIGSe films obviously need high thermal energy at 700°C to enhance grain growth. These films from the Cu-Ga-In_2Se_3 target basically had smooth and continuous surfaces.

Fig. 3 Surface SEM images of CIGSe films after deposition with a cermet target at 150°C followed by selenization at different temperatures with a two-step heating procedure. Except for 700°C-annealed CIGSe with large grains and a smooth surface, other films were covered with island-like particles and had a loose surface. The two-step selenization procedure obviously is not suitable for the CIGSe films deposited from a Cu-Ga-In_2Se_3 target. The selenization procedure becomes an important issue. The major difference in the one- and two-step procedures is the holding period at 300°C for half an hour. The holding is pretended to have Se vapor cover on as-deposited films for further reaction and selenization. If the reaction of forming CIGSe is not complete due to the insufficient thermal energy, the partially reacted Se-rich compounds will escape from substrate. The escape of partially reacted compounds leaves the voids and gaps on CIGSe films.

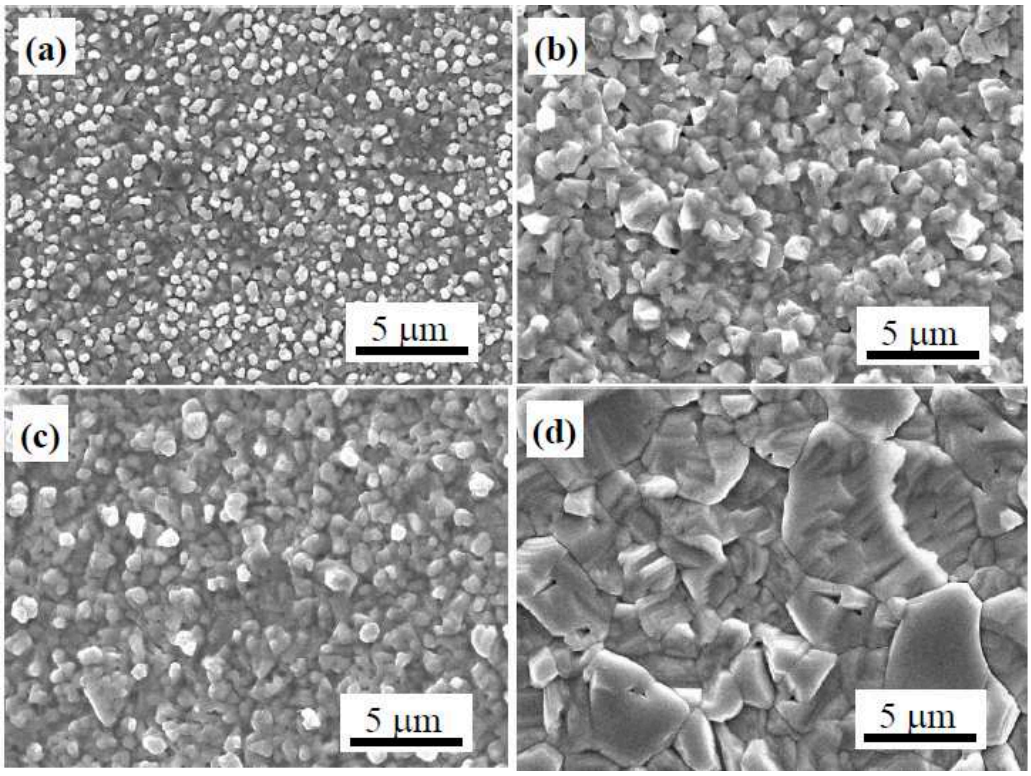


Fig. 2 Surface SEM images of CIGSe films after deposition at 150oC followed by selenization at (a) 550ºC, (b) 600ºC, (c) 650ºC and (d) 700ºC with a one-step heating procedure.

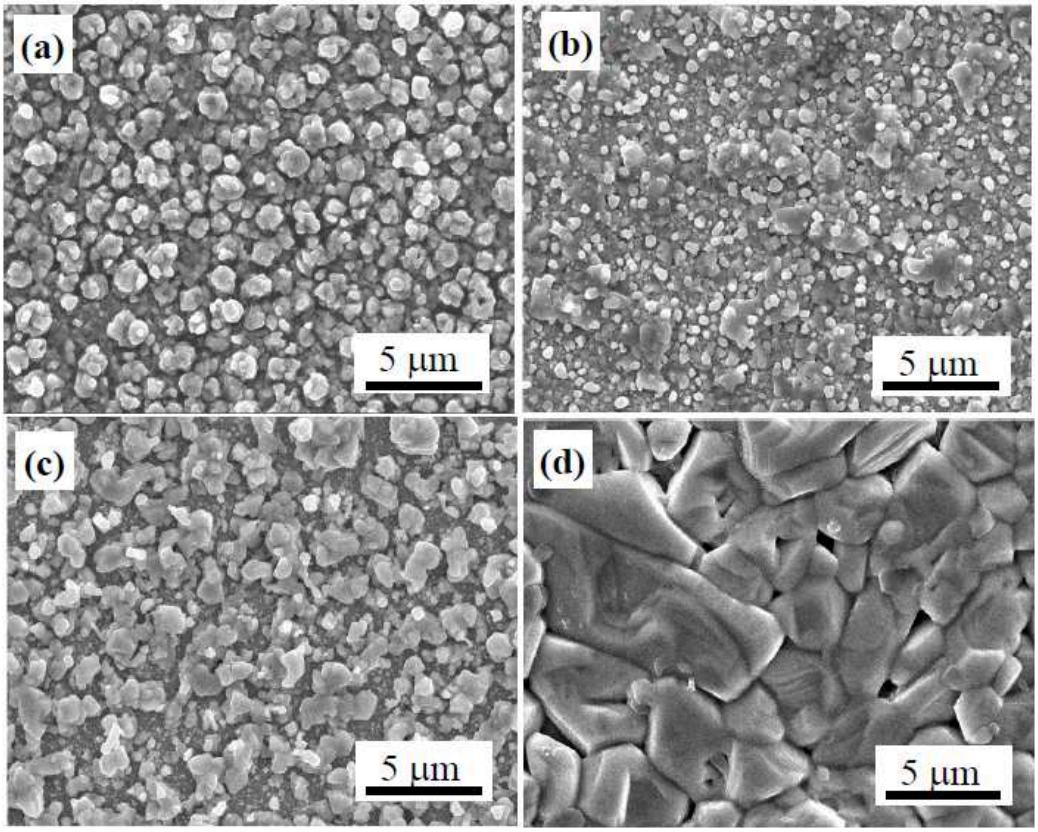


Fig. 3 Surface SEM images of CIGSe films after deposition at 150ºC followed by selenization at (a) 550ºC, (b) 600ºC, (c) 650ºC and (d) 700ºC with a two-step heating procedure.

Fig. 4 shows XRD analyses of CIGSe films obtained by sputtering and post-selenization at 550-700ºC with the (a) one-step and (b) two-step selenization procedures. The three main diffraction peaks from the (112), (220)/(204), and (312)/(116) planes were observed at 2θ angles of ~27º, 44.7º, and 53º, respectively. The Mo bottom electrode was observed for each condition. No

observable second phases were detected. The major difference for the one- and two-step processes is the peak intensity of Mo, from which we can identify that the CIGSe films after the two-step selenization procedure become much thinner. This evidence also supports the loose microstructure with voids due to the composition vaporization.

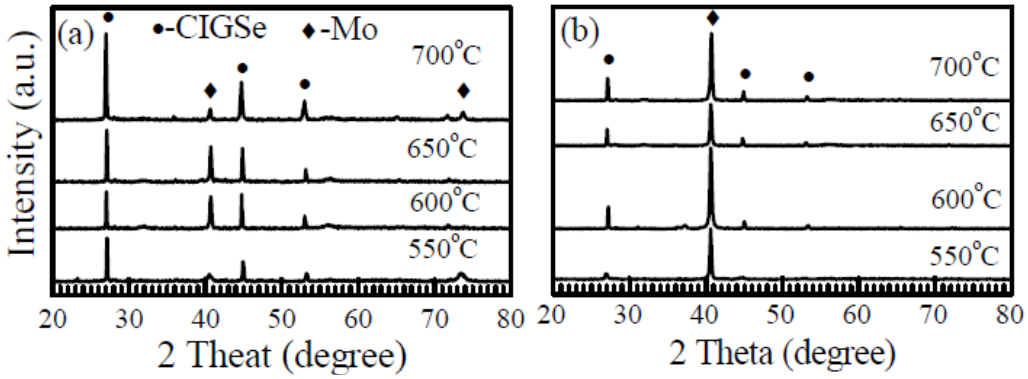


Fig. 4 XRD analyses of CIGSe films after selenization at different temperatures with the (a) one-step and (b) two-step selenization procedures.

Fig. 5 shows XRD analyses of CIGSe films obtained by sputtering and post-selenization at 550-700ºC with the (a) one-step and (b) two-step selenization procedures. For the one-step method, CIGSe films were Se excessive at low selenization temperature but became Se deficient at high temperature. The Cu ratio, on the opposite way, increased with selenization temperature. The Ga/(In+Ga) ratio was close to 0.3. For the two-step method, CIGSe films had the same Se content at ~0.5 for different conditions. The Cu ratio, relating to the Se ratio, was unchanged. The point to note is the Ga ratio decreased with the increase in selenization temperature, which made the Ga/(In+Ga) ration much lower than 0.3. From the composition analyses, the CIGSe films from the two-step procedure look the favorite. However, it has a serious problem in the film microstructure. Its loose microstructure with stable composition indicates the composition vaporization, which has caused the voids, does not have affected its crystallization, phase formation, and composition uniformity.

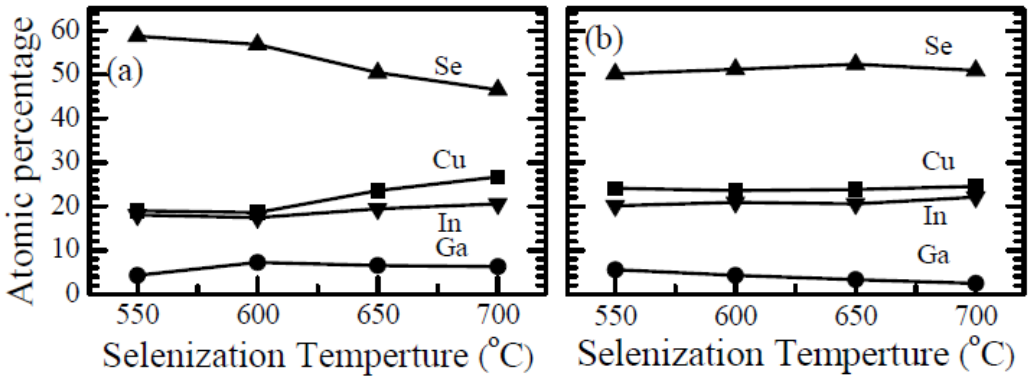


Fig. 5 Compositional analyses of CIGSe films after selenization at different temperatures with the (a) one-step and (b) two-step selenization procedures.

The mechanism of forming the loose and void microstructure needs to be classified in order to know the compositional and microstructural controls. The two-step selenization procedure with a holding at 300ºC before reaching the reaction temperature actually provides a sufficient Se vapor to condense on the as-deposited films. The Se liquid dissolutes the constituents of the as-deposited film with the formations of the selenide compounds and the Se-rich liquid solution. The major selenide is $Cu(In,Ga)Se_2$ and the Se-rich liquid solution can be easily vaporized to form the voids. Therefore, CIGSe films remains to show the CIGSe diffraction peaks and the voids after post-selenization. Because the CIGSe phase is the only phase to stay, the composition from the EDS

analyses does not have an apparent difference. On the other hand, the one-step procedure does not have the sufficient time for the Se vapor to build the over-pressure over the as-deposited films, no excessive Se species cover on the films for reactions. The Se content on the as-deposited films is not a lot to form the Se-rich liquid phase. The limited Se content on substrate reacts to form the CIGSe phase. Because there were no Se-rich species, no composition vaporization occurs and the film remains smooth. The small grain size for CIGSe films after selenization by the one-step method is attributed to the need of higher thermal energy for grain growth of ceramic-containing films deposited from the Cu-Ga-In_2Se_3 target.

Summary

Cu(In,Ga)Se_2 films were deposited by sputtering with single Cu(In,Ga)Se_2 and Cu-Ga-In_2Se_3 targets followed with a one- or two-step selenization procedure. CIGSe films from the sputtering of a CIGSe target had a severe Cu-deficient problem, but it did not occur for sputtering with a cermet target. The performance of CIGSe films from a cermet target was strongly related to the selenization procedure. The two-step procedure is to provide more Se amounts for reactions. If the reaction temperature is not high enough, the reactions are not complete and the generated Se-rich compounds will vaporize to leave a porous CIGSe film. There are no Se-rich compounds generated for the one-step procedure. The control of the Se dissolution reactions is important for the densification, grain growth and composition, which are all related to the temperature-dependent reactivity of reactants to form the CIGSe films.

References

[1] Ph. Jackson, D. Harsco's, E. Lottery, S. Patel, R. Wooers, R. Manner, W. Washman, M. Powell, New World Record Efficiency for Cu(In,Ga)Se_2 Thin-Film Solar Cells Beyond 20%, Prog. Photo volt: Res. Appl. 19 (2011) 894-897.

[2] U.P. Singh, S.P. Patrai, Progress in Polycrystalline Thin-Film Cu(In,Ga)Se_2 Solar Cells, Int. J. Photo energy 468147 (2010) 1-19.

[3] A.M. Fernandez, R.N. Bhattacharya, Electrode Position of $CuIn_{1-x}Ga_xSe_2$ Precursor Films: Optimization of Film Composition and Morphology, Thin Solid Films 474 (2005) 10-13.

[4] D.Y. Lee, M.S. Kim, L. Larine, B.T. Han, Effect of Cu Content on the Photovoltaic Properties of Cu(In,Ga)Se_2 Solar Cells Prepared by the Evaporation of Binary Selenide Sources, Electron. Mater. Lett. 4 (2008) 13-18.

[5] N. Romeo, A. Bosio, S. Mazzamuto, D. Menossi, A. Romeo, CIGS Thin Films Prepared by Sputtering and Selenization by Using In_2Se_3, Ga_2Se_3 and Cu as Sputtering Targets, 2010 10^{th} IEEE Intl. Conf. on Solid-State and Integr. Circ. Technol. (2010) 786-788.

[6] C.H. Huang, Y.C. shih, W.J. Chuang, C.P. Lin, Impacts of Process Parameters on CIGS Solar Cells Prepared by Selenization Process with Se Vapor, 2010 10^{th} IEEE Intl. Conf. on Solid-State and Integr. Circ. Technol. (2010) 2019-2021.

[7] J-H Shi, Z.Q. Li, D.W. Zang, Q.Q. Liu, Z. Sun, S.M. Huang, Fabrication of Cu(In, Ga)Se_2 Thin Films by Sputtering from a Single Quaternary Chalcogenide Target, Prog. Photovolt: Res. Appl. 19, (2011) 160-164.

Advanced Materials Research Vol. 936 (2014) pp 202-206
© (2014) Trans Tech Publications, Switzerland
doi:10.4028/www.scientific.net/AMR.936.202

Effect of hydrogen dilution ratio and substrate roughness on the microstructure of intrinsic microcrystalline silicon thin films

Baojun Yan[1,a], Shulin Liu[2,b], Xiaowei Liu[3,c], Tingting Jiang[4,d]

[1] State Key Laboratory of Particle Detection and Electronics, Institute of High Energy Physics, the Chinese Academy of Sciences, Beijing 100049, China

[2] State Key Laboratory of Particle Detection and Electronics, Institute of High Energy Physics, the Chinese Academy of Sciences, Beijing 100049, China

[3] Xi'an Institute of Applied Optics, Xi'an 710065, China

[4] Xi'an Institute of Applied Optics, Xi'an 710065, China

[a]yanbj@ihep.ac.cn, [b]liusl@ihep.ac.cn, [c]liudan928@163.com, [d]4624428@qq.com

Keywords: silicon thin film, microstructure, hydrogen dilution ratio, substrate roughness

Abstract. Intrinsic microcrystalline silicon (μc-Si:H) thin films were deposited on four kinds of substrates (polished quartz glass: PG, Rough quartz glass: RG, Textured SnO_2:F coated glass: TG, Textured ZnO:Al coated glass: ZG) by 13.56 MHz plasma enhanced chemical vapor deposition (PECVD) with different hydrogen dilution ratio (R_H=H_2/SiH_4) under the pressure of 2 Torr. The film thickness, crystalline volume fraction (X_C) and substrate surface roughness (R_a) were measured by surface profilometer, Raman spectra and atom force microscopy (AFM), respectively. The results revealed that with the increase of R_H, the deposition rate decreased and X_C increased monotonously for the films deposited on the same substrate, but the substrate R_a had an obvious impact on the film microstructure. A physical model was proposed to illustrate the growth of the μc-Si:H thin films deposited on substrates with different R_a.

Introduction

The μc-Si:H thin films were introduced by Veprek and Marecek in 1968 [1]. Since then, a lot of works have been devoted to investigate the μc-Si:H materials and solar cells [2,3]. Hydrogen dilution ratio (R_H=H_2/SiH_4) is one of the most important parameters in depositing the μc-Si:H materials. The materials with high crystalline volume fraction (X_C) can be obtained at high R_H, but with low growth rate. Then high pressure high power method is proposed to diminish the high energy ion bombardments and improve the deposition rate of the μc-Si:H thin films [4]. Although there are three interrelated models to explain the μc-Si:H growth: the surface diffusion model by Matsuda in 1983 [5,9], the chemical annealing model by Nakamura et al in 1995 [6] and the selective etching model by Tsai et al. in 1989 [7], the growth mechanism of μc-Si:H and the effect of substrate surface roughness (R_a) are not yet clear.

In this paper, the influence of RH and Ra on the microstructure of μc-Si:H thin films deposited at plasma excitation frequency 13.56 MHz by plasma enhanced chemical vapor deposition (PECVD) were investigated in detail.

Experiment

The μc-Si:H thin films were deposited in a capacitive coupled radio frequency glow discharge reactor with RH ranging from 1.1 to 25. The deposition power, the substrate temperature, the electrode gap and the deposition pressure were 200 W, 220 °C, 12 mm, and 2 Torr, respectively. The film thickness was measured by thickness profiler (Dektak 150). The crystalline volume fraction (XC) characterized by Raman scattering was determined as (Ic+Ii)/(Ia+Ic+Ii), where Ia, Ii and Ic represented the integrated intensity of amorphous, intermediate and crystalline phase peaks, respectively. The surface morphology and Ra of substrates were observed by atom force microscopy (Bruker, Model Icon).

Results and Discussion

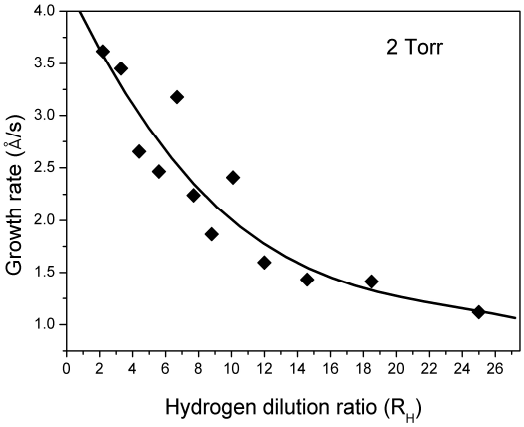


Fig. 1 Growth Rate of Thin Films Deposited on PG Substrate as a Function of R_H at 2 Torr. The Solid Line is Guide to the Eye

As seen in Fig. 1, when the RH increases from 2.2 to 25, the growth rate of thin film deposited on polished quartz glass (PG) substrate decreases slowly from 3.6 to 1.1 Å/s at 2 Torr. It is well known that there are three ways to increase the deposition rate: the first is to increase the flux of active radicals, the second is to create more sites for growth, and the third is to increase the probability for the active radical to occupy a growth site [8]. Here, we attribute the increase of the deposition rate at low RH to the increased flux of active radicals (SiH, SiH2 and SiH3) to the growth surface. And according to the 'etching model', the deposited silicon atom is easily etched and bombarded by hydrogen atom at high RH, which also results in the low deposition rate at high RH.

The crystallinity of μc-Si:H thin films is investigated by the Raman spectroscopy. The Raman spectra of the deposited thin films on four kinds of substrates (TG, ZG, PG, RG) with different RH at the deposition pressure of 2 Torr are shown in Fig. 2. The three peaks at 480 cm-1, 510 cm-1 and 520 cm-1 are attributed to amorphous phase, intermediate phase and crystalline phase, respectively. It is obviously that the Raman spectra of thin films deposited on the four kinds of substrates are different while RH is the same. The crystalline volume fraction XC was calculated by Gaussian fitting [10,11], and listed in Fig. 3. One can see from Fig. 3 that when the deposition pressure is 2 Torr, the XC increases with the RH increase on the same substrate. And when RH is the same, the film deposited on PG has the highest XC and the film on RG has the lowest XC. The deposition conditions are the same except for the type of substrates. Thus, the different kinds of substrates influence the microstructure of the μc-Si:H thin films.

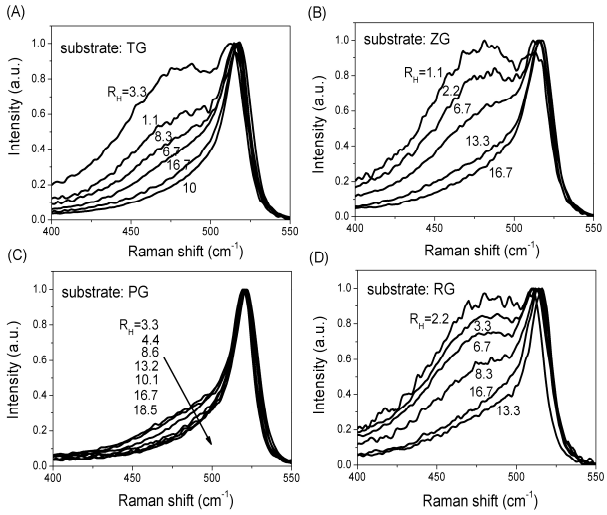


Fig. 2 Raman spectra of the thin films deposited on different substrates as a function of R_H.

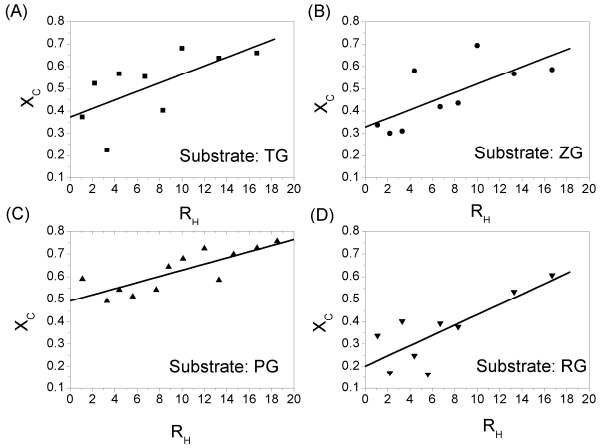


Fig. 3 Crystalline Volume Fraction X_C of the Thin Films Deposited on Different Substrates as a Function of R_H. The Solid Lines are Guides to the Eye

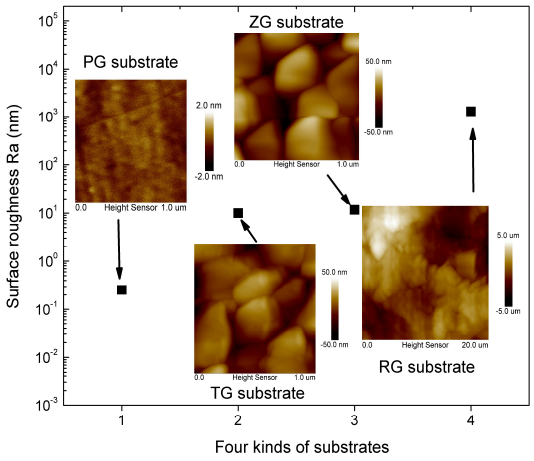


Fig. 4 Surface Roughness R_a and AFM Images of the Four Kinds of Substrate Surface

Fig. 4 shows that the surface roughness Ra of the four kinds of substrates (PG, TG, ZG and RG) is 0.255 nm, 9.94 nm, 11.17 nm and 1278 nm, respectively. However, the varied Ra of the different kinds of substrates affects the microstructure of the deposited thin films. A physical model drawn from our experimental results is proposed as the following.

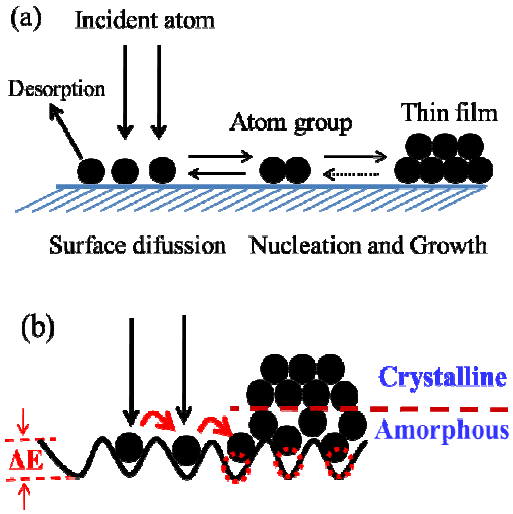


Fig. 5 A Physical Model for the Deposited Atoms with Relatively High Energy Achieving the Flat (a) and the Rough (a) Substrate Surface

The growth of silicon thin films deposited by PECVD usually goes through several processes: precursors (SiHx) in the plasma are adsorbed on the substrate surface, the absorbed precursors start to migrate on the substrate surface and make chemical bonds at the lowest energy sites, forming an amorphous or microcrystalline silicon network structure, while others are desorbed, depending on their sticking coefficients at the surface [12]. The sticking coefficients of precursors are mainly influenced by the substrate temperature [13]. In our experiment, the deposition temperature is the same for all the samples. The deposited atoms with relatively high energy achieve the substrate surface and some adatoms can cross the surface barrier (ΔE), reach the lowest energy position, and form condensation and nucleation in the growing thin films surface, shown in Fig. 5a. The rougher the substrate surface is, the greater the surface barrier ΔE will be. Then adatoms can not all find the lowest energy position (Red dotted line circle in Fig. 5b) at substrates with high Ra, and the initial stage of the film growth forms amorphous structure shown in Fig 5b, namely incubation layer [14,15]. The thickness of incubation layer is proportional to the Ra, and the low crystallization of prepared thin films forms with high Ra. Therefore, the XC of the grown films is inversely proportional to the surface Ra.

The surface coverage of the hydrogen atom is crucial in depositing high quality microcrystalline materials [16]. Then, in order to increase the atomic hydrogen flux density on the growing surface, high hydrogen dilution RH is necessary for μc-Si:H thin film growth. The high RH increases H atoms on substrate surface so as to benefit the film precursor migration on substrate surface, and influences the initial condensation and nucleation of thin films to make them crystallize easily.

Summary

The μc-Si:H thin films were deposited on four kinds of substrates (PG, RG, TG and ZG) with different Ra via PECVD method at various RH under the pressure of 2 Torr. The results revealed that with the increase of RH the deposition rate decreased and XC increased monotonously for the films deposited on the same substrate. The XC of the grown films is inversely proportional to the surface Ra. The effects of the four kinds of substrates on the microstructure and growth behavior of μc-Si:H thin films were attributed to their different surface structures.

References

[1] S. Veprek, V. Marecek. Preparation of thin layers of Ge and Si by chemical hydrogen plasma transport. Solid State Electronics 11 (1968) 683- 687.

[2] A.V. Shah, J. Meier, E. Vallat-Sauvain, N. Wyrsch, U. Kroll, C. Droz, U. Graf. Material and solar cell research in microcrystalline silicon. Solar Energy Materials and Solar cells 78 (2003) 469-491.

[3] B. Yan, G. Yue, J. Yang, S. Guha, D. Williamson, D. Han, C. Jiang. Hydrogen dilution profiling for hydrogenated microcrystalline silicon solar cells. Appl. Phys. Lett. 85 (2004) 1955-1957.

[4] M. Kondo, M. Fukawa, L. Guo, A. Matsuda. High rate growth of microcrystalline silicon at low temperatures. J. Non-Cryst. Solids 266 (2000) 84-89.

[5] A. Matsuda, Formation kinetics and control of microcrystalline in mu-Si-H from glow discharge plasma. J. Non-Cryst. Solids 59-6 (1983) 767-774.

[6] K. Nakamura, K. Yoshida, S. Takeoka, I. Shimizu. Roles of atomic hydrogen in chemical annealing. Jpn. J. Appl. Phys. 34 (1995) 442-449.

[7] C. C. Tsai, G. B. Anderson, R. Thompson, B. Wacker. Control of silicon networks structure in plasma deposition. J. Non-Cryst. Solids 114 (1989) 151-153.

[8] Y. P. Chou, S. C. Lee. Structural, optical, and electrical properties of hydrogenated amorphous silicon germanium alloys. J. Appl. Phys. 83 (1998) 4111-4123.

[9] A. Matsuda, Growth mechanism of microcrystalline silicon obtained from reactive plasmas. Thin Solid Films 337 (1999) 1-6.

[10] M. Jana, D. Das, A. K. Barua. Promotion of microcrystallization by argon in moderately hydrogen diluted silane plasma. Solar Energy Materials and Solar Cells 74 (2002) 407-413.

[11] T. Kaneko, K. Onisawa, M. Wakag, Y. Kita, T. Minemura. Crystalline fraction of microcrystalline silicon films prepared by plasma enhanced chemical vapor deposition using pulsed silane flow. Jpn. J. Appl. Phys. 32 (1993) 4907-4911.

[12] K. Tanaka, A. Matsuda. Glow-discharge amorphous silicon: growth process and structure. Materials Science Reports 2 (1987) 139-184.

[13] Bratu P, Kompa K L, Hofer U, Optical second harmonic investigations of H-2 and D-2 adsorption on Si(100)2×1: The surface temperature dependence of the sticking coefficient. Chemical Physics Letters 251 (1996) 1-7.

[14] J. Zhou, K. Ikuta, T. Yasuda, T. Umeda, S. Yamasaki, K. Tanaka. Growth of amorphous layer free microcrystalline silicon on insulating glass substrates by plasma enhanced chemical vapor deposition. Appl. Phys. Lett. 71 (1997) 1534-1536.

[15] O. Vetterl, M. Hulsbek, J. Wolff, R. Carius, E. Finger. Preparation of microcrystalline silicon seed layers with defined structural properties. Thin Solid Films 427 (2003) 46-50.

[16] J. E. Gerbi, J. R. Abelson. Deposition of microcrystalline silicon: Derect evidence for hydrogen-induced surface mobility of Si adspecies. J. Appl. Phys. 89 (2001) 1463-1469.

Advanced Materials Research Vol. 936 (2014) pp 207-211
© (2014) Trans Tech Publications, Switzerland
doi:10.4028/www.scientific.net/AMR.936.207

The photoluminescence from (Eu, Yb) co-doped silicon-rich Si oxides

Chenglin Heng[1, a], Wenyong Su[1, b], Q. W. Zhang[1], X. Q. Ren[2], P. G. Yin[2], H. P. Pan[3], S. D. Yao[3] and Terje G. Finstad[4, c]

[1] School of Physics, Beijing Institute of Technology, Beijing 100081, P. R. China

[2]School of Chemistry and Environment, Beihang University, Beijing 100191, , P. R. China

[3]School of Physics, Peking University, Beijing 100871, P. R. China

[4] Physics Department, University of Oslo, PO Box 1048, Blindern, N-0316, Oslo Norway

[a]hengcl@bit.edu.cn, [b]suwy@bit.edu.cn, [c]terje.finstad@fys.uio.no

Keywords: Silicon rich oxide; Luminescence; Eu; Yb; Rare earth compounds; Energy transfer

Abstract. We report on photoluminescence (PL) properties of europium (Eu) and ytterbium (Yb) co-doped silicon oxide films with different Si excess**.** After annealing the films in N_2, strong PL were observed from Eu and Yb^{3+} ions and their intensities are correlated. The PL intensity of Eu is mainly from 3+ for no and relatively low temperature anneals (<900 °C) while the Eu^{2+} emission is dominating for annealing at 1000 °C or above in the co-doped Si-rich oxide films. Transmission electron microscopy shows amorphous (Eu, Yb, Si, O)-containing precipitates in the Si-rich oxide during 1000-1200 °C annealing and these precipitates are considered to be responsible for the Eu^{2+}-related luminescence.

Introduction

Recently, spectral conversion in solar cells by the use of rare earth doped films has emerged as a potential application [1]. In particular, down conversion schemes using co-doping by Eu and Yb have attracted interest [2-6]. The down conversion scheme is possible by the energy of the $4f^6 5d \rightarrow 4f^7$ transition of Eu^{2+} being approximately twice that of the $^2F_{5/2} \rightarrow {}^2F_{7/2}$ transition in Yb^{3+} ions. The Yb^{3+} ions will emit photons around 980 nm, which matches the largest spectral response of crystalline Si solar cells. Eu can be found in the 3+ or the 2+ state in different host materials under different conditions and one of the challenges of the scheme has been to find a suitable host matrix for Eu and Yb that will promote the 2+ for Eu [4-7]. Si-rich silicon oxides (SRSO, composition SiO_x, $x<2$) is here chosen as host here as it's optical absorption appears suitable, partly caused by Si nanostructures. The wide band gap of Si nanostructures can also reduce energy loss in thermalization of photo exited carriers [8], and are widely studied for Si-based solar cells [9-11]. In this work, we deposited (Eu, Yb) co-doped SRSO films, and studied the effects of the SRSO matrix and the anneal temperature on the photoluminescence (PL). The emphasis is on identifying the PL contributions and the processes responsible by correlating with micro-structural characterization after annealing of samples of different composition.

Experimental Details

The (Eu, Yb) co-doped SRSO films were deposited on single crystal Si substrates by sputtering from a $Si+SiO_2+EuYbO$ composite target in a pure Ar plasma under a working gas pressure of 0.8 Pa. The EuYbO target was made by hot-pressing a mixture of high purity Eu_2O_3 (99.99%) and Yb_2O_3 (99.99%) powders. Quartz plates were attached on the surface of the EuYbO target to control the doping concentrations of Eu (Yb), and small pieces of Si plates were put on the surface of quartz plates to adjust the Si excess in the final films. We will report on samples from two different SRSO sputter runs with different Si excess, here called sample A and sample B, where B has nominally the largest Si excess. As reference we use a sputtering with no Si excess, called sample C. The

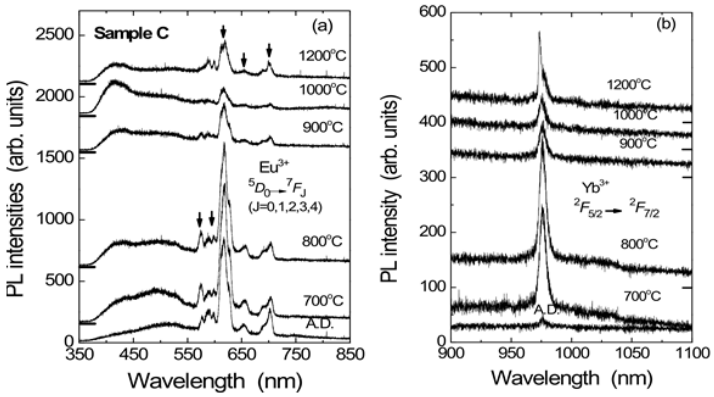
composition of the films was measured by Rutherford Backscattering Spectrometry and listed in Table I.

TABLE I. THE FILM COMPOSITIONS OF SAMPLES A, B AND C.

Sample	Si [at.%]	O [at.%]	Eu [at.%]	Yb [at.%]	Thickness [Å]
A	30.6	65.7	2.3	1.4	3900
B	33.1	63.5	1.8	1.6	3100
C	30.8	66.3	1.5	1.4	4100

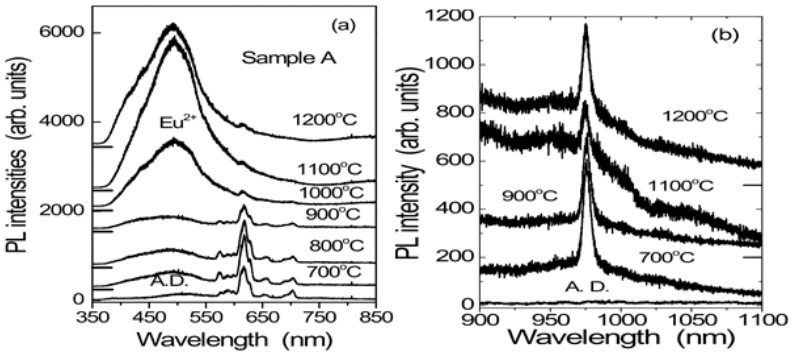
The samples were cleaved into small pieces and annealed in flowing N_2 for 30 minutes at temperatures in the range of 700-1200 °C. The structure of the films was studied by transmission electron microscopy (TEM) equipped with energy dispersive X-ray spectroscopy (EDS). The PL was excited using the 325 nm line of a He-Cd laser and was detected in the range of 350-1100 nm by a spectrometer employing a charge-coupled device (CCD) array. Time-resolved emission spectrum was recorded by using an FLS920 fluorescence spectrophotometer. All the PL measurements were performed at room temperature.

Results and Discussion



Figs. 1 The Pl Spectra of Sample c, a.d. or Annealed in N_2 for 30 Minutes at the Temperatures as Indicated.

Figure 1(a) Shows the PL spectra of sample C as-deposited (A.D.) or annealed in N_2 at the temperatures as is indicated. The spectra are recorded in the range of 350-850 nm indicative of emissions from Eu ions and the host matrix. The spectrum of the A.D. sample has a weak broad band (450-560 nm) and several sharp peaks at 579, 598, 617, 655, and 704 nm, respectively. The peaks are corresponding to the $^5D_0 \rightarrow {}^7F_J$ (J= 0, 1, 2, 3, 4) transitions of Eu^{3+} ions. Among them, the 617 nm peak is the dominant emission. After 700 °C annealing, the intensity from the Eu^{3+} 617 nm peak reaches the maximum value, the broad band is enhanced with peak position at 500 nm, and a ~ 430 nm shoulder appears on the spectrum. Increasing the anneal temperature further to 1000 °C, results in a large decrease of the Eu^{3+} emissions and the broad bands decrease in intensity leaving the 430 nm band the dominant component. However, after 1200 °C annealing, the 430 nm band intensity decreases while the Eu^{3+} peak become dominant again. Figure 1(b) shows Yb^{3+} PL spectra of the reference sample C after the above anneal temperatures. The Yb^{3+} PL from the A.D. sample is very weak which is consistent with that the excitation of Yb^{3+} ions is non-resonant to the 325 nm laser line. After 700 °C annealing, the Yb^{3+} PL increases drastically and the PL intensity reaches a maximum value for the 800 °C anneal. Then the intensity decreases gradually with increasing the anneal temperature up to 1000 °C, and the peak intensity is only 36% of the maximum value after the 1000 °C annealing. The intensity of Yb^{3+} PL increases again after the 1200 °C annealing, indicating that after annealing the variation of Yb PL is correlated to that of Eu PL. Since neither Yb^{2+} nor Yb^{3+} ions have emissions in the 450-560 nm region under UV excitation [12], it is then reasonable the broad band comprises contributions from silicon oxide matrix and Eu. Note that the intensity of the broad band decreases with increasing anneal temperature. Defects in the oxide matrix are generally believed to have such an annealing characteristic and could be the source for the band here for this sample.

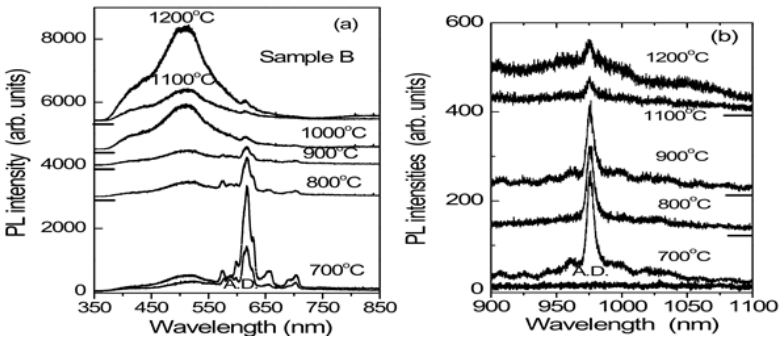


Figs. 2 The PL Spectra of Sample A, A.D. or Annealed in N_2 for 30 Minutes at the Temperatures as Indicated

Figure 2(a) shows the PL spectra of sample A as a function of the anneal temperature. It can be seen that the A.D. sample has similar spectrum to that of sample C: the Eu^{3+} 617 nm emission is the dominant peak while the 450-560 nm broad band has a peak position at around 515 nm. Also the Eu^{3+} PL intensity reaches the maximum intensity at a 700 °C anneal, the 450-560 nm broad band is enhanced but its peak position blue-shifts to ~ 490 nm. The Eu^{3+} PL intensity then decreases gradually with increasing the temperature further to 900 °C, and the PL peak intensity is 46% of the maximum value after 900 °C anneal. Interestingly, upon 1000 °C anneal the 450-560 nm broad band is enhanced significantly and becomes the dominant emission in the spectrum, while the Eu^{3+} emission peaks are much weaker, together indicating that luminescent centers have formed in the oxide upon 1000 °C anneal. After that, the spectrum intensity from the 490 nm band doubles after 1100 °C anneal, the long wavelength emissions (≥750 nm) are also enhanced implying that Si nanostructures have formed in the oxides. The PL intensity decreases at 1200 °C anneal, but the width of the 490 nm band varied little upon the 1000-1200 °C annealing indicating that the identity of the luminescence centers responsible for the strong band could be constant in this annealing range. The variation of Yb^{3+} PL from sample A with anneal temperatures is similar to that of C as is indicated in Fig. 2(b). Almost no Yb^{3+} PL were observed from the A.D. sample, and after 700 °C annealing the Yb^{3+} emission increases drastically and the PL peak intensity reaches a maximum value. Then the PL intensity decreases gradually with increasing the temperature up to 900 °C. The Yb^{3+} peak becomes stronger again upon the 1100 and 1200 °C annealing, and the peak position is superposed on the emissions possibly from the Si nanostructures, which are precipitated upon high temperature anneal.

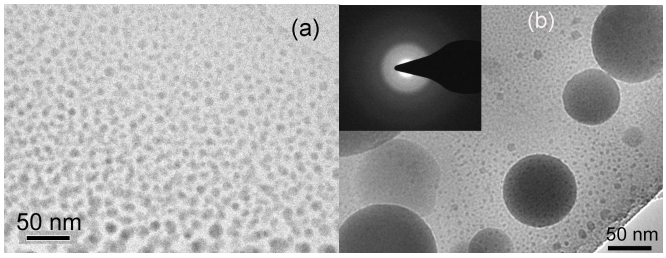
The 490 nm broad bands could be attributed to defects in the oxide matrix or to the $4f^6 5d \rightarrow 4f^7(^8S_{7/2})$ transition in Eu^{2+} [2]. The concentration of oxide defects usually decreases with increasing anneal temperature, and the strong increase in this broad band intensity after annealing to 1000 °C and higher is thus not attributed to oxide defects, but is taken as an indication of the formation of luminescent Eu^{2+}-containing silicates. Time-resolved PL of the 490 nm band (not shown) indicates that the luminescence does not have a single exponential decay but can be characterized by a mean decay lifetime (τ_{ave}) given by $\tau_{ave} = \int_0^\infty t \times I(t)dt / \int_0^\infty I(t)dt$, where I(t) is the luminescence intensity as a function of time t [4]. The average lifetime is calculated to be about 20 ns. This value does not conflict with the many indications for the radiation being due to transitions in Eu^{2+}. Luminescent Eu^{2+}-containing silicates may thus have formed in sample A.

Figures 3(a) and 3(b) show the PL spectra of sample B after annealing in N_2 at the temperatures similar to those of A. The variation of the PL spectrum with increasing anneal temperature is similar to those of A, but the Yb PL intensities decrease much, more for the B sample than for the A sample, especially upon high temperatures (1100 and 1200 °C) annealing.



Figs. 3 The PL Spectra of Sample B, A.D. or Annealed in N_2 for 30 Minutes at the Temperatures as Indicated.

TEM study was performed to investigate the correlation between structural evolutions and the PL of the films. For film A, after 700 °C annealing an unevenly distribution of grey tones was observed; some degree of phase separation seems to have occurred and precipitates are interconnected to form a network (not shown). After 1000 °C anneal, Fig. 4(a) shows that many well-defined dark dots have formed in the film with sizes of tens of nanometers. The dots are (Eu, Yb, Si, O) mixtures from EDS analysis, while the Eu and Yb concentrations remaining in the SRSO matrix are very low from EDS line-scanning analysis around the dots (not shown). Figure 4(b) shows that after 1200 °C anneal, larger precipitates have aggregated with sizes ranging from tens to hundreds of nanometers. These precipitates have amorphous nature from their selected area diffraction patterns as shown in the inset of Fig. 4b. Recalling the PL results (Fig.2(a) and Fig. 3(a)), there is a transition when the Eu^{3+} PL decrease after 800-900 °C annealing followed by an increase of Eu^{2+} PL after 1000 °C and higher temperature anneal. The amorphous (Eu, Yb, Si, O) mixtures are then believed to the silicates we above expected to be responsible for the Eu^{2+} luminescence. High resolution TEM observation confirms that Si nanocrystals have also formed after the 1200 °C annealing. The nanocrystals have clear lattice fringes with an average size of ~ 5 nm (not shown). This fact infers that tiny Si clusters (or Si-rich clusters) may have formed in sample A upon the 1000 °C or even 700 °C annealing, but are not detected by standard imaging TEM. Similar phenomena were observed in the sample B after 1200 °C anneal, but no Si nanoclusters were observed in sample C.



Figs. 4 TEM Images of Film A after Annealing in N_2 at (a) 1000 °C and (b) 1200 °C.

The decrease of Eu^{3+} PL in the samples is interpreted as part of the Eu^{3+} ions being reduced to Eu^{2+} ions. The reason for no Eu^{2+} PL being observed in the annealed samples below 1000 °C annealing, could be attributed that the Eu^{2+} ions exist dispersively in the oxides and the excited electrons in the energy levels of the Eu^{2+} ions may non-radiatively relax into the ground state, since the high covalency of Eu-O bond could produce a large offset of the 5d configuration. Similar phenomena were reported by Liu et al [13].

If we compare the visible PL intensities of the above annealed samples, those PL intensity of sample B are stronger than those of A, while those of A and C have comparable PL strength for annealing temperatures below 900 °C. The differences of the PL strengths are likely due to the highest Si excess in sample B while only a small excess in sample A. Generally a suitable Si excess will promote formation of small Si nanostructures (~ 1-3 nm) upon annealing. The nanostructures (clusters, dots, frameworks) have wide "band gaps" and enhance the Eu^{3+} emission by absorbing the radiation and transferring the excitation energy to Eu ions [14]. And for the PL intensities of samples A and B are considerably stronger than those of C upon higher temperature (≥ 1000 °C) annealing. The

overall (course) picture is that in all these samples Eu^{2+}-containing silicates have formed yielding higher PL intensity. The Yb PL intensities of sample A are several times larger than those of C, those of B are also stronger than those of C but the increments are less. Note that the Yb^{3+} PL vary correlated with the Eu^{3+} (or Eu^{2+}) PL for all the samples. This kind of correlation can be observed if there is a transfer of excitation energy from Eu to Yb, or the Yb^{3+} PL and the Eu PL are excited through a common energy transfer process such as by the oxide defects and/or Si nanostructures. Detailed excitation mechanism of Eu and Yb^{3+} ions is being examined and will be reported elsewhere.

Summary

We have investigated the annealing behaviors of PL from (Eu, Yb) co-doped in SiO_2 or SRSO sputtered films. Compared to SiO_2 host, SRSO gives stronger emissions from the Re ions. Luminescent Eu^{2+}-related silicates have formed under high temperatures annealing and the silicates seen by TEM contain (Eu, Yb, Si, O) aggregates. These results could be of interest in Si based solar cells as well as for other applications like lightening, displays and optical storage.

This work was financially supported by grant from Specialized Research Fund for the Doctoral Program of Higher Education (SRFDP) (20111101120021).

References

[1] B.M. van der Ende, L. Aarts, A. Meijerink, Lanthanide ions as spectral converters for solar cells, Phys. Chem. Chem. Phys. 11 (2009) 11081-11095.

[2] M.M. Smedskjaer, J.R. Qiu, J. Wang, Y.Z. Yue, Near-infrared emission from Eu-Yb doped silicate glasses subjected to thermal reduction, Appl. Phys. Lett. 98 (2011) 071911.

[3] J.J. Zhou, Y. Teng, S. Ye, X.F. Liu, J.R. Qiu, Broadband down-conversion spectral modification based on energy transfer, Opt. Mater. 33 (2010) 153-158.

[4] Y. Teng, J.J. Zhou, S. Ye, J.R. Qiu, Broadband Near-Infrared Quantum Cutting in Eu^{2+} and Yb^{3+} Ions Co-doped $CaAl_2O_4$ Phosphor, J. Electrochem. Soc. 157 (2010) A1073-A1075.

[5] J.J. Zhou, Y. Teng, G. Lin, X.Q. Xu, Z.J. Ma, J.R. Qiu, Broad-Band Excited Quantum Cutting in Eu^{2+}-Yb^{3+} Co-doped Aluminosilicate Glasses, J. Electrochem. Soc. 157 (2010) B1146-B1148.

[6] J.J. Zhou, Y.X. Zhuang, S. Ye, Y. Teng, G. Lin, B. Zhu, J.H. Xie, J.R. Qiu, Broadband downconversion based infrared quantum cutting by cooperative energy transfer from Eu^{2+} to Yb^{3+} in glasses, Appl. Phys. Lett. 95 (2009) 141101.

[7] H. Lin, D.Q. Chen, Y.L. Yu, Z.F. Shan, P. Huang, A.P. Yang, Y.S. Wang, Broadband UV excitable near-infrared downconversion luminescence in Eu^{2+}/Yb^{3+}:CaF_2 nanocrystals embedded glass ceramics, J. Alloy Compd. 509 (2011) 3363-3366.

[8] G. Conibeer, M. Green, R. Corkish, et al., Silicon nanostructures for third generation photovoltaic solar cells, Thin Solid Films 511 (2006) 654-662.

[9] E.C. Cho, S. Park, X.J. Hao, D.Y. Song, G. Conibeer, S.C. Park, M.A. Green, Silicon quantum dot/crystalline silicon solar cells, Nanotechnology 19 (2008) 245201.

[10] F. Gourbilleau, C. Ternon, D. Maestre, O. Palais, C. Dufour, Silicon-rich SiO_2/SiO_2 multilayers: A promising material for the third generation of solar cell, J. Appl. Phys. 106 (2009) 013501.

[11] X.D. Pi, Q. Li, D.S. Li, D.R. Yang, Spin-coating silicon-quantum-dot ink to improve solar cell efficiency, Sol. Energ. Mat. Sol. C. 95 (2011) 2941-2945.

[12] Y. Teng, J.J. Zhou, X.F. Liu, S. Ye, J.R. Qiu, Efficient broadband near-infrared quantum cutting for solar cells, Opt. Express 18 (2010) 9671-9676.

[13] G. Liu, B. Jacquier, Spectroscopic Properties of Rare Earths in Optical Materials, Springer Verlag, Berlin, 2005, p. 122.

[14] G.Z. Ran, Z.Q. Bian, S.F. Liu, C.H. Huang, G.G. Qin, Photoluminescence characterization of silicon nanoparticles hybridized europium complex, Chinese Phys. Lett. 21 (2004) 2533-2535.

Advanced Materials Research Vol. 936 (2014) pp 212-217
© (2014) Trans Tech Publications, Switzerland
doi:10.4028/www.scientific.net/AMR.936.212

Compatibility of Polyvinylidene difluorid/Polyurethane and Preparation of Composite Tubular Membrane

Dan-Ying Zuo[1], Hong-Jun Li*[2], Chang-Hai Yi[1] and Hou-Lei Gan[1]

[1] State Key Laboratory of New Textile Materials and Advanced Processing Technologies, Wuhan Textile University, Hubei, 430073, P. R. China

[2] Department of Industrial Engineering, Wuhan Textile University, Hubei, 430073, P. R. China

[1]zdy@wtu.edu.cn, [2]lihongjun@foxmail.com, *Correspondence Author

Keywords: Polyvinylidene difluorid; Polyurethane; Composite tubular membrane; Compatibility; Water flux

Abstract： The compatibility of polyvinylidene difluorid (PVDF) and polyurethane (PU), the thermodynamics of the PVDF/PU/DMF (N-N-Dimethylformamide) membrane-forming systems were studied, and the composite tubular membranes of PVDF/PU-PET knitted fabric tube were prepared by the immersion precipitation phase inversion method. The results showed that the PVDF/PU system was partly compatible by the measurements of the solubility parameter theory, the mixing enthalpy, the viscosity. With PU content increasing, the gelation values increased and the instantaneous liquid-liquid phase separation was preferred to occur. The water flux of the composite tubular membranes were enhanced from 1264.81 to 2165.35 $L/m^2.h$ with PU content increasing from 10wt% to 40wt%, which resulted from the an increment of the membrane porosity and the improvement of the hydrophilicity.

Introduction

Membrane and membrane process have been applied extensively in many application fields. Asymmetric PVDF ultrafiltration and microfiltration membranes have some advantages with a high temperature resistance, difficulty to blocking and easy to cleaning. Nevertheless, there are still some troublesome problems for PVDF ultrafiltration and microfiltration membranes. The very low surface energy of PVDF results in the poor hydrophilicity of PVDF membrane, which not only decreases low pure water fluxes, but also causes the membranes to be easily contaminated by protein and other macromolecules[1]. To prepare hydrophilic PVDF membranes, hydrophilic polymer additives[2], such as polyethylene glycol (PEG), polyvinyl-pyrrolidone (PVP), perfluorosulfonic acid and poly(methylmethacrylate) (PMMA), amphiphilic copolymers like poly(methyl methacrylate polyoxy- ethylene methacrylate), poly(ethylene oxide-polypropylene oxide- polyethylene oxide) and many inorganic nanoparticles, such astitanium dioxide (TiO_2) and aluminum oxide (Al_2O_3), have been used. Polyurethane (PU) with excellent toughness and good hydrophilicity is a proper modified material for PVDF membrane because PU could compensate greatly the tenacity and hydrophilicity. Xi et al. prepared the asymmetric blend hollow fiber membranes made from a casting dope containing poly(vinylidenefluoride)/thermoplastic polyurethane/ polyvinyl-pyrrolidone/N, N- dimethylacetamide[3]. Hu et al. fabricated the PVDF/PU blend flat membranes through the method of immersion-precipitation process[4]. On the other hand, due to the poor intensity of PVDF homogeneous membrane, the composite PVDF membranes with a support layer also have been paid more and more attentions. For example, Bottino et al. prepared

PVDF membranes cast on the outer surface of a porous braid tubular support. The stretching action of the support on the forming membrane during water coagulation may be responsible for the formation of pore with sizes in the range of a few hundred of nanometers[5]. Tang et al. fabricated the PVDF-HFP composite polymer electrolyte membranes supported by non-woven fabrics which boast good mechanical strength and excellent electrochemical properties[6].

In this work, the PVDF/PU compatibility was discussed by the solubility parameter, mixing enthalpy, the viscosity of PVDF/PU casting solutions. The composite tubular membranes of PVDF/PU-PET knitted fabric tube with high intensity and good hydrophilicity were prepared by the immersion precipitation phase inversion of a binary PVDF/ PU-solvent solution cast on the outer surface of a polyester tubular knitted fabric and the effects of PVDF/PU ratios on the structure and properties of the composite membranes were investigated.

Experimental

Materials

PVDF (FR904, Mw = 2×10^6, Mn = 4.7×10^5) was supplied by Shanghai 3F Ltd. China. PU was supplied by Yantai Wanhua Co., Ltd, China. N-N-Dimethylformamide (DMF) was the reagent grade, and used as the solvent. Polyvinylpyrrolidone (K30) was used as additives in PVDF/DMF solution. Distilled and deionized water was used as coagulant.

Preparation of Blend Solutions And Determination Of The Gel Values

A certain percentage of PVDF, PU and DMF mixtures at 60 ^{0}C were heated and stirred to dissolve, until a homogeneous solution were obtained. The viscosities of PVDF/PU blend solutions with different components were measured by the rotating viscometer. The gel values of blend solutions were determined through the turbidity method [7]. Here the gel value referred to the amount of non-solvent water that made 15g blend solution gel.

Preparation Of Pvdf/Pu Composite Tubular Membranes

Set the woven PET tube on the glass rod, and immerse the glass rod into the casting solution for 10s. The casting solution was fully saturated with the woven PET tube, then the glass rod with the woven PET tube was lift from the casting solution and the excess solution flowed into the casting solution. The tube was dipped into in deionized water, and the casting solution quickly gel to obtain the tubular composite membrane.

The Performance Determination of Pvdf/Pu Composite Tubular Membrane

Membrane module was prepared firstly. 10 tubular membranes were placed in the glass tube with a length of 30 and the inner diameter of 5cm, and both ends were encapsulated by the epoxy. Water flux was test in view of the outside pressure and the cross-flow mode. The membrane module was pre-pressured at 0.1MPa for 20min, until the water flux was basically stable, and the data were recorded. After washing with the buffer solution with pH 7.4, the static contact angles were measured for10 times. The morphologies of the membrane surfaces were examined on a scanning electronic microscope (JSM-6510, JEOL, Japan) after coating with gold under vacuum.

Results and Discussion

Prediction of PVDF/PU Compatibility with Solubility Parameter Theory

Generally, if the absolute difference of solubility parameters of the two kinds of polymers was greater than 0.5 $(J/cm^3)^{1/2}$, two kinds of polymer are partly miscible; if the absolute difference was less than 0.5 $(J/cm^3)^{1/2}$, the blend system is homogeneous miscible. That is to say, the closer the solubility parameter of two kinds of polymers, and the better the miscibility[8]. The solubility

parameter of PVDF (δ_1) is 23.2 $(J/cm^3)^{1/2}$, the solubility parameter (δ_2) of polyurethane is 20.8 $(J/cm^3)^{1/2}$. A difference of 2.4 $(J/cm^3)^{1/2}$ of the solubility parameters is greater than 0.5 $(J/cm^3)^{1/2}$, then the blend of PVDF and PU is partially compatible.

Mixing Enthalpy Calculation of the Mixture and Prediction of Blend Compatibility

It can be seen by the thermodynamic theory that polymer blends can form a fully miscible system when the free energy of mixing is less than zero ($\Delta G = \Delta H - T\Delta S < 0$). Because the change of mixing Entropy (ΔS) is small for polymer blend, mixing enthalpy (ΔH) of the system can be used to determine the miscibility. Schneier raised the mixing enthalpy calculation of two polymer blend[9].

$$\Delta H = \left\{ x_1 M_1 \rho_1 (\delta_1 - \delta_2)^2 \left[\frac{x_2}{(1-x_2)M_2\rho_2 + (1-x_1)M_1\rho_1} \right]^2 \right\}^{1/2} \quad (1)$$

Where $x_{1,2}$, $\rho_{1,2}$, and $M_{1,2}$ a are the mole fraction of polymer, the polymer density, and molecular weight of monomer unit, $\delta_{1,2}$ is the polymer solubility parameter.

The critical value of mixing enthalpy for the thermodynamic miscible system is 41.868×10^{-3} J/mol (10×10^{-3} cal/mol). When the mixing enthalpy is below the critical value, the blend system is fully miscible, when the mixing enthalpy is above the critical value, the blend system is fully immiscible, while the blend was a part compatible system, as the mixing enthalpy intersects the critical value. The mixing enthalpy was calculated with varying the ratio of PVDF and PU. The curve of the mixing enthalpy with varying the ratio of PVDF and PU was shown in Fig. 1. Mixing enthalpy curves of the blends and the baseline 41.868×10^{-3} intersected each other, which suggested that PVDF and PU blend was a partly miscible system in view of the thermodynamics. When the mass ratio of PU was less than 30%, the mixing enthalpy was lower than 41.868×10^{-3}, which suggested that polymer blends were compatible and were proper to prepare the membranes.

Viscosity of PVDF/PU Blend Solution and Compatibility

The viscosity of polymer blend solution was used to describe the compatibility. The curves of viscosities of blend solution with varying the ratio of PVDF and PU were shown in Fig. 2. If the curves were linear, the polymer blend was miscible thermodynamically. If the curves were non-linear, the polymer blend was partly miscible thermodynamically. If the curve was S-like, the polymer blend was not fully miscible thermodynamically[10]. As seen from Fig. 2, the curve of viscosity and PU mass ratio took on a non-liner relation, therefore PVDF/PU blend system was partly compatible, which accorded with the prediction above.

Thermodynamic Properties of Casting Solutions with Different PVDF/PU Ratio

Coagulation value reflects the stability of the thermodynamic properties of polymer solution[11]. As shown in Fig. 3 for PVDF/PU/DMF blend solutions, the coagulation value gradually increases with PU content increasing, which reveals that the coagulation value of neat PVDF solution is smaller than that of the neat PU solution. The gel value implies the ability to resist the gel for the polymer solution. The higher the gel value, the stronger the resistance ability to gel， and vice versa. On the phase diagram of PVDF/PU/DMF system, the area of homogeneous phase increases with the coagulation value increasing, more non-solvent was needed to make the blend solution precipitate.

PVDF is a crystalline polymer, so the solid-liquid phase separation happens, which induces the gelation of the casting solution[12]. While the liquid-liquid phase separation mainly happens for PU of a non-crystalline polymer. The gelation and crystallization starts simultaneously for crystalline polymer. On the ternary phase diagram, the line of the solid-liquid phase separation lies in the homogeneous zone of the liquid-liquid phase separation. During the coagulation process of casting solution, the components of the blending system firstly go through the line of the liquid-solid phase separation, and then reach the liquid-liquid phase separation area. Therefore, the coagulation value

causing the liquid-solid phase separation is less than that of the liquid-liquid phase separation. For PVDF and PU, with PVDF content reduction and the increase of PU content, the coagulation value increased, which suggested that the phase separation was transformed from the solid-liquid demixing to the liquid-liquid deminxing for PVDF/PU blend casting solution. As a consequence, compared with the liquid-liquid deminxing, the solid-liquid demixing was the delayed phase separation behavior. The instantaneous phase separation leads to the formation of membranes with macrovids, while the delayed phase separation easily induces the formation of the cellular pores in the membrane cross-section.

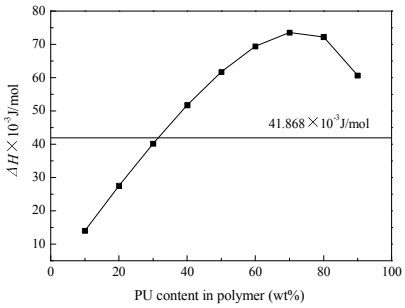


Fig. 1 The relationship of ΔH and PU content

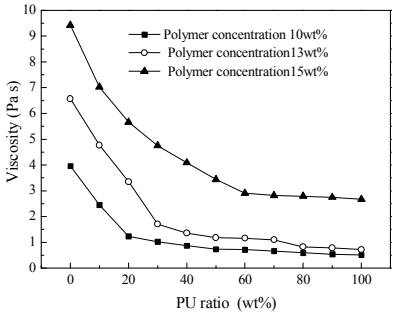


Fig. 2 Relationship between viscosity and PU content in casting solution

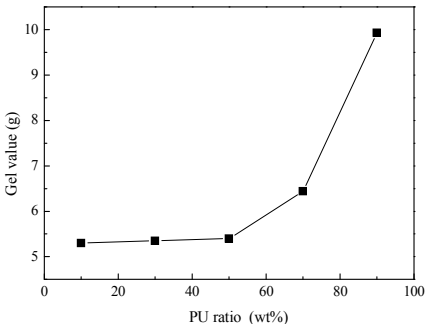


Fig. 3 The relation of gelation values of casting solution

Performance of Tubular Composite Membranes

The round tubular knitted fabric was woven on the 12-pin hand flat knitting machine weft through the way of the weft. The process parameters were as followed: 10-pin, yarn count of 32, the yarn root of 2. The parameters of woven tube are as follows, the inner diameter of 4.48mm, full coefficient of 11.28, the horizontal density of 44, the vertical density of 36, and total density of 1584. The ratio of PVDF to PU with 90/10, 80/20, 70/30, 60/40 was choose to prepare the tubular PVDF/PU-knitted fabric composite membranes. As seen from Tab. 1, the change of the tube diameters and membrane thicknesses were negligible with using different *w*(PVDF)/*w*(PU). Contact angles of several membranes changed little. But, with PU content increasing, water flux gradually increased. SEM surface photos of PVDF/PU tubular composite membranes were presented in Fig.5. With PU content increasing, surface morphologies of four types of tubular composite membranes were very distinct, and more PU was used, the membrane surface was more rough and porous, which resulted in water fluxes of composite membranes enhancing.

TAB.1 STRUCTURE AND PERFORMANCE OF FIVE TYPES OF PVDF/PU TUBULAR COMPOSITE MEMBRANES

Composite membranes	*w*(PVDF) /*w*(PU)	Outer diameter/mm	Membrane thickness/mm	Contact angle/ °	Water flux/L·(m^2·h)$^{-1}$
A	90:10	5.54	0.72	90.4	1264.81
B	80:20	5.24	0.70	86.8	1407.22
C	70:30	5.12	0.60	82.1	1521.37
D	60:40	5.44	0.60	78.2	2165.35

Note: the casting solution *w*(PVDF/PU)/*w*(PVP)/*w*(PgOH)/ *w*(H_2O)/*w*(DMF)=10:3:3:2:82.

Changes in the structure and properties of several tubular composite membranes were mainly due to the increase of PU content which decreased the viscosity of the casting solution, changed the thermodynamic properties of casting solutions and made the PVDF/PU compatibility be worse. On one hand, with PU content increasing, the decrease of the viscosity of the casting solution made the exchange speed of solvent and nonsolvent increase and speeded up the phase separation process, which was propitious to the generation of membranes with macroporous structure. On the other

hand, as described in Section 3.4, with PU content incresing, the phase separation of PVDF/PU/DMF/H_2O membrane-forming system was shift from a slow solid-liquid demixing to a rapid liquid-liquid phase separation, and then the membrane with a high porosity tended to be fabricated. As a result, the water flux was improved. In additional, the decline of PVDF/PU compatibility with PU content increasing led to the phase separation in the membrane and the formation of the interface pores, which could enhance the water flux[5]. But, as PU content increased to 30wt% and 40wt%, the size stability of the composite membrane decreased and membrane surface was coarse, therefore, PU content was controlled under 30wt%.

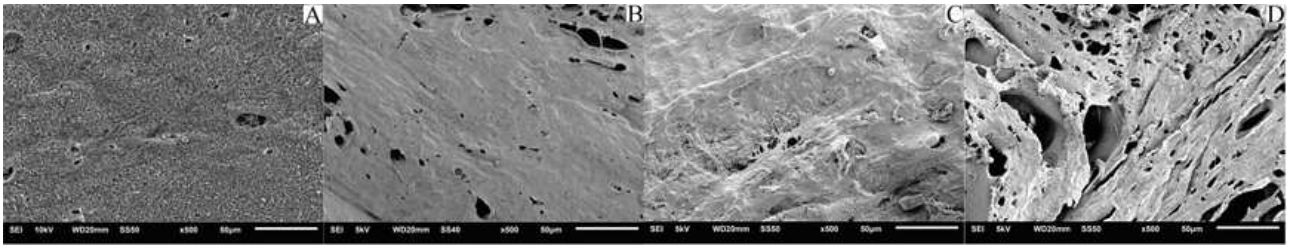


Fig 4. SEM surface photos of PVDF/PU tubular composite membranes
A: PVDF/PU=90/10 B: PVDF/PU=80/20 C: PVDF/PU=70/30 D: PVDF/PU=60/40

Conclusions

PVDF/PU blend was a partially compatible system through the measurements of solubility parameters, the theoretical calculation of the mixing enthalpy, the viscosity of PVDF/PU casting solutions and the structure of PVDF/PU flat sheet membranes. Blends significantly changed the thermodynamic properties of the PVDF/PU/DMF casting solutions. The coagulation values increased with PU content increasing, i.e. the phase behavior of the membrane-forming system transformed from the solid-liquid demixing to the liquid-liquid demixing. With PU content increasing, water flux of the composite tubular membranes of PVDF/PU-PET tube gradually increased, which resulted from the enhancement of membrane porosity and membrane hydrophilicity.

Acknowledgments

This work was supported by Research Projects of China Textile Industry Association (2011025) and the Natural Science Foundation of Hubei Province (2011CDB215).

References

[1] C. H. Loh, R. Wang, L. Shi, A. G. Fane, J. Membr. Sci., 380(2011) 114-123

[2] M. L. Yeow, Y. T. Liu, K. Li, J Appl. Polym. Sci., 92(2004) 1782-1789

[3] Y. Zhou, D. L. Xi, Desalination, 223(2008) 438-447

[4] 4 X. Y. Hu, C. F. Xiao, S. L. An, G. X. Jia, J. Mater. Sci., 42(2007) 6234-6239

[5] A. Bottino, G. Capannelli, A.Comite, Desalination, 183(2005) 375-382

[6] D. G. Tang, J. H. Liu, L. Qi, H. Chen, Y. X. Ci, Chin. Sci. Bull., 50(2005)501-504

[7] D. Y. Zuo, B. K. Zhu, Y. Y. Xu, Chin. J. Polym. Sci., 24(2006)281-285

[8] M. T. Shaw, Polym. Mater. Sci. Eng., 11(2008)91-94

[9] S. Bernard, J. Appl. Polym. Sci., 17(1973)3175-3185

[10] Y. Singh,R. P. Singh, Eur. Polym. J., 19(1983)535-541

[11] S. C. Yu, C. J. Gao, Membr. Sci. Technol. 5(1999)23-26

[12] P. van de Witte, P. J. Dijkstra, J. W. A. van den Berg, J. Feijen, J Membr Sci, 117(1996) 1-31.

Advanced Materials Research Vol. 936 (2014) pp 218-225
© (2014) Trans Tech Publications, Switzerland
doi:10.4028/www.scientific.net/AMR.936.218

Preparation and Properties of Two-Dimensional Braid Heterogeneous-Reinforced Polyvinylidene Fluoride Hollow Fiber Membrane

Quan Quan[1], Changfa Xiao [1], Hailiang Liu [1], Wei Zhao [1], Xiaoyu Hu [2] and Guolan Huan [2]

[1]State Key Laboratory of Hollow Fiber Membrane Materials and Processes, Tianjin Polytechnic University, Tianjin 300387, China

[2]Tianjin Motimo Membrane Technology Co. Ltd, Tianjin 300457, China

Corresponding author: Xiao Changfa, E-mail: xiaochangfa@163.com

Keywords: PVDF, two-dimensional braid, hollow fiber membrane, heterogeneous-reinforced

Abstract: The two-dimensional braid heterogeneous-reinforced (BHR) polyvinylidene fluoride (PVDF) hollow fiber membranes which include PVDF polymer solutions (coating layer) and the two-dimensional braid as a reinforcement were prepared through the dry-wet spinning process. The influence of PVDF concentration in polymer solutions on performance of BHR hollow fiber membranes were investigated by terms of pure water flux, protein rejection, a mechanical strength test, and morphology observations by a scanning electron microscope (SEM). The results of this study indicated that the tensile strength of the BHR PVDF hollow fiber membranes was nearly 75 MPa and the hollow fiber membranes were endowed with better flexibility performance. The BHR PVDF hollow fiber membranes had a favorable interfacial bonding between the coating layer and the two-dimensional braid. The pure water flux decreased, while the rejection ratio increased with the increase of polymer concentration.

Introduction

Nowadays, the applications of membrane technologies have been extensively used in separation facilities to separate mixtures because of their flexibility and capacity to remove contaminants from wastewater to low levels [1].The hollow fiber membranes are mechanically self-supporting and easy to assemble in modules which are attractive for industrial use. And such membranes have been widely applied in Membrane Bioreactor (MBR) systems [2]. The MBR has emerged as an attractive technology for advanced municipal and industrial wastewater treatment, and offers many advantages over conventional wastewater treatment processes, including low sludge production, very good quality effluent and reduced footprint [3]. But in the MBR filtration process, hollow fiber membranes are liable to be damaged and broken by the high-pressure water cleaning process or disturbance of the aerated airflow. In the use of such water treatment, the filtration membrane is required, not only for its being superior in separation performance and permeation performance, but also for its high mechanical property [4].

Currently, the most popularly used Ultrafiltration (UF) and Microfiltration (MF) hollow fiber membranes which composed of skin layer and support layer, are prepared through the immersion-precipitation method. Normally, these hollow fiber membranes have high permeability but low mechanical endurance [5]. As a semi-crystalline polymer, PVDF has widespread applications because of its excellent properties, such as good mechanical strength, stability against vigorous chemicals, and good thermal stability [6, 7]. In the past, PVDF membranes prepared by wet or dry–wet spinning method were known as filtration membranes. Further, since these

membranes were produced by being separated in microphase, an adequate molecular orientation is not obtained, and the tensile strength of the filtration membranes is as little as about 3 MPa [8, 9].

In this study, according to the theory of thermodynamic compatibility and the principle of skin/core composite spinning of chemical fiber, hollow fiber membranes that included PVDF casting solution as the coating layer and the two-dimensional braid which has an excellent mechanical strength as the support for the separation membrane were prepared through the dry-wet spinning process. The process was called the two-dimensional braid heterogeneous-reinforced (BHR) method. The mechanical properties of the BHR hollow fiber membranes and the effects of the PVDF concentration in the polymer solutions on the membrane structure and membrane filtration properties were studied.

Experimental

Materials

PVDF (W no. 1300 powders, Tm = 170 °C) was purchased from Kureha Chemical Industrial Co., Ltd. (Tokyo, Japan). PAN filaments were supplied by Xiangying Special Fiber Co., Ltd (Changshu, China). N,N-dimethylacetimide (DMAc, > 99%) and Polyvinylpyrrolidone (PVP,K30, Mw = 30,000) were obtained from Tiantai Fine Chemical Co., Ltd. (Tianjin, China). Tween 80 (Tw-80) was purchased from Tianjin Fengchuan Chemical Reagent Science and Technology Co., Ltd. (Tianjin, China).

Preparation of Two-Dimensional Braid Heterogeneous-Reinforced PVDF Hollow Fiber Membranes

The PAN filaments were braided into a two-dimensional hollow tubular braid as the reinforced matrix via two-dimensional braid technology. The two-dimensional braid were cleaned with a neutral liquid detergent for removing the oil which coating the PAN filaments surface during spinning process, dried at 25°C，and winded for next process. Fig.1 showed the surface SEM morphology of the two-dimensional braid which showed a rhombus structure.

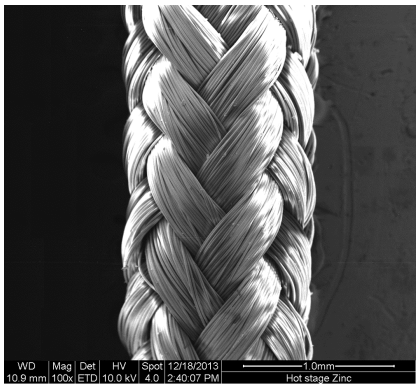


Fig.1. The two-dimensional braid structure

The BHR hollow fiber membranes were prepared using the dry–wet spinning method. Fig. 2 showed the spinning apparatus. According to the method described, the PAN two-dimensional braid were coated with the polymer solutions and guided through a precipitation bath, where the polymer solutions were converted into a microporous layer. The polymer solutions were prepared by the blending of different compositions consisting of PVDF, PVP K30, Tw-80 and DMAc (Table 1), under constant mechanical stirring in a three-necked round-bottom flask for 6 h at 70°C. All the membranes were prepared under an environmental temperature of 25°C and at an environmental

humidity of 60%. The BHR hollow fiber membranes with the different PVDF concentrations, i.e., 8, 10, 12, 14 and 16 weight (wt.%) were labeled F8, F10, F12, F14 and F16, respectively. Before the scanning electron microscope (SEM) tests, we put the resulting membranes in glycerol water solutions (three parts glycerol to two parts water) and then dried them in air, so as to retain the porous structure.

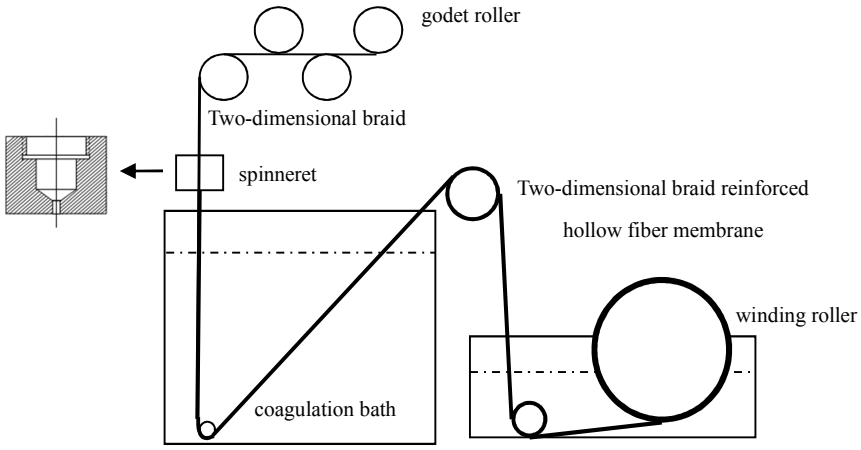


Fig.2. Schematic diagram describing the BHR PVDF hollow fiber membrane induced by the dry–wet spinning process

TABLE 1 SPINNING PARAMETERS OF BHR PVDF HOLLOW FIBER MEMBRANES WITH DIFFERENT DOPE COMPOSITION

Prepared membrane	Dope composition			
	PVDF [wt.%]	PVP [wt.%]	Tw-80 [wt.%]	DMAc [wt.%]
F8	8	8	2	82
F10	10	8	2	80
F12	12	8	2	78
F14	14	8	2	76
F16	16	8	2	74
Dope solution temperature		70 [°C]		
Extra coagulation Water		25 [°C]		
Air gap		15 [cm]		
Take up speed		15 [cm·min^{-1}]		

Membrane Characterizations

Tensile Break Strength Measurements

The tensile strength and elongation at break of the hollow fiber membranes were determined at room temperature by using a CMT4204 electronic universal testing machine (Shenzhen, China). The tensile rate was 10 mm·min^{-1}, and the clamping length was 100 mm.

Morphology Examination

The morphology of the membranes was observed using SEM (Quanta200, FEI, Czech). The samples were frozen in liquid N_2, followed by fracturing to expose their cross-sectional areas. Thereafter, they were sputtered with gold and recorded through SEM.

Membrane Permeability

The pure water flux (PWF) of the membranes was determined using Eq. (1). The pressure difference across the membrane was 1 bar under the condition of outside feeding. The membrane module contained three hollow fiber membranes with an effective length of 18–20 cm.

$$J = \frac{V}{S \times t \times P} \quad (1)$$

Where J is the PWF ($L \cdot m^{-2} \cdot h^{-1} \cdot bar^{-1}$), V is the quantity of the permeate (L), S is the membrane area (m^2), t is the testing time (h), P is the pressure (bar).

The filtration experiments were carried out using the protein solution. The rejection of the membranes was measured with 1 $g \cdot L^{-1}$ bovine serum albumin (BSA) solution and calculated using Eq. (2).

$$R\ (\%) = \left(1 - \frac{C_p}{C_f}\right) \times 100\% \quad (2)$$

Where C_p and C_f are the concentration at permeate and feed, respectively.

Each membrane was initially pressurized for 20 min at 1.5 bar. The pressure was then reduced to the operating pressure of 1 bar, and the PWF was measured. Before the protein filtration, the membranes were compacted at 1 bar for 60 min, then, the rejection was measured at 1 bar.

Porosity Determination

The membrane porosity (ε) was defined as the pores' volume divided by the total volume of the porous membrane. It can be determined by Eq. (3):

$$\varepsilon = \frac{(w_1 - w_2)/\rho_1}{(w_1 - w_2)/\rho_1 + (w_2 - w_3)/\rho_2 + w_3/\rho_3} \times 100\%, \quad (3)$$

where W_1 and W_2 are the weights of the wet and the dry membranes, respectively, W_3 is the weight of the two-dimensional braid, ρ_1 is the water density, ρ_2 is the polymer density (1.78 $g \cdot cm^{-3}$), ρ_3 is the two-dimensional braid density (1.15 $g \cdot cm^{-3}$).

Maximum Pore Size of the Membrane

The maximum pore size of the membranes was obtained using the bubble point method with alcohol as wetting liquid and calculated using Eq. (4)

$$r_p = \frac{2\gamma}{P} \quad (4)$$

Where r_p is the maximum pore size of the membrane (μm), γ is the surface tension at the alcohol/air interface ($N \cdot m^{-1}$), and P is the pressure. At room temperature (20 °C), γ is equal to 22.32 $\times 10^{-3}$ $N \cdot m^{-1}$.

Results and Discussions

Mechanical Properties of the BHR PVDF Membrane

Fig. 3 showed the tensile strength of the PAN two-dimensional braid and its heterogeneous-reinforced PVDF hollow fiber membrane. The traction of the winding device made the fibers braided into a tubular fabric such as a hollow fiber, during the two-dimensional braiding process. The different systems fibers were braided each other, and produced a lot of space between the fibers. Therefore, some of the casting solutions could infiltrate into the space in the spinning process, which could improve the interface between the two-dimensional braid and the surface separation layer after being immersed into coagulation bath [9]. When the two-dimensional braid was stretched, there was only a small tension could produce a great tensile deformation which displayed a little stress and a large tensile region before point A from Fig. 3 (a). From point A to B, with the tension increasing, the braiding angle decreased due to the deformation of the rhombus

braiding structure. At this time, if removed the tension, the deformation could be restored. But the deformation was irreversible after point B.

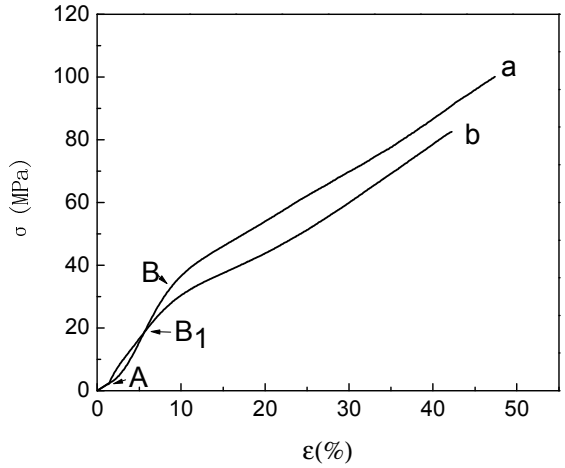


Fig.3. The mechanical properties of PAN two-dimensional braid reinforced hollow fiber membranes (a) Two-dimensional braid; (b) BHR PVDF hollow fiber membrane

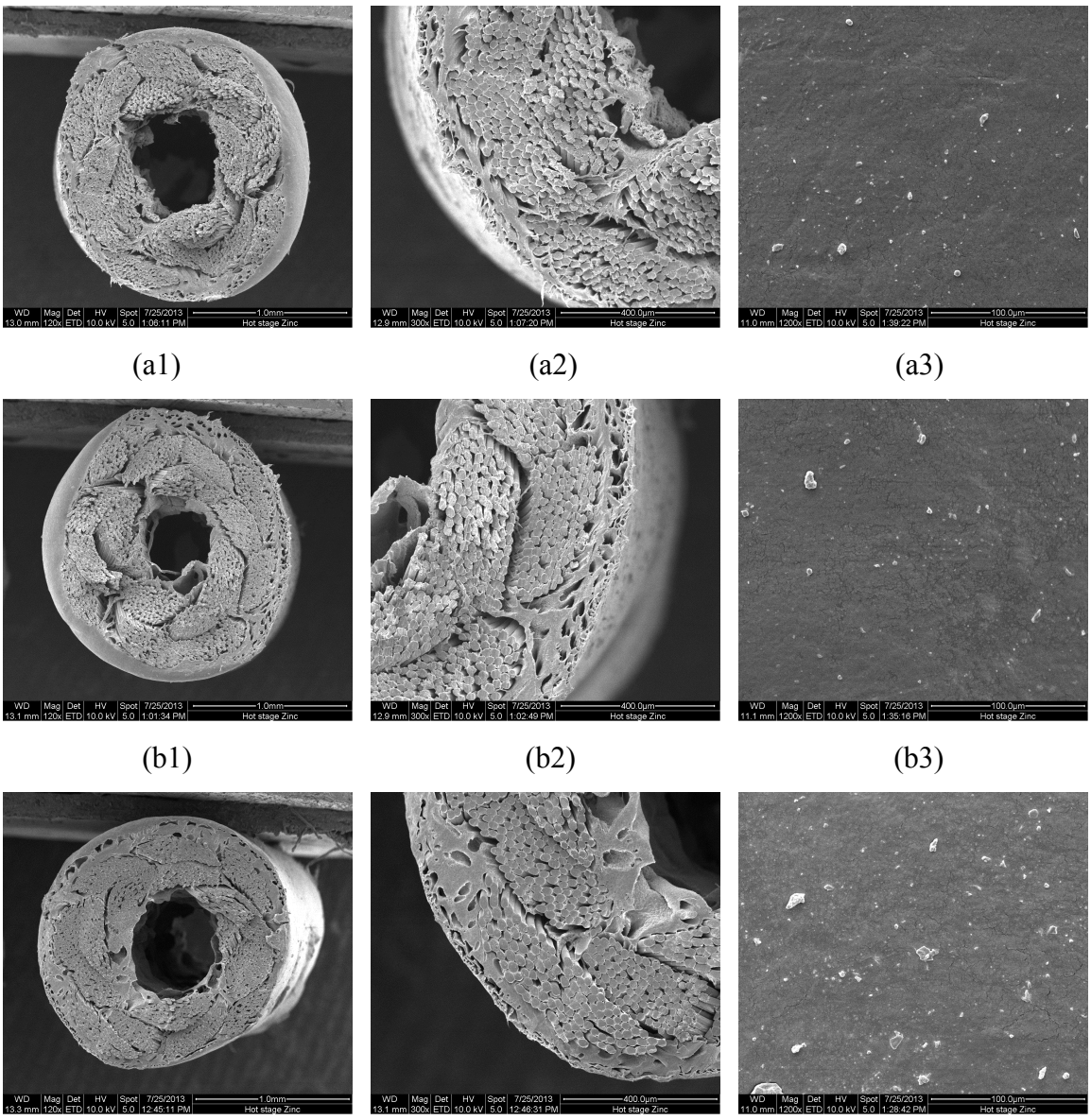
Fig. 3 showed that both of the breaking strength and breaking elongation of the BHR hollow fiber membrane were lower than that of the two-dimensional braid. But curve (b) and (a) were overlap before point A, then curve (b) was higher than curve (a) between point A and B1, and last curve (b) was lower than curve (a) after the point B1. This phenomenon occurred because the polymer solution were not only coated on the surface uniformly, but also permeated into the space of the two-dimensional braid. After immersed into coagulation bath to forming the surface separation layer which increasing the friction between the fibers and the part embedded within space which hindered the rhombus braid structure and pores deformation, thus the breaking strength and elongation of the BHR hollow fiber membrane were smaller than the two-dimensional braid. In the initial stage, before point A the polymer solution infiltrated into the partial space, but not completely filled all the interspaces, when subjected to axial tension the structure of the parts where polymer solution were not infiltrated were deformation which showed a little stress and a large tensile region. From point A to B1, with the stretch continuing the polymer that embedded in the space hindered the deformation of the braid structure. After point B1, the surface separation layer increased the friction between the fibers which made the breaking strength and breaking elongation of the BHR PVDF hollow fiber membrane lower than that of the two-dimensional braid.

We know that the tensile strength of PVDF membranes prepared by the wet spinning method was nearly to 1-3 MPa [10, 11]. A low tensile strength of PVDF membrane may easily cause fiber breakage in the state of serviceability. The BHR PVDF hollow fiber membranes prepared by the BHR method had higher mechanical properties. The tensile strength of the BHR PVDF hollow fiber membranes was nearly 75 MPa, which was adequate for MBR applications.

Morphologies of BHR PVDF Hollow Fiber Membranes

Fig. 4 showed the structure of the hollow fiber membranes prepared in different PVDF concentrations (8, 12 and 16 wt.%) in the polymer solutions by the BHR method. Fig. 4 (a1, b1, c1), (a2, b2, c2) and (a3, b3, c3) showed the whole cross-sectional structure of the membrane, the enlarged structure and outer surface, respectively. Fig. 4 (a2, b2, c2) showed three parts near the outer surface of the HR membranes. The outermost layer was the PVDF coating layer, and the

innermost layer was the two-dimensional braid. The middle layer, between the PVDF coating layer and the two-dimensional braid, was the interface layer. In the BHR process, some of the polymer solutions infiltrated into the space of the two-dimensional braid and formed the interface which endowed the BHR hollow fiber membranes with high interfacial bonding. Fig. 4 (a3, b3, c3) showed the SEM results of the outer surfaces of the hollow fiber membranes. The outer surface of the BHR PVDF hollow fiber membrane appeared a dense layer.



(a1) (a2) (a3)

(b1) (b2) (b3)

(c1) (c2) (c3)

Fig.4. Cross-sectional and outer surfaces SEM morphology of BHR PVDF hollow fiber membranes: (a) F8, (b) F12, (c) F16

Permeation Properties of the BHR PVDF Hollow Fiber Membranes

Fig. 5 showed the porosity and maximum pore size of the BHR PVDF hollow fiber membranes. The porosity and maximum pore size had the same decreasing tendency as the PVDF concentration increase in the polymer solutions. The BHR PVDF hollow fiber membranes had a denser outer surface, as shown in Fig. 4. This meant that the BHR PVDF hollow fiber membranes possessed a smaller maximum pore size which could improve the rejection of the membrane.

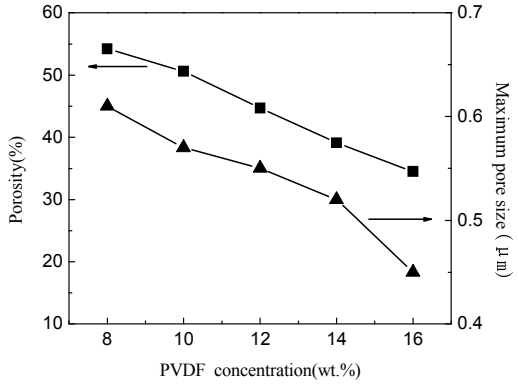


Fig.5. Effects of PVDF concentration on the porosity and maximum pore size

Fig. 6 showed the PWF and protein rejection of the prepared BHR PVDF hollow fiber membranes. According to Fig. 6, PWF of the BHR PVDF hollow fiber membranes decreased slightly from 551.8 (L·m-2·h-1·bar-1) for the F8 to 310.4 (L·m-2·h-1·bar-1) for the F16 membrane with the increase of PVDF concentration from 8 to 16 wt.%. But the rejection ratio increased with the increase of PVDF concentration. The BHR PVDF hollow fiber membranes had a thick wall, which extended the membrane filtration path and increased the intrinsic resistance of the membrane. Therefore, with the increase of PVDF concentration in the polymer solutions, the wall thickness became thicker and the PWF of the BHR PVDF hollow fiber membranes became lower. As the same time, the maximum pore size decreased with the increase of PVDF concentration in polymer solution from Fig. 5 and the pore size was a key factor impacting the membrane permeability. The rejection depended more on the denseness of the skin layer than on the structure of the cross-section [12]. The skin layers of the BHR PVDF hollow fiber membrane were dense and the maximum pore size of the BHR PVDF hollow fiber membranes were small. Thus, with the application of the BHR method, the increasing rate of the protein separation was significant for some special water treatment.

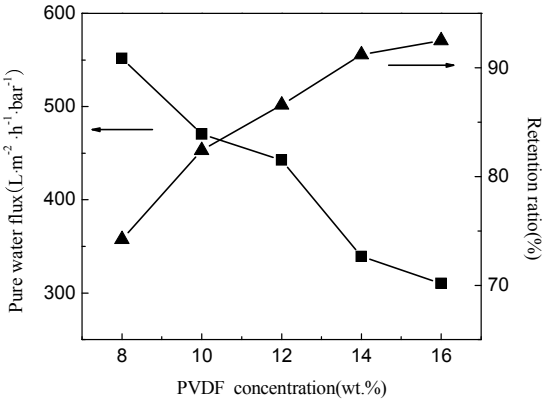


Fig.6.Effect of the PVDF concentration on pure water flux and protein rejection of the membranes

Conclusion

The BHR PVDF hollow fiber membranes were prepared through the dry–wet spinning method which coated PVDF polymer solutions on the two-dimensional braid surface. The BHR PVDF hollow fiber membranes prepared by the BHR method had excellent mechanical properties and its

tensile strength was nearly 75 MPa, which was adequate for MBR applications. The BHR PVDF hollow fiber membranes had a favorable interfacial bonding between the coating layer and two-dimensional braid due to the existence of the interface layer. The outer surface of the BHR PVDF hollow fiber membrane was a dense layer as the separating functional layer. The maximum pore size of the BHR PVDF hollow fiber membranes decreased with the increase of PVDF concentration, which could result in lower PWF and higher rejection of protein.

Acknowledgements

The authors thank the financial support of the 973 Program (2012CB722706) and 863 Program (2012AA03A603) of China, the National Natural Science Foundation of China (21274109), the Science and Technology Plans of Tianjin (12JCZDJC26600), and also the Basic Research Program of China National Textile and Apparel Council.

References

[1] E. Yuliwati, A.F. Ismail, T. Matsuura, M.A. Kassim, M.S. Abdullah, Effect of modified PVDF hollow fiber submerged ultrafiltration membrane for refinery wastewater treatment, Desalination. 283 (2011) 214–220.

[2] S.I. Patsios, A.J. Karabelas, An investigation of the long-term filtration performance of a membrane bioreactor (MBR): the role of specific organic fractions, J. Membrane Sci. 372 (2011) 102–115.

[3] M.J. Kim, B. Sankararao, C.K. Yoo, Determination of MBR fouling and chemical cleaning interval using statistical methods applied on dynamic index data, J. Membrane Sci. 375 (2011) 345–353.

[4] K. Murase, H. Habara, H. Fujiki, T. Hirane, M. Mizuta, U.S. Patent 2002/0046970A1, (2002)

[5] J. Liu, P. Li, Y. Li, L. Xie, S. Wang, Z. Wang, Preparation of PET threads reinforced PVDF hollow fiber membrane, Desalination. 249 (2009) 453–457.

[6] F. Liu, N. A. Hashim, Y. Liu, M.R.M. Abed, K. Li, Progress in the production and modification of PVDF membranes, J. Membrane Sci. 375 (2011) 1–27.

[7] X.C. Cao, J. Ma, X.H. Shi, Z.J. Ren, Effect of TiO_2 nanoparticle size on the performance of PVDF membrane, Appl. Surf. Sci. 253 (2006) 2003–2010.

[8] Q. Li, Z.-L. Xu, L.-Y. Yu, Effects of mixed solvents and PVDF types on performances of PVDF microporous membranes, J. Appl. Polym. Sci. 115 (2010) 2277–2287.

[9] P. Sukitpaneenit, T.-S. Chung, Molecular elucidation of morphology and mechanical properties of PVDF hollow fiber membranes from aspects of phase inversion, crystallization and theology, J. Membrane Sci.340 (2009) 192–205.

[10] M.-C. Yang, T.-Y. Liu, The permeation performance of polyacrylonitrile/bpolyvinylidine fluoride blend membranes, J. Membrane Sci. 226 (2003) 119–130.

[11] N. Li, C. Xiao, S. An, X. Hu, Preparation and properties of PVDF/PVA hollow fiber membranes, Desalination. 250 (2010) 530–537.

[12] M. Amirilargani, T. Mohammadi, Preparation and characterization of asymmetric polyethersulfone (PES) membranes, Polym. Advan. Technol. 20 (2009) 993–998.

Advanced Materials Research Vol. 936 (2014) pp 226-232
© (2014) Trans Tech Publications, Switzerland
doi:10.4028/www.scientific.net/AMR.936.226

Effect Of Ethanol Composition in Water Coagulation Bath on Structure and Performance of Homogeneous-Reinforced Polyvinyl Chloride Hollow Fiber Membranes

Hailiang Liu, Changfa Xiao, Qinglin Huang, Zhili Fan, Xiaoyu Hu, Wei Shu, Guolan Huan

State Key Laboratory of Hollow Fiber Membrane Materials and Processes, Tianjin Polytechnic University, Tianjin 300387, China

Corresponding author: Xiao Changfa; E-mail address: xiaochangfa@163.com (C. Xiao).

Ketwords: polyvinyl chloride; homogeneous-reinforced; hollow fiber membrane; coagulation bath

Abstract: Homogeneous-reinforced (HR) polyvinyl chloride (PVC) hollow fiber membranes consisting of coating layer and matrix layer were fabricated via coating process. The mixtures of polymer solutions were uniformly coated on the homogeneous PVC matrix membrane which was prepared by melt-spinning method. The influences of ethanol composition in water coagulation bath on structure and performance of HR membranes were investigated. The results showed that the pure water flux of the HR PVC hollow fiber membranes increased with the increase of ethanol weight fraction in coagulation bath, while the porosity changed slightly. The increase of ethanol weight fraction in coagulation bath brought about the decrease of the protein permeation flux and rejection rate. The tensile strength of HR PVC hollow fiber membranes was about 9.5 MPa, while the elongation at break was higher than 97 %.

Introduction

Dual-layer homogeneous-reinforced (HR) hollow fiber membranes were consisted of a functional outer layer and a porous matrix layer in which used the same polymer as the selective layer and the supporting layer. The HR hollow fiber membrane was prepared by HR process, which the matrix membrane was fabricated by the melt-spinning cold-stretching (MSCS) or thermally induced phase separation (TIPS) methods and the functional outer layer was fabricated by the nonsolvent induced phase separation (NIPS) method. The structure of the membrane prepared by MSCS and TIPS methods was more compact than NIPS method which gave the HR membrane the excellent mechanical property [1,2]. The membrane prepared by NIPS method usually had a dense skin layer which gave the HR membrane superior separation performance. Owing to the same polymer in the two layers of HR membrane, the adhesion of the functional outer layer to the matrix layer was better than that of the different polymers. Zhang et al. [3] prepared HR polyvinylidene fluoride (PVDF) hollow fiber membrane by HR method. They found that the HR PVDF hollow fiber membrane had a favorable interfacial bonding between the surface coating layer and the matrix membrane. Compared with the conventional polymeric membrane prepared by one single method, the HR membrane had a higher tensile strength than the membrane prepared via NIPS method, a better anti-fouling property than the membrane prepared via MSCS or TIPS method in the organic filtration.

Polyvinyl chloride (PVC) as a conventional and widely applied polymer, possessed superior performance, such as low cost, excellent physical, chemical (e.g. acids, alkalis and solvent resistance) and mechanical properties [4,5]. Thus, PVC had been widely used to prepare membranes [4-10]. In the previous studies, most of PVC hollow fiber membranes were prepared by NIPS method. These PVC hollow fiber membranes exhibited excellent water permeability, while the mechanical property of the membrane was poor [6]. Owing to the successful preparation of PVC hollow fiber membranes via MSCS method in our previous study [11]. The HR method was used to solve these problems[12] and the studies of ethanol composition in water coagulation bath effect on HR PVC hollow fiber membranes had not been found in open literature.

In this study, the HR PVC hollow fiber membranes were fabricated via coating process. During the spinning process, the mixtures of polymer solutions were coated on the homogeneous PVC hollow fiber matrix membrane uniformly. The influences of ethanol composition in water coagulation bath on structure and performance of HR membranes were investigated by morphology, pure water flux, protein permeation flux, rejection rate and mechanical property measurement.

Experimental

Materials

Polyvinyl chloride (PVC, fiber grade, DG-1000k, the average degree of polymerization is 1030±50) resin was purchased from Tianjin Dagu Chemical Plant (Tianjin, China). PVC hollow fiber matrix membrane was provided by State Key Laboratory of Hollow Fiber Membrane Materials and Processes in Tianjin Polytechnic University (Tianjin, China). N,N-dimethylacetamide (DMAc, Analytical Reagent), Ethanol (EtOH, Analytical Reagent) and Polyvinylpyrrolidone (PVP, Analytical Reagent, K30, Mw=10000) were bought from Tianjin Guangfu Fine Chemical Research Institute. Bovine serum albumin (BSA, Analytical Reagent, Mw=68000) was supplied from Beijing Aoboxing Universeen Bio-tech Co., Ltd.

Fabrication of HR PVC Hollow Fiber Membranes

The HR PVC hollow fiber membranes were fabricated via coating process[12]. The preparation process of HR PVC hollow fiber membranes were consisted of 3 steps. Firstly, the PVC hollow fiber matrix membrane went through the pre-wet solution which contained 60 wt% ethanol solutions. Secondly, the pre-wet PVC matrix membrane went through the coating device. In this process, the polymer solutions consisted of PVC, PVP and DMAc that were blended under constant mechanical stirring in a three-necked round-bottom flask for 4 h at 70 ℃ were coated on the PVC matrix membrane outer surface. Thirdly, the PVC matrix membrane coated with polymer solutions came into different ethanol fraction coagulation bath. After these 3 steps, the HR PVC hollow fiber membranes were prepared subsequently. The spinning parameters of HR PVC hollow fiber membranes were shown in Table 1.

TABLE 1 SPINNING PARAMETERS OF HR PVC HOLLOW FIBER MEMBRANES

Spinning conditions	Value
Dope composition (PVC/PVP/DMAc)/wt%	80/10/10
Matrix membrane	PVC hollow fiber membrane
Mixing temperature/℃	70.0
Spinning temperature/℃	20.0

Pre-wet solution	60wt% ethanol solution			
Pre-wet time/s	20.0			
External coagulation	Water	15wt% ethanol	30wt% ethanol	45wt% ethanol
External coagulation T/℃	20.0			
Air gap/cm	8.0			
Take up speed/m·min^{-1}	2.2			

Membrane Characterizations

Morphology Observation

Scanning electron microscope (SEM, Quanta 200, Netherlands FEI) was used to investigate the morphology of surface and cross-section of matrix and HR hollow fiber membranes. The membranes were immersed in liquid nitrogen for 10~15s and were frozen. Then the frozen membranes were broken for cross-section observation. Samples were all gold sputtered before testing.

Permeation Performance Experiments

The pure water flux (PWF) was measured with hollow fiber membranes at 0.1 MPa pressure under the condition of outside pressure and was calculated by Eq. (1):

$$J = \frac{V}{At} \tag{1}$$

Where J is the permeate flux of membrane (L·m^{-2}·h^{-1}), V is the quantity of permeation (L), A is the effective area of membrane (m^2), and t is the testing time (h).

The filtration experiments were then carried out by 1 g/L BSA solution. Before the filtration experiments, the deionized water was used to feed in the filtration experimental setup for 40 min to stabilize the permeation performance of HR PVC hollow fiber membrane at operating pressure of 0.1 MPa and temperature of 20 ^{o}C. Then the BSA solution was fed into the cross-flow membrane container. After 20 min, the protein permeation flux (PPF) was measured for 20 min and was calculated by Eq. (1). The concentration of feed solution and permeate solution were determined by UV spectroscopy at wavelength of 280 nm, using a PERSEE TU-1901 spectrophotometer (Beijing Purkinje General Instrument Co.,Ltd.). The separation efficiency of the membrane was defined by Eq. (2):

$$R = (1 - \frac{C_p}{C_f}) \times 100\% \tag{2}$$

Where C_f and C_p are the concentration of protein in the feed and the permeate solution, respectively. Porosity determination

The membrane porosity was defined as the pores volume divided by the total volume of the porous membrane. It can be determined by gravimetric method which calculated according to Eq. (3):

$$\varepsilon(\%) = \frac{W_1 - W_2}{(\pi/4)(D^2 - d^2)l\rho} \times 100\% \tag{3}$$

Where W_1 is the weight of wet membrane (g), W_2 is the weight of dry membrane (g), ρ is the water density (ρ=1.0 g·cm^{-3}), D is the outer diameter (cm), d is the inner diameter (cm) and l is the length of sample membrane (cm).

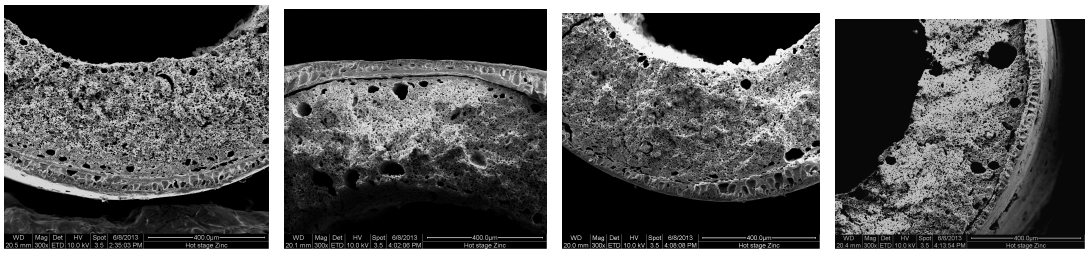
Measurement of Mechanical Property

At room temperature, mechanical properties of HR PVC hollow fiber membranes were measured by a universal mechanical testing machine (Instron3369, USA). The gripping range and the tensile rate were 50 mm and 100 mm·min^{-2}, respectively. Each sample was tested five times to evaluate the average value.

Results and Discussion

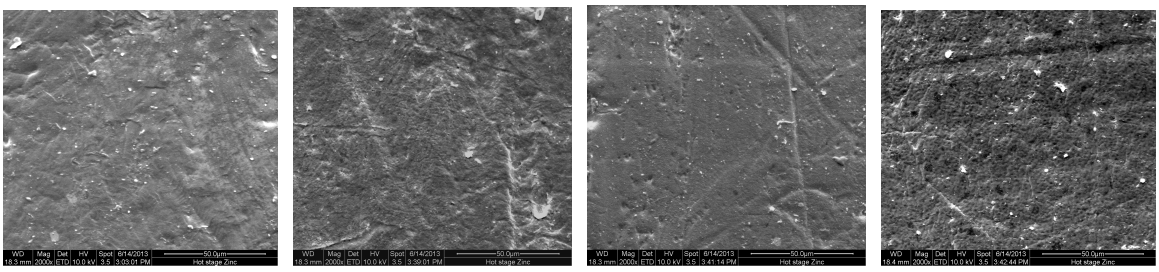
Morphologies

The PVC casting solution with 10 wt% concentration in polymer solutions were coated on the PVC hollow fiber matrix membrane to prepare the HR PVC hollow fiber membrane. The different weight fraction (0, 15, 30 and 45 wt%) of ethanol aqueous solutions as the coagulation bath were used to prepare HR PVC hollow fiber membrane. These cross sectional morphologies of prepared HR PVC hollow fiber membrane were shown in Fig. 1. It can be seen that the HR PVC hollow fiber membranes were consisted of the coating layer consisting of finger-like structure and the matrix layer consisting of sponge-like structure from Fig. 1. With the increase of ethanol weight fraction in coagulation bath from 0 to 45 wt%, the change of coating layer structure was not obvious. The outer surface morphologies of prepared HR PVC hollow fiber membrane were shown in Fig. 2. The prepared HR PVC hollow fiber membrane possessed a dense outer surface within no obvious big pores. It was obviously found that the outer surface became rough with the increase of ethanol weight fraction in coagulation bath from Fig. 2 (a), (b), (c) and (d). When the ethanol weight fraction was 45 wt%, some small pores appeared on the outer surface from Fig. 2 (d). This must be due to the delay phase separation which induced by the high ethanol weight fraction in the coagulation bath.



(a) (b) (c) (d)

Fig. 1. Cross Sectional Morphologies of HR PVC Hollow Fiber Membranes. (Ethanol Weight Fraction in Coagulation bath:a-0, b-15 wt%, c-30 wt%, d-45 wt%).



(a) (b) (c) (d)

Fig. 2. Outer Surface Morphologies of HR PVC Hollow Fiber Membranes. (Ethanol Weight Fraction in Coagulation bath:a-0, b-15 wt%, c-30 wt%, d-45 wt%).

Permeation Properties

The PWF and porosity of HR PVC hollow fiber membranes that prepared under different ethanol weight fraction in coagulation bath were shown in Fig. 3. It can be seen that the PWF first increased slowly when the ethanol weight fraction was lower than 30 wt% and then increased rapidly when the ethanol weight fraction increased from 30 to 45 wt%. But the porosity of the HR membrane was slightly changed with the change of coagulation bath. These results could be explained by the fact that the increase of the ethanol weight fraction increased the outer surface roughness from Fig. 2 and some small pores appeared on the outer surface when the ethanol weight fraction was 45 wt% (Fig. 2(d)) which decreased the filtration resistance, while the cross section morphologies of these HR PVC hollow fiber membranes almost unchanged from Fig 1.

Fig. 4 showed the PPF and rejection of HR PVC hollow fiber membranes that prepared under different ethanol weight fraction in coagulation bath. It can be seen that both of the PPF and rejection of HR PVC hollow fiber membranes decreased with the increase of ethanol weight fraction in coagulation bath. The rejection depended more on the denseness of the skin layer than on the structure of the cross section [13]. The outer surface of HR PVC hollow fiber membranes became rough and some small pores appeared on the outer surface with the increase of the ethanol weight fraction in coagulation bath from Fig. 2. Thus, the protein rejection rate decreased with the increase of the ethanol weight fraction in coagulation bath. Due to the existence of the small pores on the outer surface, the pollution of membrane inner pores became worse which decreased the membrane pores connectivity in the filtration process and increased the filtration resistance. These resulted in the decrease of the membrane PPF.

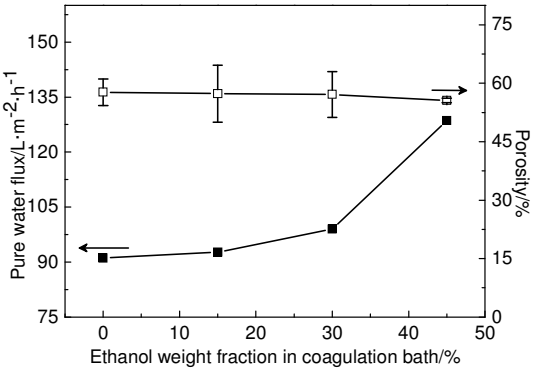


Fig. 3. Effects of Ethanol Weight Fraction in Coagulation Bath on PWF and Porosity of HR PVC Hollow Fiber membranes.

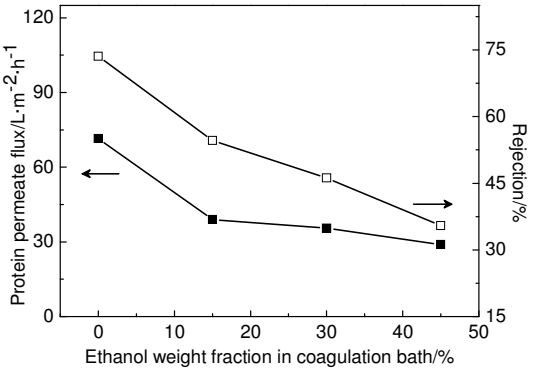


Fig. 4. Effects of Ethanol Weight Fraction in Coagulation Bath on PPF and Rejection of HR PVC Hollow Fiber Membranes.

Mechanical Properties

Fig. 5 showed the effects of ethanol weight fraction in coagulation bath on the tensile strength and elongation at break of HR PVC hollow fiber membranes. It can be seen that the tensile strength of the HR PVC hollow fiber membranes were lower than that of the matrix membrane. But the tensile strength of the HR PVC hollow fiber membranes were almost unchanged with the increase of the ethanol weight fraction in coagulation bath. The elongation at break of the HR PVC hollow fiber membranes were close to or higher than the matrix membrane. The tensile strength of HR PVC hollow fiber membranes mainly depended on the matrix membrane. In the preparation process, the dissolution of the matrix membrane in the polymer solution which contained high concentration solvent DMAc (80 wt%) might cause some unfavorable influence on the tensile strength of HR PVC hollow fiber membranes [12]. In this study, the tensile strength of HR PVC hollow fiber membranes was nearly 9.5 MPa which was higher than 1-5 MPa of membrane prepared by the wet spinning method [6]. The elongation at break of HR PVC hollow fiber membranes was higher than 97 %.

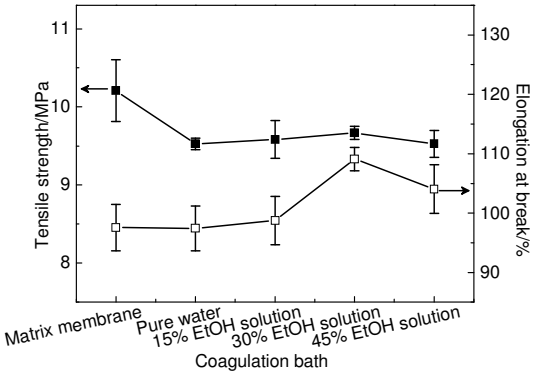


Fig. 5. Effects of Ethanol Weight Fraction in Coagulation bath on Mechanical Properties of HR PVC Hollow Fiber Membranes.

Conclusions

The HR PVC hollow fiber membranes including coating layer and matrix membrane were fabricated via coating process. The outer surface of the HR PVC hollow fiber membranes became rough with the increase of ethanol weight fraction from 0 to 45 wt% in coagulation bath. The PWF of the HR PVC hollow fiber membranes increased, while the porosity changed slightly with the increase of ethanol weight fraction in coagulation bath. The increase of ethanol weight fraction in coagulation bath also brought about the decrease of the PPF and protein rejection rate. The tensile strength of HR PVC hollow fiber membranes were lower than that of the matrix membrane and were about 9.5 MPa, while the elongation at break was higher than 97 %.

Acknowledgements

The authors gratefully acknowledge the research funding provided by the 973 Program(2012CB722706) and 863 Program(2012AA03A603) of China, the National Natural Science Foundation of China (21274109), the Science and Technology Plans of Tianjin (12JCZDJC26600), and also the Basic Research Program of China National Textile And Apparel Council.

References

[1] S.R. Rajabzadeh, C. Liang, Y. Ohmukai, T. Maruyama, H. Matsuyama, Effect of additives on the morphology and properties of poly(vinylidene fluoride) blend hollow fiber membrane prepared by the thermally induced phase separation method, J. Membr. Sci. 423-424(2012)189-194.

[2] H.L. Liu, C.F. Xiao, X.Y. Hu, M.T. Liu, Post-treatment effect on morphology and performance of polyurethane-based hollow fiber membranes through melt-spinning method, J. Membr. Sci. 427(2013)326-335.

[3] X.L. Zhang, C.F. Xiao, X.Y. Hu, Q.Q. Bai, Preparation and properties of homogeneous-reinforced polyvinylidene fluoride hollow fiber membrane, Appl. Surf. Sci. 264(2013)801-810.

[4] X.Z. Zhang, Y.S. Chen, A.H. Konsowa, X.S. Zhu, J.C. Crittenden, Evaluation of an innovative polyvinyl chloride (PVC) ultrafiltration membrane for wastewater treatment, Sep. Purif. Technol. 70(2009) 71-78.

[5] X.Y. Guo, A.J. Zhang, L. Fang, L.G. Su, Study on ultrafiltration for surface water by a polyvinylchloride hollow fiber membrane, Desalination 238(2009) 183-191.

[6] J. Xu, Z.L. Xu, Poly(vinyl chloride) (PVC) hollow fiber ultrafiltration membranes prepared from PVC/additives/solvent, J. Membr. Sci. 208(2002) 203-212.

[7] X.Y. Guo, A.J. Zhang, L. Fang, L.G. Su, Study on ultrafiltration for surface water by a polyvinylchloride hollow fiber membrane, Desalination 238(2009) 183-191.

[8] M. Khayet, M.C. Garcia-Payo, F.A. Qusay, M.A. Zubaidy, Structural and performance studies of poly(vinyl chloride) hollow fiber membranes prepared at different air gap lengths, J. Membr. Sci. 330(2009) 30-39.

[9] S. Mei, C.F. Xiao, X.Y. Hu, Preparation of porous PVC membrane via a phase inversion method from PVC/DMAc/water/addibives, J. Appl. Polym. Sci. 120(2011) 557-562.

[10] C.A. Jones, S.A. Gordeyev, S.J. Shilton, Poly(vinyl chloride) (PVC) hollow fibre membranes for gas separation, Polymer 52(2011) 901-903.

[11] H.L. Liu, C.F. Xiao, X.Y. Hu, Fabrication and properties of polyvinyl chloride hollow fiber membranes plastified by dioctyl phthalate, Desalin. Water. Treat. 51(2013) 3786-3793.

[12] H.L. Liu, C.F. Xiao, Q.L. Huang, X.Y. Hu, Structure design and performance study on homogeneous-reinforced polyvinyl chloride hollow fiber membranes, Desalination 331(2013)35-45.

[13] M. Amirilargani, T. Mohammadi, Preparation and characterization of asymmetric polyethersulfone (PES) membranes, Polym. Advan. Technol. 20(2009) 993-998.

Advanced Materials Research Vol. 936 (2014) pp 233-237
© (2014) Trans Tech Publications, Switzerland
doi:10.4028/www.scientific.net/AMR.936.233

Fabrication and Characterization of CuO Micro-dimensional Structures for Superhydrophobic Surface

Youhua Fan [1,2,a*], Zejun Chen [2], Layun Deng [2], Hong Chen [3*]

[1]Institute of Powder Metallurgy, Central South University, Changsha 410083, PR China

[2]Hunan Forestry Academy, Changsha 410004, PR China

[3]Central South University of Forestry and Technology, Changsha 410004, PR China

[a]Email:yh_fan@163.com

Keywords: Superhydrophobic surface; copper oxygen; contact angle; stearic acid

Abstract: A superhydrophobic copper oxygen (CuO) surface with hierarchical micro- and nanostructure was obtained by hydrothermally synthesized. The CuO surface was endowed with superhydrophobic property by modifying with stearic acid, which was referred to the STA-modified CuO film. The surface morphological study showed that different structures, such as petal-shaped, bulk-shaped, carambola-shaped CuO and cauliflower-shaped particles distributed on the copper substrate under the different synthesis conditions. The water contact angle and sliding angle of the as-prepared CuO surface were 157 ± 2.3º and 3º, respectively.

Introduction

Superhydrophobic surfaces with water contact angles large than 150 have recently attracted extensive attention due to their outstanding properties of self cleaning, low flow resistance, anti-sticking and anticorrosion [1,2]. It is well-known that the wettability of a solid surface is governed by both the surface chemical composition and geometrical microstructure [3]. Therefore, superhydrophobicity of a surface can thus be achieved by enhancing the surface roughness and lowering the surface energy.

Similar to many functional semiconductors, copper oxide as a kind of functional material has attracted extensive interests owing to its photoconductive and photochemical properties, which has been widely used as catalyst, gas sensors, semiconductor and solar cells[4]. Many novel CuO micro/nanostructures such as nanosheets, wheat grain-like and nanorods [5,6] structures have been fabricated by a range of techniques, including chemical vapour deposition, hydrothermal methods, and some solution processes. However, most of these reaction systems can only produce one or two morphologies. In particular, the obtained CuO nanostructures are mostly used to enhance the currently existing applications. Among these methods, the hexamethylenetetramine assisted solution method is relatively simple, inexpensive, and surfactant-free. Although this method has been used to fabricate flower-shaped or spindly-shaped CuO nanostructures, its ability to produce new structures at sufficiently large quantities for fabrication superhydrophobic CuO surface still needs to be demonstrated.

Herein, we describe a simpler one-step hydrothermal method to directly fabricate the uniform micro- and nanostructure hierarchical CuO surface on copper substrate. The so-called STA-modified CuO film, is modified with lower energy compound stearic acid at room temperature. The as-prepared CuO film exhibits good superhydrophobic property.

Experimental

Preparation of CuO Film

In a typical synthesis, the same volume ratio of the copper acetate solution and the HMTA solution with the concentration varied form 0.001 M to 0.075 M was transferred to a 100 mL Teflon-lined autoclave containing the cleaned copper substrate. The autoclave was then sealed and heated to 90 °C for 24 h. After the given reaction time, the autoclave was cooled downed to room temperature. The copper substrate was taken out from the solution. A black film was obtained (viewed through naked eye), which covered uniformly on the Cu substrate. The sample was rinsed with distilled water and dried at 60 °C for 6 h. It was then immersed in an ethanol solution (2.0 wt.%) of STA for 2 h at room temperature. The resulting film was rinsed with ethanol and then dried at 60 °C for 2 h, and then a porous superhydrophobic CuO surface with hierarchical micro- and nanostructures was obtained.

Characterization

The CuO powder was characterized by X-ray diffraction (XRD) (Rigaku D/max-2000PC) with copper target. The surface morphologies were examined by environmental scanning electron microscope (SEM) (FEI Quanta 200). The surface compositions of the samples were determined by X-ray photoelectron spectroscopy (XPS) (EscaLab 250Xi) with an Al Ka Xray source (15 kV, 10 mA) and an analytical chamber with a base pressure of 10^{-6} Pa. The sessile drop method was used for CA measurements using a Dataphysics OCA20 CA system at ambient temperature. The average CA value was obtained by measuring more than three different positions for the same sample.

Results and Discussion

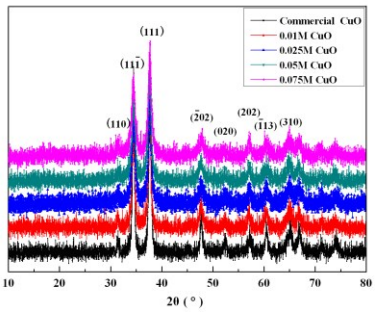


Fig. 1 XRD Patterns of the As-prepared CuO Powder

The crystalline structure of the as-prepared CuO surface was characterized using an X-ray diffraction as shown in Fig. 1. The diffraction peaks observed at 31.4, 34.5, 37.6, 47.8 and 52.5 in the XRD pattern were the typical character diffraction peaks of CuO which confirm that the formed material was copper oxygen. The main five diffraction peaks were identified to match up to the (110), ($1\,1\,\bar{1}$) and (111), ($\bar{2}02$) and (020) planes of the monoclinic CuO structure in sequence compared with the PDF card (JCPDS 45-0937). The XRD pattern showed that the samples were single-phase and no impurities were detected, indicating that the CuO powder was pure and well crystallined.

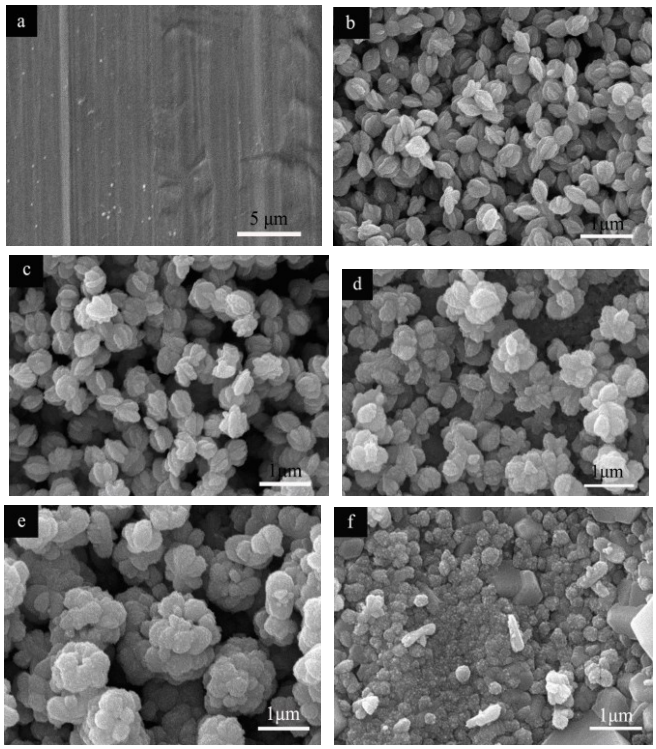


Fig. 2 SEM Images of the As-prepared CuO Surface at Different Initial Concentration (a) the Copper Substrate;

(b) 0.005 M; (c) 0.01 M; (d) 0.025 M; (e) 0.05 M; (f) 0.075 M

Fig. 2 showed the SEM images of the CuO nanostructure grown on the copper wafer substrates at different concentration. As could be seen from the top view, the different nanostructure covered the copper surface uniformly, which were different from the smooth copper substrate (Fig. 2a). When the initial concentration of the copper acetate solution and the HMTA solution increased from 0.01 M to 0.075 M, the surface morphologies of the CuO had also changed. It was clearly seen from Fig. 2b to d that the samples synthesized under the lower concentration of 0.05 M was of a carambola-shaped structure consisting of nanopetals with typical thickness of 80-120 nm. The size of a single carambola (Fig. 2c) was about 600 nm in width and 800 nm in lengths. While the initial concentration of reactants were 0.05 M, the nanopetals closely packed, gradually formed a cauliflower-shaped structure (Fig. 2e), and the size of the single cauliflower was about 1.0-1.2 μm. When the initial concentration was 0.075 M, in addition to generate a large number of carambola-shaped particle with the size of 200-300 nm, there also randomly appeared square shaped CuO particles on the copper wafer substrate. The size of the square shaped CuO particles were 1-8 μm (Fig. 2f). The above results showed that the size of the CuO increased with the increasing of the initial reactants concentration.

The CuO film was chemically modified with stearic acid, aiming at changing the surface wettability, since surface chemical composition had a remarkable effect on the hydrophobicity. Fig. 5a depicted the wide scan of the STA-modified CuO film. Fig. 5b showed the XPS spectra of the copper element obtained with copper substrate after hydrothermal synthesis. The peaks located at 932.26 eV (Cu 2p 3/2) and 952.11 eV (Cu 2p 1/2) were attributed to the Cu 2p region of metallic copper on the copper substrate. In addition to peaks at 932.26 eV (Cu 2p 3/2) and 952.11 eV (Cu 2p 1/2), there were two new peaks located at 943.61 eV (Cu 2p 3/2) and 962.31 eV (Cu 2p 1/2). It could be implied that the compound in the top surface mainly consisted of copper oxalate [7,8].

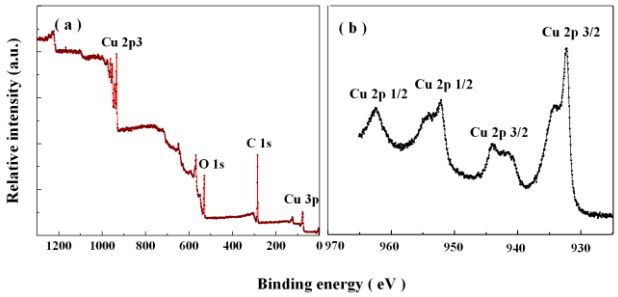


Fig. 5 (a) XPS Spectrum of the STA-modified CuO Film; (b) High Resolution Cu2p Core Level Spectrum

The nanoparticles and the particle clusters pack loosely, and a lot of pores could be observed. We tested the water contact angle of the as-prepared porous CuO surface, and the water contact angle was less than 5 ° [9], showing superhydrophilic property. In general, the wettability of a rough solid surface could be described by Wenzel [10] model shown in equation (1):

$$\cos \theta_r = r \cos \theta \quad (1)$$

Here, r was the roughness factor, and θ and θ_r were the equilibrium contact angle of a liquid on a smooth solid surface and a rough solid surface, respectively. According to the equation (1), if the roughness was increased, the contact angle of a hydrophilic solid surface would decrease. Note that CuO was an intrinsically hydrophilic material, rough surface should become more hydrophobic than those of smooth according to Wenzel model. Thus, the as-prepared CuO surface showed superhydrophilic property. However, the wettability dramatically changed after modification with stearic acid. Fig. 6a showed that the static contact angle was 157± 2.3º.on the as-prepared porous CuO surface synthesized under the conditions that the reaction time last 24 h under the initial concentration for 0.01 M at 90 ºC. Fig. 6b showed a digital photograph image of the shape of 10 µl

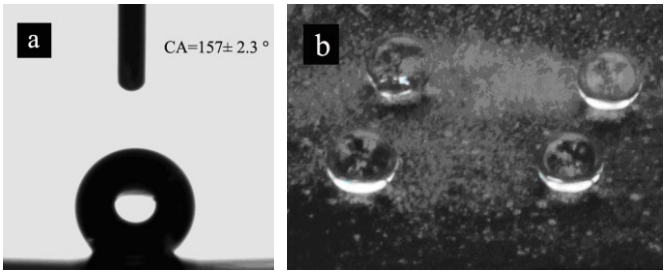


Fig. 6 (a) The Water Droplet on the As-prepared Superhydrophobic CuO Surface; (b) A photograph of Water Droplets on STA-modified CuO Film

water droplets on the superhydrophobic CuO surface. The digital photograph image of water droplets with uniform size on the surface showed a direct demonstration of the superhydrophobic property after the CuO film modified by stearic acid. A water droplet was hardly able to stick to the surface, which moved around rapidly when is was slightly disturbed, and dripped off the substrate rapidly when the substrate was tilted less than 3 º. The high water contact angle and low sliding angle indicated that the as-prepared CuO surface was a real superhydrophobic surface, which exhibited similar wettability with natural lotus leaf or rose petal. Most studies on natural and artificial superhydrophobic surfaces showed that the rough surface structure and low-surface-energy materials were crucial for a superhydrophobic surface [11,12]. Note that the water contact angle of the stearic acid surface coated on a smooth copper substrate was only 108° [9]. Therefore, it could come to the conclusion that the superhydrophobicity of the CuO surface resulted from the synergistic effect of their unique surface micro- and nanostructures and low energy compound.

Conclusions

A facile synthesis strategy for the direct construction of micro- and nanostructure CuO surface on copper substrate was investigated. The CuO surface was endowed with superhydrophobic property by modifying with stearic acid. The water contact angle and sliding angle of the as-prepared superhydrophobic CuO surface were 157 ± 2.3º and 3º, respectively. The presented method could be used to fabricate not only superhydrophobic but also superhydrophilic CuO surface. It could be easily scaled up to create large-area uniform superhydrophobic surface and could be applied in commercial manufacturing. It was believed that this method should be easily to other metals oxide, ceramics and alloys.

References

[1] W. Barthlott, C. Neinhuis, Purity of the sacred lotus, or escape from contamination in biological surfaces. Planta 202 (1997)1-8.

[2] R. Fürstner, W. Barthlott, Wetting and Self-Cleaning Properties of Artificial Superhydrophobic Surfaces. Langmuir 21 (2005) 956-961.

[3] L. Jiang, Y. Zhao, J. Zhai, A Lotus-Leaf-Like Superhydrophobic Surface: A Porous Microsphere/Nanofiber Composite Film Prepared by Electrohydrodynamics, Angew, Chem. Int. Ed 43 (2004) 4338-4341.

[4] L.B. Chen, N. Lu, C.M. Xu, H.C. Yu, T.H. Wang, Electrochemical performance of polycrystalline CuO nanowires as anode material for Li ion batteries, Electrochimica Acta 54 (2009) 4198-4201.

[5] Z.X. She, Q. Li, Z.W. Wang, .Q. Li, F.N. Chen, J.C. Zhou, Novel Method for Controllable Fabrication of a Superhydrophobic CuO Surface on AZ91D Magnesium Alloy, ACS Appl. Mater. Interfaces 4 (2012) 4348-4356.

[6] M. Basu, A.K. Sinha, M. Pradhan, S. Sarkar, Y. Negishi, T. Pal, Fabrication and functionalization of CuO for tuning superhydrophobic thin film and cotton wool, J. Phys. Chem. C 115 (2011) 20953-20963.

[7] J. Haber, T. Machej, L. Ungier, J. Ziokowski, ESCA studies of copper oxides and copper molybdates, J. Solid State Chem 25 (1978) 207-218.

[8] Z.G. Guo, J. Fang, L.B. Wang; W.M. Liu, Fabrication of superhydrophobic copper by wet chemical reaction, Thin Solid Films 515 (2007) 7190-7194

[9] Y.H. Fan, Z.J. Chen, J. Liang, Y. Wang, H. Chen, Preparation of superhydrophobic films on copper substrate for corrosion barriers, Surf. Coat. Technol (2014), http://dx.doi.org/10.1016/j.surfcoat.2014.01.005

[10] R N. Wenzel, Resistance of solid surfaces to wetting by water, Industrial & Engineering Chemistry 28 (1936) 988-994.

[11] P. Wang, D. Zhang, R. Qiu, Liquid/solid contact mode of super-hydrophobic film in aqueous solution and its effect on corrosion resistance, Corrosion Science 54 (2012) 77-84.

[12] J. Wang, D.D. Li, R. Gao, Q. Liu, X.Y. Jing, Y.L. Wang, Y. He, M.L. Zhang, Z.H. Jiang, Construction of superhydrophobic hydromagnesite films on the Mg alloy, Materials Chemistry and Physics 129 (2011) 154.

Advanced Materials Research Vol. 936 (2014) pp 238-242
© (2014) Trans Tech Publications, Switzerland
doi:10.4028/www.scientific.net/AMR.936.238

Low Temperature Preparation of Aluminum Titanate Film via Sol-Gel Method

Yi Bao[1,a], Weihui JIANG[1,2,b *], Guo FENG[1,c] Jianmin LIU[1], and Qian WU[1]

[1]School of Material Science and Engineering, Jingdezhen Ceramic Institute, Jingdezhen 333001, Jiangxi, China

[2]Jiangxi Key Laboratory of Advanced Materials, Jingdezhen 333001, Jiangxi, China

[a]baoyi0405@163.com, [b]jwhjiang@163.com, [c]243393617@qq.com

Keywords: aluminum titanate, film, sol-gel method, compound chelating agent

Abstract. Aluminum titanate(Al_2TiO_5) film was prepared via sol-gel method at low temperature, using ethyl acetoacetate and anhydrous citric acid as compound chelating agent, tetrabutyl titanate ($Ti(OC_4H_9)_4$) and aluminum chloride ($AlCl_3{\cdot}6H_2O$) as precursors, ethanol as solvent. The phase transformation of Al_2TiO_5 xerogel during heat treatment, the effect of different chelating agents on the synthesis of Al_2TiO_5, and the phase composition and morphology of film were investigated by means of differential thermal and thermo gravimetric analysis (DTA-TG), X-ray diffraction analysis (XRD), Fourier transform infrared spectroscopy (FTIR) and field-emission scanning electron microscopy (FE-SEM). The results demonstrate that Al_2TiO_5 can be synthesized at 750 ^oC by using compound chelating agent, rather than single chelating agent. Compound chelating agent contributes to the formation of Al-O-Ti heterogeneous bond, which is the key to preparing Al_2TiO_5 at low temperature. High quality Al_2TiO_5 film could be coated on the SiC substract at 750 ^oC.

Introduction

Aluminum titanate (Al_2TiO_5) is a ceramic material characterized by low thermal expansion, good thermal shock resistance, high melting point, low thermal conductivity and good corrosion resistance [1]. Al_2TiO_5 film can combine with SiC substrate firmly, which prevents the high temperature oxidation of SiC effectively, and enhances its corrosion resistance significantly [2]. In addition, Al_2TiO_5 film is a kind of ideal thermal barrier material. Therefore, Al_2TiO_5 film has appealing potential applications in the fields of aerospace, national defense and civilian industries, etc [3,4]. Various methods have been reported for the preparation of Al_2TiO_5 film, such as chemical vapor deposition method [5], radio-frequency magnetron sputtering method [6], and sol-gel method [2,4,7-9], etc.

Sol-gel method includes hydrolytic sol-gel method (HSG) and nonhydrolytic sol-gel method (NHSG). Usually, the synthesis temperature of Al_2TiO_5 film prepared by HSG method is above 1300 ^oC [2, 8]. Although Al_2TiO_5 film could be obtained via NHSG method at low temperature of 750 ^oC [9], the whole reaction process must be carried out in dry environment protected with inert gases, which is not beneficial to large scale production of Al_2TiO_5 film.

In this paper, Al_2TiO_5 film was prepared on silicon carbide (SiC) substrate at 750 ^oC in air atmosphere via sol-gel method, using ethyl acetoacetate and anhydrous citric acid as compound chelating agent, inorganic salt $AlCl_3{\cdot}6H_2O$ as aluminum source, and the crystallization water in $AlCl_3{\cdot}6H_2O$ as required water for sol-gel reaction. The reason for the low temperature synthesis of Al_2TiO_5 was investigated; meanwhile, the quality of film prepared was characterized.

Experimental

The molar ratio of aluminum chloride ($AlCl_3{\cdot}6H_2O$) to tetrabutyl titanate ($Ti(OBu)_4$) was calculated according to the chemical composition of Al_2TiO_5. A solution (S1) was prepared by dissolving $AlCl_3{\cdot}6H_2O$ (0.04 mol, 9.657 g) in ethanol (80.0 ml). Citric acid (0.02 mol, 3.842 g) dissolved in ethanol (20.0 ml), then mixed with $Ti(OBu)_4$ (0.02 mol, 6.8 ml) modified with ethyl

acetoacetate (0.04 mol, 5.1 ml) to form solution (S2). After that, solution S1 was dropwise added into solution S2. The resulting sol aged at room temperature for 48 h.

The xerogel film was prepared on clean SiC substrate by dip-coating, drying and low temperature heat treatment at 500 ^{o}C for three times. In order to obtain Al_2TiO_5 film, a high-temperature heat treatment at 750 ^{o}C was needed for the fourth coating. The heating rates of RT~500 ^{o}C and 500 ^{o}C ~750 ^{o}C were 1 ^{o}C /min and 2 ^{o}C /min, respectively.

Testing and Characterization

Differential thermal analysis (DTA) and thermo gravimetric analysis (TG) were achieved with NETZSCH STA 449C thermal analyzer. The phase compositions of samples were observed by Bruker D8 Advance X-ray diffraction (XRD) with Ni-filtered Cu Kα radiation in the 2θ angle range of 10–70°. Fourier transform infrared spectroscopy (FTIR) was carried out with Nicolet 5700 infrared spectrometer in the wavenumber range of 4000-400 cm^{-1}, and the morphology of samples was characterized by the JSM-6700F field-emission scanning electron microscopy (FE-SEM).

Results and Discussion

In order to study the phase transition of Al_2TiO_5 xerogel during the heat treatment, its DTA-TG test was carried out from room temperature to 1400 ^{o}C at the rate of 10 ^{o}C /min in argon atmosphere.

Fig. 1 shows that there is a broad endothermic peak at 217.8 ^{o}C, corresponding to 42.16% weight loss, which is due to the volatilization of organic compounds and decomposition of the residual alcohol oxygen groups from the gel [10]. The endothermic peak at 491.0 ^{o}C owes to the pyrolysis of citric acid [11]. An exothermic peak attributed to the crystallization of Al_2TiO_5 appears at 731.1 ^{o}C in the DTA curve, which can be deduced from the fact that the XRD pattern of the sample (Fig. 2) prepared at 750 ^{o}C has Al_2TiO_5 diffraction peaks while its counterpart at 700 ^{o}C has no Al_2TiO_5 diffraction peaks. Furthermore, there is an exothermic peak at 1126.8 ^{o}C and an endothermic peak at 1321.4 ^{o}C. Fig. 2 shows that there is no Al_2TiO_5 diffraction peak in the XRD pattern of the xerogel powder calcined at 1150 ^{o}C, which indicates: (1) Al_2TiO_5 formed at 750 ^{o}C decomposes into corundum and rutile, it is caused by its instability [12]; (2) the exothermic peak at 1126.8 ^{o}C can be assigned to the decomposition of Al_2TiO_5. Meanwhile, the endothermic peak at 1321.4 ^{o}C can be attributed to the synthesis of Al_2TiO_5 again, and it could be inferred from that there is Al_2TiO_5 crystal phase in the sample prepared at 1350 ^{o}C. It is noteworthy that due to the rapid weight loss before 500 ^{o}C, the heating rate should be slow in order to obtain high-quality Al_2TiO_5 film.

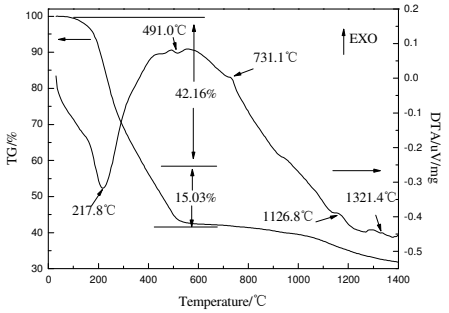


Fig. 1 DTA-TG Curves of the Xerogel

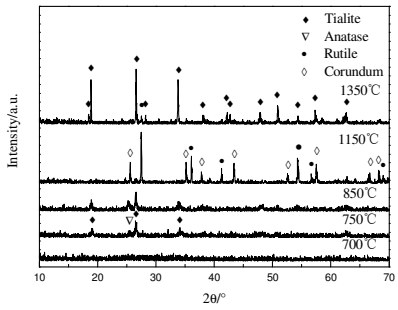


Fig. 2 XRD Patterns of the Samples Heated at Different Temperatures

Fig.3 shows the XRD patterns of samples prepared by selecting anhydrous citric acid and ethyl acetoacetate ($EC^{\#}$), ethyl acetoacetate ($E^{\#}$) and anhydrous citric acid ($C^{\#}$) as chelating agents respectively, and the calcinations temperature of samples was 850 ^{o}C. It can be seen from Fig.3 that the main crystalline phase of sample $C^{\#}$ and $E^{\#}$ is anatase. The sample $EC^{\#}$ has strong and sharp Al_2TiO_5 crystal diffraction peaks accompanied with a weak anatase crystal diffraction peak. It was apparent that Al_2TiO_5 can be prepared by using compound chelating agent, rather than the single one.

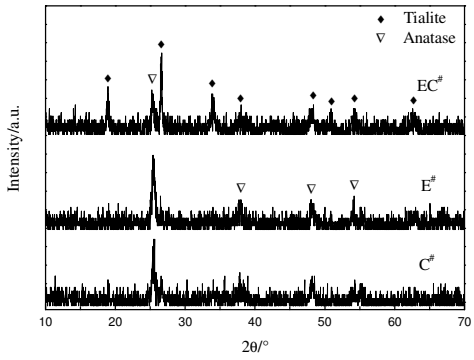


Fig. 3 XRD Patterns of Samples Prepared by Using Single and Compound Chelating Agents

In order to investigate the reason for low synthesis temperature of Al_2TiO_5, FT-IR test was performed to analyze the bonding of Al_2TiO_5 xerogel.

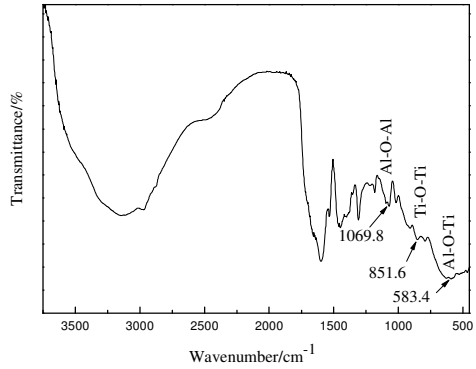


Fig. 4 FT-IR Spectrum of Aluminum Titanate Xerogel

The absorption bands at 1069 cm^{-1}, 851 cm^{-1} and 583 cm^{-1} in Fig. 4 are corresponding to the vibration of Al-O-Al, Ti-O-Ti [13] and Al-O-Ti bonds [14], respectively. The appearance of Al-O-Ti bond indicates that Al and Ti in gel have been mixed in atomic level, which is the key to synthesizing Al_2TiO_5 at 750 ^oC [14]. The reason for the formation of Al-O-Ti is as follows: the steric hindrance effect of the compound chelating agent reduces the activity of the tetrabutyl titanate, which changes the polarization of Ti-OBu in $Ti(OBu)_{4-x}(OH)_x$. This change leads to the fact that the polarization of OH in H_2O and Ti-OBu is insufficient to meet the requirement of further hydrolysis reaction [15]. Then Cl in Cl-Al= attacks on O-Bu bond in $Ti(OBu)_{4-x}(OH)_x$ to form Al-O-Ti bond. The process can be described as formula ((1)-(3)).

$$AlCl_3 \cdot 6H_2O + EtOH \longrightarrow AlCl_x(OH)_y(OEt)_z + HCl \quad (x+y+z=3) \tag{1}$$

$$Ti(OBu)_4 + xH_2O \longrightarrow Ti(OBu)_{4-x}(OH)_x + xBuOH \tag{2}$$

$$\equiv Ti-O-Bu+Cl-Al= \rightarrow =Al-O-Ti\equiv +BuCl\uparrow \tag{3}$$

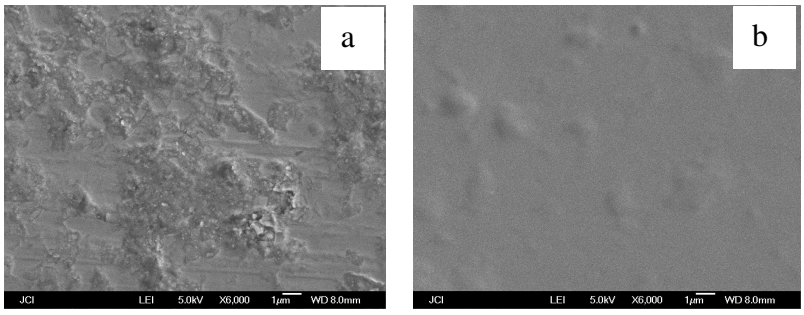


Fig.5 The Surface SEM Images of SiC(a) and Film Sample(b)

FE-SEM micrographs of the samples are shown in Fig.5. It can be seen from Fig.5 (a) that the surface of uncoated SiC substrate is rough and uneven. Comparatively, the aluminum titanate film on SiC substrate in Fig.5 (b) is smooth, homogeneous, compact and crack-free.

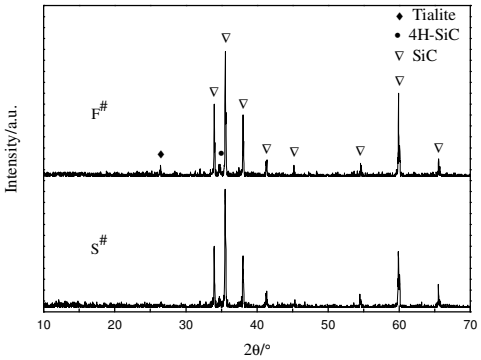


Fig.6 XRD Patterns of Silicon Carbide Substrate(S#) and Silicon Carbide Substrate Coated with Film(F#)

Fig. 6 shows the XRD of silicon carbide substrate and silicon carbide substrate coated with film. Both sample $S^{\#}$ and $F^{\#}$ contain strong diffraction peaks of SiC, however, $F^{\#}$ contains the first strong characteristic diffraction peaks of Al_2TiO_5, 2-theta angles of which is 26.62°, corresponding to (101) crystal plane of Al_2TiO_5.

Conclusions

In this paper, Al_2TiO_5 film was prepared via sol-gel method using ethyl acetoacetate and anhydrous citric acid as compound chelating agent, inorganic salt $AlCl_3{\cdot}6H_2O$ as aluminum source, and the crystallization water in $AlCl_3{\cdot}6H_2O$ as required water for sol-gel reaction. The result indicates that Al_2TiO_5 can be synthesized at low temperature by using compound chelating agent, rather than the single one. The formation of Al-O-Ti heterogeneous bond plays the key role in the low temperature synthesis of Al_2TiO_5. The Al_2TiO_5 film which is smooth, compact, homogeneous and crack-free could be coated on the SiC substract at 750 ^{o}C in air atmosphere.

Acknowledgements

The work was supported financially by National Natural Science Foundation of China (No. 51162013, 51362014); Science and Technology Supporting Plan Project of Jiangxi Province (NO.20111BBE50018); major discipline academic and technical leader training plan project of jiangxi province (NO.20113BCB22009).

References

[1] H.A.J. Thomas and R. Stevens, Aluminium titanate: a literature review. Part 2: engineering properties and thermal stability, Br. Ceram. Trans. 88 (1989) 184-190.

[2] T. Sun, N.R. Brown and J.J. Brown, U.S. Patent 5,407,479. (1995)

[3] S. Ananthakumar, M. Jayasankar and K.G.K.Warrier, Microstructure and high temperature deformation characteristics of sol-gel derived aluminium titanate–mullite composites, Mater. Chem. Phys. 117(2009) 359-364.

[4] P. Innocenzi, A. Martucci and L. Armelao, Sol-Gel Synthesis of β-Al_2TiO_5 Thin Films at Low Temperature, Chem. Mater. 12 (2000) 517-524

[5] D.H. Kuo and C.N. Shueh, Properties of aluminum titanate films prepared by chemical vapor deposition under different aluminum butoxide inputs, Thin Solid Films. 478 (2005) 109-115

[6] D.H. Kuo and K.H. Tzeng, Growth and properties of titania and aluminum titanate thin films obtained by r. f. magnetron sputtering, Thin Solid Films. 420-421 (2002) 497-502

[7] D.J. Taylor and D.P. Birnie, A Case Study in Striation Prevention by Targeted Formulation Adjustment: Aluminum Titanate Sol-Gel Coatings, Chem. Mater. 14 (2002) 1488-1492

[8] T. Sun, N.R. Brown and J.J. Brown, U.S. Patent 5,565,245. (1996)

[9] W.H. Jiang, G. Feng and J.M. Liu, Preparation of aluminum titanate film via nonhydrolytic sol-gel method and its fused salt corrosion resistance, J. Chin. Ceram. Soc. 38 (2010) 783-787(In Chinese)

[10] A. Vioux, Nonhydrolytic Sol–Gel Routes to Oxides, Chem. Mater. 11 (1997) 2292-2299.

[11] M.X. Jing, X.Q. Shen and Y.J. Shen, Preparation of nanometer nickel oxide by the citrate-gel process, J. Inorg. Mater. 19(2004) 289-294 (In Chinese)

[12] E. Kato, K. Daimon and J. Takahashi, Decomposition temperature of β-$A1_2TiO_5$, J. Am. Ceram. Soc. 63 (1980) 355-356

[13] I.H. Joe, A.K. Vasudevan and G. Aruldhas, FTIR as a tool to study high-temperature phase formation in sol-gel aluminium titanate. J. Solid State Chem. 131 (1997) 181-184.

[14] W.H. Jiang, H.Y. Wei, G. Feng, Y.H. Zhou and Y. Yu, Effect of oxygen donor alcohols no low temperature nonhydrolytic sol-gel synthesis of aluminum titanate, J. Chin. Ceram. Soc. 36 (2008). 11-16

[15] L.L. Thomson, Metal Alkoxides, New York, 1978

Advanced Materials Research Vol. 936 (2014) pp 243-247
© (2014) Trans Tech Publications, Switzerland
doi:10.4028/www.scientific.net/AMR.936.243

Multilayer Film through Inclusion Complexation

Chun-Yuan Liu[a*], Wei-In Lin[b]

Department of Chemical Engineering, I-Shou University, No.1, Sec. 1, Syuecheng Rd., Dashu District, Kaohsiung City 84001,Taiwan

[a]email: cyliu@isu.edu.tw.mail

Keywords: multilayer, inclusion chemistry, layer by layer

Abstract

In addition to traditional PEM and hydrogen-bonding methods, a polymer multilayer film could be formed via inclusion complexation,. We demonstrate this layer-by- layer method. Due to the steric hindrance of polymer segments, the thickness levels off and is generally much higher than those from PEM and hydrogen-bonding.

Introduction

Owing to its simplicity and potential applications, the layer-by-layer(LbL)[1-6] assembly, mainly relying on alternate deposition, has aroused intense interest. In addition, a wide variety of materials, including polymers, nanoparticles(NP's), functional molecules, and even living cells[7-8] can be applied via this alternate depositions technique to make multilayer films. Among all LbL techniques, assembly between oppositively charged species, polyelectrolyte multilayer(PEM), and assembly through hydrogen bonding[9-12] are the most popular LbL techniques. But under some circumstances, hydrogen bonding and ionizable monomeric units are not always available to form complexes, for example, when solution PH value is greater than a critical value, the hydrogen-bonded LbL multilayer film may disintegrate[13-15]. Consequently, some other methods are required, while very few researchers[16-18] address this problem.

With the inner hydrophobic and outer hydrophilic properties of their cavities, cyclodextrins(CD's)[19-23], the macrocyclic and water-soluble oligosaccharides, could form inclusion complexes with guest molecules selectively, and consequently, are widely used in many areas, particularly in drug research and biotechnologies. In this study, we demonstrate this unconventional method, LbL assembly through inclusion complex(IC), to form multilayer films and discuss its limitation.

To form the multilayer film, the host polymer and the guest polymer, poly(acrylic acid)(PAA) and poly(methacrylic acid)(PMA), were synthesized and labeled with ß –CD and adamantane group respectively. Then, a glass slide substrate with ß –CD labelled surface was immersed alternatively into the polymer solutions containing ß –CD and adamantane group respectively. After each immersion the substrate was rinsed thoroughly in pure water, to eliminate the excess of polymer in contact with the surface but only weakly bound to the film. The deposition cycle was repeated until the film thickness didn't increase anymore and thus, the thin multilayer film was obtained.

Furthermore, multilayer film could be formed on the interface between swelled host polymer surface and guest polymer/DMSO solution.

Experimental

Synthesis of Monomer Containing ß –CD

ß –CD was reacted with p-TsCl in dry pyridine overnight. The dry residue was dissolved in water and precipitated in acetone. The white crystal(ß–CD-6-O-TsCl) after twice recrystallization, was reacted with excess amount of ethylene diamine(EDA) for 4 hr at 60°C to obtain a white solid(EDA-6-ß–CD). Then, the ß–CD containing monomer was synthesized by reaction between EDA-6-ß–CD and glycidyl methacrylate with a small amount of 1, 4-dihydroxyl benzene as inhibitor in DMF for 8 hr. After reaction, the monomer((GMA-EDA-6-ß–CD) was obtained by precipitation the solution into acetone and vacuum drying.

Preparation of Host Polymers:

Free radical copolymerization of acrylic acid and GMA-EDA-6-ß–CD was performed to obtain PAA-based host polymer(PAA-co-GMA-EDA-EDA-6-ß-CD).

Preparation of Guest Polymers

PMA-based guest polymers(PMA-g-3AD) was prepared by labelling adamantane group onto the PMA chain. Then the guest polymer obtained was purified by reprecipitation and dialysis.

Surface Treatment of Glass Slide:

After washing, the quartz glass slides(2.5 cm x 2.5 cm x 0.1 cm) were treated with Piranha solution for 2 hr and subsequently reacted with 5% APTES/toluene solution for 12 hr. After washing with water, the slides were immersed in 5% aqueous solution of ß-CD-6-OTs for 24 hr. .

Multilayer Film Formation:

Two solutions were prepared by dissolving the PMA-based guest polymer(PMA-g-3AD) and the PAA-based host polymer (PAA-co-GMA-EDA-EDA-6-ß-CD) in water respectively, both containing 1.0 gram polymer in 100 ml water. The glass slide was immersed for 10 minutes into these two solutions alternately and after each immersion, the slide was rinsed in distilled water to remove the excess of polymer. The vacuum dried film thickness was measured by α-step and its weight was measured every five bilayers.

Results and Discusion

As shown in Table 1 was the characterization of polymers for multilayer film formation and both the contents of ß- CD and adamantane of polymers were determined by ^{1}H NMR.

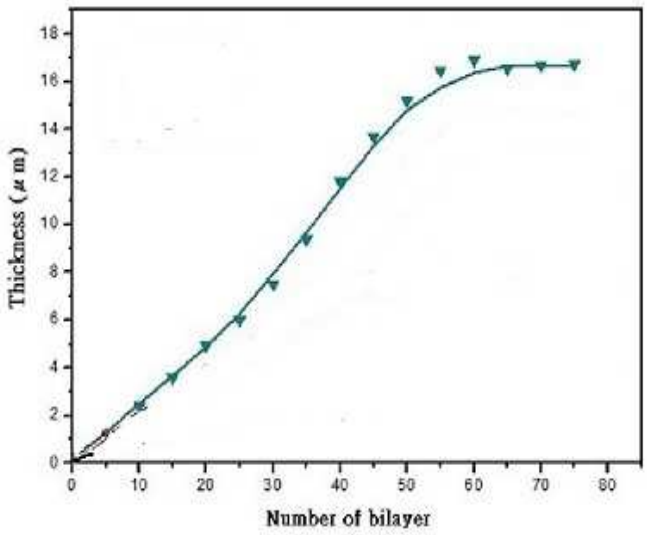
It is clearly depicted in Fig. 1, that both the film thickness and the surface mass increase layer by layer as the alternate deposition proceeds. Also performed was the blank test(fig. 2) under the same procedures by using homopolymers, PAA and PMA, instead of the host and guest polymers. In sharp contrast, no polymer film could be formed on substrate. And this also assists to verify the same conclusion. In light of the fact that the polymer chain is not extended as polyelectrolyte and it has low contents of interacting groups, it is reasonable that the thickness per

bilayer, is much larger than those from PEM. As the alternate depotision proceedes, the thickness and the surface mass of polymer film increases until it reaches their final values. We can conclude that the multilayer film formation is limited. The reason is that, due to the steric hindrance of polymer segments, the number of inclusion complexation every layer is gradually decreasing and reaches a critical value and below which, the new layer is no more stable and would be easily eliminated by water rinsing. As a result, the film thickness levels off. Future study would focus on the critical number of inclusion complexation between adjacent layers.

Table 1. Characterization of host and guest polymers

Polymers	**M.W.** **(x10^5)**	**β-CD content** **(mole %)**	**adamantane content** **(mole %)**
PAA-co-GMA-EDA-6-β-CD	**3.2**	**8.1**	**0**
PMA-g-3AD	**3.3**	**0**	**8.3**

(a)



(b)

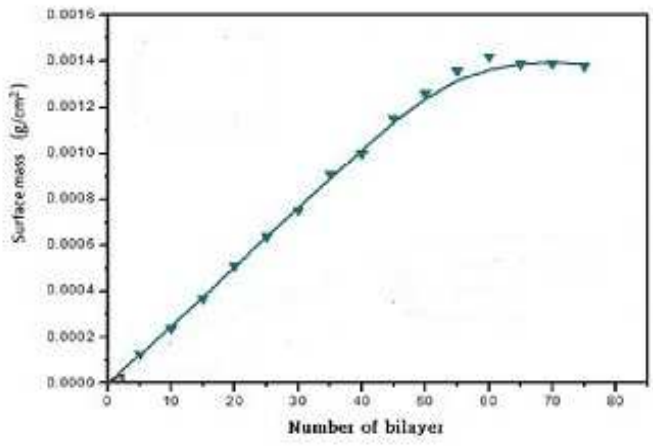


Fig. 1. Film thickness vs. number of bilayer(a); surface mass vs. number of bilayer(b)

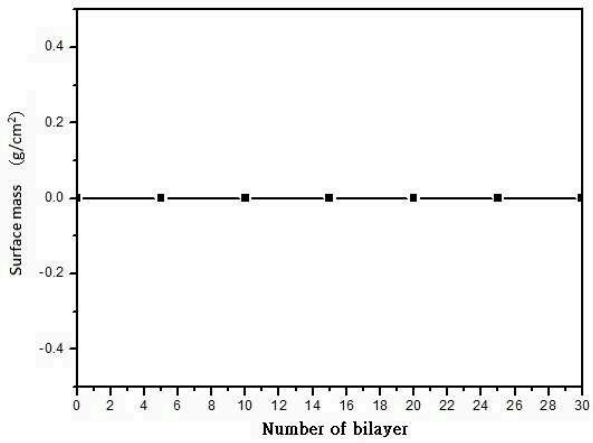


Fig. 2. Blank test with PMA and PAA, instead of host and guest polymers

Summary

Inclusion complexation could be employed to synthetic polymers to form multilayer films, in addition to traditional LbL methods. To form the multilayer film, two water-soluble polymers are synthesized and labeled with ß-CD and and adamantine group respectively. Despite its limitation to thickness, it offers a new alternative to fabricate synthetic multilayer films.

References

[1] L. Xu, D. Pritinski, A. Zhuk, L.Stooddart J. F. Ankner, and S. A. Sukhishvili, Macromolecules, **2012**, 45, 3892

[2] R. Suntivich, O. Shchepelina, I. Choi. And V.V. Tsukruk, Appl. Mater. & Interfaces, **2012**, 4, 3102

[3] G. Decher, Science,**1997,** 277, 1232

[4] G. Decher and J.B. Schlenoff (ed.), Multilayer Thin Films, 2_{nd} Ed., Wiley-VCH **2012**

[5] J. F. Quinn A.P. R. Johnston, G. K. Such, A. N. Zelin, and F. Caruso, Chem. Soc. Rev., **2007,** 36, 707

[6] Y. Jang, B. Akgun, H. Kim, S. Satija and K. Char, Macromolecules, **2012**, 45, 3542

[7] L. Grossin, D. Cortial, B. Saulnier, O. Felix, A.Chassepot, G. Decher, P. Netter, P. Schaaf, P. Gillet, D. Mainard, J.-C. Voegel, and N. Benkirane-Jesel, Adv. Mater., **2009**, 21, 650

[8] M. Matsusaki, K. Kadowaki, Y. Nakahara, and M. Akashi, Angew. Chem.Int. Ed., **2007,** 46, 4689

[9] W. B. Stockton and M. F. Rubner, Macromolecules, **1997**, 30, 2717

[10] L. Wang, Z. Wang, X. Zhang, and J.Shen, Macromol. Rapid Commun., **1997**, 18, 509

[11] L.Wang, X. Fu, Z. Wang, Y. Fan, and X. Zhang, Langmuir, **1999,** 15, 1360

[12] E. Kharlampieva and S.A.Sukhishvilli, J. Macromol. Sci., Part C, Polymer Rev., **2006**, 46, 377

[13] S. A.Sukhishvil. and S. J. Granick, J. Am. Chem. Soc., **2000,** 122, 9550

[14] S. A. Sukhishvil, Macromolecules, **2002**, 35, 301

[15] Z. Wang, Z. Feng and G. Gao, Chem. Mater., **2008**, 20, 4194

[16] Van der Heyden, M. Wilczewski, P. Labbe, and R. Auzely, Chem. Commun., 2006, 36,3220-3222

[17] X. Y. Ling, I. Y. Phang, W. Maijenburg, H. Schonherr, D. N. Reinhoudt, G. J. Vancso, and J. Huskens, Angew. Chem.Int. Edit., **2009,** 46,983

[18] X. Y. Ling, and J. Huskens, Chem. Commun., **2009**, 37, 5521

[19] C. Kretschmann. Steffens, and H. Ritter, Angew. Chemie. Int. Ed., **2007**, 46, 2708

[20] F. van de Manakker, T. Vermonden, C. F. Van Nostrum, and, W. E. Hennink, Biomacromolecules, **2009,** 10, 3157

[21] D. Tauva, A. Hashidxume, Y. Okumura, and A. Harada, Macromolecules, **2008**, 41, 3640

[22] A. Tomatsu, A. Hashidzume, and A.Harada, J. Am. Chem. Soc., **2000,** 128, 2226-2227

[23] Y. –L. Zhao and J. F. Stoddart, Langmuir, **2009**, 25, 8442

Advanced Materials Research Vol. 936 (2014) pp 248-254
© (2014) Trans Tech Publications, Switzerland
doi:10.4028/www.scientific.net/AMR.936.248

Preparation and Characterization of Bipolar Membranes Modified by Adding Multi-carboxylic Metallophthalocyanine Derivatives into the Cation Layer

Lu Min[1,a], Hu Yanyu[2,b], Chen Riyao[3,c *]

[1]College of Chemistry and Chemical Engineering, Fujian Normal University, Fuzhou 350007, People's Republic of China

[2]Department of Arts, Ningde Normal University, Ningde 352000, People's Republic of China

[3]College of Environmental Science and Engineering, Fujian Normal University, Fuzhou 350007, People's Republic of China

[a] luminjining@163.com, [b]285994926@qq.com, [c] rychen@fjnu.edu.cn

Keywords: bipolar membranes, multi-carboxylic metallophthalocyanine, modification

Abstract: The multi-carboxylic metallophthalocyanine derivatives were added into carboxymethyl cellulose cation layer to prepare the modified carboxymethyl cellulose/chitosan bipolar membranes (CMC/CS BPMs), which were characterized using electric universal testing machine, contact angle measurer and so on. The results showed that the mechanical properties were increased after modification. Moreover, the ion exchange capacity, and the hydrophilicity of the modified CMC membrane dramatically rose. As the catalytic centers, the metallophthalocyanine derivatives sped up water splitting, decreased the membrane impedance and cell voltage. In comparison with the BPMs modified by mononuclear metallophthalocyanine derivatives, the catalytic ability for water splitting of the binuclear metallophthalocyanine derivatives (especially with different central metal ions) was enhanced. At the current density of 60 $mA \cdot cm^{-2}$, the cell voltage of the BPM modified by $FeCoPc_2(COOH)_{12}$ was only 5.3V.

Introduction

At present, more and more attention has been paid to modification of cation layer or anion layer, and introduction of catalytic interlayer to promote water splitting [1]. Higher water splitting efficiency and lower membrane impedance are undoubtedly expected.

Phthalocyanine and its derivatives have aroused great interest as their distinctive structures and excellent properties such as good electrocatalytic characteristic，electrochemical behaviors [2] and high charge transfer efficiency[3,4]， which have been widely applied in the field of photoelectrochemistry [5], catalysis [6] and so on. The planar binuclear phthalocyanines have quite larger π electron conjugated system than mononuclear phthalocyanine, and exhibit high-electron storage and transfer abilities [7] .

In this paper, as a further research part of our previous study on SA/CS BPMs modified by CuTsPc and CuTAPc (here, SA: sodium alginate; CS: chitosan; CuTsPc: copper phthalocyanine tetrasulfonic acid; CuTAPc: copper tetraaminophthalocyanine)[8], the preparation and characterization of CMC/CS BPMs modified by mononuclear or planar binuclear metallophthalocyanine derivatives with carboxyl groups have been studied.

Experimental

Materials

Carboxymethyl cellulose, chitosan with an N-deacetylation degree of 90% and glutaraldehyde (25% by volume in water) were purchased from Guoyao Chemicals Co, Ltd. $FeCl_3$, $CoCl_2$ and other chemicals were analytical grade.

Preparation of BPMs

Preparation of multi-carboxylic metallophthalocyanine derivatives

The preparation method of iron(Ⅲ) octocarboxylphthalocyanine($FePc(COOH)_8$), planar binuclear iron(Ⅲ) phthalocyanine ($Fe_2Pc_2(COOH)_{12}$), planar binuclear cobalt(Ⅱ) phthalocyanine($Co_2Pc_2(COOH)_{12}$) and planar binuclear iron(Ⅲ)-cobalt(Ⅱ) phthalocyanine($FeCoPc_2(COOH)_{12}$) were detailedly described in the literature[9].

Preparation of the BPM modified by multi-carboxylic metallophthalocyanine derivatives

The multi-carboxylic metallophthalocyanine derivatives-THF solution was added into the CMC aqueous solution (3 wt.%), and then the modified CMC aqueous solution was poured onto a glass plate and dried at room temperature. The membrane was cross-linked with $CrCl_3$ solution (9 wt.%) for 30 min and dried to form the cation exchange layer (area 50 cm^2).

The CS solution was made by mixing 100 mL chitosan solution (3 wt.%) and 3 mL glutaraldehyde (0.25% by volume in water) and stirred for 30 min. The solution was poured over the prepared cation exchange layer and dried to form the modified BPM.

The $-COO^-$ groups of the multi-carboxylic metallophthalocyanine derivatives were combined with the $-COO^-$ groups of CMC by means of Cr^{3+} to form a metal chelate polymer with a net structure(*Figure 1*). At the same time, hydrogen bonds formed between the −OH groups of CMC and the $-COO^-$ groups of the multi-carboxylic metallophthalocyanine derivatives. Both of the above two factors helped to improve the dimensional stabilities of BPMs and structure stabilities of the interlayers.

Furthermore, in the CS anion membrane, the aldehyde groups of glutaraldehyde were combined with the $-NH_2$ groups of CS, which helped to form net structure in the membrane layer to improve the mechanical properties of the BPM. (*Figure 2*)

Preparation of Cr-CMC/CS BPM

In comparison with the previously prepared BPMs, the Cr-CMC/CS BPM was prepared. The preparation method was similar to the above method, except that multi-carboxylic metallophthalocyanine derivatives were not added into the CMC aqueous solution**.**

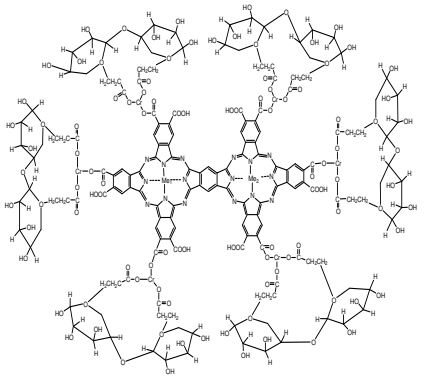


Figure 1

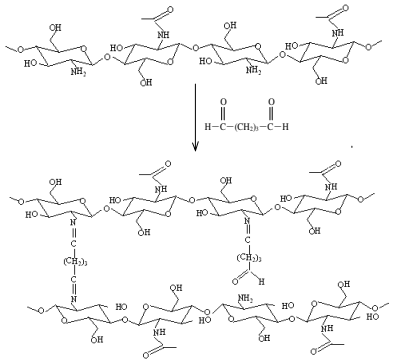


Figure 2

Figure 1 CMC modified by planar binuclear phthalocyanines and Cr^{3+} to form a metal chelate polymer with a net structure

Figure 2 CS modified by glutaraldehyde to form a net structure

Characterization of BPMs

Determination of Hydrophilicity of Cation Exchange Membrane

The contact angles of the modified CMC membranes were determined using the contact angle measurer (SL 200B, S&L (Shanghai) Inc. in China).

Determination of Ion Exchange Capacity of Cation Exchange Membrane

The determination method of the ion exchange capacity was clearly described in the literatures[10].

Determination of Mechanical Properties of BPM

The determination method of the mechanical properties was clearly described in the literatures[11].

Measurement of the Current-Voltage Curve (J-V curve) of BPM-equipped cell

The *J-V* curve of the BPM-equipped cell was measured using a direct current source (DF1720SB5A, Ningbo Zhongce Electronics Co., Ltd in China). The determination method of the current-voltage curve was clearly described in the literatures[12].

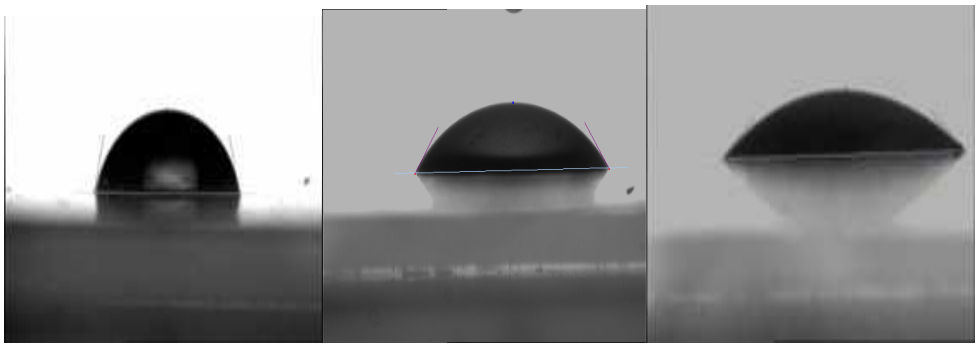
Measurement of the AC impedance spectroscopy of BPM

An electrochemical workstation (CHI660C, Shanghai Chenhua Instrument Company in China) was used to measure the AC impedance spectroscopies of the BPMs. The determination method of the AC impedance spectroscopy was clearly described in the literatures[13].

Results and discussion

The hydrophilicity of cation exchange membrane

After the modification by $FePc(COOH)_8$ and $FeCoPc_2(COOH)_{12}$, the contact angles of the CMC membrane decreased from 75.67° (*Figure 3-a*) to 54.54° (*Figure 3-b*) and 34.52° (*Figure 3-c*), respectively. Because the hydrogen bonds formed between water molecules and a large number of $–COO^-$ groups of the multi-carboxylic metallophthalocyanine derivatives, which led to the improvement in hydrophilicity of the modified CMC membrane. The good hydrophilicity could help the water in the interlayer to be supplied in time from outside of the BPM to avoid the formation of depletion layer[14].



(a) (b) (c)

Figure 3 The contact angles of the different cation exchange membranes

(a) Cr-CMC membrane (b)$FePc(COOH)_8$-CMC membrane

(c) $FeCoPc_2(COOH)_{12}$-CMC membrane

The Ion exchange capacities of cation exchange membranes

The ion exchange capacities for the different cation exchange membranes were showed in *Figure 4*. The ion exchange capacity for the unmodified Cr-CMC membrane was 14.63 $mmol \cdot g^{-1}$, and the ion exchange capacities of the modified CMC membranes dramatically rose due to a large number of $–COO^-$ groups in the multi-carboxylic metallophthalocyanine derivatives.

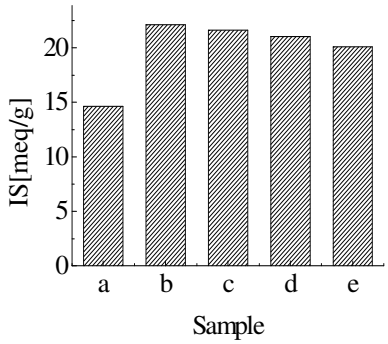


Figure 4 The ion exchange capacities of the different cation exchange membranes
(a) Cr-CMC membrane (b) $FePc(COOH)_8$-CMC membrane
(c) $Fe_2Pc_2(COOH)_{12}$-CMC membrane (d) $FeCoPc_2(COOH)_{12}$-CMC membrane
(e) $Co_2Pc_2(COOH)_{12}$-CMC membrane

The Mechanical properties of BPMs

The mechanical properties of the different BPMs were listed in *Table 1*. Because the $-COO^-$ groups of the multi-carboxylic metallophthalocyanine derivatives were combined with the $-COO^-$ groups of CMC by means of Cr^{3+} to form a metal chelate polymer with a net structure and the metallophthalocyanine derivatives were rigid molecules, the tensile strength, maximum load and Young's modulus of the modified BPMs were evidently increased, and the mechanical properties were noticeably enhanced. On the other hand, with the improvement in the rigidity of the BPMs, the molecule chains were uneasy to be stretched, and the elongation at break was declined in a way.

Table 1 Mechanics capabilities of the different BPMs

BPM	Maximum load [N]	Tensile strength [MPa]	Elongation at break [%]	Young's modulus [MPa]
Cr-CMC/CS	23.67	10.33	40.33	200.87
$FePc(COOH)_4$-CMC/CS	29.81	23.29	27.11	214.64
$FePc(COOH)_8$-CMC/CS	50.78	32.55	25.68	248.63
$FeCoPc_2(COOH)_{12}$-CMC/CS	36.88	23.95	18.76	213.11
$Co_2Pc_2(COOH)_{12}$-CMC/CS	43.78	28.43	24.62	224.58
$Fe_2Pc_2(COOH)_{12}$-CMC/CS	44.07	30.61	23.08	243.85

J-V curves of BPM-equipped cells

The *J-V* curves of the BPM-equipped cells were shown in *Figure 5*. The cell voltages of the BPM-equipped cells got larger with the increase of the current density. After modification using multi-carboxylic metallo-phthalocyanine derivatives, the cell voltages and *IR* drops of BPMs reduced obviously. Moreover, the *IR* drops for the modified BPMs changed gently with the increase of current density, due to a high charge density area formed in the interlayer of a BPM after

modification, which sped up water splitting, promoted the efficiency of water splitting and lowered the membrane impedance.

At the same current density, the cell voltages of the BPMs modified with binuclear metallophthalocyanine derivatives (especially with different central metal ions) were lower than that modified with mononuclear metallophthalocyanine derivatives. It was because that the charge density of the former was more concentrated, and their catalytic ability for water splitting was stronger than that of the latter. At the current density of 60 $mA \cdot cm^{-2}$, the cell voltage of the BPM modified by $FeCoPc_2(COOH)_{12}$ was only 5.3 V.

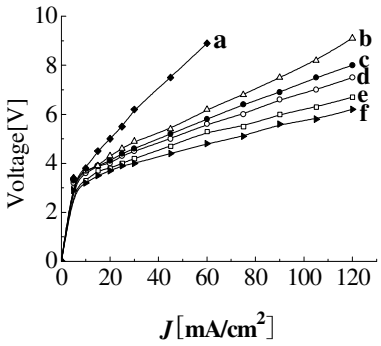


Figure 5 J-V curves of BPMs-equipped cells

(a) Cr-CMC/CS BPM (b) $FePc(COOH)_8$-CMC/CS BPM

(c) $Co_2Pc_2(COOH)_{12}$-CMC/CS BPM (d) $Fe_2Pc_2(COOH)_{12}$-CMC/CS BPM

(e) $FeCoPc_2(COOH)_{12}$-CMC/CS BPM (f) no membrane

AC impedances of BPMs

The *AC* impedance spectroscopies of the BPMs were shown in *Figure 6*. The illustration was the equivalent electrical circuit of AC impedances for the BPMs. C_d was the capacitance impedance of the interlayer, R_r was the impedance of membrane, R_l was the impedance of bulk solution. In *Figure 6*, the intersection point of the high-frequency semicircle and real aris indicated the impedance value of the membrane. The membrane impedances of the BPMs were as follows: Cr-CMC/CS BPM > $FePc(COOH)_8$-CMC/CS BPM > $Co_2Pc_2(COOH)_{12}$-CMC/CS BPM > $Fe_2Pc_2(COOH)_{12}$-CMC/CS BPM > $FeCoPc_2$- $(COOH)_{12}$-CMC/CS BPM, which corresponded to that of the cell voltages of the BPM-equipped cells at the same current density, shown in *Figure 6*.

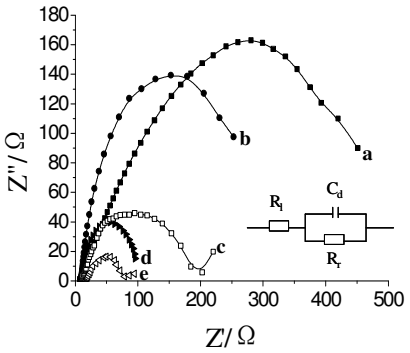


Figure 6 *AC* impedances of the different BPMs

(a)Cr-CMC/CS BPM (b)$FePc(COOH)_8$-CMC/CS BPM

(c)$Co_2Pc_2(COOH)_{12}$-CMC/CS BPM (d)$Fe_2Pc_2(COOH)_{12}$-CMC/CS BPM

(e) $FeCoPc_2(COOH)_{12}$-CMC/CS BPM

Conclusion

The multi-carboxylic metallophthalocyanine derivatives were added into CMC cation layer to prepare the modified CMC/CS BPMs, which were characterized using electric universal testing machine, contact angle measurer and so on.

The $-COO^-$groups of the multi-carboxylic metallophthalocyanine derivatives were combined with the $-COO^-$ groups of CMC by means of Cr^{3+} to form a net structure, which lowered the swelling degree of the BPMs, enhanced the dimensional stabilities, mechanical properties of the BPMs and the structure stabilities of the interlayer.

Moreover, the ion exchange capacities, and the hydrophilicity of the modified CMC membranes dramatically rose. After modification, high charge density area formed in the interlayer, which sped up water splitting, and decreased the membrane impedances and cell voltages. The charge density of the catalytic centers of the BPMs modified by binuclear metallophthalocyanine derivatives(especially with different central metal ions) was more concentrated than that modified by mononuclear metallophthalocyanine derivatives. Therefore, the catalytic ability for water splitting of the former was stronger than that of the latter. At the current density of 60 $mA \cdot cm^{-2}$, the cell voltage of the BPM modified by $FeCoPc_2(COOH)_{12}$ was only 5.3 V.

References

[1] J. H. Hao, C. X. Chen, L. Li, et al, Preparation of Bipolar Membranes (I), J. Appl. Polym. Sci. 80(2001) 1658-1663.

[2] C. Coutanceau, A. Rakotondrainibe, P. Crouigneau, et al, Spectroscopic investigations of polymer-modified electrodes containing cobalt phthalocyanine: application to the study of oxygen reduction at such electrodes, J. Electroanal. Chem. 386 (1995) 173-182.

[3] K. Mehmet, N. U. Meryem, S. Yara, K. Atıf, et al, Synthesis, characterization and electrochemistry of novel differently octasubstituted phthalocyanines, Polyhedron. 21 (3)(2002) 255-263.

[4] Y. J. Shen, Synthesis and Application of Phthalocyanine, Chemical Industry Press, Beijing, 2002.

[5] D. Schlettwein, M. Kaneko, A. Yamada, et al, Light-Induced Dioxygen Reduction at Thin Fllm Electrodes of Various Porphyrins, J. Phys. Chem. 95 (1991) 1748-1755.

[6] N. Kobayashi, P. Janda, A. B. P. Lever, Cathodic reduction of oxygen and hydrogen peroxide at cobalt and iron crowned phthalocyanines adsorbed on highly oriented pyrolytic graphite electrodes, Inorg. Chem.31 (25)(1992) 5172–5177.

[7] Zhang Y J, Li Y S, Liu Q S, et al, Molecular rectifying behaviors of a planar binuclear phthalocyanine studied by scanning tunneling microscopy, Synt. Met.128 (2002) 43-46.

[8] Ri-Yao Chen, Zhen Chen, Xi Zheng, et al, Preparation and characterization of mSA/mCS bipolar membranes modified by CuTsPc and CuTAPc, J. Member Sci. 355 (2010) 1-6.

[9] David R, Boston, John C, et al, Phthalocyanine derivatives from 1,2,4,5-Tetracyanobenzene or pyromellitic dianhydride and metal salts, Inor. Chem. 11 (7)(1972) 1578-1583.

[10] Yang J. M., Su W. Y., Leu T. L., et al. Evaluation of chitosan/PVA blended hydrogel membranes, J. Member Sci. 236 (1/2)(2004) 39-51.

[11] Zhou TJ, Hu YY, Chen RY, et al. Preparation and Characterization of bipolar membranes modified by photocatalyst nano-ZnO and nano-CeO2, Applied Surface Science, 258(8)(2012) 4023-4027.

[12] Chen Ri-yao, Chen Zhen, Zheng Xi, et al, Preparation and Characterization of CuPc(COOH)8-SA/CuTAPc-CS Bipolar Membrane, Chem. J Chinese U. 3 (2010) 530-536.
[13] Chen R Y, Chen Z, Zheng X, et al. Preparation and characterization of mSA/mCS bipolar membranes modified by CuTsPc and CuTAPc, J. Member Sci, 355(1)(2010) 1-6.
[14] Strathmann, J. Krol, H. J. Rapp, et al, Limiting current density and water dissociation in bipolar membranes, J. Member Sci.125 (1997) 123-142.

Advanced Materials Research Vol. 936 (2014) pp 255-258
© (2014) Trans Tech Publications, Switzerland
doi:10.4028/www.scientific.net/AMR.936.255

Highly Strained Silicon Nitride Thin Film Deposited by PECVD with Double Frequencies in Strained Silicon Technologies

Bin Shu *, Jingming Chen, Heming Zhang, Feng Zhu, Puli Quan, Jiangyuan Gu, Rongxi Xuan, Huiyong Hu, Jianjun Song

[1] School of Microelectronics, Xidian University, Key Laboratory of Wide Band-Gap Semiconductor Materials and Devices, Xi'an ,710071, China

binshu@xidian.edu.cn

Keywords: silicon nitride, compressive stress, tensile stress, PECVD, strained Silicon

Abstract: The mechanism of high stress in silicon nitride thin film is studied systematically in this paper. The effects of the various process parameters on the stress in silicon nitride thin film deposited by PECVD are analyzed and discussed. The silicon nitride thin film with high compressive and tensile stress has been deposited on the optimized process parameters and the compressive and tensile stress are up to -1.38GPa and 866MPa, respectively. Finally, the method of further improving the stress in silicon nitride thin film is presented.

Introduction

Strained silicon technology is the new trend in the future silicon process, which can be used to enhance the hole and electron mobility in PMOS and NMOS, not only the performance of transistors is improved, but also a lot of challenge due to the decreasing device scale can be settled [1]-[4]. There are many ways to introduce the stress to silicon. With the development of this technology, using high stress silicon nitride thin film to realize stress introduction has been a main measure in advanced Si CMOS, considering some aspects, such as cost and performance, etc., which means silicon nitride thin film is not only used as passivation layer in traditional process but also used as stress material to provide local stress. There are great deals of good qualities in silicon nitride thin film, such as good physical and chemical properties, high dielectric constant, reliable thermal endurance performance, resist performance and excellent mechanical performance. The compressive stress and the tensile stress in silicon nitride thin film deposited in current silicon nitride thin film deposition methods, such as reactive sputtering and plasma enhanced CVD (PECVD). The formation of stress in silicon nitride thin film is due to transformation from atom planar grid structure to low-energy silicon-centered cubic structure, and the atomic numbers, the magnitude and the covalent bonds of silicon atom and nitrogen in silicon nitride thin film are different, which result in the stress in silicon nitride. Silicon nitride thin film will split when it is in extra tensile stress, but, drape and flake when it is in extra compressive stress [5-8]. The mechanism of the stress formation in silicon nitride is depicted in this paper, and on the basis of this mechanism, the high compressive and tensile stress silicon nitride thin film which can be used in strained silicon technology is fabricated.

Highly Strained Silicon Nitride Thin Film

The stress in silicon nitride thin film deposited by SiH_4, ammonia and nitrogen is intrinsic tensile, but the stress in silicon nitride thin film is compressive due to the high energy particle bombardment in the low frequency power source, when both high and low frequencies are all used simultaneously.

The distortion of thin film structure due to atoms or ions combination and renewed distribution because of high energy particle can result in the compressive stress in silicon nitride thin film. And the atoms or ions combination and renewed distribution will make the thin film compact. To obtain higher and available silicon nitride thin film for actual manufacture, the process parameters, including the low frequency and high frequency ratio (LF/HF ratio), the SiH_4 and ammonia ratio (SiH_4/NH_3), temperature and pressure, etc. have been optimized to improve the effect of particle bombardment. Fourier Transform Infrared Spectrometry (FTIR) shows that the higher the hydrogen concentration is, the bigger the compressive stress is. According to the current theory, hydrogen and subsequently renewed distribution lead to the compact thin film and the stress. On the other hand, the distribution of atoms is compact and the extrusion effect of atoms is increasing because of a great deal of hydrogen atom, which can also produce the further compressive stress in silicon nitride thin film [4]. Consequently, the mechanism of the formation of the compressive stress in silicon nitride thin film is that the energy transformation makes the atoms renewed distributed more compactly because of the high energy particle bombardment in low frequency power source in microcosmic structure in reaction course, which results in the higher atoms concentration and extrusion effect, and the eventually macroscopic compressive stress in silicon nitride thin film. Similarly, macroscopic tensile stress can be obtained in silicon nitride thin film in high frequency power source.

Experiments and Result Analysis

PECVD is the integrated technology which is combined with radio frequency glow discharge physical course and chemical reaction. High energy electron and active ion (Plasma) is inspired by high frequency electric field of radio frequency source in the vacuum chamber in which there are a certain concentration of SiH_4, ammonia and nitrogen at appropriate pressure. Because of the effective collision of high energy electrons, the relative linked bonds are split, and the atoms will be renewed combined and deposited on the substrate, by which the chemical reaction course takes place and at relatively low temperature and silicon nitride thin film is deposited. To obtain the high compressive stress silicon nitride thin film, 100K~300KHz low frequency power source is used in radio frequency power source, temperature is in 200~400℃, pressure is in 300~500mτ, the SiH_4/NH_3 ratio is in 2~4, and the deposition time is in 4~5 minutes. The compressively and tensely strained silicon nitride thin film has been deposited on 4 inch silicon wafer at different process parameters, such as temperature, pressure, frequency, SiH_4/NH_3 ratio and time, etc., by PECVD. The best compressive stress results are shown in Fig.1 and Fig.2, and the compressive stress is up to -1.38GPa. In addition, the experiments show that annealing in nitrogen is helpful to higher tensile stress in silicon nitride thin film, which is mainly due to the combination and release of hydrogen atom in silicon nitride formation. The best tensile stress results are shown in Fig.3 and Fig.4, and the tensile stress is up to 866MPa. The stress in silicon nitride thin film is determined by the process parameters from the experiment results. Although the original stress are different from each other because of the different initial conditions, the stress increment in subsequent course is determined by the process parameters, such as the SiH_4/NH_3 ratio, the power and frequency in power source, under the initial conditions. Consequently, the process parameters will play a decisive role in the stress magnitude.

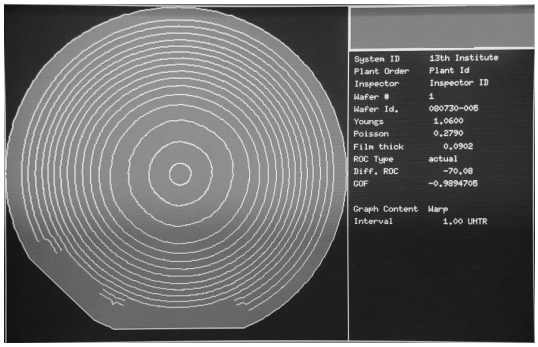


Fig.1. Compressive stress (platform)

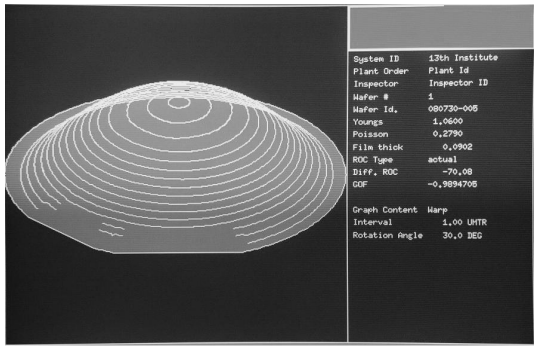


Fig.2. Compressive stress (30°rotation angle)

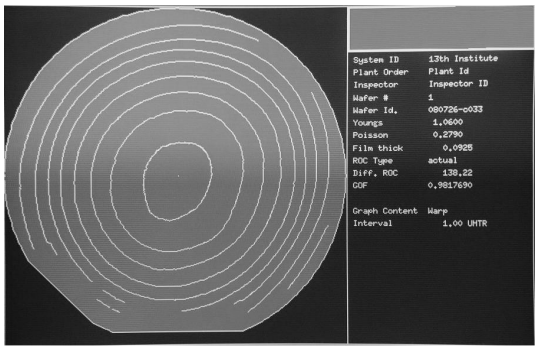


Fig.3. Tensile stress (platform)

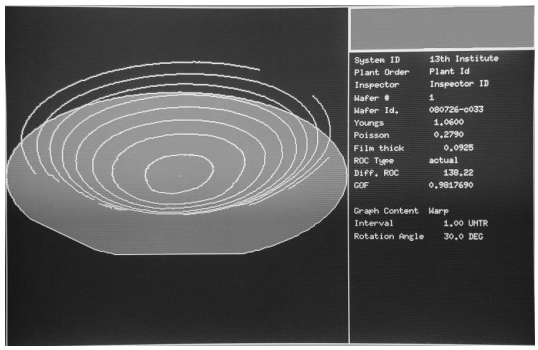


Fig.4. Tensile stress (30°rotation angle)

On the basis of the analysis to the effects of process parameters on stress in silicon nitride, we can draw the conclusion that the primary stable Si-N bond length can change in the diversified bond split and renewed combination under the certain conditions, which results in Si-N bond in excited state in the chain structure is much weaker than that in the circle structure. That is to say, under the same condition, the Si-N bond in the chain structure is easier to split than in circle structure, which means the Si-N bond in the circle structure is more stable. It is obvious that the atoms are compact, the bonds are not easy to split, and the physical and chemical properties are more stable in the circle structure, comparing these two structures. So we can infer that the chemical properties are stable, the stress is high, and the Si-N bond is not easy to split in the compact thin film. In general, the Si-N bond energy has great effect on the stress in the silicon nitride thin film, and the lower the bond energy is, the lower the stress is.

On the other hand, there are great effects of impurity on the stress in silicon nitride thin film deposited by PECVD, according to the other relative references and recent works. In the mean time, the bond length can affect the stress in silicon nitride thin film. So we can foresee that the integral stress will increase, if the ingredients are adjusted in the fabrication of silicon nitride thin film. For example, SiH_4 is replaced by SiH_3-CH_3, which adds the C-N bond in the reaction course, and the length of C-N bond is longer than that of Si-N bond, which can result in the compact atom arrangement. We obtained several sets of reasonable and optimized data from the analysis to the relative theory and the experiment results. We can obtain the higher stress thin film by not only the optimized process parameter but also the subsequent process, such as annealing, ultraviolet assisted thermal processing, etc., to improve the performance of Si CMOS devices and circuits.

Summary

The mechanism of the high stress in silicon nitride thin film is studied in this paper. The effects of the various process parameters on the stress in silicon nitride thin film by PECVD are analyzed

and discussed. The highly compressive and tensile stress in silicon nitride thin film has been obtained on the optimized process parameters, and the compressive and tensile stress are up to -1.38GPa and 866MPa, respectively. Finally, the method of further improving the stress in silicon nitride thin film is presented. The highly strained silicon nitride thin film deposited by PECVD in this paper may be used in the local strained silicon technology to improve the performance of Si CMOS devices and circuits.

References

[1] S. E. Thompson, M. Armstrong, C. Auth, A logic nanotechnology featuring strained-silicon, IEEE Electron Device Letters, 25(2004), 191-196.
[2] S. L. Wu, Y. M. Lin and S. J. Chang, Enhanced CMOS Performances Using Substrate Strained SiGe and Mechanical Strained Si Technology, IEEE Electron Device Letters, 27(2006), 46-49.
[3] R. Arghavani, L. Xia and H. M'Saad, A Reliable and Manufacturable Method to Induce a Stress of >1 GPa on a P-Channel MOSFET in High Volume Manufacturing, IEEE Electron Device Letters, 27(2006), 114-118.
[4] S. E. Thompson, M. Armstrong and C. Auth, A 90-nm Logic Technology Featuring Strained-silicon, IEEE Transactions on Electrons Devices, 51(2004), 1790-1796.
[5] J. Wang, Strained silicon Technology expanding the Moore's Law, Microelectronics. 38(2008), 50-53.
[6] C. Yu, Study of PECVD SiXNY Stress, Technology of Microelectronics, 23(2006), 19-25.
[7] Y. Yu and Y. Chen, Experimental Study of SiN Membrane, Vacuum Science and Technology, 21(2001), 51-56.
[8] Y. Chen, Q. Hao and C. Liu, Effect of Rapid Thermal Processing on PECVD Silicon Nitride Membrane Performance, Photoelectronics Laser. 19(2008), 1357-1362.

Advanced Materials Research Vol. 936 (2014) pp 259-263
© (2014) Trans Tech Publications, Switzerland
doi:10.4028/www.scientific.net/AMR.936.259

Layer Formation of SAPO-34 Zeotype Material by EPD Seeding Method Followed by Hydrothermal Secondary Growth

S.M. Hosseini Davarani[1,a], Sh. Fatemi[2,b], Z. Jabbari[3,c]

[1]School of Chemical Engineering, College of Engineering, University of Tehran,Tehran, Iran

[2]School of Chemical Engineering, College of Engineering, University of Tehran,Tehran, Iran

[3]School of Chemical Engineering, College of Engineering, University of Tehran,Tehran, Iran

[a]Sm.hosseini.d@ut.ac.ir, [b]shfatemi@ut.ac.ir, [c] zjabbari@gmail.com

Keywords: SAPO-34 Zeotype, Electrophoretic Deposition, Fine Layer Formation, Hydrothermal Crystallization

Abstract: Fine layer growth of SAPO-34 crystals on the steel and α-alumina substrates has been investigated by electrophoretic deposition (EPD) followed by secondary growth. At first step, two sizes of SAPO-34 seeds with different composition of precursor solution were synthesized. Thereafter the best quality of the seeds in term of crystal size was selected for seeding operation. All seeded samples were prepared by electrophoretic deposition (EPD) with 0.4 wt% powder in solution, voltage of 4.5 V and deposition time of 90 min, followed by the secondary growth in a Teflon lined autoclave for crystallization at 473K for 24 hr.

The prepared fine seeds characterized by XRD and SEM analysis. Also the substrates were broken and characterized by SEM methods in terms of surface coverage and mean size of the particles. The results revealed a better quality of the coated film on the surface of steel rather than α-alumina on the base of homogeneity and crystal size.

Introduction

Within the two previous decades, application of zeolite membranes for separation purposes has been widely developed. The significant mechanical resistance and suitable performance in different and even difficult conditions for temperature and pressure, is the most important specifications of these membranes [1]. Up until now, various types of zeolites with different pore size such as MFI, DDR, FAU have been used for the membrane production on different types of substrates [2]. Among various kinds of zeolites, the zeolite-like SAPO-34 having chabazite type framework with pore size of 0.038 nm, would be suitable for separating mixtures of light gases [3].

The in situ hydrothermal synthesis is the most frequently used approach for fabrication of zeolite membrane, in which the substrate is immersed into the precursor solution, and then the membrane is formed by direct crystallization [4]. However, it is difficult to fabricate high quality and defect free zeolite membrane by this method. Coating the zeolite seed on the support surface before hydrothermal synthesis has recently been developed for the preparation of zeolite membranes. This method is called secondary growth, which it's key benefit is greater control over the nucleation step and the zeolitic layer thickness by separating the crystal nucleation and growth with a shortened crystallization time [1,5].

The quality of the final membrane layer, depends entirely on the quality of the zeolite seeds [5]. Reduction in zeolite crystal size, is an important issue in recent years because the properties of the materials are greatly influenced by the change in zeolite crystal dimensions [6].

Different methods have been proposed for ceramic's seeding. Jabbari et al [7] investigated three different seeding methods including rubbing, dip-coating and EPD performed on tubular α-alumina

supports followed by one time hydrothermal crystallization, and concluded that suitable layer of SAPO-34 was formed by rubbing or EPD method of seeding.

Electrophoretic deposition (EPD) is one of the colloidal processes in ceramic production and has advantages of the short time formation, requires simple apparatus and it is less restricted by the shape of substrate [8].

In the current contribution, the comparative study between two kinds of substrates for seeding by fine SAPO-34 seeds via EPD method in constant voltage and seed concentration in aqueous solution has performed. The size of the seeds are the most influential parameter in layer formation during secondary growth and in this work two different sizes of seeds are investigated.

Experimental

Two kinds of SAPO-34 powders with stoicheometric formula of 1Al2O3:0.5SiO2:1P2O5:100H2O:mTEAOH:n Morpholin in reaction mixture were prepared for seeding operation. Aluminum isopropoxide (white powder, 98 wt%, MERK) and phosphoric acid (85 wt%, MERK) have been used as alumina and phosphorus source, respectively. The synthesis condition of making precursor solutions are shown in Table 1, for two different sizes. Aluminum isopropoxide was added to solution of H3PO4 and water to form a cream-like homogenous gel. Then, templates and silica source was added to this solution. The prepared synthesis gels were poured in Teflon lined steel autoclave and the crystallization step was performed at 473 K for 24 hr. After hydrothermal crystallization the content was washed with distilled water, centrifuged and dried at 373 K for 3 hr.

The mean particle size of each sample are calculated from SEM images from Fig. 1 and they are shown in Table 1. The results shows that using TEOS as silica source makes formation small particles even if we use a lower concentration of TEAOH.

TABLE 1: SPECIFICATION OF TWO KINDS OF SAPO-34

Sample no.	Silica source	Template	m,n	mean particle size (μm)
P1	TEOS(98% MERK)	TEAOH,(20 wt%, MERK), Morpholine	1.2,0.4	0.4
P2	Colloidal silica in water (40 wt%, MERK)	(TEAOH, 35 wt%, Aldrich)	2.2,0	1

Stainless steel tube of inner diameter 9 mm, thickness 1 mm and 10 mm length and α-alumina of inner diameter 7 mm, thickness 3 mm and 10 mm length were used as the support for synthesis of SAPO-34 membrane. Before seeding, the substrates were cleaned with deionized water in ultrasonic cleaner for 15 min.

0.4 wt % SAPO-34 seeds were dispersed in deionized water under ultrasonication for 30 min. Then the EPD operation performed with 4.5 volts and deposition time of 90 min. Thereafter, the seeded substrates were placed vertically in an autoclave. The autoclave was filled with reaction mixture having the same composition of the P1 seeds and the procedure was the same as seed synthesis. After secondary growth, the coated membrane was washed thoroughly with deionized water to approach neutral solution.

The XRD patterns of the SAPO-34 powders was obtained using high resolution X-ray diffraction, XRD, (INEL EQuinox 3000) diffractometer with the source of Cu Ka (k = 1.541874 ˚A). SAPO-34 powders and the formed membranes were analyzed by FESEM (Hitachi s-4160, at 20 keV).

Results and Discussion

The XRD pattern of Samples are shown in Fig. 1. The observed pattern confirms SAPO-34 formation by comparison with the [3,5].

Fig. 2 shows SEM image of two kinds of SAPO-34 seeds. These images clearly show that the particles P1 are smaller than the particles P2, therefore P1 was selected for seeding operation.

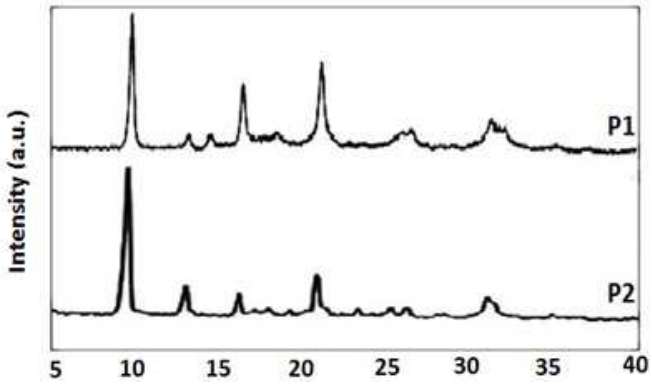


Fig. 1: XRD pattern of the as-synthesized SAPO-34 powder

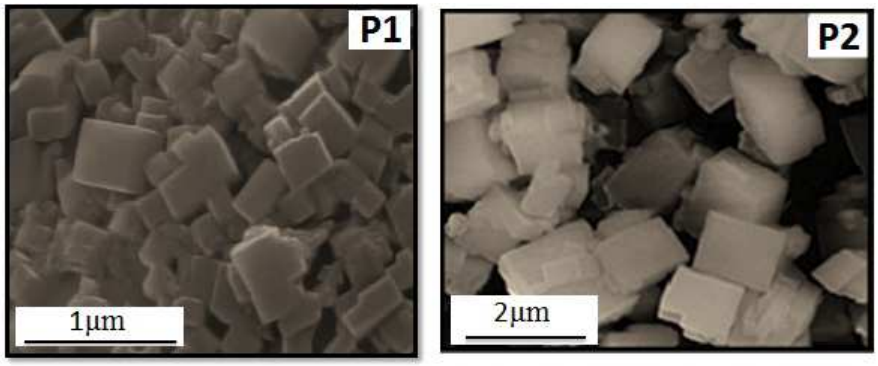


Fig. 2: SEM images of two kinds of SAPO-34 according to table 1.

Fig. 3 shows the SEM images of the top section and cross sections of the fine layers formed on each substartes. According to the SEM images, appropriate coverage has been achieved by samples using steel as the substrate rather than alumina.

Fig. 4 shows the particle size distribution of the coated particles that is measured from the top section figure. Particle size distribution of two samples are approximately the same and the mean size of the SAPO-34 particles is calculated about 0.3 μm.

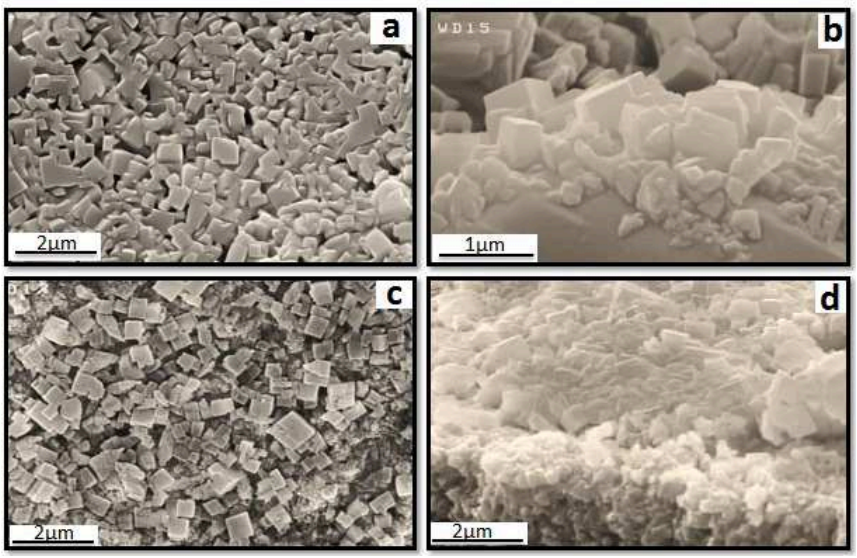


Fig. 3: SEM image of Samples, a) steel substarte top section. b) steel substarte cross section. c) α-alumina substarte top section. d) α-alumina substrate cross section

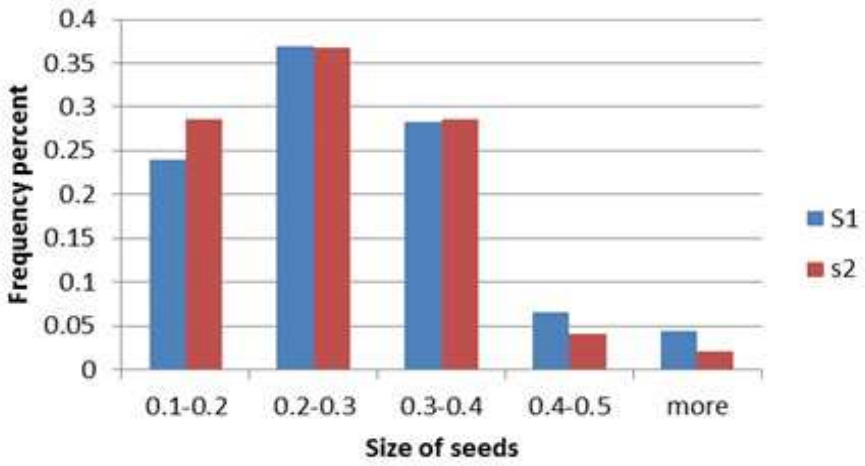


Fig. 4: Particle size distribution of samples

Conclusions

Membrane fabrication by hydrothermal method requires appropriate seeding methods for secondary growth crystallization to achieve uniform, fine and defect free membranes. EPD method would be a suitable approach to achieve this goal. Quality of the seeds prepared for EPD method and the type of substrate have shown significant role to achieve proper and uniform layer. It is concluded that the formed layer by EPD method with the uniform and less size of the particles on the surface of porous steel support is capable for qualified membrane fabrication.

References

[1] J. Caro, M. Noack, Zeolite membranes – Recent developments and progress, Microporous and Mesoporous Materials 115 (2008) 215–233

[2] Y. Hirota, K. Watanabea, Y. Uchida, Y. Egashira, K. Yoshida, Y. Sasaki, N. Nishiyama, Coke deposition in the SAPO-34 membranes for examining the effects of zeolitic and non-zeolitic pathways on the permeation and separation properties in gas and vapor permeations, Journal of Membrane Science 415–416 (2012) 176–180

[3] S. Li, J. L. Falconer, R. D. Noble, SAPO-34 membranes for CO2/CH4 separation, Journal of Membrane Science 241 (2004) 121–135

[4] J. Hedlund, J. Sterte, M. Anthonis, A.Bons, B. Carstensen, N. Corcoran, D. Cox, H. Deckman, W. D. Gijnst, P. de Moor, F. Lai, J. McHenry, W. Mortier, J. Reinoso, J. Peters, High-flux MFI membranes, Microporous and Mesoporous Materials 52 (2002) 179–189

[5] J. K. Das, N. Das, S. N. Roy, S. Bandyopadhyay, The growth of SAPO 34 membrane layer on support surface for gas permeation application, Ceramics International 38 (2012) 333–340

[6] T. L. Chew, A. L. Ahmad, S Bhatia , Rapid synthesis of thin SAPO-34 membranes using microwave heating, Journal of Porous Materials 18 (2011) 355–360

[7] Z. Jabbari, Sh. Fatemi, M. Davoodpour, Comparative study of seeding methods; dip-coating, rubbing and EPD,in SAPO-34 thin film fabrication, Advanced Powder Technology, 2013(article in press)

[8] T. Seike, M. Matsuda, M. Miyake, Fabrication of Y-type zeolite films by electrophoretic deposition, Solid State Ionics 151 (2002) 123–127

Advanced Materials Research Vol. 936 (2014) pp 264-268
© (2014) Trans Tech Publications, Switzerland
doi:10.4028/www.scientific.net/AMR.936.264

Substrate Dependence of Microcrystalline Silicon Growth with SiH_4 Diluted by Ar

Hua Cheng[a], Yongchan Qian[b], Jun Xue[c]

Changchun Institute of Engineering Technology, Changchun 130117, China

[a] chengfpf@163.com, [b] wangdibzwd@163.com, [c] xjykl@163.com

Keywords: Microcrystalline silicon film. ECR-PECVD. Substrate effect. Ar-dilution.

Abstract: Microcrystalline Si films were deposited by electron cyclotron resonance plasma-enhanced chemical vapor deposition (ECR-PECVD) using Ar diluted SiH_4 gaseous mixture. The effects of the substrate on deposition rate, preferred orientation and roughness of the films were investigated. The results show that, the influence of the substrate surface chemical nature on the deposition rate is significant in the initial stage of the growth. And considering the crystallinity and roughness of the films, the substrate is favored in its preferred orientation with a rougher surface. Based on these results, it is confirmed that the combination of diffusion and etching is indispensable to describe the deposition of μc-Si with SiH_4 diluted by Ar, and the mechanism of μc-Si growth could be controlled by diffusion of Si and etching of the Ar^+ on the film surface.

Introduction

With the developments of the solar cells industry, microcrystalline silicon films have attracted considerable attention for its high-efficiency and stability. It is attractive and desirable that direct deposition of microcrystalline silicon films at low temperature with high deposition rate by plasma enhanced chemical vapor deposition (PECVD) [1]. Microcrystalline silicon films are widely produced using SiH_4+ H_2 gaseous system because it is believed that atomic hydrogen can balance the dangling-bonding defect and hydrogen ions can etch the weak Si-Si bonds, so as to promote stability and crystallinity of the films [2]. However, H_2 dilution would limit the deposition rate seriously and great amount of H existing in the film would draw back the photoelectric efficiency of micro-Si film due to acceptor-like defect formation and light-induced defect creation [3,4].

In our previous researches, Ar was used instead of H_2, and the results demonstrated that the deposition rate was 1.5-2 times higher than using H_2 [5]. At the same time, the concentration of hydrogen in the films decreased dramatically, which would limit the creation of the light-induced defect in microcrystalline silicon [3] and enhance the photoelectric efficiency of the films. In present work, the effects of the substrate on the deposition rate, the preferred orientations, and surface image as well as roughness of the films were investigated, along with the growth mechanisms of microcrystalline silicon film with Ar dilution of SiH_4.

Experiment

The μc-Si films were deposited on general optical glass and (111) Si substrates with SiH_4/Ar by ECR-PECVD. Pre-vacuum of the reaction chamber was 6×10^{-3} Pa. The substrates were ultrasonically cleaned in alcohol and acetone solutions individually for 10min, and then cleaned in Ar^+ plasma for 10min. The substrate temperature was 300℃. The microwave power was 600W. The flow rate of SiH_4 was fixed at 10sccm，and a sequence of Ar flow rate was chosen: 20sccm, 30sccm, 40sccm, 55sccm, 70sccm, 85sccm, and 100sccm.

The preferred orientations of as-deposited films were identified by X-ray diffraction (XRD). Atom force microscopy (AFM) was utilized to characterize the topography and surface roughness of the films.

Results and Discussion

Effects of Substrate on Deposition Rate

Fig. 1 shows the deposition rate as a function of argon flow rate on different substrates. As shown in Fig. 1, the variation trends of the deposition rate with the increase of Ar flow rate on two substrates exhibit uniform. And the deposition rate on Si wafer is faster than that on general optical glass in the beginning, but the gap decreases gradually. Namely, the influence of the substrate on the deposition rate becomes minor when the technological parameter increased.

It is because that substrate contributes significantly to the film initial nucleation rate which would be determined by the critical nucleation free energy ΔG^* given by

$$\Delta G^* = \frac{16\pi\gamma_{vf}^3}{3\Delta G_V^2}\frac{(2-3\cos\theta-\cos^3\theta)}{4} \quad . \tag{1}$$

Where θ is wetting angle, G_v is unit volume free energy, γ_{vf} is boundary energy between gas and film. As shown in equation (1), ΔG^* would decrease with the decrease of θ [6] . When μc-Si film was deposited on Si substrate, θ would be smaller, so that ΔG^* would be minor than that of the film deposited on glass substrate. Consequently, Si substrate would be favored for higher film initial nucleation rate which would increase with the decrease of ΔG^*.

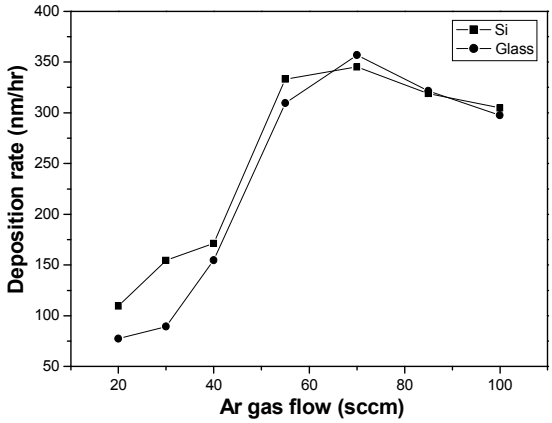


Fig. 1 Deposition rate of μ-Si films deposited on different substrates

When Ar flow rate is minor, the ionization rate of gas and the aggregation rate of atoms are lower, so that diffusion capability of active radicals are smaller and the mean staying time of sticking atoms on the film-growing surface would be shorter. The film growth depends mostly on the thermal fluctuation atoms absorbed on the surface, and nucleation would be initiated after the combination and merging of these atoms. That is to say, in this case, the contribution of initial nucleation rate to the film deposition rate would be quite major. In contrast to that the influence of initial nucleation rate on the deposition rate becomes less obvious for the improved gas ionization rate and the diffusion capability of active radicals when Ar flow rate increased. It is indicated that the substrate influence on the deposition rate would become less obvious with the increases of Ar flow rate.

Effects of Substrate on Film Preferred Orientation

The preferred orientations of the films fabricated on different substrates with different argon flow rate were characterized by XRD. As shown in Fig.2, with the increase of Ar flow rate, the dominant crystal textures of the films deposited on Si substrates are always <111> orientation, but the films deposited on glass substrate exhibit from amorphous (with Ar flow rate 20sccm, 30sccm, 40sccm, and 55sccm) to crystalline silicon whose dominant crystal textures are (111) and (220). It is suggested that the substrate would affect remarkably on the film quality, which could be explained with the surface chemisorption theory.

Many researchers have proved that, surface chemisorption would adhere to the rules of monolayer adsorption of Langmuir [7]. It is illustrated that ordering of the adsorption molecules is essential to the ordering of the film-growth. There exist great amount of dangling-bonds in the surface of (111) Si substrate, and these dangling-bonds would make the adsorption radicals resident on deposition surface for longer time, which would be favorable for crystallization. However, the radicals would be short lived on glass substrate. Some of them would depart from deposition surface, and the remains would aggregate with each other before finding proper position preparing for crystallization. So it would be easier to obtain the crystalline silicon film on (111) Si substrate than on glass substrate.

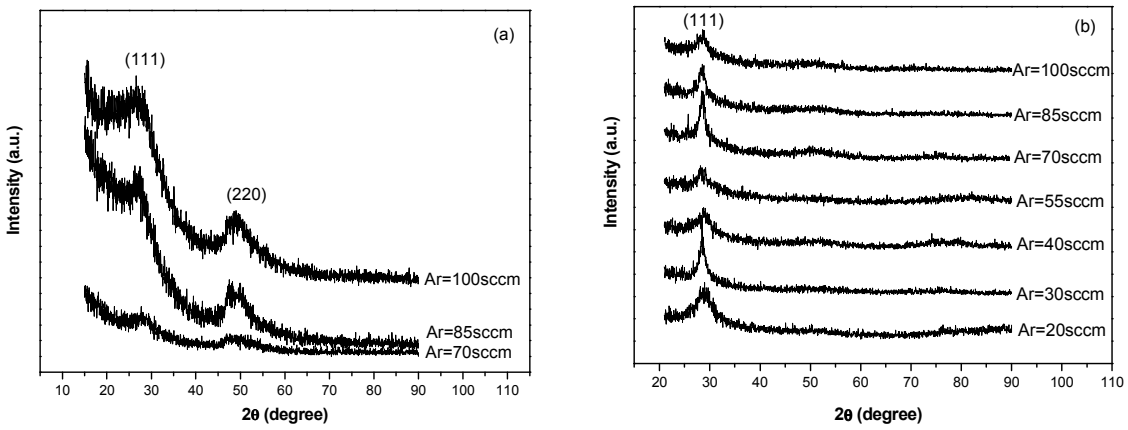


Fig. 2 XRD spectra of the films deposited with different Ar flow rate:
(a) on glass substrate, (b) on silicon substrate

On the other hand, the dominant crystal texture of the films deposited on silicon substrate is (111), which is mainly influenced by the substrate's orientation, in contrast to (111) and (220) on glass substrate. It could be explained by growth dynamics [8]. Atoms are known to be more easily absorbed on close-packed surface with higher surface energy than non close packed structure. So that the vertical growth of the non close packed plane is more rapid, and these planes would vanish gradually with the film growth. However, transversal growth of close-packed plane is quicker, resulting in that the orientations of these planes would become the film's preferred orientations, such as (111) and (220).

Effects of Substrate on Film's Surface Image and Roughness

The surface morphology of the films is a significant factor for device performance. Indeed, a rougher film allows for an increased light trapping in the acting *i*-layer of the cell, thereby to an increased short circuit current [9]. The representative surface morphologies of the films deposited on Si and glass substrates with different argon flow rate, respectively, are shown in Fig. 3.

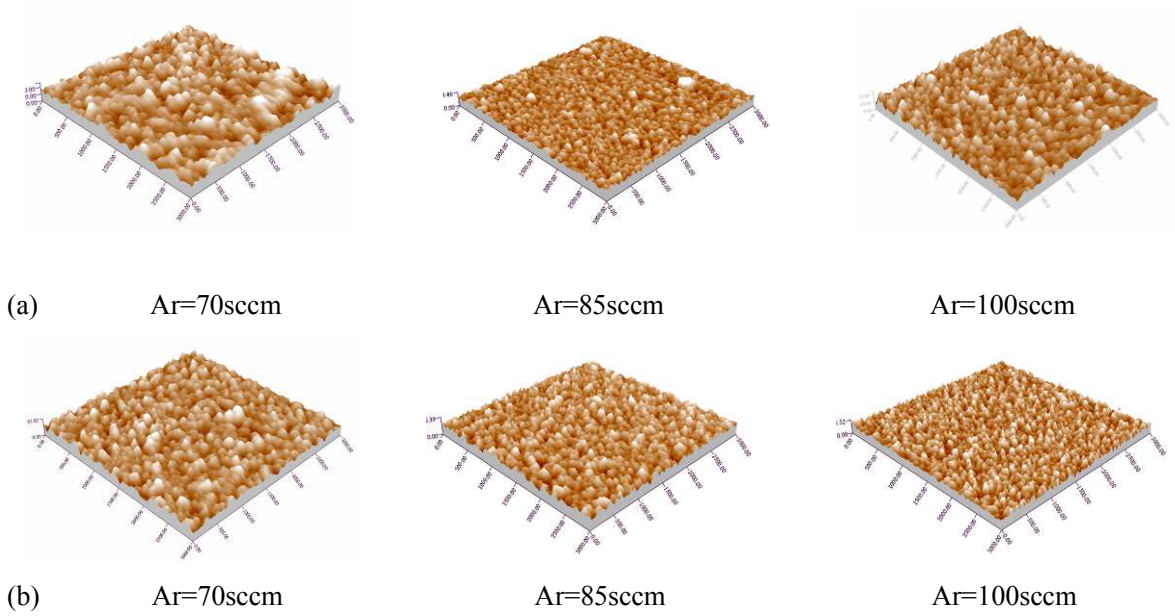


Fig. 3 AFM images of μ-Si deposited on different substrate: (a) glass, (b) Si

From Fig. 3, the distinguishing islands with a lager diameter were observed on glass, but its island density is smaller than that of on Si. It is attributed to the minor energy barrier of the film nucleation and higher nucleation rate on Si substrate than on glass. Table 1 lists surface roughness of the films shown in Fig. 3, and it is clear that the film deposited on Si is rougher. It is well known that the growth of the μc-Si film commences with the nucleation of 'islands' of the deposited material followed by columnar growth and coalescence, which makes the film more compact and continuous [10]. So a rougher film on Si substrate can be interpreted as: the vertical growth of the film is more rapid when the substrate is in its preferred orientation with a rougher surface, in contrast to a quicker transversal growth for the amorphous substrate.

TABLE 1 SURFACE ROUGHNESS OF FILMS DEPOSITED ON DIFFERENT SUBSTRATES WITH DIFFERENT ARGON FLOW RATE

Ar flow rate[sccm]	**roughness [nm]**	
	Glass substrate	**Si substrate**
70	2.95	3.27
85	3.08	4.27
100	3.7	4.38

As discussed above, substrate has a strong influence on the deposition rate and structure properties of the μc-Si film. Hence, it is necessary to analyze the growth mechanisms of microcrystalline silicon film with Ar dilution of SiH_4. Up to now details have been under discussion for μc-Si, but three models were favored: etching model, diffusion model, and chemical annealing [11].

According to our experiment results, the film crystallinity deposited on two substrates would increase with the increase of Ar flow rate, which agree with etching model. In addition, the experiment results also indicate that more exacting terms would be needed for obtaining crystalline silicon film deposited on glass substrate, which agree well with diffusion model. Above all, it is confirmed that the combination of diffusion and etching is indispensable to describe the deposition

of μc-Si with SiH_4 diluted by Ar. The growth model was considered as follows: Thermal fluctuation atoms absorbed on the growth surface plays an important role in the beginning of the film growth. Nucleation would be initiated after the combination and merging of these atoms. The dangling bond could be saturated by hydrogen atoms existing in the plasmas. Then mobility and diffusion of the SiH_x-radical on the surface of the films would remove these H atoms and produce the Si-Si bond. It is suggested that Ar^+ etching on the film surface would participate in the growth process which would remove the weak Si-Si bond and the crystalline silicon film would be formed.

Conclusions

The effects of the substrate on microcrystalline Si films deposited by ECR-PECVD using SiH_4+Ar were studied. The results indicate that the chemical nature of the substrate surface significantly influences the initial stage of the growth. Furthermore, the preferred orientation and roughness of the films would be affected remarkably by the substrate features. On the basis of the experiment results, the mechanism of μc-Si growth with SiH_4 diluted by Ar could be controlled by diffusion of Si and etching of the Ar^+ on the film surface.

References

[1] B strahm and A AAHowling: Plasma Sources Sci. Technol., Vol. 16 (2007), p. 80-89

[2] Rui Huang and Xuanying Lin: Thin Solid Films, Vol. 513 (2006), p.380-384

[3] M. Zhu and Y. Cao: Solar Energy Materials & Solar Cells, Vol. 62 (2000), p.109

[4] T. Su and P. C. Taylor: Physical Review Letters, Vol. 89 (2002), p.0155021-1

[5] Cheng Hua and Wu Aimin: Journal of Material Science and Technology, Vol. 24 (2008), p.690-692

[6] W. Z. Cui, in: *Preparation Principle, Technology, and Application of Thin Films*, edtied by Metallurgical Industry Press (2003)

[7] G. Y. Meng, in: *Chemical Vapor Deposition and Inorganic New Material*, Beijing: Science Press (1984)

[8] Chuan Jie Zhong and Hiroaki Tanaka: Thin Solid Films, Vol. 493 (2005), p.54-59

[9] E. Vallat-Sauvain and U. Kroll: Journal of Non-crystalline Solids, Vol. 266-269 (2000), p.125-130

[10] E.A.T. Dirani and A.M. Andrade: Journal of Non-Crystalline Solids, Vol. 273 (2000), p.307-313

[11] R. Terasa and M. Albert: Journal of Non-Crystalline Solids, Vol. 266-269 (2000), p.95-99

Advanced Materials Research Vol. 936 (2014) pp 269-275
© (2014) Trans Tech Publications, Switzerland
doi:10.4028/www.scientific.net/AMR.936.269

Study on the polarization reversal characteristics of a ferroelectric thin film with surface transition layers

Lian Cui[1,a]*, Zhongyang Qiu[a], Zhiyou Han[a], Ruiying Li[a], JiXin Che [2,b],

[1] Department of Physics, Daqing Normal University, Daqing 163712,China

[2] Ordnance Engineering Department, Air Force Aviation University, Changchun,130022,China

[a]* email: cl_19830422@126.com, [b]email:chejixin@126.com

Keywords: Ferroelectric thin film; Polarization reversal; Surface transition layer

Abstract. Utilizing the Landau-Khalatnikov equation of motion, the polarization reversal characteristics of a ferroelectric thin film with surface transition layers have been first investigated. We have discussed the effects of the thickness, the surface transition layer parameters and the temperature on the switching properties of a ferroelectric thin film. The results show that the stronger the surface transition layer effects are, the smaller the coercive field and switching time are.

Introduction

One of the increasingly hot topics is the polarization reversal in a ferroelectric thin film, which can provide a promising avenue for the future of nanoelectronic memories and logic devices [1-3]. To meet the need of the miniaturization of ferroelectric materials particularly in microelectronic devices, the understanding of the size and surface effects on the polarization reversal in a ferroelectric thin film is greatly urgent [4]. Therefore, the investigation for the effects of surface and film thickness on the polarization reversal properties of ferroelectric thin films has been an active research area from both a fundamental research and technological point of view [5].

Experimentally, Mitoseriu et al. [6] studied the polarization reversal properties of BaTiO3 ferroelectric ceramics at room temperature with two different grain sizes. The results showed that the switching time decreases with decreasing sizes. The thickness effects on the heteroepitaxial BaTiO3 films prepared on SrRuO3/SrTiO3 substrates by ratio-frequency magnetron sputtering employing a two-step deposition technique have been researched by Yanase et al [7]. A ferroelectric hysteresis loop was clearly observed in the heteroepitaxial BaTiO3 films even when the thickness was reduced to 12 nm, probably due to improved crystallinity at the interface between the ferroelectric film and the electrodes through optimization of the preparation technique. In theory, some models have been established to deal with the switching properties of ferroelectric thin films, such as Avrami theory [8], Kolmogorov- Avrami –Ishibashi (KAI) theory [9], non-KAI model [10], and discrete model based on the Landau-type-free energy [11, 12].

In the above theories, the surface effects on the polarization reversal in a ferroelectric thin film are not discussed. In recent years, Tilley-Zeks model of Landau Devonshire free energy expression by adding a Landau-Khalatnikov equation of motion is commonly used to study the phenomena of polarization reversal in ferroelectric thin films [13, 14]. The surface effect is considered in virtue of the extrapolation length. In this model, however, a sudden structure transition from surface to the interior for each constituent film is assumed, which is not realistic because the transition of structure

should be gradual. To avoid the insufficiencies brought by extrapolation length, the surface transition layer, representing the gradual transition of structure, was first introduced in a ferroelectric thin film by Lü and Cao [15]. They have studied the static properties (polarization distribution, phase transition temperature and dielectric susceptibility, etc.) of a ferroelectric thin film with surface transition layers [16-19]. As far as we know, the switching properties of a ferroelectric thin film by taking into account the surface transition layer have not been reported.

In this paper, we study the influences of the film thickness and temperature on the polarization switching characteristics of a ferroelectric thin film with the surface transition layers under the action of a step field, by means of the Landau- Khalatnikov equation of motion.

The model and theory

A ferroelectric thin film with surface transition layer located between two metallic electrodes is considered as the stacking of thin layers, as shown in Fig. 1. The properties of every layer with finite thickness Δz are homogeneous in planes parallel to the surface and the variation is only along the z direction. The number of the layer stack is N. Thus, the whole thickness of the ferroelectric thin film is $L = N\Delta z$. If the origin is located at the left surface, we set $z = 0$ then an arbitrary layer located at a position z can be recognized by the index i, i.e. $z = i\Delta z\ (1 \le i \le N)$.

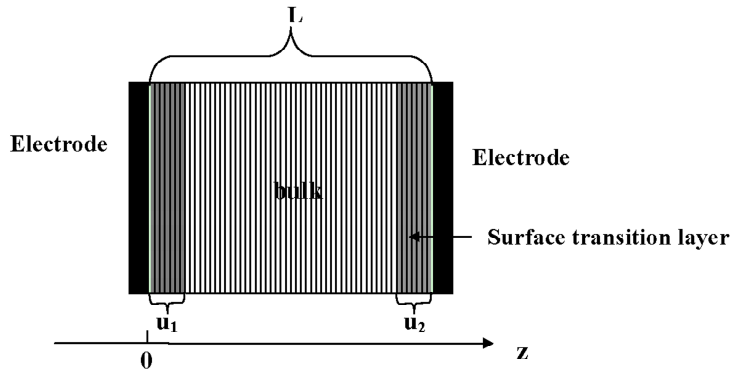


Fig. 1 Geometric structure of a ferroelectric thin film under study

To study this system, a modified Landau-type free energy for the system needs to be established. According to Ref. [16], we introduce a second power of polarization for each layer in the Landau-type free energy and assume its coefficient to be function of position in order to reflect the contribution of surface transition layers. So the free energy of the film can be expressed by Landau-type free energy expression [16, 20, 21]

$$G = \sum_{i=1}^{N}\left[\frac{1}{2}A\left(T - T_c\right)P_i^2 + \frac{1}{2}B\psi\left(z\right)P_i^2 + \frac{1}{4}CP_i^4 + K\left(P_i - P_{i-1}\right)^2 - EP_i\right], \tag{1}$$

with the boundary condition [15]

$$\left(\frac{\mathrm{d}P}{\mathrm{d}z}\right) = 0 \qquad \text{when} \quad z = 0 \text{ and } z = L, \tag{2}$$

where P_i is the polarization of the $n-$th layer; the coefficients A, B, C, and K are independent of temperature T and position z; T_c is the transition temperature of the bulk ferroelectric; E is the applied field. A new term (the second term) is added in Eq. (1) in order to reflect the contribution of the surface transition layer. Thereinto, $B>0$ denotes a decrease in the local polarization at surfaces, and $B<0$ expresses an increase in the local polarization at surfaces. In this paper, we only consider the case of $B>0$. The distribution function $\psi(z)$ reflects the surface effect. The $K\left(P_i-P_{i-1}\right)^2$ term in Eq. (1) represents the coupling effect between neighboring layers. The polarization gradient $\left(\mathrm{d}P/\mathrm{d}z\right)^2$ can be included in the finite difference expansion of the $K\left(P_i-P_{i-1}\right)^2$ term [20]. The time variation of the polarization during switching can be described by the Landau-Khalatnikov equation as follows:

$$\gamma\frac{\partial P_i}{\partial t}=-\frac{\partial G}{\partial P_i}=-A\left(T-T_c\right)P_i-B\psi\left(z\right)P_i-CP_i^3+K\left(P_{i+1}+P_{i-1}-2P_i\right)+E \tag{3}$$

where γ is the coefficient of viscosity, which causes a delay in domain motion.

It is convenient to rescale the variables into dimensionless forms. We set $f_i=P_i/P_0$ with $P_0=\sqrt{AT_c/C}$, $t_T=T/T_c$, $\delta=B/B_0$ with $B_0=AT_c$, $\zeta=z/\xi_0$ with $\xi_0=\sqrt{K/AT_c}$, $l=L/\xi_0$, $\eta=tAT_c/\gamma$, $k=K/AT_c$, $\sigma=(\varepsilon_0 AT_c)^{-1}$, $e=E/E_0$ with $E_0=P_0/\varepsilon_0$, where ε_0 is the dielectric constant of vacuum. Finally, we can obtain the normalized equation below:

$$\frac{\partial f_i}{\partial\eta}=\left(1-t_T\right)f_i-\delta\psi\left(\zeta\right)f_i-f_i^3+k\left(f_{i+1}+f_{i-1}-2f_i\right)+\sigma e \tag{4}$$

The corresponding rescaling boundary condition is

$$\left(\frac{\mathrm{d}f}{\mathrm{d}\zeta}\right)=0 \quad \text{when } \zeta=0 \text{ and } \zeta=l. \tag{5}$$

Another index j is introduced to represent the discretized time $\eta=j\Delta\eta$. The time dependent polarization at each layer is denoted as $f_{i,j}$. Through the forward difference in time for the left-hand side of Eq. (4), the difference equation for $f_{i,j}$ can be written as:

$$f_{i,j+1}=f_{i,j}+\Delta\eta\left[\left(1-t_T\right)f_{i,j}-\delta\psi\left(\zeta\right)f_{i,j}-{f_{i,j}}^3+k\left(f_{i+1,j}+f_{i-1,j}-2f_{i,j}\right)+\sigma e\right] \tag{6}$$

According to the finite difference for the derivative $\left(\mathrm{d}f/\mathrm{d}\zeta\right)$ in the second-order smallness, Eq. (5) becomes

$$\begin{cases} f_{0,1} = f_{1,j} = f_{2,j} & \zeta = 0 \\ f_{N,j} = f_{N-1,j} = f_{N-2,j} & \zeta = l \end{cases} \tag{7a, b}$$

The overall polarization of the whole film is defined as

$$\overline{f_j} = \frac{1}{N}\sum_{i=1}^{N} f_{i,j} \tag{8}$$

and the switching current is determined by

$$I_j = \frac{\mathrm{d}\overline{f_j}}{\mathrm{d}\eta} \tag{9}$$

Since there is no experimental data available on the effects of the surface transition layer, a simple form is chosen for the distribution function $\psi_i(\zeta)$. The peculiar choice of $\psi_i(\zeta)$ does not affect the generality of the results and conclusions [16]:

$$\psi_i(\zeta) = \begin{cases} \left(\dfrac{i\Delta\zeta - u_1}{\lambda_1}\right)^2 & 0 \le i < \dfrac{u_1}{\Delta\zeta} \\ 0 & \dfrac{u_1}{\Delta\zeta} \le i \le N - \dfrac{u_2}{\Delta\zeta} \\ \left(\dfrac{i\Delta\zeta - \left(N\Delta\zeta - u_2\right)}{\lambda_2}\right)^2 & N - \dfrac{u_2}{\Delta\zeta} < i \le N \end{cases} \tag{10}$$

where u_1 and u_2 are the thickness of the left and right surface transition layer, respectively. Parameter λ_1 (λ_2) reflects the variation intensity of the free energy density of each layer near the left (right) surface. For simplicity, the two surface transition layers are assumed symmetric, namely, $u = u_1 = u_2$, $\lambda = \lambda_1 = \lambda_2$.

It is useful to mention the bulk coercive field and derive from the equilibrium state as

$$e_{c0} = \pm\frac{2}{3\sqrt{3}}\left(1 - t_T\right)^{3/2} \tag{11}$$

Due to the polarization reversal often studied experimentally by a step electric field, we now show some results for switching in a step field. As stated, the polarization in the initial state is the negative remnant polarization, that is to say, the initial polarization is at zero field; then at the time $\eta = 0$ the field is switched to a positive value. The switching time is a key quantity, which is defined in several ways in the literatures. Here, we will use a definition of switching time as t_0, which is the time at which the polarization reaches zero [22].

Numerical results and discussions

The polarization profiles of the film during the switching process are shown in Fig. 2 which are calculated at selected times under different surface transition layer thickness and λ. The polarization of the film switches from the initial negative state to positive state by the applied field. From Fig. 2 (a), we can see that at the time $\eta = 0.4$, the polarization near the surfaces just starts to reverse, then gets to the interior and at the time $\eta = 0.6$ the polarization of the film has been completely switched. It is ascribed to the polarization of the surface transition layers smaller than that of the interior. The result is consistent with that obtained by Chew et al [23]. When the thickness of surface transition layer u increases (see Fig. 2(b)), the polarization near the surfaces takes a shorter time ($\eta = 0.2$) to reverse than that in Fig. 2(a). And it takes a shorter time ($\eta = 0.4$) to complete the switching process, compared with Fig. 2(a). When we decrease the value of λ, see Fig. 2(c), also a shorter time is required for reversing the polarization near the surfaces according to Fig. 2(a), but it takes a longer time to complete the switching process relative to Fig. 2(b). So the influence of the thickness of surface transition layer on the polarization distribution is more obvious than that of λ. Furthermore, with increasing the time, the polarization of the film reduces before the completion of the switching process, whereafter, the polarization of the film augments with increasing the time. Hence, it will take a shorter time to achieve the polarization reversal of the film if we increase the thickness of the surface transition layer or reduce λ.

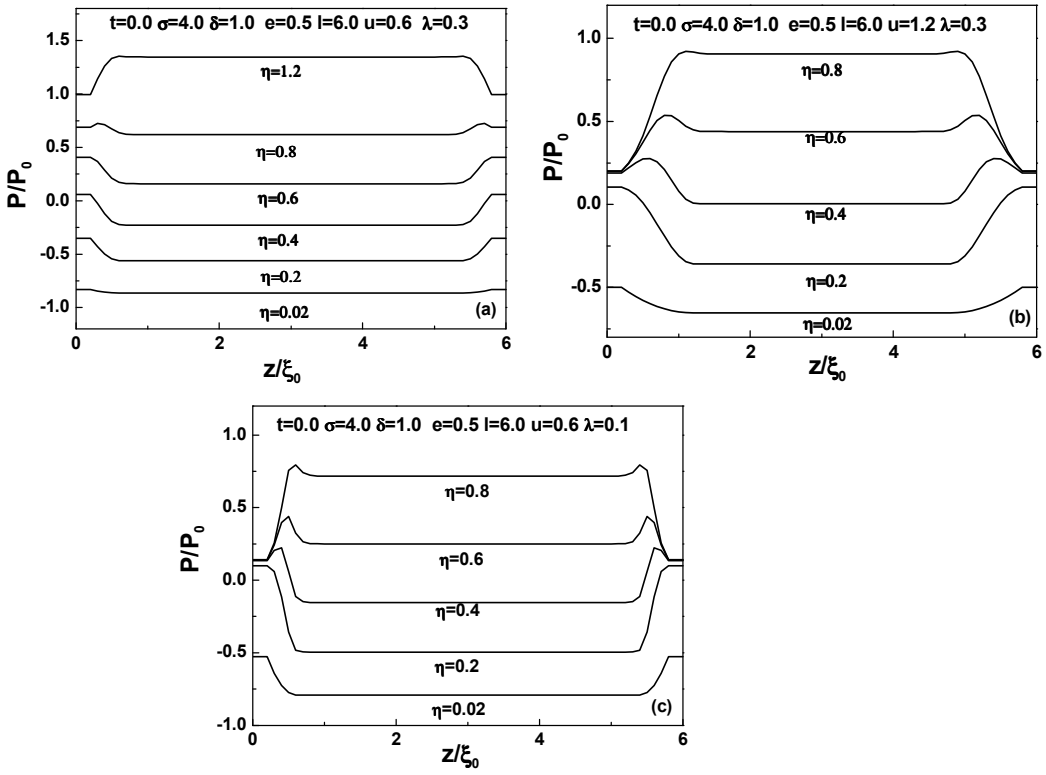


Fig. 2 Polarization distributions at selected times under different surface transition layer thickness and λ

The coercive field versus the thickness of the film for various surface transition layer thickness and λ is elucidated in Fig. 3. One can clearly see that when the surface transition layer thickness and λ are fixed, the coercive field decreases as the thickness of the film reduces. The trend is attributed to the increase of the ratio of surface transition layer to the whole film. According to Fig. 2, the stronger surface effects will make the polarization reversal of the film easier. For a given thickness of the film, the coercive field decreases with increasing the thickness of surface transition layer or reducing λ. It is worth emphasizing that the coercive field has a finite size behavior, where a phase transition from ferroelectric phase to paraelectric phase occurs at a certain critical thickness. And the critical thickness augments with increasing the thickness of surface transition layer or reducing λ. The above phenomena well coincides with those of Ref. [14]. Moreover, in accordance with Eq. (11), we gain the bulk coercive field is 0.097, which is larger than the coercive field of the film, as shown in Fig.3. That is to say, the polarization can be reversed by an electric field weaker than the bulk coercive field.

Figure 4 illustrates the switching time as a function of the thickness of the ferroelectric thin film. For a given applied field, the switching time is shorter for a thinner film, which is consistent with the experimental result of Ref. [24], and also accords with the theoretical result calculated by Wang et al. [25]. The physical reason is that as the thickness of the film reduces, the proportion of surface transition layer to the film augments. According to Fig. 2, it will take a shorter time to complete the polarization switching process with larger thickness of surface transition layer or smaller λ.

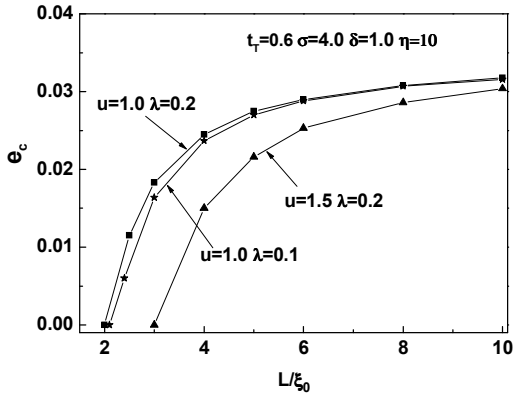


Fig. 3 Coercive field versus the thickness of the ferroelectric thin film for different surface transition layer thickness and λ

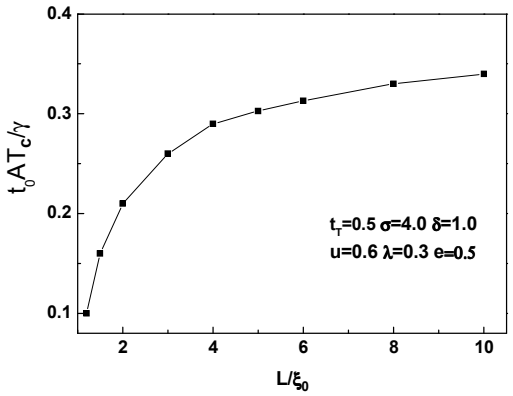


Fig. 4 Switching time as a function of the thickness of the ferroelectric thin film

Summary

In summary, we have discussed the influences of the film thickness and temperature on the polarization switching characteristics of a ferroelectric thin film with the surface transition layers using the Landau- Khalatnikov equation of motion for the first time. The results we obtained can be summarized as follows: (1) the existence of surface transition layer makes the time of polarization reversal of the film become shorter; (2) the coercive field and the switching time decrease as the thickness of the film reduces; (3) a critical thickness exists for coercive field of the film, and augments as the surface effects enhance; (4) a higher temperature can quicken the polarization switching of the film.

Acknowledgement

This work has been supported by National Natural Science Foundation of China under grant no. 11247255 and the Doctoral Start-up Fund of Daqing Normal University under Grant no. 11ZR07.

References

[1] X.H. Liu, Y. Wang, P. V. Lukashev, J. D. Burton, and E. Y. Tsymbal, Phys. Rev. B 85 (2012) 125407

[2] A. Q. Jiang, Y. Y. Lin, and T. A. Tang, J. Appl. Phys. 101 (2007) 104105

[3] J. F. Scott, Ferroelectrics Memories (Springer-Verlag, Berlin, 2000)

[4] P.-C. Ooi, Y. Ishibashi, S.-C. Lim and J. Osman, Ferroelectrics. 355 (2007) 216

[5] V. Y. Shur, A. R. Akhmatkhanov, I. S. Baturin, and E. V. Shishkina, J. Appl. Phys. 111 (2012) 014101

[6] L. Mitoseriu, D. Ricinschi, C. Harnagea, M. Okuyama, T. Tsukamoto and V. Tura, Jan. J. Appl. Phys. 35 (1996) 5210

[7] N. Yanase, K. Abe, N.Fukushima and T.Kawakubo, Jan. J. Appl. Phys. 38 (1999) 5305

[8] E.-K. Tan, J. Osman, and D.R. Tilley, Phys. Stat. Sol. (b) 228 (2001) 765

[9] A. M. Musleh, L.-H. Ong, and D. R. Tilley, J. Appl. Phys. 105 (2009) 061602

[10] A. K. Tagantsev, I. Stolichnov, N. SetterJeffrey, S. Cross and M. Tsukada, Phys. Rev. B 66 (2002) 214109

[11] M. Omura, H. Adachi and Y. Ishibashi, Jan. J. Appl. Phys. 30 (1991) 2384

[12] V. Tura, D. Ricinschi, L. Mitoseriu, C. Harnagea, S. Ando, T. Tsukamoto and M.Okuyama, Jan. J. Appl. Phys. 36 (1997) 2183

[13] L.-H. Ong and A. Musleh, Ferroelectrics. 380 (2009) 150

[14] A. Musleh A. and L.-H. Ong, J. Appl. Phys. 109 (2011) 084109

[15] T Lü and W Cao, Phys. Rev. B 66 (2002) 024102

[16] T Lü and W Cao, Microelec. Engin. 66 (2003) 818

[17] H. Chen, T.Q. Lü and W. Cao, Physica B 373 (2006) 177

[18] S. Lin, T.Q. Lüand W. Cao, Phys. Stat. Sol. (b) 243 (2006) 2952

[19] L. Cui, W. Cao, and X. Xu, J. Appl. Phys. 106 (2009) 054101

[20] V. C. Lo, J. Appl. Phys. 94 (2003) 3353

[21] V. C. Lo and Z. J. Chen, IEEE Trans. Ultrason. Ferroelectr. Freq. Control 49 (2002) 980

[22] N. T and Y. Ishibashi, J. Phys. Soc. Japan 60 (1991) 4331

[23] K.-H Chew, J. Osman, R. L. Stamps, D. R. Tilley, F. G. Shin and H. L. W. Chan, J. Appl. Phys. 93 (2003) 4215

[24] L.Mitoseriu, D. Ricincchi, C. Harnagea, and M. Okuyama, Jan. J. Appl. Phys. 35 (1996) 5210

[25] C. L. Wang and S. R. P. Smith, J. Phys.: Condens Matter. 8 (1996) 4813

Advanced Materials Research Vol. 936 (2014) pp 276-281
© (2014) Trans Tech Publications, Switzerland
doi:10.4028/www.scientific.net/AMR.936.276

Fabrication of diamond films on Cu metal substrates with buffers (SiC or MoSi2) by hot filament chemical vapor deposition

ZHAO Qi[1,2,a *], DAI Ming-jiang[2,b], TAN Di2,c,WEI Chun-bei[2,d], QIU Wan-qi[1,e], HOU Hui-jun[2,f]

[1.] School of Materials Science and Engineering, South China University of Technology, Guangzhou, 510640, China;

[2.] Guangzhou Research Institute of Non-ferrous Metals, Guangzhou 510651, China

[a]email address: zhaoqi2012yan@163.com; [b]email address: daimingjiang@tsinghua.org.cn

[c]email address:tandicqu@163.com; [d]email address:weichunb@163.com

[e]email address:mewqqiu@scut.edu.cn; [f]email address:hfg2901@126.com

Keywords: diamond films; interlayer; copper substrate; SEM; hot filament chemical vapor deposition (HFCVD)

Abstract: Diamond films were grown by hot filament chemical deposition (HFCVD) on Cu metal substrate with two different buffer layers (SiC or $MoSi_2$) synthesized by using magnetron sputtering technique. The components of films were investigated using X-ray diffraction (XRD) and laser Raman spectrum, and the surface morphology and structure were observed with scanning electron microscopy (SEM). Film adherence was investigated by micro-indentation. The results showed that the diamond films were successfully grown on Cu metal substrate with two different buffer layers. There were cracks on diamond film grown on 3μm SiC buffer layer and some SiC crystal whiskers were observed. Dense diamond films with bad adhesion were observed on 22μm $MoSi_2$ buffered copper substrate. $MoSi_2$ made chemical reaction with CH_4 and produced MoC and Mo_5Si_3 on the process of HFCVD. Conclusion: the 3μm buffer layer of SiC can't help deposit no cracking diamond film; the 22μm buffer layer of $MoSi_2$ is helpful for depositing good diamond film, but can't effectively improve the bond strength between diamond film and copper substrate.

Introduction

Diamond has a unique set of excellent physical and chemical properties and is long recognized to be a precious material for many applications. It has the highest thermal conductivity, molar density, hardness and the lowest compressibility among all materials [1~5]. Despite the huge technological and commercial benefits that it presents, it is well known that to directly deposit diamond film on ferrous substrates is difficult. So many dissertations published in literature provided the information about diamond deposition on ferrous substrates [5~7]. To improve the poor adhesion and increase the low nucleation of CVD diamond film on copper substrate, the use of interlayer is a good way to overcome the diffusion between carbon and iron. There are three interlayer categories, (i) those that is easy to form carbides, such as Si, Ti or Cr; (ii) those do not form carbides but can dissolve carbon, such as Fe, Co or Ni; (iii) those that are difficult to form a carbide and don't dissolve carbon, such as Cu and Ag. In present, the radiator used in LED is made up with diamond and copper. Chromium

and titanium, the carbide firming metal, has been utilized as a planar structured interlayer to improve bond strength between substrate and diamond film due to the formation of strong carbide bond. But the thermal conductivity of titanium is bad (Ti: about 20.4W/mK); the thermal conductivity of chromium is good (Cr: about 93.7W/mK), but chromium is easy to make chemical reaction in the processes of HFCVD and produces Cr_3C_2 with low thermal conductivity in about 19.1W/mK. So it is important to find a higher thermal conductivity interlayer in order to decrease the thermal resistance. SiC and $MoSi_2$ with high thermal conductivity (SiC: about 54.4W/mK, $MoSi_2$: about 45W/mK) can be attempted to be used as a planar structured interlayer to deposit diamond film on those and improve the composite thermal conductivity [8].

Experimental

Disks with Φ50×20mm of red copper were used as substrates. The disks were cut into cube coppers which were in 8×8×2mm. The copper substrates were first mechanically polished to get smooth surface like a mirror. Afterwards, the two different intermediate layers, SiC and $MoSi_2$, were deposited on each red copper substrate using magnetron sputtering technology. sample1: depositing SiC; sample2: depositing $MoSi_2$.

Fabrications of two different transition layers were performed in magnetron sputtering reactor, and the experimental parameters were shown at table1.

Table1: Experimental parameters in magnetron sputtering

parameters	SiC	$MoSi_2$
temperature	180°C	180°C
substrates voltage	100V	100V
ions resources	1.0A,243V	1.0A,243V
current	3.0A	3.0A
total flow rate	150ml/min	150ml/min
pressure	0.36Pa	0.36Pa
growth time	2 hours	2 hours
Rotate speed	0	0

Then the two samples were ultrasonically abraded for 30min in a suspension of 5 g-diamond powder (3.5μm) in 15 ml of ethanol, which makes diamond powder inlay into each buffer layer and is benefit to improve nucleation.

Then the diamond growth was performed in a hot filament assisted reactor in the following condition: filament temperature: 2200~2300°C, substrate temperature: 830~850 °C, distance from filament to substrate: 6mm, total flow rate: 100 ml/min of 98.35%H_2/1.65% CH_4 mixture, pressure: 5040~5100Pa, growth time: 12h.

The two samples were characterized by using scanning electron microscopy (SEM), X-ray diffraction (XRD) and Raman spectroscopy (Argon laser, λ=514.5 nm) to examine the surface morphology, residual stress, films crystallinity and phase structure, respectively. Bonding strength between diamond film and copper substrate was tested by a Rockwell indentation experiment at 300 N, using a conical diamond indenter with an included angle of 60°.

Result and discussion

Fig.1 shows the micrograph of SiC surface and cross section. As showed in Fig.1 (a), there are some scratches on SiC layer surface, and the roughness of SiC surface is about 0.96μm in Ra. The thickness of SiC layer is about 3μm. Fig.2 shows the X-ray diffraction spectrum for sample 1 before and after 12 h CVD process. XRD patterns of the films before and after the CVD process shows diamond films grown on SiC-buffered copper substrates. Peaks at 44° and 75.3° can be clearly seen in the X-ray spectrum; these peaks correspond to diamond (111) and (220), respectively. Peaks at 44.1°, 64.4° and 77.4° can be clearly seen in the X-ray spectrum; these peaks correspond to SiC (200), (220) and (311), respectively. Thus, the X-ray diffraction spectrum reveals the formation of crystalline diamond on the copper substrates buffered with SiC layer. Furthermore, weak peaks in the pattern taken before the CVD process suggest the likelihood of the presence of SiC in amorphous state. After CVD process, the enhancement in SiC peaks implies that SiC in amorphous state happens crystallization, which will be confirmed in Fig.3 (d). Few SiC whiskers were observed in Fig.3 (d). It is because the process of CVD in about 800°C~900°C provides energy for amorphous SiC converting to crystalline state. We also observed the peaks of copper, which suggests that X-ray get into the copper substrate.

The surface morphology of the diamond film on SiC coated copper substrate after 12h deposition of hot filament CVD is shown in Fig.3 (a) and (b). A continuous and uniform diamond film with well faceted grains is grown. A broad size distribution (in the range of ~1-12 μm) of particles is evident, as minority were grown from the primary nucleating agents (homo-epitaxial growth of uncovered diamond grains) and most grains are secondary nucleated particles.

Fig.3 (c) shows the Laser Raman spectrum of the diamond film on the SiC interlayer coated Cu substrate. The strong and sharp peak at 1333 cm^{-1} demonstrates the good crystalline nature of diamond. However, because 1332.5 cm^{-1} is the normal peak position of unstressed diamond, the change in the diamond peak suggests that the diamond film is under little compressive stress. In the status of biaxial stress σ, the Raman curve of polycrystalline diamond generally was split into singlet and doublets. Because no splitting peaks are observed in Fig.3 (c), the peak at 1333 cm^{-1} is regarded as an overlap of singlet and doublets, and σ can be expressed in equation (1)

$$\sigma[\mathrm{GPa}] = -0.567/[\mathrm{GPa}/\ \mathrm{cm}^{-1}](\nu_m - \nu_o)\ [\mathrm{cm}^{-1}] \quad (1)$$

Where $\Delta\nu=\nu m-\nu o$ is the difference between the measured peak wavenumber (ν_m) and the unperturbed line center wavenumber (ν_o=1332.5cm^{-1}) [9~10]. So the film average internal stress is calculated about to -0.2835 GPa. This is a very small in-plane compressive stress, which is mabye remitted by cracks as clearly seen in the SEM picture of Fig.3 (a) and (b). The cracks are probably caused by the great different thermal expansion coefficient between Cu (0.167×10^{-4} m /°C) and SiC (4.7×10^{-6}m/°C), what's more, the thickness of SiC interlayer is about 3μm, which are not enough to remit the compressive stress in diamond film. A slight broad band at 1555 cm^{-1}~1570 cm^{-1} indicates the presence of non-diamond carbon in the film[11~12].

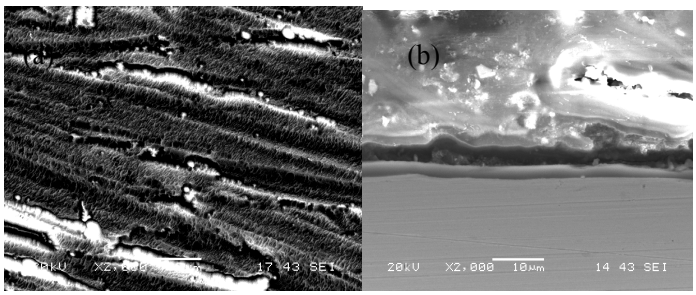


Fig.1 SEM micrograph of SiC surface (a) and cross section (b) on copper substrate

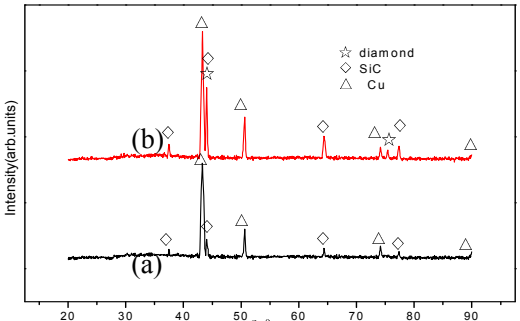


Fig.2 X-ray diffraction spectrum of sample 1 before (a) and after (b) 12 h CVD process

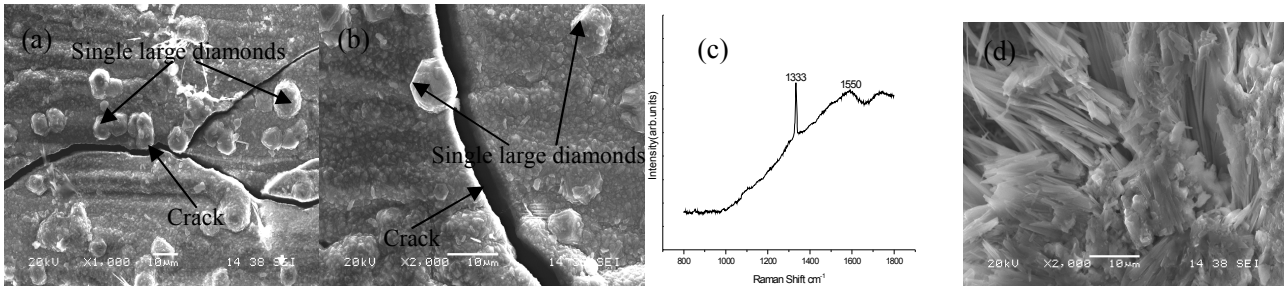


Fig.3 Surface morphology (a) (b), Raman spectrum (c) and SiC whiskers(d) of sample 1 after12 h CVD process

Fig.4 (a) and 4(b) show the micrograph of $MoSi_2$ surface and cross section respectively. As showed in Fig.4 (a), the surface roughness of $MoSi_2$ layer is about 0.72μm in Ra. The thickness of $MoSi_2$ layer is about 22μm, which is greater than the thickness of SiC layer in 2 hours. It can be explained that the bond of Si-C covalent bond is stronger than Si-Mo electrovalent bond. In same magnetron sputtering process, considering that to broke Si-Mo electrovalent bond needs less energy than Si-C covalent bond, the probability of breaking Si-Mo covalent bond is larger than Si-C. So the deposition speed $MoSi_2$ of is quicker. XRD spectrum of the film before and after the CVD process implies the continuity and crystalline in the diamond film, as showed in Fig.5. Peaks at 2θ diffraction angles of 44° and 75.3° are clearly evident, and respectively correspond to the (111) and (220) reflections of the cubic diamond structure. Furthermore, the absence of $MoSi_2$ peaks in the pattern taken before the CVD process suggests the likelihood of the presence of $MoSi_2$ in amorphous state. MoC and Mo_5Si_3 were detected after CVD process, which likely is because $MoSi_2$ is easy to make chemical reaction with CH_4 at about 800~900°C. The chemical equation can be expressed as follow:

$$MoSi_2 + CH_4 \longrightarrow MoC + Mo_5Si_3 + H_2\ (g) \qquad (2)$$

Fig.6 (b) shows Laser Raman spectrum for the diamond films deposited on $MoSi_2$-buffered copper substrates. The Raman spectrum shows a first-order Raman peak at 1339cm^{-1}, which are the sign of polycrystalline diamond and large existence of in-plane compressive stress. The spectrum contains a large band at about 1550cm^{-1}, which suggests a large number of existences of non-diamond carbon. The diamond crystals formed were highly crystalline seen in the SEM picture of Fig.6 (a). The diamonds were high dense and the diameter is in broad size distribution (in the range of ~2-12 μm). Few are grown from the primary nucleating agents and most are secondary nucleated particles. We can't observe any cracks in Fig.6 (a) despite the high compressive stress in diamond film that can be calculated to -3.86Gpa according to equation (1), which probably be explained by two reasons. Firstly, the thickness of $MoSi_2$ interlayer is about 22μm, which is sufficient to remit the inner stress in diamond film; secondly, the chemical products, MoC and Mo_5Si_3, maybe have strong bond to diamond, embed diamonds, causing a stronger combination among MoC, Mo_5Si_3 and diamonds.

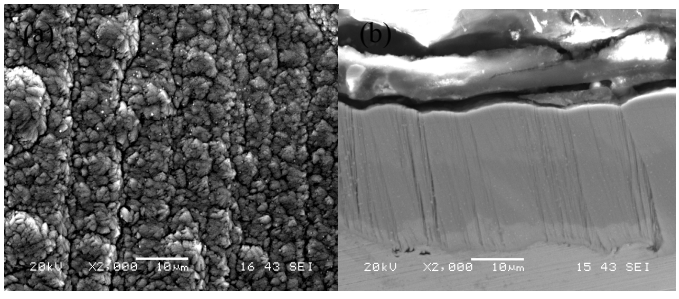


Fig.4 SEM micrograph of $MoSi_2$ surface (a) and cross section (b) on copper substrate

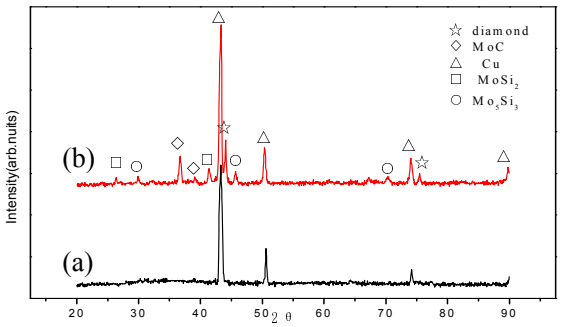


Fig.5 X-ray diffraction spectrum of sample 2 before (a) and after (b) 12 h CVD process

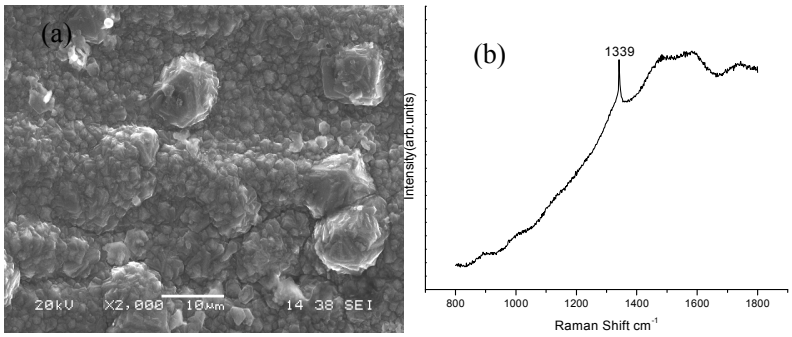


Fig.6. Surface morphology (a) and Raman spectrum (b) of the diamond films after 12 h CVD process

In order to further check the diamond film adhesion on $MoSi_2$ interlayer, Rockwell indentation experiment at 300N was carried on sample 2. Fig.7 shows the SEM image of the residual imprint of the indentation. The diameter of imprint is calculated about to 522 μm. If considering that the shape of residual imprint is same as the indenter with a half included angle of 60°, the imprint depth is calculated about to 166 μm. This imprint depth is much greater than the whole thickness of the diamond film and $MoSi_2$ interlayer (22μm), reckoning that the indenter pierced through the diamond film and the $MoSi_2$ interlayer to the copper substrate, resulting in major deformation of the residual imprint. The diamond film has been deformed and delaminated on the periphery of the indent as observed in Fig.7 (a). A magnification micrograph shows radial cracks evident on the surface of the diamond film around the indent shown in Fig.7 (b). Broken diamond grains and white small slices which are broken by the indenter during the indentation process are observed in Fig.7 (a), (c) and (d). The appearance of Radical crack and white mark surrounding the indentation spot in Fig.7 (a) shows that the adhesion strength between the diamond film and copper substrate is weak [13~14]. It suggests the 22μm buffer layer of $MoSi_2$ can't effectively improve the bond strength between diamond film and copper substrate even chemical products, MoC and Mo_5Si_3, probably causing a stronger combination among MoC, Mo_5Si_3 and diamonds.

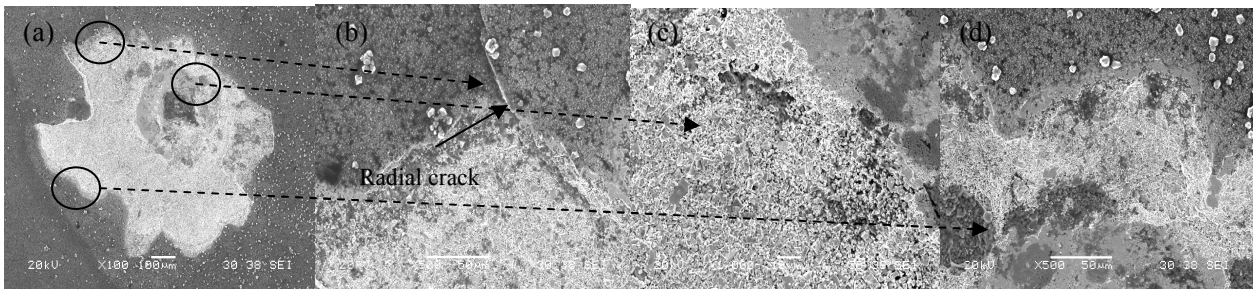


Fig.7 SEM micrographs of the indentation crater on sample2 (a) and periphery of the crater on sample2 (b), (c) and (d)

Conclusion

The present study shows that diamond films were successfully synthesized on copper substrates with two different buffer layers (SiC or $MoSi_2$) utilizing the hot filament chemical vapor deposition technique. It is demonstrated that the 3μm buffer layer of SiC can't help deposit no cracking diamond film. The 22μm buffer layer of $MoSi_2$ is helpful for depositing good diamond film, but can't effectively improve the bond strength between diamond film and copper substrate.

Acknowledgement

The research was supported by Science and Technology Planning Project of Guangdong Province, China (NO: 2011A081301003). The authors would like to thank Qiu- Wanqi, Dai-Mingjiang and Wei-Chunbei.

Reference

[1] Fang Mei, Yu Zhimin, Xiao Zhu, Chen Shuang, Chen Yongqing. Influences of substrate pre-treatments on diamond/beryllia composite, J. Materials Science and Engineering of Powder Metallurgy, 14(2009)32~36.

[2] Zhang Wenkai, Peng Fang, Guo Zhengtang, Guan Junwei, Li Rongqi. Research on Thermal Conductivity of Diamond with Cr,Ti Coating/Copper Composite Materials by Sintering under High Pressure , J. chinese journal of high pressure physics, 26(2012)306~313.

[3] S.D. Wolter, D.-A., Borca-Tasciuc, G. Chen, N. Govindaraju, R. Collazo.Thermal conductivity of epitaxially textured diamond films, J. Diamond and Related Materials, 12(2003)61~64.

[4] P. Miranzo, M.I. Osendi, E. Garcia, A.J.S. Fernandes, V.A.Silva, F.M.Costa, R.F.Silva.Thermal conductivity enhancement in cutting tools by chemical vapor deposition diamond coating, J. Diamond and Related Materials, 11(2002)703~707.

[5] Q.P. Wei, Z.M. Yu, L. Ma, D.F. Yin , J. Ye.The effects of temperature on nanocrystalline diamond films deposited on WC-13 wt.% Co substrate with W-C gradient layer, J. Applied Surface Science, 256(2009)1322-1328.

[6] Qiuping Wei, Michael N.R. Ashfold, Yu. A. Mankelevich, Z.M. Yu, P.Z. Liu, L. Ma. Diamond growth on WC-Co substrates by hot filament chemical vapor deposition: Effect of filament-substrate separation, J. Diamond and Related Materials, 20(2011) 641~650.

[7] Changzhi Gu, Zengsun Jin, Xianyi Lu, Guangtian Zou, Jifa Zhang, Rongchuan Fang. The deposition of diamond film with high thermal conductivity, J. Thin Solid Films, 311(1997)124~127.

[8] Vladimir V. Mirkovich.(Eds). Thermal conductivity 15. Canada centre for mineral and Energy technology, Ottawa, Ontario, Canada, 1978, 1~302.

[9] Leticia W. de Resende, Evaldo J. Corat, Vladimir J. Trava-Airoldi, Nelia F. Leite. Multi-layer structure for chemical vapor deposition diamond on electroplated diamond tools, J. Diamond and Related Materials, 10(2001)332~336.

[10] [Cheng Tzu Kuo, Chii Ruey Lin, How Min Lien. Origins of the residual stress in CVD diamond films, J. Thin Solid Films, 290-291(1996)254~259.

[11] May P W, Ludlow W J, Hannaway M. Raman and conductivity studies of boron doped microcrystalline diamond, J. Chemical physics Letters, 446(2007) 103~108.

[12] Wild C, Koidl P, Muller S. Chemical vapor deposition and characterization of smooth {100}-faced diamond films, J. Diamond and Related materials, 2(1993)158~168.

[13] Qiuping Wei, Z.M.Yu, Michael N.R. Ashfold, Z. Chen, L.Wang, L.Ma. Effects of thickness and cycle parameters on fretting wear behavior of CVD diamond coatings on steel substrates, J. Diamond and Related materials, 205(2010)158~167.

[14] W.Q. Qiu, A. Dasari, Y.-W. Mai. Improvement in adhesion of diamond film on Cu substrate with an inlay structured interlayer, J. Surface & Coatings Technology, 206(2011)224-227.

Advanced Materials Research Vol. 936 (2014) pp 282-286
© (2014) Trans Tech Publications, Switzerland
doi:10.4028/www.scientific.net/AMR.936.282

Epitaxial Pd-doped $LaFeO_3$ Films Grown on (100) $SrTiO_3$ by Pulsed Laser Deposition

Ying Wen Duan

Institute of Materials Science and Engineering, Lanzhou University, Lanzhou 730000, China

duanyw@lzu.edu.cn

Keywords: perovskite; precious-metal; thin films; epitaxial growth; microstructure

Abstract: Single-crystalline, epitaxial $LaFeO_3$ films with 5 at. % substitution of Pd on the Fe site are grown on (100) $SrTiO_3$ substrate by pulsed-laser deposition technique. The epitaxial orientation relationships are $(110)[001]_{LFPO}||(100)[001]_{STO}$. X-ray diffraction and transmission electron microscopy reveal that the LFPO films have high structural quality and an atomically sharp LFPO/STO interface. After reduction treatments of as-grown LFPO films, very little Pd escaped the LFPO lattice onto the film surface, the formed Pd (100) particles are oriented epitaxially, and parallel to the LFPO films surface.

Introduction

Perovskite oxides based on $LaFeO_3$ and $CaTiO_3$ have recently attracted great attention. These materials, when doped with bivalent precious metal cations such Pd^{2+} or Pt^{2+}, exhibit appealing properties of precious-metal dissolving into/segregating out of the perovskite lattice and re-forming as small metallic particles upon the oxidizing and reducing conditions, respectively [1–5]. These properties make precious-metal-doped $LaFeO_3$ and $CaTiO_3$ as ideal candidates for application in automotive exhaust-gas catalyst and for studying metal/perovskite interaction, which are widely recognized but poorly characterized in heterogeneous catalysis.

Bulk $LaFeO_3$ has an orthorhombic structure (space group *Pbnm*) with the lattice parameters of a = 5.5570 Å, b = 5.5652 Å, c = 7.8542 Å [6], which can be described in terms of a pseudo-cubic lattice with a lattice constant of 3.923 Å. At here, Pd-doped $LaFeO_3$ single-crystal films will be grown, which is ideally suited to observe the precious metal migration in the perovskite lattice due to atomic running in single crystal is slower than polycrystal for much less grain boundary. Epitaxial single-crystal films of Pd-doped $LaFeO_3$, Pd-doping level is 5 at. % of the b-site cation sublattice, were deposited on $SrTiO_3$ substrate owing to their compatible structure and relatively small lattice mismatch. $SrTiO_3$ has a cubic perovskite structure with space group $Pm\bar{3}m$ and a lattice constant of 3.905 Å. The average lattice mismatch is ~0.46% between $LaFeO_3$ and $SrTiO_3$. Such small mismatch allows the epitaxial growth of thin films with high structural quality.

In this paper, we report on the results of Pd-doped lanthanum ferrite epitaxial single-crystal films deposited by pulsed-laser deposition technique, the films were characterized by x-ray diffractometer, x-ray photoelectron spectra and transmission electron microscope were used to investigate the structure transformation of the Pd-doped $LaFeO_3$ thin films before and after thermal treatment.

Experimental

The $LaFePdO_3$ (LFPO) thin films studied in this work were deposited on (100) $SrTiO_3$ (STO) substrate by the pulsed-laser deposition (PLD) technique using a KrF excimer laser (operating at 248 nm). The LFPO deposition target was fabricated via sol-gel method, which enables the mixing of the constituents at atomic levels. La_2O_3, $Fe(NO_3)_3{\cdot}9H_2O$, $Pd(NO_3)_2{\cdot}2H_2O$ and a dispersion agent were dissolved in dilute nitric acid to get transparent solutions. Evaporating the water in the solutions, the viscous gels were dried and then calcined at 800 °C for 1 h in the air to obtain perovskite powders containing homogeneously distributed precious metals. Then powders were pressed into pellet (about 3 cm in diameter and thickness 3 mm), which was finally sintered at 1300 °C for 12 h. The planar target was mounted on a holder and the set was then assembled into the deposition chamber. The base pressure achieved in the chamber prior to deposition was 4.0×10^{-6} Torr. A stoichiometric single phase LFPO target was ablated for 60 min at a laser power of 200 mJ and a repetition rate of 10 Hz onto (100) STO substrate at a fixed growth temperature of 600 °C and an oxygen partial pressure of 5.0×10^{-2} Torr. After growth, the films were processed under various conditions of temperature, atmosphere and duration.

The crystallinity and epitaxial orientation relationship of the LFPO films were investigated by x-ray diffraction (Rigaku MiniFlex X-ray diffractometer and Bede D1 high resolution X-ray diffractometer) θ–2θ scans, ω-rocking curve measurements, and ϕ scans with a CuK_α radiation. Cross-section TEM specimens were prepared from the LFPO films by standard methods (hand-lapping and polishing, followed by argon ion milling in a Gatan precision ion polishing system until electron transparent). Electron microscopy observations were performed with a JEOL JEM-3011 high resolution transmission electron microscope (HRTEM). X-ray photoelectron spectra (XPS) were obtained on a Kratos Axis Ultra spectrometer.

Results and Discussion

Fig. 1(a) shows a typical θ-2θ scan of LFPO films grown on (100) STO. The $h00_c/hh0$ peaks series belonging to the perovskite phase is clearly visible, where $h00$ peaks are marked by pseudo-cubic indices, denoted by subscript c, the cubic-to-orthorhombic transformation of the Miller indices are 100_c to 110, 200_c to 220, 300_c to 330, no extra LFPO or impurity peaks are detected, indicating that the LFPO films grown on (100) STO with an orientation relationship of $(110)_{LFPO}||(100)_{STO}$ at out-of-plane.

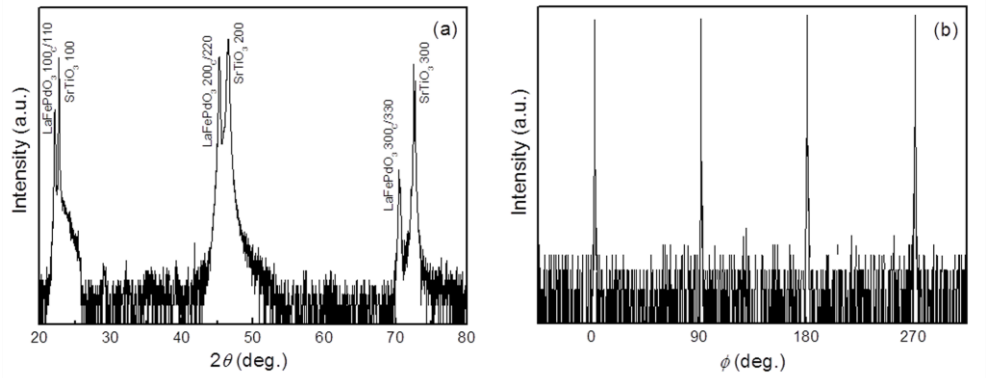


Fig. 1 (a) θ-2θ Xrd Pattern of a Lfpo Film Grown on (100) Sto Substrate, c Subscript Denotes the Pseudo-cubic Indices. (b) Xrd ϕ Scan of a Lfpo $(110)_c/200$ Peak.

Fig. 1(b) shows a ϕ scan of LFPO $110_c/200$ reflection, four sharp peaks are observed and located at the same azimuths with the STO 110 reflection, indicating that only the $100_c/110$-oriented LFPO single-crystallite was grown epitaxially on the top surface of (100) STO substrate, and in-plane orientation relationship is $[001]_{LFPO}||[001]_{STO}$. The ω-rocking curve full width at half maximum (FWHM) of $\Delta\omega = 0.05°$ for the LFPO $200_c/220$ peak indicates good crystallinity of the film.

Fig. 2(a) shows a typical low-magnification cross-sectional bright-field image of the LFPO films grown on (100) STO. It is apparent that the LFPO film has uniform thickness, both flat interface and top surface, no cracks in film. The film surface has a root-mean-square roughness of 2.69 Å measured by atomic force microscopy. The inset of (a) is the SAED pattern of film and substrate. High-resolution TEM image in Fig. 2(b) reveals an atomically sharp interface between the LFPO and STO layers, the long *c*-axis of the LFPO orthorhombic unit cell is oriented parallel to the interface and to the [001] axis of STO.

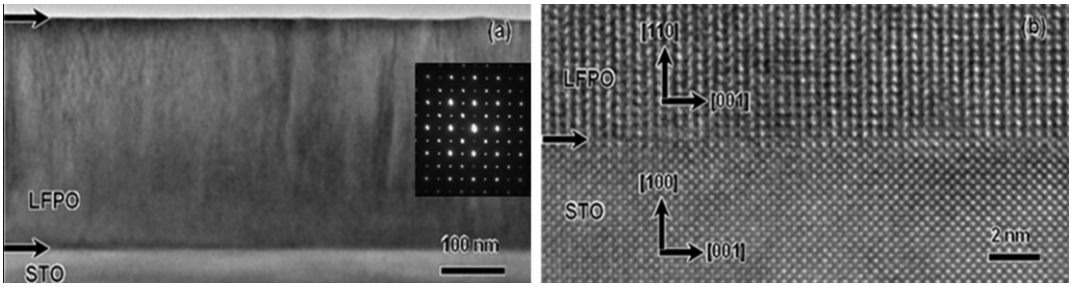


Fig. 2 (a) Cross-section TEM Image of a LFPO Film Grown on (100) STO. Arrows Denote the Top Film Surface and Film/Substrate Interface, Respectively. The Inset is the SAED Pattern of Film and Substrate. (b) HRTEM Image of the LFPO/STO Interface. The *c*-Axis of the LFPO Orthorhombic Unit Cell is Oriented Parallel to the Interface and to the [001] Axis of STO.

XPS results find the expected surface composition, Pd 3*d* spectrum shows two oxidized states of Pd ion, the signals are strong, but neither corresponding to the usual Pd^{2+} and Pd^{4+} states, and also unlike the results of Tanaka *et al* [3]. Here we think that Pd exists in the crystal of LFPO. Subsequently, the as-grown LFPO film is annealed at various thermal treatment conditions, changes in the surface compositions induced by thermal treatment are determined by XPS, results reveal that the peak position of Pd–O bonds shift toward lower binding energy for the sample as the annealing temperature and hydrogen concentration increase, and much of the Pd exist in metallic state at 800 °C in 10% H_2/N_2, as shown in Fig. 3.

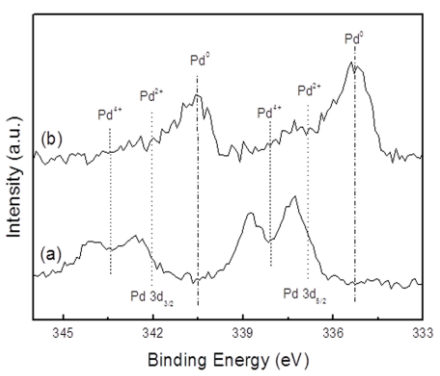


Fig. 3 XPS Scans in Pd 3d Region for LaFe0.95Pd0.05O3, (a) as-grown; (b) Reduced at 800 °C in 10% H2/N2. The Binding Energies were Corrected Based on Measured Values for C1s. Spectra Are Vertically Offset. Vertical Lines Indicate the Expected Peak Positions of the Pd Spin-orbitdoublets (3d5/2, 3d3/2) for Pd0, Pd2+, and Pd4+ [3].

Fig. 4 is HRTEM cross-sectional image of the LFPO as-grown film reduced at 800 °C in 10% H_2/N_2. It shows that the Pd in solid solution migrate to the surface region of the LFPO film, and lattice fringes of the formed Pd particles extend into the top surface of LFPO thin film, indicating that the formed Pd particles are oriented epitaxially, with Pd (100) parallel to the LFPO film surface. Maybe we can explain the above phenomena via classical nucleation model, i.e., the migration of Pd from interior toward the surface region of LFPO thin film is a thermally activated process, high heating temperature can provide a large thermal energy to overcome the high energy barrier of preventing the diffusion of Pd from interior toward surface of LFPO film, and oxygen vacancy formed under reduction atmosphere, which provide diffusion channels for Pd. Compared to out-of-plane diffusion of Pd from the interior to surface of LFPO thin film, in-plane Pd diffusion is easier. Nonstoichiometry appears in LFPO film for oxygen insufficiency during annealing, which inducing construction of new steps with high binding energy due to dangling or broken bond at the top surface of LFPO film, where the migrated Pd can be captured, and then be aggregated or coalesced into clusters or particles.

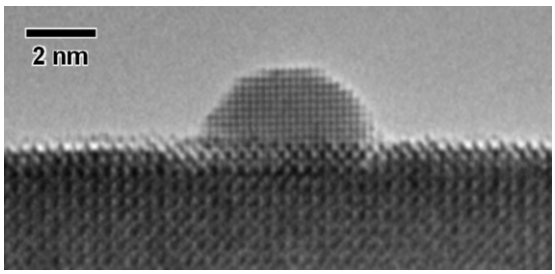


Fig. 4 HRTEM Image of a Typical Pd Particle Found on the LFPO Film Surface After Reduction.

Conclusions

Precious-metal-doped perovskite has structural and chemical transformations during annealing, and thin film materials are ideally suited to study the migration behavior of the precious-metal in the particular perovskite lattice.

Acknowledgments

This work was supported by the Natural Science Foundation of Gansu Province, China (Grant No. 1107RJZA083), finished at Prof. Xiaoqing Pan's research group of Department of Materials Science and Engineering, University of Michigan, Ann Arbor, USA. The author acknowledges Dr. Michael B. Katz for obtaining the TEM results.

References

[1] Y. Nishihata, J. Mizuki, T. Akao, H. Tanaka, M. Uenishi, M. Kimura, T. Okamoto and N. Hamada, Self-regeneration of a Pd-perovskite catalyst for automotive emissions control, Nature, 418 (2002) 164-167.

[2] D. Matsumura, Y. Nishihata, J. Mizuki, M. Taniguchi, M. Uenishi and H. Tanaka, Dynamic structural change in Pd-perovskite automotive catalyst studied by time-resolved dispersive x-ray absorption fine structure, J Appl Phys. 107 (2010) 124319-124324.

[3] H. Tanaka, I. Tan, M. Uenishi, M. Taniguchi, M. Kimura, Y. Nishihata and J. Mizuki, $LaFePdO_3$ perovskite automotive catalyst having a self-regenerative function, J Alloys Compd. 408-412 (2006) 1071-1077.

[4] M.B. Katz, G.W. Graham, Y.W. Duan, H. Liu, C. Adamo, D.G. Schlom and X.Q. Pan, Self-regeneration of Pd-$LaFeO_3$ catalysts: New insight from atomic-resolution electron microscopy, J Am Chem Soc. 133 (2011) 18090-18093.

[5] M.B. Katz, S.Y. Zhang, Y.W. Duan, H.J. Wang, M.H. Fang, K. Zhang, B.H. Li, G.W. Graham and X.Q. Pan, Reversible precipitation/dissolution of precious-metal clusters in perovskite-based catalyst materials: Bulk versus surface re-dispersion, J Catal. 293 (2012) 145-148.

[6] S.E. Dann, D.B. Currie, M.T. Weller, M.F. Thomas and A.D. Al-Rawwas, The effect of oxygen stoichiometry on phase relations and structure in the system $La_{1-x}Sr_xO_{3-\delta}$ ($0 \le x \le 1$, $0 \le \delta \le 0.5$), J Solid State Chem. 109 (1994) 134-144.

Advanced Materials Research Vol. 936 (2014) pp 287-292
© (2014) Trans Tech Publications, Switzerland
doi:10.4028/www.scientific.net/AMR.936.287

The Preparation of the Highly Preferred Orientation of Wurtzite Structure Zinc Oxide Films

Lan Lei-Lei[1,a],Zhou Dan[2,b],Gu Guang-Rui[1,c*],Wu Bao-Jia[1,d], Tian Lian-Hua[1,e]

[1] Department of Physics, College of Science, Yanbian University, Yanji 133002, China
[2] State Key Laboratory for Superhard Materials, Jilin University, Changchun 130012, China

[a] 1060760595@qq.com, [b] 747836188@qq.com, [c] grgu@ybu.edu.cn, [d] jbwu@ybu.edu.cn, [e] lhtian@ybu.edu.cn, *corresponding author

Keywords: magnetron sputtering, ZnO thin films, structure, substrate temperature

Abstract. Zinc oxide (ZnO) films are prepared on n-Si substrates by means of radio frequency (RF) magnetron sputtering method. The influences of substrate temperature on the crystal orientation and crystalline structure of ZnO films are investigated by X-ray diffraction (XRD) and Raman spectroscopy. The surface morphologies are studied by scanning electron microscope (SEM). It is indicated that ZnO films with wurtzite structure were successfully prepared. When the substrate temperature reduced to 100 ^{o}C, the wurtzite structure with highly preferred orientation along the (002) plane of the ZnO film is prepared and the elliptical shape particles distributed uniformly on the ZnO film surface. The higher substrate temperature can offer more kinetic energy for mobility of particle on the surface to achieve other crystalline growth, resulting in the highly c-axis-oriented crystalline structure is destroyed.

Introduction

In recent years, wide bandgap semiconductors have attracted much attention. Zinc oxide (ZnO) is a typical wide bandgap (3.37 eV at 300 K) semiconductor with large exciton binding energy (60meV) [1], it has more excellent properties such as good chemical stability, high melting point, excellent mechanical strength, photoelectric properties and thermal conductivity, which can be used as field emitter [2], light emitting diodes (LED) [3], laser diodes [4], ultraviolet photo detectors [5], chemical sensors [6], and so on. However, these are some problems to hinder the application and development of ZnO such as the fabrication of stable and reliable p-type ZnO thin films and the growth mechanism [7]. Therefore, the studies of preparation, properties, growth mechanism and applications of ZnO films are important significance both in basic science and practical application.

The crystal and structural properties of ZnO thin films strongly depend on growth technique and growth condition. There are several methods to fabricate high quality ZnO films, such as chemical vapor deposition (CVD) [8], sol–gel [9], pulsed laser deposition [10], sputtering [11] hydrothermal method [12], and so on. Among all these methods, reactive magnetron sputtering has been most widely used as depositing the film because of its advantages of large scale production, high maneuverability and stoichiometry controllability. So many researches have been carried out on the dependence of film properties on sputtering parameters [13-15]. In this study, we prepared a series of ZnO films by radio frequency (RF) magnetron sputtering at different substrate temperature, and discussed the influences of substrate temperature on the structure of ZnO films.

Experimental

The ZnO films are deposited on n-Si (100) substrates using a high purity (99.99%) ZnO target using RF magnetron sputtering method. Argon and oxygen are used as the working gases. The distance between the target and substrate is fixed at 50 mm. The base pressure is below 5×10^{-4} Pa. Prior to the film deposition, the substrates are ultrasonically rinsed in acetone, ethanol and distilled water sequentially and dried with nitrogen. In order to improve the crystalline quality and reduce the impact of impurities, the target is pre-sputtered with high-power for about 10 minutes. Table 1 shows the detailed deposition parameters of the ZnO films deposited by RF magnetron sputtering. The crystal structure of the ZnO films is characterized by X-ray diffraction (XRD) with Cu Ka radiation (λ=0.1541nm). Raman spectra are taken by a Renishaw micro-Raman spectroscope. The surface morphologies are examined by scanning electron microscope (SEM).

TABLE 1. THE DEPOSITION PARAMETERS OF THE ZNO FILMS DEPOSITED BY RF MAGNETRON SPUTTERING

Substrate temperature[^{o}C]	Working pressure[Pa]	Sputtering power[W]	Ar:O2	Deposition time[min]
400,300,200,100	1	150	3:1	90

Results and discussion

Fig.1 shows the XRD patterns of ZnO thin films prepared at different substrate temperature. It is revealed that the ZnO thin films have the hexagonal wurtzite crystal structure with (002) preferred orientation, and no characteristic peaks due to other impurities are observed. It is generally known that the grains are more easily grown in the planes of lower the surface energy. For the ZnO films, the (002) orientation with the lowest surface energy would be more favorable, a preferential orientation along c-axis and the grains become uniformly perpendicular to the substrate surface then form a preferred c-axis orientation, other orientations would be restrained [16]. With the decreasing substrate temperature, other ZnO crystal directions, such as (100), (110) and (103) disappear, this may be because the trend that the adsorbed atoms gain extra thermal energy and tend to move to another preferred site is restrained with the decreasing substrate temperature. The high substrate temperature can offer more kinetic energy for mobility of particle on the surface to achieve other crystalline growth [17]. It demonstrates that the films more easily became polycrystalline in high substrate temperature.

The crystal grain size at (002) peaks of the ZnO films are calculated by Scherrer formula [18]:

$$D = k\lambda / \beta\cos\theta . \quad (1)$$

where D is the crystal grain size, k is the correction factor, λ is the wavelength of the incident beam, β is the full width at half maximum (FWHM) corresponding to Bragg diffraction angle. Here, k and λ values are taken as 0.9 and 0.1541 nm. And the lattice constant for the ZnO films are calculated by the following relation [19]:

$$\lambda = 2d_{hkl}\sin\theta . \quad (2)$$

$$\frac{1}{d_{hkl}^2}=\frac{4}{3}\left(\frac{h^2+hk+k^2}{a^2}\right)+\frac{l^2}{c^2}. \quad (3)$$

where d_{hkl} is the distance between adjacent planes in the set (hkl), λ is the wavelength of the X-ray, θ is the diffraction angle, a and c is the lattice parameter, and h, k and l are the indices of the planes. The crystal grain size and lattice constant of the ZnO films deposited at different substrate temperature are shown in the table 2. From the table 2, we can see that the films showed lattice distortion comparing with the bulk ZnO (a=0.32498 nm, c=0.52066 nm), this mainly is attributed to the residual stress developed in thin films [20].

The calculation of the film residual stress is based on the biaxial strain model. The strain in the c axis can be expressed by the following formula [21]:

$$\varepsilon=(c-c_0)/c_0. \quad (4)$$

where c and c_0 are the lattice constants of ZnO films and bulk ZnO, respectively. The residual stress parallel to the film surface can be given by the following formula [22]:

$$\sigma=\frac{2c_{13}^2-c_{33}(c_{11}+c_{12})}{2c_{13}}\bullet\varepsilon. \quad (5)$$

For the elastic constants, the following values for crystal ZnO are use: c_{13}=104.2 GPa, c_{33}=213.8 GPa, c_{11}=208.8 GPa, c_{12}=119.7 GPa [23]. The residual stress of the ZnO films deposited on different substrate temperature are shown in the table 2. The ZnO film deposited at the substrate temperature of 100 ^{o}C has the minimum residual stress, indicating that it has the best crystal quality. The residual stress of the film may include a thermal stress come from the thermal mismatch between the film and Si substrate and the intrinsic stress come from the crystal defects of the films [24].

Table 2. The crystal grain size, lattice constant and residual stress of the ZnO film deposited at different substrate temperature.

Substrate temperature[^{o}C]	crystal grain size [nm]	σ [GPa]	Lattice constant[nm]	
			a	*c*
400	19.3	1.942189	0.32427	0.51632
300	20.1	-0.27298	0.32506	0.52127
200	23.2	1.038221	0.32347	0.51834
100	18.0	-0.00895	0.32308	0.52068

In order to further investigate the structure of the ZnO films, the Raman spectra of the films is measured. The broadening of the Raman peak is the result of the phonon scattering caused by stress gradients, small grains, point defects and interfaces, and the intensity and the FWHM of Raman mode can describe the crystal quality of the films [25]. The ZnO is C6v-4 (P63mc) point group symmetry and has six Raman active optical phonon modes at the center of the Brillouin zone, the frequencies of the Raman modes in ZnO are E_2 (low) = 101 cm^{-1}, E_2 (high) = 437 cm^{-1}, A_1 (TO) = 380 cm^{-1}, A_1 (LO) = 574 cm^{-1}, E_1 (TO) = 407 cm^{-1} and E_1 (LO) = 583 cm^{-1} [26]. Fig.2 shows Raman spectra of the films grown at different substrate temperature. The films exhibit two peaks located at

about 436 cm^{-1} and 580 cm^{-1} which is related to E_2 (high) mode and E_1 (LO) mode , respectively. The peak at 520 cm^{-1} derives from the Si substrate [27]. The E_2 (high) mode is corresponding to band characteristics of the wurtzite phase [28]. The E_1 (LO) mode is related to oxygen vacancies [29]. Comparing with the bulk ZnO, the Raman frequency happens shift, the shift is probably due to the effect of the impurity or defect in the crystal, the tensile strain and laser irradiation heating [30]. The E_2 (high) mode peak of the film deposited at 100 °C has a good symmetrical spectral shape, in which the FWHM value is obviously smaller and the intensity is stronger than the films deposited on higher substrate temperature. It demonstrated that the crystal quality is worse with the increasing substrate temperature. This is consistent with measuring results from the XRD pattern.

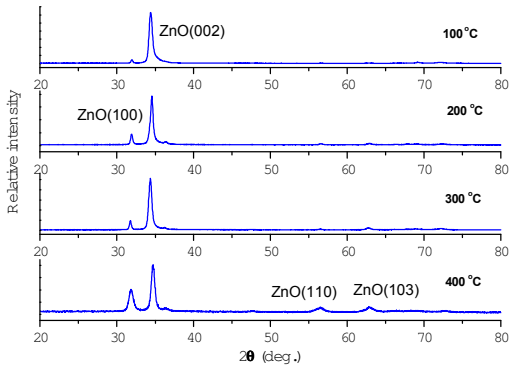


Fig. 1. XRD patterns of ZnO thin films prepared at different substrate temperature

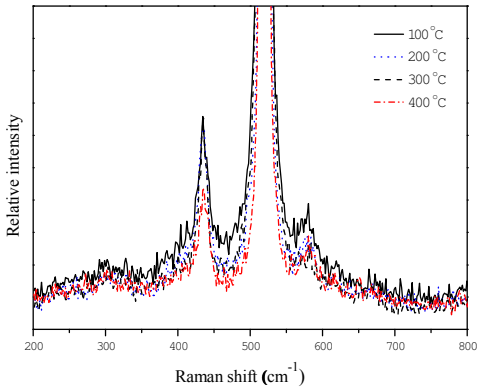


Fig. 2. The Raman spectra of the ZnO films sputtered at different substrate temperature.

In order to understand the surface features and size distribution of the deposited ZnO thin films, SEM analysis is carried out. Fig. 3 shows the surface and cross-section images of the ZnO film deposited at 100 °C, respectively. As shown in Fig. 3 (a), crystal particles with about 200 nm size and uniform top surfaces are found on the surface of the ZnO film. As shown in Fig.3 (b), the thickness of the ZnO layer is about 2.5 μm, and exhibits finer crystallinity and columnar structure with c-axis perpendicular to the Si substrate interface, which is consistent with the XRD result.

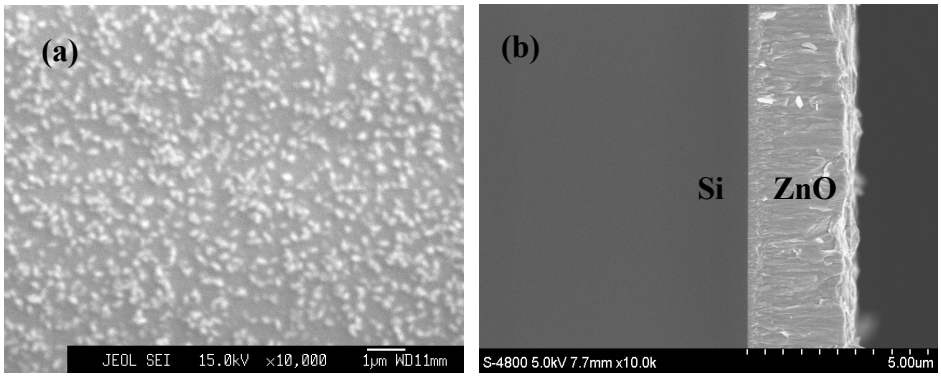


Fig. 3. The surface (a) and cross-section (b) SEM images of the ZnO film deposited at 100 °C.

Conclusions

In summary, the high crystalline quality of wurtzite structure ZnO films are prepared on n-Si substrates using RF magnetron sputtering method. The XRD shows that the films have a c-axial orientation along (002) plane and Raman spectrum measurement shows that high crystalline quality ZnO films have been obtained. In this study, highly c-axis-oriented crystalline structure is destroyed

by the increasing substrate temperature, indicating that the higher substrate temperature can offer more kinetic energy for mobility of particle on the surface to achieve other crystalline growth.

Acknowledgment

We are thankful for financial support from the National Natural Science Foundation of China (Grants No. 51272224, 11164031 and 51362028)

References

[1] D. M. Bagnall, Y. F. Chen, Z. Zhu, T. Yao, S. Koyama, M. Y. Shen, T. Goto, Optically pumped lasing of ZnO at room temperature, Appl. Phys. Lett. 70 (1997) 2230-2232.

[2] C. X. Xu, X. W. Sun, Field emission from zinc oxide nanopins, Appl. Phys. Lett. 83 (2003) 3806-3808.

[3] J. M. Bao, M. A. Zimmler, F. Capasso, X. W. Wang, Z. F. Ren, Broadband ZnO single-nanowire light-emitting diode, Nano Letters 6 (2006) 1719-1722.

[4] J. C. Johnson, H. Q. Yan, P. D. Yang, R. J. Saykally, Optical cavity effects in ZnO nanowire lasers and waveguides, J. Phys. Chem. B 107 (2003) 8816-8828.

[5] S. Liang, H. Sheng, Y. Liu, Z. Huo, Y. Lu, H. Shen, ZnO Schottky ultraviolet photodetectors, Journal of Crystal Growth 225 (2001) 110-113.

[6] P. Mitra, A. P. Chatterjee, H. S. Maiti, ZnO thin film sensor, Materials Letters 35 (1998) 33-38.

[7] L. J. Mandalapu, Z. Yang, S. Chu, J. L. Liu, Ultraviolet emission from Sb-doped p -type ZnO based heterojunction light-emitting diodes, Applied Physics Letters 92(2008) 122101.

[8] M. Purica, E. Budianu, E. Rusu, M. Danila, R. Gavrila, Optical and structural investigation of ZnO thin films prepared by chemical vapor deposition (CVD), Thin Solid Films 403(2002) 485-488.

[9] H. L. Liu, J. H. Yang, Z. Hua, Y. J. Zhang, L. L. Yang, L. Xiao, Z. Xie, The structure and magnetic properties of Cu-doped ZnO prepared by sol–gel method, Applied Surface Science 256 (2010) 4162-4165.

[10] B. J. Jin, S. H. Bae, S. Y. Lee, S. Im, Effects of native defects on optical and electrical properties of ZnO prepared by pulsed laser deposition, Materials Science and Engineering B 71 (2000) 301-305.

[11] B. G. Choi, I. H. Kim, D. H. Kim, K. S. Lee, T. S. Lee. B. Cheong, Y. -J. Baik, W. M. Kim, Electrical, optical and structural properties of transparent and conducting ZnO thin films doped with Al and F by rf magnetron sputter, Journal of the European Ceramic Society 25 (2005) 2161-2165.

[12] K. H. Tam, C. K. Cheung, Y. H. Leung, A. B. Djurisic, C. C. Ling, C. D. Beling, S. Fung, W.M. Kwok, W. K. Chan, D. L. Phillips, L. Ding, W. K. Ge, Defects in ZnO nanorods prepared by a hydrothermal method, J. Phys. Chem. B 110 (2006) 20865-20871.

[13] G. P. Daniel, V. B. Justinvictor, P. B. Nair, K. Joy, P. Koshy, P. V. Thomas, Effect of annealing temperature on the structural and optical properties of ZnO thin films prepared by RF magnetron sputtering, Physica B 405 (2010) 1782-1786.

[14] X. L. Zhang, K. N. Hui, K. S. Hui, J. Singh, Structural and optical characterization of high-quality ZnO thin films deposited by reactive RF magnetron sputtering, Materials Research Bulletin 48 (2013) 1093-1098.

[15] L. Balakrishnan, S. Gowrishankar, N. Gopalakrishnan, Fabrication of tridoped p-ZnO thin film and homojunction by RF magnetron sputtering, Ceramics International 38 (2012) 6221-6227.
[16] S. Singh, P. Chakrabarti, Comparison of the structural and optical properties of ZnO thin films deposited by three different methods for optoelectronic applications, Superlattices and Microstructures 64 (2013) 283-293.
[17] H. L. Chen, Y. M. Lu, W. S. Hwang, Characterization of sputtered NiO thin films, Surf. Coat. Technol. 198 (2005) 138-142.
[18] R. J. Hong, J. D. Shao, H. B. He, Z. X. Fan, Influence of buffer layer thickness on the structure and optical properties of ZnO thin films, Applied Surface Science 252 (2006) 2888-2893.
[19] L. G. Ma, X. Q. Ai, X. L. Huang, S. Y. Ma, Effects of the substrate and oxygen partial pressure on the microstructures and optical properties of Ti-doped ZnO thin films, Superlattices and Microstructures 50 (2011) 703–712.
[20] D. P. Zhang, P. Fan, Z. H. Zheng, L. L. Ru, J. J. Huang, X. M. Cai, T. B. Chen, Effects of different thermal treatment on optical properties and microstructure of ZnO thin films, Advanced Materials Research 197 (2011) 1766 -1770.
[21] [21] R. J. Hong, J. B. Huang, H. B. He, Z. X. Fan, J. D. Shao, Influence of different post-treatments on the structure and optical properties of zinc oxide thin films, Applied Surface Science 242 (2005) 346-352.
[22] D. P. Zhang, P. Fan, X. M. Cai, J. J. Huang, L. L. Ru, Z. H. Zheng, G. X. Liang, Y. K. Huang, Properties of ZnO thin films deposited by DC reactive magnetron sputtering under different plasma power, Applied Physics A 97 (2009) 437-441.
[23] R. Cebulla, R. Wendt, K. Ellmer, Al-doped zinc oxide films deposited by simultaneous rf and dc excitation of a magnetron plasma: Relationships between plasma parameters and structural and electrical film properties, J . Appl. Phys. 83 (1998) 1087-1095.
[24] B. Window, K. H. Muller, Strain, ion bombardment and energetic neutrals in magnetron sputtering, Thin Solid Films 171 (1989) 183-196.
[25] V. Lughi, D. R. Clarke, Defect and stress characterization of AlN films by raman spectroscopy, Appl. Phys. Lett. 89 (2006) 241911.
[26] H. Q. Bian, S. Y. Ma, F. M. Li, H. B. Zhu, Influence of ZnO buffer layer on microstructure and Raman scattering of ZnO:Ag film on Si substrate, Superlattices and Microstructures 58 (2013) 171-177.
[27] S. H. Huang, H. Xiao, S. Shou, Annealing temperature dependence of Raman scattering in Si/SiO2 superlattice prepared by magnetron sputtering, Applied Surface Science 255 (2009) 4547-4550.
[28] Z. G. Wang, H. Zang, K. F. Wei, J. R. Sun, C. F. Yao, T. L. Shen, Y. Z. Ma, L. L. Pang, Y. B. Zhu, Raman investigation of incident N-, Xe-ions induced effects in ZnO thin films, Nuclear Instruments and Methods in Physics Research B 269 (2011) 837-841.
[29] F. Rubio-Marcos, C. V. Manzano, J. J. Reinosa, I. Lorite, J. J. Romero, J. F. Fernandez, M. S. Martin-Gonzalez, Modification of optical properties in ZnO particles by surface deposition and anchoring of NiO nanoparticles, Journal of Alloys and Compounds 509 (2011) 2891-2896.
[30] R. P. Wang, G. Xu, P. Jin, Size dependence of electron-phonon coupling in ZnO nanowires, Physical Review B 69 (2004) 113303.

CHAPTER 4:

Nanomaterials and Applied Nanotechnologies

Advanced Materials Research Vol. 936 (2014) pp 295-299
© (2014) Trans Tech Publications, Switzerland
doi:10.4028/www.scientific.net/AMR.936.295

A Facile Method to Preparation of Amphiphilic Perylene Tetracarboxylic Diimide/ZnS Hybrid Nanocomposites and Improved Semiconducting Property

Jingang Song[1,a], Hongyan Wang[1,b], Nianshuai An[1,c], Yanli Chen*[1,d]

[1]Shandong Provincial Key Laboratory of Fluorine Chemistry and Chemical Materials, School of Chemistry and Chemical Engineering, University of Jinan, Jinan 250022, China

[a]songjingang1987@126.com, [b]chm_wanghy@ujn.edu.cn, [c]annianshuai@163.com, [d]chm_chenyl@ujn.edu.cn

Keywords: HH-PDI, ZnS, nanocomposite, semiconducting property.

Abstract: A self-assembled film of an amphiphilic perylene tetracarboxylic diimide derivative (N-hexane-N'-(1-phenyl-4-aminoethanol)-1,7-di(4-tert-butylphenoxy)perylene-3,4;9,10-tetracarboxy late diimide, HH-PDI) has been used as the organic template to produce the first example of monodispersed nano-particles of HH-PDI/ZnS composites. The HH-PDI pure film and HH-PDI/ZnS nanocomposites were characterized by UV-vis absorption, X-ray diffraction (XRD), scanning electron microscopy (SEM) and current-voltage (I-V) measurements. Experimental results revealed the film crystallinity and general molecular order for HH-PDI molecules in the nanocomposites are improved effectively in comparison with those in the pure film due to the introduction of ZnS nanocrystals. The electrical conductivity of the HH-PDI/ZnS nanocomposites (6.6×10^{-5} S cm^{-1}) is more than ca. 2 order of magnitude higher than that of (3.6×10^{-7} S cm^{-1}). The present result provides an efficient way to improve the performance of organic semiconductors through introducing inorganic semiconducting nanocrystals.

Introduction

Semiconductor nanomaterials can often display unique optical, electronic, and magnetic properties, whereas these properties strongly depend on the size and shape of the nanoparticles [1]. As a result, synthetic control over the morphology, size, and crystallographic orientation of materials is highly desired [2]. Among the methods for the preparation of nanomaterials, growing of inorganic structures directly on an organic template has recently emerged as a powerful technique [3]. Perylenetetracarboxylic diimide (PDI) derivatives have been extensively and intensively investigated as advanced molecular materials [4]. In particular, because of their great potential application as organic semiconductors in different molecular electronic devices, the fabrication of ordered nanostructures of these functional molecular materials has become an attracting research area in the past decade [5]. The semiconducting PDI-based organic/inorganic composites in nanoscale should be highly desired for nano-optoelectronic materials due to the possibility of combining desired properties from both. In the present paper, we reported controlled preparation of ZnS nanoparticles in a self-assembled (SA) film of amphiphilic PDI derivative modified with distinctly different hydrophobic/hydrophilic side-chains, N-hexane-N'-(1-phenyl-4-aminoethanol)-1,7-di(4-tert-butylphenoxy)perylene-3,4;9,10-tetracarboxyl ate diimide (HH-PDI), Fig. 1. By using SA film of amphiphilic HH-PDI molecules as a template, the monodisperse HH-PDI/ZnS nanocomposites were prepared at the air–water interface. The enhanced semiconducting properties were observed for the hybrid nanocomposites relative to respective the pure HH-PDI film.

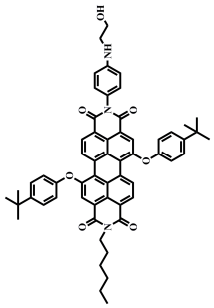


Fig. 1 The molecular structure of HH-PDI.

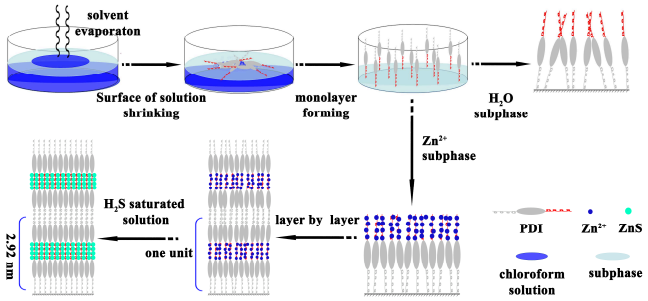


Fig. 2 Procedures for the fabrication of the HH-PDI and HH-PDI/ZnS nanocomposites.

Experimental Section

Chemicals

The sample of HH-PDI was synthesized according to previously published procedures [6]. All the chemicals are analytical reagents and used without further purification.

Preparation and characterization of the HH-PDI SA film and HH-PDI/ZnS nanocomposites

(Fig.2)**.** Prior to the deposition, substrates were successively sonicated in dichloromethane, methanol and distilled water and dried with argon gas. (i) HH-PDI (HH-PDI/Zn^{2+}) SA film: 5.0 mL of dichloroform solution (0.20 mg mL^{-1}) was put into a culture dish (diameter: 9 cm, height: 1.8 cm), then 50 mL water (or $ZnSO_4$ aqueous solution 0.081 mg mL^{-1}) was slowly added onto the surface of the solution. (caution: the amount of water added cannot cover completely the air/CH_2Cl_2 interface so as to keep the path for the evaporation of CH_2Cl_2 solvent). During solvent evaporation, HH-PDI molecules gradually assembled to form some fine nanostructures at the CH_2Cl_2-water interface. After complete evaporation of CH_2Cl_2, the densely packed film remained on the water surface. Then, the film can be easily transferred from the water surface onto a quartz or Si/SiO_2 substrate by horizontal lifting. This process was repeated to obtain the required number of layers. Residual water on the substrates, between transfer steps and after the final transfer, was removed with a stream of nitrogen. (ii) HH-PDI/ZnS nanocomposites: HH-PDI/Zn^{2+} nanocomposites were dipped to a H_2S saturated solution (~0.1 mol L^{-1} for 12 h). After being washed with water, the thin film was removed with a stream of nitrogen for SEM (Hitachi S-4300F), X-ray diffraction (Rigaku D/max-γB), UV-vis spectroscopy (Hitachi U-4100) measurements, respectively. The reactions were carried out at room temperature. The device for I-V measurements (Keithley 4200) were fabricated according to previously published procedures [7].

Results and discussion

UV-vis absorption spectra

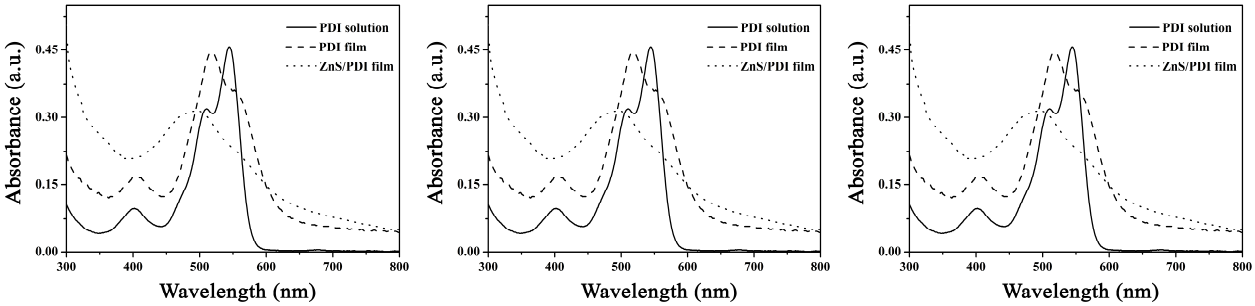


Fig. 3 UV-vis spetra of HH-PDI in dichloroform (solid line) and the HH-PDI pure film (dash line) and HH-PDI/ZnS nanocomposites (dot line). Fig. 4 The X-ray diffraction patterns of HH-PDI pure film (A) and HH-PDI/ZnS nanocomposites (B). The vertical lines show the ZnS powder diffraction pattern from the Joint Committee on Powder Diffraction Standards (JCPDS) Card No. 05-0566.

Fig. 3 displays the UV/Vis spectra of the HH-PDI pure film and HH-PDI/ZnS nanocomposites in comparison with that in the solution. As expected, HH-PDI in dichloroform showed typical feature of the non-aggregated diphenoxy-substituted PDI chromophores in the electronic absorption spectra [8]. The absorptions at about 545 and 514 nm can be attributed to the 0-0 and 0-1 vibronic band of the S_0-S_1 transition, respectively, while the observed absorption band around 402 nm is attributed to the electronic S_0-S_2 transition [6]. Note that the absorption of HH-PDI in the pure film and nanocomposites changed significantly in the ratio of the intensities of the 0-0/0-1 peaks, while peak positions of absorption maxima of HH-PDI remained almost unaltered in the pure film, and blue-shifted to ca.500 nm in the nanocomposites. Those kinds of changes implied the formation of face-to-face π stacks (H-aggregate) and stronger molecular stacking interaction between the PDI skeletons of HH-PDI in the nanocomposites than the pure film [8], which is able to provide the more efficient π stacking and in turn is responsible for the much larger carrier mobilities revealed for the devices fabricated from the former than the latter one(*vide infra*). Furthemore, by comparing the UV-vis spectra of HH-PDI pure film and HH-PDI/ZnS nanocomposites, we can find that the nanocomposites exhibits a higher absorption intensity in the wavelength region below 350 nm, which is very similar to the absorption of bulk ZnS nanoparticles [9], suggesting the ZnS nanostructures have been shaped in the nanocomposites.

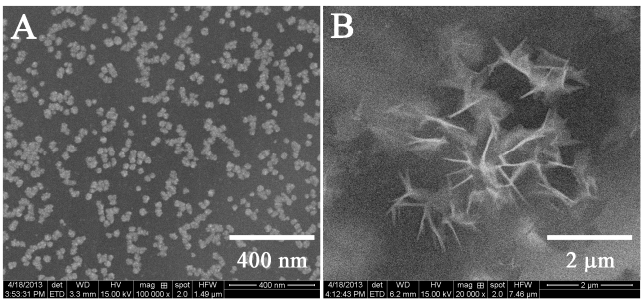


Fig. 5 SEM images of HH-PDI/ZnS nanocomposites (A) and HH-PDI pure film (B).

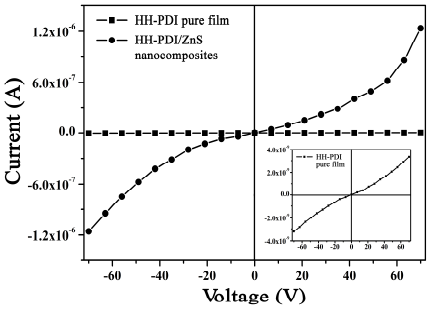


Fig. 6 The current-voltage (I-V) characteristics of the HH-PDI pure film (■), HH-PDI/ZnS nanocomposites (●).

X-ray diffraction (XRD) pattern

The XRD patterns for the HH-PDI pure film and HH-PDI/ZnS nanocomposites are shown in Fig. 4. In the nanocomposites, various diffraction peaks were observed, which were, according to JCPDS file No. 05-0566 (shown as vertical lines in Fig. 4), assigned to the (111), (220) and (311) planes of the cubic phase of zinc blende ZnS. XRD patterns in combination with UV-vis and SEM analysis (*vide infra*) of the samples provided exclusive evidence that ZnS nanoparticles formed exhibit a

highly crystalline structure. On the other hand, the XRD pattern of the HH-PDI pure film exhibits the (001) Bragg peak at 2θ = 4.48°, corresponding to a periodic spacing distance of 1.94 nm, Fig. 4A. Consequently, orientation angle of HH-PDI rings with respect to the substrate surface of ca. 59.4° are estimated for HH-PDI in pure film based on the length of HH-PDI (2.30 nm) taken from the energy-optimized structure. A slipped co-facial stacking mode with the molecular long-axis perpendicular to the substrate surface (H aggregate) was achieved for HH-PDI [10], which is in line with that UV-vis absorption. In addition, the appearance of a broad peak at 0.42 nm for the HH-PDI pure film suggested that there exists liquid-like ordered packing of long alkyl chains [6]. A sharper peak at 0.31 nm (2θ = 28.9°) obtained for the HH-PDI pure film is ascribed to π-π stacking distance of PDI rings between the adjacent molecule, implied a favorable molecular packing from co-facial conformation depending mainly on the π-π interaction between perylene rings in the HH-PDI film. However, in the HH-PDI/ZnS nanocomposites, as shown in Fig. 4B, the XRD diagram shows two well-defined low-angle diffraction peaks at 2θ = 3.01° and 6.07° (corresponding to a periodic spacing distance of 2.92 and 1.46 nm), which are ascribed to the diffractions from the (001) and (002) planes of HH-PDI, indicating the long range molecular ordering across the thickness of the nanocomposites. Due to the special asymmetric molecular structure of HH-PDI, the value of *d* (2.92 nm) in the nanocomposites is actually the thickness of the bilayer (Fig.2). Meanwhile, the diffraction at 0.42 nm disappeared, indicating that the long hydrophobic alkyl chain of HH-PDI in the nanocomposites might no longer take an extended conformation but a folded and tangled conformation instead. Consequently, a significant decreased monolayer thickness (1.46 nm) of HH-PDI obtained in the nanocomposites as compared to that in the HH-PDI pure film can be achieved. Therefore, ZnS crystals grown on HH-PDI organic template has a remarkable influence on the assemble structure of both hydrophobic and hydrophilic side-chains attached to HH-PDI in the nanocomposites.

Morphology of the HH-PDI pure film and HH-PDI/ZnS nanocomposites

As revealed by the scanning electron microscope (SEM), Fig. 5A, the unique nanoparticles were obtained with the average diameter of ca. 20 nm for HH-PDI/ZnS nanocomposites. This is in good contrast to the sheet-like microstructure with large gaps and cracks between aggregate domains observed for HH-PDI molecules in pure film, Fig. 5B, which will surely add negative effect on the electronic conductivity for the I-V devices fabricated.

Semiconducting properties

Fig. 6 shows the current-voltage (I-V) characteristics of the HH-PDI pure film and HH-PDI/ZnS nanocomposites. According to the equation reported in the literatures [7], the electronic conductivity, is calculated to be around 6.6×10^{-5} and 3.6×10^{-7} S cm^{-1} for the HH-PDI pure film and HH-PDI/ZnS nanocomposites, respectively. Comparing with the HH-PDI pure film, the improved conductivity for the nanocomposites might be attributed to readily π- stacks with adjacent planar molecules and the introduction of ZnS n-type semiconducting nanocrystal. The absence of traps or defects in these nanocomposites with more efficient π-π stacks should favour charge transport.

Summary

The well-defined HH-PDI/ZnS hybrid nanoparticles have been successfully prepared at the air-water interface by using SA film of amphiphilic HH-PDI molecules as a template. The significantly improved semiconducting properties are achieved for the resulting nanocomposites. The present result represents the first effort towards controlling the size and morphology of ZnS nanostructures via an amphiphilic asymmetric PDI derivate, which is helpful towards designing, preparing new nanomaterials and more complex nanostructures with tunable functionality.

Acknowledgment

Financial support from the Natural Science Foundation of China (21371073) and the Natural Science Foundation of Shandong Province (ZR2011BZ005) is gratefully acknowledged.

References

[1] J. H. Zhan, X. G. Yang, D. W. Wang, S. D. Li, Y. Xie, Y. Xia, Y. Qian, Polymer-Controlled Growth of CdS Nanowires, Adv. Mater. 12, (2000), 1348-1351.

[2] C. C. Chen, J. J. Lin, Controlled Growth of Cubic Cadmium Sulfide Nanoparticles Using Patterned Self-Assembled Monolayers as a Template, Adv. Mater. 13, (2001), 136-139.

[3] Y. Lu, Y. Yang, A. Sellinger, M. Lu, J. Huang, H. Fan, R. Haddad, G. Lopez, A. R. Burns, D. Y. Sasaki, J. Shelnutt, C. J. Brinker, Self-assembly of Mesoscopically Ordered Chromatic Polydiacetylene/Silica Nanocomposites, Nature 410, (2001), 913-917.

[4] F. Würthner, Perylene Bisimide Dyes as Versatile Building Blocks for Functional Supramolecular Architectures, Chem.Commun. 14, (2004), 1564-1579.

[5] J. Locklin, D. Li, S. C. B. Mannsfeld, E. J. Borkent, H. Meng, R. Advincula, Z. Bao, Organic Thin Film Transistors Based on Cyclohexyl-Substituted Organic Semiconductors, Chem. Mater. 17, (2005), 3366-3374.

[6] H. Wu, L. Xue, Y. Shi, Y. Chen, X. Li, Organogels Based on J- and H-Type Aggregates of Amphiphilic Perylenetetracarboxylic Diimides, Langmuir 27, (2011), 3074-3082.

[7] Y. Chen, M. Bouvet, T. Sizun, Y. Gao, C. Plassard, E. Lesniewska, J. Jiang, Facile approaches to build ordered amphiphilic tris(phthalocyaninato) europium triple-decker complex thin films and their comparative performances in ozone sensing, Phys. Chem. Chem. Phys. 12, (2010), 12851-12861.

[8] A. You, J. Gao, D. Li, M.l Bouvet, Y. Chen, Effects of metal–ligand coordination on the self-assembly behaviour of a crown ether functionalised perylenetetracarboxylic diimide, Supramolecular Chemistry 24, (2012), 851–858.

[9] A. Takeo, S. Shin-ichiro, S. Yoshinori, T. Hideyuki, S. Kozo, J. Balachandran, T. Kazuyuki, Cu-Doped ZnS Hollow Particle with High Activity for Hydrogen Generation from Alkaline Sulfide Solution under Visible Light, Chem. Mater. 20, (2008), 1997-2000.

[10] M. Kasha, H. R. Rawls, M. A. E. Bayoumi, The Excition Model in Molecular Spectroscopy, Pure Appl. Chem. 11, (1965), 371-392.

Advanced Materials Research Vol. 936 (2014) pp 300-303
© (2014) Trans Tech Publications, Switzerland
doi:10.4028/www.scientific.net/AMR.936.300

Pt-TiO_2 Nanocomposites in Alginate for Enhancing Photocatalytic Activity

Yunrun Wang

Department of Physics, Renmin University of China, Beijing, 100872, China

yunrunwang@163.com

Keywords: Pt/TiO_2, nanocomposite, alginate, photocatalytic activity, phenol

Abstract: A new sol-gel method was employed to synthesize Pt-containing titania composite with varied dopant concentrations using alginate as an template for preventing inorganic materials' conglomeration. During the calcination process, the Pt nanoparticles, which had been loaded in alginate porous networks, were doped into the titania system. The morphology and crystallization behavior of titania were characterized. HAAD-STEM image and EDX spectroscopy of Pt/TiO_2 composites confirmed that Pt was well embodied into the TiO_2 mesoporous network. The UV-vis diffuse reflection spectra at room temperature shown that the Pt/TiO_2 composite exhibited a marked visible light adsorption compared with a pure TiO_2 sample. The photocatalytic activities were tested using phenol as the model compound, and the results demonstrated that higher photocatalytic activity was observed at higher levels of Pt added to the titania system. The optimum dopant concentration was found to be 0.37 mol % for Pt/TiO_2 sample.

Introduction

Photocatalysis has received a great deal of attention owing to its potential application in purifying water and air by thoroughly decomposing organic compounds [1]. Among the photocatalysis, TiO_2 is known as a relatively inexpensive semiconductor exhibiting substantial photocatalytic activity, stability in aqueous solution, and nontoxicity [2]. However, titania's low quantum efficiency because of a high rate of recombination between electrons and holes and large band gap of 3.2 eV (corresponding to a wavelength of shorter than 400 nm) limit its potential application. In order to increase the photocatalytic activity, modifications of titania are involved. Metallization of TiO_2 surface with noble metals is believed to decrease the band-gap energy, and further extend its solar-driven photocatalytic applications [3]. Several noble metals, such as Pt, Ag, and Au, have been shown to promote the separation of photogenerated charge carriers, and thus to improve its photoactivity [4]. Such an enhancement in the different studies has been explained that the electrons generated by UV irradiation of the TiO_2 semiconductor quickly transfer to the metal particles loaded on the TiO_2 surface. These metal particles generate effectively enhance to the charge separation of the electrons and holes, resulting in improving the photocatalytic performance. It must be noticed that the electronic properties of the metal-TiO_2 composite is size-dependent [5].

Besides the catalytic active species, the performance and stability of the catalysts also strongly depend on the dispersion of these species and the framework designed. The sol-gel method is an attractive method for low-temperature synthesis of TiO_2, and it is easier to realize metal doping. However, the particle size of TiO_2 prepared by the sol-gel method is not uniform and it is difficult to obtain nano-sized particles using this method due to calcination posttreatments. Template synthesis by surface functionalization/stabilization is widely accepted as a simple and effective method for controlling the microstructure of catalyst material. Encouraged by the development of green chemistry, the utilization of renewable natural materials has received considerable attention. Polysaccharides and other biomacromolecules have already been utilized as templates to prepare porous metal oxide structures [6].

This paper addresses the preparation of Pt-doped TiO_2 framework synthesized by a very simple and green method. In this work, alginate gel is used as a template to avoid particle conglomeration and

fabricate nano-sized TiO_2 particles, Pt nanoparticles are embedded into the tiamnia porous network in following calcination post-treatments. The UV-vis diffuse reflection spectrocopy at room temperature show that the Pt/TiO_2 composite exhibit a marked visible light adsorption compared with a pure TiO_2 sample. The enhanced ability to absorb visible light makes this composite a potential photocatalyst for solar-driven application. The enhanced photocatalytic activities of Pt/TiO_2 have been demonstrated using phenol as the model compound. Results of the photocatalytic evaluation demonstrated that higher photocatalytic activity was observed at higher levels of Pt added to the titania system.

Experimental

Materials

Sodium alginate was purchased from Alfa Aesar. Hexachlorophlatinic acid ($H_2PtCl_6 \cdot 6H_2O$), ethanol (AR), isopropanol (AR), phenol (AR) was purchased from the Beijing Reagent Company. $CaCl_2$ was supplied by the Beijing Chemical Company. The titanium isopropoxide (TIP, 98%) was purchased from Acros. All the reagents were used as received. Deionized water was used in all experiments.

Preparation of Pt/TiO_2 nanocomposites

In a standard experiment, the desired amount of $H_2PtCl_6 \cdot 6H_2O$ solution (0.1 mL 14.5 mM) was added into 2 mL of sodium alginate (SA) aqueous solution (3.0 wt%), and the mixture was then gently heated to 100℃in an oven for 2 h for the reduction of the metal precursor. In order to prepare Pt/SA beads, the stable Pt/SA suspension was added dropwise into a $CaCl_2$ aqueous solution (50 mM) without stirring, which was then kept in a $CaCl_2$ aqueous solution and cured for at least 12 h. The resultant Pt/SA beads were washed several times using deionized water, followed by dehydration with ethanol, and were finally placed into isopropanol. The as-prepared Pt/SA beads were then soaked in 70 wt% TIP isopropanol solution for 16 h, followed by hydrolysis for 24 h in a water/isopropanol (1:5 by volume) solution. The white hybrid amorphous titania/alginate beads were dried in air at room temperature for 36 h, and then placed in an oven at 60℃ for 5 h. Finally, the samples were calcined in an oven under flowing air at 450℃ for 10 h (heating ramp 3.5℃ min^{-1}) to remove the alginate template and induce crystallization of the inorganic components.

Characterization and measurement

HAADF images were obtained from FEI TECNAI F30 STEM, and accelerating voltage was 300 kV. UV-vis diffuse reflectance spectra (UV-vis DRS) of various doped TiO_2 catalysts were recorded on Hitachi UV-vis spectrophotometer (U2800) to observe visible light adsorption of the doped TiO_2 samples. The analysis wavelength ranges from 170 to 800 nm. UV-visible absorption investigation was determined by a TU-1201 model spectrophotometer.

The photodegradation reaction were carried out at 30 ˚C using a custom-built reactor that contains 250W UV lamps (characteristic wavelength = 365 nm) mounted 10 cm away from the reaction solution. Briefly, 0.1 g Pt/TiO2 sample was mixed with a 40 mL aqueous solution containing phenol (38 mg L^{-1}). The mixture was stirred vigorously in the dark for 30 min until reaching adsorption equilibrium. The catalytic degradation of phenol was initiated by irradiating the reactive mixture. Photodegradation was monitored by measuring the absorbance of the phenol at its maximum using UV-vis system.

Results and Discussion

The facile preparation of the Pt/TiO_2 samples has been reported in zhang' work [7]. The Pt/TiO_2 composites were prepared by soaking the cross-linked Pt-Alginate beads into TIP isopropanol solution, followed by hydrolysis, drying and calcination. The TEM image showed that the prepared sample has agglomerated to large particles; However, the image revealed that the sample was consist of agglomerates of particles with an average diameter of ca. 10 nm, which was in good agreement

with the crystallite size calculated from XRD pattern [7]. This indicated that the Pt/TiO_2 sample was composed of well-crystallized anatase. Crystallization of the TiO_2 mesoporous framework was a key factor for application of the sample in photocatalysis.

High angle annular dark field (HAADF) scanning transmission electron microscopy (HAAD-STEM) images and EDX spectroscopy of Pt/TiO_2 were shown in Fig. 1. The Pt phase was clearly seen as a bright spot with Pt/TiO_2 composites. The EDX spectroscopy analysis exhibited a clear Pt signal, indicating that the Pt particles were well dispersed in the TiO_2 network.

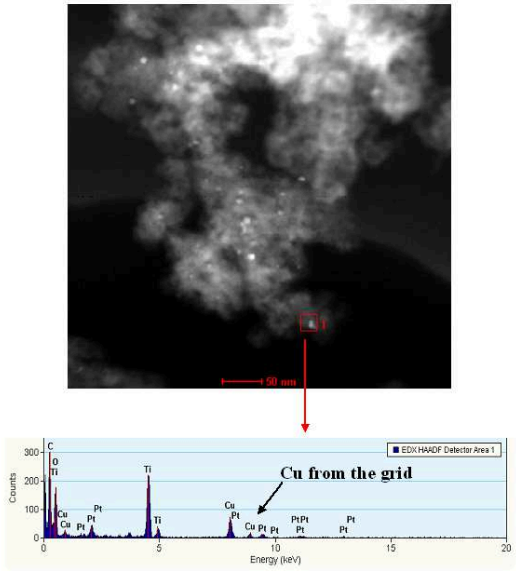


Figure 1 HAADF-STEM image and EDX spectroscopy of TiO_2 with embedded Pt nanoparticles

UV-vis DRS is useful to characterize the electronic structural property of the prepared titania nanoparticles. The UV-vis DRS of the mesoporous pure TiO_2 and Pt/TiO_2 samples were presented in Fig. 2. The spectra of the Pt-doped samples in Fig. 2 showed a red shift in the band-gap transition to longer wavelengths. The absorbance of the Pt-doped samples in the visible region was always higher than that of undoped TiO_2.

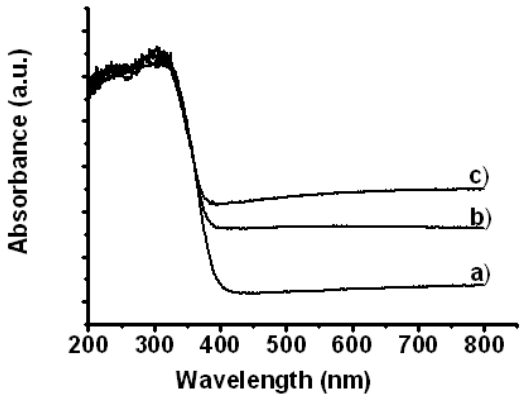


Figure 2 UV-vis diffuse reflectance spectra of (a) pure TiO_2, (b) Pt/TiO_2 (Pt: 0.18 mol-%), and (c) Pt/TiO_2 (Pt: 0.37 mol-%)

To evaluate and compare the photocatalytic performance of the mesoporous TiO_2 samples, the decomposition of phenol was used as a photoreaction probe. Results of the photocatalytic evaluation were summarized in Fig. 3. Addition of a low concentration of Pt into TiO_2 frame work could significantly improve the photocatalytic activity. The 0.37 mol % sample was found to have the

highest photocatalytic activity for the photodecomposition of phenol. The improvement of photocatalytic activity could not be expected as the Pt concentration increases further.

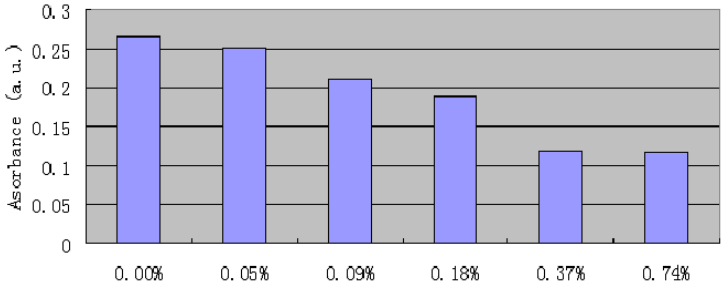


Figure 3 UV-vis absorption spectra of pure TiO_2 and different dopant (Pt) concentrations on TiO_2

Summary

A facile method was utilized to synthesize different Pt-doped TiO_2 with different dopant concentrations. Among these prepared samples, 0.37 mol % sample exhibit the highest photocatalytic activity over the degradation of phenol when 365 nm UV light was used for irradiation. The enhancement of the photoactivity can be attributed to its smallest particle size and large surface area, good dispersion of Pt over the surface of TiO_2, and suitable dopant concentration. In addition, the Pt/TiO_2 composite exhibit a marked visible light adsorption compared with a pure TiO_2 sample, which makes this composite a potential photocatalyst for solar-driven application.

References

[1] M. Sidheswaran, L. L. Tavlarides, Characterization and Visible Light Photocatalytic Activity of Cerium- and Iron-Doped Titanium Dioxide Sol−Gel Materials. Ind. Eng. Chem. Res. 48 (2009) 10292-10306.

[2] M. R. Hoffmann, S. T. Martin, W. Choi, D. W. Bahnemann, Environmental Applications of Semiconductor Photocatalysis, Chem. Rev. 95 (1995) 69-96.

[3] M. Mrowetz, W. Balcerski, A. J. Colussi, M. R. Hoffmann, Oxidative Power of Nitrogen-Doped TiO_2 Photocatalysts under Visible Illumination, J. Phys. Chem. B. 108(2004)17269-17273.

[4] A. Di Paola, G. Marci, L. Palmisano, M. Schiavello, K. Uosaki, S. Ikeda, B. Ohtani, Preparation of Polycrystalline TiO_2 Photocatalysts Impregnated with Various Transition Metal Ions: Characterization and Photocatalytic Activity for the Degradation of 4-Nitrophenol, J. Phys. Chem. B. 106 (2002) 637-645.

[5] V. Subramanian, E. E. Wolf, P. V. Kamat, Catalysis with TiO2/Gold Nanocomposites. Effect of Metal Particle Size on the Fermi Level Equilibration, J. Am. Chem. Soc. 126 (2004), 4943-4950.

[6] P. Chen, X. Zhang, Z. Miao, B. Han, G. An, Z. Liu, In-site synthesis of noble metal nanoparticles in alginate solution and their application in catalysis. J. Nanosci. Nanotechnol. 9 (2009) 2628-2632.

[7] P. Chen, X. Zhang, Fabrication of Pt/TiO_2 Nanocomposite in alginate and their applications to the degradation of phenol and methylene blue in aqueous solution, Clean. 36 (2008) 507-511.

Advanced Materials Research Vol. 936 (2014) pp 304-309
© (2014) Trans Tech Publications, Switzerland
doi:10.4028/www.scientific.net/AMR.936.304

Preparation of Carboxymethyl Chitosan Magnetic Nanoparticles and Separation of Chinese Medicines Components

YiHui Xie[1,a], YuTian Zhang[1], Xiuzhen Huang[1], Yanhua Ding[1],LiPing Huang[1,b,*]

[1]Jiangxi University of Traditional Chinese Medicine, Nanchang, Jiangxi, China

[a] email: 243619851@qq.com, [b] email: jxnchlp@163.com, *Corresponding author: LiPing Huang

Keywords: Carboxymethyl chitosan magnetic nanoparticles; Evodia rutaecarpa; Microwave reaction; Components separation

Abstract: Fe_3O_4 nanoparticles were prepared by coprecipitation method. Microwave synthesis method changed the property of the surface of chitosan, and the carboxymethyl chitosan was prepared. The carboxymethyl chitosan magnetic nanoparticle was prepared by microwave synthesis. Carboxymethyl chitosan magnetic nanoparticles were characterized by IR and SEM methods. The application conditions are discussed. Using this material to separate the alkaloid of Evodia rutaecarpa will greatly shorten the time than traditional separation method. The components will be more pure.

Introduction

Evodia rutaecarpa is the Rutaceae Evodia rutaecarpa(Juss．)Benth．dry nearly ripe fruit. This hot-natured herb was commonly used. Previous studies suggested [1] that hot-natured foundation for Evodia rutaecarpa is the N-butanol extract of Evodia rutaecarpa. This N-butanol extract mainly containing alkaloids, phenols and flavonoids components. In order to further confirm the category of hot-natured foundation for Evodia rutaecarpa, we must choose a fast, efficient and specific separation method, to separate the alkaloids of n-butanol fraction from Evodia rutaecarpa.

The conventional components separation methods of separating alkaloids of Evodia rutaecarpa have certain difficulties. It is easy to produce components cross by solvent extraction,and the Components may lossed. Small separation column is limited by capacity, so it is difficult to obtain the dose of pharmacological experiments needs.

Magnetic polymer microspheres has its unique advantages in chemical components separation like surface effect and superparamagnetism[2], it can be used for constant compositions separation, and also can be quickly and easily separated in the additional magnetic field. Functional groups on surface given by copolymerization and surface modification [3] make it adsorb some specific components. So, it is a kind of separating tool that low cost, good separated results, rapid separation, and strong selectivity.

This experiment changed the property of chitosan, and synthesized Carboxymethyl chitosan by microwave, and made Carboxymethyl chitosan magnetic nanoparticles. The alkaloids components were specific adsorbed by the carboxyl-methyl. The alkaloids from N-butanol extract of Evodia rutaecarpa was separated effectively.

Reagents and materials

Ferric chloride hexahydrate ($FeCl_3$•$6H_2O$), ferrous chloride tetrahydrate ($FeCl_2$•$4H_2O$), Tri-distilled water, the rest of the reagents are analytically pure.Chitosan, BR, Aladdin Chemistry Co. Ltd. Evodia rutaecarpa was bought in ZhangShu, appraised by teacher Liu Qinghua.G80F20CN2L-B8CRO microwave oven(Galanz appliances Co., Ltd.).Infrared spectra were measured with a VERTEX70 Fourier trans-form infrared spectrometer (Bruker, Germany). Absorption spectra were measured on a Unico UV spectrometer (St. Louis, USA). SEM were measured with a jsm6701f Scanning electron microscopy（The Japanese electronics company）.

Preparations

Preparation of Fe_30_4 nanoparticles

6.1g $FeCl_3$•$6H_2O$, 3g $FeCl_2$•$4H_2O$ were dissolved in 100ml Tri-distilled water which had been pre-degassed with nitrogen,and was heated up to 50℃. This mixed solution was added drop wise by NaOH solution ($1mol \cdot L^{-1}$) and was adjusted to pH 11, and 800 rpm mechanical stirring under nitrogen gas protection. This mixed solution was added by oleic acid 0.9g and 600 rpm mechanical stirring for 30min. This mixed solution was added by 50ml toluene, heating up to 80℃ and 600 rpm stirring for 2h. After 3minutes' standing, the toluene layer was divided and washed repetitive by tri-distilled water until it to neutral. The obtained Fe_3O_4 precipitates were separated from the reaction medium by a magnetic field, washed with ethanol and acetone five times, and then dried under vacuum at 50℃.

Preparation of Carboxymethyl chitosan

5g chitosan was swelled for 1 hour at 50℃ by isopropyl alcohol 100mL. Adding 30% sodium hydroxide solution 10mL, the mixture was stirred for 1 hour. The mixture was heated to 60℃ with microwave (800W). The mixture was reactied for 20min at 60℃ with microwave (80W) heating. The reaction product was completely dissolved in deionized water and adjusted pH value to acid with dilute hydrochloric acid solution. A white polymerization was precipitated and was filtrated with vacuum. The precipitation was washed by ethanol and acetone washing 2 times, and was dried in vacuum at 60℃.

Preparation of Carboxymethyl chitosan magnetic nanoparticles.

Carboxymethyl chitosan0.23g and 0.2g Fe_3O_4 was completely dissolved in deionized water and then an ultrasonic device is used to disperse the mixture for 20min. The mixture solution was added drop wise into the oil phase containing 35ml liquid paraffin and 0.6ml Span-80. Suspension system(W/O) was made under vigorous stirring(1000rpm) for 1 hours at room temperature. Adding 25% 4ml of glutaraldehyde,the suspension system reactied 26 min by microwave (80W) heating at 40℃. The carboxymethyl chitosan magnetic nanoparticles was separated by magnetic-iron and was washed with deionized water and ethanol 3 times, and was dewatered by Acetone. The carboxymethyl chitosan magnetic microspheres vacuum was dried 24h at 60℃.

Sample preparation

The solvent was recovered from N-butanol extract of evodia rutaecarpa. The residual was dissolved in 80% alcohol, the ethanol extract solution obtained. The mixed solution of this ethanol extract solution and 10ml 80% ethanol was adjusted to pH 5 by 0.1mol/L hydrochloric acid solution, and 0.2g carboxymethyl chitosan magnetic microspheres was added to this mixed solution. The microspheres had been dipped in 80% ethanol for 0.5 hours. Placed after 10 minutes, the mixture is placed in a magnet for 10 minutes. Carboxymethyl chitosan magnetic microspheres separated and 10ml ethanol was adjusted to pH 10 with 0.1mol/L sodium hydroxide solution. The alkaloids were eluted by ultrasound for 5 min. Separating carboxymethyl chitosan magnetic microspheres with a magnet, the alkaloid extract was obtained.

FTIR measurements

FTIR spectroscopic measurements were performed by KBr pellet method. The wave numbers of FTIR measurement range were controlled from 500 $cm^{-1}$to 4000cm^{-1}.

Determination of the content of alkaloids

The maximum absorption wavelength of evodiamine, rutaecarpine and total alkaloids of Evodia rutaecarpa were located at 361nm. And the maximum absorption wavelength of the negative solution was not in the 361nm. Therefore, the determination wavelength of alkaloid content in Evodia rutaecarpa was 360nm [4]. The 1mL test solution of Evodia rutaecarpa was diluted with ethanol into 10.00mL. Using ethanol as the blank, the absorbance of the test solution at 361nm was measured. The alkaloids amount in sample solutions was converted into rutaecarpine amount.

Static adsorption tests

Carboxymethyl chitosan magnetic nanoparticles (0.2g) were placed in a 250mL flask, and then added the alkaloid of Evodia rutaecarpa with the initial concentration ranging from 3mg/100mL to 18mg/100mL, adjusted to pH 5. The conical flasks were shaken by the oscillator for 30min and then separated carboxymethyl chitosan magnetic microspheres with a magnet. The free concentrations of alkaloid of Evodia rutaecarpa were determined by UV–visible spectrophotometer. And the acquired experimental data were analyzed by the Scatchard equation.

Identification of components

The 1ml alkaloids extract solution was removed by water bath. It showed positive reaction of alkaloid，that adding of iodine - bismuth iodide solution, the solution produced a large amount of precipitation. The results showed that the alkaloid could be successfully separated by carboxymethyl chitosan magnetic microspheres from Evodia rutaecarpa n-butanol fraction.

Adsorption time and desorption time

The n-butanol of Evodia rutaecarpa n-butanol fraction was removed by water bath. The residue was dissolved in ethanol. The ethanol solution was obtained.

The carboxymethyl chitosan magnetic microspheres 6 portions, each part 0.2g, were respectively added into 80% ethanol 20ml, and were stirred and were let stand for 20 min. The Carboxymethyl chitosan magnetic microspheres were separated by magnet. The 1mL ethanol extracts of Evodia rutaecarpa was respectively added to these Carboxymethyl chitosan magnetic microspheres, and were adjusted pH to 9, were respectively stirred for 5, 10, 15, 20, 25, 30min. The carboxymethyl chitosan magnetic microspheres after adsorption were separated from the mixture by magnet. Ethanol 20ml was respectively added into the magnetic microspheres. The mixtures were adjusted pH to 2, and were stirred, and were let stand for 20min. The carboxymethyl chitosan magnetic microspheres after desorption were separated from the mixture by magnet. The eluents were adjusted pH to neutral, and the absorbance at 361nm was measured.

The carboxymethyl chitosan magnetic microspheres 6 portions, each part 0.2g, were respectively added into 80% ethanol 20ml, and were stirred and were let stand for 20 min. The Carboxymethyl chitosan magnetic microspheres were separated by magnet. The 1mL ethanol extracts of Evodia rutaecarpa was respectively added to these Carboxymethyl chitosan magnetic microspheres, and were adjusted pH to 9, were stirred for 10min. The carboxymethyl chitosan magnetic microspheres after adsorption were separated from the mixture by magnet. Ethanol 20ml was respectively added into the magnetic microspheres. The mixtures were adjusted pH to 2, and were respectively stirred for 5, 10, 15, 20, 25, 30min, and were let stand. The carboxymethyl chitosan magnetic microspheres after desorption were separated from the mixture by magnet. The eluents were adjusted pH to neutral, and the absorbance at 361nm was measured.

Adsorption pH and desorption pH

The carboxymethyl chitosan magnetic microspheres 5 portions, each part 0.2g, were respectively added into 80% ethanol 20ml, and were stirred and were let stand for 20 min. The Carboxymethyl chitosan magnetic microspheres were separated by magnet. The 1mL ethanol extracts of Evodia rutaecarpa was respectively added to these Carboxymethyl chitosan magnetic microspheres, and were respectively adjusted pH to 4, 4.5, 5, 5.5, 6 by 1mol/L hydrochloric acid solution, and were stirred for 10min. The carboxymethyl chitosan magnetic microspheres after adsorption were separated from the mixture by magnet. Ethanol 20ml was respectively added into the magnetic microspheres. The mixtures were adjusted pH to 10 by 1mol/L sodium hydroxide solution, and were sonicated for 5 min. The carboxymethyl chitosan magnetic microspheres after desorption were separated from the mixture by magnet. The eluents were adjusted pH to neutral, and the absorbance at 361nm was measured.

The carboxymethyl chitosan magnetic microspheres 5 portions, each part 0.2g, were respectively added into 80% ethanol 20ml, and were stirred and were let stand for 20 min. The Carboxymethyl chitosan magnetic microspheres were separated by magnet. The 1mL ethanol extracts of Evodia rutaecarpa was respectively added to these Carboxymethyl chitosan magnetic microspheres, and were adjusted pH to 5 by 1mol/L hydrochloric acid solution, and were stirred for 10min. The carboxymethyl chitosan magnetic microspheres after adsorption were separated from the mixture by magnet. Ethanol 20ml was respectively added into the magnetic microspheres. The mixtures were respectively adjusted pH to 8.5, 9, 9.5, 10, 10.5 by 1mol/L sodium hydroxide solution, and were sonicated for 5 min. The carboxymethyl chitosan magnetic microspheres after desorption were separated from the mixture by magnet. The eluents were adjusted pH to neutral, and the absorbance at 361nm was measured.

Results and discussion

The characterization

Fig.1 displays the SEM image of Fe_3O_4, which illustrates the uniform size distribution of these nanoparticles. The diameter of Fe_3O_4 is in the range of 20 nm～30nm. Fig.2 displays the SEM image of Carboxymethyl chitosan magnetic microspheres, which illustrates the uniform size distribution of these nanoparticles. The diameter of Carboxymethyl chitosan magnetic microspheres is in the range of 50nm～60nm.

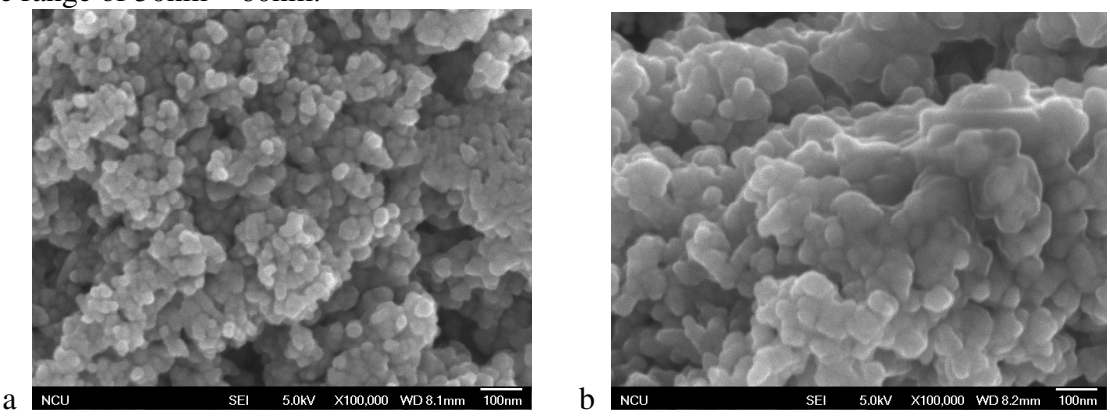


Fig1 SEM image of Fe_3O_4(a) and carboxymethyl chitosan magnetic microspheres(b)

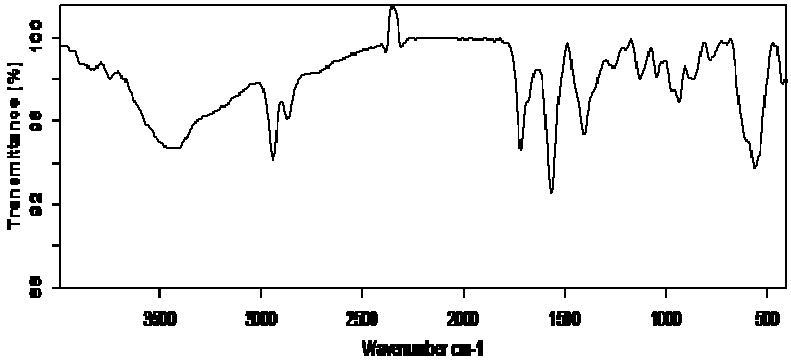


Fig.2 FTIR spectrum of Carboxymethyl chitosan magnetic nanoparticles

Fig. 2 shows FTIR spectrum of Carboxymethyl chitosan magnetic nanoparticles. Two strong O–H stretching vibration absorbance peaks in the molecule of Carboxymethyl chitosan magnetic nanoparticles are at 3300cm^{-1}~3500cm^{-1}. A stretching vibration peak of -CH_3 or -CH_2 is found at 2900- 2800cm^{-1}. A stretching vibration peak of C=O is found at 1758cm^{-1}. The absorbance peaks of —C=N— stretching, C- O or C-N stretching and Fe_3O_4 stretching are at 1566cm^{-1}, 1000-1100cm^{-1}, 580cm^{-1}, respectively. The results display that this Carboxymethyl chitosan magnetic nanoparticles was synthesized successfully.

Adsorption analysis of andrographolide

Fig. 3 describes the plot based on the Scatchard equations. The correlation coefficient (R) of regression analysis for the curve is 0.9968 for Carboxymethyl chitosan magnetic nanoparticles. It is noted that the Carboxymethyl chitosan magnetic nanoparticles has only one distinct section within the plot and inclined to a straight line, which presents that only the homogeneous affinity binding sites are formed in the polymers. From the slope ($-1/K_d$) and intercept (Q_{max}/K_d) of the Scatchard plot, the dissociation constants (K_d) and the maximum binding capacity (Q_{max}) of the Carboxymethyl chitosan magnetic nanoparticles are K_d = 2.495mg/g, Q_{max} = 34.15mg/g.

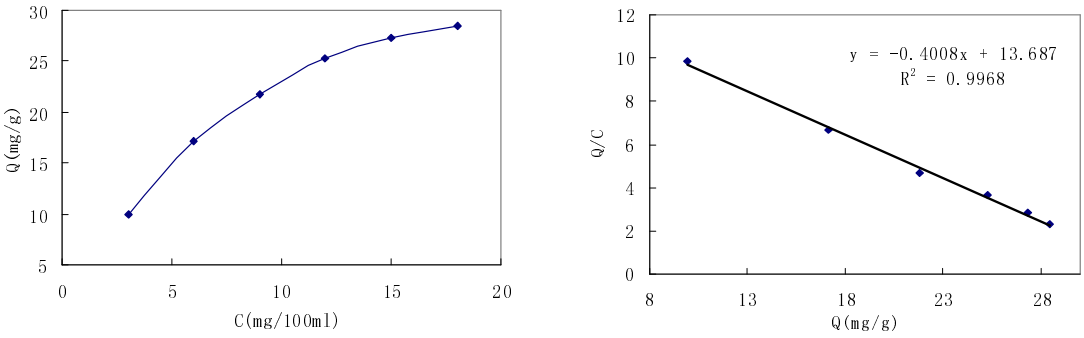


Fig. 3: Adsorption isotherm

Adsorption time and desorption time

The absorptions of each test solution of the adsorption time from 5 min to 30 min are no significant difference. These results suggest that under the experimental conditions, carboxymethyl chitosan magnetic microspheres can complete the adsorption of alkaloid components in the sample solution in 5 minutes. The desorptions of each test solution of the adsorption time from 5 min to 30 min are no significant difference. This results suggest that under the experimental conditions, carboxymethyl chitosan magnetic microspheres can complete desorption of alkaloid components in the magnetic microspheres in 5 minutes.

Adsorption pH and desorption pH

Fig. 4 and Fig.5 describes the experimental results of adsorption pH and desorption pH. When pH is 5, carboxymethyl chitosan magnetic microsphere adsorption effect is best. When pH is 10, the desorption effect is best.

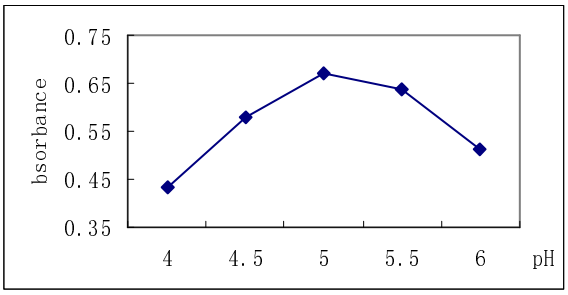


Fig. 4 Experimental results of adsorption pH

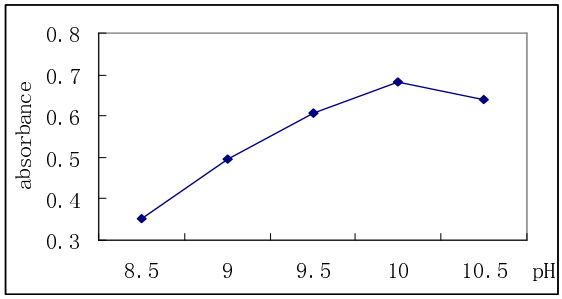


Fig.5 Experimental results of desorption pH

Discussion

In this experiment, we prepared the carboxymethyl chitosan and the carboxymethyl chitosan magnetic nanoparticles by microwave synthesis. By using this method, the reaction time is shortened about ten to twenty times than that by traditional synthesis method. According to literature references [5,6] that synthesized the carboxymethyl chitosan need 3 or 4 hours, but we just need 20 min. According to literature references [7] that synthetize the carboxymethyl chitosan magnetic nanoparticles need 7~10 hours, but we just need 26 min.

This kind of method is suitable for large doses of extraction and separation of alkaloids components in traditional chinese medicine. Comparing with acidity solvent extraction methods, new method showed advantages of short separation time, relatively pure extract, avoid cross of different solvent extraction and the broken of effective component.

Acknowledgements

This work was financially supported by the National Natural Science Foundation, PR China (Grant Nos. 30960496) and Jiangxi Provincial Department of education in Universities of science and technology research projects (Grant Nos.GJJ12521)

References

[1] Liping Huang, Shuhong Peng, Shu Zhang, et al，Hepatic energy metabolism on rats by six traditional Chinese medicine with hot property, China Journal of Chinese Materia Medica,2010,35(11):1470-1473.In Chinese

[2] J. Frenkel, J. Dorfman, Nature 126 (1930) 274.

[3] An-Hui Lu, E. L. Salabas, and Ferdi Schuth. Magnetic Nanoparticles: Synthesis, Protection, Functionalization and Application [J], Angew. Chem. Int. Ed. 2007, 46, 1222 – 1244. In Chinese

[4] Hui Zi，The compatibility of Evodia rutaecarpa and angelica medicine and structure-activity relationship study，Liaoning University of Chinese Medicine，The paper of the 2009 doctor's degree, 2009.4. In Chinese

[5] Yan Li，Preparation and application of modified chitosan magnetic microscopic particles, University Of The Sout, master's thesis, 2010. In Chinese

[6] De Wen， Study on Preparation of Magnetic polymer Microspheres，Sichuan University, master's thesis, 2007. In Chinese

[7] Dong Yun，Synthesis and Property of P(St/AA)Magnetic Polymer Microspheres，Lanzhou University of Technology, master's thesis,2008. In Chinese

Advanced Materials Research Vol. 936 (2014) pp 310-314
© (2014) Trans Tech Publications, Switzerland
doi:10.4028/www.scientific.net/AMR.936.310

Comparison Of Hydrogen Sulfide Sensing Properties Between Multiple-Walled Carbon Nanotubes (Mwnts) And Mwnts-Haucl$_4$ Materials

HE SiXuan[1,a], XIE GuangZhong[2,b*], JIANG YaDong[3,c], ZHANG GuangDi[4,d], ZHOU Yong[5,e]

State Key Laboratory of Electronic Thin Films and Integrated Devices, School of Optoelectronic Information, University of Electronic Science and Technology of China (UESTC), Chengdu 610054, China

[a]hexu.0109@163.com, [b]gzxie@uestc.edu.cn

Keywords: MWNTs, MWNTs-$HAuCl_4$, gas sensor, hydrogen sulfide

Abstract: The rapid and precise detection of hydrogen sulfide (H_2S) has great significance due to its high toxicity. In this work, the response properties of multiple-walled carbon nanotubes (MWNTs) and MWNTs-$HAuCl_4$ to H_2S at room temperature were compared. Scanning electron microscopy (SEM) technique was used to characterize MWNTs and MWNTs-HAuCl4 films. It was found that sensors with MWNTs- $HAuCl_4$ exhibited much higher response value. On the other hand, sensors with MWNTs were observed to have faster response time and better recovery properties.

Introduction

Hydrogen sulfide (H_2S) is known as a colorless, inflammable, corrosive, toxic and malodorous gas with smells like rotten eggs. When its concentration is higher than 250ppm, H_2S can be very dangerous to human health and even cause death [1]. Therefore, the rapid and sensitive detection and monitoring of hydrogen sulfide has great significance to both human daily life and industries. So far, much work on H_2S sensors has been done [2]. The majority of them are based on semiconductor sensitive membranes like WO_3 [3, 4], SnO_2 [5, 6], which exhibit good sensing properties at high working temperature.

Since the discovery by Iijima[7], carbon nanotubes (CNTs) have increasingly aroused attention as gas sensitive films. Now more experiments are focused on the methods to improve the sensing properties of CNTs through the modifications of CNTs by functionalizing, doping or coating with different materials [8].

In this paper, both MWNTs and MWNTs doped with $HAuCl_4$ (MWNTs-$HAuCl_4$) films were fabricated on the interdigitated electrodes (IDEs) through air spraying method. The results show us that sensors with MWNTs-$HAuCl_4$ exhibited much higher response, a slower response time.

Experimental

Preparation of sensitive films

In this work, pure MWNTs were purchased from Chengdu Institute of Organic, Chinese Academy of Sciences. The tube outer diameter is over 50nm, length 10～20nm, purity > 95%. The $HAuCl_4$ (99.9%-Au) was purchased from Strem Chemicals, Inc.

Fabrication of H_2S gas sensor

In this work, the structure of interdigitated electrodes is shown in Fig.1. The 0.2 ml pure MWNTs and MWNTs-$HAuCl_4$ uniform dispersion were sprayed onto the interdigitated electrodes by airbrushing method, respectively. The airbrush device is shown in Fig.2. The height from the nozzle to the sensor chip was approximately 20cm and the height was one of the influence factors on the film. Then the sensitive films were dried in a vacuum oven at 60℃ for almost 2 hours so that all the internal solvent could be volatilized.

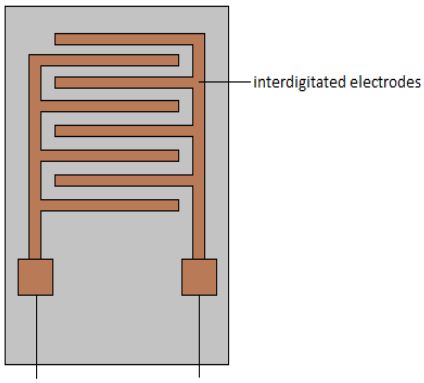


Fig. 1 Structure of interdigitated electrode

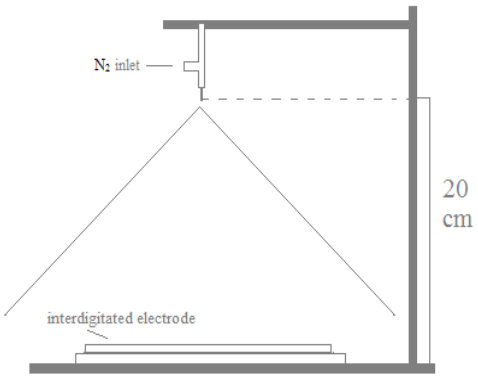


Fig. 2 Device of airbrushing

Measurement

In this work, MT50-4J flux indicator was used to produce the desired concentrations of gas mixture. The gas sensor was put into a sealed testing chamber. The electric resistance change of the sensor exposed to H_2S gas at different concentrations was monitored by keithley 2700 connected to a computer. All tests were operated at room temperature. The gas response is defined as below:

$$S=\frac{|Rg-R0|}{R0} \quad (1)$$

Where R_g and R_0 are the value of the resistance measured when the sensors were exposed to H_2S gas and N_2, respectively.

Results and discussion

Sensitivity testing

From Fig.3 and Fig.4, it's clear to see that at room temperature the sensor based on MWNTs-$HAuCl_4$ presented much higher response value than that based on pure MWNTs. When exposed to 120ppm H_2S, the response of the pure MWNTs and MWNTs-$HAuCl_4$ were 0.5% and 5%. And the response of both films when exposed to 600ppm H_2S were 2.5% and 25%, respectively. As a result, the response of MWNTs-$HAuCl_4$ film was 10 times more than that of pure MWNTs, which was a huge improvement in this regard.

The results show that both pure MWNTs and MWNTs-$HAuCl_4$ functioned as p-type semiconductor. After absorbing H_2S gas which is a kind of reducing gas, electrons transfer to the p-type materials from the gas itself. The probability that holes encounter and neutralize with electrons will increase. As a result, the conducting holes in the materials decreased which means the resistance of the films increased. When pure MWNTs were mixed with chloroaurate acid ($HAuCl_4$), the response was greatly improved. The function of $HAuCl_4$ is still not very clear.

The linearity is another important factor to characterize the static performances of a gas sensor. The linearity coefficient is used to estimate the linearity. And the closer to 1 the linearity coefficient is, the better linearity the gas sensor presents. As shown in Fig.5, the linearity coefficients of both MWNTs and MWNTs-$HAuCl_4$ films were 0.99 and 0.98, respectively. This meant that both films showed excellent linearity properties.

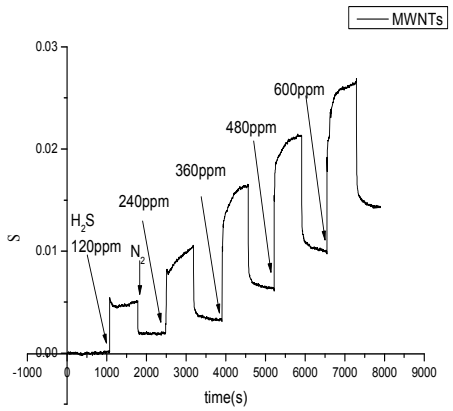


Fig. 3 The response of pure MWNTs

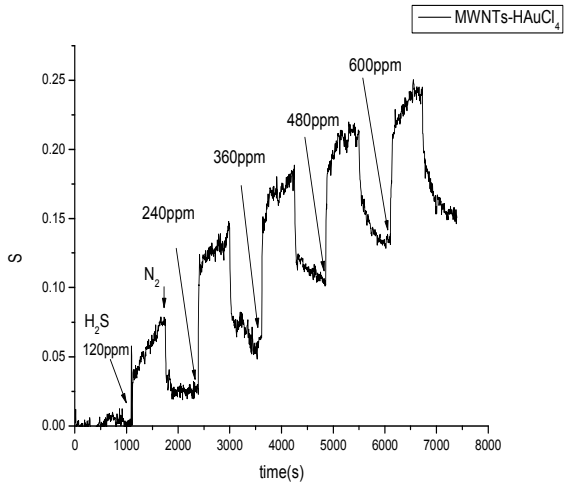


Fig. 4 The response of MWNTs-HAuCl4

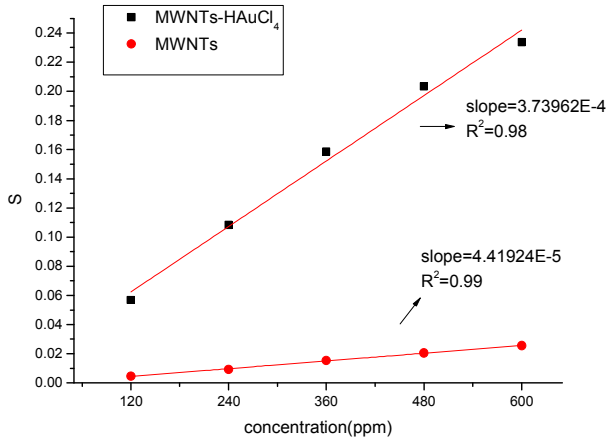


Fig. 5 The linearity of MWNTs and MWNTs-$HAuCl_4$ film

At last, the repeatability of MWNTs and MWNTs-$HAuCl_4$ films were also tested as shown in Fig.6 and Fig.7. Good repeatability is a very important property for a stable gas sensor. The cycle testing was performed at the same concentration of H_2S for five times. The original response value of MWNTs was 0.75% and the deviation of the next four test is within 0.002.It is shown that the resistance of the films could hardly return to the base line value in N_2. But it has been realized that the phenomenon is inevitable for the gas sensor. So both films were shown to present good repeatability.

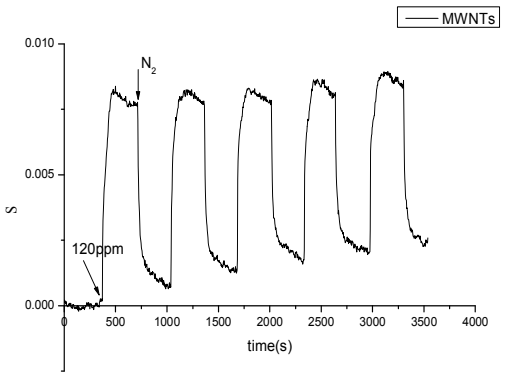


Fig. 6 The repeatability of MWNTs

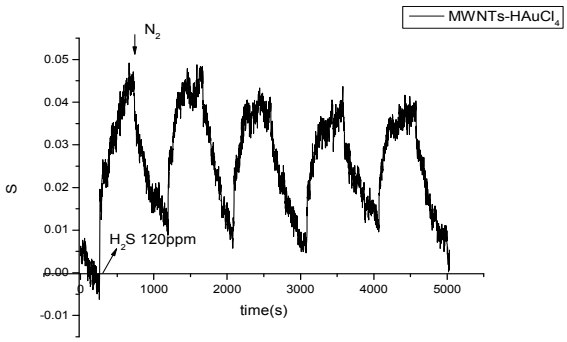


Fig. 7 The repeatability of MWNTs-$HAuCl_4$

Surface Morphology Images

In order to analyse the working mechanism of H_2S gas sensing, the surface morphology of both films were tested using SEM. It can be seen that pure MWNTs film is compact with higher density. And there are more and larger holes on the surface of MWNTs-$HAuCl_4$ film than that of pure MWNTs. The addition of holes to the surface may contribute to gas absorption. Thus more absorption sites are provided so that gas is much easier to get into the film. However, on the other hand, more holes are bad for gas desorption which leads to difficulty in the recovering of gas sensor. This result explains why MWNTs doped with $HAuCl_4$ enhanced the response to H_2S greatly, but degraded the recovering properties.

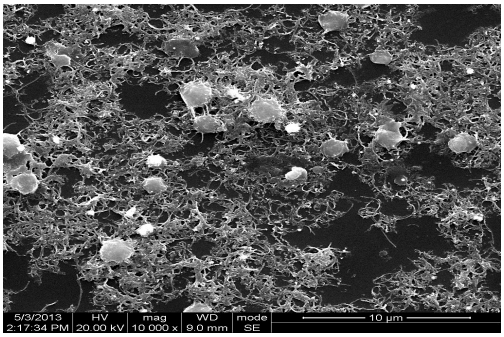


Fig. 8 The SEM images of MWNTs -$HAuCl_4$

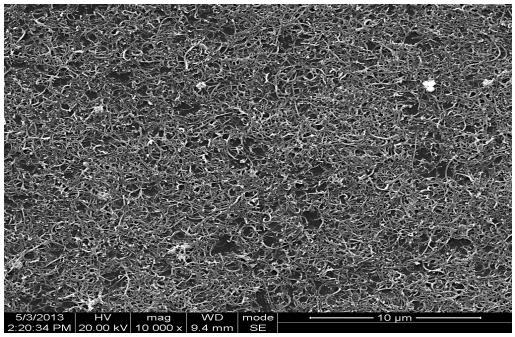


Fig. 9 The SEM images of pure MWNTs

Conclusions

In this paper, the sensing properties of MWNTs and MWNTs-$HAuCl_4$ films were compared. The results show that the response value of MWNTs-$HAuCl_4$ to H_2S was improved approximately 10 times. But on the other hand, the response and recovery times both increased. As shown in the paper, both films exhibited good linearity.

Acknowledgements

This work was supported by the National Science Foundation of China (Grant Nos.61176066 and 61101031) and Specialized Research Fund for the Doctoral Program of Higher Education (20120185110012).

References

[1] Nathan S L, James D, Richard G C. Analytical strategies for the detection of sulfide: a review. Talanta 52 (2000) 771-784

[2] Omar H, Maryam S, Martine L. Qualitative and quantitative identification of H_2S/NO_2 gaseous components in different reference atmospheres using a metal oxide sensor array. Sensors and Actuators B 103(2004) 403-408

[3] Wei H T, Ching H T. H_2S sensing properties of noble metal doped WO_3 thin film sensor fabricated by micromaching. Sensors and Actuators B 81(2002) 237-247

[4] I.Jimenez, J.Arbiol, G.Dezanneau, A.Cornet, J.R.Morante. Crystalline structure, defects and gas senor response to NO_2 and H_2S of tungsten trioxide nanopowders. Sensors and Actuators B 93(2003) 475-485

[5] Sun-Woo Choi, Jin Zhang, Katoch Akash, Sang Sub Kim. H_2S sensing performance of electrospun CuO-loaded SnO_2 nanofibers. Sensors and Actuators B 169(2012) 54-60

[6] Gong J W, Chen Q F, Lian M R, et al. Micromachined nanocrystalline silver doped SnO_2 H_2S sensor. Sensors and Actuators B 114(2006) 32-39

[7] Iijima S. Helical microtubules of graphitic carbon. Nature 1991, 354, 56-58

[8] Cheng Y W, Yang Z, Wei H, et al. Progress in carbon nanotube gas sensor research. Acta Phys. Chim. Sin. 2010, 26, 3127-3142

Advanced Materials Research Vol. 936 (2014) pp 315-321
© (2014) Trans Tech Publications, Switzerland
doi:10.4028/www.scientific.net/AMR.936.315

Effect of Cu,Cr Co-doped on Structure and Magnetic Properties of Sm_2Co_{17} Alloy Films

Wang Can[1,a *], Fang Qingqing[1,b], Wang Dangdang[1], Yang Jinjin[1], Li Jinguang[1]

[1]School of Physics and Material Science, Anhui University, Hefei 230039, PR China

[a]369909745@qq.com, [b]physfangqq@126.com

Keywords: SmCo film, co-doped, structure, coercivity, magnetic exchange bias

Abstract: Sm2Co17:Cu,Cr films growing on Cr buffer layer and Cu seed layer were prepared by pulsed laser deposition(PLD) method based on Si(100) substrate. The results showed that Cu and Cr co-doped in SmCo films made the refinement of crystal grain and the increase of coercivity of SmCo. Beside, the experiments found that the incorporation of Cu and Cr in SmCo films resulted in a positive effect of the exchange bias for SmCo-CuCr system. We suggested that the mechanism of the exchange bias origins from the interaction of ferromagnetic-antiferromagnetic state (FM-AFM, SmCo-CuCr). Meanwhile, the magnetic measurment of added magnetic field and zero-field-cooled (FC-ZFC) at temperature range of 10K~300K has further confirmed the critical value of FM-AFM tansform is about 80K, which is suggested that it was attributed to the coupling competition of FM phase and AFM phase.

Introduction

In recent years, advance rare earth permanence magnetic materials have been widely used in the communication technology, computer, medical, military and other fields. Its enormous potential has been highly concerned for researchers[1,2,3]. As a type of high coercivity material, SmCo alloy has a feature of high magnetocrystalline anisotropy, a high Curie temperature and excellent resistance to corrosion *et al*[4]. Recently, many researchers have synthesized SmCo thin films by physical and chemical methods, Junichi Sayama *et al*[5]. prepared SmCo films with perpendicular magnetic anisotropy on Cu layers by magnetron sputtering and they had investigated the influence of Cu underlayer thickness on the structure and magnetic properties of SmCo films. It is found that preparation parameters will have great impacts on the structure and magnetic properties of SmCo films[6,7]. L. N. Zhang *et al*. reported that a tantalum (Ta) seed layer can be used to decrease the Cu underlayer surface roughness, which enhanced the magnetic properties of SmCo films[8]. In this paper, Cr,Cu co-doped Sm_2Co_{17} films on Cr buffer layer and Cu seed layer were prepared by PLD, and found that Cr can restrain the grain growth of SmCo films and has great influence on the structure and propeties of SmCo films. The effects of co-doped on the structure and magnetic properties of SmCo/Cu/Cr thin films were further investigated.

Experiment

The (Sm2Co17Cux)/Cu/Cr and (Sm2Co17CuCry)/Cu(100nm)/Cr(3nm) films (x=1.5nm and 2.5nm, y = 1.6nm and 3.2nm) on Si substrates were prepared by PLD. The purity of Sm, Co, Cu and Cr metal targets are 99.99%, The background vacuum is better than 2.0 × 10-4Pa. Cr(3nm) buffer layer and Cu(100nm) seed layer are deposited on the Si (100) substrate in turn, then Sm2Co17Cux and Sm2Co17CuCry are grown on the seed layer. Beside incorporation of Cr, prepared Sm2Co17Cu(1.5nm)Cry/Cu/Cr films. The prepared samples are annealing at 680℃ under the vacuum of 10-4 Pa, holding time of 45 minutes. The structure and the surface morphology of samples are measured by X-ray diffraction(XRD) and scanning electron microscope (SEM). Magnetic properties are studied using vibrating sample magnetometer (VSM).

Results and Discussion

Structural Analysis

Figure 1 shows the XRD patterns of the Sm2Co17Cu (1.5nm) /Cu(100nm) / Cr(3nm) and Sm2Co17Cu(1.5nm)Cr(1.6nm) / Cu100nm / Cr(3nm) films. It can be observed the diffraction peaks of Sm2Co17(211) at 34.2° for fig.A and B and Sm2Co17(107) diffraction peak at 53.5° in the figure B. In addition, from the figure Cu(111) and Cr(110) diffraction peaks are also observed. To contrast figure A and B, it can also observe the Cr(110) diffraction peak of the figure A is slightly higher than the one of the figure B, which is mainly due to it contains the content of Cr (1.6nm) in SmCo. Figure 2 is the SEM spectra of the Sm2Co17Cu(1.5nm)/Cu100nm/Cr(3nm) and Sm2Co17Cu (1.5nm)Cr(1.6nm)/ Cu100nm/Cr(3nm) films. It can be seen that the fig.2(A) shows finer grain size and higher grain density as well as more uniform[9,10] than the fig.2(B) after added Cr 1.6nm, which exhibits that the small amount of doped Cr in SmCo may be helpful to refine crystal grain of film.

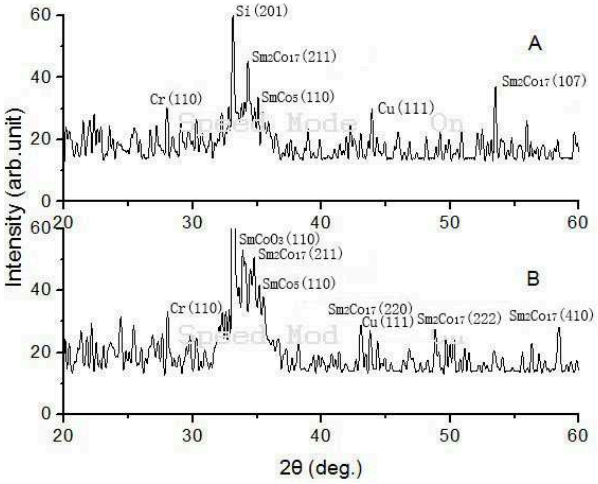
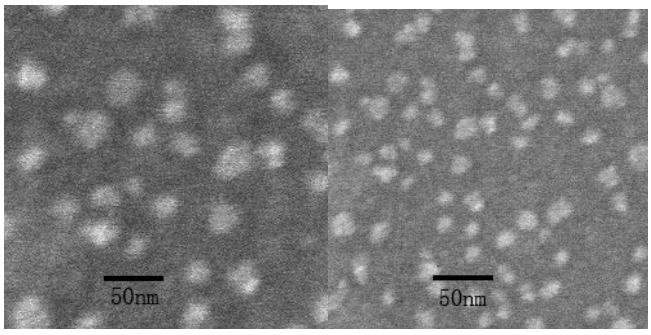


Fig.1 XRD of $Co_{17}Cu(1.5nm)Cr_y$/Cu100nm/Cr(3nm) films, A y=0, B y=1.6nm



（A） （B）

Fig.2 SEM Spectra of Sm2Co17Cu(1.5nm)Cry/Cu100nm/Cr(3nm) Films, A y=0, B y=1.6nm

Magnetic and Exchange Bias Effect

Magnetic Properties

The figure 3 gives the hysteresis loops of $Sm_2Co_{17}Cu$ (1.5nm) /Cu100nm / Cr(3nm) and $Sm_2Co_{17}Cu$ (2.5nm) /Cu100nm / Cr(3nm) films. From the figure it can be found that the H_c (1731 Oe) of SmCo layer added 1.5nm Cu has slightly larger than one (1636Oe) of SmCo layer added 2.5nm Cu. Figure 4 is the SEM spectra of two samples. It can be seen that the surface of the sample added 1.5nm Cu is more smooth than one of adding 2.5nm Cu, and the average grain size is about 50nm and about 200nm, respectively. We suggested that the more amount of Cu is not helpful to the structure growth of films[11].

Figure 5 is the hysteresis loop of $Sm_2Co_{17}Cu$ (1.5nm) /Cu100nm / Cr(3nm), $Sm_2Co_{17}Cu$(Cu1.5nm/Cr1.6nm)/Cu100nm/Cr(3nm) and $Sm_2Co_{17}Cu$(Cu1.5nm/ Cr3.2nm) / Cu100nm / Cr(3nm) films. The H_c of the film added 1.6nm Cr is 2120 Oe and one of the added 3.2nm Cr is 2554 Oe, and the H_c of the film whit no-added Cr is 1731Oe. Figure 6 is the curve of coercivity H_c as a function of Cr content y. It can be found that the coercivity of film doped Cr has higher than that of no doped Cr, and the H_c increased as the increas of the Cr content. We suggested that it was attributed to the refining effect of Cr on film grains.

Fig.7 is the SEM spectra of $Sm_2Co_{17}Cu(1.5nm)Cr_y$/Cu100nm/Cr(3nm) films, y=0, 1.6nm, and 3.2nm. It can be seen that the average grain sizes are about 10nm, 15nm and 25nm for the film C, B and A, respectively. It illustrates that doping Cr can be helpful to reduce grain size and surface roughness, which is agreement to the reports of the literature[12,13,14].

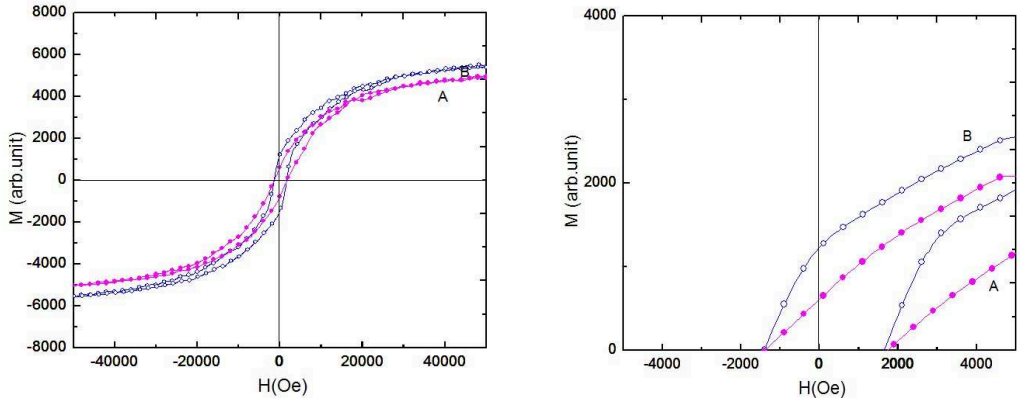
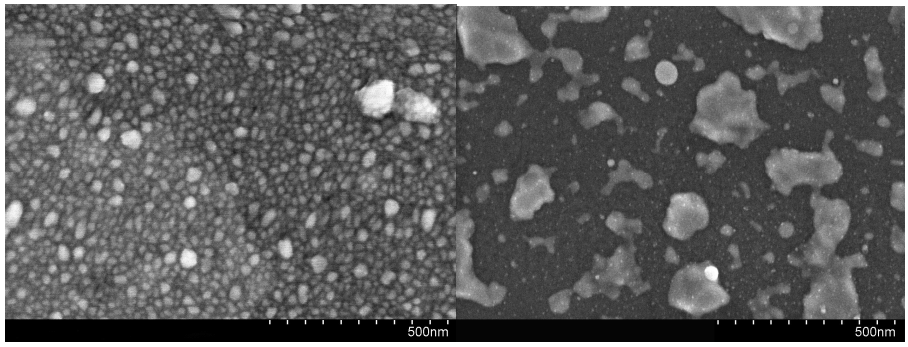


Fig.3 Hysteresis Loops of $Sm_2Co_{17}Cu_x$/Cu100nm/Cr(3nm) Films, A x=1.5nm, B x=2.5nm



（A） (B)

Fig.4 SEM Spectra of Sm2Co17Cux/Cu100nm/Cr(3nm) Films, A x=1.5nm, B x=2.5nm

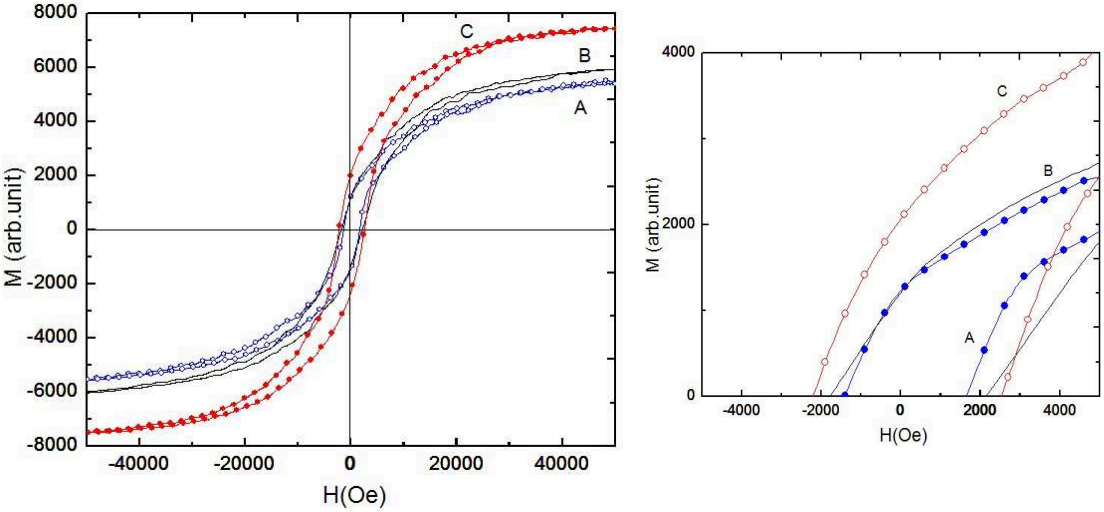


Fig.5 Hysteresis Loops of Sm2Co17Cu(1.5nm)Cry/Cu100nm/Cr(3nm) films, A y=0, B y=1.6nm, C y=3.2nm

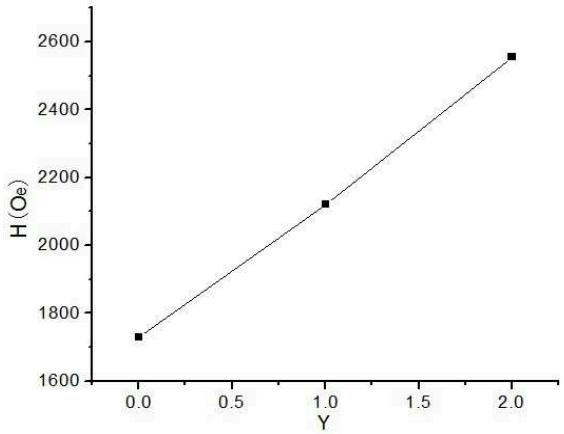
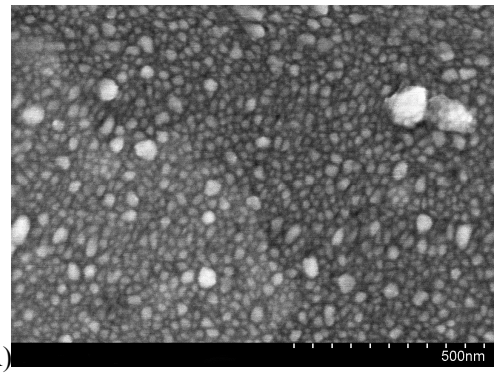
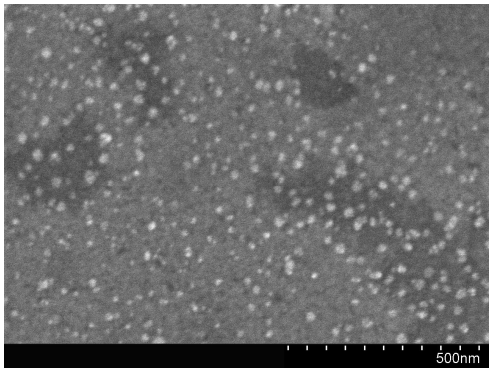
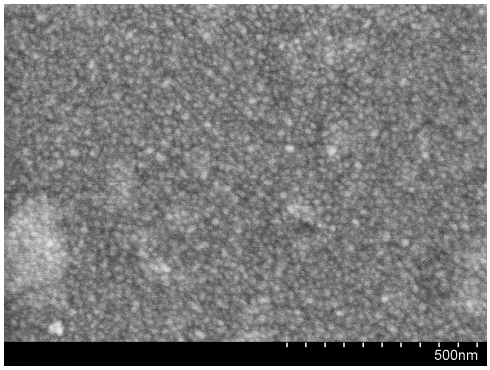


Fig.6 The Curve of Coercivity Hc as a Function of y of Cr Content for Sm2Co17Cu (Cu1.5nm/Cry)/Cu100nm/Cr(3nm) Film.



(A)





(B) (C)

Fig.7 SEM Spectra of Sm2Co17Cu(1.5nm)Cry/Cu100nm/Cr(3nm) Films, A y=0, B y=1.6nm, C y=3.2nm

Magnetic exchange bias

Figure 8 is the hysteresisloop of Sm2Co17Cu(Cu1.5nm)/Cu(100nm)/ Cr(3nm) and Sm2Co17Cu(Cu1.5nm)/Cu100nm/Cr(3nm) films. The shift of the hysteresis of A and B to right direction was seen from the figures. This indicates the appearance of the positive exchange bias effect in the SmCo-Cu system. Studies have shown that the exchange bias effect is mainly determined by the ferromagnetic-antiferromagnetic interactions in system and the coupling strength between the external field and the magnetic moment in magnetic interface. If the ferromagnetic-antiferromagnetic interaction in system shows a ferromagnetic state, exchange bias field is usually negative. If the interaction is antiferromagnetic, exchange bias field is usually positive. In a positive exchange bias system, the applied field is enough large to enable the magnetic moment in antiferromagnetic layer being arranged along the direction of the applied field, thereby the exchange bias field is positive. In the figure 8, there is a positive effect of the exchange bias, so we believe there is the competition result of ferromagnetic phase (SmCo) and anti-ferromagnetic phase (Cu) in the system[15,16,17].

The positive exchange bias effect was also found to the hysteresis loops of A, B, and C in figure 9, indicating that the exchange bias of ferromagnetic phase (SmCo) and antiferromagnetic phase (Cu,Cr) is also antiferromagnetic.

In order to confirm the above conclusions, we measured the ZFC-FC curves of the Sm2Co17Cu(Cu1.5nm/Cr3.2nm)/Cu100nm/Cr(3nm) film. Figure 10 shows the M-T curve of the sampe from 10K to 300K. It can be seen that the FC curve shows a downward trend at overall temperature range: a steep declined from 10K to 80 K, then the decline is gradual weaken after the 80K. For the ZFC curve, The magnetism decreased steeply till 80K, and there is a minimum value at about 80K, then it rises between 80 K to 260 K and has a maximum value at 260 K.

From 10 K to 80 K, FC and ZFC curves decrease monotonially, indicating the exchange interaction of film is ferromagnetic. This result is also confirmed by the figure 11, which is the hysteresis loop of the sample from fig.10 measued at 10K. From the fig.11, it can be clearly seen that the Hc changed from +450 to -583, illustrating it produced a negative magnetic bias. This approves further the exchange bias of film is ferromagnetic at low temperature. Because the thermal disturbance is weaken at low temperatures, a majority of magnetic moment in the magnetic domains is parallel, so,ferromagnetic phase has been main. On the other hand, the contents of Cr and Cu is less, so it results in the ferromagnetism being the main role.

At 80K, the ZFC curve has a minimum value, indicating the interaction of the sample transformed gradually from a ferromagnetic to an antiferromagnetc. This is due to the temperature increases and the thermal disturbance stronger. So the order arrange of magnetic moments are gradually destroyed, and the interaction is to reach equilibrium. After 80K, the ZFC curves begins rise, indicating the antiferromagnetic exchange bias begins to play a main role, which results in the hysteresis loops appears a positive exchange bias effect and the effect reaches a maximum. At 300K, the curves of FC and ZFC are to identical and is gradually to transform a paramagnetic state.

In addition, we can find that the FC and ZFC curves have a shoulder in about 50K, which may be due to the change of the exchange intensity between the ferromagnetic and the antiferromagnetic. Because the competitive of exchange interaction between ferromagnetic and antiferromagnetic is always in SmCo-Cr,Cu system. Once the antiferromagnetic is weakening, the ferromagnetic order is enhancing, and vice versa. Why the shoulder appears to 50K for our sample, we suggests that it may be related to the content of the ferromagnetic and the antiferromagnetic in the sample, the details needed to be studied further.

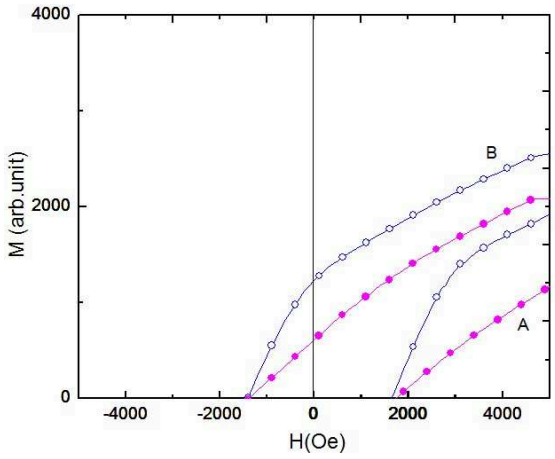


Fig.8 Hysteresis Loops of Sm2Co17Cux/Cu100nm/Cr(3nm) Films, A x=1.5nm, B x=2.5nm

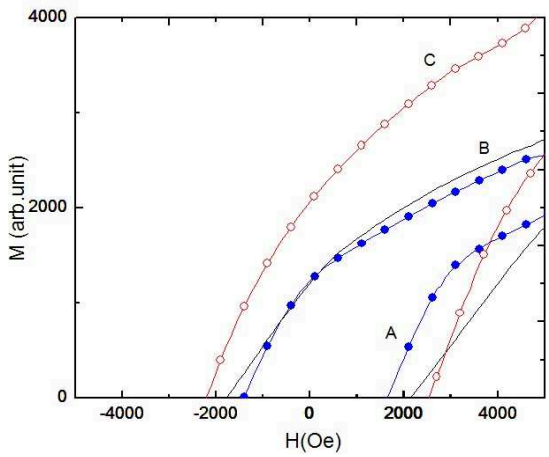


Fig.9 Hysteresis Loops of Sm2Co17Cu(1.5nm)Cry/Cu100nm/Cr(3nm) films, A y=0, B y=1.6nm, C y=3.2nm

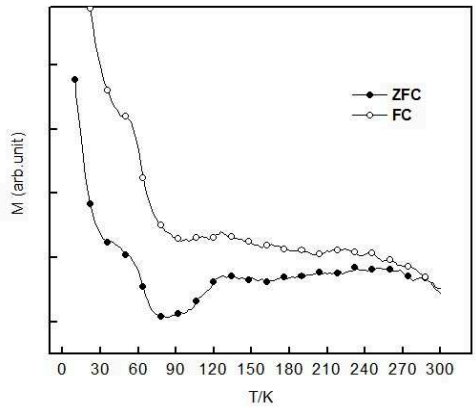


Fig.10 ZFC-FC Curve of the Sm2Co17Cu(Cu1.5nm/Cr3.2nm)/Cu100nm/Cr(3nm) Film

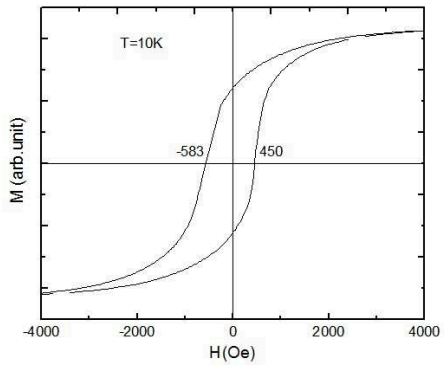


Fig.11 Hysteresis Loops of the Sm2Co17Cu(Cu1.5nm/Cr3.2nm)/Cu100nm/Cr(3nm) Film at 10K

Conclusion

In summary, the (Sm2Co17Cux)/Cu/Cr and (Sm2Co17CuCry) /Cu(100nm)/ Cr(3nm) films (x=2.5nm, y=1.6nm and 3.2nm) on Si substrates were prepared by PLD. After Cr,Cu co-doping, the case of the refinement of crystal grain and the increase of coercivity of SmCo is observed, and the most interest behave that the exchange bias in the Sm2Co17: (Cr,Cu) system was found.The incorporation of Cu and Cr in SmCo films resulted in a positive effect of the exchange bias. We suggested that the mechanism of the exchange bias origins from the interaction between the ferromagnetic state and the antiferromagnetic state in the SmCo-CuCr system, and the change of the interaction intensity results from the competition between ferromagnetic phase (SmCo) and anti-ferromagnetic phase (Cu,Cr) in the system.

Acknowledgment

This work was supported by the Key Science Found of High Education of Anhui Province (Grant No. KJ2012A002).

References

[1] S. Takei, S. Shomura, A. Morisako, M. Matsumoto, T. Haeiwa,J. Appl. Phys., 81 (1997), p. 4674

[2] J.F. Liu, T. Chui, D. Dimitrov, G.C. Hadjipanayis,J.Appl. Phys., 73 (1998), p. 3007

[3] V. Neu, S.A. Shaheen,Journal of Applied Physics, 86 (1999), p. 7006

[4] A. Yan, A. Bollero, K.H. Müller, O. Gutfleisch,Journal of Applied Physics, 91 (2000), p. 8825

[5] Junichi Sayama, Kazuki Mizutani, Toru Asahi, Jun Ariake, Kazuhiro Ouchi, Tetsuya Osaka: J.Magn. Magn. Mater. Vol. 301 (2006), p. 271

[6] Isamu Kato, Shigeto Takei, Xiaoxi Liu, and Akimitsu Morisako: IEEE, Trans. Magn. Vol. 42(2006), p. 2366

[7] J. Sayama, K. Miztutani, T. Asahi, T. Osaka: Appl. Phys. Lett. Vol. 85 (2004), p. 5640

[8] L. N. Zhang, J. S. Chen, J. Ding, et al. J. Appl. Phys., 103 (2008), 113908

[9] X. H. Liu, L. Y. Cui, S. X. Zhou, et al. Materials Science and Engineering, 304 (2001), p. 1043-1045

[10] R. Andreescu, M. J. O'Shea. J. Appl. Phys., 91 (2002), p. 8183

[11] S. Takei, A. Morisako, M. Matsumoto.J. Magn. Magn. Mater., 272 (2004), p. 1703

[12] Mitsuru Ohtake, Yuri Nukaga, Fumiyoshi Kirino, et al, J.Appl.Phys, 107(2010), 09A706

[13] Haibao Zhao, Hao Wang, Xiaoqi Liu, et al. J. Appl. Phys., 109 (2011), 07B715

[14] Chen X,Hochstrat A,Borisov P,et al.Applied Physics Letters, 89 (2006), p. 202

[15] Salaba E L,Rumplecker A,Kleitz F,et al, Nano Letters, 6 (2006), p. 2977

[16] J. Nogues, I. K. Schuller. J. Magn. Magn. Mater,192 (1999), p. 203

[17] Q. K. Ong, A. Wei, X. M. Lin, Phys. Rev. B, 80 (2009), 134418.

Advanced Materials Research Vol. 936 (2014) pp 322-326
© (2014) Trans Tech Publications, Switzerland
doi:10.4028/www.scientific.net/AMR.936.322

Hyaluronic Acid Functionalized Porous Silica Nanoparticles for Drug Delivery and Release

Lingyuan Cui, Yanhui Li*, Wei Zhang, Jingpeng Zhang and Qian Duan

Changchun University of Science and Technology, Changchun, China

email :liyanhui@ciac.ac.cn

Keywords: porous silica nanoparticle, drug delivery and release, hyaluronic acid

Abstract : In this paper, we reported a facile strategy to synthesize hyaluronic acid (HA) conjugated porous silica nanoparticles ($pSiO_2$) as drug carrier. The $pSiO_2$ were prepared by solid nano-silica nanoparticles with "surface-protected etching". Morphologies of solid and porous silica nanoparticles were characterized by SEM and TEM. Amino groups were introduced on $pSiO_2$ to graft HA as cancer targeting ligand. Then rifampicin used as model drug was loaded in $pSiO_2$-HA. The results indicate that $pSiO_2$ can perform a certain degree of slow release. Overall, the system might open the door to a new generation of carrier system for site-selective, controlled-release delivery of anticancer drugs.

Introduction

Since the discovery of ordered mesoporous silica materials, much attention has been focused on the organic moiety functionalized mesoporous silica with different potential applications due to their large surface area, uniform pore size distributions and adjustable pore sizes over the range 1.5-30 nm. Several mesoporous silica nanoparticles-based controlled-release systems have been synthesized by using different kinds of capping agents[1-4] including nucleic acids, organic molecules, inorganic nanoparticles, polymers, and superamolecular assemblies. Gary-Bobo M[5] prepared Hyaluronic acid(HA)-functionalized mesoporous silica nanoparticles for efficient photodynamic therapy. Because HA is one of cancer cell selectivity ligand linked with two kinds of cancer receptors: CD44 and RHAMM[6].

In this paper, we explored the capability of the "surface-protected etching"[7] strategy and demonstrate a simple process for the synthesis of $pSiO_2$ for Rifampicin loading. HA was introduced on $pSiO_2$ and demonstrated great potential for cell-specific targeted and drug controlled release. We hope the products will be encapsulated different drugs into respective porous space, and showing that porous silica nanoparticles can be used in for imaging, catalyze and drug delivery vectors.

Materials and methods

Materials

Tetraethyl silicate (TEOS), ammonia solution, isopropylalcohol (IPA) and Sodium hydroxide were obtained from Beijing Chemical Works with analytically pure. 3-aminoporopyl triethoxysilane (APTES), HA sodium salt, Polyvinylpyrrolidone(PVP), 1-ethyl-3-(3-dimethyl-aminopropyl) carbodiimide (EDC), N-Hydroxysuccinimde (NHS) were purchased from Aladdin Industria Corporation. Deionized water, phosphate buffer (PBS), 2-(N-morpholino) ethanesulfonic acid buffer (MES) were homemade.

Synthesis of SiO_2 Nanoparticles($sSiO_2$)

6 mL of TEOS and 20 mL of IPA were mixed in the beaker and added into the mixture of 9 mL of IPA, 20 mL of H_2O, and 8 mL of ammonia solution to stir until appeared white turbidity. Then

another stirring was continued for 15min, 3 mL of TEOS was added into the above mixture liquid, which was hydrolyzed and condensed for 4 h. Then, the products were centrifuged and washed with deionized water and ethanol several times then freeze-drying.

Synthesis of Porous SiO_2 Nanoparticles($pSiO_2$)

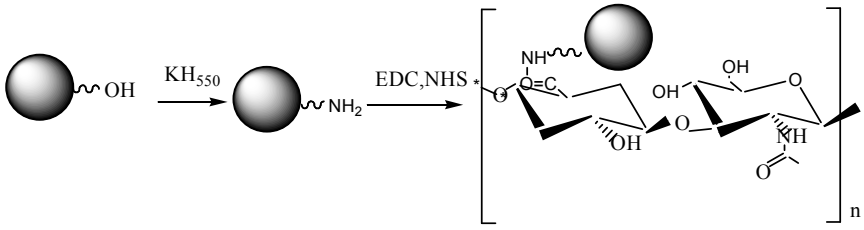
The as-prepared sSiO2 sample (200 mg) was dispersed in deionized water(20 mL) mixed mixed PVP(1.5g) at 100 ℃ for 3h. After cooling down to room temperature, NaOH aqueous solution (5 mL, 0.10 g/mL) was injected into the system to initiate etching[8]. After a defined time, the products were collected by centrifugation and washed several times by deionized water. Then the products were freeze-drying and calcined at 600℃ for 6h to get $pSiO_2$.

Amino modified Porous SiO_2 Nanoparticles(SiO_2-NH_2)

The solid and porous nano-SiO_2 microspheres were dispersed in deionized water, and then APTES was added under high-speed stirring with pH value of 10 to react at 100 ℃ for 24h. APTES and (APTES + SiO_2) molar ratio was 1:4. The products were collected by centrifugation and washed several times to freeze-dry to get SiO_2-NH_2.

HA modified porous silicon(SiO_2-NH_2-HA)

HA (30 mg) was hydrated in water overnight and then activated by EDC (6 mg) and NHS (12 mg) in MES buffer (pH=6.0) for 40 min[9]. 80 μL of PBS buffer (pH 7.4) was then added followed by the addition of 12 mg SiO_2-NH_2 at room temperature with continuous stirring for 20h. The unreacted HA was removed by centrifugation. After reaction, the products were freeze-drying to get SiO_2-NH_2-HA. The detailed process of $pSiO_2$-HA conjugates was shown as scheme 1.



Scheme 1. Synthesis of HA conjugate using amino-modified silica microspheres (SiO_2-NH_2).

Rifampicin Loading and release

The $pSiO_2$(20 mg) and Rifampicin(20 mg) were dispersed in PBS (80uL) to stir for 24h under dark conditions. The products were centrifuged and washed with PBS. Rifampicin concentration was measured by UV-vis measurements at 474 nm. Drug loading content and drug loading efficiency of Rifampicin can be calculated as follow [10]:

Drug loading content[wt.%]=(weight of loaded drug/weight of nanocomposites）×100%

Drug loading efficiency[%]=(weight of loaded drug/weight of drug in feed)×100%

The standard curve of Rifampicin was measured in the same PBS with R^2=0.9278, the equation was y=0.0044x-2.5006.

Characterization of materials

The morphologies of nanoparticles were observed through Transmission electron microscopy (TEM, JEM-2100F electron microscope) and scanning electron microscopy (SEM, JEOL JSM-6700F microscope). UV-vis spectra were recorded on a UV-3101PC Shimadzu spectroscope. The functional groups of products were emerged through infrared spectrum(8400S (Shimadzu)).

Results

Synthesis of SiO_2-NH_2 and $pSiO_2$-HA characterized by FTIR

SiO_2 and SiO_2-NH_2 were characterized by FTIR shown in fig.1. In figure 1b, the peaks at 1634 cm^{-1} and 3443cm^{-1} indicated SiO_2 surface active hydroxyl groups, the peaks at 798 cm^{-1}, 1097 cm^{-1}

and 470 cm^{-1} correspond to the Si-O-Si of antisymmetric stretching vibration, symmetric stretching vibration and bending vibration. Compared with the FTIR spectra of SiO_2 (Fig. 1b), new peaks of $pSiO_2$ were observed around 3164cm^{-1} and 1405 cm^{-1} assigned to the NH_2 vibration, the Si-CH_2 vibration. The results indicated that the SiO_2-NH_2 had been successfully prepared.

FTIR spectra of HA and $pSiO_2$-HA were shown in fig.2. The successful HA grafting was validated by the appearance more stronger absorption bands similar to HA emerged in $pSiO_2$-HA (Fig. 2a) at around 1633cm^{-1} similar to $pSiO_2$-HA(Fig. 2b), which assigned to amide C=O stretching of the carboxyl groups contained within the attached HA macromolecules.

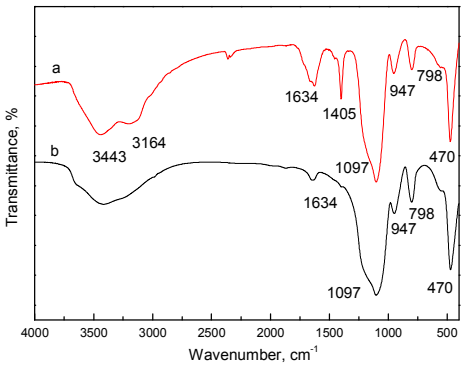


Fig. 1 FTIR spectrum of silica nanoparticles before (b) and after (a) aminaton reactiom

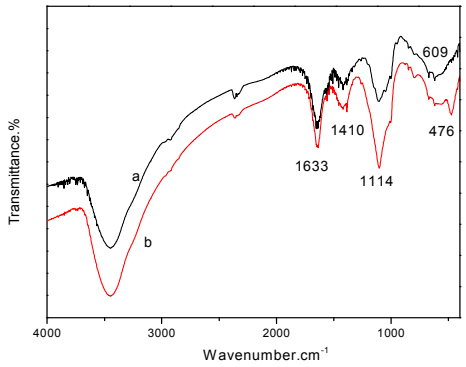


Fig. 2 FTIR spectra of HA (a), and $pSiO_2$-HA(b)

Morphologies

TEM and SEM images showed that $sSiO_2$ and $pSiO_2$ (surfactant not removed from $pSiO_2$) were of spherical morphology (Figure 3a,b), and $sSiO_2$ exhibit a smooth surface while $pSiO_2$ showed rough pore-like channels indicating the presence of pore structure.

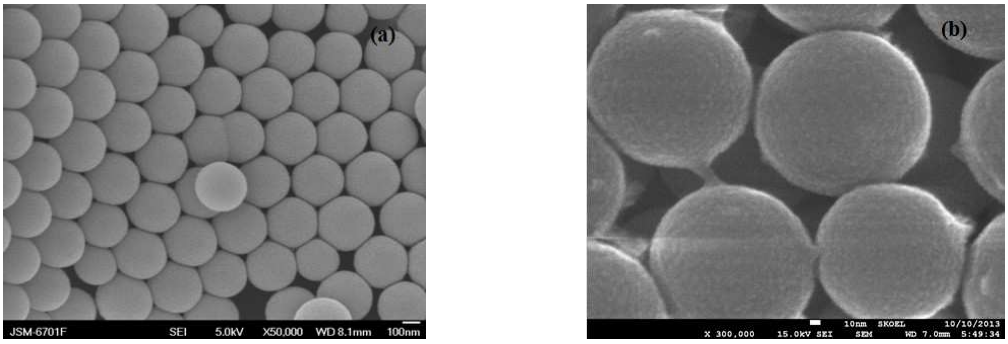


Fig. 3 SEM of $sSiO_2$ (a)(size 260nm) and $pSiO_2$(b)(size 200nm)

As seen in Fig.3, the size of $sSiO_2$ was about 240nm, while the size of $pSiO_2$was 200nm, the result indicated that the etching was successful.

Inner structure of solid and porous SiO_2 was observed by TEM as shown in fig.4.

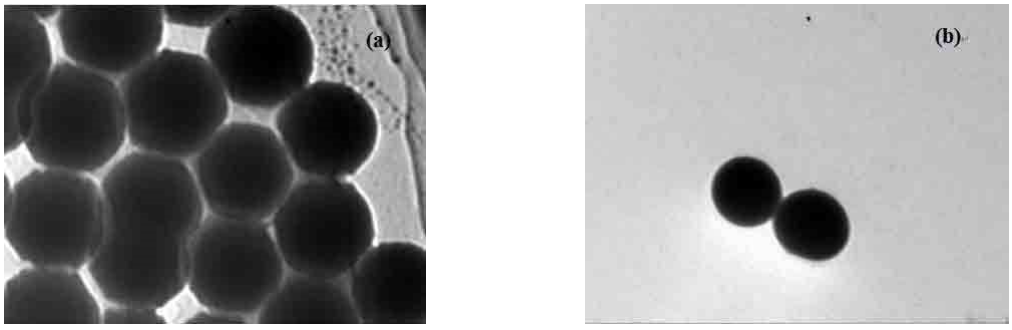


Fig. 4 TEM of $pSiO_2$ (a) and $sSiO_2$ (b)

As seen from the, there was a uniform structure in $sSiO_2$ with no difference between the internal and surface. While after NaOH dissolution, $pSiO_2$ had internal structure with the mesh from surface to inner seen from figure 4(b). In the first 70 min of reaction, the transmittance changed very slowly because the NaOH only attack the surface of silica layer which was protected by the PVP molecules. It also suggested that by controlling the reaction time the degree of etching can be controlled.

Figure 5a, b, were the SEM of nanoparticles packaged with PVP and grafted with HA, respectively.

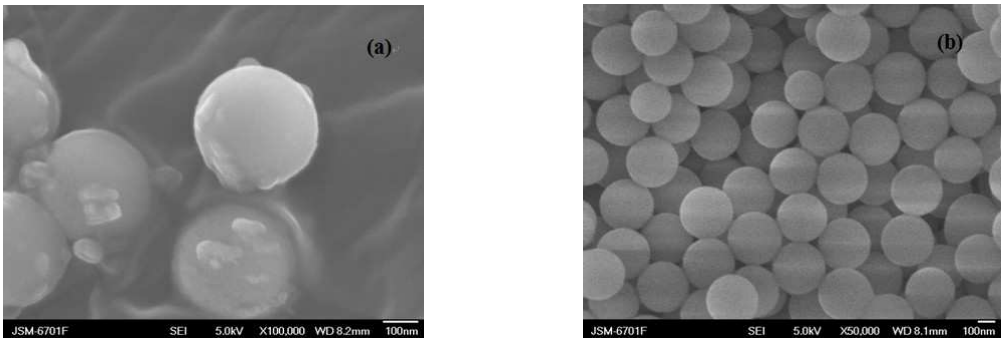


Fig. 5 SEM photos of PVP- SiO_2 nanoparticles(a) and HA-SiO_2 nanoparticles(b)

It can be seen that not only the spheres were still with the uniform size, but also possessed very good monodispersed.

Rifampicin loading and release

Drug loading content and loading efficiency of rifampicin in nanoparticles were listed in table 1.

TABLE 1 DRUG LOADING CONTENT AND DRUG LOADING EFFICIENCY

Sample	Drug loading content [wt.%]	Drug loading efficiency [%]
$sSiO_2$	20%	65%
$pSiO_2$	40%	80%

As can be seen from Table 1, rifampicin can be adsorbed in $pSiO_2$ with higher drug loading content and efficiency. The result indicated that more porous in $pSiO_2$ can load more drugs.

The experiment of Rifampicin released from $sSiO_2$ and $pSiO_2$ was performed in PBS, and the results were shown in Fig.6.

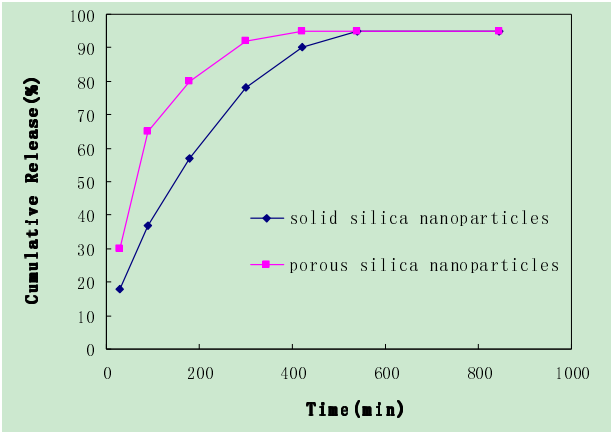


Fig. 6 Rifampicin release from solid and porous silica nanoparticles

As can be seen from Fig.6, rifampicin of solid and porous SiO_2 nanoparticles has burst release behavior, but comparatively speaking, the release rate of rifampin from $pSiO_2$ was significantly slower than $sSiO_2$. So $pSiO_2$ were more suitable for rifampicin loading and release.

Conclusion

This article prepared $sSiO_2$ by sol-gel with uniform size. Under the protection of PVP, NaOH was used to dissolute $sSiO_2$ to obtain $pSiO_2$. We can gain uniformly sized $pSiO_2$ through morphology observation in this method. But after dissolution treatment, the size of the silica sphere was slight decreased. Then HA was introduced on $pSiO_2$ to get targeting property. Based on $sSiO_2$ and $pSiO_2$, rifampicin was used as model drug to load in the paticles. The results indicated that $pSiO_2$ can load more rifampin, and release behavior has been improved. Compared with $sSiO_2$, the $pSiO_2$ was more suitable for using as drug carrier. Fortunately, we expected HA grafted on the surface of $pSiO_2$ will provide a suitable anticancer drug delivery for efficient cancer therapy.

Acknowledge

The authors are thankful to the National Natural Science Foundation of China (50903009) and the Jilin Science and Technology Bureau, Science and Technology Development Project (20100115) for financial support to this work.

References

[1] Zhang Q, Wang W, Goebl J, et al, Self-templated synthesis of hollow nanostructures, Nano Today. 4(2009) 494-507.

[2] Vallet-Regı´ M, Ra´mila A, del Real RP, Pe´rez-Pariente J, A new property of MCM-41: drug delivery system, Chem Mater. 13(2001)308-311.

[3] Vallet-Regı´M, Balas F, Arcos D, Mesoporous materials for drug delivery, Angew Chem Int Ed. 46(2007)7548-7558.

[4] Slowing II, Trewyn BG, Lin VSY, Mesoporous silica nanoparticles for intracellular delivery of membrane-impermeable proteins, J Am Chem Soc. 129(2007)8845-8849.

[5] Gary-Bobo M, Brevet D, Benkirane-Jessel N, et al, Hyaluronic acid-functionalized mesoporous silica nanoparticles for efficient photodynamic therapy of cancer cells, Photodiagnosis and Photodynamic Therapy. 9(2012)256-260.

[6] Luo, Y., Ziebell, M. R., and Prestwich, G. D, A hyaluronic acid-taxol antitumor bioconjugate targeted to cancer cells, Biomacromolecules 1(2000)208-218.

[7] Zhang, Q., Zhang, T. R., Ge, J. P., Yin, Y. D, Permeable silica shell through surface-protected etching, Nano Lett.. 8(2008)2867-2871.

[8] CUI Yuan, LI Yanhui, DUAN Qian, Preparation of Porous Silica Nanospheres and its Releasing Characterization for Insulin, Journal of the Chinese Ceramic Society. 2(2013)240-244.

[9] Chen Y, Chen H, Guo L, et al, Bioresponsive Hyaluronic Acid-Capped Mesoporous Silica Nanoparticles for Targeted Drug Delivery, Chem. Eur. 19(2013)1778-1783.

[10] Y.F. Zhu, Y. Fang, L. Borchardt, S. Kaskel, PEGylated hollow mesoporous silica nanoparticles as potential drug delivery vehicles, Microporous and Mesoporous Materials. 141(2011)199-206.

Advanced Materials Research Vol. 936 (2014) pp 327-331
© (2014) Trans Tech Publications, Switzerland
doi:10.4028/www.scientific.net/AMR.936.327

Preparation and Characterization of Fibrillated Nanofibrous Filter Material

Tian Yu[1,a], Yanbin Jiang[1,b], and Jian Hu[2,c]

[1] School of Chemistry and Chemical Engineering, South China University of Technology, Guangzhou, 510640, China

[2] State Key Lab of Pulp & Paper Engineering, South China University of Technology, Guangzhou, 510640, China

[a] tianyu163@vip.163.com, [b] cebjiang@scut.edu.cn, [c] ppjhu@scut.edu.cn

Keywords: nanofiber; fibrillation; filtration

Abstract: The nanofiber, which diameter less than 1000 nm, has been discovered as advanced fiber material for high efficiency filtration. Tencel fiber is a new kind of regenerated fiber which can be easily fibrillated by a mechanical beating process to form nanofiber morphology. The present study shows the nanofiber morphology of Tencel fiber and investigates how the structure and properties of filter material change with the impact of fibrillated nanofiber. The results show a mass of nanofibril appeared after the Tencel fiber is intensively beat. At the same time, the air permeability and pore size of filter material is decreased with the decrease of fibrillated nanofiber content while the strength gets an opposite trend. What's more, the filtration efficiency of the filter material is significantly enhanced by fibrillated nanofiber which filtration rate achieves 6.3 for particles bigger than 4 μm at 20 wt%. This paper has shed some light on the application of fibrillated fibrillated nanofiber to enhance the efficiency of filter material effectively.

Introduction

The fibers with diameter less than 1 μm are generally defined as "nanofibers" in the filtration field [1]. Owing to the ultra small diameter, nanofibers have very high surface areas that are advantageous for fibrous filtration. As a result, nanofibers become a key component of many filter material. And the filter material which have at least some fraction of nanofibers are called "nanofibrous filter material" or "nanofiber material"[2]. Nanofiber material has proved as a promising material which can provide greater filtration efficiency and higher performance than conventional filtration material.

At present, electrospinning nanofibers, improved melt-blown nanofibers and micro glass fibers are most commonly used nanofibers. While they are effective for enhance the performance of filter material, it has drawbacks. For instance, they are hard to recycle and is fairly weak which can be easily damaged in the manufacture and service process.

Tencel fiber, which is spun from a solution of cellulose in N-methylmorpholine-N-oxide (NMMO) [3-6], is a fully biodegradable cellulose fiber has almost 100% conversion efficiency from woodpulp to the final fiber. It is easily fibrillated to form highly polydisperse nanofiber morphology by a mechanical beating process[7]. As those highly fibrillated nanofibers are polydisperse fibers with perfect hydrophilicity[8], it is possible to produce nanofibrous filter material by a wet-laid process through the usage of these fibers. This is a new nanofiber material. Therefore, how to investigate the properties of this material to form new technology is of great significance.

In this paper, the morphological changes of Tencel fiber after intensively beating are characterized and their SEM pictures are observed. Then, the effect of fibrillated Tencel nanofiber（58°SR） on the structure, basic properties and filtration properties of filter material are investigated. Some light was shed on the application of fibrillated Tencel nanofibers in the nanofibrous material field.

Experimental

Materials

Tencel fiber (Fineness: 1.7dex, Length:6mm)
Hardwood fibers

Equipment

PFI-refiner: Canada LABFECH
Sheet-forming apparatus: British ME-255
Beating degree meter: Yo-2-18, Sichuan, Changjiang Paper Instruments Ltd.
Fiber length tester: Kajaani Fiber Auto Analyzer FS-200
Permeability tester: YG461E, Ningbo Textile Instrument Factory
Burst strength tester: Code 180, Lorentzen & Wettre Ltd.
Thickness gauge: YG142, Ningbo Textile Instrument Factory
Scanning electronic microscope: S3700 scanning electronic microscope, Hitachi, Japan
Pore size tester: PMI permeameter, USA

Fiber Beating

The Tencel fiber was beaten by PFI refiner with 9000 revolutions.

Sample preparation and Scanning electron micrograph observations

Nanofiber material were made from the fibrillated Tencel nanofibers with Hardwood fibers, and basis weight was 105g/m^2. In order to protect samples without destructing the original three-dimensional structure, there was no press after formation. Subsequently, the structure of samples was studied by SEM. Lastly, the effect of fibrillated Tencel nanofiber（58°SR）on the basic properties and filtration properties of filter material were investigated. The filtration properties were tested by multi-pass test method, and the schematic of test system was showed in Figure 1.

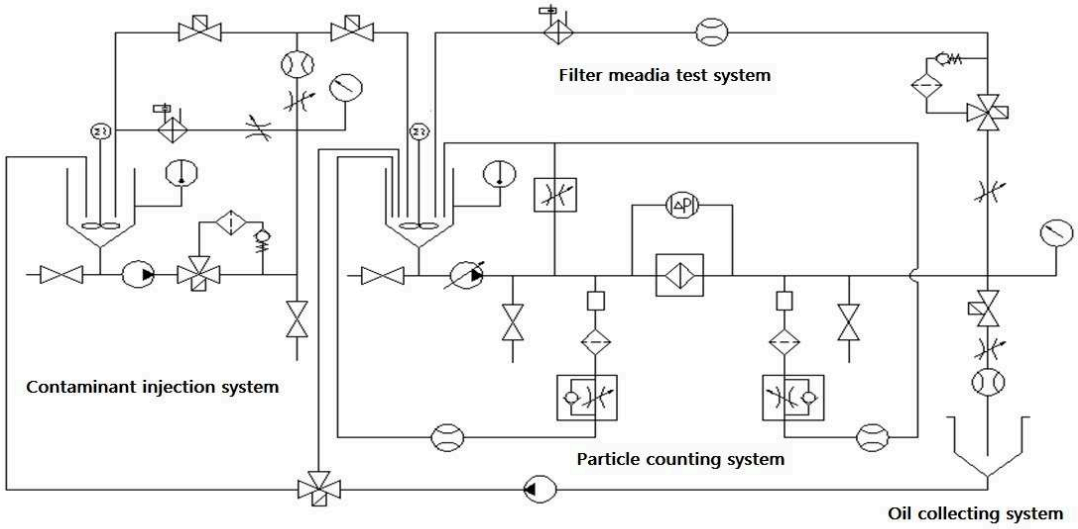


Fig. 1 The schematic of the multi-pass test method test system

Results and Discussion

Beating Properties of Tencel Fiber

After being beaten by PFI-refiner at 9000 rounds, the beating degree and the average length of Tencel fiber are listed in the following table and the un-beat fiber also listed to compare.

TABLE 1. THE EFFECT OF BEATING INTENSITY ON BEATING DEGREE AND AVERAGE LENGTH

Beating rounds	Beating degree [°SR]	The fiber's average length [mm]
0	12	6.00
9000	58	0.38

The values in the table 1 reveal that Tencel fibers are cut off instantly and their length decreases significantly after beating. Meanwhile, the beating degree is also rise obviously.

SEM Observation

Observation of Fibrillated Tencel Fibers

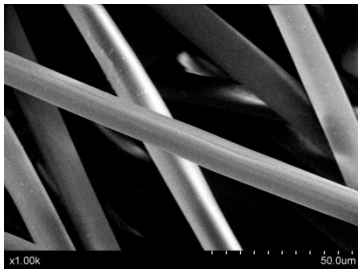


Fig. 2 Tencel fibers (×1000)

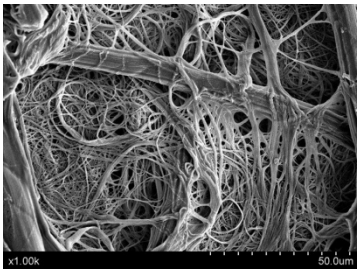


Fig. 3 Fibrillated fibers (×1000)

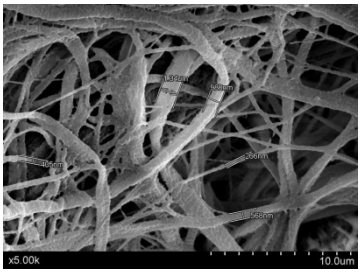


Fig. 4 Fibrillated nanofibers (×5000)

Fig.2 and fig.3 reveal the very change of morphology of Tencel fibers by beating process. Before beating (fig.2), Tencel fibers are smooth and the same size. But after beating, it can be found that a plenty of fibrils are peeled back or splintered from the trunk fiber. And from the enlarged SEM picture fig.4 with 5000 magnification, it shows the diameters of fibrils are smaller than 1 μm generally and some of them are as low as about 100 nm. They are nanofibers.

Observation of Fibrillated Nanofibrous Material

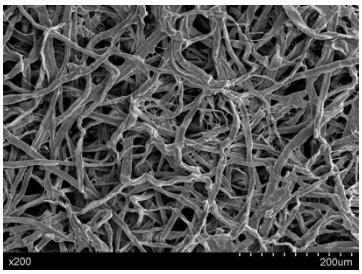


Fig. 5 5 wt% content (×200)

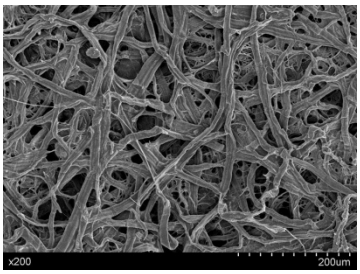


Fig. 6 10 wt% content (×200)

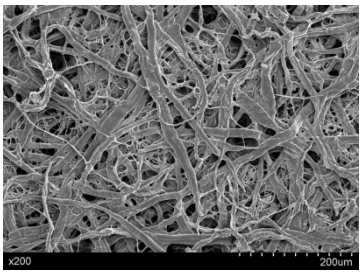


Fig. 7 20 wt% content (×200)

To understand the relationship between the properties of fibrillated nanofibrous material and its morphology, the material were studied by SEM. Fig.5 to fig.7 are the SEM pictures of fibrillated nanofibrous material. The fibrillated nanofibers content of the material are 5 wt% (fig.5), 10 wt% (fig.6) and 20 wt% (fig.7) respectively. From fig.5 to fig.7, it reveals that the fiber gaps are filled with fibrillated nanofibers quickly with the increasing of fibrillated nanofibers content. As a result, the fibrillated nanofibers make a great number of tiny pores in the material. This structure is beneficial to improve the filtration efficiency of material greatly. On the other hand, with the increasing of nanofibers' content, the bonding density of fibers in the material also increases remarkably and it might improve the strength of material effectively.

Fibrillated Nanofibrous Material Properties Test

To understand the effect of the fibrillated nanofibers on the filter material, the material properties are tested, including basic properties (burst strength, air permeability and pore size) and filtration properties (Initial pressure drop, dust retention capacity and filtration ratio). The results are listed in table 2 to table 4 respectively.

TABLE 2 BASIC PROPERTIES OF FIBRILLATED NANOFIBROUS MATERIAL

Content [wt%]	Burst Strength [Kpa]	Air Permeability [mm/s]	Max Pore Size [μm]	Mean Pore Size [μm]
0	152	114.3	24.5	9.1
5	228	62.8	17.1	6.3
10	269	48.3	16.6	5.4
20	336	29.3	13.9	3.8

From the table 2, it can be found that the properties of filter material vary a lot on the influence of fibrillated nanofibers. It means with the increase of fibrillated nanofibers' content, the air permeability and pore size decrease obviously, while the burst strength of filter material gets an opposite trend. Comparing with the material have no fibrillated nanofibers, only 5 wt% of fibrillated nanofibers have changed the performances of filter material significantly. When fibrillated nanofibers content comes to 20 wt%, the air permeability of material is quartered, pore size fells by almost half while burst strength is doubled. These results are consistent with the structure analysis above.

TABLE 3 INITIAL PRESSURE DROP AND DUST RETENTION CAPACITY OF FIBRILLATED NANOFIBROUS MATERIAL

Content [wt%]	Initial pressure drop[Kpa]	Dust retention capacity [mg/cm^2]
0	14	2.93
5	16	2.65
10	20	1.80
20	64	1.35

The results of table 3 shows with the increase of fibrillated nanofibers' content, the initial pressure drop of material is increasing while the dust retention capacity is decreasing. However, according to the test results of table 4, the filtration is radically increasing with the increase of nanofibers' content.

TABLE 4 FILTRATION RATIO OF FIBRILLATED NANOFIBROUS MATERIAL

Content [wt%]	>4μm(c)	>5μm(c)	>6μm(c)	>7μm(c)	>8μm(c)	>10μm(c)	>12μm(c)	>14μm(c)
0	/	/	/	3.91	6.04	16.00	47.54	126.24
5	/	/	/	6.44	10.55	30.84	93.87	205.51
10	/	/	7.73	14.70	29.11	106.39	294.58	/
20	6.30	18.34	41.09	82.90	146.51	/	/	/

Table 4 reveals the filtration ratio of material with different nanofibers' content. When nanofibers' content is 0%, the smallest size of detectable particle filtered by the material is 7μm, while the filtration ratio is 3.91. By contrast, when nanofibers' content reaches 20%, the filtration ratio of 7μm particles filtered by material is 80.90, 31 times as much as the material with no nanofiber. Meanwhile, when nanofibers' content reaches 20%, the smallest size of detectable particle filtered by material decreases to 4μm, while the filtration ratio is 6.3. It means the filtration efficiency of material toward to particles bigger than 4um reaches 84.12%. Fibrillated nanofiber enhances the filtration efficiency of filter material effectively.

Conclusions

The present study shows how the Tencel fiber morphology changed with intensively beating to become nanofiber and investigates the effect of this nanofiber on the structure and properties of filter material.

The results show a mass of nanofibril appeared after the Tencel fiber is intensively beat. And the fiber becomes to nanofiber. When these nanofibers are applied to filter material, the fibrillated nanofibers make a great number of tiny pores in the material. This structure is beneficial to improve the filtration efficiency of material greatly and also improve the strength of material effectively.

As a result, the test results reveal the filtration efficiency of the filter material is significantly enhanced by fibrillated nanofiber which filtration rate achieves 6.3 for particles bigger than 4 μm at 20 wt%. As to the burst strength, the filter material with 20 wt% fibrillated nanofibers is the double of non-nanofiber material.

This paper has revealed the fibrillated nanofiber is a right material to enhance the strength and filtration efficiency of filter material effectively.

Acknowledgements

The authors gratefully acknowledge the support from the National High-Tech R&D Programme of China (863 Program, 2013AA031902) and Guangdong Provincial Department of Science and Technology Program (2011A091102006).

References

[1] A. Podgorski, A. Balazy, L. Gradon, Application of nanofibers to improve the filtration efficiency of the most penetrating aerosol particles in fibrous filters, Chem. Eng. Sci. 2006, 61(20), 6804-6815.

[2] R. S. Barhate, S. J. Ramakrishna, Membrane Sci. Nanofibrous filtering media: Filtration problems and solutions from tiny materials 2007, 296(1-2), 1-8.

[3] C. C. McCorsley and J. K. Varga, U.S. Patent 4,142,913, 1979.

[4] I. Quenin, Doctoral Thesis, UJF Grenoble, 1985.

[5] J. M. Taylor, International Patent Application WO 92/01724, 1992.

[6] J. M. Taylor, International Patent Application WO 92/19807, 1992.

[7] S. Janardhnan, M. J. Sain, Bio-Treatment of Natural Fibers in Isolation of Cellulose Nanofibres: Impact of Pre-Refining of Fibers on Bio-Treatment Efficiency and Nanofiber Yield, Polym. Environ. 2011, 19(3), 615-621.

[8] V. S. Karande, S. T. Mhaske, A. K. Bharimalla, G.B. Hadge, Vigneshwaran N. Evaluation of two-stage process (refining and homogenization) for nanofibrillation of cotton fibers, Polym. Eng. Sci. 2013, 53(8), 1590-1597.

Advanced Materials Research Vol. 936 (2014) pp 332-336
© (2014) Trans Tech Publications, Switzerland
doi:10.4028/www.scientific.net/AMR.936.332

The Improvement of Pd Nanoclusters Electro-catalytic Properties for FAO by the Addition of Co Element

M. Lei[1], L.S. Wang[1, a], X.L. Liu[1], J.B. Wang[1], R. Xu[1], C.X. Lei[2], G.H. Yue[1], Y. Chen[1], D.L. Peng[1, b]

[1] Department of Materials Science and Engineering, College of Materials, Xiamen University, Xiamen 361005, China

[2]College of Materials Science and Engineering, Guangxi University, Nanning, 530004, China

Corresponding authors: [a]wangls@xmu.edu.cn; [b]pengdl@xmu.edu.cn

Keywords: Pd-based nanoclusters catalysis, Physical vapor deposition, Formic acid oxidation

Abstract. Near-monodisperse Pd and PdCo nanoclusters were synthesized by physical vapor deposition using a plasma-gas-condensation cluster deposition system and tested for catalyzing formic acid oxidation. Under the condition of high vacuum and inert gas, NCs with clean surface and uniform size were obtained. The cyclic voltammetry tests revealed that the electrochemical surface area was increased from 49.7 $m^2 g^{-1}$ to 51.7 $m^2 g^{-1}$ and the peak current density of catalyzing FAO was raised from 0.115 mA cm^{-2} to 0.125 mA cm^{-2} when about 12*wt*. % Co element was added. Additionally, the tolerance to CO poisoning of Pd could also be improved by the addition of Co. The result indicated that this method offered a chemical-free way to prepare clean and efficient Pd-based nanoscale catalytics and encouraged deeper exploration for electrochemichal catalytic reactions.

Introduction

Nowadays, the interests in the energy-converting and energy-saving technology of direct formic acid fuel cell (DFAFC) are raised significantly, due to its higher theoretical electromotive potential and less fuel crossover comparing with those of direct methanol fuel cell (DMFC) [1]. Pt as its general catalyst was challenged on account of large cost, slow reaction kinetics and the intermediate CO poisoning [2]. So one of the key issues in practical applications was to explore less or non-platinum catalysts which also could catalyze more efficiently and tolerate CO poisoning better. Recent researches showed that Pd-based catalyst could be an effective alternative to Pt in this field, due to their lower cost and higher active surface area, besides, it almost could avoid CO poisoning more effectually by the direct 2-electron catalytic process which was different from the process with the nocuous oxidation product CO of Pt-catalysts [3]. Moreover, some authors have supported that PdCo bimetallic nanoparticles (NCs) could improve the Pd electrocatalytic activity and stability for formic acid oxidation (FAO), which could be attributed to the synergistic effects within the two parts [4-6]. At present, the most commonly method to prepare bimetallic NCs was liquid-phase synthesis [7-9], however, there were several limitations, such as bad size distribution, poor surface cleanness and weak attachment. Different from the traditional liquid-phase route, the physical vapor-phase deposition method (PVD) was carried out at a high vacuum and inert gas conditions which were allowed to avoid the surface pollution and oxidation efficiently.

In this paper, the plasma-gas-condensation cluster deposition (PGCCD, see Fig. 1) system developed according to PVD technique was used to prepare Pd and PdCo bimetallic NCs. The catalytic activity and utilization efficiency of Pd could be approved by the addition of Co element. The NCs assembled films prepared by PGCCD whose packing density (P) was only about 30 % of

the bulk one [10] had a narrow size distribution and good morphology consistency. In this device, the NCs were deposited onto the glassy carbon plate (GCP) directly, therefore, the preferable contact area and adhesive strength could be maintained even without any additives. Even more important, the catalytic performance of Pd NCs for FAO and the influences of Co on the structure, morphology and electrocatalytic properties of Pd NCs were also investigated systematically in this work.

Experimental

A PGCCD system (Fig. 1) was used to synthesize Pd and PdCo NCs, and the experiment principle has been described in detail in our earlier work [11]. High-purity Pd and Co (99.99%) metal targets were installed as 100 mm apart distance, and an Ar flow rate of 350 sccm adjusted by a fine mass flow controller was injected steadily into the Sputtering chamber. In the experiment process, the pressure of the Sputtering chamber and Assembling chamber was maintained at about 100 Pa and 5×10^{-3} Pa, respectively. The high concentration Pd or Pd/Co mixed atomic vapor was generated by dc sputtering with a power of 400 W. Vapor atoms lost their kinetic energy rapidly and nucleated by collision with insert gas molecules. Then the nucleated NCs were extracted into the Assembling chamber through the nozzle located in Filter region accompanied by the Ar gas flow under the pressure differential produced by the pumping system. The NCs obtained a drift rate for the isentropic and adiabatic expansion process and softly landing and assembling onto the GCP (S = 1 cm^2).

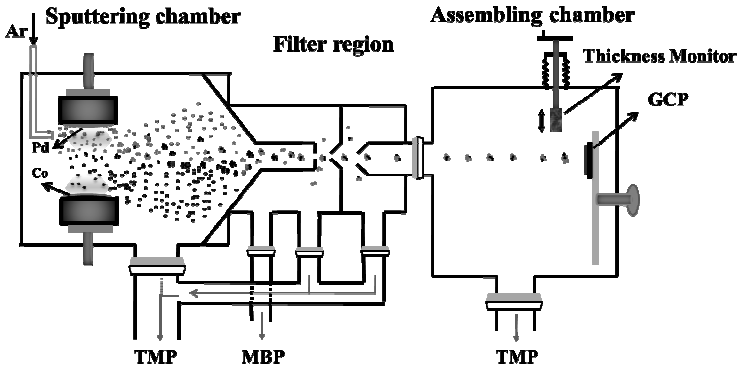


Fig. 1. Schematic Diagram of the Plasma-gas-condensation Clusters Deposition System (PGCCD)

The deposition rate of NCs was measured by a quartz oscillator-type thickness monitor located on the top of the Assembling chamber. The mass fraction of Co was measured by wavelength dispersive spectrometer (WDS, EPMA JEOL8100). The morphology and size distribution of NCs (with effect thickness of about 2.0 nm) loaded on the Cu micro grids were characterized by a transmission electron microscope (TEM, JEM2100HC). The surface morphology of the NCs assembled films (~100 nm) deposited on silicon wafers was observed though a scanning electron microscope (SEM, LEO-1530FE). Moreover, the crystalline structure of the as-prepared samples was analyzed by X-ray diffraction (XRD, Panalytical X'pert-PRO).

Electrochemical measurements were performed on an electrochemical workstation (Autolab PGSTAT302N). A standard three-electrode cell was used, which was consisted of a Pt net counter electrode, an Ag/AgCl (in saturated KCl) reference electrode and a GCP covered with 100 nm Pd or PdCo bimetallic NCs working electrode. Before deposition, the GCPs were polished with 0.3 μm alumina powder and then washed twice for 10 min each by ultrasonic in alcohol. The cyclic voltammograms (CVs) were measured in the electrolytes of 0.5 M H_2SO_4 and 0.5 M H_2SO_4 + 0.5 M HCOOH at -0.21 ~ +1.0 V with a scan rate of 50 mV s^{-1}. The potentials in electrochemical curves were reported with respect to Ag/AgCl (0.210 V vs. SHE).

Results and Discussion

The XRD patterns of the Pd and PdCo NCs assembled films were shown in Fig. 2. The main diffraction peaks located at 40.473° and 47.046° can be assigned to (111) and (200) planes of Pd_{fcc}, respectively. Besides, the additions of Co (the mass fraction was measured by WDS as 12%) didn't change the phase structure of Pd but made its crystallinity better. Fig. 3 shows the TEM and SEM images of Pd and PdCo bimetallic NCs. It can be seen form the TEM images that the Pd and PdCo NCs were spherical with small size and narrow size distribution. The particle size of PdCo NCs (6.44 nm) was larger than Pd NCs (5.15 nm), which was in accordance with the result of XRD. The SEM images show that the NCs were loosely packed on the surface of silicon wafers and formed porous films, which will be conducive to obtain large specific surface area.

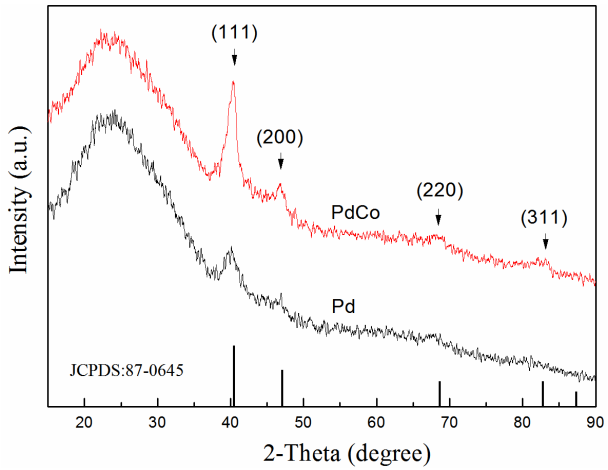


Fig. 2. XRD Patterns of Pd and PdCo NCs Synthesized by PGCCD

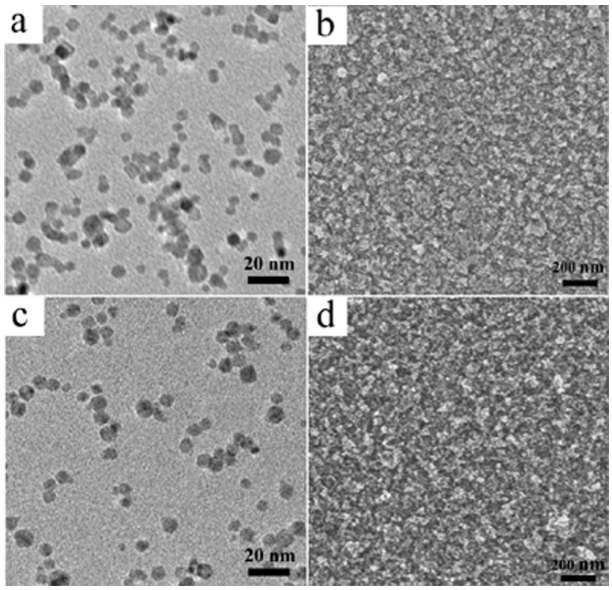


Fig. 3. TEM and SEM Images of Pd (a, b) and PdCo (c, d) NCs

Fig. 4a shows the stable CVs of Pd and PdCo NCs prepared by PGCCD and their current densities were normalized by the geometric area of catalysts. It could be found that two peaks current density (I_p) of hydrogen adsorption/desorption in the lower-potential region (-0.21 V~0.1 V). The electrochemical active area (ECSA) calculated from the integration value of the charge involved in hydrogen desorption area to reflect the real surface area of electrodes were 49.7 and 51.7 $m^2\ g^{-1}_{Pd}$ for Pd and PdCo, respectively [12]. Here, the catalysts assembled by NCs with big specific surface area and their unique spongy-network nature could enlarge the effective contact

area (ECA) and provide more active sites. On the other hand, in the anodic scan of the higher-potential region, the Pd surface oxidation could be seen at +0.55 V in forward scan and the reduction of Pd oxides (PdO) appeared at about +0.5 V in the reverse scan. It was noticed that PdCo NCs reduction peak potentials was shifted more positively than the Pd NCs, which indicated that the oxidized PdCo NCs was reduced more effortlessly. So the CVs results suggested that PdCo NCs showed a more "noble" metal character than Pd NCs.

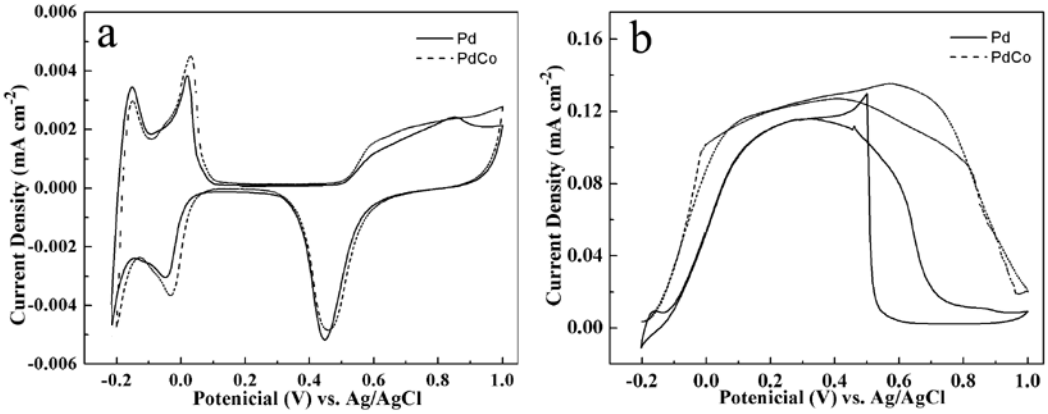


Fig. 4. CVs in N_2 Saturated 0.5 M H_2SO_4 (a) and Specific Activities (b) in 0.5 M H_2SO_4 + 0.5 M HCOOH of the As-prepared Pd and PdCo NCs

Fig. 4b reveals the responses of above-mentioned NCs catalyzing FAO and the current densities were obtained by normalizing the currents to the ECSAs (specific activities). It was observed that in the forward scan, there was a high I_p appeared near 0.3 V (the direct oxidation of formic acid to form CO_2) and a shoulder I_p near 0.6 V (the formation of intermediate CO generated from the dissociative adsorption step) [13]. The I_p of PdCo was 0.125 mA cm^{-2} which was higher than Pd (0.115 mA cm^{-2}), and its peak potential related appeared at -0.2V which was lower than Pd (-0.1V). The meaningful higher I_p of the first peak and much broader contour indicated the preferable catalytic activity to FAO and significant tolerance to CO poisoning [14]. So the PdCo NCs was capable of more rapid HCOOH absorption and activation which leaded to a kinetically faster catalytic reaction. The CVs in FAO indicated that Co doped into Pd could improve the electro-catalytic activities of Pd catalyst.

Conclusions

In this paper, a new physical vapor method to prepare Pd-based NCs catalysts was developed. By the addition of Co, the cost of Pd catalysts was reduced, and the electro-catalytic activities of Pd were improved. The ECSA was increased from 49.7 m^2 g^{-1} to 51.7 m^2 g^{-1} and the I_p of catalyzing FAO was raised from 0.115 mA cm^{-2} to 0.125 mA cm^{-2} when about 12wt. % Co element was added. Therefore, the PVD exhibits a broad application prospect in synthesizing metal NCs for applications of electrochemical catalysis.

Acknowledgements

The authors gratefully acknowledge financial support from the National Basic Research Program of China (grant no. 2012CB933103), National Outstanding Youth Science Foundation of China (grant no. 50825101), and the National Natural Science Foundation of China (grant nos. 51171158, 51371154 and 51301145).

References

[1] A.C. Chen, P. Holt-Hindle, Platinum-based nanostructured materials: synthesis, properties, and applications, Chem. Rev. 110 (2010) 3767 – 3804.
[2] J.D. Lovic, A.V. Tripkovic, S.L. Gojkovic, K.D. Popovic, D.V. Tripkovic, P. Olszewski, A. Kowal, Kinetic study of formic acid oxidation on carbon-supported platinum electrocatalyst, J. Electroanal. Chem. 581 (2005) 294–302.
[3] Z.L. Liu, L. Hong, M.P. Tham, T.H. Lim, H.X. Jiang, Nanostructured Pt/C and Pd/C catalysts for direct formic acid fuel cells, J. Power Sources 161 (2006) 831–835.
[4] X.M. Wang, Y.Y. Xia, Electrocatalytic performance of PdCo-C catalyst for formic acid oxidation, Electrochem. Commun. 10 (2008) 1644–1646.
[5] D. Wang, A. Villa, F. Porta, L. Prati, D.S. Su, Bimetallic Gold/Palladium catalysts: Correlation between nanostructure and synergistic effects, J. Phys. Chem. C 112 (2008) 8617–8622.
[6] D. Morales-Acosta, J. Ledesma-Garcia, L.A. Godinez, H.G. Rodríguez, L. Álvarez-Contreras, L.G. Arriaga, Development of Pd and Pd–Co catalysts supported on multi- walled carbon nanotubes for formic acid oxidation, J. Power Sources 195 (2010) 461–465.
[7] V. Mazumder, Y. Lee, S.H. Sun, Recent development of active nanoparticle catalysts for fuel cell reactions, Adv. Funct. Mater. 20 (2010) 1224−1231.
[8] Y.J. Xiong, Y.N. Xia, Shape-controlled synthesis of metal nanostructures: The case of palladium, Adv. Mater. 19 (2007) 3385–3391.
[9] X.M. Chen, G.H. Wu, J.M. Chen, X. Chen, Z.X. Xie, X.R. Wang, Synthesis of “Clean” and Well-Dispersive Pd Nanoparticles with Excellent Electrocatalytic Property on Graphene Oxide, J. Am. Chem. Soc. 133 (2011) 3693-3695.
[10] D.L. Peng, K. Sumiyama, K. Kumagai, T. Yamabuchi, D. Kobayashi, T. Hihara, Magnetic and electrical characteristics in dense Fe-Ni alloy cluster-assembled films prepared by energetic cluster deposition, J. Mater. Res. 23 (2008) 189-197.
[11] L.S. Wang, R.T. Wen, Y. Chen, G.H. Yue, D.L. Peng, T. Hihara, Gas-phase preparation and size control of Fe nanoparticles, Appl. Phys. A 103 (2011) 1015–1020.
[12] M. Grden, A. Piascik, Z. Koczorowski, J. Czerwinski, A. Czerwinski, Hydrogen electrosorption in Pd-Pt alloys, J. Electroanal. Chem. 532 (2002) 35–42.
[13] V. Mazumder, M. Chi, M.N. Mankin, Y. Liu, D.H. Sun, K.L. More, S.H. Sun, A facile synthesis of MPd (M = Co, Cu) nanoparticles and their catalysis for formic acid oxidation, Nano Lett. 12 (2012) 1102−1106.
[14] J.Z. Sun, Y.Z. Wang, C. Zhang, T.Y. Kou, Z.H. Zhang, Anodization driven enhancement of catalytic activity of Pd towards electro-oxidation of methanol, ethanol and formic acid, Electrochem. Commun. 21 (2012) 42– 45.

Advanced Materials Research Vol. 936 (2014) pp 337-342
© (2014) Trans Tech Publications, Switzerland
doi:10.4028/www.scientific.net/AMR.936.337

Synthesis and Characterization of Emulsion Coating of Fluorinated Polymethacrylate Modified by POSS

Baojuan Tian[1,2,a], Jungang Gao[*1,b], Chao Wang[1,c]

[1]College of Chemistry and Environmental Science, Hebei University, Baoding 071002, China

[2] College of Environmental Science and Engineering, North China Electric Power University, Baoding 071003, China

[a]tbj2001@163.com, [b]gaojg@hbu.edu.cn, [c]tony_purple@qq.com

Keywords: core-shell polymerization; silsesquioxanes; polyacrylate; nanocomposite.

Abstract: The core-shell nanocomposite particles were prepared from acrylate monomers and octavinyl polyhedral oligomeric silsesquioxane (V-POSS) by emulsion polymerization. The structure and properties of emulsion and latex film were characterized by FT-IR, dynamic mechanical analysis (DMA) and TEM and laser particle diameter analyzer (LPDA). The results showed that the V-POSS/polyacrylated (V-POSS/PMA) composite latexes was prepared and the diameter is about 36.1 nm when added 5wt% V-POSS. DMA results showed that the mechanical loss (tanδ) peak temperature (T_p) of the film enhance with increasing V-POSS content and had the best high T_p at 88.4^{o}C for added 7 wt% V-POSS, which increased 7.8 ^{o}C than had not V-POSS. Thermogravimetric analysis (TGA) showed that the addition of V-POSS can increase the thermal decomposition temperature and improved the thermal stability of polyacrylate.

Introduction

Organic-inorganic hybrid nanocomposite materials have been regarded as a new generation of high performance materials; they combine the advantages of both inorganic materials (rigidity, high thermal stability) and organic polymers (flexibility, electric insulation properties, ductility and processibility). Polyhedral oligomeric silsesquioxanes (POSS) are a relatively new type of organic-inorganic hybrid molecules. Polyhedral oligomeric silsesquioxane (POSS) are generally synthesized through the hydrolytic condensation of organotrialkoxysilanes, RSi(OR')3. POSS has a -Si-O-Si- nanostructured inorganic framework with diameters ranging between 1 and 3 nm as the core and reactive or non-reactive functional groups around the framework. The reactive functional groups on the POSS not only can further form homopolymers of the POSS, and can also be incorporated into copolymers via chemical reaction and physical blending [1-4].

Polymethacrylates are known as one of the most common commercial polymers, which had extensive applications in our daily life, for example latex coating. However, some shortcomings of these materials are relatively low glass transition temperature and poor thermal stabilities. In view of these considerations, a lot of effort has been dedicated to preparing the organic-inorganic hybrid materials with improved properties. Over the last decade, there are some reliable methods to synthesize POSS-PMMA composites to solve this problem [5,6].

In this paper, Octavinyl polyhedral oligomeric silsesquioxane (V-POSS) was synthesized through hydrolytic condensation of vinyltrimethoxysilane (CH_2=$CHSi(OCH_3)_3$), then the nano-dispersed V-POSS/PMA nanocomposite emulsion was prepared. The structure and thermal properties of emulsion and latex film were characterized through a variety of analysis methods.

Experimental section

Materials.

Vinyltrimethoxysilane was supplied by Shandong Qufu changing Chemical industry Co Ltd. 2,2,2-Trifluoroethyl Methacrylate (TFEMA) was supplied by Weihai New Era Chemical Co. Ltd. Tetramethylammonium, methyl methacrylate (MMA), methyl ethyl acrylate (EA), butyl acrylate (BA), and acrylic acid (AA), Potassium persulfate (KPS), sodium dodecyl benzene sulfonate (SDBS), isopropyl alcohol, methylbenzene, sodium chloride et al were all of analytical grade, and supplied by Tianjin Chemical Reagents Co. Octavinyl polyhedral oligoneric silsesquioxane (V-POSS) was synthesized according literature [7].

Synthesis of V-POSS.

Typically, 300 mL isopropyl alcohol, tetramethylammonium (1.053 g, 50% weight) and 10 mL deionized water were mixed in a four-necked flask, which was equipped with stirrer, dropping funnel, reflux condenser and thermometer, and then, the mixture of 30 g vinyltriethxoysilane and 50mL isopropyl alcohol was dropped slowly at 0~1 ^{o}C, he mixture was allowed to react for 24 hours at 18 ^{o}C and then isopropyl alcohol was evaporated, appropriate amount of methylbenzene was added in order to recrytallized the white power for another 4h and then cooled down to room temperature. The white crystallized power was filtered, washed with anhydrous ethanol, and vacuum dried. The yield was 82% and the epoxy value was 0.63 mol/100 g, which was closed to the theoretical value. ^{1}H-NMR (400 MHz, Bruker Co., Switzerland) and Liquid chromatography-mass spectrometry (LC/MS, Agilent 1100, Agilent Co. USA) was used for the determination of the components of the V-POSS and the detailed structure.

Synthesis of V-POSS/PMA nanocomposites emulsion.

The V-POSS/PMA latex was synthesized by using emulsion polymerization technique. The polymerization was carried out in a 100 mL four-necked glass flask fitted with a reflux condenser, stirrer, dropping funnel and thermometer. The synthesis of V-POSS/PMA which contain 1wt% V-POSS was synthesized as follow: deionized water (40 mL) and SDBS (0.471 g) were added into the flask with stirring. After the SDBS dissolved, the mixture of 0.260 g V-POSS and 10 g acrylate monomers were added with stirring quickly for 30 minutes. Then, the reaction vessel was heated to 75 ^{o}C, and then the KPS solution (0.021 g in deionized water 3 mL) as an initiator was added. The system was maintained at 75 ^{o}C for 1 h and then the rest mixture of acrylic ester monomers (MMA BA, EA and AA, total 15 g) was dropped in 1h, and adjusted to 8.0-8.5 pH with sodium carbonate, then the reaction system was heated to 80 ^{o}C and rested for another 1 h. After that, and the 5 g mixture of TFEMA and MMA was dropped in 1 h and reacted for 1 h again, then cooled down to room temperature. Finally, the fluorine-containing V-POSS/PMA nanocomposite emulsion was obtained. With the same method, the emulsion which contain 1, 3, 5, 7 and 9 wt% V-POSS was synthesized, and labeled as (b), (c), (d), (g) and (f), respectively. For comparison, the pure polyacrylate emulsion was synthesized and labeled as (a).

Testing and characterization.

Fourier transform infrared spectrometer (FTIR, FTS-40, BIO-RAD, USA) was used testing chemical reaction; Transmission electron microscope (TEM, JEM-100CX, JEOL, Japan) was used to determine the size and distribution of latex particle at 100 KV voltage and 0.14 nm resolution. The dynamic mechanical behavior of materials was characterized by dynamic mechanical analyzer (DMA, Q8000, Perkin-Elmer Co. USA). The particle diameter distribution of emulsion was determined by the laser particle diameter analyzer (LPDA, Delsa Nanoc, USA). Thermal stability of the specimens was characterized by thermogravimetric analysis (TGA, Pyris-6, Perkin-Elmer, USA) operated under 20 mL/min nitrogen flow rate. About 5mg powder of the specimens was introduced

into the thermobalance, and then heated from 30 to 500 ^{o}C at the heating rate of 5, 10, 15, 25 ^{o}C/min.

Results and discussion

Structure characterization of V-POSS and V-POSS/PMA.

Figure 1a shows the FTIR spectrum of V-POSS. In Fig. 1 (b) and (c), there is a strong absorption band at 1720 cm^{-1} which is attributed to the C=O stretching vibration, the C-H stretching vibration peak of vinyl group is located at 2941.65 cm^{-1}, the absorption band at 1118.94 cm^{-1} is the Si-O-Si stretching vibration band of POSS cage [8]. The FTIR spectra of all of the V-POSS/PMA composites are similar to that of the pure Polyacrylate, except that a symmetric absorption peak at 1118.94 cm^{-1}, which is the characteristic Si-O-Si stretching of silsesquioxane cages and the intensity increases with increasing POSS content.

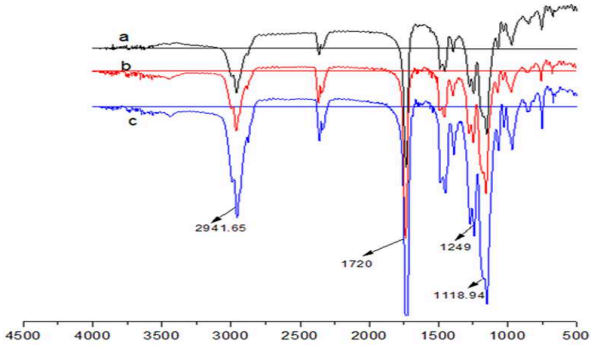


Fig.1 (a) FTIR spectra of pure PMA (b) 5 wt% V-POSS, (c) 9 wt% V-POSS

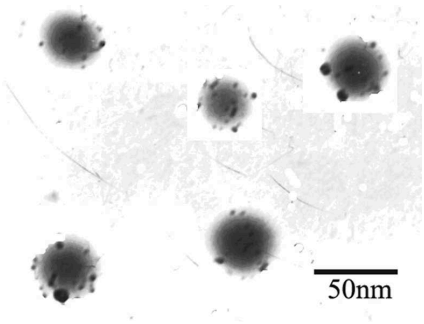


Fig. 2 TEM photograph of 5 wt% V-POSS/PMA

Figure 2 showed the TEM photograph of the 5% V-POSS/PMA latex, it can be seen that the particles are uniformly dispersed and with equirotal size of about 35 nm. Furthermore, the particles have core-shell morphology which was consisted with a copolymerized core of acrylate ester and V-POSS, and the fluorine-containing polymethacrylate shell was formed by copolymerization of TFEMA and MMA.

Particles diameter analysis of the emulsion

The effect of V-POSS/PMA on the average diameter and distribution of the composite latex particles is shown in Fig. 3. It can be seen that the diameter distribution of the composite latex with V-POSS is narrow as same as the emulsion No.0. The diameter of V-POSS/PMA and PMA is 36.1 nm and 32.9 nm respectively, the dispersing index of latex is 0.399 and 0.385, respectively. There is less difference of the average diameter between V-POSS/PMA and pure PMA. It is because that a core-shell synthesis procedure was carried out and V-POSS was packed in the core of the latex.

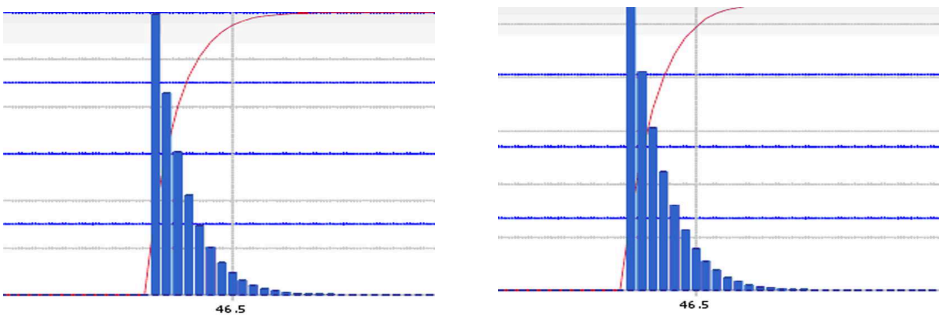


Fig.3 The diameter (nm) of composite latex particles. (a) pure PMA; (b) 5 % V-POSS/PMA

Dynamic mechanical analysis.

The glass transition temperature (T_g) may be used as a heat distortion parameter of the polymeric materials. Differential scanning calorimetry (DSC) is usually used to determine the T_g of polymers, but it is not the best method because the step in the DSC curve will be very little, inconspicuous and broadly at that time. Dynamic mechanical analysis (DMA) can be used to determine the maximal mechanical loss tanδ peak temperature (T_p) of polymers. The mechanical loss (tanδ) temperature values reflect the micro-Brownian movement of the macromolecular chain seqments. Generally, there is a one-to-one relationship between the T_g and the mechanical loss peak temperature, T_p, and the T_p is often designated as a T_g. The higher T_p, the higher T_g is, which depend on the molecular chain structure, cross-linking degree and material morphology [9].

Figure 4 shows the effect of different amount of V-POSS on the mechanical loss (tanδ) peak temperature (T_p) of coating film at a frequency of 1Hz. The Tp values of the copolymer with different V-POSS content is listed in Tab. 1. It can be observed that T_p of V-POSS/PMA increase with the increasing V-POSS content. When V-POSS content is 7 wt%, the T_p of coating film increase from 79.6 ^oC increase to 88.4 ^oC, and T_g reach the maximum value. This is because the vinyl group on the POSS reaction with acrylate monomers and increase the crosslink degree of Film. Therefore, the movement of molecular chain is blocked and become difficult, so the T_g increase. But T_g decrease with a further increase in the amount of V-POSS. The reasons are probably relative with the congregation of V-POSS and reaction one another when its content is higher than 7 wt%.

Tab.1 T_p values of polycrylate with various V-POSS content

V-POSS (wt%)	0 (a)	1 (b)	3 (c)	5 (d)	7 (e)	9 (f)
T_p(^oC)	79.6	83.4	86.8	86.7	88.4	84.5

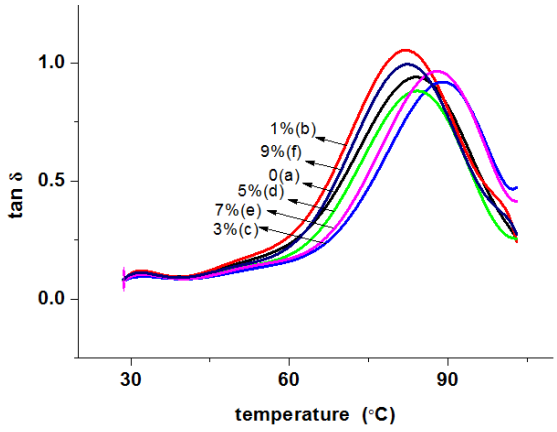


Fig. 4 DMA curves Of V-POSS/PMA

Thermal properties of V-POSS/PMA composites.

The thermal stability factors of the nanocomposites, including the initial decomposition temperature T_{id}, the temperature for mass loss of 50 wt% $T_{1/2}$, the temperature T_{md} of maximal weight loss rate. Figure 5 shows the TG curves of V-POSS/PMA composites and pure PMA with different mass samples which put in thermobalance. It can be seen from Fig. 5, all of the V-POSS/PMA nano-composites all display higher initial decomposition temperature T_{id} than the pure PMA. Figure 6 shows the initiative thermal decomposition T_{id} of the nano-composites for different V-POSS content. As seen from Fig. 6, the initiative thermal decomposition temperature T_{id} of the nano-composites is shifted to higher temperatures. When the content of V-POSS is 3 wt%, the T_{id} of the nano-composites increase about 5.5 ^oC than pure PMA; when the content of V-POSS is 9 wt%, the T_{id} increase about 19 ^oC than pure PMA. The results show that the addition of V-POSS can increase the initiative thermal decomposition temperature and improved the thermal stability of

polymethacrylate. This is because added V-POSS may increase the crosslinking density. The crosslinking density of the samples increases, the movement of molecular chain segment is limited, which is conducive to the glass transition temperature increase, and will reduce the diffusion of volatile components in the materials, so that it has also a higher thermal degradation than the pure PMA samples. The weight loss of samples at 200 to 400 ^{o}C is caused by the decomposition of polymethacrylate. The increase of residue rate after 400 ^{o}C is due to the presence of the V-POSS. The V-POSS contain the higher bond energy Si-O and Si-C bond and presence of inorganic structure similar to the SiO_2, under the high temperature it will form SiO_2 and SiC.

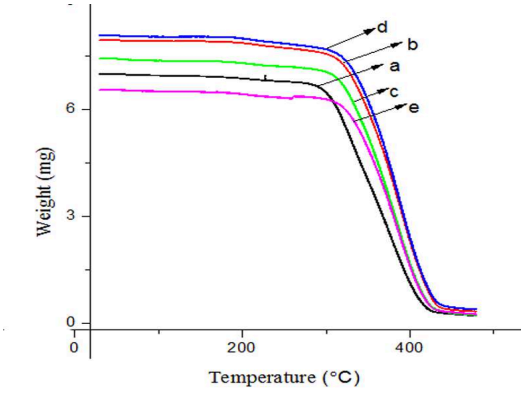


Fig.5 TGA thermograms of pure PMA (a),3~ 9% V-POSS/PMA composites (b,c,d,e)

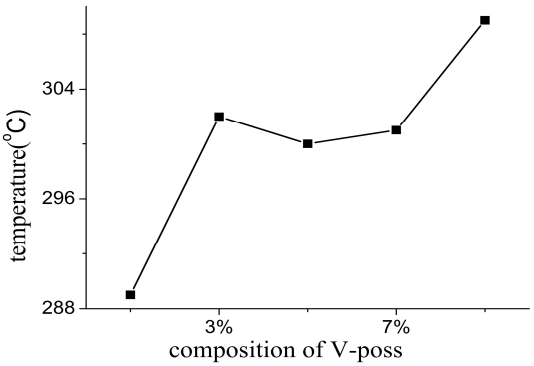


Fig.6 Initial thermal decomposition T_{id} of for the composites for different V-POSS content

Summary

The new fluorinated V-POSS/PMA core/shell nano-composite can be synthesized by using emulsion polymerization technique. The average particle diameter of core-shell latex for 5 wt% V-POSS content is bout 35nm and the dispersing index of latex is 0.399. The V-POSS can be increase the glass transition temperature (T_g) of the polyacrylates, when the content is 7 wt%, the T_g of the polyacrylate increase about 7.8 ^{o}C higher than pure polyarcylates. V-POSS can also increase the thermal decomposition temperature of the polyacrylates. When the content of V-POSS is 3 wt%, the T_{id} of the nano-composites increase about 5.5 ^{o}C than pure PMA; when the content of V-POSS is 9 wt%, the T_{id} increase about 19 ^{o}C than pure PMA.

References

[1] K. Tanaka, Y. Chujo, Advanced functional materials based on polyhedral oligomeric silsesquioxane (POSS), J. Mater. Chem. 22 (2012) 1733 - 1746.

[2] G.Z. Li, L.C. Wang, H.L. Ni, C.U.P. Jr, Polyhedral Oligomeric Silsesquioxane (POSS) Polymers and Copolymers: A Review, J. Inorg. Org. Polym. 11 (2001) 123 – 154.

[3] H. W. Milliman, H. Ishida, D. A. Schiraldi, Structure Property Relationships and the Role of Processing in the Reinforcement of Nylon 6-POSS Blends, Macromol. 45 (2012) 4650 – 4657.

[4] W.P. Wang, X.X. Jie, M. Fei, H. Jiang, Synthesis of core-shell particles by batch emulsion polymerization of styrene and octavinyl polyhedral oligomeric silsesquioxane, J. Polym. Res. 18 (2011) 13–17.

[5] W.P. Wang, B. Wang, X.M. Ma, D.R. Lu, C.Y. Pan, Synthesis and Characterization of POSS/PMMA Nano Composite Particles, Polym. Mater. Sci. Eng. 23 (2007) 96-98.

[6] J. G. Gao, H.Q. Lv, X. F. Zhang, H. C. Zhao, Synthesis and Properties of Waterborne epoxy acrylate nanocomposite coating modified by MAP-POSS, Progr. Org. Coat. 76 (2013) 1477–1483

[7] H. Saito, M. Isozaki, Japan Patent 2002-285387 (2002).

[8] D. Shen, Application of Infrared Spectrum in Polymer, Science Press, Beijing, 88 (1982).

[9] J. K. Gillham, The TBA torsion pendulum: a technique for characterizing the cure and properties of thermosetting systems. Polym. Int. 44, (**1997)**, 262276.

Advanced Materials Research Vol. 936 (2014) pp 343-346
© (2014) Trans Tech Publications, Switzerland
doi:10.4028/www.scientific.net/AMR.936.343

The Performance of Gold Nanoparticles Supported on Mesoporous Zirconia for the the Synthesis of Azoxybenzene

Meilin Jia[1, a], Mengjie Feng[1,b], Xu Li[2,c] and Zhaorigetu Bao[1,d]

[1]College of Chemistry and Environmental Science, Inner Mongolia Key Laboratory of Green Catalysis, Inner Mongolia Normal University, Hohhot, 010022, China

[2]College of Biology Science and Chemistry, Hulunbeier University, 021008, China

[a]jml@imnu.edu.cn, [b]117896472@qq.com, [c]chihu143@sina.com, [d]zrgt@imnu.edu.cn

Keywords: mesoporous zirconia, gold catalyst, azoxybenzene

Abstract. Gold nanoparticles supported on mesoporous ZrO_2 were prepared and their performance for the selective reductions of nitrobenzene to azoxybenzene was investigated. It was found that azoxybenzene could be successfully synthesized over these catalysts. Furthermore, the catalytic activity of catalysts is dependent on the pore size of catalyst. The catalyst Au/ZrO_2-PEG-1000 with pore size of 2.2 showed higher activity than Au/ZrO_2-PEG-600 with pore size of 1.9nm.

Introduction

Azoxybenzenes are important intermediates in industrial chemistry, which could be used in the production of dyes, indicators and liquid crystals. However, only very few methods have been reported for the selective reduction of nitroarenes to azoxy compounds. The most convenient method for their synthesis is the reduction of nitroarenes, which may also lead to hydroxylamine, hydrazine, azobenzene, and eventually, to aniline. Furthermore, the used reagents in most of these reactions have some shortcomings such as toxicity, complex preparation, difficult preservation and serious pollution [1-4]. Therefore, it is significant to develop a more simplified and green process to synthesis azoxybenzene.

Gold nanoparticles（Au-NPs）have many important properties, such as they can absorb visible light intensely because of so-called surface plasmon resonance (SPR) effect； and absorb ultraviolet（UV light）causing an interband excitation of electron in the Au-NPs. Zhu's group have realized to use the light adsorption of Au-NPs for driving chemical reactions, such as reduction of nitroaromatic compounds, deoxygenation of epoxide to alkenes, reduction of ketones to alcohols and hydrogenation of azobenzene to hydroazobenzene under visible or ultraviolet irradiation. They found that the light adsorption by the Au-NPs could activate the organic molecules then induce oxidation or reduction of the organic compounds. Therefore, these reactions on gold catalysts driven by light were realized at ambient temperature [5-8].

The mesoporous materials have attracted considerable attention because of their remarkably large surface areas and narrow pore size distribution, which make them ideal candidates for catalysts. It is anticipated that the use of a high surface area mesoporous ZrO_2 rather than a commercial low surface area ZrO_2 as support for gold catalysts might have some beneficial effect on the catalytic performance. Therefore, in this work, we present the study of azoxybenzene synthesis over Au-NPs supported on mesoporous ZrO_2.

Experimental

Preparation of Support

The ZrO_2 was prepared by the sol gel method with different surfactant, such as PEG-600 and PEG-1000 as structure template. The $ZrOCl_2$ solution was dropped into the surfactant solution under stirring with the final molar ratio of ZrO_2/PEG/H_2O =1/1/100. Then 1mol.L^{-1}NaOH was dropped into

the system to keep the pH of 8. After being dried at 90°C for 10h, the gel was obtained. The gel was washed with deionized water thoroughly, later dried at 80°C. Finally, the ZrO_2 was obtained after the calcination at 400°C for 2h. The ZrO_2 from different surfactant was denoted as ZrO_2-PEG-600 and ZrO_2-PEG-1000, respectively.

Preparation of Catalyst

Synthesis of catalysts was used reduction method. In the procedure of reduction method, a solution of 2.43×10^{-3}mol·L^{-1} $HAuCl_4\cdot3H_2O$ (80mL) was added to a suspension of 1.25g of the ZrO_2 supports in 50mL water, then Lysine (0.1 mol·L^{-1}, 20 mL) was added to the mixture with good stirring for 30 min. An aqueous solution of $NaBH_4$ (0.35 mol·L^{-1}, 10 mL) was added gradually within 10 min to the suspension, followed by hydrochloric acid (0.3 mol·L^{-1}, 15 mL). The mixture was left to stand for 24 h and then the solid was separated, washed with water and ethanol. After drying at 353K, 3 wt % Au/ ZrO_2 catalysts were obtained.

Catalyst Characterization

Specific surface area (BET) and pore structure were obtained on ASPA-2020 by American Micromeritics Company. The sample was vacuumed at 393K for 2h, and then began static nitrogen adsorption at 77K (liquid nitrogen). X-ray diffraction (XRD) was obtained on a Philips PW1830 diffractometer using Cu-Kα radiation (λ=0.15405 nm), operating at 40 kV and 40 mA. Profiles were recorded at 0.05°/s.

Catalytic Activity

The reactions were conducted in a one-mouth flask which contained 3 mmol of nitrobenzene, 30mL isopropyl alcohol, a solution of KOH in isopropyl alcohol (10mL, 0.1mol·L^{-1}), and 100mg catalysts. The reactions were conducted in an argon atmosphere at temperature of 333K and illuminated with incandescent light under stirring unless other specified. The resulting products were analyzed using Shimadzu GC-2014 GC with Rtx-5 column. The conversion of nitrobenzene, selectivity of azoxybenzene and azobenzene were determined by the following expressions:

$$C_{nitro} = \frac{amount\ of\ nitrobenzene\ consumed}{initial\ amount\ of\ nitrobenzene} . \quad (1)$$

$$S_{azoxy} = \frac{formation\ of\ azoxybenze\ ne}{total\ conversion\ of\ nitrobenze\ ne} . \quad (2)$$

$$S_{azo} = \frac{formation\ of\ azoxybenze\ ne}{total\ conversion\ of\ nitrobenze\ ne} . \quad (3)$$

Results and Discussion

Characterization Results

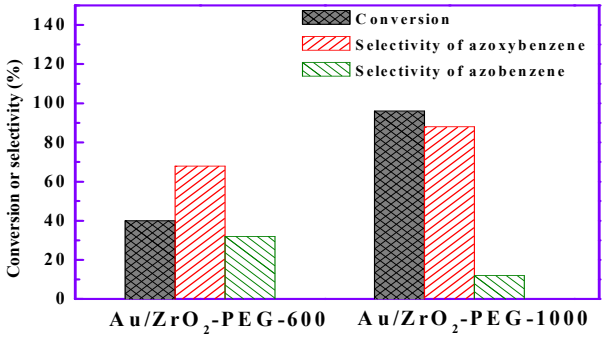


Figure 1 The Activity of Catalysts

The effect of support on the catalyst activity got at the reaction time of 3 h was presented in Fig. 1. Both ZrO_2-PEG-600 and ZrO_2-PEG-1000 supports showed imperceptible activity for the reduction in the comparison experiment. The addition of gold significantly increased the catalytic activity of the samples. From figure 1, it was observed that the property of support affected the performance of catalysts. Over the catalyst Au/ZrO_2-PEG-600, the conversion was 40% and the selectivity of azoxybenzene was about 68%. However, over Au/ZrO_2-PEG-1000, the selectivity of azoxybenzene reached 88% under the conversion of 96%. These results demonstrated that gold NPs supported on mesoporous ZrO_2 exhibited high activity for the synthesis of azoxybenzene under visible light irradiation.

TABLE.1.THE SURFACE AREA, PORE VOLUME AND PORE SIZE OF ZRO_2

support	BET surface S (m^2/g)	Pore Size nm	Catalysts	BET surface S (m^2/g)	Pore Size nm
ZrO_2-PEG-600	233	3.3	Au/ZrO_2-PEG-600	175	1.9
ZrO_2-PEG-1000	163	5.6	Au/ZrO_2-PEG-1000	115	2.2

In order to analysis the difference in the activity, the BET specific surface area, pore sizes and pore volumes based on the nitrogen adsorption/desorption isotherms were summarized in table 1. Both the ZrO_2 supports exhibited typical mesoporous structure. With the introducing of gold species, the decrease in surface area and pore diameter was observed. The pore size decreased from 5.6nm of ZrO_2-PEG-1000 to 2.2nm of Au/ZrO_2-PEG-1000 catalyst. This result indicated that part of gold particles existed inside the pore and the aggregation of gold particles could be hindered, which could result in the high performance of Au/ZrO_2-PEG-1000 catalyst.

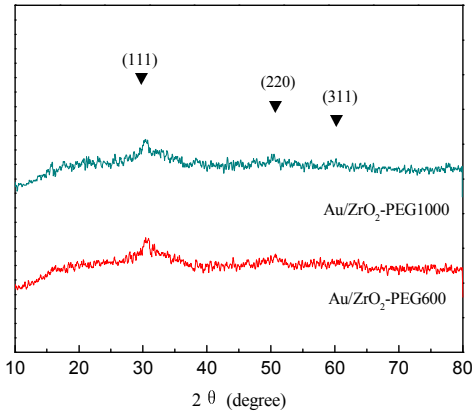


Figure 2 The XRD Patterns of Au/ZrO_2

The XRD patterns of Au/ZrO_2-PEG-1000 and Au/ZrO_2-PEG-600 were demonstrated in Fig. 2. The characteristic diffraction peaks at 30.16°, 50.60° and 66.26° verified that these supports existed in tetragonal phase. The absence of gold characteristic diffraction peak implied that the good dispersion of gold on the support.

Summary

Nanoparticle gold catalysts loaded on the ZrO_2 with different pore structure were prepared. The selective reductions of nitrobenzene to azoxybenzene were realized over these catalysts. The results demonstrated that pore size of support has effects on the activity of catalysts. Au/ZrO_2-PEG-1000 catalyst with 5 nm aperture on support prepared by non-ionic surface active agent PEG-1000 showed high activity for the reaction. The conversion of nitrobenzene reached 96% and the selectivity of azoxybenzene reached 88%.

This work was financially supported by Research Program of Science and Technology at Universities of Inner Mongolia Autonomous Region and The Region Open Major Basic Research Projects of Inner Mongolia Autonomous (20130902).

References

[1] S. Gohain, D. Prajapati, J.S. Sandhu, A new and efficient method for the selective reduction of nitroarenes: use of ammonium sulphate-sodium borohydride, Chem. Lett. 8(1995)725-726.

[2] A. Corma, P. Serna, Chemoselective hydrogenation of nitro compounds with supported gold catalysts, Science. 313(2006)332–334.

[3] A.Grirrane, A.Corma, H.Carcia, Gold-catalyzed synthesis of aromatic azo compounds from anilines and nitroaromatics, Science. 322(2008) 1661-1664.

[4] K. Schoumacker, C. Geantet, M. Lacroix, Photocatalytic synthesis of thio-organic compounds: case study of propan-1-thiol, Photochem. Photobiol. A. 152(2002)147-153.

[5] X. Chen, H.Y. Zhu, J.C. Zhao, Visible light driven oxidation of organic contaminants in air with gold nanoparticle catalysts on oxide supports, Angew. Chem. Int. Ed. 47(2008)5353-5356.

[6] M.A. Fox, M.T. Dulay, Heterogeneous photocatalysis, Chem. Rev. 83(1995)341-357.

[7] N.A. Luechinger, S. Loher, E.K. Athanassiou, Highly sensitive optical detection of humidity on polymer/metal nanoparticle hybrid films, Langmuir. 23(2007)3473-3477.

[8] K.L. Kelly, E. Coronado, L.L. Zhao, The optical properties of metal nanoparticles: the influence of size, shape and dielectric environment, J. Phys. Chem. B. 107(2003)668-677.

Advanced Materials Research Vol. 936 (2014) pp 347-351
© (2014) Trans Tech Publications, Switzerland
doi:10.4028/www.scientific.net/AMR.936.347

The Facile Hydrothermal Preparation Of Wo_3 And Its Photocatalytic Performance Under Visible-Light Irradiation

Fenfen Li[1, a], Hongtao Gao[1, b], Guangjun Liu*[2, c]

[1]Key Laboratory of Eco-chemical Engineering, Ministry of Education, College of Chemistry and Molecular Engineering, Qingdao University of Science & Technology, Qingdao 266042, P. R. China

[2]Department of Chemistry and Chemical Engineering, Jining University, Jining, 273155, P. R. China

[b]tiaozhanzhong@163.com, [b]gaohongtao@gmail.com, [c]liugjun@126.com

Keywords: WO_3 nanoplates; hydrothermal synthesis; Photocatalytic activity; RhB

Abstract: The orthorhombic WO_3 nanoplates were fabricated *via* a hydrothermal process, using HBF_4 as the acid source. They were characterized by X-ray diffraction (XRD), scanning electron microscopy (SEM), and UV-vis diffused reflectance spectroscopy (UV-Vis DRS), respectively. The WO_3 nanoplates exhibited nice UV-light driven photocatalytic performance in the degradation of Rhodamine B (RhB).

Introduction

Semiconductor photocatalysts play a significant role in the measures against energy shortage and environmental pollution. Nanostructure WO_3, with a band gap of 2.5-2.8 eV, mainly absorbed less than or equal to the wavelength of 443 nm and possesses a wide band of light absorption and light stability. Due to tungsten oxide is a versatile material, it has drawn considerable attention in these fields, such as gas sensing materials[1–3], photoluminescent[4,5] and photocatalysis[6,7]. Owing to the intriguing physiochemical properties and widespread potential applications, WO_3 has received much attention in the past few decades. Hence, people in climbing numbers pursue the synthesis of the tungsten oxide with different functions. Currently, there are many kinds of WO_3 nanomaterials. N. Le Houx showed that WO_3 nanoparticles in the 5-30 nm range have been prepared by solvothermal treatment of tungsten chloride in benzyl alcohol up to 210 ℃ followed by annealing in air[8]. Deliang Chen and Yoshiyuki Sugahara synthesized tungstate-based inorganic-organic hybrid nanobelts/nanotubes with lamellar mesostructures[9]. Jinmin Wang reported the synthesis of uniform crystalline WO_3 nanorods and their assembly without any surfactants [10].

In the present work, we report that a facile approach to synthesize WO_3 nanoplates. The obtained samples were characterized by X-ray diffraction (XRD), scanning electron microscopy (SEM), energy dispersive X-ray spectroscopy (EDX) and UV-visible diffuse reflectance spectra (UV-Vis DRS), respectively. The WO_3 nanoplates exhibited nice UV-light driven photocatalytic performance in the degradation of Rhodamine B (RhB).

Experimental

Photocatalyst preparation

All the chemicals were of analytical grade and used without further purification. A typical synthesis process for the WO_3 nanoplates were as follows: 0.005 mol $Na_2WO_4 \cdot 2H_2O$ was added into 32 mL 40% HBF_4 (0.5 M) aqueous solution while stirring. After further agitating for 1h, the yellow solution was migrated into a 50 mL Teflon-lined high-pressure reaction autoclave. The

autoclave was maintained at fixed temperature for several hours. Then the autoclave was naturally cooled to ambient temperature, and navy blue samples were collected after precipitation, washed several times with double-distilled water and absolute alcohol successively, and dried in an oven at 60 ℃ overnight.

Characterization

The XRD spectra was obtained with a Rigaku D/MAX-2000 diffractometer, using Cu Kr irradiation (λ=1.54056 Å) at 45 kV and 40 mA. The surface morphology of the samples was characterized by a JSM-7500F (JEOL Ltd, Japan) scanning electron microscope (SEM). In addition, UV-vis DRS was measured at room temperature with a UV-vis spectrometer (TU-1901; Beijing Purkinje General Instrument Co., Ltd, China).

Measurement of photocatalytic activities

The photocatalytic experiments were conducted to decompose RhB in photocatalyst aqueous suspension system, which were performed in an SGY-I photochemical reactor (Nanjing, Stonetech. EEC Ltd. Nanjing, China). A quartz cylinder (50 mm×450 mm) was placed inside the reactor and illuminated with a 300 W high-pressure mercury lamp. For each condition, WO_3 samples (0.200 g) were added into 200mL of RhB aqueous solution (10^{-5} mol·L^{-1}). Prior to irradiation, the solutions containing catalysts were stirred in the dark for 30 mins to ensure the establishment of an adsorption-desorption equilibrium between photocatalyst powders and RhB. The photocatalytic experiment was repeated under the identical reaction conditions to confirm the reproducibility. At given time intervals, 5 mL of aqueous suspension was taken from the quartz cylinder after specific intervals, centrifuged and filtered through 0.45 μm millipore filter to monitor the degradation of RhB dye. A UV spectrophotometer (UV-vis Cary50; Varian Co.) was used to monitor changes in the spectral intensity distribution of RhB.

Results and discussion

XRD analysis

XRD was used to investigate the phase and crystal structure of the products. And the XRD pattern for WO_3 prepared at different temperature is depicted in Fig. 1 (a). It was demonstrated that the crystal phase of all the products were orthorhombic. The curve a in Figure 1 (a) revealed that the crystal phase of WO_3 nanoparticles was orthorhombic structure with the diffraction peaks at about 2θ =23.1, 24.1, 28.8, 33.3, 34, 41.6, and 55.2°, which could be perfectly indexed to the (001), (200), (111), (021), (220) and (401) crystal faces of orthorhombic WO_3 (JCPDS No. 20-1324). No characteristic peaks for any other phases or impurities are observed, suggesting that the nanocrystal is composed of orthorhombic structure. It was worthwhile to note that the diffraction peaks of WO_3 at 160 ℃ in Fig. 1 (a) were sharp and intense, implying that the (001) diffraction peak of WO_3 at 160 ℃ possesses the maximum intensity and is in the best standard position (23.101°).

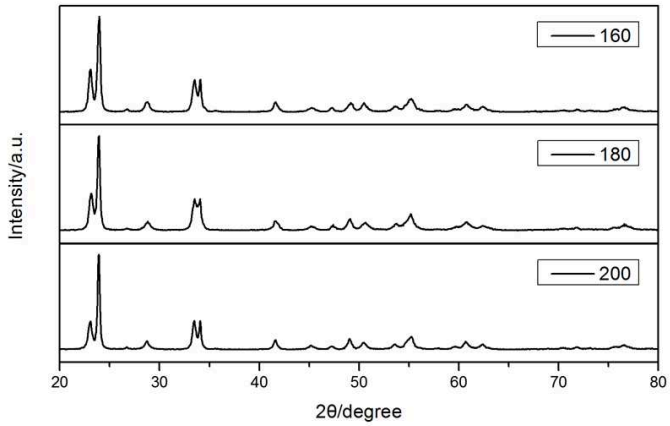


Fig. 1 (a) XRD patterns of the products synthesized at different temperature for 24 h

SEM analysis

The size and shape of the samples were further analyzed by SEM technique. The SEM images of WO_3 at different reaction conditions were exhibited in Fig. 2, which revealed the uniform nanosheets. The sizes of nanoplates decreased with the increase of the reaction temperature and increased with the increase of the reaction time. The illustration showed that the reaction time has a significant impact on controlling the growth and nucleation of tungsten oxide nanoplates. It is observed that the SEM images of specimen at 160 ℃ for 24 h existed the best morphology of cube sheets.

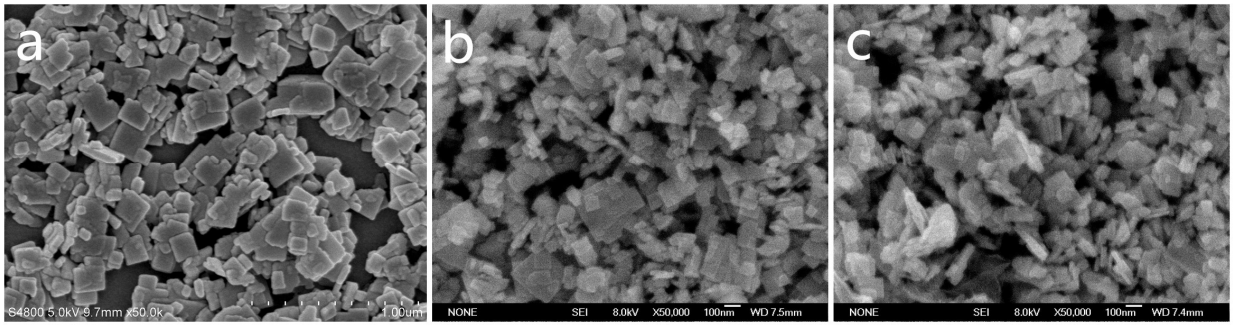


Fig. 2 SEM images of the products synthesized at reaction conditions: (a) 160 ℃ for 24 h, (b) 180 ℃ for 24 h, (c) 200 ℃ for 24 h.

UV-vis DRS analysis

The energy band structure has an influence on optical absorption property of a semiconductor. The photocatalytic activity of a semiconductor is up to this key factor. The optical absorption edge and the energy gap can be calculated via UV-Vis absorption spectrum. The UV/Vis diffuse reflectance spectra (DRS) were present in Figure 3. It indicated that the all the products exhibited strong photoabsorption in both UV and visible light area. The absorption edge can be got by the perpendicular to the abscissa axis from the point of intersection of the two tangent lines from the absorption spectrum. As it was seen in Fig. 3, WO_3 nanosheets at different conditions (160℃-24h, 180-24h and 200-24h ℃) had absorption edges at about 440 nm, 430 nm and 418 nm, which were all in the visible region (400 ~ 750 nm), and the absorption edges have shift to the long wavelength. However, it is contrary to energy gap. The E_g of the WO_3 semiconductor could be obtained by using the equation (Eq. 1):

$$\alpha hv = A(hv - E_g)^{n/2} \quad (1)$$

Where α is the absorption coefficient, hv is the discrete photon energy, and A is a constant relative to the material, and E_g is the absorption band gap, respectively. Assuming the absorption coefficient α is proportional to the Kubelka-Munk function $F(R)$, the E_g can be obtained from the plot of $[F(R)hv]^{1/n}$ *versus* hv, by extrapolation of the linear part near the onset of the absorption edge to intersect the energy axis. The energy gaps of the materials at different temperature (160, 180 and 200 ℃) for 24 hours were 2.81 eV, 2.88 eV and 2.96 eV, respectively. The band gap for WO_3 nanoplate at 160 ℃ for 24 hours was the smallest (2.81 eV). It is indicated that the photocatalyst WO_3 could exhibit photocatalytic activity under the solar light irradiation.

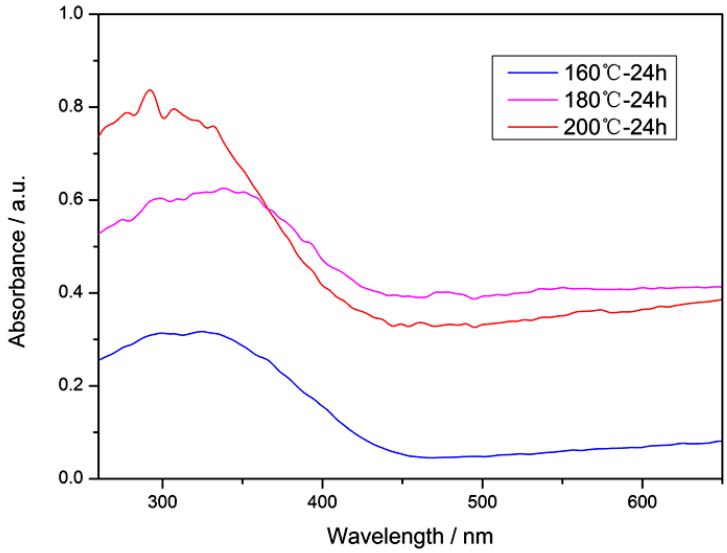


Fig. 3 UV-vis absorption spectra of the WO_3 nanocrystals

Photocatalytic activity

The photocatalytic activity of catalysts were evaluated by measuring the degradation on RhB under UV-light irradiation at room temperature. The photodegradation reaction with samples obtained from different experimental conditions. It indicated that there were obvious photocatalytic activities under irradiation for all specimens. There were evidently photocatalytic activities under UV-light irradiation for WO_3 photocatalyst. According to Fig. 4, the order of photocatalytic activity of the WO_3 nanocrystals was as following: 160-24 > 180-24 > 200-24.

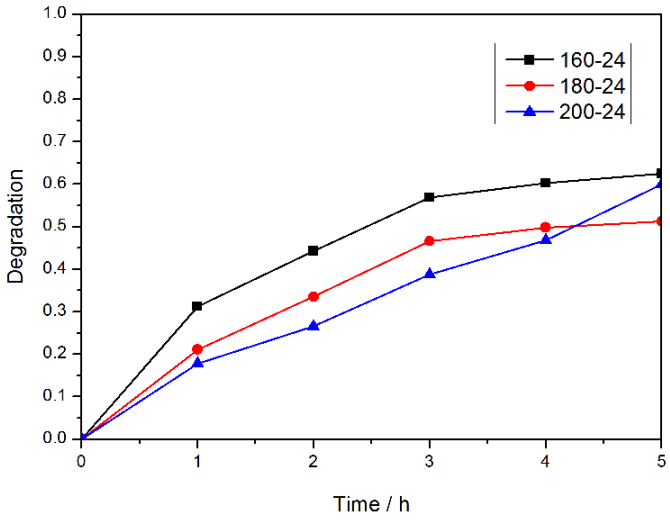


Fig. 4 Photocatalytic activity of Rhodamine B Photocatalysts under UV-light irradiation

Summary

In summary, a series of WO_3 nanoplates were prepared *via* a hydrothermal process, using HBF_4 as the acid source and structure-directing guiding agent. The products were characterized by XRD, SEM, DRS, respectively. The experimental photocatalytic degradation of RhB observations indicated that the as-prepared WO_3 photocatalysts exhibited powerful photocatalytic performance under UV-light irradiation.

Acknowledgements

This work has been supported by The National Natural Science Foundation of China (Grant No.41340037), the natural science foundation of Shandong Province (Grant No. ZR2011BL012, ZR2012EMM015) and the Scientific Research Program of Qingdao (Grant No. 11-2-4-3-15-jch).

References

[1] D.H. Yun, C.H. Kwon, H.K. Hong, H.W. Shin, S.R. Kim, K. Lee, Abnormal current-voltage characteristics of WO_3-doped SnO_2 oxide semiconductors and their applications to gas sensors, Sensors and Actuators B: Chemical. 35 (1996) 48-51.

[2] X.G. Han, X.Han, L. Li and C. Wang, Controlling the morphologies of WO_3 particles and tuning the gas sensing properties, New J.Chem. 36 (2012) 2205-2208.

[3] Z.F. Liu, M. Miyauchi, T. Yamazaki, Y.B. Shen, Facile synthesis and NO_2 gas sensing of tungsten oxide nanorods assembled microspheres, Sensors and Actuators B: Chemical. 140 (2009) 514-519.

[4] J.M. Wang, P.S. Lee, J. Ma, Synthesis, growth mechanism and room-temperature blue luminescence emission of uniform WO_3 nanosheets with W as starting material, J. Crystal Growth. 311 (2009) 316-319.

[5] M. Feng, A.L. Pan, H.R. Zhang, Z.A. Li, F. Liu, H.W. Liu, D.X. Shi, B.S. Zou, H.J. Gao, Strong photoluminescence of nanostructured crystalline tungsten oxide thin films, Applied Physics Letters. 86 (2005) 141901-141901.

[6] Y.P. Xie, G. Liu, L.C. Yin and H.M. Cheng, Crystal facet-dependent photocatalytic oxidation and reduction reactivity of monoclinic WO_3 for solar energy conversion, J. Mater. Chem. 22 (2012) 6746-6751.

[7] Z.G. Zhao, Z.F. Liu and M. Miyauchi, Nature-inspired construction, characterization, and photocatalytic properties of single-crystalline tungsten oxide octahedra, Chem. Commun. 46 (2010) 3321-3323.

[8] N.L. Houx, G. Pourroy, F. Camerel, M. Comet and D. Spitzer, WO_3 nanoparticles in the 5-30 nm range by solvothermal synthesis under microwave or resistive heating, J. Phys. Chem. C. 114 (2010) 155-161.

[9] D.L. Chen and Y. Sugahara, Tungstate-based inorganic-organic hybrid nanobelts/nanotubes with lamellar mesostructures: synthesis, characterization, and formation mechanism, Chem. Mater. 19 (2007) 1808-1815.

[10] J.M Wang, E. Khoo, P.S. Lee and J. Ma, Synthesis, Assembly, and electrochromic properties of uniform crystalline WO_3 nanorods, J. Phys. Chem. C. ,112 (2008) 14306-14312.

Advanced Materials Research Vol. 936 (2014) pp 352-358
© (2014) Trans Tech Publications, Switzerland
doi:10.4028/www.scientific.net/AMR.936.352

Hydrothermal Synthesis and Characterization of Cerium-Based Oxides

Randi Dangerfield[1], Shannon Sharp[1], Ruigang Wang[1, 2]*

[1]Department of Chemistry, Youngstown State University, OH 44555, US

[2]Materials Science and Engineering Program, Youngstown State University, OH 44555, US

*rwang01@ysu.edu

Keywords: CeO_2, nanocatalysts, automotive exhaust clean-up, hydrothermal synthesis, transmission electron microscopy.

Abstract. We report a facile hydrothermal synthesis in base solution for shape/size-controlled ceria (CeO_2) nanocrystals and CeO_2-ZrO_2 solid solution. CeO_2 nanocrystals in the shape of nanorods, nanotubes, or nanocubes with reactive {110} and {200} faces can be produced using this hydrothermal method. We found that hydrothermal reaction temperature is a critical parameter to control the shape and size of ceria nanocrystals. Above 210 ^oC, high resolution transmission electron microscopy studies revealed that the CeO_2 nanocubes expose predominant {200} crystal planes. Microscopic investigation showed that the CeO_2-ZrO_2 solid solutions synthesized using this method had high crystallinity, and compositional homogeneity, and improved low-temperature reducibility.

Introduction

Synthesizing highly reactive and selective catalysts has been an intriguing and challenging goal in heterogeneous catalysis. Ceria (cerium oxide or CeO_2) along with a few other related oxides constitute an important class of catalysts that can rapidly pick up or release molecular oxygen ($2CeO_2 \leftrightarrow Ce_2O_3+1/2O_2$) under variable reducing and oxidizing conditions, mainly by way of a reversible change of the oxidation state of the cerium ions in combination with formation or elimination of oxygen vacancies [1-10].

As for all heterogeneous catalysis processes, surfaces play a crucial role for catalytic applications involving ceria as the active species. Several theoretical studies have investigated the structure and relative stability of the surfaces of CeO_2 crystals, and the results have indicated that the compact {111} surfaces are the most stable (and are therefore the least reactive), followed by {110}, {100}, and {211} [11-13]. It has recently been reported that materials with a 1 D-like morphology, specifically if they are prepared to predominantly expose {110} and {100} surfaces, have a higher catalytic activity in CO oxidation than conventionally prepared CeO_2 particles with exposed {111} surfaces [14-15]. The generation of nanostructured ceria particles in shapes other than octahedrons, such as e.g. nanorods, nanotubes, or nanocubes, may present an opportunity for the synthesis of low-temperature catalytically active materials with more reactive surfaces such as {110}, {100}, {211} etc. accessible on the crystal surface. In this report, we describe the preparation of shape/size controlled CeO_2 nanocrytals and compositionally homogeneous CeO_2-ZrO_2 solid solution using a facile hydrothermal method in base solution. Additionally, we discuss the thermal stability of as-synthesized CeO_2-ZrO_2 solution under reducing atmosphere.

Experimental Section

Pure CeO_2 and CeO_2-ZrO_2 nanopowders were prepared by hydrothermal method in a base solution. In a typical procedure, 0.1 M $Ce(NO_3)_3$ and 0.1 M $Zr(NO_3)_3$ solutions were prepared by dissolving $Ce(NO_3)_3 \cdot 6H_2O$ and $ZrO(NO_3)_2 \cdot xH_2O$, respectively, into 200 mL distilled water, while 6 M NaOH was prepared by dissolving 48 g of NaOH into 200 mL of distilled water. As far as pure CeO_2 is concerned, the reaction mixture containing 55 mL of 0.1M $Ce(NO_3)_3$ and 5 mL of 6 M NaOH

was prepared, after which the reaction mixture was stirred vigorously for 20 minutes before loading it into the autoclave. The sampele was hydrothermally treated at 150 ^{o}C for 48 hours. On the other hand, $Ce_{0.5}Zr_{0.5}O_2$ nanopowders were synthesized in the same manner as described above except that for each reaction setup, 22.5 mL of 0.1 M $Ce(NO_3)_3$ and 22.5 mL of 0.1 M $ZrO(NO_3)_2$ solutions were thoroughly mixed together first before 5 mL of 6 M NaOH were added to the mixtures. The reaction mixture was stirred vigorously for 40 minutes. The mixtures were then poured into sealed 100 mL Teflon lined autoclaves and hydrothermally treated at 50 ^{o}C and 150 °C for 48 hours, repectively. The vessels were then cooled to room temperature. Final precipitates were then filtered and thoroughly washed with 500 mL of distilled water and 200 mL of ethanol, then dried at 40 °C for 12 hours. High-temperature reduction treatment was carried out in a tube furnace at different temperatures (900^{o}C-1100^{o}C) for 3 hours with a carrier-gas of 4%H_2/96%He mixture.

Powder X-ray diffraction (XRD) analysis was done using the Rigaku Miniflex II Desktop X-ray Diffractometer applying a scanning range of 10 to 90^{o}. Transmission electron microscopy (TEM) was performed using a JEOL 2100 that was operated at 200 kV. For the electron energy loss spectroscopy (EELS) analysis, we used the Ce $M_{4,5}$ integrated white line at 883 and 901 eV to determine the Ce oxidation state in individual nanoparticles. To avoid the electron beam damage, weak-beam technique with wide spread beam and selected area aperture were used to get the EELS spectra from individual nanoparticles in diffraction mode. Isolated nanoparticles hanging in the vacuum without overlap were selected for EELS analysis. BET surface area analysis was performed on the dry nanopowders at -196 ^{o}C using liquid nitrogen. All the samples were pretreated for 1 hour at 110 ^{o}C using helium gas before surface area measurements were conducted. Hydrogen temperature programmed reduction (H_2-TPR) experiments were performed on the samples immediately after BET surface area analysis. Both H_2-TPR and BET surface area experiments were performed in a Micromeritics AutoChem^{TM} II 2920.

Results and Discussion

Synthesis of Pure CeO_2

Figure 1 shows the typical transmission electron microscopy (TEM) images of the particles collected after a hydrothermal reaction at different temperatures (a: 70^{o}C; b: 130^{o}C; c: 210^{o}C; d: 230^{o}C). A change of the nanoparticle morphology from nanorods to nanocubes with increasing temperature of the hydrothermal reaction is clearly evident. We found that hydrothermal reaction temperature is a critical parameter to control the shape and size of ceria nanocrystals in a base solution. Initially, OH^- was introduced in Ce^{3+} aqueous solution, reacted with Ce^{3+} and formed $Ce(OH)_3$. The separated colloidal $Ce(OH)_3$ clusters in solution will act as nuclei for the growth of nanostructure during the hydrothermal growth process. At low temperature, the anisotropic growth of $Ce(OH)_3$ is favored and rod-like morphology is obtained. As the hydrothermal reaction temperature increases, the $Ce(OH)_3$ becomes unstable and starts to oxidize into CeO_2. Fine CeO_2 nuclei form spontaneously nanocubes or nanocuboids in the aqueous solution.

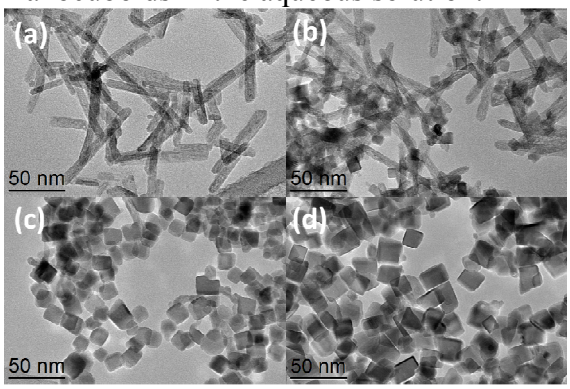


Fig 1. Some Typical Morphologies Of Ceo_2 Nanoparticles Prepared By A Facile Hydrothermal Method At Different Temperatures: (a): 70°C; (b): 130°C; (c): 210°C; (d): 230°C.

To have a better understanding of surface facets, a detailed high resolution transmission electron microscopy (HRTEM) characterization was carried out, shown in Figure 2, and HRTEM studies reveal that the CeO_2 nanocube exposes predominant {200} crystal planes.

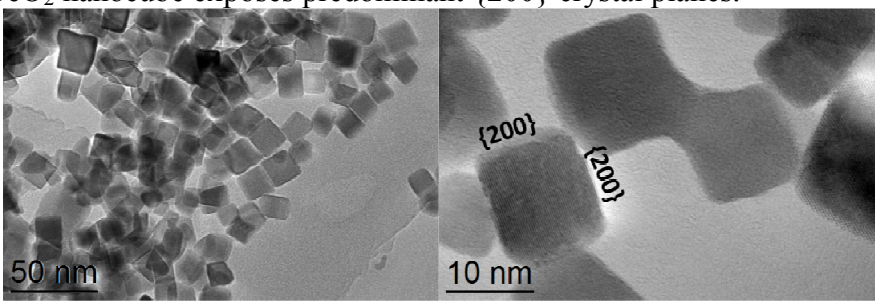


Fig 2. Low-magnification and Atomic-Level Tem Images Of Individual Ceria Nanocubes Prepared By Hydrothermal Method at 210 ^{o}C.

Synthesis of CeO_2-ZrO_2 Solid Solution

The strategy of hydrothermal synthesis was extended from pure CeO_2 to mixed cerium-based oxides as the mixed oxides present better low-temperature reducibility and superior thermal stability, compared to pure ceria [16]. In catalytic applications, a typical example of cerium-based mixed oxide is CeO_2-ZrO_2, used in commercial automotive three-way catalytic converters for its superior thermal stability and low-temperature oxygen storage capacity (OSC).

As shown in Figure 3, X-ray diffraction (XRD) data suggests that such mixed CeO_2-ZrO_2 oxides are solid solution, rather than composed of a mixture of CeO_2 and ZrO_2. For the $Ce_{0.5}Zr_{0.5}O_2$ solid solutions, the XRD lines are rather similar to those corresponding to pure ceria (face-centered cubic and fluorite structure, JCPDS 34-0394). It is clearly shown in Figure 3, that there is a shift of the XRD peaks toward higher angle for the $Ce_{0.5}Zr_{0.5}O_2$ solid solution samples. This is due to substitution of smaller Zr ion (ionic radius for Zr^{4+}: 0.84Å) for Ce (ionic radius for Ce^{4+}: 0.97Å) in the cubic ceria matrix. In addition, compared to ceria XRD peaks, the $Ce_{0.5}Zr_{0.5}O_2$ peaks are much broader. The peak widths for the sample prepared at 50 ^{o}C are broader than the sample prepared at 150 ^{o}C, indicating a better crystallinity for the sample synthesized at a higher hydrothermal reaction temperature. Since the peak widths are related to the crystalline size (without considering the strain effects) this data suggests that $Ce_{0.5}Zr_{0.5}O_2$ solid solution has a smaller crystalline size than that of pure ceria, and the $Ce_{0.5}Zr_{0.5}O_2$ sample prepared at 50 ^{o}C has a smaller crystalline szie compared with the sample prepared at 150 ^{o}C. This result is consistent with the observations of others. For examples, Sergent et al [17] found that the line widths increased with the Zr content to reach a maximum for the $Zr_{0.5}Ce_{0.5}O_2$ sample and subsequently decreased again. Their results are also in qualitative agreement with specific area data, where a maximum is obtained for the $Zr_{0.5}Ce_{0.5}O_2$ sample [17-18].

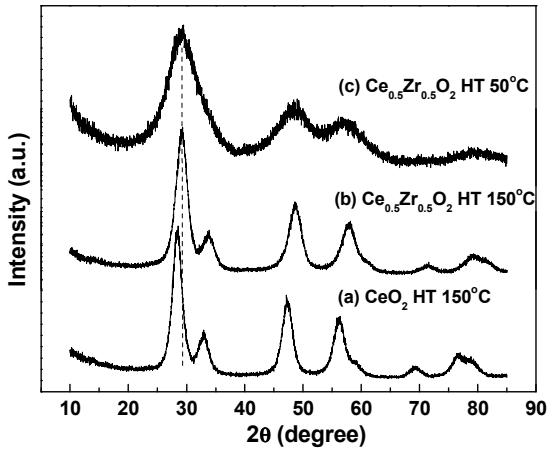


Fig3. XRD Patterns For As-Prepared Pure Ceo_2 At 150 ^{o}c And $Ce_{0.5}zr_{0.5}o_2$ Solid Solution Nanopowders Prepared At 50 ^{o}c and 150 ^{o}c using hydrothermal method. The dash line indicates the peak shift due to the doping of smaller zr ion (Zr^{4+}: 0.84 Å) In CeO_2 Lattice (Ce^{4+}: 0.97 Å).

For the catalytic redox application of cerium-based oxides, the oxygen exchange is restricted to the surface of the oxide nanoparticles. A high surface area of materials is a necessary requisite for catalyst application to maximize the gas-solid contact under reaction conditions. So we measured the BET surface areas of the CeO_2 and $Ce_{0.5}Zr_{0.5}O_2$ samples. The results are shown in Table 1. It is clear that $Ce_{0.5}Zr_{0.5}O_2$ samples have a higher surface area compared with the pure CeO_2 sample.

TABLE 1. COMPARISON OF BET SURFACE AREA OF THE CEO_2 AND $CE_{0.5}ZR_{0.5}O_2$ SAMPLES

Sample name	BET surface area
CeO_2 (150 ^oC)	111.0 m^2/g
$Ce_{0.5}Zr_{0.5}O_2$ (150 ^oC)	149.4 m^2/g
$Ce_{0.5}Zr_{0.5}O_2$ (50 ^oC)	159.8 m^2/g

Reactivity and Thermal Stability of CeO_2-ZrO_2 under Reducing Atmosphere

The reactivity of lattice oxygen in the CeO_2 and $Ce_{0.5}Zr_{0.5}O_2$ samples towards H_2 was investigated by temperature programmed reduction (TPR) technique, shown in Figure 4. The TPR profile of CeO_2 shows the "two/three-peak" pattern due to surface (low temperature peaks), and bulk reduction (high temperature peak), respectively. For the $Ce_{0.5}Zr_{0.5}O_2$ samples, only one peak is observed, in agreement with the promotion of the reduction in the bulk of mixed oxide upon doping zirconia [1-3]. This suggests that reduction of the bulk lattice oxygen must occur simultaneously with the reduction of surface oxygen.

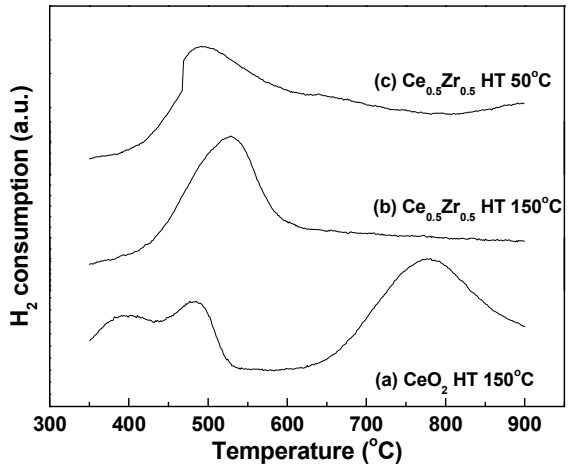


Fig 4. Temperature-programmed Redution (TPR) Profiles for Pure CeO_2 Prepared at 150 ^oC and $Ce_{0.5}Zr_{0.5}O_2$ Solid Solution Nanopowders Prepared at 50 ^oC and 150 ^oC Using Hydrothermal Method.

High temperature reduction treatments were found to favor the formation of highly active CeO_2-ZrO_2 materials [19-25]. However, there remain many questions about the role of compositional heterogeneity, cation ordering and oxygen vacancy ordering in the active component for redox reactions. Following powder synthesis, thermal treatments under reducing conditions were carried out to test the thermal stability of the CeO_2-ZrO_2 solid solution. Under a reducing atmosphere, we found that thermal treatments result in phase transformation, rather than phase separation, from fluorite structure (*Fm*3*m) to* cation-ordered pyrochlore-type superstructures (Fd-3m). Ordering of the Ce and Zr ions is clearly presented by the d-spacing doubling of the (111) peaks shown in the XRD patterns (Figure 5), which is consistent with our previous observation [9].

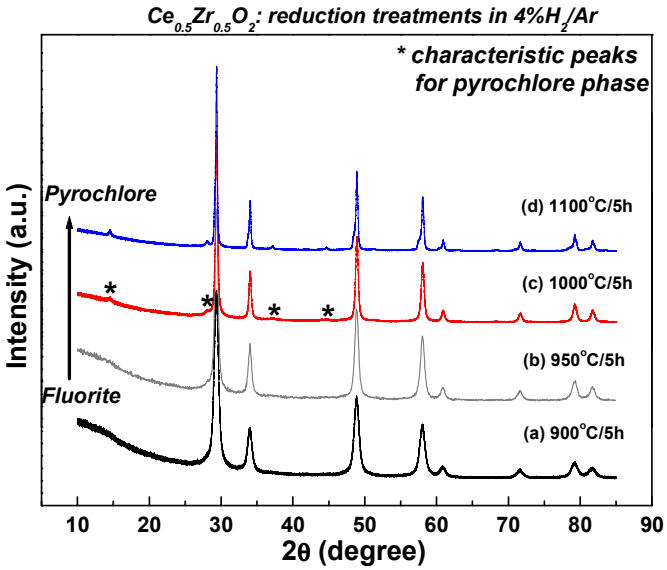


Fig 5. Phase Transformation From Fluorite To Pyrochlore Structure In Ce0.5zr0.5o2 During Thermal Treatments In Reduction Atmosphere.

Electron energy loss spectroscopy (EELS) was used to determine the Ce oxidation states for the $Ce_{0.5}Zr_{0.5}O_2$ nanoparticles in the samples before and after reduction treatments by analyzing the relative intensity of Ce $M_{4,5}$ edges. Analysis of Ce $M_{4,5}$ white line intensity ratio, obtained from EELS data indicates that the particles in raw materials is in +4 oxidation state and after reduction treatments the particles show a mixed +3/+4 oxidation states, showin in Figure 6. Statistical measurements obtained from at least 20 individual particles for each specimen. Figure 7 shows a schematic illustration of the structural transformation using $Ce_2Zr_2O_7$ unit cell and 2×2×2 CeO_2 super cell during the reduction treatment. The cation ordering along <110> is a distinguishing feature for the $Ce_2Zr_2O_7$ pyrochlore structure compared to the fluorite structure CeO_2 (Figure 7). This can be seen from the presence of pure Ce (blue), pure Zr (grey) and mixed Ce and Zr (blue/grey/blue/grey…) atom columns along <110> direction demonstrating that cation ordering is present.

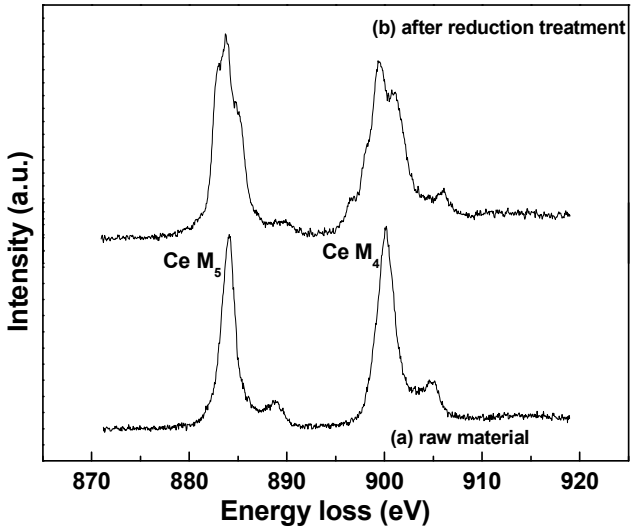
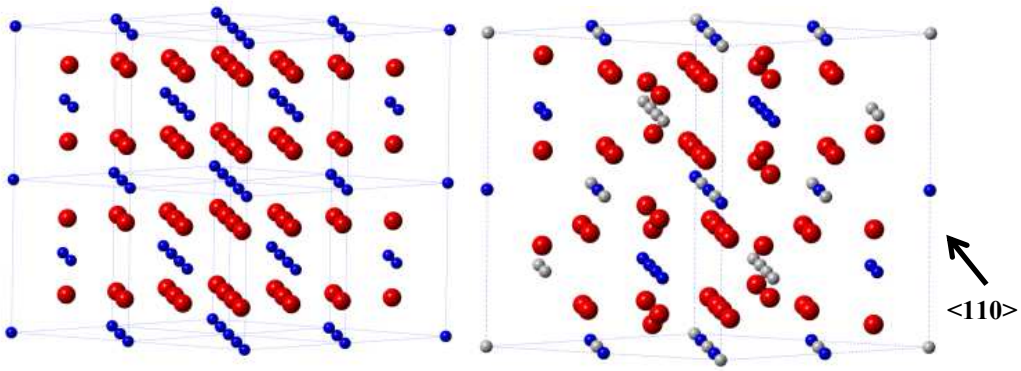


Fig 6. EELS Spectra of Ce0.5Zr0.5O2 Nanoparticles Before and after Reduction Treatment.



(a) 2×2×2 CeO_2 super cell (b) pyrochlore $Ce_2Zr_2O_7$unit cell

Fig 7. A Schematic Illustration Of The Structural Transformation From 2×2×2 Ceo2 Super Cell To Cation-Ordered Ce2zr2o7 Unit Cell During The Reduction Treatment. (Red atoms: Oxygen; Blue Atoms: Ce; Grey Atoms: Zr)

Conclusions

In summary, we have developed a facile hydrothermal method in base solution to synthesiz CeO_2 and particularly CeO_2-ZrO_2 solid solution nanopowders, with a good control over particle shape and size. By controlling the crystallization process inspired from the formation of $Ce(OH)_3$ nanocrystals, the morphology could be tuned into different regular shapes such as nanorods, nanocuboids, and nanocubes. The compositionally homogeneous CeO_2-ZrO_2 solid solution nanopowders can also readily prepared. Reduction treatment of $Ce_{0.5}Zr_{0.5}O_2$ causes a phase transformation, instead of phase separation, from fluoride to pyrochlore structure, suggesting nanoscale compositionally homogeneity of particles. We envision that the synthesis process presented here can be extended to synthesize other cerium-based mixed oxides for use in low-temperature redox active materials in automobile catalytic converter, as well as for catalysis and sensor applications.

Acknowledgements

The financial support from American Chemical Society Petroleum Research Fund (#52323), the Department of Transportation (DoT-CTME project), the Department of Energy (EE0004094), YSU University Research Council grant and the use of TEM facilities at the Center of Excellence in Materials Science and Engineering at Youngstown State University are gratefully acknowledged.

References

[1] S. Bernal, F.J. Botana, J.J. Calvino, M.A. Cauqui, G.A. Cifredo, A. Jobacho, J.M. Pintado, J.M. Rodrfguez-Izquierdo, J. Phys. Chem. 97 *(*1993) 4118-4123.

[2] P. Fornasiero, R. Dimonte, G.R. Rao, J. Kaspar, S. Meriani, A. Trovarelli, M. Graziani, J. Catal. 151(1995) 168-177.

[3] G. Balducci, J. Kaspar, P. Fornasiero, M. Graziani, M. Saiful Islam, J.D. Gale, J. Phys. Chem. B 101(1997) 1750-1753.

[4] M. Shelef, R.W. McCabe, Catalysis Today 62 (2000), 35-50.

[5] R.J. Gorte, AIChE Journal 56 (2010) 1126-1135.

[6] R. Wang, P.A. Crozier, R. Sharma, J.B. Adams, J. Phys. Chem. B 110 (2006) 18278-18285.

[7] R. Wang, P.A. Crozier, R. Sharma, J. Mater. Chem. 20 (2010) 7497-7505.

[8] R. Wang, S.I. Mutinda, Chem. Phys. Lett. 517 (2011) 186-189.

[9] R. Wang, M.H. Fang, J. Mater. Chem. 22 (2012) 1770-1773.

[10] R. Wang, P.A. Crozier, R. Sharma, J. Phys. Chem. C 113 (2009) 5700-5704.

[11] J.C. Conesa, Surf. Sci. 339 (1995) 337-352.

[12] M. Fronzi, A. Soon, B. Delley, E. Traversa, C. Stampfl, J. Chem. Phys. 131(2009) 104701.

[13] Z.X. Yang, T.K. Woo, M. Baudin, K. Hermansson, J. Chem. Phys. 120 (2004), 7741-7749.

[14] K.B. Zhou, X. Wang, X.M. Sun, Q. Peng, Y.D. Li, J. Catal. 229 (2005) 206-212.

[15] K.B. Zhou, Z.Q. Yang, S. Yang, Chem. Mater. 19 (2007) 1215-1217.

[16] P. Fornasiero, G. Balducci, R. DiMonte, J. Kaspar, V. Sergo, G. Gubitosa, A. Ferrero, M. Graziani, J. Catal. 164 (1996), 173-183.

[17] N. Sergent, J.F. Lamonier, and A. Aboukais, Chem. Mater. 12 (2000) 3830-3835.

[18] C.H. Liang, J.S. Qiu, Z.L. Li, and C. Li, Nanotechnology 15 (2004) 843-847.

[19] A. Suda, Y. Ukyo, K. Yamamura, H. Sobukawa, T. Sasaki, Y. Nagai, T. Tanabe, M. Sugiura, J. Ceram. Soc. Jap. 112 (2004) 586-589.

[20] R. Wang, P.A. Crozier, R. Sharma, J.B. Adams, Nano Letters 8(2008) 962-967.

[21] T. Montini, M. Banares, N. Hickey, R. Di Monte, P. Fornasiero, J. Kasper, M. Graziani, Phys. Chem. Chem. Phys. 6 (2004) 1-3.

[22] I. Alessandri, M. Banares, L.E. Depero, M. Ferroni, P. Fornasiero, F.C. Gennari, N. Hickey, M.V. Martinez-Huerta, T. Montini, Topics in Catalysis 41 (2006) 35-42.

[23] P.A. Crozier, R. Wang, R. Sharma, Ultramicroscopy 108 (2008) 1432-1440.

[24] J. Pérez-Omil, A.S. Bernal, J.J. Calvino, J.C. Hernández, C. Mira, M. Rodríguez-Luque, P.R. Erni, N.D. Browning, Chem. Mater. 17 (2005) 4282-4285.

[25] F. Zhang, J.M. Raitano, C. Chen, J.C. Hanson, W. Caliebe, S. Khalid, S.W. Chan, J. Appl. Phys. 99 (2006) 0843131-0843138.

Advanced Materials Research Vol. 936 (2014) pp 359-363
© (2014) Trans Tech Publications, Switzerland
doi:10.4028/www.scientific.net/AMR.936.359

Controlled Synthesis Of Core-Shell Structure Sio_2 /$Nagdf_4$:Eu^{3+} Magnetic And Optical Bifunctional Composite

Yanli Wu[a], MinLiao[b], Hanxin Ding[c], Ruchun Yang[d],

Dandan Xiong[e], Qiang Xiao*[f]

Jiangxi Key Laboratory of Organic Chemistry, Jiangxi Science and Technology Normal University,Nanchang, P.R.China

[a]e-mail：wanny118@126.com, [b]e-mai：191889585 @qq.com,

[c]e-mail:dinghaixin 2010@163.com, [d]e-mai:ouyangruchun@163.com

[e]e-mai: 1024975163 @qq.com, [f]e-mail: xiaoqiang@tsinghua.org.cn

Key words: core/shell, magnetic, optical, composite, SiO_2 /$NaGdF_4$:Eu^{3+}

Abstract: The SiO_2/$NaGdF_4$:Eu^{3+} core/shell composite was prepared by a template -mediated method, making monodispersed SiO_2 as core and $NaGdF_4$:Eu colloids as shell, the morphology and the core-shell structure of the resulting particles were analyzed by SEM，X-ray diffraction, and the photo-luminescence and magnetic properties of the microspheres were investigated too. The results shows the composite have great potential to be used as homogeneous magnetic/optical bifunctional material.

Introdution

In recent years, there has been great interesting in developing nano/micro materials with controlled size, shape and structure.[1,2]It is well known that controlling the size, structure, and shape of inorganic nano/micro structures is of fundamental and technological importance because of the strong correlation between these parameters and their chemical/physical characteristics such as magnetic, luminescent and electronic properties.[3,4] Rare Earth (RE^{3+}) doped nano/micro materials have versatile utility in biological applications because of their unique electronic and optical properties based on the 4f electrons. They can be made either as luminescent, magetic or as dual model probe by selective doping lanthanide ions.[5]

$NaREF_4$, as a excellent down-conversion (DC) and up-conversion (UC) luminescent host material have aroused intensive research in the past decade owing to the very low phonon frequencies.[6,7] In particular, lanthanide ions (Ln^{3+}) doped Gd^{3+}-based rare earth fluorides are a category of multifunctional agents for multimodal bioimaging, because the optically active Ln^{3+} ions in the fluoride lattices contribute to luminescence(optical modality), and paramagnetic property of the Gd^{3+} can introduce magnetic resonance imaging (MRI) modality. Thus, some synthetic routes have been developed to prepare the nano/micro sized $NaGdF_4$, including thermal decomposition synthesis route[8], coprecipitation method[9], hydrothermal procedure[10] and so on. However, owing to the small size and the active surface of the $NaGdF_4$ nano/micro particles prepared without modification, they are unstable and easy to gather together. That will have serious impact on their application. In order to improve the stability of the $NaGdF_4$ particles, designing a

core-shell structure with spherical morphology is a efficient way.[11] Because of non-cytotoxic, chemically inert and optically transparent at visible wavelengths, silica-based materials have been the most general choice for preparing, modifying or functionalizing some desired objects and materials, but there are few reports on silica particles used as core.

In this work, core-shell $SiO_2/NaGdF_4:Eu^{3+}$ was prepared by coating of submicron SiO_2 spheres with $NaGdF_4:Eu^{3+}$ colloids and subsequent hydrothermal treatment. Stőber method[12] was selected to prepare silica submicrospheres because of their inexpensiveness, easiness to get spherical particles with narrow size distribution. Both magnetic and luminescent properties of the obtained $SiO_2/NaGdF_4:Eu^{3+}$ submicrospheres were investigated in detail.

Experimental

Equipment

The X-ray diffraction (XRD) of the powder samples was examined on a Rigaku-Dmax 2500 diffractometer using Cu Ka radiation (k = 0.15405 nm). The morphology of the product was measured by scanning electron microscopy(FEI Quanta200F), PL was examined with F4500 Fluorescent spectroscopy and Magnetic property measurements were carried out using a vibrating sample magnetometer (MPMS XL-7, -20 to 20kOe).

Materials

Gd_2O_3(99.99%), Eu_2O_3(99.99%), Citric acid (99.5%), tetraethyl orthosilicate (TEOS) (99.0 %), $RECl_3$ (RE=Gd and Eu) salts were freshly prepared by a reaction of RE_2O_3 with dilute hydrocholic acid. All other chemicals were analytical-grade reagents and used directly without further purification.

Synthesis of silica cores

The synthesis of highly monodisperse submicron SiO_2 spheres was carried out following the modified Stőber method, i.e. the hydrolysis of tetraethoxysilane (TEOS) in an ethanol solution containing water and ammonia. This method yielded the colloidal solution of silica particles with a narrow size distribution in the submicron range, and the particle size of silica depended on the relative concentration of the reactants. In a typical experiment, the mixture of 5 mL TEOS and 45 mL EtOH was poured into another mixture of 5 mL of NH_4OH (25 wt%) , 10ml deionized water and 35ml EtOH, then stirred at room temperature for 5 h, resulting in the formation of white silica colloidal suspension. The silica particles were centrifugally separated from the suspension and washed with ethanol for four times. In order to obtain SiO_2 sphere of different particle size, the amounts of used TEOS were changed, as shown in Table1.

Coating of SiO_2 Cores with $NaGdF_4:Eu^{3+}$Shells

SiO_2 core $NaGdF_4:Eu^{3+}$shell particles ($SiO_2/NaGdF_4:Eu^{3+}$) were prepared by the following process (Fig1). First of all, SiO_2 submicospheres were dispersed in $RECl_3$ (RE=Gd, Eu) solution, because of the -OH on the surface of the silica, the RE^{3+} ions were attracted onto the surface around of the silica core, then Sodium citrate solution as a chelating agent for the metal ions was added, the molar ratio of metal ions to citric acid was 1:2. After stirring for 30 minutes, NaF solution(10 times amount of the $LnCl_3$) was poured into the mixture, then this mixture was hydrothermal treated at 180℃ for 2h, and the core-shell particles were separated by centrifugation. For the purpose of comparison, the blank sample of $NaGdF_4:Eu^{3+}$ was prepared in a similar process.

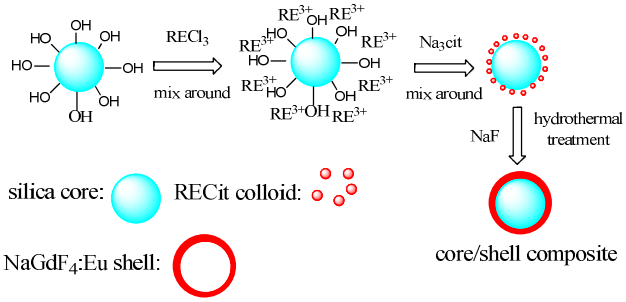


Fig.1. Formation process of $SiO_2/NaGdF_4:Eu^{3+}$

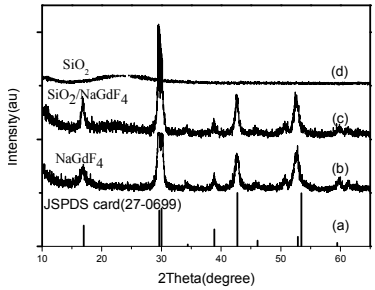


Fig.2. JSPDS card 27-0699 for β-$NaGdF_4$(a), core-shell particles and XRD patterns for pure $NaGdF_4$(b) core-shell $SiO_2/NaGdF_4$(c); pure SiO_2(d)

Results and discussion

XRD study

X-ray diffraction patterns of pure $NaGdF_4$(b), $SiO_2/NaGdF_4:Eu^{3+}$ core–shell samples (c), and bare silica spheres (d) are shown in Fig.2. In Fig.2a, the pure $NaGdF_4$ samples present several peaks that can be well indexed to hexagonal (β)-$NaGdF_4$ (JSPDS card no27-0699). For SiO_2 particles(Fig.2(d)), no diffraction peak is observed except for a broad band centered at 2θ=22.00°, which is the characteristic peak for amorphous SiO_2. For the $SiO_2/NaGdF_4:Eu^{3+}$ core–shell sample, the diffraction pattern (Fig.2(c)) consists of a broad band centered at 2θ= 22.00° and several sharp peaks, the former is due to part of amorphous SiO_2, and later is agreeing well with the XRD peaks of pure hexagonal (β)-$NaGdF_4$, no second phase was detected . The result shows that the $NaGdF_4:Eu^{3+}$ was successfully coated onto the surface of the SiO_2 core.

SEM measurements

Fig.3 shows the SEM images of the SiO_2 submicrospheres of different particle size which was obtained though changing the amount of TEOS and the SEM image of the $SiO_2/NaGdF_4:Eu^{3+}$ core/shell composite. It can be clearly observed that before coating, uniform and single-dispersed SiO_2 submicrospheres were formed, the size was changing with the amout of the TEOS which was shown in Tble 1. The diameter of the SiO_2 particles increased with the increase of the dosage of TEOS. In the Fig.3d there was obviously a thin lay onto the surface of the SiO_2 submicrospheres, that would be due to the coating of the $NaGdF_4:Eu^{3+}$ shell.

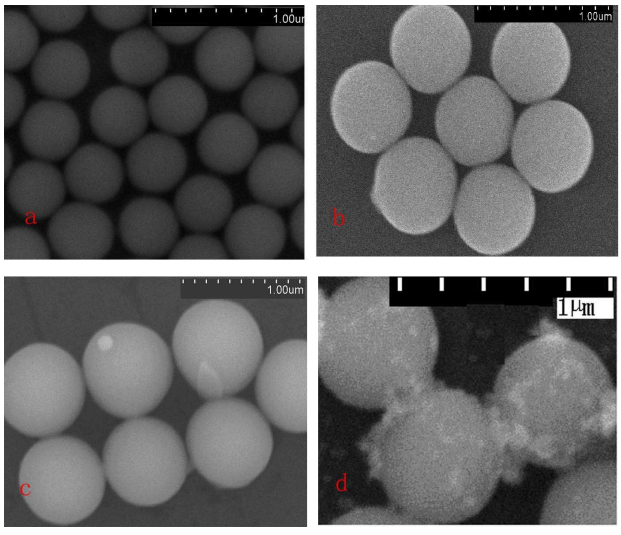


Fig.3 SEM images of SiO_2 submicrospheres of 400nm(a), 600nm(b), 680nm(c), and SEM image of the $SiO_2/NaGdF_4:Eu^{3+}$ core/shell composite (d).

TABLE 1. THE AMOUNTS OF USED TEOS CORRESPONDING TO THE DIFFERENT SIZE OF THE SIO_2

Solution A			Solution B		SEM image
H_2O/ml	EtOH/ml	NH_4OH/ml	TEOS/ml	EtOH/ml	
10	35	5	3	47	Fig.3a(400nm)
10	35	5	5	45	Fig.3b(600nm)
10	35	5	6	44	Fig.3c(680nm)

Luminescence properties

Fig.4 shows the photoluminescent spectra of the $SiO_2/NaGdF_4:Eu^{3+}$ core/shell composite at room temperature. The excitation spectrum was obtained by monitoring $^5D_0$-$^7F_2$ transition of Eu^{3+} at 614 nm (Fig.4a).There were two strong peaks at 274nm and 395nm which can be ascribled to $^8S_{7/2}$-$^6I_{11/2}$ transition of Gd^{3+} and $^7F_0$-$^5L_6$ transition of Eu^{3+} respectively. The peak at 274nm has the highest absorption relative to the others. It indicates the occurrence of an energy transfer process from Gd^{3+} to Eu^{3+} ion. Upon excitation at 274nm, $SiO_2/NaGdF_4:Eu^{3+}$ core/shell particles showed emission peaks in the range of 550–750 nm, corresponding to the transitions of $^5D_0$-$^7F_{1-4}$(Fig.4b), The strongest emission was obtained at 614nm($^5D_0$-$^7F_2$), thus giving rise to the red emission for Eu^{3+}.

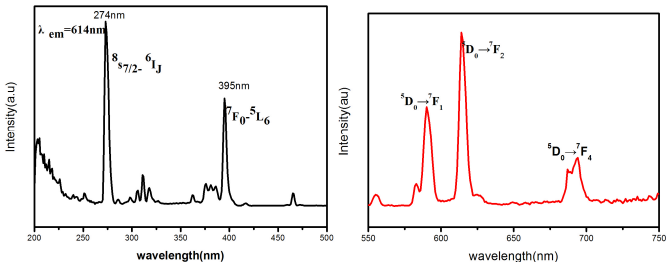


Fig.4 Excitation spectrum of $SiO_2/NaGdF_4:Eu^{3+}$ composite(a);
Emission spectrum of $SiO_2/NaGdF_4:Eu^{3+}$ composite under 274nm

Paramagnetic properties

Figure.5 shows magnetometry magnetization magnetic field (M-H) plots of $SiO_2/NaGdF_4:Eu^{3+}$ composite at 300 K. As the strength of the applied magnetic field increased, the ideal linear correlation between the magnetization and the applied magnetic field in the composite was obtained, indicating that composite possesses paramagnetism. The mass magnetic susceptibility value of the as-prepared $SiO_2/NaGdF_4:Eu^{3+}$ composite is determined to be $5.23*10^{-5}$ Oe. The paramagnetic property of the Gd^{3+} ions come from seven unpaired inner 4f electrons. $SiO_2/NaGdF_4:Eu^{3+}$ composite with paramagnetic property might be applied as MRI contrast agent.

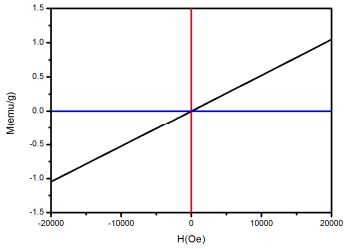


Fig.5 Magnetization versus applied magnetic field for $SiO_2/NaGdF_4:Eu^{3+}$ composite

Conclusions

$SiO_2/NaGdF_4:Eu^{3+}$ composite have been prepared by surface coating of $NaGdF_4:Eu^{3+}$ precursor on SiO_2 submicrospheres and subsequent hydrothermal treatment. The core/shell structure composite have a near perfect spherical shape with narrow size distribution, are not agglomerated. The Eu^{3+} shows a strong PL luminescence (dominated by $^5D_0$-$^7F_2$) red emission at 614 nm, and the composite shows paramagnetic property due to the 4f electron of Gd^{3+}. These properties makes it very promising for using as a dual-mode imaging nanoprobe for fluorescence and MRI analysises.

Acknowlegement

Financial support from the doctoral scientific research foundation of Jiangxi Science and Technology Normal Univsity (3000990126), the foundation of national Student innovation project (201311318005).

References

[1] S. H. Sun, H. Zeng, Size-Controlled Synthesis of Magnetite Nanoparticles, J. Am. Chem. Soc. 124 (2002) 8204-8205.

[2] L. X. Zhang, J. Luo, M. Z. Wu, H. F. Jiu, Synthesis of Eu_2O_3 hollow sub micrometer spheres through a sol-gel template approach, Mater. Lett. 61 (2007) 4452 –4455.

[3] A. Kar, A. Patra. Impacts of core–shell structures on properties of lanthanide-based nanocrystals: crystal phase, lattice strain, downconversion, upconversion and energy transfer, Nanoscale. 4 (2012) 3608-3619.

[4] D. Yang, X. Kang, P. Ma, Hollow structured upconversion luminescent $NaYF_4$: Yb^{3+}, Er^{3+} nanospheres for cell imaging and targeted anti-cancer drug delivery, Biomaterials. 34 (2013) 1601-1612.

[5] F. Wang, X. G. Liu. Recent Advances in the Chemistry of Lanthanide-Doped Upconversion nanocrystals. Chem. Soc. Rev. 38 (2009) 976-989.

[6] G. Y Chen, T. Y. Ohulchanskyy, R Kumar, H.Agren, P. N. Prasas, Ultrasmall monodisperse $NaYF_4$: Yb^{3+}/Tm^{3+} nanocrystals with enhanced near-infrared to near-infrared upconversion photoluminescence, ACS nano. 4 (2010) 3163-3168.

[7] F. He, P. P. Yang, D. Wang, N. Niu, S. L. Gai, X. B. Li, Self-Assembled β-$NaGdF_4$ Microcrystals: Hydrothermal Synthesis, Morphology Evolution, and Luminescence Properties, Inorg. Chem. 50 (2011) 4116-4124.

[8] R. Naccache, F. Vetrone, V. Mahalingam, L. A. Cuccia, J. A. Capobianco, Controlled synthesis and water dispersibility of hexagonal phase $NaGdF_4$: Ho^{3+}/Yb^{3+} nanoparticles, Chem. Mater. 21(2009) 717-723.

[9] M. Karbowiak, A. Mech, A. Bednarkiewicz, W. Strek, Structural and luminescent properties of nanostructured $KGdF_4$: Eu^{3+} synthesised by coprecipitation method, J. Alloys Compd. 380 (2004) 321-326.

[10] X. Q Zhang, X. P. Fan, X. S. Qiao, Q. Luo, $NaGdF_4$: Ce^{3+} and (Ce, Gd)F_3 nanoparticles: Hydrothermal synthesis and luminescence properties, Mater. Chem. Phys. 121 (2010) 274-279.

[11] X. H. Liu, H. S. Qian , Y. P. Ji, Z. Q. Li, Y. Shao, Y. Hu, G. X. Tong, L. C. Li, W. D. Guo, H. C. Guo, Mesoporous silica-coated $NaYF_4$ nanocrystals: facile synthesis, in vitro bioimaging and photodynamic therapy of cancer cells, RSC Advances. 2 (2012) 12263-12268.

[12] W. Stober, A. Fink, E. J. Bohn, Controlled growth of monodisperse silica spheres in the micron size range, Colloid Interface Sci. 26 (1968) 62–69.

Advanced Materials Research Vol. 936 (2014) pp 364-368
© (2014) Trans Tech Publications, Switzerland
doi:10.4028/www.scientific.net/AMR.936.364

Electrochemical Properties of Graphene Nanosheet/Polyaniline Nanocomposite as Electrode for Supercapacitors

Ran-Ran Yao[1, a], Ning-Na Yao[2, b], Dong-Lin Zhao[1, c] and Li Xu[2, d]

[1] Key Laboratory of Carbon Fiber and Functional Polymers, Ministry of Education, Beijing University of Chemical Technology, Beijing 100029, China

[2] State grid smart grid research institute, Beijing 102211, China

[a]email: 2012200501@grad.buct.edu.cn, [b]email: yaoningna@sgri.sgcc.com.cn

[c]email: dlzhao@mail.buct.edu.cn, [d]email: xuli@sgri.sgcc.com.cn

Keywords: Graphene nanosheets, Polyaniline, Supercapacitors, Electrochemical properties

Abstract. A graphene nanosheet/polyaniline (GNS/PANI) nanocomposite was synthesized using in situ polymerization. The morphology and microstructure of GNS/PANI nanocomposite were examined by transition electron microscopy (TEM) and X-ray diffraction (XRD). Electrochemical properties were characterized by cyclic voltammetry (CV) and galvanostatic charge/discharge. GNS as a support material could provide more active sites for nucleation of PANI as well as excellent electron transfer path. The GNS was homogeneously coated on both surfaces with PANI, and a high specific capacitance of 331 F g^{-1} was obtained at a current load of 0.02 A g^{-1}. The kinetics properties of GNS/PANI electrodes were investigated by AC impedance measurements. GNS/PANI electrode exhibited higher electrochemical activity and more favorable kinetic properties during charge and discharge process.

Introduction

With high requirement of energy storage systems for portable electronics, back-up power storage and hybrid electric vehicle applications, supercapacitors (also called electric double-layer capacitors) have gained an increasing attention, owing to their high power density and long cycle life compared with rechargeable batteries, and high energy density compared with conventional solid-state and electrolytic capacitors [1-3]. According to the double-layer energy-storage mechanism, the key to enhance the specific capacitance is to enlarge the specific surface area and control the pore size and distribution of the electrode material [4, 5].

Graphene is a two-dimensional carbon plane with one-atomic thickness. Since the paper on the freestanding graphene was published by Geim and co-workers [6], the preparation, structure and property of graphene have attracted great attention owing to its particular quantum Hall effect, sensitivity, mechanical hardness, electrical conductivity and so on [7–10]. These properties suggest wide applications, including field effect transistors, adsorbents, lithium-ion batteries and supercapacitors [7–11]. Recently, great effort has also been devoted to compounding graphene nanosheets (GNS) with polymers or inorganic particles. Among the conducting polymers, polyaniline (PANI) is the most investigated conducting polymer due to its low cost, easy synthesis, environmental stability, good electrical conductivity and controllable doping level [6–12]. However, it is very easy for PANI to be swelling and shrinkage in the charge–discharge process. In order to deal with this problem, it is a good methodology to compound PANI and carbon materials to increase the stability of PANI as well as to maximize the capacitance value. Among them, GNS brings many advantages that make it better than other carbon materials [13–15].

In this work, GNS/PANI nanocomposite was synthesized by in situ polymerization of aniline monomer in the presence of GNS suspension in HCl solution. The introduction of GNS into PANI could greatly enhance the electrochemical performances of the nanocomposite.

Materials and Methods

GNS was prepared in three steps: the oxidation of flake natural graphite via a modified Hummers' method, rapid heat treatment and ultrasonication. $KMnO_4$ was employed as the oxidant to obtain graphite oxide (GO). Firstly, 1 g of flake natural graphite powder with the mean diameter of 15 μm (provided by Dong Xing Electrical Carbon Co., Ltd. China) was added to 23 ml of cooled (0 ºC) concentrated H_2SO_4. Then 3 g of $KMnO_4$ was added gradually with stirring and cooling, so that the temperature of the mixture was maintained below 10 ºC. The mixture was then stirred at 35 ºC for 30 min. After this, 46 ml of distilled water was slowly added to cause an increase in temperature to 98 ºC and the mixture was maintained at that temperature for 15 min. The reaction was terminated by adding 140 ml of distilled water followed by 10 ml of 30% H_2O_2 solution. The solid product was separated by centrifugation, washed repeatedly with 5% HCl solution until sulphate could not be detected with $BaCl_2$, and then the resultant GO was dried at 65 ºC overnight. GO were quickly sent to a muffle furnace pre-heated to 1050 ºC in the air atmosphere to obtain expanded graphite. The expanded graphite was dispersed into ethanol and delaminated into GNS under a 600 W ultrasonic agitation for 15 h. The desired GNS was obtained after vacuum drying. Aniline was first distilled under vacuum to remove the oxidation impurities before using. The GNS/PANI nanocomposite was prepared by in situ polymerization. 200 mg of GNS was firstly dispersed in 100 mL of a 1 mol/L hydrochloric acid (HCl) aqueous solution and ultrasonicated for 30 min to form dispersed suspensions. The suspension was mixed with 200 mg (2.2 mmol) aniline monomer dissolved in 50 mL of a 1 mol/L HCl aqueous solution. After that, ammonium persulfate (APS, $(NH4)_2S_2O_8$) solution containing 50 mL of 1 mol/L HCl and 500 mg (2.2 mmol) of APS was added to the suspension dropwise with vigorous stirring to carry out the in situ polymerization at an ice-water bath for 24 h. The precipitated GNS/PANI nanocomposite was filtered and washed repeatedly with ethanol and de-ionized water.

The morphology and structure of the samples were observed by transmission electron microscope (TEM, Hitachi H-800). X-ray diffraction (XRD) analysis was conducted on a Rigaku D/max-2500B2+/PCX system using Cu/Kα radiation (λ = 1.5406 Å).

The electrochemical performances of GNS/PANI nanocomposite were measured with the coin-type cells. The supercapacitor electrodes were prepared by a coating method. A mixture of GNS/PANI nanocomposite, acetylene black (conductivity enhancing material) and polytetrafluoroethylene (10 wt.%, binder) with the mass ratio of 85:10:5 was dispersed in ethanol and coated on a piece of foam nickel, which was pressed under 10 MPa for 2 min and dried at 100 °C for 24 h. A two−electrode cell configuration was used to measure the performance of supercapacitors. The capacitor was constructed using a couple of electrodes face to face, with a separator inserted between these electrodes. The two identical (by weight and size) electrodes were assembled in a test cell, which consisted of two current collectors, two electrodes, and an ion-porous separator. The electrolyte was a 6 M KOH aqueous solution. Galvanostatic charge/discharge test was taken by CT2001A Battery Program Controlling Test System (China-Land Com. Ltd.) within the voltage range of 0−1 V, which was used to calculate the specific capacitance of GNS electrodes form the slope of discharge curves (dV/dt). The cyclic voltammetry and electrochemical impedance spectroscopy (EIS) were carried out on a VersaSTAT3 electrochemical working station. For the cyclic voltammetric measurements, the sweep rate ranged from 1 to 50 mV s^{-1} within a potential range of 0 to 1 V. For the EIS measurements, the frequency range was from 0.01Hz to 100 kHz.

Results and Discussion

The morphology of the obtained GNS/PANI nanocomposite was observed by TEM. Fig. 1 exhibits the TEM image of GNS/PANI nanocomposite, consisting of almost transparent carbon nanosheets with thin wrinkled structure that graphene owns intrinsically. GNS as a support material could supply a large number of active sites for nucleation of PANI, and homogeneous PANI coat on

the surfaces of GNS, which increases both the dispersion of PANI and the contact of PANI with electrolyte, and thus may be favorable for the enhancement of the electrochemical performance as an electrode for supercapacitors.

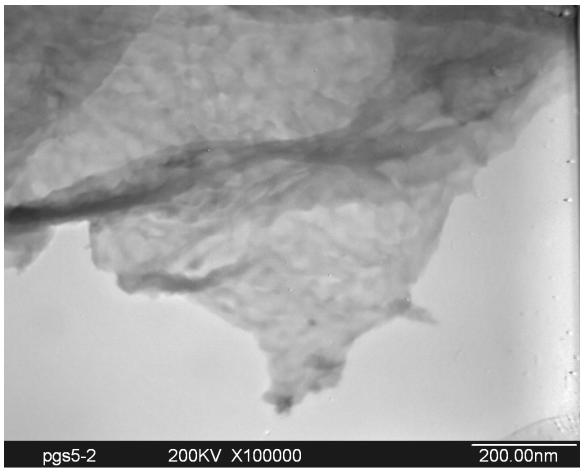


Fig. 1. TEM Images of GNS/PANI.

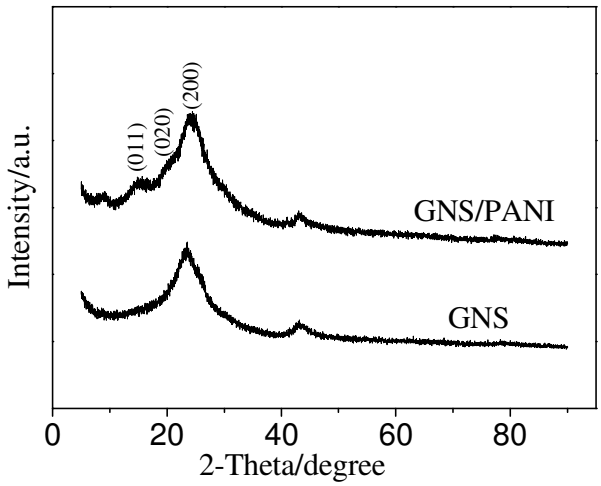


Fig. 2. XRD Patterns of GNS and GNS/PANI.

Fig. 2 shows the XRD patterns of GNS and GNS/PANI nanocomposite. For GNS, the diffraction peaks at 2θ = 24.5° and 42.8° can be attributed to the graphite-like structure (002) and (100), respectively. For GNS/PANI nanocomposite, the crystalline peaks appear at 2θ = 15.3°, 20.7° and 25.2°, corresponding to (011), (020) and (200) crystal planes of PANI in its emeraldine salt form, respectively.

Cyclic voltammetry measurements were carried out within the potential range of 0 to 1 V to analyze the electrochemical behavior of the supercapacitors. Fig. 3 presents the cyclic voltammograms of GNS/PANI electrode at scan rates varying from 1 to 20 mV s^{-1}. At low scan rates, the GNSs show typical rectangular curve without obvious oxygen and hydrogen evolution peaks, indicating good charge propagation within the electrodes. The CV curves for the GNSs still show rectangular shapes with small distortion at a scanning rate as high as 20 mV s^{-1}, suggesting that the GNS/PANI nanocomposite show a good power capability due to their uniform mesopore distribution. To investigate the electrochemical performance of GNS/PANI nanocomposite as electrodes for supercapacitors, galvanostatic charge/discharge cycling measurements were performed. Fig. 4 displays the capacitance versus cycle number curves of GNS/PANI under specific current of 0.1 A g^{-1}, and the electrode exhibits stable capacitances without fading after 500 cycles. The good cycle performances of GNS/PANI nanocomposite imply their stable energy–storage processes during long cycle charging/discharging. The electrochemical measurements show that the specific capacitance of the GNS/PANI nanocomposite maintained a stable specific capacitance of 230 F g^{-1} under specific current of 0.1 A g^{-1} for 500 cycles of charge/discharge.

To investigate the electrochemical performance of GNS/PANI nanocomposite as electrodes for supercapacitors, galvanostatic charge/discharge cycling measurements were performed. Fig. 5 shows the galvanostatic charge/discharge cycling curves for GNS/PANI nanocomposite at the current load of 0.02 A g^{-1}. From the well retained triangular-shaped curve, an apparent feature is that the electrode mainly exhibits a double–layer capacitor behavior resulted from the electrostatic attraction.

The galvanostatic charge/discharge curves of GNS/PANI nanocomposite at different specific currents are shown in Fig. 6. At 0.02 A g^{-1}, GNS/PANI nanocomposite electrodes show stable specific capacitances of 331 F g^{-1}. Higher specific capacitance values are obtained by GNS/PANI nanocomposite, which are in good accordance with its higher specific surface areas and the synergistic effect between GNS and PANI. As the specific current rises to 20 A g^{-1}, GNS/PANI electrodes show stable specific capacitances of 172 F g^{-1}, suggesting the high-rate cycle performance of GNS/PANI nanocomposite.

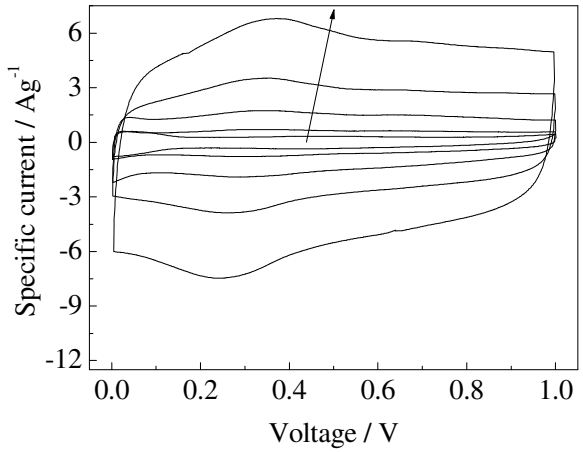


Fig. 3. Cyclic Voltammograms of GNS/PANI Electrodes at Different Sweep Rates (1, 2, 5, 10, 20 mV s−1, Direction of Arrow Shows that Sweep Rate Increases in Turn)

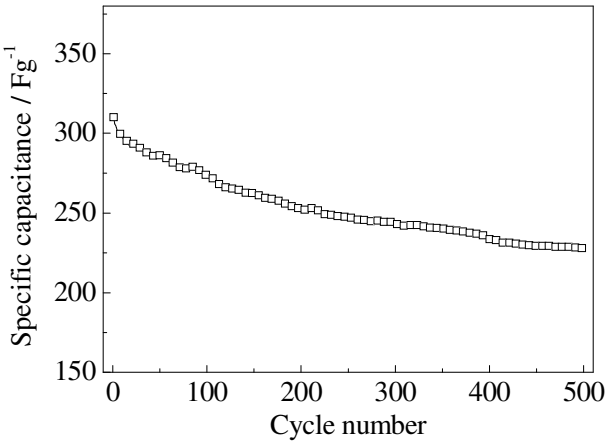


Fig. 4. The Capacitance Curve of GNSs under a Specific Current of 0.1 A g−1

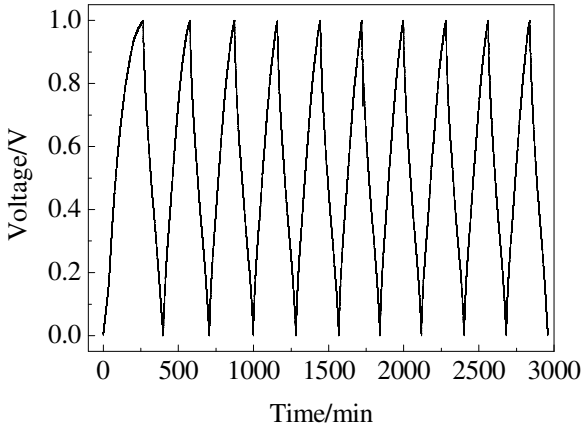


Fig. 5. Galvanostatic Charge/Discharge Cycling Curves for GNS/PANI at a Current Load of 0.02 A g -1.

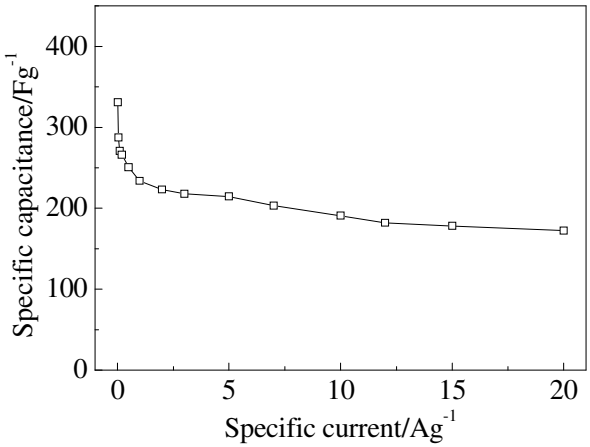


Fig. 6. The Specific Capacitances of GNS/PANI Electrodes at Various Specific Currents

Electrochemical impedance spectroscopy as a powerful technique was further employed to monitor the electrochemical behaviors of GNS/PANI nanocomposite electrodes. Impedance spectra for the electrodes are presented in Fig. 7a, where the real part (Z′) corresponds to the equivalent of ohmic resistance and the imaginary part (Z″) reflects the presence of non-resistive elements. The impedance behavior might be dominated by three major processes occurring in the high, medium and low frequency regions, respectively. The radius of semicircle in the high frequency region reflects the impedance on electrode/electrolyte interface. The slope of the 45° portion of the curve in medium frequency region is called the Warburg resistance and is a result of the frequency−dependent of ion diffusion/transport in the electrolyte. The radius of semicircle in GNS/PANI film is small, which indicates the polarization resistance of GNS/PANI nanocomposite is low. At low frequency the imaginary part of the impedance curves approaches a vertical line in GNS/PANI nanocomposite, indicating a capacitive−type behavior, in agreement with the CV results. Bode plots in Fig. 7b shows the frequency−dependent capacitance. A monotonous capacitance change is observed in the intermediate frequency region. GNS/PANI nanocomposite exhibits good frequency behavior in aqueous media, which coincide with the large volume of mesopores of GNS and the synergistic effect between GNS and PANI.

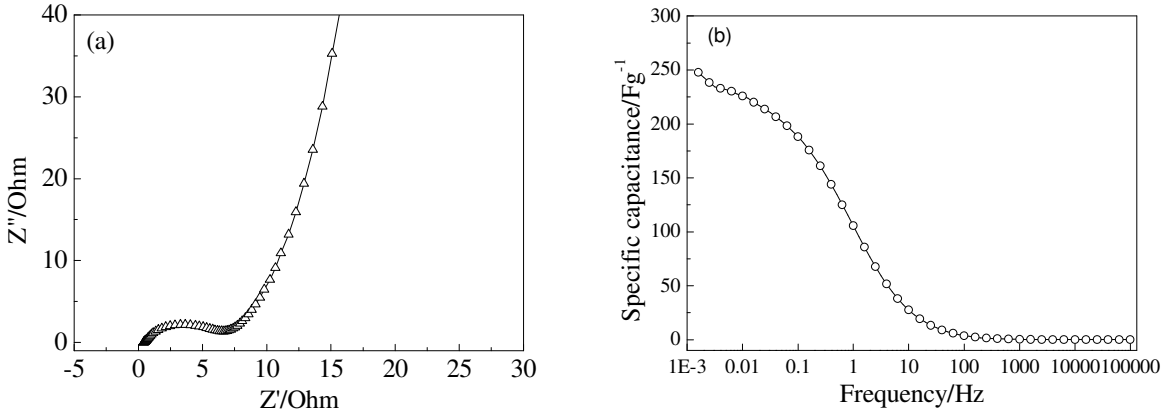


Fig. 7 Nyquist Impedance Plot for GNS Electrodes (a) and Frequency–dependent Capacitance Profile for GNS/PANI Electrodes (b).

Summary

The GNS/PANI nanocomposite was synthesized using in situ polymerization. The introduction of GNS in the nanocomposite provides high conductivity as well as a relatively large area on which to deposit the PANI, which could effectively reduce the kinetic difficulties for both charge transfer and ion transport throughout the electrode. GNS electrode maintained a stable specific capacitance of 230 F g^{-1} under specific current of 0.1 A g^{-1} for 500 cycles. The extraordinary electrochemical properties of the composites were attributed to the well designed structural advantages of binary nanocomposites and the good combination and synergistic effects between graphene and polyaniline.

References

[1] B.E. Conway and W.G. Pell: J. Solid State Electrochem. 7 (2003) 637-644.

[2] X. Du, P. Guo, H. Song and X. Chen: Electrochim. Acta 55 (2010) 4812-4819.

[3] A.G. Pandolfo and A.F. Hollenkamp: J. Power Sources 157 (2006) 11-27.

[4] A. Lewandowski and M. Galinski: J. Power Sources 173 (2007) 822-828.

[5] L. Li, H. Song and X. Chen: Electrochim. Acta 51 (2006) 5715-57-20.

[6] K.S. Novoselov, A.K. Geim, S.V. Morozov, D. Jiang, Y. Zhang, S.V. Dubonos, I.V. Grigorieva and A.A. Firsov: Science 306 (2004) 666-669.

[7] Z.-S. Wu, W. Ren, L. Gao, J. Zhao, Z. Chen, B. Liu, D. Tang, B. Yu, C. Jiang and H.-M.Cheng: ACS Nano 3 (2009) 411-417.

[8] O. Leenaerts, B. Partoens and F.M. Peeters: Microelectron. J. 40 (2009) 860-862.

[9] P. Guo, H. Song and X. Chen: Electrochem. Commun. 11 (2009) 1320-1324.

[10] C.N.R. Rao, K. Biswas, K.S. Subrahmanyam and A. Govindaraj: J. Mater. Chem. 19 (2009) 2457-2469.

[11] M.D. Stoller, S. Park, Y. Zhu, J. An and R.S. Ruoff: Nano Lett. 8 (2008) 3498-3502.

[12] K.S. Subrahmanyam, S.R.C. Vivekchand, A. Govindaraj and C.N.R. Rao: J. Mater. Chem. 18 (2008) 1517-1523.

[13] J. Yan, T. Wei, B. Shao, Z. Fan, W. Qian, M. Zhang and F. Wei: Carbon 48 (2010) 487-493.

[14] Y. Jin, S. Huang, M. Zhang, M. Jia: Synthetic Met. 168 (2013) 58-64.

[15] H. Cao, X. Zhou, Y. Zhang, L. Chen, Z. Liu: J. Power Sources 243 (2013) 715-720.

Advanced Materials Research Vol. 936 (2014) pp 369-373
© (2014) Trans Tech Publications, Switzerland
doi:10.4028/www.scientific.net/AMR.936.369

Graphene/Sulfur Nanocomposite for High Performance Lithium-Sulfur Batteries

Shao-Wu Ma[1, a], Dong-Lin Zhao[1, b], Ning-Na Yao[2, c] and Li Xu[2, d]

[1] Key Laboratory of Carbon Fiber and Functional Polymers (Beijing University of Chemical Technology), Ministry of Education, Beijing 100029, China

[2] State grid smart grid research institute, Beijing 102211, China

[a]email: masw_111@126.com, [b]email: dlzhao@mail.buct.edu.cn,

[c]email: yaoningna@sgri.sgcc.com.cn, [d]email: xuli@sgri.sgcc.com.cn

Keywords: Graphene, Sulfur, Nanocomposite, Lithium-sulfur batteries

Abstract: The graphene/sulfur nanocomposite has been synthesized by heating a mixture of graphene sheets and elemental sulfur. The morphology, structure and electrochemical performance of graphene/sulfur nanocomposite as cathode material for lithium-sulfur batteries were systematically investigated by field-emission scanning electron microscope, X-ray diffraction and a variety of electrochemical testing techniques. The graphene/sulfur nanocomposite cathodes display a high reversible capacity of 800-1200 mAh g^{-1}, and stable cycling for more than 100 deep cycles at 0.1 C. The graphene sheets have good conductivity and an extremely high surface area, and provide a robust electron transport network. The graphene network also accommodates the volume change of the electrode during the Li-S electrochemical reaction.

Introduction

Lithium–sulfur batteries have been studied as one of the most promising systems for the next generation high-energy rechargeable lithium batteries because of their high theoretical specific capacity (~1680 mAh g^{-1}) and energy density (2600 Wh kg^{-1}) [1, 2]. Other advantages are that elemental sulfur is low cost, has low toxicity, and is an abundant resource. However, the practical application of lithium–sulfur batteries is greatly hampered by two major challenges including (i) high solubility of the reaction polysulfide products, which can shuttle between the anode and cathode, forming deposits of solid Li_2S_2 and Li_2S on the cathode, causing loss of the active material, which leads to low Coulombic efficiency, low utilization of the sulfur cathode, and a severe degradation of cycle life, and (ii) the low electrical conductivity of sulfur, the intermediate polysulfide products, and the final Li_2S, affecting the reaction rate of the battery [3-6].

Extensive studies have been carried out to improve the electrical conductivity of the sulfur electrode and to confine the sulfur and polysulfides in a carbon matrix. For example, ordered mesoporous carbon, hierarchical porous carbon, microporous carbon spheres, hollow carbon spheres, carbon nanotubes/nanofibers and graphene have been investigated as the confining/conductive medium and have shown improved cyclic stability. Among these carbonaceous materials, graphene has opened new possibilities and is promising as a two-dimensional conductive support because of its high electrical conductivity, superior mechanical flexibility, high surface functionality, and large surface area [3, 7-11]

In this work, we synthesized sulfur-coated graphene nanocomposite and investigated graphene sheets as a carbon matrix to improve the performance of sulfur cathodes for rechargeable lithium sulfur batteries, the electrochemical performances of the graphene/sulfur nanocomposite were investigated by a variety of electrochemical testing techniques on the basis of the morphology and structure of the graphene/sulfur nanocomposite.

Materials and Methods

The graphene sheets were synthesized by a modified Hummers' method through three steps: the oxidation of flake natural graphite powder, rapid heat treatment and ultrasonication [12]. In the experimental process, $KMnO_4$ was employed as the oxidant to obtain graphite oxide. Firstly, 1.5 g of sodium nitrate was added to 69 ml of cooled (0 ºC) concentrated H_2SO_4. Then 3 g of flake natural graphite with the mean diameter of 15 μm (provided by Dong Xing Electrical Carbon Co., Ltd. China) was added gradually under stirring for 15 min. At the same time, the temperature of the mixture was maintained below 10 ºC. Then 9.0 g $KMnO_4$ was added slowly to the solution and stirred for 20 min below 20 ºC. In the following 10 min, the experimental temperature was heated up to 35 ºC and kept for 1 h. Then 138 ml of distilled water was slowly added to cause an increase in temperature to 98 ºC and the mixture was maintained at that temperature for 15 min. The reaction was terminated by adding 420 ml of distilled water followed by 30 ml of 30% H_2O_2 solution. The solid product was separated by centrifugation, washed repeatedly with 5% HCl solution until sulphate could not be detected with $BaCl_2$, and then the resultant graphite oxide was dried at 65 ºC overnight. The graphite oxide was quickly sent to a muffle furnace pre-heated to 1050 ºC in the air atmosphere to obtain expanded graphite. The expanded graphite was dispersed into ethanol and delaminated into graphene sheets under a 600 W ultrasonic agitation for 15 h. The desired graphene sheets were obtained after vacuum drying. The graphene sheets were mixed with elemental sulfur S in the weight ratio of 1:1. Then, the mixture was held at 200 ºC for 6 h to allow the melted elemental sulfur to infiltrate into the layer of graphene. The temperature was increased to and held at 300 ºC for 3h, so that the vaporized sulfur was coated onto the graphene.

The morphologies and structures of graphene/sulfur nanocomposite were observed by field-emission scanning electron microscope (FESEM, Hitachi S-4700) and X-ray diffraction (XRD) analysis was conducted on a Rigaku D/max-2500B2+/PCX system using Cu/Kα radiation (λ =1.5406 Å).

The working electrodes were prepared as following: graphene/sulfur nanocomposite, acetylene black and poly(vinylidene fluoride) binder at the weight ratio of 80:10:10 were homogenously mixed and pasted on an aluminium foil, then dried at 80 °C for 10 h in a vacuum oven. The foil was pressed between twin rollers, shaped into a circular pellet with a diameter of 12 mm, and used as a cathode. The electrolyte was 1.0 M lithium bis-trifluoromethanesulfonylimide in 1,3-dioxolane and 1,2-dimethoxyethane (1:1 by volume) with 0.5 wt % $LiNO_3$ additive. A 2032 type stainless steel coin cell was used to assemble a test cell. A lithium metal foil was used as the anode, and a graphene/sulfur slice as the cathode. The Celgard 2325 microporous polypropylene film was used as separator. Electrochemical properties of the coin type cells were galvanostatically charged and discharged in the voltage range of 1.3-3.0 V vs. Li/Li^+ using LANDCT2001A. Cyclic voltammetry curves were measured at 0.1 mV s^{-1} within the range of 1.5-2.8 V using an electrochemical work station (VersaSTAT3). Electrochemical impedance studies of the coin cells were performed using an electrochemical work station (VersaSTAT3) by applying sine wave with amplitude of 10.0 mV in the frequency range of 100 kHz to 0.01 Hz.

Results and Discussion

The morphology and structure of graphene sheets and graphene/sulfur nanocomposite were characterized by FESEM and their images are shown in Fig. 1. Fig. 1a exhibits the SEM image image of graphene sheet agglomerate, consisting of almost transparent carbon nanosheets with thin wrinkled structure. The graphene sheets are entangled with each other and resemble crumpled papers. Moreover, the thin wrinkled structure represents a curled and corrugated structure that the graphene owns intrinsically. Fig. 1b exhibits the SEM image image of graphene/sulfur nanocomposite. After heat treatment of the mixture of S and graphene sheets, the microsized S particles were melted and covered the graphene nanosheets. The embedded sulfur exists in fine particles and a highly dispersed state, with the crystalline sulfur most likely converted to amorphous sulfur by the heat treatment. When the mixture of sulfur and graphene was thermally treated at 200

ºC, sulfur would be expected to melt and coat the graphene sheets. At the higher temperature of 300 ºC, sulfur existing on the external surface of the graphene sheets was sublimed. At the same time, sulfur gas could also diffuse into the pores of graphene [6]. Fig. 2 exhibits the XRD patterns of graphene, graphene/sulfur nanocomposite and sulfur.

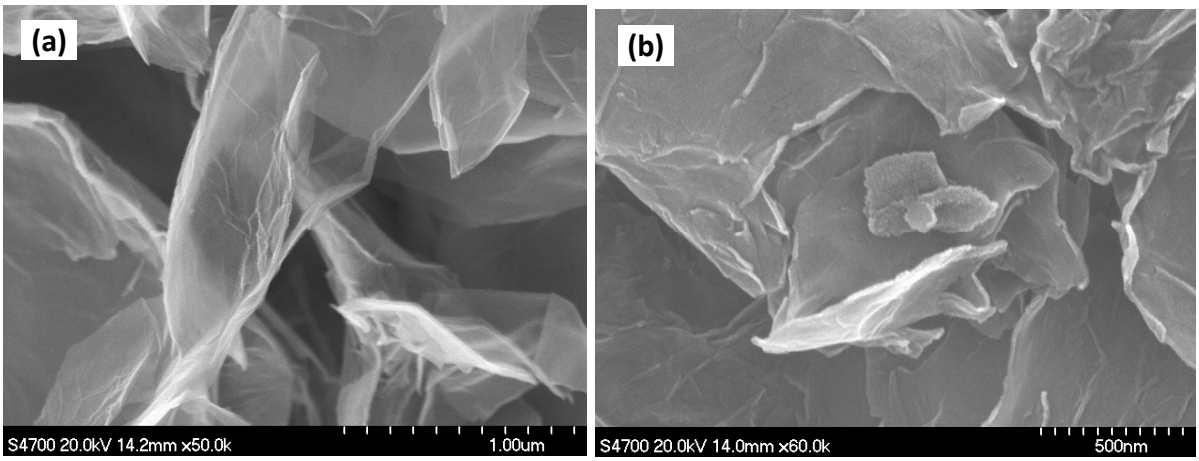


Fig. 1 SEM images of graphene (a) and graphene/sulfur nanocomposite (b).

Cyclic voltammetry (CV) was used to reveal the electrochemical reaction mechanism of the graphene/sulfur cathode measured between 1.5 and 2.8 V at a sweep rate of 0.1 mV s^{-1}, as shown in Fig. 3. During the first cathodic reduction process, three peaks at approximately 2.3, 2.0, and 1.8 V (vs Li/Li^+) were observed. The peak at 2.3 V corresponds to the reduction of sulfur to higher order polysulfides (Li_2Sx, $4<x<8$) [5]. The peaks at 2.0 and 1.8 V are related to the reduction of higher-order polysulfides to lower-order polysulfides (such as Li_2S_4, Li_2S_3, Li_2S_2) and Li_2S [3, 7]. In the subsequent anodic scan, one asymmetric oxidation peak (which can be divided into two peaks) is observed at about 2.5 V and is attributed to the conversion of lithium sulfides to polysulfides and sulfur. These results are in agreement with galvanostatic charge/discharge curves (Fig. 4) and similar to other reports [3]. From the second cycle, both the CV peak positions and areas remain almost unchanged, suggesting relatively good capacity retention.

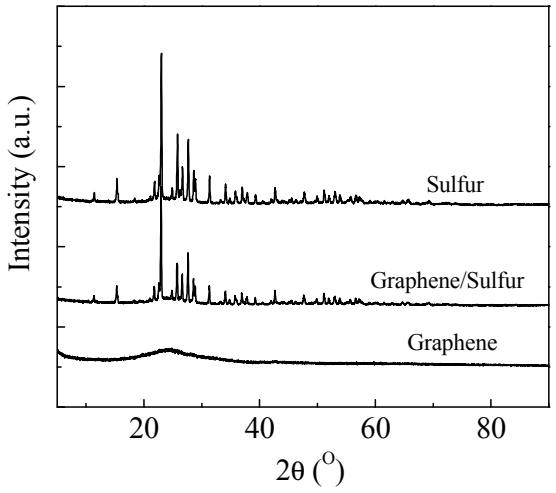


Fig. 2. XRD patterns of graphene sheets, graphene/sulfur nanocomposite and sulfur.

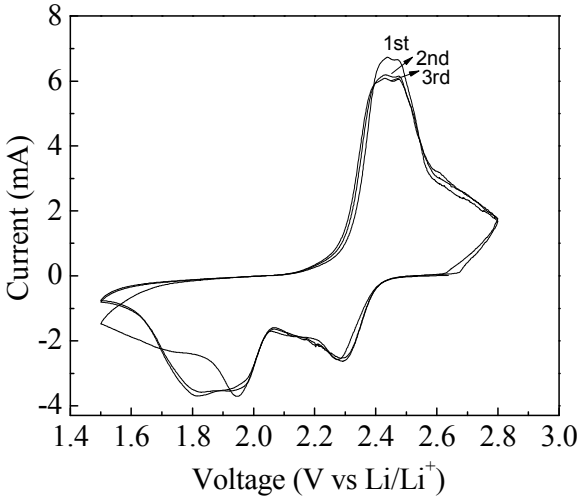


Fig. 3 CVs of the graphene/sulfur cathode at 0.1 mV s^{-1} in a potential window from 1.5 to 2.8 V vs Li/Li^+.

The electrochemical performance of the graphene/sulfur cathode electrode was examined by galvanostatic measurements. Fig.4 depicts the galvanostatic charge/discharge profiles of the graphene/sulfur cathode electrode at a current density of 0.1 C (1C=1675 mA g^{-1}) and the voltage rang 1.3-3.0 V, respectively. In the first cycle, an initial reversible discharge capacity of 1210 mA h g^{-1} is achieved. The characteristic voltage profiles are preserved during cycling, while a specific

capacity of 1189 and 1184 mA h g^{-1} is retained in the second and third cycle respectively, which indicates the good reversibility of the electrode materials. Fig. 5 shows charge/discharge capacity versus cycle number for cells made with the sulfur and graphene/sulfur electrodes. The initial capacity of the graphene/sulfur electrode is much higher than that of the pure sulfur electrode. Furthermore, the cycling stability of the graphene/sulfur nanocomposite is also improved. After more than 100 cycles at the same rate, the reversible capacity remains at 814 mAh g^{-1} (with a coulombic efficiency of about 97.8%), indicating very stable reversibility of the electrochemical reactions and excellent capacity retention. The graphene/sulfur electrode displays improved coulombic efficiencies compared to the pure sulfur electrode (Fig. 6). The improvement in the capacity and cycling stability of the cell with the graphene/sulfur nanocomposite electrode may be because the graphene in the nanocomposite can improve the conductivity of the electrode.

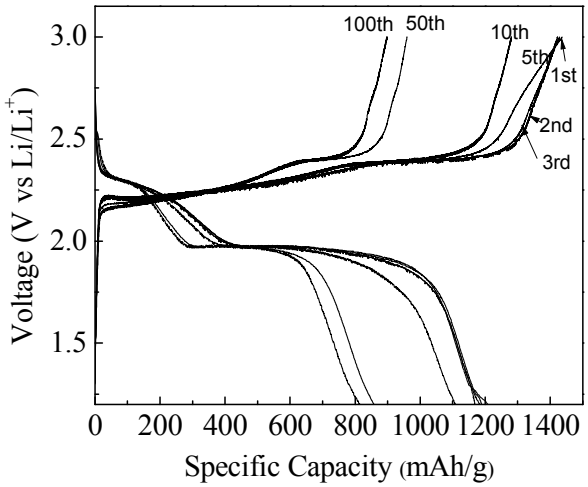


Fig. 4 Galvanostatic charge/discharge curves of graphene/sulfur cathode at 0.1 C.

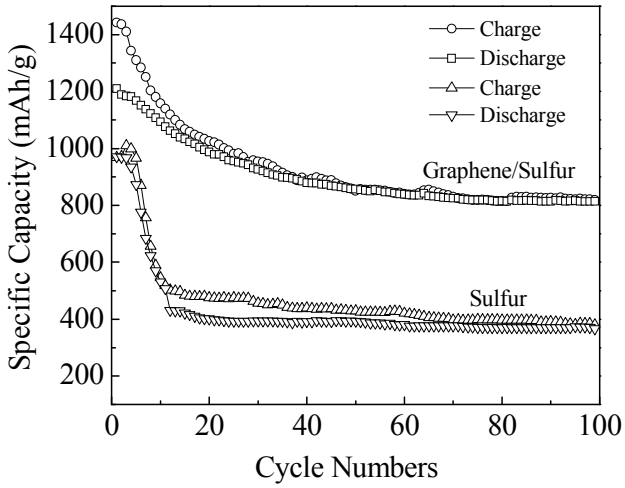


Fig. 5 Cyclic performance of graphene- sulfur cathode at 0.1 C for 100 cycles.

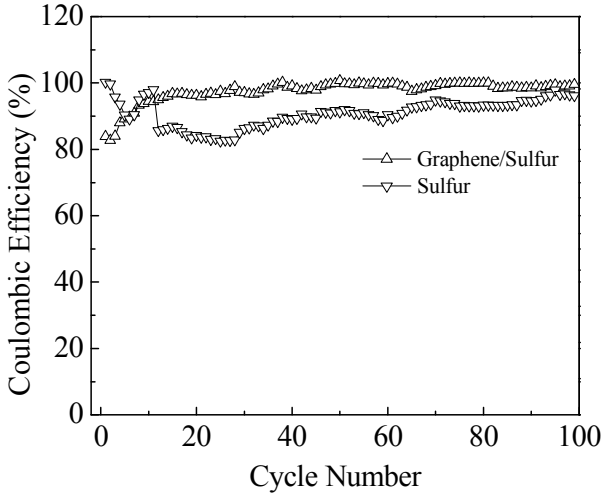


Fig. 6 Coulombic efficiency of sulfur and graphene/ sulfur cathode at 0.1C for 100 cycles.

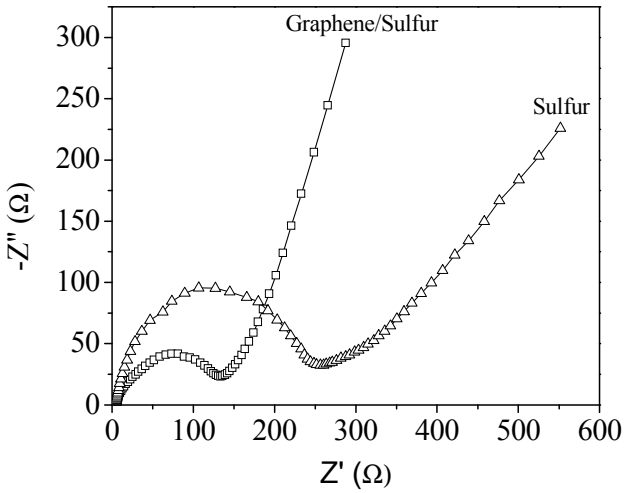


Fig. 7 Impedance plots for electrodes of sulfur and graphene/sulfur nanocomposite.

In order to verify that the graphene is responsible for the good performance of the cell with the graphene/sulfur electrode, electrochemical impedance spectroscopy measurements were performed on the pure sulfur and graphene/sulfur electrodes. Impedance spectra for the electrodes are presented in Fig. 7, where the real part (Z′) corresponds to the equivalent of ohmic resistance and the imaginary part (Z″) reflects the presence of non-resistive elements. The impedance behavior might be dominated by three major processes occurring in the high, medium and low frequency

regions, respectively. The radius of semicircle in the high frequency region reflects the impedance on electrode/electrolyte interface. The slope of the 45º portion of the curve in medium frequency region is called the Warburg resistance and is a result of the frequency−dependent of ion diffusion/transport in the electrolyte. At high frequencies, the impedance response exhibits a semicircular loop. The diameter of this semicircle gives the charge-transfer resistance, which is a measure of the charge transfer kinetics. The results show that the charge-transfer resistance of the cell with graphene/sulfur electrode is lower than for the cell made from pure sulfur electrode. This indicates that the nanocomposite of sulfur with graphene can improve the electrochemical kinetics of the sulfur in rechargeable lithium batteries.

Summary

In summary, the graphene/sulfur nanocomposite was synthesized by heating a mixture of elemental sulfur and graphene sheets. The graphene/sulfur nanocomposite shows a significantly improved capacity and cycle life compared to the bare sulfur electrode. The unique structure of the graphene/sulfur nanocomposite can improve the overall electrochemical performance when it is used as a cathode material for lithium-sulfur batteries. It can accommodate the significant volume changes of S as it is converted to Li_2S on discharge, and back to elemental S on recharge. In addition, the graphene with its large surface area along with ubiquitous cavities can establish more intimate electronic contact with S and avoid aggregation and loss of electrical contact with the current collector.

References

[1] N. Li, M. Zheng, H. Lu, Z. Hu, C. Shen, X. Chang, G. Ji, J. Cao and Y. Shi: Chem. Commun. 48 (2012) 4106-4108.
[2] R. Dominko, R.D. Cakan, M. Morcrette and J. M. Tarascon: Electrochem. Commun. 13 (2011) 117-120.
[3] G. Zhou, L.C. Yin, D.W. Wang, L. Li, S. Pe, I. R. Gentle, F. Li, and H.M. Cheng: ACS Nano 7 (2013) 53676-5375.
[4] X. Ji and L. F. Narzar: J. Mater. Chem. 20 (2010) 9821-9826.
[5] L.F. Xiao, Y. L. Cao, J. Xiao, B. Schwenzer, M.H. Engelhard, L.V. Saraf, Z.M. Nie, G.J. Exarhos, J. Liu: Adv. Mater. 24 (2012) 1176-1181.
[6] J.Z. Wang, L. Lu, M. Choucair, J.A. Stride, X. Xu, and H.K. Liu: J. Power Sources 196 (2011) 7030-7034.
[7] G.M. Zhou, D.W. Wang, F. Li, P.X. Hou, L. Yin, C. Liu, G.Q. Lu, I. R. Gentle and H.M. Cheng, Energy Environ. Sci. 5 (2012) 8901-8906.
[8] X.L. Ji, K.T. Lee and L.F. Nazar: Nat. Mater. 8 (2009) 500-506.
[9] J. Schuster, G. He, B. Mandlmeier, T. Yim, K.T. Lee, T. Bein and L.F. Nazar: Angew. Chem. Int. Ed. 51 (2012) 3591-3595.
[10] M.Q. Zhao, X.F. Liu, Q. Zhang, G.L. Tian, J.Q. Huang, W. Zhu and F. Wei: ACS Nano 6 (2012) 10759-10769.
[11] J.Q. Huang, X.F. Liu, Q. Zhang, C.M. Chen, M.Q. Zhao, S.M. Zhang, W. Zhu, W.Z. Qian and F. Wei: Nano Energy 2 (2013) 314-321.
[12] L. Z. Bai, D.L. Zhao, Z.T. Zhang, W.G. Xie and J.M. Zhang: Electrochim. Acta 107 (2013) 555-561.

Advanced Materials Research Vol. 936 (2014) pp 374-378
© (2014) Trans Tech Publications, Switzerland
doi:10.4028/www.scientific.net/AMR.936.374

Preparation And Characterization Of Magnesium Oxide Aerogels

Jiawen Wu[1,a], Lanfang Yao[1*,b], Jun Shen[2,c], Guoqing Zu[2,d], Fang Wang[1,e]

[1] College of science, University of Shanghai for Science and Technology, Shanghai 200093, china

[2] Shanghai key laboratory of special artifical microstructure materials and technology, pohl institute of solid state physics, tongji university, shanghai 200092, China.

[a]reassure@live.cn, [b]yao_lanfang@126.com, [c] shenjun67@tongji.edu.cn, [d]zuguoqing863@gmail.com, [e]407356153@qq.com

[*] Corresponding author: Yao Lanfang, Assoc. Prof ; Ph D; Email: yao_lanfang@126.com

Keywords: magnesium oxide, aerogel, sol-gel.

Abstract: Magnesium-based aerogels were prepared by sol-gel technology and drying with supercritical fluid dry process in 245℃. The structure and properties of the magnesium-based aerogels were featured by TEM, XRD and BET. The densities of the prepared samples were about 0.34~0.59 g/m^3. The results show that the MgO aerogel has a high surface area.

Introduction

The extraordinary properties of aerogels including high surface areas, low refractive indices, low dielectric constants, low thermal loss coefficients and low sound velocities lead to potential applications such as: ultra-low dielectric constant interlayer dielectrics, sensors, and acoustic impedance matching.

The most outstanding feature of nano-sized MgO aerogel and other aerogel-prepared nanocrystalline metal oxides is their high efficiency in chemisorption of such toxic gases as NO_2, SO_2 , SO_3 , HCl, as well as chlorinated and phosphorous-containing compound. The interaction of such gases with the surface of the nanoparticles is referred to as destructive sorption as both the surface and the bulk chemical composition of the oxides are often subjected to significant changes during this process [1].MgO, an insulator, is traditionally used for the preparation of cement, medicines, insulators, desiccants, and optical materials. In recent decades, people have given attention to the synthesis of MgO nanomaterials with different morphologies—nanoparticles, nanotubes, and nanorods—which have been investigated for different purposes; MgO nanomaterials have been investigated as catalysts, adsorbents, and destructive adsorbents for toxins, including chemical warfare agents [2].

Method of precipitation is the most used technique to prepared Nano-sized MgO. Although Method of precipitation has a few merits such as cheap materials resource, simple process, the product of MgO powder's diameter was big and would distribute in a big range. Compared to the precipitation method, the sol-gel method could prepare MgO powder with tiny diameter and narrow the diameter distribution range.

There is considerable interest in the synthesis of nanoscale MgO and magnesium hydroxide $Mg(OH)_2$ particles via the magnesium alkoxide $Mg(OR)_2$ route. Generally, an alkoxide is hydrolyzed in an alcohol solvent to yield the hydroxide, which is followed by isolation and thermal dehydration. A modified autoclave hypercritical drying procedure has been developed to prepare nanoscale MgO particles. These nanoscale materials exhibit unusual surface chemistry and catalytic

properties and, compared to other MgO samples, are more chemically reactive. They have been extensively studied as destructive adsorbents for a variety of toxic substances [3].

There are many reports about the preparation and properties of silica aerogels and carbon aerogels etc. However, there are relatively few reports about the preparation and characterization of magnesium oxide aerogels though the MgO aerogel have a plenty of great applications.

To prepare MgO aerogel which was made by sol-gel technology, methanol as solvent, water and magnesium methoxide were used in the experiment. Drying it with supercritical process in autoclave 245℃. Then Calcined at 500℃. It has a huge potential of application that could be found in further study.

Experimental

Preparation

$Mg(OCH_3)_2$ solution was prepared by the process as follows. First, immersing the Mg ribbon into the diluted hydrochloric acid to remove the MgO on the Mg ribbon's surface. Then, the treated Mg ribbon was dissolved in methanol to give $Mg(OCH_3)_2$.

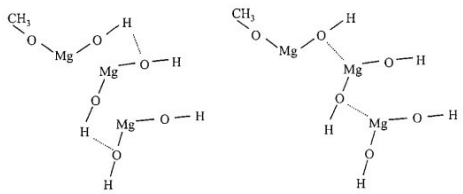
$$Mg+CH_3OH \rightarrow Mg(OCH_3)_2+H_2 \quad (1)$$

The wet gels were prepared according to the following to the following steps. Appropriate amount of water and methanol were mixed in a beaker in 10 minutes. Then added the designed amount of $Mg(OCH_3)$ solution into the water-methanol solvent very quickly. The typical mole ratios were $Mg(OCH_3)_2:H_2O:CH_3OH=1:2:32$ and other ratios were tried too. The mixture would become transparent wet gel in less then 1minute.

$$Mg(OCH_3)_2+2H_2O \rightarrow Mg(OH)_2+2CH_3OH \quad (2)$$

The wet gels were conventionally aged for 48 hours followed by washing with methanol for 4 times (each 12 hours). To obtain dried gels, the nature evaporation process is unacceptable. Because it will destroy $Mg(OH)_2$ aerogel's porous structure. The wet gel was dried under a supercritical condition using ethanol as the drying agent.

To fit the required condition, the wet gel was placed in an autoclave that partially filled with ethanol and sealed. The ultra pure, dry nitrogen gas was flushed in the autoclave to have the oxygen free atmosphere and for safety precautions. Rising the temperature to 245℃ at the rate of 2℃/min while the pressure rose and was controlled at about 10MPa. When temperature reached the target limit, the autoclave was decompressed slowly at a rate of 40kPa/min. Finally, the system was cooled down to room temperature naturally and the aerogel was taken out. Then the samples were heated to 500℃ in Muffle furnace.



(1)hydrogen bonding (2)Mg-O bonding

Fig 1 Structure of interconnected gel molecules

Characterization

The bulk of density of the aerogels were determined by grinding the aerogel into powder and filling a small square container to measure its volume and mass. The nature of phases at the aerogels was analyzed by powder X-ray diffraction (XRD) in a Rigata/max-C diffractometer using the Cu-Kα radiation. The microstructures of the samples were characterized by a transmission election microscope (TEM). The pore size distribution and specific surface area of sample were tested by a N_2 adsorption analyzer (TriStar 3000, USA).

Result and Discussion

The combinations of $Mg(OCH_3)_2$ and H_2O happened in really short time . The longest gelling time was less than 10 seconds. In all cases, hydrolysis resulted in the formation of totally clear gels. The reason of gel that were turned to brown after supercritical drying process was that there were plenty of carbonaceous residuals linked to the network structure of the MgO aerogel. It shrunk more then 40% and turned into white and opaque after 500℃ heat treatment for 4 hour. The dried magnesium aerogel was transparent with the density about 0.34 to 0.59g/m^3.

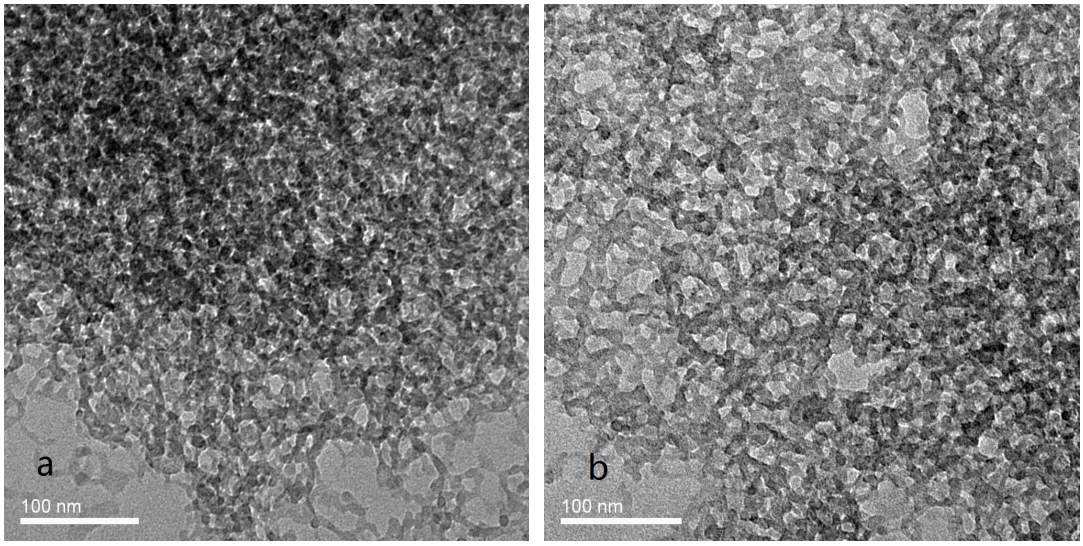


Fig 2 (a) The sample after supercritical drying process (b) sample calcined at 500℃

The TEM photographs of original and heated samples are showed in Fig 2. The micrographs suggest the existence of a polymer network which appears under the microscope as a multitude of thin strands to give a porous web-like matrix. It shows that the magnesium aerogel exhibits randomly interconnected networks consist of nanometer-sized fibrous particles with varying diameters ranging from 20 to 30nm. After 500℃ heat treatment by 4 hours, the magnesium aerogel remains its interconnected network structure. To get more information on the hydrolysis products, the wet gel was dried according to the previously mentioned drying procedure.

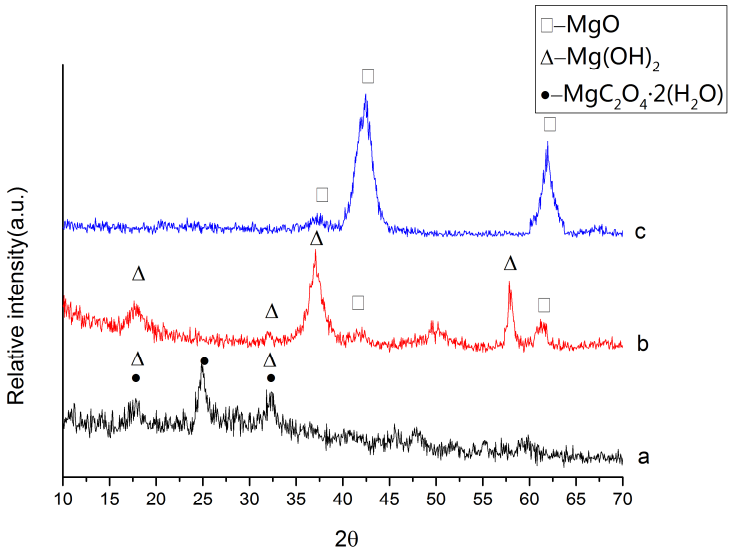


Fig 3. XRD sample of (a) the aerogel before calcination (b) aerogel calcined at 500℃ by 1hour (c) aerogel calcined at 500℃ by 4 hours

Figure 3 illustrates the XRD pattern of the dried gel and calcined gels respectively. From the Fig 3(a) the diffraction peak are largely fit the magnesium oxalate dihydrate and magnesium hydroxide ($Mg(OH)_2$) (JCPDS 86-0441) phase, it indicates that magnesium oxalate dehydrate and magnesium hydroxide are present in large amounts the aerogel before calcination. After 1 hour 500℃ heat treatment, the diffraction peaks which were showed in Fig 3(b) inferred that magnesium hydroxide and magnesium oxide's existence and the phase of magnesium oxalate dihydrate was dissapper. It prove that magnesium oxalate dehydrate was broke into magnesium hydroxide and magnesium oxide. After 4 hour heat treatment the XRD pattern from Fig 3(c) demonstrated that all the diffraction peaks of the samples were entirely consistent with the periclase structure (JCPDS 87-0653) which means that the rest of $Mg(OH)_2$ has been removed totally and there is magnesium oxide in aerogel calcined at 500℃ by 4hour .

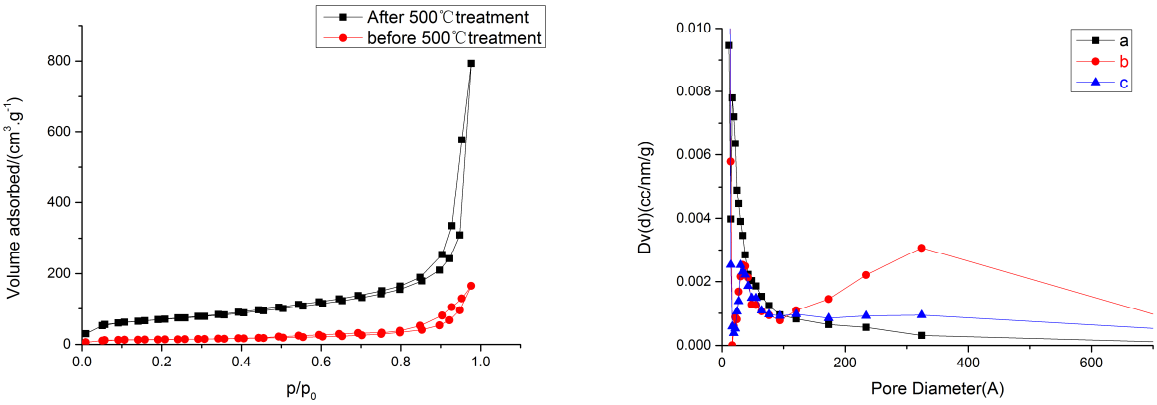


Fig 4. (A)N2 adsorption-desorption isotherms and (B)Pore size distribution for the samples (a) mole ratio Mg(OCH3)2:CH3OH=1:32 (b) Mg(OCH3)2:CH3OH=1:48 (c) Mg(OCH3)2:CH3OH=1:64

N_2 adsorption-desorption isotherms provide information about the microstructure of MgO aerogels before and after 500℃ hour heat treatment by 4hour. According to the IUPAC classification[4], the adsorption isotherms exhibit the H3 hysteresis loop to both MgO aerogels that before and after 500℃ heat treatment by 4hour, it inferred that the MgO aerogel is a fractured nanoporous magnesium material and has mesoporous structure and large pore size distribution. The

corresponding pore-size distributions were given in Fig 4(B), It's specific areas of the magnesium oxide aerogel are about to 220~291m^2/g. The main pore size are concentrated on the 30nm which are in good agreement with the trends discussed above. In those three sample, sample (b) has the most high surface areas 291 m^2/g. It means $Mg(OCH_3)_2$:CH_3OH=1:48 would be the best stoichiometry probably.

Conclusions

Magnesium aerogels were prepared by sol-gel method with the ethanol supercritical drying technique. This method afforded high surface area and transparent magnesium aerogel without the use of dangerous and complex agents. The aerogel possessed a web-like network microstructure consist with a high surface area of 291m^2/g. Since the technique of making magnesium aerogel was rarely reported, it has a huge potential of application that could be found in further study.

The project was supported by the National key Technology R&D Program of China (2013BAJ01B01), National Natural Science Foundation of China (U1230113), 863 Program of Ministry of Science and Technology of China, Shanghai Committee of Science and Technology (11nm0501600，12nm0503001) and Fundamental Research Funds for the Central Universities.

References

[1] Ryan M. Richards, Alexander M. Volodin, Alexander F. Bedilo and Kenneth J. Klabunde, ESR study of nanocrystalline aerogel-prepared magnesium oxide, Phys. Chem. Chem. Phys., 2003, 5, 4299–4305

[2] Khadga M. Shrestha, Christopher M. Sorensen, Kenneth J. Klabunde, MgO–TiO2 mixed oxide nanoparticles: Comparison of flame synthesis versus aerogel method J. Mater. Res., 2013, 28, (3), 431- 439

[3] Yulu Diao, Walter P. Walawender, Christopher M. Sorensen, Kenneth J. Klabunde, and Thomas Ricker, Hydrolysis of Magnesium Methoxide. Effects of Toluene on Gel Structure and Gel Chemistry, Chem. Mater. 2002, 14, 362-368

[4] Sing, K.S.W.; Everett, D. H.; Haul, R.A.W.; Moscou, L.; Pierotti, R.A.; ROUQUEROL, J.; Siemieniewska, T. Pure Appl. Chem. 1985, 57, 603.

Advanced Materials Research Vol. 936 (2014) pp 379-383
© (2014) Trans Tech Publications, Switzerland
doi:10.4028/www.scientific.net/AMR.936.379

Enhanced Field Emission Characteristics of ZnS Dentalation Nanostructures

Junjie Qi[a], Zhanqiang Deng[b], Zhao Wu[c], Yue Zhang[d]

School of Materials Science and Engineering, University of Science and Technology Beijing, Beijing 100083, P. R. China

[a]junjieqi@ustb.edu.cn, [b]dengzq@126.com, [c]wz2007340218@163.com, [d]yuezhang@ustb.edu.cn

Keywords: ZnS, Nanomaterials, Microstructure, Field emission

Abstract: Large quantities of ZnS dentalation nanostructures were synthesized successfully at low temperature using a simple chemical vapor deposition method, and the microstructures and field emission properties of the dentalation structures were investigated. The results indicated that the stem of the dentalation structures is single-crystalline but the surfaces of the teeth are amorphous. The photoluminescence properties show a strong green emission at 520.89 nm due to S vacancy. Investigations on the field emission properties of the ZnS dentalation nanostructures imply that the turn-on field is about 5.56V/μm at an anode-cathode distance of 150μm, which should be attributed to the specific sharp tips and high aspect ratios of the present needle-shaped structure. The field emission behavior of the ZnS obeys Fowler-Nordheim relationship. The results could be valuable for using the ZnS nanostructure as cold-cathode field-emission materials.

Introduction

With a direct wide bandgap of 3.7~3.9 eV, which is higher than that of ZnO (3.37 eV), GaN (3.39 eV), and 4H-SiC (3.27 eV), ZnS is one of the most important II-VI semiconductors compounds, and exhibits the luminescence of short wave centered near 337 nm. Compared with the room-temperature thermal energy (25 eV), ZnS exhibits significantly large exciton binding of 40 eV, which makes the exciton's threshold much lower, so ZnS is an excellent candidate for efficient room-temperature exciton short-wave devices[1]. Latest achievements have shown ZnS has remarkable fundamental properties versatility and a promise for novel diverse applications [2-5], including field emitters, field effect transistors (FETs), light-emitting diodes (LEDs), UV-light and chemical sensors and biosensors, etc.

Although the structure and most properties of ZnS are comparable to more popular and widely known ZnO, certain properties pertaining to ZnS are unique and advantageous. However, the nanostructures of ZnS have not been investigated in much detail relative to ZnO nanostructures. Recently various morphologies of ZnS nanostructures have been fabricated while the ZnS dentalation nanostructures have been reported rarely[6-12], and the fabrication temperature of one-dimensional ZnS nanostructures is usually very high. Moore et al succeeded in the synthesis of nanoteeth-shaped ZnS by direct evaporation of ZnS powder at relatively high temperature of 1000℃[13-14].

With respect to field emission applications, it is also well known that the needle-shaped tips can significantly enhance the material field emission properties. The synthesis of microstructures with sharp tips is always the center of field emission research and application. In recent years, much attention has been paid to explore the prospects of inorganic semiconductor nanostructures including CNTs, ZnO, SiC etc, as field emitters due to their low work functions, high aspect ratios,

high mechanical stability, and high conductivity [15-19]. But few studies on the field emission properties of ZnS nanostructures has been reported [20,21], and it is still a question whether it is possible to make excellent field emitters out of various ZnS nanostructures by some facile routes. Chang et al investigated the field emission property of ZnS nanowire but a relatively high turn-on field of 12V/μm was achieved [22].

In this letter, Compared with the traditional thermal evaporation techniques (above 1000℃), ZnS dentalation nanostructures have been synthesized in a large scale by simple thermal evaporation method at lower temperature (800℃) with Au as catalyst, the microstructure and the field emission property of the product have been analyzed.

Experimental Section

The ZnS nanowires were synthesized by hydrogen-assistant thermal evaporation method through the direct reaction of Zn vapor with S vapor in a furnace with a horizontal quartz tube. First, Zn powder and S powder with the molar ratio of Zn : S= 1:2 were thoroughly grinded into a mixture before being loaded into a quartz boat. Then, the Si substrate with 10 nm Au catalyst with the polished side facing powder was fixed upon the boat, and the boat with the mixture was placed at the center of the furnace. A carrier gas of high-purity argon premixed with 3% hydrogen was kept flowing through the tube at a high flow rate (>400 sccm) (standard cubic centimeters per minute) for 1 h. The process was carried out at 800°C for 1 h with Ar flow rate of 50 sccm. After the reaction was completed, the product was collected from the Si substrate.

The morphologies and structures of the synthesized product were characterized using X-ray diffraction (XRD) (Rigaku DMAX-RB, Japan), field emission scanning electron microscopy (FESEM) (LEO1530, Japan), high-resolution transmission electron microscopy (HRTEM) (JEOL-2010, Japan), and energy dispersive x-ray spectroscopy (EDS). Photoluminescence (PL) measurements (HORIBA Jobin Yvon，labRAM HR) were performed at room temperature using a He-Cd laser line of 325 nm as the excitation source. The measurements of field emission characteristics of the products were carried out in a vacuum chamber maintained at a base pressure of ~10^{-5}Pa. A keithley 2410 sourcemeter was used for performing I-V measurements. DC voltages were employed between the flat anode and cathode in the examination of the emission process.

Results and Discussion

A typical SEM and XRD patterns of the as-grown ZnS nanostructures are shown in Figure 1. Figure 1(a) shows the SEM micrographs of the as-prepared nanostructures. The stem of the ZnS dentalation nanostructres is straight nanorod with smooth surface, and the diameter is about 50~200nm. The cone-shaped teeth of the nanostructure with the tip diameter of 10~30nm grow perpendicular to the stem. All main diffraction peaks in Figure 1(b) can be perfectly indexed to the hexagonal wurtzite structure of ZnS (JCPDS，No.75-1534) with lattice constants corresponding to a=b=3.242 Å and c=5.194 Å, and no other peaks were clearly detected.

TEM analysis was employed to further confirm the microstructure of nanostructures. Figure 2(a) shows the enlarged TEM micrographs of the as-prepared dentalation nanostructrues. The HRTEM image (Figure 2(b)) of the stem shows clear lattice fringes, which confirm the single-crystalline nature and the corresponding SAED patterns demonstrate that the stem could be indexed to a hexagonal structure growing along $[10\bar{1}0]$ direction. Figure 2(c) displays the HRTEM micrographs

and the corresponding SAED patterns of the teeth of the dentalation nanostructrues, indicating that the teeth is not fully crystallized but showing a polycrystalline morphology, and the surfaces of the teeth are covered by a layer of amorphous. This may be related to the reaction time. The EDS spectra (Figure 2(d)) imply that Zn and S are major elements, Cu comes from the Cu grid, no other elements were found in the microstructure.

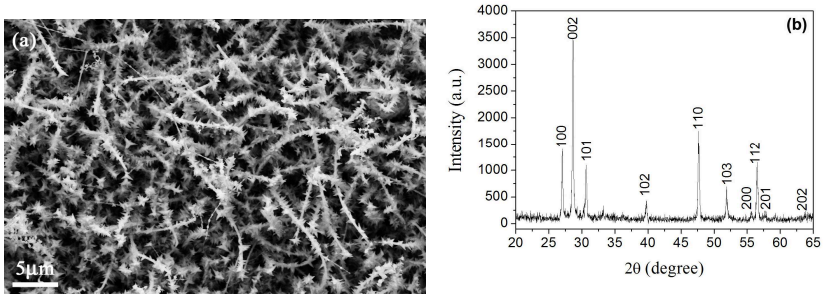


Fig. 1 Typical SEM (a) and XRD patterns (b) of the As-grown ZnS Nanostructures

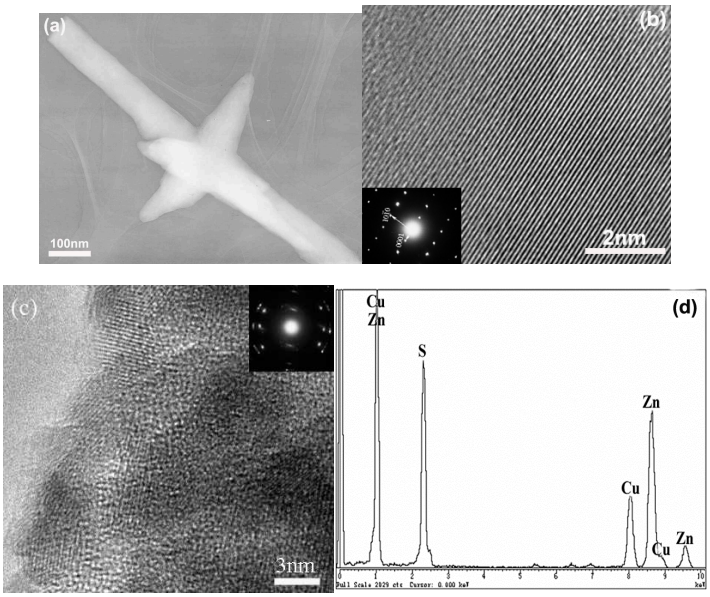


Fig. 2 (a) The Enlarged TEM Micrographs of the As-prepared Dentalation Nanostructrues. (b) HRTEM Image of the Stem and the Inset is the Corresponding SAED Patterns. (c) HRTEM Micrographs of the Teeth and the Inset is the Corresponding SAED Patterns. (d) EDS Spectra of the Dentalation Nanostructrues.

Room temperature photoluminescence (PL) spectra of the as-synthesized ZnS nanostructures were measured with excitation wavelengths of 325 nm as shown in Figure 3. The spectrum exhibit a strong emission centered at 520.89 nm corresponding to the characteristic green emission. The green emission observed here might be caused by the S vacancy due to the shortage of S source when heating the S powder.

The field emission current of the samples was measured at room temperature using a Keithley 2410 source-meter. The anode was a stainless steel plate with a diameter 5 mm, and the distance between the anode and cathode was 150μm. Figure 4 shows the field emission characteristics of the ZnS nanostructures. The current data was acquired by varying the applied voltage between the cathode and anode from 0 to 1100V with a step of 10V. The relatively smooth and consistent curves indicate the stability of emission from the dentalation emitters. From the relation curve of the emission current density vs. applied electric field, the turn-on field was extrapolated to be about 5.56V/μm, which is lower than that reported result from ZnS nanowires [22]. The possession of

decent turn-on field should be attributed to the specific sharp tips and high aspect ratios of the present needle-shaped structure.

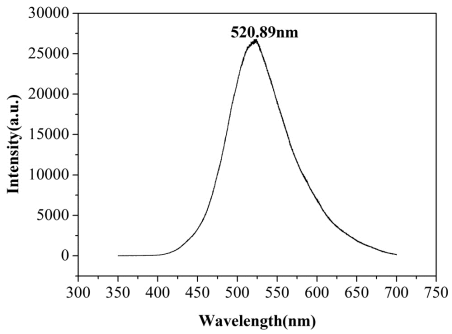


Fig. 3 Room Temperature Photoluminescence Spectra of the As-synthesized ZnS Nanostructures

The FE *I-V* characteristics can be analyzed by a simplified Fowler-Nordheim (F-N) equation:

$$J = \frac{A\beta^2 E^2}{\phi} \exp\left(-B\frac{\phi^{3/2}}{\beta E}\right) \tag{1}$$

Where J is the emission current density, E is the macroscopic field, ϕ is the work function of the emitter, A and B are the constants with values of $1.56\times10^{-10}AV^{-2}eV$ and $6.83\times10^{3}VeV^{-3/2}\mu m^{-1}$, respectively [23]. The β is the FE enhancement factor that represents the true value of the electric field at the tip compared to its average macroscopic value. The β can be calculated from the slope of the FN plot [$\ln(J/E^2)$vs1/E plot] if the work function is known. The inset in Figure 4 shows the F-N plot of the field emission result, and the emission process obeying the law well. Assuming the work function of ZnS to be 5.4eV [23], from the slope of curve shown in the inset of Fig. 4, the factor β can be calculated from the following equation:

$$\beta = -6.83\times10^{3}\frac{\phi^{3/2}}{S} \tag{2}$$

S is the slope of the straight line in Figure 4, the experimental value of β is estimated to be 554 for the ZnS dentalation structures. The factor β is strongly affected by the nanostructure density, the emitter geometry (such as aspect ratios), its crystal structure, and vacuum gaps. The relatively lower β value may be attributed to the low quality crystalline of the teeth. While since the dentalation structures shape gives them the advantage of having many sharp tips and edges, the electrons can be emitted easily form the ZnS thin layer even if a small voltage is applied on those sharp tips, exhibiting decent emission performance.

Summary

The synthesis of microstructures with sharp tips is always the center of field emission research and application. In this letter, compared with the traditional thermal evaporation techniques (above 1000℃), ZnS dentalation nanostructures have been synthesized in a large scale by simple thermal evaporation method at lower temperature with Au as catalyst. The turn-on field was extrapolated to be about 5.56V/μm. The possession of decent turn-on field should be attributed to the specific sharp tips and high aspect ratios of the present needle-shaped structure. The present nanostructures are expected to become valuable in fundamental field emission research and device applications

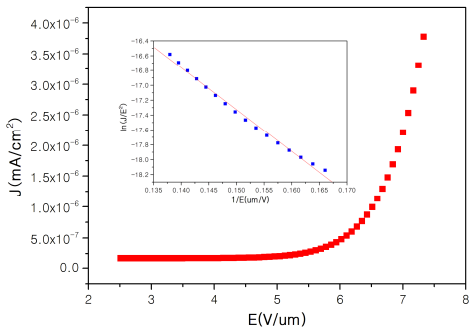


Fig. 4 Field Emission Characteristics of the ZnS Nanostructures Recorded at the Anode-cathode Distances of 150μm Showing J-E Curve and the Corresponding F-N Plot (inset)

Acknowledgment

This work was supported by the National Major Research Program of China (2013CB932600), the Program of International S&T Cooperation (2012DFA50990), NSFC (51232001, 51172022), the Research Fund of Co-construction Program from Beijing Municipal Commission of Education, the Fundamental Research Funds for the Central Universities, Program for Changjiang Scholars and Innovative Research Team in University.

References

[1] S. Velumani, J.A. Ascencio: Appl. Phys. A: Mater. Sci. Process. Vol. 79 (2004), p. 153
[2] W. Park, J.S. King, C.W. Neff and C. Summers: Phys. Status Solidi B. Vol. 229 (2002), p. 7949
[3] E. Monroy, F. Omnes, F. Calle: Semicond. Sci. Technol. Vol. 18 (2003), p. R33
[4] R.N. Bhargava, D. Gallagher, X. Hong, D. Nurminkko: Phys. Rev. Lett. Vol. 72 (1994), p. 416
[5] E. Monroy, F. Omnes, F. Calle: Semicond. Sci. Technol. Vol. 18 (2003), p. R33
[6] Y. Jiang, X.M. Meng, J. Liu, Z.Y. Xie, C.S. Lee, S.T. Lee: Adv. Mater. Vol. 15 (2003), p. 323
[7] Y. Jiang, X.M. Meng, J. Liu, Z.R. Hong, C.S. Lee, S.T. Lee: Adv. Mater. Vol. 15 (2003), p. 1195
[8] X.H. Zhang, Y. Zhang, Y.P. Song, Z. Wang, D.P. Yu: Physica E. Vol. 28 (2005), p. 1
[9] L.W. Yin, Y.S. Bando, J.H. Zhan, M.S. Li, D. Golberg: Adv. Mater. Vol. 17 (2005), p. 1972
[10] Y.C. Zhu, Y.S. Bando, D.F. Xue, D. Golberg: J. Am. Chem. Soc. Vol. 125 (2003), p. 16196
[11] J.F. Gong, S.G. Yang, H.B. Huang, J.H. Duan, H.W. Liu, Y.W. Du: Small. Vol. 2 (2006), p. 732
[12] Z.Q. Deng, J.J. Qi, Y. Zhang, Q.L. Liao, Y.H. Huang: Nanotechnology. Vol. 18 (2007), p. 475603
[13] D. Moore, Y. Ding, Z. L. Wang: Angew. Chem. Vol. 118 (2006), p. 5274
[14] D. Moore, Z. L. Wang: J. Mater. Chem. Vol. 16 (2006), p. 3898
[15] Q.L. Liao, Y. Zhang, L.S. Xia, J.J. Qi, Z.Q. Deng: Acta Phys. Sin. Vol. 57 (2008), p. 2328
[16] C.J. Lee, T.J. Lee, S.C. Lyu: Appl. Phys. Lett. Vol. 81 (2002), p. 3648
[17] G. Hang, Q.F. Zhang, Y. Pei: Vacuum. Vol. 56 (2004), p. 53
[18] K.W. Wong, X.T. Zhou, C.K. Au: Appl. Phys. Lett. Vol. 75 (1999), p. 2918
[19] Y.W. Zhu, T. Yu, F.C. Cheong : Nanotechnology. Vol. 16 (2005), p. 88
[20] X. Fang, T. Zhai, Y. Bando, D. Golberg: Progress in Materials Science. Vol. 56 (2011), p.175
[21] F. Lu, W. P. Cai, Y. G. Zhang : Appl. Phys. Lett. Vol. 89 (2006), p. 231928
[22] Y.Q. Chang, M.W. Wang, X.H. Chen: Solid State Communications. Vol. 142 (2007), p. 295
[23] F. Lu, W.P. Cai, Y.G. Zhang: Appl. Phys. Lett. Vol. 89 (2006), p. 231928

Advanced Materials Research Vol. 936 (2014) pp 384-389
© (2014) Trans Tech Publications, Switzerland
doi:10.4028/www.scientific.net/AMR.936.384

Enhancement of Titania Photocatalytic Properties by Fabrication of MWCNT-TiO_2 Nanocomposites

E. Soroodan Miandoab[1,a], Sh. Fatemi[2,b]

[1]School of Chemical Engineering, College of Engineering, University of Tehran, Enghelab Street, Tehran, Iran

[2]School of Chemical Engineering, College of Engineering, University of Tehran, Enghelab Street, Tehran, Iran

[a]ehsan.soroodan@ut.ac.ir, [b]shfatemi@ut.ac.ir

Keywords: nanocomposite, sol-gel, nano-tube TiO_2, photocatalyst

Abstract: Multi- walled carbon nanotube and nano TiO_2 composite,(MWCNT)-TiO_2,was synthesized via sol-gel deposition method. The product was characterized with FE-SEM and XRD analysis and the results were compared with nano-tube TiO_2 prepared by thermal treatment of the produced nano-composite. Photocatalytic degradation of acetaldehyde, under UV and visible light irradiation, was performed in a continuos flow reactor equiped with 80W Hg lamp and the results were compared with commercial TiO_2 powder (P25). Results showed considerable decrease in concentration of acetaldehyde fed into the reactor during a short time (70 min) for hybrid materials in comparison to nano-tube TiO_2. Furthemore, under visible light irradiation nanocomposite materials revealed good improvement in photocatalytic efficiency with respect to P25 powder.

Introduction

In recent years, attention to the environmental issues has become a driving force to develop new methods of removing pollutants. Photocatalytic degradation of environmentally inadaptable materials is a powerful method to gain this aim. Among photocatalysts, titanium dioxide, with a band gap of 3.25 eV (anatase), can absorb light with wavelengths of 385 nm and below to activate water molecules to create strongly oxidizing hydroxyl radicals and strongly reducing dioxygen ions (O_2^-) [1,2]. Absorption of a photon by TiO_2 crystals, promotes electrons to the conduction band and leaves a hole in the valence band [3]. High performance of titanium dioxide is also investigated in the so-called dye-sensitized solar cells[4]. To enhance the photocatalytic activity of TiO_2, firstly improving the surface and adsorption properties are necessary. Some methods have been investigated including reduction the particle size to nano scale and making porous nano TiO_2. Some others are the formation of composite materials that can enhance the adsorption properties, therefore better electron –hole transfer and higher rate of reaction than pure TiO_2 can be occurred. Coupling carbonaceous materials with TiO_2, is a new and effective route to improve the adsorption and photocatalytic activity owing to their exceptional optical, physical, chemical and thermal properties. As an example, the photocatalytic efficiency of TiO_2 was improved by combining it with activated carbon into nanocomposite [5,6].Due to the unique electronic properties of graphene, in the last years some investigations have been reported about titania-graphene composite to enhance photovoltaic behaviors of pure titania [7-9]. Among carbonaceous materials, carbon nanotube (CNT) have been found considerable attractions owing to its superior properties. CNTs can act as supports to concentrate organic pollutants on the composite surface and more importantly to extend electron-hole (e-h) recombination time as electron scavengers [10].

The present investigation, focuses on the improvement of TiO_2 photocatalytic properties by incorporation of carbon nanotube in its structure under the visible light irradiation.For comparison, nano-tube TiO_2 was prepared by thermal treatment on MWCNT-TiO_2 nanocomposite to remove carbonacious material and its ability to degrade gaseous phase acetaldehyde was examined.

Materials and Methods

Materials

MWCNTs with 20-40 nm in diameters and one micron in length (Nutrino, Iran), Ethanol (C_2H_5OH, Merck, 99% pure), Titanium tetraisopropoxide ($Ti(i\text{-}C_3H_7O_2)_4$, Panreac, 97% pure), Benzyl alcohol (C_7H_8O, Merck, 99% pure), Acetaldehyde (CH_3CHO, Merck, 99% pure) and commercial TiO_2 powder (Sigma Aldrich) were used as received.

Preparation of nanocomposites and nano-tube TiO_2

In a typical experiment MWCNTs were dispersed in ethanol and vigorously stirred. After stirring, deionized water and benzyl alcohol, were added to the suspension. Titanium tetraisopropoxide (TTIP) was dissolved in ethanol and slowly dropped to the CNT suspension. The final molar ratio of TTIP:ethanol:water:BA was 1:30:6:3. The entire mixture was stirred at for 1 hour. After that, the precipitate was filtered and dried in air at 100°C for 6 hours. The dried sample, was calcined in air at 400°C (with a ramp of 5°C per minute) to get the desired anatase crystalline phase. After formation MWCNT-TiO_2 nanocomposite further heat treatment was used in air at temperatures up to 550°C, to form nano-tube TiO_2 with decomposition and oxidation of the MWCNTs.

Photocatalytic experiments

To perform photocatalytic tests, 15 mlit/min acetaldehyde with initial concentration of 1000 ppm, was fed into the reactor and at a distance of about 3 cm from top of it, 80W Hg lamp was placed. 0.1 gr catalysts were distributed on a filter paper and were placed on a stainless steel support. The reactor was kept in dark for 1 hr to compelete adsorption of acetaldehyde by the catalysts. The acetaldehyde concentration variations as a function of time were monitored using VARIAN CP-3800 FID detector Gas Chromatograph. To eliminate UV irradiation in visible light experiments, a UV cutter (HOYA-HMC) was used.

Characterization techniques

The X-ray diffraction (XRD) patterns of the prepared samples were collected with a Phillips diffractometer using CuKα (λ=1.54056A) radiation in angular domain of $0 < 2\theta < 80$. The morphology of the samples was investigated by field emission scanning electron microscopy (FE-SEM) with a Hitachi-F4160. Powder surface area was determined from N_2 gas-adsorption data using Brunauer–Emmett–Teller technique (BET) with Belsorb II.

Results and Discussion

FE-SEM analysis

The morphological structure of the samples has been shown in Fig.1. According to FE-SEM images and comparison of the bare MWCNTs with produced samples, formation of desired structures is observed. However, the presence of aglomerated particles in the mixture is not controllable and the stoichiometric ratios of primary materials in the synthesis procedure, affects the amount of produced grains and aglomerates.

X-ray diffraction analysis

The XRD patterns of the prepared samples are shown in Fig.2. These patterns reveals that the entire crystallite phase is anatase; because there is no rutile peak. Comparison with P25 XRD pattern (Fig.3), verifies this claim.

The average crystallite size of the synthesized samples was calculated from the XRD data according to the Scherrer's equation [11]:

$$d = \frac{k\lambda}{\beta \cos\theta} \qquad [1]$$

where d is the crystallite size, k is a constant (0.9), λ is the wave-length of X-ray (CuKα), β is the half-peak width in radians and θ is the Bragg's diffraction angle in degree. Crystallite size and wieght percentage of crystalline phases are listed in Table.1. It can be seen from Table.1 that further thermal treatment to remove carbon nanotubes have enlarged crystallite size of nano-tube TiO_2. This phenomenon decreases the specific surface area.

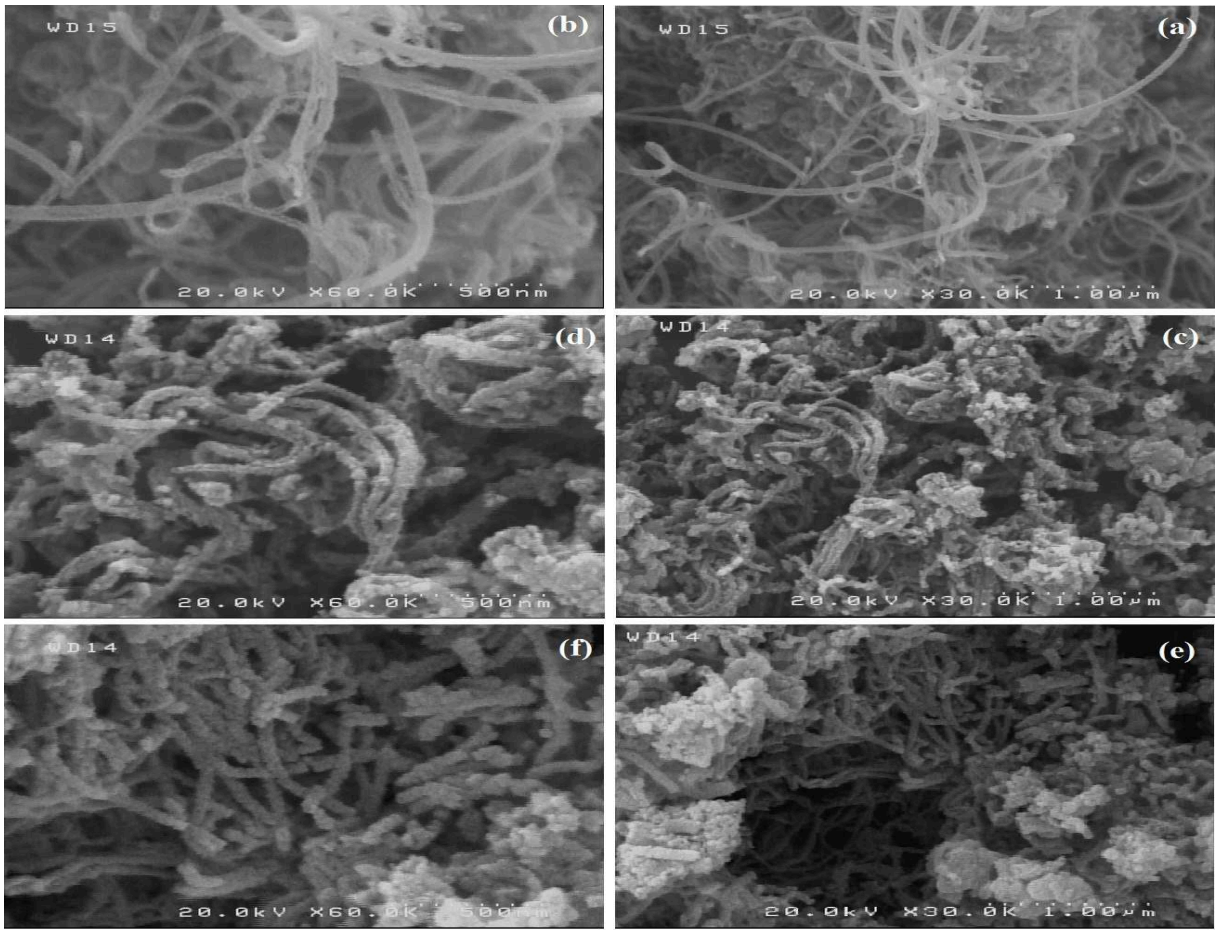


Fig. 1-FE-SEM images of (a,b) bare MWCNTs (c,d) MWCNT-TiO2 nanocomposites (e,f) nano-tube TiO_2

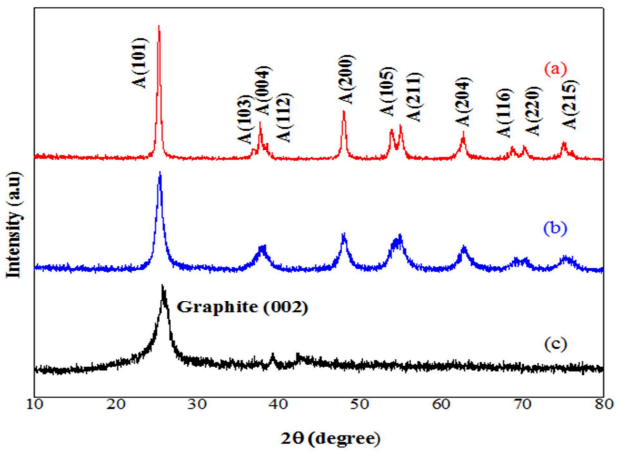


Fig. 2- XRD patterns (a) nano-tube TiO2 (b) MWCNT-TiO_2 nanocomposites (c) pure CNTs

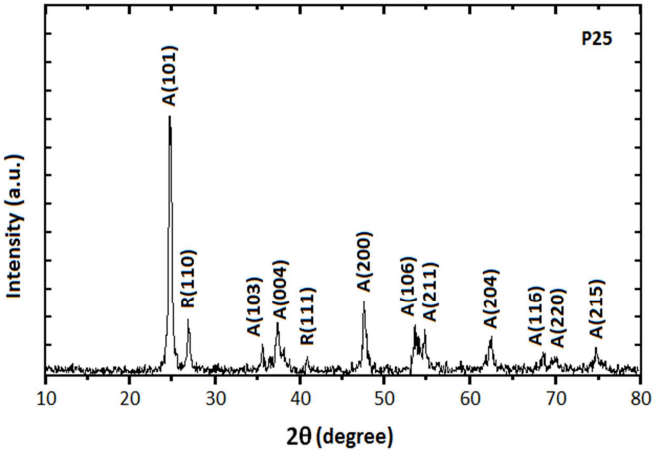


Fig. 3-XRD pattern of P25 (with the permission of ref [11])

TABLE 1- XRD RESULTS

Sample	Crystallite size (nm)	Anatase (%)	Rutile (%)
P25	25	80	20
MWCNT-TiO_2	59	100	-
Nano-tube TiO_2	165	100	-

Photocatalytic Activity

The photocatalytic activities of the nanocomposite and naotubes were determined comparatively by degradation of acetaldehyde in the air and were presented in Fig.4 and Fig.5. As can be seen

from the figures, under UV irradiation P25 shows the largest actitivity to decrease the concentration of acetaldehyde but in the case of visible light, nanocomposite sample is the most efficient material and gives the highest pollutant degradation efficiency. This can be explained by the synergystic effect of carbon nanotubes. Carbon nanotubes can act either electron sink or source. Two mechanisms are being discussed to explain the enhancement of the photocatalytic properties of CNT–TiO_2 composites. The first mechanism proposes that a high-energy photon excites an electron from the valence band to the conduction band of anatase TiO_2. Photo-generated electrons formed in the space-charge regions are transferred into the CNTs, and holes remain on the TiO_2 to take part in redox reactions. In the second mechanism, the photogenerated electron is injected into the conduction band of the TiO_2, allowing for the formation of superoxide radicals by adsorbed molecular oxygen. Once this occurs, the positively charged nanotubes remove an electron from the valence band of the TiO_2 leaving a hole. The now positively charged TiO_2 can then react with adsorbed water to form hydroxyl radicals.Also nano-tube TiO_2 has less activity. This is related to large crystallite size (acording to XRD results) and lack of enough active sites to promote degradation process.

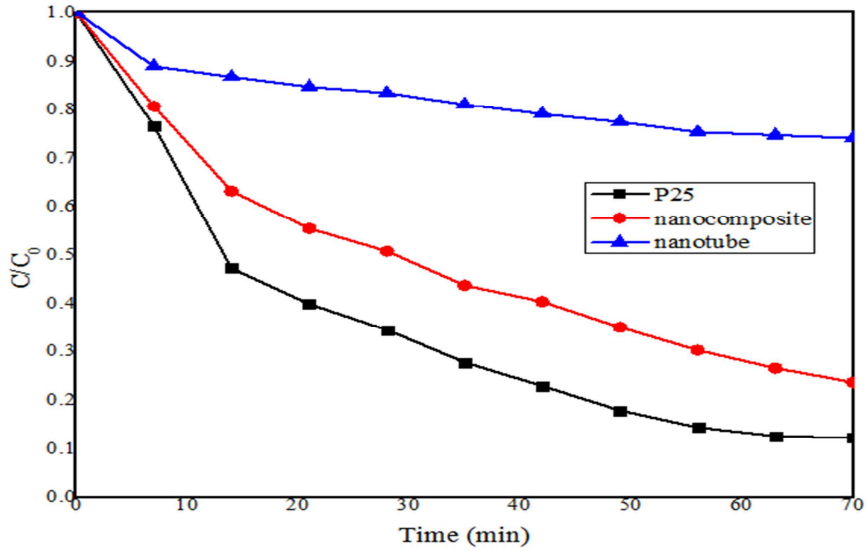


Figure 2- Photocatalytic activity under UV light

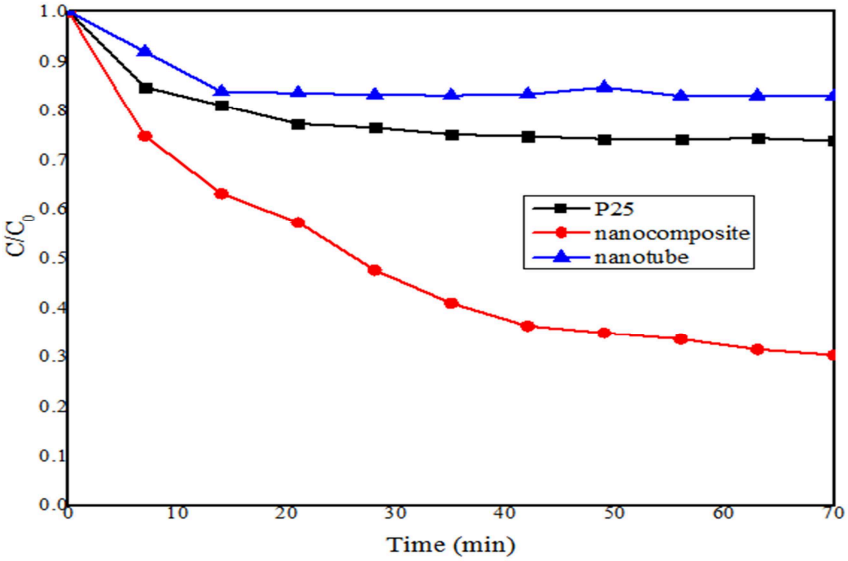


Figure 3- Photocatalytic activity under visible light

Conclusion

Nanocomposite MWCNTs - TiO_2 was synthesised by the sol-gel method. The prepared material was treated under thermal oxidation to prepare TiO2 nantube after removing the base carbon

material. The remained product after thermal treatment was a mixture of nanotube TiO2 and agglomerated TiO2 crystals in which the fraction of nanotube to the nanograin was influenced by the stoichiometry of primary materials used in the synthesis gel. Also, XRD patterns authorized pure anatase phase in the produced composite samples. In the visible light region, nanocomposite sample upgraded photocatalytic activity and showed good efficiency to remove organic pollutant in the contineous reactor. On the othre hand the nano-TiO_2 tubes could not show remarkable photoactivity towards visible light irradiation.

References

[1] Eder, D. and A. H. Windle , Morphology control of CNT-TiO_2 hybrid materials and rutile nanotubes, Journal of Materials Chemistry 18(17): 2036-2043.
[2] Carp, O., C. Huisman, et al. (2004)Photoinduced reactivity of titanium dioxide." Progress in solid state chemistry **32**(1): 33-177
[3] Rajeshwar K (1995) J Appl Electrochem 25:1067
[4] B. O'Regan and M. Graetzel, Nature, 1991, 353(6346), 737–740.
[5] Kudo A, Miseki Y. Heterogeneous photocatalyst materials for water splitting. Chem Soc Rev 2009;38:253–78.
[6] J. Matos, J. Laine, J.-M. Herrmann, Appl. Catal. B: Environ. 18 (1998) 281.
[7] C.G. Silva, J.L. Faria, J. Photochem. Photobiol. A 155 (2003) 133.
[8] G. Colón, M.C. Hidalgo, M. Macías, J.A. Navío, J.M. Doña, Appl. Catal. B: Environ. 43 (2003) 163.
[9] B. Tryba, A.W. Morawski, M. Inagaki, Appl. Catal. B: Environ. 41 (2003) 427.
[10] Q.Cao, G.Yu, Q.Yu, Des.W, Connell, Titania/carbon nanotube composite (TiO_2/CNT) and its application for removal of organic pollutants, Clean Techn Environ Policy
[11] Habibi, S., S. Fatemi, et al. (2012). "TiO< sub> 2</sub> nanoparticle layer formation on ceramic support, a statistical approach to control influential synthesis parameters." Powder Technology **229**: 51-60.
[12] Leary, R. and A. Westwood (2011). "Carbonaceous nanomaterials for the enhancement of TiO_2 photocatalysis." Carbon **49**(3): 741-772.

Advanced Materials Research Vol. 936 (2014) pp 390-393
© (2014) Trans Tech Publications, Switzerland
doi:10.4028/www.scientific.net/AMR.936.390

Study on tensile and impact performance for the MWCNTs/EP composite

Fei Yan[2, a], Jingwen Fu[2, b], Dongyu Zhao[1, 2, C, *]

[1] Key Laboratory of Chemical Engineering Process & Technology for High-efficiency Conversion, College of Heilongjiang Province, Harbin, China

[2] School of Chemistry and Materials Science, Heilongjiang University, Harbin, China

[a]yanfei731.love@163.com, [b]591641326@qq.com, [c]zhaodyu@aliyun.com

Keywords: Multiwalled carbon nanotubes; Epoxy resins; Nanocomposite

Abstract: In this paper, multiwalled carbon nanotubes (MWCNTs)/epoxy resins (EP) composite was prepared by situ polymerization. MWCNTs/EP composites were prepared with different content of MWCNTs. The study of morphology and properties showed certain content of MWCNTs can well homogeneous dispersed in EP. Since of interface interaction between MWCNTs and EP, the glass transition temperature (T_g), strength and toughness of MWCNTs/EP composites were improved. Compared to the neat EP, composites prepared with 10 wt% MWCNTs showed 20 ℃ rising in T_g and nine orders of magnitude reduce in volume resistivity. The percolation thresholds between 4 wt% and 6 wt% are observed. Compared to the neat EP, composites prepared with 6 wt% MWCNTs showed with 83 % increase in tensile strength, 83 % increase in elastic modulus and 89 % increase in impact strength.

Introduction

Since the considerable discovery of carbon nanotubes in 1991 by Iijima [1], they had inspired scientists to consider them for a range of potential application and have become one of the most promising fillers for reinforcement of muti-functional nanocomposites. Their remarkable mechanical [2-4] and geometrical properties (extremely high aspect ratio, nanometer-range diameter), made them ideal candidates for fibre reinforcement in composites materials.

Epoxy resins (EP) are one of the most important thermoset polymers and have been used extensively because of their performance. EP have been widely used in practical applications [5] such as adhesives, construction materials, composites, laminates and coatings owing to their excellent mechanical properties, ease of processing, low cost, and good chemical resistance. A number of recent research efforts have used CNTs for polymer composites' reinforcement [6-7]. Compared to those of the neat EP, the electrical and mechanical properties of the composites could increase.

In this paper, we described the influence of different contents of MWCNTs in the EP. The loss factor, volume resistivity, mechanical properties were tested and will be discussed.

Experimental

Mixture of MWCNTs/EP

Multiwalled carbon nanotubes with average length and diameter of 5-15 μm and 40-60 nm were obtained from Shenzhen nanoport PRC China. Epoxy resin (EP-51) was obtained from Wuxi resin factory of blue star new chemical materials CO, LTD. MWCNTs with different contents was added in the EP, and then MWCNTs were dispersed in the EP by emulsifying machine to obtained MWCNTs/EP mixture.

Preparation of MWCNTs/EP composite

The MWCNTs/EP mixture and 45wt% curing agent PA651 were put respectively in an oven at 60℃ for 2h. Then mixed and stirred at 100r/min to obtain a mixture. The mixture was put into the rectangular mold and then cured in an oven at 70℃/2h, 125℃/2.5h, and 150℃/1h.

Results and discussion

In the research, the addition of 2, 4, 6, 8 and 10wt%WMCNTs to EP was compared with neat EP. Fig.1 showed the loss factor tanδ as a function of MWCNTs contents. The results showed that compared with neat EP, the loss factor peak of MWCNTs/EP composites was shifted to higher temperature, namely T_g increased with the addition of MWCNTs. Because the MWCNTs had good thermal stability and MWCNTs can promote curing reaction of EP, so that the crosslinking density and curing degree increased, at the same time, free volume decreased and mobility of chains were reduced due to the addition of MWCNTs. At the other hand, acid-treated MWCNTs formed chemical bonds with the EP, so that the resistance of molecular chain movement increased. Therefore, dispersing the MWCNTs in EP could improve T_g.

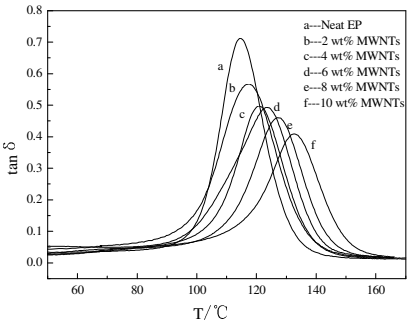


Fig. 1 Influence of MWCNTs content on the T_g of MWCNTs/EP composites

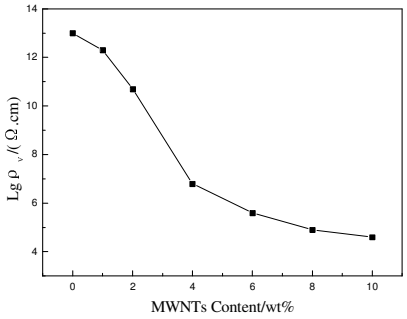


Fig. 2 Influence of MWCNTs content on the volume resistivity of MWCNTs/EP composites

Fig.2 showed volume resistivity as a function of weight fraction of MWCNTs in the EP. The volume resistivity of MWCNTs/EP composites is lower than neat EP, namely conductivity increased. Increasing additions of MWCNTs from 0 to 10wt% resulted in an almost 9 orders of magnitude reduction in resistivity. As the concentration of MWCNTs increased, the average distance between MWCNTs decreased until an effective interconnectivity of MWCNTs in the EP matrix is formed, and electron transport is then facilitated through tunneling throughout the polymer. So the electrical resistivity for this EP reduced and conductivity increased greatly. The percolation threshold was in 4-6wt%.

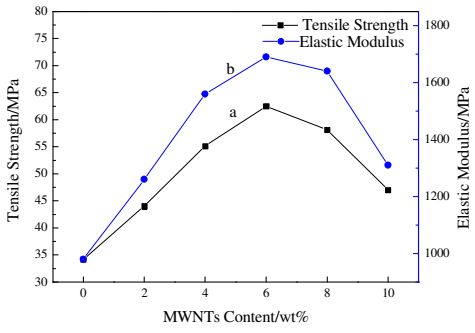


Fig. 3 Influence of MWCNTs content on the tensile strength and elastic modulus of MWCNTs/EP composites

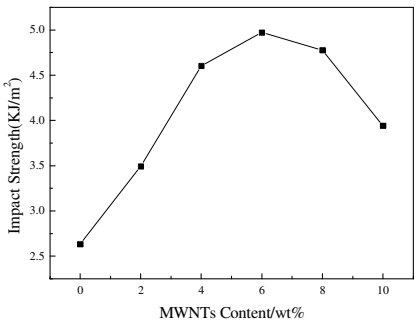


Fig. 4 Influence of MWCNTs content on the impact strength of MWCNTs/EP composites

Fig.3 (a) showed the tensile strength as a function of weight fraction of MWCNTs in the EP, and (b) showed the elastic modulus as a function of weight fraction of MWCNTs in the EP. Fig.4 showed the impact strength as a function of weight fraction of MWCNTs in the EP. All date sets reveal the increase and then decrease as a function of MWCNTs weight fraction. When the fraction of MWCNTs in the EP is 6% by weight, the tensile strength and the elastic modulus increased 83% and the impact strength increased 89% compared with neat EP. Owing to the excellent mechanical properties, high strength and good toughness of MWCNTs. Acid-treated MWCNTs were difficult aggregation in the EP, so it could form a good interface in the composites. The force on the composites effectively transferred to the MWCNTs through the interface and prevented the stress concentrations, thus the tensile strength and the impact strength increased. But when the MWCNTs is increased to a certain amount, they were easy aggregation again, and couldn't form a good interface, even formed defects in the matrix, so this made the stress concentrations, and tensile strength, elastic modulus and impact strength decreased.

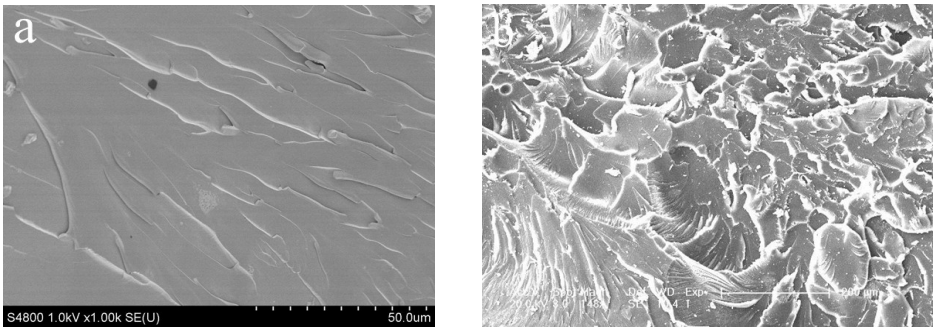


Fig. 5 SEM micrographs of fracture surfaces of neat EP and MWCNTs/EP composites

(a) cured neat EP , (b) 6wt% MWCNTs

The morphology and extent of dispersion of MWCNTs in the EP was investigated using scanning electron microscopy (SEM). The fracture surface of neat EP (Fig.5a) indicated brittle fracture of the materials. The MWCNTs/EP composites showed a somewhat rougher fracture surface which is a corroboration of the observed increase in fracture energy. After adding a certain amount of MWCNTs, the fracture surface of MWCNTs/EP composites became rougher than neat EP, and the fracture surface of the composites exhibited clear features of the toughness. So it indicated MWCNTs could increase the strength and toughness of EP, due to their mechanical properties, the fibre-shaped structure (high aspect ratio) and the huge interface provided. And in the Fig.5 (b) a good dispersion of the MWCNTs in the EP could be observed.

Acknowledgments

The work was supported by Harbin Scientific and Technological Special Fund for Innovative Talents (Grant Num 2012RFXXG093).

References

[1] S. Iijima, Helical microtubules of graphitic carbon. Nature 354, 56(1991).

[2] Yu MF, Lourie O, Dyer MJ, Moloni K, Kelly TF, Ruoff RS, Strength and breaking mechanism of mutiwalled carbon nanotubes under tensile load. Science 2000; 287:637-40.

[3] Yu MF, Files BS, Arepalli S, Ruoff RS, Tensile loading of ropes of single wall carbon nanotubes and their mechanical properties. Phys Rev Lett 2000; 84:5552-5.

[4] Li C, Chou TW, Elastic moduli of multi-walled carbon nanotubes and the effect of van der Waals forces. Compos Sci Technol 2003; 63:1517-24.

[5] Rosu D, Cascaval CN, Mustata F, Ciobanu C (2002) Thermochim Acta 383(1-2): 119.

[6] Coleman JN, Khan U, Gun'ko YK, Mechanical reinforcement of polymers using carbon nanotubes, Adv Mater 2006; 18(6):689-706.

[7] Zhu J, Kim J, Peng H, Margrave JL, Khabashesku VN, Barrera EV, Improving the dispersion and integration of single-walled carbon nanotubes in epoxy composites through functionalization. Nano Lett 2003; 3(8):1107-13.

Advanced Materials Research Vol. 936 (2014) pp 394-399
© (2014) Trans Tech Publications, Switzerland
doi:10.4028/www.scientific.net/AMR.936.394

The Natural Rubber/Zinc Oxide Nanocomposites: Its Morphology, Mechanical and Thermal Decomposing Properties

Ming-zhe Lv[1], Lei Fang[1] ,Pu-wang Li [1]and Chun-Liang Yang[1,*]

[1.]Agricultural Product Processing Research Institute, Chinese Academy of Tropical Agricultural Science, Guangdong, Zhanjiang, 524001

*Corresponding Author. Tel: +86 759 2272708; fax: +86 759 2208758.
Email address: zjyangcl@126.com.

Key words: Natural Rubber; zinc oxide; nanocomposite; dispersion; anti-bacterial property.

Abstract: Natural rubber /Zinc Oxide (NR/ZnO) nanocomposites are fabricated by blending natural rubber latex with aqueous suspension of nano-ZnO particles. Its morphology and thermal/thermooxidative ageing resistance are investigated with scanning electron microscopy (SEM) and thermogravimetric analyzer (TGA). The results show that the mechanical properties of NR is greatly improved by the incorporation of nano–ZnO, nanoparticles, which are homogenously distributed throughout NR matrix as nano-clusters with an average size of 80 nm when the ZnO loading is less than 4 wt%. The thermal/thermooxidative aging resistance of NR/ZnO nanocomposites is compared to the pure NR. It is found that the introduction of nano-ZnO has no obvious impact to the thermal decomposing properties of NR matrix. ZnO/NR composites possess excellent antibacterial effect.

Introduction

Natural rubber latex, as one of the most important natural polymers, has been widely used in various areas. Many medical products such as medical glove, condom, blood transfusion tubing, catheter, injector closure and safe bag are made from natural rubber latex due to its excellent elasticity, flexibility, anti-virus permeation, human body compatibility and good formability.

Low tensile strength and poor tear resistance are the other major drawbacks of NRL products, however, especially for medical gloves and condoms. In the past attempts have been made to reinforce NRL products by using of carbon black, ultra-fine calcium carbonate , modified montmorillonite , silica and starch[1-4].

Nano-ZnO, as one of the multifunctional inorganic nanoparticles, has drawn increasing attention in recent years due to its many significant physical and chemical properties. The introduction of nano-ZnO into polymers could improve the mechanical and optical properties of the polymers due to a strong interfacial interaction between the organic polymer and the inorganic nanoparticles. Consequently, this nanoparticle could be widely applied in coatings, rubbers, plastics, sealants, fibers and other applications.

In this article, natural rubber latex/ZnO nanocomposites were prepared.The dispersion of nano-ZnO in the NR matrix was observed with SEM, and the effect of the addition of nano-ZnO on the thermal decomposition of NR was characterized by thermal analyses.

EXPERIMENTAL

Materials

Natural Rubber latex (NRL) with a total solid content of 60% was purchased from Shuguang Rubber Plantation (Maoming, China), and zinc oxide nanoparticles (average diameter: 40 nm, purity: 99.99%) from were purchased from the market.

Preparation of natural rubber latex/ ZnO nanocomposites

The natural rubber latex/ZnO nanocomposites were prepared by using of blending methods. Briefly, natural rubber latex and different contents of nano-ZnO slurry was blended under high shear stirring. The surface of nano-ZnO was treated through some methods before blending. Then the composites were vulcanized by the recipe for vulcanization: S,1； ZDC, 0.4； ZnO, 0.2.

Characterizations

Tensile and tear resistance testing were conducted on an Instron Series 3365 Automated Materials Testing System (Instron, USA) with a crosshead speed of 500 mm/min. The measurement was done under at room temperature.

Scannning electron microscopy (SEM) of the nanocomposites were taken with a Philips XL 30 FEG-SEW instrument (Philips, Eindhoven, Netherlands) at an acceleration voltage of 10 kV. The fracture surface was obtained by splitting the bulk sample quenched in liquid nitrogen. A sputter coater was used to pre-coat conductive gold onto the fracture surface before SEM observation.

A STA449C thermogravimetric analyzer (TGA) (NETZSCH, DE) was used for thermal and thermooxidative decomposition measurement. In nitrogen or air, the measurement of the films (ca.10 mg) was carried out from 50℃ to 650 ℃ at a heating rate of 10℃/min. The flow rate of the carrying gas is 50 ml/min.

RESULTS AND DSCUSSION

Mechanical property

The incorporation of inorganic nanoparticales into elastomer matrix leads to a significant improvement in the mechanical properties of the host elastomer. Table 1 lists the mechanical properties of the pure NR and NR/ZnO nanocomposites with different ZnO loading.

As shown in table 1 the introducing ZnO into NR can significantly improve its tensile strength. The tensile strength increases with an increasing ZnO loading. At ZnO content of 2 wt%, the tensile strength has increased by 13 MPa compared to the pure NR. However, when the nano-ZnO content of the sample is more than 2 wt%, the tensile strength decreases.

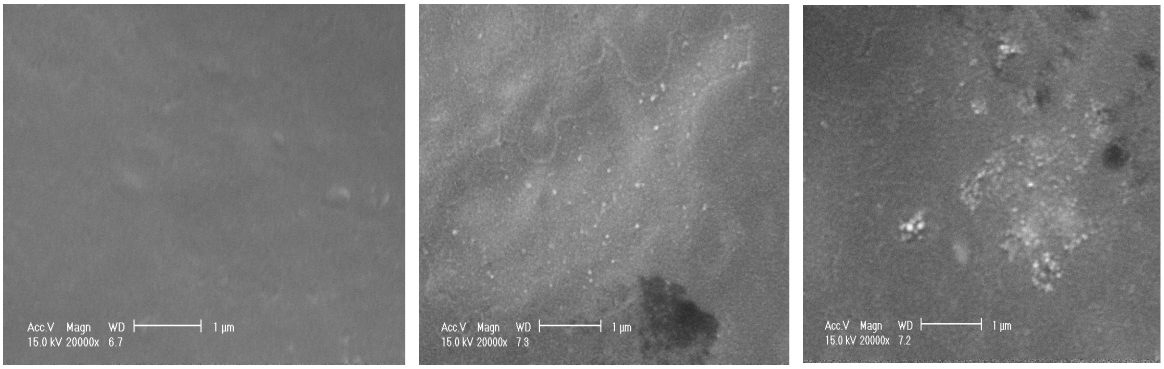
Another noticeable improvement is observed in tear resistance. Poor tear resistance is one of the major problems for NRL product. Introducing nano-ZnO into NR can significantly improve its tear resistance. The tear strength increases with an increasing ZnO loading. At nano-ZnO content of 4 wt%, the tear strength (60.9 kN/m) is higher that of the pure NR (37.4 kN/m). However, the tear strength decrease significantly at the nano-ZnO content of 5 wt%.

However, the ZnO reduces the flexibility of NR due to the restriction of molecular chain slipping along the filler surface. The influence of ZnO on NR's elongation at break seems relatively unnoticeable at low ZnO (less than 3 wt%) , while it plays a critical role at higher loading of ZnO. Particularly, the elongation at break of the sample with the ZnO content of 5 wt% has a increase compared to that (880%) of the sample with ZnO content of 4 wt%.

TABLE 1 MECHANICAL PROPERTIES OF THE PURE NR AND NR/ZNO NANOCOMPOSITES

Nano-ZnO loading (wt%)	0	0.5	1.0	2.0	3.0	4.0	5.0
Tensile strength (MPa)	23.6	32.9	35.5	36.6	34.4	33.0	29.3
100% elongation (Mpa)	0.67	0.71	0.72	0.75	0.76	0.79	0.76
300% elongation (Mpa)	1.16	1.26	1.30	1.33	1.33	1.40	1.32
Elongation at break (%)	963	987	928	887	882	880	906
Tear strength (MPa)	37.4	40.8	43.0	45.2	47.5	60.9	51.9

Morphology of NRL/ZnO nanocomposite



(a) (b) (c)

Fig. 1 The morphology of NR/ZnO nanocomposites:(a)the pure NR, (b) NR with 2% nano-ZnO, (c)NR with 4% nano-ZnO.

Figure 1 shows the morphology fracfure obtained by splitting the bulk sample quenched nitrogen. There are a little amount of ZnO of larger sizes as the vulcanizing agent in the control sample (a);In the sample with a loading of 2% of nano-ZnO, it can be found that the ZnO dispersed evenly in the NR matrix, which had basicly reached dispersion state of nano-meter scale(about 80 nm),with a fuzzy interface between the ZnO and NR matrix, indicating that there is a strong interaction between ZnO and NR to comes the improvement in the physical properties of NR. However, when the content of ZnO was increased to over 4%, the physical properties decressed due to the large agglomeration the uneven dispersion of ZnO in the NR matrix.

Thermal and Thermooxidative Ageing Resistance

The thermal and thermooxidative ageing resistance of NR/ZnO nanocpmposite can be assessed, respectively, by the investigation of thermal and thermooxidative decomposition. Figure 2 shows TG and DTG curves of the pure NR and NR/ZnO nanocomposite in nitrogen. There is only one obvious thermal decomposition step of NR molecular chains, primarily initiated by thermal scission of C-C chain bonds accompanying by a transfer of hydrogen at the site scission.

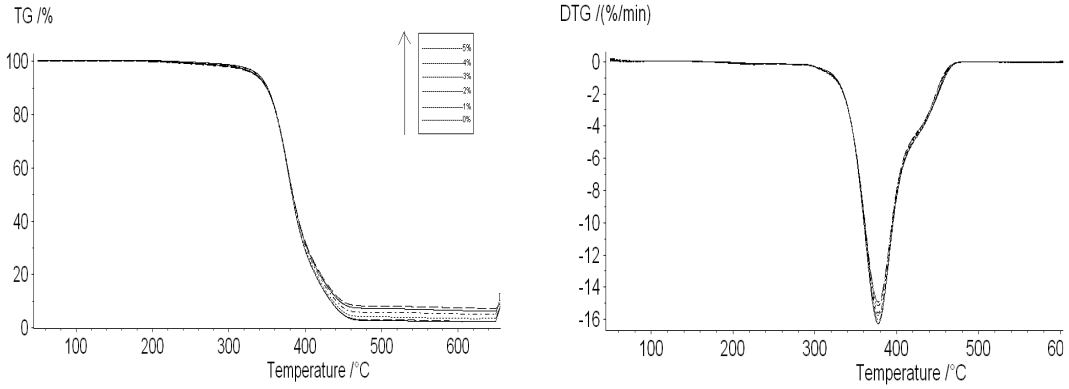


Fig. 2 TG and DTG curves for pure NR and NR/ZnO nanocomposites in nitrogen

The thermooxidative decomposition is obviously different from the thermal decomposition as shown in Figure 3, which are the TG and DTG curves of the pure NR and NR/ZnO nanocomposites in air, respectively. The first large decomposition peak is caused by oxidative dehydrogenation accompanying hydrogen abstraction, while the second weak peak is resulted from the oxidative reaction of residual carbon.

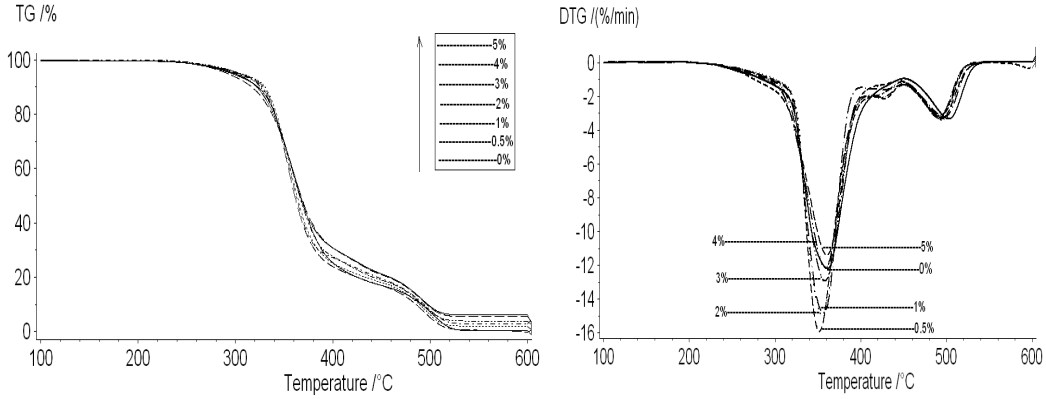


Fig. 3 TG and DTG curves for pure NR and NR/ZnO nanocomposites in air

The initial (T_0), maximal (T_p) and final (T_f) temperatures of decomposing are calculated from the TG and DTG curves. The temperature range of the thermal degradation, an important parameter to evaluate the degree of degradation, is expressed as $\Delta T = T_p - T_0$. These characteristic temperatures are summarized in Table 2.

TABLE 2 CHARACTERISTIC TEMPERATURES OF THERMAL AND THERMOOXIDATIVE DECOMPOSITION FOR PURE NR AND NR/ZNO NANOCOMPOSITES WITH DIFFERENT NANO-ZNO CONTENTS

Sample	Thermal decomposition				Thermooxidative decomposition			
	T_0(℃)	T_p(℃)	T_f(℃)	ΔT(℃)	T_0(℃)	T_p(℃)	T_f(℃)	ΔT(℃)
NR	353.2	377.9	412.0	24.7	332.6	361.4	388.0	28.8
0.5%	353.4	378.2	412.2	24.8	332.1	352.2	375.4	20.1
1%	352.8	377.9	412.2	25.1	331.3	355.3	378.1	24.0
2%	352.7	377.9	412.2	25.2	330.1	356.7	374.7	26.6
3%	353.0	378.2	411.9	25.2	328.9	358.4	381.3	29.5
4%	352.6	377.9	412.3	25.3	326.6	359.0	379.6	32.4
5%	352.4	377.9	412.3	25.5	324.8	360.7	382.1	35.9

When the ZnO/NR nanocomposite was degraded in air, the initial (T_0), maximal (T_p) and final (T_f) temperatures of decomposing were all lower that those of control sample, which is different from the simplely accelerating or delaying of degradation abilities demonstrated by the addition general kinds of nanoparticles such as SiO_2 into rubber. With the increment in nano-ZnO content, the initial decomposing temperature decreased, the maximal decomposing temperature, however, decreased then increased and finally approached that of pure NR. Previous studies [5-7] had shown that, the metal consists of variable valence would cause electron transferring and accelerate the production of free radicals to speed up the rupture of rubber hydrocarbons, resulting in the thermal degradation of rubber hydrocarbons and the production in ageing resistance. And the Zinc ion in the Nano-ZnO just possesses such a function. With the increment in nano-ZnO content, the physical shielding exhibited by ZnO caused the improvement in thermal degradation and ageing resistance; when the content of nano-ZnO was increased to a certain amount, however, the thermal decomposing and ageing resistance tended to approach thet of NR sample without the addition of nano-ZnO.

Anti-bacterial property

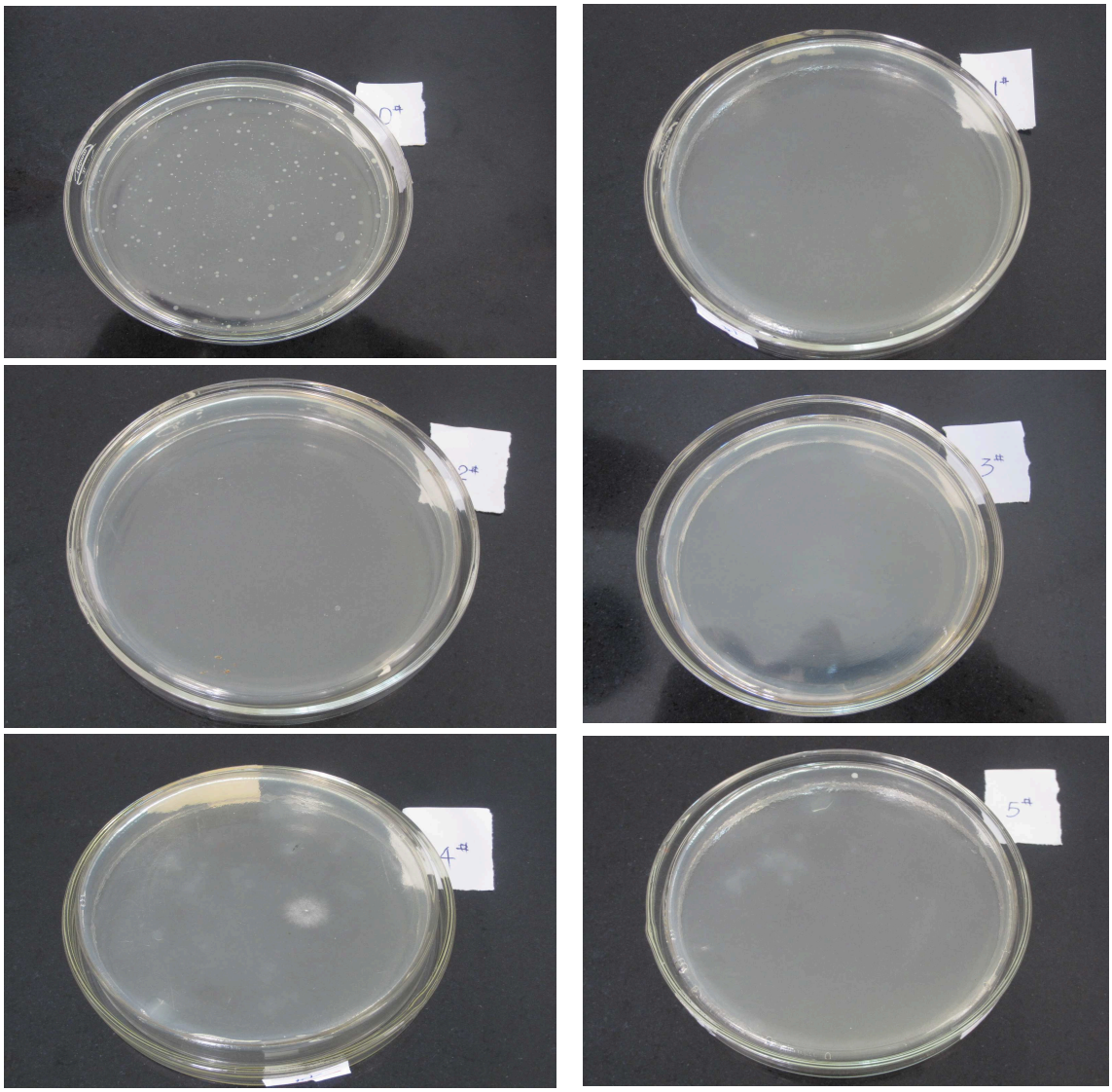


Fig.4 The colony's morphology of (0#) pure NR sample and (1#~5#) ZnO/NR nanocomposites

Fig.4 show the colony morphology of pure NR and ZnO/NR nanocomposites, and the number of Escherichia coli colony which had been cultivated at the antibacterial experiment for 24 hours.The number of Escherichia coli colony reached 70 cfu for each piece of the pure NR material. However, less than 10 cfu for each piece of ZnO/NR nanocomposites was observed. It is evident that the ZnO/NR nanocomposites possess excellent antibacterial property. Furthermore, the antibacterial rate didn't increase with the increasing loading of ZnO in nanocomposites.

Materials possess anti-bacterial function if its anti-bacterial rate is above 90%, according to antibacterial plastics standard (QB/T 2591-2003). In the current work we found that the antibacterial rate of ZnO/NR composite was all higher than 90%, which confirmed the fact that the ZnO/NR composites possess excellent antibacterial effect.

CONCLUSIONS

Natural rubber/ZnO nanocomposites was fabricated, and its physical properties, were investigated. The mechanical properties of NR are observed to improve by the incorporation of nano -ZnO. It can seen from the SEM micrograph that the nano-ZnO was dispersed evenly in the NR matrix in nano dimension..The thermooxidative decomposing temperature was reduced to some extent by the loading of nano-ZnO, however, with the increment in the ZnO content, the maximum decomposing temperature tended to approach that of pure NR sample. ZnO/NR composites possess excellent antibacterial effect.

References

[1] J. J. C. Busfield, C. Deeprasertkul and A. G. Thomas.The effect of liquids on the dynamic properties of carbon black filled natural rubber as a function of pre-strain[J].Polymer, 2000,**41**:9219-9225.

[2] H. H. Cai, S. D. Li, T. G. Rian, H. B. Wang and J. H. Wang.Reinforcement of natural rubber latex film by ultrafine calcium carbonate[J]. Appl. Polym. Sci., 2003,**87**: 982-985.

[3] M. Arroyo, M. A. Lopez-Manchado and B. Herrero, Organo-montmorillonite as substitute of carbon black in natural rubber compounds[J].Polymer, 2003,**44**:2447-2453.

[4] L. Jose and R. Joseph, Study of the effect of polyethylene-glycol in field natural-rubber latex vulcanizates Kaut[J]. Gummi. Kunstst., 1993,**46**: 220-222.

[5] Jadrnicek B R, Stivala S S, Reich L．J．Polym Sci．1971, A-19：231.

[6] Albert H E, Smith G E P, Gottschalk G W．Effect of iron on of GR-S[J]．Rubber Chemistry and Technology. 1948, **21**：877-888.

[7] Villain H, The action of copper and manganese on the ageing of rubber[J]．Rubber Chemistry and Technology, 1950, **23**：252-361.

Advanced Materials Research Vol. 936 (2014) pp 400-408
© (2014) Trans Tech Publications, Switzerland
doi:10.4028/www.scientific.net/AMR.936.400

Effect of Grain Size on the Fracture Toughness of Bimodal Nanocrystalline Materials

Yingguang Liu[1,a*], Xiaodong Mi[1,b], Songfeng Tian[1,c]

[1]School of Energy and Power Engineering, North China Electric Power University, Baoding 071003, Hebei, People's Republic of China

[a]yingguang266@126.com, [b]mixiao.dong@163.com, [c]tiansongfeng@163.com

Keywords: Bimodal nanocrystalline materials; Cohesive zone; Fracture toughness; Grain size

Abstract: To research the effect of grain size on the fracture toughness of bimodal nanocrystalline (BNC) materials which are composed of nanocrystalline (NC) matrix and coarse grains, we have developed a theoretical model to study the critical stress intensity factor K_{IC} (which characterizes toughness) of BNC materials by considering a typical case where crack lies at the interface of two neighboring NC grains and the crack tip intersect at the grain boundary of the coarse grain, the cohesive zone size is assumed to be equal to the grain size d of the NC matrix. Blunting and propagating processes of the crack is controlled by a combined effect of dislocation and cohesive zone. Edge dislocations emit from the cohesive crack tip and make a shielding effect on the crack. It was found that the critical stress intensity factor K_{IC} increases with the increasing of grain size d of the NC matrix as well as the coarse grain size D. Moreover, the fracture toughness is relatively more sensitive to the coarse grain size rather than that of NC matrix.

Introduction

Even though exhibiting remarkable improvement in strength, most of the experimental studies reveal that NC materials generally possess insufficient ductility compared with their coarse-grained conventional counterparts [1, 2]. However, the evidence of tensile superplasticity in NC materials has been reported, but these cases appear to be not numerous, and often occur only at high temperatures, or with micro tensile samples using specialized testing method [3-5].

As the deficiency of low ductility and the associated loss of toughness in some materials stop their applications in engineering. According to engineering practice and theoretical experience, people always build a composite structure to enhance the ductility of such materials [6-8]. Many approaches have been proposed to enhance the ductility of NC materials [9-12]. One of the several strategies that have been suggested for enhancing ductility in NC materials is to develop a bimodal grain size distribution, in which fine grains can provide high strength, whereas coarse grains can enable strain hardening to enhance ductility [13-15].

It can be seen from the above literatures that even though there are many experiment observations that the ductility of NC materials with a bimodal grain size distribution can be enhanced, there are few literatures doing quantitative study on the fracture toughness of BNC materials. For instance, Ovid'ko and Sheinerman [16] built a theoretical model that describes the generation of nanoscale cracks of BNC materials, in the frame work of their model, cracks were generated in the stress field of interfacial disclination dipoles formed at the interfaces between larger grains and NC matrix during plastic deformation. But, it did not consider the critical stress intensity factors. Fan et al. [17] studied the plastic deformation and fracture of ultrafine-grained Al–Mg alloys with a bimodal grain size distribution, the Ramberg–Osgood equation was used to fit the compressive stress–strain curves of the bimodal ultrafine-grained (ufg) alloys, it was found that the plastic deformation of the ufg Al–Mg alloys with a bimodal microstructure was highly localized. The fracture of the alloys was attributed to shear localization under the compressive tests and to a combination of shear localization, cavitation and necking under the tensile tests. However, the grain

size of their ufg matrix did not reach the nano-scale. Han et al. [18] investigated the strain rate sensitivity and the strain rate effect on the ductility of bimodal 5083 Al alloys, the mechanical responses of several bimodal 5083 Al alloys with different fractions of coarse grains were studied at different strain rates. It was found that the failure strain increases with decreasing strain rate for the plastic deformation when the strain rate is less than $10^{-1}\ s^{-1}$, but it was very difficult to conduct quantitative calculation using their model. Zhu et al. [19-20] built two statistical models to study the strength and ductility of BNC materials. The calculating results show that nano micro cracks don't lead to catastrophic failure, instead, they induce the back stress for strain hardening in BNC materials; However, their models did not consider the crack propagation and calculate the critical stress intensity factor. We [21] also built a constitutive model of BNC materials based on a strain-gradient plasticity theory, but we did not consider the fracture of such materials.

Besides, there are many other literatures to study BNC materials [22-24] and most of them mainly described the experimental phenomena rather than established a mathematical model to take quantitative analysis. During the last few decades, cohesive model of fracture has gradually evolved as an attractive tool to model crack initiation and propagation [25-28]. As can be seen from the above literatures, most of the cohesive zone models are used to study the fracture of coarse grained materials rather than NC/BNC materials. The present paper is aimed at studying the fracture toughness of BNC materials by using a combined dislocation—cohesive zone model.

Dislocations cohesive model

In this paper, we will focus on the dislocation shielding on a Dugdale [29] cohesive crack under mode I dominant conditions (Fig. 1). The crack lies at the interface of two adjacent NC grains with the crack tip intersecting at the grain boundary of the coarse grain. The rectangular cohesive law of Dugdale, as shown in Fig. 1 (b), is assumed to govern the traction within the cohesive zone OO' of length L. The origin of the (x, y) coordinate system (point O) is located at the tip of the cohesive zone. With increased external load, *N* edge dislocations will emit from the crack tip, and it is assumed that the emitted dislocation is retarded at the opposite grain boundary of the coarse grain, as shown in Fig. 1 (a).

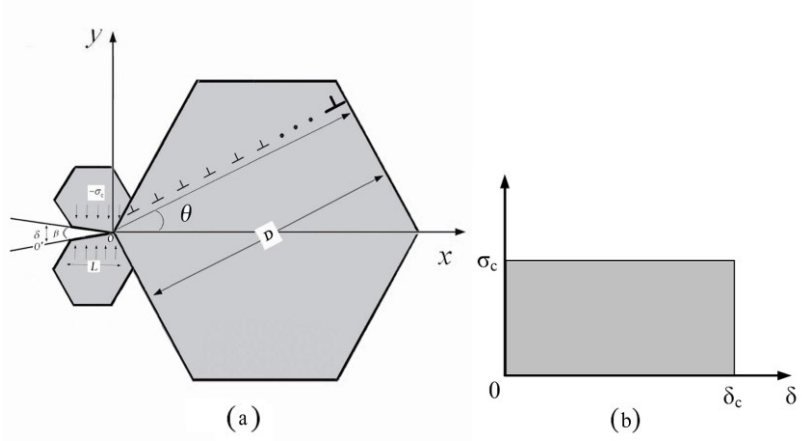


Fig.1 (a) A Dugdale cohesive crack, subjected to a remote mode-I loading, lies at the interface of two adjacent grains with the crack tip intersecting the grain boundary of the third grain. N edge dislocations with Burgers vectors b emit from the crack tip and slip to the opposite grain boundary, the crack tip cohesive zone size is L. The cohesive zone starts at O' where the crack-opening displacement is calculated. (b) Dugdale's (rectangular) cohesive law with cohesive strength σ_c and critical displacement δ_c.

The stress intensity factor K_{IC} at O is calculated as

$$K_{IC} = \sqrt{(K_{IC}^{c})^2 - (k_{II}^{dis})^2} - k_{I}^{dis} \quad (1)$$

where, K_{IC}^{c} is the intensity factor for the cohesive stress σ_c, while k_{I}^{dis} and k_{II}^{dis} are , respectively, the intensity factors for the normal (to the crack line) and shear stresses created by the generated dislocations. The mode I stress intensity factor for a semi-infinite crack subjected to a distribution of normal traction p(*x*) along the crack surfaces [30] is

$$K_{\mathrm{I}} = \sqrt{\frac{2}{\pi}} \int_{-\infty}^{0} \frac{p(t)}{\sqrt{-t}} dt \tag{2}$$

In the Dugdale model, the cohesive traction is $p_{\mathrm{c}}(t) = -\sigma_{\mathrm{c}}$ for $-L \le t \le 0$ and vanishes over the rest of the crack faces, as shown in Fig. 1 (b). The corresponding stress intensity facto at point O is [31]

$$K_{\mathrm{IC}}^{\mathrm{c}} = -\sigma_{\mathrm{c}} \sqrt{\frac{8L}{\pi}} \tag{3}$$

Note that in the Dugdale model, the cohesive stress σ_{c} is equal to the yield strength σ_y. However, all other cohesive zone models suggest that in the traction-separation process, the cohesive stress varies with the opening displacement, and there exists a maximum cohesive stress $\sigma_{\max}$ with value being a few times of the yield strength σ_y.[32] In the present paper, we will use equation (4) which provides a relation between the cohesive stress $\sigma_{\max}$ and the yield strength σ_y [33]

$$\sigma_{\max} = \frac{\sigma_y}{\sqrt{\alpha^2 - \alpha + 1}} \left[\frac{2E}{\sigma_y} \frac{\alpha + 1}{2 - \alpha} C e^{-1.5 H_0} + 1 \right]^n \tag{4}$$

where $\alpha = \sigma_{\mathrm{II}} / \sigma_{\mathrm{I}}$ is the bi-axiality ratio that defines the stress triaxiality, which is shown in Fig. 2. H_0 is set to a constant value of 0.5, an average value chosen to represent the equivalent plastic strain failure locus for lower triaxialities encountered in plane stress, C is a material dependent non-dimensional parameter. σ_y can be obtained by the well-known Hall-Petch relationship:

$$\sigma_y = \sigma_0 + \frac{k}{\sqrt{d}} \tag{5}$$

where σ_0 is the lattice friction stress, k is the H–P constant and d is the grain size. It should be noted that: 1) Many NC materials do not obey the Hall–Petch relation when the grain size decrease to a critical value (3-20 nm) [34-37]. Therefore, in this paper, we will not consider the NC materials with a grain size below 20 nm; 2) We assume that the crack tip curvature radius $\rho = 0$, it can be seen from Fig. 1 (a) that in the cohesive zone, the maximum opening displacement $\delta_{\mathrm{c}} = L\beta$, where β is the crack tip opening angle. In general, $1\mathrm{nm} \le \delta_{\mathrm{c}} \le 10\mathrm{nm}$ in the cohesive models [32], thus, in the present paper, we fix the cohesive zone $L \le 100\mathrm{nm}$, and the suggested model is questionable for the solids with grain sizes that exceed a hundred nanometers. By putting σ_0=25MPa and $k = 0.11 \times 10^6$ for NC copper into Eq. (4), we obtained the dependence of $\sigma_{\max}$ on grain size d for NC copper, as shown in Fig. 3.

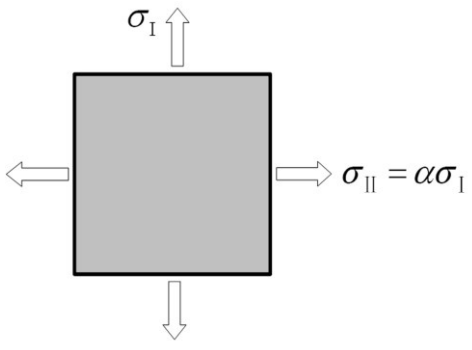


Fig.2 Schematic diagram of bi-axiality ratio, α, under conditions of plane stress.

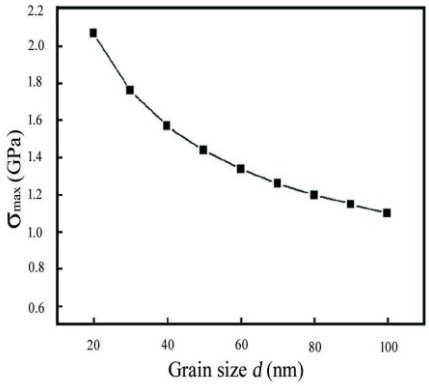


Fig. 3 Dependence of critical cohesive stress $\sigma_{\max}$ on grain size d.

Next, we will calculate the stress intensity factors $k_{\mathrm{I}}^{\mathrm{dis}}$ and $k_{\mathrm{II}}^{\mathrm{dis}}$. In doing so, as shown in Fig. 1 (a), θ is the angle made by the boundary plane (the dislocation Burgers vector) and the crack propagating direction. The stress intensity factors $k_{\mathrm{I}}^{\mathrm{dis}}$ and $k_{\mathrm{II}}^{\mathrm{dis}}$ for the dislocation-induced stresses can be calculated by [38]

$$k_{\mathrm{I}}^{\mathrm{dis}} = -\frac{3\pi D b_{\mathrm{T}} \sin\theta\cos(\theta/2)}{\sqrt{2\pi r_0}}\ ,\ k_{\mathrm{II}}^{\mathrm{dis}} = -\frac{\pi D b_{\mathrm{T}}[\cos(\theta/2)+3\cos(3\theta/2)]}{2\sqrt{2\pi r_0}} \tag{6}$$

where $D = G\ /[2(1-\nu)]$, D is the shear modulus, $b_{\mathrm{T}} = N\mathrm{b}$, is the sum of all the emitted dislocations, b =0.256 nm, denotes the Burgers vector magnitude of the edge dislocation, ν is the Poisson's ratio, r_0 is the distance between the edge dislocation and the crack tip.

Let us calculate *N*--the number of dislocations emitted from a crack tip and retarded at the opposite grain boundaries of the coarse grain. In the quasi-equilibrium state, the Burgers vector magnitude Nb corresponds to a minimum of the energy change ΔW within the dislocation generation process (Fig. 1). ΔW has three terms:

$$\Delta W = W_{\mathrm{s}} + W_{\mathrm{c}} - A \tag{7}$$

where W_{s} is the proper elastic energy of the dislocation, W_{c} is the dislocation core energy, A denotes the work spent to the generation of dislocations and the movement of dislocation from the crack tip to its final position.

Since the dislocation is located near the crack free surface, its stresses are screened. The proper energy of the dislocation can be calculated, with the aid of the formula taking into account the image forces that characterizes the screening effect, as [39]

$$W_{\mathrm{s}} \approx \frac{D b_{\mathrm{T}}^2}{2} \ln\frac{r}{r_{\mathrm{c}}} \tag{8}$$

where r_{c} is the dislocation core radius. The dislocation core energy W_c under the standard approximation is given as [16]

$$W_{\mathrm{c}} \approx D b_{\mathrm{T}}^2 / 2 \tag{9}$$

The work A spent on generation of the dislocation and the movement of the dislocation from the crack tip to its final position, is calculated in the standard way. The work A is represented in the following form:

$$A = b_{\mathrm{T}} \int_0^{\mathrm{r}} \sigma_{r\theta}^{K_I}(r,\theta)\, d\rho \tag{10}$$

Here $\sigma_{r\theta}^{K_I}(r,\theta)$, written in the polar coordinate system (r,θ) with the origin at the crack tip can be given by

$$\sigma_{r\theta}^{K_{\mathrm{I}}}(r,\theta) = \frac{K_{\mathrm{I}}^{\mathrm{c}} \sin\theta\cos(\theta/2)}{2\sqrt{2\pi r}} \tag{11}$$

According to formula (10-11), one will obtain

$$A = b_T r\left(\frac{K_I^c \sin\theta\cos(\theta/2)}{\sqrt{2\pi r}}\right) \quad (12)$$

Then, with formulas (8-12), we obtain the following formula for the characteristic energy change ΔW

$$\Delta W = \frac{Db_T^2}{2}\left(\ln\frac{r}{r_c}+1\right) - \frac{b_T r K_I^c \sin\theta\cos(\theta/2)}{\sqrt{2\pi r}} \quad (13)$$

With the condition $\partial(\Delta W)/\partial b_T = 0$ of the minimum of the energy change ΔW, one finds the following expression for the number of emitted dislocations:

$$N = \frac{(1-v)K_I^c \sin\theta\cos(\theta/2)\sqrt{2\pi r}}{b\mathrm{G}[\ln(r/r_c)+1]} . \quad (14)$$

In the present work, it is assumed that all the emitted dislocations will reach the opposite grain boundary, that is, each dislocation will slip the same distance which equals to the coarse grain size *D*.

In our previous paper [40], we have calculated the critical crack intensity factor K_{IC} as a function of θ for NC Ni, as shown in Fig. 4. It can be seen from Fig. 4 that the critical intensity factor K_{IC} reaches the maximum value when the boundary plane makes the angle θ of around 70° with the direction of crack growth. By putting $\theta = 70^\circ$, we obtained the relationship between *N* and *D* the coarse grain size for NC copper which is shown in Fig. 5. It shows that *N* increases with increasing the coarse grain size *D*. It should be noted that the value of *N* is relatively small and the increase rate tends to be reduced. This means that for small grain sizes, dislocation emission along one slip plane cannot lead to a significant crack blunting and the crack can easily grow. It is because that the driving force being exerted on the dislocations will be getting smaller as the dislocations move far away from the crack tip, and the dislocations are arrested at grain boundaries which make the sliding of later emitted dislocations become more and more difficult.

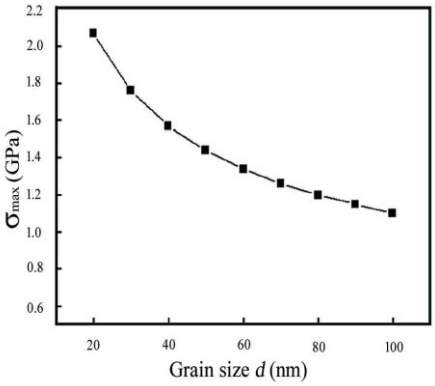


Fig.4 Dependence of critical crack intensity factor K_{IC} on the angle θ made by the boundary plane and the crack growth direction for NC nickel.

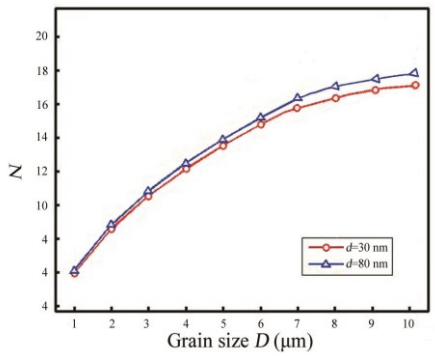


Fig.5 The maximum number *N* of edge dislocations that can be emitted from the crack tip along one slip plane as a function of coarse grain size *D* in NC copper.

Results and discussion

To understand the fracture toughness of BNC materials，numerical simulation based on the aforementioned model were carried out for the cases of BNC copper. Detailed information about the parameters of BNC copper is listed in Table 1.

TABLE 1 MATERIAL PARAMETERS IN CALCULATIONS FOR CU.

Description	Notation	Value
Magnitude of the burgers vector	G	0.256×10^{-9}m
Shear modulus of copper	b	42GPa
Poisson ratio	ν	0.3
Friction stress	σ_0	25MPa
H–P constant	k	0.11×10^{6}
Distance between the edge dislocation and the crack tip	r_0	1μm
Angle made by the boundary plane (the dislocation burgers vector) and the crack propagating direction	θ	70°
Dislocation core radius	r_c	0.256×10^{-9}m

When the grain size d of NC matrix is constant, with Eq. (6) and Eq. (3) substituted to Eq. (1), one will obtain the relationship between the fracture toughness and the coarse grain size D. Fig. 6 shows our calculating result which demonstrates that when the grain size d of NC matrix is constant, the critical stress intensity factor K_{IC} .increases with the increased coarse grain size D, and the change is obvious. For example, when the grain size of the NC matrix d=30 nm, the fracture toughness increases by 31.6% as the coarse grain size D increases from 1 to 10 μm. It is because that the number of emitted dislocations N increases with increasing the coarse grain size D which can prove more shielding effect on crack.

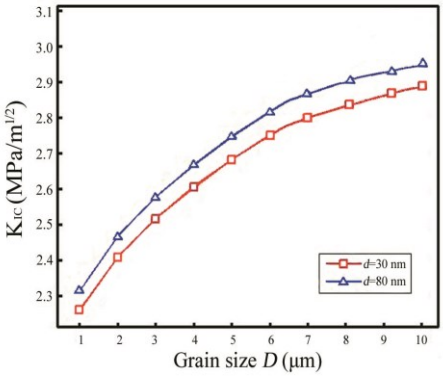


Fig. 6 Critical stress intensity factor KIC vs. coarse grain size D in NC copper.

With the same calculation procedure, when the coarse grain size D is fixed can obtain the relationship between the fracture toughness and the grain size d of the NC matrix. Fig. 7 shows our calculating result which suggests that when the coarse grain size D is constant, the critical stress intensity factor increases with the increased grain size d, and the increase is relatively small. For example, as D is set to be 5 μm, K_{IC} increases by 4.2% when the grain size d increases from 20 to 100 nm. It demonstrates that the fracture toughness of BNC materials is not highly sensitively to the grain size d of the NC matrix. In addition, our calculated fracture toughness values are between 2 and 3 MPa/m1/2, which are smaller than the experimental data. This can be explained by two reasons: 1) In the present model, we did not consider the dislocations already existing in real materials but the dislocations emitting from crack tip, 2) we did not consider the alternative

deformations such as grain boundary sliding, diffusional creep, rotational deformation and nanoscale twin which are capable of causing good toughness of BNC materials under certain conditions.

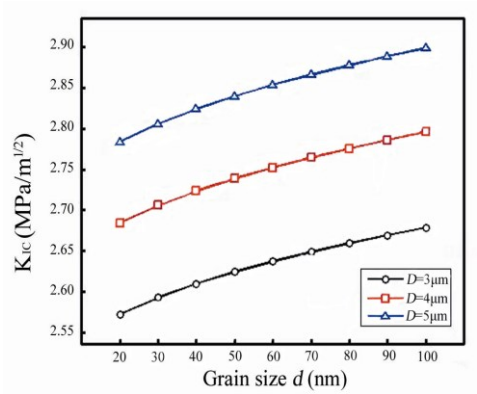


Fig.7 Critical stress intensity factor K_{IC} vs. grain size d in NC copper.

Conclusions and prospects

In the present work, we have developed a theoretical model to study the critical stress intensity factor K_{IC} of BNC materials: the cohesive stress near crack tip in the NC matrix initiates edge dislocations which move from the grain boundary of the coarse grain to the opposite one. The emitted dislocations provide a shielding effect on the crack. The dependence of both the maximum number of dislocations, emitted from a crack, and the critical stress intensity factor on grain size d of the NC matrix (ranging from 20 to 100 nm) as well as to the coarse grain size D (ranging from 1 to 10 μm) for Cu were calculated. The calculating results show that: i) BNC materials have higher fracture toughness than NC materials, ii) when the grain size d of NC matrix is constant, the critical stress intensity factor increases with increased coarse grain size D , and the change is obvious, iii) as the coarse grain D is fixed, the critical stress intensity factor increases with the increased grain size d of NC matrix, and the increase is relatively small. In this model, we only consider the K_{IC} of the BNC materials in a certain case: the crack lies at two neighboring NC grains and the crack tip intersect at the grain boundary of the coarse grain. It is known that the crack blunting and growth processes are strongly influenced or even controlled by alternate deformation modes (e.g., diffusional creep, rotational, grain boundary sliding and twin deformation), these deformation modes may cause high toughness of NC materials under certain conditions, and the influence of alternative deformation modes on the toughness of NC materials is largely unknown and needs further study.

Acknowledgements

The authors are grateful for the funding of the National Natural Science Foundation of China (51301069).

References

[1] C.C. Koch, D.G. Morris, K. Lu, A. Inoue, Ductility of nanostructured materials, MRS Bull. 24 (1999) 54–58.

[2] K.S. Kumar, V. Swygenhoven, S. Suresh, Mechanical behavior of nanocrystalline metals and alloys, Acta Mater. 51 (2003) 5743–5774.

[3] S. Zhang, H. Wang, R.O. Scattergood, J. Narayan, C.C. Koch, A.V. Sergueeva, et al, Tensile elongation (110%) observed in ultra-fine-grained Zn at room temperature, Appl. Phys. Lett. 81 (2002) 823–825.

[4] A.A. Karimpoor, U. Erb, K.T. Aust, G. Palumbo, High strength nanocrystalline cobalt with high tensile ductility, Scr. Mater. 49 (2003) 651–656.

[5] R.Z. Valiev, I.V. Alexandrov, Y.T. Zhu, T.C. Lowe, Paradox of strength and ductility in metals processed by severe plastic deformation, J. Mater. Res. 17 (2002) 5–8.

[6] A.E. Pasto, D.N. Braski,T.R. Watkins, W.D.Porter, E. Lara-Curzio, S.B. McSpadden, Characterization techniques for composites and other advanced materials, Composites: Part B 30 (1999) 631–646.

[7] G.X. Cao, X. Chen, Z.H. Xu, X.D. Li, Measuring mechanical properties of micro- and nano-fibers embedded in an elastic substrate: theoretical framework and experiment. Composites Part B 41(2010) 33–41.

[8] S. Neralla, D.Kumar, S. Yarmolenko, J. Sankar, Mechanical properties of nanocomposite metal–ceramic thin films, Composites: Part B 35 (2004)157–162.

[9] M. Dao, L. Lu, R.J. Asaro, J.T.M.D. Hosson, E. Ma, Toward a quantitative understanding of mechanical behavior of nanocrystalline metals, Acta Mater. 55 (2007) 4041–4065.

[10] X. Zhang, H. Wang, C.C. Koch, Mechanical behavior of bulk ultrafine-grained and nanocrystalline Zn, Rev. Adv. Mater. Sci. 6 (2004) 53–99.

[11] B.Q. Han, E. Lavernia, F.A. Mohamed, Mechanical properties of nanostructured materials, Rev. Adv. Mater. Sci. 9 (2005) 1–16.

[12] I.A. Ovid'ko, Rev. Adv. Superplasticity and ductility of superstrong nanomaterials, Mater. Sci. 10 (2005) 89–104.

[13] Y. Wang, M. Chen, F. Zhou, E. Ma, High tensile ductility in a nanostructured, Metal Nature 419 (2002) 912–915.

[14] Y.M. Wang, E. Ma, M.W. Chen, Enhanced tensile ductility in nanostructured Cu, Appl. Phys. Lett. 80 (2002) 2395–2397.

[15] A.H. Chokshi, A.K. Mukherjee, A topological study of superplastic deformation in an Al–Li alloy with a bimodal grain size distribution, Metall. Trans. A 19 (1988) 1621–1624.

[16] I.A. Ovid'ko, A.G. Sheinerman, Ductile vs. brittle behavior of pre-cracked nanocrystalline and ultrafine-grained materials, Acta Mater. 58 (2010) 5286-5294.

[17] G.J. Fan, H. Choo, P.K. Liaw, E.J. Lavernia, Plastic deformation and fracture ofultrafine-grained Al–Mg alloys with a bimodal grain size distribution, Acta Mater. 54 (2006) 1759–1766.

[18] B.Q. Han, J.Y. Huang, Y.T. Zhu, E.J. Lavernia, Strain rate dependence of properties of cryomilled bimodal 5083 Al alloys, Acta Mater. 54 (2006) 3015–3024.

[19] L.L. Zhu, S.Q. Shi, K. Lu, J. Lu, A statistical model for predicting the mechanical properties of nanostructured metals with bimodal grain size distribution, Acta Mater. 60 (2012) 5762–5772.

[20] L.L. Zhu, J. Lu, Modelling the plastic deformation of nanostructured metals with bimodal grain size distribution, Int. J. Plast. 30–31 (2012) 166–184.

[21] Y.G. Liu, J.Q. Zhou, H. David, A strain-gradient plasticity theory of bimodal nanocrystalline materials with composite structure, Composites Part B 43 (2012) 249–254.

[22] B.Q. Han, Z. Lee, D. Witkin, S. Nutt, E.J. Laveravi, Deformation behavior of bimodal nanostructured 5083 Al alloys, Metall. Mater. Trans. A 36 (2005) 957–965.

[23] M.J.N.V. Prasad, S. Suwas, A.H. Chokshi, Microstructural evolution and mechanical characteristics in nanocrystalline nickel with a bimodal grain-size distribution, Mater. Sci. Eng. A 503 (2009) 86–91.

[24] Z. Lee, D.B. Witkin, V. Radmilovic, E.J. Lavernia, S.R. Nutt, Microstructural evolution and mechanical characteristics in nanocrystalline nickel with a bimodal grain-size distribution, Mater. Sci. Eng. A 410 (2005) 462–467.

[25] A. Needleman, A continuum model for void nucleation by inclusion debonding, J. Appl. Mech. 54 (1987) 525-531.

[26] V. Tvergaard, J.W. Hutchinson, The relation between crack growth resistance and fracture process parameters in elastic-plastic solids, J. Mech. Phys. Solids. 40 (1992) 1377-1397.

[27] N.G. Broedling, A. Hartmaier, H.J. Gao, A combined dislocation-cohesive zone model for fracture in a confined ductile layer, Int. J. Fract. 140 (2006) 169-181.

[28] V.S. Deshpande, A. Needleman, E. Van der Giessen, A discrete dislocation analysis of near-threshold fatigue crack growth, Acta Mater. 49 (2001) 3189-3203.

[29] D.S. Dugdale, Yielding of steel sheets containing slits, J. Mech. Phys. Solids. 8 (1960) 100-104.

[30] T.K. Bhandakkar, A.C. Chng, W.A. Curtin, H.J. Gao, Dislocation shielding of a cohesive crack, J. Mech. Phys. Solids. 58 (2010) 530-541.

[31] V.S. Deshpande, A. Needleman, E. Van der Giessen, Discrete dislocation modeling of fatigue crack propagation, Acta Mater. 50 (2002) 831-846.

[32] N. Chandra, H. Li, C. Shet, H. Ghonem, Some issues in the application of cohesive zone models for metal–ceramic interfaces, Int. J. Sol. Struct. 39 (2002) 2827-2855.

[33] I. Scheider, M. Rajendran, A. Banerjee, Comparison of different stress-state dependent cohesive zone models applied to thin-walled structures, Eng. Fract. Mech. 78 (2011) 534-543.

[34] A.H. Chokshi, A. Rosen, J. Karch, H. Gleiter, On the validity of the Hall-Petch relationship in nanocrystalline materials, Scr. Metall. Mater. 23 (1989) 1679-1683.

[35] D.K. Kim, K. Okazaki, Processing of superconducting composite materials by electro-discharge compaction, Mater. Sci. Forum 553 (1992) 88–90.

[36] T.D. Shen, R.B. Schwarz, S. Feng, J.G. Swadener, J.Y. Huang, M. Tang, J.Z. Zhang, S.C. Vogel, Y.S. Zhao, Effect of solute segregation on the strength of nanocrystalline alloys: Inverse Hall-Petch relation, Acta Mater. 55 (2007) 5007-5013.

[37] G. Palumbo, U. Erb, K.T. Aust, Triple line disclination effects on the mechanical behaviour of materials, Scr. Metall. Mater. 24 (1990) 2347-2350.

[38] T.Y. Zhang, J.C.M. Li, Image forces and shielding effects of an edge dislocation near a finite length crack, Acta Metall. Mater. 39 (1991) 2739-2744.

[39] I.H. Lin, R. Thomson, Dislocation emission, and shielding for cracks under general loading, Acta Metall. 34 (1986) 187-206.

[40] Y.G. Liu, J.Q. Zhou, L. Wang, S. Zhang, Y. Wang, Grain size dependent fracture toughness of nanocrystalline materials, Mater. Sci. Eng. A 528 (2011) 4615-4619.

Advanced Materials Research Vol. 936 (2014) pp 409-414
© (2014) Trans Tech Publications, Switzerland
doi:10.4028/www.scientific.net/AMR.936.409

Numerical Simulation of Synthetic Heat Transfer in Laminar Nano-fluid in a Horizontal Pipe

Mohsen Mirzaei[1, a], Mostafa Jafari Gishin[2,b] and Mohammad Abbaspour[3,c]

[1]Engineering Department, ValiAsr University of Rafsanjan, Iran

[2] Engineering Department, Kar Higher Education institute, Rafsanjan, Iran

[3] Shiraz University of Technology,Shiraz, Iran

[a] m.mirzaei@vru.ac.ir, [b]Jafari@kar.au.ir, [c] abbaspour.mohammad@gmail.com

Keywords: Numerical simulations, Nano-fluid, grashof number.

Abstract. In this study, the effect of solid-liquid volumetric ratio in laminar flow of nano-fluid has been investigated numerically. The conservation equations are utilized in three dimensional elliptical forms for laminar and steady flow, and the effects of adding aluminum oxide nano-particles to water based-fluid are studied. First, the influence of solid-liquid volumetric ratio on the secondary flow vortices, non-dimensional temperature is investigated for a flow with a fixed low Reynolds number and different Grashof numbers in a horizontal pipe. Then, the effect of variation in solid-liquid volumetric ratio on Nusselt number and convective heat transfer coefficient along the pipe is studied. The results of this study are in good agreement with the current literatures.

Introduction

With the progress of sciences and developing the fields related to heat, lots of efforts have been made to enhance heat transfer. Among these researches, using additive materials to improve the fluid properties, relating to heat transfer, has been the subject of most researches in this field [1,2]. Nano-fluid concept refers to a new type of heat transfer fluids in which metallic or non-metallic nano-particles are added to the fluid, and since these particles are too small, in order of the based fluid molecules, they are suspended in the fluid and the fluid remains homogenous and particle deposition does not occur. Moreover, nano-particles do not cause blocked ducts, pipe erosion and also pressure drop in pipes. Nano-particles strongly enhance heat conductivity of the based fluid [3-6]. Pec and Chou [7] studied experimentally mixture friction and heat transfer behaviors of two types of nano-fluids. They used aluminum oxide (Al_2O_3) and titanium oxide (TiO_2) nano-particles into water as the based fluid. The results have shown the Nusselt number for both nano-fluids increases with solid volumetric ratio and Reynolds number. Wang et al. [8] proposed a model based on experiments to predict the effective heat conduction of nano-fluids. They used non-metallic copper oxide nano-particles with the volumetric ratios of less than 0.5%.

Governing Equations

In this study, the conservation equations are utilized in three-dimensional elliptical form for laminar and steady flow. Physical properties are considered to be constant except the density variations which are obtained by Boussinesq approximation. Therefore, with ignoring viscose dissipation, the conservation equations are given as follows:

Continuity equation:

$$\frac{\partial u_j}{\partial x_j} = 0 \qquad (1)$$

Momentum equation:

$$\frac{\partial}{\partial x_j}(\rho_{nf} u_i u_j) = \frac{\partial}{\partial x_j}\left[\mu_{eff}(\frac{\partial u_i}{\partial x_j})\right] - \frac{\partial p}{\partial x_i} - \rho_{nf,0} g_i \beta_{nf}(T - T_0) \quad (2)$$

Energy equation:

$$\frac{\partial}{\partial x_i}\left[(\rho c_p)_{nf} u_i T\right] = \frac{\partial}{\partial x_i}\left(k_{eff}\frac{\partial T}{\partial x_i}\right) \quad (3)$$

And the boundary conditions are:

$$V = Const., \quad T = Const., \quad at \quad z = 0$$
$$\frac{\partial T}{\partial r} = q'', \quad u_j = 0, \quad at \quad r = a \quad (4)$$

Non-dimensional numbers Prandtl, Reynolds, Grashof and local Nusselt numbers are as follows:

$$Pr_{nf} = \frac{\upsilon_{nf}}{\alpha_{nf}} \quad (5)$$

$$Re_{nf} = \frac{u_m d}{\upsilon_{nf}} \quad (6)$$

$$Gr = \frac{g_i \beta_f q'' d^4}{k_{ef} \upsilon_f^2} \quad (7)$$

$$Nu_\theta = \frac{q'' d}{k_{eff}(T_w - T_b)} \quad (8)$$

Numerical Solution

Governing equations are solved for laminar flow heat transfer. Figure 1 shows that structured grid was used for the solution domain (pipe). In order to discretize the governing equations, finite volume method was applied. Second order upwind difference scheme was used to discretize convective term in governing equations. SIMPLEC algorithm was utilized for the coupling between velocity and pressure since it is suitable for incompressible pipe flow. In addition, energy equation was discretized via second order upwind difference scheme.

To assure the validity of the results, first, the grid independency of the results was investigated. In this regard, different computational grids were studied and finally, it was observed that the results of the grid with the size of 36*160*36 are independent of grid size in perimeter, axial and radial directions, respectively.

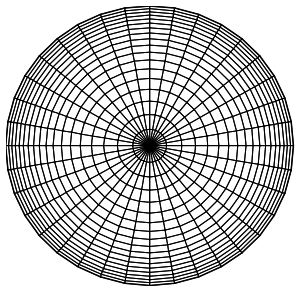


Fig 1. Computational Grid in Two-dimensional Outlet Plane with the Meshes with Similar Distances

Investigation of Variation in Nusslet Number and Convective Heat Transfer in Regard to Increasing Solid-Liquid Volumetric Ratio

Figure 2 shows the variations of Nusselt number which represent the ratio of convective heat transfer to conductive (molecular) heat transfer in terms of non-dimensional length of the pipe.

It is observed that Nusselt number decreases with increasing metallic solid nano-particles volumetric ratio i.e. molecular heat transfer increase relative to conductive heat transfer with increment of metallic solid nano-particles volumetric ratio. However, this phenomenon does not imply decreasing the heat transfer because the outlet temperature of the nano-fluid is more than that of based fluid and even the outlet temperature of the nano-fluid increases with increasing the volumetric ratio of nano-particles. Therefore, it can be concluded that molecular heat transfer (conduction) of the nano-fluid is more than that of based fluid. This fact was predictable since heat conductivity of nano-fluid is more than that of base fluid.

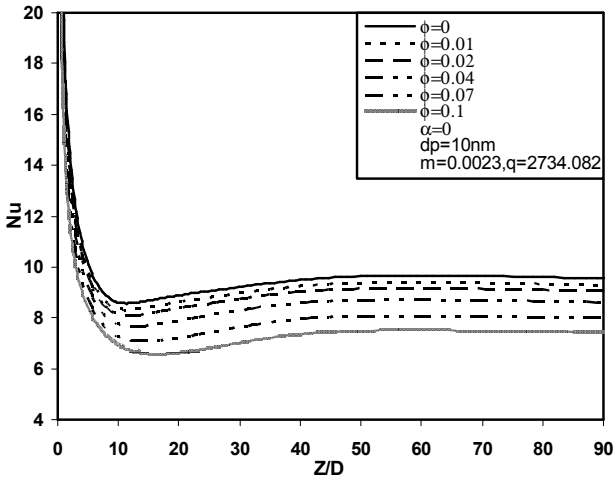


Fig 2- Nusselt Number Variations

Investigation was also done on coefficient of convective heat transfer (h) of the nano-fluid. Figure 3 shows the variations of convective heat transfer coefficient of nano-fluid in terms of a function of non-dimensional length.

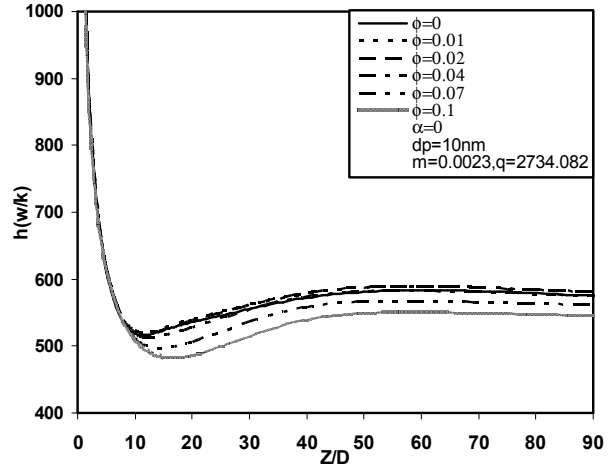


Fig 3- Variation of Heat Convection Coefficient in Terms of a Function of Non-dimensional Length

As it is obvious, first, the heat convection coefficient decreases with the increment of volumetric ratio of nano-particles and then increases. So it can be predicted nano-fluid temperature increases with volumetric concentration of solid particles and also the mean temperature of nano-fluid becomes closer to wall temperature. In this case, the thickness of thermal boundary layer is less hence, heat convection coefficient of nano-fluid increased with volumetric concentration of solid particles. But, when volumetric concentration of solid particles increases in a constant heat flux, buoyancy forces

reduce, yielding decrement of secondary velocities and consequently heat convection coefficient. Hence, for the cases with low volumetric ratios, which secondary velocities do not decrease so much, the coefficient of convective heat transfer of nano-fluid is more than that of the based fluid. But for high volumetric ratios, although the nano-fluid mean temperature approaches the wall temperature, secondary velocities decrease to some extent, leading the heat convection coefficient of nano-fluid lessens the heat convection coefficient of the based fluid (water).

Investigation on the Effects of Solid-Liquid Volumetric Ratio on Secondary Velocities and Non-Dimensional Temperature Contours

From figures showing secondary velocity vectors, decrement of buoyancy forces reduces the secondary velocity vectors and consequently, heat convection coefficient of nano-fluid decreases with increment of nano-particle concentration. This phenomenon can be justified in regard to the constant heat flux, changing the physical properties of nano-fluid and reduction of Grashof number.

Figures 4 to 7 illustrate secondary velocity vectors for a middle cross section. Obviously, increasing volumetric ratio of nano-particles and with constant heat flux and constant mass flow rate, leads to decrement of these vectors. Non-dimensional temperature contours are also shown in figure 4 to 7, in which the maximum temperature is above the pipe axis and close to upper wall, and the minimum temperature is below pipe axis and close to lower part of the wall. This is due to displacement of cool and warm fluid (secondary flows).

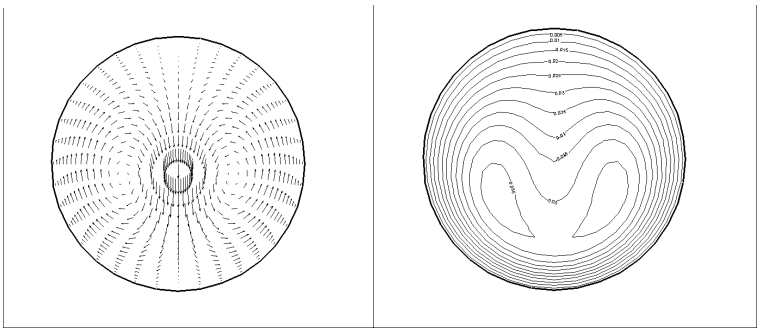


Fig- Secondary Velocity Vectors and Non-dimensional Temperature Contour for Volumetric Ratio of $\varphi = 0.02$

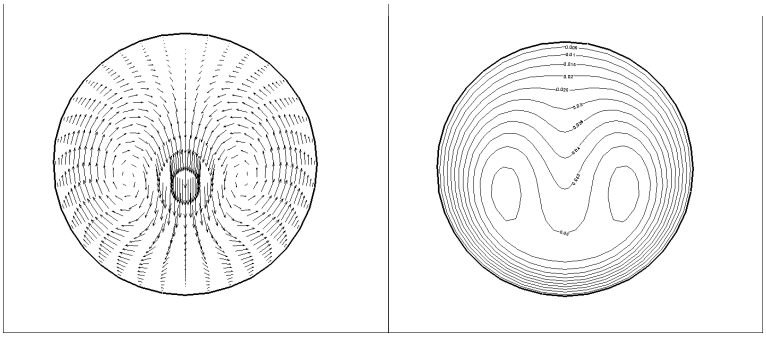


Fig- Secondary Velocity Vectors and Non-dimensional Temperature Contour for Volumetric Ratio of $\varphi = 0.04$

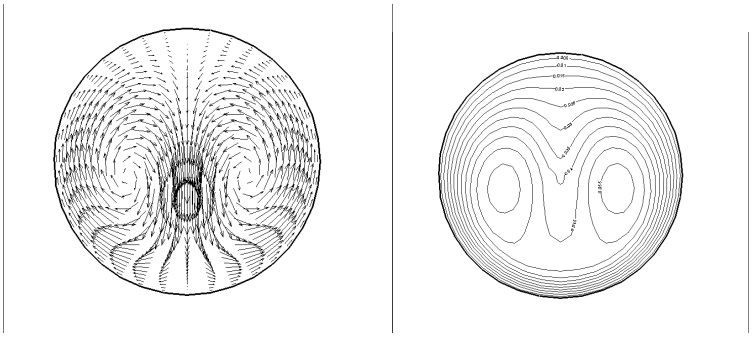


Figure 6- Secondary Velocity Vectors and Non-dimensional Temperature Contour for Volumetric Ratio of $\varphi = 0.08$

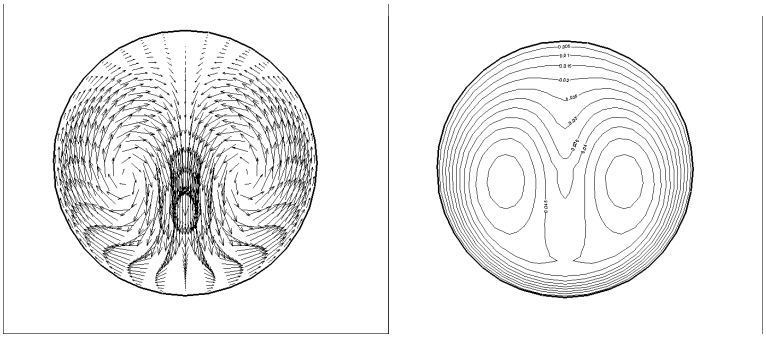


Figure 7- Secondary Velocity Vectors and Non-dimensional Temperature Contour for Volumetric Ratio of $\varphi = 0.1$

Conclusion

In this article, solid-liquid volumetric ratio of a nano-fluid in a laminar pipe flow has been investigated numerically. The nano-fluid included water as based fluid and Al_2O_3 nano-particles. The nano-fluid flow in a horizontal pipe was studied numerically considering synthetic heat transfer. The results have shown increasing volumetric ratio of nano-particles leads to increment of secondary velocity vectors and consequently, the temperature of nano-fluid in the transverse section of the pipe becomes homogenous. It is also observed adding solid nano-particles increases convective heat transfer coefficient for constant values Grashof and Reynolds number. For low volumetric ratios, the convective heat transfer coefficient of nano-fluid is more than that of based fluid due to the fact that in this case, there is no significant reduction in secondary velocities. But for high volumetric ratios, although the mean temperature of nano-fluid becomes closer to the wall temperature, secondary velocities decrease and hence, the convective heat transfer coefficient of nano-fluid becomes less than that of based fluid (water). Furthermore, the maximum temperature is above the pipe axis and near the upper part of the wall and the minimum temperature is below the pipe axis and near the lower part of the wall which is due to displacement of cool and warm fluids (secondary flows).

References

[1] K. V. Liu, S. U. Choi, K. E. Kasza, Measurements of pressure drop and heat transfer in turbulent pipe flows of particulate slurries, report, Argonne National Laboratory, aNL-88 15,1988.

[2] L. R. Webb,Principles of enhancement heat transfer, John Wiely & sons, New York.

[3] X. Wang, X. Xu, S. U. S. Choi, Thermal conductivity of nanoparticle-fluid mixture, J. Thermophys. Heat Transfer, vol. 13, No. 4, pp. 474-480, 1999.

[4] S.Lee, S.U.S.Choi,S.Li,J.A.Eastman, Measuring Thermal Conductivity of fluids containing Oxide Nanoparticles, Int. J. ASME ,Vol. 121 ,pp.280-288, 1999.

[5] Q.Li, Y.Xuan, Experimental investigation on transport properties of nano fluid,heat Transfer Science and Technology, Wang Buxuan ,edu., Higher Education, Press, pp. 757-762, 2000.

[6] Y.Xuan, Q.Li, Heat transfer enhansment of nanofluids, Int. J. Heat and fluid flow, vol. 21, pp.58-64, 2000.

[7] B.C.Pak, Y. I. Cho, Hydrodynamic and heat transfer of dispersed fluid with submicron metallic oxide particles, Exp. Heat Transfer, vol. 11, pp. 151-170, 1998.

[8] B.X.Wang, L.P.Zhou, X.F.Peng, A fractal model predicting the effective thermal conductivity of liquid with suspension of nanoparticles, Int. J. Heat and Mass Transfer, vol. 46, (2003), pp. 2665-2672.

Advanced Materials Research Vol. 936 (2014) pp 415-418
© (2014) Trans Tech Publications, Switzerland
doi:10.4028/www.scientific.net/AMR.936.415

Particle Swarm Optimization Technique for DNA Sensor Model Based Nanostructured Graphene

Vladimir Popov[1,a]

[1]Ural Federal University, 620083, Ekaterinburg, Russia

[a]popovvvv@gmail.com

Keywords: DNA biosensors, Nanomaterials, Particle swarm optimization, Genetic algorithm, Runge Kutta neural network.

Abstract: DNA biosensors has received significant attention. In particular, we can mention the model of a graphene-based DNA sensor which is used for electrical detection of DNA molecules. In this paper, we consider a method of selection of PSO parameters for optimization of the analytical model of a graphene-based DNA sensor. In particular, we consider genetic algorithms, multilayer perceptron networks with gradient learning algorithm, recurrent neural networks with gradient learning algorithm, and 4-order Runge Kutta neural networks with different learning algorithms. Also, we present experimental results for different intelligent algorithms.

Introduction

Biological DNA sensors has during the past years received significant attention (see e.g. [1]). In particular, DNA sensors have been commonly considered for diagnostic prediction in genetic research such as cancer or hereditary disease (see e.g. [2,3]). It should be noted that different interfaces between nanomaterials and biosystems are widely studied (see e.g. [4]). In particular, the limit of planar semiconductor devices is well known. In order to overcome the limit, various nanomaterials are widely proposed in sensor platform (see e.g. [5,6]). In particular, we can mention graphene with a two-dimensional thick monoatomic block of a carbon allotrope. It offers a large detection area for DNA sensing [7-10]. In paper [11], a particle swarm optimization method (PSO) was proposed to optimize the analytical model of a graphene-based DNA sensor which is used for electrical detection of DNA molecules.

PSO is a well-known computational method [12]. The method allows us to optimize a problem by iteratively trying to improve a candidate solution with regard to a given measure of quality.

It should be noted that PSO is one of the most efficient methods. The method is extensively used to solve many problems.

However, different PSO parameters significantly affect the quality of solutions [12]. There are a number of different strategies for setting PSO parameters [12]. In this paper, we consider a method of selection of PSO parameters for optimization of the analytical model of a graphene-based DNA sensor.

Implementation of PSO in DNA Sensor

In this section, we consider the implementation of PSO in DNA sensor that presented in the paper [11]. It should be noted that in our experiments we use basic definition and the general scheme of the implementation of PSO in DNA sensor. Following [11], we consider the DNA concentration model (see [13]):

$$I_d = \frac{3q^2(3\pi a^3 t^3 k_{BT})^{1/2}}{hL}\left(J_{-1/2}(\eta) + J_{-1/2}(-\eta)\right)\left(\frac{AF^2 + BF + C}{F}V_{gs(withoutDNA)} - V_t\right).$$

The parameters to be optimized in the DNA sensor model are A, B, and C coefficients in polynomial function

$$AF^2 + BF + C$$

that models iteration method of the DNA molecules adsorbed on graphene surface (see [11,13]). Vector

$$V[i] = (A[i,k+1] - A[i,k], B[i,k+1] - B[i,k], C[i,k+1] - C[i,k])$$

is the movement velocity vector of the particle i. Following [11], we assume that the number of particles is equal to 200, the number of dimensions is equal to 3, the maximum number of iteration is equal to 300, c1=2, c2=2.

The fitness function is the sum of squares of differences of the modeled current waveform for particle and the experimental current of the DNA sensor [11]. Mean absolute percentage error (MAPE) index is used as an error evaluation parameter to evaluate the quality of the obtained waveforms with respect to the experimental results [11].

Inertia Weight

In paper [11], inertia weight W was given by relations 0.4 < W < 1.2. However, any clear evidence of such choice was not given.

It is natural to consider some intelligent algorithm for the prediction of the value of W. In our computational experiments, we consider genetic algorithms (GA), multilayer perceptron networks (MPN) with gradient learning algorithm, recurrent neural networks (RN) with gradient learning algorithm.

Let f(x) be the best fitness value for x iterations and fixed value of W. Let fT(x) be the best fitness value for x iterations and values of W that predicted by intelligent algorithm T. It is clear that we can consider f[T,x] = fT(x) / f(x) as a measure of the quality of the convergence of the optimization process using PSO with intelligent algorithm T for prediction of W. Selected experimental results for different intelligent algorithms are given in Table 1 and Table 2.

Table 1. The convergence of the optimization process using pso with different intelligent algorithms for w.

x	10	20	40	60	100	200	300
F[GA,x]	0.954	0.976	0.989	0.993	0.994	0.998	0.999
F[MPN,x]	0.937	0.941	0.973	0.988	0.992	0.995	0.996
F[RN,x]	0.879	0.898	0.942	0.964	0.985	0.991	0.993

Table 2. Accuracy based on mape value for pso with different intelligent algorithms for w.

Concentration *F* (nM)	W = *const*	GA	MPN	RN
F = 0.01	95.42 %	95.32 %	96.03 %	96.37 %
F = 0.1	96.48 %	95.77 %	96.18 %	96.69 %
F = 1	96.67 %	95.81 %	96.42 %	96.73 %
F = 10	96.61 %	96.01 %	96.71 %	96.77 %
F = 100	96.48 %	96.11 %	96.54 %	96.81 %
F = 500	96.06 %	96.43 %	96.38 %	96.52 %

In Table 2, we use results for W = const from [11]. It is easy to see that we obtain only small difference for the convergence of the optimization process using PSO with different intelligent algorithms for W. However, it is clear that RN gives us some better results for the convergence of the optimization process using PSO.

It should be noted that W = const gives some better accuracy based on MAPE value for some values of concentration F then GA and MPN. However, we obtain slightly better results for accuracy based on MAPE value for PSO with RN.

Fitness Function

In this section, we continue the investigation of the prediction of the value of W by recurrent neural networks. In particular, we consider the optimization process using PSO with RN and the fitness function that predicted by 4-order Runge Kutta neural networks (see [14]). We consider 4-order Runge Kutta neural networks with the zero-order nonlinear recursive least square learning algorithm (RK[0]) and the first-order nonlinear recursive least square learning algorithm (RK[1]). We assume that the fitness function is a polynomial function that depends from differences of the modeled current waveform for particle and the experimental current of the DNA sensor.

Let fRK[j](x) be the best fitness value for x iterations where values of W were predicted by RN and the fitness function was predicted by 4-order Runge Kutta neural network RK[j]. Let f[RK[j],x] = fRK[j](x) / f(x). Selected experimental results for PSO with RN for W and 4-order Runge Kutta neural network for the fitness function are given in Table 3 and Table 4.

Table 3. The convergence of the optimization process using PSO with RN for W and 4-order Runge Kutta neural network for the fitness function.

x	10	20	40	60	100	200	300
F[RK[0],x]	0.821	0.863	0.911	0.933	0.933	0.933	0.933
F[RK[1],x]	0.544	0.673	0.789	0.791	0.791	0.791	0.791

Table 4. Accuracy based on MAPE value for PSO with RN for W and 4-order Runge Kutta neural network for the fitness function.

Concentration *F* (nM)	W = *const*	RK[0]	RK[1]
F = 0.01	95.42 %	96.49 %	98.13 %
F = 0.1	96.48 %	96.74 %	98.32 %
F = 1	96.67 %	96.83 %	98.47 %
F = 10	96.61 %	97.05 %	98.55 %
F = 100	96.48 %	96.92 %	98.12 %
F = 500	96.06 %	96.73 %	97.91 %

It is easy to see that we obtain significantly better convergence of the optimization process using PSO with 4-order Runge Kutta neural network for the fitness function. It is clear that RK[0] not gives us significant advantage for the accuracy based on MAPE value. However, we obtain considerably better results for accuracy based on MAPE value for PSO with RK[1].

Summary

In this paper, we have considered a method of selection of different PSO parameters for optimization of the analytical model of a graphene-based DNA sensor. In particular, we have considered inertia weight W and the fitness function. We have used genetic algorithms, multilayer perceptron networks with gradient learning algorithm, recurrent neural networks with gradient

learning algorithm, and 4-order Runge Kutta neural networks with different learning algorithms. We have presented experimental results for different intelligent algorithms. The best results we have obtained for simultaneous use of 4-order Runge Kutta neural networks with the first-order nonlinear recursive least square learning algorithm and recurrent neural networks with gradient learning algorithm.

Acknowledgement

This research was partially financially supported by RFBR, research project No. 13-01-00048 a, and under the Agreement 02.A03.21.0006 of 27.08.2013 between the Ministry of Education and Science of the Russian Federation and Ural Federal University.

References

[1] K. Ishii, C. Tang, Biological DNA Sensor, Academic Press, Chennai, 2013.
[2] J.L. Su, B.-S. Youn, W.P. Ji, J.H. Niazi, S.K. Yeon, B.G. Man, ssDNA aptamer-based surface plasmon resonance biosensor for the detection of retinol binding protein 4 for the early diagnosis of type 2 diabetes, Anal. Chem. 80 (2008) 2867-2873.
[3] A.L. Liu, G.X. Zhong, J.Y. Chen, S.H. Weng, H.N. Huang, W. Chen, L.Q. Lin, Y. Lei, F.H. Fu, Z.L. Sun, X.H. Lin, J.H. Lin, S.Y. Yang, A sandwich-type DNA biosensor based on electrochemical co-reduction synthesis of graphene-three dimensional nanostructure gold nanocomposite films, Anal. Chim. Acta 767 (2013) 50-58.
[4] X. Dong, Y. Shi, W. Huang, P. Chen, L.-J. Li, Electrical detection of DNA hybridization with single-base specificity using transistors based on CVD-grown graphene sheets, Adv. Mater. 22 (2010) 1649-1653.
[5] Y. Cui, Q. Wei, H. Park, C.M. Lieber, Nanowire nanosensors for highly sensitive and selective detection of biological and chemical species, Science 293 (2001) 1289-1292.
[6] P.R. Nair, M.A. Alam, Performance limits of nanobiosensors, Appl. Phys. Lett. 88 (2006) 233120-233123.
[7] N. Mohanty, V. Berry, Graphene-based single-bacterium resolution biodevice and DNA transistor: interfacing graphene derivatives with nanoscale and microscale biocomponents, Nano Lett. 8 (2008) 4469-4476.
[8] X. Dong, X. Zhao, L. Wang, W. Huang, Synthesis and application of graphene nanoribbons, Curr. Phys. Chem. 3 (2013) 291-301.
[9] F. Chen, Q. Qing, J. Xia, N. Tao, Graphene field-effect transistors: electrochemical gating, interfacial capacitance, and biosensing applications, Chem. 5 (2010) 2144-2153.
[10] M. Zheng, A. Jagota, E.D. Semke, B.A. Diner, R.S. Mclean, S.R. Lustig, R.E. Richardson, N.G. Tassi, DNA-assisted dispersion and separation of carbon nanotubes, Nature Mater. 2 (2003) 338-342.
[11] H. Karimi, R. Yusof, R. Rahmani, M. Ahmadi, Optimization of DNA Sensor Model Based Nanostructured Graphene Using Particle Swarm Optimization Technique, J. Nanomater. 2013 (2013) Article ID 789454.
[12] A. Jordehi, J. Jasni, Parameter selection in particle swarm optimisation: a survey, J. Exp. Theor. Artif. In. 25 (2013) 527-542.
[13] H.K.F. Abadi, R. Yusof, S.M. Eshrati, S.D. Naghib, M. Rahmani, M. Ghadiri, E. Akbari, M.T. Ahmadi, Current—voltage modeling of graphene-based DNA sensor, Neural Comput. Appl. 24 (2014) 85-89.
[14] Y.-J. Wang, C.-T. Lin, Runge-Kutta neural network for identification of dynamical systems in high accuracy, IEEE T. Neural Networ. 9 (1998) 294-307.

Advanced Materials Research Vol. 936 (2014) pp 419-423
© (2014) Trans Tech Publications, Switzerland
doi:10.4028/www.scientific.net/AMR.936.419

Preparation of Ethanol-sensing Gas Sensor Based on PECH /Multi-Wall Carbon Nanotubes Sensitive Films

Wei Yao, Guang-Zhong Xie[a,*], Hui-Ling Tai[b,*], Ya-Dong Jiang, Yong Zhou

School of Optoelectronic Information, State Key Laboratory of Electronic Thin Films and Integrated Devices, University of Electronic Science and Technology of China (UESTC), Chengdu 610054, China

[a]gzxie@uestc.edu.cn , [b]taitai1980@uestc.edu.cn

Keywords: gas sensor, PECH, ethanol, MWCNTs, two-layer film, composite film

Abstract. In this paper, Polyepichlorohyron(PECH)/multi-wall carbon nanotubes(MWCNTs) composite films and PECH/multi-wall carbon nanotubes two-layer film were deposited on interdigitated electrodes by airbrush technology to detect ethanol vapor of various concentrations at room temperature. Thickness and structure of the film were taken into account, so films of different thicknesses and with different structures were prepared respectively. The responses of the sensors to ethanol showed that composite film had a higher response than two-layer film, and the thick composite film performed better than its counterpart when they were exposed to ethanol vapor.

Introduction

Ethanol is liquid at atmospheric pressure and room temperature, but it is very easy to volatilize and belongs to volatile organic compounds (VOCs). It is combustible in air, so the detection of ethanol is very necessary, and much research has been done on the detection of ethanol. Wang, T.H. et al. fabricated the ZnO nanowires ethanol gas sensor [1,2]. Tomoki Maekawa et al developed ethanol gas sensor based on SnO2, which had showed high performance [3,4,5]. However, gas sensors based on semiconductor metal oxide have high power consumption because most of them work at high temperature operation [6,7]. As a result, the research of gas sensor working at room temperature is of great value. Gas sensors based on organic materials like polymers are thought to be a good choice [8,9].Polymer sensing materials have been used in various devices such as quartz crystal microbalance [10], surface acoustic wave (SAW) [11] device, opto-chemical device and chemical resistance. In this paper, gas sensors were prepared by using PECH combined with multi-wall carbon nanotubes to detect ethanol. In order to consider different factors affecting the response of the sensors, three different devices were prepared, one was made by depositing two-layer film with PECH upside and MWCNTs downside, the other two were made of PECH/MWCNTs composite film with different thicknesses. The testing result showed that composite film showed better response and linearity than two-layer film, and the sensor with a thicker film performed better in term of response and linearity than its counterpart.

Experimental

Materials

PECH was purchased from Alfa Aesar. Tetrahydrofuran, toluene and MWNTs (Outer diameter >50 nm, length 10-20um, 3.6 wt% in isopropanol) were purchased from Chengdu Organic Chemicals Co. Ltd, Chinese Academy of Sciences. All of these chemicals were utilized without further purification.

Preparation of Sensitive Films

In this experiment, the interdigitated electrode pairs (IDTs) with gold electrodes (width and gap of interdigitated electrodes were 50 um) on a silicon substrate with a sensing area of 5×8 mm2 were used. The structure of ethanol gas sensor was shown in the Fig.1. The sensitive films were fabricated as follows:

(1)Preparation of PECH and MWCNTs two-layer films: MWCNTs (3.6wt% in isopropanol) was diluted 20 times in isopropanol and then ultra-sonicated for ten minutes. Then 0.2 ml MWCNTs solution (0.18wt% in isopropanol) was airbrushed on the interdigitated electrodes, and 0.2 ml PECH (dissolved in THF, 10 mg/ml) airbrushed on the MWCNTs. All devices were dried at 60℃ in vacuum oven for 24 hours.

(2)Preparation of PECH and MWCNTs composite films: MWCNTs (3.6 wt% in isopropanol) was diluted 20 times in isopropanol followed and ultra-sonicated for ten minutes, then mixed with the PECH (dissolved in THF, 10 mg/ml) with the weight ratio of 1:1. And 0.2 ml of the mixture was airbrushed on the interdigitated electrodes after it was sonicated for ten minutes. In contract, another device was prepared with 0.4 ml of the mixture airbrushed. All devices were dried in a vacuum oven at 60℃ for 24 hours.

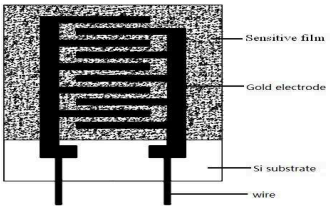


Fig.1 Structure of Toluene Gas Sensor

Experimental Procedures

The concentrations of ethanol vapor were controlled by MF-3C liquid organic solvent dynamic gas distribution device. N2 was used as a carrier gas. The changes of electric resistance caused by adsorption and desorption of alcohols were monitored by Keithley 2700, and the data was received by a computer system via a GPIB interface board. All experiments were carried out at room temperature.

Results and Discussions

The Sensitive Properties of the Films with Different Structures

In this paragraph, the dynamic response of the sensors with composite film exposed to different concentrations of ethanol was showed in Fig.2. The resistance of the sensors increased when they were exposed to the ethanol vapors at room temperature, which can be explained by "swelling effect". The distance of the conductive particles continuously increased and decreased through swelling/shrinking due to the adsorption/desorption of ethanol vapor, resulting in the increase and decrease of the whole resistance. Fig.3 showed the sensitivity curves of the sensors with different structures, one was made by depositing the polymer upside and MWCNTs downside. The other was made as the composite film, the response(S) was defined as (Rg-Ra)/Ra×100%， where Ra was the initial resistance of the sensor and Rg was the resistance of the sensor exposed to ethanol vapor. It could be clearly observed that the PECH/MWCNTs composite film showed a much better response to the ethanol vapors than the PECH/MWCNTs two-layer film. The response of the composite film to 2000ppm was 5.8%, while the response of the two-layer film to 2000 ppm was only 2.6%. Moreover, the sensitivity of the composite film is 2.75E-5/ ppm compared to 1.355E-5/ ppm of the two-layer film, which meant that the composite film had a larger sensitivity than the two-layer film.

In addition, the response time and the recovery time were defined as 90 percent and 10 percent of the time for sensors to arrive at its stable state after exposure to ethanol vapor or nitrogen, respectively. It was found that both the response time and recovery time of the sensor with two-layer film were 250s; while the response time and recovery time of the composite film were 200s. So the composite film was better than that of layer film.

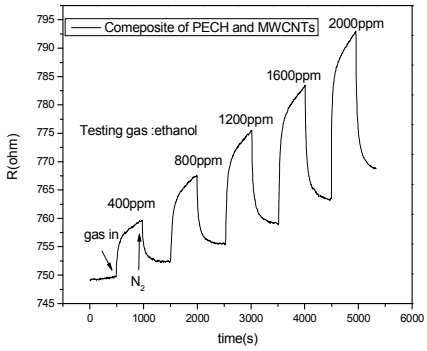


Fig.2 Real Resistance-time Curve of the Composite Film to the Ethanol Vapor Ranged from 400 ppm to 2000 ppm at Room Temperature

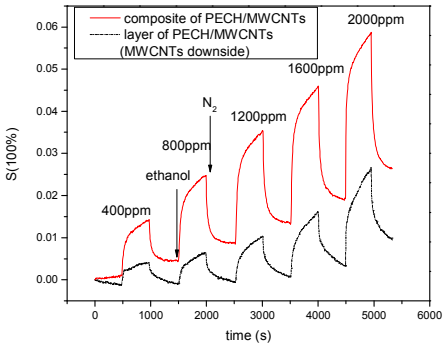


Fig.3 Dynamic Response Curves of the Composite and Two-layer Films to the Ethanol Vapor Ranged from 400ppm to 2000ppm at Room Temperature

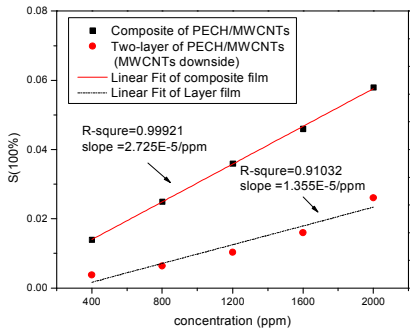


Fig.4 Sensitive Properties of the Composite and Two-layer Films with Ethanol Concentration Change Ranging from 400ppm to 2000ppm

The Sensitive Properties of Composite Films with Different Thicknesses

In order to study the effect of different thicknesses on the response of sensors, two sensors of composite films with different thicknesses were fabricated, one was airbrushed with 0.4 ml of the PECH/MWCNTs solution, and the other was airbrushed half quantity of that. The dynamic response curves of the two sensors were showed in Fig.5 (the sensors airbrushed with 0.4 ml and 0.2 ml of the solution were marked as sensor 1 and sensor 2, respectively). The initial resistance of sensor 1 was about 330Ω, while the initial resistance of sensor 2 was about 5720Ω, it could be seen that the sensor 1 had a better performance than sensor 2, i.e, the response of sensor 1 was about 5.69% when exposed to 2000 ppm of ethanol vapors, while the response of sensor 2 could only reach to about 3.0% at the same concentration. In addition, it could be seen from Fig.5 that the dynamic response curve of sensor 1 was much smoother than that of sensor 2, which meant that the signal noise ratio of sensor 1 was larger than that of senor 2. It could be seen from Fig.6 that the sensitivity of sensor 1 was 2.625E-5/ ppm, which was higher than 1.595E-5/ppm of sensor 2, which meant that sensor 1 had a better sensitivity to ethanol than sensor 2. Moreover, the R2 of the two sensors were 0.99674 and 0.9275 respectively, i.e, sensor 1 had a better linearity than sensor 2.

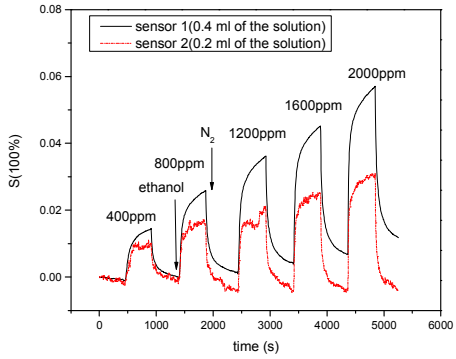


Fig.5 Dynamic Response Curves of the Two Different Composite Films to the Ethanol Vapor Ranged from 400ppm to 2000ppm

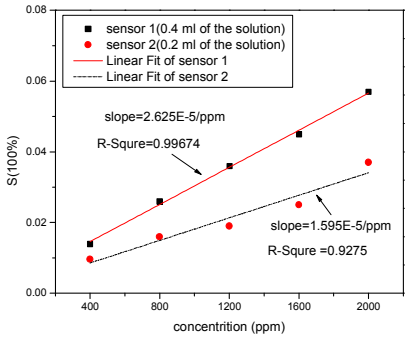


Fig.6 Sensitive Properties of the two Different Composite Films with Ethanol Concentration Change Ranging from 400ppm to 2000ppm.

The Selectivity of PECH Toward Ethanol

Selectivity is one of the most important elements of an excellent gas sensor. However, the VOC gas sensors perform a bad selectivity to testing gas because most of the VOC gases can cause the change of the resistance of the sensor. In order to test the selectivity of the sensors, the composite film sensor was exposed to vapors (the concentration is 2000ppm) of methanol, ethanol, acetone and isopropanol. Fig.7 showed that the responses of the sensor toward ethanol, methanol, acetone, isopropanol were 0.06, 0.02, 0.035 and 0.045, respectively, which showed that the response of the sensor to ethanol were the largest, so the sensor has an excellent selectivity toward ethanol.

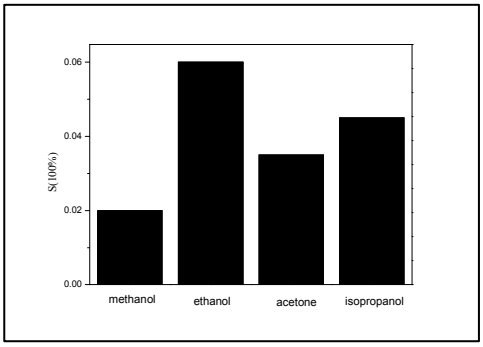


Fig.7 Selectivity of the Sensor with Composite film

In order to find out the reason why the sensor with composite film and the sensor with a thicker film had a better response, the morphologies of the surface of the sensitive films were observed by scanning electron microscope, and the SEM images were showed in Fig.8, Fig.9 and Fig.10, respectively. It can be observed from the Fig.8 and Fig.9 that the surface of the composite film had a much rougher surface than the two layer film, and the much rougher surface can preferably absorb the target gas because it had a lager contact area to the target gas. Similarly, the surface of sensor 1 had a rougher surface than sensor 2 although they were both composite films. So sensor 1 had a better response than sensor 2. Moreover, the amount of the PECH polymer may also be one of the reasons.

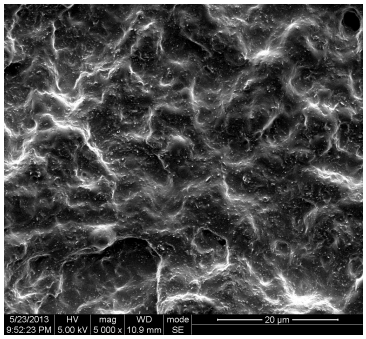


Fig.8 SEM Images of the Surface of PECH/MWCNTs Composite Film of Sensor 1

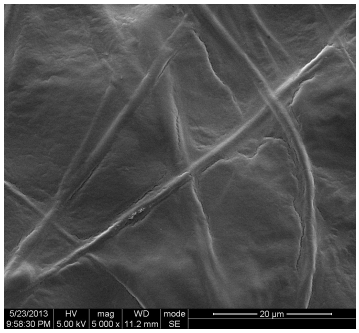


Fig.9 SEM Images of the Surface of PECH/MWCNTs two Layer Film

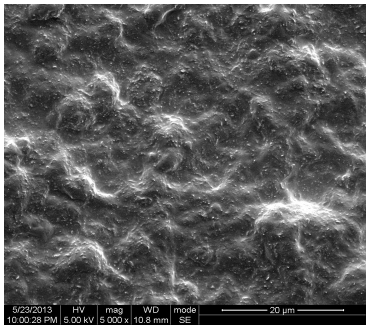


Fig.10 SEM Images of the Surface of PECH/MWCNTs Composite Film of Sensor 2

Conclusions

In this paper, three gas sensors were fabricated with different structures and different thicknesses by using PECH and MWCNTs. It was found that sensor with composite film had a better response and lineality than the two layer one, and the sensor with a thicker film performed better than its counterpart when exposed to ethanol gas.

Acknowledgements

This work was partially supported by Natural Science Foundation of China (NSFC) under grant nos. 61176066 and 61101031 and Specialized Research Fund for the Doctoral Program of High Education (20120185110012)

References

[1] Li, Q.H. ,Chen, Y.J. ,Wang, T.H.Applied Physics Letters Vol,84 , pp3654-3656(2004).

[2] O.k.Tan,W.Zhu.Q.Yan.L.B.Kong. Sensors and Actuators B:Chemical,Vol,65,pp361-365(2000).

[3] Tomoki Maekawa.,Jun Tamaki.,Norio Miura, Sensors and Actuators B Vol.9, pp 63-69,(1992).

[4] Chu Xiangfeng,Jiang Dongli,Guo Yu. Sensors and Actuators B: ChemicalVol, 120, pp.177-181.

[5] B.Bhooloka Rao.Materials Chemistry and Physics Vol,64 ,pp62-65(2000).

[6] Ting-Jen Hsueh,Cheng-Liang Hsu,. Sensors and Actuators B Vol. 126, pp. 473-477,(2007).

[7] Y.K.Fang,J.J.Lee. Thin Solid Films Vol,169,pp51-56 (1989).

[8] Xie H., Yang Q., Sun X.,Yang J., Huang Y. Sensors Actuators B Vol. 113, pp. 887, (2006).

[9] Yong Shin Kim,Seung-Chul Ha. Sensors and Actuators B Vol. 122,pp.211-218 (2007).

[10] K. Henkel, A. Oprea, I. Paloumpa, G. Apple, Selective polypyrrole electrodes for quart microbalance:NO2 and gas flux sensitivities, Sensors and Actuators B 76(2001) 124-129.

[11] N. Levit, D. Pestov, G. Tepper, High surface area polymer coatings for SAW-based chemical sensor applications ,Sensors and Actuators B 82(2002)241-249.

Advanced Materials Research Vol. 936 (2014) pp 424-428
© (2014) Trans Tech Publications, Switzerland
doi:10.4028/www.scientific.net/AMR.936.424

Preparation and Characterization of Polyacetylene/Expanded Graphite Composites

Mingming Hu[1,a], Linhua Song[2,b *] and Binglin Tao[1,c]

[1]College of Chemical Engineering, China University of Petroleum (East China), Qingdao 266580, PR China

[2]College of Science, China University of Petroleum (East China), Qingdao 266580, PR China

[a]humm0918@gmail.com, [b]281170984@qq.com, [c]taobinglin@126.com

Keywords: polyacetylene, expanded graphite, composites

Abstract. Expanded graphite (EG) is a promising conducting filler to enhance the conductivity of the polyacetylene (PA)/EG composites and also an ideal support to catalyst PA to polymerize on the surface of EG. The expanded interlayers of EG prepared by chemical oxidation is between 100 and 1500 nm. Diameters of the $Fe(naph)_3$ nanoparticles deposited on the external surface and internal surface (i.e. surface of the expanded graphitic layers) of EG range from 7 to15 nm. PA/EG composites were prepared by heterogeneous polymerization. PA catalyzed by $Fe(naph)_3$ nanoparticles supported on the external surface and at the edge of the expanded layers was inclined to form bigger aggregation, while PA grown between the interlayers exhibit smaller size. The bulk conductivity of the prepared composites is 5.78×10^3 $S\cdot m^{-1}$.

Introduction

Composites of conducting polymers with carbon materials have attracted a great of interests due to their unique electrical and mechanical properties and their potential applications in light emitting devices, batteries and electromagnetic shielding coating [1-4]. Carbon nanotubes (CNTs) as conducting fillers have been used to enhance the conductivity of the conducting polymers. Polyaniline/multiwalled carbon nanotube (MWNT) composites have been fabricated by in situ polymerization with bulk conductivity of 5180 $S\cdot m^{-1}$ [5]. Polypyrrole/carbon nanotube composites have been prepared by electropolymerization with a DC conductivity of 3965 $S\cdot m^{-1}$ [6]. In the previus work, polyacetylene (PA)/MWNT nanocomposites with core-shell structure were prepared and the bulk conductivity of the nanocomposites is about 240 $S\cdot m^{-1}$ [7].

Graphites are also an promising conducting filler, which are abundant in mineral reserves, highly conductive and lower cost than CNTs. Expanded graphites (EG) synthized from graphite by intercalation of oxidants and expansion at high temperature [8, 9] maintain the excellent electrical property and thereafter become an ideal catalyst support [10]. The conductivity of poly (phenylene sulfide)/EG composites reach 10^{-1} $S\cdot m^{-1}$ after the introduction of EG to the composites [11]. Although the polymethyl methacrylate (PMMA) is an insulator with conductivity of 10^{-14} $S\cdot m^{-1}$, the conductivity of PMMA/EG could be increased to 10^{-2} $S\cdot m^{-1}$ [12]. In addition, the special sandwich structure and long distance between the graphitic layers of EG make it easy to intercalate atoms and molecules into the expanded interlayers.

In this paper, natural flake graphite was used to synthize EG by chemical oxidation. Prior to polymerization, $Fe(naph)_3$ nanoparticles was supported on the surface of EG by a process of impregnation. EG performed not only as the conducting filler to improve the electrical properties of the PA/EG composites, but also as the catalyst support during polymerization in which PA grown on

the sueface of the EG. The bulk conductivity of the PA/EG composites is 5.78×10^3 $S\cdot m^{-1}$ which is measured by a four-probe approach.

Experimental

Synthesis of EG.

EG was prepared from natural flake graphite by chemical oxidation [8, 10]. 3.0 g of natural flake graphite was first treated with 30 mL mixed acid consisting of perchloric acid and phosphoric acid with a volume ratio of 5:1. Subsequently, 0.3 g of potassium permanganate was added into the mixed acid solution bit by bit to form graphite intercalated compound (GIC). The mixture was magnetically stirred for 1 h. 100 mL of deionized water was used to dilute the viscous mixture. 30 mL of hydogen peroxide was then added into the mixture to reduce the residual potassium permanganate and the reduzate of manganese dioxide into bivalent manganese ion. Graphite oxide was separated by centrifugalization for 15 min at 3000 $r\cdot min^{-1}$, followed by washing with distilled water to reach neutral. GIC was dried in an oven at 60 °C for 12 h. GIC (1.0-2.0 g) was explosively expanded at 900 °C for 10-20 s in an electric furnance to form EG.

Preparation of PA/EG composites.

0.5 g of EG was first impregnated with 1.0g of $Fe(naph)_3$ in 10 mL toluene under magnetically stirring for 48 h at room temperature. The suspension was separated by filtration and the $Fe(naph)_3$/EG was obtained after drying in an oven at 90 °C for 3 h. PA/EG composites was prepared by a method of heterogeneous polymerization based on a previous work [7]. 0.5 g of $Fe(naph)_3$/EG and 40 mL of anhydrous toluene were mixed in a 250 mL three-necked flask which was primarily purged with dry nitrogen for 20 min to remove oxygen. Subsequently, 0.02 mol of $Al(i\text{-}Bu)_3$ was added into the flask in nitrogen atmosphere. Upon the introduction of acetylene gas, polymerization started to run under stirring and lasted for 40 min at room temperature. The mixture after reaction presented purple. Toluene and ethanol solvents containing hydrochloric acid (volume ratio of 2 to 1) were used to wash the products until the filtrate became colourless. The product was dried under vacuum at room temperature overnight. For comparison with the composites, PA was prepared following the same protocols except substituting $Fe(naph)_3$/EG with $Fe(naph)_3$.

Characterization.

The morphologies and structures of the samples were analyzed using a JEM-2100UHR high resolution transmission electron microscope (HRTEM) with an accelerating voltage of 200 kV. A Hitachi S4800 scanning electron (SEM) was used to analyze the samples with an accelerating voltage of 5 kV. Fourier-transform infrared spectroscopy (FTIR) analyses were performed on a NEXUS FTIR spectrometer using KBr tablets. The bulk conductivity of the samples were measured by a four-probe approach at room temperature.

Results and dissussion

Morphology of the EG is revealed by SEM image. As shown in Fig. 1a, the prepared EG has a legume-like structure which can be attributed to the opening of plannar graphite networks caused by the rapid gasification of the itercalation compounds and surface oxygen groups. As a result of expansion, the EG exhibits a loose and porous structure with interlayer spacing between 100 and 1500 nm. This structure endows the EG with high surface area and large pore size. Thus, the EG is able to effectively support the $Fe(naph)_3$ catalyst which disperse on the surface and into the expanded graphite interlayers which is indicated by the SEM images. During impregnation process, the $Fe(naph)_3$ catalyst is easy to disperse into the expanded interlayer. And the expanded interlayer

has enough space to accommodate the $Fe(naph)_3$ nanoparticles which formed after being heated at at 90 °C for 3 h.

Representative TEM image of $Fe(naph)_3$/EG is shown in Fig. 1b. $Fe(naph)_3$ nanoparticles are well dispersed on the external and internal surface of EG with diameters of 7-15 nm. The TEM image also comfirms the loose structure of the EG.

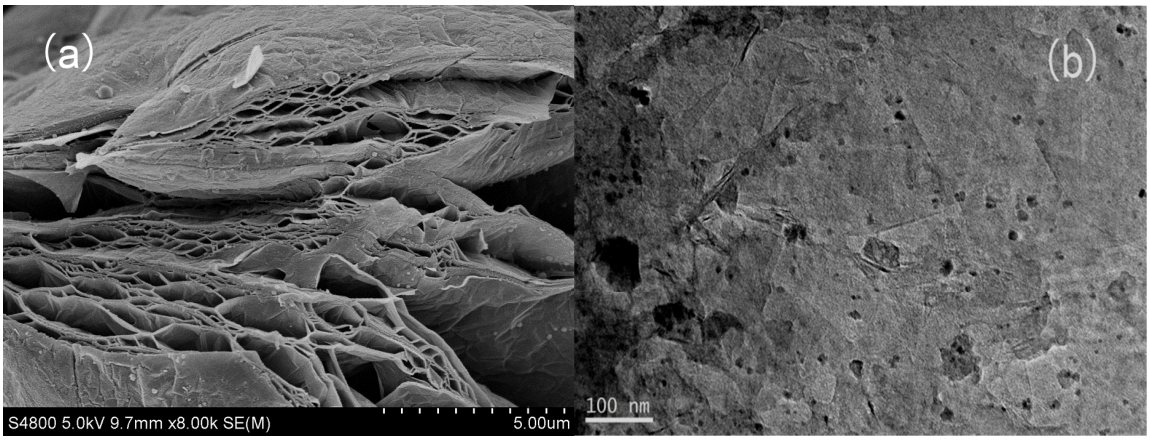


Fig 1 SEM image of EG (a) and TEM image of $Fe(naph)_3$/EG

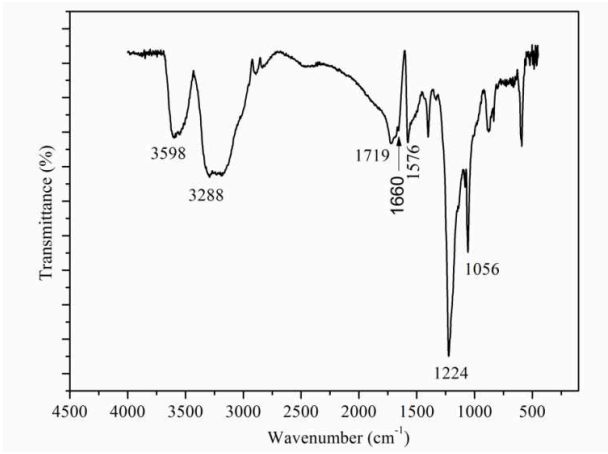


Fig. 2 FT-IR spectrum of PA/EG composites

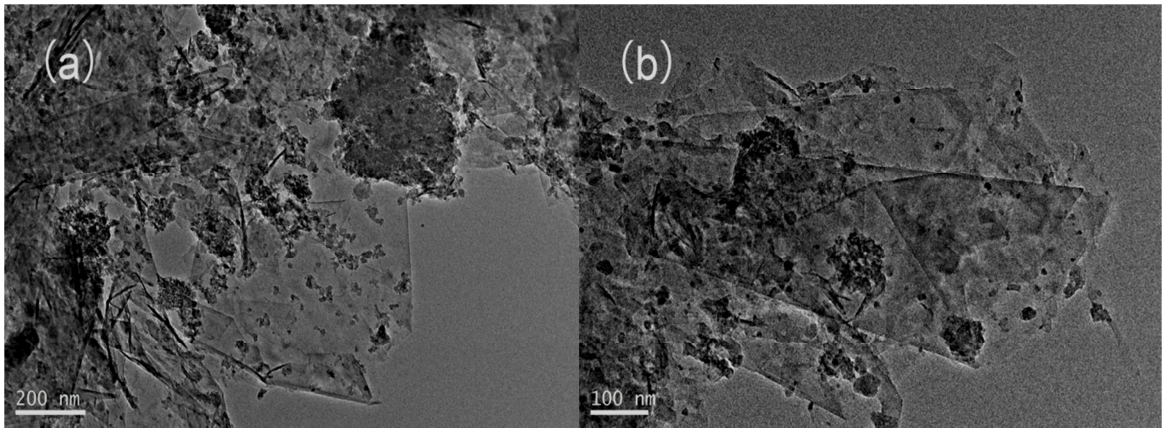


Fig. 3 TEM images of PA/EG composites

FTIR spectrum of PA/EG composites is shown in Fig. 2. The adsorption band at 3288 cm^{-1} corresponds to the hydroxy group which derives from oxidation of PA. And the peaks at 1660 and 1719 cm^{-1} can be asigned to α, β-unsaturated ketone and isolated ketone chromophores which is from the oxidation of C=C of PA [13]. Thus, PA formed on the surface of the EG and PA/EG were successfully prepared.

TEM images of the prepared PA/EG composites are shown in Fig. 3a and b. PA contained in the PA/EG composites are inclined to aggregate with different sizes. Because the acetylene monomers polymerized on the external and internal surface of the EG were through a process of heterogeneous polymerization [14] which was catalyzed by $Fe(naph)_3$ nanoparticles. The $Fe(naph)_3$ nanoparticles dispersed on the external surface and at the edge surface of the expanded layers are easy to contact with the acetylene monomer. As a result, the PA formed in bigger aggregation on the external surface. However, the $Fe(naph)_3$ nanoparticles deposited on the internal surface contact with less acetylene monomers which led to PA with smaller size. In addtion, PA formed at the edge surface of the expanded layers prevent the $Fe(naph)_3$ nanoparticles deposited on the internal surface of the expanded layers from contacting with acetylene monomer. Therefore, many $Fe(naph)_3$ nanoparticles are still contianed in the PA/EG composites after acid washing.

The bulk conductivity of the PA/EG composites is 5.78×10^{3} $S\cdot m^{-1}$ lower than that of EG (3.43×10^{4} $S\cdot m^{-1}$). Compared with PA (4.55×10^{-10} $S\cdot m^{-1}$) preapred by the same method, the bulk conductivity of PA/EG composites increases by 13 orders of magnitude. This reason can be attributed to the synergistic effects between PA and EG [15]. Electron of the graphite layer only flow horizontally to form a two dimentional conductive netmork. But, after filled with PA between the interlayers, the conjugated electron of PA and EG may have chance to exchange, which form a three dimentional conductive network. Thus, the bulk conductivity of the PA/EG composites could be increased to 5.78×10^{3} $S\cdot m^{-1}$ after the introduction of EG.

Summary

EG as a conducting filler was supported with $Fe(naph)_3$ nanoparticles to prepare PA/EG composites by a process of heterogeneous polymerization. The $Fe(naph)_3$ nanoparticles dispersed well on the external and internal surface of the EG. But the PA grown on the surface of EG is un-uniform. EG plays a more important role to improve the bulk conductivity of the PA/EG composites.

References

[1] H. Ago, K. Petritsch, M.S.P. Shaffer, A.H. Windle, and R.H. Friend, Composites of carbon nanotubes and conjugated polymers for photovoltaic devices, Adv. Mater. 11 (1999) 1281-1285.

[2] Y.Y. Meng, S.J. Zhou, S.Y. Xie, R.B. Huang and L.S. Zheng, Composites of oxidized boron carbonitride nanotubes with polyaniline preparation and conductivity studies, J. Phys. Chem. C 114 (2010) 13421-13426.

[3] H.S. Peng, X.M. Sun, F.J. Cai, X.C., Y.L. Chen. Y.C. Zhu, G.P. Liao, D.Y. Chen, Q.W. Li, Y.F. Lu, Y.T. Zhu and Q.X. Jia, Electrochromatic carbon nanotube/polydiacetylene nanocomposite fibres, Nat. Nanotechnol. 4 (2009) 738-741.

[4] K. Jurewicz, S. Delpeux, V. Bertagna, F. Béguin and E. Frackowiak, Superconductors from nanotubes/polypyrrole composites, Chem. Phys. Lett. 347 (2001) 36-40.

[5] T.M. Wu, Y.W. Lin, C.S. Liao, Preparation and characterization of polyaniline/multi-walled carbon nanotube composites Carbon 43 (2005) 734-740.

[6] P. Hojati-Talemi, G.P. Simon, Electropolymerization of polypyrrole/carbon nanotube nanocomposite films over an electrically nonconductive membrane, J. Phys. Chem. C 114 (2010): 13962-13966.

[7] M.M. Hu, L. H. Song, C.Y. Jiang, Multi-walled carbon nanotubes-supported Fe(naph)$_3$ nanoparticles to prepare polyacetylene/multi-walled carbonnanotubes nanocomposites, J. Mater. Sci. - Mater. Electron. 24 (2013) 2357-2361.

[8] G.H. Zheng, J.S. Wu, W.P. Wang and C.Y. Pan, Characterizations of expanded graphite/polymer composites prepared by in situ polymerization, Carbon 42 (2004) 2839-2847.

[9] SS S. R. Dhakate, M. Borah, R. B. Mathur, and T. L. Dhami (2008) Energy & Fuels 22: 3329.

[10] W. Li, C, Han, W. Liu, M.H. Zhang and K.Y. Tao, Expanded graphite applied in the catalytic process as a catalyst support Catalysis Today 125 (2007) 278-281.

[11] Y.F. Zhao, M. Xiao, S.J. Wang, X.C. Ge and Y.Z. Meng, Preparation and properties of electrically conductive PPS/expanded graphite nanocomposites, Compos. Sci. Technol. 67 (2007) 2528-2534.

[12] W.G. Zheng, S.C. Wong, Electrical conductivity and dielectric properties of PMMA/expanded graphite composites, Compos. Sci. Technol. 63 (2003) 225-235.

[13] H.W. Gibson, J.M. Pochan, Oxidation of Polyacetylene, Macromolecules 15 (1982) 242-247.

[14] W. Liu, Z.M. Cui, Q. Liu, D.W. Yan, J.Y. Wu, H.J. Yan, Y.L. Guo, C.R. Wang, W.G. Song, Y.Q. Liu, and L.J. Wan, Catalytic synthesis and structural characterizations of a highly crystalline polyphenylacetylene nanobelt array, J. Am. Chem. Soc. 129 (2007) 12922-12923.

[15] M.L. Clingerman, E.H. Weber, J.A. King and K.H. Schulz, Synergistic effects of carbon fillers in electrically conductive nylon 6,6 and polycarbonate based resins, Polym. Compos. 23 (2002) 911-924.

Advanced Materials Research Vol. 936 (2014) pp 429-433
© (2014) Trans Tech Publications, Switzerland
doi:10.4028/www.scientific.net/AMR.936.429

Preparation and Mechanics Properties of the EP/SiO_2 Nanocomposites

Wenfu Zeng[1,2], Yong Jiang[1,2,*], Shaofen Bu[1,2], Yanhuai Ding[1,2], Jiuren Yin[1,2]

[1]College of Civil Engineering & Mechanics, Xiangtan University, Xiangtan 411105, China;

[2]Institute of Rheology Mechanics, Xiangtan University, Xiangtan 411105, China;

*Corresponding author. E-mail address: jiangy@xtu.edu.cn

Keywords: epoxy resin；SiO_2；the compressive mechanics properties

ABSTRACT: The EP/SiO_2 nanocomposites were prepared by using epoxy resin as matrix, nano-SiO_2 as the modifier, polyamide as curing agent. The surface morphology of nano-SiO_2 was observed, the average particle diameter of nano-SiO_2 is 20nm. Their mechanics properties were studied and the experiment results were analyzed. The results indicated that the compressive stress-strain curves of the nanocomposites had obvious three phases characters, i.e., linear elastic phase, plastic yield flat phase and compact phase. Along with the nanograins content of the nanocomposites increasing, the compressive elastic modulus and compressive strength of the nanocomposites augmented. When the nanograins content is 5% and the transfiguration speed is 10mm/min, the compressive elastic modulus and compressive strength of the nanocomposites respectively improved 22.7% and 35.2% comparing with their of the pure epoxy resin. At the same nanograins content, with the transfiguration speed increasing, their compressive strength added.

Introduction

Epoxy resin (EP) as a typical representative of the thermosetting resin, with adhesive properties, mechanical properties, excellent insulating properties and shrinkage of small, low cost and other advantages, has been widely used in mang areas such as adhesives, paint, construction materials and composite matrix etc.. But cured EP which is brittle, fatigue resistance, heat resistance, impact resistance, poor, largely limits its application in some fields [1]. Therefore, in the premise of ensuring the EP of excellent performance, the toughening modification has become a hot research topic concerned in recent years.

The modified method of epoxy resin has use elastomer, thermoplastic resin, liquid crystal polymer blends [2-3], also has the nanocomposite modification techniques, such as nano-Al_2O_3 [4], nano carbon black [5], nano-Si_3N_4 [6], nano-SiO_2 [7-10], nano-TiO_2 [11], nano-ZnO [12], etc.. The nanocomposite modification techniques can improve greatly the toughness, strength, wear resistance and heat resistance of epoxy resin.

In this paper, the EP/SiO_2 nanocomposites were prepared by using epoxy resin as matrix, nano-SiO_2 as the modifier, polyamide as curing agent. The surface morphology of nano silica was observed, and the compression mechanical properties of the composite were experimentally studied.

Experiment

Preparation of the Nanocomposite Materials

Preparation of Nano-SiO_2

The right amount of anhydrous ethanol, distilled water and concentrated ammonia have been put in a clean beaker successively and be mixed uniformly. In the case of stirring, a certain amount

mixed solution of TEOS and ethanol have been dropped in the beaker slowly. After dripping finished, the solution were continued to stir about 2 hours. A white powder was obtained by vacuum filtration the solution, washing it by distilled water, drying, calcining in the muffle furnace; nano-SiO_2 powder was obtained.

Preparation of the EP/SiO_2 Nanocomposites

We measure out 20ml acetone and put into the beaker, then adding a certain amount of nano-SiO_2 powder. At first the solution were stirring for 15 minutes with a magnetic stirrer, then placed the beaker in ultrasonic cleaning instrument and ultrasound for 1 hour.

8g epoxy resin (E-44) preheated to 80℃ was added into the beaker and stirred for 10 minutes, then ultrasound for 30 minutes. Next, the beaker were put into the electric air blowing drying box and keep warm at 90℃ for 24 hours.

7.5g polyamide curing agent preheated to 80℃ was added into the beaker and stirred for 10 minutes, then the viscous liquid in the beaker was pouringed to self-made mold. Putting the mold into the electric air blowing drying box and keeping warm at 90℃ for 6 hours, the EP/SiO_2 nanocomposites were obtained.

Preparation and Analysis of the Samples

Referring to the test method for properties of resin casting body (GB2567-2008), the specimen was got by self-made mold and was cylinder specimen. Samples of five different nano-SiO_2 contents were prepared. The nano-SiO_2 contents (relative to the quality of epoxy resin matrix) are respectively 0%, 0.5%, 1%, 3% and 5%. The size of compressed sample was about diameter 19mm and height 40mm.

The surface morphology of nano-SiO_2 was observed by scanning electron microscope.

The uniaxial compression experiment was carried out under the conditions of 20℃and relative humidity 50%. The stress-strain curves of specimens were obtained by electronic universal testing machine at the deformation rate of 1mm/min, 5mm/min and 10mm/min respectively.

Results and discussion

Surface Morphology of Nano-SiO_2

Fig.1 was the SEM picture of nano-SiO_2. From the picture, we could see that the particle size of nano-SiO_2 was uniform and was about 20nm.

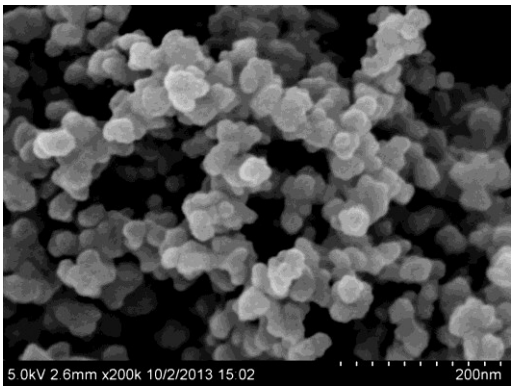
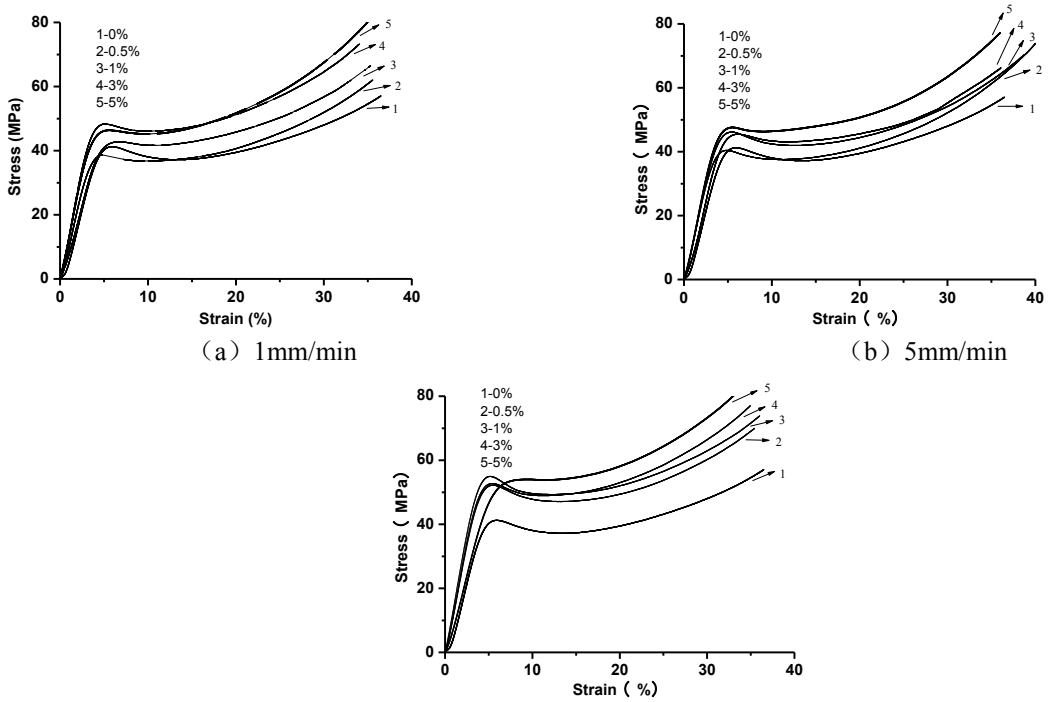


Fig.1 SEM Picture of Nano-SiO_2

Effect of Nano-SiO_2 Content on the Compression Properties of EP/SiO_2 Nanocomposites

Fig.2 was the compression stress-strain curves of the composites with different nano-SiO_2 contents at different deformation rates. As could be seen from Fig.2, the experimental curves had three stages, namely the linear elastic, plastic yield plateau region and densification section. With the increasing of the nano-SiO_2 content, the compressive strength of the composites increased.



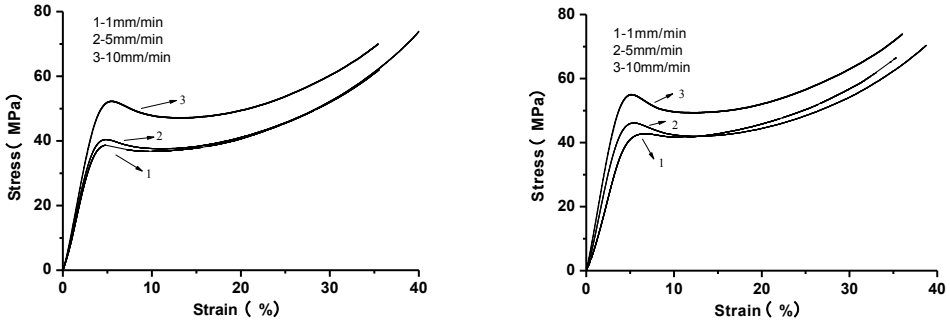
（a）1mm/min （b）5mm/min

（c）10mm/min

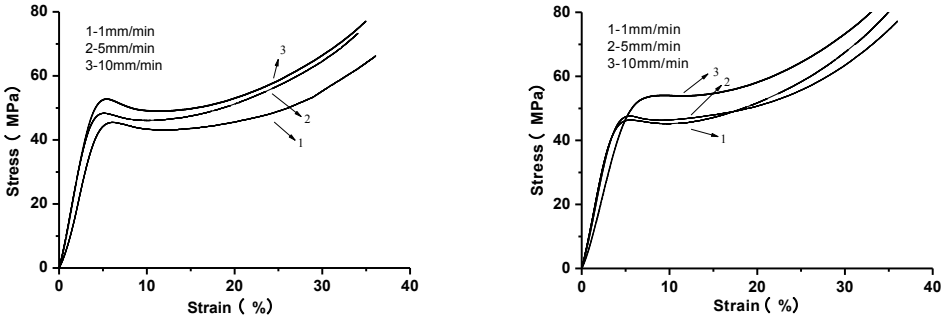
Fig.2 Effects of the Nano-Sio_2 Contents on the Stress-Strain Curves of the Composites At Different Deformation Rates

Effect of the Deformation Rate on the Compression Properties of EP/SiO_2 Nanocomposites

Fig.3 was the compression stress-strain curves of the composites at different deformation rates. From fig.3, we could seen that at elastic segment, with the increasing strain rate, the corresponding stress value of the sample which had the same nano-SiO_2 content was not obviously increased when it achieved to the same strain. That suggested the EP/SiO_2 nanocomposites did not have obvious strain rate effect under quasi-static compression process.



（a）0.5% （b）1%



（c）3% （d）5%

Fig.2 Effects of the Nano-SiO_2 Contents on the Stress-strain Curves of the Composites at Different Deformation Rates

The Compression Properties of EP/SiO_2 Nanocomposites

According to the experimental curve, we obtained the compression mechanical properties of the EP/SiO_2 nanocomposite (when the deformation was 5%, the corresponding stress and strain were used to calculate the modulus of elasticity in compression of the EP/SiO_2 nanocomposites), the results in table 1.

From table 1, we could seen that with the increasing of nano-SiO_2 content in the composite, the compression elastic modulus and compressive strength of that increased; while the nano-SiO_2 content was same, with the increasing of strain rate, compressive strength of the composite increased.

TABLE 1 COMPRESSIVE MECHANICAL PROPERTIES OF EP/SIO_2 NANOCOMPOSITES WITH DIFFERENT NANO-SIO_2 CONTENTS

SiO_2 [%]	Strain rate [mm/min]	Elastic modulus [MPa]	Average elastic modulus [MPa]	Compressive strength [MPa]
0	1	802.50	803.76	59.64
	5	803.88		62.43
	10	804.91		63.79
0.5%	1	800.33	875.84	63.97
	5	808.62		65.71
	10	1018.56		70.01
1%	1	819.42	929.08	66.62
	5	919.13		72.11
	10	1048.69		74.21
3%	1	966.71	959.51	72.21
	5	889.76		75.06
	10	1022.07		78.56
5%	1	943.18	985.88	77.09
	5	1028.21		81.42
	10	986.24		86.24

Conclusion

(1) The EP/SiO_2 nanocomposite materials were prepared by using epoxy resin as matrix, silica nanoparticles as modifier, polyamide as curing agent. This method is simple and easy to operate.

(2) The compressive stress-strain curve of EP/SiO_2 nanocomposite had three stages, namely the linear elastic, plastic yield plateau and tight stage. That does not have obvious strain rate effect in the quasi-static compression process. With the increasing of nano-SiO_2 content in the composite, the

compression elastic modulus and the compressive strength of it increased. When the nano-SiO_2 content was 5%, at 10mm/min deformation rate, the compression elastic modulus and compressive strength of the nanocomposites improved by 22.7% and 35.2% than those of pure epoxy resin were. For the composite of the same content, with the increasing of deformation rate, compressive strength of the nanocomposites increased.

Acknowledgement

This work was supported by the National Natural Science Foundation of China (No. 51002128).

References

[1] Chen xiangbao, Handbook of polymer matrix composite materials, Chemical Industry Press, Beijing, 2004.

[2] Lopez J, Rico M, Montero B, et a1, Polymer blends based on an epoxy-amine thermoset and a thermoplastic: Effect of thermo-plastic on cure reaction and thermal stability of the system, J. Therm. Anal. Cal., 2009, 95(2):369-376.

[3] Zhang Jiaoxia, Zheng Yaping, Xu Lei, Developments of toughening and modifying of epoxy resin, Adhesion in China, 2008, 29(9):39-42.

[4] Zhou Hongjun, Yin Guoqiang, Lin Xuan, et al, Curing kinetics of epoxy/activated nano-Al_2O_3 composites, Journal of Chemical Industry and Engineering (China), 2011, 62(6):1749-1755.

[5] Zhou Hongjun, Yin Guoqiang, Wu Wanshuang, et al, curing kinetics of epoxy resin/modified nano-carbon black composite, China Plastics, 2011, 25(4):33-37.

[6] Ji Xiaoli, Xu Guocai, Wang Jun, Effect of nano Si_3N_4 on the cure reaction of epoxy resin, Thermosetting Resin, 2009, 24(5):17-20.

[7] Lu Shaorong, Zhang Hailiang, Wang Xiayu, Preparation and properties of EP/SiO_2 hybrid materials, Polymer Materials Science & Engineering, 2005, 21(5):261-265.

[8] Yang Yanqing, Xu Liang, Preparation and property characterization of spherical silica epoxy resin composites, Plastics Science and Technology, 2010, 38(2):74-77.

[9] Zhai Xiaoyu, Zhang Qiuyu, Ai Qiushi, et al, Preparation of nano-SiO_2 and its application in epoxy resin, China Adhesives, 2009, 18(6):62-65.

[10] Tian Chao, Yang Li, Ma Hanbing, Properties of epoxy resin toughened by adding nano-SiO_2, Journal of Southwest University of Science and Technology, 2012, 27(4):11-14.

[11] Dong Yuancai, Meng Wei, Wei Xin, et al, Preparation and property of EP/TiO_2 nanocomposite, China Plastics Industry, 1999, 27(6):37-38.

[12] Zhang Rongliang, Liu Yashu, Jin Yunxue, Preparation of EP/ZnO composites with needle nano-ZnO and its mechanical properties, Journal of Materials Engineering, 2011, 12(1):78-82.

Advanced Materials Research Vol. 936 (2014) pp 434-438
© (2014) Trans Tech Publications, Switzerland
doi:10.4028/www.scientific.net/AMR.936.434

Effects on Characteristics of the SiO_2-to-Na_2O Ratio on Nano-SiO_2 Metakaolin-based Geopolymers

Kae-Long Lin[1, a], Kang Gao[2, b], De-Ying Wang[2, c], Kang-Wei Luo[1, d], Wen-Hsuan Chang[1, e] Dian Yi Huang[1, f], Hui Cheng[2, g] and Rong Cui[2, h]

[1] Department of Environmental Engineering, National Ilan University, Yilan, 26047, Taiwan

[2] Department of Environmental and Material Engineering, Yan-Tai University, China

[a]kllin@niu.edu.tw, [b]gaokang19891201@163.com, [c]wdy591118@163.com, [d]dark83054689@yahoo.com.tw, [e]g9567419@yahoo.com.tw, [f]m13225647@gmail.com, [g,] chenghui6@126.com, [h] glorytre@163.com

Keywords: Geopolymer, metakaolin, nano-SiO_2, SiO_2/Na_2O molar ratio, microstructure

Abstract. This study explores the effects of the SiO_2/Na_2O molar ratio (1.0-2.0) on the properties of 1% nano-SiO_2 metakaolin-based geopolymers. The porosity, flexural strength, DTA/ TGA, and NMR are investigated to study the mechanical and microstructure properties of the geopolymers. The results show that the flexural strength increased, and that the products of geopolymerization filled pores with curing time, causing the microstructure to become denser. Moreover, a nano-SiO_2 metakaolin-based geopolymer sample with a SiO_2/Na_2O ratio of 1.5 exhibited more strength and less porosity. Applying the 1% nano-SiO_2 to a geopolymer enhances compactness, improves uniformity, and increases strength.

Introduction

Geopolymers are amorphous three dimensional aluminosilicate materials with ceramic-like properties that are produced and hardened at ambient temperature. Geopolymeric materials are attractive because they exhibit desirable properties, such as rapid compressive strength development, low permeability, resistance to acid, resistance to freeze-thaw cycles, and a tendency to drastically decrease the mobility of most heavy metal ions within the geopolymeric structure [1-3].These characteristics make geopolymers promising building, toxic waste immobilizing, sealing, and temperature-resistant materials [4]. Their porosity can be less than that of cements or mortars and thus superior mechanical properties are obtained [5]. Geopolymer production generates almost no NOx, SOx, CO, and only emits small amounts of CO_2 [6].

Nanoparticles are particles between 1 and 100 nm that create volume and surface effects. Nanoparticle preparation and application and their size and surface effects offer various benefits; they can be used to develop high-performance polymers [7]. Nanosynthesis technology has been widely applied to develop novel materials with better properties and to improve conventional material properties. Studies have been conducted on nanocoatings, high-strength structural materials, macromolecular-based nanocomposites, magnetic materials, optical materials, and bionic materials [8]. To understand the effects of different SiO_2-to-Na_2O molar ratios (1.00-2.00) on the 1% nano-SiO_2-metakaolin-based geopolymers. The mechanical properties were determined by porosity and flexural. Moreover, the microstructure of all samples were determined by DTA/ TGA, and NMR.

Materials and Methods

Materials

Metakaolin was calcined using kaolin at 650 °C for 3 h. The Na_2SiO_3 solution was produced in Taiwan. It was composed of 29.5% SiO_2, 9.1% Na_2O, 61.4% H_2O, and the Ms (SiO_2/Na_2O) was 3.4. Analytical-grade 99% pure NaOH was used. The nano-SiO_2 used was a white powder. The SiO_2

content was 99.9%, the average particle size was approximately 10 nm, and the specific surface area was 670 m^2/g.

Sample Preparation

NaOH and distilled water were mixed with a Na_2SiO_3 solution and allowed to cool to room temperature. With constant stirring, nano-SiO_2 was added to the alkali activator. The SiO_2/Na_2O ratio were 1.00, 1.25, 1.50, 1.75 and 2.00; the solid-to-liquid ratios was 1.03; and the nano-SiO_2 additions were 1%. The alkali activator solution was prepared 24 h before use to ensure that the activator component was mixed uniformly. Table 1 shows the mixture proportions. A mechanical mixer was used to mix the activator solution and 1000 g metakaolin for a few minutes. The fresh paste was then rapidly poured into plastic molds (5 × 5 × 5 cm). Samples were placed into an oven at 80 °C for 24 h. Mechanical properties and the microstructure performance of specimens were tested after 1, 7, 14, 28 and 60 days.

TABLE 1 THE MIXTURE PROPORTIONS OF SAMPLES

SiO_2/Na_2O	Nano-SiO_2 addition(%)	Mixture proportion by weight (g)				
		Metakaolin	Nano-SiO_2	Na_2SiO_3	NaOH	H_2O
1.00	1	1000	10	575.1	158.3	350.8
1.25	1	1000	10	718.9	141.4	289.7
1.50	1	1000	10	862.7	124.5	228.5
1.75	1	1000	10	1006.5	107.6	167.3
2.00	1	1000	10	1150.3	90.7	106.2

Results and Discussion

Material characteristics

The metakaolin used in this study was obtained from kaolin calcined at 650 °C for 3 h. It was slightly pink. Before and after calcination, the proportions of kaolin and metakaolin were 3.35 (compared to kerosene). However, the pH values of kaolin and metakaolin were 6.52 and 5.74, respectively. This is because dehydroxylation during calcination makes metakaolin weakly acidic. The chemical composition of raw materials was determined using X-ray fluorescence. The results show that kaolin is mainly composed of SiO_2 (53.7%) and Al_2O_3 (37.88%). Metakaolin is composed of 59.6% SiO_2 and 38% Al_2O_3. Table 2 shows the chemical composition of the raw materials.

TABLE 2 CHEMICAL COMPOSITION OF THE RAW MATERIALS

Composition	Kaolinite	Metakaolin
SiO_2 (%)	53.70	59.60
Al_2O_3 (%)	37.88	38.00
Fe_2O_3 (%)	0.88	1.30
CaO (%)	0.20	0.24
K_2O (%)	0.34	0.32

Flexural strength

Figure 1 showed the flexural strength of 1% nano-SiO_2-metakaolin-based geopolymers with various SiO_2-to-Na_2O ratios. It can be concluded that flexural strength of geopolymers with different SiO_2-to-Na_2O ratio at 60 days were 14.5 MPa, 14.7MPa, 15.4 MPa,13.9 MPa and 12.9 MPa, respectively. It indicated that the flexural strength of metakaolin-based geopolymer whose SiO_2-to-Na_2O ratio of 1.5 was the largest. The increase of the SiO_2/Na_2O ratio in the geopolymeric system caused the dissolution of considerable aluminosilicates and the subsequent gradual shift of the

chemical system from the monosilicate chains and cyclic trimers to species with larger rings and complex structures and polymers, resulting in the 3D polymeric framework and increasing the mechanical properties of the resulting geopolymeric materials. When the SiO_2/Na_2O ratio continued to increase from 1.75 to 2.00, the metakaolin-based geopolymer strength decreased. When the SiO_2/Na_2O ratio increased, the high content of the sodium-silicate solution caused the geopolymer paste to become sticky because of the viscous nature of the sodium-silicate solution. The high amount of the sodium-silicate solution may inhibit the geopolymerization process.

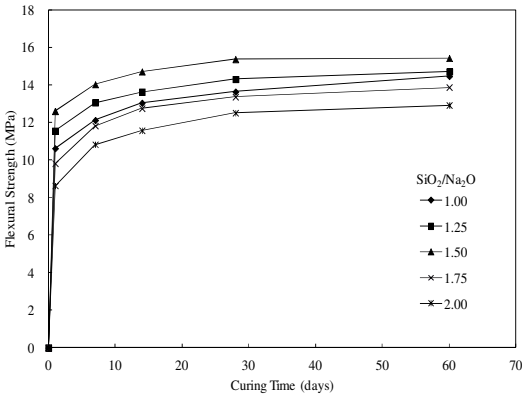


Figure 1 Flexural strength of geopolymers.

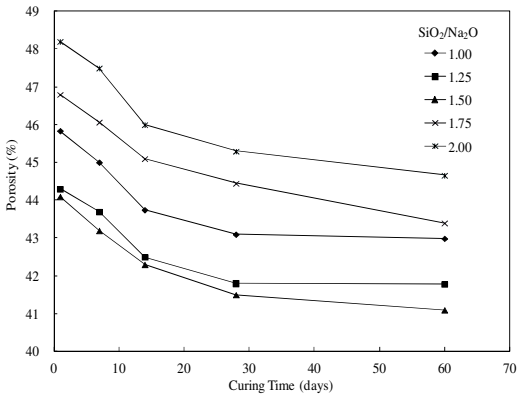


Figure 2 Porosity of geopolymers.

Porosity

Figure 2 presents the porosity is a main factor of affecting the sample's mechanical characteristics. The structure tends to be denser and the strength will be enhanced if the porosity gets lower. Figure 2 shows the porosity of nano-SiO_2-metakaolin-based geopolymers with various solid-to-liquid ratios after 1, 7, 14, 28 and 60 days of curing. The porosity range is between 41.1% and 48.2%. The results displayed that the porosity would decrease slightly with the growth of the curing time. When the SiO_2/Na_2O ratio was 1.50, the geopolymer porosity was the smallest, which is consistent with the following higher mechanical strength and smaller cumulative pores.

TG/DTA analysis

Figure 3 shows the thermogravimetric analysis of 1% nano-SiO_2-metakaolin-based geopolymers with various SiO_2-to-Na_2O ratios. Three distinct endothermic peaks appear in the DTA spectra: 130 °C, 450 °C, and 650 °C. Therefore, the whole area was divided into three sections: 50–350 °C, 350–550 °C, and 550–690 °C. Although the first endothermic peak was not completely symmetrical, it can be assumed that two or more endothermic peaks overlapped part of this temperature range. The weight loss occurring at the temperature range of 50–340 °C was primarily caused by the dissipation of free water in the pores. A further increase in temperature produces shrinkage, and finally damages the geopolymer structure. The continuous weight loss at 350–550 °C was due to the evaporation of structural water. Because water is a vital aspect of the final geopolymer structure ($Mn((SiO_2)z–AlO_2)n\cdot wH_2O$), an adequate water content should be present in the initial geopolymer paste to proceed reactions.

Table 3 shows the weight loss of nano-SiO_2-metakaolin-based geopolymers. The weight losses occurring at 350–550 °C during the polymerization reaction were related to gels. When SiO_2/Na_2O ratio was 1.5, the weight loss of the nano-SiO_2-metakaolin-based geopolymers was slightly higher due to forming more gels than other ratios. At SiO_2/Na_2O ratio was 1.5, the weight losses of the geopolymer at 350–550 °C and 550–690 °C were relatively high. When the curing time increased, the weight loss at a temperature range of 350–550 °C gradually increased. As the curing time increased, the polymerization reaction became more thorough, and the structure of the specimen became gradually denser. Therefore, the weight loss in the two highest temperature ranges was greater. These results are consistent with the previous mechanical characteristics.

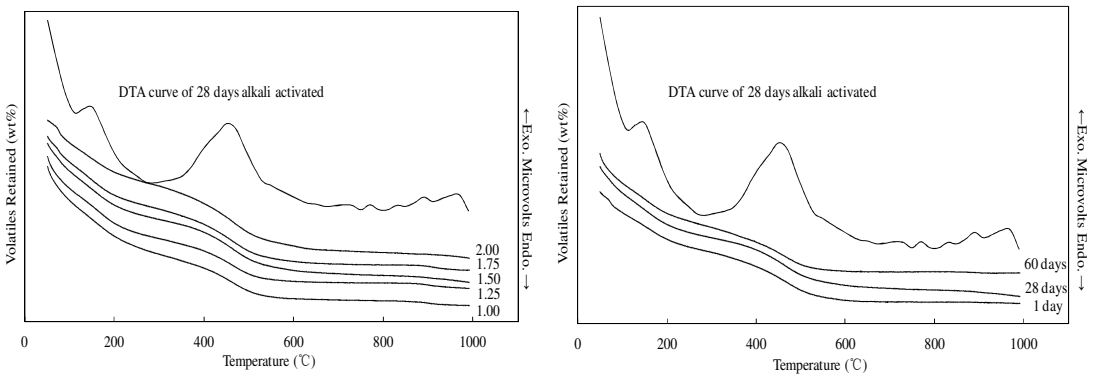


Figure 3 TG/DTA of 1% nano-SiO_2-metakaolin-based geopolymers with various SiO_2/Na_2O ratios.

TABLE 3 WEIGHT LOSS OF NANO-SIO_2-METAKAOLIN-BASED GEOPOLYMERS

SiO_2/Na_2O	Nano-SiO_2 addition (%)	Curing Time (days)	Temperature (℃)		
			50-350	350-550	550-690
1.00	1	28	19.60	8.63	1.21
1.25	1	28	18.37	8.77	1.43
1.50	1	28	16.90	9.87	1.84
1.75	1	28	16.73	7.45	0.63
2.00	1	28	15.19	7.35	0.64
1.50	1	1	18.16	8.54	1.07
1.50	1	28	16.90	9.87	1.84
1.50	1	60	14.87	9.91	1.93

NMR Analysis. The main characteristics of the geopolymer structure, such as the elements location of Si and Al, coordination, cross-linking degree of the tetrahedral, can be analyzed by MAS-NMR to obtain a better understanding of the structural properties and the geopolymerization process. Figures 4 and 5 show the ^{29}Si MAS NMR spectra of nano-SiO_2-metakaolin-based geopolymers. The ^{29}Si MAS NMR spectra of samples are broad, diffuse, and have no sharp peaks. ^{29}Si chemical shifts are sensitive to changes in the coordination of the Si atom. The Q^0 species, which denote silicate ions with no bridging oxygen atoms, typically exhibit ^{29}Si chemical shifts of approximately -65 ppm. For each of the additional bridging oxygen atoms, a shift of approximately 10 ppm to the shielded region; that is, the ^{29}Si chemical shift of the fully polymerized silicon species (Q^4) is approximately -110 ppm.

Figures 4 and 5 show that the resonance of nano-SiO_2-metakaolin-based geopolymers of the two major components are -90 and -97 ppm, which can be assigned to Q^4 (3Al) and Q^4 (2Al), respectively. Compared with MK, the signal center shifted to a lower magnetic field, and was still positioned in the range of geopolymer resonance. This indicates a change in the environment of the Si atoms. Furthermore, the changes of peak location, intensity, and full width at half maximum in ^{29}Si NMR spectra are caused by different Si/Al molar ratios, the type of cation used, and the adsorbed molecules of the sample structure.

Summary

This study presents the effects of different SiO_2-to-Na_2O molar ratios (1.00-2.00) on the 1% nano-SiO_2-metakaolin-based geopolymers.The geopolymer with the optimal SiO_2-to-Na_2O molar ratio and nano-SiO_2 addition level contained more structural water and gels that are beneficial to structure development. In summary, the application of nano-SiO_2 to a geopolymer enhanced its

compactness and increased its strength. Moreover, a nano-SiO_2 metakaolin-based geopolymer sample with a SiO_2/Na_2O ratio of 1.5 exhibited more strength and less porosity. Applying the 1% nano-SiO_2 to a geopolymer enhances compactness, improves uniformity, and increases strength.

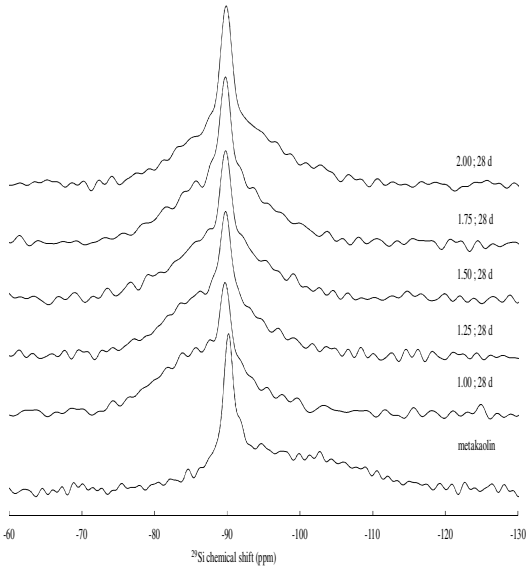


Figure 4 NMR spectra of geopolymers (28 days).

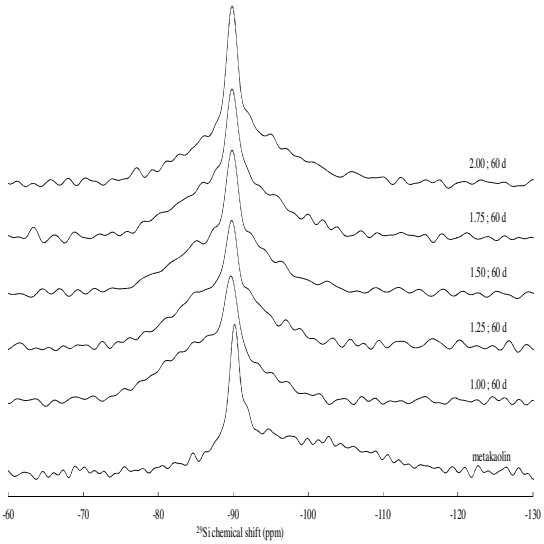


Figure 5 NMR spectra of geopolymers (60 days).

References

[1] J. Davidovits, Geopolymers and geopolymer new materials, J. Therm. Anal. 35 (1989) 429-441.

[2] J.G.S. Van Jaarsveld, J.S.J. Van Deventer, L. Lorenzen, The potential use of geopolymer materials to immobilize toxic metals: part I: Theory and applications, Miner. Eng. 10 (1997) 659-669.

[3] Y.S. Zhang, W. Sun, Z.J. Li, Composition design and microstructural characterization of calcined kaolin-based geopolymer cement, App. Clay Sci. 47 (2010) 271-275.

[4] E. Álvarez-Ayuso, X. Querol, F. Plana, A. Alastuey, N. Moreno, M. Izquierdo, O. Font, T. Moreno, S. Diez, E. Vazquez, M. Barra, Environmental, physical and structural characterisation of geopolymer matrixes synthesised from coal (co-)combustion fly ashes, J. Hazard. Mater. 154 (2008) 175-183.

[5] A. Komnitsas, Potential of geopolymer technology towards green buildings and sustainable cities, Procedia Eng. 21 (2011) 1023 – 1032.

[6] J.L. Provis, P. Duxson, R.M. Harrex, C.Z. Yong, J.S.J. Van Deventer, Valorisation of fly ashes by geopolymerisation, Global Nest J. 11(2) (2009) 147-154.

[7] M. Aly, M.S.J. Hashmi, A.G. Olabi, M. Messeiry, E.F. Abadir, A.I. Hussain, Effect of colloidal nano-silica on the mechanical and physical behavior of waste-glass cement mortar, Mater. Design. 33 (2012) 127–135.

[8] E.D. Rodríguez, S. A. Bernal, J.L. Provis, J. Paya, J.M. Monzo, M.V. Borrachero, Effect of nanosilica-based activators on the performance of an alkali-activated fly ash binder, Cem. Concr. Compos. 35 (2013) 1–11.

Advanced Materials Research Vol. 936 (2014) pp 439-443
© (2014) Trans Tech Publications, Switzerland
doi:10.4028/www.scientific.net/AMR.936.439

Microstructures of ZnO electrospun nanofibers on AZO glass

Xiuzhen Lu, Yanyan Chang, Mingtao Xu and Bo Peng

Key Laboratory of Advanced Display and System Applications, Ministry of Education and SMIT Center, School of Mechatronic Engineering and Automation, Shanghai University, Shanghai, 200072, China

Email: xzlu@shu.edu.cn

Key words: ZnO nanofibers; electrospinning; AZO glass;

Abstract: ZnO electrospun nanofibers were considered to be potential novel materials in applications of photovoltaic devices and sensors. AZO glass was usually used in those devices as transparent electrodes. ZnO nanofibers on AZO glass were synthesized by electrospinning and calcination process. Scanning electron microscopy (SEM), transmission electron microscopy (TEM), Raman spectroscopy and photoluminescence (PL) spectrum was employed to investigate the morphology, structure and optical performance of ZnO nanofibers. Network structure composed of sheet ZnO was observed. Raman spectra and PL spectrum indicated the existence of defect states in the ZnO nanofibers.

Introduction

Electrospinning technology, created by Formhals in 1934 [1], is a process that allows the continuous production of fibers ranging from several nm to over 1μm. And it was thought to be a simple, versatile and convenient method and potential for textile processing firstly due to its characteristics of easy control and low cost. In recent year, electrospun nanofibers were found to have wide application prospect on the photovoltaic devices, and bioscoffolds result from its high surface-to-volume ratio and large specific surface area [2, 3]. Zinc Oxide (ZnO) electrospun nanofibers with the advantages of ZnO one-dimensional nanostructure and electrospun nanofibers have attached much attention in the past ten years [4-7]. Great improvement of ZnO electrospun nanofibers had been achieved in the application of solar cell, sensor, photo catalytic activity, detector *etc.* in past five years, which demonstrated ZnO electrospun nanofibers as a novel 1D semiconductive materials have a huge application potential [8-11].

In particular, most of the applications in devices need electrodes to connect with an external circuit. AZO film was an appreciated material usually used as electrodes in optoelectronic devices, especially in devices with ZnO structure. Therefore, we will report the ZnO electrospun nanofibers synthesis on a glass with AZO film coated on surface in this paper. The ZnO nanofibers were successfully synthesized by electrospun technology and calcinations on AZO glass. The morphology, microstructure and optical properties are studied subsequently.

Experimental procedure

Polyvinyl alcohol (PVA) and $Zn(CH_3COO)_2 \cdot 2H_2O$ was used as the precursor for ZnO nanofibers synthesis by electrospun technology. A PVA aqueous solution was prepared firstly by solving 10 g PVA in distilled water with a weight ratio of 10%. Then 0.6 g $Zn(CH_3COO)_2 \cdot 2H_2O$ was added into the PVA solution with constant stirring until the transparent solution was obtained. The obtained

solution was placed in a plastic syringe and fed through a metal capillary with flat tip and a diameter d=0.4 mm. The syringe with solution was then fixed on the electrospun system (shown in figure 1) with a distance of 15 cm between the tip of capillary and the collector. AZO glass was placed on the metal roller as collectors. Electrospun was carried out at a voltage of 18 kV and a rotation speed of 4000 r/min at room temperature. After dried at 100 °C for 1 hour, the composite nanofibers were calcined at 400 °C and 600 °C temperatures in air to get ZnO nanofibers. X-ray diffraction (XRD), scanning electron microscopy (SEM), transmission electron microscopy (TEM), Raman spectroscopy and PL spectra were employed for analysis of microstructure, morphology and photoluminescence emission properties.

Results and analysis

Fig.1 shows the SEM images of aligned ZnO nanofibers on AZO glass. The morphology shown in fig.1 (a) indicated the volatilization of solvent was incomplete. After calcination, a network structure with flat ZnO nanofibers was formed, which indicated the morphology of ZnO nanofibers was not the typical ones. The shape of a single fiber was not columniform. TEM was employed to examine the microstructure of ZnO nanofibers in greater detail. Fig.2 shows the TEM images of different magnifications of ZnO nanofibers calcined at 400 °C and 600 °C for 2 hours. The low-magnification TEM micrograph (fig.2 (a, c)) shows the sheet structure of a single fiber. The network structure was shown by HRTEM shown in fig.2 (c) clearly. The polycrystalline structure of ZnO nanofibers was clearly observed at higher magnification, as shown in fig.2 (b, d). Figure 2 (b) shows the nanofibers calcined at 400 °C were composed of small grains with a diameter of no more than 10 nm. Grain coarsening was occurred at high calcination temperature, which was shown in fig.2 (d). The ZnO grain with diameter of tens of nanometers was obtained in the nanofibers calcined at 600 °C.

The Raman scattering was performed to investigate the vibrational properties of ZnO nanofibers on AZO glass at room temperature. Fig.3 (a) shows one normal mode at 436 cm^{-1} was observed in the Raman spectra of ZnO nanofibers calcined at 400 °C, which was corresponding to E_{2H} phonon scattering mode. The appearance of E_{2H} confirmed the wurtzite crystal structure of ZnO nanofibers since E_{2H} mode is related to the band characteristic of wurtzite phase [12]. However, the peak of E_{2H} was very weak, which indicated the low crystalline structure of ZnO nanofibers. The peaks of ZnO at 328, 436 and 584 cm^{-1} were observed clearly in the Raman spectra of ZnO nanofibers calcined at 600°C, which were assigned to E_{2H-2L}, E_{2H} and E_{1L}, respectively [13]. The strong E_{2H} peak demonstrated higher crystalline structure of ZnO, while the appearance of E_{1L} peak was attributed to the formation of oxygen deficiency, interstitial Zn and free carrier [14]. The peak at 328 cm^{-1} was ascribed to the multiple phonon scattering [15]. More peaks were observed in the Raman spectra of ZnO nanofibers treated at 600 °C. The strong and sharp peak of E_{2H} indicated the perfect wurtzite structure and high crystalline of ZnO nanofibers. The peak at 384 cm^{-1} corresponds to A1 symmetry with TO mode. Meanwhile, the peak of E_{1L} was considered to be related to the defect states.

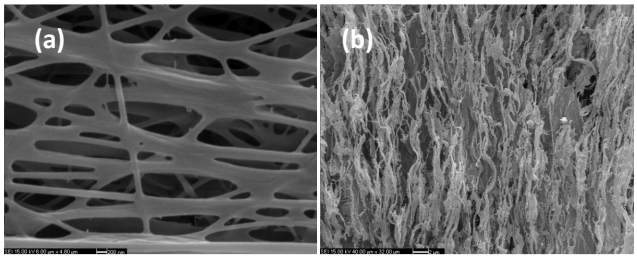


Fig. 1 SEM images of PVA/ Zn $(CH_3COO)_2 \cdot 2H_2O$ composite electrospun nanofibers and ZnO nanofibers calcined at 600 °C.

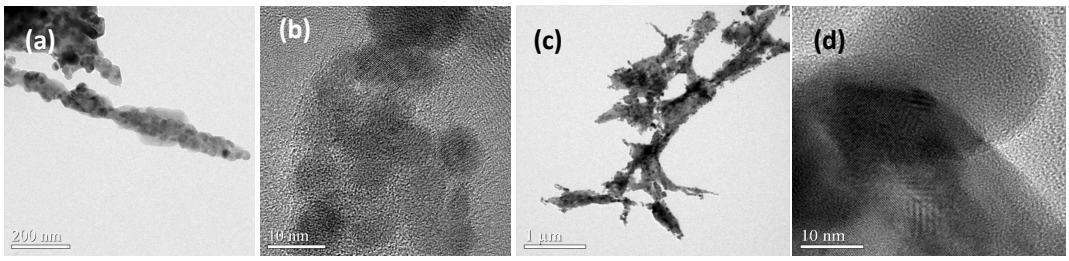


Fig. 2 (a) TEM images of ZnO nanofibers calcined at 400 °C for 2 hours on AZO glass. (b) HRTEM images of ZnO naonofibers shown in (a). (c) TEM images of ZnO nanofibers calcined at 600 °C for 2 hours on AZO glass. (d) HRTEM micrograph of ZnO nanofibers shown in (c).

The photoluminescence (PL) spectrum of ZnO nanofibers on AZO glass calcined at 400 °C and 600 °C measured at room temperature with excitation wavelength of 325 nm was shown in fig. 4. Emission peaks at 396, 450, 467nm were observed in ZnO nanofibers calcined at 400 °C. Ultraviolet (UV) emission around 396 nm was attributed to the exciton recombination related to the near band edge emission of ZnO [16]. The blue emission of 450 and 467 nm could be considered originating from the intrinsic defects in the ZnO nanofibers, such as Zn interstitial and oxygen vacancies. Emission peaks at 395, 450, 468 and 516 nm were observed in ZnO nanofibers calcined at 600 °C. The weak and broad green peak around 516 nm was owing to the transitions in defect states [17]. The existence of defect states in ZnO nanofibers demonstrated by PL results was in well agreement with the results of Raman analysis.

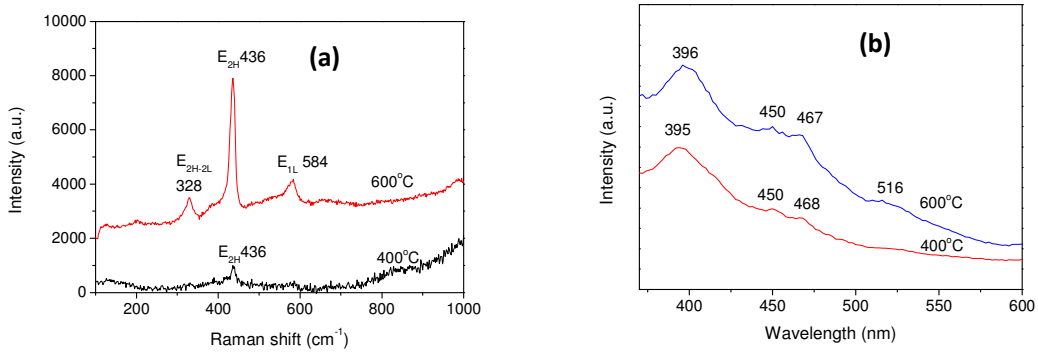


Fig. 3 (a) Raman spectra of ZnO nanofibers on AZO glass calcined at 400 °C and 600 °C. (b) Room temperature photoluminescence spectrum of ZnO nanofibers on AZO glass calcined at 400 °C and 600 °C.

Conclusion

ZnO electrospun nanofibers on AZO glass were obtained after calcinations at 400 and 600°C. Network structure composed of sheet ZnO was formed after electrospinning and calcination. Small grains with diameter of no more than 10 nm and big gains with diameter of tens nanometers were observed in the ZnO nanofibers calcined at 400 and 600°C respectively. The existence of defect states in the ZnO nanofibers was determined by the appearance of E_{1L} peak in Raman spectra and peak of 516 nm in PL spectrum.

Acknowledgement

This work was financial supported under the National Natural Science Foundation of China (NSFC) under Grant No. 51102161.

References

[1] Formhals A, U. S. Patent 1975504, (1934).

[2] Sining Yun, Sangwoo Lim, Improved conversion efficiency in dye-sensitized solar cells based on electrospun Al-doped ZnO nanofiber electrodes prepared by seed layer treatment, Journal of Solid State Chemistry. 184 (2011) 273–279.

[3] Shawn H. Lim a, Hai-Quan Mao, Electrospun scaffolds for stem cell engineering, Advanced Drug Delivery Reviews. 61 (2009) 1084-1096.

[4] Xinghua Yang, Changlu Shao, Hongyu Guan, Xiliang Li, Jian Gong, Preparation and characterization of ZnO nanofibers by using electrospun PVA/zinc acetate composite fiber as precursor, Inorganic Chemistry Communications. 7 (2004) 176-178.

[5] Bin Ding, Tasuku Ogawa, Jinho Kim, Kouji Fujimoto, Seimei Shiratori, Fabrication of a super-hydrophobic nanofibrous zinc oxide film surface by electrospinning, Thin Solid Films. 516 (2008) 2495-2501.

[6] Yuval Shmueli, Gennady E. Shter, Ossama Assad, and Hossam Haick, Structure and electrical properties of single Ga/ZnO nanofibers synthesized by electrospinning, Journal of Material Research Society. 27 (2012) 1672-1678.

[7] Jin-Ah Park, Jaehyun Moon, Su-Jae Lee, Sang-Chul Lim, Taehyoung Zyung, Fabrication and characterization of ZnO nanofibers by electrospinning, Current Applied Physics. 9 (2009) S210–S212.

[8] Sujuan Wu, Jinhua Li, Shing-Chung Lo, Qidong Tai, Feng Yan, Enhanced performance of hybrid solar cells based on ordered electrospun ZnO nanofibers modified with CdS on the surface, Organic Electronics. 13 (2012) 1569-1575.

[9] Xinchang Wang, Minggang Zhao, Fang Liu, Jianfeng Jia, Xinjian Li, Liangliang Cao, C_2H_2 gas sensor based on Ni-doped ZnO electrospun nanofibers, Ceramics International. 39 (2013) 2883-2887.

[10] Ayman Yousef, Nasser A.M. Barakat, Salem S. Al-Deyab, R. Nirmala, Bishweshwar Pant, Hak Yong Kim, Encapsulation of CdO/ZnO NPs in PU electrospun nanofibers as novel strategy for effective immobilization of the photocatalysts, Colloids and Surfaces A: Physicochem. Eng. Aspects. 401 (2012) 8-16.

[11] Wei Tian, Tianyou Zhai, Chao Zhang, Song-Lin Li, Xi Wang, Fei Liu, Dequan Liu, Xingke Cai, Kazuhito Tsukagoshi, Dmitri Golberg, and Yoshio Bando, Low-cost fully transparent ultraviolet photodetectors based on electrospun ZnO-SnO_2 heterojunction nanofibers, Advanced Materials. 25 (2013) 4625-4630.

[12] Jae Young Park and Sang Sub Kim, Growth of nanograins in electrospun ZnO nanofibers, Journal of the American Ceramic Society. 92 (2009) 1691-1694.

[13] T. C. Damen, S. P. S. Porto, and B. Tell, Ramaneffect in zinc oxide, Physical Review. 42 (1966) 570-574.

[14] Ji Nan Zeng, Juay Kiang Low, Zhong Min Ren, Thomas Liew, Yong Feng Lu, Effect of deposition conditions on optical and electrical properties of ZnO films prepared by pulsed laser deposition, Applied Surface Science, 197-198 (2002) 362-367.

[15] Puneet Singh, Kunal Mondal, Ashutosh Sharma, Reusable electrospun mesoporous ZnO nanofiber mats for photocatalytic degradation of polycyclic aromatic hydrocarbon dyes in waste water, Journal of Colloid and Interface Science, 394 (2013) 208-215.

[16] Ye Zhang, Hongbo Jia, Rongming Wang, Chinping Chen, Xuhui Luo, and Dapeng Yu, Cheoljin Lee, Low-temperature growth and Raman scattering study of vertically aligned ZnO nanowires on Si substrate, Applied Physics Letters. 83 (2003) 4631-4633.

[17] K. Vanhausden, WL Warren, CH Seager, DR Tallant, JA Voigt, and BE Gnade, Mechanisms behind green photoluminescence in ZnO phosphor powders, Journal of Applied Physics. 79 (1996) 7983-7990.

CHAPTER 5:

Materials for Energy Sources and Energy Supply

Advanced Materials Research Vol. 936 (2014) pp 447-451
© (2014) Trans Tech Publications, Switzerland
doi:10.4028/www.scientific.net/AMR.936.447

Research of properties on Li-Ion batteries based on a polypyrrole derivative bearing TEMPO as a cathode material

Lihuan Xu[1, a], Fang Yang[2,b] , Chang Su[2, c], Cheng Zhang[2]

[1] College of Chemical Engineering, Shenyang University of Chemical Technology

[2] International Sci. &Tech. Cooperation Base of Energy Materials and Application, College of Chemical Engineering and Materials Science, Zhejiang University of Technology, Hangzhou, P. R., China

[a]xulihuanss@163.com, [b] yfzjut@gmal.com, [c]suchang@zjut.edu.cn,

* Corresponding author. Email address: xulihuanss@163.com

Keywords: PolyPyrrole; 2,2,6,6-tetramethylpiperidin(TEMPO); Cathode; Li-ion Battery

Abstract: 4-(3-(Pyrrol-1-yl) butyric acid base)-2,2,6,6-tetramethylpiperidin(Py-B-TEMPO) was synthesized by etherification reaction of 4-hydroxy-2,2,6,6-tetramethylpiperidin-1-yloxy. And the polymer of its monomer was prepared by chemical oxidative polymerization and the chemical structure and battery performance of the prepared materials were characterized comparably by Mass spectrometry, ^{1}H NMR, FT-IR spectra and galvanostatic charge-discharge testing using simulant lithium ion half-cell method, respectively. The results shows that the introduction of the TEMPO group to the pyrrole could prevent the polymer from agglomeration and optimize the particle morphology of the resulting polymers, all of which made it demonstrate a significantly improved specific capacity of 86.5 $mAh \cdot g^{-1}$ (99% of the theoretical capacity) compared with PPy (21.7 $mAh \cdot g^{-1}$). Moreover, it gives an obvious voltage plateau of nearly 3.5 V which is comparable to the redox potential of TEMPO.

Introduction

Recently, the need for human beings to manufacture a more lightweight, safety and high energy-density power source becomes increasingly important. Li-ion battery as its widely applied in portable electronic devices has been considered to be the most promising technology for future.[1-3] The application of electroactive conducting polymers (e.g., polyacetylene, polyaniline, polypyrrole, polythiophene) in Li-ion battery have been widely studied.[4, 5] Among the conducting polymers, polypyrrole (PPy) is one of the most popular for use as a cathode for its high specific energy (ranging from 80 to 390 $W \cdot h \cdot kg^{-1}$)[4]. However, the specific capacity of undoped PPy is always low (only about 20 $mA \cdot h \cdot g^{-1}$). This has limited the commercial application of PPy as a cathode material. However, the usage of electroactive conducting polymers in rechargeable batteries has been hampered, because they exhibit low doping levels, this drawback lower their capacities which limit charge/discharge rates of the batteries.[6] As an alternative, using molecular design to improve the doping levels and accelerate the electrode kinetics may be useful. Recently the radical polymers bearing organic redox radicals as pendant groups on their structural unit have been researched, because of their high electrical storage capacity and high charge-discharge rate capability since PTMA was reported by Nakahara's group in 2002.[7]

In this work, we synthesized a compound of a polypyrrole derivative bearing TEMPO, and then the polymer of the prepared monomer is synthesized by chemical oxidation polymerization. The structure and morphological analysis of the polymers is characterized. Coin cells are assembled to evaluate the electrochemical performance of the polymers as a cathode material.

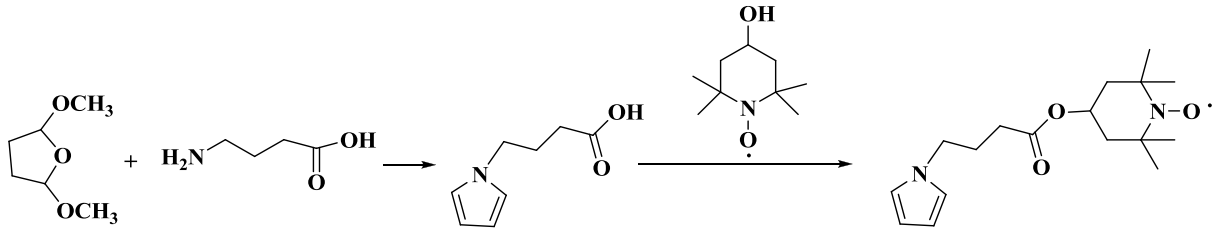
Experimental

Materials.

4-Hydroxy-2,2,6,6-tetramethylpiperidine 1-Oxyl Free Radial (99%), 4-Amino butyric acid (98%), 2,5-dimethoxytetrahydrofuran (98%), pyrrole were purchased from Aladdin. All other reagents were received as analytical grade and used without further purification.

Synthesis of Py-B-TEMPO.

The synthesis of Py-B-TEMPO is shown in Scheme 1.



Scheme 1. The synthesis route to Py-B-TEMPO.

Synthesis of pyrrole butyric acid[8].

2,5-dimethoxytetrahydrofuran (6.61g, 0.05mol) and 4-Amino butyric acid (4.12g, 0.04mol) were dissolved in a mixture of 30ml deionized water and 20ml glacial acetic acid and heated reflux(60 °C) for 1h until the solution turned jacinth. The reaction mixture was then cooled and extracted with CH_2Cl_2, and the organic fraction was washed with saturated brine for three times. The organic phase was separated, dried, and evaporated to dryness. Flash chromatography of the residue (silica gel, petrol ether/EtzO 20:1) afforded the title compound (4.34 g, 71.1% yield) as a white liquid. 1H NMR ($CDCl_3$, 400 MHz) d/ppm: 2.19 (t, 2H), 2.43 (t, 2H), 4.05 (t, 2H), 6.29 (t, 2H), 6.77 (t, 2H), 11.56(s, 1H).

Synthesis of Py-B-TEMPO.

4-hydroxy-2,2,6,6-tetramethylpiperidin-1-yloxy (2.1g) and Pyrrole butyric acid (2.4g) was dissolved in 40ml dichloromethane in the pre-dried three-necked flask, then 2.76g 1-(3-Dimethylaminopropyl)-3-ethylcarbodiimide hydrochloride as dehydrating agent and 0.73g 4-dimethylaminopyridine was added as acylating catalyst, and stirring for 24h at room temperature. The reaction mixture was then separated by vacuum filtration. The filtrate was washed with saturated brine for three times. Organic phase was dried over sodium sulfate. The ester was purified by column chromatography using silica gel and petroleum ether/ethyl acetate afforded the title compound as golden flakes like crystals. Mass spectrometry (MS) $[M]^+$. Found: 307.4.

Chemical Polymerization of Py-B-TEMPO.

A solution of Py-B-TEMPO (0.3 g) was dissolved in CCl_4 (20ml), and then was added into a 250 ml boiling flask-3-neck. To this solution, 10ml of CH_3NO_2 containing 0.63 g of $FeCl_3$ was added drop wise for about 0.5 h, with magnetic stirring at near 0 °C. With increasing of density of $FeCl_3$•$6H_2O$ in the reactor, the mixture turned black. After the addition was completed, the stirring was continued overnight at room temperature. After completion of the reaction, 100ml deionized water was added to deposit the copolymer, which was then filtered and washed with methanol and water alternately for several times, until the filtrate became colorless. Finally, the black powder was dried in vacuum at 60 °C for 24 h, and 0.3 g black powder was obtained. Yieds: 75%.

Characterization.

FT-IR spectra of PPy-B-TEMPO and PPy were recorded with KBr pellet method on Nicolet 6700 spectrometer (Thermo Fisher Nicolet, USA) in the frequency range of 4000-400 cm^{-1}. Morphological analysis was examined using a Hitachi S-4800 scanning electron microscopy (Hitachi, Japan).

Electrochemical Measurement.

The PPy-B-TEMPO and PPy electrode was prepared by coating a mixture containing 50% prepared materials, 40% acetylene black, 10 % PVDF binder on circular Al current collector foils, followed by drying at 60 °C for 24 h. After that, the cells were assembled with lithium foil as the

anode, the prepared electrodes as cathode and 1 M LiPF6 dissolved in ethylenecarbonate (EC) and dimethylcarbonate (DMC) (EC/DMC = 1:1 wt) as the electrolyte. The charge-discharge measurements were carried out on a LAND CT2001A in the voltage range of 2.5-4.2 V versus Li/Li^+, using a constant current density of $20mA \cdot g^{-1}$ at room temperature.

Results and Discussion.

Materials Characterization.

As shown in Fig. 1, the two samples exhibited the characteristic bands of PPy,[9] involving the pyrrole ring fundamental vibration at 1545 cm^{-1} and 1459cm^{-1}, the C-H in-plane vibration at 1286 cm^{-1} and 1045 cm^{-1} and the C-N stretching vibration at 1172 cm^{-1}. We can observe that PPy-B-TEMPO has similar peaks which are assigned to the polypyrrole ring stretching. As expected, the spectrum of PPy-B-TEMPO also shows the characteristic absorption peaks at 1733, 1167 and 1365 cm^{-1}, corresponding to the C=O, C-O and nitroxyl radical groups, respectively.[10] This indicates the 4-hydroxy-2,2,6,6-tetramethylpiperidin-1-yloxy group has been successfully introduced into the pyrrole butyric acid and the nitroxyl radical has not been destroyed during the polymerization progress.

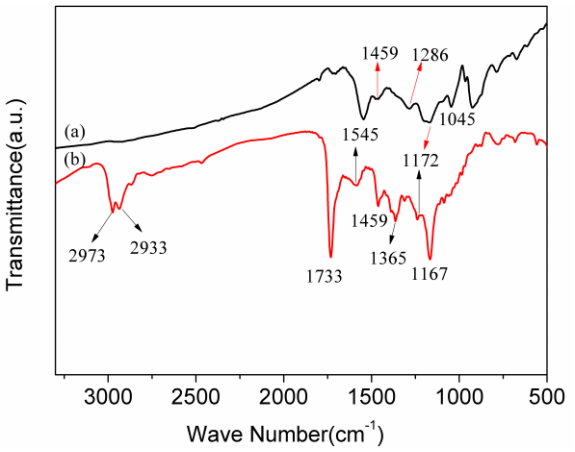


Fig. 1 FT-IR spectra of a) PPy and b) PPy-B-TEMPO

Fig. 2 shows the morphological analysis of the PPy-B-TEMPO and PPy polymer. As shown in Fig. 2 (a), the PPy polymer has a dense packing structure as plate-like and the aggregation of PPy particles can be noticed obviously. While, as shown in Fig.2 (b), the polymer of PPy-B-TEMPO shows a loose stacking structure. This open structure of PPy-B-TEMPO with the porous morphologies is in favor of the contact of electrode-active material and electrolyte; as a result, much more electrode-active material is effectively utilized and the electrochemical properties of PPy-B-TEMPO is obviously improved. All of those are very important to prepare a good cathode material for Li-ion batteries.

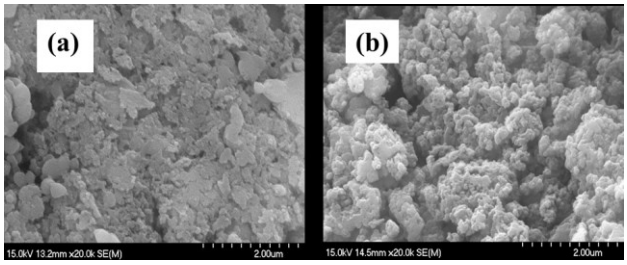


Fig. 2 SEM images of (a) PPy and (b) PPy-B-TEMPO.

Charge/Discharge Performance.

Fig. 3 a) shows the charge/discharge curves (initial cycle) of PPy and PPy-B-TEMPO cathodes in $LiPF_6$ EC/DMC (v/v, 1:1) electrolyte at a constant current of 20 $mA \cdot g^{-1}$ between 2.5 and 4.2 V. At low current density of 20 $mA \cdot g^{-1}$, an initial discharge capacity of PPy-B-TEMPO up to 86.5 $mAh \cdot g^{-1}$ can be obtained, which is higher than that of PPy electrode of 21.7 $mAh \cdot g^{-1}$. It can be ascribed to the contribution of redox-active nitroxyl radical, as well as the prominent structure features of PPy-B-TEMPO, which can allow the electrolyte to better infiltrate into the polymer and provide ionic channels for polymeric electrode redox reactions. Also, we notice that it gives an obvious voltage plateau of nearly 3.5 V which is comparable to the redox potential of TEMPO.

Discharge profiles of the polymer material at 20 $mA \cdot g^{-1}$ are shown in Fig. 3 b), compared with the PPy, the cycling stability of PPy-B-TEMPO exhibits a serious capacity degeneration, which is possibly caused by the seriously re-aggregation of PPy-B-TEMPO during the repeated charge and discharge process, due to the pristine looser stacking micro-structure of PPy-B-TEMPO than that of PPy. However, it is noteworthy that a flat voltage plateaus is still obviously observed in the charge-discharge curves of the PPy-B-TEMPO even at 50^{th} cycles, implying that PPy-B-TEMPO electrodes has a lower polarization during the charge-discharge process.

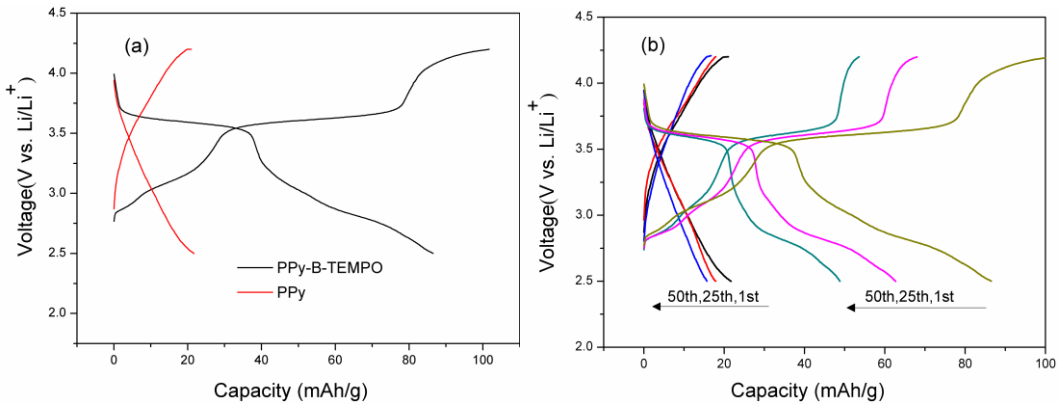


Fig. 3 Charge/discharge curves of PPy and PPy-B-TEMPO in LiPF6 EC/DMC (v/v, 1:1) electrolyte at a constant current of 20 mA g−1. b) Discharge profiles of PPy and PPy-B-TEMP

Conclusions

The monomer of Py-B-TEMPO was prepared by the reported method. And the polymer of PPy-B-TEMPO was synthesized by chemical oxidation polymerization. The charge/discharge measurements show that the PPy-B-TEMPO had high capacity of 86.5 $mAh \cdot g^{-1}$, which was significant higher than PPy of 22.6 $mAh \cdot g^{-1}$. The PPy-B-TEMPO electrode also shows an obvious voltage plateau of nearly 3.5 V, compared to the pristine PPy-based electrode and was promising as advanced cathode material.

Acknowledgements

The authors gratefully thank the National Natural Science Foundation of China (NSFC, No. 51003095, No. 51103132) and Research on Public Welfare Technology Application Projects of Zhejiang Province, China (2010C31121) for financial support. This work also was supported by the analysis and testing foundation of Zhejiang University of Technology.

References

[1] J. M. Tarascon, M. Armand: Nature. Vol. 414 (2001), p. 359-367

[2] Y. Nishi: J. Power Sources. Vol. 100 (2001), p. 101-106

[3] M. Armand, J. M. Tarascon: Nature. Vol. 451 (2008), p. 652-657

[4] P. Novak, K. Muller, K.S.V. Santhanam, O. Haas: Chem. Rev. Vol. 97 (1997), p. 207-281

[5] H.E. Katz, P.C. Searson, T.O. Poehler: J. Mater. Res. Vol. 25 (2010), p. 1561-1574

[6] M. Aydın, B. Esat: European Polymer Journal. Vol. 47 (2011), p. 2283–2294

[7] K. Nakahara, S. Iwasa, M. Satoh: Chemical Physics Letters. Vol. 359 (2002), p. 351–354

[8] S. Thomas, M. Eva: Sensors and Actuators B. Vol. 4 (1991), p. 273-281

[9] Xiao Liang, Yu Liu: Journal of Power Sources. Vol. 196 (2011), p. 6951–6955

[10] Wei Guo, Yaxia Yin: Energy Environ. Sci. Vol. 5 (2012), p. 5221–5225

[11] J. K. Kim et al: Met. Mater. Int. Vol. 15 (2009), p. 77-82

Advanced Materials Research Vol. 936 (2014) pp 452-458
© (2014) Trans Tech Publications, Switzerland
doi:10.4028/www.scientific.net/AMR.936.452

Nanostructured Morphology of Spinel $LiMn_2O_4$ Oxide under Microwave Heating

Di Huo

Key Laboratory of Anisotropy and Texture of Materials (Ministry of Education), Northeastern University, Shenyang 110819, Liaoning, P R China

Email: dhuo@mail.neu.edu.cn

Key words: $LiMn_2O_4$; surface morphology; microwave heating; nanorod; nanowhisker.

Abstract: The surface morphology and structure of the cubic stoichiometric spinel $LiMn_2O_4$ powder prepared by microwave heating were examined using X-ray diffraction, scanning electron microscopy and transmittance electron microcopy. It is shown that the surface morphology of $LiMn_2O_4$ particle changed with increasing preparing temperature, while the crystal structure kept unchanged. Novel nanostructured morphologies including nanorods and nanowhiskers were formed under appropriate synthesis conditions. The growth mechanism of the nanostructured morphology of spinel $LiMn_2O_4$ was discussed in accordance with period bonding chains (PBCs) theory.

Introduction

Stoichiometric spinel $LiMn_2O_4$ has attracted considerable attention as an active cathode material in Lithium ion batteries. It is commonly regarded as a potential candidate material to replace $LiCoO_2$ and $LiNiO_2$ due to the advantages of low cost, environmental benignity and operational safety of the manganese element [1, 2]. However, the poor performances such as considerable capacity fading on cycling at an elevated temperature and low capacity of the micrometer-sized grade $LiMn_2O_4$ powder restricted its wide practical applications [3]. Therefore, various efforts had been made to enhance the electrochemical properties of spinel $LiMn_2O_4$ cathode.

The stoichiometry, crystal structure and morphology of the cathode materials in Lithium ion batteries are crucial for its electrochemical properties [4]. In recent years, substantial researches have confirmed that crystalline $LiMn_2O_4$ powders with specific nanostructured morphological features possessed improved electrochemically performances. For instances, the nanosized $LiMn_2O_4$ particles exhibit excellent rate performance and capacity retention on cycling at 30-50℃, and structural stability [5,6]. In particular, one-dimensional ultrathin $LiMn_2O_4$ nanowire showed very good electrochemical performances at high current rate in a large compositional range [7, 8]. These improved properties are mainly attributed to the merits of morphological and structural features of the nanostructured spinel $LiMn_2O_4$.

The particle size and morphology of $LiMn_2O_4$ are directly related to synthesis method and conditions. Until now, sol-gel [9] and hydrothermal plus ion exchange [10] or hydrothermal [11] methods were used to make the one-dimensional crystalline $LiMn_2O_4$. It was also mentioned that spinel $LiMn_2O_4$ powder with needle-like morphology was obtained under microwave heating by using γ-MnOOH and $LiOH \cdot H_2O$ as starting precursors [12]. In this paper the cubic spinel $LiMn_2O_4$ powders with nanostructured surface morphologies were found under conditions of high temperature and oxygen flow protection using microwave heating, and the growth mechanism of the nanostructrured surface morphologies was also discussed.

Experimental

Commercial analytical grade MnO_2 and Li_2CO_3 were used as starting materials without further treatment. The reactants were weighed on mole ratio of $LiMn_2O_4$ stoichiometrically, and then mixed and ball milled in ethanol for 8 hours. After drying at 100℃, the mixture was put into a SiC crucible with a diameter of 20 mm and a height of 40 mm which was also used as an inductor to microwave energy. The crucible was then placed in a quartz tube which inserted vertically in TE_{101} microwave heating cylinder cavity. The employed microwave frequency is 2.45GHz and the power input is in range of 300-500W. The heating temperature was controlled in the range of 850-1200℃, the duration time was 20-30min and the samples were ground intermittently 2-3 times during this process. Oxygen was used as protection gas, and the flow rate was 1.2mL/min. An infrared thermo detector （WGG2-201, Shanghai, China）was used to monitor surface temperature of the powder in crucible.

Phase composition of the as-synthesized $LiMn_2O_4$ powder was examined by X-ray diffractometer （XRD, Model D/max-rA, Rigaku, Japan）employing graphite-monochromated CuK_α radiation. After being dispersed in ultrasonic bath and surface coated with gold, the morphology and surface composition of the $LiMn_2O_4$ powders were characterized by field emission scanning microscopy （FESEM, JEOL，JSM-6301F）equipped with EDS(Oxford). Transmission electron micrographs and selected area diffraction pattern were obtained using an analytical Transmission Electron Microscopy (TEM, Philip, EM420, Holland).

Results and Discussion

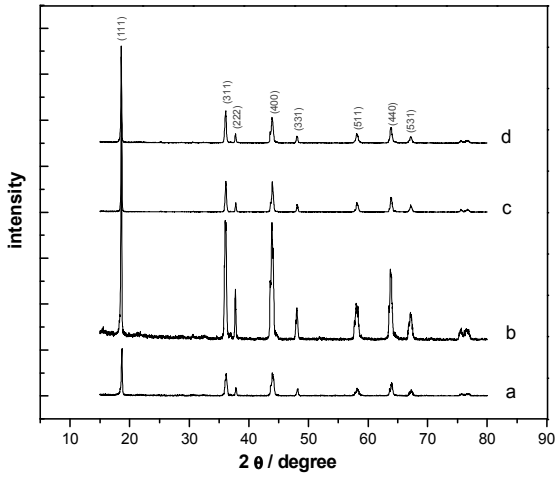


Fig.1. XRD spectra of the as-calcined $LiMn_2O_4$ powder under microwave heating at: 850℃ (a); 1000℃ (b); 1100℃ (c); 1200℃ (d)

Fig. 1 shows XRD spectra of the $LiMn_2O_4$ powders calcined at different temperatures by microwave. It is shown that in the temperature range of 850-1200℃ and under flow oxygen protection, the crystalline phase of the stoichiometric $LiMn_2O_4$ powder had predominately been single spinel phase which can be indexed with standard cubic spinel structure (JCPDS No.35-0782, space symmetry group Fd3m). In fact, the X–ray diffraction peaks splits of several crystallographic planes of the lower temperature synthesized $LiMn_2O_4$ samples almost completely disappeared as the temperature increased to 1100℃. It had been mentioned that there was a wide range of solid solution within the Li-Mn-O family of spinel compounds, and a number of discrete phases with

different crystallographic structures were formed as the temperature was raised from 800℃ to 1200℃ in conventional solid state synthesis [13]. Different from the above phenomenon, in this experiment the highest symmetry of spinel cubic crystal structure was achieved as the sample was heated in range of 1000℃ to 1100℃, and the phase composition remain unchanged till 1200℃ under flow oxygen. The cubic crystalline $LiMn_2O_4$ spinel demonstrated higher crystal structure stability under microwave heating than that under the conventional heating in the same temperature range. This probably is due to the microwave heating features of faster heating and cooling, shorter duration time and also higher partial oxygen pressure utilized.

On the contrary to the high stability of cubic spinel crystal structure of $LiMn_2O_4$ powders, their surface morphologies were varied obviously in the temperature range of 850-1200℃. Fig. 2 (a) shows SEM micrograph of the $LiMn_2O_4$ powder heated by microwave at 850℃. It can be found the crystalline particles exhibit very flat and well developed crystallographic facets. Theoretically, the $LiMn_2O_4$ crystalline particle exhibits regular polyhedral shape which is bounded by the planes of {111}, {110} and the truncated {100}, therein some {111} facets presents almost perfect triangle shape. Here, the marked feature of microwave irradiated $LiMn_2O_4$ powders at 850℃ is that the faceting planes of {111} show very flat and sharp terrace-edges between the crystallographic planes on the crystalline particle surfaces.

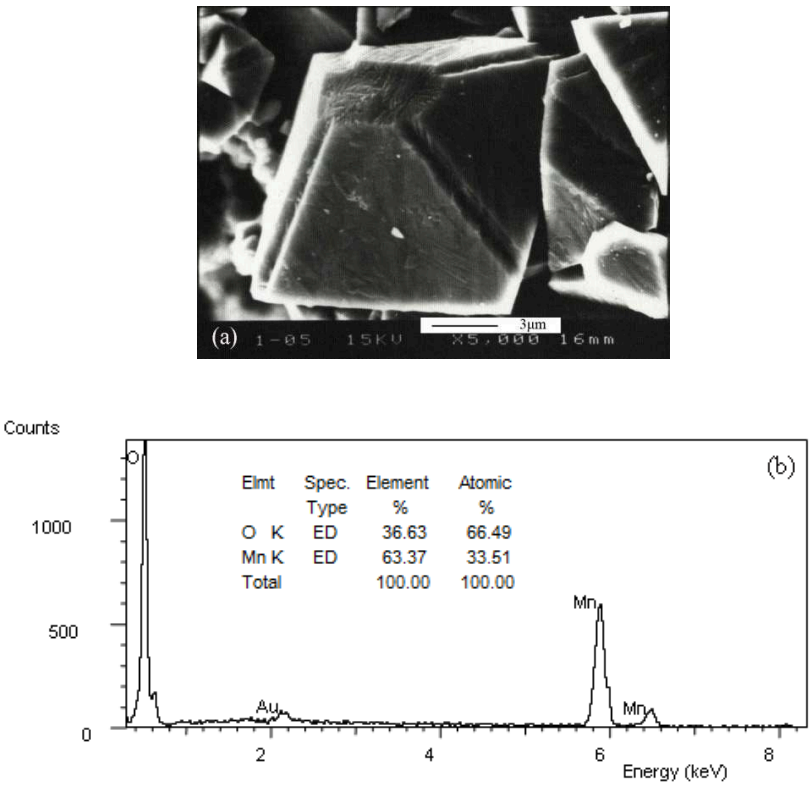


Fig. 2. SEM micrograph of the spinel $LiMn_2O_4$ particles heated at 850℃(a); EDS analysis of surface composition of the spinel particles (b)

The morphology of crystal depends kinetically on the growth rate of crystallographic planes, and the crystal planes with higher growth rate usually disappear from crystal forms, so the equilibrium shape of crystal is generally bounded by crystal planes having the lowest growth rate [14]. Periodic Bond Chains (PBCs) theory is useful for building up the relation between crystal structure and crystal growth morphology [15]. The {111} planes of spinel $LiMn_2O_4$ crystal can be assigned to F plane of the PBCs theory, and it can be predicted that the equilibrium morphology of spinel crystals

should be an octahedral shape composed of six {111} triangular planes for their lowest surface energy [16,17]. However, the $LiMn_2O_4$ particles prepared by microwave heating showed predominately an polyhedral form exhibiting faceting of {111}, {100} and {110}, and this equilibrium growth particle shape is similar to the one found in conventional solid state synthesized $LiMn_2O_4$ powders [18], except that there is no round transition facets between the crystallographic faces. Generally, due to the dangling or unsaturated bonds among the ions in crystal surface layers, the coordination relations of the ions near the crystal surface can affect their geometric profile. The EDS results of in this work showed that the ratio of Mn/O on particles surface is closer to its theoretical value, as shown in Fig. 2(b). It means that no or less of chemical composition on particles surface layer is lost, for which an ideal coordination relation among the ions and configuration near to theoretical value are achieved, so the majority {111} planes on polyhedral shape particles show more flat and smooth layered characters.

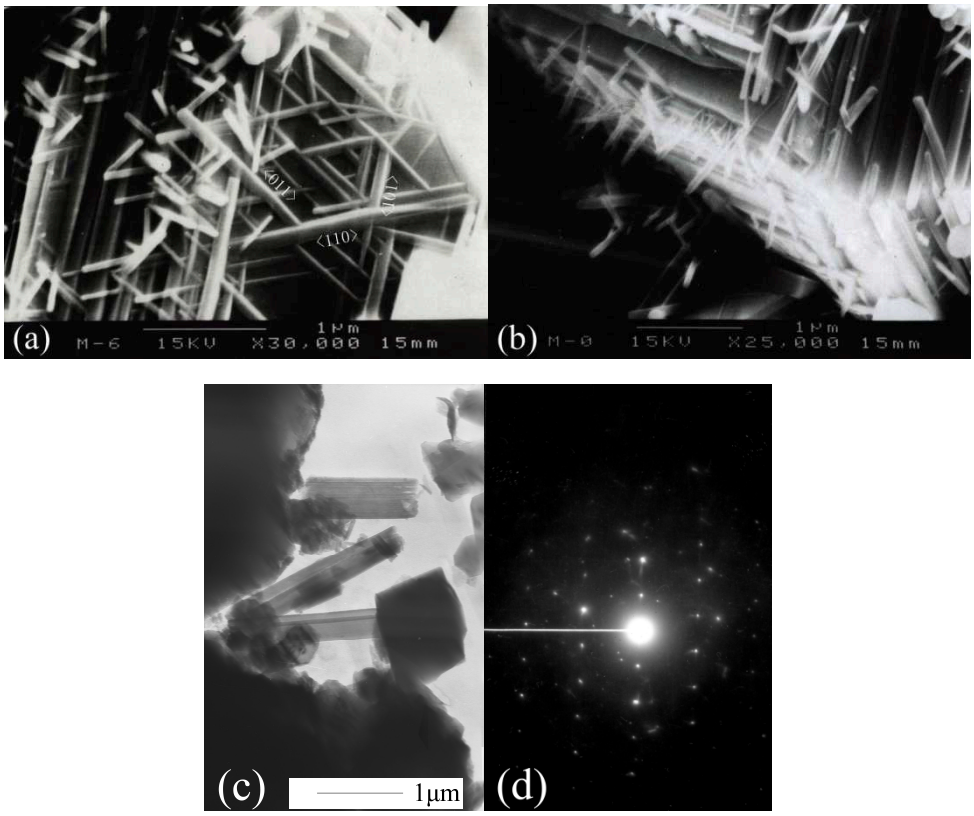


Fig. 3. SEM Micrographs of the nanorods formed on {111} surfaces (a) and on corner (b) of spinel $LiMn_2O_4$ particles at 1000℃, and TEM image(c) and SAED pattern (d) of the spinel nanorod

The surface morphology of spinel crystalline particles changed tremendously with increasing microwave heating temperature. When the reactant mixture was microwave heated at 1000℃, it was found that on the surface of some particles a lots of one-dimensional crystals nucleated along the [110]directions on spinel triangular {111} planes, as shown in Fig. 3a. Some of them grew habitually into nanorod and out of particles surface with about 100nm in diameter and several micrometers in length. All of these one-dimensional nanorods predominately nucleated on the layered slice planes of {111}, and strictly keeping crystallographic directions of [110] on {111} faces, i e., {111}[110] of spinel $LiMn_2O_4$ crystal, as shown in Fig. 3b. The TEM image of the nanorods and its selected area electron diffraction pattern (SAED) are shown in Fig. 3c and 3d, which also indicate the cubic spinel crystal structure of the nanorod $LiMn_2O_4$.

When the temperature was increased to 1100℃, some peculiar morphologies were generated on {111}, {110} and truncated {100} faces of the original equilibrium particles. It is admitted that there was uneven temperature distribution in the SiC crucible. In relatively lower temperature zones, the truncated {100} face and the vicinal {110} face between the {111} faces were still covered with a thin layer before the powder decomposed as shown in Fig. 4a. With the temperature increased, the thin layer on {110} step facets and {100} rough facets eroded away, so the kinked surface of {100} (K face of PBCs) and stepped surface of {110} （S face of PBCs）of the crystal began to emerge. It can also be noted that the decomposed original {110} step faces are virtually consisted of even fine sub-steps of several nanometer high.

However, in relatively higher temperature zones, the growth of nanowhiskers at the expense of dissociation of {110} and {100} surface planes of the spinel crystal become pronounced and then new crystal morphologies were formed. Different from the nanorod crystals observed above, a quantity of nanosized whisker crystals with about 1 micrometer in length and 10 nanometers in diameter nucleated and grew on the layered growth {111} faces, and all these newly formed crystals tend to align along the [110] direction of the crystal and some of the nanowhiskers have also grown out of the crystal surface, as shown in Fig. 4b. The same as the growth of nanowhisker on layered eroded {110} crystal faces, a large number of nanowhiskers can be seen on the truncated {100} crystal faces and they also kept with [110] directions. The crystallographic configuration of these nanowhiskers is totally in the same way as that of the nanorods in Fig. 3a.

It is reasonable to postulate that the growth of crystalline spinel $LiMn_2O_4$ powders prepared by microwave solid state synthesis is by way of both diffusion and vapor-condensation mechanisms. As using microwave to heat the mixture of MnO_2 and Li_2CO_3 reactants, MnO_2 has higher ability of coupling with and absorbing microwave energy [18]. With heating temperature increased the phase transformation process can be in the thermodynamically sequence of MnO_2-Mn_2O_3-Mn_3O_4, therein the last ferrite phase Mn_3O_4 has the highest dielectric couple loss to microwave energy, which means microwave energy can be effectively used to heat the reactants. This may also be the reason that the heating rate of the reactant mixtures became accelerated in later period of microwave synthesis in this experiment. The ability of coupling with or absorbing microwave energy of Li_2CO_3 is relatively low, it can thus be thought that Li_2CO_3 was heated by conduction heat from the microwave inductor SiC crucible and the high temperature of heated MnO_2, and then the heated Li_2CO_3 decomposed and reacted with MnO_2 and gradually intercalated into MnO_2 to form $LiMn_2O_4$ spinel composite oxide. If the temperature was increased to even higher temperature, not only solid diffusion mechanism, but vapor-condensation mechanism for mass transport will play an important role in the nucleation and growth of $LiMn_2O_4$ crystal, so the surface morphology of $LiMn_2O_4$ becomes various kinds due to this change.

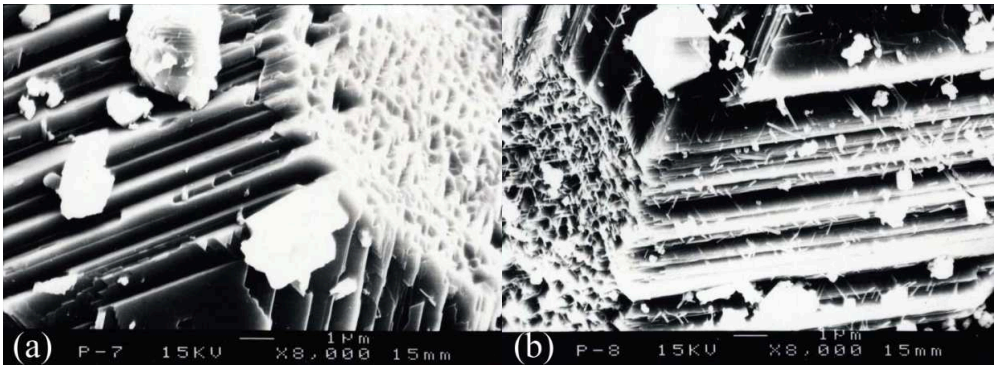


Fig.4. SEM surface morphologies of the spinel formed at the temperature of 1100℃ (a) and 1150 ℃ (b)

External conditions, such as the supersaturation and temperature at the surface, can definitely influence crystal shape. The existence of various kinds of morphological crystals may indicate that the mechanisms of nucleation and growth changed when the powder mixture was heated at higher temperatures. In view that cubic structure of $LiMn_2O_4$ standard spinel belongs to Fd3m space group, oxygen ions occupied the 32e crystallographic position and arranged according to the a-b-c-a-b-c----- sequence to form face centered cubic close packing [19]. The closest packed {111} planes consisted of oxygen anions are the first atomic vicinal plane, and crystal directions of {111}[110] are the most dense package direction of Mn ion at 16d octahedral position, which also means {111}[110] that the crystallographic direction is stronger periodic bond chain sectors. Due to higher bond energy in the periodic bond chains sector direction, the growing units can readily adhere to and integrate into the crystals [14]. Therefore under appropriate conditions, the reactant ions detached and/or diffused away from {110} and {100} crystal faces, and then incorporated into and grew quickly along with the {111}[110] crystallographic directions, finally leading to one-dimensional nanorod or nanowhisker crystals. The theoretical calculation [20] and experimental result [16] confirmed that the most stable crystallographic plane with the lowest solid–to–vapor surface energy of spinel $LiMn_2O_4$ is {111} planes, which abide with increasing sequence of $\gamma_{SV\{111\}}<\gamma_{SV\{100\}}<\gamma_{SV\{110\}}$. So, under the even higher temperatures, the decomposed crystal planes of {110} and {100} will lead to more supersaturated concentration of reactant ions around the crystal, which results in different crystal morphologies other than nanorods on the $LiMn_2O_4$ powder surface. As shown in this work, when the microwave heating temperature was increased to 1200℃ a lots of sub-micron sized round island crystals emerged on the {111} planes besides the one-dimensional nanostructured crystals.

Conclusion

The intrinsic characters of microwave heating such as fast kinetic, short duration time and selectively internal heating are beneficial for increasing mass transport rate which may involve evaporation-condensation mechanism. With microwave heating combined with oxygen flow protection, a number of novel nanostructured surface morphologies of spinel $LiMn_2O_4$ oxide were formed in the temperature range of 850-1100℃, while the crystal structure kept unchanged. It may be indicated that under a certain condition one-dimensional $LiMn_2O_4$ nanorods or nanowires can be prepared in a facile and fast way by microwave heating.

Acknowledgements

I would like to thank Mrs. Yanfeng Guo for her assistance on SEM observation and analysis, and also thank Professor Jiguang Li for his comments and reviewing on this manuscript.

References

[1] M. M. Thackeray, P. J. Johnson, L. A. Picciotto, P. G. Bruce, J. B. Goodenough, Electrochemical extraction of lithium of $LiMn_2O_4$, Mater. Res. Bull. 19 (1984) 179-187.

[2] T. M. Tarascon, E. Wang, F. K. Shokoohi, The Spinel phase of $LiMn_2O_4$ as a cathode in secondary lithium cells, J. Electrochem. Soc. 138 (1991) 2859-2864.

[3] M. M. Thackeray, Spinel electrodes for lithium batteries, J. Am. Ceram. Soc. 82 (1999) 3347-3354.

[4] H. Gadjov, M Gorova, V. Kotzeva, $LiMn_2O_4$ prepared by different methods at identical thermal treatment conditions: structural, morphological and electrochemical characteristics, J. Power Sources. 134 (2004) 110-117.

[5] K. M. Shaju, P. G. Bruce, A stoichiometric nano-$LiMn_2O_4$ Spinel electrode exhibiting high power and stable cycling, Chem. Mater. 20 (2008) 5557-5562.

[6] T. Doi, T. Yahiro, S. Okada, Electrochemical insertion and extraction of lithium-ion at nano-sized $LiMn_2O_4$ particles prepared by a spray pyrolysis method, Electrochem. Acta 53 (2008) 8064-8069.

[7] D. K. Kim, P. Muralidharan, H. W. Lee, Spinel $LiMn_2O_4$ nanorods as lithium ion battery cathodes,Nano. Letters. 8 (2008) 3948-3952.

[8] E. Hosono, H. Matsuda, T. Saito, Synthesis of single crystalline $Li_{0.44}MnO_2$ nanowires with large specific capacity and good high current density property for a positive electrode of Li ion battery, J. Power Sources. 195 (2010) 7098-7101.

[9] Y. Zhou, C.Chen, J. Huang, Synthesis of high-ordered $LiMn_2O_4$ nanowire arrays by AAO template and its structural properties, Mater. Sci. Eng. B. 95 (2002) 77-82.

[10] J. Y. Luo, D.D. Xiong, Y. Xiao, $LiMn_2O_4$ nanorods, nano-thorn microsphere and hollow nanospheres as enhanced cathode materials of lithium-ion battery, J. Phys. Chem. C. 112 (2008) 12051-12057.

[11] Q. Liu, D. Mao, C. Chang, F. Huang, Phase conversion and morphology evolution during hydrothermal preparation of orthorhombic $LiMnO_2$ nanorods for lithium ion battery application, J. Power Sources. 173 (2007) 538-544.

[12] P. S. Whitfield, J. J. Davidson, Microwave synthesis of $Li_{1.025}Mn_{1.975}M_4$ and $Li_{1+x}Mn_{2-x}O_{4-y}F_y$, J. Electrochem. Soc. 147(2000) 4476-4484.

[13] M. M. Thackeray, M, F, Mansuetto, D. W. Dees, The thermal stability of lithium-manganese-oxide spinel phases, Mater. Res. Bull. 31 (1996) 133-140.

[14] M. A. Lovette, A. R. Browning, D. W. Griffin, Crystal shape engineering, Ind. Eng. Chem. Res. 47 (2008) 9812-9833.

[15] P. Hartman, W. G. Perdok, On the relation between structure and morphology of crystals, Acta.

[16] Crystallogr. 8 (1955) 48-52.

[17] M. R. Huang, C. W. Lin, H. Y. Lu, Crystallographic facetting in solid state reacted $LiMn_2O_4$ spinel powder, Appl. Surf. Sci. 177 (2001) 103-113.

[18] R. Dekkers, C. F. Woensdregt, Crystal structural control on surface topology and crystal morphology or normal spinel ($MgAl_2O_4$), J. Cryst. Growth. 236 (2002) 441-454.

[19] S. L. Sui, E. Vilemo and Q. H Zhang. Microwave induced chemical reaction in synthesis and catalysis, in: D. E. Clark, W. H. Sutton, D. A. Lewis (Eds), Microwaves: theory and application in materials processing IV[C]. Ceramic transactions, American Ceramic Society, Westerville, OH, 1997, 80, pp. 331-339.

[20] K. E. Sickafus, J. M.Wills, Structure of spinel, J. Am. Ceram. Soc. 82 (1999) 3279-3292.

[21] R. K. Misha, G. Thomas, Surface energy of spinel, J. Appl. Phys. 48 (1977) 4576-4580.

Advanced Materials Research Vol. 936 (2014) pp 459-463
© (2014) Trans Tech Publications, Switzerland
doi:10.4028/www.scientific.net/AMR.936.459

Effect of SnO_2 particle size on properties of Ag-SnO_2 electrical contact materials prepared by the reductive precipitation method

Zhijie Lin[1, a], Xudong Sun[1,b], Shaohong Liu[1,2,c], Jialin Chen[2,d], Ming Xie[2,e], Ji-Guang Li[3,f], Xiaodong Li[1,g], Di Huo[1,h], Mu Zhang[1,i] and Qi Zhu[1,j]

[1] Key Laboratory for Anisotropy and Texture of Materials (Ministry of Education), School of Materials and Metallurgy, Northeastern University, Shenyang, Liaoning 110819, China

[2] State Key Laboratory of Advanced Technologies for Comprehensive Utilization of Platinum Metals, Kunming Institute of Precious Metals, Kunming 650106, China

[3] Advanced Materils Processing Unit, National Institute for Materials Science, Sengen 1-2-1, Tsukuba, Ibaraki 305-0047, Japan

[a]fuanlzj@foxmail.com, [b]xdsun@mail.neu.edu.cn, [c]liush@smm.neu.edu.cn, [d]cjl@ipm.com.cn, [e]powder@ipm.com.cn, [f]lijg@smm.neu.edu.cn, [g]lixd@atm.neu.edu.cn, [h]huod@smm.neu.edu.cn, [i]muzhang@mech.uwa.edu.au, [j]Zhuq@smm.neu.edu.cn,

Keywords: electrical contact materials; chemical reductive precipitation; particle size; hardness; electrical conductivity.

Abstract: Performances of Ag-SnO_2 electrical contact materials can be strongly affected by the microstructure. In this work, Ag-SnO_2 composite powders were synthesized by chemical reductive precipitation method. During the precipitation process, Ag particle was deposited onto the surface of SnO_2 particle with the assistance of citric acid. The microstructure and properties were analyzed for the prepared Ag-SnO_2 electrical contact materials. Our research reveals that the particle size of SnO_2 has significant influence on the morphology of the Ag-SnO_2 composite powders, and therefore on the microstructure and physical properties of the electrical contact materials. With the decrease of particle size of SnO_2, hardness of the Ag-SnO_2 electrical contact materials increases, while electrical conductivity decreases.

Introduction

Silver-tin oxide composite materials have been widely applied to low voltage switch in the past two decades [1]. In practice, the advantages of eco-friendly, low temperature rising and anti-welding behaviors makes them the most attractive replacement for Ag-CdO electrical contact materials. For Ag-MeO electrical contact materials, microstructural control has been considered to be the decisive factor for high performances [2]. Various preparation [3-7] and processing [8, 9] methods have been used for microstructural optimization of the Ag-MeO electrical contact materials. Previous research [7, 10] has revealed that homogeneous distribution of SnO_2 in Ag matrix is beneficial to good electrical and mechanical properties. An chemical reductive precipitation method was once developed by Wolmer et al. [5] to prevent SnO_2 from aggregation. Paul et al. [6] investigated the effects of coating process, and the results indicate that chemical plating can also enhance the wettability between SnO_2 particles and Ag matrix, and improve the thermal and electrical conductivity of the Ag-SnO_2 electrical contact materials. Whereas, a fundamental research describing the influence of the particle size on the basic properties of Ag-SnO_2 electrical contact materials was scarce but urgently need.

In this work, the chemical reductive precipitation method was successfully used to prepare the Ag-SnO_2 composite powders with different particle sizes of SnO_2. The influence of SnO_2 particle size on microstructure and properties of the electrical contact materials was systematically investigated.

Experiment Details

Reagents

Silver nitrate ($AgNO_3$, analytical reagent) was provided by the Sino-platinum Metals. Tin (IV) chloride ($SnCl_4 \cdot 5H_2O$, analytical reagent), tin (II) chloride ($SnCl_2 \cdot 4H_2O$, analytical reagent), citric acid anhydride ($C_6H_8O_7 \cdot H_2O$, analytical reagent), urea ($CO(NH_2)_2$, analytical reagent) and Ascorbic acid ($C_6H_8O_6$, analytical reagent) were purchased from Sinopharm Chemical Reagent Co.. These chemicals were used as received without further purification. Four kinds of SnO_2 particles, S1, S2, S3 and S4, were used for the preparation of the electrical contact materials, as shown in Table 1. The precursor of S1 was synthesized via direct hydrolyzing of Tin (IV) chloride. The precursor of S2 was synthesized via the homogenous precipitation of tin (II) chloride. The obtained precursors were transformed into SnO_2 by calcining at 600 ^oC in air. S3 and S4 were purchased from Luoyang Found New Materials Technology Co., Ltd..

TABLE 1. PARTICLE SIZE OF THE SNO_2 PARTICLES.

Sample	S1	S2	S3	S4
Mean diameter (nm)	15	608	1807	4685

Synthesis Of The Ag-Sno_2 Composite Powders And Contact Materials

The mass radio of Ag to SnO_2 is 88:12 in the final electrical contact materials. In a typical synthesis, SnO_2 and $AgNO_3$ was added to a strongly stirred 2M citric acid solution, and then followed by a ultrasonic dispersion. Afterwards, the silver was slowly reduced by dropwise addition of ascorbic acid solution. The obtained precipitates were aged for 30 min at room temperature, and then dried at 80 ^oC after rinsing with deionized water and ethanol. The dried cakes were lightly crushed with an agate pestle and mortar, and then calcinated in air at 600 ^oC to obtain the Ag-SnO_2 composite powders. The as-prepared composite powders were then hot-pressed to fabricate the electrical contact materials (Φ12×5 mm) in a graphite die at 700 ^oC with a pressure of 60 MPa under the protection of argon.

Characterization Techniques

Density of the Ag-SnO_2 contact materials was measured by the Archimedes method. Hardness was determined using a Vickers hardness tester. An FQR 7051 vortex conductivity apparatus was used to investigate the electric conductivity of the Ag-SnO_2 contact materials. XRD analysis was conducted under 40 kV/40 mA using nickel-filtered Cu Kα radiation (Model PW 3040/60; PANALYTICAL B.V, Almelo, the Netherlands). Particle size distributions were analyzed by the Laser particle size analyzer (LA-920; HORIBA, Kyoto, Japan). Particle morphologies were observed via field emission scanning electron microscope (FE-SEM) with an acceleration voltage of 10 kV (Model JSM-7001F; JEOL, Tokyo, Japan). Microstructures of the Ag-SnO_2 electrical contact materials were examined by scanning electron microscope (SEM, JSM-6510A; JEOL, Tokyo, Japan).

Results and Disccusion

Morphology of the SnO_2 particles

The mean sizes of the used SnO_2 particles are shown in Table 1. The morphologies of the SnO_2 are presented in Figure 1. All the four kinds of particles show narrow size distribution and loose aggregation, which is also verified by the analysis of particle size distribution (Figure 2). The grain size of S1 is about 15 nm calculated by the Scherer formula, which is out of the range of Laser particle size analyzer.

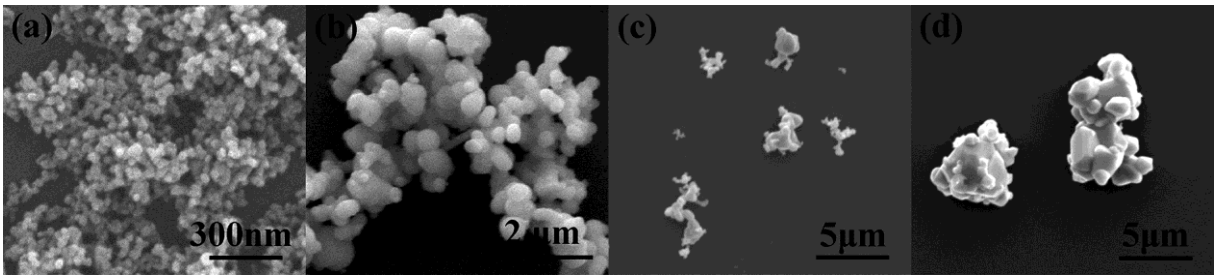


Fig. 1 FE-SEM micrographs show the morphologies of the original SnO2 core: (a) S1; (b) S2; (c) S3; and (d) S4.

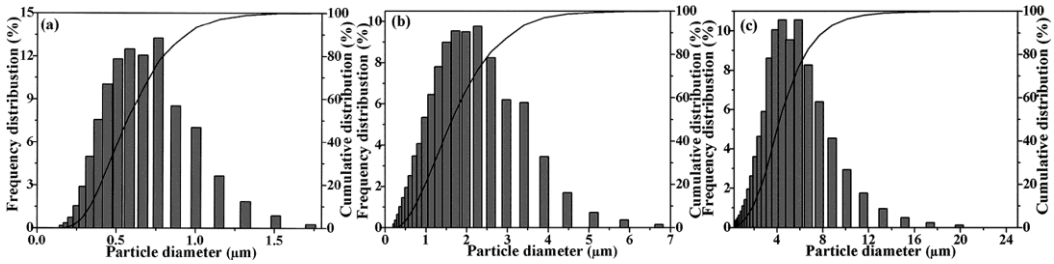


Fig. 2 Particle size distribution of the SnO_2 powders. (a) S2; (b) S3; (c) S4.

The coating of SnO_2 by Ag

During the reduction process, Ag particles are precipitated onto the surface of the SnO_2 particles. The citrate ion has two effects: one is to absorb onto the surface of SnO_2 particles to prevent them from aggregation by the electrostatic force; the other is Ag^+ ion and citrate ion have a tendency to form a complex, which is beneficial to the homogeneous coating of Ag onto the surface of SnO_2 cores.

The morphologies of the as-prepared Ag-SnO_2 composite powders were observed by FE-SEM, as shown in Figure 3. The composite powders show narrow size distribution, which is due to the homogenous reaction in the system. Particle size of the composite powders increases with increasing particle size of SnO_2. Thus, particle size of the composite powders can be adjusted by the SnO_2 particle size. The smaller the SnO_2 particle size, the higher the specific surface area, and thus the more the nucleation sites of Ag.

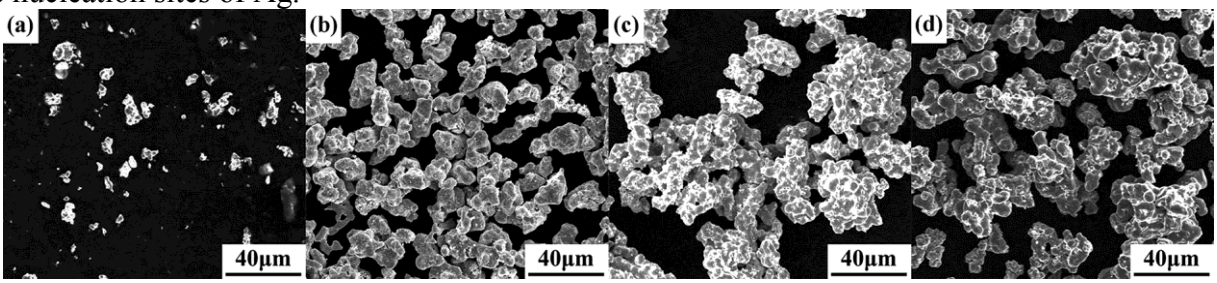


Fig. 3 Morphology of the Ag-SnO_2 composite powders with different particle size of SnO_2: (a) S1; (b) S2; (c) S3; (d) S4.

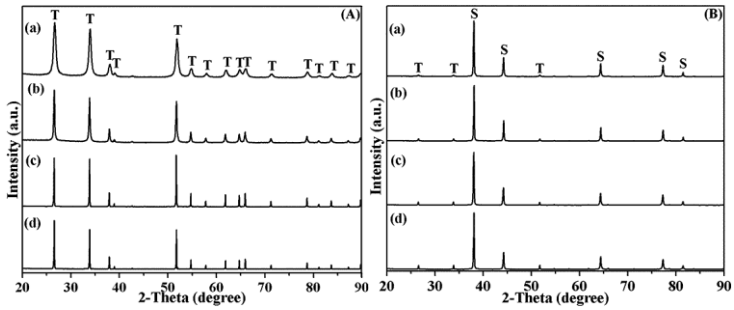


Fig. 4 XRD patterns of (A) the original SnO_2 particles, and (B) the corresponding Ag-SnO_2 composite materials: (a) S1; (b) S2; (c) S3; and (d) S4. Letters T and S represent tin oxide and silver, respectively.

XRD analysis (Figure 4) shows that the original particles are all pure rutile tetragonal structured SnO_2, and the as-prepared Ag-SnO_2 composites are all composed of face-centered cubic Ag and rutile tetragonal structured SnO_2. No other phases were observed.

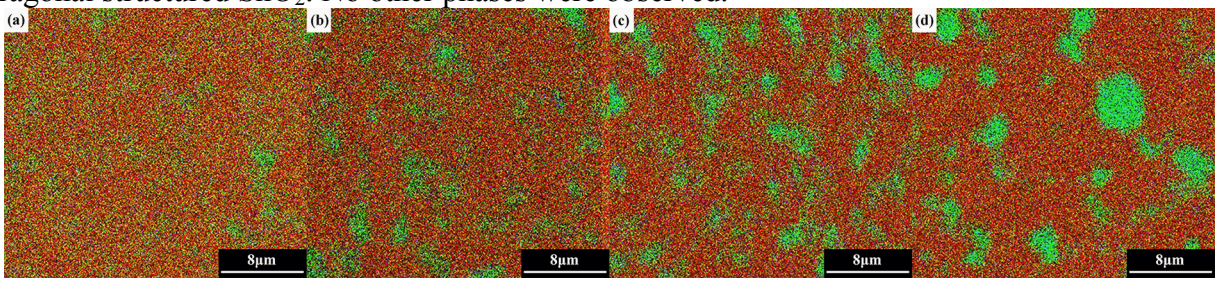


Fig. 5 EDX element mapping shows the element distribution in Ag-SnO_2 electrical contact materials (red-Ag rich zone, and green-Sn rich zone): (a) S1; (b) S2; (c) S3; (d) S4.

Element distributions in the Ag-SnO_2 electrical contact materials were analyzed by EDX, as shown in Figure 5. The second phase SnO_2 particles are all uniformly dispersed in the Ag matrix with low degree of aggregation. The size of Sn rich area is consistent with the initial sizes of the SnO_2 particles.

Properties of the Ag-SnO_2 electrical contact materials

Hardness and electric conductivety are of great importance to the electrical contact materials. The effect of particle size of SnO_2 on hardness and electric conductively were shown in Figure 6.

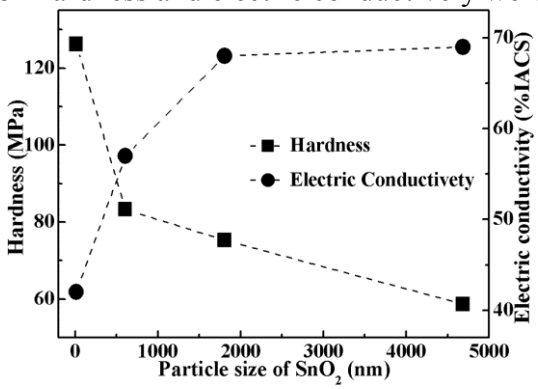


Fig. 6 The influence of particle size of SnO_2 on hardness and electric conductively of the bulk Ag-SnO_2 contact materials

With the increase of SnO_2 particle size, hardness decreases while electric conductivety increases for the Ag-SnO_2 electrical contact materials. For the incoherent interface between SnO_2 and Ag, the flow stress, $\Delta\sigma$, of the Ag-SnO_2 electrical contact materials can be described by the Orowan mechanism [10].

$$\Delta\sigma \propto \frac{G \cdot b}{L} \tag{1}$$

where G is shear modulus, b is the value of Burgers vector, and L is mean free spacing between SnO_2 particles. It can be seen that flow stress increases with the increase of amount of oxide particles in the silver matrix. The strengthening of Ag-SnO_2 electrical contact materials is beneficial to the wear resistance from the point of view applications. However, high hardness is detrimental to mechanical processing.

It is believed that electric conductivity is achieved the transmission of the conduction electrons, which can be weaken by the interface scattering in the Ag-SnO_2 interfaces [11]. The smaller the SnO_2 particle size, the higher the specific surface area, and thus the stronger of interface scattering, due to lower electric conductivity.

Conclusion

Ag-SnO_2 composite powders were successfully prepared by the chemical reductive precipitation of Ag particles onto the surface of SnO_2 particles. Citric acid was introduced as both dispersant for forming SnO_2 suspension, and coordination connection between Ag and SnO_2 particles in the reaction system. Therefore, the silver particle was deposited onto the surface of SnO_2 particles by heterogeneous nucleation. As a consequence, the particle size of the Ag-SnO_2 composite powders decreases with decreasing particle size of SnO_2. It was observed that SnO_2 particles are all uniformly dispersed in the Ag matrix. With the increase of SnO_2 particle size, hardness decreases and electric conductivity increases.

Acknowledgments

This work was supported by the National Natural Science Foundation of China (Grants No. U1302272), the Fundamental Research Funds for the Central Universities (Grants Nos. N120402002 and N110802001), and the fund of the State Key Laboratory of Advanced Technologies for Comprehensive Utilization of Platinum Metals (SKM-SPM-201214 and SKL-SPM-201206).

References

[1] A. Kratzschmar, R. Herbst, T. Mulzel, R. Niederreuther, P. Braumann, Basic Investigations on the Behavior of Advanced Ag/SnO2 Materials for Contactor Applications, Electrical Contacts (2010) 127-133.

[2] E. Hetzmannseder, W.F. Rieder, Make-and-Break Erosion of Ag/MeO Contact Materials.Components, Packaging, and Manufacturing Technology, Part A 19 (1996) 397-403.

[3] Ć. Vladan, Ć. Aleksandar, T. Nadežda, Ž. Dragana, M. Dragan, M. Duško, Improving dispersion of SnO_2 nanoparticles in Ag-SnO_2 electrical contact materials using template method, J. Alloy. Compd. 567 (2013) 33-39.

[4] T. Z. Yang, Z. J. Du, Y. Y. Gu, X. Y. Qiu, M. X. Jiang, G. Chu, Preparation of $AgSnO_2$ composite powders by hydrothermal process, T. Nonferr. Metal. Soc. 17 (2007) 434-438.

[5] R. Wolmer, M. Mueller, F. Heringhaus, D. Ruehlicke and D. Goia, U.S. Patent 6,409,794. (2002)

[6] X. M. Liu, S. L. Wu, P. K. Chu, C. Y. Chung, J. Zheng, S. L. Li, Effects of coating process on the characteristics of Ag-SnO_2 contact materials. Mater. Chem. Phys. 98 (2006) 477-480.

[7] Z.J. Lin, S.H. Liu, X.D. Sun, M. Xie, J.G. Li, X.D. Li, Y.T. Chen, J.L. Chen, D. Huo, M. Zhang, Q. Zhu and M.M. Liu, The effects of citric acid on the synthesis and performance of silver-tin oxide electrical contact materials, J. Alloy. Compd. 588 (2014) 30-35.

[8] Y. L. Chen, C. F. Yang, J. W. Yeh, S. S. Hung, S. W. Lee, A novel process for fabricating electrical contact SnO_2/Ag composites by reciprocating extrusion, Metall. Mat. Trans. A. 36 (2005) 2441-2447.

[9] C.H. Xu, D.Q. Yi, C.P. Wu, H.Q. Liu, W.Z. Li, Microstructures and properties of silver-based contact material fabricated by hot extrusion of internal oxidized Ag-Sn-Sb alloy powders, Mat. Sci. Eng. A 538 (2012) 202-209.

[10] F. Heringhaus, P. Braumann, D. Rühlicke, E. Susnik, R. Wolmer, On the improvement of dispersion in Ag-SnO_2-based contact materials, proceedings of 20th International conference on Electrical contacts, 2000.

[11] Y.G. Du, S.X. Bai, Y. Yi, J.C. Zhang, The resistance of tin-oxide particulate-reinforced silver composite materials, J. Funct. Mater. 25 (1994) 150-153.

Advanced Materials Research Vol. 936 (2014) pp 464-470
© (2014) Trans Tech Publications, Switzerland
doi:10.4028/www.scientific.net/AMR.936.464

Electrochemical Investigation of $La_{0.2}Sr_{0.8}TiO_{3+\delta}$-$Ce_{0.8}Sm_{0.2}O_{2-\delta}$ Composite Cathode for the Direct High Temperature Steam Electrolysis

Guojian Wu[1], Kui Xie[1, 2] *, Yucheng Wu [1, 2] *

[1]School of Materials Science and Engineering, Hefei University of Technology, Hefei, Anhui, China.

[2]Key Laboratory of Advanced Functional Materials and Devices of Anhui Province, Anhui, China.

[*] corresponding author, Email: xiekui@hfut.edu.cn; ycwu@hfut.edu.cn;

Keywords: Steam; Electrolysis; Solid oxide electrolyzer; Strontium titanate

Abstract: This paper investigates a composite cathode $La_{0.2}Sr_{0.8}TiO_{3+\delta}$-$Ce_{0.8}Sm_{0.2}O_{2-\delta}$ (LSTO-SDC) for the direct steam electrolysis in an oxide-ion-conducting solid oxide electrolyzer. The dependences of electrical conductivity of the reduced LSTO on temperature and oxygen partial pressure are studied and further correlated to the electrochemical properties of the cathode in symmetric cell LSTO-SDC/YSZ/LSTO-SDC and solid oxide electrolyzer LSTO-SDC/YSZ/LSM-SDC, respectively. Current efficiencies of the solid oxide electrolyzer with LSTO-SDC cathode were found to be 92.38% and 91.17% with or without reducing gas flowing over them under the applied voltage of 1.8 V at 800 ^{o}C, respectively.

Introduction

Hydrogen is an environmental-friendly fuel, it is regard as the candidate fuel because it has the potential to solve the environmental and energy shortage issues associated with fossil fuel [1-2]. Many processes have been used to promote the sequestration of steam including photosynthesis, heterogeneous catalysis and steam electrolysis [3-4]. The high-temperature steam electrolysis in a solid oxide electrolyzer (SOE) stands out for its possibility to operate in high efficiency and can be further combined with renewable electricity to effectively exploit available heat streams [5]. Solid oxide electrolyzer is the reverse process of solid oxide fuel cell, which can directly convert the electrical energy into chemical energy and recently it has attracted a lot of interests. A solid oxide electrolyzer operates at high temperature which could partially offer energy for molecular dissociation, leads to more favorable kinetics and thermodynamics. Using external electricity, an oxide-ion-conducting solid oxide electrolyzer can electrolyze steam into hydrogen and oxygen. At the cathode, H_2O molecules are electrochemically reduced into H_2 under applied potential, while the generated O^{2-} transports through the electrolyte to the anode where O_2 gas is formed [6].

Composite Ni-YSZ cathode has been preferentially used for the high temperature steam electrolysis in an oxide-ion-conducting solid oxide electrolyzer [7]. However, the composite cathode can only work in an atmosphere with a significant concentration of H_2, or the oxidation of Ni to NiO at high temperature would occur and further cause a loss of electronic conductivity and the failure of the composite cathode. The poor redox cycling is also the critical problem for a Ni-YSZ cathode [8]. Irvine et al. have demonstrated an efficient ceramic $(La_{0.75}Sr_{0.25})_{0.95}Mn_{0.5}Cr_{0.5}O_3$ (LSCM) cathode for the direct steam electrolysis [9]. Recently, we demonstrated that some adverse chemical changes may occur in LSCM cathode under strong reducing potentials when perform high-temperature steam electrolysis, which further degrades the Faradic current efficiency and the

electrode performances [10]. On the other hand, the p-type conduction in LSCM is restricted when high voltage is applied to cathode for electrochemical reduction of steam [11]. Therefore, a cathode that has n-type conduction with sufficient electro-catalytic activity seems more suitable in cathode atmosphere. The $La_xSr_{1-x}TiO_{3-\delta}$ (LSTO) perovskite is an active and redox-stable material that has high n-type conductivity upon reduction atmosphere, which has attracted a lot of attentions in the field of solid oxide fuel cell anode materials [12]. Perovskite $La_{0.2}Sr_{0.8}TiO_{3+\delta}$ would well fit the cathode atmosphere in an oxide-ion-conducting solid oxide electrolyzer.

In this work, a composite cathode $La_{0.2}Sr_{0.8}TiO_{3+\delta}$-$Ce_{0.8}Sm_{0.2}O_{2-\delta}$ is prepared and utilized for the direct steam electrolysis in an oxide-ion-conducting solid oxide electrolyzer. The electrical properties of $La_{0.2}Sr_{0.8}TiO_{3+\delta}$ are studied and then correlated to the cathode performance. High temperature steam electrolysis is then systematically investigated and evaluated with a solid oxide electrolyzer- (cathode) $La_{0.2}Sr_{0.8}TiO_{3+\delta}$-$Ce_{0.8}Sm_{0.2}O_{2-\delta}$/YSZ/$(La_{0.8}Sr_{0.2})_{0.95}MnO_{3-\delta}$-$Ce_{0.8}Sm_{0.2}O_{2-\delta}$ (anode).

Experimental

$La_{0.2}Sr_{0.8}TiO_{3+\delta}$ (LSTO) powders were synthesized by a traditional solid-state reaction method [13]. The phase formations of the LSTO powders were analyzed by X-ray diffraction (XRD, $2\theta=3^{o}\cdot min^{-1}$, D/MAX2500V, Rigaku Corporation, Japan). Subsequently, the sintered samples were reduced at 1400 ºC for 12 h in 5%H_2/Ar. The conductivity test was performed using a DC four-terminal method from 130 to 800 ºC in 5%H_2/Ar atmosphere. The 8YSZ powders were dry-pressed into a green disk with a diameter of 20 mm followed by a sintering in air at 1450 ºC (3 $ºC\cdot min^{-1}$) for 10 h to obtain a 2-mm-thick electrolyte support. The composite electrodes LSTO-SDC and LSM-SDC slurries were prepared by milling the SDC powders with the LSTO and LSM powders at a weight ratio of 35:65 in the alpha-terpineol with the cellulose additive, respectively. The silver paste (SS-8060, Xinluyi, Shanghai, China) was printed onto both electrode surfaces for current collection. Scanning electron microscope (SEM, JSM-6490LV, JEOL Ltd, Japan) was used to observe the microstructure of the as-prepared electrolyzers.

The AC impedance of symmetric cells were tested at the open circuit voltage (OCV) in different hydrogen pressure at 800 ^{o}C using the electrochemical workstation (IM6, Zahner, Germany). The single solid oxide electrolyzers were sealed to a home-made testing jig by using ceramic paste (JD-767, Jiudian, Dongguan, China) for electrochemical measurements including the AC impedance and Current-Voltage (I-V) curve. The direct electrolysis of steam was performed at 1.2, 1.6 and 1.8 V with the as-prepared single solid oxide electrolyzers at 800 ^{o}C, respectively. The output gas from the cathode was analyzed using an online gas chromatograph (GC9790II, Fuli, Zhejiang, China) to detect the concentration of generated hydrogen.

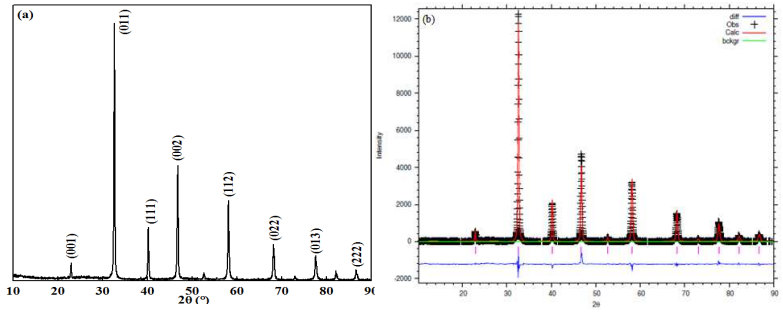


Fig. 1 (a) XRD Patterns and (b) Rietveld Refinement of $La_{0.2}Sr_{0.8}TiO_{3+\delta}$ (LSTO) Powders.

Results and Discussion

Fig. 1(a) shows the XRD patterns of LSTO powders. The results show pure phase according to the references [14], and the XRD patterns are indexed according to its PDF card (LSTO: No.52-1769). These two oxides belong to the same space group; however, the chemical compositions are different. The LSTO refinement gives χ^2, wRp and Rp values of 1.425, 2.23% and 1.21%, respectively, and the cell parameters of LSTO are a=b=c=3.88139 Å, α=β=γ=90 º.

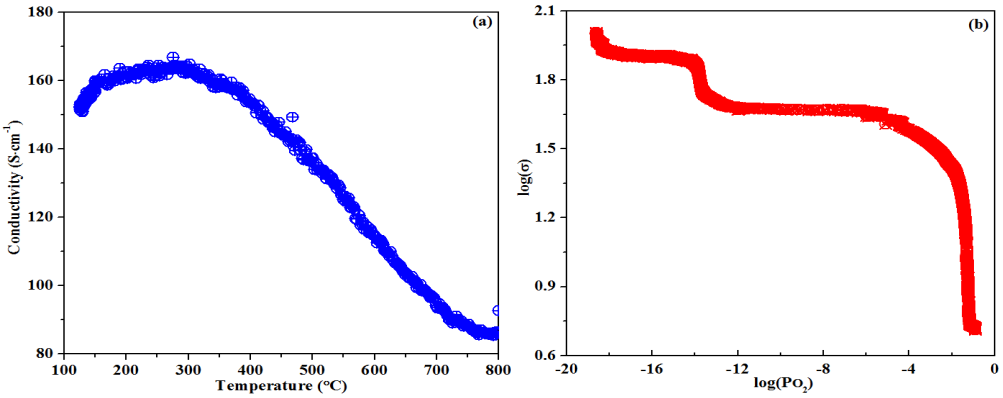


Fig. 2 The Conductivity of LSTO Versus (a) Temperature in 5%H2/Ar and (b) the Oxygen Partial Pressure.

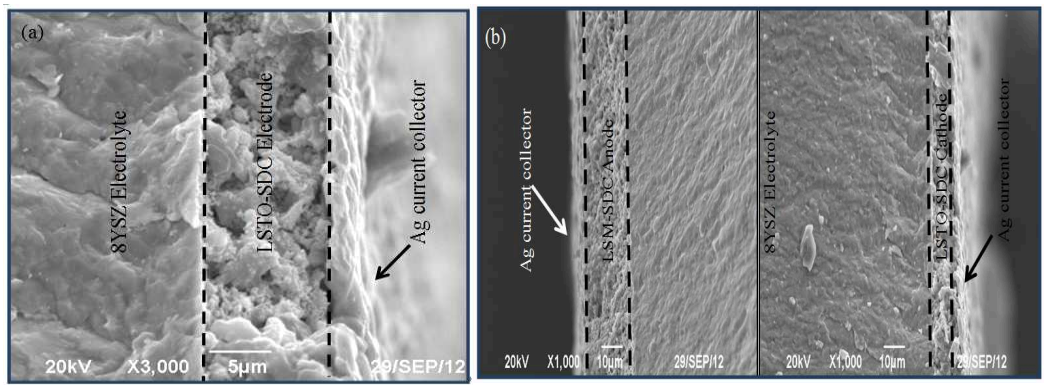


Fig. 3 (a) Microstructure of the Symmetric Solid Oxide Electrolyzer; (b) Microstructure of the Single Solid Oxide Electrolyzer

The reduced LSTO sample is an n-type electronic conductor which is expected to show a typical metallic behavior in H_2/Ar gas; however, an increase in conductivity is observed when the temperature increases from 130 ºC to 247 ºC as shown in Fig. 2 (a). It is attributed to the oxidized and p-type LSTO layer on the sample surface which is produced by the absorption of oxygen on the surface of the reduced sample. The atmospheric oxygen would easily and quickly oxidize Ti^{3+} to Ti^{4+} and causes the loss of conductivity of the reduced sample at low temperatures; however, the oxidized layer would be gradually and sufficiently reduced by H_2 up to the 247 ºC and enhance the conductivity though the conductivity of n-type conductor would decrease with temperature. The maximum conductivity reaches approximately 160 $S \cdot cm^{-1}$ at 247 ºC and drops to about 85 $S \cdot cm^{-1}$ at 800 ºC which is in good accordance with the n-type conductor behavior. Fig. 2 (b) shows the dependence of conductivity of the reduced LSTO on the PO_2. It is observed that the conductivity is increasing versus PO_2, especially at low oxygen partial pressure region. The reduction of Ti^{4+} to Ti^{3+} is promoted to generate higher concentrations of the charge carriers and enhances the conductivity, which further confirms the n-type conduction mechanism.

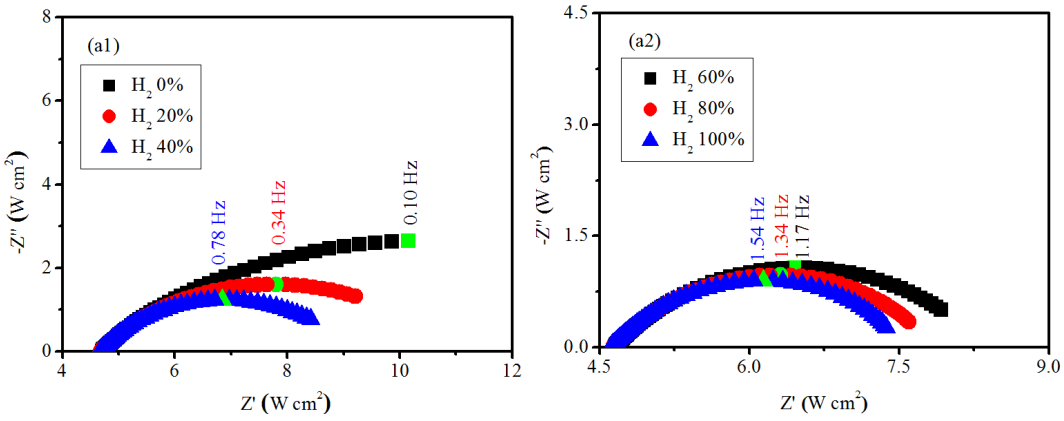


Fig. 4 The AC Impendence of the Symmetric Cells for LSTO Composite Cathode.

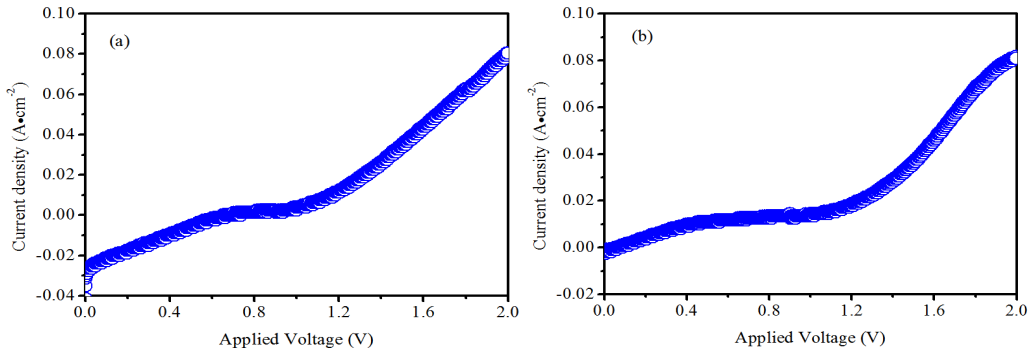


Fig. 5 The I-V Curves of the Electrolyzer with LSTO Cathode at 800 oC in Different Atmospheres (a) 5%H2O/5%H2/Ar and (b) 5%H2O/Ar.

Fig. 3 shows the microstructures of the symmetric cell and the single cell. The adhesion between dense electrolyte and the porous electrodes layers with a thickness of 10-μm seems very well. The outer porous silver current collector layer is only about 2 μm in thickness. Fig. 4 (a) shows the AC impendence of symmetric cell tested in different hydrogen pressure at 800 ºC. The electrode polarization resistance (Rp) of symmetric cell based on LSTO-SDC decreases from approximately 10 $\Omega \cdot cm^2$ to 1.5 $\Omega \cdot cm^2$ with the hydrogen partial pressure ranging from 0% to 100%. The low Rp in a stronger reducing atmosphere may be related to the improved electrocatalytic activity of the composite electrodes. A low oxygen partial pressure was also favorable to increasing electrical conductivity of the reduced LSTO, which also improved the electrode performances. The LSTO is efficiently activated at higher temperature in H_2 atmosphere and could be a good cathode candidate.

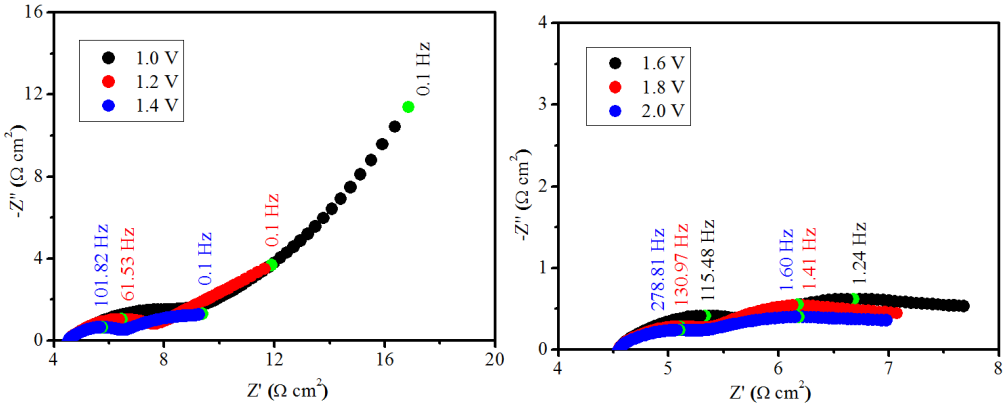


Fig. 6 The AC Impendence of the Electrolysis Cells Based on LSTO with the Flow of 5%H2O/5%H2/Ar at 800 oC.

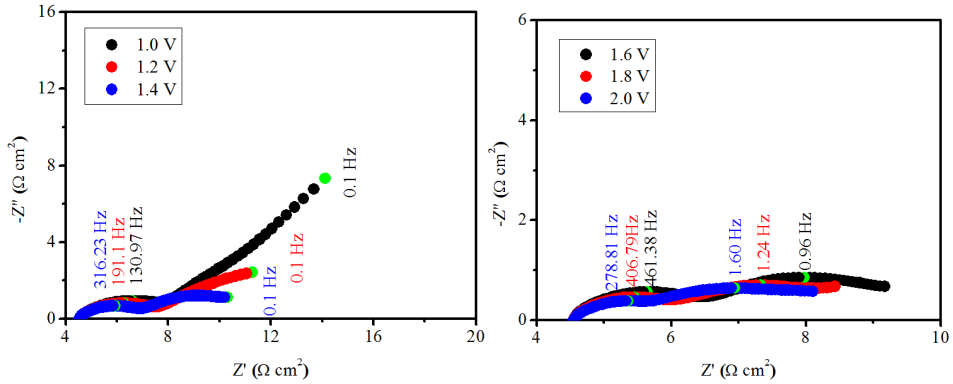


Fig. 7 The AC Impendence of the Electrolysis Cells Based on LSTO with the Flow of 5%H2O/Ar at 800 oC.

Fig. 5 shows the current density with the applied voltage (I-V curve) of the electrolyzer under different testing conditions. The open circuit voltages of the single electrolyzers in 5% H_2O/5% H_2/Ar are 0.9 V as shown in Fig. 5 (a). The relationship between the current density and applied voltage are far from linear, and clear changes in slope can be observed above 1.2 V. The maximum current density reaches 0.0822 A cm^2 at 2.0 V based on LSTO-SDC composite cathodes; As shown in Fig. 5 (b), the current density reached 0.0807 A cm^2 at 2.0 V with LSTO-SDC composite cathodes in 5% H_2O/Ar. It should also be noted that the current densities based on LSTO-SDC in 5% H_2O/5% H_2/Ar is slightly larger than it in 5% H_2O/Ar, which might be attributed to the better catalytic performances and mixed conductivities of the composite electrodes in more reducing conditions. To further study the electrochemical performance of the electrodes, in-situ AC impedance spectroscopy was conducted to investigate the change of cell resistance under different voltages.

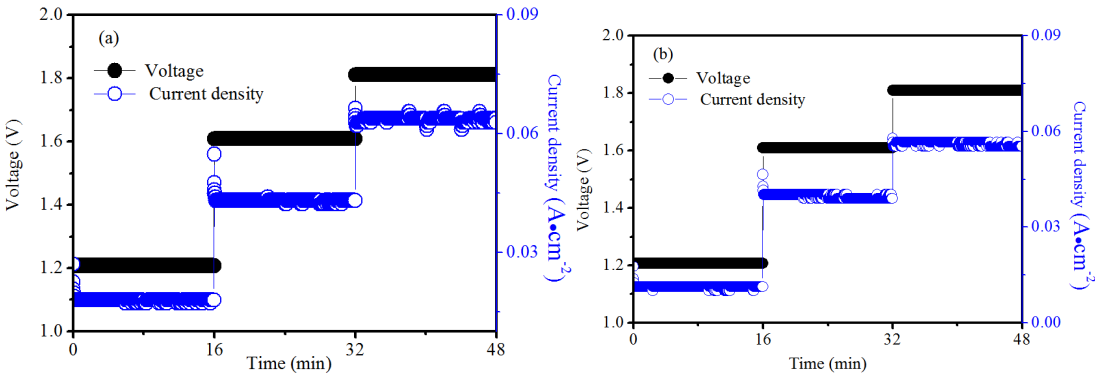


Fig. 8 The Performances of Steam Electrolysis for the Electrolyzer in Different Atmosphere (a) 5%H2O/5%H2/Ar and (b) 5%H2O/Ar at 800 oC.

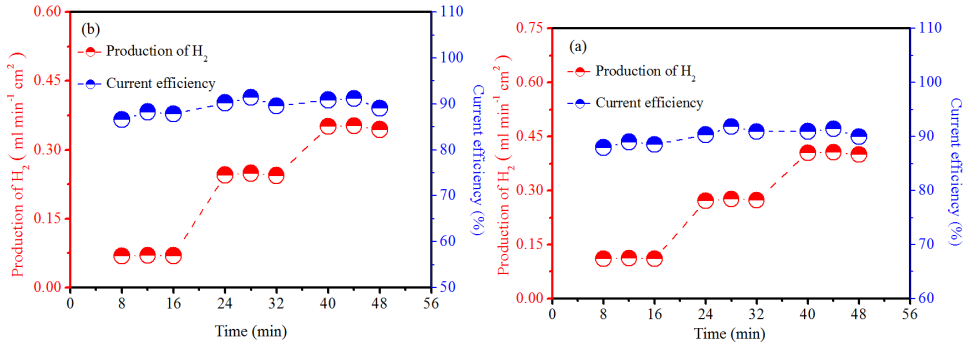


Fig. 9 The Hydrogen Production and Current Efficiency (a) for the Electrolyzer with the flow of 5%H2O/5%H2/Ar; (b) with the Flow of 5%H2O/Ar.

Fig. 6 and 7 show the in-situ AC impendence of solid oxide electrolyzers under a series of external voltages ranging from 1.0 to 2.0 V, at 800 ºC in 5% H_2O/5% H_2/Ar and 5% H_2O/Ar, respectively. As shownin the figures, the electrode polarization resistance Rp is quite large at low voltages, whereas the increasing voltages make the Rp drop considerably at high voltages, which may be attributed to the fact that the applied voltage not only activates the electrode but also electrochemically reduces the composite LSTO-SDC electrode and enhances the mixed conductivity. The Rp is only 3.5 $\Omega \cdot cm^2$ at 1.6 V and further drops to 2.5 $\Omega \cdot cm^2$ at 2.0 V in 5% H_2O/5% H_2/Ar with LSTO-SDC cathode; A promising electrochemical performance with the LSTO-SDC composite cathodes was also obtained in the 5% H_2O/Ar atmosphere for direct steam electrolysis as shown in Fig. 7. Direct steam electrolysis was achieved with the composite cathode, and a comparable performance with electrolyzers in 5% H_2O/Ar was obtained. The electrode polarization resistance with the LSTO-SDC cathode, Rp, is approximately 4.5 $\Omega \cdot cm^2$ at 1.6 V and finally drops to 3.5 $\Omega \cdot cm^2$ at 2.0 V, which is comparable but slightly larger than the values in 5% H_2O/5% H_2/Ar, which is most likely because the direct steam electrolysis produces a less reducing atmosphere that decreases the mixed conductivity of the LSTO-SDC composite electrodes.

As shown in Fig. 8, the current density vessus time with the applied voltage of 1.2, 1.6 and 1.8 V were also recorded to further investigate the process of steam electrolysis. It is clear that the current densities increased with the applied voltage and the performance was stable at a certain potential load. It can also be observed that the current density reached approximately 0.0637 A cm^2 at 1.8 V with the LSTO-SDC electrodes in 5% H_2O/5% H_2/Ar. In addition, the current density with the LSTO-SDC cathodes still reached a comparable 0.0553 A cm^2 in 5% H_2O/Ar for direct steam electrolysis. Fig. 9 shows the hydrogen production rate, and current efficiency with the LSTO-SDC cathodes under different applied voltages for steam electrolysis in 5% H_2O/5% H_2/Ar and 3% H_2O/Ar at 800 ºC, respectively. The production of H_2 reached 0.406 ml min^{-1} cm^2 at 1.8 V with the LSTO-SDC composite electrode in 5% H_2O/5% H_2/Ar. More importantly, direct steam electrolysis was achieved with the LSTO-SDC composite cathodes in the 5% H_2O/Ar atmosphere. The hydrogen generation from the direct electrolysis of 5% H_2O/Ar reaches 0.353 ml min^{-1} cm^2 for the LSTO-SDC composite cathodes. The result suggests that the redox-stable LSTO-SDC leads to the improved cathode performances for direct steam electrolysis and desired short-term stability. The corresponding current efficiency reached 92.38% and 91.17% at 1.8 V with the LSTO-SDC cathodes in 5% H_2O/5% H_2/Ar and 5% H_2O/Ar.

Conclusion

In this work, a composite electrode based on $La_{0.2}Sr_{0.8}TiO_{3+\delta}$ (LSTO) is investigated in an oxide-ion-conducting solid oxide electrolyzer with a configuration of LSTO-SDC/YSZ/LSM-SDC for the direct steam electrolysis at 800ºC. AC impedance spectroscopy and I-V tests demonstrate two main processes from 0 to 2.0 V with steam versus air: the reduction of the LSTO electrode below 1.0 V and the electrolysis of steam above 1.0 V. The applied voltage improves the cathode performance and the current efficiency is 92.38% and 91.17% with or without reducing gas flowing over them under the applied voltage of 1.8 V at 800 ^oC, respectively.

References

[1] G. Tsekouras and J.T.S. Irvine, The role of defect chemistry in strontium titanates utilised for high temperature steam electrolysis, J. Mater. Chem. 21 (2011) 9367-9376.

[2] S. Sista, Z. Hong, L. Chen, Y. Yang, Tandem polymer photovoltaic cells—current status, challenges and future outlook, Energy Environ. Sci. 4 (2011) 1606-1620.

[3] N.V. Gnanapragasam, B.V. Reddy, M.A. Rosen, Feasibility of an energy conversion system in Canada involving large-scale integrated hydrogen production using solid fuels, Int. J. Hydrogen Energy 35 (2010) 4788-4807.

[4] A. Hauch, S.D. Ebbesen, S.H. Jensen, M. Mogensen, Highly efficient high temperature electrolysis, J. Mater. Chem. 18 (2008) 2331-2340.

[5] M. Ni, M.K.H. Leung, D.Y.C. Leung, Technological development of hydrogen production by solid oxide electrolyzer cell (SOEC), Int. J. Hydrogen Energy 33 (2008) 2337-2354.

[6] [6] K. Xie, Y.Q. Zhang, G.Y. Meng, J.T.S. Irive, Direct synthesis of methane from CO2/H2O in an oxygen-ion conducting solid oxide electrolyser, Energy Environ. Sci. 4 (2011) 2218-2222.

[7] E.C. Shin, P.A. Ahn, H.H. Seo, J.M. Jo, S.K. Woo, Polarization mechanism of high temperature electrolysis in a Ni-YSZ/YSZ/LSM solid oxide cell by parametric impedance analysis, Solid State Ion. 232 (2013) 80-96.

[8] M. Pihlatie, A. Kaiser, M. Mogensen, Redox stability of SOFC: Thermal analysis of Ni-YSZ composites, Solid State Ion. 180 (232) 1100-1112.

[9] S.W. Tao, J.T.S. Irvine, A redox-stable efficient anode for solid-oxide fuel cells, A redox-stable efficient anode for solid-oxide fuel cells. Nat. Mater. 2 (2003) 320-323.

[10] S.S. Xu, S.G. Chen, M. Li, K. Xie, Y. Wang, Y.C. Wu, Composite cathode based on Fe-loaded LSCM for steam electrolysis in an oxide-ion-conducting solid oxide electrolyser, J. Power Sources 239 (2013) 332-340.

[11] X.B. Zhu, Z. Lu, B. Wei, M.L. Liu, X.Q. Huang, W.H. Su, A comparison of La0.75Sr0.25Cr0.5Mn0.5O3−δ and Ni impregnated porous YSZ anodes fabricated in two different ways for SOFCs, Electrochim. Acta 55(2010) 3932-3938.

[12] Y. Gan, Q.Q. Qin, S.G. Chen, Y. Wang, D.H. Dong, K. Xie, Composite cathode La0.4Sr0.4TiO3-Ce0.8Sm0.2O2-δ impregnated with Ni for high-temperature steam electrolysis, J. Power Sources 245 (2014) 245-255.

[13] D. Neagu, J.T.S. Irvine, Structure and properties of La0.4Sr0.4TiO3 ceramics for use as anode materials in solid oxide fuel cells, Chem. Mater. 22 (2010) 5042-5053.

[14] J. Canales-Vazquez, M.J. Smith, J.T.S. Irvine, W.Z. Zhou, Studies on the Reorganization of Extended Defects with Increasing *n* in the Perovskite-Based La4Sr*n*–4Ti*n*O3*n*+2 Series, Adv. Funct. Mater. 15 (2005) 1000-1008.

Advanced Materials Research Vol. 936 (2014) pp 471-475
© (2014) Trans Tech Publications, Switzerland
doi:10.4028/www.scientific.net/AMR.936.471

Highly hydroxylated graphite felts used as electrodes for a vanadium redox flow battery

LI Wen-Wen, CHU You-Qun, MA Chun-An

College of Chemical Engineering, Zhejiang University of Technology, Hangzhou 310014, China,

E-mail: chuyq@zjut.edu.cn

Keywords: Vanadium redox flow battery, graphite felt, electrochemical activity

Abstract: The highly hydroxylated graphite felts (GFs) were obtained by treating in mixed acids ($V(HNO_3)/V(H_3PO_4)$=3:1) for different time at 80℃, and used as the electrodes for all vanadium redox flow battery (VRB). The physical, chemical and electrochemical characteristics of these GFs are characterized by X-ray photoelectron spectroscopy, scanning electron microscopy, cyclic voltametry, electrochemical impedance spectroscopy and charge/discharge test. The excellent electrochemical properties of the treated GFs to VRB electrode reactions can be ascribed to the enhancement of the interaction between vanadium ions with –OH groups introduced by acid treatment. Using GFs treated in the mixed acids for 8 h as electrodes, the VRB exhibits excellent performance under a current density of 20 mA/cm^2. The average current efficiency, voltage efficiency and energy efficiency are about 97%, 83.3% and 78%, respectively.

Introduction

Recently, the all vanadium redox flow battery (VRB) has attracted great attention due to its excellent merits, such as long cycle life, deep discharge capability, fast response time, flexible design, low cost, etc. Graphite felts (GFs) are the most commonly used electrode materials for VRB due to their great specific surface area, high strength and broad potential window[1]. But these materials have been proven to show a poor electrochemical activity[2]. Considerable efforts have been devoted in introducing oxygen-containing groups such as hydroxyl, carbonyl and carboxyl for the purpose of improving the electrochemical properties of GFs[3-13]. Despite a large number of literature reports on the modification of the GF surface nature, but it still need further research to enrich the surface modification method to meet the steep demands for the practical application of VRB in large scale energy storage domain.

In this study, we developed a new method to treat GFs in mixed acids $V(H_2SO_4)/V(HNO_4)$=3:1 to get the hydroxylated surface of GFs. The effects of treatments on the surface of GFs were characterized by X-ray photoelectron spectroscopy (XPS), scanning electron microscopy (SEM). And their electrochemical properties to the redox reaction of V(IV)/V(V) were also investigated using cyclic voltammetry (CV), electrochemical impedance spectroscopy (EIS) and charge/discharge test of a small-size VRB.

Experimental

PAN-graphite felt with the thickness of 10 mm was purchased from Shanghai XinXing Carbon Co. Ltd., China. HNO_3 (68 wt %) was provided by Zhejiang Zhongxing Chemical Co. China. H_3PO_4 (> 85wt %) was purchased from Guoyao Chemical Co. China.

The raw GFs were heated at 520±10 ℃ for 3 h under air atmosphere to produce R-GF. The R-GF of 1 cm×1 cm was treated in a sealed Teflon-lined stainless steel autoclave containing 70 mL mixed acids $V(HNO_3)/V(H_3PO_4)$=3:1 for different time at 80℃, then the GFs were washed with distilled water until pH of the rinsed water was neutral and dried for 3 h at 60℃. The GFs after acid treating were denoted as AGF-X, where X represents the treating time.

XPS spectra were obtained with an ESCALab220i-XL electron spectrometer from VG Scientific using 300W Al-Kα radiation. The base pressure was about 3×10^{-9} mbar. The binding energies were

referenced to the C1s line at 284.6 eV from adventitious carbon. The spectra were analyzed using Spectrum software (XPSPEAK). The surface morphologies of the GFs were observed using a Hitachi S-4800 scanning electron microscopy (SEM) at an acceleration voltage of 20 kV.

For cyclic voltammetry (CV) and the electrochemical impedance spectroscopy (EIS, 0.01–10^5 Hz, amplitude=5mV) measurements, a three-electrode cell was used with GF as the working electrode, a saturated calomel electrode (SCE) as the reference electrode and graphite plate as the counter electrode. The measurements were performed with an Iviumstat electrochemical workstation (Ivium Technologies BV, The Netherlands) in 3.0 M H_2SO_4 + 0.1 M $VOSO_4$ solution at room temperature.

The constant current charge/discharge test was carried out by using a small-size VRB with symmetrical structure on an Arbin BT2000 battery testing system (Arbin Instruments, USA). Two pieces of GFs with area of 9 cm^2 (3.0 × 3.0 cm) were used as positive electrode and negative electrode, respectively. The chambers of positive electrode and negative electrode were separated by a Nafion 117 cation exchange membrane. The initial anolyte was 40 ml 1.0 M V(VI)+3.0 M H_2SO_4, and catholyte was 40 ml 1.0 M V(III)+3.0 M H_2SO_4. The cells were charged and discharged at the current density of 20 mA/cm^2 and the voltage range was fixed between 1.65 and 0.8 V.

Results and Discussions

SEM analysis. It can be seen from Fig.1 that the impurities on the GF surface were eliminated by treating in the mixed acids. The surface of GF before acid treatment (R-GF) is smoother than those treated in the acids. With the extension of processing time, the increasing of cavities on the surface of GF fibres can be observed. The increasing of cavities could increase the specific surface area of the GFs, which may beneficial to the VRB reactions. But the GF structure was destroyed when the processing time extended to 14h, which may have negative impacts on the electrochemical performance. This indicates that the processing time should not last more than 8 h.

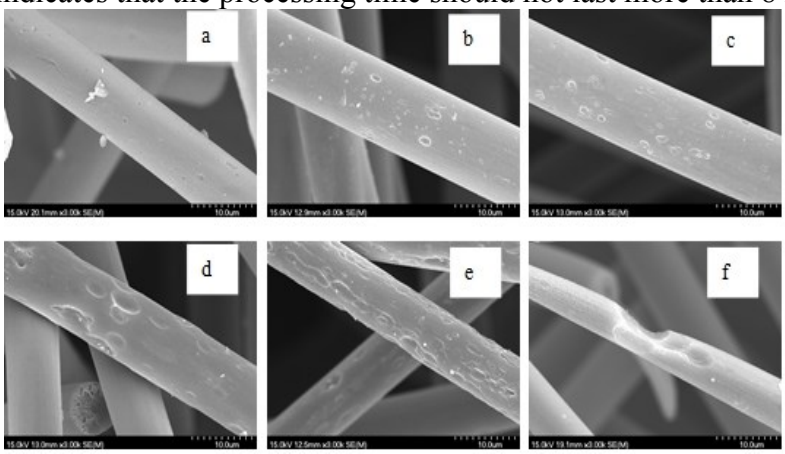


Fig.1. SEM images of R-GF(a), AGF-2(b), AGF-4(c), AGF-6 (d), AGF-8 (e) and AGF-14 (f)

XPS analysis. To elucidating surface nature of GFs before and after treatments, XPS is a suitable technique particularly for monitoring the functional groups in the surface region. With the increase of treatment time, the intensity of the O1s peak at the binding energy of 532 eV increases significantly with concerning to that of the C1s peak at the binding energy of 284.7 eV (shown in Fig. 2), and corresponding O content at the surface of GFs increase gradually from 10.10 at% to 13.28 at% (listed in Table 1).

In the case of O1s deconvolution for R-GF, three main peaks were observed at 531.7, 532.4, and 534.4eV, which correspond to C=O, -OH and H-O-H[14-16]. The C=O groups mainly come from the further oxidization of -OH groups which result from the breakage of C=C bonds on the fragments under strong oxidation [17]. As the increase of the treatment time, almost all the C=C bonds on the fragments are broken and all the carbons from the broken bonds transform into -OH groups.

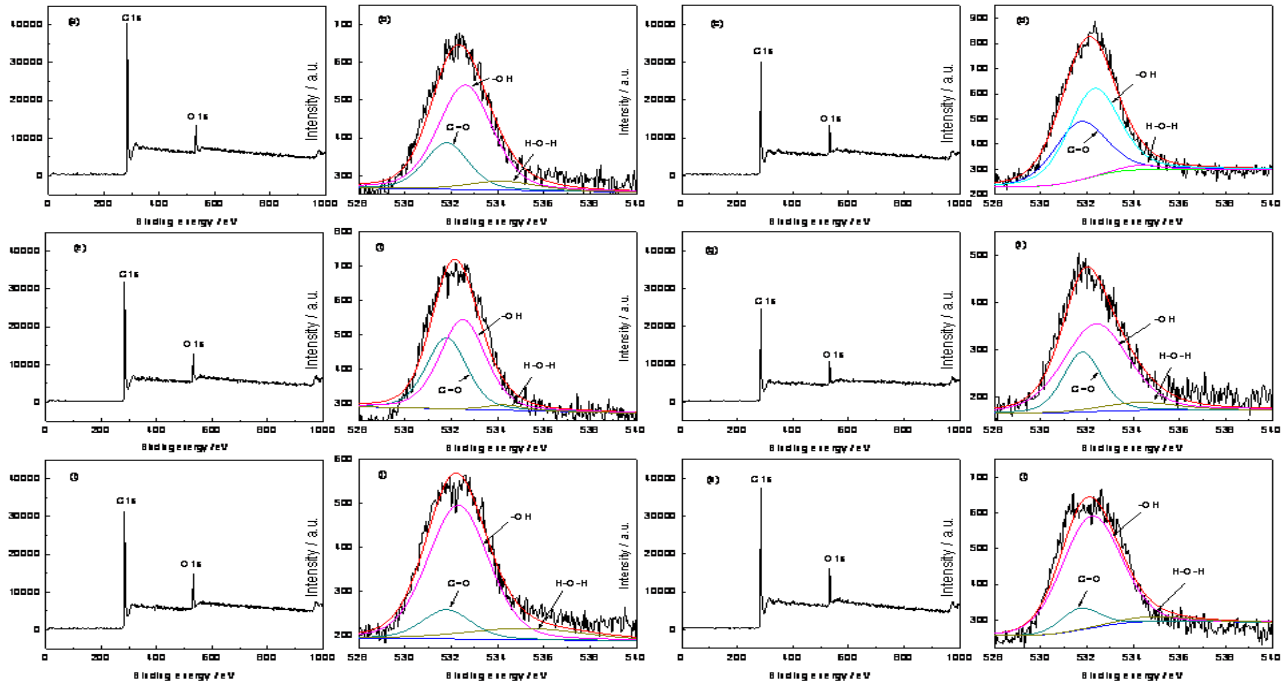


Fig. 2 XPS of (a,b) R-GF, (c,d)AGF-2, (e,f)AGF-4, (g,h)AGF-6, (i,j)AGF-8, and (k,l)AGF-14 h

Table 1 XPS surface elemental analysis parameters of the untreated and treated GFs

Times (h)	Content(at%)					
	C1s	O1s	N1s	C=O	-OH	H-O-H
0	89.90	10.10	-	2.5	6.9	0.7
2	87.71	11.21	1.09	4.4	6.5	0.3
4	86.69	12.10	1.21	4.9	6.9	0.3
6	86.61	12.32	1.07	3.3	8.2	0.8
8	85.67	12.92	1.41	1.5	8.4	1.43
14	85.59	13.28	1.12	1.4	11.2	0.64

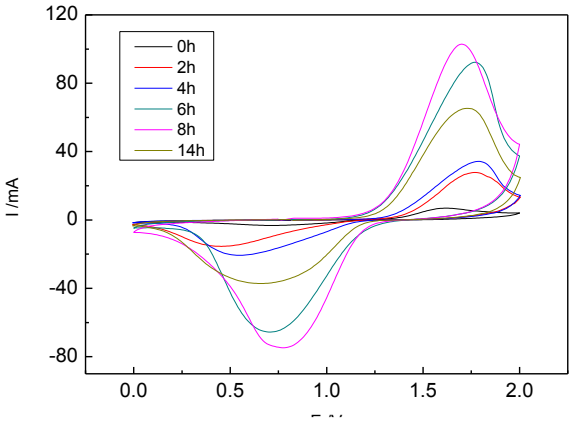


Fig.3 Cyclic voltammograms of the untreated and treated GFs obtained at 10 mVs^{-1}

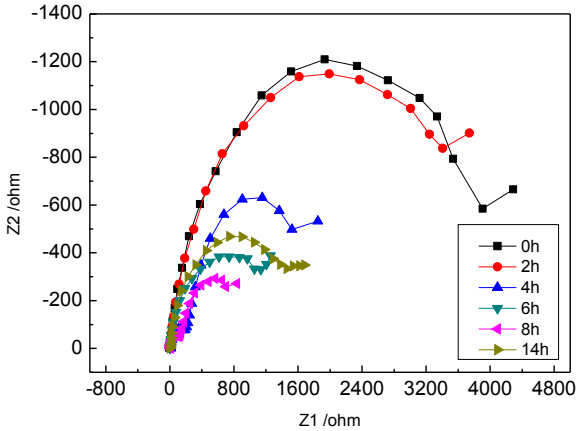


Fig. 4 Nyquist plots of GF electrodes

Cyclic voltammetric behavior. As shown in Fig. 3, the activities of GFs toward V(IV)/V(V) redox reaction have been improved after the treatment in mixed acids. The anodic peak appears at 1.46-1.49 V corresponding to V(IV)/V(V) redox reaction. Much higher current responses were obtained with those treated samples, this can be attributed to the enhanced interaction between the vanadium ion with the -OH groups formed during the acid treatment. Among them, AGF-8 exhibits

the highest activity. Although AGF-14 has the highest -OH group contents, showing poorer activity than AGF-8, this can be ascribed to the structural damage of the GF treated for 14 h.

EIS analysis. A comparison of impedance (Nyquist) plots is shown in Fig.4. The Nyquist plots include a semicircle part and a linear part, indicating that the V(IV)/V(V) redox reactions on these GF electrodes are all mix-controlled by charge transfer and diffusion steps. The semicircle part at high frequencies reflects the charge transfer process and the linear part at low frequencies reflects the diffusion processes in pore channel of GF[19-22]. In addition, it can be seen that the reaction resistance decreases gradually with the prolonging of processing time, and the smallest reaction resistance is achieved with AGF-8. This further proves that the hydroxylation of GF surface is beneficial to the electrode reaction. The increasing of reaction resistance of AGF-14 can also attributed to the structural failure of GF.

Charge-discharge test. Fig.5 and Fig.6 show the charge/discharge characteristics of VRBs using R-GF and AGF-8 as electrodes. It can be seen from Fig.5 that the VRB using AGF-8 (Fig.5a) as electrodes has lower charging voltage and higher discharging voltageusing compared to the VRB using R-GF as electrodes (Fig.5b). This implies that AGF-8 has better electrocatalytic actives for the VRB reactions than R-GF. This is in complete accord with the results obtained by CV and EIS. In addition, both VRBs show no significant performance degradation after 50 times charge/discharge cycles at current density of 20 mA/cm^2. The current efficencies of both VRBs are about 97%, while the VRB using AGF-8 as electrodes has higher voltage efficency and energy efficiency, 83.3% and 78%.

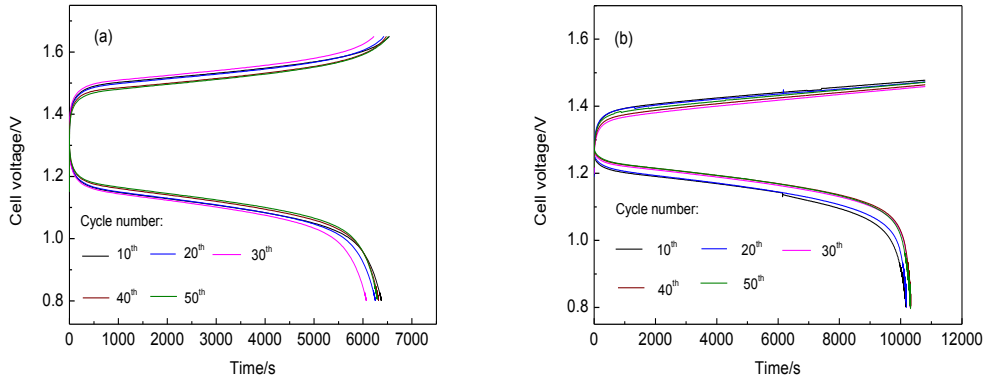


Fig. 5. Charge/discharge curves of VRBs using R-GF(a) and AGF-8(b) at 20 mA/cm^2

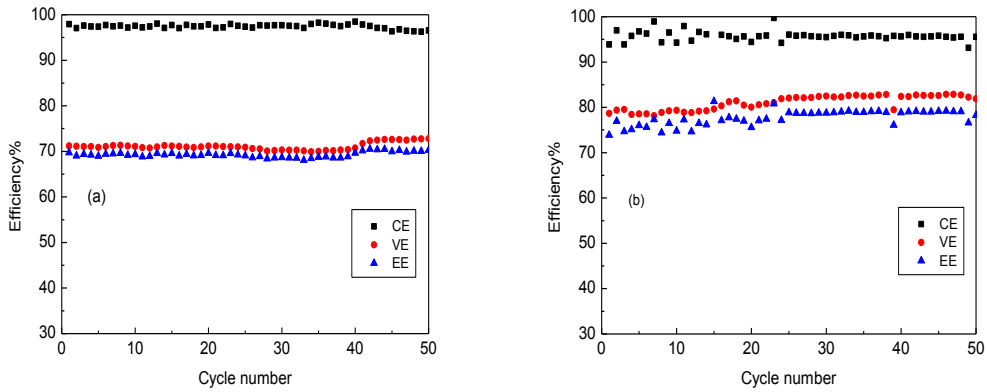


Fig. 6. Charge/discharge performance of VRBs using R-GF(a) and AGF-8(b) at 20 mA/cm^2.

Conclutions

The GF surface was successfully hydroxylated through the treatment in mixed acids V(HNO_3)/V(H_3PO_4)=3:1. The introduction of –OH groups onto GF surface can significantly improve its electrocatalytic activities for VRB reactions. This can be ascribed to the enhancement of interaction between vanadium ions and -OH functional groups formed on the GF surface, which

makes the electron transfer reaction of vanadium ions at the GF surface easier. The appreciate time for treating GF in the mixed acids is 8 h, and the GF structure will be destroyed if the time further prolongs. The VRB using AGF-8(GF treated in the mixed acid for 8 h) as electrodes exhibits excellent performance under a current density of 20 mA/cm^2. The average current efficiency, voltage efficiency are about 97%, 83.3%, and 78%, respectively.

Acknowledgements

This study was financially supported by Innovative Team Program of Science Technology Department of Zhejiang Province (No. 2011R09002-05).

References

[1] Kamarudin S K, Daud WRW, Ho SL, et al. J. Power Sources, 163 (2007) 743-54.
[2] Fabjan C, Garche J, Harrer B, et al. Electrochim. Acta, 47 (2001) 825-31.
[3] Zhou C F, Kumar S, Doyle C D. Chem Mater., 17 (2005) 1997-2002.
[4] Tseng C H, Wang C C, Chen C Y. Chem Mater., 19 (2007) 308-15.
[5] Shen W Z, Wang H, Guan R G, et al. Colloids Surf. A: Physicochem. Eng. Aspects, 331 (2008) 263-267.
[6] Zhao P, Zhang H M, Zhou H T, et al. Electrochim. Acta, 51 (2005) 1091-1098.
[7] Yang D, Guo G Q, Hu J H, et al. J. Mater. Chem., 18 (2008) 350-354.
[8] Kang Z H, Wang E B, Mao B D, et al. Appl. Catal. A, 299 (2006) 212-217.
[9] Wu Z H, Pittman C U, Gardner S D. Carbon, 33 (1995) 597-605.
[10] Sun B, Skyllas-Kazacos M. Electrochim. Acta, 37 (1992) 2459-2465.
[11] Yue L, Li W S, Sun F Q. Carbon, 48 (2010) 3079-3090.
[12] Laachachi A, Vivet A, Nouet G, et al. Mater. Lett., 62 (2008) 394-397.
[13] Rasheed A, Howe J Y, Dadmun M D, et al. Carbon, 45 (2007):1072-1080.
[14] Kim K J, Kim Y J, Kim J H, et al. Mater. Chem. Phys. 131 (2011) 547-553.
[15] Yue L., Li W., Sun F., et al. Carbon, 48 (2010) 3079-3090.
[16] Lu Y, Chen J, Cui H, et al. Compos. Sci. Technol., 68 (2008) 3278-3284.
[17] Mawhinney D B, Naumenko V, Kuznetsova A, et al. Chem. Phys. Lett. 324 (2000) 213-216.
[18] Zhang L S, Shao Z G, Wang X Y. J. Power Sources, 242 (2013) 15-22.
[19] Ahn S, Tatarchuk B J. J. Electrochem. Soc., 142 (1995) 4169-4175.
[20] Arai H, Muller S, Haas O. J. Electrochem. Soc., 147 (2000) 3584-3591.
[21] Li W Y, Liu J G, Yan C W. Carbon, 49 (2011) 3463-3470.
[22] Wang W H, Wang X D. Electrochim. Acta, 52 (2007): 6755-6762.

Advanced Materials Research Vol. 936 (2014) pp 476-479
© (2014) Trans Tech Publications, Switzerland
doi:10.4028/www.scientific.net/AMR.936.476

A Novel Route to Prepare Titanium Doped Mesoporous Carbon

Hao Tian[1, a], Yan Zhang[1,b*] and Yujian Liu[1,c]

[1]Key Laboratory for Specially Functional Polymers and Related Technology of Ministry of Education, School of Materials Science and Engineering, East China University of Science and Technology, MeiLong Road 130, Shanghai 200237, PR China

[b]email: yzhang@ecust.edu.cn

Keywords: Mesoporous carbon, titanium, nanocomposite, self-assembly

Abstract: A series of titanium doped ordered mesoporous carbons (Ti-OMCs) were prepared by employing titanium modified resol as source for the first time. The effect of titanium content and F127 content on the microstructure of Ti-OMCs was investigated by X-ray diffraction (XRD), N_2 sorption isothermal and Transmission electron microscopy (TEM). The results showed that regularity of products decreased with the increase of titanium content. A mesophase transformation from 2-D hexagonal(P6mm) to body-centered cubic ($Im\bar{3}m$) structure can be achieved by decreasing F127 content.

Introduction

Titanium-doped ordered mesoporous carbons (Ti-OMCs) have aroused much interest for their wide potential application in the field of photo-catalysts Li-ion battery, protein immobilization, etc [1,2]. A variety of strategies have been developed to prepare Ti-OMCs, such as impregnating pores of CMK-3 with titanium precursor to form TiO_2/CMK-3 materials [3], synthesis of Ti-OMCs by the aid of evaporation-induced self-assembly (EISA) method [4]. In general, titanium complex is almost doped by physical hybrid, which leads to the poor compatibility between titanium complex and carbon matrix. If heteroatom could be anchored on the backbone of resol through chemical reaction, interface compatibility would be improved. Meanwhile, heteroatom would be well dispersed in the OMC because of the dispersion of modified resol during EISA. Recently, this new route is applied to prepare B doped OMC [5]. Nevertheless, to the best of our knowledge, no metal atom was doped through this novel route, presumably because it's tough to obtain appropriate metal modified resol. Previously, our group reported a facile way to synthesis titanium modified phenolic resin [6], which might be a candidate for fabrication Ti-OMCs. Herein, we prepared a series of Ti-OMCs by employing titanium modified resol as source for the first time. The effect of titanium contents and F127 contents on the mesostructure was investigated by XRD, N_2 sorption and TEM.

Experimental

Preparation of titanium modified resol was according to our previous report [6].

Ti-OMC was synthesized by a modified solvent evaporation induced self-assembly (EISA) method. The final products are denoted as Ti-OMC-X-Y while X represents the molar ratio of titanium and phenol, and Y represents the mass ratio of F127 and carbon source.

Transmission electron microscopy (TEM) images were obtained on JEOL-1400. Nitrogen adsorption experiments were performed at 77 K using a Micromeritics ASAP 2010. Pore size distribution and the BET surface area of samples were calculated by the BET method from the N2 adsorption isotherm data. Powder X-ray diffraction (XRD) patterns were recorded on Rigaku D/MAX-2550 diffractometer using Cu-Kα radiation.

Results and discussion

Influence of titanium content

Fig. 1 shows the small angle XRD (SAXRD) and wide angle XRD (WAXRD) results of samples with different titanium content. As shown in fig 1a, Ti-OMC-0.015-1 revealed obvious diffraction peak, indicating its well-ordered framework. However, the intensity decreased dramatically with the increase of titanium content, which implied the collapse of regular structure. In all the WAXRD spectra, two broad diffraction peaks emerge around 22° and 44°, corresponding to (002) and (001) diffractions of amorphous carbon respectively. Besides, a tiny peak mainly attributed to Ti7O13 (JCPDS 50-0780) was observed only for Ti-OMC-0.037-1. No other typical peaks attributed to titanium species could be detected probably due to excellent compatibility between carbon and titanium or low titanium content. Thus, to obtain Ti-OMCs with well-ordered structure, the molar ratio of titanium/phenol is 0.015 in following study.

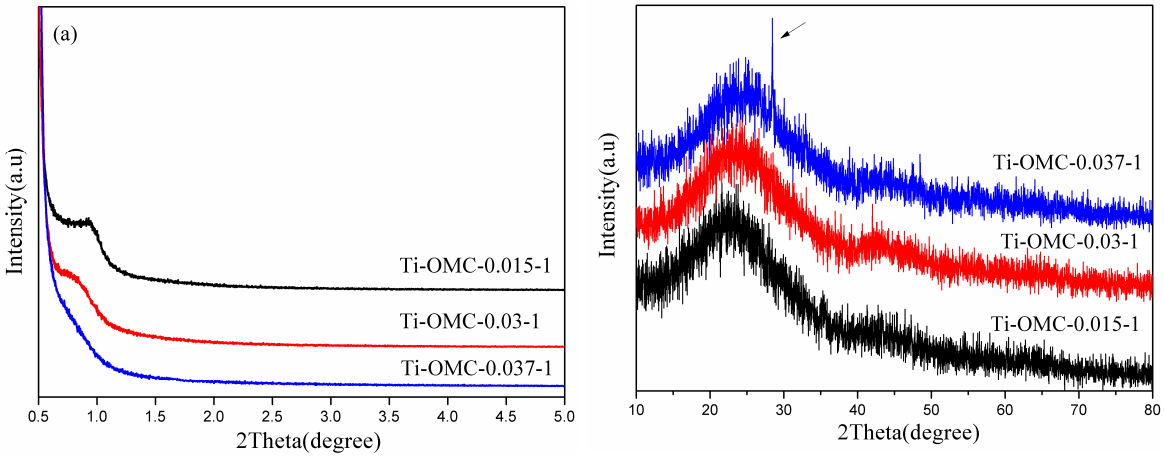


Fig. 1 Small angle XRD (a) and wide angle XRD patterns of Ti-OMCs

Influence of F127 content

The surfactant F127 has been used as the structure directing agent in the synthesis of ordered mesoporous carbon, and previous research shows its content might affect the structure of the final products. In this work, the influence of the amount of F127 on the structure of Ti-OMCs was also investigated. With F127 content decreasing from 1 to 0.5, a slight enhancement in diffraction intensity (Fig 2) is observed. However, the peak disappeared while F127 content is 0.1.

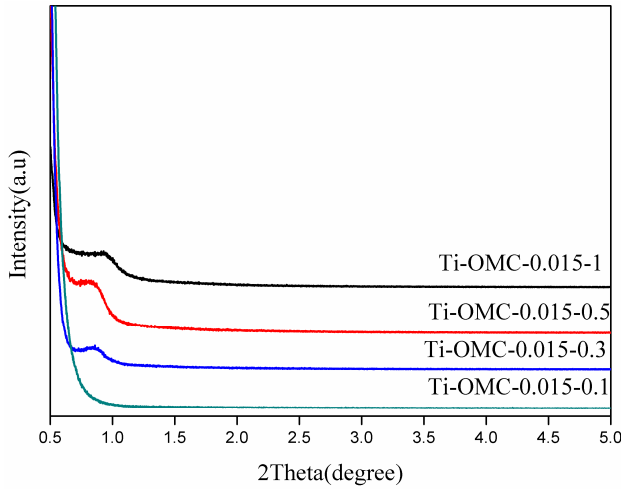


Fig. 2 Small angle XRD patterns of Ti-OMCs prepared with different F127 contents

Figure 3 represents N2 sorption isotherms and pore size distribution curves of samples prepared with different F127 contents. It can be seen that sample Ti-OMC-0.015-1, Ti-OMC-0.015-0.5, Ti-OMC-0.015-0.3 display typical IV isothermals with a sharp capillary condensation step at

P/Po=0.35-0.7, indicating the mesoporous character of these materials. And they all posses samilar pore size at about 3.5nm according to fig. 3(b). However, Ti-0.015-0.1-OMC posesses typical I sorption isothermal, suggesting no mesopores in this sample. This is because F127 content is too low to form polymer aggeration , which is the template of mesopores.

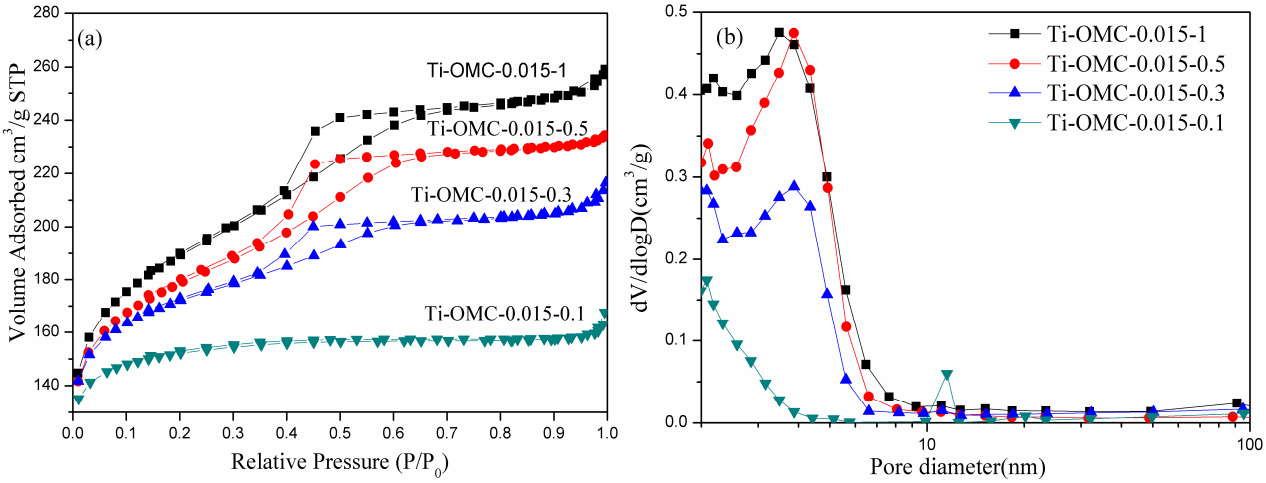


Fig. 3 N_2 adsorption-desorption isothermals of Ti-OMCs (a) and pore size distributions of Ti-OMCs (b)

Fig 4 reveals the TEM images of samples prepared with different F127 contents. Ti-OMC-0.015-1 and Ti-OMC-0.015-0.5 show strip-like channels, which are typical images of 2-D hexagonal structure. However, when F127 content is 0.3, TEM image of body-centered cubic structure is observed in Fig. 4 (c). This phenonemon indicat that a mesophase transformation from 2-D hexagonal(P6mm) to body-centered cubic ($Im\bar{3}m$) structure is occured with the decrease of F127 content. F127 contents can influence both regularity and symmetry structure of Ti-OMCs.

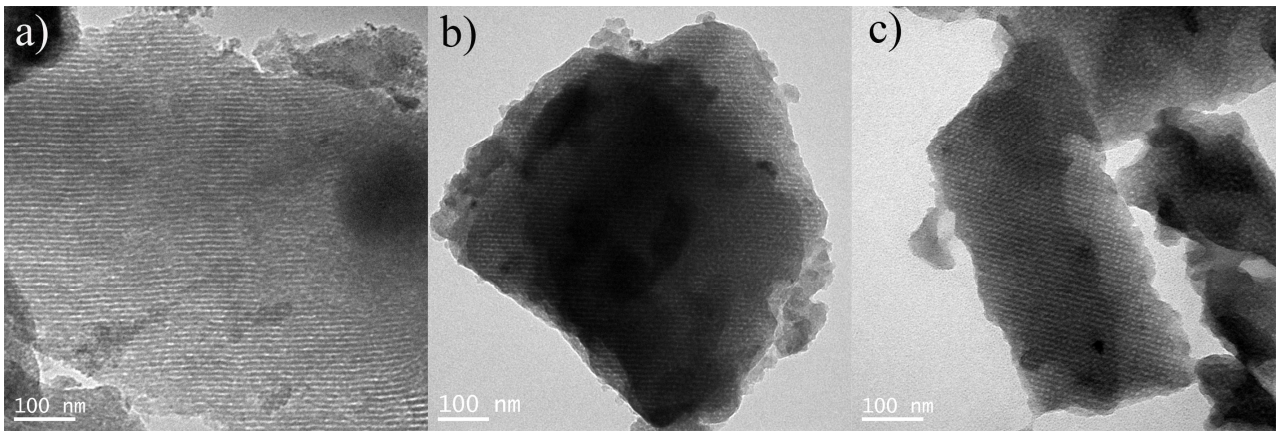


Fig. 4 TEM images of Ti-OMCs. (a) Ti-OMC-0.015-1, (b) Ti-OMC-0.015-0.5, (c) Ti-OMC-0.015-0.3

Conclusion

In summary, a series of Ti-OMCs were prepared by employing titanium modified resol as source for the first time. The results show that regularity of products decreased with the increase of titanium content. A mesophase transformation from 2-D hexagonal (P6mm) to body-centered cubic ($Im\bar{3}m$) structure can be achieved by decreasing F127 content.

Acknowlegement

The work was supported by the National Natural Science Foundation of China (51303054), National Basic Research Program of China (No. 2013CB035505), Shanghai Leading Academic Discipline Project (B502).

References

[1] Chang PY, Huang CH, Doong RA. Ordered mesoporous carbon–TiO_2 materials for improved electrochemical performance of lithium ion battery. Carbon. 50 (2012) 4259-68.

[2] Huang CH, Gu D, Zhao DY, Doong RA. Direct Synthesis of Controllable Microstructures of Thermally Stable and Ordered Mesoporous Crystalline Titanium Oxides and Carbide/Carbon Composites. Chemistry of Materials. 22 (2010) 1760-1767.

[3] Park IS, Choi SY, Ha JS. High-performance titanium dioxide photocatalyst on ordered mesoporous carbon support. Chem Phys Lett. 456 (2008) 198-201.

[4] Yu T, Deng YH, Wang L, Liu RL, Zhang LJ, Tu B, et al. Ordered mesoporous nanocrystalline titanium-carbide/carbon composites from in situ carbothermal reduction. Advanced Materials. 19 (2007) 2301-2306.

[5] Zhao X, Zhang Q, Zhang B, Chen C-M, Xu J, Wang A, et al. Decorated resol derived mesoporous carbon: highly ordered microstructure, rich boron incorporation, and excellent electrochemical capacitance. Rsc Adv. 3 (2013) 3578-3584

[6] Zhang Y, Shen S, Liu Y. The effect of titanium incorporation on the thermal stability of phenol-formaldehyde resin and its carbonization microstructure. Polymer Degradation and Stability. 98 (2013) 514-518.

Advanced Materials Research Vol. 936 (2014) pp 480-485
© (2014) Trans Tech Publications, Switzerland
doi:10.4028/www.scientific.net/AMR.936.480

Enhanced Electrochemical Performances Of Lifepo$_4$/C Cathode Materials By Deposited With Ge Film

Yandan Huang[1,2], Yingbin Lin[1,2],Zhigao Huang[1,2]

[1]College of Physics and Energy, Fujian Normal University, Fuzhou 350108, China

[2]Fujian Provincial Key Laboratory of Quantum Manipulation and New Energy Materials, Fuzhou 350108, China

Ydhuang0749@163.com, yblin@fjnu.edu.cn, zghuang@fjnu.edu.cn

Keywords: Li-ion battery, $LiFePO_4$, Ge film, Rate capability.

Abstract: $LiFePO_4$/C-Ge electrodes were prepared with vacuum thermal evaporation deposition by depositing Ge films on as-prepared $LiFePO_4$/C electrodes. The effect of Ge film on the electrochemical performances of $LiFePO_4$/C cells was investigated systematically by charge/discharge testing, cyclic voltammograms and AC impedance spectroscopy, respectively. It was found that Ge-film-surface modified $LiFePO_4$/C showed excellent electrochemical performances compared to that of the pristine one in terms of cyclability and rate capability. At 60℃, $LiFePO_4$/C-Ge film exhibited outstanding cyclability with less than 5% capacity fade after 50 cycles while the pristine one suffers 15%. Analysis from the electrochemical measurements showed that the presence of Ge film on the $LiFePO_4$/C electrode would protect active material from HF generated by the decomposition of $LiPF_6$ in the electrolyte and stabilize the surface structure of active material during the charge and discharge cycle. Electrochemical impedance spectroscopy (EIS) results indicated that Ge film mainly reduced the charge transfer resistance R_{ct} of $LiFePO_4$/C electrode, resulting from the suppression of the solid electrolyte interfacial (SEI) film.

Introduction

With the development of the electric vehicles and hybrid electric vehicles, olivine-structured orthophosphate $LiFePO_4$ has been considered as one of the most promising candidates for cathode materials due to its high theoretical capacity(170mAhg^{-1}), flat voltage profile, high thermal stability as well as environment benignity[1-4]. However, this material suffers from the low intrinsic electronic conductivity (~10^{-8} to 10^{-10} Scm^{-1}) and lithium-ion diffusivity (~10^{-18} cm^{2}s^{-1}), which become major obstacles to extraction of lithium and result in steep falling in capacity at high rates[5-7]. Tremendous efforts have been devoted to improve electronic conductivity and overall electrochemical performance of $LiFePO_4$. The surface coating with a more conductive material such as carbon is well-known as an effective way in improving the rate performance of $LiFePO_4$ cathode[8-10]. For instance, Tang et al.[8] coated $LiFePO_4$ with $Li_{0.34}La_{0.51}TiO_{2.94}$ by rheological phase reaction method, and revealed that the surface modification of $LiFePO_4$ obviously enhanced the rate performance. The samples exhibited high discharge capacity of 109.9mAhg^{-1} at 10C. Sun et al.[9] reported that the surface modified $LiFePO_4$ by three-dimensional carbon networks exhibited better cyclic performance. Zhang et al.[10] revealed that the surface coating with Li_4SiO_4 was a feasible approach for improving the discharge capacity, cycling stability and interfacial resistance of $LiFePO_4$.

In contrast, germanium seems to be more promising surface-modification material due to its favorable electronic conductivity (2.1 S m^{-1}) and ionic diffusivity (1.9x10^{-14} cm^2 s^{-1})[11, 12]. Combining the above ideas, composing $LiFePO_4$ with germanium would be reasonably beneficial for improving rate capability and cyclic reversibility. In this paper, germanium film was deposited on $LiFePO_4$/C electrode by vacuum thermal evaporation. Compared to the pristine $LiFePO_4$/C, the as-prepared LiFePO4/C-Ge film exhibited better electrochemical performances.

Experimental

Preparation and characterization of $LiFePO_4$/C cathode material

Carbon coated $LiFePO_4$ composite materials were first prepared by a carbothermal reduction method. Firstly, $LiCH_3COO \cdot 2H_2O$(AR), $FeC_2O_4 \cdot 2H_2O$(AR), and $NH_3H_2PO_4$(AR) in stoichiometric amounts were thoroughly planetary milled in mortar for 48 h in ethanol containing proper amount of tartaric acid as carbon source. The obtained slurry was dried at 70℃ and then pressed into pellets. These pellets were transferred to a temperature-controlled tube furnace equipped with flowing Ar gas, calcined at 350℃ for 6 h and subsequently sintered at 700℃ for 12 h to obtain $LiFePO_4$/C. The phase analysis of the $LiFePO_4$/C composite was characterized by X-ray diffraction (XRD, Rigaku MiniFlex II) with monochromatized Cu Kαradiation source (λ=0.15405 nm). The morphology was observed by scanning electronic microscopy (SEM, JSM-7500F, Japan). The carbon content in $LiFePO_4$/C was determined by simultaneous thermal analyzer (STA 449 F3) with a heating rate of 10℃/min up to 900℃ in oxygen ambient.

Deposition of Ge film on $LiFePO_4$/C electrode

The cathode electrodes were prepared by homogeneously pasting a slurry containing 80 wt.% active material, 10 wt.% super-P and 10 wt.% polyvinylidene fluoride (PVDF) which was dissolved in N-methyl-2-pyrrolidone on an Al foil and subsequently dried at 110℃ for 12h in vacuum. Ge film was deposited onto the cathode electrode by thermal evaporation at a base pressure of 3×10^{-3} Pa with crystalline Ge as the vaporization source.

Cell fabrication and characterization

The coin cells (R2025) were assembled in an argon-filled glove box (O_2 <3ppm and H_2O<3ppm, Mikrouna, Super 1220/750, China) with Li metal as anode and counter electrode, Celgard 2300 microporous polyethylene membrane as separator and 1M $LiPF_6$ in a mixture of ethyl carbonate (EC) and dimethyl carbonate (DMC) (1:1 in vol. ratio) as electrolyte. Galvanstatic charge/discharge tests were carried out in the voltage range of 2.0-4.5V with a battery cycler (LAND, CT2001A, China). Cyclic voltammograms (CV) and electrochemical impedance spectra (EIS) measurements were performed by the electrochemical workstation (CHI660C). EIS analysis was recorded in a frequency range from 10 mHz to 100 KHz with a sinusoidal perturbation of 5 mV.

Results and discussion

Fig.1 shows XRD pattern of $LiFePO_4$/C powder. All the observed diffraction peaks for as-prepares powder can be indexed well based on an olivine-type phase structure with a space group of Pmnb (JCPDS No. 40-1499), indicating the successful synthesis of phase pure $LiFePO_4$[13,14].

Fig. 2 presents the surface morphology of $LiFePO_4$/C powder examined by SEM, which indicates the homogeneous $LiFePO_4$ particles with the order of ~200 nm are coated by carbon layers. The tartaric acid in reactants is considered to prevent the agglomeration of $LiFePO_4$ and protect $LiFePO_4$ from oxidation during the calcinations. The 3D carbon network would facilitate electron transport effectively among particles and consequently improve the electrochemical performances[9].

The carbon content in $LiFePO_4$/C composite was confirmed by simultaneous thermal analyzer. Fig.3 presents TG curve of as-prepared $LiFePO_4$/C in oxygen ambient. The weight loss between 200 and 700 °C might result from the reaction of carbon and oxygen. Analysis from the TGA measurements reveals that the carbon content was 7.5wt.% approximately.

To examine the effect of Ge film on improving the rate performances, the discharge capacities and the cycle numbers for $LiFePO_4$/C and $LiFePO_4$/C-Ge film at different current densities (0.2C, 0.5C, 1C, 2C, 3C, 1C = 170 $mAhg^{-1}$) between 2.0 and 4.5 V at 25 ℃ were investigated, as shown in Fig.4. It was found that with the deposition of Ge film on the electrode, $LiFePO_4$/C-Ge film (0.2C: 146 $mAhg^{-1}$; 0.5C: 131 $mAhg^{-1}$; 1C: 117 $mAhg^{-1}$; 2C: 104 $mAhg^{-1}$; 3C: 89 $mAhg^{-1}$, respectively) exhibited higher capacity than that of $LiFePO_4$/C (0.2C: 140 $mAhg^{-1}$; 0.5C: 120 $mAhg^{-1}$; 1C: 99$mAhg^{-1}$; 2C: 81 $mAhg^{-1}$; 3C: 65 $mAhg^{-1}$, respectively), especially at higher rates. The enhancement

in rate performances indicated that high conductive Ge film would facilitate Li^+ ion diffusion in the electrode, especially at high rates[15-17].

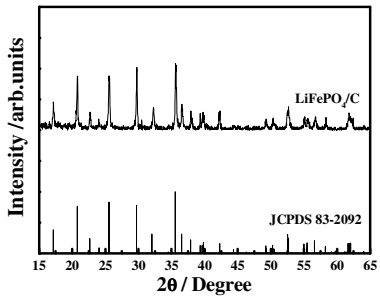


Fig.1 XRD pattern of LiFePO4/C powder

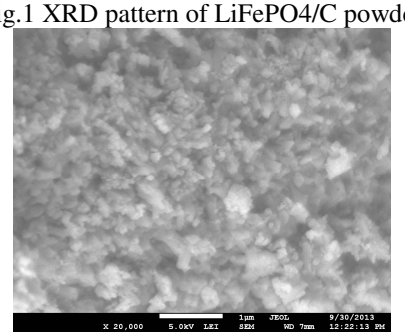


Fig.2 SEM images of LiFePO4/C powder

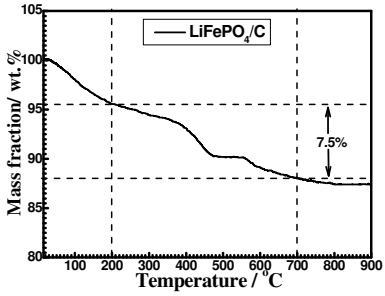


Fig.3 TGA curve of of as-prepared LiFePO4/C powder

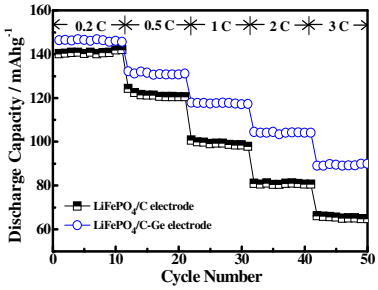


Fig. 4 Rate capabilities of the pristine LiFePO4/C and LiFePO4/C-Ge film at 25℃

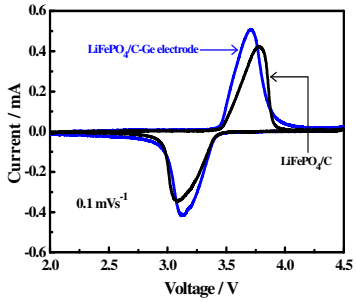


Fig. 5 Cyclic voltammograms of LiFePO4/C and LiFePO4/C-Ge film

Fig.5 show the CV curves of $LiFePO_4$/C and $LiFePO_4$/C-Ge film at a scanning rate of 0.1mV/s in the potential range from 2.0 to 4.5 V. Both curves shows a couple of peaks around 3.4 V, which correspond to the redox reaction of Fe^{2+}/Fe^{3+} couple[18]. The higher intensity of the redox peaks of $LiFePO_4$/C-Ge film than that of $LiFePO_4$/C further indicates that Ge-depositing should facilitate

li-ion transportation in the electrodes[19]. On the other hand, the separation between the anodic and cathodic peaks of $LiFePO_4$/C-Ge film (0.57 V) is lower than that of $LiFePO_4$/C (0.71 V), suggesting the outstanding reversibility of lithium intercalation into and de-intercalation from $LiFePO_4$/C-Ge film[20].

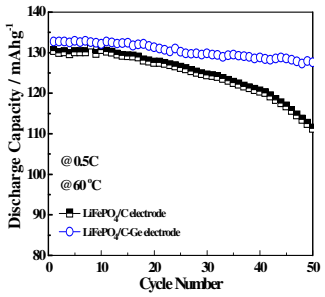


Fig. 6 Cycling performances of $LiFePO_4$/C and $LiFePO_4$/C-Ge film at 0.5C and 60℃;

Fig. 6 shows the capacity cyclabilities of $LiFePO_4$/C and $LiFePO_4$/C-Ge film at 0.5C at 60℃, respectively. It is clear that $LiFePO_4$/C-Ge film shows superior capacity cyclability in comparison with $LiFePO_4$/C. The $LiFePO_4$/C shows initial capacity of 130.5 $mAh \cdot g^{-1}$ and fades faster to 111.3 $mAh \cdot g^{-1}$ after 50 cycles, suffering a more than 15% capacity loss. The fade in capacity mainly results from the dissolution of Fe caused by in LiPF6-based electrolyte[21,22], especially at the elevated temperatures. In $LiFePO_4$/C-Ge film, Ge film provices protection to $LiFePO_4$/C from the erosion of HF[23], keeping crystal structure stable during charge/discharge process and consequently resulting in improved cyclic stability.

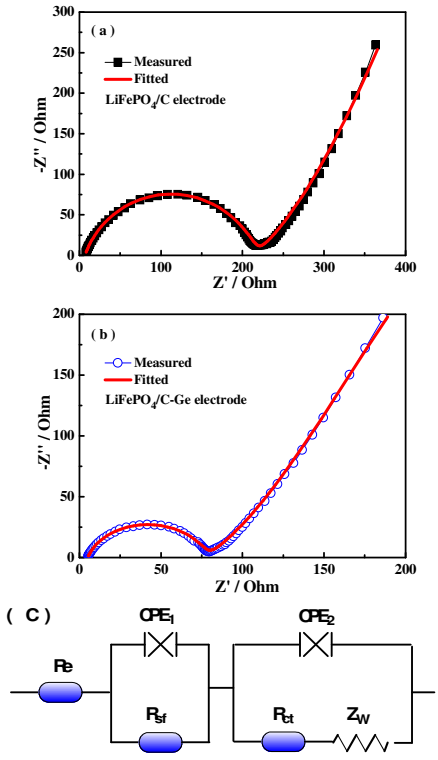


Fig.7 Nyquist plots and equivalent circuit of LiFePO4/C electrode and LiFePO4/C-Ge electrode after 10 cycles at charged state.

Figs. 7(a) and (b) present impedance spectra of the pristine $LiFePO_4$/C and $LiFePO_4$/C-Ge film in the fully discharged state after 50 cycles at 0.5C rate in 60 ℃, respectively. Both EIS profiles are composed of a depressed semicircle at high frequencies and a spike at low frequencies. The depressed semicircle in high frequency region on the real axis is mainly attributed to the charge transfer

process[24] and the sloping line in low frequency region is ascribed to the warburg impedance associated with lithium ion diffusion[25]. It is found that $LiFePO_4$/C-Ge film has smaller charge-transfer resistance (R_{ct} = 72.73Ω) than that of the pristine one (=209.6Ω), which is ascribed to the highly conductive Ge film on the $LiFePO_4$/C electrode and the suppression of SEI layer. The decrease in R_{ct} is expected to overcome the kinetics restrictions and consequently enlarge the depth of Li ion insertion/extraction[26].

Summary

$LiFePO_4$/C-Ge film was synthesized by depositing Ge on $LiFePO_4$/C electrode in vacuum. Compared to the pristine $LiFePO_4$/C, $LiFePO_4$/C-Ge film exhibited superior rate performance and cyclic stability. The obtained results indicate that the presence of Ge film on $LiFePO_4$/C surface plays an important role in reducing polarization of electrode, enhancing lithium diffusion rate and protecting $LiFePO_4$ from the erosion of HF in the $LiPF_6$ based electrolyte.

Acknowledgements

This work was supported by a grant from Natural Science Foundation of Fujian Province (No. 2013J01007), Natural Science Foundation of China (No.11344008) and National Key Project for Basic Research of China under Grant No. 2011CBA00200.

References

[1] K. Xu, Nonaqueous liquid electrolytes for lithium-based rechargeable batteries, Chem. Rev, 104 (2004) 4303-4418.

[2] Z. Y. Chen, B. L. Du, M. Xu, et al., Polyacene coated carbon/$LiFePO_4$ cathode for Li ion batteries: Understanding the stabilized double coating structure and enhanced lithium ion diffusion kinetics, Electrocheimica Acta, 109 (2013) 262-268.

[3] J. Zhou, B. H. Liu, Z. P. Li, Nanostructure optimization of $LiFePO_4$/carbon aerogel composites for performance enhancement, Solid State Ionics, 244 (2013) 23-29.

[4] H. M. Xie, R. S. Wang, J. R. Ying, et al., Optimized $LiFePO_4$–Polyacene Cathode Material for Lithium-Ion Batteries, Advanced Materials, 18 (2006) 2609-2613.

[5] K. Zaghib, A. Mauger, J. B. Goodenough, et al., Electronic, optical, and magnetic properties of $LiFePO_4$: small magnetic polaron effects, Chemistry of materials, 19 (2007) 3740-3747.

[6] Z. Li, D. Zhang, F. Yang, Developments of lithium-ion batteries and challenges of $LiFePO_4$ as one promising cathode material, Journal of materials science, 44 (2009) 2435-2443.

[7] H. Huang, S. C. Yin, L. F. Nazar, Approaching theoretical capacity of $LiFePO_4$ at room temperature at high rates, Electrochemical and Solid-State Letters, 4 (2001) A170-A172.

[8] H. Tang, J. Xu, Enhanced electrochemical performance of $LiFePO_4$ coated with $Li_{0.34}La_{0.51}TiO_{2.94}$ by rheological phase reaction method, Materials Science and Engineering: B, 178 (2013) 1503-1508.

[9] W. J. Sun, C. H. Deng, H. H, et al., Improved cyclic performance of $LiFePO_4$ coated with three-dimensional carbon networks, Materials Letters, 93 (2013) 49-51.

[10] Q. Zhang, W. W. Jiang, Z. F. Zhou, et al., Enhanced electrochemical performance of Li_4SiO_4-coated $LiFePO_4$ prepared by sol-gel method and microwave heating, Solid state ionics, 218 (2012) 31-34.

[11] J. Graetz, C. C. Ahn, R. Yazami,et al., Nanocrystalline and thin film germanium electrodes with high lithium capacity and high rate capabilities, Journal of The Electrochemical Society, 151 (2004) A698-A702.

[12] C. S. Fuller, J. C. Mobility of impurity ions in germanium and silicon, Severiens, 96 (1954) 21-24.

[13] Y. Lin, B. Z. Zeng, Y. B. Lin, et al., Electrochemical properties of carbon-coated $LiFePO_4$ and $LiFe_{0.98}Mn_{0.02}PO_4$ cathode materials synthesized by solid-state reaction, Rare Metals, 31 (2012) 145-149.

[14] S. Uchida, M. Yamagata, M. Ishikawa, Optimized condition of high-frequency induction heating for $LiFePO_4$ with ideal crystal structure, Journal of Power Sources, 243 (2013) 617-621.

[15] C. H. Mi, X. B. Zhao, G. S. Cao, et al., In situ synthesis and properties of carbon-coated $LiFePO_4$ as Li-ion battery cathodes, Journal of The Electrochemical Society, 152 (2005) A483-A487.

[16] J. Morales, R. Trócoli, E. Rodríguez-Castellón, et al., Effect of C and Au additives produced by simple coaters on the surface and the electrochemical properties of nanosized $LiFePO_4$, Journal of Electroanalytical Chemistry. 631 (2009) 29-35.

[17] Y. Lin, M. X. Gao, D. Zhu, et al., Effects of carbon coating and iron phosphides on the electrochemical properties of $LiFePO_4$/C, Journal of Power Sources, 184 (2008) 444-448.

[18] M. Konarova, I. Taniguchi, Synthesis of carbon-coated $LiFePO_4$ nanoparticles with high rate performance in lithium secondary batteries, Journal of Power Sources, 195 (2010) 3661-3667.

[19] Y. Feng, The preparation and electrochemical performances of $LiFePO_4$ multiwalled nanotubes composite cathode materials for lithium ion batteries, Materials Chemistry and Physics, 121 (2010) 302-307.

[20] T. F. Yi, J. Shu, Y. R. Zhu, et al., Advanced electrochemical performance of $Li_4Ti_{4.95}V_{0.05}O_{12}$ as a reversible anode material down to 0V, Journal of Power Sources, 195 (2010) 285-288.

[21] H. H. Chang, C.C. Chang, C. Y. Su, et al., Effects of TiO_2 coating on high-temperature cycle performance of $LiFePO_4$ based lithium-ion batteries, Journal of Power Sources, 185 (2008) 466-472.

[22] D. Aurbach, B. Markovsky, Y. Talyossef, et al., Studies of cycling behavior, ageing, and interfacial reactions of $LiNi_{0.5}Mn_{1.5}O_4$ and carbon electrodes for lithium-ion 5-V cells, J. Power Sources, 162 (2006) 780-789.

[23] Y. K. Sun, K.-J. Hong, Jai Prakash, et al., Electrochemical performance of nano-sized ZnO-coated $LiNi_{0.5}Mn_{1.5}O_4$ spinel as 5 V materials at elevated temperatures, Electrochemistry Communications, 4 (2002) 344-348.

[24] P. J. Zuo, T. Wang, G. Cheng, et al., Effects of carbon on the structure and electrochemical performance of Li_2FeSiO_4 cathode materials for lithium-ion batteries, Rsc Advances, 2 (2012) 6994-6998.

[25] Y. B. Lin, Y. M. Yang, Y. Lin, et al., Improvement of electrochemical and thermal stability of $LiFePO_4$@C batteries by depositing amorphous silicon film, Electrochimica Acta, 56 (2011) 4937-4941.

[26] Y. B. Lin, Y. Lin, T. Zhou, et al., Electrochemical performance of $LiFePO_4$/Si composites as cathode material for lithium ion batteries, Materials Chemistry and Physics, 138 (2013) 313-318.

Advanced Materials Research Vol. 936 (2014) pp 486-490
© (2014) Trans Tech Publications, Switzerland
doi:10.4028/www.scientific.net/AMR.936.486

Study on $Ag/SnO_2/TiO_2$ Electrical Contact Materials Prepared by Liquid Phase In-situ Chemical Route

ZHU Yancai[1,a],WANG Jingqin[1,b], AN Liqiang[2,c],WANG Haitao[1,d]

[1]Hebei University of Technology, Tianjin 300130 China

[2] Hebei construction group, Shijiazhuang 050051 China

[a]zhuyancai@hebut.edu.cn,[b]jqwang@hebut.edu.cn,[c]alq12@163.com,[d]wanght@hebut.edu.cn

Key words: contact material; $Ag/SnO_2/TiO_2$; mechanical property; electrical property

Abstract. In order to improve the machinability and electrical performance of the Ag electrical contact materials. A new kind of nano-Ag/SnO_2-TiO_2 electrical contact materials were prepared by liquid phase in-situ chemical route. The distribution state of elements titanium in copper and their effects on the microstructures and properties have been studied. The results of SEM show that SnO_2-TiO_2 powders are small, uniform and with no obvious phenomenon of reunion. At last, Ag/SnO_2-TiO_2 electrical contact materials were prepared by powder metallurgy method and electrical performance were done. Test results show that the electrical properties of Ag/SnO_2-TiO_2 are superior to the electrical properties of Ag/SnO_2. Hence Ag/SnO_2-TiO_2 may become a new contact material which can replace Ag/SnO_2.

Introduction

Ag/CdO contact material is known for its goog switching performance. At present, traditional Ag/CdO materials have been replaced gradually by some new contact material such as Ag/SnO_2 because of its damages to the environment and human health in the process of making and using[1-2].But Ag/SnO_2 materials have innate shortcomings. First, the electrical performance such as contact resistance and temperature rise of Ag/SnO_2 is higher than Ag/CdO, and we have not yet found a satisfactory solution to it at home and abroad. Secondly, because of the large particles and high hardness of SnO_2, so the plasticity and ductility of Ag/SnO_2 is poor and have bad formability. All of the above limited the manufacturing and application of Ag/SnO_2 electrical contact materials greatly. Applying different additives to improve the performance of Ag/SnO_2 contact material is studied by many scholars. The most widely used additions are other metal oxides[3-4].

The deposit of titanium element is very large in China. It have the similar chemical properties and show +4 valence in the usual conditions. It combine with oxygen to form stable oxide TiO_2 easily. The dielectric constant of TiO_2 is high, so it has excellent electrical performance. TiO_2 has the performance of the semiconductor, its electrical conductivity increased rapidly with temperature rising[5-7].

The aim of this study is to develop a new kind of contact material $Ag/SnO_2/TiO_2$ by liquid phase in-situ chemical route and powder metallurgy technology. The new $Ag/SnO_2/TiO_2$ has excellent mechanical properties and electrical property. The new material improved the electrical appliances work performance and improved Chinese electrical products market competitiveness.

Research Steps and Experimental Means

The main work of this research includes experimental raw material and additive amount selection, powder preparation, powder performance characterization and the preparation of electrical contact materials and performance test and so on. The designed composition is shown in table1.

TABLE 1 THE COMPOSITION OF THE NEW MATERIAL

10	Ag	SnO_2	TiO_2
Mass fraction/%	allowance	10	1～3

The morphologies of SnO_2-TiO_2 powders and electrical contact materials were observed by scanning electron microscopy (TDCLS4800).The test parameters of the electrical contact material comprehensive parameter tester were 17V and 20A DC, contact pressure was 80Cn and the space was 2.0 mm. The test conditions and parameters are shown in table 2.

TABLE 2 ELECTRICAL PERFORMANCE TEST CONDITIONS AND PARAMETERS

Test conditions	Environment temperature(℃)	20	Test parameters	Duty ratio（%）		40
	Environmental humidity(%)	60		Interval of measuring contact resistance(time)		1000
	Air pressure(kPa)	101		Minimum arc voltage(V)		10
	Power source type	DC		Minimum arc current(A)		0.7
	Load type	Resistive		Contact from(mm)		1.5
	Operating frequency (time/minute)	60		Contact closure pressure(g)		100
	Test voltage(V)	24		Failure to determine	Great powers welding(g)	100
	Test current (A)	20			Number of consecutive (time)	5

Results and Discussion

Physical Properties

The additive and physical properties of the homemade materials are shown in table 3.

TABLE 3 EXPERIMENT WITH ADDITIVE AND PHYSICAL PROPERTIES OF THE HOMEMADE MATERIALS

Serial number	Material	Additive	Additive amount	Hardness (HV)	Electrical conductivity (%IACS)
1#	Ag/SnO_2(10)-T	—	—	760.4	62.48
2#	Ag/SnO_2(10)-T	TiO_2	1%	774.5	61.19
3#	Ag/SnO_2(10)-T	TiO_2	2%	795.6	60.17
4#	Ag/SnO_2(10)-T	TiO_2	3%	869.4	59.24

From the table, it can be seen that the hardness of the materials are all improved after Ti doped. The higher the Ti content, the greater the materials' hardness. On the contrary,the electrical conductivity decreased with the increase of Ti content.

Microstructure Analysis

The SEM images of SnO_2-TiO_2 powders with different content of TiO_2 are shown in Fig. 1.

From Fig.1 we can learn that the SnO_2 particles exhibit larger size and nonuniform. But the SnO_2 particles doped Ti^{4+} exhibit small size and almost uniform distribution.The small white particles exhibit smaller size(about a few nanometers), the large gray particles are dozens of nanometers because of a few soft reunion phenomenon while gel-drying process. Furthermore, SnO_2 particles doped 2% Ti^{4+} are more fruity compared to other ones. Ti^{4+} doping is beneficial to enhance the strength of the contact materials due to the excellent wettability and fine distribution. This also strongly accounts for the markedly improved mechanical properties and processing performance of Ag/SnO_2[8-10].

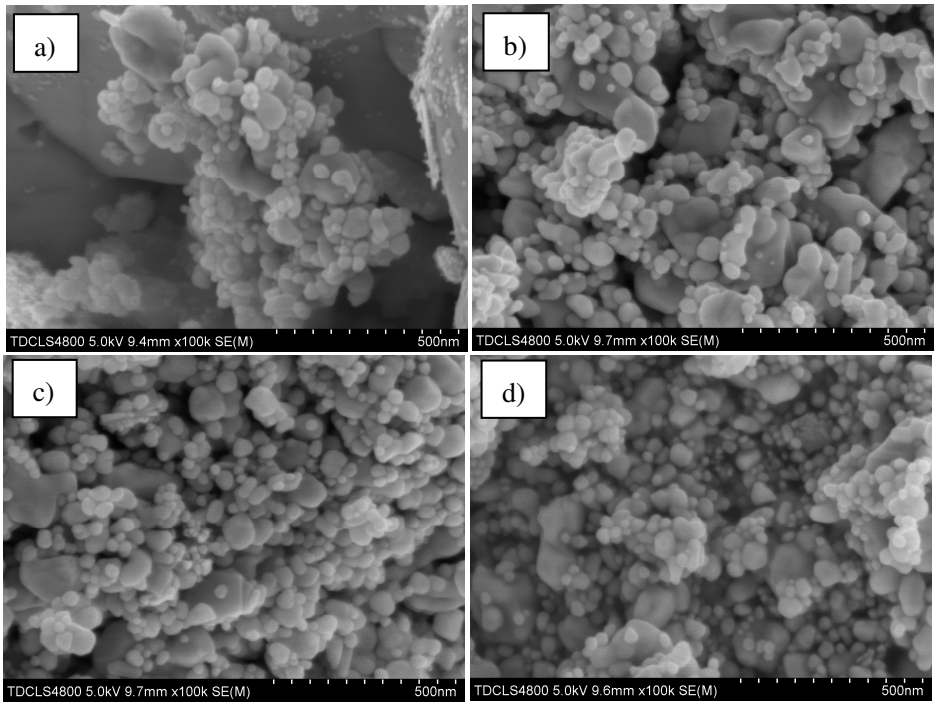


Fig.1 The SEM Images of Oxide Powders with Different Content of TiO_2

(a) 0%;(b)1%;(c)2%;(d)3%

The SEM images of composite materials with different SnO_2-TiO_2 content are shown in Fig. 2.

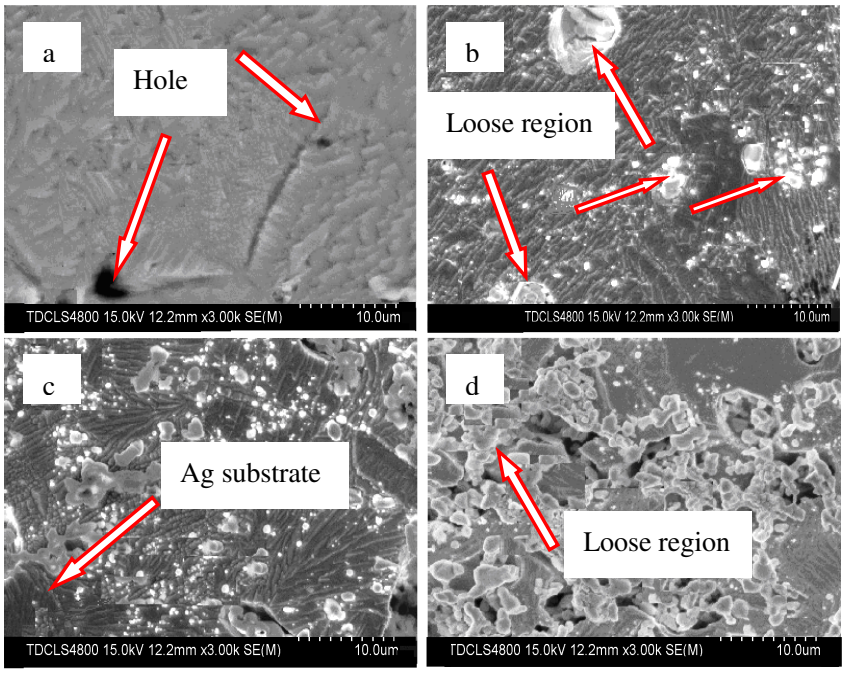


Fig.2 SEM Images of Composite Materials with Different SnO_2-TiO_2 Content (a)10%;(b)11%,(c)12%;(d)13%

From Fig.2 we can learn that the white area on the surface of the sample is the reunion of oxide particles.The defects such as holes and loose increased with the increase of SnO_2-TiO_2 content.There is a big loose zone when the content of SnO_2-TiO_2 is 13%. However,When the oxide content increased from 11% to 12%, there are not obvious defects such as holes and loose region. Comprehensive 3.1 and 3.2 we can learn that when the SnO_2-TiO_2 content is 12%, the microstructure and physical properties of the materials is best.

Electrical Performance Test Results

The morphologies of the contactor which through electrical performance test were observed by scanning electron microscopy (TDCLS4800). The SEM images of Ag/SnO_2(10) and Ag/SnO_2-TiO_2(12) after arc erosion are shown in Fig. 3.

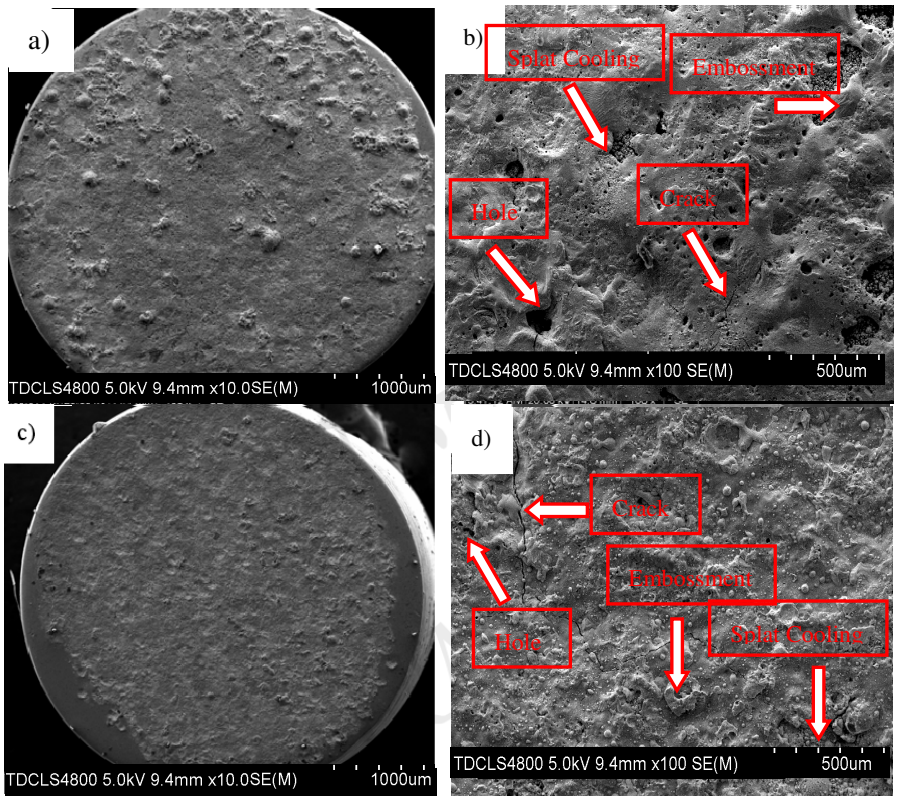


Fig.3 SEM Images of Homemade Materials after Arc Erosion (a)ag/sno$_2$(10); (b)Enlarge figure of Fig.3(a);(c) Ag/SnO_2-TiO_2(12);(d)Enlarge figure of Fig.3(c)

Comparative Fig.3(a) and Fig.3(c)we found that the ablation area is larger and there are more trunk and potholes on the surface of Ag/SnO_2(10) sample than that of on the surface of Ag/SnO_2-TiO_2(12). It can be seen that Ti coating on SnO_2 particles improves the wet ability of Ag to SnO_2 and prevents the temperature arising owing to the formation of SnO_2 insulation layer and thus significantly improves the electrical properties, such as the electrical life,anti-fusion welding ability, electrical arc resistance of the materials. Because the electrical conductivities of Ag/SnO_2 contact materials depend strongly on the condition of the interface between SnO_2 and Ag[11-12].

Temperature Rise Test

The conditions of the test are as follows:electric current(40A), on-load factor(100%), environment temperature(22℃), connection wire specifications(10mm^2/m). The temperature rise of terminals were measured using thermocouple. The results are shown in table 4.

TABLE 4 RESULTS OF TEMPERATURE RISE BETWEEN HOMEMADE CONTACT AND EXISTING CONTACT AT HOME AND ABROAD

Measurement Locations		Measured maximum temperature rise (K)		
		Ag/SnO_2-TiO_2 (Homemade contact)	Ag/SnO_2-In_2O_3 (Foreign contact)	Ag/SnO_2 (Domestic contact)
Terminals	Inlet A	21.6	18.7	23.6
	Inlet B	25.4	21.9	26.0
	Inlet C	22.2	21.1	22.6
	Outlet A	20.7	20.2	21.7
	Outlet B	21.4	23.7	22.6
	Outlet C	20.1	18.9	21.8

Summary

Ti doped is beneficial to enhance the density and strength and improve mechanical properties and processing performance of the contact materials due to the excellent wettability and fine distribution. This also strongly accounts for the markedly improved electrical properties of Ag/SnO_2.

Scientific research project:Z2013052

References

[1] J.G.Lu, J.Q.Wang and J.Y.Zhao: submitted to Rare Metals(2002)

[2] S.G.Cao, M.Xie and L.Chen:submitted to Precious Metals(2005)

[3] J.B.Wang, Y.Zhang and M.G.Yang:submitted to Materials Science and Engineering (2006)

[4] S.J.Fu, M.Xie and L.Chen:submitted to Rare Metals(2005)

[5] J.Zheng,S.L.Li,F.Q.Dou and T.H.Li:submitted to Rare Metals(2009)

[6] X.M.Liu,S.L.Wu,P.K. Chu and J. Zheng:submitted to Materials Science and Engineering(2006)

[7] J.B.Wang, Y.Liu and C.Fu: submitted to Rare Metal Materials and Engineering(2009)

[8] W.S.Lin, N.X.Fang andB.Lin: submitted to Powder metallurgy technology(2002)

[9] Z.M.Deng, X.Y.Lu and F.Q.Zheng: submitted to Precious Metals(2001)

[10] H.T.Wang,J.Q.Wang and Y.C.Zhu: submitted to Low Voltage Electrical Apparatus(2006)

[11] X.H.Chen,C.C.Jia and X.B.Liu: submitted to Powder Metallurgy Industry(2009)

[12] J.Q.Wang,H.T.Wang,M.Wen and Y.C.Zhu:submitted to Journal of Zhejiang University SCIENCE A(2007)

Advanced Materials Research Vol. 936 (2014) pp 491-495
© (2014) Trans Tech Publications, Switzerland
doi:10.4028/www.scientific.net/AMR.936.491

A novel synthesis of nanometer spherical β-$Ni(OH)_2$ cathode materials with high electrochemical performances

Li Chen[1,a], YanMing Wang[1,b], Juan Liu[1,c], XingYao Wang[1,d]*

[1]Department of Chemistry, School of Science, Tianjin University, Tianjin, China

[a]Email wshrcn@163.com,[b]email estherwym@126.com, [c]emai liujuansd@163.com,

[d]email wxyghw@tju.edu.cn

Keywords: Hydrothermal stripping, nano-β-$Ni(OH)_2$, cathode materials, electrochemical performances

Abstract: A novel hydrothermal stripping technique synthesis route, in which the nickel-loaded organic phase of naphthenic acid was directly stripped by water at 140-240 °C for 2.0 h to recover nickel as hydroxide precipitates, has been firstly developed. The nickel hydroxide powders synthesized by this route was the spherical β-$Ni(OH)_2$ and had a small particle size in the range of 20-100 nm shown by XRD and TEM test. The results of electrochemical performances show that the nanometer β-$Ni(OH)_2$ cathode materials have much higher discharge specific capacity, excellent capacity retention and cycle performances.

Introduction

Nickel hydroxide ($Ni(OH)_2$) is a very important cathode material in a number of alkaline rechargeable batteries, which are the most widely used in many applications ranging from power tools to portable electronics and electric vehicles [1-8]. Many synthesis methods have been proposed for controlling the physical and chemical characteristics of $Ni(OH)_2$ by controlling the structure, morphology and particle size. Recently, β-$Ni(OH)_2$ with a small crystalline size and spherical shape has attracted enormous interest due to their novel physical properties and excellent electrochemical performance, and its synthesis has been the focus of significant interest in materials chemistry [9-17]. The nanometer spherical β-$Ni(OH)_2$ can be synthesized by different techniques such as solid-state reaction, precipitation and hydrothermal method, etc [6-12].

Hydrothermal stripping synthesis is a promising method for synthesizing oxide ceramic powders for high-performance applications [18-26]. Compared with the previous works, the hydrothermal stripping synthesis as reported in this paper has some advantages: effectively reaction control, which will help control the product morphology and particle size at low-temperature, environmentally friendly and low costly processes, in which the product was formed and the organic phase was released and can be reused. The nanometer spherical β-$Ni(OH)_2$ synthesized by this route has good electrochemical performances.

Experimental

The hydrothermal stripping synthesis route is started with water and organic phase. The nickel-loaded organic phase of naphthenic acid (RCOOH) was prepared by solvent extraction from an aqueous nickel sulfate solution. In each stripping experiment the water and organic phase were transferred into a stainless steel autoclave, heated to the experimental temperature. After being cooled, the precipitates were segregated by centrifugation and washed several times with distilled water. Then the samples were dried at 80℃ for 2.0 h in an oven and the samples were numbered as A, B, C, D and E according to different synthesis conditions (See Table 1).

Table 1 Samples synthesized from nickel-loaded organic phase of naphthenic acid

Samples	**A**	**B**	**C**	**D**	**E**
Temperature /[°C]	**80**	**140**	**200**	**240**	**240**
Time /[h]	**2.0**	**2.0**	**2.0**	**2.0**	**4.0**

The crystal phase structure of sample was investigated using an X-ray diffractometer (XRD) (BDX-3300 made by Peking University Instrument Co, China). A Transmission Electron Microscope (TEM) (100CX-II made by JEOL, Tokyo, Japan) and Field Emission Gun Scanning Electron Microscope (SEM) (100CX-II made by JEOL) were used to characterize the sample with respect to their morphology and particle size. Simulated battery was prepared to study the electrochemical performance of the nickel hydroxide electrode with 60 mass% β-$Ni(OH)_2$, 10% CoO and 30% Ni powder.

Results and discussion

Structure analysis

Fig. 1 shows the XRD patterns of the samples synthesized from nickel-loaded naphthenic acid (RCOOH) at different temperature. It can be found from the XRD patterns that sample B, C and D exhibits the standard XRD characteristics of β-$Ni(OH)_2$ phase (JCPDS 14-0117), and sample A has several clutter peaks due to unidentified crystalline phase. The fact that pure water is used as the reactant means the sample is uncontaminated.

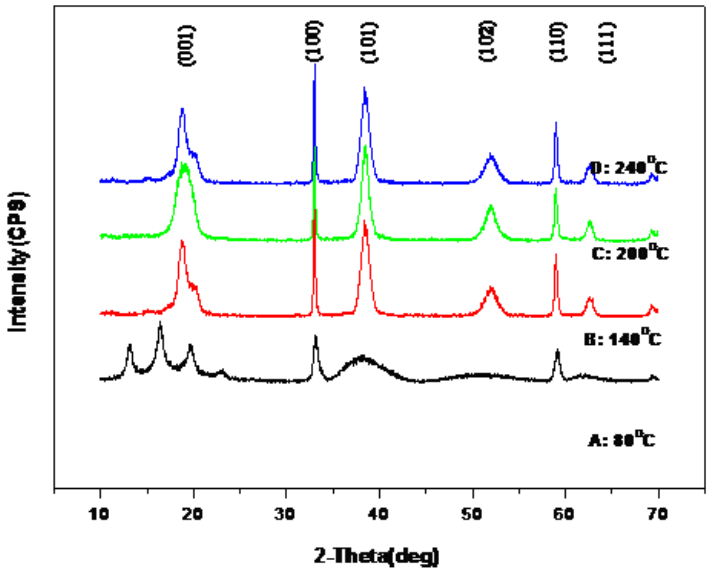


Fig. 1. XRD patterns of samples

Morphology and particle analysis

The typical TEM images in Fig. 2 show that the samples are the uniform distribution of spherical β-$Ni(OH)_2$ without agglomeration, of which the particle size was smaller than that of literature reported [20-22] and synthesized by precipitation transformation (2). It can be seen from Fig. 2 that the average particle size was related with the stripping temperature and time, and the size becomes larger with the increase of temperature (B, C and D) and time (D and E). The average particle size of sample C, which was synthesized at 200 ℃ for 2.0 h, is measured to be about 34 nm by observation. As a contrast, the size of C is 33.61 nm, which was estimated from the Cherrer's formula according to the full width at half-maximum (fwhm) of the diffraction peaks (Seen Fig. 1).

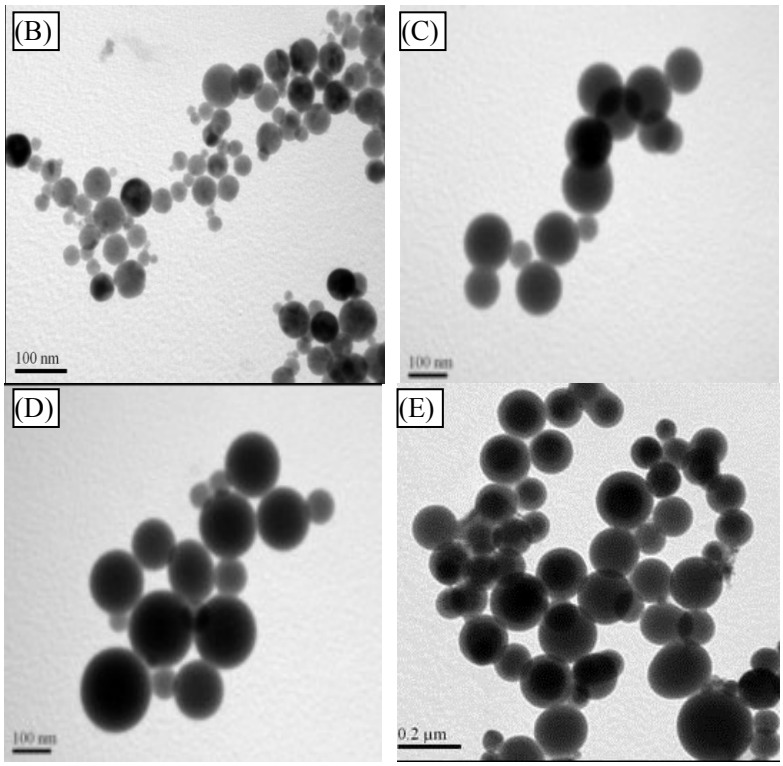


Fig. 2. TEM images of (B), (C), (D) and (E)

Electrochemical performance

Fig. 3 (a) displays the typical charge-discharge voltage profiles of the samples synthesized by hydrothermal stripping. The fact that charging potential plateaus is lower and the discharging potential plateau is higher suggests that the charge–discharge process can be taken place more easily and more reversibly on the nanometer β-$Ni(OH)_2$ electrode.

Cycle performance is an important index for MH-Ni batteries. Fig. 3 (b) displays the typical cycle performance of the samples synthesized by hydrothermal stripping method. At a constant current rate of C/5, the cell prepared with nano-$Ni(OH)_2$ shows the discharge capacity of 289 $mA{\cdot}hg^{-1}$. This shows hat the nanometer β-$Ni(OH)_2$ cathode materials have much higher discharge specific capacity . As seen in Fig. 3 (b), the nanometer β-$Ni(OH)_2$ sample at C/5 manifests a good cycling performance with initial discharge capacity of 289$mA{\cdot}hg^{-1}$, and discharge capacity of 285 $mA{\cdot}hg^{-1}$ after 58 cycles. The 1.7% loss of specific capacitance after 58 cycles indicates that the repetitive charge-discharges do not induce noticeable degradation of the nanometer β-$Ni(OH)_2$. The spherical nanometer particles, which has larger real superficial area, can provide more chances for the β-$Ni(OH)_2$ to contact the electrolyte solution, therefore proton diffusion is enhanced, which in turn will accelerate the electrode reaction. The charge–discharge process can be taken place more easily and more reversibly on the β-$Ni(OH)_2$ electrodes than that on the microsized β-$Ni(OH)_2$ electrode.

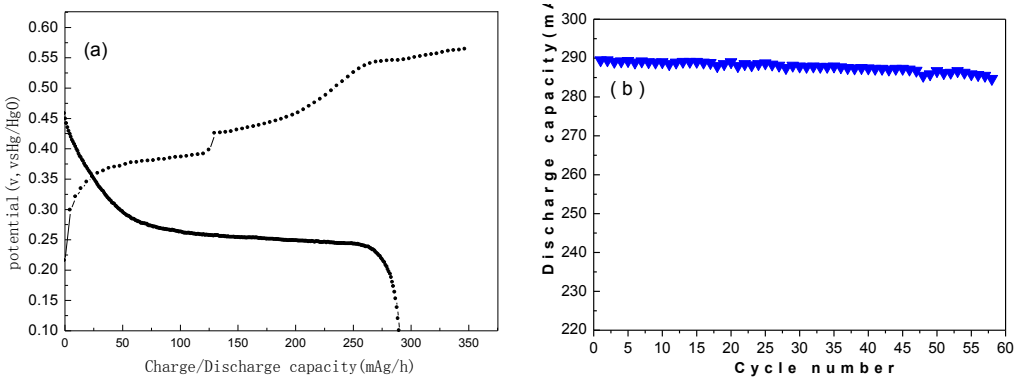


Fig.3. Charge and discharge curves (a) and cycle performance (b) of samples

Conclusions

In summary, the spherical nanometer β-$Ni(OH)_2$ were successfully synthesized by the hydrothermal stripping route, in which the nickel-loaded organic phase was directly stripped by pure water at 140-240 °C for 2.0-4.0 h. The nanometer β-$Ni(OH)_2$ sample at C/5 manifests a good cycling performance with initial discharge capacity of 289mAh·g^{-1}, and discharge capacity of 285 mAh·g^{-1} after 58 cycles. The excellent performances of the present samples in our work are due to the spherical and smaller β-$Ni(OH)_2$ particles. This can makes it feasible as a promising additive material for Ni/MH battery. Hydrothermal stripping route is an effective and green solution-phase synthetic method for synthesizing nanometer β-$Ni(OH)_2$ cathode materials and other high quality materials.

Acknowledgments

This work was financially supported by the National Natural Science Foundation of China (No. 21276185).

References

[1] W.K. Zhang, X.H. Xia, H. Huang, Y.P. Gan, J.B. Wu, J.P.Tu, High-rate discharge properties of nickel hydroxide/carbon composite as positive electrode for Ni/MH batteries, J.Power Sources. 184(2008) 646–651.

[2] W. Zhang, W. Jiang, Yu L, Z. Fu, W. Xia, M. Yang, Effect of nickel hydroxide composition on the electrochemical performance of spherical $Ni(OH)_2$ positive materials for Ni–MH batteries, J. Hydrogen Energy. 34(2009) 473– 480.

[3] H. Jiang, T. Zhao, C.Z. Li, J. Ma, Hierarchical self-assembly of ultrathin nickel hydroxide nanoflakes for high-performance supercapacitors, J. Mater. Chem. 21(2011) 3818-3823.

[4] C. Jinho, P. Mira, H. Dukho, S.B. Ogale, S.M. Rajaram, S.H. Han, .Liquid-phase synthesized mesoporous electrochemical supercapacitors of nickel hydroxide, Electrochim.Acta. 53(2008) 5016–5021.

[5] X.Y. Guan, J.C. Deng, Preparation and electrochemical performance of nano-scale nickel hydroxide with different shapes, Mater. Lett. 61(2007) 621–625.

[6] D.B. Kuang, B.X. Lei, Y.P. Pan, X.Y. Yu, C.Y. Su,Fabrication of Novel Hierarchical β-$Ni(OH)_2$ and NiO Microspheres via an Easy Hydrothermal Process, J.Phys. Chem. C. 113(2009) 5508–5513.

[7] U.M. Patil, K.V. Gurav, V.J. Fulari, C.D. Lokhande, O.S. Joo, Characterization of honeycomb-like "β-$Ni(OH)_2$" thin films synthesized by chemical bath deposition method and their supercapacitor application, J. Power Sources. 188(2009)338–342.

[8] X.J. Hana, P. Xu, C.Q. Xu, L. Zhao, Z.B. Mo, T. Liu, Study of the effects of nanometer β-Ni(OH)2 in nickel hydroxide electrodes, Electrochim. Acta. 50(2005) 2763–2769.

[9] L. Kumari, W.Z. Li, Self-assembly of β-$Ni(OH)_2$ nanoflakelets to form hollow submicrospheres by hydrothermal route, Physica E. 41(2009)1289–1292.

[10] M.A. Kiani, M.F. Mousavi, S. Ghasemi,Size effect investigation on battery performance: Comparison between micro- and nano-particles of β-$Ni(OH)_2$ as nickel battery cathode material, J.Power Sources. 195(2010) 5794–5800.

[11] X.J. Han, P. Xu, C.Q. Xu, L. Zhao, Z.B. Mo, T. Liu, Study of the effects of nanometer β-$Ni(OH)_2$ in nickel hydroxide electrodes, Electrochim. Acta. 50(2005) 2763-2769.

[12] T. Adschiri, Y. Hakuta, K. Arai, Hydrothermal Synthesis of Metal Oxide Fine Particles at Supercritical Conditions, Ind. Eng. Chem. Res. 39, 12(2000) 4901-4907.

[13] A.G. Kanaras, C. So¨nnichsen, H. Liu, A.P. Alivisatos, Controlled Synthesis of Hyperbranched Inorganic Nanocrystals with Rich Three-Dimensional Structures, Nano Letts. *5*(11) (2005), 2164–2167.

[14] L. Dong, Y. Chu, W. Sun, Controllable Synthesis of Nickel Hydroxide and Porous Nickel , Oxide Nanostructures with Different Morphologies**,** Chem. Eur. J. 14(2008) 5064 – 5072.

[15] D. Chen, L. Gao, A new and facile route to ultrafine nanowires, superthin flakes and uniform nanodisks of nickel hydroxide, Chenical physics letters. 405(2005) 159-164.

[16]M.Fathima Parveen, S.Umapathy, V.D.Hanalakshmi, R.Anbarasan, Synthesis and characterizations of nano-sized Ni(OH)2 and Ni(OH)2/poly(vinyl alcohol) nano composite, J .Mater. Sci .44 (2009) 5852-5860.

[17] Y. Konish, T. Kawamura, S. Asai, Preparation and Characterization of Ultrafine Nickel Ferrite Powders by Hydrolysis of Iron(III)−Nickel Carboxylate Dissolved in Organic Solvent, Ind. Eng. Chem. Res. 35, 1(1996) 320-325.

[18] Y. Konishi, D. Satoh, K. T akano. Precipitation of Nickel Hydroxide by Hydrolytic Stripping of Nickel Phosphinate Dissolved in Organic Solvent, Ind. Eng. Chem. Res. 41(2002) 3999-4003.

[19] Y. Konishi, T. Nomura, D. Satoh, Solvothermal Preparation of Cuprous Oxide Fine Particles by Hydrolysis of Copper(II) Carboxylate in Two-Phase Liquid−Liquid System, Ind. Eng.Chem. Res. 43(2004) 2088-2092.

[20] Y. Konishi, T. Noshiyuki, K. Mizoe, K. Nakata, Preparation of Cobalt Ferrite Nanoparticles by Hydrolysis of Cobalt-Iron (III) Carboxylate Dissolved in Organic Solvent,Mater. Trans. 45, 1(2004) 81~85.

[21] X.Y Wang, J.Y. Han, L.Z Lu, H.Q Xie, X.H Kang, Kinetic study of hydrothermal stripping from iron-loaded organic phase, Transactions of Tianjin Univer. 13,2(2007) 113-116.

[22] X,Y. Wang, X.H. Kang, H.Q. Xie, L.Z. Lu, Studies of heterogeneous hydrothermal stripping from iron-loaded naphthenic acid-alcohol-kerosene, Chin. J. Process Eng. 3,2(2003) 109-115.

[23] X.Y. Wang, X.H. Kang, H.Q. Xie, L.Z. Lu, Preparation of Nanosized α-Fe_2O_3 by Hydrothermal Stripping Process, J. Appl. Chem. 21,7(2004) 655-659.

[24] X.Y. Wang, J.Y. Han., J. Wang, G.Q. Yang, Synthesis of spinel $MgFe_2O_4$ nano-powder by hydrothermal stripping Source, Cailiao Gongcheng/J. Mate. Eng. 10(2008)98-100.

[25] X.Y. Wang, C. Miao, J. Zhou, C. Ma, H.F. Wang, S.Q. Sun, A novel synthesis of spherical $LiFePO_4$ nanoparticles, Mater. Lett. 65(2011) 2096–2099.

[26] X.Y. Wang, J. Zhou, C. Miao, Y.M. Wang, H.F. Wang, C. Ma, S.Q.Sun, Synthesis and size control of ferric oxide nanoparticles via a hydrothermal stripping route, J.Nanopart Res. 14(2012):783.

Advanced Materials Research Vol. 936 (2014) pp 496-502
© (2014) Trans Tech Publications, Switzerland
doi:10.4028/www.scientific.net/AMR.936.496

A high Rate, High Capacity and Long Life $(LiFePO_4+AC)/Li_4Ti_5O_{12}$ Hybrid Battery-Supercapacitor

Xuebu Hu[1,2,a], Ziji Lin[3,4], Yonglong Zhang[1]

[1] College of Chemistry and Chemical Engineering, Chongqing University of Technology, Chongqing 400054, China

[2] Chongqing Enterprise Engineering Technology Research Center for Phosgene Derivatives, Changshou, Chongqing 401252, China

[3] Sichuan Provincial Centre for Quality Supervision & Inspection of Alcohol Packaging Products, Luzhou, Sichuan 646000, China

[4] Luzhou Products Quality Supervision & Inspection Institute, Luzhou, Sichuan 646000, China

[a]Xuebu8006@126.com

Keywords: Hybrid battery-supercapacitor; $(LiFeO_4+AC)/Li_4Ti_5O_{12}$; High rate; High capacity; Long life

Abstract:A hybrid battery-supercapacitor $(LiFePO_4+AC)/Li_4Ti_5O_{12}$ using a $Li_4Ti_5O_{12}$ anode and a $LiFePO_4$/activated carbon(AC) composite cathode was built. The electrochemical performances of the hybrid battery-supercapacitor $(LiFePO_4+AC)/Li_4Ti_5O_{12}$ were characterized by constant current charge-discharge, rate charge-discharge, electrochemical impedance spectra, internal resistance, leakage current, self-discharge and cycle performance testing. The results show that $(LiFePO_4+AC)/Li_4Ti_5O_{12}$ hybrid battery-supercapacitors have rapid charge-discharge performance, high energy density, long cycle life, low resistance, low leakage current and self-discharge rate, which meet the requirements of practical power supply and can be applied in auxiliary power supplies for hybrid electric vehicles. At 4C rate, the capacity loss of $(LiFePO_4+AC)/Li_4Ti_5O_{12}$ hybrid battery-supercapacitors in constant current mode is no more than 7.71% after 2000 cycles, and the capacity loss in constant current- constant voltage mode is no more than 4.51% after 1500 cycles.

Introduction

Due to the lack of energy and increasingly serious pollution, hybrid electric vehicles (HEVs) has become a research hotspot in automotive industry [1,2]. But neither secondary batteries (low power density) nor supercapacitors (low energy density) as a single power source can be applied in HEVs [3-9]. Therefore, the demand for electrochemical energy storage devices with high energy density and high power density is urgent. Hybrid battery-supercapacitor is a kind of combination of secondary battery and supercapacitor. It has high energy density as the secondary battery and also high power density as the supercapacitor [10-13]. This makes it one of the most possible auxiliary power supplies for hybrid electric vehicles (HEVs). The authors previously synthesized a composite cathode material containing $LiFePO_4$ and activated carbon (AC) abbreviated as LAC, by an in-situ synthesis method, and then assembled a hybrid battery-supercapacitor device with a $Li_4Ti_5O_{12}$ anode to form the $LAC/Li_4Ti_5O_{12}$ system. Although the hybrid battery-supercapacitor $LAC/Li_4Ti_5O_{12}$ showed the advantages of high rate capability and high capacity [11], the in-situ synthesis requires high system stability. It's hard to control product performance, stability and consistency, particularly accurate content of $LiFePO_4$ in composite materials. The shortage of in-situ synthesis increase difficulty in industrial production. One possible solution to this problem is to synthesize products by a direct mixing technique. The direct mixing technique synthesizes the composite materials via high-speed mechanical mixing, which is simple and can control accurate content of each component in composite materials.

In this paper, we used a composite material from $LiFePO_4$ and AC, as the composite cathode, and then assembled a hybrid battery-supercapacitor device with $Li_4Ti_5O_{12}$ anode to form the system. The

electrochemical properties of ($LiFePO_4$+AC)/$Li_4Ti_5O_{12}$ hybrid battery-supercapacitors were investigated. The study summed up ($LiFePO_4$+AC)/$Li_4Ti_5O_{12}$ hybrid battery-supercapacitors application characteristics and rules. These results may provide the theoretical basis and practical reason for the need of practical application for HEVs.

Experimental

Synthesis of electrode materials

$Li_4Ti_5O_{12}$ powder was prepared via a solid-state reaction as described in Ref. [11].

Cells assembly

Cathodes were prepared with $LiFePO_4$ (STL, China) and AC (GH-6, China). The conductive additives used were colloidal graphite (F-0, China) and conductive carbon black (SuperP, TIMCAL) termed SP hereinafter. The binder used was LA132 (Indigo, China). Anodes were prepared in the same way, using $Li_4Ti_5O_{12}$ as active material. The electrodes formulations are summarized in Table 1.

TABLE 1. FORMULATIONS OF THE ELECTRODES TESTED.

Electrode	Active material	Conductive additives	Binder
15% LFP + AC	$LiFePO_4$ 15% + AC 60%	F-0 12% + SP 6%	LA132 7%
22.5% LFP + AC	$LiFePO_4$ 22.5% + AC 52.5%	F-0 12% + SP 6%	LA132 7%
30% LFP + AC	$LiFePO_4$ 30% + AC 45%	F-0 12% + SP 6%	LA132 7%
LTO	$Li_4Ti_5O_{12}$ 86%	F-0 6% + SP 4%	LA132 4%

The cells were assembled in an argon-filled dry box by pressing a $LiFePO_4$/AC cathode, a Celgard 2400 polypropylene membrane, and a $Li_4Ti_5O_{12}$ anode. Al foil was used as electrode current collectors. The electrolyte was a 1.0M $LiPF_6$ solution in the mixture of ethylene carbonate, dimethyl carbonate and ethylene methyl carbonate (1:1:1 by weight). The cells were packaged with aluminum-plastic membrane and shaped. The final size of hybrid battery-supercapacitor is 4.5mm × 30mm × 48mm (thickness × width × length, Fig. 1). For comparison, the capacitors of AC/AC and AC/$Li_4Ti_5O_{12}$ and the battery $LiFePO_4$/$Li_4Ti_5O_{12}$ were also assembled in the same way.



Fig. 1. Hybrid battery-supercapacitor obtained.

Performance evaluation

Rate capability and cycle performance of the hybrid battery-supercapacitor and capacitor were tested on a Repower Battery Tester (China). Cycle performance tests were divided into two modes: constant current mode (CC mode) and constant current-constant voltage mode (CC-CV mode). In CC mode, the hybrid battery-supercapacitors were charge-discharge cycled over a cell-voltage window of between 2.6V and 1.0V at a constant current. In CC-CV mode, for each cycle, after resting for 5 minutes, the hybrid battery-supercapacitors were charged with constant current to 2.6V and with constant voltage at 2.6V till charge current declined to 5mA. Then, they were rested for 5 minutes. After that, they were discharged to 1.0V at a constant current. Electrochemical impedance spectra were investigated by a Solartron 1260/1287 (UK) in the frequency range of 10^{-1}–10^5Hz. Internal resistance of the cells was investigated by a BK-300 Precision Internal Resistance Tester (1000Hz,

20mA, China). Leakage current and self-discharge behaviors of the cells were characterized using an Arbin instrument (USA). All the tests were carried out at 20 ℃.

Results and discussion

Physical properties of electrode materials

The particle size distribution of $LiFePO_4$, AC and $Li_4Ti_5O_{12}$ is depicted in Fig. 2. As is seen in this figure, the average particle size of $LiFePO_4$, AC and $Li_4Ti_5O_{12}$ is 3.27, 12.11 and 0.303μm, respectively. The BET of $LiFePO_4$, AC and $Li_4Ti_5O_{12}$ is listed in Table 2.

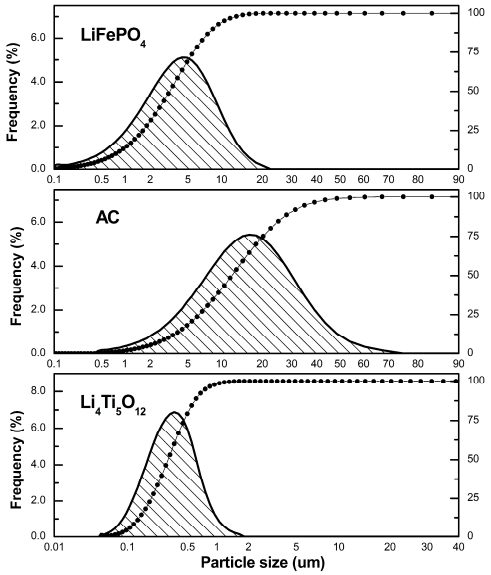


Fig. 2. The particle size distribution of $LiFePO_4$, AC and $Li_4Ti_5O_{12}$.

TABLE 2. THE PARTICLE SIZE DISTRIBUTION AND BET OF $LIFEPO_4$, AC AND $LI_4TI_5O_{12}$.

	D_{10}(μm)	D_{50}(μm)	D_{90}(μm)	$D_{(4,3)}$(μm)	BET($m^2 \cdot g^{-1}$)
$LiFePO_4$	0.765	3.27	8.43	4.06	2.41
AC	3.09	12.11	29.40	14.53	581.7
$Li_4Ti_5O_{12}$	0.128	0.303	0.638	0.352	10.67

Charge/discharge behavior of hybrid battery-supercapacitor

Fig. 3 shows a whole charge-discharge process of ($LiFePO_4$+AC)/$Li_4Ti_5O_{12}$ hybrid battery-supercapacitors with different $LiFePO_4$ contents. The whole charge-discharge process of ($LiFePO_4$+AC)/$Li_4Ti_5O_{12}$ battery-supercapacitor includes six steps that are A～B，B～C，C～D，D～E，E～F and F～G [11]. Step B～C is the middle stage of the charge process, which is also the slow charge process during which the capacity is increased but the voltage is kept constant. It belongs to the process of Li-ion extraction/oxidation in $LiFePO_4$ and Li-ion insertion/reduction in $Li_4Ti_5O_{12}$, and presents Faradaic energy storage. Step C～D is the final stage of the charge process, i.e. the slow charge process during which the capacity increases linearly with voltage, which is the characteristic charge process of electric double-layer electrostatic adsorbing PF_6^{-1} in AC and Li-ion insertion/reduction in $Li_4Ti_5O_{12}$, and presents energy storage of electric double-layer electrostatic adsorption. Step A～B is the early stage of charge, i.e. slow charge process capacitor shows a non-linear increase with voltage, which has the characteristics of B～C and C～D stages. The steps D～E，E～F and F～G are the reversible discharge processes of C～D，B～C and A～B steps respectively. In two modes, with the increase of $LiFePO_4$ content in composite cathodes, the platform region of hybrid battery-supercapacitors correspondingly adds and the platform performance strengthens. Compared with CC and CC-CV modes, discharge capacity of CC-CV mode is slightly

larger than that of CC mode under the same conditions, which is resulted from adding the process of constant voltage charge.

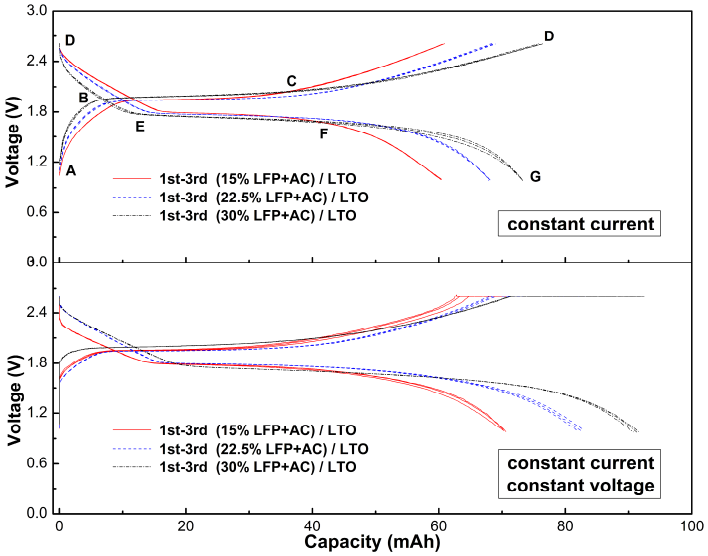


Fig. 3. Charge-discharge curves of the hybrid battery-supercapacitor.

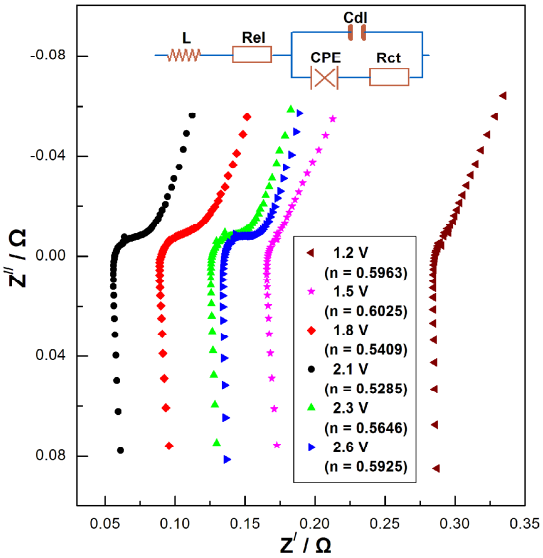


Fig. 4. EIS of the hybrid battery-supercapacitor at various potentials.

Electrochemical impedance spectra (EIS) of hybrid battery-supercapacitor

Fig. 4 shows EIS of hybrid battery-supercapacitor (22.5%$LiFePO_4$+AC)/$Li_4Ti_5O_{12}$ at various potentials. It is apparent that Nyquist plots at various potentials are very similar, which is composed of two parts: an almost vertically straight line & semicircle in the high frequency range and a slash in the low frequency range. The equivalent circuit is made of a connector's inductance (L), an electrolyte resistance (Rel), a charge-transfer resistance (Rct), a double-layer capacitance (Cdl), and a constant phase element (CPE). CPE reflects capacitance characteristics of the hybrid battery-supercapacitor. With the increase of potential, n of CPE increases firstly (from 1.2V to 1.5V), then decreases (from 1.8V to 2.1V) and finally increases again (from 2.3V to 2.6V). These results indicate that with the increase of potential the hybrid battery-supercapacitor shows firstly the capacitance characteristics, then transfers to the battery characteristics and finally shows capacitance characteristics again. This demonstrates that energy storage process in the hybrid battery-supercapacitor is gradually transferred from energy storage of electric double-layer electrostatic adsorption to Faradaic energy storage, then to energy storage of electric double-layer electrostatic adsorption. These facts illustrate that the Nyquist plot of ($LiFePO_4$+AC)/$Li_4Ti_5O_{12}$ hybrid battery–supercapacitor is consistent with the charge-discharge cycle curve.

Energy density of hybrid battery-supercapacitor

Table 3 shows the results of the energy densities of the hybrid battery-supercapacitors in CC and CC-CV modes. In two modes, the mass and volume energy densities of ($LiFePO_4$+AC)/$Li_4Ti_5O_{12}$ hybrid battery-supercapacitors with various $LiFePO_4$ contents all exceed 10.9 $Wh \cdot kg^{-1}$ and 16.8 $Wh \cdot kg^{-1}$, respectively. The energy densities of the hybrid battery-supercapacitors are significantly higher than that of AC/$Li_4Ti_5O_{12}$ hybrid capacitor and AC/AC electric double-layer capacitor, also higher than that of commercial supercapacitors (1~10 $Wh \cdot kg^{-1}$). Moreover, the energy density of hybrid battery-supercapacitor is enhanced when the content of $LiFePO_4$ is added in composite cathode. When the content of $LiFePO_4$ in composite cathode is 30 wt% in CC-CV mode, the mass and volume energy densities of ($LiFePO_4$+AC)/$Li_4Ti_5O_{12}$ hybrid battery-supercapacitor reach 15.56 $Wh \cdot kg^{-1}$ and 24.02 $Wh \cdot kg^{-1}$, respectively. The Energy densities of the hybrid battery-supercapacitors will be increased (especially for volume energy density) if the monomer cell is assembled. These results demonstrate ($LiFePO_4$+AC)/$Li_4Ti_5O_{12}$ hybrid battery-supercapacitors have high energy density at 4C rate.

TABLE 3. ENERGY DENSITIES OF HYBRID BATTERY-SUPERCAPACITORS AT 4C RATE.

Type		Energy density	
		($Wh \cdot kg^{-1}$)	($Wh \cdot L^{-1}$)
AC/AC (DLC306)		4.17	6.44
AC/AC		2.31	3.56
AC/LTO		5.77	8.91
CC mode	(15%LFP+AC)/LTO	10.92	16.85
	(22.5%LFP+AC)/LTO	12.07	18.63
	(30%LFP+AC)/LTO	12.98	20.02
CC-CV mode	(15%LFP+AC)/LTO	12.36	19.08
	(22.5%LFP+AC)/LTO	14.81	22.86
	(30%LFP+AC)/LTO	15.56	24.02

Resistance characteristics of hybrid battery-supercapacitor

Table 4 shows the results of alternating current resistance of the hybrid battery-supercapacitors. After formation process, alternating current resistances of all devices decrease. With the increase of $LiFePO_4$ content in composite cathodes, the alternating current resistances of the hybrid battery-supercapacitors slightly increase, also slightly higher than AC/$Li_4Ti_5O_{12}$ hybrid capacitor and AC/AC electric double-layer capacitor.

TABLE 4. ALTERNATING CURRENT IMPEDANCE OF THE HYBRID BATTERY-SUPERCAPACITORS.

Type		Before formation (mΩ)	After formation (mΩ)	2000 cycles(4C) (mΩ)
AC/AC (DLC306)		12.6	12.2	29.3
AC/AC		27.3	27.3	30.3
AC/LTO		32.9	32.8	32.8
CC mode	(15%LFP+AC)/LTO	27.6	27.3	33.8
	(22.5%LFP+AC)/LTO	29.9	28.8	34.0
	(30%LFP+AC)/LTO	33.4	32.4	40.0
CC-CV mode	(15%LFP+AC)/LTO	27.9	27.1	32.5
	(22.5%LFP+AC)/LTO	29.5	28.7	33.5
	(30%LFP+AC)/LTO	33.3	33.0	39.8

Leakage current

Leakage current can be used as an important evaluation index of energy storage devices performance. In Fig. 5, all devices were charged with constant voltage for 72 hours. The constant voltage is 2.6V for ($LiFePO_4$+AC)/$Li_4Ti_5O_{12}$ hybrid battery-supercapacitor and $LiFePO_4$/$Li_4Ti_5O_{12}$ battery, 2.7V for AC/AC electric double-layer capacitor, and 2.8V for AC/$Li_4Ti_5O_{12}$ hybrid capacitor. As shown in the figure, the hybrid battery-supercapacitors present good leakage current performance, which is the same as other energy storage devices.

Self-discharge

Fig. 6 shows self-discharge performance of all devices. After charging with constant voltage for 0.5 hour, all devices were placed in an open-circuit state for 72 hours. The constant voltage is 2.6V for ($LiFePO_4$+AC)/$Li_4Ti_5O_{12}$ hybrid battery-supercapacitor and $LiFePO_4$/$Li_4Ti_5O_{12}$ battery, 2.7V for AC/AC electric double-layer capacitor, and 2.8V for AC/$Li_4Ti_5O_{12}$ hybrid capacitor. As shown in the figure, the order of voltage drop is AC/AC > $LiFePO_4$/$Li_4Ti_5O_{12}$ > ($LiFePO_4$+AC)/$Li_4Ti_5O_{12}$ > AC/$Li_4Ti_5O_{12}$. With the increase of $LiFePO_4$ content in composite cathodes, the self-discharge curve

of the hybrid battery-supercapacitors is gradually closer to that of $LiFePO_4/Li_4Ti_5O_{12}$ battery. These results demonstrate $(LiFePO_4+AC)/Li_4Ti_5O_{12}$ hybrid battery-supercapacitors have low self-discharge performance.

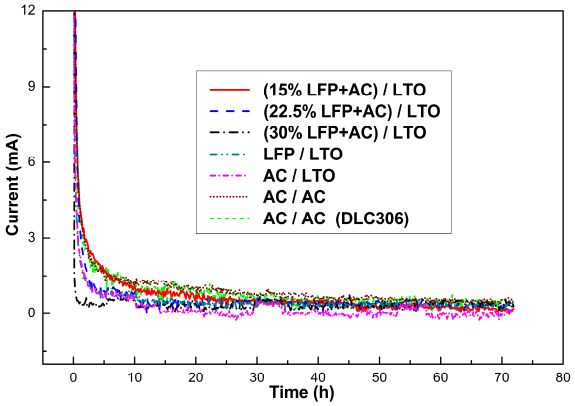


Fig. 5. Leakage current curves of all devices.

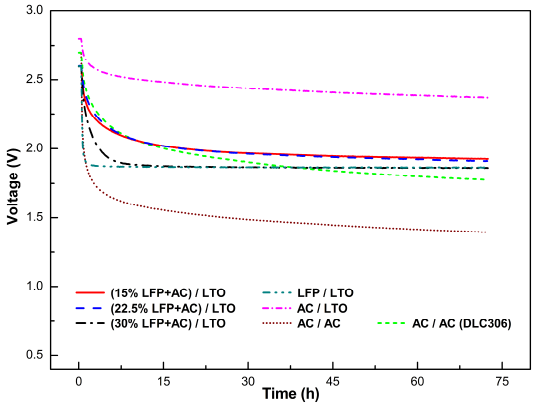


Fig. 6. Self-discharge curves of all devices.

Cycle life performance of hybrid battery-supercapacitor

The results for cycle life of the hybrid battery-supercapacitors at 4C rate are shown in Fig. 7. As is seen in the figure, the capacity losses of AC/AC electric double-layer capacitors are less than 3.00% after 2000 cycles, which demonstrates that they have excellent cycling performance. However, their discharge capacities are low. In contrast, $AC/Li_4Ti_5O_{12}$ hybrid capacitor has larger capacity, but its capacity retention remains poor. It is obvious that AC/AC electric double-layer capacitors and $AC/Li_4Ti_5O_{12}$ hybrid capacitor have not high capacity and long life performances at high rate. $(LiFePO_4+AC)/Li_4Ti_5O_{12}$ hybrid battery-supercapacitors in two modes provide high coulombic efficiencies closed to 100%. In CC mode, when the content of $LiFePO_4$ in composite cathode is 15, 22.5 and 30 wt%, after 2000 cycles the capacity loss of $(LiFePO_4+AC)/Li_4Ti_5O_{12}$ hybrid battery-supercapacitor is 6.04%, 7.48% and 7.71%, respectively. Clearly, all the value is no more than 7.71%. However, if in CC-CV mode, after 1500 cycles the capacity loss will be 2.71%, 4.51% and 3.60%, respectively, and noticeably, all the value is no more than 4.51%. The results show that $(LiFePO_4+AC)/Li_4Ti_5O_{12}$ hybrid battery-supercapacitors have high capacity and good cycle life performance at high rate.

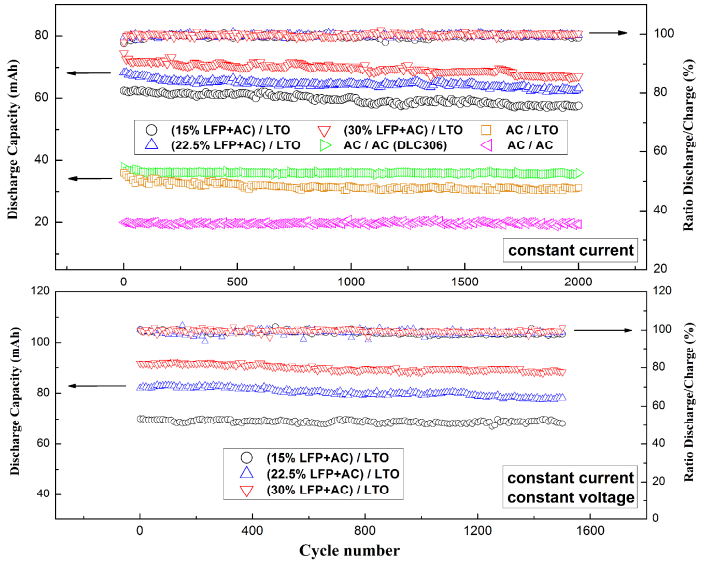


Fig. 7. Discharge capacity and discharge/charge ratio vs. cycle number for hybrid battery-supercapacitors at 4C rate.

Conclusions

The hybrid battery-supercapacitors ($LiFePO_4$+AC)/$Li_4Ti_5O_{12}$ have the advantages of high rate, high capacity and long life. At 4C rate, when the content of $LiFePO_4$ in composite cathode is 30 wt% in CC-CV mode, the mass and volume energy densities of the monomer ($LiFePO_4$+AC)/$Li_4Ti_5O_{12}$ hybrid battery-supercapacitor reach 15.56 $Wh \cdot kg^{-1}$ and 24.02 $Wh \cdot kg^{-1}$, respectively, which is significantly higher than that of AC/$Li_4Ti_5O_{12}$ hybrid capacitor and AC/AC electric double-layer capacitor. The capacity loss of ($LiFePO_4$+AC)/$Li_4Ti_5O_{12}$ hybrid battery-supercapacitors in CC mode is no more than 7.71% after 2000 cycles, and the capacity loss in CC-CV mode is no more than 4.51% after 1500 cycles. Moreover, low resistance, leakage current and self-discharge rate of the hybrid battery-supercapacitors are in accordance with the requirements of practical power supply, and expected to further optimize and improve their electrochemical performance. In a word, ($LiFePO_4$+AC)/$Li_4Ti_5O_{12}$ hybrid battery-supercapacitors have rapid charge-discharge performance, high energy density, long cycle life, low resistance, low leakage current and self-discharge rate, which can be applied in auxiliary power supplies for HEVs.

Acknowledgements

This work was supported by Program for Chongqing Science & Technology Innovation Talents (cstc2013kjrc-qnrc50006) and the National Natural Science Foundation of China (No. 21206203).

References

[1] A.O. Johansson, E.M. Fonte, P.A. Selonge, Power source management requirements in some types of road vehicles with electric traction, J. Busan, Korea, Oct. 2002, pp. 19-23.
[2] J.V. Mierlo, L. Vereecken, G. Maggetto, V. Favrel, S. Meyer, W. Hecq, Int. J. Automotive Technol. 4 (2003) 77-86.
[3] A. Guerfi, M. Dontigny, P. Charest, M. Petitclerc, M. Lagace, A. Vijh, K. Zaghib, Improved electrolytes for Li-ion batteries: Mixtures of ionic liquid and organic electrolyte with enhanced safety and electrochemical performance, J. Power Sources. 195 (2010) 845-852.
[4] V. Sauvant-Moynot, J. Bernard, R. Mingant, A. Delaille, F. Mattera, S. Mailley, J. L. Hognon, F. Huet, ALIDISSI, a Research Program to Evaluate Electrochemical Impedance Spectroscopy as a SoC and SoH Diagnosis Tool for Li-ion Batteries, Oil Gas Sci. Technol. 65 (2010) 79-89.
[5] D. Yoshikawa, Y. Kadoma, J.-M. Kim, K. Ui, N. Kumagai, N. Kitamura, Y. Idemoto, Spray-drying synthesized lithium-excess $Li_{4+x}Ti_{5-x}O_{12-\delta}$ and its electrochemical property as negative electrode material for Li-ion batteries, Electrochim. Acta. 55 (2010) 1872-1879.
[6] E. Karden, S. Ploumen, B. Fricke, T. Miller, K. Snyder, Energy storage devices for future hybrid electric vehicles, J. Power Sources. 168 (2007) 2-11.
[7] S.Y. Kan, M. Verwaal, H. Broekhuizen, The use of battery-capacitor combinations in photovoltaic powered products, J. Power Sources. 162 (2006) 971-974.
[8] C.E. Holland, J.W. Weidner, R.A. Dougal, R.E. White, Experimental characterization of hybrid power systems under pulse current loads, J. Power Sources. 109 (2002) 32-37.
[9] A.C. Baisden, A. Emadi, Advisor-based model of a battery and an ultra-capacitor energy source for hybrid electric vehicles, Ieee T. Veh. Technol. 53 (2004) 199-205.
[10] A.D. Pasquier, I. Plitz, J. Gural, F. Badway, G.G. Amatucci, Power-ion battery: bridging the gap between Li-ion and supercapacitor chemistries, J. Power Sources. 136 (2004) 160-170 .
[11] X.B. Hu, Y.J. Huai, Z.J. Lin, J.S. Suo, Z.H. Deng, A ($LiFePO_4$-AC)/ $Li_4Ti_5O_{12}$ Hybrid Battery Capacitor, J. Electrochem. Soc. 154 (2007) A1026-A1030.
[12] L.T. Lam, R. Louey, Development of ultra-battery for hybrid-electric vehicle applications, J. Power Sources. 158 (2006) 1140-1148.
[13] G.G. Amatucci, U.S. Patent. 6,517,972B1 (2003)

CHAPTER 6:

Chemical Physics

Advanced Materials Research Vol. 936 (2014) pp 505-508
© (2014) Trans Tech Publications, Switzerland
doi:10.4028/www.scientific.net/AMR.936.505

Modeling of Recrystallization Texture of Rolled Polycrystalline Aluminium

Krzysztof Wierzbanowski[1,a *], Michał Kotra[1,b], Marcin Wronski[1,c], Krzysztof Sztwiertnia[2,d]

[1] AGH University of Science and Technology, Faculty of Physics and Applied Computer Science, al. Mickiewicza 30, 30-059 Kraków, Poland

[2] Institute of Metallurgy and Materials Science, Polish Academy of Sciences, ul. Reymonta 25, 30-059 Kraków, Poland

[a]wierzbanowski@fis.agh.edu.pl, [b]michalkotra@motorolasolutions.com, [c]mwronskii@gmail.com, [d]k.sztwiertnia@imim.pl

Keywords: recrystallization modeling, texture, polycrystalline aluminium, oriented growth

Abstract: In many metallic materials the dominating recrystallization mechanism can be described by the oriented growth behavior. Phenomenological laws state that only these nuclei grow intensively which have a given misorientation with the deformed matrix. This description is frequently verified in f.c.c. metals and generally reported misorientations are between 30^0 and 50^0 rotations around the <111> axis. Basing on the above ideas the recrystallization model was formulated and applied to the study of recrystallization textures in rolled polycrystalline aluminium.

Introduction

Texture development in f.c.c. metals was studied and described in literature using various models (eg. [1-5]. In many of these models the stored energy and residual stresses play the essential role (e.g., [3-6]). However, a relatively simple orientation relationship between growing nuclei and deformed matrix was found in aluminium, which can explain the formation of its recrystallization texture. Preferred misorientations, Δg, between nuclei and deformed grains, correspond to high mobility of grain boundaries. They are traditionally described as a rotation $\omega_0 \cong 40^o$ around one of <111> axes. Therefore, the velocity of grain boundary, u, between a nucleus and the deformed matrix depends very strongly on misorientation Δg. This relation was reported in [7] and [8]. Based on the above assumptions, a successful recrystallization model was formulated [9,10]. It was also shown that predicted results are much improved if the so called *compromise condition* and, consequently, the *compromise function* are used. Let us describe now in more details the recrystallization model used in the present calculations.

Recrystallization Model

Boundary Migration Rate

Each deformed grain is statistically consumed by many nuclei but at very different rates. The crystal misorientation Δg_{ij} between the nucleus i and the deformed grain j is expressed by the rotation axis $\mathbf{r}_{ij}$ and the misorientation angle ω_{ij}. Obviously, in general the determined rotation axis $\mathbf{r}_{ij}$ does not exactly coincides with one of <111> axes; let us assume that it is deviated of the angle α_{ij} from the nearest <111> axis. Similarly, the ω_{ij} misorientation angle does not equal exactly to ω_0 (corresponding to the maximum migration rate). Therefore,

basing on the results presented in [7] and [8] the boundary migration rate, u_{ij} (ω_{ij}, α_{ij}) between the nucleus *i* and deformed grain *j*, was approximated as:

$$u_{ij}(\omega_{ij},\alpha_{ij}) = u_{max}\, e^{\frac{-(\omega_{ij}-\omega_0)^2}{\Delta\omega^2}} \cdot e^{\frac{-\alpha_{ij}^2}{\Delta\alpha^2}} \tag{1}$$

The first exponential function in the above equation describes the relation of the migration rate on the misorientation angle ω_{ij}, assuming that the maximum migration rate corresponds to ω_0. In the second exponential function the effect of deviation of a current rotation axis $\mathbf{r}_{ij}$ from the nearest 'ideal' <111> of α_{ij} angle is taken into account. In the above formula the following constants were adjusted from experimental data [9,10]: ω_0=40^0, $\Delta\omega$=13.7^0, $\Delta\alpha$, $\Delta\alpha$=7.5^0 and u_{max}=4.56 mm/min corresponds to the maximum value of the boundary migration rate.

Compromise Function

The compromise function is defined as a volume fraction of all deformed grains, which can be potentially 'consumed' by a nucleus of a given orientation:

$$S(g_i) = \frac{\sum_j V_j}{V_0} \tag{2}$$

where V_j is the volume of the *j-th* deformed grain and the following condition has to be fulfilled: the i-th nucleus can grow into j-th grain with the migration rate exceeding some minimal value, i.e., $u_{ij} \geq u_{min}$. The value u_{min}=0.001 mm/min used.

Calculation of Recrystallization Texture

The deformation matrix is presented as *N*=5000 grains of the same volume with crystal orientation distribution corresponding to the deformation texture. We generate *M*=6859 nuclei with crystal orientations contained in the range of Euler angles space corresponding to the cubic crystal and sample orthorhombic symmetries, i.e.: $: 0 \leq \phi \leq \pi/2,\ 0 \leq \varphi_2 \leq \pi/2$ oraz $0 \leq \varphi_1 \leq \pi/2$ (i.e., every 5^0 with respect to each Euler angle). Next, we define a step function *c(g)*, basing on the compromise function, which decides whether a given nucleus with orientation g_i will grow or not:

$$c(g_i) = \begin{cases} 1, & if \quad S(g_i) \geq s_0 \\ 0, & if \quad S(g_i) < s_0 \end{cases} \tag{3}$$

where s_0 is the assumed level of compromise [3].

The volume ΔV_{ij} of the *j-th* deformed grain consumed by the *i-th* nucleus is:

$$\Delta V_{ij} = \frac{u_{ij}}{\sum_{k=1}^{M} u_{kj}} \cdot V_j \tag{4}$$

where V_j is the initial volume of the j-th grain and the summation on *k* is done on growing nuclei (those which fulfill the compromise condition).

The total volume of the deformed matrix, 'consumed' by *i-th* nucleus is:

$$\Delta V(g_i) = \sum_{j=1}^{N} V_{ij} \tag{5}$$

where N is total number of deformed grains. And finally, the recrystallization texture is calculated as:

$$f(g_i) = a \cdot n(g_i) \Delta V(g_i) \cdot c(g_i) \tag{6}$$

where: $n(g_i)$ is the volume fraction of nuclei with g_i orientations and *a* is a normalization constant.

Results

The example result of our calculations is shown in Fig. 1.

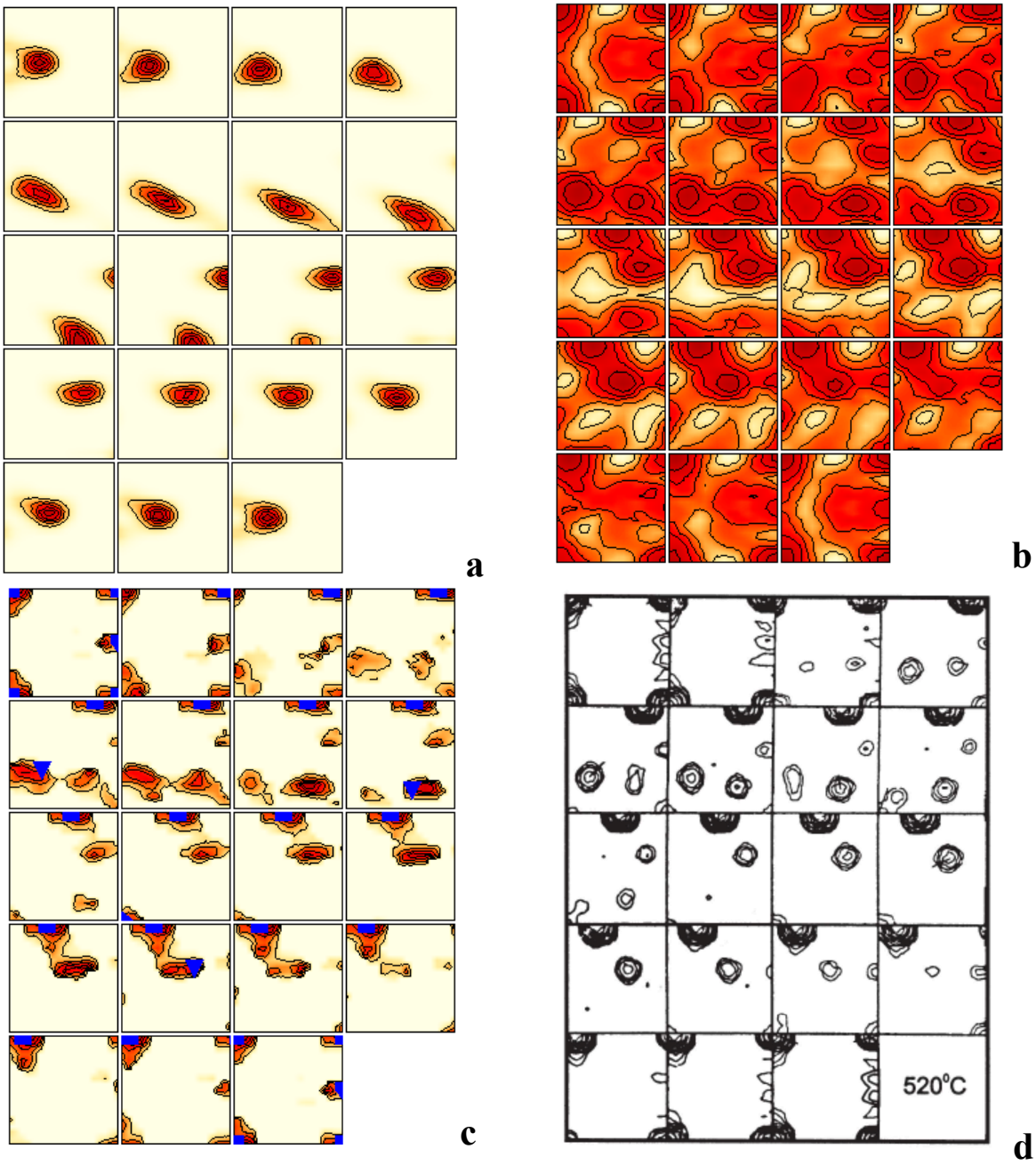


***Fig. 1**. a) Rolling texture of aluminium (reduction 60%, max. intensity: 18), b) calculated compromise function S(g); max. intensity: 0.67, c) predicted recrystallization texture; max. intensity: 11; texture components marked: cube (■), S (▼), rotated Goss (◣), d) experimental recrystallization texture of aluminium annealed at 520^0; max. intensity: 70 (after [4]).*

The starting rolling texture of aluminium (60% rolling reduction) is shown in Fig. 1a, while the compromise function, S(g), calculated on the basis of the deformation texture, is shown in Fig. 1b. The recrystallization texture (Fig. 1c) was calculated assuming the compromise threshold s_0=0.45 and is compared with experimental recrystallization texture of aluminium (Fig. 1d). We observe surprisingly good agreement between the calculated and experimental recrystallization textures - the same texture maxima appear in the two compared orientation distribution functions. Three ideal orientations are marked in recrystallization texture (Fig. 1c): the dominating cube component (0^0, 0^0, 0^0), S component (26^0, 58^0,19^0) and also rotated Goss component (0^0, 90^0, 45^0). It should be noted that already the shape of the compromise function is very similar to the experimental

recrystallization texture of aluminium. Therefore, we conclude that the compromise condition is a very important factor in recrystallization textures modeling.

Conclusions

The concept of preferred growth, defined by specific misorientations between nuclei and matrix, leads to a very good prediction of aluminium recrystallization texture. The compromise condition was included in our calculations in order to obtain a better texture prediction. The question is why this relatively simple approach, used in the presented calculations, leads to so good result in the case of aluminium. One argument can be based on the fact that there is principally one preferred misorientation relation found in f.c.c. metals (40^{o}<111>), while more complex descriptions of the oriented growth relations are reported for other metals (e.g., for b.c.c. metals).

Acknowledgment

This study was financed by the Polish National Centre for Science (NCN) under decision number: DEC-2011/01/B/ST8/07394.

The support of the Polish Ministry of Science and Higher Education is also appreciated.

References

[1] J. Humphreys, M. Hatherly, Recrystallization and Related Annealing Phenomena, Elsevier, 2004

[2] K. Lücke, The Formation of Recrystallization Textures in Metals and Alloys, Proc. 7-th Int. Conf. on Textures of Materials, Eds. Brakman et al., Noordwijkerhout, The Netherlands, 1984, pp. 195-210.

[3] K. Piękoś, J. Tarasiuk, K. Wierzbanowski and B. Bacroix, Generalized vertex model of recrystallization – Application to Polycrystalline Copper, Comp. Mat. Sci., 42 (2008) 584-594

[4] K. Piękoś, J. Tarasiuk, K. Wierzbanowski and B. Bacroix, Stochastic vertex model of recrystallization, Comp. Mat. Sci., 42 (2008) 36-42

[5] K. Wierzbanowski, J. Tarasiuk, B. Bacroix, A. Miroux and O. Castelnau, Deformation Characteristics Important for Nucleation Process. Case of Low-Carbon Steels, Arch. Metall., 44 (1999) 183- 201

[6] A. Baczmański, K. Wierzbanowski, J. Tarasiuk, M. Ceretti, A. Lodini, Anisotropy of Micro-Stress - Measured by Diffraction, Revue de Metallurgie, 94 (1997) 1467- 1474

[7] B. Liebmann, K. Lücke, and G. Masing, Untersuchungen über die Orientierungs-abhängigkeit der Wachstumsgeschwindigkeit bei der primaren Rekristallisation von Aluminium-Einkristallen, Z. Metallkde, 47 (1956) 57-63

[8] Y. Huang, F.J. Humphreys, Measurement of Grain Boundary Mobility During Recrystallization of a Single Phase Aluminium Alloy, Acta Mater., 47 (1999) 2259-2268

[9] K. Sztwiertnia, Simulation of Compromise Textures, Arch. Metall., 41 (1996) 101-116

[10] Wierzbanowski, J. Tarasiuk, B. Bacroix, K. Sztwiertnia, P. Gerber, Recrystallization Textures - Two Types of Modelling, Metals and Materials International, 9 (2003) 9-14

Advanced Materials Research Vol. 936 (2014) pp 509-514
© (2014) Trans Tech Publications, Switzerland
doi:10.4028/www.scientific.net/AMR.936.509

Numerical Analysis on Decay Heat Power of Weapon-grade Uranium and Depleted Uranium

WANG Yuling[a],YU Wenli,WANG Tao,DONG Sanqiang

Xi'an Research Inst of Hi-Tech, Xi'an 710025, Shanxi, China

[a]wangyulingsa@126.com

Keywords: weapon-grade uranium; depleted uranium; heat power; numerical analysis

Abstract: In order to exactly master effect of uranium material's heat power on safety and reliability of nuclear weapon, weapon-grade uranium(WgU) and depleted uranium(DU) were regarded as research object in this paper. According to their component, decay heat power of WgU and DU per kilogram was calculated through dynamic decay cascade and decay law of uranium. Decay heat power of WgU and DU was respectively 1.8152 and 0.4075 milliwatt per kilogram. Main nuclide influencing on decay heat power of WgU and DU is uranium-234(U-234).

Introduction

All kinds of nuclear weapon all have at least several kilogram fission materials. Uranium and plutonium are major fission material，these material mainly are weapon-grade plutonium(WgPu) and WgU. In addition DU also exists in definite radioactivity[1]. These materials can emit a great of energy during radioactivity decay and nuclear fission, at the same time the energy can be used to elevate temperature of their surrounding material. On the one hand it can lead to detonate explosive, on the other hand it can lead to deform surrounding material[2]. These will affect performance of whole nuclear explosive device. In order to exactly grasp effect of heat-producing power of nuclear material on store safety and reliability of nuclear explosive device, heat power of these materials must be firstly known. This paper regards uranium as research object and analyzes heat power of WgU and DU. Because uranium can produce alpha decay reaction, spontaneous fission, gamma decay reaction, and so on, but heat power of spontaneous fission is far less than other nuclear reactions[3]. Therefore decay heat power of uranium will be considered in this paper.

Component and decay law of WgU and DU

Component of WgU and DU

Uranium-235(U-235) content is only 0.7% in natural uranium. Concentration of U-235 must reach certain value in order to realize self-sustaining chain reaction. Critical mass of uranium is very big and already can't be made nuclear weapon when its concentration is fewer than 20%. According to use way of uranium, uranium is defined as different grade[4]. When U-235 content is less than 0.711%，uranium is termed depleted uranium. U-235 Content is equal to 0.711% in natural uranium. U-235 content is from 0.711% to 20% in low enrichment uranium. U-235 content is equal or greater than 20% in high enrichment uranium. Generally it is defined as weapon-grade uranium when U-235 content is excess 90%. Component of WgU and DU and atomic mass of their isotopes are shown in Table one[5-6].

TABLE 1 COMPONENT AND THEIR MASS PERCENT ABOUT WGU AND DU

Nuclear material	Isotope	Mass percent (%)	Atomic mass(u)
WgU	uranium-234	1%	234.040975
	uranium-235	93.3%	235.043944
	uranium-238	5.5%	238.050816
DU	uranium-234	0.2%	234.040975
	uranium-235	0.4%	235.043944
	uranium-238	99.4%	238.050816

Decay law of WgU and DU

Most nuclide can become steady nuclide by continuous disintegration. For simple dynamic decay cascade lies in A→B→C, disintegration of nuclide A complies with the law of exponential decay, as well as nuclide B constantly decays nuclide C, on the other hand nuclide B constantly gains supplement from nuclide A. So change of nuclide B with time is shown in below formula:

$$\frac{dN_B}{dt} = \lambda_A N_A - \lambda_B N_B$$

It can be gained by integral about above formula:

$$N_B = N_{A0} \frac{\lambda_A}{\lambda_B - \lambda_A} (e^{-\lambda_A t} - e^{-\lambda_B t})$$

Thus it can be seen, change law of nuclide B is not only correlative with its disintegration constant λ_B, but also is correlative with disintegration constant λ_A of matrix A. In the same way it can be gained that change law of nuclide C is not only correlative with its disintegration constant λ_C, but also is correlative with disintegration constant λ_A of matrix A and disintegration constant λ_B of nuclide B.

For continuous disintegration, whole disintegration can reach perennial balance after enough time if radioactive half-life of matrix A is far long than radioactive half-life of its nuclide. In other words activity of matrix A is equal with its nuclide[7]. Therefore some nuclide must be considered besides main nuclide when radioactivity intensity of uranium is calculated.

Decay cascade of isotopes in WgU and DU are shown in Figure one.

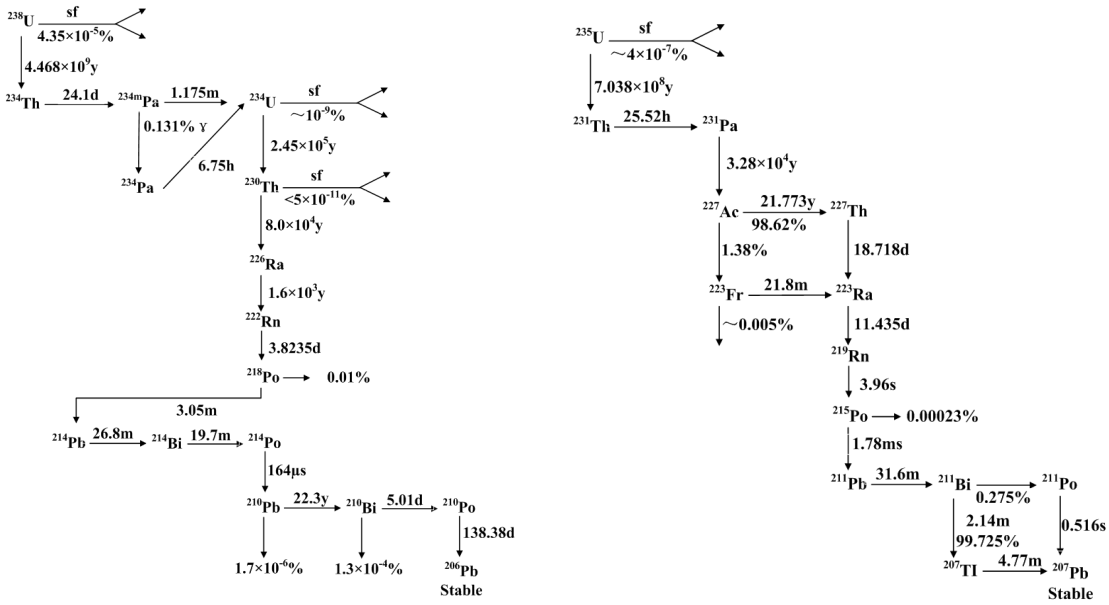


Fig.1 Decay cascade of isotopes in WgU and DU

Atom number calculation of WgU and DU isotope

If initial component content of WgU and DU are shown in Fig.1, atomic number of each nuclide in per kilogram WgU and DU can be calculated by below formula:

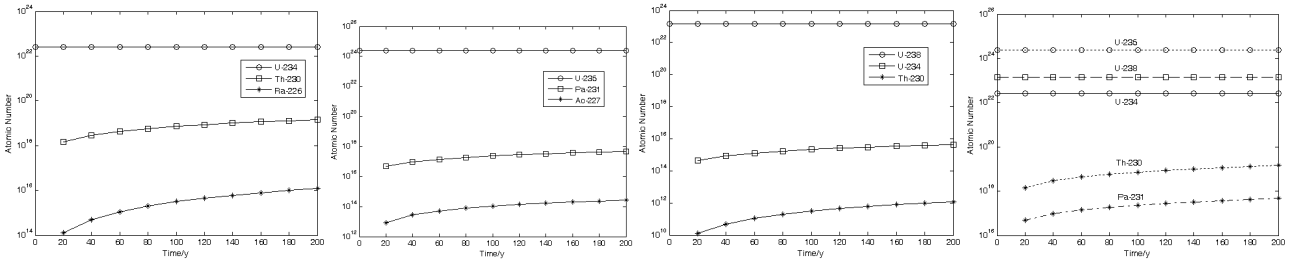
$N_i(0)=percent\%/m_i$

Where i=1,2,3,4,5.

From disintegration process of U-235 we can get that radioactive half-life is 7.038×10^8 years from U-235 to thorium-231(Th-231), radioactive half-life is 25.52 hours from Th-231 to protactinium-231(Pa-231), radioactive half-life is 3.28×10^4 years from Pa-231 to actinium-227(Ac-227), radioactive half-life is 21.773 years from Ac-227 to thorium-227(Th-227), it need about 30 days from Th-227 decaying to steady nuclide plumbum-207(Pb-227). It is thus clear that we only need calculate atomic number from U-235 decaying to Th-227. Because it only need 25.52 hours from Th-231 to Pa-231, atomic number after Th-231 decaying won't be considered.

Atom number calculation of WgU isotope

According to decay cascade of isotopes, we can gain atomic number of isotopes in WgU and total atomic number versus time are shown in Fig.2(a)-2(d).



(a) (b) (c) (d)

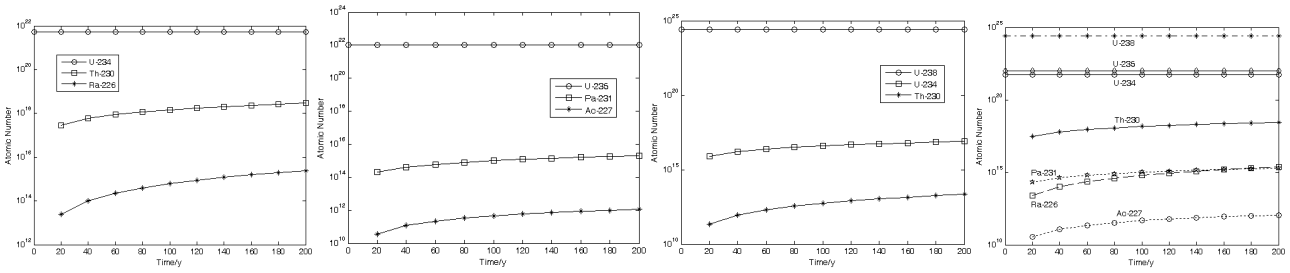
Fig.2 Atomic number of WgU and its isotopes versus time

From computational formula of decay heat power for isotope, we can get that decay heat power is not only relative to its disintegration energy, but also is relative to radioactive half-life and atomic number. Decay heat power varies inversely with radioactive half-life isotope and directly with atomic number. It is thus clear that atomic number is more its decay heat power is maybe bigger.

From Fig.2(a) it can be seen that main nuclide influencing decay heat power on U-234 is itself. From Fig.2(b) and Fig.2(c) can be seen that main nuclide influencing decay heat power on U-235 and U-238 is also respectively itself. From Fig.2(d) it can be seen that main nuclide influencing decay heat power on WgU is U-234, U-235 and U-238. At the same time that it can be seen that atomic number of U-235 is most, atomic number of U-234 is least. This explains that atomic number of isotopes is related to isotope content and they are direct ratio. Moreover from above figures we can find that decay atomic number of various isotopes are almost constant in two hundred years.

Atom number calculation of DU isotope

According to decay cascade of isotopes, we can gain atomic number of isotopes in DU and total atomic number versus time are shown in Fig.3(a)-3(d).



(a) (b) (c) (d)

Fig.3 Atomic number of DU and its isotopes versus time

From above figures we can find that decay atomic number of various isotopes in uranium isotope are almost constant in two hundred years. Among them, it can be seen that atomic number of U-238 is most; atomic number of U-234 is least. This explains that atomic number of isotopes is related to isotope content and they are direct ratio.

Calculation about decay heat power of WgU and DU

According to dynamic decay cascade, atomic number of nuclide is more its radioactive half-life is longer. So heat power of latter nuclide is less contributed to total heat power and they can be ignored. When calculating decay heat power of WgU and DU, the several earlier disintegrations are calculated.

Suppose atomic number of matrix is $N_i(0)$ at begin and disintegration coefficient of j grade nuclide is λ_{ij} during dynamic decay cascade process for i matrix. Disintegration formulas are shown as below:

$$\begin{cases} N_{i1}(t) = N_i(0)e^{-\lambda_{i1}t} \\ N_{i2}(t) = \lambda_{i1}N_i(0)\left(\dfrac{e^{-\lambda_{i1}t}}{\lambda_{i2}-\lambda_{i1}} + \dfrac{e^{-\lambda_{i2}t}}{\lambda_{i1}-\lambda_{i2}}\right) \\ N_{i3}(t) = \lambda_{i1}\lambda_{i2}N_i(0)\left[\dfrac{e^{-\lambda_{i1}t}}{(\lambda_{i2}-\lambda_{i1})(\lambda_{i3}-\lambda_{i1})} + \dfrac{e^{-\lambda_{i2}t}}{(\lambda_{i1}-\lambda_{i2})(\lambda_{i3}-\lambda_{i2})} + \dfrac{e^{-\lambda_{i3}t}}{(\lambda_{i1}-\lambda_{i3})(\lambda_{i2}-\lambda_{i3})}\right] \\ \cdots\cdots\cdots\cdots \\ N_{ij}(t) = \lambda_{i1}\lambda_{i2}\cdots\lambda_{ij-1}N_i(0)\left[h_{i1}e^{-\lambda_{i1}t} + h_{i2}e^{-\lambda_{i2}t} + \cdots + h_{ij}e^{-\lambda_{ij}t}\right] \end{cases}$$

Where each h_{ij} can be gained by below formulas:

$$\begin{cases} h_{i1} = 1/\left[(\lambda_{i2}-\lambda_{i1})(\lambda_{i3}-\lambda_{i1})\cdots(\lambda_{ij}-\lambda_{i1})\right] \\ h_{i2} = 1/\left[(\lambda_{i1}-\lambda_{i2})(\lambda_{i3}-\lambda_{i2})\cdots(\lambda_{ij}-\lambda_{i2})\right] \\ \cdots\cdots\cdots\cdots \\ h_{ij} = 1/\left[(\lambda_{i1}-\lambda_{ij})(\lambda_{i2}-\lambda_{ij})\cdots(\lambda_{ij-1}-\lambda_{ij})\right] \end{cases}$$

We can gain j order decay heat power of matrix nuclide M_{ij} in i branch by below formula:

$P_{ij}=E_{ij}A_{ij}=E_{ij}\lambda_{ij}N_{ij}$

Calculation about decay heat power of WgU

According to above formula, we can calculate decay heat power of each isotope in WgU. Then we can get total decay heat power of WgU per kilogram by accumulation. Decay heat power of WgU and its isotopes versus time are shown in Fig.4.

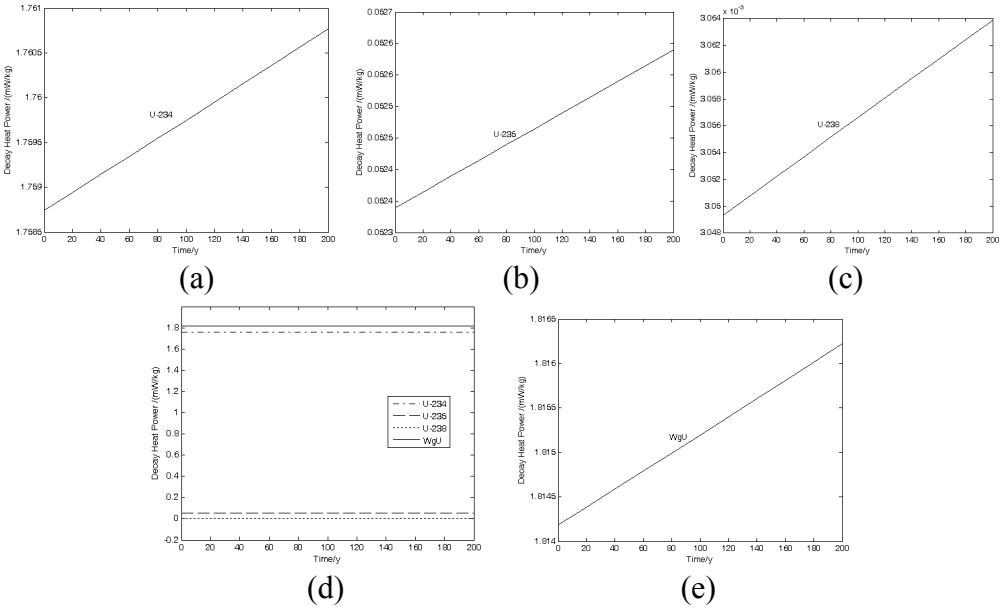


Fig.4 Decay heat power of WgU and its isotopes versus time

From Fig.4(a) it can be seen that decay heat power of U-234 increases linearly with time, but it's change is very small and is only 0.0021 milliwatt per kilogram in two hundred years. Therefore decay heat power of U-234 can be regarded as constant and is 1.76 milliwatt per kilogram. From Fig.4(b) and Fig.4(c) they can be seen that decay heat power of U-235 and U-238 both are constant and are respectively 0.0525 and 0.003058 milliwatt per kilogram. From Fig.4(d) it can be seen that U-234 contributes to decay heat power of WgU is maximum, but contribution of U-238 can be neglected. From Fig.4(e) it can be seen that decay heat power of WgU increases linearly with time, but it's change is very small and is only 0.002 milliwatt per kilogram in two hundred years. Therefore decay heat power of WgU can be regarded as constant and is 1.8152 milliwatt per kilogram.

Calculation about decay heat power of DU

According to above formula, we can calculate decay heat power of each isotope in DU, then we can gain total decay heat power of DU per kilogram by accumulation. Decay heat power of DU and its isotopes versus time are shown in Fig.5.

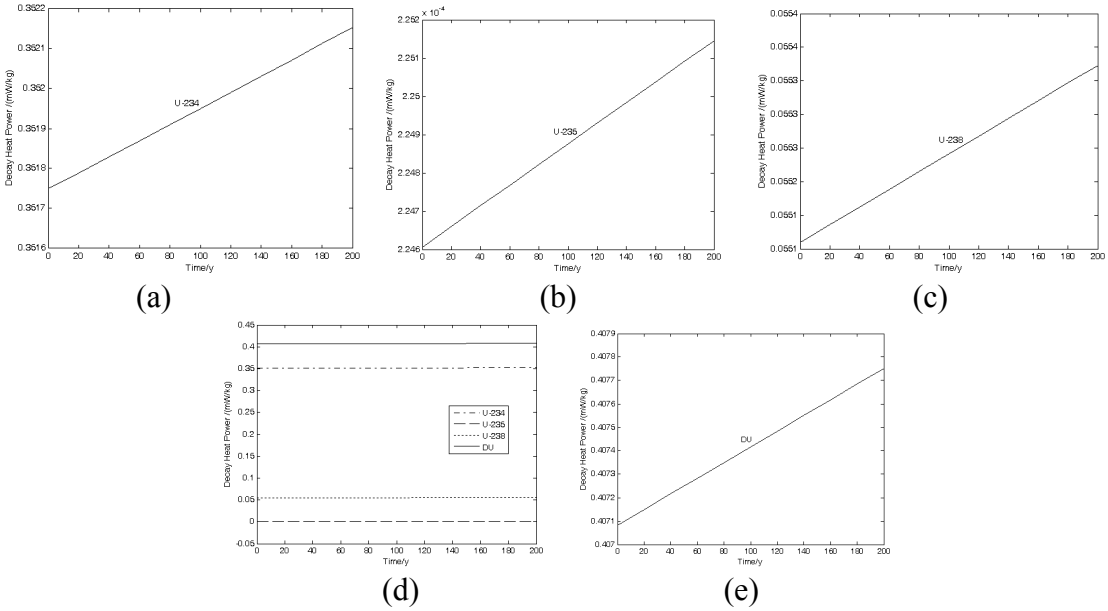


Fig.5 Decay heat power of DU and its isotopes versus time

From Fig.5(a) it can be seen that decay heat power of U-234 increases linearly with time, but it's change is very small and is only 0.0005 milliwatt per kilogram in two hundred years. Therefore decay heat power of U-234 can be regarded as constant and is 0.352 milliwatt per kilogram. Similarly from Fig.5(b) and Fig.5(c) they can be seen that decay heat power of U-235 and U-238 both are constant and are respectively 0.000225 and 0.0553 milliwatt per kilogram. From Fig.5(d) it can be seen that U-234 contributes to decay heat power of DU is maximum, but contribution of U-235 can be neglected. From Fig.5(e) it can be seen that decay heat power of DU increases linearly with time, but it's change is very small and is only 0.002 milliwatt per kilogram in two hundred years. Therefore decay heat power of DU can be regarded as constant and is 0.4075 milliwatt per kilogram.

Conclusions

(1) Decay heat power of WgU is approximately 1.8152 milliwatt per kilogram. Among them, contribution of U-234, U-235 and U-238 is respectively 1.76, 0.0525 and 0.003058 milliwatt per kilogram.

(2) Decay heat power of DU is approximately 0.4075 milliwatt per kilogram. Among them, contribution of U-234, U-235 and U-238 is respectively 0.352, 0.000225 and 0.0553 milliwatt per kilogram.

(3) U-234 contributing to decay heat power of WgU and DU is maximum. However U-238 contributing to decay heat power of WgU can be neglected. U-235 contributing to decay heat power of DU can be neglected. These explain that U-235 and U-238 contributing to decay heat power of uranium is related to their content in nuclear material.

(4) If some nuclear weapon has ten kilogram uranium, decay heat power of uranium is only ten milliwatt more. So small power is equivalently that 10 milliwatt electric lamp can emit heat. It is thus clear that decay heat power of uranium contributing to nuclear weapon can be neglected.

References

[1] Zhengming Gao, Bin He, Juan Zhao. Thermal Dynamics Study of Nuclear Explosive Device[J]. Atomic Energy Science and Technology, 2010,44(3):331-338(In Chinese).

[2] Gang Xiao, Kaiwen Zhu. Numerical Simulation for Three Dimensional Temperature Fields of Composite Body with Plutonum-239[J].Acta Armamentar, 2005,26(1):140-142(In Chinese).

[3] Jun Wu. Numerical simulate on detection technique of nuclear bomb[D]. Chinese Academy of Engineering Physics, 2003(In Chinese).

[4] Hua Chen, Xinxian Li, Caike Wang. Study on radiation field of special nuclear material[C]. 6th academic seminar on nuclear monitor, 2005:25-29(In Chinese).

[5] Xin Tian, Shanqiang Wang.Calculation of Radiant Field about Special Nuclear Material[R]. The seventh session of national nuclear survey academic conference, 2009:210-217(In Chinese).

[6] Authorized team of nuclide diagram. Usual datasheet of nuclide[M].Beijing: Atomic Energy Publisher, 1977:500-502(In Chinese).

[7] Yansen Wang, Futing Shi. Atomic Nuclear Physics[M]. Beijing: Atomic Energy Publisher, 1998:138-139(In Chinese).

[8] Yunzuo Liu. Disintegration diagram of usual radioactive nuclide[M]. Beijing: Atomic Energy Publisher, 1982:418-446(In Chinese).

Advanced Materials Research Vol. 936 (2014) pp 515-522
© (2014) Trans Tech Publications, Switzerland
doi:10.4028/www.scientific.net/AMR.936.515

Hydrogen Storage Mechanism of Fe_3O_4: A First-principles Study

Hao Zhang[1, a] , Nanpu Cheng[1,b], zhiqian Chen[1,c] and Qun Hui[1,d *]

[1]Faculty of Materials and Energy, Southwest University, Chongqing, 400715, China

[a]zhangh710021@163.com, [b]chen_zq@swu.edu.cn, [c]cheng_np@swu.edu.cn, [d]qhui01@swu.edu.cn

Keywords: Hydrogen

Abstract: The adsorption and dissociative adsorption of a hydrogen molecule on Fe_{tet1}- terminated Fe_3O_4 (111) surfaces are investigated within the framework of density function theory. The surface Fe_{tet1} atom site with the parallel mode of hydrogen molecule is found to be the most stable equilibrium adsorption state. The most possible dissociative adsorption pathway of a hydrogen molecule needs an energy barrier of 2.85 or 2.87 eV at the surface O_a or O_c atom site, and generates a water molecule, remarkably in agreement with Otsuka.K's conclusion on the reaction condition and hydrogen storage mechanism of Fe_3O_4 from microscopic point of view. The calculation of the electronic properties of the termination states with the adsorption and dissociative adsorption of a hydrogen molecule shows strong interactions between atomic hydrogen and Fe_3O_4 (111) surface.

Introduction

Magnetite Fe_3O_4, a promising alternative to hydrogen storage proposed by Otsuka et al [1-3], has attracted extensive attention. Basing on the old steam-iron process to produce hydrogen-rich fuel gas [4], it achieves the hydrogen storage-release processes by a simple redox reaction as following procedure:

Step1: Chemical hydrogen storage (reduction)

$$Fe_3O_4+4H_2 \rightarrow 3Fe+4H_2O \quad (1)$$

Step2: Hydrogen recovery (oxidization)

$$3Fe+4H_2O \rightarrow Fe_3O_4+4H_2 \quad (2)$$

Due to the fact that the standard experimental methods, such as low-energy electron diffraction, X-ray photo-electron spectroscopy and Auger electron spectroscopy, are not able to detect the positions of hydrogen atoms, experimental researches on the adsorptions of hydrogen atoms and molecules at Fe_3O_4 surface are very limited. The theoretical calculations are even less. X. Sun et al [5] confirmed that the adsorption of an atomic hydrogen on Fe_3O_4 (100) is chemical sorption and induces the reappearance of half-metal behavior in the surface structure around the Fermi level by a density-functional theory (DFT) calculation. To understand the surface structure and activity which are essential for the catalytic mechanism of water gas shift (WGS) and Fischer-Tropsch synthesis (FTS) processes, Y. Tao et al [6] investigated the dissociation of hydrogen molecules on Fe_{tet}- and Fe_{oct}- terminated Fe_3O_4 (111) surfaces at different coverage values based on DFT and drew the conclusion that the most favored adsorption of a hydrogen molecule on Fe_{tet}- terminated surface is homolytic and dissociative on two non-adjacent O atoms with more dangling bonds, which is not consistent with the conclusion obtained by the redox reaction.

In this work, we report a DFT study on atomic and molecular hydrogen adsorption on Fe_{tet1}-terminated Fe_3O_4 (111) surfaces to understand the reaction condition and hydrogen storage mechanism of Fe_3O_4 from microscopic point of view. The Linear synchronous transit/quadratic synchronous transit (LST/QST) methods are used to search for the transition states. The activation energies and energy barriers are calculated to determine the dissociative adsorption pathway. In

addition, the density of the states of Fe_{tet1}- terminated Fe_3O_4 (111) surface including the adsorption and dissociative adsorption of a hydrogen molecule are analyzed in detail to understand the interaction between atomic hydrogen and Fe_3O_4 (111) surface.

Computation Models and Methods

All calculations are performed using the plane-wave pseudopotential method based on DFT. This method is implemented in the CASTEP (Cambridge Sequential Total Energy Package) [7] code. The Perdew-Burke-Ernzerhof (PBE) version of the generalized gradient approximation (GGA) [8-11] is used for the exchange and correlation effects. The interaction between valence electron and ion core is described by ultrasoft pseudopotential [12], and the electronic wave functions are expanded in a plane wave basis set with an energy cut-off of 340 eV to ensure convergence [13]. Brillouin zone integration is carried out using K- point sampling, which is generated by the Monkhorst-Pack scheme [14]. For Fe_3O_4 bulk model and 1×1 Fe_3O_4 (111) surface slab model, the K- point grid are 2×2×2 and 2×2×1, respectively. The density-mixing scheme based on the Pulay algorithm [15] is used for self-consistent-field (SCF) calculation. The SCF tolerance is set at 1×10^{-6}eV/atom. The spin polarization of Fe atom in Fe_3O_4 is considered in the calculations as a spin polarization has significant effect on magnetic system [16,17]. The pseudopotentials are obtained by including a partial core charge in the treatment of the exchange and correlation in spin-polarized calculation to account for the nonlinear core corrections [18].

Fe_3O_4 has a cubic inverse spinel structure with a lattice parameter of 8.394 Å [19]. Fe_3O_4 (111) surface is a predominant natural growth face and may be more active for reactions than other surfaces [20, 21]. There are six non-equivalent terminations along Fe_3O_4 (111) stacking sequence. Fe_{tet1}- and Fe_{oct2}- terminated surfaces, which have the least dangling bonds, are proposed to be the most stable terminations. The calculated energy difference of the two terminated surfaces is only 0.03eV [22] indicating the possibility of their coexistence. In this work, the Fetet1- terminated surface is chosen to investigate the adsorption of hydrogen atoms and molecules. For each calculation, a periodic eight-layer slab model in which the top four layers of atoms are relaxed and the bottom four layers of atoms are fixed in their optimized bulk positions is constructed and separated from its neighboring image in the direction normal to the surface by a vacuum spacing of 10 Å. The adsorbed hydrogen atom or molecule is on the one side of the slab and fully relaxed with the top four layers of atoms.

The adsorption energies of surfaces with an adsorbed hydrogen molecule and atom, E_{ads-H_2/Fe_3O_4} and E_{ads-H/Fe_3O_4}, are defined as:

$$E_{ads-H_2/Fe_3O_4} = E_{H_2/Fe_3O_4} - (E_{Fe_3O_4} + E_{H_2}) \tag{3}$$

and

$$E_{ads-H/Fe_3O_4} = E_{H/Fe_3O_4} - (E_{Fe_3O_4} + E_H) \tag{4}$$

Where E_{H_2} and E_H are the total energies of a hydrogen molecule and atom, respectively; $E_{Fe_3O_4}$ is the total energy of Fe_3O_4 (111) slab without adsorbed species; and E_{H_2/Fe_3O_4} and E_{H/Fe_3O_4} are the total energies of surfaces with an adsorbed hydrogen molecule and atom, respectively. With this definition, a negative value of E_{ads} indicates that the adsorption is an exothermic (stable) reaction, and a positive value indicates the adsorption is an endothermic (unstable) reaction. The calculated adsorption energies do not include zero point energy corrections.

Results and Discussion

The Optimization of Fe_{tet1}- Terminated Fe_3O_4 (111) Clean Surfaces

The total energies of an isolated hydrogen atom and molecule are calculated in an orthorhombic cell of 10×10×10 Å3. The bond length r(H-H) and bond dissociative adsorption energy E_{BDE} of a hydrogen molecule are 0.0747 nm and 433.9 kj/mol, which are in good agreement with the experimental values of 0.0740 nm[23] and 436.1 kj/mol[24]. The calculated lattice constant of bulk Fe_3O_4 and magnetic moments are 0.8350 nm and 4.0 uB in comparison with the experimental value of 0.8394 nm [19] and 4.1 uB [25]. The deviation of the calculated values from the experimental values is only around 1%. The results allow us to be confident in making the next calculations, namely the interactions of hydrogen atoms with Fe_3O_4 (111) surface and the interactions of hydrogen molecules with Fe_3O_4 (111) surface.

The model of Fe_{tet1}- terminated Fe_3O_4 (111) surfaces is constructed as shown in Fig.1 It consists of eight layers of atoms in which Fe_{tet1} atom bonds with three O atoms in the next layer consisting of four O atoms and forms three Fe_{tet1}-O bonds which have nearly the same bond lengths. It is clearly seen that both Fe_{tet1} atom and the four O atoms are exposed nearly in the surface plane. The possible adsorption sites Fe_{tet1}, O_a, O_b, O_c and O_d are also shown in Fig. 1.

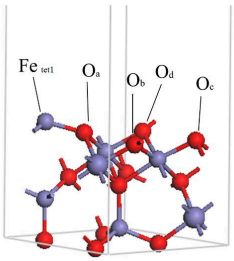


Fig. 1 The optimized configurations of Fe_{tet1}- and Fe_{oct2}- terminated Fe_3O_4 (111) clean surfaces and the presentation of the possible adsorption sites.

Adsorption of a Hydrogen Atom on Fe_{tet1}- terminated Fe_3O_4 (111) Surfaces

The calculated adsorption energies, adsorption heights and distances of H atom adsorbed on the possible adsorption sites on Fe_{tet1}- terminated surfaces are listed in Table 1. The results indicate that the surface O_c atom site is the most stable adsorption site. The adsorption energies are -3.15eV, and the distances are 0.0980 nm.

TABLE 1. THE CALCULATED ADSORPTION ENERGIES (E_{ADS}), ADSORPTION HEIGHTS (H) AND DISTANCES (D) OF A HYDROGEN ATOM ADSORBED ON THE POSSIBLE ADSORPTION SITES IN FE_{TET1}-TERMINATED SURFACE.

Models	H[nm]	D[nm]	E_{ads}[eV]
On-Fe_{tet1}	0.1585	0.1585	-1.79
On-O_a	0.0822	0.0983	-2.93
On-O_b	0.0635	0.0985	-2.81
On-O_c	0.0979	0.0980	-3.15
On-O_d	0.0759	0.0984	-2.83

Adsorption of a hydrogen molecule on Fe_{tet1}- terminated Fe_3O_4 (111) surfaces

In the adsorption of a hydrogen molecule on Fe_{tet1}- terminated Fe_3O_4 (111) surfaces, parallel and vertical types are considered for each possible adsorption site. Parallel type is the side-on type that an adsorbed hydrogen molecule is parallel to an adsorption atom site (denoted as E-), and vertical type is the end-on type that an adsorbed hydrogen molecule is vertical to an adsorption atom site (denoted as S-). They are depicted in Fig. 2. For Fe_{tet1}- terminated surface, there are ten adsorption models, denoted as E1-O_a, E1-O_b, E1-O_c, E1-O_d, E1-Fe_{tet1}, S1-O_a, S1-O_b, S1-O_c, S1-O_d, S1-Fe_{tet1}.

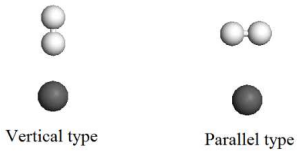


Fig. 2 Parallel type and vertical type of a hydrogen molecule adsorbed on an adsorption site. The white spheres represent hydrogen atoms, and the gray spheres represent adsorption atom sites.

The calculated adsorption energies, H-H bond lengths, distances between H' atom of the adsorbed hydrogen molecule and the adsorption sites, and distances between H" atom of the adsorbed hydrogen molecule and the adsorption sites are given in Table 2 Obviously, the adsorptions of an hydrogen molecule on the possible adsorption sites in the surface are physical adsorptions, less stable than those of a hydrogen atom. In the case of model E1-O_c, the optimized adsorption energy is positive and the hydrogen molecule is inclined to keep away from the surface. In the each case of model E1-O_a, E1-O_b, E1-O_d and E1-Fe_{tet1}, the hydrogen molecule is adsorbed in oriented arrangement with respect to the surface. The H-H bond lengths in the above four adsorption models change slightly, ranging from 0.0756 to 0.0769 nm. In the each case of model S1-O_c and S1-O_d, the hydrogen molecule is inclined to keep away from the surface, and the adsorption energy is positive, indicating the adsorption model is unstable. In the case of model S1-Fe_{tet1}, the H-H bond length elongates to 0.0771 nm, and the adsorption energy is the lowest (-0.38 eV), indicating model S1-Fe_{tet1} is the most stable.

TABLE 2. THE CALCULATED ADSORPTION ENERGIES (E_{ADS}), BOND LENGTHS OF H-H BOND (D_{H-H}), DISTANCES BETWEEN H' ATOM OF THE ADSORBED HYDROGEN MOLECULE AND THE ADSORPTION SITES ($D_{M-H'}$), AND DISTANCE BETWEEN H" ATOM OF THE ADSORBED HYDROGEN MOLECULE AND THE ADSORPTION SITES ($D_{M-H"}$) FOR FE_{TET1}- TERMINATED SURFACE.

Mode	D_{H-H}[nm]	$D_{M-H'}$[nm]	$D_{M-H"}$[nm]	E_{ads}[eV]
E1-O_a	0.0758	0.3131	0.3404	-0.18
E1-O_b	0.0756	0.2477	0.2961	-0.23
E1-O_c	0.0756	0.2138	0.2894	0.01
E1-O_d	0.0769	0.2250	0.2839	-0.18
E1-Fe_{tet1}	0.0751	0.1995	0.2736	-0.17
S1-O_a	0.0761	0.2591	0.2669	-0.27
S1-O_b	0.0755	0.2835	0.3055	-0.07
S1-O_c	0.0770	0.2257	0.2297	0.21
S1-O_d	0.0747	0.2465	0.2551	0.02
S1-Fe_{tet1}	0.0771	0.1978	0.1988	-0.38

Dissociative adsorption of a hydrogen molecule on Fe_{tet1}- terminated Fe_3O_4 (111) surfaces

To study the dissociative adsorptions of an hydrogen molecule on Fe_{tet1}- terminated Fe_3O_4 (111) surfaces, the most stable adsorption model of an hydrogen molecule calculated in section 3.3 is considered as the initial reactant, and the possible final geometric models of the dissociative adsorption are proposed as the products. The LST/QST methods are used to search for the transition states. The activation energies and energy barriers are calculated to determine the possible dissociative adsorption pathway.

Three possible dissociative adsorption models are proposed after performing a quantitative calculation of the adsorption energies of different dissociative adsorption models: (a) dissociative adsorption of a hydrogen molecule on the surface O_a atom site; (b) dissociative adsorption of a hydrogen molecule on the surface O_c atom site; (c) dissociative adsorption of a hydrogen molecule on both the surface O_a and O_c atom sites. The optimized geometric configurations are depicted in Fig. 3.

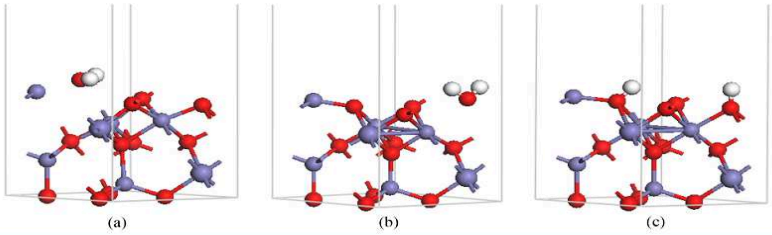


Fig. 3 The optimized geometric configurations: (a) dissociative adsorption of a hydrogen molecule on the surface O_a atom site; (b) dissociative adsorption of a hydrogen molecule on the surface O_c atom site; (c) dissociative adsorption of a hydrogen molecule on both the surface O_a and O_c atom sites. The gray spheres represent H atoms, the blue spheres stand for Fe atoms and the red spheres refer to O atoms.

The calculated total energies, adsorption energies, distances between the two H atoms of the adsorbed H_2, distances between H' atom of the adsorbed H_2 and the adsorption sites, and distance between H" atom of the adsorbed H_2 and the adsorption sites are listed in Table 3 for the three possible dissociative adsorption models. It is found that the adsorption energies of the three models are much higher than those of adsorption models calculated in section 3.3. The value range of the adsorption energies indicates these dissociative adsorptions are chemisorptions. In the dissociative adsorption of a hydrogen molecule on O_a (or O_c) atom site, the original O-Fe^{3+} and H-H bond are broken, and the two H atoms are both adsorbed on O_a (or O_c) atom site to form a water molecule as the bond length and bond angle (0.098nm and 107.9°) are in the range of those at the ground state (Normally for a water molecule, O-H bond length is between 0.957 Å ~1.00 Å and H-O-H bond angle is between 104.52° ~109.5°). In the dissociative adsorption of a hydrogen molecule on both O_a and O_c atom sites, the hydrogen molecule dissociates into two separate hydrogen atoms which are adsorbed on O_a and O_c atom sites respectively. The total energy and adsorption energy are the lowest, indicating the dissociative adsorption is the most stable. It is unclear, however, whether the dissociative adsorption is ease to occur. The possible dissociative adsorption pathways are then analyzed for this purpose.

The optimized S1-Fe_{tet1} adsorption model is chosen as the initial state (IS) since it is the most stable adsorption model for a hydrogen molecule adsorbed on Fe_{tet1}- terminated surface, and the three possible dissociative adsorption models are considered as the final states (FS). The complete LST/QST methods are used to search for the transition states. The activation energies and energy barriers are calculated to determine the most possible dissociative adsorption pathway of a hydrogen molecule. The calculated results are shown in Table 4 and the geometry of the calculated dissociative adsorption pathways are plotted in Fig.4 in which the IS, transition states, and FS are shown as insets. In S1-Fe_{tet1} adsorption model, the hydrogen molecule adsorption is physical adsorption with the H-H bond length 0.0771 nm (see the illustration in section 3.3). Only one transition state along each pathway occurs. The hydrogen molecule moves to the surface, and the distance between the two hydrogen atoms is elongated to 0.1337, 0.1433 and 0.2495 nm in each transition state respectively. The calculated energy barrier of S1-Fe_{tet1}--O_a and O_c dissociative adsorption pathway is 5.201 eV, higher than those of S1-Fe_{tet1}--O_a (2.850 eV) and S1-Fe_{tet1}--O_c (2.871 eV) dissociative adsorption pathways. Hence, S1-Fe_{tet1}--O_a and S1-Fe_{tet1}--O_c dissociative adsorption pathways have priority over S1-Fe_{tet1}--O_a and O_c dissociative adsorption pathway under an external condition. In the two most possible dissociative adsorption pathways, water molecules are generated on Fe_{tet1}- terminated surface, remarkably in agreement with Otsuka.K's conclusion on the reaction condition and hydrogen storage mechanism of Fe_3O_4 from microscopic point of view.

TABLE 3. THE CALCULATED TOTAL ENERGIES (E_{TOTAL}), ADSORPTION ENERGIES (E_{ADS}), DISTANCES BETWEEN THE TWO H ATOMS OF THE ADSORBED H_2 (D_{H-H}), DISTANCES BETWEEN H' ATOM OF THE ADSORBED H_2 AND THE ADSORPTION SITES ($D_{H'-O}$), AND DISTANCES BETWEEN H" ATOM OF THE ADSORBED H_2 AND THE ADSORPTION SITES ($D_{H"-O}$) FOR THE THREE POSSIBLE DISSOCIATIVE ADSORPTION MODELS OF A HYDROGEN MOLECULE ON FE_{TET1}- TERMINATED FE_3O_4 (111) SURFACE.

Models	E_{total}[eV]	E_{ads}[eV]	D_{H-H}[nm]	$D_{H'-O}$[nm]	$D_{H"-O}$[nm]
O_a	-11321.24	-0.77	0.1609	0.0985	0.0976
O_c	-11321.20	-0.73	0.1594	0.1000	0.0971
O_a and O_c	-11322.02	-1.55	0.2978	0.0984	0.0975

TABLE 4. THE CALCULATED TOTAL ENERGIES OF THE TRANSITION STATES (E_T), ENERGY BARRIERS (E_B) AND ACTIVATION ENERGIES (E_A) FOR THE THREE POSSIBLE DISSOCIATIVE ADSORPTION PATHWAYS OF A HYDROGEN MOLECULE ON FE_{TET1}- TERMINATED FE_3O_4 (111) SURFACE.

Pathways	E_t[eV]	E_b[eV]	E_a[eV]
S1-Fe_{tet1}--O_a	-11317.997	2.850	-0.5010
S1-Fe_{tet1}--O_c	-11317.976	2.871	-0.5010
S1-Fe_{tet1}--O_a and O_c	-11315.709	5.201	-1.1858

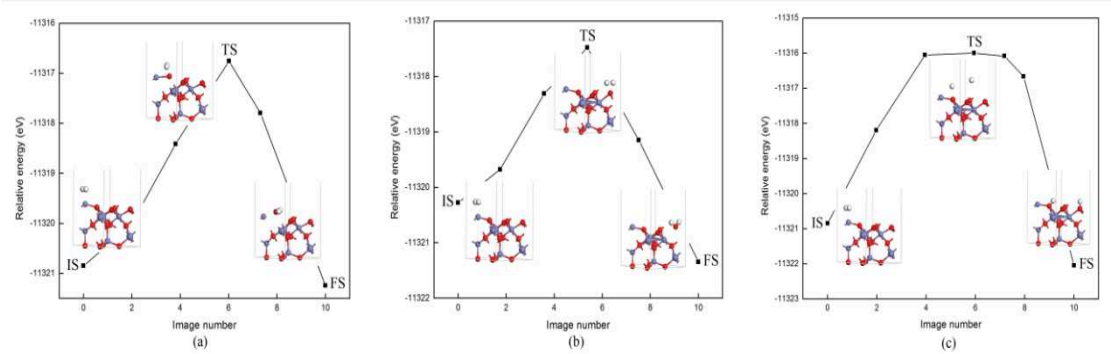


Fig.4 Schematics of the three possible dissociation pathways of a hydrogen molecule on Fe_{tet1}- terminated Fe_3O_4 (111) surface:（a）S1-Fe_{tet1}--O_a;（b）S1-F e_{tet1}--O_c;（c）S1-Fe_{tet1}--O_a and O_c.

Electronic structures of a hydrogen molecule adsorption and dissociative adsorption on Fe_{tet1}-terminated Fe_3O_4 (111) surface

The density of states (DOS) of a Fe_{tet1}- terminated Fe_3O_4 (111) surface and free H_2, the partial density of states (PDOS) of Fe(III) atoms and O atoms are presented in Fig. 5a. The valence bands ranging from -7.5eV~2.5eV are mainly composed of the 2p states of O atoms and 3d states of Fe(III) atoms, the valence bands ranging from -20eV~-18eV are mainly contributed by the 2s states of O atoms and 3d states of Fe (III) atoms, and the valence bands ranging from -18eV~-15eV are mainly caused by the 3d states of Fe (II) atoms. Fe (II) atoms have no effect on the adsorption of hydrogen molecule and are not considered. The DOS values of a free H_2 are near the Fermi level. The DOS of a Fe_{tet1}- terminated Fe_3O_4 (111) surface in which an adsorbed H_2 is vertical to Fe_{tet1} atom site (S1-Fe_{tet1} model) and the adsorbed H_2, the PDOS of Fe(III) atoms and O atoms are presented in Fig. 5b. The DOS values of the adsorbed H_2 move from the Fermi level to lower energy region. The DOS of the surface has a weak peak near -7.5eV which is contributed by the 1s states of the atoms of H_2 and 3d states of Fe (III) atoms, indicating the H_2 is adsorbed on Fe_{tet1} atom site. The DOS of a Fe_{tet1}-terminated Fe_3O_4 (111) surface in which an H_2 is dissociated and adsorbed on O_a (or O_c) atom site and the adsorbed H_2, PDOS of Fe(III) atom and O atom are presented in Fig.5c (or Fig. 5d). The valence bands ranging from -24 eV and -22 eV are mainly dominated by the 1s states of H atoms and 2s states of O atoms, and the valence bands ranging from -11 eV and -8 eV are mainly dominated by the 1s states of H atoms and 2p states of O atoms, indicating the dissociated H atoms are adsorbed on the surface O atoms. The electronic structure of Fe_{tet1}- terminated Fe_3O_4 (111) surface is obviously changed with the adsorption and dissociative adsorption of H_2. The 1s states of H atoms form a series of hybrid peaks with the 3d states of Fe (III) atoms, 2s and 2p states of O atoms, indicating that there are interactions between H atoms and Fe_{tet1}- terminated Fe_3O_4 (111) surface.

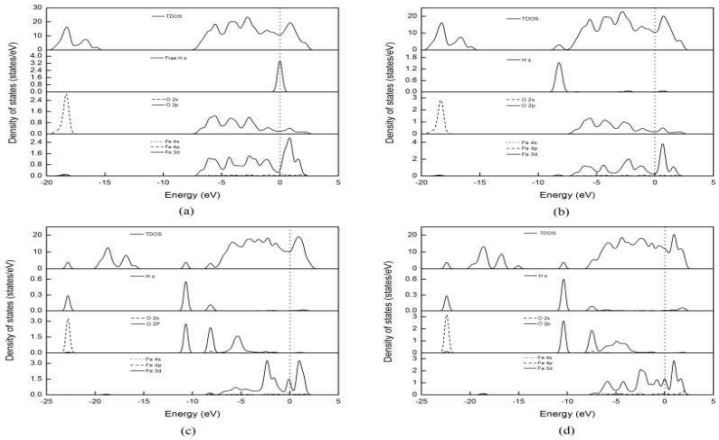


Fig. 5 (a) The DOS of a free H_2 and clean Fe_{tet1}- terminated Fe_3O_4 (111) surface; (b) The DOS of S1-Fe_{tet1} model; (c) The DOS of O_a dissociative adsorption model; (d) The DOS of O_c dissociative adsorption model.

Summary

A detailed density functional study is performed on the adsorption and dissociative adsorption of an H_2 on Fe_{tet1}- terminated Fe_3O_4 (111) surfaces. Our results show clearly that S-Fe_{tet1} model is the most stable adsorption configurations for an H_2 on Fe_{tet1}- terminated Fe_3O_4 (111) surfaces with adsorption energy of -0.38eV. The dissociative adsorption pathway of an H_2 is from S1-Fe_{tet1} to O_a or O_c via a transition state with adsorption energy of -0.77 eV or -0.73eV. Water molecules are generated on Fe_{tet1}- terminated surface, remarkably in agreement with Otsuka.K's conclusion. Finally, the density of states of an H_2 adsorption and dissociative adsorption on the termination surface is calculated, indicating that the models of dissociative adsorption of H_2 on Fe_3O_4 (111) surface are more tempting.

Acknowledgments

This work is supported by the Fundamental Research Funds for the Central Universities (Grant No. XDJK2010C017) and National Natural Science Foundation of China (Grant No. 51171156).

References

[1] Otsuka K, Yamada C, Kaburagi T, et al. Hydrogen storage and production by redox of iron oxide for polymer electrolyte fuel cell vehicles, International journal of hydrogen energy. 28 (2003) 335-342

[2] Otsuka K, Kaburagi T, Yamada C, et al. Chemical storage of hydrogen by modified iron oxides, Journal of power sources. 122 (2003) 111-121

[3] Takenaka S, Kaburagi T, Otsuka K, et al. Storage and supply of hydrogen by means of the redox of the iron oxides modified with Mo and Rh species, J. Catal. 228 (2004) 66-74.

[4] Hacker V, Faleschini G, et al. Usage of biomass gas for fuel cells by the SIR process, J. Power Sources. 71 (1998) 226-230.

[5] Sun X, Kurahashi M, Pratt A, et al. First-principles study of atomic hydrogen adsorption on Fe3O4 (100), Surface Science. 605 (2011) 1067-1073

[6] Yang T, Wen X D, Huo C F, et al. Structure and energetics of hydrogen adsorption on Fe3O4 (111), Journal of Molecular Catalysis A: Chemical. , 302 (2009) 129-136

[7] Perdew J P, Burke K, Ernzerhof M. Phys.Rev.Lett. 77 (1996) 3865-3868.

[8] Perdew J P, Burke K, Ernzerhof M. Phys.Rev.Lett. 78 (1997) 1396.

[9] Perdew J P, Ruzsinszky A, Tao J, et al. J.Chem.Phys. 123 (2005) 62201.

[10] Perdew J P, Burke K, Wang Y, Phys.Rev.B. 54 (1996) 16533.

[11] Milman V, Winkler B, White J A, et al. Electronic structure, properties, and phase stability of inorganic crystals: A pseudopotential plane-wave study, Int.J.Quantum Chem. 77(2000) 895-910.

[12] Vanderbilt D. Soft self-consistent pseudopotentials in a generalized eigenvalue formalism. Phys.Rev.B. 41 (1990) 7892–7895.

[13] Lin J S, Qteish A, Payne M C, et al. Optimized and transferable nonlocal separable ab initio pseudopotentials, Physical Review B. 47 (1993) 4174- 4180

[14] Monkhorst H J, Pack J D. Special points for Brillouin-zone integrations, Physical Review B. 13 (1976) 5188-5192

[15] Pulay P. Ab initio calculation of force constants and equilibrium geometries in polyatomic molecules: I, Theory, Molecular Physics. 17 (1969) 197-204

[16] Nayak S K, Nooijen M, Bernasek S L, et al. Electronic structure study of CO adsorption on the Fe (001) surface, The Journal of Physical Chemistry B. 105 (2001) 164-172

[17] Cheng H, Reiser D B, Dean S W, et al. Structure and energetics of iron pentacarbonyl formation at an Fe(100) surface, The Journal of Physical Chemistry B. 105 (2001) 12547-12552

[18] Louie S G, Froyen S, Cohen M L. Nonlinear ionic pseudopotentials in spin-density-functional calculations, Physical Review B. 26 (1982) 1738-1742

[19] Fleet M E. The structure of magnetite, Acta Crystallographica Section B: Structural Crystallography and Crystal Chemistry. 37(1981): 917-920

[20] Henrich V E, Shaikhutdinov S K. Atomic geometry of steps on metal-oxide single crystals, Surface science. 574 (2005) 306-316

[21] Zhu L,Yao K L,Liu Z L. First-principles study of the polar (111)surface of Fe3O4, Phys Rev B. 74 (2006) 035409-035418.

[22] Yang T, Wen X D, Ren J, et al. Surface structures of Fe3O4 (111),(110), and (001): A density functional theory study, Journal of Fuel Chemistry and Technology. 38 (2010) 121-128

[23] Wu G, Zhang J, Wu Y, et al. The effect of defects on the hydrogenation in Mg (0001) surface, Applied Surface Science. 256 (2009) 46-51

[24] Kerr J A. CRC handbook of chemistry and physics 1999-2000: a ready-reference book of chemical and physical data, in: D.R. Lide (Ed.), CRC Handbook of Chemistry and Physics, 81st ed., CRC Press, Boca Raton, FL, USA, 2000

[25] Szotek Z, Temmerman W M, Svane A, et al. Ab initio study of charge order in Fe3O4, Physical Review B. 68 (2003) 054415-054423

Advanced Materials Research Vol. 936 (2014) pp 523-528
© (2014) Trans Tech Publications, Switzerland
doi:10.4028/www.scientific.net/AMR.936.523

Phase-field crystal study for the effect of heating rate on the premelting of grain boundary

Yanli Lu[1,a], Tingting Hu[1,b] and Hong Mu[1,c]

[1]State Key Laboratory of Solidification Processing, Northwestern Polytechnical University, Xi'an 710072, China

[a] luyanli@nwpu.edu.cn, [b] tingting@mail.nwpu.edu.cn,[c] hongmu@mail.nwpu.edu.cn

Keywords: heating rate; grain boundary premelting; phase-field crystal; liquid film width

Abstract. The effect of heating rates on the premelting of grain boundary (GB) is investigated by the phase-field crystal method. The microstructure evolution of premelting under different heating rates are discussed, and the film width of GB is quantitatively calculated in terms of the excess mass method. Results show that the liquid film appears as the melting point (T_m) is approached from below and that the film thickness is affected by heating rate. In heating process, at the same temperature (close to T_m), the liquid film width is larger when the temperature increases with lower rate. In insulation process, the liquid film thickness increase until to its equilibrium value with holding time prolonging. For low-angle GBs, the higher heating rate the system has during heating stage, the lager equilibrium value of liquid film will be reached during insulation stage. For high-angle GBs, the liquid film thickness has the same equilibrium value during the insulation process although the heating rate is different during heating process.

Introduction

The grain boundary (GB) is the area where numerous phase transformations easily occur, leading to dramatic changes on the mechanical and physical properties of polycrystalline materials [1,2]. The liquid film at GB is preformed at temperatures below the melting point, which is called GB premelting[3]. The presence of premelting significantly affects the strength and fracture properties of polycrystalline materials. The premelting of GB are research hot spots in materials [4, 5]. Heating rate is an important factor of the GB premelting. Observing GB directly by experimental methods is difficult because it is only a few atoms thick. Hence, solving GB problems through computer simulation presents unique advantages. Keblinnski et al. [6] proved through molecular dynamics simulation that a GB disorder layer exists at different temperatures above and below the melting point. Tang et al. [7] characterized the morphology of the film between the subsolidus during premelting transition. Kikuchi and Cahn [5] approximately estimated the thermodynamic properties of GB premelting using a lattice gas model and a cluster variation approximation.

Although the above methods have been used to confirm and simulate the GB premelting, they did not quantitatively study the relationship between the width of GB premelting layer and atomic GB structure because of the limitation imposed by these models. Phase-field crystal (PFC) inspired from the density functional theory [8] has shown unique advantages of resolving the atomic scale density-wave structure of polycrystalline materials [9-11]. The film width can be quantified and its relationship with atomic GB structure can be clarified by studying the thermodynamic properties of premelted GB because the order parameter of PFC is the periodic local number density of atoms. In this work, we used PFC to study the microstructure evolution of premelting under different heating rates and mainly discussed the effect of heating rates on the film width of GB.

Theoretical Modeling

PFC model

PFC model describes periodic structure on atomic length and diffusive timescales by introducing a free energy that is functional of the local-time-averaged density field ρ(**r**,*t*). We consider the simplest PFC model defined by the dimensionless free-energy functional [9]:

$$F = \int d\vec{r}\left\{\frac{\rho}{2}\left[r + (\nabla^2 + 1)^2\right]\rho + \frac{1}{4}\rho^4\right\} \tag{1}$$

where F is the dimensionless free energy; ρ represents the atomic density field; r is variable related to temperature, the larger value of r corresponds to the higher temperature.

The density is uniform in the liquid. The free energy function reaches the minimum through $\rho(x, y)$. In this instance, we will use the one-mode approximation for the density field. Then, the density for two-dimensional hexagonal structure can be written as: $\rho_s(x, y) = \overline{\rho} + A_t[\cos(qx)\cos(qy/\sqrt{3}) - 1/2\cos(2qy/\sqrt{3})]$. where A_t is density wave amplitude function of hexagonal phase. Substituting the expression into Eq. (1) and minimizing with A_t and q .we can obtain $A_t = 4/5(\overline{\rho} \pm 1/3\sqrt{-15r - 36\overline{\rho}^2})$,where the $\pm$ signs are for positive and negative $\overline{\rho}$, respectively, and $q = \sqrt{3}/2$. The phase diagram of this model has been discussed previously in Ref. [9], and we know that the phase diagram is symmetric in $\overline{\rho}$.

Numerical methods and the choice of simulation parameters

The standard equation of motion of the PFC model is

$$\frac{\partial \rho}{\partial t} = \nabla^2\left(\frac{\delta F}{\delta \rho}\right) = (1 + r)\nabla^2\rho + 2\nabla^4\rho + \nabla^6\rho + \nabla^2\rho^3 \tag{2}$$

Eq. (2) reflects the fact that the density field ρ is a locally conserved quantity and they achieve their equilibrium state through self-diffusion. The Eq. (2) can be efficiently solved by using a semi-implicit Fourier spectral formulation.

The simulation is performed in a system of size $512\Delta x \times 512\Delta y$ with periodic boundary conditions, where $\Delta x = \Delta y = \pi/4$ and the time step $\Delta t = 0.1$. The initial condition used to simulate GBs begin with two large grains, which are rotated by angle $\theta/2$ in opposite directions, are placed into a supercooled liquid. This work mainly studied the relationship between heating rate and liquid film width. Several misorientation angles are selected: 6.2°, 9.6°, and 32.5°. We set $\rho_0 = -0.1969$. In the first simulation stage, r is set as -0.3 until the system reaches to the equilibrium state of solid. Then, the temperature coefficient is increased from $r = -0.3$ to $r = -0.1$ (the melting point (T_m) of pure substance with $\rho_0 = -0.1969$ is $r = -0.09$) with different heating rates ($k = 4\times10^{-6}$, $k = 4\times10^{-7}$, $k = 4\times10^{-8}$) and then keep the system at $r = -0.1$ for 150,000 time steps. As time is prolonged, various premelting phenomena occur in the system .

Simulation Results and Discussions

Effect of heating rate on the premelting and melting of low-angle GBs

Fig. 1 and 2 show separately the structure of a low-angle GB at misorientation angle 9.6° for $r = -0.1$ under different heating rates and its density distributions. Low-angle GB consists of individual dislocations separated by distances that are larger than a few lattice spacing. The dislocations are surrounded by individual 'liquid pools'. The lower the heating rate is, the larger 'liquid pools' has in the GB region [Fig. 1(b)]. The density distribution curves present the vibration form. The peak value of the atomic density of the GB region is lower than the atomic density inside the system, which indicates that 'liquid' appears at this time and that atoms appear disordered. The vibration amplitude of density curves increases as the atom location gradually close to the GB. The

reason for this result is that the Burgers vectors of adjacent dislocations at the GB are different, the atoms

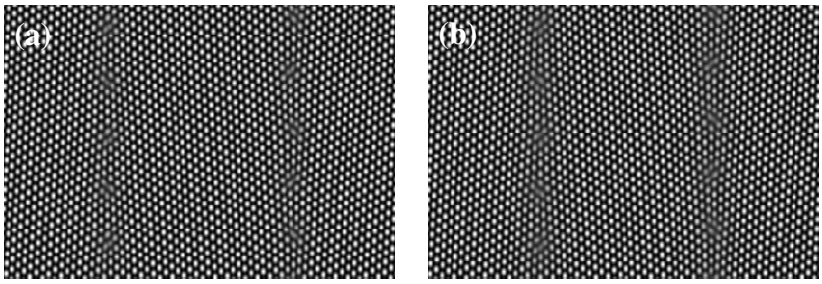


Figure 1. Snapshots of a low-angle grain boundary at misorientation angle 9.6° for $r = -0.1$ under different heating rates (a) $k = 4\times10^{-6}$; (b) $k = 4\times10^{-8}$.

around the dislocation have different degrees of deviation from its original equilibrium position and they are distributed uniformly on both sides of GB. The vibration amplitude of atomic density with heating rate

$k = 4\times10^{-8}$ is lower than that with $k = 4\times10^{-6}$ in near-GB and GB region [Fig. 2(b)]. This is indicated that the arrangement of atoms in GB region is more disordered and the width of liquid film may higher with lower heating rate.

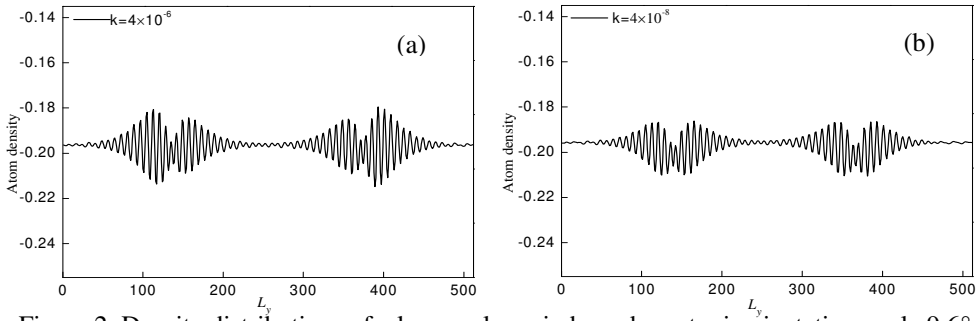


Figure 2. Density distributions of a low-angle grain boundary at misorientation angle 9.6° for $r = -0.1$ under different heating rates (a) $k = 4\times10^{-6}$; (b) $k = 4\times10^{-8}$.

We use excess mass theory of Mellenthin [12] to calculate the liquid film thickness of GB. An excess mass per unit length of GB can be defined by subtracting the mass of the homogeneous solid at the same chemical potential from the actual mass contained in the system. The total mass is fixed in the system and the film thickness can be extracted with good precision from measured the chemical potential $\mu(\rho)$. The liquid film thickness can be defined as follow:

$$w = \frac{L_y\left[\mu - \mu_s(\rho)\right]}{\mu_l(\rho) - \mu_s(\rho)} \tag{5}$$

where $\mu_l(\rho)$ and $\mu_s(\rho)$ are respectively the chemical potential of bulk liquid and bulk solid phases at the same condition, and μ is the total chemical potential in the system. L_y is the boundary length perpendicular to the GB, and the lattice constant $a = 2\pi / q$.

Fig. 3 shows the variation in liquid film width of low-angle GB $\theta = 9.6°$ with temperature r . As the temperature rises, the liquid film width increase flatly when the temperature is far below T_m and then increases rapidly when the temperature is close to T_m . Temperature almost has no effect on the liquid film width when the temperature is relatively low because low-angle GB is formed by the dislocation networks and its structure is complex. At low temperature, atomic diffusion is relatively slow. As a result, the heating rate elicits minimal effect on the liquid region on the GB and the three curves almost coincide. When temperature is close to the T_m , the liquid film width rapidly increases. Furthermore, at the same temperature (close to T_m), the liquid film width is larger when the heating rate is smaller. Because the thermal motion of atom aggravates near the melting point and atoms can

diffuse fully with low heating rates. So, when the system reaches to the same temperature with lower heating rate, the liquid film width is larger.

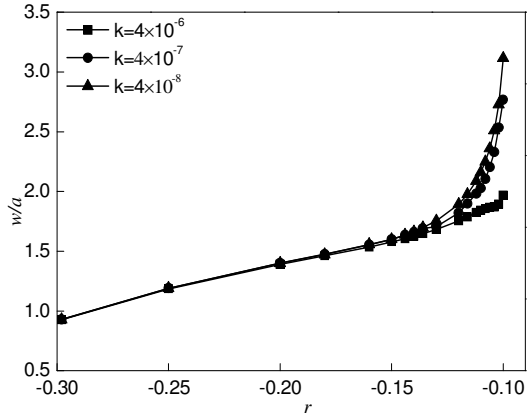


Figure 3. Film thickness w as a function of temperature r under different heating rates at misorientation angle 9.6°.

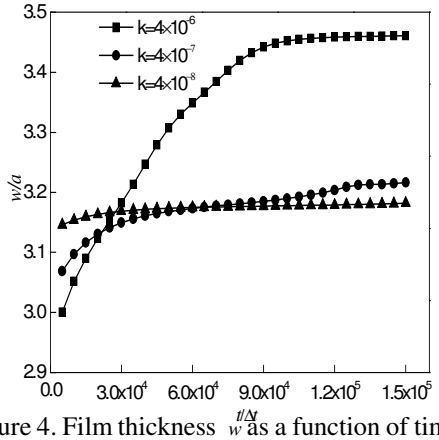


Figure 4. Film thickness w as a function of time t after Different heating rates for $\theta = 9.6^\circ$ at $r = -0.1$

Fig. 4 shows the curves of liquid film thickness w versus holding time t during heat preservation stage after different heating process. We can observe that as the holding time is prolonged, the liquid film thickness increase until to its equilibrium value, and then the liquid film thickness is no longer increase with holding time and keep its equilibrium value. This is due to the diffusion of atoms is in the dominant position in the initial stage of heat preservation, and the driving force of diffusion decreases with the holding time prolonging. The migration of liquid-solid interface gradually stabilizes and the liquid film thickness tends to stop increasing. In the initial stage of insulation, the film thickness in the system with high heating rates is less than that in the system with low heat rates. This finding is consistent with the change of film width in the heating stage. As time is prolonged, the film thickness in the system with high heating rates exceeds that of the system with low heating rates. This is because atoms cannot diffuse sufficiently in the system with high heating rates during the heating process, and dislocations on the GB lead to lattice distortion, allow storage of high distortion energy and increase the internal energy of the system, indicating that the system is unstable. In the consequent insulation stage, the system would be changed to reduce the free energy. The strain energy of dislocation becomes the diffusion driving force. The system with high heating rates during the heating stage has higher diffusion driving force during the insulation stage than that with low heating rates, allowing the "liquid pool" to obtain high driving force to merge and the liquid film thickness to have a dramatically increase during the insulation stage. The higher heating rate the system has during heating stage, the lager equilibrium value of liquid film will be reached during insulation stage.

Effect of heating rate on the premelting and melting of high-angle GB

Fig. 5 and 6 show separately the structure of a high-angle GB at misorientation angle 32.5° for $r = -0.1$ under different heating rates and its density distributions. The liquid film constructed by the fuzzy lattice structure forms the connected "pipe." The liquid film is rather homogeneous, that is, it has approximately the same width at each point. The film width increases with heating rate decreasing [Fig. 5(b)]. In the density distribution curve, no vibration trend can be found in the high-angle GB, but obvious valley is formed. With increasing heating rate, the atomic average density in bulk crystal region is smaller, whereas that in the region of GB is larger. We can observe that the liquid film thickness is larger when the temperature increases to the same value $r = -0.1$ with a smaller rate [Fig. 6].

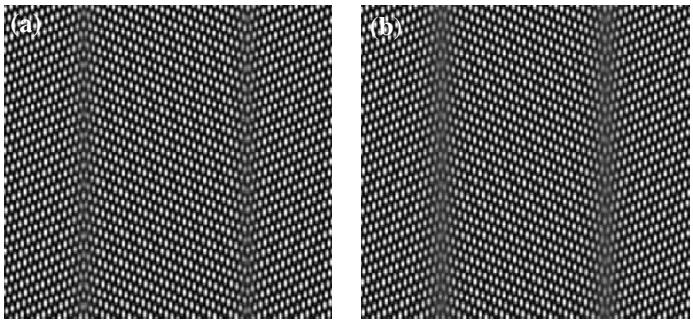


Figure 5. Snapshots of a high-angle grain boundary at misorientation angle 32.5° for $r=-0.1$ under different heating rates (a) $k=4\times10^{-6}$; (b) $k=4\times10^{-8}$.

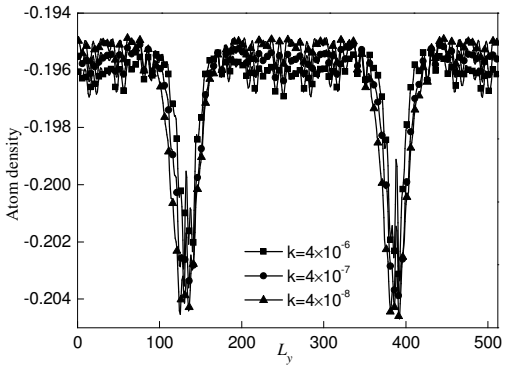


Figure 6. Density distributions of a high-angle grain boundary at misorientation angle 32.5° for $r=-0.1$ under different heating rates.

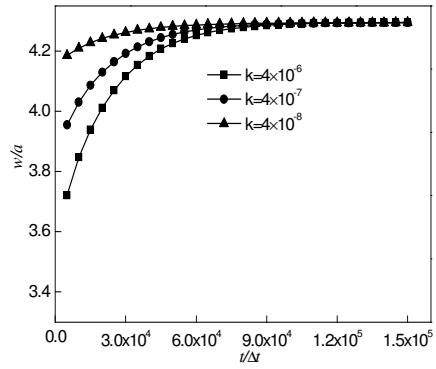


Figure 7 Film thickness w as a function of time t under different heating rates with misorientation angle $\theta=32.5^{\circ}$.

The curve of film width w versus temperature r for high-angle GB $\theta=32.5^{\circ}$ under different heating rates is similar to Fig. 3. At the beginning, the film width flatly increases with temperature, and heating rates exhibit no obvious effect on the film width. When the melting point is reached, the film width rapidly increases, and at the same temperature, the liquid film width is larger when temperature rises with lower heating rate.

Fig. 7 depicts the curves of film thickness w of high-angle GBs versus holding time t during the insulation stage after different heating process. The same point with Fig. 4 is that as the holding time prolonging, the liquid film thickness increase until to its equilibrium value, and then keeps the equilibrium value with holding time prolonging. The difference from Fig. 4 is that the liquid film thickness has the same equilibrium value during the entire insulation process although the heating rate is different during heating process. For high-angle GBs, the liquid is distributed homogeneously along the GB, thereby providing the convenience channel for the thermally activated motion of atoms so that atoms can fully diffuse during the heating process. As the liquid film thickness is lager in the system with lower rate during heating process, atoms can use the larger channel to diffuse, and the liquid film thickness in the system is still larger before achieving the equilibrium value; that is, the three curves have no intersections in this stage. However, the system can store more distortional energy with higher rate during heating process, which can lead the atoms to diffuse quickly, and in the stage before liquid film width achieving stability, the increasing rate of liquid film width is larger in the system. The final state is that the system with different heating rates reaches to the same value of equilibrium liquid film width.

Conclusions

The PFC model is used to study the effect of heating rate on the GB premelting. The liquid film thickness is calculated by excess mass theory. Our results show that the liquid film appears as the melting point is approached from below, and the liquid film width of GB is related to heating rate and misorientation angle. In the heating process, the liquid film width increase flatly when the

temperature is far below T_m, and then increases rapidly when the temperature is close to T_m.At the same temperature(close to T_m), the liquid film width is large when the temperature increases with low heating rate. In the insulation process, the liquid film thickness increase until to its equilibrium value, and then the liquid film thickness is no longer increase with holding time. For low-angle GBs, the higher heating rate the system has during heating stage, the lager equilibrium value of liquid film will be reached during insulation stage. For high-angle GBs, the liquid film thickness has the same equilibrium value during the insulation process although the heating rate is different during heating process.

Acknowledgments

The authors gratefully acknowledge the financial support from the National Natural Science Foundation of China (Grant No. 51174168, 51274167) and the "111" Project (Grant No. B08040).

References

[1] Z.Q. Guo ,W.M. Parlinska, G.Blugan, T. Graule, J.R. Mike and J. Kuebler, The influence of the grain boundary phase on the mechanical properties of Si_3N_4-$MoSi_2$ composites, Acta Mater. 55(2007) 2875-84.
[2] B. Straumal, B. Baretzky, Grain boundary phase transitions and their influence on properties of polycrystals, Interface Sci. 12(2004) 147-155.
[3] F. Inoko, T. Okada, T. Muraga and Y. Nakano, Strain induced grain boundary premelting in bulk copper bicrystals, Interface Sci. 4(1997) 263-72.
[4] A. Suzuki, Y. Mishin, Atomic mechanisms of grain boundary diffusion: Low versus high temperatures, J. Mater. Sci. 40(2005) 3155-61.
[5] R. Kikuchi, J.W. Cahn, Grain-boundary melting transition in a two-dimensional lattice-gas model, Phys Rev B 21(1980) 1893.
[6] P. Keblinski, S.R. Phillpot, D.Wolf and H. Gleiter, Amorphous structure of grain boundaries and grain junctions in nanocrystalline silicon by molecular-dynamics simulation, Acta Mater 45(1997) 987-98.
[7] M. Tang, W.C. Carter and R.W. Cannon, Grain boundary transitions in binary alloys, Phys Rev Lett 97(2006) 075502.
[8] T.V. Ramakrishnan, M. Yussouff, First-principles order-parameter theory of freezing, Phys Rev B 19(1979) 2775.
[9] K.R. Elder, M. Grant, Modeling elastic and plastic deformations in non-equilibrium processing using phase field crystals, Phys Rev E 70(2004) 051605.
[10] J. Berry, M. Grant and K.R. Elder, Diffusive atomistic dynamics of edge dislocations in two dimensions, Phys Rev E 73(2006) 031609.
[11] K.A. Wu, A Karma, J.J. Hoyt and Asta, Ginzburg-Landau theory of crystalline anisotropy for bcc-liquid interfaces, Phys Rev B 73(2006) 094101.
[12] J. Mellenthin, A. Karma and M. Plapp, Phase-field crystal study of grain-boundary premelting, Phys Rev B 78(2008) 184110.

Advanced Materials Research Vol. 936 (2014) pp 529-533
© (2014) Trans Tech Publications, Switzerland
doi:10.4028/www.scientific.net/AMR.936.529

A First-principles study on electronic properties of Ce/N codoped anatase TiO2

Siyu Yang[a], Lanfang Yao* [b]and Hao Cheng[c]

College of science, University of Shanghai for Science and Technology, Shanghai 200093, China
*Corresponding author: Assoc. Prof ; Ph D; Email：yao_lanfang@126.com

[a]yangsiyu321@126.com, [b]yao_lanfang@126.com, [c]ch122211604@aliyun.com

Keywords: first-principles, Ce/N co-doped TiO2, electronic properties, photocatalytic activity

Abstract. Density function theory is performed in order to investigate the effect of Ce/N co-doping on geometry structure, electronic and optical properties of anatase TiO2. Comparing the energy band and density of states of pure TiO2 and Ce/N doped anatase TiO2. We can conclude that, the valence band of pure TiO2 is main composed of O 2p states and the conduction is mainly composed of Ti 3d states. For N-doped TiO2, the topmost part of the valence band is mainly occupied by N 2p states which is higher than that of the O 2p states which can narrowed the band gap. Ce doping will introduce 4f states which is involved in the conduction band. These may lead the conduction band move down. As for Ce and N co-doped, the top of the valence band is mainly occupied by an admixture N 2p, O 2p and the bottom of the conduction band is predominantly occupied by an admixture of Ce 4f ,Ti 3d. The strong interaction between the dopants and the ions lead the band gap get narrower. We predict that Ce+N doping is one of the best choices for enhancing the photoelectrochemical activity of TiO2.

Introduction

TiO2 photo catalysts has received more and more attention as a promising material due to its wide range of potential application. such photolysis of water, as solar cells, photocatalytic degradation of organic compounds , purifying water and air. Many researches have proved that TiO2 is the most preferable photocatalytic semiconductor because of its low price, non-toxicity, chemical stability and photocatalytic activity. However, as a large band gap (3.2eV for anatase and 3.0eV for rutile), TiO2 can be activated only by UV light which accounts for a small part(~4%) of solar energy. Therefore, many studies have been done to improve photocatalytic activity of TiO2 under visible-light irradiation. An effective method is doping the TiO2 with non-metal or metal elements.

Among non-metal doped TiO2 materials, doping with nitrogen atom is considered to be one of the most effective methods and it has been studied thoroughly via both experimental and theoretical methods. For example, Asahi et al. discovered that band gap energy of TiO2 was narrowed when TiO2 doped with N , which is further studied by other theoretical and experimental[1] tools to support their views. However Irie et al.suggested that the isolated N-2p states are above the valence-band maximum of TiO2, which is consistent with several recent experimental studies. The localized N-2p states act as the trap for photo generated carriers and decreases the photo-generated current which consequently limits the efficiency of N-doped TiO2 in the photocatalytic process. On the other hand, many attempts have been made to improve the photocatalytic activity of TiO2 by preparing Ce-doped TiO2. Tong et al.[2] figure out doping Ce^{4+} effectively improves the photocatalytic activity under both UV light irradiation and visible light irradiation with an optimal doping concentration of 0.2% and 0.4%, respectively. Fu et al.[3] studied the electronic and optical properties of Ce^{3+}-doped TiO2, and indicated that the Ce incorporation leads to a decrease of Ti 3d states and enhancement of 4f states in the bottom of conduction band. Recently, some researchers attempted to improve the photocatalytic activity of TiO2 by preparing Ce and N co-doped TiO2. Zhang et al.[4] studied the electronic properties of Ce/N-Coped TiO2, and found that Ce+N doping results in band gap narrowing and also leads to a red-shift of the absorption edge of TiO2.

In order to explain the reason of the enhanced photocatalytic activity and red shift of optical absorption, in this report the crystal structures, band structures and density of states between pure anatase TiO2 and Ce, N-doped anatase TiO2 are studied using the plane-wave ultrasoft pseudopotential method of density functional theory(DFT).

Model and Method of Calculation

The doped system consists of 2×2×1 anatase TiO2 super cell with 48 atoms in total. The Ce-doped configuration was constructed by replacing one Ti atom with one Ce atom, and similarly N-doped configuration was constructed when the O atom was replaced by N atom with a doing molar concentration 6.25%. For co-doping(Fig .1), One Ti atom was replaced by Ce atom while one O atom near the Ce atom was replaced by one N atom with a doping molar concentration of 3.125% .

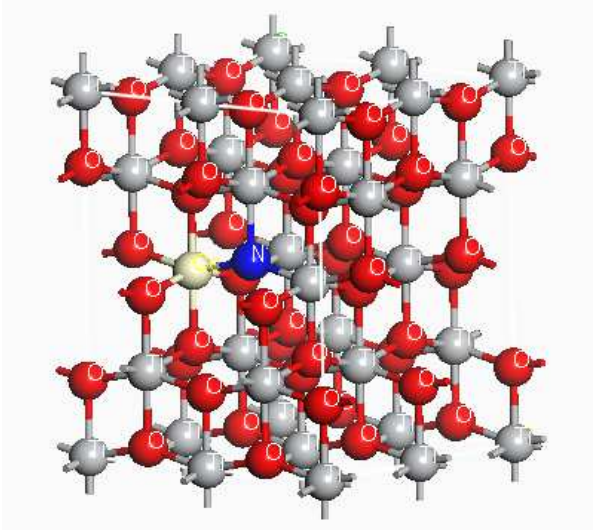


Fig. 1 Super cell models of Ce/N-co-doped TiO2

All of the calculations have been performed using Cambridge Serial Total Energy Package (CASTEP) module in Materials Studio 6.0.The electronic exchange-correlation energy is treated within the framework of the generalized gradient approximation (GGA) with the Perdew-Burke-Ernzerhof (PBE). The planewave expansion is truncated by the cutoff energy of 380ev. Monkhorst-Pack grid parameter for K-point simpling was 3×3×2 for all models. The convergences are set as 1.0×10^{-3} Å for maximum displacement tolerances, 8.5×10^{-3} eV/Å for maximum force, 0.01GPa for maximum stress and 5×10^{-7} eV/atom. The valence electrons configuration for the O,Ti,N, and Ce was $2s^2\ 2p^4$,$3s^2\ 3p^6\ 3d^2\ 4s^2$,$2s^2 2p^3$ and $4f^1\ 5s^2\ 5p^6\ 5d^1 6s^2$, respectively. Considering the influence of the doping on the lattice, the first step is geometrical optimization.

Results and Discussion

Optimized Structure Properties. After optimizing the geometry, we got the lattice parameters of pure TiO2 (a=3.802 Å ,and c=9.721 Å) which are close to the experimental data (a=3.782 Å and c=9.502 Å [5]). In order to study further , we also got the average bond lengths of pure TiO2 and doped TiO2 . We can find that the lattice parameters of doped TiO2 are bigger than pure TiO2 . This is due to the lager radius of N and Ce than those of O and Ti atoms, respectively. In N doped TiO2, the Ti-N (2.040 Å) bond lengths are similar with Ti-O (2.005 Å) in pure TiO2. However, in Ce doped TiO2, the Ce-O (2.164 Å) is slightly longer than Ti-O (2.076 Å) ones. The more powerful ionicity of Ce than Ti is due to the Mulliken charges of Ce (1.80) is larger than Ti (1.26). In Ce+N doped TiO2, the bond length of Ce-N (2.193 Å)and Ti-N (2.020 Å)are shorter than Ce-O (2.205 Å)and Ti-O (2.535 Å). These show strong covalent interaction for the Mulliken charges of Ce(1.74) is larger than

Ti (1.24), meanwhile, N (-0.66) and O (-0.65) are basically the same. These can explain the situation that the lattice parameters became bigger after doping. These Ti-O bonds are close the doped ions.

Electronic Properties. In order to analyze the electronic properties of co-doped anatase TiO2, the calculated band structures of the pure TiO2 and different doped models are presented in Fig. 2. From Fig.2(a), we could know the band gap of the pure anatase TiO2 is about 2.2eV, which is less than the experimental data of 3.20eV due to the limitation of GGA. But the results is close to the calculation of Shi and his workers[6] using the generalized gradient approximation (GGA) function (2.18eV). Although the drawback in DFT, the calculation results are reasonable for a comparison. The top of valence band maximum (VBM) and the bottom of conduction band minimum (CMB) are located at same points, indicating that pure anatase TiO2 is a direct-gap semiconductor material.

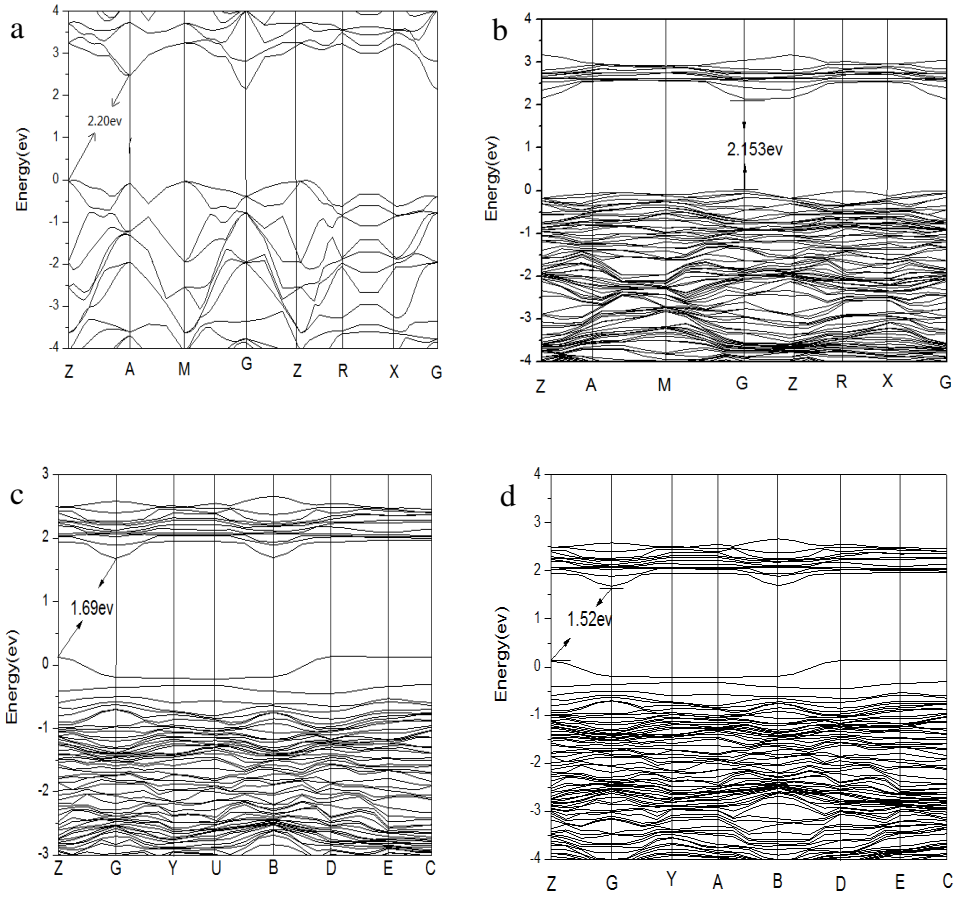


Fig. 2. Band structures plots of (a) pure anatase TiO2, (b) Ce-doped TiO2, (c) N-doped TiO2 and (d) Ce/N.

For Ce doped TiO2 Fig.2(b), The valence band and the conduction band became dense and the band gap is effectively narrowed by introducing impurity states below the conduction band. In this case, the band gap is about 2.153eV, which is less than the band gap of pure TiO2 (2.2eV). For N doped TiO2 Fig.2(c), an unoccupied acceptor state is introduced above the valence band which reduced band gap of TiO2 from 2.20eV to 1.69eV. This narrowed band gap may lead to the reduction of photoelectron transition energy, which shift the optical absorption edge to the visible light region. For Ce/N co-doped TiO2 Fig.2(d), the CBM is located at the G point, and VBM is at the Z point. The calculated indirect band gap is about 1.52eV. The band gap is get narrower and the unoccupied acceptor state is also introduced. Consequently, the probability of electrons being excited from the valence band to the conduction band increases, which may contribute significantly to the visible-light optical absorption.

To further study the modifications in band structure, the density of states (DOS) of different doped models have been calculated as indicated in Fig. 3. Total density of states (TDOS) of the pure TiO2 as well as of the different doped models (Fig.3a) shows that the valence band maximum (VBM) of all the doped models has no obvious shift from that of pure TiO2 , however, the conduction band

minimum (CBM) of Ce doped (Fig.3b) model declines about 0.48eV and N (Fig.3c) doped/Ce+N co-doped models(Fig.3d) declines about 1.0eV. Obviously, the smaller band gap of doped models may results in red-shift of the optical absorption. In pure anatase TiO2, the valence band which is close to the zero point energy is main composed of O 2p states and has a large bandwidth of about 4.93eV. Meanwhile, the conduction is mainly composed of Ti 3d states and has a bandwidth about 5.41eV. Ti^{4+} is surrounded by six O^{2-} which consisted octahedral structure. According to the crystal field theory, Ti 3d states split into t2g and eg states, and thereby the conduction band is divided into two parts, of which part of higher energy consists of O2p states and eg states of Ti atoms, and lower part consists of O2p states and t2g states of Ti atoms.

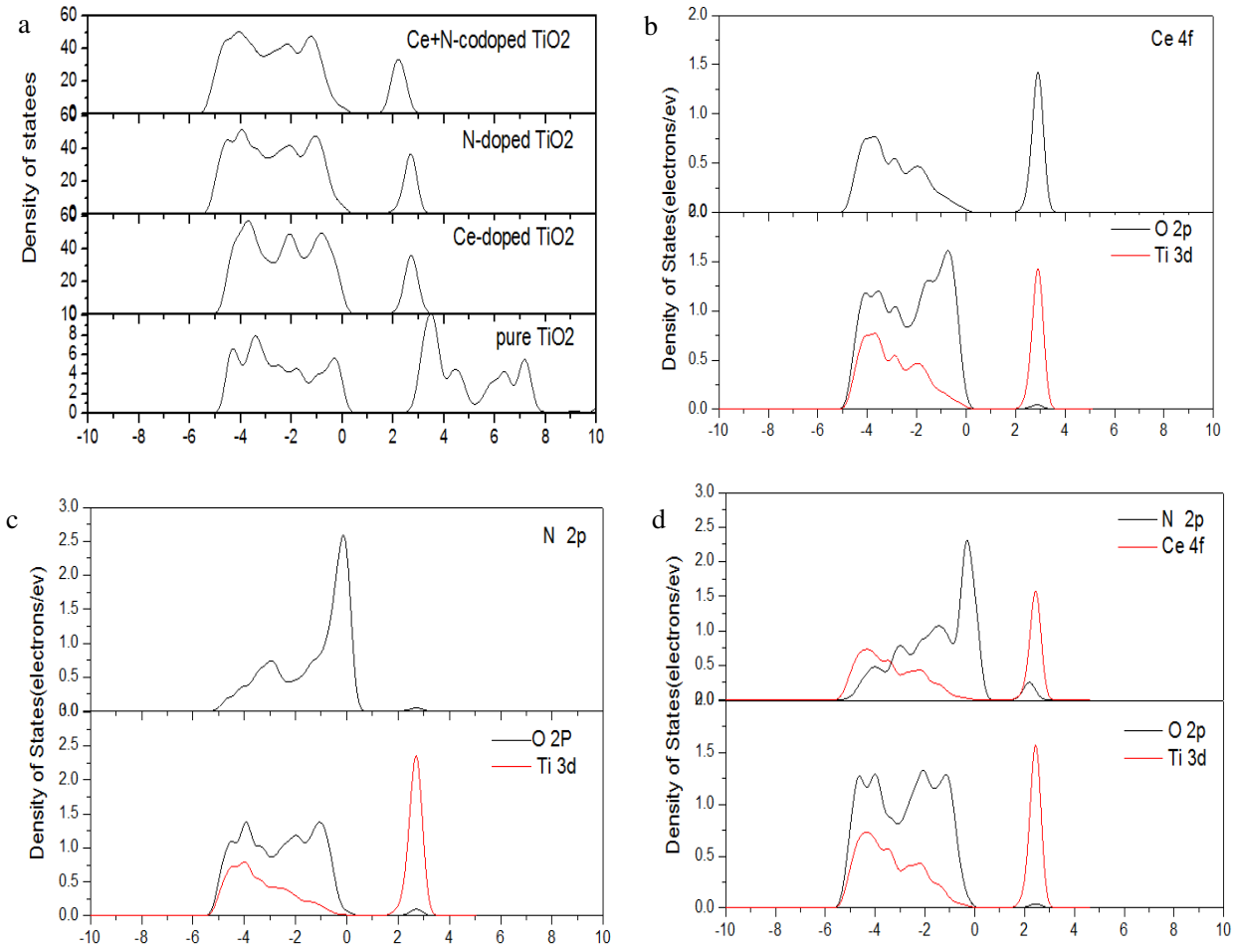


Fig. 3. (a) The calculated and comparison TDOS of different ions doped TiO2, calculated PDOS of (b) Ce-doped TiO2, (c) N-doped TiO2, (d) Ce/N.

As to Ce-doped TiO2, an Ti atom was replaced by a Ce atom which introduced 4f states. (Fig.3b) shows that the valence band is main composed of O 2p states and Ce 4f states and conduction band is predominantly composed of Ti 3d and Ce 4f. It is found that the conduction band moved left(about 0.583eV), improves the mobility of photo-generated electrons. The higher mobility of the photo-generated carriers, the better performance of the photocatalyst. This is same with the situation we found from the band structures of pure anatase TiO2 and Ce-doped anatase TiO2.

With respect to N-doped TiO2, N atom substitute one O atom. The N atom can obtain two electrons and its 2p states are not fully occupied (seen from Fig.3c), leading to the creation of acceptor N 2p states located at above the valence band maximum of TiO2. The bottom of the conduction band is mainly consisted of Ti 3d states. However, the topmost part of the valence band is mainly occupied by N 2p states which is higher than that of the O 2p states. This N 2p states are

responsible for the band gap narrowing. Unfortunately, unoccupied N 2p states may act as recombinations, which promote the electron-hole recombination rates.

For Ce/N-co-doped TiO2, the top of the valence band is mainly occupied by the N 2p states and the bottom of the conduction band is predominantly occupied by an admixture of Ce 4f and Ti 3d. The N impurity level appears above the VBM similar to the N-doped. In this case, the band gap is narrowed because of the decline of the conduction band. All the doped models have narrowed band gap, and thus they may induce a red shift of the optical absorption edge.

Conclusions

In summary, the crystal structures, band structures, density of states of pure anatase TiO2 , N-TiO2, Ce-TiO2 and (Ce,N) co-doped anatase TiO2 have been calculated and analyzed. We came to the conclusion that: N doping will effectively reduce the gap of anatase TiO2, but unoccupied N 2p states promote the recombination rates. Ce doping will introduce 5d states which are involved in the valence band and conduction band. These formed hybrid orbitals narrowed the band gap of anatase TiO2. For Ce and N doped, the top of the valence band is mainly occupied by an admixture N 2p, O 2p and the bottom of the conduction band is predominantly occupied by an admixture of Ce 4f , Ti 3d. The strong interaction between the dopants and the ions in anatase TiO2 is the main reason for its band gap narrowing. Maybe Ce and N doping is the best method which can effectively improve the photocatalytic activity.

References

[1] Y. Yin, W. Zhang, S. Chen, S. Yu, Mater. Chem. Phys. 113 (2009) 982.

[2] T.Z.Tong, J.L. Zhang, B.Z. Tian, Journal of Colloid and Interface Science 315 (2007) 382–388

[3] C. Fu, T.Z. Li, J.S. Qi, J. Phys. Chem. 494 (2010) 117–122.

[4] Y.G.Zhang,Dai, Y. X.Wang,Journal of Applied physics 110, 033519 (2011)

[5] K. Yang, Y. Dai, B. Huang, Chem. Phys. Lett. 456 (2008) 71.

[6] W.M. Shi, Q.F. Chen, Y.X.Applied Surface Science 257 (2011) 3000–3006.

Advanced Materials Research Vol. 936 (2014) pp 534-539
© (2014) Trans Tech Publications, Switzerland
doi:10.4028/www.scientific.net/AMR.936.534

Effective Nuclear Field Measurement in a Single Quantum Well via Time-Resolved Kerr Rotation Technique

Li-Ping Yan[a], Reina Kaji[b] and Satoru Adachi[c *]

Graduate School of Engineering, Hokkaido University, N13W8, Kitaku, Sapporo 060-8628, Japan

[a]email: liping.yan@eng.hokudai.ac.jp, [b]email: r-kaji@eng.hokudai.ac.jp,
[c]email: adachi-s@eng.hokudai.ac.jp

Keywords: Nuclear field, Quantum well, Spin dephasing, Time-resolved Kerr rotation

Abstract: Effective magnetic field of nuclear spin polarization (NSP) under circularly polarized pumps excitation and the dephasing time of resident electron spin polarization under pump and control excitation has been detected in a single CdTe quantum well (QW) by a time-resolved Kerr rotation (TRKR) technique. We deduced that the experimental method is verified with the effect, to a certain extent, through confirming the external magnetic field results. In addition, the nuclear field is revealed to be increased with the increasing electron spin component due to the enhanced electron-nuclear hyperfine interaction. Significant nuclear field is observed as 1.85 mT with the applied magnetic field tilted by about 15 degree. What is more, we found the spin dephasing time (SDT) has little relation with the created NSP field, but it decreases largely with the increasing spin polarization magnitude under pump excitation and the spin vector dispersions induced by control pulses.

Introduction

Optically injected spin-polarized electrons polarize and depolarize nuclear spins through dynamic nuclear polarization (DNP) by the contact hyperfine interaction between electron and nuclear spins. The hyperfine interaction between the electron and the ensemble nuclear spins recently has attracted considerable attentions due to the potential applications in spin-based quantum information processing (QIP) [1,2]. Nuclear spins, as ideal quantum bits, play important roles in utilizing spin degree of freedom of semiconductor spintronic devices. Thus, the dynamical nuclear spin polarization created by optically injected spin-polarized electrons via hyperfine interaction has been largely observed in the past in bulk semiconductors [3] and quantum wells (QWs) [4-6], and quantum dots (QDs) [7-9]. However, the contact hyperfine interaction will modify their spin Hamiltonians, such that the spin splitting. This inherent feedback in the Hamiltonian leads to the bistability and hysteresis in the electron-nuclear spin system [8,9]. Therefore we have great interests on the manipulation and detection of effective nuclear field from NSP with keeping the long electron coherence at the same time.

For the applications by using an electron spin, its decoherence via NSP fluctuation becomes a large obstacle, especially for the QIP devices using QDs or QWs. NSP fluctuation limits the number of quantum operations and reduces the potential performance [7]. From this viewpoint, II-VI compound semiconductors such as CdTe [6] are preferable since those generally have a smaller hyperfine constant compared to III-V compound materials such as GaAs [5], and could expect smaller influence for electron spins coherence. However, precise measurements of the NSP amount with this order of magnitude hold several experimental challenges and additional difficulties in the valuation of nuclear field effects. For example, it is difficult to study nuclear spins by creating equilibrium nuclear polarization directly due to the small value of nuclear magnetic moment. Therefore, we try to measure the small NSP in a single CdTe QW by a TRKR method accurately.

Also, the SDT in turn would be influenced by NSP field reaction and the electron spin behaviours. In particular, resident electron spins have a long dephasing time in a QW [10] . Now that we know recent studies have revealed that SDT can be affected by magnetic field, temperature and spin density [11]. Therefore, it is necessary to discuss the dependence of ensemble electron SDT on controllable spin polarization and spin vector distribution, since the comprehensive researches of SDT related to spin polarization and spin dispersion have been a few so far.

In this study, we first have measured the dynamical nuclear-spin field in a single CdTe QW with negative charged excitons (X^-). We will show that the optically-polarized electron can effectively polarize nuclear spins, which is found to produce a few mT of effective nuclear field. The value depends drastically on the applied external magnetic field and photoinjected electron spin polarization. Afterwards, we investigated the SDTs derived from Kerr rotation signals using double circularly (σ^+/σ^+) laser pulses excitation. Which demonstrated that the electron SDT can be changed largely by the spin polarization magnitude modification in each independent subensemble of electrons and the dispersions of inhomo-geneous spin vectors.

Experiments and Analysis of Results

Effective Nuclear Field Under Tilted Magnetic Field.

The sample used here is a single CdTe/$Cd_{1-x}Mg_xTe$ (x=0.15) QW with the thickness of 100 Å. The resident electrons in a QW show the formation of the negative trions, consisting of spin-paired electrons and a hole [12]. Under the excitation of trion resonance, the photocreated electron-hole pair captures one of the resident electrons with a certain spin, leaving the polarizing residual electron ensemble to the opposite spin polarization since the initial polarization of resident electron emsemble is zero. The hole-in-trion spin relaxation time is rather smaller compared with the trion recombination time. Therefore, the effect of the remaining depolarized excited electrons can be ignored and never affect the temporal evolution of the ensemble resident electrons polarization.

The sample was excited by σ^+ (σ^-) circularly polarized picosecond pulses (duration~5 ps) with 769.6 nm near normal incidence and the generated spin polarization was measured by the linearly polarized probe pulse with the controlled delay time. The external magnetic field B up to ~170 mT was applied in Voigt configuration. The sample was mounted in a cryostat and was kept at 10 K through the measurements.

The linearly polarized probe beam was modulated by a photo-elastic modulator set as half wave retard at 50 kHz for a lock-in detection. And circularly polarized pump beam which was created by a quarter-wave plate (QWP) was modulated by a mechanical chopper at 120 Hz. In addition to the laser pump beam modulation, a combination of a half wave plate and a wollaston prism was set in front of a balanced photo-detector in order to cancel the static Kerr rotation with no pump pulses and reduce the influence of the scattered pump beam on the measured signal.

Fig. 1 shows the temporal evolution of the electron spins, which were generated by the circularly polarized pump pulses, was recorded by measuring Kerr rotation angle $\theta_K(\Delta t)$ of the linearly polarized probe pulse with delay time Δt**.** The observed signal can be fitted by exponentially damped oscillations function containing the beating frequency ω_L and a single decay time T^*:

$$\Delta\theta_K = A * \exp\left(\frac{-\Delta t}{T^*}\right)\cos\left(\omega_L \Delta t + \phi\right) \tag{1}$$

where the coefficient A is the initial amplitude of electron spin polarization, T^* is the transverse spin-relaxation time, ω_L is the electron Larmor frequency. Φ is an apparent initial phases for spin precession.

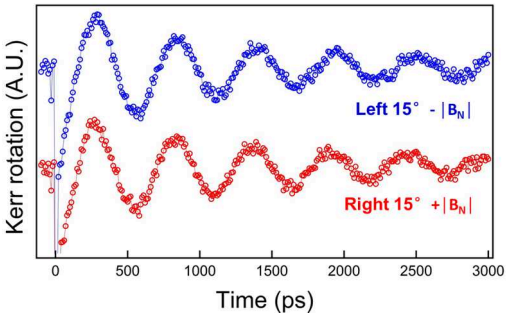


Fig. 1. TRKR signals for σ- pumps excitation in +15°/-15° geometry at T=10 K under 86.6 mT external field.

The Larmor frequency ω_L is shown in the following function:

$$\omega_L = g'_e \mu_B (B_e \pm B_N) / \hbar \tag{2}$$

where anisotropic $g`_e$ is the electron g factor in the magnetic field direction, B is an oblique applied magnetic field , and B_N is a created nuclear field. The direction of B_N depends on the direction of the excited electron spin polarization. Therefore, the nuclear field influences the electron spins precession, as is shown in Fig. 1.

As we mentioned before, this NSP effect only occurs if an applied magnetic field is used at an oblique angle and does not occur in the true Voigt geometry (i.e. right angle case). A longitudinal component of electron spin polarization is necessary to observe an spin precession frequency shift via B_N. Spins are, in principle, injected perpendicular to the field in the Voigt geometry and DNP should not be observed since the longitudinal spin polarization averages to zero. In a word, a direct longitudinal component of spin-injection can be created by simply tilting the applied magnetic field. From this process, we also calculated the exact external magnetic field (shown in Eq. 3) by TRKR measurement. For this technique, the magnitude of the effective field $|B_N|$ should be produced as the equal value at an equal angle of external field tilted to left and to right. Therefore, the measured total effective field B_{left} (B_e+B_N) and B_{right} (B_e-B_N) acting the electron spins can conclude the precise external field.

$$B_e = (B_{left} + B_{right}) / 2 \tag{3}$$

The tilted angle dependence of the applied magnetic field deduced from TRKR experiments is displayed in Fig. 2. As shown by the blue curve derived from σ^- pumps excited experiments and the red curve from σ^+ pumps excited measurements. At the same angle, the nuclear field could vary with different pump pulses, yet the applied magnetic field is a certain mount. Thus we deduced a series of applied magnetic field with the titled angle. As a result, the average measuring error of the detected external magnetic field for equal tilted angle from σ^+ experiments and from σ^- experiments is 0.0406 roughly, which verifies that this measurement method is also quite accurate to nuclear field at some degree.

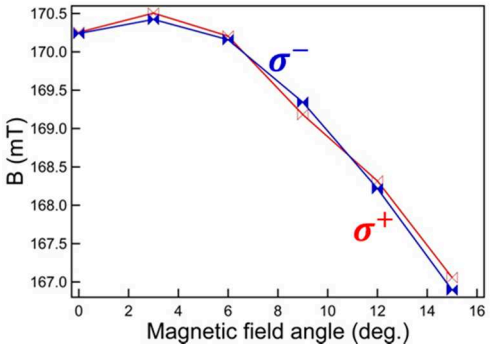


Fig. 2. External magnetic field B_e deduced from TRKR measurement.

In consequence, $B_{N\text{-}total}$ value can be obtained for any angle of external field inclination, which is indicated by Eq. 4:

$$B_{N\text{-}total} = B_{left} - B_{right} \tag{4}$$

Nuclear field absolute value tends to increase as the external magnetic field angle increases, as shown in Fig. 3. This is because the spin components that paralleled to external field increase with the increasing inclination of applied magnetic field. And we can notice that the nuclear field value B_N changed in the way that is almost proportional to the slant angle. Moreover, the largest nuclear field turned out to be 1.85 mT at the angle of 15° under σ^- pumps excitation. In the same way, nuclear field is also increased with the increasing of electron spin polarization, which is shown in Fig. 4. In all of the above experiments, the average electron spin transverse time is about 1400 ps, which is influenced a little by NSP effective magnetic field for this QW, in contrast to other influences, even the spin precession frequency spread causing spin dephasing [13].

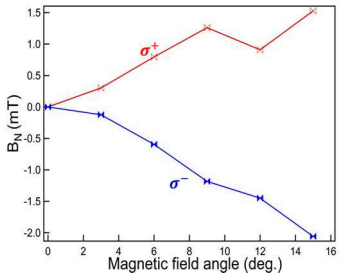


Fig. 3. Effective nuclei field under varied external field slope angle.

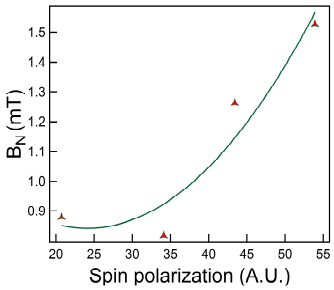


Fig. 4. Effective nuclei field under σ^+ pump excitation with different power around the external field slope angle of 15°.

Electron Spin Dephasing Under an Un-tilted Magnetic Field

The residual electron SDT could be affected by the magnitude and distribution of electron spins polarizations. Therefore, this electron SDT study was carried out by σ^+ pump around the normal external magnetic field B up to 205 mT applied in the same Voigt configuration. Moreover, a control pulse circular polarization was injected at a given controlled timing in the different Larmor period stages. That is because the distribution and magnitude of the resident electron spin polarizations can be varied by control pulse with the same phase and different phase relative to pump, as shown in Fig. 5. The total spin polarization generated by the pump and control excitations in the same phase has a higher polarization. However, the total spin polarization in 1/4 phase difference displays the nearly equal polarization magnitude as that of pump excitation and also shows up a phase shift. Otherwise, the dispersion (φ) increases with the increasing phase difference. For the same phase difference, φ rises with reducing relative magnitude difference of spin polarization excited by pump and control pulses.

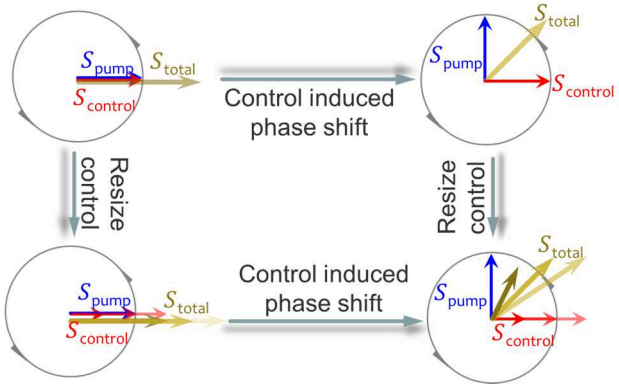


Fig. 5. Combined spin vector superposition (yellow arrow) of pump and control excitation (spin polarizations are presented by blue and red arrows, respectively) precess around normal applied magnetic field.

The SDTs were obtained from fitting the measured Kerr rotation signals on the control-probe delay Δt, and were plotted in Fig. 6. Figure shows the clear dependences of electron SDTs on the spin polarization magnitude under different excitation powers: (a) σ^+ pump; (b) σ^+ control; (c) σ^+ pump fixed at 5 mW and σ^+ control from 1 mW to 9 mW with same phase; (d) σ^+ pump fixed at 5 mW and σ^+ control from 1 mW to 9 mW with a quarter phase difference. There is a directly inverse linear relationship between the transverse electron SDT and the spin polarization (P) for an individual ensemble spin polarization under pump or control pulse excitation seen from Fig. 6(a) or Fig. 6(b).

However, the spin dephasing is slowed down by the spin phase dispersion of electron spins formed in different phase shown by Fig. 6(d), in which the dispersion of spin vectors is considered to firstly increase in the region of control < pump, and then decrease with increasing the spins excited by control pulse. Also, the plot of Fig. 6(c) shows a little deviation from linear correlation, which can be explained by the potential spin heating and a little spin vectors diffusion due to some experimental errors.

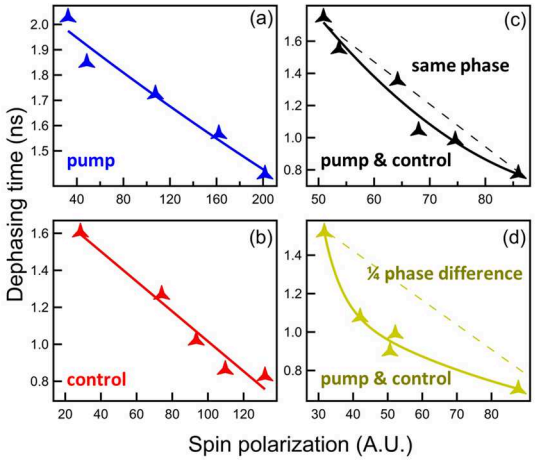
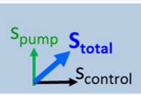


Fig. 6. Electron SDT versus spin polarization under different excitation intensities: (a) σ^+ pump; (b) σ^+ control; (c) σ^+ pump and σ^+ control with the same phase; (d) σ^+ pump and σ^+ control with a quarter phase difference.

Table 1 exhibits the main relationship of the spin vectors of pump-excited spins (green arrow), control-excited spins (black arrow) and the total spins (blue arrow). The measured electron spin polarization ratio derived from Kerr signal amplitudes and the fitted dephasing times (1550 ps: 2018 ps: 1519 ps ≈ 1: 1.3 :1) from Kerr rotation signals by pump and control with a quarter phase difference, pump alone, pump and control with the same phase, respectively, are summarized.

TABLE 1. SPIN VECTOR AND SDT.

Experiment excitation	Only pump	Pump and control with same phase	Pump and control with ¼ phase difference
Spin vector			
Total Polarization	1	1.8	1
Dephasing time [ps]	2018	1550	1519

From the spin polarization analysis above, it can be inferred that the electron spin dephasing is induced by two main aspects: the P magnitude of individual spin vector and the spin distribution φ of more than one spin vectors. According to Fig. 6(a) and Fig. 6(b) along with the left two columns of Table 1, the SDT decreases with the increasing P. Also, as seen in Fig. 6(d) and the right two columns of Table 1, the SDT is reduced by the diffused spin vectors dispersion φ, compared to a concentrated spin for the equal spin polarization value. In addition, from the left and right columns of Table 1 for the pump and control with different phases, the following is concluded: the sum of spin vector modules seemingly largely determines the dephasing time rather than the measurable total spin polarization.

From the above analysis, we can easily reach a conclusion that:

$$\mathrm{SDT} \propto 1/(\varphi * P) \tag{5}$$

Eq. 5 indicates that SDT and spin polarization has a directly negative linear relation as the spins vector dispersions are identical. While the spin polarizations are equal, SDT is supposed to decrease with the increase of ensemble spins dispersion.

Summary

In conclusion, it was shown experimentally that the nuclear field was obtained accurately by TRKR measurements through verifying the acquired precise external magnetic field value in a single QW. In the present of external magnetic field at 15 degree inclination to the sample, the nuclear field was about 1.85 mT when a small magnetic field of 170 mT is applied, being mainly determined by the electron-nuclear interaction. In addition, its value went up with the increasing external magnetic field slant angle and electron spin polarization respectively. However, the residual electron SDT reduced with the increasing spin polarization and dispersion of spin vectors.

References

[1] X.M. Dou, B.Q. Sun, D.S. Jiang, H.Q. Ni, Z.C. Niu, Electron spin relaxation in a single InAs quantum dot measured by tunable nuclear spins, Phys. Rev. B, 84 (2011) 033302.

[2] J. Fischer, D. Loss, Hybridization and Spin Decoherence in Heavy-Hole Quantum Dots, Phys. Rev. Lett., 105 (2010) 266603.

[3] G. Sukhodub, F. Hohls, R.J. Haug, D.K. Maude, D. Reuter, A.D. Wieck, Dynamics of nuclear spins appearing in transport measurements of an inter-edge spin diode in tilted magnetic fields, Physica E: Low-dimensional Systems and Nanostructures, 34 (2006) 355-358.

[4] J. Ishihara, M. Ono, G. Sato, S. Matsuzaka, Y. Ohno, H. Ohno, Magnetic Field Dependence of Quadrupolar Splitting and Nuclear Spin Coherence Time in a Strained (110) GaAs Quantum Well, Jpn. J. Appl. Phys., 50 (2011) 04DM03.

[5] V.K. Kalevich, V.L. Korenev, Optical Polarization of Nuclei and ODNMR in GaAs/AlGaAs Quantum Wells, Appl. Magn. Reson., 2 (1991) 397-411.

[6] B. Li, P. Coles, J.A. Reimer, P. Dawson, C.A. Meriles, Optical pumping of nuclear spin magnetization in GaAs/AlAs quantum wells of variable electron density, Solid State Commun., 150 (2010) 450-453.

[7] R. Kaji, S. Adachi, H. Sasakura, S. Muto, Direct observation of nuclear field fluctuations in single quantum dots, Phys. Rev. B, 85 (2012) 155315.

[8] P. Maletinsky, A. Badolato, A. Imamoglu, Dynamics of quantum dot nuclear spin polarization controlled by a single electron, Phys. Rev. Lett., 99 (2007) 056804.

[9] R. Kaji, S. Adachi, H. Sasakura, S. Muto, Hysteretic response of the electron-nuclear spin system in single In(0.75)Al(0.25)As quantum dots: Dependences on excitation power and polarization, Phys. Rev. B, 77 (2008) 115345.

[10] E.A. Zhukov, O.A. Yugov, I.A. Yugova, D.R. Yakovlev, G. Karczewski, T. Wojtowicz, J. Kossut, M. Bayer, Resonant spin amplification of resident electrons in CdTe/(Cd,Mg)Te quantum wells subject to tilted magnetic fields, Phys. Rev. B, 86 (2012) 245314.

[11] E.A. Zhukov, D.R. Yakovlev, M. Bayer, M.M. Glazov, E.L. Ivchenko, G. Karczewski, T. Wojtowicz, J. Kossut, Spin coherence of a two-dimensional electron gas induced by resonant excitation of trions and excitons in CdTe/(Cd,Mg)Te quantum wells, Phys. Rev. B, 76 (2007) 205310.

[12] N.J. Harmon, W.O. Putikka, R. Joynt, Theory of electron spin relaxation in n-doped quantum wells, Phys. Rev. B, 81 (2010) 085320.

[13] I.A. Yugova, M.M. Glazov, D.R. Yakovlev, A.A. Sokolova, M. Bayer, Coherent spin dynamics of electrons and holes in semiconductor quantum wells and quantum dots under periodical optical excitation: Resonant spin amplification versus spin mode locking, Phys. Rev. B, 85 (2012) 125304.

Advanced Materials Research Vol. 936 (2014) pp 540-544
© (2014) Trans Tech Publications, Switzerland
doi:10.4028/www.scientific.net/AMR.936.540

Theoretical investigation on rearrangement mechanism of fluoroalkylsilane

ZHOU Yu Fang[1,a]*, MA Qing Yu[2,b]

[1]School of Physics, Shandong University, Jinan 250100, China

[2]School of Materials Science and Engineering, University of Jinan, Jinan 250022, China

[a]yfz@sdu.edu.cn, [b]mse_maqy@ujn.edu.cn

*The corresponding author

Keywords: quantum chemical DFT methods. rearrangement mechanism. fluoroalkylsilane

Abstract: Fluoroalkylsilanes are a kind of important carbofunctionalized silanes and applied in many fields. while the rearrangement and decomposition reactions could easily occur for these compounds under a certain high temperature or catalysis. In this work, we selected $CH_3H_2SiCH_2F$ as the molecular sample and investigated the mechanism of rearrangement reaction by using quantum chemical DFT methods. The results showed the rearrangement occurred via a transition state, in which the fluorine atom migrated from carbon to silicon and the hydrogen atom migrated from silicon to carbon. To understant the the process details the atomic charge distribution and electronic transfer were analyzed. And atomic vibrations spectra was discussed as well.

Introduction

Organosilicon materials have been widely applied in all fields of national economy because of their many unique and notable properties [1]. For example, the methylsiloxane-based materials are main representatives and possess many prominent advantages, such as high and low temperature resistance, weather resistance, ozone resistance, electrical characteristics, physiological inert [2]. Thus these materials have extensive and important applications, including aerospace, electric, medicine, construction, machinery [3]. Carbofunctionalized polysiloxanes are functional organosilicon materials and have been widely utilized in coating industry, textile industry, daily-use chemical industry, polymer modifications [4]. Meanwhile, carbofunctionalized silanes ($\equiv Si(CH_2)_nX$, X = halogen) are a kind of important organosilicon products and the appearance of these products especially promote the development of polymer composites [5]. However, the rearrangement and decomposition reactions could easily occur for these compounds under a certain high temperature or catalysis, because silicon atom owns empty *3d* orbits and can accept the electron from adjacent electron-rich carbon-containing functional groups. These drawbacks limit their applications [6]. Therefore, it is significant for their applications and developments to investigate the mechanisms of thermal rearrangement and decomposition reactions.

Fluoroalkylsilanes ($\equiv Si(CH_2)_nF$) are a kind of carbofunctionalized silanes and have important applications [7-12]. However, these compounds can also rearrange and decompose under a certain high temperature or catalysis. It is beneficial to find out the mechanisms of rearrangement and decomposition reactions and guide the reasonable utilization. Thus based on the mechanisms, avoid, control or use these reactions. It is facile and efficient to investigate theoretically and the theoretical results can provide the basis for the experimental research. Therefore, herein we selected $CH_3H_2SiCH_2F$ as the model and related information was obtained by using density functional theory (DFT) method. To understand details of the mechanism we will discuss the rearrangement in three aspects as described below.

Theoretical methods

The molecular sample of CH_3SiCH_2F was selected to investigate in this work. To understand the process of thermal arrangement reaction, all molecular structures for reactant, product, as well as its transition state were optimized by using quantum chemical DFT methods at the 6-311G(d, p) level. And the harmonic vibrational frequencies were calculated for these structures at the same level. The result shown there is only one imaginary frequency for the transition state, confirming the certainty of transition state. The intrinsic reaction coordinate (IRC) calculation was further more used to demonstrate the rationality of the reaction pathway. Gaussian 03 software was used for all calculations in this work.

Results and discussion

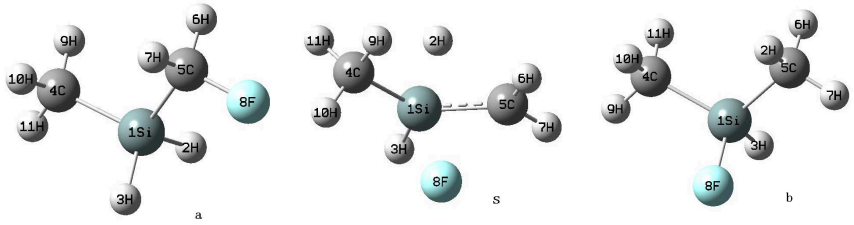


Fig.1 Geometries of the reactant(a), transition state(s), and product(b) of fluoroalkylsilane.

According to the principal of minimum energy, geometries of reactant ($CH_3H_2SiCH_2F$), its rearrangement product ($CH_3HSiFCH_3$), as well as the corresponding transition state were determined through all structures optimized. The structures were schemed the figure 1. Molecular energies for three structures with partial bond-lengths were listed in table 1. Table 2 gave the distribution of atomic charges and electronic transfer among atoms.

Stationary points and energies.

As shown in figure 1, rearrangement occurred from reactant of $CH_3SiH_2CH_2F$, via transition state, to product of $CH_3SiHFCH_3$. In this process, the fluorine atom deviated from the carbon atom step by step, and the hydrogen atom deviated from the silicon atom at the same time, forming the transition state of higher energy. The state possessed energy value of -469.68 a.u and was 205.05 kJ mol^{-1} more than the reactant. That means the reactant should overcome 205.05 kJ mol^{-1} energy barrier to form the transition state. After the fluorine atom migrated from carbon to silicon and the hydrogen atom migrated from silicon to carbon, the transition state transited to its rearrangement product. Compared with reactant, the product was in lower energy level, with energy value of -469.85 a.u and 238.92 kJ mol^{-1} less than the reactant, suggesting the stability of the product.

In the process of rearrangement, some atomic bonds changed obviously. As seen in table 1, when forming transition state the bonds of 1Si-2H and 5C-8F were weakened gradually. The lengths of 1Si-2H and 5C-8F increased 0.12 $\mathring{A}$ and 0.70 $\mathring{A}$ respectively in transition state. Meanwhile, 8F approached 1Si greatly, forming a 1Si-8F bond of 1.83 $\mathring{A}$. Another notable change was the bond of 1Si-5C. From reactant, via transition state to product the length slightly shortened 0.059 $\mathring{A}$ and then enlarged 0.022 $\mathring{A}$.

Table 1. Zero-point energies, absolute energies, relative energies, partial lengths ($\mathring{A}$) of reactant, transition state, and product, calculated at the B3LYP/6-311(d, p) level

species	E_{ZP} (kJ mol^{-1})	E (a.u)	E_R (kJ mol^{-1})	1Si-5C	1Si-2H	1Si-8F	5C-8F
a ($CH_3H_2SiCH_2F$)	218.3397	-469.7549	0.0	1.8857	1.4860	2.7181	1.4087
S	205.6793	-469.6768	205.0499	1.8264	1.6066	1.8315	2.1121
b ($CH_3HSiFCH_3$)	223.1026	-469.8459	-238.9186	1.8686	2.4743	1.6345	2.8402

Atom electronic transfer.

Mulliken atomic charges calculated with above method were listed in table 2. In the rearrangement reaction, those of electronic charges transferred obviously were atoms of 1Si, 2H, 5C and 8F. Due to the interaction of the empty 3d orbit of the silicon atom and the lone pair of electrons of the fluorine atom, partial valence electrons of the silicon atom transferred to the fluorine atom. In the process, the interaction of 5C with 8F weakened gradually, while the interaction of 1Si with 8F enhanced gradually, benefiting formation the transition state. Another active atom of 2H, migrated from 1Si with negative charge to 5C with positive charge, total 0.27 electronic charge transferred. The atom 5C obtained negative charge mainly from 1Si and 2H.

Table 2. Atomic charges in reactant, transition state, and product calculated at the B3LYP/6-311(d, p) level

species	1Si	2H	3H	4C	5C	6H	7H	8F	9H	10H	11H
a ($CH_3H_2SiCH_2F$)	0.735	-0.131	-0.131	-0.631	-0.187	0.115	0.115	-0.289	0.132	0.132	0.140
S	0.939	-0.212	-0.125	-0.598	-0.294	0.177	0.173	-0.446	0.119	0.128	0.140
b ($CH_3HSiFCH_3$)	1.096	0.140	-0.189	-0.640	-0.640	0.125	0.136	-0.430	0.125	0.136	0.140

Vibration frequencies.

Infrared spectra of atomic vibrations were shown in figure 2. Some of the vibrational peaks changed in position and intensity obviously. In figure 2 (a), two strong peaks were located in 906cm-1 and 2225cm-1, one represented the bending vibration of CH_3-SiH_2 group, the other correlated the stretching vibration of two hydrogen atoms relative to the silicon atom. Another major peak located in 1019cm-1, its strength was weaker than the formers, and was caused by the stretching vibration of the C-F bond. When the molecule reached its transition state, obvious changes had taken place in the infrared spectrum. Firstly, the noticeable fact, there was a imaginary frequency at -587cm-1, which was representation of transition state flag. Besides, there appeared many new peaks which were different from that of the reactant. Among them, the strongest one, located at 1669cm-1, was due to the stretching vibration of active H atom relative Si atom, which would weaken the Si-H bond until the disconnect. In 422cm-1 there was a new stronger peak, this was because in the process of forming transition state, fluorine atom migrated to silicon atom to form F-Si bond and the stretching vibration of F-Si bond contributed the infrared spectrum. For the

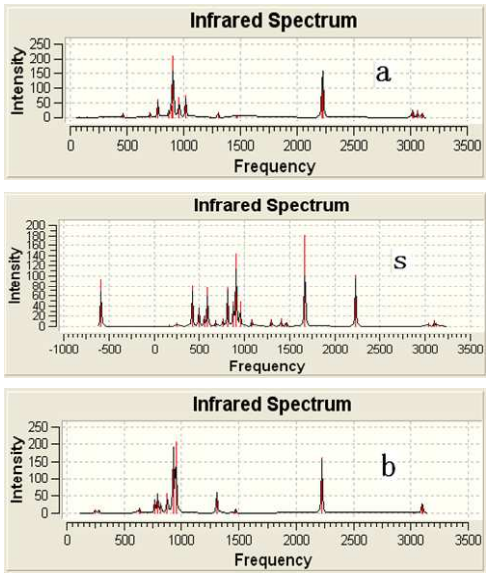


Fig.2 Infrared spectra reactant(a), transition state(s), and product(b) of fluoroalkylsilane.

infrared spectrum of the product, seen figure 2 (b), there were some obvious differences compared with the reactant. In the vicinity of 900cm-1 the original single line in reactant changed to double lines in product. One line at 819cm-1 was the F-Si-H stretching vibration. The additional spectral lines were also observed in the range of 700-800cm-1. And the line of 765cm-1 corresponded to the bending vibration of H-Si-F.

Conclousion

The discussion about rearrangement mechanism of the fluoroalkylsilane showed the reactant would occur rearrangement through a transition state to the product. In the process of rearrangement the fluorine atom migrated from carbon to silicon and the hydrogen atom migrated from silicon to carbon. Part of the electronic charge transferred between atoms, making certain bonds fractured and others formed. The difference of molecular vibrational spectra further confirmed adjustment of the structure as well as the bonding property.

Acknowledgments

This work was supported by the National Natural Science Foundation of China (51373069) and the Natural Science Foundation of Shandong Province (ZR2013BM005).

References

[1] C. Liu, W. Wu, X. Zhang, Y. Man, Research progress of photocurable silicone material，Materials Review. 4 (2006) 44-48.

[2] (1) H. Li, Development and application of organosilicon materials, Silicon Material. 20 (2006) 212-217. (2) H. J. Naghash, R. Mohammadrahimpanah, Synthesis and characterization of new polysiloxane bearing vinylic function and its application for the preparation of poly (silicone-co-acrylate)/montmorillonite nanocomposite emulsion, Progress in Organic Coatings. 70 (2011) 32-38.

[3] S. Mikhalovsky, V. Nikolaev, Biodefence (Eds.), Biodefence, NATO Science for Peace and Security Series A: Chemistry and Biology, Springer Netherlands, 2011, pp199-221.

[4] S. Feng, J. Zhang, M. Li, Q. Zhu, Organosilicon Polymers and Applications, Chemical Industry Press, Beijing, 2004.

[5] (1) M. Kathalewar, A. Sabnis, G. Waghoo, Effect of incorporation of surface treated zinc oxide on non-isocyanate polyurethane based nano-composite coatings, Progress in Organic Coatings, 76(2013) 1215-1229. (2) X. Li, L. Tabil, S. Panigrahi, Chemical treatments of natural fiber for use in natural fiber-reinforced composites, Journal of Polymer Environment, 15(2007) 25-33.

[6] Z. Du, J. Chen, X. Bei, C. Zhou, Organosilicon Chemistry, Chemical Industry Press, Beijing, 1989.

[7] C. Yi, J. Guo, Q. Gao, Z. Xu, Preparation and application of fluorosilicone polymer, Polymer Bulletin. 7(2006) 77-81.

[8] H. Chen, B. Liu, R. Luo, Recent progress and modification on emulsion polymerization of acrylate, West Leather. 12(2007) 18-22.

[9] R. R. Thomas, D. R. Anton, W. F. Graham, M. J. Darmon, K. M. Stika, Films containing reactive mixtures of perfluoroalkylethyl methacrylate copolymers and fluorinated isocyanates: synthesis and surface properties, Macromolecules, 31(1998) 4595-4604.

[10] M. Mazzola, P. Frediani, S. Bracci, A. S, New strategies for the synthesis of partially fluorinated acrylic polymers as possible materials for the protection of stone monuments, European Polymer Journal, 39(2003) 1995-2003.
[11] H. Zhou, H. Wang, H. Niu, A. Gestos, X. Wang, T. Lin, Fluoroalkyl silane modified silicone rubber/nanoparticle composite: A super durable, robust superhydrophobic fabric coating, Advanced Materials, 24(2012) 2409-2412.
[12] A. Nakajima, K. Hashimoto, T. Watanabe, K. Takai, G. Yamauchi, A. Fujishima, Transparent superhydrophobic thin films with self-cleaning properties, Langmuir. 16(2000) 7044-7047.
[13] Y. Chen, Y. Lu, H. Chen, Y. Zhang, Z. Song, F. Song, China Patent 101593584, (2011).
[14] T. He, Z. Luo, C. Lin, L. Dai, Progress in development of marine antifouling coatings, Paint & Coatings Industry.37(2007) 59-62.
[15] J. Beom, J. Ha, D. Kim, J. Kim, J. Kim, K. Kim, K. Lee, S. Lee, I. Park, W. So, Super-water repellent organic/Inorganic composite particles, and process for preparing them, Korea Patent 20050033330 (2005).

Advanced Materials Research Vol. 936 (2014) pp 545-551
© (2014) Trans Tech Publications, Switzerland
doi:10.4028/www.scientific.net/AMR.936.545

Assessments of Impurity Diffusion Coefficients of Selected Pure Metals in Fcc Fe

Xianxian Hu[a], Xiao-Gang Lu[b],Yanlin He[c]

School of Materials Science and Engineering, Shanghai University, China

[a]ddanydany@126.com, [b]xglu@shu.edu.cn, [c]ylhe@staff.shu.edu.cn

Keywords: fcc Fe; impurity diffusion; atomic mobility; CALPHAD; DICTRA

Abstract: The atomic mobilities for impurity diffusion of Al, Au, Co, Cu, Mn, Mo, Nb, Ni, Pt, Sn and Zn in fcc Fe have been critically assessed based on the experimental diffusion coefficient data available in the literature. The impurity diffusion coefficients calculated from the atomic mobilities agree reasonably well with the reliable experimental data. This work provides a helpful guidance for the establishment of a general Fe-based mobility database to design new Fe-based alloys for practical purposes.

Introduction

There are many phenomena associated with diffusion in metallic materials during production and service, such as smelting, crystallization, segregation, equalization, heat treatment, welding. Diffusion is a basic and important factor that should be considered in design of metallic materials. Impurity diffusion refers to the diffusion of impurity atoms (or ions) A in pure metal B at an extremely small concentration. It is not only of practical importance, but also of theoretical interest to describe the diffusion behavior [1].

In the framework of computational thermodynamics and kinetics (also known as CALPHAD), all kinds of diffusion coefficients contribute to assess the atomic mobilities of species in multicomponent materials. When the atomic mobility and thermodynamic data are available, various diffusion coefficients can be readily calculated [1–7] which is especially significant for multicomponent materials. To realize the goal, a software tool, DICTRA (DIffusion-Controlled TRAnsformations) is developed [4, 8]. It is capable of simulating diffusion-controlled phase transformations in multicomponent materials by coupling thermodynamic data with mobility data stored in databases.

The aim of the present work is to use DICTRA to critically assess the atomic mobilities for impurity diffusion of Al, Au, Co, Cu, Mn, Mo, Nb, Ni, Pt, Sn and Zn in fcc Fe based on the experimental diffusion data available in the literature. The evaluated parameters are validated by comparing the calculated diffusion coefficients with measured data and can be easily incorporated into a general Fe-based mobility database for practical purposes.

Modelling of the Atomic Mobility

Almost 20 years ago, Andersson and Ågren [9] and Jönsson [10] modeled the temperature, pressure and composition dependencies of atomic mobility in multi-component solution phases. According to the absolute rate theory, the atomic mobility of element B, denoted by M_B, can be divided into a frequency factor M_B, and an activation enthalpy Q_B, as follows [9-13]:

$$M_B = M_B^0 \exp\left(\frac{-Q_B}{RT}\right)\frac{1}{RT}\Omega^{mag}, \quad (1)$$

where R is the gas constant; T is the temperature; Ω^{mag} is a factor taking into account the effect of the ferromagnetic transition. For the fcc phase, Ω^{mag} can be regarded as 1 [14, 15]. So for the fcc phase, the atomic mobility M_B can be further modified to:

$$M_B = \frac{1}{RT}\exp\left(\frac{-Q_B + RT\ln\left(M_B^0\right)}{RT}\right) = \frac{1}{RT}\exp\left(\frac{\Phi_B}{RT}\right), \quad (2)$$

where Φ_B is a temperature-dependent parameter. Since the impurity diffusion coefficient is directly related to the atomic mobility by the Einstein relation:

$$D_B^* = RTM_B \quad (3)$$

Therefore Φ_B can be easily evaluated from the impurity diffusion coefficient.

Results and Discussion

To assess the atomic mobility parameters, the experimental data are collected and the optimization is performed in the PARROT module in DICTRA, which is based on the minimization of the residual between the calculated and measured diffusion coefficients.

Table 1 summarizes the experimental data utilized in the assessment, together with the temperature range and experimental methods. The work uses the book by Neumann and Tuijn[16] as the main reference from which most of the literature are incorporated and critically classified Additional experimental data are collected by literature research. In the following, these experimental impurity diffusion data are critically evaluated.

Table 1 Experimental information for impurity diffusion in fcc Fe utilized in this work.

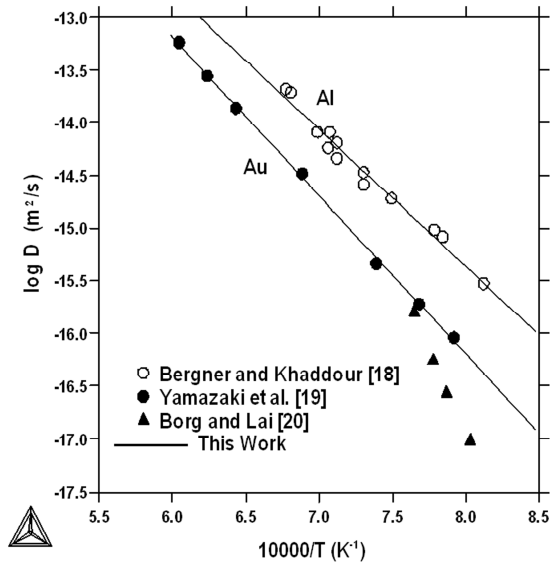
Diffusion data	Temperature [K]	Method	References
Al in Fe	1003-1673	Polycrystals, 99.9%; XRD; diffraction method	[17]
	1230-1473	Fe (1.5%Al)/Fe/Fe(1.5% Al); diffusion couple; EPMA	[18]
Au in Fe	1263-1653	diffusion couple ; EPMA	[19]
	1245-1307	^{195}Au; polycrystals; 99.999 %; residual activity	[20]
Co in Fe	1478–1535	^{60}Co; electroplated; lathe	[21]
	1409–1633	Co, polycrystals, 99.999 %; diffusion couple and thin film; EPMA	[22]
	1223-1593	Co, polycrystals, 99.99 %; diffusion couple; EPMA	[23]
	1233-1493	^{60}Co, polycrystals, 99.9 %; residual activity	[24]
Cu in Fe	1202–1293	Cu, polycrystals; EPMA	[25]
	1558–1641	Cu, single crystals, 99.91%; 64Cu; vapour deposition; grinder	[26]

		sectioning	
	1203–1283	Cu; Cu/Fe diffusion couples; EPMA	[27]
	1198–1323	Cu, polycrystal, 99.999%; vapour deposition (4 mm film); EPMA	[28]
Mn in Fe	1193–1553	Mn, polycrystals, 99.97%; ^{54}Mn, electroplated; residual activity	[29]
Nb in Fe	1435–1607	^{95}Nb; electroplated; residual activity	[30]
	1221–1474	Nb, polycrystals, 99.99 %; ^{95}Nb; electroplated; serial sectioning	[31]
	1210–1604	Nb, polycrystals, 99.97 %; ^{95}Nb; dried-on from oxalate solution; microtome sectioning	[32]
Mo in Fe	1217–1573	^{99}Mo; residual activity	[33]
Ni in Fe	1425–1673	^{63}Ni; electroplated; absorption	[34]
	1409–1633	Ni, polycrystals, 99.999%; diffusion couple and thin film; EPMA	[22]
Pt in Fe	1183–1533	Pt, polycrystals;^{193}Pt; electroplated; residual activity	[35]
Sn in Fe	1197–1653	Sn, polycrystals, >99.97%; ^{113}Sn; dried-on from salt solution; serial sectioning	[36]
Zn in Fe	1273–1425	Zn; Fe/Fe (3% Zn) diffusion couple; EPMA	[37]

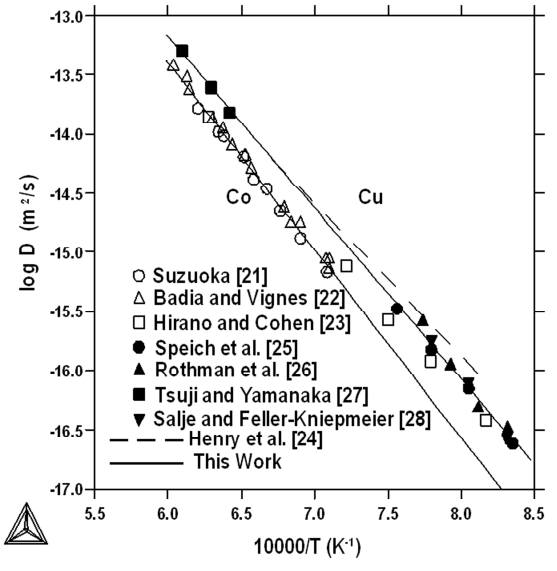
Note: EPMA= electron probe microanalysis.

For the impurity diffusivities of Al in fcc Fe, the data reported by Akimova et al. [17] are nearly ten times larger than those measured by Bergner and Khaddour [18]. In addition, no influence of bcc/fcc transition were observed by Akimova et al. In the present work, only Bergner and Khaddour's data were used in the assessment. In the case of Au, more recent data by Yamazaki et al. [19] were adopted in the assessment. The impurity diffusion coefficients of Co measured by Henry et al. [24] are larger than those of Suzuoka [21], Badia and Vignes [22], their data are not consistent with the interdiffusion coefficients measured for fcc Fe-Co alloys and not selected in the assessment. Hirano and Cohen's[23] data were also not used, because the data are larger in the low-temperature region. For the impurity diffusivities of Mn, Mo, Pt, Sn and Zn in fcc Fe, only one set of experimental data was found and used to assess the corresponding atomic mobilities.

Table 2 lists the assessed mobility parameters for impurity diffusion of eleven elements. The calculated diffusion coefficients are shown in Fig. 1. As can be seen, the calculated values agree well with the measured values for the eleven elements.



(a)



(b)

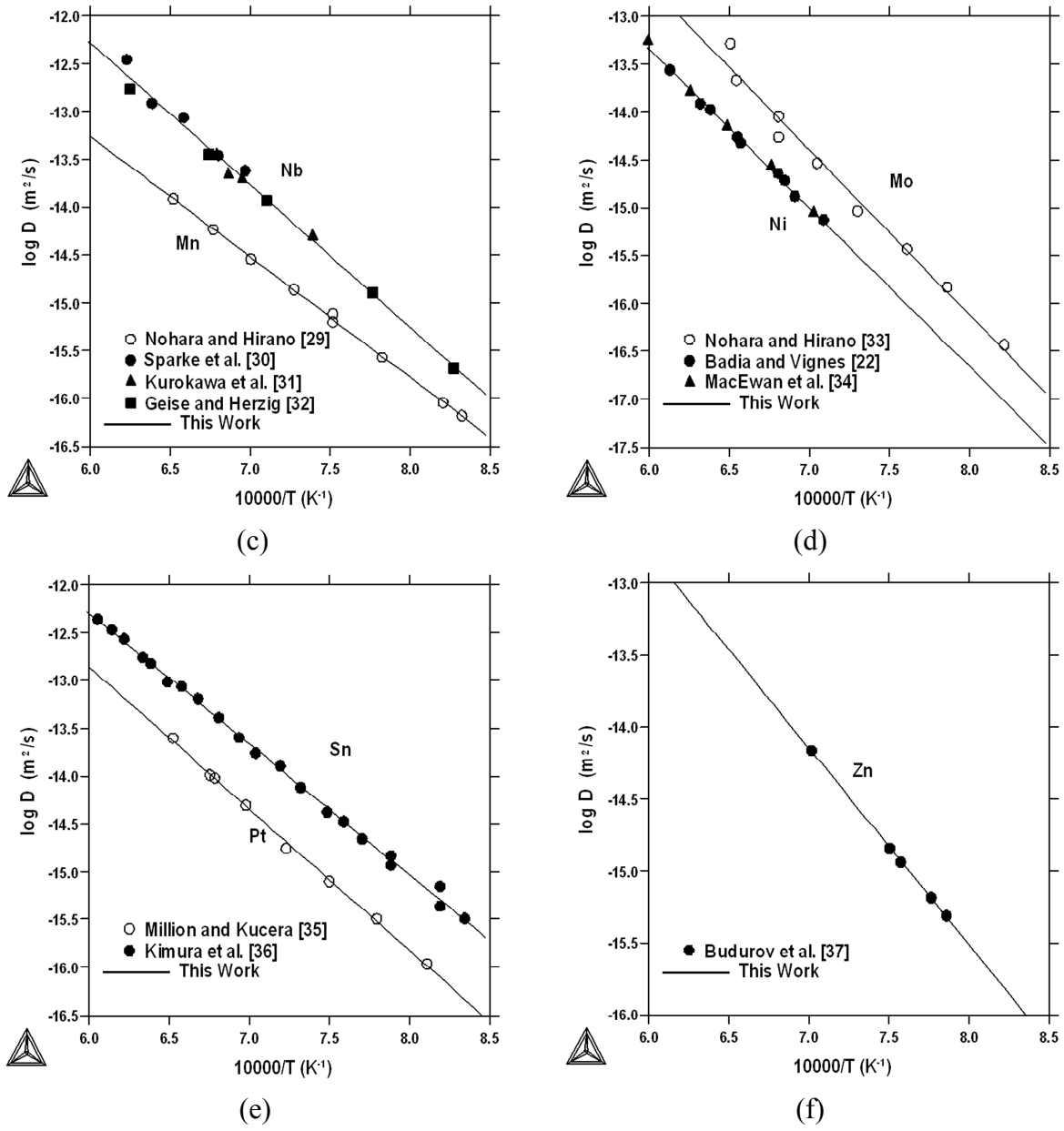


Fig. 1. Impurity diffusion coefficients in fcc Fe plotted against inversed temperature. Note that the filled symbols represent experimental data for one element and the unfilled for another. (a) Al and Au ; (b) Co and Cu. Note that the dashed line is for Co; (c) Mn and Nb ; (d) Mo and Ni ; (e) Pt and Sn ; (f) Zn

Table 2 Assessed atomic mobilities for the impurity diffusion in fcc Fe

Phase	Mobility	Parameters
fcc	Al	$\Phi_{Al}^{Fe} = -249274 + R*T*\ln(1.1222E-5)$
	Au	$\Phi_{Au}^{Fe} = -287984 + R*T*\ln(6.8076E-5)$
	Co	$\Phi_{Co}^{Fe} = -303256 + R*T*\ln(1.2749E-4)$
	Cu	$\Phi_{Cu}^{Fe} = -276942 + R*T*\ln(3.1610E-5)$

Mn	$\Phi_{Mn}^{Fe} = -240863 + R*T*\ln(1.9202E-6)$
Nb	$\Phi_{Nb}^{Fe} = -284913 + R*T*\ln(4.4564E-4)$
Mo	$\Phi_{Mo}^{Fe} = -329743 + R*T*\ln(4.5296E-3)$
Ni	$\Phi_{Ni}^{Fe} = -318009 + R*T*\ln(4.2063E-4)$
Pt	$\Phi_{Pt}^{Fe} = -283464 + R*T*\ln(1.0428E-4)$
Sn	$\Phi_{Sn}^{Fe} = -262349 + R*T*\ln(8.4284E-5)$
Zn	$\Phi_{Zn}^{Fe} = -261602 + R*T*\ln(2.6024E-5)$

Summary

Based on the PARROT module in DICTRA and various diffusion data available in the literature, the impurity diffusion coefficients for Al, Au, Co, Cu, Mn, Mo, Nb, Ni, Pt, Sn and Zn in fcc Fe have been critically evaluated. The computed impurity diffusion coefficients resulting from the assessed diffusion parameters agree reasonably with the reliable experimental data. The presently obtained impurity diffusion coefficients are of both technological and theoretical importance.

Acknowledgements

The financial support from the National Key Project of Science and Technology (Grant number: 2012ZX06004-012) is gratefully acknowledged.

References

[1] J.-O. Andersson, L. Hoglund, B. Jonsson, J. Agren, in: G.R. Purdy (Ed.), Fundamentals and Applications of Ternary Diffusion, Pergamon Press, New York, 1990, p. 153.

[2] B. Jönsson, Assessment of the mobilities of Cr, Fe and Ni in binary FCC Cr-Fe and Cr-Ni alloys, Scand. J. Metall. 24 (1995) 21-27.

[3] B. Jönsson, Mobilities in Fe-Ni alloys: assessment of the mobilities of Fe and Ni in fcc Fe-Ni alloys, Scand. J. Metall. 23 (1994) 201-208.

[4] A. Borgenstam, A. Engstrom, L. Hoglund, J. Agren, DICTRA, a tool for simulation of diffusion transformations in alloys, J. Phase Equilib. 21 (2000) 269-280.

[5] Y. Du, J.C. Schuster, Assessment of Diffusional Mobilities of Cr, Ni, and Si in fcc Cr-Ni-Si Alloys, Z. Metallkd. 92 (2001) 28-31.

[6] Y. Du, J.C. Schuster, An effective approach to describe growth of binary intermediate phases with narrow ranges of homogeneity, Metall. Mater. Trans. A 32 (2001) 2396-2400.

[7] C.E. Campbell, W.J. Boettinger, U.R. Kattner, Development of a diffusion mobility database for Ni-base superalloys, Acta Mater. 50 (2002) 775-792.

[8] J.-O. Andersson, T. Helander, L.H. Hoglund, et al. Thermo-Calc and DICTRA, computational tools for materials science, Calphad 26 (2002)273-312.

[9] J.-O. Andersson, J. Ågren, Models for numerical treatment of multicomponent diffusion in simple phases, J. Appl. Phys. 72 (1992) 1350-1355.
[10] B. Jönsson, Assessment of the Mobilities of Cr, Fe and Ni in bcc Cr-Fe-Ni Alloys, ISIJ Int. 35 (1995) 1415-1421.
[11] G. Ghosh, Dissolution and interfacial reactions of thin-film Ti/Ni/Ag metallizations in solder joints, Acta Mater. 49 (2001) 2609-2624.
[12] T. Helander, J. Ågren, A phenomenological treatment of diffusion in Al-Fe and Al-Ni alloys having B2-bcc ordered structure, Acta Mater. 47 (1999) 1141-1152.
[13] T. Helander, J. Ågren, Diffusion in the B2-bcc phase of the Al-Fe-Ni system application of a phenomenological model, Acta Mater. 47 (1999) 3291-3300.
[14] B. Jönsson, On Ferromagnetic Ordering and Lattice Diffusion: A Simple Model, Z. Metallkd. 83 (1992) 349-355.
[15] B. Jönsson, Ferromagnetic Ordering and Diffusion of Carbon and Nitrogen in bcc Cr-Fe-Ni Alloys, Z. Metallkd., 85 (1994) 498-501.
[16] G. Neumann, C. Tuijn, Self-Diffusion and Impurity Diffusion in Pure Metals: Handbook of Experimental Data, first ed., Great Britain, 2009.
[17] L.A. Akimova, V.M. Mironov, A.V. Pokoyev, Fiz. Met. Metalloved. 56 (1983) 1225.
[18] D. Bergner, Y. Khaddour, Impurity and Chemical Diffusion of Al in BCC and FCC Iron, Defect and Diffusion Forum 95-98 (1993) 709-714.
[19] Y. Yamazaki, Y. Iijima, M. Okada, Enhanced diffusion of Au in γ-Fe by vacancies induced under elevated hydrogen pressure, Acta Mater. 52 (2004) 1247-1254.
[20] R.J. Borg, D.Y.F. Lai, Acta Metall. The diffusion of gold, nickel, and cobalt in alpha iron: A study of the effect of ferromagnetism upon diffusion, 11 (1963) 861.
[21] T. Suzuoka, Lattice diffusion and grain boundary diffusion of cobalt·in Iron, Trans. Jpn. Inst. Metals 2 (1961) 176-181.
[22] M. Badia, A. Vignes, Iron, nickel and cobalt diffusion in transition metals of iron group, Acta Metall. 17 (1969) 177-187.
[23] K. Hirano, M. Cohen, Diffusion of Cobalt in Iron-Cobalt Alloys, Trans. Jpn. Inst. Metals 13 (1972) 96.
[24] G. Henry, G. Barreau, G. Cizcron, Coefficients of volume diffusion of Co in gamma Fe and in Fe-Co alloys, C. R. Acad. Sci., (Paris) 280 (1975) 1007-1010.
[25] G.R. Speich, J.A. Gula, R.M. Fisher, T.D. McKinley, K.F.J. Heinrich, D.B. Wittry (Eds.), The Electron Microprobe, Wiley, New York, 1966, pp. 525-542.
[26] S.J. Rothman, N.L. Peterson, C.M. Walter, L.J. Nowicki, The Diffusion of Copper in Iron, J. Appl. Phys. 39 (1968) 5041.
[27] S. Tsuji, K. Yamanaka, Interdiffusion Coefficients and Moving Rates of Phase Interfaces for Reaction-Diffusion in the Cu-Fe System, J. Jpn. Inst. Metals 38 (1974) 415-421.
[28] G. Salje, M. Feller-Kniepmeier, The diffusion and solubility of copper in iron, J. Appl. Phys. 48 (1977) 1833-1839.
[29] K. Nohara, K. Hirano, Proceedings of International Conference on Science and Technology of Iron and Steel, Trans. Iron Steel Inst. Jpn. (Suppl.) 11 (1971) 1267.
[30] B. Sparke, D.W. James, G.M. Leak, J. Iron Steel Inst. 203 (1965) 152.
[31] S. Kurokawa, J.E. Ruzzante, A.M. Hey, F. Dyment, Diffusion of Nb in Fe and Fe alloys, Met. Sci. 17 (1983) 433-438.
[32] J. Geise, Ch. Herzig, Lattice and grain boundary diffusion of niobium in iron, Z. Metallk. 76 (1985) 622-626.

[33] K. Nohara, K.-I. Hirano, Self-diffusion in the iron-molybdenum system. [Impurity diffusivity of Mo in pure Fe. Transformations], J. Jpn. Inst. Metals 40 (1976) 1053-1061.

[34] J.R. MacEwan, J.U. MacEwan, L. Yaffe, Diffusion of Ni^{63} in iron, cobalt, nickel, and two iron-nickel alloys, Can. J. Chem. 37 (1959) 1629-1636.

[35] B. Million, J. Kučera, Diffusion of Pt-193 m in platinum, gamma-iron, cobalt and nickel, Kovové Mater. 11 (1973) 300-306.

[36] K. Kimura, Y. Iijima, K. Hirano, Diffusion of tin in gamma-iron, Trans. Jpn. Inst. Metals 27 (1986) 1-4.

[37] S. Budurov, P. Kovatchev, Z. Kamenova, Chemical diffusion of zinc into gamma- and alpha-iron, Z. Metallk. 64 (1973) 652-654.

Advanced Materials Research Vol. 936 (2014) pp 552-561
© (2014) Trans Tech Publications, Switzerland
doi:10.4028/www.scientific.net/AMR.936.552

The properties of a novel green long afterglow phosphor $Zn_2GeO_4:Mn^{2+}_{0.01}, Pr^{3+}_{0.01}$

Minhua Wan[a], Yinhai Wang[a*], Xiansheng Wang[a], Hui Zhao[a], Zhengfa Hu[a], Cheng Wang[b]

[a.] School of Physics and Optoelectronic Engineering, Guangdong University of Technology, Waihuan Xi Road, No.100, Guangzhou 510006, PR China

[b.] State Key Laboratory of Rare Earth Resource Utilization, Changchun Institute of Applied Chemistry, Chinese Academy of Sciences, Changchun 130022, PR China

Keyword: Zn_2GeO_4 afterglow traps Mn^{2+}

Abstract: $Zn_2GeO_4:Mn^{2+}_{0.01}$, $Pr^{3+}_{0.01}$ long afterglow phosphors were synthesized by the high temperature solid state reaction. The X-Ray diffraction (XRD), emission spectra, afterglow spectra, decay curve and thermoluminescence curve were utilized to characterize the sample. The X-Ray diffraction phases indicate that the sample have a crystal structure of Zn_2GeO_4 and was not influenced by co-doped Mn^{2+}, Pr^{3+} no influence for crystal structure. According to the emission spectra, we found that the $Zn_2GeO_4:Mn^{2+}_{0.01}$, $Pr^{3+}_{0.01}$ exhibit a narrow band emission with the peak at 532nm, which could be ascribed to Mn^{2+} transition between $^4T_1$ and $^6A_1$ electron configurations. The green long afterglow of $Zn_2GeO_4:Mn^{2+}_{0.01}$,$Pr^{3+}_{0.01}$ could be observed for three hours by naked eyes at room temperature under 254 nm UV excitation. The thermoluminescence (TL) curve is employed for the discussion of the origin of the traps and the mechanism of the persistent luminescence. The results indicate that $Zn_2GeO_4:Mn^{2+}_{0.01}$, $Pr^{3+}_{0.01}$ may be an excellent green long afterglow material and the Pr^{3+} ions behave as the electron trapping centers to be associated with the occurrence of the ultra-long afterglow.

Introduction

Persistent luminescence is a phenomenon whereby luminescence can last for hours after the stop of the excitation. Phosphors with persistent luminescence have been rapidly developed in the past decade, largely stimulated by the widely used in many areas such as the traffic signs, emergency signage, display, optical memory, imaging storage and high energy ray detection [1]. Therefore, many efforts have been made to discover long afterglow host material as well as activators with high performance. In recent years, germanates has attracted considerable attention and have been widely investigated as new host materials for light emitting devices [2]. Among germanates, zinc germanate (Zn_2GeO_4) is an excellent candidate due to its reasonable conductivity and high stability. As is reported, Zn_2GeO_4 has been discovered to be a self-activated white-blue phosphor, whose emission may be due to a radiative transition from a donor of oxygen vacancy ($V^{\bullet}_{O}$) or Zn interstitial ($Zn^{\bullet}_{i}$) to an acceptor of germanium vacancy (V_{Ge}) or zinc vacancy ($V^{''}_{Zn}$) [3,4]. Especially, the Mn^{2+} activated Zn_2GeO_4 phosphors exhibit more saturated green emission than the commercial FEDs phosphor ZnO:Zn, and it expected that these phosphors are promising for application in field-emission displays [5]. By our knowledge, Zn_2GeO_4 have played an important

role as new host material for field emission displays but few literatures focus on its potential as long afterglow host material. Zinc germanate can acts as long afterglow host material for high luminance and long persistence of phosphorescence phosphors when doped with appropriate active center. As the previous reported [4], transition metal Mn^{2+} ions can serve as luminescence center and exhibit high luminescent output in inorganic oxide compounds, the rare earth Pr^{3+} ions could act as the electron trapping centers to enhance the long afterglow time. Therefore, the $Zn_2GeO_4:Mn^{2+}_{0.01}$, $Pr^{3+}_{0.01}$ phosphor with high luminescence intensity and saturated color have been investigated in the present study. Mn^{2+} ions are centers capable of emitting radiation after being excited, Pr^{3+} store excitation energy and release it gradually to emitters (Mn^{2+}) owing to thermal stimulations. This new persistent material has potential application in optical memory, traffic signs, display, emergency signage and so on. As far as the author's knowledge, the long afterglow property and mechanism of $Zn_2GeO_4:Mn^{2+}_{0.01}$, $Pr^{3+}_{0.01}$ are first reported by the present work and a new member of green long afterglow phosphors based on zinc germinates is added. Up to now, the $Zn_2GeO_4:Mn^{2+}_{0.01}$, $Pr^{3+}_{0.01}$ may be the longest and the brightest green long afterglow materials base on Mn^{2+} as luminescence center. The luminescent properties of $Zn_2GeO_4:Mn^{2+}_{0.01}$, $Pr^{3+}_{0.01}$ as a long afterglow phosphor have been investigated in detail by measuring the emission spectra, afterglow spectra, the decay curve and the thermoluminescence curve. According to the TL curves, the mechanism of afterglow decay is analyzed in depth based on electron transfer between the traps and energy bands.

Experimental

The sample $Zn_2GeO_4:Mn^{2+}_{0.01}$, $Pr^{3+}_{0.01}$ was synthesized via high temperature solid-state reaction of constituent oxides, namely, ZnO, GeO_2, Pr_2O_3. Manganese was added in the form of manganous carbonate. The raw powders were weighed according to the nominally compositions and the mixture was milled for about 1h in an agate mortar. Subsequently, the mixed powders were moved into a corundum crucible and sintered at 1300℃ for 5h in an air ambient. Meanwhile, we synthesized $Zn_2GeO_4:Mn^{2+}_{0.01}$ for comparing.

The crystal structure of the powder phosphor was analyzed by X-ray powder diffraction (XRD) using Cu Kα (λ=0.15418 Å) irradiation operating at 36 kV and 20 mA. The emission, excite spectra and afterglow spectra were performed by means of a Hitachi F-700 fluorescence spectrophotometer. Prior to the afterglow spectra measurements, the sample was exposed to radiation from a UV lamp with 254nm wavelength for 3 minutes. The afterglow decay curves were detected via GFZF-2A single-photon counter system after the samples were irradiated with a conventional tricolor fluorescence tube. A FJ27A1 thermoluminescent dosimeter was used to record thermoluminescence curve with the heating rate of 1℃/s, the measurement started after switching off the light source 5 minutes.

Results and discussion

phase structure

Structure of the $Zn_2GeO_4:Mn^{2+}_{0.01}$, $Pr^{3+}_{0.01}$ powder was studied by means of the XRD power diffraction technique. As shown in Fig.1, all the diffraction peaks are consistent with the standard JCPDS card NO.11-0687, which indicates that the co-doped Mn^{2+}, Pr^{3+} have little influence on the crystal structure of Zn_2GeO_4, and all of the peaks are assigned to the phase of Zn_2GeO_4. The Zn_2GeO_4, whose structure is constructed by corner-shared ZnO_4 tetrahedral and GeO4 tetrahedral, has a rhombohedra until cell with space group $R\bar{3}$ [5] and has a phenacite structure with lattice constants of a=b=14.231Å and c=9.53Å. The coordination number of Zn, Ge, O atoms is 4, 4, 3,

respectively [6]. Considering the ionic radii of Zn^{2+} (0.60Å), Mn^{2+}(0.66Å), Pr^{3+}(0.99Å) and Ge^{4+}(0.39Å) ions in the site of CN(coordination number)=4, it is expected that the Pr^{3+} ions substitute the Zn^{2+} ions. Meanwhile, it is also expected that the Mn^{2+} ions substitute the Zn^{2+} ions due to the close radius in $Zn_2GeO_4:Mn^{2+}_{0.01}$, $Pr^{3+}{}_{0.01}$ phosphor.

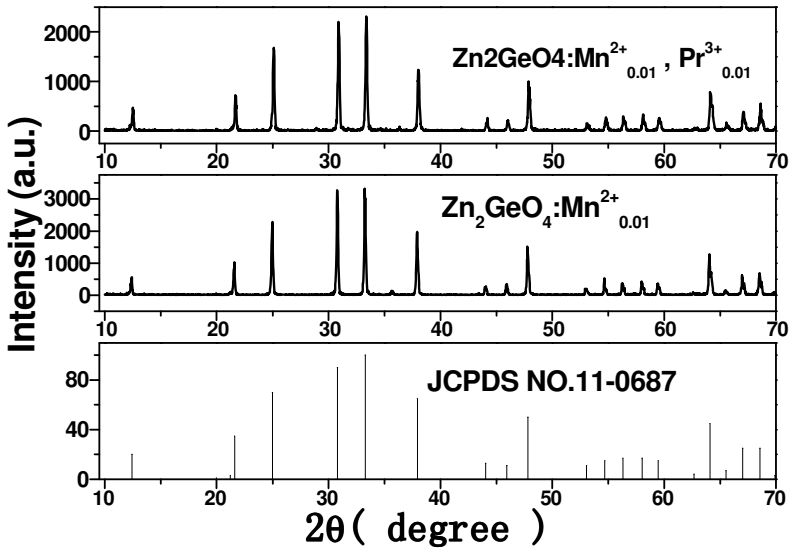


Fig.1. XRD patterns of the as-prepared sample and the pattern of JCPDS NO.11-0687 for Zn_2GeO_4

Luminescence properties

In order to study the photoluminescence properties of the phosphor, the PL emission spectrum of a $Zn_2GeO_4:Mn^{2+}_{0.01}$, $Pr^{3+}{}_{0.01}$ at room temperature is shown in Fig.3. As we know, the Mn^{2+} ions activated phosphors can give green or red emission, which depends on the crystal field condition. The Mn^{2+} ion yields green luminescence when it is tetrahedrally coordinated (CN=4) in the lattice whereas it emits red luminescence in octahedral coordination (CN=6) [5]. As mentioned earlier, there are only the tetrahedral Zn^{2+} sites available for Mn^{2+} ions in the rhombohedral Zn_2GeO_4 host. Therefore, Mn^{2+} gives green emission, which is consistent with the spectral result. Just as Fig.3 shows, we can observe that photoluminescence spectrum of $Zn_2GeO_4:Mn^{2+}_{0.01}$, $Pr^{3+}{}_{0.01}$ exhibits symmetric emission band at about 532nm could be attributed to the $^4T_1$（^4G）$\rightarrow{}^6A_1$（^6S）transition of Mn^{2+} ions which occupy the tetrahedral coordination. Additional, we can infer from the emission spectrum that the Pr^{3+} ions act as electron trap center instead of luminescence center in our research. And the Pr^{3+} ions behave as the electron trapping center to be associated with the occurrence of the long afterglow will be discuss in detail later.

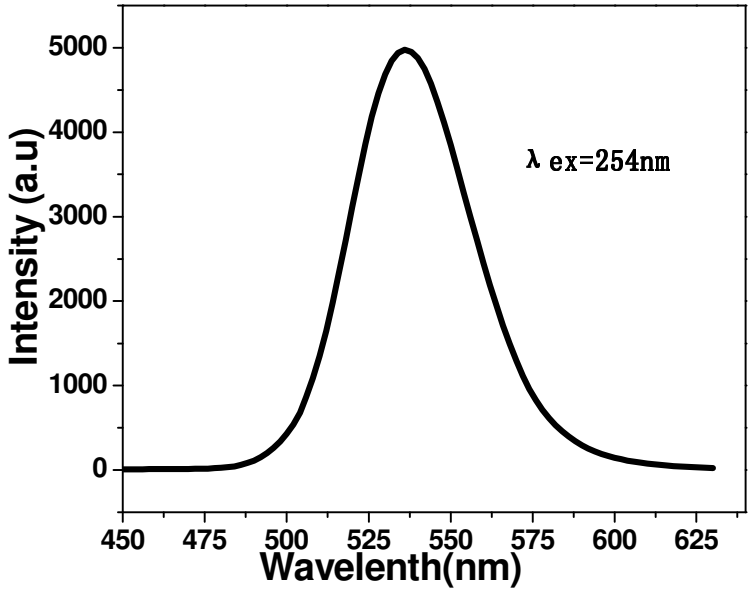


Fig.3 The emission spectrum of $Zn_2GeO_4:Mn^{2+}_{0.01}$, $Pr^{3+}_{0.01}$ under the excitation of 254nm at room temperature

Long afterglow properties

Afterglow spectra

Besides the intense photoluminescence, the excitation of UV light can also induce long-lasting persistent luminescence in $Zn_2GeO_4:Mn^{2+}_{0.01}$, $Pr^{3+}_{0.01}$ phosphor with a persistent times ＞3h (here the persistent times is defined as the duration for which the naked eyes can see). Fig.3a displays typical time-resolved photoluminescence spectra of $Zn_2GeO_4:Mn^{2+}_{0.01}$, $Pr^{3+}_{0.01}$ phosphor. The emission peak at about 532nm in the afterglow photoluminescence remain the same without any change, indicating that the afterglow characteristics of the as-prepared sample can be considered coming from the $^4T_1$ to $^6A_1$ transition of Mn^{2+} ions, it has also indicated that the Pr^{3+} ions only serve as the trap center, not as the luminescent center. As can be seen in the Fig.3a, the afterglow intensity of 0min is remarkably stronger than that of 2 min, while the intensity is no significant difference of 4 min, 6 min, and 8 min. The long-lasting persistent luminescence of the $Zn_2GeO_4:Mn^{2+}_{0.01}$, $Pr^{3+}_{0.01}$ phosphor discs were also visually evaluated using a fluorescence microscopy in the dark room. Fig.3b-f show the changes of green emission “brightness” with a decay time up to 3h for three $Zn_2GeO_4:Mn^{2+}_{0.01}$, $Pr^{3+}_{0.01}$ discs after exposure to a 4w 254nm lamp for 30s, 3min, 5min. Fig.3b-f clearly shows that the $Zn_2GeO_4:Mn^{2+}_{0.01}$, $Pr^{3+}_{0.01}$ discs can be effectively activated by a 254nm UV lamp and seconds to minutes of irradiation can result in 3h of persistent green emission.

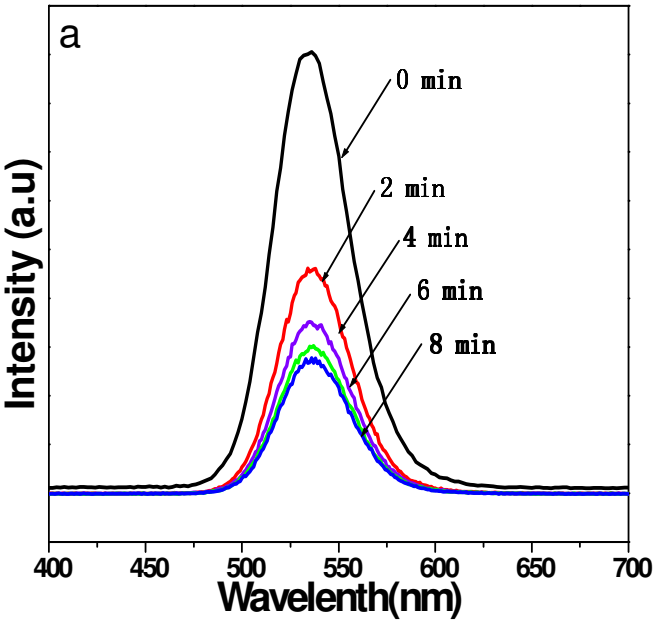


Fig.3a. Long afterglow spectra of $Zn_2GeO_4:Mn^{2+}_{0.01}$, $Pr^{3+}_{0.01}$.

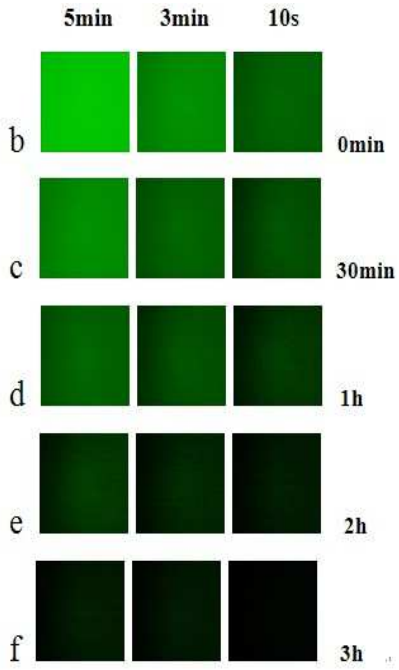


Fig.4b. Time-resolved photoluminescence spectra of $Zn_2GeO_4:Mn^{2+}_{0.01}$, $Pr^{3+}_{0.01}$ phosphor which were examined in 0,2,4,6,8min after the 254nm ultraviolet lamp excitation for 5min at room temperature. Fig.4b-f. images of three discs taken at different persistence luminescence times after irradiated by a 254nm lamp for 10s, 3min, 5min, respectively.

Decay characteristics

In order to investigate the decay characteristics, Fig.4 shows the persistent luminescence decay curve of $Zn_2GeO_4:Mn^{2+}_{0.01}$, $Pr^{3+}_{0.01}$ phosphor disc monitored at 532nm after irradiation by 254nm UV light for 5min. The recording lasted for 1h. As can be seen, the persistence luminescence intensity drops quickly in the first several minutes and then decays slow. After an hour of persistent emission, the persistence luminescence intensity is still significantly high, indicating that the persistent luminescence should last much longer than 1h. After switch off the exciting resource for 3h, we can see the emission still by the naked eyes. The upper inset of Fig.4 shows a persistence luminescence emission spectrum recorded at 1h after the stop of 254nm UV light irradiation. The profile of the persistence luminescence emission spectrum is almost identical to that of photoluminescence emission spectrum, indicating that the persistence luminescence originates from Mn^{2+} emitting center. The afterglow characteristics are evaluated using the curve fitting, since the decay process of the phosphor contains the rapid–decaying process and the slow-decaying process which has mentioned in the previous study [13,14]. In our work, the double exponential function is utilized to fit into the decay curves. The formation of the function is as follows:

$$I = I_1 \exp(\frac{-t}{\tau_1}) + I_2 \exp(\frac{-t}{\tau_2}) \quad (1)$$

Where t is the decay time; I (t) represent the phosphorescent intensity at the t time; I_1 and I_2 are constants which depend on the rapid and slow initial luminescent intensity at t=0; τ_1 and τ_2 time of $Zn_2GeO_4:Mn^{2+}_{0.01}$, $Pr^{3+}_{0.01}$ phosphor is up to 843s. And we discover that the $Zn_2GeO_4:Mn^{2+}_{0.01}$,

$Pr^{3+}_{0.01}$ phosphor exhibits a much longer slow-decaying time than that of $Zn_2GeO_4:Mn^{2+}_{0.01}$ phosphor. It indicates that the co-doping with Pr^{3+} ions can strongly prolong the afterglow duration of the $Zn_2GeO_4:Mn^{2+}_{0.01}$ phosphor. The main reason why co-doping Pr^{3+} could enhance the decay characteristics will discuss in detail latter.

Table 1 Simulated results for the afterglow curves of $Zn_2GeO_4:Mn_{0.01}^{2+}$, Pr^{3+} and $Zn_2GeO_4:Mn_{0.01}^{2+}$

Phosphor composition	τ_1(s)	τ_2(s)
Zn2GeO4:Mn2+，Pr3+	58	843
Zn2GeO4:Mn2+	24	144

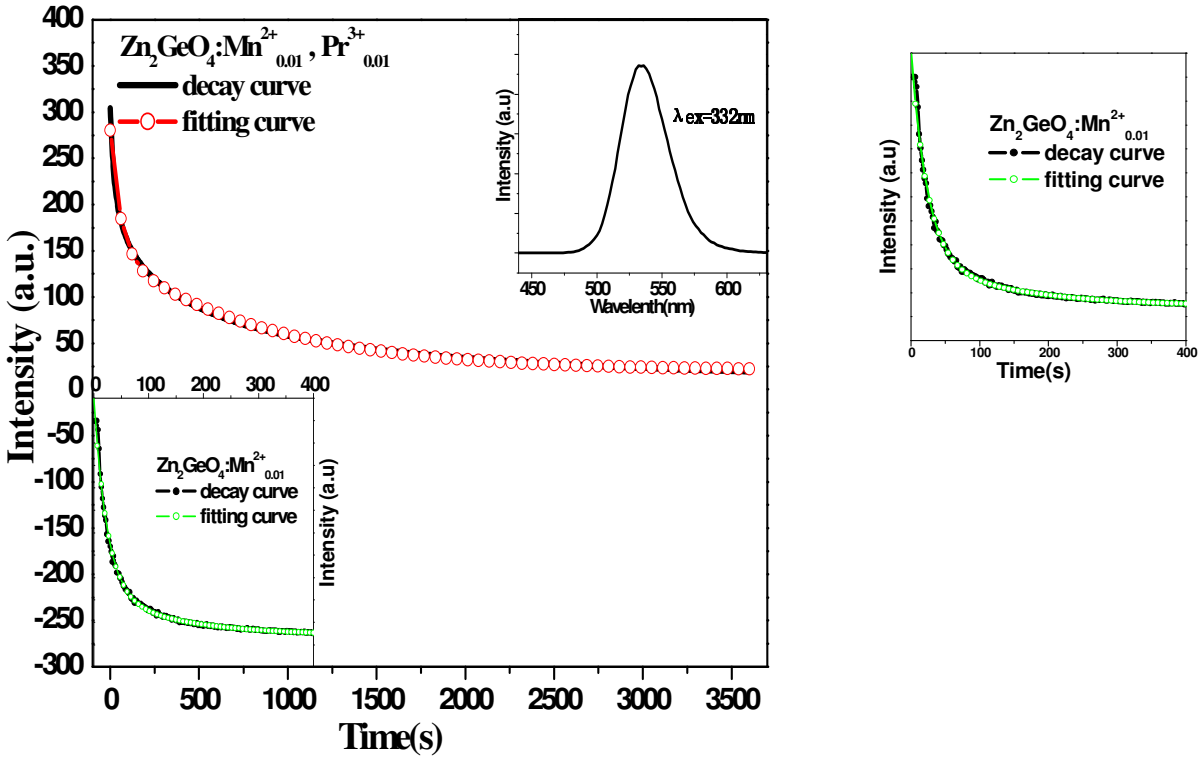


Fig.4 Afterglow decay curve of $Zn_2GeO_4:Mn_{0.02}^{2+}$, Pr^{3+} excited by a 254nm ultraviolet lamp at room temperature. The bottom inset is the afterglow decay curve of $Zn_2GeO_4:Mn_{0.02}^{2+}$ excited by a 254nm ultraviolet lamp at room temperature. Long afterglow intensity (I) monitored at 532nm as a function of time (t). The phosphors were irradiated for 5 minutes. The fitting curves are shown as green line and red line with empty circle. The upper inset shows the persistent luminescence emission spectrum recorded at 1h after the stop of the irradiation.

Thermoluminesecence characteristics

As already known, the afterglow of the phosphors is considered to be generated by the detrapped carriers which recombine in the luminescent centers accompanied by the decay emission, hence the traps which induced by the lattice defects in the phosphor play an important role on the afterglow. In order to investigate the relationship between the long afterglow and the trap energy level, the thermoluminescence curve which reflect the trapping property of defects were recorded and shown in Fig.4. As can be seen in Fig.4, only one peak is observed above room temperature which resides around 68℃, indicating that the sample only have one trap in the range from 25℃ to 250℃. The

TL parameters of the thermal activation energy E which is associated with the trap depth can be obtained by fitting experimental data to the general order kinetics formula. The TL intensity I as a function of the temperature T is described as follows [13,14]

$$I(T) = S\, n_0 \exp(-\frac{E_t}{k_B T}) \times [\frac{(l-1)s}{\beta} \times \int_{T_0}^{T} \exp(-\frac{E_t}{k_B T})\ dT + 1]^{-l/(l-1)} \quad (3)$$

Where I(T) is the TL intensity; E is the activation energy (trap depth); n_0 is the concentration of trap carries(electrons or holes) at t=0; s is the frequency factor; k_B is the Boltzmann's constant; β is heating rate (1℃/s in this study), and l is the order of kinetics. In this research, as the effect of s on T_m (the temperature of glow peak) is neglected and the frequency of an electron escaping from the trap is 1/s, then the thermal activation energy E(eV) could be estimated by the formula of E=T_m(K)/500 [15]. Where T_m is the temperature of the glow peak in the thermoluminesecence curve. Therefore, we can calculate the trap depth of Zn_2GeO_4:$Mn^{2+}_{0.01}$, $Pr^{3+}_{0.01}$ is 0.69eV. Generally, for phosphor, in order to exhibit long afterglow at room temperature, it is crucial to have a suitable trap level and trap density. If the depth of the trap level is too low, the electron in the trap can return to the energy level of the excited state easily, thus resulting in poor afterglow property. On the other hand, if the trap depth is too deep, the energy necessary for the electron to return to the excited state level is so difficult to obtain at room temperature, also resulting in short afterglow time. As previous reported, the trap energy(0.65eV-0.75eV) whose TL peaks located at 50~110℃ can generate optimal long afterglow at room temperature [16]. According to the calculated trap depth and the position of TL peak, we believe that the Zn_2GeO_4:$Mn^{2+}_{0.01}$, $Pr^{3+}_{0.01}$ phosphor have an opportune trap depth so that the sample could exhibit excellent afterglow at room temperature.

In the previous research, we know that Zn_2GeO_4 was a native defect material whose lattice defects have already existed even without (co-)doping other ions [15]. When Pr^{3+} ions were doped into Zn_2GeO_4, they would substitute the divalent cation Zn^{2+}, which have mentioned in the part of phase structure. As the introduction of Pr^{3+} ions, the periodic structure is distorted and the disturbances in the crystal planes are generated since the radius of Pr^{3+} is much bigger than that of Zn^{2+} [20]. It means that the addition of Pr^{3+} ions in the Zn_2GeO_4 lattice results in cationic distortion and new defects. Meanwhile, the addition of Pr^{3+} ions in the lattice also results of the charge compensation. As two Pr^{3+} ions substitute two Zn^{2+} sites, in order to keep the charge balance, one cation vacancy, which possesses two negative charges, is created in the vicinity. So the depth of traps formed by the lattice defects would modify by the clustering of the Pr^{3+} ions which lead to the disturbances and cation vacancies. Those increase lattice defects may have contribution on the modification of the trap depth and the new depth of trap is suitable for generating afterglow. Additional, since the Pr^{3+} is difficult to be reduced to Pr^{2+}. When two Pr^{3+} ions substitute two Zn^{2+} sites, two positive defects of $Pr^{\bullet}_{Zn}$ and one vacancy defect represented as $V^{''}_{Zn}$ with two negative charges would be created by each substitution of every two Pr^{3+} ions in the compound of Zn_2GeO_4:$Eu^{3+}_{0.01}$. From the previous knowledge about the long afterglow, the energy transfer from Pr^{3+} or various vacancies to Mn^{2+} in long-lasting afterglow may be possible. So the $Pr^{\bullet}_{Zn}$ defects may act as electron traps which are connected by $V^{''}_{Zn}$ and the part of the electrons trapped by oxygen vacancies transfer to the Pr^{3+}, forming Pr^{3+} reduce to Pr^{2+}or $Pr^{3+} + e^{-}$. The detrapping of electrons delays the emission then could prolong the persistent luminescence.

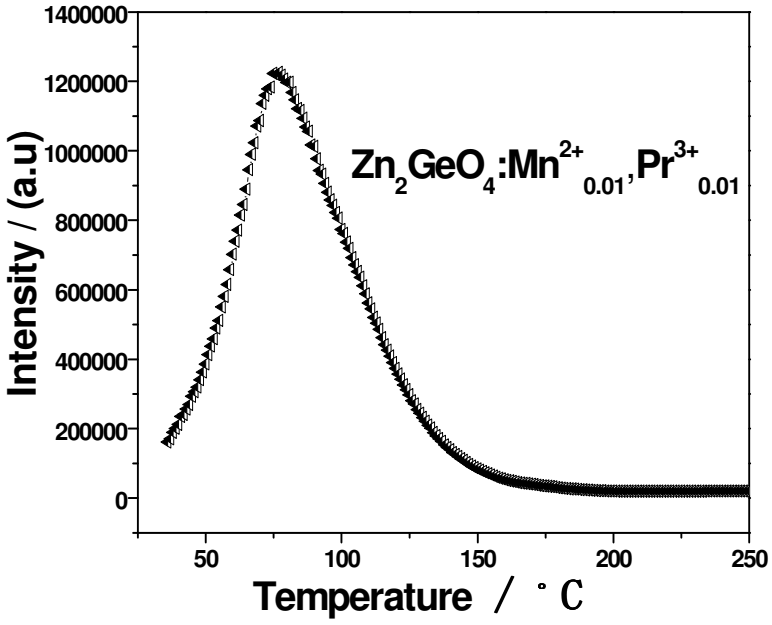


Fig.4. Thermoluminescence curve of $Zn_2GeO_4:Mn^{2+},Pr^{3+}$phosphor at region of 30℃～250℃. The sample was irradiated for 5 minutes before the measurement, with the excitation of a UV (about 254nm) lamp for 3 minutes first.

Previous studies [20] and the above results lead to a possible mechanism of long-lasting afterglow of Mn^{2+} and Pr^{3+} co-doped Zn_2GeO_4. A general schematic of the afterglow process in $Zn_2GeO_4:Mn_{0.01}{}^{2+}$, Pr^{3+} is illustrated in Fig.5. As the oxygen vacancy ($V^{\bullet}_O$) or Zn interstitial ($Zn^{\bullet}_i$) is positive charged, it will act as electron traps. The germanium vacancy (V_{Ge}) or zinc vacancy ($V^{''}_{Zn}$) is negative charged and it can trap holes. Firstly, upon ultraviolet light irradiation, a large number of holes and electrons created(progress①). Then the energy associated with the excited carriers (electrons or holes) will be transferred via the lattice directly to the luminescence centers Mn^{2+}, followed by the Mn^{2+} $^4T_1 \rightarrow {}^6A_1$ emission as the immediate luminescence (progress②). However, part of the excitations trapped by the oxygen vacancies may transfer to the Pr^{3+} and form Pr^{2+}or $Pr^{3+} + e^-$ in the clusters, instead of returning to the ground state (progress③). After stopping UV irradiation, with the thermal disturbance at proper temperature, these electrons trapped by Pr^{3+} will be released from the traps and transferred via the host to the luminescence center then recombine with the opposite charge, followed by the characteristic Mn^{2+} emissions as long afterglow (progress④).

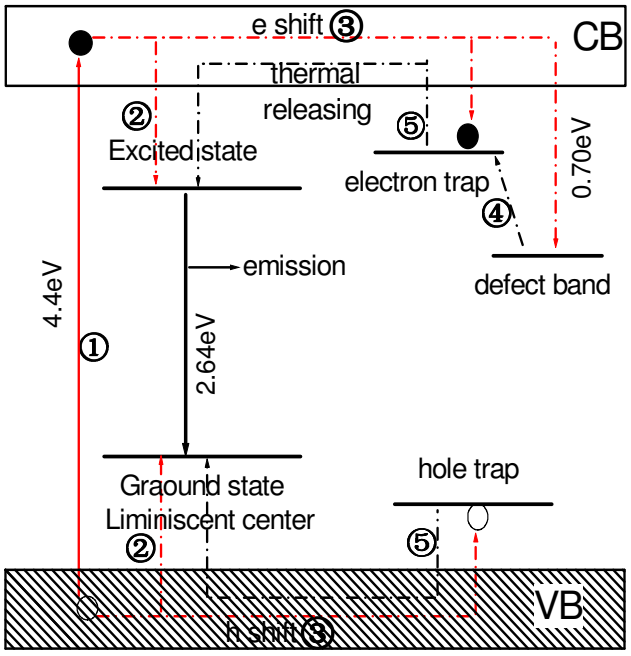


Fig.5 The schematic diagram of the long-lasting luminescence mechanism

Conclusion

In the present study, a novel phosphor $Zn_2GeO_4:Mn^{2+},Pr^{3+}$ were prepared by a high temperature solid state reaction in air atmosphere at 1300℃for 5 h. The investigation of the luminescent properties the $Zn_2GeO_4:Mn^{2+},Pr^{3+}$ phosphor has been carried out. The doped of Mn^{2+} or Pr^{3+} has little influence on the structure of the Zn_2GeO_4 lattice. The results showed that the emission spectra and afterglow spectra of $Zn_2GeO_4:Mn^{2+}$, Pr^{3+} exhibited a narrow emission band at 532 nm due to the $^4T_1 \rightarrow {}^6A_1$ transition of Mn^{2+} ions. With the Pr^{3+} ions co-doping in $Zn_2GeO_4:Mn^{2+}$, the afterglow characteristic was found to be enhanced greatly. It is ascribes to the trap which is created by the disturbances in the crystal planes and the introduction of the cation vacancies. Further analysis showed that the Pr^{3+} ions may behave as the electron trapping centers and the traps induced by Pr^{3+} possess an optimum depth for detrapping, so the Pr^{3+} doping prolonged the persistent luminescence. According to the results in this paper, we may arrive the conclusion that the $Zn_2GeO_4:Mn^{2+},Pr^{3+}$ may be a novel and promising long afterglow phosphor which have a potential application in many areas such as the traffic signs, emergency signage, display, optical memory and imaging storage.

Acknowledgement

This work is supported by the National Nature Science Foundation of China (No. 21271048) and State Key Laboratory of Rare Earth Resource Utilization open projects (RERU2013007).

References

[1] H.Y. Wu, Y.H. Hu, Y.H. Wang, C.J. Fu, J. Alloys Compd. 497 (2010) 330-335.

[2] Z.X. Yuan, C.K. Chang, D.L. M, W.J. Ying, J. Alloys Compd. 377 (2004) 268-271.

[3] Z.S. Liu, X.P. Jiang, L.X. Wang, J. Electrochem. Soc. 154 (2007) H500-H506.

[4] Q.H. Zhang, J. Wang, Appl. Phys A. 108 (2012) 943-948.

[5] S. Takeshit, J. Honda, T. Isobe, T. Sawayama, S. Niikura, J. Solid State Chem. 189 (2012) 112-116.

[6] M.M. Shang, G.G. Li, D. M. Yang, X.J. Kang, C. Peng, Z.Y. Cheng, J. Lin, Dalton Trans. 40 (2011) 9379-9387.

[7] T. Sanada, H. Seto, Y. Morimoto, K. Yamamoto, N. Wada, K. Kojima, J. Sol-Gel Sci Technol. 56 (2010) 82-86.

[8] P.J. Yadav, C.P. Joshi, S.V. Moharil, J. Lumin. 132(2012) 2799-2801.

[9] M.Y. Tsai, C.Y. Yu, C.C .Wang, T.P. Perng, Cryst. Growth Des. 8(2008) 2264-2269.

[10] M. Vasile, P. Vlazan, N.M. Avram, J. Alloys Compd. 500 (2010) 185-189.

[11] M.Y. Peng, Z.W. Pei, G.Y. Hong, Q. Su, J. Chem. Phys. Lett. 371 (2003) 1-6.

[12] Q.S. Qing, M.H. Yu , H.L. Zhou, J.C. Zhang, Acta Phys. Sin. 60 (2011) 0678021-8.

[13] D.W. Cook, B.L. Bennett, E.H. Farnum, W.L. Hults, Appl. Phys. Lett. 70(1997) 3594-3596.

[14] E.W. Forsythe, D.C. Morton, C.W. Tang, Y.L. Gao, Appl. Phys. Lett. 73(1998) 1457-1459.

[15] J.T. Randall, M.H.F. Wilkins, Proc. Royal. Soc. A. 184(1945) 366-389.

[16] S.W.S. Mckeever, Thermoluminescence of solids, Cambridge university press, Cambridge, 1985, p.99.

[17] T. Matsuzawa，Y. Aoki，N. Takeuchi, J. Electrochem. Soc. 143 (1996) 2670-2673.

[18] F.L. Song, D.H. Chen, Y.H. Yuan, J. Alloys Compd. 458 (2008) 564-568.

[19] H. Furusho, J. Hölsä, T. Laamanen, M. Lastusaari, J. Niittykoski, Y. Okajima, A.Yamamoto, J. Lumin. 128 (2008) 881-884.

[20] J. Hölsä, T. Aitasalo, H. Jungner, M. Lastusaari, J. Niittykoski, G. Spano, J. Alloys Compd. 374 (2004) 56-59.

[21] H.Y. Wu, Y.H. Hu, Y.H. Wang, B.D. Zeng, Z.F. Mou, J. Alloys Compd. 486 (2009) 549-553.

Advanced Materials Research Vol. 936 (2014) pp 562-570
© (2014) Trans Tech Publications, Switzerland
doi:10.4028/www.scientific.net/AMR.936.562

Dy^{3+} Doping Blue-Green $Sr_4Al_{14}O_{25}:Eu^{2+}$ Phosphor for Enhancing Luminescent Properties and the Mechanism Study

Zhe Kong[1,a], Hongbo Wang[2,b], Erpan Zhang[1,c], Tao Qiu[1,d], Jun Zhang[1,e], Zhenguo Ji[1, 3,f*]

[1.] College of Materials and Environmental Engineering, Hangzhou Dianzi University. Hangzhou, Zhejiang 310018, China

[2.] College of Automation, Hangzhou Dianzi University. Hangzhou, Zhejiang 310018, China

[3.] State key laboratory for silicon materials, Zhejiang University. Hangzhou, Zhejiang 310027, China
[a]zhekong@hdu.edu.cn, [b]wanghb@hdu.edu.cn, [c]epzhang@hdu.edu.cn, [d]646563579@qq.com, [e]zhangj@hdu.edu.cn, [f] jizg@hdu.edu.cn

Keywords: long afterglow phosphors; $Sr_4Al_{14}O_{25}:Eu^{2+}$; luminescent properties; luminescent mechanism

Abstract: Dy^{3+} doped blue-green Eu^{2+} doped strontium aluminate ($Sr_4Al_{14}O_{25}:Eu^{2+}$) phosphor was prepared using a high temperature solid state method and the influence of the doped Dy3+ on the luminescent properties was studied using X-ray diffraction, scanning electron microscopy, fluorescence spectroscopy and a series of other characterization methods. It is found that Dy3+ doping can enhance the luminescent intensity and extend the afterglow time. The luminescent mechanism of rare earth ions doped strontium aluminate phosphor was also discussed deeply, the effects of the doping amount on the luminescent properties has been made detailed explanation and description. This work has important theoretical significance for the development of higher brightness and longer afterglow blue-green phosphors.

Intruduction

Despite the long afterglow phosphors and its associated light-emitting products have been gradually realized in industrialization and commercialization, it still needs further research. As a kind of "green" and no pollution cold source, rare earth doped $MAl_2O_4:Eu^{2+}$ (M=Mg, Ca, Sr, Ba) has been called the second generation of long afterglow phosphors, which also has great application prospects in the field of printing, dyeing, ceramics, decorative, military, traffic signs and other aspects. This kind of luminescent materials has excellent afterglow luminescent properties, such as: long afterglow, high luminescent intensity, stable chemical property, etc., which is one of the main developing directions of luminescent materials.

The internal structure and the performance will be different if the crystalline of substances are different. For example, the $SrAl_2O_4:Eu^{2+}$ phosphor issues yellow-green light [1], but $SrAl_4O_7:Eu^{2+}$ phosphor shows blue long afterglow luminescence [2], while $Sr_4Al_{14}O_{25}:Eu^{2+}$ phosphor mainly characterizes blue-green light [3]. The research of strontium aluminate phosphors mainly focuses on $SrAl_2O_4:Eu^{2+}$[4-12], while the study of other strontium aluminate crystallines is relatively less. The common problem of the prepared blue or blue-green long afterglow luminescent materials are that the afterglow is short, and the research of the relationships between the structure of the material, the sintering temperature, the excitation light, the trap depth, and the afterglow time are still not sufficient, the unified and complete theoretical system of the luminescent mechanism is also not formed. So the exploration of the impact of additives on the blue-green long afterglow materials is one of the most urgent problems to be solved for the research field of the rare earth doped strontium aluminate phosphors.

The blue-green strontium aluminate ($Sr_4Al_{14}O_{25}:Eu^{2+}$) phosphor has been studied in this paper, the long afterglow luminescent mechanism has been explored through the research of the influence of assistant activator Dy on the luminescent properties, and combined with external morphology, internal structure, and the relationship between these factor and the luminescent performance. The research of the effect of activators on the performance and mechanism of the phosphors has great significance on the preparation of better blue-green $Sr_4Al_{14}O_{25}:Eu^{2+}$ long afterglow phosphor.

Experimental section

Material preparation

In accordance with the stoichiometry of $Sr_4Al_{14}O_{25}$ chemical formula, the raw materials have been accurately weighed. The strontium carbonate ($SrCO_3$) and alumina (Al_2O_3) were acted as a matrix material. Boric acid (H_3BO_3) was acted as a flux, and its addition amount was set at 10 mol% of Al_2O_3 on the basis of the pre-process optimization. Europium oxide (Eu_2O_3) was an activation agent, its addition amount was Eu / Sr = 2 mol%. The samples were prepared by high temperature solid state method, and the carbon powder (C) was selected as the reductant in order to reduce costs and operate safely. The reductant C was added in sufficient quantities to make the raw materials fully reduced. Dysprosium oxide (Dy_2O_3) was added as an assistant activator, the doping amount of Dy was Dy / Sr = 0 mol% , 0.2 mol%, 0.5 mol% , 1 mol% , 2 mol% , 3 mol% , with the samples labeled as D0 , D1, D2 , D3 , D4, D5, respectively.

The reaction raw materials were sufficiently mixed and grinded in an agate mortar for 20 minutes, then, placed in the corundum boat and heated for 1 hour in the incubator at 90 ℃.

Experimental scheme

After the raw materials being dried, it was pushed into the center of the high-temperature program-controlled atmosphere heat treatment furnace. Then, set the heating-cooling process and sintered the $Sr_4Al_{14}O_{25}:Eu^{2+}$, Dy^{3+} phosphor. The heating rate was set to 4 ℃ / min, the sintering temperature was 1400℃, and the holding time was set to be 2 hours. When the process finished, the sample cooled to room temperature naturally, removed from the furnace, and grinded to powder in the agate mortar.

The chemical reactions occurred in the pipe furnace were as follows:

$$SrCO_3 \xrightarrow{\Delta} SrO+CO_2\uparrow \quad (1)$$

$$C+CO_2 \xrightarrow{\Delta} 2CO \quad (2)$$

$$4SrO+7Al_2O_3 \xrightarrow{\Delta} Sr_4Al_{14}O_{25} \quad (3)$$

$$Eu_2O_3+Dy_2O_3+Sr_4Al_{14}O_{25}+CO \xrightarrow{\Delta} Sr_4Al_{14}O_{25}:Eu^{2+},Dy^{3+}+CO_2 \quad (4)$$

Testing equipments

X-Ray diffractometer

XRD (X-Ray diffractometer system, Dandong Tongda TD-3500 instrument manufacturing) was used to analyze the crystal structure of the luminescent powder. The testing result was compared with the standard JCPDF card. Cu Ka radiation (λ = 1.5406 nm) was used when testing, the tube voltage was 35 kv, tube current was 30 mA, scanning speed was 0.05 degrees/s and the scan area was arranging form 10 degrees to 80 degrees.

Scanning electron microscope

The surface morphology of the samples was examined by scanning electron microscopy (SEM, SU1510, Hitachi, Japan) with the operating voltage of 25 kV. All the samples were evaluated without any pretreatment.

Fluorescence spectrometer

The RF-5301 PC fluorescence spectrometer was used to analyze the fluorescence spectral characteristics of the luminescent materials. The slow scanning speed and low sensitivity were selected.

Results and discussion

The influence of Dy2O3 doping amount on the crystal phase

The matrix structure of materials has great influence on the luminescent performance of phosphors. So, it is necessary to analyze the crystal phase of the samples prepared in the experiments. The XRD pattern of $Sr_4Al_{14}O_{25}:Eu^{2+}$, Dy^{3+} phosphors prepared with different Dy_2O_3 doping amount was shown in Figure 1.

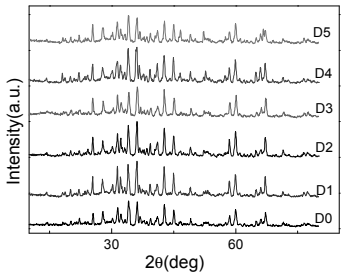


Figure 1 The XRD pattern of $Sr_4Al_{14}O_{25}:Eu^{2+}$, Dy^{3+} phosphors with different Dy_2O_3 doping amount.

In this figure, the diffraction peaks displayed are consistent with the standard map JSPDS74-1810, which shows that, the strontium aluminate obtained by the experiment is the monoclinic phase of $Sr_4Al_{14}O_{25}$. It is known from the curve that, the diffraction peaks are basically identical with each other, the crystal structure changes a lot bit, and the crystal type transformation is good. This result proves that, the matrix phase composition not change when the Dy_2O_3 doping amount is different. But the diffraction peak intensity of each sample are different, as the doping concentration of Dy_2O_3 increases, the diffraction peak presents the trend of increases first, then decreases.

The influence of Dy2O3 doping amount on the morphology

According to the microstructure, grain boundary, grain size, agglomeration degree and crystal growth situation, the luminescent performance of the samples could be analyzed. The SEM diagram of $Sr_4Al_{14}O_{25}:Eu^{2+}$, Dy^{3+} phosphors with different Dy_2O_3 doping amount was shown in Figure 2.

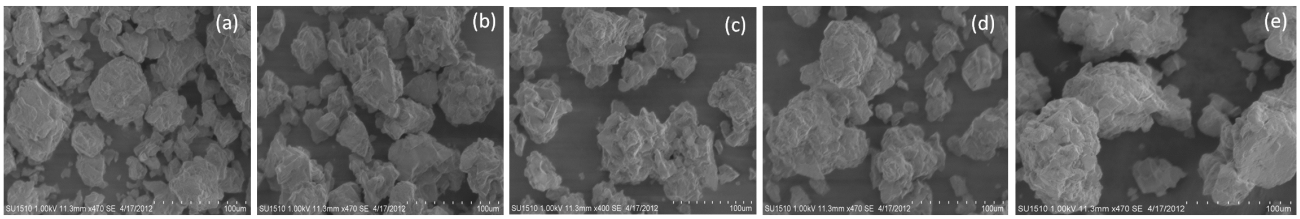


Figure 2 The SEM figure of $Sr_4Al_{14}O_{25}:Eu^{2+}$, Dy^{3+} phosphors with different Dy_2O_3 doping amount. (a) Dy/Sr=0%; (b) Dy/Sr=0.2%; (c) Dy/Sr=0.5%; (d) Dy/Sr=1%; (e) Dy/Sr=2%

It is obtained from the figure that, the crystal edge and crystal plane are very clear, and the particle size are quite large for all the samples, which shows that, the crystalline state of the samples are very well, and the impact of Dy_2O_3 doping amount on the particle size of the phosphor is not big. This is consistent with the results of the XRD detection.

The influence of Dy2O3 doping amount on the fluorescence spectrum

The excitation and emission spectrum are important parameters for luminescent materials. The excitation spectrum of the sample was tested firstly to get the optimal excitation wavelength. Then, under the excitation of this wavelength, the emission spectrum was measured to obtain the emission wavelength of sample, which revealed the luminescent color of the sample. The excitation and emission spectrum of $Sr_4Al_{14}O_{25}:Eu^{2+}$, Dy^{3+} with different Dy_2O_3 doping amount were shown in Figure 3 and Figure 4, respectively.

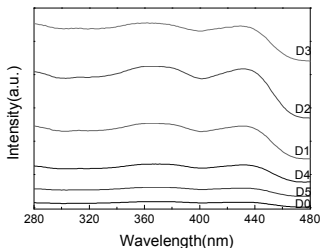


Figure 3 The excitation spectrum of $Sr_4Al_{14}O_{25}:Eu^{2+}$, Dy^{3+} with different Dy_2O_3 doping amount. The slit width was 3 nm.

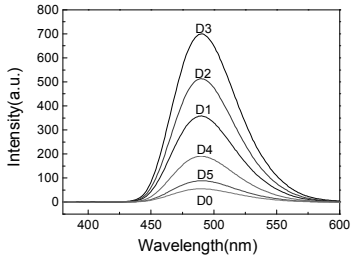


Figure 4 The emission spectrum of $Sr_4Al_{14}O_{25}:Eu^{2+}$, Dy^{3+} with different Dy_2O_3 doping amount. The excitation wavelength was 370 nm, the slit width was 3 nm.

It can be seen from the excitation spectrum that, the excitation peaks of each samples are all broadband peak and the peak position is near 370 nm and 430 nm, which mean that, these samples can be stimulated by visible light. The intensity of the excitation peaks changes regularly as the Dy_2O_3 doping amount increasing, the peak intensity increases first, then decreases. It might be relevant with the ability of the electron capturing and hole formation of Dy^{3+}.

From Figure 4, it is clear that, the emission peak is very weak without Dy_2O_3. As the Dy_2O_3 doping concentration increasing from 0 to 1%, the samples has the same emission spectrum shape, the peak position is about 490 nm, and the peak intensity increases gradually. The emission peak intensity reaches the maximum value when the doping content of Dy_2O_3 is 1%, and the values decrease as the doping amount increases continuously.

Because of the radius of Dy^{3+} and Al^{3+} is so different that, Dy^{3+} cannot occupy Al^{3+} in the $Sr_4Al_{14}O_{25}$ matrix. So, when Dy^{3+} is introduced into the lattice, it will take the place of Sr^{2+}. For this is an inequivalent replacement, the electronic trap will be formed. It is known that, the intensity of emission spectrum has great relationship with the density of electronic trap. So, when the doping amount of Dy^{3+} is small, the electronic trap density will be low, and the speed of electronic releasing will be slow. Under this condition, the composition of the electron (which released by electron trap) and the hole (which released by the hole trap) around the Eu^{2+} luminescent center will be slow, then, the releasing speed of photon will be slow too, which resulting the wake emission peak intensity. With the increases of Dy_2O_3 doping amount, the electronic trap goes denser, the electronic release rate become quicker, the composition rate of the electron and the hole become quicker, so, the emission peak intensity gradually increase. When the Dy_2O_3 doping amount increases to a certain extent, the electronic trap density will become too big that the release rate of photons in the luminescent center will be affected, the concentration quenching will be occurred and the emission peak intensity will be decreased. So, in order to obtain the biggest emission intensity, the doping amount of Dy_2O_3 should be controlled at an optimum concentration.

The influence of Dy2O3 doping amount on the afterglow properties

Long afterglow phosphors have an afterglow decay process, that is, after the external excitation stopping, the materials still can shine for a period of time, the luminescent intensity becomes wake and wake until the intensity reduced to 0.32 mcd/m^2, which cannot be seen by naked eyes. The afterglow decay process can be divided to two processes: fast decaying and slow decaying. The afterglow time and persistence brightness are two important parameters to evaluate the light storage performance of long afterglow luminescent materials, which can influence the application prospect and application scope of the luminescent materials to a great extent. The persistence characteristics are different for different materials, which can be expressed by the following formula [13]:

$$I = \alpha_1 \exp(-t/\tau_1) + \alpha_2 \exp(-t/\tau_2) + \alpha_3 \exp(-t/\tau_3) + \cdots \quad (5)$$

where, I is luminescent intensity, t is time, α_1, α_2, α_3 are constant, τ_1, τ_2, τ_3 are index afterglow time.

The luminescent brightness and persistence performance of the samples prepared in our experiment are very well, the afterglow time is more than 24h by visual observation. The equipment detection method of the persistence characteristic is as follows: After located in dark room for 24 h, the $Sr_4Al_{14}O_{25}:Eu^{2+}$, Dy^{3+} phosphor is put into the fluorescence spectrometer, then, set the parameters, open the xenon lamp 20 min to exposure the phosphor and then close the light source, test the afterglow decay curve. The excitation wavelength is set for 370 nm, and emission wavelength is 490 nm when testing. The exponential decay curve of $Sr_4Al_{14}O_{25}:Eu^{2+}$, Dy^{3+} phosphor with different Dy_2O_3 doping amount are shown in Figure 5. From this figure, it can clearly see the fast decaying and slow decaying of the afterglow decay process. The relationship between afterglow time and Dy^{3+} doping concentration is shown in Figure 6.

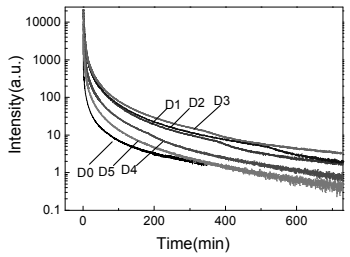


Figure 5 The exponential decay curve of $Sr_4Al_{14}O_{25}:Eu^{2+}$, Dy^{3+} phosphor with different Dy_2O_3 doping amount.

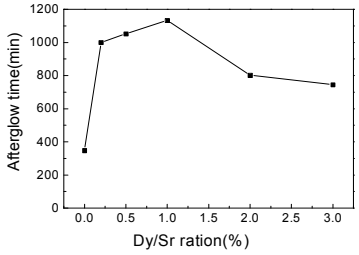


Figure 6 The relationship between Dy_2O_3 doping concentration and long afterglow time.

It can be seen from the afterglow decay curves that, the afterglow time is very short without the doping of Dy_2O_3. As one of the assistant activator, Dy^{3+} do not act as luminescent center [14, 15] in the strontium aluminate matrix, but it has appropriate radius and optical electronegativity, which can slowly release the trapped electrons or holes to the $4f^6 5d^1$ excited state of Eu^{2+}, and produce long afterglow luminescence. For it has been discussed that, the addition of Dy^{3+} can induce inequivalent replacement, and the traps of the $Sr_4Al_{14}O_{25}:Eu^{2+}$ matrix will be increased and the luminescence will be enhanced. So, the initial brightness will be improved accordingly. When the doping concentration of Dy^{3+} is 0, the initial brightness is low, and the composition of electron and hole is less, the afterglow time will be short. As the doping concentration increases, the depth of the electronic trap become deeper and the density of electronic trap increase. So, when the doping concentration increases from 0.2% to 1%, more and more electrons can be captured and then released slowly under the action of thermal disturbance, which resulting the better initial brightness and longer afterglow time. But, when still increase the doping amount, because of the depth of the electronic traps is too deep and the density is too big that the composition of electron and hole will be bounded, which will result low initial brightness and short afterglow time.

The influence of additives on the long afterglow luminescent mechanism

The luminescent mechanism models including hole transfer model, location coordinate model, electronic transfer model, energy transfer model, thermal luminescent model, etc [16-19]. These mechanistic models all give some interpretation and speculation in different extent about the afterglow behavior of rare earth activated strontium aluminate phosphors. However, there are still lack of a complete, accurate, and universal significant theory. The most commonly recognized statement of the previous mechanism is that, the luminescent phenomenon of Eu^{2+} activated strontium aluminate phosphor is caused by the $4f^6 5d^1$- $4f^7$energy level transition of Eu^{2+} in the lattice. When the phosphor is irradiated by the external light, the $4f^7$ ground state electron will be inspired to the excited state. The excited electron can transform to the ground state after the excitation stopped, and emit light. In this section, the long afterglow luminescent mechanism of BO_3^{3-} and Dy^{3+} doped $Sr_4Al_{14}O_{25}:Eu^{2+}$ phosphor was systematically discussed based on the previous research and the results of our experiment.

In the preparation process of $Sr_4Al_{14}O_{25}:Eu^{2+}$, Dy^{3+} phosphor, both the doping of rare earth ions and the changing of matrix composition can lead to the point defect. Because the ion radius of Eu^{2+} and Dy^{3+} is close to Sr^{2+}, and much bigger than that of the Al^{3+}, this two doped ions will take place of Sr^{2+}. The radius of B^{3+} is smaller than Al^{3+}, but the electronegativity of B^{3+} is greater than that of Al^{3+}. After doped into the matrix, BO_4^{5-} will partial substitute AlO_4^{5-} to obtain stronger ionicity [20]. The XRD results of this experiment also prove that, the doping of Eu^{2+}, Dy^{3+} and BO_3^{3-} does not change the crystal phase of $Sr_4Al_{14}O_{25}$, only affects the diffraction peak intensity.

When the position of Sr^{2+} is replaced by Eu^{2+}, the point defect (Eu_{Sr}) and (V''_O) will be occurred. Where, (Eu_{Sr}) acts as luminescent center and (V''_O) acts as electronic trap. But the doping of Dy^{3+} is an unequivalent substitution, which will produce three kinds of point defects for once two Dy^{3+} doped into the lattice, one Sr^{2+} vacancy will be formed in order to keep the charge balance. This will form ($Dy^{\cdot}_{Sr}$), (V''_O) and (V''_{Sr}) three point defects [21]. Under the carbon powder reduction atmosphere, Eu^{3+} will be reduced to Eu^{2+}, at the same time, one O atom will be removed from BO_4^{5-} and the (BO_3''') vacancy will be formed. So, the main point defects in the $Sr_4Al_{14}O_{25}:Eu^{2+}$, Dy^{3+} lattice are as follows: ($Dy^{\cdot}_{Sr}$) and (V''_O) are positively charged, which called electronic trap for they can capture electrons, (V''_{Sr}) and (BO_3''') are negatively charged, which called hole trap for they have the ability of capturing holes.

The long afterglow luminescent mechanism of $Sr_4Al_{14}O_{25}:Eu^{2+}$, Dy^{3+} phosphor can be explained through the following process, which is displayed in Figure 7:

(1) Under the excitation of ultraviolet visible light, the electron – hole pairs are produced in the conduction band and valence band of $Sr_4Al_{14}O_{25}:Eu^{2+}$, Dy^{3+}, respectively, as shown in Figure 7, process (1).

(2) These electrons and holes move freely in the band. Through the heat balance, electrons drop to the bottom of conduction band quickly, while holes quickly rise to the top of the valence band. The electrons captured by the electronic trap ($Dy^{\cdot}_{Sr}$) and (V''_O) when diffusing in the conduction band. During this process, the electronic traps can store a lot of electrons and form ($Dy^{\cdot}_{Sr}e'$) and ($V''_O 2e'$), as shown in Figure 7, process (2).

(3) Partial trapped electrons can transit back to the conduction band under the action of thermal disturbance. As shown in Figure 7, process (3).

(4) The similar process also occurred in the valence band. Holes trapped by the hole traps (V''_{Sr}) and (BO_3''') to form ($V''_{Sr}2h^{\bullet}$) and ($BO_3'''3h^{\bullet}$). As shown in Figure 7, process (4).

(5) Partial trapped holes also can transit back to the valence band through the action of thermal disturbance. As shown in Figure 7, process (5).

When ($Dy^{\cdot}_{Sr}e'$), ($V''_{O}2e'$), ($V''_{Sr}2h^{\bullet}$) and ($BO_3'''3h^{\bullet}$) are excited by the thermal disturbance of the environmental temperature, the following reactions can be occurred, electrons and holes will be released.

$$(Dy^{\cdot}_{Sr}e') \longrightarrow Dy^{\cdot}_{Sr} + e' \quad (6)$$

$$(V''_{O}2e') \longrightarrow V''_{O} + 2e' \quad (7)$$

$$(V''_{Sr}2h^{\bullet}) \longrightarrow V''_{Sr} + 2h^{\bullet} \quad (8)$$

$$(BO_3'''3h^{\bullet}) \longrightarrow BO_3''' + 3h^{\bullet} \quad (9)$$

(6) The released electrons and holes can also composite in the (Eu_{sr}) luminescent center, which will release photon and produce long afterglow luminescent phenomenon. As shown in Figure 7, process (6).

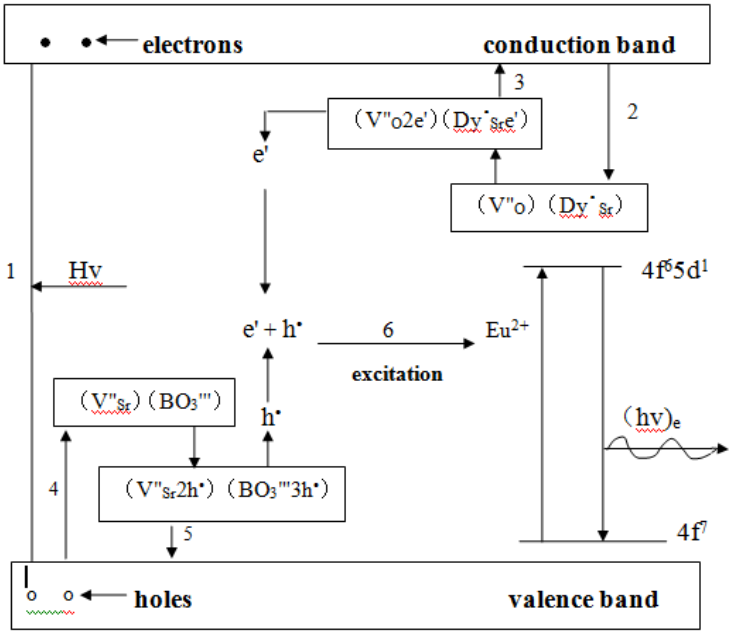


Figure 7 The schematic diagram of the luminescent mechanism for $Sr_4Al_{14}O_{25}:Eu^{2+}$, Dy^{3+} phosphor.

The fast and slow decaying process of afterglow decay phenomenon can be explained by the above process. After the excitation of the external light, the electrons and holes in a shallow trap can quickly get rid of the trap under the thermal disturbance of the environmental temperature, then composite and emit light in the Eu^{2+} luminescent center. This is the fast decay process of the long afterglow luminescence. In the deep traps, the releasing probability of the trapped electrons or holes is small, they can only slowly released to the conduction band or valence band, their composition and emitting is slowly too, which will result slow decay process of the long afterglow luminescence for few minutes or several hours.

Experiments have proved that, the doping amount of the additive has great effect on the luminescent performance of the phosphors. The luminescent performance has the characteristics of enhanced firstly then weakened with the increasing of the doping amount. When the doping concentration of other additive is not changed and the doping amount of Dy^{3+} is low, the formation of (V''_{O}) and ($Dy^{\cdot}_{Sr}$) is less, for Dy^{3+} has little opportunity the doping into the lattice and replace the position of Sr^{2+}. The trapping and releasing of electrons or holes will be less, and the photons released from the composition will be less too, which will result low initial brightness and short afterglow time. As the doping concentration increases, more Dy^{3+} will replace the poison of the Sr^{2+}, and the depth and density of the electronic traps will be increased, which will lead to stronger initial

brightness and longer afterglow time. But when the doping concentration exceed to the critical concentration, the electronic trap is too deep and the density is too large that, the composition of electrons and holes will be bounded, and the releasing speed of the photon also will be slow down, which will result lower initial brightness and shorter afterglow time. That is to say, when the doping amount exceed to the critical concentration, concentration quenching phenomenon will be happened.

The influence of other addictive on the phosphors can be explained similar as the above discussion. In the preparation process of the $Sr_4Al_{14}O_{25}:Eu^{2+}$, Dy^{3+} phosphor, the addition of H_3BO_3 also can increase the electronic traps and the hole traps. As the concentration of H_3BO_3 increase, on the one hand, the formation of $Sr_4Al_{14}O_{25}$ crystal phase will become easy and the preparation temperature could be reduced, on the other hand, the depth of the traps becomes deeper, and the density of the traps increases too. But, if too much H_3BO_3 is added, the glass state borate will be separated out, the formation ratio of the $Sr_4Al_{14}O_{25}$ crystal phase will be decrease, and resulting low luminescent intensity.

Conclusions

The Dy^{3+} doped $Sr_4Al_{14}O_{25}:Eu^{2+}$ phosphor has been prepared by the high temperature solid state method. The afterglow time of the phosphors prepared in our experiments was more than 24 h. A series of characterization means have been used to study the influence of doping amount on the luminescent performance of the phosphor. The results proved that, the doping of Dy^{3+} has little influence on the crystal phase and the morphology, but has great effect on the luminescent performance of the phosphor. The emission peak intensity of the $Sr_4Al_{14}O_{25}:Eu^{2+}$ sample increased as the doping concentration of Dy_2O_3 increasing in the range of 0 to 1%. While, the intensity decreased as the concentration increasing in the range of 1% to 3%. With the increasing of the Dy^{3+} doping concentration, the afterglow time of the samples also expressed the similar tendency. Based on the above results, the important role of additives (Dy^{3+} and BO_3^{3-}) in the luminescent mechanism of phosphor has been further discussed. The reason of why the doping amount can greatly influence the photoluminescent properties also has been explained in detail. This study can provide useful theoretical guidance for the preparation of more excellent long afterglow phosphors.

Acknowledgements

The financial support of the Zhejiang Provincial Natural Science Foundation of China (No. LQ12F05001, LY13F04006) and the Educational Commission of Zhejiang Province (No. Y201121341) is gratefully acknowledged.

References

[1] Matsuzawa T, Aoki Y, Takeuchi N, *et al*. A new long phosphorescent phosphor with high brightness, $SrAl_2O_4:Eu^{2+}$, Dy^{3+}. J. Electrochem. Soc. 143 (1996) 2670-2673.

[2] Sophya Preethi K R, Lu C H, Thirumalai J, *et al*. $SrAl_4O_7$: Eu^{2+} nanocrystals: Synthesis and fluorescence properties. J. Phys. D: Appl. Phys. 37 (2004) 2664.

[3] Suriyanurthy N and Panigrahi B S. Luminescence studies during combustion synthesis of a long afterglow phosphor $Sr_4Al_{14}O_{25}:Eu^{2+}$, Dy^{3+}. Indian J. Eng. Mater. Sci. 16 (2009) 178-180.

[4] Clabau F, Rocquefelte X, Jobic S, *et al*. On the phosphorescence mechanism in $SrAl_2O_4:Eu^{2+}$ and its codoped derivatives. Solid State Sci. 9 (2007) 608-612.

[5] Arellano-Tánori O, Meléndrez R, Pedroza-Montero M, *et al*. Persistent luminescence dosimetric properties of UV-irradiated $SrAl_2O_4:Eu^{2+}$, Dy^{3+} phosphor. J. Lumin. 128 (2008) 173-184.

[6] Yamamoto H and Matsuzawa T. Mechanism of long phosphorescence of $SrAl_2O_4:Eu^{2+}$, Dy^{3+} and $CaAl_2O_4:Eu^{2+}$, Nd^{3+}. J. Lumin. 72-74 (1997) 287-289.

[7] Liu X J, Li H L, Xie R J, *et al*. Cerium-doped lutetium aluminum garnet optically transparent ceramics fabricated by a sol-gel combustion process. J. Mater. Res. 21 (2006) 1519-1525.

[8] Xiao L Y, Xiao Q, and Liu Y L. Preparation and characterization of flower-like $SrAl_2O_4:Eu^{2+}$, Dy^{3+} phosphors bysol-gel process. J. Rare Earth. 29 (2011) 39-43.

[9] Zhan T Z, Xu C N, Yamada H, *et al*. Enhancement of afterglow in $SrAl_2O_4:Eu^{2+}$ long-lasting phosphor with swift heavy ion irradiation. RSC Adv. 2 (2012) 328-332.

[10] Yu N Y, Liu F, Li X F, *et al*. Near infrared long-persistent phosphorescence in $SrAl_2O_4:Eu^{2+}$, Dy^{3+}, Er^{3+} phosphors based on persistent energy transfer. Appl. Phys. Lett. 95 (2009) 231110.

[11] Clabau F, Rocquefelte X, Jobic S, *et al*. Mechanism of Phosphorescence Appropriate for the Long-Lasting Phosphors Eu^{2+}-Doped $SrAl_2O_4$ with Codopants Dy^{3+} and B^{3+}. Chem. Mater. 17 (2005) 3904-3912.

[12] Song H J, Chen D H, Tang W J, *et al*. Synthesis of $SrAl_2O_4$: Eu^{2+}, Dy^{3+}, Gd^{3+} phosphor by combustion method and its phosphorescence properties. Display. 29 (2008) 41-44.

[13] Nag A and Kutty T R N. Role of B_2O_3 on the phase stability and long phosphorescence of $SrAl_2O_4$:Eu, Dy. J. Alloy. Comp. 354 (2003) 221-231.

[14] Peng T Y, Yang H P, Pu X L, *et al*. Combustion synthesis and photoluminescence of $SrAl_2O_4$: Eu^{2+}, Dy^{3+} phosphor nanoparticles. Matter. Lett. 58 (2004) 352-356.

[15] Lu X D and Shu W G. Roles of crystal defects in the persistent luminescence of Eu, Dy co-doped strontium aluminate based phosphors. Rare Metal. 26 (2007) 305.

[16] Qiu J R, Kawasaki M, Tanaka K, *et al*. Phenomenon and mechanism of long-lasting phosphorescence in Eu^{2+}-doped aluminosilicate glasses. J. Phys. Chem. Solid. 59 (1998) 1521-1525.

[17] Aitasalo T, Deem P and Holsa J. Persistent luminescence Phenomena in materials doped with rare earth ions. J. Solid State Chem. 171 (2003) 114-122.

[18] Aitasalo T, Holsa J, Jungner H, *et al*. Mechanisms of persistent luminescence in Eu^{2+}, RE^{3+} doped alkaline earth aluminates. J. Lumin. 76-77 (1998) 424.

[19] Holsa J, Jungner H and Lastusaari M. Persistent luminescence of Eu^{2+} Doped alkaline earth aluminates, $MAl_2O_4:Eu^{2+}$. J. Alloy. Comp. 323-324 (2001) 362-330.

[20] Nag A and Kutty T R N. The mechanism of long phosphorescence of $SrAl_{2-x}B_xO_4$ ($0<x<0.2$) and $Sr_4Al_{14-x}B_xO_{25}$ ($0.1<x<0.4$) co-doped with $Eu^{2+}$and Dy^{3+}. Mater. Res. Bull. 39 (2004) 331-342.

[21] Lu X D and Shu W G. Chin. Formation and roles of point defects in $SrAl_2O_4:Eu^{2+}$, Dy^{3+} phosphors. J. Inorg. Chem. 22 (2006) 808-812.

Advanced Materials Research Vol. 936 (2014) pp 571-576
© (2014) Trans Tech Publications, Switzerland
doi:10.4028/www.scientific.net/AMR.936.571

Magnetic and Electrical Property in Mg^{2+} Deficient $La_{1.4}Sr_{1.6}Mn_2O_7$ Perovskite

ZONG Yun[1,2,a], ZHAO Xu[2,b] and CHEN Wei[2,c]

[1]Department of Computer Science, Shijia-zhuang Information Engineering Vocational College, Shijiazhuang 050035, China

[2]Department of Physics, and Hebei Advanced Thin Film Laboratory, Hebei Normal University, Shijiazhuang 050016, China

[a]1148843246@qq.com, [b]1171337248@qq.com, [c]chen07308@mail.hebtu.edu.cn

Keywords: bilayered perovskites; magnetic property; electrical property

Abstract: The nominal compositions of $La_{1.4}Sr_{1.6-x}Mg_xM_{n2}O_7$ (x=0, 0.1, 0.2, 0.3, 0.4) have been synthesized using solid-state reaction method. The XRD analyses show that the x=0 compound is pure I4/mmm tetragonal bilayered perovskites phase, while they are mixture of an orthorhombic ABO_3-type perovskite and tetragonal bilayered perovskites for x=0.1, 0.2 and 0.3). When x is 0.4, the compound is pure orthorhombic ABO3-type perovskite. For lightly doped samples (x=0.1 and 0.2), the Curie and Nair temperature decreases with the increasing Mg^{2+} doping, while the metal-insulation transformation temperature is 90K and 140K, respectively. For heavy doped samples (x=0.3 and 0.4), the magnetic property shows spin-glass state, and the resistance increases nearly 4 order of magnitudes.

Introduction

The magnetoresistance effect of manganites with ABO_3 type perovskite structure can be improved by means of doping in A or B bit, which has attracted quite large attention in recent years [1-2]. The doping for A bit includes the doping of divalent alkaline earth ions and the mutual doping of rare earth ions. The doping practice can change the size of lattices and influence the changes of Mn-O bond length and Mn-O-Mn bond angles, thus further influencing the double-exchange interaction, and it can also indirectly change Mn^{3+}/Mn^{4+} ratio through replacement among icons with various valence states; besides, the changes of average ionic radius after doping can strengthen the distortion of lattices, all of which can influence the magnetoresistance effect of materials.

Many researchers have researched the replacement in La/Sr and Mn bits of double-layer perovskite compound $La_{1.4}Sr_{1.6}Mn_2O_7$ [3-4]. We have also researched the structure, magnetism and magnetic entropy property of $La_{1.4}Sr_{1.6-x}Ca_xMn_2O_7$. The reason why we select Ca^{2+} ion to replace Sr^{2+} ion is that the two ions have the same valence state, thanks to which Mn^{3+}/Mn^{4+} ratio in Mn bit can remain unchanged after their replacement; besides, the radius of Ca^{2+} ion (1.0Å) is lower than that of Sr^{2+} ion (1.26 Å), and great disputes have remained among various research groups in terms of the synthesis of $La_{1.4}Ca_{1.6}Mn_2O_7$ compound. Therefore, the influence of Ca ion replacement on the structure and magnetism of $La_{1.4}Sr_{1.6-x}Ca_xMn_2O_7$ is investigated. Double-layer perovskite structure can still be formed until x=0.8, while the structure is completely disappeared and replaced by ABO_3 type perovskite phase and CaO with x>0.8, which suggest that the mismatching of ionic radiuses can directly influence the phase stability of double-layer perovskite structural $La_{1.4}Sr_{1.6}Mn_2O_7$.

In periodic table of elements, the radius of Mg^{2+} ion is relatively small (0.72 Å) under the same valence state. If we conduct Mg^{2+} ion replacement in Sr bit, will the mismatching between ions with relatively large radius difference still be able to ensure the entry of Mg^{2+} ion into the Sr bit of double-layer perovskite structure, and how will it change the structure of the double-layer perovskite oxide $La_{1.4}Sr_{1.6}Mn_2O_7$ Few reports related to the above issue have been published at present, considering which we synthesized the series of oxides with $La_{1.4}Sr_{1.6-x}Mg_xMn_2O_7$ as the nominal component and researched certain properties related to their structure, magnetism and magnetoresistance.

Sample Preparation

Polycrystalline oxides with $La1.4Sr_{1.6-x}Mg_xMn_2O_7$ (x=0, 0.1, 0.2, 0.3, 0.4) as nominal components were synthesized by a solid state method. Firstly, the raw materials of La_2O_3, $SrCO_3$, MgO and MnO_2 with high purity were mixed according to the stoichiometric ratio, and then calcined for 4 hours at 900 °C after fully grounded. Finally the calcined powder was sintered for another 20 hours at 1,400 °C after another grinding and performing for them.

XRD data related to the series of compounds were collected by means of X'Pert Pro type X-ray diffractometer supplied by PANalytical Company in Netherlands. Cu target Kα rayand Nioptical filter were adopted in the diffraction experiment, during which the voltage and current were 40kV and 40mA respectively. The data were collected by continuous scanning method with a step length of 0.0167°, a rate of 30s/step and the scanning angle ranging from 20°to 120°.

The magnetism and electrical properties of the materials were tested by means of PPMS supplied by American Quantum Company. The Curie temperature (T_C) of samples was determined according to the temperature corresponding to the maximum value of low-field magnetization curve(0.05T)derivative of the temperature.

Experimental Results and Discussions

Figures1 shows the X ray diffraction patterns of $La_{1.4}Sr_{1.6-x}Mg_xMn_2O_7$ compounds with x=0.0, 0.1, 0.2, 0.3, 0.4. When x=0, the compound show a $Sr_3Ti_2O_7$ type (Type 327) tetragonal system perovskite structure with a space group of I4/mmm; crystal face indices of its main diffraction peaks are shown in Figure 3.1 respectively. When x = 0.1, new diffraction peaks appeared at 2θ of 23.02° and 40.39° respectively. The intensity of the two diffraction peaks is also gradually strengthened with the increase of x content; meanwhile, the intensity of diffraction peaks such as (105),(116),(0010) and (2010) belonging to double-layer perovskite structure is gradually reduced with the increase of x content. The new diffraction peaks belong to ABO_3type (Type113) perovskite manganite with rhombohedral structure in $R3\bar{c}$ space group.

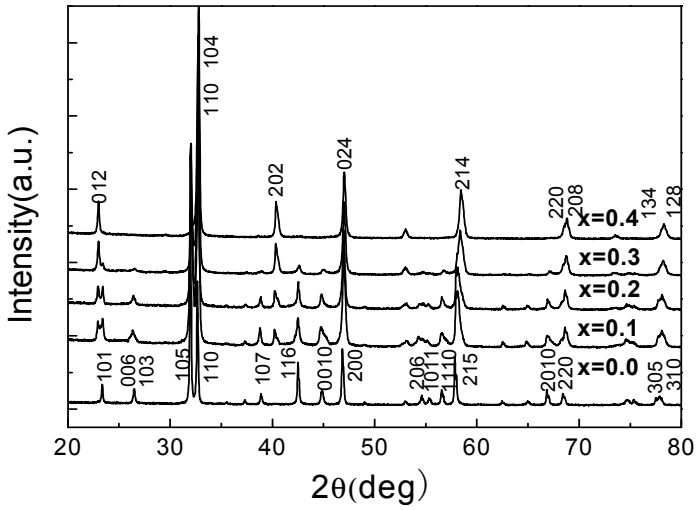


Fig1 The X ray diffraction pattern of $La_{1.4}Sr_{1.6-x}Mg_xMn_2O_7$series of compounds ($x$=0.0,0.1,0.2,0.3,0.4)

We find that Mg^{2+}ion with the radius of 0.72 Å actually enters the Mn bit of perovskite structure owing to the intensified mismatching degree of ionic radius in A bit, thus forming $La_{1.4}Sr_{1.6}Mn_{2-2y}Mg_{2y}O_7/La_{0.67}Sr_{0.33}Mn_{1-y}Mg_yO_3$(327/113) composite. Besides, with the increase of x content, the content of Phase 327 belonging to double-layer perovskite is gradually reduced, while the content of Phase113 belonging to the perovskite with infinite layers is gradually increased.

Figures2 represents variation of magnetization intensity with temperature for $La_{1.4}Sr_{1.6-x}Mg_xMn_2O_7$ under the applied magnetic field of 500Oe. According to our analysis, the sample with x=0 shows antiferromagnetic (ATM) property under 60 K: The magnetization intensity is obviously reduced with the reduction of temperature, and a peak appeared when the temperature reaches Neel temperature T_N (60 K); the magnetization intensity is rapidly reduced when the temperature is above 60 K, accompanied with self-spinning ferromagnetic orderliness and the antiferromagnetic coupling within the double layers of MnO_6[5]; when the temperature ranges from 100 K to 250K, a section of platform approximating the shape of a straight line is formed in M-T curve, which represents two-dimensional ferromagnetic orderliness; when the temperature is above 250K, the material is in the paramagnetic state.

For x=0.1 sample, the component and corresponding content are refined as 72.9(5)% $La_{1.4}Sr_{1.6}Mn_{1.9}Mg_{0.1}O_7$ and 27.0(5)% $La_{0.67}Sr_{0.33}Mn_{0.95}Mg_{0.05}O_3$.Two transformation temperatures are obviously formed in the material: T_N of Phase 327 is reduced to roughly 20K, while *Tc* of Phase 113 is transformed to roughly 320K (the Curie temperature of pure $La_{0.67}Sr_{0.33}MnO_3$is 360K[6]). Two main reasons are suggested for the change in the transition temperature: Firstly, since Mg ion is nonmagnetic, its doping can reduce the total magnetic moment in the system; owing to the random place holding of Mg ion, the original long-range ferromagnetic order of the material is damaged, thus making the double-exchange interaction in Mn^{3+}-O-Mn^{4+} net structure restrained.

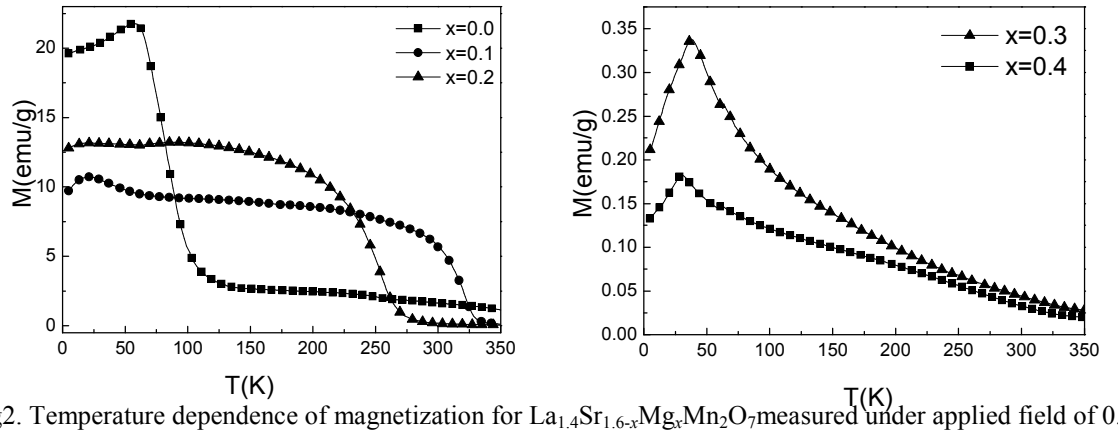


Fig2. Temperature dependence of magnetization for $La_{1.4}Sr_{1.6-x}Mg_xMn_2O_7$measured under applied field of 0.05 T.

When the nominal doping quantity of Mg is increased to such a degree that x=0.2, the component of Phase 327 change into $La_{1.4}Sr_{1.6}Mn_{1.82}Mg_{0.18}O_7$ with the lower content of 58.3(1)%. The reduction of the content and the increase of Mg ion in Mn bit result in the decrease of antiferromagnetic transformation temperature in the low-temperature area of the material; meanwhile, the increase of Phase 113 increases the ferromagnetic component in the low-temperature area, which dominates the higher magnetization intensity of the sample with x = 0.2in the low-temperature area. Similarly, the further increase of Mg content in Mn bit makes the Curie temperature of the material reduced to roughly 250K in high-temperature area.

When the nominal doping quantity of Mg reaches x = 0.3 or 0.4,the magnetization intensity of the material shows obviously different characteristics. Firstly, the numerical value of the magnetization intensity is reduced by nearly 2 orders of magnitude; secondly, the Curie temperature Tc in the high-temperature area disappears, while in the M-T curves, there is an extremely sharp maximum value when the temperature is near 39K for *x*=0.3 and 30K for *x*=0.4 in the low-temperature area, which could be attributed to the high proportion of Phase 113 in the two compositions (70.5(7)% and 100% for x = 0.3 and 0.4, respectively), and the high practical Mg content of 0.13 and 0.17 respectively. Therefore, the magnetic property of $La_{0.67}Sr_{0.33}Mn_{1-x}Mg_xO_3$of Phase 113 is mainly represented in the two materials [7].

Figures3 shows the variation in the specific resistance with temperature. For sample with x=0.0, the specific resistance shows a sharp maximum value at its Curie temperature around 103K, which is corresponding with the insulation-metal transition temperature. When the temperature is higher than the corresponding temperature, the compound shows the semi-conductive property, otherwise, it represents metallicity. Therefore, this temperature is determined as an insulation-metal transformation temperature (Tρ). The sharp reduction of specific resistance below Tρ is closely related to 3D ferromagnetic self-spinning and ordering. The specific resistance of the material represents semi-conductive property when the temperature is further reduced to the Neel temperature T_N (60K). According to researches on neutron scattering[8], when the temperature is lower than T_C, the arrangement of 3D ferromagnetic orderliness will prevail with the ferromagnetic orderliness between two tilting double layers. When the temperature is lower than T_N, the stratiform antiferromagnetic orderliness will prevail. In the antiferromagnetic state, the two layers of ferromagnetic orderliness are coupled along the direction of c axis (perpendicular to the plane) in the antiferromagnetic way. Compared to the mutual ferromagnetic effect in the layer, the mutual antiferromagnetic effect between layers is weaker. Such antiferromagnetic coupling between layers may result from the obstructed tunneling penetration between layers of spin-polarized electrons , which dominates the disappearance of metallicity and the obvious enlargement of the specific resistance.

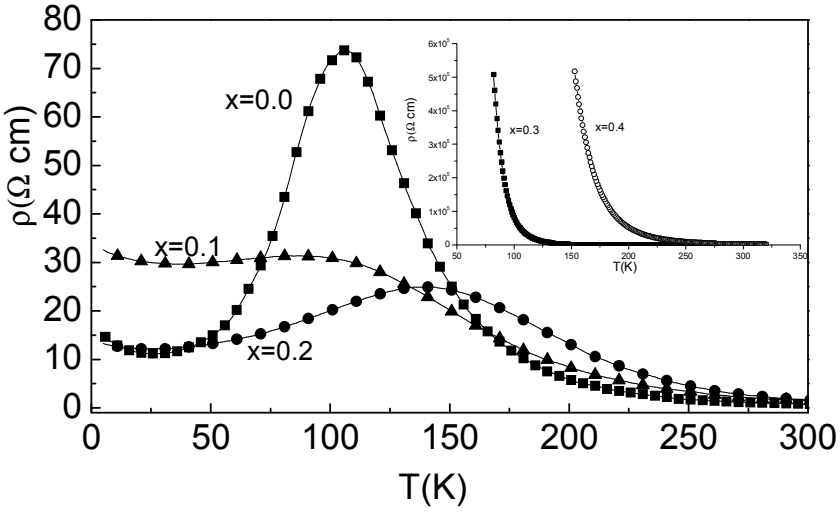


Fig3 The curve showing changes of the specific resistance of sample with $La_{1.4}Sr_{1.6-x}Mg_xMn_2O_7$ as its nominal component with temperature variation

The specific resistance of samples with x=0.1 and x=0.2 is obviously reduced with the increase of Mg content. For sample with x=0.1, its specific resistance has a T_ρ transformation temperature near 90K, while for sample with x=0.2, the T_ρ transformation temperature is near 140 K. Both transformation temperatures are lower than their Curie temperatures in the high-temperature area respectively. As is shown in the illustration of Figure 4, both the specific resistances of samples with x=0.3 and x=0.4 experience a mutation. Firstly, the numerical value of the specific resistance increases by nearly 4 orders of magnitude; secondly, the metal-insulation temperatures disappear, and the temperature zone represents insulativity throughout the measurement. The rules for the changes of the specific resistance are quite approximate to the electrical property of $La_{0.67}Sr_{0.33}Mn_{1-x}Mg_xO_3$series of compounds [9].

Conclusion

We have investigated the structure, magnetic and electrical properties of the nominal compositions $La_{1.4}Sr_{1.6-x}Mg_xMn_2O_7$. The samples are tetragonal bilayered perovskite with space group I4/mmm in the x=0 sample, while they are composed of ABO_3-type perovskite structure with space group Pbnm and tetragonal bilayered perovskite in the $0.1 \leq x \leq 0.3$ dopant regimes. When x is 0.4, the compound is pure orthorhombic ABO_3-type perovskite. For the magnetic properties, the Curie and Nair temperature first decreases with the increasing Mg^{2+} doping in the x=0.1 and 0.2 samples, then shows spin-glass state in the x=0.3 and 0.4 samples. For the electrical properties, the metal-insulation transformation temperature is 90K and 140K in the x=0.1 and 0.2 samples, respectively, and then the resistance increases nearly 4 order of magnitudes in the x=0.3 and 0.4 samples.

References

[1] Raveau B, Martin C, Maignan A. What about the role of B elements in the CMR properties of ABO_3 perovskites.[J]. J Alloys and Comps, 1998, 275-277: 461-467.

[2] Ogale S B, Shreekala R, Bathe R, et al. Transport properties, magnetic ordering, and hyperfine interactions in Fe-doped $La_{0.75}Ca_{0.25}MnO_3$: Localization-delocalization transition[J]. Phys Rev B, 1998, 57: 7841-7845.

[3] Hirot K, Ishihar S, Fujiol H, et al. Spin dynamical properties and orbital states of the layered perovskite $La_{2-2x}Sr_{1+2x}Mn_2O_7(0.3<\sim x<0.5)$[J]. Phys. Rev. B, 2002, 65: 064414 (1-10).

[4] Zhang J, Wang F W, Zhang P L, et al. Effect of Fe doping on magnetic properties and magnetoresistance in $La_{1.2}Sr_{1.8}Mn_2O_7$[J]. J. Appl. Phys., 1999, 86: 1604-1606.

[5] Hayashi T, Miura N, Tokunaga M, et al. Magnetic properties and CMR effect in layer type manganite $LaSr_2Mn_2O_7$ under high magnetic fields[J]. J. Phys.: Condens. Matter, 1998, 10: 11525-11529.

[6] Urushibara A, Moritomo Y, Arima T, et al. Insulator-metal transition and giant magnetoresistance in $La_{1-x}Sr_xMnO_3$[J]. Phys. Rev. B, 1995, 51: 14103-14109.

[7] Fan J Y, Pi L, Tong W, et al. Percolative conductivity in the $La_{0.67}Sr_{0.33}Mn_{1-x}Mg_xO_3$ system[J]. Phys. Rev. B, 2003, 68: 092407 (1-4).

[8] Perring T G, Aeppli G, Kimura T, et al. Ordered stack of spin valves in a layered magnetoresistive perovskite[J]. Phys. Rev. B, 1998, 58: R14693- R14696.

[9] Battle P D,Millburn J E,Rosseinsky M J,et al. Neutron Diffraction Study of the Structural and Electronic Properties of Sr2HoMn2O7 and Sr2YMn2O7[J]. Chem.Mater., 1997, 9: 3136–3143.

Advanced Materials Research Vol. 936 (2014) pp 577-584
© (2014) Trans Tech Publications, Switzerland
doi:10.4028/www.scientific.net/AMR.936.577

The ideal "defects" of the crystal structure of GaAs

Kulpash Iskakova[1, a], Rif Akhmaltdinov[2, b], Aisara Amanova[3, c]

[1]Kazakh National Pedagogical University, Almaty, Kazakhstan

[2]Caspian Public University, Almaty, Kazakhstan

[3]Kazakh National University, Almaty, Kazakhstan

[a]ahmanovakulpash@yahoo.com, [b]my_3d_email@mail.ru, [c]princessaa94@mail.ru

Keywords: semiconductors, GaAs, simulation, structure.

Abstract: The current industry needs for new results require current capabilities of computer technology can solve problems on a whole new level. This article briefly describes the algorithms for obtaining the structures and the appearance of discontinuities in the growth of crystals.

Introduction

Solution of some technological issues requires study the internal structure of electron shells. There is a problem of explaining the phenomenon of increasing orders of the electronic resistivity silicon with the introduction of a probe by the diffusion of electrons. To elucidate the structure of the outer electron shells of the 18 copper is an essential knowledge of the inner radius of these shells that is the outer radius of the lower shells. Reference data on X-ray spectra have become an important and reliable source of information on the geometrical dimensions of the inner electron shells of atoms of any chemical element.

Computer simulation of Cu structure

For example, for copper Z=29, R=0.004915 nm. Computer simulation was carried out in the cluster approximation, which consists in the fact that the volume of the crystal was cut limited selection, the initial positions of the atoms which correspond to their positions in the nodes of the real crystal lattice. For copper in Fig. 1 is shown the sphere-rod model third sphere of the fcc lattice with 24 atoms, but the model is rotated 45º around the axis z. In Fig. 2 is shown the sphere-rod model seventh sphere fcc lattice with 48 atoms. The model is rotated 45º about the axis of x. Atoms and bond rods are shown in different colors.

The modeling of properties shows that the crystal structure within a certain distance a gap of uniform growth occurs in the distances from the central atom. For copper, a spatial gap occurs after 321-th atomic node in the cluster. Further, these discontinuities are repeated periodically. And this is a defect associated with impaired growth are not in real crystals and the properties of the ideal lattice. The instability of the first cluster and the introduction of a defect in the corresponding crystal structure is the very first principle on which to conduct a fairly accurate analysis of the growth process of a real crystal and the resulting defects in it.

Copper is a metal, but also for semiconductors, computer simulation provides essential information for subsequent analysis of the process of their growth and ultimate properties. For example, computer simulation was conducted for the GaAs in the cluster approximation, which consists in the fact that the volume of the crystal was cut limited selection, the initial positions of the atoms of which comply with their provisions at the nodes of the real crystal lattice.

The lattice with a radius of 6 in her coverage of the atomic cores is considered. Calculation of the GaAs parameters were performed using the package we have created programs. As a cluster model was chosen 918-atom fragment of the crystal lattice of quantum dots based on GaAs. The properties of clusters depend on their size. Electron spectroscopy gives information averaged over the ensemble non isometric clusters on the surface and in the bulk solid. Therefore, to improve the accuracy and reliability of the information is necessary to create ensembles of clusters with a low dimensional variance.

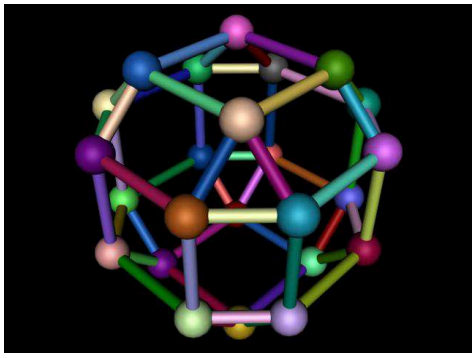


Fig. 1. The sphere-rod model third sphere model of the fcc lattice with 24 atoms. The model is rotated 45º around the axis *z*. Atoms and bond rods are shown in different colors.

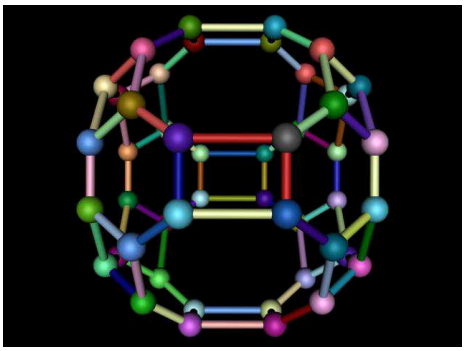


Fig. 2. The sphere-rod model seventh sphere model of the fcc lattice with 48 atoms. The model is rotated 45º about the axis of *x*. Atoms and bond rods are shown in different colors.

Consider the finite crystal with unbroken intervals (except for the crystal boundary violation). For simplicity, we take a large number of cores, when there is a nearly ideal periodicity of the crystal. In this case, the parameters obtained from the mathematical formalism for the analysis of the band spectrum are periodic functions, except for the boundary of the crystal. The crystal potential and wave functions have a period equal to the distance between the cores, depending on the chosen direction.

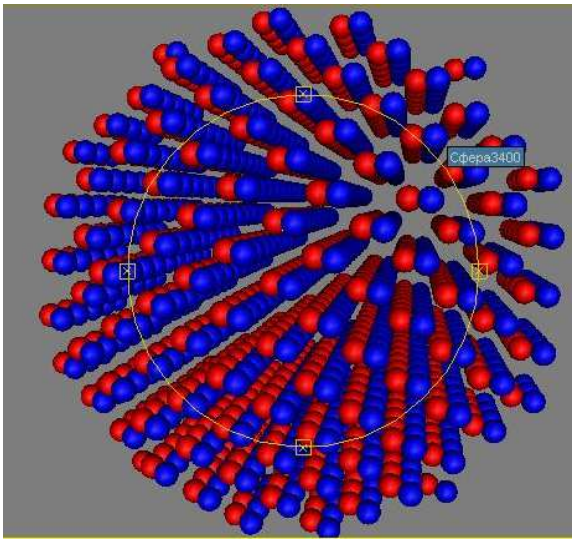


Fig. 3. The As atoms and Ga for the radius of coverage 6. Red marked atoms As, in blue denote atoms Ga. Central atom is As.

The energies have multiple frequency modulus of the wave vector in the quasi-momentum space [1]-[3]. Now turn to the crystal with a very small number of cores. In such a crystal frequency is not as ideal as in the previous case. The simulation of such a crystal is insurmountable difficulties for traditional methods, but this is the case is taken by us as a basic demonstration version. The object in question is distant from a perfect crystal due to its limited size. And despite this, the technique presented by us showed the periodicity of the above parameters. Thus in our problems are not used the condition of periodicity and Bloch's theorem as the necessary initial conditions. The Fig. 3 shows it on the example of GaAs.

Computer modeling of the crystal structure of GaAs

In computer modeling of the crystal structure of GaAs, combined with three-and five-valent elements are observed the following regularities (see Table 1). When the radius of coverage is two in this range there are 38 cores. As the first atomic core in the center of origin, the four Ga atoms are located at a distance of 3 next 12 As atoms at a distance of 8. Nine Ga atoms at a distance there are 11. Six As atoms at a distance of 16, three Ga at a distance of 19 and three Ga at a distance of 27.

Table 1. The Combined lattice GaAs

№	*x*	*y*	*z*	d^2	*Ion*		№	*x*	*y*	*z*	d^2	*Ion*	
0	0	0	0	0	As		19	–3	1	1	11	Ga	
1	–1	–1	1	3	Ga	breaking	20	–1	3	1	11	Ga	
2	–1	1	–1	3	Ga		21	3	1	–1	11	Ga	
3	1	–1	–1	3	Ga		22	1	–3	1	11	Ga	
4	1	1	1	3	Ga		23	–1	1	3	11	Ga	
5	0	2	–2	8	As	breaking	24	3	–1	1	11	Ga	
6	0	2	2	8	As		25	1	1	–3	11	Ga	
7	0	–2	–2	8	As		26	0	4	0	16	As	breaking
8	0	–2	2	8	As		27	–4	0	0	16	As	
9	–2	2	0	8	As		28	4	0	0	16	As	
10	–2	–2	0	8	As		29	0	0	–4	16	As	
11	2	2	0	8	As		30	0	0	4	16	As	
12	2	–2	0	8	As		31	0	–4	0	16	As	
13	–2	0	2	8	As		32	3	3	1	19	Ga	breaking
14	–2	0	–2	8	As		33	1	3	3	19	Ga	
15	2	0	2	8	As		34	3	1	3	19	Ga	
16	2	0	–2	8	As		35	1	5	1	27	Ga	breaking
17	1	3	–1	11	Ga	breaking	36	5	1	1	27	Ga	
18	1	–1	3	11	Ga		37	1	1	5	27	Ga	
19	–3	1	1	11	Ga		19	–3	1	1	11	Ga	

Total number of cores with zero: 38

We observe quasiperiodic change in the difference. At the border radius of coverage this periodicity is broken. When increasing the radius of coverage this periodicity is restored to the previous radius, but is broken on the new range. Thus, the boundary conditions lead to a violation of the periodicity. Simulated lattice shown in the following figures. The first figure shows the four first neighbors As in the lattice. Neighbors' ions Ga (blue) form a tetrahedron with the center of As (red). The boundary atoms can approximately account for modeling the interface of the quantum dot with the matrix. The Fig. 1 shows the grid with a radius of coverage 6. There are 918 atomic cores in it. There is a periodic step structure. The structure of the previous lattice is preserved. And the structure of the central ion and its neighbors on the tetrahedron is stored and located in the center of this lattice. It can be seen as an increase in the radius of coverage is restored periodicity in the lattice covered by the previous radius and there is a new violation of the periodicity on the boundary spanning lattice. The depth of violation increases with the radius of coverage. This is well observed in the tables you demonstrated for different cores. On the basis of the direct lattice can construct the reciprocal lattice and define the properties of the Fermi surface. And the radius of coverage can be taken arbitrary (millions of skeletons). The calculated structure allows to reach a real-time implementation and to take into account of defects and of real devices based on GaAs, because these are high-speed computing now by our proposed method. On the basis of the direct lattice we can also construct the reciprocal lattice and define the properties of the Fermi surface. And the radius of coverage can be taken arbitrary (millions of skeletons). High-speed computing enables a dynamic computer simulation of the properties of real crystals of the GaAs. Since the GaAs lattice is identical to the lattice of Si, sphalerite and diamond, we can apply the technology provided by and for these substances. In calculating of coordination spheres cells of FCC- and BCC-lattices are presented as superlattice structure to fill own nodes by atoms of cells and additional nodes of the simple cubic lattices (SCL) — interstitial atoms [2]. The completing of coordination spheres with atoms is determined on the basis of a small SC-lattice, taking into account octahedral, tetrahedral internodes. If atoms in the lattice arrange with the dense packing, P-nodes are centers of the inter-body lattices in the methods of presentment of the spatial distribution of atoms and internodes along the coordination spheres in the crystals. Tetrahedral and octahedral internodes in the ion-interionic terminology mean inter-body lattice space surrounded by the atoms in the crystal lattice nodes. Table 1 contains the number of atoms and the distance from the central

atom of the diamond-like structure. The distance is given in units of the lattice constant a. Let us choose the maximum distance based on these conditions, forming a set of atoms contributions on which the calculation of the potential are taken into account.

The crystal potential for crystals with the diamond structure

In this work we consider the crystal potential for crystals with the diamond structure. The Coulomb potential is the sum of the capacity building of the nucleus and the electrons occupied levels:

$$U_c = U_n + U_0, \tag{1}$$

where $U_n = -2Z/r$. Here, Z — number of the element, r — distance from the atom to the specified point.

Potential U_0 is a solution of the Poisson equation:

$$\nabla^2 U_0 = -8\,\pi\rho_0(r), \tag{2}$$

where $\rho_0(r)$ — the density of the electrons of the occupied levels at the distance r from the center of the atom. The density is calculated as follows:

$$\rho_0(r) = \sum_{n,l} r^2 R_{nl}^2(r). \tag{3}$$

Function $R_{nl}(r)$ — the radial part of the electron wave function for a hydrogen atom [4], [5]. Using the principle of superposition of the electronic densities and the additivity of the integral Eq. 3 can solve as follows:

$$U_0(r) = \sum_{i=0}^{I} u(r_i), \tag{4}$$

$$u(r_i) = \sum_{n,l} u_{nl}(r_i), \tag{5}$$

where I — the set of the number of atoms minus one, r_i — the distance from the center of the i-th atom to the specified point

$$\vec{r}_i = \vec{r} - \vec{a}_i. \tag{6}$$

Here a_i — the radius-vector of the i-th atom with respect to the center of origin. Let us obtain the Poisson equation for an electron of i-th atom:

$$\nabla^2 u_{nl}(\vec{r}_i) = -8\,\pi\, r_i^2 R_{nl}^2(\vec{r}_i). \tag{7}$$

Solving (8), we obtain

$$u(\vec{r}_i) = -8\,\pi \sum_{n,l} \iint u_{nl}(\vec{r}_i)\, d\vec{r}_i^{\,2}\ . \tag{8}$$

Directly using the functions (Eq.4, Eq.5, Eq.6, Eq.7, Eq.8) we find the potential U_0(r). This approach allows us to calculate effectively and accurately the electronic potential. We rewrite Eq. 2 accounted for the entire set of atoms:

$$U_c(\vec{r}) = \sum_i U_n(\vec{r}_i) + U_0(\vec{r})\,. \tag{9}$$

Thus, the Coulomb potential is calculated from all the surrounding atoms [1], [6]. This approach allows us to select any line capacity in any direction from the lattice points, and may be any length of line. Moreover, we can specify a curved line capacity. The cell potential near the nucleus has a singularity, and the distance from the nucleus is close to zero in hyperbole. For a single atom inside the Wigner-Seitz sphere the main contribution comes from the nucleus of an atom [6], [7]. Consider

the cell potential obtained at the line potential. In this case, clearly seen the potential frequency, which is created by all the atoms are now set. In passing through the core potential becomes singular. The potential between the atoms is identical and negligible in the magnitude. There is a little effect of the atoms located at the centers of the faces of the two face-centered cubic lattices [8].

The obtained simulation results show the crystal potential, the crystal can be modeled with all its features. In contrast to known methods of calculating of the crystal potential as described in the engineering calculations of the crystal potential is universal. It gives the results without making any correction factors, does not require the use of logarithmic scales, and other non-uniform, allows you to quickly calculate the crystalline potential for all elements of the given crystal structure. There are facilities for the further developments of such technology in the direction of accounting for various disturbances. It will allow a calculating the electronic potential even more precisely. However, even without taking into account the properties of an ideal crystal, this calculation provides sufficiently accurate results. To illustrate the power and versatility of the described technique for the calculating of the potential capabilities it is shown an interaction potential on line drawn along the main diagonals of the two face-centered cubic lattices in Fig. 4.

In determining the energy spectra of quantum-mechanical problems for periodic structures, it often uses methods of the broadcast. In particular, semiconductors have a periodic structure. The crystal potential, having the grating period, usually modeled by the expression [1], [9]:

$$V(\vec{r}) = \left[\sum_{i=0}^{N} V_{\text{n}}(\vec{r}_i)\right] + U_0(\vec{r}) + V_{\text{exh}}(\vec{r}). \tag{10}$$

where $V_{\text{n}}(\mathbf{r}_i)$ — the potential created by the i-th nucleus at the point $\mathbf{r}$; $U_0(\mathbf{r})$ — the electronic potential, formed by the electrons of the core at some point r and is determined from the Poisson equation

$$\nabla^2 U_0(\vec{r}) = -8\pi\rho_0(\vec{r}). \tag{11}$$

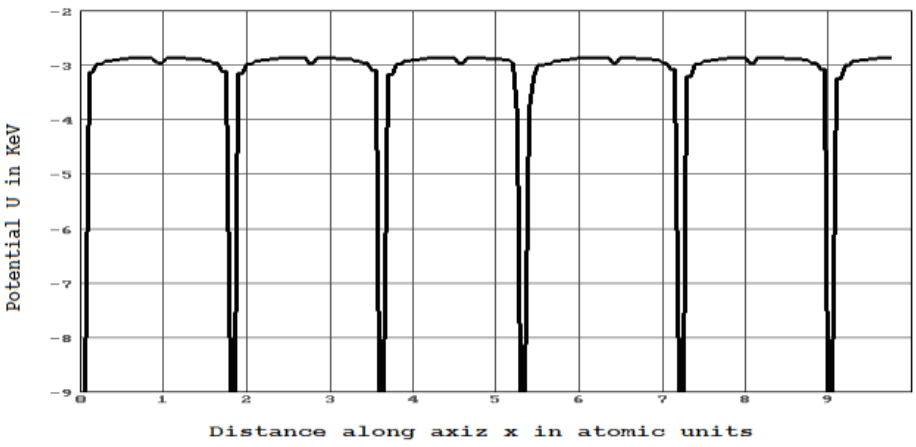


Fig. 4. An interaction potential on line drawn along the main diagonals of the two face-centered cubic lattice

Here $\rho_0(\mathbf{r})$ — the electronic density of the occupied levels at a distance r from the center of the atom; $V_{\text{exh}}(\mathbf{r})$ —the exchange potential at point $\mathbf{r}$; $\mathbf{r}_i = |\mathbf{r}\text{-}\mathbf{a}_i|$ — the distance from the i-th node to the point $\mathbf{r}$; $\mathbf{a}_i$ — the node location; N — the number of neighbors taken into account relatively to the cores. The solution of Schrödinger equation based on the potential (11) is carried out by the Hartree-Fock-Slater. The specificity of a solid compared to other bodies, is the decisive role of spatial-structural properties: a lattice type, a location and an interaction of the defects, a structure of core lattices and inter-ionic space. The period of the inter-ionic lattice coincides with the period of the core lattice. Spatially periodic structure of two weakly coupled and oppositely charged objects is the cause of the stability of rigid body — in this case the semiconductor GaAs — because between these objects appear spatially periodic Coulomb forces. In the geometric structure of each inter-ionic space surrounded on six sides by positive ion cores, and the ionic core in turn — intervals. For a uniform distribution of

electrons in the space of interaction between them becomes energetically unfavorable. There is the possibility of an orderly arrangement of electrons in space, the emergence of the so-called Wigner or “electron crystal”. The geometrical structure of the crystal consists not only of the atomic cores, but inter-ionic space intervals. The valence electrons in inter-ionic space intervals are also elements of the crystal, along with the atomic cores. The inter-ionic space is gap, i.e. the most probable location of the valence electrons. In addition, inter-ionic space intervals are also still a kind of “elements” of the crystal. But then the conclusion is that in the crystal lattice there are two — the well-known lattice consisting of the atomic cores, and another, equally important for the existence of the crystal lattice of the valence electrons are concentrated between the cores. The lattice periodicity of the atomic cores immediately implies the lattice periodicity of the inter-ionic space. Even more natural in such a conclusion, if you do not forget that the atomic cores of the crystal lattice — not a point in space, but the figures, which occupy a significant part of the whole space of the crystal, and inter-ionic space also has a periodic structure, as well as skeletons. The period of this lattice coincides with the usual of the core of the lattice. Fig. 5 shows a two-dimensional lattice with the lattice constant a_0. The coordinate origin of the system Oxy is at the center of one of the cores, and the origin of the coordinate system $O'x'y'$ is located in the center of one of the inter-ionic cells. The coordinate system $O'x'y'$ is formed by the translation of the coordinate system Oxy in $a_0n/2$, where $n = \{0, 1, 2, ...\}$. We assume inter-ionic intervals are the inter-ionic elements of the lattice, which is shifted with respect to a core of the lattice by half a lattice constant in all coordinate axes.

The energies have multiple frequency modulus of the wave vector in the quasi-momentum space [1]-[3]. Now turn to the crystal with a very small number of cores. In such a crystal frequency is not as ideal as in the previous case. The simulation of such a crystal is insurmountable difficulties for traditional methods, but this is the case is taken by us as a basic demonstration version. The object in question is distant from a perfect crystal due to its limited size. And despite this, the technique presented by us showed the periodicity of the above parameters. Thus in our problems are not used the condition of periodicity and Bloch's theorem as the necessary initial conditions. The Fig. 3 shows it on the example of GaAs.

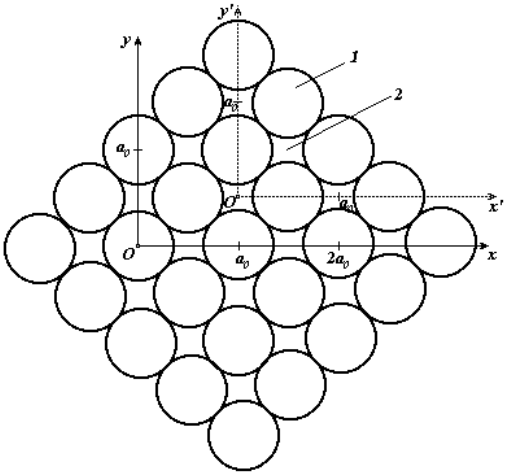


Fig. 5. A two-dimensional lattice with the lattice constant a_0. Cores and inter-ionic space two-dimensional lattice include 1) frame, 2) inter-ionic space.

The determining the location of the centers of the location of the centers of the inter-ionic intervals can be easily receive from the definition of the basis vector for the nodes of the crystal (the core) of the lattice with any structure. But it should be noted that by increasing the radius of inter-ionic volumes (not just their centers) there is a change the number under the consideration inter-ionic space compared to the amount covered by the cores. Since you want to cover all inter-ionic space surrounding covered the skeletons, the radius of coverage inter-ionic space few more skeletons examined. Crystal is in a stable condition thanks to the orderly arrangement of opposite charges. Most of the properties of crystals (eg, electrical conductivity, magnetic susceptibility), are caused not only property of the host lattice, but also the existence of inter-ionic lattice. This inter-ion lattice in addition to the core determines the physical properties of the crystal. Specificity of a solid compared to other bodies is that in them play crucial role spatial structural properties: the lattice type, location and interaction of defects, the structure of the nucleus and inter-ion lattice. The period of the inter-ion lattice coincides with the period of the core lattice. Spatially periodic structure of two weakly coupled and oppositely charged objects is the cause of the stability of rigid body — in this case the GaAs — because between these

objects appear spatially periodic Coulomb forces. In the geometric structure of each inter-ionic cell surrounded on six sides by positive ion cores, and the ionic core in turn — the inter-ionic gaps.

Discussion

Computer simulation of the properties of the crystal lattice gives to use up to 1010 ÷ 1012 atoms. Using the described technique can be obtained from any of these atomic systems, as well as changes in the radii of coordination spheres at various distances. Simultaneously, you can get a number of nearby neighbors, the location of atoms on the coordination sphere.

Thus, algorithms are developed for the FCC, BCC and diamond-like structures for determining the orderly and semiregular Archimedean and Platonic figures, as well as their complexes.

We can develop an algorithm for constructing the structure of compound semiconductor-type A^3B^5, based on this principle. For example, to the type of A^3B^5 of semiconductor compounds it is used compound GaAs. It is crystal lattice of two face-centered cubic lattices shifted relative to each other at *j* spatial diagonal. Each Ga atom has four nearest neighbors located at the tops of a tetrahedron. Each ion is surrounded by four nearest neighboring ions of opposite sign. There are four ions with $q_i\ q_j = -1$ at a distance $a_0 2½/2$, eight ions of opposite sign of $q_i\ q_j = +1$ at the 2 distance $a_0 2½$. The system of links of the GaAs structure establishes the order of the atomic body along tetrahedral combinations [2], [3]. For such compounds of the tetrahedral group of atoms is one-eighth of the basic lattice, so it is convenient to consider as a superstructure. The cell of the GaAs lattice consists of four tetrahedral sublattices.

One of the advantages of the described technique is its application to systems with short-range order, which does not use Bloch's theorem as the initial conditions. This was possible due to the fact that translational invariance follows as a consequence of the calculations, and not postulated initially. Thus, translational invariance in real space and in the quasi-momentum space is not a prerequisite for the determination of the crystal potential, wave functions and energies in wave vector space.

This, in turn, allows you to define these parameters not only for infinite crystals, but also for the real limits on the size of the crystals. Therefore, it is possible to determine the properties of crystals with impaired structure of a single scheme, with no additional idealizations. Individual interest is a violation of the periodicity on the boundary of the crystal. In fact, it is inherent in all real crystals violation of the ideal (i.e. infinite) crystal structure.

The violation of a perfect crystal at the border no doubt affects the theoretical study of the band spectrum. Boundary effects appear in the form of decay phase portraits of the main parameters (the crystal potential, the wave functions and energies in wave vector space) in all directions of the crystal boundaries (in our case spherical).

Summary

In the study of solid-state we considered two sites within the crystal, virtually connected to each other. A theoretical study of solid-state is easily accomplished with the use of these facilities both qualitative and quantitative methods. But the most effective way of investigating solids is to use a direct computer simulation, and that we have done for simple structures.

Thus, the use of techniques discussed in the article allows the calculation of real properties of GaAs crystals with defects and other constraints.

References

[1] T. Loucks, Augmented plane wave method. New York, W. A. Bendjamin Inc., 1967, p. 12-62.

[2] Iskakova K.A., Ahmaltdinov R.F., Possibilities of the modifications of the method of calculation of wave function and zonal spectrum of crystal structure, PCI-2010 «12th International Conference on the Physics and Chemistry of Ice». Sapporo, Japan.

[3] Iskakova K.A., Ahmaltdinov R.F., Modelling and calculation of FCC structures and principles of the algorithm structure Si, 88th annual meeting of the German Mineralogical Society, 19–22. September 2010 Munster, Germany.

[4] Bugaev V.N., Chepulski R. V. 1. Basic theory. The symmetry of interatomic lattice potentials in general crystal structures. – Acta crystallogr. 1995, v. 51, No 4, p. 456–462.

[5] Sowa E.C., Gonis A. A multisite interaction expansion of the total energy in metals. Instrum. and Meth. Phys. Res. B. 1995, v. 102, No 1–4, p. 1–2.

[6] Korhonen T., Puska M. I., Nieminen R. M. Vacancy formation energies for fcc and bcc transition metals. Phys. Rev. B. 1995, v. 51, No 15, p. 9526–9532.

[7] Mirabella D.A., Aldao C.M. Effects of orbital nonorthogonality on band structure within the hight binding scheme. Phys. Rev. B. 1994, v. 50, No 16,p. 12152–12155.

[8] Andrews Lawrence C., Bernstein Herbert I. Bravais lattice invariants. Acta Crystallogr. A. 1995, v. 51, No 3, p. 413–416.

[9] Krimmel H.G., Ehmann I., Elsasser C. Calculation of atomic forces using the lineorized – augmented – plane wave method. Phys. Rev. B. 1994, v. 50, No 12,p. 8846–8848.

Advanced Materials Research Vol. 936 (2014) pp 585-590
© (2014) Trans Tech Publications, Switzerland
doi:10.4028/www.scientific.net/AMR.936.585

Cooperative Energy Transfer of Er-Gd-Tb System in Tb^{3+}, Er^{3+} Co-doped $K_2GdZr(PO_4)_3$ as a Potential Visible Quantum Cutting Phosphor

Liangfeng Niu[1, a], Wei Liang[2, b*], Changzeng Wu[1] and Yuhua Wang[3]

[1]School of Chemistry and Chemical Engineering, Xuchang University, Xu Chang, He Nan, 461000, P.R. China

[2]School of New Materials and Energy, Xuchang University, Xu Chang, He Nan, 461000, P.R. China

[3]Department of Materials Science, School of Physical Science and Technology, Lanzhou University, Lanzhou 730000, P. R. China

[a]hnbfnlf@126.com, [b]lawe_13@163.com

Keywords: cooperative energy transfer, visible quantum cutting, spectral characteristics, $K_2GdZr(PO_4)_3$:Tb^{3+},Er^{3+}.

Abstract. Tb^{3+}, Er^{3+} co-doped $K_2GdZr(PO_4)_3$ samples were prepared by solid-state reaction method and their photoluminescence (PL) properties were investigated in ultra-violet (UV) and vacuum ultra-violet (VUV) region. The results indicate that the energy transfers from Er^{3+} to Gd^{3+} and from Gd^{3+} to Tb^{3+} required for occurring of visible quantum cutting through down-conversion are efficient. In this cooperative energy transfer process, Gd^{3+} is used as an intermediate of energy transfer between Er^{3+} and Tb^{3+}. The optimal quantum efficiency (QE) of this co-doped system $K_2GdZr(PO_4)_3$: Er^{3+}, Tb^{3+} phosphor reached to 110%, suggesting a potential visible quantum cutting phosphor in practical application.

Introduction

In recent several years, the spectral characteristics of phosphors with quantum efficiency higher than 100% have become a new focal point in the field of luminescent materials research.[1-7] This is due to the emerging need for new vacuum ultraviolet (VUV) phosphors in applications such as mercury-free fluorescent tubes and plasma display panels (PDP).[4,8,10] Research on the phenomenon of generating two or more visible photons for each incident VUV photon absorbed by phosphors (quantum cutting) started on Pr^{3+}-doped YF_3 in the early 1970s.[5-7] Up to now, the quantum cutting process and its possibilities in other rare earth ions and host materials have been investigated extensively.[12-19] However, no perfect phosphor for practical applications has been discovered so far. Based on the prediction expected by Van der Kolk et al.[7,8], host materials with weak crystal field, low phonon energies, larger band gap, large cation-anion distance and large coordination number for the substitution site are considered important to exhibit quantum cutting (QC) phenomenon. Besides, as is known to all, fluoride phosphors are unsuitable for lighting and display applications. In contrast, rare-earth phosphates have many advantages over fluorides, such as high VUV absorption efficiency, high physical-chemical and thermal stability, easy fabrication, low solubility, transparent and low cost, which are more useful in practical applications. The particular structure of $K_2GdZr(PO_4)_3$ exhibited in Ref. [11,21] indicates that it could be an ideal host to fulfill the above requirements of QC process. In addition, an efficient visible QC has also been obtained in Er^{3+} - Gd^{3+} - Tb^{3+} system with a maximum quantum efficiency (QE) of 130%.[12] However, to the best of our knowledge, no report has focused on the QC phenomenon in Tb^{3+}, Er^{3+} co-doped $K_2GdZr(PO_4)_3$ phosphor.

Herein, in this paper, the photoluminescence (PL) and spectroscopic characteristics studies of $K_2Gd_{1-x-y}Zr(PO_4)_3$: Tb^{3+}, Er^{3+} (0.5 mol. % $\leq$ x $\leq$ 5 mol. %, 1 mol. % $\leq$ y $\leq$ 5 mol. %) were presented. The cooperative energy transfer (down-conversion) process of Er^{3+} - Gd^{3+} - Tb^{3+} system was also investigated and the quantum efficiency for $K_2GdZr(PO_4)_3$ co-doped with Tb^{3+} and Er^{3+} was evaluated.

Experimental

Sample Preparation.

The samples of $K_2Gd_{1-x-y}Zr(PO_4)_3 : Tb^{3+}$, Er^{3+} (0.5 mol. % ≤ x ≤ 5 mol. %, 1 mol. % ≤ y ≤ 5 mol. %) were prepared by solid-state reaction method. K_2CO_3 (99.0%, AR), ZrO_2 (99.0%, AR), $(NH_4)_2HPO_4$ (98.5%, AR), Gd_2O_3 (99.99%), Tb_4O_7 (99.99%) and Er_2O_3 (99.99%) were used as raw materials. They were thoroughly mixed in stoichiometric proportions. The mixtures were heated at 980 °C (optimal synthesis temperature) for 8 h in reducing atmosphere and finally cooled to room temperature. The phases of as-prepared samples were characterized by monochromatic Cu K_α X-ray powder diffraction (XRD) analysis (Rigaku D/max-2400). During the XRD measurement, the data were obtained by step scanning with an increment of 0.02° (2θ) in the diffraction angles of 10° ~ 80°. The XRD patterns are shown in Fig. 1. All the samples are indexed to the phase of $K_2GdZr(PO_4)_3$ (JCPDF No. 49-0634) with the space group of P_{2_13} and there is no extra peaks corresponding to any other phases. Therefore, the expected compounds were synthesized in this work.

Spectroscopic Properties Analysis.

The UV PL properties were analyzed using an Edinburgh Instruments FLS-920T combined fluorescence lifetime and steady-state spectrophotometer with Xe900 (450W xenon arc lamp) as excitation source. The VUV excitation and emission spectra were measured with FLS-920T and the vacuum monochromator (VM504, Acton Research Corporation, ARC). The VUV light source was a 150W Deuterium lamp (Cathodeon Incorporated). The VUV excitation spectra were corrected by dividing the excitation intensity of sodium salicylate at the same measurement condition. All the spectra were recorded at room temperature.

Results and Discussion

Mechanism of Cooperative Energy Transfer for Er^{3+} - Gd^{3+} - Tb^{3+}.

The possible mechanism for visible quantum cutting through down-conversion in the Gd^{3+}-based host material co-doped with Er^{3+} and Tb^{3+} is illustrated in a schematic energy level diagram[12,16] shown in Fig. 2.

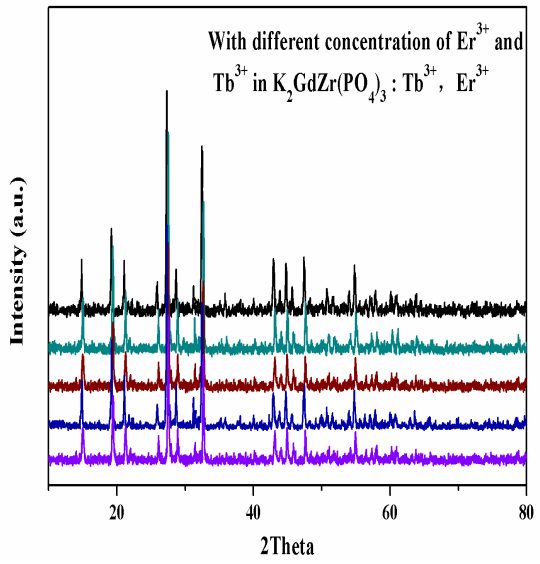


Figure 1 XRD Patterns of $K_2Gd_{1-x-y}Zr(PO_4)_3 : Tb^{3+}$, Er^{3+} (0.5 mol. % ≤ x ≤ 5 mol. %, 1 mol. % ≤ y ≤ 5 mol. %)

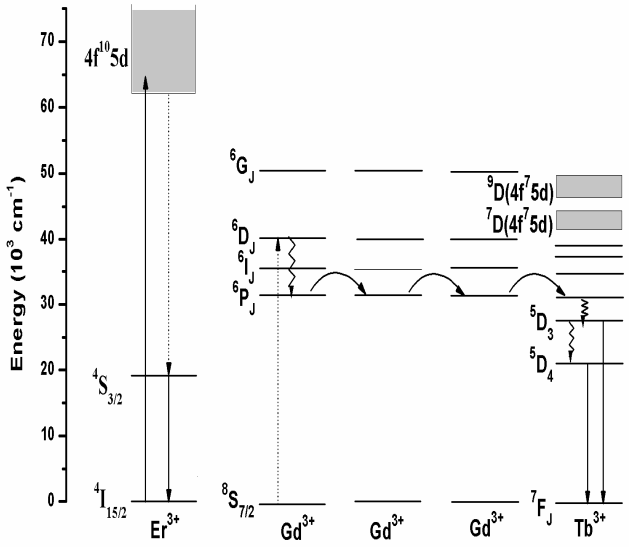


Figure 2 Part of Approximate Energy Level Diagram for Er^{3+}, Gd^{3+} and Tb^{3+}, Showing the Cooperative Energy Transfer Process of the Er-Gd-Tb System and the Possibility for Visible Quantum Cutting Via the Energy Transfer upon Excitation in the $4f^{10}5d$ State of Er^{3+}.[12,16]

According to the energy-matching relationship between Er^{3+}, Gd^{3+} and Tb^{3+}, the quantum cutting process takes place on Er^{3+} upon excitation in its $4f^{10}5d$ levels which are situated in the VUV range. After non-radiative relaxation to the lowest $4f^{10}5d$ state of Er^{3+}, the energy can be transferred to Gd^{3+} by cross-relaxation and excites Gd^{3+} into ^6P_J, ^6I_J or ^6D_J states.[12,13] Then Er^{3+} transfers back to the level in or above the $^4S_{3/2}$ excited state and emits a green photon due to the $^4S_{3/2} \rightarrow {}^4I_{15/2}$ transition of Er^{3+}. Subsequently, the energy transferred to Gd^{3+} migrates over the Gd^{3+} sublattice before reaching to a high-energy state of Tb^{3+}, emitting another green photon corresponding to the Tb^{3+} $^5D_J \rightarrow {}^7F_J$ transition by fast non-radiative relaxation to its ^5D_J states.[14, 17-19] In this process, Gd^{3+} is used as an intermediate of energy transfer between Er^{3+} and Tb^{3+}.[12,20]

PL and Spectroscopic Properties.

In Fig. 3 (a) and (b), the relevant excitation and emission spectra of Er^{3+} single doped $K_2GdZr(PO_4)_3$ under VUV excitation is exhibited. The strong excitation band centered at around 132 nm in the region of 125 ~ 155 nm in Fig. 3(a) is assigned to the spin-allowed transition to low-spin $4f^{10}5d$ state of Er^{3+} as well as the Gd^{3+} f-d transition. The weak band at 163 nm overlapping with the band of transitions originating from the $4f^7$ configuration of Gd^{3+} corresponding to the spin-forbidden transition to Er^{3+}'s high-spin $4f^{10}5d$ level. Besides, the $^8S_{7/2} \rightarrow {}^6D_J$ and $^8S_{7/2} \rightarrow {}^6I_J$ transitions of Gd^{3+} can also been observed. As it shown in Fig. 3 (b), under 147 nm excitation, the emission peaks corresponding to the $^6P_{7/2} \rightarrow {}^8S_{7/2}$ transition at 311 nm of Gd^{3+}, and the $^2P_{3/2} \rightarrow {}^4I_{13/2}$ at 405 nm, $^4F_{5/2} \rightarrow {}^4I_{15/2}$ at 460 nm, $^4S_{3/2} \rightarrow {}^4I_{15/2}$ at 547 nm, $^4F_{9/2} \rightarrow {}^4I_{15/2}$ at 648 nm transitions of Er^{3+}, respectively. The occurring of energy transfer from Er^{3+} to Gd^{3+} plays an important role in the investigation on the probability of quantum cutting. The spectral overlap between Er^{3+} and Gd^{3+} shown in Fig. 3 (a) indicates that the Er^{3+} (f-d) $\rightarrow$ Gd^{3+} (f-f) energy transfer process could be effective, providing a theoretical possibility for the occurrence of visible quantum cutting through the down-conversion process. Fig. 4(a) and (b) exhibit the excitation spectra of Tb^{3+} single doped $K_2GdZr(PO_4)_3$ phosphor in UV and VUV range, monitoring the Tb^{3+}'s 550 nm emission. In the region of 100 ~ 200 nm, the excitation spectra consists of several overlapped excitation bands, which can be ascribed to the Gd^{3+} f-d and $^8S_{7/2} \rightarrow {}^6G_J$ transitions, P-O band covalency, O^{2-} - Tb^{3+} and O^{2-} - Gd^{3+} charge transfer band (CTB), the $4f^8 \rightarrow 4f^75d^1$ transition of Tb^{3+}, respectively. The excitation lines shown in Fig. 4(b) at about 274, 311 and 300 ~ 380 nm range corresponds to the $^8S_{7/2} \rightarrow {}^6I_J$ and $^8S_{7/2} \rightarrow {}^6P_{7/2}$ transitions of Gd^{3+} as well as the f-f transition of Tb^{3+}, respectively. It is clear that there are several cases of good spectral overlap between Gd^{3+} and Tb^{3+}, providing a condition for the energy transfer from Gd^{3+} to Tb^{3+}. The emission spectra of Tb^{3+} single doped sample under 254, 274, 212 and 147 nm excitation in Fig. 5 display that the emission peaks corresponding to the $^5D_3 \rightarrow {}^7F_5$ (416 nm), $^5D_3 \rightarrow {}^7F_4$ (435 nm), $^5D_3 \rightarrow {}^7F_3$ (457 nm), $^5D_4 \rightarrow {}^7F_6$ (490 nm), $^5D_4 \rightarrow {}^7F_5$ (550 nm), $^5D_4 \rightarrow {}^7F_4$ (583 nm) and $^5D_4 \rightarrow {}^7F_3$ (620 nm) transitions of Tb^{3+} are obtained.

As shown in Fig. 5, the emission intensity of the sample excited by 274 nm (Gd^{3+} $^8S_{7/2} \rightarrow {}^6I_J$ transition) is higher than that excited by 254 nm. It suggests that the energy of Gd^{3+} is transferred to Tb^{3+} effectively. Figs. 6, 7(a) and (b) show the excitation and emission spectra of Tb^{3+}, Er^{3+} co-doped $K_2GdZr(PO_4)_3$ under UV and VUV excitation. The excitation bands exhibited in Fig. 6 are due to the f-d, $^8S_{7/2} \rightarrow {}^6G_J$, $^8S_{7/2} \rightarrow {}^6I_J$ and $^8S_{7/2} \rightarrow {}^6P_{7/2}$ transitions of Gd^{3+}, $4f^8 \rightarrow 4f^75d^1$ (low-spin) and f-f transitions of Tb^{3+}, Er^{3+}'s spin-allowed and spin-forbidden f-d transition, respectively. In Fig. 7(a) and (b) the emission spectra in the region of 300 ~ 700 nm under 274 and 147 nm excitations are presented, next to the Er^{3+} and Gd^{3+} emissions, a number of strong emissions which are all assigned to the Tb^{3+} transitions are observed. The most intense $^5D_4$ emission of Tb^{3+}, the $^5D_4 \rightarrow {}^7F_5$ transition (green), overlaps with the Er^{3+} $^4S_{3/2} \rightarrow {}^4I_{15/2}$ transition, emitting two green photons. The results in Fig. 7 prove that a significant part of the Gd^{3+} excitation energy is transferred to Tb^{3+}, resulting in a green photon emission. In addition, the increase of the Er^{3+}'s $^4S_{3/2}$ emission (another green photon)[15] can be seen relative to the other emissions in Fig. 7(a), indicating that the cross-relaxation required for visible quantum cutting via down-conversion occurs.

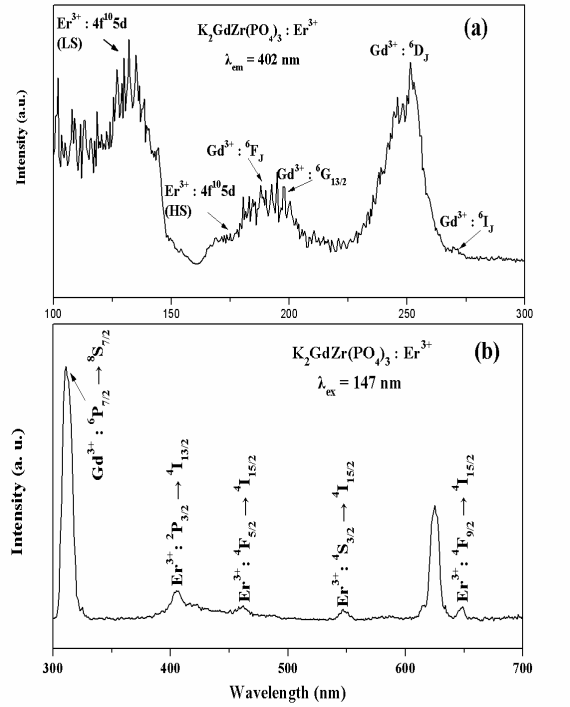


Figure 3 (a) Excitation Spectra of Er^{3+} Single Doped $K_2GdZr(PO_4)_3$ Sample Monitored at 402nm; (b) Emission Spectra of Er^{3+} Single Doped $K_2GdZr(PO_4)_3$ under 147 nm Excitation.

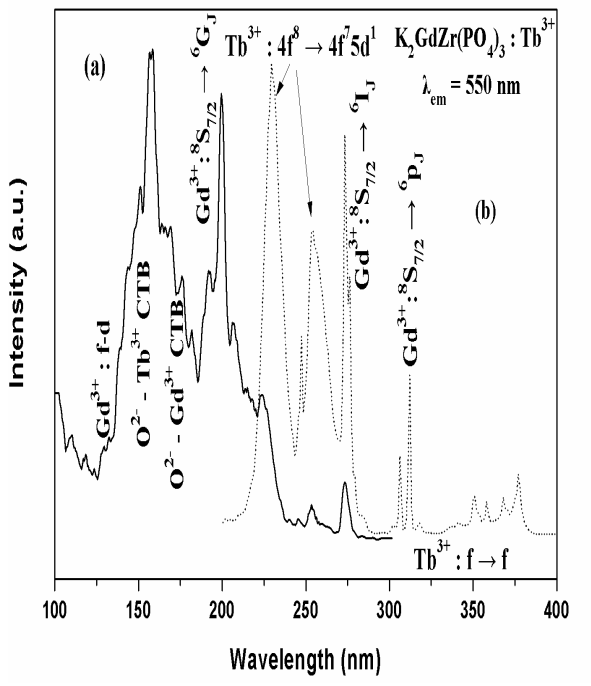


Figure 4 Excitation Spectra of Tb^{3+} Single Doped $K_2GdZr(PO_4)_3$ Sample in the (b) UV and (a) VUV Range, Monitored at 550 nm.

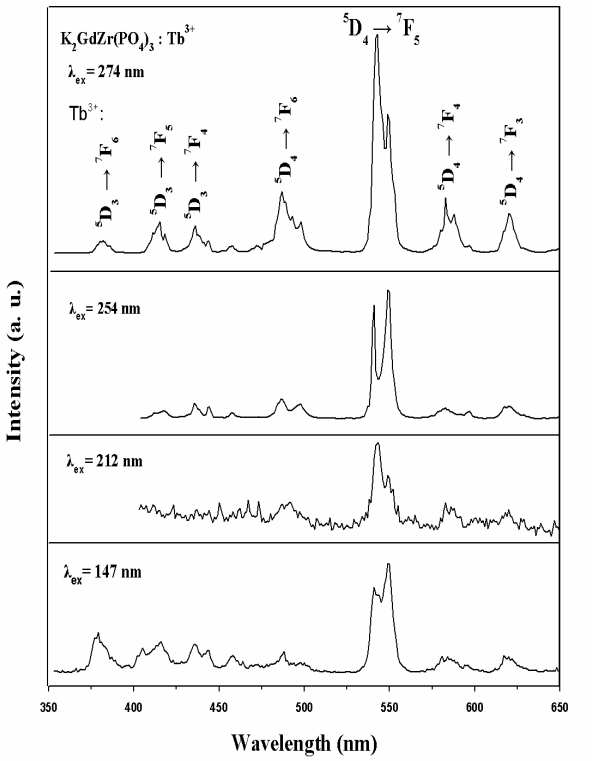


Figure 5 Emission Spectra of Tb^{3+} Single Doped $K_2GdZr(PO_4)_3$ Sample under 254, 274, 212 and 147 nm Excitation, Respectively.

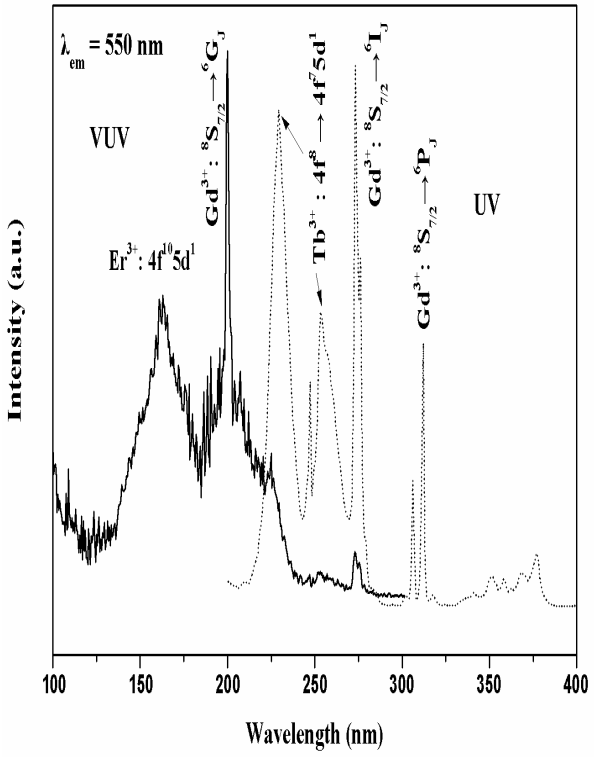


Figure 6 Excitation Spectra of $K_2Gd_{1-x-y}Zr(PO_4)_3$: Tb^{3+}, Er^{3+} (0.5 mol. % ≤ x ≤ 5 mol. %, 1 mol. % ≤ y ≤ 5 mol. %) under UV and VUV Excitation, Monitored at 550 nm.

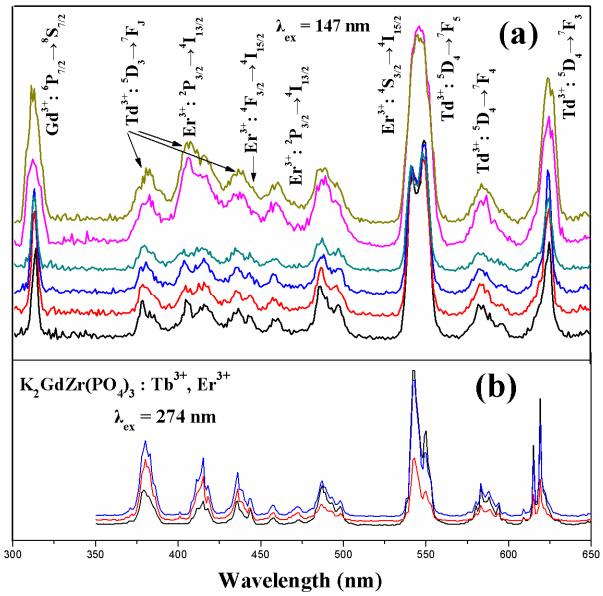


Figure 7 (a) Emission Spectra of $K_2Gd_{1-x-y}Zr(PO_4)_3$: Tb^{3+}, Er^{3+} (0.5 mol. % ≤ x ≤ 5 mol. %, 1 mol. % ≤ y ≤ 5 mol. %) under 147 nm Excitation; (b) Emission Spectra of Tb^{3+}, Er^{3+} Co-doped $K_2Gd_{1-x-y}Zr(PO_4)_3$ Samples under 274 nm Excitation.

Calculation of the Quantum Efficiency

On the basis of the operation explored by Wegh et al., the approximate efficiency of the cross-relaxation needed for visible quantum cutting occurring in $K_2GdZr(PO_4)_3$ co-doped with Tb^{3+} and Er^{3+} can be estimated by comparing the increase in the intensity of Er^{3+} $^4S_{3/2}$ emission with the intensities of other emissions in the emission spectra under UV and VUV excitation. If it is assumed that, in the 300 ~ 700 nm region, all the excited Gd^{3+} result in the emission of one visible photon, either on Er^{3+} or Tb^{3+}. In this process, some emissions of Er^{3+} in the infrared spectral region are so weak that they can be neglected. Thus, the energy transfer efficiency in the Er - Gd -Tb system can be estimated by the following formula[12]:

$$\frac{P_{ET_+}}{P_{ET_+} + P_{ET_-}} = \frac{R(^4S_{3/2} / \text{rest})_{Er^{3+}} - R(^4S_{3/2} / \text{rest})_{Gd^{3+}}}{R(^4S_{3/2} / \text{rest})_{Gd^{3+}} + 1} \quad (1)$$

where P_{ET+} and P_{ET-} are the probabilities of the desired and undesired energy transfer possibilities from the Er^{3+} $4f^{10}5d$ states to Gd^{3+}, respectively. $R(^4S_{3/2} / \text{rest})_{Er^{3+}}$ and $R(^4S_{3/2} / \text{rest})_{Gd^{3+}}$ are the intensity ratios of Er^{3+} $^4S_{3/2}$ emission to all the remaining emissions upon the f-d excitation of Er^{3+} and the ^6I_J excitation of Gd^{3+}, respectively. If the non-radiative losses because of energy transfer at the defects and impurities could be ignored, the quantum efficiency (η) of this Tb^{3+}, Er^{3+} co-doped $K_2GdZr(PO_4)_3$ phosphor can be given by $\eta = (P_{ET+} / P_{ET+} + P_{ET-}) + 1$. From the emission spectra shown in Fig. 5, the optical quantum efficiency was evaluated to be 110 %. That is to say, approximately 10 % of the Er^{3+} exited into the $4f^{10}5d$ levels yields an additional visible photon via cross-relaxation with Gd^{3+}. Although the calculated result of energy transfer efficiency in this phosphor was not very ideal, it was clear that the visible quantum cutting through cooperative energy transfer between Er^{3+}, Gd^{3+} and Tb^{3+} did indeed occur. This could be hopeful for the further development of $K_2GdZr(PO_4)_3$ co-doped with Tb^{3+} and Er^{3+} as a potential VUV phosphor with visible quantum efficiency higher than unity.

Summary

A potential visible quantum cutting phosphor, $K_2GdZr(PO_4)_3$: Tb^{3+}, Er^{3+}, was prepared successfully by solid-state reaction method. Its luminescence excitation and emission properties were

studied at room temperature. Based on the results of experiment in this paper, the visible quantum cutting via energy transfer down-conversion can occur upon the excitation of Er^{3+} in the $4f^{10}5d$ levels followed by the emission of two green photons and the quantum efficiency for this Tb^{3+}, Er^{3+} co-doped $K_2GdZr(PO_4)_3$ phosphor can be calculated to be near 110 %.

Acknowledgements

This work was supported by the Intramural Research Funds of Xuchang University (NO. 2013071), the Natural Science Foundation of Education Department of Henan Province(NO. 14A150056) and National Natural Science Foundation of China (NSFC 21271152).

References

[1] Y. F. Li, M. Yin, H. Guo, V. N. Makhov, N. M. Khaidukov, J. C. Krupa, J. Phys.: Condens. Matter 15 (2003) 7117.

[2] R. P. Rao, D. J. Devine, J. Lumin. 87–89 (2000) 1260.

[3] R. T. Wegh, H. Donker, E. V. D. van Loef, K. D. Oskam, A. Meijerink, J. Lumin. 87–89 (2000) 1017.

[4] Y. R. Do, J. W. Bae, J Appl Phys. 88 (2000) 4660.

[5] N. Murase, C. L. Li, J. Lumin. 128 (2008) 1896.

[6] B. Moine, L. Beauzamy, P. Gredin, G. Wallez, J. Labeguerie, Opt. Mater. 30 (2008) 1083.

[7] Q.Y. Zhang, X.Y. Huang, Prog. Mater Sci. 55 (2010) 353.

[8] E. van der Kolk, P. Dorenbos, A. P. Vink, R. C. Perego, C. W. E. van Eijk, A. R. Lakshmanan, Phys. Rev. B. 64 (2001) 195129.

[9] K. D. Oskam, R. T. Wegh, H. Donker, E. V. D. van Loef , A. Meijerink, J. Alloys. Compd. 300–301 (2000) 421.

[10] T. Jüstel, H. Nikol: Adv. Mater. 12 (2000) 527.

[11] I. V. Ogorodnyk, I. V. Zatovsky, V. N. Baumer, N. S. Slobodyanik, O. V. Shishkin, Cryst. Res. Technol. 42 (2007) 1076.

[12] R.T. Wegh, E.V.D. van Loef, A. Meijerink, J. Lumin. 90 (2000) 111.

[13] Q. H. Xu, B. C. Lin, Y. L. Mao, J. Lumin. 128 (2008) 1965

[14] L.Y. Zhou, J. S. Wei, J. X. Shi, M. L. Gong, H. B. Liang, J. Lumin. 128 (2008) 1262.

[15] N. Jaba, M. Ajroud, G. Panczer, M. Férid, H. Maaref, Opt. Mater. 32 (2010) 479.

[16] P. S. Peijzel, A. Meijerink, Chem. Phys. Lett. 401 (2005) 241.

[17] T. J. Lee, L. Y. Luo, E. W. G. Diau, T. M. Chen, B. M. Cheng, C. Y. Tung, Appl. Phys. Lett. 89 (2006) 131121.

[18] H. Y. Tzeng, B. M. Cheng, T. M. Chen, J. Lumin. 122–123 (2007) 917.

[19] Q. Y. Zhang, C. H. Yang, Y. X. Pan, Appl. Phys. Lett. 90 (2007) 021107.

[20] H. Kondo, T. Hirai, S. Hashimoto, J. Lumin. 102–103 (2003) 727.

[21] W. Liang, Y. H. Wang, Mater. Chem. Phys. 119 (2010) 214.

Advanced Materials Research Vol. 936 (2014) pp 591-595
© (2014) Trans Tech Publications, Switzerland
doi:10.4028/www.scientific.net/AMR.936.591

First-principles investigations of electronic, dynamic and thermodynamic properties of α-MnO_2

Aimin Hao* and Naqi Wang

Hebei Provincial Laboratory for Dielectric and Electrolyte Materials, School of Resources and Materials, Northeastern University at Qinhuangdao, Qinhuangdao, 066004, China

haoam@neuq.edu.cn

Keywords: first-principles calculations, electronic properties, dynamic properties, thermodynamic properties

Abstract: We investigate the electronic, dynamic and thermodynamic properties of α-MnO_2 using first-principles calculations based on density functional theory (DFT) with the GGA+*U* method. The results of electronic structures show that α-MnO_2 is a semiconductor with a direct band gap of 1.4 eV at Γ point. The results of dynamic properties indicate that the structure of α-MnO_2 is dynamically unstable at ground-state. Several important thermodynamic quantities, such as entropy, enthalpy and Gibbs free energy, et al each as a function of temperature were presented.

Introduction

Manganese dioxide (MnO_2) has a huge structural flexibility and appears in a number of crystallgraphic polymorphs, such as α-, β-, γ-, δ-, and ε-MnO_2, which are widely used as catalysts [1], electrode materials in Li/MnO_2 batteries [2,3] and supercapacitors [4-7].

The equilibrium phase of MnO_2 at standard temperature and pressure is β-MnO_2. The electrochemical properties of MnO_2 strongly depend on its particle size, morphology, crystalline structure and bulk density. Gao et al. [8] discussed lattice vibrational properties of β-MnO_2 and α-MnO_2 using Raman scattering spectroscopy. Yang et al. [9] studied the effect of the synthetic condition, morphology and crystallographic structure of MnO_2 on its electrochemical behavior. Lee et al. [10] reported the use of MnO_2 as a positive electrode material in Fuel Cell/Battery systems. They observed that MnO_2 possesses redox capabilities as a positive electrode of a secondary battery when it is subject to charge/discharge cycles.

Sato et al. [11] investigated transport properties and magnetic susceptibility of β-MnO_2. Kim et al. [12] demonstrated the presence of ε-MnO_2 as a major component of electrolytic manganese dioxide. Li et al. [13] successfully synthesized single crystalline α-MnO_2 nanotubes based on the redox reaction of $MnCl_2$ and $KMnO_4$ in the presence of sodium polyacrylate via a soft chemical method for the first time. α-MnO_2 nanotubes may provide novel peoperties, which will offer more application in nanotechnology. Zhang et al. [14] studied reversible Mg insertion and extraction behaviors of α-MnO_2 using discharge-charge cycling.

Franchini et al. [15] have presented a comprehensive study of the ground-state properties of MnO, Mn_3O_4, α-MnO_2 and β-MnO_2 using four different methods to treat exchange and correlation. Cockayne and Li [16] theoretically investigated electronic and magnetic properties of α-MnO_2 using first-principles calculations. The results show that α-MnO_2 is a semiconductor with an indirect band gap of 1.3 eV.

Form the fundamental point of view, manganese oxide material have gained much attention because of the presumably rather strong electron correlation, which leads to interesting phenomena such as colossal magnetoresistance, orbital ordering, and exotic magnetic structure [17,18]. Despite the fact that MnO_2 have been extensively studied for the past several decades, many details of their atomic structures are poorly understood. To our best knowledge, the dynamic property and thermodynamic properties of α-MnO_2 are not even known.

The ability to successfully model and predict the chemical and thermodynamic properties of Mn oxide depends to a large degree on a detailed understanding of their crystal structure [19]. In this work, we systematically investigated the electronic, dynamic and thermodynamic properties of

α-MnO_2 using first-principles calculations to gain a comprehensive understanding of the ground-state properties of α-MnO_2.

Computational details

In this work, the calculations were performed using the plane-wave pseudopotential DFT method as implemented in the CASTEP simulation package [20]. The ultrasoft pseudpotential with GGA+*U* method was employed to model the ion-electron interaction. The GGA+*U* theory is designed to give the self-energy correction to localized states embedded in delocalized states. The localized states have a large Coulomb correlation which is accounted for by the *U*-term whereas the delocalized states are well described by the GGA [21]. The advantage of the GGA+*U* method is the ability to treat simultaneously delocalized conduction band electrons and localized d/f electrons in the same computational scheme. The GGA+*U* method was proved to be very efficient and reliable for the electronic structure calculations of systems where the Coulomb interaction is strong enough to cause the localization of the electrons [22]. The convergence criteria for structure optimization and energy calculation were set to ultrafine quality with a kinetic energy cutoff of 340 eV and *k*-point meshes of 5×5×2. The self-consistent convergence accuracy was set to be 5.0×10^{-6} eV/atom. The convergence criterion for the maximal force between atoms was 0.01 eV/Å. The maximum displacement was 5.0×10^{-4} Å, and the stress was set to be 0.02 GPa.

Results and discussions

Electronic properties

The GGA+*U* method takes into account orbital dependence of the Coulomb and gives a qualitative improvement not only for excited-state properties such as energy gaps but also for ground-state properties such as magnetic moments. In this study, the GGA+*U* method (U = 2.5 eV) is used to correct the strong on-site Coulomb repulsion of Mn 3*d* states.

Because Mn^{4+} is a magnetic ion, it is crucial to include the effects of magnetism in electronic structure studies of manganese oxides. We have carried out spin-polarized electronic band structure calculations of α-MnO_2, as shown in Fig. 1. From Fig. 1, one can see that there is a significant difference between the band structure of majority-spin and minority-spin states. This is because Mn-3*d* electrons quantity of the spin-up state is different from the quantity of the spin-down state.

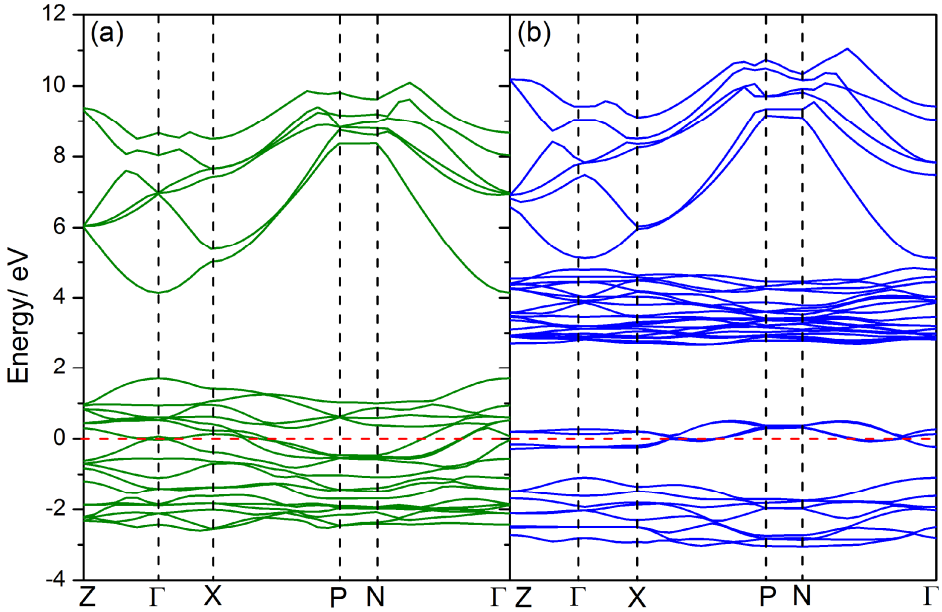


Fig. 1. Calculated band structures of α-MnO_2 at ground-state. (a) the majority- spin state; (b) the minority-spin states

Our result shows that α-MnO_2 is a semiconductor with a direct band gap of 1.4 eV at the high symmetry *Γ* point, which is in good agreement with the previous calculations [16]. The effect of electron-electron correlations is to enhance the hybridization and open the gap around the Fermi

level. It will shift the position of the Fermi level to the lowest conduction states and away from the highest valence states.

Partial density of states of O-*sp* and Mn-*spd* electrons of α-MnO_2 are shown in Fig.s 2 and 3, respectively. Form Fig. 2, it can be seen that around -18 eV are the O 2*s* bands in both of the spin channels with a small exchange splitting. Just below the Fermi energy, the states are predominantly due to the contributions of O 2*p* electrons in both of the spin channels without splitting. This indicates that the contributions of O-*sp* electrons to the magnetic properties are almost zero.

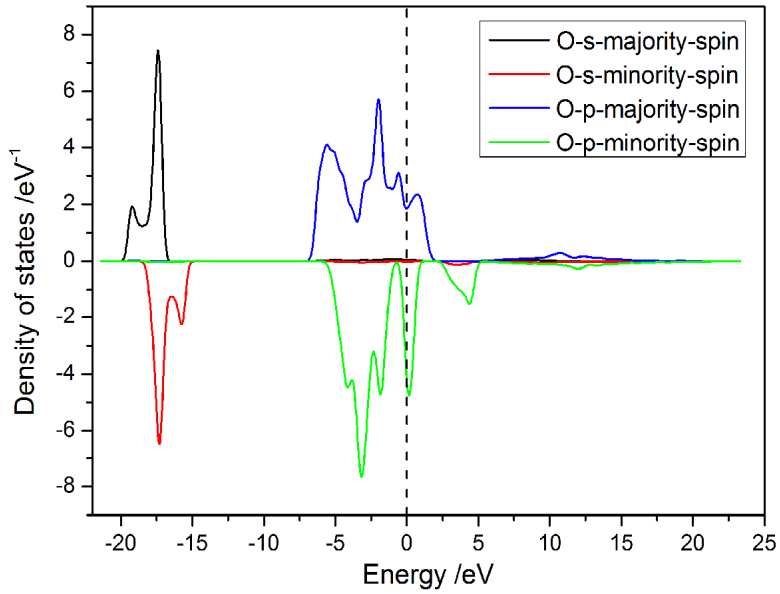


Fig. 2. The partial density of states of α-MnO_2 for O 2*s* and 2*p* states, respectively. The vertical dash line at zero indicates the Fermi energy level.

From Fig. 3, it can be clearly seen that some of the Mn-3*d* bands from the majority-spin crosses the Fermi level (E_f). Above E_f are the contributions of the minority-spin states of Mn-3*d* electrons with some hybridization yielding small contributions from Mn-4*s* and -3*p* electrons. This distribution makes Mn mostly responsible for the magnetism.

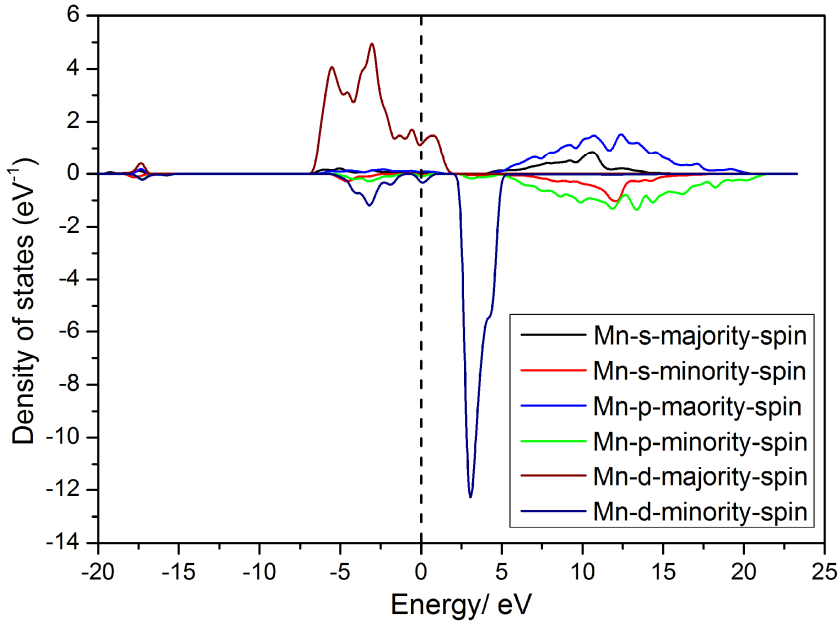


Fig. 3. The partial density of states of α-MnO_2 for Mn 3*p*, 3*d* and 4*s* states, respectively. The vertical dash line at zero indicates the Fermi energy level.

Dynamic properties

Many physical properties of solids depend on their phonon properties, such as specific heat, thermal expansion, heat conduction and electron-phonon interaction. To our knowledge, no

experimental or other theoretical works exist on the lattice dynamics of α-MnO_2. The phonon dispersion curves and density of states of ground-state of α-MnO_2 along the high-symmetry directions are shown in Fig. 4. Form Fig. 4, it can be clearly seen that imaginary frequencies occur at *Z*, *Γ* and *X* high-symmetry points. This indicates that the structure of α-MnO_2 is dynamically unstable at ground-state. As stated above, the equilibrium phase of MnO_2 at standard temperature and pressure is β-MnO_2. This indicates that our result is consistent with experimental result.

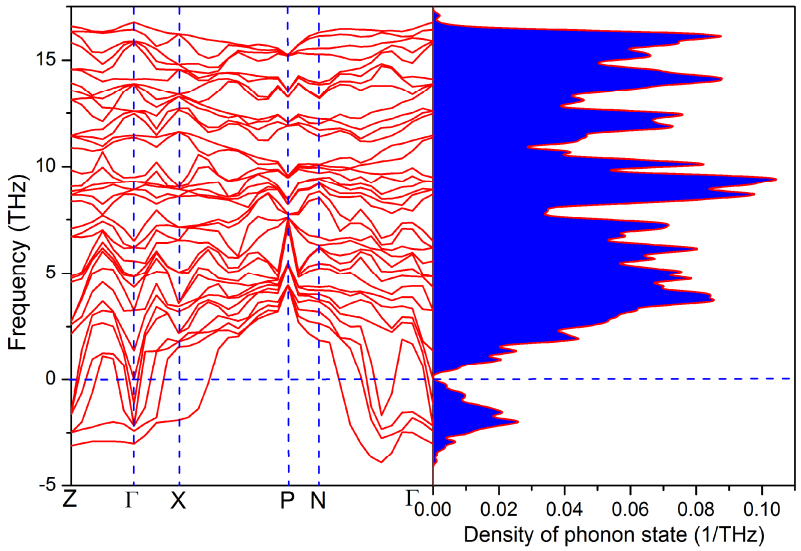


Fig. 4. Calculated phonon dispersion curves of ground-state of α-MnO_2 at zero pressure.

Temperature dependence of thermodynamic quantities

As is known, first-principles phonon calculations are limited to T = 0 K and thermodynamic properties of the crystals are determined in detail by phonons. The quasi-harmonic approximation can describe such properties satisfactorily. In the general Gibbs free energy expression $G(T,P) = F(T,V)+PV$, the free energy $F(T,V)$ of a crystal is the sum of the ground state energy $E(V)$ and the phonon free energy $F_{phon}(T,V)$, the temperature T appears in $F(T,V)$ via the phonon term [23]. The more explicit forms of the internal energy, free energy, entropy, and heat capacity in the harmonic approximation per primitive unit cell are given as follows:

$$E = \frac{1}{2} r \int_0^\infty g(\omega) \hbar\omega \coth\left(\frac{\hbar\omega}{2k_B T}\right) d\omega \tag{1}$$

$$F = r k_B T \int g(\omega) \ln\left[2\sinh\left(\frac{\hbar\omega}{2k_B T}\right)\right] d\omega \tag{2}$$

$$S = r k_B \int_0^\infty g(\omega) \left\{\frac{\hbar\omega}{2k_B T}\left[\coth\left(\frac{\hbar\omega}{2k_B T}\right) - 1\right] - \ln\left[1 - \exp\left(\frac{\hbar\omega}{2k_B T}\right)\right]\right\} d\omega \tag{3}$$

where r is the number of degrees of freedom in the unit cell, h the Plank's constant, and k_B the Boltzmann's constant.

The above formulae were used to plot the temperature dependence of several thermodynamic quantities of α-MnO_2. Figure5 shows the variations of enthalpy, phonon free energy, and entropy with temperature of α-MnO_2. From Fig. 5, it can clearly be seen that enthalpy and product of temperature (T) and entropy increase with increasing temperature. While phonon free energy decreases with increasing temperature.

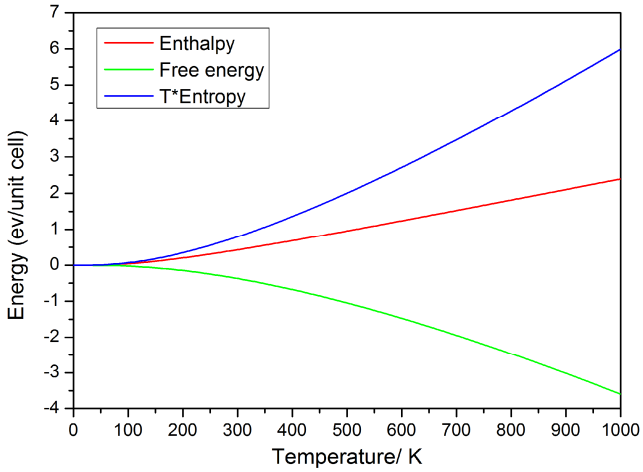


Fig. 5. Temperature dependence of enthalpy, free energy, and entropy of α-MnO_2

Conclusions

First-principles density functional theory calculations were used to investigate the electronic, dynamic and thermodynamic properties. The hybridization of O-2*p* orbitals with Mn-3*p* orbitals is the main contribution to the top of valence bands. α-MnO_2 is a semiconductor with a direct band gap of 1.4 eV at *Γ* point. The dynamic property indicates that the structure of α-MnO_2 is dynamically unstable at ground-state. We presented several import important thermodynamic quantities, such as entropy, enthalpy and Gibbs free energy, et al each as a function of temperature.

References

[1] S.L. Suib, J. Mater. Chem. 18 (2008) 1623.
[2] A.R. Armstrong, P.G. Bruce, Nature 381 (1996) 499.
[3] B. Annundsen, J. Paulsen, Advan. Mater. 13 (2001) 943.
[4] W. Xiao, H. Xia, J.Y.H. Fuh, L. Lu, J. Power Sources 193 (2009) 935.
[5] M.W. Xu, W. Jia , S.J. Bao, Z. Su, B. Dong, Electrochimica Acta 55 (2010) 5117.
[6] D.Y. Sung, I.Y. Kim, T.W. Kim, M.S. Song, S.J. Hwang, J. Phys. Chem. C 115 (2011) 13171.
[7] Y.C. Chen,Y.K. Hsu, Y.G. Lin, Y.K. Lin, Y.Y. Horng, L.C. Chen, K.H. Chen, Electrochimica Acta 56 (2011) 7124.
[8] T. Gao, H. Fjellvag, P. Norby, Anal. Chim. Acta 648 (2009) 235.
[9] Y.J. Yang, C.D. Huang, J. Solid State Electrochem. 14 (2010) 1293.
[10] S. Lee, B. Choi, N. Hamasuna, C. Fushimi, A. Tsutsumi, J. Power Sources 181 (2008) 177.
[11] H. Sato, T. Enoki, M. Isobe,Y. Ueda, Phys. Rev. B 61 (2000) 3563.
[12] C.H. Kim, Z. Akase, L. Zhang, A.H. Heuer, A.E. Newman, P.J. Hughes, J. Solid State Chem. 179 (2006) 753.
[13] H. Li, W. Wang, F. Pan, X. Xin, Q. Chang, X. Liu, Mater. Sci. Eng. B 176 (2011) 1054.
[14] R. Zhang, X. Yu, K.W. Nam, C. Ling, T.S. Arthur, W. Song, A.M. Knap, S.N. Ehrlich, X.Q. Yang, M. Matsui, Electrochem. Comun. 23 (2012) 110.
[15] C. Franchini, Podloucky, J. Paier, M. Marsman, G. Kresse, Phys. Rev. B 75 (2007) 195128.
[16] E. Cockayne, L. Li, Chem. Phys. Lett. 544 (2012) 53.
[17] S. Massidda, A. Continenza, M. Posternak, A. Baldereschi, Phys. Rev. Lett. 74 (1995) 2323.
[18] X. Feng, Phys. Rev. B 69 (2004) 155107.
[19] J.E. Post, Proc. Natl. Acad. Sci. USA 96 (1999) 3447.
[20] S. Clark, M. Segall, C. Pickard, P. Hasnip, K. Refson, M. Payne, Z. Kristallogr. 220 (2005) 567.
[21] V.I. Anisimov, F. Aryasetiawan, A.I. Lichtenstein, J. Phys.: Condes. Matter 9 (1997) 767.
[22] Hao, X. Yang, L. Zhang, Y. Zhu, J. Phys. Chem. Solids 74 (2013) 1504.
[23] E. Tuncel, K. Colakoglu, E. Deligoz, Y.O. Ciftci, J. Phys. Chem. Solids 70 (2009) 371.

CHAPTER 7:

Materials and Technologies in Microelectronics

Advanced Materials Research Vol. 936 (2014) pp 599-602
© (2014) Trans Tech Publications, Switzerland
doi:10.4028/www.scientific.net/AMR.936.599

Ultra-Multilevel-Storage Phase-Change Memory

You Yin[a], and Sumio Hosaka

Division of Electronics and Informatics, Faculty of Science and Technology, Gunma University,

1-5-1 Tenjin, Kiryu, Gunma 376-8515, Japan

[a]yinyou@gunma-u.ac.jp

Keywords: Phase-change memory, Multilevel Storage, Lateral structures

Abstract. In this study, we investigated ultra-multilevel-storage (UMLS) in lateral phase-change memory (PCM) on the basis of device structure, reliability and programming method. We found that the number of resistance levels was limited strictly by the number of PC layers in multilayer multilevel cell (ML-MLC). A number of distinct levels up to 16 were obtained using a simple single-layer multilevel cell (SL-MLC). And material engineering is expected to greatly improve the reliability of MLS. We believe that fast-freely-achievable (FFA)-MLC by stair-like-pulse programming is a very promising method for future's application.

Introduction

Large capacity is required for memory nowadays. One of the most effective approaches to increase the memory capacity is the multilevel storage (MLS), by which much more information can be stored without increasing memory size. Phase-change memory (PCM) [1-6] based on amorphous-crystalline transition is expected to apply to MLS [7-12] since a lot of intermediate resistance levels are possible by controlling the total crystallinity between electrodes. On the other hand, lateral PCMs have been demonstrated to have many advantages such as low-power consumption over vertical ones [13-14].

In this study, we report two structures of lateral MLS PCM: multilayer multilevel cell (ML-MLC) and single layer (SL-) ultra-MLC (UMLC). And then we discuss how to obtain high reliability for MLC based on material engineering. Staircase-like shaped pulse programming is finally shown for the future's application of fast-freely-achievable (FFA) MLC.

Multilayer MLC and Single-layer UMLC

The phase-change layer of SbTeN (STN) is firstly adopted in these devices. STN shows a gradual resistivity drop and good phase stability with temperature, a characteristic which makes it suitable for MLS applications. [7, 8, 10, 15]

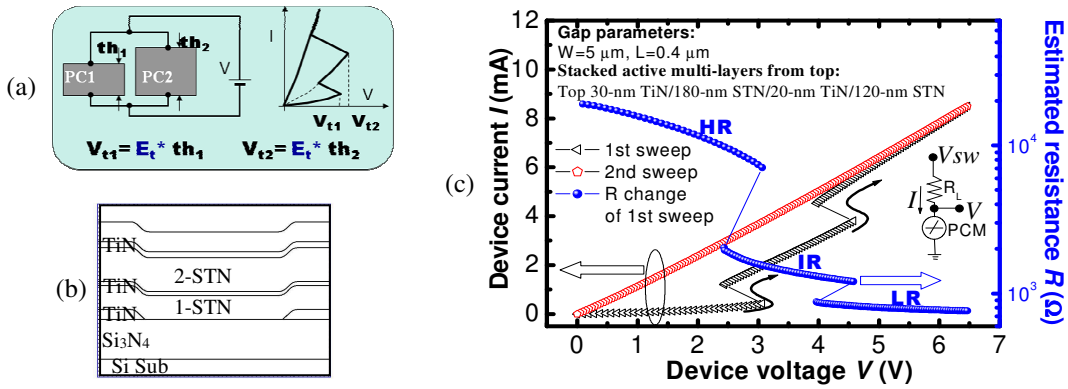


Fig. 1. (a) Principle of Multilevel Storage of ML-MLC With Different Thicknesses of PC layers. (b) Structure of Lateral ML-MLC. (c) I-V Characteristics And Resistance Change With Device Voltage of ML-MLC.

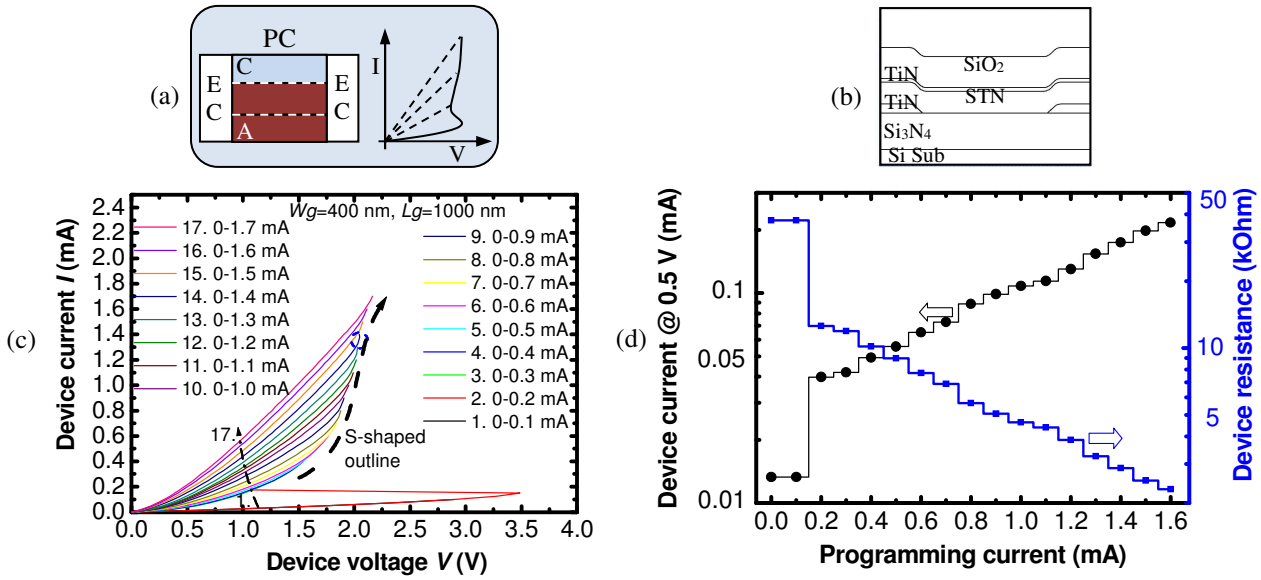


Fig. 2. (a) Principle of Multilevel Storage of SL-MLC with a Single PC layer. (b) Structure of Lateral SL-MLC. (c) I-V Characteristics. (d) Resistance Change with Device Voltage of ML-MLC.

We propose MLS based on multiple phase-change (PC) layers of different thicknesses as shown in Fig. 1(a). For two PC layers, three levels are expected to be obtained due to the two switchings at two threshold voltages. A top 30-nm TiN/180-nm STN/20-nm TiN/bottom 120-nm STN stacked structure is experimentally adopted as the active medium in the multi-layer devices, as shown in Fig. 1(b). Three stable and distinct device resistance levels are demonstrated in switching characteristics, as shown in Fig. 1(c). From the principle and analysis of this ML-MLC, the available number of resistance levels is strictly limited to be n+1 by the number of PC layers n.

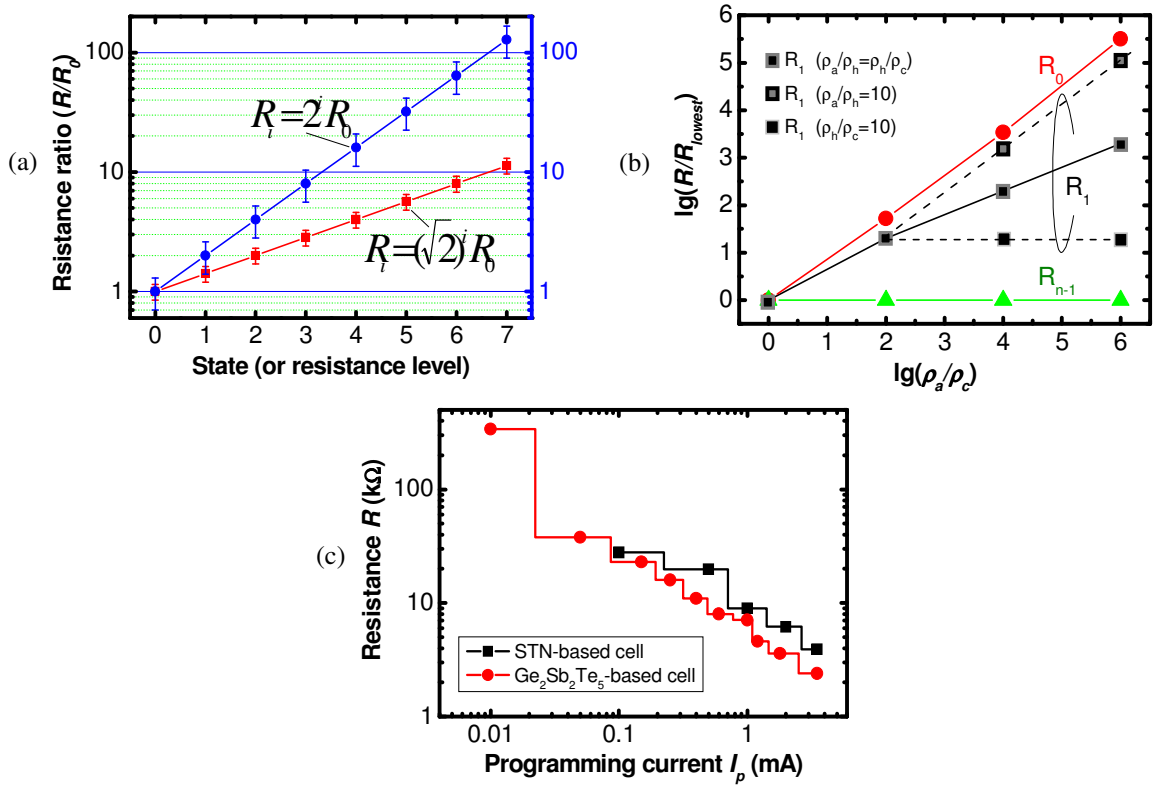


Fig. 3. (a) Larger Resistance Change Implies Higher Reliability. (b) Resistance Change of Lateral SL-MLC Depends Strongly on Material Properties. (c) Lateral GST-based SL-MLC Exhibited Higher Resistance Change than STN-based SL-MLC.

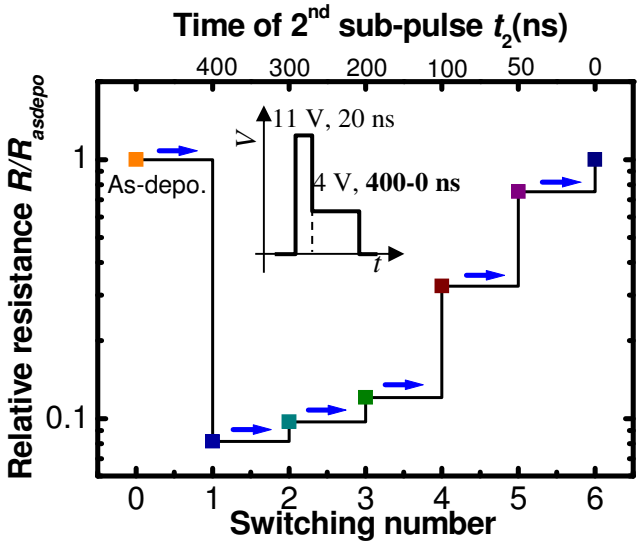


Fig. 4. Fast-freely-achievable MLC by Stair-like-pulse Programming.

To overcome the above limit, we propose SL-UMLC to obtain much more resistance levels as shown in Fig. 2(a). Principally, the MLS results mainly from the gradual enlargement of crystalline (C) region between electrodes (EC) by Joule heating. The active layers of SL-UMLC consist of 150-nm-thick STN layer with an additional top 50-nm-thick TiN layer, as shown in Fig. 2(b). Experimental results, as shown in Fig. 2 (c-d), exhibit a number of levels up to 16 are distinct and stable, which are induced by electric currents.

High-Reliability MLC by Material Engineering

Reliability (or stability) is the critical characteristics for MLC. In order to improve reliability of SL-UMLS, there are two effective approaches, (i) enlargement of the ratio between resistance levels as shown in Figs. 3(a) and (b), and (ii) reduction of scattering of resistance level. On the basis of our experimental results, it is demonstrated that the $Ge_2Sb_2Te_5$ (GST)-based double-layered cell has a high ratio of highest to lowest levels up to two-to-three orders of magnitude, implying high reliability, as shown in Fig. 3(c).

FFA-MLC by Stair-like-pulse Programming

The effect of the staircase-like shaped pulse with two sub-pulses on programming characteristics is investigated in SL-UMLS for fast-freely-achievable MLS. Phase-change material is melt by the first sub-pulse while the second one is used for controlling the total crystallinity after melting by crystallization time. Our finite-element analysis shows that the shorter the second sub-pulse is, the lower the crystallinity is. It is experimentally demonstrated that the device resistance increases with reducing the width of second sub-pulse due to the decreasing crystallinity, as shown in Fig. 4. This implies that any resistance levels are expected to be freely achieved by staircase-like shaped pulse programming.

Summary

MLS in lateral PCM was investigated from device structure, reliability and programming method. The number of resistance levels was limited strictly by the number of PC layers in ML-MLC. Simple SL-UMLC exhibited potential to obtain a number of distinct levels up to 16. And reliability can be expected to be greatly improved by material engineering. FFA-MLC by stair-like-pulse programming is very promising for future's application.

Acknowledgments

This work was financially supported by Grant-in-Aid for Young Scientists and Grant-in-Aid for Scientific Research from the Ministry of Education, Culture, Sports, Science and Technology of Japan (Nos. 24686042, and No. 24360003).

References

[1] S. Lai: Tech. Dig. IEDM (2003), p. 255.

[2] Y. Yin, D. Niida, K. Ota, H. Sone and S. Hosaka: Rev. Sci. Instrum. Vol. 78 (2007), p. 126101.

[3] H. Y. Cheng, Y. C. Chen, R. J. Chung and T. S Chin: Semicond. Sci. Technol. Vol. 21 (2006), p. 1196.

[4] J. M. Yoon, D. O. Shin, Y. Yin, H. K. Seo, D. Kim, J. H. Jin, Y. T. Kim, B-S Bae, S. O. Kim, and J. Y. Lee: Nanotechnology Vol. 23 (2012), p. 255301.

[5] A. Pirovano, A. L. Lacaita, A. Benvenuti, F. Pellizzer and R. Bez: IEEE Trans. Electron Devices Vol. 51 (2004), p. 452.

[6] J. M. Yoon, H. Y. Jeong, S. H. Hong, Y. Yin, H. S. Moon, S. J. Jeong, J. H. Han, Y. I. Kim, Y. T. Kim, H. Lee, S. O. Kim, and J. Y. Lee: Journal of Materials Chemistry, Vol. 22 (2012), p. 1347.

[7] Y. Yin, H. Sone and S. Hosaka: Microelectron. Eng. Vol. 84 (2007), p. 2901.

[8] Y. Yin, N. Higano, H. Sone, and S. Hosaka, Appl. Phys. Lett. Vol. 92 (2008), p. 163509.

[9] T. J. Feng, Y. F. Lai, B. W. Qiao, B. C. Cai, Y. Y. Lin, T. A. Tang, and B. Chen: Jpn. J. Appl. Phys. Vol. 46 (2007), p. 5724.

[10] Y. Yin, T. Noguchi and S. Hosaka: Jpn. J. Appl. Phys. Vol. 50 (2011), p.105201.

[11] Y. Yin and S. Hosaka, Appl. Phys. Lett. Vol. 100 (2012), p. 253503.

[12] T. Nirschl, J. B. Philipp, T. D. Happ, *et al*. Tech. Dig. IEDM (2007), p. 461.

[13] Y. Yin, A. Miyachi, D. Niida, H. Sone, and S. Hosaka: Jpn. J. Appl. Phys. Vol. 45 (2006), p. L726.

[14] M. Lankhorst, B. Ketelaars, and R. Wolters: Nat. Mater. Vol. 4 (2005), p. 347.

[15] Y. Yin, H. Sone, and S. Hosaka: J. Appl. Phys., Vol. 102 (2007), p. 064503.

Advanced Materials Research Vol. 936 (2014) pp 603-606
© (2014) Trans Tech Publications, Switzerland
doi:10.4028/www.scientific.net/AMR.936.603

Surface Passivation of Crystalline Silicon by a-Si:H Thin Films

Yin Wang[a], Wei Li[b,*], An-ran Guo, Feng Yu, Jian He, Ya-dong Jiang

State Key Laboratory of Electronic Thin Films and Integrated Devices, University of Electronic Science and Technology of China, No.4, Section 2, North Jianshe Road, Chengdu, China 610054

[a]445964943@qq.com, [b]wli@uestc.edu.cn

Keywords: surface passivation, the minority carrier lifetime, hydrogen flow rate.

Abstract: Surface passivation of c-Si by a-Si:H thin films has been studied. In this paper, the minority carrier lifetime of 345μs (from 85μs) is obtained at optimal hydrogen flow rate (8.0sccm) by using RF-magnetron sputtering method.

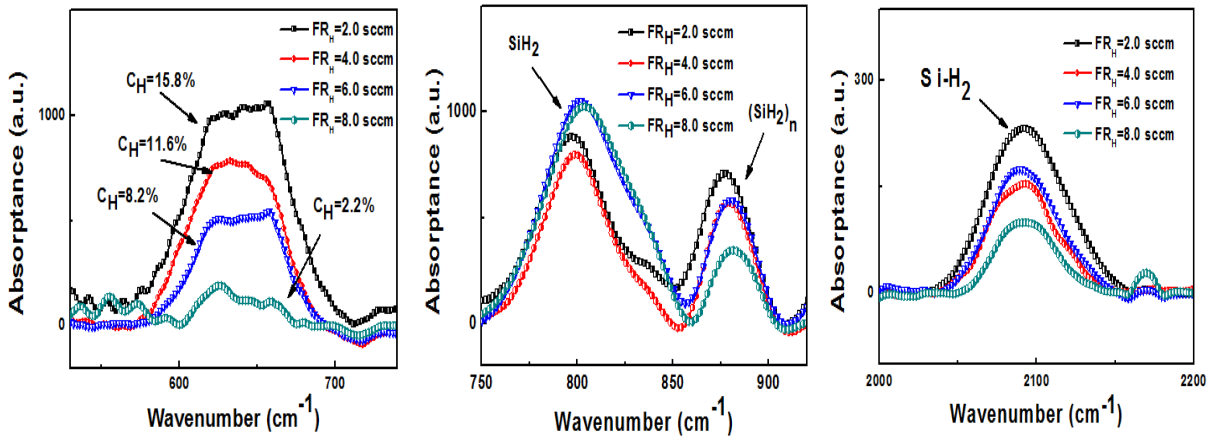
Introduction

With the further promotion of semiconductor applications, crystalline silicon surface passivation for improving the performance of the devices got more and more research, especially the hydrogenated amorphous silicon (a-Si:H) thin films deposited on c-Si surfaces as passivation layers. As in laminated film solar cells, the photoelectric conversion efficiency, the device performance and stability depend on strongly the surface cleanliness and the surface recombination center density related to the passivation effect. In all known strategies, a-Si:H is still the best candidate for many silicon devices compared with the others, it is due to the simple processing without the introduction of any atoms other than silicon and hydrogen and the excellent passivation properties obtained at low deposition temperatures. The a-Si:H on crystalline silicon surface as a passivation layer can achieve the minimization of electronic losses by reducing the semiconductor surface activity and the surface recombination velocity [1-3]. For the termination of dangling bonds on the cysalline silicon surface, the hydrogen in a-Si:H is a key factor, which affects directly the passivation quality. So it is necessary to study the crystalline silicon surface passivation using the a-Si:H with different hydrogen content.

Results and Discussion

The FTIR spectra of the thin films deposited with various FR_H are shown in Fig.1. There are three bands related to Si-H bond within wavenumber range of 500-2300cm^{-1}. The first one located at near 630 cm^{-1} is attributed to Si-H rocking/wagging mode. It is observed from Fig.1.(a) that the intensity of the absorption peak at around 630 cm^{-1} decreases apparently with the increasing FR_H. Combined with the film thickness obtained from SE850, we can figure out the hydrogen contents in varying FR_H from the infrared results. The hydrogen content decreases with the increasing hydrogen flow rate. The hydrogen contents in a-Si:H thin films deposited at hydrogen (H_2) flow rates of 2.0 sccm, 4.0 sccm, 6.0 sccm and 8.0 sccm are 15.8%, 11.6%, 8.2%, 2.2%, respectively. According to the TO peaks mentioned in the above Raman spectra, we can deduce that hydrogen ion etching effect has influence on the hydrogen content. The second one is a doublet at 800-900 cm^{-1} which is associated with the dihydrides SiH_2 scissoring mode and the polysilanes $(SiH_2)_n$ bending mode, respectively. From Fig.1.(b), it is obviously shown that the absorption bands present near 800 cm^{-1} increase with the increasing FR_H, which can be due to the increase of the amount of

SiH_2 in a-Si:H thin films. The opposite phenomenon appears around 870 cm^{-1}, which reflects the reduction of the amount of $(SiH_2)_n$ in a-Si:H thin films. The third one at ~2100 cm^{-1} is recognized as the SiH_x (with x=2 or 3) stretching mode [4]. In Fig.1.(c), we can see that the signals at ~2090cm^{-1}, which mean stretching mode of Si-H_2 bond, become weak with the increasing FR_H.



(a) (b) (c)

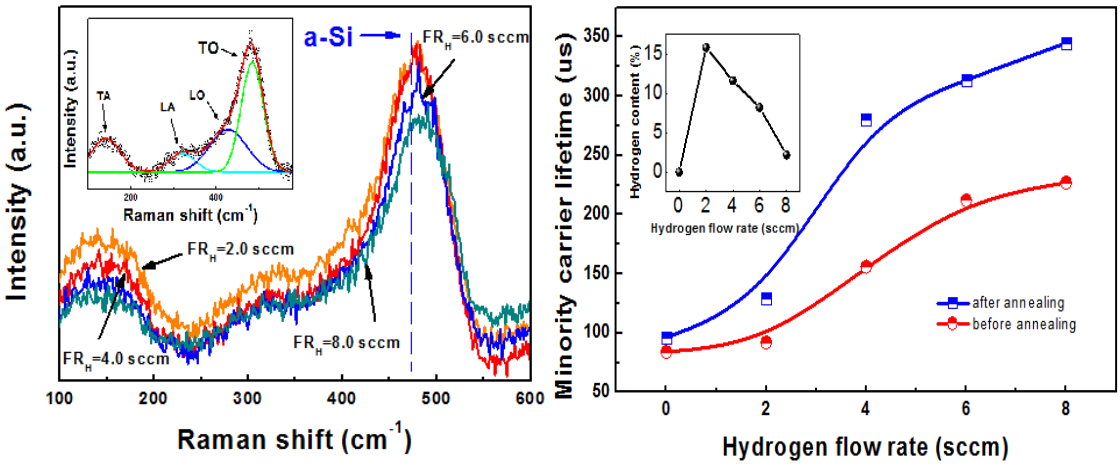
Fig.1 Ir Absorption Spectra Of Thin Films In Various Absorption Regions. (a) A Bending Mode At Near 630 Cm^{-1}; (b) A Doublet At 750-950 Cm^{-1} Which Is Associated With The Dihydrides Sih_2 Scissoring Mode And The Polysilanes $(Sih_2)_N$ Bending Mode, Respectively; (c) A Stretching Mode Centered At Approximately 2090 Cm^{-1}.

The Raman scattering are used to estimate the crystal phase information in the thin films due to its sensitivity to the structural disorder in solids. A typical deconvolution result is shown in the inset of Fig.2.(a), the Raman spectra of a-Si:H film prepared at hydrogen flow rate of 6.0 sccm, where curves (from left to right) denote the TA bond, LA bond, LO bond and TO bond, respectively. The TO phonon band at about ω_{TO}=480 cm^{-1} is sensitive to the short-range order (SRO) of amorphous network. Fig.2.(a) includes the Raman spectra of a-Si:H thin films prepared at various FR_H. The corresponding characteristic parameters are listed in Table 1. It can be seen that the all curves have the broad TO peak at near 480 cm^{-1}, namely Raman features of typical a-Si. The increase in MRO is characterized by the decrease in the ratio I_{TA}/I_{TO} in experiment. As shown in Table 1, there are a decrease in value of I_{TA}/I_{TO} from 0.63 to 0.39, a narrowing of Γ_{TO} by ~2.5 cm^{-1}, a blue-shift by ~3.1 cm^{-1}, and a decrease in the average bond angle deviation $\Delta\theta$ by ~0.41°, indicating that the amorphous network becomes more ordered on both short and intermediate scales. In addition to the structural disorder, the shift of ω_{TO} also depends on the intrinsic stress in the thin film [5]. It is seen from Table 1 that as FR_H increases from 2.0 sccm to 8.0 sccm, the ratios of I_{LA}/I_{TO} and I_{LO}/I_{TO} decrease from 0.3 and 0.64 down to 0.19 and 0.58, respectively. In our present study, the decrease in LA (near 300 cm^{-1}) and LO (near 410 cm^{-1}) strength associated with coordination defects, can be attributed to the reduction of silicon coordination defects and closed rings in the amorphous network due to a higher FR_H. It is verified that the amorphous network of a-Si:H films become more ordered on short and intermediate scales. We find that with the increase of hydrogen flow rate, E_{opt} collapse from 1.78 eV to 1.67 eV by UV-VIS test.

TABLE.1 RAMAN CHARACTERISTIC PARAMETERS OF THIN FILMS. THE AVERAGE BOND ANGLE DEVIATION $\Delta\theta$ IS CALCULATED BY THE EMPIRICAL FORMULA $\Gamma_{TO}=15+6\Delta\theta$

Sample	FR_H (sccm)	ω_{TO} (cm^{-1})	Γ_{TO} (cm^{-1})	$\Delta\theta$ (°)	I_{TA}/I_{TO}	I_{LA}/I_{TO}	I_{LO}/I_{TO}
A	2.0	482.07	54.68	6.61	0.63	0.30	0.64
B	4.0	482.87	53.32	6.39	0.58	0.28	0.61
C	6.0	484.54	52.26	6.21	0.42	0.21	0.59
D	8.0	485.17	52.18	6.20	0.39	0.19	0.58

In our study, the in-situ annealing treatment in vacuum is performed on the prepared samples. The annealing time is kept constant for 2 h, and the annealing temperature is 300 ℃. The FR_H dependent effective lifetime τ_{eff} is shown in Fig.2.(b) Comparing the minority carrier lifetime before and after annealing treatment, while the τ_{eff} increased with increasing FR_H in both cases, but the minority lifetime improved more obviously after annealing. As a result, the maximum value of carrier lifetime ～345 μs was obtained in the annealed sample deposited at a FR_H of 8.0 sccm. Accordingly, it can be concluded that the hydrogen atoms in the films were activated and the weak bonding, Si-H_2mode, were rearranged to Si-H mode by annealing treatment [6].



(a) (b)

Fig.2 (a) Raman Spectra Of A-Si:H Films Prepared At Various Hydrogen Flow Rates And The Inset Shows A Typical Deconvolution Result (Raman Spectra Of A-Si:H Film Prepared At Hydrogen Flow Rate Of 6.0 Sccm); (b) The Minority Carrier Lifetime Before And After Annealing Treatment In A-Si:H Films Deposited At Fr_h Of 2.0, 4.0, 6.0 And 8.0 Sccm And The Inset Shows Variations Of Hydrogen Content (C_H).

Conclusion

In summary, a-Si:H thin films were deposited using radio-frequency magnetron sputtering method at various FR_H. The passivation effects of these thin films on crystalline silicon display the dependence on hydrogen flow rates. Our experiment demonstrated that the variation of the hydrogen content not only affects the nature of the film itself, but also the c-Si surface passivation. The in-situ annealing can also enhance the lifetime value through hydrogen diffusion toward to the interface. These are attributed to the saturation effect of the dangling bond and the stability of Si-H

bond. Optimal hydrogen flow rate as 8.0 sccm was obtained in this experimental conditions. Moreover, the further improvements of effective carrier lifetime in the prepared samples were found after in-situ annealing at 300℃ for 2 h. Base on these results, we realized that the combination of the RF-magnetron sputtering deposition and the thermal annealing of a-Si:H film are essential for improving the surface passivation.

References

[1] Mueller T, Schwertheim S, Scherff M, et al. High quality passivation for heterojunction solar cells by hydrogenated amorphous silicon suboxide films[J]. Applied Physics Letters, 2008, 92(3): 033504-033504-3.

[2] Jeon M, Yoshiba S, Kamisako K. Hydrogenated amorphous silicon film as intrinsic passivation layer deposited at various temperatures using RF remote-PECVD technique[J]. Current Applied Physics, 2010, 10(2): S237-S240.

[3] Zhou H P, Wei D Y, Xu S, et al. Crystalline silicon surface passivation by intrinsic silicon thin films deposited by low-frequency inductively coupled plasma[J]. Journal of Applied Physics, 2012, 112(1): 013708-013708-9.

[4] Touir H, Zellama K, Morhange J F. Local Si-H bonding environment in hydrogenated amorphous silicon films in relation to structural inhomogeneities[J]. Physical Review B, 1999, 59(15): 10076.

[5] Li Z, Li W, Jiang Y, et al. Raman characterization of the structural evolution in amorphous and partially nanocrystalline hydrogenated silicon thin films prepared by PECVD[J]. Journal of Raman Spectroscopy, 2011, 42(3): 415-421.

[6] Jeon M, Yoshiba S, Kamisako K. Hydrogenated amorphous silicon film as intrinsic passivation layer deposited at various temperatures using RF remote-PECVD technique[J]. Current Applied Physics, 2010, 10(2): S237-S240.

Advanced Materials Research Vol. 936 (2014) pp 607-612
© (2014) Trans Tech Publications, Switzerland
doi:10.4028/www.scientific.net/AMR.936.607

Microwave-assisted Synthesis of Graphene Oxide-MnO_2 Composites for Supercapacitors

Ying Wen Duan[a*], Xun Sun[b], Hong Yu Zhao[c] and Zhi Bo Liu[d]

Institute of Materials Science and Engineering, Lanzhou University, Lanzhou 730000, China

[a]duanyw@lzu.edu.cn, [b]sunx_2010@lzu.edu.cn, [c]zhaohy10@lzu.edu.cn, [d]lzb867266@163.com

Keywords: grapheme oxide-MnO_2 composites; microwave-assisted synthesis; electrochemical property; supercapacitor

Abstract: Graphene oxide-MnO_2 (GO-MnO_2) was successfully synthesized by microwave -assisted method with the substrate of GO covered by MnO_2. MnO_2 contained disordered pore structure and aggregate of random shape. GO exhibited layer-like shape and had a large numbers of functional groups on its surface. The electrochemical measurements were employed by cyclic voltammetry (CV) and galvanostatic charge/discharge (GCD), the results showed that the GO-MnO_2 composite had good capacitive performance, the maximum of specific capacitance was 127 F g^{-1} at the current density of 100 mA g^{-1}.

Introduction

In recent years, tremendous effort has been devoted to the development of new energy storage devices due to their excellent electrochemical property, which can be used in different electric devices to meet the requirement of energy application, ranging from hybrid vehicles to portable electronics and large industrial equipment [1]. Supercapacitors, also named electrochemical capacitors (ECs) or ultracapacitors, have attracted incredible attention with their outstanding chemical and physical properties such as longer cycle life, higher power and energy densities than conventional electrical capacitors and secondary batteries [2]. Two types of supercapacitors, electrical double layer capacitor (EDLC) and pseudocapacitor, have been currently developed. The EDLC stores the electric energy from the electrostatic charges at the interface between the electrode and electrolyte [3], and the pseudocapacitor generally uses active metal oxides as its electrode, transferring their faradic charges by fast and reversible redox through a conducting polymer [4].

Metal oxide-carbon composites have gained extraordinary interest owing to their superior and additional electrochemical functions for pseudocapacitor and EDLC. Graphene oxide (GO), one of the most valuable derivatives of graphene, well-dispersed in aqueous solution due to its electrostatic repulsion [5], is a kind of carbon material that has been intensively employed for EDLC. The material with a two dimensional plane has plenty of oxygen functional groups bearing on the surface and edges [6]. The function groups are capable of immobilizing nanoparticles of metal oxides for charge storage [7]. Transition-metal oxides are fundamental candidates which are used as supercapacitor electrode materials [8]. As for the transition-metal oxides, RuO_2, one of the most popular electrode materials, exhibits prominent capacitive properties [9], but the high cost of Ru limits the commercial acceptance for practical application [10].

Manganese oxides have received considerable attention for supercapacitors due to its high theoretical specific capacitance, low cost, and good eco-friendly properties [11]. Recently, various research groups have worked with the syntheses of MnO_2 and carbon-based materials, including various methods such as thermal decomposition, electrodeposition, physical mixing and redox reaction [12,13]. The synthesis process usually uses hydrazine, sodium borohydride, ethylenediamine or oleic acid as reducing agents [14].

Being widely used in daily life and academic research, microwave irradiation has been a fast growing research field in the materials synthesis due to its dramatic reduction in reaction time and high internal heating rate, which are not possible to achieve by conventional heating methods. Manganese oxides can be prepared via dielectric heating by microwave irradiation [11], meanwhile, graphene oxides are perfect absorbents of microwave energy owing to the electrical conductive properties that can absorb a considerable fraction of irradiation [15]. The rapid and internal heating process has provided a remarkable efficiency to large-scale synthesis of carbon materials and their composites. In our work, we synthesize GO-MnO_2 composites by microwave irradiation, the experimental results reveal that the produced materials via this simple method have a good electrochemical performance for supercapacitor electrodes.

Experimental Method

Synthesis of Graphene Materials

GO was prepared from natural graphite (99.9999%, 200 mesh, Alfa Aesar) by a modified hummer method [16]. The as-prepared GO (0.27 g) was dispersed in deionized (DI) water and subjected to ultrasonic vibration for 2 h. Then 0.81 g $KMnO_4$ powder (99.99% J.T. Baker) was dissolved in DI water. Subsequently, $KMnO_4$ suspension was added dropwise into GO suspension under vigorous stirring. The mass ratio of GO:$KMnO_4$ was 1:3. The solution mixture was placed in a microwave reactor (Discover, CEM, USA) and heated at 150 °C for 10 min under 300 W. The resulting mixture turned to a brownish color. After cooling to room temperature, the deposit was filtered, washed several times with DI water and ethanol, and dried at 60 °C for 12 h in a vacuum oven. For comparison, 1.00 g $KMnO_4$ was dissolved in DI water to prepare pure MnO_2 following the same rest steps directly.

Preparation of Electrodes

The fabrication of working electrodes was carried out as follows. Briefly, the as-prepared composites, carbon black and poly (vinylidene fluoride) (PVDF) were mixed in a mass ratio of 80:10:10 and dispersed in the N-methyl-2-baredpolyvinylpyrrolidone (NMP) solvent. Then the slurry was coated onto the stainless steel substrate (1 cm × 2 cm) with a spatula, which was followed by drying at 100 °C for 12 h in a vacuum oven. Pure MnO_2 also used the same proportion and the step for preparing an electrode.

Characterization

The crystallographic structure of the materials was determined by powder X-ray diffraction (Shimadzu Labx XRD-6000) equipped with Cu K_α radiation (λ=1.5406 Å). Fourier transform infrared (FT-IR) spectrum was recorded on a Nicolet Nexus spectrometer with the standard KBr pellet method. The morphology of the sample was investigated by a scanning electron microscopy (SEM, JEOL JSM 5600).

Electrochemical Measurement

Electrochemical characterization was carried out using a three electrode configuration. A conductive substrate coated with GO-MnO_2 composites served as the working electrode, a platinum sheet and a saturated calomel electrode (SCE) served as the counter and reference

electrodes, respectively. The CV and GCD were employed by a CHI 614D electrochemical workstation in 1 M Na_2SO_4 aqueous solution. CV was applied between -0.1 and 0.9 V (vs. SCE) at different scan rates of 50, 100, 200 and 500 mV s^{-1}. GCD characteristics were measured in the potential range of -0.1–0.9 V (vs. SCE) with different current densities of 100, 200, 500 and 1000 mA g^{-1}. All the electrochemical experiments were carried out at room temperature.

Results and Discussion

Materials Characterization

In Fig. 1, the pure MnO_2 with the broad peaks shows poorly crystallized compound. The XRD pattern of GO shows sharp peaks at 11.5° and 43° corresponding to the diffraction of (002) and (100) planes, respectively. The sharp and strong peaks suggest a high crystalline structure of the GO. Calculated by Bragg's law, the basal spacing of GO (0.81 nm) is larger than that of the origin graphite (0.17 nm), indicating the interlayer distance is greatly expanded after the excellent oxidation of graphite into the GO. Three broad peaks of GO-MnO_2 at 12°, 37° and 66° are corresponding to the diffraction of (002), (006) and (119) planes of birnessite-type MnO_2 (JCPDS 18-0802, a=5.82 Å, c=14.62 Å), respectively. Herein, the diffraction peaks of GO cannot be observed, we think that the surfaces of graphene are covered by loaded MnO_2. The graphene content is estimated to be about 16 wt% by TGA. The broad and weak diffraction peaks of MnO_2 suggest the crystallization of MnO_2 is not complete.

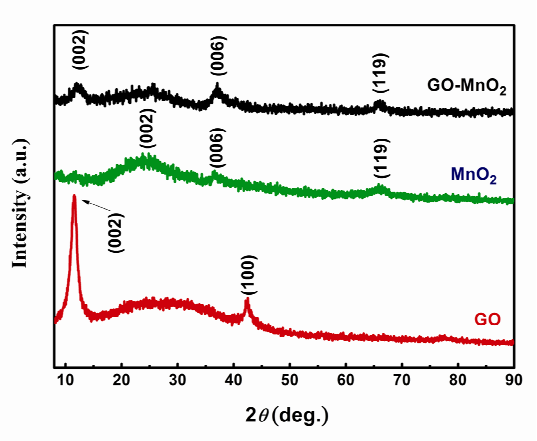


Fig. 1 XRD patterns of the MnO_2, GO and GO-MnO_2 composites.

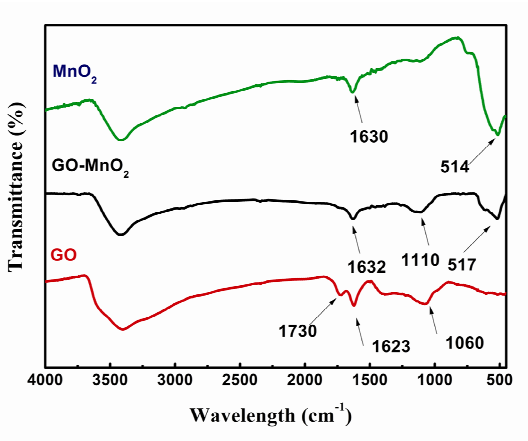


Fig. 2 FT-IR spectra of the MnO_2, GO and GO-MnO_2 composites.

Fig. 2 represents the FT-IR spectrum of the MnO_2, GO and GO-MnO_2 composites. The broad peak at 3250–3500 cm^{-1} is linked to the stretching vibration of water molecule and hydroxyl groups in the lattice. The 1630 cm^{-1} band is assigned to the C=C stretching, and the 1730 cm^{-1} band is usually attributed to the COOH groups of GO. The 1632, 1623 cm^{-1} band and the 1060, 1110 cm^{-1} band are usually attributed to the O-H bending vibration combined with Mn atoms of MnO_2 and composite. The band located at 517 and 514 cm^{-1} can be ascribed to the Mn-O vibrations of MnO_2. The FT-IR studies confirm the successful synthesis of GO-MnO_2 composites with plenty of functional groups on the surface.

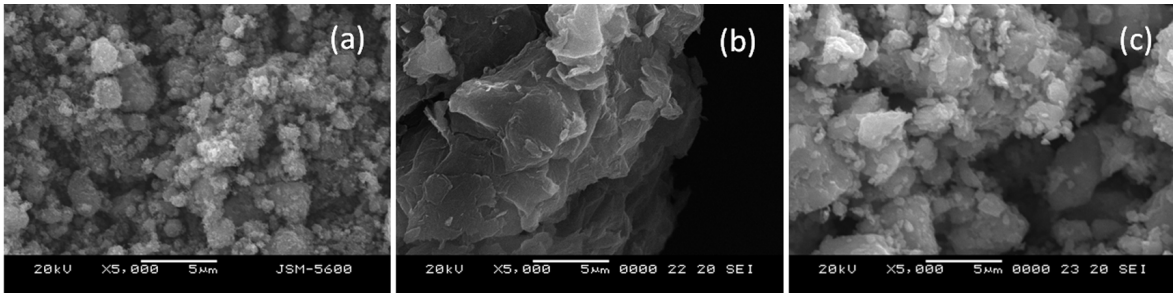


Fig. 3 SEM images of (a) MnO_2; (b) graphene oxide; (c) GO-MnO_2 composites.

The pure MnO_2 with a flower-like structure is not uniform with chunk presence in Fig. 3(a). The graphene oxide exhibits curved and layer-like shape with smooth surface in Fig. 3(b). The GO sheets are formed due to van der Waals interactions between layers [8]. Fig. 3(c) shows that the graphene sheets were coated on all surfaces with MnO_2, which contains disordered pore structure and aggregates of random shapes with different sizes from hundreds of nanometers to a few micrometers. The formation mechanism of as-obtained composite is due to plenty of functional groups on the basal planes and edges of GO, which provides the anchor sites to enable the MnO_2 attaching on these sides, i.e., the graphene oxides with carbonyl, carboxyl, and/or hydroxyl groups are more active and vulnerable to anchor metal oxides than the defect-free graphene surface [13].

Electrochemical Performance

Fig. 4(a) shows the CV curves of GO-MnO_2 and MnO_2 electrodes in 1 M Na_2SO_4 electrolyte at scan rate of 100 mV s^{-1}. The CV curve of GO-MnO_2 shows larger area compared with that of MnO_2. The specific capacitance of material is in proportion to the area of its CV curve, thus the electrochemical capacitance of GO-MnO_2 as electrode is larger than that of MnO_2 in 1 M Na_2SO_4 aqueous solution. The graphene sheet with inter-spacing expanded in the GO-MnO_2 composite electrode facilitates the penetration of the electrolyte into electrode. With additional and abundant micropores, MnO_2 coated on GO sheets shows good capacitive behavior due to the significant reducing of Na^+ diffusion length during the process of charge/discharge.

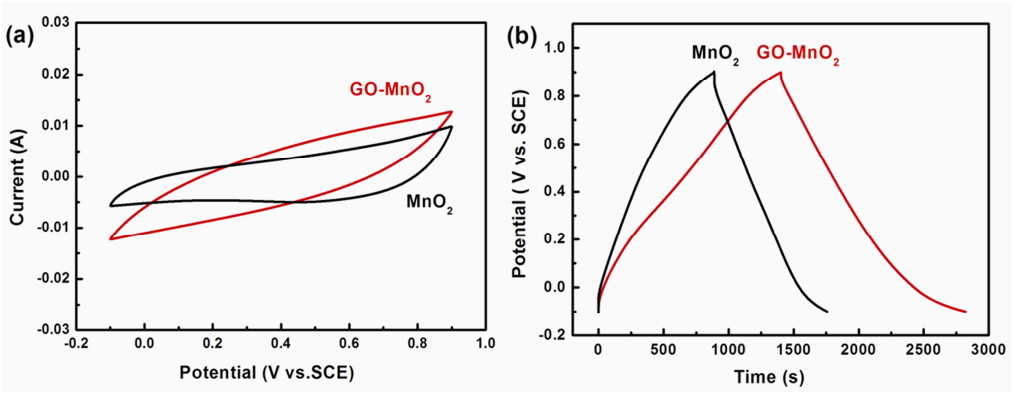


Fig. 4 (a) CV curves of GO-MnO_2 and MnO_2 electrode in 1 M Na_2SO_4 solution at scan rate of 100 mV s^{-1}; (b) GCD curves of GO-MnO_2 and MnO_2 electrode and pure MnO_2 in 1 M Na_2SO_4 solution under a current loading density of 100 mA g^{-1}.

Fig. 4(b) shows the GCD curves of the GO-MnO_2 and MnO_2 electrodes in 1 M Na_2SO_4 aqueous solution at a current density of 100 mA g^{-1}. It is clearly observed that the charge curve is symmetric to its corresponding discharge counterpart with a negligible curvature, which suggests the pseudocapacitive performance along with double layer contribution [6]. The C_s is calculated

according to $C_s=I\times\Delta t/(\Delta V\times m)$ from the discharge curves, where I is the constant discharge current, Δt is the total discharge time, and ΔV is the potential drop during discharge and C_s is the specific capacitance. The C_s is calculated to be about 127 and 50 F g^{-1} for GO-MnO_2 and MnO_2 electrode, respectively. Here, GO is not involved in the comparison due to the poor electrical conductivity and low faradic reaction rate as reported elsewhere [17], the electrochemical performance of GO is generally below 30 F g^{-1}.

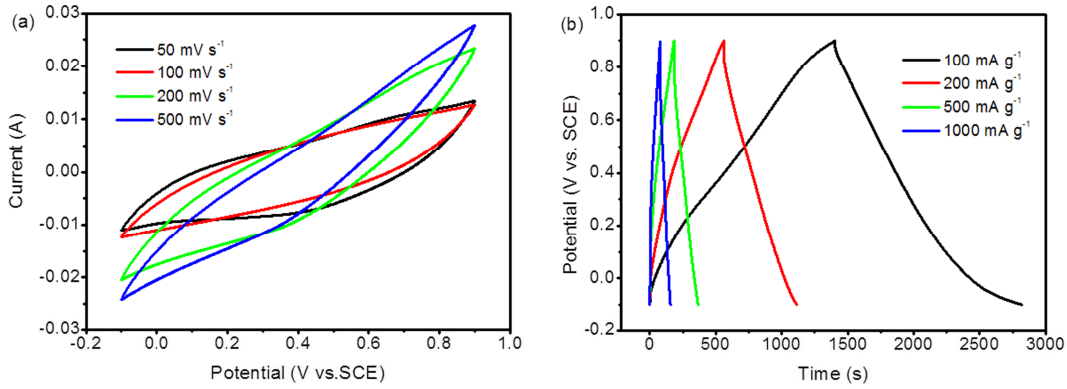


Fig. 5 (a) CV curves of GO-MnO_2 electrode in 1 M Na_2SO_4 solution under different scan rates; (b) GCD curves of GO-MnO_2 electrode in 1 M Na_2SO_4 solution under different current loading density.

To further evaluate the electrochemical performance of the as-synthesized GO-MnO_2 as electrode materials for supercapacitors, changing scan rates and current densities during the CV and GCD measurements are conducted. Fig. 5(a) shows the CV curves of the GO-MnO_2 electrode in 1 M Na_2SO_4 electrolyte under different scanning rates. The CV curves still retain a similar shape without obvious distortion and no redox peaks appear at different scan rates in the CV curves, proving that the electrode is charged and discharged at a pseudo-constant rate over the complete voltammetric cycle. Fig. 5(b) shows the GCD curves of the GO-MnO_2 electrode in 1 M Na_2SO_4 electrolyte under different loading current densities. The charge curve is almost symmetric to its corresponding discharge counterpart with a slight curvature, indicating the pseudocapacitive contribution along with the double layer contribution. The specific capacitances are calculated to be about 127, 116, 102 and 92 F g^{-1} at 100, 200, 500 and 1000 mA g^{-1}, respectively.

Conclusions

We have demonstrated a one-pot method to prepare GO-MnO_2 composites assisted by microwave irradiation without any chemical reductant. Compared with specific capacitance of 50 F g^{-1} for MnO_2, GO-MnO_2 composites exhibit a higher specific capacitance of 127 F g^{-1} at the current density of 100 mA g^{-1}, which derives from the disordered pore structure of the MnO_2 and expands inter-spacing of the GO-MnO_2 composite, i.e., MnO_2 anchored on the GO sheet improves the charge transfer and diffusion rate, and the graphene sheet with expanded layer structure in the GO-MnO_2 composite electrode facilitates the penetration of the electrolyte into electrode.

Acknowledgment

This work was supported by the Natural Science Foundation of Gansu Province, China (Grant No. 1107RJZA083).

References

[1] Y. Zhu, S. Murali, M.D. Stoller, K.J. Ganesh, W. Cai, P.J. Ferreira, A. Pirkle, R.M. Wallace, K.A. Cychosz, M. Thommes, D. Su, E.A. Stach, R.S. Ruoff, Carbon-based supercapacitors produced by activation of graphene, Science, 332 (2011) 1537-1541.

[2] P. Yu, X. Zhang, Y. Chen, Y.W. Ma, Z.P. Qi, Preparation and pseudo-capacitance of birnessite-type MnO_2 nanostructures via microwave-assisted emulsion method, Mater. Chem. Phys., 118 (2009) 303-307.

[3] Q. Cheng, J. Tang, J. Ma, H. Zhang, N. Shinya, L.C. Qin, Graphene and nanostructured MnO_2 composite electrodes for supercapacitors, Carbon, 49 (2011) 2917-2925.

[4] Z.J. Li, B.C. Yang, S.R. Zhang, C.M. Zhao, Graphene oxide with improved electrical conductivity for supercapacitor electrodes, Appl. Surf. Sci., 258 (2012) 3726-3731.

[5] C.S. Liao, C.T. Liao, C.Y. Tso, H.J. Shy, Microwave-polyol synthesis and electrocatalytic performance of Pt/graphene nanocomposites, Mater. Chem. Phys., 130 (2011) 270-274.

[6] S. Chen, J. Zhu, X. Wu, Q. Han, X. Wang, Graphene Oxide-MnO_2 Nanocomposites for supercapacitors, Am. Chem. Soc. Nano., 4 (2010) 2822-2830.

[7] L. Li, Z. Du, S. Liu, Q. Hao, Y. Wang, Q. Li, T. Wang, A novel nonenzymatic hydrogen peroxide sensor based on MnO_2/graphene oxide nanocomposite, Talanta, 82 (2010) 1637-1641.

[8] J. Yan, T. Wei, B. Shao, F. Ma, Z. Fan, M. Zhang, C. Zheng, Y. Shang, W. Qian, F. Wei, Electrochemical properties of graphene nanosheet/carbon black composites as electrodes for supercapacitors, Carbon, 48 (2010) 1731-1737.

[9] G. Arabale, D. Wagh, M. Kulkarni, I.S. Mulla, S.P. Vernekar, K. Vijayamohanan, A.M. Rao, Enhanced supercapacitance of multiwalled carbon nanotubes functionalized with ruthenium oxide, Chem. Phys. Lett., 376 (2003) 207-213.

[10] Z. Fan, Z. Qie, T. Wei, J. Yan, S. Wang, Preparation and characteristics of nanostructured MnO_2/MWCNTs using microwave irradiation method, Mater. Lett., 62 (2008) 3345-3348.

[11] J. Yan, Z. Fan, T. Wei, J. Cheng, B. Shao, K. Wang, L. Song, M. Zhang, Carbon nanotube/MnO_2 composites synthesized by microwave-assisted method for supercapacitors with high power and energy densities, J Power Sources, 194 (2009) 1202-1207.

[12] X. Jin, W. Zhou, S. Zhang, G.Z. Chen, Nanoscale microelectrochemical cells on carbon nanotubes, Small, 3 (2007) 1513-1517.

[13] E. Raymundo-Pinero, V. Khomenko, E. Frackowiak, F. Beguin, Performance of manganese oxide/CNTs composites as electrode materials for electrochemical capacitors, J Electrochem. Soc., 152 (2005) A229-A235.

[14] K. Wang, T. Feng, M. Qian, H. Ding, Y. Chen, Z. Sun, The field emission of vacuum filtered graphene films reduced by microwave, Appl. Surf. Sci., 257 (2011) 5808-5812.

[15] J.A. Menéndez, A. Arenillas, B. Fidalgo, Y. Fernández, L. Zubizarreta, E.G. Calvo, J.M. Bermúdez, Microwave heating processes involving carbon materials, Fuel Process. Technol., 91 (2010) 1-8.

[16] W.S. Hummers, R.E. Offeman, Preparation of graphitic oxide, J Am. Chem. Soc., 80 (1958) 1339-1339.

[17] L.F. Lai, L. L.W. Chen, D. Zhan, L. Sun, J.P. Liu, S.H. Lim, C.K. Poh. Z.X. Shen, J.Y. Lin, One-step synthesis of NH_2-graphene from in situ graphene-oxide reduction and its improved electrochemical properties, Carbon, 49 (2011) 3250-3257.

Advanced Materials Research Vol. 936 (2014) pp 613-617
© (2014) Trans Tech Publications, Switzerland
doi:10.4028/www.scientific.net/AMR.936.613

Te inclusions in CdMnTe crystal grown by the traveling heater method and their effects on the electrical properties

Ping Shen[a] , Jijun Zhang*, Linjun Wang, Jiahua Min, Jian Huang, Xiaoyan Liang, Ke Tang, Min Shen, Lin Wang and Yiben Xia

School of Materials science and engineering, Shanghai University, Nanchen Road 333, Shanghai 200444, PR China

[a]shenping0724@163.com

*zhangjijun222@shu.edu.cn

Keywords: CdMnTe, Te inclusions, Distribution, Infrared microscopic, Traveling Heater Method.

Abstract. The concentration and size distribution of Te inclusions in CdMnTe (CMT) are key factors in nuclear devices' performance. High-concentration and large-size Te inclusions degrade the performance drastically, especially for electrical properties. In this paper, the Te inclusions along the axial and radial directions in CMT crystal grown by the Traveling Heater Method (THM) were revealed by Infrared Microscopic System. The size of Te inclusions is 5-17 μm and the concentration is (2.5-4.6) $\times 10^5$ cm^{-3}. The Current-Voltage measurements were performed and the resistivity of the CdMnTe crystal with excess Te was in the range of 10^8-10^9 Ω•cm, and the correlation between the Te inclusions and resistivity was investigated. The large size (>17 μm) and high concentration (4.5 of $\times 10^5$ cm^{-3}) Te inclusion decrease the resistivity of the CMT crystal seriously.

Introduction

The $Cd_{1-x}Mn_xTe$ (CMT) crystals belong to group II-VI compound semiconductors and they are the excellent materials for developing X-ray, γ-ray detector and magneto-optical isolator [1-2]. It possesses several opportune properties, such as large band gap (1.53-2.54 eV), high density (5.2-5.9 g/cm^3), and good electronic-transport properties (10^{-3}-10^{-5} cm^2/V), making it a very attractive material to be used as room-temperature nuclear-detectors for homeland security, astronomy, and medical imaging [3]. In addition, because the segregation coefficient of Mn in CdTe is about 1, the distribution of Mn in crystal is uniform along axial-direction, which makes CMT a promising material for nuclear-detectors instead of $Cd_{1-x}Zn_xTe$ (CZT) [4].

The devices usages demand monocrystalline CMT crystals with good compositional homogeneity, free from macroscopic defects, such as grain boundaries, twins, and large Te inclusions. CMT crystals are usually grown by the conventional Bridgman method [5]. However, the high growth temperature (1120 ℃) causes the crystal many kinds of defects which degrade the electrical properties of CMT crystal [6]. The THM has been proven to be a promising method in yielding large-size, uniform single-crystalline CZT and CdTe ingots [7, 8]. By THM, crystals can be grown at relatively low temperatures (900 ℃) compared with the melt growth, and the Te solution absorbs the impurity from the source materials and growth crucibl，therefore, crystals can be grown with less thermal stresses and high purity. However, the THM method has a major disadvantage that the Te solution introduces Te inclusions in the ingots because of the microscopically irregular melt–solid interfaces during growth, which can trap the Te-rich CMT solution forming inclusions [9-11]. It decreases the resistance of CMT and traps electron-hole when exerting bias voltage on CMT wafer. In this study, the CMT crystal was grown by the THM method and Te inclusions along the axial and radial directions of the CMT ingot were revealed by the Infrared microscopic system BX51-IR. Then the resistivity of the CMT wafers was measured by the current-voltage curves using Keithley 4200-SCS electrometer, and the relationship of the Te inclusions and the resistivity was investigated.

Experiments

All the CMT(x=0.1) crystals were grown by the THM technique from a Te-rich solution. The crystal growth was unseeded, carried out in conically tipped quartz ampoules, with a graphite coating on their inner walls. We loaded the required amount of CMT source and excess 6N purity Te, as well as 6N purity indium as a dopant, in the ampoule of 26-mm inner diameter. The ampoule was subsequently sealed under a vacuum of 1 $\times 10^{-4}$ Pa. The sealed ampoule was loaded into a three zone vertical tubular furnace. The temperatures of the three zones were set to achieve the required temperature gradient near the growth interface. A very low-speed DC motor was used for lowering the crucible into the furnace. Lowering rate from 3 to 5 mm/day was used for the growth and the temperature gradient near the growth interface was between 20 and 50 ℃/cm. The crucible was rotated in a speed from 3 r/min to 10 r/min. Finally, ingots were cooled at a rate of 100 ℃/h to room temperature after the growth was completed.

To study the distribution of Te inclusions, the crystal ingots were sliced into wafers with the thickness 2-5 mm perpendicular to axial-direction with inner circle cutting machine, then the wafers were sliced-into pieces with 8×8 mm^2 area using an inside-diamond wire saw machine. The testing samples were from different parts of the ingot, as shown in Fig.1.

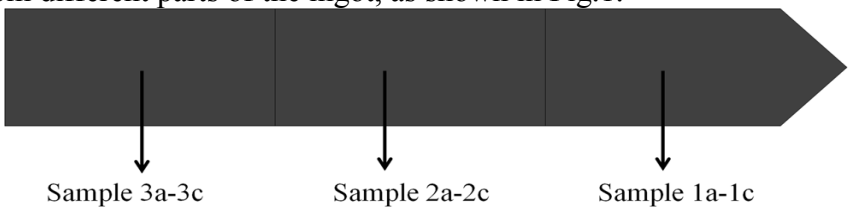


Fig.1 The samples from the different region of the ingot

The samples were mechanically polished with 0.3 mm alumina and 0.05 mm alumina suspensions to obtain mirror-like wafer surfaces. An Infrared Transmission Microscopy was employed to record the concentration and size distribution of Te inclusions in CMT. The current-voltage curves of the samples were measured at room temperature to evaluate the electrical behaviors. The wafer surfaces were passivated using BM (Br_2 and Methanol) and LB (Br_2 + Lactic Acid + Glycol) for 2 minutes, separately. Deposited gold was used for contact metallization.

Results and discussion

The IR transmission microscopy is known to be one of the most effective ways of detecting Te inclusions in CZT and CMT. Fig.2 shows the typical IR microscopic images of Te inclusions with regular triangular or hexagon shapes in the CMT wafers grown by THM. Taking into account the isotropy of melt, the trapped Te-rich droplet will tend to stabilize into a spherical shape due to surface tension. However, Te-rich droplet gradually becomes a polyhedral such as triangular or hexagon because of the deformation of CMT lattice and the anisotropic growth of Te inclusions.

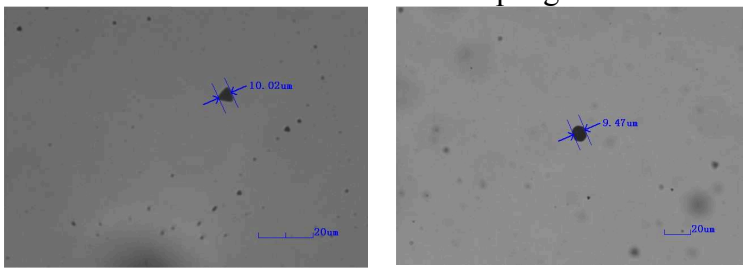


Fig. 2 The typical Infrared microscopic images of Te inclusion

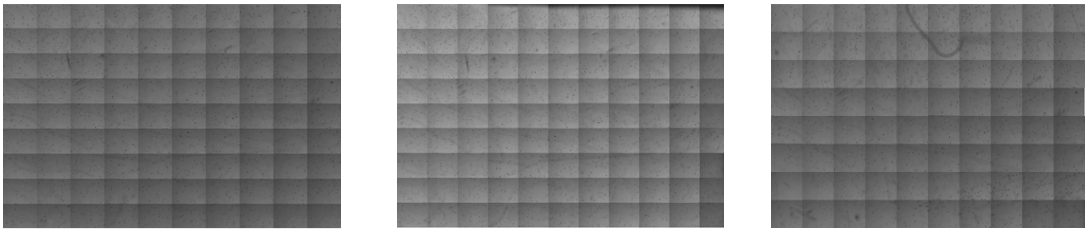
Fig. 3 shows the IR transmission images of Te inclusion in the samples from the first-to-freeze, stable-to-freeze and last-to-freeze parts of the ingot named with (a） CMT1b, (b) CMT2b and (c) CMT3b. It reveals that Te inclusions were randomly distributed throughout the samples. The size of those inclusions is mostly less than 20 μm, and their concentration is about 10^5 cm^{-3}. In order to reveal

the concentration and size distribution of Te inclusions intuitively, we change the actual datum of Te inclusions in Fig. 3 into a column chart, as shown in Fig. 4.

It's found that, in the first-to-freeze region, the size of Te inclusion is small, about 6 μm and the concentration is high, about 4.5×105 cm^{-3}. In the stable-to-freeze region, the size becomes larger, about 10 μm and the concentration decreases to 2.5×10^5 cm^{-3}. In the last-to-freeze region, the size is about 17 μm and the concentration is about 4.2×10^5 cm^{-3}. The size of Te inclusion varies in connection with the annealing time of ingot. From the first-to-freeze to the last-to-freeze part of the ingot, the time becomes less, so the size keeps on growing. The concentration is affected by the stability of interface and the excessive Te. In the first-to-freeze region, the excessive Te is small but the interface is unstable, so the concentration is high. With the stable interface in the stable-to-freeze region, the concentration of Te inclusion decreases. In the last-to-freeze region, the concentration is still high with the large excessive Te.The concentration of Te inclusion is mainly effected by Table 1 gives the Te inclusions in the radial direction of CMT samples. The results shown that the Te inclusions are almost the same in the equal radial direction, which indicate a planar solid-liquid interface during the THM growth.

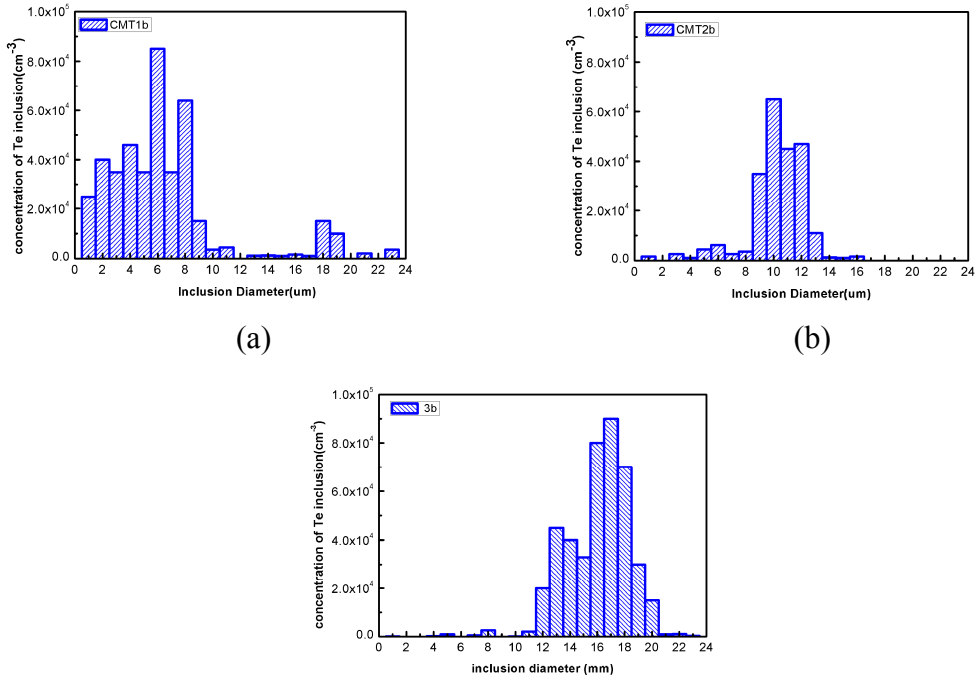
Table 1 The concentration and size of the samples of Te inclusions

Sample	1a	1b	1c	2a	2b	2c	3a	3b	3c
$D_{Te}[10^5cm^{-3}]$	4.6	4.52	4.46	2.45	2.50	2.53	4.3	4.19	4.10
Size[μm]	5.7	6.1	6.4	8.8	10.2	9.6	16.8	17.1	17.2



(a) (b) (c)

Fig. 3 Te inclusion of one face in samples （a）CMT1b（b）CMT2b（c）CMT3b



(a) (b)

(c)

Fig.4 Histogram of the Te inclusions size distribution in CMT samples（a）CMT1b（b）CMT2b（c）CMT3b

The current-voltage (I-V) curves of the samples are measured at room temperature. The typical I-V curves of sample 1b, 2b and 3b are shown in Fig. 5. The corresponding bulk resistivity of the three

wafers were 2.3×10^8 Ω•cm, 4.4×10^9 Ω•cm, 6.6×10^8 Ω•cm respectively. The results were shown in table 2. From CMT1b to CMT3b, with the size of Te inclusion becoming larger and the concentration tardily becoming lower then high, the resistivity of sample first becomes high then becomes low. Te inclusion in the crystal not only reduces the lifetime of electron-hole but also absorbs other impurities. When the size of Te inclusion is small, it is unable to degrade the lifetime, thus the resistivity is low. With the size becoming lager, the shorter the lifetime of electron-hole is, the high resistivity of the samples is. But when the size of Te inclusion increases to 20 μm, it also absorbs other impurity, the resistivity of the samples is low again. Consequently, the resistivity is not only related to the size of Te inclusion but also related to the concentration. The larger the size and the higher the concentration of Te inclusion are, the lower the resistivity of CMT is.

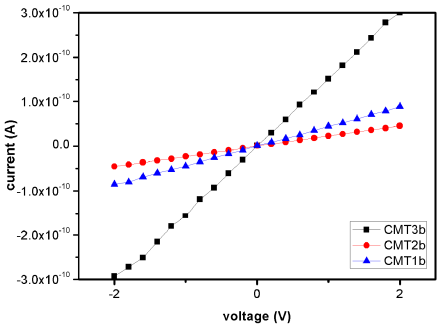


Fig.5 I-V curves of the CMT samples from different parts by THM

Table 2 The size and concentration of Te inclusion and the resistivity of sample

	CMT1b	CMT2b	CMT3b
$D_{Te}[cm^{-3}]$	4.5×10^5	2.5×10^5	4.2×10^5
Size[μm]	6	10	17
ρ [Ω.cm]	2.3×10^9	7.4×10^9	6.6×10^8

Summary

1) Te inclusion with regular triangular or circular shapes is randomly distributed throughout CMT crystal by THM.

2) In the first-to-freeze region, the size of Te inclusion is about 6μm and the concentration is 4.5×10^5 cm^{-3}; In stable-to-freeze region, the size is about 9 μm and the concentration is 2.5×10^5 cm^{-3}; In the last-to-freeze region, the size is about 17 μm and the concentration is about 4.2×10^5 cm^{-3} μm.The rate of the radial directions is almost the same.

3) The resistivity of the CMT is low to high to low from the first-to-freeze to the last-to-freeze region. The large size and high concentration of Te inclusion seriously decrease the resistivity of the CMT crystal.

Acknowledgements

This work was supported by the Na-tional Natural Science Foundations of China (No. 50902091, No. 11375112, and No. 11275122),Science and Technology Commission of Shanghai (No. 11530500200), and Innovation Program of Shanghai Mu-nicipal Education Commission (No.12ZZ096).

References

[1] H L Ding, X F Zhang, Compound semiconductor detector and its application, J. Atomic Energy Press, BeiJing, 1994: 1-114 (in Chinese) .

[2] L Y Shi, J J ZHANG, L J WANG, et al. Study on defects in $Cd_{1-x}Mn_xTe$ crystals by Vertical Bridgman Method , J. Journal of Synthetic Crystals, 2011, 40(3):543-551 (in Chinese) .

[3] X C Shen. Spectrum and Optical Properties of Semiconductors, M. Beijing: Science Press, 2003: 276.

[4] Burger A, Chattopadhyay K, H T Chen, et al. Crystal growth, fabrication and evaluation of cadmium manganese telluride Gamma ray detectors, J. Journal of Crystal Growth, 1999, 198/199:872-876.

[5] J J Zhang, W Q Jie, T Wang, et al. Vertical Bridgman growth and characterization of CdMnTe substrates for HgCdTe epitaxy, J. Journal of Crystal Growth, 2008,310:3203-3207 (in Chinese).

[6] Klapper H. Structural defects in techniques for their detection, J. Material Science. 1998, 276/277: 291-306.

[7] Y C Liu, DOST S, LENT B, RED DEN R F. A three-dimensional numerical simulation model for the growth of CdTe single crystals by the Traveling Heater Method under magnetic field , Journal of Crystal Growth, 2003, 254(3-4): 285-297.

[8] Roy U N, Weiler S, Tein J.S. Growth and interface study of 2 in diameter CdZnTe by THM technique, J. Journal of Crystal Growth, 2010, 312(19): 2840-2845.

[9] Y Wang, KUDO K, INATOMI Y, et al. Growth and Structure of CdZnTe crystal from Te solution with THM technique under static magnetic field, J. Journal of Crystal Growth, 2005, 275(1 −2): e1551 −e1556.

[10] BABALOLA O S, BOLOTNIKOV A E, GROZA M, et al. Study of Te inclusions in CdMnTe crystals for nuclear detector applications, J. Journal of Crystal Growth, 2009, 311(14): 3702 −3707.

[11] Schwarz R, Benz K W. Thermal. Field influence on the formation of Te inclusions in CdTe grown by the Travelling Heater Method,J.Journal of Crystal growth,1994, 144(3-4):150-156.

Advanced Materials Research Vol. 936 (2014) pp 618-623
© (2014) Trans Tech Publications, Switzerland
doi:10.4028/www.scientific.net/AMR.936.618

The effect of the Cu Source on Optical Properties of Cu-doped ZnO Films

Lung-Chien Chen [1, a], Xiu-Yu Zhang [1, b] and Kuan-Lin Lee[1, c]

[1] Department of Electro-optical Engineering, National Taipei University of Technology, No.1, Sec. 3, Chung-Hsiao E. Rd., Taipei 106, Taiwan

[a]ocean@ntut.edu.tw, [b]t101658072@ntut.edu.tw, [c]zwl44@yahoo.com.tw

Keywords: Cu-doped ZnO film, Copper source, Optical properties

Abstract: Cu-doped ZnO (CZO) films have been widely discussed due to its potential applications in semiconductor devices, such as gas sensors or solar cells, but few articles were reported to show the effect on properties of CZO films by using different Cu sources. The article demonstrates that CZO films have been prepared by using different Cu source via a simple ultrasonic spray method, in which copper nitrate and copper acetate were used as copper sources. Optical properties of CZO films prepared by copper nitrate and copper acetate were investigated by transmittance and photoluminescence measurement. The X-ray diffraction analysis and field emission scanning electron microscopy were used to investigate the composition and the morphology of the films. The CZO films prepared by using copper acetate shows better optical properties by comprehensive analysis.

Introduction

It is well known that zinc oxide (ZnO) is a wide direct bandgap (3.36eV) II-VI compound semiconductor, which has a large exciton binding energy of 60mV with a hexagonal wurtzite structure [1]. On the other hand, copper oxide is one kind of semiconductor with a band gap of 1.4eV and absorbs strongly in visible spectrum [2]. The Cu-doped ZnO film (CZO) which is combined by ZnO and CuO has been widely researched due to its potential application in many fields, such as gas sensors, solar cells and so on [3~9]. The common copper source used for CZO film via ultrasonic spray method are copper nitrate and copper acetate [10,11]. There are few papers reported to discuss the physical properties of the CZO films using different copper sources.

In this study, ultrasonic spray method is employed to prepare CZO films with different Cu sources and the structures, morphologies, and properties were measured by various techniques. The ultrasonic spray method was used because it has the advantage of high growth rate, large area uniformity, and inexpensive preparation [12].

Experimental Details

CZO films were deposited by ultrasonic spraying technique at atmospheric pressure on a glass substrate. Before deposition, the glass substrates were first cleaned in Acetone and Methanol. Then the substrates were rinsed in de-ionized water and dried in the flowing Nitrogen. To obtain the precursor solution, three kinds of aqueous solution, zinc acetate, and ammonium acetate were chosen as the sources of zinc and nitrogen, copper acetate or copper nitrate as the source of copper respectively. The molar concentration of zinc acetate and ammonium acetate solution were 0.05M and 0.45M and the copper acetate or copper nitrate is 0.1M. The solutions were stirred at room temperature for 1h and then moved into a commercial ultrasonic nebulizer where makes the solutions be aerosol. The aerosol was transported to the substrate by high-purity nitrogen gas and the substrate was kept at 500°C. The deposition time lasts for 15 minutes.

The crystalline microstructure of the films were determined by a PANalytical X'Pert Pro DY2840 X-ray diffraction with Cu-Kα radiation (λ=0.1541nm) in the scanning range between 2θ=20° and 60°. Surface morphology was studied by a JEOL JSM-5600LV scanning electron microscope. Optical

transmission properties were measured in the range of 300-1000nm using by a Hitachi U-2001 Ultraviolet-Visible spectrophotometer. Photoluminescence (PL) spectra were excited by a He-Cd laser (325nm) and collected by a Dongwoo spectrophotometer at room temperature.

Results and Discussion

Crystalline structure

Fig.1 shows the XRD patterns of CZO films deposited on glass substrates. The CZO film using copper acetate have several peaks, which show that the film has both ZnO and CuO phases. The diffraction peaks marked as "Z" were observed at 2θ=31.86°, 34.57°, 36.39°, 47.66°and 56.71°, which can be corresponded to (1 0 0), (0 0 2), (1 0 1), (0 1 2), and (1 1 0) planes of ZnO phase. This result showed the thin film was polycrystalline and had a hexagonal wurtzite structure of ZnO phase. For the peaks marked as "C" and observed at 2θ= 35.60°, 38.76°, 48.95°, and 58.30° are corresponding to (1 1 -1), (1 1 1), (2 0 -2), and (2 0 2) planes of CuO with monoclinic structure. The peaks observed above are fully matched with the hexagonal wurtzite structure ZnO (JCPDF # 75-0576) and monoclinic structure CuO (JCPDF # 89-5895). On the other hand, the film using copper nitrate only shows two diffraction peaks which are corresponding to (1 1 -1), (1 1 1) planes of CuO with monoclinic structure and the intensity of the peaks are lower than that of the former. From Fig.1 it is evident that the film using copper acetate has both CuO and ZnO phases and the intensity difference between two films implies that the film using copper acetate has better crystalline.

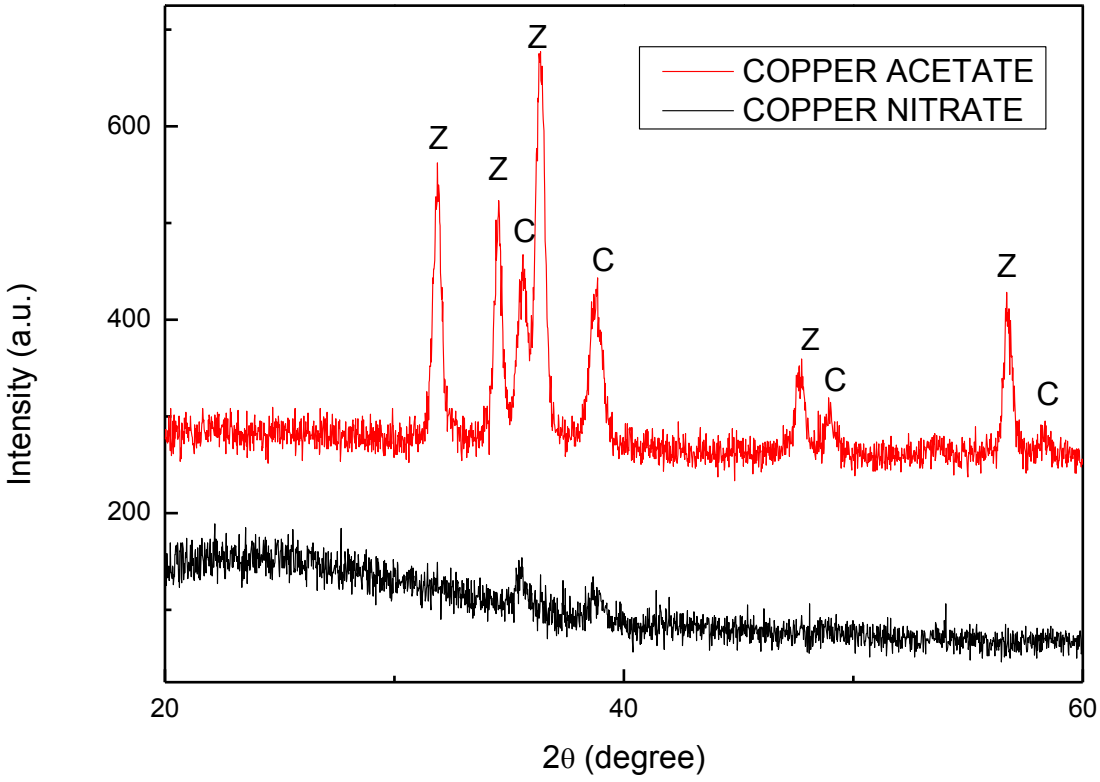


Fig. 1 XRD Patterns of CZO thin Films Using Different Copper Sources.

Fig. 2 depicts the scanning electronic microscopy (SEM) images of the surface morphology of CZO films were observed. As shown in the figure, the morphology of the films using different copper sources are quite different from each other. The film using copper acetate formed small island

structure with about 1 micrometer diameter on the films and the film thickness is about 500nm. The deposited film using copper nitrate failed to cover the whole glass substrate and form uniform and dense layer. The dark background of the SEM image is corresponding to glass substrate and the bright areas is CZO film with sheet morphology structure. The SEM images show that the film using copper nitrate has poor crystalline which is in keeping with the result of XRD analysis and also imply that the film deposition velocity is much slower when using copper nitrate as copper source.

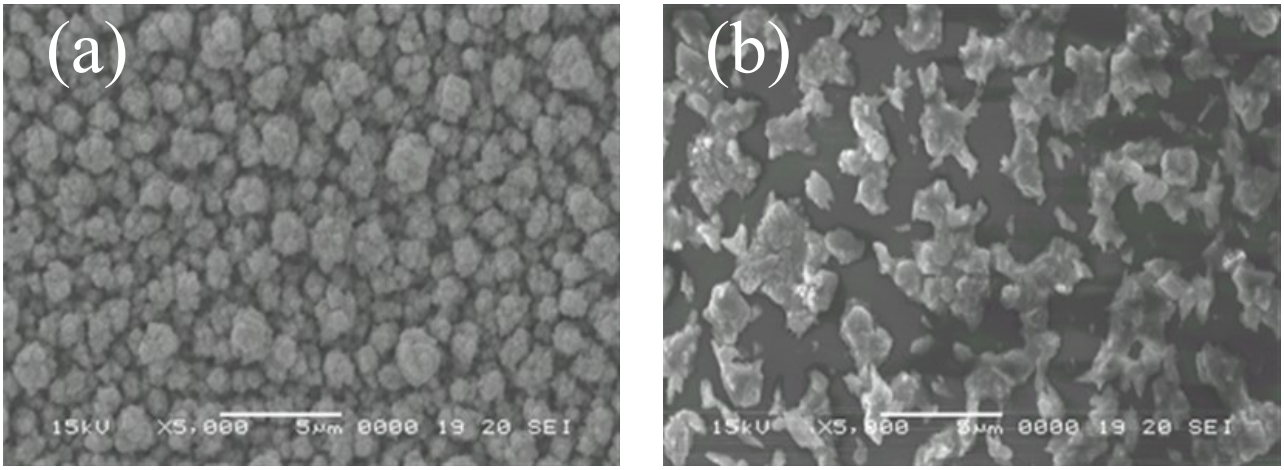


Fig. 2 SEM Images of CZO Films Using Different Copper Sources, (a) Copper Acetate, (b) Copper nitrate.

Optical characteristics

The optical transmittance spectra of CZO films are shown in Fig. 3(a). Due to the film using copper nitrate failed to cover the whole substrate, the lowest value of the transmittance spectrum of the film using copper nitrate isn't zero, and the value of transmittance spectrum is about 19% from 300nm to 700nm which means that about 80% region of the substrate were covered with CZO film. It can be observed from the spectrum that the film using copper acetate has strong absorption in visible region. It's similar to the properties of CuO film.

The direct optical band-gap E_g of the films as shown in Fig. 3(b) was obtained from the transmission spectra using the following relationships:

$$\alpha d = -\ln T \tag{1}$$

$$(\alpha hv)^2 = A\left(hv - E_g\right) \tag{2}$$

Where α is the absorption coefficient values; d is the film thickness; T is the transmittance spectra of thin films; A is a constant; hv is the photon energy and E_g is the optical band-gap of the semiconductor.

The graph of α^2 versus hv plots for the film using copper acetate is shown in Fig. 3 (b). It can be seen that the extrapolation of linear portion of the graph to energy axis at $(\alpha hv)^2=0$ gives the E_g value. The optical band-gap of the film using copper acetate is 1.8eV which is in the interval of the band-gap of CuO (1.4eV) and ZnO (3.36eV). The optical band-gap of the film using copper acetate were failed to be calculated by this way because the film thickness were hard to measure.

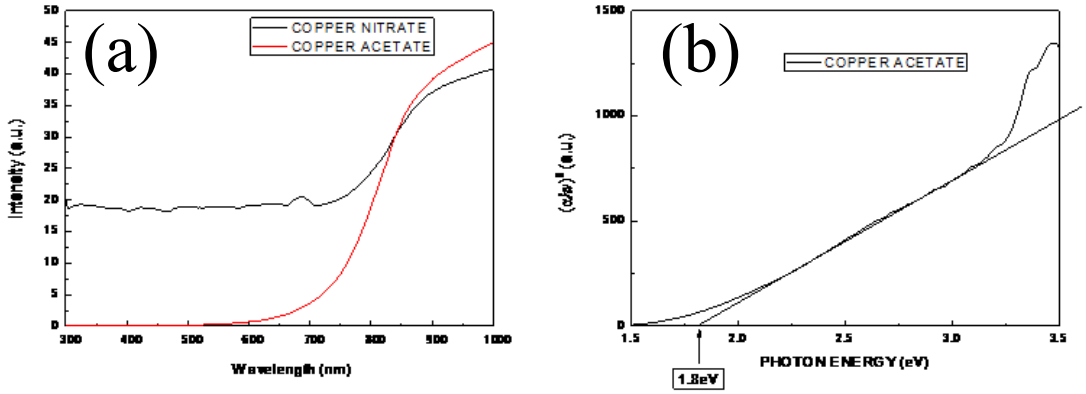


Fig. 3 Transmittance Properties and Variation of the CZO Films: (a) Optical Transmission Spectra of the CZO Films, (b) the Graph of $(\alpha hv)^2$ vs. hv Plots For the Film Using Copper Acetate.

Photoluminescence (PL) measurement of the CZO films was carried out to gather further information of optical properties. Fig. 4 shows the PL spectra of the films. The peaks of the film using copper acetate was indicated at 665nm and 760nm. The peak centered at 665nm is corresponding to the optical band-gap of the CZO film and is close to the band observed in a single ZnO film, which is also attributed to the single and double ionized oxygen vacancies [13,14]. Many groups postulated that the near-IR emission at about 760nm originates from defects similar to those responsible for the red emission in ZnO, i.e. oxygen vacancy [15,16]. It's obvious that the CZO film using copper nitrate shows weak Near-IR emission which is centered at 760nm and mainly caused by oxygen-related defects.

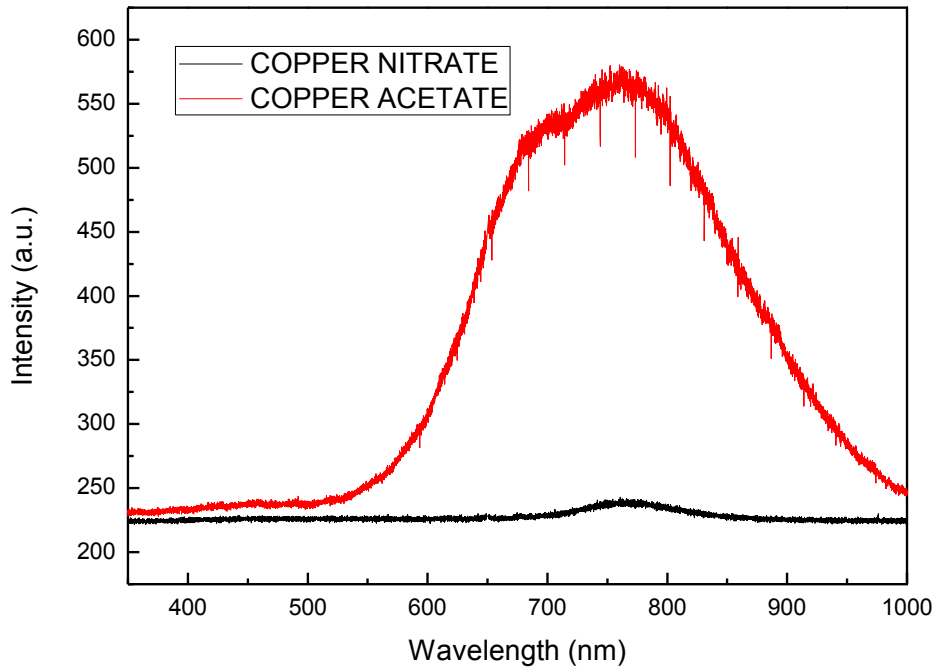


Fig. 4 Room Temperature PL Spectra of CZO Films.

Conclusion

The structural, morphological, and optical properties of the CZO films using different copper sources prepared via ultrasonic spray method were investigated. The XRD patterns showed that the film using copper acetate are polycrystalline with both ZnO and CuO phase and has better crystalline. The transmission measurement related to the optical band-gap of the film using copper acetate showed the film having strong absorption in visible region as expect and the optical band-gap is about 1.8eV. The film using copper acetate showed strong Near-IR emission of photoluminescence features. All these analysis indicates that the prepared CZO films using copper acetate has better crystalline and optical properties than using copper nitrate.

References

[1] Y. Chen, D. M. Bagnall, H. Koh, K. Park, K. Hiraga, Z. Zhu, and T. Yao, Plasma assisted molecular beam epitaxy of ZnO on c -plane sapphire: Growth and characterization, Journal of Applied Physics, 84 (1998) 81-98.

[2] J. Ghijsen, L. H. Tjeng, J. van Elp, H. Eskes, J. Westerink, and G. A. Sawatzky, Electronic structure of Cu2O and CuO, Physics Review B, 38 (1988) 322-330.

[3] D.H. Yoon, J.H. Yu, and G.M. Choi, CO gas sensing properties of ZnO-CuO composite, Sensors and Actuators B, 46 (1998) 15-23.

[4] E.N. Muhamad, R. Irmawati, Y.H. Taufiq-Yap, A.H. Abdullah, B.L. Kniep, F. Girgsdies b, T. Ressler, Comparative study of Cu/ZnO catalysts derived from different precursors as a function of aging, Catalysis Today, 131 (2008) 118-124.

[5] P. K.Sharma, R. K.Dutta, A. C.Pandey, Doping dependent room-temperature ferromagnetism and structural properties of dilute magnetic semiconductor ZnO:Cu^{2+} nanorods, Journal of Magnetism and Magnetic Materials, 321 (2009) 4001-4005.

[6] D.Y. Benjamin and P. Yang, Nanowire-Based All-Oxide Solar Cells, Journal of American Chemistry Society, 131 (2009) 3756-3761.

[7] M. B. Rahmani, S. H. Keshmiri, M. Shafiei, K. Latham, W. Wlodarski, J. du Plessis, and K. Kalantar-Zadeh, Transition from n- to p-Type of Spray Pyrolysis Deposited Cu Doped ZnO Thin Films for NO_2 Sensing, Sensor Letters, 7 (2009) 1-8.

[8] H. Ma, L. Yue, C. Yu, X. Dong, X. Zhang, M. Xue, X. Zhang and Y. Fu, Synthesis, characterization and photocatalytic activity of Cu-doped Zn/ZnO photocatalyst with carbon modification, Journal of Materials Chemistry, 22 (2012) 23780-23788.

[9] L. Chowa, O. Lupana, G. Chaia, H. Khallafa, L.K. Onoa, B. Roldan Cuenyaa, I.M. Tiginyanu, V.V. Ursaki, V. Sontea, A. Schulte, Synthesis and characterization of Cu-doped ZnO one-dimensional structures for miniaturized sensor applications with faster response, Sensors and Actuators A: Physical, 189 (2013), 399-408.

[10] G.K. Mani, J.B.B. Rayappan, Influence of copper doping on structural, optical and sensing propertiesof spray deposited zinc oxide thin films, Journal of Alloys and Compounds 582 (2014) 414–419.

[11] S. Wei, Y. Chen, Y. Ma, Z. Shao, Fabrication of CuO/ZnO composite films with cathodic co-electrodeposition and their photocatalytic performance, Journal of Molecular Catalysis A: Chemical, 331 (2010) 112–116.

[12] J.G. Lu, Z.Z. Ye, L. Wang, B.H. Zhao, J.Y. Huang, Preparation and properties of N-doped p-type ZnO films by solid sorce chemical vapor deposition with the c-axis parallel to the substrate, Chinese Physics Letter, 19 (2002) 1494-1497.

[13] Z. Fan, P. Chang, and Jia G. Lu, Photoluminescence and polarized photodetection of single ZnO nanowires, Applied Physics Letters, 85 (2004) 6128-6130

[14] Y. G. Wang, S. P. Lau, H. W. Lee, S. F. Yu, and B. K. Tay, Photoluminescence study of ZnO films prepared by thermal oxidation of Zn metallic films in air, Journal of Applied Physics, 94 (2003) 354-358.

[15] R.B.M Cross, M.M.D. Souza and E.M. Sankara Narayanan, A low temperature combination method for the production of ZnO nanowires, Nanotechnology, 16 (2005) 2188-2192.

[16] B. Lin, Z. Fu, and Y. Jia, Green luminescent center in undoped zinc oxide films deposited on silicon substrates, Appl. Phys. Lett. 79 (2001) 943.

Advanced Materials Research Vol. 936 (2014) pp 624-627
© (2014) Trans Tech Publications, Switzerland
doi:10.4028/www.scientific.net/AMR.936.624

The Model of Nano-scale Cu-particle Removal in CO_2-based Micelle Solutions with Different Surfactants

Yunrun Wang

Department of Physics, Renmin University of China, Beijing, 100872, China

yunrunwang@163.com

Keywords: equilibrium separation distance, net adhesion force, high pressure, carbon dioxide, surfactant

Abstract: This work focused on the analysis of static forces of a Cu particle in CO2-based micelle solutions with different surfactant, including fluorinated surfactants PFPE COO-NH4+, 8FS(EO)2 and hydrocarbon surfactants L31, DiF8-PO4-Na+. Calculations demonstrated that high pressure could impose enough capillary pressure effect beneath a particle to compete with the net adhesion force and increase the particle surface separation distance. The ESD for the micelle solutions had the similar behavior, otherwise, the value of NAF for the micelle solution with surfactant DiF8-PO4-Na+ had the minimum relative to other surfactant micelle solutions, suggesting that Cu particles would be more easily removed in micelle solution with DiF8-PO4-Na+ surfactant.

Introduction

Copper has replaced aluminum for interconnectors in semiconductor industry to satisfy the demand for better performance [1]. During the cleaning units in semiconductor industry, residues on the via sidewall and bottom of the trenches must be removed. As the characteristic dimension in wafers shrink to nano-scale dimension, the ability of cleaning solutions to penetrate small features and contact the residues will become significantly challenging. Generally, external pressure must be exerted on the fluid to penetrate the features. In addition, the cleaning solution will be difficult to remove due to Laplace pressure. Therefore, novel concepts in cleaning processes are required to overcome these challenges.

Water and carbon dioxide constitute two of the most abundant and environmentally benign solvents on earth. Dense CO2, liquid and supercritical, has many desirable properties for cleaning wafers. It is inexpensive, essentially nontoxic, inert, and nonflammable. The surface tension of liquid carbon dioxide is only 1.5 mN/m at 25 ºC and reaches zero at the critical point, where liquid droplets are no longer formed [2]. The beneficial interfacial property promotes the penetration of small features. The formation of water-in-CO2 (W/C) microemulsions has spawned novel applications for CO2. The H2O-CO2 systems with surfactants are being explored for cleaning of wafers in microelectronics processes. The introduction of excess amount of solution into CO2 solvent forms a fluid bridge between microscopic particles and surfaces, which makes the static-force system more susceptible to pressure changes. This second fluid phase forms a well-defined phase interface with the bulk CO2 solvent. Because of the curvature of this phase interface, there is a pressure change within the entrapped fluid bridge, which can be calculated by the Kelvin equation [3]. The entrapped fluid brings two opposing forces on the particle, one adding to the adsorption forces, the other acting to counteract those forces [4].

In this study, the net adhesion forces (NAF) and equilibrium separation distance (ESD) of a copper particle adhering on silicon wafer in CO2-based micelle solution with different surfactants were calculated. The calculated results demonstrated that elevated pressure applied in cleaning system can significantly alter the static force balance on adhered particles.

Model Description and Procedure

In the general way, adsorption forces consist of Van der Waals force, classical Coulombic attraction (electrostatic image force), contact potential force, and fluid bridge force. These forces act as an obstacle for removing particles adhering to the surface. With regard to the fluid bridge entrapped between the particle and the surface, there is an opposing force or the capillary pressure due to the curvature of the interface acting against the adsorption force. We adopted the model and procedure intruduced by the reference [4], and caculated the net adhesion forces (NAF) and equilibrium separation distance (ESD) of a copper particle adhering on silicon wafer in CO2-based micelle solution with different surfactants. In the calculation, we introduced a variable (immersion height d) to represent the depth of the particle beneath the heavy phase of the CO2-based solutions.

Results and Discussion

The NAF is the sum of all of the forces which adheres the particle to the substrate. The ESD is a static particle-substrate separation distance where the all of the downwards forces imposed on the particle and the upwards forces are equal in magnitude. The calculation focused on the copper particles with different radius (50 nm~300 nm) in CO2-based micelle solution with fluorinated surfactant PFPE COO-NH4+, 8FS(EO)2 and hydrocarbon surfactants L31, DiF8-PO4-Na+ under different pressures. In the calculation, the data of surface tension and entrapped fluid dielectric constant of CO2-based solutions at certain pressure and temperature were taken from references [4].

Generally, a particle with larger ESD and smaller NAF would be removed more easily. Chai' research work demonstrated that high pressure could increase the particle-substrate separation distance in the regions of pressures studied and this effect might be coupled with a decrease in NAF for the CO2-H2O system, suggesting that particles would be removed more easily at high pressure.

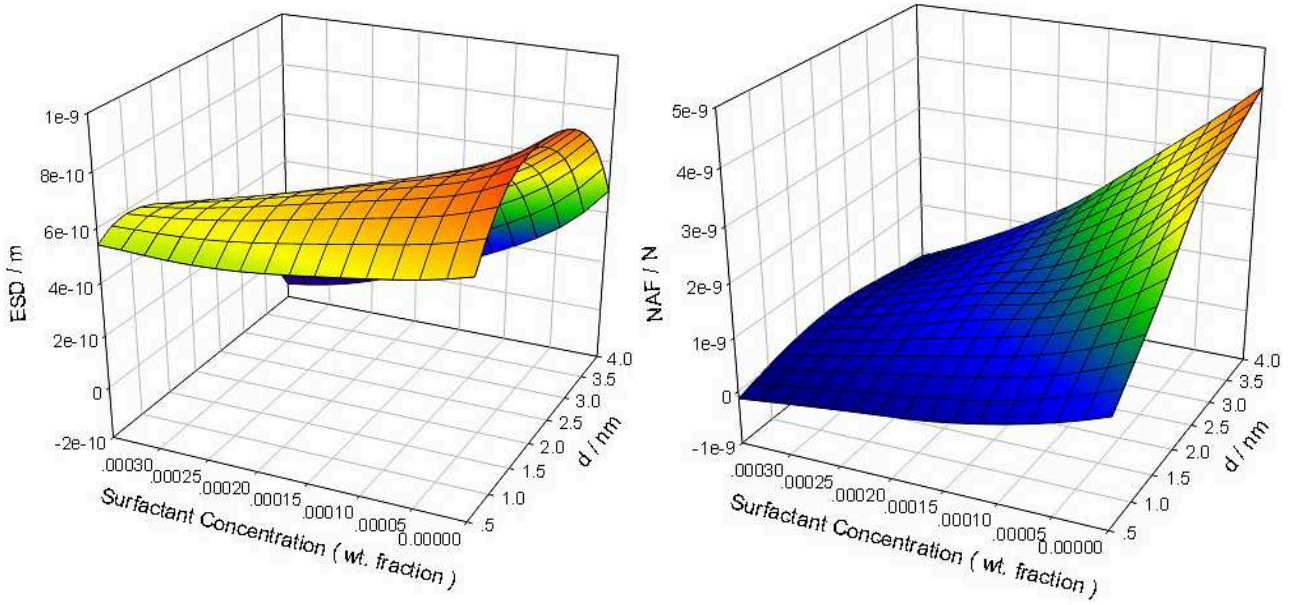


Figure 1. ESD and NAF as a function of the surfactant concentration and submersion height (d) in CO_2-based micelle solution at 313 K and 25 MPa, surfactant: PFPE COO-NH4+, particle radius: 50 nm.

In this work, a copper particle with 50 nm radius in CO2-based micelle solutions with surfactants PFPE COO-NH4+,8FS(EO)2, L31 and DiF8-PO4-Na+ was be given the object of study. Figures 1 to 4 showed the NAF and ESD as a function of surfactant concentration and immersion height in CO2-based micelle solutions. The value of ESD in CO2-based micelle solution was nearly independent of surfactant concentration as the immersion height was fixed, and the value of NAF decreased with increased surfactant concentration. As the surfactant concentration was given, the value of NAF decreased with the decrease of immersion height. Unlike the trends of NAF, the value of ESD had a maximum in the immersion height ranges for both surfactant systems. The ESD for the micelle solutions has the similar behavior, otherwise, the value of NAF for the micelle solution with surfactant DiF8-PO4-Na+ had the minimum relative to other surfactant micelle solutions, suggesting that Cu particles would be more easily removed in micelle solution with DiF8-PO4-Na+ surfactant. From the calculation results, we could see that in order for particles to remove, entrapped fluid layer between the particle and substrate is needed. Holding the certain value of immersion height will be favorable to particle removal.

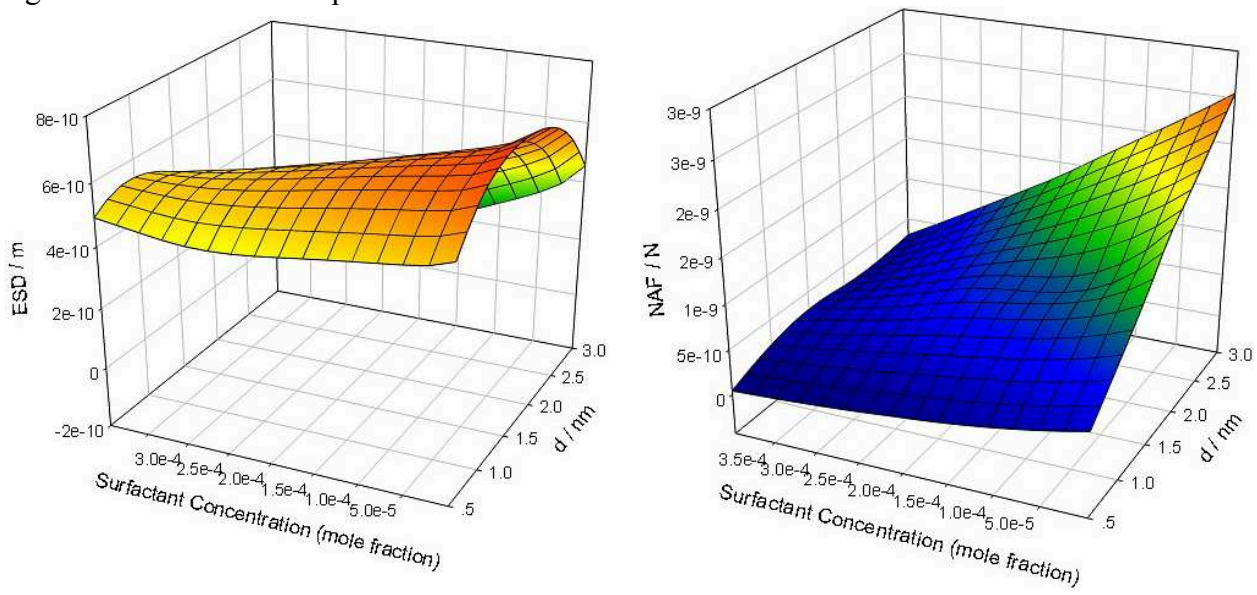


Figure 2. ESD and NAF as a function of the surfactant concentration and submersion height (d) in CO_2-based micelle solution at 313 K and 25 MPa, surfactant: L31, particle radius: 50 nm.

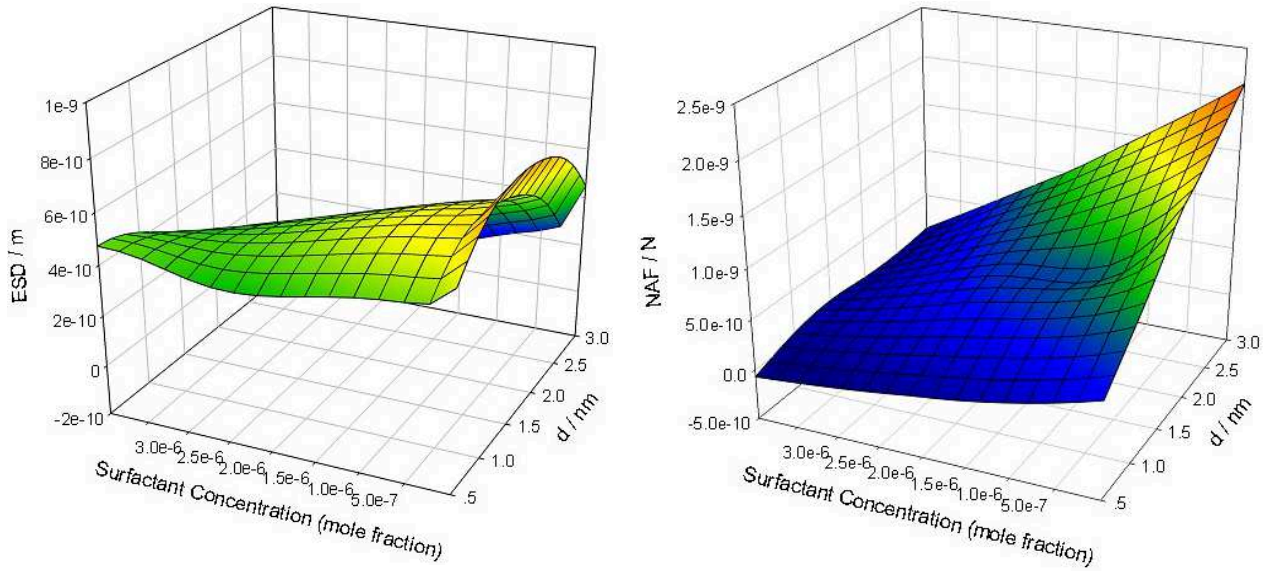


Figure 3. ESD and NAF as a function of the surfactant concentration and submersion height (d) in CO_2-based micelle solution at 313 K and 25 MPa, surfactant: 8FS(EO)2, particle radius: 50 nm.

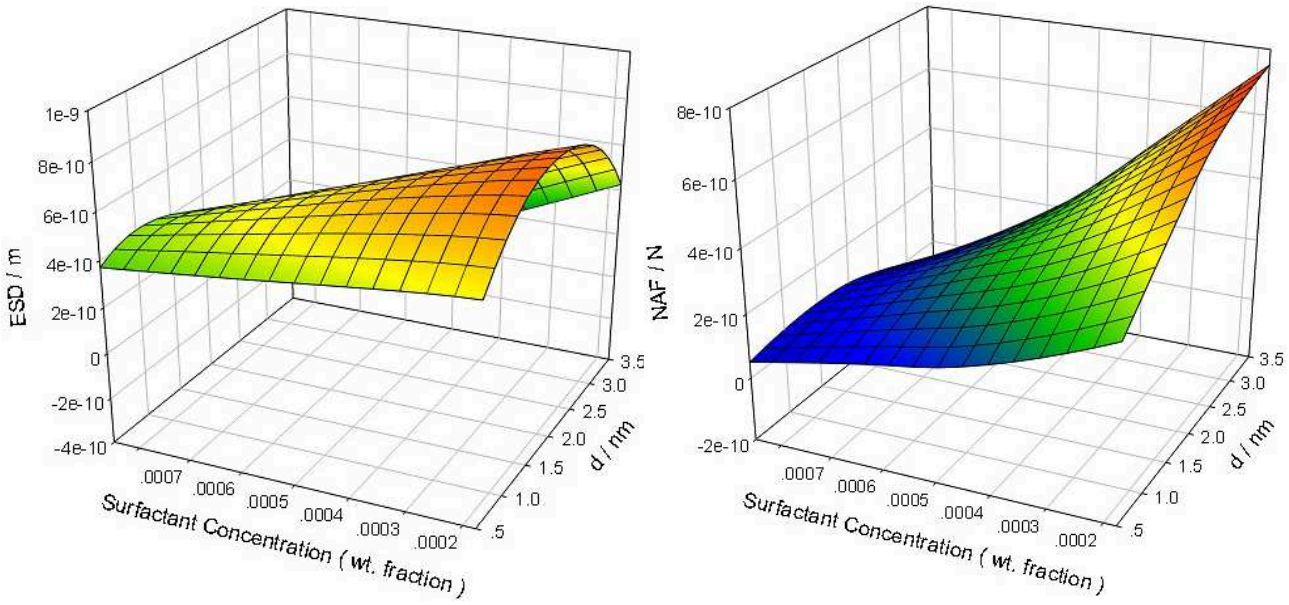


Figure 4. ESD and NAF as a function of the surfactant concentration and submersion height (d) in CO_2-based micelle solution at 313 K and 25 MPa, surfactant: DiF8-PO4-Na+, particle radius: 50 nm.

Summary

A physical model was presented to illustrate the behavior of all kinds of static forces existed in nano-scale Cu particle on flat surface with a fluid layers on the substrate. the values of NAF and ESD in CO2-based micelle solutions with different surfactants were calculated. The results demonstrated that high pressure could impose enough capillary pressure effect beneath a particle to compete with the net adhesion force and increase the particle surface separation distance. The existence of entrapped fluid layer between the particle and substrate favor the particle removal. The ESD for the two micelle solutions had the similar behavior, otherwise, the value of NAF for the micelle solution with surfactant DiF8-PO4-Na+ had the minimum relative to other surfactant micelle solutions, suggesting that Cu particles would be more easily removed in micelle solution with DiF8-PO4-Na+ surfactant. The model is expected to be helpful to design and analysis of high pressure CO2-based micelle cleaning systems.

References

[1] X. Xie, C. C. Finstad and A. J. Muscat, Chem. Mater. 17 (2005), p. 1753.
[2] Y. Fukushima, H. Wakayama, J. Chem. Phys. B 103 (1999), p 3062.
[3] F. R. E. De Bisschop and W. J. L. Rigole, J. Colloid Interface Sci. 88 (1982), p.117.
[4] X. Tan, J. Chai, X. Zhang and J. Chen, J. Nanosci. Nanotech. 11 (2011), p. 10782.
[5] J. Chai, X. Zhang, J. Huang, X. Tan, and G. Dai, J. Supercrit. Fluids. 49 (2009), p.182.

Advanced Materials Research Vol. 936 (2014) pp 628-632
© (2014) Trans Tech Publications, Switzerland
doi:10.4028/www.scientific.net/AMR.936.628

Failure Analysis of the Solder Joints in Flip-Chip BGA Packages under Free-Drop Test

Guozheng Yuan, Xia Chen, Xuefeng Shu*

Institute of Applied Mechanics & biomedical engineering, Taiyuan University of Technology, Taiyuan, Shanxi 030024,China,

*Corresponding author: shuxuefeng@tyut.edu.cn, 0351-6014455

Key words: free-drop, failure analysis, BGA Packages, drop test

Abstract: The failure of plastic ball grid array under intense dynamic loading was studied in the project. This paper presents the drop test reliability results of SnPb flip-chip on a standard JEDEC drop reliability test board. The failure mode and mechanism of planar array package in the drop test was comprehensively analyzed. High acceleration dropping test method was used to research the reliability of BGA (ball grid array) packages during the free-drop impact process. The model RS-DP-03A drop device was used to simulate the falling behavior of BGA chip packages under the real conditions, The drop condition meets the JEDEC22-B111 standards (pulse peak 1500g, pulse duration 0.5 ms)when dropping from the 650mm height . In the testing, according to the real-time changes of dynamic voltage, the relationship between drop times and different phases of package failure was analyzed. With the dye -penetrated method and optical microscopy, it was easy to observe the internal crack and failure locations. The growth mechanism of the cracks in solder joints under the condition of drop-free was analyzed and discussed.

Introduction

Along with the rapid development of the electronic industry, the electronic products are regenerated more and more quickly. Handheld electronic products are developed to miniaturization and multifunction, such as mobile, camera, DV and tablet computer. These electronic products have been widely used in people's daily life. In using process of customers, sudden falls occur frequently. The drop impacts not only destroy the shell of electronic products, but damage internal encapsulation of components seriously. The drop events may result in failure of solder joints inside these devices.

There has been a significant amount of research which were done in the last few years on drop impact reliability. BGA package solder ball faces such drop impact test. Recently, the research about drop test is more and more subtle. Numbers of boundary bolts can influence the chip's service life greatly[1]. To edge combined the chip package, different combine material have different influence on the service life[2]. Combining with the finite-element simulation, the dynamic performance of the test board can be obtained completely. Qin Fei etc analyze the mechanical behavior of solder ball with the Johnson-Cook model in drop test [3]. Liu Fang etc get the fracture mode of Lead-free solder ball is the brittle fracture of the IMC layer [4]; In abroad, It is one of the hot issues to research the reliability behavior of package drop. They use many methods to analyze the package dynamic mechanics performance, such as using the finite element analysis, improving the experiment instrument, changing weld layer of the internal encapsulation components [5-7].

In this article, the drop tester was different from JEDEC standard. In order to imitate the electronic components free-drop conditions, the drop test of BGA packages was conducted. The plane-hit destruction causes and failure mechanism of the packages are analyzed through the test.

This paper presents the drop test reliability for edge-bonded 0.5mm pitch lead-free chip scale packages on a standard JEDEC drop reliability test board, the failure mode and mechanism of planar array package in the drop test are comprehensively analyzed.

Experiment

Specimen preparation

The chip components in the test are 12 x 12 ball grid array packages, the solder pitch is 1.27 mm, diameter of the solder joints is 0.6 mm, welding plate size is 0.45 mm, solder joints arrangement is shown in figure 1. The solder joints of the BGA package constitute two "Daisy chains", the number of nodes around is used to test the failure position of solder joints. PCB substrate is coated of copper and sinker gold for the surface of FR-4 fiber glass, the size of PCB board is 54 mm x 45 mm x 0.5 mm.

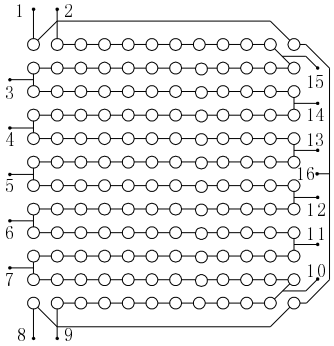


Fig. 1 BGA Solder joint arrangement

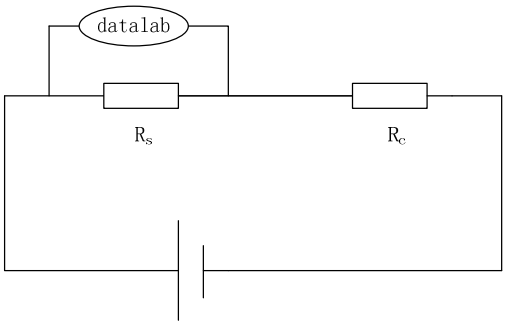


Fig. 2 DC series voltage divider circuit

JEDEC22-B111 standard which recommended drop/ impact test method was adopted. RS-DP-03A drop tester was used to imitate the free-drop of the product under the real condition. The drop tester consists of vacuum head, digital control panel, and rigid base. There was a felt on the rigid base to control the duration of acceleration. Before the test, checked up the conductivity of the chip first, then connected the 2 Daisy chains to test system. The strain gauges were posted on PCB for recording PCB bending deformation in dropping impact process. Acceleration sensors installed in drop specimens were used to collect acceleration curve during the drops. In the experiment, specimens and vacuum head dropped from 650 mm in height freely, then they separated at 300 mm in height, and specimens fell with the same speed before separation. Dropping specimens stroke on the rigid base with the fixed posture, producing the specified pulse curve (pulse peak 1500 g, pulse duration 0.5 ms). With the real-time data acquisition system, the impact pulse, strain curve of PCB and voltage curve during drop were collected.

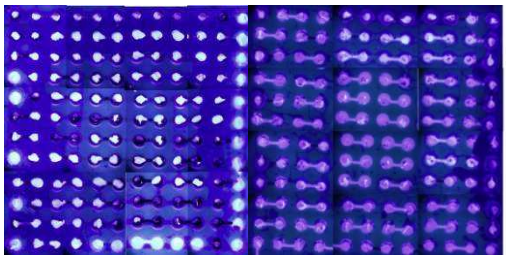
Experimental procedure

The daisy chains are placed in a DC series circuit with a static resistor (R_s) whose value is known as $100\,\Omega$ to construct a voltage divider circuit as shown in Fig. 2. The monitoring system record the voltage (V_s) which is the voltage of R_s .The relation between the dynamic resistance of daisy-chained solder joints and V_s can be described by EQ. 1.

$$V_s = \frac{V_{DC} R_s}{R_s + R_c} \tag{1}$$

The voltage curve of the encapsulation can indicate the crack inside the solder joints. The greater the fluctuation, the longer the cracks. The system registers a decline in voltage($V_s \to 0$) while the resistance rises ($R_c \to \infty$).When the dynamic voltage waves to zero, the package is invalid transiently. During 5 subsequent drops, if there are 3 additional transient failure, it is called the permanent failure of the packages[8]. Dyeing method was adopted to mark the dangerous area of the packages and the crack situation of solder joints. The morphology of internal cracks in solder joints was observed by optical microscope.

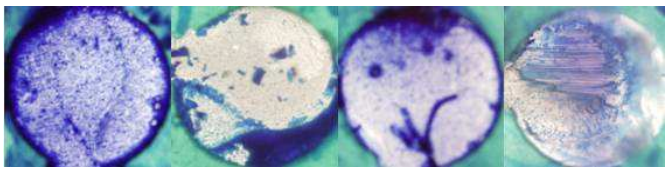
Experiment result



(a) (b)

Fig. 3 Solder joints dyeing photos

PCB and package were parted for observation of dyed solder joints as shown in figure 3. BGA was fixed in the center of the PCB board before the test, and the four corners in Figure 3 (a) are corresponding to the ones in figure 3 (b). The black spots on PCB are the solder joints which remain on the PCB after division. The closer to the boundary, the more the dyed solder joints . The completely dyed solder joint in the upper left explains that the solder joint is completely invalid, as shown in figure 4. That is to say, in the BGA package, the outermost area is the dangerous area solder ball, the solder joints in the outermost corners are trend to be invalid.



a. b. c. d.

Fig. 4 Main failure modes of chip packages (×60)
a-Failure between bonding pad and substrate;
b-IMC layer failure; c-Base board failure; d-Bonding pad fatigue

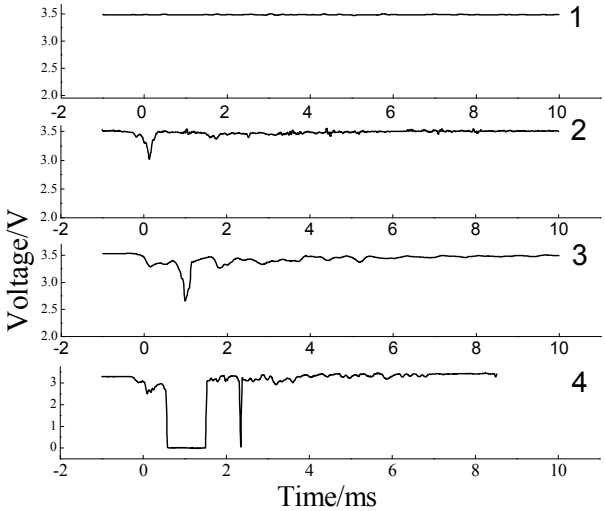


Fig. 5 Typical test data curve (resistance)

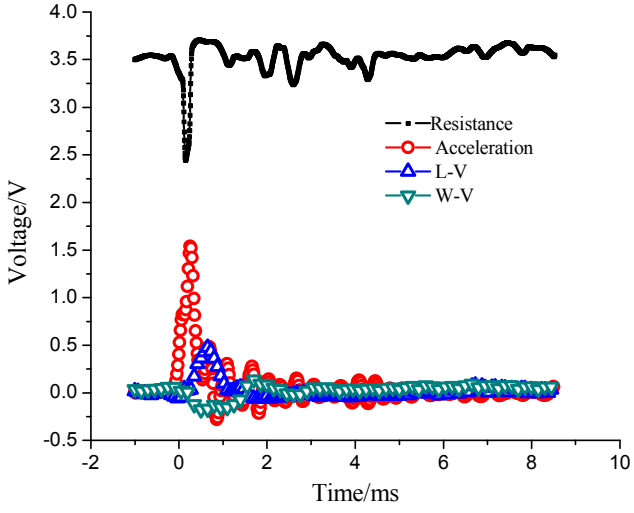


Fig. 6 Typical test data curve (acceleration&strain)

Solder joints' failure modes are different. The different failure modes of solder joints result to the different morphology after dyeing, as shown in figure 4. PCB substrate bends up and down repeatedly , creating the coupling effect of periodic tensile stress, compressive stress and shear stress in the solder joints [9]. Edge fatigue failure happened in the solder joint under the effect of stress firstly. The main failure mode along the plate width of solder joints is welding plate fracture failure, as shown in figure 5. Along the width direction of the board, the failure modes of solder joints are welding plate fracture, welding and welding plate of the ball between the IMC layer failure. Real-time dynamic pulse signal, PCB dynamic strain signal and the dynamic voltage signal were collected the moment the chip dropping on the block. In the drop test, the typical characteristic curve of the crack in the solder joints is shown in figure 6. As can be seen from the graph, the strain signal delays in pulse (acceleration) signal about 0.4 ms when pulse energy transfers to the PCB. The bending deformation in PCB length direction is bigger than the width of the direction, but the duration of deformation in the width direction is longer than length direction. Dynamic voltage fluctuation which shows the change of chip resistor is consistent with the impact pulse in the 0.5ms. During that time, PCB substrate have not bended, that is to say, the first factor which cause the cracks in solder ball is dropping impact energy, not reciprocating bending deformation of PCB.

Along with the increase of drop times, the cracks of solder joints propagate quickly, eventually chip become invalid. Figure 5 shows the typical dynamic voltage curves in different phases of a chip. Dynamic voltage curve 1 has no waves, so the solder joints are in a steady stage, and the chip could work regularly. Significant fluctuations appear firstly in dynamic voltage curve 2, and impact energy is the cause of the appearance of the cracks in solder ball .Dynamic voltage curve 3 appears the fluctuation twice as big as the one in curve 2, it is because that the bending of PCB makes the cracks continue expanding, and solder joints damage situation become worse. Curve 2, 3 are the derivative crack phases. The stages of encapsulation chip solder ball have effect on the crack, electric properties fall. Dynamic voltage curve 4 appears big fluctuations, dropping impact energy causes fluctuations firstly, too. Then the PCB board bending causes solder ball fracture, during the drop, dynamic voltage approach to zero, visible PCB reciprocating bending is the main factor. Observing curve 2, 3 and 4 , before 0.5ms, the first ball cracks emerge , after 0.5 ms, PCB board begin to bend, causing solder joint crack grows and eventually opens.

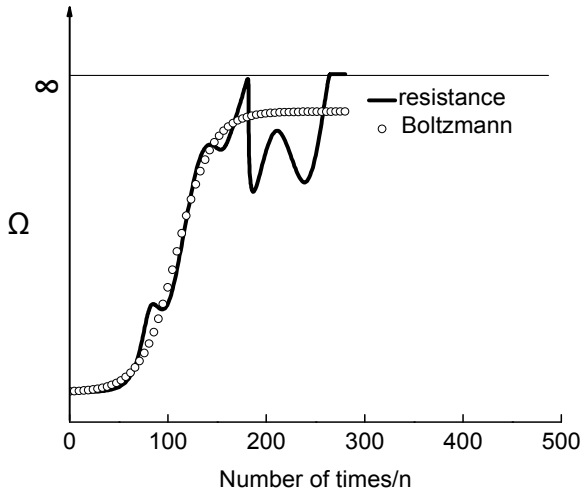


Fig.7 Relationship of chip peak resistor and drop times:

Stage 1: not produced crack area; Stage 2: the fatigue and growth area; Stage 3: failure area

The dynamic relationship between drop times and the peak resistance is available, according to the relation between the dynamic voltage and resistance. With the increase of drop times, the collected dynamic resistance peak curve can be divided into three stages. Drop times from 0 to 82 times are in the first stage. Electric resistance of this stage is in the steady state district, and does not change significantly. In this stage solder ball does not appear crack, and the chip works regularly. From 82 to 182 times, resistance has shown a sharp trend of crack expansion in the solder joints. Between 182 and 263 times, the cracks also in the expanding, and transient and steady state failure of solder joints happen（Transient failure in the test is defined as the first time in continuous

discontinuous circumstances; the first event of intermittent discontinuity as defined above followed by 3 additional such events during 5 subsequent drops）. In Transient failure, chip can continue to work, but its reliable performance has been greatly reduced. Continuous transient failure would cause the steady-state limitation, then chip function has been lost, and the chip become invalid.

Conclusions

In the free-drop test, impact energy is the cause of the appearance of cracks in solder ball .After crack appears, the reciprocating bending deformation of PCB is the main factors which lead to the propagation of cracks and the failure of package eventually. In drop process, substrate length direction has bigger value of bending deformation, shorter duration , and more effect on solder joints than the width direction. The deformation of PCB causes the cracks to open or close. With the increase of drop times, it can cause internal resistance of chip to reach to the peak of the dynamic change. Chip resistor peak steady-state continues growing until infinite, reflecting the process of the produces, expansion, and failure of the cracks. With the increase of dropping times, chip resistor peak showed "S" type of growth trend which fits poll Boltzmann curve, in the area to prevent possible failure at any time, for possible function is lost to prevent preparation, the failure of chip has certain tip role. The primary failure mode is pad cratering which indicates that solder joints may not be the weakest link of the assembly in this study.

Acknowledgments

The project supported by Youth Foundation of Taiyuan University of Technology (No. 2012L093), the National Natural Science Foundation of China (Grant No. 11172195) , the Natural Science Foundation of Hebei Province, China(Grant No. A2012201003), the Natural Science Foundation of Shanxi Province, China(Grant No. 2012011019-4).

References

[1] Luan J E, Tee T Y, Pek E, et al, Dynamic responses and solder joint reliability under board level drop test, J. Micro- electronics Reliability, Vol. 47,No. 2-3(2007), pp. 450-460.

[2] Farris A, Pan J B, Liddicoat A, et al, Drop impact reliability of edge-bonded lead-free chip scale packages, J.Microelectronics Reliability, Vol. 49, No. 7(2009), pp. 761-770.

[3] Liu F, Meng G, Zhao Z, et al, Researches of lead-free solder joint reliability under board-level drop impact, J. Acta Electronica Sinica, Vol. 35, No. 11(2007), pp. 2083-2086.

[4] Zhou C Y, Yu C X, Lee S W, Drop/impact tests and analysis of typical portable electronic devices, J.International Journal of Mechanical Sciences, Vol. 50, No. 5(2008), pp. 905-917.

[5] Wong E H, Seah S K W, Selvanayagam C S, et al, High-speed cyclic bend tests and board-level drop tests for evaluating the robustness of solder joints in printed circuit board assemblies, J.Journal of Electronic Materials, Vol. 38, No. 6(2009), pp. 884-895.

[6] Hochstenbach P H, Van Driel W D, Yang D G, et al, Designing for reliability using a new Wafer Level Package structure, J. Microelectronics Reliability, Vol. 50, No. 4(2010), pp. 528-535.

[7] Cédric L C, Tougui A, Stempin M P, et al, Experimental study of WL-CSP reliability subjected to a four-point bend-test, J. Microelectronics Reliability, Vol. 50, No. 7(2010), pp. 1007-1013.

Advanced Materials Research Vol. 936 (2014) pp 633-638
© (2014) Trans Tech Publications, Switzerland
doi:10.4028/www.scientific.net/AMR.936.633

The advantages of Ga-graded obtained by growth profile modification and Na incorporation on $Cu(In,Ga)Se_2$ solar cells

Rachsak Sakdanuphab[1,a], Sojiphong Chatraphorn[2,b] and Kajornyod Yoodee[2,c]

[1]College of Data Storage Innovation, King Mongkut's Institute of Technology Ladkrabang, Bangkok, 10520 Thailand

[2]Semiconductor Physics Research Laboratory, Department of Physics, Faculty of Science, Chulalongkorn University, Bangkok, 10300 Thailand

[a]ksrachsa@kmitl.ac.th, [b]sojiphong.c@chula.ac.th, [c]kajornyod.y@chula.ac.th

Keywords: $Cu(In,Ga)Se_2$; band gap grading; Ga-Graded; solar cell.

Abstract: $Cu(In,Ga)Se_2$ (CIGS) compound is a p-type semiconductor that has been used as light absorber layer in high efficiency thin film solar cell. The CIGS compound can be adjusted the band gap energy by varying the ratio of [Ga]/([In] +[Ga]) ratio (x). From theoretical and simulation, it was found that band gap grading in CIGS thin films showed the advantages to increase the efficiency of solar cells. Generally, the band gap grading can be done by the growth of non homogeneous x-ratio in depth of CIGS thin films. In this work, we develop two approaches to create band gap grading in CIGS thin films; (1) modifying the growth profile and (2) using Na incorporation in the growth process. The effects of Ga-graded would be revealed and compared with homogeneous CIGS thin films. CIGS thin films were grown on soda-lime glass and Al_2O_3 coated soda-lime glass substrates by molecular beam deposition method. The growth process was based on 2-stage and 3-stage growth profiles. The as grown films were characterized for their structural property, chemical composition and optical transmission as well as solar cell performance. The Auger electron spectroscopy in depth profiles revealed the variation of x- ratio increasing from the surface toward the back contact in CIGS films with our modified growth profile and Na incorporation. This result indicated Ga-graded in CIGS thin films. The structural property of Ga-graded CIGS films showed the (112) preferred orientation of the chalcopyrite structure with a broad asymmetric spectrum related to the inhomogeneous structure. The optical transmission measurements of the Ga-graded CIGS film showed the broad transition near the absorption edge indicating the effect of the band gap grading as a result of the variation in depth of the Ga-content. From I-V measurements, the solar cell efficiencies significantly increase due to the advantages of Ga-graded constitute.

Introduction

Solar energy is an important alternative energy. It reduces the CO_2 emission and other greenhouse gases that are the cause of climate change and global warming problems [1]. Solar cell is a semiconductor device that can directly convert the light energy into the electrical energy by using a photovoltaic (PV) effect. Over the past three decades, the technology of solar cell has been developed in order to achieve high electrical conversion efficiency. Solar cells based on thin film technology have attracted commercials because of their high efficiency, low material usage and high yield processes. One of the most interesting thin film solar cells is $Cu(In,Ga)Se_2$ or CIGS based solar cell. CIGS solar cells are the 2nd generation of solar cell which have the high efficiency solar energy conversion. The world record of CIGS solar cells efficiency in lab scale is nearly 20 percent demonstrated by NREL [2].

CIGS is a ternary-compound semiconductor with a direct band gap. Due to its high absorption coefficient and sufficient long-term stability [3], it is then used as a photon absorber layer in high efficiency thin film solar cell with Ni-Al grid/ZnO/CdS/CIGS/Mo structure. A special property of CIGS material is that its band gap energy can be adjusted in the range between 1.04 -1.68 eV by

varying the [Ga]/([In]+[Ga] ratio (x). The composition of group III elements plays an important role to the performance of solar cell. The high efficiency solar cells of homogeneous CIGS thin films have been achieved with [Ga]/([In]+[Ga]) ratio about 0.3. A method that helps to increase the solar cell efficiency in CIGS thin film known as band gap grading has been proposed [4]. The variation of the band gap energy towards the back contact causes the electric field, namely back-surface field (BSF) [5]. It assists in sweeping electrons in the quasi-neutral region of absorbers across the junction, resulting in the increase of the minority carrier's life time and diffusion length as well as reduction of the recombination [6]. Thus the solar cell efficiency improves by the increase of probability for carrier collection. The variation of Ga-content in CIGS thin film can be obtained by growing the non-homogeneous [Ga]/([In]+[Ga]) ratio at different depths in the CIGS film. However, there is a trade-off between the increase of carrier collection and the loss of created electron-hole pair from low-energy photons due to the increase in band gap. The band gap grading is beneficial in reducing the thickness of the absorber layer. The optimization would be calculated by simulation and verified by experiment.

In order to obtain band gap grading, we develop two approaches (1) modifying the growth profile; the standard 2-stage was modified into double Ga-graded profile and (2) using Na incorporation; Na precursor was incorporated before the growth process was begun. O. Lundberga *et al*. reported the effect of Na on diffusion of Ga and In in CIGS thin film. The presence of Na reduces the inter-diffusion of In and Ga that could be observed in the broad peak of X-ray diffraction [7]. The properties of Ga-graded CIGS films such as chemical composition in depth profile, structural orientation and optical transmission as well as device performance were studied and compared with the standard homogeneous CIGS thin film solar cell.

Methodology

Substrate preparation

SLG commercial substrates (2 mm thick with the area of 3×3 cm^2) were sonicated in an ultrasonic bath with a mixture of detergent and deionized water at 60ºC for one hour. Then, the substrates were rinsed with deionized water and ultrasonic cleaned again in deionized water at 60ºC for one hour to completely decompose the detergent. Finally, the substrates were dried with compressed nitrogen gas. To reduce or block sodium from SLG, the Al_2O_3 films (alkaline barrier) were deposited on the SLG substrate using a 4-inch Al_2O_3 target. The thickness of Al_2O_3 layer was about 800 nm. The Al_2O_3 film was an amorphous structure, smooth surface with a nanoscale grain size. Then Mo films were deposited on SLG by DC magnetron sputtering from 4 inch in diameter Mo target using Univex 350 sputtering system. The thickness was about 0.6 μm. Note that, Mo/SLG and Mo/Al_2O_3/SLG substrates were used in the 1st approach and 2nd approach, respectively.

Growth profile of CIGS thin film

$CuIn_{1-x}Ga_xSe_2$ thin films were grown by molecular beam deposition (MBD) technique using molecular beam epitaxial (MBE) system (EIKO EW100) under a based pressure of 10^{-9} Torr. The element sources of Cu, In, Ga and Se were evaporated form Knudsen cells (K-cells) and the temperatures of these sources were calibrated by quartz crystal monitor (QCM) and beam flux monitor for the corresponding compositions of each element. The *in situ* monitoring signals were employed for process control and end point detection (EPD) [8].

The 2-stage growth process was used in the growth of the CIGS films as shown in Fig. 1(a). For the standard growth profile, the [Ga]/([In]+[Ga]) ratio (x) was always a constant x=0.3 (thick line) and [Cu]/([In]+[Ga]) ratio (y) was constant at 1.2 in the 1st stage. The substrate temperature was 550°C. The growth process time was about 160 minutes which typical yield the thickness of CIGS of about 1.5 μm. In the 1st approach, we modified 2-stage profile and used only a half process time (80 minutes) with the decreasing of substrate temperature (480°C). The profile began with x=1.0 about 25% of the process time and subsequently deposits with x=0 about 50% of the process time. Finally, In, Ga and Se vapor with x=0.35 were supplied until the end of the process as seen in Fig.

1(b). The process time was within 80 minutes for 0.7 μm thick of Ga-graded CIGS film. From the assumption, the inter-diffusion of Ga and In between the interface layer could create the variation of Ga-content.

The 3-stage process was used in the growth of high quality $Cu(In,Ga)Se_2$ thin film. The growth profile was shown in Fig. 1(c). The process started with the deposition of In, Ga and Se at a substrate temperature (T_{sub}) of 340°C in the first stage for a formation of $(In,Ga)_2Se_3$ layer. In the second stage, only Cu and Se vapors were allowed at T_{sub} of 550°C at which there was a transformation from $(In,Ga)_2Se_3$ layer via γ-CI(G)S and β–CI(G)S to α–CI(G)S. The formation of polycrystalline $Cu(In,Ga)Se_2$ occured until the composition of film is slightly Cu-rich (y>1) at the end of the second stage. Our standard three-stage process used y = 1.2. During the last stage, the deposition of In, Ga and Se at T_{sub} of 550 °C converted excess Cu_xSe entirely into Cu-poor at EPD (y=0.9). The duration of the growth process was about 90-120 minutes which typically yielded the thickness of CIGS of about 1.25-1.5 μm. In the 2nd approach, we studied the effects of Ga-graded due to Na incorporation. NaF precursors as a Na source with 50 Å thick were evaporated on $Mo/Al_2O_3/SLG$ substrates before growing the CIGS film. The critical thickness was optimized to gain the maximum solar cell efficiency.

The microstructure of the as grown films was characterized by scanning electron microscope (SEM). The crystal structure was measured by X-ray diffraction (Bruker model D8 x-ray diffractometer) and the chemical composition of CIGS was revealed by Auger electron spectroscopy (PHI700 AES) in the depth profile.

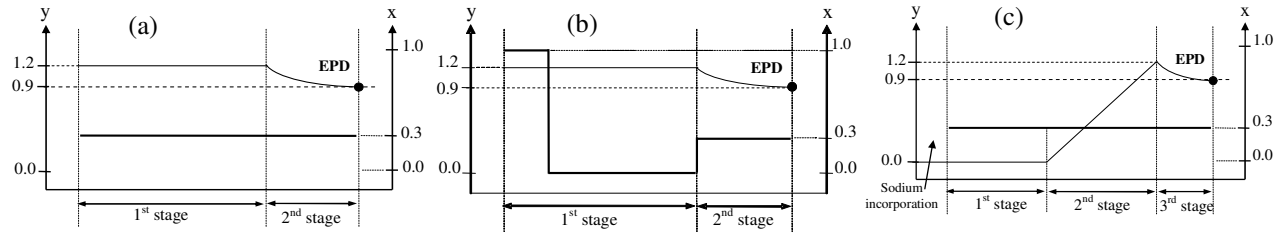


Fig. 1 The growth profile of CIGS thin films; (a) two-stage (b) modified two-stage and (c) three-stage with sodium incorporation where [Cu]/([In]+[Ga]) ratio (y) and [Ga]/([In]+[Ga]) ratio (x).

Solar cell fabrication

Photovoltaic devices were then prepared by chemical bath deposition (CBD) of 500 Å of CdS, followed by RF magnetron reactive sputtering of about 500 Å of intrinsic ZnO and 5000 Å of Al-doped ZnO. The solar cell devices were completed by the evaporation of 2 μm of Ni/Al grid contacts though a metal mask. The sample consisted of 10 solar cells per sample. The total area of each cell was about 0.5 cm^2 with approximately 2.5% shading loss. The current-voltage characteristics and device efficiencies were obtained by I-V solar simulator (YSS-50A).

Results and Discussion

Microstructure and Structural Property

SEM was used to characterize microstructure of CIGS thin films. The surface morphologies of the CIGS films typically showed rough surface consisting small and large grains as illustrated in Fig. 2. The CIGS film grown by modifying 2-stage had smoother surface than the film grown by 2-stage profile as seen from Fig. 2(b). The CIGS films grown on $Mo/Al_2O_3/SLG$ substrate showed flat round grains as shown in Fig. 2(c), whereas the CIGS films grown with Na incorporation on $Mo/Al_2O_3/SLG$ revealed relatively sharp grains as shown in Fig. 2(d). These results indicate that the growth profile and Na incorporation affected to the surface morphology of the CIGS films.

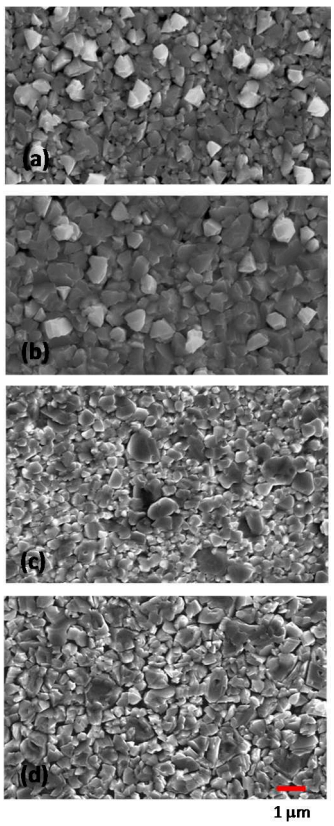


Fig. 2 Surface morphologies of the CIGS films grown by (a) standard 2-stage profile (b) modified two-stage (c) standard 3-stage profile and (d) Na incorporation in 3-stage profile.

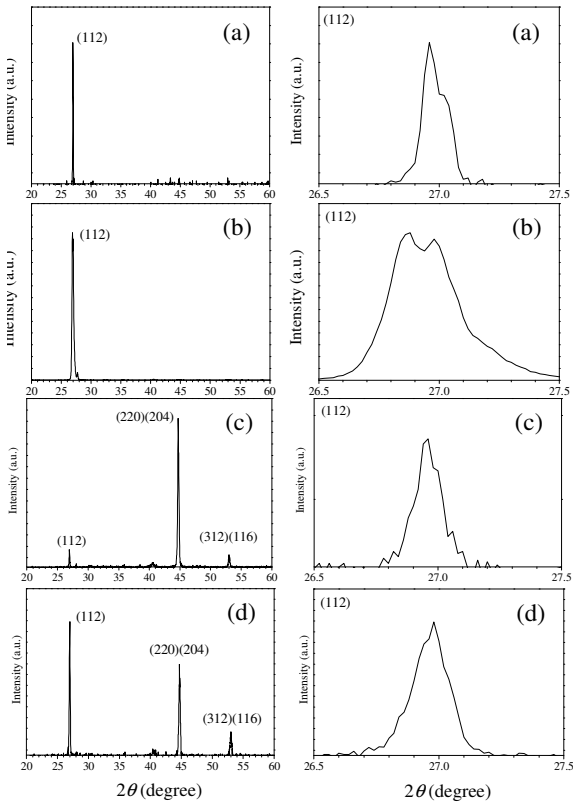


Fig. 3 XRD spectra of the CIGS films grown by (a) standard 2-stage profile (b) modified two-stage (c) standard 3-stage profile and (d) Na incorporation in 3-stage profile.

The structural property was determined from X-ray diffraction (XRD) as shown in Fig. 3. CIGS films grown by 2-stage profile showed (112) preferred orientation of the chalcopyrite structure. The standard CIGS film had a high sharp intensity peak corresponding to the homogeneous structure. However, the (112) oriented peak of the Ga-graded film had a broad asymmetric spectrum related to the inhomogeneous structure as seen in Fig. 3(b).This result indicated the variation of lattice constant due to the variation of [Ga]/([In]+[Ga]) ratio inside the CIGS film. XRD spectra of 3-stage CIGS films revealed that the CIGS thin films showed (220)(204) preferred orientation chalcopyrite structure that dominated by nature of three-stage growth process as seen in Fig. 3(c). However, Na affected to the change of preferred orientation from (220)(204) to (112) as seen in Fig. 3(d).

By considering the centers of the (112) CIGS peaks, they were nearly at the same positions in 2-stage and 3-stage profiles excepted in the modified 2-stage. Note that, the second peak with half intensity occurred by $Cu_{K\alpha 2}$ x-ray sources. The changes of preferred orientation directly related to the appearance of the surface morphology as seen from SEM images. The increase of (112) texture leaded to the increase of sharp grains that looked like the triangle shape. And the increase of (220)(204) texture leaded to the increase of flat grains as seen from surface morphology.

Optical Transmission (%T)

Optical property of semiconductor films could be determined by transmission and reflection measurements. Perkin Elmer model Lamba 900 double beam spectrometer in the wavelength 200-2600 nm was used to measure the CIGS thin films on an area of uncoated Mo film. The optical transmittance of the selective standard 2-stage and modified 2-stage CIGS films were shown in Fig. 4. We could see that the Ga-graded CIGS film had the lower thickness according to the number of interference fringes. The standard 2-stage CIGS film showed a sharp cut off band edge with small band tail near the absorption edge. The energy gap of 1.22 eV was calculated from both sharp cut

off and center of (112) peak in the following XRD result. For the modified 2-stage CIGS film, the band gap could not be calculated due to a broad of absorption band edge. This result indicated the variation of band gap grading CIGS film due to the Ga-graded.

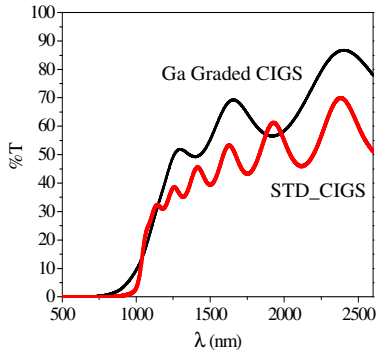


Fig.4 Optical transmission spectra of the CIGS film grown by (a) standard 2-stage profile (b) modified two-stage.

Auger electron spectroscopy depth profile

The compositional depth profiles of the CIGS films were characterized by Auger electron spectroscopy (AES). The depth profiles of the 2-stage and Ga-graded CIGS films were shown in Fig. 5(a) and 5(b). It revealed that the standard CIGS film had a uniform [Ga]/([In]+[Ga]) ratio about 0.3. However, the modified 2-stage CIGS films had the variation of [Ga]/([In]+[Ga]) ratio that increased from the surface toward the back contact due to the inter-diffusion of Ga and In between the interface layer. In another approach, the variations of [Ga]/([In]+[Ga]) in the film with Na incorporation could be observed but the slope was less than the modified 2-stage as shown in Fig. 5(d). The Ga grading was automatically obtained in the films with Na incorporation in 3-stage growth profile. In other words, Na affects the inter-diffusion between In and Ga in the CIGS film during the growth process of CIGS films. We suggested that Na atom would disturb the mobility of Ga that created Ga-graded through the back contact.

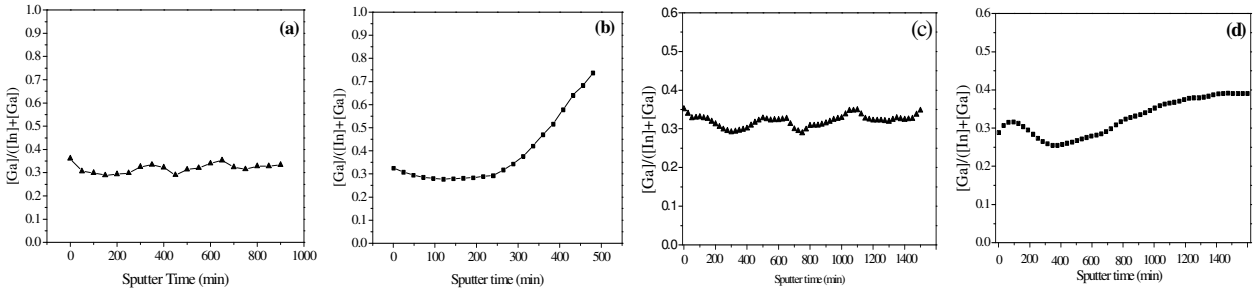


Fig. 5 AES depth profiling for the CIGS film grown by (a) standard 2-stage profile (b) modified two-stage (c) standard 3-stage profile and (d) Na incorporation in 3-stage profile.

Device Performance

The average device performances obtained from the I-V measurement were shown in Table 1. The standard 2-stage CIGS solar cells had the efficiency about 14% with 1.5 μm thick of absorber layer. However, we achieved the efficiency of 14% with only 0.7 μm thick of absorber layer by using the Ga-graded CIGS solar cells. It could be seen from the increasing of the short circuit current density as expected from band gap grading in the absorber layer. The solar cell using Mo/Al_2O_3/SLG substrate had a relatively lower efficiency compared to that of the solar cell using Mo/SLG substrate. It could be seen from the decrease of open circuit voltage (V_{oc}) and fill factor (*FF*). The decrease of V_{oc} directly corresponded with the mainly decrease of doping level or p-type defects in the CIGS film because the internal Na diffusion was interrupted by the Al_2O_3 barrier [9]. This result indicated the necessary of Na incorporation in CIGS thin film solar cells. However, the solar cell using a small amount of Na incorporation on Mo/Al_2O_3/SLG substrate showed the significantly increasing of the V_{oc}, *FF* and the solar cell efficiency. The increasing of the V_{oc} and *FF* related to

the increase doping in CIGS films and the junction formation respectively. The improvement of crystal quality and the increase of p-type defects as well as constitute of Ga-graded were the main parameters to gain the solar cell efficiency.

Table 1 Device performance of CIGS and Ga-graded CIGS solar cells; where V_{oc} = open-circuit voltage, J_{sc} = short-circuit current density, FF = fill factor and η = efficiency

Sample	V_{oc} (mV)	J_{sc} (mA/cm^2)	FF (%)	η (%)
2-stage Profile	620	32.7	70	14.2
Modified 2-stage Profile	600	34.5	70	14.5
3-stage Profile	530	33.6	61	10.6
Na incorporate 3-stage profile	651	35.5	67	15.5

Conclusion

We have obtained the approaches to grow the Ga-graded CIGS thin films for increasing the efficiency solar cell. AES confirmed the variation in depth of composition, i.e. [Ga]/([In]+[Ga]) ratio that increased from the surface toward the back contact by modifying growth profile and using Na incorporation. The XRD spectrum of Ga-graded films showed the broad asymmetric intensity with variations of lattice. The optical transmittance showed the variation of band gap in Ga-graded CIGS absorber. Because of the lower material used and the device performances increasing compared with standard device, these were the advantages of Ga-graded due to the band gap grading in CIGS thin film solar cells.

Acknowledgment

The authors would like to thank the Department of Physics, Faculty of Science, Chulalongkorn University for financial support as well as the Department of Geology, Faculty of Science, Chulalongkorn University for allowing us to use their XRD. Finally, we gratefully acknowledged Dr. Suwat Sopitpan at Thai Microelectronics Center (TMEC) for his help on AES.

References

[1] M.Z. Jacobson, Review of Solutions to Global Warming, Air Pollution, and Energy Security, Energy Environ. Sci. 2 (2009) 148-173.

[2] I. Repins, M. Contreras, B. Egaas, C. DeHart, J. Scharf, C. Perkins, B. To, R. Noufi, 19.9%-efficient ZnO/CdS/CuInGaSe$_2$ solar cell with 81.2% fill factor, Prog. Photovolt. Res. Appl. 16 (2008) 235–239.

[3] R.W. Birkmire. Compound polycrystalline solar cells: Recent progress and Y2K perspective, Sol. Energy. Mater. Sol. Cells 65(1-4) (2001) 17-28.

[4] J. Song, S.S. Li, C.H. Huang, O.D. Crisalle, T.J. Anderson, Device modeling and simulation of the performance of Cu(In$_{1-x}$,Ga$_x$)Se$_2$ solar cells, Solid-State Electronics 48 (2004) 73–79.

[5] M. Gloeckler, J.R. Sites, Band-gap grading in Cu(In,Ga)Se$_2$ solar cells, J. Phys. Chem. Solids 66 (2005) 1891–1894.

[6] O. Lundberg, M. Edoff, L. Stolt, The effect of Ga-grading in CIGS thin film solar cells, Thin Solid Films 480-481 (2005) 520–525.

[7] O. Lundberg, J. Lu, A. Rockett, M. Edoff, L. Stolt, Diffusion of indium and gallium in Cu(In,Ga)Se$_2$ thin film solar cells, J. Phys. Chem. Solids 64 (2003) 1499–1504.

[8] C. Chityuttakan, P. Chinvetkitvanich, K. Yoodee, S. Chatraphorn, In situ monitoring of the growth of Cu(In,Ga)Se$_2$ thin films, Sol. Energy Mater. Sol. Cells 90 (2006) 18-19.

[9] R. Sakdanuphab, C. Chityuttakan, A. Pankiew, N. Somwang, K. Yoodee, S. Chatraphorn, Growth characteristics of Cu(In,Ga)Se$_2$ thin films using 3-stage deposition process with a NaF precursor, J. Crystal Growth 319 (2011) 44-48.

Advanced Materials Research Vol. 936 (2014) pp 639-642
© (2014) Trans Tech Publications, Switzerland
doi:10.4028/www.scientific.net/AMR.936.639

Near-Field Broadband Light Transparency via Tunneling and Cavity Effects

Xiang-nan Zhang[1,a], Gui-qiang Liu[1,b]*, Zheng-qi Liu[1,c] and Yuan-hao Chen[1,d]

[1]Laboratory of Nanomaterials and Senors, College of Physics and Communication Electronics, Jiangxi Normal University, Nanchang 330022, China

[a]zxn0111@163.com, [b]*liugq@jxnu.edu.cn, [c]liuz@jxnu.edu.cn, [d]120427846@qq.com

Keywords: Light transparency; plasmon resonance; cavity effects; transmission.

Abstract: This work presents a broadband optical transparency structure consisting of a metal film perforated by an array of strip cavities. We theoretically demonstrate the metal film with side-coupled grooves system in model structure by the coupled model theory. The transparent light with a great bandwidth is obtained as a result of the tunneling and the resonance effect of the cavities by employing the finite-difference time-domain method simulation. By changing the parameter of the grooves in the structure, the transparency property shows a great adjustment in both wavelength and bandwidth. These structures have potential applications for transparent conductor devices.

Introduction

Surface plasmon polaritons (SPPs) are electromagnetic surface waves at an interface between metal and dielectric [1]. One typical way to realize the excitations and control the propagations of SPPs by incident light is to corrugate periodical subwavelength metallic grooves on the interface [2,3]. This way has attracted great attention due to its potential applications in optoelectronics, such as the enhancement of light absorption in solar cells and the optical elements of switching and transparent conductors. It is well known that metal transparent conductors are essential components of modern flat panel displays, and light emitting diodes (LEDs). On a flat metal surface, the electronic charges concentrate on the interface and decay exponentially into both media. As a result, the localized SPP modes occur in the grooves or grating, and the resonant tunneling effect caused by the excitation of standing waves of SPPs in the grooves on two opposite surfaces can lead to great enhanced transmission [4]. Therefore, thanks to the advantage of metal film with grooves or gratings, the study of resonant tunneling of localized SPP modes play an great important on the optical transparent phenomena both the fundamental theory and device applications. To the best of our knowledge, the extraordinary optical enhanced behaviors depend on the geometry shape of grooves largely [5].

In this paper, we theoretically demonstrate the transmission behavior in coupled grooves by using coupled model theory [6]. The thin metal film perforated grooves on the up or down sides are investigated respectively in this paper. Their optical properties are calculated and analyzed by employing the finite-difference time-domain (FDTD) method accompanied with the perfectly matched layer. The parameters of the shape of grooves are investigated to obtain the perfect transparent spectra in the metal film with grooves. After the analysis and optimization, a great broad near-field optical transparency is achieved in the metal film with one-side coupled grooves. These results may be helpful for the new study and designing of transparent conductor devices.

Structure Model and Simulation

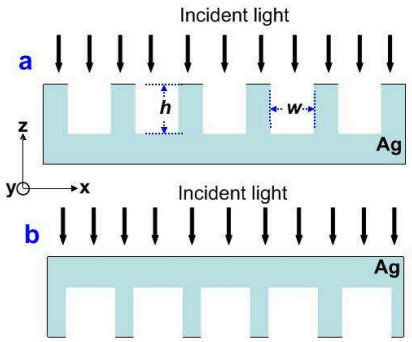


Fig. 1. Schematic diagrams of the optically transparent structure with upside (a) and downside (b) coupled grooves.

The proposed structures are shown in Fig. 1. Fig. 1 (a) shows the silver film with side coupled grooves on the upside, where the height and width of the rectangular grooves is denoted by h and w, respectively. Fig. 1 (b) shows the silver film with side coupled grooves on the downside. The light is directly incident on the top of the structures along the negative z axis direction. Periodic boundary conditions are utilized in the x and y directions and perfectly match layer (PML) boundary condition is employed in the z direction. The thickness of silver film is fixed at 60 nm. We first set h = 40 nm, w = 60 nm to study the optical phenomenon. The single groove can be considered as a lossy optical resonator. The resonant frequency can be tuned by the parameters of the grooves including h and w. Simulation calculations were performed using the three-dimensional (FDTD) method to obtain the optical transmission spectra.

It is necessary to note that the similar physical model in isolated groove acting as a Fabry-Pérot has been proposed by Lin *et al* [7]. When the light with transverse magnetic polarization is launched normally on the grooves, it will be reflected at both the mouth and the bottom of the grooves. The amplitude of the localized mode is a, the resonant frequency is ω_0. γ_{ref} and γ_{sca} represent the decay rate of reflected, and the scattering wave, respectively. γ_0 denote the total decay rate of a, which includes scattering, excitation of SPPs, and absorption in other channels, *i.e.* $\gamma_0 = \gamma_{sca} + \gamma_{spp} + \gamma_{ab.}$ s_{in} and s_{ref} represent normalized amplitudes of the incident and reflected waves, respectively. As a result, the reflectance is $R = |s_{ref}/s_{in}|$ the localized energy in the groove, expressed as $|a|^2$. The relationship equations can be obtained:

$$\frac{d_a}{d_t} = \left(j\omega_0 - \gamma_{ref} - \gamma_0\right)a + \sqrt{2\gamma_{ref}}\, s_{in} \tag{1}$$

$$s_{ref} = -s_{in} + \sqrt{2\gamma_{ref}}\, a \tag{2}$$

$$R = \frac{(\omega-\omega_0)^2 + (\gamma_{ref} - \gamma_0)^2}{(\omega-\omega_0)^2 + (\gamma_{ref} + \gamma_0)^2} \tag{3}$$

$$|a|^2 = \frac{2\gamma_{ref}}{(\omega-\omega_0)^2 + (\gamma_0 + \gamma_{ref})^2}\,|s_{in}|^2 \tag{4}$$

Results and Discussion

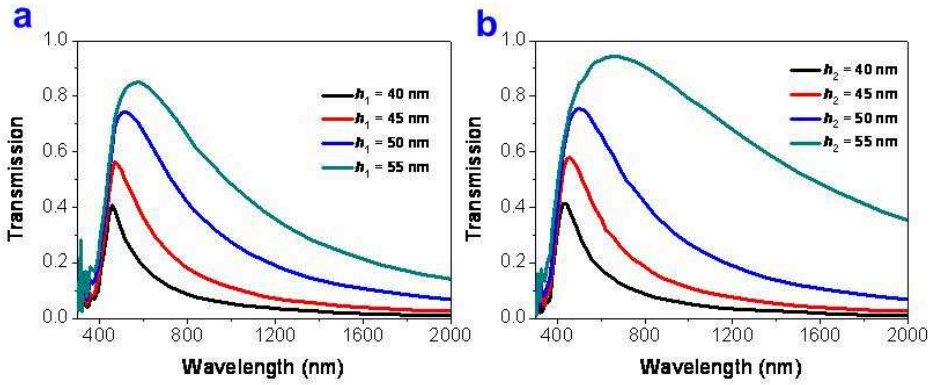


Fig. 2. The power transmission spectra of a pure Ag film perforated by an array of rectangular grooves on its upside (a), or on its downside (b) as a function of the height of the grooves. h_1, h_2 represent the height of the up and down groove, respectively. The width (w) is kept 60 nm.

The transmission behaviors of the proposed structure with the upside coupled grooves and the downside coupled grooves are investigated respectively, as shown in Fig. 2 (a) and (b). Clearly, the transmission intensity show a great increase accompanied by a slightly red-shift in peak position as h_1 changes from 40 to 55 nm. The tremendous increase in bandwidth is also observed. The transmission maximum is exceeding 88% and the bandwidth ($T > 50\%$) is even over 600 nm, shown in Fig. 2(a). And T is transmittance. In addition, it is interesting to note similar responses are also observed in Fig. 2(b), which indicates the same physical mechanism in the downside coupled grooves structure. The higher transmission intensity with broader bandwidth occurs when h_2 increases. The transmission maximum even exceeding 95% with the bandwidth ($T > 50\%$) over 1200 nm is obtained, which implies the tunneling effect in downside grooves structure is more efficient than that in upside grooves structure. The change of transmission behaviors result from resonant mode depends on the shape of the grooves. The tunneling and cavity resonant effect mainly contribute to the broadband transparent property in our proposed structures.

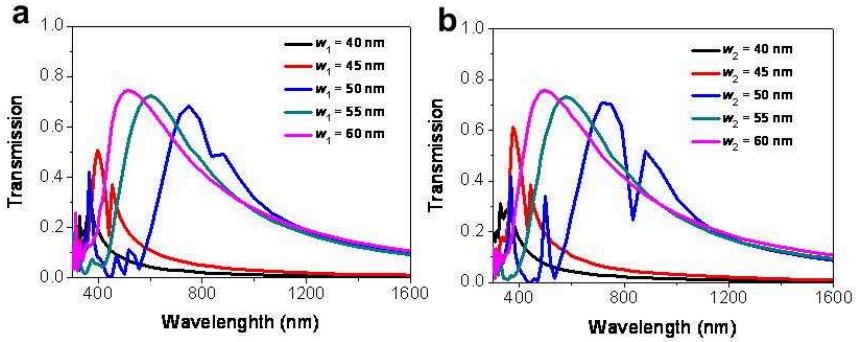


Fig. 3. The power transmission spectra of a pure Ag film perforated an array of rectangular grooves on its upside (a), on its downside (b) as a function of the width of the grooves. w_1, w_2 represent the width of the up and down groove, respectively. The height (h) is kept 50 nm.

Inspired of the extremely broad transparency phenomenon by changing the height of grooves, we further investigate the effect of the width on the spectra response. Contrast with the red-shift in Fig. 2 (a) and (b), an obvious blue-shift is observed in Fig. 3 (a) and (b) as a function of the width of the grooves in the structures. The wavelength center position of peak with high transmission intensity

changes from 800 nm to 500 nm. The transmission maximum is close 0.78 and the bandwidth is over 300 nm when w_1 is set to 60 nm. In addition, the spectra in two structure are very similar, which indicates the same physical mechanism both the tunneling and cavities effects are suitable for the structure with downside coupled grooves. In addition, the tunneling effect is more intense in the downside coupled groove structure, causing a more transparent bandwidth. These results indicate our structure has great potential applications in transparent conductor devices due to its highly tunable peak position and bandwidth and the perfect conductivity of silver.

Summary

In this paper, we theoretically investigate two metal transparent structures of the thin metal film with upside or downside coupled grooves. A great broad transparent with high transmission is obtained due to the tunneling and cavity model effects in the grooves in our structures. The FDTD with perfect matched layers are employed to calculate the optical transmission response. The peak position and transparent bandwidth show a great adjustable property by changing the height and width of the grooves in our proposed structures. After the analysis and optimization, the transmission maximum exceeding 95% with the bandwidth (T > 50%) over 1200 nm in optical frequency range is obtained in the upside coupled grooves structures. It has potential applications for solar cells and other optoelectronic devices. These results may be helpful for the new study and designing of transparent conductor devices.

Acknowledgments

Work was funded by the National Natural Science Foundation of China (Nos.11004088, 11264017), Natural Science Foundation of Jiangxi Province (No. 20122BAB202006), Scientific and Technological Supporting Projects of Jiangxi Province (No.20112BBE50033), and Jiangxi Provincial Education Department (No.GJJ13234).

References

[1] W. L. Barnes, A. Dereux, T.W. Ebbesen. Surface plasmon subwavelength optics, Nature. 424 (2003) 824-830.

[2] N. Anttu, Z.Q. Guan, U. Hakanson, H. X. Xu, H. Q. Xu. Excitations of surface plasmon polaritons in double layer metal grating structures, Appl. Phys. Lett. 100 (2012) 091111-091111-3.

[3] Z.Q. Liu, G.Q. Liu, X.S. Liu, K. Huang, Y.H. Chen, Y. Hu, G.L. Fu, Tunable Plasmon-induced transparency of double continuous metal films sandwiched with a plasmonic array, Plasmonics. 24 (2013) 1-8.

[4] Y.C. Lan, C.J. Chang, P.H. Lee, Resonant tunneling effects on cavity-embedded metal film caused by surface-plasmon excitation, Opt. lett. 34 (2009) 25-27.

[5] A.C.R. Pipino, G.C. Schatz, Surface-profile dependence of photon-plasmon- polariton coupling at a corrugated silver surface, JOSA B. 11 (1994) 2036-2045.

[6] H.A. Haus, Wave and fields in optoelectronics. Prentice-Hall, New Jersey, 1984.

[7] X.S. Lin, S. Lan, Design of optical filters with flat-on-top transmission lineshapes based on two side-coupled metallic grooves, Plasmonics. 8 (2013) 283-287.

Advanced Materials Research Vol. 936 (2014) pp 643-650
© (2014) Trans Tech Publications, Switzerland
doi:10.4028/www.scientific.net/AMR.936.643

Modification of epoxy Resin with Silicone for Electronic Encapsulation Application

Lixin Chen[1,a*], Lingyu Fan[2,b] and Lishuai Gao[3,c]

[1,2,3]Department of Applied Chemistry, School of Science, Northwestern Polytechnical University, Xi'an, 710072, China

[a*]lixin@nwpu.edu.cn, [b]fanfly1701@163.com, [c]497306793@qq.com

Keywords: DHDPS, PTS, Epoxy resin, Modification, Encapsulant

Abstract: The reaction was carried out with a solventless (hot-melt) method using epoxy resin (E-20) as a base material and dihydroxydiphenylsilane (DHDPS) or polymethyltriethoxysilane (PTS) as a modifier. IR spectrum, epoxy value of modified epoxy resins indicated that DHDPS and PTS were incorporated into epoxy resin respectively. The influences of silicone contents on softening point and thermal resistance of cured silicone modified epoxy resin systems were studied. The thermal stability was investigated by thermogravimetic analysis (TGA). Effects of the viscosity of packaging slurry on the performance of encapsulated electronic elements were also investigated. In contrast to ED-20 cured system, the thermal resistance, toughness, humidity resistance of ETS-20 cured systems improved more obvious. And ETS-20 has exhibited excellent resistance to the thermal shock cycling test. It indicated that ETS-20 can be applicated for electronic encapsulation. The viscosity of packaging slurry was most appropriate when it was 170~200 mPa•s.

Introduction

Epoxy encapsulat is one of the main materials used in encapaulation for semiconductor. It is composed of many raw materials, which contains epoxy resin, curing agent, curing accelereator, ionrganic filler, pigment, etc. Epoxy encapsulat is the resin indispensably employed to encapsulate electronic elements because of its wellbalanced properties including low curing shrinkage, excellent moisture, superior mechanical and electrical properties, and good adherence to many substrates [1,2,3]. However, in the crosslinked state, they are intrinsically brittle[4,5,6] with very low fracture energy [7]. Also, they have comparatively low hydrophobicity[8] and poor weathering resistance [9]. Major disadvantage for their application are their thermal resistance and low impact resistance [10,11]. The low pigment-holding ability and yellowing of epoxy resins further resist their wide application in coatings [12].

Hence, modification of epoxy resins with flexible polymeric segments like rubber, polyurethane, silicone and some other thermoplastics are mandatory as these modifiers when incorporated with epoxy resin have been proved to improve its thermal and mechanical properties [13-17]. Silicone is considered to be one of the suitable modifiers for epoxy resins, owing to its superior thermal and thermo-oxidative stability, excellent moisture resistance, low surface energy, free rotation of chains about Si-O bonds and good hydrophobicity [15,18]. However, silicones possess poor mechanical properties. The incorporation of silicone in epoxy resin results in the enhancement of physico-mechanical properties, thermal stability and so on. The latter can be attributed to the high bond dissociation energy of Si-O unit bond i.e. 443.7 KJ/mol, compared to those of C-O bond (357.9 KJ/mol) [4,19-21].

In recent years, there are more researches on silicone modified epoxy resins, but the properties of the modified epoxy resin encapsulat are reported relatively less. In this study, E-20 was modifide by DHDPS and PTS respectively through some chemical reaction. The structure of modified epoxy resins (ED and ETS) were confirmed by FT-IR. The physicochemical test such as epoxy values

(EV), softening point were carried out by ring and ball method. ED and ETS were further formulated into encapsulant and packaging slurry. The coating vehicle was cured by trimellitic anhydride (TMA) and aluminum(III) acetylacetonate. The performance of ED and ETS cured systems and packaging slurries were evaluated by standard methods. The electronic elements encapsulated by modified epoxy resins were also evaluated by the thermal shock cycling test.

Experimental

Materials

Epoxy resin, E-20 (epoxy equivalent 455–556, softening point 64~76°C).

DHDPS and PTS were used as modifiers. Stannous octanoate (the concentration of petroleum ether liquor is 30%) and dibutyltindilaurate (DBTDL) were used as catalysts. TMA was used as a curing agent. Aluminum(III) acetylacetonate was used as a curing accelerator. Filler were used as extenders. Acetone and methanol were used as solvents.

Synthesis of DHDPS-modified epoxy resin

E-20 was placed in a three-necked flask fitted with a mechanical stirrer, thermometer and a reflux condensation unit. The resin was melted at 120°C for 30 min under a reduced pressure (ca. 37.5 mm Hg) to remove water and solvent. The melted epoxy resin and DHDPS in 10:0.5, 10:1, 10:2 ratio (by weight) was taken into the three-necked flask. 1% (mass fraction) of stannous octanoate was added. The reactants was maintained at 120°C along with constant stirring for 2h. Epoxy values and softening point of modified epoxy resins (EDs) were determined. The structure of ED was confirmed by FT-IR spectral analysis.

Synthesis of PTS-modified epoxy resin

E-20 was placed in a four-necked flask fitted with a mechanical stirrer, thermometer, a reflux condensation unit and a constant pressure funnel. The resin was melted at 120°C for 30 min under a reduced pressure (ca. 37.5 mmHg) to remove water and solvent. The melted epoxy resin and PTS in 10:1, 10:2, 10:3 ratio (by weight) was taken into the four-necked flask when the temperature fell to 100°C. A few distilled water and 0.5% (mass fraction) of DBTDL was added in drops within 20~30 min and then maintained for 4h at 100°C. The resultant product was further removed small moleculars which were produced during the progress of the reaction under full vacuum for 30 min at 100°C. Epoxy values and softening point of modified epoxy resin (ETSs) were determined. The structure of ETS was confirmed by FT-IR spectral analysis.

Curing procedure

The unmodified and the modified epoxy resins were dissolved in cetone in 3/1 ratio (by weight) and mixed with a stoichiometric amount of TMA. Moderate Aluminum(III) acetylacetonate was also added as a curing accelerator. The mixture was stirred uniformly and transferred to a vacuum oven to remove the solvent. The solvent-free epoxy/curing agent system was cured at 120°C for 2h and then post-cured at 160°C for 2h.

Characterizations

The pure epoxy (E-20) and silicone modified epoxy resins were characterized by FT-IR spectroscopic techniques. FT-IR spectra of these resins were taken on a model WQF-310 FT-IR spectrophotometer (The second optical instrument factory, Beijing, China) with KBr pellet. The thermal analyses of these resins was carried out via thermogravimetric analysis (TGA) (SDTQ600, TA Instrument, USA) in nitrogen atmosphere. Scanning electron micrograph (SEM) of fracture surfaces of cured resins were also taken on a model VEGA 3 XMU/XMH tester (TESCAN Instrument, CZE) scanning electron microscope under gold film.

Formulation of silicone modified epoxy resins-based packaging slurries

The modified resin, curing agent, curing accelerator, filler were weighed according to a certain proportion. In order to obtain even powder encapsulant, the mixture was premixed under a mill machine with high speed. In this study, electronic elements were encapsulanted by solvent method. The packaging slurry was made of powder encapsulants and mixed solvent of acetone and methanol.

Testing of silicone modified epoxy encapsulant

The fluidity of powder encapsulant was characterized by the length of flow trace (WH/WI-03) and the gel time (IEC 60455-2-2). The viscosity of packaging slurry was measured via a model NDJ-79 rotational viscometer. The encapuslated film hardness was measured by a QHQ-A type pencil hardness test apparatus. The physical properties such as water absorption, drying time, solvent resistance and temperatureshock strength were evaluated by standard methods.

Results and discussion

Synthesis and characterization

Stannous octanoate which is known as a condensation catalyst is used to aid the reaction between the OH or silanol groups of silicone and the groups of epoxy resin. There will be two kinds of reactions between the OH of DHDPS and epoxy resin. The one is the ring opening addition reaction of epoxy groups with DHDPS, the other one is the condensation reaction of OH groups of epoxy resin with DHDPS. In addtion, the autocondensation between DHDPS will also take place. Table 1 shows an reduce in the epoxy values from pure epoxy to siloxane-modified epoxy system. In contrast to the theoretical values of epoxy values, which dose't consumpt epoxy group during the reaction, the measured values are lower. This shows that the ring opening addition reaction has occured.

Compared with stannous octanoate, the catalytic activity of DBTDL is lower. Due to Si-OR is sensitive to water, the PTS will produce more pendent functional groups of OH under catalysis. In this study, DBTDL was used to aid the polycondensation reaction between the OH groups of silicone and the OH groups of epoxy resin. The measured and calculated EV of PTS-modified resins and pure epoxy are listed in Table 2. EV calculation is made based on the proposed reaction which doesn't involve the ring opening of the epoxy.

TABLE 1 EPOXY VALUES OF E-20/DHDPS SYSTEMS

m(E-20):m(DHDPS)	Theoretical value/(eq/100g)	Measured value/(eq/100g)
10:0	0.214	0.214
10:0.5	0.204	0.179
10:1	0.195	0.172
10:2	0.178	0.153

TABLE 2 EPOXY VALUES OF E-20/PTS SYSTEMS

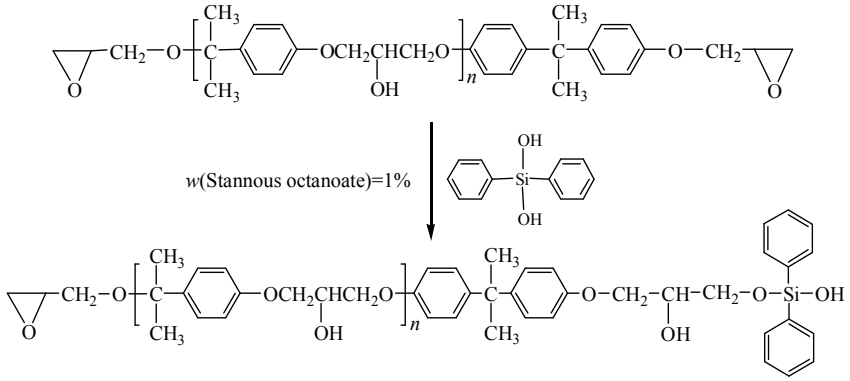
m(E-20):m(PTS)	Theoretical value/(eq/100g)	Measured value/(eq/100g)
10:0	0.214	0.214
10:1	0.195	0.189
10:2	0.178	0.178
10:3	0.165	0.164

Scheme 1 shows the chemical reaction between E-20 and DHDPS to form ED. Scheme 2 shows the hydrolysis of PTS. Scheme 3 shows the chemical reaction between E-20 and PTS to form ETS. The proposed structure of ED and ETS were confirmed by FT-IR.

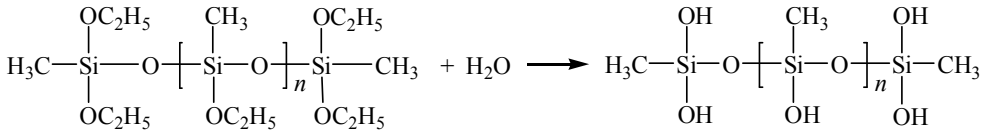
Pure epoxy (IR, cm^{-1}): 1297–1182 (C-O-C, aryl alkyl ether, asym str), 1087 (aryl alkyl ether, sym str), 2964 (-CH_3 of quaternary carbon), 3036, 1581, 828, 770 (aromatic rings, str), 2929 (-CH_2 sym str), 2871 (-CH_2 asym str), 912.7 (oxirane ring), 1384 $(CH_3)_2C$), 3432.5 (-OH) [4].

In case of IR spectra of ED, the bands of oxirane ring are found to be shorter than those of pure epoxy; the band at 3432.5cm^{-1} for the OH stronger. A characteristic pronounced band appears at 1127.4cm^{-1} for Si-O-C confirming the occurrence of ring opening addition reaction between epoxy and DHDPS [17,19]. The chemically bonded silicon in the back bone of the silicone modified epoxy resin enhance the stiffness, thermal stability and hydrophobicity of the resin, which ultimately influence the physico-mechanical.

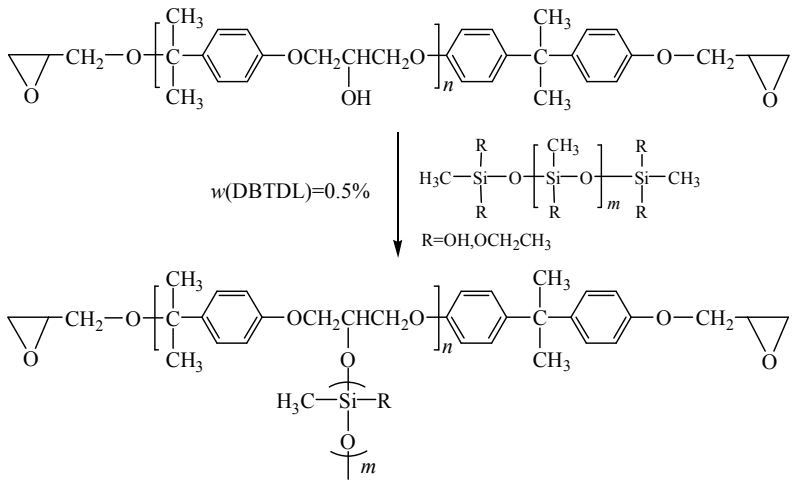
From the IR spectra of ETS, the bands of oxirane ring are almost invariant. The Si-O-C absorption at 1107.7 cm^{-1} can be seen in Figure 1 (C) [17,19]. The reaction between E-20 and PTS can form a modified epoxy resins with moderate crosslinking density, which can not only reduce the internal stress of epoxy resin, improve the compatibility of the systems, but also enhance the thermal stability and so on.



Scheme 1 Synthesis of ED



Scheme 2 The hydrolysis of PTS



Scheme 3 Synthesis of ETS

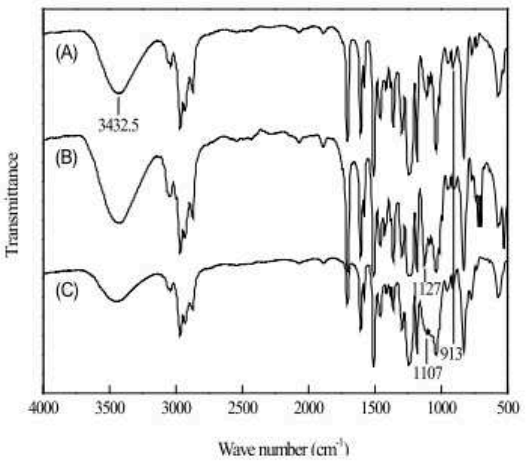


Fig.1 FTIR spectra of E-20 (A), ED (B) and ETS(C)

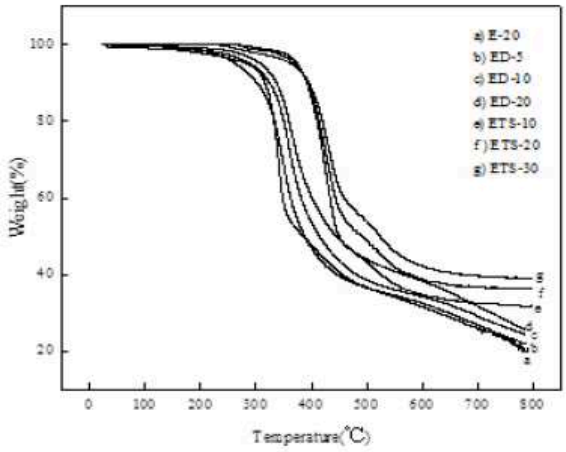


Fig.2 TGA thermogram for the cured systems E-20, DHDPS and PTS modified epoxy resin

Softening point analysis

The softening point has a great impact on the performance of epoxy encapsulat. On the one hand, the encapsulat shows good fluidity but is easy to sag with low softening point. On the other hand, the encapsulat shows poor fluidity, leveling, gloss and is easy to crust with high softening point. Thus the softening point is most appropriate when it is 65~90°C. Table 3 shows that the softening point of DHDPS-modified epoxy resins and ETS-20 meet the requirement.

TABLE 3 SOFTENING POINT OF MODIFIED EPOXY RESIN

Sample number	E-20	ED-5	ED-10	ED-20	ETS-10	ETS-20	ETS-30
Softening point /°C	67	66	67	65	58	66	62

Thermal analysis

The effects of different contents of silicone on the thermal stability of ED and ETS have been investigated by TGA. The results for TGA thermogram (Fig.2) of cured systems reveal that the temperature for 5 wt.% decomposition of E-20, ED-20 and ETS-20 are 263.8, 308.3 and 368.6 °C, respectively, while the tempareture for 50% weight loss are 382.3, 445.0 and 491.2 °C. And the residue percent of E-20, ED-20 and ETS-20 at 800 °C are 20.3%, 25.9% and 36.2%. These results also show that the presence of siloxane in epoxy noticeably enhances the thermal stability of E-20. The increase in thermal stability can be attributed to higher bond dissociation energy of Si-O bond [22]. In addition, it forms a moderate crosslinked network since PTS is introduced into epoxy resin, which contains more reactive groups. The crosslinked network can increase crosslinking degree, so that ETS has a greater improvement of thermal stability.

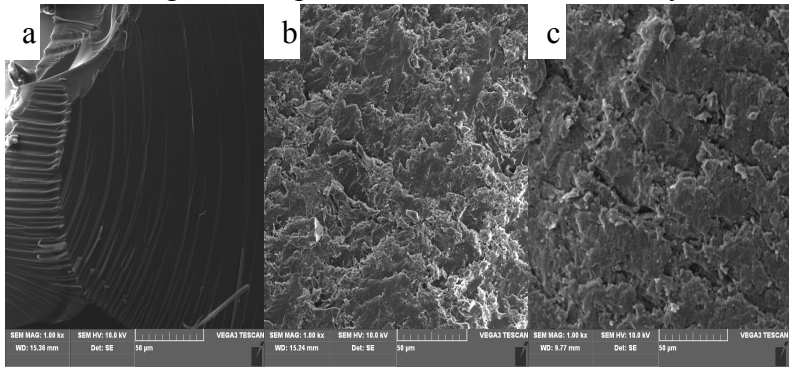


Fig.3 SEM micrograph of fractured surfaces of E-20 (a), ED (b) and ETS (c) cured system

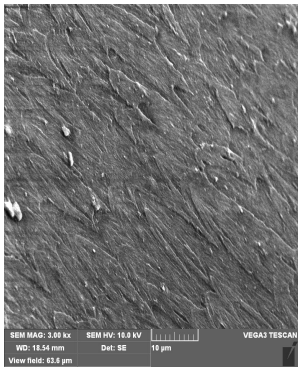


Fig.4 SEM micrograph of fractured surfaces of ETS-20

Scanning electron micrograph

The scanning electron micrograph (Fig.3) studies of unmodified and modified epoxy cured systems at 1000 magnifications show that the limits of fractured surface of unmodified epoxy resin is clear, and the propagating direction of the cracks is relatively concentrate. However, the limits of fractured surface of ED and ETS are blur, and the propagating direction of the cracks is dispersive. The above shows the toughening of silicone modified epoxy resins is obvious. Also Fig.4 shows no sign of phase separation of modified epoxy resin. The interface between epoxy resin and silicone is blur, which reveals the two are interconnected by chemicalbonds and have good compatibility.

The viscosity of packaging slurries

The influencing factors of the viscosity of packaging slurry include temperature, proportion of powders, solvent quantity, ect. The study between solvent quantity and the performance of encapsulation was carried out at a certain temperature and percentage of resin and filler. The performance of encapsulation and drying time are influenced by the viscosity of packaging slurry. As shown in Table 4, with increasing of the viscosity of slurry, the surface drying time is shortened. But the excessive viscosity will result in poor fluidity and leveling. Also with increasing of the viscosity of slurry, the actual drying time is lengthened. The actual drying time is more than 24h when the viscosity is 290 mPa•s, which dosen't meet the requirements of electronic encapsulation. The surface performance of cured encapsulated electronic elements is shown in Table 4. The surface occurs sag when the viscosity is less than 140 mPa•s. The surface is smooth and non-cracking when the viscosity is 170~200 mPa•s. The surface occurs cracks when the viscosity is more than 200 mPa•s. The solvent volatilizes uneasily in the internal of paint film at room temperature when the viscosity is excessive. And the solvent volatilizes quickly during high temperature curing, which lead to cracks on the surface of encapsulated electronic elements. By comprehensive consideration, the viscosity of packaging slurries is most appropriate when it is 170~200 mPa•s.

TABLE 4 EFFECT OF THE VISCOSITY ON THE PERFORMANCE OF ENCAPSULATION

Viscosity /mPa·s	140	170	200	230	260	290
Surface drying time	5h25min	5h10min	5h5min	4h55min	4h45min	4h20min
Actual drying time	＜24h	＜24h	＜24h	＜24h	＜24h	＞24h
Surface performance	sag	smooth/non-cracking	smooth/non-cracking	microcracks	microcracks	cracks

The properties of encapsulat powder and cured resins

Table 5 provides information about the properties of encapsulat powder and cured resins. A considerable improvemens were achieved in the water absorption, which can be attributed to the hydrophobic nature of the methyl or phenyl groups as well as the hydrophobic nature of the silicones, which hindered the ingress of water molecules [8,12].

The systems were subjected to an solvent resistance performance evaluation under solvents. The ED-20 and ETS-20 encapsulat systems showed a fair-to-satisfactory performance when immersed in mixed solvent [acetone:methanol (3:1) (m/m)] for 15 min after cured. The highly crosslinked network of ED-20 and ETS-20 hindered the easy penetration of solvent into the encapsulat system and thus enhanced the solvent resistance performance.

The pencil hardness of ETS-20 encapsulat systems is greater than ED-20 encapsulat systems. The result was in contrast to our expectations because DHDPS contains hard benzene rings,

whereas PTS have unusual flexibility on account of the flexible Si-O linkages and mobile silicone chains, which possess poor mechanical characteristics [12]. However, in this case, PTS incorporation actually enhanced the physicomechanical properties. It is assumed that in ETS-20 encapsulat systems, the siloxane behaves as chain entanglements rather than as a flexibilizer [11]. The long, mobile siloxane chains assist in the formation of a highly crosslinked network between two E-20 molecular units through a curing agent. Thus it leads to the formation of a highly crosslinked network and dense structure and results in a tremendous increase in the pencil hardness.

The modified epoxy resin were used to encapsulate the electronic elements and the encapsulated elements were subjected to a thermal shock cycling test. The thermal shock cycling test involves cycling the encapsulated elements at -55 and 125°C and observing the crack (failure) of encapsulated elements at a cycle (both of the low temperature and high temperature keep 30 min). The result indicates that failure happened after 3 cycles for ED-20 encapsulat. Compared with above, non-cracking occurs to ETS-20 encapsulated elements after 5 cycles. PTS-modified epoxy resin has much better thermal shock resistance and lower stress than ED-20.

TABLE 5 THE PROPERTIES OF ENCAPSULAT POWDER AND CURED RESINS

	Test condition	System		Reference
		ED-20	ETS-20	
Length of flow trace, mm	150°C, 45° inclined plate	28.14	27.31	18~30
Gel time, s	150°C	187	193	50~200
Water absorption, %	25°C/24h	0.34	0.36	⩽0.4
Solvent resistance	acetone:methanol (3:1) (m/m)	eligible	eligible	non-swelling, non-cracking, non-peeling
Pencil hardness	—	H	2H	⩾H
Thermal shock cycling test	-55°C~125°C	microcracks	non-cracking	non-cracking after 5 cycles

Conclusions

Modified epoxy resins (ED and ETS) were synthesized by the reaction of DHDPS and PTS with E-20 respectively. FT-IR was used to characterize the structure of the synthesized ED and ETS. The morphology of fractured surface of unmodified and modified epoxy resin cured systems was observed via SEM. It revealed that the two are interconnected by chemicalbonds and no sign of phase separation. The thermal analysis through TGA confirmed that the incorporation of Si into the E backbone had a synergistic effect on its thermal stability, especially ETS cured systems. Fairly good physicomechanical properties were achieved for ED-20 and ETS-20 encapsulat systems. Electronic elements encapsulated with ETS-20 encapsulat system have exhibited excellent resistance to the thermal shock cycling test. In addtion, the viscosity of packaging slurries was most appropriate when it was 170~200 mPa•s at a certain temperature and percentage of resin and filler.

References

[1] P. Khurana, S. Aggarwal, A.K. Narula, et al. Studies on the curing and thermal behaviour of DGEBA in the presence of bis (4-carboxyphenyl) dimethyl silane. Polym Int. 52 (2003) 908-917.

[2] E. Sharmin, L. Imo, S.M. Ashraf, et al. Acrylic-melamine modified DGEBA-epoxy coatings and their anticorrosive behavior. Prog Org Coat. 50 (2004) 47-54.

[3] T.H. Ho and C.S. Wang. Modification of epoxy resin with siloxane containing phenol aralkyl epoxy resin for electronic encapsulation application. Eur Polym J. 37 (2001) 267-274.

[4] S.S. Hou, Y.P. Chung, C.K. Chan, et al. Function and performance of silicone copolymer. Part IV. Curing behavior and characterization of epoxy-siloxane copolymers blended with diglycidyl ether of bisphenol-A. Polymer. 41 (2000) 3263-3272.
[5] S.A. Kumar and T.S.N.S. Narayana. Thermal properties of siliconized epoxy interpenetrating coatings. Prog Org Coat. 45 (2002) 323-330.
[6] S. Bhuniya and B. Adhikari. Toughening of epoxy resins by hydroxy-terminated, silicon-modified polyurethane oligomers. J Appl Polym Sci. 90 (2003) 1497-1506.
[7] S. Ahmad, S.M. Ashraf, A. Hasnat, et al. Studies on epoxidised oil and its blend with polystyrene and poly(methyl methacrylate). Indian J Chem Technol. 8 (2001) 176-180.
[8] T.V.T. Velan and I.M. Bilal. Aliphatic amine cured PDMS-epoxy interpenetrating network system for high performance engineering applications—Development and characterization. Bull Mater Sci. 23 (2000) 425-429.
[9] W.C. Shih and M.M.A. Chen-Chi. Tetrafunctional aliphatic epoxy I. Synthesis and characterization. J Appl Polym Sci. 69 (1998) 51-58.
[10] A.A. Kumar, M. Alagar and R.M.V.G.K. Rao. Studies on thermal and morphological behavior of siliconized epoxy bismaleimide matrices. J Appl Polym Sci. 81 (2001) 2330-2346.
[11] M. Alagar, A.A. Kumar, K.P.O. Mahesh, et al. Studies on thermal and morphological characteristics of E-glass/Kevlar 49 reinforced siliconized epoxy composites. Eur Polym J. 36 (2000) 2449-2454.
[12] S. Ahmad, S.M. Ashraf, S.N. Hassan, et al. Synthesis, characterization, and performance evaluation of hard, anticorrosive coating materials derived from diglycidyl ether of bisphenol A acrylates and methacrylates. J Appl Polym Sci. 95 (2005) 494-501.
[13] P.H. Sung and C.Y. Lin. Polysiloxane-modified epoxy polymer networks – I. Graft interpenetrating polymeric networks. Eur Polym J. 33 (1997) 903-906.
[14] H. Deligoz, T. Yalcinyuva and S. Ozgumus. A noval type of Sicontaining poly (urethane-imide)s: synthesis, chracterization and electrical properties. Eur Polym J. 41 (2005) 771-781.
[15] U. Lauter, S.W. Kantor, K. Schmidt-Rohr, et al. Vinylsubstituted silphenylene siloxane copolymers: noval high temperature elastomers. Macromolecules. 32 (1999) 3426-3431.
[16] P.R. Dvornic, H.J. Perpall, P.C. Uden, et al. Exactly alternating silarylene-siloxane polymers. VII. Thermal stability and degradation behavior of *p*-silphenylene-siloxane polymers with methyl, vinyl, hydrido, and/or fluoroalkyl side groups. Polym Sci Part A Polym Chem. 27 (1989) 3503-3514.
[17] A.A. Kumar, M. Alagar and R.M.V.G.K. Rao. Preparation and characterization of siliconized epoxy/bismaleimide (*N*,*N*-bismaleimido-4,4-diphenyl methane) intercrosslinked matrices for engineering applications. J Appl Polym Sci. 81 (2001) 38-46.
[18] J. Chojnowski, M. Cypryk, W. Fortuniak, et al. Controlled synthesis of vinylmethylsiloxane-dimethylsiloxane gradient, block and alternate copolymers by anionic ROP of cyclotrisiloxanes. Polymer. 43 (2002) 1993-2001.
[19] S. Ahmad, A.P. Gupta, E. Sharmin, et al. Synthesis, characterization and development of high performance siloxane-modified epoxy paints. Prog Org Coat. 54 (2005) 248-255.
[20] S.T. Lin and S.K. Huang. Preparation and structural determination of siloxane-modified sulfone-containing epoxy resin. J Polym Sci Part A: Polym Chem. 34 (1996) 869-884.
[21] G.H. Hsiue, W.J. Wang and F.C. Chang. Synthesis, chracterization, thermal and flame-retardant properties of silicone-based epoxy resin. J Appl Polym Sci. 73 (1999) 1231-1238.
[22] C.L. Homrighausen and T.M. Keller. Synthesis and chracterization of a silarylene-siloxane-diacetylene polymer and its conversion to thermosetting plastic. Polymer. 43 (2002) 2619-2623.

Advanced Materials Research Vol. 936 (2014) pp 651-655
© (2014) Trans Tech Publications, Switzerland
doi:10.4028/www.scientific.net/AMR.936.651

Effect of annealing oxygen flow rate on the properties of vanadium oxide films deposited by reactive magnetron sputtering

Huafu Zhang[1, a], Zhiming Wu[2,b], Xuefei Wu[3,c] and Yadong Jiang[4,d]

[1] School of Optoelectronic Information, State Key Laboratory of Electronic Thin Films and Integrated Devices, University of Electronic Science and Technology of China,Chengdu 610054, P. R. China

[2] School of Optoelectronic Information, State Key Laboratory of Electronic Thin Films and Integrated Devices, University of Electronic Science and Technology of China,Chengdu 610054, P. R. China

[3] School of Optoelectronic Information, State Key Laboratory of Electronic Thin Films and Integrated Devices, University of Electronic Science and Technology of China,Chengdu 610054, P. R. China

[4] School of Optoelectronic Information, State Key Laboratory of Electronic Thin Films and Integrated Devices, University of Electronic Science and Technology of China,Chengdu 610054, P. R. China

[a]huafuzhang@126.com, [b]zmwu@uestc.edu.cn

Keywords: Vanadium oxide; Annealing oxygen flow rate; Insulator-metal transition; Thin films

Abstract: Vanadium oxide films were prepared on indium-tin oxide glass substrates at low temperature by means of reactive direct current magnetron sputtering and subsequent in-situ annealing process in pure oxygen ambient. In the process of annealing, the oxygen flow rates were varied from 0 to 15 SCCM in order to investigate the effect of annealing oxygen flow rates on the properties of the deposited films. The experimental results indicate that only the vanadium oxide films annealed under relatively high oxygen flow rates (≥ 0.8 SCCM) displayed insulator-metal transition. In addition, it was found that vanadium valence states, surface morphology, optical transmittance and phase transition temperature of the deposited films were sensitive to the annealing oxygen flow rates while the width of thermal hysteresis was relatively insensitive to the annealing oxygen flow rates.

Introduction

Vanadium oxide (VOx) films have been intensively investigated due to their potential applications in switching elements, storage devices, smart windows and terahertz modulators [1-3]. Up to now, many techniques including reactive magnetron sputtering, pulsed laser deposition, laser ablation, chemical vapour deposition, ion implantation, polymer-assisted deposition and sol-gel method have been used to prepare VOx films [2-4]. Among these techniques, reactive magnetron sputtering is outstanding for low deposition temperature, high growth rate and good adhension [3]. For reactive magnetron sputtering, the annealing process is commonly needed in order to improve the properties of the deposited films. In the case of reactive magnetron sputtering, the annealing oxygen flow rate was a key parameter and would affect the films' properties. However, to the best of our knowledge, the effect of annealing oxygen flow rate on the properties of VOx films was rarely studied. Thus, it is necessary to investigate the effect of annealing oxygen flow rate on the properties of the sputtered VOx films.

In this work, VOx films were deposited by reactive direct current magnetron sputtering followed by in-situ annealing process in pure oxygen ambient. The effect of annealing oxygen flow rate on the vanadium valence states, surface morphology, optical transmittance and insulator-metal transition properties of the deposited films was investigated in detail.

Experimental details

VOx films were deposited on indium-tin-oxide (15 nm thickness) coated glass substrate by direct current magnetron sputtering from a metallic vanadium target (99.9% purity) in $Ar+O_2$ atmosphere

and subsequent in-situ annealing in high-purity O_2 ambient. In the process of preparation, the annealing oxygen flow rate was varied from 0 to 15 SCCM. The film annealed at an oxygen flow rate of 0, 0.8, 5 and 15 SCCM was named S1, S2, S3 and S4, respectively. Both sputtering time and annealing time are 30 min. The substrate temperature and annealing temperature are 100 and 300 ^{o}C, respectively. The other detailed experimental conditions as well as the cleaning of substrates have been described in our previous work [3].

X-ray photoelectron spectroscopy (XPS, XSAM 800), field emission scanning electron microscope (SEM, Hitachi S4800) and UV–vis spectrophotometers (Shimadzu, Spec-1700) were used to characterize the valence and composition, the surface morphology, the thermochromic properties of the deposited VOx films, respectively.

Results and discussions

XPS analysis. Fig.1 shows the XPS spectra of S2 and S4. Obviously, the vanadium exists in two valences, namely, +4 valence with the binding energy of 516.06-516.24 eV [3,5] and +5 valence with the binding energy of 517.37-517.69 eV [6]. According to the corresponding areas and atom sensitive factors, the atom concentrations of +5 valences for S2 and S4 were evaluated as 35.6 and 64.4 %, respectively. This indicates that the annealing oxygen flow rates have a significant effect on the vanadium valence states.

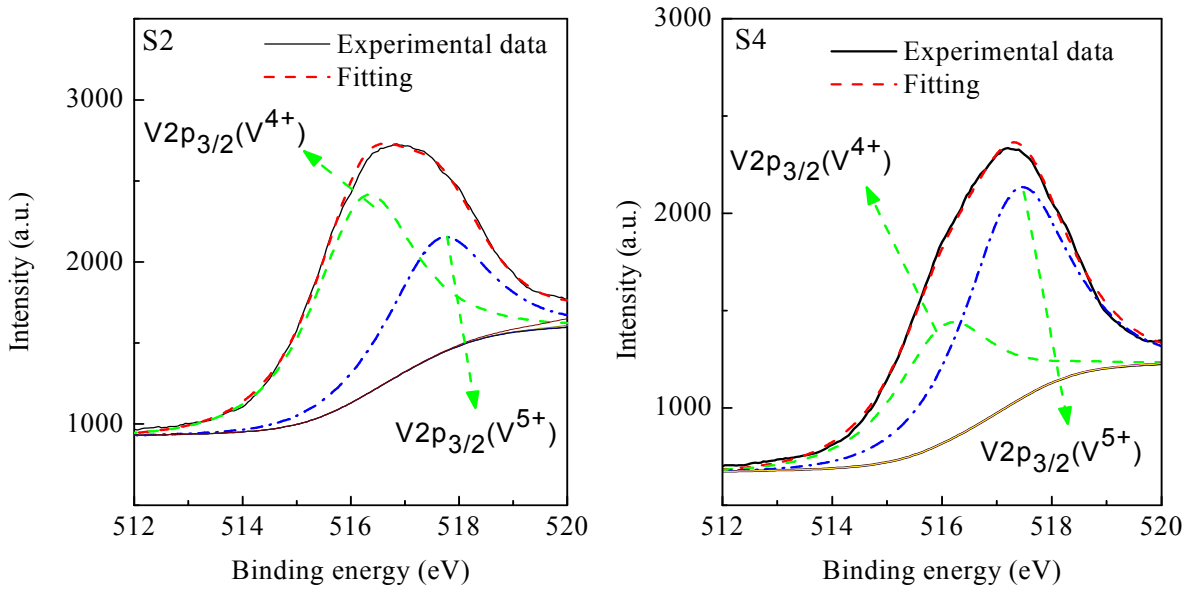


Fig.1 XPS spectra for S2 and S4.

Surface morphology. Fig.2 shows the surface morphologies for S2, S3 and S4. It can be seen that the surface morphologies of the deposited films are strongly dependent on the annealing oxygen flow rate. For a small annealing oxygen flow rate of 0.8 SCCM, the film surface of S2 is smooth and compact although a few cracks are found. As the annealing oxygen flow rate increases, the film surface begins to become loosely. One can also find that the grain size increases obviously as the annealing oxygen flow rate increases.

Thermochromic properties. Fig.3 shows the transmittance spectra of the films below and above the transition temperature. The films annealed at a small oxygen flow rate (<0.8 SCCM) did not show insulator-metal transition while the films annealed at high oxygen flow rates displayed obvious insulator-metal transition. It can be seen that the higher the annealing oxygen flow rate, the higher the transmittance of the films at room temperature (RT). However, the transmittance at high temperature (HT) was almost independent of the annealing oxygen flow rate.

The details of temperature dependence of transmittance at the infrared light of 1100 nm and the corresponding plots of $d(Tr)/d(T) - T$ were shown in Fig.4 and Fig.5, respectively. Tr and T represent

the corresponding optical transmittance and the temperature, respectively. T_{TC} and T_{TH} represent the phase transition temperature upon cooling and heating, respectively. The width of the hysteresis loops is defined as $\triangle H=T_{TH}-T_{TC}$. It can be seen from Fig.4 and Fig.5 that the phase transition temperature increases obviously with the increase in annealing oxygen flow rate. However, the width of the hysteresis loops was found to be relatively insensitive to the annealing oxygen flow rate. This agrees with the reported results that transition temperature is dependent on the oxygen content while the width of the hysteresis loops is not related to the oxygen content [7].

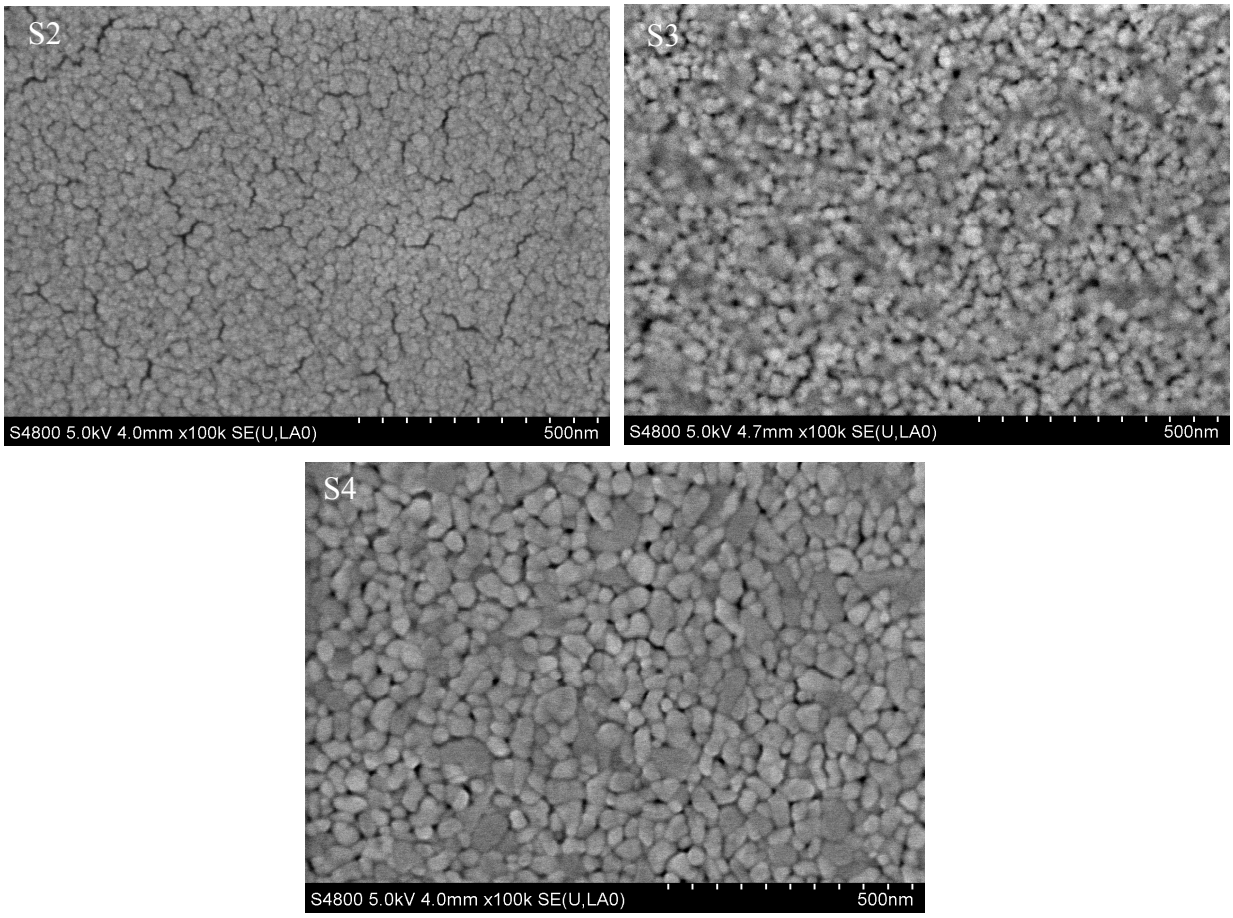


Fig.2 The surface morphologies for S2, S3 and S4.

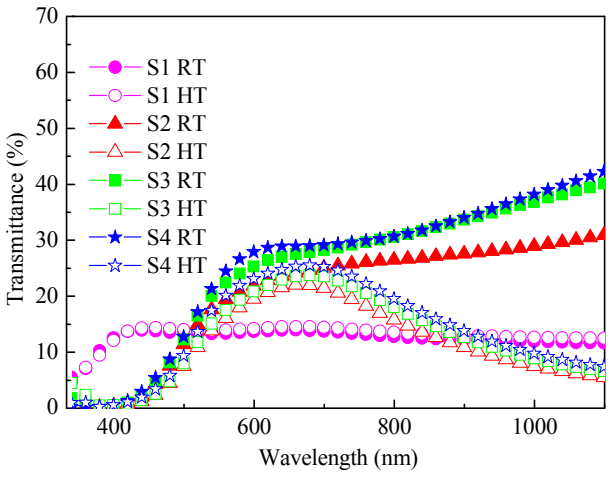


Fig. 3 The transmittance spectra of the films

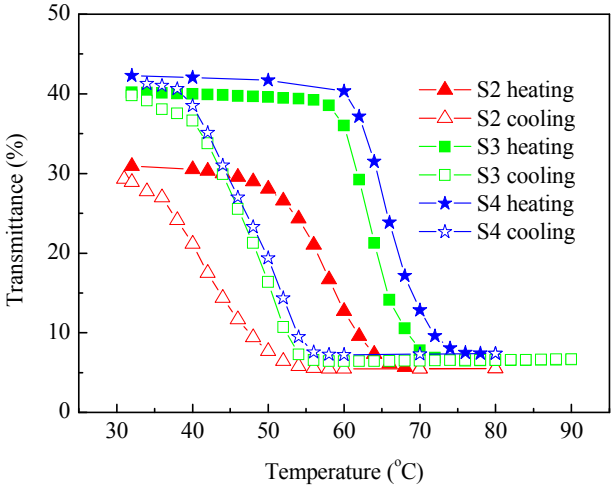


Fig.4 Temperature dependence of transmittance

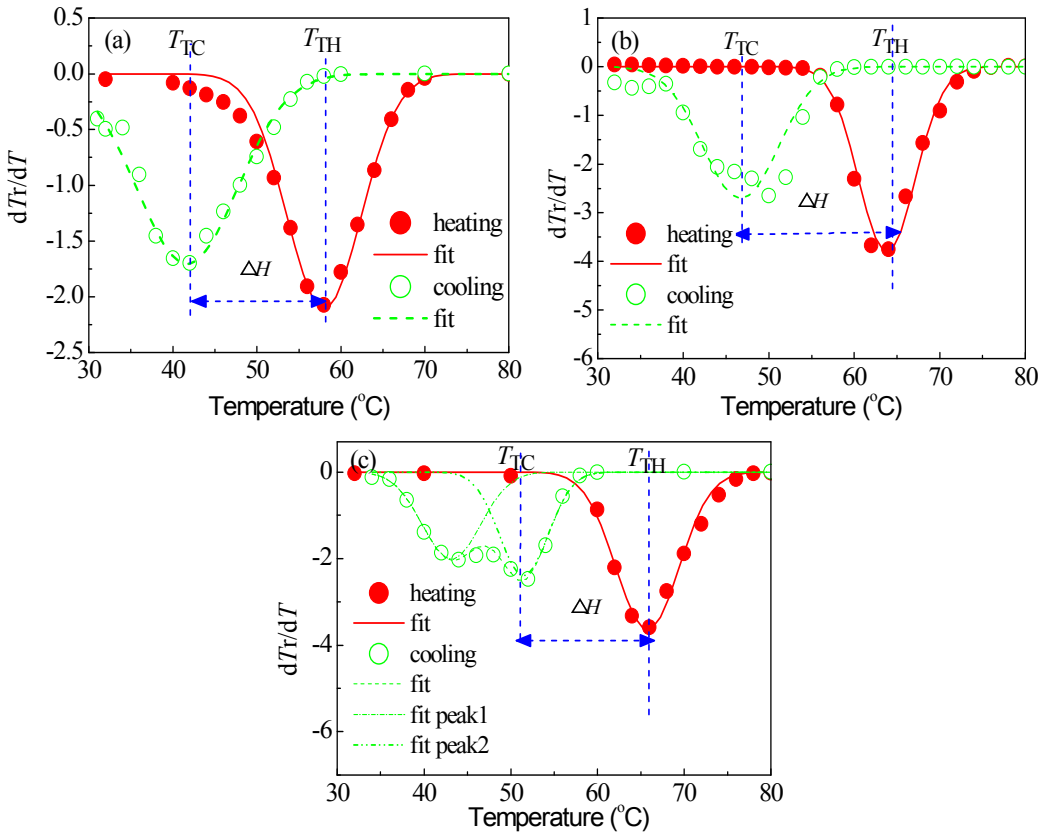


Fig.5 The plots of d(*Tr*)/d(*T*) – *T* for S2 (a), S3 (b) and S4 (c).

Conclusions

Using reactive direct current magnetron sputtering technique, we prepared VOx films and investigated the effect of the annealing oxygen flow rate on the properties of the deposited films. The experimental results indicate that only the vanadium oxide films annealed under relatively high oxygen flow rates (≥ 0.8 SCCM) displayed insulator-metal transition. In addition, it was found that vanadium valence states, surface morphology, optical transmittance and phase transition temperature of the deposited films were sensitive to the annealing oxygen flow rate while the width of thermal hysteresis was relatively insensitive to the annealing oxygen flow rate.

Acknowledgements

This work was financially supported by National Natural Science Foundation of China (grant no.61235006).

References

[1] R. Lopez, L.A. Boatner, T.E. Haynes, L.C. Feldman, R.F. Haglund, Synthesis and characterization of size-controlled vanadium dioxide nanocrystals in a fused silica matrix, J. Appl. Phys. 92 (2002) 4031-4036.

[2] Z.H. Zhang, Z.M. Wu, D.W. Yan, X.X. Dong,Y.D. Jiang,Tunable hysteresis in metal-insulator transition of nanostructured vanadium oxide thin films deposited by reactive direct current magnetron sputtering, Thin Solid Films, 552 (2014) 218-224.

[3] Z.H. Zhang, Z.M. Wu, Q. He,Y.D. Jiang, Preparation and investigation of sputtered vanadium dioxide films with large phase-transition hysteresis loops, Appl. Surf. Sci. 277 (2013) 218-222.

[4] J. Du, Y.F. Gao, H.J. Luo, Z.T. Zhang, L.T. Kang, Z. Chen, Formation andmetal-to-insulator transition properties of VO2–ZrV2O7 composite films by polymer-assisted deposition, Sol. Energy. Mat. Sol. C Vol. 95 (2011) 1604-1069

[5] N. Alov, D. Kutsko, I. Spirovova′, Z. Bastl, XPS study of vanadium surface oxidation by oxygen ion bombardment, Surf. Sci. 600 (2006) 1628-1631

[6]Y.L. Wang, X.K. Chen, M.C. Li, R. Wang, G. Wu, J.P. Yang, W.H. Han,S.Z. Cao, L.C. Zhao, Phase composition and valence of pulsed laser deposited vanadium oxide thin films at different oxygen pressures, Surf. Coat. Tech. 201 (2007) 5344-5347

[7] R. Lopez, T. E. Haynes, L. A. Boatner, L. C. Feldman, R. F. Haglund Jr, Size effects in the structural phase transition of VO2 nanoparticles, Phys. Rev. B 65 (2002) 224113-1-5

Advanced Materials Research Vol. 936 (2014) pp 656-660
© (2014) Trans Tech Publications, Switzerland
doi:10.4028/www.scientific.net/AMR.936.656

TEM Study of AlGaN/GaN on Hexagonal SiC Substrates

Alexandra Gkanatsiou[1,a], Christos B. Lioutas[1,b], Nikolaos Frangis[1,c], Narendraraj Chandran[1,d], Efstathios K. Polychroniadis[1,e *], Pawel Prystawko[2,3,f], Mike Leszczynski[3,2,g]

[1] Department of Physics, Aristotle University of Thessaloniki 54124, Greece

[2] Institute of High Pressure Physics "Unipress", Polish Academy of Sciences

Sokolowska 29/37, 01-142 Warsaw, Poland

[3]TopGaN Ltd, Sokolowska 29/37, 01-142 Warsaw, Poland

[a]alexgkan@auth.gr, [b]lioutas@physics.auth.gr, [c]frangis@auth.gr, [d]naren@physics.auth.gr, [e]polychr@auth.gr, [f]pprysta@unipress.waw.pl, [g]mike@unipress.waw.pl

Keywords: GaN, SiC, heteroepitaxy, TEM

Abstract. The present work concerns the microstructural characterization of a multi-component (based on GaN and related materials) and multi-layered (5 layers) film, grown on 6H-SiC substrate (with a misorientation of 1 degree off from the (0001) plane), using transmission electron microscopy (TEM). The TEM characterization showed no surface undulation, despite the presence of steps in the SiC/AlN interface.

Introduction

Switching from silicon electronics to wide bandgap alternatives promises to deliver improvements in the performance of electronic devices. Nowadays, there has been an increasing interest for GaN- and SiC-based electronic devices, although both kinds of devices have their advantages and disadvantages. GaN-based devices have higher electron mobility and saturation velocity, as well as a variable band gap due to the alloying with AlN and InN (realizing higher frequency devices [1]). SiC-based devices have a higher thermal conductivity and a higher breakdown voltage (realizing higher power devices [2]).

A high quality GaN film is essential for device fabrication. Due to the lack of sufficiently high quality bulk GaN substrate, the growth of GaN epitaxial layer has so far been carried out on various foreign substrates such as sapphire and silicon carbide (SiC). Most commercially available GaN-based devices are normally grown on sapphire substrates because of the relatively low cost and general availability, although their lattice parameter and coefficient of thermal expansion are significantly different from that of GaN. For power device applications, however, it is desirable for a substrate with higher thermal conductivity, such as SiC.

6H-SiC has a thermal conductivity coefficient (room temperature) of 4.9 W/(cm·K), which is an order of magnitude higher than sapphire (0.5 W/(cm·K)). Meanwhile, SiC also has a lower lattice mismatch to GaN (~3.5%) and AlN (~1%) compared to sapphire. However, the thermal expansion coefficient of 6H-SiC (4.2×10^{-6} K^{-1}) is lower than that of GaN (5.59×10^{-6} K^{-1}), which produces a strain of ~0.1% for a growth temperature of 1000°C [3]. As a result, GaN layers grown directly on SiC (0001) are usually under tensile strain at room temperature and there are high amounts of dislocations and even cracks in the GaN films caused by strain. To resolve the problems, an AlN buffer layer has been widely used to reduce this tensile strain and even producing compressively strained GaN layers grown on SiC [4-7] and AlN buffer has been repeatedly found to be necessary to achieve a GaN layer with a smooth surface and a reasonably low density of threading dislocations via the metal organic chemical vapor deposition technique (MOCVD) [3].

So far, most of the SiC homoepitaxy has been realized on 8-degree-off and 4-degree-off substrates, whereas GaN heteroepitaxy is done on SiC on-axis (up to 0.3 degrees off) [8]. As 6-inch SiC wafers are being introduced into the market, a decrease of the substrate cut-off to 2 degrees for SiC

homoepitaxy is desirable to reduce the manufacturing costs. The purpose of this paper is to show the microstructural and morphological characteristics of the AlGaN/GaN HEMT structure and to study the influence of the off-axis angle on the surface quality of the device.

Experimental results

A sample of AlGaN/GaN HEMT structure was grown on a 1-degree-off 6H-SiC substrate. An EMCORE D75 MOVPE system was used for the growth. The AlGaN/GaN heterostructure was grown on 6H-SiC substrate sandwiched with an AlN spacer layer. The complete structure of the sample consists of an AlN nucleation layer, a GaN buffer, a GaN undoped thin AlN spacer, a AlGaN layer and finally a GaN cap layer. The layers are grown epitaxially, which is confirmed from the corresponding electron diffraction patterns (with the [0001] SiC direction parallel to the [0001] GaN direction). A typical electron diffraction pattern is shown in Fig. 1.

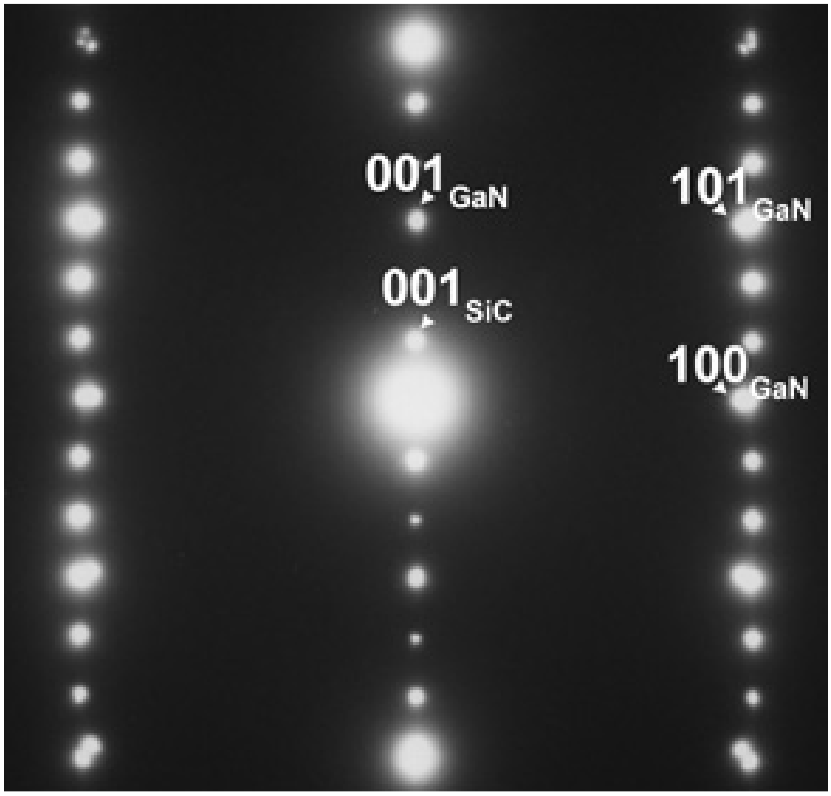


Fig. 1. An electron diffraction pattern taken close to SiC /GaN interface, revealing the very good epitaxial growth of GaN on the 6H-SiC substrate.

The conventional bright field TEM image of Fig. 2 shows the structure of the sample and allows the accurate measurement of the layers' thickness. Sharp interfaces are observed between most of the layers. The layers of the upper part of the structure are not clearly distinguished in this magnification, so for this reason higher magnification TEM images are needed and shown below.



Fig. 2. A multilayer structure grown on a 6H-SiC substrate. Five layers were grown epitaxially on the substrate.

The black colored rectangular marked in the upper part of Fig. 2 is magnified and showed in Fig. 3. In this HRTEM image, which reveals the upper part of the multilayer structure, the surface of the GaN cap layer appears atomically flat (despite the cut-off substrate).

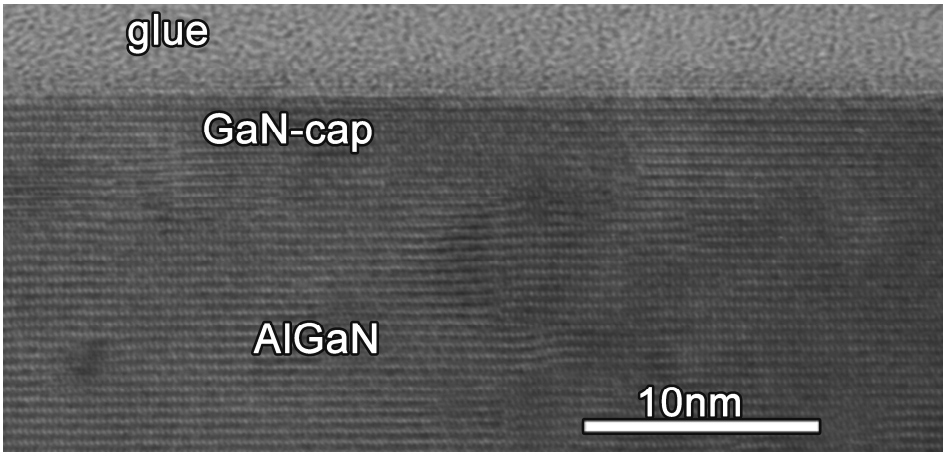


Fig. 3. HRTEM image showing the upper part of the multilayer structure

In Table 1 the nominal and experimental thicknesses of the multilayer structure are presented.

Table 1: Nominal and experimental thicknesses of the structure

Layers (top to bottom)	Nominal thickness [nm]	Experimental thickness [nm]
GaN cap	2-2.5	20-21
AlGaN (~20%Al)	20	
AlN spacer	1	2-4
GaN undoped channel	80	1680-1700
GaN buffer	2500	
AlN nucleation layer	60-90	13-33
Substrate 6H-SiC (1° off)		

It is obvious that on the surface of the 1-degree cut-off substrate characteristic steps would appear. The High Resolution TEM (HRTEM) image of Fig. 4 shows these steps at the interface between the 6H-SiC substrate and the AlN nucleation layer. The white colored arrows indicate the steps' positions. The characteristic contrast suggests the growth of threading dislocations in the AlN layer that begin from the SiC/AlN interface at the steps' positions.

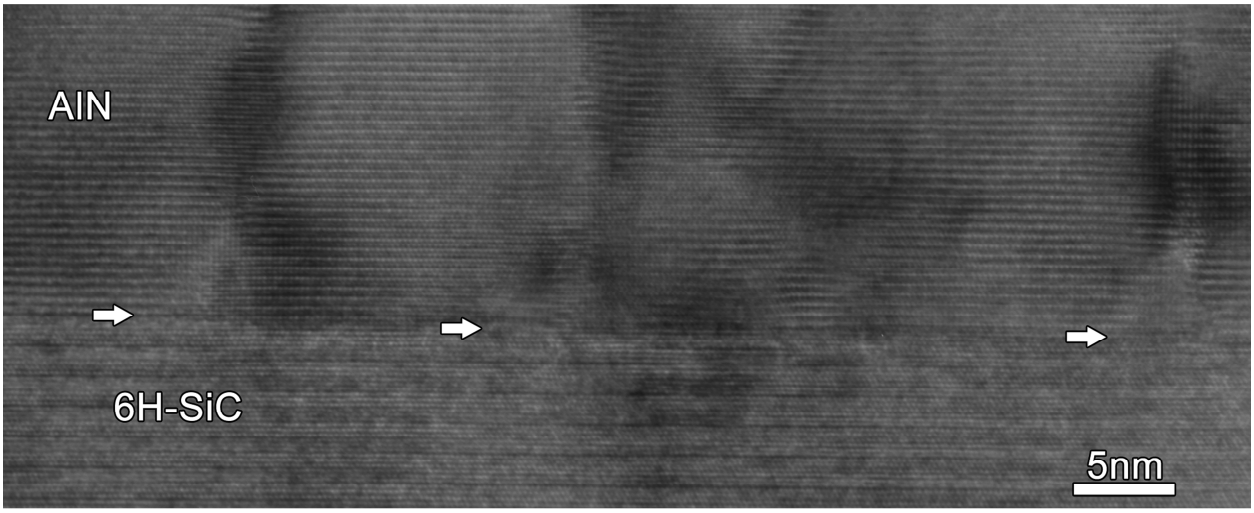


Fig. 4. HRTEM image revealing the steps in the SiC/AlN interface indicated by white colored arrows

Summary

In this paper, we showed that the AlGaN/GaN HEMT structure grown on a 1-degree-off 6H-SiC substrate appears to have an atomically flat free surface, although the SiC/AlN interface shows the expected steps.

Acknowledgements

This work was supported by the JU ENIAC Project LAST POWER Grant agreement no. 120218 and the Greek General Secretariat for Research and Technology, contract SAE 013/8 - 2009SE 01380012.

References

[1] J. W. Chung, W. E. Hoke, and E. M. Chumbes, and T. Palacios, IEEE Electron Device Letters 31 (2010) 195

[2] S. Sundaresan, M. Digangi, and, R. Singh, GeneSiC Semiconductor, Inc. Power Electronics Technology (2010) 21

[3] Ding Guojian, Guo Liwei, Xing Zhigang, Chen Yao, Xu Peiqiang, Jia Haiqiang, Zhou Junming, and Chen Hong, Journal of Semiconductors 31 (2010) 033003-5

[4] Davydov V Y, Averkiev N S, Goncharuk I N, et al., J. Appl. Phys. 82 (1997) 5097

[5] Skromme B J, Zhao H, Wang D, et al., Appl. Phys. Lett. 71 (1997), 829

[6] Perry W G, Zheleva T, Bremser M D, et al., J. Electron. Mater. 26 (1997) 224

[7] Waltereit P, Brandt O, Trampert A, et al., Appl. Phys. Lett., 74 (1999), 3660

[8] A. Trampert, O Brandt, B Yang, B Jenichen, Klaus H Ploog, J. Crystal Growth 201-202 (1999) 407-410

CHAPTER 8:

Biomaterials, Biotechnologies and Pharmaceutics

Advanced Materials Research Vol. 936 (2014) pp 663-668
© (2014) Trans Tech Publications, Switzerland
doi:10.4028/www.scientific.net/AMR.936.663

Protein Adsorption on Titanium Surface Functionalized with Bioactive Gelatin Methacrylate Hydrogel Coating

Guoxin Tan[1, a *], Ying Tan[1, b], Chengyun Ning[2, c], Lin Zhang[3, d], Lei Zhou[1, e], Hang Wang[1, f]

[1]School of Chemical Engineering and Light Industry, Guangdong University of Technology, Guangzhou, China, 510006

[2]College of Materials Science and Technology, South China University of Technology, Guangzhou, China, 510641

[3]Guangdong Medical Device Quality Surveillance and Test Institute, Guangzhou, China, 510663

[a]tanguoxin@126.com, [b]tanying223@163.com, [c]imcyning@scut.edu.cn, [d]zl8224256@163.com, [e]zhoulei7170@126.com, [f]wh-0518@163.com

Keywords: Gelatin methacrylate hydrogel; Protein adsorption; Titanium surface modification

Abstract: Gelatin methacrylate (GelMA) hydrogel comprised of modified natural extracellular matrix (ECM) components, making it a potentially attractive material for surface modification. In this paper, we hypothesize that establishing a GelMA hydrogel coating on titanium surface will accelerate osseointegration. Titanium substrates were silanized with 3-Aminopropyltriethoxysilane (APTES), which was treated by alkali-heated treatment firstly. The GelMA hydrogel coating was constructed on the silanized titanium surface by in situ photopolymerization under UV illumination. Adsorption of bovine serum albumin (BSA) onto modifed titanium surfaces was investigated. The results showed that GelMA-coated titanium adsorbed greater amount of protein than other Ti surfaces. The differences in protein adsorption behavior could result in very different initial cellular behavior on GelMA-coated titanium implant surfaces.

Introduction

Titanium (Ti) is widely used as orthopedic implants because of its good biocompatibility, superior mechanical properties and excellent corrosion resistance. However, it cannot meet clinical requirements due to the lack in integration with the surrounding bone environment. Protein adsorption mediated cell behavior is regarded as a fundamental reaction at biomaterial/tissue interface. It is well recognized that protein adsorption is sensitive to physicochemical surface properties of the implant. Various surface modifications have been developed to facilitate bone tissue responses toward titanium surfaces including hydroxyapatite coating, biomolecular immobilization [1], and control of the surface topography [2].

Gelatin is partially denatured derivative of collagen and it is biodegradable, biocompatible and non-immunogenic. Furthermore, due to the large number of functional side groups, gelatin readily undergoes chemical cross-linking, which is very important for its widely use in tissue engineering and drug delivery system [3]. It has been reported that hydrogels based on methacrylamide-modified gelatin were attractive materials for biomedical applications because of their controllable chemical networks, high water content, biocompatibility and mechanical properties [4]. In this paper, we supposed that establishing a gelatin methacrylate (GelMA) hydrogel coating on titanium surface would be a potential surface optimization method to enhance osseointegration of titanium implant. For one thing, the hydrogel can mimic extracellular matrix (ECM) to be beneficial for biomaterial/tissue interface and gelatin has been previously reported to act as nucleators of mineral deposition onto biomaterials [5]. Besides, its macroporous topographical features may promote cell adhesion, differentiation and proliferation, as reported previously [6]. Therefore, the objective of this study was to construct and characterize macroporous GelMA hydrogel coating on Ti by

photopolymerization, and focuse the study on the potential of protein adsorption onto this coating. We hypothesized that this modified gelatin coating would be helpful for enhancing protein adsorption on titanium substrates, which would enhance subsequent cellular binding.

Experimental Procedures

Fabrication of GelMA Hydrogel Coating on Ti Surface

Commercially pure titanium sheets (0.1mm thick) were etched in a mixture of HF, HNO_3 and distilled water and named as "Ti". The NaOH-heat-treated and 3-Aminopropyltriethoxysilane (APTES, 99.0 %, Acros) -silanized titanium samples were prepared as described [7] and denoted as Ti-OH and Ti-APTES respectively. Gelatin methacrylate were synthesized with gelatin (Sigma) and methacrylic anhydride (Sigma) using techniques previously demonstrated [4]. The GelMA-coated Ti sample was prepared as follows. Briefly, GelMA macromonomer solution in PBS (10%, w/v) containing the photoinitiator Irgacure 2959 (1%, w/v) was pipetted between a Ti-APTES plate and an octadecyltrichlorosilane (OST, Sigma) modified coverslip separated by a 500μm spacer, then irradiated with UV light (6.9 mW/cm^2, Omnicure S1500, Canada). After that, the GelMA-coated Ti samples were incubated in milliQ-water for 3h in order to remove the GelMA physically adsorbed on Ti surface, and then lyophilized.

Protein Adsorption

Bovine serum albumin (Sigma, purity of 99.8%) was dissolved in phosphate buffered saline (PBS) buffer one day before use. To investigate the protein adsorption kinetics, titanium samples were immersed in 1.5 mg/mL BSA solution and protein concentration of different time points was determined by using the bicinchoninic acid (BCA) assay according to the instruction of the manufacturer. The analysis was performed by using a microplatereader (RT-2100C, Rayto, China) at 595nm ($n=3$, $p<0.05$). The adsorbed amount was determined by subtracting the residual protein from the initial added protein.

Surface Analysis

The topography of the modified titanium surfaces was measured by scanning electronic microscopy (SEM). Attenuated total refraction-Fourier transform infrared spectroscopy (ATR-FTIR, FTS400 spectrometer, Shimadzu) was employed to determine the surface chemical changes after samples incubation in 1.5 mg/mL BSA solution for 6h. After incubation in Cy3-labeled bovine serum albumin (Beijing Biosynthesis Biotechnology Co., LCD) solution (50 μg/mL in 0 .01M PBS buffer) for 60 min at 37 ℃, samples were washed twice with PBS buffer and observed by fluorescent microscope (Zeiss Axioskop 40 POL, Germany).

Results and Discussion

As shown in Fig. 1A, gelatin molecule was introduced methacrylate pendant groups by reacting with methacrylic anhydride (MA). To enhance the stability of GelMA coating, titanium substrates were firstly silanized using APTES (Fig. 1B), which could become a "molecular bridge" between the interface of organic materials and inorganic substrates. Then GelMA hydrogel was immobilized onto titanium surfaces by applying a photochemical reaction. After photo-crosslinking, GelMA hydrogel coatings on titanium surface showed interconnected macroporous structure with the pore size ranging from 20-200μm. When incubated in BSA solution, the amino and carboxyl groups in GelMA structure will be charged and they will interact with the charged amino acid residues presented on the outside of protein by forming hydrogen bonds and electrostatic force. Meanwhile, the mesh size of hydrogel was large enough to allow diffusion of BSA into the internal structure. Therefore, protein can be adsorbed within membrane pores and on the surface as well. It is reasonable to suspect that the GelMA hydrogel coating will promote the protein adsorption on titanium.

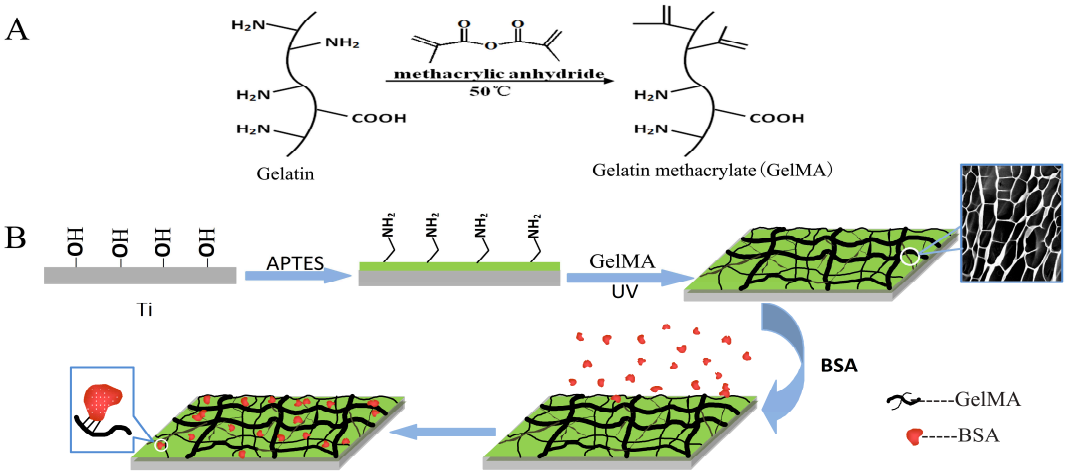


Fig. 1. Schematic illustration of **(A)** synthesis of gelatin methacrylate (GelMA) and **(B)** construction of GelMA coating on titanium surface.

Fig. 2A showed the ATR-FTIR spectra corresponding to samples by different treatments. Ti-OH sample exhibited the typical hydroxyl group peak at around 3235 cm^{-1} and 1625 cm^{-1}, respectively. After bonding the APTES films, the hydroxyl group disappeared and new peaks located around 1090cm^{-1} (Si –O –Si) and 1199 cm^{-1} ($–OCH_2CH_3$) indicated that silane agent had been grafted onto the surface of Ti-OH substrate. The characteristic bands for GelMA functionalized titanium surface were observed at 1645 cm^{-1} (amide I), 1530 cm^{-1} (amide II) and 1446 cm^{-1} (amide III), corresponding to the stretching of C=O bond, bending of N-H bond and plane vibration of C-N and N-H, respectively [8]. The observation of characteristic peaks of -CONH- and $-NH_2$ in the spectrum of Ti-GelMA suggested the successful immobilization of GelMA hydrogel coating on titanium surface.

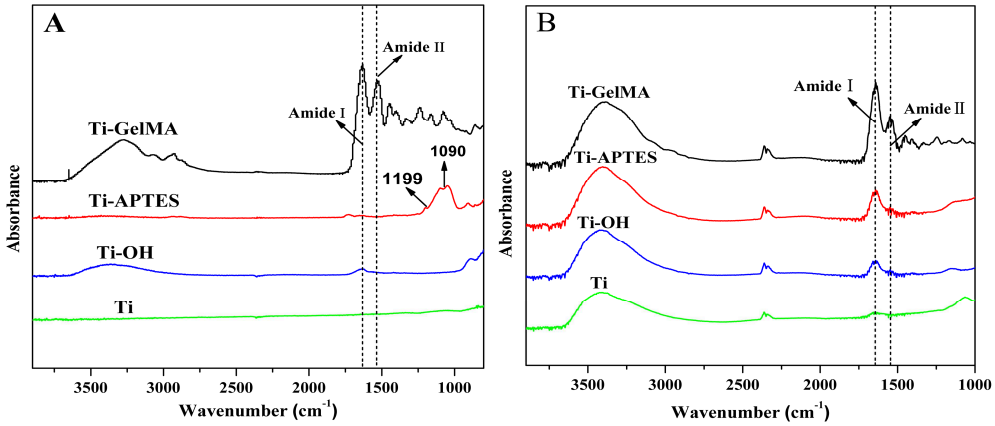


Fig. 2. ATR-FTIR spectra of (A) before and (B) after the protein adsorbed samples.

After the protein adsorption (Fig. 2B), both amide I (centered at 1645 cm^{-1}) and amide II (centered at 1540 cm^{-1}) adsorption bands can be observed in the ATR-FTIR spectra of the protein adsorbed samples. The relative intensity of signals corresponding amide I was significantly higher for Ti-GelMA sample than for all other groups, which partly came from the amide I of molecular structure of GelMA itself. In contrast, the amides I and II bands were hardly to be observed on Ti sample. It has been reported that peak intensity of amide I increases linearly with the amount of protein statistically adsorbed on the surface [9]. Therefore, we can assume that Ti sample adsorbed least BSA for a given geometric surface area than other three titanium surfaces and no significant change was observed for Ti-OH and Ti-APTES samples. In order to verify that Ti-GelMA surface adsorbed most protein, quantitative analysis of protein adsorption on modified titanium surfaces was discussed in the next chapter.

For evaluation of protein adsorption properties of GelMA coating, modified titanium samples were incubated with fluorescently labeled BSA. Integration time was kept constant for all samples to allow compatibility of the results. Sporadic fluorescence was observed on the control Ti surface (Fig. 3a),

indicating minimized protein adsorption. The fluorescence intensity of the other three Ti samples was larger than the control Ti, especially for Ti-GelMA sample with the strongest fluorescence. Proteins tend to adhere more strongly to charged than to uncharged substrates [10]. Therefore, negatively charged Ti-OH, positively charged APTES film and zwitterionic GelMA coating could adsorb more proteins than the neutral Ti sample. Besides the functional groups, topography also plays a significant role in protein adsorption and that not just the size distribution, but also the detailed shape of topographical features is of paramount importance [11]. As shown in Fig.3d, fluorescence could be observed in the inner region of the GelMA hydrogel, implying that the labeled protein could diffuse into and form bind with the network structure. The amount of protein adhered on the nanoporous structure (Fig. 3b and 3c) was higher than that on nanosteps-like structure of control Ti (Fig. 3a), suggesting that increased surface roughness provides more surface area for protein adsorption. A similar result has been reported previously [12]. As shown in the figure proteins adhered on the Ti-APTES surface in slightly higher amounts than on Ti-OH surface. This is because the $-NH_2$ of APTES could be the binding sites for protein to form hydrogen bonding .

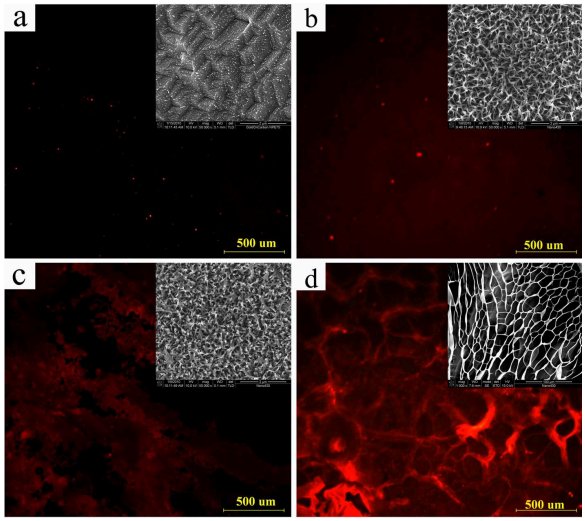


Fig. 3. Fluorescence images of BSA absorbed for 60min on different Ti surfaces with SEM images (a-c: 50000×, d: 1000×) inserted (a: Ti, b: Ti-OH, c: Ti-APTES, d: Ti-GelMA)

The protein adsorption onto the surfaces of titanium may proceed in two different processes [13]. The first process is the direct attachment of the protein molecules. The second process probably involves the slow rearrangement of the adsorbed layer due to the changes of orientation and conformation of the adsorbed molecules. Protein absorption kinetics of BSA on modified titanium surfaces was showed in Fig. 4. At the first 3 h, the degree of BSA adsorption was similar for all treatment groups. The amount of BSA adsorbed on Ti-GelMA samples was statistically significantly higher than other groups after 5 hours incubation. Equilibrium adsorption occurred at 8h for all samples. Hydrophobic surfaces tend to adsorb more proteins. Adsorption reached the maximum on the Ti-GelMA with a surface coverage of 0.97 mg/m2, and got less on the hydrophilic Ti-OH sample (approximately 0.64mg/m^2). As the cellular response to implant surface topography is governed by the adsorbed protein layer, it is assumed that the GelMA hydrogel coating would enhance subsequent cellular binding. There was no statistically significant difference between Ti-APTES and Ti-OH samples in BSA adsorption, which was in accord with the results mentioned above. Taken together, each of surface properties such as chemistry, charge, morphology and wettability can affect protein adsorption differently. While these surface properties are connected, it is difficult to distinguish the effect of individual surface properties on protein adsorption since changing one property often changes others. To understand the mechanism of protein-material interaction, further studies are in progress.

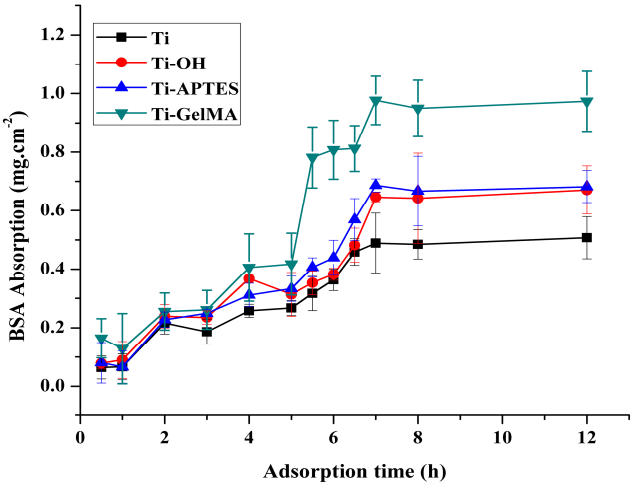


Fig. 4. Kinetics of BSA adsorption on different titanium surfaces (mean±standard deviation).

Conclusions

We have developed a simple method for fabricating macroporous GelMA hydrogel coating on titanium by using the combination of silanization and photochemical cross-linking. In contrast to uncoated titanium surface, GelMA hydrogel coating showed a good bioactivity with higher affinity to proteins, presumably due to the interconnected network structure and change of adhesion sites for proteins. It is envisioned that our method could be an optimized surface modification method to accelerate osseointegration.

Acknowledgment

We gratefully acknowledge the financial support of National Basic Research Program of China (2012CB619100), the National Natural Science Foundation of China (Grant 51072057, 81271957, 51372087).

References

[1] C.D. Reyes, T. A. Petrie, K. L. Burns, Zvi Schwartz, A. J. García, Biomolecular surface coating to enhance orthopaedic tissue healing and integration, Biomaterials. 28 (2007) 3228-3235.

[2] K. S. Brammer, S. Oh, C. J. Cobb, L.M. Bjursten, H. Heyde, S. Jin, Improved bone-forming functionality on diameter-controlled TiO2nanotube surface, Acta Biomaterialia.5 (2009) 3215-3223.

[3] M.Peter, N.S.Binulal, S.V.Nair, N.Selvamurugan, H.Tamura, R.Jayakumar,Novel biodegradable chitosan-gelatin/nano-bioactive glass ceramic composite scaffolds for alveolar bone tissue engineering, Chem. Eng. J. 158 (2010) 353-361.

[4] A.V. Bulcke, B. Bogdanov, N. D. Rooze, E. H. Schacht, M. Cornelissen, H. Berghmans, Structural and Rheological Properties of Methacrylamide Modified Gelatin Hydrogels Biomacromolecules. 1 (2000) 31-38.

[5] M.C. Chang, C. C. Ko, W.H. Douglas, Preparation of hydroxyapatite–gelatin nanocomposite, Biomaterials. 24 (2003) 2853-2862.

[6] V. Karageorgiou, D. Kaplan, Porosity of 3D biomaterial scaffolds and osteogenesis, Biomaterials. 26 (2005) 5474-5491.

[7] G. Tan, L. Zhang, C.Ning, X. Liu, J.Liao, Preparation and characterization of APTES films on modification titanium by SAMs, Thin. Sol. Fil. 519 (2011) 4997-5001.

[8] Z.A. Nur Hanani, Y.H. Roos, J.P. Kerry, Use of beef, pork and fish gelatin sources in the manufacture of films and assessment of their composition and mechanical properties, Food Hydrocolloids. 29 (2012) 144-151.

[9] J.Xie, C. Riley, M. Kumar, K.Chittur, FTIR/ATR study of protein adsorption and brushite transformation to hydroxyapatite, Biomaterials. 23 (2002) 3609.
[10] S. Patil, A. Sandberg, E. Heckert, W.Self, S. Seal, Protein adsorption and cellular uptake of cerium oxide nanoparticles as a function of zeta potential, Biomaterials. 28 (2007) 4600-4607.
[11] M. S. Lord, M. Foss, F. Besenbacher, Influence of nanoscale surface topography on protein adsorption and cellular response, Nano Today. 5 (2010) 66-78.
[12] [12] P. E. Scopelliti, A. Borgonovo, M. Indrieri, L. Giorgetti, G. Bongiorno, R. Carbone, A.Podestà, P. Milani, The effect of surface nanometre-scale morphology on protein adsorption, PloS One. 5 (2010) e11862.
[13] T. Sakiyama, J. Tomura, K. Imamur, K. Nakanishi, Adsorption characteristics of bovine serum albumin and its peptide fragments on a stainless steel surface, Colloids & Surf B. 33 (2004) 77.

Advanced Materials Research Vol. 936 (2014) pp 669-673
© (2014) Trans Tech Publications, Switzerland
doi:10.4028/www.scientific.net/AMR.936.669

Extraction and Antifungal Activity of a Lipopeptide Biosurfactant

Fanren Fang[b],Sheng Zhong[a*] ,Yan Dong and Lijing Gong

School of Chemical Engineering, University of Science and Technology Liaoning, Anshan, Liaoning, China

[a]shengzh-99@163.com

[b]fang_fanren@126.com

Keywords: Biosurfacant; Lipopeptide; Antimicrobial activity

Abstract: A kind of biosurfactant produced by ascendant strain BS01 was screened by detecting the surface tension , diameter of oil spreading. The structure of the biosurfactant extracted from fermentation broth of strain BS01 was verified by IR and UV .It has superior surfactive properties. Its critical micelle concentration (CMC) is 25mg/l and the surface tension is 29.6mN/m in CMC. The biosurfactant shows excellent antibacterial spectrum against agricultural pathogenic fungi and human pathogenic bacteria. Especially, it presents good antibiotic activity against Sclerotinia sclerotiorum ,staphylococcus aureus Rosenbach and pseudomonas aeruginosa .

Introduction

Biosurfactants take advantages over synthetic surfactants from the viewpoint of their biodegradability, lower toxicity, stable activities at extreme temperature, pH and salinity when applied for enhancing bioremediation, food processing and crude oil drilling[1]. Thus, biosurfactants have been a research hot spot in the last decade. In view of a short metabolism period of biosurfactant produced by microorganisms, the preparation of the biosurfactant has great economic benefits by means of microorganism fermentation. Lipopeptide is an amphiphilic biosurfactant containing lipid and peptide as hydrophobic and hydrophilic moiety, respectively.Lipopeptide biosurfactants exhibit some powerful biological actions such as plant diseases control [2], anti-tumour and anti-viral activities[3] and awide antimicrobial spectrum. [4] The latter is due to their exceptional surface activity that allows modifications of the bacterial surface hydrophobicity and can consequently interfere with the microbial adhesion to solid surfaces, like those of medical devices. [5] However, while the industrial demand for surfactants has increased nearly 300% in the US chemical industry during the last decade, all these usable surfactants in practice originate from chemical synthesis strategies at present. This fact, an increasing demand of high-quality surfactants (for example, environmentally friendly biosurfactants) and the lack of cost-competitive bioprocess of biosurfactants for commercial utilization, motivates researchers to develop cost-effective strategies for biosurfactant production[6]. To solve this problem, new biosurfactant producers with stable surface-active properties need to be investigated and their cultural conditions also need to be optimized. Here, we isolated a strain from waste soybean oil and named to BS01. The strain produced new biosurfactant and it has very strong emulsification activity for hydrophobic materials. In addition, we purified and characterized the biosurfactant then its antibacterial and antifungal properties were researched.

Methods

Preliminary Screening Assays for Biosurfactant Production

In order to determine the ability of the strain to produce biosurfactant, the pure culture was subjected to preliminary screening methods namely oil displacement test and emulsification assay., All the above mentioned experiments were carried out based on the methodology previously described in Sriram et al. [7]All the experiments were done in triplicates.

Production Media Composition and Cultivation Conditions

Using the nutrient broth (NB) media (HiMedia, Mumbai, India), inoculum was prepared and incubated at 37 ℃ for 12 h. The seedculture at 3% was utilized to inoculate the biosurfactant production media of 100 ml in a 500 ml Erlenmeyer conical flask and incubated at 160 rpm at 37 ℃ for 5 days. The production media contained (g/L): $(NH_4)_2SO_4$, 10; NaCl, 1.1; KCl, 1.1; $FeSO_4$.7H2O, 2.8 X 10-4;$K_2HPO_4.3H_2O$, 4.4; KH_2PO_4, 3.4; $MgSO_4$, 0.5; Yeast Extract, 0.5; trace elements solution, 0.5 ml/L and diesel oil, 2% (v/v) as the sole carbon source. The composition of trace elements solution involved (g/L): $CaCl_2$, 0.24; $ZnSO_4$, 0.29; $MnSO_4$, 0.17 and $CuSO_4$, 0.25. After the production media was autoclaved, the trace elements solution was added prior to inoculation by filtering it with a 0.22 lm pore membrane [8].

Solation, Extraction and Purification of Biosurfactant

The cell free supernatant was obtained by centrifuging the broth culture at 4,000 rpm at 4℃ for 20 min. The supernatant was acidified with 6 N HCl, thereby reducing its pH to 2.0 and then incubated overnight at 4℃. It was further extracted twice with chloroform–methanol (2:1, v/v).then selected the lower organic layer ,removed the solvent by rotary evaporation,and lyophilization, Yellow powdered solid was obtained . After the coarse product was reduced to powder,it was extracted by methylene chloride for 24h.then the solvent was removed and the solid was washed with hexane , Purification of biosurfactant was achieved by recrystallization. White powdered solid was obtained .

Chemical Characterization of Biosurfactant

The primary characterization of the biosurfactant was carried through TLC as per the methodology described above in purification and the separated compound was visualized under UV light. Further characterization was accomplished with the help of IR and UV spectrum.

Critical Micelle Concentration

Surface tension measurements were carried out using De–Nouy Tensiometer Kruss K-6 with platinum ring. Freshly prepared aqueous solutions of surfactants were used with concentration range of 0–100 mg/L at 25℃. The critical micelle concentration (CMC) values were estimated from the break point of each surface tension versus concentration (on log scale) curves at 25℃.

The Diameter of Oil Spreading

To 15cm diameter dish, adding 60mL of distilled water, adding 2mL water liquid paraffin, uniform and stable film to be formed, the center of the film gradually added 2mL fermentation broth of the test, the oil film formed around the exhaust is discharged to circle. Circle area with rows of biosurfactants content into a linear relationship. The oil phase and the aqueous phase component is small, images acquisition time, be unable to record clear oil discharge ring. the oil phase can be stained with Sudan, Between the oil phase and the water phase is formed a good color. Its can be clearly observed oil spreading.

Antimicrobial Studies

The antibacterial activities of the biosurfactant were tested with *PDA* medium against various agricultural pathomycetes such as Cordana musae, Sclerotinia, sclerotiorum, Cladosporium cucumerinum, Fusarium roseum, Colletotrichum atramentarium, Fusarium oxysporum f.sp., Fusarium moniliforme, Rhizoctonia cerealisRhizoctonia solani, Phytophthora capsici, Cladosporium cucumerinum by using agar well diffusion method at 1g/L, Aditionnally, the effect of the biosurfactant on E. Coli, Staphyloccocus aureus Rosenbach, P.Aeruginosa were detected with beef extract andpeptone medium using the previous mentioned method.

Results and Discussion

Screening Assays for Biosurfactant Production

After Preliminary screening assays for biosurfactant production ,we cultivated four bacteria strains named BS01, BS02, BS03 and BS04. Preliminary stains medium were fermented for 72 hours,then were centrifuged twice for each time 15 min on the condition of low temperature and 4000r/min. Leave to rest for 30 minutes.surface tension and oil displacement of the supernatant were tested.

Table 1 showed that stain BS01 posses lower surface tension and better oil displacement compared with other three preliminary screened stains BS02~BS04.Consequently,we selected BS01 as the following test stain.

TABLE 1 THE ISOLATION OF MICROORGANISMS PRODUCTING BIOSURIFACTANTS

strain	Surface tension（mN m）	The diameter of oil spreading (mm)
BS01	35.6	12.6
BS02	37.2	11.0
BS03	39.6	10.2
BS04	40.4	9.6

Isolation, extraction and purification of biosurfactant

This crude biosurfactant was further purified by using the Silicagel TLC plates. Different mobile phase system were detected. TLC plates were in stiu acid hydrolysized ,and regularly sprayed with chromogenic agent ninhydrin ,a yellow spot with the Rf value of 0.51 confirms the presence of amino acids.We deduced the biosurfactant extracted from stain BS01 is a kind of lipopeptide biosurfactant.

Characterization of biosurfactant

The structure of biosurfactant was detected by IR (Fig.1) and UV(Fig.2)The N-H stretching vibrations in the transmittance range 3282cm^{-1} and 3064 cm^{-1} indicated the presence of N-H group.The distinct peak values observed at and 1645 cm^{-1} and 1535 cm^{-1} corresponded to the hydrophilic lipopeptide bond. The peak of 2924 cm^{-1}, 2854 cm^{-1}, 1469 cm^{-1} and 1381 cm^{-1} are attibuted to the hydrophobic hydrocarbon chains.The IR spectra revealed the biosurfactant was a type of lipopeptide biosurfactant.

Fig2 showed the tensive peak of 215nm firmly confirmed the biosurfactant containning lipopeptide chain,which is accordance with the privious refered reviews.

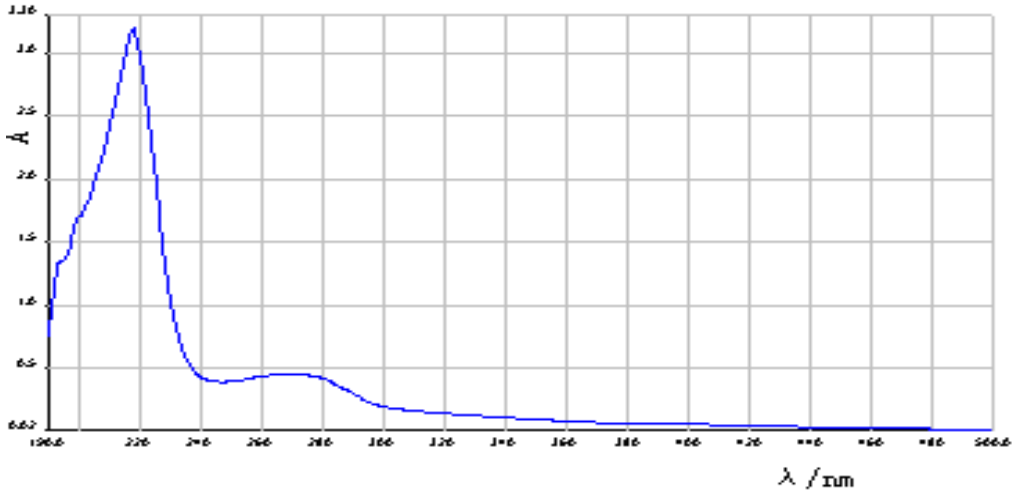


Fig. 2 The UV spectra of the biosurfactant

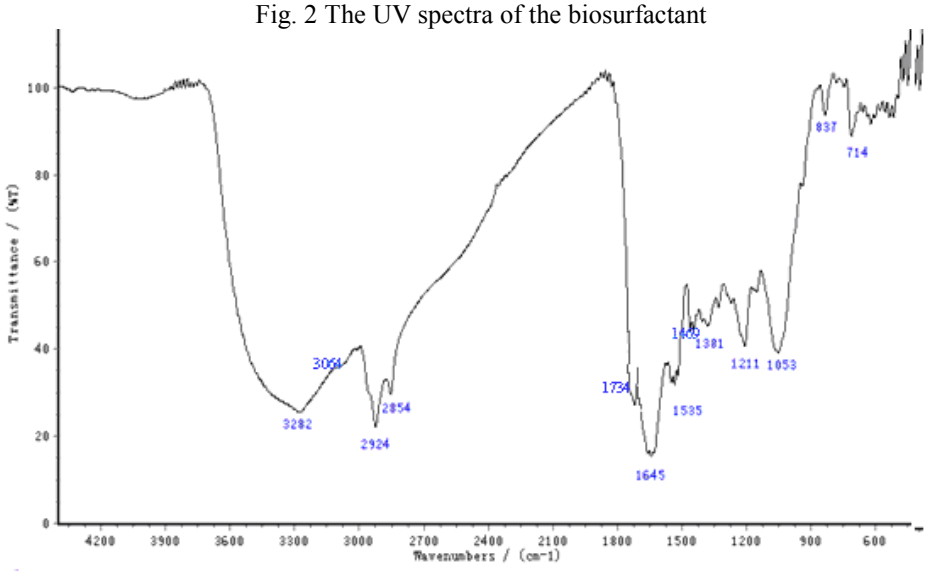


Fig. 1 The IR spectra of the biosurfactant

Critical micelle concentration

The variation of the surface tensionγ with the biosurfactant concentration are shown in the Fig. 3. The plot of γ vs logC show a break at a concentration corresponding to the CMC. The value of CMC is 25mg/l and the value ofγat the CMC is 29.6mN/m. The surface activity of the biosurfactant is significant.

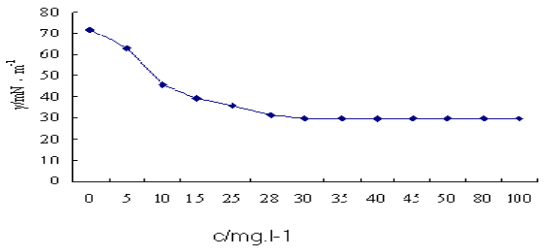


Fig. 3 The curves of relationship between the surfacetension of the biosurfactants aqueous solution and concentration

Antimicrobial Activity

The biosurfactant was screened for their antimicrobial activity against 11 kinds of agricultural pathomycetes and three human pathogenic bacteria as shown in Table.2.

The biosurfactant exhibited extensive inhibitive activity against 11 type of agricultural pathogenic fungi. Notely, it produced the halo of diameter 31mm against the *Sclerotiniasclerotiorum*. Additonally, it was found that the biosurfactant posses good anti bacteria ability against *Staptehyloccocus aureus Rosenbach* and *P.Aeruginosa.*

The adsorption of the amphipathic biosurfactant at the cellular membranes reaches its maximum extent at higher dose leading to complete coverage of the membranes by the surfactant molecules. After the complete coverage, the molecules penetrate through it. Furthermore, the positive charges in the cationic molecules neutralize the negative charges on the bacterial cell membranes. Accordingly, the selective permeability which characterizes the outer cellular membrane is completely deactivated. Hence, the vital transportation of essential components for cell bioreactions and activities is disturbed, causing death for these microorganisms.

Conclusions

In this work, a lipopeptide biosurfactant was isolated, extracted and purified from BS01 stain. The lipopeptide biosurfactant represent great significance in surface activity and extensive inhibition performance. We have full confidence to believe the it will be a potential , effective and broad -spectrum antimicrobial agents.

TABLE.2 INHIBITION OF LIPOPEPTIDE ON PLANT PATHOGENS AND HUMAN PATHOGENIC BACTERIA

Entry	Type of pathogenic bacteria	Inhibition zone diameter [a](mm)
1	*Cordana musae*	12
2	*Sclerotinia sclerotiorum*	31
3	*Cladosporium orbiculare*	14
4	*Fusarium roseum*	24
5	*Colletotrichum atramentarium*	23
6	*Fusarium oxysporum f.sp.*	22
7	*Fusarium moniliforme*	9
8	*Rhizoctonia cerealis*	18
9	*Rhizoctonia solani*	23
10	*Phytophthora capsici*	24
11	*Cladosporium cucumerinum*	15
12	*E. coli*	15.5
13	*Staptehyloccocus aureus Rosenbach*	26
14	*P.Aeruginosa*	26

Acknowledgements

This work was financially supported by science and technology support program of Anshan in China .

References

[1] J. Chen, P.T. Huang, K.Y. Zhan and F.R. Ding： Journal of Applied Microbiology. 112 (2012)660-671.
[2] Ongena, MARCJacques, Philippe: Trends in microbiology. 16(2008)115-125.
[3] Fukushima M: Eicosanoids. 3(1990)189-199.
[4] Diego Romero, Antonio de Vicente: A.P.S. Journals. 20(2007)430-440.
[5] Ylenia Pecci, Fabrizio Rivardo, Maria: Journal of Mass Spectrometry .2010, pp. 772–778 .
[6] Kiran, G.S., Hema, T.A., Gandhimathi, R., Selvin, J., Thomas, T.A., Ravji, T.R. and Natarajaseenivasan, K: Colloids Sur B Biointerfaces. 73(2009)250–256.
[7] Muthu Irulappan Sriram: Bioresource Technology. 102(2011)9291-9295.
[8] Wei Wu ,Yang Wang, Li Que: European Journal of Pharmaceutics and Biopharmaceutics**.** 63(2006)288-294.

Advanced Materials Research Vol. 936 (2014) pp 674-680
© (2014) Trans Tech Publications, Switzerland
doi:10.4028/www.scientific.net/AMR.936.674

Immobilized recombinant chitinase and its inhibition effect on Botrytis cinerea

Zhang Na[1,a], Yan Rui-xiang[2,b*], Guan Wenqiang[3,c]

[1,2.]National Engineering and Technology Research Center for Preservation of Agricultural Products, Tianjin Key Laboratory of Postharvest Physiology and Storage of Agricultural Products, Tianjin 300384, China;

[3.]Tianjin Key Laboratory of Food Biotechnology, College of Biotechnology and Food Science, Tianjin University of Commerce, Tianjin 300134

[a] wuaidehua@163.com, [*b]yrxan@163.com, [c]gwq18@163.com

Keywords: magnetic nanoparticles; carboxyl; recombinant chitinase; immobilized enzyme; Botrytis cinerea

Abstract: To isolate recombinant chitinase quickly and boost its anti-fungi activities in vitro, functional magnetic nanometer carrier was used to immobilize recombinant chitinase from the crude enzyme solution and immobilized recombinant chitinase was applied to test whether it would inhibit the growth of gray mold from fruits. In this study, the carboxyl magnetic carrier was produced by solvent thermal reduction method and characterized by scanning electron microscope (SEM) and fourier transform infrared spectrometer (FTIR). Then, the carboxyl magnetic carrier activated by EDC/NHS was applied to immobilize recombinant chitinase and the immobilization efficiency was investigated by quantitative analysis. To obtain the highest immobilization efficiency, reaction conditions were optimized through combining different pH, temperature and reaction period. The results show that the surface of magnetic carrier was successfully carboxyl and the average diameter was 200nm. The immobilization efdiciency could reach the peak 64.43% after 7h reaction at the condition of pH 6 and 25℃. It also shows that immobilized recombinant chitinase can significantly inhibit the growth of gray mold isolated from table grape compared with the enzyme without immobilization with magnetic nanometer carrier.

Introduction

Fungus as an serious pathogenic factor for postharvest fruits and vegetables have been included in the HACCP system (hazard analysis and critical control point system), since they generally cause postharvest diseases and finally result in large decay of fruits and vegetables [1]. Botrytis cinerea is one such major pathogenic fungal that cause postharvest diseases. Chitinase from plant have been shown the abilities to make most of the pathogenic fungi lose the ability of infecting and causing diseases of plants. These suggest an important role of chitinase in plant disease resistance[2, 3]. However, chitinase is less stable, and difficult to be purified and reused. All these restrain its wide application to protection of the postharvest fruits and vegetables from fungal.

In order to increase chitinase's stability and extend the period for its activity, magnetic carrier was introduced to immobilize chitinase. Magnetic carrier is consist of magnetic nanoparticles coated with organic polymer shell and can be introduced with a variety of function groups, such as epoxy group, carboxyl, chloride, aldehyde, etc.. Magnetic carrier can immobilize enzyme by covalent bond which is generally very stable. Then, magnetic field can be used to easily separate magnetic carrier covalent with enzyme. Therefore, magnetic carrier as one kind of new functional

polymer materials in recent years are widely used in drug controlled release, the immune test, magnetic resonance imaging, medical diagnosis, enzyme immobilization and biological separation, and so on[1].

The magnetic carrier covalent with carboxyl group was used to immobilize recombinant chitinase in this study, realizing the pupose of fast purifing chitinase, boosting the stability of purified chitinase, prolonging the active period of the purified chitinase. This study could provide theoretical basis and technical support for the application of restructuring chitinase in industry. Meanwhile，this study shows some insights into the inhibition of mycelium of grey mould (Botrytis cinerea) with immobilized recombinant chitinase.

Materials and methods

Synthesis of carboxyl magnetic carriers

To synthesize magnetic carriers covalent with carboxyl, 1.08g of FeCl3·6H2O, 2.4g of anhydrous sodium acetate, 2.4g of sodium citrate soluble and 40ml of ethylene glycol were mixed and stirred for 30min. Then the mixture was turned into the reaction kettle for 10h at 200℃. Thereafter, the carboxyl Fe3O4 magnetic microspheres were synthesized. The carriers were collected with external magnet and washed with high pure water followed by ethanol at least 3 times. Then, the carriers were dried at 60℃ under vacuum for at least 8 hours.

Characterization of carboxyl magnetic carrier

A small amount of magnetic carrier was sprayed with gold. The morphology of magnetic nanoparticles was observed by the scanning electron microscope (SEM, Japanese Seiko JEOL).

The carboxyl magnetic carriers were mixed with KBr and sample slices were made with the . The FT-IR spectra of the mixture were recorded by using a Spectrophotometer (Brook instruments, VECTOR22).

Preparation of the immobilized chitinases

30mg of the magnetic carriers was mixed with 1.0ml of MES buffer (25mmol/L, pH5.0) and shaked at 40 rpm for 24h. 100μL of the magnetic particle solution was mixed with, 50μL of 50mmol/ml EDC and NHS solution and shaked at 40 rpm for 30min at room temperature. Under magnetic field, supernatant was discarded and the carriers were, washed with MES solution for 3 times.

The activated carrier were added into the crude recombinant chitinase solution, and shaked for 5h at 25℃ and 40 rpm. Then, the immobilized chitinase was washed 3 times with phosphate buffer solution（0.1mol/L, pH6.0）. The elution was collected to detect the amount of residual chitinase. The resulting immobilized chitinases were held at 4℃ prior to use.

The amount of protein in the crude enzyme solution of recombinant chitinase and in supernatant after immobilization was determined by the Bradford method [2].

Protein load=(weight of crude enzyme protein–weight of residual protein after immobilization)/weight of carboxyl magnetic carrier

Immobilization efficiency=(weight of protein crude enzyme–weight of residual protein after immobilization)/weight of crude enzyme protein

Determination of activity

Determination of activity of free chitinases activity and immobilized chitinases was based on reference Tan[3].

The enzyme action of 1 ml enzyme solution to release the 1μg N-acetyl-D-glucosamine in a minute was defined as enzyme activity units (U). The enzyme activity of U (u/g) =OD585/ (a * tmin), where a is the parameters of enzyme activity linear regression equation, a=0.009

Specific activity of enzyme = enzyme activity / protein content;

Purification factor = immobilized enzyme specific activity / free specific activity of enzyme;

The relative activity (%) was the ratio between the activity of every sample and the maximum activity of sample.

Optimum conditions of chitinases immobilization

The optimum reaction conditions of immobilized chitinase were determined based on the relative activity under a variety of pH (from5.0 to 7.5) value, reaction temperature (from15 to 40℃) and reaction time (from 1-11h).

2.6 Inhibition effect of immobilized chitinases on Botrytis cinerea mycelium

Botrytis cinerea involved in the test was separated and purified from the grapes fruit, which provided by Tianjin key laboratory of postharvest physiology and storage of agricultural products.

Six pieces of diameter 0.06cm bacteria cake was placed into 50mL culture medium, ten parallel samples were followed by adding immobilized chitinase and free chitinase which have been placed for 0d, 2 d, 4 d and 6 d, inactivation of immobilized enzyme and free chitinase as the control. The treatment was shacked in water bath for 3 days at 26±0.5℃. The mycelia was acquired by filtering medium then was washed three times, and then drying to constant weight at 105℃. The experiment was repeated for three times.

The inhibitory rate=(weight of control sample-weight of mycelium mycelial)/(weightof control mycelial)*100%.

Results and discussion

Characterization of magnetic carriers

The size and morphology of carboxyl functional Fe3O4 magnetic carriers were characterized by scanning electron microscopy (SEM) and shown in figure 1. Results showed that the carboxyl Fe3O4 magnetic carriers appear spherical shapes, uniform dispersion, smooth surface, with a mean diameter of 200 nm. This study adopted solvent thermal reduction method. Ethylene glycol as solvent, sodium citrate as complexing agent and sodium acetic acid as reducing agent were used to prepare carboxyl magnetic carrier in the reaction kettle of coating with PTFE. Based on the theory of homogeneous nucleation of LaMer model [4], after the crystal nucleus formation, the more slowly particle formation rate, the narrower nanoparticles size distribution was. Therefore, the surface of Fe ions form complexes after suitable amount of sodium citrate was added into the reaction system. The concentration of Fe ion was reduced, so the generation rate of Fe atoms was reduced. The new crystal nucleus formation was obstructed in the growing process of the old crystal nucleus. All Fe atoms can evenly add to previously crystal nucleus, so Fe particles grew up at uniform rate. In this case, particle size distribution of ferromagnetic nanoparticles is more narrow, even get monodisperse nanoparticles might be obtained[5].

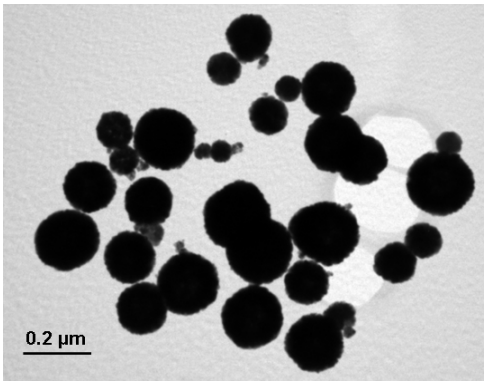


Fig.1 SEM Photos of magnetic carriers

FT-IR analysis

FTIR spectra of carboxyl magnetic carrier were shown in figure 2. The absorption peaks of the stretching vibration of Fe-O keys from Fe3O4 should be at 570cm-1 and 375cm-1 in the macroscopic state. When the size of Fe3O4 was reduced to nanoscale, a large number of cohesion among surface atoms were damaged, leading to the particle's surface electron rearrangement. Therefore, the absorption peaks of Fe-O keys from Fe3O4 appear blue shift phenomenon and characteristic absorption at 430cm-1 and 580cm-1 appeared in the FTIR spectra figure [9]. FTIR results also showed that the absorption peaks presented at 3400 cm-1 and 1652 and1396cm-1 should be attached to the stretching vibrations of O–H, C=O and C–O from carboxyl groups respectively. All these suggest that carboxyl group was successfully introduced to the surface of the magnetic microspheres.

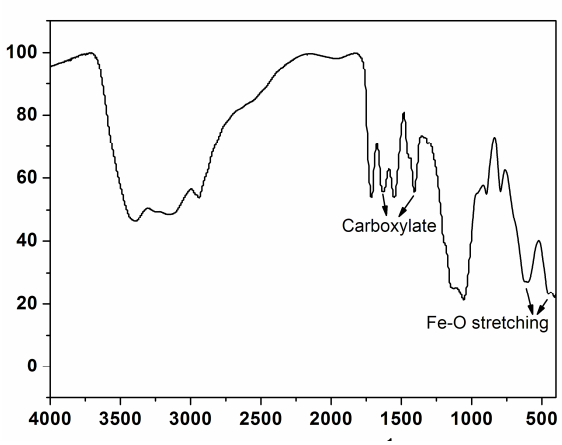


Fig.2 FTIR of magnetic carrier

The effect of temperature on enzyme activity of the immbilized recombinant chitinase

The effects of temperature on the enzyme activity of immobilized recombinant chitinase were shown in figure 3.

It shows that immobilized temperature evidently affects enzyme activity. When the temperature is below 25℃, the higher the temperature was, the higher the relative enzyme activity showed. However, when the temperature exceeds 25℃, the relative enzyme activity decreased linearly, which suggesting that free enzyme quickly deactivated in the immobilization process with increasing temperature increasing. Therefore, the suitable immobilized temperature was 25℃.

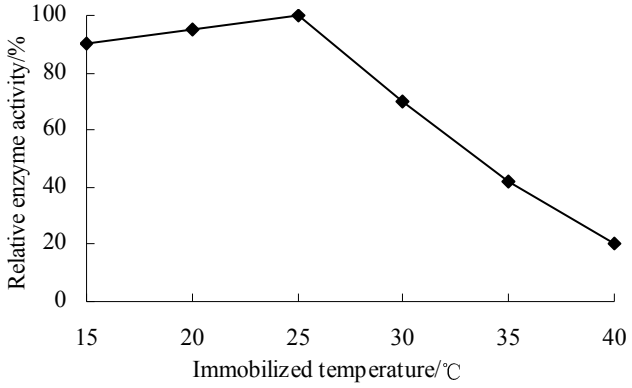


Fig. 3 The effect of immobilized temperature on the relative enzyme activity of immobilized chitinase

The effect of immobilized time on enzyme activity of the immobilized recombinant chitinase

The effects of immobilized time on the enzyme activity of immobilized recombinant chitinase were shown in figure 4.

It can be seen that the enzyme activity of the immobilized enzyme increased with the increasing of immobilization time. When the immobilized time was 7h, the enzyme activity reached maximum. Thereafter, the immobilized enzyme activity slightly decreased.

With the extension of immobilization time, more enzyme molecules combined to binding sites of the carriers. When the binding site reached saturation, the enzyme molecules could not bind up to the sites. Therefore, longer immobilized time will lead to the steric hindrance of enzyme molecules [10], wich will reduce the affinity between enzyme and immobilized carriers and prevent enzyme and substrate binding. These would result in the decrease of enzyme activity. Therefore, 7h should be the right immobilized time in this study.

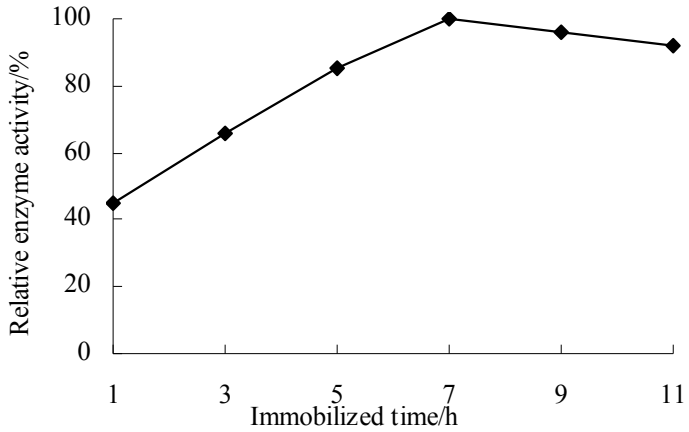


Fig.4 The effect of immobilized time of magnetic carrier on the relative enzyme activity

The effect of immobilized pH on enzyme activity of the recombinant chitinase

Reactions catalyzed by enzymes are very sensitive to the pH value. The effect of immobilized pH on the recombinant chitinase enzyme activity was shown in figure 5.

It shows that the activity of immobilized enzyme increased gradually with the increasing of pH value. When pH value reached 6, the immobilized enzyme activity reached a maximum value. When the pH continue to increase, activity of immobilized enzyme rapidly declined,indicating that immobilized enzyme is sensitive to the change of pH value and pH 6 seems to be the opitimum value for the immobilized chitinase.

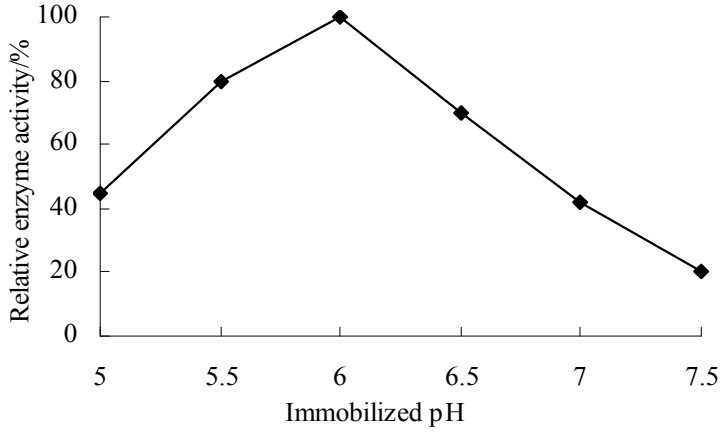


Fig.5 The effect of immobilized pH on the relative enzyme activity

The immobilized efficiency of magnetic carrier on recombinant chitinase

The recombinant chitinase crude enzyme was immobilized by the carboxyl functional magnetic carrier, then the total protein content of crude enzyme and the supernatant was determined to calculate immobilization efficiency. Thereafter, the enzyme activity of crude enzyme and immobilized enzyme was determined to calculate purification multiple. Results were shown in table 1.

As seen in table 1, immobilized efficiency of carboxyl functional magnetic carrier to recombinant chitinase was 64.43%, and purification rate was 3.47, which means the magnetic carrier is a nice way of purification and separation of recombinant chitinase.

Table1 The immobilization rate of magnetic carrier

Crude enzyme protein content (mg/L)	Crude enzyme activity (U/g)	Residue protein content (mg/L)	Immobilized enzyme activity (U/g)	Protein loading (mg/g)	The immobilized efficiency (%)	purification multiple
85.43	9.21	30.39	20.57	55.04	64.43	3.47

Inhibition of Botrytis cinerea mycelium by immobilized recombinant chitinase

Immobilized chitinase enzyme and free chitinase both can inhibit Botrytis cinerea mycelium to grow. As seen in Fig6, the inhibitory rate decreased with the increasing of enzyme storage period, but the inhibition rate of immobilized chitinase decreased more slowly than free enzyme. This is mainly because the stability of immobilized enzyme was better. After stored for 2-6 d, Immobilized enzyme still had strong inhibitory effects on Botrytis cinerea hyphae. However, free enzyme's inhibitory effect on Botrytis cinerea hyphae was significantly decreased and the inhibition rate of Botrytis cinerea hyphae dropped to 5% after 4 d storage of free chitinase enzyme. After 6 d storage, the free enzyme completely loss activity and the inhibition rate fell to 0%. Although inhibition of the immobilized chitinase after storage is gradually reduced, but the inhibitory effect of immobilized enzyme on mycelium was still higher than free enzyme stored for the same period. These demonstrate that enzyme immobilization reaction can keep the activity of chitinase enzyme and improve enzyme stability. Generally, this immobilized recombinant chitinase is conducive to the application in postharvest diseases control.

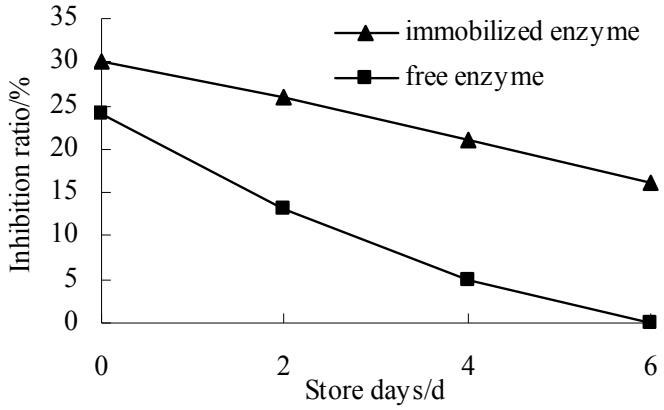


Fig.6 Inhibitory effect of chitinase and immobilized chitinase on Botrytis cinerea in liquid cultures

Conclusions

(1)The carboxyl magnetic nanoparticles that prepared by solvent melting method is functional and the average diameter was 200nm. (2)The magnetic carrier activated by EDC and NHS can stably bind recombinant chitinase and keep the enzyme activity. This suugests that the carboxyl magnetic carrier activated by EDC and NHS might also be stably combined with other enzyme/protein. (3) The optimum immobilized conditions of recombinant chitinase immobilized by carboxyl magnetic carrier are that pH value equals 6, temperature is 25℃, immobilized time is for 7h. (4)Immobilization efficiency of carboxyl magnetic carrier on recombinant chitinase is 64.43%, and purification multiple was 3.47. (5) Immobilized recombinant chitinase could inhibit the growth of Botrytis cinerea hypha of postharvest fruits and vegetables, and the inhibitory effect of immobilized enzyme on hypha only reduced by half after stored for 6d, significantly better than the free enzyme. However, the detailed mechanism how the inhibitory effect on the gray mold on the surface of fruits and vegetables need to be further studied in the future.

Acknowledgments

This research was supported by the National Natural Science Foundation of China (Grant No. 31 101362).

References

[1] L. Xu Sh.Y. Zhang, Y.W Wang et al., Pathogenicity of botrytis cinerea on postharvest grape berrie, ACTA Phytopathologica Sinica. 36(1)(2006) 74-79.

[2] Boller T, Hudroxytic enzymes in plant disease resistance, Plant-Microbe interaction: molecular and genetic perspectives. 2(1987)385-413.

[3] Zh. G.Wu, X.F. Zhu, Molecular biology characterization and application in transgenic plant for chintinase, Chinese Bulletin of Life Sciences. 14(2) (2002)117-121.

[4] G. D. Sturbaum, P. T. Klonicki, Immunomagnetic separation(IMS)-fluorescent antibody detection and IMS-PCR detection of seeded Cryptosporidium parvumo ocysts in natural waters and their limitations, Applied and Environmental Microbiology. 68(2002)2991-2996.

[5] J.Zh. Wang, F.Ming, Protein technology,Beijing: Sinence Press.,2000.

[6] J.X. Tan, Zh.Y Chen, J. Zhang, Isolation and identification of chitinolytic strains and preliminary study on the antifungal activity of its crude chitinases, Plant Protection,27(2001) 1-3.

[7] V. K. Lamer, R.H. Dinegar, Theory, production and mechanism of formation of monodispersed hydrosols,J Am Chem Soc., 72(1950) 4847-4854.

[8] J.W. Guo, T. S. Zhao, J. Pranhuram, et al., Preparation of the physical/ electrochemical properties of a Pt/C nano-catalyst stabilized by citric acid for polymer electrolyte fuel cells, Electrochimica Acta. 50 (2005)1973-1 983.

[9] L. J. Bellamy, The Infrared spectra of complex molecules.Wiley, NewYork: Springer, 1975.

[10] Y. Wang, X. Wang, G. Luo, et al., Adsorption of bovin serum albumin(BSA) onto the magnetic chitosan nanoparticles prepared by a microemulsion system, Bioresource Technology. 99(2009) 3881-3884.

Advanced Materials Research Vol. 936 (2014) pp 681-686
© (2014) Trans Tech Publications, Switzerland
doi:10.4028/www.scientific.net/AMR.936.681

Electrospinning synthesis of PLA fiber film containing antimicrobial silver nanorods

Jiaqi Bai[1], Yanhui Li[2], Qian Duan[2], Jingjing Chang[1*]

[1]School of Chemistry and environmental engineering, Changchun university of Science and Technology, Changchun , China, 130022

[2]School of material science and engineering, Changchun university of Science and Technology, Changchun , China, 130022

sarahchangcpp@gmail.com

Keywords: PLA; Silver nanorods; Antimicrobial properties

Abstract: Poly(L-lactide) (PLA) fiber film containing silver nanorods were prepared via electrospinning. Morphology of the PLA/Ag fibers and distribution of the silver nanoparticles were characterized. These fibers showed antimicrobial activities against Gram-negative E. coli, because of the presence of a small amount of silver nanorods.

Introduction

Poly(L-lactide) (PLA) is a kind of biodegradable material. PLA has good biocompatibility, biodegradability, and non-toxic. In orthopedic fixation repair, artificial skin and tissue engineering and other fields have a wide range of applications. The electrospinning fibers of polymer, which have great specific surface area and high porosity, developed in the wound dressing has a great advantage.

In the past decades, metal nanostructures, for instance nanorods, nanowires and tetrahedron have been widely researched. They were different from other materials, because of their thermal, catalytic and other excellent properties. Silver is a powerful antimicrobial agent, which fit three antimicrobial methods such as antiadhesive, biocide release and contactactive antimicrobial modification [1]. Silver nanorods have been used in medical polymer materials in this paper. Electrospinning technology has received much more interested in fabricating medical polymer fiber film materials which have high specific surface areas [2]. The fibers are collected as a porous fiber film which is suitable for biomedical use such as wound dressing [3-5].

In this study, we added the silver nanorods into spinning dope which used to obtain the PLA composite fiber film. We tested the antibacterial properties of this fiber film. The experimental results were indicated that the film of PLA fibers has antimicrobial effect because of the containing of a small amount of silver nanorods.

Experimental

Materials

Poly(L-lactide) (PLA) (Mw=8,000) was purchased from Changchun institute of applied chemistry academy of sciences. Methylene chloride, silver nitrate ($AgNO_3$), ferric chloride, ethylene glycol (EG), and polyvinyl pyrrolidone (PVP) were all purchased from Beijing chemical factory.

Synthesis and Electrospinning process

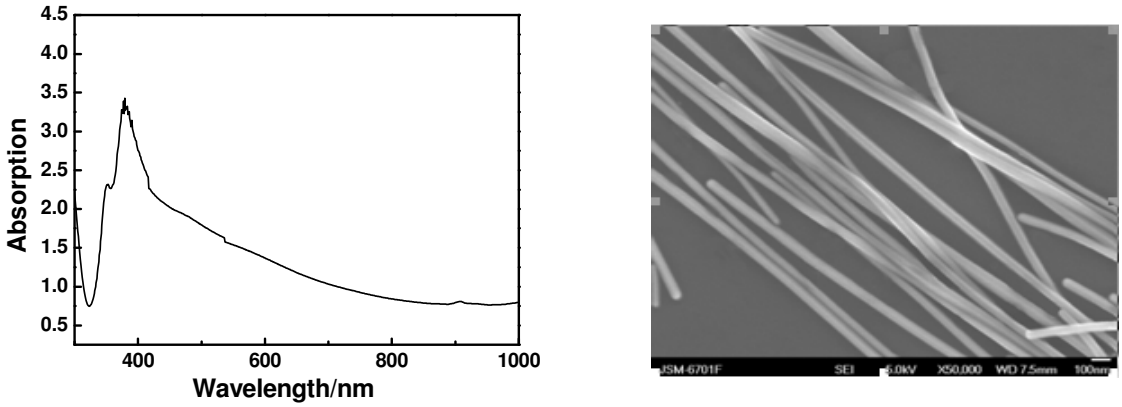
In the process of synthesis, 13 ml solution of $FeCl_3 \cdot 6H_2O$ (4.62×10^{-5} mol L^{-1}, in EG) in a conical flask which was heated to 130 ℃ for 10 min, after that 12 ml of EG dissolve including 0.098 mol L^{-1} $AgNO_3$ and 0.061 mol L^{-1} PVP (Mw=90 000) mixture solution was mixed into the previous hot solution. The mixture was kept at 130 ℃ until all the $AgNO_3$ was dissolved completely, which lasted 1.5 h. With the purpose of examine the morphology of Ag nanorods, 1 mL of the resulted suspension solution was centrifuged at 9000 rpm for 10 min then washed with ethanol, three times. The precipitate was diluted with 10 ml of ethanol, measured as the sample of UV-vis and scanning electron microscopy (SEM) [6].

The electrospinning experiments were performed at 22 ℃, and the electrospinning equipment was assembled according to Lee et al. [7]. The polymer solution was placed in a syringe with the needle attached to a metal clamp, which connected to the high voltage power supply. It offered a positive voltage of 15 KV. An aluminum foil as a negative electrode was placed 15 cm away from the tip.

Measurements

The UV-vis spectrum was taken at room temperature with a Shimadzu UVmini-1240 spectrometer. The morphology of the electrospinning fibers were observed by using a field emission scanning electron microscope (JEOL JSM-6701F). The FTIR spectra were acquired using Shimadzu IR-8400s spectrometer. The X-ray diffraction (Bruker D8 Advance) patterns were performed in a 2-theta scan configuration in the range of 10-80°.

Results and discussion



(a) (b)

Fig. 1 UV–vis absorption spectra (a) and SEM image (b) of silver nanorods.

Fig. 1 (a) shows the UV–vis absorption spectrum of silver nanorods product. The spectrum of precipitation clearly exhibits two surface plasmon resonance peaks at 350 and 380 nm, which are the optical finger prints of silver nanorods [8-10]. Fig. 1 (b) shows the SEM image of silver nanorods that have a length of about 5 μm and a diameter of about 46 nm.

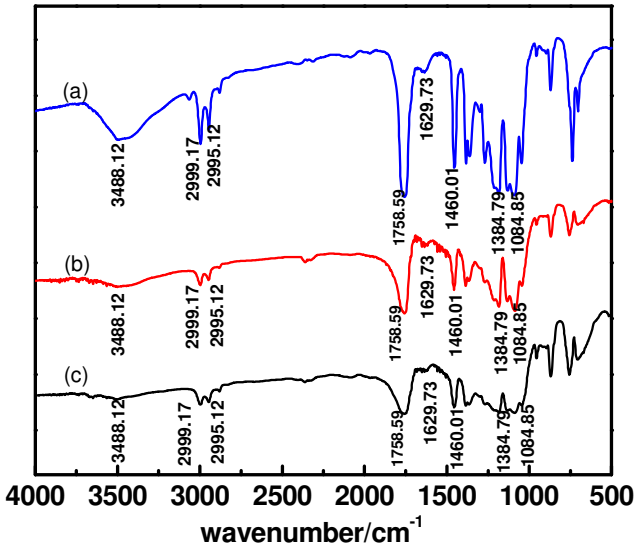


Fig. 2 FTIR spectra of PLA in methylene chloride (a), PLA/Ag fibers (b) and PLA fiber film (c)

The FTIR spectra of PLA in methylene chloride, PLA/Ag fibers and PLA fiber film shows in Fig. 2 respectively. The characteristic peaks of the hydroxy group (3488.12 cm^{-1}) can be seen obviously in Fig. 2 (b) and (c), which indicate the disappearance of hydrogen bonds that presents between PLA and methylene chloride. 2997.17 cm^{-1} and 1629.73 cm^{-1} belongs to methyl stretching and bending vibration peaks, 2995.12 cm^{-1} and 1758.59 cm^{-1} belongs to methyne stretching and bending vibration peak, 1460.01 cm^{-1} belongs to carbonyl stretching vibration peak and 1384.79 cm^{-1}, 1085.84 cm^{-1} belongs to carbony antisymmetric and symmetric stretching vibration peak. But, methyne stretching and bending vibration peak in Fig. 2 (a) are stronger than that in (b) and (c) because they are methylene chloride solvent peaks. The spectra of FTIR prove that dichloromethane solvents can be volatile out completely during the process of spinning.

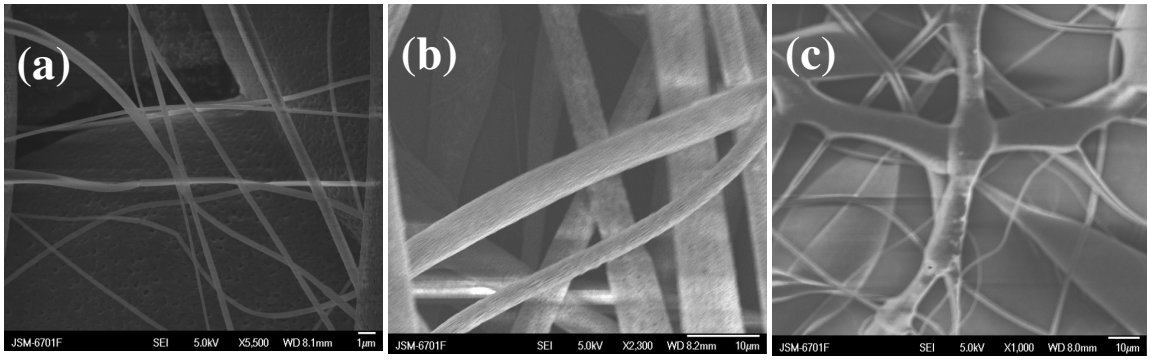


Fig. 3 SEM images of (a) 8 wt% PLA, (b)10 wt% PLA and (c)12 wt%PLA electrospnning fibers

Fig. 3 demonstrates SEM images of the electrospnning fibers of PLA of 8 wt%, 10 wt% and 12 wt%. The SEM results show that the electrospinning get best film properties in three conditions of PLA mass fraction of 10 wt%, spinning voltage of 15 KV and receiving distance of 15 cm.

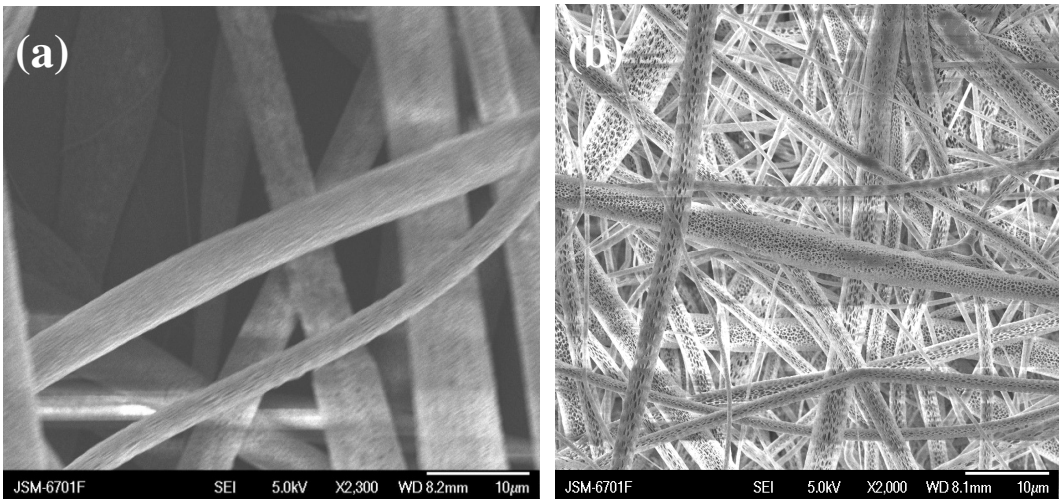


Fig. 4 SEM images of (a) PLA and (b) PLA/Ag 0.1 electrospinning fibers.

Fig. 4 illustrates SEM images of electrospinning fibers from 10 wt% PLA and 10 wt% PLA/Ag 0.1 solution. The average diameter of the fibers slightly decreased from 10 μm in Fig. 4 (a) to 6 μm in Fig. 4 (b), as the silver content increased [11]. A porous fiber film was observed. With the addition of nanorods, the filbers appear the porous structure that increase the specific surface area of fiber film, which improved the application as a biological material.

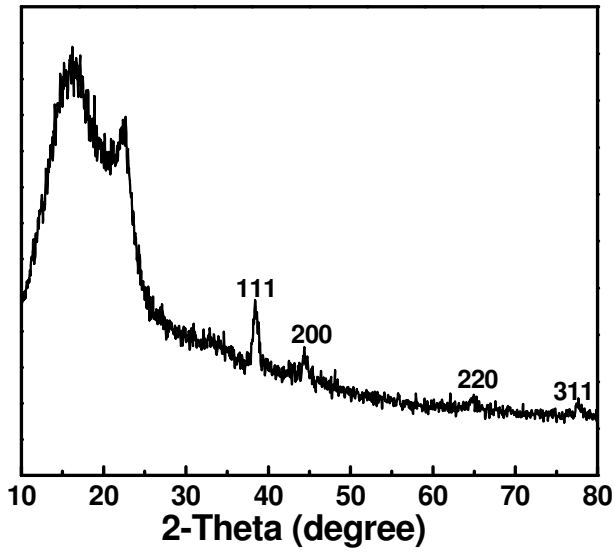


Fig. 5 XRD patterns of PLA/Ag composite fibers

Fig. 5 shows the XRD patterns of PLA/Ag composite fiber film. They respectively corresponding to the diffraction planes of (111), (200), (220) and (311) of silver [12]. It proves that the silver nanorods are embedded in the PLA fibers.

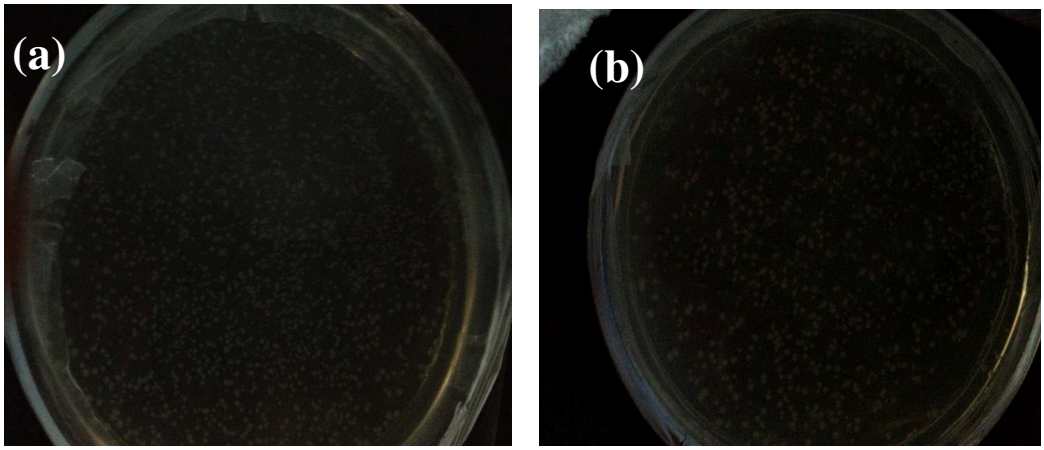


Figure 6 The antibacterial experiments of PLA(a) and PLA/Ag 0.1 fiber film

Fig. 6 shows the result of the antibacterial test for the PLA and PLA/Ag 0.1 fiber film against Gram-negative E. coli. As a result, the PLA fiber films containing silver nanorods have a certain role of inhibited the proliferation of Gram-negative E. coli. These results illustrate the silver nanorods in charge of the antibacterial activity of the composite fibers. The antibacterial improving experiments will report in future.

Summary

PLA fiber film containing silver nanorods were successfully prepared via electrospinning and characterized by multiple characterization methods. The results show that electrospinning synthesis of PLA fiber film containing silver nanorods have a structure of porous fiber film. The PLA fiber film containing silver nanorods have a certain role of inhibited the proliferation of Gram-negative E. coli. The antimicrobial porous fiber film of PLA containing silver nanorods could have a good application as wound dressing.

Acknowledgment

We thank the helpful comments and suggestions from our colleagues in Chemical and environmental engineering, Changchun university of Science and Technology at Changchun. Financial support was provided by the Provincial Science and Technology Departant (the project development plan of science and technology of Jilin Province No.201201120).

References

[1] C.H. Ho, I. Tobis, C. Sprich, R. Thomann, J.C. Tiller, Nanoseparated polymeric networks with multiple antimicrobial properties, Adv Mater. 16 (2004) 957-961.

[2] X. Xu, Q. Yang, Y. Wang, et al, Biodegradable electrospun poly (L-lactide) fibers containing antibacterial silver nanoparticles, Eur. Polym. J. 42 (2006) 2081–2087.

[3] P.L. Taylor, A.L. Ussher, R.E. Burrell, Impact of heat on nanocrystalline silver dressings: Part I: Chemical and biological properties, Biomaterials. 26 (2005) 7221–7229.

[4] Z.C. Xing, W.P. Chae, M.W. Huh, et al, In vitro assessment of antibacterial activity and cytocompatibility of silver-containing PHBV nanofibrous scaffolds for tissue engineering, Biomacromolecules. 11 (2010) 1248–1253.

[5] K. Vasilev, J. Cook, H.J. Griesser, Antibacterial surfaces for biomedical devices, Expert Review of Medical Devices. 6 (2009) 553-567.

[6] J. Jiu, K. Murai, D. Kim, et al, Preparation of Ag nanorods with high yield by polyol process, Mater. Chem. Phys. 114 (2009) 333-338.

[7] K.H. Lee, H.Y. Kim, Y.J. Ryu, et al, Mechanical behavior of electrospun fiber mats of poly (vinyl chloride)/polyurethane polyblends, J. Polym. Sci., Part A: Polym. Chem. 41 (2003) 1256–1262.

[8] V.F. Puntes, K.M. Krishnan, A.P. Alivisatos, Colloidal nanocrystal shape and size control: the case of cobalt, Science. 291 (2001) 2115-2117.

[9] Y. Sun, B. Gates, B. Mayers, Y. Xia, Crystalline silver nanowires by soft solution processing, Nano Lett. 2 (2002) 165-168.

[10] Y. Sun, Y. Yin, B. Mayer, T. Herricks, Y. Xia, Uniform silver nanowires synthesis by reducing $AgNO_3$ with ethylene glycol in the presence of seeds and poly (vinyl pyrrolidone), Chem. Mater. 14 (2002) 4736-4745.

[11] K. Ohkawa, K.I. Minato, G. Kumagai, S. Hayashi, H. Yamamoto, Chitosan nanofiber, Biomacromolecules. 7 (2006) 3291–3294.

[12] H.J. Jeon, S.C. Yi, S.G. Oh, Preparation and antibacterial effects of $Ag–SiO_2$ thin films by sol–gel method, Biomaterials. 24 (2003) 4921-4928.

Advanced Materials Research Vol. 936 (2014) pp 687-694
© (2014) Trans Tech Publications, Switzerland
doi:10.4028/www.scientific.net/AMR.936.687

Characterization of Three Calcium Phosphate Microporous Granulated Bioceramics

Nelson H. A. Camargo[1a], Priscila F. Franczak[1b], Enori Gemelli[1c,]
Bruna Ditzel da Costa[2a] Aury Nunes de Moraes[2b]

[1] Santa Catarina State University – UDESC, Materials Science and Engineering Program PGCEM Mechanical Engineering Department, Rua: Paulo Malschitski S/N – Zona Industrial Norte 89.219-710 – Joinville – SC – Brazil

[2] Santa Catarina State University – UDESC Centro de Agroveterinário –CAV, Av. Luiz de Camões,2090, Bairro Contadinheiro – 88.520-000 – Lages SC. Brazil

[a]dem2nhac@joinville.udesc.br, [b]Priscila_jlle@yahoo.com.br, [c]enori@joinville.udesc.br, [a]bruna_ditzel@yahoo.com.br [b]a2anm@cav.udesc.br

Keywords: Bioceramics, Microstructure, Microporosity, Characterization.

Abstract: The calcium phosphate microporous bioceramics, and hydroxyapatite (HA) and β-tricalcium phosphate (β-TCP) biphasic compositions, in the granular form of microporous biomaterials, are research themes and present potential biomedical applications in rebuilding and repairing maxillofacial bone and tooth structure and in orthopedic applications. This is associated with microstructural characteristics of biocompatibility and bioactivity and osteoconductivity properties that these biomaterials offer when applied *in vivo* or in simulated environment. Another differential point of these biomaterials is the solubilization capacity that they present when applied in the biological environment. These compositions of calcium phosphates (hydroxyapatite matrix and/or β-tricalcium phosphate) allow for the gradual release of calcium and phosphate ions for the biological environment, which are absorbed and promote the formation of new bone tissue. These materials are also promising in applications in the field of traumatology as in the repair of traumatized bone tissue and drugs controlled release and bone structure treatments. The favorable results of these biomaterials as bone reconstruction matrix and drugs controlled release are associated with crystallographic characteristics, morphology, surface and solubility that these biomaterials present when in contact with body fluids. This work aimed to describe three types of calcium phosphate microporous granulated biomaterials. The biomaterials used were provided by the Biomaterials' Group from Universidade do Estado de Santa Catarina - UDESC and are: hydroxyapatite, β-tricalcium phosphate and biphasic composition 60% hydroxyapatite/40% β-tricalcium phosphate. The Scanning Electron Microscopy technique (SEM) was used for carrying out the morphological characterization and microstructure studies of granulated biomaterials. The X-Ray Diffractometry (XRD) served for characterization of crystalline phases. Arthur Method was used for determining open porosity and hydrostatic density of biomaterials. The BET technique served to support determination of the surface area of microporous granulated biomaterials. The results are encouraging and show that these biomaterials present promising morphological characteristics and microporous microstructure as wettability and capillarity. These characteristics may contribute to biomaterial osteointegration by new tissue, bone formation and mineralization process.

Introduction

The calcium phosphate bioceramics and hydroxyapatite–β-tricalcium phosphate biphasic compositions are biocompatible biomaterials and present crystallographic similarity to bone tissue and teeth apatites and play the role of osteoinduction and osteointegration when applied *in vivo* [1,2,3,4].

The calcium phosphate bioceramics in the form of granules or microporous blocks had been featured in research as materials for repairing defects and bone tissue reconstruction, as already

observed by different authors, who performed *in vitro* and *in vivo* tests and observed the good performance of these bioceramics in bone neoformation [5, 6, 7, 8]. This is because these biomaterials have bioactivity, solubilization capacity, wettability and interconnected microporous microstructures and high grain surface area and micropores [9, 10, 11]. These properties are promising for adhesion of osteoblasts cells on the granules surface through the inter-granular micropores. These microporous microstructures also favor the extension of osteoblasts cells to the interior of the interconnected microporosity of granulated biomaterial, providing better conditions for bone tissue mineralization [12,13]. These bioceramics are generally manufactured with an architecture composed of macro and microporosity, which has generated favorable results to the mechanism of adhesion and cell proliferation, thus contributing to the osteoinduction system, bone tissue repair and reconstruction [13, 14, 15, 16].

The biomaterials used in this study were obtained by the wet synthesis method, through the dissolution/precipitation of liquid-solid phase involving CaO and phosphoric acid solution necessary for formation of Ca/P molar compositions. Three compositions of granulated materials were used as follows: microporous hydroxyapatite, β-tricalcium phosphate and a biphasic composition of 60% hydroxyapatite /40% β-tricalcium phosphate.

The results presented refer to studies of morphological, microstructural, physical and chemical characterization. The characterization studies were carried out with the help of the Scanning Electron Microscopy technique (SEM), X-Ray Diffractometry (DRX). and by Fourier Transform Infra-Red spectrometry (FTIR).The hydrostatic density and open porosity were determined by Arthur Method and surface area by BET.

Experimental Method

Three compositions of calcium phosphate microporous granulated biomaterials were used in this work: hydroxyapatite, β-tricalcium phosphate and biphasic 60% HA/40%β-TCP (HA/β-TCP). These were elaborated in the microporous granulated biomaterials form with size between 200μm and 500μm.

The preparation of nanostructured powders was performed with help of a high-energy NETZSCH attrition mill, with zircon beads with a diameter of 2.0 mm and distilled water. The attrition mill process was conducted with a solid/liquid concentration of 50%/50% in volume. This process in attrition mill was kept under stirring for a period of one hour, as described by [10, 17].

The colloidal suspension retrieved from the attrition mill was dried in rotary evaporator, providing agglomerated calcium phosphates nanostructured powders. These pellets went through the process of classification by sieves through #500 mesh and the accumulated granulated material was recovered in #200 mesh.

The granulated material obtained was submitted to sintering at a temperature of 1100ºC/2h, providing microporous granulated biomaterials.

Morphological and microstructural characterization studies of microporous granulated biomaterials were carried out with the help of a ZEISS scanning electron microscope, model DSM 940A, through the secondary electrons system (SE) and retro-scattered (BSE).

In order to facilitate the characterization work through the scanning electron microscopy technique, the biomaterials were prepared using a disc sample holder made of aluminum with smooth surface. A double-sided carbon ribbon was attached on the smooth surface of the disc, on which the biomaterials were deposited.

In order to avoid the charge effects inside the chamber, all biomaterials underwent metallization process by sputtering, with deposition of a gold film on the surface of the samples. This deposition was performed through Bal-Tec model SCD 050 Sputter Coater. The ion-deposition parameters were set as follows: temperature at 25ºC in metallization chamber, 40mA current, 2kV voltage and deposition time of 140 seconds, providing a gold film on the samples surface at order of 30nm [18].

For the determination of open porosity (%) and hydrostatic density (g/cm^3), the Arthur Method was used [19]. Previously the granulated biomaterials were dried in a kiln at temperature of

100°C/24h. This method consists in measuring the weight of air-dried samples (*Par*), then they are soaked with xylene inside a vacuum chamber at about 10^{-3}mbar and this low pressure is maintained for 20 minutes, then the vacuum is broken and the granulated biomaterial is removed for realization of measures of weight of microporous biomaterial soaked in xylene (*Pxa*); shortly after, the weight of biomaterial soaked in xylene immersed in distilled water (*Pxe*) is measured. With the results of these measurements the values of open porosity and hydrostatic density are determined, with the help of the (Eq. 01) about open porosity (%) and with the (Eq. 02) about hydrostatic density (g/cm^3). These calculations were performed for the granulated biomaterials: HA, β-TCP and biphasic composition 60% HA/40% β-TCP.

$$d_h = \frac{Par.de}{Pxa - Pxe} \quad (1)$$

$$P.A. = \frac{(Pxa - Par).de}{(Pxa - Pxe).dx}.100 \quad (2)$$

With:

Par – air-dried weight (g);
Pxa – soaked in xylene weight (g);
Pxe – soaked in xylene immersed in distilled water weight (g);
d_h – hydrostatic density (g/cm^3);
dx – xylene density (0,8802 g/cm^3);
de – water density (g/cm^3);
P.A – open porosity (%).

The BET method (Brunauer, Emmett and Teller) was used in this study to determine surface area of microporous granulated biomaterials: HA, β-TCP and biphasic 60% HA/40% β-TCP. This method consists of physical absorption of a gas (N_2, H_2 or He) at low temperature, on open porosity and on the grains surface and micropores of granulated biomaterial, thus filling the entire surface of the microporous granulated biomaterials.

The x-ray diffractometry (XRD) served on crystallographic characterization of microporous granulated biomaterials. In this study a SHIMADZU x-ray diffractometer model XRD LAB X-6000, with anti-cathode copper tube, was used. To obtain the x-rays diffraction, a 40kV voltage and current of 30mA were used, being the scanning angular range from 5° to 80°, with a goniometer speed of 2º/min in function of 2θ.

The Fourier Transform Infrared Spectroscopy technique assisted in this characterization study of microporous granulated biomaterials. This method consists of identifying the vibrational modes of the OH^- and PO_4^{-3}grouping. The analyses were carried out in the wavelength range from 4000 to 500cm^{-1} with 4.0cm^{-1} precision.

Results and Discussion

The results of morphological and microstructural characterization obtained from microporous granulated biomaterials revealed, through their micrographs, the granules morphology, with irregular shapes presenting sizes between 200μm and 500μm, as can be observed in figures 1a, 2b and 1c. Another observation was the interconnected microporous microstructure of granulated biomaterials, as shown on the micrographs represented in figures 2a, 2b and 2c. Relating the micrographs obtained from microstructure of microporous granulated biomaterials, it was observed there is finer grain morphology, indicating there is greater microporosity for HA granulated biomaterials and biphasic composition, compared to β-TCP granulated biomaterial.

The open porosity in percent and the hydrostatic density were determined using the Arthur Method [19]. Open porosity and hydrostatic density measurements were performed for the different compositions of microporous granulated biomaterials: HA, β-TCP and biphasic 60%HA/40%β-TCP, obtained from the sintering at temperature of 1100ºC/2h. The results are represented in table1.

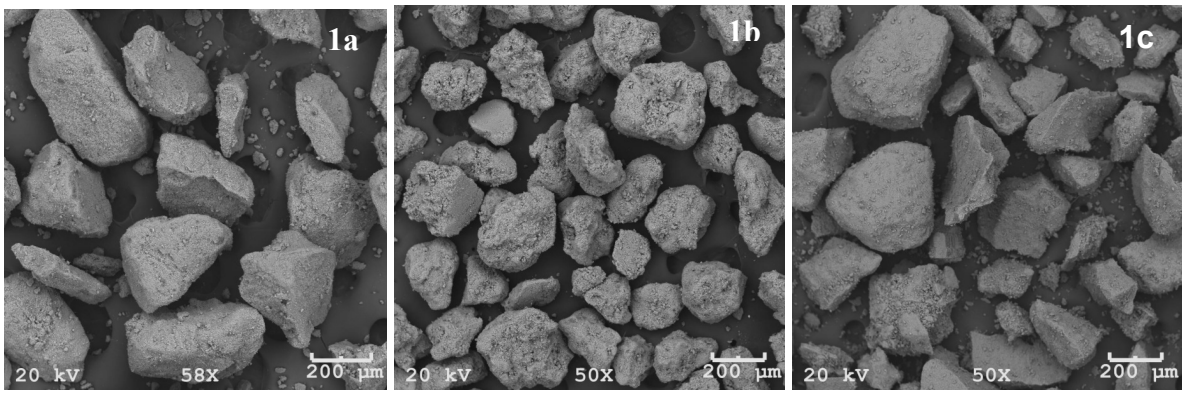


Figure (1a). Hydroxyapatite (HA) granulated biomaterial morphology; (1b). β-TCP granulated biomaterial morphology and (1c) Biphasic 60%HA/40%β-TCP granulated biomaterial morphology

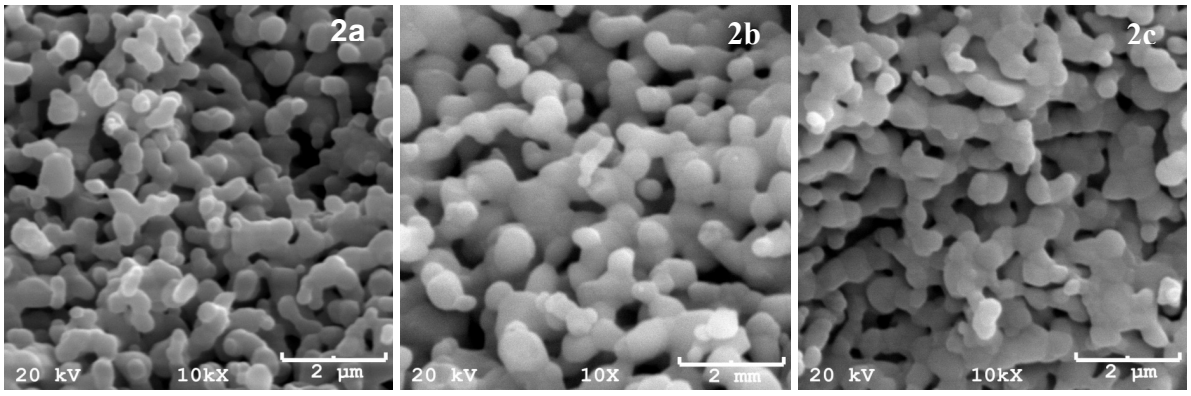


Figure (2a). HA granulated biomaterial microstructure; (2b) β-TCP granulated biomaterial microstructure and (2c) 60%HA/40%β-TCP biphasic granulated biomaterial microstructure

TABLE 1. OPEN POROSITY, THEORETICAL DENSITY AND HYDROSTATIC DENSITY RESULTS OBTAINED FOR THE MICROPOROUS GRANULATED BIOMATERIALS.

Granulated Biomaterial	PA (%)	d_{th} (g/cm^3)	d_h (g/cm^3)
HA	77.64±1.67	3.16±0.001	1.96±0.04
β-TCP	76.57±0.82	3.07±0.001	2.18±0.04
60%HA/40%β-TCP	77.76±1.69	3.12±0.004	1.87±0.03

PA = open porosity; $\mathbf{d_{th}}$ = theoretical density; $\mathbf{d_h}$ = hydrostatic density

The results about open porosity presented in table 1 showed approximate values between microporous granulated biomaterials. A slight variation between the hydrostatic density values was also found, showing lower value for the biphasic granulated microporous biomaterial (1.87 g/cm^3). The bibliography shows that calcium phosphate biomaterials with interconnected microporous microstructures are promising in biomedical applications, in defects repairing and bone tissue reconstruction. These interconnected microporous microstructures formed by fine grains offer the best conditions of wettability, capillarity, oxygenation, cellular adhesion on the grain and micropores surface, promoting osteoinduction, osteointegration and new bone tissue neoformation, as already observed by different authors [3, 4, 5, 6, 20].

The surface area analysis was performed to microporous granulated biomaterials: HA, β-TCP and biphasic 60%HA/40%β-TCP. The results are shown in table 2, compared to the values obtained from the open porosity and hydrostatic density. It can be noticed in the table 2 that surface area values are close between the microporous granulated biomaterials in study, showing greater surface area value for the hydroxyapatite granulated biomaterial: 3.62 m^2/g. The explanation is that hydroxyapatite biomaterials present slightly finer grain morphology in relation to other biomaterials in study, as can be observed in micrographs represented in figures 2a, 2b and 2c.

TABLE 2. SURFACE AREA, OPEN POROSITY, THEORETICAL DENSITY AND HYDROSTATIC DENSITY RESULTS FOR THE MICROPOROUS GRANULATED BIOMATERIALS STUDIED.

Granulated Biomaterial	BET (m^2/g)	PA (%)	$d_{th}(g/cm^3)$	$d_h(g/cm^3)$
HA	3.62	77.64 ± 1.67	3.16 ± 0.001	1.96 ± 0.04
β-TCP	2.67	73.67 ± 0.82	3.07 ± 0.001	2.33 ± 0.04
HA/β-TCP	2.78	77.96 ± 1.69	3.12 ± 0.004	1.87 ± 0.03

The results obtained by x-ray diffractometry of the granulated biomaterials clearly revealed in their x-ray diffractograms the presence of hydroxyapatite phase, β-tricalcium phosphate and hydroxyapatite/β-tricalcium phosphate for biphasic composition, as shown in the x-ray diffractograms represented in figures 3, 4 and 5. In figure 3 the presence of well-defined peaks of stoichiometric hydroxyapatite phase in the composition $Ca_{10}(PO_4)_6(OH)_2$ can be noticed, with main diffraction plane of [211] and hexagonal crystalline structural system.

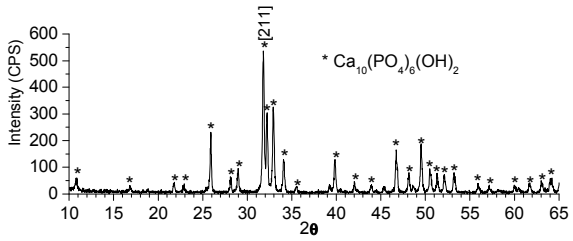


Figure 3. X-ray diffractograms obtained from HA granulated biomaterial.

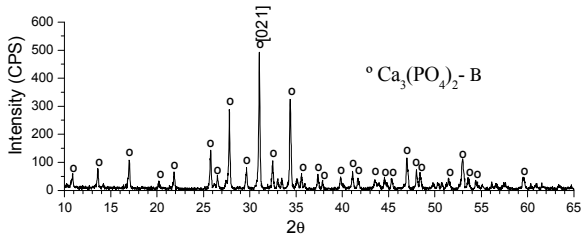


Figure 4. X-ray diffractograms obtained from β-TCP granulated biomaterial.

Figure 4 illustrates the diffractogram obtained from β-tricalcium phosphate granulated biomaterial. The well-defined peaks of β-TCP (Whitlockite) phase at composition β-$Ca_3(PO_4)_2$ rhombohedral crystalline system can be noticed, with main diffraction plane of [021].

Figure 5 illustrates the diffractogram obtained from biphasic 60% HA/40% β-TCP granulated biomaterial. The representative peaks of stoichiometric hydroxyapatite phase and β-TCP phase are noticeable in the diffractogram, with main plane of diffraction [211] to HA phase and [021] for β-TCP phase.

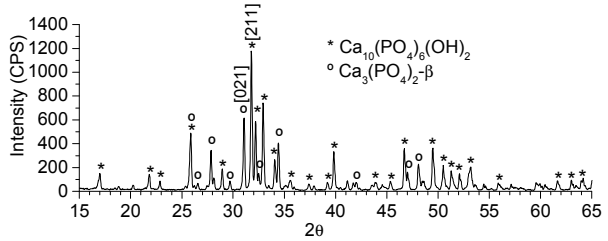


Figure 5. X-ray diffractograms obtained from biphasic HA/β-TCP granulated biomaterial.

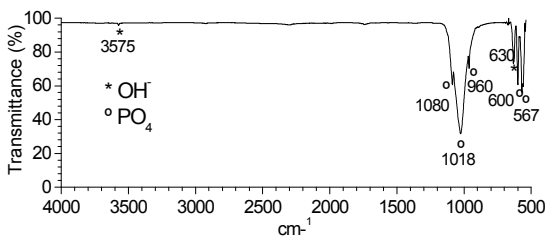


Figure 6. Spectrogram obtained from HA granulated biomaterial.

The infrared spectroscopy technique was used to complement the characterization studies about microporous granulated biomaterials. This method allowed the identification of the vibrational bands of functional PO_4^{-3} and OH^- groupings. Figure 6 shows the spectrogram obtained from granulated microporous HA. The presence of the vibrational bands in 3575cm^{-1} and 630cm^{-1} is observed, indicating the presence of vibrational OH^- grouping. PO_4 groupings are also noted in the spectrogram, evidenced by presence of the vibrational bands in 1087cm^{-1}, 1022cm^{-1}, 960cm^{-1}, 600cm^{-1}, 567cm^{-1}. This result clearly shows the vibrational bands of the OH^- and PO_4 groupings, typical from hydroxyapatite biomaterial, as already observed by other authors [2.9, 21, 22, 23]. The result obtained by FTIR confirms those already obtained by x-ray diffractometry, which indicated the hydroxyapatite phase (Fig. 3).

In the case of β-TCP microporous granulated biomaterials (Fig. 7), only the PO_4 grouping in 1083cm^{-1}, 1080cm^{-1}, 976cm^{-1}, 943cm^{-1} and 600cm^{-1}, that are typical to the β-TCP, is noted in the spectrogram. These same vibrational bands have already been noted by other authors [24]. These analyzed results along with the results obtained by x-ray diffractometry show that the biomaterial is formed by β-TCP phase (Fig. 4).

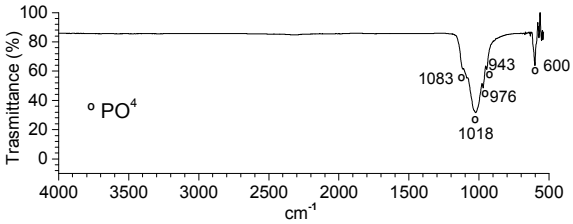


Figure 7. Spectrogram obtained from β-TCP granulated biomaterial.

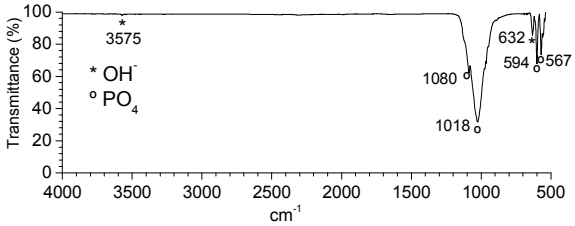


Figure 8. Spectrogram obtained from HA/β-TCP granulated biomaterial.

For the biphasic composition 60% HA/40% β-TCP (Fig. 8), the OH^- grouping in 3575cm^{-1} and 632cm^{-1} was observed. The vibrational PO_4 groupings are present in 1080cm^{-1}, 1018cm^{-1}, 594cm^{-1} and 567cm^{-1}, as can be seen in figure 8, as already observed for the hydroxyapatite and β-tricalcium phosphate biomaterials.

Conclusion

The microstructural and morphological characterization clearly showed that the biomaterials are formed by granules with various forms, which presented microporous microstructures formed by fine grains with equiaxial forms. These properties are promising to adhesion and cell proliferation in micropores and grain surface.

The open porosity and hydrostatic density studies highlighted the presence of significant porosity for all biomaterials, showing open porosity's best result for the biphasic biomaterial HA/β-TCP. This result certainly can contribute in the process of osteointegration of biomaterial and new bone tissue mineralization.

The results obtained by BET showed greater value of surface area for the biomaterial HA (3,62 m^2/g), which is justified by the slightly inferior grain morphology than other biomaterials and also due to its microporosity.

The results obtained by x-ray diffractometry showed the presence of the respective phases for each composition: hydroxyapatite, β-tricalcium phosphate and biphasic composition HA/β-TCP.

The result obtained by FTIR clearly showed the presence of the vibrational bands of PO_4^{-3} and OH^-, present in calcium phosphates. This result came to supplement those obtained by x-ray diffractometry, showing that the biomaterials are formed by HA and β-TCP phases respectively.

The results found in this work are encouraging and show that microporous granulated biomaterials are promising for use as bone substitutes. This is associated with the interconnected microporous microstructures formed by fine grains and their porosity higher than 70%. These

properties are favorable to wettability, capillary action, cell adhesion on the surface of grains and micropores, thus giving better conditions to osteoinduction and osteointegration process and formation of new bone tissue.

References

[1] Camargo, N. H. A. ; Lima, Sarah Amin de ; Souza, J. C. P. ; Aguiar, Juliana Francine de ; Gemelli, Enori ; Meier, M. M. ; Cardoso ; Mittelstädt . Synthesis and Characterization of Nanostructured Ceramic Powders of Calcium Phosphate and Hydroxyapatite for Dental Applications. Key Engineering Materials, v. 398, (2009), p. 619-622.

[2] Huipin Yuan, Kenji Kurashia, Joost D. de Bruijn, Yubao Li, K. de Groot, Xingdong Zhang; A preliminary study on osteoinduction of two kinds calcium phosphate ceramics. Biomaterials nº 20, (1999), p. 1799-1806.

[3] Oliver Gathier, Jean-Michel Bouler, Eric Aguado, Paul Pilet Guy Daculsi; Macroporous biphasic calcium phosphate ceramics: Influence of macropore diameter and macroporosity percentage on bone ingrowth. Biomaterials nº 19, (1998), p. 133-139.

[4] K. Kurashina, H. Kurita, Q. Wu, A. Ohtsuka, H. Kobayashi; Ectopic osteogenesis with biphasic ceramics of hydroxyapatite and tricalcium phosphate in rabbits. Biomaterials, nº 23, (2002), p. 407-412.

[5] Shahram Ghanaati, Mike Barbeck, Carina Orth, Ines Willershausen, Benjamin W. Thimm, Christane Hoffmann, Angela Rasic, Robert A. Sader, Ronald E. Unger, Fabian Peters, C. James Kirkpatrick Influence of β-tricalcium phosphate granule size and morphology on tissue reaction in vivo. Acta Biomaterialia, nº 6, (2010), p. 4476-4487.

[6] T. L. Livingston, S. Gordon, M. Archambault, S. Kadiyala, K. Mcintosh, A. Smith, S. J. Peter; Mesenchymal stem cells combined with biphasic calcium phosphate ceramics promote bone regeneration. Journal of Materials Science: Matrials in Medicine nº 14, (2003), p. 211-218.

[7] Jianxin Wang, Weiqun Chen, Yubao Li, Sanjun Fan, Jie Weng, Xinggdong Zhag; Biological evaluation of biphasic calcium phosphate ceramic vertebral laminae. Biomaterilas, nº 19, (1998), p. 1387-1392.

[8] T. Tanaka, S. Kitasato, M. Chazono, Y. Kumagga, T. Iida, M. Mitsuhashi, A. Kakuta and K. Marumo. Use of an injeectable complex of β-tricalcium phosphate granules, hyaluronate, and fibroblast growth factor-2 on repair of unstable intertrochanteric fractures. The Open Biomedical Engineering Journal, nº 6, (2012), p. 98-103.

[9] Nelson H. A. Camargo, Sarah A. de Lima, Enori Gemelli; Synthesis and Characterization of Hydroxyapatite/TiO_{2n} Nanocomposites for Bone Tissue Regeneration, American Journal of Biomedical Engineering, vol. 2, (2012), p. 41-47.

[10] Dalmônico, G. M. L., Síntese e caracterização de fosfato de cálcio e de hidroxiapatita: elaboração de composições bifásicas HA/TCP-β para aplicações biomédicas. Dissertação de mestrado em Ciência e Engenharia de Materiais, Universidade do Estado de Santa Catarina, Joinville-SC, ((2012), P. 95.

[11] B. Lautre, M. Descamps, C. Delecourt, M. Blary, P. Hardouin; Porous HA ceramic for bone replacement: role of the pores and interconnections experimental study in the rabbit, The Journal of Materials Science: Materials in Medicine nº 12, (2001), p. 679–682.

[12] A. L. Rosa, M. M. Beloti, P. T. Oliveira, R. Van Noort. Osseointegration and osseoconductivity of hydroxyapatite of different microporosite. Journal of Materials Science: Materials in Medicine nº 13 (2002), p. 1071-1075.

[13] Satyavrata Samavedi, Abby R. Whittington, Aaron S. Goldstein. Calcium phosphate ceramics in bone tissue engineering: A review of properties and their influence on cell behavior. Acta Biomaterialia, nº 9, (2013), p. 8037-8045.

[14] Sergey V. Dorozhkin, Biphasic, triphasic and multiphasic calcium phosphetes. Acta Biomaterialia, nº 8, (2012), p. 963-977.

[15] Hassna R. R. Ramay, M. Zhang; Biphasic calcium phosphate nanocomposite porous scaffolds for load-bearing bone tissue engineering. Biomaterials, nº 25, (2004), p. 5171-5180.

[16] Dubois, J. C., Souchier, C., Couble, M. L., Exbrayat, P., Lissac, M. Na image analysis method for the study of cell adhesion to biomaterials. Biomaterials vol. 20, (1999), p. 1841-1849.

[17] Delima, S.; Souza, J.; Camargo, N.; Pupio, F.; Santos, R.; Gemelli, E. Síntese e Caracterização de Pós Nanoestruturados de Hidroxiapatita. 5º Congresso Latino Americano de órgãos Artificiais e Biomateriais - COLAOB'2008, Ouro Preto - MG. v. 1. (2008), p. 1-6.

[18] Silva, R.F. Estudo de Caracterização de Pós Nanoestruturados de Fosfato de Cálcio e Nanocompósitos Fosfato de cálcio/SiO_2n Para Aplicações Biomédicas. Dissertação de Mestrado - UDESC/Joinville, (2007), p. 96.

[19] Pennings, E.C.M.; Grellner, W. Precise non destrutive determination of the density of ceramic. Journal American Ceramic. Society, v. 72, n.7, (1989), p. 1268-1270.

[20] João Costa-Rodrigues, Anabela Fernandes, Maria A. Lopes, Maria H. FERNANDES Hydroxyapatite surface roughness: Complex modulation of the osteoclastogenesis of human precursor cells. Acta Materialia, vol. 8, (2012), p. 1137-1145.

[21] H. Ivankvic, G. Gallego Ferrer, E. Tkalcec, S. Orlic, M. Ivankovic Preparation of highly porous hydroxyapatite from cuttlefish bone. J. Mater. Sci: Mater. Med. Vol. 20, (2009), p. 1039-1046.

[22] B. Viswanath, N. Ravishankar, Controlled synthesis of plate-shaped hydroxyapatite and implications for the morphology of the apatite phase in bone. Biomaterials, vol. 29, (2008), p. 4855-4863.

[23] Chun-Jen Liao, Feng-Huei Lin, Ko-Shao Chen, Jui-Sheng Sun, Thermal decomposition and reconstitution of hydroxyapatite in air atmosphere. Biomaterials, vol. 20, (1999), p. 1807-1813.

[24] Daiwon Choi, Prashant N. Kumta, Mechano-chimical synthesis and characterization of nanostructured b-TCP powder. Materials Science & Engineering C, vol. 27, (2007), p. 377-381.

Advanced Materials Research Vol. 936 (2014) pp 695-700
© (2014) Trans Tech Publications, Switzerland
doi:10.4028/www.scientific.net/AMR.936.695

CHARACTERIZATION OF DIFFERENT NANOSTRUCTURED BONE SUBSTITUTE BIOMATERIALS

Nelson Levandowski Jr.[1,a], Nelson H.A. Camargo[1,b], Daiara F. Silva[1,c], Gisele M.L. Dalmônico[1,d], Priscila F. Franczak[1,e]

[1] Universidade do Estado de Santa Catarina (UDESC), Centro de Ciências Tecnológicas (CCT), Campus Universitário Prof. Avelino Marcante S/N - Bairro Bom Retiro - Joinville - SC – Brasil

[a]levandowski.jr@gmail.com; [b]dem2nhac@joinville.udesc.br; [c]daiara.floriano@gmail.com
[d]gidalmonico@gmail.com, [e]priscila_jlle@yahoo.com.br

Keywords: Calcium phosphates; Hydroxyapatite; Nanostructure; Bone substitutes; Biomaterials.

Abstract: The present research paper centers on physicochemical characterization of six nanostructured alloplastic bone substitutes developed at Santa Catarina State University (UDESC – Brazil). In addition to identifying the main phases, the focus was to measure the morphological and microstructural features, which are believed to be crucial for controlling and guiding biological and molecular events. The studied samples exhibited rounded granules measuring 200μm <d <500μm. It was observed the presence of nanograins (<100nm) for all samples, with average grain diameter under 300nm. Hydroxyapatite [$Ca_{10}(PO_4)_6(OH)_2$] was found as main phase for HAp, BCP and HAp/Al_2O_3 biomaterials. For HAp/TiO2n, HAp/SiO_2n and β-TCP, the major phase was beta tricalcium phosphate [$Ca_3(PO_4)_2$-β]. The results demonstrate that the presence of a second phase of nanometer order, at a hydroxyapatite bioceramic matrix, may modify the surface diffusion of the grains and the phase transformation kinetics of hydroxyapatite and beta tricalcium phosphate at temperatures up to 1100°C.

Introduction

The marked increase in world population, combined with an increment of life expectancy in the last century, leads to enormous demands each year for various biomedical implants to repair diseased or lost bone tissue. However, conventional tissue replacements (such as autografts and allografts) have a variety of problems that cannot satisfy high performance demands necessary for today's patient [1]. Alloplastic biomaterials have the property of not transmitting any pathogen, since they can be synthesized in a safe environment and sterilized to prevent handling contamination. Of these, calcium phosphates (CaP) biomaterials such as hydroxyapatite (HAp) and beta tricalcium phosphate (β-TCP) have been extensively studied and employed for the last thirty years as bone graft substitutes, mostly due to their composition closely resembling the inorganic phase of bone [2].

Some studies suggest that in addition to chemical and crystallographic properties, the microstructure seems to be a key factor for calcium phosphates bioactivity [3-5]. Indeed, there is clear evidence that surfaces exert a differential activity on proteins by promoting or limiting their adhesion to the substrate. In particular, nanoscale surface cues are pivotal in controlling and guiding biological and molecular events [6]. The present research aims to characterize six different compounds of nanostructured calcium phosphate biomaterials developed at Santa Catarina State University (UDESC – Brazil).

Materials and Methods

The examined biomaterials included three compounds of calcium phosphate: HAp, β-TCP and a biphasic calcium phosphate (BCP) composed of HAp and β-TCP at a concentration of 60/40 by volume; and three hydroxyapatite matrices added 5% of nanostructured secondary phases: Al2O3-αn, TiO2n or SiO2n (Table 1). All of the biomaterials were supplied by the Biomaterials Research Group of Santa Catarina State University (UDESC - Brazil). The biomaterials were produced by attrition milling process, sintered at 1100°C for 2 hours and provided in a granular form.

TABLE 1. LIST OF EVALUATED BIOMATERIALS AND RELATED CHEMICAL FORMULA.

HAp	β-TCP	BCP	HAp/Al_2O_3	HAp/TiO2	HAp/SiO_2n
$Ca_{10}(PO_4)_6(OH)_2$	$Ca_3(PO_4)_2$-β	60% $Ca_{10}(PO_4)_6(OH)_2$ 40% $Ca_3(PO_4)_2$-β	95% $Ca_{10}(PO_4)_6(OH)_2$ 5% Al_2O_3-αn	95% $Ca_{10}(PO_4)_6(OH)_2$ 5% TiO_2n	95% $Ca_{10}(PO_4)_6(OH)_2$ 5% SiO_2n

To identify phase and composition features, X-ray diffraction (XRD) was used. Diffraction data were collected using an SHIMADZU XRD-6000 (Shimadzu, Tokyo, Japan), operating with Cu-Kα radiation (λ = 1.54060 Å) at a current of 30mA and an accelerating voltage of 40kV. Spectra were recorded in the range of 5º < 2θ < 80° at a scanning speed of 2º/min. The obtained X-ray patterns were compared to corresponding data from International Centre for Diffraction Data (ICDD).

Fourier transform infrared spectroscopy (FTIR) was employed to provide information concerning the chemical composition and the major functional groups. FTIR spectra were obtained within the range between 4000 and 450 cm^{-1}, with resolution of 4cm^{-1}, and the number of scans was 32. Total reflectance (ATR) technique was used at room temperature.

Studies of morphological and microstructural characterization were carried out by scanning electron microscopy (SEM) with ZEISS DSM 940A microscope (Carl Zeiss, Oberkochen, Germany), through the method of secondary electrons (SE), with a working distance of 10 mm and accelerating voltage of electrons of 20 kV. The samples were mounted on double-coated, carbon-conductive tape and then sputter-coated with gold.

The grain size of the biomaterials was measured through SEM images. Five different samples of each biomaterial were obtained at 5000x magnification. The perimeter of the grains was manually demarcated within the images, and the average diameter calculation was carried out with ImageJ software (v. 1.43, National Institutes of Health, USA).

Results

The results of morphological and microstructural characterization were conducted on the different biomaterials using the technique of scanning electron microscopy (SEM). Results are illustrated in Fig. 1 (a-f) and exhibited slight variations. The morphology revealed rounded granules with size between 200μm <d <500μm. Extensively interconnected microporous microstructure was also observed, formed by fine grains with a few preferred sinterability regions.

The image analysis method for grain size measuring allowed a statistical statement average of grains diameter. The data are depicted in Table 2. It was noticed an average diameter below 300 nm for all biomaterials, with the presence of nanostructured grains (d < 100nm).

TABLE 2. RESULTS FOR AVERAGE GRAINS SIZE FOR THE DIFFERENT BIOMATERIALS (SD = STANDARD DEVIATION).

Biomaterial	Average (nm)	SD (nm)	Minimum (nm)	Maximum (nm)
HAp	279	111	80	541
β-TCP	294	95	76	678
BCP	288	90	92	560
HAp/Al_2O_3	204	85	72	482
HAp/TiO_2	249	128	49	625
HAp/SiO_2	207	99	62	487

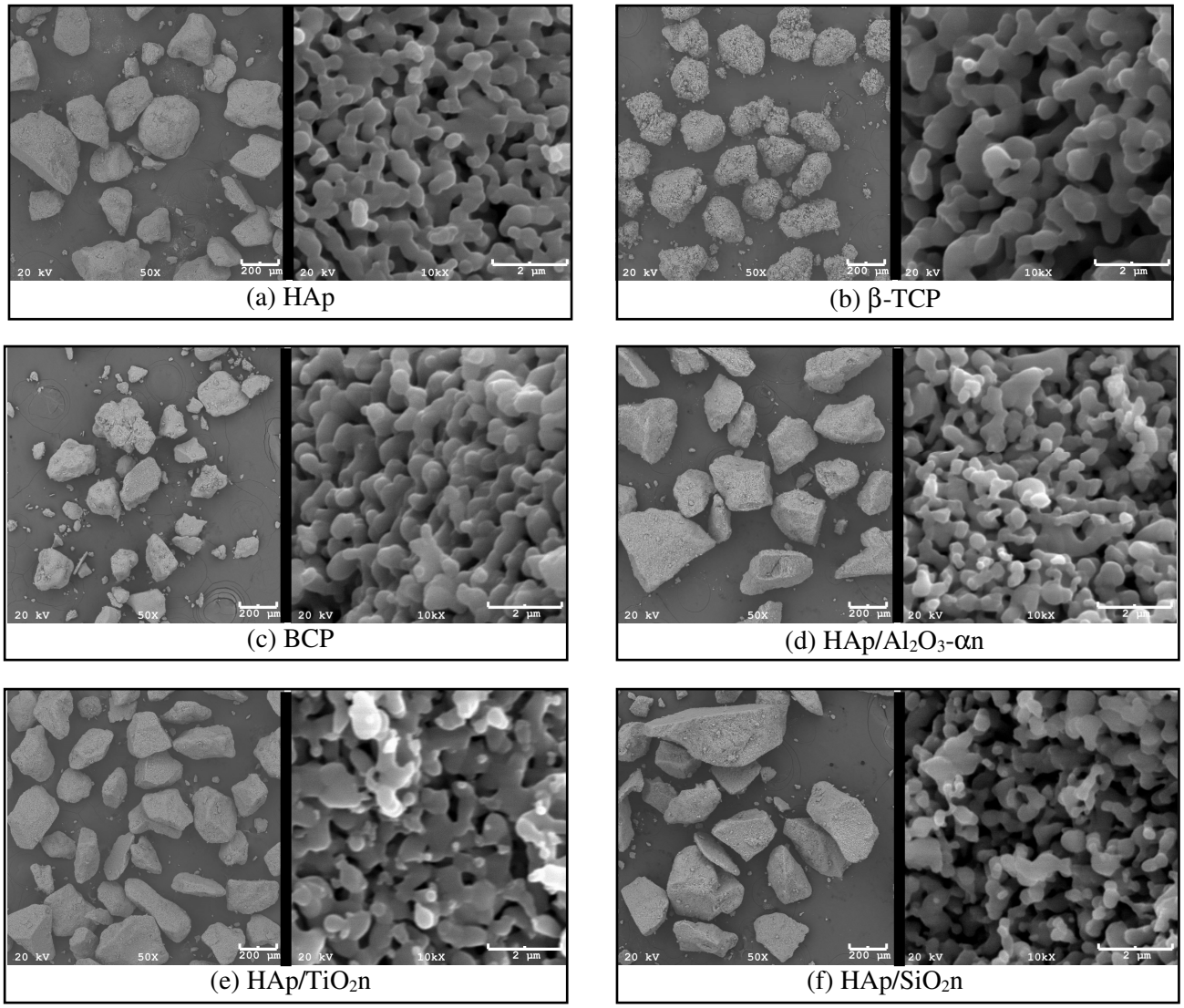


Fig. 1. Morphology (50X magnification) and microstructure (10kX magnification) of the granular biomaterials: (a) hydroxyapatite, (b) beta tricalcium phosphate, (c) 60/40 biphasic HAp/β-TCP, (d) nanocomposite HAp/Al_2O_3, (e) nanocomposite HAp/TiO_2, and (f) nanocomposite HAp/SiO_2.

The XRD technique was used for phase identification of different biomaterials (Figs. 2 and 3). The diffractograms were compared with ICDD data and pertinent literature. All samples presented high degree of crystallinity. As expected, the XRD results of HAp and β-TCP showed coincident peak positions and intensities with their related ICDD patterns. BCP presented peak positions of HAp and β-TCP in the estimated proportion of 60/40 (Fig. 2). The secondary phases of 5% nanocomposites (Al_2O_3, TiO_2 and SiO_2) were not identified at diffractograms (Fig. 3). The main finding at nanocomposites diffractograms was the appearance of peaks of an undesigned phase: β-TCP. Its amount ranged from 24% for HAp/Al_2O_3 sample, to about 83% for HAp/TiO2 and HAp/SiO_2 nanocomposites.

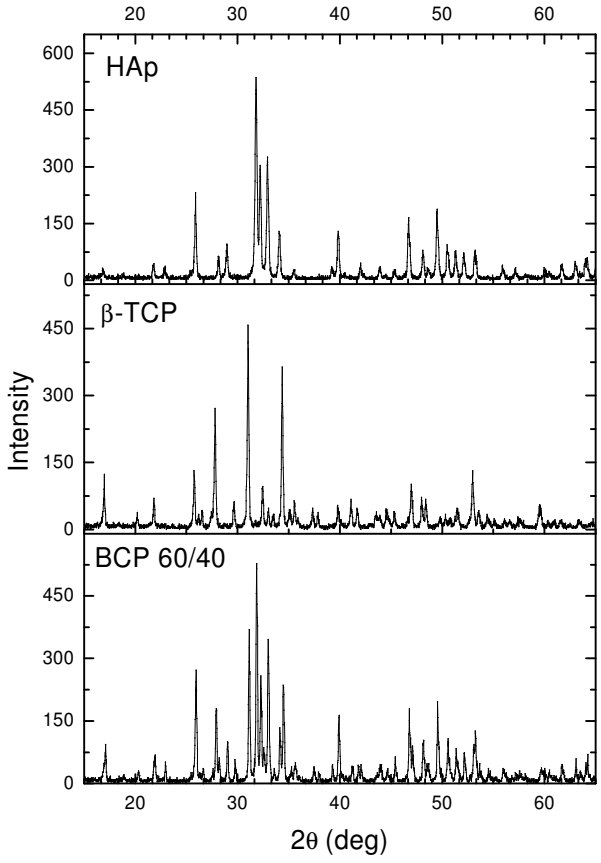


Fig. 2. Diffractograms of HAp, β-TCP and BCP, with peaks related to their own composition.

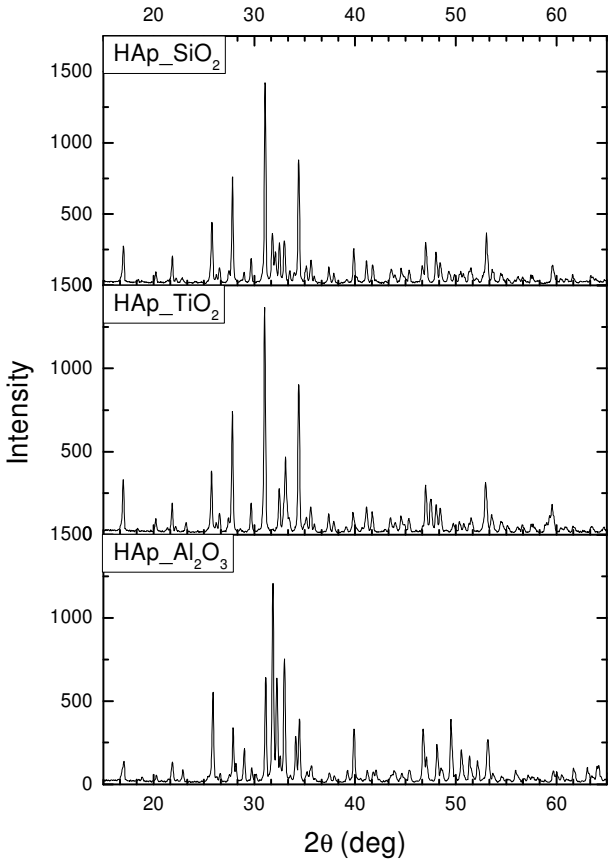


Fig. 3. Diffractograms of HAp/Al_2O_3, HAp/TiO2 and HAp/SiO_2 nanocomposites, with peaks of β-TCP phase in addition to HAp matrix peaks.

The β-TCP phase formation could also be visualized at FTIR. The infrared spectra are given in Figs. 4 and 5. All of them showed the typical bands originated mainly by phosphate molecule (PO_4^{3-}), with more intense phosphate stretching bands observed at around 1025 cm^{-1}, 600 cm^{-1} and 565 cm^{-1}. Figs. 6 and 7 display a higher magnification of the interest region of the spectra. Vibrational bands of 630 cm^{-1}, related to hydroxide anion (associated to hydroxyapatite) are well visualized at spectra of Fig. 6. The vibrational bands of 570 cm^{-1} 556 cm^{-1} evidenced at Fig. 7 suggest formation of β-TCP phase.

Discussion

Morphological and microstructural results demonstrated that the evaluated biomaterials exhibited extensively interconnected microporous microstructure, formed by fine grains with a few preferred sinterability regions. These features that may be favorable to wettability, capillarity and capillary and cell proliferation through surface of the biomaterial [3-5]. Furthermore, nanometer and submicron grain size presented at its structure may enhance the adsorption of proteins, the adhesion and cell proliferation, as well as the deposition of bone tissue [6-8].

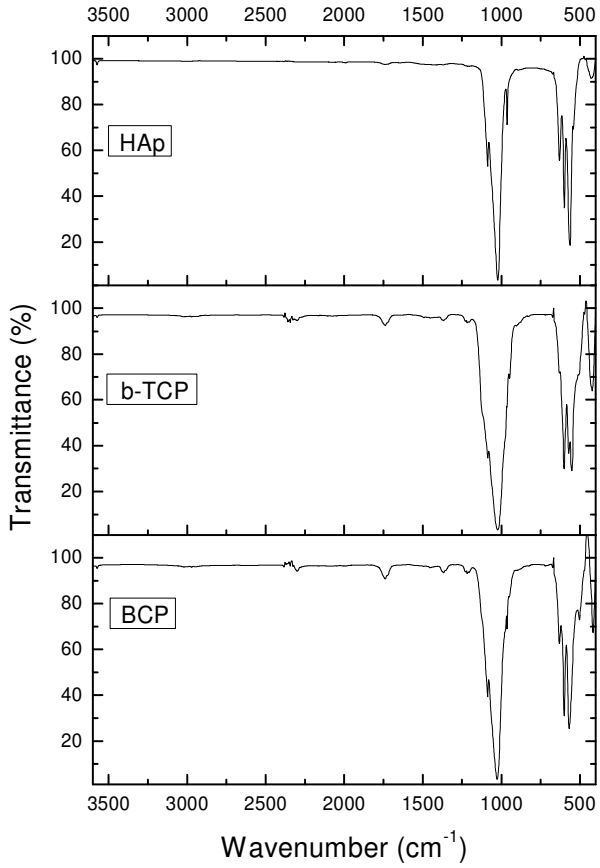


Fig. 4. FTIR spectra of HAp, β-TCP and BCP, essentially consisting of bands of phosphate molecules.

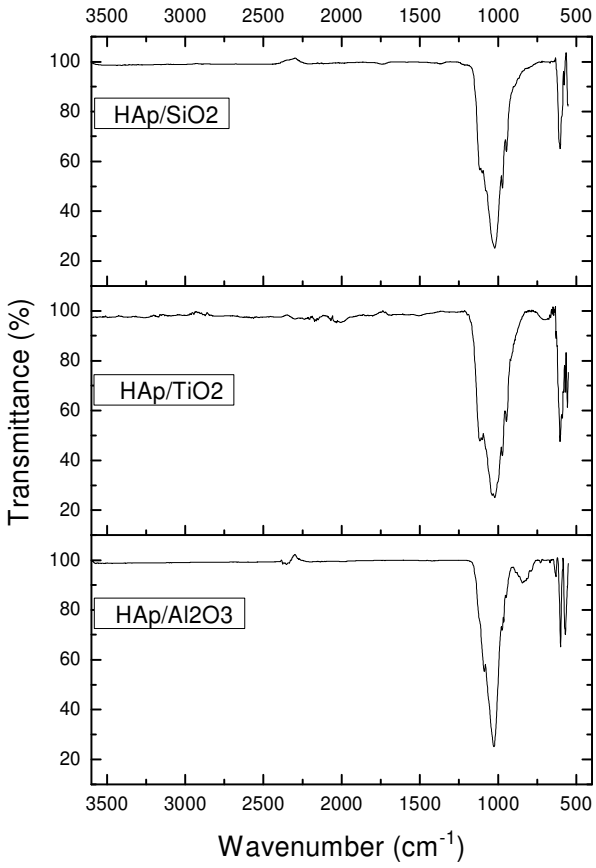


Fig. 5. FTIR spectra of HAp/Al_2O_3, HAp/TiO2 and HAp/SiO_2 nanocomposites, essentially consisting of bands of phosphate molecules.

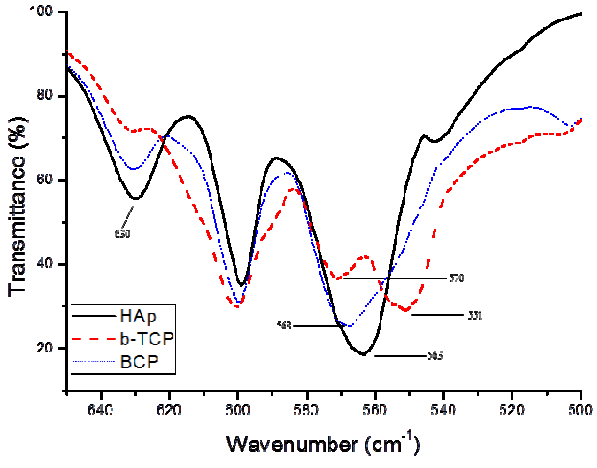


Fig. 6. Higher magnification of Fig. 4 spectra. In addition of phosphate typical vibrational bands, it can be seen (OH^-) vibrational band at $630cm^{-1}$.

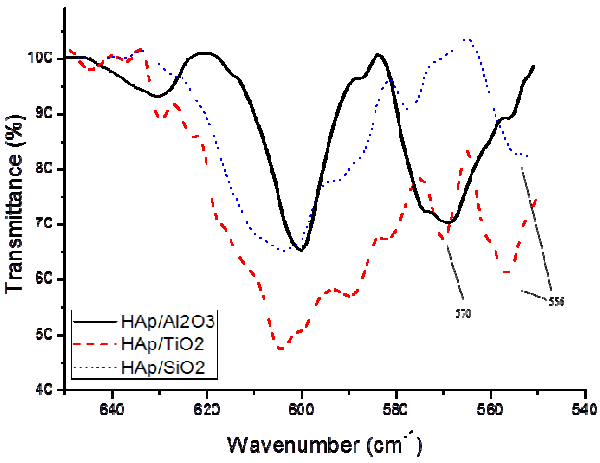


Fig. 7. Higher magnification of Fig. 5 spectra. It is possible to note lower intensity to (OH^-) vibrational band, and higher intensity to signals associated to (PO_4^{3-}) of β-TCP at $570cm^{-1}$ and $556cm^{-1}$.

The results obtained by XRD showed that the presence of a second phase of nanometer order, at a hydroxyapatite bioceramic matrix, may modify the surface diffusion of the grains and the kinetics of phase transformation of hydroxyapatite and beta tricalcium phosphate at a temperature of 1100°C. This temperature is below usual temperature expected for phase transformation of HAp/β-

TCP [9-10]. Beyond XRD, it can be realized at FTIR spectra that the intensity of 630 cm^{-1} band decrease according to β-TCP content, i.e., the presence of β-TCP phase within a composition of hydroxyapatite, can conduct to the attenuation of this band. It is related to the fact that beta tricalcium phosphate does not exhibit the hydroxyl group in its structure. Also, the presence of this β-TCP phase at hydroxyapatite composition may have modified the refraction indices, thereby altering the wavelength region at intensity of 551 cm^{-1} both for BCP as well as for nanocomposites. This wavelength (551 cm^{-1}) may be restricted to vibrational mode of PO_4^{3-} at β-TCP [11,12].

Conclusion

In the present work, six different nanostructured biomaterials were evaluated. Morphological and microstructural results demonstrated that the evaluated biomaterials exhibited extensively interconnected microporous microstructure, formed by fine grains with a few preferred sinterability regions. It was noticed an average diameter under 300 nm for all biomaterials, with the presence of nanostructured grains ($d < 100nm$). The results obtained by XRD and FTIR showed that the presence of a second phase of nanometer order, at a hydroxyapatite bioceramic matrix, may modify the surface diffusion of the grains and the kinetics of phase transformation of hydroxyapatite and beta tricalcium phosphate at a temperature up to 1100°C.

References

[1] L. Zhang, T.J. Webster. Nanotechnology and nanomaterials: Promises for improved tissue regeneration. Nano Today, 4 (2009) 66-80.

[2] R.Z. Legeros, G. Daculsi, J.P. Legeros. Bioactive Bioceramics. In W.S. Pietrzak. Musculo-skeletal tissue regeneration: biological materials and methods, Humana Press, Totowa, 2008.

[3] H. Yuan, K. Kurashina, J. D. de Bruijn, Y. Li, K. de Groot, X. Zhang. A preliminary study on osteoinduction of two kinds of calcium phosphate ceramics. Biomaterials, (20) 1999 1799-1806.

[4] D. Le Nihouannen, G. Daculsi, A. Saffarzadeh, O. Gauthier, S. Delplace, P. Pileta, P. Layrolle. Ectopic bone formation by microporous calcium phosphate ceramic particles in sheep muscles. Bone 36 (2005) 1086-1093.

[5] K.A Hing, B. Annaz, S. Saeed, P.A. Revell, T. Buckland. Microporosity enhances bioactivity of synthetic bone graft substitutes. Journal of Materials Science: Materials in Medicine, 16 (2005) 467– 475.

[6] L. Richert, F. Variola, F. Rosei, J. D. Wuestd, A. Nanci. Adsorption of proteins on nanoporous Ti surfaces. Surface Science 604 (2010) 1445–1451.

[7] Z. Evis, M. Sato, T. J. Webster. Increased osteoblast adhesion on nanograined hydroxyapatite and partially stabilized zirconia composites. J Biomed Mater Res A, 78 (2006) 500-507.

[8] J.W. Park, E.S. Kim, J.H. Jang, J.Y. Suh, K.B. Park, T. Hanawa. Healing of rabbit calvarial bone defects using biphasic calcium phosphate ceramics made of submicron-sized grains with a hierarchical pore structure. Clin. Oral. Implants Res. 21 (2010) 268-276.

[9] N. Kivrak, A. C. Tas. Synthesis of Calcium Hydroxyapatite–Tricalcium Phosphate (HA–TCP) Composite Bioceramic Powders and Their Sintering Behavior. J. Am. Ceram. Soc., 81 (1998) 2245–52.

[10] S. Raynaud, E. Champion, D. Bernache-Assollant. Calcium phosphate apatites with variable Ca/P atomic ratio II. Calcination and sintering. Biomaterials 23 (2002) 1073-1080.

[11] J Peña, M. Vallet-Regi. Hydroxyapatite, tricalcium phosphate and biphasic materials prepared by a liquid mix technique. Journal of the European Ceramic Society, 23 (2003) 1687-1696.

[12] P. Layrolle, G. Daculsi. Physicochemistry of Apatite and Its Related Calcium Phosphates. In: B. León, J.A. Jansen. Thin calcium phosphate coatings for medical implants. Springer, New York, 2009.

Advanced Materials Research Vol. 936 (2014) pp 701-706
© (2014) Trans Tech Publications, Switzerland
doi:10.4028/www.scientific.net/AMR.936.701

Sintering and Characterization of Calcium Phosphate Biomaterials Elaborated From Fossilized Calcareous Shell

Daiara F.Silva[1,a], Nelson H. A. Camargo[1,b], Nelson Levandowski Jr. [1,c], Priscila F. Franczak[1,d], Mônica S. Schneider[1,e]

[1] Universidade do Estado de Santa Catarina (UDESC), Centro de Ciências Tecnológicas (CCT), Campus Universitário Prof. Avelino Marcante S/N - Bairro Bom Retiro - Joinville - SC – Brasil

[a]daiara.floriano@gmail.com, [b]dem2nhac@joinville.udesc.br, [c]levandowski.jr@gmail.com; [d]priscila_jlle@yahoo.com.br; [e]monicaschnei@gmail.com

Keywords: Calcareous Shell, Biomaterial, Calcium Phosphate, Sintering and Characterization.

Abstract: Bioceramics of calcium phosphate, obtained from natural raw materials, are promising as bone substitutes because they exhibit crystallographic similarity with the bone tissue. This work deals with the sintering and characterization of calcium phosphate biomaterials from fossilized calcareous shells. Four compositions of biomaterials were prepared with Ca/P molar ratio ranging from 1.4 to 1.67. They were synthesized using a wet method and calcined at 900°C/2h providing calcium phosphate powder, then compressed into a metallic mould. The samples obtained from this compression were sintered at 1200ºC for 2h. The biomaterials recovered from sintering were subjected to a microstructural characterization by scanning electron microscopy [SEM] and by X-ray diffraction [XRD]. Mechanical properties were determined by compression tests. Finally, the Arthur method was used for determining the hydrostatic density and open porosity from these biomaterials. The value of fracture strength was between 54 and 84 MPa for compositions 1.5, 1.67 and 1.6 molar and for composition 1.4 molar about 328 Mpa. The results also showed was the amount of open porosity which ranged between 35 and 54% with increasing Ca/P molar ratio. These studies demonstrate that the production of biomaterials from fossilized calcareous shells may be a new alternative to the production of biomaterials for bone reconstruction.

Introduction

Hydroxyapatite (HAp) and beta tricalcium phosphate (β-TCP) are calcium phosphate bioceramics widely employed as bone substitutes. In addition to presenting chemical and crystallographic similarity to bone structure, they may also exhibit bioactivity and biocompatibility [1,2]. Natural raw materials, as marine coral, fossilized calcareous shells, sea urchins, oyster shells, egg shells and bovine cortical bone have been studied as bone substitute biomaterials [3,4]. Calcium phosphate powder has been previously developed with raw materials by wet method involving solid phase/liquid $CaCO_3$ and phosphoric acid [5].This method was able to provide hydrated calcium phosphate nanosized powders, which subsequently calcination at 900ºC/2h engendered biomaterials with new morphological characteristics and high surface area [5]. The microstructure of biomaterials obtained from fossilized calcareous shells present interconnected porosity, wettability, capillarity, and better cell matrix interactions [3,6]. The results presented here concern the sinterability and characterization of calcium phosphates biomaterials obtained of sintering at 1200°C/2h.

Materials and Methods

Initial powders were obtained from fossilized calcareous shells and were described elsewhere [5]. This synthesis method consists primarily of wet solid/liquid method with decarbonation of $CaCO_3$ from shells. Phosphoric acid addition formed precipitates of hydrated calcium phosphate which was subsequently calcined at 900ºC/2h providing the calcium phosphate powder. For the present characterization studies, four different compositions of calcium phosphate powder achieved from above mentioned method were packed in a metallic matrix with dimensions of 12mm in height and 5mm in diameter, with compression load applied to 30MPa. Uniaxial compaction process was

carried using a universal mechanical testing machine EMIC model DL30000 with displacement rate of the beam of 0.3 mm/min. The samples were sintered in a Linberg/Blue muffle furnace, with a heating rate of 5°C/min, level of sintering at 1200°C/2h, followed by cooling to room temperature.

Sintered samples of four different compositions were subjected to compression testing. All samples were dried 60ºC/24h before and the mechanical tests were performed in EMIC with load cell capacity of 1,000 kgf; beam displacement rate of 0.1mm/min. The tests were performed according to standard ASTM E9-89a.

The X-ray diffraction technique (XRD) was used in order to identify the phases present in the sintered biomaterials. The studies were performed using SHIMADZU X-ray diffractometer model XRD LAB X-6000, with anti-cathode cobalt tube [λ 1.78897Å]. The scanning angular range from 10° to 80° was used with a goniometer speed of 2º/min in function of 2θ, voltage 40kV and current of 30mA.

Microstructural characterization were carried out on fracture surface using the scanning electron microscopy technique (SEM) with ZEISS DSM 940A, through the secondary electrons (SE) method with working distance of 10 mm and voltage to 20kV.

The hydrostatic density and open porosity was determined used Arthur method [8]. This method consists of measuring the weight of the sample in air [Pair], and then the weight of the sample wet in xylene [Pxa]; xylene penetrates the open pores and then measured the weight of the sample with xylene after immersed in distilled water [Pxe]. After performing these measurements was determined hydrostatic density values through [Eq.1]; open porosity, with [Eq.2 and Eq.3] by the relation between the hydrostatic density and theoretical density in percent. The Fig.1 shows a schematic of how to perform the steps of the weight test samples dried, wet in xylene, and embedded in xylene in water.

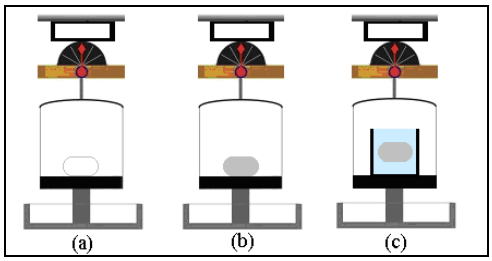


Fig. 1. Process measures: (a) P_{air} - air, (b) P_{xa} - air dipped in xylene, (c) P_{xe} - dipped in xylene in water [9].

Through these measures are determined the values of the hydrostatic density, open porosity and relationship between the hydrostatic density and the theoretical density (Eq.1, 2 and 3).

- Hydrostatic density:

$$dh = \frac{Par.de}{Pxa - Pxe} \quad (1)$$

- Open porosity:

$$P.A. = \frac{(Pxa - Par).de}{(Pxa - Pxe).dx}.100 \quad (2)$$

- Theoretical density in Percent:

$$\frac{dh}{dth} = \frac{Par.de}{(Pxa - Pxe).dx}.100 \quad (3)$$

With:
P_{air} – air-dried weight (g);
P_{xa} - soaked in xylene in air weight (g);
P_{xe} – soaked in xylene immersed in distilled water weight (g);
dh - hydrostatic density (g/cm^3);
dth - theoretical density of the material (g/cm^3);
dx - xylene density (0.8802 g/cm^3);
de - water density (g/cm^3);
P.A. - open porosity in %.

The hydrostatic density and open porosity measurements were performed using three samples of each composition initially dried in an oven to 100°C/24h to remove humidity present in the grain surfaces and micropores. After weighing on a precision balance, the samples were embedded in

xylene [dx=0.8802 g/cm^3] with a desiccator connected to a vacuum pump for 30 minutes. Once removed from the desiccator, the samples were weighed quickly in air [Pxa] and immersed in distilled water [Pxe].

Results

The results showed coarsening calcium phosphate grains to Ca/P molar ratio 1.4 and 1.5 [Fig.2 and 3]. The Ca/P molar ratio biomaterials 1.6 and 1.67 presented microporous microstructure formed by fine grains with micropores volume of 44.42% to ratio 1.6 and 54% to 1.67, as shown on the micrographs represented in Figs. 4, 5 and Table 1.

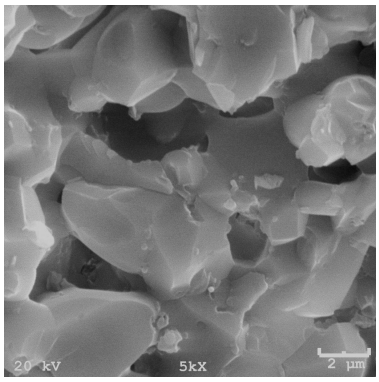


Fig.2. Ca/P molar ratio 1.4 biomaterial morphology

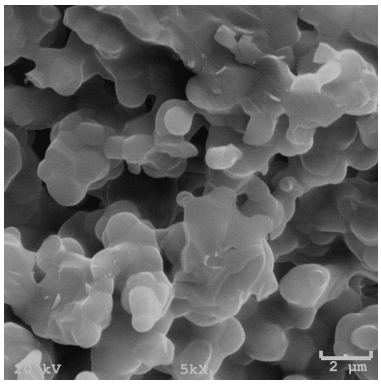


Fig.3. Ca/P molar ratio 1.5 biomaterial morphology

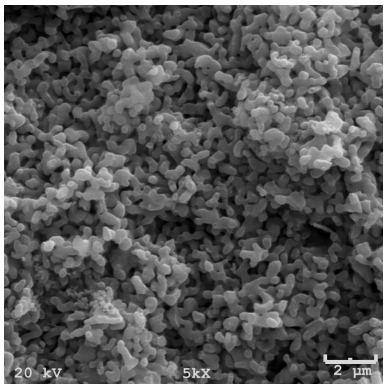


Fig.4. Ca/P molar ratio 1.6 biomaterial morphology

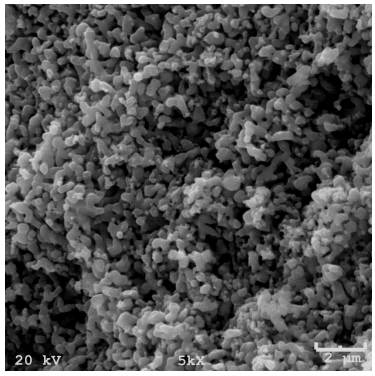


Fig.5. Ca/P molar ratio 1.67 biomaterial morphology

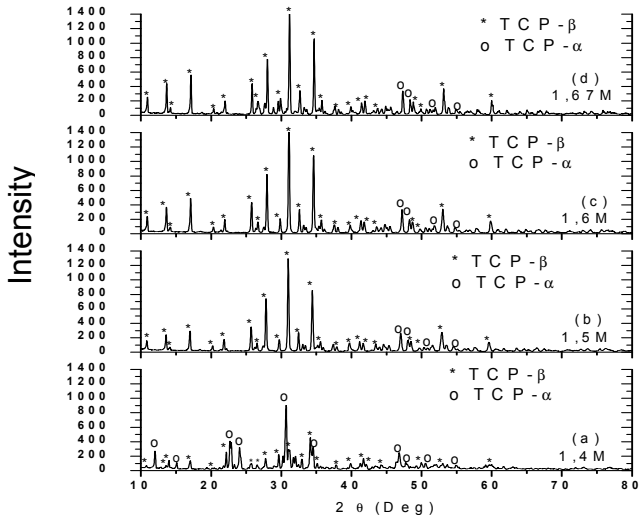


Fig.6. X-ray diffraction patterns of sintered biomaterials at 1200°C/2h

The X-ray diffraction results from the different biomaterials showed the presence of β-calcium phosphate [β-TCP] and α-calcium phosphate [α-TCP] phases, according to the Fig. 6.

The open porosity and hydrostatic density results showed an increase on porosity and reduction of density with variation Ca/P molar ratio. The values are shown in Table 1.

TABLE1. DATA OPEN POROSITY [P.A], HYDROSTATIC DENSITY [DH] AND THEORETICAL DENSITY [DH/DTH]

Compositions	P.A. (%)	dth(g/cm^3)	dh(g/cm^3)	dh/dth (%)
Ca/P 1.4 M	37.71± 2.00	3.07	2.25± 0.06	73.38± 2.00
Ca/P 1.5 M	41.80± 0.13	3.07	1.8± 0	58.76± 0.13
Ca/P 1.6 M	44.42± 0.49	3.07	1.55± 0.06	50.78± 0.49
Ca/P 1.67M	54.40± 0.95	3.10	1.45± 0.02	46.94± 0.95

The compression test results showed that Ca/P molar ratio can certainly influence the biomaterial sinterability, as shown in Table 2.

TABLE 2. BIOMATERIALS FRACTURE STRENGTH

Compositions	Fracture strength (MPa)
1.4 M	328.00 ± 68.90
1.5 M	84.68 ± 8.26
1.6 M	8.15 ± 9.02
1.7 M	54.24 ± 9.12

Discussion

The Ca/P molar ratio biomaterials 1.4 and 1.5 presented calcium phosphate grain coalescence during the sintering process. This coalescence led to the achievement of grain interface quality, which contributed to biomaterial sinterability, with grain boundaries and interfaces with well-defined open microporosity volume about 37.71% for the biomaterial with Ca/P molar ratio 1.4 and 41.42% for Ca/P molar ratio 1.5 [Figs. 2 and 3] and table 1.There was a microporous microstructure composed of fine grains to Ca/P molar ratio1.67 and 1.6 biomaterials [Figs. 4 and 5]. It is known that for the calcium phosphate biomaterials, interconnected microporosity, grain surface and micropores are favorable to wettability, solubility, cell adhesion of osteoblasts on the surface of grains and micropores, which is associated with the volume of micropores already existing and known by the bioactivity of calcium phosphate biomaterials [7]. These properties can contribute to the osteointegration and bone formation process.

The X-ray diffraction results [Figure 6] revealed to 1.4 ratio molar the presence of the higher concentrations of α-calcium phosphate, may explain the better biomaterial sinterability, which also contributed significantly to superior mechanical properties for this composition.

The open porosity and hydrostatic density results observed the highest density value for the biomaterial in the Ca/P molar ratio 1.4 and a lower value for the biomaterial Ca/P molar ratio 1.67. The same way, there was a higher value of open porosity for biomaterial in the Ca/P molar ratio 1.67 with 54 %, observed in Table 1. A comparative study relating the hydrostatic density with the theoretical density [d_h/d_{th}] in percentage between the biomaterials was performed to evaluate the approach of theoretical density with hydrostatic. Relating (the open porosity results) with those obtained by the scanning electron microscopy technique, one can say that, while varying the Ca/P molar ratio from 1.4 to 1.67, there was a change in the sinterability of these biomaterials, which can be explained by the presence of α-calcium phosphate phase in the compositions. For the biomaterial composition Ca/P molar 1.67, there was a higher value for the porosity and smaller grain size [Table 1] and [Fig. 5]. This result demonstrated that the Ca/P molar ratio and the synthesis process influence directly on the powder sinterability.

The biomaterial interconnected microporous microstructure is a promising property in biomedical applications, as already observed by [10]. It is known that calcium phosphate microporous biomaterials have a better response as biomaterials for repairing defects or as guide plates for bone tissue reconstruction [11], as confirmed by other authors who produced microporous calcium phosphates from natural raw materials, using other synthesis methods [1,2,10,11].

The presence of α-calcium phosphate phase in the compression tests can influenced the biomaterial sinterability and mechanical properties, observing a higher value of fracture strength to Ca/P molar ratio 1.4, which had a 328.00 ± 68.90 value. This type of biomaterial can be improved and used in the near future as a bone implant. Another observation was the smallest open porosity value, better grain interface quality, which confer biomaterial sinterability and mechanical properties [Table 2] [Fig. 2]. In what concern the compositions on the Ca/P molar ratio 1.5 and 1.6 and 1.67 these values showed similar fracture strength, these values are presented close to those found in the literature, for human cortical bone results in compression and bending [80-200MPa] [13]. This result can be explained by the presence of open porosity, fine grain morphology and grain boundaries connection interface, which inhibit the biomaterial mechanical properties.

Conclusion

Fossilized natural materials may be an alternative for the development biomaterials in biomedical applications, due to these natural raw materials have differentiated morphological characteristics according with variable Ca/P molar ratio within the range 1.4-1.67. These materials are also promising in orthopedic applications, tooth structure repairing and traumatology, as well as biomaterials capable of exercising drug delivery in cancer treatment. It is known that the grain morphology, interconnected microporosity, surface area of grain and micropores are prerequisites for a favorable biomaterial provides a means to oxygenation, wettability, capillarity, osteoinduction, osteointegration and bone formation.

References

[1] Xu, Y., Wang, D., Yang, L., Tang, H. Hydrothermal conversion of coral into hydroxyapatite. Materials Characterization; 2001; 47, 83-87.

[2] Shahgaldi, B.F. Coral graft restoration of osteochondral defects. Biomaterials. ; 1998; 19, 205-213.

[3] Almeida, U. Análise e utilização de biomaterial confeccionado a partir das conchas de Crassostrea gigas em defeito periodontal em ratos. Dissertação de Mestrado – Universidade Positivo - Curitiba. 2010; p.59.

[4] Tanur, A.E., Gunari N, Sullan RAM, Kavanagh CJ, Walker GC. Insights into the composition, morphology, and formation of the calcareous shell of the serpulid Hydroides dianthus. Journal of Estructural Biology. 2010; p.145-160.

[5] Silva, D. F. Síntese e caracterização de pós de fosfatos de cálcio a partir de conchas calcárias fossilizadas. Dissertação de mestrado, CCT/UDESC – Joinville, 2012; p. 124.

[6] Weiner, S, Dove, P M. An overview of biomineralization processes and the problem of thevital effect. In Biomineralization, Series: Reviews in Mineralogy and Geochemistry. Mineralogical Society of America: Washington, D.C., USA, 2003; 54:1-29.

[7] Camargo, N.H.A., Delima, S.A., Gemelli, E. Synthesis and characterization of hydroxyapatite/tio$_2$n nanocomposites for bone tissue regeneration. American Journal of Biomedical Engineering. 2012; 2(2):41-47.

[8] Pennings, E.C.M, Grellner, W. Precise non destrutive determination of the density of ceramic. Journal American Ceramic. Society. 1989, 72(7):1268-1270.

[9] Dalmônico, G.M.L. Síntese e caracterização de fosfato de cálcio e hidroxiapatita: elaboração de composições bifásicas HA/TCP-β para aplicações biomédicas.'' Dissertação de Mestrado. CCT/UDESC, 2011, p.103.

[10] Li, W.M. Chen S.Y, Liu D.M. In situ doxorubicin-CaP shell formation on amphiphilic gelatin-iron oxide core as a multifunctional drug delivery system with improved cytocompatibility, pH-responsive drug release and MR imaging Acta Biomaterialia Volume 9, Issue 2, 2013, Pages 5360-5368.

[11] Vecchio, K.S.; Zhang, X.; Massie, J.B.; Wang, M.; Kim, C.W. ‘‘Conversion of bulk seashells to biocompatible hydroxyapatite for bone implants.’’ Acta Biomaterialia, , 2007; 910–8.

[12] Demers, C.; Hamdy, R.C.; Corsi, K..; Chellat, F.; Tabrizian, M.; Yahia, L. ‘‘Natural coral exoskeleton as a boné graft substitute: A Review.’’ Bio-Medical Materials and Engineering, 2001 ; p 1-21.

[13] Bignon Bignon, L. “Optimization de la structure poreuse d´implants en phosphate de calcium our application de comblement osseux et relargage in situ d´un principe actif.” Tese de doutorado, Institut National de Sciences Appliquées de Lyon 2002.

Advanced Materials Research Vol. 936 (2014) pp 707-711
© (2014) Trans Tech Publications, Switzerland
doi:10.4028/www.scientific.net/AMR.936.707

The content of physiologically active substances in several medicinal mushrooms with various doses of γ-irradiation

Shih-Jeng Huang[1,a], Ya-Ling Liu[2,b], Jeng-Leun Mau[3,c], Shu-Yao Tasi[4,d*]

[1] Chung Chou University of Science and Technology, Yuanlin, Changhua 51003, Taiwan, ROC

[2] Grape King Bio, Zhong-Li, Taoyuan 320, Taiwan, ROC

[3] National Chung Hsing University, 250 Kuokuang Road, Taichung 40227, Taiwan, ROC

[4] Asia University, 500 Lioufeng Road, Wufeng, Taichung 41354, Taiwan, ROC

[a]hsj1030@gmail.com, [b]yaling.liu@grapeking.com.tw, [c]jlmau@dragon.nchu.edu.tw, [*d]sytsai@asia.edu.tw

Keywords: Gamma-irradiation, Edible mushroom, Medicinal mushroom, Physiologically active component

Abstract: Dry samples of fruit bodies of *Cordyceps militaris* and *Agariucs blazei,* mycelia of *Antrodia camphorata*, and hot water extracts of *Ganoderma tsugae* were ground and irradiated with γ-rays at doses of 0, 2.5, 5, and 10 kGy. After γ-irradiation, the content of γ-aminobutyric acid, adenosine, cordycepin, and triterpenoids in medicinal mushrooms did not significantly change. Gamma-irradiation only affects *A. camphorata* mycelia polysaccharide content, and an increase in irradiation dose (0-10 kGy) significantly reduces its content (111.85-101.88 mg/g). The content of high molecular weight (2.7×10^5 Da) polysaccharide in *G. tsugae* by γ-irradiation with increasing doses gradually increased. Gamma-irradiation could significantly affect the content of vitamin D_2 and ergosterol. However, ergosterol content in non-irradiated *C. militaris*, *A. blazei*, *A. camphorata*, and *G. tsugae* was 2.34, 1.31, 2.33, and 1.15 mg/g, and of that in 10 kGy γ-irradiated mushrooms was 2.75, 1.88, 2.19, and 0.94 mg/g, respectively. Summarily, γ-irradiation does change some medicinal mushrooms by the content of physiologically active substances. When using γ-irradiation sterilization to maintain the physiological activity of mushroom products, one should consider its impact on the physiologically active substances.

Introduction

Mushrooms have recently become attractive as functional food, considered a source for biological and useful substances material. Edible and medicinal mushrooms contain many physiologically active substances, including γ-aminobutyric acid, adenosine, cordycepin, triterpenoids, polysaccharide, vitamin D and ergosterol [1]. Several methods for the prevention the contamination have been developed, such as the exposure to ionizing radiation: γ-rays [2]. Irradiation with an average dose of 10 kGy has shown no toxicological hazards and introduced no specific microbial and nutritional problems [3]. Several studies on γ-irradiation of spices at the doses up to 10-15 kGy have shown that no substantial changes occurred in volatile oils, flavor profiles, spicing power [3] and antioxidant properties [4]. However, the effect of γ-irradiation on medicinal mushrooms has not been investigated.

Medicinal mushrooms are important for developing health foods in Taiwan, and γ-irradiation is a technique for elongation of their shelf life. However, the content of physiologically activity substances (γ-aminobutyric acid, adenosine, cordycepin triterpenoids, polysaccharide, vitamin D_2, and ergosterol) in medicinal mushrooms with γ-irradiation is unknown. Our objective was to study the content of physiologically activity substances in medicinal mushrooms (*C. militaris*, *A. blazei*, *A. camphorata* and *G. tsugae*) with various doses (0, 2.5, 5, and 10 kGy) of γ-irradiation.

Experimental and method

Mushrooms and γ-irradiated

Fresh fruit bodies of *A. blazei* were originally obtained from the Rich-Year Farm, Puli, Nantou County, Taiwan. Fresh fruit bodies of *C. militaris* were originally obtained from the Star-Ocean International Co., Taichung City, Taiwan. Extracts of *G. tsugae* were obtained from the Yen-Ten Farm, Zhongpu, Chiayi County, Taiwan. Mycelia of *A. camphorata* were obtained from the Biotechnology Center, Grape King Inc., Chungli, Taiwan. Images of the four samples are displayed in Fig. 1. Sample (20 g) was packaged in polyethylene packaging. After packaging, mushrooms were transported to the China Biotech Corp., Taichung City, Taiwan. Mushrooms were either unirradiated (control) or γ-irradiated with doses of 2.5, 5 and 10 (± 10%) kGy 60Co (600000 Ci, 6.78×10^2 kGy/h) at ambient temperature.

Color Measurement

The reflective surface color of steamed buns was measured on crumbs using an S80 color measuring system (Nippon Denshoku Inc., Tokyo, Japan) and L, a and b values were recorded. A standard white plate (X = 91.98, Y = 93.97 and Z = 110.41) was used to standardize the instrument. Whiteness index (WI) was calculated based on the following equation [5]:

$$WI = 100 - \sqrt{(100 - L)^2 + a^2 + b^2}$$

Gamma-aminobutyric acid, adenosine, cordycepin, triterpenoids, vitamin D_2 and ergosterol assays

Each γ-aminobutyric acid [6], adenosine [7], cordycepin [7], triterpenoids [8], vitamin D_2 [9] and ergosterol [9] were identified using the authentic compound (Sigma) and quantified by its respective calibration curve.

Polysaccharides content and molecular weight assays

Mushroom powder (1 g) was refluxed with 50 mL of deionized water for 30 min. The filtrate was dialyzed using a Cellu Sep T2 tubular membrane (MWCO: 6,000-8,000, Membrane Filtration Products, Seguin, TX, USA) for 24 h. The polysaccharide content was then determined by the phenol–sulfuric acid assay according to Dubois et al [10]. The polysaccharide molecular weights were analyzed according to the method of Hsieh et al. [11].

Statistical analysis

All the measurements were determined in triplicate. The experimental data were subjected to an analysis of variance for a completely random design to determine the Fisher's least significant difference among means at $P < 0.05$.

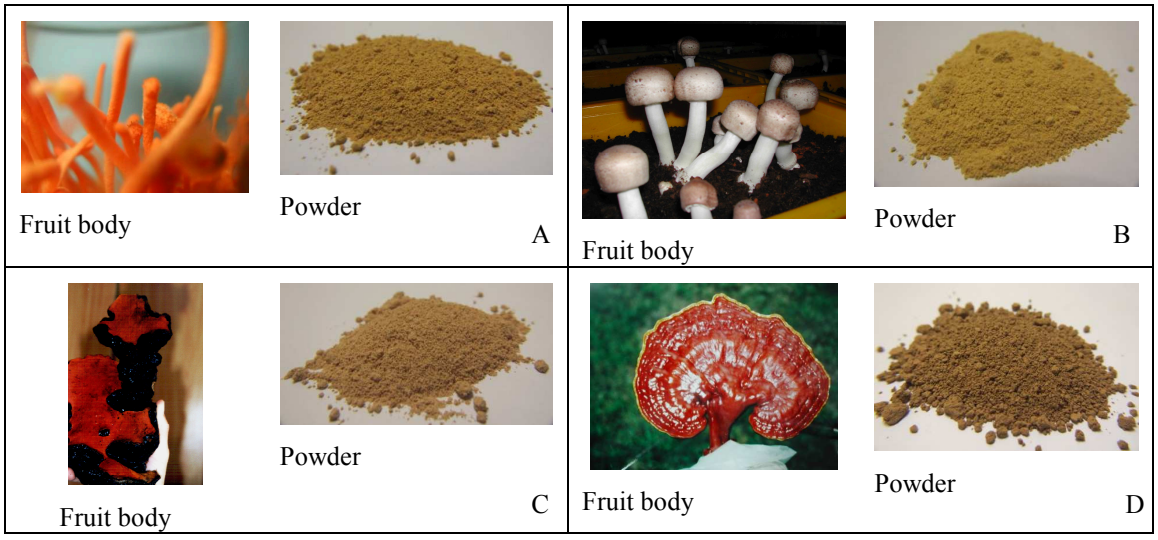


Fig. 1 Photographs of (A) *C. militaris*, (B) *A. blazei*, (C) *A. camphorata* and (D) *G. tsugae*, respectively.

Results and discussion

Color properties

G. tsuge showed lower lightness and WI values than *C. militaris*, *A. blazei*, and *A. camphorata* (Table 1). With regard to a and b values, *A. blazei* showed low redness and more yellowness. After γ-irradiation, the color properties in *C. militaris*, *A. blazei*, *A. camphorata* and *G. tsugae* did not significantly change.

TABLE 1 THE COLOR PROPERTIES OF MEDICINAL MUSHROOMS WITH VARIOUS DOSES OF Γ-IRRADIATION.

	C. militaris	*A. blazei*	*A. camphorata*	*G. tsugae*
L	67.19-68.94	71.87-71.92	66.46-66.90	49.36-50.07
a	12.25-12.29	7.92-8.04	12.35-12.39	13.16-13.22
b	34.94-36.56	38.73-38.80	24.40-24.41	25.02-25.14
WI	50.32-50.72	51.44-51.49	56.71-57.06	41.99-42.61

Physiologically active substances contents

The γ-aminobutyric acid and adenosine content of *A. blazei* was significantly higher than that in *C. militaris*, *A. camphorata* and *G. tsugae* (Table 2). Surprisingly, γ-aminobutyric acid (GABA), a hypotensive agent [12], was found in these four mushrooms. Cordycepin was detected in *C. militaris* (2.35-2.39 mg/g) but not detected in *A. blazei*, *A. camphorata* and *G. tsugae*. The content of triterpenoids in *C. militaris*, *A. blazei*, *A. camphorata* and *G. tsugae* was 21.12-23.27, 18.88-21.46, 22.81-23.57 and 18.36-20.14 mg/g, respectively. After γ-irradiation, the content of γ-aminobutyric acid, adenosine, cordycepin, and triterpenoids in medicinal mushrooms did not significantly change.

TABLE 2 CONTENT OF PHYSIOLOGICALLY ACTIVE SUBSTANCES IN MEDICINAL MUSHROOMS WITH VARIOUS DOSES OF Γ-IRRADIATION.

	Contents（mg/g dry weight）			
Physiologically active substances	*C. militaris*	*A. blazei*	*A. camphorata*	*G. tsugae*
γ-Aminobutyric acid	1.27-1.35	13.02-13.43	2.12-2.23	0.14-0.15
Adenosine	1.56-1.60	4.61-4.65	2.17-2.20	0.12
Cordycepin	2.35-2.39	nd	nd	nd
Triterpenoids	21.12-23.27	18.88-21.46	22.81-23.57	18.36-20.14

Vitamin D_2 and ergosterol content

The content of vitamin D_2 in *C. militaris, A. blazei, A. camphorata* and *G. tsugae* was 2.31-2.75, 1.33-1.88, 2.19-2.53 and 0.94-1.18 μg/g, respectively (Fig. 2A). The content of ergosterol in *C. militaris, A. blazei, A. camphorata and G. tsugae* was 18.41-22.87, 4.80-7.45, 0.28-13.98 and 14.29-17.78 mg/g, respectively (Fig. 2B). It seems that the increase of vitamin D_2 and ergosterol content is not dose-dependent. About the fresh common mushrooms, Simon et al. [13] found that no significant difference in ergosterol concentration was detected between the UVB light treated and control mushrooms, which contained 5.80 mg/g and 5.78 mg/g, respectively, but sunlight exposure could significantly increase ergosterol concentration (6.33 mg/g). Fortunately, mushrooms process a large amount of ergosterol that can be converted to vitamin D under ultraviolet light irradiation or pulsed ultraviolet light [14-15]. Our results showed that γ-irradiation is a new method to produce vitamin D_2 in medicinal mushrooms.

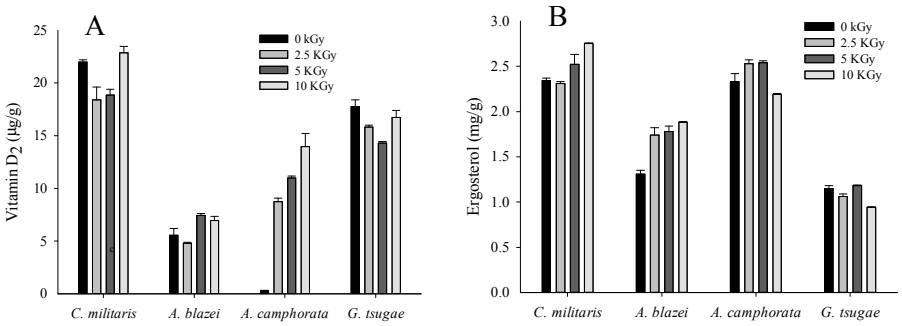


Fig. 2 Effect of γ-irradiation on vitamin D_2 (A) and ergosterol (B) content of medicinal mushrooms.

Polysaccharide content and molecular weight

The content of polysaccharide in *C. militaris*, *A. blazei*, *A. camphorata* and *G. tsugae* was 30.99-31.41, 71.29-71.67, 101.88-111.85 and 176.08-181.58 mg/g, respectively (Table 3). However, polysaccharide content in *A. camphorata* decreased after γ-irradiation. The γ-irradiation might cause the decomposition of polysaccharides in *A. camphorata* mycelia. The content of high molecular

TABLE 3. CONTENT OF POLYSACCHARIDES IN EDIBLE MUSHROOMS WITH VARIOUS DOSES OF Γ-IRRADIATION.

	Polysaccharides Content [1] （mg/g dry weight）			
edible mushrooms	0 kGy	2.5 kGy	5 kGy	10 kGy
Fruit bodies of *C. militaris*	31.25 ± 0.85 ^{A}	31.41 ± 0.60 ^{A}	31.13 ± 0.28 ^{A}	30.99 ± 0.59 ^{A}
Fruit bodies of *A. blazei*	71.25 ± 0.71 ^{A}	71.39 ± 0.60 ^{A}	71.67 ± 0.75 ^{A}	71.29 ± 1.27 ^{A}
Mycelia of *A. camphorata*	111.85 ± 1.96 ^{A}	106.75 ± 1.06 ^{B}	105.24 ± 2.32 ^{BC}	101.88 ± 1.87 ^{C}
Extracts of *G. tsugae* fruit bodies	179.32 ± 3.83 ^{A}	176.08 ± 3.85 ^{A}	181.58 ± 3.58 ^{A}	176.53 ± 2.56 ^{A}

[1] Each value is expressed as mean ± SD (n=3). Means with different letters within a row are significantly different ($p < 0.05$).

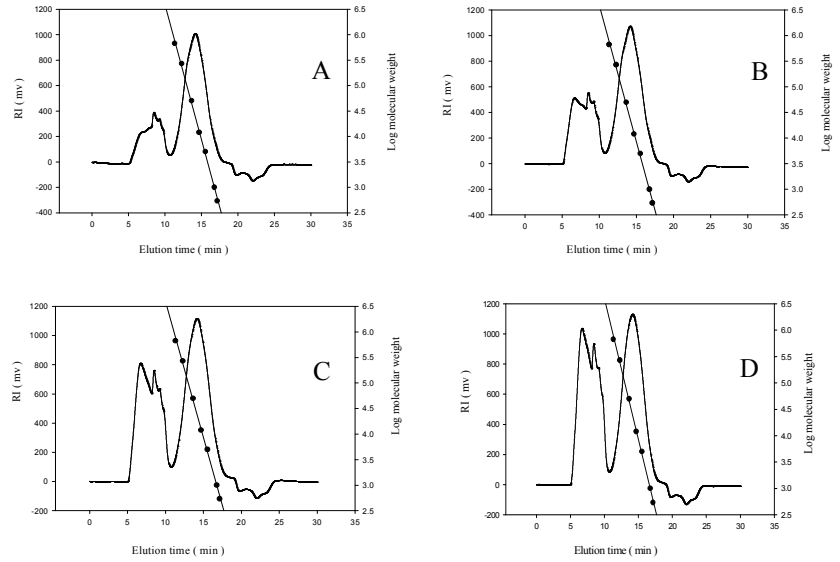


Fig. 3 The chromatography of polysaccharides from extract of *G. tsugae* fruit bodies with (A) 0 kGy, (B) 2.5 KGy (C)5 KGy and (D)10 kGy of γ-irradiation.

weight (2.7×10^5 Da) polysaccharide in *G. tsugae* by γ-irradiation with increasing doses gradually increased (Fig. 3). After γ-irradiation, the molecular of polysaccharide in *C. militaris*, *A. blazei* and *A. camphorata* did not have significant effects (data no shown).

Conclusions

Based on the results obtained, γ-irradiation did not markedly change the content of physiologically active substances. When using γ-irradiation sterilization to maintain the physiological activity of mushroom products, one should consider its impact on the physiologically active substances.

Acknowledgments

This study was supported by grants from the National Science Council of Taiwan (NSC 95-2313-B-235-003) and Asia University (101-asia-46).

References

[1] P. Kalac, A review of chemical composition and nutritional value of wild growing and cultivated mushrooms, J. Sci. Food Agr. 93 (2013) 209-218.

[2] M. Adamo, D. Capitani, L. Mannina, M. Cristinzio, P. Ragni, A. Tata, R, Coppola, Truffles decontamination treatment by ionizing radiation, Rad. Phys. Chem. 71 (2004) 165-168.

[3] International Atomic Energy Agency, Irradiation of spices herbs and other vegetable seasonings. A compilation of technical data for its authorization and control, IAEA-TECDOC-639 (1992) pp.16-17.

[4] D.P. Kuruppu, J. Schmidt, D.I. Langerak, D.A. Van Duren, J. Farkas, The effect of irradiation and fumigation on the antioxidant properties of some spices, Acta. Alimentaria. 14 (1985) 343-353.

[5] C.-L. Hsu, W. Chen, Y.-M. Weng, C.-Y, Tseng, Chemical composition, physical properties, and antioxidant activities of yam flours as affected by different drying methods, Food Chem. 83 (2003) 85-89.

[6] J.-L. Mau, C.-C. Chyau, J.-Y. Li, Y.-H. Tseng, Flavor compounds in straw mushrooms *Volvariella volvacea* harvested at different stages of maturity, J. Agric. Food Chem. 45 (1997) 4726-4729.

[7] M. Masuda, U. Eriko, S. Akihiko, S. Mikio, Production of cordycepin by surface culture using the medicinal mushroom *Cordyceps militaris*, Enzyme Microb. Technol. 39 (2006) 641-646.

[8] S.-C. Lee, Studies of the mycelium of *Antrodia camphorata*：In vivo protection against CCl_4-induced liver damage and its aqueous extract's effect in matrix metalloproteinases in vitro. Master thesis, National Chung-Hsing University (2003).

[9] C.-H. Tung, H.-H. Kung, W.C. Chen, J.-Q. Pan, S.-S, Chou, Survey on compliance of labelling of vitamin D and calcium on dietary supplements with regulations in Taiwan, Annual Report of BFDA, Taiwan, R.O.C. 25 (2007) 163-170.

[10] M. Dubois, K.A. Gilles, J.K. Hamilton, P.A. Rebers, F. Smith, Colorimetric method for determination of sugars and related substances, Anal. Chem. 28 (1956) 350-356.

[11] C.Y. Hsieh, M.H. Tseng, C.J. Liu, Production of polysaccharides from *Ganoderma lucidum* (CCRC 36041) under limitations of nutrients, Enzyme Microb. Technol. 38 (2006) 109-117.

[12] Y. Kohama, S. Matsumoto, T. Mimura, N. Tanabe, A. Inada, T. Nakanishi, Isolation and identification of hypotensive principles in red-mold rice, Chem. Pharm. Bulletin 35 (1987) 2484-2489.

[13] R.R. Simon, K.M. Phillips, R.L. Horst, I.C. Munro, Vitamin D mushrooms: comparison of the composition of button mushrooms (*Agaricus bisporus*) treated postharvest with UVB light or sunlight, J. Agr. Food Chem. 59 (2011) 8724-8732.

[14] M.D. Kalaras, R.B. Beelman, R.J. Elias, Effects of postharvest pulsed UV light treatment of white button mushrooms (*Agaricus bisporus*) on vitamin D_2 content and quality attributes, J. Agr. Food Chem. 60 (2012) 220–225.

[15] H.L. Kristensen, E. Rosenqvist, J. Jakobsen, Increase of vitamin D_2 by UV-B exposure during the growth phase of white button mushroom (*Agaricus bisporus*), Food Nutr. Res. 56 (2012) 7114-7121.

Advanced Materials Research Vol. 936 (2014) pp 712-716
© (2014) Trans Tech Publications, Switzerland
doi:10.4028/www.scientific.net/AMR.936.712

Synthesis and Characterization of Three Hydrated Calcium Phosphates used as Biocement Precursors

Priscila Ferraz FRANCZAK[1,a], Nelson Heriberto Almeida CAMARGO[1,b], Nelson LEVANDOWSKI Jr.[1,c] and Daiara Floriano da SILVA[1,d]

[1]Universidade do Estado de Santa Catarina – UDESC. Programa de Pós-Graduação em Ciência e Engenharia de Materiais – PGCEM.
Rua Paulo Malschitzki, s/n. Zona Industrial Norte – Joinville – SC.

[a]priscila_jlle@yahoo.com.br, [b]dem2nhac@joinville.udesc.br, [c]levandowski.jr@gmail.com, [d]by-daya@hotmail.com

Keywords: biocements, synthesis, characterization.

Abstract. Calcium phosphates biocements are biomaterials that present crystallographic and mineralogical characteristics similar to human skeletal structure. This has led to the development of new calcium phosphates biomaterials for biomedical applications, especially biomaterials for repairing defects and bone reconstruction. Calcium phosphates biocements are a promising alternative in biomedical applications, for they are easy to mold, they have good wettability, hydration and hardening capacity during its application in biological environment. This work aimed at the synthesis of hydrated calcium phosphates powder, precursor to late biocements development. Three calcium phosphates compositions were produced via $CaCO_3$/phosphoric acid reactive method in the ratios Ca/P = 1,5; 1,6 e 1,67 molar. The presented results are associated to hydrated powder morphology and synthesis process control. Field Electronic Microscope helped with the morphological characterization of the powders, Fourier Transformed Infrared Spectroscopy (FTIR) gave support to the identification of H_2O e PO_4^{3-} grouping vibrational bands and x-ray diffractometry (XRD) served on crystallographic characterization of hydrated calcium phosphates. The work showed that for the different powder compositions the hydrated calcium phosphate phase is formed by clustered fine particles. This demonstrated that the chosen synthesis method permits the obtaining nanoparticles of hydrated calcium phosphates, precursors for later biocement production.

Introduction

Materials and tissue engineering contribute to the development of new biomaterials and to the assessment of their behavior in *in vivo* studies. The results obtained from different studies show that calcium phosphate biomaterials are promising as post traumatic bone restoration, surgical or pathological injuries materials, such as bone tumors or osteoporosis. Calcium phosphate biocements can be used not only as bone replacement, but also as vehicles for controlled drug supply, being also widely used as medication carrier systems [1, 2, 3].

Calcium phosphate cements are produced from cement paste composed of calcium phosphate and a aqueous liquid [4] and present high osteoconductivity and easy manipulation, giving it high potential for application in orthopedics, for the correction of bone malformations that don't receive heavy loads [5, 6], having as main advantage it's capacity to easily adapt to the bone defect. Due to its molding capacity, these biocements can fit perfectly into the filling or restoration place, optimizing bone-biomaterial contact, even in geometrically complex bone defects, being considered the most promising biomaterials for minimally invasive surgeries [7].

This work aimed at the synthesis and characterization of hydrated calcium phosphate powders, precursors for later elaboration of biocements. The presented results are associated to the synthesis process and morphology control of hydrated powders. Scanning Electron Microscopy (SEM) helped with the powder's morphological characterization, laser analysis method was used to determine particle size and Fourier Transform Infra-Red (FTIR) gave support to the identification of vibrational bands of H_2O and PO_4^{3-} groupings.

Materials and Methods

The process of obtaining hydrated calcium phosphate powder, precursor of biocement, was performed using the reactive calcium carbonate / phosphoric acid method in the quantities required for forming the desired molar ratio of Ca/P. Three compositions of hydrated calcium phosphates were prepared on the molar ratios Ca/P = 1,5; 1,6 e 1,67.

Synthesis of Hydrated Calcium Phosphate Powders

The synthesis of hydrated calcium phosphate powders was performed by sequence shown in figure 1:

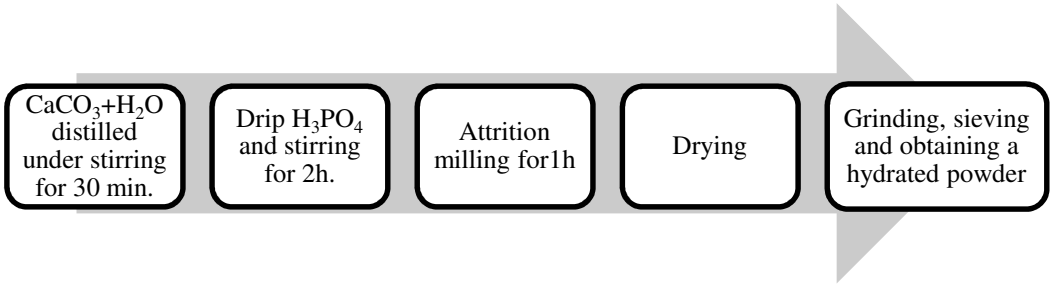


Figure 1: Synthesis flowchart of powders from hydrated calcium phosphate.

Morphological Characterization

Morphological characterization studies were performed with the help of a JEOL Field Electronic Microscope (Field Emission Gun–FEG). Observation studies were performed with hydrated calcium phosphate powders recovered by sieving at 100μm through secondary electrons system.

Chemical Characterization by Fourier Transform Infrared Spectroscopy (FTIR)

Fourier Transform Infra Red Spectroscopy technique (FTIR) was used for chemical analysis, which allowed the identification of OH^-, HPO_4^{2-} and PO_4^{3-} groupings vibrational bands present on hydrated calcium phosphates. Studies were performed using a Perkin Elmer Spectrum equipment, with attenuated reflectance, with resolution of 4,00 cm^{-1}.

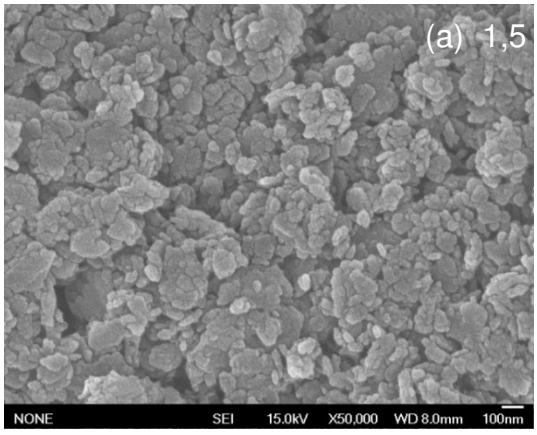
Physical Characterization by XRD

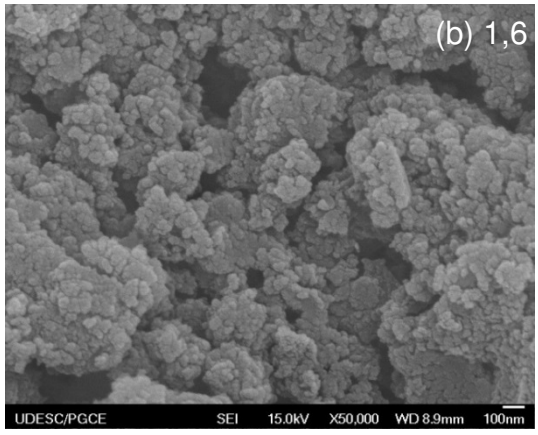
X-ray diffractometry served on crystallographic characterization of hydrated calcium phosphates. In this study a SHIMADZU x-ray diffractometer model XRD LAB X-6000, with anti-cathode copper tube, was used. To obtain the x-ray diffraction, a 40 kV voltage and current of 30mA were used, being the scanning angular range from 5° to 80°, with a goniometer speed of 2º/min in function of 2θ.

Results and Discussion

Morphological Characterization

Morphological characterization studies obtained from the hydrated calcium phosphate powders showed for ratios Ca/P = 1,5; 1,6 e 1,67 molar a morphology of fine clustered particles, as seen on figure 2(a), 2(b) and 2(c).





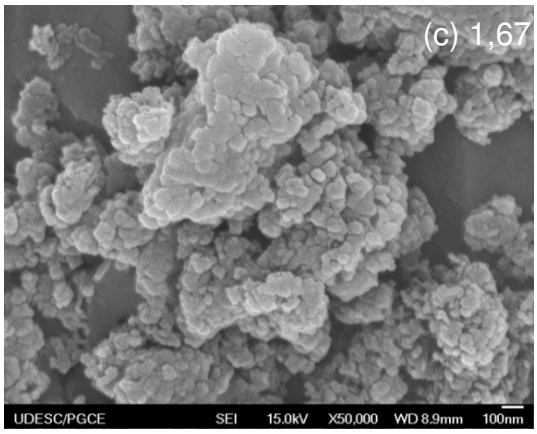


Figure 2. Micrographs obtained for the different compositions of hydrated calcium phosphate (a) Ca/P 1,5 molar; (b) Ca/P 1,6 molar e (c) Ca/P 1,67 molar.

Chemical Characterization by Fourier Transform Infrared Spectroscopy (FTIR)

Figure 3 presents the FTIR spectogram obtained from the Ca/P = 1,5 molar ratio powder, noticing the presence of the vibrational band at 1650 and 633cm^{-1}, indicating the presence of water molecules on the surface of the particles. OH^- grouping is represented by vibrational bands between 2900 and 3600cm^{-1}, typical for hydrated calcium phosphates, as already observed by other authors [8]. Vibrational frequencie at 1450cm^{-1} correspond to the CO_3^{2-} grouping bond. Vibrational bands at 562, 600, 960, 1027 and 1094cm^{-1} were also noticed, which are associated to PO_4^{3-} groupings. Also oberved was the 875 cm^{-1} band, associated to HPO_4^{2-}, as observed by other authors [9].

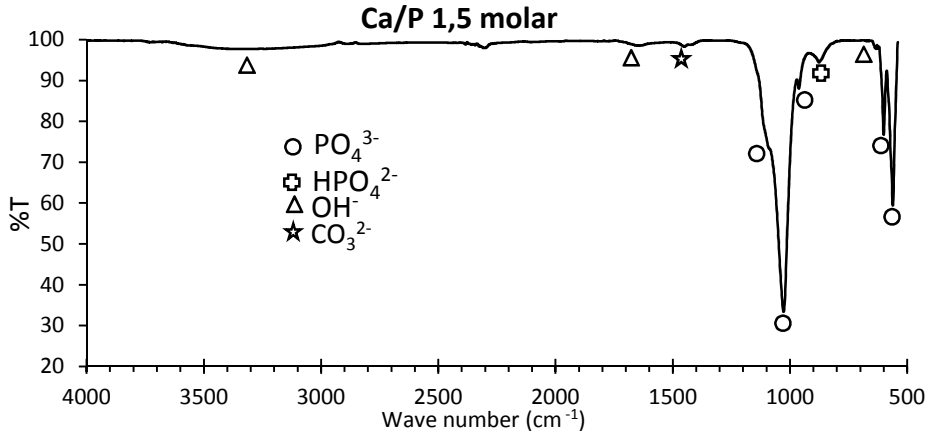


Figure 3: FTIR spectrum of hydrated calcium phosphate of molar ratio Ca/P = 1,5.

At ratio Ca/P = 1,6 molar, figure 4 shows that the PO_4^{3-} grouping appeared at 561, 600, 960 and 1025 cm^{-1}. Just like for Ca/P = 1,5 molar ratio, the vibrational band of the grouping HPO_4^{2-} was also observed at 875 cm^{-1}. Grouping CO_3^{2-} shows at 1450 cm^{-1}, indicating residual carbonate, and OH^- is shown at 1650 cm^{-1}. Adsorved water is between 3000 and 3600 cm^{-1} (which will became narrower under the influence of thermal treatment).

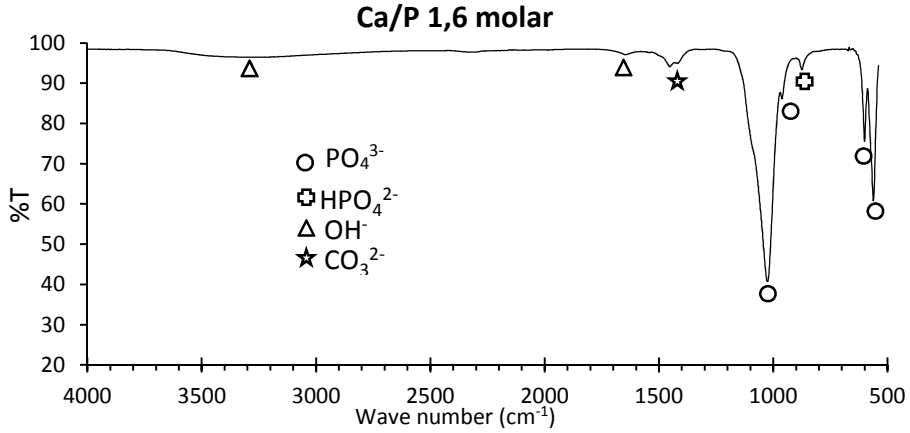


Figure 4: FTIR spectrum of hydrated calcium phosphate of molar ratio Ca/P = 1,6.

The spectrogram of molar ratio Ca/P = 1,67 appeared similar to the ratio Ca/P = 1,5 and 1,6, however with more accentuated CO_3^{2-} e HPO_4^{2-} grouping bands, as shown on figure 5, due to increase of molar ratio.

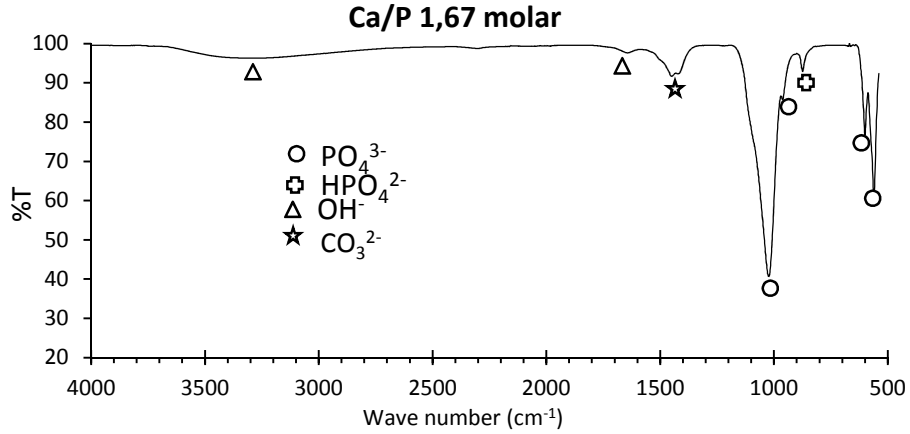
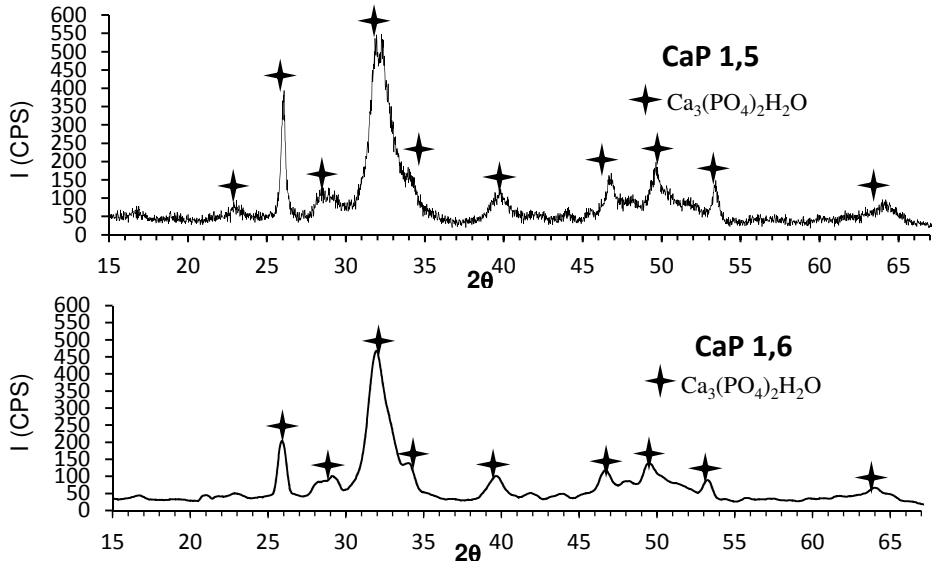


Figure 5: FTIR spectrum of hydrated calcium phosphate of molar ratio Ca/P = 1,67.

Physical Characterization by XRD

The results obtained by x-ray diffractometry of the powders recovered from rotatory evaporator revealed in their x-ray diffractograms the presence of hydrated calcium phosphates, as shown in the x-ray diffractograms in figure 6, in the composition $Ca_3(PO_4)_2H_2O$ for three molar ratios studied.



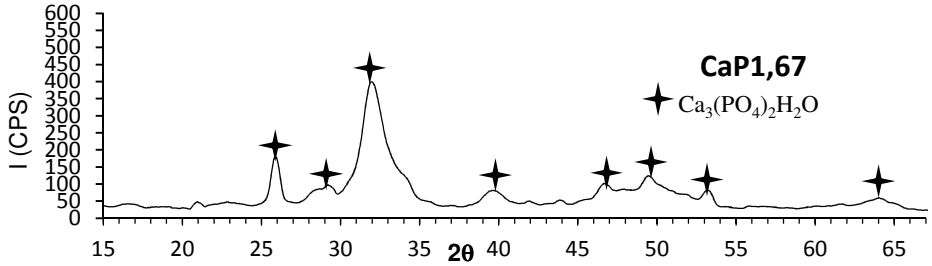


Figure 6. X-ray diffractograms obtained from molar ratios Ca/P = 1,5, Ca/P = 1,6 and Ca/P = 1,67.

Conclusions

The reactive calcium carbonate / phosphoric acid method allowed to obtain hydrated calcium phosphates. It was found in the results obtained for different compositions of calcium phosphate hydrated powders, a morphology composed of fine agglomerated particles. The FTIR spectra clearly showed the presence of PO_4^{3-} vibrational bands, indicating the presence of hydrated calcium phosphate phase in the compositions, which was proved by x-ray diffractrograms.

It is concluded that the synthesis method used allows obtaining precursors of hydrated calcium phosphate for subsequent preparation of biocements.

REFERENCES

[1] VERRON, E.; BOULER, J.M.; GUICHEUX, J. Controlling the biological function of calcium phosphate bone substitutes with drugs. Acta Biomaterialia, v. 8 (2012) p. 3541 – 3551.

[2] GINEBRA, Maria-Pau; Traykova, Tania; PLANELL, Josep A. Calcium phosphate cements: Competitive drug carriers for the musculoskeletal system. Biomaterials, v. 27 (2006) p. 2171 – 2177.

[3] CAMARGO, N.H.A.; SOARES, C.; GEMELLI, E. Elaboration and Characterization of Nanostructured Biocements for Biomedical Applications. Materials Research, v. 10, n. 2, (2007) p. 135-140.

[4] LILLEY, K. J.; GBURECK, U.; WRIGHT, A. J.; FARRAR, D. F.; BARRALET, J. E. Cement from nanocrystalline hydroxyapatite: Effect of calcium phosphate ratio. Journal of Materials Science: Materials in Medicine, v. 16 (2005) p. 1185 – 1190.

[5] DOROZHKIN, Sergey V. Calcium orthophosphate cements for biomedical application. Journal of Materials Science, v. 43, 9 (2008).

[6] YUASA, Tetsuya et. al. Effects of apatite cements on proliferation and differentiation of human osteoblasts in vitro. Biomaterials, v. 25 (2004) p. 1159 – 1166.

[7] MIRTCHI, A. A.; LEMAITRE, J; MUNTING, E. Calcium-phosphate cements–action of setting regulators on the properties of the beta-tricalcium phosphate monocalcium phosphate cements. Biomaterials, v. 10 (1989) p. 634 – 638.

[8] RAYNAUD, S.; CHAMPION, E., BERNACHE-ASSOLLANT, D., THOMAS, P. ‘‘Calcium phosphate apatites with variable Ca/P atomic ratio I. Synthesis, Characterization and thermal stability of powders.’’ Biomaterials, v. 23 (2002) p. 1005-1072.

[9] DESTAINVILLE A., CHAMPION E., BERNACHE-ASSOLLANTE D., et al. Synthesis, characterization and thermal behavior of apatite tricalcium phosphate. Materials Chemistry and Physics, n. 80 (2003) p. 269 – 277.

Advanced Materials Research Vol. 936 (2014) pp 717-722
© (2014) Trans Tech Publications, Switzerland
doi:10.4028/www.scientific.net/AMR.936.717

Preparation And Release Profiles Of A Solid Oleoylchitosan Coated Poly (Lactic-Co-Glycolic Acid) Nanoparticles

Yanyan Li[a,*], Fengsong Liu[b]

College of Life Sciences, HeBei University, 180# WuSi East Road, Baoding, P.R.China, 071002, Peoples' Republic of China

[a] E-mail address: liyanyan203@hotmail.com [b] E-mail address: liufengsong@hbu.cn

Keyword: oleoylchitosan; Poly (lactic-co-glycolic acid); nanoparticles; drug delivery system

Abstract: A solid oleoylchitosan (OCS) coated Poly (lactic-co-glycolic acid) (PLGA) nanoparticles (OCS-coated PLGA NPs) were prepared using the emulsification–evaporation method. The nanoparticles in suspension (TEM) and solid state (SEM) were spherical and very regular and compact. The effects of OCS concentration, PLGA concentration, drug concentration, and release media on drug entrapment efficiency and in vitro drug release behavior were investigated for the release properties using rifampicin (RFP) as a model drug. Both the increase of PLGA concentration and the increase of OCS concentration could decrease the drug release rates. The RFP release rates decreased as the RFP concentration increased. The RFP release rate was sensitive to the pH of the release media.

Introduction

Recently, much attention has been drawn to various amphiphilic block polymers, because they can form self-assembled nanoparticles and because they exhibit unique physicochemical characteristics such as a nanoparticle structure, biodegradability, and thermodynamic stability. [1, 2] The drug can be loaded into a polymeric micelle in three ways: simple physical embedding, electrostatic interactions or chemical bonding method. [3,4] The drug release rate is largely determined by the stability of the micelles, physical state of micelle core, drug molecular size, the position of drug in micelles, and the dissociation rate. Sometimes in order to delay drug release rate, further crosslink can be used including nuclear crosslinked micelles and micelles crosslinked hydrophilic shell. [5]

Chitosan, its unique characteristics such as positive charge, biodegradability, biocompatibility, and nontoxicity make this macromolecule ideal as a drug carrier and delivery material.[6,7] PLGA is by far the most common biodegradable polymer used for the controlled delivery of drugs due to its early use and approval as compatible biomaterial in humans. [8]

The author has prepared oleoylchitosan nanoparticles (OCS) and illustrated the OCS had good biocompatibility from the cytotoxicity testing and erythrocyte toxicity assay. [9] The hydrophobic drugs can be directly wrapped into OCS micelle core and drug release by passive diffusion out from the micelles. Thus, it was expected that the introduction of PLGA to the core of OCS micelles would delay the release of drug. Herein, we prepare the OCS coated PLGA nanoparticles (OCS-coated PLGA NPs) and study the characteristic and in vitro release profiles of the nanoparticles.

Experiment

Materials

Chitosan, degree of deacetylation 82%, molecular weight 38 KDa, was purchased from Biotech Co. (Mokpo, Korea). PLGA (MW 60KDa, 50/150) were purchased from Sigma Chemicals. Rifampicin was kindly donated by the Jiangbei Pharmaceutical Factory (Zhejiang, China).

Preparation of OCS-coated PLGA NPs

The OCS-coated PLGA NPs were prepared using the emulsification–evaporation method.[10]

Fourier Transform Infrared Spectroscopy (FT-IR)

The FT-IR spectra of OCS NPs and OCS-coated were recorded using a an Avater-360 Fourier transform infrared spectrometer. [11]

Morphology of the OCS-coated PLGA NPs

The morphology of the OCS-coated PLGA NPs suspension was observed by transmission electron microscope (TEM, JEM-2010). The morphology of the OCS-coated PLGA NPs powder was observed by a scanning electron microscope (SEM, JSM-T330A, Nihon Denshi, Japan).

Evaluation of in vitro drug release

The rifampicin (RFP) loaded nanoparticles were prepared by dissolving RFP in methylene chloride and subsequently as above described to prepare blank nanoparticles.

A cellulose membrane (8,000-10,000) tube containing 3 ml of the RFP loaded nanoparticles solution was placed in 97 ml of buffer at 37℃ under protection from light. The amount of released RFP was assayed by spectrophotometry at 475 nm in comparison to the standard curve. [12]

Results and Discussion

FT-IR of OCS Coated PLGA Nanoparticles

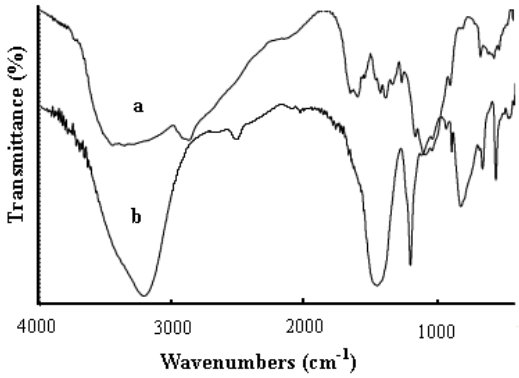


Figure 1 FT-IR of OCS NPs (a) and OCS-coated PLGA NPs (b)

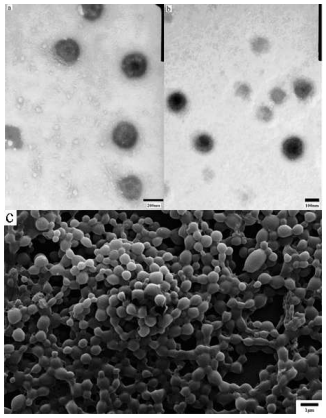


Figure 2 TEM and SEM photographs of OCS-coated PLGA NPs (a)TEM: 40000×; (b) TEM: 50000×; (c)SEM

The FT-IR spectra of OCS NPs and OCS-coated PLGA NPs are shown in Figure 1. The OCS had the basic characteristics (Figure 1 a) at: 3455 cm^{-1} (O–H stretch), 2900 cm^{-1} (C–H stretch), 1596 cm^{-1} (N–H bend), 1154 cm^{-1} (bridge-O- stretch), and 1094 cm^{-1} (C–O stretch). The spectra of OCS-coated PLGA NPs (Figure 1 b) exhibited alterations compare to OCS NPs. It had characteristic peaks of PLGA at 3326 cm^{-1}(C-H), 2400 cm^{-1}, 1750 cm^{-1}(C=O), 1100 cm^{-1}(C-O). These results indicated the success of the preparation of OCS-coated PLGA NPs.

Morphology of OCS-coated PLGA NPs

The TEM image of OCS-coated PLGA NPs is shown in Figure 2 (a, b). It could be confirmed that polymeric micelles are spherical in shape and a light circle could be seen around the nanoparticles. The hydrophilic groups could form hydrated layer in aqueous media to avoid the aggregation of the micelles. The results also suggested that the OCS-coated PLGA NPs were fairly dispersed in aqueous media and formed homogeneous small-sized micellar structures. The majority number of the particles was around 200 nm in size.

TABLE 1 EFFECTS OF OCS, PLGA, AND RFP ON DRUG LOADING AND ENCAPSULATION EFFICIENCY

	(g/L)	Encapsulation efficiency (%)	Drug loading (%)
OCS	1.00	76.75±2.90	65.12±1.02
	2.00	81.03±3.01	54.71±3.50
	3.00	83.75±4.01	47.63±2.56
PLGA	0	80.10±2.18	61.53±1.56
	0.65	81.03±3.01	54.71±3.50
	2.00	81.30±1.97	44.50±4.20
RFP	2.00	83.05±2.36	38.52±3.01
	4.00	81.03±3.01	54.71±3.50
	6.00	74.75±1.02	62.62±1.29

AS for the solid state of OCS-coated PLGA NPs, SEM was used to observe the morphology Figure 2 (c). The images revealed that formulated OCS-coated PLGA NPs have regular spherical shape with narrow size distribution and smooth surface without any noticeable pinholes, tiny pores or cracks at the resolution level within the equipment resolution.

In Vitro Release Of Rifampicin From Nanoparticles

The encapsulation efficiency (EE) and drug loading (DL) of RFP loaded nanoparticles with different PLGA concentrations was listed in Table 1. It can be found that all formulations gave high EE, which higher than 80%. There was no significant difference in EE in the samples with different concentration of PLGA. Figure 3 (a) shows the release profile of RFP from OCS-coated PLGA NPs prepared with different PLGA concentrations. It could be found that the release rate of RFP from nanoparticles decrease with an increase of PLGA concentrations. The nanoparticles prepared with PLGA concentration 2.00g/L, 0.65g/L, 0 released 35.46%, 46.08%, 59.12% after 36 h, respectively. This result could be explained by polymeric micelles formed by OCS solubilize hydrophobic drugs RFP suffering from poor water solubility. RFP was physically entrapped in the hydrophobic core of the micelle. Accordingly, the in vitro release behaviors of a drug from these polymeric micellar systems are largely affected by its inner core with hydrophobic properties. The nanoparticles might act as a barrier against the release of drug. Therefore, as the PLGA concentration inceresed, resulting in the decrease of drug release rates. [13, 14]

The EE and DL of RFP-loaded nanoparticles with different OCS concentrations was listed in Table 1. The EE increased as the increase of OCS concentration. And the DL decreased as the increase of OCS concentration. The increase of OCS concentration can increase the number of nanoaprticles. Accordingly, the EE increase as the increase of OCS concentration. Figure 3 (b) shows release profiles of RFP from samples with different concentration of OCS. It could be found that the release rate of RFP from nanoparticles decrease with an increase of OCS concentrations. The nanoparticles prepared with OCS concentration 1.00g/L,2.00g/L, 3.00g/L released 52.87%, 46.08%, 39.13% after 36 h, respectively. OCS is an amphiphilic polymer which can increase the wetting behaviors between oil phase and water phase and reduce the surface free energy of droplet.[15] The surfactants may be formed on the surface of droplet of a protective film to prevent the formation of agglomeration. Thus, the addition of OCS contributed to the formation of stable and homogeneous nanoparticles. Therefore, as the OCS concentration inceresed, the physically bound and binding affinity to drug increased, resulting in the decrease of drug release rates.

The EE and DL of RFP-loaded nanoparticles with different RFP concentrations was listed in Table 1. The DL increased as the increase of RFP concentration while the EE decreased as the increase of RFP concentration. Figure 3 (c) shows release profiles of RFP from samples with different concentration of RFP. The nanoparticles prepared with RFP concentration 6.00g/L, 4.00g/L, 2.00g/L released 28.84%, 46.08%, 52.84% after 36 h, respectively.

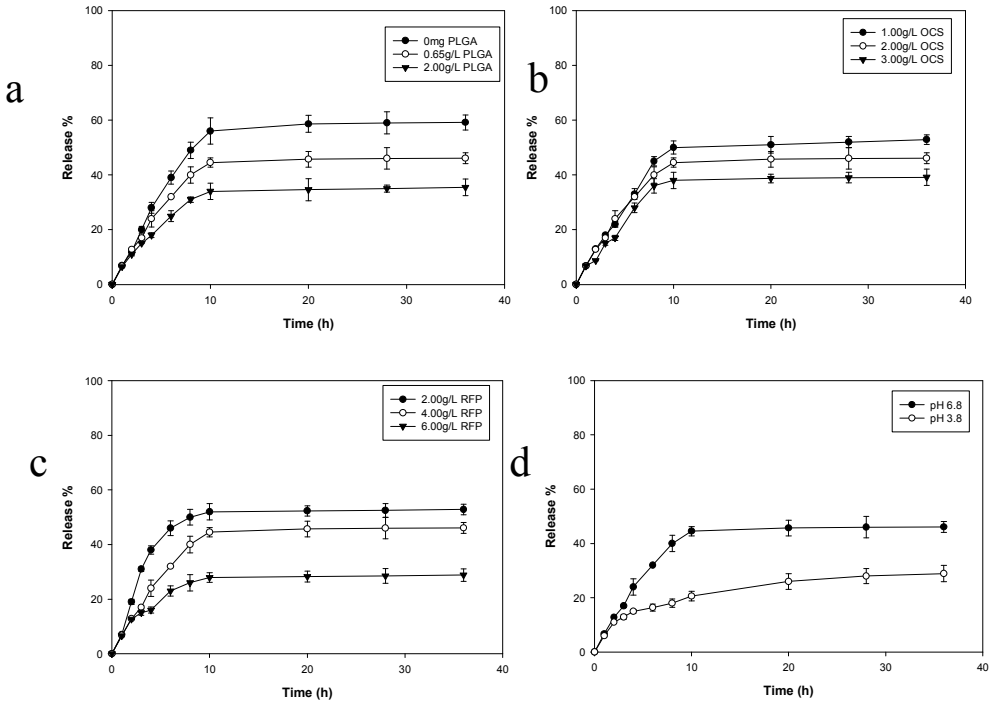


Figure 3 The effects of PLGA concentration (a), OCS concentration (b), drug concentration (c), and release media (d) on drug release behavior

The release profile of RFP from the nanoparticles in intro in different buffer solution was shown in Figure 3 (d). From the release profile, we can see that the release of rifampicin from solution with pH 6.8 was rapid. The release from solution with pH 3.8 had the slower rate. That was related to the stability of the nanoparticles in the solution. OCS was soluble in an aqueous acidic solution below pH 6.5. However, it was not soluble at neutral or alkali pH. That made the nanoprticles was less stable in the system above pH 6.5 than in the system below pH 6.5. And that also made the release of drug from solution below pH 6.5 slower than from solution above pH 6.5.

Conclusion

In this study, OCS-coated PLGA NPs were prepared using an emulsification–evaporation method. The nanoparticles in suspension were spherical and very regular and compact. AS for the solid state, the OCS-coated PLGA NPs had regular spherical shape with narrow size distribution and smooth surface without noticeable pinholes, tiny pores or cracks. The effects of OCS concentration, PLGA concentration, RFP concentration and release media on drug entrapment efficiency and in vitro drug release behavior were investigated for the release properties. There was no significant difference in DL and EE in the samples with different concentration of PLGA. The RFP release rates decreased as the PLGA concentration increased. As the PLGA concentration inceresed, the physically bound and binding affinity to drug increased, resulting in the decrease of drug release rates. The EE increase as the increase of OCS concentration. While the DL decrease as the increase of OCS concentration. As the OCS concentration increased, the physically bound and binding affinity to RFP increased, resulting in the decrease of drug release rates. The RFP release rates decreased as the RFP concentration increased. The RFP release rate was sensitive to the pH of the release media.

Acknowledgements

The authors are indebted to the financial support from the Project Supported by Hebei Provincial Natural Science Foundation of China—Shijiazhuang Pharmaceutical Group (CSPC) Foundation (E2013201205) and Hebei Province Department of Education Fund (Q2012140) and Startup Project of Doctor scientific research of HeBei Univeisity (2009-174).

References

[1] C.J. Rijcken, O. Soga, W.E. Hennink, C.F. van Nostrum, Triggered destabilisation of polymeric micelles and vesicles by changing polymers polarity: an attractive tool for drug delivery. J. Control. Release. 120(2007) 131-148.

[2] K.M. Huh, H.S. Min, S.C. Lee, H.J. Lee, S. Kim, K. Park, A new hydrotropic block copolymer micelle system for aqueous solubilization of paclitaxel. J. Control. Release.126(2008) 122-129.

[3] L.Y. Qiu, Y,H. Bae, Self-assembled polyethylenimine-graft-poly (ε-caprolactone) micelles as potential dual carriers of genes and anticancer drugs. Biomaterials. 28(2007) 4132-4142.

[4] F.Q. Hu, M.D. Zhao, H. Yuan, J. You, Y.Z. Du, S. Zeng, A novel chitosan oligosaccharide–stearic acid micelles for gene delivery: Properties and in vitro transfection studies. Int. J. Pharm. 315(2006)158-166.

[5] D.J. Bharali, S.K. Sahoo, S. Mozumdar, A. Maitra, Cross-linked polyvinylpyrrolidone nanoparticles: A potential carrier for hydrophilic drugs. J. Colloid Interf. Sci. 258(2003) 415-423.

[6] B.Q. Wang, C.B. He, C. Tang, C.H. Yin, Effects of hydrophobic and hydrophilic modifications on gene delivery of amphiphilic chitosan based nanocarriers. Biomaterials. 32(2011)4630-4638.

[7] Y. Jeong, S.G. Jin, I.Y. Kim, J. Pei, M. Wen, T.Y. Jung, K.S. Moon, S. Jung, Doxorubicin-incorporated nanoparticles composed of poly(ethylene glycol)-grafted carboxymethyl chitosan and antitumor activity against glioma cells *in vitro*. Colloid. Surface. B. 79(2010) 149-155.

[8] R.M. Mainardes, R.C. Evangelista, PLGA nanoparticles containing praziquantel: effect of formulation variables on size distribution. Int. J. Pharm. 290(2005) 137-144.

[9] Y.Y. Li, X.G. Chen, J. Zhang, C.S. Liu, Y.P. Xue, G.Z. Sun, W.F. Zhang, In Vitro Release of Rifampicin and Biocompatibility of Oleoylchitosan Nanoparticles. J. Appl. Polym. Sci. 111(2009) 2269-2274.

[10] B. Semete, L. Booysen, Y. Lemmer, L. Kalombo, L. Katata, J. Verschoor, H.S. Swai, Kalombo In vivo evaluation of the biodistribution and safety of PLGA nanoparticles as drug delivery systems. Nanomed-Nanotechnol. 6(2010) 662-671.

[11] Y. Shigemasa, H. Matsuura, H. Sashiwa, H. Saimoto, Evaluation of different absorbance ratios from infrared spectroscopy for analyzing the degree of deacetylation in chitin. Int. J. Biol. Macromol. 18(1996) 237-242.

[12] T. Udayakumar, M. Vasudevan, Novel Sustained Release Swellable Bioadhesive Floating Gastroretentive Drug Delivery System of Bilayer Tablets Containing Rifampicin and Isoniazid. Int. J. Pharm. Sci. Letters. 1(2012) 21-24.

[13] M.C. Jones, J.C. Leroux, Polymeric micelles—a new generation of colloidal drug carriers. Eur. J. Pharm. 48(1999)101-111.

[14] Y.J. Son, J.S. Jang, Y.W. Cho, H. Chung, R.W. Park, I.C. Kwon, I.S. Kim, J.Y. Park, S.B. Seo, C.R. Park, S.Y. Jeong, Biodistribution and anti-tumor efficacy of doxorubicin loaded glycol-chitosan nanoaggregates by EPR effect. J. Control. Release. 91(2003) 135-145.

[15] S.Y. Teh, R. Lin, L.H. Hung, A.P. Lee, Droplet microfluidics. Lab. Chip. 8(2008)198-220.

Advanced Materials Research Vol. 936 (2014) pp 723-727
© (2014) Trans Tech Publications, Switzerland
doi:10.4028/www.scientific.net/AMR.936.723

Polymer-tethered pH-sensitive Magnetic Nanoparticles for Targeted Delivery of Anti-cancer Drug

Yueqing Shen[1,a], Menglu Pu[1,b], Wei Jiang[1,c*]

[1]National Special Superfine Powder Engineering Research Center, Nanjing University of Science and Technology, Nanjing 210094, China

[a]shenyueqing@126.com, [b]494591992@qq.com, [c]climentjw@126.com

Keywords: pH-sensitive;Magnetic nanoparticles;Drug delivery;Doxorubicin

Abstract: Efficient delivery of drug to tumor cells is one of the crucial issues in cancer therapy. This letter addresses for the first time that poly(acrylic acid) (PAA), a pH-sensitive polymer, is tethered to the surface of the nanoparticles by chemical grafting. The release rates of doxorubicin (DOX) are subsequently studied in vitro. The results reveal that DOX can be released preferentially at the desired lysosomal pH, and show that the anti-cancer drug carrier can be applied to the biomedical applications.

Introduction

In recent years, magnetic nanoparticle-based drug delivery systems have shown high degree of efficiency in cancer treatments because they can improve pharmacokinetics and bio-distribution profiles via the enhanced permeability and retention (EPR) effect.[1-3] However, the poor cellular internalization and insufficient drug release limits the dosages of anticancer drugs to level below the optimum therapeutic value.[1] Therefore, the effective absorption and release of anticancer drugs is of vital importance in ensuring the tumor targeting and choosing the suitable targeting ligand. Recently, some stimuli-sensitive materials have been reported to improve the absorption of anticancer drugs because they can make sharp respond according to the changs in microenvironment of some pathological sites, such as heat, light, or acidic conditions.[4-6] Among the various stimuli, pH is the most widely used chemical stimuli because pH values vary significantly in different tissues and cellular compartments. Futhermore, introduction of specific ligands such as folic acid (FA) can also help the magnetic nanoparticles (MNPs) deliver the dugs to the targeted cells via the receptor mediated endocytosis.[7]

In this work, a biocompatible and very sensitive to pH and ionic strength material, i.e., PAA, is chosen for improving the absorption of the magnetic nanoparticles-based drug. In addition, it provokes little antigenic reaction in vivo.[8] In fact, PAA has already been used for the synthesis of PAA coated magnetic nanoparticles with the potential application as solvent absorbers and drug delivery devices.[8,9] However, in these studies, PAA is attached to the magnetic nanoparticles through electrostatic interaction, which is not stable enough in the acid and alkaline environment. In this paper, we present an efficient method to prepare magnetic nanoparticles containing PAA and FA via the method of chemical grafting, which are stable in acid and alkaline environment and exhibite high encapsulation efficiency and loading capacity, as well as good pH-responsive release profile. In addition, the magnetic nanoparticles can also realize passive targeting and active targeting at the same time.

Experiment

The initial chemical agents were ferric chloride, ferrous sulfate, ammonia (25 wt%), 3-aminopropyl triethoxysilane (APTES), N-hydroxysuccinamide (NHS), 1-[3-(dimethylamino)propyl]-3-ethylcarbodiimide hydrochloride (EDC), poly(acrylic acid) (PAA), folic acid (FA), Doxorubicin hydrochloride (DOX·HCl). In an experimental procedure, PAA was dissolved into distilled water, and then EDC and NHS was also dissolved into distilled water with stirring. The pH value of the system was maintained at 7.0-7.5 with dilute NaOH solution. The molar ratio of PAA:EDC:NHS was 1:2:2. The obtained transparent solution was carried out at RT for 4h. Then amine functionalized magnetic nanoparticles (NH_2-MNPs) which were prepared by grafting APTES described in previous reports[2] were dispersed into water by sonication and added into the above solution and carried out at RT for 24 h. The mass ratio of NH_2-MNPs:PAA was 150:1. Thereafter, the PAA modified magnetic nanoparticles (PAA-MNPs) were magnetically precipitated and washed several times with distilled water. Finally FA was connected to the as-prepared PAA-NMPs (FA-PAA-MNPs) according to the reported procedure with little modification.3 DOX, an anticancer drug, was loaded into the pH-sensitive Magnetic nanoparticles (DOX-MNPs). In brief, 5 mg FA-PAA-MNPs were added to 5 mL 0.3 mg mL^{-1} DOX solution and the mixture was kept in a shaker for 24 h. The release rates of DOX were subsequently studied in vitro at 37℃ in simulate environments with different pH values, corresponding to the physiological condition of the blood (pH 7.4) and acidic environment in intracellular lysosomes (pH 5.0).

The sizes and shapes of these samples were observed by transmission electron microscopy (TEM, Model Tecnai 12, Philips Co. Ltd., Holland). Magnetic properties of the particles were measured at room temperature using a vibrating sample magnetometer (VSM, Model 7410, Lake Shore Co. Ltd., USA). The thermal stability was detected by thermogravimetricanalysis (TGA, Model TA 2100, TA Instruments, USA) under an inert atmosphere (N_2). DOX content was determined by measuring ultraviolet and visible spectrum (UV759S, Shanghai Precision & Scientific Instrument Co. Ltd., China).

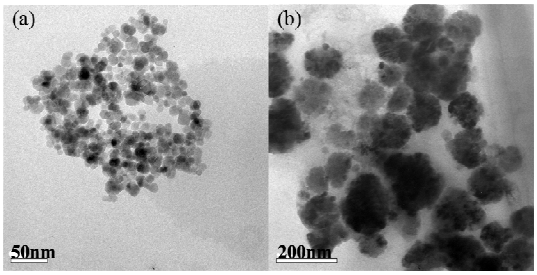


Figure 1 (a) TEM image of NH_2-MNPs and (b) TEM image of FA-PAA-MNPs

Figure 1 (a), 1 (b) show the TEM image of the NH2-MNPs (a) and the FA-PAA-MNPs (b). In Fig. 1 (a), the nanoparticles are well dispersed, spherical in nature with average particle size 10-15 nm. In Fig.1 (b), almost spherical nanocomposites can be observed and the dispersion of the nanoparticles is also well. The majority of the nanoparticles have a diameter size of about 100-160 nm. Shivang has summarized that NPs should typically be between 100 and 200 nm to avoid sequestration and extravasation to the tissues in order to maximize confinement to the vasculature.1 This means the size of nanoparticles is well within the preferred range of the nanoparticles useful for effective drug-delivery.

Figure 2 (a) displays the magnetic properties of various nanoparticles where typical ferromagnetic behavior can be observed. The saturated magnetization values (Ms) for NH2-MNPs, PAA-MNPs and FA-PAA-MNPs are calculated to be 62, 51, and 46 emu/g, respectively. Gradual decrease in the Ms values with surface modification is due to decrease in magnetic dipolar

interaction with diamagnetic coating. In each stage of nanoparticles preparation and subsequent surface modification, the nanoparticles are isolated from the aqueous dispersion by simple magnetic precipitation. From magnetic studies, it may be concluded that these magnetic particles show a high enough Ms value which have the potential ability to be used in magnet-guided drug delivery applications.

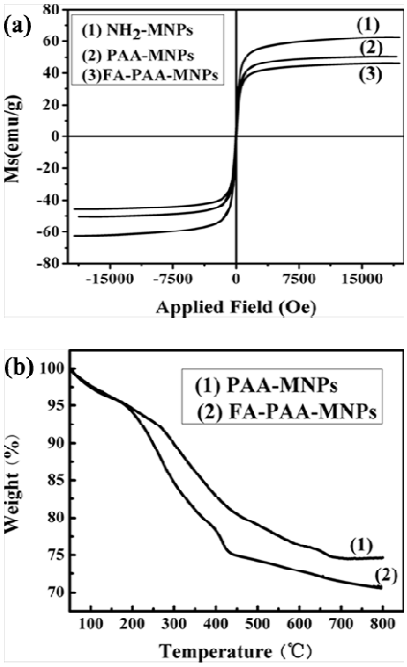


Figure 2 The VSM and the TG measurement results

Fig. 2 (b) displays the TG measurement result of the PAA-MNPs and FA-PAA-MNPs, respectively. In Fig. 2 (b) (2), the first stage is a weight loss of up to less than 3% in the range of 50–100 ℃, mainly relates to the evaporation of the physically adsorbed water of the sample. The second stage appears in the temperature range of 200 – 420 ℃, which has a weight loss of up to 19%. It is due to dehydration and decarboxylation of the carboxylic acid groups of PAA polymers and the degradation of APTES and FA. The third stage appears in the temperature range of 420 – 800 ℃ which has a weight loss of up to 5%, and it is mainly associated with the degradation of PAA polymer backbone and the remaining part of FA. Combined with TEM, VSM and TG results, it is suggested that Fe3O4 nanoparticles have been coated by PAA and FA in the chemical grafting process.

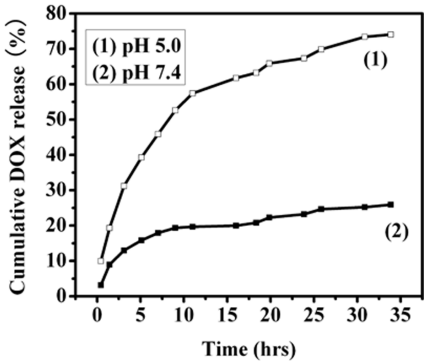


Fig 3 Release curves of DOX-MNPs with time (1) pH 5.0 and (2) pH 7.4

DOX possesses an ionizable amino group on the sugar ring when DOX is in the form of hydrochloride. DOX can be binded to nanoparticles through ionic interaction as sodium ions on the PAA form a salt bridge and produce sodium chloride as a byproduct. The loading content = weight of drug in nanoparticle/weight of nanoparticles taken, The entrapment efficiency = weight of drug

in nanoparticle/weight of drug injected. According to these equations, the loading content and entrapment efficiency of DOX in FA-PAA-MNPs are found to be 23.2% and 79.5%, respectively. The DOX loading amount in the polymeric shell observed here are found to be much higher than those in other polymer shells as suggested in earlier reports.4,10,11 In vitro, the release of DOX from DOX-MNPs at different conditions is shown in Fig.3. The release performance is studied at both physiological and lysosomal pH conditions at 37 ℃. The drug release profile reveals that the release rate is pH-dependent. About 74% of the loaded DOX is released in the stage of 0–35 h at pH 5.0 at 37 ℃, whereas only about 26% drug is released at pH 7.4 at the same time interval and temperature. Compared with pH 7.4, there is a drastic increase in drug release amount and rate at pH 5.0, indicating that the release amount and rate are dependent on pH. The result owing to the protonation of carboxylic groups of PAA at pH 5.0, the DOX-MNPs interaction becomes weak and DOX is released at a much faster rate and in larger amount. The drug release pattern indicates that the pH responsive polymer plays a key role on release of loaded drug in a desired fashion.

Summary

In summary, we have shown that the pH-sensitive nanoparticles prepared by chemical grafting is in desired size-range for drug delivery application. They possess high saturation magnetizations and good stability in physiology medium. Moreover, the loading content and entrapment efficiency can reach as high as 23.2% and 79.5%, respectively. It means the outer PAA and FA shell encapsulate large amount of DOX. Further, the drug release study reveals that DOX-MNPs release DOX preferably at pH 5.0, meaning that the as-prepared nanoparticles achieve excellent efficiency for simultaneous targeting. It is expected that the magnetic nanoparticles have applications in the biomedical field.

Acknowledgements

The authors are grateful for the financial support of National Natural Science Foundation of China (Nos. 50602024, 50972060), the Scientific and Technical Supporting Programs of Jiangsu province (BE2012758) and the Scientific Research Fund from NJUST Research Funding (No. 2010ZDJH06), the Fundamental Research Funds for the Central Universities (No. 30920130112003).

References

[1] Shivang R. Dave1, X. Gao, Monodisperse magnetic nanoparticles for biodetection, imaging, and drug delivery: a versatile and evolving technology, Nanobiotechnol. 1 (2009) 583–609.

[2] S. Nie, Y. Xing, G.J. Kim, J.W. Simons, Nanotechnology Applications in Cancer, Annu Rev Biomed Eng. 9 (2007) 257-288.

[3] C. Xu, S. Sun, Monodisperse magnetic nanoparticles for biomedical applications, *Polym. Int*. 56 (2007) 821-826.

[4] E.R. Gillies, J.M.J. Fréchet, pH-Responsive Copolymer Assemblies for Controlled Release of Doxorubicin, *Bioconjugate Chem*. 16 (2005) 361-368.

[5] S. Kumar, Y.L. Dory, M. Lepage, Y. Zhao, Surface-Grafted Stimuli-Responsive Block Copolymer Brushes for the Thermo-, Photo- and pH-Sensitive Release of Dye Molecules, *Macromolecules* 44 (2011) 7385-7393.

[6] Y. Chang, X. Meng, Y. Zhao, K. Li, B. Zhao, M. Zhu, Y. Li, X. Chen, J. Wang, Novel water-soluble and pH-responsive anticancer drug nanocarriers: Doxorubicin–PAMAM dendrimer conjugates attached to superparamagnetic iron oxide nanoparticles (IONPs), Journal of Colloid and Interface Science 363 (2011) 403-409.

[7] A. Sulistio, J. Lowenthal, A. Blencowe, M.N. Bongiovanni, L. Ong, S.L. Gras, X. Zhang, G.G. Qiao, Folic Acid Conjugated Amino Acid-Based Star Polymers for Active Targeting of Cancer Cells, *Biomacromolecules* 12 (2011) 3469-3477.

[8] X. Yang, W. Jiang, L. Liu, B. Chen, S. Wu, D. Sun, F. Li, One-step hydrothermal synthesis of highly water-soluble secondary structural Fe_3O_4 nanoparticles, *J. Magn. Magn. Mater.* 324 (2012) 2249-2257.

[9] O. Moscoso-Londoño, J.S. Gonzalez, D. Muraca, C.E. Hoppe, V.A. Alvarez, A. López-Quintela, L.M. Socolovsky, K.R. Pirota, Structural and magnetic behavior of ferrogels obtained by freezing thawing of polyvinyl alcohol/poly(acrylic acid) (PAA)-coated iron oxide nanoparticles, *Eur. Polym. J.* 49 (2013) 279-289.

[10] L. Zhou, J. Yuan, W. Yuan, X. Sui, S. Wu, Z. Li, D. Shen, Synthesis, characterization, and controllable drug release of pH-sensitive hybrid magnetic nanoparticles, *J. Magn. Magn. Mater.* 321 (2009) 2799-2804.

[11] B. Gaihre, M. Khil, D. Lee, H. Kim, Gelatin-coated magnetic iron oxide nanoparticles as carrier system: Drug loading and in vitro drug release study, *Int. J. Pharm.* 365 (2009) 180-189.

Advanced Materials Research Vol. 936 (2014) pp 728-733
© (2014) Trans Tech Publications, Switzerland
doi:10.4028/www.scientific.net/AMR.936.728

Preparation and Anti-Tumor Activity of Polysaccharides From Phellinus Pini Mycelia

An-jun Liu[1,a], Hong-chen Sun[1,b], Ying Chen[1,c,*], Wen-hang Wang[1,d],

Cai-hong Liu[1,e], Yue-meng Wang[1,f]

[1]Key Laboratory of Food Nutrition and Safety, Ministry of Education, College of Food Engineering and Biotechnology, Tianjin University of Science and Technology, Tianjin 300457, P.R. China

[a]laj-tj@hotmail.com, [b]sun_hongchen@163.com, [c]chenying2001@126.com, [d]wangwenhang@tust.edu.cn, [e]caihongL58@163.com, [f]wangyuemeng1990@163.com

Keywords: Phellinus pini, polysaccharide, preparation, anti-tumor activity

Abstract: Polysaccharides PS Ⅰ and PS Ⅱ were isolated from liquid-cultured mycelia of *Phellinus pini*. The average molecular weight: PS Ⅰ 36 kDa, PS Ⅱ 49 kDa; sulfate content: PS Ⅰ 5.25%, PS Ⅱ 0.65%; monosaccharide composition: PS Ⅰ glucose, galactose and mannitose; PS Ⅱ glucose, mannitose and xylose. Anti-tumor activities of PS Ⅰ and PS Ⅱ (400 mg/kg·d, i.g.) were investigated in S180-bearing mice. Results indicated that PS Ⅰ and PS Ⅱ significantly inhibited the growth of S180-solid tumors. PS Ⅰ and PS Ⅱ effectively protected immune organs (thymus and spleen) and increased activities of immune cells (NK cells, macrophages, T and B lymphocytes). Results suggest that polysaccharides PS Ⅰ and PS Ⅱ from *Phellinus pini* have potential anti-tumor activities, which might attributed partly to their immunomodulatory properties.

Introduction

Mushroom polysaccharides have attracted considerable attention due to their various and potentially significant pharmacological activities and low toxicity[1-3]. The genus *Phellinus* includes many species, of which *Phellinus linteus*, *Phellinus baumii Pilát* and *Phellinus igniarius* are well-known traditional medicinal mushrooms in Eastern countries such as China, Korea and Japan[4-6]. Many researchers have investigated the biological activities of polysaccharides isolated from these *Phellinus* species in recent years. Results indicated that polysaccharides isolated from *Phellinus linteus*, *Phellinus igniarius*, etc. exerted anti-tumor effects by activating immune cells (e.g., T cells, B cells, dendritic cells (DC) and macrophages) and directly acting on the tumor cells[5-7].

Due to the limited resource of the genus *Phellinus* in nature and some disadvantages associated with traditional solid culture, the submerged fermentation technology has been applied to obtain mycelia for the production of polysaccharides[8-11]. A higher mycelia production in a more-compact space over a shorter time could be achieved using submerged culture technology. *Phellinus pini* is a species belonging to the genus *Phellinus* that fructifies over the stem of *Pinus pinaster*. Being exploited lately, there are few reports focusing on the bioactivities of polysaccharides from *Phellinus pini*. In the present study, the immunologically active polysaccharides PS Ⅰ and PS Ⅱ were prepared from *Phellinus pini* mycelia, which was obtained using submerged culture technology. The anti-tumor activities of PS Ⅰ and PS Ⅱ *in vivo* were investigated in S180-bearing mice. Results of this study suggest that polysaccharides PS Ⅰ and PS Ⅱ from *Phellinus pini* have potential anti-tumor activities, which might attributed partly to their immunomodulatory properties.

Materials and methods

Fermentation and preparation of crude polysaccharides.

The submerged-fermentation of *Phellinus pini* were performed under the following conditions: 26℃, pH 7.0, 160 r/min, seed age 3 d, inoculum size 15%, bottling capacity 70 mL/250 mL, 7 d; carbon resource: glucose 2.66%, soluble starch 2.11%, nitrogen resource: yeast extract 0.76%, peptone 0.82%. The crude polysaccharides were applied to a DEAE-cellulose column and further purified by gel filtration chromatography on Sepharose CL-4B and Sepharose CL-6B column. Two fractions were concentrated, dialyzed, lyophilized and named as PS Ⅰ and PS Ⅱ, respectively.

Composition analysis of PS Ⅰ and PS Ⅱ.

The total polysaccharide content was determined using the phenol-sulfuric acid method and the protein content was measured by Lowry method using D-glucose and bovine serum albumin as standard, respectively. The sulfur content was determined by sodium rhodizonate method. Gas chromatography analysis of monosaccharide composition was performed on a Shimadzu GC-9A instrument: hydrogen flame ionization detector (FID), the flow rate of N_2, H_2 and air were 40 mL/min, 50 mL/min and 500 mL/min, respectively; the column temperature: 180℃; the inlet temperature: 210℃. Standard monosaccharides (xylose, ribose, mannose, galactose and glucose) were used as standards. The average molecular weight of PS Ⅰ and PS Ⅱ was determined by high-performance size-exclusion chromatography (HPSEC) on an Ultrahydrogel^{TM}1000 column. The calibration curve was made with the T-series Dextran standards (Dextran T-10, T-40, T-70, T-110, T-500 and T-2000).

Animals and experimental design.

Animals (*Kunming* mice, male/female, 6-8 weeks old, 20-22 g) were randomly divided into four groups (n=10 in each group). PS Ⅰ group and PS Ⅱ group were treated once daily with an oral administration of PS Ⅰ (400 mg/kg·bw) or PS Ⅱ (400 mg/kg·bw) for 28 days, respectively. Control group and Model group were administered with an equal volume of distilled water. On day 14, Sarcoma 180 tumor cells (1×10^7 cells/ml, 0.2 ml) were inoculated subcutaneously into the left armpit of the mice in Model, PS Ⅰ and PS Ⅱ groups. All animal experiments were performed in strict accordance with the National Institutes of Health Guidelines for the Care and Use of Laboratory animals. Animals were weighed every two days. The length (L) and width (W) of solid tumors were measured using a caliper. After 28 days of oral administration, mice were sacrificed by cervical dislocation. Thymus index and spleen index were defined as the ratio of the corresponding organ's weight (mg) to the body weight (g).

Assay of natural killer (NK) cells activity.

The activity of NK cells were assayed by MTT method. Spleen cells (2×10^6 cells/ml) together with S-180 cells (1×10^5 cells/ml) were incubated overnight at 37℃ in a 96-well culture plate. 10 μl MTT (5 mg/ml) was added to each well. After another 4 h of incubation, 150 μl DMSO was added to each well and shaken until all crystals dissolved. The wells of target cells control, blank control and effector cells control were treated simultaneously. The absorbance of each well was recorded at 570 nm.

Macrophage phagocytosis assay.

Mice were injected intraperitoneally with 1 mL sterile soluble starch (5%) daily for 3 days. Peritoneal exudates were harvested by a lavage of the peritoneal cavity with 5 ml of PBS on day 4. Cells were added (100 μl/well) into a 96-well plate, and incubated for 3 h at 37℃. After washed twice with PBS, 0.073% neutral red was added (200 μL/well) and incubated for another 3 h. Each well was added 100 μl cell lysis solution (acetic acid: anhydrous ethanol= 1:1) and incubated overnight. The absorbance was read at 540 nm.

Lymphocyte proliferation assay.

A single spleen cell suspension was prepared. Cells were pipetted into a 96-well flat-bottom plate (100 μl/well) in the presence or absence of Con A (5 μg/ml) or LPS (10 μg/ml). After incubation at 37℃ for 44 h in a 5% CO_2 incubator, 20 μl MTT solution (5 mg/ml) was added to each well and the plate was further incubated for 4 h. 150 μl DMSO was added to each well and shaken until all crystals dissolved. The absorbance was detected at 570 nm.

Statistical analysis.

Results were expressed as the means±SD. Statistical analysis was performed by the Student's *t*-test. $p<0.05$ was considered statistically significant.

Results and discussion

Preparation and composition analysis of PS Ⅰ and PS Ⅱ.

In the present study, an artificial cultivation of *Phellinus pini* mycelia was performed using submerged fermentation technology. The yield of crude polysaccharide from *Phellinus pini* mycelia was 6.70%. Two purified fractions PS Ⅰ and PS Ⅱ were obtained. Composition analysis of PS Ⅰ and PS Ⅱ indicated: the total sugar content of PS Ⅰ 75.31%, PS Ⅱ 86.28%; protein content: PS Ⅰ 4.52%, PS Ⅱ 6.87%; sulfate content: PS Ⅰ 5.25%, PS Ⅱ 0.65%; the average molecular weight: PS Ⅰ 36 kDa, PS Ⅱ 49 kDa. And the results of monosaccharide composition analysis indicated that PS Ⅰ was mainly composed of hexose (92%) and the molar ratio of glucose, galactose and mannitose was 68:15:7; PS Ⅱ was composed of hexose (95%, glucose: mannitose 86:8) and pentose (5%, mainly xylose).

Anti-tumor activity of PS Ⅰ and PS Ⅱ.

Anti-tumor activity of PS Ⅰ and PS Ⅱ *in vivo* were investigated in S180-bearing mice in the present study. Results indicated that both polysaccharides PS Ⅰ and PS Ⅱ (400 mg/kg·d, i.g.) significantly inhibited the growth of S180-solid tumors. The tumor inhibition ratio of PS Ⅰ and PS Ⅱ was 94.58% and 84.65%, respectively.

Effects of PS Ⅰ and PS Ⅱ on immune organ index.

Thymus and spleen are important immune organs. In the present study, the effects of PS Ⅰ and PS Ⅱ on the immune organs (thymus and spleen) were investigated. As shown in Fig.1, the thymus index and spleen index in PS Ⅰ and PS Ⅱ treatment groups were significantly increased (PS Ⅰ: $p<0.05$, $p<0.05$; PS Ⅱ: $p<0.05$, $p<0.05$ vs. S-180 model group), indicating the protective effects of PS Ⅰ and PS Ⅱ on the immune organs.

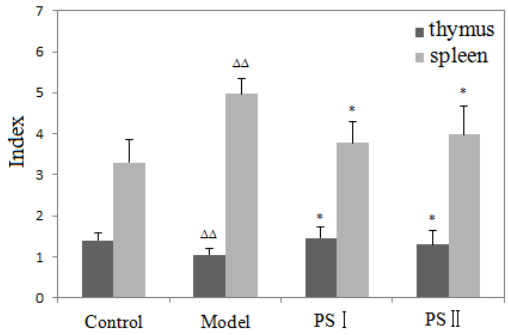


Fig.1 Comparison of thymus and spleen index of mice from different groups

ΔΔp<0.01 vs. Control group; *p<0.05 vs. Model group

Effects of PS Ⅰ and PS Ⅱ on NK cell activity.

Natural killer (NK) cells are important lymphocytes of the innate immune system. There is accumulating evidence of the crucial contribution of NK cells to the immunosurveillance of tumor. The effects of PS Ⅰ and PS Ⅱ on NK cell activity in S180-bearing mice were investigated in the present study. As shown in Fig.2, the NK cell activities were significantly increased in the PS Ⅰ- and PS Ⅱ-treated animals (PS Ⅰ: $p<0.05$; PS Ⅱ: $p<0.05$) .

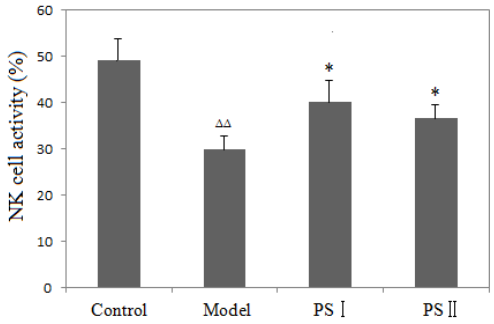


Fig.2 Effect of PS Ⅰ, PS Ⅱ on splenic NK cell activity in S180-bearing mice

ΔΔp<0.01 vs. Control group; *p<0.05 vs. Model group

Effects of PS Ⅰ and PS Ⅱ on phagocytic activity of macrophages.

The effects of PS Ⅰ and PS Ⅱ on the phagocytic activity of macrophages were investigated in the present study. Macrophages are considered as the important immunocytes in the host defense system. The phagocytic activities of peritoneal macrophages in PS Ⅰ- and PS Ⅱ-treated animals were significantly increased ($p<0.01$, $p<0.01$ vs. Model group, Fig.3), and a greater increment was observed in PS Ⅰ group ($p<0.05$ vs. PS Ⅱ group), which might be related to their different chemical structures, e.g. molecular weight, monosaccharide composition.

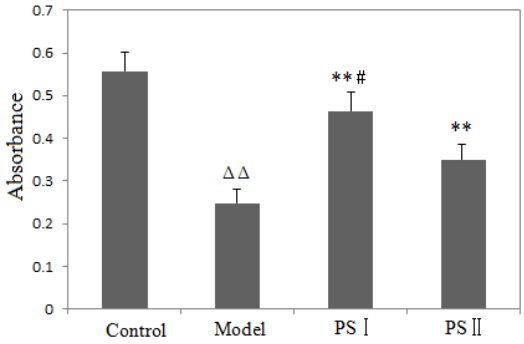


Fig.3 Effect of PS Ⅰ, PS Ⅱ on phagocytic activity of peritoneal macrophages in S180-bearing mice

ΔΔp<0.01 vs. Control group; **p<0.01 vs. Model group; #p<0.05 vs. PS Ⅱ group

Effects of PS Ⅰ and PS Ⅱ on lymphocyte proliferation.

As shown in Fig.4, both PS Ⅰ and PS Ⅱ significantly increased (PS Ⅰ: $p<0.05$; PS Ⅱ: $p<0.05$) splenic lymphocytes proliferation in the presence of Con A (stimulates T lymphocytes). The effects of PS Ⅰ and PS Ⅱ were more obvious (PS Ⅰ: $p<0.01$; PS Ⅱ: $p<0.01$) in the presence of LPS (stimulates B lymphocytes) and significant difference ($p<0.05$) was observed between PS Ⅰ and PS Ⅱ. Lymphocytes play significant roles in the host defense against tumor cells. Results of this study indicated that the stimulating effects of PS Ⅰ and PS Ⅱ on proliferative activity of lymphocytes especially B lymphocytes might contribute greatly to the anti-tumor activities of PS Ⅰ and PS Ⅱ.

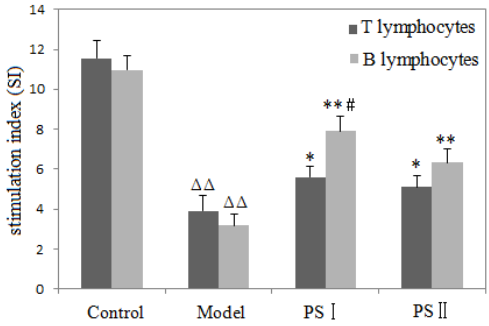


Fig.4 Effect of PS Ⅰ, PS Ⅱ on splenic lymphocyte proliferation of S180-bearing mice (n=8)

ΔΔp<0.01 vs. Control group; *p<0.05, **p<0.01 vs. Model group; #p<0.05 vs. PS Ⅱ Group

Conclusions

In the present study, polysaccharides PS Ⅰ and PS Ⅱ were prepared from *Phellinus pini* mycelia, which was obtained using submerged fermentation technology. Composition analysis of PS Ⅰ and PS Ⅱ was performed. The anti-tumor activities of PS Ⅰ and PS Ⅱ were investigated in S180-bearing mice. Results indicated PS Ⅰ and PS Ⅱ significantly inhibited the growth of S180-solid tumors and effectively protected immune organs and activated immune cells. Although further studies are needed, the results of this study suggest that polysaccharides PS Ⅰ and PS Ⅱ from *Phellinus pini* have potential anti-tumor activities and the difference observed between PS Ⅰ and PS Ⅱ might be related to their different chemical structures.

Acknowledgements

The research received financial support from National High Technology Research and Development Program 863: Special food protein binders for research and development of key technologies (SS2013AA100204).

References

[1] P. Seephonkai, S. Samchai, A. Thongsom, et al. DPPH radical scavenging activity and total phenolics of Phellinus mushroom extracts collected from northeast of Thailand. CJNM. 9(2011) 0441-0445.

[2] H.Y. Huang, S.Y. Chieh, T.K. Tso, et al. Orally administered mycelial culture of Phellinus linteus exhibits antitumor effects in hepatoma cell-bearing mice. J. Ethnopharmacol. 133(2011) 460-466.

[3] M. Kozarski, A. Klaus, M. Niksic, et al. Antioxidative and immunomodulating activities of polysaccharide extracts of the medicinal mushrooms Agaricus bisporus, Agaricus brasiliensis, Ganoderma lucidum and Phellinus linteus. Food Chem. 129(2011)1667-1675.

[4] C.F. Yuan, X.N. Huang, Li Cheng, et al. Evaluation of antioxidant and immune activity of Phellinus ribis glucan in mice. Food Chem. 115(2009)581-584.

[5] L. Chen, J.Z.Pan, X. Li, et al. Endo-polysaccharide of Phellinus igniarius exhibited anti-tumor effect through enhancement of cell mediated immunity. Int. Immunopharmacol.11(2011)255-259.

[6] Y.G. Li, D.F. Ji, S. Zhong, et al. Anti-tumor effects of proteoglycan from Phellinus linteus by immunomodulating and inhibiting Reg IV/EGFR/Akt signaling pathway in colorectal carcinoma. Int. J. Biol. Macromol. 48(2011)511-517.

[7] Z.Y. Wang, C.Y. Wang, Y. Quan. Extraction of polysaccharides from Phellinus nigricans mycelia and their antioxidant activities in vitro. Carbohydr. Polym. 99(2014) 110-115.

[8] J.G. Luo, Jun Liu, C.L. Ke, et al. Optimization of medium composition for the production of exopolysaccharides from Phellinus baumii Pilát in submerged culture and the immuno-stimulating activity of exopolysaccharides. Carbohydr. Polym. 78(2009) 409- 415.

[9] J.G. Luo, J. Liu, Y. Sun, et al. Medium optimization, preliminary characterization and antioxidant activity in vivo of mycelical polysaccharide from Phellinus baumii Pilát. Carbohydr. Polym. 81(2010) 533-540.

[10] X. Guo, X. Zou, M. Sun. Optimization of extraction process by response surface methodology and preliminary characterization of polysaccharides from Phellinus igniarius. Carbohydr. Polym. 80(2010) 344-349.

[11] B.Z. Zhang, P.S.Yan, H. Chen, et al. Optimization of production conditions for mushroom polysaccharides with high yield and antitumor activity. Carbohydr. Polym. 87(2012) 2569-2575.

Advanced Materials Research Vol. 936 (2014) pp 734-739
© (2014) Trans Tech Publications, Switzerland
doi:10.4028/www.scientific.net/AMR.936.734

A Facile Method to Synthesize Responsive Magnetic Polymer Composite Nanoparticles with Multifunctional Groups

Menglu Pu[1,a], Wei Jiang[2, b *], Yueqing Shen[3,c]

[1,2,3]National Special Superfine Powder Engineering Research Center, Nanjing University of Science and Technology, Nanjing 210094, China

[a]menglu521@qq.com, [b]climentjw@126.com, [c]shenyueqing@126.com

Keywords: magnetic nanoparticles; composite particles; emulsion polymerization; high saturation magnetization; biomedical application

Abstract: Magnetite nanoparticles (MNPs) coated with poly(divinylbenzene-co-glycidyl methacrylate) particles (mPDGs) are prepared by co-polymerization of 1,4-divinylbenzene and glycidyl methacrylate monomers via batch emulsion polymerization. The Fe_3O_4 nanoparticles modified by oleic acid are obtained by chemical precipitation. The chemical composition, morphology, magnetic content, magnetic properties and particle size of the composite particles are investigated using transmission electron microscopy, thermogravimetric analysis, vibrating sample magnetometer, and dynamic light scattering, respectively. The results show that the magnetic nanoparticles have been coated by 1,4-divinylbenzene and glycidyl methacrylate, with the high saturation magnetization being 33.66 emu/g. The mean size of the mPDGs with good dispersion is about 200 nm. Subsequently, the polymer shell with reactive epoxy group is expected to be useful for chemical grafting of any biomolecule containing reactive functional groups (-NH_2, -OH, -COOH, etc) or can be chemically modified to desired functional groups. These magnetic nanospheres with multifunctional groups have potential application in biomedical applications.

Introduction

Recently, MNPs have generated considerable interests in various areas, especially in the biomedicine field,[1] which is attributed to their small size, large surface-to-volume ratio and size dependent magnetic properties.[2] Magnetite nanoparticles possess magnetism in the magnetic field. Owing to this character, MNPs may be used as drug carriers because it can transfer the carried particle to the chosen site with the help of localized magnetic field. Moreover, the MNPs can be held by the magnetic field until finish of the therapy and finally can be removed by the magnetic field.[3] Unfortunately, only small amount of drugs can be carried by MNPs, and the biocompatibility and stability of the MNPs should be improved.

It has been reported that coating the surfaces of MNPs with polymers to form functional magnetic polymer nanoparticles or microspheres (FMPLs) is a good way to solve these problems. By coating the polymer shell, appreciable amount of drugs can be loaded onto the surfaces of the polymer shell, and aggregation of Fe_3O_4 nanoparticles is prevented both in biological medium and magnetic field, meaning that the stability of the Fe_3O_4 nanoparticles is improved.[4-7] Moreover, the surfaces of magnetic nanoparticles modified by polymers are suitable for further functionalization by the attachment of various bioactive molecules.[8]

In general, all biomedical applications of magnetic nanoparticles require that nanospheres should fulfill certain criteria, for example, no sedimentation, uniform size, high saturation magnetization, and abundant functional groups. In the last decade, several interesting approaches have been developed to prepare these hybrid particles, including classical heterogeneous polymerization processes using mini-emulsions, inverse emulsions or inverse micro-emulsions, as well as some multi-step synthesis procedures.[9,10]

Mini-emulsion polymerization has been used for the preparation of carboxylated magnetic polymer nanoparticles by Zheng et al.[11] and epoxy-functionalized magnetic polymer microspheres by Lee et al.[12] However, these obtained magnetic spheres cannot match the above-mentioned biomedical requirements simultaneously. Batch polymerization process is reported to be the most

widely used method to synthesize microgel materials.[13] Montagne et al.[14] have firstly reported the use of o/w magnetic emulsion droplets as the seed in emulsion polymerization. This new approach is based on the transformation of magnetic emulsion droplets into magnetic latex particles by emulsion polymerization using hydrophobic monomers such as styrene.[15] Homogeneous encapsulation of Fe_3O_4 nanoparticles can also be efficiently achieved using a styrene/1,4-divinylbenzene (DVB) monomer mixture in the presence of potassium persulfate (KPS) as initiator. The magnetic seeds used are submicron droplets of a highly stable magnetic emulsion and the particle size distribution of the magnetic polymer emulsion is controlled by the size distribution of the initial magnetic emulsion. In this article, poly(divinylbenzene-co-glycidyl methacrylate) microspheres are prepared by batch emulsion copolymerization[16] in the presence of o/w magnetic emulsion droplets as the seed. It is a facile method to synthesize responsive magnetic polymer composite nanoparticles. The difference between this work and that of Montagne *et al*. is that magnetic seeds with grain sizes of about 10 nm in diameter are used in this work while submicron magnetic seeds are applied by Montagne et al. The embedding of oleic acid modified Fe_3O_4 nanoparticles within polymeric matrices prevents the aggregation of Fe_3O_4 magnetic seeds in physiological media and the physicochemical properties of Fe_3O_4 magnetic seeds can be preserved. This method can control the particle size distribution and magnetic content of the composite particles. This study provides a route to prepare a new material, which might be useful in biomedical applications especially drug releasing coatings for medical devices. As a result, medical devices may be implanted or inserted into the body because magnetite nanoparticles have extensive biomedical applications due to their biocompatibility.[17,18]

Experiment

Materials

Divinyl benzene (DVB, 80%) and Glycidyl methacrylate (GMA, 98%) were purchased from Aldrich Chemical Co.Ltd.. The monomers were purified of inhibitors by washing with 5% NaOH solution before use. Ferric chloride ($FeCl_3 \cdot 6H_2O$, analytically pure grade), ferrous sulfate ($FeSO_4 \cdot 7H_2O$, analytically pure grade), sodium dodecyl sulfate ($C_{18}H_{29}NaO_3S$, SDS, chemically pure grade) were supplied by Sinopharm Chemical Reagent Co. Ltd., Shanghai, China. Oleic acid ($CH_3(CH_2)_7CH=CH(CH_2)_7COOH$, OA, chemically pure grade), potassium persulfate ($K_2S_2O_8$, analytically pure grade) and n-Octane (C_8H_{20}, chemically pure grade) were obtained from Shanghai Linfeng Chemical Reagent Co. Ltd., Shanghai, China. Ammonia ($NH_3 \cdot H_2O$, 25 wt % NH_3, analytically pure grade) was purchased from Nanjing Chemical Reagent Co. Ltd., Nanjing, China. All the chemical agents were used as-received without further purification.

Preparation of Fe_3O_4 ferrofluid

Fe_3O_4 NPs were prepared by chemical coprecipitation of Fe^{3+}: Fe^{2+} in the ratio of 1.5: 1 as described in previous reports.[19] The procedure preparing ferrofluids was showed as follows. Briefly, $FeCl_3 \cdot 6H_2O$ and $FeSO_4 \cdot 7H_2O$ were dissolved in distilled water with vigorously stirring to dissolve completely, and then heated to 70 ℃ under the protection of nitrogen atmosphere followed by adding ammonia to the flask. After 10 min, OA was added into the solution and continuously stirred at 70 ℃ for 1 h. Then, the solution was heated to 85 ℃ and kept at this temperature for 30 min in order to evaporate NH_3. After finishing the reaction, the solution was cooled to room temperature and washed with deionized water for several times. Finally, the products were dispersed in octane to get magnetic fluid with magnetite content of 8 wt %.

Preparation of epoxy-functionalized magnetic colloidal particles

The reactions were conducted by batch emulsion polymerization in the presence of o/w magnetic emulsion droplets as the seed, as illustrated schematically in Fig. 3. DVB (1.0 mL) and GMA (0.5 mL) were added in magnetic emulsion (50 mL) in the presence of KPS as initiator. The mixture was then carried out at 70 ℃ with stirring (300 rpm) under N_2 atmosphere for 24 h, and then terminated by cooling at room temperature. The obtained epoxy-functionalized magnetic colloidal particles were collected with a magnet and washed with distilled water for several times.

Characterization

The sizes and morphologies of the samples were investigated by transmission electron microscopy (TEM, Model Tecnai 12, Philips Co. Ltd., Holland). The particle size distributions of samples were determined by dynamic light scattering instrument (DLS, Zetasizer, Malvern, UK). The thermal stability of the dried sample was measured by thermogravimetric analysis (TGA, Model TA 2100, TA Instruments, USA) at a heating rate of 10 ℃/min in N_2 over the range of 50-700 ℃. Magnetic properties of the particles were detected at room temperature using vibrating sample magnetometer (VSM, Model 7410, Lake Shore Co. Ltd., USA).

Results and discussions

Characterization of sample

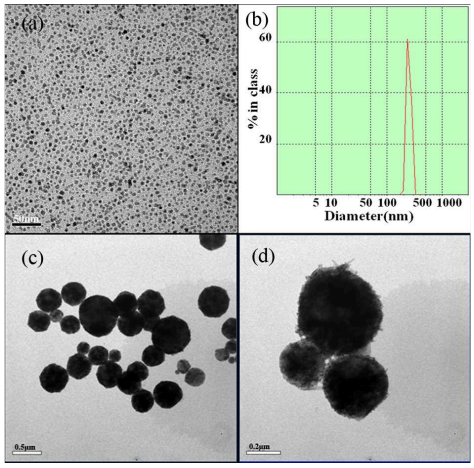


Figure 1 Transmission electron microscope images of (a) the OA modified Fe_3O_4 particles, (c, d) mPDGs and (b) dynamic light scattering graph of mPDGs.

The morphologies of the OA modified Fe_3O_4 particles and the mPDGs are investigated by TEM, as shown in Fig. 1. From Fig. 1 (a), we can see that the modified Fe_3O_4 particles can be well dispersed in octane, and the mean size of nanoparticles is about 10 nm, which is similar to our previous results.[19] In Fig. 1 (c) and (d), the TEM images present well-defined polymer microspheres with a mean diameter of about 200 nm. Fig. 1 (b) shows that the sizes of mPDGs determined by DLS are in the range of 150-350 nm, and the majority of the particles have a grain size of about 250 nm.

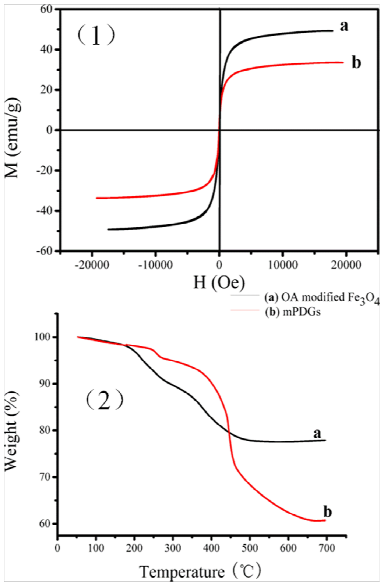


Fig. 2 VSM measurement results (1) and the TG measurement results (2) of (a) the OA modified Fe_3O_4 particles and (b) mPDGs.

Fig. 2 (1) shows the magnetic properties of the Fe_3O_4 particles before and after coating with poly(divinylbenzene-co-glycidylmethacrylate). It can be seen from Fig. 2 (1) that the saturation magnetization (M_s) value of the OA modified Fe_3O_4 particles is 48.25 emu/g while the M_s of mPDGs is 33.66 emu/g. Interestingly, ferromagnetism is preserved, demonstrating that the polymerization conditions have a little influence on the as-synthesized nanoparticles. Therefore, these magnetic materials can be easily controlled by an external magnetic field which is significant for applying to bioconjugation and biomedical fields.

The magnetic contents of the samples are evaluated by TGA. Fig. 2 (2) presents the thermal degradation curves for (a) OA-coated Fe_3O_4 nanoparticles and (b) mPDGs, respectively. As can be seen from curve a, a very moderate decrease before 150 ℃ is mainly attributed to the release of moisture entrapped by the emulsified Fe_3O_4 nanoparticles. Upon heating to 500 ℃, owing to decomposition of the organic layer, a larger loss (19.5 wt % (a) weight loss) appears, so it is concluded that OA decomposes in the range of 300-500 ℃, and this means that about 78% of the magnetite particles are coated with OA. From the curve of mPDGs, the weight of mPDGs begin to decrease rapidly at 400-700 ℃ and the residual mass percentage is 60 wt % at 700 ℃, which means a thicker polymer shell on the surfaces of the MNPs. These results demonstrate that the magnetic ferrofluids have been coated by divinylbenzene-co-glycidyl methacrylate and mPDGs can keep its structural and functional stability for further research.

Reaction procedure

The possible reaction procedure of the mPDGs by the batch emulsion polymerization method is presented in Fig. 3. The oil-soluble Fe_3O_4 ferrofluids are first dropped into lauryl sodium sulfate solution and emulsified to form Fe_3O_4 magnetic emulsion droplets as the seeds. Emulsifier molecules gather together to form emulsifier micelle when lauryl sodium sulfate is dissolved in the solvent. When KPS is added to the emulsion as water-soluble initiator, it will generate SO_4^{2-} ions in water. Some of the sulfate ions directly spread into the inner part of emulsifier micelle, inducing polymerization reaction. The others sulfate ions are captured by the double bond on the surfaces of Fe_3O_4 particles in the emulsion. They further spread into the micelle to induce polymerization between the activated double bond on the surfaces of Fe_3O_4 particles and the double bond of the hydrophobic DVB monomer in the micelle. New reactive epoxy-functionalized mPDGs are synthetized using seed emulsion polymerization of DVB and GMA monomers in the presence of Fe_3O_4 magnetic emulsion droplets as the seed. In the synthesis of reactive functional polymers, GMA contains a polymerizable double bond and a reactive epoxy group in its chemical structure, which are useful for chemical grafting of any biomolecule containing reactive functional groups.

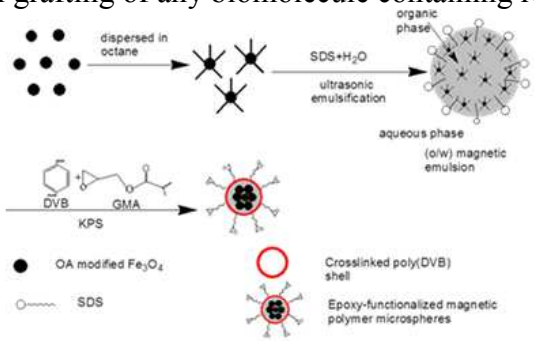


Fig. 3 Schematic illustration of the reaction mechanism of mPDGs.

Conclusion

Through the batch emulsion polymerization method, we have successfully synthesized the magnetic responsive poly(divinylbenzene-co-glycidyl methacrylate
) colloidal particles (mPDGs). The materials possess structural stability, high biocompatibility and biodegradability, and they would be a promising drug carrier. Furthermore, we have enough reasons to believe its application in the biomedical field. Further study on their biomedical application is being conducted in our team.

Acknowledgements

The authors are grateful for the financial support of National Natural Science Foundation of China (Nos. 50602024, 50972060), the Scientific and Technical Supporting Programs of Jiangsu province (BE2012758) and the Scientific Research Fund from NJUST Research Funding (No.2010ZDJH06), the Fundamental Research Funds for the Central Universities (No.30920130112003).

References

[1] A. S. Lübbe, C. Alexiou, C. Bergemann, Clinical applications of magnetic drug targeting, J. *Surgical Res*. 95 (2001) 200-206.

[2] H. Maeda, J. Wu, T. Sawa, Tumor vascular permeability and the EPR effect in macromolecular therapeutics: a review, J. Controlled Release. 65 (2000) 271-284.

[3] S. Dietrich, S. Chandra, C. Georgi, Design, characterization and magnetic properties of Fe_3O_4-nanoparticle arrays coated with PEGylated-dendrimers, Mater. Chem. Phys. 132 (2012) 292-299.

[4] Y. Wang, H-J. Kim, G. Vunjak-Novakovic, Stem cell-based tissue engineering with silk biomaterials, Biomaterials. 27 (2006) 6064-6082.

[5] J. K. Oh, J. M. Park, Iron oxide-based superparamagnetic polymeric nanomaterials: Design, preparation, and biomedical application, Prog. Polym. Sci. 36 (2011) 168-189.

[6] M. Lattuada, T. A. Hatton, Functionalization of monodisperse magnetic nanoparticles, Langmuir. 23 (2007) 2158-2168.

[7] X. Shi, T. P. Thomas, L. A. Myc, Synthesis, characterization, and intracellular uptake of carboxyl-terminated poly(amidoamine) dendrimer-stabilized iron oxide nanoparticles, PCCP. 9 (2007) 5712-5720.

[8] X. Liu, Q. Dai, L. Austin, A One-step homogeneous immunoassay for cancer biomarker detection using gold nanoparticle probes coupled with dynamic light scattering, J. Amer. Chem. Soc. 130 (2008) 2780-2782.

[9] P. Tartaj, M. del Puerto Morales, S. Veintemillas-Verdaguer, The preparation of magnetic nanoparticles for applications in biomedicine, J. Phys. D: Appl. Phys. 36 (2003) R182.

[10] R. Hidalgo-Álvarez, *Structure and functional properties of colloidal systems*, CRC Press, 2010.

[11] W. Zheng, F. Gao, H. Gu, Carboxylated magnetic polymer nanolatexes: Preparation, characterization and biomedical applications, J. Magn. Magn. Mater. 293 (2005) 199-205.

[12] S. S. Lee, K. Y. Park, J. Y. Kim, Effect of GMA on monodisperse epoxy-functionalized polymer microsphere particles by dispersion copolymerization of styrene with glycidyl methacrylate, J. Appl. Polym. Sci. 80 (2001) 1206-1212.

[13] R. A. Ramli, S. Hashim, W. A. Laftah, Synthesis, characterization, and morphology study of poly(acrylamide-*co*-acrylic acid)-*grafted*-poly(styrene-*co*-methyl methacrylate) "raspberry"-shape like structure microgels by pre-emulsified semi-batch emulsion polymerization, J. Colloid Interface Sci. 391 (2013) 86-94.

[14] F. Montagne, O. Mondain-Monval, C. Pichot, Highly magnetic latexes from submicrometer oil in water ferrofluid emulsions, J. Polym. Sci. Part A: Polym. Chem. 44 (2006) 2642-2656.

[15] J. Zhang, D. Yu, W. Chen, Preparation of poly(styrene-glucidylmethacrylate)/Fe_3O_4 composite microspheres with high magnetite contents, J. Magn. Magn. Mater. 321 (2009) 572-577.

[16] M. M. Eissa, M. Rahman, N. Zine, Reactive magnetic poly(divinylbenzene-co-glycidyl methacrylate) colloidal particles for specific antigen detection using microcontact printing technique, Acta biomaterialia. 9 (2013) 5573-5582.

[17] V. R. Babu, M. Sairam, K. M. Hosamani, Development of 5-fluorouracil loaded poly(acrylamide-*co*-methylmethacrylate) novel core-shell microspheres: *In vitro* release studies, Int. J. Pharm. 325 (2006) 55-62.

[18] T. Begam, R. Tomar, A. Nagpal, Synthesis of poly(acrylamide-*co*-methyl methacrylate-*co*-vinyl amine-*co*-acrylic acid) hydrogels by Hoffman degradation and their interactions with acetaminophen, J. Appl. Polym. Sci. 94 (2004) 40-52.

[19] S. Wu, W. Jiang, Z. Sun, Preparation of novel magnetic fluorescent nanospheres by sonochemical method, J. Magn. Magn. Mater. 323 (2011) 2170-2173.

Advanced Materials Research Vol. 936 (2014) pp 740-745
© (2014) Trans Tech Publications, Switzerland
doi:10.4028/www.scientific.net/AMR.936.740

The effects of immobilization conditions and materials on the desulfurization performance of immobilized UP-3

Ning Guo[1,2,a], Yingfei Hou[2, b*], Yaya Gu [2,c] and Chunhu Li [1,d]

[1] College of Chemistry and Chemical Engineering, Ocean University of China, Shandong Qingdao 266100, China

[2] State Key Laboratory of Heavy Oil Processing, China University of Petroleum (East China), Qingdao 266580, China

[a]guoningjh@sina.com, [b]houyf@upc.edu.cn, [c] yayagu1989@gmail.com, [d]lichunhu@ouc.edu.cn

Keywords: Biodesulfurization, Immobilized cells, Sodium alginate, Polyvinyl alcohol.

Abstract: Immobilization of the bacterium *Agrobacterium tumefaciens UP-3*, which was isolated from soil and sewage in the Shengli Oilfield, was studied in this paper. The suitable culture condition of growth cells was determined. The effects of immobilization conditions and materials on the desulfurization performance of immobilized cells were investigated. The results showed that the immobilized cells with mixture of sodium alginate(SA) and polyvinyl alcohol(PVA) as the immobilized carrier had good biodesulfurization characteristics; The optimum operation immobilization conditions are 4° C, the concentration of SA being 3% (w), the concentration of PVA and SA being 7% (w), and the ratio of carriers (ml) and cells (g) being 20. When DBT addition is 2.7 mM, the DBT degradation rate of immbobilized cells is above 60%.

Introduction

People were forcing to develop new technology of clean fuel production. Biodesulfurization (BDS) at room temperature and atmospheric pressure could selective oxidize the sulfide due to the effect of air, water and bio-catalytic, and then remove the sulfur atom or sulfide [1]. It has advantages of low cost, mild operating conditions, no need for hydrogen and effectively desulfurization heterocyclic sulfur compounds which is difficult for hydrodesulphurization. The researcher abroad have been isolated a variety of bacteria with the ability of desulfurization [2-7]. Less research on the oil biodesulfurization has been done and the progress was quite slow. Thus there is an urgent need to strengthen the basis technical reserves for petroleum biodesulfurization.

Immobilized microorganisms has now become a research hotspot, since immobilization through regeneration and activation can significantly improve the life of biocatalytic desulfurization catalyst; maintain the original state of the enzyme; enhance the stability of the biocatalyst performance; increase the cell density and resistance to pollution; avoid the loss of cells; save the subsequent separation process of the reaction system. Highly efficient and stable biological desulfurization catalyst is the premise of the industrialization of biocatalytic desulfurization, and the immobilization of desulfurization microbe strain is one of effective ways to obtain a highly efficient and stable biological desulfurization catalyst. The research on immobilization related to the oil desulfurization microbe strain which have been reported at abroad were only Je Hwan Chang, Manabu Naito etc[4]. This article uses *Agrobacterium tumefaciens UP-3* with independent intellectual property rights of our own as the oil biodesulfurization bacterium. Its desulfurization performance and immobilized study at home and abroad have not been reported yet. In this paper, the immobilization technique of embedding was adopted to research the immobilization of *Agrobacterium tumefaciens UP-3*, and we also explored the influence of immobilization conditions and materials on the catalytic desulfurization performance of the biocatalyst.

Materials and methods

Strain

The microbe strain, identified by Chinese Academy of Sciences as *Agrobacterium tumefaciens*(named: *Agrobacterium tumefaciens UP-3*), was isolated from the oil contaminated soil and sewage of Shengli Oilfield, obtained after the process of the separation, purification, mutation, screening and rescreening.

The media

Santes medium: soybean peptone 10 g, yeast extract powder 2 g, enzymatic hydrolysis of casein, 2 g, NaCl 6g, glucose 10g, distilled water 1000ml, with NaOH adjusted to pH 7.3～7.5.

Phosphate buffer: $Na_2HPO_4 \cdot 12H_2O$ 71.36g, $NaH_2PO_4 \cdot 2H_2O$ 31.20g, deionized water 1000ml, the PH 7.5.

Basic salt solution: Na_2HPO_4 4 g, $(NH4)_2SO_4$ 2 g, $MgSO_4.7H_2O$ 0.2 g and $CaCl_2$ 0.001 g, $FeSO_4.7H_2O$ 0.001 g, distilled water 1000 ml, pH 7.0.

The other main material

Sodium alginate, polyvinyl alcohol, agar, calcium chloride, boric acid, dibenzothiophene (DBT), diatomaceous earth, activated carbon.

Strain cultivation and collection

Cultured in shaking table with a speed of 200r/min. At the temperature of 31° C, with 250 mL flask, 50 mL medium, cultured for 24 hours, then centrifuge, centrifuge operating conditions: -4 ° C, 10000r/min.

Immobilization method

When adsorption immobilized method was used, add sterilized carrier to the medium which have been cultivate for 24 hours, adsorb 15 to 18 hours, then remove, wash for standby; while for embedding immobilized method, put collected bacterium washed several times with phosphate buffer. After centrifugation, add to the dissolved immobilized carrier glue, then using a syringe drip the 4 ° C gel solution into ball under stirring condition, cross linking and precipitate 24 hours, make the strength of the immobilized ball stable, and then wash it three times with distilled water for further use.

Desulfurization test

Oil biodesulfurization technology developed earlier at abroad, and many studies used dibenzo thiophene as model compounds [4-7], Mainly because it is relatively difficult to remove the sulfur compounds of thiophene compounds (especially dibenzo thiophene and its derivatives) in the existing oil products. Similarly, we also used DBT as a model compound to conduct biological desulphurization experiment. The specific methods were as follows: adding the growth cells or immobilized cells to sterile reaction model system containing DBT concentration of 2.7 mM, putting into the constant temperature shaking table for reaction.

Determination of desulfurization effect

By using 0.8 volume of extract liquid, the remaining DBT in the culture medium after reaction was extracted. After full concussion, take 1μl of the top extraction phase into the chromatographic for the determination of residual content of DBT which could be used to calculate the effect of desulfurization. Chromatographic conditions were as follows: WCOT FUSED SILICA 30m × 0.25mm capillary column, FID detector, the initial temperature of column box : 80° C, heated up to 300° C at the speed of 20°C / min, inlet temperature 320° C, flame ionization detector temperature 325 ° C, gas flow tail-blowing 25ml/min, H_2 30 ml/min, air 300 ml/min.

Results and discussion

Desulfurization performance of growth cells

The growth of microorganisms was not only affected by the medium, but also greatly influenced by temperature, pH, pressure, ventilation status and other factors of growth environment. In the previous

study we have identified the optimum culture conditions of UP-3 as follows: atmospheric pressure, 31 °C, pH value of 7.3 to 7.5, aerobic conditions.

Resting cells refer to cells that basically stopped growing in the culture medium and with a poor nutritional status. In order to check whether UP-3 strains of resting cells could degrade DBT or not, the cells were suspended in phosphate buffer with no nutrients. The experimental results of degradation of DBT showed that the UP-3 cells in poor nutritional status had a quite limited capacity of degradation. When the DBT concentration was 2.7mM, the best degradation effect is only about 13%.

Influent of the immobilization materials on desulfurization performance

The common immobilization methods includes adsorption, embedding and cross-linking, of which cross-linking has a large impact on the activity of the microorganisms and relatively harsh operating conditions [8], thus this paper initially chose adsorption and embedding. Among them, the immobilized material is an important factor affecting the immobilized effect, and the principle of selection of the immobilized material is low cost, easy operation, high activity of immobilized microorganisms, long life and so on. We used three kinds of adsorption carrier and two embedding vectors, and the results were shown in Table 1. It can be seen that adsorption immobilization effect of the UP-3 were generally lower than the embedding method, and the adsorption effect of silica gel got the best which was still much lower than the immobilized effect of the embedding; while among the embedding method due to slower rate of cross-linking and difficult operation of PVA we improved its operability through the addition of SA and meanwhile its mechanical strength has been greatly improved as well as the drop of desulfurization activity was not very clear compared with SA immobilized ball. Then we mainly studied the immobilized cells which was based SA and PVA as the immobilized carrier.

TABLE 1 PERFORMANCE COMPARE OF IMMOBILIZATION CARRIERS

Item	Adsorption			Encapsulation	
	Active carbon	Kieselguhr	Silica gel	SA	PVA and SA
Mobilization degree	Middle	Bad	Middle	Good	Excellent
Activity	13.76	16.38	34.96	67.70	66.13
Longevity	400	400	400	600	650

Influent of the immobilization conditions on desulfurization performance. The preparation conditions include pH value, temperature, concentrations of carriers and precipitators, etc. According to the previously mentioned investigations of the cells performance, the optimum pH value of UP-3 cells is 7.3-7.5. So the preparation of immobilized cells is also operated under that pH value. In table 2, the influence of temperature on desulfurization of immobilized cells is showed. The relatively ideal temperature for the immobilization preparation is at 4 ° C when the immobilized cells perform the highest activity and the best degradation ability. It is found that the metabolism of microorganisms is slower at 4° C and the influence of preparation conditions on the performance of microorganisms is smaller, causing less activity loss.

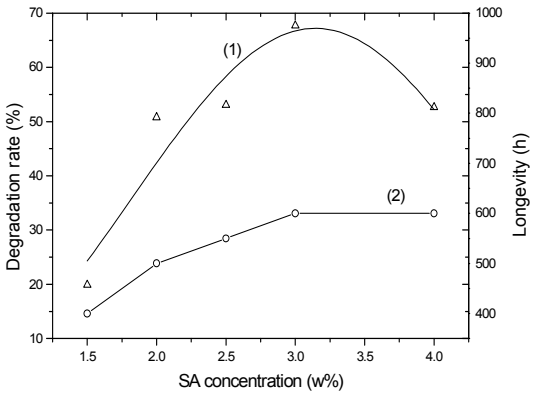
TABLE 2 INFLUENCE OF TEMPERATURE ON DESULFURIZATION OF IMMOBILIZED CELLS

Immobilization temperature (° C)	4	15	25
First degradation rate (%)	53.10	29.46	28.40
Second degradation rate (%)	45.98	16.35	19.86

The SA aqueous solution which is a polyelectrolyte with higher charge density could experience gel transformation due to the divalent cations. PVA could also experience cross-linking reaction in the saturated boron solutions. In this paper, the higher concentration of embedding carriers results in

the greater viscosity bringing inconvenience to granulation and producing irregular balls. In addition the compact structure of immobilized balls could lead to the slow diffusion. On the other hand, the lower concentration of embedding carriers results in the lower viscosity and porous structure promoting diffusion. But during the granulation process agglomerate is likely to take place, which causes the lower strength, the easier loss of cells and the decrease of desulphurization performance. So it's necessary to select the proper concentration in order to facilitate the immobilization process and keep the better mechanical strength.

Figure 1 shows the influence of sodium alginate concentration on immobilization. It is observed that when the concentration of SA is 3wt%, the degradation ability of immobilized cells achieves the best and the longevity almost reaches the maximum. It is found that with the lower concentration of SA, the structure of granulation is looser and the pore size is larger, which reduces the fixation strength of microorganisms as well as the UP-3 cells and makes degradation affected by biochemical reaction. In addition, as the concentration of SA increases, the performance of fixation and desulphurization is gradually improved. Especially beyond a critical concentration of SA, the amount of embedded microorganisms is invariable and the degradation performance is controlled by diffusion. With the higher concentration of SA, the structure of granulation becomes much compacter while the desulphurization performance is reduced.



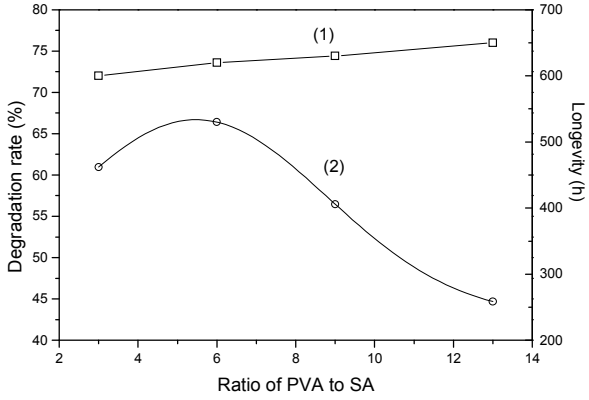
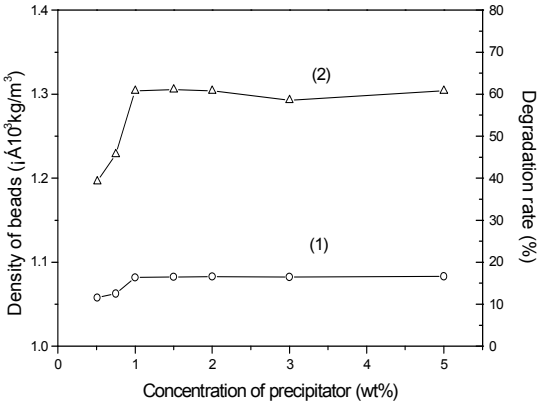


Fig 1. Influence of SA concentration on immobilization Fig 2. Influence of ratio of PVA to SA on immobilization

Figure 2 shows the influence of ratio of PVA to SA on immobilization. The total concentration of PVA and SA is 7wt%. Form figure 2, as the ratio of PVA to SA increases, the degradation rate of immobilized cells rises and then declines while the longevity keeps growing. It is found through analysis that with the lower concentration of PVA and SA, the higher SA content affects the performance of cross-linking and immobilization. Then the decrease of the concentration of SA prevents the agglomeration of PVA, reduces the influence on immobilization, and promotes granulation as well as the embedding performance of UP-3 with PVA. But when the SA concentration further reduces with PVA concentration rising, the inner structure of immobilized balls becomes much compacter, affecting the diffusion of substrates and reaction products, reducing the activity of embedded cells and the degradation performance of immobilized cells. As it is showed in figure 2, the proper concentration ratio of PVA to SA is 6.

In this part the density variation of immobilized balls and the desulphurization performance of immobilized cells are studied. Figure 3 shows the influence of precipitator on immobilization. It is observed that when the concentration of precipitator is beyond 1wt%, the concentration variation has little effect on the density of immobilized balls and the desulphurization performance of immobilized cells. It is considered through analysis that the selected carriers could be immobilized by cation exchange. So according to the stoichiometric calculations, the mass ratio of precipitator cation to carrier cation should be 1:3.92. When the carrier concentration is 3wt%, accordingly the stoichiometric concentration of precipitators is 0.77wt%. Because of the influence of inner diffusion of immobilized balls on cation exchange and the lower water content of alginate during the

granulation process, the practical concentration of carrier increases in a certain extent. As a result, even though the precipitator concentration is above 1wt%，the precipitator almost has little impact on the immobilization performance.



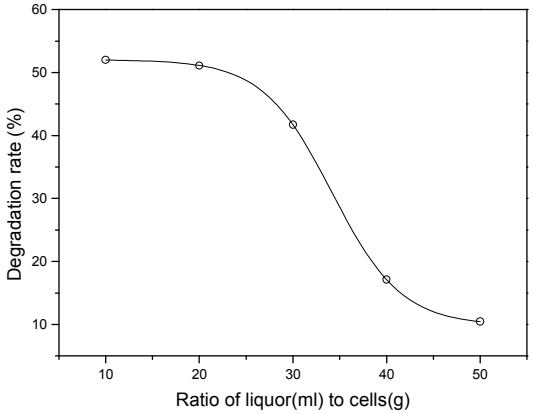


Fig.3 Influence of precipitator on immobilization Fig.4 Relationship of DBT degradation with ratio of SA and PVA

The concentration of embedded cells is another key factor to influence the desulphurization performance of the immobilized cells. Figure 4 indicates the relationship of DBT degradation with ratio of sodium alginate (ml) to cells (g). The degradation rate reduces with the increase of that ration. When the ratio is below 20, the degradation rate increases slowly with the ratio reduces. Considering the optimum usage amount and the activity of immobilized cells, the ratio of sodium alginate to cells is selected 20.

Influent immobilization conditions and materials on degradation time.

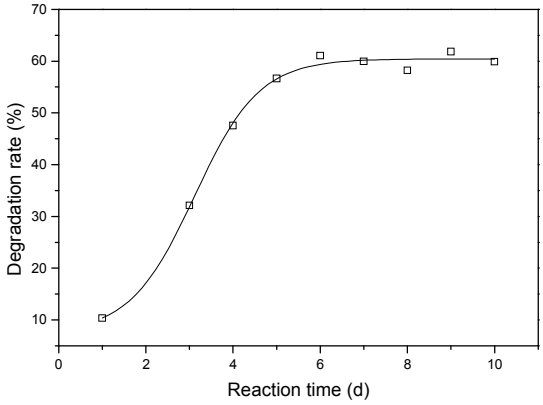


Fig.5 Relationship of DBT degradation with degradation time

The desulphurization performance obviously decreased and the desulphurization rate also slowed after UP1 cells were immobilized. Figure 5 indicates the relationship of DBT degradation of immobilized UP1 cells with degradation time. As shown, the degradation rate rises significantly when the reaction time is below 6h. And then the rate varies slightly. Those results are caused by feedback inhibition and diffusion effect during the reaction process of microorganisms. At the beginning of reactions, because of the higher activity of enzyme systems and the higher concentration of the substrates, the effect of feedback inhibition is smaller and the reaction rate is faster, which enlarges the concentration difference of products between inside and outside of colloidal particle and the diffusion driving force, leading to the easier diffusion of products into the water phase outside the colloidal particle and the faster degradation rate. With the reaction carried through, the concentration of substrates decreases while the concentration of products increases compared to that of substrates. Then the effect of feedback inhibition is enforced and reaction rate falls down, which leads to the slow

rise of degradation rate. When the concentration of products and/or substrates in water phase is equal or close to that inside the colloidal particle, the diffusion driving force is approximates zero. So products don't diffuse into the water phase and substrates in water phase also don't enter the colloidal particle. That is the end of reaction which indicates the maximum of degradation rate.

Conclusions

The immobilized research on oil biodesulfurization bacteria—*Agrobacterium tumefaciens* UP-3 have not been reported yet at home or abroad. In this article, the mixture of SA and PVA was selected, the SA and PVA as the immobilization carrier, and optimized the immobilization conditions of UP-3 so as to prepared immobilized UP-3 which had a great desulfurization performance. When the DBT concentration reaching 2.7 mM, the degradation rate reached more than 60 percent of DBT; and the optimum degradation time of the immobilized UP-3 cells was 6 d. Excellent desulfurization capacity was shown by the immobilized UP-3 cells as well as mild using conditions with a broad prospects for industrial applications.

Acknowledgements

This work is supported by the Innovation Foundation of CNPC, and Shandong Provincial Natural Science Foundation（No.ZR2011EL031 and No.ZR2012BL15）, China.

References

[1] J. van der Geer, J.A.J. Hanraads, R.A. Lupton, The art of writing a scientific article, J. Sci. Commun. 163 (2000) 51-59.

[2] H.M. Chen, Retrospective review of annual meeting of NPRA and prospect on world petroleum refining technologies, Petroleum Refining Engineering. 9 (2001) 1-5

[3] Y. Tanaka, T. Matsui, J. Konishi, et al. Isolation and characterization of a moderate thermophile, Mycobacterium phlei GTIS10, capable of dibenzothiophene desulfurization Applied Microbiology And Biotechnology, 59 (2002) 325-328

[4] J.H. Chang, Y.K. Chang, H.W Ryu, et al. Desulfurization of light gas oil in Immobilized-cell systems of Gordona sp. CYKS1 and Nocardia sp. CYKS2, FEMS Microbiol Letter, 182 (2000) 309-312

[5] M. Naito, T. Kawamoto, K. Fujino et al, Long-term repeated biodesulfurization by immobilized Rhodococcus erthropollis KA2-5-1, Applied Microbiology And Biotechnology. 55 (2001) 374-378

[6] K. Kirimura, T. Furuya, Y. Nishii, et al. Biodesulfurization of dibenzothiophene and its derivatives through the selective cleavage of carbon-sulfur bonds by a moderately thermophilic bacterium Bacillus subtilis WU-S2B, Journal Biosicence and Bioengineering, 3(2001)262-267

[7] K. Kirimura, T. Furuya, Y. Nishii, Y. Ishii, et al. Thermophilic biodesulfurization of dibenzothiophene and its derivatives by Mycobacterium phlei WU-F1, FEMS Microbiology Letter. 9 (2001)129-133

[8] J. Konishi, T. Onaka, Y. Ishii, M. Suzuki, et al. Demonstration of the carbon-sulfur bond targeted desulfurization of benzothiophene by thermophilic Paenibacillus sp. strain A11-2 capable of desulfurizing dibenzothiophene, Journal Biosicence and Bioengineering. 2(2001)193-196

[9] Z. Z. Li. Biochemical Engineering Fundamentals, Chemistry Industry, Press Beijing,1999, pp.104-107

[10] X. M. Zhai, D. T. Li. Organic Micropolluted Source Water Treatment by Immobilized Cells. Environmental Science. 6 (2000) 80-84

[11] J. L. Wang, H. Ch. Shi. Study and Advance on Polyvinyl Alcohol (PVA) as Entrapping Agents for Immobilizing microbial. Industrial Microbiology. 2 (1998) 35-39

Advanced Materials Research Vol. 936 (2014) pp 746-750
© (2014) Trans Tech Publications, Switzerland
doi:10.4028/www.scientific.net/AMR.936.746

The Release characteristics of Different Model Drugs from Medicated PLGA Microspheres

Tong chen[1, a], Yuanyuan Liang[2, b],Yingge Zhao[3, c], Xiaoyun Zhang[4, d], Tongsheng Qi[5, e], Qing Shang*[, f]

[1, 2, 3, 4, *]School of Chemical and Pharmaceutical Engineering, Hebei University of Science and Technology, 050000, Hebei, China

[5]Hebei Veyong Bio-Chemical Co. Ltd, 050000, Hebei, China

[a]xiaowazaijiayou@163.com, [b]liangyuanyuan1010@163.com, [c]15131100826@163.com, [d]hbzyzxy@163.com,[e]13833102862@163.com, [f]shangqingyl@163.com,

Keywords: PLGA microspheres, in vitro release, different drugs, degradation

Abstract In this study, four model drugs, i.e., Meloxicam (MEL), Risperidone (RIS), Eprinomectin (EPR), and Bull Serum Albumin (BSA), were encapsulated in PLGA microspheres *via* solvent evaporation methods. The encapsulation efficiency and *in vitro* release profiles of different drugs with various water solubilities from medicated PLGA microspheres were investigated. The surface morphologies of microspheres were detected by scanning electron microscope (SEM). The release characteristics of the model drugs from the medicated microspheres were carried out in the phosphate buffer solution (PBS), pH7.4, at 37 °C. Studies found that the water solubility of model drugs had significant influences on their *in vitro* release profiles and the release rates of four model drugs were in the orders of BSA＞MEL＞RIS＞EPR.

Introduction

For the past few years, PLGA microspheres were widely used as the carriers of sustained and targeted drug delivery systems due to its excellent biocompatibility and biodegradation [1]. At present, eight kinds of microsphere formulations had been on market [2]. Recently, the studies of medicated PLGA microspheres were mainly concentrated on the influences of the drug-loading, encapsulation efficiency and *in vitro* release profiles under different conditions. For example, Ito and Wang improve the encapsulation efficiency of hydrophilic drugs by putting some additives into the internal water phase [3, 4]. Aamir discussed the *in vitro* release dynamics of tramadol hydrochloride-loaded microspheres [5]. However, in present literatures, people were mainly focus on the research of the *in vitro* release about a single drug from microspheres, but fewer researches take the solubility of model drugs into consideration in drug release. Fewer people make a comparative study on the release profiles of different drugs with various water solubilities. Therefore, it is meaningful to study the *in vitro* release profiles from different drug-loaded microspheres.

In this study, BSA, MEL, RIS and EPR were chosen as the model drugs and encapsulated into PLGA microspheres by solvent evaporation methods. The morphologies were observed by scanning electron microscope (SEM). The drug-loading and different release profiles of various model drugs were revealed. All experimental data might have the significance of theoretical and practical applications.

Experimental

Materials

Poly (D, L-lactide-co-glycolide) (PLGA, lactide/glycolide ratio 50:50) was obtained from Lakeshore Biomaterials. Poly (vinyl alcohol) (PVA17-99, 88% hydrolyzed) was the product of Tianjin Institute of Chemical Reagents (Tianjin, China). MEL and RIS were received from Jiangsu Nhwa Pharmaceutical Corporation Limited. EPR was purchased from Hebei Veyong Bio-Chemical

Co. Ltd. BSA (fraction V) was supplied by Shanghai Institute of Lianshuo biological science and technology. Some important information of model drugs was summarized in Table 1.

Preparation of microspheres

Model drug-loaded PLGA microspheres were prepared through solvent evaporation technology. Approximately 25 mg of model drugs (MLX, RIS, EPR) were dissolved into 10 mL of PLGA/dichloromethane solution (10 mg/ mL) to obtain a homogeneous solution. Then, 500 mL PVA/water solution (1.0 %, w/v) was added into above solution *via* an LSP01-1A micro-injection pump (Baoding Longer Precision Pump Co Ltd, China) at the speed of 0.5 mL/min. After stirring at 1200 rpm for 20 min, the stirring rate was reduced to 400 rpm for another 5 h to evaporate methylene dichloride. Subsequently, the resultant microspheres were washed three times using deionized water. The medicated microspheres were freeze-dried for 24h under the condition of vacuum, -40°C, using a LGJ-10 vacuum freeze drier (Beijing Songyuan Huaxing Science and Technology Corporation, China) for further study.

BSA-loaded PLGA microspheres were usually prepared through a double emulsion solvent evaporation method. 25 mg of BSA was dissolved into 1.0 mL deionized water using as internal water phase. Then, above solution was dispersed into 10 mL PLGA/methylene dichloride solution (10 mg/mL) and mixed with a vortex mixer (QL-861, Haimen Qi Lin Beier Instrument Manufacturing Co. Ltd, China) to obtain a homogeneous W/O emulsion. Subsequently, the formed emulsion was added into 500 mL PVA/water solution (1.0 %, w/v) using an LSP01-1A micro-injection pump at a rate of 0.5 mL/min. The following steps were carried out as the forward descriptions. All the obtained dry-microspheres were stored at -20 °C for further usage.

TABLE 1: THE PHYSICOCHEMICAL PROPERTIES OF FOUR MODEL DRUGS

Materials	Molecular mass(D)	Melting temperature (°C)	Water solubility (mg/mL)	pKa
MLX	351.40	260.00	8.10	4.50± 1.00
RIS	410.50	170.00	0.16	8.10 ± 0.10
EPR	914.10	161.00~166.00	0.02	12.40 ± 0.70
BSA	66400.00	—	≥40.00	—

Morphology of microspheres

The morphologies of the lyophilized drug-loaded microspheres were observed by an S-4800 SEM (Hitachi, Japan) after coating the dried samples with gold films under vacuum.

Drug-loading and encapsulation efficiency

For the three hydrophobic drugs, approximately 10 mg of medicated microspheres were dissolved into 2 mL dichloromethane, and then diluted with alcohol to 50 mL. The amount of drugs entrapped into microspheres were analyzed by 2400 PC UV spectroscopy (Shanghai Shunheng Corporation, China) [6-8], while the drug loading of BSA microspheres were determined by an extraction method [9]. 10 mg of medicated microspheres were dissolved into 1 mL dichloromethane for 10min and then 1.5 mL PBS was added. The mixture was vigorously shaken for 1 min in order to extract BSA into PBS from the organic solution. After centrifuging, the PBS solution was withdrawn and the BSA was extracted again. The BSA content of the solution was analyzed using BCA kit [10]. The drug loading and encapsulation efficiency was calculated as the following Eq.1, Eq.2 [11], where m_d is the weight of drug entrapped, m_s is the weight of microspheres used, E_a represents the actual drug-loading and E_t is the theoretical drug-loading. The results were reported as the mean ± SD.

$$\text{Drug-loading}(\%) = (m_d/m_s) \times 100\% \quad (1)$$

$$\text{Encapsulation Efficiency}(\%) = (E_a/E_t)\times 100\% \quad (2)$$

In vitro release profiles

Four different forms of lyophilized drug-loaded microspheres were individually placed in test tubes and suspended in 4 mL of PBS (pH 7.4) containing 0.02 % sodium azide. Samples were

incubated at 37 °C on a ZHWY-100H oscillator (ZHICHENG analytical instrument manufacturing, China) at the shaken speed of 100 rpm. At appropriate time intervals, the samples were collected and centrifuged for 10 min at 4000 r/m. 3 mL of PBS was removed and replaced with equivalent fresh medium. The concentrations of model drugs in the PBS was analyzed by 2400 PC UV spectroscopy (Shanghai Shunheng Corporation, China). All the drug release tests were carried out in triplicate and the results were presented as average.

Results and Discussion

Morphological characterization of microspheres

The representative SEM images of four kind of medicated microspheres were shown in Fig. 1 (a-d). It was clearly seen that the obtained microspheres were smooth, rounded and mono-dispersed spheres with the particle size distribution of 60-140 μm. However, the striking distinctions were observed on their surface. Some micro-pores were markedly observed on the surface of BSA/PLGA microspheres in Fig. 1 (d), while others were not found on the surfaces clearly.

The encapsulation efficiency of microspheres

The encapsulation efficiency were calculated and shown in Fig. 2. It could be seen that the encapsulation efficiencies were followed the orders of EPR > RIS > MLX >BSA. The reason mainly came from their natural characters [12]. Table 1 showed that the water partition coefficient (log P) of MLX, RIS and EPR was 2.66±0.85, 2.68±0.41 and 5.95±0.86, respectively. Some researches revealed that the substance was amphipathic when its log P was between -0.30 and 4.50. It was hydrophobic if its log P > 4.50 [13]. Therefore, MLX and RIS were the amphipathic molecules, and EPR was lipotropic. Accordingly, EPR could easily dissolve in the organic phase on the basis of the similarity-intermiscibility theory. It was hard to transfer into the water phase during the preparation. However, amphiphilic MLX and RIS could dissolve into water phase more or less, which led to a lower drug-loading. The BSA exhibited the lowest encapsulation, which was only 50.60±6.01%. The possible reason might be due to the strongest water solubility of BSA, which made serious drug-leakage during the preparation of BSA-loaded microspheres.

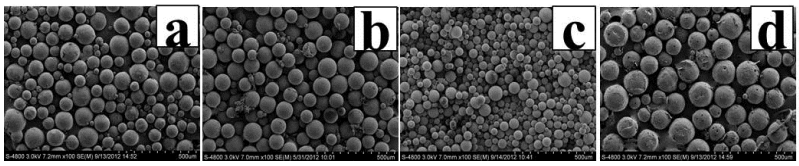


Fig. 1: SEM photographs of four types of microspheres: (a) MEL, (b) RIS, (c) EPR, and (d) BSA.

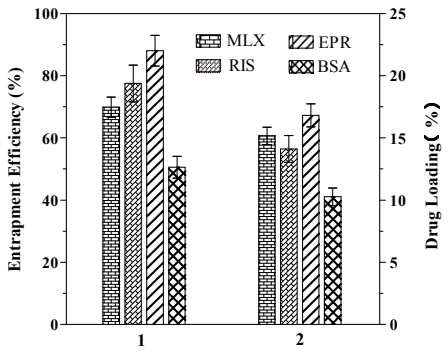


Fig. 2: Drug loading and encapsulation efficiency of four model drug-loaded PLGA microspheres, 1 was the encapsulations of four types of microspheres, 2 was the drug-loading of four model drug-loaded microspheres.

The in vitro release and degradation of microspheres

The cumulative release profiles of the four drugs were shown in Fig. 3. At 24 h, the cumulative release percent of drugs were 9.07±5.18% (MLX), 4.67±1.15% (RIS), 2.73±4.18% (EPR), and 53.03±5.10% (BSA), respectively. It was clear that BSA showed the fastest release rate. After 12 d, the cumulative release amount of BSA reached to 96.14±2.55%. MLX-loaded microspheres reached the equilibrium state of release at the 18 d with the cumulative release percent of 94.51±2.67%. In

contrast, the release of RIS and EPR were relatively slow, and the released amount of both drugs was 86.69±4.56% and 75.32±3.64%. The release rates followed the orders of BSA > MLX > RIS > EPR. The degradation of different medicated microspheres was distinguishing and it could be clearly seen that the MLX-loaded microspheres exhibited a fast erosion process in Fig. $4a_{1\text{-}3}$. In the 21st day, cracks were appeared on the microspheres, and these microspheres lost their spherical shapes in the 28th day. The degradation rate of RIS-loaded microspheres (Fig. $4b_{1\text{-}3}$) was similar to that of MLX. However, EPR (Fig $4c_{1\text{-}3}$) almost maintained its sphere without collapsing at the 28th day, and only some surface corrosion and irregularity were observed. Compared with other microspheres, the BSA-loaded microspheres exhibited the fastest degradation process. Fig. $4d_{1\text{-}3}$ showed that big and dense channels were shown on the surface of spheres in the 15th day, and it was broken into fragments in the 21st day. The differences among these release profiles might be attributed to the different physicochemical properties of drugs and the structures of medicated microspheres. The percent release of drugs from polymers, at a fixed time point, depended on the drug solubility in water, It seemed reasonable that hydrophilic drugs with high solubility might increase the rate of water diffusion into the matrix, thereby accelerating release and bulk erosion, while highly hydrophobic drugs with low solubility would inhibit water diffusion into the matrix, thereby slowing the release rate [12].

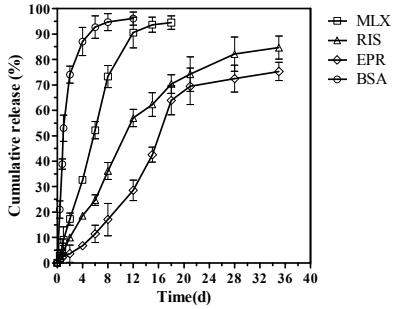


Fig. 3: Cumulative release profiles of model drugs, (a) MEL, (b) RIS, (c) EPR, and (d) BSA-loaded PLGA microspheres during 0-35 d.

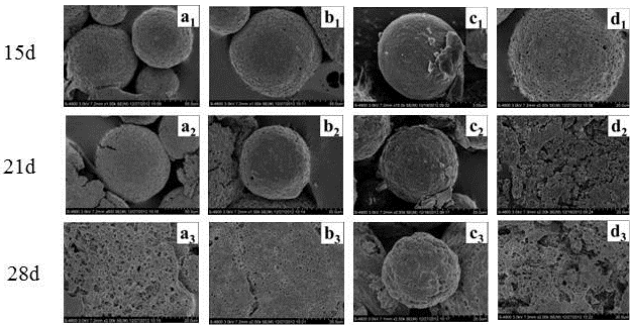


Fig. 4: Representative SEM images of the degradation of medicated microspheres on the day of 15, 21, and 28, respectively. a) was MEL-loaded microspheres, b) RIS-loaded microspheres, c) EPR-loaded microspheres and d) was BSA-loaded microspheres

Conclusions

In this study, four kinds of drug-loaded PLGA microspheres were fabricated by solvent evaporation technique. The resultant microspheres were smooth and spherical and the encapsulation efficiencies of four drugs were following the orders of BSA ＜ MLX ＜ RIS ＜EPR medicated microspheres. In addition, the release profiles of four kinds of drugs-loaded PLGA microspheres showed that the drug release rate of microspheres was BSA ＞ MLX ＞ RIS ＞ EPR. We found that the release rate were vary as the different drugs, the water solubility of drugs played an important role in drug release and the degradation of microspheres matrix. Therefore, overall drugs release profiles from medicated microspheres must take the properties of drugs into consideration.

Acknowledgements

This work had been supported by a grant from Natural Science Foundation of Hebei province, China (No. C2011208111).

References

[1] A. Frank, S.K. Rath, S.S. Venkatraman, Controlled release from bioerodible polymers: effect of drug type and polymer composition, J. Control. Release. 102(2005) 333-344.

[2] K. Maryam, B. Ali, Preparation and In Vitro Evaluation of a Microballoon Delivery System for Theophylline, Iran. J. Pharm. Res. 6(2007) 35-42.

[3] I. Fuminori, F. Hiroyuki, M. Kimiko, Incorporation of water-soluble drugs in PLGA microspheres, Colloids Surf. B. Biointerfaces. 54(2007) 173-178.

[4] J. Wang, B.M. Wang, S.P. Schwendenman, Mechanistic evaluation of the glucose-induced reduction in initial burst release of octreotide acetate from poly(d,l-lactide-co-glycolide) microspheres, Biomaterials. 25(2004) 1919-1927.

[5] M.N. Aamir, M. Ahmad, N. Akhtar, G. Murtaza, S.A. Khan, S. Zaman, A. Nokhodchi, Development and in vitro–in vivo relationship of controlled-release micro-particles loaded with tramadol hydrochloride, Int. J. Pharm. 407(2011) 38-43.

[6] G.G. Chen, J. Tang, X.M. Li, Study on sustained-release risperidone biodegradable microspheres, Chin. J. Pharm. Univ. 37(2006) 512-5.

[7] F.Y. Ke, T. Zhen, Y.H. Zhang, Q. Shang, Preparation and performance of meloxicam loaded PLA sustained-release microspheres, Mod. Chem. Ind. 31(2011) 232-235.

[8] S.Y. Ci, L.J. Ma, S.Y. He, RP-HPLC determination of eprinomectin, Chin. J. Pharm. Anal. 30(2010) 1129-1131.

[9] Y.Y. Yang, T.S. Chung, N.P. Ng, Morphology, drug distribution and in vitro release profiles of biodegradable polymeric microspheres containing protein fabricated by double-emulsion solvent extraction/evaporation method, Biomaterials. 22(2001) 231-241.

[10] Q. Shang, Y.H. Zhang, T. Chen, Y.Y. Liang, Y.L. Shi, Preliminary studies on pH-sensitive hydrogels and in vitro release profiles of two model drugs, J. Biomat. Sci. Polym. E. 24(2013) 1459-1471.

[11] F. Wang, Y.L. Song, C.X. Li, D. Li, H.P. Zhang, A.J. Ma, X.Q. Xi, N. Zhang, B.G. Wang, Y. Wang, W. Zhou, Sustained release of insulin-like growth factor-1 from poly(lactide-co-glycolide)microspheres improves osseointegration of dental implants in type 2 diabetic rats, Eur. J. Pharm. 640 (2010) 226-232.

[12] S. Kiortosis, K. Kachrimanis, Th. Broussali, S. Malamataris, Drug release from tableted wet granulations comprising cellulosic (HPMC or HPC) and hydrophobic component, Europ. J. Pharma. Biopharma. 59(2005) 73–83.

[13] S.X. Hou, T. Chen, Y. Lu, The preparation of three kinds of carriers and the comparation of their encapsulation and vitro release, Chin. J. Chin. Material Medica. 31(2006) 728-730.

Advanced Materials Research Vol. 936 (2014) pp 751-756
© (2014) Trans Tech Publications, Switzerland
doi:10.4028/www.scientific.net/AMR.936.751

Synthesis and Performance of pH-sensitive Hydrogel Microspheres and In Vitro Evaluation as Potential Drug Carriers

Yuanyuan Liang[1, a], Tong Chen[2, b], Yuqin Cui[3, c], Ruiqiong Tian[4, d], Tongsheng Qi[5, e] and Qing Shang*[, f]

[1, 2, 3, 4, *]School of Chemical and Pharmaceutical Engineering, Hebei University of Science and Technology, 050000, Hebei, China

[5]Hebei Veyong Bio-Chemical Co. Ltd, 050000, Hebei, China

[a]liangyuanyuan1010@163.com, [b]xiaowazaijiayou@163.com, [c]cyqspc1003@163.com, [d]trqjiayou@163.com, [e]13833102862@163.com, [f]shangqingyl@163.com

Keywords: hydrogel microspheres, pH-sensitive, swelling behaviour, BSA.

Abstract. To accelerate the response rate of smart hydrogels to the environmental conditions, a novel pH-sensitive hydrogel microsphere with the controlled shapes and sizes were developed. Such monodispersed microspheres were synthesized *via* free radical polymerization under the protection of a multilayer stability system. The pH-responsibility of hydrogel microspheres was tested with the hydrogel bulk as a control. *In vitro* release studies were conducted in the simulated gastric fluid and intestinal juice with bovine serum albumin (BSA) as a model drug. The large specific surface areas endowed hydrogel microspheres a faster pH-responsibility than that of bulk ones. Therefore, such microspheres showed potential applications as the oral protein drugs carrier.

Introduction

The pH-sensitive hydrogel is a kind of crosslinked polymer with three-dimensional network structure, which can shrink or swell with the changing of environmental conditions [1]. As a common pH-responsible hydrogel, acrylic-based hydrogels have aroused widely attention in recent years due to their excellent pH-sensitivity, specific shape and mechanical strength [2-4]. In acid conditions (*i.e.* stomach juice), acrylic-based hydrogel shrinks and blocks model drug to leak out. On the contrary, they will swell in alkaline solutions (*i.e.* small intestine fluid) and release drug quickly. Therefore, it can be used to fixed-point release drug in intestinal tract and avoid the protein drugs to be destroyed by pepsase [5, 6]. Mariko Morishita *et al.* fabricated a pH-responsive poly (methacrylic acid) hydrogel. In the *in vivo* trial, a significant glucose reduction is observed for oral insulin delivery [7].

The previously research reveals that it takes over 10 h to reach the release equilibrium for a drug-loaded hydrogel bulks [8]. It is just meet the time of drug transfer in the small intestine, which may cause the drug released from hydrogel incompletely and influence the drug efficacy. The hydrogel microspheres have some discrepancies of small radius and large specific surface areas compared with hydrogel bulks, which guarantees them larger contact areas with release medium and a rapid drug release profile. Morishita et al. crush and sieve the hydrogel bulks into powders with diameters of < 53 μm and 212-300 μm. Results show that the smaller sized microparticles induce larger hypoglycaemic effects and the maximal hypoglycaemic effects are achieved at 4 h [7]. Now hydrogel microparticles of small size are almost obtained after processing the hydrogel bulks. It may lead to the destruction of the internal network of hydrogels.

In this study, a batch of hydrogel microspheres was developed *via* a heat-initiated suspension polymerization. The molar ratio of methacrylic acid (MAA) and Poly (ethylene glycol) methyl ether methacrylate (PEGMA475) was an important influence factor in the fabrication of monodisperse hydrogels microspheres [9]. To overcome the aggregation of hydrogel microspheres in the polymerization process, a multilayer stability system was constructed. The swelling characteristics

of hydrogel microspheres and the drug release profiles from medicated hydrogel microspheres were also evaluated.

Experimental

Materials

Before usage, MAA was purified *via* vacuum distillation to remove the polymerization inhibitor. Poly(vinyl alcohol) (PVA 1799) with an alcoholysis degree of 99% and an average polymerization degree of 1750 ± 50. PEGMA475, Triethylene glycol dimethacrylate (TRGDMA) and BSA were purchased from Sigma-Aldrich (USA). All the chemical agents were AR.

Preparation of pH-sensitive hydrogel microspheres

7.2 g PVA aqueous solution (2 wt%) and 0.05 g Tween 80 were added into a 25 mL three-necked flask equipped with a thermometer, a reflux condenser and magnetic stirring. Fixing the monomers at 3wt% (based on the total mass of reaction system), the compositions of different hydrogels were weighed according to Table 1. After adjusting the pH of above solution to 7.0, the mixed solutions were added dropwise and reacted 30 min under the temperature of 82 ± 0.5 °C. When the reaction system became turbid, uniform particle size and monodisperse hydrogel microspheres were obtained. The resulting products were centrifugal washed with the deionized water for five days. Consequently, the p(PEGMA-g-MAA) hydrogel microspheres were fabricated and preserved for the further studies.

TABLE 1: COMPOSITION OF PREPARED HYDROGEL MICROSPHERES

Sample code	Molar ratio (MAA:EG) [a]	AIBN(mg)	TEGDMA(mol%) [b]
PM1	3:1	7.5	1.50
PM2	2:1	7.5	1.50
PM3	1:1	7.5	1.50
PM4	1:2	7.5	1.50
PM5	1:3	7.5	1.50
PMT	1:2	7.5	1.25

FTIR studies

The FTIR spectra of hydrogels and raw materials were determined by a Spectrum 100 Fourier transform infrared spectrometer (PerkinElmer, China). The freeze-dried samples were tested directly after grinding and tabletting with KBr powder.

Morphology observation

The morphologies of hydrogel microspheres were observed *via* a B1 electron microscope (Motic, China). An S-4800-I SEM (HITACHI, Japan) was used to observe the morphology lyophilized hydrogel microspheres.

Swelling studies

Five copies of hydrogel microspheres (PM1, PM2, PM3, PM4 and PM5) were used to study their swelling behaviors. PBS with the pH values of 1.2 and 7.4 were used to simulate gastric fluid and small intestine fluid, respectively. The specific process was carried out following the previous study.

A certain amount of lyophilized hydrogel microspheres (PMT) was immersed into PBS (pH 7.4) for 34 h. Then, they were transferred into the PBS (pH 1.2). This swelling procedure was repeated twice. The swelling ratios were determined after sampling at certain points of time during whole process [8].

Drug incorporation

The lyophilized hydrogel microspheres (PMT) were immersed into the BSA solutions (2 mg/mL). After 24 h, they were freeze-dried, and then immersed into 30 mL PBS (pH 7.4) for 24 h. The BSA concentrations were determined by the BCA protein assay through 2400 PC UV spectroscopy (Shanghai Shunheng Corporation, China). The incorporation of BSA was calculated according to Eq. 1:

Incorporation of BSA (mg/g, w/w) $=M_i/W_{hm} \times 100\%$ (1)

Where: M_i was the amount of BSA incorporated into hydrogel microspheres,
W_{hm} was the weight of lyophilized hydrogel microspheres.

In vitro drug release

To investigate the *in vitro* release properties of hydrogel microspheres, pH1.2 (simulated gastric juice) PBS and pH 7.4 (simulated intestinal fluid) PBS were chosen for the release test. The specific process was carried out following the previous study [8].

Results and discussion

Preparation of pH-sensitive hydrogel microspheres

The hydrogel microspheres were prepared by the heat-initiated radical polymerization. The hydrogen bonds would result in the aggregation of final microspheres. To solve this problem, a multi-layers protection system of Tween-80, PVA and $-COO^-$ were constructed. Tween-80 would be adsorbed on the surface of particles, which isolated particles from agglomeration with each other. PVA could increase the viscosity of the continuous phase. The steric hindrance formed from PVA would inhibit hydrogel microspheres from gathering. Importantly, –COOH groups were ionized into $–COO^-$ by controlling the pH above 7.0. The electrostatic repulsions among electriferous microspheres would inhibit them from aggregation.

The distribution states of different hydrogel microspheres with various monomer ratios were depicted. With the molar ratios of MAA/EG changing from 3:1 to 1:3, the hydrogel microspheres gradually transited from much pieces to complete spheres, and their diameters were in the range of 20-100 μm. The obtained hydrogel was fragmented when the molar ratio of MAA/EG was 3:1. Because of MAA was a hard monomer, and higher MAA content in reaction systems made the resulting hydrogel microspheres fragile [10]. When MAA/EG was changed to 1:2 or 1:3, the hydrogel microspheres became relatively uniform spherical particles. Higher content of EG in the molecular chains made the hydrogel microspheres more flexible.

In FTIR spectra (Fig. 1), the absorption bands observed at 1680-1600 cm^{-1} in PEGMA and MAA were attributed to the stretching of C=C groups, which were disappeared in the spectrum of the hydrogel microspheres, Fig. 1(c). The sharp peaks observed at about 1700 cm^{-1} in monomers were representing the stretching vibration of –C=O groups. For the distribution of ether linkage in PEGMA, spectrum (b) exhibited the stretching vibration bands of C-O at about ~1113.1 cm^{-1}. These peaks were also observed in the spectrum of hydrogel microspheres. Accordingly, these data suggested that the hydrogel microspheres was successful prepared.

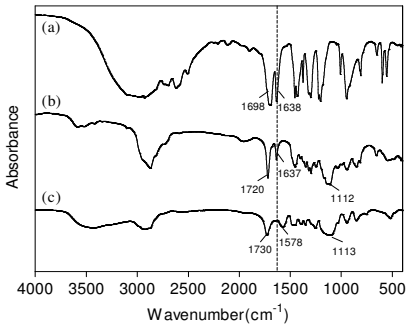


Fig. 1: FTIR spectra of (a) PEGMA, (b) MAA and (c) hydrogel microspheres.

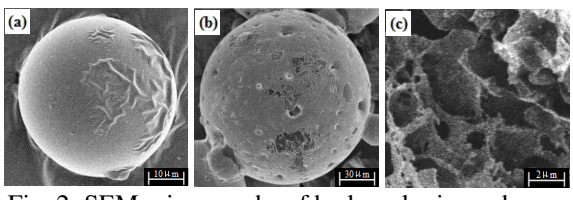


Fig. 2: SEM micrographs of hydrogel microspheres.

The SEM detection was carried out and shown in Figure. 2. As to the hydrogel microsphere (Fig. 2 (a)), its particle size was about 50 μm and the surface was slightly wrinkled. However, the size of

hydrogel microsphere was increased to 100 μm after swelling in PBS (pH 7.4). After lyophilizing, the swollen hydrogel microspheres showed some pores on its surface (Fig. 2 (b)), which might be due to the fast lose of moisture during the lyophilization. The internal structures of hydrogel microspheres were three dimensional networks, Fig. 2 (c) [8].

Swelling behaviour

PBS with pH values of 1.2 and 7.4 were used to mimic gastric juice and small intestinal juice, respectively. Five kinds of hydrogel microspheres showed above 3 times swelling ratios in pH 7.4 than those in pH 1.2, Fig. 3. A *t*-test showed that the differences between the swelling ratios in pH 1.2 and pH 7.4 were significant ($p < 0.05$) (the portion with dashed line).

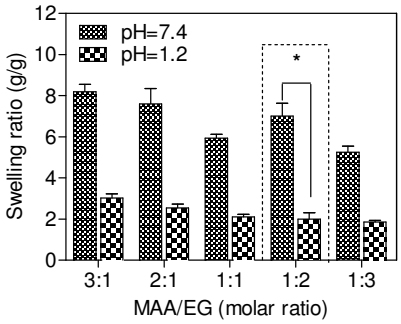


Fig. 3: Swelling ratios of hydrogel microspheres prepared with five monomers ratios in PBS with the pH values of 1.2 and 7.4.

The swelling hydrogel microspheres were shrank in the acidic buffer solutions. After swelling in alkaline buffer solution again, the swelling ratio was still high. It performed good swelling reversibility. The comparison of the swelling reversibility between hydrogel microspheres (PMT) and hydrogel bulks (TMP475) was carried out [8]. In PBS (pH 7.4), the swelling ratio of the hydrogel microspheres was about 11 times of lyophilized microspheres, and the equilibrium swelling time was only 6 h. Whereas, the swelling ratio of hydrogel bulks might increase to 35 folds of the original hydrogels with the equilibrium swelling time of 24 h. Though the swelling ratio of hydrogel microspheres was low, the equilibrium swelling was quick, Fig. 4. The hydrogel microspheres had lager special surface areas than hydrogel bulks, and the particles responded quickly to the environment stimuli. Therefore, the hydrogel microspheres with a high response rate might be useful for the quickly releasing of macromolecular hydrophilic drugs into the intestine by the oral administration.

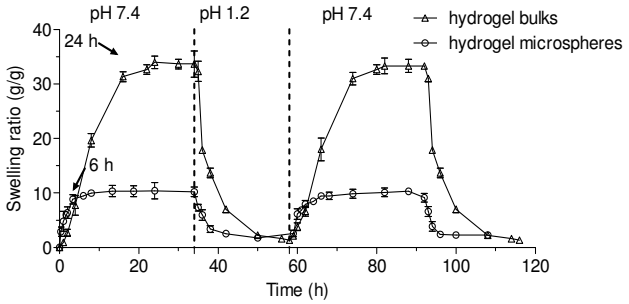


Fig. 4: Equilibrium swelling and reversibility studies of hydrogel microsphere and hydrogel bulks.

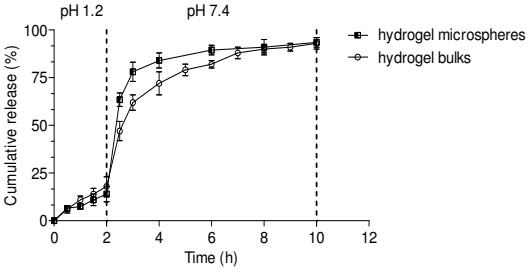


Fig. 5: The cumulate BSA released from medicated hydrogel microsphere and hydrogel bulks.

In vitro release

The BSA loading efficiency of hydrogel microspheres was 87.7 % and the hydrogel bulks' was 71.4 %. Though the hydrogel microspheres had a low swelling ratio, the BSA loading efficiency was higher than those of hydrogel bulks. *In vitro* release, less than 20 % BSA were released from the medicated hydrogels under acidic conditions (pH 1.2) at the first 2 hours, Fig. 5. In the alkaline conditions (pH 7.4), the cumulative release of BSA was reached above 75 % in 3h. Consequently, the release rate gradually slowed down and reached to the equilibrium state at 6 h. The maximum cumulative release of BSA was above 90%. Whereas, the cumulative release of BSA of hydrogel bulks was 65% in 3h. Compared with hydrogel bulks, the medicated hydrogel microspheres released smaller amount of BSA under acidic conditions, but BSA released more quickly under alkaline condition. These results indicated that hydrogel microspheres had the compact internal structure and could prevent drug leakage under acidic conditions. The characteristic of them might have potential advantages to the oral delivery of protein drugs.

Conclusions

A pH-sensitive hydrogel microsphere was developed *via* thermally initiated radical polymerization under the protection of the multilayer stability system. The monodisperse hydrogel microspheres with a good swelling property were obtained. *In vitro* release experiments revealed that the BSA-loaded hydrogel microspheres released faster than that of hydrogel bulks. The hydrogel microspheres had fast response to the environment conditions.

Acknowledgements

The authors would like to thank the financial support by the Natural Science Foundation of Hebei province, China (No. C2011208111).

References

[1] C. Phithupha, S. Anuvat, N. Sumonman, C. Datchanee, V.P. Kwanchanok, Controlled transdermal iontophoresis of sulfosalicylic acid from polypyrrole/poly (acrylic acid) hydrogel, Int. J. Pharm. 381 (2009) 25–33.

[2] J. Yun, H.I. Kim, Preparation of poly(vinyl alcohol)/poly(acrylic acid) microcapsules and microspheres and their pH-responsive release behaviour, J. Ind. Eng. Chem. 15 (2009) 902–906.

[3] Q. Wang, J.P. Zhang, A.Q. Wang, Preparation and characterization of a novel pH-sensitive chitosan-g-poly (acrylic acid)/attapulgite/sodium alginate composite hydrogel bead for controlled release of diclofenac sodium, Carbohyd. Polym. 78 (2009) 731–737.

[4] X.Y. Gao, C.L. He, C.S. Xiao, X.L. Zhuang, X.S. Chen, Biodegradable pH-responsive polyacrylic acid derivative hydrogels with tunable swelling behavior for oral delivery of insulin, Polymer. 54 (2013) 1786-1793.

[5] X. Jin, Y.L. Hsieh, pH-responsive swelling behavior of poly(vinyl alcohol)/poly(acrylic acid) bi-component fibrous hydrogel membranes, Polymer. 46 (2005) 5149–5160.

[6] M.C.I.M. Amin, N. Ahmad, N. Halib, I. Ahmad, Synthesis and characterization of thermo- and pH-responsive bacterial cellulose/acrylic acid hydrogels for drug delivery, Carbohyd. Polym. 88 (2012) 465–473.

[7] M. Mariko, G. Takahiro, N. Koji, M.L. Anthony, T. Kozo, A.P. Nicholas, Novel oral insulin delivery systems based on complexation polymer hydrogels: Single and multiple administration studies in type 1 and 2 diabetic rats, J. Control. Release. 110 (2006) 587–594.

[8] Q. Shang, Y.H. Zhang, T. Chen, Y.Y. Liang, Y.L. Shi, Preliminary studies on pH-sensitive hydrogels and in vitro release profiles of two model drugs, J. Biomat. Sci-Polyme. E. 24 (2013) 1459–1471.

[9] X. Li, S.M. Xu, J.D. Wang, X.Z. Chen, S. Feng, Structure and characterization of amphoteric semi-IPN hydrogel based on cationic starch, Carbohyd. Polym. 75 (2009) 688-693.

[10] A. Pourjavadi, S. Barzegar, F. Zeidabadi, Synthesis and properties of biodegradable hydrogels of κ-carrageenan grafted acrylic acid-co-2-acrylamido-2-methylpropanesulfonic acid as candidates for drug delivery systems, React. Funct. Polym. 67 (2007) 644–654.

Advanced Materials Research Vol. 936 (2014) pp 757-762
© (2014) Trans Tech Publications, Switzerland
doi:10.4028/www.scientific.net/AMR.936.757

Study On Structure Analysis and Cell Toxicity Of Okra Polysaccharide

Min Li-jing[1]

School of Life Science, Huzhou Teachers College, Huzhou, Zhejiang 313000

Keyword: okra polysaccharide; structure; cytotoxicity assay

Abstract: The aim is to analysis okra polysaccharide component and structure, and study on the cell toxicity.[Method] In this paper, we used okra seeds as raw material, extracted okra polysaccharide by boiled alcohol sink method extraction, purified it, studied the mono-saccharide composition, and did okra polysaccharide cytotoxicity assay.[Results]The results show sugar content is 28.15% in the extracts form okra seeds, and the okra polysaccharides are composed of rhamnose, Arabian sugar, D-xylose, D - fructose and D-glucose as well as several monosaccharide composition, cytotoxicity assay shows that the cell toxicity of okra polysaccharide is similar to that of glucose. [Conclusion]This study provided experimental basis for the optimization and development of polysaccharide resources from okra. Polysaccharides are from cell wall of plants, animal cell membrane, multi hydroxyl polymer of microbial cell wall[1]. Polysaccharide is second only to coal, oil and natural gas in the world's fourth largest energy[2]. Plant polysaccharide has many physiological activities, no cytotoxicity, and become the research hotspot [1].Okra polysaccharides extracted from okra fruit has the activities of lipid-lowering, antihypertensive, anticancer, anti stress, anti fatigue activity, and etc [2].In the paper, we extracted polysaccharides from Okra Seed, puried by column purification, hydrolyzed by acid hydrolysis, and then studied its monosaccharide composition and the cytotoxicity of okra polysaccharide, to provide the experimental basis for further development of okra polysaccharide.

Reagent and Instrument

Reagents

Okra seeds, bought from the farmers market; anthrone (analytical pure), sulfuric acid (analysis purity), trifluoroacetic acid (analysis purity), methanol (analytical pure), acetonitrile (analytical pure) Shuanglin Chemical Reagent Factory; Dextran standard, rhamnose standard, D- xylose standard, xylitol standard, fucose standard, D- fructose standard, D- glucose standard, galactose mannose standard, Shanghai Xi Bao Biotechnology Co. Ltd; Sephadex HW-40C, TOSOH company; methyl thiazolyl tetrazolium (MTT), trypsin were purchased from sigma-Adrich company; DMEM was purchased from Gino biological Co. Ltd.; calf serum (FCS) were purchased from Hangzhou Sijiqing biological engineering materials Co., ltd..

SMMC-7721 cells (HCC) was cultured in 1640 containing 10% calf serum medium, which offered by Zhejiang University tumor immunity.

Phosphate buffer solution (PBS): 8.0gNaCl, 3.4785gNa_2HPO_4, 12H_2O, 2.9g NaH_2PO_4, 0.2 g KCl, 0.2 g KH_2PO_4 were dissolved in 1000mL distilled water;MTT solution: 5 mg/mL methyl thiazolyl tetrazolium was dissolved in PBS liquid, filtering, sterilizing, stored at 20℃ in dark;

Main instruments

Dialysis membrane (MW8000-14400) was purchased from Pierce company; FD-1 freeze dryer was purchased from Beijing De Tianyou Technology Development Co., Ltd.; VV1800PC scanning UV VIS spectrophotometer, Shanghai mapada Instruments Co. Ltd.; Themo Forma thermostatic shaker; Sony -80 ℃ cold box; Thermo Mulitiskan Mk3 microplate, Thermo company.

Method

Extracted and purified okra polysaccharide[3]

Okra fruits were soaked in water, counter-flow at 100℃ for 4h (×4 times), filter to obtain filtrate, combined filtrate, concentrated, dripped ethanol (v/v:1:3), 4000rmp centrifugal to obtain precipitation, added water to dialysis for 48h (MW:8000-14400), 4000rmp centrifugal to obtain supernatant, dryed to obtain crude, the crude was dissolve in water and puried from column (Sephadex, HW-40C), freeze-dried into light yellow powder.

Determined the content of okra polysaccharide with anthrone sulfuric acid method[4]

Standard curve of glucose: 0.05g glucose standard was dissolved in pure water, constanted volume for the glucose standard solution of 0.5g/L, as the stock solution. Remove stock solution to configure for the series of standard solution concentration of 5 μ g/mL, 15 μ g/mL, 40 μ g/mL, 60 μ g/mL, 80 μ g/mL. Orderly we shifted 1mL standard solution for different concentration in the colorimetric tubes, and added 4mL 2g/L anthrone-sulfuric acid solution, the ice water bath, after that bathed in boiling water for 10 min, removed to cool it at room temperature for 10min. Using distilled water as blank, measured absorbance at 621nm, and the standard working curve were obtained by the least squares method, the regression equation is: A=0.0093C+0.0312 (R^2=0.9779). As the absorbance value changes with the sugar concentration is linear, we can determine the sugar content in the samples with the external standard one point method, as for:

$$\frac{A_{s\tan dard}}{A_{sample}} = \frac{C_{s\tan dard}}{C_{\mathrm{x}}} \qquad (1)$$

$$\text{sugar content}\% = \frac{C_{\mathrm{x}}}{C_{\text{stoste}}} \times 100\% \qquad (2)$$

$A_{s\tan dard}$: standard absorbance: Abs; A_{sample} : sample absorbance: Abs;

$C_{s\tan dard}$: standard concentration: μg/mL; C_{x} : okra polysaccharide concentration of sample: μg/mL;

C_{stoste} : okra polysaccharide apparent concentration of sample: μg / mL.

Okra polysaccharide powder was dissolved in water into 100mL volume, removed 1mL this solution to determine the sugar content operated as above.

Gel permeation chromatography (GPC) determination of okra polysaccharide molecular weight

The molecular weights were 10500, 43200, 76900, 188000Da of the standard products of dextran as standard, GPC determination of retention time, as the standard working curve were obtained by the least squares method, the regression equation is: y=-1.5319x+21.653 (R^2=0.9955).

Chromatographic conditions were: Agilent 1100, SEDEX75 type evaporative light scattering detector (ELSD), detector sensitivity: 7, atomization temperature: 55℃, atomization pressure: 3.06bar,: Tsk-GeL 3000PWXL column (7.8 × 300mm), column temperature: 30℃, mobile phase: water /N_2, flow rate: 1mL/min.

Acid hydrolysis of polysaccharide chain

Some okra polysaccharide sample was added 2mL2.0mol $L^{-1}CF_3COOH$, , constant temperature oil bath at 110°C, reflux for 2h, taken a sample every 0.5h to 8h after hydrolysis and then low concentration at 45°C , the HPLC tests components.

Chromatographic conditions were: Agilent 1100, SEDEX55 type evaporative light scattering detector (ELSD), detector sensitivity: 5, atomization temperature: 40 ℃, atomization pressure: 3.0bar chromatographic column: HypersilNH25 μm (4.6mm × 250mm), column temperature: 25 ° C, mobile phase: acetonitrile water (v:v = 82: 18), flow rate: 1mL/min, injection volume: 10 μ L.

HPLC analysis monosaccharide composition

Chromatographic conditions were: Agilent 1100, SEDEX55 type evaporative light scattering detector (ELSD), detector sensitivity: 5, atomization temperature: 40℃, atomization pressure: 3.0bar chromatographic column: HypersilNH25 μm (4.6mm × 250mm), column temperature: 25°C, mobile phase of methanol: acetonitrile water (v:v = 85: 10:5) ,flow rate: 1mL/min, injection volume: 10μL.

cytotoxic assay

Cos-7 cells were inoculated into 96 well plate, 5000 cells / well, culture 24h., absorbed the old culture each bore liquid. Okra polysaccharide and glucose standard in 10%FCS containing DMEM were prepared into solution concentration gradient is 0.01, 0.025, 0.05, 0.1, 0.25, 0.5 and 1mg/mL. Each hole was added 0.15mL this solution, 4 holes for 24h cocultured with cell culture liquid sugar, suction to the old, then added serum free DMEM per hole 100 μ L containing 5 μ g/mLMTT (5mg/mL MTT10mL into 90 μ LDMEM), cultured for 4H at 37 ℃. Turning plate method to discard the liquid, each hole was added with 100 μ LDMSO 10min, concussion, determined the OD value at the wavelength of 570nm in the ELISA detecting instrument. At the same time for the cell alive and cell death were all control, all 6 holes.

$$\text{cytotoxicity}\ (\%) = \frac{X - X_{0\%}}{X_{100\%} - X_{0\%}} \times 100\% \tag{3}$$

X： the value of OD after cocultured with okra polysaccharide; $X_{0\%}$： the value of OD cell death control;

$X_{100\%}$： the value of OD cell alive control.

Results and analysis

Determined the content of okra polysaccharide with anthrone sulfuric acid method

TABLE 1 DETERMINED THE CONTENT OF OKRA POLYSACCHARIDE WITH ANTHRONE SULFURIC ACID METHOD

No	stoste Concentration（μg/mL）	absorbance（Abs）	sugar concentration（μg/mL）	sugar content（%）	Average（%）
standard	30	0.2142			
1	188	0.3747	52.48	27.91	
2	188	0.3802	53.25	28.32	28.15
3	188	0.3790	53.08	28.23	

Gel permeation chromatography (GPC) determination of okra polysaccharide molecular weight

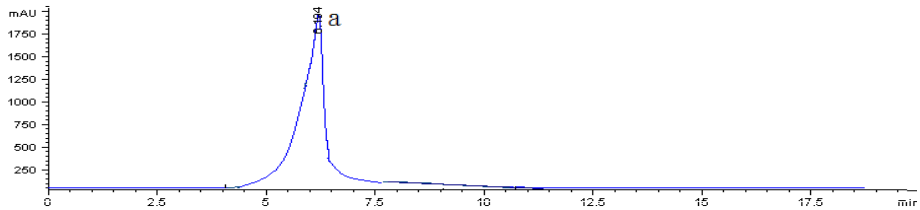


Fig1 Gel permeation chromatography (GPC) determination of okra polysaccharide molecular weight

The spectrogram showed that retention time of okra polysaccharide wsa 6.194min, so it's molecular weight was 191,838.9Da.

Acid hydrolysis of polysaccharide chain

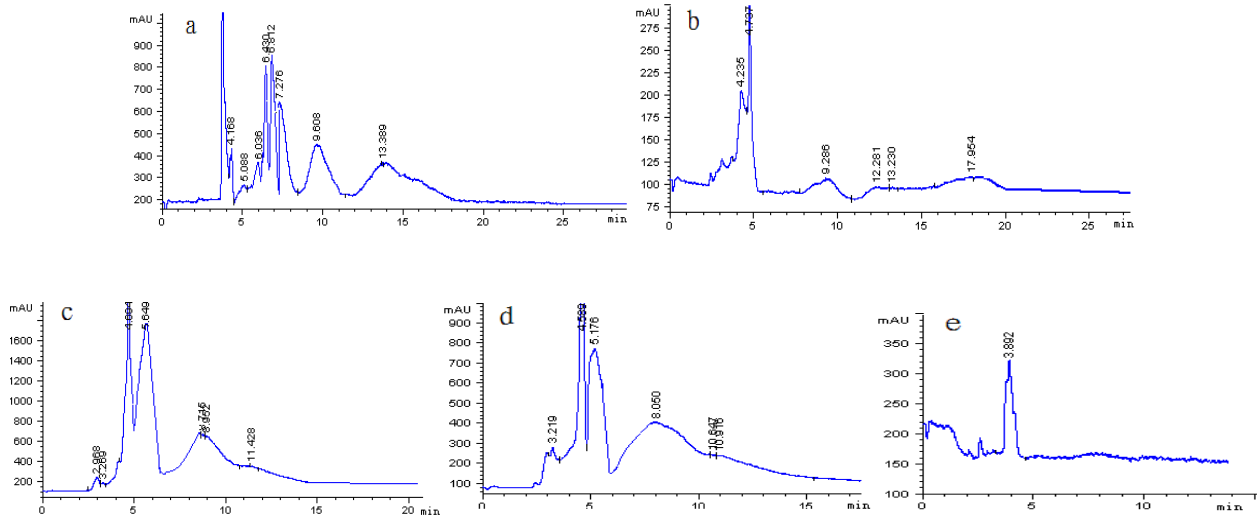


Fig2 The chromatograms of the sample of Okra polysaccharide in different hydrolysis time

a 2h；b 2.5h；c 3h；d 3.5h；e 8h

Observation of okra polysaccharide hydrolysis series map, we found that the hydrolysis products became more and more simple along with the hydrolysis time, this may be due to residual damage acid with the degradation of hydrolysate hydrolyzed liquid, especially in the hydrolysis of 8h

hydrolysis products had all degradation. And the selection should be relatively mild, hydrolysis time shoulds not be too long hydrolysis for okra polysaccharide, generally the best choice of the hydrolysis time was 2h for the best effect. The change in retention time between 11-13min peak displacement, may be D – glucose was shaped into in enolate anion, and then converted to the mixture of fructose, mannose and glucose in the action of dilute acid.

The retention time of CF_3COOH was 2.4-2.9min, while around 4.9min was the peak of CH_3CN. There was no disaccharides in liquid solution of polysaccharide, all ingredients were monosaccharides.

HPLC analysis of monosaccharide composition

Taking retention time may influence on each other after mixing the monosaccharide standard into account, so we determined their retention time of each component after the monosaccharide mixed, basing on determination retention time the monosaccharide standard single injection.

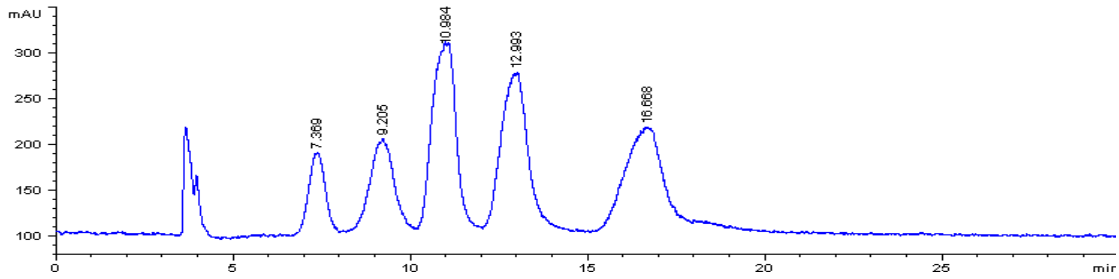


Fig3 The retention time of each component in mixed monosaccharide standard

We added methanol in the mobile phase in the monosaccharide composition analysis, because the time interval sampling data in okra polysaccharide acid hydrolysis liquid, we found that each component had adhesion retention time, to decrease the mobile phase polarity, component retention time shiftted, the retention time was about 3.3-3.9min for CF_3COOH solvent peak, about 5.0min was mobile phase CH_3CN peak. We found of existence of rhamnose, arabinose, D-xylose, D-fructose and glucose monosaccharide in okra polysaccharide acid hydrolysate.

TABLE 2 THE RETENTION TIME OF EACH MONOSACCHARIDE COMPOSITION OF OKRA POLYSACCHARIDE ACID HYDROLYSATE

retention time (t_R/min)	monosaccharide compositio
7.014	rhamnose
8.754	arabinose
9.957	D-xylose
12.490	D－ fructose
15.084	D－glucose

Cytotoxic assay

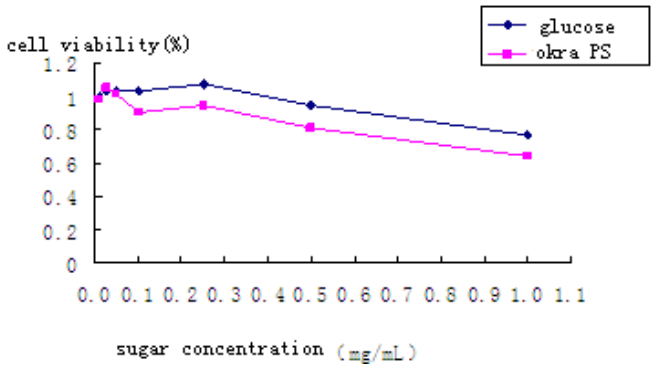


Fig4 The data of cytotoxic assay

Figure4 shows the observed cytotoxicity, okra polysaccharide and glucose similar, belong to low toxicity materials, good biological compatibility. These results provide an experimental data support for the further development and utilization of okra polysaccharide.

In this paper, okra polysaccharide was extracted from okra seeds, and is mainly composed of rhamnose, glucose, xylose, D-Arabia, D- fructose and glucose, several kinds of monosaccharide composition, and the material of low cytotoxicity, good biological compatibility, is expected to develop the use of depth.

Reference

[1] Zhou jinghua,Shao yuan. Research Advances on biological activities of polysaccharides of plant [J]. Journal of Dali University,2012,11(6):36-37

[2] Fang xiangru.The prospect of energy resources in alternative way of biomass[J]. Progress in chemical industry,2011,30(11):2333-2339

[3] Li xin. Introduces a kind of medicinal and edible vegetables -- Okra[J]. Famous quality,2012(10):50

[4] Fang jinian. Purification and identification of polysaccharide purity, molecular weight determination[J]. Pharmaceutical Bulletin,1984(19):622-5

Advanced Materials Research Vol. 936 (2014) pp 763-769
© (2014) Trans Tech Publications, Switzerland
doi:10.4028/www.scientific.net/AMR.936.763

Resveratrol Loaded Self-Microemulsifying Drug Delivery System (SMEDDS): Development and Optimization

Liu Guoqing[1, a], Zhou Huafeng[1, 2, 3, b], Zhang Jing[2, c], Yan Zemin[3, d], Duan Mingxing[2, e], Long Yingfang[2, f], Xia Qiang[1*, g]

[1]State Key Laboratory of Bioelectronics, School of Biological Science and Medical Engineering, Southeast University, Nanjing 210096, China

[2]State-key Laboratory of Biomembrane and Membrane Biotechnology, School of Life Sciences, Tsinghua University, 100084 Beijing, China

[3]Jiangsu Longliqi Bioscience Co., Ltd., 215555 Suzhou, China

[a]liugq1988@gmail.com, [b]zhouhf@mail.tsinghua.edu.cn, [c]fossezhang@126.com, [d]zhf031689@163.com, [e]duanmx@mail.tsinghua.edu.cn, [f]longyf2013@126.com, [g]xiaq@seu.edu.cn

Keywords: Resveratrol; SMEDDS; Development; Optimization

Abstract. We developed a SMEDDS to enhance the oral delivery of resveratrol by using high performance liquid chromatography, a pseudo ternary phase diagram and a central composite design (CCD). We found that the optimal formulation of 12.69% greoil gtcc, 62.29% Cremophor EL, and 25.02% Labrasol. We characterized the particle size and zeta potential of the final SMEDDS.

Introduction

Resveratrol is a polyphenol occurring naturally in several plants [1, 2]. Previous studies have shown that resveratrol has many physiological properties, such as cardio protective actions, cancer preventive and therapeutic effects [3]. It also has the potential as an anti-obesity compound and a potent new antioxidant in skin care formulations [4, 5]. However, the oral delivery of resveratrol is very low in humans [6]. Therefore, a drug delivery system to improve oral delivery is crucial.

In recent years, many researchers have focused on SMEDDS to improve oral delivery of some drugs. SMEDDS is a mix of oil, target drugs, surfactant and cosurfactant that emulsify under gentle agitation [7]. A SMEDDS can improve oral delivery because it offers a large inter facial area for drug diffusion with nano size [8]. SMEDDS has been successfully established in improving the oral bioavailability of cyclosporine, coenzyme Q10, tacrolimus and oridonin [8-12]. However, only few studies have described the use of SMEDDS for resveratrol.

Generally speaking, it is important to optimize the SMEDDS. And it is easier to conduct investigations by changing one variable while keeping all others constant. However, this approach was difficult to determine interactions among the variables. One common way is to use CCD [13]. The CCD is a composite of the factorial experiment, axial points, and centre point, and it is widely used for the response variable that abolishes the need for a complete three-level factorial experiment [14]. CCDs have been used in the optimization of formulations such as the nanostructured lipid carrier system for econazole nitrate, α-tocopherol-loaded solid lipid nanoparticles [15, 16].

In this study, a high performance liquid chromatography (HPLC) method was established for the determination of the solubility of resveratrol in different oils, surfactants and cosurfactants. The effects of the surfactants, cosurfactants, and oils on the microemulsion were investigated using the pseudo ternary phase diagrams. A CCD was used to study the effect of formulation variables (oil content and Km value) on the response variables, including droplet size, polydispersity index (PI) and drug loading. The optimal preparation was characterized preliminarily

Materials and Methods

Materials

Resveratrol (purity: 98%) was purchased from Tianjin Jianfeng Natural Product R&D Co., Ltd, China. Cremophor EL and Cremophor RH 40 were supplied by BASF, Germany. Labrasol, Maisine 35-1, Peceol, Lauroglycol 90, Labrafil M 1944CS, Plurol OleiqueCC497, and Plurol Diisostearique were obtained from Gattefosse, France. Greoil gtcc, 1,2-propanediol, oleic acid, propylene glycol esters offatty acid, Tween 80, and PEG400 were provided by Beijing Fengli Jingqiu Commerce and Tarde Co., Ltd, China. HPLC grade methanol and acetonitrile were supplied by DikmaPure, China. All other chemicals used were of analytical grade and were commercially available products. MilliQ water was used in all the experiments.

Solubility of resveratrol

Excess amount of resveratrol was placed in dark brown screw-capped bottles with 1 mL different vehicles and mixed by vortexing. Mixtures were allowed to agitate on a shaker (Zhicheng ZHWY-103D, China) at 37 °C for 48 h. After that, the samples were centrifuged at 10000 rpm for 15 min. The supernatant was diluted with methanol and then passed through 0.45 μm membrane filters (Millipore, America). And an HPLC 1200 system (Agilent, America) with an Agilent Extend C18 column (5 μm, 4.6×250 mm) was used. The mobile phase was a mixture of water and acetonitrile (73:27, v/v) at a flow rate of 0.8 mL/min. The resveratrol concentration was quantified at 306 nm, and the column temperature was 30 °C. The inter- and intra-day variance was within the acceptable range. The solubility studies were repeated three times.

Preparation of SMEDDS formulations

SMEDDS of resveratrol were prepared by dissolving resveratrol into the mixture of surfactant, cosurfactant and oil. And it was vigorous vortexing adequately in a water bath at 37 °C. All formulations were stored at room temperature before use.

Construction of pseudo ternary phase diagrams

Pseudo ternary phase diagrams of the selected compositions of SMEDDS were constructed by titration of homogenous liquid mixtures of oil, surfactant and cosurfactant with 0.1 M HCL. And they were used to identify the self-microemulsifying regions and to find the preliminary optimal component concentrations. With Km values of 3, 2, 1, 1/2 and 1/3 (w/w), the surfactant and cosurfactant mixture was warmed and then mixed with oil. The ratio of oil to surfactant varied as 1:9, 2:8, 3:7, 4:6, 5:5, 6:4, 7:3, 8:2 and 9:1 (w/w). These mixtures were slowly titrated with aliquots of 0.1 M HCl at 37 °C until they became turbid. Clear and isotropic samples were deemed within the self-microemulsifying regions [17]. All experiments were repeated three times, and similar observations were made across all replications.

CCD. In our study, the oil content and Km value were identified as the studied factors of SMEDDS. And the droplet size, PI and drug loading were the responses. The CCD was created by Design Expert 8.0. The three responses were suitable for a second order polynomial model (Eq. 1). In the equation, X_1 and X_2 correspond to the studied factors, Y represents the measured response, A_0 is an intercept, and A_1–A_5 are the regression coefficients. The signal to noise ratio, adeq Precision, was employed to validate the resulting model. A ratio greater than 4 is desirable.

$$Y=A_0+A_1\times X_1+A_2\times X_2+A_3\times X_1^2+A_4\times X_2^2+A_5\times X_1\times X_2. \quad (1)$$

The desirability function is used to treat the multicriteria problem as a single criterion problem. The response to be minimized is Eq. 1. In the two equations, Y_{min} represents the lowest possible value, Y_{max} represents the highest possible value, and Y_i indicates the experimental value. As a global desirability function, an overall desirability (D) is calculated using the geometric mean.

$$d=\begin{cases} 0 & (Y_i \geq Y_{max}) \\ \dfrac{Y_i - Y_{min}}{Y_{max} - Y_{min}} & (Y_{min} < Y_i < Y_{max}) \\ 1 & (Y_i \leq Y_{min}) \end{cases} \quad (2)$$

$$d=\begin{cases} 1 & (Y_i \geq Y_{max}) \\ \dfrac{Y_{max} - Y_i}{Y_{max} - Y_{min}} & (Y_{min} < Y_i < Y_{max}) \\ 0 & (Y_i \leq Y_{min}) \end{cases} \quad (3)$$

Characterization of SMEDDS

Prior to the droplet size, PI and zeta potential measurement, SMEDDS of resveratrol was diluted with water 200 times and gently stirred. They were determined using a Malvern Zetasizer ZS90 (Malvern Instruments, UK). Each sample was analysed in triplicate.

The drug loading of SMEDDS was determined with the blank SMEDDS (absence of the drug). And the experiment method was the same with the investigation of solubility of resveratrol.

Results and Discussion

Solubility Studies

The solubility of resveratrol in various materials is presented in Fig. 1. The solubility of resveratrol was very low in the oil phase for the oils tested compared to some surfactants and cosurfactants. Therefore, the solubility of resveratrol can be increased by SMEDDS. Finally, greoil gtcc was selected for the oil phase because it is widely used in the pharmaceutical and food industries. Among the surfactants, Cremophor EL showed the highest solubility for resveratrol. Labrasol was selected as a cosurfactant for its high resveratrol solubility and for its improved intestinal absorption of drugs [17].

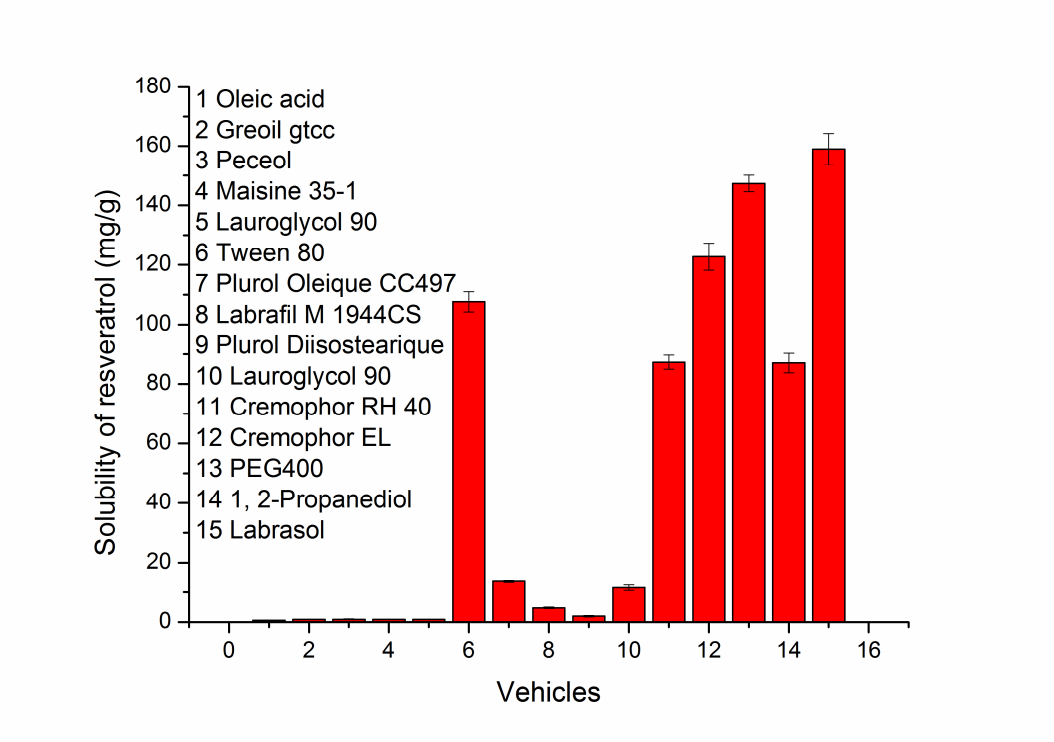


Fig. 1 The solubility of different vehicles

Construction of pseudo ternary phase diagrams

As Fig. 2 shows, the self-microemulsifying region expands as the Km value increases, with the maximum self-microemulsifying region at the Km value of 3, indicating that the Km values are effective for a stable and efficient SMEDDS formation. The appropriate formation and the specific formulation could not be determined and confirmed in this experiment. Therefore, some formulations were selected and used for the CCD experiment.

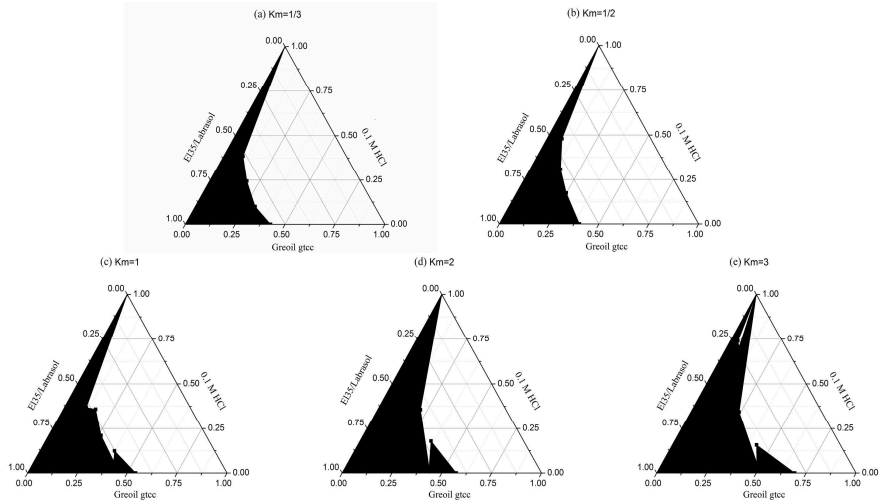


Fig. 2 The pseudo-ternary phase diagrams of greoil gtcc, 0.1 M HCl, Cremophor EL and Labrasol

CCD. The responses for oil content (X_1), Km value (X_2), droplet size (Y_1), PI (Y_2) and drug loading (Y_3) were included in the CCD, and the three responses Y_1–Y_3 were significant for assessing the SMEDDS's quality. Among these objectives, Y_1 and Y_2 were minimized, while Y_3 was maximized. D was calculated for each run. Design Expert was used to fit these responses using Eq. 1. The fitting parameters are shown in Table 1. The Adeq Precision of the responses and the desirability indicated that the model was significant and could be used to navigate the design spaces.

TABLE 1: THE FITTING PARAMETERS OF THE RESPONSES AND THE DESIRABILITY

	A_0	A_1	A_2	A_3	A_4	A_5	Adeq Precision
Droplet size	5.40	4.11	5.13	-0.055	-7.99	0.21	20.46
PI	0.35	-0.0077	-0.037	0	0	0.0028	11.18
Drug loading	119.72	-2.21	-9.10	0.030	0.95	0.011	25.88
Desirability	0.53	-0.0016	0.0011	0	-0.088	-0.0031	11.58

A 3D colour map of the three responses and D was drawn using Origin 8.5 (Fig. 3). Fig. 3a shows the 3D colour map for droplet size and reflects the relationship between the droplet size and the two factors. A droplet size smaller than 50 nm could be observed in the domain containing an oil content of less than 20%. When the oil content was more than 30% and the Km value was less than 2, the droplet size was greater than 80 nm.

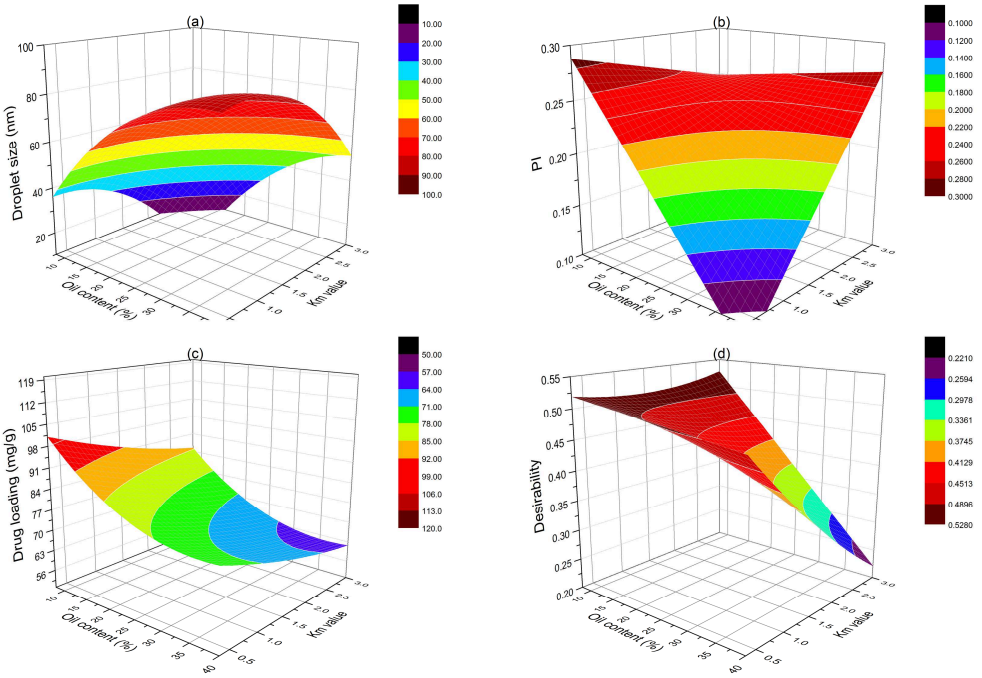


Fig. 3 The 3d colour map of the three responses and the desirability

The PI reflects the size distribution generated by the SMEDDS dispersion in an aqueous media. The optimal oil content was greater than 25% for achieving a minimum PI within a Km value less than 1.5 (Fig. 3b). As shown in Fig. 3c, the effect of the oil content on the drug loading was critical. When the Km value remained constant, the increase in oil content resulted in decreased solubility.

For further optimization of the formulation, D function was used to optimize the three responses simultaneously. The 3D colour map for D is shown in Fig. 3d. D was greatly affected by the oil content, which was important to maintain the stability of the formulation. The solution for the cosurfactant looked better than the solution for the surfactant, indicating that the Km value was responsible for dissolving more resveratrol. The final formulation that was chosen by the Design-Expert software was X_1=12.69%, X_2=2.49, and D = 0.541. Thus, the final optimal formulation of the SMEDDS was 12.69% greoil gtcc, 62.29% Cremophor EL and 25.02% Labrasol.

Characterization of SMEDDS

The droplet size was 20.51±0.63 nm, PI was 0.241±0.016, and drug loading was 76.45±3.23 mg/g. The zeta potential was -1.12±0.21 mV for the formulation.

Conclusion

We developed a potentially useful method for local delivery of orally ingested resveratrol. The selection of the optimal SMEDDS composition for resveratrol might offer an advantage as an alternative oral dosage form. The optimization of the SMEDDS formulation for resveratrol was conducted using CCD combined with a desirability function. And it was efficient for modelling and optimization of resveratrol in a SMEDDS as well as for understanding how the formulation factors influence the properties of a SMEDDS.

Acknowledgements

This work was supported by Program (CC201213) from Changshu Science and Technology Bureau, Program (ZXG2012034) from Suzhou Science and Technology Bureau and International Scientific Cooperation Project of Suzhou (No. SH201204).

References

[1] Choi JS, Choi BC, Kang KW. Effect of resveratrol on the pharmacokinetics of oral and intravenous nicardipine in rats: possible role of P-glycoprotein inhibition by resveratrol. Die Pharmazie 2009;64:49-52.

[2] Cottart CH, Nivet-Antoine V, Laguillier-Morizot C, Beaudeux JL. Resveratrol bioavailability and toxicity in humans. Molecular nutrition & food research 2010;54:7-16.

[3] Bhat KPL, Kosmeder JW, 2nd, Pezzuto JM. Biological effects of resveratrol. Antioxidants & redox signaling 2001;3:1041-64.

[4] Baxter RA. Anti-aging properties of resveratrol: review and report of a potent new antioxidant skin care formulation. Journal of cosmetic dermatology 2008;7:2-7.

[5] Macarulla MT, Alberdi G, Gomez S, Tueros I, Bald C, Rodriguez VM, et al. Effects of different doses of resveratrol on body fat and serum parameters in rats fed a hypercaloric diet. Journal of physiology and biochemistry 2009;65:369-76.

[6] Walle T HF, DeLegge MH, Oatis JE Jr, Walle UK. High absorption but very low bioavailability of oral resveratrol in humans. Drug Metabolism And Disposition 2004;32:1377-82.

[7] Balakrishnan P, Lee BJ, Oh DH, Kim JO, Hong MJ, Jee JP, et al. Enhanced oral bioavailability of dexibuprofen by a novel solid self-emulsifying drug delivery system (SEDDS). European journal of pharmaceutics and biopharmaceutics : official journal of Arbeitsgemeinschaft fur Pharmazeutische Verfahrenstechnik eV 2009;72:539-45.

[8] Von Suesskind-Schwendi M, Gruber M, Touraud D, Kunz W, Schmid C, Hirt SW, et al. Pharmacokinetics of a self-microemulsifying drug delivery system of tacrolimus. Biomedicine & pharmacotherapy = Biomedecine & pharmacotherapie 2013;67:469-73.

[9] Vonderscher J, Meinzer A. Rationale for the development of Sandimmune Neoral. Transplantation proceedings 1994;26:2925-7.

[10] Gershanik T, Benita S. Self-dispersing lipid formulations for improving oral absorption of lipophilic drugs. European journal of pharmaceutics and biopharmaceutics : official journal of Arbeitsgemeinschaft fur Pharmazeutische Verfahrenstechnik eV 2000;50:179-88.

[11] Kommuru TR, Gurley B, Khan MA, Reddy IK. Self-emulsifying drug delivery systems (SEDDS) of coenzyme Q10: formulation development and bioavailability assessment. International journal of pharmaceutics 2001;212:233-46.

[12] Zhang P, Liu Y, Feng N, Xu J. Preparation and evaluation of self-microemulsifying drug delivery system of oridonin. International journal of pharmaceutics 2008;355:269-76.

[13] Georgiou SD, Stylianou S, Aggarwal M. A class of composite designs for response surface methodology. Computational Statistics & Data Analysis 2013.

[14] Diler EA, Ipek R. Main and interaction effects of matrix particle size, reinforcement particle size and volume fraction on wear characteristics of Al–SiCp composites using central composite design. Composites Part B: Engineering 2013;50:371-80.
[15] De Carvalho SM, Noronha CM, Floriani CL, Lino RC, Rocha G, Bellettini IC, et al. Optimization of α-tocopherol loaded solid lipid nanoparticles by central composite design. Industrial Crops and Products 2013;49:278-85.
[16] Lav Keshri KP. Development of thermodynamically stable nanostructured lipid carrier system using central composite design for zero order permeation of Econazole nitrate through epidermis. Pharmaceutical development and technology 2012;18:634-44.
[17] Wei Y, Ye X, Shang X, Peng X, Bao Q, Liu M, et al. Enhanced oral bioavailability of silybin by a supersaturatable self-emulsifying drug delivery system (S-SEDDS). Colloids and Surfaces A: Physicochemical and Engineering Aspects 2012;396:22-8.

Advanced Materials Research Vol. 936 (2014) pp 770-775
© (2014) Trans Tech Publications, Switzerland
doi:10.4028/www.scientific.net/AMR.936.770

Stress Analysis of the Hip Joint Endoprosthesis Ceramic Head for Different Values of Shape Deviations

Vladimír Fuis[1, a] and Premysl Janicek[2,b]

[1] Institute of Thermomechanics Academy of Sciences of Czech Republic, Dolejskova 5, 182 00, Prague, Czech Republic

[2] Institute of Thermomechanics Academy of Sciences of Czech Republic, Dolejskova 5, 182 00, Prague, Czech Republic

[a] fuis@fme.vutbr.cz, [b] janicek@fme.vutbr.cz

Keywords: Hip joint endoprosthesis, ceramic head, shape deviations, cone contact areas, tensile stress, failure probability.

Abstract: The paper deals with the problems of ceramic head of hip joint endoprosthesis destructions, and with assessing the impact of shape deviations of conical surfaces on the tensile stress under ISO 7206-5 loading. The failure of the hip joint endoprosthesis ceramic head has always traumatic consequences for the patient, since a part of or even the whole endoprosthesis has to be reoperated. Hence, it is desired to reduce the number of implant re-operations to the minimum. Therefore the computational modelling of the stress of the head was realised. The shape deviations of the ideal contact cone areas of the head and stem are parameters that significantly influence the tensile stress in the head and its reliability. The assumed shape deviations of the head's and stem's cones are macro shape deviations (different cone taper) and micro shape deviations (unevennes) measured using the IMS-UMPIRE equipment. The stress state in the ceramic heads was solved using the FEM and head's failure probability is based on the Weibull weakest link theory [4, 5 and 9].

Introduction

One of the most frequently operated joints of the human body is the hip joint [1]. In young patients, the operation is mostly aimed at reconstructing the joint's pathologically developed geometry [6]. In older age, operations prevail in which the patients are provided with partial or total endoprostheses [8, 13]. These may be of different design solutions, with various materials being used in the endoprosthesis' individual parts. In a design solution which used ceramic heads, the destruction of the



Fig. 1. *In vivo* destructed ceramic heads

head has occurred in vivo. In one hospital of the Czech Republic, more than 1 % of applied endoprostheses had to be reoperated (Fig. 1). That is why the state of stress and the reliability of ceramic heads of total endoprosthesis is being intensively analysed by means of computational modelling.

The analysis of the head fracture surface orientation showed that the meridionally oriented fracture surfaces prevail (Fig. 1). Since ceramics is a material characterised by the limit state of brittle strength, the cohesion failure starting in directions perpendicular to the direction of the maximum principal tensile stress, then the stress responsible for the failure of head cohesion should be the hoop stress [3]. An effective method of solving the problem of reliability is computational modelling combined with experiments. For solving the strain/stress states in the head, the finite elements method was used, namely the ANSYS program system.

Computational modelling

The topology of the elements of the total hip joint endoprosthesis follows from Fig. 2 with the basic macro-dimensions of elements. Computational modelling of the strain/stress states in the head was implemented on a system whose elements were parts of the stem and the head.

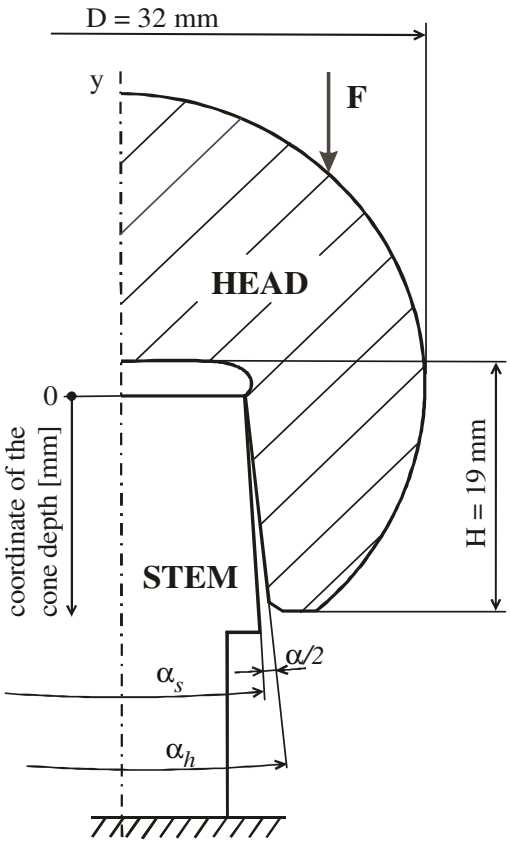


Fig. 2. Topology and macro shape deviation



Fig. 3. Measure device IMS-UMPIRE

In order to implement computational modelling of the impact of shape deviations of the cones of stems and heads of hip joint endoprostheses, which has a stochastic character, the measurement of these deviations was carried out using the IMS-UMPIRE measuring equipment (Fig. 3). The quality of the measured contact surface of both cones can be expressed by macro-parameters (deviations) – the most important is angle of the taper of the head and the stem and straight line character), and micro-parameters (deviations) – local micro-unevenness of surface. As regards the inclination angles of the elements of ruled surfaces (degree of taper) one can say that the manufacturing documentation permits only an alternative in which the vertex angle of the head (angle α_h) is greater than the vertex

angle of the stem (angle α_s) – Fig. 2 (the value of the angle α can be found from zero to 10'), and the circularity of the individual sections (perpendicular to the y-axis) is less than 10 µm [2 and 7].

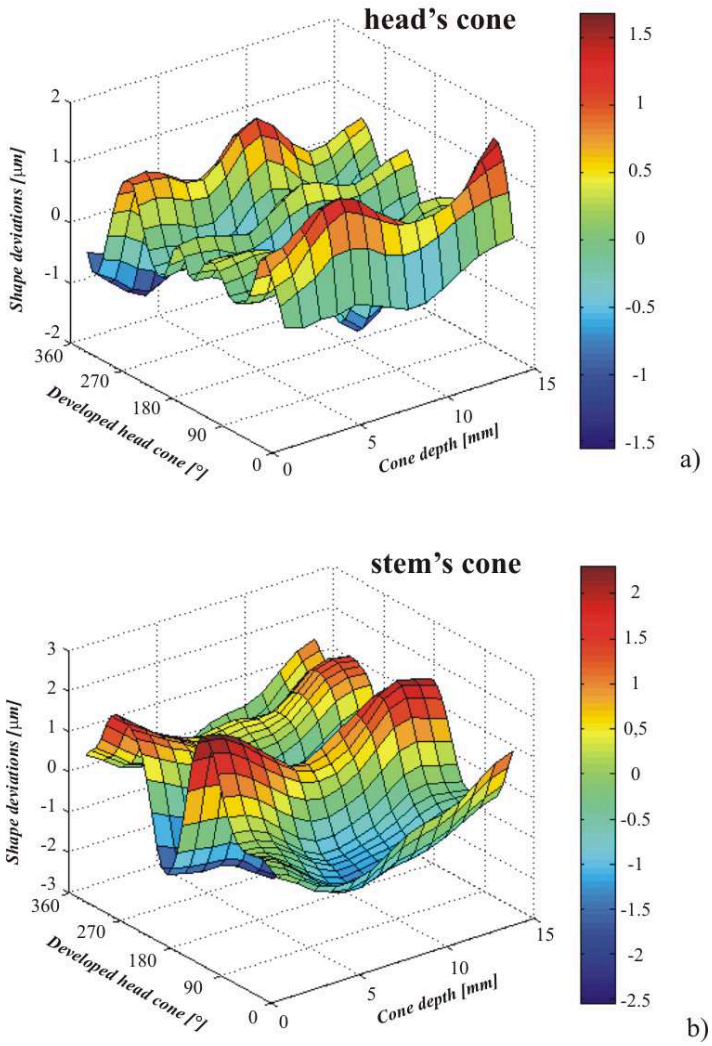


Fig. 4. Micro shape deviation of the: a) head cone and b) stem cone

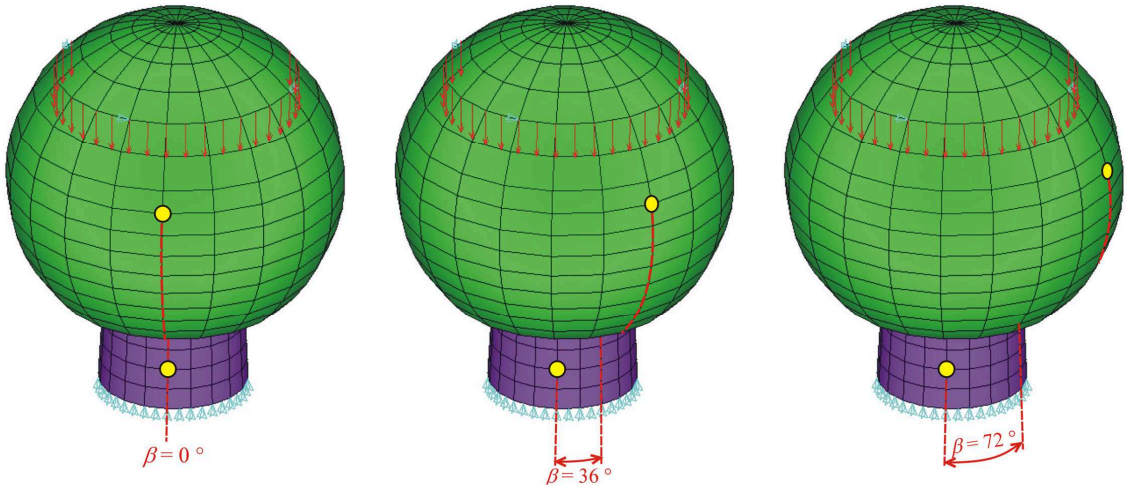


Fig. 5. Representation of various head to stem positions - angle β

The measured micro shape deviations from the ideal conical shape for cone of head are illustrated by the developed cones in Fig. 4a (from -1.5 to 1.5 μm). The micro shape deviations of the stem cone are show in Fig. 4b (from -2.5 to 1.5 μm). The mentioned head with macro and micro shape deviations was put and loaded on the stem cones under ISO 7206-5 loading (Fig. 2).

The state of stress of the ceramic head of endoprosthesis can be strongly affected by the process of endoprosthesis implantation, when the surgeon fits the head on the cone of the stem. The fitting of the head on the cone of the stem is a random process, in view of the mutual position of the head to the stem (in sense of the head's slight turning around the y-axis, defined by angle β – Fig. 5) [10, 11]. The question is, whether the local shape deviations of the cones, in case of random completing, can produce high tensile stresses that might reduce the reliability of the head. For this reason, a series of computations will be made for each pair and for various positions of the head towards the stem.

For computational analyses of the head's cohesion failure, the head was loaded with linear forces acting on a circle, the carrier of the resulting force F being identical with the axis of the stem, Fig. 2. This way of loading complies with the ISO 7206-5 standard, according to which the reliability of ceramic heads is tested for failure of cohesion.

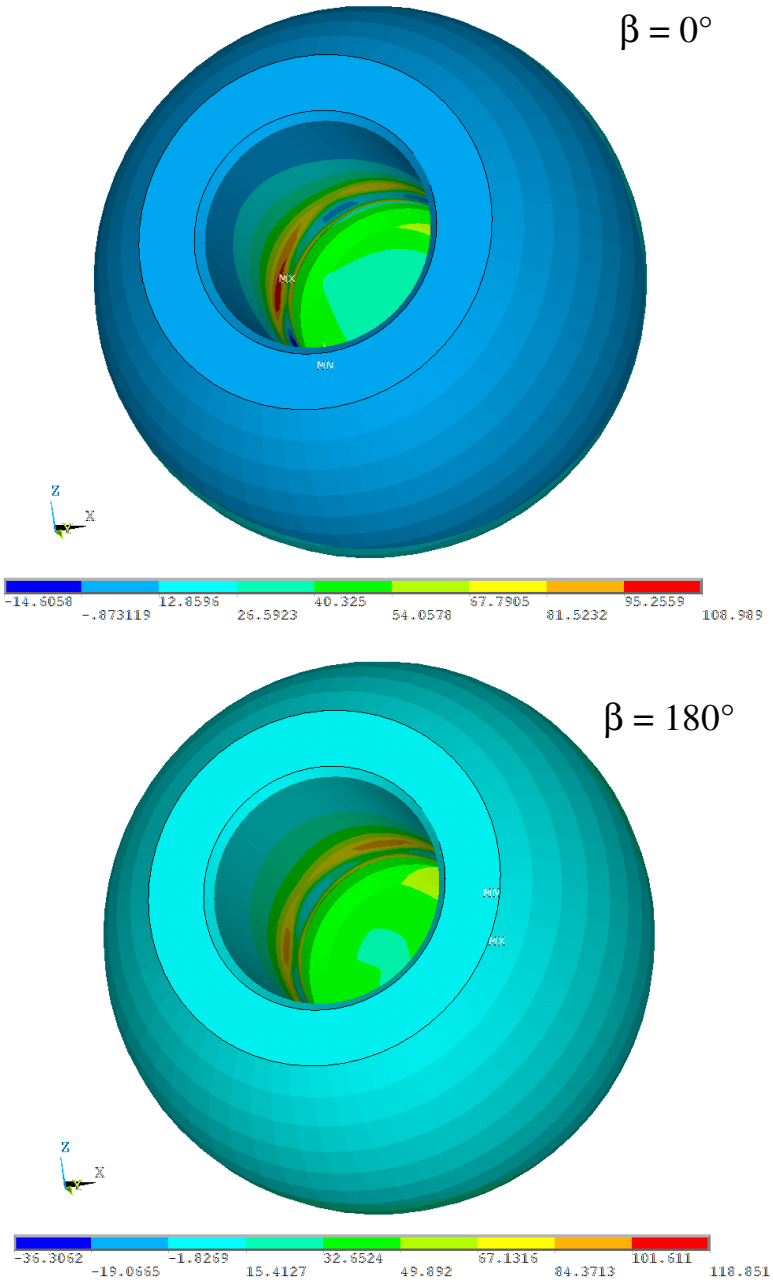


Fig. 6. First principal stress isolines (in MPa) for loading F = 4 kN and α = 10’ and for two different angles β

The material of the head and the stem was considered to be a linear isotropic continuum. The stem was made of steel and the following constitutive characteristics were taken into account in the calculation: E = 210 GPa μ = 0.3. The material of the head was ceramics on the basis of aluminium oxide Al_2O_3, for which the following constitutive characteristics were considered: E = 390 GPa, μ = 0.23. Contact between the head and the stem is modelled as elastic Coulomb friction with coefficient of friction f = 0.15 [7, 8 and 12].

Results and Discussions

The negative behavior of the ceramics is the brittleness and therefore the tensile stresses in the ceramic head will be analysed in detail [8]. The maximum tensile stress in the head is located on the contact surface near the contact region. The size of the contact region is influenced of the position of micro shape deviations of the stem and the head cone. Fig. 6 shows the isolines of the first principal stress in the head

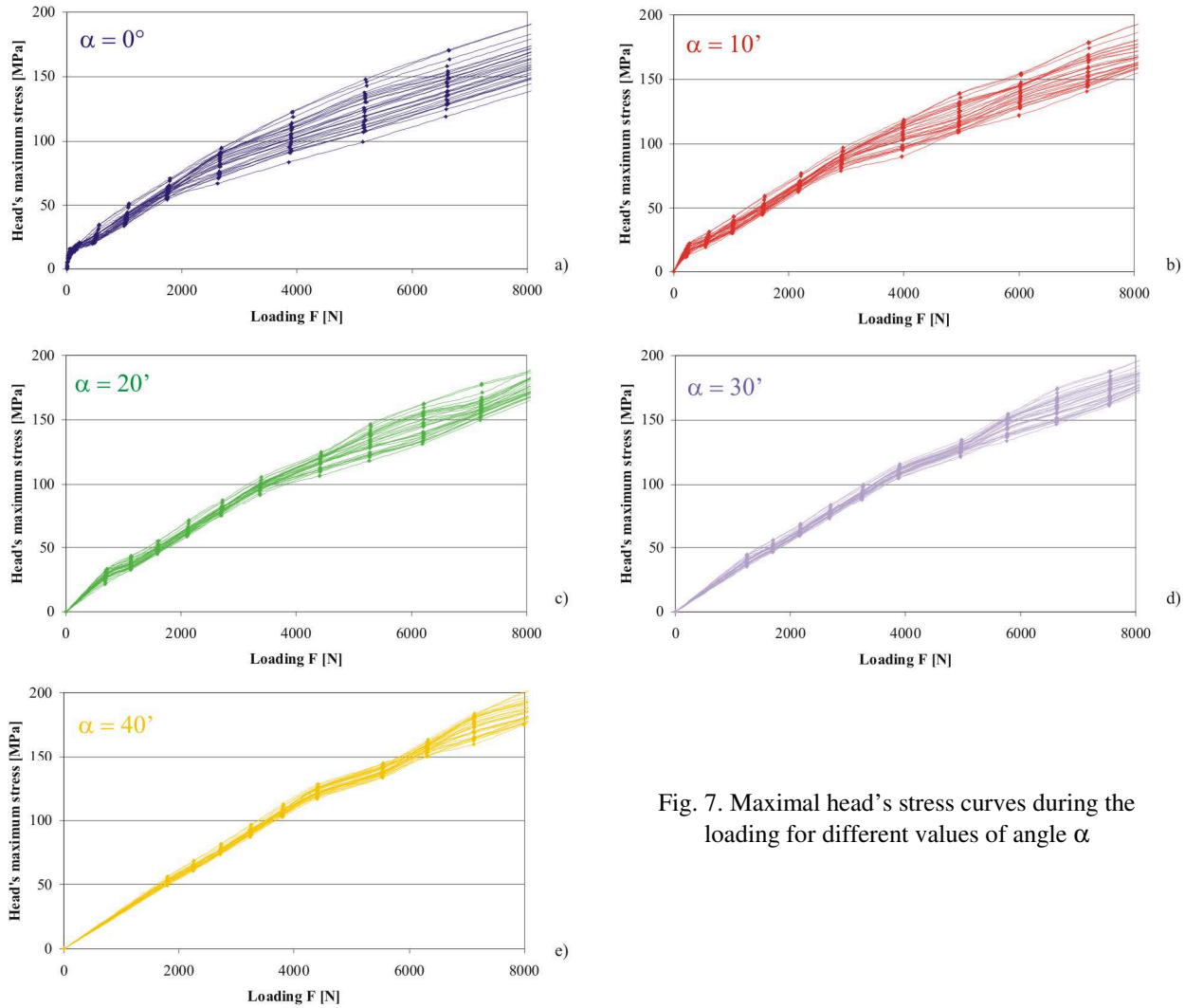


Fig. 7. Maximal head's stress curves during the loading for different values of angle α

(F = 4 kN and α = 10') for different position of the head and the stem (β = 0° and β = 180°). The location of the maximum tensile stress and the shape of the isolines are different for both analysed angles β due to the relative location of the micro deviations of the head's and stem's cones.

The distribution of maximum values of tensile stresses in the ceramic head (σ_{max}), in dependence on the value of the head's load and on value of the α, is shown in Fig. 7a-e. The width of the curves is decresed with increasing angle α. This is due to the fact that in case the zero angle α (ideal case when the cone angle of the head and stem is the same) is in the contact local shape deviations on the entire tapered surface. Increasing of the angle α value caused the reduction of the contact area and this contact area is localized to the area of the smallest diameter of the cone. Then the smaller number of the local shape deviations are in contact and extreme tensile stress in the head has a smaller variance (width of curves in Fig. 7).

Conclusions

By computational modelling it has been proved that the character and the size of micro and macro shape deviations on a conical contact area between the stem and the head of hip joint endoprosthesis have a pronounced influence on the character and the value of stress in the head and, hence, on the probability of the head's cohesion failure. The increasing of the stress and the failure of cohesion of ceramic heads illustrate how the ignorance of the influence of micro-dimensions on macro-behaviour of parts may have negative and even traumatising consequences.

Acknowledgement

The research has been supported by the project of the Czech Science Foundation GA CR nr. 13-34632S.

References

[1] A. O. Andrisano, E. Dragoni, A. Strozzi, Axisymmetric mechanical analysis of ceramic heads for total hip replacement. Proc. Inst. Mech. Engrs, Part H, Vol. 204 (1990) 157-167.

[2] V. Fuis, P. Janicek, Stress and reliability analyses of damaged ceramic femoral heads, Conference on Damage and Fracture Mechanics, Maui Hawaii, Structures and Materials Vol. 12, (2002) 475-485.

[3] V. Fuis, M. Koukal, Z. Florian, Shape Deviations of the Contact Areas of the Total Hip Replacement, 9th International Conference on Mechatronics, Warsaw, Poland (2011) 203-212.

[4] D. Bush, Designing Ceramic Components for Structural Applications, J. Mater. Eng. Perf. ASM Int., Vol. 2, (1993) 851-862.

[5] V. Fuis, M. Malek, P. Janicek, Probability of destruction of Ceramics using Weibull's Theory, 17th International Conference on Engineering Mechanics, Svratka, Czech Rep. (2011) 155-158.

[6] S. H. Teoh, W. H. Chan, R. Thampuran, An Elasto-plastic Finite Element Model for Polyethylene Wear in Total Hip Arthroplasty, J Biomech (2002) 35: 323-330.

[7] V. Fuis, P. Janicek, L. Houfek, Stress and Reliability Analyses of the Hip Joint Endoprosthesis Ceramic Head with Macro and Micro Shape Deviations, Proc. vol. 23, Issue 1-3, International Conference on Biomedical Engineering, Singapore (2008) 1580-1583.

[8] V. Fuis, Stress and reliability analyses of ceramic femoral heads with 3D manufacturing inaccuracies, 11th World Congress in Mechanism and Machine Science, Tianjin, China (2004) 2197-2201.

[9] A. F. McLean, D. L. Hartsock, Engineered materials handbook, Vol. 4, Ceramics and Glasses. ASM International (1991) 676-689.

[10] V. Fuis, T. Navrat, P. Hlavon et al., Reliability of the Ceramic Head of the Total Hip Joint Endoprosthesis Using Weibull's Weakest-link Theory, IFMBE Proc. vol. 14, World Congress on Medical Physics and Biomedical Engineering, Seoul, South Korea (2006) 2941-2944.

[11] V. Fuis, Tensile Stress Analysis of the Ceramic Head with Micro and Macro Shape Deviations of the Contact Areas, RECENT ADVANCES IN MECHATRONICS: 2008-2009, Proc. International Conference on Mechatronics, Brno, Czech Rep., (2009) 425-430.

[12] V. Fuis, J. Varga, Stress Analyses of the Hip Joint Endoprosthesis Ceramic Head with Different Shapes of the Cone Opening. 13th International Conference on Biomedical Engineering, IFMBE Proceedings, Vol. 23, Iss. 1-3, (2009) 2012-2015.

[13] L. Houfek, et al, Development of Experimental Devices for Testing of the Biomechanical Systems, Conference: 13th International Conference on Biomedical Engineering (ICBME), IFMBE Proceedings, Vol. 23, Issue 1-3, pp. 2005-2008, (2009).

Advanced Materials Research Vol. 936 (2014) pp 776-779
© (2014) Trans Tech Publications, Switzerland
doi:10.4028/www.scientific.net/AMR.936.776

Synthesis and Characterization of Amphiphilic Copolymer poly [2-(dimethylamino)ethyl methacrylate-Co-methyl Methacrylate]

FangPing Wang[a], Ting Yuan[b], Wanxia Li[c], Junying Zhang[d], Qi zhao Wang[e]

Key Laboratory of Bioelectrochemistry & Environmental Analysis of Gansu Province, Key Laboratory of Eco-Environment-Related Polymer Materials, Ministry of Education of China, College of Chemistry and Chemical Engineering,

Northwest Normal University, Anning Road 967,Lanzhou 730070, China

[a] wangfp@nwnu.edu.cn, [b] yuanting@163.com , [c] liwx@126.com

[d] zhangjunying@126.com , [e] wangqizhao@163.com

Keywords: Amphiphilic copolymer, RAFT, Polymerization, Methyl methacrylate

Abstract： A novel, well-defined, amphiphilic block copolymer was synthesized by RAFT copolymerization of 2-(dimethylamino) ethyl methacrylate (DMAEMA) and methyl methacrylate (MMA). The polymer structure was characterized by ^1H *NMR* , GPC and TEM. It was found that the stable spherical micelles with core-shell structure are formed and good solubility in water. The copolymer would have great potential in drug delivery systems.

Introduction

Amphiphilic copolymers are able to self-assemble into micelles having a hydrophobic inner core and a hydrophilic outer shell. In recent years, polymeric micelles used as nanoscale drug carriers have attracted much attention for their pharmaceutical or diagnostic applications [1] and a variety of anticancer drugs, such as paclitaxel [2] and doxorubicin [3, 4] were incorporated into the hydrophobic inner core for the controlled release. The precise control of polymer architectures as well as the properties of self-assembled micelles is of great importance for drug delivery [5-8].

Poly[2-(dimethylamino) ethyl methacrylate] (PDMAEMA) is a special polymer containing tertiary amino groups and exhibits pH-sensitivity which can be protonized in acidic solution [9-11]. Due to the unique property, a series of pH responsive copolymers have been synthesized from PDMAEMA for application as controlled drug delivery system [12-14].

In this study, a novel amphiphilic block copolymer(Poly (DMAEMA-co-MMA) was synthesized by RAFT and the structure was characterized by ^1H *NMR* , GPC and TEM. The amphiphilic copolymers are able to self-assemble into micelles having a hydrophobic inner core (MMA) and a hydrophilic (DMAEMA) outer shell. The results suggest that the micelles would have great potential in drug delivery systems.

Experimental

Materials

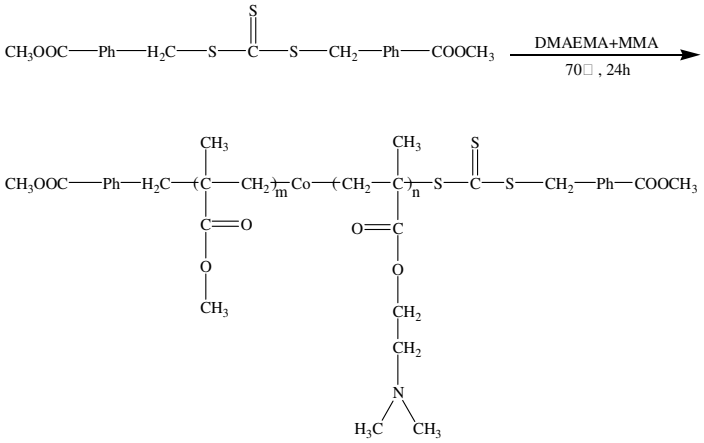
Trithiocarbonate RAFT agent had been synthesized in our laboratory according to the literature [15]. DMAEMA(Tianjin Fuchen Chemicals,China) and MMA(Tianjin Fuchen Chemicals,China) were dried over CaH_2 and distilled under reduced. All other reagents and solvents were used as received without further purification.

Measurements

Fourier transform infrared spectra were recorded on a Nicolet 670 spectrometer. The ^{1}H-NMR and measurements were obtained with a Mercury Plus AS400 spectrometer at room temperature in $CDCl_3$. GPC measurements were conducted on an Alli-ance GPCV2000 instrument (Milford, MA, USA) with THF as the eluent. TEM images were obtained using a JEM 1200 EX transmission electron microscope.

Copolymer Synthesis

The Amphiphilic copolymer Poly (DMAEMA-co-MMA) was synthesized by RAFT polymerization of 2-(dimethylamino) ethyl methacrylate (DMAEMA) and methyl Methacrylate (MMA). The reaction process as shown in Scheme 1.



Scheme 1 Synthesis of the Amphiphilic Poly(MMA-co-DMAEMA)

TEM Experiments

Transmission electron microscopy (TEM) was performed on a JEM 1200 EX, a drop of sample solution was placed onto a copper grid coated with carbon. Water was allowed to evaporate from the grids at room temperature.

Results and Discussion

1H NMR

The ^{1}H-NMR spectra of Poly(MMA-co-DMAEMA) is shown in Fig.1. The characteristic chemical shifts of polymer are clearly assigned: 0.871-1.291(-CCH_2C$\underline{H}_3$), 1.419-1.989(-CC$\underline{H}_2$CH_3), 2.01-2.364(-N(C$\underline{H}_3$)$_2$), 2.614(C$\underline{H}_2$N(CH_3)$_2$), 3.583 (-OCOC$\underline{H}_3$), 4.055 (-OCOC$\underline{H}_2$-), The ^{1}H NMR result is thus consistent with the structure of the copolymer.

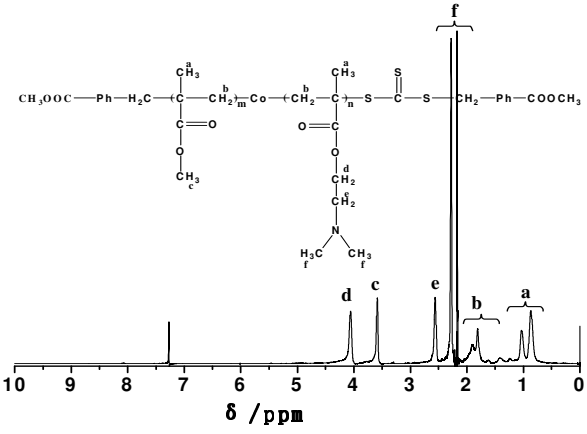


Fig. 1 ^{1}H-NMR spectra of the amphiphilic Poly(DMAEMA-co- MMA) in $CDCl_3$

GPC

The number-average molecular weight were determined by GPC with polystyrene standards to be 1.83×10^4 , weight-average molecular weight (Mw) / number-average molecular weight (Mn) =1.15. The GPC trace (Fig.2)of the graft copolymer showed a unimodal shape. This further indicated that the polymerization was completed successfully and that there was no homopolymer in the reaction product.

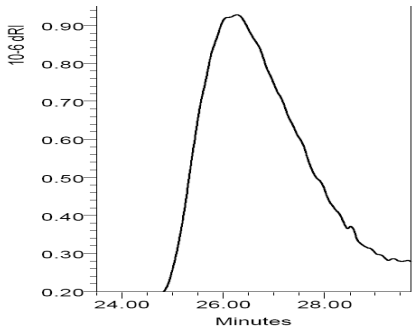


Fig. 2 GPC curve of the copolymer

TEM

The morphology of copolymer in aqueous solution was studied by TEM at room temperature are show in Fig.3. At a concentration of 1.0×10^{-4} g·mL^{-1} (Fig. 3a)， the micelles are globular, with the micellar size varying from 150 to 170 nm. Further increasing concentration, the micelles size start to increase, at a concentration of 3.0×10^{-4} g·mL^{-1}, the micelles are globular , with the micellar size varying from 300 to 320nm in Fig. 3b.

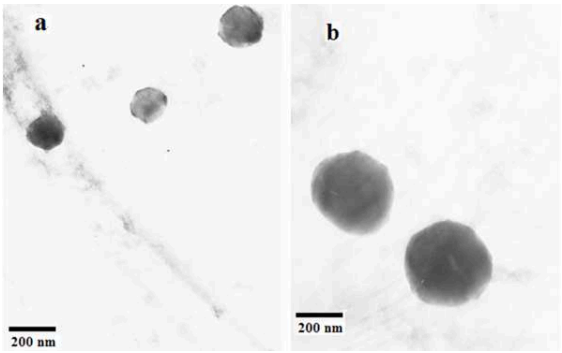


Fig. 3 TEM image of copolymer micelles in aqueous solution

Conclusions

In this study, a novel amphiphilic block copolymer Poly(MMA-co-DMAEMA) was successfully synthesized by RAFT copolymerization. The polymer structure was characterized by ^1H *NMR* , GPC and TEM. The results show that Poly(MMA-co-DMAEMA can form stable micelles in queous solution, the sizes of micelles was found to be related with the copolymer concentration, the sizes increased with concentration. More attention will be paid to the study of the supramolecular self-assembly behavior of the copolymer in aqueous solution and organic solvents in the future.

Acknowledgements

This work was financially supported by the National Natural Science Foundation of China (21065010, 51262028), the Key Laboratory of Eco-Environment-Related Polymer Materials Ministry of Education and the Key Laboratory of Polymer Materials of Gansu Province of China.

References

[1] W.Y. Seow, J.M. Xue, Y.Y. Yang: Biomaterials 28(2007), p.1730

[2] K.S. Soppimath, L.H. Liu, W.Y. Seow, S.Q. Liu, R. Powell, P. Chan, Y.Y. Yang: Adv Funct Mater 17(2007), p.355

[3] E.S. Lee, K. Na, Y.H. Bae: Nano Lett 5(2005), p.325

[4] Y.Z. Wang, L.Yu, L.M. Han, X.Y. Sha, X.L. Fang: Int J Pharm 337(2007), p.63

[5] J. Wang, R. Wang, L.B. Li: J Colloid Interface Sci 336(2009), p.808

[6] D. Velluto, C. Wandrey, D. Demurtas, J. Dubochet: J Control Release 137(2009), p.146

[7] Y. Yang, J.C. Wang, X. Zhang, W.L. Lu, Q. Zhang: J Control Release 135(2009), p.75

[8] C.F. Mu, P. Balakrishnan, F.D. Cui, Y.M. Yin, Y.B. Lee, H.G. Choi: Biomaterials 31(2010), p.2371

[9] S.D. Li, L. Huang : Mol Pharm 5(2008), p.496

[10] C.M. Hu, L.F. Zhang : Curr Drug Metab 10(2009), p.836

[11] S. Dai, P. Ravi, K.C. Tam: Soft Matter 4(2008), p.435

[12] B.Y. Zhang, W.D. He, W.T. Li, L.Y. Li, K.R. Zhang, H. Zhang: Polymer 51(2010), p.3039

[13] S.M.Timol, D. Jhurry: Eur Polym J 43(2007), p.3042

[14] J. Chen, M.Z. Liu, N.Y. Zhang, P.P. Dai, C.M. Gao, L.W. Ma, H.L. Liu: Sens Actuators B 149(2010), p.34

[15] A. Naoto, E. Takeshi: Journal of Polymer Science: Part A: Polymer Chemistry, 47(2009), p.3702

Advanced Materials Research Vol. 936 (2014) pp 780-783
© (2014) Trans Tech Publications, Switzerland
doi:10.4028/www.scientific.net/AMR.936.780

Assessment Antibacterial Activities on Essential Oil of Plant Extract

Chih-Chung Shiao[1,2], Chih-Ming Ma[1,a], Bor-Yann Chen[3,b] , Hua-Wei Chen[1,a]

[1]Department of Cosmetic Application and Management, St. Mary's Junior College of Medicine, Nursing and Management, No. 100, Lane 265, San-Shing Rd., Sec.2, San-Shing Shiang, Yilan, 266, Taiwan

[2]Department of Internal Medicine, Saint Mary's Hospital Luodong, No. 160 Chong-Cheng South Road, Loudong 265, Yilan, Taiwan.

[3]Department of Chemical and Materials Engineering, National I-Lan University, No. 1 Sheen-Long Road, I-Lan City, 260, Taiwan

Corresponding author: [a]cmma@smc.edu.tw, [b]bychen@niu.edu.tw

Keywords: antibacterial, essential oil, Eugenol

Abstract. Essential oils are produced by plants for many reasons including protection against various bacterial and fungal. This study provides a dose-response analysis for antibacterial activity assessment using *Escherichia coli* DH5 as indicator microorganism. In this work it has been shown that it is possible to extract antibacterial activities using a simple process.

Introduction

The essential oils are volatile liquids extracted from various plants that generally grow in tropical countries [1]. Plant essential oil is reported to be a rich source of bioactive compounds like benzalde-hyde, carvacrol, carvone, cineole, cinnamaldehyde, citral, cymene, estragole, eugenol, geraniol, limonene, menthol, pinene, terpenene,terpineol, thymol and vanillin. These bioactive compounds of plant origin exhibit antibacterial, antifungal, antigiardia and antioxidant. Plant essential oils are potentially useful sources of naturally derived antimicrobial compounds. They not only have pleasant fragrances, but also possess many useful biological activities [2-5]. The essential oils from a number of aromatic crops are extracted through steam distillation, with each plant species often having a distinct temperature and duration of the distillation process. The steam distillation of any aromatic crop results in four products: (i) essential oil; (ii) steam-distilled (residual) plant material; (iii) residual water; and (iv) hydrolat. Eugenol (4-allyl-2- methoxyphenol) is the major constituent of several important essential oils such as clove, pimento berry, bay, nutmeg and cinnamon oil. It is commonly used as a fragrance and flavoring agent in a variety of cosmetics, and food products. Eugenol has shown antimicrobial, antioxidant, anti-inflammatory, antispas- modic, antidepressant, antigenotoxic, and anticarcinogenic properties [1, 6] .

The essential oils from plants play an important role in medicine and cosmetic industry. Since their discovery, antimicrobial drugs have proved remarkably effective for the control of bacterial infections. The antimicrobial compounds from plants may inhibit bacterial growth by different mechanisms than those presently used antimicrobials and may have a significant clinical value in treatment of resistant microbial strains. Examples of some microorganisms that gained resistance to antimicrobials are: *Escherichia coli* and *Streptococcus faecalis.* This study provides dose-response relations which are regularly used in antibacterial activity, as a quantitative analysis to show the criteria of 50% effective concentration EC_{50} [7]. The principle of antibacterial activity indicated that for all materials there is a minimum concentration. In this study, the essential oil extraction technique was used steam distillation; the aim of this work was to evaluate the influence of essential oil and eugenol of antibacterial activities.

Materials and Methods

Fresh plant (200 g) was placed in a flask which was connected to a boiler. The steam was produced in the boiler by electrical heating of distilled water. As the water started to boil, the vapor from the boiler went through the fresh plant. Then the vapor and the essential oil extracted from the plant passed through the cooler, where both the oil and water were condensed and collected (Fig. 1). The operation lasted 2 h.

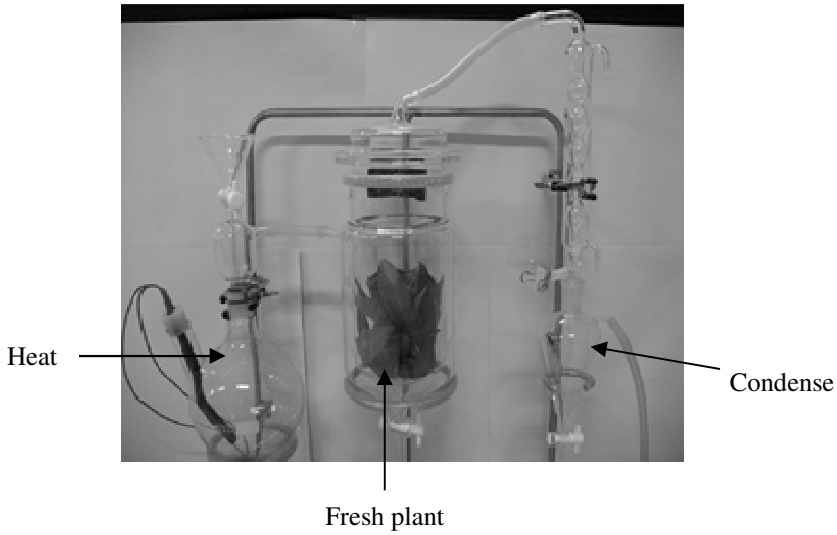


Fig. 1 Experiment equipment

As E. coli is commonly found in the lower intestine of human body, we intentionally selected E. coli as an indicator microorganism to reveal preliminary screening of antibacterial activity of plant extracts. The E. coli DH5α used in this study was provided by Professor Bor-Yann Chen, NIU, Taiwan. E. coli DH5α was pre-cultured in Luria-Bertani (LB) broth (10 g/L tryptone, 5 g/L yeast extract, 10 g/L NaCl) at 37 °C, 125 rpm for 12 h. All the essential oils used in this study were high-purity liquid from steam distillation method. Each essential oils was diluted to various concentrations, and mixed with sodium citrate buffer solution, 0.5× LB, and deionized water to formulate essential oil solutions ranging between 0 mg/L and 2000 mg/L. Subsequently, cultured E. coli DH5α solutions were added to each essential oil solution at a volume ratio of 1:100. The E. coli DH5α concentration was then determined by measuring the of the cell solution optical density (OD) value every 30 min for the initial 5 h, and then every 1 h up until 24 h. The cell solution OD value was measured at 600 nm (OD600) in a spectrophotometer (GENESYS 20, Thermo Scientific) using cultured broth as the blank cuvette [8-9].

Results and Discussion

Probit analysis [10] was adopted to reveal dose response curves of various metal ions. The probit model postulates that the tolerance capacity of individuals in response to toxic material in a given population is Log-normal distribution. A semilogarithmic plot of metal concentration versus the provoked response is assumed to reveal a linear relation. The probit model converts sigmoid-shaped dose-response curve into a linear normal equivalent deviation scale. For example, the 50% and 84.1% response correspond to the NED scale in 0 and 1, respectively. In addition, a probit unit in the model equals NED scale plus 5. The conversion formula are shown as follows:

$$Y = A + B \log_{10} Z$$

$$P = \frac{1}{2}\left\{1 + erf\left(\frac{Y-5}{\sqrt{2}}\right)\right\}$$

$$erf(x) = \frac{2}{\sqrt{\pi}}\int_0^x e^{-\xi^2} d\xi$$

where A and B denote the intercept and slope of dose–response relation, Z and Y are metal concentration (mg/l) and probit unit, respectively; P is the response (%) corresponding to administered metal, erf(x) is an error function. Note that the response variable is normalized to be located between 0 and 1. The conversion relation between the probit unit and provoked response is listed in Table 1. For example, 55 and 85% of response correspond to probit unit of 5.13 and 6.04, respectively. The responses for antibacterial activities are determined by $1-\mu/\mu_0$ and $1-L_0/L$, respectively, where μ and L denote the maximum specific growth rate and the adaptation lag time. [8-9].

TABLE 1. CONVERSION RELATION BETWEEN ANTIBACTERIAL ACTIVITIES RESPONSE (%) AND PROBIT UNIT

%.	0	1	2	3	4	5	6	7	8	9
0	2.60	2.67	2.95	3.12	3.25	3.36	3.45	3.52	3.59	3.66
10	3.72	3.77	3.82	3.87	3.92	3.96	4.01	4.05	4.08	4.12
20	4.16	4.19	4.23	4.26	4.29	4.33	4.36	4.39	4.42	4.45
30	4.48	4.50	4.53	4.56	4.59	4.61	4.64	4.67	4.69	4.72
40	4.75	4.77	4.80	4.82	4.85	4.87	4.90	4.92	4.95	4.97
50	5.00	5.03	5.05	5.08	5.10	5.13	5.15	5.18	5.20	5.23
60	5.25	5.28	5.31	5.33	5.36	5.39	5.41	5.44	5.47	5.50
70	5.52	5.55	5.58	5.61	5.64	5.67	5.71	5.74	5.77	5.81
80	5.84	5.88	5.92	5.95	5.99	6.04	6.08	6.13	6.18	6.23
90	6.28	6.34	6.41	6.48	6.55	6.64	6.75	6.88	7.05	7.33
100	8.10									

Probit unit of 2.60, 4.16 and 5.00 correspond to the threshold (bottom; EC0), EC20 and median effective response (EC50), respectively. (Chen et al., 2004, 2006).

The conversion relation between the probit unit and response could be calculated from Eqs. (1)-(3) and simulated results were listed in Table 2. As indicated in Table 2 for antibacterial activities of essential oils, EC_{20} and EC_{50} values all point to the essential oils series being *Eugenol* > *Melaleuca alternifolia essential oil* > *Basil essential oil*.

TABLE 2. CRITICAL EFFECTIVE CONCENTRATIONS OF 'ANTIBACTERIAL ACTIVITIES' PREDICTED FROM THE PROBIT MODEL

	EC_{20}(mg L^{-1})	EC_{50}(mg L^{-1})
Eugenol	718.7	1463.5
Basil essential oil	987.2	1724.3
Melaleuca alternifolia essential oil	930.4	1682.6

Summary

In recent years, the essential oils and the herbal extracts from various plants have attracted a great deal of scientific interest due to their potential as a source of natural agents to increase the safety and shelf life of cosmetic active compounds. In this work it has been shown that it is possible to extract antibacterial activities using a simple process (steam distillation extraction). Based on these conclusions, future investigations will focus the research on the in extraction techniques and on chemical identification of the antimicrobial ingredients.

References

[1] N. Chaibakhsh, M. Basri, S. H. M. Anuar, M. B. A. Rahman and M. Rezayee, Optimization of enzymatic synthesis of eugenol ester using statistical approaches, Biocatalysis and Agricultural Biotechnology. 1 (2012) 226-231.

[2] A. Wattanasatchaa, S. Rengpipatb and S. Wanichwecharungruang, Thymol nanospheres as an effective anti-bacterial agent, Int. J. Pharm. 434 (2012) 360-365.

[3] J. Maree, G. Kamatou, S. Gibbons, A. Viljoena and S. V. Vuuren, The application of GC-MS combined with chemometrics for the identification of antimicrobial compounds from selected commercial essential oils, Chemometrics Intell. Lab. Syst. 130 (2014) 172-181.

[4] P. Goni, P. Lopez b, C. Sanchez, R. Gomez-Lus, R. Becerril and C. Nerin, Antimicrobial activity in the vapour phase of a combination of cinnamon and clove essential oils, Food Chem. 116 (2009) 982-989.

[5] V. Ghosh, A. Mukherjee and N. Chandrasekaran, Eugenol-loaded antimicrobial nanoemulsion preserves fruit juiceagainst, microbial spoilage, Colloids and Surfaces B: Biointerfaces, 114 (2014) 392-397.

[6] A. Navarrete, M. Herrero, A. Martin, M. J. Cocero and E. Ibanez, Valorization of solid wastes from essential oil industry, J. Food Eng. 104 (2011) 196-201.

[7] B. Y. Chen, Induction threshold of the Q mutant of bacteriophage in *Escherichia coli*. Biotechnol Tech. 11 (1997) 709-12.

[8] B. Y. Chen, H. L. Liu, Y. W. Chen and Y. C. Cheng, Dose–response assessment of metal toxicity upon indigenous *Thiobacillus thiooxidans* BC1, Process Biochemistry 39 (2004) 735-745.

[9] Chen BY, Chang JS. Characterization and theoretical analysis on toxicological threshold of mercuric ions to *Pseudomonas aeruginosa* PU21 (Rip64). Bioproc. Eng. 23 (2000) 675-80.

[10] Finney DJ. Probit analysis. London: Cambridge Univ. Press, 1971.

Advanced Materials Research Vol. 936 (2014) pp 784-788
© (2014) Trans Tech Publications, Switzerland
doi:10.4028/www.scientific.net/AMR.936.784

Preparation, Characterization of Cellulose Fibers Grafting by β-cyclodextrin and Their Application for Antibacterial Products

Chao Dong[1,a], Ying Ye[1,b], Liying Qian[1,c*], Beihai He[1,d], Huining Xiao[2,e]

[1]State Key Laboratory of Pulping and Papermaking Engineering, South China University of Technology, Guangzhou, 510640, PR China

[2]Department of Chemical Engineering, University of New Brunswick, Fredericton, N.B., Canada E3B 5A3

[a]Cdong2012@126.com,[b]105460562@qq.com, [c*]lyqian@scut.edu.cn, [d]ppebhhe@scut.edu.cn, [e]hxiao@unb.ca

Keywords: cellulose fibers; β-cyclodextrin; FTIR; CP-MAS NMR; antibacterial activity

Abstract: Cyclodextrins (CDs) can form inclusion complexes with a variety of molecules making them very attractive in different areas, such as pharmaceutics, biochemistry, food chemistry and papermaking. In this communication the preparation of β-cyclodextrin-grafted cellulose fibers was carried out by reacting β-cyclodextrin with cellulose fiber via citric acid (CA). Both fourier transform infrared (FTIR) and cross polarization magic angle spinning solid state nuclear magnetic resonance (CP-MAS NMR) indicated that β-CDs had been chemically attached to cellulose backbone through the formation of ester bonds. Furthermore, the β-CD-grafted cellulose fibers formed inclusion complexes with ciprofloxacin hydrochloride (CipHCl). And the β-CD-grafted cellulose fibers loaded with CipHCl showed excellent antibacterial activity against *E.coli* and *S.aureus*.

Introduction

β-Cyclodextrins (β-CDs) are cyclic oligosaccharides containing seven D-glucose units linked by α-1, 4 glycosidic bonds and they contain a hydrophobic cavity which can entrap small molecules. β-CDs can also be grafted onto macromolecules with cross-linkers to make the substrate functionalized by hosting some small agents [1,2].

Cellulose is the abundant natural polymers on earth. It is virtual and inexhaustible source of raw materials for environmentally friendly, biocompatible, renewable and modifiable polymers which makes it one of the most promising feedstocks for industry in the future [3]. In order to increase the functionality of cellulose, synthesis procedures have been developed. In fact, the modification and functionalization of nature fibers with CDs is being implemented. A number of cross-linking agents are utilized to graft β-CD onto cellulose, such as epichlorohydrin, cyanuric chloride, N-methylol acrylamide, polycarboxylic acids [4-6]. In this paper, β-CD was grafted onto the cellulose fiber with citric acid as cross-linkage, and the modified cellulose fibers were characterized by means of FTIR spectroscopy, solid-state NMR, TGA and SEM. Moreover, ciprofloxacin hydrochloride was loaded into grafted β-CD to obtain the antimicrobial cellulose fiber and the inhibition activities of β-CD grafted cellulose fibers containing the antibiotics against gram-negative and gram-positive bacteria were also investigated.

Experimental Procedure

β-cyclodextrin citrate (CA-β-CD) was prepared firstly by semidry reaction between β-CD and citrate acid [7]. The obtained CA-β-CD (0.3g) and SHP (0.1g) was dissolved in distilled water (10mL), followed by adding cellulose fiber (1.0g) and cured at 160℃ for 15 min. FT-IR (Vector 33; Bruker) and solid-state CP/MAS ^{13}C-NMR (AVANCE 300; Bruker) was applied to characterize the structures of modified cellulose fibers. Thermal analysis was performed using TGA (Q500, TA Instruments) and the morphology of modified cellulose fibers was investigated by SEM (S3700, Hitachi).

β-cyclodextrin-grafted cellulose fibers (1g) were immersed into CipHCl aqueous solution (100mg/g oven dry fiber) for 4h. The obtained samples were washed with distilled water and dried at 60℃ for 24h.

The inhibition efficiency of the cellulose fibers with antibiotics against *E.coli* was assessed with a shaking flask method [8].

Results and Discussion

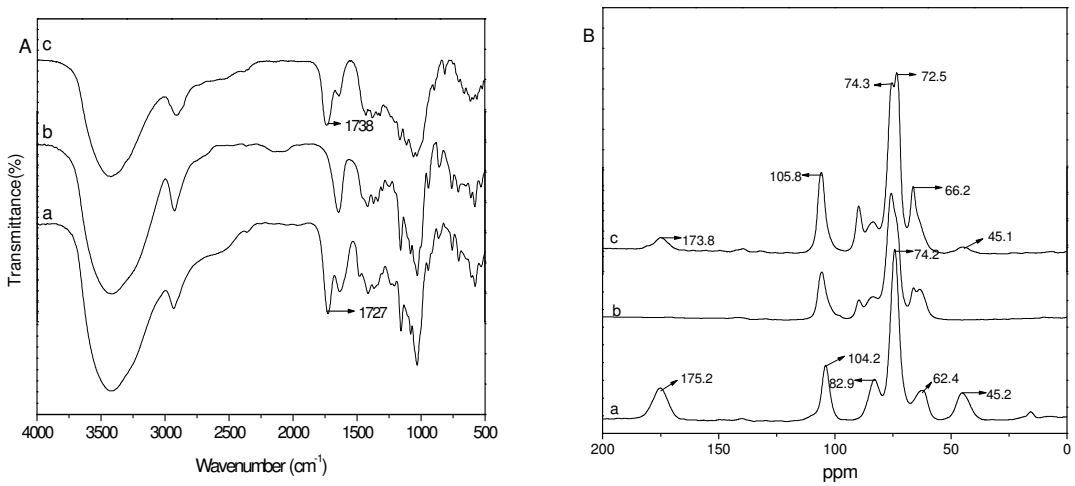


Fig. 1 FT-IR spectra (A) and solid-state CP/MAS ^{13}C-NMR spectra (B) of CA-β-CD (a), native cellulose fibers (b) and β-CD-grafted cellulose fibers (c)

The FT-IR spectra of CA-β-CD, native cellulose fibers and β-CD-grafted cellulose fibers are shown in Fig. 1A. For the free β-CD, the adsorption at 3404, 2933, 1416, 1370, 1180, 1029 cm^{-1} are an indicative of β-CD [9]. Comparatively, the bands in CA-β-CD are qualitatively the same except a new vibration at 1727cm^{-1}, which is indicative of ester group, suggesting that esterification reaction occurred between β-CD and CA. From the spectra of unmodified and modified cellulose fibers, A new vibration at 1738 cm^{-1} can be observed in modified cellulose fibers and assigned to a C=O stretching vibration mode characteristic for an ester bond. This suggests that the carboxylic acid from CA-β-CD forms ester bonds with the hydroxyl groups from cellulose fiber at elevated temperature. The results showed that β-CD had been successfully grafted onto cellulose fiber by this approach.

The esterification has also been confirmed by solid-state CP/MAS ^{13}C-NMR spectra (Fig.2 B). It has already been shown that the spectra of the free β-CD is relatively poorly resolved due to the presence of multiple resonances for the C-atoms of the glucose unites (C2, C3, C3,C4, C5 and C6), which can be ascribe to the co-existence of different structural arrangements induced by partial

hydration of the sample [10]. The signals between 55 and 110ppm are assigned to the C-atoms, and the assignments of each carbon were made with reference to the literature [11]. Compared with the free β-CD, a significant signal is present at 175.2ppm assigned to carbonyl group, indicating that the esterification reaction occurred between β-CD and CA. For the cellulose fibers，the signals between 55 and 110 ppm are attributed to carbon in the carbohydrate, while the small signal peaks between 110 and 160ppm are assigned to carbon of lignin. The next two peaks at 74.8 and 72.5 ppm are from cellulose C2 and C3. Finally, the peak at 105.8 ppm is due to the C1 of cellulose. Comparatively, a new signal at 173.8 ppm is assigned to the carbonyl group of modified cellulose fibers for an ester bond which confirms the reaction between carboxylic acid from CA-β-CD and hydroxyl groups from cellulose fibers. In addition, an obvious signal at 45.1 ppm is due to $–CH_2$ from CA. This also confirmed the reaction between CA-β-CD and cellulose, therefore β-CD was grafted onto cellulose fibers with citric acid as a bridging.

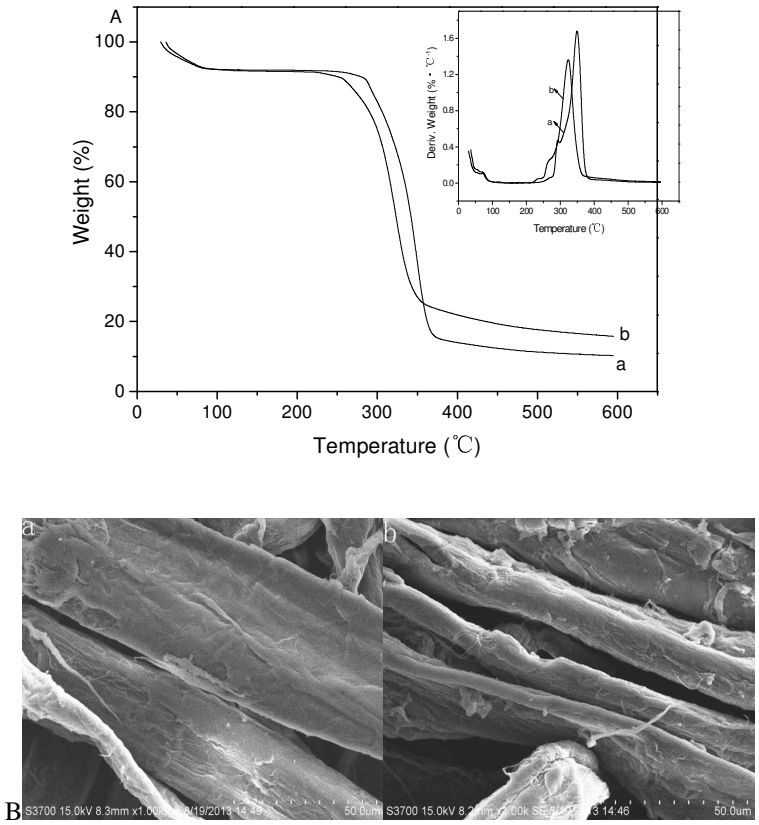


Fig. 2 TG and DTG (A) profiles and SEM (B) of native cellulose fibers (a), β-CD-grafted cellulose fibers (b)

The thermogravimetric behaviors of native cellulose fibers and cellulose fibers grafted with β-CD are illustrated in Fig. 2A. Two degradation steps can be observed up to 600℃: the first one at a temperature around 100℃ is due to the loss of water evaporation, while the second one is due to the start decomposition of various compositions in samples. The remainder weights at 600℃ were 11% and 13% for native cellulose fibers and β-CD-grafted cellulose fibers, respectively. Moreover, the temperatures at the maximum degradation rate (T_{max}) of all samples were determined from the maximum of DTG curves. The peaks corresponding to the maximum weight loss rate were present 350℃ with 60% weight loss for native cellulose fibers, while at 292℃ with 15% weight loss and 348℃with 63% weight loss for cellulose fibers grafted with β-CD. The incorporation of β-CD into cellulose fibers lead to a decrease in the T_{max}, which might be attributed to the presence of β-CD and an increase in the disorder of cellulose molecular packing.

Fig. 2B shows the morphologies of cellulose fibers before and after modification. The morphology of cellulose fibers after esterification is similar with unmodified cellulose fibers because of the occurrence of chemical modification on the surface of cellulose fibers and no serious disruption inside.

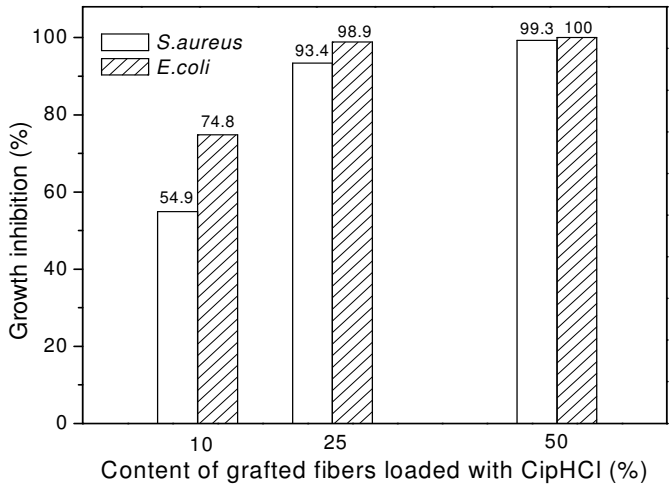


Fig. 3 Effect of β-CD grafted fibers loaded with CipHCl content on the growth inhibition of sheets against E.coli and S.aureu

The effect of modified cellulose fiber content on the growth inhibition of sheets with the shaking flask method is shown in Fig. 3. With the increasing of modified cellulose fiber content, the growth inhibition against *E.coli* and *S.aureu* both increase. The growth inhibition against *E.coli* and *S.aureu* both reach about 100% when modified cellulose fiber content is 50%, suggesting that all the bacteria were killed. Moreover, the growth inhibition of sheets against *E.coli* is higher than that against *S.aureu*, probably due to the difference in walls between Gram-negative and Gram-positive bacteria.

Conclusion

Cellulose functionalization is still a hot topic. FTIR and solid-state CP/MAS ^{13}C-NMR showed that β-cyclodextrin had been successfully grafted onto cellulose fibers. And the β-CD grafted fibers loaded with CipHCl exhibited excellent antibacterial activities against *E.coli* and *S.aureus*. This approach opens the way to develop antibacterial paper products that may be useful to prevent wound and nosocomial infections in medical and packaging fields.

Acknowledgement

This work was supported by the grants from the National Natural Science Foundation of China (Grant No.31200457), NSERC SENTINEL Bioactive Paper Network (Canada) and the Fundamental Research Funds for the Central Universities (2013ZZ0072).

References

[1] R. Peila, C. Vineis, A. Varesano. Different methods for β-cyclodextrin/triclosan complexation as antibacterial treatment of cellulose substrate, Cellulose. 20 (2013) 1-9.

[2] G. Astray, C. Gonzalez-Barreiro, J.C. Mejuto, et al. A review on the use of cyclodextrins in foods, Food Hydrocolloids. 23 (2009) 1631-1640.

[3] B. Medronho, R. Andrade, V. Vivod, et al. Cyclodextrin-grafted cellulose: Physico-chemical characterization, Carbohydr. Polym. 93(2013) 324-330.

[4] J. Szejtli. Introduction and general overview of cyclodextrin chemistry, Chem. Rev. 98 (1998) 1743-1753.

[5] M.H. Lee, K.J. Yoon, S. Ko. Synthesis of a vinyl monomer containing β-cyclodextrin and grafting onto cotton fiber, J. Appl. Polym. Sci. 80 (2001) 438-446.

[6] B. Martel, M. Weltrowski, D. Ruffin, et al. Polycarboxylic acids as crosslinking agents for grafting cyclodextrins onto cotton and wool fabrics: study of the process parameters, J. Appl. Polym. Sci. 83 (2002) 1449-1456.

[7] K. El-Tahlawy, M.A. Gaffar, S. El-Rafie. Novel method for preparation of β-cyclodextrin/grafted chitosan and it's application, Carbohydr. Polym. 63 (2006) 385-392.

[8] L. Qian, Y. Guan, Z. Ziaee, et al. Rendering cellulose fibers antimicrobial using cationic β-cyclodextrin-based polymers included with antibiotics, Cellulose. 16 (2009) 309-317.

[9] A. Rukmani, M. Sundrarajan. Inclusion of antibacterial agent thymol on β-cyclodextrin-grafted organic cotton, J. Ind. Text. 42 (2012) 132-144.

[10] A.H. Karoyo, P.S. Sidhu, L. Wilson, et al. Characterization and dynamic properties for the solid inclusion complexes of β-cyclodextrin and perfluorooctanoic acid, J. Phys. Chem. B. 16 (2013) 8269-8282.

[11] A.I. Ramos, T.M. Braga, J.A. Fernandes, et al. Analysis of the microcrystalline inclusion compounds of triclosan with β-cyclodextrin and its tris-O-methylated derivative, J. Pharm. Biomed. Anal. 30 (2013) 34-43.

Advanced Materials Research Vol. 936 (2014) pp 789-794
© (2014) Trans Tech Publications, Switzerland
doi:10.4028/www.scientific.net/AMR.936.789

Detoxification Capabilities of Adsorbents for Artificial Liver Support Devices: A Comparison

Weiping Ding[1, a], Lili Zou[1], Yingying Pei[1], Sijie Sun[2] and Dayong Gao[2]

[1]Center for Biomedical Engineering, Department of Electronic Science and Technology, University of Science and Technology of China, Hefei, Anhui 230027, China

[2]Department of Bioengineering, University of Washington, Seattle, WA 98195, USA

[a] Corresponding Author: wpdings@ustc.edu.cn

Keywords: adsorption; artificial liver; equilibrium isotherm; kinetic adsorption; toxin

Abstract: Adsorption performances of activated carbon Norit RO 0.8, neutral resin Amberlite XAD-7, anion resin Dowex 1x4 and cation resin Dowex 50wx4 were investigated in detail for artificial liver support devices. Firstly, equilibrium adsorption experiments of these adsorbents to albumin, creatinine, bilirubin, tryptophan and cholic acid were conducted respectively. Then their adsorption capacities were obtained by curve fitting. The results indicate that activated carbon Norit RO 0.8 and anion resin Dowex 1x4 are two better adsorbents for removing toxins. Lastly, adsorption rate constants of activated carbon Norit RO 0.8 and anion resin Dowex 1x4 to all above solutes were studied with pseudo-first and second-order kinetic adsorption models. The results show that the toxin adsorption rate of anion resin Dowex 1x4 is faster than that of activated carbon Norit RO 0.8. The systematical experimental results in this paper are very important references for researchers in the field of blood purification based on adsorption technology.

Introduction

Adsorbents are key parts of artificial liver support devices. They dominate the clearance of toxins in patients with liver failure. Therefore, the selection of adsorbents is very crucial. Since the concept of adsorption is introduced into artificial liver devices, many efforts have been focusing on the selection/search of adsorbents with specific adsorption, high adsorption capacity and good biocompatibility.

Activated carbon is a widely used adsorbent in artificial liver support devices [1-3]. Generally, powdered activated carbon, because of its large surface area, can removed more toxins than granular activated carbon; however, it easily causes a large pressure drop across the detoxifying column [4]. In order to improve biocompatibility, activated carbon usually is coated with albumin or cellulose [5]. Activated carbon is a non-specific adsorbent. It removes not only harmful toxins but also useful substances. In order to improve specificity, lots of resins are being tried. There are three types of resins: anion, neutral and cation. In general, anion exchange resin are used to remove protein-bound toxins, e.g. bile acids; cation exchange resins are for ammonium [6]; neutral resins are for the adsorption of water-insoluble substances, e.g. aromatic amino acids [7]. As ammonium can be removed by dialysis, cation exchange resin could be of no major benefit to the liver therapy [6]. Currently, Molecular Adsorbent Recirculating System uses activated carbon and anion exchange resin whereas Prometheus System uses neutral and anion exchange resins [8, 9]. Although various adsorbents are investigated in/for artificial liver support devices, the study of the measurement of the basic adsorption parameters of these adsorbents is scattered and also is relatively little in the literature.

The measurement of adsorption parameters of adsorbents to toxins is a basic and important research. It not only can estimate the use or regeneration time of adsorbent cartridges for artificial liver support devices, but also can facilitate the development of mathematical models to predict the adsorption efficiency of artificial liver support devices. In this paper, based on the literature, four typical adsorbents i.e. activated carbon Norit RO 0.8, neutral resin Amberlite XAD-7, anion resin

Dowex 1x4 and cation resin Dowex 50wx4 were chosen as candidates because of their highly frequent appearance in removing harmful substances or drugs. Then, adsorption parameters i.e. adsorption capacities and kinetic adsorption rate constants of these adsorbents to albumin, creatinine, bilirubin, tryptophan and cholic acid were studied systematically.

Materials and Methods

Bovine serum albumin (Cohn fraction V, MW = 66,000), creatinine, tryptophan, cholic acid, dimethyl sulfoxide (DMSO, ≥99.5%), sodium carbonate (anhydrous, ≥99.95%), activated carbon (Norit® RO 0.8), resins Amberlite XAD-7 Dowex 1x4 and 50wx4 were bought from Sigma-Aldrich, USA. Bilirubin (MW = 584.68) was from VWR, USA. Hydrochloride acid (1.0N) was purchased from Chemistry Store at the University of Washington. The hemodialyzer was Gambro® Phoenix™.

Batch experiments were performed to determine all adsorption parameters. Each adsorption experiment generally includes five steps: adsorbent preparation, solution preparation, equilibrium/kinetic adsorption, concentration test, and data analysis. All kinetic adsorption experiments almost were the same as equilibrium experiments except that the real-time samples were taken from flasks quickly. Take the case of bilirubin adsorption onto activated carbon, detailed operations are as follows:

Activated Carbon Preparation

Before experiments, a given amount of activated carbon (dry), e.g. 0.5g, was weighed and placed in a 50 ml plastic tube flask. Dialysate, prepared from the Gambro machine, was added into the tube and the tube was placed for at least 48h to remove air bubble and then was washed to remove carbon ash and small debris. Generally, for each case, at least 5 concentration situations were considered, so 5 activated carbon samples were prepared. Sometimes 5 concentrations were not enough to determine the adsorption parameters. Under this situation, multiple concentrations were conducted.

Bilirubin Solution Preparation

First, dialysate was produced by the hemodialysis machine. Second, it was used to prepare the bilirubin mother solution with 2% albumin and 200mg/l bilirubin (During the process, DMSO was added into the weight boat to dissolve the bilirubin powder, 0.25M Na_2CO_3 solution was used to help dissolution, and 1.0N HCl solution was added drop by drop to adjust the pH value of the solution to about 7.3). Third, according to the experimental requirement, the bilirubin mother solution was diluted step by step to obtain serial concentrations with the 2% albumin solution, e.g., 200, 150, 100, 50, 10mg/l.

Bilirubin Adsorption

Before experiments, dialysate in each sample tube was carefully sucked out using pipettes. Then, for each solution, take one sample for testing the initial concentration and add the given volume (usually 25ml) into one tube. Finally all tubes were horizontally placed on an oscillator shaker with 60rpm (KJ-201BJ). Samples were taken after 24 hours in equilibrium experiments or at desired time in kinetic experiments. All experiments were repeated at least 3 times.

Bilirubin Concentration Test

The spectrophotometer (Spectra Max 190) was used to test all concentrations of solutes. All samples were tested in 3 days. Albumin (BCG), creatinine and total bilirubin (Diazonium Salt) reagents were from Fisher Scientific, USA. All methods for testing solute concentrations were from the product specifications or [10]. Each sample was tested at least 3 times and an average value was used.

Equilibrium Isotherm

The Langmuir isotherm is a simple model frequently used to understand adsorption under a variety of situations. Although one might like to use other adsorption isotherms such as the Freundlich isotherm and the Toth isotherm to describe the adsorption phenomena, in all cases except bilirubin in this study, the Langmuir isotherm is good enough. The Langmuir equation is expressed as $q_e=ac_e/(1+bc_e)=q_mbc_e/(1+bc_e)$, where, q_e (mg/g) is the toxin adsorbed by an adsorbent at equilibrium,

c_e (mg/l) the toxin concentration at equilibrium, q_m (mg/g) the maximum value of the toxin adsorbed by an adsorbent (on the first layer), a the fitted constant, and b the fitted constant.

Regarding the bilirubin adsorption, the Langmuir isotherm is used under the condition of low bilirubin concentrations [11]; however, in the broad range of bilirubin concentrations, the experimental results could be apt to BET isotherm [12]. The Langmuir isotherm is a monolayer model whereas the BET isotherm is a multilayer adsorption model. In this study, the modified BET isotherm for the liquid phase adsorption was used [13]: $q_e=q_m k_s c_e/[(1-k_l c_e)(1-k_l c_e+k_s c_e)]$, where, k_l and k_s are constants.

Kinetic Adsorption

Several kinetic models can be used to examine the mechanism of adsorption process. In this study, pseudo-first-order and pseudo-second-order equations, which derive from chemical/reaction kinetics, were used. The pseudo-first and second-order equations [14, 15] are expressed as $dq_t/dt = k_1(q_e-q_t)$ and $dq_t/dt = k_2(q_e-q_t)^2$, respectively, where, q_e and q_t are the toxins adsorbed at equilibrium and time t, respectively, k_1 and k_2 the fitted rate constants of pseudo-first and second-order adsorptions, respectively.

Results and discussion

Adsorption capacity is an important parameter for artificial liver support devices. In this study, equilibrium adsorption experiments were conducted. Fig.1 shows two typical examples of equilibrium isotherms with respect to different adsorbents. Equilibrium adsorptions of all solutes except bilirubin can be described by the Langmuir isotherm. Compared to the cholic acid adsorption (Fig.1, left), the bilirubin adsorption isotherms are more complicated (Fig.1, right). The results show that when the resin Dowex 1x4 or 50wx4 is used, the experimental adsorption curve agrees with the Langmuir isotherm. However, when activated carbon or resin XAD-7 is used, it is apt to the BET isotherm.

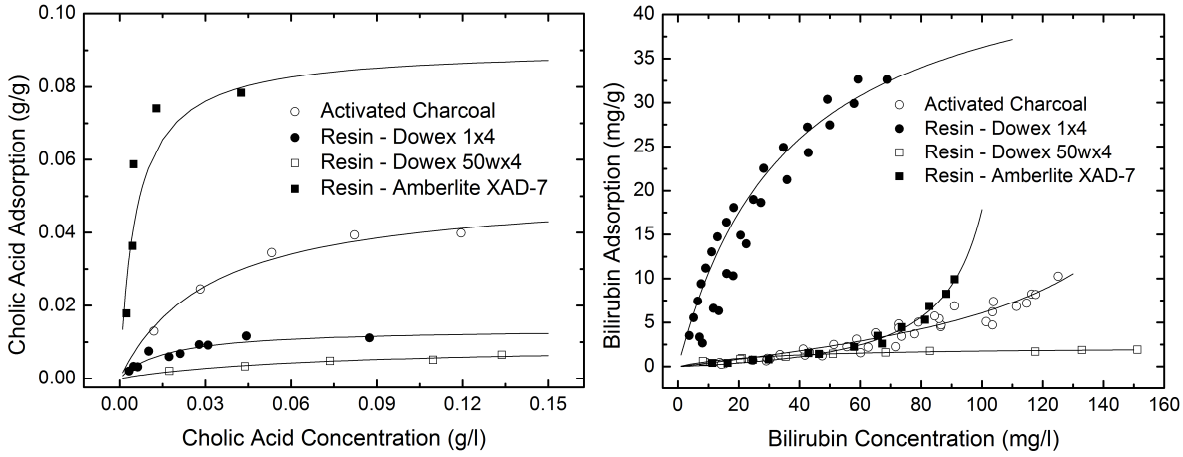


Figure 1 Equilibrium adsorption of cholic acid (left) and bilirubin (right)

Bilirubin is a specific albumin-bound toxin. Comparing to tryptophan and cholic acid, its solubility is relatively low. Without the help of albumin, it is hard to be dissolved. Therefore, the adsorption of bilirubin strongly depends on albumin conditions. Activated carbon or resin XAD-7 can absorb albumin molecules only in large pores. In the space with small pores, almost no carriers, i.e. albumin molecules appear. For free bilirubin molecules in the internal space, they have two possible directions to go. One is to arrive at the void site in small pores; the other is to reunite with bilirubin already adsorbed on the surface and form multilayer adsorption. The tendency depends on affinity. Possibly, the affinity between bilirubin and activate carbon or resin XAD-7 is weaker than that between bilirubin molecules. As time goes on, the bilirubin multilayer adsorption becomes more and more notable. Finally, the adsorption isotherm is similar to BET. The affinity between bilirubin and resin 1x4 could be stronger. Then, the adsorption of bilirubin onto resin 1x4 is close to the Langmuir isotherm.

Adsorption capacities of all adsorbents were obtained by curve fitting, which are listed in Tables 1 and 2. The results indicate that creatinine is only adsorbed by activated carbon. Resin XAD-7 adsorbs a lot of albumin whereas others slightly adsorb albumin. Tryptophan is mainly adsorbed by activated carbon. For the removal of cholic acid, activated carbon and resin XAD-7 are better choices. With respect to bilirubin, the best adsorbent is resin 1x4.

Albumin is a very important protein in carrying non-water-soluble toxins. The loss of albumin is not expected during the treatment with artificial liver support devices. Therefore, the adsorbent which adsorbs fewer albumin molecules is better. Resin XAD-7 can remove more cholic acids; however, it also loses more albumin molecules. So, resin XAD-7 is not an ideal choice. Resin 50wx4 can remove tryptophan, cholic acid and bilirubin, but the capacities are relatively low. Considering all aspects, activated carbon and anion resin Dowex 1x4 are two better choices. Then, in the following kinetic adsorption, only activated carbon and resin 1x4 are used.

TABLE 1 EQUILIBRIUM ADSORPTION PARAMETERS FOR CREATININE, ALBUMIN, TRYPTOPHAN AND CHOLIC ACID

Solute	**Adsorbent**	**a**	**b**	q_m **(g/g)**	$\mathbf{R^2}$
Creatinine	Carbon	16.273	0.0763	0.2132	0.9964
Albumin	Carbon	0.0762	1.9199	0.0397	0.9285
Albumin	Resin 1x4	0.0368	2.6189	0.0141	0.9602
Albumin	50wx4	0.0427	2.0388	0.0210	0.9627
Albumin	XAD-7	1.1064	3.7888	0.2920	0.9893
Tryptophan	Carbon	10.352	34.356	0.3013	0.9991
Tryptophan	Resin 1x4	0.0611	0.5193	0.1176	0.9995
Tryptophan	XAD-7	0.0178	0.2008	0.0886	0.8346
Cholic Acid	Carbon	1.6485	31.663	0.0521	0.9877
Cholic Acid	Resin 1x4	0.8387	61.011	0.0137	0.9595
Cholic Acid	50wx4	0.1344	14.666	0.0092	0.9282
Cholic Acid	XAD-7	15.823	174.76	0.0905	0.9691

TABLE 2 BILIRUBIN EQUILIBRIUM ADSORPTION PARAMETERS

Adsorbent	k_l	k_s	q_m **(mg/g)**	$\mathbf{R^2}$
Carbon	4.86E-03	7.47E-03	5.316	0.9134
XAD-7	8.68E-03	5.41E-03	2.936	0.9872
Adsorbent	**a**	**b**	q_m **(mg/g)**	$\mathbf{R^2}$
Resin 1x4	1.3563	0.02740	45.504	0.9231
50wx4	0.0791	0.03495	2.2619	0.9902

Adsorption rate constant is another important parameter in evaluating the performance of adsorbents. Small adsorption rate constant means that it takes long time for toxins to be removed. In order to reduce the toxin level in patients to normal range, the treatment time would have to been prolonged. In clinic, it is not acceptable because long treat time means high risk.

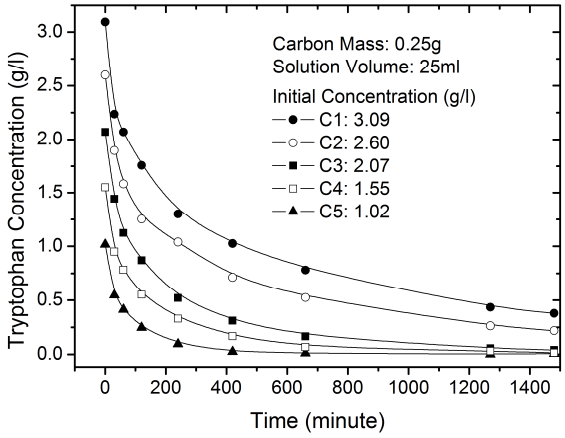


Figure 2 Tryptophan kinetic adsorption onto activated carbon

In the kinetic adsorption experiments, five different initial concentrations were used. Fig. 2 shows curves of tryptophan kinetic adsorptions onto activated carbon. The results show that the concentration of tryptophan decreases as time increases. According to these data, pseudo-first and second-order kinetic adsorption parameters can be obtained by curve fitting, which are listed in Tables 3 and 4, respectively.

Generally, the smaller the molecule is, the faster the adsorption is. Take the case of activated carbon. Among all solutes, creatinine molecule weight is the smallest, so the adsorption is the fastest. Tryptophan is the second solute regarding adsorption rates. Both bilirubin and cholic acid adsorption rates are close for their molecule weights are close. In addition, the adsorption rate constant could depend on the initial concentration because the experimental results indicate that the adsorption rate constant increases as the initial concentration decreases (in Tables 3 and 4, the initial concentration decreases from C1 to C5). This is especially obvious when the pseudo-second-order kinetic is used. The results also show that the toxin adsorption rate of resin 1x4 is faster than that of activated carbon.

TABLE 3 PSEUDO-FIRST-ORDER KINETIC ADSORPTION PARAMETER (UNIT: 1/MIN; VALUE: ×10-3)

Adsorbent	Solute	C1	C2	C3	C4	C5
Carbon	Creatinine	53.6	49.8	51.5	60.9	50.6
Carbon	Bilirubin	6.06	5.48	5.32	6.60	6.72
Carbon	Tryptophan	3.98	4.46	6.38	7.85	12.9
Carbon	Cholic Acid	3.61	4.06	4.02	5.32	7.82
Resin 1x4	Bilirubin	10.8	10.7	11.5	9.97	7.65
Resin 1x4	Tryptophan	20.4	20.7	19.0	21.8	23.6
Resin 1x4	Cholic Acid	9.88	13.6	17.5	12.6	19.5

TABLE 4 PSEUDO-SECOND-ORDER KINETIC ADSORPTION PARAMETER (UNIT: G /(MG · MIN); VALUE: $\times 10^{-3}$)

Adsorbent	Solute	C1	C2	C3	C4	C5
Carbon	Creatinine	0.352	0.322	0.402	0.646	0.640
Carbon	Bilirubin	1.868	2.414	2.143	2.970	1.107
Carbon	Tryptophan	26.35	34.52	55.14	97.43	281.4
Carbon	Cholic Acid	74.70	157.2	225.9	463.9	1681
Resin 1x4	Bilirubin	16.56	18.07	23.03	23.20	24.80
Resin 1x4	Tryptophan	468.4	570.9	547.6	839.9	1215
Resin 1x4	Cholic Acid	895.9	1389	2547	3206	12082

Theoretically, for a given situation, the adsorption rate should be a constant. However, in practice, it is related to the operation. For example, the adsorption rate constant is affected by stir speed. In our experiments, the speed 60rpm guarantees the solution mixed well; however, it is hard to know if 60rpm is an optimal rotation speed or not. One might increase rotation speeds, but have to take the risk of solution stability or the carbon debris, which could consequently result in the fake increase of toxin adsorption rates. In this study, all kinetic adsorption experiments were done under the same conditions. The speed 60rpm is an eclectic protocol, which balances all pros and cons.

Conclusions

In this paper, the equilibrium adsorption experiments of activated carbon, resin Amberlite XAD-7, resin Dowex 1x4 and resin Dowex 50wx4 to albumin, creatinine, bilirubin, tryptophan and cholic acid were conducted respectively. Then, adsorption capacities of different adsorbents to different solutes were obtained by curve fitting. Based on adsorption capacities, Norit RO 0.8 activated carbon and Dowex 1x4 anion resin are better for artificial liver support devices. After the equilibrium adsorption experiments, the kinetic adsorption experiments were performed. Kinetic adsorption rate constants of creatinine, bilirubin, tryptophan and cholic acid onto activated carbon and resin Dowex 1x4 were obtained by curve fitting. The results show that the toxin adsorption rate of anion resin Dowex 1x4 is faster than that of activated carbon Norit RO 0.8. Because the systematic measurement

of the basic adsorption parameters in the area of blood purification based on adsorption technology is relatively little in the literature, the systematic results in this paper are important references for researchers in their future work.

References

[1] B. Carpentier, A. Gautier, and C. Legallais, "Artificial and bioartificial liver devices: present and future," *Gut*, vol. 58, pp. 1690-1702, 2009.

[2] B. Carpentier and S. R. Ash, "Sorbent-based artificial liver devices: principles of operation, chemical effects and clinical results," *Expert Review of Medical Devices*, vol. 4, pp. 839-861, 2007.

[3] S. R. Ash, "Extracorporeal blood detoxification by sorbents in treatment of hepatic encephalopathy," *Advances in Renal Replacement Therapy*, vol. 9, pp. 3-18, 2002.

[4] S. R. Ash, T. A. Sullivan, and D. J. Carr, "Sorbent suspensions vs. sorbent columns for extracorporeal detoxification in hepatic failure," *Therapeutic Apheresis and Dialysis*, vol. 10, pp. 145-153, 2006.

[5] V. V. Sarnatskaya, W. E. Lindup, P. Walther, V. N. Maslenny, L. A. Yushko, A. S. Sidorenko, A. V. Nikolaev, and V. G. Nikolaev, "Albumin, bilirubin, and activated carbon: New edges of an old triangle," *Artificial Cells Blood Substitutes and Immobilization Biotechnology*, vol. 30, pp. 113-126, 2002.

[6] S. R. Ash, D. J. Carr, and T. A. Sullivan, "Sorbent suspension reactor for extracorporeal detoxification in hepatic failure or drug overdose," *Asaio Journal*, vol. 50, pp. Lviii-Lxv, 2004.

[7] K. Rifai, T. Ernst, U. Kretschmer, M. J. Bahr, A. Schneider, C. Hafer, H. Haller, M. P. Manns, and D. Fliser, "Prometheus (R) - a new extracorporeal system for the treatment of liver failure," *Journal of Hepatology*, vol. 39, pp. 984-990, 2003.

[8] F. Wong, "Drug Insight: the role of albumin in the management of chronic liver disease," *Nature Clinical Practice Gastroenterology & Hepatology*, vol. 4, pp. 43-51, 2007.

[9] P. Krisper and R. E. Stauber, "Technology Insight: artificial extracorporeal liver support - how does Prometheus (R) compare with MARS (R)?," *Nature Clinical Practice Nephrology*, vol. 3, pp. 267-276, 2007.

[10] J. L. Irvin, C. G. Johnston, and J. Kopala, "A photometric method for the determination of cholates in bile and blood," *Journal of Biological Chemistry*, vol. 153, pp. 439-457, 1944.

[11] M. C. Annesini, C. Di Carlo, V. Piemonte, and L. Turchetti, "Bilirubin and tryptophan adsorption in albumin-containing solutions. I. Equilibrium isotherms on activated carbon," *Biochemical Engineering Journal*, vol. 40, pp. 205-210, 2008.

[12] V. G. Nikolaev, V. V. Sarnatskaya, V. L. Sigal, V. N. Klevtsov, K. E. Makhorin, and L. A. Yushko, "High-porosity activated carbons for bilirubin removal," *International Journal of Artificial Organs*, vol. 14, pp. 179-185, 1991.

[13] A. Ebadi, J. S. S. Mohammadzadeh, and A. Khudiev, "What is the correct form of BET isotherm for modeling liquid phase adsorption?," *Adsorption-Journal of the International Adsorption Society*, vol. 15, pp. 65-73, 2009.

[14] Y. Onal, C. Akmil-Basar, D. Eren, C. Sarici-Ozdemir, and T. Depci, "Adsorption kinetics of malachite green onto activated carbon prepared from Tuncbilek lignite," *Journal of Hazardous Materials*, vol. 128, pp. 150-157, 2006.

[15] Y. S. Ho and G. McKay, "Sorption of dye from aqueous solution by peat," *Chemical Engineering Journal*, vol. 70, pp. 115-124, 1998.

Advanced Materials Research Vol. 936 (2014) pp 795-800
© (2014) Trans Tech Publications, Switzerland
doi:10.4028/www.scientific.net/AMR.936.795

Prediction of the Tertiary Structure and the Dimerization Interface of FNR Protein in Klebsiella pneumoniae

Qing-rui Zhang[a *], Xia Li[b]·

College of Chemical Engineering, Qingdao University of Science and Technology, Qingdao 266042, China

[a]zhangqingrui@qust.edu.cn, [b]xiali520310@163.com

Keywords: homology modelling;· FNR; protein·dimerization interface;

Abstract. FNR (fumarate nitrate reduction regulator) is an important oxygen regulation protein, which plays a major role in altering gene expression between aerobic and anaerobic conditions. In this study, the tertiary structure of FNR protein in *Klebsiella pneumoniae* was established using homology modelling. The model was modified and optimized using molecular mechanics and molecular dynamics simulations. In addition, Support Vector Machines (SVMs) was applied to predict the possible binding sites patches of FNR. The residues conservations were further analyzed and it was found that the Asn138-Ser162 region of FNR protein was the putative dimerization interface.

Introduction

1,3-propanediol as a monomer of polyesters, polyehters or polyurethanes can be produced by glycerol in *Klebsiella pneumoniae* under anerobic and aerobic conditions[1]. The oxygen regulation mechanism has attracted increasing interest. Fumarate & nitrate reduction (FNR) was the primary oxygen sensor. It controls the physiological switch between aerobic and anaerobic growth conditions [2]. Although some researches about FNR in *Escherichia coli* were reported[3], little information is known about the oxygen regulation mechanism in *K. pneumoniae*. Shaw et al [4] presented that *K. pneumoniae* FNR gene showed high similarities to *E. coli* FNR gene (98% amino acid identity), which brought great help to study the oxygen signaling systems of *K. pneumoniae*. FNR was predicted consisting of a C-terminal DNA-binding domain, which recognizes specific binding sites within FNR-controlled promoters, and an N-terminal sensory domain containing four cysteine residues (Cys20, Cys23, Cys29, and Cys122) ligated with the $[4Fe\text{-}4S]^{2+}$ cluster [5]. Under anaerobic conditions, FNR exists as a homodimer, with each monomer containing a $[4Fe\text{-}4S]^{2+}$, which promotes dimerization, site-specific DNA binding and the gene regulation. Upon a switch to aerobic conditions, the $[4Fe\text{-}4S]^{2+}$ cluster is converted to a $[2Fe\text{-}2S]^{2+}$ cluster, triggering conformational changes that induce monomerization, preventing DNA binding and hence productive interactions with RNA polymerase [6]. The oxygen regulation mechanism of FNR is not very clear and the FNR structure has not been known. The FNR structure of *E. coli* lacking the parts of N and C terminals was modeled by Moore and Crack based on the CRP structure [7]. Therefore, it is important to build the complete structure of FNR monomerization. FNR is an active homodimer in the absense of oxygen, it is necessary to analyze the dimerization interface. Several studies about protein-protein interactions had been reported, which could be helpful to find the dimerization interface of FNR protein[8,9].

In this work, the complete FNR structure of *K. pneumoniae* was constructed using homology modelling, then the model was modified and optimized using molecular mechanics and molecular dynamics simulations. The possible binding regions of FNR dimmer were predicted by Support Vector Machines (SVMs). In addition, residues conservation were analyzed, it was suggested that Asn138-Ser162 residues region was the dimerization interface.

Materials and Methods

Model Building. The FNR protein amino acid sequence of *K. pneumoniae* was obtained from the SWISS-PROT protein sequence database. The homology modelling of FNR tertiary structure was performed using Swiss-Model based on the CRP and endonuclease Ⅲ as the templates.

The function domain of FNR is similar with CRP, and the identity between FNR protein and CRP protein was 29%. However, it only showed residues Ile30-Asp237 homologous structure of FNR protein. The position of residue Cys122 was known and could be connected to one Fe atom of $[4Fe\text{-}4S]^{2+}$ cluster, but Cys20,Cys23 and Cys29 were not sure how to be connected to the rest Fe atoms of $[4Fe\text{-}4S]^{2+}$ cluster. Jervis et al[10] presented that endonuclease III structure was known and had the iron-sulfur clusters ligated by an FNR-like CysXXCysXXXXXCys motif. Then residues Cys20-Cys29 structure of FNR bounding with a [4Fe-4S] cluster was modeled by SWISS-MODEL Server using endonuclease III as a template.

Residues Met1-His19 and Leu238-Ala250 tertiary structures of FNR protein were modeled by Insight II MODELLER module, according to the results obtained from secondary structure prediction ExPASy Server. The parameters in calculations were used as the default values unless the special illustration.

Model Refinement and Validation. The molecular mechanisms and molecular dynamics were performed for the FNR model obtained from homology modeling using the DISCOVER module of Insight II and a CVFF force field. Firstly, the model was put through energy minimization for 20000 steps of the steepest descent method. Then, the model was further subjected to energy minimization for 7000 steps of the conjugate gradient technique that led to refined structure of FNR with RMS deviation less than 0.001kal/mol. Next, a water layer was set up and the molecule was positioned at the centre of the layer by defining a 1nm distance between the protein and the layer edge. FNR model was subjected to molecular dynamics run at 300K for 500000 fsec with 1 fsec each step. The output conformers were collected at every 5000 fsec. The energy profile was analyzed using Analysis module of Insight II. The reliability of the model was verified by assessment with PROCHECK.

Interface Prediction. The interface residues of FNR monomer were predicted by PPI-Pred server combined with interface analysis. The electrostatic potential of the model was calculated using the Delphi module implemented in Insight II using the continuum dielectric approach to solve the Poisson-Boltzmann equation by the finite difference method. In the calculations, the dielectric constants for FNR and the solvent were taken to be 2.0 and 80.0, respectively. The radius of solvent was 0.14nm and the specific force field PROTEIN FORMAL in Delphi was applied. In addition, the hydrophobic interaction was analyzed using Insight II.

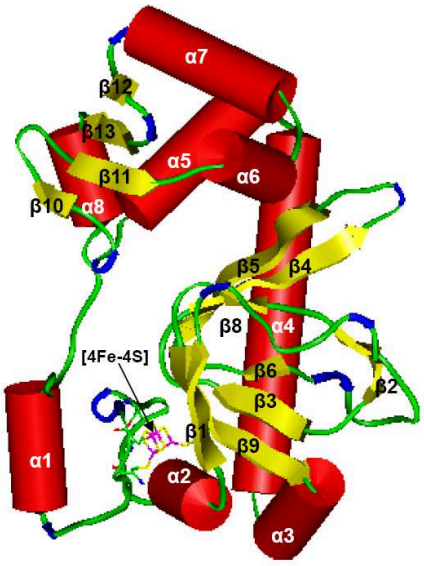


Fig. 1 The tertiary structure of FNR protein

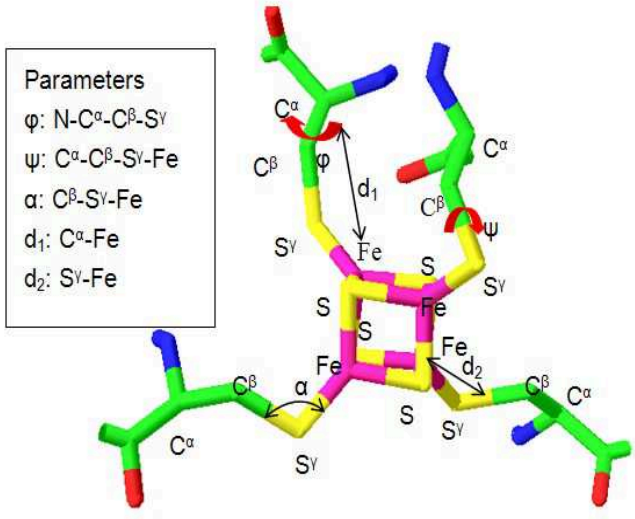


Fig. 2 Geometrical presentation of the parameters analyzed for the [4Fe-4S] cluster

Table 1 Analysis of Selected Parameters of Cysteine Residues within FNR

	Cys-20	Cys-23	Cys-29	Cys-122
φ[°]	-89.42	-73.98	-89.00	-94.21
ψ[°]	113.40	112.66	-23.79	104.35
α [°]	105.14	121.92	107.13	113.13
d_1[Å]	3.70	4.48	4.03	4.53
d_2[Å]	2.22	2.28	2.31	2.35

Results and Discussion

Description of the FNR model. The optimized FNR model was illustrated in Fig. 1. The model is mainly comprised of 8 helices, 13 β-sheets, 20 coils and a [4Fe-4S] cluster. The [4Fe-4S] cluster in FNR protein is equivalent to the oxygen-responsive molecular switches[7]. A theoretical conformational analysis of [4Fe-4S] cluster was carried out. Relevant structural parameters(i.e., φ and ψ dihedrals, α angles, and distances involving the topology of the Fe atoms) were shown in Fig 2 and summarized in Table 1. The dihedral ψ (C^{α}-C^{β}-S^{γ}-Fe) varied between -23.79° and 113.40°, and the angle α (C^{β}-S^{γ}-Fe) ranged from 105.14° to 121.92°. On the other hand, the distances d_1(C-Fe) and d_2(S-Fe) showed only minor deviations from an average value of 4.19Å and 2.29Å, respectively. The dihedral φ showed nearly a *trans* conformation for coordinating Cys20, Cys23, Cys29 and Cys122. Obviously, all cysteine residues were oriented by adopting a low-energy conformation for their side-chain-torsion.

MD Simulation and Quality Assessment of the Model. The change of potential energy with time was shown in Fig. 3. It was seen that the potential energy decreased quickly in the first 100 ps, then decreased slowly to around 7010Kcal/mol after 200ps. The conformation at 500 ps was chosen as the final 3D structure for the further study.

The model was analyzed using PROCHECK program. The Ramachandran plot was shown in Fig. 4. It was seen that 94.4% residues were in the most favoured regions, 4.5% residues were in additional allowed regions, 0.4% residues were in generously allowed regions and 0.4% residues were in disallowed regions respectively. The model is considered as a high quality model as the ratio of the residues in the most favoured regions to all residues is more than 90%. This revealed that the main chain structure modeling of FNR protein was reasonable.

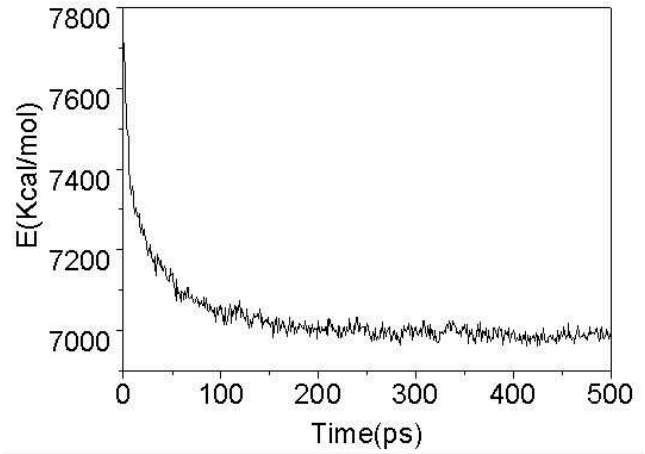


Fig. 3 Potential energy changed with the time

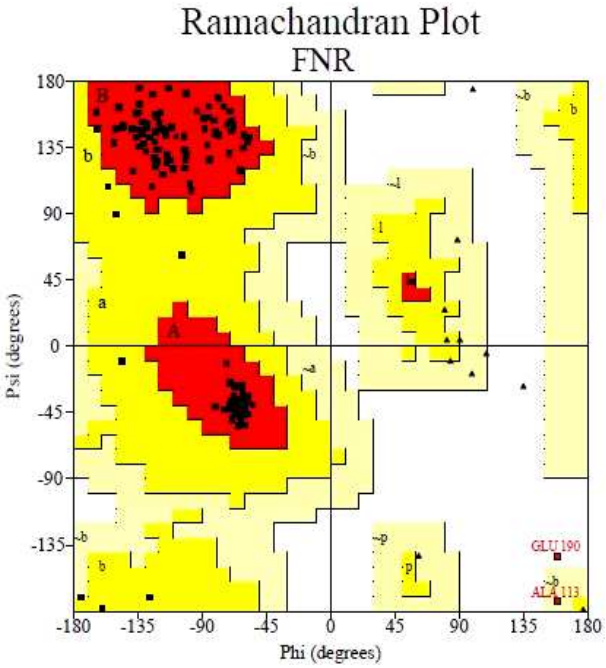


Fig. 4 The Ramachandran plot of FNR protein

Determining the Dimerization Interface of FNR Protein. The binding sites patches of unbound FNR monomer structure were predicted by PPI-Pred server combined with interface analysis. Three possible interaction binding sites patches were predicted by PPI-Pred Server. The amino acid sequences corresponding to the three different patches were shown in Fig. 5. The highest scoring patches which were most likely to be part of the protein-protein binding sites were indicated in red, and the second highest scoring patches and the third highest scoring patches were indicated in blue and green, respectively. It was found that the green patches were close to N terminal and the blue patches were close to C terminal of the FNR, respectively. The red patches were mainly located on the middle parts of the FNR amino acid sequences. In the following part, residues conservations were used to find the interaction binding sites of the dimerization interface.

MIPEKRIIRR	10	IQSGGCAIHC	20	QDCSISQLCI	30	PFTLNEHELD	40	QLDNIIERKK	50
PIQKGQTLFK	60	AGDELKSLYA	70	IRSGTIKSYT	80	ITEQGDEQIT	90	GFHLAGDLVG	100
FDAIGTGHHP	110	SFAQALETSM	120	VCEIPFETLD	130	DLSGKMPNLR	140	QQMMRLMSGE	150
IKGDQDMILL	160	LSKKNAEERL	170	AAFIYNLSRR	180	FAQRGFSPRE	190	FRLTMTRGDI	200
GNYLGLTVET	210	ISRLLGRFQK	220	SGMLAVKGKY	230	ITIENNDALA	240	QLAGHARNVA	250

Fig. 5 The possible binding sites of FNR were colored differently to show the location of three patches on the amino acid sequences.

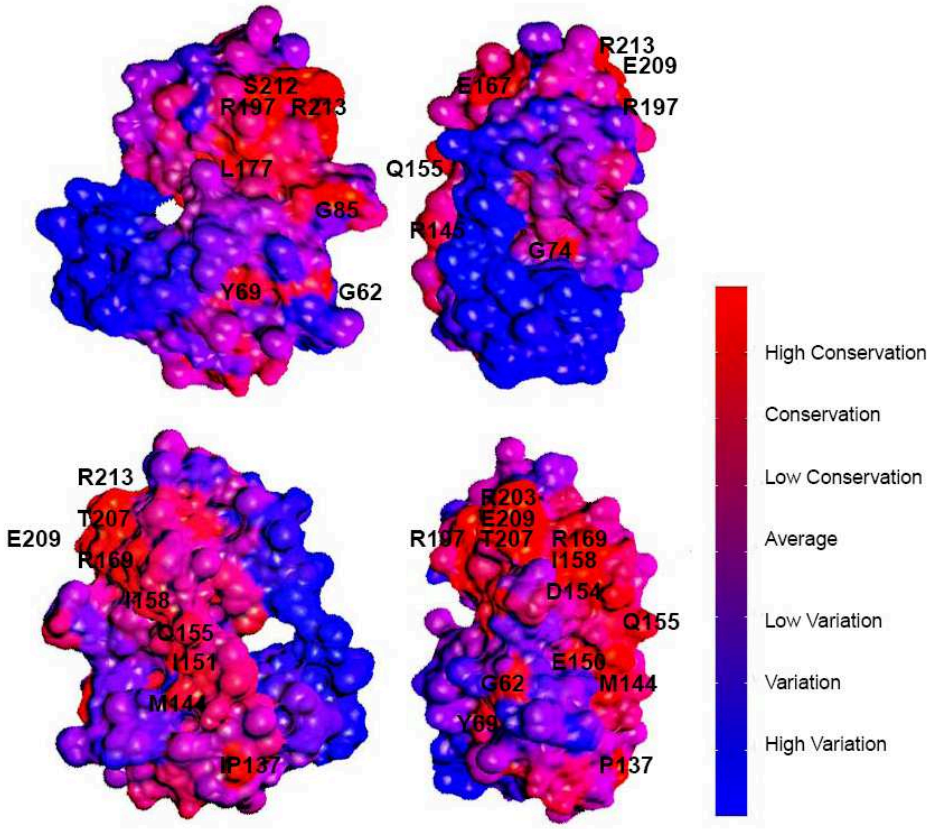


Fig. 6 The surface models of residues conservation of FNR protein predicted by PPI-Pred Server, the four views were rotated about vertical axis by 90°. Highly conserved residues were shown in Red and residues without conservation were shown in blue.

Conservations. Compared to surface residues, residues in the interface region are thought to be evolving at a slower rate. So evolutionary conservation of the residues is an important property of

the interface regions[11]. It was found that residues at the interface were more conserved than those occurring elsewhere on the protein surface in homodimer[12]. The residues conservation of FNR protein was predicted by PPI-Pred Server (Fig.6), it was observed that the highly conserved residues including: Gly62, Tyr69, Gly74, Gly85, Glu87, Asp137, Met144, Arg145, Glu150, Ile151, Asp154, Gln155, Ile158, D156, I158, Glu167, Arg169, Leu177, Arg180, Thr196, Arg197, Thr207, Glu209, Arg213, Phe218. However, not all the above residues were the residues in the interface.

The four residues of Thr207, Glu209, Arg213, Phe218 were located on the helix-turn- helix region which was the sites binding with DNA. So, the four residues were rejected. The five residues of Gly62, Tyr69, Gly74, Gly85, Glu87 were located on the ninth β-sheets region. The two residues of Tyr69 and Gly74 were not possible the residues in the interface as they were in the molecule inside. The nine residues of Met144, Arg145, Glu150, Ile151, Asp154, Gln155, Ile158, D156 and I158 were located in the α4 region. The residual residues of Glu167, Arg169, Leu177 and Arg180 were located in the α5 region. In general, the interface of dimer was big and planar. The number of conserved residues on the β-sheets was little and the interface was small and uneven. Although the interface of α5 region was planar, it was not the possible interface as the number of conserved residues was little and the α5 region was blocked by α8. The number of conserved residues on the α4 region was the most and the interface was big and planar. The residues Asn138-Ser162 of FNR were analogous to the residues of the CRP α-helix which promotes subunit interactions through formation of a coiled coil. Therefore, it was predicted that the α4 region including Asn138-Ser162 was the most probable dimerization interface.

Conclusion

In this work, the tertiary structure of FNR in *K. pneumoniae* was modeled using homology modeling and was refined by using molecular mechanics and molecular dynamics. The refined structure was validated to be reliable by using of protein validation tools. The interaction binding sites patches were predicted by PPI-Pred server. It was suggest that the Asn138-Ser162 region was the putative dimerization interface.

Acknowledgments

This work was supported by the grant from the natural science foundation of Shandong Province (ZR2013BM001).

References

[1] E. Celinska, *Klebsiella spp* as a 1,3-propanediol producer- the metabolic engineering approach, Crit. Rev. Biotechnol. 32 (2012) 274-288.

[2] R. Grabbe, A. Kuhn, R.A. Schmitz, Cloning ,sequencing and characterization of Fnr From *Klebsiella pneumonia*, Antonie. Van. Leeuwenhoek. 79 (2001) 319-326.

[3] K.S. Myers, H.H. Yan, I.M. ong, D.J. Chung, K. liang, F. Tran, S. Keles, R. Landick, P. J. Kiley, Genome-scale analysis of Escherichia coli FNR reveals complex features of transcription factor binding, PLoS. Genet. 9 (2013) e1003565.

[4] D.J. Shaw, J.R. Guest, Nucleotide sequence of the FNR gene and primary structure of the FNR protein of *E. coli*, Nucleic. Acids. Res. 10 (1982) 6119-6130.

[5] S. Spiro, K.L. Gaston, A.I. Bell, R.E. Robert, S.J. Busby, J.R. Guest, Interconvertion of the DNA-binding specificities of two related transcriptional regulators, CRP and FNR, Mol. Microbiol. 4 (1990) 1831-1838.

[6] V.R. Sutton, E.L. Mettert, H. Beinert, P.J. Kiley, Kinetic analysis of the oxidative conversion of the [4Fe-4S]2+ cluster of FNR to a [2Fe-2S]2+ cluster, J. Bacteriol. 186 (2004) 8018-8025.

[7] J.C. Crack, A.J. Jervis, A.A. Gaskell, G.F. White, J. Green, A.J. Thomson, N.E. Le Brun, Signal perception by FNR: the role of the iron-sulfur cluster, Biochem. Soc. Trans. 35 (2008)1144-1148.

[8] N. Tuncbag, G. Kar, O. Keskin, A. Gursoy, R. Nussinov, A survey of available tools and web servers for analysis of protein-protein interactions and interfaces, Brief. Bioinform. 10 (2009) 217-232.

[9] S. Sonavane, P. Chakrabarti, Prediction of active site cleft using support vector machines, J. Chem. Inf. Model. 50 (2010) 2266-2273.

[10] A.J. Jervis, J.C. Crack, G. White, P.J. Artymiuk, M.R. Cheesman, A.J. Thomson, N.E. Le Brun, J. Green, The O2 sensitivity of the transcription factor FNR is controlled by Ser24 modulating the kinetics of [4Fe-4S] to [2Fe-2S] conversion, Proc. Natl. Acad. Sci. USA. 106 (2009) 4659-4664.

[11] O. Keskin, N. Tuncbag, A. Gursoy, Characterization and prediction of protein interfaces to infer protein-protein interaction networks, Curr. Pharm. Biotechnol. 9 (2008) 67-76.

[12] R.P. Bahadur, M. Zacharias, The interface of protein-protein complexes: Analysis of contacts and prediction of interactions, Cell. Mol. Life. Sci. 65 (2008) 1059-1072.

Advanced Materials Research Vol. 936 (2014) pp 801-805
© (2014) Trans Tech Publications, Switzerland
doi:10.4028/www.scientific.net/AMR.936.801

Potassium Dichromate Surface Modification of Poly-lactic Acid(PLA) and Poly-Lactide-Co-Glycolide(PGLA) Fibers

WANG Bi-qiao[1, a], ZHANG Pei-hua[1,b] and FANG Mei-han[1,c]

[1]College of Textiles, Donghua University, Shanghai 200051,China

[a]wbq@mail.dhu.edu.cn, [b]phzh@dhu.edu.cn, [c]fangmeihan@163.com

Keywords: Potassium Dichromate($K_2Cr_2O_7$), Surface Modification, hydrophilicity, PLA,PGLA.

Abstract: PLA and PGLA, as biodegradable polymers, are widely used in the biomedical field, such as in surgical sutures, drug delivery devices, and tissue engineering research and so on. However, the lack of hydrophilic groups on their surfaces limit their application. For improving hydrophilicity of PGA and PGLA fibers, and preserving fiber mechanical property at the same time, PLA and PGLA fibers were modified by potassium dichromate solution for different processing time for optimizing modification parameter. Breaking strength and water contact angle were tested to observe the change of properties, differential scanning calorimeter (DSC) and fourier transform infrared spectrometry (FTIR) were used to analyse the change of molecular structure and functional groups. Experimental results showed that 6min was the most suitable time for improving hydrophilicity of PLA and PGLA fibers and preserve fiber mechanical property.

Introduction

Poly-lactic acid (PLA) and poly-lactide-co-glycolide(PGLA) are thermoplastic polymers with hydrolytically labile aliphatic ester linkages[1].Their most notable includes its excellent fiber-forming ability, biodegradability and controllable hydrolytic degradation. Because of excellent properties, they are widely used in the biomedical field, such as in surgical sutures, drug delivery devices, tissue engineering research and so on[2].

However，their existing properties, such as hydrophily, can not meet the demands of tissue engineering[3]. The lack of hydrophilic groups on their surfaces also influences their biocompatibility.Therefore many researchers focus on surface modification on these materials[4,5]. Some researchers used PGLA microparticles surface-attached with TNF-related apoptosis-inducing ligand(TRAIL) to incorporated doxorubicin for inhalation treatment of metastatic lung cancer[6]. Cationic, anionic or nonionic PLA microspheres were prepared with different surface charges surfactants, and embedded on PLA membranes. The modified PLA membranes could improve the cell compatibility[7]. Some researchers grafted β-cyclodextrin(β-CD) on PLA to obtain a copolymer, which had better hydrophilicity than PLA homopolymer[8]. However, these approaches were either decreased the mechanical properties of the polymer, or too complex.

In the recent study, we attempted an easy operating and effective method to encourages the surface property of PLA and PGLA fiber, meanwhile maintains the good mechanical performance. The ester backbone can hydrolyze under the acidic condition, and the terminal hydroxyls may be oxidized. These reactions may improve hydrophilic functional groups on the surface. In this study, the mixed solution of potassium dichromate($K_2Cr_2O_7$) and sulfuric acid(H_2SO_4) was attempted to encourage hydrolyzation and biocompatibility of PLA and PGLA fibers.

Experimental

Materials

Fibers of PLA, PGLA (GA:LA=90:10) are provide by Shanghai Tianqing Biomaterial Co., LTD. The basic properties were shown in Table 1.

TABLE1 THE BASIC PERFORMANCE OF PLA AND PGLA FIBERS

Sample	Linear density[dtex]	Breaking strength[cN]	Elongation[%]
PLA	5.19	15.72	39.68
PGLA(90:10)	2.75	16.23	42.39

Potassium dichromate ($K_2Cr_2O_7$) and sulfuric acid (H_2SO_4) were analytically pure and used without further purification.

Potassium Dichromate Surface Modification

Both mass fraction of $K_2Cr_2O_7$ and H_2SO_4 solution is 10%. $K_2Cr_2O_7$ and H_2SO_4 solution were mixed with volume ratio 1:6. Samples were dipped into mixed solution for deferent period: 2min, 4min, 6min, 8min, 10min, then cleaned by deionized water three times, and dried in a vacuum frozen dryer for 2 hours.

Tensile Properties

The tensile test was made with an electronic single fiber strength tester(LLY06E, Laizhou electron instrument co.,LTD, China). Gauge length was 10 mm, stretch speed was 20mm/min. The sample number was 30.

Water Contact Angle

Water contact angle measurements of unmodified and modified fibers were undertaken by the sessile drop technique using a contact angle goniometer(JC2000A, Shanghai Zhongchen, China) under standard condition.

DSC Analysis

Fiber samples(3~5mg) were placed in crucible, tested their thermodynamic performance by Differential Scanning Calorimeter (DSC,Pyris-1, PerkinElmer, US). Samples were kept warm for 2 min at 40℃, then heated up from 40℃ to 250℃ with a heating rate of 20℃/min. The DSC automatic calculated thermal melting point (Tm) and crystallinity.

FTIR Analysis

Fibers were tested by FTIR spectrometer (NEXUS 670, Thermo Nicolet Corporation, US) in the range of 400-4000 cm-1 with a resolution of 1 cm^{-1}.

Results and Discussion

Breaking Strength of Fiber

The relationship between fiber breaking strength and $K_2Cr_2O_7$ surface modification process-time was shown in Fig.1.

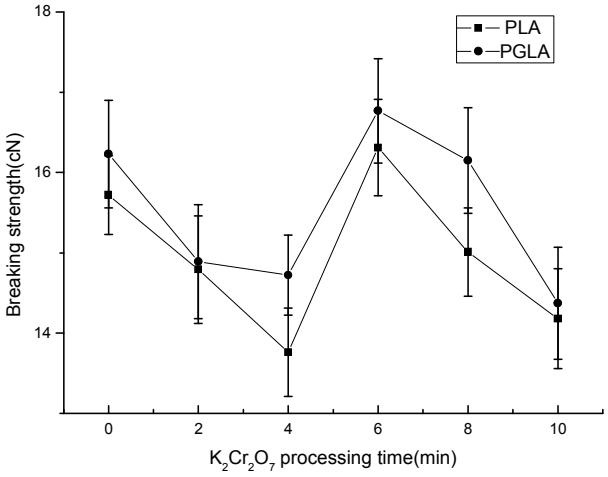


Fig.1 Change of fiber breaking strength with deferent $K_2Cr_2O_7$ process-time

Overall, the value of breaking strength had not change a lot. It indicated $K_2Cr_2O_7$ surface modification had little impact on fiber breaking strength. The breaking strength curve of PLA and

PGLA fibers dropped at the processing time of 2min and 4min. Curves reached their peak at 6min, then dropped again. That may be because joint effect of fiber molecular chain and fiber inner structure. On one hand, fiber surface molecular chain breaking caused dropping of breaking strength. On the other hand, swelling changed fiber inner structure and made it uniform. In swelling process, water molecules got inside of fibers, enhanced the fiber intermolecular distance, decreased the difference between crystalline region and amorphous region, thus made fiber inner structure uniform. Uniform structure may decrease inside stress and increase fiber breaking strength. The joint effect of two factors made breaking strength curve fluctuation.

Water Contact Angle of Fibers

The relationship between fiber contact angle and $K_2Cr_2O_7$ process-time was shown in Fig.2. Totally, contact angles of PLA were larger than PGLA. It can be seen that the contact angles of PLA and PGLA fiber increased after 2 min treatment. With the passage of time, contact angles of PLA and PGLA fibers were decreasing until 6min, then it increased once again. The lowest point of contact angle curve appeared at 6 min. Overall, appearance of two kind fibers was similar.

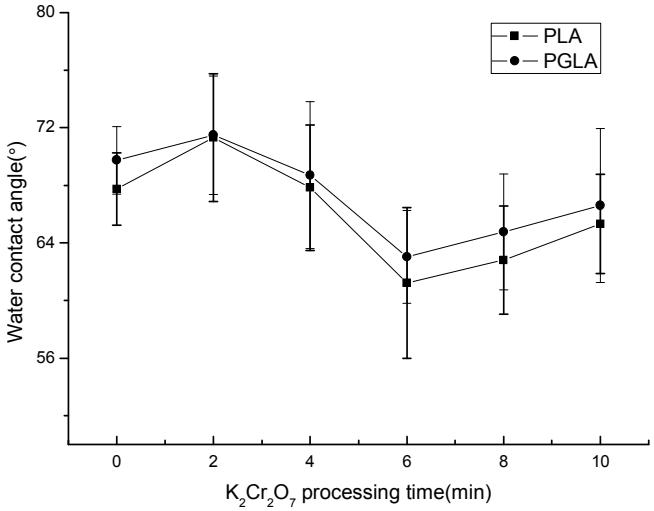


Fig.2 Change of fiber contact angle with deferent $K_2Cr_2O_7$ process-time

Under the same test method and condition, two important influencing factors of material contact angle were material surface morphology and surface molecule polarity[5]. Molecule of PLA was more lyophobic than PGLA, so contact angle of PLA fiber was higher than PGLA fiber. Furthermore, surface modification can promote ester bond hydrolysis and increase of polar groups. This was beneficial to reduce the water contact angle. On the other hand, fiber surface roughness should increase because of the chemical reagent erosion. However, the swelling effect had a contrary and made fiber surface smooth. To a certain extent, the increase of surface roughness can reduce the water contact angle. Due to the joint effect, the contact angle curves with deferent process-time of PLA and PGLA showed fluctuation. At the beginning, the chemical reagent just reacted, and the polar groups produced by reaction were very limited. At the same time, the swelling effect made fiber surface roughness decreased and played a main role, so the contact angle increased. As time passing, many polar groups were produced and surface roughness increased, so the contact angel decreased gradually. However, the reaction stopped after the reactant completely consuming. Meanwhile, the swelling was going on.So the contact angle increase once again.

Because decreased of contact angle means improving of hydrophilicity, 6min treated PLA and PGLA got the best hydrophilicity. In consideration of fiber breaking strength, controlling process-time as 6min seems reasonable.

Thermal Melting Point (T_m) and Crystallinity

Results of the thermal melting point (T_m) and crystallinity of PLA and PGLA fiber after 6min surface modification were compared with untreated samples in Table 2. It's obviously that T_m of PLA and PGLA almost had no change after treated, as the crystallinity decreased clearly, especially PLA dropped about 27.41%. This experimental result of maintaining of T_m indicated that the change of fibers chemical constituents was very limited, and might concentrate on surface. The sharp decrease of crystallinity showed that structure of fibers had changed obviously. It seems $K_2Cr_2O_7$ surface modification had less impact on crystallinity of GA-component than PLA or LA-component. Decreased of fiber crystallinity means increasing of amorphous region, which was beneficial to absorb moisture. This change may have positive effect on improving of hydrophilic.

TABLE 2 THE THERMAL MELTING POINT (TM) AND CRYSTALLINITY BEFORE AND AFTER K2CR2O7 TREATED

Samples	Untreated		$K_2Cr_2O_7$ treated	
	T_m[℃]	Crystallinity[%]	T_m[℃]	Crystallinity[%]
PLA	176.53	86.52	176.27	59.11
PGLA	206.27	44.66	206.90	34.88

FTIR Spectrometry

FTIR spectrum of PLA before and after $K_2Cr_2O_7$ treated was shown in Fig. 3.

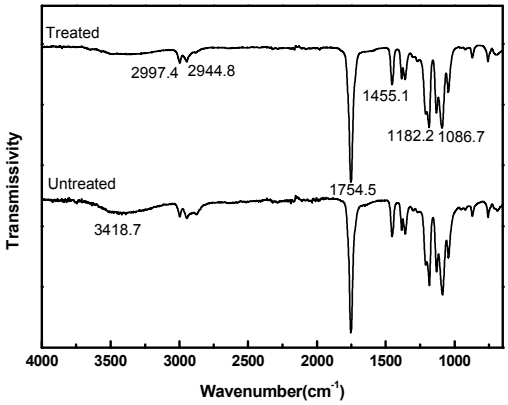


Fig.3 FTIR spectrum of PLA before and after $K_2Cr_2O_7$ treated

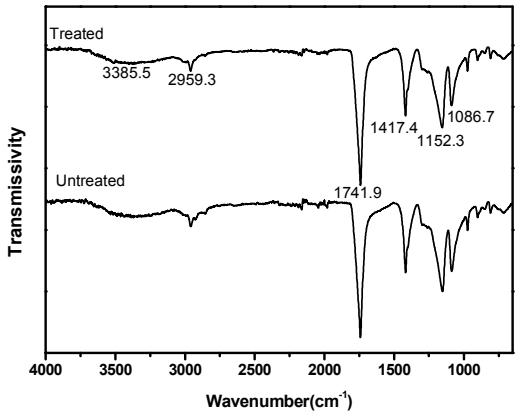


Fig.4 FTIR spectrum of PGLA before and after $K_2Cr_2O_7$ treated

The main change was the intermolecular hydrogen-bonding O-H absorption peak at 3418.7 cm^{-1} region reduced. It means that O-H hydrogen-bonding broke, and probably formed free O-H groups. As one kind of polar groups, the free O-H groups can improve the hydrophilicity of material.

FTIR spectrum of PGLA was shown in Fig.4.Before and after $K_2Cr_2O_7$ treated, infrared spectrum of PGLA fiber had no many change, besides remarkable decrease of absorption peak at 1086.7 cm^{-1} (lactone C-O-C stretch) and 1152.3cm^{-1}(bridge ester C-O-C stretch).The change means amount of

ester bond linkages decreased. It indicates the ester bond linkage of PGLA fibers were partly hydrolyzed, and might cause the increase of molecular-end polar groups.

Conclusion

In this article, $K_2Cr_2O_7$ and H_2SO_4 mixed solution was used to surface modify PLA and PGLA fibers with different time, then modifying parameter was optimize. Consideration of fiber hydrophilicity and breaking strength, the best potassium dichromate surface modification processing time was 6min. The crystallinity decreased clearly, which meant structure of fibers had changed. It meant increasing of amorphous region, which was beneficial to absorb moisture, and it's a positive change for hydrophilic. The FTIR spectrum shown that ester bonds of PLA and PGLA fibers surface were hydrolysis, and PGLA macromolecules end-groups may be oxidized. In conclusion, this modified method can improve the hydrophilicity of PLA and PGLA fibers and preserve fiber mechanical property.

Acknowledgements

Supported by the Shanghai Science and Technical Committee(Project Number 12DZ194030) and State Key Laboratory for Modification of Chemical fibers and Polymer Materials(Project Number LZ0902).

References

[1] C.K.Pillai, C.P.Sharmaa, Review paper: absorbable polymeric surgical sutures: chemistry, production, properties, biodegradability, and performance, J.Biomater. Appl. 25(2010)291-366.

[2] B.Talor , A.Bayat . Basic plastic surgery techniques and principles: choosing the right suture material, Stud. BMJ.11(2003)140-141.

[3] Y.Young, W. L.Sung, In vitro degradation behavior of non-porous ultra- fine poly (glycolic acid)/poly (L-lactic acid) fibers and porous ultra-fine poly (glycolic acid) fibers, Polym. Degrad. Stabil. 90(2005)441-444.

[4] Y.Wang, D.K. Wang , N.Sun, Nano and micro technologies for delivering macromolecular therapeutics using poly(lactide-co-glycolide),Chin. J. Pharm. 7(2009)205-211.

[5] R. Chen, J.A.Hun, Biomimetic materials processing for tissue-engineering processes, J. Mater. Res. 17(2007)3974-3979.

[6] Kim I; Byeon H J; Kim T H, et al. Doxorubicin-loaded porous PLGA microparticles with surface attached TRAIL for the inhalation treatment of metastatic lung cancer, Biomaterials 34(2013)6444-6453.

[7] D.Chen, J.Ji , J. C.Shen, A Study on Cytocompatibility of Poly (lacticacid) Membrane Modified by Polymer Microspheres with Different Surface Charges. J Biomed Eng.22(2005) 966-970.

[8] Y.S.Qi, B.H. Luo, C.R. Zhou, Preparation for polylactide-grafted copolymer of β-cyclodextrin with microwave irradiation, J. Changshu Inst. Technol.(Nat.Sci.)25(2011) 68-70.

CHAPTER 9:

Materials and Technologies in Environmental Engineering

Advanced Materials Research Vol. 936 (2014) pp 809-813
© (2014) Trans Tech Publications, Switzerland
doi:10.4028/www.scientific.net/AMR.936.809

Preparation and Photocatalytic Performance Study of La-WO_3 Co-doping TiO_2

Xianzhen Diao, Dong Zhou

Chemistry and Chemical Engineering College, Chongqing Institute of Science and Technology, Chongqing 401331,China
xianzhen81@126.com

Keywords：titanium dioxide; photocatalytic properties; La;WO_3; sol-gel method

Abstract：Butyl titanate as titanium source, anhydrous ethanol as solvent, glacial acetic acid as inhibitor, La-WO_3/TiO_2, La/TiO_2, WO_3/TiO_2 and pure TiO_2 photocatalysts were prepared through sol-gel method; At the same time, both of which were characterized by infrared spectrometer and uv-vis spectrophotometer; With methyl orange as simulated target degradation material, heat treatment temperature, different dopants, etc. on photocatalytic performance influences of TiO_2 were studied by spectrophotometer. Experimental results show that doping can improve obviously the photocatalytic activity of TiO_2. When calcination temperature is 500 ℃, dosage of catalyst is 0.25 g, pH is 1, and methyl orange concentration is 10 mg/L, La-WO_3/TiO_2 photocatalytic effect is best, and degradation rate is 46.18%.

Introduction

With rapid development of industrial production and a lot of industrial waste gas pollutants discharged into nature unceasingly, it makes human survival environment deteriorated, in which water environment problem is acute particularly. More than one million tons of synthetic dyes, pigments are produced and used in printing and dyeing industry each year in the world. Scientists have expected about 10% with the waste water discharged, which contain a lot of biological refractory materials, such as polycyclic aromatic hydrocarbon, polychlorinated biphenyls(PCBS), etc. Because their biological toxicity is bigger, there is a serious threat to human health and life security. Improving the environment condition and eliminating the organic pollutants in the water are current major problems to be solved to the human.

Photocatalytic materials has been the hot topics in the study of catalytic science and material science in recent years. Titanium dioxide as a kind of important inorganic semiconductor material has important application prospect in the solar water splitting, sewage treatment, etc. However, because anatase TiO_2 forbidden band width is large (Eg-3.2ev), solar energy utilization rate is low, and there is light composite problems such as electrons and holes, TiO_2 surface catalytic technology is limited in the practical application[1,2]. A lot of research experiments show that doping, precious metal deposition, semiconductor compositing[3-6] can improve effectively photocatalytic activity of TiO_2, broaden its range of light response, further improve its sun light energy use efficiency. In this paper, butyl titanate as titanium source, anhydrous ethanol as solvent, La, WO_3 doped TiO_2 photocatalysts were prepared by sol-gel method, and its photocatalytic activity was studied using uv-vis spectrophotometer and infrared spectrometer.

Experiments

La-WO_3 co-doped TiO_2 photocatalyst preparation

Under vigorous stirring, a certain amount of butyl titanate was added to 20mL anhydrous ethanol and 2.0 mL glacial acetic acid mixture slowly, stirring after 30 min, getting light yellow uniform transparent solution A; Soluble metal salt lanthanum nitrate and sodium tungstate mixture were added into 7mL anhydrous ethanol and 1.8mL distilled water mixed solution, adjusting the solution pH value(pH=2), getting the solution B. Then under the intense mixing, B liquid was added to A liquid dropwise, continuing to stir 2 h until the transparent sol. the sol was aged at room temperature for 1 d, getting silvery white gel. After the gel dried 12 h under 100 ℃ in the oven, dry gel powder was got after grinding. In the end, titanium dioxide powder was heated treatment 2h under 500 ℃ temperature in the muffle furnace, cooling, pure TiO_2, La doped TiO_2, WO_3 doped TiO_2 and La-WO_3 co-doped TiO_2 were got.

Infrared spectrum study

Molecular structures of samples analysed by German Bruker company's Equinox 55 type Fourier infrared spectrometer, scope of its wave number: 4000-400cm^{-1}; Accuracy of wave number: ≤4cm^{-1}(4000-2000), ≤2cm^{-1}(2000-400); Resolution: 1.5 cm $^{-1}$; Through the rate of accuracy: ±0.2%T; l_0 line straightness:≤±2%T.

Photocatalytic performance study

Configuration 500 ml10mg/L methyl orange solution, and measuring 60 ml methyl orange were poured into with 0.1g pure TiO_2, La doped TiO_2, WO_3 doped TiO_2, La-WO_3 co-doped TiO_2 in the beaker respectively; Stirring after 5min, dark treatment for 20min,under the irradiation of ultraviolet lamp at 30w, and liquid level 10cm from the light source, then every 30 min sampling, centrifugal separation, taking the supernatant fluid, and measuring its absorbance. The absorbance(A) of maximum absorption wavelength of 465nm was measured with visible spectrophotometer, and thus the degradation rate was calculated .

At low concentration range, it is directly proportional to the concentration and absorbance of the methyl orange solution(the concentration of methyl orange solution for 10 mg/L in this experiment), so photocatalytic degradation rate of sample can be represented as Eq. 1.

$$D=[(A_o-A_1)/A_o]\times 100\%. \quad (1)$$

In the formula, D for degradation rate; A_o for initial absorbance of methyl orange solution;A_1 for the absorbance of methyl orange solution after photocatalysis.

Results and discussion

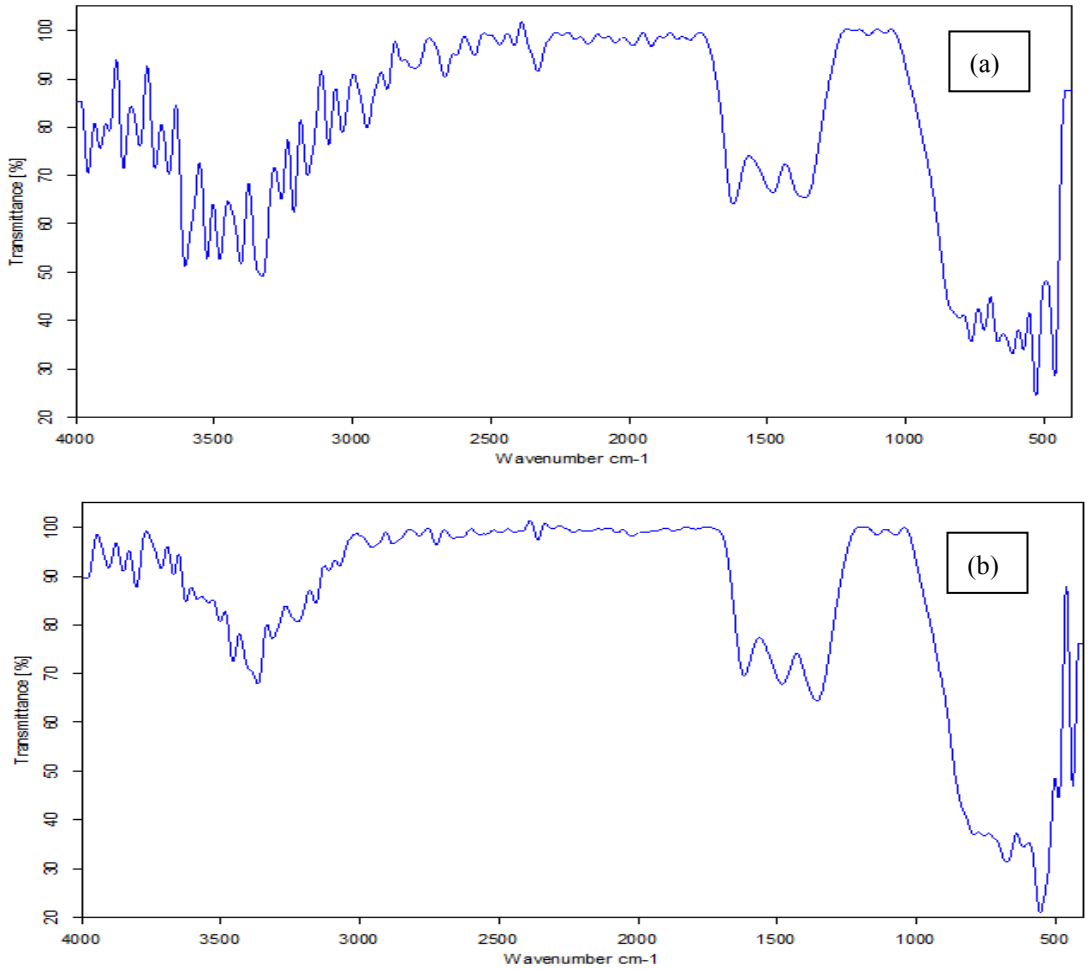
Infrared spectrum analysis

Fig.1 are infrared spectrograms of pure TiO_2, La-WO_3/TiO_2 powders after 500 ℃ calcination.The visible on the drawing, a wide absorption peak in the vicinity of 3380cm^{-1} appears from all samples, corresponding to the stretching vibration peak of the TiO_2 surface hydroxyl. In photocatalytic oxidation reaction, the amount of catalyst surface hydroxyl and light catalytic

reactivity is directly related[17], because it not only can easily generate hydroxyl free radical (·OH) by capturing the hole, but also can improve O_2's ability to capture electron to generate more ·OH. Other, absorption peak near 1640cm^{-1} is free water H-O-H bending vibration peak, which explains the surface of samples have already been hydroxylated. Between 800-420cm^{-1} wide absorption peak attributable to Ti-O keys vibration of amorphous TiO_2[19]. And 500-800^{cm-1} appears a broad peak of Ti-O stretching vibration absorption peak. In 2440cm^{-1}, 2380cm^{-1}, 1320 cm^{-1} and 1260cm^{-1} more wide absorption peaks may be the interaction of TiO_2 and W, La formed Ti-O-W, Ti-O-La, La-O-Ti-O-W keys and appear the peaks. Also can be seen that the presence of TiO_2 makes the surface hydroxyl peak wider and stronger, and doped catalysts have more abundant surface hydroxyl. This may be due to the presence of metal ions to improve the properties of TiO_2 catalysts specific surface area, etc. And in the photocatalytic degradation organic matter molecular reaction, ·OH is the main active species of oxy-genated. Therefore, after the compound TiO_2, photocatalytic performance will be improved.

Photocatalytic performance analysis

Fig.2 is different calcination temperature of La-WO_3/TiO_2 photocatalytic degradation methyl orange diagram in 10 mg/L methyl orange solution at 465nm, addition amount of photocatalyst for



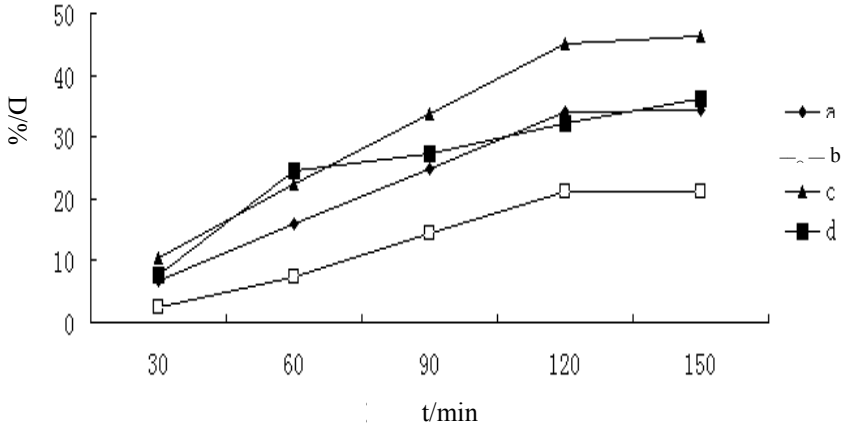
(a) pure TiO_2 (b)La-WO_3/TiO_2

Fig.1 The infrared spectrograms of TiO_2

0.25g, pH for 1. Fig.2 shows that illumination after 150 min, the degradation rates of La-WO_3/TiO_2 at 300 ℃, 400 ℃, 500 ℃, 600 ℃ heat treatment after 2h are 21. 27%, 34. 30%, 46. 18%, 36. 05% respectively. Because in low temperature calcination, TiO_2 is amorphous structure and

exists defects more, a lot of defects become the center of electrons and holes in the compound, electron and hole structure is difficult to reach surface involved in photocatalytic reaction, thus TiO_2 has lower light catalytic activity; With the increase of calcination temperature, the degree of crystallization and the density of surface structure are improved, its internal fewer defects become the center of electrons and holes in the compound, thus TiO_2 has higher photocatalytic activity. When calcining temperature is too high, however, grain growth, the effective surface area of TiO_2 is reduced, REDOX ability is reduced, TiO_2 surface active hydroxyl amount is reduced, and high temperature calcining can make the crystal structure of TiO_2 from anatase to rutile type, so its photocatalytic activity also decreases.

Fig.3 is pure TiO_2 powder, single doped and co-doping titanium dioxide powder photocatalytic degradation rate figure in10mg/L methyl orange solution,0.25g photocatalyst, pH=1, at 465nm. From figure 4.9 can be seen, as the growth of the illumination time, TiO_2 samples to methyl orange degradation rate increased gradually. At the same time, doping can improve obviously the photocatalytic activity of TiO_2, the degradation efficiency from big to small order for: La-WO_3/TiO_2>La/TiO_2>WO_3/TiO_2>pure TiO_2. Therefore, photocatalytic effect of co-doping titanium dioxide is better than single doped and pure TiO_2. Lanthanum doped with tungsten trioxide improve photocatalytic activity of TiO_2 is caused by their synergism. Because lanthanum metal ion

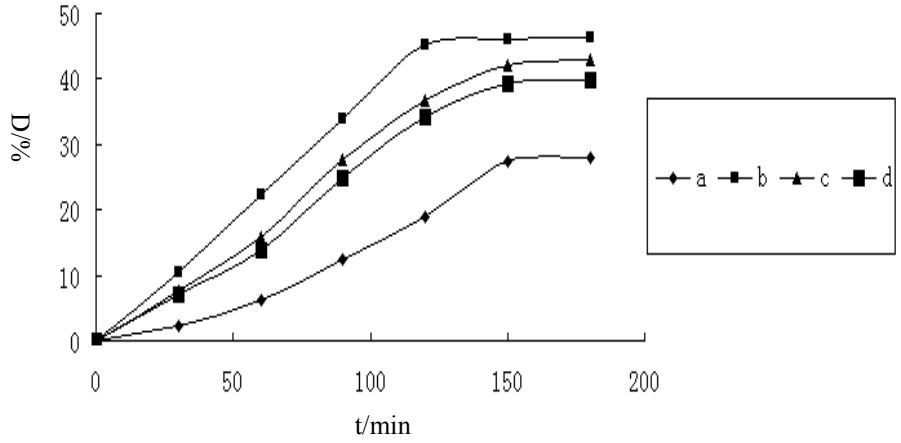


(a) 400℃ (b) 300℃ (c) 500℃ (d) 600℃

Fig.2 Heat treatment temperature on the influence of La -WO_3/TiO_2 photocatalytic degradation rate

radius is bigger than titanium, lanthanum can enter the lattice of TiO_2 rarely.When doping lanthanum quantity is small, lanthanum of entering lattice of TiO_2 is +3 valence. According to the band theory of solid state physics, La^{3+} doped into TiO_2 can replace Ti^{4+} lattice position, TiO_2 crystal lattice will lack an electron, which can strengthen tungsten-titanium system charge imbalance, and reduce electronic-hole composite risk, improv its photocatalytic performance.

In addition, also can be seen from the figure, photocatalytic activities of single lanthanum doped and tungsten trioxide doped TiO_2 are higher than that of pure TiO_2, the reason is that doping metal ions could enter titanium dioxide lattice, change TiO_2 crystal lattice distortion, and lead to phase transformation, make absorption wavelength of TiO_2 extending to the visible light region.



(a) pure TiO_2 (b) La-WO_3/TiO_2 (c) La/TiO_2 (d) WO_3/TiO_2

Fig.3 Different dopant on the influence of TiO_2 photocatalytic degradation rate

Conclusions

Butyl titanate as titanium source, anhydrous ethanol as solvent, glacial acetic acid as inhibitor, La-WO_3/TiO_2, La/TiO_2,WO_3/TiO_2 and pure TiO_2 photocatalysts were prepared through sol-gel method in this paper; At the same time, photocatalytic performance of /TiO_2 was studied by infrared spectrometer and spectrophotometer; With methyl orange as simulated target degradation material, heat treatment temperature, dopant, etc. on photocatalytic performance of TiO_2 affect were analysed. Experimental results show that doping can improve obviously the photocatalytic activity of TiO_2. When calcination temperature is 500 ℃, dosage of catalyst is 0.25 g, pH is 1, methyl orange concentration is10 mg/L, La-WO_3/TiO_2 photocatalytic effect is best, and degradation rate is 46.18%.

References

[1] Yong Wang, Yan Zhang, Yawei Zhao, et al. The preparation, modification and Application research progress of nanometer titanium dioxide [J]. Chemical research, 2010，21(2) .

[2] Imai H，Ohgi H. Takezawa Y，et al. Control of nanoscale morphology of oxide crystals using aqueous solution systems[J].Key Eng Mater,2006,301:211-214.

[3] GAO H T, ZHOU J, DAI D M, et al. Photocatalytic activities and electronic structure analysis of N_2 doped anatase TiO_2 : a combined experimental and theoretical study[J]. Chem Eng Technol, 2009, 32 (6) : 867-872.

[4] RAMARKR ISHNA G, H IRENDRA N G. Emission from the charge transfer state of xanthene dye sensitized TiO_2 nanoparticles: a new app roach to determining back electron transfer rate and verifying the marcus ilnverted regime [J]. J Phys Chem B, 2001, 105: 7000-7008.

[5] XING C J, ZHANG Y J , GUO L J, et a1. Band structure controlled solid solution of $Cd_{1-x}Zn_x$ photocatalyst for hydrogen production by water splitting[J]. Int J Hydrogen Energy, 2006, 31 (14) : 2018-2024.

[6] JANG J S, L IW, SE H O, et a1. Fabrication of CdS/TiO_2 nano-bulk composite photocatalysts for hydrogen production from aqueous H_2S solution under visible light[J]. Chem Phys Lett, 2006, 425 (4 /5 /6) : 278- 282.

Advanced Materials Research Vol. 936 (2014) pp 814-818
© (2014) Trans Tech Publications, Switzerland
doi:10.4028/www.scientific.net/AMR.936.814

Preparation and photocatalytic performances of F-doped TiO_2

Xianzhen Diao , Xili Zhang

Chemistry and Chemical Engineering College, Chongqing Institute of Science and Technology, Chongqing 401331,China

Xianzhen81@126.com

Keywords：titanium dioxide; photocatalytic properties; sol-gel method; doping

Abstract：Butyl acetate titanate as precursors, no water ethanol as solvent, pure TiO_2 and different doping ratio of F/TiO_2 photocatalysts were prepared through sol-gel method; And F doping amount on photocatalytic activity of TiO_2 influences were analysed systematically through uv-vis spectrophotometer, infrared spectrometer, etc. Experimental results show that photocatalytic activity of TiO_2 is better when the mole ratio of F is between 10% and 20%; When F doping amount is 20%, catalyst amount is 25g, the photocatalytic degradation rate of F/TiO_2 can reach 85.74% in10%wt methylene blue solution under 250W high-voltage mercury lamp illumination after 2 hours and the area of illumination $6.94\times10^{-3}m^2$. In the same way, the photocatalytic degradation rate of pure TiO_2 is just 35.39 %. It proves that F/TiO_2 catalyst of doping amount 20% presents the best photocatalytic activity.

Introduction

Along with the increasingly serious environmental problems and the demand of new energy, because its application and prospect in environmental pollution purification, energy regeneration is very broad and photocatalytic technology has been attracted much attention. Photocatalytic technology has some unique properties, which can use directly sunlight at room temperature to all kinds of organic pollutants completely mineralized and no secondary pollution, and it become a kind of ideal environmental pollution control technology, so it has become one of the most active area of research at home and abroad in recent years[1].Nano TiO_2 photocatalyst as a kind of excellent performance has many advantages of suitable width of forbidden band, large specific surface area, high photochemical stability, and high catalytic efficiency, non-toxic, low cost. It is of great significance to reduce running costs, protect the environment, maintaining ecological balance, and realizing the sustainable development, so it has a broad and attractive prospects in the control environmental pollution and so on many fields [2,3].But TiO_2 sunlight utilization rate is low and raw electronic light- hole is easy to composite, which results in the decrease of the photocatalytic efficiency. So how to improve the range of spectral response and catalytic efficiency of TiO_2, shorten the reaction required time is the emphases and difficulties and development direction of the current research.Researches show that nonmetal doping modification TiO_2[4-7]can significantly improve the photocatalytic activity of TiO_2.

In this paper, butyl titanate as precursor, anhydrous ethanol as solvent, the F/TiO_2 light catalyst was prepared by the sol gel method, and its photocatalytic activity was studied using the uv-vis spectrophotometer, infrared spectrometer, etc.

Experiments

F-doped TiO_2 powder preparation

Chemical pure butyl titanate/Ti $(OC_4O_9)_4$ as raw material, anhydrous ethanol as solvent and glacial acetic acid as inhibitor, a certain amount of distilled water, anhydrous ethanol, a small amount of nitric acid and NH_4F solutions were mixed, fully stirring, mixing, as A solution; A certain amount of acetic acid, butyl titanate and glacial acetic acid were slowly added to in 60 ml anhydrous ethanol under the magnetic force agitator, as B liquid. Under the magnetic force agitator the A solution was slowly dripped into to the B solution, got uniform transparent solution. After waiting for gel formation, stopped stirring, placed in the air, then aged 12h above; Under the condition of 120 ℃constant temperature dried about 2h, got yellow crystals; The white powder after crystal grinding would put into the muffle furnace, high temperature calcination 2h, and white fluorine doped TiO2 nano powder was got.

Catalyst characterization

Samples of components were analysed by the Germany Tensor-27 Fourier infrared spectrometer (FT-IR) ; Samples of light absorption performance and light catalytic degradation performance were tested by UV1102 ultraviolet-visible spectrophotometer of Shanghai day science co., LTD production .

Photocatalytic performance study

Research of photocatalytic performance is to use 250 w of straight pipe shape uv high pressure mercury lamp (wavelength of 253.7nm) irradiation TiO_2 degradation methylene blue solution completion. A certain amount of titanium dioxide photocatalyst was dipped to 20 ml, 10 mg/L of methylene blue solution under ultraviolet light (light source only 20 cm from the surface, the area light is $6.94*10^{-3}$ m^2), then was measured the absorbance at 464 nm every 30min, recording data, degradation rate of measured target degradation solution under uv irradiation was got by absorbance data calculated as Eq. 1.

$$D=(1-A_t/A_0)\times 100\%. \quad (1)$$

Among them: D for degradation rate; A_t for the of target degradation solution after the reaction; A_0 for the absorbance of target degradation solution before the reaction.The photocatalytic degradation rate of samples was got by the formulas.

Results and discussion

Infrared spectral analysis

Figure 1, figure 2 are pure TiO_2, F/TiO_2 infrared spectrograms. From figures illustrates that the wide and strong absorption peak in 400 ~ 1000 cm^{-1} is caused by TiO_2 crystals on the surface of Ti - O key stretching vibration.Relative to the pure TiO_2, waves obviously increases a lot after doping F. Because the F-O key antisymmetric stretching vibration absorption peak are between 1000 ~ 1700 cm^{-1}, so it can be thought that 1637 cm^{-1} , 1407 cm^{-1} peaks are infrared absorption peaks of F atom surface chelation in the TiO_2 and double complexing adsorption. It can be concluded the F element is doped in the TiO_2 catalyst effectively.

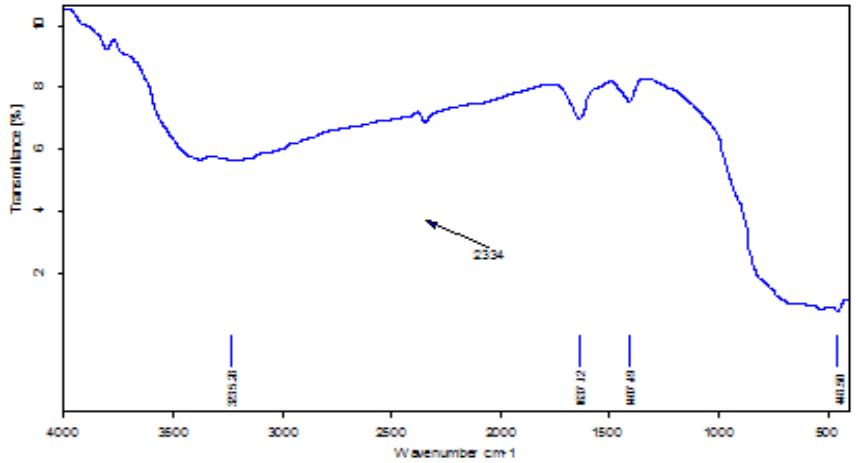


Fig.1 Pure TiO_2 FT-IR spectra

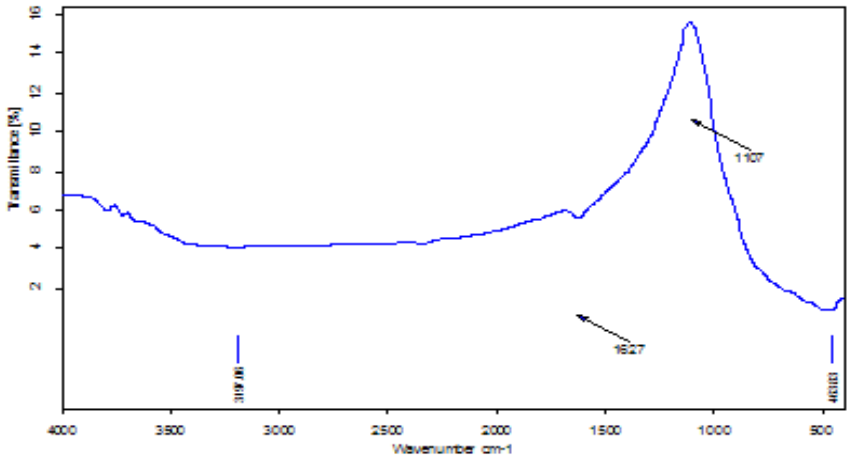


Fig.2 F/TiO_2 FT-IR spectra

Absorption spectrum analysis

Fig.3 is the uv-visible absorption spectrum of TiO_2 catalyst under the condition of PH = 2, 400 ℃, F doping amount respectively 0%, 5%, 10%, 20%, 30%.

Can be more intuitive to see from the figure, the samples of TiO_2 doped fluoride absorption sideband is more pure TiO_2 obvious red shift; With the increase of fluorine doping amount, TiO_2 nanoparticles of spectral response range expands to visible light area, and absorption of visible light increases. When fluorine doping amount increase to 20%, the ultraviolet absorption spectrum sideband from pure TiO_2' 400nm expands to 450 nm, the red shift phenomenon is more obvious. At the same time also can be seen from the picture, along with the increases of the doping amount, TiO_2 sample absorbance value also increase. When the mixing amount of fluoride is 20%, absorbance values is the most biggest; But continuing to increase the fluorine doping amount, its absorbance reduces. Thus fluorine doping amount of TiO_2 is greatly influenced by light absorption performance.

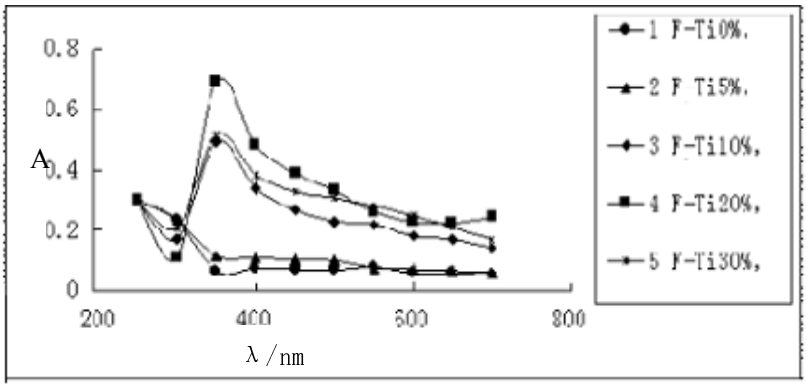


Fig.3 Uv visible absorption spectra of different doping amounts F/TiO_2

Photocatalytic Activity Analysis

Fig.4 shows 25g F/TiO_2 photocatalytic degradation rate change over time under the condition of 400 ℃, PH = 2, F doping amount respectively 0%, 5%, 10%, 20%, 30% .

The figure shows that doped fluoride of titanium dioxide photocatalyst of degradation rates increased significantly, and with the increase of illumination time, photocatalytic effect is more and more better. Doping ratio for 10% and 20% of F/TiO_2 photocatalyst of degradation rate after two hours sunlight were 82.64% and 82.64% respectively; But pure TiO_2 of degradation rate is 35.39% under the same condition. It can be attributed that F element doping can reduce light electrons and holes in the compound, restrain grain growth, and improve photocatalytic degradation rate[8]. Therefore, fluorine doping amount of TiO_2 photocatalyst has a great influence on photocatalytic degradation rate.

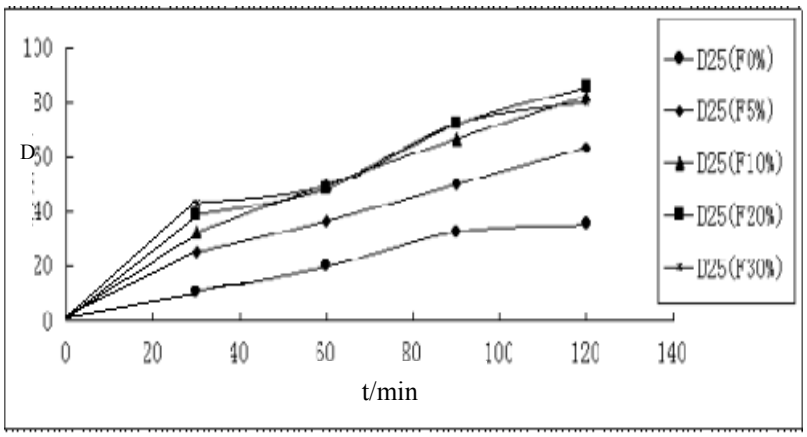


Fig.4 TiO_2 photocatalytic degradation rate chart of different F doping amount

Conclusions

Butyl acetate titanate as precursors, no water ethanol as solvent, pure TiO_2 and different doping ratio F/TiO_2 photocatalysts were prepared through sol-gel method. By means of uv-visible absorption spectrum and photocatalytic activity of study of TiO_2, results show that fluorine doping make the absorption spectrum of TiO_2 photocatalyst moving towards long wave, and within the scope of the visible light absorption enhancement; And photocatalytic degradation performance has increased significantly. When fluorine doping ratio is 20%, light time are two hours, TiO_2 catalyst for degradation rate of methylene blue solution can reach 85.74%, photocatalytic degradation effect is better.

References

[1] Yizhong Wang. Eight kinds of dyes in the pulp suspension system of TiO_2 sunlight catalytic oxidation degradation [J]. Journal of catalysis, 2000, 21 (4) : 327-330.

[2] ChenJian Zhang, Kunmin Guo, Lan Ma, Gongyang Zhao. Reaction kinetics model of gas pollutants degradation onTiO_2/AC photocatalyst [J]. Journal of catalysis, 2006, 27:853

[3] Aihua Chen, Aiping Chen, Chitao Ceng, Wei Liu, Zhiming Dai. Deactivation research of load type catalyst[J]. Journal of chemical university of technology, 2003, 29 (4) : 376-379.

[4] Huijing Liu, Yuan Bai, Hongqi Sun, etc. Mechanism study of doped groups influence on nitrogen modified TiO_2 ultraviolet catalytic activity[J]. Journal of inorganic materials, 2009, 24 (3) : 443-447.

[5] Periyat P, Pillai S C, McCormack D E, et al. Improved High-Temperature Stability and Sun-Light-Driven PhotocatalyticActivity of Sulfur-Doped Anatase TiO_2[J]. J Phys Chem C, 2008,112:7644-7652.

[6] Ren WJ，Ai ZH, Jia FL, et al. Low Temperature Preparation and Visible Light Photocatalytic Activity of Mesoporous Carbon-Doped Crystalline TiO_2[J]. Appl Catal B-Environ，2007，69: 138- 144.

[7] Lu N，Quan X，Li J Y，et al. Fabrication of Boron-Doped TiO2 Nanotube Array Electrode and Investigation of Its Photoelectrochemical Capability[J]. J Phys Chem C,2007,111: 11836-11842.

[8] Qingju Liu. Research of department of TiO_2 photocatalysis super hydrophilic film [D]. Kunming: kunming university of science and technology, 2003.

Advanced Materials Research Vol. 936 (2014) pp 819-821
© (2014) Trans Tech Publications, Switzerland
doi:10.4028/www.scientific.net/AMR.936.819

Preparation of Doped TiO_2 Responded to Visible Light

Yanhuai Zhou[1,a], Xinghe Wang[1,b], Jia Chen[1], Rui Pu[1]

[1]School of Physics and Technology, Nanjing Normal University, Nanjing 210023, China

[a]zhouyanhuai@njnu.edu.cn,[b]wangxinghe@njnu.edu.cn,

Keywords: TiO_2; sol-gel method; photocatalytic degradation

Abstract. Cu-N co-doped TiO_2 powder was prepared by sol-gel method. The Powder was characterized by X-ray diffraction (XRD) and UV-Visible absorbance spectroscopy (UV-Vis). The X-ray results indicated that Cu-N co-doped has no effect on its anatase type. The UV-Vis results show that the absorb threshold has extend to visible-light, the absorbility of co-doped TiO_2 is higher than that of pure TiO_2, and the Photocatalytic activity has been increased.

Introduction

In recent 20 years, more and more researchers pay their attention to nanometer TiO_2, since TiO_2 has many advantages, for example, better chemical stability, highly reactive, nontoxicity, cheapness and making direct use of solar energy, it is a promising material in photoelectric conversion, chemical synthesis and photodegradation of organic pollutions in water and air. However, TiO．only absorb ultraviolet light, and it has a low utilization ratio of the sunlight (3%~4%). So, it is meaningful if the absorb threshold of TiO_2 can be extended to visible light.

A lot of researches show that dopant can improve visible light absorbility of TiO_2. At present, there has many essays about doping metallic or nonmetallic elements into TiO_2 to extend its absorb threshold. But doping metallic and nonmetallic elements at the same time is not much to see.

In this paper, metallic and nonmetallic elements co-doped TiO_2 were prepared by sol-gel method, the result of characterization and photocatalytic of co-doped TiO_2 is good.

Experimental Details

Chemical Reagent

Tetrabutyl titanate, absolute alcohol, glacial acetic acid, secondary water.

The Synthesis of Samples

Solution A: acetic acid(4ml) and tetrabutyl titanate(4ml) were added to the absolute alcohol(20ml) and stirred them strongly in the same time. Solution B: acetic acid(2ml), secondary water(2.5ml),$Cu(NO_3)_2.3H_2O$(0.0361g)and $CO(NH_2)_2$(0.5231g) were added to absolute alcohol(10ml) , dissolved them by means of ultrasonic dissolution. In conditions of strongly stirring, added B into A slowly and stirred for about 3 hours, we got stable gel after left them stand for 24h, the gel turned into dry glue after dry them at temperatures 80℃, then , the Cu-N co-doped TiO_2 powder was prepared by roasting the dry glue in muffle burner at 450℃ for 3h. For compassion, pure TiO_2 was prepared under the same conditions.

Characterization of Samples

The crystal construction of samples was characterized by using **X**-ray diffraction (D/max2500VL/Pc) with CuKa radiation, the angle of diffraction was 2θ，the step was 0.02℃, scan speed was 5℃/min, the voltage was 40 KV, the current was 50mA. Ultraviolet/visible/near infrared spectrograph (Cary5000) made by Varian Corporation was applied to Uv-Vis diffuse reflectance spectroscopy , Standard BaSO4 board was used to adjust the instrument baseline.

Photocatalytic Activity Test

The center light of photochemical reactor is 500W high-pressure mercury-arc lamps outside is circulating water cooling trap, catalyst was the powder of pure TiO_2 and co-doped TiO_2, added the powder into secondary water at the level of 1.0g/L, the original level of degrading methyl orange was 200mg/L. The solution was kept away from the light and stirred for 30min to make sure adsorption reaction of reactants reach balance at room temperature.

Results

Uv-Vis Diffuse Reflectance Spectroscopy

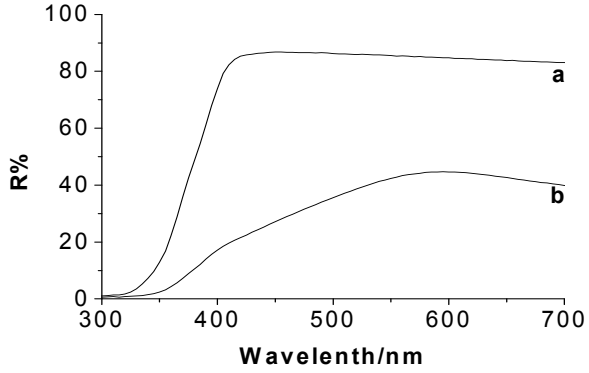


Figure1. Uv-Vis Diffuse Reflectance Spectrum Of (A) Pure Tio_2 And (B) Co-Doped Tio_2

Figure1 shows, compared with pure TiO_2, a red shift was happened in co-doped TiO_2 spectrum from 380nm to 590nm, the corresponding energy dropped from 3.2ev to 2.14ev, the strength of spectrum absorption was greatly improved. The reason might be the nitrogen-atoms incorporated into crystal lattices and replaced oxygen-atoms, and then Cu^{2+} interacted with TiO_2, since nitrogen's electronegativity is lower than oxygen's, electronic hybrid of nitrogen and oxygen leaded to the decrease of band-gap energy. The result indicated the absorption threshold could be broadened after co-doped metallic and nonmetallic elements into TiO_2.

Analysis of Samples Crystal Phase Structure

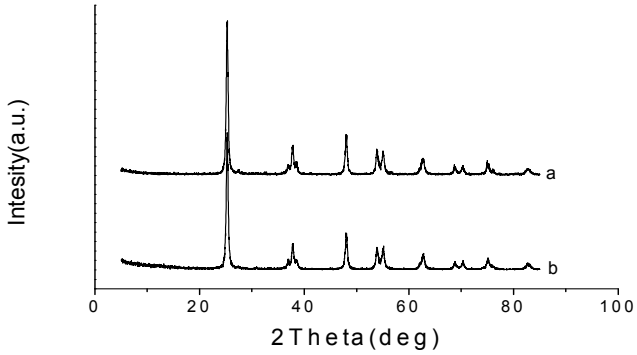


Figure2. Xrd Spectrum Of (A) Pure Tio_2 And (B) Co-Doped Tio_2

Figure2 is XRD spectrum of (a) pure TiO_2 and (b) co-doped TiO_2, the result turned that a and b were anatase types. According to the formula of Scherrer, samples' average size $D=K\lambda/\beta\cos\theta$(β, half band width of the anatase phase; λ,wavelength of X-ray; K, Scherrer constant=0.89). The

average sizes of pure TiO_2 and co-doped TiO_2 are 7.0nm and 4.9nm respectively. The size of co-doped TiO_2 became smaller, the reasons might be the dopant incorporated into TiO_2 lattices and interacted with TiO_2.

Photoreactivitie of Samples

Measured photocatalytic degradation reaction of pure TiO_2 and co-doped TiO_2 with xylenol orange by Uv-Vis spectroscopy. The absorbance of xylenol orange changed at 433nm, according to Beer law, A=KC (K, absorption coefficient; C, level of samples). Degradation rate of xylenol orange is $D=(\Delta C/C_0)\times 100\%=(A_0-A/A_0)\times 100\%$ (D, degradation rate; C_0 , the original concentration of xylenol orange; ΔC, differences between original and final concentration; A_0, the absorbance of original xylenol orange at 433nm; A, the absorbance of final xylenol orange).

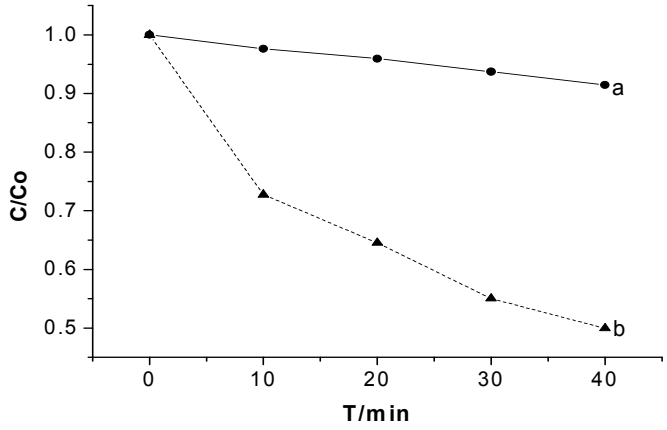


Figure3. Photocatalytic Degradation Reaction Of (A)Pure Tio_2 And (B) Co-Doped Tio_2 With Xylenol Orange

Form Figure 3, we know Photoreactivitie of dopant is higher than pure TiO_2, after 40min catalysts, photocatalytic degradation rate of dopant is 51%, the pure is only about 10%

Conclusion

The absorb threshold of Cu-N co-doped TiO_2 powder prepared by sol-gel method has extend to visible-light. The test of xylenol orange photocatalytic degradation shows Photoreactivitie of dopant is 40% higher than pure TiO_2, Photoreactivitie of catalyst is strengthened obviously.

References

[1] J Mater Res, Haro Poniatowsh E, Crystallization of nanosized titania particles prepared by the Sol--Gel process, 1994 ,9(8) :210222108.

[2] Yang Songwang，Gao Lian，Simple and Effective Preparation of N-doped Nanocrystallites with Visible-light Activities, Journal of Inorganic Materials，2005，2(4)：785-788.

[3] Choi W, Termin A, Hoffmann M R, The role metal of ion do pants in quantum sized TiO_2: Correlation between photo reactivity and charge carrier recombination dynamics [J]. J Phys-Chem , 1999, 98: 13669 - 13679.

Advanced Materials Research Vol. 936 (2014) pp 822-828
© (2014) Trans Tech Publications, Switzerland
doi:10.4028/www.scientific.net/AMR.936.822

Development and Comparative Analysis of Aluminosilicate Based Ceramic Filters for Ground Water Defluoridation

Johnson Kwame Efavi[a*], Abu Yaya[a], SolomonAdeborna[a], Julius Fobil[b]

[a]Department of Materials Science and Engineering, University of Ghana, Legon

[b]Department of Biological, Environmental and Occupational Health Sciences School of Public Health University of Ghana, Legon

[*]Corresponding Author: Materials Science and Engineering Department, University of Ghana, Legon, Accra-Ghana. Tel.: +233244111217, Email Address: jkefavi@ug.edu.gh

KeyWords: Kaolin, Flouride, Porous Ceramics, Ghana,Water Contamination, Aluminosilicates

Abstract. Low levels of fluoride in drinking water is healthy for the teeth enamel, however, higher concentrations result in dental fluorosis with prolonged exposures leading to skeletal fluorosis. Fluoride removal capacities of ceramic filters using aluminosilicates (Anfoega clay, Kibi kaolin, Laterite soil and Termitaria earth) samples from Ghana Geological Survey Department have been investigated and analysed for possible application in the Bongo District of Ghana noted forhavinghigh fluoride concentration in its ground water. Batch sorption studies conducted revealed that the amount of fluoride ions removed increased proportionally with increasing filter thickness, temperature and contact time to an optimum value. Using particle size ranges of <355µm and 1cm filter thickness at room temperature, the percentage of fluoride removed by the samples reached an optimum value after 70mins. Increases in filter thickness, contact time or temperatureincreased the amount of fluoride ions removedand the time required to reach the optimum value reduced significantly.

Introduction

Water is a natural resource vital for the healthy growthof mankind. In the rural regions of most developing nations however, there is inadequate access to potable waterand the water sources are contaminated with disease vectors, pathogen, toxins, suspended solids and excessive amount of minerals and organic matter [1, 2].

Ground water is one of the major sources of water for domestic purposes in the rural regions of the world. Due to earth coverings that acts like a filter, ground is considered to be pure and unpolluted by rural indigenes if it is odorless, free from turbidity etc. This perception has however, changed due to proven scientific results showing that water, no matter how colourless, may be polluted by rock bearing minerals rich in As, F- ions[1,3]. Fluoride contaminations in ground water have been observed to occur in two distinct ways: naturally in ground water resources and as toxic waste [4, 5, 6].

Many domestic water purification processes are available and research works have shown that ion exchange techniques, activated carbon, bone char, reverse osmosis and chemical precipitation techniques are capable of removing fluoride ions and other volatile organic compounds (VOCs) very effectively [3, 4, 5]. Due to the complexities and cost involved in these technologies, their applicability in rural regions of sub-Saharan Africa is challenging and often unavailable.

Research reports have also shown thatclays and laterites have high tendencies to effectively remove anions and many other volatile organic compounds from contaminated water bodies by adsorption mechanismbecause they contain minerals such as kaolinite, smectite, amorphous minerals etc that have exchangeable OH groups in the mineral structure [6,7]. Different technological concepts for fluoride adsorption onto Al and Fe based oxides have also been reported [7, 8, 9] and they are well recognized in sub-Saharan Africa [10, 11]. These efforts have helped to effectively reduce turbidity, bacterial and protozoan contamination.The inability of these technologies to substantially

reduce chemical pollutants especially fluoride ions, leaves much to be desired and have been largely attributed to structural changes, influence of pH on adsorption capacity as well as slow kinetics [12].

The Bongo district in the upper east region of Ghana has been associated with high incidence of dental cavities and mottled teeth. In 1993, a dental health survey of 1558 students indicated that 62% had fluorisis and a monitoring programme by then Ghana Water and Sewage Corporation on 93 boreholes and shallow wells indicate 63.5% had fluoride levels in excess of 1.0mg/l. An innovative simple alternative to solve ground water fluoride contamination problems in rural regions is therefore required.

This worktherefore seeks to developcheap, efficient and sustainable porous ceramic bodies (filters) from alumino-silicates (Al oxides) based materials for the potential adsorption of fluoride ions from contaminated water bodies in the Bongo district of Ghana to levels accepted by WHO standards [13,14]. The chemical composition of various aluminosilicate ores will be sampled and analysed. The effect of preheating high temperature processing will also be observed.

Materials &Methods

Raw Materials and Preparation

The porous media (filter) used for this investigation was based on aluminosilicates and includes Anfoega clay deposits in Anfoega- Volta region of Ghana, Kibi Kaolin deposits in Kibi- Eastern region of Ghana. Laterite and Termataria Earth received from Ghana Geological Survey Department (GGSD) sampled from the Bongo region in Ghana was also included in this investigation. Mortar and pestle were used to ground the sample in order to reduce the particle size. We then sized the ground samples using a sieve stack of:500µm, 355µm, 90µm and 63µm.Saw dust was used for the formation of pores in the aluminosilicates materials (Anfoega clay, Kibi Kaolin and Laterite as well as Termataria Earth). The sawdust was obtained from a local sawmill and it was dried in an oven at 80˚C for 1 hour.

Chemical Analysis

The chemical analysis of the aluminosilicate samples used in this investigation was done with SpectroXLab 2000 X-Ray fluorescence spectrometer (AMETEK, USA) at the Ghana Geological Survey Department. The aluminosilicate samples to be analysed were sieved in a 106um sieve after which 4 grams of each was mixed with aucowax powder acting as a binder. We then milled the mixture was for about 3minutes in a Retich milling machine (model MM 301) and the mixture was later pressed in an XRF pellet press. The samples were then loaded into a Spectra Xlab 2000 sample holders for the analysis.

Porous Ceramics Filter Preparation

We prepared batch formulations comprising of the aluminosilicates test samples, sawdust and water. The batch green bodies (unfired clay) were subsequently formed by slip casting using a funnel connected to a suction pump. After the suction pump had taken all the moisture from the slip, the green body was left to dry in the open air for 4 hours before transferring the mass to a drying oven maintained 110˚C to completely dry. The formed bodies were fired to 850˚C using a CSIR manufactured gas furnace. When the desired firing temperature was reached, it was held constant for 2 hours (“Soaking Period”). The firing process burns off the saw dust after which the kiln was left to cool for 24 hours before the fired filters were removed. We observed dimensional stability and modulus of rupture (MOR) test conducted on the filters. The batch formulations experiment was repeated for thicknesses of 0.5cm, 1.0cm, 1.5cm, 2.0cm and 2.5cm.

Batch Sorption Test

Fluoride concentration in Bongo ground water has been reported in excess of 4mg/l to as high as 6mg/l [16]. As a baseline guide a stock solution of NaF containing 6mg/l was prepared to serve as contaminated fluoride water for the fluoride sorption studies. The NaF powder was dried in a drying oven for 1 hour at 100˚C; 6g of the dried NaF was weighed and dissolved in deionized water and it was then diluted to 1000ml in a volumetric flask.

The adsorption capacity of the different ceramic filters at room temperature and at higher temperature up to 100ºC was tested. The flow rate studies of the ceramic filters were conducted by

first soaking the filters completely inside a bowl of the stock solution for 2 hours and the time it takes for 10ml of the stock solution to completely pass through the filters was observed and recorded. The concentration of fluoride in the filtrate was also recorded.

Results and Discussion

Physical Properties Evaluation

Shrinkage after drying and firing was observed. The degree of shrinkage was independent of the pore formers (saw dust) used. As seen in Fig. 1, Anfoega clay which was observed to be more plastic during the test processes exhibited a much higher strength.Observed variation in the strength of the filters as measured by the MOR test and is expected due to differences in mineralogical composition as well as the plastic nature of the alumino-silicate samples used.

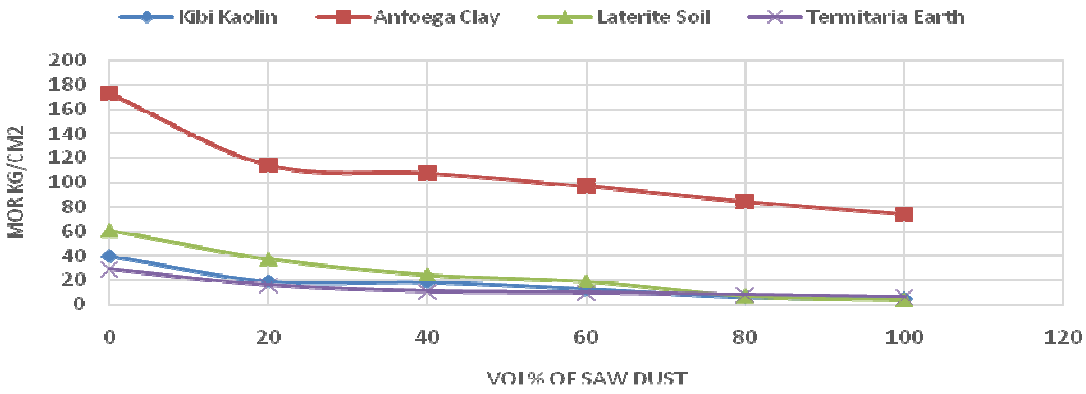


Fig 1 Effect of Pore Formers on MOR

Chemical Composition

Table 1 shows the chemical composition of the alumino-silicate samples used in this investigation. The samples have varying degrees of SiO2, Al2O3 and Fe2O3 because they represent a group of mineral deposits consisting of residual insoluble ferric and aluminum oxides, clay minerals and quartz formed by weathering of rocks [12].

Table 1: Chemical Compositions of Samples (%)

	Afoega Clay	Kaolin, Kibi	Laterite	Termataria, GGSD
Si02	**66.09**	45.81	48.2	57.6
Al2O3	23.15	41.64	22.2	9.8
Fe2O3	2.55	0.95	12.1	7.1
FeO	-	-	0.63	-
MgO	0.5	-	0.43	0.07
CaO	0.7	0.01	0.05	1.5
Na2O	1.43	0.02	0.13	1.21
K2O	2.35	0.84	0.3	-
TiO2	1.14	1.46	0.96	0.92
MnO2	0.0026	<0.01	0.03	-
P2O5	0.12	0.06	0.14	0.12
BeO	-	-	-	0.08
SO3	0.22	0.01	-	0.08
Cl-	0.026	<0.01	-	0

Fluoride Removal Capacity

The filter prepared from 850˚C fired Anfoega clay, Kibi kaolin, Laterite soil and Termitaria earth demonstrated different fluoride adsorption capacities at different dose thicknesses as seen in Fig. 2.

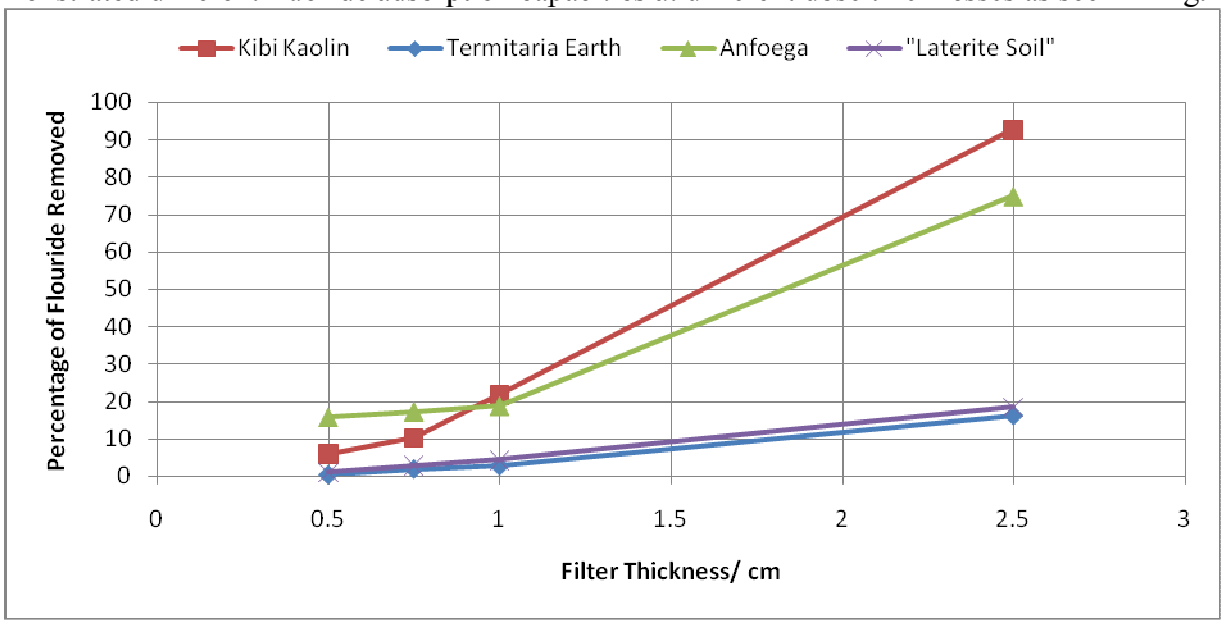


Fig 2 Effect of Filter Thickness on Fluoride Adsorption

At very low thickness below 1cm, Anfoega Clay removed more fluoride ions than the other batch samples. However, when the thickness of the samples was increased Kibi kaolin removed more of the fluoride than the other formulations. This indicates that the Kibi based filters performs better when the filters are thick and the solution contact the material for a longer period. From this observation, it was also calculated that 0.5cm of Anfoega clay and Kibi kaolin filters fired to 850˚C and having a particle size range of <355µm will take away 6mg/l of fluoride in 100ml beaker in less than 20 minutes, while Laterite soil and Termitaria earth will require 2.5cm thickness to achieve the same effect.

Effect of Contact Time on Fluoride Adsorption

Fig. 3, shows the percentage of defluoridation of Anfoega clay, Kibi kaolin, Laterite soil and Termitaria earth with time using a filter thickness 1.0cm. The percentage of fluoride removed increased steadily during the period. Laterite and Termataria earth showed lower degree of fluoride removal strength. This indicates that Anfoega clay particles and Kibi kaolin have more specific surface area for the adsorption of fluoride than Laterite soil and Termitaria earth.

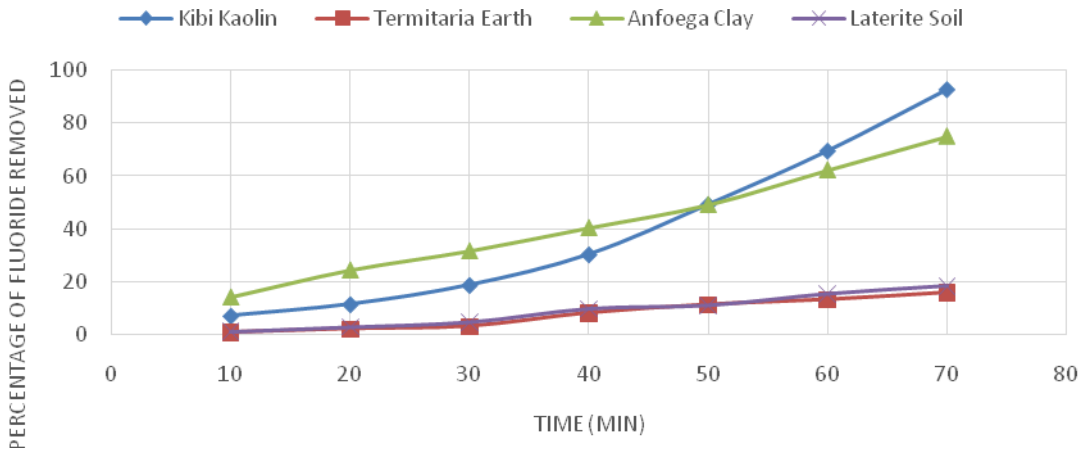


Fig 3 Effect of Contact Time on Fluoride Adsorption

Effect of Flow Rate on Fluoride Sorption

The highest flow rate achieved in the composed ceramic filters showed in Fig. 4 was 0.3ml/s and the lowest flow rate was 0.0029ml/s. Even though a high flow rate was desirable, it decreased the amount of fluoride removed. To compensate this effect the filtration process would have to be repeated to allow more time for the fluoride to be removed. Low flow rate is undesirable even though it results in better fluoride removal.

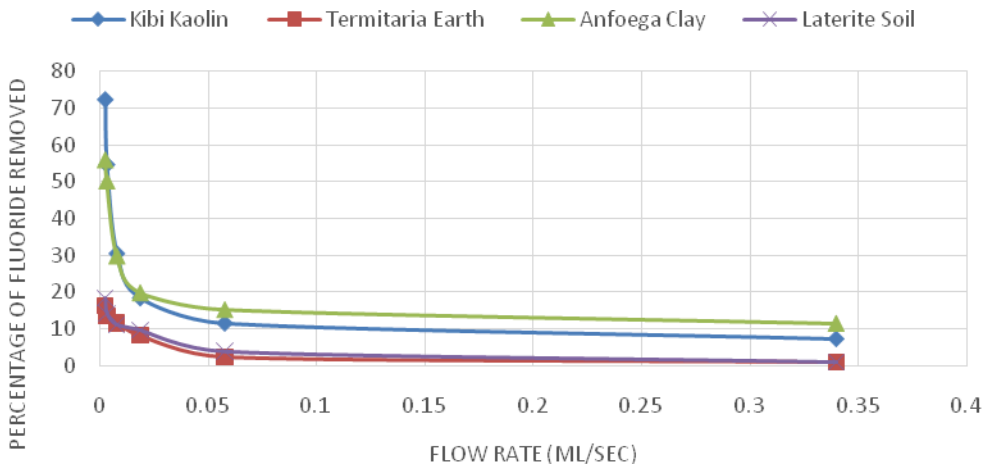


Fig 4 Effect of Flow Rate on Fluoride Adsorption

Effect of Temperature on Fluoride Adsorption

The temperature dependence of fluoride adsorption by Anfoega clay, Kibi kaolin, Laterite soil and Termitaria earth was studied over the range of 24-100˚C. Above 70˚C, it was observed that all the samples removed significant amount of fluoride ion and approached completion as the temperature further increased as seen in Fig. 5. This shows that, if the Bongo ground water is boiled before passing it through any of the formulated filters, fluoride contamination of the water will be reduced significantly. This is attributed to thermodynamics and kinetics of the adsorption reaction which are temperature dependent through $\Delta G = -RT\ln Kc$ [13].

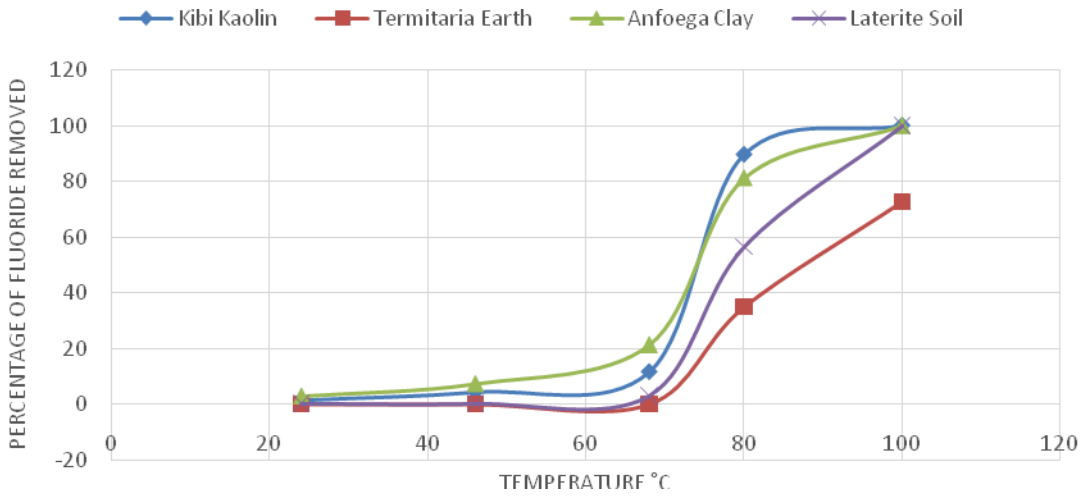


Fig 5 Effect of Temperature on Fluoride Adsorption

Micrograph Results

Fig. 6 shows optical micrographs of the ceramic filters produced. The observed dimensional stability of the porous media in the thickness ranges investigated confirms the feasibility of producing such filters for rural household usage.



Fig 6 Optical Micrograph of Ceramic Filters

Conclusions

Fluoride contamination of water in rural regions of Ghana especially in the Bongo district of the Northern Ghana causes a number of health related problems for the indigenes living in such communities. The possibility of using porous ceramic bodies (filters) as fluoride removal media have been successfully investigated in this work.

The results showed that excess fluoride ions in ground water can be removed to different levels using aluminosilicate based mineral deposits and that preheating to temperatures above 70˚C improved the adsorption characteristics of the filters.

Acknowledgement

The authors will like to thank Ghana Geological Survey Department and the Council Centre for Scientific and Industrial Research for making their facilities available for this investigation. The authors are also grateful to University of Ghana for financial assistance received in the course of this work.

References

[1] Sarma, J., Sarma, G. A., 2011 , Study of the Removal of Toxic Anions from Contaminated Water Utilizing Natural Kaolinite Clay of Assam, International Journal of Research in Chemistry and Environment.

[2] Gyau-Boakye, P. and Dapaah-Siakwan, S., 2012, Groundwater: Solution to Ghana's Rural Water Supply Industry, http://www.africantechnologyforum.com/GhIE/ruralwtr/ruralwtr.htm

[3] Bårdsen, A. and Bjorvatn, K., 1995, Fluoride Sorption Isotherm on Fired Clay, 1st International Workshop on Fluorosis Prevention and Defluoridation of Water, International Society of Fluoride Research.

[4] Mohapatra,M.,Anand,S., Mishra,B. K., Giles, D. E., Singh, P. "Review of fluoride removal from drinking water, Journal of Environmental Management Vol.91(1), pp 67-77 (2009).

[5] MMWR Fluoridation of drinking water to prevent dental caries, 1999, Morbidity and Mortality Weekly Report, 48 (41), 933–940. Ottawa, Canada.

[6] The Story of Fluoridation, National Institute of Dental and Craniofacial Research, http://www.nidcr.nih.gov/oralhealth/topics/fluoride/thestoryoffluoridation.htm,(accessed on January 23, 2012).

[7] Kau, P.M.H., Smith, D.W., Binning, P.1998, Experimental sorption of fluoride by kaolinite and bentonite, Geoderma Vol.84 No. 1-3.

[8] Feenstra, L.Vasak, L.,Griffioen, J., 2007, Fluoride in groundwater: Overview and evaluation of removal methods, Utrecht.

[9] N. Chen, Z. Zhang, C. Feng, M. Li, An Excellent Fluoride Sorption Behaviour of Ceramic Adsorbent, Journal of Hazardous Materials, 183, 2010.

[10] Chibi, C. and Haarhoff, J., 2000, A Promising Approach to Fluoride Removal in Rural Drinking Water Supplies, Presented at WISA 2000 Biennial Conference, Sun City, South Africa.

[11] Coetzee1, P.P., Coetzee, L.L.,Puka, R., Mubenga, S., 2003,Characterisation of selected South African clays for defluoridation of natural waters, Water SA Vol. 29 No. 3.

[12] Y. Shen, H. Guo, Chemical Engineering Journal, 223 (2013)

[13] Kerbyson, J.D. and Scherdorf, J.R.H., 1948-1963, Chemical Analysis of Ghana Rocks, Ores and Minerals, Geological Survey Bulletin No. 42.

[14] WHO (World Health Organization) Guidelines for Drinking Water quality, WHO, Geneva, 1993.

[15] F. A. Atipoka, Water Supply Challenges in Rural Ghana, Desalination, 251 (2010).

[16] H. Mjengera, G. Mkorfo, Appropriate Deflouridation Technology for use in flouridic areas in Tanzania, Physical, Chemical, Earth 28 (2003)1097-1104.

[17] A. Bhatnagor, E. Kumar, M. Sillanpaa, Flouride Removal from Water by Adsorption a Review Chemical Engineering Journal 17 (2011) 811-840.

[18] S. Ayooh, A. K. Gupta, Performance evaluation of alumina cement granules in removing fluoride from natural water, Chemical Engineering Journal, 36 (2006) 433-487

Advanced Materials Research Vol. 936 (2014) pp 829-833
© (2014) Trans Tech Publications, Switzerland
doi:10.4028/www.scientific.net/AMR.936.829

Adsorption of Ni (Ⅱ) from aqueous Solution Based on Porous Magnetic/Chitosan Resin

Hai song[1, a], Xinghai Yu[1*, b], Xiaoqin Zhang[2, a], Guifang YAN[2, b], Yuanzhi Zheng[2,c]

[1] College of Chemistry and Chemical Engineering, Hexi University, Zhangye, 734000, China

[2] Key Laboratory of Resources and Environment Chemistry of West China, Hexi University, Zhangye, 734000, China.

Keywords: Magnetic chitosan resin, biosorbents, adsorption, nickel (II).

Abstract: The purpose of this work is to prepare a low-cost biosorbent, Magnetic chitosan resin (MCR), and determine the ability of this biosorbent to removing Ni (II) ion from aqueous medium. Both kinetics and thermodynamic parameters of the adsorption process were also estimated. The thermodynamic parameters indicated an exothermic spontaneous process and the kinetics followed the second-order adsorption process.

Introduction

Heavy metals are potentially hazardous to human beings and environment. Various industrial processes result in the production of considerable residual water contaminated with heavy metals [1]. Metallic nickel and nickel compounds have many industrial and commercial applications including use in stainless steels and other nickel alloys, catalysts, batteries, pigments, and ceramics [2, 3]. Nickel and nickel compounds generally cause a variety of pathologic effects like skin allergy, lung fibrosis and human carcinogen. Therefore, Nickel removal from aqueous waste streams is currently of great concern for public health and environmental conservation. Several treatment methods have been developed to remove nickel from aqueous waste streams, such as adsorption [4], ion exchange [5], microfiltration and chemical precipitation [6]. Adsorption is considered an effective and economical method among the treatment. Recently utilize low-cost adsorbents has become a new focus point mainly using biopolymers, which obtained from renewable sources and adsorbed metallic ions selectively and effectively. As available biopolymers in nature, chitosan attracted much consideration because of its excellent features, such as biocompatibility, biodegradability, and anti-bacterial properties [7]. Further physical and chemical modification of chitosan has been developed to improve mechanical strength, selectivity and capacity for the adsorption of metals. Magnetic chitosan resin (MCR) is a typical modification method which keeps the properties of chitosan for the adsorption of metal ions, and moreover, techniques employing magnetism are imparted to resins facilitating their trapping from the medium using a magnetic field compared to the centrifugal methods. So it has been widely used in various applications such as enzyme purification, cell separation, and waste treatment [8]. In our present work, we aim to prepare a Magnetic chitosan resin（(MCR) adsorbent and determine the ability of this biosorbent to removing Ni(II) ion from aqueous medium.

EXPERIMENTAL

Preparation of Magnetic chitosan resins (MCR) adsorbent

Chitosan powder (1.0g) was dissolved in 2.0% aqueous acetic acid (200 ml) and 5 g magnetite was added and stirred at room temperature for 2h until the mixture dispersed sufficiently. Next, the magnetic chitosan precipitation was obtained after the addition of ethanol. After dried at 80 ℃, it was placed in ethanol solution in contact with 5% of glutaraldehyde for 2 h, according to the chemical crosslinking with glutaraldehyde occurs by Schiff's reaction. Next the magnetic chitosan resins were collected by magnetic separation and further washed with distilled water and ethanol in order to

remove the unreacted glutaraldehyde. At last, it was dried at 80 ℃ and the magnetic chitosan resin (MCR) was finally prepared. The characteristic of magnetism provides an easy and efficient way to separate the MCR from aqueous solutions. It can be seen that the magnetic chitosan resins with adsorbed Ni could be easily separated by a magnetic field, resulting in clean water (Fig. 1).

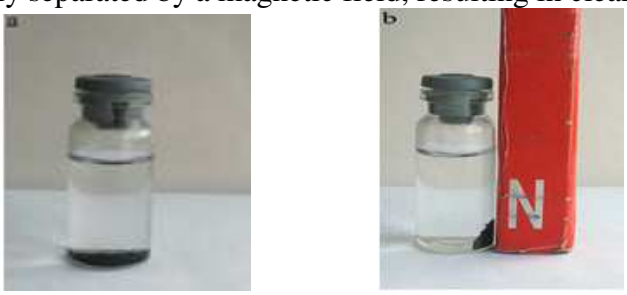


Fig.1 MCR gathered in solution (a) and separated with magnet (b)

Adsorption experiments

The sorption experiments were studied by batch technique. 0.2g MCR were equilibrated with 50 mL of aqueous $Ni(NO_3)_2$ solution with 50mg·L^{-1} in a 100 mL glass stoppered Erlenmeyer flask at 30±2 ℃ in a shaking bath. The initial pH was adjusted with HNO_3 (0.1M) or NaOH (0.1M) before adding the adsorbent. After shaking for 150 min to ensure full equilibration, the MCR were collected and the concentration of nickel (Ⅱ) ions in the supernatant was estimated by monitoring with atomic absorption spectrophotometer. The adsorption capacity was calculated from the following expression:

$$Q = \frac{(C_i - C_t)V}{m} \tag{1}$$

where, Q is the adsorption capacity of the adsorbent (mg/g), C_i and C_t (mg/L) are the initial and terminal concentrations of Ni(Ⅱ) respectively, m (g) is the mass of adsorbent, and V is volume of solution liters.

RESULTS AND DISCUSSION

Kinetics Of Adsorption

The experimental results of Ni (II) adsorption on MCR versus time are shown in Fig.2 The extent of adsorption increases with time and attained equilibrium near 150 minutes. After this equilibrium period, the amount of metal adsorbed did not change remarkably with time. Many researchers have found that if the reaction rate is chemically controlled, the pseudo-second-order model [9] will be the most appropriate model to describe the reaction [10] The experimental data were tested by the pseudo-second-order model whose expression is given as follows：

$$\frac{dq_t}{dt} = k(q_e - q_t) \tag{2}$$

For boundary conditions t=0 for Q_t =0 and t=t for $Q_t = Q_t$, integrating Eq (2) gives below:

$$\frac{t}{q_t} = \frac{1}{kq_e^2} + \frac{t}{q_e} \tag{3}$$

where q_t (mg/g) and q_e (mg/g) are the absorbances at time t and at equilibrium respectively. The slope and intercept of plot of t/Q_t vs. t were used to calculate the pseudo-second-order rate constant k and q_e.

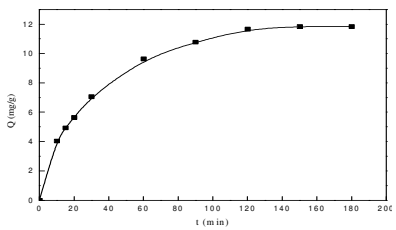


Fig. 2 Effect of adsorption time on adsorption capacity of Ni (II)

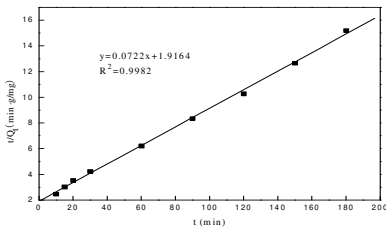


Fig. 3 Pseudo-second-order equation for the adsorption of Ni (II) on MCR

As illustrated in Fig.3, the pseudo-second-order model fitted well with the kinetic experimental data and the correlation coefficients were greater than 0.99. Therefore, the Ni (II) adsorption process is controlled by the chemical process.

Equilibrium isotherm of adsorption

Analysis of the equilibrium data is the most significant to accurately represent the adsorption isotherm. Langmuir and Freundlich adsorption isotherms were often used to fit the experimental data [11]. The Langmuir isotherms assume monolayer coverage of adsorption of each molecule onto the surface has equal sorption activation energy and no interaction between sorbed species. It has traditionally been used to quantify and contrast the performance of different biosorbents. In mathematical form, it is written as:

$$\frac{C_e}{Q_e} = \frac{Ce}{Q_m} + \frac{1}{(Q_m b)} \tag{4}$$

where C_e is the equilibrium concentration of metal ions ((mg·L^{-1}), Q_e is the amount of metal ions adsorbed ((mg·g^{-1}), Q_m is the maximum adsorption capacity of metal ions (mg·g^{-1}), and b is the Langmuir adsorption equilibrium constant (L·mg^{-1}). Therefore, the polt of C_e/Q_e against C_e gives a straight line with a slope of $1/Q_m$ and an intercept of $1/(Q_m b)$ (Fig 4 and Table 1). Table 1 indicates that Langmuir model has perfectly application for nickel (II) sorption with a regression coefficient. The maximum sorption capacity revealed MCR can remove Ni (II) with a higher affinity compared to chitosan in its natural form and most of the modified forms reported in the literature [12].

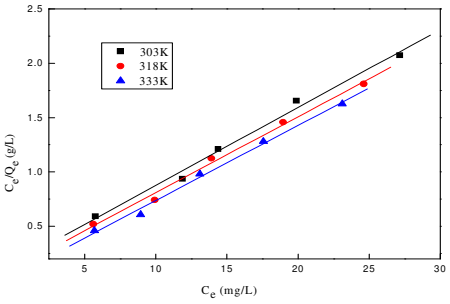


Fig.4 Langmuir isotherms for the adsorption of nickel (II) on MCR

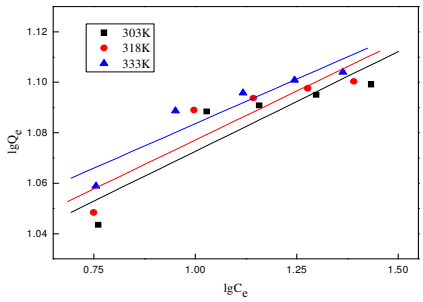


Fig.5 Freundlich isotherms for the adsorption of nickel (II) on MCR

Table 1 Langmuir and Freundlich constants for Ni (II) biosorption on MCR

Temperature	Langmuir constants			Freundlich constants		
(K)	Q_m (mg/g)	b (L/mg)	R^2	K_f	n	R^2
303	13.93	0.4503	0.9908	9.861	12.66	0.8134
318	14.29	0.6393	0.9936	9.992	12.91	0.8270
333	14.47	1.509	0.9942	10.31	14.18	0.8712

The equilibrium adsorption data were applied to the Freundlich isotherm equation for multilayer adsorption isotherm on heterogeneous surfaces. The Freundlich isotherm is an empirical equation based on an exponential distribution of sorption sites and energies. In mathematical form, it is represented as:

$$Q_e = K_f C_e^{1/n} \tag{5}$$

$$\lg Q_e = \lg K_f + \frac{1}{n} \lg C_e \tag{6}$$

In the equations, C_e and Q_e are equilibrium Ni (II) ion concentration (mg/L) and equilibrium adsorption capacity (mg/g), respectively. Freundlich constants, K_f and n can be determined from a liner plot of $\lg Q_e$ versus $\lg C_e$, which affect the adsorption process such as adsorption capacity and intensity of adsorption, respectively. Fig. 5 depicts the plots obtained by the Freundlich isotherm for the adsorbents along with their R^2 values. The Freundlich constants for the adsorption were also

presented in Table 1. As can be seen, the experimental data did not fit well in the Freundlich isotherm equation with low correlation coefficients from 0.81 to 0.87.

Thermodynamic parameters of adsorption

In order to explain the effect of temperature on the adsorption thermodynamic parameters, the adsorption behavior of Ni (II) on the adsorbent at different temperatures were also investigated (Fig. 6). The results showed that as the temperature increased, the value of Q increased, which implied that the adsorption process was endothermic.

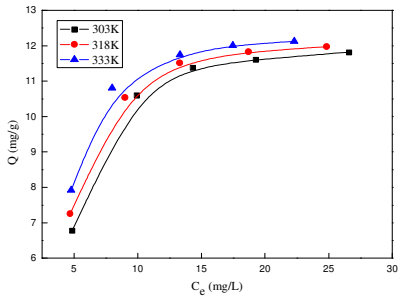


Fig. 6 Equilibrium isotherms for the adsorption of nickel (II) on MCR at different temperature

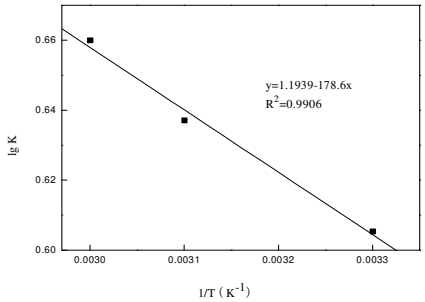


Fig. 7 Van't Hoff plot for the adsorption of nickel (II) on MCR

The thermodynamic equilibrium constant (K) for each system was obtained by calculating the apparent equilibrium constant K'_c at different initial concentration of Ni (II) and extrapolating the same to zero.

$$K_c^{'} = \frac{C_a}{C_e} \tag{7}$$

where C_a is the concentration of Ni(II) on the adsorbent at equilibrium in mg/L and C_e is the equilibrium concentration of Ni(II) in solution in $mg \cdot L^{-1}$. The adsorption parameters thermodynamic standard enthalpy (ΔH^{θ}), standard entropy (ΔS^{θ}), and standard Gibbs free energy (ΔG^{θ}) can be calculated by the thermodynamic equation [13] :

$$\lg K = \frac{\Delta S^{\theta}}{2.303R} - \frac{\Delta H^{\theta}}{2.303RT} \tag{8}$$

$$\Delta G^{\theta} = \Delta H^{\theta} - T\Delta S^{\theta} \tag{9}$$

In the Eq (8), R is the gas constant, 8.314×10^{-3} (kJ/mol·K), T is absolute temperature, K is equilibrium constant at the temperature T, respectively. When lgK is plotted against 1/T, a straight line with slope $\Delta H/2.303RT$, and intercept $\Delta S/2.303R$ were obtained (Fig. 7). The values of ΔH^{θ} and ΔS^{θ} were also obtained from the slope and intercept of the Van't Hoff plots of lnK versus 1/T (Fig.7). The thermodynamic parameters for the adsorption process are given in Table 2. It can be observed that the positive value of ΔH^{θ} indicates the adsorption is endothermic and higher temperature makes the adsorption easier. In addition, this also indicates that adsorption of Ni (II) on MCR is rather chemical process. If it was only physisorption process, the enthalpy of the system would be exothermic [14]. The positive value of ΔS^{θ} indicates that there is an increase in the randomness at the solid/solution interface during the adsorption process [15]. The negative value of ΔG^{θ} decreases with the increase of temperature indicating that the spontaneous nature of adsorption of Ni (II) are inversely proportional to the temperature, and the adsorption is more favorable at high temperatures.

TABLE 2 THERMODYNAMIC PARAMETERS FOR FOR NI (II) BIOSORPTION ON MCR

Temperature (K)	$\triangle G^{\theta}$ (kJ • mol $^{-1}$)	$\triangle H^{\theta}$ (kJ • mol $^{-1}$)	$\triangle S$ (J • mol $^{-1}$ • K $^{-1}$)
303	-3.506		
318	-3.848	3.421	22.86
333	-4.191		

CONCLUSIONS

In this study, a low-cost biosorbent, Magnetic chitosan resin (MCR) was prepared by cheap and environmentally friendly chitosan and iron salts. The biosorbent could remove nickel (II) ions from aqueous solution efficiently via the chemical adsorption process which can be described by pseudo-second rate model. The Langmuir adsorption model and Freundlich equation were used for the mathematical description of the adsorption, and the results showed that the Langmuir isotherm was better compared with the Freundlich isotherm. And the adsorption thermodynamic parameters demonstrated the adsorption process was endothermic.

REFERENCES

[1] Y.Vijaya, S.RM. opuri, V.M. Boddu, A. Krishnaiah, Modified chitosan and calcium alginate biopolymersorbents for removal of nickel (II) through adsorption, Carbohyd. Polym, 72(2008) 261-265.

[2] J.W.Wang, Y. M. Kuo, Preparation and adsorption properties of chitosan-poly(acrylic acid) nanoparticles for removal of Ni(II) ions, J. Appl. Polym. Sci, 107 (2008) 2333-2337.

[3] K. Thamaraiselvi, C. Namasivayam, Adsorption of nickel (II) from aqueous olution onto activated carbon prepared from coirpith, Purif. Techno, 24 (2001) 497-499.

[4] A.Thevannan, R.Mungroo, C. H. Niu, Biosorption of Nickel with Barley Straw, Bioresour.Techno, 101 (2010) 76-81.

[5] C. Aydiner, M. Bayramoglu, B. Keskinder, O. Ince, Behavior of Inorganic Nanoparticles in Silver polymerlectrolytes and Their Effects on Silver Ion Activity for Facilitated Olefin Transport, Ind. Eng. Chem. Res, 131 (2009) 48-53.

[6] T. Fukuta, H. Matsuda, F.Seto, K. Yagishita, Sulfuration treatment of electroplating wastewater for selective recovery of copper, zinc and nickel resource, Global Nest. J, 8 (2006) 131-137.

[7] N.V. Majeti, R. Kumar, A review of chitin and chitosan applications, React. Funct. Polym, 46, (2000)1-5.

[8] H. Peniche, A. Osorio, N. Acosta, A. Campa, Preparation and characterization of superparamagnetic chitosan microspheres: Application as a support for the immobilization of tyrosinase, J. Appl. Polym. Sci, 98, (2005) 651-656.

[9] Y.S. Ho, G. Mckay, Process Saf., Kinetic models for the sorption of dye from aqueous solution by wood, Environ Prot, 76 (1998) 183-187.

[10] D. Karadag, M. Turan, E. Akgul, S. Tok, A. Faki, The biosorption data for removal of Reactive Black 5 were readily modeled using the Langmuir adsorption isotherm, J. Chem. Eng. Data, 52 (2007) 1615-1620.

[11] A.H. Chen, C.Y. Yang, C.Y. Chen, M. R. Liu, The chemically crosslinked metal-complexed chitosans for comparative adsorptions of Cu (II), Zn (II), Ni (II) and Pb (II) ions in aqueous medium, J. Hazard. Mater, 163**,** (2009) 1068-1073.

[12] C. Huang, Y.C. Chung, R.L. Ming, Adsorption of Cu (II) and Ni (II) by pelletized biopolymer, J. Hazard. Mater, 45 (1996) 265-272.

[13] S. I. Lyubchik, A. I. Lyubchik, O. L. Galushko, et al., Kinetics and thermodynamics of the Cr(Ⅲ)adsorption on the activated carbon fromco-mingled wastes, Colloids and Surfaces A: Physicochem. Eng. Aspects, 42 (2004) 151-156.

[14] M. Ajmal, A. Khan, S. Ahmad, A. Ahmad, Role of sawdust in the removal of copper (II) from industrial Wastes, Water Res, 32 (1998) 3085 -3089.

[15] N. Sankararamakrishnan, A. Dixit, L. Iyengar, R. Sanghi, Removal of hexavalent Chromium using a novel cross linked xanthated chitosan, Bioresour. Technol, 97 (2006) 2377-2382.

Advanced Materials Research Vol. 936 (2014) pp 834-842
© (2014) Trans Tech Publications, Switzerland
doi:10.4028/www.scientific.net/AMR.936.834

Highly Efficient Adsorption of Eriochrome black T in Wastewater on Mesoporous Alumina sphere

Heng Liu[1,a,*], Na Tian[2,b], Yayang Tian[2,c], Chu Dai[2,d], Yanxin Wang[1,e]

[1]School of Environmental Studies, China University of Geosciences, Wuhan 430074, P.R. China

[2]Faculty of Material and Chemistry, China University of Geosciences, Wuhan 430074, P.R. China

[a]kyc08@cug.edu.cn, [b]nzhxxue365@163.com, [c]yayang907@163.com, [d]326930327@qq.com, [e]yx.wang@cug.edu.cn

Keywords: adsorption; Eriochrome black T; mesoporous alumina sphere

Abstract. The present study presents the adsorption behavior of mesoporous alumina sphere for Eriochrome black T (EBT) azo dyes. The batch adsorption experiments were carried out to optimize various experimental parameters such as contact time and dye concentration. The maximum adsorption of EBT was achieved 312.5mg/g. The kinetic studies revealed that the adsorption process followed the pseudo-second-order kinetic model. The adsorption behavior was analyzed by Langmuir and Freundlich isotherms. The values of correlation coefficients (R) showed that the Langmuir isotherm model found to be best fit. Results of study showed that Mesoporous alumina sphere proved to be highly effective for the removal of selected azo dyes.

Introduction

Dyes and pigments as additive materials have been widely used in many industries such as textiles, rubber, paper, and plastics. Recently, over 7×10^5 tons of dyes and pigments are produced annually, of which more than 10% of them persist in the waste effluents of these industries [1]. As the disposal of these effluents into the receiving water body may cause severe damage to aquatic biota and humans due to mutagenic and carcinogenic effects [2], it is of great importance to provide waste-treatment facilities for minimizing these substances in the effluents before discharge.

Hence, the removal of color from waste effluents has significant importance to the environment [3,4]. Various techniques have been employed for the removal of dyes from wastewaters. Due to the low biodegradability of dyes, a conventional biological treatment process is not very effective. Dye laden wastewaters are usually treated by physical or chemical processes. The conventional methods for treating dyes containing wastewaters are coagulation and flocculation [5], oxidation or ozonation [6-7], membrane separation [8,9] and adsorption [10-12]. Among them, adsorption has been found to be a proficient and economic method, and a successful and widely in use for wastewater treatment [13,14]. Conventional porous adsorbent such as activated carbon, peat, chitin, silica, fly ash and clay with nonuniform pore size and discontinuous pore structure, normally showed lower absorption capacity and adsorption efficiency. Therefore, to enhance the sorption performance new sorbents are still under investigation [15].

Mesoporous materials, whose pore sizes range from 2 to 50 nm, are of interest because of their potential use in various fields such as heterogeneous catalysis, energy, biotechnology and nanodevices [16-17]. Owing to their large pore sizes and high surface areas, mesoporous materials are also promising adsorbents for various pollutants in water. From a viewpoint of practical use, the adsorbents themselves should readily be prepared and they should not be toxic. Recently, mesoporous alumina with high surface area, uniform pore-size distribution, a spongelike interlinked

pore system [18,19], large pore size and easy of regeneration can be an alternative for organic pollutants removal. However, the research of dye adsorption on mesoporous alumina was seldom reported.

The main objective of the present research is to investigate the azo dye pollutants removal capacity of mesoporous alumina from aqueous solutions as a possible adsorbent. Here EBT was selected as typical organic pollutants in wastewater. The kinetics and isotherm of EBT adsorption onto mesoporous alumina were also investigated in view of understanding the nature of adsorption.

Experimental

Synthesis and Characterization of Adsorbent.

Mesoporous alumina powders were synthesized using the procedure, which was similar to that reported by Wang et al.[20]. In a typical synthesis, 1.0 g of P123 was dissolved in 25.0 mL of anhydrous ethanol and stirred for 3 h at 40℃. 20 mmol of aluminum nitrate (or aluminum chloride) was then dissolved in a mixed solvent composed of 3.0 mL of 37 wt.% hydrochloric acid and 12 mL of anhydrous ethanol. Once dissolved, two solutions were mixed and vigorous stirred at 40℃. Then the homogeneous sol was transferred to a flat-bottomed flask with plug and aging for 4 d at 40℃. After that, the aged sol evaporation was performed at 70℃ for 48 h in a drying oven without stirring. The resulting solid was calcined at 400℃ for 4 h in muffle furnace at a heating rate of 1.0 ℃ min^{-1}. At last, white alumina powders were obtained. The final powdery sample was labeled as N-MA (aluminum nitrate) and Cl-MA (aluminum chloride).

The synthesized mesoporous alumina was thoroughly characterized using powder X-ray diffraction (XRD), Transmission electron microscopy (TEM) and BET surface area analysis. The Powder X-ray diffraction (XRD) patterns were recorded with a (Rigaku D/max-βB) diffract meter using a Cu Kα radiation at 40 KV and 50 mA. Transmission electron microscopy (TEM) images were obtained on a (JEOL 2000 EX) electron microscope operating at an accelerating voltage of 200 KV. Nitrogen adsorption–desorption isotherm measurements were performed on a Micrometitics ASAP 2020 volumetric adsorption analyzer at 77 K. Before adsorption–desorption isotherm measurements, the samples were out gassed at 150 ℃ for 4 h in the degas port of the analyzer. The Brunauer-Emmett-Teller (BET) method was utilized to calculate the specific surface area of each sample and the pore-size distribution was derived from the adsorption branch of the corresponding isotherm using the Barrett-Joyner-Halenda (BJH) method. The total pore volume was estimated from the amount adsorbed at a relative pressure of $P/P_0 = 0.99$.

Batch adsorption studies.

Adsorption of EBT on mesoporous alumina was studied by batch experiments. A stock solution (1.0 g L^{-1}) of EBT was prepared from analytical-reagent product. The stock solution was then diluted to give a series of standard solutions in different concentrations. Batch adsorption experiments were carried out using a model SHA-C thermo stated shaker (Changzhou Boyuan Experimental Analysis Instrument Manufacture, China) at 100 rpm. Typically, adsorption volume of solution was 40ml and 10 mg mesoporous alumina were used in each adsorption at giving time intervals, the suspension containing adsorbents was extracted and adsorbents were collected using 0.25 μm Millipore filtration. EBT concentration in supernate after separation was monitored by UV-vis 722 spectrophotometer (Shanghai precision Instrument CO., Ltd) at λ_{max} =540 nm. The adsorption capacity (q_t: mg g^{-1}) and percent adsorption (r) were calculated from the change of EBT concentration according to the following equation (1) and (2), respectively:

$$q_t = \frac{(C_0 - C_t) \times V}{m} = \frac{C_0 - C_t}{m_c} \quad (1) \qquad r = \frac{C_0 - C_t}{C_0} \times 100 \quad (2)$$

Where C_0 is initial EBT concentration (mg L^{-1}); C_t is the instantaneous EBT concentrations (mg L^{-1}); m_c is the weight of the adsorbent (g) and V is the volume of the solution (L).

Regeneration experiments.

Mesoporous alumina (50 mg) were suspended in 400 mL of EBT solution (100 mg L^{-1}) and the adsorption was conducted with constant shaking for 24 h at a pH of 6.8 ± 0.05. Then the solution was filtered and the adsorbent was calcinated at 350 ℃ for 2 h in the air to remove the adsorbed EBT after which the morphology and structure of adsorbent were characterized by TEM and infrared spectrum.

Results and discussion

Characterization of mesoporous alumina.

Powder X-ray diffraction (XRD) patterns of the calcined mesoporous alumina samples designated as N-MA and Cl-MA are shown in Fig. 1. Both N-MA and Cl-MA exhibited only single XRD peak at 2θ values around 0.8, which indicates a mesoporous structure without a long range order, but having a fairly uniform pore size. It is worth mentioning that the single low angle XRD peak in mesoporous alumina does not necessarily prove well-ordered mesoporous material with uniform pores [21]. Low angle peak remained intact after calcinations at 400℃, which implies the structural stability of the materials during and after the removal of surfactant. As shown by the wide angle XRD patterns of samples (inset of the Fig. 1) no discernable diffraction peak were observed which indicated that the structure character of mesoporous alumina powders was amorphous (the pore wall is not crystalline) [22]. Fig. 2 shows TEM images of mesoporous alumina samples used in this work. Both N-MA and Cl-MA show a typical sphere structure with different diameter from tens to hundreds nano-meter and wormhole-like morphology mesoporous structure were observed. The interconnected pore system of mesoporous alumina can reduce transport limitations, enhance accessibility to the active sites [23-24], and contribute to the adsorption uptake elevation [25]. The textural property of the samples was determined by N_2 adsorption–desorption. As can be seen from Fig.3, nitrogen adsorption–desorption isotherms of mesoporous alumina sphere were typically IV type with large hysteresis loops, which suggested the existence of mesoporous framework. A BJH analysis (inset in Fig.3) of the desorption branch of the isotherm indicates that N-MA and Cl-MA with mesoporous structure possess a mean pore size of 10.0 nm and 14.6 nm with pore volume bearing 0.33 $cm^2 g^{-1}$ and 0.35 $cm^2 g^{-1}$ respectively. The mesoporous sphere exhibited relatively high specific surface area and the BET surface area is 127.1 $m^2 g^{-1}$ and 95.68 $m^2 g^{-1}$ respectively. We deduce that the increase of the specific surface area among the as-synthesized mesoporous structure can be ascribed to the interactions between anionic and surfactant. The higher surface area and interlink pore system structure will facilitate more active sites exposed and enhance the adsorption property of mesoporous materials. According to Yuan [26] that NO_3^- does not strongly influence the self-assembly process because of its weak complexation ability, however, chloride ion can strongly coordinate with aluminum ions, and disturb the assembly process, leading to long-range disordered mesostructures.

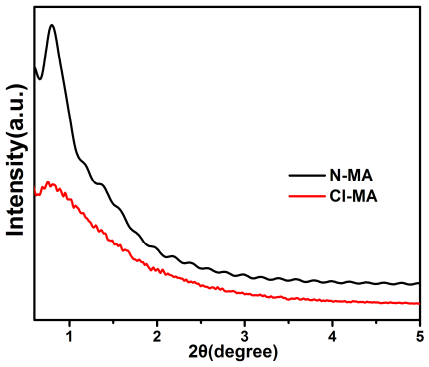


Fig. 1 Small-angle and wide-angle XRD patterns for N-MA and Cl-MA.

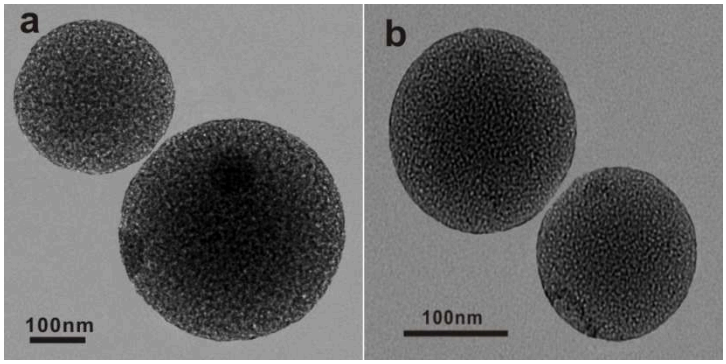


Fig. 2 The TEM images of mesoporous alumina: (a) N-MA; (b) Cl-MA.

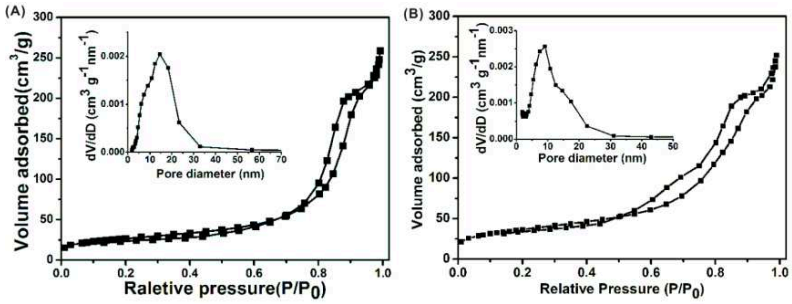


Fig. 3 The nitrogen adsorption–desorption Isotherms and pore size distributions (inset) of mesoporous alumina: (A) N-MA; (B) Cl-MA.

Effect of contact time.

The effect of contact time on the adsorption of EBT was studied to determine the time taken by N-MA and Cl-MA to remove 100.0 mg L^{-1} EBT solution. The results are shown in Fig. 4. Sorption equilibrium was reached after 15 hours with two samples. The adsorption capacity of N-MA and Cl-MA were 312.5 and 135 mg g^{-1}respectively, which means the adsorption capacity of N-MA was about one time higher than that of Cl-MA. These preliminary results led us to deduce that the higher surface area, narrower pore size distribution and interlinked pore system of N-MA results in a better acid dye sorption capacity. This investigation is only devoted to the N-MA, which is more efficient than Cl-MA in the acid dye removal process. In the following discussion N-MA, as its superior adsorption capacity was selected as the adsorbent for EBT removal.

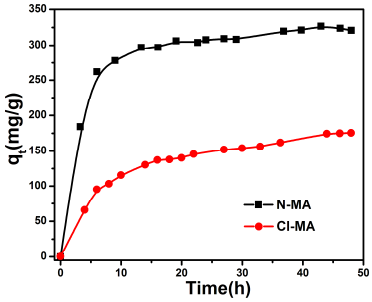


Fig. 4 Effect of contact time on EBT adsorption rate for different mesoporous alumina.

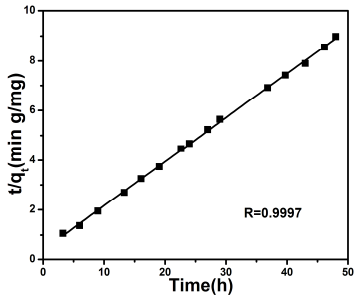


Fig. 5 The pseudo-second-order kinetic plots for the adsorption of EBT onto N-MA at various time intervals.

TABLE 1. KINETIC PARAMETERS FOR THE ADSORPTION OF EBT ONTO AL$(NO_3)_3$-MA AT VARIOUS TIME INTERVALS

sorbent	qexp (mg/g)	k1 (min-1)	|r1|	qe1 (mg/g)	k2 (g/mg·min)	|r2|	qe2 (mg/g)
Al(NO3)3-MA	307.75	3.22*10-2	0.938	177.95	2.29*10-5	0.9997	333.33

Adsorption kinetic models.

Adsorption kinetics, demonstrating the uptake rate of pollutants, is one of the most important characteristics representing the adsorption efficiency of mesoporous alumina. The Lagergren's first order kinetic model [27-28] and the Ho's pseudo second order model [29-30] are the most frequently used in the literature to describe the sorption process. The Lagergren's first order model is expressed by the equation:

$$\lg(q_{e1} - q_t) = \lg q_{e1} - k_1 t / 2.303 \quad (3)$$

Where q_t and q_{e1} (mg g^{-1}) are the amounts of dye adsorbed per unit mass of the adsorbent at time t and at equilibrium, respectively and k_1 (min^{-1}) is the first order rate constant of adsorption. Eq. (3) shows a linear relationship between $\lg(q_{e1} - q_t)$ and t. Linear regression calculations allow to obtain the values of the rate constant k_1 and the equilibrium removal capacity q_{e1}. These parameters (k_1, q_e) were calculated for the sorption of EBT on N-MA and were reported in Table 1. The calculated values from the first order kinetic model show that the experimental results fit this model with determination coefficient values of 0.938. Moreover, large differences between experimental and calculated values of the equilibrium sorption capacities are observed (Table 1). We conclude that the first order kinetic model is not adequate to describe the sorption process. Due to its good correlation with the experimental results, pseudo second order model has been extensively used by several researchers in the same field. This model is expressed by equation:

$$\frac{t}{q_t} = \frac{1}{k_2 q_{e2}^2} + \frac{1}{q_{e2}} t \quad (4)$$

Where k_2 is the second order rate constant (g mg^{-1} min^{-1}). The plots of t/qt versus t should give straight lines where slopes and intercepts are respectively $1/q_{e2}$ and $1/(k_2 q^2_{e2})$ (Fig.5). The values of the rate constant k_2 and of the equilibrium sorption capacity q_{e2} are calculated from these parameters. The calculated k_2 and q_{e2} values and the corresponding linear regression determination coefficient R values for 100 mg L^{-1} (EBT) initial concentrations are also reported in Table 1. Good correlation is observed between experimental data and the pseudo second order kinetic model with determination coefficient values higher than 0.9997. These results implied that the pseudo-second-order kinetics model fitted better with kinetic data than pseudo-first-order kinetic model.

Effect of EBT initial concentration.

The experiments studying the effect of EBT initial concentration were carried out using 10 mg of N-MA for 24 h at room temperature. The results of the experiments with varying EBT initial concentrations were shown in Fig. 6. With an increasing of the EBT initial concentration, from 15 to 180 mg L^{-1}, the adsorption capacity at equilibrium rose significantly and then the increasing trend became smaller. The percentage of EBT removal reached 100 % when the initial concentration was

as low as 28.01 mg L^{-1} or lower, and the color of the EBT solution changed from purple to clarification.

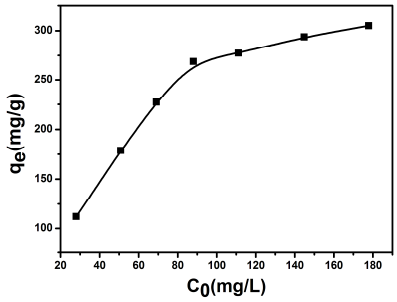


Fig. 6 Effect of initial concentration of EBT on the adsorption of EBT onto N-MA.

TABLE 2. THE ADSORPTION ISOTHERM CONSTANTS FOR THE ADSORPTION OF EBT ONTO AL$(NO_3)_3$-MA AT VARIOUS INITIAL CONCENTRATIONS OF EBT.

Sorbent	Langmuir				Freundlich		
	q_{max}	k_L	r_L	R_L	n	k_F	r_F
Al$(NO_3)_3$-MA	312.5	0.215	0.995	0.0255	5.679	141.55	0.942

Equilibrium isotherms.

Equilibrium studies were carried out in order to determine the optimum conditions for maximum EBT removal by N-MA. Two general-purpose equilibrium models and a modified combined model were used in an attempt to fit the experimental data: (i) the Langmuir model (Eq. (5)), and (ii) the Freundlich model (Eq. (6)).

$$\frac{1}{q_e} = \frac{1}{q_{\max}} + \left(\frac{1}{k_L q_{\max}} \right) \frac{1}{C_e} \tag{5}$$

$$\lg q_e = \lg k_F + \frac{1}{n} \lg C_e \tag{6}$$

Where q_{max} and K_L are constants related to the loading capacity and the free energy of adsorption; K_F and n are the Freundlich temperature-dependent constants; Ce is the equilibrium concentration (mg L^{-1}) and q_e is the amount adsorbed at equilibrium (mg L^{-1}). The Langmuir and Freundlich parameters for the adsorption of EBT are list in Table 2. The results shows that the Langmuir isotherm model gives a better fit to the experimental isotherm than Freundlich isotherms based on regression coefficients (R_L=0.995, R_F=0.942). The best-fit Langmuir parameters are q_{max}= 312.5 mg g^{-1}, K_L=0.215 L mg^{-1}.

The effect of isotherm shape has been discussed [31] with a view to predict whether an adsorption system is favorable or unfavorable. The essential feature of the Langmuir isotherm can be expressed by means of 'R_L', a dimensionless constant referred to as separation factor or equilibrium parameter. R_L is calculated using the following equation:

$$R_L = 1/(1+K_L C_0) \tag{7}$$

Where C_0 is the highest initial dye concentration (mg L^{-1}). As the R_L values lie between 0 and 1, the adsorption process is favorable [31]. The R_L value for the adsorption of EBT is 0.0255 indicating that the adsorption is favorable.

Regeneration Studies

Desorption studies help to elucidate the nature of adsorption and recycling of the spent adsorbent and the EBT. After adsorption, the adsorbent was calcined at 350 ℃ for 2 h to remove the adsorbed organic matter. Then, the obtained sample was used to repeat adsorption experiment for about several times and the adsorption capacity of adsorbent were calculated. The results showed that the adsorption capacity of N-MA could be maintained to 237.74 mg g^{-1} after three times of regeneration experiment, which indicated that the adsorbent has excellent regeneration capacity.

Conclusion

In summary, regular mesoporous alumina spheres were prepared by a simple evaporation induced self assembly procedure. The high surface area and interconnected pore system of mesoporous alumina can reduce transport limitations and enhance accessibility to the active sites that highly increase the adsorption property of mesoporous alumina. The adsorption experiment of EBT solution showed that the as-synthesized mesoporous alumina sphere can effectively remove EBT from aqueous solutions and the adsorption capacity was 312.5 mg L^{-1}. The percentage of EBT removal by mesoporous alumina sphere reached 100 % when the initial concentration of adsorbate is or below 28.01 mg L^{-1}. The kinetic and sorption data fitted well with the second order kinetic model and the Langmuir model respectively. Regeneration experiment showed that the adsorption capacity was still 237.74 mg g^{-1} after three times of simple calcined desorption treatment. Hence, it is suggested that these mesoporous alumina sphere have higher potential to be employed as a highly efficient alternative adsorbent for azo dye wastewater.

Acknowledgement

This work was financially supported by the National Basic Research Program of China (Grant No. 2011CB933700). We are grateful to the National Natural Science Foundation of China (Grant NO. 50904054) and Fundamental Research Funds for the Central Universities for financial support.

References

[1] T. Deveci, A. Unyayar, M.A. Mazmanci, Production of Remazol Brilliant Blue R decolourising oxygenase from the culture filtrate of Funalia trogii ATCC 200800, Journal of Molecular Catalysis B: Enzymatic, 30 (2004) 25-32.

[2] G. Crini, Non-conventional low-cost adsorbents for dye removal: a review, Bioresource Technology, 97 (2006) 1061-1085.

[3] M. Chiou, H. Li, Adsorption behavior of reactive dye in aqueous solution on chemical cross-linked chitosan beads, Chemosphere, 50 (2003) 1095-1105.

[4] M.S. Chiou, H.Y. Li, Equilibrium and kinetic modeling of adsorption of reactive dye on cross-linked chitosan beads, Journal of hazardous materials, 93 (2002) 233-248.

[5] T. Panswad, S. Wongchaisuwan, Mechanisms of dye wastewater colour removal by magnesium carbonate-hydrated basic, Water Science and Technology WSTED 4, 18 (1986).

[6] V. Santos, M. Pereira, P. Faria, J. ¨Decolourisation of dye solutions by oxidation with H2O2 in the presence of modified activated carbons, Journal of hazardous materials, 162 (2009) 736-742.

[7] M. Koch, A. Yediler, D. Lienert, G. Insel, A. Kettrup, Ozonation of hydrolyzed azo dye reactive yellow 84 (CI), Chemosphere, 46 (2002) 109-113.

[8] F. Harrelkas, A. Azizi, A. Yaacoubi, A. Benhammou, M.N. Pons, Treatment of textile dye effluents using coagulation-flocculation coupled with membrane processes or adsorption on powdered activated carbon, Desalination, 235 (2009) 330-339.

[9] G. Ciardelli, L. Corsi, M. Marcucci, Membrane separation for wastewater reuse in the textile industry, Resources, conservation and recycling, 31 (2001) 189-197.

[10] R. Couto, Dye removal by immobilised fungi, Biotechnology advances, 27 (2009) 227-235.

[11] F.C. Wu, R.L. Tseng, High adsorption capacity NaOH-activated carbon for dye removal from aqueous solution, Journal of hazardous materials, 152 (2008) 1256-1267.

[12] M. Anbia, S.E. Moradi, Adsorption of naphthalene-derived compounds from water by chemically oxidized nanoporous carbon, Chemical Engineering Journal, 148 (2009) 452-458.

[13] C. Namasivayam, R. Radhika, S. Suba, Uptake of dyes by a promising locally available agricultural solid waste: coir pith, Waste Management, 21 (2001) 381-387.

[14] A. Namane, A. Mekarzia, K. Benrachedi, N. Belhaneche-Bensemra, A. Hellal, Determination of the adsorption capacity of activated carbon made from coffee grounds by chemical activation with ZnCl2 and H3PO4, Journal of hazardous materials, 119 (2005) 189-194.

[15] I. Uzun, Kinetics of the adsorption of reactive dyes by chitosan, Dyes and pigments, 70 (2006) 76-83.

[16] M. Hartmann, Ordered mesoporous materials for bioadsorption and biocatalysis, Chemistry of materials, 17 (2005) 4577-4593.

[17] S.W. Boettcher, J. Fan, C.K. Tsung, Q. Shi, G.D. Stucky, Harnessing the sol-gel process for the assembly of non-silicate mesostructured oxide materials, Accounts of chemical research, 40 (2007) 784-792.

[18] Y. Kim, C. Kim, I. Choi, S. Rengaraj, J. Yi, Arsenic removal using mesoporous alumina prepared via a templating method, Environ. Sci. Technol., 38 (2004) 924-931.

[19] S. Rengaraj, Y. Kim, C.K. Joo, J. Yi, Removal of copper from aqueous solution by aminated and protonated mesoporous aluminas: kinetics and equilibrium, Journal of colloid and interface science, 273 (2004) 14-21.

[20] Z. Wang, X. Tian, C. Yang, Y. Zhao, Z. Pi, Synthesis, Characterization and Catalytic Applications in Propane Dehydrogenation of Ordered Mesoporous Alumina, Journal of Nanoscience and Nanotechnology, 9 (2009) 6876-6882.

[21] B. Xu, T. Xiao, Z. Yan, X. Sun, J. Sloan, S.L. Gonzalez-Cortes, F. Alshahrani, M.L.H. Green, Synthesis of mesoporous alumina with highly thermal stability using glucose template in aqueous system, Microporous and mesoporous materials, 91 (2006) 293-295.

[22] W. Deng, P. Bodart, M. Pruski, B. Shanks, Characterization of mesoporous alumina molecular sieves synthesized by nonionic templating, Microporous and Mesoporous Materials, 52 (2002) 169-177.

[23] Y.S. Cho, J.C. Park, B. Lee, Y. Kim, J.H. Yi, Preparation of mesoporous catalyst supported on silica with finely dispersed Ni particles, Catalysis Letters, 81 (2002) 89-96.

[24] Y. Kim, P. Kim, C. Kim, J. Yi, A novel method for synthesis of a Ni/Al2O3 catalyst with a mesoporous structure using stearic acid salts, Journal of Materials Chemistry, 13 (2003) 2353-2358.

[25] A. Corma, From microporous to mesoporous molecular sieve materials and their use in catalysis, Chemical Reviews, 97 (1997) 2373-2419.

[26] Q. Yuan, A.X. Yin, C. Luo, L.D. Sun, Y.W. Zhang, W.T. Duan, H.C. Liu, C.H. Yan, Facile synthesis for ordered mesoporous ¦Ã-aluminas with high thermal stability, Journal of the American Chemical Society, 130 (2008) 3465-3472.

[27] S. Rengaraj, Y. Kim, C. Joo, J. Yi, Removal of copper from aqueous solution by aminated and protonated mesoporous aluminas: kinetics and equilibrium, Journal of Colloid and Interface Science, 273 (2004) 14-21.

[28] S. Rengaraj, K.-H. Yeon, S.-H. Moon, Removal of chromium from water and wastewater by ion exchange resins, Journal of Hazardous Materials, 87 (2001) 273-287.

[29] Y. Ho, C. Chiang, Sorption studies of acid dye by mixed sorbents, Adsorption, 7 (2001) 139-147.

[30] P. Selvam, S. Preethi, P. Basakaralingam, Removal of rhodamine B from aqueous solution by adsorption onto sodium montmorillonite, Journal of Hazardous Materials, 155 (2008) 39-44.

[31] K. Hall, L. Eagleton, A. Acrivos, T. Vermeulen, Pore-and solid-diffusion kinetics in fixed-bed adsorption under constant-pattern conditions, Industrial & Engineering Chemistry Fundamentals, 5 (1966) 212-223.

Advanced Materials Research Vol. 936 (2014) pp 843-849
© (2014) Trans Tech Publications, Switzerland
doi:10.4028/www.scientific.net/AMR.936.843

Construction and Application of Molecularly Imprinted Film Sensor on Determination of Chlorpyrifos in Water

Guifeng Lin[1, a] ,Yanhong Wang[2, b*] ,Guochen Li[3,c]
Wen Bai [4, d],Hong Zhang[5, e] ,Shicheng Wang[6, f]

[1,2,3,5,6]Key laboratory of Pollution Ecology and Environmental Engineering
Institute of Applied Ecology, Chinese Academy of Sciences Shenyang, China

[4]College of Quartermaster Technology Jilin University Changchun, China

[a]lingf@iae.ac.cn,[b*]wangyh@iae.ac.cn,[c]ligc@iae.ac.cn,
[d]wenwen503@sina.com,[e] zhanghong@iae.ac.cn, [f] wangsc@iae.ac.cn

Keywords: chlorpyrifos; molecular imprinted film; sensor;water

Abstract. Molecularly imprinted microspheres for recognition of chlorpyrifos were prepared by thermal initiation and precipitation polymerization, and were characterized using scanning electron microscope and infrared spectroscopy. Binding characteristics of the microspheres were also investigated. Sensitive film electrode of chlorpyrifos was prepared using the microspheres above on the surface of gold electrode by spin coating. Electrochemical sensor was constructed with the electrode prepared above as recognition element, and the response characteristics of the sensor to chlorpyrifos in water were investigated based on constant-current potentiometry. It was shown that a reasonable linear response curve between potential and concentration was obtained from 1.0×10^{-12} mol/L to 2.0×10^{-8} mol/L, with a detection limit of 1.0×10^{-13}mol/L. The suitable pH was 2.2～3.4， and response time was 10 min. The imprinted electrode showed relatively high selectivity to chlorpyrifos and was applied to the analysis of chlorpyrifos in the simulated river samples with recovery rates ranging from 89% to 105%.

Introduction

Chlorpyrifos (CPF) is widely-used as a pesticides as well as a herbicide given its low toxicity and high efficiency [1]. Due to its low degradation speed, frequent existence in the surface water and crops, and the potential carcinogenic effects to human body, it is quite necessary to detect CPF residues in both environment and food [2,3]. At present, the national standard detection methods for CPF are mostly based on the liquid-liquid extraction-gas chromatography, which require complex operation, long time, and large amount of organic reagents[4,5]. Therefore, it is significantly important to develop a new efficient, low-cost, and simple method for CPF determination.

Molecular imprinting technique (MIT) is a hot applied technology by synthesizing molecular imprinted polymers (MIPs) with peculiar selectivity for special molecules. In recent decades, MIT has been widely developed for solid extraction[6,7,8],chromatographic separation[9,10], chiral resolution[11,12]. For the outstanding advantages like strong tolerability, low cost, good stability, MIPs have also been used as the recognition elements in sensors research [13-17]. Recently, molecularly imprinted sensor technology has been applied to analyze pesticides. For example, Zhao Jun et al [15] prepared an aminophenol isoproturon imprinted film sensor on gold electrode by electric polymerization. With the use of K3Fe(CN)6 as the probe between imprinted electrode and base solution, a detection method of isoproturon was developed . Peini Zhao et al [18] prepared a chemiluminescence molecularly imprinting sensor for the determination of glyphosate in the food. However, MIT used for analyzing CPF is seldom reported. Furthermore, such sensors still have some problems including relatively high test concentration range. In this study, an imprinted sensitive film electrode of CPF was prepared on the surface of gold electrode by spin coating method, and then a highly sensitive film electrode sensor was constructed. A reasonable result was achieved rapidly when the sensor was preliminary applied to the actual water samples.

Experimental

Apparatuses and Reagents

Potentiostat/Galvanostat Model 273 electrochemical workstation(PE Company, USA); three-electrode system(the MIPs sensor developed in this study was used as working electrode, with a saturated calomel electrode (SCE) and a Pt filament electrode being respectively used as reference electrode and counter electrode); portable acidity meter pH B-5(Hangzhou Ray Magnetic Analysis Instrument Factory, China); the XL-30FEG scanning electron microscope (Philips Company, Holland); Nicolet MAGNA-IR 560 infrared spectrometer (Thermoelectric Co., USA).

CPF(95% of the technical grade of pesticide, Shenyang Dongda Dick Bio-pharmaceutical Co. Ltd., China) were purified by recrystallization in our laboratory; 2-2' azoisobutyronitrile(AIBN) (chemical grade, Tianjin Bodi Chemical Co., Ltd., China); Methacrylic acid(MAA) (analytical grade, Tianjin Regent Chemicals Co. Ltd, China); Ethylene glycol dimethacrylate (EGDMA) (98%, Shanghai crystal pure reagent Co. Ltd, China); Polyvinyl chloride powder (PVC) (National Key Laboratory of Sichuan University Materials Engineering). all the reagents were all of the analytical grade and were purchased from Bodi Chemical Co.Ltd. Mill-Q ultra-pure water was used.

Construction of Molecular Imprinted Electrochemical Sensor

1)Preparation of molecular imprinted microspheres

The molecularly imprinted polymers (MIPs) for CPF were synthesized according to literature[19] and part of the preparation steps were modified. 175 mg of CPF (0.5 mmol) and 0.17 mL of MAA (2mmol) were dissolved in 40 mL acetonitrile. After shaking for 60min at room temperature, the solution was placed into the refrigerator for overnight to complete the reaction. 1.7 mL of EDMA (10mmol) and 10mg of AIBN (0.06mmol) were then added. After nitrogen gas sparged into the mixture for 10min, the solution system was sealed and kept in a constant temperature water-bath at 60°C for 24 h. Then the polymerization products were taken out, cooled to room temperature, and centrifuged to obtain the polymer microspheres.

The microspheres were washed with a mixture of methanol-acetic acid((9:1, v/v) until the template molecule of CPF was no longer detected in the elution, and then rinsed with methanol to wash off acetic acid to ensure the neutralization of hydrogen ion. The microspheres were dried to constant weight in vacuum, resulting in the desired imprinted microspheres (MIPs). For comparison, the non-imprinted polymers were also prepared using the same steps without the addition of CPF

2) Pretreatment of gold electrode

The gold electrode was polished carefully with sand paper of 3000#, polishing paper (either withα-Al2O3 polishing powder of 30 nm~50 nm) and chamois successively, and then sonicated in ultra-pure water for 5 min. The procedure was repeated for three times.

3) Preparation of molecularly imprinted film electrode

5 mg of PVC powder and 15 mg of imprinted microspheres(MIPs) were dissolved in 20mL of tetrahydrofuran and then sonicated for 30 min. 20 μL of the above solution was coated on the surface of the gold electrode using the self-made spin coating device. After complete evaporation of the tetrahydrofuran, the MIPs microspheres were deposited uniformly. The above spin coating operation was repeated for 4 times, thus shaping the film electrode. The prepared film electrode was placed at 4℃ in the refrigerator overnight for use.

Test Method

A three-electrode system was adopted in our experiment. The working electrode was the prepared sensitive film electrode, the reference electrode was the Ag/AgCl electrode and the counter electrode was the Pt filament. The constant current potentionmetric method was used for

testing and the response time was 10min. Before the test, the film electrode was placed in the blank solution for activation for 5 min. The blank and test solution both contained 0.03 mol/L of HCl and 0.02 mol/L of KCl.

Results and Discussion

Scanning Electron Microscopic Observation and Infrared Spectrum Analysis of MIPs

Bulk polymerization was the regular preparation method of MIP. However, its preparation required grinding and screening, which caused serious damage to the hole, irregular particle and poor uniformity. In this study, CPF molecularly imprinted microspheres was prepared by thermal initiation and settlement polymerization in the presence of acetonitrile solvent. Then, SEM was used for morphology analysis of the polymer microspheres (see Fig.1). As Fig. 1 showed the products were spherical, uniform particles, of which the diameter ranged from100 nm to 200 nm.

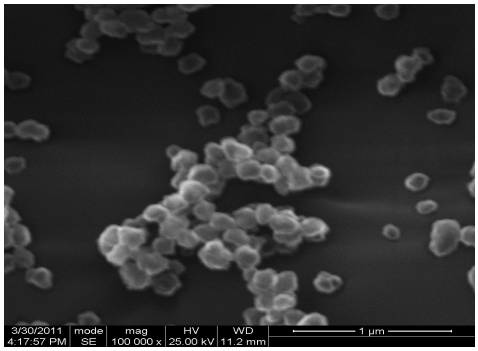


Fig.1 Scanning Electron Micrograph of CPF

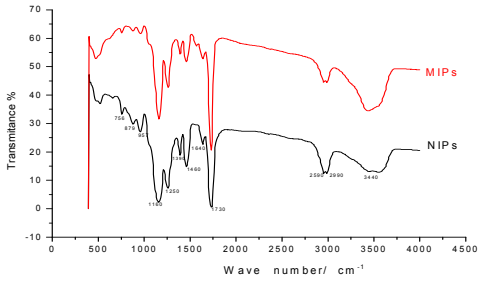


Fig.2 IR Spectra of MIPs and NIPs Molecularly Imprinted Polymer MIP_S: Imprinted Microspheres; NIP_S: Non-imprinted Microspheres.

Infrared spectrometer was used for the analysis of the functional group of the polymer.(see Fig. 2) As Fig. 2 showed - stretching vibration absorption of -C=C double bond near 1640 cm^{-1} was very small, which illustrated that the cross-linking agent and functional monomer polymerized mostly, and the template molecules could be crosslinked to the polymers. The infrared spectra of MIPs and NIPs were nearly consistent in peak shape and peak position, indicating that CPF template molecules in the MIPs were completely eluted [20]. Meanwhile, the absorption peak near 3400 cm^{-1} was the -OH characteristic absorption peak of -COOH functional group in MAA. The peak strength of MIPs near 3400 cm^{-1} was higher than NIPs obviously, indicating that the holes formed in MIPs made -OH active groups increase significantly, which can produce more hydrogen bonds function to help the combination and adsorption of the template molecules.

Adsorption Capacity of MIPs

The adsorption isotherm of CPF onto imprinted microspheres and non-imprinted microspheres were drawed at CPF 10^{-5} mol/L~10^{-7} mol/L with static adsorption method (see Fig. 3).With the increase of concentration of CPF, the adsorbance of the imprinted microspheres increased significantly and then reached a saturation value. However, the adsorbance of CPF onto non-imprinted microspheres was few and it did not change significantly along with the concentration of CPF. It showed that the adsorption of imprinted microspheres to CPF was due to the specific combination on the selective binding sites. The experiment results were analyzed with Scatchard method (see Fig.4).The figure was comprised of two straight lines with good linear relationships, which indicated that in the studied concentration range, it existed two non-equivalent binding sites between CPF and imprinted microspheres at the molecular level, that caused a significant adsorption behavior, and provided the necessary conditions for the sensor study.

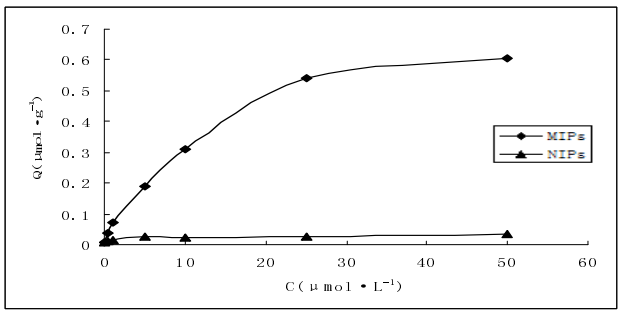


Fig.3 Binding isotherm of MIPs-CPF and NIPs-CPF (20℃) MIP_S: imprinted microspheres; NIP_S: non-imprinted microspheres.

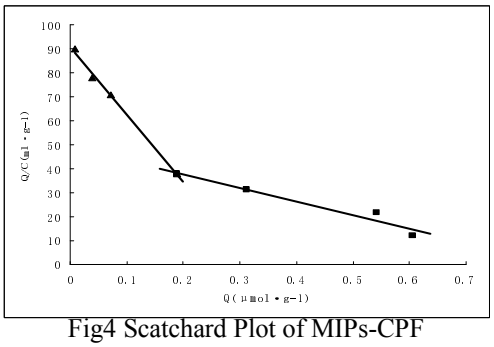


Fig4 Scatchard Plot of MIPs-CPF

Optimization of Imprinted Film Electrode Preparation

Film-forming material is one of the basic materials for film electrode preparation. Materials such as PVC SG-2, PVC SG-3, PSH-10, and PSH-30 were compared in the study. According to the operation of Ⅱ,B,3), PVC SG -2 showed better hardness, toughness and adhesion onto the electrode than other materials.

The effect of THF solvent volume and the times of spin-coating on the film quality and sensor property were also investigated. It indicated that the film showed good uniformity and the film electrode showed good repeatability with appropriate response time when 20mL THF and 4 times of spin-coating were adopted.

Effect of pH Value on the Film Electrode Test

For 1.0×10^{-10} mol/L of CPF solution, the potential under different pH values was recorded using the film electrode.It was shown in the E-pH curve (see Fig.5) that when the pH ranged from 2.2 to 3.4, the potential value was basically stable; when the pH was greater than 3.4, the potential value obviously declined. In order to reduce the effect of pH value on the accuracy of results, 2.2 to 3.4 of pH range was selected for testing.

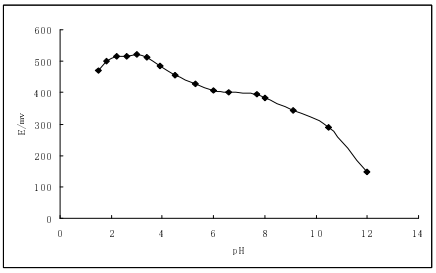


Fig.5 The effect of pH value

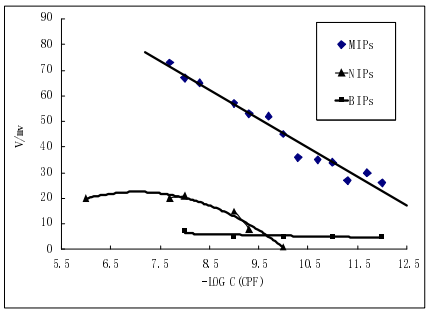


Fig.6 Analysis of Molecular Imprinting Effect
mip_S: Imprinted Film Electrode; Nip_S: Non-imprinted Film Electrode;
Bip_S: Bare Gold Electrode.

Analysis of Molecularly Imprinting Effect

Response of bare gold electrode, non-imprinted film electrode and imprinted film electrode to different concentrations of CPF were tested in this study,(see Fig. 6). The results showed that the bare gold electrode had no apparent responses to different concentrations of CPF solution; the non-imprinted film electrode showed a certain responses when CPF concentration varied from 1.0×10^{-10} mol/L to 2.0×10^{-6} mol/L without a linear relationship, which quickly approached an equilibrium in 3 min; for CPF concentration ranging from 1.0×10^{-12} mol/L~2.0×10^{-8} mol/L, there existed a good negative linear relationship between potential and CPF concentrations.. It can be concluded that recognition site formed in the imprinting polymer film played an important role.

Electrochemical Response of Imprinted Film Electrode

Using constant current-potential, the response of film electrode to CPF was detected. A good linear relationship was achieved when the concentration of CPF ranged from 1.0×10^{-12} mol/L to 2.0×10^{-8} mol/L. With the minus logarithm of test concentration(m) as abscissa and potential difference (V) between test solution and blank solution as ordinate, the linear equation was V=11.26m +157.9 (R2 = 0.9897). The detection limit was 1.0×10^{-13} mol/L, which was significantly lower than previous research [14, 17]. Hereby, samples with low content of CPF can be determined directly without preconcentration which is time-consuming and complex.

Investigation of the Sensor Selectivity

The selectivity of film electrode to dimethoate, malathion, phorate and atrazine were investigated. The results showed that the sensor exhibited a weak response to dimethoate, malathion, phorate and atrazine, with the reduction of potential significantly less than that for CPF under the same concentration of solution. The response to phorate was more obvious, but the response potential was instable with great fluctuation of the potential value. Possible reasons were that the molecular structure of dimethoate, malathion and atrazine was quite different from CPF, and did not match the electrode surface holes, so could not close to the holes. But non-specific adsorption could still cause a weak response which did not interfere with the determination of CPF. However, phorate which was small molecule could enter the hole freely, closed part of the hole to some extent, and objectively impeded the diffusion of ions in the solution. However, this random combination was not firm, showing an instable response value [21]. As a whole, the sensor showed a relatively good selectivity to CPF.

Sample Analysis

Three samples of river water were adjusted to pH 2.8 for recovery test carried out with the calibration curve method. Three samples of river water were adjusted to pH 2.8 for recovery test carried out with the calibration curve method. 1.0×10^{-9} mol/L, 5.0×10^{-9} mol/L, and 1.0×10^{-8} mol/L CPF were added into three river water samples respectively. As shown in Table1, the average recovery rate ranged from 88% to 105%, and RSD(n=3) ranged from 5.8% to 8.6%. It showed that this method had good accuracy and precision.

TABLE 1 RECOVERY OF CPF WITH CALIBRATION METHOD

Sample	Addcd (mol/L)	Meaured (mol/L)（n=3）	Recovery rate (%) (n=3)	RSD (%) (n=3)
1	1.0×10^{-9}	1.05×10^{-9}	105	8.6
2	5.0×10^{-9}	4.4×10^{-9}	88	6.4
3	1.0×10^{-8}	0.90×10^{-8}	90	5.8

Conclusions

It was reported in this paper a method of molecularly imprinted film sensor on determination of CPF in water. Compared with sensors for determining other pesticides, this sensor has relatively higher sensitivity with lower detection limit and wider linear concentration range. A good result was achieved when this method was applied to the actual water samples with only a simple adjustment of pH. There are many advantages of this method, including easy and time-saving operation, low cost, and low toxicity because toxic organic solvents were generally avoided. And so it was a good alternative for some of costly instrumental methods such as gas chromatography. A follow-up study will focus on optimizing the procedure of film-coating and improving sensor’s reused times.

Acknowledgment

This study was financially supported by the import direction project of Chinese Academy of Sciences (project No: KSCX2-YW-N-035), the plan of science and technology of Liaoning province (project No: 201041501).The authors are highly indebted to colleagues who participated in the fieldwork and data processing.

References

[1] G Z Zheng,J Zhi,Research development on the toxicity of chlorpyrifos,China Pub. Health. 18(4) (2002)496-498

[2] A W Abu-Qare, M B Abou-Donia, Quantification of nicotine, chlorpyrifos and their metabolites in rat plasma and urine using high-performance liquid chromatography,J.Chromatogr.B,757(2) (2001)295-300.

[3] C. R.A Michael, M D, S Claudine, L Jay, F Charles, C K Lynch, B Joseph, J A H ane, P. S Dale, C Joseph,T Kent,B Aaron,Pesticides and lung cancer risk in the agricultural health study cohort ,Am. J.Epidemiol., 160(9) (2004)876-885.

[4] Standard examination methods for drinking water –Pesticides parameters. National standards of the people's republic of china,GB/T 5750.9-2006.

[5] Pesticide multiresidue screen methods for determination of organophosphorus pesticides,organochlorine pesticides, pyrethroid pesticides and carbamate pesticides in vegebables and fruits.Ministry of agriculture standards of the people's republic of china,NY/T761- 2008.

[6] G L Yang, H Y Liu, M M Wang, S B Liu, Y Chen,Chromatographic characterization and solid-phase extraction on dinicunazole-imprinted polymers stationary phase. React Funct Polym, 66(2006)579- 583.

[7] Prieto, a, S. Schradera, C. Bauera and M. Mödera. Synthesis of a molecularly imprinted polymer and its application for microextraction by packed sorbent for the determination of fluoroquinolone related compounds in water. Analytica Chimica Acta,685(2) (2011)146-152

[8] Y H Wang,J P Huo, H Zhang,et a1, Preparation and application of atrazine molecularly imprinted solid phase extraction pillar. Chinese Ana1.Chem., 38(5) (2010)678-682.

[9] J Takeuchi Matsui, Miniaturized molecularly imprinted continuous polymer rods.J High Resolut Chromatogr, 2 3(1) (2000) 44- 46 .

[10] J J Ou, L H Hu, X Li, H F Zou, Determination of phenolic compounds in river water with on-line coupling bisphenol A imprinted monolithc precolumn with high performance liquid chromatography.Talanta, 69(4) (2006) 1001- 1006.

[11] M. Monier, D.M. Ayad, Y. Wei and A.A. Sarhan, Preparation of cross-linked chitosan/glyoxal molecularly imprinted resin for efficient chiral resolution of aspartic acid isomers, Biochem. Eng. J, 3 (2010) 140-146.

[12] K Hosoya,Mo1ecular1y imprinted chiral stationary phase prepared with racemic template . Ana1. chem, 70(5) (1998)943.

[13] P A Lieberzeit, F L Dicke,Molecularly imprinted polymers in clinical diagnostics-future potential and existing problems,Ana1.Bioana1.Chem, 391(5) (2008)1629-1639.

[14] S A Piletsky,N W Turner, P Laitenberger,Molecularly imprinted polymers in clinical diagnostics-Future potential and existing problems,Medical Engineering&Physics,28(10) (2006)971-977.

[15] J Zhao, J P Li,F Y Jiang,Isoproturon sensor based on molecularly imprinted electropolymer molecularly imprinted polymers in clinical diagnostics-Future potential and existing problems, Chinese Ana1．Chem, 37(8) (2009)1219-1222.

[16] M Pesavento,G D Agostino， R Biesuz,G Albeni, Molecularly imprinted polymer-based sensors for amperometric determination of nonelectroactive,Electroanalysis, 21(3) (2009)604-611.

[17] N W Zhang, M X Ding,G Y Liu,W W Song, C Y Chai, Preparation of chloramphenicol succinate molecularly imprinted membrane and study of its absorption characteristic,Chinese Ana1.Chem., 36(10) (2008)1380-1384 .

[18] P N Zhao, M Yan, C C Zhang, R X Peng, D S Ma, J H Yu.,Determination of glyphosate in foodstuff by one novel chemiluminescence-molecular imprinting sensor,Spectrochimica Acta Part A , 78(5) (2011) 1482-1486.

[19] X F Liu, B Yao, G Y Liu, C Y Chai, Bionic sensor for detection of diazepam in meat using molecularly imprinted film,Chinese Ana1.Chem., 38(5)(2010)683-687.

[20] X F Liu, F Li, B Yao, L Wang, G Y Liu, C Y Chai,Spectroscopic Study of Diazepam Molecularly Imprinted Polymers and Initiative Application to Conductimetric Sensor Based on Molecularly Imprinted Films,Spectroscopy and Spectral Analysis, 30(8) (2010)2228-2231.

[21] X H Luo,K Liu,H Y,Huang Determination of l-Serine with self-assembled molecular imprinted monolayer modified electrode,Journal of instrumental analysis ,28(3) (2009)349-352.

Advanced Materials Research Vol. 936 (2014) pp 850-853
© (2014) Trans Tech Publications, Switzerland
doi:10.4028/www.scientific.net/AMR.936.850

An Investigation Of Some Factors Affecting The Dispersant Nno Adsorption On Imidacloprid Particle

Han Hao[1,a], Jianguo Feng[2,b], Xinyu Guo[1,c], Wenjun Liu[3,d], Xuemin Wu*[,1,e]

[1:] College of science, China Agricultural University, Beijing 100193, China

[2:] College of Horticulture and Plant Protection, Yangzhou University, Yangzhou, Jiangsu, 225009, China

[3:] State Intellectual Property Office, Beijing 100088, China

[a] haohan@cau.edu.cn, [b] fengjianguo2003@163.com,

[c] 370827245@qq.com, [d] mmjjuuyy@sohu.com,

*,[e] wuxuemin@cau.edu.cn

Keywords: NNO; Imidacloprid; Adsorption; Dispersant

Abstract: Some factors such as imidacloprid dose, contact time, initial NNO concentration, stirring speed and temperature affecting the dispersant NNO (formaldehyde condensate sodium salt of naphthalene sulfonic acid) adsorption on imidacloprid particle was investigated in this paper. It demonstrated that NNO adsorption amount decreased with the increasing imidacloprid dose and temperature, but increased with the increasing contact time, initial NNO concentration and stirring speed. The results implied that the dispersant NNO was adsorbed on imidacloprid particle physically and exothermically.

Introduction

For the successful utilization of imidacloprid aqueous suspension concentrate (SC) in commercial products, a high imidacloprid concentration is desired, and it is necessary for imidacloprid SC to display good fluidity and stability for its handling in preparation, storage and transport processes. The proper type and dosage of dispersants are crucial to obtain commercially suitable imidacloprid SC, these dispersants adsorb on imidacloprid particle surface, and modifying properties of particle surface[1]. The main objective of this paper is to investigate some factors, including imidacloprid dose, contact time, initial NNO concentration, stirring speed and temperature, affect the dispersant NNO adsorption, and the results provide useful data for manufacturing commercially suitable imidacloprid SC.

Experimental Section

Imidacloprid (purity 97 %) was obtained from Sigma-Aldrich. The chemical structure of imidacloprid and dispersant NNO were presented in Fig.1. The NNO solution (1000 $mg \cdot L^{-1}$) was prepared by dissolving weighted proper NNO powders in distilled water, which was diluted with appropriate volumes of distilled water into dispersant NNO solutions at different concentrations.

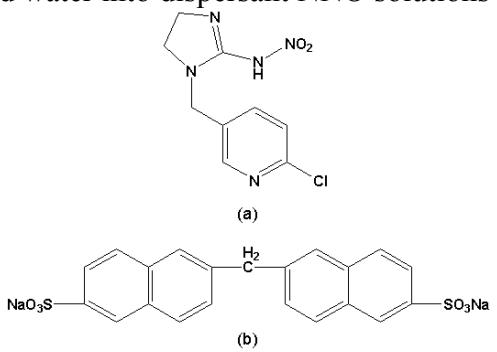


Fig. 1 Chemical structure of imidacloprid (a) and NNO (b)

Batch adsorption studies were conducted at different imidacloprid doses (0.5-2.0 g·L^{-1}), contact times (0-30 min), initial NNO concentrations (250-1000 mg·L^{-1}), stirring speeds (50-250 rpm) and temperatures (298-328 K) with 50 mL of NNO solution in a water bath to optimize the adsorption conditions. At last, dispersant NNO and imidacloprid particles were separated by centrifugation (Hettich universal 320R) at 5000 rpm for 20 min, and NNO concentration in solution was determined using a UV-visible spectrophotometer (Shimazu UV-1800) by monitoring the absorbance changes at 225 nm. Moreover, the amounts of NNO at time t (min) and equilibrium were calculated by Eq. 1 and 2, respectively:

$$q_t = (c_0 - c_t)V/M \quad (1)$$

$$q_e = (c_0 - c_e)V/M \quad (2)$$

Results and Discussion

The plot of NNO adsorption amount versus imidacloprid doses (0.5-2.0 g·L^{-1}) was shown in Fig. 2. It was found that NNO adsorption amount decreased with the increasing imidacloprid dose. This is due to aggregation or overlapping of adsorption sites on imidacloprid particle surface. That is, the diffusion path length increase and available total imidacloprid surface area decrease with the increasing imidacloprid dose[2].

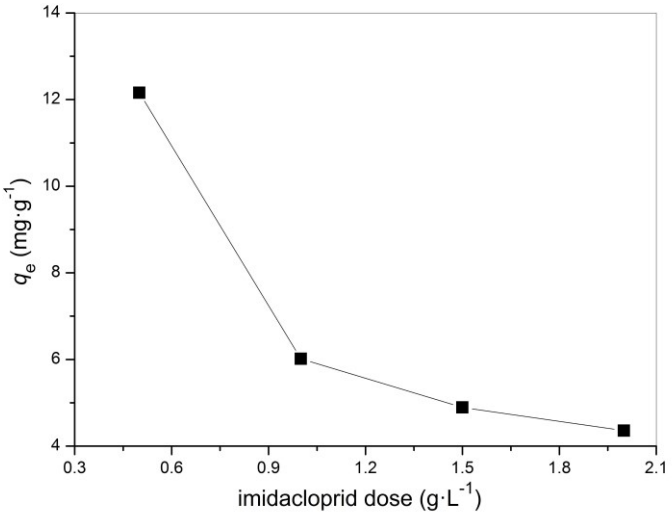


Fig. 2 Effect of imidacloprid dose on the adsorption of NNO. (c_0 = 500 mg·L^{-1}; stirring speed 200 rpm; T = 298 K; t = 30 min)

The plot of NNO adsorption amount versus contact time at initial NNO concentration of 250-1000 mg·L^{-1} was shown in Fig. 3. NNO adsorption amount increased rapidly with elapsed contact time at the beginning stage of adsorption, then the adsorption rate decreased gradually. At last, NNO adsorption amount did not change significantly after 15 min when there was a dynamic equilibrium between desorption and adsorption.

In addition, Fig. 3 indicated that NNO adsorption amount was increased with an increase in the initial NNO concentration. It is attributed to that initial NNO concentration provides a principal driving force to overcome mass transfer resistances of all molecules between the aqueous (dispersant NNO solution) and solid phases (imidacloprid particle)[3].

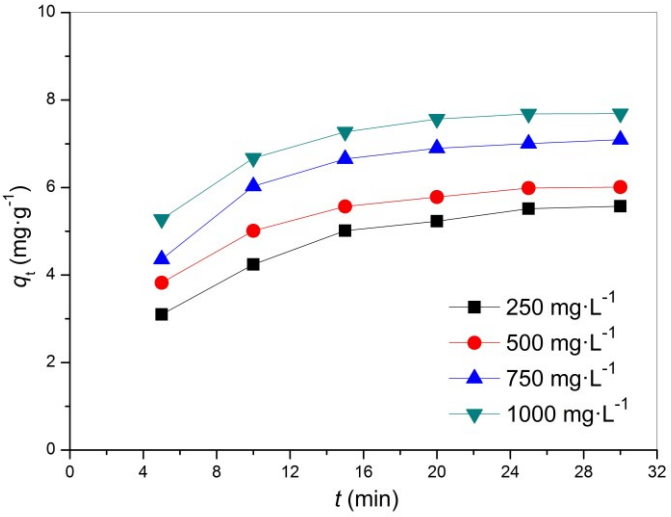


Fig. 3 Effect of contact time and initial NNO concentration on the adsorption of NNO. (imidacloprid dose 1.0 g·L^{-1}; stirring speed 200 rpm; T = 298 K)

The effects of stirring speed on NNO adsorption amount were analyzed at 50-250 rpm (Fig. 4). NNO adsorption amount was significantly augmented as the stirring speed increased from 50 rpm to 200 rpm, which is attributed to the increase in turbulence and the decrease in boundary layer thickness around imidacloprid particles as a result of increase in the degree of mixing[4]. However, NNO adsorption amount remained approximately constant when the stirring speed reached over 200 rpm.

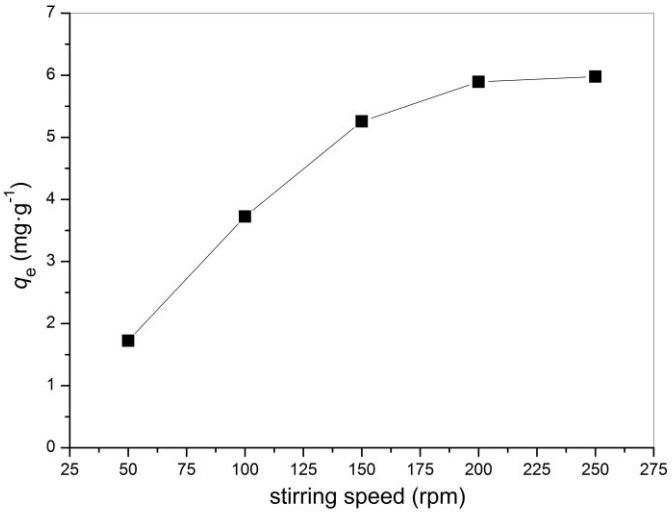


Fig. 4 Effect of stirring speed on the adsorption of NNO. (c_0 = 500 mg·L^{-1}; imidacloprid dose 1.0 g·L^{-1}; T = 298 K; t = 30 min)

The effects of temperature on that adsorption were investigated at 298-328 K (Fig. 5). NNO adsorption amount slightly decreased with increasing temperature, which implied that dispersant NNO was mainly adsorbed physically rather than chemically as an exothermic process on imidacloprid particle surface.

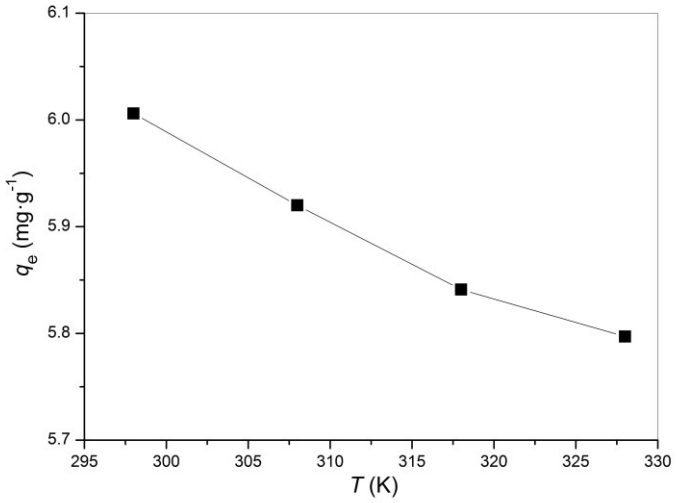


Fig. 5 Effect of temperature on the adsorption of NNO. (c_0 = 500 mg·L^{-1}; imidacloprid dose 1.0 g·L^{-1}; stirring speed 200 rpm; t = 30 min)

Nomenclature

c_0 — initial NNO concentration, mg·L^{-1}
c_e — equilibrium NNO concentration in the solution, mg·L^{-1}
c_t — NNO concentration at any time t, mg·L^{-1}
M — mass of imidacloprid, g
q_e — amount of NNO adsorbed at equilibrium, mg·g^{-1}
q_t — amount of NNO adsorbed at any time t, mg·g^{-1}
T — temperature, K
t — contact time, min
V — volume of dispersant NNO solution, mL

References

[1] N. Hua, Y. Lin, Influence Pesticides SC Physical Stability Factor and Solutions, Agrochemicals 51 (2012) 163-167.

[2] G. Crini, C. Robert, F. Gimbert, B. Martel, O. Adam, F. De Giorgi, The removal of Basic Blue 3 from aqueous solutions by chitosan-based adsorbent: batch studies, J. Hazard. Mater. 153 (2008) 96-106.

[3] G. Donmez, Z. Aksu, Removal of chromium (VI) from saline wastewaters by *Dunaliella* species, Process Biochem. 38 (2002) 751-762.

[4] W.R. Weber Jr., F.A. DiGiano, Process Dynamic in Environmental Systems, John Wiley & Sons, New York, 1996.

Advanced Materials Research Vol. 936 (2014) pp 854-858
© (2014) Trans Tech Publications, Switzerland
doi:10.4028/www.scientific.net/AMR.936.854

Adsorption studies of methacrylic acid-styrene-acrylic polyethers copolymer on imidacloprid particles

Han Hao[1,a], Jianguo Feng[2,b], Tengfei Fan[1,c], Wenjun Liu[3,d], Xuemin Wu*[,1,e]

[1:] College of science, China Agricultural University, Beijing 100193, China

[2:] College of Horticulture and Plant Protection, Yangzhou University, Yangzhou, Jiangsu, 225009, China

[3:] State Intellectual Property Office, Beijing 100088, China

[a] haohan@cau.edu.cn, [b] fengjianguo2003@163.com,

[c] 380055961@qq.com, [d] mmjjuuyy@sohu.com,

*,[e] wuxuemin@cau.edu.cn

Keywords: Adsorption; Imidacloprid; Methacrylic acid-styrene-acrylic polyether copolymer; Kinetic; Thermodynamics

Abstract: The adsorption of methacrylic acid-styrene-acrylic polyethers (MAA-St-APEG) copolymer on the insecticide imidacloprid particles was studied to calculate the kinetic, isotherm and thermodynamic parameters. The kinetic data followed the pseudo-second order kinetic model, and the equilibrium data were well fitted by the Langmuir isotherm model with the maximum adsorption amount of 7.610 $mg \cdot g^{-1}$ at 298 K. The calculated thermodynamic parameters including ΔG, ΔH and ΔS, demonstrated that this adsorption was a spontaneous and exothermic process in nature. Therefore, MAA-St-APEG copolymer are eligible for the dispersion of imidacloprid particles in aqueous solution as a effective dispersant.

Introduction

The poly-carboxylic acid copolymer hyper-dispersant has attracted much attention, and it is actively researched and developed because of its characteristics of keeping the dispersion of particles and the stability of dispersion system. Methacrylic acid-styrene-acrylic polyethers (MAA-St-APEG) copolymer were used to be a dispersant on pesticide aqueous suspension concentrate (SC) in recent years. However, a proper dispersant is vitally important to improve the stability of SC[1]. The adsorption kinetic, isotherm and thermodynamic of MAA-St-APEG copolymer on imidacloprid particles was studied in this paper, which provide experimental data for using MAA-St-APEG copolymer in imidacloprid SC as a dispersant.

Experimental section

Analytical-grade NaOH and HCl were obtain from Sinopharm Chemical Reagent Co., Ltd. Imidacloprid (purity 97 %) was purchased from Sigma-Aldrich, the chemical structure was showed in Fig.1. The chemical structure of MAA-St-APEG copolymer was presented in Fig.2. The MAA-St-APEG copolymer solution (2000 $mg \cdot L^{-1}$) was prepared by dissolving weighted appropriate copolymer particles in distilled water, which was diluted with appropriate volumes of distilled water into experimental solutions at different concentrations.

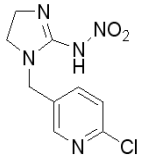


Fig. 1 Chemical structure of imidacloprid

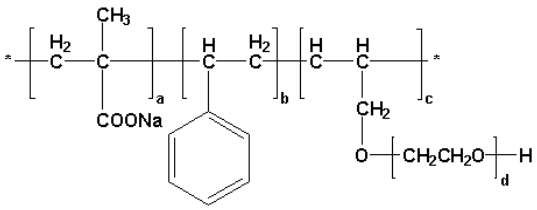


Fig. 2 Chemical structure of MAA-St-APEG copolymer

The weight average molecular weight, number average molecular weight and polydispersity of MAA-St-APEG copolymer were obtained by gel permeation chromatography (GPC), the carboxyl group content of MAA-St-APEG copolymer were determined by conductometric titration using 0.1 mol·L^{-1} NaOH and HCl solution, and these results are summarized in Table 1.

Table 1 Molecular weight and carboxyl content of MAA-St-APEG copolymer

M_w / Da	M_n / Da	Polydispersity	Carboxy content / mmol·g^{-1}
13886	7690	1.806	1.328

2.0 g of imidacloprid particles were mixed with 50 mL of MAA-St-APEG copolymer solution and shaken at 200 rpm in a 250 mL conical flask, and duplicate samples were obtained at different time intervals at 298, 308, 318 and 328 K.

At the end of adsorption, imidacloprid particles and MAA-St-APEG copolymer were separated by centrifugation (Hettich universal 320R, Germany) at 5000 rpm for 10 min, then MAA-St-APEG copolymer concentration was determined by monitoring the absorbance changes at 191 nm using a UV-visible spectrophotometer (Shimazu UV-1800, Japan).

The amount of MAA-St-APEG copolymer at equilibrium was obtained from the mass balance equation:

$$q_e = (c_0 - c_e)V/M \tag{1}$$

Standard deviation (SD) and chi-square test (χ^2) combined with correlation coefficient (R^2) are commonly used to quantitatively compare the applicabilities of different kinetic and isotherm models, respectively. Higher R^2, lower SD and χ^2 values represent a better fitting of the model, and the SD and χ^2 values can be calculated by eq. 2 and 3, respectively[2].

$$SD = \{\Sigma[(q_{t,exp} - q_{t,cal}) / q_{t,exp}]^2 / (p - 1)\}^{0.5} \tag{2}$$

$$\chi^2 = \Sigma[(q_{e,exp} - q_{e,cal})^2 / q_{e,exp}] \tag{3}$$

Results and discussion

It is most important to predict the adsorption rate in adsorption system design with the adsorbate contact time and the reactor dimensions controlled by the kinetics[3]. In this study, the pseudo-first order and pseudo-second order models were used to test the experimental data[4-5]. All of calculated kinetic parameters were showed in Table 2.

Table 2 Kinetic parameters for the adsorption at 298 K.

c_0 / mg·L^{-1}	$q_{e,exp}$ / mg·g^{-1}	Pseudo-first-order kinetic model			
		$\ln(q_e - q_t) = \ln q_e - k_1 t$			
		$q_{e,cal}$ / mg·g^{-1}	k_1 / min^{-1}	R^2	SD
400	4.720	8.532	0.211	0.905	0.401
800	6.948	8.361	0.202	0.880	0.122
1200	7.397	7.477	0.189	0.863	0.113

c_0 / mg·L^{-1}	$q_{e,exp}$ / mg·g^{-1}	Pseudo-second-order kinetic model			
		$t/q_t = 1/k_2q_e^2 + (1/q_e)t$			
		$q_{e,cal}$ / mg·g^{-1}	$k_2 \times 10^{-2}$ / g·mg^{-1}·min^{-1}	R^2	SD
400	4.720	5.450	3.569	0.996	0.097
800	6.948	7.524	3.387	0.992	0.060
1200	7.397	7.663	3.181	0.994	0.085

As seen in Table 2, it was found that the adsorption process of MAA-St-APEG copolymer on imidacloprid particles were well represented by the pseudo-second order kinetic model due to high R^2 and low SD values.

To optimize the adsorption process of MAA-St-APEG copolymer on imidacloprid particles, it is essential to establish a most appropriate adsorption isotherm using equilibrium data. Two well-known models including the Langmuir and Freundlich isotherm models were used to fit the equilibrium data, and the results were summarized in Table 3[6-7].

Considering the R^2 and χ^2 values in Table 3, the adsorption of MAA-St-APEG copolymer on imidacloprid particles followed the Langmuir isotherms due to high R^2 and low χ^2 values.

Table 3 Isotherms parameters for the adsorption at different temperatures

Temperature / K	Langmuir isotherm			
	$c_e/q_e = 1/bq_m + c_e/q_m$			
	q_m / mg·g^{-1}	$K_L \times 10^{-2}$ / g·mL^{-1}	R^2	χ^2
298	7.610	13.663	0.998	0.460
308	7.450	11.364	0.997	0.283
318	7.348	10.995	0.995	0.227
328	7.243	10.823	0.999	0.168
Temperature / K	Freundlich isotherm			
	$\ln q_e = (1/n_f)\ln c_e + \ln K_f$			
	n_f	K_f / mg·g^{-1}·(L·mg^{-1})$^{1/n}$	R^2	χ^2
298	5.784	2.710	0.847	0.814
308	5.459	2.510	0.815	0.966
318	5.414	2.461	0.808	0.979
328	5.316	2.378	0.785	1.062

To reveal the thermodynamic behavior of MAA-St-APEG copolymer adsorption, thermodynamic parameters, such as Gibbs free energy change (ΔG), entropy change (ΔS) and enthalpy change (ΔH) were calculated (eq. 4-6):[8]

$$K_D = q_e/(c_e \cdot 10^{-3}) \quad (4)$$

$$\ln K_D = (\Delta S/R) - (\Delta H/RT) \quad (5)$$

$$\Delta G = \Delta H - T \cdot \Delta S \quad (6)$$

Table 4 Thermodynamic parameters for the adsorption

c_0 / mg·L^{-1}	ΔS / J·mol^{-1}·K^{-1}	ΔH / kJ·mol^{-1}	ΔG / kJ·mol^{-1}			
			298 K	308 K	318 K	328 K
400	12.004	−10.236	−13.815	−13.935	−14.055	−14.175
800	22.337	−5.223	−11.883	−12.106	−12.330	−12.553
1200	21.640	−3.402	−9.854	−10.070	−10.287	−10.503

The calculated values of ΔG, ΔH, and ΔS for the adsorption of MAA-St-APEG copolymer on imidacloprid particles are listed in Table 4. The negative values of ΔG reflected that this adsorption process was spontaneous[9]. The negative value of ΔH (absolute values < 20 kJ·mol^{-1}) indicated that the adsorption of MAA-St-APEG copolymer on imidacloprid particles was exothermic in nature, and

involved a physisorption process mainly[10]. The positive value of ΔS indicated the increased randomness at the solid-solution interface in this sorption process. Thus, it was feasible for the adsorption of MAA-St-APEG copolymer on imidacloprid particles.

Nomenclature

c_0 — initial MAA-St-APEG copolymer concentration, $mg \cdot L^{-1}$

c_e — equilibrium MAA-St-APEG copolymer concentration in the solution, $mg \cdot L^{-1}$

ΔG — Gibbs free energy change, $kJ \cdot mol^{-1}$

ΔH — enthalpy change, $kJ \cdot mol^{-1}$

k_1 — pseudo first order rate constant of adsorption, min^{-1}

k_2 — pseudo second order rate constant of adsorption, $g \cdot mg^{-1} \cdot min^{-1}$

K_D — distribution coefficient, dimensionless

K_f — Freundlich constant correlated to the maximum multilayer adsorption capacity, $L \cdot g^{-1}$

K_L — Langmuir adsorption constant, $L \cdot mg^{-1}$

M — mass of adsorbent, g

M_n — weight average molecular weight, Da

M_w — number average molecular weight, Da

n_f — experimental constant indicative of the adsorption intensity, dimensionless

p — the number of experimental data

q_e — amount of MAA-St-APEG copolymer adsorbed at equilibrium, $mg \cdot g^{-1}$

$q_{e,\,cal}$ — amount of MAA-St-APEG copolymer adsorbed at equilibrium (calculated), $mg \cdot g^{-1}$

$q_{e,\,exp}$ — amount of MAA-St-APEG copolymer adsorbed at equilibrium (experimental), $mg \cdot g^{-1}$

q_m — maximum sorption capacity, $mg \cdot g^{-1}$

q_t — amount of MAA-St-APEG copolymer adsorbed at any time t, $mg \cdot g^{-1}$

$q_{t,\,cal}$ — amount of MAA-St-APEG copolymer adsorbed at any time t (calculated), $mg \cdot g^{-1}$

$q_{t,\,exp}$ — amount of MAA-St-APEG copolymer adsorbed at any time t (experimental), $mg \cdot g^{-1}$

R — molar gas constant, 8.314 $J \cdot K^{-1}$

R^2 — correlation coefficient

ΔS — entropy change, $J \cdot mol^{-1} \cdot K^{-1}$

T — temperature, K

t — adsorption time, min

V — volume of MAA-St-APEG copolymer solution, mL

References

[1] N. Hua, Y. Lin, Influence Pesticides SC Physical Stability Factor and Solutions, Agrochemicals 51 (2012) 163-167.

[2] L. Ding, X. Lu, H. Deng, X. Zhang, Adsorptive Removal of 2,4-Dichlorophenoxyacetic Acid (2,4-D) from Aqueous Solutions Using MIEX Resin, Ind. Eng. Chem. Res. 51 (2012) 11226-11235.

[3] S. Venkata Mohan, S.V. Ramanaiah, B. Rajkumar, P.N. Sarma, Removal of fluoride from aqueous phase by biosorption onto algal biosorbent *Spirogyra* sp.-I02: sorption mechanism elucidation. J. Hazard. Mater. 141 (2007) 465-474.

[4] S. Lagergren, Zur theorie der sogenannten adsorption gelöster stoffe, Veternskapsakad Handlinger 24 (1898) 1-39.

[5] Y.S. Ho, G. McKay, Pseudo-second order model for sorption processes, Process Biochem. 34 (1999) 450-465.

[6] I. Langmuir, The adsorption of gases on plane surfaces of glass, mica and platinum, J. Am. Chem. Soc. 40 (1918) 1361-1403.

[7] H.M.F. Freundlich, Over the adsorption in the solution, Zeitschriftfür Physikalische Chemie 57 (1906) 385-470.

[8] M. Saleem, M. Afzal, R. qadeer, J. Hanif, Selective Adsorption of Uranium on Activated Charcoal from Electrolytic Solutions, Sep. Sci. Technol. 27 (1992) 239-253.

[9] A. Sari, M. Tuzen, Equilibrium, thermodynamic and kinetic studies on aluminum biosorption from aqueous solution by brown algae (*Padina pavonica*) biomass, J. Hazard. Mater. 171 (2009) 973-979.

[10] Y.S. Ho, A.E. Ofomaja, Kinetics and thermodynamics of lead ion sorption on palm kernel fibre from aqueous solution, Process Biochem. 40 (2005) 3455-3461.

Advanced Materials Research Vol. 936 (2014) pp 859-863
© (2014) Trans Tech Publications, Switzerland
doi:10.4028/www.scientific.net/AMR.936.859

Adsorption Characteristics of Methacrylic Acid-Styrene Copolymer onto Azoxystrobin Particles Surfaces

Han Hao[1,a], Jianguo Feng[2,b], Weitao Chen[1,c], Wenjun Liu[3,d], Xuemin Wu*[,1,e]

[1:] College of science, China Agricultural University, Beijing 100193, China

[2:] College of Horticulture and Plant Protection, Yangzhou University, Yangzhou, Jiangsu, 225009, China

[3:] State Intellectual Property Office, Beijing 100088, China

[a] haohan@cau.edu.cn, [b] fengjianguo2003@163.com,

[c] cwt06100103@126.com, [d] mmjjuuyy@sohu.com,

*,[e] wuxuemin@cau.edu.cn

Keywords: Azoxystrobin; Methacrylic acid-styrene copolymer; Kinetic; Thermodynamics; Adsorption

Abstract: In order to investigate the feasibility of using methacrylic acid (MAA)-styrene (St) copolymer as dispersants to disperse azoxystrobin particles in aqueous suspension, the adsorption kinetics, isotherm and thermodynamics of MAA-St copolymer onto azoxystrobin particle surfaces were studied by batch equilibrium experiments. The results showed that the adsorption process followed the pseudo-second-order kinetic model with the entire adsorption, adsorption rate decreased with the initial concentration of MAA-St copolymer increasing. The equilibrium data were fitted with Langmuir isotherm equation better. The thermodynamic parameters were calculated, which indicated that the adsorption was a spontaneous and exothermic process in nature, and higher temperature is not beneficial to that adsorption process.

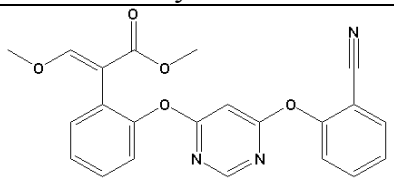
Introduction

Aqueous suspension concentrate (SC) is a very important environment friendly modern agrochemical formulation, and has a bright developing foreground for less dust pollution problem and favorable bioactivity. Choosing a proper dispersant is a key point in improving the stability of SC[1]. In this paper, the adsorption characteristics of MAA-St copolymer on azoxystrobin particles surface was studied, which provide a theoretical basis for choosing the optimal quantity of MAA-St copolymer as dispersant, developing stable and environmental friendly pesticide SC.

Experimental Section

Analytical-grade HCl and NaOH were purchased from Sinopharm Chemical Reagent Co., Ltd. azoxystrobin with the purity of 99 % was purchased from Sigma-Aldrich, the chemical structure and physical properties are shown in Table 1. Methacrylic acid (MAA)-styrene (St) copolymer were purchased from Beijing Grand AgroChem., Ltd, and the chemical structure is shown in Fig. 1. The stock MAA-St copolymer solution (2000 $mg \cdot L^{-1}$) was prepared by dissolving accurately weighted MAA-St copolymer particles in distilled water, which was diluted with appropriate volumes of distilled water into experimental copolymer solutions at various concentrations.

TABLE 1 ELEMENTAL PROPERTIES OF AZOXYSTROBIN

Adsorbent	azoxystrobin
Chemical structure	
Molecular Weight	403.39
Solubility in Water / mg·L^{-1}	6.0 (293 K); 10.0 (298 K)
log K_{ow}	2.64

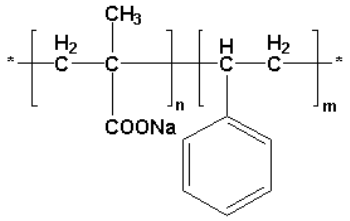


Fig. 1 Chemical Structure of MAA-St Copolymer

The weight average molecular weight (M_w), number average molecular weight (M_n) and polydispersity of MAA-St copolymer were determined by gel permeation chromatography, the carboxyl group content of MAA-St copolymer were obtained by conductometric titration using 0.1 mol·L^{-1} HCl and NaOH solution. Finally, the results obtained are summarized in Table 2.

TABLE 2 MOLECULAR WEIGHT AND CARBOXYL CONTENT OF MAA-ST COPOLYMER

M_w / Da	M_n / Da	Polydispersity	Carboxy content / mmol·g^{-1}
9442	5976	1.580	2.784

Azoxystrobin particles (2.0 g) were mixed with 50 mL of MAA-St copolymer solution and shaken at 220 rpm in a 250 mL conical flask. Duplicate samples were obtained at various time intervals at 288, 298, 308, and 318 K.

At the end of adsorption experiments, all samples were separated from the adsorbent by centrifugation (Hettich universal 320R, Germany) at 3500 rpm for 15 min, and then the MAA-St copolymer concentration was evaluated using a UV-visible spectrophotometer (Shimazu UV-1800, Japan) by monitoring the absorbance changes at 191 nm.

The amount of MAA-St copolymer adsorbed into azoxystrobin at equilibrium was calculated from the mass balance equation:

$$Q_e = (c_i - c_e)V/M \quad (1)$$

Results and Discussion

Two well-known kinetic models including the pseudo-first order and pseudo-second order equation were employed in investigating the mechanism of the MAA-St copolymer adsorption on azoxystrobin particles[2-3]. The results of kinetic parameters and the correlation coefficients were calculated and listed in Table 3.

TABLE 3 FITTED VALUES OF TWO KINETIC EQUATION FOR THE ADSORPTION AT 298 K.

c_i / mg·L^{-1}	$Q_{e,exp}$ / mg·g^{-1}	Pseudo-first order Kinetic model		
		$\ln(Q_e-Q_t)=\ln Q_e-k_1t$		
		$Q_{e,cal}$ / mg·g^{-1}	k_1 / min^{-1}	R^2
400	4.105	4.954	0.209	0.878
800	5.115	4.818	0.183	0.819
1200	5.324	4.253	0.164	0.809
c_i / mg·L^{-1}	$Q_{e,exp}$ / mg·g^{-1}	Pseudo-second order Kinetic model		
		$t/Q_t=1/k_2Q_e^2+(1/Q_e)t$		
		$Q_{e,cal}$ / mg·g^{-1}	k_2 / ×10^{-2} g·mg^{-1}·min^{-1}	R^2
400	4.105	4.690	4.783	0.989
800	5.115	5.522	4.201	0.981
1200	5.324	5.679	4.093	0.987

The results presented in Table 3 indicate that the adsorption of MAA-St copolymer on azoxystrobin particles were well represented by the pseudo-second order kinetic model due to high R^2 values. In addition, the rate constant of adsorption decreased with increasing MAA-St copolymer concentration due to more intensive competition for adsorption sites on azoxystrobin particles surface.

To optimize the design of an adsorption system, it is crucial to establish the most appropriate correlation for the equilibrium curves. The Langmuir and Freundlich models were used to fit the equilibrium data, and the results were showed in Table 4[4-5].

TABLE 4 FITTED VALUES OF TWO ISOTHERMS FOR THE ADSORPTION AT DIFFERENT TEMPERATURES

Temperature / K	Langmuir Isotherm		
	$c_e/Q_e=1/bQ_m+c_e/Q_m$		
	$b\times10^{-2}$ / g·mL^{-1}	Q_m / mg·g^{-1}	R^2
288	4.492	5.612	0.996
298	4.275	5.482	0.998
308	3.957	5.325	0.997
318	3.562	5.128	0.996
Temperature / K	Freundlich Isotherm		
	$\ln Q_e=(1/n_f)\ln c_e+\ln K_f$		
	n_f	K_f / mg·g^{-1}·(L·mg^{-1})$^{1/n}$	R^2
288	5.005	1.548	0.876
298	4.854	1.446	0.828
308	4.817	1.382	0.777
318	4.647	1.275	0.787

All of calculated isotherm parameters were summarized in Table 4. It was found that the adsorption of MAA-St on azoxystrobin particles was fitted better by the Langmuir model than the Freundlich model due to high R^2 values. Moreover, The maximum adsorption amount of MAA-St copolymer slightly decreased with increasing temperature, suggesting that the adsorption was mainly physical rather than chemical as an exothermic process.

Theoretically, thermodynamic parameters imply the feasibility of adsorption process. In this paper, thermodynamic parameters were calculated by using the following equations:[6]

$$K_D = Q_e/(c_e\cdot10^{-3}) \quad (2)$$

$$\ln K_D = (\Delta S^0/R)-(\Delta H^0/RT) \quad (3)$$

$$\Delta G^0 = \Delta H^0 - T\cdot\Delta S^0 \quad (4)$$

The plot of $\ln K_D$ versus $1/T$ gave straight lines with the intercept of $(\Delta S^0/R)$ and the slope of $(-\Delta H^0/R)$, and the thermodynamic parameters are listed in Table 5. As seen in Table 5, the negative values of ΔG^0 and ΔH^0 implied that the adsorption process was spontaneous and exothermic in nature. The positive value of ΔS^0 suggested that randomness at the solid-solution interface increased during the adsorption of MAA-St copolymer on azoxystrobin particles. The ΔG^0 values for physisorption range between −20 and 0 kJ·mol^{-1}, but those for chemisorption range from −80 to −400 kJ·mol^{-1}[7].As evidenced by the calculated ΔG^0 values, physisorption was the dominant mechanism.

TABLE 5 DETERMINATION RESULT OF THERMODYNAMICS

c_i / mg·L^{-1}	ΔS^0 / J·mol^{-1}·K^{-1}	ΔH^0 / kJ·mol^{-1}	ΔG^0 / kJ·mol^{-1}			
			288 K	298 K	308 K	318 K
400	15.134	−5.440	−9.801	−9.952	−10.104	−10.255
800	7.817	−4.094	−6.346	−6.425	−6.503	−6.581
1200	4.391	−3.318	−4.583	−4.627	−4.671	−4.715

Nomenclature

b — Langmuir adsorption constant, L·mg^{-1}

c_i — initial MAA-St copolymer concentration, mg·L^{-1}

c_e — equilibrium MAA-St copolymer concentration in the solution, mg·L^{-1}

ΔG^0 — standard Gibbs free energy, kJ·mol^{-1}

ΔH^0 — standard enthalpy, kJ·mol^{-1}

k_1 — pseudo first order rate constant of adsorption, min^{-1}

k_2 — pseudo second order rate constant of adsorption, g·mg^{-1}·min^{-1}

K_D — distribution coefficient, dimensionless

K_f — Freundlich constant correlated to the maximum multilayer adsorption capacity, L·g^{-1}

M — mass of adsorbent, g

M_n — weight average molecular weight, Da

M_w — number average molecular weight, Da

n_f — experimental constant indicative of the adsorption intensity, dimensionless

Q_e — amount of MAA-St copolymer adsorbed at equilibrium, mg·g^{-1}

$Q_{e,\,cal}$ — amount of MAA-St copolymer adsorbed at equilibrium (calculated), mg·g^{-1}

$Q_{e,\,exp}$ — amount of MAA-St copolymer adsorbed at equilibrium (experimental), mg·g^{-1}

Q_m — maximum sorption capacity, mg·g^{-1}

Q_t — amount of MAA-St copolymer adsorbed at any time t, mg·g^{-1}

$Q_{t,\,cal}$ — amount of MAA-St copolymer adsorbed at any time t (calculated), mg·g^{-1}

$Q_{t,\,exp}$ — amount of MAA-St copolymer adsorbed at any time t (experimental), mg·g^{-1}

R — molar gas constant, 8.314 J·K^{-1}

R^2 — correlation coefficient, dimensionless

ΔS^0 — standard entropy, J·mol^{-1}·K^{-1}

T — temperature, K

t — adsorption time, min

V — volume of MAA-St copolymer solution, mL

References

[1] N. Hua, Y. Lin, Influence Pesticides SC Physical Stability Factor and Solutions, Agrochemicals 51 (2012) 163-167.

[2] S. Lagergren, Zur theorie der sogenannten adsorption gelöster stoffe, Veternskapsakad Handlinger 24 (1898) 1-39.

[3] Y.S. Ho, G. McKay, Pseudo-second order model for sorption processes, Process Biochem. 34 (1999) 450-465.

[4] I. Langmuir, The adsorption of gases on plane surfaces of glass, mica and platinum, J. Am. Chem. Soc. 40 (1918) 1361-1403.

[5] H.M.F. Freundlich, Over the adsorption in the solution, Zeitschriftfür Physikalische Chemie. 57 (1906) 385-470.

[6] M. Saleem, M. Afzal, R. Qadeer, J. Hanif, Selective Adsorption of Uranium on Activated Charcoal from Electrolytic Solutions, Sep. Sci. Technol. 27 (1992) 239-253.

[7] M.J. Jaycock, G.D. Parfitt, Chemistry of Interfaces, Ellis Horwood, Onichester, 1981.

Advanced Materials Research Vol. 936 (2014) pp 864-867
© (2014) Trans Tech Publications, Switzerland
doi:10.4028/www.scientific.net/AMR.936.864

Preparation of 5-sulfosalicylic Acid Modified Silica Gel and Its Adsorption Performances for Lead

Wu Xiongzhi[1,a], Meng Jiao [1,b], Li Feiping[1,c], Luo Liangliang[1,d]

[1]Department of Chemistry and Biological Engineering, Guilin University of Technology, Guilin 541004, China

[a]2004046@glut.edu.cn, [b]meng87meng87@126.com, [c]420041173@qq.com, [d]380664562@qq.com

Keywords: Silica gel; 5-sulfosalicylic acid; enrichment; Lead

Abstract：A new sorbent (SSA-SG) with 5-sulfosalicylic acid as functional group has been prepared and characterized with FTIR and then used as micro-column packing for enrichment of Pb(II). Enrichment conditions of lead were optimized. The enrichment factor reaches 200 and the dynamic sorption capacity was 15.46 mg•g^{-1} for Pb(II). The proposed column enrichment procedure was applied for the preconcentration/separation and atomic absorption spectrometry (AAS) determination of Pb (II) in water samples successfully.

Introduction

Lead is one of the toxic elements and can enter the organism by food, drinking water and air and accumulate in human body, which carry high risk to human health. Lead pollution has been paid more attention and the analysis of lead is an important research field. Atomic absorption spectrometry and mass spectrometry are the most used methods for the analysis of lead. Considering the low lead concentration and interferences in environmental samples, enrichment techniques are often necessary. Solid-phase extraction (SPE) is one of the most interesting enrichment procedures. Chelating sorbents, such as silica gel[1], chelating resin [2], activated carbon [3] are often used extraction materials.

In the present work, 5-sulfosalicylic acid modified silica gel was prepared and its performance of adsorption for lead was investigated. It was used as the micro-column packing for enrichment of Pb (II) in water samples successfully.

Experimental

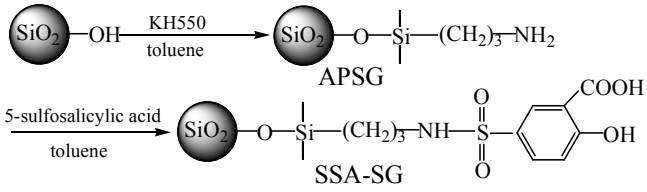
Apparatus and Reagents

Atomic absorption spectrometer (TAS-990AFG) of Beijing Purkinje General Instrument Co., Ltd. (China) was employed. Peristaltic pump (BT01S-YZ1515) of Yi Kang Xin Da Technology Co., Ltd (China) and a self made micro-column (7 cm × 0.5mm i.d.) were used. PTFE tubing (0.8mm i.d.) was used for connections.

Silica gel (Qingdao Shuoyuan Chemical Co. Ltd., China) was 60–100 meshes, and its surface area was 300-600 m^2•g^{-1}. γ-Aminopropyltriethoxysilane (Beijing Shenda Fine Chemical Co. Ltd., China) was purified by distillation at 123℃ under 10 mm Hg. All of the other reagents were analytical reagent grade. Distilled water was used throughout. Stock solution of Pb(II) (1000 mg• L^{-1}) was prepared by dissolving appropriate amounts of analytical pure $Pb(NO_3)_2$ in pH=2 HNO_3 solution. Standard solutions of Pb(II) were prepared by dilution of the stock solution just before use.

Preparation of SSA-SG

APSG and SSA-SG was prepared according to reference [4] and [5]. 5.0g 5-sulfosalicylic acid was added to a 250mL flask and dissolved with 20ml dimethyl sulfoxide. 20.0g APSG and 80ml toluene were added to the flask and the mixture was stirred for 8h at 80℃. The resulting solid product was filtered off and washed in order with dimethyl sulfoxide, toluene and ethanol respectively for 3 times. Then the solid product was dried at 70℃ for 7h. The synthesis routine to SSA-SG is shown schematically in Scheme 1.



Scheme 1 The Synthetic Route for SSA-SG

Enrichment Procedures

One end of the micro-column was packed with polypropylene fiber, SSA-SG was packed in micro-column, then the other end was packed with polypropylene fiber, two ends were connected with suitable silicone tubing. In Step 1, the blank solution (its pH is the same as Pb (II) standard solution) was pumped through micro-column with flow rate of 1.2 mL•min^{-1}. In Step 2, the Pb(II) solution was pumped through micro-column with flow rate of 1.2 mL•min^{-1}. In Step 3, the blank solution was pumped through micro-column with the same flow rate. In Step 4, the eluent solution was introduced through micro-column in the reverse direction with flow rate of 2.4 ml•min^{-1}. Then the eluent solution was determined with flame atomic absorption spectrometry (FAAS).

Sample Pretreatment

2500ml water sample was acidified with 5 mL of HNO_3 and kept in refrigerator for 3 days and then filtered. 95 ml filtrate was adjusted to pH 5, transferred to 100 ml flask and then its volume was adjusted to 100 ml pH=5 HCl solution. Then Pb(II) in the solution was preconcentrated and determined with FAAS.

Results and Discussion

Characterization of Sorbent

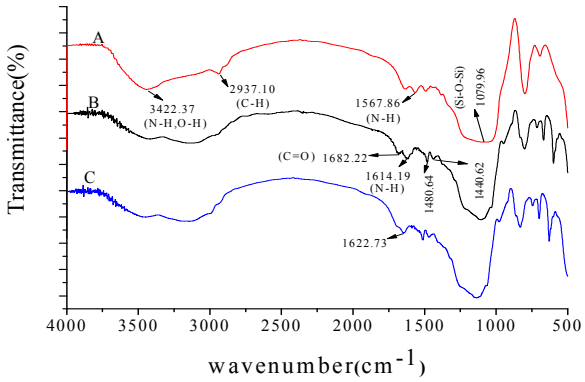


Fig.1 Infrared Spectra

A:APSG B:SSA-SG C: SSA-SG (Pb(II) was absorbed)

Fig.1 are the Fourier transmission infra-red (FTIR) spectra of APSG, SSA-SG and SSA-SG after Pb(II) was absorbed. In FTIR spectra of A, B and C, the absorption of 1079.96 cm^{-1}and 798.39cm^{-1} cm^{-1} are characteristic of Si-O-Si skeleton, and the absorption at 3422.37cm^{-1} is characteristic of

-OH and $-NH_2$ groups. In the FTIR spectra of B and C, the absorption at 1682.22 cm^{-1} is characteristic of carboxyl groups. The changes of FTIR spectra suggested 5-sulfosalicylic acid was successfully introduced to the surface of silica-gel.

Effect of pH

In the range from 2 to 10, adsorption rate of Pb(II) reached more than 95% when pH is in the range of 5-6. The solution of pH=5 was selected as the sample medium.

Effect of Eluent Concentration

In the range of 0.05~4 .0 mol•L^{-1}, when the concentration of HCl was more than 1.0 mol•L^{-1}, elution recovery of Pb(II) could reach more than 95%, but high concentration of HCl would effect adsorption rate of next sample loading. So 1.0 mol•L^{-1} HCl was selected as eluent.

Effect of Flow Rate

In the range of 0.6–6.0 ml•min^{-1}, when sample solution flow rate was not more than 1.2 ml•min^{-1}, adsorption rate of Pb(II) reached more than 95%. So 1.2 ml•min^{-1} was used as the sample solution flow rate. When the eluting flow rate was 2.4 ml•min^{-1}, elution recovery could reach more than 98%. So 2.4 ml•min^{-1} was used as eluting flow rate.

Effect of Sample and Eluent Solution Volume

Under the above selected conditions, different volume (5.0-50.0 ml) sample solution of 5.0 μg•mL^{-1} Pb(II) was used respectively for sample loading. When sample solution volume was not more than 10.0 ml, adsorption rate of Pb(II) were more than 98%. So sample solution volume was 10.0 ml. Different volume (5.0-25.0 ml) HCl solution (1.0 mol•L^{-1})was used as eluent, and elution recovery of Pb(II) could reach more than 95%. So 5.0 ml eluent was used in the further experiments.

Interference of Co-exiting Ions

The effects of anions and co-existing metal ions were tested when 10 ml sample solution with 5.0 μg•ml^{-1} Pb(II) was determined. More than 25 μg•ml^{-1} of co-existing metal ions (Na^+, K^+, Ca^{2+}, Mg^{2+}, Zn^{2+}, Al^{3+}, Mn^{2+}, Cu^{2+}, Cr^{3+}, Co^{2+}, Cd^{2+}, Ni^{2+}, NH_4^+) and 1000 μg•$ml^{-1}$of anions (PO_3^{4-}, SO_4^{2-}, NO_3^-, CH_3COO^-, Cl^-) (added as sodium salts) did not interfere with the enrichment and determination.

Saturated Adsorption Capacity

5.0 μg•mL^{-1} Pb(II) solution (pH=5.0) passed through micro-column with flow rate of 1.2 ml•min^{-1} to obtain the break-through curve. The saturated adsorption capacity of SSA-SG for Pb(II) was 15.46 mg•g^{-1}. Pseudo-first kinetic model and quasi-two kinetic model fitting results showed that quasi-two kinetic model was suitable for describing the adsorption of Pb(II) on SSA-SG.

Low concentration Enrichment

Different volume solutions with 50 μg Pb(II) were respectively preconcentrated according to the enrichment procedure, and then Pb (II) was eluted with 5.0 ml eluent and determined. When solution volume reached 1000 ml (larger volume solution was not tested), Pb(II) could be quantitatively preconcentrated on SSA-SG. The enrichment factor was 200.

Water Sample Analysis

In order to test the applicability of sorbent, SSA-SG was applied for the enrichment of Pb (II) in water samples. The analysis results listed in Table1 demonstrated that SSA-SG is suitable for quantitative preconcentration of Pb (II) from water samples.

TABLE 1 DETERMINATION OF PB(II) IN WATER SAMPLES AND ADDITION–RECOVERY TESTS

Sample	Added ($\mu g\ ml^{-1}$)	Found ($\mu g\ ml^{-1}$)	RSD (%)	Recovery (%)
Tap water	0	unfound	---	---
	1.0	1.02	2.1	102
	3.0	3.29	5.0	109.8
Lijiang River water	0	1.78	1.4	---
	1.0	2.78	0.8	100
	3.0	4.88	3.3	103.3

Summary

SSA-SG sorbent with 5-sulfosalicylic acid as functional group has been synthesized and characterized with FTIR, then enrichment conditions for Pb(II) was investigated. After being used for no less than 200 times of enrichment cycle, the performance of SSA-SG has not changed yet. SSA-SG showed good characteristics, such as simplicity, fast extraction, stability, selectivity for Pb(II). It was used as the microcolumn packing for enrichment coupled with FAAS determination of Pb(II) in water samples successfully.

Acknowledgements

The financial support of the National Natural Science Foundation of China (No. 51262005) was gratefully acknowledged.

References

[1] M. Ezoddin, F. Shemirani, Kh. Abdi, M. K. Saghezchi, M.R. Jamali, Application of modified nano-alumina as a solid phase extraction sorbent for the preconcentration of Cd and Pb in water and herbal samples prior to flame atomic absorption spectrometry determination, Journal of Hazardous Materials 178 (2010) 900–905.

[2] X.P. Huang, X.J. Chang, Q. He, Y.M. Cui, Y.H. Zhai, N. Jiang, Tris(2-aminoethyl) amine functionalized silica gel for solid-phase extraction and preconcentration of Cr(III), Cd(II) and Pb(II) from waters, Journal of Hazardous Materials 157 (2008) 154–160.

[3] M. Ghaedi, F. Ahmadi, Z. Tavakoli, M. Montazerozohori, A. Khanmohammadi, M. Soylak, Three modified activated carbons by different ligands for the solid phase extraction of copper and lead, J. Hazard. Mater. 152 (2008) 1248-1255.

[4] X.Z. Wu, P. Liu, Q.S. Pu, Q.Y. Sun, Z.X. Su, Preparation of dendrimer-like polyamidoamine immobilized silica gel and its application to online preconcentration and separation palladium prior to FAAS determination, Talanta 62 (2004) 918-923.

[5] Y.M. CUI, X.J.CHANG, X.B. ZHU, N. Jiang, Z. Hu, N. Lian, Nanometer SiO_2 modified with 5~sulfosalicylic acid as selective solid~phase extractant for Fe (III) determination by ICP-AES from biological and natural water samples. Microchemical journal 86 (2007) 23-28.

Advanced Materials Research Vol. 936 (2014) pp 868-874
© (2014) Trans Tech Publications, Switzerland
doi:10.4028/www.scientific.net/AMR.936.868

Preparation and characterization of mesoporous activated carbon from alligator weed with H_3PO_4

Huimin Xu[1,a],Guofu He[1,b,*],Mintao Shi[1,c],Jun Tu[1,d],Wei Liu[1,e],Weining Xiang[1,2,f]

[1] College of Ecological and Environmental Science, East China Normal University, Shanghai, China

[2] Shanghai Key Lab for Urban Ecological and Eco-Restoration, Shanghai, China

[a]huimin0905@163.com, [b]gfhe@des.ecnu.edu.cn, [c] 464954084@qq.com, [d]463647471@qq.com, [e]370275381@qq.com, [f]wnxiang@mail.ecnu.edu.cn;

Keywords: Alligator weed; Mesoporous activated carbon; Chemical activation; Optimum condition; Phosphoric acid

Abstract: Alligator weed, containing ash of 8.56 wt.% (dry basis), is a low-cost and renewable material for preparing activated carbon (AC) by chemical activation. Yield and iodine number results of orthogonal experiments showed H_3PO_4 was the optimal activator comparing with NaOH and $(NH_4)_2HPO_4$. And optimal condition was at impregnation ratio of 4 to 1 with the impregnation time of 6h, carbonization temperature of 873K and carbonization time of 1h. According to calculation of Brunauer-Emmett-Teller (BET), the surface area of P1 (AC prepared by H_3PO_4 under optimum condition) attained the value of 1100.720 m^2/g. Calculated by Barrett-Joyner-Halenda (BJH), the total pore volume and average pore size of P1 were 0.610 cm^3/g and 2.216nm. The rate of mesoporous range, as high as 72.00%, revealed P1 was mesoporous AC. FT-IR spectrum suggested P1 contained carboxyl, phenol, ether and other functional groups. XRD showed a graphitization degree of 65.12% indicating its high stability in application.

Introduction

Alligator weed (*Alternanthera philoxeroides* (Mart.) Grisebach) is a famous invasive weedy species originated in South America [1]. Since it has been introduced into China in the 1930s, alligator weed has rapidly expanded in 18 of 31 provinces bringing direct economic loss of 10 billion yuan per year [2]. To control its expansion, every year billions of tons of alligator weed have been weeded or salvaged as agricultural wastes [3]. Discarding arbitrarily and setting on fire are traditional methods of deposing these wastes, while the former is useless since the broken stems from the parental plants can rapidly grow root systems, and soon anchor on soil and develop into complete plants and the latter can cause serious air pollution [1, 4]. The utilization of large quantity of alligator weed debris yielded as agriculture wastes every year in China has not been well understood. Thus, development of methods to re-use these waste materials is greatly desired.

Preparing activated carbon from environmental wastes has attached many researchers attention which is motivated by strong market position and growing need for activated carbon and also helpful for solving environmental problems. Philip and Girgis[5] succeeded in preparing microporous activated carbon from apricot stone shells by phosphoric acid with a BET surface area of 1000 m^2/g. Tseng [6] published that mesoporous activated carbon was prepared from corncob by NaOH with high surface area in narrow range from 2318 to 2474 m^2/g. Shi et al. [7] proved that cattail could also be prepared to activated carbon by H_3PO_4 and activated temperature had the greatest effects on surface area of resulting activated carbon. Gao et al. [8] reported the preparation of activated carbon from rice straw by $(NH_4)_2HPO_4$ with apparent surface area of 1154 m^2/g. Based

on the above results, characteristics and constituents of alligator weed on a dry basis was analyzed. As shown in Table 1, low content of ash, high content of cellulose and renewable characteristic show that alligator weed is potential as precursor to active carbon [9].

Table 1. Characteristics and constituents of alligator weed (dry basis)

Component analysis (wt.%)	Moisture	Cellulose	Lignin	Ash
	2.76	23.5	9.9	8.56
Ultimate analysis (wt.%)	C	H	O*	N
	39.31	5.23	53.15	2.45
* Calculated by difference.				

The purposes of the present work were to prepare activated carbon from alligator weed by chemical activation and achieve the optimal activator and condition. The characteristics (surface area, pore volume, functional groups and so on) of activated carbon obtained by optimum activator under optimum condition were also detected.

Experimental

Raw material

Alligator weed used in this study was obtained from Xiaoshahe River, a branch of Nansihu basin, Shandong, China. All reagents were analytically graded.

Preparation of Activated Carbon and Orthogonal Experiment

Pre-oxidation experiment: Alligator weed was dried in an oven kept at 378 K for 24 h and then cut into short sections with 2-3cm in length each. The dried short sections were soaked in a solution of NaOH (2 wt. %) for 24h to remove wax, ash and other water-soluble impurities on the surface. After alkaline liquor pretreatment, they were washed with distilled water to neutral pH and then dried in an oven kept at 473 K for 1h.

Orthogonal experiment: Using activator H_3PO_4 (85 wt. %), NaOH (solid) and $(NH_4)_2HPO_4$ (30 wt. %), three series experiments, each series of 9 experiments, were made following $OA_9(3^4)$ matrix. The factors and levels of orthogonal experiment are presented in **Table 2**. The pre-oxidization samples were mixed with a solution of activator with varying ratios (3-5) and times (6-24). Then impregnated samples were loaded on ceramic crucibles and placed inside a muffle furnace heating up for carbonization at heating rate of 10K/min. After cooling to room temperature in muffle furnace, they were washed with hot distilled water to remove the remaining activator and filtered, and finally dried at 373 K for 24 h in a thermostatically controlled oven. The washing and filtration steps were repeated until the filtrate reached neutral pH. All activated carbon products were kept in screw-cap bottles.

Table 2. Factors and levels of the orthogonal experiment

Level	Impregnation ratio(A)	Impregnation time (B)	Carbonization temperature(C)	Carbonization time(D)
1	3	6 h	773 K	1 h
2	4	12 h	873 K	2 h
3	5	24 h	973 K	3 h

Yield and Adsorptive Properties

The yield was based on the following equation:

Yield=weight of prepared activated carbon / weight of sample after alkaline pretreatment

Adsorptive properties were described by the iodine adsorption which gave the information on the quantity of pores larger than 1 nm. The amount of iodine absorbed (in milligrams) by 1 g of

carbon was called the iodine number. The iodine adsorption was measured by the sodium thiosulfate volumetric method.

Characterization of Prepared Activated Carbons

Activated carbon prepared under optimum activator and condition was characterized by N_2 adsorption at 77K, Fourier Transform Infrared Spectrometer (FT-IR), X-ray Powder Diffraction Pattern (XRD) and Scanning Electron Micrograph (SEM).

The adsorption isotherm of N_2 on the prepared activated carbon was measured at 77 K using the constant volume adsorption apparatus (Quanta chrome Autosorb-3B, JAPAN, Inc.). The surface area of the activated carbon was calculated by the Brunauer-Emmett-Teller (BET) method using the adsorption isotherm data of N_2. The micropore volume (V_{micro}) was calculated from the amount of N_2 adsorbed at a relative pressure P/P^0 of 0.1, and the mesopore volume (V_{meso}) was estimated from the amount adsorbed between relative pressures of 0.1 and 0.95. The total pore volume (V_t) was evaluated from the volume adsorbed at the relative pressure of 0.98. FT-IR was determined at Nexus 670 FT-IR spectrometer to characterize the functional groups of activated carbon sample which determined the adsorption of activated carbon. X-ray powder diffraction pattern was determined at D/texultra (Rigaku, Japan) with Cu Kα radiation at a step of 0.01°. XRD results helped to characterize the crystal structure of activated carbon sample. Scanning electron micrographs carried out in secondary electron imaging mode was measured by a Hitachi DSM-4600, after plating the sample with gold.

Results and Discussion

Yield and Iodine Number

The average values of yield of AC prepared by H_3PO_4, NaOH and $(NH_4)_2HPO_4$ are 34.7%, 25.8% and 33.4%. The average values of iodine number of AC prepared by H_3PO_4, NaOH and $(NH_4)_2HPO_4$ are 726 mg/g, 521 mg/g and 396 mg/g. With comprehensive consideration of yield and iodine number, we come to a conclusion that H_3PO_4 is the optimal activator.

The analysis results presented in

Table 3 reveal that yield and iodine number of activated carbon prepared by H_3PO_4 are variously affected by impregnation ratio impregnation time, carbonization temperature and carbonization time. According to the range analysis of yield, with the decrease sequence of range R, the order of factors is C>A>D>B. The range analysis of iodine number is consistent with that of yield.

The result of K (the average of yield and iodine number for each factor at different levels) is K_2(C) >K_2 (A) >K_1 (D) >K_1 (B). Thus, the best combination is $A_2B_1C_2D_1$, which means the optimum condition possibly has an impregnation ratio of 4, impregnation time of 6h, carbonization temperature of 873K and carbonization time of 1h.

Table 3. Range analysis results of yield ratio and adsorption of I_2 of H_3PO_4

	Level	Impregnation ratio(A)	Impregnation time (B)	Carbonization temperature(C)	Carbonization time(D)
Yield	K 1	38.50	35.70	31.87	36.35
	K2	32.17	35.30	38.80	34.22
	K3	33.31	32.98	33.31	33.41
	R	6.33	2.72	6.93	2.94
Iodine number	K1	730.97	731.41	740.60	737.36
	K2	739.19	720.79	729.56	734.23
	K3	708.35	726.32	708.35	706.93
	R	30.84	10.62	32.25	30.43

Additional Verification Experiment

An additional experiment was carried out to verify whether the combination of $A_2B_1C_2D_1$ was optimum condition or not. The results of yield and iodine number in additional experiments were 37.44% and 752.36mg/g, which were both higher than the average of the orthogonal experiments. It proves that optimum condition of preparing activator carbon from alligator weed by H_3PO_4 is exactly $A_2B_1C_2D_1$. The activated carbon prepared under optimum condition was named P1 and characterized by N_2 adsorption, FT-IR, XRD and SEM.

N_2 adsorption at 77 K

According to the classification standard of International Union of Pure and Applied Chemistry (IUPAC), the N_2/77K adsorption/desorption isotherm of P1 is classified as a type IV, as shown in **Fig. 1**. It indicates that P1 has apparent mesoporous structure and the aperture is mainly between 2 to 50 nm. Furthermore, the inconsistency between adsorption and desorption isotherm, with the formation of hysteresis loop of a type H4, shows P1 contains a narrow wedge-shaped hole [10].

The surface area of P1 is calculated by the equation of Brunauer-Emmett-Teller (BET) and pore size distribution is calculated by the Barrett-Joyner-Halenda (BJH) model. The results shows P1 is mesoporous activated carbon, which is coincident with N_2/77K adsorption/desorption isotherm, with surface area of 1100.720 m^2/g, total volume of 0.610 cm^3/g , mesoporous volume of 0.540 cm^3/g and average pore diameter of 2.216nm.

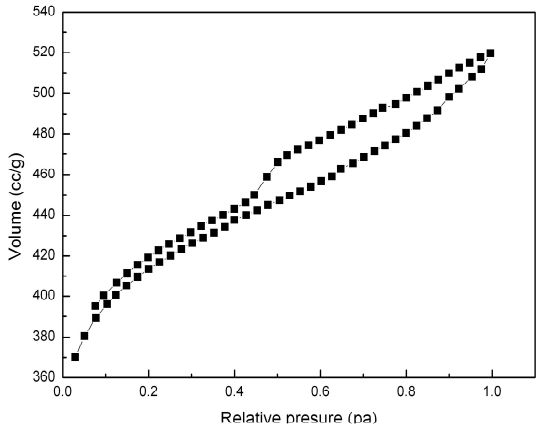


Fig. 1. Adsorption and desorption isotherms of N_2/77K on P1

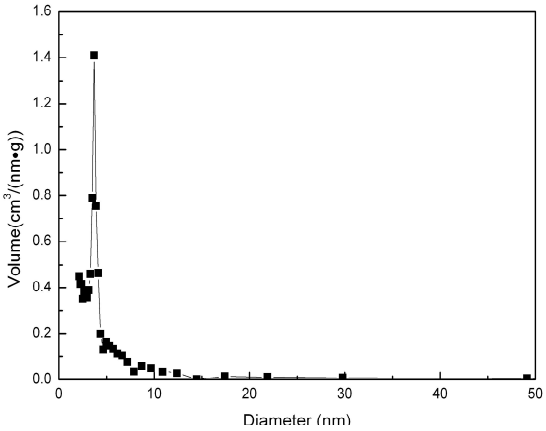


Fig. 2.Mesopore size distributions of P1

The rate of mesoporous range of P1 obtains 72.00% and pore size distribution is mainly concentrated in the 2-5 nm as shown in **Fig. 2**. The study of Wang et al. [11] showed that lignin played a major role in the formation of microporous, while cellulose is important to the formation of mesoporous.

FT-IR

FT-IR is useful to analyze the function groups and chemical structure of P1 qualitatively. **Fig. 3** shows the FT-IR spectrum of P1. A broad band around 3430 cm^{-1} is most likely caused by hydroxyl (OH) or carboxyl (COOH). The weak band around 2922 cm^{-1} can be attributed to the stretching vibration of CH_2 groups, while the relatively strong band located around 1600 cm^{-1} is attributed to C=C, C=O, NHCO or NH_2. The band around 1384 cm^{-1} may be caused by aliphatic or aromatic compounds which means such substances haven't degraded or volatilized completely during the carbonization process. The stretching vibration of ether or alcohol groups may lead to a band located around 1162cm^{-1}. The band in the region of 1003-714cm^{-1} is caused by bending vibration of tertiary amine possibly. The FT-IR spectrum obtained is in agreement with the results reported in the studies of preparing activated carbon from bamboo and rice bran [12-14].

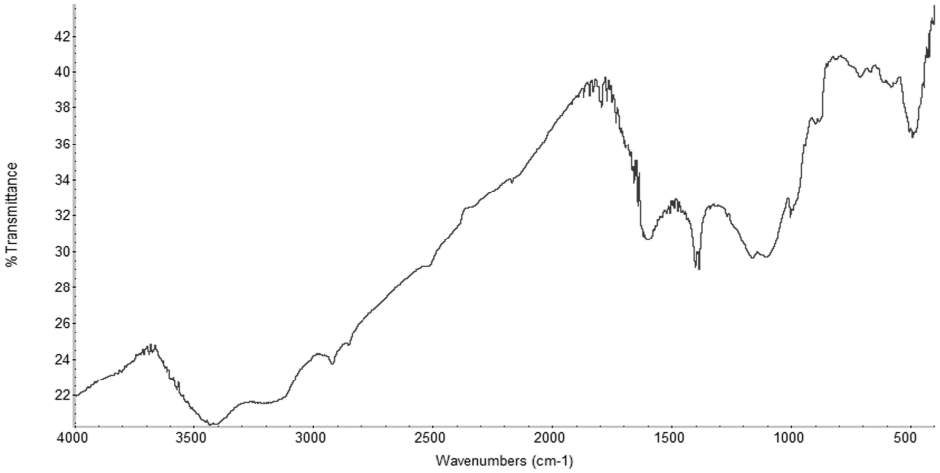


Figure 3. FT-IR spectrum of P1

XRD

XRD pattern of P1 is given in **Fig. 4**. It is clear that when 2<theta> is nearly 26°, there is an obvious diffraction peak. The reason for this phenomenon is that during the carbonization procedure of P1, some carbon atoms formed into relatively stable structure of lamellar graphite. The other amorphous structure leads to the increase of lamellar gap and surface area of P1. In addition, there is a relatively weaker peak at 42° which may be caused by the elimination of distortion or defects in the graphite crystal. It is because that under high temperature, P atoms enter into the microcrystalline layer and makes catalytic oxidation reaction with carbon atoms [15].

From the position of the peak around 26°, an estimate of the interplanar spacing, d_{002}, can be calculated by application of the Bragg's Law [7]. On this basis, we summarize a calculation method from previous studies and calculate that the graphitization degree of P1 is 65.12% [16]. The higher graphitization degree, the better stability of activated carbon in subsequent application it is.

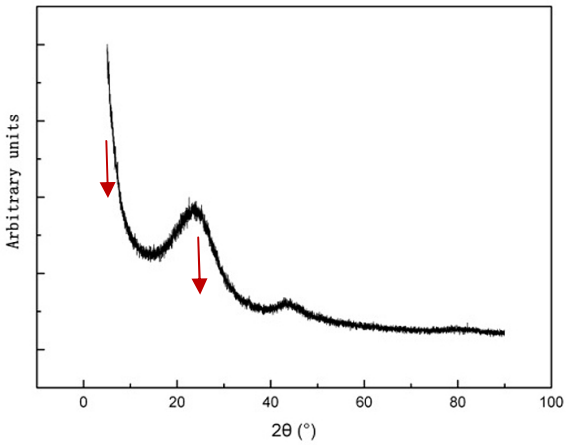


Fig. 4. XRD of activated carbon P1

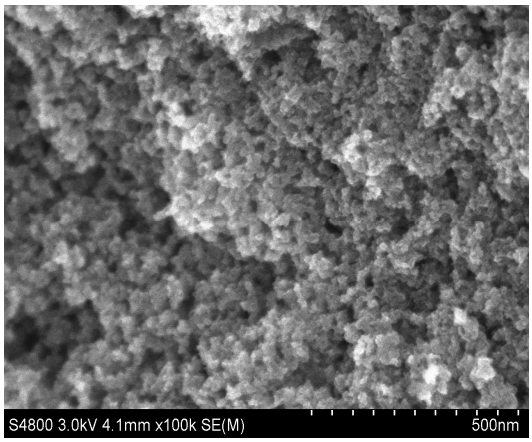


Fig. 5. SEM of P1 enlarged 100K

SEM

The scanning electron micrograph of P1 enlarged 100K is shown in **Fig. 5**. From the shape of pore, it is observed that the surface of activated carbon is the distribution of well developed porous with various shapes. Some of them are oval shape, and others are crack and irregular shape. In addition, surface morphology of P1 is rough, showing an uneven and honeycomb structure. From the size of pore, mesoporous and microporous are the majority with the distribution of few macroporous.

Conclusions

To prepare activated carbon from alligator weed by chemical activation, H_3PO_4 is demonstrated to be an optimal agent as the results of yield and iodine number in orthogonal experiments. The optimal condition appears to be impregnation ratio of 4, impregnation time of 6h, carbonization temperature of 873K, and carbonization time of 1h. High-performance activated carbon has been prepared with surface area, total pore volume and average pore size as high as 1100.720m^2/g, 0.610cm^3/g and 2.216nm, respectively. This work confirms that alligator weed can be employed as a good material in preparing mesoporous activated carbon which has a promising precursor in removing relatively macromolecular pollutants.

Acknowledgements

The work was supported by the National Science and Technology Major Project (NO. 2009ZX07210).

References

[1] C. Y. Xu, W. J. Zhang, C. Z. Fu, B. R. Lu, Genetic diversity of alligator weed in China by RAPD analysis. Biodivers. Conserv. 12 (2003) 637–645.

[2] Y. Li, China Flora of Weeds. Beijing: Chinese Agricultural Press, 1998.

[3] G. Sainty, G. Mccorkelle, M. Julien, Control and spread of alligator weed Alternanthera Philoxeroides(Mart.)Griseb, in Australia: lesson for other regions. Wetl. Ecol. and Manag. 5(1998) 195-201.

[4] S. H. Chen, J. Zhan, C. L. Zhang, Equilibrium and kinetic studies of methyl orange and methyl violet adsorption on activated carbon derived from Phragmites australis. Desalination 252(2010) 149-156.

[5] C. A. Philip, B. S. Girgis, Adsorption characteristics of microporous carbons from apricot stones activated by phosphoric acid. J. Chem. Tech. Biotechnol. 67(1996) 248-254.

[6] Rajeshwarisivaraj, S. Sivakumar, P. Senthilkumar, V. Subburam, Carbon from Cassava peel, an agricultural waste, as an adsorbent in the removal of dyes and metal ions from aqueous solution. Bioresour. Technol. 3(2001), 233–235.

[7] Q. Q. Shi, J. Zhang, C. Li, B. Zhang, Preparation of activated carbon from cattail and its application for dyes removal. J. Environ. Sci. 22(2009) 91-97.

[8] P. Gao, Z. H. Liu, G. Xue, B. Han, M. H. Zhou, Preparation and characterization of activated carbon produced from rice straw by $(NH_4)_2HPO_4$ activation. Bioresour. Technol. 102(2011), 3645–3648.

[9] W. Heschel, E. Klose, On the suitability of agricultural by-products for the manufacture of granular activated carbon. Fuel 12(1995), 1786-1791.

[10] Y. Guo, D. A. Rockstraw, Physical and chemical properties of carbons synthesized from xylan, cellulose, and Kraftlignin by H3PO4 activation. Carbon 44(2006), 1464-1475.

[11] Z. F. Wang, Z. Zheng, X. Z. Luo, J. B. Zhang, Preparation of activated carbon from S. Altreniflora by H_3PO_4 chemical activation. Environ. Chem. 30(2011) 530-537.

[12] S. Y. Wang, M. H. Tsai, S. F. Lo, Effects of manufacturing conditions on the adsorption capacity of heavy metal ions by Mkkino bamboo charcoal. Bioresour. Technol. 99(2008) 7027-7033.

[13] F. C. Wu, R. L. Tseng, R. S. Juang, Preparation of activated carbons from bamboo and their adsorption abilities for dyes and phenol. J. Environ. Sci. Heal. A. 34(1999) 1753-1775.

[14] R. M. Suzuki, A. D. Andrade, J. C. Sousa, M. C. Rollemberg, Preparation and characterization of activated carbon from rice bran. Bioresour. Technol. 98(2007), 1985-1991.
[15] S. J. Greeg, K. S. Sing, Adsorption, surface area and porosity. New York: Academic Press, 1982.
[16] P. J. M. Carrott, J. M. V. Nabaisa, M. M. L. Ribeiro Carrotta, J. A. Pajares, Preparation of activated carbon fibres from acrylic textile fibres. Carbon 39(2001) 1543-1555.

Advanced Materials Research Vol. 936 (2014) pp 875-880
© (2014) Trans Tech Publications, Switzerland
doi:10.4028/www.scientific.net/AMR.936.875

Silica gel as an Adsorbent in the Removal of Cationic Blue X-Bl From Aqueous Solutions and its Regeneration by UV-Fenton Oxidation

Qiuyuan Xiong[1,2]

[1] Changzhou key Laboratory of New textile material, Changzhou,213164, China
[2] Changzhou Textile Garment Institute, Changzhou, Jiangsu Province, 213164, China
libin5008@126.com

Keywords: Silica gel; Adsorption; Dye; Regeneration; Oxidation

Abstract. The removal of cationic Blue X-BL in aqueous solution by adsorption of silica gel was investigated. Effects of pH, initial concentration of dye solution and temperature on the adsorption of Cationic Blue X-BL onto silica gel were studied. When the initial concentration of the blue dye was 100 mg/dm^3, silica gel is 0.6 g at pH 9.3 and at 303 K, adsorption reached equilibrium after 2 h with the final adsorption quantity 16.38 mg/g. Fenton reaction with UV light was applied in the regeneration operation of silica gel which can transmit most of the UV light. The concentration of Fe^{2+} and H_2O_2 was evaluated and when the concentration of Fe^{2+} and H_2O_2 were 0.05 mmol/dm^3 and 0.132 mol/dm^3, the first, second, third and forth regeneration efficiency were 84.68 %, 82.05 %, 65.26% and 50.73 %, respectively. In order to improve the regeneration capacity and silica gel's reuse times, acid washing was introduced in the forth regeneration after Fenton reaction, which can enhance the regeneration efficiency to 92.19%.

Introduction

Many of dyes can cause health problems such as allergic dermatitis, skin irritation, cancer and mutation in human [1]. While adsorption techniques have found many practical applications as it can aggregate dyes to high concentration especially for the non-biodegradable dyes [2]. Among numerous absorbents, silica gel deserves particular attention, considering its high thermal and chemical stability, controlled porosity, swelling resistance, relative rapidity in reaching equilibrium, high surface area and inexpensive cost [1,2]. UV-Fenton reaction has its own unique advantage in the degradation of pollutants as one of advanced oxidation processes (AOPs) [3].

In this work, the influence of pH, initial concentration of dye solution and temperature were evaluated on the adsorption behavior of Cationic Blue X-BL by silica gel to get the most optimizing adsorption condition. UV-Fenton reaction was applied to regenerate silica gel loaded with dyes.

Materials and methods

Materials

Silica gel (Sanpont Co., China), for column chromatography, presenting particle size and average pore size of 100–200 mesh and 60 Å, respectively, was used in the present work. H_2O_2 (30%), $FeSO_4 \cdot 7H_2O$, NaOH and H_2SO_4 were analytical grade. The dye, commercially available as Cationic Blue X-BL were gifts from Runtu Co., China (see to Fig. 1). shows the chemical structure of the dye. Model 2100UV spectrophotometer(Unico Inc., Shanghai, China).

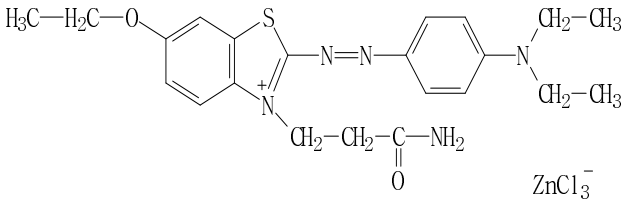


Fig.1. The chemical structure of Cationic Blue X-BL

Preparation of Dye Solution and Concentration Measurements

Stock solution (1 g/dm^3) of the blue dye was prepared in distilled water. The desired concentrations were obtained by dilution. The concentrations of the studied dyes were measured using spectro- photometric method. Calibration curves of the blue dye were prepared by measuring their absorbance against concentration at λ_{max} 622 nm. The amount of the adsorbed dye on the investigated silica was determined using the following mass balance equation: $q=(C_0-C_i)\times V/W$. Where q represents the amount of the dye adsorbed (mg/g), C_0 and C_i the initial and final concentrations (mg/dm^3) of dye, V is the volume (dm^3) of adsorption solution and W is the weight (g) of silica gel.

Adsorption Experiment

A 0.6 g of dry silica gel samples were placed in a series of flasks containing 100 cm^3 of dye stock solution with different initial concentration of the dye. The various pH was adjusted using 0.1 mol/dm^3 H_2SO_4 and 0.1 mol/dm^3 NaOH. The flasks were equilibrated on a digital control thermostat water bath shaker, at 100 r/min and different temperature for 2 h. Get the concentration of the dye solution measured at time interval after shaking, respectively. The residual concentration of the dye was determined at λ_{max} 622 nm by UNIC-2100 spectrophotometer.

Regeneration of Silica Gel

Regeneration of Silica Gel by UV-Fenton Oxidation and Evaluation of the Regenerative Capability of Silica Gel.The regeneration experiments were carried out inside photochemistry reactor XPA-II, Xujiang Electromechanical Plant, Nanjing, China. Fig. 2 shows structural drawings of the photochemistry reactor. A UV lamp (300W) of medium pressure mercury positioned in the center of reactor was used as an irradiation source. The container was stirred magnetically during irradiation. In this process, The contact time was 90 min and solution pH (adjusted by H_2SO_4) was 2.8. After 90min the solution was centrifuged to separate regenerated silica gel from the solution. Then get the silica gel dried treated with or without acid washing (H_2SO_4 1 mol/dm^3, 100 cm^3), waiting for the adsorption process to evaluate the regenerative capacity. Regeneration efficiency was calculated according to the following equation: $R= q_i/q_e$. Where R represents the regeneration efficiency (%), q_i the equilibrium adsorption (mg/g) of regenerated silica gel and q_e is 16.38 mg/g.

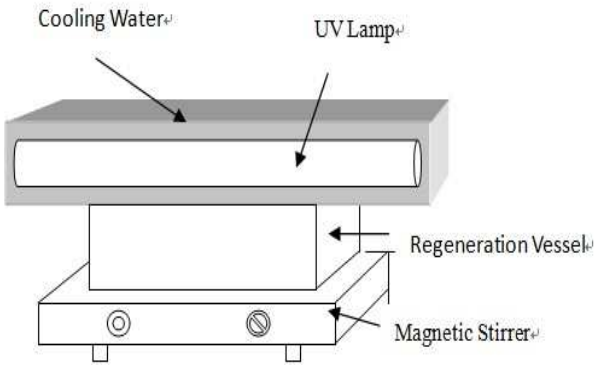


Fig. 2. Structure chart of photochemistry reactor

Results and discussion

Effect of pH on the adsorption of the investigated dye

The role of pH playing on the adsorption of the blue dye onto silica gel is shown in Fig. 3. It shows that pH has a powerful impact on the adsorption and the maximum adsorption rate occurs at pH 10.96. Adsorption performs well when pH is above 4. As the pH value of the solution of the investigated dye is 9.3, pH at 9.3 is used in the latter adsorption.

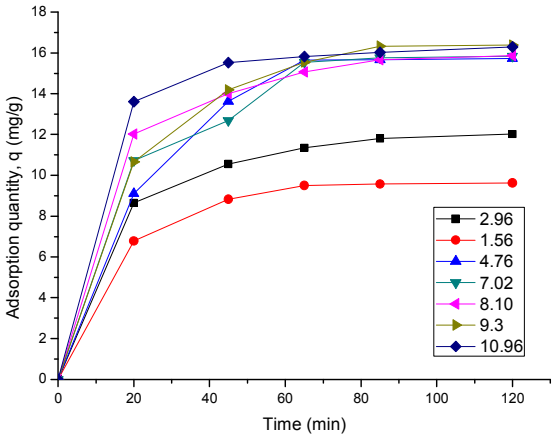


Fig.3. Effect of pH on the adsorption of the investigated dye with initial concentration of 100mg/dm^3 in 2 h and at 303K

Effect of Initial Dye Concentration

The effect of initial concentration of the investigated dye solution on the adsorption onto silica is displayed in Fig. 4. All of the adsorption with different initial dye concentrations occur mainly in the first 80 minutes and get finished after processed 100 minutes. With the consideration of industries wastewater with low concentration, the initial concentration of 100 mg/dm^3, which can contribute to both high adsorption rate and large adsorption quantity, is introduced into latter test.

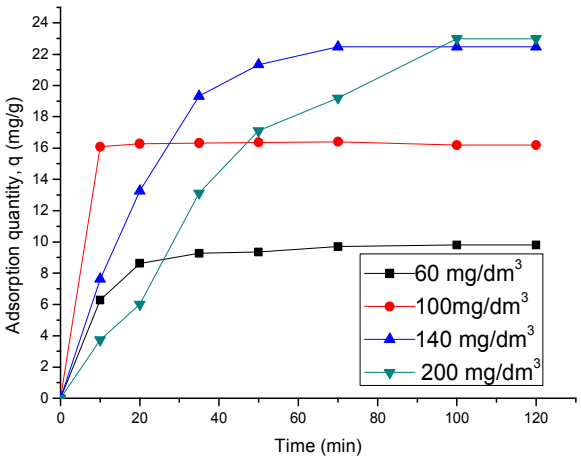


Fig. 4. Effect of initial concentration on the adsorption of the dye at 303 K and in 2 h.

Effect of Temperature

Fig. 5 displays that adsorption rate increases as the adsorption temperature goes up. After 80 minutes, all of the adsorption under different temperature reached equilibrium and when temperature higher than 303K equilibrium adsorption can be easily got just in 20 minutes. This may be attributed to high temperature providing a large diffuse rate. Considering both adsorption rate and final adsorption efficiency, 303 K is accepted.

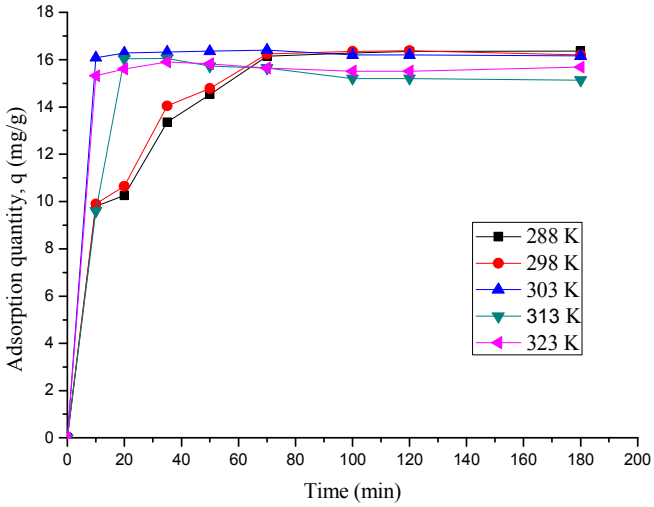


Fig. 5. Effect of temperature on the adsorption of the investigated Dye with initial concentration of 100 mg/dm^3 in 2 h.

The Regeneration of Dye-loaded Silica Gel

Fig. 6 shows that silica gel has very low absorptivity in the range of UV-VIS part, especially from wavelength 380 nm to 780 nm lower than 10 %. This indicates that silica gel has a good performance in transmitting UV-VIS light. The influence of the concentration of H_2O_2 on the regeneration operation of silica gel is presented in fig. 7. Too high or too low concentration of H_2O_2 both resulted poor regeneration capacity. Table1 provides the role of Fe^{2+} playing on the regeneration effect of silica gel. Regenerations with concentration of Fe^{2+} in the range of 0.05 to 0.10 did not have much different in regeneration capacity. So the proper regeneration process are regeneration with concentration of H_2O_2 0.132 mol/dm^3, concentration of Fe^{2+} 0.05 mmol/dm^3, contact time 90 min

and at pH 2.8. Table 2 provides the regeneration efficiency data. After four times regeneration, adsorption of silica gel decreased to 50.73 %. For overcoming the above problem, acid washing was applied after the forth regeneration and it enhanced the regeneration efficiency to 92.19 %.

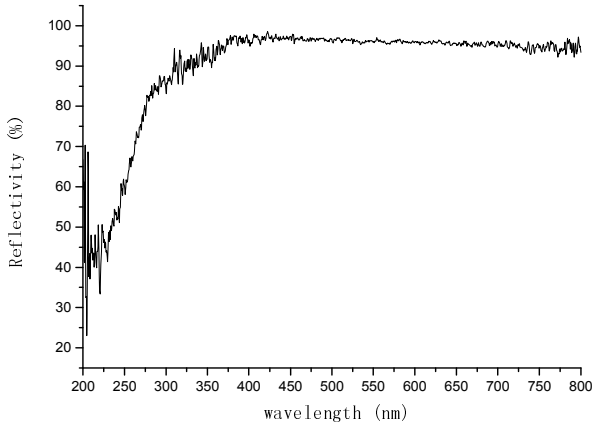


Figure 6.The Diffuse Reflection Spectrum Of Silica Gel

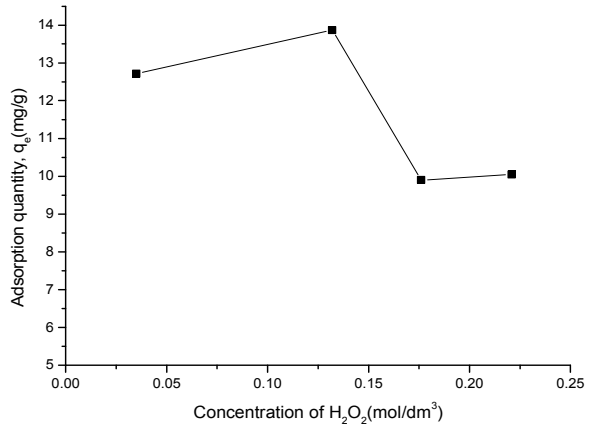


Figure 7. Effect of the concentration of H_2O_2 on the regenerative capacity of silica gel at pH 2.8 and the concentration of Fe^{2+} is 0.075mmol/dm^3.

TABLE1 EFFECT OF FE^{2+} ON THE REGENERATION CAPACITY OF SILICA GEL

C_{Fe}^{2+}(m mol/dm^3)	0.05	0.075	0.10
q_e(mg/g)	13.2	13.14	13.16

TABLE 2 REGENERATION CYCLES AND REGENERATION EFFICIENCY

Number of recycling processes	1	2	3	4
Regeneration Efficiency (%)	84.68	82.5	65.26	50.73

Summary

In this work, the satisfying adsorption quantity 16.38 mg/g was obtained when the initial concentration of the blue dye was 100 mg/dm^3 with 0.6 g silica gel at pH 9.3 and 303 K after 2 h. As Fenton reaction is environmentally benign, fast, cheap and relatively easy to obtain and handle, and silica gel have the ability to penetrate most of the UV light, Heterogeneous Fenton reaction with aid of UV light was adopted in the regeneration of silica gel. When the concentration of Fe^{2+} 0.05 mmol/dm^3 and H_2O_2 0.132 mol/dm^3, the first, second, third and forth regeneration efficiency were 84.68%, 82.05%, 65.26% and 50.73 %, respectively. An acid washing after the forth regeneration can enhance the regeneration efficiency to 92.19%.

References

[1] Ahmed M. Donia, Asem A. Atia ,Waheeba A. Al-amrani, Ahmed M. El-Nahas, J. Hazard. Mater. 161(2009) 1543-1545.

[2] Antonio R. Cestari, Eunice F.S. Vieira, Glaucia S. Vieira, Luiz P. da Costa, Andre a M.G.Tavares,Watson Loh, Claudio Airoldi, J. Hazard. Mater. 161(2009) 306-308.

[3] Yi Li, Fu-Shen Zhang,Chem. Eng. J. 158(2010)146-148.

Advanced Materials Research Vol. 936 (2014) pp 881-886
© (2014) Trans Tech Publications, Switzerland
doi:10.4028/www.scientific.net/AMR.936.881

Optimization and Evaluation of Preparation Process of Activated Carbon Loaded ZrO_2 Catalyst for Oxidative Desulfurization

Yang Chong[1,a], Hou Yingfei[1,b], Liu Min[1,c] , Guo Ning[1,2,d] and Zhang Jianhui[3,e]

[1]State Key Laboratory of Heavy Oil Processing, China University of Petroleum (East China), Shandong Qingdao 266580, China

[2]College of Chemistry and Chemical Engineering, Ocean University of China, Shandong Qingdao 266100, China

[3]China Petroleum Engineering Co., ltd, Beijing 10085, China

[a]ycghupc1988@163.com, [b]houyf@upc.edu.cn, [c]1039579551@qq.com,

[d]guoningjh@sina.com, [e]zhjianhui@cnpc.com.cn

Keywords: activated carbon; oxidation desulfurization; SO_4^{2-}/ ZrO_2; catalyst

Abstract: This paper studied how DBT oxidation was influenced by different preparation conditions of diesel desulfurization catalyst. Fuel oil oxidation and desulfurization technology has been studied by using solid superacid prepared by activated carbon loaded SO_4^{2-}/ ZrO_2 as catalyst instead of the traditional liquid acid, hydrogen peroxide as oxidant, in mild conditions. Impacting factors on removal sulfur have been investigated such as soaking time, burning temperature, burning time, active ingredient content and concentration of sulfuric acid, etc. The results show that soaking time is 6h, burning temperature is 500 ℃, burning time is 2.5h, the mass ratio of the active ingredient is 3:100 ZrO_2 and activated carbon, sulfuric acid concentration is 0.5mol/L. The desulfurization rate is over 93% and raffinate oil recovery can reach more than 86% under this optimum condition.

Introduction

Organic sulfur in diesel generates SO_x during combustion and pollutes the environment and endangers human health. Faced with increasingly stringent diesel sulfur content standards and huge market demand for low-sulfur clean diesel, the world's countries have committed to developing a variety of diesel desulfurization technologies[1-3].

Currently, diesel desulfurization consists of two ways, hydrodesulfurization (HDS) and non-hydrodesulfurization. Due to the harsh conditions of hydrodesulfurization reaction and a large requirement for investment in equipment, non-hydrodesulfurization becomes a hot topic. Methods for non-hydrodesulfurization include oxidative desulfurization, adsorption desulfurization, extraction desulfurization, membrane desulfurization and complex biological desulfurization[4-9]. Among them, oxidative desulfurization (ODS) as an alternative process to the traditional processes has received much attention for deep desulfurization of fuels for a number of reasons. This is because the ODS process has two main advantages compared to the HDS process. First, the most refractory sulfur-containing compounds to the HDS process, (e.g., DBT and its derivatives) show high reactivity toward the oxidation by this method. Second, the ODS process can be carried out in the liquid phase and under very mild operating conditions[4].

Oxidative desulfurization technology is a method for deep desulfurization at room temperature, atmospheric pressure and the presence of catalyst, the organic sulfur compounds being converted into polar substances and separated by extraction[10-12]. The choice of catalyst is the core factor affecting the desulfurization effect. Taking into account the requirements of clean production, hydrogen peroxide is frequently used as the oxidant in a variety of oxidative desulfurization methods having been reported, and usually organic acid is used as a catalyst[13-14]. While the oxidative desulfurization system of hydrogen peroxide/organic acids can achieve high desulfurization rate, the organic acids may partially dissolve in the fuel oil, which would affect the quality of fuel oil, and organic acid can corrode the equipment easily, causing high recovery costs. There are many researches and reports about solid superacid catalyzed hydrogen peroxide desulfurization systems home and abroad in recent years[15-16]. Solid superacid catalyst for oxidative desulfurization can simplify the catalyst regeneration cycle links. Separation and recovery of the catalyst is easy and it does not affect the fuel oil quality. Raw materials are fully utilized.

For the above reasons, the present study uses hydrogen peroxide as the oxidant, solid super-acid,instead of liquid acid, as the catalyst to find cheap catalyst, so as to achieve the purpose of the production of ultra low sulfur diesel.

Experimental

Materials, Reagents and Equipment. Materials: model diesel (dibenzothiophene and dodecane mixture, the total sulfur content 400ug/g). Reagents: dodecane(AR); dibenzothiophene(AR); hydrogen peroxide, with a purity of 30%(AR); ammonia purity of 25%-28%; N,N-dimethyl-formamide (DMF, AR); $Zr(NO_3)_4 \cdot 5H_2O$(AR); activated carbon(20-40mesh). Instrument: KQ3200DB CNC ultrasonic cleaner, Kunshan Ultrasonic Instrument Co., Ltd.; SZCL-3A-type digital temperature magnetic stirrer functions, Gongyi Branch Equipment Co., Ltd.; centrifuges, Shanghai Anting Scientific Instrument Manufacturing; tube furnace, Anhui BEQ Equipment Technology Co., Ltd.; fluorescence sulfur analyzer TEA-6000, Taizhou Suntoc Precision Instrument Co., Ltd..

Experimental Process. Catalyst preparation. A certain amount of activated carbon (20-40 mesh) was added to Zr $(NO_3)_4 \cdot 5H_2O$ dispersed by ultrasonic cleaner and immersed in aqueous solution at room temperature for 10h, aqueous ammonia with a mass fraction of 25% -28% was added to adjust the PH to 9-10 to precipitate. Aged at room temperature for 12h, the activated carbon was washed with ultrapure water and dried for 12h at 110 ℃. Then, impregnated the activated carbon with H_2SO_4. Filtered, dried and then roasted in a tubular furnace filled with nitrogen. That was activated carbon loaded SO_4^{2-}/ZrO_2 catalyst (denoted as SO_4^{2-}/ZrO^{2-}AC).

Catalytic Oxidative Desulfurization. Catalytic oxidative desulfurization process is divided into two parts: the catalytic oxidation and solvent extraction. Oxidation: a certain amount of diesel model was put into the reactor vessel and the right amount of self-made catalyst and hydrogen peroxide were added. The reaction vessel was placed in a water bath at a set temperature(60℃). After reacting for a certain period in a reflux condenser with magnetic stirring, the reaction system was then cooled. After cooling to room temperature, the catalyst was recovered by centrifugal separation, the reaction solution was desulfurized. Solvent Extraction: The desulfurization reaction solution was poured into a separatory funnel, adding a certain amount of DMF, the solution was extracted at room temperature after being thoroughly shaken. The oil phase and the extract phase were collected , recovery and sulfur content of the collected oil phase were determined.

Determination of Sulfur Content. Determination of total sulfur content: sulfur content of model diesel and diesel fuel after desulfurization were analyzed by fluorescence sulfur analyzer. Fluorescence sulfur analyzer trace of liquid injection, the temperature is set to 1000 ℃, pyrolysis oxygen flow 400ml/min, import oxygen flow rate 80ml/min, an argon flow of 160ml/min. Desulfurization rate is calculated based on the measured total sulfur content. It is calculated as follows:

$$\eta = \frac{C_0 - C_x}{C_0} \times 100\%$$

of which:

η——the desulfurization rate,%;

C_0 —— the sulfur content of diesel models, ug/g;

C_x —— the sulfur content of diese model after desulfurization, ug / g.

Results and Discussion

Effect of Sulfuric Acid Soaking Time on the Desulfurization Rate. Experimental conditions for the desulfurization was that the mass ratio of the active ingredient was 3:100 ZrO_2 and activated carbon, sulfuric acid concentration of 0.5mol/ L, calcined at 500 ℃ for 3h, soaking time was 2h, 4h, 6h, 8h and 10h. Performance of the catalyst prepared was shown in Fig.1.

As can be seen from Fig.1 that with the increase of soaking time below 6h, the removal sulfur increased. When the soaking time was above 6h, desulfurization rate was decreased, this may be because the soaking time was too short, the loaded active centers on the catalyst surface could not be sufficient, resulting in the reduction of desulfurization rate. The soaking time was too long, the effect would be a salt of sulfuric acid, it could also affect the performance of the catalyst, so the optimum soaking time was 6h.

Effect of Burning Temperature on the Desulfurization Rate. Experimental conditions for the desulfurization was that the mass ratio of the active ingredient was 3:100 ZrO_2 and activated carbon, sulfuric acid concentration of 0.5mol/L, soaking time was 6h, calcined at 400℃, 450℃, 500℃, 550℃ and 600℃ for 3h respectively. Performance of the catalyst prepared was shown in Fig.2.

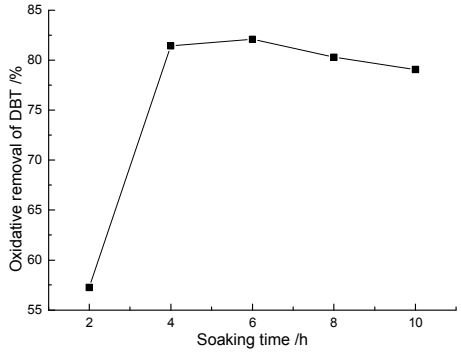


Fig.1. The connection between the soaking time and removal of DBT

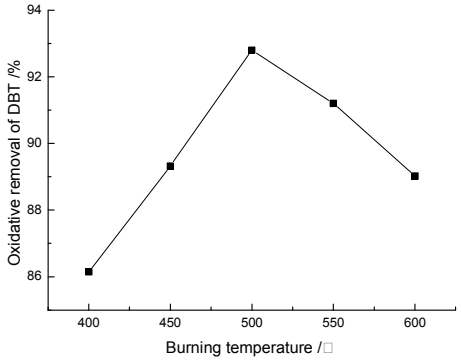


Fig.2. The connection between the burning temperature and removal of DBT

Calcination temperature significantly affected the performance of catalytic desulfurization, different calcination temperatures can form SO_4^{2-}/M_nO_m-AC superacid catalysts with different acid strength and acid distribution. As can be seen from Fig.2 that the calcination temperature was

500 ℃, the desulfurization rate was highest; with the increase of calcination temperature below 500℃, the removal sulfur rised. When the soaking time was above 6h, the desulfurization rate decreased. This may be because the calcination temperature was too low, it can not form a sufficient number of acid centers; the calcination temperature was too high, the acid center of superacid would decompose, reducing the number of catalytically active centers due to the loss of sulfate, and the surface area decreased.Strong acid center of SO_4^{2-}/M_xO_y-AC solid superacid can be formed to appropriate temperature in the Process for preparing the solid acid, which is because ion type S-O bond in high temperature can be converted into the covalent S = O bond, the covalent bond has the capacity of inducing effect to make metal ion has a strong electron withdrawing ability to be acidic. There is also a suitable calcining temperature range determined by type of crystalline metal oxide of catalyst surface and the sulfur content.

Effect of Burning Time on the Desulfurization Rate. Experimental conditions for desulfurization was set as follows: the mass ratio of the active ingredient was 3:100 ZrO_2 and activated carbon, sulfuric acid concentration of 0.5mol/L, soaking time was 6h, calcined at 500℃ for 1.5h, 2h, 2.5h, 3h, 3.5h and 4h respectively. Performance of the catalyst prepared was shown in Fig.3.

As can be seen from Fig.3 that when the burning time is 2.5h, the desulfurization activation was highest. The burning time was too short, it can not form sufficient acid centers; burning time was more than 2.5h, the formation of acid sites may be decomposed, reaction reactivity was decreased. That the burning time was too long would reduce specific surface area of the solid acid, and a large number of square phase ZrO_2 was converted into monoclinic phase ZrO_2, sulfur species were not firmly bonded to the surface, reducing the number of acid sites , the catalytic activity was not high.

Effect of Active Ingredient Content on the Desulfurization Rate. Experimental conditions:the mass ratio of the active ingredient was n:100 (n=1, 2, 3, 4, 5, 6) ZrO_2 and activated carbon, sulfuric acid concentration of 0.5mol/L, soaking time was 6h, calcined at 500℃ for 2.5h. Performance of the catalyst prepared was shown in Fig.4.

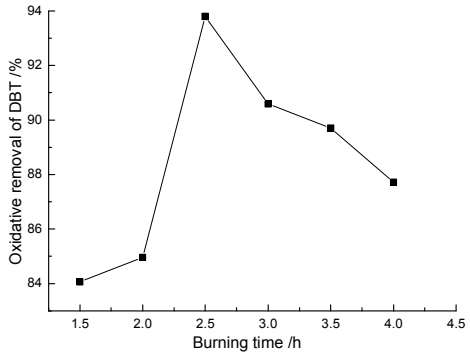


Fig.3. The connection between the burning time and removal of DBT

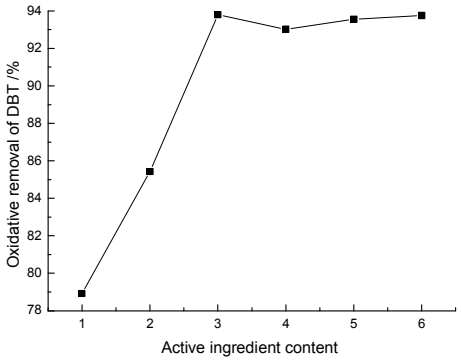


Fig.4. The connection between the active ingredient content and removal of DBT

H_2O_2 under acidic conditions produce hydroxyl radicals with a very strong oxidation strength, even oxidize thiophenic sulfur to sulfate sulfur. Small amount of catalyst can speed the oxidation rate, and increase the desulfurization rate. As can be seen from Fig.4 that with the increase of the active ingredient content, the number of active centers was larger, the oxidation effect was more significant. When the mass ratio of the active ingredient is 3:100 ZrO_2 and activated carbon, desulfurization rate is 93.80%. And then the desulfurization little change with increasing active

ingredient content, this may be because when mass ratio is 3:100, providing sufficient catalytic activity center. Then the content of the active ingredient increased, no increase in catalytic activity.

Effect of the Concentration of Sulfuric Acid on the Desulfurization Rate. Experimental conditions:the mass ratio of the active ingredient was 3:100 ZrO_2 and activated carbon, soaking time was 6h, calcined at 500℃ for 2.5h, sulfuric acid concentration of 0.25mol/L, 0.5mol/L, 0.75mol/L, 1.0mol/L and 1.25mol/L. Performance of the catalyst prepared was shown below.

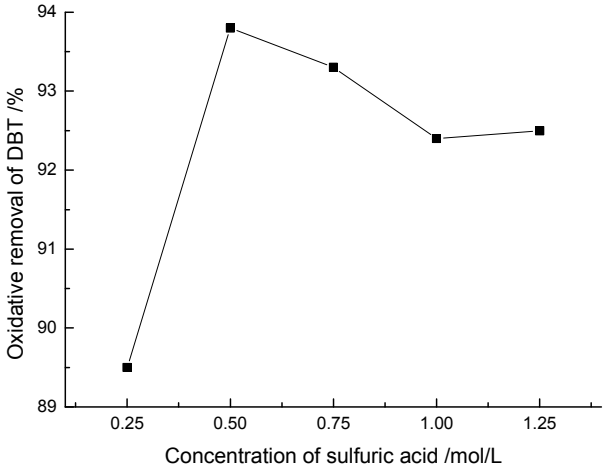


Fig.5. The connection between the concentration of sulfuric acid and removal of DBT

As can be seen from Fig.5 that SO_4^{2-} concentration was too low, the acidity of solid acid wasn't enough, insufficient amount of acid and unevenly distributed. SO_4^{2-}concentration was too high, the sulfate would block pores of catalyst, reducing the specific surface area, reducing the amount of acid, or sulfuric acid could cause side reactions with the metal oxide to form sulfate. For the reasons above, the optimum concentration of sulfuric acid was 0.5mol/L.

Conclusion

In this study, activated carbon loaded ZrO_2 solid acid catalyst for the desulfurization was investigated, the optimal preparation conditions of oxidative desulfurization catalyst: the mass ratio of the active ingredient is 3:100 ZrO_2 and activated carbon, 0.5 mol/L sulfuric acid soaked for 6h, resulting catalyst calcined at 500 ℃ for 2.5h, activated carbon loaded solid super acid catalyst desulfurization rate can reach over 93%, raffinate oil recovery can reach more than 86% under this optimum condition.

Acknowledgements

The study was supported by the Natural Science Foundation of Shandong Province (ZR2012BL15), and the Fundamental Research Funds for the Central Universities.

References

[1] C.S. Song, An overview of new approaches to deep desulfurization for ultra-clean gasoline, diesel fuel and jet fuel, J. Catalysis today. 86.1 (2003) 211-263.

[2] C.S. Song, X.L. Ma, New design approaches to ultra-clean diesel fuels by deep desulfurization and deep dearomatization, J. Applied Catalysis B: Environmental. 41.1 (2003) 207-238.

[3] D. Shekhawat, T.H. Gardner, D.A. Berry, et al. Catalytic partial oxidation of n-tetradecane in the presence of sulfur or polynuclear aromatics: Effects of support and metal, J. Applied Catalysis A: General. 311 (2006) 8-16.

[4] A.M. Dehkordi, Z. Kiaei, M.A. Sobati, Oxidative desulfurization of simulated light fuel oil and untreated kerosene, J. Fuel Processing Technology, 90.3 (2009) 435-445.

[5] K.M. Dooley, D.X. Liu, A.M. Madrid, F.C. Knopf, Oxidative desulfurization of diesel with oxygen: Reaction pathways on supported metal and metal oxide catalysts, J. Applied Catalysis A: General. 468(2013) 143-149.

[6] J. Chaichanawong, T. Yamamoto, T. Ohmori, Adsorptive desulfurization of bioethanol using activated carbon loaded with zinc oxide, J. Chemical Engineering Journal. 165.1 (2010) 218-224.

[7] J.L. Wang, D.S. Zhao, E.P. Zhou, Z. Dong, Desulfurization of gasoline by extraction with N-alkyl-pyridinium-based ionic liquids, J. Journal of fuel chemistry and technology. 35.3 (2007) 293-296.

[8] L.G. Lin, G. Wang, H.M. Q, J.R. Yang, Y.F. Wang, D.Q. Shi, Y. Kong, Pervaporation performance of crosslinked polyethylene glycol membranes for deep desulfurization of FCC gasoline, J. Journal of membrane science. 280.1 (2006) 651-658.

[9] Y.F. Hou, Y. Kong, J.R. Yang, Biodesulfurization of dibenzothiophene by immobilized cells of pseudomonas stutzeri UP-1, J. Fuel. 84 (2005) 1975-1979.

[10][10] L.A. Gonzalez, P. Kracke, W.H. Green, Oxidative desulfurization of middle-distillate fuels using activated carbon and power ultrasound, J. Energy & Fuels. 26.8 (2012) 5164-5176.

[11] D. Wang, E.W. Qian, H. Amano, Oxidative desulfurization of fuel oil: Part I. Oxidation of dibenzothiophenes using tert-butyl hydroperoxide, J. Applied Catalysis A: General. 253 (2003) 91-99.

[12] M. Sersdych, C.T. Wu, P. Brender, Role of phosphorus in carbon matrix in desulfurization of diesel fuel using adsorption process, J. Fuel. 92 (2012) 318-326.

[13] J.L. Wang, D.S. Zhao, K.X. Li, Oxidative desulfurization of dibenzothiophene using ozone and hydrogen peroxide in ionic liquid, J. Energy & Fuels. 24.4 (2010) 2527-2529.

[14] G.X. Yu, S.X. Lu, H. Chen, Z.N. Zhu, Oxidative desulfurization of diesel fuels with hydrogen peroxide in the presence of activated carbon and formic acid, J. Energy & Fuels. 19.2 (2005) 447-452.

[15] A. Jatia, C. Chang, J.D. Macleod, ZrO_2 promoted with sulfate, iron and manganese: a solid superacid catalyst capable of low temperaturen-butane isomerization, J. Catalysis letters. 25 (1994) 21-28.

[16] S. Furuta, H. Matsuhashi, K. Arata, Biodiesel fuel production with solid superacid catalysis in fixed bed reactor under atmospheric pressure, J. Catalysis communications. 5.12 (2004) 721-723.

Advanced Materials Research Vol. 936 (2014) pp 887-891
© (2014) Trans Tech Publications, Switzerland
doi:10.4028/www.scientific.net/AMR.936.887

Research on the Quicklime Treatment Dewatered Sludge Technology and Mechanical

Jieliang Chen[1, a], ZhenDeng[1,b], Ranling Zhang[1,c], Penglai Zhu[2,d], Weiwei Ding[2]

[1]Water treatment facility construction and development center in Hangzhou, China

[2]College of Civil Engineering and Architecture, Zhejiang University, China

[a]13116793075@163.com,[b]447496015@qq.com, [d]zhupl@zju.edu.cn

Keywords: quicklime treatment;sludge semi-dry;dewatered sludge;mechanical design parameters.

Abstract: The fundamentals of lime treatment for dewatered sludge and main factors which affect the treatment process are introduced in this study. According to the results, higher effective calcium oxide content in lime contributes to faster heating rate of the semi-dry system and better effects of semi-dry process. Sludge at the moisture content of 45%-55% after the semi-dry process can be well balled while that at the moisture content of 35% can easily get collapsed and has hard surface. Mechanical design parameters are determined by experiments. The optimum stirring time is 5-10mins when well stirred and the stirring rate should be slow. Heat preservation jacket is needed for the machine and the water vapor, which is produced by heating, should be exhausted in time.

Introduction

Lime treatment for dewatered sludge is the oldest one of the methods to be applied. Through adding Calcium oxide, this method can increase the PH and temperature to achieve the sludge solidification. Besides, the nature of the sludge may be effectively changed by choosing appropriate mixing conditions and equipment in the process. Treated sludge become particles [1] that have good fluidity and lower moisture content, thus storage and transportation could be much easier. In addition to meet the hygiene index, it is mainly used as pretreatment method of sanitary landfill or building materials using. This paper studies on the technical parameters of lime Semi-dry System and puts forward reasonable mechanical design parameters.

Theory of the Increased Calcium Material Semi-dry System

The Fundamentals of Lime Treatment for Dewatered Sludge

Mixing the sludge with calcium oxide, calcium oxide and water contained in the sludge will produce exothermic reaction and generate calcium hydroxide or calcium hydrate [3] . Quicklime can produce following reaction (Eq. 1 and Eq. 2) per kilogram:

$$1kgCaO+0.32kgH_2O \rightarrow 1.32kgCa(OH)_2+1177KJ \quad (1)$$

$$H_2O\ (l)+2258KJ/kg \rightarrow H_2O\ (g) \quad (2)$$

According to this reaction(Eq. 1 and Eq. 2), 1kg calcium oxide is combined with 0.32 kg water to become calcium hydroxide, the reaction heat generated is equivalent to about 0.5 kg water evaporation heat required. Thus, the method, using calcium oxide to generate heat and absorb water to make sludge achieved semi-dry state, is theoretically feasible.To the drying, chemical reaction heat released of calcium oxide have bigger contribution than the chemical reaction itself.

The Main Factors that Affect the Treatment Process

Determination of Industrial Lime Effective Calcium Oxide Content

During the reaction process of lime and sludge, the heating rate and the temperature height are subject to the restrictions of calcium oxide content. So, it need to determine the content of effective calcium oxide before making semi-dry, The test methods are according to JTG - E51-2009 " Highway Engineering inorganic binder stabilized material testing procedures“ T0811-1994. The effectively calcium oxide content is calculated according to the following formula(Eq. 3).

$$X = \frac{V_5 \times M \times 0.028}{m_1} \times 100 \quad (3)$$

The formula:X—The effectively calcium oxide content(%);

V_5—The volume of consumption of hydrochloric acid standard solution while titration(mL)

0.028—Calcium oxide mg equivalent

m_1—The quality of the sample(g)

M—The molar concentration of hydrochloric acid standard solution (mol/L)

Laboratory determine 4 kinds of samples according to the method, effective calcium oxide content were 98%, 68%, 60%, 55%.The common effective calcium oxide content of industrial lime is between 60% ~ 70%.

Analysis of Industrial Lime Reaction Rate

While using quick lime to semi-dry sludge, the heating rate is determined by the effective calcium oxide content. Figure 1 is the internal heating rate figure that lime whose effective calcium oxide content are 98%, 68%, 60%, 55% 30% outer doped (ratio with sludge mass) sludge with 80.5% moisture content. The test method is puting semi-drying sludge into heat preservation box, to determinate the effect of sludge internal heating.

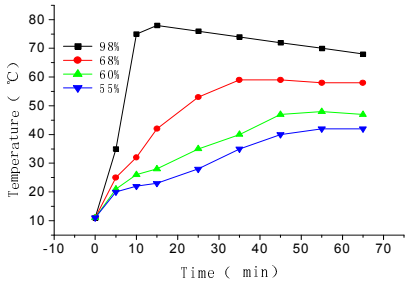


Fig.1 Internal heating curve of sluge- different quality lime(outer doped 30%)

As shown in figure 2, higher effective calcium oxide content in lime contributes to faster heating rate and reaction rate of the semi-dry system outer doped with 30% lime. Lime that have 98% effective calcium oxide content make the internal temperature of mixture system up to 78 ℃ in 15 min,produce large amounts of water vapo. Lime that have 98% effective calcium oxide content raise up to the highest temperature(53℃) in 35min, and the temperature maintained well. The temperature of lime that have 60% and 55% effective calcium oxide content heat up slowly, it still raise slowly after 70min. In such mixture system, the reaction rate is lower and temperature hysteresis is serious.

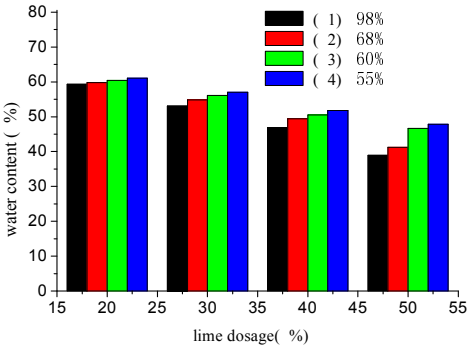


Fig.2 The relation figure of lime dosage- moisture content

Analysis of Effects About Semi-dry Process

The quality of the effect of semi-dry is determined by the sludge moisture content. Moisture content testing method according to the CJ/T221-2005 "test method of urban sludge treatment plant sludge", section 2, the determination of city sludge moisture content (gravimetric method).

We studied the semi-dry effect of different dosage of lime according to the content of calcium oxide, the results shown in fig.2. Fig.2 is the effect figure of semi-dry sludge about the lime with calcium oxide content of 98%, 68%, 60%, 55%. As, we can see, higher effective calcium oxide content in lime and higher dosage of lime contributes to better effects of semi-dry process. Dewatered sludge moisture content of 80.5%, mixed 20% different quick lime has little distinction that the moisture content reduced to（60±1）%, the surface of sludge is wet and easy to be reunited. When the dosage is changed up to 50%, the moisture content of No.1 is 38.9%, No.4 is 48.8%, both moisture content difference of nearly 10%. Adding 30% lime, the moisture content of sludge is (55 + 1) %, after semi-drying the industrial quick lime, sludge can be well balled.



60% 55% 45% 35%

Fig.3 Moisture content figure

The condition of semi-dried sludge is shown in Fig.3. Fig.3 is the condition of mixed lime and sludge which was stirred 2min slowly and layed up 30min in net cement slurry mixer. The lower moisture content of sludge has whiter color and harder surface. The process of semi-drying sludge with strong ammonia smell increases with the increase of dosage of lime. the sludge will have a sticky surface and easy to be reunited when the moisture content figure is 60%. The white particles in the figure are calcium hydroxide produced by the reaction of calcium oxide and water. Sludge at the moisture content of 45%-55% after the semi-dry process can be well balled while that at the moisture content of 35% can easily get collapsed and has hard surface.

The Determination of Lime Semi-drying Machine Designed Parameters

The Mechanical Stirring Time and Stirring Speed

The semi-drying mechanical stirring time and stirring speed is Directly determines the production of dry sludge, it is also directly related to mechanical efficiency.Fig.4 is the diagram of stirring time and moisture content. After adding 30% quick lime, along with the increase of mixing time, moisture content is not significantly reduced. The reaction rate of lime and water is quickly completed within 5 min. the moisture evaporation rate is low without heat preservation measures.

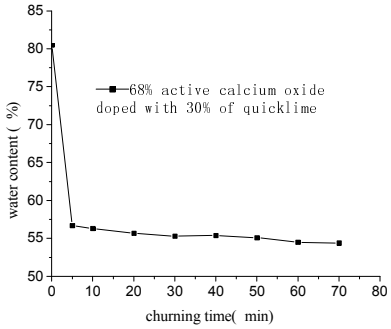


Fig.4 The diagram of stirring time and moisture content



stirring 2min *stirring 5min* *stirring 10min*



stirring 20min *stirring 2min, laying up30min* *stirring 30min*

Fig.5 Stirring time and the condition of sludge

Fig.5 is the condition of sludge with different stirring time. As the extension of stirring time, the sludge get wetter on the surface, the viscosity increased gradually.Along with the increasing of stirring time , the internal capillary bound water and combined water of the sludge are destroyed and appear on the surface. And the faster the stirring speed, the greater the shearing action of sludge is, the easier to release the moisture inside package. Thus, stirring speed is not the sooner the better, time also is not as long as possible. Contrast the sludge that is stirred 2min and layed up 30min to the one that is stirred slowly all the time, difference of the two sludge surface state is very big, the former sludge can be cut into pieces, can into the ball; The latter is wet, sticky.the former sludge can be cutted into pieces, can be balled; The latter is wet, sticky. According to fig.4, the optimum stirring time is 5-10mins when well stirred and the stirring rate should be slow.

Mechanical External Thermal Insulation Jacket Design.

The process of semi-drying can release a large amount of heat, moisture in the sludge can be evaporated. The amount of evaporation is related to the temperature inside the sludge,Fig.6 is internal temperature curve with heat preservation measures or not.Fig.7 is Natural moisture evaporation rate with heat preservation measures or not. The heat preservation measures is puting sludge into foam insulation box. No heat preservation measures is placing dry sludge in indoor and the temperature is 20 ℃. Botth of them need to exhaust air slowly.

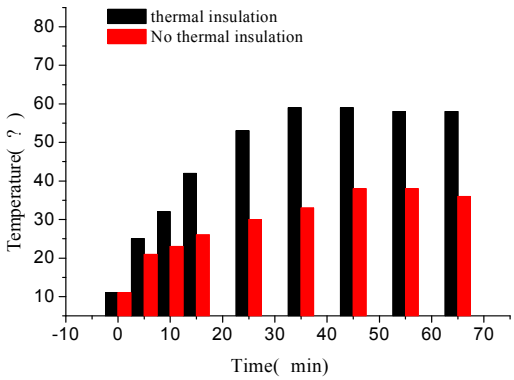


Fig.6 Temperature curve with 30% lime.

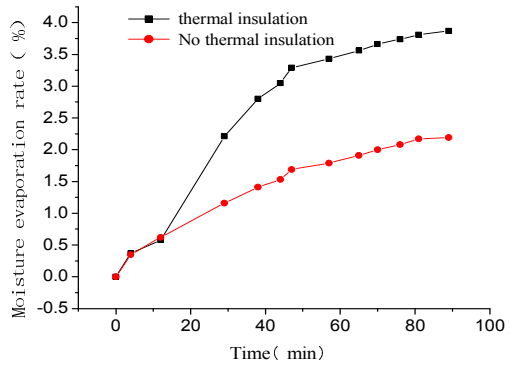


Fig.7 The moisture evaporation rate diagram with 30% lime.

From figure 6 can be seen that the maximum temperature difference is 20 ℃. Figure 7 shows the biggest difference of moisture evaporation rate reached 1.7% within 90 min, and the difference showed a trend of gradual increase. That both shows the The importance of the heat preservation measure. Thus, heat preservation jacket is needed for the machine and the water vapor, which is produced by heating, should be exhausted in time that to improve the rate of evaporation as far as possible for making semi-dry mechanical effectively.

Summary

The method of using increased calcium material to semi-dry sludge is economic and reasonable, convenient and easy.

(1) Higher effective calcium oxide content in lime contributes to faster heating rate of the semi-dry system and better effects of semi-dry process

(2) Sludge basic has no smell after semi-drying.Sludge at the moisture content of 45%-55% after the semi-dry process can be well balled while that at the moisture content of 35% can easily get collapsed and has hard surface. Storage and transportation could be much easier.

(3) The optimum stirring time is 5-10mins when well stirred and the stirring rate should be slow.

(4) Heat preservation jacket is needed for the machine and the water vapor, which is produced by heating, should be exhausted in time to improve the rate of evaporation as far as possible for making semi-dry mechanical effectively.

References

[1] Jian Zhang, The material and energy flow analysis in the process of sludge treatment, J. Water supply and drainage. 2008,34(Supplement) :54-58

[2] Meijuan Ying, Zhenfeng Zhao, Xilong Cui, etc., Lime sludge drying process application in the sewage plant of the little red door of Beijing, J. China Water & Wastewater.2011,27(6):75-78.

[3] Shuiying Zhang, Hui Zhang, Research on urban sewage treatment plant sludge lime stable drying technology application, J. Water purification technology. 2009,28（1）:75-77.

[4] Meijuan Ying, Zhenfeng Zhao, Xilong Cui, etc.,: Analysis of dewatered sludge lime process ,J. China Water & Wastewater, 2011, 27（18）： 14-16.

Advanced Materials Research Vol. 936 (2014) pp 892-897
© (2014) Trans Tech Publications, Switzerland
doi:10.4028/www.scientific.net/AMR.936.892

Simultaneous Reduction and Immobilization of $Cr_2O_7^{2-}$ in Metakaolinite-based Geopolymer Complexed Reductant

Jieyu Chen[1, 2,a *], Xinrong Lei[1,2], Sun Tao[1]

[1] Faculty of Material Science and Chemistry, China University of Geosciences, Wuhan 430074, PR China

[2] Engineering Research Center of Nano-Geo Materials of Ministry of Education, China University of Geosciences, Wuhan 430074, PR China

[a] chenjieyu@cug.edu.cn

Keywords: geopolymer; chromium; Geopolymerization; immobilization

Abstract: Reduction and immobilization of Cr(VI) as $Cr_2O_7^{2-}$ is investigated by using metakaolinite-based geopolymer complexed reductant. Without reductants, the leached Cr concentration from metakaolinite-based geopolymer containing Cr(VI) is very high. Adding reductants as $FeCl_2 \cdot 4H_2O$, $FeSO_4 \cdot 7H_2O$, and $Na_2S \cdot 9H_2O$ respectively during geopolymerization, the leached Cr concentration is below 5 mg L^{-1} with high Cr immobilization rate above 99 %. By comparison with the immobilization of Cr (III), the added reductants reduced Cr (VI) to Cr (III) which can be locked successfully in the amorphous structure of geopolymer. Meanwhile, Cr (VI) initial concentration is lower than 0.7 wt. % in metakaolinite-based geopolymer, the above reductants can all meet the requirements. While for Cr (VI) initial concentration larger than 0.7 wt. %, $Na_2S \cdot 9H_2O$ is more appropriate. Such a simultaneous reduction and immoboilization process enables the feasibility of using metakaolinite-based geopolymer complexed reductant to implement a one-step procedure for chromite ore processing residue cleanup.

Introduction

Chromite ore processing residue (COPR) from the high-lime chromium extraction industry has already been recognized as one of the most hazardous industrial waste. The inherent chromium ions, with the total amount up to 5 wt. % in COPR samples, appear mainly as hexavalent-Cr(VI) and trivalent-Cr(III) oxidation states. However, the Cr(VI) species is severely toxic at moderate doses and has been classified as a respiratory carcinogen to human health [1]. Although the high-lime process has been abandoned in US and UK at later 1960s, however, it is still adopted in developing countries such as China and India [2]. Each year, Chinese chromium industry generates 600,000 tons of COPR and over the years accumulated about 3 million tons in heaps [3]. In fact, millions of tons of COPR have been dumped at urban areas throughout the world waiting for cleanup [4-5]. Unfortunately, due to its highly water-soluble nature, Cr(VI) species can be easily leached out from COPR upon natural exposure and then enter into the vicinal groundwater, streams, soil and atmosphere, leading to severe harmful pollution towards health of living beings.

Several detoxication technologies aiming to reduce Cr(VI) to low-toxic Cr(III) species, including the high-temperature detoxication method [6-9], wet-process, reduction and immobilization of Cr(VI) using nanoscale zero-valent iron [10] and microwave process[11, 12], have been developed. However in the above technologies, the stabilization/immobilization of the reduced product Cr (Ⅲ) is seldom considered and apparently they are not applicable for large-scale processing of COPR. Another potential risk is the fact that Cr (III) ions in the post-processed COPR

may be reoxidized to Cr(VI) upon exposure in air. Consequently, besides Cr (VI) detoxication, the successive immobilization of Cr (III) is another key procedure for the cleanup of COPR. Recently, a low-cost and easily-operated method, named the stabilization/solidification (S/S) technique, which utilizes reductant (such as $FeSO_4$) for Cr(VI) and Portland cement as stabilizer for Cr(III), might be a potential possible solution to meet the industrial desires [13-15]. However, due to the limited lifespan and low acidic resistivity of cement, the immobilized Cr species has to encounter the potential threaten of being leached out again to environment.

In comparison, geopolymer with amorphous network structure, mainly constructed by aluminosilicates, hosts much better acidic resistivity, durability in nature, low permeability and high compressive strength compared with cement [16, 17]. So it attracts more attention in immobilizing heavy metals and has been widely applied to immobilize Zn^{2+}, Co^{2+}, Pb^{2+}, Cu^{2+}, Cr^{3+} and Cd^{2+} [18-22], but fails to deal with Cr(VI) as $Cr_2O_7^{2-}$ [23, 24]. This motivates us to envision the adaptability and feasibility of the geopolymer method coupling with reductant for reduction and immobilization of Cr(VI) in contaminated solid waste, especially COPR.

In the present work, we report a new method of simultaneous reduction and immobilization of Cr(VI) by selecting Fe^{2+}, SO_3^{2-} and S^{2-} as reductant for reducing Cr(VI) to Cr(III) and employing the metakaolinite-based geopolymer to shed light on the immobilization of Cr(III). Using this method, reduction and immobilization of chromium can be realized by one-step procedure of geopolymerization, in which reduced Cr^{3+} is locked in the amorphous structure of geopolymer instead of being re-oxidized. The method is low-cost and simple with high efficient for Cr(VI) cleanup. Thus it provides a highly applicable alternative technique for large-scale cleanup for COPR or other Cr (VI)-contaminated solid waste.

Material And Methods

Materials

Coal-series kaolinite with 86% particles size below 2 μm was obtained from Datong, Shanxi province, China. The chemical composition of the kaolinite sample shown in Table 1 was determined by the X-ray fluorescence (XRF). Before geopolymerization, kaolinite was calcined at 600 ºC for 4 h to harvest metakaolinite product with high pozzolanic activity.

TABLE 1 CHEMICAL COMPOSITION OF KAOLINITE AS OXIDES

Composition	SiO_2	Al_2O_3	Fe_2O_3	TiO_2	CaO	MgO	Na_2O	K_2O	P_2O_5	LOI [a]
wt. %	45.36	38.49	0.32	0.44	0.16	0.08	0.088	0.053	0.18	14.33

[a] LOI: Loss on ignition at 1000ºC

Analytical-grade reagents NaOH, $K_2Cr_2O_7$, $CrCl_3 \cdot 6H_2O$, $FeSO_4 \cdot 7H_2O$, $FeCl_2 \cdot 4H_2O$, $Na_2S \cdot 9H_2O$ and Na_2SO_3 were obtained from Sinopharm Chemical Reagent Co., Ltd (China). Sodium silicate solution with the Baume degree of 45% - 47% and the modulus of 2.6-2.8 was purchased from Foshan Zhongfa sodium silicate factory (China).

Geopolymerization of metakaolinite-based geopolymers

The metakaolinite, sodium silicate solution and NaOH with a mass ratio of 6:5:1 were first mixed and stirred for 20 min until the formation of homogeneous colloid. The colloid was then casted into a 20 mm × 20 mm × 20 mm mold and vibrated for 2 min to eliminate air bubbles therein. After that, the mold was put in an oven with a constant temperature of 90 °C and a fixed humidity of 100% for 30 min. Then the sample was demolded. The samples with brick-shape were obtained. Finally, the brick was sealed with polyethylene (PE) film and immersed in a 60 °C water bath for 1 h. The pure metakaolinite-based geopolymer was obtained and denoted as MP. For justifying the immobilization efficiency of MP towards Cr(III) and Cr(VI), $CrCl_3 \cdot 6H_2O$ and $K_2Cr_2O_7$ saturated

solutions with certain Cr weight percentage were introduced into the colloid, respectively. For those colloids with Cr (VI), the reductants ($FeCl_2 \cdot 4H_2O$, $FeSO_4 \cdot 7H_2O$, $Na_2S \cdot 9H_2O$ and Na_2SO_3 saturated solution) were successively added with specific molar ratio to Cr(VI) before casting. The denoted names of the brick samples with the detailed reagent composition are listed in Table 2. Before the subsequent measurements, all bricks were stored under ambient condition with the protection of the PE film.

TABLE 2 EXPERIMENTS OF GEOPOLYMERIZATION

Sample	Cr / wt%	Cr species	Reductant	Reductant: Cr
MP	-	-	-	
MP-T-1	0.025	$CrCl_3 \cdot 6H_2O$	-	
MP-T-2	0.2	$CrCl_3 \cdot 6H_2O$	-	
MP-T-3	0.5	$CrCl_3 \cdot 6H_2O$	-	
MP-T-4	0.75	$CrCl_3 \cdot 6H_2O$	-	
MP-T-5	1	$CrCl_3 \cdot 6H_2O$	-	
MP-H	0.025	$K_2Cr_2O_7$	-	
MP-H-FC	0.025~0.7	$K_2Cr_2O_7$	$FeCl_2 \cdot 4H_2O$	3:1
MP-H-FS	0.025~0.7	$K_2Cr_2O_7$	$FeSO_4 \cdot 7H_2O$	3:1
MP-H-NS	0.025~0.7	$K_2Cr_2O_7$	$Na_2S \cdot 9H_2O$	0.5
MP-H-SO	0.025	$K_2Cr_2O_7$	Na_2SO_3	1.5

Test method

The leaching tests of chromium in the samples were conducted according to the No.1311 USEPA TCLP (toxicity characteristic) leaching procedure method [25]. And the leached Cr concentration of the filtrates was determined using atomic absorption spectrometry (AAS, Hitachi180-70). The immobilization performance of MP towards chromium was consequently evaluated by the percentage content of chromium immobilized in MP, which was called *immobilization* rate in the following paper. It was calculated according to the leached Cr versus the chromium added in MP.

Results and discussion

Immobilization of Cr(III)

Since the product of detoxicated Cr(VI) is Cr(III), using MP to immobilize Cr(III), similar to those reported for Zn^{2+}, Co^{2+}, Pb^{2+}, Cu^{2+} and Cd^{2+}, has become the first critical issue to match the fundamental requirement of COPR processing. Fig. 1 depicts the total leached chromium concentration and the immobilization rate of the MP-T-x samples from the TCLP experiments. At low initial introduced Cr(III) concentration (≤ 0.2 wt.%), immobilization rate of > 99.99% can be reached with the leached Cr concentration below 0.1 $mg \cdot L^{-1}$. While with the initial introduced Cr(III) concentration increases to 1.0 wt.%, the leached concentration varies quasi-linearly within a small range of 0.1-0.2 mg L^{-1}, far below the current regulatory limit of 5 mg L^{-1} for nonhazardous wastes proposed by the US EPA. Furthermore, all the samples show very high immobilization rate of beyond 99.0%. The result indicates that the MP matrix is capable of immobilizing the Cr(III) species with high efficiency once Cr(VI) is reduced to Cr(III).

Reduction of Cr(VI) and the successive immobilization

Another critical issue arising is whether the Cr(VI) species, generally appears as $Cr_2O_7^{2-}$, can be reduced and immobilized simultaneously. We then fixed the initial Cr(VI) concentration to be

0.025 wt.% and selected various reductants, including Na_2SO_3, $Na_2S·9H_2O$, $FeCl_2·4H_2O$ and $FeSO_4·7H_2O$ (denoted as MP-H-SO, MP-H-NS, MP-H-FC and MP-H-FS, respectively) as well as a blank benchmark (MP-H), to evaluate the feasibility of the proposed process. The result is shown in Fig. 2 Without reductant, the leached Cr concentration is up to 8.233 mg L^{-1}, with a low immobilization rate of 34.14%. While the Na_2SO_3 additive can moderately decrease the leached Cr concentration to 5.286 mg L^{-1} with the immobilization rate of above 50%. It is found that Fe^{2+} and S^{2-} additives can reduce greatly the leached Cr concentration. MP-H-NS, MP-H-FC and MP-H-FS all show the leached Cr concentration far below 5 mg L^{-1} of the regulatory limit for nonhazardous wastes proposed by the US EPA. And the immobilization rate is enhanced dramastically up to 99.0%. The above data confirm that Cr(VI) species as $Cr_2O_7^{2-}$ cannot be directly stabilized by the pure MP system. However, the appropriate reductive agents introduced can help stabilization of Cr in MP and prevent it from leaching out. Obviously, redox reaction happens in the geopolymerization in which Cr(VI) as $Cr_2O_7^{2-}$ is reduced to Cr(III) species as Cr^{3+} under the reductant action which are oxidized conversely and then Cr(III) is stabilized in MP .

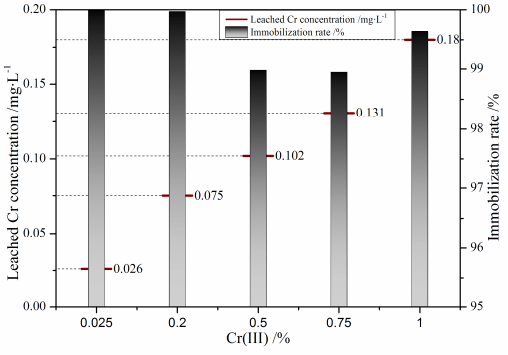


Fig.1.Immobilization performance of Cr (III).

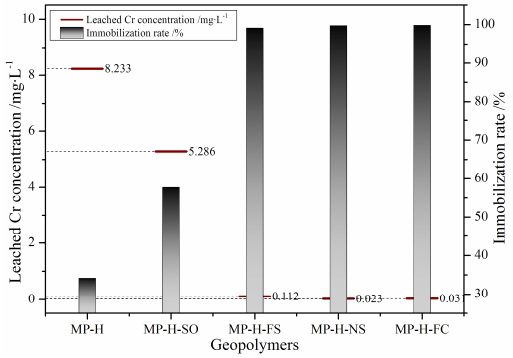


Fig.2. Iobilization rate of performance of Cr (VI

In the above successful experiments, only 0.025% of initial Cr(VI) concentration in MP was studied. But Cr(VI) content is often far higher than this value in Cr(VI)-contaminated solid waste, especially COPR, up to 1%. Five initial Cr(VI) concentrations, ranging from 0.1 wt% to 1.0 wt%, were studied according to the same procedure for the MP-H-FC, MP-H-FS and MP-H-NS systems.The results are summarized in Table 3. It is confirmed that all the MP-H-FC, MP-H-FS and MP-H-NS samples exhibit excellent immobilization rate of above 99.0%, with slight differences on the leached chromium concentration, when the initial Cr(VI) concentrations is from 0.1 wt.% to 0.7 wt.%. However, when the initial Cr(VI) concentration is 1.0 wt.%, MP-H-FC and MP-H-FS bricks could not be prepared because the colloids lose the cementitious activity by adding 1.0 wt.% Cr (VI) and moderate Fe^{2+}. The result further confirms that MP-H-NS bricks can be formed successfully regardless of the initial Cr(VI) concentration. And all the leached concentrations are below the US EPA limitation of 5 mg L^{-1}. If the amount of reductants were set to be appropriate towards the initial Cr(VI) content, Fe^{2+} and S^{2-} both can serve as the additive to the geopolymer matrix to simultaneously realize the reduction and stabilization of Cr(VI) with concentration below 0.7 wt.%. For Cr(VI) concentration larger than 0.7%, S^{2-} can be more appropriate and further study about the mechanism of Cr(VI) reduction and immoboilization is required.

TABLE.3. LEACHED CR CONCENTRATION AND IMMOBILIZATION RATE IN THE BRICKS WITH INCREASED CR (VI) CONTENT

Cr(VI) /%	$FeCl_2·6H_2O$		$FeSO_4·7H_2O$		$Na_2S·9H_2O$	
	leached Cr concentration /mg L^{-1}	immobilization rate /%	leached Cr concentration /mg L^{-1}	immobilization rate /%	leached Cr concentration /mg L^{-1}	immobilization rate /%

0.1	0.042	99.36	0.015	99.83	0.131	99.74
0.3	0.060	99.96	0.023	99.98	0.136	99.91
0.5	0.041	99.99	0.049	99.98	0.180	99.93
0.7	0.049	99.99	0.034	99.99	0.220	99.95
1.0	lose cementitious activity				0.230	99.98

Conclusion

Cr(VI) is a high toxic substance and due to the high water solubility, direct detoxification and immobilization of Cr(VI) within natural environment is technologically difficult. In this paper, simultaneous reduction and immobilization of Cr(VI) as $Cr_2O_7^{2-}$ is investigated by one-step procedure using metakaolinite-based geopolymer added reductant. Cr added as Cr^{3+} can be locked successfully in the amorphous structure in geopolymer and leached Cr concentration is lower 5 mg L^{-1} when initial Cr(Ⅲ) concentration is less than 1 wt.%. Cr(Ⅲ) has slightly influenced on the compressive strength of the sample bricks. On the base of Cr^{3+} immobilized successfully in geopolymer, reductant was introduced to reduce Cr(VI) to Cr(Ⅲ) and the metakaolinite-based geopolymer was applied to immobilize Cr(III). In the absence of reductants, Cr added as $Cr_2O_7^{2-}$ is highly leachable. But addition of $FeCl_2 \cdot 4H_2O$, $FeSO_4 \cdot 7H_2O$ and $Na_2S \cdot 9H_2O$ by certain proportion respectively towards Cr(VI) reduced greatly the leached Cr concentration in metakaolinite-based geopolymer. Under these reductants, Cr(VI) was reduced to Cr(III) and Cr(III) was then locked in geopolymers. When initial Cr(VI) concentration is lower than 0.7% in metakaolinite-based geopolymer, the leached Cr concentration is below 5 mg L^{-1} and Cr immobilization rate above 99%. When initial Cr(VI) concentration is larger than 0.7%, the geopolymer bricks added $FeCl_2 \cdot 4H_2O$ and $FeSO_4 \cdot 7H_2O$ could not be prepared because the colloids lose the cementitious activity. So, $Na_2S \cdot 9H_2O$ may be the best reductant not only to achieve good Cr immobilization effiency. Such a simultaneous reduction/immoboilization process enables the feasibility of using metakaolinite-based geopolymer complexed reductant to implement a one-step procedure for COPR cleanup.

Acknowledgements

The authors acknowledge the financial support from National Natural Science Foundation of China (41102025) and the Fundamental Research Funds for the Central Universities, China University of Geosciences (Wuhan) (No. CUG120118). T

References

[1] M. Wazne, D.H. Moon, S.C. Jagupilla, S.C. Jagupilla, C. Christodoulatos, D. Dermatas, M. Chrysochoou, Remediation of chromite ore processing residue using ferrous sulfate and calcium polysulfide, Geosci. J., 11 (2007) 105-110.

[2] S. Dantu, Heavy metals concentration in soils of southeastern part of Ranga Reddy district, Andhra Pradesh, India, Environ. Monit. Assess., 149 (2009) 213-222.

[3] D. Zhang, S. He, R. Cai, K. Peng, Z. Hu, H. Pang, H. Kong, F. Zhang, Study on the remediation of chromite ore processing residue by pyrolysis process, Environ. Pollut. & Control., 31 (2009) 1-5.

[4] M.C. Graham, J.G. Farmer, P. Anderson, E. Paterson, S. Hillier, D.G. Lumsdon, R.J.F. Bewley, Calcium polysulfide remediation of hexavalent chromium contamination from chromite ore processing residue, Sci. Total Environ., 364 (2006) 32-44.

[5] J.G. Farmer, E. Paterson, R.J.F. Bewley, J.S. Geelhoed, S. Hillier, J.C.L. Meeussen, D.G. Lumsdon, R.P. Thomas, M.C. Graham, The implications of integrated assessment and modelling studies for the future remediation of chromite ore processing residue disposal sites, Sci. Total Environ., 360 (2006) 90-97.

[6] T. Wang, M. He, Q. Pan, A new method for the treatment of chromite ore processing residues, J. Hazard. Mater., 149 (2007) 440-444.
[7] Y.L. Wei, H.F. Hsieh, Y.S. Peng, J.C. Yang, H. Paul Wang, C.Y. Lin, W.L. Shih, C.C. Hsu, Thermal detoxification and bloating of chromium(VI) with bentonite, Nucl. Instrum. Methods Phys. Res., Sect. A, 619 (2010) 108-111.
[8] C. Wu, H. Zhang, P. He, L. Shao, Thermal stabilization of chromium slag by sewage sludge: Effects of sludge quantity and temperature, J. Environ. Sci.-China, 22 (2010) 1110-1115.
[9] D. Zhang, S. He, L. Dai, X. Hu, D. Wu, K. Peng, G. Bu, H. Pang, H. Kong, Treatment of Chromite Ore Processing Residue by pyrolysis with rice straw, Chemosphere, 77 (2009) 1143-1145.
[10] J. Du, J. Lu, Q. Wu, C. Jing, Reduction and immobilization of chromate in chromite ore processing residue with nanoscale zero-valent iron, J. Hazard. Mater., 215-216 (2012) 152-158.
[11] H.-S. Tai, C.-J.G. Jou, Immobilization of chromium-contaminated soil by means of microwave energy, J. Hazard. Mater., 65 (1999) 267-275.
[12] L. Yang, Y. Wang, L. Li, H. Liang, H. Gao, X. Su, J. Fan, L. Zhang, Technologic research on detoxification of residue with chromium through radiation of microwave, Chin. J. Environ. Eng., 2 (2008) 820-825.
[13] T.L. Rinehart, D.G. Schulze, R.M. Bricka, S. Bajt, E.R. Blatchley, Chromium leaching vs. oxidation state for a contaminated solidified/stabilized soil, J. Hazard. Mater., 52 (1997) 213-221.
[14] R. Badreddine, A.N. Humez, U. Mingelgrin, A. Benchara, F. Meducin, R. Prost, Retention of trace metals by solidified/stabilized wastes: Assessment of long-term metal release, Environ. Sci. Technol., 38 (2004) 1383-1398.
[15] H.-S. Shi, L.-L. Kan, Study on the properties of chromium residue-cement matrices (CRCM) and the influences of superplasticizers on chromium(VI)-immobilising capability of cement matrices, J. Hazard. Mater., 162 (2009) 913-919.
[16] J. Davidovits, 30 years of successes and failures in geopolymer applications. Market trends and potential breakthroughs, in: Keynote Conference on Geopolymer Conference, 2002.
[17] J.G.S. Van Jaarsveld, J.S.J. Van Deventer, A. Schwartzman, The potential use of geopolymeric materials to immobilise toxic metals: Part II. Material and leaching characteristics, Miner. Eng., 12 (1999) 75-91.
[18] S.F. Liu, P.M. Wang, Z.J. Li, I.M.C. Lo, An FTIR and XPS study of immobilization of chromium with fly ash based geopolymers, Spectrosc. Spect. Anal., 28 (2008) 67-71.
[19] Y. Luna, X. Querol, D. Antenucci, E.-A. Jdid, C. Fernandez-Pereira, J. Vale, Immobilization of a metallurgical waste using fly ash-based geopolymers, in: 2007 World of Coal Ash, Covington, Kentucky, USA, (2007) 7-10.
[20] M.T. Jin, Q. Zhang, M.X. Lou, L.J. Wang, Immobilization of Heavy Metal Ions in Fly Flashed-Geopolymer, Bull. Chin. Ceram. Soc., 3 (2007) 011.
[21] J.Z. Xu, Y.L. Zhou, R.X. Tang, Study on the solidification of heavy metals by fly ash based geopolymers, J. Build. Mater., 9 (2006) 341-346.
[22] Y.S. Zhang, W. Sun, Q.L. Chen, L. Chen, Synthesis and heavy metal immobilization behaviors of slag based geopolymer, J. Hazard. Mater., 143 (2007) 206-213.
[23] J. Zhang, J.L. Provis, D. Feng, J.S.J. van Deventer, Geopolymers for immobilization of Cr^{6+}, Cd^{2+}, and Pb^{2+}, J. Hazard. Mater., 157 (2008) 587-598.
[24] Q.Y. Lu, Research of preparation ang application of geopolymer, in, Fu Zhou University, 2005.
[25] U.S. EPA, Toxicity Characteristic Leaching Procedure, Method 1311, in: E.P. Agency (Ed.), Washington, DC, USA, 1992.

CHAPTER 10:

Materials and Technologies of Chemical Industry

Advanced Materials Research Vol. 936 (2014) pp 901-904
© (2014) Trans Tech Publications, Switzerland
doi:10.4028/www.scientific.net/AMR.936.901

Construction of a Novel 3D Indium Phosphate–Phosphite with Extra-Large 16-MRs Channels: Synthesis, Structure and Fluorescence Property

LI Hui-Duan[1, a *]

[1]Department of Chemistry and Life Science, Chuxiong Normal University, Chuxiong 675000, P. R. China

[a]email: lhd08@cxtc.edu.cn

Keywords: hydrothermal synthesis; indium phosphate–phosphite; structure directing agent; fluorescence property.

Abstract. A novel 3D anionic indium phosphate–phosphite, formulated as $|(C_{10}H_{10}N_2)_{1.5}(H_3O)_3|[In_{18}(H_2O)_{12}(HPO_4)_{12}(HPO_3)_{16}(H_2PO_3)_6]$ (1), was hydrothermally prepared by using 4, 4′-bipyridine (4, 4′-bipy) as a structure directing agent (SDA). Single-crystal X-ray diffraction analysis reveals that compound 1 crystallizes in the hexagonal system space group $P6_3/m$ (No. 176) having unit cell parameters a = 13.7843(19) Å, b = 13.7843(19) Å, c = 28.058(6) Å, V = 4617.0(13) Å^3. Compound 1 exhibits a unique pillar-layer open-framework constructed from InO_6 octahedra, HPO_3 pseudo-tetrahedra and HPO_4 tetrahedra, resulting extra-large 16-MRs channels. Synthesis, crystal structure and fluorescence property for compound 1 were reported in this paper.

Introduction

Metal phosphates and phosphites exhibiting open architectures have been recognized for their potential applications in magnetism, nonlinear optics, renewable catalysis, ion exchange and host-guest assembly [1-3]. Numerous metal phosphates have been reported relating to aluminum, gallium and indium metal ions [4-7]. In these years, HPO_3 pseudo-tetrahedral were introduced to explore the design and synthesis of novel open architectures. The replacement of the phosphate group with phosphite forbids self-interpenetration and offers the potential to construct porous solids with extra-large channels[8-12].

Here, We reported the synthesis and structure of a novel 3D indium phosphate–phosphite, $|(C_{10}H_{10}N_2)_{1.5}(H_3O)_3|[In_{18}(H_2O)_{12}(HPO_4)_{12}(HPO_3)_{16}(H_2PO_3)_6]$ (1). Further characterizations for 1 were performed using powder X-ray diffraction (PXRD), infrared spectra (IR), thermal gravimetric analyses, solid fluorescence property, inductively coupled plasma and elemental analyses.

Experiment

Synthesis. Compound 1 was hydrothermally synthesized: 100 mg $In(NO_3)_3 \cdot 4H_2O$, 64 mg $H_2C_2O_4$ and 120 mg H_3PO_3 were dispersed into 6 mL H_2O with stirring. Then, 48mg of 4, 4′-bipy was added. After stirring for 30 min, the mixture was transferred into a sealed Teflon-lined steel autoclave and heated at 160ºC for 3 days. Colorless prism-like crystals of compound 1 were collected and air-dried at room temperature (53% yield based on Indium).

Determination of crystal structure. Suitable single crystal of 1 (0.20 × 0.20 × 0.08 mm^3) was selected for single-crystal X-ray diffraction analyses. The data was collected on a Bruker Smart CCD diffractometer (λ(Mo-Kα) = 0.71073Å). A total of 33564 reflections with 3921 unique reflections (R_{int} = 0.0629) were collected. Data processing was accomplished with the SAINT processing program. The structure was solved by direct methods and refined by full-matrix least-squares on F^2 using SHELXTL 5.1 software package [13]. First, the In and P atoms were located, followed by location of O, N and C atoms. The hydrogen atoms from framework were located from difference Fourier maps. While the hydrogen atoms from guest molecules were placed geometrically. For the

final refinement, all the non-hydrogen atoms were refined anisotropically. It was noteworthy that P(4) atoms were disordered over two positions with an equal occupancy. Detailed crystallographic data for 1 was presented in Table 1.

Table 1 Crystal data and structure refinement for 1

Empirical formula	|(C10H10N2)1.5(H3O)3|[In18(H2O)12(HPO4)12(HPO3)16(H2PO3)6]
Temperature (K)	298(2)
Wavelength (Å)	0.71073
Formula weight	5446.62
Crystal system	Hexagonal
Space group	P63/m
a (Å); b (Å); c (Å)	13.7843(19); 13.7843(19); 28.058(6)
γ (°)	120
Volume (Å3)	4617.0(13)
Z	1
Dcalc (mg m-3)	1.959
Absorption coefficient (mm-1)	2.592
F(000)	2599
Crystal size (mm)	0.20 × 0.20 × 0.08
θ range (o)	1.85 to 28.44
Limiting indices	-12≤h≤18; -18≤k≤15; -35≤l≤37
Reflections collected	33564 / 3921
Reflections unique	3921 [R(int) = 0.0629]
Completeness to θ = 24.98	98.5 %
Refinement method	Full-matrix least-squares on F2
Data / restraints / parameters	3921 / 68 / 167
Goodness-of-fit on F2	1.330
Final R indices [I>2σ(I)]a,b	R1 = 0.1105; wR2 = 0.2561
R indices (all data)a,b	R1 = 0.1306; wR2 = 0.2669
Largest diff. peak and hole	2.684 and -2.498 e Å-3

[a] $R_1=\sum||F_o|-|F_c||/\sum|F_o|$. [b] $wR_2=[\sum[w(F_o^2-F_c^2)^2]/\sum[w(F_o^2)^2]]^{1/2}$.

Results and discussion

Description of crystal structure for 1. Single-crystal X-ray diffraction analyses reveals that 1 crystallizes in the hexagonal space group $P6_3/m$ (No. 176), formulated as $|(C_{10}H_{10}N_2)_{1.5}(H_3O)_3|[In_{18}(H_2O)_{12}(HPO_4)_{12}\ (HPO_3)_{16}(H_2PO_3)_6]$. As shown in Fig. 1a, each asymmetric unit contains three crystallographically independent In atoms, four crystallographically independent P atoms, eleven oxygen atoms, one guest water molecule and one 4, 4′-bipy molecule. All the three In atoms were octahedrally coordinated. The coordinated environment for In(2) and In(3) atoms were similar, six vertex oxygen atoms were shared with adjacent P atoms. The coordinated environment for In(1) was different, whereby, five vertex oxygen atoms were shared with adjacent P atom. The remaining coordination site was occupied by a coordinated water molecule, as indicated by the In(1)-O(4) bond length of 2.259(12) Å. The coordination fashion for P(1), P(3) and P(4) were pseudo-tetrahedra. The P(2) atom was tetrahedrally coordinated. It was connected to three In atoms via oxygen atoms bearing a terminal –OH group. All bond lengths and angles in the crystal structure of 1 were similar to those reported in the literature.

The novel 3D open-frameworks for compound 1 were constructed from InO_6 octahedra, HPO_3 pseudo-tetrahedra and HPO_4 tetrahedra, featuring intersecting extra-large 16-MRs channels. The guest water molecular and 4, 4′-bipy molecular were deposited in these channels (as shown in Fig. 1b).

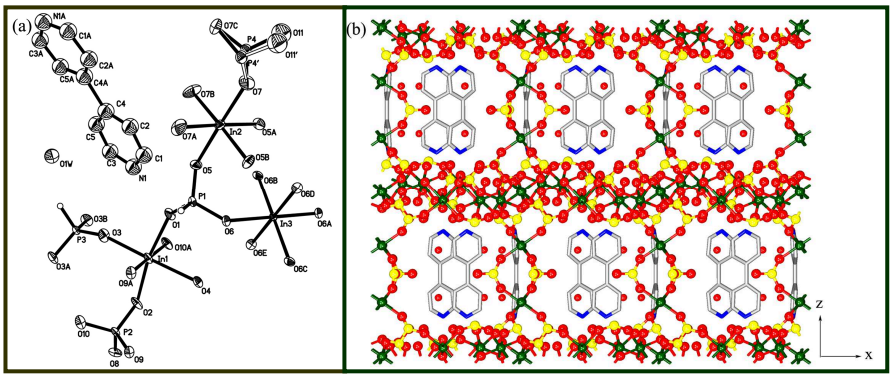


Fig. 1 (a) ORTEP view of the asymmetric unit of compound 1; (b) Ball and stick view of the structure of compound 1 with 4, 4′-bipy deposited in the 16-rings channels.

Characterization for compound 1. The purity of 1 was confirmed by comparison of the experimental PXRD pattern to the calculated ones based on single-crystal structure (as shown in Fig. 2a). The result of elemental analysis for 1 was consistent well with the theoretical values. Analysis found (%): In, 37.56; P, 19.20; C, 3.24; H, 1.50; N 0.66. Calcd. (%): In, 37.61; P, 19.17; C, 3.28; H, 1.61; N 0.76.

IR spectrum for 1 was shown in Fig. 2b, The bands in the range of 3500–3000 cm^{-1} are associated with stretching vibrations of N-H, O-H and C-H groups. The band at 2410 cm^{-1} was ascribed to vibrations of the P-H. The multi-fold bands in the region of 1600-1400cm^{-1} should be attributed to pyridyl rings. The stretching and bending vibration absorption peaks for In-O, P-O and In–O–P were featured in the region of 1200-900cm^{-1} and 600–400 cm^{-1}, respectively.

TG analysis curve for 1 showed two steps of weight loss from 40 to 1000 °C (Fig. 2c). The first step weight loss of 7.87 wt% before 400 °C was attributed to the removal of water molecular and the release of partial 4, 4′-bipy molecules. On further heating, the second step weight loss of 12.50 wt%, which is attributed to the release of residual organic amine. The total observed weight loss 20.37 wt% for the above two steps matches well with the calculated value based on the structure. PXRD studies indicated that the post-residue is a mixture of $InPO_4$ (JCPDS:08-0052) and $In_4(P_2O_7)_3$(JCPDS: 53-1018).

Fluorescence property for compound 1. The guests 4, 4′-bipy molecular acted as SADs to form the large pore structure of 1, which were deposited in the 16-rings channels with the two pyridyl rings twisted at an angle of 59.19°. Compound 1 presented the same solid fluorescence property as the 4, 4′-bipy, attributing to the intraligand π-π* transition in the structure (Fig. 2d).

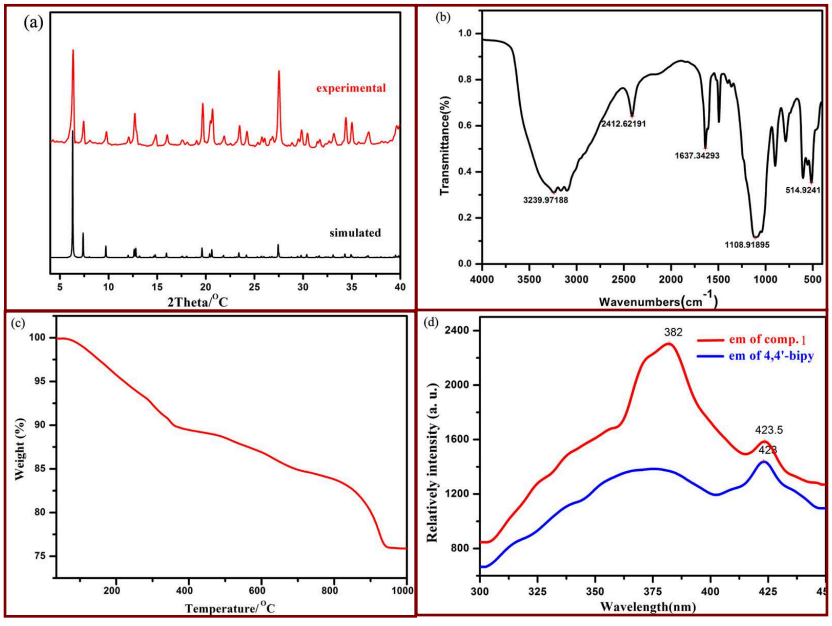


Fig. 2 Structure characterizations for compound 1

Conclusion

In conclusion, a novel indium phosphate–phosphite was synthesized under hydrothermal conditions by using 4, 4′-bipy as a SDA. The construction of InO_6 octahedra, HPO_3 pseudo-tetrahedra and HPO_4 tetrahedra leads to the assembly of 3D open-framework with intersecting extra-large 16-rings channels. The guests 4, 4'-bipy molecular were deposited in the channels. Solid fluorescence property for compound **1** was also studied in this paper. Further investigations on assembly novel indium phosphites and potential applications for these materials are underway.

Acknowledgements

The authors acknowledge the financial support of the Natural Science Foundation of Yunnan province (Grant No. 2012FD050) and the State Key Laboratory of Inorganic Synthesis and Preparative Chemistry of Jilin University.

References

[1] R. Murugavel, A. Choudhury, M. G. Walawalkar, R. Pothiraja, C. N. R. Rao, Metal Complexes of Organophosphate Esters and Open-Framework Metal Phosphates: Synthesis, Structure, Transformations, and Applications, Chem. Rev. 108 (2008), 3549-3655.

[2] J. Yu, R. Xu, Insight into the construction of open-framework aluminophosphates, Chem. Soc. Rev., 35 (2006) 593-604.

[3] C. N. R. Rao, S. Natarajan, A. Choudhury, S. Neeraj, A. A. Ayi, Aufbau Principle of Complex Open-Framework Structures of Metal Phosphates with Different Dimensionalities, Acc. Chem. Res., 34 (2001) 80-87.

[4] A. K. Cheetham, G. Férey, T. Loiseau, Angew. Chem. Int. Ed., 38 (1999) 3268, and references therein.

[5] D. Maspoch, D. Ruiz-Molina, J. Veciana, Chem. Soc. Rev., 36 (2007) 770, and references therein.

[6] T. Rojo, J. L. Mesa, J. Lago, B. Bazan, J. L. Pizarro, M. I. Arriortua, Organically templated open-framework phosphites, J. Mater. Chem., 19 (2009) 3793-3818.

[7] S. Natarajan, S. Mandal, Open-Framework Structures of Transition-Metal Compounds, Angew. Chem. Int. Ed., 47 (2008) 4798-4828.

[8] L. Wang, T. Song, J. Xu, Y. Wang, Z. Tian. S. Shi, Synthesis and characterization of two new organically templated indium phosphites built from one-dimensional ladders, Micropor. Mesoporo. Mater., 96 (2006) 287-292.

[9] L. Huang, T. Song, Y. Fan, L. Yang, L. Wang, H. Zhang, L. Wang, J. Xu, Hydrothermal syntheses, characterizations of novel three-dimensional indium phosphite and indium phosphite–phosphate with intersecting 8-membered ring channels: $[In_3(H_2PO_3)_3(HPO_3)_4]\cdot(trans\text{-}C_6N_2H_{16})$ and $[In_6(HPO_3)_8(H_2PO_3)_5(H_2PO_4)]\cdot(C_3N_2H_{12})_2$, Micropor. Mesoporo. Mater., 132 (2010) 409-413.

[10] Z. Dong, Y. Yan, Y. Li, J. Li, J. Yu, R. Xu, A new open-framework indium phosphate–phosphite containing intersecting extra-large 16-ring channels, Inorg. Chem. Commun., 14 (2011), 727–730

[11] H. Li, L. Zhang, L. Liu, T. Jiang, Y. Yu, G. Li, Q. Huo, Y. Liu, Organic template-directed indium phosphite-oxalate hybrid material: Synthesis and characterization of a novel 3D $|C_6H_{14}N_2|[In_2(HPO_3)_3(C_2O_4)]$ compound with intersecting channels, Inorg. Chem. Commun., 12 (2009) 1020-1023.

[12] H. Li, L. Zhang, Q. Huo, Y. Liu, Construction of two novel indium phosphites with (3,6)- and (3,5)-connected frameworks: Synthesis, structure and characterization, J. Solid State Chem., 197 (2013) 75-80

[13] G. M. Sheldrick, SHELXTL-NT, Version 5.1, Bruker AXS Inc. Madison, WI, 1997.

Advanced Materials Research Vol. 936 (2014) pp 905-910
© (2014) Trans Tech Publications, Switzerland
doi:10.4028/www.scientific.net/AMR.936.905

The Effect of Polyvinyl Pyrrolidone and Nickel Acetylacetonate on the Fabrication of Polyacrylonitrile Precursor Fiber

WANG Zhi-hui [1, a], RONG Hai-qin, XU Ao-yun[1, b], LIN Hui-min and ZHAO Shu-hui[1,c]

[1] College of Chemistry, Chemical Engineering and Biotechnology, Donghua University, Shanghai 201620, China

[a]wangzhihui200803@163.com, [b]aoyunxu@163.com, [c]shzhao@dhu.edu.cn

Keywords: polyvinyl pyrrolidone; polyacrylonitrile; fiber precursor; nickel acetylacetonate

Abstract. The effect of polyvinyl pyrrolidone (K30) and nickel acetylacetonate ($Ni(acac)_2$) on the fabrication of polyacrylonitrile(PAN) fiber was investigated. K30 and $Ni(acac)_2$ were chosen as pore-forming agents to prepare mesoporous carbon fibers.Meanwhile, the concentration of K30 and $Ni(acac)_2$, the mass ratio of pore-forming agent to PAN, the rheological properties of spinning dope, the mechanical properties, thermal performance of fiber precursor were also characterized. Furthermore, the precursor fibers and the carbon fibers were researched by FTIR analysis, TG analysis and static benzene adsorption. Based on the research, when the concentration of K30 and $Ni(acac)_2$ was 5%, the mass ratio of K30/$Ni(acac)_2$ to PAN was 7:3, the fiber precursors had excellent properties. Adding poreforming agent, the pore distribution was controlled.

Introduction

As a type of effective carbonaceous adsorbent, activated carbon fibers (ACF) have attracted considerable interest because of their numerous special features compared to conventional activated carbon[1]. ACF have uniform pore distribution, large specific surface area and performance of heat-resisting, acid-resisting, alkali-resisting, the high electric and thermal conductivity. They generally have narrower pore size distribution and allow greater accessibility of adsorbates to their micropores. These properties have endowed ACF with high adsorption capacity for small-molecular-size pollutants. However, these features might not always be advantageous, especially when ACF are being used as electrodes/capacitor materials or adsorbents for larger-molecular-size pollutants[2]. In microporous carbon materials, adsorption occurs in pores with sizes about 1.7 times larger than the second widest dimension of the adsorbate molecules[3]. As reported previously, the fabrication of mesoporous carbon fibers become a hot research field [4].

At present, the mesoporous ACF was mainly prepared by changing activation process and using additives. Gan Yongjin [5] from Jilin University has researched mesoporous ACF. But he made it mainly from changing activation process to improve the volume of mesopore. Adding additives especially K30 and Ni(acac)2 to prepare mesoporous ACF has not been reported at home and abroad. In this work, the main aim was to select K30 and Ni(acac)2 as pore-forming material. Ni(acac)2 is not only as pore-forming agent, but also it acts as catalyst in activation process. By adding Ni(acac)2, aperture distribution can be controlled [6,7].

To prepare original fiber, dissolve the pore-forming material in the solvent and then mix with PAN slurry to form homogeneous system, finally fulfill the deaeration and wet spinning process. In the whole process, the content of pore-forming material, the ratio of K30 and Ni(acac)2 to PAN and spinning conditions had important influence on the rheological behavior of slurry, the thermodynamics properties and mechanical properties. Furthermore, they would affect the temperature of carbonization and activation.

Experimental

Materials and Agents

PAN copolymers slurry (acrylonitrile: methylacrylate: itaconic acid = 96:3:1), with a viscosity-average molecular weight $M\eta=1.25\times105$g.mol-1 were prepared by our laboratory. DMSO (AR) was purchased from Shanghai Boer Chemical Reagent. K30 and Ni(acac)2 was purchased from Aladdin Chemistry Co., Ltd.

Fabrication Methods

The Fabrication of Spinning Solution

The dried PAN copolymers, K30 and Ni(acac)2 which the mass concentration were 18 wt% and 5 wt% respectively were dissolved in DMSO, then mixed by mechanically stirring to produce a homogeneous viscous solution. Four spinning solution were prepared with different mass ratio of PAN slurry to pore-forming solution of 10:0,9:1,8:2,7:3.The resulting slurry was swollen at 60℃for 24h to make sure that there were no bubbles in the spinning solution.

The Fabrication of PAN Precursor by Wet Spinning

The spinneret was used in this experiment with 6 holes of 0.25mm, which was heated in the oven at 70℃for 24h, then poured into the spinning solution in the charging barrel under 60℃. 40% DMSO at 5℃was used as the coagulation bath. Then heat them up to 100℃.

The wet spinning process in this experiment was depicted as follows:

Preparation before spinning →spinning→coagulation→stretching→boil water stretching

Applying oil →densification →winder

Pre-oxidation, Carbonization and Activation of Fiber Precursor

Put the dried fiber precursor in the furnace and rise temperature to 800 ℃, then keep at this temperature for 2 hours, take out the carbon fibers after pre-oxidation, carbonization and activation.

Characterization

Fourier transformed infrared spectroscopy (FTIR) was recorded between 4,000cm-1 and 400cm-1 on USA Nicolet FTIR 670 NEXUS spectrophotometer at room temperature. The thermal gravimetric analyses (TGA, TG209 T1) were used to characterize the thermal performance of original fiber at a heating rate of 10℃/min under flowing nitrogen, and the temperature rose from room temperature to 900℃. The rheological measurements were carried out on a rotational rheometer (ARES-RFS, TA company), the concentric parallel plate geometry (diameter: 25mm) was utilized, the chosen gap was 1mm for all measurement. Steady shear profiles were examined at constant temperature of 60 ± 0.01℃ covering a shear-rate range from 0.1-100Hz.The mechanical properties were tested by single fiber strength instrument(LLY-06,China).The microstructure was examined using a scanning electron microscope (SEM, TM-1000, Japan).

Results and Discussion

The Effect of Concentration of Pore-forming Solution on Spinning Performance

In this experiment, K30 and Ni(acac)2 as pore-forming agent had important influence on the spinning performance. The slurry was prone to crust in the air and water which would lead to spinneret block and affecting spinning. The dosage of K30 and Ni(acac)2 were determined through testing the thickness of slurry block.

Prepare different mass concentration of the solution of K30/ Ni(acac)2/DMSO by 18%, 9%, 5%, 1% respectively. Pour the solution on the glass plate and observe the crust phenomenon. The result was shown in table 1.

TABLE 1 THE CRUST EXPERIMENT ON DIFFERENT CONCENTRATIONS OF K30/ NI(ACAC)$_2$/ DMSO SYSTEM

Solution	Concentration[%]	The thickness of crust
K30 /Ni(acac)2/DMSO	18	thicker
	9	thick
	5	thin
	1	less

Table 1 showed that the crust phenomenon were more serious in the dense solution, but the voids content of mesoporous activated carbon fibers would be affect if the concentration was too small. Above all, the concentration of 5% was the optimum condition of spinning. The concentration of K30 /Ni(acac)2/DMSO was 5% in the following experiment.

The Rheology of Spinning Solution

Rheology was a significant property of slurry. Through testing the rheology of different ratios of PAN to K30 /Ni(acac)2, the optimum condition of spinning can be achieved. Prepare different ratios of PAN to K30 /Ni(acac)2 with 10:0(S0), 9:1(S1), 8:2(S2), 7:3(S3) [8-9]respectively.

Fig.2 showed the effect of different ratios on the complex viscosity of slurry. From the curves, the complex viscosity (η*) heavily decreased with the increase of shear rate and gradually went back to a point. This might be the reason for the orientation of polymer, polymer molecular chain tended to be orientation under shearing force, so the movement of molecular chain enhanced which led to the decrease of complex viscosity.

Fig.1 shown that the complex viscosity (η*) decreased with the dosage of K30 /Ni(acac)2 increasing. The reason was that when mixed K30/ Ni(acac)2 with PAN, some PAN chains broke up which leaded to moving easily. The more the dosage of K30/ Ni(acac)2 was, the more easily the chains moved[10-13]. According to experiment data, when the mass of PAN to K30 /Ni(acac)2 was 7:3, the complex viscosity was so little that it was the optimum condition of spinning.

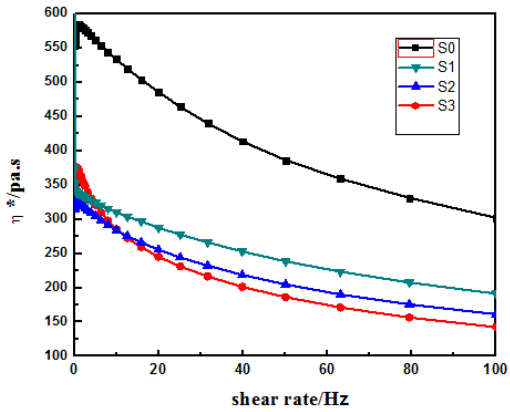
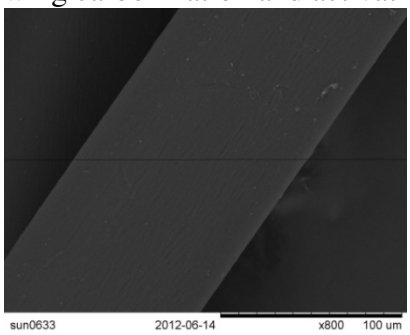


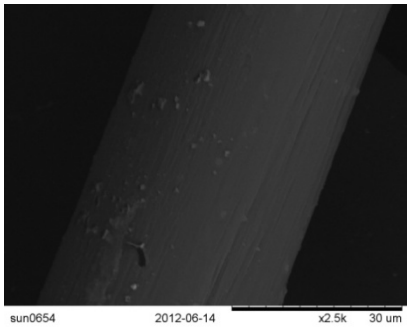
Fig.1 The Influence of Different Ratios on the Complex Viscosity

Morphology of PAN/K30 /Ni(acac)$_2$ fiber

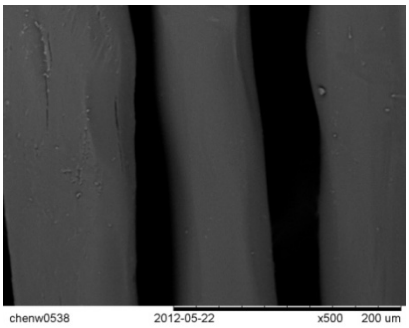
The fiber uniformity could improve strength, from SEM the microstructure can be clearly seen. SEM images of PAN/ K30 /Ni(acac)2 fiber were shown in Fig.2, It should be noted that fiber were mostly smooth and round and texture was clear along the axial direction which would be helpful for the following carbonization and activation.

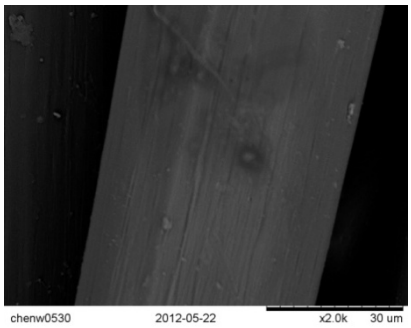


(a) PAN Fiber Precursor



(b) m(PAN):m(K30/Ni(acac)2)=7:3





(c) m(PAN):m(K30/Ni(acac)2)=8:2 (d) m(PAN) : m(K30/Ni(acac)2)=9:1

Fig.2 The SEM Images of PAN/ K30 /Ni(acac)2 Fibers

Mechanical Properties of Single Fiber

The strength of fiber usually refers to the relative strength, which was also the fracture point of unite load. The strength of fiber was mostly caused by the flaws, namely the starting point of fracture. The data of the testing was shown in table 2. It was clearly observed that the presence of K30 /Ni(acac)2 led to deterioration of tensile properties. Moreover, the strength of fiber decreased heavily with the increase of K30 /Ni(acac)2 which were closely related to the morphology in previous section. Enhance the strength of the fiber by improving the draw ratio.

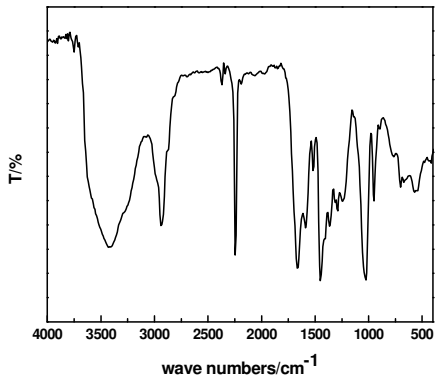
TABLE 2 THE STRENGTH TEST OF SINGLE FIBER

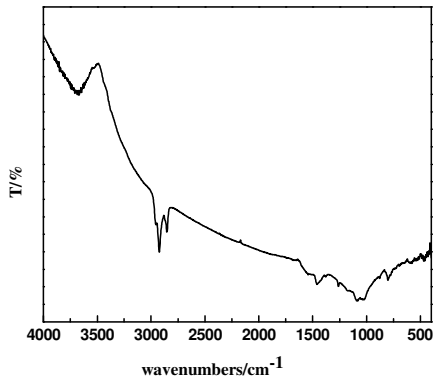
NO.	Strength[CN]	Breaking elongation[%]	Line density [dtex]	Modulus [CN/dtex]
S0(1)	142.64	27.3	40.5	3.52
S0(2)	106.00	44.27	29.70	4.80
S1(1)	54.62	18.65	46.28	1.18
S1(2)	58.61	17.68	32.92	1.78
S2(1)	37.67	15.41	26.89	1.40
S2(2)	33.29	13.29	23.69	1.41
S3(1)	38.64	13.69	37.05	1.04
S3(2)	34.29	13.69	31.75	1.08

Note:(1) stands for that draw ratio is one, (2) stands for that draw ratio is two.

FTIR Analysis[5-7]

Fig.3 shows FTIR spectra of fiber precursor and carbon fibers.





(a) Fiber precursor (b) Carbon fibers

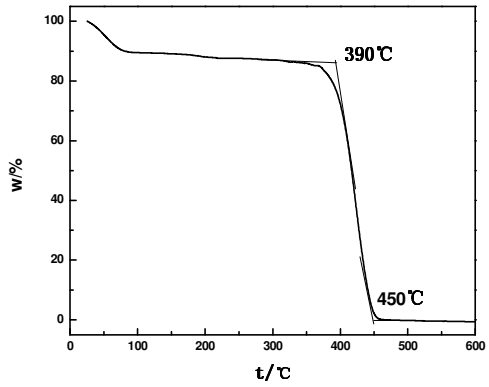
Fig.3 FTIR spectra of fiber precursor(a) and carbon fibers(b)

Fig.3 shows that most of the functional groups disappeared after pre-oxidation, carbonization and activation, the residual functional groups were the basic carbon skeleton. It indicated that the pore-forming agents were decomposed in the process of carbonization and activation.

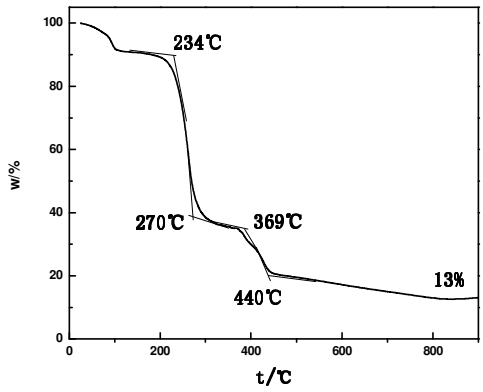
TG-DT Analysis

The TG analysis on the material had an important effect on carbonization and activation. Fig.4 showed TG-DT analysis of K30, Ni(acac)2 and carbon fibers. It can be seen from the curve that the onset decomposition temperature of K30 was 390℃, when the temperature rised to 450℃, the decomposition rate of K30 reached the maximal nearly 100%, the decomposition rate of Ni(acac)2 reached about 87% at 600℃, so K30 and Ni(acac)2 as pore-forming agent were suitable for mesporous activated carbon fibers.

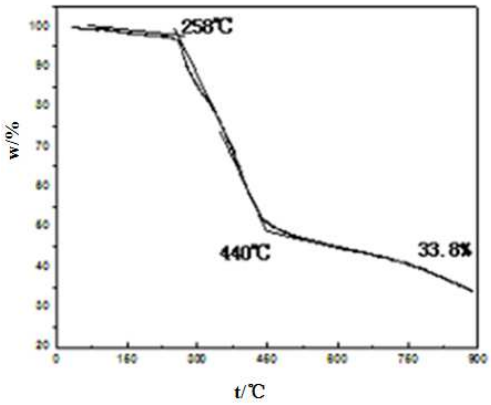
It can be seen from Fig.5(d), the decomposition rate of precursor fiber reached about 74.2% after 900℃, which was much high compared with the decomposition rate of fiber(c).



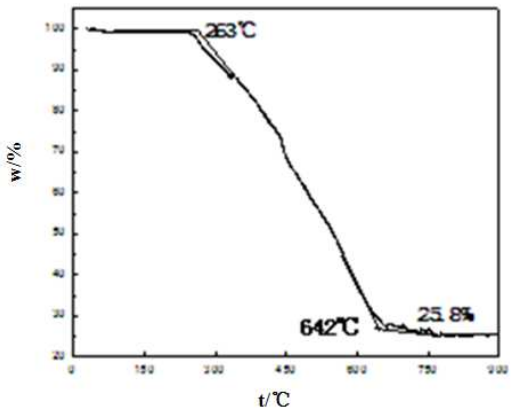
(a) TG Analysis of Raw Material K30



（b） TG Analysis of Raw Material Ni(acac)2



（c） Precursor Fiber without Pore-forming agent



（d） TG Analysis of Precursor Fiber with K30/Ni(acac)2

Fig.4 The TG test of Raw Material and PAN Precursor Fiber

Static Benzene Adsorption of Carbon Fibers

TABLE 3 THE VALUES OF STATIC BENZENE ADSORPTION

NO.	S0	S1	S2	S3
Value of static benzene adsorption [%]	0.15	8.5	13.6	29.8

Table 3 showed the values of static benzene adsorption increased by adding K30/ Ni(acac)2. It indicated that K30/Ni(acac)2 played the role of pore-forming agent which influenced the pore size distribution.

Conclusions

(1) The best condition of spinning was achieved with the concentration of K30 and Ni(acac)2 of 5% and the mass ratio of K30/Ni(acac)2 to PAN of 7:3.

(2) The spinning solutions exhibited appreciable shear thinning behaviors in a high rate range with the dosage of PAN increased.

(3) The morphology of K30/ Ni(acac)2 /fiber was smooth and round ,which would be appropriate for following carbonization and activation and the fiber precursor had excellent properties.

(4) The value of static benzene adsorption greatly increased by adding pore-forming agent.

References

[1] Zhang S J; Yu H Q; Feng H M. PVA–based Activated Carbon Fibers with Lotus Root-like Axially Porous Structure[J]. *Carbon*, 2006, 44:2059-2068

[2] Feng H M; Zhang S J; Chen Y Z, et al. Fabrication and Evaluation of Mesporous Poly (vinyl alcohol) -based Activated Carbon Fibers[J]. *Ind. Eng. Chem. Res*，2009, 48:3398-3402

[3] Yuan R S; Guan R B; Zheng J T. Effect of the Pore Size of TiO_2 –Loaded Activated Carbon Fiber on its Photocatalytic Activity[J]. *Scr.Mater*, 2005, 52: 1329-1335

[4] XU B, WU F, CHEN R J, et al. Mesoporous activated carbon fiber as electrode material for high-performance electrochemical double layer capacitors with ionic liquid electrolyte[J]. Journal of Power Sources, 2010, 195(2): 2118–2124.

[5] Chen D S; Gan Y J. The preparation of Activated carbon fiber (ACF) and its recent progress[J]. *Journal of Jilin college of engineering*,1996,6(4):76-77.(in chinese)

[6] Zhang Z H; Sun R J; Ma H F. Preparation and Characterization of Modified Collagen/PAN Blending Fibers[J]. *Fibers and Polymers*, 2008,9(5):551-555

[7] Zhang S J; Feng H M; Wang J P, et al. Structure Evolution and Optimization in the Fabrication of PVA-based Activated Carbon Fibers[J]. *Journal of Colloid and Interface Science*, 2008,321:96-102

[8] Zhu X J; Wang X; Chen X; et al. Rhelogy of Poly (acrylonitrile–co- acrylamide) / 1-buty1-3-methylimidazolium chloride Solution with Various Molecular Weights[C]. Proceedings of 2011 International Conference on Advanced Fibers and Polymer Material, Shanghai, 2011:120-122.

[9] Li L; Wang B; Wen Z W. Rheological Behavior of Polybenzimidazole /[Bmim]Cl Solutions. Proceedings of 2011 International Conference on Advanced Fibers and Polymer Material, Shanghai, 2011:50-52

[10] Xin C; David P K; Frita V. Rheological Characterization of Nephila Spidroin Solution[J]. Biomacromolecules, 2002,3(4):644-648

[11] Shilton S J ; Bell G. The Rheology of Fiber Spinning and the Properties of Hollow Fiber Membranes for Gas Separation[J]. Polymer,1994,35(24):5327-5335

[12] James L W. Dynamics of Ziscoelsatic Fluids, Melt Fracture, and the Rheology of Fiber Spinning[J]. Journal of Applied Polymer Science, 2003,8(5):2339-2357

[13] Larson R G. The Structure and Rheology of Comples Fluids[M]. Oxford University Press, New York,1999:425-456

Advanced Materials Research Vol. 936 (2014) pp 911-914
© (2014) Trans Tech Publications, Switzerland
doi:10.4028/www.scientific.net/AMR.936.911

Morphology and Conductivity of Self-Assembled Pyrene-Perylenetetracarboxylic diimide Dyad

Yan Shi , Xiyou Li[a]

Key Laboratory of Colloid and Interface Chemistry, Ministry of Education, Department of Chemistry, Shandong University, Jinan, 250100, China

[a]xiyouli@sdu.edu.cn

Keywords: Perylenetetracarboxy diimides, Self-assembly, Morphology, Conductivity

Abstract. One perylenetetracarboxylic diimide (PDI) derivatives (**PDI 1**) linked with pyrene by flexible chain at the bay positions was synthesized and the molecular structure was characterized by ^{1}H NMR, MALDI-TOF mass spectra as well as elemental analysis. The molecular self-assembly were prepared from solution via a slow evaporation of solvent. The properties of these molecular aggregates were studied by electronic absorption and fluorescence spectra. The morphologies and structures were examined by scanning electronic microscopy (SEM) and X-ray diffraction (XRD) techniques. The conducting properties were evaluated by current–voltage (I–V) measurements. The results revealed highly ordered structure for these molecular self-assembly. The thin solid film fabricated from these molecular self-assembly show an electric conductivity as high as 4.85×10^{-4} S cm^{-1} under the ambient light, which means this compound might be used as a semiconductor in nano-electronics.

Introduction

Perylenetetracarboxylic diimide derivatives (PDIs), as an important functional dye with outstanding photo and chemical stability as well as interesting photophysical and photochemical properties, have been intensively studied for several decades [1]. Because of their great potential application as organic semiconductors in different molecular electronic devices, the fabrication of ordered nanostructures of this functional molecular material has become an attracting research area recently [2]. Studies have revealed that the self-assemble process of PDI molecules is dominated by π–π interactions between the conjugated perylene rings [3]. Increase the molecular interaction by introducing different side groups is proved to be an efficient way to achieve an ordered structure with novel electronic or photophysical properties [4].

Pyrene is a well known fluorescent molecule, which has been widely used as fluorescent sensors or as organic semiconductors in solar cell. A recent review has described the recent progress of the pyrene based organic electronic materials [5]. Pyrene is proved to be an electron or energy donor when it is connected with PDI [6]. More importantly, pyrene has very strong π-π interactions and form self-assembly easily in solution. Therefore, it is expected that connection of pyrene with PDI might lead to a new molecule with novel self-assemble and physical properties.

In this letter, we report a new PDI molecule, which linked with a pyrene group by a flexible linkage at the bay position, **PDI 1** (Fig. 1). Introduction of pyrene, which can be an electron or energy donor, can bring some new photophysical process for this molecule. More importantly, the strong π-π interactions between the pyrene units can tune the self-assemble process of PDI, which may lead to a new nanostructure for the self-assembly of this compound.

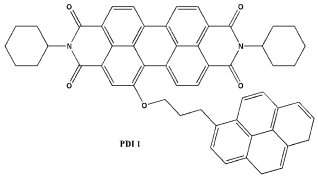


Fig. 1 The molecular structure of **PDI 1**

Results and Discussion

Electronic Absorption and Fluorescence Spectra. The absorption spectra of **PDI 1** in $CHCl_3$ solution and the aggregates on the SiO_2 surface by using solution-based quasi-Langmuir-Shäfer (QLS) [7] are shown in Fig. 2A. In chloroform, the absorption at about 553 and 519 nm can be attributed to the 0-0 and 0-1 vibronic band of the $S_0 - S_1$ transition, respectively, while the observed absorption band around 407 nm is attributed to the electronic S_0-S_2 transition [8]. The absorptions peaks at 345 and 328 can be attributed to the absorption of pyrene. In the QLS aggregates, an enhanced 0-1 vibronic band at 524 nm is observed. Such a spectral change implies strong molecular stacking between the PDI skeletons and the formation of face-to-face stacked structure (H-aggregate) [9]. Beside the changes on the absorption spectrum of PDI part, the absorption of pyrene part at about 350 nm red-shifted for about 6 nm in the solid film compared with that in solution, which means that the pyrenes are also interacted with each other in the solid films. Consistent with the absorption measurement, the emission spectrum of the aggregates of **PDI 1**, as shown in Fig. 2B, shows one new emission band at approximately 707 nm, which should be attributed to emission from the excimer-like states of the molecular aggregates formed by the co-facial arranged adjacent **PDI 1** molecules [10].

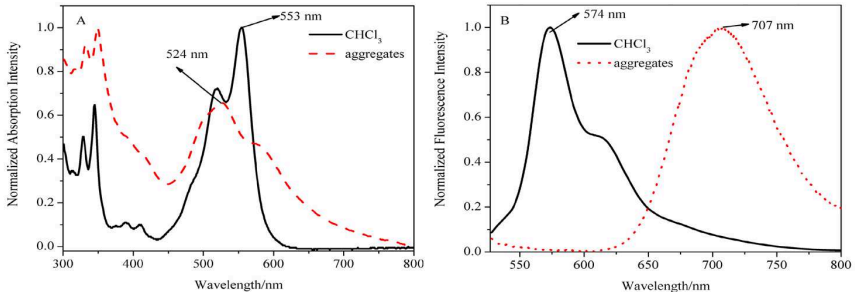


Fig. 2 Normalized electronic absorption (A) and fluorescence emission (B) spectra of **PDI 1**. The excited wavelength was 500 nm.

X-ray diffraction patterns of the aggregates. The internal structure of self-assembled nanostructures of this compound was investigated by XRD analysis. As shown in Fig. 3, in the low angle range, the XRD diagram shows one clear diffraction peak at $2\theta = 4.54°$(1.95 nm), which is close to the length of molecule (2.0 nm) read from the minimized molecular structure. This results suggest that the molecules in the aggregates take an edge-on configuration with the long axis of the molecule perpendicular to the surface of the substrate. Due to the direction of the face-to-face stacking parallel to the surface of the substrate, the in plane charge moving in this solid film should be favorable [11]. In the wide angle region, the XRD pattern presents additional diffraction at 0.31 nm, which can be attributed to the π–π stacking distance of PDI rings between the adjacent molecules [12]. This is in line with the conclusion resulted from the electronic absorption spectroscopic properties as detailed above.

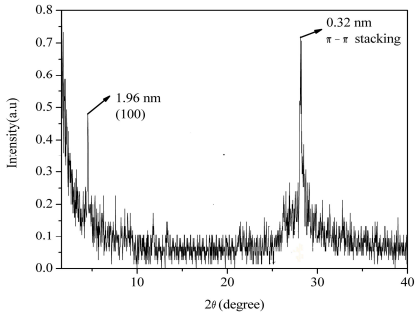


Fig. 3 X-ray diffraction patterns of the nanostructures of **PDI 1** by QLS method.

Morphology of the Aggregates. The morphology of the aggregates formed was examined by scanning electron microscopy (SEM). Fig. 4 displays SEM images of the molecular aggregates. **PDI 1** assembled into nanostructures with belt-like morphology with uniform size. The nanobelts were

over 50 μm in length with average width of ca. 230 nm, leading to an aspect ratio (length over thickness) of 200. This one dimensional structure is favorable for the device application in photovoltaics and field effect transistors [13]. It is worth noting that the size- as well as morphology-adjustable nanomaterials are highly desired for fabricating nanoscale molecular (opto) electronic devices which often require a wide variety of channel dimensions to achieve the optimum gate or optical modulation.

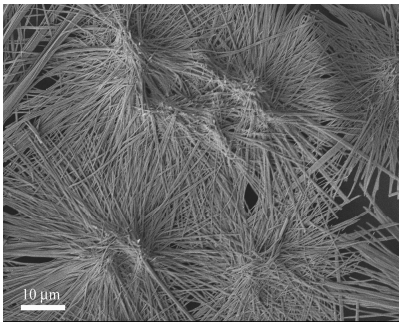


Fig. 4 SEM images of the nanobelts of **PDI 1** fabricated by QLS method.

I–V properties. The uniform aggregates of **PDI 1** with well-defined nanostructures would be promising candidates for applications in electronic devices. To demonstrate the potentials of these nanostructures, the molecular aggregates of **PDI 1** prepared by QLS method was suspended into methanol and carefully dropped onto glass substrates with ITO IDEs. After complete evaporation of the solvents, densely packed nanostructural films remained and adhere to ITO IDEs/glass substrate tightly. The electron conductivity measurement was then performed for this film. Fig. 5 shows the current-voltage (I-V) characteristics of nanobelts of **PDI 1**. According to the equation reported in the literatures [7], the electronic conductivity is calculated to be around 4.85 × 10^{-4} S cm^{-1} for the nanobelts of **PDI 1** under the ambient light, whereas the same device in dark shows an electronic conductivity of 1.31× 10^{-6} S cm^{-1}. The electronic conductivity on/off ratio is ca. 3×10^{2}, which is expected to be much larger if higher power irradiation and/or longer electrode pairs were employed for the photocurrent measurement [14]. This unexpected good conductivity of the nanobelts of **PDI 1** might be attributed to both readily π-stacks with adjacent planar molecules and higher-ordered crystalline molecular arrangement [15]. When the perylene cores of **PDI 1** are organized in one-dimensional and stack into nanobelts, they may show favorable charge transport. The interactions between the π systems of pyrene as revealed by the absorption spectra might also benefit the charge transport. These aggregates with highly current modulation could be useful for a wide range of electronic and sensor devices. The efforts to explore such opportunities are underway.

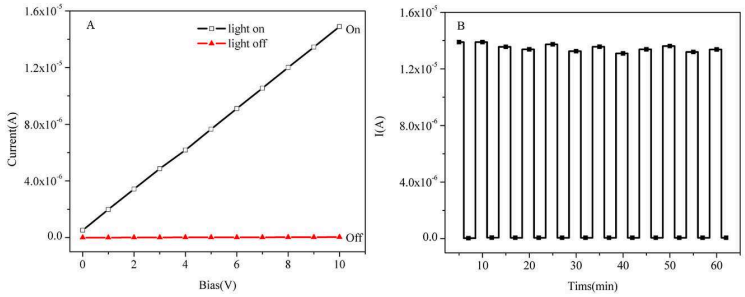


Fig. 5 (A) I-V curves measured on nanobelts from **PDI 1** under ambient light(□) and in the dark(▲). (B) photocurrent (at 10 V) in response to turning on and off the irradiation (white light).

Summary

Aggregates of **PDI 1**with ordered nanobelt structure was controllably prepared by QLS method. The I-V experimental results revealed good semiconductivity for this material and suggest that this PDI molecules might serve as a functional material for nano-electronics. It will be valuable for the design and preparation of PDI-based nano-electronic and nano-optoelectronic devices.

References

[1] X. Li, L.E. Sinks, B. Rybtchinski, M.R. Wasielewski, Ultrafast Aggregate-to-Aggregate Energy Transfer within Self-assembled Light-Harvesting Columns of Zinc Phthalocyanine Tetrakis(Perylenediimide) J. Am. Chem. Soc. 126 (2004) 10810-10811.

[2] Y. Chen, L. Chen, G. Qi, H. Wu, Y. Zhang, L. Xue, P. Zhu, P. Ma, X. Li, Self-Assembled Organic−Inorganic Hybrid Nanocomposite of a Perylenetetracarboxylic Diimide Derivative and CdS, Langmuir 26 (2010) 12473-12478.

[3] L.E. Sinks, B. Rybtchinski, M. Iimura, B.A. Jones, A.J. Goshe, X. Zuo, D.M. Tiede, X. Li, M.R. Wasielewski, Self-Assembly of Photofunctional Cylindrical Nanostructures Based on Perylene-3,4:9,10-bis(dicarboximide), Chem. Mater. 17 (2005) 6295-6303.

[4] L. Xue, H. Wu, Y, Shi, H. Liu, Y. Chen, Xi. Li, Supramolecular Organogels Based on Perylenetetracarboylic Diimide Dimer or Hexamer, Soft. Matt. 7 (2011) 6213-6221.

[5] T. M. Figueira-Duarte, K. Müllen, Pyrene-Based Materials for Organic Electronics, Chem. Rev. 111 (2011) 7260-7314.

[6] B. K. Kaletas, R. Dobrawa, A. Sautter, F. Würthner, M. Zimine, L. De Cola, W. René M, Photoinduced Electron and Energy Transfer Processes in a Bichromophoric Pyrene-Perylene Bisimide System,J. Phys. Chem. A 108 (2004) 1900-1909.

[7] Y. Chen, M. Bouvet, T. Sizun, Y. Gao, C. Plassard, E. Lesniewska, J. Jiang, Facile approaches to build ordered amphiphilic tris(phthalocyaninato) europium triple-decker complex thin films and their comparative performances in ozone sensing, Phys. Chem. Chem. Phys. 12 (2010) 12851-12861.

[8] Y. Chen, Y. Feng, J. Gao, M. Bouvet, Self-assembled aggregates of amphiphilic perylene diimide–based semiconductor molecules: Effect of morphology on conductivity J. Colloid Interface Sci. 368 (2012) 387–394.

[9] S. Vajiravelu, L. Ramunas, G.J. Vidas, G. Valentas, J. Vygintas, S. Valiyaveettil, Effect of substituents on the transport properties of bay substituted perylene diimide derivatives, J. Mater. Chem. 19 (2009) 4268-4275.

[10] F. Würthner, C. Thalacker, S. Diele, C. Tschierske, Fluorescent J-type Aggregates and Thermotropic Columnar Mesophases of Perylene Bisimide Dyes, Chem. Eur. J. 7 (2001) 2245-2253.

[11] D. Schlettwein, H. Graaf, J.-P. Meyer, T. Oekermann, N.I. Jaeger, Molecular Interactions in Thin Films of Hexadecafluorophthalocyaninatozinc (F16PcZn) as Compared to Islands of N,N'-Dimethylperylene-3,4,9,10-biscarboximide (MePTCDI) J. Phys. Chem. B 103 (1999) 3078-3086.

[12] Z. Chen, V. Stepanenko, V. Dehm, P. Prins, L. D. A. Siebbeles, J. Seibt, P. Marquetand, V. Engel, F. Würthner, Photoluminescence and Conductivity of Self-Assembled π–π Stacks of Perylene Bisimide Dyes, Chem. Eur. J. 13 (2007) 436-439.

[13] A. Babel, S.A. Jenekhe, High Electron Mobility in Ladder Polymer Field-Effect Transistors, J. Am. Chem. Soc. 125 (2003) 13656-13657.

[14] Y. Che, X. Yang, G. Liu, C. Yu, H. Ji, J. Zuo, J. Zhao, L. Zang, Ultrathin n-Type Organic Nanoribbons with High Photoconductivity and Application in Optoelectronic Vapor Sensing of Explosives, J. Am. Chem. Soc. 132 (2010) 5743-5750.

[15] Z. Wang, C.J. Medforth, J.A. Shelnutt, Porphyrin Nanotubes by Ionic Self-Assembly, J. Am. Chem. Soc. 126 (2004) 15954-14955.

Advanced Materials Research Vol. 936 (2014) pp 915-918
© (2014) Trans Tech Publications, Switzerland
doi:10.4028/www.scientific.net/AMR.936.915

Synthesis, structure and characterization of a novel 3D zinc organophosphonate

LI Hui-duan [1, a *]

[1] Department of Chemistry and Life Science, Chuxiong Normal University, Chuxiong 675000, PR China

[a]email: lhd08@cxtc.edu.cn

Keywords: [piperazine-1,4-diyldi(methylene)]bis(phosphonic acid); zinc organophosphonate; Solvothermal synthesis.

Abstract. A novel zinc organophosphonate was synthesized under solvothermal conditions by using [piperazine-1,4-diyldi(methylene)]bis(phosphonic acid) as a organic ligand. Single-crystal X-ray diffraction analysis reveals that compound 1 crystallized in the triclinic space group P-1 (No. 2). Compound 1 formulated as $Zn(O_3PCH_2NHC_4H_8NHCH_2PO_3)\cdot H_2O$. Compound 1 featured a 3D open-framework. Notably, the structure of compound 1 featured one-dimensional channel in the [001] direction. Water molecules were located in these channels. Further characterizations of compound 1 have been performed, including X-ray powder diffraction, IR, ICP and CHN analyses.

Introduction

In the past two decades, hybrid organic - inorganic porous materials exhibiting open architectures have been widely investigated for their potential applications in gas adsorption, asymmetric catalysis, ion exchange and proton conduction [1-5]. Organic phosphonic acid have been extensively studied as primary building blocks to synthesize hybrid metal phosphonate for their strongly coordinated ability , diverse coordination modes and high thermal stability [6-10] . [piperazine-1,4-diyldi(methylene)]bis(phosphonic acid), formulated as $H_2O_3PCH_2NC_4H_8NCH_2PO_3H_2$, was explored to construct novel metal phosphonate complexes in the literature[11-18]. Here, A novel zinc organophosphonate, $Zn(O_3PCH_2NHC_4H_8NHCH_2PO_3)\cdot H_2O$ (**1**), was synthesized under solvothermal conditions by using [piperazine-1,4-diyldi(methylene)]bis(phosphonic acid) as a organic ligand. Synthesis, structure and characterization of **1** were reported in this paper.

Experiment

Synthesis

Compound **1** was synthesized under solvothermal conditions: 30 mg $ZnNO_3\cdot 6H_2O$, and 54 mg $H_2O_3PCH_2NC_4H_8NCH_2PO_3H_2$ were dispersed into a mixture of 5 mL H_2O and 5 mL DMFwith stirring. Then, 10 mg of 2, 2′-bipy was added. After stirring for 30 min, the mixture was transferred into a sealed Teflon-lined steel autoclave and heated at 180^{o}C for 5 days. Colorless block-like crystals of **1** were collected and air-dried at room temperature (67% yield based on zinc).

Determination of Crystal Structure

Suitable single crystal of **1** (0.23 × 0.19 × 0.16 mm^3) was selected for single-crystal X-ray diffraction analyses. The data was collected on a Rigaku RAXIS-RAPID IP diffractometer (λ(Mo-Kα) = 0.71073Å). A total of 5872 reflections with 2680 unique reflections (R_{int} = 0.0461) were collected. Data processing was accomplished with the Process-auto processing program. The structure was solved by direct methods and refined by full-matrix least-squares on F^2 using SHELXTL-97 software package. First, the Zn and P atoms were located, followed by location of O, N and C atoms. The hydrogen atoms from guest molecules and organic phosphonic acid were placed geometrically. All the non-hydrogen atoms were refined anisotropically for the final refinement. Detailed crystallographic data for **1** was presented in Table 1.

Table 1 Crystal data and structure refinement for compound 1

Empirical formula	$C_6H_{16}N_2O_7P_2Zn$
Formula weight	355.52
Temperature (K)	293(2)
Wavelength (Å)	0.71073
Crystal system	Triclinic
Space group	*P*-1
a (Å)	8.3287(17)
b (Å)	8.9106(18)
c (Å)	8.9825(18)
α(°)	64.27(3)
β (°)	86.00(3)
γ(°)	78.90(3)
Volume ($Å^3$)	589.2(2)
Z	2
Dcalc (mg m^{-3})	2.004
Absorption coefficient (mm^{-1})	2.385
F(000)	364
Crystal size (mm)	0.23 × 0.19 × 0.16
θ range (°)	3.25 - 27.44
Limiting indices	-10≤h≤10, -11≤k≤11, -11≤l≤11
Reflections collected	5872 / 2680
Reflections unique	2680 [R(int) = 0.0461]
Completeness to θ = 24.98	99.0 %
Refinement method	Full-matrix least-squares on F^2
Data / restraints / parameters	2680 / 3 / 175
Goodness-of-fit on F^2	1.044
Final R indices [I>2σ(I)][a,b]	R_1 = 0.0448，wR_2 = 0.0860
R indices (all data)[a,b]	R_1 = 0.0578, wR_2 = 0.0917
Largest diff. peak and hole	0.620 and -0.607 e $Å^{-3}$

[a] $R_1=\sum||F_o|-|F_c||/\sum|F_o|$. [b] $wR_2=[\sum[w(F_o^2-F_c^2)^2]/\sum[w(F_o^2)^2]]^{1/2}$.

Results and Discussion

Description of Crystal Structure for 1

Single-crystal X-ray diffraction analyses reveals that **1** crystallizes in the triclinic space group *P*-1 (No. 2), formulated as $Zn(O_3PCH_2NHC_4H_8NHCH_2PO_3)\cdot H_2O$. As shown in figure 1a, each asymmetric unit contains one crystallographically independent Zn atoms, one crystallographically independent organic phosphonic acid and one guest water molecule. Zn (1) atom was tetrahedrally coordinated, which was coordinated with four different organic ligands through O(1), O(3), O(4) and O(6) atoms. The average bond lengths of Zn (1)-O were in the range of 1.920(3)–1.956(3) Å. All bond lengths and angles in the crystal structure of **1** were similar to those reported in the literature[11-18].

In the structure of **1**, the organic phosphonic acid adopted two similar coordinated environments. one chelated with two Zn (1) atoms through O(1) and O(3), resulting a 8-rings described as P(1) – O(1) – Zn (1) – O(3) – P(1) – O(1) – Zn (1) – O(3); another one chelated with two Zn (1) atoms through O(2) and O(4), resulting a 8-rings described as P(2) – O(4) – Zn (1) – O(6) – P(2) – O(4) – Zn (1) – O(6). The 8-rings interconnect each other base on vertex-sharing resulting in 1D chain (figure 1b). These 1D chains were further constructed into the open architectures of **1** by piperazine from the organic ligand. Guest water molecules were deposited in the 1D channels in the [001] direction (figure 1c).

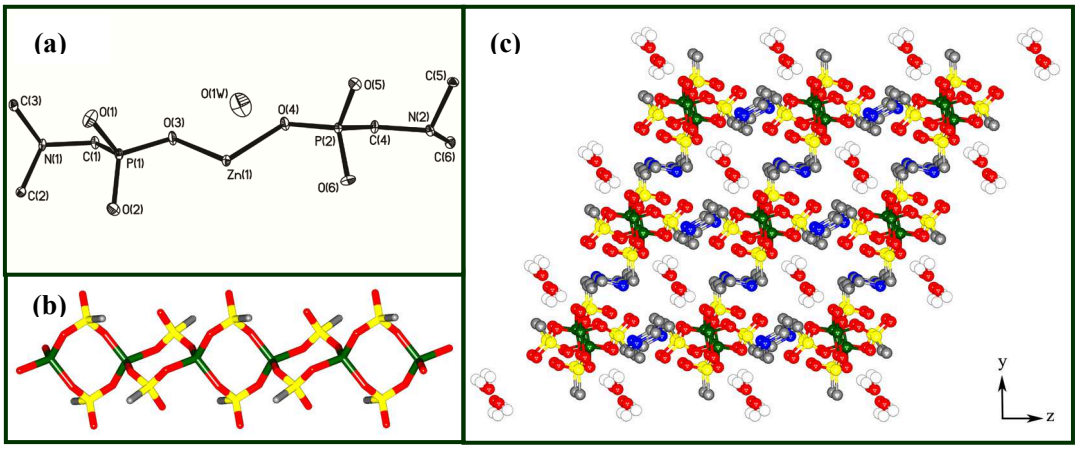


Figure 1 (a) ORTEP view of the asymmetric unit of 1; (b) 1D chain in the structure 1; (c) open architectures of 1 with water molecules deposited in the channels.

Characterization for Compound 1

The purity of **1** was confirmed by comparison of the experimental PXRD pattern to the calculated ones based on single-crystal structure (as shown in figure 2). The result of elemental analysis for **1** was consistent well with the theoretical values. Analysis found (%): Zn, 40.12; P, 17.64; C, 20.24; H, 4.20; N 7.62. Calcd. (%): Zn, 40.40; P, 17.42; C, 20.27; H, 4.54; N 7.88.

IR spectrum for **1** was shown in figure 2, The bands of 3026, 3025 and 2895 cm^{-1} were associated with stretching vibrations of O-H, N-H and C-H groups. The multi-fold bands in the region of 1600-1300cm^{-1} were ascribed to bending vibrations of O-H, N-H and C-H groups. The stretching and bending vibration absorption peaks for CPO_3, N–C and C–C were featured in the region of 1200-900 cm^{-1} and 600–400 cm^{-1}, respectively.

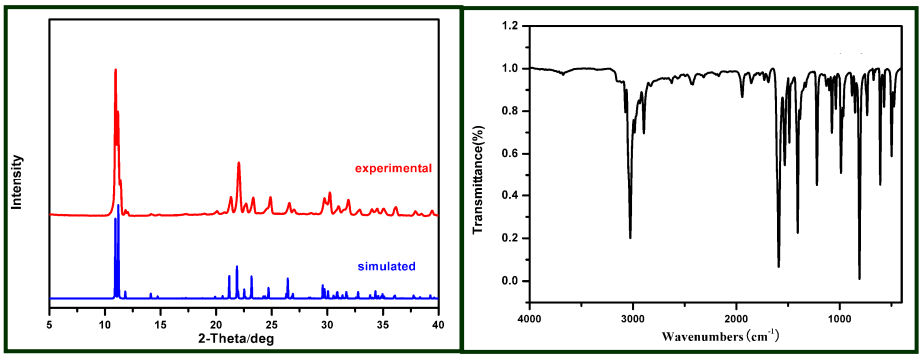


Figure 2 Simulated and experimental PXRD patterns for 1(left) ; IR spectrum for 1(right)

Conclusion

In conclusion, a novel zinc organophosphonate exibiting open architectures was synthesized under solvothermal conditions by using [piperazine-1,4-diyldi(methylene)]bis(phosphonic acid) as a organic ligand. The coordination of organic phosphonic acid with zinc resulted the assembly of 3D structure for **1**. The guests water molecules were deposited in these 1D channels. Further investigations on assembly novel metal organophosphonate and potential applications for these materials are underway.

Acknowledgements

The authors acknowledge the financial support of the Natural Science Foundation of Yunnan province (Grant No. 2012FD050) and the State Key Laboratory of Inorganic Synthesis and Preparative Chemistry of Jilin University.

References

[1] YAGHI O M, O'KEEFFE M, OCKWIG N W. Reticular synthesis and the design of new materials[J]. 2003, 423: 705-714.

[2] FÉREY G, MELLOT-DRAZNIEKS C, SERRE C, et al. Crystallized Frameworks with Giant Pores: Are There Limits to the Possible? [J]. Acc. Chem. Res., 2005, 38(4): 217–225.

[3] FÉREY, G. Hybrid porous solids: past, present, future [J]. Chem. Soc. Rev., 2008, 37, 191–214.

[4] YOON M, SRIRAMBALAJI R, KIM K, Homochiral metal-organic frameworks for asymmetric heterogeneous catalysis[J]. Chem. Rev., 2012, 112: 1196–1231.

[5] ADHIKARY C, KONER S, Structural and magnetic studies on copper(II) azido complexes[J]. Coord. Chem. Rev., 2010, 254: 2933–2958.

[6] NGO H-L, LIN Wen-Bin. Chiral crown ether pillared lamellar lanthanide phosphonates[J]. J Am. Chem. Soc., 2002, 124(48): 14298-14299.

[7] Mao Jiang-Gao. Structures and luminescent properties of lanthanide phosphonates[J]. Coord. Chem. Rev., 2007, 251: 1493-1520.

[8] SONNAUER A, NÄTHER C, HÖPPE H A, et al. Systematic Investigation of Lanthanide Phosphonatoethanesulfonate Framework Structures by High-Throughput Methods, $Ln(O_3P{-}C_2H_4{-}SO_3)(H_2O)$ (Ln = La−Dy) [J]. Inorg. Chem., 2007, 46(23): 9968−9974.

[9] HUANG Y-L, HUANG M-Y, CHAN T-H, et al. Synthesis, Structural Characterization, and Luminescence Properties of Lanthanide Oxalatophosphonates: $Na[M_3(H_2O)_4(C_2O_4)_4(CH_3PO_3)]\cdot 2H_2O$ (M = Nd and Pr) [J]. Chem. Mater., 2007, 19: 3232–3237.

[10] LIU Xun-Gao, ZHOU Kai, DONG Jia, et al. Homochiral Lanthanide Phosphonates with Brick-Wall-Shaped Layer Structures Showing Chiroptical and Catalytical Properties [J]. Inorg. Chem., 2009, 48(5): 1901–1905.

[11] DU Zi-Yi, XU Hai-Bing, MAO Jiang-Gao. Rational Design of 0D, 1D, and 3D Open Frameworks Based on Tetranuclear Lanthanide(III) Sulfonate−Phosphonate Clusters[J]. Inorg. Chem., 2006, 45: 9780–9788.

[12] DU Zi-Yi, XIE Yong-Rong, WEN He-Rui. Novel open-framework architecture in strontium(II) phosphonate[J]. Inorg. Chimi. Acta., 2009, 362: 351–354.

[13] MILLER S R, PEARCE G M, WRIGHT P A, et al. Structural Transformations and Adsorption of Fuel-Related Gases of a Structurally Responsive Nickel Phosphonate Metal-Organic Framework, Ni-STA-12[J]. J. Am. Chem. Soc., 2008, 130: 15967–15981.

[14] GROVES J A, WRIGHT P A, LIGHTFOOT P, Two Closely Related Lanthanum Phosphonate Frameworks Formed by Anion-Directed Linking of Inorganic Chains[J]. Inorg. Chem., 2005, 44: 1736–1739.

[15] GROVES J A, STEPHENS N F, WRIGHT P A, et al. Novel open-framework architectures in lanthanide phosphonates [J]. Solid State Sci., 2006, 8: 397–403.

[16] SERRE C, GROVES J A, LIGHTFOOT P, et al. Synthesis, Structure and Properties of Related Microporous *N*,*N*'-Piperazinebismethylenephosphonates of Aluminum and Titanium[J]. Chem. Mater., 2006, 18: 1451–1457.

[17] Groves J A, Wright P A, Lightfoot P. The pH-controlled hydrothermal synthesis and crystal structures of two zinc *N*, *N*'-piperazinebis(methylenephosphonate) frameworks[J]. Dalton Trans., 2005: 2007–2010

[18] GROVES J A, MILLER S R, WARRENDER S J, et al. The first route to large pore metal phosphonates [J]. Chem. Commun., 2006: 3305–3307.

Advanced Materials Research Vol. 936 (2014) pp 919-928
© (2014) Trans Tech Publications, Switzerland
doi:10.4028/www.scientific.net/AMR.936.919

Hydrothermal synthesis and characterization of hexagonal $Mg(OH)_2$ flame retardant with bischofite and NH_3

Xuexue Song[1,a], Lijuan Li[1,b,*], Zhiqi Liu[1]

[1]Qinghai Institute of Salt Lakes, Chinese Academy of Sciences, Xining, 810008, China

[a]songxuexue123@163.com, [b]lilj@isl.ac.cn, [*]correspondence author

Keywords: hydrothermal modification; flame retardant magnesium hydroxide; ammonia gas; high slurry concentration

Abstract: Regular hexagonal plates of magnesium hydroxide with high slurry concentration were prepared by hydrothermal reaction without any organic additive or catalyst using bischofite and ammonia as raw materials. The effects of hydrothermal temperature, stirring speed, hydrothermal duration, and dilution multiple on the preparation of $Mg(OH)_2$ flame retardant were investigated. Scanning electron microscopy, X-ray diffraction, and laser particle analysis were performed to characterize the product morphologies, structures, and size distributions. Results indicated that the growth direction of $Mg(OH)_2$ crystal changed, and the regular hexagonal plates of $Mg(OH)_2$ with uniform particle size and high dispersion characteristic formed after hydrothermal modification treatment. A mass fraction of 15.50% $Mg(OH)_2$ of magnesium hydroxide slurry was obtained by high-concentration (4.30mol/L) magnesium chloride and ammonia as the raw materials.

Introduction

Magnesium hydroxide (MH) is an important multifunctional material that has elicited scientific interest[1–3] and is widely used in flame retardants[4,5], wastewater treatment[6], flue gas desulfurization[7,8], medicines[9], etc. MH produces an environment-friendly flame retardant that simultaneously acts as a smoke suppressant, with no evolution of hazardous by-products[10,11]. Caustic soda method[12–14], lime cream method[15], and ammonia method[16,17] are the three important methods for preparation of MH. Among these three methods, the ammonia method for MH synthesis is used predominantly in industrial production. However, $Mg(OH)_2$ particles synthesized at room temperature are usually ready to aggregate with each other because of poor crystal formation and small particle size, which cause a lack of compatibility and reduce the mechanical properties of the corresponding composite. One of the effective approaches to improve the dispersion of $Mg(OH)_2$ is to recrystallize the particles at hydrothermal[18] conditions. The hydrothermal technique facilitates the processing of monodispersed and highly homogeneous particles and is defined as any heterogeneous reaction in the presence of aqueous solvents or mineralizers under high pressure and temperature conditions that dissolve and recrystallize materials that are relatively insoluble under ordinary conditions.

Jin et al.[19] obtained an $Mg(OH)_2$ product that exhibits a uniform lamella-like hexagonal structure with approximately 40 nm thickness after hydrothermal modification at 150 °C for 24 h. Henrist et al. [10] obtained larger, well-defined $Mg(OH)_2$ particles after hydrothermal treatment at 170 °C for 7 d. An overall enhancement of the crystallinity is clearly visible because the intensity of the diffraction peaks is remarkably increased in the curve from X-ray diffraction (XRD) patterns of the sample. Wu et al. [20] obtained dispersive $Mg(OH)_2$ particles with an average particle size of

approximately 0.3 μm-0.7 μm, an average agglomerate size of 1.2 μm, and Brunauer-Emmett-Teller surface area of 10.5 m^2/g after hydrothermal treatment in 1.0 g/L $CaCl_2$ aqueous solution at 200 °C for 4.0 h. Ji et al.[21] prepared a spherical crystalline MH that has a symmetrical and regular crystal morphology when the reaction temperature is 180 °C and the reaction time ranges from 4 h to 8 h, the MH and organic modifier solution concentrations were 5% and 4 mol/L, respectively. Yan et al.[22] obtained $Mg(OH)_2$ with mean size of 400 nm and a thickness of 60 nm after hydrothermal treatment at 150 °C for 6 h at pH 11 with Mg^{2+}/CTAB molar ratio of 80. Chen et al.[23] obtained 90 nm-130 nm thickness of the $Mg(OH)_2$ plates after hydrothermal modification at 200 °C for 6 h in solutions containing 4 mol/L KOH.

However, the MH slurry concentration synthesized is too low when aqueous ammonia, NaOH aqueous solution, and lime milk were used for precipitation. High MH slurry concentration can be prepared if NH_3 is chosen as precipitant because no water was channeled when the precipitant NH_3 was introduced into the reaction system. The optimum processing conditions through the direct precipitation method without any additives were obtained in the Pre-Work. In the present study, we performed hydrothermal modification and characterization of the synthesized MH slurry in the optimum processing conditions. The effects of hydrothermal temperature, stirring speed, hydrothermal duration, and dilution multiple were investigated for preparation of $Mg(OH)_2$ flame retardant.

Experimental

Materials

Bischofite ($MgCl_2$•$6H_2O$ 95.62%) was obtained from Qinghai Kunlun magnesium Co., LTD. Ammonia (NH_3 99.15%) was obtained from Qinghai LaoQian gas Co., LTD. All the chemical reagents used in this experiment were analytical grade.

Experimental Procedures

Ammonia was used as precipitating agent for MH preparation and bischofite, which is abundant in salt lakes, was used in the experiments as raw material. The detailed synthesis procedures will be described in the following section.

A solution with 4.30 mol/L concentration of bischofite was prepared and insoluble impurities were removed through filtration. Ammonia was then added to the prepared solution via a gas flowmeter working at a discharge rate of 320 ml/min whereas the suspension was maintained at 60 °C with constant stirring at 350 r/min. After the addition of the ammonia gas, the slurry was aged for 90 min at 60 °C and 350 r/min. The MH slurry was transferred into a teflon-lined high pressure reaction kettle. The high-pressure reaction kettle was then maintained at 100 °C-180 °C with stirring at 0 r/min-700 r/min for 0.5 h-4 h. After passively cooling down to 60 °C, the white powders were collected, filtered, and washed with deionized water. Finally, the samples were air-dried at 110 °C for 10 h.

Analysis And Characterization

The morphology of the particles was analyzed using a scanning electron microscope (JSM-5610LY, Japan). The crystalline form of the sample was characterized by XRD (X'PRO Pert, USA) using Cu Kα radiation (λ=0.154 nm) with an X-ray tube at 40 kV and 30 mA. XRD data were collected at room temperature over the 2θ range from 5° to 80° at a step size of 0.0167°/s. The particle size and distribution of the sample were measured with an ultrasonic particle size analyzer (BT-9300S, China).

Results and Discussion

Effect Of Hydrothermal Temperature

The particle size distribution patterns of the products of different hydrothermal temperatures are shown in Fig. 1. The hydrothermal modifications of MH were done at 100, 130, 160, and 180 °C with stirring at 500 r/min for 4 h. As shown in the particle size distribution pattern, particle size distribution changed after hydrothermal modification. The mean sizes of particles were 1.08, 1.24, 1.93, and 2.40 μm at 100, 130, 160, and 180 °C, respectively, and it was 1.38 μm before hydrothermal modification. Therefore, hydrothermal temperature had an important effect on particles size. Higher hydrothermal temperature results in bigger particles. Thus, the hydrothermal modification of $Mg(OH)_2$ may be performed via the dissolution-precipitation mechanism. The intergranular reunion and coupling of the normal temperature product were destroyed in the initial stage, the smaller particles were dissolved in hydrothermal media, and then deposited on the larger particle surface with a certain pattern because smaller particles have large specific surface area and high reactivity. High hydrothermal temperature results in faster dissolution-recrystallization process and bigger particles.

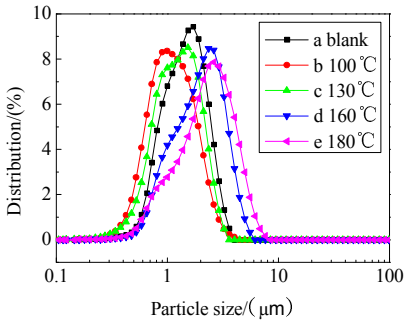


Fig. 1 Particle size distribution pattern of products of different hydrothermal temperatures, blank: without hydrothermal modification.

The XRD patterns of the products of different hydrothermal temperatures are shown in Fig.2. As shown in the XRD patterns, all diffraction peaks of each sample could be indexed as the hexagonal structure of MH with lattice constants comparable to the values of JCPDS 7-239. No XRD peaks arising from impurities were detected. Therefore, the synthesis phase corresponds to pure MH, which suggests a complete synthesis reaction. The intensity of each peak of the sample synthesized at room temperature is weak, and the peak strength of the (001) plane, a non-polar plane, was similar to that of the (101) plane, a polar plane. However, the intensity of each peak of the sample is stronger after hydrothermal treatment, and the strength of the (001) plane became remarkably stronger than that of the (101) plane. Thus, the $Mg(OH)_2$ powder is well-crystallized and the weakening of the polarity of $Mg(OH)_2$ after hydrothermal modification was favorable for the dispersion of $Mg(OH)_2$ particles. Further analysis of the XRD data in Fig. 2 indicated that the strength of the (001) plane increased with the increase in hydrothermal temperature, which results in the decrease in micro-strain, increase in the thickness, and improvement of the dispersion of $Mg(OH)_2$ particles with the increase in hydrothermal temperature.

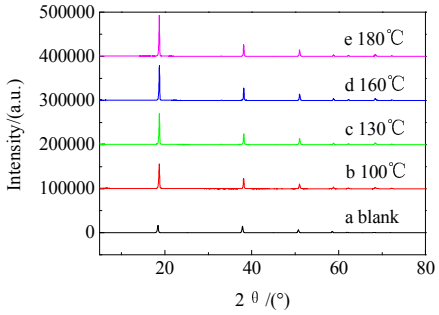
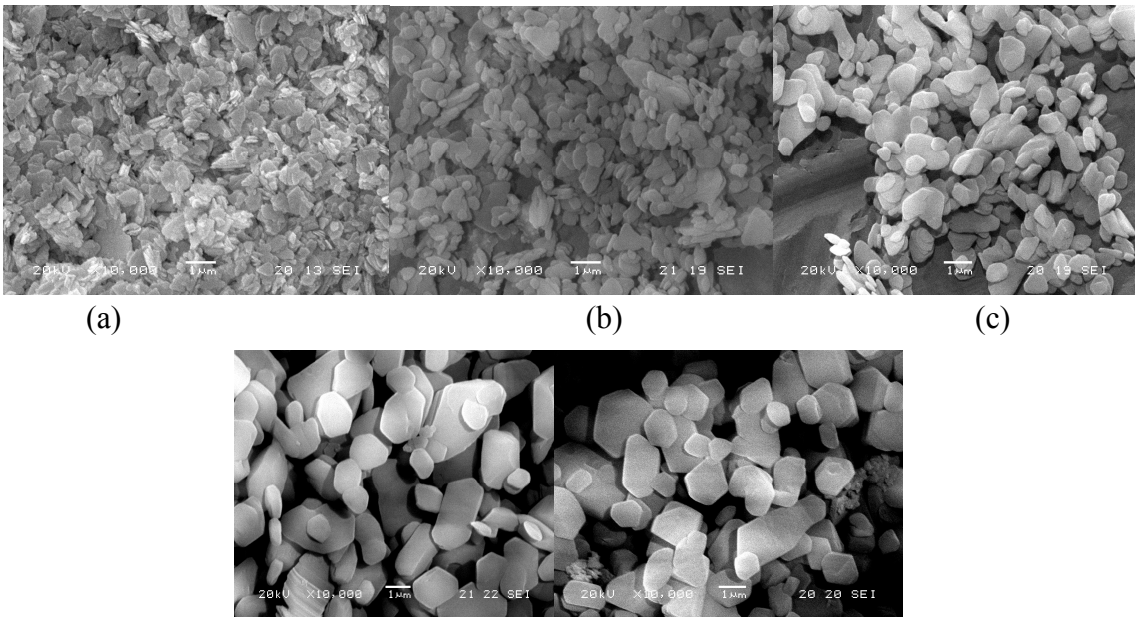


Fig. 2 XRD pattern of the products of different hydrothermal temperatures.

The morphologies of the products of different hydrothermal temperatures are shown in Fig. 3. The shape evolution process of particles at various temperatures was noted. Based on the morphology, self-aggregation of $Mg(OH)_2$ particles occurred and only minimal single $Mg(OH)_2$ particles with precipitates formed at room temperature because of their higher surface energy. By contrast, $Mg(OH)_2$ particles are modified after hydrothermal treatment; thus, the self-aggregation of the particles disappears and results in better dispersion. The gradual formation of the bigger plates and the disappearance of the smaller plates confirmed that the hydrothermal modification of $Mg(OH)_2$ may be performed via the dissolution-precipitation mechanism. The increase of temperature from 100°C to 180°C resulted in the formation of $Mg(OH)_2$ plates with bigger size, more regular hexagonal plates, increased thickness, and better dispersion. These results are consistent with the XRD and SEM data.



(a) (b) (c)

(d) (e)

Fig. 3 Morphologies of the products of different hydrothermal temperatures: (a) blank, (b) 100 °C, (c) 130°C, (d) 160 °C, (e) 180 °C.

Effect of Stirring Speed

The particle size distribution patterns of the products at different stirring speeds are shown in Fig. 4. Hydrothermal modification of MH was performed at 0, 300, 500, and 700 r/min at 160 °C for 4 h. The mean sizes of particles were 1.14, 1.93, 1.93, and 1.96 μm for the 0, 300, 500, and 700 r/min speeds, respectively. The particle size produced without stirring was smaller than the particles size produced with stirring. Thus, the diffusion velocity of the solute molecules is too slow without

stirring, which slows down the dissolution-recrystallization process, especially for the recrystallization process, because the diffusion of solute molecules has greater effect on recrystallization. The mean size of the particles increased minimally with increasing stirring speed, which could be because the solution viscosity decreases with rising temperature. The solution viscosity decreased by approximately two orders of magnitude at these high hydrothermal temperatures compared with room temperature. Therefore, the dielectric constant of the solution decreased considerably, diffusion coefficients increased considerably, and the apparent concentration decreased considerably, which usually lead to the minimal increase in dispersive effect of the solution with increasing stirring speed. All these factors could have contributed to the minimal increase in mean particle size with stirring speed.

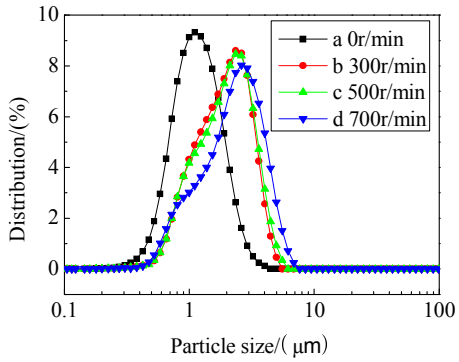


Fig. 4 Particle size distribution pattern of products of different stirring speeds.

The XRD patterns of the products at different stirring speeds are shown in Fig. 5. The intensity of each peak of the sample increased minimally with increasing stirring speed. However, when the stirring speed was increased up to 700 r/min, the strength of the (001) plane of the product was slightly less compared with the particles obtained with other stirring speeds. This result might be attributed to the spatter of the $Mg(OH)_2$ slurry under such high stirring speed. It is speculated that less strength of the (001) plane results in bigger and thinner particles under the same size distribution.

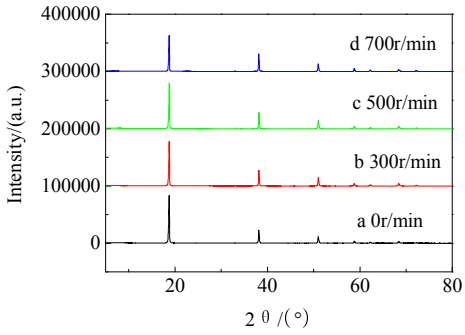
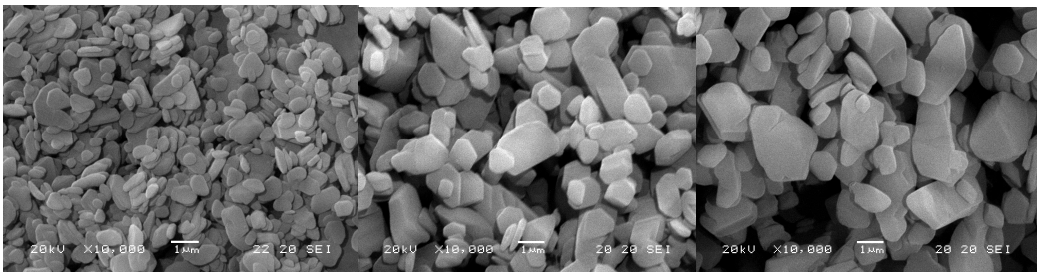


Fig. 5 XRD pattern of the products with different stirring speeds.

The morphologies of the products at different stirring speed are shown in Figs. 6 and 3d. These results are the same as the experimental results of SEM wherein the mean size of the particles produced without stirring is smaller than the particles size produced with stirring. The difference is that the product of hydrothermal modification at 700 r/min is bigger and thinner than at 300 and 500 r/min. This difference could be because the mean size of the equivalent volume sphere was

measured with laser diffusion on a suspension in water and the size and thickness were measured by image analysis on the basis of SEM micrographs taken on the dry powder. However, the XRD pattern of products reflects that hydrothermal modification at 700 r/min produced different results compared with the 300 and 500 r/min modifications.



(a) (b) (c)

Fig. 6 Morphologies of products of different stirring speeds: (a) 0 r/min, (b) 300 r/min, (c) 700 r/min.

Effect of Hydrothermal Duration

The particle size distribution patterns of the products of different hydrothermal durations are shown in Fig. 7. Modifications of hydrothermal durations of MH were performed at 0.5, 2, and 4 h at 160 °C and 500 r/min. The mean sizes of particles were 1.24, 1.36, and 1.93 μm, respectively. At 0.5h, the particle size distribution of the product was uneven and had two peaks; at 2 h, the product had small size and narrow size distribution; and at 4 h, the product had larger size. These results could be because of the requirement of sufficient time to finish processes. If sufficient time is allowed, intergranular reunion and coupling of the normal temperature product will be destroyed, smaller particles will be dissolved, and particles can grow to larger sizes. Thus, not enough time was allowed to form a better crystal, and the intergranular reunion and coupling still exist at 0.5 h. However, as the duration was extended to 2 h, destruction of the intergranular reunion and coupling has been basically completed and the smaller particles were dissolved, which allowed continuous growth of larger particles. Thus, the self-aggregation of particles disappears and the formation of $Mg(OH)_2$ plates is enhanced. In longer durations, the dissolution of smaller particles and growth of larger particles mainly occur; thus, particles size is increased.

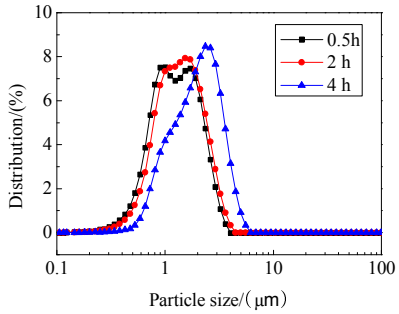


Fig. 7 Particle size distribution pattern of the products of different hydrothermal durations.

The XRD patterns of the products of different hydrothermal durations are shown in Fig. 8. Based on the XRD patterns, the strength of the (001) plane increased and the (101) plane decreased with increase in hydrothermal duration. This result leads to the decrease in micro-strain, increase in thickness, and improvement of the dispersion of $Mg(OH)_2$ particles accompanying the increase in hydrothermal duration.

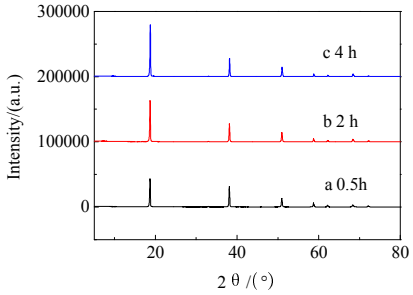
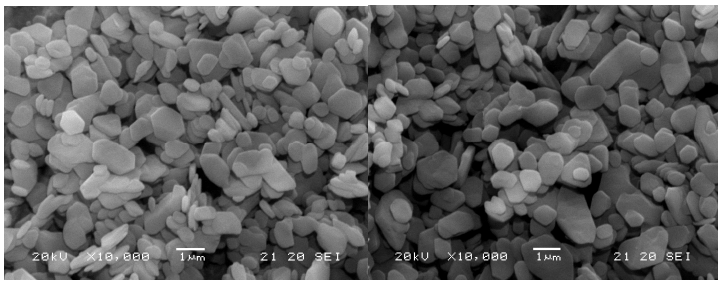


Fig. 8 XRD patterns of products of different hydrothermal durations.

The morphologies of the products with different hydrothermal durations are shown in Figs. 9 and 3d. As shown in the XRD patterns, particles are thin and the intergranular reunion and coupling still exist at 0.5 h. Moreover, the extent of time from 0.5 h to 4 h resulted in the formation of $Mg(OH)_2$ plates with bigger size, more regular shape, increased thickness, and better dispersion. This result is consistent with XRD and SEM data.



(a) (b)

Fig. 9 Morphologies of products of different hydrothermal durations: 0.5 h, (b) 2h.

Effect of Dilution Multiple

Results of different dilution multiples are summarized in Figs. 10, 11, 12 and 3d. The dilution multiple of the MH slurry was diluted five times (20% of original slurry), thrice (33.33% of original slurry), and once (100% of original slurry) at 160 °C and 500 r/min for 4 h. The mean sizes of the particles were 1.95, 1.98, and 1.93 μm, respectively. The intensity of each peak of the samples and the XRD patterns was minimally changed. Thus, the impact of dilution multiple on hydrothermal modification of MH is minimal. This minimal effect could be attributed to the drop in solution viscosity of approximately two orders of magnitude at these high hydrothermal temperatures compared with room temperature. This change favors electro-static interactions, lowers kinetic barriers, and accelerates the ripening processes. Therefore, the dispersive effect of the solution minimally increases with increase in dilution multiple.

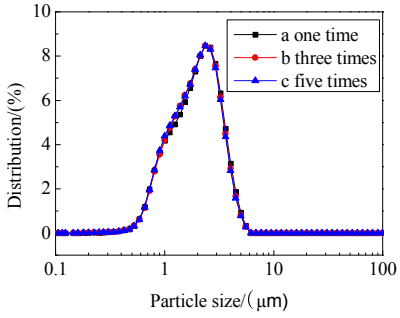


Fig. 10 Particle size distribution patterns of the products of different dilution multiples.

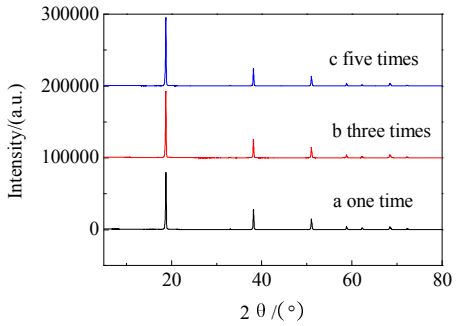
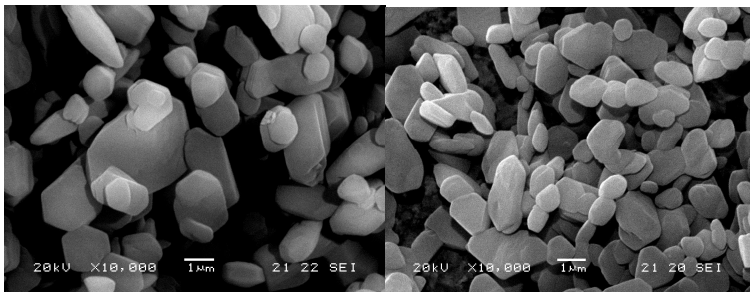


Fig. 11 XRD patterns of the products of different dilution multiples.



(a) (b)

Fig. 12 Morphologies of the products with different dilution multiples: (a) three times, (b) five times.

MH slurry concentrations were 15.50%, 5.12% and 2.71% when the slurry was diluted once, thrice, and five times, respectively. In this paper, a mass fraction of 15.50% $Mg(OH)_2$ in the MH slurry was obtained by high concentration (4.30 mol/L) magnesium chloride and ammonia as the raw materials. The concentration of magnesium chloride was high and did not attract water when the precipitant ammonia was introduced into the reaction system. Therefore, this study produces high yield with unit equipment.

Conclusions

In this study, uniform lamellar hexagonal structure MH at high slurry content was prepared using bischofite and ammonia as raw materials. The influences exerted by several hydrothermal modification parameters on the size distribution, structure, and morphology of MH particles precipitated were studied. The intensity of each peak of the sample was strong and the strength of the (001) plane became stronger than that of the (101) plane after hydrothermal treatment. Self-aggregation of the particles disappears, MH hexagonal structures form, and disperses better after hydrothermal treatment. Hydrothermal temperature exhibits important effects on size distribution, structure, and morphology of the particles. The increase in temperature resulted in the formation of $Mg(OH)_2$ plates with bigger size, more stable structure, more regular shape, increased thickness, and with better dispersion. Stirring speed also has some effect on MH crystals. Particles size produced without stirring is smaller than particles size produced with stirring. However, the minimal increase in MH crystal size with stirring speed as solution viscosity significantly decreases at these high hydrothermal temperatures compared with room temperature. Hydrothermal duration exhibits important effects on MH crystals. If hydrothermal duration was too short, the intergranular reunion and coupling still exist and the recrystallization process is not complete. With longer durations, $Mg(OH)_2$ plates formed with bigger size, more stable structure, more regular shape, increased thickness, and better dispersion. The effect of the dilution multiple of hydrothermal

modification on MH is small. In this paper, mass fraction of 15.50% $Mg(OH)_2$ of MH slurry is obtained by high concentration magnesium chloride of 4.30 mol/L and ammonia as raw materials. Therefore, this study demonstrated that bigger size, more stable structure, more regular shape, increased thickness, and better dispersion of the hexagonal structure of MH at high slurry content was obtained by hydrothermal modification.

Acknowledgements

This work was financially supported by the Funding Project of Qinghai Science and Technology Agency (2010-G-221A), Technology Innovation Project of CAS Graduate Science (2008-34) and Western Light (2011-1).

References

[1] M.J. Solomon, A.S. Almusallam, K.F. Seefeldt, A. Somwangthanaroj, P. Varadan, Rheology of polypropylene/clay hybrid materials, J. Macromolecules. 34 (2001) 1864-1872.

[2] J. Lv, L.Z. Qiu and B.J. Qu, Controlled synthesis of magnesium hydroxide nanoparticles with different morphological structures and related properties in flame retardant ethylene-vinyl acetate blends, J. Nanotechnology. 15 (2004) 1576-1581.

[3] Y.H. Hu and S.F. Li, The effects of magnesium hydroxide on flash pyrolysis of polystyrene, J. Journal of Analytical and Applied Pyrolysis. 78 (2007) 32-39.

[4] S.Y. Lu and I. Hamerton, Recent developments in the chemistry of halogen-free flame retardant polymers, J. Progress in Polymer Science. 27 (2002) 1661-1712.

[5] P.R. Hornsby and A. Mthupha, Rheological Characterization of Polypropylene Filled with Magnesium-Hydroxide, J. Journal of Materials Science. 29 (1994) 5293-5301.

[6] L.E. De-Bashan and Y. Bashan, Recent advances in removing phosphorus from wastewater and its future use as fertilizer (1997-2003) , J. Water Research. 38 (2004) 4222-4246.

[7] M.K. Mondal, Absorption equilibria of dilute sulphur dioxide in $Mg(OH)_2$ slurry, J. Fluid Phase Equilibria. 262 (2007) 111-120.

[8] M.V. Dagaonkar, A.A.C.M. Beenackers and V.G. Pangarkar, Absorption of sulfur dioxide into aqueous reactive slurries of calcium and magnesium hydroxide in a stirred cell, J. Chemical Engineering Science. 56 (2001) 1095-1101.

[9] J.C. Kang and S.P. Schwendeman, Comparison of the effects of $Mg(OH)_2$ and sucrose on the stability of bovine serum albumin encapsulated in injectable poly(D,L-lactide-co-glycolide) implants, J. Biomaterials. 23 (2002) 239-245.

[10] C. Henrist, J.P. Mathieu, C. Vogels, A. Rulmont, R. Cloots, Morphological study of magnesium hydroxide nanoparticles precipitated in dilute aqueous solution, J. Journal of Crystal Growth. 249 (2003) 321-330.

[11] R.N. Rothon and P.R. Hornsby, Flame retardant effects of magnesium hydroxide, J. Polymer Degradation and Stability. 54 (1996) 383-385.

[12] P. Jeevanandam, R.S. Mulukutla, Z. Yang, H. Kwen, K.J. Klabunde, Nanocrystals to nanorods: A precursor approach for the synthesis of magnesium hydroxide nanorods from magnesium oxychloride nanorods starting from nanocrystalline magnesium oxide, J. Chemistry of Materials. 19 (2007) 5395-5403.

[13] W.J. Jiang, X. Hua, Q.F. Han, X.J. Yang, L.D. Lu, X. Wang, Preparation of lamellar magnesium hydroxide nanoparticles via precipitation method, J. Powder Technology. 191 (2009) 227-230.

[14] L.Z. Qiu, R.C. Xie, P. Ding, B.J. Qu, Preparation and characterization of $Mg(OH)_2$ nanoparticles and flame-retardant property of its nanocomposites with EVA, J. Composite Structures. 62 (2003) 391-395.

[15] Y.Q. Zhang, X.C. Ye and L.J. Zhang, Preparation of magnesium hydroxide by improved brine-lime rout, J. Journal of Nanjing University of Technology (Natural Science Edition). 30 (2008) 54-58.

[16] X. Li, G.B. Ma, and Y.Y. Liu, Synthesis and Characterization of Magnesium Hydroxide Using a Bubbling Setup, J. Industrial & Engineering Chemistry Research. 48 (2009) 763-768.

[17] C.L. Yan, D.F. Xue, L.J. Zou, X.X. Yan, W. Wang, Preparation of magnesium hydroxide nanoflowers, J. Journal of Crystal Growth. 282 (2005) 448-454.

[18] D.F. Xue, X.X. Yan, and L. Wang, Production of specific $Mg(OH)_2$ granules by modifying crystallization conditions, J. Powder Technology. 191 (2009) 98-106.

[19] D.L. Jin, X.Y. Gu, X.J. Yu, G.S. Ding, H.L. Zhu, K.H. Yao, Hydrothermal synthesis and characterization of hexagonal $Mg(OH)_2$ nano-flake as a flame retardant, J. Materials Chemistry and Physics. 112 (2008) 962-965.

[20] Q.L. Wu, L. Xiang and Y. Jin, Influence of $CaCl_2$ on the hydrothermal modification of $Mg(OH)_2$, J. Powder Technology. 165 (2006) 100-104.

[21] L.M. Ji, L.J. Li, Z.Q. Liu, B. Zhang, F. Nie, Z.M. Zeng, F.G. Song, Y.H. Zhang, X.H. Jia, Preparation and characterization of $Mg(OH)_2$ flame-retardant with particular morphology via hydrothermal process, J. Emerging Focus on Advanced Materials, Pts 1 and 2. 306-307 (2011) 1311-1316.

[22] H. Yan, X.H. Zhang, J.M. Wu, L.Q. Wei, X.G. Liu, B.S. Xu, The use of CTAB to improve the crystallinity and dispersibility of ultrafine magnesium hydroxide by hydrothermal route, J. Powder Technology. 188 (2008) 128-132.

[23] J.M. Chen, L. Lin, Y.H. Song, L. Shao, Influence of KOH on the hydrothermal modification of $Mg(OH)_2$ crystals, J. Journal of Crystal Growth. 311 (2009) 2405-2408.

Advanced Materials Research Vol. 936 (2014) pp 929-932
© (2014) Trans Tech Publications, Switzerland
doi:10.4028/www.scientific.net/AMR.936.929

Effect of Solvent Properties on the Swelling Assisted with Protrusion of PS@TiO_2

Baoling Chen[1, a], Longhui Zheng[1, b], Junhui He[1, c], Qinhui Chen[1, 2, d] and Jinhuo Lin[1, 2, e*]

[1]College of Material Science and Engineering, Fujian Normal University, Fuzhou 350007, China

[2]Fujian Key Laboratory of Polymer Materials, Fuzhou 350007, China

[a]chenbaoling1989@163.com, [b]lhzheng88@163.com, [c]hjunhui616@163.com,[d]chenqh@fjnu.edu.cn, [e]jhlin@fjnu.edu.cn

Keywords: swelling; core-shell microspheres; Janus; solubility parameter; polar fraction

Abstract. Janus particles have particular properties and potential application for their asymmetry dual-faced structure. In this report, we study the effect of the solubility parameter and the polar fraction of solvent on the swelling assisted with protrusion of polystyrene @ titanium dioxide (PS@TiO_2) core-shell microspheres. The resultant titanium dioxide/polystyrene (TiO_2/PS) Janus particles were characterized by scanning electron microscope. Results indicated that solvent with the solubility parameter of about 9.3 $(cal/cm^3)^{1/2}$ and with low polarity such as dimethylbenzene, carbon disulfide and methyl methacrylate exhibited the preferable swelling efficiency.

Introduction

Janus particles are regarded as some of the most complicated colloidal particles in existence. Janus particles with different composition and structure may have different assembly behaviors and properties such as surfactants [1], biosensors [2], directional catalysis [3], biological probe [4], electronic devices and photonic crystal [5] and so on. Many synthesis approaches have been developed for the fabrication of Janus particles, including biphasic grafting [6], the Pickering emulsion method [7-9], asymmetric wet-etching [10-12], solvent-free method [13], and seeded emulsion polymerization [14]. However, these methods are difficult to achieve accurate control of the surface chemical partition and microstructure of Janus particles, also unable to undertake large-scale production. Recently, Yang [15,16] synthesized the polymer/inorganic asymmetric Janus particles by emulsion swelling core-shell composite particle. This method is not only easy to operate but also provides possibility of mass production. In this report, we synthesized titanium dioxide/polystyrene (TiO_2/PS) Janus particles by using single solvent with different solubility parameter and polar fraction to swell core-shell microspheres and investigated the effect of solvent properties on the swelling assisted with protrusion of polystyrene @ titanium dioxide (PS@TiO_2).

Experimental

Materials

Ethanol, styrene, n-hexane, acetone, dimethylbenzene, carbon disulfide, methyl methacrylate, butyl alcohol and sodium dodecyl sulfate (SDS) were all A. R. and purchased from Sinopharm Chemical Reagent Co., Ltd.

Synthesis of the Janus composite particles of TiO_2/PS

The core-shell composite particles of PS@TiO_2 were prepared by the method reported in the literature [17]. 0.05 g of freeze-dried PS@TiO_2 composite particle was dispersed in 5 mL of aqueous solution containing 10 $mg \cdot mL^{-1}$ of SDS. 0.2 mL of different kind of solvent and 5 mL of aqueous solution containing 10 $mg \cdot mL^{-1}$ of SDS were emulsified at ambient temperature under ultrasonication for 5 min. The emulsion was added into the composite dispersion within 1 min

under stirring at ambient temperature, and the system stood there for 20 min to control swelling extent. The swelling was terminated by adding excess ethanol. The samples were centrifuged and washed with ethanol to remove solvent. The Janus composite particles of TiO_2/PS were obtained after freeze-drying.

Characterization

The morphologies of the Janus composite particles of TiO_2/PS swelling by the single solvent were performed on a JSM-7500F scanning electron microscope (SEM) at an accelerating voltage of 5 kV.

Results and discussion

Effect of the solubility parameter of solvent on swelling

The solubility parameter and polar fraction of the solvents were listed on Table 1. The SEM images of the Janus composite particles of PS@TiO_2 swelled by the emulsion of different solvents for 20 min at room temperature were shown in Fig. 1. The solubility parameter of PS is about 9.3 $(cal/cm^3)^{1/2}$. When the solvent with low solubility parameter such as n-hexane which solubility parameter is 7.3 $(cal/cm^3)^{1/2}$ was used to swell PS@TiO_2 core-shell structure, the inner osmotic pressure could not increase sufficiently to crack the TiO_2 shell. The PS core could not protrude under swelling (Fig.1 a). With the increase of solubility parameter of solvent, swelling ability of solvent improved obviously so the inner osmotic pressure would enhance sufficiently to form a tiny crevice on the surface of TiO_2 shell. Part of the PS core was protruded through the crevice and formed a lobe anchored onto the surface of TiO_2 shell [8] (Fig.1 b and Fig.1 c). However, when the gap of solubility parameters between solvent and PS became larger, the heat of mixing of PS largen and the swelling ability of solvent decreased (Fig.1 d).

Effect of the polar fraction of solvent on swelling

The solvents with weak polarity, such as dimethylbenzene and methyl methacrylate, are beneficial to preparing TiO_2/PS Janus particles by swelling the core-shell microspheres (Fig.1 b and Fig.1 e) because the polarity of PS is low. The TiO_2/PS Janus particles could not obtain when the core–shell composite particles of PS@TiO_2 were put into the single solvent which has large polarity (Fig.1 f), for example, the butyl alcohol that the polarity is 11.4 $(cal/cm^3)^{1/2}$.

TABLE 1 THE SOLUBILITY PARAMETER AND POLAR FRACTION OF THE SOLVENTS

Solvent	Solubility parameter/ $(cal/cm^3)^{1/2}$	Polar fraction
n-hexane	7.3	0
dimethylbenzene	8.8	0
carbon disulfide	10.0	0
methyl methacrylate	8.7	0.149
acetone	10.0	0.695
butyl alcohol	11.4	0.096

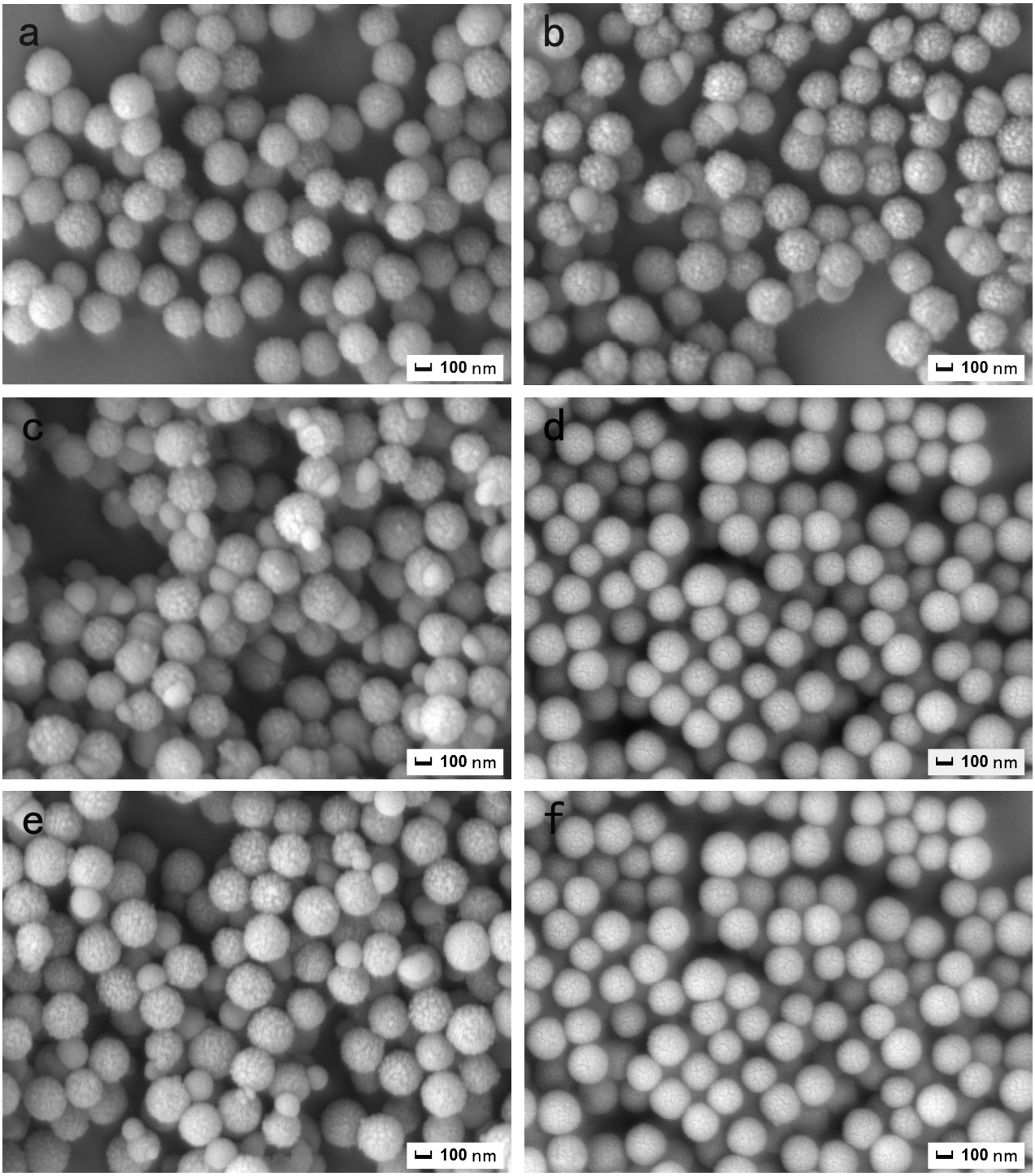


Fig. 1 SEM images of the TiO_2/PS Janus particles prepared with different solvent. (a) n-hexane; (b) dimethylbenzene; (c) carbon disulfide; (d) butyl alcohol; (e) methyl methacrylate; (f) acetone

Conclusion

The core of PS in the shell of TiO_2 is more likely to swell and form the TiO_2/PS Janus particles when solvent has the similar solubility parameters with PS which solubility parameter is about 9.3 $(cal/cm^3)^{1/2}$. Moreover, solvent with low polarity is benefit for the formation of Janus particles because PS is a kind of polymer with low polarity.

Acknowledgments

This work is supported by the National Natural Science Foundation of China (No. 51103024) and Fujian Normal University Foundation for Excellent Young Teachers (No. fjsdky2012004).

References

[1] J. Hu, S. Zhou, Y. Sun, X. Fang, L. Wu, Fabrication, properties and applications of Janus particles, Chem. Soc. Rev. 41 (2012) 4356-4378.

[2] J. Lee, J. Kim, Multiphasic Sensory Alginate Particle Having Polydiacetylene Liposome for Selective and More Sensitive Multitargeting Detection, Chem. Mater. 24 (2012) 2817-2822.

[3] D.J. Cole-Hamilton, Janus catalysts direct nanoparticle reactivity, Science. 327 (2010) 41-42.

[4] M. Himmelhaus, H. Takei, Cap-shaped gold nanoparticles for an optical biosensor, Sen. Act.B: Chem. 63 (2000) 24-30.

[5] E. Yablonovitch, T. Gmitter, K. Leung, Photonic band structure: The face-centered-cubic case employing nonspherical atoms, Phys. Rev. Lett. 67 (1991) 2295-2298.

[6] B. Liu, W. Wei, X. Qu, Z. Yang, Janus colloids formed by biphasic grafting at a Pickering emulsion interface, Angew Chem Int Ed Engl. 47 (2008) 3973-3975.

[7] Q.H. Chen, B.L. Chen, L.H. Zheng, J.H. Lin, Preparation of Polyaniline / Polystyrene Janus Composite Particles, Chem. J. Chinese Univ. 34 (2013) 1788-1793.

[8] Q.H. Chen, L.H. Zheng, B.L. Chen, J.H. Lin, Scalable synthesis of TiO_2–Ag Janus composite particles, Eur. Polym. J. 49 (2013) 2610-2616.

[9] J. Zhang, J. Jin, H. Zhao, Surface-initiated free radical polymerization at the liquid-liquid interface: a one-step approach for the synthesis of amphiphilic janus silica particles, Langmuir. 25 (2009) 6431-6437.

[10] W. Lu, M. Chen, L. Wu, One-step synthesis of organic-inorganic hybrid asymmetric dimer particles via miniemulsion polymerization and functionalization with silver, J. Colloid Interface Sci. 328 (2008) 98-102.

[11] B. Liu, C. Zhang, J. Liu, X. Qu, Z. Yang, Janus non-spherical colloids by asymmetric wet-etching, Chem Commun. (2009) 3871-3873.

[12] C. Zhang, B. Liu, C. Tang, J. Liu, X. Qu, J. Li, Z. Yang, Large scale synthesis of Janus submicron sized colloids by wet etching anisotropic ones, Chem. Commun. 46 (2010) 4610-4612.

[13] S. Jiang, M.J. Schultz, Q. Chen, J.S. Moore, S. Granick, Solvent-Free Synthesis of Janus Colloidal Particles, Langmuir. 24 (2008) 10073-10077.

[14] S.p. Reculusa, C.l. Poncet-Legrand, A. Perro, E. Duguet, E. Bourgeat-Lami, C. Mingotaud, S. Ravaine, Hybrid Dissymmetrical Colloidal Particles, Chem. Mater. 17 (2005) 3338-3344.

[15] C. Tang, C. Zhang, J. Liu, X. Qu, J. Li, Z. Yang, Large Scale Synthesis of Janus Submicrometer Sized Colloids by Seeded Emulsion Polymerization, Macromolecules. 43 (2010) 5114-5120.

[16] B. Liu, J. Liu, F. Liang, Q. Wang, C. Zhang, X. Qu, J. Li, D. Qiu, Z. Yang, Robust Anisotropic Composite Particles with Tunable Janus Balance, Macromolecules. 45 (2012) 5176-5184.

[17] Z. Yang, Z. Niu, Y. Lu, Z. Hu, C.C. Han, Templated Synthesis of Inorganic Hollow Spheres with a Tunable Cavity Size onto Core-Shell Gel Particles, Angew. Chem. Int. Ed. 115 (2003) 1987-1989.

Advanced Materials Research Vol. 936 (2014) pp 933-937
© (2014) Trans Tech Publications, Switzerland
doi:10.4028/www.scientific.net/AMR.936.933

Non-isothermal Crystallization Kinetics of Semi-aromatic Polyamide and the Preparation of its Fiber

Chen Yuejun[1,a], Wu Pingting[1,b] , Xu Huajun[1,c], Wang Dan[1,d], Wang Yimin[2,e], Wang Yanping[2,f]

[1.] College of Material Science and Engineering, Donghua University, Shanghai 201620, China;

[2.] State Key Laboratory for Modification of Chemical Fibers and Polymer Materials, Donghua University, Shanghai 201620, China

[a]chyj897@163.com, [b]175799172@qq.com, [c]huajun87@hotmail.com, [d]wangdan0211@126.com, [e]ymw@dhu.edu.cn, [f]wyp@dhu.edu.cn

Keywords: semi-aromatic polyamide, non-isothermal crystallization kinetics, heat treatment, mechanical properties.

Abstract: In order to meet the new requirement of polyamide materials on the thermal behavior, the aromatic rings were introduced into the main chain to synthesize semi-aromatic polyamide. In this paper, the non-isothermal crystallization kinetics of semi-aromatic polyamide was studied with Mo method. It was found that the crystallization rate slowed down with the increase of crystallinity. Spinning experiments showed that the semi-aromatic polyamide fibers could be prepared by melt spinning. Heat treatment can improve the mechanical properties of the as spun fibers obviously. Considering the impact on the mechanical properties, heat treatment time under 60 min was optimum.

Introduction

At present, the main varieties of semi-aromatic polyamides are nylon MXD6, PA6T, PA9T, PA10T[1-2] and so on. Semi-aromatic polyamide has many outstanding properties, for example, good heat resistance, excellent chemical resistance, high fracture strength and perfect electrical insulation. Now, this new type of polyamide possessing both the advantages of aromatic and aliphatic polyamide has become a hot research area. In this paper, the non-isothermal crystallization kinetics of the semi-aromatic polyamide was analyzed. The fibers of semi-aromatic polyamide were made through melt spinning and the effects of heat treatment time on mechanical properties of semi-aromatic PA fibers were also studied.

Experimental

Materia

The sample of semi-aromatic polyamide was provided by School of Chemical Engineering Donghua University with a melt index of 17.72 g/min.

Non-Isothermal Crystallization Measurement

Non-isothermal crystallization kinetics was carried out using a differential scanning calorimeter (DSC, TA2910, USA). The non-isothermal crystallization was performed as follows: the sample was heated to 350℃ at the heating rate of 20℃/min, stayed there for 2 min, then cooling the melt to crystallize at cooling rates of 10,15,20 and 25 ℃/min.

Melt Spinning

The dried semi-aromatic polyamide chips were put into the screw extruder to melt and extruded through spinneret. The screw extruder temperatures were set as 290, 295, 305, 310, 315℃, respectively from the inlet to the outlet. The winding speed was set at 450m/min and the metering pump rotation speed was 12.5 rpm. At last heat treatment was required to enhance mechanical properties of the as spun fiber. Some groups of as spun fibers were kept in the vacuum oven under a sustained stress of 40cN to heat. The heat treatment time was set as 20,40,60,90 min under the unchanged heat treatment temperature of 160℃， respectively.

Results and Discussions

Non-Isothermal Crystallization Kinetics

Figure 1 shows the DSC crystallization exothermal curves of semi-aromatic polyamide samples at different hearting rate.

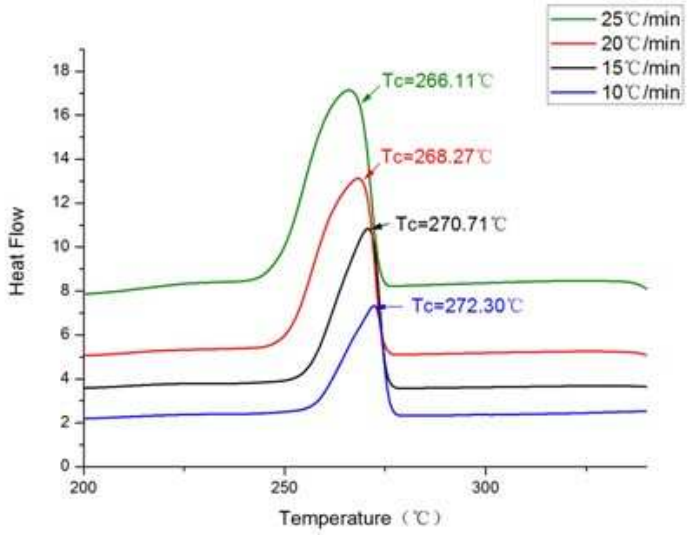


Fig.1 Non-isothermal crystallization curves of semi-aromatic polyamide

As seen from Fig 1, the crystallization exotherm becomes broader and shifts to lower temperatures with the increase of cooling rate. The reason may be that, at a lower cooling rate, polymer chain has enough time to transfer from the melt to the surface of the crystal [5]. So crystallization can occur at higher temperature.

The non-isothermal crystallization kinetics of semi-aromatic polyamide fibers was studied with Mo method[4,5] in this paper. Based on the assumption that the degree of crystallinity is correlated to the cooling rate and crystallization time, the non-isothermal crystallization process can be effectively characterized by using the combined Avrami/Ozawa equation[6],that is Mo method. The Avrami[7] equation is expressed as,

$$1-\mathrm{X(t)} = \exp(-\mathrm{Z}_t t^n). \quad (1)$$

Taking a double logarithm of Eq. (1) gives:

$$\lg[-\ln(1-X(t))] = \lg Z_t + n\lg t. \quad (2)$$

where n is the Avrami exponent, which depends on the nucleation mechanism and growth geometry, Zt is the crystallization rate constant, X(t) is the relative degree of crystallinity at certain time.

Ozawa[8] equation is an extension of the Avrami equation to the non-isothermal condition. In the Ozawa approach, the time variable in the Avrami equation is replaced by the cooling rate. Thus the relative crystallinity degree is described as a function of constant cooling rate:

$$1-X_t=\exp(-K(T)/\theta^m)\,. \tag{3}$$

Using Eq. (3) in double-logarithmic form:

$$\lg(-\ln(1-X_t))=\lg K(T)-m\lg\theta\,. \tag{4}$$

Where K(T) is a function of temperature, m is the Ozawa exponent, and θ is the cooling rates. Merging the Eqs. (2) and (4) in the following form:

$$\lg Z_t+n\lg t=\lg K(T)-m\lg\theta\,. \tag{5}$$

And by rearrangement:

$$\lg\theta=\lg F(T)-a\lg t\,. \tag{6}$$

where the kinetic parameter $F(T)=[K(T)/Z_t]^{1/m}$ refers to the cooling rate that needs to be selected within a unit of crystallization time when the measured system amounts to a certain degree of crystallinity, and a is the ratio of the Avrami exponent n to the Ozawa exponent m. The value of a is closely related to the fitness of the Mo method. According to Eq.6, for a given relative crystallinity, from the plot of lgθ against lg t, the values of F(T) and a can be determined from the intercept and the slope of the line, respectively. The plot of lgθ versus lgt for semi-aromatic polyamide with different crystallinity was given in Fig. 2. The values of F(T) and a were listed in Table 1.

TABLE 1 NON-ISOTHERMAL CRYSTALLIZATION KINETIC PARAMETERS OF SEMI-AROMATIC PA

X_t (%)	a	lg F(T)
20	1.43	0.93
40	1.45	1.06
60	1.46	1.12
80	1.46	1.15

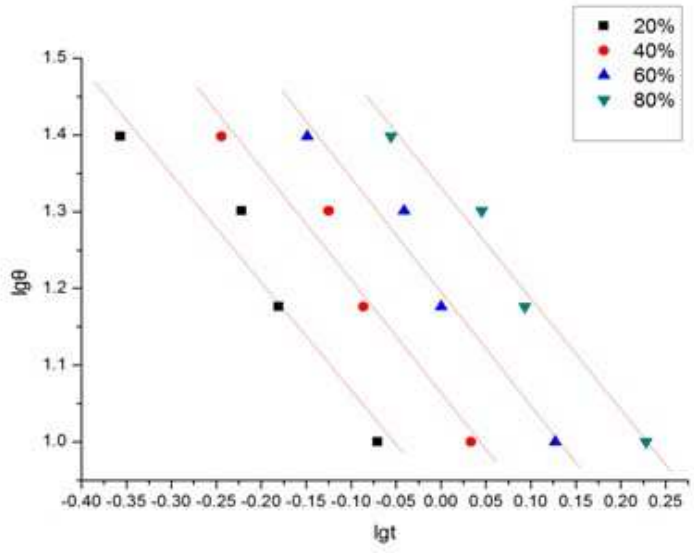


Fig.2 The plots of $\lg\theta$ versus log t for semi-aromatic polyamide

Table 1 shows that the values of a are in the range of 1.43~1.46 with the average of 1.45, changing slightly at different relative crystallinity. It means this method has been proven to be applicable for the crystalline process of semi-aromatic polyamide. It also can be seen that the values of lg F(T) become larger with the relative crystallinity increasing, which shows that the cooling rate should be increased to achieve a higher relative crystallinity in unit crystallization time.

The Mechanical Properties of the Semi-aromatic PA Fiber

The mechanical properties of the fibers under different heat treatment time were tested and listed in Table 2. The heat treatment temperature was set at 160℃, and remained unchanged.

TABLE 2 THE MECHANICAL PROPERTIES OF THE FIBERS UNDER DIFFERENT HEAT TREATMENT TIME

Heat Treatment Time (min)	Tensile Strength (MPa)	Young's Modulus (GPa)	Elongation at break (%)
as-spun fiber	357.86	5.38	63.8
20	660.91	10.32	8.7
40	692.68	10.82	7.6
60	760.04	12.33	6.2
90	749.85	11.88	6.6

Table 2 shows that the tensile strength and the modulus of the fibers increase obviously with the increase of heat treatment time at first. When the time was 60min, the tensile strength and the modulus reached the highest point. It is because the molecular chain starts to reorganize and orient along the fiber direction. So the optimal heat treatment time of the fibers is about 60min. Then the values decrease with the time extension because of the disorientation caused by the too long time in high temperature.

Conclusions

(1) Mo method can describe non-crystallization kinetics of semi-aromatic polyamide well. To realize a higher relative crystallinity in unit time, a faster cooling rate is needed.

(2) The semi-aromatic PA fiber can be prepared by melt spinning, with a winding speed of 450m/min. Heat treatment can improve the mechanical properties of the fibers obviously. The results demonstrate that 60min is the best heat treatment time, under which the tensile strength can reach to 760MPa and the modulus can reach to the maximum of 12.3GPa.

References

[1] S. Naudy, L.David, C.Rochas, R, Fulchiron. Shear induced crystallization of poly(m-xylylene adipamide) with and without nucleating additives. Polymer, 2007, 48:3273-3285.

[2] A.Ballistreri, D.Garozzo, M.Giuffrida, P.Maravigna, G.Montaudo. Thermal decomposition processes in aliphatic-aromatic polyamides investigated by mass spectrometry. Macromolecules, 1986, 19: 2693-2699.

[3] H.S.Yuani,D.Qiang. Non-isothermal crystallization kinetics of β-nucleated isotactic polypropylene.

[4] J.P.Liu, Z.S.Mo, Y.C.Qi, H.F.Zhang, D.L.Chen. Kinetics of non-isothermal crystallization of PEO/PBHE blends. Acta Polymerica Sinica, 1993, 1: 12-16.

[5] C.S.Zhu, X.D.Li, J.W.Wang, H.G.Li, S.T.Pu. Study on the spherulites of nylon 1010 with unusual optic property. Polymeric Materials Science and Engineering, 1992, 3: 61-64

[6] M.M.Nia, M.R.Memarzadeh. Characterization and non-isothermal crystallization behavior of biodegradable poly(ethylene sebacate)/SiO_2 nanocomposites. Polym.Bull, 2013, 70:2471–2491.

[7] M.J.He, W.X.Chen, X.X.Dong. Polymer Physics. Fudan University Press, 1997, 156-171.

[8] T. Ozawa. Kinetics of non-isothermal crystallization. Polymer, 1971, 12: 150-158.

Advanced Materials Research Vol. 936 (2014) pp 938-941
© (2014) Trans Tech Publications, Switzerland
doi:10.4028/www.scientific.net/AMR.936.938

Recycled Paper Cellulose Aerogel Synthesis and Water Absorption Properties

Jingduo Feng[1, a], Son T. Nguyen[1, b], Hai M. Duong[1, c *]

[1]Material Laboratory, Department of Mechanical Engineering, National University of Singapore,9 Engineering Drive 1, Singapore 117576

[a]verafeng1988@gmail.com,[b]mpents@nus.edu.sg,[c]mpedhm@nus.edu.sg

Keywords: recycled cellulose aerogel, water absorption

Abstract: By applying sodium hydroxide/urea and a sample freeze drying method, we successfully synthesized green cellulose aerogel from paper waste for the first time. We adjusted the cellulose concentration from 1.5 percents to 4 percents in the initial hydrogel. They yielded densities changing from 0.03-0.1 g/cm^3.The absorption capacities varied from 9 to 20 times of their own weight. To investigate the water absorption capacity in relationship with the initial chemical dosage, we changed the input amount of urea and sodium hydroxide, which is the first study ever. The thermal conductivity of the 2 percents sample ranged from 0.029-0.032 W/mK. Besides, the material has a high potential to be used in diaper industry as it is biodegradable which is better than most super absorbent polymers.

Introduction

Most diapers in market are composed of super absorbent polymers, which are not biodegradable. Averagely a baby needs more than 5,000 diapers before it is potty-trained [1]. Adult diapers are also requested in large amount every day. Huge amount of diapers is consumed daily in this world. Nowadays, as super absorbent polymer is not biodegradable. The used diapers waste large amount of land to store them. Our paper gives a potential alternative of traditional diapers-Cellulose aerogel, which with high absorbent capacity (almost 20 times) and also biodegradable can be used to replace the non-biodegradable super absorbent polymer. Cellulose aerogel can be derived from paper. Only United States alone used 85.5 million tons of paper per year [2]. This huge amount of used paper needs to be recycled and functions as useful material to prevent waste. Our group converts the recycled cellulose to cellulose aerogel. Aerogel is porous material with more than 90 percents pores in the volume. Most aerogel are silica or carbon aerogel. Cellulose aerogel is a new material.

Materials and Chemicals

Sodium hydroxide, urea, and ethanol are purchased from Sigma-Aldrich. Commercial recycled cellulose fibers are donated by Insul-Dek Engineering Pte. Ltd., Singapore.

Synthesis Procedure

For standard sample, urea (13.7 wt%, 5.025g) and sodium hydroxide (1.9 wt%, 0.725g) were dispersed in DI water (30g), which is dispersed by a magnetic stir. Recycled cellulose (2 wt%, 0.75g) was added to the transparent solution, pre-cooled in ice/water bath for 10 minutes, then

sonication for 10 minutes. Thereafter, the solution was placed in refrigerator for more than 24 h to allow gelation of the solution. After the solution was frozen, it was then thawed at room temperature and then followed by immersing into ethanol (99 vol %) for coagulation for two days. After coagulation, solvent exchange was carried out by immersing the gel in de-ionised (DI) water for 2 days. The sample was then frozen in a freezer at – 18 ℃ for 24 h. After that, freeze drying is carried out for 2 days with a ScanVac CoolSafe 95-15 Pro freeze dryer (Denmark) to obtain the desired aerogel. Other samples were prepared by the same method by varying one component of the standard sample. Detail refers to the Table 1.

TABLE 1 PARAMETERS USED IN MORPHOLOGY CONTROL OF CELLULOSE AEROGEL

Group 1	cellulose amount	cellulose concentration
G1_015	0.5444[g]	1.50%
standard	0.75[g]	2%
G1_03	1.1057[g]	3%
G1_04	1.4896[g]	4%
Group 2	urea amount	urea concentration
G2_10	3.4972[g]	10%
standard	5.025[g]	13.76%
G2_15	5.5544[g]	15%
G2_20	7.8688[g]	20%
Group 3	NaOH amount	NaOH concentration
G3_015	0.5448[g]	1.50%
standard	0.725[g]	1.90%
G3_025	0.9173[g]	2.50%
G3_03	1.1064[g]	3%

Characterization

Thermal conductivity measurement.

C-Therm TCi Thermal Conductivity Analyzer (C-Therm Technologies, Canada) was used to measure the thermal conductivity of the aerogel.

Water absorption test.

This test was carried out in DI water, followed by modified ASTM D570-98 standard, refer to Figure.1.



Figure 1 The setting of water absorption test

Results and Discussion

The thermal conductivity of the standard sample was 0.03 $Wm^{-1}K^{-1}$. It is comparable to silica aerogels (0.026 $Wm^{-1}K^{-1}$) and wool (0.03-0.04 $Wm^{-1}K^{-1}$) [3].

TABLE 2 CELLULOSE CONCENTRATION AFFECTS WATER UPTAKE RATIO AND POROSITY

Sample No	Dry Weight [g]	Wet Weight [g]	Water uptake Ratio	Porosity	Density [g/cm^3]
G1_015	0.3928	8.3431	20.24	0.984	0.03
Standard	0.7280	13.4140	17.43	0.978	0.04
G1_03	0.8976	12.3885	12.80	0.970	0.05
G1_04	2.4507	24.4634	8.98	0.935	0.10

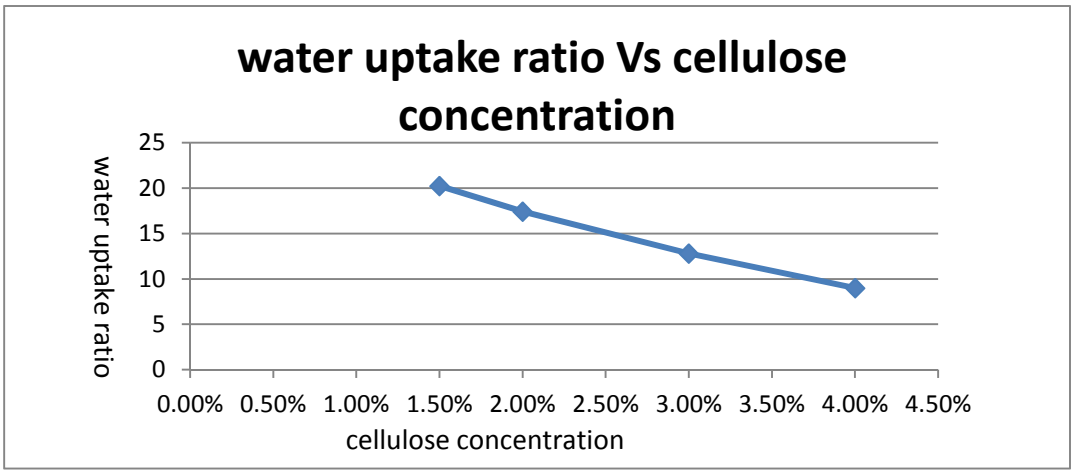


Figure 2 The water uptake ratio change with cellulose concentration

Cellulose concentration varies from 1.5% to 4%, while the water uptake ratio drops from 20 to 9. Their relationship is quite linear. By increasing cellulose content in one sample, the density of the solution is also increased, but the structure of the aerogel is more compacted. Hence, the porosity is decreased (see Table 2), resulting in less space for water molecular being taken in. As the result, Water uptake ratio linear decrease with an increase cellulose concentration, referring to Figure. 2.

TABLE 3 UREA AMOUNT AFFECTS WATER UPTAKE RATIO AND POROSITY

Sample No	Dry Weight [g]	Wet Weight [g]	Water uptake Ratio	Porosity
G2_10	0.6712	14.1073	20.02	0.978
standard	0.7280	13.4140	17.43	0.978
G2_15	0.7532	14.5129	18.27	0.975
G2_20	0.6985	13.1829	17.87	0.978

Urea forms urea hydrate in the solution. Urea hydrate helps prevent cellulose molecule come near to each other. Hence, urea restrains the formation of hydrogen bond among cellulose. The experiment results about water up take ratio are without much difference in this group. It may be caused by the urea amount that plays an insignificant role about porosity. However, the porosity is not as the same as the water up take ratio results suggest, referring to Table 3. It is may be due to measure errors, as the porosity is calculated by weight divided by volume. Volume is derived from diameter and height of the cellulose samples, and then determined by cylinder volume calculation formula. The diameter is determined by the average of three readings. Errors may be generated in the process, as the sample is not exactly cylindrical shape. However, we could see all the data are the same in the first two digits regards to porosity.

Part of sodium hydroxide can be bound to cellulose, which improves the dissolve of cellulose. More sodium hydroxide causes less hydrogen bonding among cellulose, which leads to less porosity and thus less water uptake ratio, referring to Table 4. However, when sodium hydroxide changes from 2.5 percents to 3 percents, the water uptake ratio does not drop further. It is due to 2.5 percents of sodium hydroxide is the maximum amount needed to bound with cellulose. More sodium hydroxide will not further the reaction.

TABLE 4 SODIUM HYDROXIDE AMOUNT AFFECTS WATER UPTAKE RATIO AND POROSITY

Sample No	Dry Weight [g]	Wet Weight [g]	Water uptake Ratio	Porosity
G3_015	0.5925	11.9001	19.08	0.983
standard	0.7280	13.4140	17.43	0.978
G3_025	0.7639	12.6251	15.53	0.974
G3_03	0.7066	11.3263	15.03	0.976

Summary

Our group successfully synthesized recycled cellulose aerogel from paper waste. The newly developed material is with high absorption capacity. Sodium hydroxide amount and cellulose concentration alter the water uptake ratio of cellulose aerogel greatly, while urea amount do not play a significant role in the water uptake ratio.

References

[1] Information on http://www.enfamil.com/app/iwp/enf10/content.do?dm=enf&id=/Consumer_Home3/Prenatal 3/Prenatal_Articles/changingdiaper&iwpst=B2C&ls=0&csred=1&r=3557620074

[2] Information on http://www3.niu.edu/recycling/alum_facts/page5.html

[3] S. Sequeira; D.V. Evtuguin; I. Portugal, Preparation and properties of cellulose/silica hybrid composites. Polymer Composites. 30 (2009) 1275-1282.

Advanced Materials Research Vol. 936 (2014) pp 942-949
© (2014) Trans Tech Publications, Switzerland
doi:10.4028/www.scientific.net/AMR.936.942

Preparation of P(GMA-co-EGDMA) Monolithic Columns with Adjustable Porous Properties

Haotian Zhang, Qiuyu Zhang [a]*, Baoliang Zhang and Chunmei Li

Key Laboratory of Applied Physics and Chemistry in Space of Ministry of Education, School of Natural and Applied Sciences, Northwestern Polytechnical University, Xi'an 710072, China

[a]qyzhang@nwpu.edu.cn

Keywords: Monolithic column; Polyacrylate; Adjustable porous properties; Porogenic system

Abstract. Porous properties have notable effect on separating effect of organic polymer-based monolithic column. Different applications of monolithic columns require tailored pore size distributions. On account of that, P(GMA-co-EGDMA) monolithic columns were prepared with novel ternary porogenic agents. Glass tubes was chosen as polymerization mold. Moreover, factors influencing the inner pore morphology, pore size and specific surface area were investigated systematically. The results showed that the increasing of the solubility of porogenic agents and the amount of crosslinker, the decreasing of the amount of porogenic agents and temperature rising all could give rise to the decreasing of pore size. Remarkably, the effect of initiator was studied for the first time. The results showed that amount of initiator had no remarkable influence on porous properties. By controlling effect factors, P(GMA-co-EGDMA) Monolithic Columns with pore size from dozens to thousands of nanometer, which can be applied in separation of molecules with different size.

Introduction

Organic polymer-based monolithic columns can be used as stationary phase of various chromatography with its widespread sources of raw material, large range of pH, excellent biocompatibility and accessibility for chemical modification[1-4]. Its typical preparation process is as follows: homogenous polymerization mixture of monomers, porogenic agents, crosslinker and initiator is put into a mold which polymerization reaction takes place in. Due to its formed interconnected pore and channels, it allows high flow velocity under moderate pressure[5,6]. Common materials of the mold include stainless steel [7], glass [8], silica capillary [9] and so on. In recent years, organic polymer-based monolithic columns are applied in the area such as separation of biomacromolecule[10-15], inorganic ion[16] and detection in solid phase[17,18] by virtue of its high efficiency, high throughput and low back pressure in the process of separation.

Porous properties have great effect on separating effect of organic polymer-based monolithic column. Different applications of monolithic columns require tailored pore size distributions. The monolithic with dozens nanometers pore size can be used for separation of small molecules, such as aminoacid[19]; micrometer-scale pore is for separation of large molecules, just like proteins[20]. Therefore, it is of great importance to realize the preparation of controllable pore structure.

Based on the above knowledge, P(GMA-co-EGDMA) monolithic columns, which are most widely applied, were prepared choosing glass tube as polymerization mold. Meanwhile, influencing factors on the porous properties of P(GMA-co-EGDMA) monolithic columns were investigated systematically, including kind and amount of porogenic agents, amount of crosslinker, amount of initiator and reaction temperature. The aims of this work were revealed the influence law of these reaction conditions and technology. So as to laid the foundations for preparation of P(GMA-co-EGDMA) monolithic columns with controllable pore structure.

Experimental

Materials

Glycidyl methacrylate(GMA, AR) and ethylene glycol dimethacrylate(EGDMA, AR) were purchased from SARTOMER; cyclohexanol(AR), 1,4-butanediol(AR), 1-propanol(AR), 1-dodecanol(AR), acetone(AR) and azobisisobutyronitrile(AIBN, CP) were purchased from Sinopharm Chemical Reagent Co.,Ltd. The water used throughout the work was produced by AJY-2002-U ultra-pure water machine from Aquapro.

Preparation of P(GMA-co-EGDMA) monolithic columns

The homogenous mixtures consisting of GMA, EGDMA, 1-propanol, 1-dodecanol, water and AIBN were injected into glass tubes after being sparged with nitrogen for 10 min. The sealed glass tubes were then put straightly into an electric blast drying oven to polymerize for 24 h at 50 ℃. The resulting monolithic columns were washed by acetone and water successively, and vacuum dried for later experiment.

Monomer(2.06 g of GMA), crosslinker(0.50 g of EGDMA) and initiator (24 mg of AIBN) were dissolved in a ternary porogenic mixture consisting of 1-propanol(1.69 g), water(0.30 g) and the third component(1.22 g). Cyclohexanol, 1,4-butanediol, 1-dodecanol were chosen as the third component respectively.

Determining 1-dodecanol as the third component, we investigated the effects of proportion of porogenic agents, amount of initiator，crosslinking degree and reaction temperature on the porous properties of monolithic columns systematically. The dosage of components and reaction conditions were as shown in Table1.

Table 1 Dosage of each components and reaction conditions of P(GMA-co-EGDMA) monolithic columns with porogenic system of 1-dodecanol

Sample	GMA [g]	EGDMA [g]	AIBN [mg]	1-propanol [g]	1-dodecanol [g]	Water [g]	TA[a] [g]	Tempreture [℃]
MC-1	2.06	0.50	24	1.69	1.00	0.30	2.99	50
MC-2	2.06	0.50	24	1.69	1.22	0.30	3.21	50
MC-3	2.06	0.50	24	1.69	1.40	0.30	3.39	50
MC-4	2.06	0.50	24	1.69	1.60	0.30	3.59	50
MC-5	2.06	0.50	24	1.49	1.60	0.30	3.39	50
MC-6	2.06	0.50	24	1.89	1.20	0.30	3.39	50
MC-7	2.06	0.50	24	2.09	1.00	0.30	3.39	50
MC-8	2.06	0.50	24	2.29	0.80	0.30	3.39	50
MC-9	2.30	0.26	24	1.69	1.40	0.30	3.39	50
MC-10	2.18	0.38	24	1.69	1.40	0.30	3.39	50
MC-11	1.92	0.64	24	1.69	1.40	0.30	3.39	50
MC-12	1.79	0.77	24	1.69	1.40	0.30	3.39	50
MC-13	2.06	0.50	16	1.69	1.40	0.30	3.39	50
MC-14	2.06	0.50	20	1.69	1.40	0.30	3.39	50
MC-15	2.06	0.50	28	1.69	1.40	0.30	3.39	50
MC-16	2.06	0.50	32	1.69	1.40	0.30	3.39	50
MC-17	2.06	0.50	24	1.69	1.40	0.30	3.39	40
MC-18	2.06	0.50	24	1.69	1.40	0.30	3.39	60

Characterization

The microstructure of the monolithic columns was characterized by a Scanning Electron Microscope (SEM, JEOL JSM-6700F). The porous properties was measured by means of a mercury porosimeter instrument (AutoPore IV 9500, USA). The pressure range was 0.10~60000.00 psia; the equilibration time was 10 seconds.

Results and discussion

Different porogenic system effect on porous properties

The porous properties of the monolithic columns prepared by changing the third component are as shown in Table2. From Table2 it can be seen that the order of pore size is: 1-dodecanol > 1,4-butanediol > cyclohexanol. Fig.1 shows the pore size distribution curves of the monolithic columns with three different porogenic systems. It can be seen that the pore size of the monolithic column with porogenic system of cyclohexanol distributed dispersedly around 0~100 nm. The monolithic column with porogenic system of 1,4-butanediol had a pore size of about 120 nm at the highest peak in the distribution profile curve. Compared to the former two columns, the monolithic column with porogenic system of 1-dodecanol had a larger pore size of about 300 nm at the highest peak. As shown in Fig. 2 cumulative pore area changes as a function of pressure. As can be seen, the monolithic column with porogenic system of cyclohexanol had the largest cumulative pore area, and its cumulative pore area increased steadily with the increasing of pressure, which indicated that its pore distributed dispersedly. Otherwise than that, the monolithic column with porogenic system of 1-dodecanol had the smallest cumulative pore area, and its cumulative pore area didn't change much after the pressure reached 2500 psia, which indicated that its pore size had the characteristics of concentrated distribution. The curve of 1,4-butanediol presented two platforms, indicating that there were two kinds of pore with different size, which is consistent with the information presented by the pore size distribution curves.

All the results above can be explained by phase separation theory and swelling theory[1]. A poorer solvent to the system results in an earlier phase separation in the polymer. The new phase swells with the monomers because these are thermodynamically better solvents for the polymer than the porogenic solvent. Therefore, the local concentration of monomers in the swollen gel nuclei is higher than that in the surrounding solution and the polymerization reaction proceeds mainly in these swollen nuclei rather than in the solution. Those nuclei formed are likely to be adsorbed by the large preglobules developed earlier by coalescence of many nuclei, increasing the size of the preglobules. Thus, the globules formed in the system are larger and the voids between pores are larger as well. Contrarily, if the solvent quality improves, the good solvent competes with monomers in the solvation of nuclei, the local monomer concentration is lower and the globules are smaller. As a result, porous polymers formed have smaller pores. The order of compatibility to the system is cyclohexanol > 1,4-butanediol > 1-dodecanol. Through the theoretical analysis, the order of pore size should be 1-dodecanol > 1,4-butanediol > cyclohexanol, which consistents with the results from the experiments.

Table 2 Porous properties of the monolithic columns with different porogenic systems

Porogenic system	cyclohexanol	1,4- butanediol	1-dodecanol
Specific surface area[m^2/g]	85.62	46.05	18.89
Average pore size[nm]	26.9	105.0	308.8

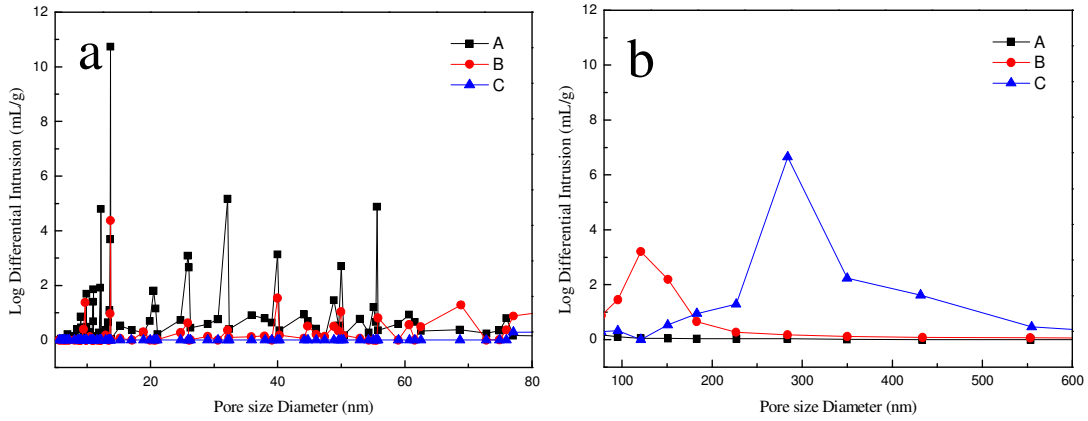


Fig. 1 Pore size distribution curves of the monolithic columns with three different porogenic systems（a: 5-80 nm, b: 80-600 nm）: cyclohexanol（A）; 1,4-butanediol（B）; 1-dodecanol（C）

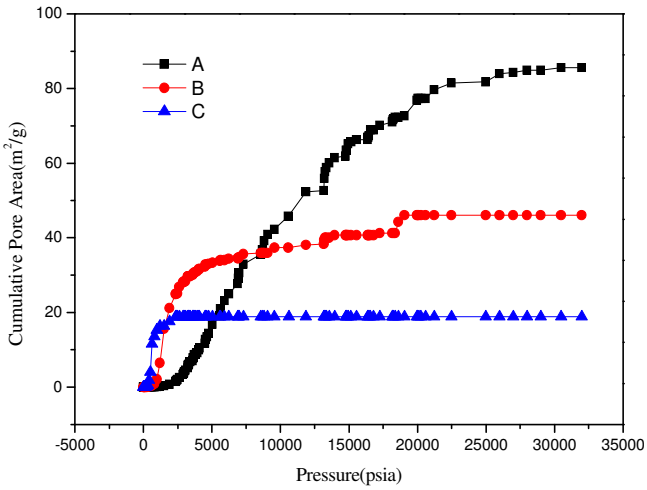


Fig. 2 Cumulative pore area changing as a function of pressure: cyclohexanol(A);1,4-butanediol（B);1-dodecanol（C）

Addition amount of porogenic agents effect on porous properties

The effects of amount of porogenic agents on porous properties were investigated by regulating the amount of 1-dodecanol of ternary porogenic system. Table3 gives the data of porous properties. As can be seen, as the amount of 1-dodecanol increased, the average pore size increased while the specific surface area decreased. Fig. 3 shows the pore size distribution curves of the monolithic columns with different amount of 1-dodecanol. The pore of MC-1 mainly distributed on the small pore interval(0~75 nm). MC-2 had a pore size of 300 nm at the highest peak in the distribution profile curve with a narrow distribution. MC-3 and MC-4 had a similar pore size distribution. Both of them had peaks in the interval of 0~15 nm and 2000~6000 nm, and most of pores distributed in the large pore interval. On the one hand, increasing the amount of porogenic agent could increase the porosity. On the other hand, the compatibility of the system to polymer decreased with the increasing of amount of 1-dodecanol. Consequently, those nuclei formed are likely to absorb monomers in the surrounding solution to increase their size. Thus, the globules formed are larger and the voids between pores are larger as well while the specific surface area decreasing.

Table 3 Pore properties of monolithic columns with different amount of 1-dodecanol

Sample	1-dodecanol[g]	Specific surface area[m^2/g]	Average pore size[nm]
MC-1	1.00	38.58	131.4
MC-2	1.22	18.87	308.8
MC-3	1.40	12.99	509.0
MC-4	1.60	12.00	630.8

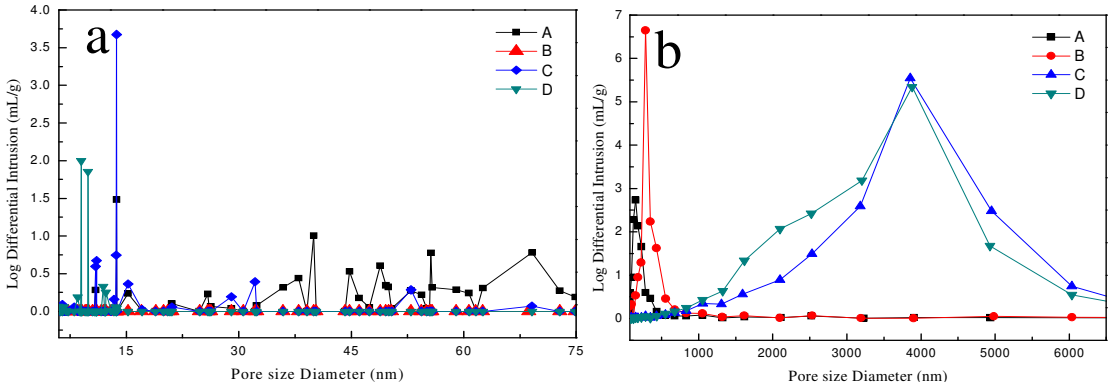


Fig. 3 The pore size distribution curves of the monolithic columns with different amount of 1-dodecanol（a: 5-75 nm, b: 75-6500 nm）, A：MC-1；B：MC-2；C：MC-3；D：MC-4

Proportion of porogenic agents effect on porous properties

As in Fig. 4, the SEM images of monolithic columns prepared by changing the proportion of porogenic agents. As shown, due to the increasing of compatibility of the system to polymer, with the increasing of amount of 1-propanol pore size decreased. Furthermore, the average pore size of MC-8 is 307.4 nm, and the specific surface area is 19.22 m2/g.

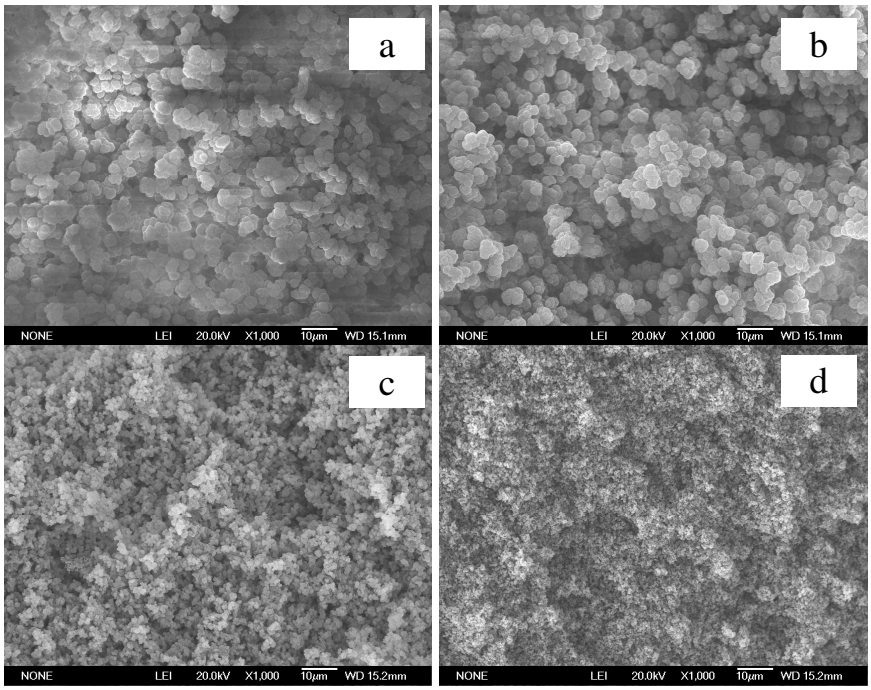


Fig. 4 The SEM images of monolithic columns prepared by changing the proportion of porogenic agents, a：MC-5；b：MC-6；c：MC-7；d：MC-8

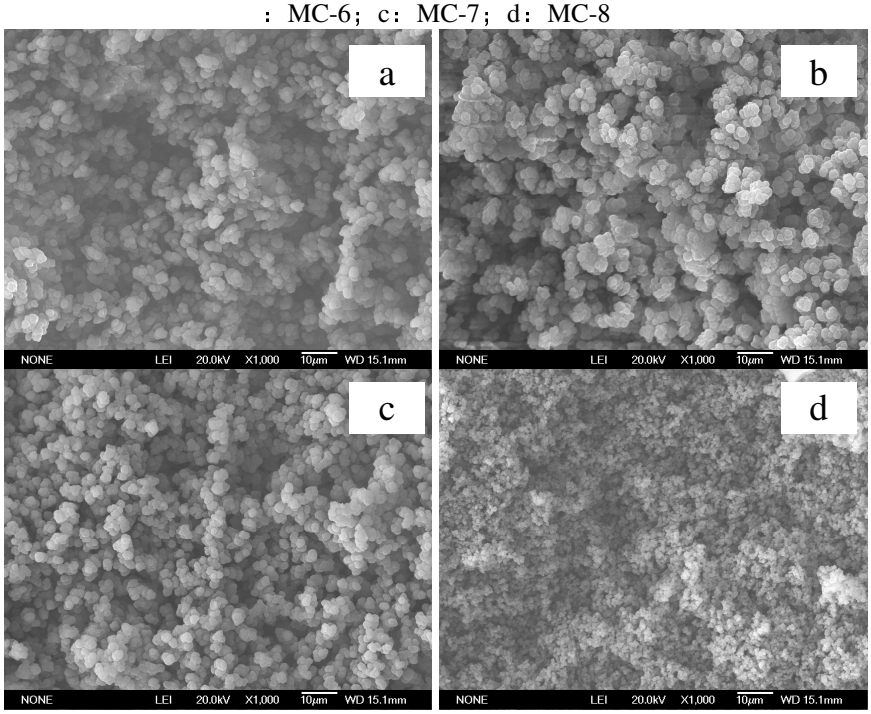


Fig. 5 The SEM images of monolithic columns prepared by changing the amount of crosslinker, a：MC-9；b：MC-10；c：MC-11；d：MC-12

Addition amount of crosslinker effect on porous properties

Fig. 5 shows the scanning electron microscopic images of monolithic columns prepared by changing the amount of crosslinker. As shown, pore size decreased with increasing of proportion of EGDMA, meanwhile, it had a more compact structure. Increasing the proportion of EGDMA resulted in an earlier phase separation in the polymer hence forming more nuclei. Besides, the increasing of crosslinking density restricted swelling of nuclei. Consequently, the globules formed in the system became smaller and the voids between them are smaller as well. The conclusion drawn is that increasing the proportion of crosslinker resulted in the decreasing of pore size. The average pore size of MC-12 is 438.4 nm, and the specific surface area is 14.88 m2/g. The pore size distribution curve of MC-12 is shown as Fig. 6. From Fig. 6 it can be seen that it had two remarkable peaks at about 11 nm and 1000 nm. It makes a conclusion that larger pores were formed by stacking of globules while smaller pores were within globules.

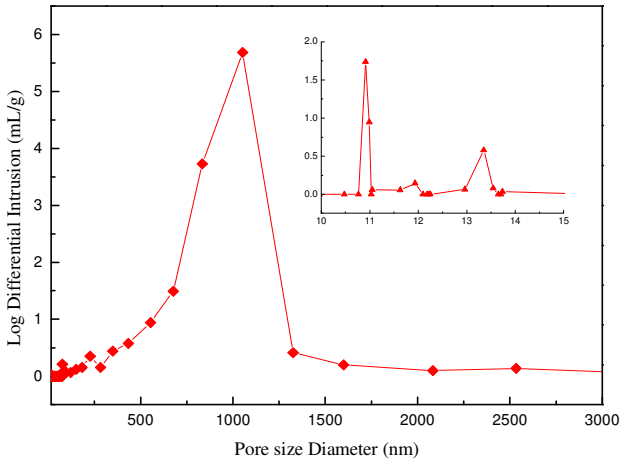


Fig. 6 The pore size distribution curve of MC-12

Addition amount of initiator effect on porous properties

Fig. 7 shows the SEM images of monolithic columns prepared by changing the amount of initiator. As shown, with increasing of amount of AIBN, pore size didn't change much. However, contrasting MC-13 and MC-16 it can be seen that MC-16 had a relatively smaller pore with a more compact structure. It can be explained that the increasing of initiator increased the amount of free radicals during the early stage of reaction. Consequently, more globules formed and the size of them decreased, which resulted in a smaller pore size. It makes a conclusion that increasing the amount of initiator results in a smaller pore size while the effects are not remarkable.

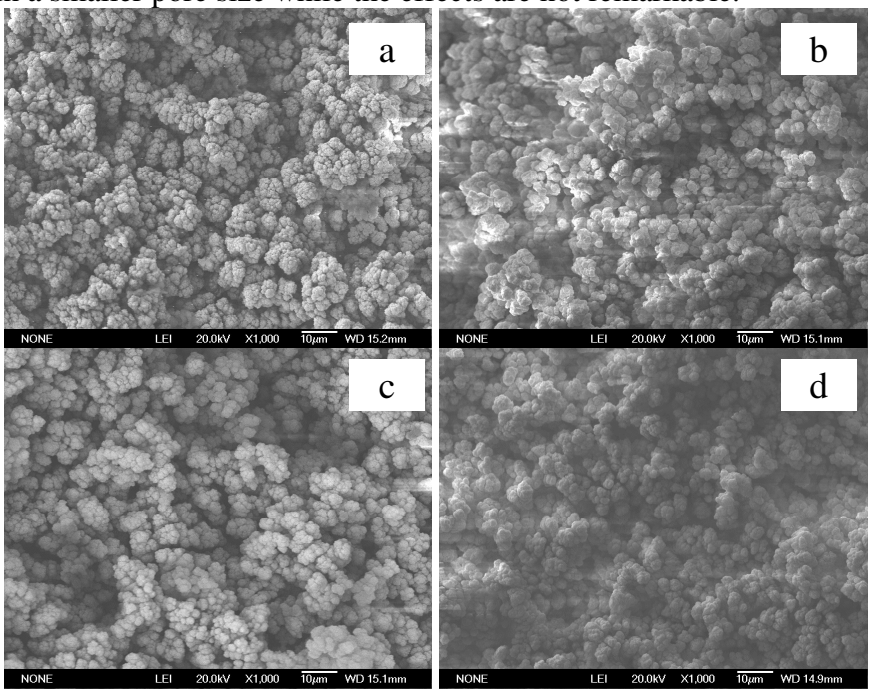


Fig. 7 The SEM images of monolithic columns prepared by changing the amount of initiator, a: MC-13; b: MC-14; c: MC-15; d: MC-16

The effects of reaction temperature on porous properties

Preparing monolithic columns at 40 ℃, 50 ℃ and 60 ℃ respectively to investigate the effects of reaction temperature on porous properties, the results indicated that MC-17 reacted incompletely as a result of the slow reaction rate. MC-18 and MC-3 reacted completely, and their SEM images were shown in Fig. 8. MC-3 had smaller globules, nevertheless, those small globules formed large clusters which made a more compact structure. The higher the reaction temperature, the greater the number of free-radicals generated per unit of time and the greater the number of nuclei and microspheres formed. Increasing the number of nuclei and microspheres necessarily decreases their size. Those nuclei preferred to gather into clusters before increasing their size. Besides, clusters formed went against

swelling. All of above restricted increasing of globules. Consequently, increasing the number of globules necessarily decreased their size so that smaller voids or pores between them appeared in the final copolymer.

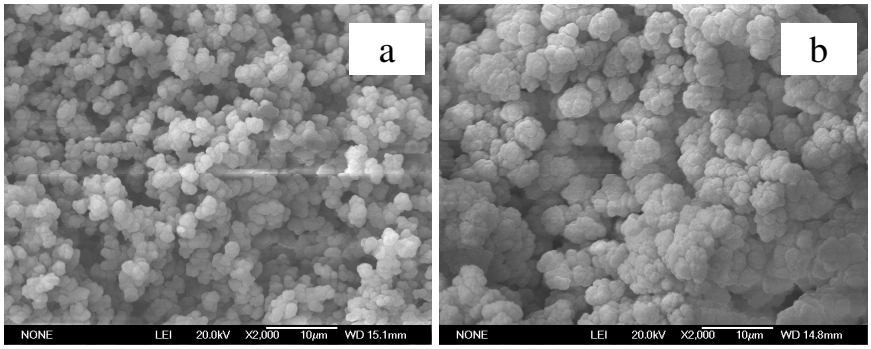


Fig. 8 The SEM images of monolithic columns prepared by changing reaction temperature, a：MC-3；b：MC-18

Conclusions

By means of investigating the effects of kind and amount of porogenic agents, amount of crosslinkers, amount of initiator and reaction temperature on porous properties of monolithic columns systematically, the influence rules of those factors were obtained. Results indicated that pore size decreased with the solubility of porogenic agents getting better. Monolithic columns prepared by the porogenic system of 1-dodecanol had the largest pore size, and increasing the amount of 1-dodecanol made the pore size increase with the largest average pore size reaching 630.8 nm. Increasing the amount of porogenic agents, decreasing the degree of crosslinking and decreasing the reaction temperature all could make pore size increase obviously. However, the amount of initiator didn't influence porous properties so much.

Acknowledgements

Financial support from National High-tech R&D Program of China(2012AA02A404), the National Natural Science Foundation of China (No.51173146, NO.51173147), Key Project of Space Foundation (CASC201106), Basic Research Fund of Northwestern Polytechnical University (JC20120248).

References

[1] M. Petro, F. Svec, J.M.J. Fréchet, Molded continuous poly(styrene-co- divinylbenzene) rod as a separation medium for the very fast separation of polymers comarison of the chromatographic properties of monolithic rod with columns packed with porous and non-porous beads in high-performance liquid chromatography of polystyrenes, J. Chromatogr. A, 752(1996) 59-66.

[2] H. Oberarcher, A. Premstaller, C. G. Huber, Characterization of some physical and chromatographic properties of monolithic poly(styrene-co-divinylbenzene) columns, J. Chromatogr. A, 1030(2004) 201-208.

[3] H Chen, Rejtar T, V. Andreev, et al, High-speed, High-resolution monolithic capillary LC-MALDI MS using an off-line continuous deposition interface for proteomic analysis, Anal. hem., 7(2005) 2323-2331.

[4] Ruben Dario Arrua, Miriam Cristina Strumia, Cecilia Inés Alvarez Igarzabal, Macroporous Monolithic Polymers: Preparation and Applications, Materials, 2(2009) 2429-2466.

[5] M. AL-Bokary, D. Cherrak, G. Guiochon, Determination of the porosities of monolithic columns by inverse size-exclusion chromatography, J.Chromatogr. A, 975(2002) 275-284.

[6] B. Bidlingmaier, K.K. Unger, N. Vondoehren, Comparative study on the column performance of microparticulate 5-μm C18-bonded and monolithic C18-bonded reverse-phase columns in high-performance liquid chromatography, J. Chromatogr. A, 832(1999)11-16.

[7] F. Svec, J.M.J. Fréchet, Continuous Rods of Macroporous Polymer as High-Performance Liquid Chromatography Separation Media, Anal. Chem., 64(1992) 820-822.

[8] R.D. Arrua, M. Strumia, G. Pastrana, et al, Synthesis of macroporous polymer rods based on an acrylamide derivative monomer, J.Polym.Sci. A Polym. Chem., 44(2006) 6616-6623.

[9] Xin Chen, H. Dennis Tolley, Milton L. Lee, Monolithic capillary columns synthesized from a single phosphate-containing dimethacrylate monomer for cation-exchange chromatography of peptides and proteins, J. Chromatogr. A, 1218(2011) 4322-4331.

[10] Lidija Urbas, Bostjan Kosir, Matjaz Peterka, et al, Reversed phase monolithic analytical columns for the determination of HA1 subunit of influenza virus haemagglutinin, J. Chromatogr. A, 1218 (2011) 2432-2437.

[11] Alen Albreht, Irena Vovk, Applicability of analytical and preparative monolithic columns to the separation and isolation of major whey proteins, J. Chromatogr. A, 1227(2012) 210-218.

[12] Dubravko Forcic, Marija Brgles, Jelena Ivancic-Jelecki, et al, Concentration and purification of rubella virus using monolithic chromatographic support, J. Chromatogr. B, 879(2011) 981-986.

[13] Marija Brgles, James Clifton, Robert Walsh, Selectivity of monolithic supports under overloading conditions and their use for separation of human plasma and isolation of low abundance proteins, J. Chromatogr. A, 1218 (2011) 2389- 2395.

[14] F. Svec, J.M.J. Frechet, Modified poly(glycidyl methacrylate-co-ethylene dimethacrylate) continuous rod columns for preparative-scale ion-exchange chromatography of proteins, J. Chromatogr. A, 702(1995) 89-95.

[15] C. Virklund, F. Svec, J.M.J. Frechet, Fast ion-exchage HPLC of proteins using porous poly(glycidyl methacrylate-co-ethylene dimethacrylate) monolithic grafted with poly(2-acrylamido-2-methy-1-propanesulfonic acid), Biotech Prog, 13(1997) 597-603.

[16] Mutsumi Takahashi, Tomohiko Hirano, Shinya Kitagawa, et al, Separation of small inorganic anions using methacrylate-based anion-exchange monolithic column prepared by low temperature UV photo-polymerization, J. Chromatogr. A , 1232(2012) 123-127.

[17] Zeid A. Al-Othman, Ahmad Aqel, Muteb K.E. Alharbi, et al, Fast chromatographic determination of caffeine in food using a capillary hexyl methacrylate monolithic column, Food Chemistry, 132(2012) 2217-2223.

[18] He Zhang, Yunyun Jiang, Jun Wen, et al, Rapid determination of telmisartan in human plasma by HPLC using a monolithic column with fluorescence detection and its application to a bioequivalence study, J. Chromatogr. B, 877(2009) 3729-3733.

[19] Qi Liang Deng, Yan Li Li, Li Hua Zhang, Molecularly imprinted macroporous monolithic materials for protein recognition, Chinese Chemical Letters, 22(2011) 1351-1354.

[20] B. Schlemmer, R. Bandari, L. Rosenkranz, et al, Electron beam triggered, free radical polymerization-derivedmonolithic capillary columns for high -performanceliquid chromatography, J. Chromatogr. A, 1216(2009) 2664- 2670.

Advanced Materials Research Vol. 936 (2014) pp 950-954
© (2014) Trans Tech Publications, Switzerland
doi:10.4028/www.scientific.net/AMR.936.950

The Synthesis and Electro-optical Properties of Perylene Dicarboximide Dimer with Electron Withdrawing Groups

Huimin Wei,[1] Nan Zhao,[1] Nan Jiang,[1] Wenfeng Duan,[1] Baoxiang Gao[1,2,a]

[1]College of Chemistry and Environmental Science, Hebei University, Baoding, 071002, P. R. China.

[2] Key Laboratory of Medicinal Chemistry and Molecular Diagnosis, Ministry of Education

[a]bxgao@hbu.edu.cn

Keywords: Perylene dicarboximide, Electron withdrawing groups, Optoelectronic properties, Extinction coefficient, Fluorescence quantum yield.

Abstract: Perylene dicarboximide dimer with electron withdrawing groups were synthesized and fully characterized by ^{1}H-NMR and ^{13}C-NMR spectra. The effects of the substituted groups on the optical and electrochemical properties of the two compounds were investigated. The π–π* absorption peak of the perylene dicarboximide dimer compounds were red shifted from 525nm to 535nm. The band gaps of the dimer could be tuned from 2.28 eV to 2.13 eV. The first reduction wave of the dimer with electron withdrawing groups is shifted by 60 mV to more positive potential compared to that of perylene dicarboximide, suggesting the enhanced electron affinity. Furthemore, the dimer exhibited intermolecular aggregation, and decrease fluorescence quantum yield.

Introduction

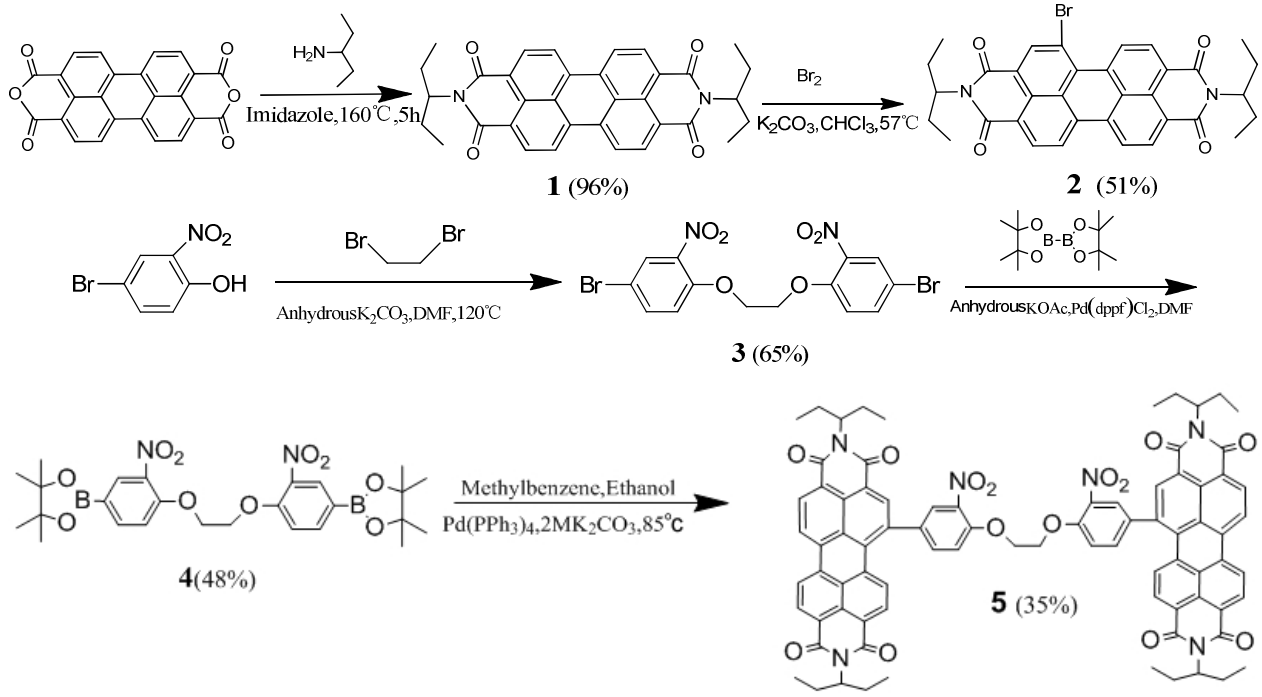
Rylenes and their dicarboxylic imide derivatives are key chromophores due to their excellent chemical and photostability [1,2]. The absorption, and emission behavior of this class of materials can be efficiently controlled by functionalization using a variety of different synthetic procedures[3]. Up to now, perylenebis(dicarboximide) and higher rylenes, namely terrylene, quaterrylene, pentarylene, and hexarylene, have been synthesized[4,7]. Perylene dicarboximide *(PDIs)*, the well-known rylenes, have received considerable attention in dye chemistry, supramolecular assemblies, and optoelectronic applications because of their exceptional properties, such as photochemical stabilities, high quantum yields[8], and ability to self-assemble into ordered supramolecular structures[9]. Modifications of PDIs have been concentrated on the bay regions, at which chemical substitution can dramatically alter the intermolecular interactions, and the optical electronic properties[10,11]. Furthermore, the core-extended of PDIs attract huge interest and offer access to various biological [12] as well as organic electronic applications[13].

Our current interests are development of the new rylenes dicarboxylic imide compounds with functional groups for use as stable fluorophores[14,15,16]. In this paper, the synthesis of the perylene diimides dimer with electron withdrawing groups was present, and their optical and electrochemical properties were further investigated.

Results and Discussion

The synthetic approach of compound 1 and 5 is outlined in Scheme 1. Compound 1 and Compound 2 were synthesized according to literature methods. Imidazole melting method between

perylene tetracarboxylic acid dianhydride and 3-aminopentane to give compound 1, which was brominated to afford compound 2. Electrophilic substitution between 4-bromo-2-nitrophenol and 1,2-dibromoethane gave the intermediate compound 3 (1,2-bis(4-bromo-2-nitrophenoxy)ethane) in a yield of 65%. Conversion of 3 into diboronate ester 4 was achieved under Miyaura reaction conditions in the presence of bis(pinacolato)diborane, $Pd(dppf)_2Cl_2$ and KOAc with dry DMF as the solvent. The objective product compound 5 was obtained by Pd-catalyzed Suzuki coupling reaction between compound 2 and compound 4. After purification by silica gel column chromatography, pure compound 5 was obtained in good yield of 35%. Structures of all these products were confirmed by ^{1}H-NMR and ^{13}C-NMR spectra.



Scheme.1, Synthetic sequence of perylene dicarboximide dimer compound.

The absorption of compound 1 and 5 was recorded in dichloromethane (Fig. 1, A). The absorption bands of compound 1 with peak at 525 nm are attributed to the perylene dicarboximide core π–π* transition, along with two higher vibronic transitions located at 495 and 462 nm, which is a typical dissolved PDI molecule (Fig. 1, A). Compared with compound 1, the π–π* transition absorption of compound 5 are red shifted from 525 nm to 535 nm. This is because the reinforcing of the conjugation between perylene diimides core and benzene on the bay region. The compound 1 exhibits a very high fluorescence quantum efficiency, almost 100%. When the solution concentration increases from 10^{-5}mol L^{-1} to 10^{-4}mol L^{-1}, the fluorescence quantum efficiency of compound 1 almost unchanged. The compound 5 exhibited a 62% fluorescence quantum yield in a low concentration of 10^{-5}mol L^{-1}. However, at a high concentrations of 10^{-4}mol L^{-1}, the fluorescence quantum efficiency reduced to 45%(Fig. 1, B). This is due to the behavior of dimer intermolecular aggregation , leading to a decrease in the fluorescence quantum efficiency.

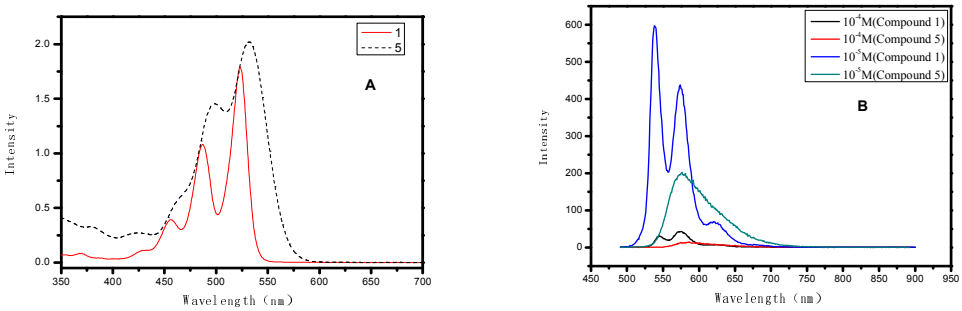


Fig. 1, The absorption spectra(A) and fluorescence emission spectrum(B) of compounds 1 and 5 in CH_2Cl_2 solution with a concentration of 2×10^{-5}mol L^{-1}.

The aggregation behaviors of PDIs in dichloromethane solution were studied by the concentration-dependent UV-vis absorption spectroscopy (Fig. 2). The aggregation in CH_2Cl_2 solution was further supported by the changes in the absorption extinction coefficient at different concentrations. Upon increasing the concentration range from 1.0×10^{-5} mol L^{-1} to 1.0×10^{-4}mol L^{-1}. the extinction coefficient (0–0 transition) of compound 1 did not change. Due to the aggregation, a non-Lambert–Beer law behavior was observed for the investigated compound 5. In the same concentration range, the extinction coefficient (0–0 transition) of compound 5 decreased by 33% (14.7×10^{-4} $M^{-1}cm^{-1}$ to 9.9×10^{-4} $M^{-1}cm^{-1}$). This indicates, the dimer molecule exhibited aggregation behavior in a relatively high concentration.

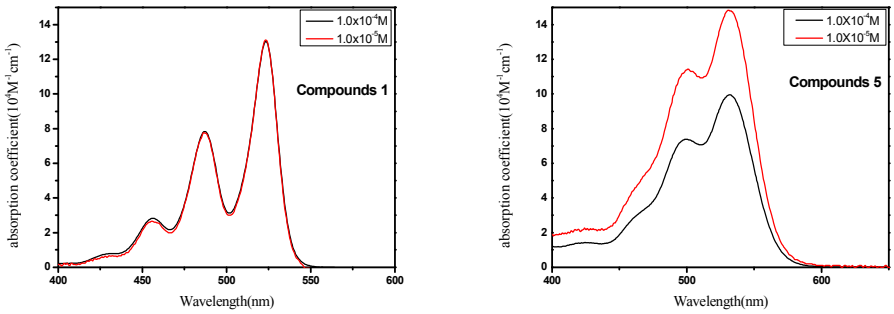


Fig. 2, Concentration-dependent UV-vis absorption spectra of compound 1 and 5 in CH_2Cl_2 solution at 20℃.

The electrochemical properties of compounds 1 and 5 were studied by cyclic voltammetry (CV)experiments. Cyclic voltammetry was performed on a CHI-660b electrochemical analyzer with a three-electrode cell in 2-3mg/mL compound dichloromethane solution with 0.1 M tetrabutylammonium hexafluorophosphate at a scan rate of 100 mV/s. A Pt disk (2-mm diameter) was used as working electrode with a Pt wire as the counter electrode and a calomel electrode as the reference electrode. The redox potential was calibrated with ferrocene/ferrocenium (0.44 V vs Calomel). The corresponding data are collected in Table 1. Figure 3 shows the cyclic voltammograms of compound 1 and 5. The CV scan for compound 1 and 5 with anodic scanning from 0 to 2 V shows no peaks. On cathodic scanning, compound 1 exhibits one reversible reduction wave at -0.66 V versus Calomel and the second irreversible reduction wave at -0.89 V. Compounds 5 also exhibit two reduction waves. The first reduction wave of compound 5 is shifted by 60 mV to more positive potential compared to that of compound 1, suggesting the enhanced electron affinity. Compound 5 has one electron-withdrawing groups in the bay region of the PDIs, which is a polarized species and enhanced the reduction potentials dramatically.

The optical band gap (E^o_g) levels, the lowest unoccupied molecular orbital (LUMO) and the highest occupied molecular orbital (HOMO) of these compounds were determined from their

electrochemical data and their absorption data. Optical band gap was obtained from the Eq. 1. The LUMO was estimated from the onset reduction potentials(Eq. 2), and the HOMO of these compounds was estimated from the Eq. 3. The E^o_g levels of compound 5 are shifted from 2.28 to 2.13eV compared with compound 1. The LUMO of compound 5 is -3.80eV , reduced 60mV compared with compound 1. The HOMO of compounds 1 and 5 are -5.93 and -6.02 eV, respectively. In comparison, compound 5 has relatively lower LUMO and small band gap. This indicates that the LUMO lie on the polarized electron-deficient parts of compound 5, and the HOMO lie on the perylene dicarboximide core.

TABLE 1 OPTICAL AND ELECTROCHEMICAL PROPERTIES AND BAND GAP DATA OF COMPOUND 1 AND 2

Compound	λ_{onset}(nm)	E^0_g(eV)	LUMO(eV)	E_{red}(eV)	HOMO(eV)
1	543.93	2.28	-3.74	-0.66	-5.93
5	581.40	2.13	-3.80	-0.60	-6.02

$$E^o_g = 1240/\lambda^{abs}{}_{onset}. \quad (1)$$

$$LUMO = -(4.40 + E_{red}). \quad (2)$$

$$HOMO = LUMO - E^o_g. \quad (3)$$

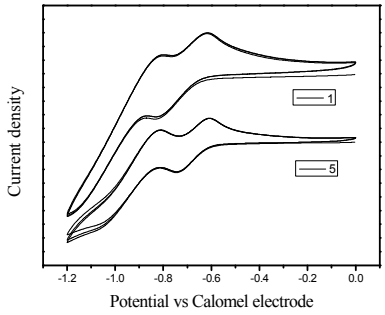


Fig. 3, Cyclic voltammograms of compounds 1 and 5 were performed with a three-electrode cell in dichloromethane solution.

Conclusions

In summary, the perylene dicarboximide dimer with electron withdrawing groups have been successfully designed and synthesized. The optical and electrochemical properties and band gap of the dimer and compound 1 were investigated. Introduction of aromatic substituent on the bay of the perylene dicarboximide resulted in the red shifted π–π* transition absorption and smaller band gap. The dimer molecule exhibited aggregation behavior, which lead to low extinction coefficient and fluorescence quantum efficiency. The addition of electronwithdrawing groups onto the lead to a high electron-accepting capability and lower LUMO level.

Acknowledgment

This work was supported by Hebei Province for Distinguished Young Scholar (B2012201031), the National Natural Science Foundation of China (21274036), the Program for New Century

Excellent Talents in University (NCET-12-0684), Training Program for Innovative Research Team and Leading talent in Hebei Province University (LJRC024).

References

[1] W. Herbst, K. Hunger, Industrial Organic Pigments: Production, Properties, Applications, Wiley-VCH, Weinheim, 3rd edn, 2004.

[2] X.W. Zhan, A. Facchetti, S. Barlow, T.J. Marks, M.A. Ratner, M.R. Wasielewski, S.R. Marder, Rylene and related diimides for organic electronics, Adv. Mater. 23(2011) 268–284.

[3] Y. Avlasevich, C. Li, K. Müllen, Synthesis and applications of core-enlarged perylene dyes, J. Mater. Chem. 20(2010) 3814–3826.

[4] L.E. Sinks, B. Rybtchinski, M. Iimura, B.A. Jones, A.J. Goshe, X.B. Zuo, D.M. Tiede, X.Y. Li, M.R. Wasielewski, Self-Assembly of photofunctional cylindrical nanostructures based on perylene-3,4:9,10-bis(dicarboximide)**,** Chem. Mater. 17(2005) 6295–6303.

[5] F.O. Hortrup, G.R.J. Müller, H. Quante, S. de Feyter, F.C. de Schryver, K. Müllen, Terrylenimides: New NIR fluorescent dyes, Chem. Eur. J. 3(1997) 219–225.

[6] H. Quante, K. Müllen, Quaterrylenebis(dicarboximides), Angew. Chem., Int. Ed. Engl. 34(1995) 1323–1325.

[7] N.G. Pschirer, C. Kohl, F. Nolde, J. Qu, K. Müllen, Pentarylene and hexarylenebis (dicarboximide)s: Near-Infrared-Absorbing polyaromatic dyes, Angew. Chem., Int. Ed. 45(2006) 1401–1404.

[8] Y. Nagao, T. Misono, Synthesis and properties of N-alkyl-N′-aryl-3,4:9,10-perylenebis (dicarboximide), Dyes Pigm. 5 (1984) 171-188.

[9] Z. Chen, A. Lohr, C.R. Saha-Möller, F. Würthner, Self-assembled π-stacks of functional dyes in solution: structural and thermodynamic features, Chem. Soc. Rev. 38(2009) 564-584.

[10] U. Rohr, P. Schlichting, A. Böhm, M. Gross, K. Meerholz, C. Bräuchle, K. Müllen, Liquid crystalline coronene derivatives with extraordinary fluorescence properties, Angew. Chem. Int. Ed. 37(1998) 1434-1437.

[11] H.A. (a) Wegner, L.T. Scott, A. de Meijere, A New Suzuki−Heck-Type Coupling Cascade: Indeno[1,2,3]-Annelation of polycyclic aromatic hydrocarbons, J. Org. Chem. 68(2003) 883-887.

[12] M. Franceschin, A. Alvino, V. Casagrande, C. Mauriello, E. Pascucci, M. Savino, G. Ortaggi, A. Bianco, Specific interactions with intra- and intermolecular G-quadruplex DNA structures by hydrosoluble coronene derivatives: A new class of telomerase inhibitors, Bioorg. Med. Chem. 15(2007) 1848-1858.

[13] P. Samorì, N. Severin, C.D. Simpson, K. Müllen, J.P. Rabe, Epitaxial composite layers of electron donors and acceptors from very large polycyclic aromatic hydrocarbons, J. Am.Chem. Soc. 124(2002) 9454-9457.

[14] B.X. Gao, H.X. Li, H.M. Liu, L.C. Zhang, Q.Q. Bai, X.W. Ba, Water-soluble and fluorescent dendritic perylene bisimides for live-cell imaging, Chem. Commun. 47(2011) 3894–3896.

[15] B.X. Gao, D.F. Xia, L.C. Zhang, Q.Q. Bai, L.B. Bai, T. Yang, X.W. Ba, Helical columnar liquid crystals based on dendritic peptides substituted perylene bisimides, J.Mater.Chem. 21(2011) 15975-15980.

[16] Q.Q. Bai, B.X. Gao, Q. Ai, Y.G. Wu, X.W. Ba, Core-Extended terrylene diimide on the bay region: synthesis and optical and electrochemical properties, Org. Lett. 13 (2011) 6484-6487.

Advanced Materials Research Vol. 936 (2014) pp 955-959
© (2014) Trans Tech Publications, Switzerland
doi:10.4028/www.scientific.net/AMR.936.955

Effect of aniline oligomer on the electrosynthesis of polyaniline fibres

Baosong Li[1,a] Lei Zhang[1,a] Weiwei Zhang[2,b] and Yang Yu[1,a]

[1]College of Mechanics and Materials, Hohai University, Nanjing 210098, China

[2]College of Mechanical and Electrical Engineering, Hohai University, Changzhou 213022, China

[a]bsli@hhu.du.cn, [b]zdzdq@126.com

Keywords: polyanilne fibres, electrochemical polymerization, p-aminodiphenylamine, oligomer; conductive polymer

Abstract: In this paper, polyaniline(PANI) fibres were prepared by electrochemical polymerization from the solutions of aniline and hydrochloric acid in the presence of different concentrations of aniline oligomer. The influences of adding a small amount of aniline oligomeric additives, such as p-aminodiphenylamine (PADPA), p-phenylenediamine (PPDA) to the electrochemical polymerization system of aniline on polyaniline fibres have been investigated. Change in fibre diameter with the concentration of aniline oligomer were investigated. Morphologies of PANI fibres were characterized by scanning electron microscopy (SEM). Electrochemical behaviors of PANI fibres were studied by cyclic voltammetry (CV). The results show that with the addition of PADPA, PPDA to aniline polymerization system, the rate of polymerization increases greatly, and more lower potentials can be applied to generate electroactive PANI fibres with more finer and uniform structure.

Introduction

It is known that the polymerization of aniline is an autocatalytic process[1]. With potentiostatic techniques the initial formation of PANI on the surface of the electrode is slow, but the initially formed PANI accelerated the polymer growth greatly. However, the quantitative description and interpretation of this process are still unclear. The role played by PADPA during the electrochemical polymerization of aniline in acid medium on platinum electrodes was proposed for the first time by Mohilner in the early 1960s[2]. The polymerization mechanism involved a so-called “head-to-tail” coupling of two aniline radical cations that, as it was pointed out, gave rise to the PADPA and subsequently to an oligomeric growth. This hypothesis was confirmed some years later by Bacon and Adams, who identified PADPA as the main product formed during the initial stages of aniline oxidation on carbon paste electrodes[1]. In the present paper, a small amount of aniline oligomeric additives, such as PADPA , PPDA is intentionally introduced in the aniline polymerization system. The effects of the additives on the rate of electrochemical polymerization of aniline are investigated. The morphologies of the PANI prepared in the presence of the additives are studied by scanning electron microscopy. The results are discussed in relation to the mechanism of polymerization of aniline.

Experimental Section

Aniline was purchased from Sinopharm Chem. Reagent Co. Ltd (Beijing, China) and were doubly distilled under reduced pressure before use. The PADPA, PPDA supplied by Aldrich were used without further purification. The monomers employed for the polymerization reaction were of reagent grade. Electrochemical polymerization of aniline was performed by CHI660D electrochemistry work-station (Shanghai Chenhua Instrument CO., Ltd.) under programmed computer control. A three-electrode cell was employed with a saturated calomel electrode (SCE) as reference electrode. Platinum foils were used as both the counter electrode (3.0 cm^2) and the working electrode whose size varied in each specific experiment. Platinum electrodes were pretreated by dipping in hydrochloric acid for 1 minute, followed by wash in acetone and deionized water. PANI were prepared on a

platinum working electrode in a 1.0 M hydrochloric acid, 0.2 M aniline aqueous solution with 0-2.0 mM additives at room temperature.

Results and Discussion

Effects of PADPA and PPDA on electrochemical polymerization of PANI

The anodic peak at near 0.18 V vs SCE in Fig. 1(a) has been well understood as the oxidation of PANI deposited on the electrodes which corresponds to the conversion of amine units to radical cations. At this potential, neither polymerization of aniline nor other side reactions were observed. The peak current increased continually with successive potential scans, indicating the build up of the electroactive PANI in the solution. However, the corresponding reduction peak is not obvious. It can been seen that there is no PANI formed on the electrode surface without additives when switch potential is 0.8V.

When the electrochemical polymerization switch potential is increased to 1.0V, as shown in Fig. 1(b), the redox peaks of aniline in the electrochemical polymerization are greatly increased. This indicates that the rate of the electrochemical polymerization increased significantly. In the first scan of Fig. 1(c), an anodic peak due to the oxidation of the PADPA appeared at +0.48 V vs. SCE, whereas no reaction occurs at this potential for the system without PADPA. In general, characteristics of the cyclic voltammograms are similar in this systems. The anodic peak at +0.17-0.19 V can be assigned to the oxidation of PANI deposited on the electrode, corresponding to the conversion of amine units to radical cations in the polymer chain. It was found that the mass and thickness of the PANI film formed on the electrode are proportional to the anodic peak current at +0.18 V[13]. Therefore, the rate of polymerization can be measured by the rate of increase in this peak current. There are two pairs of redox peaks, at 017-0.19/0.03V, 0.48/0.44V, corresponding to the different redox patterns, respectively, as shown in Fig. 1(c). This indicates that the presence of PADPA will lower the polymerization potential and accelerate the rate of polymerization, which would produce more finer fibres. Fig.1(d) indicates that the addition of PPDA to the aniline system will increase the rate of polymerization and lower the polymerization potential[4, 5]. In addition, more finer and longer fibres could be obtained.

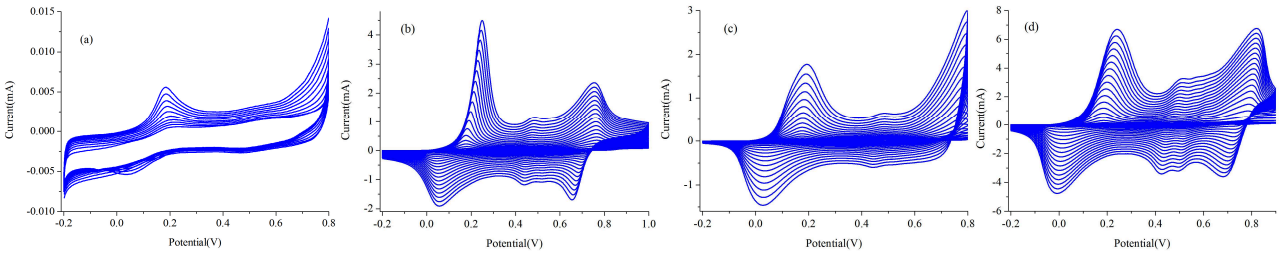


Fig. 1 Cyclic voltammograms of aniline polymerization in a 1.0 M HCl aqueous solution containing 0.2 M of aniline at 50 mV·s-1, (a) no additives, scanning between -0.2 and 0.8V, (b) no additives, scanning between -0.2 and 1.0 V, (c) 2.0 mM PADPA, scanning between -0.2 and 0.8V, (d) 5.0 mM PPDA, scanning between -0.2 and 0.9V.

It is apparent that the growth of the PANI film is faster for the system with the additives than that without the additives. Similar to what has been usually accepted for PANI, it can be assumed that the mass of the PANI film deposited onto the electrode surface is proportional to the peak current measured on the cyclic voltammograms. When the amount of PANI deposited on the electrode is higher, the rate of polymer formation slows down. This could be attributed to an increase in the film thickness as the amount of polymer on the electrode increases. Thus, in order to accelerate the polymerization, the polymer has to be in contact with the solution, i.e., with the monomer. When the polymer film thickness increases, the polymer that has been produced during the earlier period of reaction will be covered by the polymer that has been produced later, even though the effective surface area of the polymer may increase with the reaction time due to a fibrillar morphology. As a result, the polymer deposited earlier will no longer be in contact with solution, and it will contribute no effect to the reaction rate.

Morphology and structure of PANI

Scanning electron microscopy was used to examine the morphology of PANI prepared with different concentrations of PADPA, PPDA additives. A fibrillar morphology was observed for all the samples. The PANI film prepared with the PADPA, PPDA was more finer than that without the additives. Furthermore, the uniformity of the film also increased with an increase in the switch potential. These results agree well with the proposed mechanism. Thus, both the addition of the additives and the higher switch potential would result in more initiation species on which the polymer chains grow. Fig. 2 show the SEM of PANI prepared by potentiostatic 0.8 V for 2000 s, in 1 M HCl and 0.3 M aniline solution containing different concentrations of PADPA. As can be seen in Fig. 2, the diameter of the PANI fibres become smaller with the increasing of PADPA. At 0.3 mM PADPA, the PANI fibres are wider in diameter. From 0.3 mM to 2.4 mM, the diameter of the PANI fibres is decreasing. This indicates that the PADPA could accelerate the polymerization rate and make the fibres more finer.

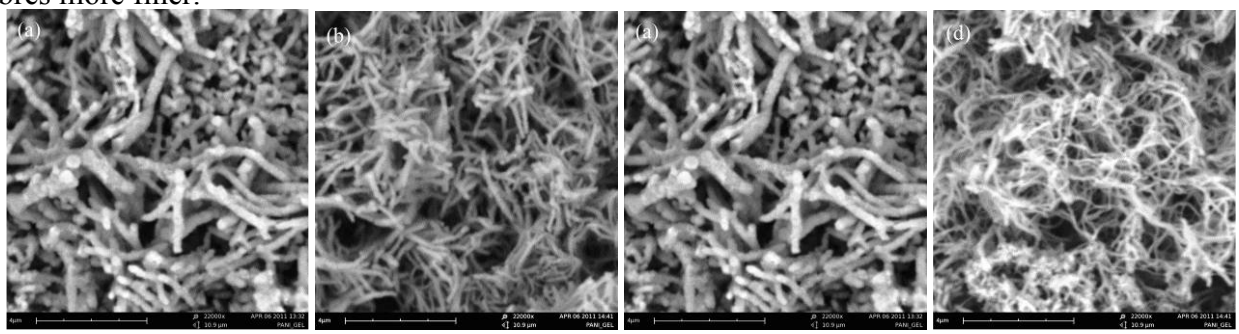


Fig. 2 SEM of PANI prepared by potentiostatic 0.8V for 2000s, in 1M HCl and 0.3M aniline solution containing PADPA: (a) 0.3 mM, (b) 1.0 mM, (c)1.7 mM, (d)2.4 mM.

Fig. 3 shows the SEM of PANI prepared by potentiostatic 0.8 V for 2000 s, in 1 M HCl and 0.3 M aniline solution containing different concentrations of PPDA. As can be seen in Fig. 3, the diameter of the PANI fibres become finer with the increasing of PPDA. However, this trend is not very obvious compared to PADPA. It shows that, compared with the PADPA, PPDA has more effect on the length of the fibres. In the presence of PPDA, the length of the PANI fibres formed is obvious longer than in the presence of PADPA. The growing mechamism for longer fibres is probably related to the two amidos of PPDA which give it more reaction positions. This makes it possibility that more uniform PANI could be obtained.

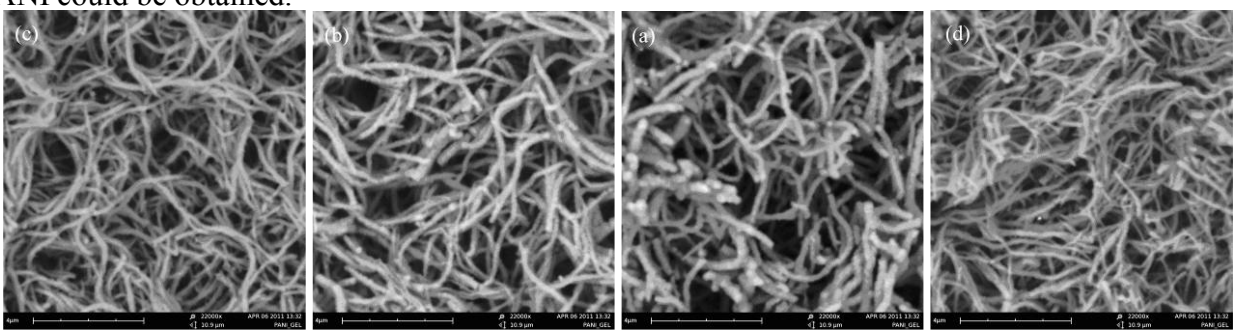


Fig. 3 SEM of PANI prepared by potentiostatic 0.8 V for (a) 2000 s, (b) to (e) 1000 s, in 1 M HCl and 0.3 M aniline solution containing PPDA (a) 0.3 mM, (b) 1.0 mM, (c) 1.7 mM, (d) 2.4 mM.

It can be seen that the fibre will become finer with the addition of oligomeric additives, such as PADPA, PPDA. As for PADPA in Fig.4, the diameter decreases greatly from about 480 nm to 220 nm with the concentrations of PADPA increasing from 0.1 mM to 1.0 mM. The fibre decreases slowly to 160 nm in diameter when PADPA was 2.4 mM. As for PPDA, the diameter decreases greatly from about 480 nm to 321 nm with the concentrations of PPDA increasing from 0.1 mM to 0.5 mM. Then the fibre decreases slowly to 208 nm in diameter when PADPA was 2.4 mM. It can be concluded that the addition of PADPA or PPDA could modify the diameter of the PANI fibres.

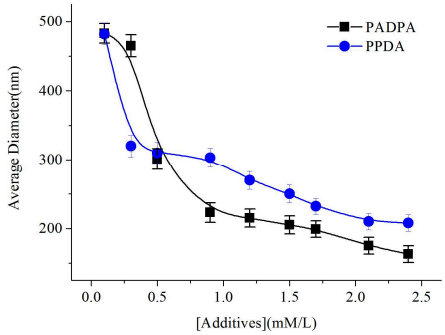


Fig. 4 The average diameter of the PANI fibre.

Electrochemical characterization of the PANI formed

Fig. 5 shows that cyclic voltammograms of PANI at a scan rate of 50 mV·s-1 in 1.0 M HCl aqueous solution without aniline. Fig. 5(a) is cyclic voltammograms of PANI formed according to electrochemical polymerization conditions of Fig. 1(b) without additives. Fig. 5(b) and (c) is in the presence of 2.0 mM PADPA and 1.2 mM PPDA, respectively. In comparison with these three Fig.s, it can be seen that the anodic peaks at 0.24, 0.21 and 0.23 V respectively. It indicates that the polymerization potential is lower about 30 mV in the presence of 2.0 mM PADPA. The results obtained confirm the earlier established catalytic effect on the potential of the redox reaction by shifting it to more negative values. In the presence of PPDA, the potential of the redox reaction did not change much, however, the fibres will grow more longer and finer. This has been proved by the SEM data.

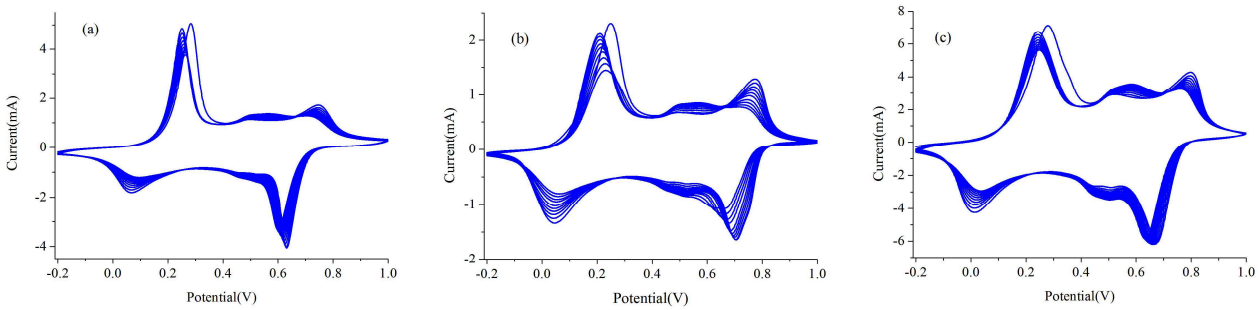


Fig. 5 Cyclic voltammograms of PANI at 50 mV·s-1 in 1.0 M HCl aqueous solution without aniline. PANI formed (a) no additives, polymerization conditions of Fig. 1(b); (b) with 2.0 mM PADPA, Fig. 1(c); (c) with 1.2 mM PADPA , polymerization conditions of Fig. 1(d).

The effects of switch potential on the rate of polymerization with or without the additives are compared. In general, a higher rate of polymerization can be achieved by increasing the switch potential, at the risk, however, of polymer degradation and other undesired side reactions. The polymerization of aniline in the presence of the PADPA, PPDA can proceed at lower switch potentials without sacrificing the rate of polymerization. PANI was formed at a potential as low as +0.55 V in the presence of the PADPA, whereas no polymer formed at this potential in the absence of the PADPA within a reasonable time span. When the switch potential was increased to +0.9 V or above, the rates of polymerization became essentially the same for the system with the additives and for that without.

Conclusions

The results of these investigations confirm that the addition of PADPA, PPDA to aniline monomers polymerization solution can fast the polymerization rate, lower the polymerization potential, and produce electroactive PANI with more finer or longer fibrillar structure. The PADPA have more effect on forming finer fibres and PPDA is contribute to form longer fibres. This results in a more compact, uniform and finer PANI compared to pure aniline solution, indicating that by administering a predetermined concentration of PADPA, PPDA, the morphology and structure of the resulting PANI could be tailored.

Acknowledgments

This work was supported by the National Natural Science Foundation of China (Grant No. 51301061), the Fundamental Research Funds for the Central Universities of Hohai Uinversity, China(Grant No. 2013B32614) and the Application Research Foundation of Nantong(Grant No. BK2012059).

References

[1] J.Bacon, R.Adams: J. Am. Chem. Soc. Vol. 90 (1968) p. 6596
[2] D. Mohilner, R. Adams, W. Argersinger: J. Am. Chem. Soc. Vol. 84 (1962) p. 3618
[3] Y.Wei, X.Jia, D.Jin, F.Davisa : Macromol. Rnpid Cornniun. Vol. 17 (1996) p. 897
[4] M. Oyharcabal, T. Olinga, M. Foulc : Composites Sci. Technol. Vol. 74 (2013) p. 107
[5] M. She, R. Ho : Polymer Vol. 53 (2012) p. 2628

Advanced Materials Research Vol. 936 (2014) pp 960-964
© (2014) Trans Tech Publications, Switzerland
doi:10.4028/www.scientific.net/AMR.936.960

Preparation and properties of electroactive PANI by electrodeposition

Baosong Li[1,a] Yang Yu[1,a] Weiwei Zhang[2,b] and Lei Zhang[1,a]

[1]College of Mechanics and Materials, Hohai University, Nanjing 210098, China

[2]College of Mechanical and Electrical Engineering, Hohai University, Changzhou 213022, China

[a]bsli@hhu.du.cn, [b]zdzdq@126.com

Keywords: polyaniline fibres, electrodeposition, cyclic voltammetry, morphology

Abstract. Electroactive polyaniline fibres have been prepared by eletrodeposition in aniline and hydrochloric acid aqueous media. The influence of applied potential and polymerization time on the electrochemical polymerization of polyaniline fibres have been investigated. Morphology and structure of PANI were characterized by scanning electron microscopy. Electrochemical behaviors of PANI were studied by cyclic voltammetry. The results show that the applied potential and the polymerization time have a crucial influence on the polymerization rate and conductivity of the PANI prepared. It indicates that the properties, as well as the morphology of PANI, could be changed by applied potential and po-lymerization time, etc. This change might result in the quality of PANI suitable for specific applications.

Introduction

Among all of CPs, PANI is a particularly attractive material because it has a moderately high electrical conductivity upon doping with protonic acids and its interesting electrochemical behavior [1, 2]. PANI can be prepared either chemically or electrochemically. Although polyaniline have been studied much, many problem are still not solved about polyaniline fibres which quality suitable for specific ap-plications.

In the present paper, the influence of applied potential and polymerization time on the electrochemical polymerization of polyaniline fibres have been investigated. With hydrochloric acid, as doping acids, the polyaniline fibres were obtained. The structure and morphology of PANI were characterized. The elec-trochemical properties of the polyaniline fibres were studied by CV. The results are discussed in relation to the mechanism of polymerization of aniline.

Experimental Section

Materials

Aniline (analytical pure grade) was purchased from Sinopharm Chem. Reagent Co. Ltd (Beijing, China) and were doubly distilled under reduced pressure before use. Hydrochloric acid (analytical pure grade) were bought from Beijing Chem. Reagent Co. (Beijing, China) and were used without further purifica-tion.

Preparation and characterization of polyaniline fibres

Electrochemical polymerization of aniline was performed by CHI660D electrochemistry work-station (Shanghai Chenhua Instrument CO., Ltd.). A three-electrode cell was employed with a saturated calomel electrode (SCE) as reference electrode. Platinum foils were used as counter electrode and working elec-trode. Platinum electrodes were pretreated by dipping in hydrochloric acid for 1 minute, followed by wash in acetone and deionized water. Polyaniline fibres were prepared on a platinum working electrode in a 0.5 M aniline aqueous solution with 1.0 M hydrochloric acid at room temperature. The electrochemical properties of the polyaniline fibres were characterized in an aniline free, 1.0 M hydrochloric acid aqueous solution. The microstructure of the PANI was examined by SEM.

Result s and Discussion

Electrochemical polymerization of polyaniline

Fig. 1(a) shows the cyclic voltammogram transients traced during the PANI polyaniline fibres with Pt electrode at a scan rate of 20 mV/s in an solution of 0.5 M aniline and 1 M HCl, scanning beween 0.2 V and 1.25 V. It can be seen in Fig. 1(a) that there are three anodic peaks, and these anodic peak current is gradually increased with the scanning numbers. The peak potentials are shifting to more positive potential with scanning cycles. This indicates that the quantity of PANI formed is increasing, and the electrochemical stability is improved. As the energy barrier which initiates the polymerization is higher than the energy barrier which maintains the reaction, polymerization proceeds slowly in the initiation stage. PANI polymerization is a selfcatalytic reaction process, and the generated PANI could accelerate the following reaction. In the fifth cycle, the first anodic peak is at 0.57 V, the second anodic peak is at 0.83 V and the third anodic peak is at 1.17 V. However, in the twentieth cycle, the first anodic peak is at 0.74 V, the second anodic peak is at 0.94 V and the third anodic peak is at 1.15 V. This indicates the changes of the electroactivity of PANI fibres formed. PANI prepared by electrochemically is fibrous morphology. Compared with the electrochemical and chemical polymerization methods, the fibres formed by electrochemically is longer than formed by chemically. It indicates that uniform and conductive PANI fibres was easy to be produced by electrochemical methods.

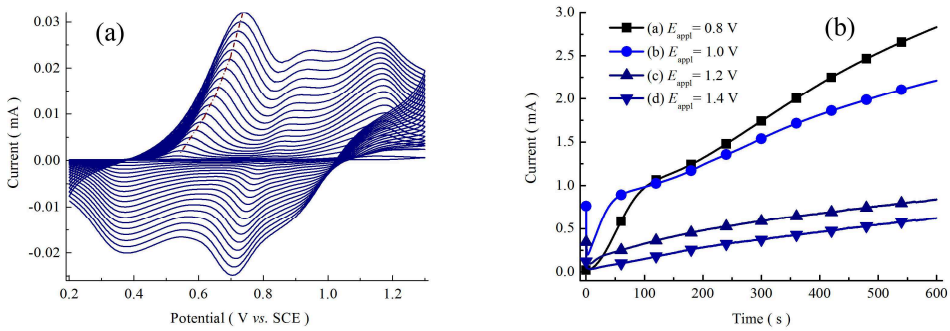


Fig. 1 (a) Cyclic voltammogram transients traced during the PANI fibres polymerization in 0.5 M aniline and 1 M HCl, v =20 mV/s, 20 cycles.(b) Potentiostatic current-time curves of the PANI fibres electrosynthesis process in 0.3 M aniline and 1 M HCl solution at different applied potentials(E_{appl}).

When the amount of PANI deposited on the electrode is higher, the rate of polymer formation slows down. This could be attributed to an increase in the film thickness as the amount of polymer on the electrode increases. Thus, in order to accelerate the polymerization, the polymer has to be in contact with the solution, i.e., with the monomer[3, 4]. When the polymer film thickness increases, the polymer that has been produced during the earlier period of reaction will be covered by the polymer that has been produced later, even though the effective surface area of the polymer may increase with the reaction time due to a fibrillar morphology. As a result, the polymer deposited earlier will no longer be in contact with solution, and it will contribute no effect on the reaction rate.

Previous studies have shown that when PANI polymerization potential is higher than 0.8 V, the π conjugated structure of polymer could be partly destroyed for the overoxidation, which could reduce it's conductivity[5]. However, when the polymerization potential is lower than 0.6 V, the electrosynthesis is difficult to proceed and could not form a film on the electrodes effectively. Fig. 1(b) shows the potentiostatic currenttime curves of the PANI fibres electrosynthesis process in a 0.3 M aniline and 1 M HCl solution at different applied potentials. It is accepted that the reaction current is proportional to the rate of polymerization[6]. Then, it could be concluded that the reaction rate is decreasing with the increasing of applied potentials from 0.8 V to 1.4 V. As for 1.4 V, the rate of polymerization is the lowest. Considering the polymerization rate, electrical conductivity and other physical and chemical properties, PANI polymerization potential is generally between 0.7-1.0 V, and the optimized applied potential is about 0.7-0.8 V.

Morphology and structure of PANI

Scanning electron microscopy was used to examine the morphology of PANI fibres with different applied potential and polymerization time. It was observed that the PANI prepared with hydrochloric acid was fibrillar morphology. Fig. 2 shows the SEM images of PANI electrodeposited on Pt at different constant potential in an solution of 0.3 M aniline and 1 M HCl. The morphology of the PANI prepared at different applied potential is similar to each other. However, the fibres prepared at 0.8 V is finer and sparseness compared to others formed at higher applied potential. The electroactive area of the PANI is decreasing with the increasing of the applied potential from 0.8 V to 1.4 V. At 1.2 V, the diameter of the fibre is wider than low potential produced. In order to obtain large electroactive area and high conductivity of PANI, the optimized applied potential is between 0.8 V and 1.0 V.

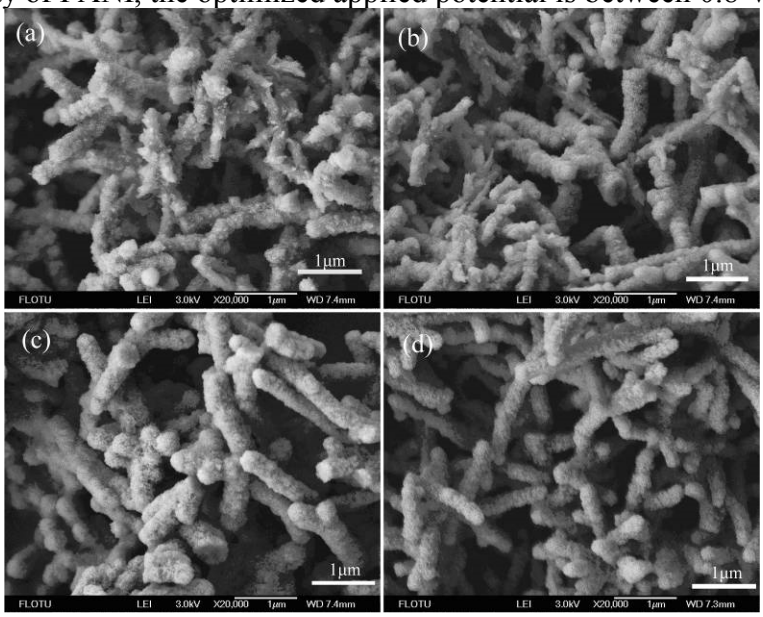


Fig. 2 SEM images of PANI fibres electrodeposited on Pt at different constant potential Eappl in an solution of 0.3 M aniline and 1 M HCl.: (a) 0.8V, (b) 1.0 V, (c) 1.2V and (d) 1.4V, time (a)-(c) 600s, (d) 300s.

Fig. 3 shows the SEM images of PANI electrosynthesized on Pt at 0.85 V for different time in an solution of 0.3 M aniline and 1 M HCl. As can be seen in Fig. 3, the diameter of the PANI fibres become wider with the polymerization time increasing. The PANI fibre is fine and short when polymerization 180s. With the polymerization time increasing, the fibre is becoming more and more wider in diameter and longer in length. It indicates that the molecular weight grows with the polymerization time. As Fig. 3(d) shows, the fibre is about 500 nm in diameter and is longer than 5 μm in length. In this view, the solubility and physical property could be modulated.

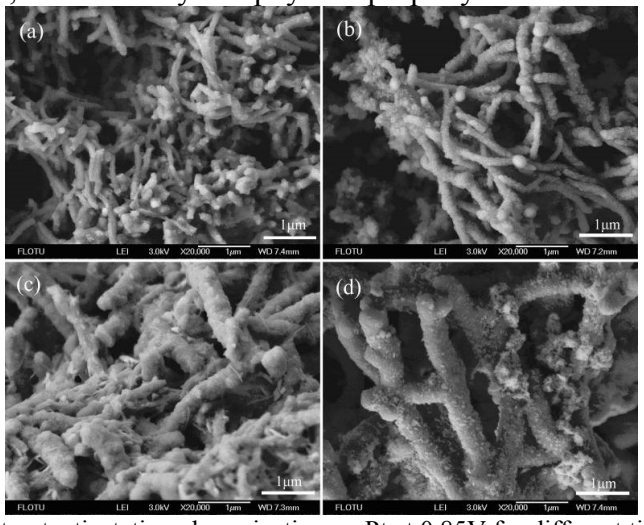


Fig. 3 SEM images of PANI at potentiostatic polymerization on Pt at 0.85V for different time in an solution of 0.3 M An and 1 M HCl.: (a) 180s, (b) 360s, (c) 720s and (d) 1440s.

Electrochemical characterization of the PANI

Fig. 4 shows cyclic voltammograms of PANI fibres synthesized by potentiostatic method at different applied potential, where the electrode potential was continuously swept between -0.2 and 1.0 V vs SCE at a scan rate of 100 $mV \cdot s^{-1}$. As can be seen in Fig. 4, with different synthesized potential, the peak potential will shift. When the synthesized potential is 0.8 V, anodic peak potential is about 0.17 V, the peak current is 0.71 mA. As for PANI fibres prepared at 1.1 V, the anodic peak potential is shift to 0.27 V, and the peak current is increasing to 0.83 mA. With the synthesized potential increasing to 1.4 V, the anodic peak potential is about 0.26 V, however, the peak current is decreasing much to 0.39 mA. Fig. 4 shows that the anodic peak potential of PANI fibres synthesized at 0.8 V is more negative than that synthesized at 1.1V and 1.4V. Compared with the Fig. 4(b) and (c), it can be observed that the peak current of 1.4V is lower than that of 1.1V. This indicates that PANI fibres synthesized at about 0.8 V has lower anodic peak potential and have good electroactivity. When the potential is higher than 1.1 V, the peak current is decreasing and it will damage the electroactivity and conductivity. The optimized applied potential is between 0.7-0.9 V vs SCE. In general, a higher rate of polymerization can be achieved by increasing the synthesize potential, at the risk, however, of polymer degradation and other undesired side reactions. When the potential was increased to +1.1 V or above, the rates of polymerization is fast, which could be attributed to that the amount of oligomer species generated from the oxidation of aniline itself was sufficient enough to sustain the polymerization at the high applied potentials. It indicates that the properties, as well as the morphology of PANI, could be changed by applied potential and polymerization time, etc. This change deserves to be studied, because it might result in the quality of PANI fibres suitable for specific applications.

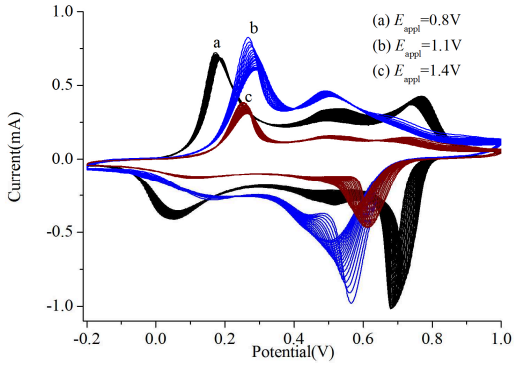


Fig. 4 Cyclic voltammogram of PANI fibres in an solution of 1M HCl, with Potentiostatic synthesized (a)0.8V, (b)1.1V, (c)1.4V, -0.2 V to 1.0 V, v = 100 mV/s.

Conclusions

The results show that the applied potential and the polymerization time have a crucial influence on the polymerization rate and the conductivity of the PANI fibres prepared. PANI prepared with hydrochloric acid was fibrillar morphology, the diameter of the PANI fibres become wider with the polymerization time increasing, the optimized applied potential is between 0.8 V and 1.0 V. It indicates that the properties, as well as the morphology of PANI fibres, could be changed by applied potential and polymerization time, etc. This change deserves to be studied, because it might result in the quality of PANI suitable for specific applications.

Acknowledgments

This work was supported by the National Natural Science Foundation of China (Grant No. 51301061), the Fundamental Research Funds for the Central Universities of Hohai Uinversity, China(Grant No. 2013B32614) and the Application Research Foundation of Nantong(Grant No. BK2012059).

References

[1] I. Falina, N. Berezina and A. Sytcheva: J. Solid State Electrochem. Vol. 16 (2012) pp. 1983-1991
[2] D. Mohilner, R. Adams, W. Argersinger: J. Am. Chem. Soc. Vol. 84 (1962) p. 3618.
[3] L.D. Arsov, W. Plieth, G. Koûmehl: J. Solid State Electrochem. Vol. 2 (1998) pp. 355-361
[4] R. Guo, Z. Li, T. Liu: J. Polym. Sci. A-Polym. Chem. Vol. 44 (2006) pp. 2388-2394
[5] Y. Sahin, S. Percin, M. Sahin, G. Ozkan: J. Appl. Polym. Sci. Vol. 91 (2004) pp. 2302–2312.
[6] H. Zhou, H. Chen, S. Luo, G. Lu, W. Wei: Polymer Bulletin Vol. 45 (2000) pp. 113-120.

Advanced Materials Research Vol. 936 (2014) pp 965-969
© (2014) Trans Tech Publications, Switzerland
doi:10.4028/www.scientific.net/AMR.936.965

Electrocatalytic Hydrogenation Of Oxalic Acid To Glyoxylic Acid On A Self-Organized Tio_2 Nanotube Electrode

Qian Yang, Zhao Fengming, Qiu Qingqing and Ma Chun-an*

College of Chemical Engineering and Materials, Zhejiang University of Technology,

Hangzhou City 310032, Zhejiang, PR China

E-mail: science@zjut.edu.cn; zhaofm@zjut.edu.cn

Keywords: anodic oxidation; self-organized; TiO_2 nanotube; electrocatalytic hydrogenation

Abstract: A study for electrocatalytic hydrogenation of oxalic acid has been reported using the self-organized TiO_2 nanotube electrode prepared by anodic oxidation method. The prepared electrode was characterized by SEM and XPS. The electrocatalytic activity of the TiO_2 nanotube electrode was evaluated by CV and galvanostatic electrolysis. The CV studies and electrochemical experiments showed that TiO_2 nanotube electrode exhibited high electrocatalytic activity. In addition, the surface of TiO_2 nanotube electrode developed into a periodic lattice of nanopores after electrolysis, which makes it find a potential application as electrocatalysts.

Introduction

Since electrochemical methods are simple and considerably avoid environmental pollution, many organic compounds are synthesized by such methods[1, 2]. Organic electrosynthesis is a method of the sustainable development of green chemistry, owing to its distinct properties such as environmental friendly and mild reaction conditions which has become one of the important frontiers of chemical research. The indirect electrosynthesis using mediator as oxidant and reductant is mostly homogeneous electrocatalytic process. Heterogeneous catalytic hydrogenation is widely used for the addition of hydrogen to olefinic (C=C), carbonyl (C=O) groups[2-5]. Compared with homogeneous catalysis, heterogeneous catalysis has more significant advantages. For instance, it can be performed at more mild conditions (room temperature and normal pressure)[6]. In most cases, industry favors heterogeneous over homogeneous catalysts because of the formers ease of handling and simple work-up[7].

Electrocatalytic reduction of maleic acid, oxalic acid and other unsaturated carbon bonds compounds using the lead cathode have been studied[8-11]. But the lead cathode can be easily deactivated[12, 13] which is the key problem and has been incompletely resolved. So, it is very necessary to find replaceable cathode materials for the reduction of these compounds. Some researchers have proposed to use the TiO_2 film electrode replacing lead electrode to electroreduction of these compounds[5, 14, 15]. In addition, our previous work using TiO_2 film electrode prepared by anodic oxidation method to electrocatalytic reduction of maleic acid and oxalic acid have been reported[3, 5]. Consequently, we found that the TiO_2 film electrode with a high electrocatalytic activity is attributed to the function of $TiO_2/Ti(OH)_3$ redox couple and its larger surface area which have many active sites[16]so that substances can be adsorbed in large quantities onto the TiO_2 surface.

In this paper, we first use the self-organized TiO_2 nanotube electrode to study the electrocatalytic hydrogenation of oxalic to glyoxylic acid. The mechanism of oxalic acid reduction on the self-organized TiO_2 nanotube electrode has been discussed. The prepared electrode exhibited higher electrocatalytic activity for the reduction of oxalic acid than that of the polished Ti electrode. Using this heterogeneous catalyst with higher electrocatalytic activity would contribute to starting a new research field for the application of TiO_2 nanotube electrode in other organic electrosynthesis.

Experimental

Preparation Of Tio_2 Nanotube Electrode

Titanium foils (0.5 mm, 99.6% purity) were polished in a mixed solution of 6 mL nitric acid, 6 mL hydrogen peroxide, 2.5 g ammonium fluoride and 0.15 g urea for 30 seconds. Then the polished titanium foils were ultrasonically cleaned in acetone and deionized water followed by rinsing with deionized water. The TiO_2 nanotubes were prepared by means of an anodic oxidation developed in glycerol solution with 0.2 M Na_2SO_4 and 0.5 wt% NaF at 20 V for 1.5 h.

Characterization

The morphology of the electrode surface was characterized using a Hitachi s-4700 field emission scanning electron microscope (FE-SEM). The analysis of the surface valence state of titanium was conducted by X-ray photoelectron spectroscopy with a Kratos Axis Ultra DLD spectrometer using a focused monochromatized Al Kα operated at 300 W.

Cyclic Voltammetric Studies

Cyclic voltammetry measurements were carried out using CHI660D electrochemical analyzer. The TiO_2 nanotube electrode and polished Ti sheet (surface area of 1 cm^2) served as the working electrode, a platinum sheet and a saturated calomel electrode（SCE）served as the counter electrode and reference electrode respectively. All CV experiments were performed in three electrochemical cells at a constant temperature of 20 ℃.

Preparative Electrolysis Experiments

The electrolysis on a preparative scale was carried out according to previous report[5]. The concentration of titanium ion during the electrolysis processes were monitored and analyzed by ICP (Inductively Coupled Plasma).

Results and discussion

Sem And Xps Characterization Of Tio_2 Nanotube Electrode

Fig.1 show the top-view morphology of TiO_2 nanotube by anodization and polished Ti sheet. It confirmed the formation of self-organized oxide layers on Ti sheet. It was found that the self-organized tubes were formed with the average diameter of 90 nm (Fig. 1A). After electrolysis experiments with the TiO_2 nanotube and polished Ti electrode, the surface of TiO_2 nanotube electrode developed into a periodic lattice (Fig.1 B) . Comparing to the nanotube electrode, surface of the polished Ti sheet remained little change (Fig.1 C and D).

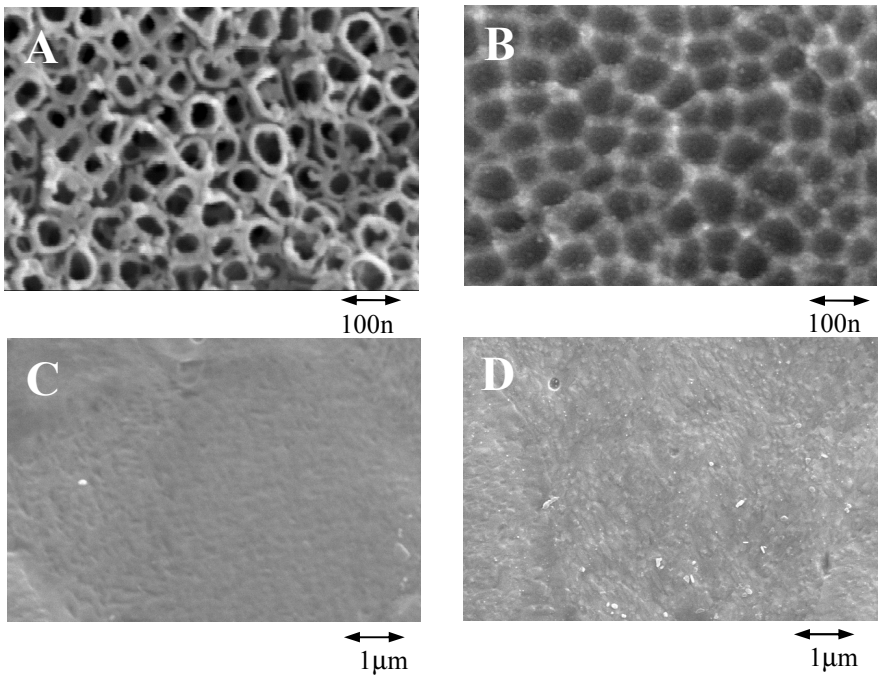


Fig.1 SEM of TiO_2 nanotube before electrolysis(A) and after electrolysis(B); polished Ti sheet before electrolysis(C) and after electrolysis(D).

XPS characterization was carried out to explore the valence state of titanium on surface of TiO_2 nanotube before and after electrolysis. The corresponding titanium 2p1/2 and 2p3/2 peaks before electrolysis were centered at 461.1 eV and 455.4 eV and after electrolysis two peaks for the titanium 2p of the electrodes were observed at 461.9 eV and 455.6 eV, which are assigned to Ti^{4+} species[17] and the other valence state of titanium was not found from Fig.2. These results further confirmed that the surface of nanotube electrode was composed of TiO_2 before and after electrolysis.

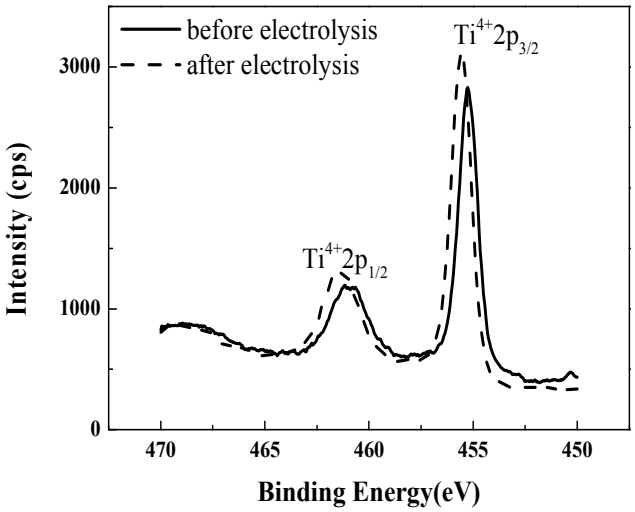


Fig. 2 XPS spectra of the TiO_2 nanotube electrode

Cyclic Voltammetric Studies

The cyclic voltammograms of the TiO_2 nanotube electrode in 1M sulfuric acid solution and 1M sulfuric acid + 1M oxalic acid solution at a scan rate of 0.05 V/s are shown in Fig. 3 (a). It can be seen that the reduction peak of the TiO_2 nanotube electrode was characterized by an irreversible reduction. Compared the reduction peaks, we found that there were two reduction peaks in 1M sulfuric acid + 1M oxalic acid solution which illustrated that the reduction of oxalic acid occurred on the surface of TiO_2 nanotube electrode.

Fig. 3 (b) shows cyclic voltammograms obtained in 1 M oxalic acid solution at TiO_2 nanotube electrode and polished Ti electrode with the scan rate of 0.05 V/s. As can be seen, an irreversible reduction peak of the TiO_2 nanotube electrode was characterized. However, this irreversible reduction peak cannot be observed at the polished Ti electrode. The irreversible reduction peak was attributed to the following reaction:

$$TiO_2 + H_2O + H^+ + e \rightarrow Ti(OH)_3 \quad (1)$$

Then the Ti (Ⅲ) species reduced the oxalic acid to gelyoxylic acid and Ti (Ⅳ) was regenerated. It's obviously that the reduction process of oxalic acid at the TiO_2 nanotube electrode was different from that at the polished Ti electrode. The results showed that the TiO_2 nanotube electrode have higher electrocatalytic activity for the reduction of oxalic acid. The increase of current value may be due to the large amount of Ti (Ⅳ) species generated instantaneously by the fast chemical reaction[3, 18]. The TiO_2 nanotube electrode with a higher peak current may attribute to its special structure which is good for the adsorption the Ti (Ⅲ) species and reduction the oxalic acid. The CV studies have revealed that TiO_2 nanotube electrode behaves higher electrocatalytic activity than the polished Ti electrode.

The CV behavior of the TiO_2 nanotube electrode in 1M oxalic acid solution and 1M oxalic + 1M sulfuric acid solution at the scan rate of 0.05 V/s are shown in Fig. 3 (c). It can be seen that the initial potential of reduction peak in 1M oxalic acid solution move negatively. This illustrated that the polarization effect of the TiO_2 nanotube electrode was higher in 1M oxalic acid solution than that in 1M oxalic acid + 1 M sulfuric acid solution.

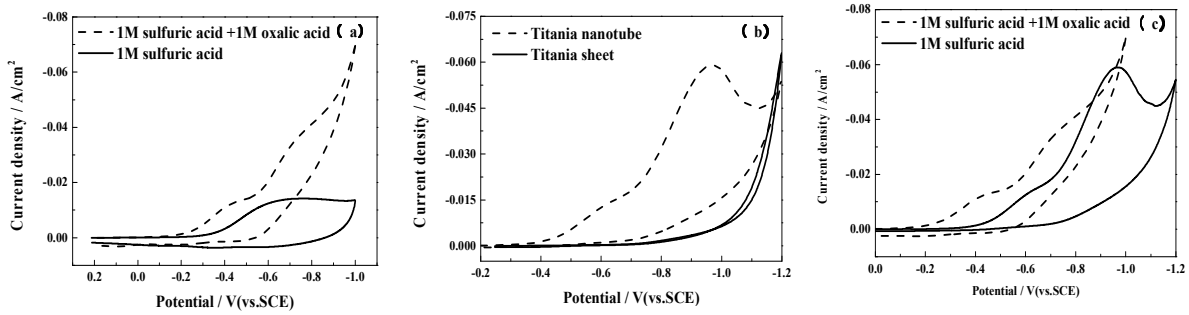


Fig.3 CV behavior of (a) TiO_2 nanotube electrode in 1M sulfuric acid and 1M sulfuric acid+1M oxalic acid; (b) TiO_2 nanotube and polished Ti electrode in 1 M oxalic acid solution; (c) TiO_2 nanotube electrode in 1M oxalic acid solution and 1M oxalic +1M sulfuric acid solution.

The whole CV studies have revealed that the TiO_2 nanotube electrode behaves as a good heterogeneous catalytic electrode and the reduction mechanism of oxalic acid at the the TiO_2 nanotube electrode is proposed as follow:

$$TiO_2 + H_2O + H^+ + e^- \longrightarrow Ti(OH)_3 \qquad (2)$$

$$HOC(=O)-COH + Ti(OH)_3 + H^+ \longrightarrow TiO_2 + HOC(=O)-CH + 2\,H_2O \qquad (3)$$

Preparative Electrolysis Studies

The electrolysis on a preparative scale was carried out at constant current density 30 mA/cm^2 for 4 hours in different oxalic acid solutions at 20℃. The results of the preparative electrolysis experiments are reported in table1. It was found that the current efficiency increased with the oxalic acid concentration. While the yield of glyoxylic on the TiO_2 nanotube electrode showed a trend of first increase and then decrease. The maximum yield was 72.05% in 0.3 M oxalic acid. The electrodes were characterized by SEM after electrolysis (Fig.1B and D). On the surface of TiO_2 electrode, the self-organized nanotubes developed into a periodic lattice of nanopores (Fig. 1B). However the surface of the polished Ti electrode did not change after electrolysis (Fig. 1D). The reason of the changes was that the TiO_2 as the active centers were reduced to $Ti(OH)_3$ and dissolved, then $Ti(OH)_3$ reduced oxalic acid to glyoxylic acid[[5]]. In addition, the nanopores structure was good for adsorption of the electrogenerated Ti (Ⅲ) species and reduction of oxalic acid which can improve the electrochemical activity of the TiO_2 nanotube electrode[19, 20]. Based on the results above, it is strongly suggested that the special surface structure change will benefit the application of the TiO_2 nanotube electrode in organic electrosynthesis.

TABLE 1. ELECTROLYSIS RESULTS ON TIO_2 NANOTUBE AND POLISHED TI ELECTRODE, T = 4 [H], T = 20 [℃], I = 30 [MA/CM^2]

Electrode	$C_{0\ \text{oxalic acid}}$ [mol/l]	Conversion [%]	Yield [%]	Current efficiency [%]
TiO_2 Nanotube	0.1	76.09	70.21	29.45
	0.3	78.27	72.05	88.23
	0.5	67.89	39.46	77.61
	0.8	38.98	30.52	91.11
	1.0	48.20	21.37	95.84
Polished Ti	0.1	75.96	89.95	37.73
	0.3	60.96	55.68	68.69
	0.5	38.14	38.60	75.90
	0.8	23.91	29.70	88.66
	1.0	24.10	21.25	95.31

Summary

In this paper, the TiO_2 nanotube electrode was obtained by anodic oxidation method. XPS results showed that the surface of nanotube was composed of TiO_2 before and after electrolysis. The SEM confirmed that the surface of TiO_2 nanotube electrode developed into a periodic lattice of nanopores after electrolysis which was good for adsorption of the electrogenerated Ti (Ⅲ) species and reduction of oxalic acid which can improve the electrochemical activity of the TiO_2 nanotube electrode. The CV studies and electrochemical experiments presented that the electrocatalytic activity of the TiO_2 nanotube electrode was higher than that of the polished Ti electrode. These results demonstrated that the TiO_2 nanotube electrode is a useful electrode material for reducing oxalic acid and it is also a potential candidate as a heterogeneous catalytic for the electroreduction.

Acknowledgements

This work was supported by the National Basic Research Program of China (973 Program) (No. 2012CB722604) and the National Natural Science Foundation of China (21106133)

References

[1] G. Chamoulaud, D. Floner, C. Moinet, et al., Electrochim. Acta. 46 (2001) 2757-2760.

[2] D. B. Chu, M. Xu, J. Lu, et al., Electrochem. Commun. 10 (2008) 350-353.

[3] F. M. Zhao, F. Yan, Y. Qian, et al., Int. J. Electrochem. Sci. 7 (2012) 12931-12940.

[4] D. B. Chu, X. H. Li, X. Y. Liu, et al., Chin. J. Chem. 22 (2004) 1231-1234.

[5] F. M. Zhao, F. Yan, Y. Qian, et al., J. Electroanal. Chem. 698 (2013) 31-38.

[6] M. Vilar, J. L. Oliveira, M. Navarro, Appl. Catal., A 372 (2010) 1-7.

[7] M. L. Kantam, S. Laha, J. Yadav, et al., Tetrahedron Lett. 47 (2006) 6213-6216.

[8] S. S. Vaghela, G. Ramachandraiah, P. K. Ghosh, et al., J. Appl. Electrochem. 32 (2002) 1189-1192.

[9] J. R. Ochoa, A. Diego,J . Santa-Olalla, J. Appl. Electrochem. 23 (1993) 905-909.

[10] K. Scott, A. P. Colbourne, S. D. Perry, Electrochim. Acta. 35 (1990) 621-623.

[11] D. J. Pickett, K. S. Yap, J. Appl. Electrochem. 4 (1974) 17-23.

[12] J. Li, X. Hu, Y. Su, et al., Chem. Eng. Sci. 62 (2007) 6784-6793.

[13] Y. L. Zhou, X. S. Zhang, Y. C. Dai, et al., Chem. Eng. Sci. 58 (2003) 1021-1027.

[14] J. S. Gu, D. B. Chu, X. F. Zhou, et al., Acta Chim. Sinica. 61 (2003) 1405-1409.

[15] D. B. Chu, G. X. Qin, X. M. Yuan, et al., J. Porous Mat. 15 (2008) 661-665.

[16] C. T. Kresge, M. E. Leonowicz, W. J. Roth, et al., Nature. 359 (1992) 710-712.

[17] L. C. Chen, T. C. Chou, Ind. Eng. Chem. Res. 33 (1994) 1436-1443.

[18] Y. Gan, W. Zhang, H. Huang, et al., Chin. J. Chem. Eng. 14 (2006) 649-653.

[19] A. Vittadini, A. Selloni, F. P. Rotzinger, et al., J. Phys. Chem. B 104 (2000) 1300-1306.

[20] A. Vittadini, A. Selloni, F. P. Rotzinger, et al., Phys. Rev. Leet. 81 (1998) 2954-2957.

Advanced Materials Research Vol. 936 (2014) pp 970-974
© (2014) Trans Tech Publications, Switzerland
doi:10.4028/www.scientific.net/AMR.936.970

Preparation of Zircon Whiskers via Non-hydrolytic Sol-gel Process Combined with Molten Salt Method

Hongda WANG[1,a], Weihui JIANG[1,2,b *], Guo FENG[1,c], Jianmin LIU[1], Qian WU[1], and Lifeng MIAO[1]

[1]School of Material Science and Engineering, Jingdezhen Ceramic Institute, Jingdezhen 333000, Jiangxi, China

[2]Jiangxi Key Laboratory of Advanced Materials, Jingdezhen 333000, Jiangxi, China

[a]whd19890819@163.com, [b]jwhjiang@163.com, [c]243393617@qq.com

Key words: Zircon; Whiskers; Non-hydrolytic sol-gel process; Molten salt method

Abstract: Zircon whiskers were prepared via non-hydrolytic sol-gel process combined with molten salt method, using $Si(OC_2H_5)_4$ (TEOS) and $ZrCl_4$ as raw materials, LiF as mineralizer, and Na_2WO_4 as molten salt. The phase composition, morphology and microstructure of the samples were characterized by X-ray diffraction analysis (XRD), field emission scanning electron microscopy (FE-SEM) and transmission electron microscopy (TEM). The influence of introducing molten salt and calcination temperature on the synthesis and morphology of zircon crystals was investigated. The results show that the introduction of Na_2WO_4 contributes to the one-dimensional preferential growth of zircon. Zircon whiskers elongated along the c-axis, with diameter of ~100nm and aspect ratio of more than 15, are achieved at the temperature of 850 ^oC, and neither over low nor over high calcination temperature is conducive to the growth of zircon whiskers.

Introduction

Whisker is fiber-like single crystal, with aspect ratio of more than 10 [1]. It has well-ordered atomic arrangement and complete structure, which endows the whisker material with high strength [2]. And because its strength is close to the theoretical value of crystal, whisker is used as reinforcing phase in composite materials [3].

Zircon ($ZrSiO_4$) is a kind of structure ceramic material with excellent properties, such as high melt point, low thermal conductivity, low thermal expansion coefficient, high index of refraction, ultimate chemical durability and phase stability [2,4,5]. In addition, the zircon has higher thermal shock resistance than that of mullite and alumina [6]. Due to these advantages, zircon is widely used in refractory, opacifying glaze, high temperature structural ceramics, and so on. As a new type of composite material reinforcement, zircon whisker owning the properties of both zircon and whisker has vast potential applications.

Non-hydrolytic sol-gel (NHSG) process is a very effective method for low-temperature synthesis of composite oxide [7], and molten salt method can provide a liquid state environment for the anisotropic growth of crystal [8]. Therefore, in this paper, zircon whiskers were prepared via NHSG process combined with molten salt method. The influence of introducing molten salt and calcination temperature on the synthesis and morphology of zircon crystal was researched.

Experimental Procedures

With the Si/Zr and Li/Zr molar ratio being 1.2 and 0.36 [9], respectively, 8 mL TEOS was mixed with $ZrCl_4$ and LiF. 30 mL ethanol was added into the above mixture with stirring, and then transparent solution was obtained. After reflux and drying, the dried gel was formed. The gel was pre-calcined at 400 ^oC for 30 min, then muddled uniformly with Na_2WO_4 molten salt and calcined at different temperatures. Finally, the samples were achieved by washing with dilute HF acid and distilled water for several times.

The phase composition of samples was analyzed by X-ray diffraction (XRD, D8 Advance, Bruker AXS Co. Ltd.) and CuKα radiation (λ = 0.154 nm), with scanning range of 5 °~70 ° 2θ. The morphologic information of samples was obtained by field emission scanning electron microscopy (SEM, JSM-6700F, JEOL) and transmission electron microscopy (TEM, JEM-2010, JEOL). And TEM was also used to characterize and analyze the microstructure and growth direction of whisker.

Results and Discussion

In order to investigate the effect of molten salt added on the one-dimensional preferential growth of zircon, the phase composition and morphology of the samples calcined at 800 °C were analyzed by XRD and SEM as shown in Fig. 1 and Fig. 2, respectively.

It can be seen that the samples with or without molten salt are all composed of single $ZrSiO_4$ crystal phase (Fig. 1), indicating that the addition of Na_2WO_4 molten salt doesn't hinder the synthesis of zircon. As can be seen from Fig. 2, the sample with molten salt mainly consists of rod-like $ZrSiO_4$ whiskers, while the sample without molten salt entirely composed of zircon grains.

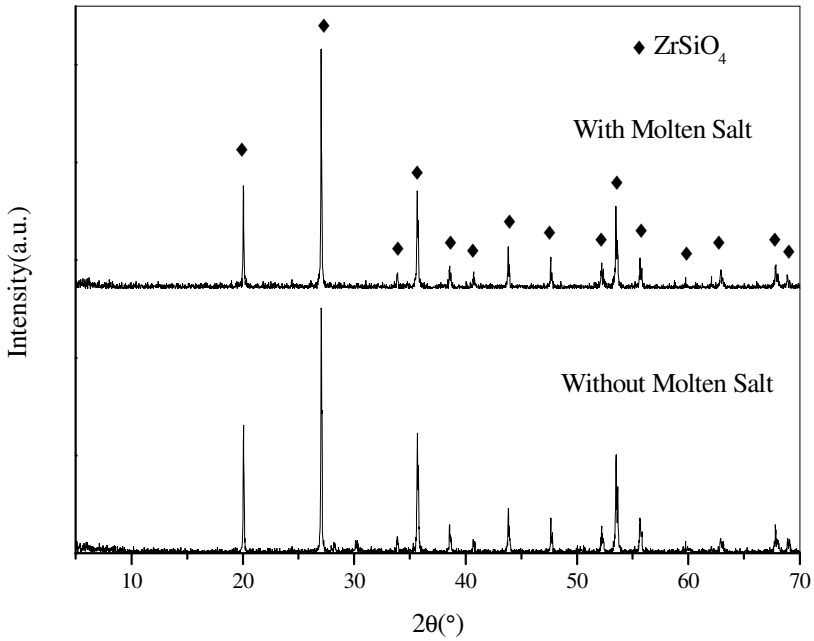


Fig. 1 XRD patterns of samples without or with molten salt

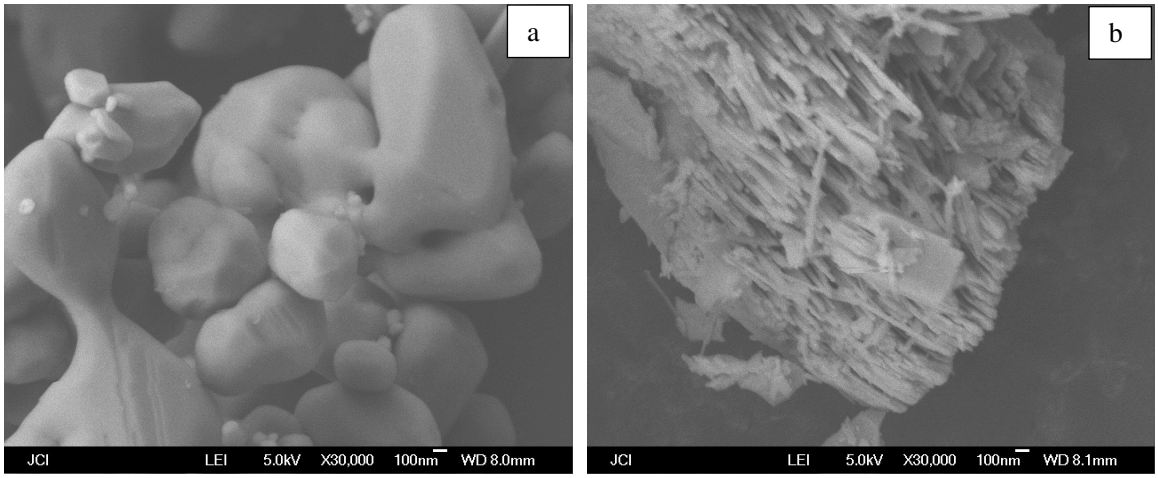


Fig. 2 FE-SEM micrographs of samples (a) without molten salt; (b) with molten salt

The XRD patterns of samples with Na_2WO_4 molten salt calcined at different temperatures are shown in Fig. 3. At 650 °C, the diffraction peaks agree well with $Na_7Zr_6F_{31}$ phase (PDF#10-0177),

and no characteristic diffraction peak corresponding to $ZrSiO_4$ is detected. As the calcination temperature increases to 700 °C, the sample mainly consists of $ZrSiO_4$ crystal phase, as well as a small amount of $Na_7Zr_6F_{31}$ phase. When the temperature rises to 750 °C or higher gradually, $Na_7Zr_6F_{31}$ phase disappears and the samples are entirely composed of $ZrSiO_4$ crystal phase.

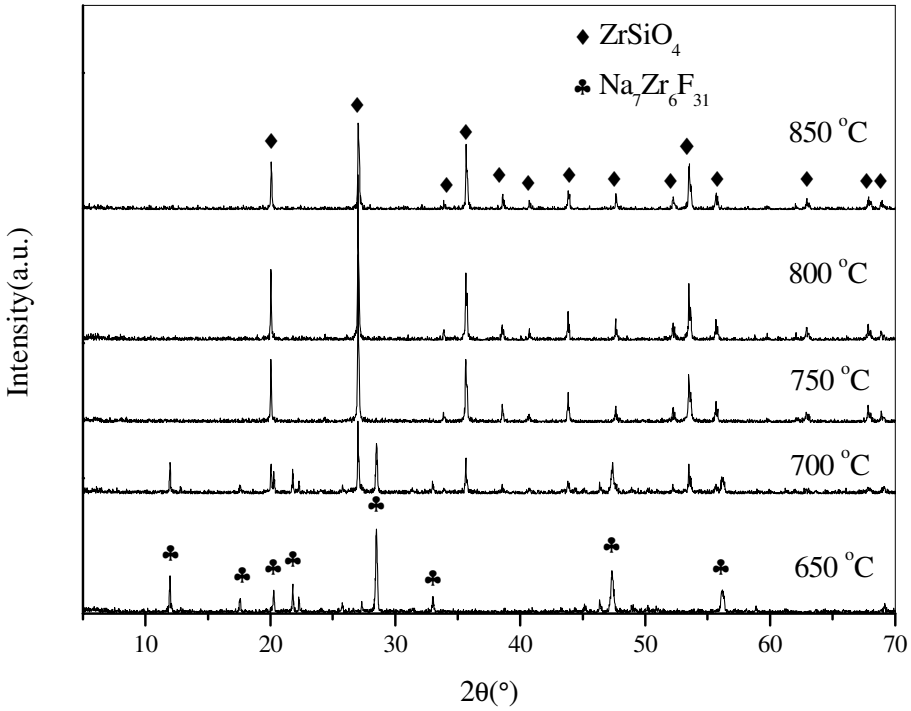


Fig. 3 XRD patterns of samples with molten salt calcined at different temperatures

Based on the analysis above, the forming process of $ZrSiO_4$ whisker can be implied as follows: the dry gel of zircon acts with molten salt to form $Na_7Zr_6F_{31}$ at 650 °C. When Na_2WO_4 molten salt (m.p. 695 °C) melts at 700 °C, zircon crystal phase forms gradually, and the sample is mainly composed of zircon and $Na_7Zr_6F_{31}$ crystal phases. With the temperature further rising, zircon and $Na_7Zr_6F_{31}$ crystal phases are dissolved in liquid molten salt to form supersaturated solution of zircon. Due to the anisotropic characteristics of zircon crystal, and the liquid state environment produced by adding molten salt that is beneficial to the one-dimensional preferential growth of crystal than solid state recation, zircon appears and grows into whisker under the appropriate supersaturated condition.

The FE-SEM micrographs of the samples are shown in Fig. 4 The samples calcined at 750 °C and 800 °C are both composed of massive zircon crystals and whiskers with small diameter and short length. When the temperature rises to 850 °C, the sample mainly consists of well-developed zircon whiskers with average diameter of ~100 nm and aspect ratio of more than 15, accompanied by a small number of zircon grains. With the temperature further increasing to 900 °C, zircon whiskers disappear, and the sample is basically composed of massive zircon crystals. Consequently, it can be concluded that both over low and over high calcination temperatures are not conducive to the growth of zircon whiskers.

Usually, the viscosity of molten salt rapidly decreases with increasing of the calcination temperature. The one-dimensional preferential growth of zircon are destroyed at over low temperature due to the insufficiency of zircon growth dynamic and the high viscosity of molten salt. Thus the massive zircon crystals and zircon whiskers with small diameter and short length coexist in the samples calcined at 750 °C and 800 °C. Nevertheless, the growth rate differences along three-dimensional direction will obviously be reduced at over high temperature, which are also not conducive to the one-dimensional preferential growth of zircon crystals. Only at 850 °C, the combined effect of sufficiency growth dynamic, appropriate viscosity of molt salt, and larger three-dimensional growth rate differences promote the growth and development of zircon whiskers.

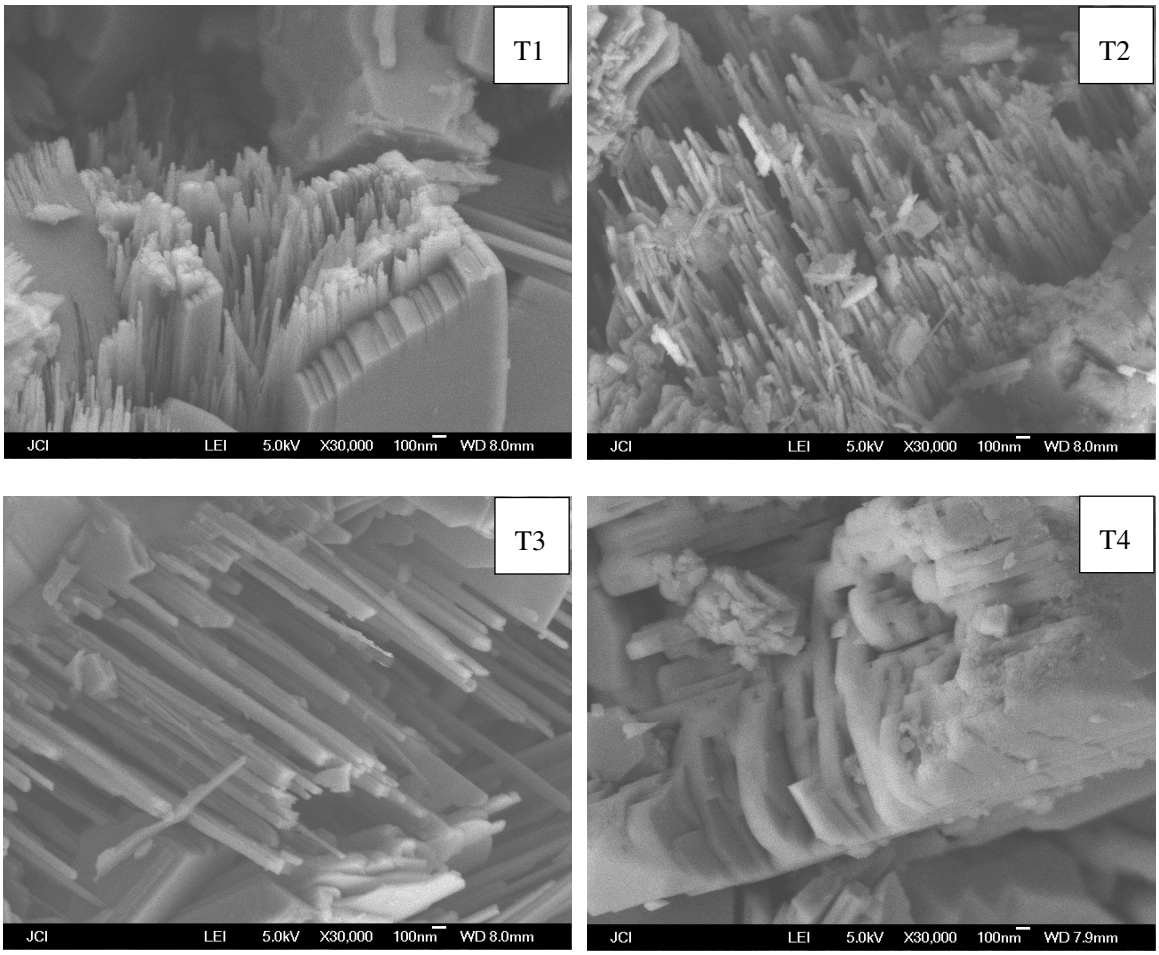


Fig. 4 FE-SEM morphologies of samples calcined at different temperatures
(T1: 750 ^{o}C; T2: 800 ^{o}C; T3: 850 ^{o}C; T4: 900 ^{o}C)

The TEM, SAED and HRTEM micrographs of zircon whisker obtained at 850 ^{o}C are showed in Fig. 5. The unit cell parameters (a = b = 6.686 Å, c = 5.595 Å) are calculated by analyzing the SAED and HRTEM micrographs, which are consistent with standard diffraction card of zircon (PDF#06-0266). Moreover, the single crystal structure of zircon whisker is confirmed by SAED [10]. And the elongated direction of zircon whisker is parallel to c-axis, as shown in HRTEM micrograph.

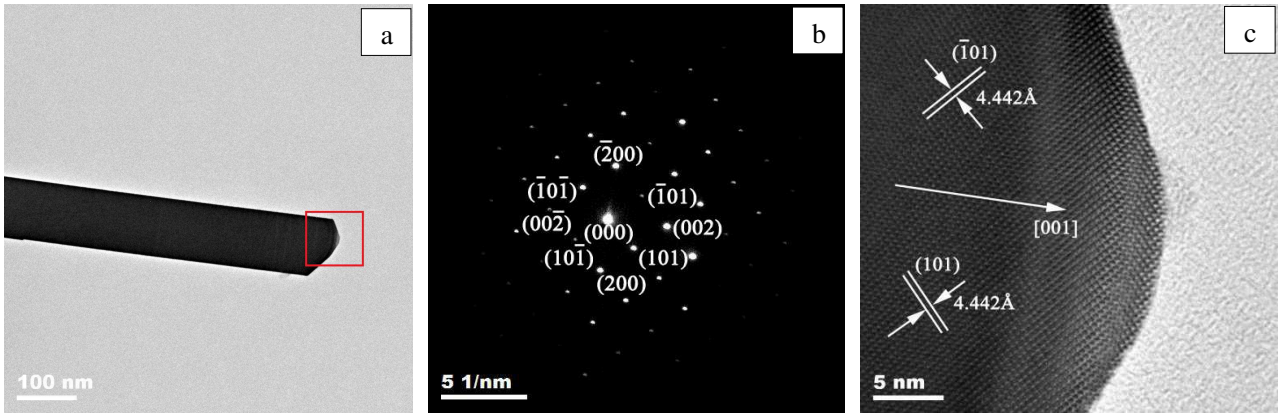


Fig. 5 (a) TEM, (b) SAED and (c) HRTEM of zircon whisker

Conclusions

Zircon whiskers were prepared via NHSG process combined with molten salt method. The addition of Na_2WO_4 molten salt contributes to the one-dimensional growth of zircon crystals significantly. Optimized zircon whiskers, with diameter of ~100 nm, aspect ratio of more than 15, can be obtained at 850 ^oC, and the growth direction of whiskers is along c-axis. Both over low and over high calcination temperatures count against the growth of zircon whiskers. NHSG process could realize the low temperature synthesis of zircon, and Na_2WO_4 molt salt provides a suitable liquid environment, both of which promote the growth of zircon whiskers.

Acknowledgements

This research is supported by National Natural Science Foundation of China (No. 51162013, 51362014), Major Discipline Academic and Technical Leader Training Plan Project of Jiangxi Province (NO.20113BCB22009), and Science and Technology Supporting Plan Project of Jiangxi Province (NO.20111BBE50018).

Reference

[1] C. C. Evans, Whiskers, Mills and Boon, London, 1972.

[2] W. Li, Inorganic Whisker (In Chinese), Chemistry and applied chemistry Press, Beijing, 2005.

[3] G. L. Converse, T. L. Conrad, C. H. Merrill, and R. K. Roeder, Hydroxyapatite whisker-reinforced polyetherketoneketone bone ingrowth scaffolds, Acta biomaterialia. 6 (2010) 856-863.

[4] M. Shoyama, N. Matsumoto, T. Hashimoto, H. Nasu, and K. Kamiya, Sol–gel synthesis of zircon–effect of addition of lithium ions, J. Mater. Sci. 33 (1998) 4821-4828.

[5] P. Tartaj, Zircon formation from nanosized powders obtained by a reverse micelle process, J. Am. Ceram. Soc. 88 (2005) 222–224.

[6] T. Mori, H. Yamamura, H. Kobayashi, T. Mitamura, Preparation of high-purity $ZrSiO_4$ powder using sol–gel processing and mechanical properties of the sintered body, J. Am. Ceram. Soc. 75 (1992) 2420-2426.

[7] Y. Dimitriev, Y. Ivanova, and R. Iordanova, History of sol-gel science and technology, Journal of UCTM. 43 (2008) 181-192.

[8] J. F. Hou, Z. J. Wu, Y. T. Wang, and M. F. Bi, Research progress in preparation of anisometric single-crystal particles by molten salt synthesis method (In Chinese), China Ceramics. 2 (2012) 1-3.

[9] W. H. Jiang, T. Zhang, Q. X. Zhu, and J. M. Liu, Effect of non-hydrolytic gelation process on synthesis of zircon at low temperature (In Chinese), J. Chin. Ceram. Soc. 39 (2011) 383-386.

[10] N. Jiang, J. C. Spence, Radiation damage in zircon by high-energy electron beams, J. Appl. Phys. 105 (2009) 123517.

Advanced Materials Research Vol. 936 (2014) pp 975-980
© (2014) Trans Tech Publications, Switzerland
doi:10.4028/www.scientific.net/AMR.936.975

Low Temperature Preparation of Mullite Whisker via Non-hydrolytic Sol-gel Process Combined with Molten Salt Method

Kailin Fu[1,a], Weihui Jiang[1,2,b *], Guo Feng[1,c], Jianmin Liu[1], Qian Wu[1], Lifeng Miao[1], Ting Chen[1], Quan Zhang[1], Hongda Wang[1], Jianrui Zha[1]

[1]School of Material Science and Engineering, Jingdezhen Ceramic Institute, Jingdezhen 333001, Jiangxi, China,

[2]Jiangxi Key Laboratory of Advanced Ceramic Materials, Jingdezhen 333001, Jiangxi, China

[a]jd_a1092683@163.com, [b]jwhjiang@163.com, [c]243393617@qq.com

Keywords: mullite whisker, non-hydrolytic sol-gel process, molten salt method, crystal growth

Abstract. Mullite whisker was prepared at low temperature via non-hydrolytic sol-gel (NHSG) process combined with molten salt method. The influence of heat treatment temperature was studied on the morphology and the microstructure of whisker, and its growth mechanism was also described. The results show that the mullite whisker appears at the lowest temperature of 750 ºC, and optimized mullite whisker can be prepared at 850 ºC with the growth direction of [001], whose diameter is in the range of 170~300 nm with the aspect ratio of >30.

Introduction

Mullite is widely used as high temperature engineering material and refractory material because of its excellent high temperature strength and creep resistance, low thermal expansion coefficient and good chemical stability [1-4]. Mullite whisker has attracted much attention due to its serving as a reinforcement phase in high temperature ceramic composites [5-8]. Various processing routes have been reported for the preparation of mullite whisker, such as mineral decomposition method [9], oxide doping method [10], sol–gel process combined with vapour-phase reaction method [11], molten salt method [12], sol-gel process combined with molten salt method [13], non-hydrolytic sol-gel process combined with vapour-phase reaction method [14]. Nevertheless, the above mentioned methods generally require an annealing temperature of above 1000 ºC [13]. Non-hydrolytic sol-gel (NHSG) process simplifies the sol-gel process, and especially makes the sol homogeneous at the atomic level during the sol-gel process, thus greatly reducing the synthesis temperature of multicomponent oxides [15,16]. Meanwhile, molten salt method has been employed to prepare mullite whisker because molten salt provides liquid environment in which the whisker growth is easily accelerated. However, to the best of our knowledge, there is no report on the mullite whisker prepared by NHSG process combined with molybdate molten salt.

In this paper, mullite whisker was prepared by the combination of NHSG process with molten salt method. The influence of heat treatment temperature was studied on the whisker, and its growth mechanism was also discussed.

Experimental

Preparation

Anhydrous aluminum chloride ($AlCl_3$, AR, Shanghai), tetraethoxysilane ($Si(OC_2H_5)_4$, AR, Shanghai) and anhydrous ether (EtOEt, AR, Shanghai) were used as precursors and mixed in a conical flask with the nominal composition of mullite ($3Al_2O_3 \cdot 2SiO_2$). The reaction mixture was continuously heated under reflux at 110 ºC for 24 h to obtain the mullite xerogel via non-hydrolytic sol-gel process. The xerogel was calcined at 910 ºC for 10 min to prepare mullite crystal seed. Then mullite crystal seed and molybdate with the mass ratio of 1:1 were ball-milled for 2 min. The milled mixture was heated to the final temperature and then held for 6 h. The prepared samples were

crushed and washed with 10 vol.% HF solution to remove the molybdate. Finally, white powder was obtained after filtrating, washing and drying. Based on the eutectic composition (at 523 ºC) in the lithia-molybdena phase diagram [17], the molten salt of molybdate was prepared using lithium carbonate and molybdenum oxide as raw materials.

Characterization

Differential thermal analysis (DTA) and thermo gravimetric analysis (TG) were carried out by using NETZSCH STA 449C thermal analyzer. Infrared spectroscopy (IR) studies were performed with Nicolet 5700 infrared spectrometer in the wavenumber range of 4000-400 cm^{-1}. The phase compositions of samples were determine by the Bruker D8 Advance X-ray diffraction (XRD), and their morphology was observed by the JSM-6700F scanning electron microscopy (FE-SEM). Microstructure of the whiskers was investigated by using JEM-2010 transmission electron microscope (TEM).

Results and Discussion

In order to study the phase transition of mullite xerogel during the heat treatment, its DTA–TG test was carried out from room temperature to 1300 °C at the rate of 10 °C/min in nitrogen atmosphere. There is a broad endothermic peak in the DTA curve with the peak temperature of 181 °C, which is due to the volatilization of organic compounds and decomposition of the ethyoxyl groups in the xerogel, and correspondingly there is a 47.48 % weight loss in the TG curve (Fig. 1(a)).

At 905 °C, the DTA curve also shows a sharp exothermic peak attributed to the crystallization of mullite. This can be deduced from the fact that the XRD pattern of the sample prepared at 910 °C has mullite diffraction peaks while its counterpart at 880 °C has no mullite peaks (Fig. 1(b)). It is noteworthy that the background strength in the XRD pattern is relatively high at 910 °C, which suggests that there is a great deal of amorphous phase due to the short holding time of only 10 min. The existing amorphous mullite is easier to dissolve in molybdate melt than the crystalline mullite. At the same time, a small amount of crystalline mullite, as crystal seed, plays an important role in the whisker growth process.

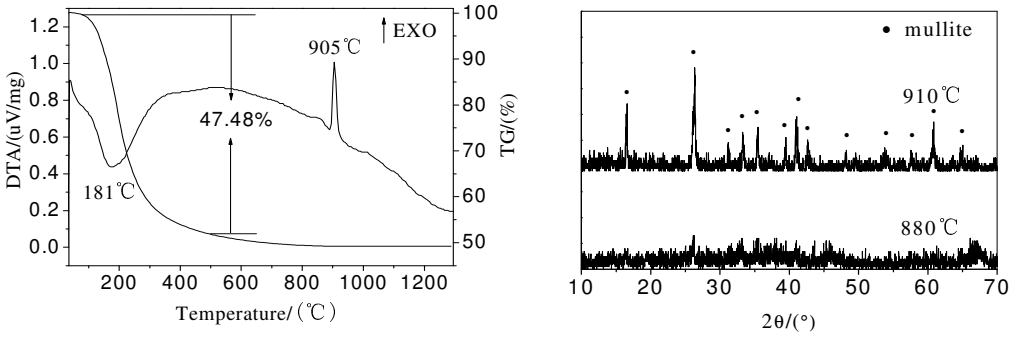


Fig. 1 (a) DTA-TG curves of the xerogel powder, (b) XRD patterns of the samples heat treated at different temperatures.

In order to verify why NHSG method can synthesize mullite at the much lower temperature of 910 ºC than both traditional solid phase method and hydrolytic sol-gel method, FT-IR test was performed to analyse the bonding of mullite xerogel prepared via NHSG method. Two absorption bands at 1090 cm_{-1} and 610 cm_{-1} appeared in the the FT-IR spectrum of mullite xerogel (Fig. 2), which were ascribed to the vibration of Al-O-Si [18,19]. The reaction process can be described as the following formula:

$$Si(OC_2H_5)_4 + AlCl_3 + C_2H_5OC_2H_5 \xrightarrow{NHSG} = Al - O - Si \equiv + C_2H_5Cl \uparrow \quad (1\text{-}1)$$

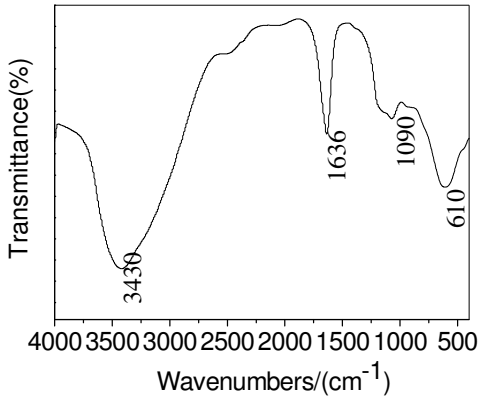


Fig. 2 FT-IR spectrum of mullite xerogel prepared via NHSG method.

According to the formula, the C-Cl absorption peak should have existed in the infrared spectrum. However, it doesn't appear in the spectrum because C_2H_5Cl is gaseous at room temperature [20] and can escape during the exothermic reaction. The key to synthesizing mullite at low temperature lies in the formation of Al-O-Si heterocondensational bond through the non-hydrolytic process.

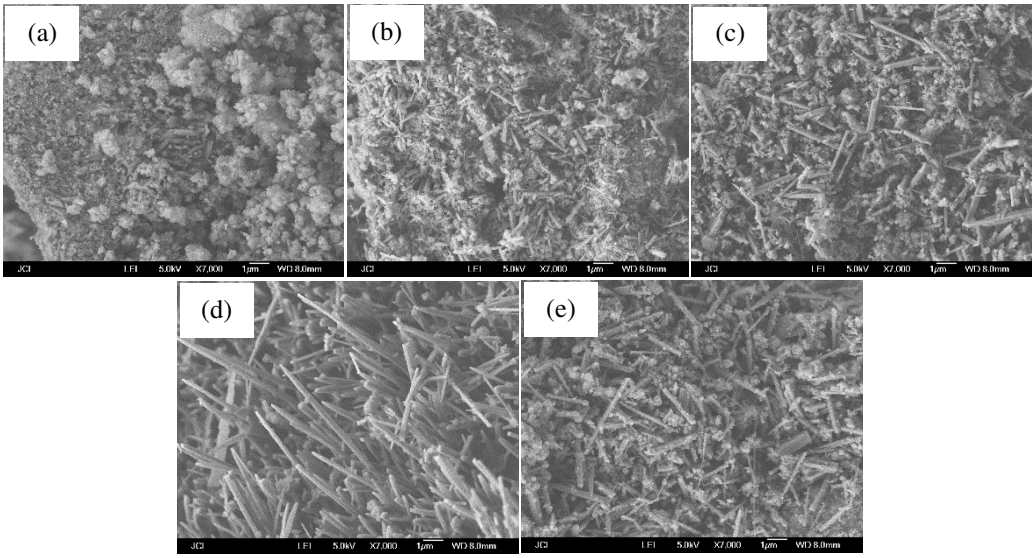


Fig. 3 FE-SEM micrographs of the samples heat treated at different temperatures: (a) 700 °C, (b) 750 °C, (c) 800 °C, (d) 850 °C and (e) 900 °C.

FE-SEM micrographs of the samples heat treated at 700 ºC, 750 ºC, 800 ºC, 850 ºC and 900 ºC are shown in Fig. 3. It can be seen from Fig. 3 that heat treating temperature has great influence on the formation of mullite whisker: there is no mullite whisker present after 700 °C heat treatment, and the short rod-like mullite whisker appears with the aspect ratio of about 12 and with the length of 1~2 μm through 750 °C annealing (Fig. 3(b)); with the increase of heat treating temperature, both dimension and amount of the mullite whisker increase (Fig. 3(b-d)), and the optimized temperature of 850 ºC results in the well-developed mullite whisker with the diameter in the range of 170-300 nm and the aspect ratio of >30 (Fig. 3(d)); when the temperature raises up to 900 °C, the whisker begins to decrease in both length and amount, and what is more, it is mingled with a lot of fine mullite particles and some thick whisker, which is probably due to the fast evaporation of molten salt and the reduction in the three-dimensional growth rate difference with the increase of temperature.

Fig. 4 shows the TEM micrograph of the representative whisker, the selected area electron diffraction (SAED) pattern and the lattice image of the sample heat treated at 850 ℃. The SAED pattern (Fig. 4(b)) as well as the measured lattice spacing confirms that the whisker is single-crystal

of mullite, which is in good agreement with the XRD analysis, and the whisker growth direction can be identified as [001]. The interplanar spacing of (110) can be determined to be 5.39 Å from Fig. 4(c).

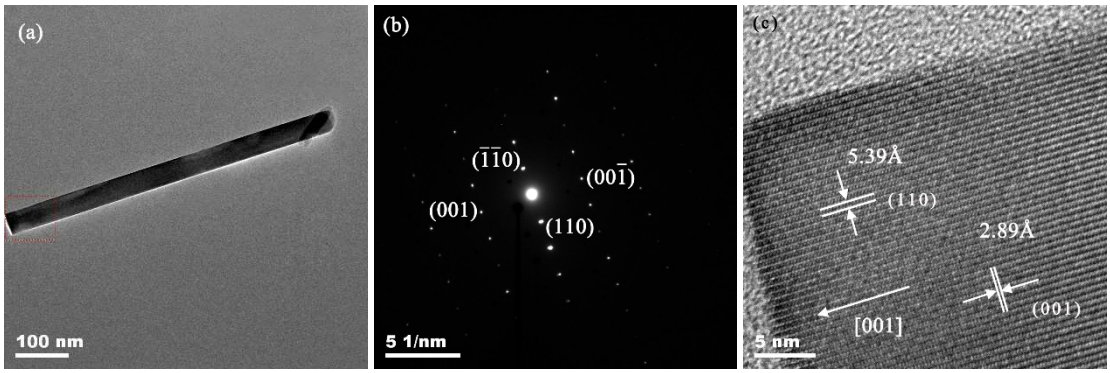


Fig. 4 TEM, SAED and HR-TEM photographs of whisker.

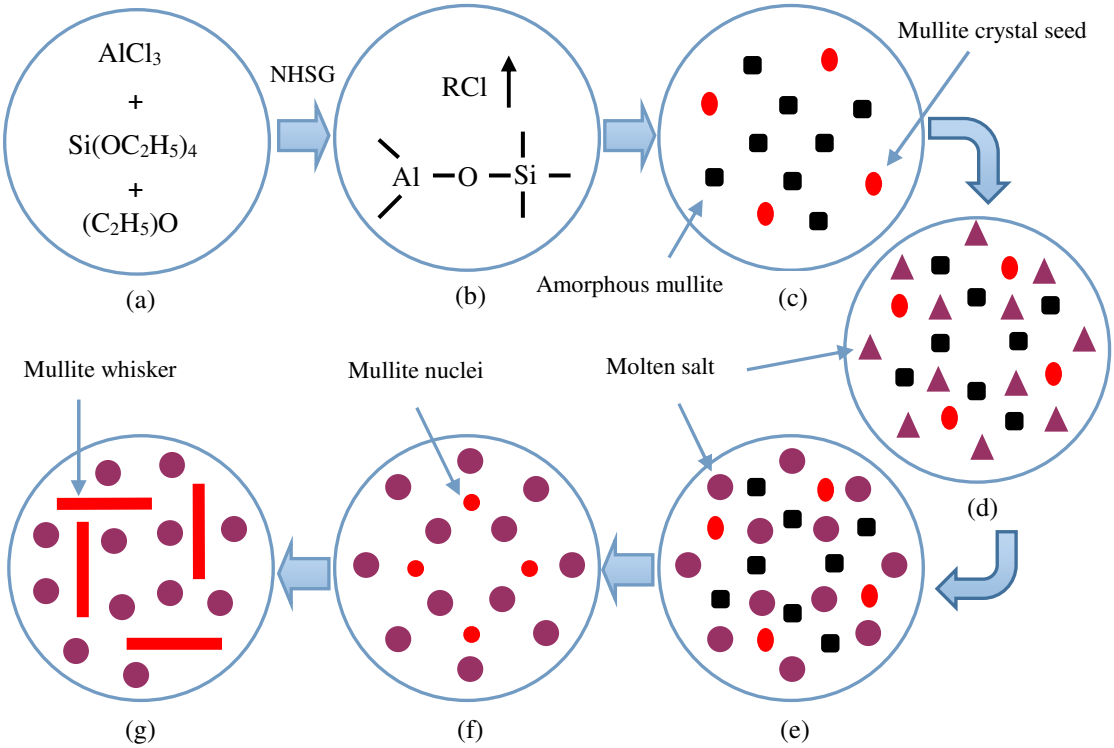


Fig. 5 Schematic of the mullite whisker growth process: (a) precursors, (b) reaction products via NHSG process, (c) mullite crystal seed with its amorphous phase after annealing at 910 °C, (d) mixture of mullite crystal seed, amorphous mullite and molten salt, (e) molten salt melting at over the eutectic temperature, (f) amorphous mullite dissolution in molten salt, (g) whisker growth.

Fig. 5 shows the schematic of the mullite whisker growth process. Firstly, the precursors (Fig. 5(a)) reacted to form mullite xerogel via NHSG process (Fig. 5(b)), and mullite crystal seed came into existence with a great deal of amorphous phase at 910 °C (Fig. 5(c)). The amorphous mullite is easy to dissolve into the molten salt due to its fine particle size and high activity. Then, mullite crystal seed with amorphous phase and molybdate molten salt were mixed at room temperature (Fig. 5(d)), and the molten salt melted at more than 523 °C (Fig. 5(e)). Thirdly, amorphous mullite began to dissolve into the molten salt with the size decrease of the mullite seed (Fig. 5(f)). Finally, from the supersaturated molten salt, mullite crystallizes on the surface of the mullite seed and continues to grow into whisker (Fig. 5(g)).

Conclusions

The formation of Al-O-Si bond in the mullite xerogel via NHSG route plays the key role in the low temperature synthesis of mullite crystal seed. With the aid of the prepared seed and the molybdate molten salt, the mullite whisker can be formed at the lowest temperature of 750 °C, and at 850 °C, the optimized mullite whisker was prepared with the growth direction of [001], the diameters in the range of 170~300 nm and the aspect ratio of >30. Overhigh or overlow annealing temperature is not beneficial to the growth of mullite whisker.

Acknowledgements

The work was supported financially by National Natural Science Foundation of China (No.51362014, No.51162013), major discipline academic and technical leader training plan project of Jiangxi province (No.20113BCB22009), Science and Technology Supporting Plan Project of Jiangxi Province (NO.20111BBE50018).

References

[1] J.S. Hong, X.X. Huang, J.K. Guo, Synthesis and sintered properties of mullite powder from seeded diphasic Al_2O_3-SiO_2 gel, Mater. Lett. 24 (1995) 327-331.

[2] J. Ossaka, Tetragonal mullite-like phase from co-precipitated gels, Nature. 191 (1961) 1000-1001.

[3] C. Aksel, The role of fine alumina and mullite particles on the thermomechanical behaviour of alumina–mullite refractory materials, Mater. Lett. 57 (2002) 708-714.

[4] I.A. Aksay, J.A. Pask, The silica-alumina system: stable and metastable equilibria at 1.0 atmosphere, Science. 183 (1974) 69-71.

[5] A.R. Guo, J.C. Liu, Y. Wang, H. Xu, Preparation of porous lamellar mullite ceramics with whisker skeletons by electrospinning and pressure molding, Mater. Lett. 74 (2012) 107-110.

[6] X. Miao, Porous mullite ceramics from natural topaz, Mater. Lett. 38 (1999) 167-172.

[7] B.M. Kim, Y.K. Cho, S.Y. Yoon, R. Stevens, H.C. Park, Mullite whiskers derived from kaolin, Ceram. Int. 35 (2009) 579-583.

[8] W.H. Jiang, Q. Wu, J.M. Liu, Q.X. Zhu, L.F. Miao, Low temperature synthesis of mullite whisker by nonhydrolytic sol-gel process combined with molten salt method, Adv. Mater. Res. 538-541 (2012) 2346-2349.

[9] P. Peng, C. Sorrell, Preparation of mullite whiskers from topaz decomposition, Mater. Lett. 58 (2004) 1288-1291.

[10] L.B. Kong, H. Huang, T.S. Zhang, J. Ma, F. Boey, R.F. Zhang, Growth of mullite whiskers in mechanochemically activated oxides doped with WO_3, J. Eur. Ceram. Soc. 23 (2003) 2257-2264.

[11] K. Okada, N. Otsuka, Synthesis of mullite whiskers and their application in composites, J. Am. Ceram. Soc. 74 (1991) 2414-2418.

[12] W. Wang, H.W. Li, K.R. Lai, K.H. Du, Preparation and characterization of mullite whiskers from silica fume by using a low temperature molten salt method, J. Alloys. Compd. 510 (2012) 92-96.

[13] P.Y. Zhang, J.C. Liu, H.Y. Du, Z.Q. Li, S. Li, R. Xu, Molten salt synthesis of mullite whiskers from various alumina precursors, J. Alloys. Compd. 491 (2010) 447-451.

[14] W.H. Jiang, Y.F. Peng, J.M. Liu, G. Feng, X.Y. Tan, Y. Yu, Preparation of mullite whisker via non-hydrolytic sol-gel route, J. Inorg. Mater. 25 (2010) 532-536.

[15] L.L. Hench, J.K. West, The sol-gel process, Chem. Rev. 90 (1990) 33-72.

[16] W.H. Jiang, H.Y. Wei, G. Feng, Y.H. Zhou, Y. Yu, Effect of oxygen donor alcohols on low temperature nonhydrolytic sol-gel synthesis of aluminum titanate, J. Chin. Ceram. Soc. 36 (2008) 11-16.

[17] W.S. Brower, H.S. Park, R.S. Roth, J.L. Waring, Phase equilibrium and crystal growth in the system lithium oxide-molybdenum oxide, J. Cryst. Growth. 16 (1972) 15-20.

[18] S. Konduri, S. Mukherjee, S. Nair, Strain energy minimum and vibrational properties of single-walled aluminosilicate nanotube, Phys. Rev. B. 74 (2006) 0334011-0334014.

[19] A. Hidalgo, S. Petit, C. Domingo, C. Alonso, C. Andrade, Microstructural characterization of leaching effects in cement pastes due to neutralisation of their alkaline nature: Part I: Portland cement pastes, Cement. Concrete. Res. 37 (2007) 63-70.

[20] W.P. Hu, D.G. Truhlar, Factors affecting competitive ion-molecule reactions: $ClO^-+C_2H_5Cl$ and C_2D_5Cl via E2 and S_N2 channelsm, J. Am. Chem. Soc. 118 (1996) 860-869.

Advanced Materials Research Vol. 936 (2014) pp 981-985
© (2014) Trans Tech Publications, Switzerland
doi:10.4028/www.scientific.net/AMR.936.981

Co-Ni Bimetallic Catalysts Coated on Cordierite Monoliths for Hydrazine Decomposition

Shahram Ghanbari Pakdehi [a,*], Mozaffar Salimi [b], Maryam Rasoolzadeh [c]

Faculty of Chemistry and Chemical Engineering, Malek Ashtar University of Technology, Tehran, Iran

[a,*] ghanbari.shahram60@gmail.com, [b] salimi.mozaffar@gmail.com, [c] rasoolzadeh21@gmail.com

Keywords: Monolith, γ-Alumina Washcoat, Cobalt-Nickel, Active Phase Loading.

Abstract: The preparation conditions to obtain cobalt-nickel monolithic catalyst with high loading and homogeneous distribution are studied. Washcoating of raw monolith with gamma alumina solution was examined and characterized by SEM. A uniform layer of alumina washcoat as a support for active phase was achieved in this process. Also the effect of the molarity of solution and the number of impregnation were studied to obtain different loading of active phase on monolith walls. Catalysts with 38.81, 20.44 and 3.22 wt.% of loading were obtained by four steps of impregnation in active phase solution with 3.33, 1.42, 0.3 of molarity, respectively. It was found that increase in concentration of active phase loading leads to increase in active phase loading but reduces the uniformity of active phase distribution.

Introduction

Monolithic catalysts are one of the most attractive structures that have sensible application in catalytic reaction engineering and industrial catalysis [1-3]. This is due to the commercial success of such well-known environmental catalysis processes as the purification of exhaust gases from automobiles, the abatement of NO_x emitted in the stack gases from power stations by the selective catalytic reduction process, and the catalytic combustion of VOCs. The main reason for focusing research on monoliths was their low pressure drop [2, 4, 5].

The most common material for monolithic structures is cordierite (a ceramic material consisting of magnesia, silica, and alumina ($2MgO.2Al_2O_3.5SiO_2$)). Cordierite has several critical properties such as high mechanical resistance and high thermal shock resistance that are required for many processes in chemical engineering. Generally cordierite monoliths have a low specific surface area, usually less than 1 m^2/g, so it is essential to coat monolith surface with a high surface material to increase the surface area and provide a suitable bed for active phase deposition [6]. Washcoat materials, most often gamma alumina (γ-Al_2O_3), are used to increase the surface area and distribute the catalyst on the surface of the monolith to process a monolith into an active monolithic catalyst. The interior walls of monolith are coated with a layer of a γ-Al_2O_3, called the washcoat. Finally, within the matrix of the washcoat, incorporate the noble metals that catalyze the conversion reactions of the various reactants [7, 8].

Hydrazine (N_2H_4) as a hydrogen rich material has an extensive usage in fuel cells and gas generators. This material can decompose over supported catalysts and produce nitrogen, hydrogen and ammonia. The catalytic decomposition of hydrazine can be occurred as Eq. 1 and 2 [9, 10]:

$$3N_2H_4\ (g) \rightarrow 4NH_3\ (g) + N_2\ (g) \quad \Delta H = -157\ kJ\ mol^{-1} \tag{1}$$

$$2NH_3\ (g) \rightarrow N_2\ (g) + 3H_2\ (g) \qquad \Delta H = 46.2\ kJ\ mol^{-1} \tag{2}$$

Several transition metals, such as Ir, Ni, Co, Pt, Ru, Pd, Ag, Cu, Fe and W, are active catalysts for the decomposition of hydrazine [11, 12]. These catalysts have several advantages and disadvantages that have been discussed in literatures. These catalysts are generally in pellet shapes. This kind of support forms causes several problems like high pressure drop and low strength hydrazine decomposition reactor. It is proposed that using of monoliths as supports in hydrazine decomposition catalysts can improve transporting phenomena properties during the reaction [13].

In this study, the first objective was to develop a simple procedure leading to washcoat of monolith with γ-Al_2O_3 and obtain a washcoat with uniform distribution. This washcoated monolith was used as a support to deposition of cobalt-nickel as a usual bimetallic catalyst in hydrazine decomposition. Then cobalt-nickel active phase as a usual catalyst in hydrazine decomposition was impregnated in washcoated monolith. Effects of molarity of solution on active phase was examined and studied in details. The ultimate goal of the impregnation process is the loading of the monolith with a high amount of active phase in the form of a homogeneous layer on monolith walls.

Experimental

Washcoating of Monolith

The γ-alumina slurry was prepared to coat raw monolith. For the preparation of γ-alumina slurry, a commercial γ-alumina powder (Alfa Aesar, USA, mean particle size: 3μm) was employed. An aqueous slurry of this powder was prepared with addition of γ-Al_2O_3 powder to water solution under mixing to gain a solution with 25 wt.%. HCl and NaOH were employed for setting the pH and stabilization of the slurry.

Subsequently, cubic cordierite samples with 2 cm length (supplied by Iran Delco, Iran) and 600 cells per square inch (CPSI) were used. The cell shape of the monolithic channels is square cross section with channel width 1.08 ± 0.02 mm. As the first step in monolith preparation for washcoat, it is necessary to remove physical impurities on the surface of monolith by washing monoliths with acetone [14]. After washing with acetone, the acid treatment (washing with HNO_3) was done to increase in the specific surface area [6]. Finally raw monoliths were calcinated at 600 ℃ to improve the characteristic specific of surface. Pre-treatment monoliths were then dipped in the gamma alumina slurry prepared by solving gamma alumina in distilled water. The loaded specimens were withdrawn and excess slurry was removed by blowing air (60℃, 10 min) through the monolith channels. Then the samples were dried at 110℃ for 1.5 h and finally calcined at 560℃ for 2 h.

Ni-Co was then co-impregnated with an aqueous solutions of $Ni(NO_3)_2 \cdot 6H_2O$ (Sigma – Aldrich, USA) and $Co(NO_3)_2 \cdot 6H_2O$ (Sigma – Aldrich, USA). Solutions were prepared by solving equal amounts of these salts in different mL of distilled water to obtain solutions with 0.3, 1.42 and 3.33 M (10, 30 and 50 wt.% respectively). Washcoated samples were dipped in these solutions for 4 hours, and then excess slurries were removed by blowing air, dried at 100℃ for 2 hours calcined at 460℃ for 2 hours. Impregnation, drying and calcination was repeated respectively for four steps to achieve desirable loading. Loading percentage was determined from the increase of monolith weight after every impregnation step.

Characterization

Catalysts were characterized by X-ray diffractometer (Philips model: D6792) using a copper target at 40 kV × 100 mA at 25℃. Also the coated monoliths were examined with a scanning electron microscope SEM in a Philips XL30 ESEM microscope. The SEM images were collected to identify the average thickness of washcoat layer and study the homogeneity of washcoat.

Results and Discussion

SEM Analysis

SEM analyses of washcoated monolith are shown in Fig 1. SEM images represent suitable quality of washcoat on monolith surface. The coat layer is deposited on the channel walls of the support. It is clear that washcoat layer of γ-alumina shows no cracks or peels on monolith surface. The thickness of the alumina washcoat is about 50 microns in the middle of a channel (flat part) up to 100 micron in the corners. The γ-Al_2O_3 layer penetrated the surface open macro-pores of the cordierite, which represents a good anchoring onto the support.

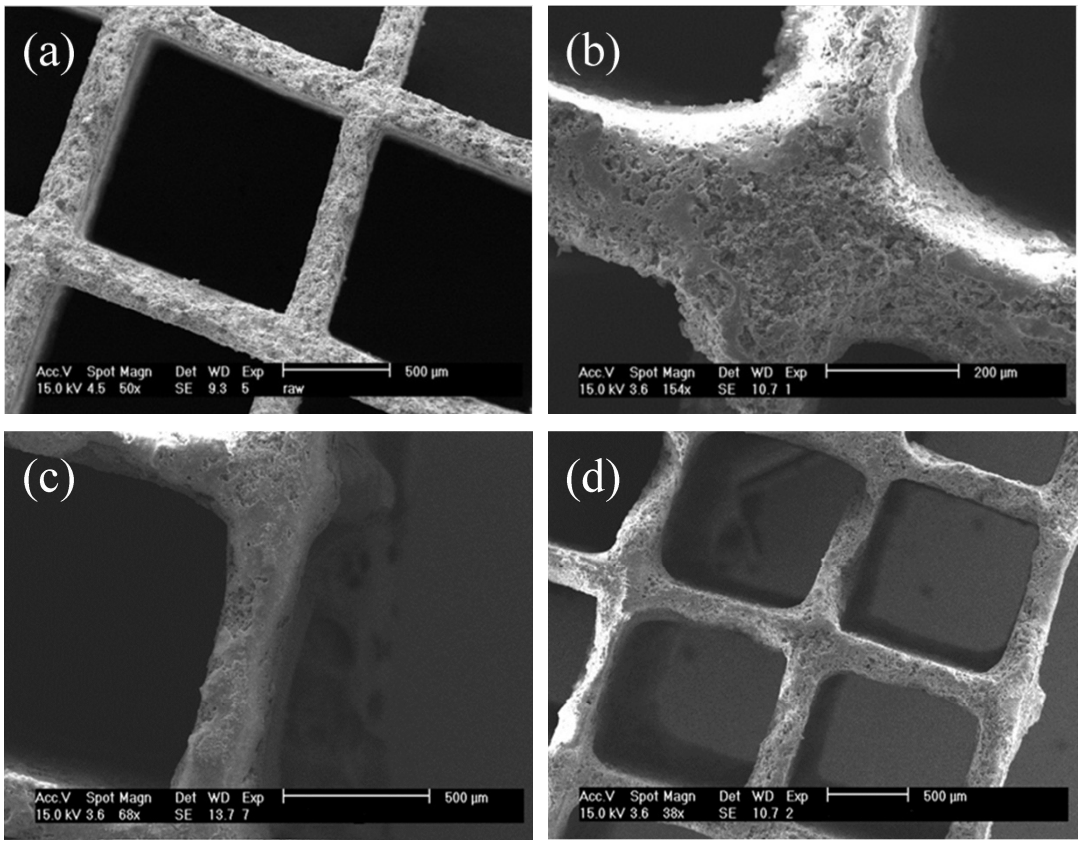


Fig 1. SEM of raw and coated monolith with γ-Al_2O_3; (a): raw monolith; (b), (c) and (d): Coated monolith with γ-Al_2O_3.

XRD analysis

The result of X-ray diffraction corresponding to the monolithic catalysts is presented in Fig. 2. This diffractogram shows the characteristic peaks of the cordierite, gamma alumina, cobalt oxide (Co_3O_4) and nickel oxide (NiO). The presence of bulk $NiAl_2O_4$ could not be confirmed by this technique.

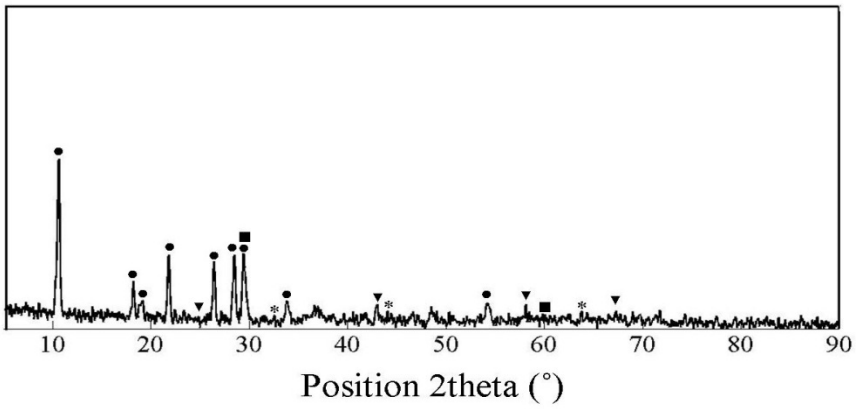


Fig 2. X-ray diffraction pattern of the Ni-Co bimetal monolithic catalyst: cordierite: ●; γ-Al_2O_3: ♥ ; Co_3O_4: ■ ; NiO: ★.

Co-Ni Loading

The required loading of the active phase on washcoated monolith is a key factor in heterogeneous catalysts synthesizing especially hydrazine decomposition catalysts. This loading was achieved with successive impregnation until the total amount of active phase loading is deposited upon the washcoated monolith. Percentage loading of active phase per number of impregnation in different solution is shown in Fig 3. The amount of loading increased with increasing in steps of impregnation. The cobalt-nickel content of the catalysts, was 3.22, 20.44 and 38.81 wt.% respectively, after four steps of impregnation with a 0.3, 1.42, 3.33 M of cobalt-nickel

active phase solution. Increase in active phase concentration leads to increase in solution viscosity and then increase in loading.

It is important to synthesize monolithic catalysts with suitable distribution and dispersion of the active phase loading. Besides, it is a key factor to achieve high loading of active phase in production of hydrazine decomposition catalysts. So it is essential to obtain a high loading, a high dispersion, and a uniform of cobalt-nickel distribution over the surface area of the washcoated monolith. Increasing in molarity of active phase loading leads to the increasing in active phase loading on monolith surface, but causes non-uniformity of active phase deposition. In other hands, increasing cobalt-nickel concentration in the impregnation solution caused in increasing the region in which cobalt-nickel accumulates. This phenomenon can be observed obviously in monolith impregnated with solution of 3.33 molarity.

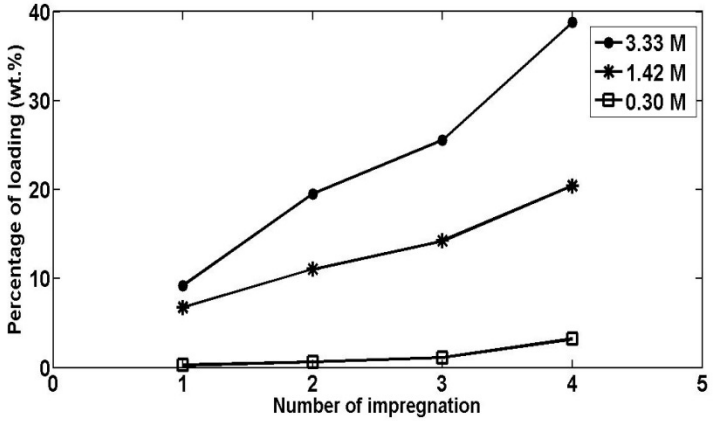


Fig 3. Percentage loading of active phase per number of impregnation in different solution with 3.33, 1.42 and 0.3 of molarity

Calcination immediately after drying is an important factor that was considered. This process prevents dissolving of previous layers of coated layer in active phase solution in every steps of impregnation. So a high loading of active phase on washcoated monolith was achieved.

Summary

Synthesize of cobalt-nickel monolithic catalyst used in hydrazine decomposition studied. A uniform layer of gamma alumina washcoat was prepared on raw monolith surface. In this way, SEM images were employed to show the morphology of coated monolith. Also XRD pattern showed cordierite, alumina, cobalt oxide and nickel oxide characteristic picks as the main compounds in synthesized catalyst. It observed that the molarity of active phase solution has high influence on loading of active phase. Increase in concentration of solution increased the percentage loading but caused uniformity of active phase distribution.

References

[1] Chen and Z. Ring, Monolith Catalysts/Reactors and Their Industrial Applications, 2007, Research Scientist and Manager, Secondary Upgrading and Refining Group National Centre for Upgrading Technology: Canada.

[2] T. Boger, Monolithic Catalysts for the Chemical Industry, Ind. Eng. Chem. Res. . 43, (2004) 4602-4611.

[3] R.M. Heck, S. Gulati and R.J. Farrauto, The application of monoliths for gas phase catalytic reactions, Chem. Eng. J . 82, (2001) 149–156.

[4] S. Yasaki, Y. Yoshino, K. Ihara and K. Ohkubo, Method of manufacturing an exhaust gas purifying catalyst, 1993.

[5] A. Cybulski and J.A. Moulijn, "Structured catalysts and reactors", USA: Marcel Dekker, Inc., 1998.
[6] A.N. Shigapov, G.W. Graham, R.W. McCabe, M.P. Peck and H.K.P. Jr, The preparation of high-surface-area cordierite monolith by acid treatment, App. Catal. A. 182, (1999) 137-146.
[7] A. Cybulski and J.A. Moulijn., "Stuctured catalysts and reactors", ed. New York: Marcel Dekker, Inc., 1998.
[8] M. Valentini, G. Groppi, C. Cristiani, M. Levi, E. Tronconi and P. Forzatti, The deposition of gamma-Al2O3 layers on ceramic and metallic supports for the preparation of structured catalysts, Catal. Today. 69, (2001) 307–314.
[9] G. A. F., Development of Hydrazine as a Monopropellant and Gas Generant, 1950, Report 9-1. Jet Propulsion Laboratory, Pasadena, Calif.
[10] W.E. Armstrong, L.B. Ryland and H.H. Voge, Catalyst for hydrazine decomposition and method for preparing such catalyst, 1980.
[11] J.B.O. Santos, G.P. Valenca and J.A.J. Rodrigues, Catalytic Decomposition of Hydrazine on Tungsten Carbide: The Influence of Adsorbed Oxygen, J .Catal. 210, (2002) 1-6.
[12] M. Zheng, R. Cheng, X. Chen, N. Li, L. Li, X. Wang and T. Zhang, Anovel approach for CO-freeH2 production via catalytic decomposition of hydrazine, Int. J .Hydrogen Energy. 30, (2005) 1081-1089.
[13] E.W. Schmidt, "Hydrazine and its Derivatives. preparation, properties, Applications". 2 ed: AJOHN Wiely & Sons, 2001.
[14] M. Valentini, G. Groppi, C. Cristiani, M. Levi, E. Tronconi and P. Forzatti, The deposition of γ-Al_2O_3 layers on ceramic and metallic supports for the preparation of structured catalysts, Catal. Today. 69, (2001) 307–314.

Advanced Materials Research Vol. 936 (2014) pp 986-991
© (2014) Trans Tech Publications, Switzerland
doi:10.4028/www.scientific.net/AMR.936.986

Low-cost Synthesis and Morphology Control of Magnesium Oxysulfate Hydrate Whiskers

ChuanHui Gao[a], Li Ding[b], YuMin Wu[c], ChuanXing Wang[d], Jun Xu[e]

College of Chemical Engineering, Qingdao University of Science & Technology, Qingdao 266042, China

[a]chuanhuigao@126.com, [b]dingli@qust.edu.cn, [c]wuyumin005@163.com, [d]wangchuanxing@qust.edu.cn, [e]xujun@qust.edu.cn

Key words: bittern; magnesium oxysulfate hydrate; morphology control; dislocation

Abstract: A low-cost raw material, bittern obtained from the production process of sea salt, was used to prepare magnesium oxysulfate hydrate ($MgSO_4 \cdot 5Mg(OH)_2 \cdot 2H_2O$, abbreviated as 152MOS) whiskers via hydrothermal synthesis with ammonia and magnesium sulfate as the other starting raw materials. The bittern was firstly filtered and then used directly without de-coloring. X-ray powder diffraction (XRD), transmission electron microscope (TEM), selected area electron diffraction (SAED), energy dispersive X-ray spectroscopy (EDX) and scanning electron microscope (SEM) were employed to investigate the composition and morphology of the products. It was found that the 152MOS whiskers synthesized from bittern at 190℃ for 3 hours exhibited fanlike morphology. The formation of the fanlike whiskers was inhibited and most of the whiskers presented as single fibers when ethanol was used as crystal control agent in the hydrothermal process. From the two-dimensional steps observed at tips of the whiskers, a possible growth mechanism was speculated that it was the extension of dislocations that made the growth of the whiskers.

Introduction

It is a well known technique to add inorganic whiskers, such as silicon carbide, calcium carbonate, magnesium hydroxide and potassium titanate, to polymers with the aim of enhancing the latter's mechanical properties and thermal stability [1–4]. As one-dimensional functional materials, whiskers have attracted great attention because of their curious structure and various remarkable physical, chemical and mechanical properties which are distinctive from those of conventional bulk materials [5]. Among the various whiskers, magnesium oxysulfate hydrate (MOS) whiskers, being proved to be well-suited as an additive for polymers and plastics [6,7], have been paid much attention since they are economically attractive and environmentally benign.

Magnesium oxysulfate hydrate can also be called basic magnesium sulfate or a solid solution in the xMgSO4·yMg(OH)2·zH2O system. By varying the ratio of these three moieties, the family of MOS comprises no less than 20 members [8]. Although previous papers had reported preparation, characterization and potential applications of the whiskers [9-13], almost all work in the literature used magnesium chloride or magnesium hydroxide as raw materials to synthesize MOS. Herein, the MgSO4·5Mg(OH)2·2H2O whiskers were prepared using bittern as raw material directly by hydrothermal synthesis without de-coloring process. It was of great interest for cost reduction, and also a new way for bittern utilization. In order to inhibit the aggregation of single whisker and enhance its application performance, several chemical additives were added, and morphology of the whisker was effectively regulated and controlled.

Experimental

Hydrothermal synthesis of MOS whiskers

The MOS whiskers were synthesized by a hydrothermal procedure in autoclave without additional template [14]. Briefly, ammonia solution was added dropwise into concentrated bittern [15] at room temperature. The slurry was filtrated, the solid filtrate was transferred to autoclave, and then magnesium sulfate was added. The autoclave was heated gradually to 190℃ and kept stirred (400 rpm) for 3 hours. A white precipitate was obtained after the autoclave was cooled down to room temperature. After filtration, the precipitate was washed with distilled water several times and dried in a vacuum oven at 100℃ for 3 hours. Then the product was obtained.

Experimental procedures and characterizations

X-ray powder diffraction (XRD) patterns were obtained with a Rigaku D/max-rA X-ray diffractometer with graphite monochromatized Cu *K*α radiation ($\lambda = 1.542$ Å), with a scanning rate of $4°\cdot min^{-1}$. The operation voltage and current were maintained at 40 kV and 50 mA, respectively.

The morphology of the products was observed on both TEM (JEM-1200EX, JEOL, Japan) at an accelerating voltage of 160 kV and SEM (JSM-6700F, JEOL, Japan) at an accelerating voltage of 12 kV. The structure was also elucidated based on both SAED on TEM and EDX on SEM.

Results and Discussion

Influence of reactants on the formation of the whiskers

Fig. 1 showed the influence of the starting raw material on morphology and composition of the hydrothermal products. Whiskers in Fig. 1a and Fig. 1b were synthesized at 190℃ for 3 hours using $MgCl_2$ and bittern as one of the starting raw materials, respectively. As could be observed the products prepared from $MgCl_2$, ammonia and magnesium sulfate exhibited a randomly arranged, long straight needle-like morphology with an average diameter of 20-40 nm and aspect ratios between 50 and 200 (Fig. 1a). While the products from bittern in replacement of $MgCl_2$ grew to fanlike whiskers, and many whiskers reunited in the same point as shown in Fig. 1b. The corresponding EDX patterns of fanlike whiskers were presented in Fig. $1b_1$ and Fig. $1b_2$. It was shown from the EDX analysis that the elementary composition at the intersection point (Fig. $1b_1$) was consistent with that in the main body (Fig. $1b_2$). The elements of O, Mg and S were observed in both cases. It meant that in the hydrothermal process, bittern could be used as one of the raw materials instead of $MgCl_2$ without de-colouring, which was of great interest for cost reduction. But except for Mg^{2+} and SO_4^{2-} it also contains many other kinds of inorganic ions such as borate ion, K^+, Cl^- and Li^+ in bittern. The crystal nucleation and growth may be influenced by the impurity ions which led to the occurrence of aggregation.

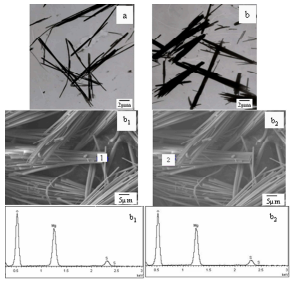


Fig. 1 Influence of starting raw materials on the morphology and composition of the whisker products. (a) and (b) are TEM images of the products with $MgCl_2$ and bittern as the staring materials, respectively. (b1) and（b2）are SEM images and the corresponding EDX spectra at the intersection point (b1) and the main body (b2) of the fanlike whiskers in Fig b

Morphology control of the whiskers

As one-dimensional functional materials, magnesium oxysulfate hydrate whiskers have been proved to be well suited as additives for polymers such as resins and plastics, acting as fillers or reinforcers with the aim of enhancing the polymers' mechanical properties and thermal stability. However, as shown in Fig. 1b, the whiskers synthesized using bittern in replacement of $MgCl_2$ agglomerated and grew to fanlike whiskers. It may be caused by the impurity ions in brine. The dispersed effect of whiskers in polymer matrix will be obviously decreased by the agglomeration which greatly restricts the use of magnesium oxysulfate hydrate whiskers.

As reported in some articles, many inorganic substances and organic compounds can be added as crystal control agents [16-18]. In order to improve the application effect, acetic acid, EDTA and ethanol were added respectively in the hydrothermal process and the morphology of whiskers was effectively controlled. It can be seen from Fig. 2 that when using acetic acid (Fig. 2b) and EDTA (Fig. 2c) as crystal control agents, the whiskers aggregated more severely with increased aspect ratios. It indicated that the presence of organic acids was favorable for the crystallization and growth of 1D $MgSO_4 \cdot 5Mg(OH)_2 \cdot 2H_2O$ whiskers [19]. While most of the whiskers presented as single fibers (Fig. 2d) with less aggregation and better dispersion when ethanol was added. The hydroxyl group in ethanol can form hydrogen bond with -OH group contained in $MgSO_4 \cdot 5Mg(OH)_2 \cdot 2H_2O$. Therefore, the surface energy of crystal nucleus was reduced and the aggregation was prevented.

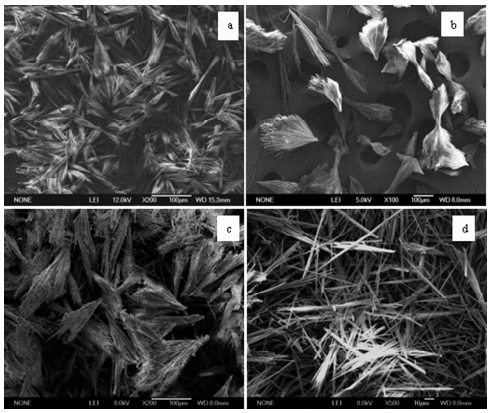


Fig. 2 Effect of additive on morphology of the products: (a) no additive，(b) acetic acid，(c) EDTA , (d) ethanol

Influence of reaction time on the formation of the whiskers

It was found that reaction time had a strong effect on the formation of 152MOS whiskers. Fig. 3 showed the TEM images of the products obtained from hydrothermal reaction of $MgCl_2$, ammonia and $MgSO_4$ at 190℃ with different reaction time and the high-magnification SEM image of the whiskers synthesized at 190℃ for 3h. As can be seen from Fig. 3a, there were some needle-like whiskers coexisted with plate particles when the reaction was maintained for 1h. The XRD pattern in Fig. 4a indicated that the products were mixture of $Mg(OH)_2$ particles and MOS whiskers when the reaction was 1h. The SAED pattern of the plate particles (shown in the inset of Fig. 3a) indicated that the particles were typical polycrystalline $Mg(OH)_2$. With hydrothermal time prolonged, the plate particles disappeared and all the products presented needle-like morphology with aspect ratios between 50 and 200. The SAED pattern of the whiskers shown in the inset of Fig. 3b suggested that the 152MOS whiskers were typical single crystal structure.

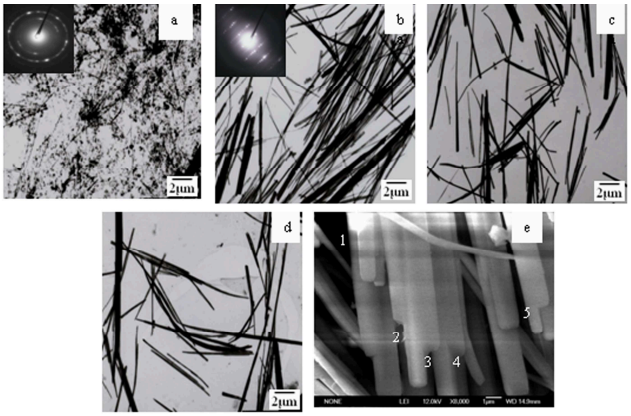


Fig.3 TEM images of the hydrothermal products synthesized at 190℃ for (a) 1h, (b) 3h, (c) 5h and (d) 20h, respectively. (e) is the high-magnification SEM image of the product shown in Fig 3b. The insets in Fig 3a and 3b are the corresponding SAED patterns of the plate particles and the whiskers, respectively

From the XRD patterns shown in Fig. 4a it could be found that the products were high purity MOS whiskers when the hydrothermal time was more than 3 hours. The 2θ values of the major peaks correspond to crystal faces of (201), (202), (203), (111), (114) and (513), respectively. The intensive XRD peaks suggested that the MOS whiskers were structurally highly ordered with high crystallinity.

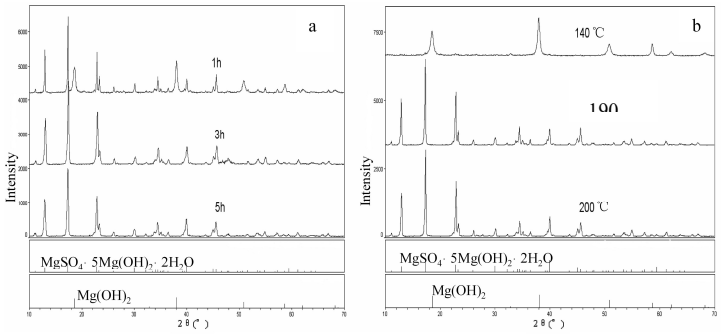


Fig. 4 XRD patterns of the hydrothermal products formed (a) at 190℃ for various reaction times, and (b) at different temperatures for 3h. The bottom bars in the figures are the major diffraction peaks of MgSO4⊙5Mg(OH)2⊙2H2O and Mg(OH)2 standards, respectively, as references

It was also seen that once all the plate $Mg(OH)_2$ particles were converted to needle-like MOS whiskers, the reaction time had no obvious effect on the morphology of the whiskers as shown in Fig. 3c and 3d, which was also in consistent with the XRD patterns in Fig. 4a.

Fig. 3e showed a part of the enlarged view of Fig. 3b, in which many two-dimensional steps can be observed. It was speculated that these steps were formed during crystal growing process as a result of crystal dislocations. Whiskers were preferentially grown crystals, and the formation includes supersaturation of the medium, crystal nucleation, dislocation nucleation and dislocation extension (crystal growth). It was exactly the extension of dislocations that made the growth of the whiskers [20]. Therefore, it was speculated that the growth of 152MOS whiskers was a result of dislocation extension.

Conclusions

152MOS whiskers were hydrothermally prepared using bittern, ammonia and magnesium sulfate as raw materials. The best hydrothermal condition was at 190℃ for 3 hours. The whiskers were preferentially grown single crystal structure and the growth mechanism was ascribed to the result of dislocation extension. The products prepared from bittern without de-coloring aggregated, reunited

in the same point and grew to fan-like whiskers. The whiskers morphology was effectively controlled and its dispersity was correspondingly improved by adding ethanol as crystal control agent. Using the magnesium resources in bittern to prepare magnesium oxysulfate hydrate whiskers is an effective way for cost reduction, and also a newly-proposed way for bittern utilization.

Acknowledgements

This work is supported by the National Natural Science Foundation of China (21106075) and Promotive research fund for excellent young and middle-aged scientisits of Shandong Province (BS2012CL016).

References

[1] Han S, Chung DDL, Mechanical energy dissipation using carbon fiber polymer–matrix structural composites with filler incorporation, J. Mater. Sci. 47 (2012) 2434–2453.
[2] Tjong SC, Meng YZ, Properties and morphology of polyamide 6 hybrid composites ontaining potassium titanate whisker and liquid crystalline copolyester, Polymer. 40 (1999)1109-1117.
[3] Chen LF, Hong YP, Zhang Y, et al, Fabrication of polymer matrix composites reinforced with controllably oriented whiskers, J. Mater. Sci. 35(2000)5309-5312.
[4] Zhou Y, Liu C, He M, et al, Splitting behavior and structural transformation process of $K_2Ti_6O_{13}$ whiskers under hydrothermal conditions, J. Mater. Sci. 43(2008)155–163.
[5] Yue T, Gao SY, Zhu LX, et al, Morphological study on the growth of $5MgSO_4 \cdot Mg(OH)_2 \cdot 2H_2O$ whiskers, Chin. J. Inorg Chem. 18 (2002)313–315.
[6] Xiang L, Liu F, Li J, et al. Hydrothermal formation and characterization of magnesium oxysulfate whiskers, Mater. Chem. Phys. 87(2004) 424-429.
[7] Dong DQ, Wang J, Yang JQ, et al. Preparation of basic magnesium sulfate whiskers, Functional. Mater. 30(1999)559-560.
[8] Yue T, Gao SY, Zhu LX, et al, Crystal growth and crystal structure of magnesium oxysulfate $2MgSO_4 \cdot Mg(OH)_2 \cdot 2H_2O$, J. Mol. Struct. 616(2002)247-252.
[9] Ding Y, Zhao HZ, Sun YG, et al, Superstructured magnesium hydroxide sulfate hydrate fibres photoluminescence study, Int. J. Inorg. Mater. 3 (2001)151-156.
[10] Y Ding, GT Zhang, SY Zhang, et al, Preparation and characterization of magnesium hydroxide sulfate hydrate whiskers, Chem. Mater. 12 (2000)2845-2852.
[11] Yan XX, Xu DL, Xue DF, SO_4^{2-} ions direct the one-dimensional growth of $5Mg(OH)_2 \cdot MgSO_4 \cdot 2H_2O$,. Acta. Mater. 55(2007)5747-5757.
[12] Wei ZQ, Qi H, Ma P et al (2002) A new route to prepare magnesium oxide whisker. Inorg Chem Commun 5:147-149
[13] Zhu LX, Yue T, GaoSY, et al, Hydrothermal sythesis and the effect of reaction time on morphology of $MgSO_4 \cdot 5Mg(OH)_2 \cdot 3H_2O$, Chin. J. Inorg. Chem. 19(2003)99-102.
[14] C Gao, X Li, L Feng, et al, Preparation and thermal decomposition of $5Mg(OH)_2 \cdot MgSO_4 \cdot 2H_2O$ nanowhiskers, Chem. Eng. J. 150(2009)551-554.
[15] Li DY, Li XG, Feng LJ, et al, One-step Hydrothermal Synthesis of Magnesium Hydroxide Sulfate Hydrate Whiskers Using Brine as Raw Material, Adv. Mater. Res. (233-235) (2011)2545-2548.
[16] Sugimoto T, Wang Y, Itoh H, et al, Systematic control of size, shape and internal structure of momodisperse a-Fe_2O_3 particles, Colloids. Surf. A 3(1998) 265-279.

[17] Sudakar C, Subbanna GN, Kutty TRN, Effect of cationic substituents on particlemorphology of goethite and the magnetic properties of maghemite derived from substituted goethite, J. Mater. Sci. 39(2004)4271-4286.

[18] Neira IS, Guitia´n F, Taniguchi T, et al, Hydrothermal synthesis of hydroxyapatite whiskers with sharp faceted hexagonal morphology, J. Mater. Sci. 43(2008)2171-2178.

[19] Sun XT, Shi WT, Xiang L, et al, Controllable Synthesis of Magnesium Oxysulfate Nanowires with Different Morphologies, Nanoscale. Res. Lett .3(2008)386-389.

[20] Wei ZQ, Qi H, Ma P, Mechanism of whisker growth from solution system, J. Salt Lake Sci. 3(1995)57-65.

Advanced Materials Research Vol. 936 (2014) pp 992-996
© (2014) Trans Tech Publications, Switzerland
doi:10.4028/www.scientific.net/AMR.936.992

The Preparation of Starch Sodium Octenyl Succinate and its Application as Surface Sizing Agent

Chenwei Tang[1,a], Zhaoli Liu[1,b] ,Yafeng Cao[1,c] ,Fengzhi Tan[1,d],
Yuan Li[1,e]

[1]School of Light Industry and Chemical Engineering, Dalian Polytechnic University,1 Qinggongyuan, 116034 Dalian, China

[a]tangwei5918@163.com,
[b]liuzl@dlpu.edu.cn,[c]yafeng0929@163.com,[d]fz_tan@126.com,[e]liyuan@dlpu.edu.cn

Keywords: SSOS, degree of substitution, surface sizing

Abstract: The preparation of Starch sodium octenyl Succinate(SSOS) and its application as a surface sizing agent in papermaking was studied in this paper. The effect of different reaction conditions on esterification of starch was firstly discussed. Based on which, SSOS with different degree of substitution (DS) was obtained and its surface sizing performance was researched. The results showed that the optimal esterification conditions were as follows: When pH is 8.5, reaction emperature is 35°C, reaction time is 3h, the maximum reaction efficiency can be achieved. The study of surface sizing performance of SSOS showed that when solid content of SSOS was 0.8613 and its DS was 0.0381, the picking speed of paper was up to a maximum value. SSOS showed a good film-forming property when its concentration was 3%.

Introductions

SSOS is an effective modified starch, which is widely used in industry such as food and paper making. Research on properties and applications of SSOS has aroused increasingly more attention [1,2]. Due to limitations of raw materials and different pulps in paper making industry of our country, the surface-strength of paper isn't high, which lead to farina or fibrilla desquamation from the paper during the printing process. Thus it is necessary to increase the strength of paper by some way. Because the special structure of SSOS, its good biodegradability and non-toxicity, it can be used as surface sizing agent in papermaking [3].In this paper SSOS is synthesized by esterification of starch and its reaction conditions were discussed firstly. Then the produced SSOS was used in surface sizing for papermaking, and its performance was analyzed.

Materials and Methods

Material and Equipment. Corn starch was purchased from Huanglong Food Industry Co. (Changchun, China); Octenyl Succinic Anhydride(OSA) was from Wei-hua Spices Chemical Co. (Hangzhou, China); reed paddle board and printing ink(medium viscosity) were provided by lab of light chemical engineering of our university; All other chemicals such as pure alcohol, solid natrium hydroxide, ammonium thiocyanate, and ferric trichloride were purchased locally and used as received without any further purification.

Methods. Preparation of Starch Sodium Octenyl Succinate. Corn starch was suspended in appropriate amount of deionized water in a beaker, which was then put in a thermostat water-bath to control the reaction temperature at a given value; The PH was adjusted to a given value by 1mol/L sodium hydrate. Then OSA, which dissolved in ethanol, was dropped in for one hour, with constant

stirring. During which 1mol/L sodium hydrate was dropped in to control the pH. At the end of reaction, 1mol/L hydrochloric acid was used to adjust the PH value to 7. Then the product was filtered and washed three times with 40% ethanol, Followed which it was dried at 55ºC overnight, crashed, and sieved.

Paper preparation. The raw materials, reed paddle board, was rived, marinated, and pulped by PFI vertical milling machine (35-39°SR). Then Paper was obtained only by adding filler, CaCO3, without squeezing . Then SSOS with different degree of substitution was cast to the surface of paper and the product was set aside for 24 hours and then tested in a constant temperature, pressure and humidity.

Tests. Determination of the degree of substitution and solid content. 5g SSOS was accurately weight and diluted with tiny amounts of ethanol, then.2.5mol/L hydrochloric acid in ethanol (25ml) was added. The slurry was magnetic stirred for 30 minutes, then added 90% ethanol(100ml) and stirred for 10 minutes. The suspension was filtrated again, and the residue was washed with 90% ethanol until no Cl- could be detected any longer and then moved to 500ml beaker. The SSOS was re-dispersed in 300 mL of distilled water, and then heated in a boiling water for 10 min. The starch solution was titrated with 0.1 M standard NaOH solution, using phenolphthalein as an indicato. According to the following formula to calculate the degree of substitution (DS) [8]:

$$DS = \frac{0.1624A}{1 - 0.210A} \quad . \tag{1}$$

A is the amount of sodium hydroxide consumed (mmol/g SSOS). Solid content(SC) was difference value of quality before painting on the paper, then divided by the area[9].

Surface strength. Surface strength of the paper was tested by printing adaptability instrument. 5 scrip specimens were cut from the paper according to the standard sample size. The sample was put between the paper clips, rotating fan handle which touched the rubber roller, then proper speeds were used to test the picking speed [7]. The sample was quickly got after printing, using a magnifying glass to observe surface condition with the aid of fluorescent, fluff position was recorded if the sample fluffing. The distance from starting point of printing to fluff pares crack point was measured, and then picking speed was got according to the speed curve diagram.

Waterproofness. According to the stockigt measurement [5], 5*5cm pattern was folded into boat. 1% $FeCl_3$ solution was dripped on the inside of paper. The boat was put on the 2% NH_4CNS solution, and at the same time the stopwatch started to time. The time when $FeCl_3$ reacted with NH_4CNS to produce red colour was recorded as the degree of sizing.

$$FeCl_3 + 3NH_4CNS \longrightarrow [Fe(CNS)_3] + 3NH_4Cl. \tag{2}$$

Results and Discussion

Influences of the preparation of SSOS. The DS of SSOS was closely related to the reactions conditions such as PH value, addition of OSA, reaction time, reaction temperature and so on.

Effect of temperature on esterification. Effect of temperature on esterification was shown in Fig 1. The results showed that the optimum temperature of esterification was 35 ºC. The DS was increased with the increase of temperature firstly and then decreased. This was perhaps because that the solubility and diffusion ability of OSA was increased when the temperature raised. But when the temperature is too high, it can lead to a faster decomposition of SSOS than that of lower temperature. Thus the optimal temperature was 35 ºC.

Effect of reaction time on esterification. The effect of reaction time on esterification was shown in Fig 2. The DS of the product was increased firstly and then decreased with the increment of reaction time. The DS was up to the highest at the traction time of 3h. It may be due to that esterification is reversible, which caused the decrease of DS when the reaction time beyond 3h.

Effect of PH on esterification. The effect of pH on esterification was shown in Fig 3. The results showed that when PH was 8.5，the DS of SSOS reached to its maximum value. It was because that with the increase of pH and amount of sodium hydrate, and starch was prone to be gelatinized. Besides, with the increment of the alkaline, much OSA would react with alkali instead of starch, which led to the decrease of DS.

Effect of dosage of the OSA on esterification reaction. To investigate the effect of time on esterification reaction in Fig.4, PH 8.5, 3h, 35 ℃, and the dosage of the starch milk was 0.25mg/L. Seen from Fig.4 , the DS kept increasing with the increase of the OSA, . The different DS was made for the experiment.

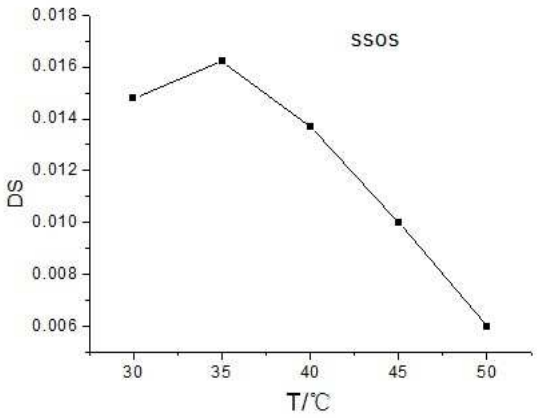


Fig 1 Effect of temperature on esterification

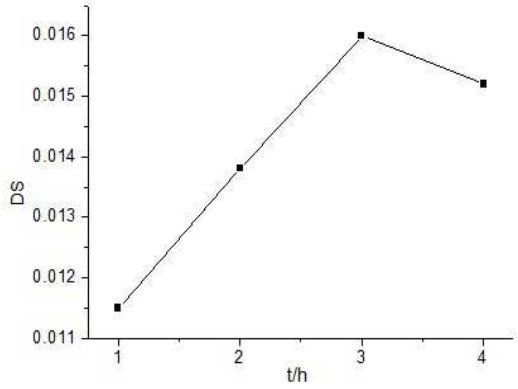


Fig 2 Effect of reaction time on esterification

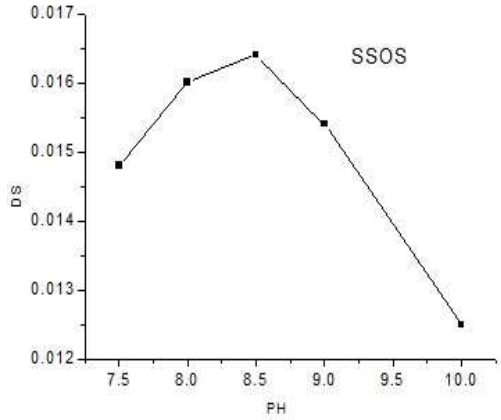


Fig 3 Effect of PH on esterification

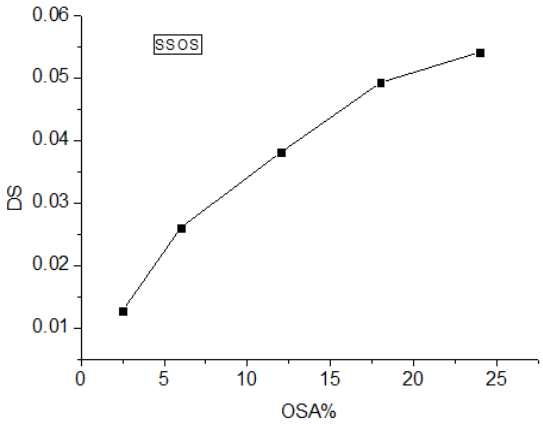


Fig 4 Effect of dosage of the OSA on esterification

Surface sizing performance of SSOS. Strength of the surface of paper was also called anti-dropping anti-blockage, which showed that the resistance ability of off powder and dropping in the printing process. Dropping and off powder was a common phenomenon in paper making industry, which was the paper defects. The mechanism is that when surface tension of the paper was less than external mechanical forces, some stuff like fiber fines, fragment, filler particles, sizing agent, and pigment particle were fell off the edge of paper under the action of mechanical force. SSOS was used to size the paper surface and its ability of resistance of the off power was studied, the sizing effect was measured at the same time.

Effect of DS and solid content on the surface strength of the paper. Printing adaptability test was made to assess SSOS sized paper and the result was shown in fig. 5. Each trend line represented different solid content of SSOS. The results showed that while the solid content was constant, the surface strength of paper increased with the increase of DS of SSOS. Native starch was illiquid, on the contrary, the modified starch, which infiltrated into the paper surface formed hydrogen bonds with the paper fiber, was greatly increased the surface strength of paper. At the same time, the hydrophobic alkenyl was directionally distributed on the fiber surface, which gave water resistence performance of the paper[4,6]. The higher the DS, the more the double bonds combined, which led to increased picking speed of paper. Meanwhile, the sizing effect enhanced with the increase of solid content under the same DS of SSOS. Starch and paper fiber were combined more closely when the solid content of SSOS was increased, thus increased surface strength of the paper obviously.

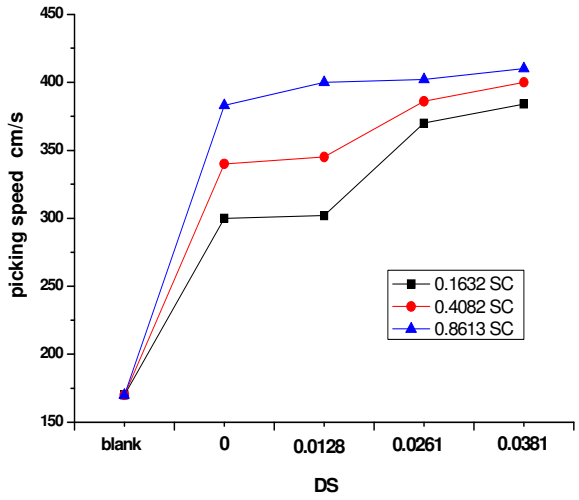


Fig. 5 Effect of DS and solid content on the surface strength

Effect of DS and solid content on water resistance of paper. Stockigt method was adopted to assess sizing effect whether good or not. SSOS with concentration of 1%, 3%, and 5%, respectively, was used as surface sizing agent and the results was shown in Fig. 6. It can be observed that the sizing effect enhanced with the increase of DS, no matter what concentration of the SSOS. It perhaps because that the modified starch which infiltrated into the paper surface formed hydrogen bonds with the paper fiber, while the hydrophobic alkenyl was directionally distributed on the fiber surface, which gave the paper water resistence performance. The more the alkenyl chains, the better the sizing effect. The results also showed that the solution with concentration of 3% had the best surface sizing performance. May be it formed a more impeccable layer than that of lower concentration. Thus its water resistance was better. Solution of 1% has very good liquidity, which led to a thin film, and it is hard to be stripped. When the concentration is more than 5% starch solution had poor liquidity, which cannot form an integrated layer, and its barrier property and water resistance decreased. So the best performance of SSOS was 3% concentration.

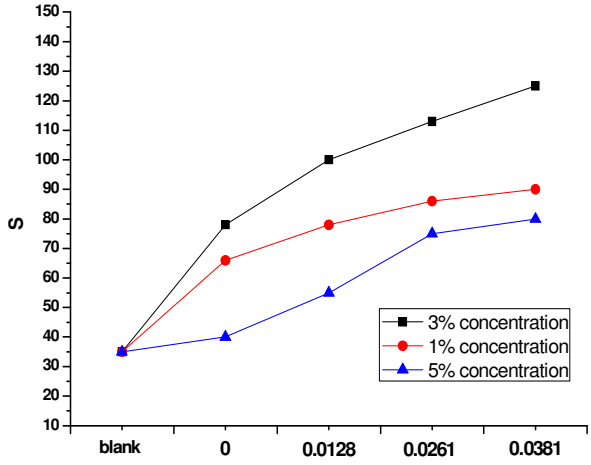


Fig.6 Modified starch of three different solid content starch

Conclusion

SSOS was prepared by using corn starch as the raw materials, and the optimum conditions of esterification were investigated firstly. Then surface sizing performance of SSOS on paper was studied. The influence of DS of SSOS and its solid content on the surface strength and water resistance of paper were discussed. Firstly, the optimal conditions of preparation of SSOS were that temperature of 35 ºC, pH of 8.5, and reaction time of 3h. Picking speed test showed maximum value when the DS was 0.0381 and solid content of SSOS was 0.8613 g/m2. The result indicated that the solid content and the DS of SSOS were two important factors that affect paper surface sizing performance of SSOS.

References

[1] Guangxun Song, Guangzhu Feng, Heping Li. Grain and oil processing 2006(8):81-84.

[2] Yuanchao Fang, Ming Cai, Wei Wang. 2004(2): 86-89.

[3] Xifeng Xu, Guangxiu Jin. Paper and papermaking 2007, 26(5): 2-3

[4] Jianmin Zhao. Shenyang chemical industry.2000, 29(4): 221-223

[5] Yunlong Pan. Wochenblatt fur papierfabrikation .1982(11):5-6.

[6] Junjian An, Guangyan Zhang. Hubei papermaking. 2010, 4: 13-16..

[7] Rui Zhou. Paper Science&Technology. 2007, 3: 011

[8] SHI Ying, LIU Zhaoli, Li Yuan. Journal of Dalian Polytechnic University, 20013, 32(1):39-42.

[9] Chen Haihong，Chen Zhonghua. Electroplating & Finishing, 2009, 28(11): 51-53.

Advanced Materials Research Vol. 936 (2014) pp 997-1001
© (2014) Trans Tech Publications, Switzerland
doi:10.4028/www.scientific.net/AMR.936.997

Structure and Property Development of Polyacrylonitrile Fiber with Ionic Liquid as Solvent During Spinning Process

Haiming Cheng[a], Enjie Zhang[b], Xuemin Yin[c], Yumei Zhang[d*], Huaping Wang[e]

College of Materials Science and Engineering, State Key Laboratory for Modification of Chemical Fibers and Polymer Materials, Donghua University, Shanghai, 201620, China

[a] chenghaiming1989@126.com, [b] zhangej1234@163.com, [c] zamoxite@126.com,

[d*] zhangym@dhu.edu.cn (corresponding author), [e] wanghp@dhu.edu.cn

Keywords: polyacrylonitrile, ionic liquid, dry-jet wet spinning, structure, property

Abstract: In order to study the structure and property development of polyacrylonitrile fiber during spinning process with ionic liquid as solvent, the 13 wt% PAN/[BMIM]Cl solution was prepared by dissolving polyacrylonitrile (PAN) in 1-butyl-3-methylimidazolium chloride ([BMIM]Cl). The dry-jet wet spinning of PAN/[BMIM]Cl was carried out to obtain the samples along spinning line. The mechanical properties, dynamic mechanical properties (DMA) and supramolecular structure of PAN fiber were analyzed. It is found that along spinning line tensile strength of PAN fiber increased significantly; initially, elongation at break increased followed by subsequent decrease. The fiber's glass transition temperature (T_g) drops initially and later becomes constant; however, the fiber's crystallinity and orientation increased.

Introduction

Polyacrylonitrile (PAN) fiber was widely used in costumes, decorations and industrial applications because of its excellent flexibility, fluffy texture, exhibits acid and light sensitivity and other properties. There are some strong dipole interactions resulting from（-C≡N）in the polyacrylonitrile (PAN). It causes that the fiber's melting point to become relatively higher than the decomposition temperature (T_d). Therefore，Polyacrylonitrile was dissolved in some strongly polar solvents such as N, N-dimethylformamide (DMF), N, N-dimethylacetamide (DMAc), dimethyl sulfoxide (DMSO) and aqueous solution of sodium thiocyanate etc.

In 2004, Cheng *et al.* [1] found that the ionic liquid (IL) was good solvent for polymerization and dissolution of acrylonitrile. Then the dissolution and regeneration of polyacrylonitrile in ILs have been investigated [2]. PAN/[BMIM]Cl solution has a higher apparent viscosity and significant shear thinning properties. The elastic characteristics of the solution were conducive to spinning and stretching [3, 4]. Wan and Yin *et al*. [5, 6] studied the structure of PAN fibers prepared with ionic liquid as a solvent by dry-jet wet spinning.

Previous studies have shown that polyacrylonitrile with IL as solvent has imparted some different characteristics in dissolution [1, 7, 8], solution properties [3, 4] and spinning [5, 6] compared to conventional solvents. As we all known, solution spinning is a complex process and each procedure has significant impact on the final structure and properties of the fibers. Ji [9] studied the relationship between techniques and properties during PAN fiber formation process and suggested that the crystal structure of the fibers has formed basically during the coagulation stage. Both drawing and removal of solvent can increase the mechanical properties of the fibers. Liang *et al*. [10] discussed the changes in formation and evolution of porosity structure during spinning process and found that porosity structure can affect the fiber's resultant physical properties. However, after-processing,

stretching can reduce fiber pores, thus fiber density, mechanical properties, crystallinity would increase. The study of the relationship between structure evolution and mechanical properties during the spinning process of PAN fiber in the [BMIM]Cl system have yet to be further explored. In this work the macromolecular structure of PAN fiber during the spinning process was evaluated using wide-angle X-ray synchrotron radiation diffraction (WAXD) technique. The relationship between the structure and properties during the spinning process was investigated by combining mechanical testing and dynamic mechanical analysis (DMA).

Experimental

Samples

Materials

The copolymer poly(AN-co-MA) (Acrylonitrile : methyl acrylate = 9:1) was provided by Shanghai Petrochemical Co. Ltd. (Shanghai, China) with a viscosity average molecular (Mv) of 9.0×10^4g/mol. The ionic liquid [BMIM]Cl was synthesized and purified according to the literature[11].

Polyacrylonitrile fibers preparation

The 13 wt% PAN/[BMIM]Cl solutions were prepared by dissolving PAN in [BMIM]Cl by kneading. PAN fibers were prepared by the dry–jet wet spinning process with a lab scaled spinning machine with the following process diagram and conditions, shown in Fig. 1.

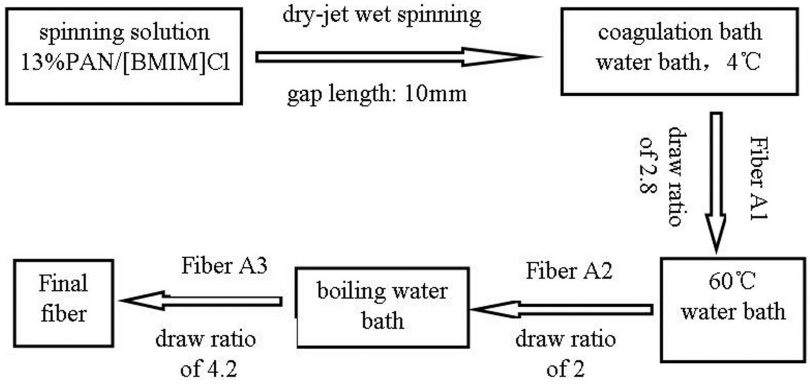


Fig. 1 The flow-process diagram of dry-jet wet spinning process for PAN fibers

Fiber diameter

Fiber diameters were measured by Polarizing microscope WT-MV3100H (Shanghai Science and Technology Development Co., Ltd.). At least 15 measurements were taken as the average value.

Mechanical properties

Samples were washed with hot water to remove residual solvents and dried to constant weight. The stress-strain curves of a single fiber were recorded using a XQ-1A tensile tester with a gauge length of 20 mm and an extension rate of 20 mm/min. At least 20 samples were tested for each samples and the tenacity, elongation at break and initial modulus were calculated averagely.

Fiber birefringence

Fiber's birefringence was measured using Mongolian compensation method by Motic BA300Pol polarizing microscope. The compensation angle θ (^{o}) of fiber was measured using a polarizing microscope. The birefringence was calculated according to Eq. (1).

$$\Delta n = \theta\lambda / 180^o d \tag{1}$$

Where Δn is the birefringence, $\lambda=0.589\times10^{-9}$ m is the wavelength of sodium, θ is compensation angle, d is the fiber's diameter (m).

Wide-angle X-ray diffraction

Wide-angle X-ray diffraction (WAXD) characterizations of fibers were carried out at the Shanghai Synchrotron Radiation Facility (SSRF) on beam line (BL14B). The X-ray wavelength was 1.24Å. The 2θ vs. intensity curves were obtained by integrating using FIT2D software based on fiber's diffraction curves. The content of crystal phase and mesophase, orientation factor and crystallite size were calculated according to the reference[12].

The Dynamic Mechanical Analysis

The dynamic mechanical Analysis (DMA) was carried out by TA Q800 instrument to obtain the loss factor (tanδ). The frequency applied was 1 Hz over a temperature range from 25 °C to 400 °C in the temperature-frequency sweeping mode. Heating rate is 5°C/min and the amplitude is 15μm.

Results and discussion

Mechanical properties of PAN fiber during spinning process

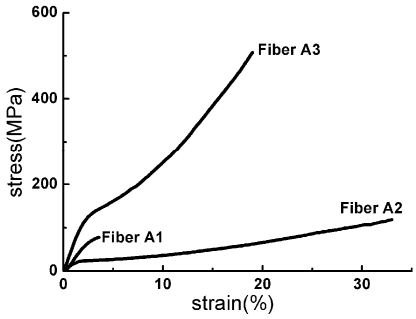


Fig. 2 The stress-strain curves of PAN fiber during spinning process

TABLE 1 MECHANICAL PROPERTIES OF PAN FIBER DURING SPINNING PROCESS

Samples	Diameter [μm]	Tensile strength [MPa]	Elongation at break [%]	Initial modulus [GPa]
Fiber A1	59.26	70.71	3.51	2.99
Fiber A2	51.40	101.85	33.00	2.21
Fiber A3	25.68	500.81	19.01	6.29

The stress-strain curves of the washed and dried PAN fibers obtained from spinning line were shown in Fig.2. It is found that along spinning line the fiber's tensile strength increased significantly while initial modulus and elongation at break showed different regulation. Fiber A1 is brittle and has no apparent yield behavior. However, fiber A2 and fiber A3 got plastic deformation under load and exhibited obvious yield behaviors. Fiber A2 and A3 were in elastic region before the yield point. After the yield point, plastic deformation occurred but no obvious phenomenon of the narrow neck. Then, with the strain increase, the tensile stress continued to increase.

DMA of PAN Fiber During Spinning Process

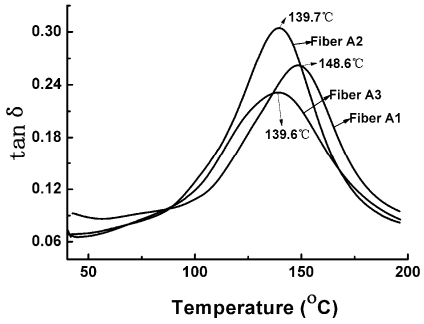


Fig. 3 Curves of tanδ vs. temperature of PAN fibers during spinning process

As shown in Fig. 3, only the glass transition peak was observed in the temperature-tanδ curves. It can be seen from the curves the Tg of Fiber A1 is the largest, which attributes to the entanglement of macromolecular chain in amorphous regions[13]. After the pre-drawing in water bath, the macromolecular chains of amorphous region began to be oriented and the entanglements reduced so the Tg decreases.

Supermolecular structure of PAN fibers during spinning process

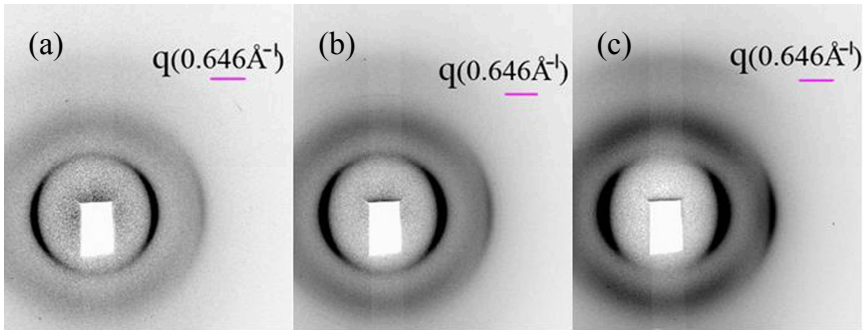


Fig. 4 WAXD patterns of PAN fibers during spinning process, (a) Fiber A1, (b) Fiber A2 and (c) Fiber A3

Table 2 Parameters of supermolecular structure of PAN fibers during spinning process

Samples	Percent of crystal phase[%]	Percent of mesophase [%]	Crystallite size of (100) [nm]	Birefringence [$\Delta n \times 10^2$]	Crystal orientation factor [f_c]
Fiber A1	44.8	30.8	4.44	0.31	0.66
Fiber A2	45.3	31.5	4.09	0.54	0.69
Fiber A3	49.5	31.1	4.36	0.87	0.77

From Fig. 4, the image of dimensional WAXD of fiber A1 showed an obvious long diffraction arc indicated a low orientation in crystal phase. The diffraction arcs of fiber A2 and A3 gradually become short and the strength is increased after the drawing. The $2\theta=16.9°$ and $2\theta=29.5°$ in the equatorial line show apparent reflex arc which belong to hexagonal crystal system [14], corresponding to the (100) plane and the ($2\bar{1}0$) plane.

From the calculation results shown in Table 2, it is clear that the content of crystal phase, the birefringence and crystal orientation factor increased along the spinning line, which caused the increase of tenacity of the fibers. And the change of crystallite size could be the corresponding to the change of initial modulus of the PAN fibers because the larger crystallite often caused larger initial modulus of fiber.

Summary

From the analysis of properties and structure of the PAN fiber during spinning process, it is found the increase of the content of crystal phase and orientation both in crystal phase and non-crystal phase resulted in the increase of tenacity along spinning line. While the different change of initial modulus was resulted from the variation of the crystallite size as the larger crystallite leaded to the larger initial modulus. And the higher Tg was observed in the coagulated PAN fiber (Fiber A1) which was caused by the strong entanglements of the molecular chains in the amorphous phase due to the low orientation of Fiber A1.

Acknowledgements

This work was financially supported National Natural Science Foundation of China (51273041).

References

[1] L. Cheng, Y. Zhang, T. Zhao, H. Wang, Free radical polymerization of acrylonitrile in green ionic liquids, Macromol Symp. 216 (2004), 9-16.

[2] W. Zheng, B. Cheng, H. Zang, B. Liu, Study of solubility properties of ionic liquids to PAN, J. Tianjin polytechnic univ. (2008) 13-15.

[3] G. Yan, W. Dong, X. Chen, Y. Zhang, H. Wang, Rheological behavior of polyacrylonitrile /ionic liquid solution, China Synth Fiber Ind. (2010) 33-35.

[4] X. Chen, Y. Zhang, H. Wang, S. Wang, S. Liang, RH. Colby, Solution rheology of cellulose in 1-butyl-3-methyl imidazolium chloride, J. Rheol. 55 (2011) 485.

[5] S. Wan, Y. Zhang, H. Wang, Acrylic fibers processing with ionic liquid as solvent, Polym. Adv. Technol. 20 (2009) 857–862.

[6] X. Yin, L. Zhang, X. Chen, H. Wang, Y. Zhang. Effect of secondary drawing rate in boiling water on structure and properties of polyacrylonitrile fiber. China Synth Fiber Ind. (2013) 23-26.

[7] D. Li, Y. Zhang, H. Wang, J. Tang, B. Wang. Free-radical copolymerization kinetics of acrylonitrile and methyl acrylate in [BMIM]BF_4, J. Appl. Polym. Sci. 102 (2006) 4254-4257.

[8] Y. Chen, Y. Zhang, F. Ke, J. Zhou, H. Wang, D. Liang. Solubility of neutral and charged polymers in ionic liquids studied by laser light scattering, Polymer. 52 (2011) 481-488.

[9] B. Ji, Relationship between technics and properties during PAN precursors formation process, C. In. (2011) 1148-1151.

[10] Y. Liang, W. Jiang, S. Zhang, R. Zhou, J. Zhao, Y. Zhang, D. Pan, Formation and evolution of porosity structure of PAN precursor during fiber formation process, China Synth Fiber Ind. (2010) 5-7.

[11] S. Csihony, C. Fischmeister, C. Bruneau, IT. Horváth, PH. Dixneuf, First ring-opening metathesis polymerization in an ionic liquid. Efficient recycling of a catalyst generated from a cationic ruthenium allenylidene complex, New J Chem. 26 (2002) 1667–1670.

[12] X. Yin, L. Zhang, X. Zhu, H. Wang, Y. Zhang, Phase structure of acrylic fibers processed with ionic liquid as solvent, AMR. 560-561 (2012) 41-45.

[13] Z. Bashir, The hexagonal mesophase in atactic polyacrylonitrile: A new interpretation of the phase transitions in the polymer, J. Macromol. Sci. B40 (2001) 41–67.

[14] X. Liu, W. Ruland, X-Ray studies on the structure of polyacrylonitrile fibers, Macromolecules. 26 (1993) 3030-3036.

Advanced Materials Research Vol. 936 (2014) pp 1002-1006
© (2014) Trans Tech Publications, Switzerland
doi:10.4028/www.scientific.net/AMR.936.1002

Plasticization of cellulose diacetate by Ionic liquid

Na Liu[1, a], Jingwen Zhang[1,b] and Huaping Wang[1,c]

[1] State Key Laboratory for Modification of Chemical Fibers and Polymer Materials, College of Materials Science and Engineering, Donghua University, Shanghai 201620, P. R. China

[a]liuna@dhu.edu.cn, [b]1065600813@qq.com, [c]wanghp@dhu.edu.cn

Keywords: cellulose diacetate; ionic liquid; plasticization

Abstract: Three ionic liquids, 1-butyl-3-methylimidazolium terafluoroborate ($BMIMBF_4$), 1-butyl-3-methylimidazolium trifluoromethanesulfonate (BMIMOTF) and 1-butyl-3-methylimidazolium hexafluorophosphate($BMIMPF_6$) were applied as the plasticizers of CDA. Among three ILs, $BMIMBF_4$ was considered to be the most effective plasticizer, which was confirmed by TGA and DMA. The interaction between ILs and CDA was also investigated.

Introduction

In recent years, cellulose material has become one of the focuses as a replacement of petroleum-based material in the field of fibers and textiles due to the anxiety about exhaustible resources[1-3]. However, limited by the strong intermolecular interactions of a large number of hydrogen bonds among hydroxyl groups of the anhydroglucose units in cellulose (Fig 1)[4-7], its processing is basically realized by solvation and derivatization to weaken and unlock the intermolecular hydrogen bonds[8-9], which is nongreen and raises a lot of environment problems. Cellulose cannot be melt processed for its higher melting processing temperature (T_m) than decomposition temperature (T_d), resulting from the strong intermolecular interactions. Although acetyl groups substituting the hydroxyl group in Cellulose diacetate (CDA) making it thermoplastic[10], CDA cannot be melt processed either without any modification dut to its melting processing temperature (T_m) close to decomposition temperature (T_d) [11].

To improve the melt processability and facilitate processing of CDA, it is commonly modified by low molecular weight plasticizers like phthalates, glycerine and phosphates because of their low cost and facility of compounding, while a serious problem of plasticizer leaching occurs which is responsible for the lowering of the mechanical properties of molded CDA products[12-13]. To solve this migration problems, some attempts have been made by introducing long chain to CDA, i.e. chemical modification. Polylactic acid (PLA) and caprolactone (CL) are commonly practiced to graft CDA, main role being to destroy the cellulose crystalline structure and lead to a lower glass transition temperature[14-19]. However, chemical modification depends very much on the degree of substitution, and often, external plasticizers and catalysts have been used to assist grafting. Despite of the good modification effect of introduction of side chain, it also causes some problems to be solved such as side chain flow and increased brittleness of products and so on[20].

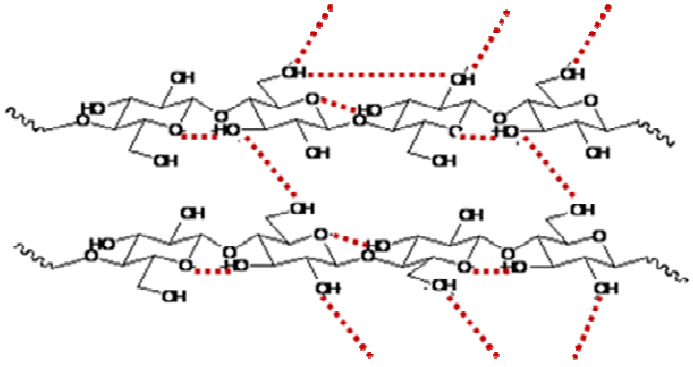


Fig. 1 Schematic Diagram of H-bondings in Cellulose

Ionic liquids (ILs) are low melting point salts being entirely composed of ions. They have been extensively investigated in the last decade due to their many unique properties such as recyclablility, negligible vapor pressure, thermal and chemical stability and non-flammablility[21-23]. It is also reported that ILs containing imidazolium or pyridinium cations are similar to some conventional plasticizers, containing an aromatic core and pendant alkyl groups[24]. Moreover, ILs exhibit many of ideal plasticizer characteristics such as low volatility, low leachability, high and low thermal stability, thermodynamic compatibility with polymers, with performance, reproducibility, and wide thermal range being some of greatest advantages over traditional plasticizing agent, which attract many interest in the studies on the plasticizing effect of ILs as plasticizer of polymer. However, to the best of our knowledge, very little effort has been devoted to the preparation of cellulose material by ILs plasticizing, not to mention the subsequent processing.

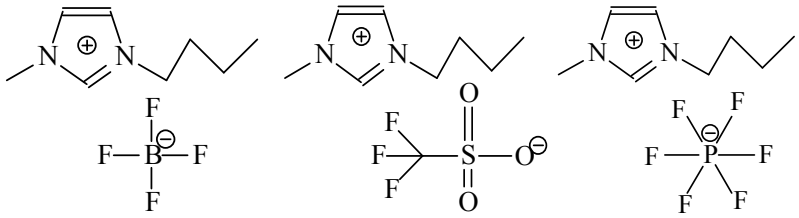


Fig. 2 Chemical Structure of plasticizing agents investigated

In this paper, the plasticization effect of ILs and the interaction between ILs and CDA were investigated. Firstly the solubility of CDA in different ILs were studied, considering that the interaction between ILs and CDA was more easier to observe in solution than in plasticized mass. By comparison, the solubility of cellulose in defferent ILs were also investigated(as shown in table 1). It was found that cellulose could not be solved in 1-butyl-3-methylimidazolium terafluoroborate ($BMIMBF_4$), 1-butyl-3-methylimidazolium trifluoromethanesulfonate (BMIMOTF) and 1-butyl-3-methylimidazolium hexafluorophosphate($BMIMPF_6$), which is in consistent with literature, while CDA exhibited the opposite solubility in these three ILs. In consideration of the difference of structure between cellulose and CDA, we inferred that it was the acetyl groups that played an important role in interaction with those three ILs.

Table 1. The solubility of CDA and cellulose in different ILs at 30°C

	BMIMOTF	$BMIMPF_6$	$BMIMBF_4$	BMIMCOOH
CDA	soluble	soluble	soluble	insoluble
cellulose	insoluble	insoluble	insoluble	soluble

In the further exploration, $BMIMBF_4$, BMIMOTF and $BMIMPF_6$ were used as plasticizer. ILs and CDA with a certain mass ratio were mixed and dissolved in acetone. Colorless and transparent solutions were prepared and then were casted in aluminum foil. Thin plasticizing film samples were recovered after acetone volatilization.

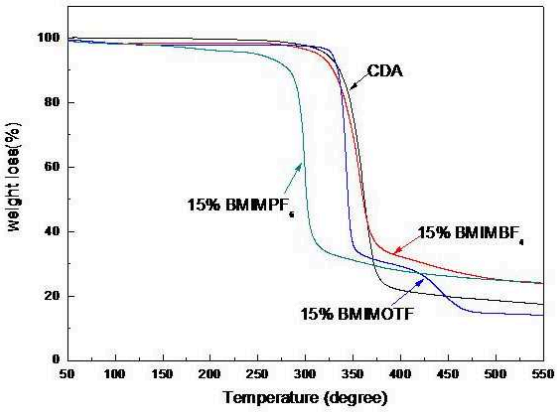


Fig. 3 Thermal stability of CDA and plasticized CDAs by different ILs

The plasticized samples were tested for thermal stability. It was evident from Fig. 3 that CDA sample plasticized with 15 wt% $BMIMBF_4$ had a similar thermal stability with CDA, which was more stable than those plasticized by BMIMOTF and $BMIMPF_6$ (Table 2). The glass transition temperatures of CDA and plasticized CDAs samples were also tested by DMA. As shown in Table 2, T_g of plasticized CDAs were much lower than CDA, while the differences in T_d were not significant, especially in the case of $BMIMBF_4$ as plasticizer. It is indicated that ILs as plasticizer can be effective in broadening the processing temperature by reducing T_g of plasticized CDA, resulting in improving the processability of CDA. Among three ILs, $BMIMBF_4$ was considered to be the most effective plasticizer.

Table 2. T_g and T_d at 5%, 10%, 50% weight loss of CDA and plasticized CDA (15 wt% ILs)

samples	T_g	$T_{d,5\%}$	$T_{d,10\%}$	$T_{d,50\%}$
CDA	231 °C	318.3 °C	333.8 °C	363.2 °C
CDA/$BMIMBF_4$	161 °C	311.8 °C	328.1 °C	360.8 °C
CDA/BMIMOTF	163 °C	327.3 °C	332.9 °C	344.4 °C
CDA/$BMIMPF_6$	176 °C	234.4 °C	282.9 °C	301.1°C

The interaction between $BMIMBF_4$ and CDA in plasticized samples was investigated by FT-IR (Fig.4). It could be noticed that the O-H stretching decreased in intensity and the peak position assigned to C=O in acetyl groups[25] moved to higher wavenumber with the introduction of $BMIMBF_4$, meanwhile, the peak position assigned to C-H in imidazolium ring[26] moved to lower wavenumber, which indicated that the hydrogen-band matrix in CDA was weakened and partly destroyed by the interaction between CDA and $BMIMBF_4$. And it was also indicated that when the ILs serve as solvents, the same interaction occurs in the solvation(as shown in figure 5).

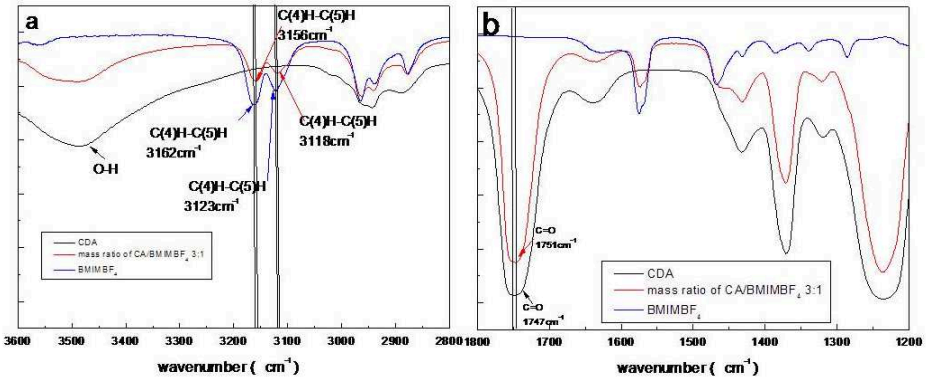


Fig. 4 IR spectra of CDA, $[BMIM]BF_4$ and CDA/25wt%$[BMIM]BF_4$ in the region (a)from 3600 cm^{-1} to 2800 cm^{-1}; (b)from 1800 cm^{-1} to 1200 cm^{-1}

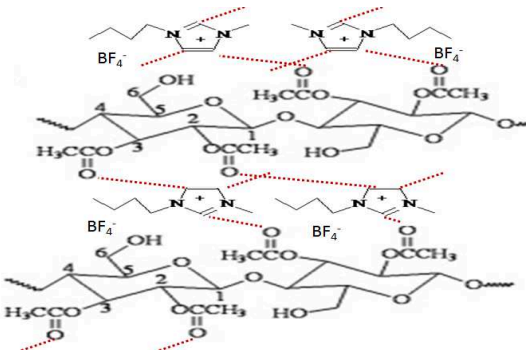


Fig. 5 Proposed schematic diagram for the interactions between repeating monomer units of CDA and [BMIM]BF_4

The application of $BMIMPF_6$, BMIMOTF and $BMIMBF_4$ as plasticizer of CDA is very promising in processing of CDA material allowing CDA to have a wider range of working temperatures. Among these three ILs, $BMIMBF_4$ was regarded as the most effective plasticizer. The interaction between ILs and CDA or the plasticization mechanism will be further investigated in our future work.

Acknowledgement: This work was financially supported by The National Natural Science Foundation of China (51273041) and the Fundamental Research Funds for the Central Universities.

References

[1] I.S. Kim, J.P. Kim, S.Y. Kwak, et al, Novel regenerated cellulosic material prepared by an environmentally-friendly process, Polymer. 2006 (47) 1333-1339.

[2] Q. Chen, S. Nattatan, X. Y. Ni, et al, The effect of fibre volume fraction and mercerization on the properties of all-cellulose composites, Carbohydrate Polymers. 2008 (71) 458-467.

[3] Y.B. Song, J.P. Zhou, L.N. Zhang, et al, Homogenous modification of cellulose with acrylamide in NaOH/urea aqueous solutions, Carbohydrate Polymers. 2008 (73) 18-25.

[4] J. Schroeter, F. Felix, Melting cellulose, Cellulose. 2005 (12) 159-165.

[5] H.P. Fink, P. Weigel, H.J. Purz, et al, Structure formation of regenerated cellulose materials from NMMO-solutions, Progress in Polymer Science. 2001 (26) 1473-1524.

[6] P. Zugenmaier, Conformation and packing of various crystalline cellulose fibers, Progress in Polymer Science. 2001 (26) 1341-1417.

[7] X.M. Chen, C. Burger, D.F. Fang, et al, X-ray studies of regenerated cellulose fibers wet spun from cotton linter pulp in NaOH/thiourea aqueous solutions, Polymer. 2006 (47) 2839-2848.

[8] T. Heinze, New ionic polymers by cellulose functionalization, Macromolecular Chemistry and Physics. 1998 (199) 2341-2364.

[9] T. Heinze, T. Liebert, P. Klüfers, et al, Carboxymethylation of cellulose in unconventional media, Cellulose. 1999 (6) 153-165.

[10] T. Heinze, T. Liebert, Chemical characteristics of cellulose acetate, Macromolecular symposia. 2004 (208) 167-237.

[11] P. Zugenmaier, Characterization and physical properties of cellulose acetates, Macromolecular symposia. 2004 (208) 81-166.

[12] V.E. Yarsley, W. Flavell, P.S. Adamson, N.G. Perkins, Cellulosic plastics; cellulose acetate; cellulose ethers; regenerated cellulose; cellulose nitrate. London, 1964.

[13] C.R. Fordyce, L.W.A. Meyer, Plasticizers for cellulose acetate and cellulose acetate butyrute, Industrial and Engineering Chemistry. 1940 (32) 1053-1060.

[14] S.H. Lee, N. Shiraishi, Plasticization of cellulose diacetate by reaction with maleic anhydride, glycerol, and citrate esters during melt processing, J. Appl. Polym. Sci. 2001 (81) 243-50.

[15] M. Yoshioka, N. Hagiwara, N. Shiraishi, Thermoplasticization of cellulose acetates by grafting of cyclic esters, Cellulose. 1999 (6) 193-212.

[16] H. Hatakeyama, T. Yoshida, T. Hatakeyama, The effect of side chain association on thermal and viscoelastic properties. Cellulose acetate based polycaprolactones, J. Thermal. Anal. 2000 (59) 157-68.

[17] K.H. Guruprasad, G.M. Shashidhara, Grafting, blending, and biodegradability of cellulose acetate, J. Appl. Polym. Sci. 2004 (91) 1716-23.

[18] H. Warth, R. Mülhaupt, J Schätzle, Thermoplastic cellulose acetate and cellulose acetate compounds prepared by reactive processing, J. Appl. Polym. Sci. 1997 (64) 231-42.

[19] H. VazquezTorres, C.A. Cruzramos, Blends of cellulosic esters with poly(caprolactone)-characterization by DSC, DMA, and WAXS, J. Appl. Polym. Sci. 1994 (8) 1141-1159.

[20] Aranishi Y, Yamada H, Maeda Y, Takahashi H, Ozaki M, Nishio Y, Yoshioka M. Thernoplastic Cellulose Derivative Composition and Fiber Comprising the same. U.S. Patent 6,984,631. (2006)

[21] M. Yoshioka, T. Miyazaki, N. Shiraishi, Plasticization of Cellulose Derivatives by Reactive Plasticizers. 1. Plasticization of Cellulose Acetate by Kneading Reaction using Dibasic Acid Anhydrides and Monoepoxides, Mokuzai Gakkaishi, 1996(4) 406-416.

[22] R. P. Swatloski, S.K. Spear, J.D. Holbrey, R.D. Rogers, Dissolution of Cellulose with Ionic Liquids. J. Ameri. Chemi. Socie. 2002 (1) 4974-4976.

[23] H. Zhang, J. Wu, J. Zhang, J. He, 1-Allyl-3-methylimidazolium Chloride Room Temperature Ionic Liquid: A New and Powerful Nonderivatizing Solvent for Cellulose, Macromolecules. 2005 (38) 8272-8277.

[24] M.P. Scott, C.S. Brazel, M.G. Benton, et al, Application of ionic liquids as plasticizers for poly(methyl methacrylate), Chemical Communications. 2002 (2) 1370-1371.

[25] Y.L. Guo, P.Y. Wu, Investigation of the hydrogen-bond structure of cellulose diacetate by two-dimensional infrared correlation spectroscopy, Carbohydrate Polymers. 2008 (74) 509-513.

[26] J.M. Andanson, F. Jutz, A. Bailer, Investigation of Binary and Ternary Systems of Ionic Liquids with Water and/or Supercritical CO2 by in Situ Attenuated Total Reflection Infrared Spectroscopy, Journal of Polymer Science Part B: Polymer Physics. 2010 (6) 2111-2117.

Advanced Materials Research Vol. 936 (2014) pp 1007-1011
© (2014) Trans Tech Publications, Switzerland
doi:10.4028/www.scientific.net/AMR.936.1007

Studies of Vapor-Liquid Equilibrium of Meta-Xylylenediamine-Aniline System

Xiaohong Wang

(College of Chemical Engineering, QingDao University of Science and Technology, QingDao, 266042, Shandong, China)

E-mail: wxhlee@sohu.com

Keywords: m-xylylenediamine (MXDA); aniline; vapor-liquid equilibrium; Wilson equation

Abstract: The saturated vapor pressures of m-xylylenediamine (MXDA) were measured with the static method at the temperatures between 150-180℃, and the Antoine parameters of MXDA were regressed. The Vapor-Liquid Equilibrium (VLE) data of aniline-MXDA system at pressure of 4 kPa were determined. The VLE data were tested by the integral method proposed by Herington and showed to meet thermodynamic consistency. Wilson Equation was used to correlate the experimental data and the model parameters were determined. The calculated data from Wilson Equation agreed well with the experimental data of the above binary system.

Introduction

MXDA is an aliphatic diamine having benzene ring produced from isophthalonitrile (IPN).

MXDA is used as an epoxy resin hardener directly and is useful as a chemical intersolvent in the plastic and polymer fields.[1-3] Zhang Peng et al[4] prepared the amorphous Ni-Al alloy thin strip with quenched to make high activity skeleton nickel and the molar yield of MXDA was up to 96%. With Co-Ti/diatomite catalyst, the yield of MXD to 94% was made for UOP Inc.[5] In this hydrogenation reaction, optimum reaction conditions are crucial to produce a high grade of MXDA. The solubility of IPN in several commonly used solvent is compared with each other in literature.[6]

Because the solubility of aniline to IPN is very big and aniline does not participate in this reaction[7], aniline is determined for the reaction solvent in this paper. In the subsequent design of the reaction product separation, the VLE data of aniline-MXDA system are essential which are not reported now. The VLE data of aniline-MXDA system are determined at pressure of 4 kPa with gas-liquid dual-loop method and Wilson Equation is used to correlate the experimental data in this paper.

Experimental

Experimental principle. The VLE data of aniline-MXDA system are determined with the loop method used widely in this paper. When the vapor-liquid equilibrium is reached, in addition to the pressure and the temperature of the two-phase is equal respectively, the chemical potentials of each phase is equal too, that means the fugacity of each phase is equal. When these VLE data are determined at pressure of 4 kPa, the activity coefficients of the different components can be calculated by equation (1), then, Wilson equation is used to correlate the activity coefficients with the compositions of the different components by equation (2). The Wilson parameter— Λij can be changed with the temperature changing and $\ln \Lambda ij$ can be expressed as a function of temperature shown in equation (3). The binary interaction parameters—a_{ij}, b_{ij}, c_{ij}, d_{ij} included in equation (3) can be regressed with the VLE data and the saturated vapor pressures data of the pure component determined in this paper, then, the vapor-liquid equilibrium equation can be got.

$$\gamma_i = \frac{Py_i}{P_i^0 x_i} \quad (1)$$

$$\ln \gamma_i = 1 - \ln(\sum_j \Lambda_{ij} x_1) - \sum_j \frac{\Lambda_{ji} x_j}{\sum_k \Lambda_{jk} x_k} \quad (2)$$

$$\ln \Lambda_{ij} = a_{ij} + b_{ij}/T + c_{ij} \ln T + d_{ij} T \quad (3)$$

Materials. IPN (purity≥99.9%), aniline(purity≥99.5%), methanol (purity≥99.5%)，and the origins of the chemicals is from Sinopharm Chemical Reagent Co., Ltd.

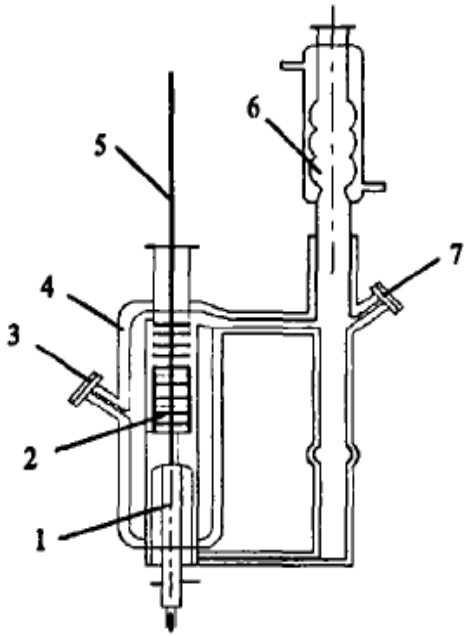


Fig.1 Sketch of EC-2 VLE equipment

1.heating rod 2.temperature point

3.liquid phase sample connection 4.glass VEL kettle

5.thermometer 6.condenser 7.vapor phase sample connection

Experimental procedure. This experiment is conducted in the gas-liquid equilibrium kettle shown as Figure 1. First, some tested solution is put into the gas-liquid equilibrium kettle, then, the cooling water is entered and the kettle is heated slowly. When the condensate of the gas phase begins to reflux, this refluxing operation can be stable through controlling the heating. After this refluxing operation has been stabilized for 30min, the gas and liquid samples are taken with the syringe, the compositions of them are analyzed respectively and the equilibrium temperature and pressure are recorded at the same time (thermometer calibration accuracy ±0.01K). The pressure of this system is controlled with a Nessler vacuum pump and is determined with a U-shaped mercury manometer (accuracy±0.067 kPa). In order to examine the device reliability, the vapor-liquid equilibrium data of the binary system of benzene and toluene are determined. The average deviation of the equilibrium temperature is 0.70K and it of the gas and liquid composition is less than 0.008.

Analytical technique. Analytical instruments：Agilent 7890A gas chromatograph with hydrogen flame (FID) detector: Chromatograph column: DB-1(Φ0.25×30m, membrane thickness: 0.25μm). Chromatograph conditions: column temperature box: initiation temperature: 100℃(remaining 3 min), heating rate: 30 K/min, termination of temperature: 250℃(remaining 2 min), vaporizer temperature: 250℃, Detector: 250℃ (hydrogen flow rate: 40 ml/min, air flow rate: 400ml/min,

mixing gas flow rate: 35ml/min）, speed：1.0mL/min, split ratio: 100:1, the injection volume: 0.2μL. The area normalization method is used for the quantitative analysis.

Results and Discussion

Determination and fitting of saturated vapor pressures of MXDA. As section 2.1 described, the activity coefficients of the different components are needed for the correlation of the thermodynamic equation, but the data of saturated vapor pressures of MXDA are not reported completely. The saturated vapor pressures of MXDA are measured with the static method at the temperatures between 150-180℃ and they are regressed with the 5 Parameters Antoine equation shown in equation (4).

$$\ln p = c_1 + c_2/(T + c_3) + c_4 T + c_5 \ln T \tag{4}$$

Where: p is used to express the saturated vapor pressures of MXDA and its unit is kPa; T is used to express the temperature and its unit is ℃; Antoine equation parameters can be expressed with c_1, c_2, c_3, c_4 and c_5.

The data of saturated vapor pressure of MXDA determined in this paper is given in Table 1 which is used to fit the Antoine equation parameters and the Antoine equation for MXDA is described as equation (5).

Table 1 The saturated vapor pressure data of MXDA

T(℃)	150	153	157.5	165	168	170	172.5	178	180
P(kPa)	3.689	3.708	3.823	4.46	4.641	5.174	5.835	7.307	8.480

$$\ln p = 2337.57 - 9786.71/(T - 8.003) + 1.005T - 451.5 \ln T \tag{5}$$

The average relative deviation expressed in equation (6) between the calculated results and the regressed values is 1.24％.

$$ARD = \frac{1}{k}\sum_{i=1}^{k}\left|\frac{x_{\exp} - x_{cal}}{x_{\exp}}\right| \times 100\% \tag{6}$$

Where: x_{exp} is used to express the experimental values, x_{cal} is used to express the calculated results, k is used to express the experimental points.

Thermodynamic consistency test. Whether the VLE data determined in this paper is reliable, the thermodynamic general relationship can be used to test. If the VLE data can be conformed to the thermodynamic relationship, they can be thought having the thermodynamic consistency. The VLE data are tested for the thermodynamic consistency by the Herington area test method which is based on Gibbs-Duhem law, then, the activity coefficients of the two components are calculated by the VLE experimental data and the area of the $\ln(\gamma_1/\gamma_2)$—x_1 of the area test figure is calculated with the area integration method, the values of D and J can be calculated finally. If D<J or D-J<10, The VLE experimental data can be considered to conform the demand of the thermodynamic consistency.

$I = \int_0^1 \ln\frac{\gamma_1}{\gamma_2} dx_1$, $\Sigma = \int_0^1 \left|\ln\frac{\gamma_1}{\gamma_2}\right| dx_1$, $D = \frac{|I|}{\Sigma} \times 100$, $J = \frac{150\theta}{T_m}$, Where: T_m is the lowest boiling point, K； θ is the boiling point difference of aniline－MXDA.

The test results of the thermodynamic consistency are given in Table 2.

Table 2 Results of thermodynamic consistency test

system	D-J
binary equilibrium system at pressure of 4 (kPa)	-8.21
binary equilibrium system at pressure of 6.67 (kPa)	-13.67

As Table 2 shows, the demand of the thermodynamic consistency can be conformed for these VLE experimental data because of D<J for the two systems.

Determination and fitting of the VLE data of aniline-MXDA system. The VLE data of aniline-MXDA system at pressure of 4 kPa are determined and the binary interaction parameters of aniline-MXDA for Wilson equation are regressed through these VLE data, shown in Table 3.

Table 3 Wilson binary interaction parameters

i= Aniline j= MXDA	a_{ij}	a_{ji}	b_{ij}	b_{ji}	c_{ij}	c_{ji}	d_{ij}	d_{ji}
P=4(kPa)	253.302	771.065	47063.48	154491.4	15.813	52.543	0.2935	0.8366

The VLE values of aniline-MXDA system are calculated with Wilson equation and the calculation results and the experimental data are given in Table 4. The data in the tables show, at the pressure of 4 kPa, the average absolute error of the calculation results and the experimental data of the VLE temperature is -0.768K, the average absolute error of the calculation results and the experimental data of the vapor composition of aniline is -0.0867. The above results prove the regressed Wilson equation parameters of aniline-MXDA can be used to calculate the phase equilibrium data of aniline-MXDA system.

Table 4 Experimental and calculated VLE data of the binary system (Aniline(1)- MXDA) at 4 kPa

NO.	Experimental data			Calculated data		Absolute deviation	
	T_{exp} (℃)	x_{exp}	y_{exp}	T_{cal} (℃)	y_{cal}	ΔT (K)	Δy
1	90.95	1.0000	1.0000	91.02	1.0000	-7.00E-02	0.00E+00
2	91.5	0.8544	0.9995	94.22	0.9991	-2.72E+00	-4.00E-04
3	92.3	0.7264	0.9985	95.31	0.9971	-3.01E+00	-1.40E-03
4	97.1	0.4969	0.9961	98.86	0.9798	-1.76E+00	-1.63E-02
5	100.7	0.4074	0.9704	100.59	0.9403	1.10E-01	-3.01E-02
6	106.5	0.2863	0.9641	106.41	0.7552	9.00E-02	-2.09E-01
7	115.9	0.1847	0.8974	115.91	0.5412	-1.00E-02	-3.56E-01
8	124.7	0.1169	0.6956	125.57	0.4427	-8.70E-01	-2.53E-01
9	133.8	0.0741	0.5742	134.04	0.4041	-2.40E-01	-1.70E-01
10	145.6	0.0355	0.2997	145.59	0.3822	1.00E-02	8.25E-02
11	160.75	0	0	160.73	0	2.00E-02	0.00E+00
AAD*						-7.68E-01	-8.67E-02

* AAD is the average absolute error.

Conclusion

The saturated vapor pressures of MXDA are measured at the temperatures between 150-180℃ and the expanding Antoine equation is used to correlate them. The VLE data of aniline-MXDA system at pressure of 4 kPa are determined and Wilson Equation is used to correlate the experimental data and the model parameters are regressed. The regression values are compared with the experimental data and the average relative error is within 5%.

References

[1] Yang Hai-kun. Production and requirement situation of meta-xylenediamine in domestic and international. Fine. Spec. Chem. (China). 1998, 13:1-3.

[2] Zhang Hua. Technical development and market application of meta-xylenediamine. Chem. Intermed. (China). 2002, 7:13-14.

[3] Ma Lei, Kong Ling-qi, Li Yu-gang. Research progress of proparing meta-xylylenediamine by hydrogenation by catalyst from isophthalonitrile. Chem. Ind. Eng. Prog. (China). 2011, 30(4): 766-770.

[4] Zhang Peng, Wang Yue, Lv Lianhai. Mild Hydrogenation of Isophthalonitrile to m-Xylylenediamine Catalyzed by Highly Active Skeletal Nickel. Fine. Chem. (China). 2008, 25(2): 201-204.

[5] Liu Zhongneng. Synthesis of m-Phenyldimethylamine via Catalytic Hydrogenating Isophthalonitrile. Fine. Spec. Chem. (China). 2000, 8(18): 25-26.

[6] Tae Young Chae，Sung Wook Row，Kye Sang Yoo, et al. Hydrogenation of isophthalonitrile with 1-methylimidazole as an effective solvent for m-xylenediamine production. Bull. Korean Chem. Soc. 2006, 27: 361-362.

[7] Shen Qin, Liu Zhong-neng, Hou Min-bo, *et al*. Synthesis of m-xylenediamine by hydrogenation with modified Raney-Ni catalyst. Fine. Chem.(China). 2000, 17(9): 544-546.

[8] Carl L.Yaws. Chemical Properties Handbook[M]. Beijing: McGraw-Hill Book Co, 1999.

Advanced Materials Research Vol. 936 (2014) pp 1012-1016
© (2014) Trans Tech Publications, Switzerland
doi:10.4028/www.scientific.net/AMR.936.1012

Experimental Studies of Catalytic Hydrogenation of Isophthalonitrile for Meta-Xylenediamine Preparation

Yugang Li

(Research Center for Computer and Chemical Engineering, QingDao University of Science and Technology，QingDao, 266042, Shandong，China)

E-mail: lyg@putech.com.cn

Keywords: meta-xylenediamine（MXDA）; isophthalonitrile（IPN）; hydrogenation; catalyze

Abstract: With Raney nickel catalyst, the process of catalytic hydrogenation of isophthalonitrile for meta-xylenediamine preparation using aniline as the solvent is studied in this paper. The effect of the amount of catalyst, the reaction pressure and temperature is discussed. The results show that: on the conditions of the initial raw materials concentration for 2.0mol/L, the ratio of the catalyst quality and the IPN quality for 1/10, the reaction temperature for 100°C, the reaction pressure for 35bar, the reaction inhibitor NaOH for 0.6g and some additives, the reaction is conducted for 80min and the quality yield of meta-xylenediamine is up to 98.58%.

Introduction

MXDA is a kind of high performance epoxy resin curing agent, and is an important chemical intermediates. The process of ammoxidation of meta-xylene to make IPN is a mature technology, while the technology of catalytic hydrogenation of IPN to prepare MXDA is not yet mature. Therefore, people did a lot of studies for this system and some progress was obtained in recent years.

Zhang Peng et al [1] prepared the amorphous Ni-Al alloy thin strip with quenched to make high activity skeleton nickel and the molar yield of MXDA was up to 96%. With Co-Ti/diatomite catalyst, the yield of MXD to 94% was made for UOP Inc.[2]

When the effects of the reaction conditions is discussed, organic amines, aromatic hydrocarbons, alcohols, ethers, lower aliphatic amide and aromatic monoamines[3,4] can be used as the reaction solvent, and the solubility of IPN in several commonly used solvent is compared with each other in literature.[5] The right choosing of the initial concentration is conducive to the full use of the catalyst active site, then, the utilization rate of the catalyst is improved. Different catalytic hydrogenation reactions need difference optimal pressure and usually 1.5-15MPa is kept. Different catalytic hydrogenation reaction needs difference optimal reaction temperature and the range of 70°C to 130°C is maintained basically.

With the high activity nickel catalyst, the optimum experimental conditions of catalytic hydrogenation of IPN to make MXDA using aniline as the solvent is discussed in this paper.

Experimental

The details of the experimental set-up, experimental procedures and analytical techniques are presented in this section.

Materials

IPN(purity≥99%), methanol(purity≥99.5%), toluene(purity≥99.5%), aniline (purity≥99.5%), hydrogen, deionized water.

Catalyst: high activity Raney nickel catalyst with nickel, aluminum, molybdenum, chromium, iron. The physical properties of this catalyst are shown in Table 1.

TABLE.1 PHYSICAL PROPERTIES OF CATALYST

Physical characteristics	unit	specification	remarks
shape	-	black metal powder	-
particle size	(mu)	400	average particle size
BET-specific surface area	(m^2/g)	⩾100	-
packing density	(kg/L)	1.3	-

Experimental set-up

The experiment of catalytic hydrogenation of IPN to make MXDA is conducted in a 1L büchiglas high-pressure hydrogenation reactor which can provide 100bar pressure safely and the highest temperature is for 250°C. The hydrogenation reactor is made of stainless steel materials and the catalyst can be fully stirred up from the bottom of the reactor by the stirrer which is the type of hydrogen absorbing turbine, then, the gas-liquid-solid three-phase full mixing in this hydrogenation reactor can be achieved. The kettle of the reactor is arranged with the coil pipe and jacket which is used to heat the raw materials in the reaction forepart time and to remove the heat with cooling oil in the reaction process. The structure of this hydrogenation reactor with the complex mixing agitator is shown in Fig.1 and the schematic diagram of the experimental set-up is exhibited in Fig. 2.

Experimental procedure

The raw material (IPN), solvent (aniline), catalyst (high activity Raney nickel catalyst), reaction inhibitor NaOH and some additives are put into the high-pressure reactor from the feed inlet together, then, the reactor is sealed. The mixture in the reactor is heated with the temperature controller while the stirrer is started with 100r/min speed. When the specified reaction temperature is reached, the BPC is opened to enter hydrogen and the stirrer is closed at the same time. When the specified reaction pressure is reached, the stirrer is opened again with 100r/min speed, meanwhile, the hydrogen consumption is recorded with the specific computer software. When the hydrogen consumption is not changed within 30min, the reaction is considered to end, then, the sample can be taken from the high pressure sampler and be analyzed.

Analytical technique

The qualitative analysis of the sample is conducted with GC-MS and the quantitative analysis of the sample is achieved with GC-MS single particle scanning. The internal standard method is used for the quantitative analysis.

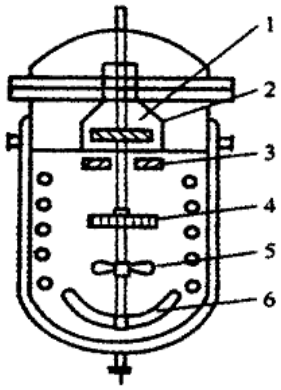


Fig.1 Reactor with multiple stirrer

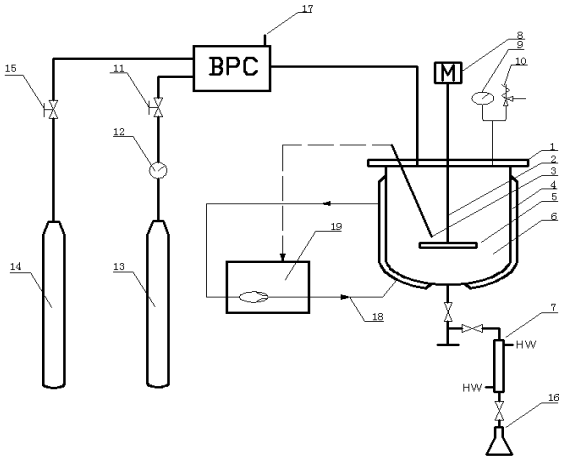


Fig.2 Schematic diagram of the experiment set-up

1-fan stirring; 2-dome; 3-fixed impeller;
4-curved blade turbine; 5-propeller type agitator;
6- anchored agitator

1.reactor cover 2.stirring shaft 3.thermocouple 4.jacket
5.agitator 6.reactor 7.high- pressure sampling device
8.motor 9.reactor pressure gauge 10.safety valve
11.nitrogen inlet valve 12. nitrogen pressure gauge
13.nitrogen cylinder 14.hydrogen cylinder
15.hydrogen inlet valve 16.receiver 17.BPC
18.heat transfer oils 19. temperature control system

Results and discussion

The effect of several chemical and physical parameters which affect the reaction rate and the yield is studied. The amount of catalyst and reaction inhibitor, the reaction temperature and pressure is included mainly.

When the initial raw materials concentration is high, the materials can't be dissolved in the solvent, then, the materials can't be absorbed by the activity site of catalyst fully, thus, it is not conducive to the hydrogenation reaction similarly. Thus, the initial raw material concentration is set to 2.0mol/L in this paper.

Effect of the amount of catalyst

As Figure 3 shows, when the ratio of the catalyst quality and the IPN quality is between 1/8-1/10, the product yield is higher, otherwise, the product yield begins to reduce. Figure 4 indicates the relationship between the ratio of the catalyst quality and the IPN quality and the hydrogen consumption rate. The hydrogen consumption rate is reduced with the reduction of the catalyst/IPN ratio, which means the amount of catalyst is bigger, the reaction speed is faster, as the results, a lot of MXDA is produced in a short time. But some polymerization reactions occur easily within these MXDA molecules at this time and the secondary and tertiary amines can be produced which leads to the reduction of product yield. Comprehensive considering the influence of the product yield, reaction time and economic factors, the ratio of the catalyst quality and the IPN quality is set to 1/10 in this paper.

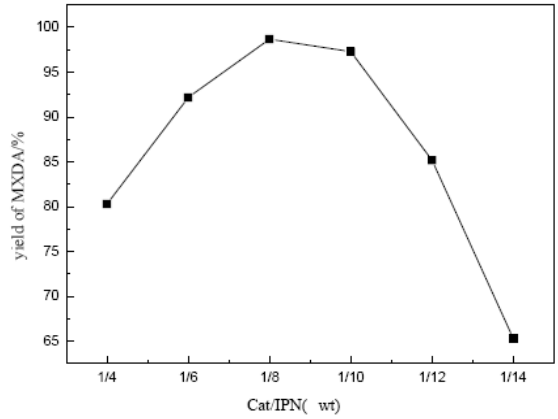


Fig.3 Relationship between catalyst/IPN mass ratio and yield of MXDA

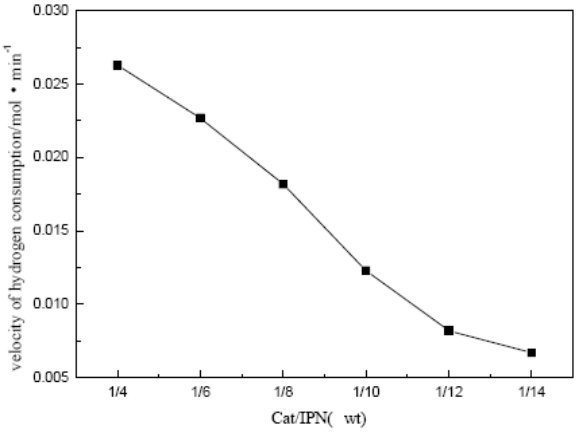


Fig.4 Relationship between catalyst/IPN and velocity of hydrogen consumption

(*reaction condition*: aniline:300ml, IPN:80g, NaOH: 0.6g, water:2ml, temperature:100℃, pressure: 40bar)

Effect of reaction temperature

As Figure 5 shows, the influence of the temperature for the product yield is very significant and there is a peak between 90°Cand 100°C. Because ammonia produced by the side reaction of MXDA deamination can escapes easily at the high temperature which can promote the main equilibrium reaction to the side reaction of MXDA deamination direction. The relationship between the reaction temperature and the reaction time is indicated in Figure 6. Although the product yield at 90°C and it at 100°C is very similar, the reaction time at 100°C is less than it at 90°C for 45min, thus, the optimal reaction temperature is set to 100°C in this paper.

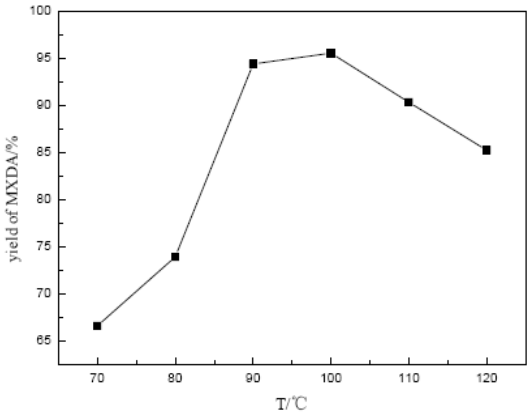


Fig.5 Relationship between temperature MXDA

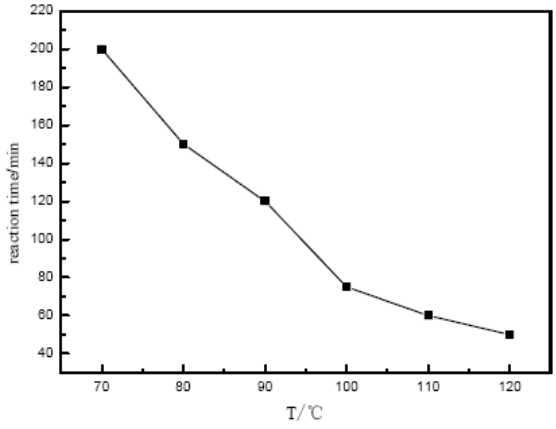


Fig.6 Relationship between temperature and and yield of reaction time

(*reaction condition*: aniline:300ml, IPN: 80g, catalyst: 8g, NaOH: 0.6g, water:2ml, pressure: 40bar)

Effect of reaction pressure

Because the dissolved and adsorbed hydrogen concentration of the reaction system can be improved under the high reaction pressure, the collision probability of IPN and hydrogen with the catalyst activity center is increased, thus, the yield of MXDA and the reaction speed can be improved. As Figure 7 shows, the yield of MXDA is improved with the pressure increasing. When

the pressure reaches 35bar, the product yield is fixed and maintained at a higher level basically.Considering the high producing costs with the higher reaction pressure, the optimal reaction pressure is set to 35bar in this paper.

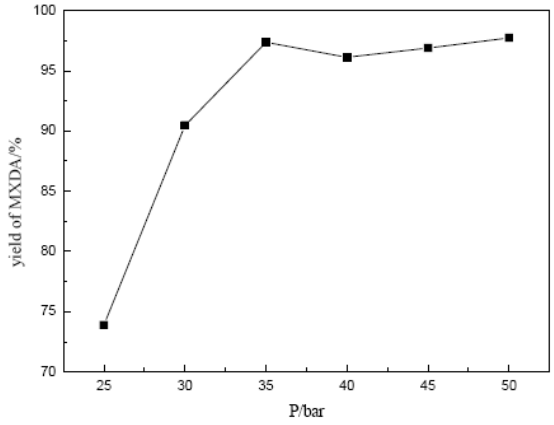


Fig.7 Relationship between pressure and yield of MXDA

(*reaction condition*: aniline:300ml, IPN:80g, catalyst:8g, NaOH:0.6g, water:2ml, temperature: 100℃)

Conclusions

The experimental studies of the catalytic hydrogenation of IPN to make MXDA are conducted in this paper and the optimal reaction conditions are got. With Raney nickel catalyst and aniline solvent, the initial raw material concentration is 2.0mol/L, the ratio of the catalyst quality and the IPN quality is 1/10, the reaction temperature is 100°C, the reaction pressure is 35bar. With above optimal reaction conditions, MXDA quality yield reaches 98.58%. These results can provide the accurate basis for the industrialization of this reaction.

References

[1] Zhang Peng, Wang Yue, Lv Lianhai. Mild Hydrogenation of Isophthalonitrile to m-Xylylenediamine Catalyzed by Highly Active Skeletal Nickel. Fine Chemicals (China). 2008, 25(2): 201-204.

[2] Liu Zhongneng. Synthesis of m-Phenyldimethylamine via Catalytic Hydrogenating Isophthalonitrile. Fine and Specialty Chemicals (China). 2000, 8(18): 25-26.

[3] Qin Yisheng, Qin Xudong, Zhu Debao, et al.A continuous method of hydrogenation of isophthalonitrile for meta-xylenediamine preparation. China, Patent 101337893A (2009).

[4] Qin Yisheng, Qin Xudong, Zhu Debao, et al. A stirred tank continuous hydrogenation of isophthalonitrile for meta-xylenediamine preparation. China, Patent 101337894A (2009).

[5] Tae Young Chae，Sung Wook Row，Kye Sang Yoo, et al. Hydrogenation of isophthalonitrile with 1-methylimidazole as an effective solvent for m-xylenediamine production. Bull. Korean Chem. Soc. 2006, 27：361-362.

Advanced Materials Research Vol. 936 (2014) pp 1017-1021
© (2014) Trans Tech Publications, Switzerland
doi:10.4028/www.scientific.net/AMR.936.1017

Orthogonal Investigation of Influencing Factors on the Modification of Montmorillonite By Thpc in Acid Conditions

Pan Chen, Wang Jincheng*

College of Chemistry and Chemical Engineering, Shanghai University of Engineering Science, Shanghai 201620, P.R.China.

wjc406@263.net

Keywords: montmorillonite, modification, THPC, influencing factors

Abstract. Na-MMT was modified with quaternary phosphonium salts, tetramethylolphosphonium chloride (THPC), via ion-exchange reactions, in acid conditions. Different factors such as reaction time , reaction temperature, the types of solvent, and CEC ratios, were investigated using orthogonal test. Results showed that the best combination of these four factors were $A_1B_3C_1D_1$, that is, the type of the solvent was acetone and water (1:1), reaction time was 3h, CEC ratio was 1:1, and the reaction temperature was 80°C.

Introduction

Montmorillonite (MMT) has now been receiving special attention in the field of reinforcement because of its submicroparticle size and intercalation properties. Composites containing intercalated organic montmorillonite (OMMT) particles exhibit improved moduli, decreased gas permeability, and enhanced thermal stabilities [1,2].

In practice, the use of organoclays prepared by alkyl ammonium salts to manufacture polymer-clay nanocomposites is limited by the clay properties. For instance, the alkyl ammonium salts decompose about 170-180°C and are not suitable for high temperature melt processing techniques. The decomposition products impart an undesirable color, odor, and taste.

Efforts have been made to synthesize thermally stable organo-clays based on stibonium [3], phosphonium [4], or imidazolium surfactants [5]. The montmorillonites modified with such thermally stable cations had higher onset temperature of thermal degradation as well as peak degradation temperature values, thus, allowing them to retain their structural integrity during compounding. We have prepared tetramethylolphosphonium chloride (THPC) modified organoclays in different pH values [6]. Results revealed that the use of acid conditions can increase the d-spacing and thermal stability of the organic silicate layers.

However, different factors have different effect on the preparation and characteristics of this THPC-OMMT even in acid conditions. In the present work, we investigated the factors such as reaction time, reaction temperature, the types of solvent, and CEC ratios on the silicate spacing of this organo-clays.

Design of orthogonal test

The reaction time, reaction temperature, the types of solvent, and CEC ratios were combined with different amounts. For different combining ratio had different effect on the silicate spacing of OMMT, following orthogonal test was used to find out the most effective combination of above four factors. In this test, silicate spacing was used to evaluate the effect of this intercalation performance. Conditions and results were shown in Table 1 and 2.

Table 1. Orthogonal parameters of intercalation and their levels.

Factors / Levels	Reaction time (h)	Reaction temperature (°C)	Types of solvent*	CEC ratios**
Level-1	3	40	acetone：water (1:1)	1.5
Level-2	5	60	methanol：water (1:1)	2
Level-3	7	80	water	1

*The ratio of acetone with methanol and water referred to volume ratio.
** The CEC ratio was the ration of the molar values of cations in THPC and the cations in MMT.

Table 2. Design of orthogonal test for Na-MMT modification.

Factors / Experiments	Reaction time (h)	Reaction temperature (°C)	Types of solvent	CEC ratios
1	3	40	acetone：water(1:1)	1.5
2	3	60	methanol：water(1:1)	2
3	3	80	water	1
4	5	40	methanol：water(1:1)	1
5	5	60	water	1.5
6	5	80	acetone：water(1:1)	2
7	7	40	water	2
8	7	60	acetone：water(1:1)	1
9	7	80	acetone：water(1:1)	1.5

Results of orthogonal test

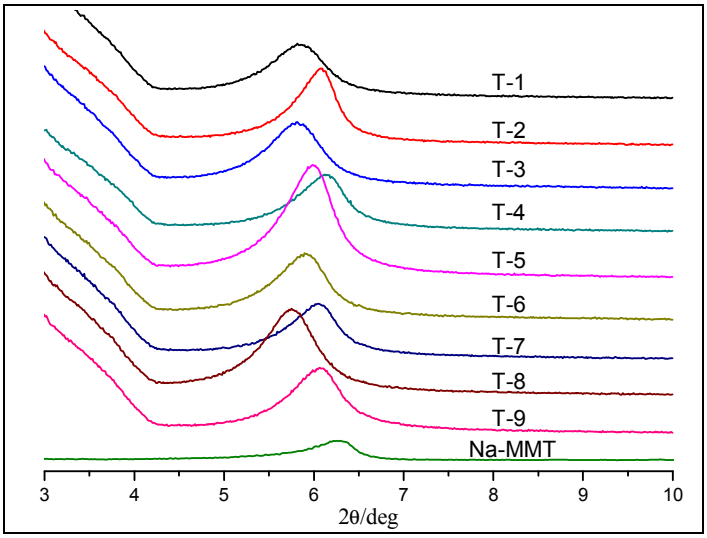


Figure 1. X-ray diffraction (XRD) patterns of different types of OMMT.

Figure 1 compared XRD patterns of OMMT prepared under different environmental conditions. Their d-spacing data were calculated by Bragg formula: $2d\sin\theta=n\lambda$. In curve a, only one peak appeared in the XRD spectrum, indicating only one interlayer space existing in Na-MMT. The XRD of the MMT sample showed a peak at the same position as for the neat silicate that corresponded to a gallery spacing of 1.43 nm. The large full width at half maximum of the as-received clay represented a large inhomogeneity of the intergallery spacings, which were a result of the poorly crystalline nature and the turbostratic packing of smectite minerals.

From Figure 1, we can see that the interlayer spacing of these OMMTs was changed due to the different environmental conditions during the intercalation process. The d-spacing depends on the organic modifier's packing status and the amount readily adsorbed inside the clay galleries. Since none of the clay modifiers was adsorbed to the same extent, relative to each other, no conclusions could be drawn in terms of their respective types of packing or interaction within the clay galleries.

Table 3. Orthogonal test results of different types of OMMT.

Factors / Experiments	A*	B*	C*	D*	Silicate spacing /nm
1	1	1	1	1	1.52
2	1	2	2	2	1.45
3	1	3	3	3	1.52
4	2	1	2	3	1.44
5	2	2	3	1	1.47
6	2	3	1	2	1.50
7	3	1	3	2	1.46
8	3	2	1	3	1.53
9	3	3	2	1	1.46
Average value K_1	1.497	1.473	1.517	1.483	
Average value K_2	1.470	1.483	1.450	1.470	
Average value K_3	1.483	1.493	1.483	1.497	
Range, R	0.027	0.020	0.067	0.027	

*: A=reaction time（h），B=reaction temperature（°C），C=Types of solvent，D=CEC ratios.

From the calculated results and the range values listed in Table 3, it was clear that the types of solvent was the main factor that influenced the silicate spacing of OMMT. The reaction time and CEC ratio were less important but more important than that of reaction temperature.

The influencing behavior of above four factors were summarized in Figure 2. The types of solvent had an important influence on the intercalation of OMMT. Its mechanism depended on the polarity of MMT and the solvent, which strongly influenced the hydrogen bonds developed during preparation process. When water was used as the solvent in the preparation process of OMMT, many hydrogen bonds may be produced and this may hinder the THPC molecules to be intercalated into the interlayer sapcing of MMT. The mixture of methanol and water also had this problem due to the increasing amount of hydrogen bonds produced by methanol. However, when acetone was mixed with water, the hydrogen bonds may decrease and this was beneficial for the intercalation process. Thus, MMT modified by THPC in this environment had larger d-spacing value.

The effect of reaction time on the interlayer spacing of OMMT was such an extent that a shorter reaction time yielded a larger d-spacing. This was due to the intercalation process may be already finished during 3 hours of the intercalation process. When more reaction time was given, the interlayer spacing was not larger. This may be due to other environmental conditions which can decrease the interlayers spacing.

To investigate the effect of CEC ratio on the interlayer spacing of OMMT, the ratio was varied from 1:1 to 2:1. At lower CEC ratio, the intercalation process may be successfully accomplished and a larger d-spacing was obtained. When CEC ratio was increased, more THPC molecules were not easily intercalated and smaller d-spacing was thus obtained.

The effect of reaction temperature had different influence on the silicate spacing of OMMT. With the increase of reaction temperature, the interlayer spacing was increased. It was concluded that more energy was useful for the intercalation process and was beneficial for the enlarging of the interlayer spacing of OMMT.

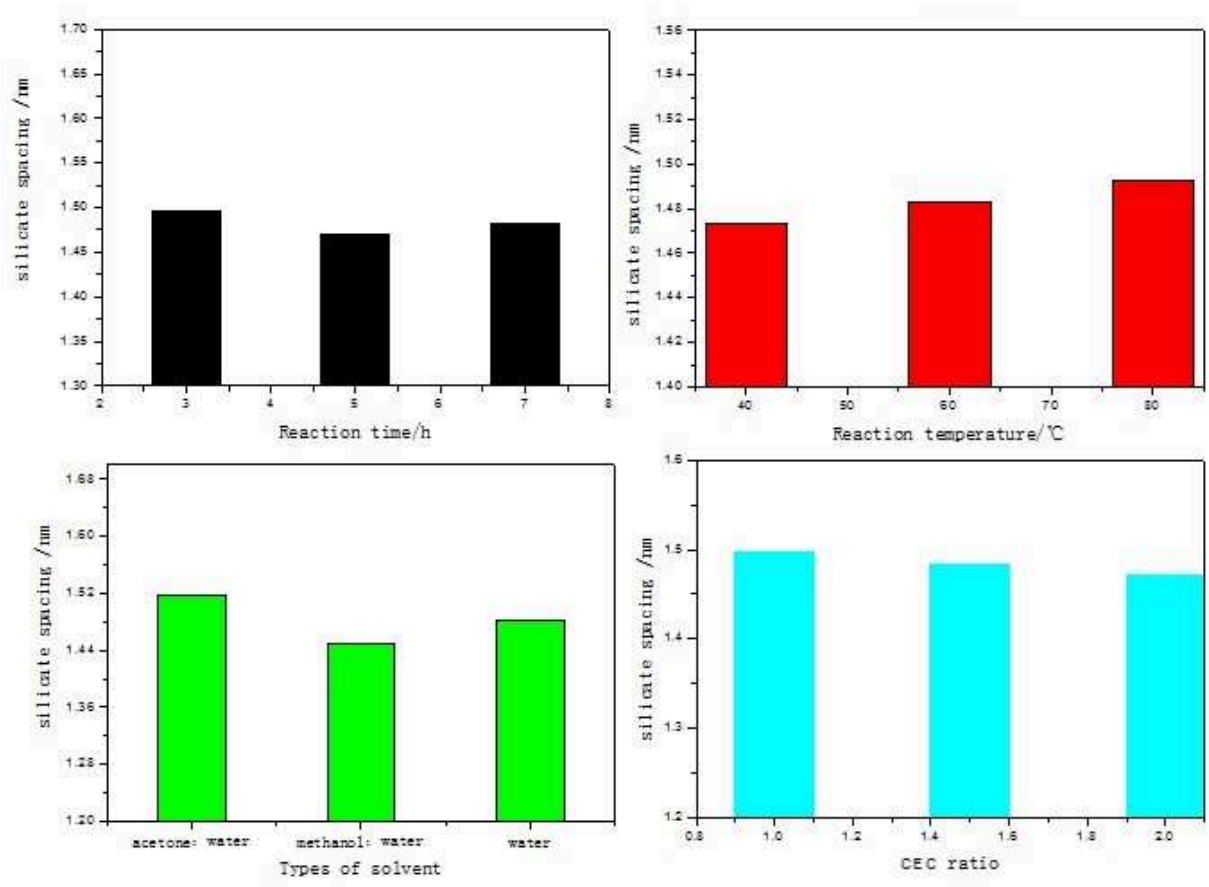


Figure 2. Influencing behavior of interlayer spacing by different factors.

Conclusion

The effect of influencing factors on the modification of MMT by THPC in acid conditions was analyzed by orthogonal test. The levels were chosen according to the preparation process. Results showed that the most satisfactory combination of the four factors was $A_1B_3C_1D_1$, that is, the type of the solvent was acetone and water (1:1), reaction time was 3h, CEC ratio was 1:1, and the reaction temperature was 80°C.

Acknowledgemenst

This work was financially supported by "National Natural Science Funds (Project No.51173102 and No. 51210105020)", "'Shu Guang' project (Project No. 10SG53)","Special Funds for Science and Technology Development of Shanghai University of Engineering Science (Project No. 2012td10 and 2012zh05) ", and "Students Research and Training Project of Shanghai University of Engineering Science (Project No. cs1304001 and cs1204003).

References

[1] Xi,Y., Frost, R.L., He, H., Kloprogge, T., Bostrom, T. Modification of Wyoming montmorillonite surfaces using a cationic surfactant. Langmuir, 2005, 21: 8675-8680.

[2] Wang, J.C., Chen, Y.H., Jin, Q.Q. Preparation and characteristics of a novel silicone rubber nanocomposite based on organophilic montmorillonite. High Performance Polymers, 2006, 18: 325-340.

[3] Wang, D., Wilkie, C. A stibonium-modified clay and its polystyrene nanocomposite. Polym. Degrad. Stab., 2003, 82: 309-315.

[4] Arroyo, M., Suarez, R., López-Manchado, M., Fernández, J. Relevant features of bentonite modification with a phosphonium salt. J. Nanosci. Nanotechno., 2006, 7: 2151-2154.

[5] Bourbigot, S. , Vanderhart, D., Gilman, J., Awad, W., Davis, R., Morgan,A., Wilkie, C.J. Investigation of nanodispersion in polystyrene-montmorillonite nanocomposites by solid-state NMR. Polym. Sci., Part B, Polym. Phys., 2003, 41:3188-3213.

[6] Wang, J.C., Du, Y.C., Sun, K., Sun, Y.B., Pan, C., Zhao, Y. Organoclays prepared from montmorillonites with tetramethylolphosphonium chloride in different pH conditions. Powder Tecnhoplogy, 2013, 247:178-187.

CHAPTER 11:

Corrosion and Surface of Materials, Technologies of Coatings

Advanced Materials Research Vol. 936 (2014) pp 1025-1030
© (2014) Trans Tech Publications, Switzerland
doi:10.4028/www.scientific.net/AMR.936.1025

The effects of PTFE content on microstructures and properties of composite brushing plating coating

Yang Wang[a], Xiufang Cui[a], Guo Jin[a,*] , Haipeng Li[a], Wei Zheng[b],

Xuming Zhang[b]

[a]Institute of Surface/Interface Science and Technology, School of Materials Science and Chemical Engineering, Harbin Engineering University, Harbin 150001, China

[b]School of Materials Science and Chemical Engineering, Harbin Engineering University, Harbin 150001, China

Keywords: Brush plating, PTFE, Structure, Performance

Abstract. Polytetrafluoroethylene (PTFE) is known as a solid material with high lubricating property and low friction coefficient. The application of PTFE is significant to improve the tribological properties of coating. In this paper, Scanning electron microscopy (SEM), Energy Dispersive Spectrometer (EDS), X-ray diffractometry (XRD), Microhardness test and friction and wear experiment are adopted to study the effects of PTFE content on the structure, morphology and properties of coating. The results show that the addition of PTFE particles can reduce spherical particle size and increase the hardness and friction properties of coating when typical cauliflower shaped druse and excellent interface binding characteristics are maintained. If the content of PTFE is too much, some area of coating is prone to powder hoarding which may lead to the decrease of coating density, hardness, and friction coefficient stability.

Introduction

Wear is one of the major failure forms of mechanical parts and engineering components [1-3]. According to the importance of Engineering, adopt reasonable surface protective measures to control surface damage and material loss without influencing the functions of parts [4-8]. Brush plating offers a possible, flexible and high quality deposit technology, which occupies a very important position in surface engineering [9-11]. It is found that in a large number of engineering applications, single metal and alloy brush plating do not present ideal tribological properties [12-15]. The application of PTFE can improve tribological performance of coatings due to its higher lubricity and the lowest friction coefficient [14-16].

Current studies on brush plating are not as many as those on chemical deposit. There are large differences between them, therefore, it is significant to study the effects of PTFE on the structure, morphology and performance of brush plating coating, so as to improve the comprehensive performance of brush plating, enrich connotation of PTFE tribology and perfect brush plating process category. Based on the studies both home and abroad, Ni/PTFE suspensions with different content of PTFE will be prepared by optimized PTFE dispersion process. This paper will analyze the effects of composite coatings with different content of PTFE prepared by brush plating on coatings' structure, morphology and performance.

Experimental Materials and Methods

Materials and Preparation. Matrix material is FV520(B) steel, grinded by 240#, 320#, 600#, 800# emery papers respectively and then dropped into alcohol for ultrasonic cleaning for 10 min. Then wipe it by degreasing cotton with alcohol, dry and put it into drying vessel.

Fast speed nickel plating solution is chosen as matrix solution, and PTFE powder of 5μm as a composite. Suspension ensures uniform and qualified coating, so sixteen alkyl three-methy bromide and OP-10 emulsifier are selected as activating agent through process optimization, which is helpful to uniform dispersal of PTFE in the solution.

Brush plating adopts DSD-30-QA DC power supply and ZDB-1 plating pen. Plating rate is 8~12m/min and plating time lasts 10min. After brush plating, the pen should be rinsed with distilled water and dried with a hairdryer stand-by.

Characterization and Testing

The Analysis of Structure, Morphology and Component. Scanning electron microscopy (Quanta 200 SEM) is used to scrutinize the morphology of coatings. Energy Dispersive Spectrometer EDS (genesis xm-2) is used to analyze the components of coatings. X-ray diffraction (XRD) is adopted to confirm the phase structure of coatings, Cu as radiation source. Scanning angles range from 20°to 80° in steps of 0.05°. Kaλ is 1.54056 Å, voltage 45 kV, current 100 mA and scanning speed $4^{o}min^{-1}$.

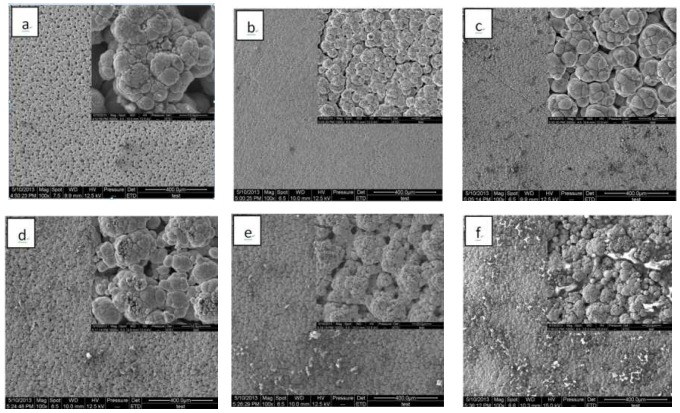
Performance Testing

Digital micro hardness tester HVS-1000 is adopted in the testing. The load is 100g, and load time is 10s. The average value of five points is taken as microhardness. In the process of measurement, hardness is measured gradually by taking points from the border to the center of coatings. Abandon the obvious deviation data and analyze the hardness of coatings based on the acquired data.

The samples cleaned at room temperature are placed in the friction and wear tester, loading weight 200g. Analyze the friction and wear properties based on friction coefficient curves obtained after data processing. Each set of samples before and after the experiment is weighed by electronic weighing scales, and compare the different values to get the amount of wear and measure the abrasion resistance of coatings.

Results and Discussion

The Effect of PTFE Content on Coating Morphology. Fig. 1 shows that PTFE particles help reduce spherical particle size and increase coating compactness, but they do not change the micromorphology of coatings-typical cauliflower shaped druse. The agglomerated particles become smaller and the coatings become more compact when the content of PTFE ranges from 5 g/L to 20 g/L. But when the content of PTFE is between 20g/L and 40g/L, the particles become larger and the coatings become looser. In the meantime, with the increase of PTFE content, more and more white accumulation appears on coatings' surfaces. The coating with PTFE content of 40g/L is analyzed by energy spectrum in order to know the components of the white precipitate. The results are shown in Fig. 2. It mainly consists of PTFE and nickel. Therefore, with the increase of PTFE, some of the powder is agglomerated on the coating surface and then enwrapped by the deposition of nickel due to difficult dispersal and easy aggregation.



(a) 0g/L, (b) 10g/L, (c) 15g/L, (d) 20g/L, (e) 30g/L, (f) 40g/L

Fig. 1 Surface morphologies of coatings with different PTFE contents

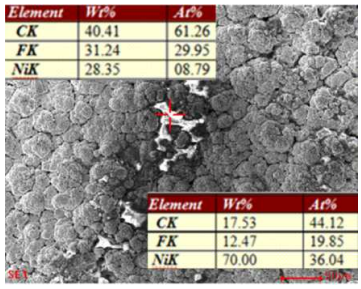
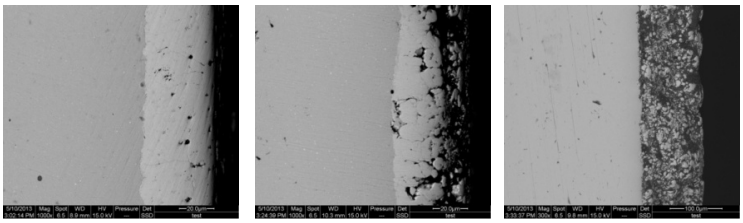


Fig. 2 Spectrum of the coating with PTFE content of 40g/L

Fig. 3 is cross-sectional morphology of the coatings with different PTFE contents. By comparison, interface morphology changes significantly, but the combination of coatings and substrate are not affected.

According to Fig. 3a, b, c, the cross-sectional morphology of these coatings presents accumulation of particle aggregates, which is different from that of nickel coating. When powder content increases, PTFE embedded in the gap between particles will increase. But too large powder content will lead to unevenly dispersal and powder accumulation (Fig. 3c). Thus, it can be concluded that nickel ions are continuously deoxidized to metallic Ni and deposit on the substrate surface together with PTFE in the solution.

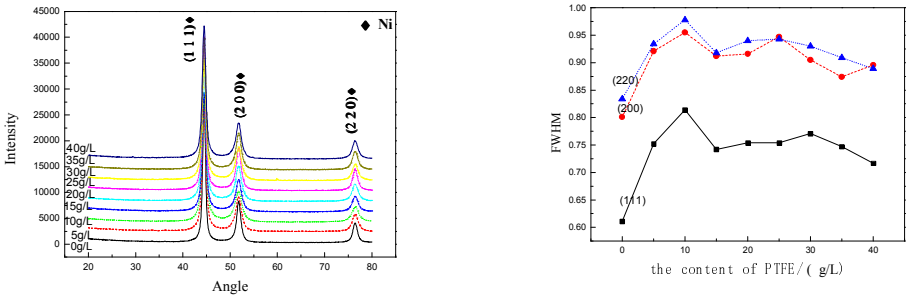


(a) 0g/L (b) 10g/L (c) 30g/L

Fig. 3 Cross-sectional morphology of coatings with different PTFE contents

The Effect of PTFE Content on Coating Structure. Fig. 4a shows XRD results of Nickel coatings with different PTFE contents. The analysis by Jade software marks out just crystal indice of Ni and its three strong peaks. There is no diffraction peaks of element F and C. Fig. 4b indicates that the height of three strong peaks of PTFE coatings is significantly lower than that of coatings without PTFE. But the half-width of PTFE coatings is obviously higher. The narrower the peak is, the larger the grains are. The addition of PTFE can remarkably refine coating grains. Diffraction curves of PTFE coatings do not change much in height and width. But the coating with PTFE

content of 10 g/L stands out with obviously lower peak height and higher peak width, which means the finest grains. Therefore, the solution with PTFE of 10 g/L has the best refining effect.



(a) XRD patterns of coatings (b) FWHM of three strong peaks

Fig. 4 XRD analysis of coatings with different PTFE contents

The Effect of PTFE Content on Coating Properties. Fig. 5 shows the microhardness of coatings with different PTFE contents. The results show that in the initial stage, microhardness is in proportion to PTFE content. When PTFE content reaches 10g/L, coatings achieve the maximum microhardness. With the gradual increase of PTFE, microhardness begins to decrease and when PTFE content is more than 25g/L, microhardness becomes smaller than that of coatings without PTFE. When PTFE content is larger than 30g/L, microhardness remains stable with tiny changes. Too much PTFE results in saturation, therefore, under the same plating process, microhardness does not change too much and PTFE are soft particles, high PTFE content will reduce microhardness of coatings.

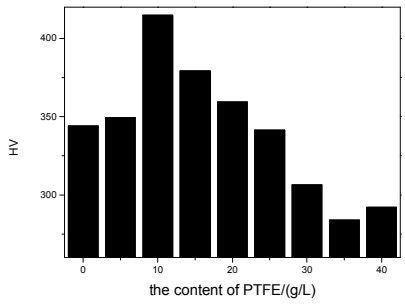
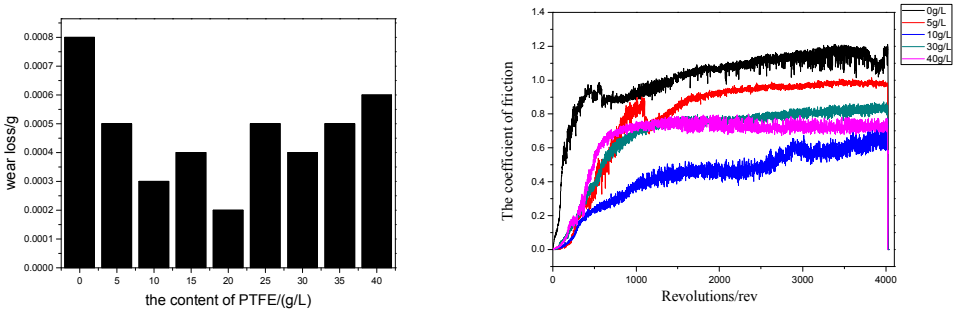


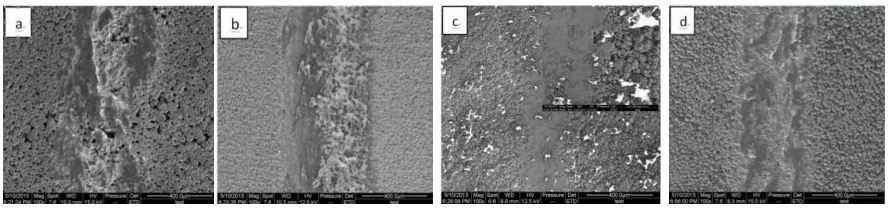
Fig. 5 Microhardness of coatings with different PTFE contents

Fig. 6 and Fig. 7 show the result of Friction and wear experiments. As is seen in Fig. 6a, the wear loss of 20g/L coating is less than other PTFE groups by comparison. Fig.6b is the comparison among dry friction coefficients. When PTFE content is 20g/L, the friction coefficient of coating is minimum and steady. When it is less than 20g/L, the friction coefficient is in inverse proportion to PTFE content. When the PTFE content is more than 20g/L, the friction coefficient increases with the increase of PTFE content. When PTFE content reaches 35g/L, the friction coefficient becomes unstable. The friction coefficient of 20g/L coating has been around 0.09 and the sliding friction coefficient of coating without PTFE is about 0.85. It can be found that the 20g/L coating has better uniformity and self lubricity. Its sliding friction coefficient is only 1/10 of that of a single metal Nickel coating, which can effectively improve the wear resistance of coating. So too much PTFE will have negative effects on the stability of sliding friction coefficient and wear resistance of coatings due to uneven powder distribution. On the contrary, low content of PTFE contributes to more uniform coatings, more stable sliding friction coefficient and better wear resistance.



(a) wear loss (b) friction coefficient

Fig. 6 Wear loss and friction coefficient of coatings with different PTFE contents



(a) 0g/L (b) 10g/L (c) 20g/L (d) 30g/L

Fig. 7 Wear morphology of coatings with different PTFE contents

Fig. 7 shows SEM images of coatings after wear tests. The coating without the addition of PTFE is worn out by pressure head. Its trajectory is not continuous, but wears tracks of other coatings present good continuity. Coatings significantly become soft, and friction coefficients are effectively reduced and wear resistance is increased. Fig. 7b indicates that wear tracks of coatings are visible with low content of PTFE due to insufficient PTFE powder for lubrication, and the stability of sliding friction coefficient is also influenced. The solution is hard to scatter with high PTFE content, which easily causes uneven distribution of powder in coatings. So wear tracks are also uneven and incoherent, obviously in some places and no signs in other places. Friction coefficient is not stable as well and wear resistance is affected. Fig. 8c shows that PTFE powder hoards a little and disperses unevenly in the 20g/L coating, which can significantly reduce sliding friction coefficient and increase wear resistance. The wear track is smooth and continuous in the right corner of enlargement, so the wear resistance of the 20g/L coating is superior.

Conclusion

Grains are refined significantly in PTFE coatings. The 10g/L PTFE coating has the minimum grains and the maximum microhardness. PTFE content in solution greatly affects grain size and coating compactness. The 20g/L PTFE coating gets smaller clusters and higher compactness. Deposition rate is in proportion to PTFE content and reaches the maximum when PTFE content is 25g/L. Then it experiences up and down and gradually tends toward stability. Therefore, the 20g/L PTFE coating possesses the smallest sliding friction coefficient, good self-lubrication and good wear resistance.

Acknowledgement

This work was financially supported by National Basic Research Program of China (973 Program) (No. 2011CB013404), National Natural Science Foundation of China (No. 51275105, 51375106), Fundamental Research Funds for the Central Universities (No. HEUCF20130910003).

Reference

[1] Stefan Olovsjö, Richard Johanson, Flor Falsafi, Ulf Bexell, Mikael Olsson. Surface failure and wear of cemented carbide rock drill buttons-The importance of sample preparation and optimized microscopy settings, Wear. 302 (2013) 1546-1554.

[2] Kun Zhang, Jinyong Yao, Tongmin Jiang. Degradation assessment and life prediction of electro-hydraulic servo valve under erosion wear ,Engineering Failure Analysis. 36 (2014) 284-300.

[3] G. Fedorko, V. Molnár, J. Živčák, M. Dovica, N. Husáková. Failure analysis of textile rubber conveyor belt damaged by dynamic wear , Engineering Failure Analysis. 28 (2013) 103-114.

[4] M.H. Enayati, F. Karimzadeh, M. Jafari, A. Markazi, A. Tahvilian. Microstructural and wear characteristics of HVOF-sprayed nanocrystalline NiAl coating , Wear. 309 (2014) 192-199.

[5] Q. Bi, M. Niu, J. Yang, W. Liu. Tribological behavior of Ni Al matrix composites with addition of oxides at high temperatures , Wear. 274–275 (2012) 423–434.

[7] Y. Wang, S. Jiang, M.D. Wang, S.H. Wang, T.D. Xiao, P.R. Strutt. Abrasive wear characteristics of plasma sprayed nanostructured alumina/titania coatings, Wear. 237 (2000)176–185.

[8] B. Mallia, P.A. Dearnley. Exploring new W-B coating materials for the aqueous corrosion-wear protection of austenitic stainless steel, Thin Solid Films. 549 (2013) 204-215.

[9] Xu Bin-shi, Wang Hai-dou, Dong Shi-yun, Jiang Bin. Fretting wear-resistance of Ni-base electro-brush plating coating reinforced by nano-alumina grains, Materials Letters. 60 (2006) 710-713.

[10] Zhongzhi Han, Yu Zuo, Pengfei Ju, Yuming Tang, Xuhui Zhao, Junlei Tang . The preparation and characteristics of a rare earth/nano-TiO2 composite coating on aluminum alloy by brush plating, Surface and Coatings Technology. 206 (2012) 3264-3269.

[11] Xiangliang Li, Xibao Wang, Rui Gao, Li Sun. Study of deposition patterns of plating layers in SiC/Cu composites by electro-brush plating, Applied Surface Science. 257 (2011) 10294-10299.

[12] Guozheng Ma, Binshi Xu, Haidou Wang, Xiaohe Wang, Guolu Li, Sen Zhang. Research on the microstructure and space tribology properties of electric-brush plated Ni/MoS2-C composite coating, Surface and Coatings Technology. 221 (2013) 142-149.

[13] Xian-Hua Zhang, Jia-Jun Liu, Bao-Liang Zhu. The tribological performance of Ni/MoS2 composite brush plating layer in vacuum, Wear, 157 (1992) 381-387.

[15] Prasanta Sahoo, Suman Kalyan Das. Tribology of electroless nickel coatings-A review, Materials & Design. 32 (2011) 1760-1775.

[16] Jae-Ho Kim, Susumu Yonezawa, Masayuki Takashima. Preparation and characterization of C/Ni-PTFE electrode using Ni-PTFE composite plating for alkaline fuel cells. International Journal of Hydrogen Energy, 36 (2011) 1720-1729.

Advanced Materials Research Vol. 936 (2014) pp 1031-1034
© (2014) Trans Tech Publications, Switzerland
doi:10.4028/www.scientific.net/AMR.936.1031

Novel infrared stealth Properties of cotton Fabric with ZnO: (Al, In) coating

Xi-Li Yu, Lin-Ping Zhang*, Yi Zhong, Hong Xu, Zhi-Ping Mao*

Key Laboratory of Science & Technology of Eco-Textile (Ministry of Education), Donghua University, Shanghai 201620, P. R. China.

. *Email address: zhpmao@dhu.edu.cn (Z. Mao);

zhang_lp@dhu.edu.cn (L. Zhang)

Keywords: ZnO: (Al, In), coated fabric, infrared emissivity, infrared stealth.

Abstract. In this paper, we report a study on the infrared stealth properties of cotton fabrics with ZnO: (Al,In) coating. Al, In doped ZnO samples were prepared through sol-gel method. The crystalline phase of the ZnO: (Al, In) solids were determined by XRD. IR-2 Dual-Band Infrared Emissivity Measuring Instrument was used to test the infrared emissivity of the coated fabric. Infrared stealth effect of ZnO: (Al, In) coated fabric was measured using thermal infrared photospectrometry instrument. It was found that the ZnO: (Al, In) thin film has a low infrared emission in the range of 8 ~ 14μm wavelengths, and the addition of Al and In leaded to a better infrared stealth effect.

Introduction

Doped ZnO as filler material could be used to make low infrared emissivity coatings on the target objects, such as thermal camouflage coatings [1], thermal deformation camouflage screen (thermal camouflage net) [2], infrared smoke screen [3] and infrared decoys [4], etc.

In this paper, the sol-gel process was adapted to prepare Al, In doped ZnO. The prepared Al, In doped ZnO solids were coated on cotton fabrics to prepare infrared stealth material. The influence of doped concentration of In on emissivity property and the microstructure were discussed in detail.

Experimental section

ZnO: (Al, In) coated fabric

Al, In doped ZnO was prepared by sol-gel process. Zinc nitrate dihydrate, isopropanol, monoethanolamine were mixed in a flask equipped with a thermometer placed in a constant temperature oil bath pot at 75-85°C and stirred for 1h. Then aluminum chloride hexahydrate and Indiumnitrate were added into the mixture until dissolved. The concentrations of In were 1wt%, 2wt%, 3wt%, 4wt%, 5wt% and 6wt% respectively for six ZnO: (Al, In) sol samples (the concentrations of Al were maintained 2 wt%). The prepared ZnO: (Al, In) gel was heated in a muffle furnace at 400°C for 4h, and calcined at 1100℃ at a heating rate of 2 °C / min when the organic solvent was removed in order to get the ZnO: (Al, In) solids.

The ZnO: (Al, In) solids with 3% molar ratio of In and 2% molar ratio of Al were mixed with zirconia beads, sodium hexametaphosphate (a kind of dispersant), and ethanol, at a weight ratio of 1:50:0.1:10 in a milling instrument dispersion at a rotational speed of 800r/min for5h,10h,15h,20h,25h,30h and 40h. Then the ZnO: (Al, In) suspension was carefully added to the polyvinyl acetate emulsion adhesive and stirred for 30 minutes. The above solution was deposited on the cotton fabric fixed on the glass plate, and uniformly scratched with a stainless steel rod. Then the obtained ZnO: (Al, In) coated fabric was dried at 180°C for 1-2 minutes with a shaping machine.

Characterization

The crystalline phase of the ZnO: (Al, In) films were determined using X-ray diffraction (XRD) diffractometer (D/Max-2550 PC). IR-2 Dual-Band Infrared Emissivity Measuring Instrument was used to test the infrared emissivity of the coated fabric. Infrared stealth effect of ZnO: (Al, In) film was measured using thermal infrared photospectrometry instrument. The granularity of milled ZnO: (Al, In) were analyzed using Nano-ZS English Malvern Instruments.

Results and Discussion

Characterization of ZnO: (Al, In) Film

Figure 1 showed X-ray diffraction pattern of the pure ZnO and ZnO: (Al, In) solids with different In doped molar ratio from 1% to 6%. All the diffraction peaks were indexed according to ZnO standard [PDF#05-0664] indicating that both pure ZnO and (Al,In) doped ZnO have hexagonal wurtzite structure. It meant that Al and In dope effectively.

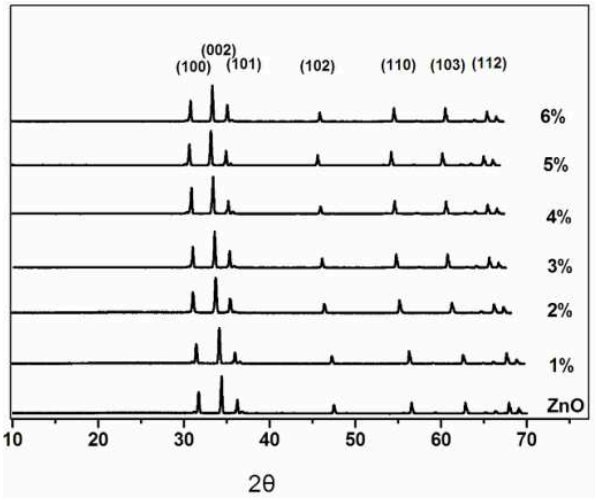


Fig.1. X ray diffraction pattern of pure ZnO and ZnO: (Al, In) with different doping contents of In(Al, 2%)

Effect of Particle Size on the Infrared Emissivity of Coated Fabrics

As shown in table 1, the average particle sizes of ZnO: (Al, In) particles decreased with the increase of milling time. The average particle size is samllest after 30 hrs milling, when the welding and fracture mechanisms come into a balance.

Table 1 Milling time effect on average particle size of ZnO: (Al, In) particles (2% Al and 3% In doping contents)

Milling time/h	5	10	15	20	25	30	40
Average particle size/nm	359	275	233	210	198	180	185

ZnO: (Al, In) particles through different wet-grinding time (5h, 10h, 15h, 20h, 30h,40h) was coated on cotton fabrics with polyvinyl acetate emulsion adhesive. As shown in figure 2, the infrared emissivity of the ZnO: (Al, In) decreased with the average particle size decreasing. The optical infrared emissivity could reach 0.715 at a minimum for sample: ZnO: (Al, In) with 2% Al and 3% In doping contents, 80% ZnO: (Al La) and 20% polyvinyl acetate, particle size was 180nm milled at 30 hrs. The softy of this coated fabric was satisfied at this time. So 30 hrs was better wet-milling time.

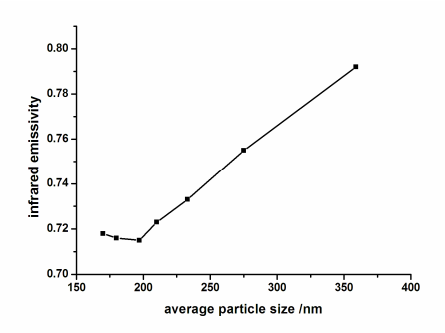


Fig. 2 Effect of particle size on infrared emissivity ZnO: (Al, In) coated fabrics.

Effect of doping In content on infrared emissivity of coated fabrics

The Effect of In doping content on infrared emissivity of ZnO: (Al, In) film with AL molar ratio of 2% was shown in Figure 3. The infrared emissivity of the pure ZnO in the band of 8-14 μm is 0.832, but the infrared emissivity of ZnO: (Al, In) coated fabrics significantly decreased with an increasing of In doping contents from 1% to 3% and the lowest infrared emissivity was 0.715 at 3% In molar concentration. However, the infrared emissivity rose when In concentration continued improving to 4%.This is because the addition of Al and In is favorable for providing more free electrons and improving scattering of infrared photon. Furthermore, increase amount of Al and In could bring new gap as infrared photon scattering centers and reduced the adsorption of infrared ray.

Thermography

The thermal infrared image of ZnO: (Al, In) coated fabrics, with 2% Al and 3% In doping contents was shown in Figure 4. It illustrated that the samples infrared stealth effect were obviously improved with 2% Al and 3% In doping contents.

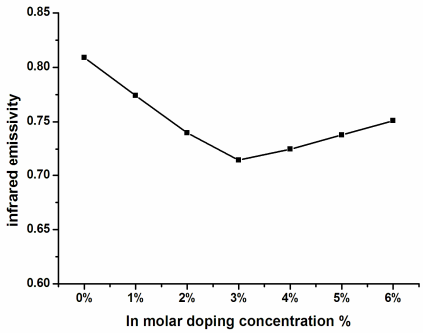
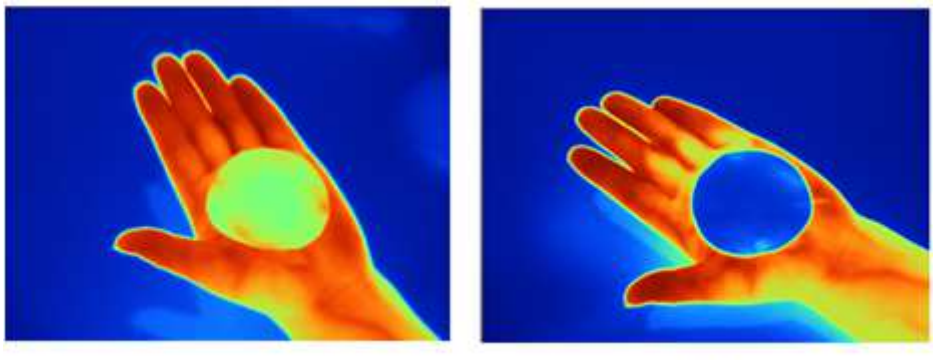


Fig. 3. The infrared emissivity of ZnO: (Al, In) coated fabrics with different In doping contents



(a) (b)

Fig. 4. Thermographies of pure ZnO (a) and ZnO: (Al, In) coated fabrics with 3% In molar ratio (Al , 2%)

Conclusion

ZnO: (Al, In) was synthesized by the sol-gel method and coated on cotton fabric, forming a thin film to reduce infrared emissivity of the fabric.

The addition of Al and In leaded to a better infrared stealth effect. The optimum coated fabric was soft and its infrared emissivity was 0.718, when the mass percentage of adhesive was80%, with 2% Al and 3% In doping contents.

Acknowledgements

This work was financially supported by the National Key Technology R & D Program (No. 2011BAE07B08).

Reference

[1] H. Wu, W. Guo, Z.Z. Zheng. China Supf. Een. 24(2011) 7-8.

[2] F. Zhang, J.Y. Wang, H.Y. Du. National Defense Sci. Tech.. 3(2003) 23-24.

[3] X. Zhang, J.Q. Zhang, W. Jin. Acta Photonica Sinica, 38(2009) 1221-1225.

[4] Y.L. Gan, X.F. Wang, B.L. Guo. Ship. Elec. Eng..9(2009):23-27.

Advanced Materials Research Vol. 936 (2014) pp 1035-1041
© (2014) Trans Tech Publications, Switzerland
doi:10.4028/www.scientific.net/AMR.936.1035

Research on Influencing Factors of Adiabatic Coating Performance

CAO Guangyuan[1,a], GUO Hanjie[1,b*], LI Lin[1,2], LI Yongqi[1], PENG Jie[1]

([1]School of Metallurgical and Ecological Engineering, University of Science and Technology Beijing, Beijing 100083; China;

[2]Beijing Shougang International Engineering Technology Co., Ltd. Beijing 100043; China)

[a]libatistu@163.com, [b]13031128987@163.com

Keywords: Adiabatic coating, Hollow tiny bead, Agglutinating reagent, Thickener

Abstract: Microcosmic features of adiabatic coating was observed, influencing factors of adiabatic coating performance were studied by 4 types of agglutinating reagents when the size of hollow tiny bead was 2.5-60 μm. Next, carboxymethyl cellulose was introduced, 2.6 μm hollow tiny bead was selected to testify antifatigue performance of coating, transmission principle was applied to build one-dimensional mathematic model of adiabatic coating for testifying experimental value, industry test was conducted to check performance of coating in 30 t ladle.

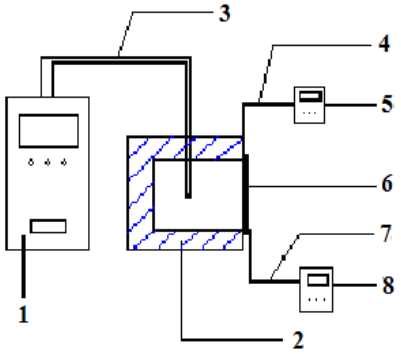
Introduction

Adiabatic materials have heat resistance performance. Adiabatic level is R-33.3, heat reflectivity is 89%, heat conductivity is 0.03 W/(m·°C). 0.3-0.5 mm coating is painted on object surface with some virtues, such as heat insulation, anticorrosion and waterproof. Technical ideas of foreign related products were brought, adiabatic coatings formed integrated development trend, such as high efficiency, thin layer, energy saving, waterproof. Nowadays, little reports are about the application of adiabatic coatings, especially for metallurgical energy saving[1].

New adiabatic coatings must be developed, adiabatic performances were studied from some aspects, such as the size of hollow tiny bead, agglutinating reagent, coating thickness, antifatigue performance. One-dimensional mathematic model was made to testify experimental data by theory calculation. Industry test was conducted to check adiabatic performance in 30 t ladle. Research on adiabatic performance is significant to metallurgical energy saving.

Experiments

The size of steel plate is 1.5×280×300 mm, adiabatic coating was painted on one side of steel plate, formula design was shown in table.1. After dried, coatings were heated by muffle furnace to detect temperature difference on two sides of steel plate, temperature differences were detected by 2 thermocouples, temperature value was recorded from 150°C. Fig.1 expressed experimental equipments[2].



1. cabinet; 2. resistance furnace; 3. thermocouple for temperature control; 4. No.1 thermocouple; 5. No.1 temperature controller; 6. steel plate; 7. No.2 thermocouple; 8. No.2 temperature controller;
Fig.1 Experimental Equipments

Raw materials:

Hollow tiny bead (main ingredients are SiO_2 and Al_2O_3), silicone (agglutinating reagent, XR-500), Na_2SiO_3 (hydrophilic adhesion agent), sodium alginate (thickener, $(C_6H_7NaO_6)_x$), silicone resin and E 800-800^oC hydrophilic inorganic heat-resistant resin (thickener), A3 steel plate (1.5×280×300 mm).

Ingredients:

Adiabatic performance and microstructure are tightly related to the ingredients, table.1 was the experimental ingredients of adiabatic coatings[3].

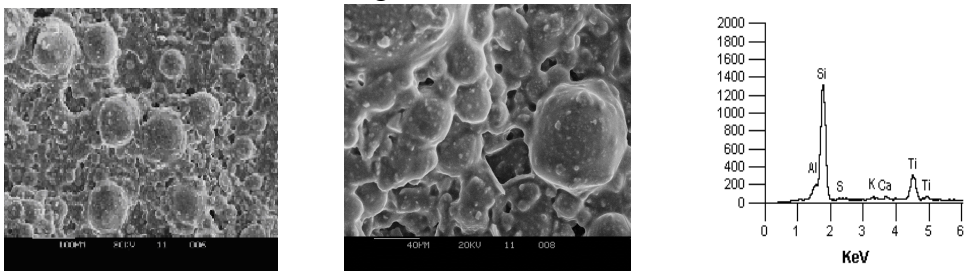
TABLE.1 EXPERIMENTAL INGREDIENTS OF ADIABATIC COATINGS

Number	Agglutinating reagent	Thickener	Bead size(μm)	Coating thickness (mm)			
1#	Silicone	$(C_6H_7NaO_6)_x$	58	0.5			
2#	Silicone	None	58	0.5		0.9	
3#	Na_2SiO_3	$(C_6H_7NaO_6)_x$	58	0.5		0.9	
4#	None	Silicone resin	10	0.45			
5#	None	Hydrophilic inorganic heat-resistant resin	15	0.23	0.45	0.59	0.80
			10	0.21	0.41	0.60	0.76
			2.6	0.23	0.45	0.59	0.80

Result and Analysis

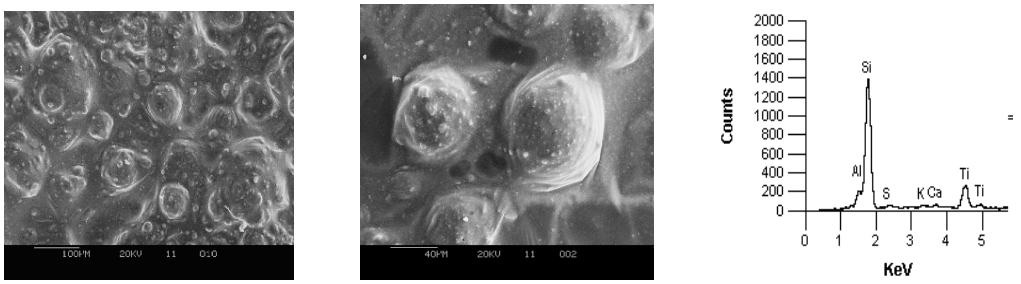
Microstructure and ingredients of No.1-No.3 coatings were analyzed by SEM. the size, the particle distribution and the ingredients were displayed in Fig.2-Fig.4. The size of hollow tiny dead is 50-130 μm, pelleting ability brought about good anti-radiation performance. Microporous structure led to low heat conductivity, air molecules can't form convection and Brownian motion, so favorable adiabatic performances were got.

Fig.2 showed that thickener caused porosity structure, but no porosity structure was expressed in Fig.3. Morphology in Fig.4 was different from that in Fig.2 and Fig.3. Coating itself had more air porosity in Fig.4, agglutinating reagent was Na_2SiO_3. The ingredients of agglutinating reagent in No.3 coating were different from that in No.1 and No.2 coatings. No.3 coating had lower Si content and more Al, Si and K content than other coatings, furthermore, it had Zn and Fe, but no Ti and S.



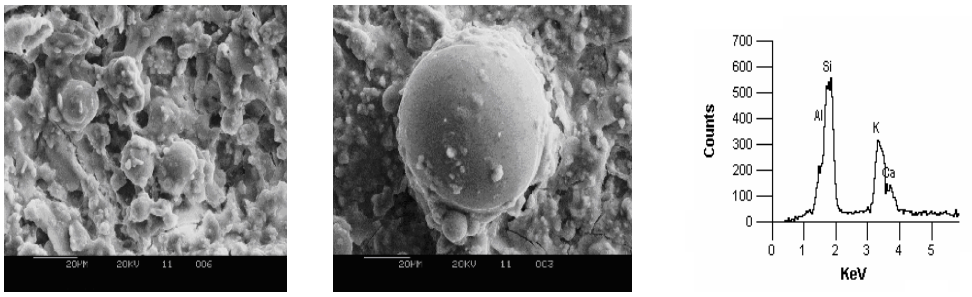
(a) Morphology magnified 200 times (b) Morphology magnified 500 times (c) Energy spectrum

Fig.2 SEM morphological observation and energy spectrum analysis of No.1 coating



(a) Morphology magnified 200 times (b) Morphology magnified 500 times (c) Energy spectrum

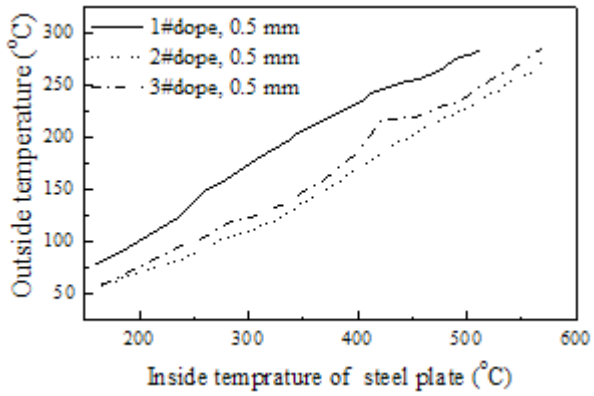
Fig.3 SEM morphological observation and energy spectrum analysis of No.2 coating



(a) Morphology magnified 200 times (b) Morphology magnified 500 times (c) Energy spectrum

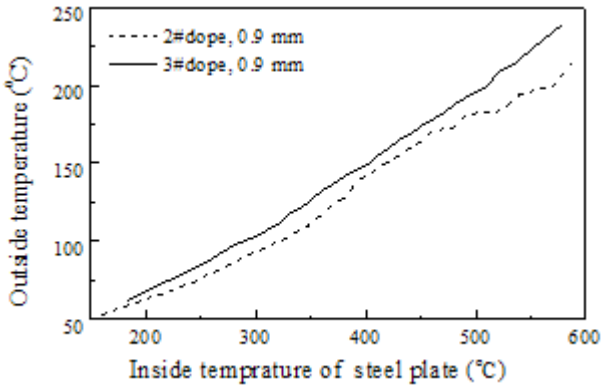
Fig.4 SEM morphological observation and energy spectrum analysis of No.3 coating

To study effect of base material on performance of adiabatic coating, No.1-3 coatings were used, same size of hollow tiny bead, same coating thickness, different base material, see Fig.5-Fig.7. In Fig.5, same 0.5 mm coating and inside temperature of steel plate, highest outside temperature of steel plate appeared in No.1 coating, outside temperature of No.2 coating was close to that of No.3 coating. So No.1 coating had worst adiabatic performance. Fig.6 expressed temperature difference of steel plates with 0.9 mm coating. Combined with Fig.5 and Fig.6, No.3 coating had best adiabatic performance.



(a)

Fig.5 Experimental chart with 0.5mm coating



(b)

Fig.6 Experimental chart with 0.9mm coating

Next, experimental datum of No.3- No.5 coatings were showed in Fig.7. adiabatic performance of No.3 coating was best at lower temperature, but No.4 and No.5 coatings had better performance at high temperature. No.5 coating has no crack phenomenon after high temperature experiment, so No.5 coating got best adiabatic performance in all coatings.

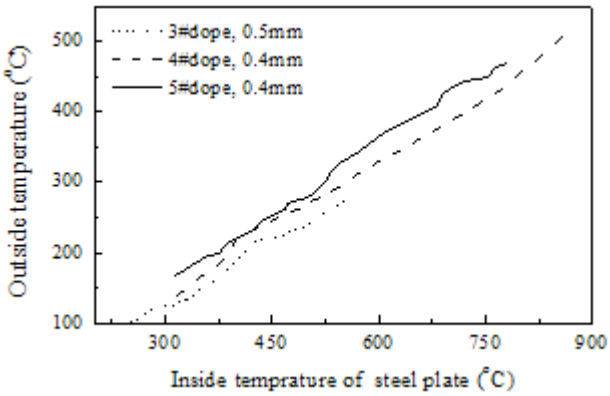
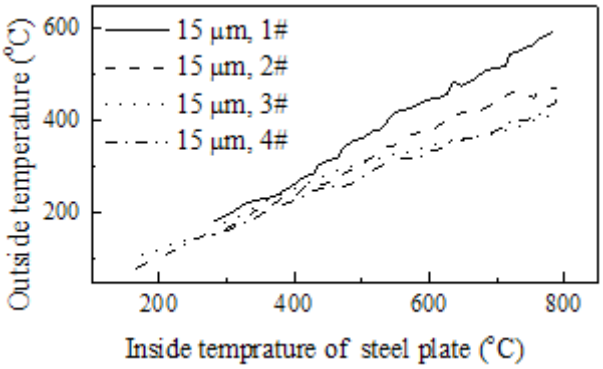


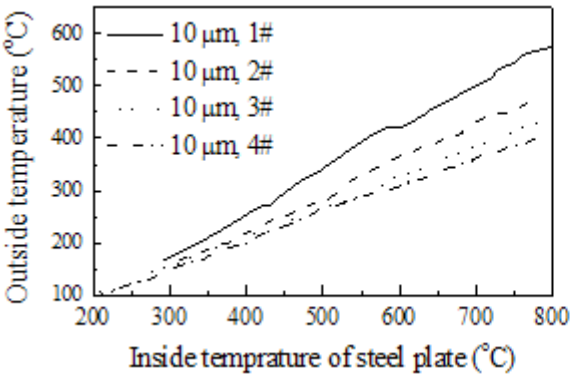
Fig.7 Inside And Outside Temperature On No.3-No.5 Coatings

To study effect of the thickness on adiabatic performance, No.5 coating was classified as 3 sizes, 15 μm, 10 μm, 2.6 μm, No.1-No.4 steel plates (0.2-0.8 mm coating) were respectively tested, see Fig.8. Fig.8 illustrated that outside temperature of steel plate decreased with the increase of thickness

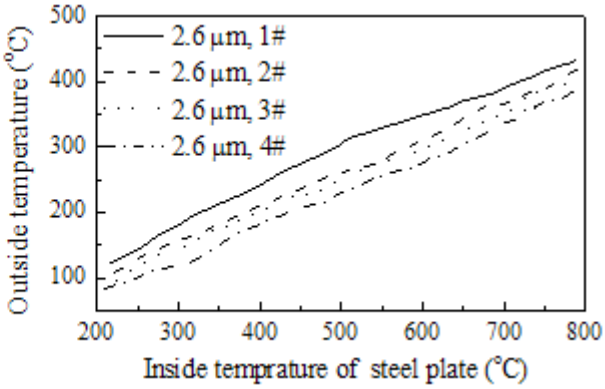
at same inside temperature of steel plate, and the temperature difference of inside and outside was proportional to inside temperature. Generally, the thicker coating may get better adiabatic performance[4].



(a)



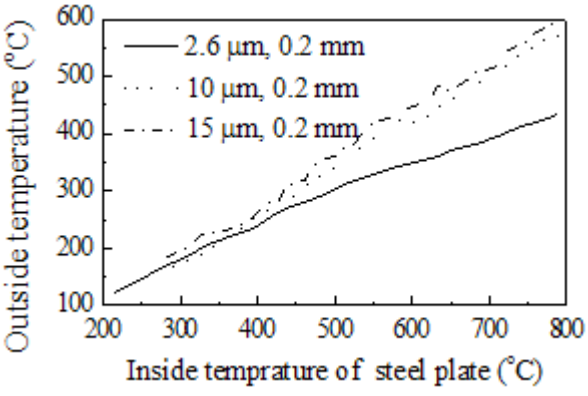
(b)



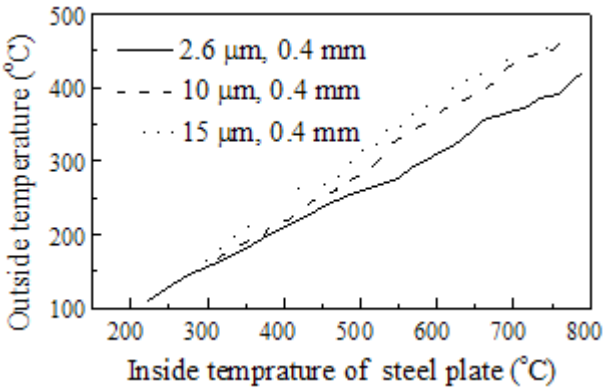
(c)

Fig.8 Inside And Outside Temperature Of Steel Plate With Different Size Of Hollow Tiny Bead

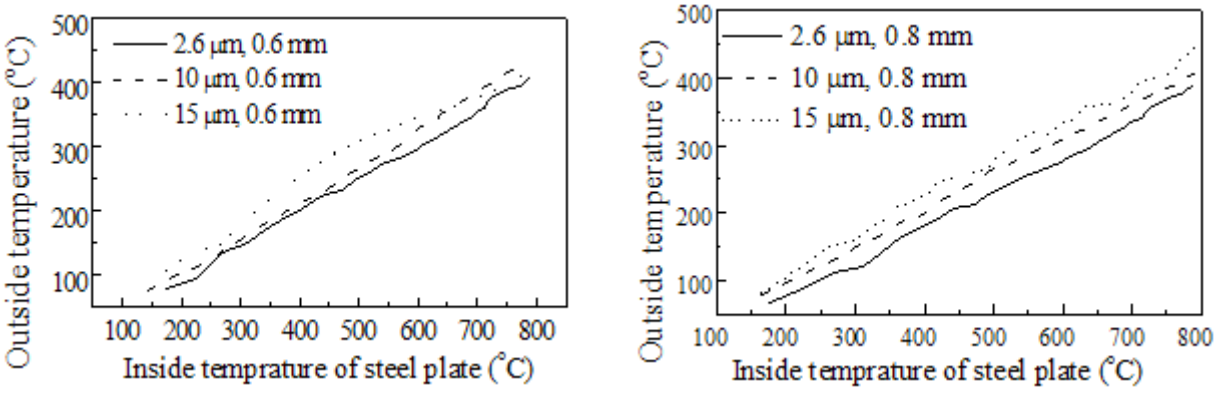
To research effect of hollow tiny bead size on adiabatic performance, No.5 coating was classified as 3 types with different hollow tiny bead size, 15 μm, 10 μm and 2.6 μm. Fig.9 showed that 2.6 μm tiny bead received best adiabatic performance. Experimental temperature had more obvious effect on adiabatic performance of thinner coating. 3 types of coatings had no obvious difference at lower temperature, but remarkable difference appeared at higher temperature (inside temperature of steel plate was more than 500°C). Smallest bead size can get optimal adiabatic performance, see Fig.9. 0.8 mm coating and 2.6 μm tiny bead may reach best adiabatic performance[5].



(a)



(b)



(c) (d)

Fig.9 Inside And Outside Temperature Of Steel Plate With 0.2-0.8mm Coating

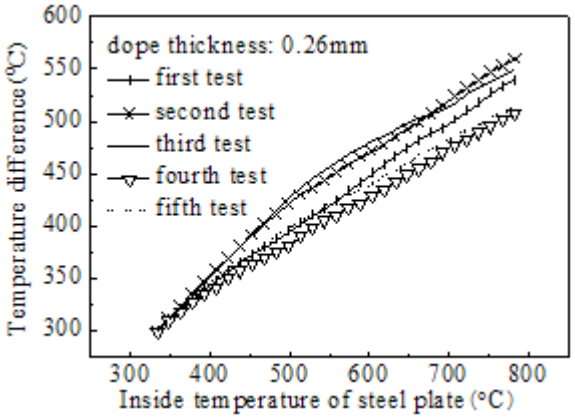


Fig.10 Antifatigue Experiment With 0.26mm Coating

After carboxymethyl cellulose was introduced as thickener, base experiments illustrated that coating didn't crack at 800 °C, so carboxymethyl cellulose, Na_2SiO_3 solution and 2.6 μm tiny bead were applied to produce the coatings for antifatigue experiment. Steel plate that had 0.26 mm coating experienced temperature rise experiments for 5 times, the results that inside-outside temperature difference changed with inside temperature were illustrated in Fig.10. After experiments for 5 times, coating still kept in good condition, this result was imperative to next industry application.

One-Dimensional Unstable State Heat Transfer Model

No.5 coating had best adiabatic performance by experiments, heat transfer model is made to analyze by applying Fourier law and energy conservation law. 1.5x100x200 mm A3 steel plate, 15 μm hollow tiny bead, different coating thickness, No.5 coating is introduced to build mathematic model. There is no inner heat source in heating period, convection occurs on outer boundary of steel plate, outside temperature changes with inside temperature. Following hypothesis is made to build one-dimensional unstable-state heat transfer model: uniform internal components of coating, isotropic nature, heat transfer that occurs in one section doesn't be influenced by other adjacent sections.

Based on above-mentioned hypothesis and theory, math model is given in Eq.1.

$$\frac{\partial}{\partial x}\left(\lambda\frac{\partial \mathrm{T}}{\partial x}\right)+q_v=\rho c_p\frac{\partial T}{\partial \tau} \tag{1}$$

$q_v = 0$ (no inside heat source)， Eq.1 is in unstable state.

λ: the conductivity (W/(m·°C)); c_p: mass heat capacities at constant pressure (J/(kg·°C)); ρ: the density (kg/m^3); T: the temperature (°C); τ: heating time; x: coordinate in thickness direction. Test result is: ρ: 1200 (kg/m^3); c_p: 1000 (J/(kg·°C)); λ (known boundary condition): 0.03-0.12

(W/(m·°C)), at the beginning of test, inside temperature of coating is 25°C, inside-outside temperature difference of steel plate increases gradually, heat transfer proceeds on outside of steel plate, heat transfer coefficient (α) is 20 W/(m^2·°C).

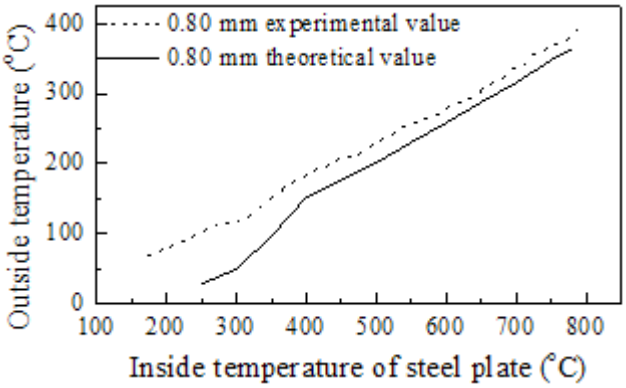
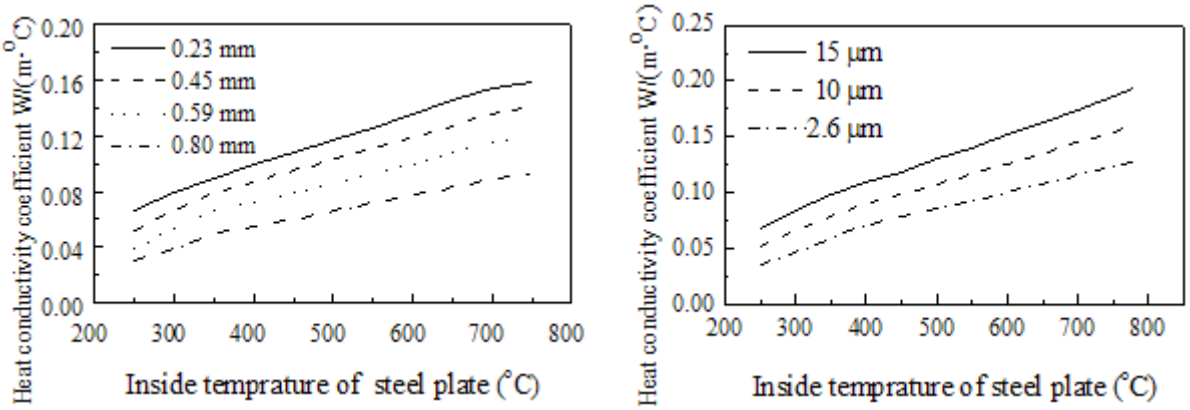


Fig.11 The comparison of outside temperature with 0.8mm coating

Fig.11 was the comparison of theory and experiment. Experiment value was close to theory value at thicker coating. At low temperature (<400°C), the higher temperature and thinner coating reduce the difference between theory and experiment. Generally, the results between theory and experiment were most similar at 0.8 mm coating.



(a) (b)

Fig.12 Inside temperature and heat conductivity coefficient at different status

When hollow tiny bead size was 2.6 μm, heat conductivity of coatings with different thickness was shown in Fig.12. Heat conductivity was inversely proportional to coating thickness at same inside temperature of steel plate. Heat conductivity increased with inside temperature, hollow tiny bead size had more obvious influence on heat conductivity at higher temperature. Bigger hollow tiny bead size was corresponding to lower heat conductivity and better adiabatic performance[6].

Industry Test On Ladle

Based on lab experiments, adiabatic coating was used in 30 t ladles of a steel plant. In terms of proportion of mixture in lab experiments, mixture contained 2.6 μm hollow tiny bead, sodium silicate, pure water, carboxymethyl cellulose. After weighed respectively, these substances were mixed evenly, then the coating was painted on internal surface of ladle. During the test period, operators recorded detailed datum. Statistics illustrated that average temperature drop on testing ladle was 2.3 °C/min, but that on normal ladle was 2.71 °C/min, so adiabatic coating had significant effect on molten steel.

Conclusion

Influencing factors of adiabatic performance were studied by experiments, antifatigue ability was tested, one-dimensional heat transfer model was made to testify experimental value. The conclusions are as follows:

(1) Na_2SiO_3 improves adiabatic performance at lower temperature, but it's not suitable for high temperature. Performance of hydrophilic inorganic heat-resistant resin is better than that of silicone resin at higher temperature[7].

(2) Experimental results expressed that thicker coating can get better adiabatic performance, but rational and affordable thickness should be determined.

(3) Smaller size of hollow tiny bead may realize better effect. The size of hollow tiny bead, coating thickness and experimental temperature affect adiabatic performance commonly. Generally, smaller size of hollow tiny bead and thicker coating are better choice.

(4) Antifatigue experiment showed that adiabatic performance has no direct relation with experiment time, so adiabatic coating can be applied in industrial production.

(5) After lab experiments, adiabatic coating was used in ladles of a steel plant. Test result expressed that temperature drop of molten steel can be decreased, it may reduce energy consumption for steelmaking, bring economic benefit for steel plants.

Acknowledgement

First and foremost, I would like to show my deepest gratitude to my teacher, Dr. GUO Hanjie, a respectable, responsible doctor, who has provided me with valuable guidance in every stage of the writing of this thesis. His keen and vigorous academic observation enlightens me in this thesis and my future work. Last but not least, I' d like to thank Dr. LI Lin and Dr. LI Yongqi, especially for their encouragement and support, they are my sincere friends.

References

[1] LV Xia, YU Chengbing, ZHANG Yun, etal. *Present and Future of Heat Insulation Coatings* [J]. Paint and Coatings Industry, 2011, 41(3): 45-47. In Chinese.

[2] LI Lin, ZANG Ruoyu, LI Yongqi, etal. *Research Development on Performance of Industrial Insulation Coating* [J]. Advanced Material Research, 2013(744): 278-282. In Chinese.

[3] YU Mingtao, WAN Long, LIU Xiaopan. *Formulation Design of Silicate Heat-insulating Coatings* [J]. Paint and Coatings Industry, 2007, 37(9): 26-28. In Chinese.

[4] LIU Jie, LI Xiang. *Properties of Waterbome Solar-reflective Heat-insulating Coatings* [J]. Journal of Beijing University of Chemical Technology, 2009, 36(1): 47-49. In Chinese.

[5] YIN Wu, KONG Zhiyuan, CAI Qingqing, etal. *Development of Novel Thin Film Thermal Insulation Coatings* [J]. Paint and Coatings Industry, 2010, 40(2): 28-29. In Chinese.

[6] HONG Xiao. *Development of Inorganic Transparency and Insulating Paint* [J]. New Building Materials, 2008(2): 57-58. In Chinese.

[7] ZHANG Ruizhi, ZHANG Xiongfei, LIN Cuihua. *Influence of Xonotlite-type Calcium Silicate on Heat Insulation Properties of Coatings* [J]. Paint and Coatings Industry, 2010, 40(9): 35-36. In Chinese.

Advanced Materials Research Vol. 936 (2014) pp 1042-1046
© (2014) Trans Tech Publications, Switzerland
doi:10.4028/www.scientific.net/AMR.936.1042

One-step processing to fabricate highly transparent superhydrophobic surface via granuliform silica aerogels

Bi Xu[1,a *], Jingjing Ge[1,b] and Zaisheng Cai[1,c]

[1]College of Chemistry, Chemical Engineering and Biotechnology, Donghua University, Shanghai, China 201620

[a]xubi@dhu.edu.cn, [b]sunnyjingge@163.com, [c]zshcai@dhu.edu.cn

Keywords: Superhydrophobicity, Transparency, Silica aerogel.

Abstract. A simple, versatile method has been developed to fabricate the transparent superhydrophobic surface via granuliform silica aerogels. The effect of ageing on the wettability, microstructure morphology and chemical structure of the dried gels has been investigated. Silica aerogel (dried alcogel with ageing) has a 3D porous network exhibiting the high surface area and pore volume. In comparison, large aggregates of silica nanoparticles exist within the backbone of the silica xerogel (dried alcogel without ageing). Both the aerogel and xerogel exhibit analogous chemical composition with abundant of methyl groups on the surface. The rough surface due to the high porosity and low surface energy provided by the methyl groups of aerogel contribute to the superhydrophobicity. Meanwhile, glass slides coated with aerogel film is highly transparent because the roughness created by the aerogel film is limited.

Introduction

A superhydrophobic surface with a water contact angle (WCA) greater than 150° and low contact angle hysteresis (CAH) has been extensively investigated due to its importance in both fundamental research and practical applications[1,2]. Since the wettability of a solid surface is mainly dependent on its chemical composition and the geometrical structure[3,4], a variety of techniques[5-7] have been developed to fabricate superhydrophobic surface. However, tedious procedures and unique equipment are always essential for most of these techniques.

SiO2 aerogel is such a kind of solid material which consists of SiO2 nanoparticles and has a continuous random structure filling with gaseous dispersive medium[8]. SiO2 aerogel shows an instinct rough surface due to its extremely high porosity. Meanwhile, selecting proper precursors can introduce the chemical groups with low surface energy into the structure of the prepared aerogel [9]. Therefore, rough surface and hydrophobization can be realized via one-step processing, which is beneficial for the highly efficient fabrication of superhydrophobic surface[10].

In our previous work, methyltrimethoxysilane (MTMS) was chosen as the precursor and monolithic aerogels with low bulk densities were produced at ambient pressure without the need for any solvent exchange and surface modification[11,12]. It is observed the high concentration of methyl groups attached to network skeleton and the extremely porous structure of the areogel render the superhydrophobic property of the MTMS derived aerogel. In this study, we develop a simple method to fabricate highly transparent superhydrophobic solid surface via granuliform silica aerogels. The effect of aging on the chemical composition, the geometrical structure and the wettability of the prepared aerogel is systematically investigated.

Experiment

Materials

All chemicals used including methanol (MeOH, 99.8% purity), MTMS (95% purity), oxalic acid, ammonium hydroxide were purchased from Sinopharm Chemical Reagent Co. Ltd. (Shanghai, China) and used as received.

The Preparation of Silica Alcogel

The silica alcogel was prepared via a two-step, acid-base catalysis sol-gel process[11]. In the first step, MTMS was mixed with MeOH while fixing the MeOH/MTMS molar ratio of 21. The aqueous solution of oxalic acid (0.01M), as an acidic catalyst, was then added to the reaction media. The mixture was stirred at room temperature for 24 hours to complete the hydrolysis process. In the second step, the aqueous solution of ammonium hydroxide (10M), acting as a basic catalyst, was added dropwise to the as-prepared silica sol while stirring. Molar ratio of MTMS/the oxalic acid solution/the ammonium hydroxide solution was kept constant at 1:4:4. The prepared silica alcosol was transferred into a glass test tube which was then made air-tight and placed at 30 °C for the gelation. After gelation, some amounts of fresh MeOH were added into the test tube and the alcogel was aged in MeOH for 48 hours at 60 °C. At last, the MeOH solvent was removed from the test tube and the aged alcogel were obatined. Meanwhile, the alcogel without ageing was also prepared.

The Fabrication of Superhydrophobic Glass Surface

The silica dispersion was prepared by homogenizing the above alcogel with MeOH using an ultrasonic cell disruptor for 3 minutes. The as-obtained homogenized alcoholic dispersion was spin-coated on glass slides which were pretreated in an ultrasonic cleaner by soap-suds, deionized water and MeOH respectively. At last, the coated glass slides were dried in an oven at 40 °C.

Characterisation

The adsorption–desorption isotherms of the aerogels for nitrogen at 77 K were obtained using a Micromeritics TriStar II 3020 analyzer. The microstructure of the aerogels were examined by transmission electron microscopy (TEM, JEM 2100F), scanning electron microscopy (SEM, Hitachi S4800) and a scanning probe microscope (SPM, NanoScope IV). The chemical structure of the aerogels was characterized by an infrared spectrometer (ATR-IR, Nicolet Avatar380). The hydrophobicity of the glass slides was evaluated using a contact angle system (Kruss DSA 30) . The optical transparency of the glass slides were measured by a UV-vis spectrophotometer (Hitachi U-3310).

Results and Discussion

Contact Angel

In this study, the wettability of various glass slides was investigated (Fig. 1). The pristine glass shows a hydrophilic surface with a static contact angle of 22.1° (Fig. 1a). When the alcogel was directly homogenized after gelling without ageing and subsequently spin-coated onto a glass slide, the contact angle of the coated glass slide increased to 144.0° (Fig. 1b). Once the alcogel was aged in MeOH at 60 °C for 48 hours before homogenization and coating, the wettability of the coated glass slide shows superhydrophobicity and the contact angle reaches to 175.5° (Fig. 1c). Meanwhile, it is widely recognized that lower CAH plays a more significant role in determining hydrophobicity than the static WCA. The glass slide coated with aerogel exhibits very low CAH and the water droplets can easily roll away on these surfaces by a gentle vibration, while the glass slide coated with xerogel shows much higher CAH.

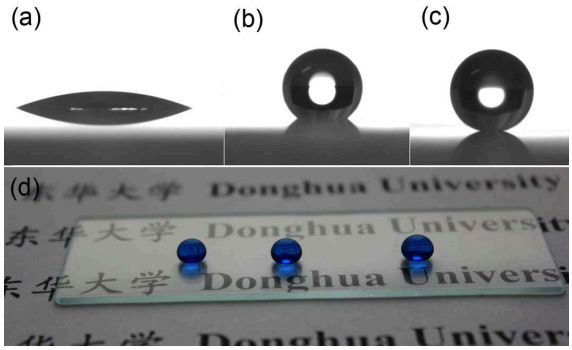


Fig. 1. Optical Images of Water Droplets on a Pristine Glass (a), Glass Coated with the Xerogel (b), Glass Coated with the Aerogel with Ageing (c) and a Photograph of Water Droplets (Colored with DyStar Procion blue H-ERD) on the Glass Coated with the Aerogel

SEM and TEM

SEM and TEM were used to investigate the effect of ageing on the geometrical structure. Fig. 2(a, b, c) shows the FESEM images of the xerogel with different magnifications. It is obvious that large voids and aggregates can be confirmed within the gel backbone network. Fig. 2(d, e, f) exhibit the FESEM images of the aerogel, in which small clusters and highly homogeneous pore structure can be confirmed. Both samples exhibit rough surface while larger fraction of air can be trapped within the network of aerogel in comparison with the xerogel. During ageing, the conversion of unreacted Si-OH to Si-O-Si continued and the alcogel network is further strengthened. Therefore, the skeleton of the aged gel can withstand high interfacial forces (capillary force) during the ensuing ambient pressure drying, resulting in low volume shrinkage and high porosity. Meanwhile, the pore structure collapses and small particles firmly connect with each other within the xerogel.

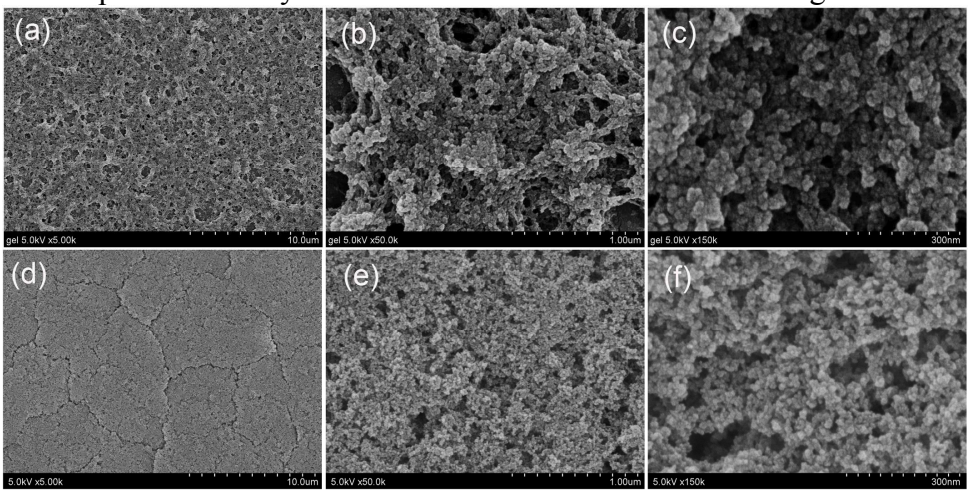


Fig. 2. FESEM Images of the Xerogel and the Aerogel with Different Magnifications (a,d) Scale Bar 10um , (b,e) Scale Bar 1um ,(c,f) Scale Bar 300nm

Fig. 3 demonstrates the HRTEM images of the xerogel (Fig. 3a, 3b) and aerogel (Fig. 3c, 3d). Both samples are composed of interconnected approximately 15 nm sized particles. However, larger aggregates can be obviously observed in the xerogel comparing with the aerogel. This is consistent with the FESEM results. According to the Cassie-Baxter model, increasing the fraction of air between water and the solid surface is advantageous to obtain superhydrophobic surface with a high WCA and low CAH.

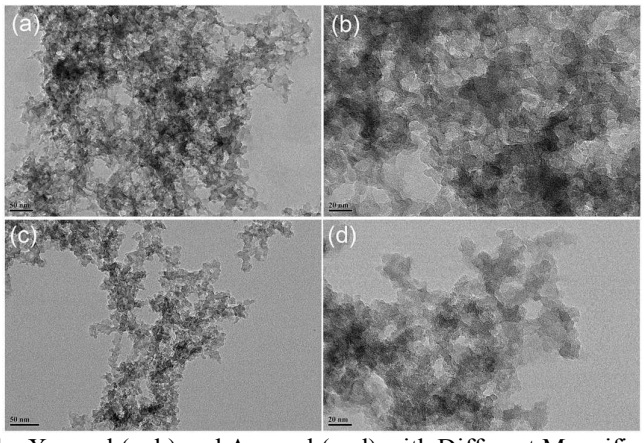


Fig. 3. HRTEM Images of the Xerogel (a, b) and Aerogel (c, d) with Different Magnifications (a, c) Scale Bar 50nm, (b, d) Scale Bar 20nm

BET Surface Area And Pore Size Distribution

Fig. 4 shows the nitrogen adsorption-desorption isotherms and pore size distributions of xerogel and aerogel. Both samples show a type Ⅳ isotherm, while the aerogel exhibits a much higher specific surface area and total pore volume than the xerogel. Meanwhile, the pore size of the aerogel shifts to larger range than the xerogel. For the xerogel, numerous smaller particles aggregate together to form large clusters after ambient pressure drying. That's the reason why the xerogel displays small pore sizes. Ageing leads the aclogel to a stiffer gel network, resulting in more resistance to gel shrinkage

during drying. Therefore, the strengthened gel network and relatively large pores ensure that the porous structure can be maintained in the prepared aerogel. This is in agreement with the previous FESEM and HRTEM results.

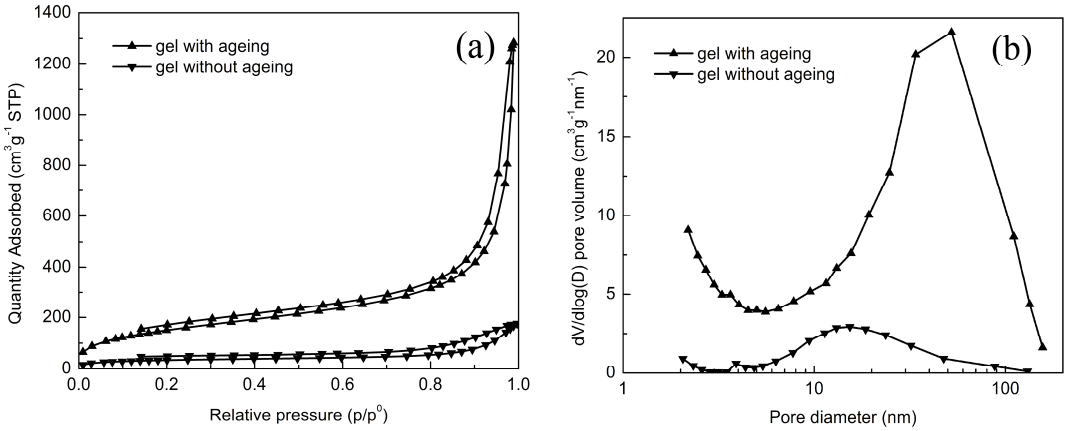


Fig. 4. Nitrogen Adsorption-desorption Isotherm (a) and Pore Size Distribution (b) of Xerogel and Aerogel

FTIR

The chemical composition and functional group were identified by ATR-IR (Fig. 5). Fig. 5a shows ATR-IR spectrum of MTMS. The peaks at 1193 and 1087 cm-1 are assigned to C-O stretching vibration mode of Si-O-CH3 while the peaks at 2841 and 1460 cm-1 are assigned to C-H stretching vibration and bending vibration mode of Si-O-CH3. All these peaks disappear in the MTMS based xerogel and aerogel, demonstrating that MTMS has been fully hydrolyzed. ATR-IR spectra of MTMS based xerogel and aerogel in Fig. 5b and 5c show the peaks around 1030 and 1110 cm-1 which are assigned to stretching mode of Si-O-Si. Meanwhile, the peaks around 2971, 1409 and 1272 cm-1 which are attributed to C-H stretching and bending vibration modes of Si-CH3 are sustained in the MTMS based xerogel and aerogel, indicating the condensation of hydrolyzed MTMS and the presence of methyl group. Fig. 5b and 5c have a high similarity except that the MTMS based xerogel shows a higher intensity of the band of Si-OH stretching vibration (~919 cm-1) than the areogel, implying more residual silanol group and incomplete condensation between hydrolyzed MTMS in the xerogel.

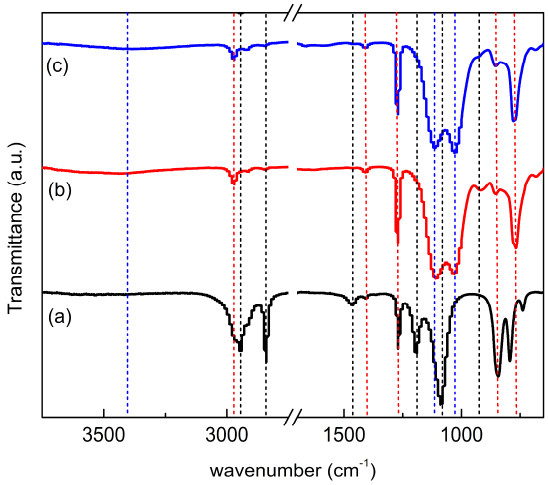


Fig. 5. ATR-IR Spectra of MTMS (a), MTMS Based Xerogel (b) and MTMS Based Aerogel (c)

Light Transmission

Since transparency is a very important property during the application of superhydrophobic surface (e.g. solar cell, glass) [13], Transmittance of the aerogel coated glass was investigated (Fig. 6). The underlying text can be clearly seen, indicating that the coated glass is highly transparent. The transmittance of the glass coated with the silica aerogel is further investigated by the UV-vis spectra. The coated glass exhibits the similar transmittance in the range of 600-800 nm and a slightly lower transmittance in the range of 400-600 nm.

Rough surface fabrication, which is important in preparing superhydrophobic surface, may lead to the decrease of the transparency because of the Mie scattering from the rough surface. The roughness

dimension of the surface must be controlled less than 100 nm to achieve high transparency. AFM was used to investigate the surface topography of the glasses. The surface roughness, rms, increases from 0.248 nm for the pristine glass to 77.288 nm for the spin coated glass. The relatively low surface roughness (<100 nm) renders the coated glass transparency.

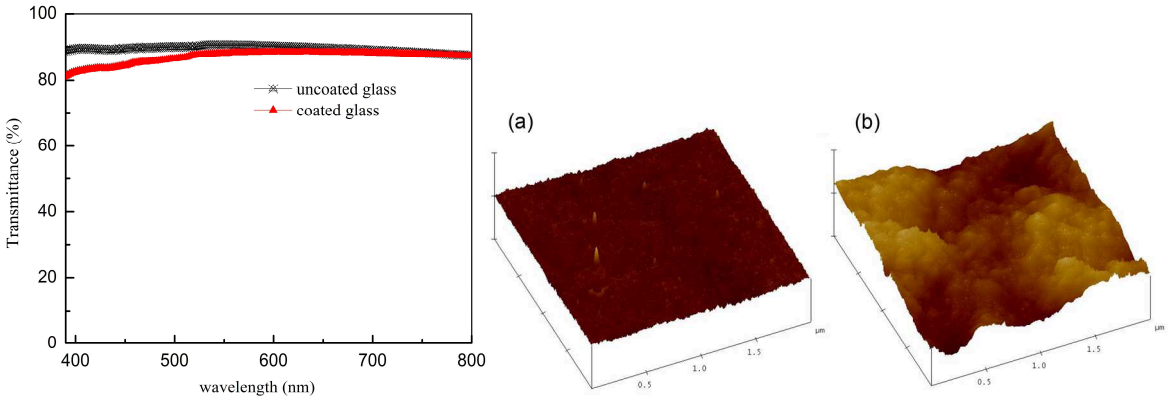


Fig. 6. Transmittance and AFM Images of the Pristine Glass (a), the Glass Coated with the Aergel (b)

Summary

In conclusion, a simple method to create the highly transparent superhydrophobic surface (static WCA larger than 175°) has been developed by spin-coating granuliform silica aerogel particles on the solid substrate. SEM and TEM images indicate that the ageing of the alcogel would provide the aerogel with a very porous 3D network structure while the xerogel without ageing shows large clusters and voids within its structure. IR spectrum demonstrates that complete hydrolysis and condensation take place for the areogel and abundant of methyl groups with low surface energy exist on its structure. Furthermore, the film shows a high transparency because the roughness dimension of the aerogel film is within 100 nm. This method can be extended to a wide range of substrates to prepare surperhydrophobic surface.

References

[1] D. Xia, L.M. Johnson, G.P. Lopez, Adv. Mater. 24 (2012) 1287-1302.

[2] Y.L. Zhang, H. Xia, E. Kim, H.B. Sun, Soft Matter 8 (2012) 11217-11231.

[3] X.F. Gao, L. Jiang, Nature 432 (2004) 36-36.

[4] J. Groten, J. Ruhe, Langmuir 29 (2013) 3765-3772.

[5] R. Jafari, S. Asadollahi, M. Farzaneh, Plasma Chem. Plasma Process. 33 (2013) 177-200.

[6] X. Wang, B. Ding, J. Yu, M. Wang, Nano Today 6 (2011) 510-530.

[7] Y. Liu, J.H. Xin, C.-H. Choi, Langmuir 28 (2012) 17426-17434.

[8] D.W. Schaefer, K.D. Keefer, Phys. Rev. Lett. 56 (1986) 2199-2202.

[9] N.D. Hegde, H. Hirashima, A.V. Rao, J. Porous. Mater. 14 (2007) 165-171.

[10] H. Budunoglu, A. Yildirim, M.O. Guler, M. Bayindir, Acs Appl. Mater. Interfaces 3 (2011) 539-545.

[11] B. Xu, J.Y. Cai, N. Finn, Z. Cai, Micropor. Mesopor. Mater. 148 (2012) 145-151.

[12] B. Xu, J.Y. Cai, Z. Xie, L. Wang, I. Burgar, N. Finn, Z. Cai, L. Wong, Micropor. Mesopor. Mater. 148 (2012) 152-158.

[13] D. Ebert, B. Bhushan, Langmuir 28 (2012) 11391-11399.

Advanced Materials Research Vol. 936 (2014) pp 1047-1055
© (2014) Trans Tech Publications, Switzerland
doi:10.4028/www.scientific.net/AMR.936.1047

Deep Cryogenic Treatment and CrN Coating Effects on Micro-Scale Abrasion of Aluminum Alloy AA 6101-T4

E.S. Ashiuchi[1,a], V.F. Steier[1,b], C.R.M. da Silva[1,c], T.D. Barbosa[1,d], T.F.O. Melo[1,e], J.A. Araújo[1,f]

[1]Department of Mechanical Engineering, University of Brasilia, 70.910-900 Brasilia, DF, Brazil

[a]eashiuchi@gmail.com, [b]volkersteier@gmx.de,

[c]cosmeroberto@gmail.com,[d]thales.dbarbosa@gmail.com, [e]tiago@kryos.com.br , [f]alex07@unb.br ,

Keywords: Cryogenic treatment, coating, chromium nitrite, CrN, PVD, aluminum, ULTP, micro-scale abrasion.

Abstract: The endurance of components made of aluminum and aluminum alloys is often limited by their low yield strength and by their low wear resistance. The aim of this paper is to investigate the effect of different methods that can improve wear resistance of aluminum alloys. As a first approach, a highly wear resistant chromium nitrite layer was deposited by plasma vapor deposition on the surface of the aluminum alloy AA 6101-T4. In the second method, an ultra-deep cryogenic treatment was selected. Both methods have been previously used to improve the wear resistance of other harder substrate materials, like tool steel. To investigate the impact of the two methods on the wear resistance of such alloy, micro abrasive wear tests were carried out and an analysis based on the Archard's law was considered. The results showed a decrease of the wear rate by 29% and 26% for the coated and for the cryogenically treated specimens, respectively, when compared to the as received material. The work also investigated the performance of three different methods (Allsopp, Double Intercept and Polynomial AT) usually considered to calculate the wear rate of coated samples. The three methods presented similar measures of wear rate for the substrate and for the coating.

Introduction

Aluminum and aluminum alloys are rarely used for mechanical applications subjected to highly abrasive environment, since their wear resistance are known to be low [1,2]. For this reason, there is a limited amount of published material on the wear of aluminum and its alloys. The advantages of aluminum are the low costs of production and manufacturing, its good resistance against corrosion [3], its low density among others [4]. However, in some applications aluminum components are exposed to damage mechanisms such as fretting fatigue or fretting wear. These mechanisms either damage the component due to an irrecoverable material loss or lead to premature crack initiation, which can drastically reduce the strength of the component [5].

One example where aluminum components are exposed to an abrasive environment, is the overhead conductor used to transmit electrical energy. The conductors are usually made of aluminum or of aluminum alloys wires wrapped together. The damage normally occurs in points where the displacement of the cable due to Aeolian vibration is restricted, as in the assemblies between cable and suspension clamps, which are fixed to the towers [6]. Due to this oscillatory movement of the conductor a minute relative displacement will occur in the interface between cable and clamp, generating fretting wear and fretting fatigue [6].

The damage of overhead conductors leads to high maintenance costs and sometimes even to extensive black outs if a conductor experiences complete failure. The increase of the wear resistance of aluminum alloys can provide longer operational lives for these lines and reduce the costs of repairing. In this setting, this paper investigates the application of two different treatments in order to improve the wear resistance of aluminum. The deposition of wear resistant coatings is a technique that works well for hard materials like tool steels. However, more recently the deposition of wear resistant coatings for soft materials like aluminum and polymers [1,2,7] have been successful. Here, the effect of a chromium nitrite (CrN) layer deposited on an AA 6101-T4 alloy was examined.

Deep cryogenic treatments (Ultra Low Temperature Process, ULTP) have also been used as an alternative to improve the wear resistance (not only on the surface but also in the core) of tool steels [8]. The effects of cryogenic treatment on steels is somehow well understood [8,9,10]. For these materials the cryogenic treatment leads to the precipitation of hard carbides in the microstructure [11,12,13], which are believed to be the main factors in the improvement of their wear resistance. There are evidences that a ULTP can improve the mechanical properties of other metallic alloys [12,18,19]. In this setting, the effect of a ULTP on the wear resistance of the AA 6101-T4 alloy was also investigated in this work.

Materials and Methods

To carry out the micro abrasive tests extruded bars of AA 6101-T4 aluminum alloy were provided by an electrical fittings producer. The extruded bar was cut in small block specimens with dimensions 25×20×13 mm. All specimens were extracted from the same bar. The chemical composition of the alloy was determined in laboratory to confirm its specification and is reported in Table 1.

Table 1: Elements contained in the aluminum alloy in %.

Cu	Si	Mn	Cr	Fe	Zn	Mg	Ti	Al
< 0.01	0.50	< 0.01	< 0.01	0.18	< 0.01	0.49	0.01	> 98.78

To generate similar surface conditions among the specimens their surfaces were grinded with sandpaper P 600 (particle size 25 μm). The surface preparation occurred before the studied processes were applied. To investigate the effect of the different treatments, a series of three specimens was considered.

The first treatment, a chromium nitride (CrN) coating was executed by a company (Platit) in Brazil. According to the manufacturer, the temperature occurring on the surface of the specimens during the PVD process was 100 °C. The deep cryogenic treatment was also performed by contract work from an external company (Kryos Cryogenic Engineering, Brazil). The deep cryogenic process starts at room temperature and goes down to the target level (190 ºC) within a period of 12 h. This target temperature is then maintained for further 12 h. After this dwell time, the temperature is increased to room temperature within the same 12 h ramp. Before the liquid nitrogen was induced in the chamber, it is evaporated to enable a controlled cooling and to prevent a severe gradient of temperature between the surface and the core of the specimens [11].

In order to examine the wear resistance of the different specimens, micro abrasive wear tests were performed. The micro-scale abrasion device uses a free-ball system (Calowear, CSM instruments). Due to the fact that the tested aluminum alloy can be classified as a soft material, the test conditions needed to be properly adjusted [1,2,15]. In order to generate craters with the negative shape of the rotating balls, the following test parameters were set:

(i) the contact force, (ii) the abrasive and (iii) the velocity.

The load applied during the tests was 50 mN (0.05N). This load proved enough to generate the crater shape sought and also to generate a three body wear regime in the crater [15]. The force reduction was reached by positioning the ball close to the center of the drive shaft, as shown in Fig. 2 (a). This position reduces the contact force, which is only generated by the weight of the ball. All tests were carried out using alumina (Al_2O_3) with a mean particle size of 1μm as abrasive slurry. A concentration of Vol. 10 % Al_2O_3 was dispersed in deionized water [16]. The abrasive slurry was dripped at a rate of at least ten drops per minute. For the tests, a steel ball with the radius of 10 mm was used. The sliding velocity adjusted at approximately 0.1 m/s. On each specimen a series of six craters were generated with distinct sliding distances. After the predefined sliding distances were reached, the tests were interrupted and the diameter of the crater was measured. The interruptions of the tests occurred at a sliding distance of 21, 32, 48, 64, 80 and 107 m. The diameter of the crater generated by the rotating ball was measured subsequently. The mean external diameter *b*, which is used in the analysis, was determined from two measurements taken in a 90 ° angle to each other, being one parallel and the other perpendicular to the sliding direction (Fig. 1).

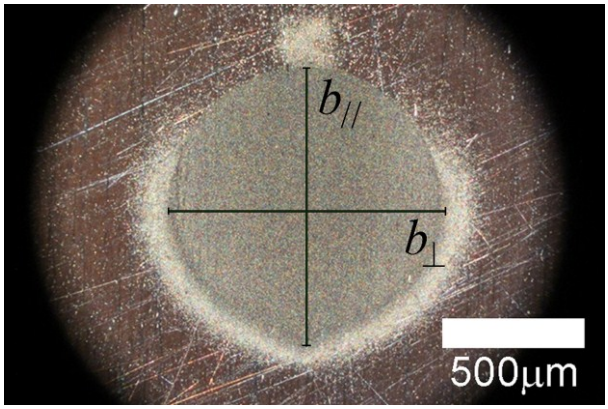


Fig. 1. Exemplary measurement of the crater diameter of an uncoated specimen. Three body wear was found.

All the tests were conducted using the same experimental routine. The applied wear rate calculation is based on the Archard's law (Eq. 1), which implies that the removed volume V depends on the sliding distance S and on the contact force N. The mean wear rate of all specimens was calculated using such law [14]. In Eq. 1 the volume is summarized in the second term, where b is the diameter of the crater and R is the diameter of the ball.

$$\kappa = \frac{1}{SN}\frac{\pi b^4}{64R} \tag{1}$$

In order to enrich the analyses, the coated samples were submitted to a second analysis as proposed by Gee et al [16]. According to Eq. 2 from Rutherford and Hutchings [17], the wear rates of the substrate and of the coating ? o_s and ? o_c respectively, can be calculated separately using the volume of the substrate V_s and the volume of the coating V_c.

$$SN = \frac{V_c}{\kappa_c} + \frac{V_s}{\kappa_s} \tag{2}$$

Three methods were selected to calculate the wear rates ? o_s and ? o_c. These methods (methods that perforate the coating) do not measure the values of κ_c and κ_s directly, but can numerically determine them. To calculate ? o_s and ? o_c directly, non-perforating methods can be used. However, as the thickness of the deposited CrN layer was too low these methods could not be considered in this work.

Allsopp Method: The first method used was the so called Allsopp or Vc-AT method (Eq. 3).

$$\frac{SN}{V_c} = \frac{1}{\kappa_s}\frac{V_s}{V_c} + \frac{1}{\kappa_c} \tag{3}$$

With this method, the wear rates can be calculated with the inclination and with the interception of the linear regression for the data plotted in a graph of SN/V_c against V_s/V_c. The volumes V_s and V_c can be obtained from a pre-determined value of the coating thickness t and the measured outer diameter of the crater b.

$$V_c \approx \frac{\pi t}{4}\left(b^2 - 4Rt\right) \tag{4}$$

$$V_s \approx \frac{\pi b^4}{64R} - \frac{\pi t}{4}\left(b^2 - 4Rt\right) \tag{5}$$

Double Intercept Method: The double intercept method (DI) (Eq. 6) is another rearrangement of Eq. 2 and offers another option to calculate the different wear rates [16].

$$\frac{1}{\kappa_s}\frac{V_s}{SN}+\frac{1}{\kappa_c}\frac{V_c}{SN}=1 \tag{6}$$

The DI method calculates the wear rates by the interceptions of a linear fit of V_c/SN versus V_s/SN with the axes of ordinate and abscissa.

Polynomial AT Method: The third option is the polynomial AT method (Poly-AT) (Eq. 7). In this case, the wear rates can be calculated with the inner crater diameter a and the coating thickness t.

$$SN=\frac{\pi}{64R\kappa_s}a^4+\frac{\pi t}{4\kappa_c}a^2+\frac{\pi R t^2}{\kappa_c} \tag{7}$$

Since the inner crater diameter was not measurable (Fig. 1), a was calculated using the predetermined values of t and the outer crater diameter b.

$$t\approx\frac{1}{8R}(b^2-a^2) \tag{8}$$

The measurement of the coating thickness could be only conducted using a scanning electron microscope (SEM) and a special technique to prepare the specimens, which was developed during this research. The preparation technique is called half corner crater preparation (HCC). Within this technique, a crater analog to the wear tests is generated on the edge of the specimens (Fig. 2b). With the HCC the coating thickness can be measured accurately, since no polishing that normally causes rounded edges is needed. To determine the coating thickness a crater needs to be generated on the edge of the specimen (Fig. 2a). The coated side of the specimen is facing to the down side. Using this specimen position, the crater is generated orthogonal to the coated surface. To reach a reasonable crater depth, the sliding distance should be sufficient to remove the rounding of the edge. The HCC was generated under the same conditions of the micro-scale abrasion tests (abrasive, force, velocity).

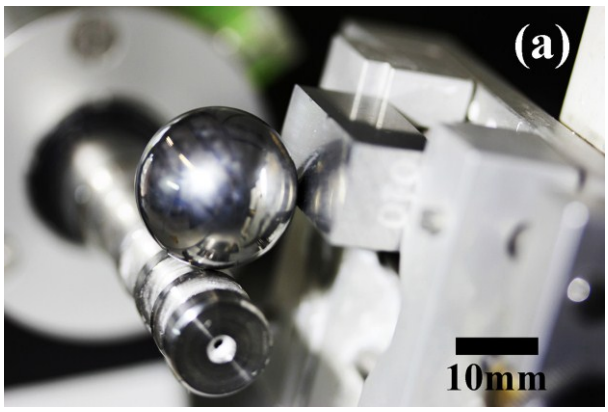


Fig. 2. (a): Illustrative position of the ball to produce a HCC.

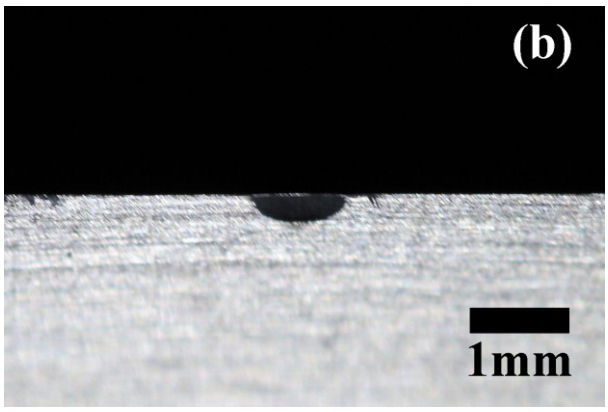


Fig. 2 (b): HCC on the edge of the specimen.

Results

As described already in the introduction, the shape of the crater can influence the measurement significantly. In order to prove if the shape of the crater is comparable to the shape of the ball, profilometric measurements were performed with a Mitutoyo SJ201 contact roughness tester (Fig. 3a). If the shape of the crater differs from the shape of the ball, the calculated removed volumes do not represent the actually removed volume. In Fig. 3a the profile measurement of one crater is plotted. Above the measurement shown as a black line, the theoretical profile of the ball is shown in red with a distance of 1 µm. This gap corresponds to the used mean particle size of the abrasive slurry.

Due to the low thickness of the surface coating, the coating thickness could not be measured using the images of the craters. To determine the coating thickness, SEM investigations were carried out. In Fig. 3 b, one coated specimen is shown.

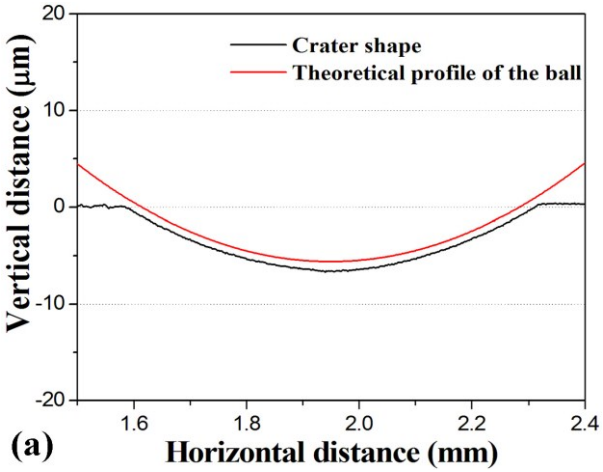


Fig. 3 (a): Geometry of crater depth against the theoretical profile of the ball.

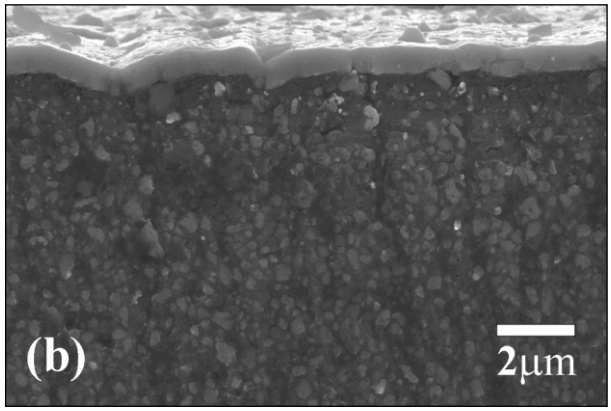


Fig. 3 (b). Determination of the coating thickness using SEM.

Fig. 3 b illustrates the sectional view of a coated specimen. The bright area on top of the picture shows the coated surface of the specimen. The darker area represents the bulk material of the aluminum alloy in a 90 ° angle to the coated surface. In between these areas, a section though the CrN layer is presented (light gray layer). Based on a series of SEM pictures, a mean coating thickness of 660 nm was measured. This value was used for the wear rate calculations of the coated specimens.

The results of the wear tests are shown in fig.4. fig.4a shows the removed volume over the sliding distance multiplied by the contact force of the different test series.fig.4b illustrates the wear rate of the same specimens using the same scale and unity for the x-axis.

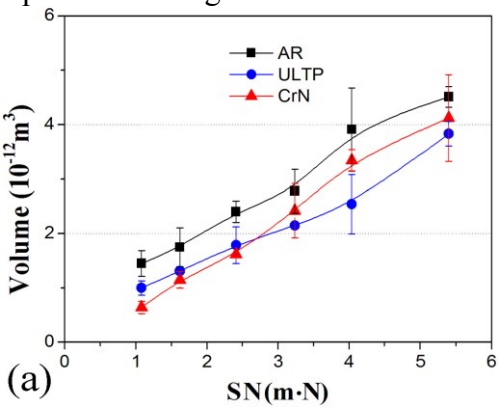


Fig. 4a. Removed volume *versus* the sliding distance multiplied by the contact load.

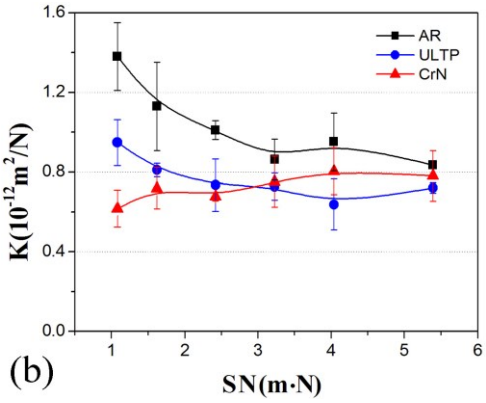


Fig.4b. Wear rate versus sliding distance multiplied by the contact load.

As expected, the amount of removed volume increases with an increasing sliding distance, whereas the AR specimens show the highest volume loss in all measurement points. A reduced removed volume was measured for the coated and the cryogenically treated specimens. Comparing

the results of the coated and cryogenically treated specimens, an intersection of both curves can be recognized. The wear rate of the test series shown in Fig.4b show a comparable behavior. The specimens tested AR have the highest wear rates, which is decreasing with SN. Analog to the analysis of the removed volume, the curves of the treated specimens are crossing each other. This means that the wear rate of the coated specimens is increasing with SN. A contrast behavior was found for the cryogenically treated specimens.

To compare the wear rates at all measurement points with each other, the mean wear rates are shown in Fig. 5a. Each bar represents the mean wear rate of three equally treated specimens. On each of them, six craters were generated. The shown error bars illustrate the standard deviation between the mean wear rates calculated for each specimen. In Fig. 5b, the calculated wear rates of the coated specimens are shown. To compare the calculated values with the reference materials (AR), the wear rate of the untreated specimens is additionally shown in the graph.

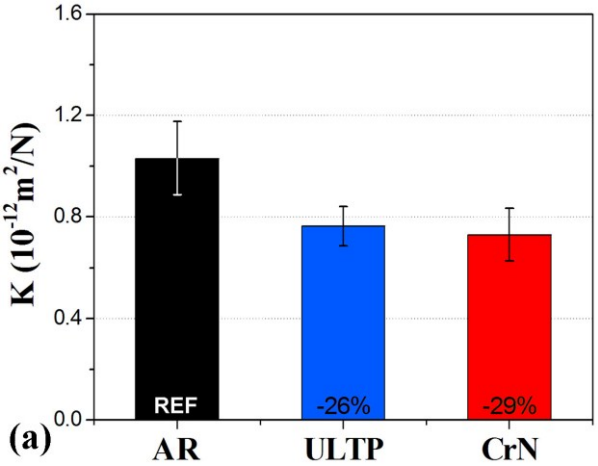


Fig. 5. (a): Mean wear rates of the investigated test series.

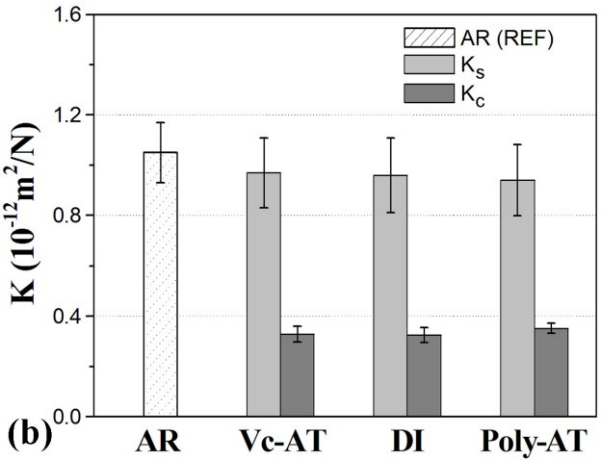


Fig. 5(b): Comparison of the applied analysis methods for the coated specimens.

The applied treatments show a significant effect on the wear behavior of the tested aluminum alloy. A reduction of 26 % was measured for the cryogenically treated specimens. The specimens coated with CrN show a wear rate reduction of 29 %, compared to the AR specimens.

In Fig. 5b the wear rate of the specimens tested AR are compared with the calculated wear rates of the bulk material using the calculation methods Vc-AT, DI and Poly-AT. Furthermore, the calculated wear rate of the CrN coating are shown. The calculated values for ? o_s agree well with the reference material. Furthermore, only very small differences between the single calculation methods were found. The wear rate ? o_c is significant lower than the wear rate of the substrate. Likewise to the ? o_s, only slight differences can be seen between the single calculation methods.

Discussion and Conclusion

As shown in Fig 4a, all tested specimens showed higher volume loss with an increasing SN. For this graph, the removed volume is plotted versus the contact force multiplied by the sliding distance. Since the contact force was kept constant during the tests, the Archard's theory, which claims that the volume increase with the sliding distance, can be confirmed. As expected, the as received specimens show the highest volume loss at all measured sliding distances. It is worth of notice in this figure that the curves of the coated and of the cryogenically treated specimens cross each other after the third measurement point. This effect can be explained by the effective range of the applied wear improving treatments. As the surface coating only increases the wear resistance on the surface, the effect of it to reduce the volume of material removed mainly occurs at low sliding distances. After the coating is perforated, the contact area between the rotating ball and the specimen involves a zone of CrN coating and another zone of the aluminum alloy. With an increased wear volume, the coating/aluminum ratio in the contact area decreases significantly. For this reason, the wear rate of the coated and of the as received specimens converges with an increase in the sliding distance. On the

other hand, the curve progression of the cryogenically treated specimens shows a reverse effect. At low sliding distances, the volume loss of the cryogenically treated specimens is lower than the untreated specimens, but higher than the coated ones. Since the effect of the cryogenic treatment is not limited to the surface area [13], the improved wear resistance can also be felt (and then measured) at higher sliding distances.

The same tendency can be seen for the results of the wear rate (Fig. 4b). In theory, the wear rate of the uncoated and the cryogenically treated specimens should be constant over the whole sliding distance [14]. Anyhow, several effects can influence the wear rate in dependency of the sliding distance. The most probable effect for the difference observed in the wear rate is an overestimation of the removed volume at low wear rates due to the difficulty to measure the diameter of the crater [16]. As shown in Fig. 1, the uncoated specimens show a large scuffed area around the crater. This turns the measurement of its diameter and consequently of the volume loss a less precise task. Other authors found similar behavior for uncoated soft materials [15]. Besides this, further measurement difficulties in this test can be caused by craters that do not mirror exactly the shape of the ball. Other scientists report about two possible effects [17]: first, a ridge can be formed around the crater. This mainly happens if soft materials are used, which was the case here. To avoid or at least minimize this effect the contact force was reduced to 50mN (0.05N). Second, the crater can show an elliptical shape (sectional view) with softened edges. In both cases, the calculated volume does not represent the actual removed Volume. In order to verify if such phenomena occurred, contact profilometry was used to determine the shape of the craters. As shown in Fig. 3a, none of such effects could be found in the tested specimens.

The results also showed (Fig. 5a) that the cryogenic treatment reduces the wear rate in 26% (over the whole sliding distance) compared to the as received specimens. This represents a clear improvement in the wear properties of this aluminum alloy associated to such treatment. Less clear at this stage of the work are the material changes that cause such improvement. Other authors raise the possibility of the formation of hard second phases, which could be formed during the cryogenic treatment [12,18,19]. Some possible second phases found by other researchers that also researched about the effect of cryogenic treatments on comparable aluminum alloys are $Mg_{17}Al_{12}$, $AlCu_3$, Al_7Cu_2Fe, $MgZn_2$ or Al_2Cu [12,18,20,21]. As shown in Table 1, the elements Mg, Cu and Fe are present in the tested aluminum alloy. In order to investigate the formation of the mentioned phases, XRD measurements will be carried out in the near future. Furthermore, a microstructure analysis and a micro hardness measurements will be performed.

A wear rate reduction of 29 % could be reached due to the coating with CrN. CrN is known to be a good wear resistant coating, for which reason a reduction of the wear rate was expected [1,2]. The coating of soft materials is not riskless, since delamination or crack formation can occur easily in the case of high contact loads or deformation of the substrate [7]. Due to the low contact forces used between the rotating ball and the specimens, none of the mentioned failures was found. The wear rate reduction of 29 % is anyhow higher than expected, since the coating is just 660 nm thick.

As already mentioned in Methods section, the coating thickness could not be measured with an optical microscope after the wear tests, what would be the classically used method. The small thickness of the coating avoided a measurement of the inner crater radius. For this reason, the coating thickness was measured inside an independent crater generated from the test series, which was placed on the specimens edges. The already described HCC preparation was the only possibility to measure the coating thickness without an interference of the polishing process which would produce rounding edge effects.

The determined coating thickness was used to calculate the wear rate of the substrate and the wear rate of the coating within the same analysis. Three different analysis methods have been tested. These methods showed similar results, despite their different ranges of emphasis. All the methods are based on the Archard's law and use the volume loss and the diameter of the crater to calculate the wear rates [22]. Each calculation method has some positive and negative aspects. For this reason, the result of each method is slightly different. The double intercept method, for example, puts emphasis to low sliding distances, which are normally the ones with the highest possibility for inaccurate

measurements. On the other hand, both wear rate are divided by SN, which can be measured much more accurately than the diameter of the craters, what decreases the measurement deviations [22]. The Allsopp (Vc-AT) method also puts high emphasis to the smallest craters, since it is using a linear regression to calculate the ? o_s. The problematic involved in the analysis based on linear regression is the big weight of single measurement points. Therefore, the third method works with a fit of a polynomial function to avoid this huge influence. Using this method, the emphasis is on larger craters [22].

References

[1] F. Zhou, C.-M. Suh, S.-S. Kim, and R.-I. Murakami, Sliding-Wear Behavior of TiN- and CrN-Coated 2024 Aluminum Alloy Against an Al2O3 Ball. Tribology Letters 13, (2002) 173-178.

[2] F. Zhou, C.-M. Suh, S.-S. Kim, and R.-I. Murakami, Tribological behavior of CrN coating on aluminum alloys deposited by arc ion plating. Journal of Materials Research 17, (2011) 3133-3138.

[3] W.J. Liang, P.A. Rometsch, L.F. Cao, N. Birbilis, General aspects related to corrosion of 6xxx series aluminium alloys: Exploring the influence of Mg/Si ratio and Cu, Corrosion Science 76, (2013) 119-128.

[4] Metals Handbook, Properties and Selection: Nonferrous Alloys and Special-Purpose Materials, ASM International 2 (10) (1990).

[5]J. A. Araújo, & D. Nowell, The effect of rapidly varying contact stress fields on fretting fatigue, International Journal of Fatigue 24 (7), (2002) 763-775.

[6] A.A. Fadel, D. Rosa, L.B. Murça, J.L.A Ferreira, J.A. Araújo, Effect of high mean tensile stress on the fretting fatigue life of a Ibis steel reinforced aluminum conductor, International Journal of Fatigue 42, (2012) 24-34.

[7] S. Guanhong, H. Xiaodong, J. Jiuxing, and S. Yue, Parametric study of Al and Al2O3 ceramic coatings deposited by air plasma spray onto polymer substrate, Applied Surface Science 257, (2011) 7864-7870.

[8] F. Meng, K. Tagashira, R. Azuma, H. Sohma, Role of eta-carbide precipitations in the wear resistance improvements of Fe-12Cr-Mo-V-1.4C tool steel by cryogenic treatment, ISIJ International 34 (1994). 205-210.

[9] R.F. Barron, Cryogenic treatment of metals to improve wear resistance, Cryogenics 22 (8), (1982) 409-4013.

[10] F.J. da Silva, S.D. Franco, Sinésio, A.R. Machado, E.O. Ezugwu, A.M. Souza Jr, Performance of cryogenically treated HSS tolls, Wear 261 (2006) 674-685.

[11] W. E. Bryson, Cryogenics, Hanser Gardner Publications, 1999, 210p.

[12] S. Zhirafar, Effect of cryogenic treatment on the mechanical properties of steel and aluminum alloys, Mechanical and industrial Engineering, Thesis Master of Applied Science. (Library and Archies Canada: Concordia University Quebec) (2005).

[13] B. Podgornik, F. Majdic, V. Leskovsek , and J. Vizintin. Improving tribological properties of tool steels through combination of deep-cryogenic treatment and plasma nitriding. Wear 288, (2012) 88-93.

[14] J.F. Archard, Contact and Rubbing of Flat Surfaces, Journal of Applied Physics 24, (1953) 981-988.

[15] R.I. Trezona and I.M. Hutchings, Three-body abrasive wear testing of soft materials, Wear 233–235, (1999) 209-221.

[16] M.G. Gee, A.J. Gant, I.M. Hutchings, Y. Kusano, K. Shiffman, K. Van Acker, S. Poulat, Y. Gachon, J. von Stebut, P. Hatto, G. Plint, Results from an interlaboratory exercise to validate the micro-scale abrasion test, Wear 259 (2005) 27-35.

[17] K.I. Schiffmann, R. Bethke, and N. Kristen, Analysis of perforating and non-perforating micro-scale abrasion tests on coated substrates, Surface and Coatings Technology 200, (2005) 2348-2357.

[18] Gui Rong Li, Hong MingWang., Yun Cai, Xue Ting Yuan, Behavior of β(Mg17Al12) Phases in Mg-Al Alloy Subject to Cycling Cryogenic Treatment, Key Engineering Materials 575 - 576, (2013) 390-393.

[19] J. Liu, G. Li, D. Chen, and Z. Chen, Effect of Cryogenic Treatment on Deformation Behavior of As-cast AZ91 Mg Alloy, Chinese Journal of Aeronautics 25 ,(2012) 931-936.

[20] C.-C. Jain, C.-Y.Bai, S.-W. Chen, and C.-H. Koo, The Microstructure and Mechanical Properties of AZ31-xRE Magnesium Alloys, Materials Transactions 48, (2007) 1149 to 1156.

[21] P. Wang, W. Lu , Y. Wang, J. Liu, and R. Zhang, Effects of cryogenic treatment on the thermal physical properties of Cu76.12Al23.88 alloy, Rare Metals 30, (2011) 644-649.

[22] Y. Kusano, K. Van Acker, I.M. Hutchings, Methods of data analysis for the micro-scale abrasion test on coated substrates, Surface and Coatings Technology 183 (2004) 312-327.

Advanced Materials Research Vol. 936 (2014) pp 1056-1065
© (2014) Trans Tech Publications, Switzerland
doi:10.4028/www.scientific.net/AMR.936.1056

Wear Resistance of Ti-40Zr Alloy with TiN and ZrN Multilayer Coatings

DIAS, F.C.[1a], SILVA, C.R.M.[1b], MUTERLLE, P.V.[1c],
HENRIQUES,V. A. R. [2d],ARAUJO, J.A.A.[1e]

[1]University of Brasília, Faculty of Technology. UnB – Mechanical Engineering Department - Campus Universitário Darcy Ribeiro, Asa Norte. 70910-900 - BRASILIA, DF – Brasil

[2]Instituto Tecnológico da Aeronáutica, São José dos Campos,SP, Brasil

[a]felipedias.mat@gmail.com, [b]cosmeroberto@unb.br, [c]palloma@unb.br, [d]vinicius@iae.cta.br,[e]jaaunb@gmail.com

Keywords: wear, pvd thin films, TiN, ZrN

Abstract: Production and processing of titanium alloys are expensive and its alloys show low wear resistance. Substrates of Ti-40Zr, used for orthopedic implants, were obtained from the elemental mixture of hydrogenated powders, followed by a sequence of cold uniaxial and isostatic pressing and vacuum sintering. Aiming wear resistance increase, samples were coated by physical vapor deposition using electron beam technique (EB-PVD). Multilayer coatings with three different configurations were undertaken: Ti/TiN, Ti/TiN/ZrN and Ti/TiN/ZrN/TiN. Micro-abrasive wear tests were conducted by ball-cratering, with abrasive slurry of silicon carbide (SiC). The wear craters were measured at intervals corresponding to increments in the sliding distance of approximately 14 m. Range of the normal force were between 0.35 and 0,45 N. Scanning electron microscopy was used to evaluate the wear crater and the wear mode. All experiments showed three-body abrasive wear and a reduction of one order of magnitude in wear coefficient for two coated samples: $2{,}58\cdot10^{-12}$ $m^3(Nm)^{-1}$ to substrate, $5{,}4\cdot10^{-13}$ $m^3(Nm)^{-1}$ to Ti+TiN film and $7{,}22\cdot10^{-13}$ $m^3(Nm)^{-1}$ to Ti+TiN+ZrN film. In the Ti+TiN+ZrN+TiN experiment the wear coefficient of film is nearer to the substrate, $7{,}58\cdot10^{-13}$ $m^3(Nm)^{-1}$. The multi-layers containing ZrN presented wear coefficient higher than Ti/TiN films, possibly due to existing residual stresses.

Introduction

Biomaterials application has expressive market worldwide, and its increase reached over 150 % from 2009 to 2012 [1]. Considering the increase of life expectance and rise of traffic accidents, gross import and export of implants in Brazil had financial transactions reaching nearly 750 million of dollars, only in 2011 [2-4]. Among several materials used as biomaterials, titanium and its alloys prevails considering its appropriate properties such as: good ratio between density and mechanical properties, low thermal expansion coefficient, compatibility with human tissue and high corrosion resistance [5,6]. Despite its good properties as biomaterial, titanium alloys have poor tribological properties such as low wear resistance and high coefficient of friction [7].

Titanium prosthesis fabrication with powder metallurgy can be an economic alternative, taking into account parts with high precision and porosity control. This process must consider contamination with titanium stable oxides considering that they cannot be removed during manufacturing. Aiming to improve tribological performance, surface coating via physical vapor deposition is being used nowadays. Basically consists on substrate coating with more abrasive resistant material, and is mainly applied to orthopedic implants [8-10]. The objective of this work was to evaluate wear behavior of samples of Ti-40Zr alloys coated with multi-layer films of TiN and ZrN.

Wear volume, V, from material without coating, is related to sliding distance, L, and with contact normal force, N, by a wear model equivalent to the following Archard equation:

$$L \cdot N = \frac{V}{k} \quad (1)$$

where *k* is the material wear coefficient.

However, when there is a coating on the material, and each material has it own specific wear coefficient, Rutherford e Hutchings (1996) propose an extension of Eq (1) [11].

$$L \cdot N = \frac{V_c}{k_c} + \frac{V_s}{k_s} \quad (2)$$

where índex c and s are related to coating and substrate, respectively.

From Eq (2) is possible to establish wear coefficient values, both coating and substrate, by linear adjustment of data. Kusano et al. (2004) evaluated several methods aiming wear coefficient determination [12]. The best results were obtained by Eq.(2) rearrangement, dividing its terms on one hand by coating volume, Vc, and on the other hand by substrate volume, Vs, represented respectively by the equations (3) and (4):

$$\frac{S \cdot N}{V_c} = \frac{1}{k_s} \cdot \frac{V_s}{V_c} + \frac{1}{k_c} \quad (3)$$

$$\frac{S \cdot N}{V_s} = \frac{1}{k_c} \cdot \frac{V_c}{V_s} + \frac{1}{k_s} \quad (4)$$

Using this method, both the wear coefficients of coating, k_c, and substrate, k_s, can be determined in just one experiment, from the coefficients of linear adjustment of graphic SN/Vc against Vs/Vc or SN/Vs against Vc/Vs.

According to Trezona et al (1999) the usefulness of wear coefficient as abrasive wear measurement occur by direct proportionality between worn volume and sliding distance times loading[13].

Figure 1 shows schematically the cap geometry at microabrasive wear test with sphere of radius R. Parameters *t* and *h* are film thickness and total height of cap, respectively, and *a* and *b* are internal and external cap diameter.

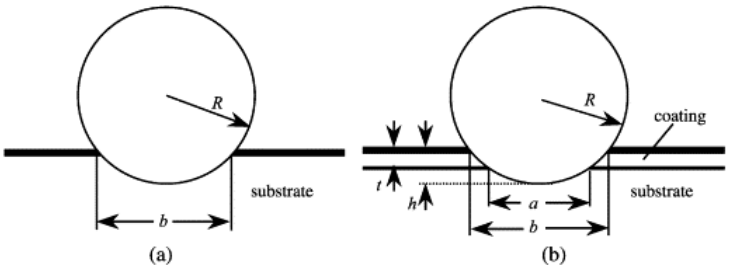


Fig. 1 – Schematic representation of cap geometry at microabrasive wear test with sphere of radius R: (a) uncoated and (b) coated material [12].

Worn volume calculation, either from coating or substrate, can be written either as a function either of external diameter, b, or internal diameter, a, and film thickness, by the following expressions:

$$V_c = \frac{\pi}{64R}(b^4 - a^4) = \frac{\pi t}{4}(a^2 + 4Rt) \quad (5)$$

$$V_s = \frac{\pi a^4}{64R} \quad (6)$$

Materials and Experimental Procedure

PVD coating

The raw materials for samples manufacture was produced by Brazilian Aerospace Institute by hydrogenation process. Titanium and zirconium powders where washed with organic solvent and

dried in air. Hydrogenation process occurred at 500 ^{0}C, in a high vacuum furnace, during approximately 3 hours. After cooling, friable material was blended under 0,23 Pa pressure at titanium grinder, aiming contamination avoidance.

Samples of Ti-40Zr alloys were obtained by blended- elemental technique (BE), from hydrogenated powders, followed by cold uniaxial pressure (with compaction pressure of 60 MPa during 30s), and cold isostatic pressure (pressure of 450 MPa and 30s) and vacuum sintering.

Samples dimensions were 12mm diameter and 3 mm thickness, with and without coating. All samples were grinded and polished before the film deposition process [14.15].

Coatings were carried out via physical vapor deposition by electron beam (EB-PVD), divided in three different experiments, aiming to evaluate the multi-layer films performance. Table 1 shows films coating process and the adopted nomenclature for each sample in this work. The evaporation containing Ti was carried out with current of 0,05 A and those with Zr with current of 0,15 A.

TABLE 1 – NOMENCLATURE ADOPTED FOR EACH COATING PROCESS

Sample	Coating Process
E1	Ti evaporation during 5 minutes + Evaporation of ($Ti+N_2$) during 20 minutes
E2	Ti evaporation during 5 minutes + Evaporation of ($Ti+N_2$) during 20 minutes + Evaporation of ($Zr+N_2$) during 30 minutes
E3	Ti evaporation during 5 minutes + Evaporation of ($Ti+N_2$) during 10 minutes + Evaporation of ($Zr+N_2$) during 30 minutes + Evaporation of ($Ti+N_2$) during 10 minutes

Microbrasive wear tests were carried out with a free sphere equipment CSM, model Calowear.

Normal loads were between 0,37 and 0,45 N (±0,001N) as showed at figure 2. The used sphere was steel 100Cr6, with diameter of 20mm. The abrasive slurry was silicon carbide suspension, with volumetric concentration of approximately 0,20 corresponding to 75g of abrasive in 100 cm^3 of distilled water.

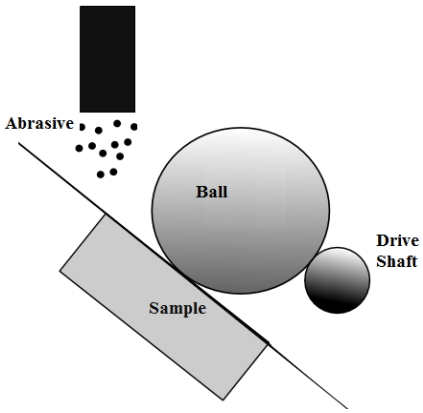


Fig. 2 – Schematic model of microabrasive wear [16]

Scanning Electron Microscopy

Scanning electron microscopy was carried out at samples cross sections aiming coatings thickness measurement. Samples were grinded and polished followed by ultrasonic washing with organic solvent during 30 min. Afterwards the samples were etched at acid solution (10ml of HF, 5 ml of HNO_3 and 85 ml of H_2O) in 30 s [19]. Coating thickness was measured with software installed at SEM

Cap wear was evaluated by scanning electron microscopy, using a FEI Quanta 450. Image of wear crater was collected using backscattered mode aiming to identify differences between atoms from different layer. Vickers microhardness was carried out with a Microhardness Tester FM 700 under 50, 100, 300 e 500 gf (0.49, 0.98, 2.94,4.9 N).

Results and Discussion

Vickers Microhardness

Vickers microhardness was carried out on samples with and without coating aiming to evaluate the performance of coated material. Table 2 shows average microhardness values for each load and its respective standard deviation. Figure 3 show graphically these values.

TABLE 2 – VICKERS MICROHARDNESS VALUES FOR EACH LOAD AND DEVIATIONS

Load (gf)	Substrate		E1		E2		E3	
	Aver.	Dev.	Aver.	Dev.	Aver.	Dev.	Aver.	Dev.
50	401,36	39,04	839,53	81,65	743,59	58,15	922,89	62,07
100	396,24	46,18	710,11	31,53	700,8	39,83	744,37	54,51
300	374,6	29,42	609,03	44,52	597,8	25,61	675,93	72,66
500	393,19	8,85	531,13	46,98	516,71	44,14	576,4	33,14

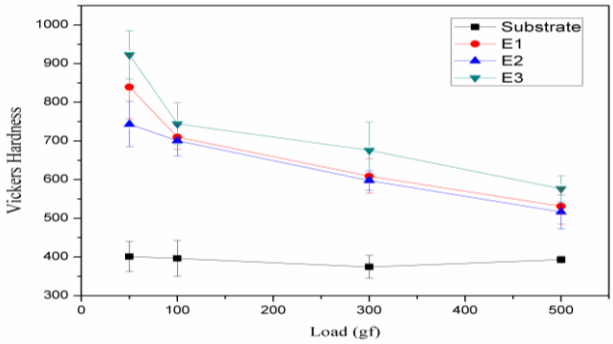


Fig. 3 – Vickers microhardness as function of load

Previous result for microhardness of Ti-40Zr alloy without coating is approximately 350 HV [17,18] and for pure Ti is between 90 and 160 HV. The alloy without coating has hardness values below all coated samples, regardless the used coating.

Comparing the coated samples, one can see that samples where TiN was the last coating (E1 and E3) have better performance at microhardness test. These results can be correlated to surface characteristics of ZrN coating. With load increase hardness values of coated samples has sharp decrease. This result can be correlated to increase of the depth reached by Vickers indenter [9].

Scanning Electron Microscopy

Medium silicon carbide particle size was around 4 μm, as can be seen in Figure 4.

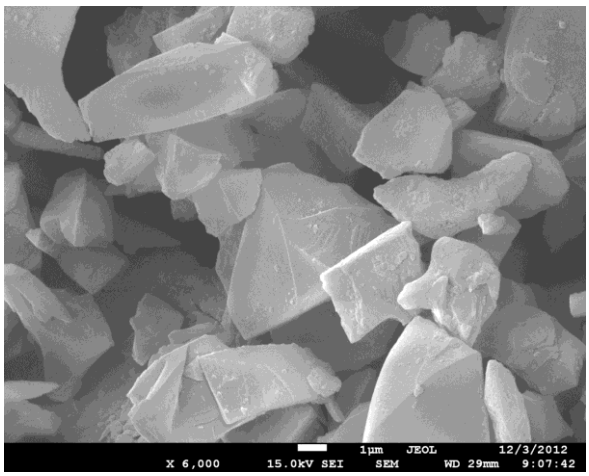


Fig. 4 - SEM image of SiC particles

Table 3 presents the average thickness values. Figures 5,6 and 7 show micrograph of samples cross sections used for films thickness measurements.

TABLE 3 – AVERAGE COATING THICKNESS

Sample	Average (m)	Standard Deviation
E1	2,45E-06	2,40E-07
E2	2,16E-06	9,64E-08
E3	4,91E-06	4,13E-07

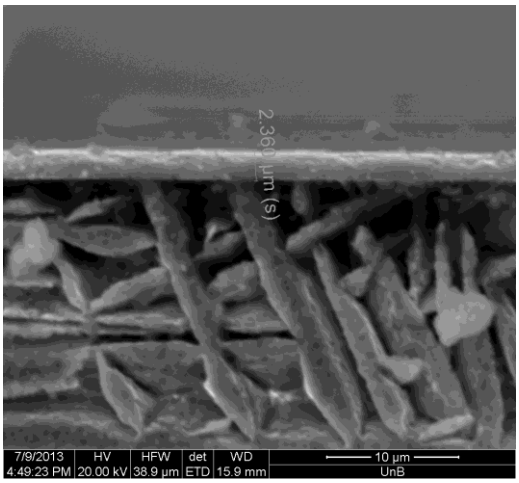


Fig. 5 – SEM of sample cross section of sample E1 with coating thickness measurement.

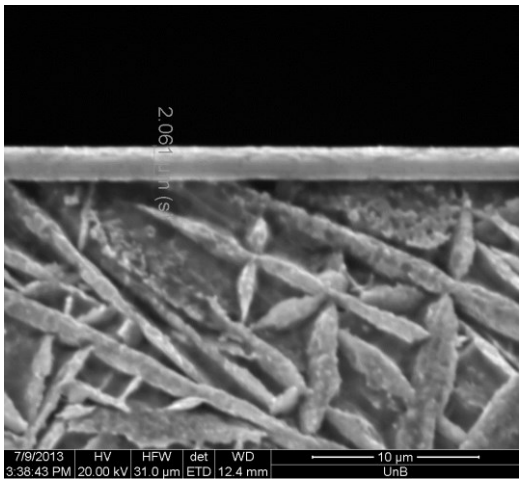


Fig. 6 – SEM of sample cross section of sample E2 with coating thickness measurement

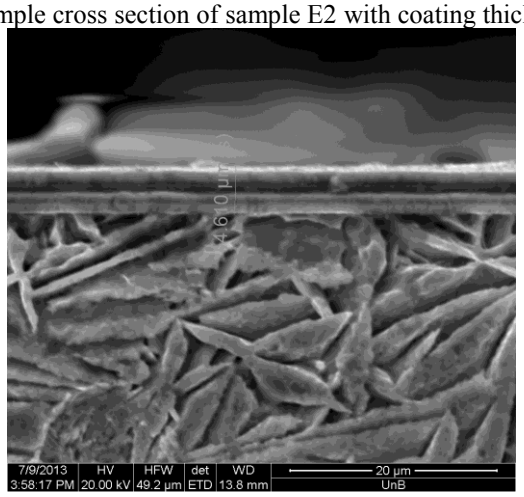


Fig. 7 – SEM of sample cross section of sample E3 image with coating thickness measurement

Figure 8 shows variation of wear crater diameter as a function of time of test, for coated material. It is possible to identify small variations at external and internal diameters. Such variations can be explained by the difficulty of accurate diameter measurements for this sort of experiments. Gee et al. (2003)[16]. Figure 9 shows image of external diameter and the region defined as “scuffing”,

where grooves around the edge of external crater of wear cause difficulties in diameter determination.

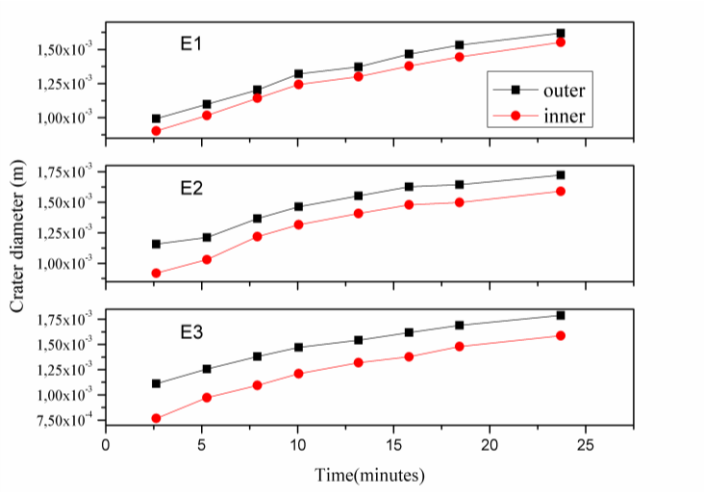


Fig. 8 – Evolution of wear crater diameter with test time.

For wear volume calculation, aiming reduction on edge effect, internal diameter values of wear crater has been used.

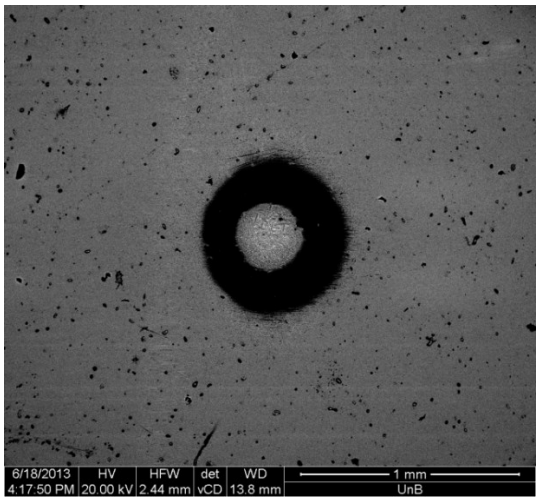


Fig. 9 – Edge effect of wear crater

Figure 10 shows total wear volume as function of sliding distance. According Trezona et al. (1999) the linear behavior of this volume is indicative that the permanent wear regime was reached [13].

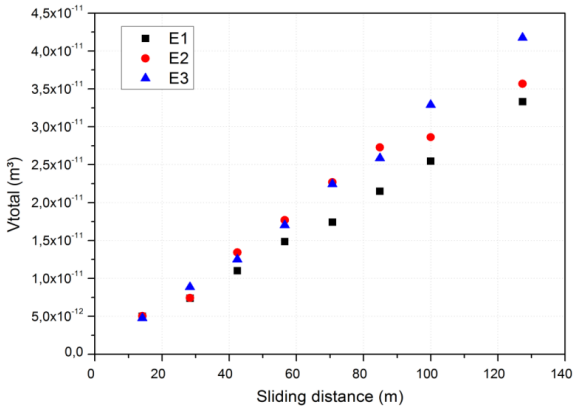
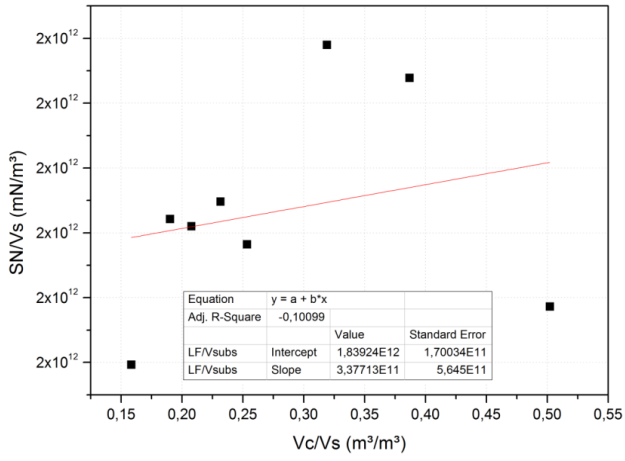
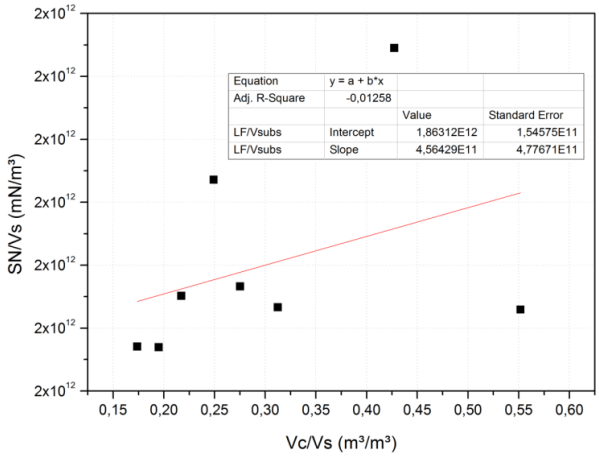


Fig.10 – Worn volume as function of sliding distance.

Figures 11 and 13 show the graphic SN/Vs against Vc/Vs, used to calculate wear coefficients k_c and k_s, according to Eq. (4).

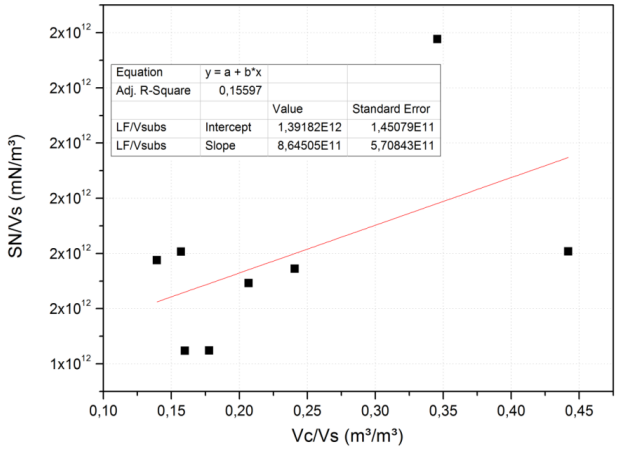


(a)

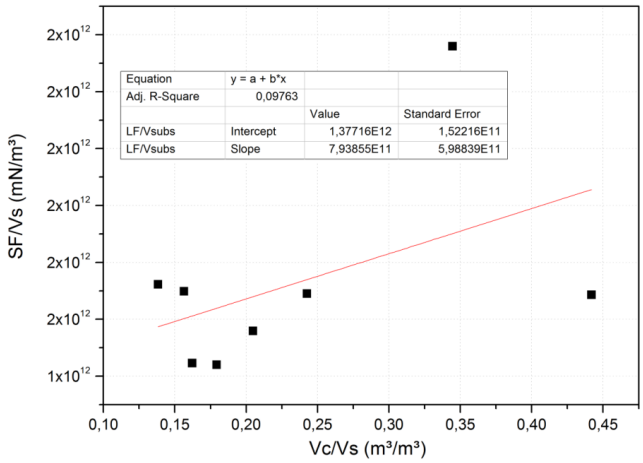


(b)

Fig. 11 – Graphic of SN/Vs against Vc/Vs for coating E1: (a) sample 1 and (b) sample 2

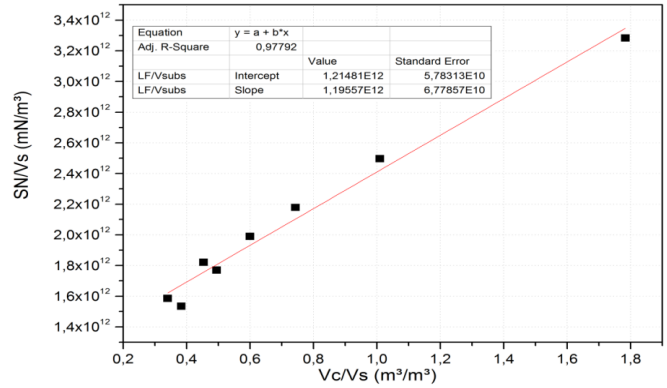


(a)

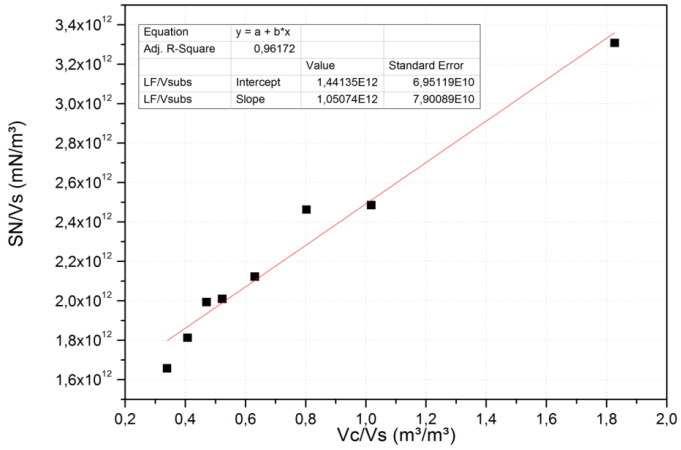


(b)

Fig. 12 – Graphic of SN/Vs against Vc/Vs for coating E2: (a) sample 1 and (b) sample 2



(a)



(b)

Fig. 13 – Graphic of SN/Vs against Vc/Vs for coating E3: (a) sample 1 and (b) sample 2

With these graphics it was possible the wear coefficient determination for coatings and substrate, according Table 4.

TABLE 4 – WEAR COEFFICIENT VALUES FOR COATINGS AND SUBSTRATE, FOR EACH SAMPLE.

Sample	**E1**		**E2**		**E3**	
	k_c	**k_s**	**k_c**	**k_s**	**k_c**	**k_s**
Sample 1	5,44E-13	2,96E-12	7,18E-13	1,16E-12	8,23E-13	8,36E-13
Sample 2	5,37E-13	2,19E-12	7,26E-13	1,25E-12	6,94E-13	9,51E-13
Average	5,40E-13	2,58E-12	7,22E-13	1,2E-12	7,58E-13	8,94E-13

In accordance with Table 4, all values of k_c were below the k_s values, although at sample E3 these values remained at the same order of magnitude. The biggest difference was at E1, where there is no ZrN coating.

For samples E2 and E3, where the coefficients values are nearer, there is ZrN coatings. Despite being a material with high hardness, the ZrN coating can generate residual stresses and, as a result, low-adhesion and lower wear resistance [8].

Another possibility is higher coating roughness of ZrN coating, lowering its tribological performance [20-22]

Conclusions

The titanium coating applied before deposition of nitride films contributed to coating good adhesion. All coated samples showed higher Vickers microhardness than the substrate without coating. Multilayer coating with high hardness, such those applied to E3 samples had better performance is this test, followed by samples E2 and E3. With the load increase, hardness values present reduction and become similar to substrate hardness, probable because the indenter cracks the coating for higher load.

Samples coating is effective to increase wear resistance of substrate, for silicon carbide abrasive. All coatings from this work showed wear coefficient lower than the measured in the substrate. For the different coated samples, those without ZrN showed lower wear coefficients. A possible explanation for this behavior is the existing residual stress between TiN and ZrN films. Additional evaluation using low angle X-ray diffraction can indicate these stresses.

References

[1] MarketandMarkets. Global Biomaterials Market worth US$58.1 Billion by 2014. Disponível em <http://www.marketsandmarkets.com/PressReleases/global-biomaterials-market-worth-US58.1-Billion-by-2014.asp>. Acessed on feb. 2012.

[2] BRASIL. Instituto Brasileiro de Geografia e Estatística (IBGE). Em 2010, esperança de vida ao nascer era de 73,48 anos. Disponível em <http://www.ibge.gov.br/home/presidencia/noticias/noticia_visualiza.php?id_noticia=2032&id_pagina=1&titulo=Em-2010,-esperanca-de-vida-ao-nascer-era-de-73,48-anos>

[3] BRASIL. Departamento Nacional de Infraestrutura de Transportes (DNIT). Estatística de acidentes em estradas federais: Número de condutores envolvidos por sexo e idade do condutor ano de 2011. Disponível em: <http://www.dnit.gov.br/rodovias/operacoes-rodoviarias/estatisticas-de-acidentes/quadro-0302-numero-de-condutores-envolvidos-por-sexo-e-idade-do-condutor-ano-de-2011.pdf>

[4] ABIMO. Dados econômicos. Disponível em <http://www.abimo.org.br/modules/content/content.php?page=dados-economicos>. Acessed on feb. 2012.

[5] M. Niinomi, Mechanical biocompatibilities of titanium alloys for biomedical applications. Journal of the Mechanical Behavior of Biomedical Materials, 19(18), (2008). pp. 1621 – 1639

[6] M. Geetha, A. K. Singh, R.A. sokamani, A. K. Gogia, Ti based biomaterials, the ultimate choice for orthopaedic implants – A review. Progress im materials science, 54, (2009). pp 397-425

[7] A. Zhecheva, W. Sha, S. Malinov, A. Long, Enhacing the microstructure and properties of titanium alloys through nitriding and other surface engineering methods. Surface & Coatings Technology, 200, (2005), p. 2192 – 2207.

[8] C. J. Tavares et al., Mechanical characterization of TiN/ZrN multi-layered coatings. Journal of Materials Processing Technology 92-93, (1999), p. 177 – 183.

[9] Y.Tamura et al., Mechanical properties of surface nitrided titanium for abrasion resistant implant materials. Materials Transactions, vol 43 (12), (2002), p. 3043 – 3051.

[10] D. K. Boampong, The wear behaviour of ion implanted biomaterials. 2003. 276 p. Tese, Durham University. Reino Unido.

[11] K.L. Rutherford, I.M. Hutchings, A micro-abrasive wear test, with particular application to coated systems. Surface & Coatings Technology, 79, (1996), p. 231 – 239.

[12] Y.Kusano, K. Van Acker, I.M. Hutchings, Methods of data analysis for the micro-scale test on coated systems. Surface & Coating Technology, 183, (2004), p. 312 - 327

[13] R. I. Trezona, D. N. Allsopp, I. M. Hutchings, Transitions between two-body and three-body abrasive wear: influence of test conditions in microscale abrasive wear test. Wear, 225 – 229, (1999), p. 205 – 214.

[14] E. T. Galvani, Obtenção de revestimentos de nitreto de titânio por meio de deposição física de vapores em ligas de titânio obtidas por metalurgia do pó. 2011. 218p. Tese, Instituto Tecnológico da Aeronáutica. Brasil.

[15] L.M. Gammon, et al. Metallography and microstructures of Titanium and its alloys, *Metallography and Microstructures,* Vol 9, *ASM Handbook*, ASM International, 2004, p. 899–917.

[16] M.G.Gee et al., Progress towards standardization of ball cratering. Wear, 255, (2003), p. 1-13.

[17] W.F. Ho, et al. Structure, mechanical properties and grindability of dental Ti-Zr alloys. Journal of Materials Science: Materials in Medicine, 19, (2008), p. 3179 – 3186.

[18] http://www.infomet.com.br/metais-e-ligas-conteudos.php?cod_tema=10&cod_secao=14&cod_assunto=93, acessed on 06/10/2013.

[19] R. B. Boyer, Titanium and titanium alloys: metallographic techniques and microstructure. *Metallography and Microstructures,* Vol 9, *ASM Handbook*, ASM International, (1992), p. 968–975.

[20] I. Wadsworth, D. B Lewis, G. Williams, Structural studies of TiN/ZrN multilayer coating deposited by physical vapour deposition. Journal of Materials Science, 31, (1996), p. 5907 – 5914.

[21] O. B. Soroka, S. A. Klymenko, Evaluation of residual stress in PVD coating. Part 2. Strength of Materials, 42 (4), (2010), p. 450 – 458.

[22] J.A. Ortega-Saenz et al., Comparison of wear processes of biomaterials used in hip joint implants. Scientific Problems of Machine Operation and Maintenance, 4 (156), (2008), p. 15 – 26.

Advanced Materials Research Vol. 936 (2014) pp 1066-1070
© (2014) Trans Tech Publications, Switzerland
doi:10.4028/www.scientific.net/AMR.936.1066

Preparation and Tribological Property Of Novel Self-Assembled Composite Films On Silicon

Shu-Hua Teng[1, a], He Pan[2, b]

[1]School of Materials Science and Engineering, China University of Mining and Technology, Xuzhou 221116, China

[2]Xuzhou Technician College, Xuzhou 221151, China

[a]email: shteng425@qq.com, [b]email: sideno311@163.com

Keywords: Self-assembly; Deposition; Composite films; Multilayer structure; Tribological property

Abstract: Self-assembled composite films of APTES-GA-APTES were successfully prepared on single-crystal silicon substrates through the cross-linking reaction between glutaraldehyde (GA) and two layers of 3-aminopropyltriethoxysilane (APTES). The optimal time to deposit the GA layer on the APTES monolayer was 3 h, during which most amino groups of APTES reacted with the aldehyde groups of GA to form smooth and uniform APTES-GA composite films. The further deposition of another APTES layer led to the generation of three-layer APTES-GA-APTES composite films. Compared to the APTES self-assembled monolayers, the three-layer films displayed a similar surface morphology but a reduced friction coefficient from 0.23 to 0.15 and an extended wear life from 50 s to 820 s due to the introduction of GA.

Introduction

Self-assembled monlayers (SAMs) have gained growing interest over the past few decades due to their effectiveness in improving the reliability and stability of the microelectromechanical systems (MEMS) by reducing friction and adhesion on the surface of the devices [1,2]. Silicon is the basically used material for most electromechanical components. However, silicon is not a good tribological material because of its high friction, adhesion and wear during sliding. Therefore, various types of SAMs have been constructed on silicon to improve their tribological properties [3-5], among which 3-aminopropyltriethoxysilane (APTES) SAMs have been extensively studied [6,7]. Nevertheless, despite the low friction coefficient, the APTES SAMs exhibit poor antiwear and load-carrying capacities, which will greatly limit their promising applications in the lubrication of MEMS [8].

The durability and load-carrying capability of the organic monolayers can be significantly enhanced by constructing self-assembled multilayer films [9,10]. The high activity of the amino groups (-NH_2) of the APTES molecules makes it possible to prepare APTES-based multilayer films by further chemically adsorbing another molecular layer onto the amino-terminated surface of the APTES SAMs [11-13]. In this study, glutaraldehyde (GA) was chosen for the first time as a cross-linker to prepare the APTES-GA-APTES composite films via the reaction between the amino and aldehyde groups. It is expected that the chemical bonding between GA and two layers of APTES would generate stable multilayer films with improved tribological properties as compared to the APTES SAMs.

Experimental Procedure

The preparation of APTES SAMs was performed according to the method reported in the literature [8]. Briefly, the P-type polished (100) Si wafers were sufficiently cleaned and then hydroxylated in a piranha solution (7:3 volume ratio of concentrated H_2SO_4 and 30% H_2O_2) at 90°C for 30 min. After being rinsed with distilled water and dried, the wafers were immersed in the freshly prepared toluene solution containing 1 mM APTES (99%, Sigma-Aldrich) for 30 min. Then, the wafers were taken out and ultrasonically washed, followed by thermal treatment at 100°C for 1 h to generate stable APTES

SAMs. Subsequently, the Si substrates modified by APTES SAMs were placed in an aqueous solution of 0.5% (w/w) GA for several hours. After being ultrasonically washed with distilled water and dried, the substrates were heat-treated at 100°C for 1 h to allow the formation of the dual-layer APTES-GA films. Finally, the three-layer APTES-GA-APTES films were obtained by immersing the APTES-GA films in 1 mM APTES-toluene solution and following the same procedure for the preparation of the APTES SAMs.

The surface morphology of the films was observed in tapping mode with an atomic force microscope (AFM, Nanoman VS), and their surface roughness was also evaluated. The chemical states of the elements on the film surface were detected by X-ray photoelectron spectroscopy (XPS, Thermo ESCALAB 250Xi). The tribological behaviors of the films were investigated in a ball-on-plate contact configuration using a tribometer (UMT-2MT). The films coated on silicon slid reciprocally against Si_3N_4 balls (φ 4 mm). The sliding speed, normal load and sliding distance were kept constant at 2 mm/s, 0.2 N and 5 mm, respectively. The friction coefficient-versus-time curves were recorded automatically.

Results and Discussion

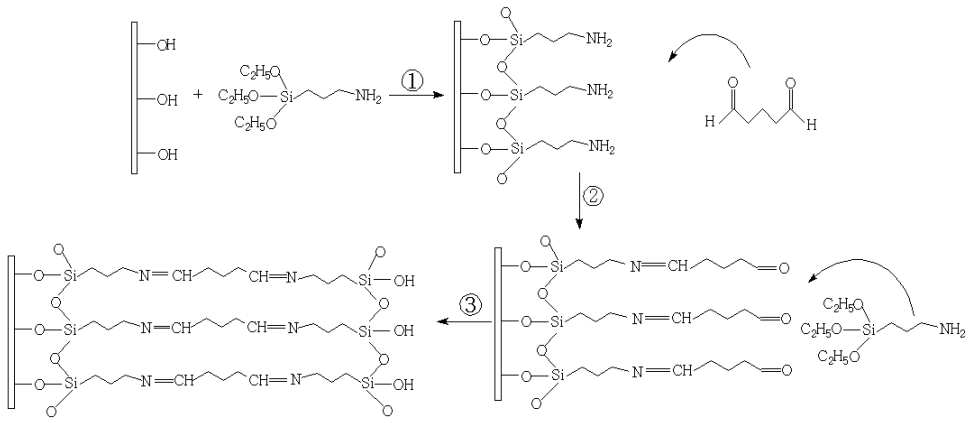


Fig. 1 Schematic diagram of the formation of the APTES-GA-APTES composite films.

Figure 1 schematically shows the formation of the APTES-GA-APTES composite films on Si (110) substrates. Firstly, the APTES SAMs were deposited on the silicon surface through a self-assembly process, as illustrated in step 1. Secondly, the GA layer was chemically grafted to the surface of the APTES SAMs via the reaction between the amino groups of APTES and the aldehyde groups of GA, which led to the formation of the APTES-GA composite films (Step 2). Finally, another APTES monolayer was chemically adsorbed onto the aldehyde-terminated surface and polymerized to attain the APTES-GA-APTES composite films (Step 3). In brief, a novel three-layer film of APTES-GA-APTES was successfully constructed on silicon through a multistep self-assembly process.

Figure 2 shows a series of AFM images taken at various deposition stages of films. It can be observed from Fig. 2(a) that the surface of the APTES SAMs were rough with an average roughness of about 0.951 nm over a scanning area of 10 × 10 μm^2. The film surface seemed still rough after reacting with GA for 1 h (Fig. 2(b)), whereas it became quite smooth and homogeneous after reacting for 3 h (Fig. 2(c)). However, a further prolongation of the reaction time to 5 h led to an increased surface roughness (Fig. 2(d)). The average surface roughness over a 10 × 10 μm^2 area was 0.657, 0.380 and 0.515 nm for the APTES-GA composite films obtained by reacting with GA for 1, 3 and 5 h, respectively. Therefore, it could be suggested that the best time to form the GA layer on the APTES monolayer was 3 h, during which most amino groups of APTES reacted with the aldehyde groups of GA to generate the APTES-GA films with the lowest surface roughness. When the reaction time was

further extended, the remaining GA molecules in the solution might be deposited disorderly onto the smooth GA layer via physical absorption, thereby increasing the surface roughness.

After reacting with GA for 3 h, the substrates were once again immersed in the APTES solution to prepare the APTES-GA-APTES composite films. As shown in Fig. 2(e), the films presented a similar surface morphology to the APTES SAMs (Fig. 2(a)), with the average roughness of 0.786 nm which was slightly lower than that of the APTES SAMs but higher than that of the APTES-GA composite films. These results indicated that a second layer of APTES was successfully formed on the Si substrates by self-assembly.

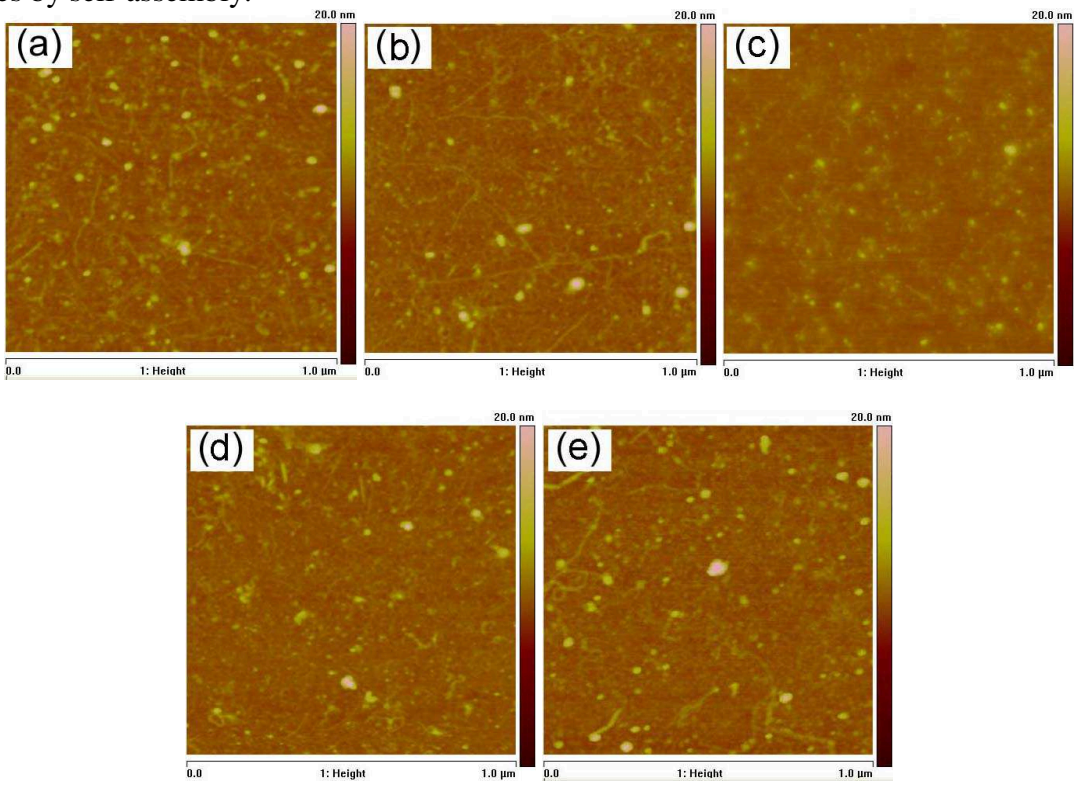


Fig. 2 AFM images of different types of the self-assembled films: (a) APTES SAMs; APTES-GA films obtained by reacting with GA for (b) 1 h, (c) 3 h and (d) 5 h; (e) APTES-GA-APTES films.

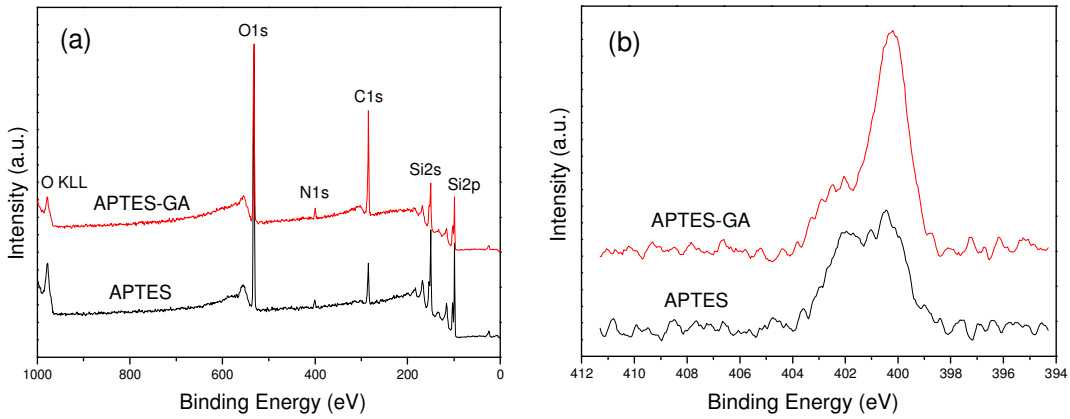


Fig. 3 XPS spectra of APTES SAMs and APTES-GA films: (a) survey scan and (b) N1s regions.

The XPS spectra of the APTES SAMs and APTES-GA composite films were presented in Fig. 3. It could be found in Fig. 3(a) that, except the intensity increase of the C1s and O1s peaks, the APTES-GA composite films displayed almost the same spectrum with the APTEM SAMs. This was because the deposition of the GA layer on the APTES SAMs did not introduce any new elements, but enhance considerably the contents of the C and O elements existing in the films. Furthermore, with the formation of the GA layer on the APTES SAMs, three peaks of N1s positioned at approximately

400.4, 401.0 and 402.0 eV were replaced by a single strong peak at 400.1 eV corresponding to the C=N bonds [14] (Fig. 3(b)). It was inferred that most amino groups remaining on the APTES SAMs had formed a Schiff-base linkage with the aldehyde groups of GA.

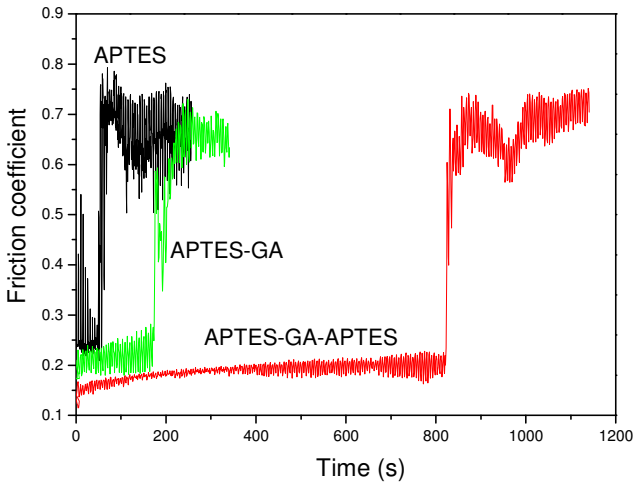


Fig. 4 Curves of friction coefficient vs. time for different types of self-assembled films.

The friction coefficient versus time curves of the self-assembled films were illustrated in Fig. 4.

It was assumed that the lubrication failure of the films occurred when the friction coefficient rose abruptly to a stable value of about 0.7 (a typical value of friction coefficient for the silicon wafer). As shown in Fig. 4, the APTES SAMs revealed a low friction coefficient of ~0.23, but they were easily destroyed in ~50 s under a load of 0.2 N. After being modified with GA, the APTES-GA films exhibited a friction coefficient of about 0.20 and an antiwear life about 170 s, slightly superior to the APTES SAMs. Furthermore, the APTES-GA-APTES composite films displayed a greatly improved tribological properties characterized by a much lower friction coefficient of about 0.15 and a greatly longer antiwear life over 820 s, as compared to both the APTES SAMs and the APTES-GA films.

The remarkable increase in the wear-resistance ability of the APTES-GA-APTES films might be mainly correlated with their stable multilayer structure. As discussed above (Fig. 1), the APTES-GA-APTES films were formed by the cross-linking reaction of GA with the two layers of APTES. Thus, the interlayer combinations of the films as well as the adhesion to the Si substrates were all accomplished by the chemical bonding, which will contribute to the enhancement of the mechanical stability and wear-resistance capacity of the films. In addition, the multilayer structure of the APTES-GA-APTES films permitted the transfer of the films from the Si substrates to the surface of the Si_3N_4 balls after the outer APTES layer was destroyed. It was desirable that the transfer film efficiently improve the tribological properties of the films by reducing the friction and wear.

Conclusions

In this study, a multistep self-assembly strategy was proposed to deposit the APTES-GA-APTES composite films on the single-crystal silicon substrates via the reaction between the amino and aldehyde groups. The composition, morphology and tribological properties at various stages of the film preparation were investigated. The results showed that the APTES-GA dual-layer films with a smooth and uniform surface were obtained after depositing the GA layer for 3 h. The further deposition of another APTES layer led to the generation of the three-layer APTES-GA-APTES composite films which displayed a similar surface morphology to the APTES SAMs. Moreover, as compared to the conventional APTES SAMs, the three-layer films possessed a greatly improved tribological properties characterized by a much lower friction coefficient and a greatly longer antiwear life, thus potentially more suitable for the MEMS applications.

Acknowledgements

The authors are grateful to the Fundamental Research Funds for the Central Universities (No. 2011QNA06), the Natural Science Foundation of Jiangsu Province of China (No. BK20130173), the National Natural Science Foundation of China (No. 51303207) and the Vital Foundational 973 Program of China (No. 2011CB707603) for financial support.

References

[1] E. Gnecco, E. Meyer, Fundamentals of Friction and Wear on Nanoscale, 1st ed. Springer, Heidelberg, 2007.

[2] L.H. Xu, Z.D. Zhou, S.H. Teng, L. Jiang, J.L. Liu, Interfacial properties and tribological behavior of 3-mercaptopropyltrimethoxysilane self-assembled film, J. Dispersion Sci. Technol. 33 (2012) 1093-1096.

[3] H.S. Ahn, P.D. Cuong, S. Park, Y.W. Kim, J.C. Lim, Effect of molecular structure of self-assembled monolayers on their tribological behaviors in nano- and microscales, Wear 255 (2003) 819-825.

[4] Y.Cheng, B. Zheng, P. Chuang, S. Hsieh, Solvent effects on molecular packing and tribological properties of octadecyltrichlorosilane films on silicon, Langmuir 26 (2010) 8256-8261.

[5] T. Bai, X.H. Cheng, Investigation of the tribological behavior of 3-mercaptopropyl trimethoxysilane deposited on silicon, Wear 261 (2006) 730-737.

[6] Q. Gu, X. Cheng, Tribological behaviors of self-assembled 3-aminopropyltriethoxysilane films on silicon, Curr. Appl. Phys. 8 (2008) 583–588.

[7] J. Li, X.Z. Li, The preparation and tribological characteristics of phosphorylated 3-aminopropyltriethoxysilane self-assembeld film, Appl. Surf. Sci. 255 (2009) 6159-6163.

[8] H. Pan, S.H. Teng, C.C. Ding, Preparation and tribologcial properties of self-assembled composite films on silicon surface, Acta Phys.-Chim. Sin. 28 (2012) 917-922.

[9] J.Q. Ma, C.J. Pang, Y.F. Mo, M.W. Bai, Preparation and tribological properties of multiply-alkylated cyclopentane (MAC)-octadecyltrichlorosilane (OTS) double-layer film on silicon, Wear 263 (2007) 1000-1007.

[10] B. Yu, L. Qian, J. Yu, Z. Zhou, Effect of tail group and chain length on the tribological behaviors of self-assembled dual-layer films in atmosphere and in vacuum, Tribol. Lett. 34 (2008) 1-10.

[11] J. Zhao, M. Chen, J. Liu, F. Yan, Preparation and tribological studies of self-assembled triple-layer films, Thin Solid Films 517 (2009) 3752-3759.

[12] Y. Mo, M. Zhu, M. Bai, Preparation and nano/microtribological properties of perfluorododecanoic acid (PFDA)-3-aminopropyltriethoxysilane (APS) self-assembled dual-layer film deposited on silicon, Colloids Surf. A 322 (2008) 170-176.

[13] J. Ou, J. Wang, S. Liu, J. Zhou, S. Yang, Self-Assembly and tribological property of a novel 3-layer organic film on silicon wafer with polydopamine coating as the Interlayer, J. Phys. Chem. C 113 (2009) 20429-20434.

[14] H. Mineo, H. Masaru, Carbon nanowalls: synthesis and emerging applications. 1st ed. Springer, Wien, 2010.

Advanced Materials Research Vol. 936 (2014) pp 1071-1076
© (2014) Trans Tech Publications, Switzerland
doi:10.4028/www.scientific.net/AMR.936.1071

Study on the BTSPS Silane Film prepared on the Surface of the 2A12 Aluminum Alloy

Longjiang Peng[1,a], Shaohui Chen[2,b], Yingning Feng[3,c] and Tianyi Li[*4,d]

[1,3,4]School of Chemical Engineering, ChangChun University of Technology, Changchun, China

[2]COFCO Corporation, China

[a]firedragon2011@126.com,[b]chenshaohui@cofco.com,[c]FYN18633089537@163.com,

[d]litianyi@mail.ccut.edu.cn. *correspondence author

Keywords: 2A12 Aluminum Alloy, Corrosion Protection, Silane Film, Surface Treatment

Abstract: The protective silane film BTSPS was prepared on the surface of 2A12 aluminum alloys by dip-coating method in this paper. The influence factors such as the volume fraction, hydrolysis time, hydrolysis temperature and dip-coating time of BTSPS were studied through orthogonal experiment. The optimum conditions is: the volume fraction is 5%; hydrolysis time is 180min; Hydrolysis temperature is 20℃; Dipping time is 10 min. The silane film performance was investigated by electrochemical test, sodium chloride solution immersion and scanning electron microscope (SEM). The results show that the corrosion resistance of the 2A12 aluminum alloy coated with BTSPS is improved greatly.

Introduction

The 2A12 aluminum alloy is a kind of high-strength aluminum alloy.It is extensively used in making all kinds of parts that can support high load and components (but not including stamping forgings),such as the frame part,skin,frame,ribs,wing beam,rivets and other parts which work under 150℃.However,its corrosion resistance is weak, so its surface must be pretreated before application generally. Traditionally, industrial phosphating and chromate passivation process was applied in large-scale . Although the anticorrosion effect by such a pretreated process is good, but it will cause serious environmental pollution problems .

With the improvement of the public awareness of environmental protection and environmental requirements , the development of environment -friendly metal surface pretreatment and corrosion protection technology instead of the traditional phosphating and chromate passivation process has become more and more urgent. Organosilane treatment is a new type of surface protection technology compared with traditionally Large-Scale application of phosphating and chromium passivation process. It has the advantages of energy-saving, environment friendly, and low cost. However,the silanated effect is not as well as phosphating and chromate passivation currently.

Therefore,how to study the best film-forming process of the silane processing completely instead of toxic and hazardous phosphide chromate passivation process has very important significance.

The studies[1,2,3,4] showed that the dual silane has a greater advantage in the protection of the metal.This paper chose bis-[3-(triethoxysilyl)propyl]tetrasulfide (BTSPS),and the formula is $(H_5C_2O)_3Si(CH_2)_3S_4(CH_2)_3Si(OC_2H_5)_3$, it can inhibit zinc, aluminum and its alloy[5,6], magnesium [7], copper, galvanized steel[8], hot dipping steel[9] and all kinds of metal corrosion. Although some literatures have researched on BTSPS[10~11], but did not introduce the hydrolysis process and the film-forming process.

This article obtained the optimum conditions for BTSPS film preparation on the 2A12 aluminum alloy surface .The results show that it presents good anticorrosion performance throughout the experiments and corrosion test.

Experimental

Materials

Silane coupling agent(BTSPS), used as coupling agent in the research, was purchased from Anhui Xiangfei Lipai Organosilicon New Material Co., Ltd.,China. acetone(analytically pure), supplied by Beijing north Fine Chemicals Co., Ltd.,China,was used as oil cleaning agent.deionized water(homemade),Anhydrous ethanol(analytically pure),supplied by Tianjin Tiantai Fine Chemicals Co., Ltd.,China,was used as the solvent for dissolving silane. Sodium chloride solution and all other chemicals used were of analytical reagent grades.

Instruments

DDS-11 Conductivity Meter,used for measuring the electrical conductivity of silane solution,were obtained from Tianjin second analytical instrument factory, China.DF-101S Collector-type magnetic stirrer was purchased from Jintan Scientific Analytical Instruments Co., Ltd.,China. 501 super thermostat,supplied by Shanghai Experimental Instrument Co., Ltd.,China.KH-700B CNC ultrasonic cleaning instrument was purchased from Kunshan Hechuang Ultrasonic Instrument Co., Ltd.,China.CHI-660D electrochemical workstation was purchased from Shanghai Chen Hua Co., Ltd.,China.DZF-6050 vacuum oven supplied by Shanghai JingHong Experimental Equipment Co., Ltd.,China.And some other commonly used laboratory instruments.

Experimental Procedure

2A12 aluminum alloy surface pretreatment.Concrete steps: polished by fine sandpaper→washed twice with distilled water→ultrasonically cleaned in acetone(65 to 70℃,10min)→ultrasonically cleaned in methanol(60 to 65℃, 15min)→washed twice with deionized water
→drying with vacuum oven→reserve.

Preparation of silane films by the dipping method. Aluminum alloy specimen fully immersed into the hydrolysis of the silane solution,uniform velocity ,removed after a certain time,residual liquid dried by hair dryer,placed it in a vacuum oven, curing and forming.

The hydrolysis solution configurated by BTSPS,ethanol,deionized water with the proportion of 5:5:90, and fully stired 3h in the collector magnetic stirrer, the electrodes of the conductivity meter is inserted into the hydrolysis solution, and detected the conductivity of the solution online. Then the metal substrate is immersed in the hydrolysis solution with 6 min, 8 min, 10 min, 12 min and 14min respectively. The polarization resistance values of each group have been tested by electrochemical workstation.

Results and discussion

The Experimental Results to Discuss.

The Impact of BTSPS Volume Fraction and the Hydrolysis Time

As shown in Fig. 1, when BTSPS volume fraction is 1~5%, hydrolysis time is 2~4h, the conductivity of solution no longer changes, indicating that the solution has stabilized; and when the volume fraction is 7~9%, the conductivity is still changing after it reaches the maximum value, indicating that the solution is unstable. Therefore, in the BTSPS hydrolysis process, the volume fraction should be between 1~5%, and the hydrolysis time should be 2~4h.

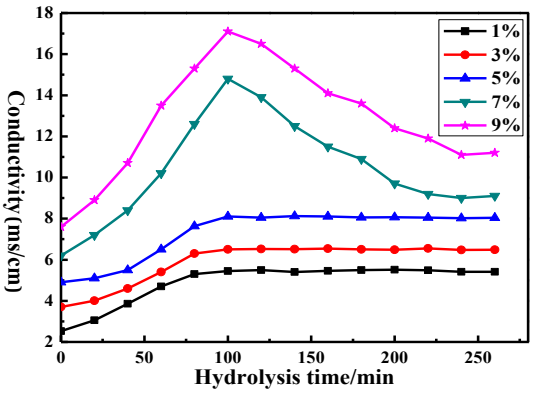


Fig.1 Variation diagram of conductivity with time under different BTSPS volume fraction

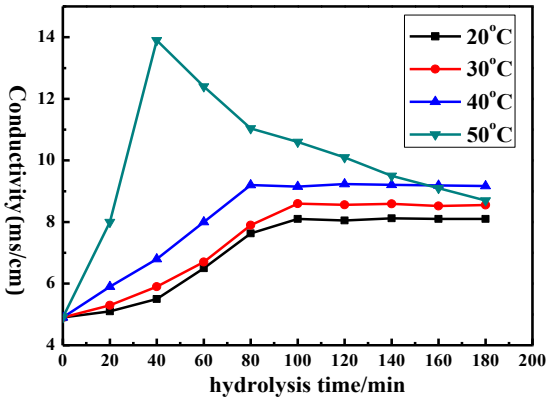


Fig.2 Variation diagram of conductivity with time under different hydrolysis temperature

The Impact of Hydrolysis Temperature

As can be seen from Fig. 2, the higher temperature, the shorter time to achieve the highest conductivity value, but when the temperature was 50℃, the solution is very unstable. And when the temperature is 20~40℃,the solution basically stabilizes after hydrolysis time is more than 2h. Therefore, in the BTSPS hydrolysis process, the optimal hydrolysis temperature should be from 20℃ to 40℃.

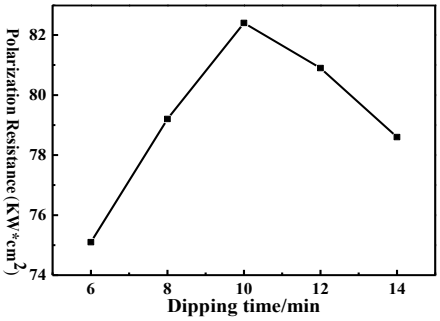


Fig.3 Variation diagram of polarization resistance with dipping time

Dipping Time of the Substrate in BTSPS Solution

As can be seen form Fig. 3, when the dipping time is 8min, 10min and 12min,the anticorrsion effects of the silane films prepared is better than the other two groups. Therefore, in the process of BTSPS film, the optimum dipping time for the metal material in the hydrolysed solution is 8~12min.

Orthogonal Analysis

The analysis results using by the orthogonal experiment software were shown in the following table

TABLE 1 ORTHOGONAL EXPERIMENTAL DESIGN

Factors / E[n]	The silane Volume Fraction[%]	Dipping Time[min]	Hydrolysis Temperature[℃]	Hydrolysis Time[min]	The Experimental Results
E1	1	8	20	60	72.9
E2	1	10	30	120	78.2
E3	1	12	40	180	85.2
E4	3	8	30	180	104.5
E5	3	10	40	120	128.3
E6	3	12	20	60	120.3
E7	5	8	40	120	100.1
E8	5	10	20	180	105.6
E9	5	12	30	60	112.8

MV 1	145.433	159.168	336.933	70.333	
MV 2	217.700	274.700	197.500	99.533	
MV 3	375.833	205.100	104.533	269.300	
ED	258.133	155.533	232.400	170.800	
E:Experiment		MV: Mean Value		ED: Extreme difference	

As can be seen from the table 1, the sequence of influence on the performance of the BTSPS film is: the volume fraction of BTSPS>hydrolysis temperature>hydrolysis time>dipping time.

By the mean size can be seen:

The Best Volume Fraction of BTSPS is 5%

If the volume fraction of BTSPS is too low, the silane molecule adsorbed on the aluminum alloy surface will be few,the film thickness will be thiner, the corrosion resistance of the obtained silane film is poor.

The Best Dipping Time is 10min

The dipping time is shorter, the film formation time is shorter and film corrosion resistance is poorer; The dipping time is longer, it will not increase the corrosion resistance of the film, instead it will deteriorate the performance of the film.

The Best Hydrolysis Temperature is 20℃

The hydrolysis reaction of BTSPS is an exothermic reaction, the condensation is an endothermic reaction, if the temperature is too high, it will inhibit the hydrolysis reaction and promote the condensation reaction. Thereforea lot of silane condense silicone that is not conducive to formate the silane film.

The Best Hydrolysis Time is 180min

If the hydrolysis time is too short, and the number of silanols in the hydrolysis solution will be few, the formed film will be thin, and the corrosion resistance of film is poor.

The Corrosion Resistance of Silane Film on the Substrate Surface

Electrochemical Tests

The substrates were used as working electrode, a saturated calomel electrode(SCE) and a platinum mesh were used as the reference and counter electrodes respectively. and electrochemical tests have been conducted using the integrated test system for electrochemical workstation.The eletrolytic solution is a solution of 3.5% NaCl (mass fraction); the scan rate applied here was 10 mV/s; the sample test area approximately 6 cm^2.

First of all, the resulting polarization curves were used for qualitative analysis using the logarithmic of corrosion current density lg(i_{corr}, A/cm^2) as Ordinate and the corrosion potential (E_{corr}, mv) as abscissa.

As can be seen from Fig.4 that the polarization curves of black experimental group have been moved to the right significantly, and show that the corrosion resistance of the material of the experimental group improved greatly than blank group[12].

Then, the polarization resistance value obtained using an electrochemical test software is used to quantitative analysis the corrosion resistance of material coated with BTSPS film. The polarization resistance value obtained in experimental group is 156.8KΩ·cm^2, and the polarization resistance value of blank group is 1.9KΩ·cm^2, the polarization resistance of experimental group is 82 times of blank group. It's show that the corrosion resistance of material in the experimental group have been improved greatly.

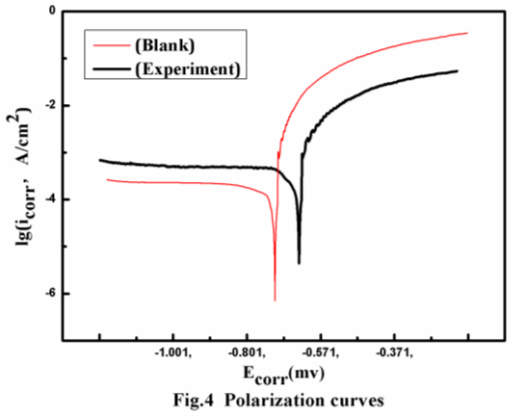


Fig.4 Polarization curves


Fig. 5 Effect diagram of experimental samples were soaked

Immersion Test

Researchers often used seawater or sodium chloride solution immersion test in the study of metal protection intuitive to understanding of the corrosion resistance of the materials[13]. The experimental samples were soaked in 5 mol/L sodium chloride solution for 7 days in this work. As shown in Fig. 5.

In Fig 5, the left part of the aluminum plate was coated with a silane film, while the right part of baseplate was uncoated. It can be seen that the corrosion of the right part of the baseplate was obvious, while that of the left part was slight after soaked in sodium chloride solution, This indicates that the silane film can significantly enhance the corrosion resistance of aluminum alloy.

Detection of SEM

In order to further describe the corrosion resistance of the experimental group of material qualitatively, blank and experimental groups material before and after the immersion test were observed by SEM. As shown in Fig. 6.

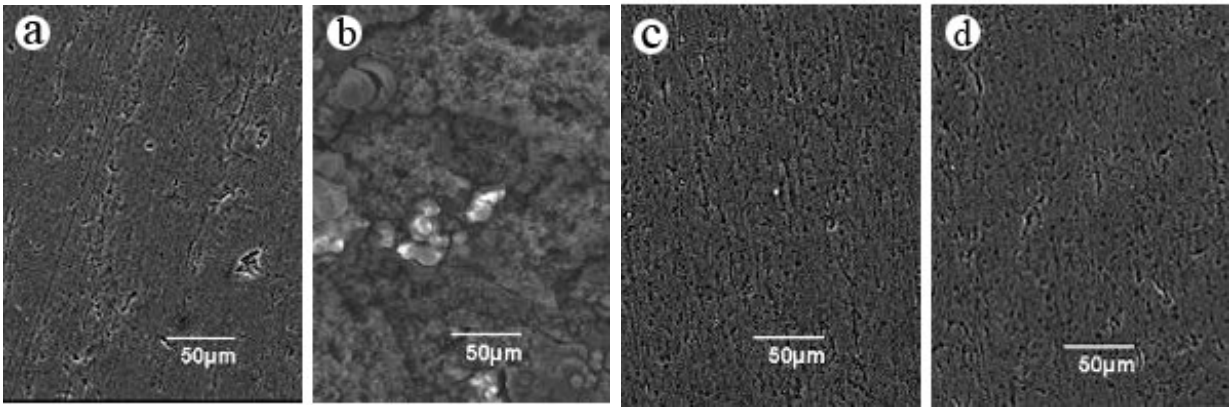


Fig.6 SEM Images

In Fig. 6, Fig. a and Fig. b represent the blank group before and after immersion test respectively, and Fig. c and Fig. d represent the experimental group before and after immersion test respectively. Compared fig. a with fig. c, it can be seen that the surface of material exist scratches and small gaps before treated with the silane; while become smooth and uniform after treated with the silane. In fig. b, the surface of the blank group have been damaged severely after immersion with 7 days; but fig. d shows that no significant changes on the surface of the experimental group before and after the immersion test.

Conclusions

The following conclusions obtained through the above experiment:

Obtained BTSPS hydrolysis conditions after conductivity experiment:the volume fraction is 1%~5%; hydrolysis time is 2~4h; hydrolysis temperature is 20~40℃.

The single-factor tests of BTSPS film dipping time result show that the dipping time is 8~12 min.

The optimum conditions for preparation of BTSPS film obtained through orthogonal experiment: the volume fraction is 5%; dipping time is 10 min; hydrolysis temperature is 20℃; hydrolysis time is 180min.

After electrochemical test,immersion test and SEM experiment,We can see BTSPS film prepared under the optimum conditions rapidly improved the corrosion resistance of the material.

References

[1] Subramanian V, W.J. van Ooij, Effect of the Amine Functional Group on Corrosion Rate of Iron Coat with Films of Organofunctional Silanes, Corrosion. 54 (1998) 204-215.

[2] Subramanian V,W.J. van Ooij, Silane based Metal pretreatments as Alternatives to Chromating,Surface Engineering. 15 (1999) 1-5.

[3] Zucchi F, Grassi V, Frignani A, et al, Inhibition of copper corrosion by silane coatings, Corrosion Science. 46 (2004) 2853-2865.

[4] Susac D, Leung C W, Sun X, Comparison of a chromic acid and BTSE final rinse applied to phosphated 2024-T3 aluminum alloy, Surface and Coatings Technology. 187 (2004) 216-224.

[5] Vignesh Palanivel, D. Zhu, W.J. van Ooij, Nanoparticle-filled silane films as chromate replacements for aluminum alloys, Progress in Organic Coatings. 47 (2003) 384-392.

[6] A.Cabral, R.G.Duarte, M.F. Montemor, Analytical characterisation and corrosion behaviour of bis-[triethoxysilylpropyl]tetrasulphide pre-treated AA2024-T3, Corrosion Science. 47 (2005) 869-881.

[7] M.F. Montemor, M.S.G Ferreira, Electrochemical study of modified bis-[triethoxysilylpropyl] tetrasulfide silane films applied on the AZ31 Mg alloy, Electrochimica Acta. 52 (2007) 7486-7495.

[8] Sundararajan G P,W.J. van Ooij, Silane based pretreatments for automotive steels, Surface Engineering. 16 (2000) 315-320.

[9] M.S.G Ferreira, R.G.Duarte, M.F. Montemor, Silanes and rare earth salts as chromate replacers for pretreatments on galvanised steel, Electrochim Acta. 49(2004) 2927-2935.

[10] D. Zhu, W.J. van Ooij, Corrosion protection of AA 2024-T3 by bis-[3-(triethoxysilyl)propyl] tetrasulfide in neutral sodium chloride solution, Part 1: corrosion of AA 2024-T3, Corrosion Science. 45 (2003) 2163-2175.

[11] D. Zhu, W.J. van Ooij, Corrosion protection of AA 2024-T3 by bis-[3-(triethoxysilyl)propyl] tetrasulfide in sodium chloride solution, Part 2: mechanism for corrosion protection, Corrosion Science. 45 (2003) 2177-2197.

[12] C.N. Cao, Principles of Electrochemistry of Corrosion, third ed., Chemical Industry Press,Beijing 2008.

[13] D. Zhu, W.J. van Ooij, Corrosion protection of metals by water-based silane mixtures of bis-[trimethoxysilylpropyl]amine and vinyltriacetoxysilane, Progress in Organic Coatings. 49 (2004) 42-53.

Advanced Materials Research Vol. 936 (2014) pp 1077-1081
© (2014) Trans Tech Publications, Switzerland
doi:10.4028/www.scientific.net/AMR.936.1077

Hydrophobicity of Beeswax-chitosan Latex Coated Paper

Weiwei Zhang[1,2,a], Liying Qian[1,b], Huining Xiao[1,2,c*]

[1.] State Key Laboratory of Pulp and Paper Engineering, South China University of Technology, Guangzhou, Guangdong, 510640, China

[2.] Department of Chemical Engineering, University of New Brunswick, Fredericton, NB, E3B 5A3, Canada

[a]zhangww1166@gmail.com, [b]lyqian@scut.edu.cn, [c]hxiao@unb.ca

Keywords: beeswax-chitosan latex, water vapour transmission rate, contact angle

Abstract: Both water repellency and water vapour barrier properties were endowed at paper surface by coating with beeswax-chitosan latex. It was found that the water vapour transmission rate of coated paper decreased as the drying temperature increased. However, water contact angle was not affected with it. Although the surface morphology deformed at high drying temperature, the roughness values maintained at micro-scale. Further analysis indicated that the water vapour barrier property of coated paper was influenced by the density of the coating layer.

Introduction

As a natural, biodegradable and renewable polymer, chitosan exhibits excellent film-forming properties. Chitosan possesses good mechanical properties, thus its film is tough, long-lasting, flexible and difficult to tear. More than that, excellent gas-barrier (such as oxygen, nitrogen, carbon dioxide[1]) properties are found in chitosan film due to its high crystallinity and hydrogen bonds between the molecular chains[2, 3]. However, because of the same polar groups, chitosan film easily absorbs water or water vapour and the swelled film leads to a loss of the gas barrier properties. Studies of chitosan coatings on paper and paperboard revealed an improved moisture barrier properties but not sufficient for food application[4]. The hydrophilicity of coating surface was too high that its water sorption was found to be greater than the fibre sorption in the base paper[1].

A feasible approach to improve the water or water vapour barrier properties is to combine hydrophobic lipid materials to form composite films in a form of emulsion coating or bilayer coating. Although the water vapour barrier ability of bilayer coating is superior to that of emulsion coating, the later shows better adhesion onto any substrate due to its hydrophilic and lipophilic nature[5]. The coating process can also be carried out at room temperature, which can be applied on fruits and vegetables to extend shelf lives[6].

The objective of this study is to investigate the abilities of water vapour barrier and water repellency of emulsion coated paper. It is the first time to produce beeswax-chitosan latex with beeswax composition over than 90 wt% in the final solid coating layer, so that both high water repellency and water vapour barrier properties are obtained.

Experimental Details

Preparation of Beeswax-chitosan Latex

Beeswax-chitosan latex was produced by melting beeswax (Aldrich, Canada) in chitosan (Aldrich, Canada) solution (glycerol : chitosan = 1:4 in weight ratio) under acidic conditions at 80 ^{o}C. After stirring with magnetic stirrer for 5 min, each mixture solution was homogenized using a high-shear probe mixer (Power Tool X120, Ingenieurbüro CAT, Germany) for 3 min at 28,000 rpm. Upon completion of homogenization, the hot beeswax-chitosan latex was quickly cooled to room temperature in an ice-bath.

Paper Surface Coating

Copy paper (Xerox Corporation, Canada) was coated with beeswax-chitosan latex using K303 Multilayer (RK Print Coat Instruments Ltd, U.K.) with a bar coating speed of 10 m/min and then dried at different temperatures for 2 h.

Characterization

The particle size of beeswax-latex was tested using Brookhaven ZetaPlus zeta potential analyser. The paper weight and thickness was measured before and after coating, respectively. The water repellency was characterized by water contact angle using Attension Theta Optical tensiometer (Finland) and the water vapour barrier property was measured by water vapour transmission rate (WVTR) on IGA-003 (Hiden-Isochema, Warrington, UK) according to TAPPI standard T464 om-12[7]. The morphology of coated paper was determined using AFM (Nanoscope IIIa from Veeco Instruments Inc., Santa Barbara, CA) with a silicon tapping probe (NP-S20).

Results and Discussion

The Effect of Drying Temperature

Under acidic condition, chitosan was considered to be a good emulsifier to prepare stable lipid latex, because of the interaction between positively-charged chitosan with negatively-charged lipids[8]. The particle size of beeswax-chitosan latex ranged from 150 nm to 650 nm and phase separation occurred after standing for more than ten days. This stability of beeswax-chitosan latex was good enough for paper surface coating. The viscoelastic beeswax was proved previously to be more effectively to reduce water vapour permeation (WVP) than carnauba and candelilla wax in whey protein/lipid emulsion film, and the WVP decreased as the fat concentration increased. Here, beeswax composition of the final coating layer was set as high as 96 wt% to investigate the effect of drying temperature on water contact angle and WVTR of coated paper.

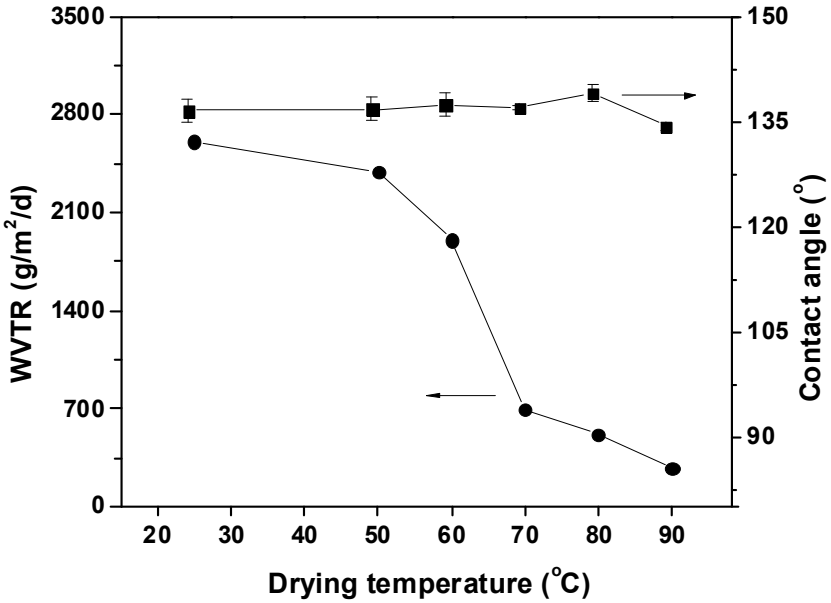


Figure 1. The effect of drying temperature on WVTR and contact angle of chitosan-beeswax coated paper. The beeswax latex was prepared by 1.2 wt% chitosan solution and beeswax composition in the coating layer was 96 wt%.

As seen in Fig. 1, the drying process after coating influenced the water vapour barrier property strongly. The WVTR of latex coated paper reduced from 2610.6 to 273.6 g/m^2/d as the drying temperature increased from 25 to 90 ^{o}C. The degree of viscoelasticity of lipids determined water

vapour resistance property as those viscoelastic lipid droplets might deform, merge and aggregate into network of lipids within the emulsion film[9, 10]. This viewpoint was also certificated by the sharp drop in the WVTR of beeswax-chitosan emulsion coated paper at around 60 °C which was exactly the melting point of beeswax. With drying temperature larger than 60 °C, the enhancement of reduction in WVTR became moderated. An interesting discovering is that the water contact angle of latex coated paper seemed to be almost unaffected by drying temperature, with value of approximate 135°. Since the chemical composition of this surface was same, it could be concluded that surface morphology might be changed slightly during drying process.

Surface Morphology

The AFM height images of different drying temperatures were obtained in an area of 15×15 μm in Fig. 2. Individual beeswax particles distributed over the entire scanning area in the samples dried at room temperature. As the drying temperature increased, beeswax particles began to partially melt to form larger agglomeration. When the drying temperature was higher than its melting point, beeswax particles melted completely to form annular-folds at the surface. The roughness values, Rq, of the beeswax-chitosan coated papers were 614, 876, 969,642, 611, 540 nm, corresponding to drying temperature of 25, 50, 60, 70, 80, 90 °C, respectively. The Rq fluctuated within micro-scale, indicating that the area fraction of the liquid-solid contact was likely unchanged according to Cassie-Baxter model[11] for determining surface wettability.

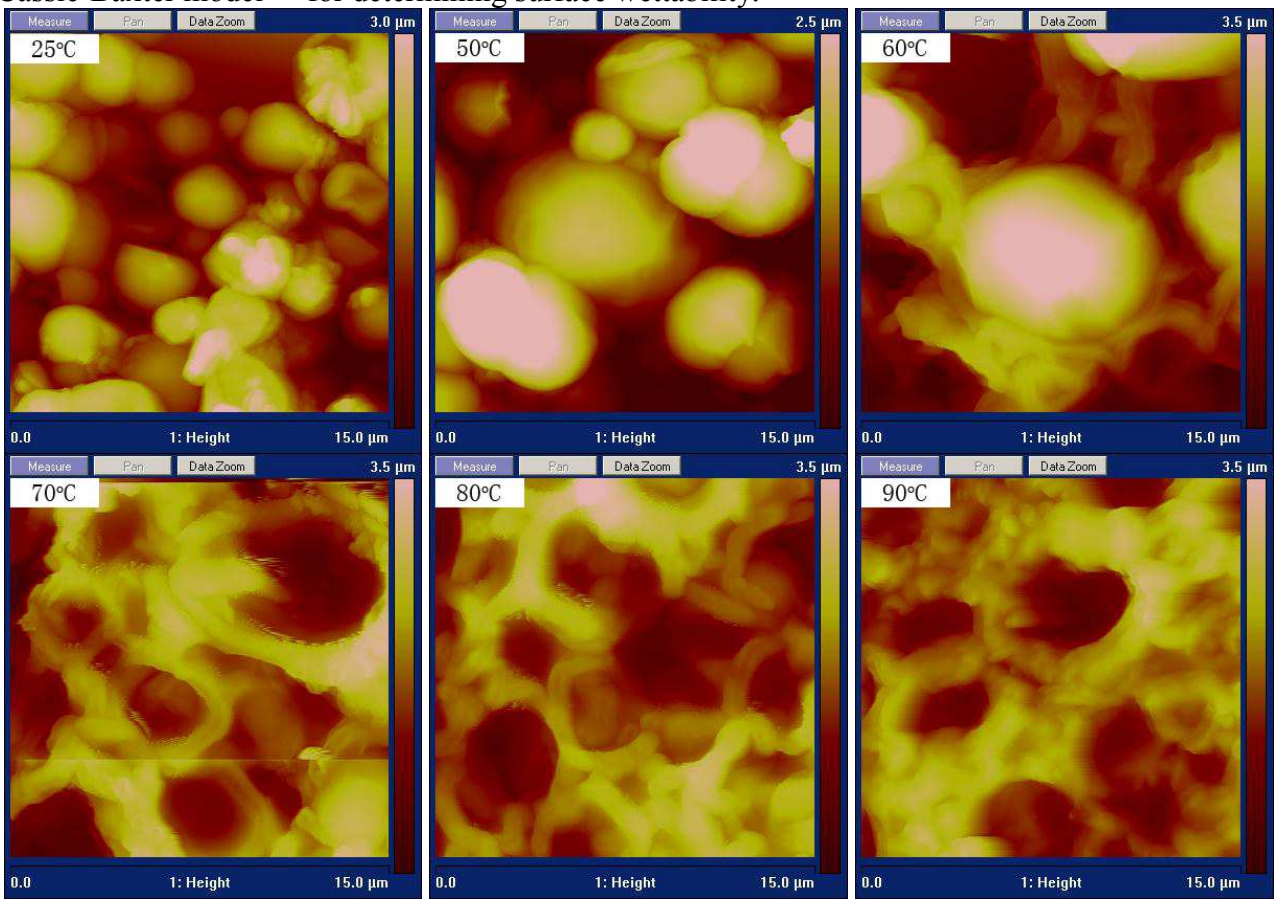


Figure 2. AFM measurements of beeswax-chitosan coated papers at various temperatures.

The Effect of Coating Layer Density

It is a fact that the final barrier properties of coated paper is affected by chitosan concentration, beeswax composition and drying temperature. An indirect factor, coating layer density which was calculated based on the coating weight and thickness, was used to combine these three direct factors together. An interesting relationship between WVTR and density of coating layer was found in Fig. 3. When the density was lower than about 800 kg/m^3, the water vapour resistance property of coated

paper was almost unchanged compared to blank paper. After the turning point, increasing the density of the coating layer correlated with a linear decrease in WVTR of coated paper. The surface and internal structural reconfiguration of beeswax led to the formation of more compact structure which lowered water vapour permeability.

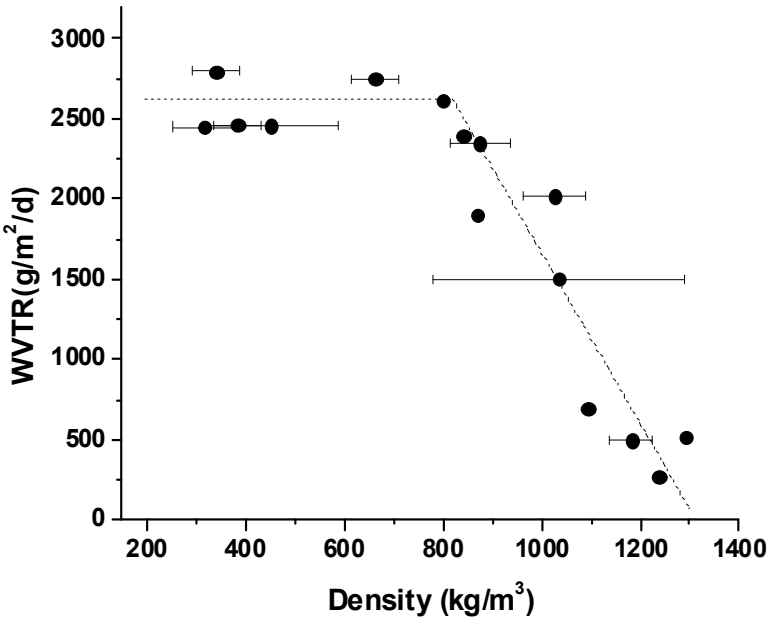


Figure 3. The relationship between WVTR and density of composite coating layer

Conclusion

Hydrophobic paper with low WVTR and high water contact angle was prepared by coating with beeswax-chitosan latex in this study. Water vapour barrier property of emulsion coating was improved through increasing lipid content and drying temperature. It could be explained by deformation and aggregation of lipid within and without of the emulsion coating layer. Although the surface morphology changed, the roughness values fluctuated within micro-scale, which limited the enhancement of water repellence property.

Acknowledgement

Authors greatly thank NSERC Green Wood Fibre Network (Canada), National Science Foundation of China (Grant No. 31200457) and the Fundamental Research Funds for the Central Universities (2013ZZ0072) for funding this project.

References

[1] Kjellgren H, Gällstedt M, Engström G, et al. Barrier and surface properties of chitosan-coated greaseproof paper, Carbohydrate polymers. 65 (2006) 453-460.

[2] Kittur F S, Kumar K R, Tharanathan R N. Functional packaging properties of chitosan films, European Food Research and Technology. 206 (1998) 44-47.

[3] Gällstedt M. Packaging related properties of uncoated, coated and laminated whey protein and chitosan films, KTH, 2001.

[4] Bordenave N, Grelier S, Pichavant F, et al. Water and Moisture Susceptibility of Chitosan and Paper-Based Materials: Structure – Property Relationships, Journal of Agricultural and Food Chemistry. 55(2007) 9479-9488.

[5] Khwaldia K, Arab Tehrany E, Desobry S. Biopolymer coatings on paper packaging materials, Comprehensive Reviews in Food Science and Food Safety. 9(2010) 82-91.

[6] Navarro-Tarazaga M L, Sothornvit R, Pe´rez-Gago M B. Effect of Plasticizer Type and Amount on Hydroxypropyl Methylcellulose–Beeswax Edible Film Properties and Postharvest Quality of Coated Plums (Cv. Angeleno), Journal of Agricultural and Food Chemistry. 56(2008) 9502-9509.

[7] Water vapor transmission rate of paper and paperboard at high temperature and humidity, Test Method T 464 om-12. Tappi, 2012.

[8] Jumaa M, Müller B W. Physicochemical properties of chitosan-lipid emulsions and their stability during the autoclaving process, International journal of pharmaceutics. 183(1999) 175-184.

[9] Shellhammer T H, Krochta J M. Whey Protein Emulsion Film Performance as Affected by Lipid Type and Amount, Journal of Food Science. 62(1997) 390-394.

[10] Perez-Gago M B, Krochta J M. Drying temperature effect on water vapor permeability and mechanical properties of whey protein-lipid emulsion films, Journal of agricultural and food chemistry. 48(2000) 2687-2692.

[11] Cassie A, Baxter S. Wettability of porous surfaces, Transactions of the Faraday Society. 40(1944) 546-551.

Advanced Materials Research Vol. 936 (2014) pp 1082-1085
© (2014) Trans Tech Publications, Switzerland
doi:10.4028/www.scientific.net/AMR.936.1082

Research on Cerium Conversion Coating on ZM5 magnesium alloy

ZHU Rong-xia[a,*], GAO Guo-mian and MIAO Zheng

The College of Science, Air Force Engineering University, Xi'an, Shaanxi, China

[a]email:zhx40@sohu.com

Keywords: magnesium alloy, Corrosion resistance, conversion coatings

Abstract. The conversion coating formed by immersion in a solution containing cerium salt on ZM5 magnesium alloy was studied and the corrosion resistance was evaluated as well. These micrographs of specimen surface were investigated by metallographic microscope. The corrosion behaviors of ZM5 magnesium alloy and conversion coating were assessed by means of potentiodynamic polarization curves and immersion tests. The experimental results indicated that a yellow-brown conversion coating was formed subsequently on the specimen surface. The results of electrochemical measurements and immersion tests revealed that the cerium conversion coating possessed better corrosion resistance than the substrate. In this study, cerium conversion coatings formed on ZM5 magnesium alloy were characterized and the formation mechanism was discussed.

Introduction

Magnesium alloys have quite special properties which lead to specific applications. The high strength-to-weight ratio of magnesium alloys makes the alloys extremely attractive for applications requiring light weight, such as applications in transport and aerospace. However, magnesium alloys are still not as popular as aluminum alloys because of their poor corrosion resistance. So, some sort of surface treatments or coating treatments should be applied to magnesium alloys in order to meet the requirement in practical applications.

Among various surface treatments, chemical conversion treatments for magnesium alloys， for example chromate[1], permanganate-phosphate[2], stannate[3], vanadium[4], organic baths[5], phytic[6] and cerium[7], were extensively investigated. The most successful conversion treatment is based on the use of chromates, in which can give rise to contamination by hexavalent ion of chromium and is strictly controlled due to recent environmental legislation in worldwide application. Therefore, new systems, showing environmental friendliness, must be studied and developed. Among of them, cerium chemical conversion coatings for magnesium alloys are considered to be environmentally acceptable.

Experiment

Cerium Conversion Treatment

The treatments described in this study were performed on 30×20×5 mm die cast plates of ZM5 magnesium alloy, with chemical composition (wt%): Al 8.3%, Zn 0.5%, Mn 0.3%, Si 0.25%, Ni 0.01%, Cu 0.1%, Fe 0.08%. A hole of 2 mm in diameter was drilled in the middle of one edge of each specimen for convenient hanging up in the solution during treatments. The chemical conversion on the magnesium alloy was investigated on the specimens using the following sequence of operations:

(1) Surface polished

The surfaces of the specimens were mechanically polished with abrasive paper (grade 360, 600, 1000 and 2000), ultrasonically cleaned in acetone and rinsed with distilled water, then dried by air.

(2) Alkaline cleaning

Sodium hydroxide，25 g/L NaOH，Sodium carbonate，10 g/L Na_2CO_3．Temperature: 343 K，Time: 10 min，Post treatment: Water rinse．

(3) Chemical conversion

Potassium permanganate, 5g/L $KMnO_4$，Cerium chloride, 3g/L $CeCl_3 \cdot H_2O$. Temperature: at room temperature; Time: 30 min; Post treatment: hot air drying.

Coating Characterization

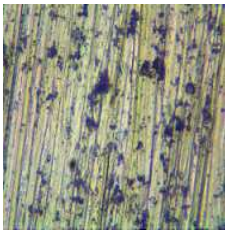
These micrographs of specimen surface were investigated by XJZ2-1A metallographic microscope. The mass of the specimen was measured with a BS210S electronic scale with an accuracy of 0.1 mg**.** The substrate and the conversion coated specimens were immersed in 3.5 wt. % NaCl solution in 96 hours and degree of corrosion of different specimens was observed.

The anticorrosion performance was evaluated by recording the corrosion potential of the specimens in the corrosive medium upon immersion, which was conducted on a CHI660D electrochemical workstation. A classic three electrode system was used, which contained a working electrode (the epoxy-sealed sample with exposed area 1.0 cm^2), a reference electrode (a saturated calomel electrode), and a counter electrode (a platinum foil). The corrosive medium was 3.5 wt. % NaCl solution at room temperature.

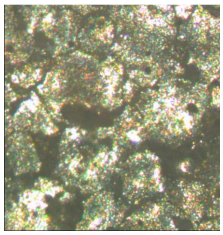
Results and Discussion

Chemical Conversion Coating Morphology

Specimen topography of chemical conversion process is shown in Fig. 1. Fig. 1(a) show that magnesium alloy substrate surface has many tiny holes and processing traces and other defects exist. Fig.1(b) showed that the cerium coating was generated by the cerium conversion treatment and completely covered the surface of the substrate with conversing to 30 minutes.



(a) substrate surface



(b)cerium coating

Fig. 1. Metallographic microscope of specimen

Corrosion Resistance of the Coating

The specimen's macrographs of the substrate and the cerium conversion coating are provided in Fig.2. Compared Fig.2 (a) with Fig.2 (b), it showed that the specimen's surface of the cerium coating has a yellow-brown conversion coating. The specimen's corrosion macrographs of the substrate and the cerium conversion coating are provided in Fig.3. Fig.3 showed the surface of the substrate specimen (only at 6 hours) showed a lot of corrosion pits and the specimen's surface of the cerium coating no corrosion pits, after immersed in 3.5 wt. % NaCl solution. So corrosion resistance of the cerium coating is very good.

The effect of conversion coating on the corrosion resistance of ZM5 alloy was studied by electrochemical tests. Fig. 4 showed the potentiodynamic polarization curves for ZM5 alloy substrate and cerium conversion coating in 3.5 wt.% NaCl solution. The cathode reaction in the polarization curves corresponded to the evolution of the hydrogen, and the anodic polarization curve controlled with active dissolution reaction was the most important features related to the corrosion resistance. The hydrogen evolution rate diminished after ZM5 alloy was covered with conversion coating. The shape of anodic curves was obviously different. The anodic current density increased smoothly with the increasing of anodic potential, indicating that the ZM5 substrate was dissolved gradually. For the cerium conversion coating, the corrosion current density increased slowly when the potential was more positive than −1.2 V_{SCE}. Revealing that no severe dissolution reaction was observed until the potential was more positive than −1.2 V_{SCE}. The corrosion current density *I*corr obtained from polarization curves was summarized in Table 1. As it was scientific to evaluate the corrosion rate by corrosion current density, it can be seen that cerium conversion coating presented a noticeable reduction in *I*corr relative to the substrate alloy. Thus, the cerium conversion coating was the most effective in 3.5 wt.% NaCl solution.



(a) substrate (b) cerium coating

Fig.2 A photograph of cerium conversion coating



(a) substrate (b) cerium coating

Fig.3 A corrosion photograph of cerium coating

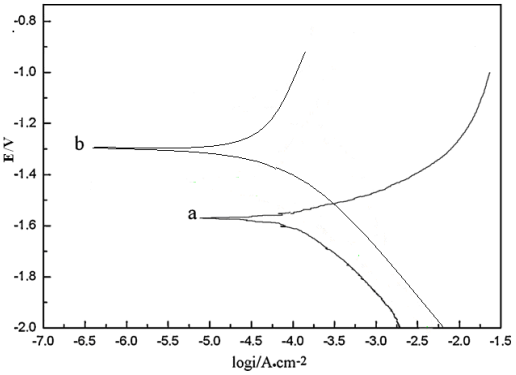


Fig. 4 The potentiodynamic polarization curves of substrate (a) and cerium conversion coating (b)

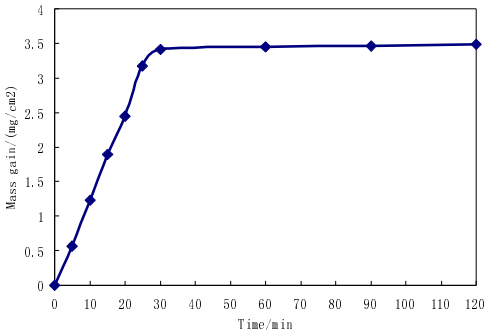


Fig.5 Mass gain of cerium conversion coating upon formation

Table 1 The values of *I*corr for the coating extracted from the polarization curves.

Parameters	Substrate alloy	cerium conversion coating
*I*corr (A/cm^2)	1.294×10^{-4}	3.162×10^{-5}

Formation Kinetics and Mechanism

It is well known that Mg^{2+} is the sole stable magnesium species in aqueous solution with pH value less than 8.50. Once the ZM5 magnesium alloy substrate contacts with cerium conversion treating solution, the preformed native (hydr)oxide coating on the substrate surface immediately dissolves. After the dissolution of the (hydr)oxide coating, primary anodic reaction[8] (the dissolution of magnesium) occurs:

$Mg \rightarrow Mg^{2+} + 2e$

Spontaneously, cathodic reaction (the reduction of protons) occurs:

$2H_2O+2e \rightarrow 2OH^- + H_2$

The metallic ions dissolved into the solution and the H_2 escaped from the solution to the ambient atmosphere. The reduction of H^+ resulted in a decrease of the acidic value of the cathodic site, thus the pH value of these local cathodic sites increased. This resulted in the formation of hydroxide. Simultaneously, $KMnO_4$ oxidized the Ce^{3+} to Ce^{4+} and was deoxidized to MnO_2 and MnO, then MnO, MnO_2, $Ce(OH)_4$, and $Mg(OH)_2$ deposited on the surface of the alloy[30], Finally, the hydroxide was dehydrated and conversion coatings were formed on the alloy surface.

$4Ce^{3+} + MnO_4^- + 8H^+ + 2H_2O \rightarrow 4Ce^{4+} + Mn(H_2O)_6^{3+}$

$2\ Mn(H_2O)_6^{3+} \rightarrow MnO_2 + Mn^{2+} + 10H_2O + 4H^+$

$Mg(OH)_2 \rightarrow MgO + H_2O$

$Ce(OH)_4 \rightarrow CeO_2 + 2H_2O$

In addition, the above formation mechanism is used to interpret the coating formation kinetics and anticorrosion performance. Fig.5 illustrates the mass gain curve of the coating upon treating, which describes the coating formation kinetics. At the beginning of treating process, in 0-30 min, mass gain linear increase with time. It showed that the coating formation is rapid at the beginning of cerium conversion treatment. The substrate intimately contacts the conversion solution. and the formation rate is mainly controlled by the producing rate of OH^- or the coupled anodic reaction (the dissolution of magnesium) rate.

As the coating formation proceeds, the substrate surface is gradually covered with cerium or magnesium hydroxides/oxides. The transportation of reacting ions and molecules through the covered layer is necessary for the further formation of the coating, which is limited by the diffusion of various reaction species. The rate of coating formation then gradually slows down. Fig.5 showed that mass gain increase slowly after cerium conversion treatment proceeds is 30min, so the best time of cerium conversion treatment is 30 min.

Summary

(1) After treatment in the bath, a red-brown coating could be formed on the AZ91 magnesium alloy and mainly composed of CeO2, MnO, MnO2, MgO, Mg(OH)2 and Ce(OH)4.

(2) The corrosion resistance of the bare ZM5 alloy in 3.5 wt. % NaCl solution was limited, and the attack morphology was pitting corrosion.

(3) The corrosion resistance of the ZM5 alloy was improved by the cerium conversion treatment.

(4) Before 30 minutes of cerium conversion treating process, mass gain was a linear growth with time. After 30min, mass gain was a slow growth or almost no growth.

References

[1] CHEN Zhen-hua. Magnesium alloys. Beijing: Chemical Industry Press, 2004: 385. (in Chinese)

[2] Ying-hui Wei, Li-jing Yang, Li-feng Hou, Yao-wen Guo, Bing-she Xu. Formation process of bright spots on surfaces of die-cast magnesium alloy components after chemical conversion treatment. Eng. Fail. Anal. 2009,16: 19~25.

[3] HANDY A S. The effect of surface modification and stannate concentration on the corrosion protection performance of magnesium alloys. Surf. Coat. Technol. 2008, 203: 240~249.

[4] YANG K H, GER M D, HWU W H, SUNG Y, LIU Y C. Study of vanadium-based chemical conversion coating on the corrosion resistance of magnesium alloy. Mater. Chem. Phys. 2007, 101: 480~485.

[5] ZHAO Ming, WU Shu-sen, AN Ping, FUKUDA Y, NAKAE H. Growth of multi-elements complex coating on AZ91D magnesium alloy through conversion treatment. J. Alloy Comp. 2007, 427: 310~315.

[6] CUI Hu-fang, LI Qing-fen, LI Ying, WANG Fu-hui, JIN Guo, DING Ming-hui. Microstructure and corrosion resistance of phytic acid conversion coatings for magnesium alloy. Appl. Surf. Sci. 2008, 255: 2098-2103.

[7] Manuele Dabala, Katya Brunellia, Enrico Napolitanib, Maurizio Magrini.Cerium-based chemical conversion coating on AZ63 magnesium alloy. Surf. Coat.Technol. 2003, 172: 227~232.

[8] R.F. Zheng, C.H. Liang. Conversion coating treatment for AZ91 magnesium alloys by a permanganate-REMS bath. Mater. Corros. 2007, 58(3):193~197.

Advanced Materials Research Vol. 936 (2014) pp 1086-1090
© (2014) Trans Tech Publications, Switzerland
doi:10.4028/www.scientific.net/AMR.936.1086

Microstructure And Properties of Laser Surface Carburized Titanium And Titanium Alloys

Jingjie Dai*, a1,2, Chuanzhong Chen[b], Shouying Li[1], Lei Zhuang[1]

[1,] Qingdao Binhai University, Qingdao Shandong 266555, PR China

[2,] School of Materials Science and Engineering, Shandong University, Jinan Shandong 250061, PR China

*,[a]Corresponding author, daijingjie1979@163.com

[b]czchen@sdu.edu.cn

Keywords: Laser surface carburizing; Titanium and titanium alloys; Growth morphology; Formation mechanism

Abstract: Titanium and titanium alloys are widely used in many fields due to their some characteristics such as light density, high strength and excellent corrosion resistance. However, their practical applications are limited by their poor surface mechanical properties. Laser surface carburizing can improve the surface properties of titanium and titanium via the formation of titanium carbide and other reinforcing phases. In this paper, the properties of the alloyed coatings, the growth morphologies and the formation mechanism of titanium carbide are discussed.

Introduction

Owing to their excellent properties such as specific strength and corrosion resistance, titanium and its alloys are widely used in many areas such as aerospace, military, sport equipment, chemical engineering, biomedical engineering, etc. However, they are currently restricted to nontribological applications, owing to their poor friction and wear resistance, and high tendency to galling [1-3]. Titanium carbide, TiC, is a refractory material which has a melting temperature about 3170 ℃ and a high hardness ranging between 2500 and 3000 HV. It is widely used as a reinforcing phase to improve the surface properties of titanium and titanium due to its ultra-high hardness. On the other hand, laser surface alloying offers an excellent scope for tailoring the surface microstructure and/or composition of a component and proves superior to conventionally practiced surface engineering. Laser surface alloying involves melting of a pre-deposited coating or concomitantly added alloying elements/compounds with a part of the underlying substrate by the directed energy laser beam to form an alloyed zone confined to a shallow depth within a very short interaction time. In addition, laser surface alloying can overcome some disadvantages of the conventional strengthening methods and has the major advantages of the ability to control the power density precisely, minimum heat affected zone, and processing of inaccessible and localized areas [4]. And it has been actively investigated and applied to improve wear and corrosion properties for various steels, aluminum and titanium alloys.

Laser surface carburizing is a method of laser surface alloying using carbon or graphite as the mainly alloying powder to fabricate the alloyed coating. The surface properties of the metal components are significantly improved due to the formation of hardening titanium carbide. In this paper, recent research progress on laser surface carburizing of titanium and titanium alloys is reviewed.

Laser surface carburizing

Laser surface carburizing uses carbon or graphite as the complete alloying powder and the alloyed coating reinforced by hardening titanium carbide phase is fabricated on the substrate of titanium and titanium alloys. And many researches have been carried out. Laser surface carburizing of pure titanium with graphite powder shows that some above 800 μm thicknesses of the alloyed

coatings, mainly consisting of dendritic TiC, are fabricated on the substrate, which increase the hardness from the substrate about 210 $HV_{0.1}$ to 1200 $HV_{0.1}$ and decrease the wear coefficient from 0.5 to 0.3. The result of dry-sliding friction test of laser carburized pure titanium shows that dry-sliding friction between ceramic and titanium is minimized whereas adhesive wear of the metal is reduced much and its abrasive wear is prevented, which can be attributed to the formation of hardening titanium carbide phase and the self-lubricating action of the rest of graphite powder [5-7]. In addition, Ref. [6] also confirms that titanium carbide phase formed in the alloyed coating is non-stoichiometric carbide phase TiC_{1-x} owing to non-equilibrium solidification. Laser surface carburizing of Ti-46Al-2Cr-1.5Nb-1V with graphite and C + Nb shows that the oxidation and wear resistance of the alloyed coating, consisting of in-situ produced TiC particles, improve obviously, and the sample alloyed with C + Nb exhibits the best oxidation and wear resistance [8-9]. The alloyed coating, with gradient distributed TiC reinforcing phase, is successfully fabricated on γ-TiAl alloy by laser surface carburizing with carbon [10]. The result of high-temperature sliding wear test indicates that the alloyed coating has excellent high-temperature sliding wear resistance. The high hardness and excellent wear resistance of the alloyed coating is the result of the refined rapidly solidified microstructure and the presence of hardening ceramic phase TiC. But it must be noted that although hardening ceramic phase TiC can improve the wear resistance of the samples, excessive volume fraction of TiC in the alloyed layer increases the brittleness and decreases the wear resistance of the alloyed coating.

Laser surface composite carburizing

Laser surface composite carburizing uses mixed powders consisting of C and other powders as the alloying powders to fabricate the alloyed coatings, which consist of TiC and other reinforcing phases. According to the reinforcing phases formed in the alloyed layers, the extra addition powders are divided into the following two kinds: one is the powders formed hard ceramic phases with titanium; the other is the powders formed intermetallic compounds with titanium.

The alloyed layer reinforced by multiple ceramic phases could be achieved better effectiveness than by only one ceramic phase. Laser surface alloying of Ti-6Al-4V with graphite and boron mixed powders shows that the coatings, consisting of TiC, TiB_2 and TiB, have higher hardness (about 1250-1700HV) and are more resistant to wear than the as-received sample [11]. And the composite coating produced by laser alloying with boron and carbon mixed powders has better properties than that alloyed with boron and carbon separately. As is well known, rare earth (RE) oxides are effective in grain refinement of many metallic alloys and thus improve the mechanical properties. Compared with the result of Ref. [11], the microstructures of the coatings are refiner through the addition of rare earth oxides Ce_2O_3 and Y_2O_3 into graphite and boron mixed powders [12]. The mechanism of the microstructural refinement is mainly attributed to the surface activity of the elements Ce and Y, the function of the Ce_2O_3 and Y_2O_3 particles acting as heterogeneous nuclei, and the grain growth resistance of the elements Ce and Y and their oxides. Laser melted BN + C coating on the Ti-6Al-4V titanium alloy has produced the alloyed coating, consisting of hard ceramic TiC, TiN and TiB particles spaced in ductile martensitic matrix, which has a high hardness level of 920 HV [13]. The fracture examination of laser treated zones shows that the heat affected zone displays ductile fracture whereas inside of alloyed zone displays the complex character of fracture. And the propagating crack penetrates the area of martensitic phase and can be stopped on particles of TiC, TiB and TiN phases.

Titanium silicides such as Ti_5Si_3 is confirmed to be good reinforcements for titanium alloys because of its excellent capability including high hardness and wear resistance in many tribological systems, thermal stability at high temperature, high elastic modulus and the similar density to pure titanium. Surface modification of titanium alloys with titanium carbides or silicides is considered to be effective method to improve the wear resistance of titanium alloys Composite coatings consisting of preeutectic TiC and eutectic Ti_5Si_3 + β- (Ti) were fabricated by laser alloying of titanium alloy Ti-6Al-4V with graphite and silicon mixed powders [14]. The test results show that the composite coatings, thickness of about 0.6 mm, surface microhardness of about 1500 $HV_{0.1}$, have a

lower friction coefficient and a much higher wear resistance than the as-received sample. In addition, the analysis also shows the combination of C with Ti at relatively higher temperature results in a shorter diffusion time of the C atoms in the melt pool and thus the titanium carbides formed in the top layer of the coatings. On the other hand, the titanium silicides formed at a relatively lower temperature results in the Si atoms having more time to diffuse deep into the melt pool. So, the compounds in the inner layer of the coatings are mainly titanium silicides.

Growth morphology analysis of titanium carbide

TiC has a NaCl-type crystal structure and is face center cubic crystal. Ti atoms array fcc sub-lattice, while carbon atoms occupy the free place of octahedral configuration forming another fcc sub-lattice [15]. They are completely symmetry with sub-lattice of Ti and carbon. The growth morphology of TiC is a regular octahedron under equilibrium solidification and free growth conditions, and each of the corners is faceted by {111} planes, requiring that growth velocity $V_{\{111\}}$ normal to each {111} planes must be equal. However, the carbide growth morphologies under non-equilibrium solidification conditions often deviate from its equilibrium growth morphology, indicating sufficiently that growth morphology of TiC carbide depends strongly upon solidification conditions. It is well known that the final growth morphology of a crystal is controlled by the following factors: (1) crystal structure; (2) thermodynamic properties such as interfacial energy and phase transformation entropy; (3) growth kinetics and mechanism; and (4) thermal and mass transportation in melt. It is commonly known that a change in solidification conditions must affect the thermal and mass transport in melt. As a result, distribution of thermal field and solute field in the melt would deviate from that under equilibrium solidification conditions, leading to a variety of growth morphologies.

Chen et al. find in their experiment that different morphologies of titanium carbide dendrite are formed in the carburized coating with different laser scanning velocity. Dendritic titanium carbide is the most common morphology in laser carburized coatings. It having a platelet/catenulate growth characteristic on dendrite arms is formed with lower laser scanning velocity, while a well-developed dendrite having a three-dimensional network growth characteristic is formed with higher laser scanning velocity. In addition, different morphologies of titanium carbide are also formed under different cooling rate. With an increase of cooling rate, the growth morphologies of titanium carbide change from well-developed dendrite, cross-petal microstructure to blocky microstructure [16]. Platelet-like microstructure is also observed in laser carburized TiAl coating [17]. Laser carburizing of pure titanium with graphite shows that cellular dendrite and globular microstructure are formed with different laser parameters [7]. In present author's work [18], different morphologies of titanium carbide including globular microstructure, well-developed dendrite, cross-petal microstructure and cellular microstructure are observed orderly from the top surface to the bottom of the carburized coating, as shown in Fig. 1. These differently morphologic titanium carbides correspond to different carbon contents. And there is a strong relationship between the carbon content and the mean microhardness, namely high carbon content corresponds to high hardness. The dense and coarse titanium carbide has higher carbon content, and consequently has higher microhardness. While the finer and shorter titanium carbide has lower carbon content, consequently has lower microhardness. During solidification, the alloying primitive content C_0, the temperature gradient of the liquid phase on solid-liquid interface G and solidification rate R are the chiefly influencing factors on crystal morphology.

Otherwise, laser scanning velocity has an important effect on the microstructures of the alloyed coating. When the scanning velocity is lower, there is a longer laser irradiation time which results in the melt pool absorbing more heat energy. The melt thus takes a longer time for solidification to start and the temperature of the base material becomes higher which results in lower temperature gradient and cooling rate, and prolongs the interaction time between molted Ti and C and the grain growth time. The resulting microstructure exhibits a dense and coarse morphology. With an increasing of the scanning velocity, the laser irradiation time reduces, which induces the decreases of the interaction time and the grain growth time. The microstructure is finer and shorter.

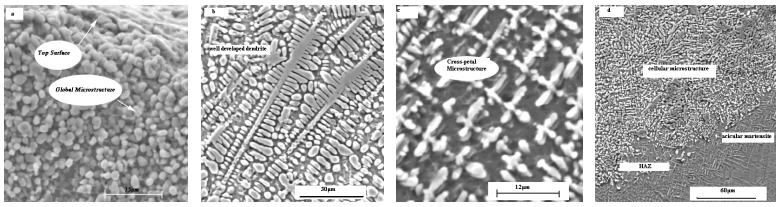


Fig. 1 SEM micrographs of different morphologies of titanium carbide

Formation mechanism of titanium carbide

The formation mechanism of TiC is related to the highest processing temperature. It can be classified into two mechanisms according to the highest temperature: diffusion mechanism and solution-precipitation mechanism [19]. Thermodynamic and kinetic calculations of TiC show that the formation mechanism is diffusion mechanism when processing temperature is lower than 1554K, while the formation mechanism is solution-precipitation mechanism when the processing temperature is above 1554K [20]. Since the processing temperature of laser surface alloying is much higher than 1554K, the formation mechanism of TiC is solution-precipitation mechanism. The formation of TiC particles in liquid titanium can be considered in the following ways:

$$Ti_{(l)} + C_{(s)} \rightarrow TiC_{(l)} + Q_1 \qquad [1]$$

$$TiC_{(l)} \rightarrow TiC_{(s)} + Q_2 \qquad [2]$$

where $C_{(s)}$ is the carbon particle precursor, Q_1 is the heat of reaction, and Q_2 is the heat of solidification. Equation [1] shows a liquid-solid reaction process. The carbon particle diffuses into laser melted pool during laser irradiation. Then, the molten titanium surrounds the carbon particle and reacts at its outer interface. The molten titanium diffuses through TiC layer to react with the unreacted portion of the carbon particle, and TiC dissolves in the liquid phase. As the reaction progresses, the carbon particle and titanium concentrations in melted pool decrease, and the product concentration increases with time. Equation [2] shows a precipitation process. TiC particles precipitate from liquid phase and different morphologies of TiC are formed in this process. The sketch of the formation of TiC is showed in Fig.2 [18].



Fig.2 Sketch of the formation of TiC

a-activated carbon preplaced on the substrate, b-diffusion C into liquid titanium, c-reaction between C and Ti, d-precipitation of TiC

References

[1] K.E.Budinski, Tribological properties of titanium alloys, Wear. 151 (1991) 203-217.

[2] J. Komotori, B.J. Lee, H. Dong, P.A. Dearnley, Corrosion response of surface engineered titanium alloys damaged by prior abrasion, Wear. 251 (2001) 1239-1249.

[3] M. Kulka, N. Makuch, P. Dziarski, A. Piasecki, A. Miklaszewski, Microstructure and properties of laser-borided composite layers formed on commercially pure titanium, Optics & Laser Technology. 56 (2014) 409-424.

[4] Y.S. Tian C.Z. Chen, D.Y. Wang and T.Q. Lei, Laser surface modification of titanium alloys—a review, Surface Review and Letters.12 (2005) 123-130.

[5] Tian Yong-sheng, Chen Chuan-zhong, Wang De-yun, Xu Ying, Lei Ting-quan, Analysis of the growth mechanism of TiC crystal and the mechanical properties of the laser alloyed layer on the surface of pure titanium, Laser Technology. 29 (2005) 113-116 (in Chinese).

[6] B. Courant, J.J. Hantzpergue, S. Benayoun, Surface treatment of titanium by laser irradiation to improve resistance to dry-sliding friction, Wear. 236 (1999) 39-46.

[7] Bruno Courant, Jean Jacques Hantzpergue, Ludovic Avril, Stéphane Benayoun, Structure and hardness of titanium surfaces carburized by pulsed laser melting with graphite addition, Journal of Materials Processing Technology. 160 (2005) 374-381.

[8] Xin Yanhui, Lin Jianguo, Ren Zhiang, Microstructure Characteristics and Oxidation Resistance Properties of "in-situ" TiC Particle Reinforce Coatings by Laser Surface Alloying, Rare Metal Materials and Engineering. 34 (2005) 899-902 (in Chinese).

[9] Xin Yanhui, Lin Jianguo, Ren Zhiang, Microstructure Characteristics and Wear Resistance of TiC Particle Reinforced Coatings by Laser Surface Alloying in a Ti-Al-Cr-Nb-V Alloy, Transactions of Materials and Heat Treatment. 25 (2004) 63-67 (in Chinese).

[10] Y. Chen, H.M. Wang, Microstructure and high-temperature wear resistance of a laser surface alloyed g-TiAl with carbon, Applied Surface Science. 220 (2003) 186-192.

[11] N. Makuch, M.Kulka, P.Dziarski, D.Przestacki, Laser surface alloying of commercially pure titanium with boron and carbon, Optics and Lasers in Engineering. 57 (2014) 64-81.

[12] Y.S. Tian, C.Z. Chen, L.X. Chen, Q.H. Huo, Effect of RE oxides on the microstructure of the coatings fabricated on titanium alloys by laser alloying technique, Scripta Materialia. 54 (2006) 847-852.

[13] R. Filip, Alloying of surface layer of the Ti-6Al-4V titanium alloy through the laser treatment, Journal of Achievements in Materials and Manufacturing Engineering. 15 (2006) 173-179.

[14] Y.S. Tian, C.Z. Chen, L.X. Chen, Q.H. Huo, Microstructures and wear properties of composite coatings produced by laser alloying of Ti–6Al–4V with graphite and silicon mixed powders, Materials Letters. 60 (2006) 109 -113.

[15] ZHANG Er-lin , JIN Yun-xue, ZENG Song-yan, ZHU Zhao-jun, Microstructure of in-situ TiC particle reinforced titanium alloy matrix composites, Trans. Nonferrous Met. Soc. China. 10 (2000) 764-768.

[16] Y. Chen, H.M. Wang, Microstructure and high-temperature wear resistance of a laser surface alloyed γ-TiAl with carbon, Applied Surface Science. 220 (2003) 186-192.

[17] Y. Chen, H.M. Wang, Rapidly solidified MC carbide morphologies of a pulsed laser surface alloyed γ-TiAl intermetallic with carbon, Scripta Materialia. 50 (2004) 507-510.

[18] Dai Jingjie, Experimental and Mechanism Study of TA2 Fabricated by Laser Surface Modification, Master Degree These, Lanzhou University of Technology, China. 2006 (in Chinese).

[19] Nukami T, Flemings M C, In situ Synthesis of TiC Particulate Reinforced Aluminum Matrix Composite, Metallurgical and Materials Transactions. 26 (1995) 1877-1884.

[20] Tong X C, Fang H S, Al-TiC Composites in situ Processed by Ingot Metallurgy and Rapid Solidification Techology: part1, Microstructural Evolution. Metallurgical and Materials Transactions. 29 (1998) 875-891.

Advanced Materials Research Vol. 936 (2014) pp 1091-1096
© (2014) Trans Tech Publications, Switzerland
doi:10.4028/www.scientific.net/AMR.936.1091

The Application Research of Ship Metal Corrosion in Marine Environment

Chunyong Hu[1,a*], Shengwei Kou [2,b], Jingjing Guo [3,c]

[1]School of Mechanical and Electrical Engineering of Hainan University, Haikou, China

[2]School of Material and Chemical Engineering of Hainan University, Haikou, China

[a]1940282472@qq.com [b]253985282@qq.com [c]844614452@qq.com

Keywords: corrosion mechanism; corrosion inhibitors

Abstract: In this paper, we state the corrosion mechanism of carbon steel, copper, aluminum and other non-ferrous metal in the seawater; analyze the types and mechanism of corrosion inhibitors. By experiments, we have a good knowledge of the function of corrosion inhibitors to metal in the seawater. We also analyze the application prospects of corrosion inhibitors' application to metallic corrosion inhibition in ocean environment.

Introduction

At present, most ships use metal shells sailing in the ocean, however metal will be influenced by the temperature of seawater, the salinity of seawater, the marine atmosphere temperature and the marine microorganism in ocean environment, so the corrosion degree of metal will be serious. Corrosion not only can reduce the ships' structural strength and service life but also can increase the sailing resistance, reduce the speed of sailing, make the ships' sailing hard and have negative effects on the navigation safety. If the ships have already been corroded under the effects of the external world and there are cracks and perforation, which can lead to the happening of marine casualty and cause heavy losses to people's lives and property. Twenty to thirty bilion yuan will be lost because of metal corrosion every year, of which the corrosion of ship accounts for a very big part.

Since most ships use metal shells, and hull parts touching with the seawater directly are coated with anticorrosive paint, at the same time, protected by the system of the impressed current or sacrificial anode cathodic protection system. When the anticorrosive coatings are washed by seawater off or when the anode is used up, the ships will still be corroded, even the corrosion rate will be faster, shortening the service life of the ships. Therefore, studying how to minimize the corrosion rate when the hull has been corroded is especially important. That is to say, it is important to study the applications and application effect of metal corrosion inhibitor in marine environment.

Mechanism Of Metal Corrosion In The Marine Environment

Corrosion is material's damage or deterioration under the effect of the external environment, including chemical corrosion, electrochemical corrosion and biological corrosion. Materials mentioned here include metal and nonmetal. Metal corrosion is the damage that metal interacts with surrounding medium by chemical or electrochemical reaction, sometimes accompanied by mechanical, physical and biological effects. Non-metallic corrosion is non-metallic materials' damage due to the direct chemical action (such as oxidation, dissolving and swelling, aging, etc). Because most of corrosion in ships occurred in metal, so we will mainly discuss the metal hull corrosion and research the anticorrosive measures of the metal hull.

Chemical composition and environment of seawater are complex, so there are many factors leading to corrosion of metal hull. In addition to the composition of seawater that can cause all sorts of chemical reaction with the metal hull, a lot of factors outside such as temperature, will be the reasons of accelerating hull's metal corrosion.

For hull, corrosion mainly occurs in the underbody and water line. The hull underwater is corroded by electrochemical corrosion and the hull's corrosion at the water line is mainly the chemical corrosion and electrochemical corrosion. The hull underwater is completely immersed in seawater, which is equivalent to immerse in the electrolyte solution.

Carbon Steel Corrosion Mechanism

Carbon steel con tains various components, which mainly are ferrite and cementite (Fe3C). The former is a body centered cubic lattice pure iron, and the latter is a kind of iron-carbon compounds whose electrochemical properties are similar to graphite. When carbon steel is immersed in aqueous solution.

TABLE I. MAIN SALT CONTENT IN THE WATER

composition		NaCl	MgCl2	MgSO4	CaSO4
The percentage of	total salinity/%	77.8	10.9	4.7	3.6
composition		K2SO4	CaCO3	MgBr2	total
The percentage of	total salinity/%	2.5	0.3	0.2	100

Electric potential difference between ferrite and cementite is caused by the electrode potential difference. Ferrite' electrode potential is negative and is the anode, however, cementite' is positive and is the cathode. And the two components are arranged closely cross together, because they are connected by point, free electrons will flow from the ferrite to the cementite. When carbon steel is immersed in aqueous solution, the dissolved oxygen in the aqueous solution will absorb the electron which is released because of iron corrosion in the surface of the cementite to make the corrosion process go on.

And the equation for anodic reaction as in $Fe \rightarrow Fe^{2+} + 2e^{-}$. (1)

The equation for cathodic reaction as in $O_2 + 2H_2O + 4e^{-} \rightarrow 4OH^{-}$. (2)

Solubility of corrosion products Fe(OH)2 is small, depositing and coating on metal surface. And Fe(OH)2 can be further oxidized to Fe(OH)3 which generates rust Fe2O3 dehydrating nH2O. The equation for anodic reaction, as in $4Fe(OH)_2 + 2H_2O + O_2 \rightarrow 4Fe(OH)_3$. (3)

The cathodic reaction equation, as in $2Fe(OH)_3 \rightarrow Fe_2O_3 + 3H_2O$. (4)

Furthermore, Fe2+and Cl- in the sea water will generate FeCl2 dissolving in water, and then spread to the anode zone, generating Fe(OH)2 known as brown rust with OH- of the bulk solution or cathode zone, quickly converting into other forms of rust when encountering the water in the pore liquid and oxygen. FeCl2 generates Fe(OH)2 and it will release a Cl- at the same time, the new Cl- and migrate to the anode area, bring out moreFe2+, accelerating the anodic process. We usually refer to the accelerating anodic process as anodic polarization, Cl-'s t function is anode depolarization.And the anodic reaction equation, as in

$2Cl^{-} + Fe + 6H_2O + 2Fe^{3+} = 3Fe(OH)_2 + 6H^{+} + 2Cl^{-}$. (5)

The cathodic reaction equation, as in

$4Fe(OH)_2 + 2H_2O + O_2 \rightarrow 4Fe(OH)_3$. (6)

Mechanism of Non-Ferrous Metal Corrosion in the Seawater

Copper will be affected by different degree of corrosion in the flowing seawater, the equation that copper is corroded in seawater,equation for anodic reaction, as in $2Cu \rightarrow 2Cu^{2+} + 4e^{-}$. (7)

And the equation of cathodic reaction, as in $O_2 + 2H_2O + 4e^{-} \rightarrow 4OH^{-}$. (8)

Aluminum's corrosion degree is related to its purity in seawater, the purity is smaller, the more serious corrosion. aluminum of not high purity will be a galvanic cell with internal impurities, also electrochemical corrosion in the absence of protection, and the equation of Anodic reaction, as in

$$4Al \rightarrow 4Al^{3+} + 12e^{-} \quad (9)$$

Cathodic reaction equation, as in $3O_2 + 3H_2O + 12e^{-} \rightarrow 12OH^{-}$ (10)

In addition, unprotected aluminum in seawater will appear cavitation erosion intergranular corrosion and stress corrosion cracking.

Corrosion of the Hull Waterline Part

Because the hull waterline part's environment is alternation between sea and air, impacted by sea and air alternately, subjected to chemical and electrochemical corrosion, as a result, its rate is faster; In spite of the waterline coated with anti-corrosion layers, but these layers will fall off under the impact of the water of the sea.

The corrosion reactions above are functioning well when water and the metal are not influenced by the special conditions. In the Marine environment, there are all kinds of variable factors outside, for example change of temperature, the flow rate of seawater and the pressure of seawater. These factors will accelerate the chemical corrosion and electrochemistry corrosion of metal in the seawater, increasing the degree of metal corrosion. So we must take enough consideration to these areas when we research on metal corrosion in seawater factors.

Species And The Corrosion Mechanism Of Metal Corrosion Inhibitors

Corrosion inhibitor is chemical substances or compounds that exists in the appropriate concentration and form in the environment, can prevent or reduce corrosion of material. According to medium, we can make the classification: acid restrainer, alkaline, corrosion inhibitor, neutral corrosion inhibitor, oil soluble corrosion inhibitor and volatile corrosion inhibitor and so on. Now, what corrosion inhibitors people use most are volatile corrosion inhibitor an liquid corrosion inhibitor. So far, main organic corrosion inhibitors people have developed are Low molecular weight amines, dicyclohexyl ammonium nitrite, gasifiable amino acid alkyl ester, heterocyclic compounds, for example: isopropyl amine, β - amino acids, thiazole derivatives were, three nitrogen truxene azole derivatives, morpholine derivative and so on. Liquid phase corrosion inhibitors such as hydrochloric acid pickling corrosion inhibitors are widely used. Moreover, vapor phase corrosion inhibitors are often made into gas liquid corrosion inhibitor with liquid corrosion inhibitor or into composite vapor-phase corrosion inhibitor with several kinds of gas phase corrosion inhibitors .Because metal's environment is not just a simple liquid or gas phase environment, but as a complex multiphase coexistence environment in the real production practice, we should consider materials' erosion of the multiphase flow.

Based on the Influence of the Electrode

For cathode: By changing reaction process of the cathode, to make the corrosion potential negatively shift, reducing the cathodic process, to make metal corrosion potential into passivity potential area, which plays an important role in the corrosion; for anode: the anions of metal corrosion inhibitor of anode type move toward the anode and passivate the metal(oxidization), forming a compact passivation membrane(oxidation membrane),so as to inhibit the corrosion of metals.

Corrosion inhibitors change the process of the electrode reaction, destroy the corrosion of electrochemical corrosion, as a result, the iron, copper and other metal can not react with each other in the way of electrochemical reaction, to have the effect of slowing down the metal corrosion. But if anodic corrosion inhibitor dosage is insufficient, is not fully covering the surface of the anode, as a result, there will be forming small anode and large cathode's batteries of corrosion, which can accelerate the corrosion of metals, it will become a dangerous corrosion inhibitor, instead. On the other hand, the cathode corrosion inhibitors become secure corrosion inhibitor.

Forming a Protective Membrane on the Metal Surface

Some corrosion inhibitors will form dense and adhesional oxide membrane on the metal surface, when the thickness of the oxide membrane reaches a certain level, which will slow down the rate of oxidation reaction, the protective membrane will stop growing; and some corrosion inhibitors and ionic of medium will react with each other generating the undissolved material which directly precipitates on the metal surface to form the precipitation membrane of corrosion resistance, to have played an important role in protecting the metal. This kind of protective membrane attached to the metal surface will separate the metal from the surrounding sea water and air in the seawater, reducing their exposure, which can effectively block the electrochemical corrosion of the underbody and nonferrous metals, also dual corrosion of topsides, to protect the hull.

The Adsorption of Polar Groups and Non-polar Groups

Polar groups make corrosion inhibitor molecules adsorbed on the metal surface, which changes the charged state of the metal surface and interface properties, leads energy state on the surface of the metal to the stabilization, and increases activation energy of the metal reaction, so that the rate of metal corrosion slows down. Non-polar groups can form hydrophobic protective membrane to prevent the corrosive medium or water molecules from spreading to the metal surface diffusion, at the same time, and to prevent the dissolution and diffusion of metalion.

Experiment Analysis

In order to prove that the metal corrosion inhibitor is useful for corrosion and rust of metal in the marine environment, we need to use black and non-ferrous metal to do the experiment.

Nonferrous Metals

1) Experimental material

We chose the fine copper as test object of all the non-Ferrous Metal, and make the sample into $25\text{mm}\times 25mm\times 2mm$.

2) Sample Pretreatment

Samples are copper pieces and should be polished through the 120 mesh and 240 mesh dry abrasive paper step by step, then washed with distilled water.

Divide the preprocessed samples into two groups, the sample surface is coated with metal corrosion inhibitors (group 1), as showing in figure 1, in the first group, when the metal corrosion inhibitor on the surface is dry, put them separately in the seawater prepared ahead of time; While the other group do not do any processing(group 2), as showing in figure 2, and put them separately in the seawater prepared in advance with group 1 at the same time, and immerse respectively for 5 days and 15 days, and analysis their metallographic, compare with the experimental results of two groups which are as follows. And the experimental temperature of immersion is $(25\pm2)^0$C.



Figure 1 Group 1: sample surface is coated with metal corrosion inhibitors



Figure2. Group 2: samples without any processing

3) Comparison of Results (the experimental temperature of seawater immersion is 250C)
4) By comparing the experiment results of two groups, we find that corrosional phenomena of group 2(without any process) is more obvious.

The Ferrous Metals

1) Experimental Material

We chose the industrial steel plate as test object of all the ferrous metals, and make the sample into 25mm×25mm×2mm.

2) Sample Pretreatment

Samples should be polished respectively through the 120 mesh and 240 mesh dry abrasive paper step by step, then washed with distilled water.

Divide the preprocessed samples into three groups, each group into two small groups, the sample surface is coated with metal corrosion inhibitors (group 1) in each group of the first group, as shown in figure 3, when the metal corrosion inhibitor on the surface is dry, we can do the experiment; While the other group do not do any processing(group 2). After tested respectively for 15 days, and analysis their metallographic, finally compare test results of two groups. And the temperature of soak testing is(25±2)0C.In the experiment, the samples of the first group， as showing in figure 3, are all in the water; each of samples in second group is half in seawater, the other in the outside, as showing in figure 4; the samples of group 3 suspended above the seawater, don't immersed in seawater,as showing in figure 5.

3) Comparison of Results

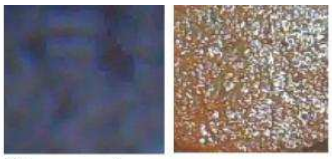


Figure3. Comparison of results for group 1



Figure4. Comparison of results for group 2

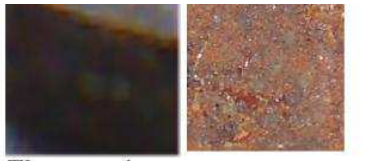


Figure5 . Comparison of results for group 3

Conclusion

By comparing the experiment above and results, we find that the sample whose metal surface is daubed with corrosion inhibitor, is no matter in sea water environment, or atmospheric environment of sea water, its corrosion is lighter or can slow down the corrosion of metal corrosion for a long time, to prove that the metal corrosion inhibitors on the metal surface have antiseptic gentle erosion effect on metal in seawater and marine environment, to prolong the service life of metal material and reduce the costs of maintenance and after-sales service. The application prospect of metal corrosion inhibitor: the metal applied corrosion inhibitor can effectively prevent metal corrosion and slow down the rate of corrosion in the seawater environment, also prolongs service life of metal. Therefore, the metal corrosion inhibitor can be applied to corrosion protection system of the hull part under sea water. Before launching, we can evenly daube it on the hull part of underwater and between wind and water, constituting the anti-corrosion system of ships together with corrosion protection measures such as anti-corrosion coating and cathodic protection technology, as the last line of defense system, which can effectively prolong the service life of ship and greatly reduce the costs of each year for hull anticorrosion and the loss of life and property for this reason. At the same time, on one hand we should use the corrosion inhibitors which are harmless to sea water and marine living beings, on the other hand we should strengthen the research of environmental friendly and anticorrosive effect better corrosion inhibitor.

Acknowledgment

2012 education, teaching research subject of Hainan University(Program No :hdjy1222).

References

[1] Qinxia Li, “The ultrasonic hull corrosion situation and development trend,” Journal of Testing Technology, vol. 12, pp.65-67, March 1998.

[2] Guangzhi Zhang, “The protection measures and regular pattern of hull corrosion,” Chinese Journal of Ship Repairing, vol. 16, pp, 53-58, May 2003.

[3] Youlin Xu, “Application and development of the hull anticorrosion technology,” Chinese Journal of Ship Repairing, vol. 21, pp. 43-46, July 2008.

[4] Qiuyu Zhang, The Research Progress of Gas Phase Delay Etchant, 2008.

[5] Chunfang Chang, The Corrosion Inhibition Effect and the Meehanism of New Complexes as Inhibitors on Carbon Seel and Coppe; East China University Of Science, 2011.

Advanced Materials Research Vol. 936 (2014) pp 1097-1101
© (2014) Trans Tech Publications, Switzerland
doi:10.4028/www.scientific.net/AMR.936.1097

Corrosion Resistance of Three 316 stainless Steels

Janshu Lu[1,a] , Qinsong Lu[2,b] , Jin Xue[1,c]

[1] Materials Chemistry Laboratory, Department of Materials Science and Engineering, Zhejiang University of Technology, Hangzhou, Zhejiang Province, 310014, P. R. China

[2] Zhejiang Yinlun Machinery Co. Ltd, Tiantai County, Zhejiang Province, 317200, P. R. China

[a]Jianshul@zjut.edu.cn, [b]luqinsong@yinlun.cn, [c]zcpsic@zjut.edu.cn

Keywords: stainless steel, corrosion resistance, EGR

Abstract. 316L stainless steel is a well known advanced material for its good corrosion resistance in many aggressive situations. As the quality of different manufacturer of the stainless steel may vary in some degree, this paper studied the corrosion resistances of three 316L stainless steels which supplied by three manufacturers. The results show that the difference of the corrosion rates of the three 316L stainless steels in 5% H_2SO_4 or 3.5%NaCl solutions is one time in quantity. The reasons for the difference can be explained by compositional and metallographic factors.

Introduction

Exhaust gas recycle (EGR) system can be used in many vehicles (especially for heavy trucks) for more efficient energy usage and less pollutant emission [1-4]. A problem of EGR system is the corrosion of the construction materials which are often stainless steels. Because combustion reactions in engine will more or less produce nitrogen oxide (NOx). Also, most oils contain small amount of sulfur which is the source of sulfur oxides (SO_2, SO_3) in exhaust gas . As water is the inevitably product of hydrocarbon combustion reaction, nitric acid and sulfuric acid may formed in the cold region of EGR system. So, high corrosion resistance of the materials in EGR system is required. 316L stainless steel is widely used in chemical industry and many other demanding applications. It is a good candidate material for EGR system. There are many 316L stainless steel manufacturers in the world. The quality of their products may vary in some degree. In this paper, the corrosion resistances of three 316L stainless steels supplied by three manufacturers were tested by weight loss method and electrochemical method. Optical metallographic and scanning electron microscope examination were used for the material characterization.

Experiment

The Materials

The three 316L stainless steels which were supplied by three manufactures were named as 316L-A, 316L-B and 316L-C in this study. All the material samples were in plate form with thickness vary from 0.27 to 0.48mm. Table 1 shows the compositions of the three 316L stainless steels.

Table 1 The compositions of the three stainless steels (% in weight)

Element	C	Cr	Ni	Mo	Mn	Si	S	P	Cu	N
316L-A	0.027	16.80	10.20	2.00	1.07	0.47	0.001	0.036	0.17	/
316L-B	0.022	16.00	10.17	2.03	1.45	0.57	0.001	0.031	0.13	0.025
316L-C	0.026	17.10	12.14	2.08	0.97	0.62	0.004	0.031	/	/

Dip tests and electrochemical tests

Stainless steel rectangular samples with dimension of 40×30mm were used for dip test. The sample surfaces were first sanded with 1500# SiC paper and then washed in flowing water and cleaned ultrasonically in ethanol for 15min. The samples were weighted by electronic microbalance and were dipped in 5%H_2SO_4 at the boiling temperature for 6hours. After that the samples were taken out and washed with water. The corrosion products on the sample surfaces were removed by dipping in 30% HNO_3 with ultrasonic resonance. The samples were weighted again and kept in dryer for examination.

Two electrochemical test techniques were used. One is corrosion potential measurement. Another is Tafel test. The instrument for the electrochemical test is P4000 of Princeton Applied Research Company.

Metallographic Examinations

The microstructures of the stainless steels were examined both by optical microscope and scanning electron microscope (SEM). A MR5000 microscope was used for optical metallographic examination and a Inspect S50 scanning electron microscope was used for finer examination. For optical metallographic examination the stainless steel samples were first embedded in epoxy resin and then polished with fine alumina and last etched in acid $FeCl_3$ solution. For SEM observation, stainless steel plate specimens were fractured by a tensile tester. The fractured surfaces were observed for microstructure characterization of the materials.

Results and Discussion

Dip Test

Three parallel samples for each kind of 316L stainless steel were used in the dip test. Each sample has 16cm^2 surface area. Table 2 shows the result of the test. The average corrosion rates of the three stainless steels in boiling 5% sulfuric acid are 10.0 g/m^2h or 12.0 mm/a for 316L-A, 18.0 g/m^2h or 20.2 mm/a for 316L-B and 7.2g/m^2h or 8.1mm/a for 316L-C. 316L-C shows the best corrosion resistance in the solution. The corrosion rate of 316L-B is more than one time higher than that of 316L-C. From Table 1 we know that 316L-C has higher Cr and Ni content than 316L-A and 316L-B. So, higher Cr and Ni content are beneficial for corrosion resistance of this type of stainless steel.

Table 2 Test result of three stainless steels dipped in boiling 5% sulfuric acid for 6h

Sample	thickness [mm]	weight1# [g]	weight2* [g]	weight loss [g]	corrosion rate [g/m^2.h]	average [g/m^2.h]
316L-A-1	0.41	2.5875	2.4837	0.1038	10.8	
316L-A-2	0.41	2.5865	2.4857	0.1008	10.5	10.0
316L-A-3	0.41	2.5694	/ $	/	/	
316L-B-1	0.38	2.3764	2.2002	0.1762	18.4	
316L-B-2	0.38	2.3749	2.2021	0.1728	18.0	18.0
316L-B-3	0.38	2.3708	2.2005	0.1703	17.7	
316L-C-1	0.48	3.1554	3.0857	0.0697	7.3	
316L-C-2	0.48	3.1379	3.0698	0.0681	7.1	7.2
316L-C-3	0.48	3.1599	3.0901	0.0698	7.3	

#:weight1=weight before dip, * weight2=weight after dip, $: test failure due to instrument problem

Electrochemical Test

Fig. 1 shows the open circuit potential measurements of the stainless steels in 3.5%NaCl solution. The measurement duration was 2 hours. The potential of 316L-A is relatively stable over the time and it was -0.174V(SCE) at the end of the measurement. The potentials of 316L-B and

316L-C varied a lot over the time and they were -0.234V(SCE) and -0.101V(SCE) respectively at the end of the measurement. There were many abrupt changes of the potential of 316L-B. As 316L-B is the worst of the corrosion resistance among the three stainless steels, the abrupt changes of potential may be the show of less protective property of the passive film of the stainless steel. 316L-C has the highest open circuit potential. It also has the highest corrosion resistance. So, open circuit potential is an important parameter for corrosion resistance measurement of stainless steels.

Fig.2 shows the Tafel plot of the polarization curves of the three stainless steels in 3.5%NaCl solution. From Fig.2, both corrosion potential and corrosion rate can be obtained. For 316L-A, they are -0.257V(SCE) and 6.3×10^{-6}A/cm^2. For 316L-B, they are -0.252V(SCE) and 7.9×10^{-6}A/cm^2. For 316L-C, they are -0.241V(SCE) and 4.0×10^{-6}A/cm^2. Again, 316L-C shows the best corrosion resistance of the three stainless steels. And the corrosion rate of 316L-B is approximately one time higher than that of 316L-C.

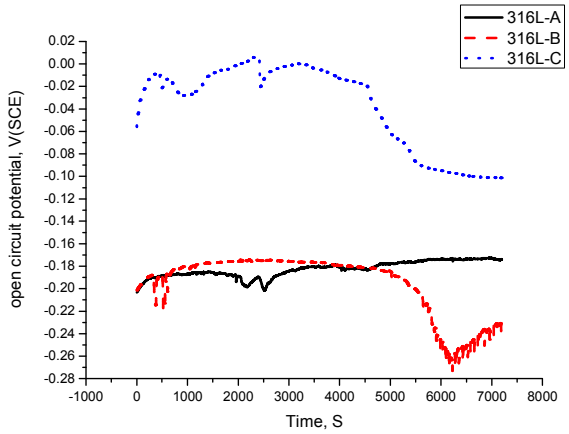


Fig.1 Corrosion potential of the three 316L stainless steel in 3.5%NaCl

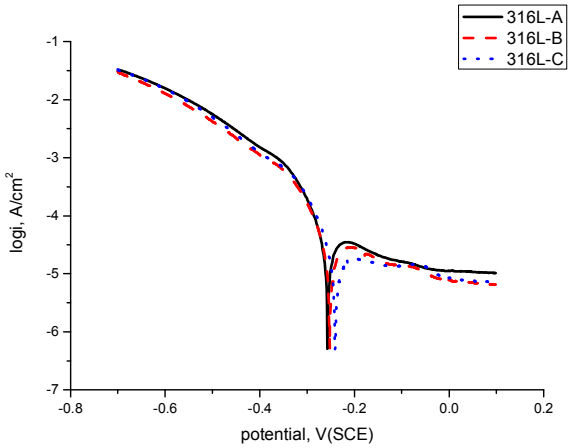
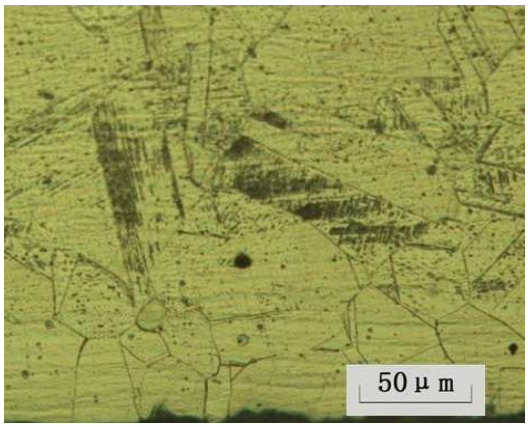


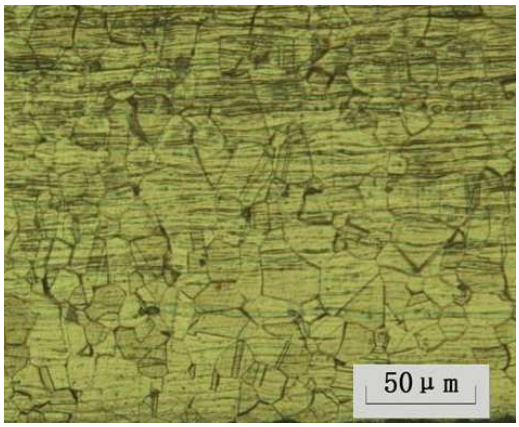
Fig.2 Tafel plot of polarization curves of three stainless steels in 3.5%NaCl

Metallographic Examinations

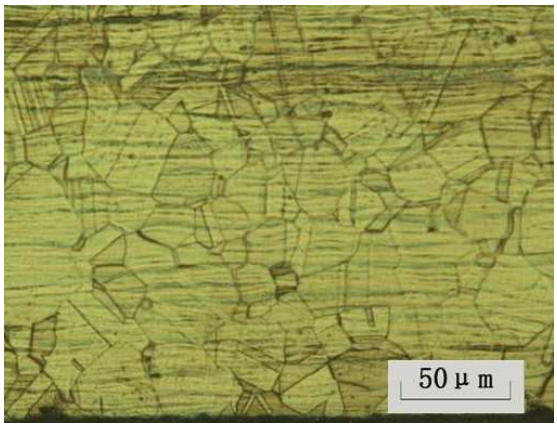
Fig.3 shows the results of optical microscope examination and SEM examination of the three stainless steels. The optical metallographs (Fig.3 a, b, c) show that 316L-A has larger grain size than 316L-B and 316L-C. It also shows that 316L-C has fewer inclusions than 316L-A and 316L-B. The SEM photos (Fig.3 d,e,f) also show the existence of more inclusions in 316L-A and 316L-B.



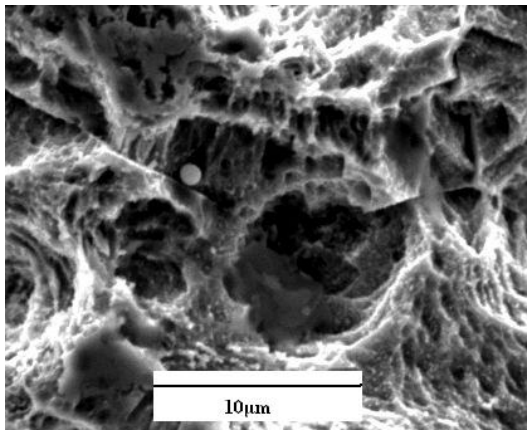
a 316L-A



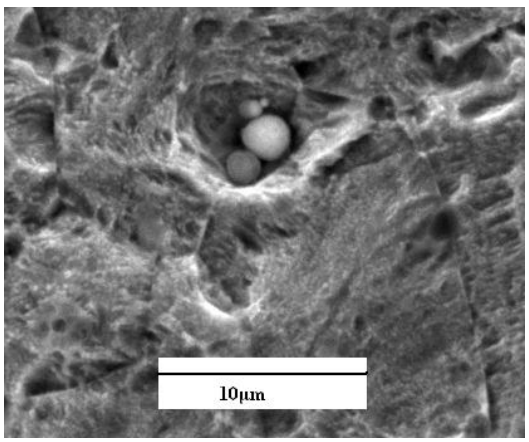
b 316L-B



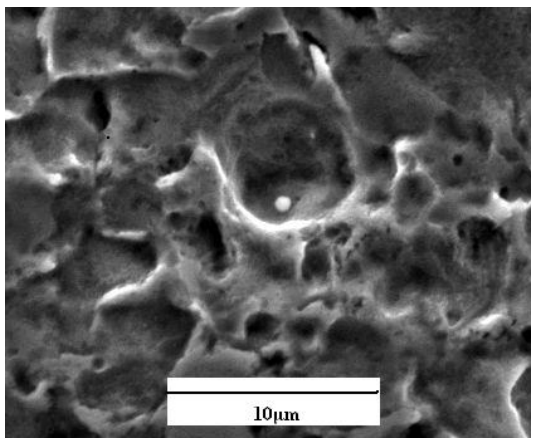
c 316L-C



d 316L-A



e 316L-B



f 316L-C

Fig.3 Results of metallographic examination of the three 316L stainless steels

Discussions

The above results show that the corrosion resistances of the three 316L stainless steels are different. Corrosion rate of 316L-B in 5%H_2SO_4 or 3.5%NaCl was approximately one time higher than 316L-C. The result of the dip test was in consistent with the electrochemical test. To explain the result, both chemical compositional factor and metallographic factor of the materials are needed to consider. To examine Table 1, we find that 316L-C has higher Cr and Ni contents than 316L-A and 316L-B. This is in consistent with the well known rule that higher Cr and Ni content in stainless steel are beneficial for its corrosion resistance. Many present stainless steel standards (such as AISI

in US and GB in China) specify chemical compositions of stainless steel in a range. For example, the Cr and Ni content of 316L stainless steel can be 16-18% and 10-14% respectively [5]. For economic consideration, some manufactures control the Cr and Ni content in stainless steel in the low limit. This study has showed that the corrosion resistance (and the quality) of their products are actually related closely to the Cr and Ni content in the materials.

The SEM micrographs in Fig.3 show the existence of inclusions in all the stainless steels Inclusion composition and morphology is an important factor affecting corrosion resistance of stainless steels [6-8]. It can be seen that 316L-C has fewer inclusions in comparison with 316L-A and 316L-B. This may be one of the reasons why 316L-C has superior corrosion resistance.

Conclusions

From the above results, following conclusions can be obtained: even slight compositional (especially chromium and nickel content) variance and metallographic difference in 316L stainless steel will cause the change of its corrosion resistance.

Reference

[1] S. Weng,C. Chen, C. J. Shang, J. Y. Weng, D. Y. Li, Corrosion behavior of a new developed ferritic stainless steels used in automobile exhaust system, Advanced Materials Research, 89-91 (2010) 102-106

[2] Saedlou, P. Santacreu, Suitable stainless steel selection for exhaust line containing a Selective Catalytic Reduction (SCR) system, *SAE 2011 World Congress and Exhibition*, 2011

[3] M. Barteri, F. Fazio, S. Fortunati, Stainless steels in car exhaust gas systems**,** Metallurgia Italiana, 91, 5 (1999) 31-36,

[4] A. Miyazaki, J. Hirasawa, S. Satoh, Advanced stainless steels for stricter regulations of automotive exhaust gas, Kawasaki Steel Technical Report, 43 (2000) 21-28

[5] T. L. Sudesh, L. Wijesinghe, D. J. Blackwood, characterization of passive films of 300 series stainless steels, Applied Surface Science, 253(2006) 1006-1009

[6] T. L. Sudesh, L. Wijesinghe, D. J. Blackwood, Real time pit initiation studies on stainless steels: the effects of sulfide inclusion. Corrosion Science, 49 (2007) 1755-1764

[7] L. M. Cabalin, M. P. Mateo, J. J. Laserna, Larger area mapping of non metallic inclusions in stainless steel by an automated system based on laser ablation, Spectrochimica Acta Part B 59 (2004) 567-575

[8] D. E. Williams, M. R. Kilburn, J. Cliff, G. I. N. Waterhouse, Compositional change around sulphide inclusions in stainless steels and implications for the initiation of pitting corrosion, Corrosion Science, 52 (2010) 3702-3716

Advanced Materials Research Vol. 936 (2014) pp 1102-1105
© (2014) Trans Tech Publications, Switzerland
doi:10.4028/www.scientific.net/AMR.936.1102

The Corrosion Behavior of Cu-Ni-Si alloy in Sea Water with Deep-Sea Bacteria

SHEN Yuan Yuan [1], ZHANG Li [2,a*], DONG Li Hua [2,b], LIU Tao [2], LEI Qian [3] and LI Zhou [3]

[1]Department of naval architecture and ocean engineering, Merchant Marine Academy, Shanghai Marine University, Haigang Road NO.1550,Pudong new area, Shanghai 201306, China

[2]College of Ocean Science and Engineering, Shanghai Maritime University, 1550 Haigang Av. Lingang New City, Shanghai 201306, China

[3] School of Materials Science and Engineering, Central South University, Changsha 410083, China

[a] zhangli@shmtu.edu.cn, [b]lhdong@shmtu.edu.cn

Keywords: Cu-Ni-Si alloy, corrosion behavior; EIS; seawater

Abstract: The corrosion behavior of Cu-Ni-Si alloy exposed to a nutrient-rich simulated seawater-based nutrient-rich medium in the presence of a deep-sea bacterial (*Erythrobacter pelagi sp.nov*) was investigated by metallographic microstructure observation, electrochemical impedance spectroscopy (EIS) measurement. It was demonstrated that the charge transfer resistance (Rct) and the resistance of oxide film(R_f) dramatically increased within 2 days then gradually decrease and becoming stable because of an patchy or blotchy biofilm formed on the surface of the alloy.

Introduction

Copper-nickel alloys are now being used extensively in electric power, electronics and instrumentation applications due to their electrical and thermal conductivity , excellent mechinability and corrosion resistance [1-3,7-8] .Cu-Ni-Si alloy is one of the most outstanding one due to its combination of high electrical conductivity and high strength, which has been considered as one of ideal materials used for electrical devices, such as semiconductor lead-frames, connectors, high-speed train contact wire clamps, and wear-resistant parts [4]. As a typical age-hardening alloy, this alloy is usually used in an over-aging condition [5-6]. The precipitates responsible for the strengthening effect have been identified as δ-Ni_2Si. So Cu-Ni-Si alloy have a good prospect used in deep-sea environment. It is obvious that previous investigations focused mainly on the properties of Cu-Ni-Si alloy used on land, while few published studies have documented the corrosion behavior of Cu-Ni-Si alloys in seawater environment. It is therefore significant to determine the corrosion behavior of Cu-Ni-Si alloy in the medium with deep-sea bacterial. The present study seeks to gain a better understanding on the influence of deep-sea bacterial on the corrosion behavior of the Cu-Ni-Si alloy as a function of time using electrochemical method.

Experimental Details

Test Specimen

The chemical composition (wt. %) of Cu-Ni-Si alloy in this work is: 90.83Cu, 7.54Ni and 1.63Si. The alloy was supplied as plate with planar dimensions of 100×500mm and a thickness of 1mm.

Metallographic Examination

Specimens were cut from the original plate samples with sizes of 10×10×1mm. Prior to the experiments, the specimens were sequentially ground using a series of grit (400, 800, 1000, 1500, and 2000) silicon carbide emery paper to a smooth surface, rubbed against smooth cloth using diamond (2.5μm) polishing liquid till reaching a mirror bright surface, rinsed with distilled water, and then immersed in solution (2g $K_2Cr_2O_7$，8mL H_2SO_4，4mL saturated sodium chloride solution，100mLH_2O) for etching.

Electrochemical Measurements

Specimens were welded with copper wire, and then encapsulated bare copper wire and weld surface with ethoxyline resin. Exposure area was 1 cm^2. After solidification, the exposure face was sequentially ground using a series of grit (400 and 800) silicon carbide emery paper to a smooth surface, and degreased with acetone and ethanol, then rinsed with distilled water, and finally dried in drying vessel. The electrochemical impedance investigations and polarization measurements were performed using Autolab electrochemical workstation. A conventional three-electrode glass corrosion cell was used. A saturated calomel electrode (SCE) was used as the reference electrode， a platinum slice which area was 4 cm^2 was used as the counter electrode and the Cu-Ni-Si alloy was used as working electrode. Text medium is a 3.5% sodium chloride solution to make sure the corrosion medium is the same. Before EIS measurements, the specimens should be immersed in medium for 30min at room temperature in order to make sure the test process is stable. For all EIS measurements， an excitation amplitude of 10 mV peak-to-peak was used. The frequency range is from 0.01 Hz to 10 kHz.

Results and Discussion

Metallographic Examination

In order to observe the microstructure of Cu-Ni-Si alloy, metallographic examination is carried out on the surface of the alloy. Figs. 1 show the metallographic images of the Cu-Ni-Si alloy. We can clearly observe the rolling direct and some intermetallic compounds. The grain size is about 10~20μm.

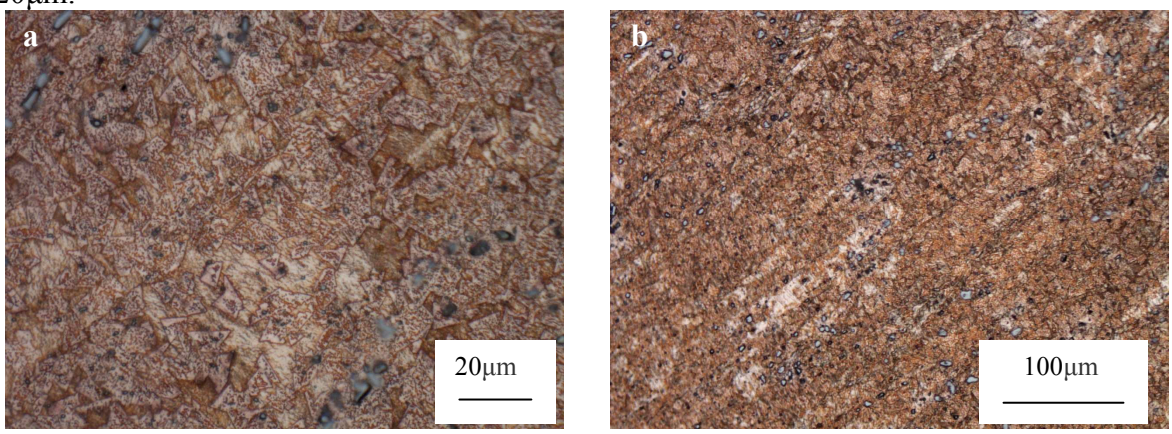


Fig.1. Metallographic structure of the Cu-Ni-Si alloy (a. 200× b. 100×)

Electrochemical Impedance Spectroscopy

Electrochemical impedance spectroscopy (EIS) is a powerful, non-destructive electrochemical technique for characterizing electrochemical reactions at the metal/electrolyte interface and the formation of corrosion products. Impedance spectra are normally displayed either in the form of a Nyquist (i.e., complex plane) plot or a Bode plot [9].Herein, impedance spectra of Cu-Ni-Si alloy immersed in medium with and without bacterial are recorded at the open circuit potential after 1, 2, 3, 4, 5, 6, and 7 days to monitor the corrosion behavior of Cu-Ni-Si alloy. Fig. 2 shows the impedance spectra in medium with deep-sea bacterial as a function of time. As shown in Fig. 2a, it is remarkable that the diameters of impedance loops increased first and then decreased with the immersion time from 0 to 7 days, which suggested first increase and then decrease in the corrosion rates of alloy specimen with time. The variation regulation of impedance loop diameters could be attributed to a corrosion produce film formed on the surface of Cu-Ni-Si alloy. At second day, the number of bacterial was the largest, the metabolic products were the most and the biofilm was thick. This suggested that Cu-Ni-Si alloy could form a biofilm during corrosion and the biofilm could improve the corrosion resistance of Cu-Ni-Si alloy. As shown in the phase angel Bode plots, there are two maxima, one located in higher frequency range and the other in the lower frequency range. Two peak

maxima changed to one from fifth day, this is because the number of bacterial decreased slightly and the biofilm became thinner with time.

The impedance spectra in medium without deep-sea bacterial after different immersion time were illustrated as Fig.3. The diameters of impedance loops fluctuated and the number of maxima varied between one and two. This demonstrated that the Cu-Ni-Si alloy immersed in the abiotic medium did not form biofilm on the surface. So the corrosion rate of alloy did not decreased with immersion time.

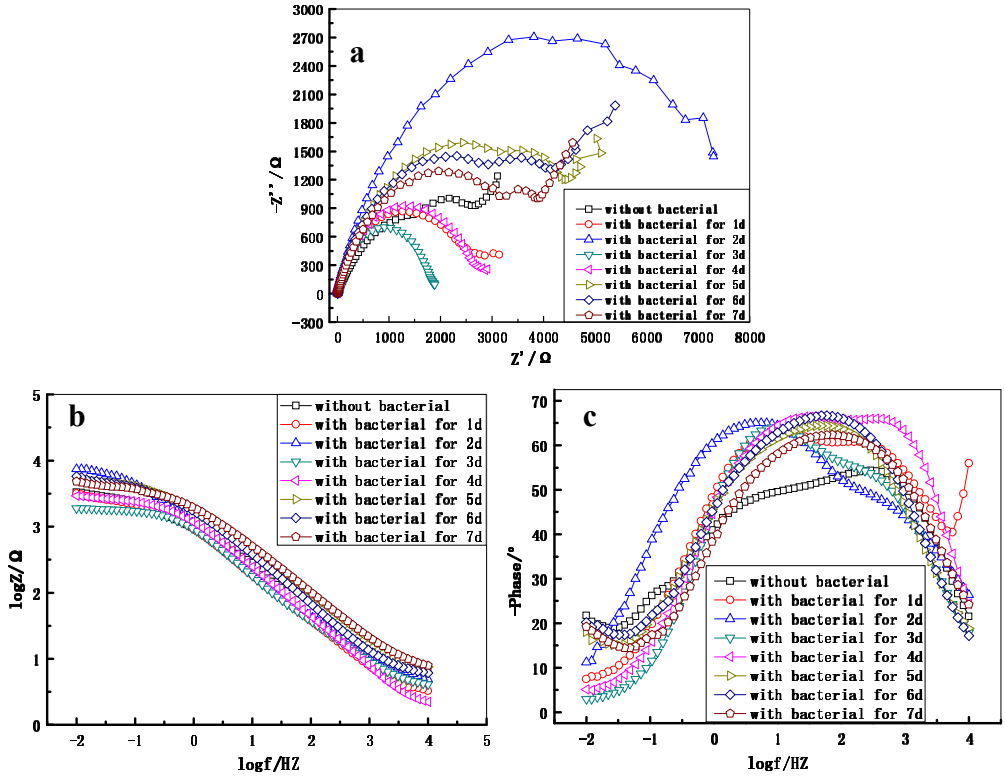


Fig.2. Impedance spectra of the Cu-Ni-Si alloy recorded at the open circuit potential immersed in medium with deep-sea bacterial for 7days (metabolic cycle of deep-sea bacterial)

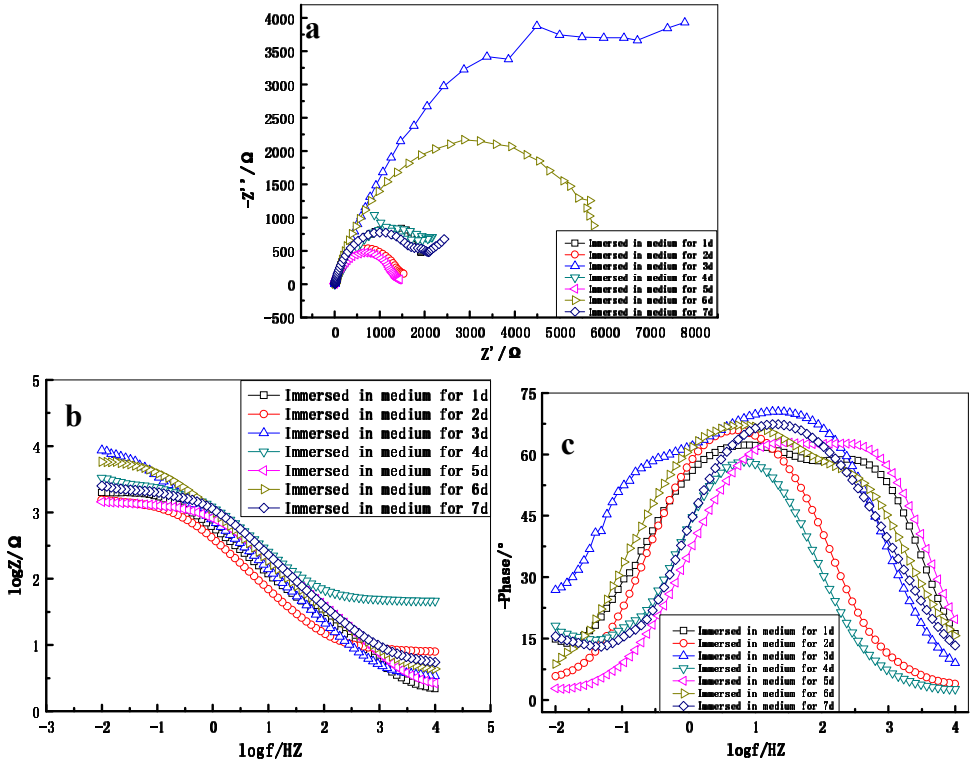


Fig.3. Impedance spectra of the Cu-Ni-Si alloy recorded at the open circuit potential immersed in medium without deep-sea bacterial for 7days

Summary

The corrosion behavior of the Cu-Ni-Si alloy in the absence and presence of a deep-sea bacterial (*Erythrobacter pelagi sp. nov*)in a nutrient-rich simulated seawater based medium as a function of immersion time were investigated using electrochemical methods. The EIS data showed that the corrosion rates of the alloy specimens gradually decreased under the attack of the bacterial cells and its EPS. A patchy or blotchy biofilm was formed on the surface of the alloy and protect inhibit the corrosion of the alloy. While in the abiltic medium, the EIS results showed that the Cu_2O thin oxide film of the alloy was destroyed by chloride ions then the immerged fresh surface was oxidized quickly by oxygen in seawater. The processes of destroy and rebuilt of oxide film occurred continuously, which caused the corrosion resistance of Cu-Ni-Si alloy decreased.

Acknowledgements

This work was financially supported by the National Basic Research Program of China (2014CB643306), National Natural Science Foundation (51101098, 51003056), Shanghai Foundation for Development of Science and Technology (12231204102) and Ph.D. Programs Foundation of Ministry of Education of China(20103121110003).

References

[1] Božić D, Dimčić O, Dimčić B, Cvijović I, Rajković V, The combination of precipitation and dispersion hardening in powder metallurgy produced Cu-Ti-Si alloy, Materials Characterization 59 (2008) 1122-1126.

[2] Lee Jeong-Keun, On the effect of substituting copper powder with cupric salt for the sintering process of W-Cu MIM Parts, Int J Refract Met Hard Mater, 26(2008)290-294.

[3] Abdel Yazid Khereddine, Faycal Hadj Larbi, Hiba Azzeddine, Thierry Baudin, Francois Brisset ,Anne-Laure Helbert , Marie-Helene Mathon, Megumi Kawasaki, Djamel Bradai, Terence G. Langdon , Microstructures and textures of a Cu-Ni-Si alloy processed by high-pressure torsion, Journal of Alloys and Compounds, 574(2013) 361-367.

[4] Ryoichi Monzen, Chihiro Watanabe, Microstructure and mechanical properties of Cu–Ni–Si alloys, Materials Science and Engineering A , 483-484(2008) 117-119.

[5] LEI Qian, LI Zhou, PAN Zhi-yong, WANG Ming-pu, XIAO Zhu, CHEN Chang, Dynamics of phase transformation of Cu-Ni-Si alloy with super-high strength and high conductivity during aging, Transactions of Nonferrous Metals Society of China, (2010) 1006-1011.

[6] Q. Lei, Z. Li, T. Xiao, Y. Pang, Z.Q. Xiang , W.T. Qiu, Z. Xiao, A new ultrahigh strength Cu-Ni-Si alloy , Intermetallics, 42(2013) 77-84.

[7] M. Metikoš-Hukovic´, R. Babic´, I. škugor , Z. Grubac, Copper-nickel alloys modified with thin surface films: Corrosion behavior in the presence of chloride ions, Corrosion Science 53 (2011) 347-352.

[8] Weihua Sun, Honghui Xu, Shuhong Liu, Yong Du, Zhaohui Yuan, Baiyun Huang, Phase equilibria of the Cu-Ni-Si system at 700℃ , Journal of Alloys and Compounds 509 (2011) 9776-9781.

[9] S.J. Yuan, S.O. Pehkonen, Surface characterization and corrosion behavior of 70/30 Cu-Ni alloy in pristine and sulfide-containing simulated seawater, Corrosion Science 49 (2007) 1276-1304.

Advanced Materials Research Vol. 936 (2014) pp 1106-1111
© (2014) Trans Tech Publications, Switzerland
doi:10.4028/www.scientific.net/AMR.936.1106

Corrosion performance of medical titanium alloy with different surface morphology

Zhang Jie[1a] Zhang Song-ying[1] Liu Bin[1b*] Li Ming-xin[1] Lin Qian-qian[1]
Wang Jin-qing[2c*]

[1] School of Stomatology, Lanzhou University, Lanzhou 730000

[2] State Key Laboratory of Solid Lubrication, Lanzhou Institute of Chemical Physics, Chinese Academy of Sciences, Lanzhou 730000

[a]zhangjie@lzu.edu.cn, [b]liubkq@lzu.edu.cn, [c]Jqwang@licp.cas.cn

Supported by:Foundation for Openning project of State Key Laboratory of Solid Lubrication, Lanzhou Institute of Chemical Physics, Chinese Academy of Sciences.No:LSL-1208

Keywords: titanium alloy, sand blasting and acid etching , corrosion resistance

Abstract. [Objective] The purpose of this study was to evaluate the variation of surface morphology of titanium alloy after sand blasting with different particle sizes of Al_2O_3 sand and acid etching, and its corrosion resistance property. **[Methods]** The surfaces of titanium alloy were first treated with the different sands and then acid etched with mixture of 18% HCl and 48% H_2SO_4. The morphology of samples was investigated by scanning electron microscopy (SEM). The potentiodynamic polarization curves of the various surfaces were obtained by electrochemical workstation (CHI 660E) in simulated body fluid (SBF). **[Results and conclusions]** It is observed that pore sizes on surface increases with the increase of sand grain diameter while there is no obvious change after acid etching. After sand blasting and acid etching, the corrosion resistance of titanium alloy was improved. However, as the pore size of the surface increases, the corrosion resistance gradually degrades and this becomes even more obvious after acid etching. The investigation of the corrosion rate indicates there is an increasing trend with the emergence of small pores.

Introduction

Titanium alloy has a well application prospect in oral medicine due to following characteris：low density，high intensity，suitable thermal conductivity,good biocompatibility and corrosion，no-toxicity，and low mass[1] In recent years,there are researches focus to take titanium alloy as dental implant instead of natural root [2-4]. As an implant, the surface of titanium alloy should be modified with the aim of optimizing osseointegration and stability. Previous studies reported that rough surface was better than smooth surface to increase the mechanical stability of the implant, stimulate cell growth and promote early osseointegration [5, 6]. Sand blasting with acid etching is considered one of the common surface treatment techniques, which has shown great superiority in clinical applications because of increasing the surface roughness and the area contacting with bone [7]. The body fluid is a kind of electrolyte solution containing a variety of organic acid, protein and alkali metal ion, which is a dynamic oxidation environment including protein [8]. After being implanted into the bone, titanium alloy will be immersed in the complex environment for a long time. Under the action of proteins, enzymes and cells, there will produce the corrosion substances such as ions, oxide and chloride around the implant, which contact with adjacent tissue, even infiltrate into the normal tissue or the whole biological system. These factors will affect or stimulate the normal tissue impacting on long-term success rate of implant [9].

Recently, the research of titanium alloy with rough surface mainly focused on the positive aspect of improving osseointegration, while paid little attention to negative effects resulting from the roughing treatment. The study found that the change of titanium alloy surface morphology was likely to

associate with its corrosion resistance. For example, Lautenschlager et al. [10] early evaluated the corrosion behavior of porous metal surface by electrochemistry method. They found that the corrosion resistance property of porous metal was the same with the substrate. And by metal ion dissolution experiments, Cao et al. [11] indirectly proved that the rough surface resulting from sand blasting and acid etching reduced the corrosion resistance property of titanium alloy. At the same time, another [12, 13] reported the different surface roughness could be obtained on the smooth surface of titanium alloy by sand blasting and acid etching. With the increase of surface roughness, its corrosion resistance reduced. Micro-rough surface than macro rough surface had better corrosion resistance. But there were also researchers [14] thought the difference between sand particle diameter and corrosion resistance was no statistical significance. Other relevant researches [15, 16] showed the corrosion rate of the porous implant with higher surface area was higher, but the increase of surface area (5 ~ 10 times) was beneficial to the long-term security of the implant. In this paper, first by sand blasting and acid etching using Al_2O_3 with different particle sizes we produced different rough topography on titanium alloy surface. Then its morphology and structure were analyzed and the corrosion resistance of the different surface was measured by electrochemistry method, aiming to investigate the relationship between the morphology and structure and the corrosion resistance of titanium alloy.

Materials and methods

Preparation of titanium samples

The Ti-6Al-4V were suitably cut into small samples of approximately 10mm× 10mm×1mm and polished using silicon carbide (SiC) papers successively from grade 600, 1000 to1500 grit to remove surface oxidation layer. The alumina (Al_2O_3) particles was loaded into the sandblasting equipment and then titanium alloy surfaces were blasted by alumina (Al_2O_3) particles in the condition of 10cm distance, an incidence angle of 90° and 0.6 MPa pressure for 30s through a blasting nozzle. After treatments, all samples were acid etched with an equal volume of mixed acid solution of 18% HCl and 48% H_2SO_4 (v/v) by immersing in ultrasonic bath for 45min (ultrasonic conditions: temperature 36℃, frequency: 70Hz) and afterwards, the samples were ultrasonic cleaned in distilled water for 10min and then dried by N_2 before using.

Group of experiments

The pretreated titanium alloy samples were randomly divided into four groups: Group 1: Control (Ti). Untreated titanium alloy surface. Group 2: Blasted titanium (S). Divided into three groups, titanium alloy surfaces were blasted by alumina (Al_2O_3) particles with three types of 36#(S36), 60#(S60) and 100#(S100). Group 3: Etched titanium (ATi).Pretreated titanium alloy surfaces were etched with mixed acid solution. Group 4: Sand blasted and acid etched titanium (SA). Divided into three groups, titanium alloy surfaces were blasted by alumina (Al_2O_3) particles with three types of 36#(S36), 60#(S60) and 100#(S100). Next, these blasted surfaces were etched as described above.

Characterization of morphology

The surface morphology of the samples was examined by scanning electron microscopy. In order to improve the electrical conductivity of titanium, gold were produced by sputtering on each sample.

Electrochemical test

Containing 10% fetal bovine serum simulated body fluid (SBF) as medium, the potentiodynamic polarization curves of the various surfaces were obtained by electrochemical workstation (CHI 660E) in simulated body fluid (SBF). The experiment was carried out in the condition of platinum sheet as the auxiliary electrode, saturated calomel electrode as the reference electrode, the samples as the working electrode, initial scan voltage of -2.0V, terminate scan voltage of -0.2V, and scan speed of 0.01V/S. The potentiodynamic polarization curves were obtained by electrochemical workstation and measurement software, to obtain the corrosion potential and corrosion current. At last, we calculated corrosion current density of samples through the formula: corrosion current density = corrosion current / corrosion area.

Results and discussion

SEM

Figure 1 shows the surfaces of sand blasting (S) group and sand blasting and acid etching (SA) group are irregular concave or convex structure resembling crater shape, which of the control group (Ti) are uniform scratches (Fig. 1 a). After sand blasting, the surfaces fluctuate largely. The biger concave pits are up to about 50 microns in diameter (Fig. 1 b); c is less than b, less than 30 microns in diameter; d is less than c, less than 10 microns in diameter. After acid etching, three groups are all visible to the big concave pits inlaid with little secondary pits, and the diameter of secondary pits are about 0.1 ~ 1.0 microns. The surfaces of g and h are obtuse and no gap with honeycomb structure. f shows the excessive concave pits, discontinuous edges. SEM reveals surface concave size obtained by 60# is closest to osteoblast diameter (about 10um), which is most suitable for the growth of osteoblast by previous biology experiments. The roughness has no obvious difference before and after the acid etching, which shows acid etching does not change the rough topography obtained by sand blasting. Combined with Fig.1, the acid etching can make the surface obtuse, and form secondary pitting concaves of 1um average diameter within the primary holes. Zeng et al. [17] investigated the morphology changes of titanium plate after sand blasting and acid etching in HCl/H_2SO_4 mixed acid under 75℃ with 10 to 60 min. They found the etching time of 30min could form 1 ~ 5um small pitting concave in the rough surface obtained by sand blasting, and the surface was uniform.

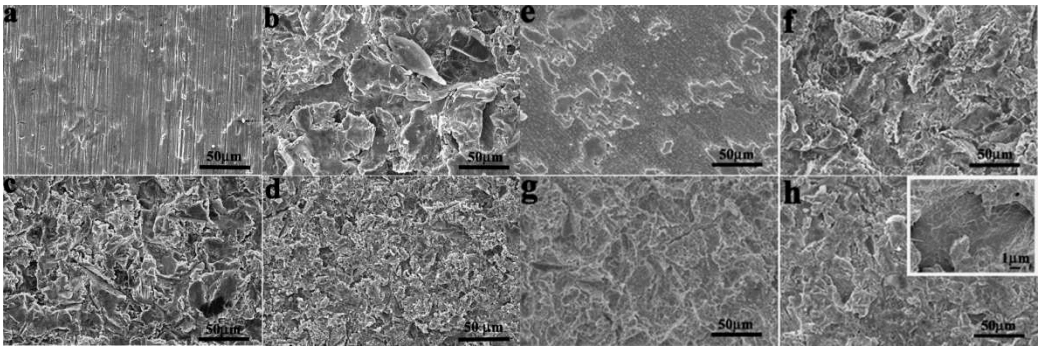


Fig 1 Left: SEM images of Ti alloy after sand blasting with different types of sand. Right: SEM images of Ti alloy after sand blasting and acid etching using 18% HCl and 48% H_2SO_4. ae: control group, bf: 36#, cg: 60#, dh: 100#.

Corrosion Resistance

Fig.2 shows the Tafel curves of titanium alloy in SBF by electrochemical workstation after different treatment. It can be seen that the shape of Tafel curves is basically the same in SBF, which of S60 group is at the right hand side, and ATi group at the left side. The curves of ATi, SA36, SA60 and SA100 are all in the left side of corresponding Ti, S36, S60 and S100. By Tafel curves, the corrosion potential (V) and the corrosion current density (A/cm^2) of different surfaces are figured out, as shown in Tab.1. We find that the negative value of the corrosion potential in S60 group is smallest (-0.9213V). After acid etching the negative values all increase, and ATi group is largest (-1.2893 V). The minimum corrosion current density is 2.874 x 10-6 A/cm^2 in Ti group, which of all groups increase after sand blasting and acid etching and SA36 group is largest (27.425×10^{-6} A/cm^2).

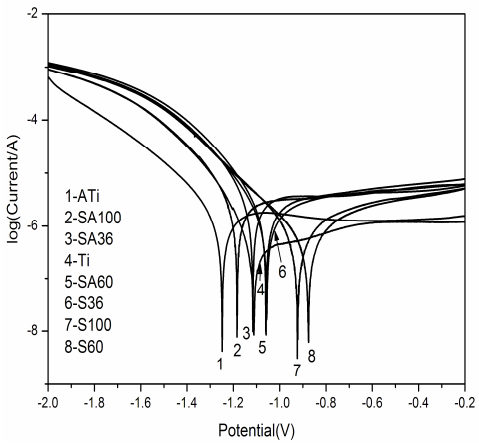


Fig 2 The Tafel curves of the different surfaces in SBF

Tab 1 Corrosion potential and corrosion current density of the different surfaces

	Ti	S36	S60	S100	ATi	SA36	SA60	SA100
Corrosion voltage (V)	**-1.1385**	**-1.0369**	**-0.9213**	**-0.9378**	**-1.2893**	**-1.1212**	**-1.0517**	**-1.1713**
Current density ($\times 10^{-6}$A/cm^2)	**2.874**	**11.250**	**5.300**	**4.038**	**12.867**	**27.425**	**15.643**	**21.450**

About the phenomenon of metal corrosion, some scholars put forward "model of corroded galvanic cell" [18]. The formation of galvanic cell results in the corrosion of the metal, which weaken the intensity and hardness of implant and also shorten the clinical survivorship. Even the corrosion products make the body produce a variety of adverse reactions, including the local or systemic damage [19]. According to the electrochemical theory，the greater the negative value of corrosion potential, the greater the tendency of metal corrosion, and the greater the positive value of corrosion potential, the smaller the tendency of metal corrosion. Correspondingly, the larger the corrosion current density, the faster the corrosion rate of metal, and the smaller the corrosion current density, the slower the corrosion rate of metal.

The results showed the corrosion resistance of sandblasted samples were better than untreated titanium alloy. In addition, there were no statistical differences between the S60 and S100 group ($P > 0.05$), but both were significantly better than the S36 group. After acid etching, the corrosion resistance of titanium alloy was all significantly weaker, as the ATi group was smallest. When the titanium alloy was acid etched, under the effect of the H^+, there were pitting corrosion reactions, which caused decrease of corrosion resistance and acceleration of corrosion [20]. The corrosion rate of the treated groups was significantly greater than untreated titanium, and with the increase of surface roughness, the speed of corrosion was presented increased trend. Correlation theory [18] has reported most pitting corrosion was occurred on metal materials with passive film or protective film on the surface. When the defective materials were soaked in the electrolyte solution containing the halogen elements such as chlorine, they were more likely to produce pitting corrosion, because the defects of the surface film of the metal were exposed and activated. After acid etching, some small pitting concaves were formed in the passivation film under the effect of acid, thus the corrosion resistance was decreased. Xue et al. [21] investigated the influence of rough surface on metal chemical corrosion, and thought that irregular topography of rough metal surface greatly affected the amount of chemical corrosion reaction thermodynamics, causing or accelerating the chemical corrosion. Li et al. [22] researched the effects of different surface morphologies on metal corrosion and electrochemical behavior and they found that the corrosion rate of the rough surface with small pits is greater, which is consistent with the results obtained in this experiment.

Conclusions

The conclusions of this work are summarized as follows. Different surface roughness can be obtained by using Al_2O_3 with different particle sizes, while there is no obvious change after acid etching. After sand blasting and acid etching, surface morphology and crystal structure are changed, which have an impact on the corrosion resistance of titanium alloy. Corrosion resistance is improved by sand blasting, but with the increase of surface roughness, the corrosion resistance gradually degrades and the decline is even more obvious after acid etching. The investigation of the corrosion rate indicates there is an increasing trend with the increase of surface roughness and emergence of small pores. To conclude, some measures should be taken to avoid corrosion of titanium alloys by simulated body fluid. For this reason， following implantation into oral cavity , implant top should be well protected .

References

[1] Zhang Dong,Zhang Pu-liang,Pan Xiao-jing,et al. Corrosion performance of medical titanium alloys in three different physiological electrolytes[J]. Journal of Clinical Rehabilitative Tissue Engineering Research,2009,13(34):6689-6692.

[2] M. J. Werbitt, P. V. Goldberg. The immediate implant: bone preservation and bone regeneration [J]. The International Journal of Periodontics & Restorative Dentistry, 1992, 12(3): 206-217.

[3] S. A. Jovanovic, H. Spiekermann, E. J. Richter. Bone regeneration around titanium dental implants in dehisced defect sites: a clinical study[J]. International Journal of Oral and Maxillofacial Implants, 1992, 7(2): 233-245.

[4] A. Wennerberg, T. Albrektsson. Effects of titanium surface topography on bone integration: a systematic review[J]. Clinical Oral Implant Research, 2009, 20(Supplement s4): 172–184.

[5] Z. Qu, X. H. Rausch-Fan, M. Wieland, et al. The initial attachment and subsequent behavior regulation of osteoblasts by dental implant surface modification[J]. Journal of Biomedical Materials Research Part A, 2007, 82A (3): 658-668.

[6] A. Wennerberg. The importance of surface roughness for implant incorporation[J]. Int. J. Mach. Tools Manufact, 1998, 38(S5-6): 657-662.

[7] S. Szmukler-Moncler, D. Perrin, V. Ahossi, et al. Biological properties of acid etched titanium implants: effect of sandblasting on bone anchorage[J]. Journal of Biomedical Materials Research Part B: Applied Biomaterials, 2004, 68B(2): 149-159.

[8] R. N. Pierson, J. Wang, E. W. Colt, P. Neumann. Body composition measurements in normal man: The potassium, sodium, sulfate and tritium spaces in 58 adults[J]. Journal of Chronic Diseases, 1982, 35(6): 419-428.

[9] Wang Ming, Song Xiping. Study actuality of corrosion, mechanical compatibility and biocompatibility of titanium alloys for medical application[J]. Titanium industry progress, 2008, 25(2): 13-18.

[10] E. P. Lautenschlager, N. K. Sarker, A. Acharya, et al. Anodic polarization of porous fiber metals[J]. J. Biomed. Mater. Res., 1974, 8(2): 189–191.

[11] Cao Hongdan. The study on properties of surfaces of titanium implants treated by different roughing methods[D]. Sichuan University, 2005.

[12] L. Joska, J. Fojt. Corrosion behaviour of titanium after short-term exposure to an acidic environment containing fluoride ions[J]. J Mater Sci: Mater Med, 2010, 21(2):481–488.

[13] Yan Honghai, Hu Linghua, Huang Hairong. Corrosion resistance of pure titanium implant with different surface micro roughness[J]. Chinese Journal of Oral Implantology, 2008, 13(4): 175-179.

[14] C. Aparicio, F. J. Gil, C. Fonseca, et al. Corrosion behaviour of commercially pure titanium shot blasted with different materials and sizes of shot particles for dental implant applications[J]. Biomaterials, 2003, 24(2): 263-273.

[15] R. M. Pilliar. Porous-surfaced metallic implants for orthopedic applications[J]. Journal of Biomedical Materials Research, 1987, 21(A1 Suppl): 1-33.
[16] Lv Yupeng, Zhu Ruifu, Ma Quansheng, et al. Current evolution of biomedical titanium and its alloy implant materials[J]. Chinese Journal of Oral Implantology, 2000, 5(1): 43-49.
[17] Z. Lin, Y. Wang, D. N. Wang, et al. Porous structure preparation and wetability control on titanium implant[J]. Surface and Coatings Technology, 2013, 228(Supplement 1): S131–S136.
[18] Cao Chunan. Principles of electrochemistry of corrosion[M]. Beijing: Chemical Industry Press, 2008.
[19] A. S. Hiyasat, O. M. Bashabsheh, H. Darmani. Elements released from dental casting alloys and their cytotoxic effects[J]. Int J Prosthodont, 2002, 15(5): 473 – 478.
[20] Liu Li, Mao Yingjie, Chen Zhihong. The effect on the corrosion resistance of titanium alloy in the artificial saliva with different ph value[J]. Chinese Journal of Biomedical Engineering, 2006, 25(2): 166-169.
[21] Xue Yongqiang, Luan Chunhui, Fan Jinchuan. The Effect of Rough Surfaces on Chemical Corrosions of Metals[J]. Materials Review, 1998, 12(2): 23-24.
[22] W. Li, D.Y. Li. Influence of surface morphology on corrosion and electronic behavior[J]. Acta Materialia, 2006, 54(2): 445–452.

Advanced Materials Research Vol. 936 (2014) pp 1112-1115
© (2014) Trans Tech Publications, Switzerland
doi:10.4028/www.scientific.net/AMR.936.1112

Analyzing the Corrosion of "Hai Yang Shi You 931"Jack-up Drilling Unit

Wang Hong[1, a], Xu Zhi[2,b]

[1]Bohai Shipbuilding Vocational college, China

[2]China Shipping Industry (Jiangsu) Co.,Ltd, China

[a]bhcy_wanhng@163.com, [b]xuzhi@cic-jsshipyard.com

Keywords: Cathodic Protection; anode; jack-up; corrosion

Abstract. Severe corrosion was found on structures and spud leg of "Hai Yang Shi You 931" jack-up drilling unit according to the data of inspection. Some analysis and corrective action was required for Cathodic Protection system. The reason was concluded according to the environmental condition, service life, coating surface area, coating breakdown area, protection surface area and chemical test of anode etc. The electrochemical reaction was rapid suppressed and lost its due utility with the anode was covered by "Sacrifice" product and marine growth. Near the waterline, the oxygen strong bad battery effect was easy to form, and the chance and degree of corrosion occurrence was increased on spud leg.

Introduction

Severe corrosion was found on structures and spud leg of "Hai Yang Shi You 931" jack-up drilling unit according to the data of 2013 inspection. Some analysis and corrective action was required for Cathodic Protection system. But the original calculation sheet and layout plan for Sacrificial Anode system was not found, then the Sacrificial anodes system layout plan that designed by Whale Kapper in 2008 was not approved by CCS and the layout plan for three spud legs was lost. As requirement of client, we carry out inspection, calculation and analysis on anode system of "Hai Yang Shi You 931". According to the environmental condition, service life, coating surface area, coating breakdown area, protection surface area and the type of anode etc., we performed the calculation and assessment for the Sacrificial Anode system of platform and make sure whether the anode is satisfied with the requirement.

Site Survey

Anodes.

There were two types anode on the Spud leg such as shown in fig.1.



Fig. 1 The anode on spud leg and spud can

One was "0"type anode (Size: 55cm×15cm×19cm) which the integrity rate was more than 90%. It was installed on most parts of #1,2,3 spud leg. There were 6 pieces of anode on level poles each layer and installation position was about 50cm from column. Another was "1"type anode (Size: 90cm×12cm×9cm) which the integrity rate was more than 95%. It was only installed on level poles of

6 ~ 12 layer under # 1 spud leg. There were 6 pieces of anode on level poles each layer and installation position was about 65cm from column.

Only one type anodes (size: 150cm×8cm×8cm) were installed on outside surface of three spud can. There some anodes were not found. The corrosion of anodes was more differences in individual.



Fig. 2 Corrosion of jack-up drilling unit

There were two types anode (One: 147cm×5cm×7cm. Another: 20cm ×7cm×15cm) inside spud can. The corrosion of anodes was more differences in individual.

Only one type anodes (size: 150cm×8cm×8cm) were installed on the frame of submersible pump. The corrosion of anodes was more differences in individual.

Site Survey Illustration for Construction Coating

Antiseptic treatment for serious corrosion was performed near the waterline of spud leg. Because the surface of the spud leg was covered by marine growth within approximately 10 meters above spud can, the intuitive judgment should be not taken for the coating condition. The surface coating was in good basic condition on the rest part of the spud leg underwater. The pitting, caviation was found on several coating damage of the pipe. The coating outside spud can was in good basic condition and the obvious corrosion was not found. The mostly surface was covered by rust inside spud can, but the obvious pitting, caviation was not found. The coating of the submersible pump frame was in good basic condition and the obvious corrosion was not found.

The Sampling Introductions.

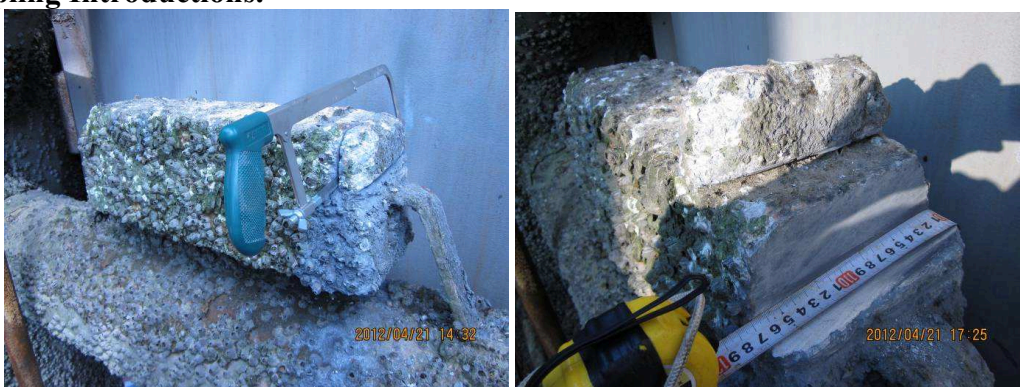


Fig. 3 The sampling of anodes

The "0"type anode on #3 spud leg was random sampled by hand saw. (number:931-0)

The "1"type anode on #1 spud leg was random sampled by hand saw. (number:931-1)

Analysis

Observational Check on Coating

The coating was general in good condition under water, but the obvious corrosion was found on several coating damage.

The main protection was provided by coating for the hull.

The obvious corrosion was found on splash zone.

The coating was damage easily for impacted by wave flow on splash zone.

In the air, sea water near the oxygen strong bad battery effect was formed, and the corrosion was increased on spud leg.

Near the waterline or seafloor, the oxygen strong bad battery effect was also formed due to some places attached marine growth and some places not attached on the spud leg, thus the corrosion was increased.

Check on the Remaining Quantity of Anodes.

A. The anode on spud leg was not obviously consumed and the Integrity rate was more than 90%. According to the calculation, the "0"type anodes lifetime was 15.2 years and the "1"type anodes lifetime was 7.37 years.

The 931 platform has been worked 10 years from 1993, the integrity rate of the mostly anodes should be 0~50% because some anodes was only replaced in 2008 and the others was original.
The actual consumptions of these anodes ("0"type and "1"type") was not satisfied with the design and the rules.

The anodes near the region where the serious corrosion was found after the coating damage on spud leg was not obvious consumed and cathodic protection was not provided.

B. The corrosion situation of anodes outside spud can were more differences in individual and integrity rate was 70~95%.

The anode lifetime was 14.6 years in the position. The integrity rate should be 75% after it served 4 years.

The actual consumption of these anodes was corresponded to the code and did not see the obvious flaws.

C. The corrosion situation of anodes inside spud can were more differences in individual and integrity rate was 0~95%.

The anode lifetime was 4 years in the position. The anodes should be exhausted after it served 4 years.

The actual consumption of these anodes was corresponded to the expectation.

D. The corrosion situation of anodes on the submersible pump frame were more differences in individual and integrity rate was 0~90%.

The situation of these anodes was similiar to that outside spud can. At present the integrity rate should be 75%.

The anodic dissolution was nonuniform for the environmental factor (the position was difference, for example, meet the water, negative side water etc.) was differences.

Electric Potential Inspection Underwater

Anode: -1068~ -1026mv，metal base: -1017~ -970mv.

The electric potential was normal range. In clearing the surface attachments of the anode, potential detection data showed that the anode protection system is in normal operation condition.

Chemical Composition of the Sample

The anode samples was submitted to Guangzhou mechanical and electrical industry physical and chemical measurement center, and material chemical component test was completed, the results such as shown in table 1

TABLE 1 ANODE CHEMICAL COMPOSITION

composition	Zn	In	Cd	Sn	Mg	Ti	Si	Fe	Cu
Inspection Results	4.1~ 4.5	0.008~ 0.0095	<0.01	<0.002	0.003	0.004	0.066	0.063~ 0.079	0.0051
Normal value(scope)	4.0~ 7.0	0.02~ 0.05	-	-	0.5~ 1.5	0.01~ 0.08	<0.1	<0.15	<0.01

The chemical composition of the "0"type anode was closed to the "1"type anode, but it was not c with five types Al-Zn-In sacrificial anode that approved by the national standard

If the anode impurities such as Si, Fe were too much, they could make the anode surface oxidation product not easy to fall off, and then the anodic dissolution was uneven. And indium In was the main elements of aluminium alloy anode, it could partly suppressed the bad influence of the

electrochemical properties caused by Si, Fe of anode impurities. But the sample chemical composition analysis results showed that content of indium In was quite low.

Electrochemical properties test of the sample

TABLE 2 THE RESULTS OF ELECTROCHEMICAL PROPERTIES

	open circuit potential	working potential	actual electric capacity	current efficiency	Consumption rate	Dissolution status
Inspection Results	-1.125 ~ -1.113V	-1.125 ~ -1.055V	2613～ 2631Ah/kg	90.4~ 91.0%	3.35 kg/(A·a)	dissolve uneven
Normal value (scope)	-1.18 ~ -1.10V	-1.12 ~ -1.05V	≥ 2600Ah/kg	≥90%	≤3.37 kg/(A·a)	dissolve even, product easy to fall off

The related performance and parameters of the "0"type and "1"type anode were corresponded to requirements of the rules.

Because the sample anode dissolution was uneven and oxidation product was not easy to fall off, the anode protection ability was rapid decline with the time passing.

Summary

The "0" type and "1" type anodes were not standard type aluminum alloy anode. "Sacrifice" product of the anode was uneven dissolved and not easy to fall off. The electrochemical reaction was rapid suppressed and lost its due utility with the anode was covered by "Sacrifice" product and marine growth. Therefore, normally, the above two kinds of sizes, aluminum alloy anode couldn't meet the practical requirements. In addition, other parts of the anode material were unknown, actual effect had not seen the obvious flaws.

For the splash area was relatively serious corrosion phenomena, we think that we should pay attention to the following factors:

The coating (especially poor quality) was easy to damage when it was impacted by the wave flow.

Near the waterline, the oxygen strong bad battery effect was easy to form, and the chance and degree of corrosion occurrence was increased on spud leg.

Near the waterline or seafloor, the oxygen strong bad battery effect was also formed due to some places attached marine growth and the others not attached on the spud leg , thus the corrosion was increased.

References

[1] Ba FaHai, Li Ling, Lu Zhou, Fracture Wires Causes Analysis of Steel Wire Rope for Port Machine, J. Materials for Mechanical Engineering. 33 (2009) 90-93.

[2] M.B. Kermani, A. Morshed, The Carbon dioxide corrosion in oil and gas production-A Compendium, J. Corrosion. 2003.59 (8):659.

[3] Zhang DeYing, Shan LianMin, Analyses of Failure for Breaking of Wire Rope, J. Journal of GuiZhou University of Technology. 30 (2001) 23-25.

Advanced Materials Research Vol. 936 (2014) pp 1116-1119
© (2014) Trans Tech Publications, Switzerland
doi:10.4028/www.scientific.net/AMR.936.1116

Effects of Soil Type of Shanghai and Electrode Potential on Near-Neutral pH Stress Corrosion Cracking of Pipeline Steel X60

Guangfu LI[1, a], Dafeng Yan[2,b]

[1] Shanghai Research Institute of Materials, Shanghai Key Lab for Engineering Materials Evaluation, National Quality Supervision Testing Center for Metallic Materials, Shanghai/200437, China

[2]Shanghai Natural Gas Pipeline Network Company Ltd, Shanghai/201204, China

[a]guangfuli8298@vip.sina.com, [b] besttudor@hotmail.com

Keywords: pipeline steel; near-neutral pH stress corrosion cracking; electrode potential; soil type; X60

Abstract. The effects of soil type of Shanghai and electrode potential from cathodic protection point on near-neutral pH stress corrosion cracking (SCC) behavior of pipeline steel X60 has been investigated for structural integrity assessment. The SCC behavior was evaluated through slow strain rate tests (SSRT) at various electrode potentials in three solutions containing different typical soils. Results showed that the SCC susceptibility generally increased with decreasing electrode potential in all the three environments, with quick increase happening in the range from -1500 to -700mV(SCE). It is suggested that hydrogen induced cracking should dominate the SCC at low potentials. In cathodic potential range, the rank of the SCC susceptibility for soil type was Near-city soil > Cyan-purple soil > Cyan-yellow soil. In anodic potential range, SCC susceptibility curves mixed each other in the three solutions.

Introduction

SCC from the soil side has become one of the most important issues in the structural integrity of high pressure pipeline, which have resulted in many severe failures of underground pipelines for long distance transmission of gas or oil in the world. The SCC of pipelines is usually divided into two basic forms, that is, high pH SCC occurring in concentrated carbonate-bicarbonate solution and near-neutral pH SCC taking place in dilute carbonate-bicarbonate solutions containing small amount of chloride and sulfate. The latter form was firstly reported in Canada in 1985, with transgranular cracking mode, which has become a common failure mode [1]. Many researches have been attracted to the cracking behavior and prediction methodology. The soil type and electrode potential have been regarded as vital environmental factors in the cracking characterization and prediction, from both academic and engineering points [2-6]) . However, the effects and the mechanism have not been made clear enough. In this work, SCC behavior of X60 used for high pressure gas pipeline network around Shanghai in near-neutral pH soil environments has been studied for structural integrity assessment.

Experimental Procedures

The chemical composition of X60 steel used was (mass %): 0.050C，0.22Si，1.51Mn，0.001S，0.014P，0.044V，<0.02Ti，0.049Nb, 0.042Cr, 0.18Mo and Fe balance. The mechanical properties at room temperature were 650MPa for ultimate tensile strength, 524MPa for yield strength, 18.6% for elongation and 83% for reduction in area (RA). Cylinder specimens with a gauge dimension of Φ4×25 mm were machined from a pipeline in the transverse direction for SSRT

Three soil solutions were prepared for the tests, which were made with deionized water and three types of soils, i.e. Cyan-yellow soil, Cyan-purple soil and Near-city soil, in Shanghai with a ratio of water/soil=1/1 (by weight). All the solutions were kept at 30°C and purged with 5%CO_2 +95%N_2 in tests to simulate near neutral pH environments. Table 1 gives the main chemical characteristics of the soils which were sampled according to soil type distribution and X60 pipeline distribution around Shanghai.

Table 1- Main chemical characteristics of typical soils for X60 around Shanghai

Soil Type	pH[1]	NO_3 [%]	Cl^- [%]	SO_4^{2-} [%]	HCO_3 [%]	CO_3^{2} [%]	Na^+ [%]	All salt [%]	$\Lambda^{2.}$ [MΩ^{1}/cm]	Λ^{3} [MΩ^{1}/cm]
Cyan-yellow soil	8.24	0.000405	0.00345	0.0312	0.0286	Not found	0.00685	0.0823	0.118	0.144
Cyan-purple soil	8.2	0.000368	0.00731	0.0264	0.0274	Not found	0.0112	0.0833	0.142	0.168
Near-city soil	7.76	0.00091	0.00332	0.0912	0.0248	Not found	0.00495	0.154	0.340	0.406

Notes: 1. pH of the solution with a ratio of water/soil: 1/2.5 (by weight);
2. Λ^2, the conductivity of the lixivium with a ratio of water/soil: 1/5 (by weight) ;
3. Λ^3, the conductivity of the mud

In a test, a saturated calomel electrode (SCE) was used as reference electrode. SSRT was conducted at a strain rate about 1×10^{-6} 1/s. The susceptibility to SCC is expressed by using SCC susceptibility index I_{SCC} ($I_{SCC}=1-RA_S/RA_0$, where RA_S and RA_0 were RA values in solution and in air respectively). The bigger the values of I_{SCC}, the higher the susceptibility to SCC. The fracture surfaces of the tested specimens were examined with optical and scanning electron microscopy. Some specimens were sectioned for further observation of the cracks.

Results and Discussion

Measurements showed that the pH values of the three test soil solutions were reduced into a similar range of 6.1 ~ 6.5. The reduction of pH value as compared with the numbers in Table 1 can be mainly attributed to the continuous purging of 5%CO_2. The corrosion potentials of the steel were in the range of -755~ -720 mV in Cyan-yellow soil solution, in the range of -772~ -723 mV in Cyan-purple soil solution, in the range of -761~ -715mV in Near-city soil solution, respectively.

Effect of electrode potential: The variations of SCC susceptibility index I_{SCC} with electrode potential for the steel in the three soil solutions are shown in Figure 1. In Near-city soil solution and Cyan-yellow soil solution, the susceptibility almost monotonously increased with decreasing electrode potential. Although there were some waves, the susceptibility in Cyan-purple soil solution also basically exhibited similar trend. Fast increase of I_{SCC} happened when potential decreased in the range of -1500 ~ -700mV. The increase tended to be saturated when potentials decreased further.

Examination with scanning electron microscopy showed that the SCC mode was transgranular cracking. Similarly in all the three soil solutions, the SCC cracks produced at potentials typical lower than -700mV were long, deep, in quasi-cleavage type and mainly at 90° to tensile direction, corresponding to high SCC susceptibility. When tested at higher potentials, the cracks were small and mainly at 45° to the tensile direction, corresponding to low SCC susceptibility, as shown in Figure 2.

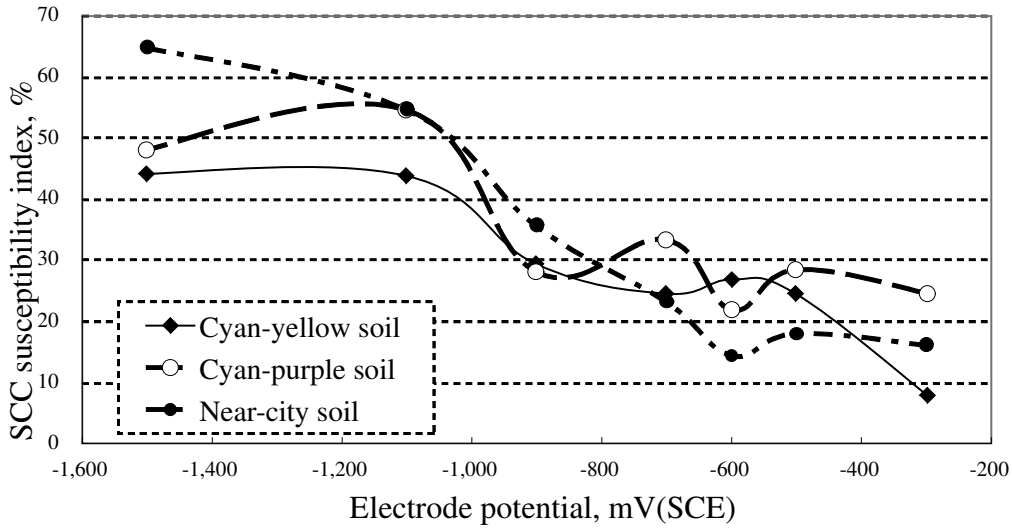
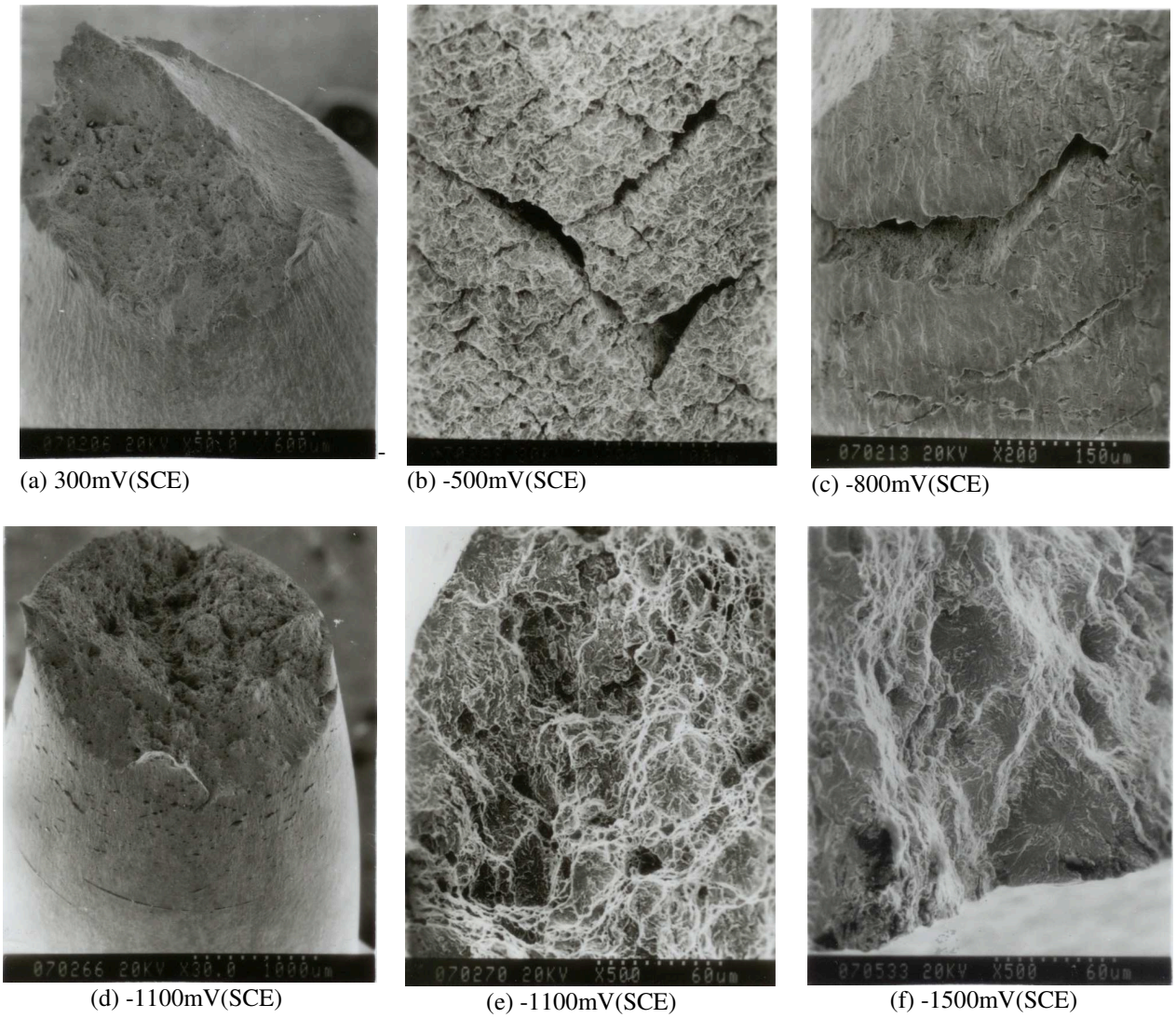


Figure 1. SCC susceptibility index as a function of electrode potential for X60 in three near neutral-pH soil solutions at 30 C



(a) 300mV(SCE) (b) -500mV(SCE) (c) -800mV(SCE)

(d) -1100mV(SCE) (e) -1100mV(SCE) (f) -1500mV(SCE)

Figure 2. Fracture surface morphologies of X60 tested at different potentials in near neutral-pH Cyan-yellow soil solution at 30°C

Above general trend of SCC behavior as a function of electrode potential suggests that hydrogen induced cracking (HIC) should be vital in the cracking mechanism at low potentials. Parkins [7] pointed out that the equilibrium potential for hydrogen discharge ($H_2 = 2H^+ + 2e$), E_{H_2/H^+} or simply

refers to E_H, should be the highest potential for HIC happening system. Based on the pH of the solutions and widely-used Nernst equation, the E_H value was calculated as about -635mV (SCE), as shown in Figure 1, close to the boundary between the low and high SCC susceptibility areas. Based on above results, the cracking mechanism of X60 in the near neutral pH soil solutions is suggested as follows:

When $E \leq EH$ (about -635mV), HIC should be dominant in the SCC, causing the long, deep, 90° cracks and high SCC susceptibility;

When $E > EH$, other mechanism, maybe anodic dissolution, should be important in the SCC, causing the small and 45° cracks and relatively low SCC susceptibility.

From structural integrity point, the parameters of cathodic protection should be carefully optimized in engineering using X60 pipeline steel to avoid possible SCC.

Effect of soil type: It can be seen from Figure 1 that in the cathodic potential range (< -750mV), the I_{SCC} curve for Cyan-yellow soil solution was almost always the lowest, that for Near-city soil solution almost always the highest among the three solutions. In the anodic potential range (> -700mV), three curves for three solutions mixed each other. Presently it is still difficult to explain the complex difference among the SCC behaviors in different soil solutions. However, the results are important for structural integrity assessment of the pipeline buried in the three soils.

Conclusions

1. In three near neutral pH solutions containing typical soils around Shanghai, the SCC susceptibilities of pipeline steel X60 generally increased with decreasing electrode potential. It is suggested that hydrogen induced cracking should dominate the SCC at low potentials.

2. In cathodic potential range, the rank of the SCC susceptibility for soil type was Near-city soil > Cyan-purple soil > Cyan-yellow soil. In anodic potential range, the SCC susceptibility curves mixed each other in the three soil solutions.

Acknowledgement

This work was financially supported by both The Science and Technology Commission of Shanghai Municipalityand Shanghai Natural Gas Pipeline Network Company LTD. Mr. Guoliang Zhang, Mr. Wu Yang, Mr. Zhenhua Sun, Mr. Jiahua Fang joined some parts of the research. The authors are grateful for above supports.

References

[1] R. N.Parkins, A review of stress corrosion cracking of high strength gas pipelines, Proceedings of CORROSION/2000, NACE International, Houston, 2000, Paper No. 00363

[2] W. Chen, F. King, T.R. Jack, and M.J.Wilmott, Environmental aspects of near-neutral pH stress corrosion cracking of pipeline steels， Metall. Mater. Trans. 33A (2002) 1429-1436

[3] J.A.Beavers, C.L.Durr, D.M. Delanty, and R.L.Sutherby, Near-neutral pH SCC in susceptible soil environments , Proceedings of CORROSION/2001, NACE International, Houston , 2001, Paper No. 01217

[4] J.A.Beavers and W.V.Harper, Stress corrosion cracking prediction model, Proceedings of CORROSION/2004, NACE International, Houston, 2004, Paper No. 04189

[5] GUO Hao，LI Guangfu，CAI Xun，ZHOU Jianjiang，YANG Wu, SCC Behaviour of X-70 Pipeline Steel in Near-Neutral pH Solutions， J. Materials Science and Technology, 21（2005）33-38

[6] GUO Hao，LI Guangfu，CAI Xun，YANG Ruipeng, YANG Wu. Effect of cyclic loading on SCC Behaviour of X-70 Pipeline Steel in Near-Neutral pH Solutions, Journal of Materials Science and Technology，21(2005)459-464.

[7] R. N.Parkins, , Stress corrosion cracking, Uhlig's Corrosion Handbook, Second Edition, Edited by R. Winston Revie, New York etc, John Wiley & Sons, Inc., 2000, pp.191-204

Advanced Materials Research Vol. 936 (2014) pp 1120-1124
© (2014) Trans Tech Publications, Switzerland
doi:10.4028/www.scientific.net/AMR.936.1120

The Effects Of Hydrogen On Properties Of Surface Films Formed On Iron In Sulfate Solutions

Ahsan Ejaz, Zhanpeng Lu*, Junjie Chen, Xiaofeng Xia, Qian Xiao, Bo Lu

Institute of Materials Science, School of Materials Science and Engineering, Shanghai University, Shanghai 200072, China

* Corresponding author, zplu@shu.edu.cn

Keywords: Iron; Hydrogen; Corrosion; XRD; Raman spectroscopy

Abstract: The effects of charged hydrogen in iron on surface properties of iron in pure water and sodium sulfate solutions of various concentrations were investigsted by open circuit potential monitoring, surface morphology observations, Raman spectroscopy and XRD measurements. Hydrogen in iron shifed the open circuit potential in the negative directions. Hydrogen could change the types of oxide film on iron. Effects of hydrogen on corrosion of iron was More significant in pure water and dilute sodium solutions than those in concentrated solutions.

Introduction

The effects of hydrogen in metal on metallic corrosion and passivation were reported[1-5]. Zeng et al. [2] investigated the effect of charged hydrogen on electronic properties of passive film of iron. Hydrogen decreases the pitting resistance and the stability of passive films [4, 5]. In this work, the effects of hydrogen on corrosion behavior of iron in various concentrations of sodium sulfate solutions were studied by open circuit potential monitoring, surface observation, Raman spectroscopy and XRD measurements, for understanding the combined effects of solution composition and hydrogen in metal on corrosion morphology and corrosion products.

Experimental procedures

Pure iron was used in corrosion tests and electrochemical measurements. Pure iron was annealed at 940℃for 2 h before using. The size of working electrodes was 8×8×2.5 mm. The iron electrode was embedded with epoxy resin with an exposed area of 0.64 cm^2 to test solutions. The surface of the iron electrode was grinded to 1500-grit SiC emery paper and then cleaned in ethanol and in acetone prior to the electrochemical measurements. All tests were carried out in naturally aerated sulfate solutions. Hydrogen charging of iron electrodes was performed by applying a cathodic current density of 0.2 mA/cm^2 in 0.5 mol/L H_2SO_4+1g/L thiourea for 1h at room temperature of around 25℃. The hydrogen-charged iron electrodes were lightly polished by 1500-grit emery paper and cleaned by ethanol and acetone before the corrosion tests. Un-charged and hydrogen-charged iron electrodes were immersed in pure water and in 10^{-4} to 0.5 mol/L Na_2SO_4 solutions for 21 h. Open circuit potentials (OCP) during the immersion tests were monitored by an electrochemical workstation with saturated calomel electrode (SCE) as the reference electrode. The potentials were cited versus SCE. After the immersion tests, the specimens were taken out carefully to keep the corrosion product in the original condition. XRD and Raman spectroscopy measurements were used to characterize the corrosion products formed on iron electrodes after corrosion immersion tests.

Results and discussion

The surface morphologies, open circuit potential versus immersion time, Raman spectra and XRD patterns of uncharged and hydrogen-charged iron electrodes after the immersion tests in pure water, 10^{-4} mol/L Na_2SO_4, 10^{-3} mol/L Na_2SO_4, 10^{-2} mol/L Na_2SO_4 and 0.5 mol/L Na_2SO_4, solutions for 21 h are shown in Figs. 1-20. Results in Figs. 3, 6, 13 and 18 showed that the OCP of un-charged iron moved in the negative direction with increasing immersion time, while the OCP of

hydrogen-charged iron moved in the positive direction with increasing immersion time. The OCP of hydrogen iron was more negative than that of un-charged iron. The difference between OCP (uncharged) and OCP (hydrogen-charged) decreased with time. After 21h immersion test, OCP values of uncharged iron and hydrogen-charged iron in 10^{-4} to 0.5 mol/L Na_2SO_4 solutions, while in pure water the OCP of hydrogen-charged iron were still more negative than that of un-charged iron.

Figures 1,2, 4, 5, 9-12, 16 and 17 showed that charged-hydrogen in iron significantly affected the surface morphologies of iron after immersion tests. After 21h immersion in pure water, un-charged iron only showed several local corroded sites of yellow color while the hydrogen-charged iron was mainly covered by a dark surface layer with local yellow sites of rusts (Fig. 1 and 2). After 21 h immersion in 10^{-4} mol/L Na_2SO_4 solution, the un-charged iron was partly covered with yellow corrosion rusts and partly bright, and the hydrogen-charged iron was mainly covered with a dark layer with several bands of yellow rusts (Figs. 4 and 5). After 21 h immersion in 10^{-3} mol/L Na_2SO_4 solution, the un-charged iron was mainly covered with yellow corrosion rust sites, and the hydrogen-charged iron was partly covered with a dark layer and partly covered with yellow rusts (Figs. 9 and 10). After 21 h immersion in 10^{-2} mol/L Na_2SO_4 solution, the un-charged iron was partly bright and partly covered with a brown rust layer, and the hydrogen-charged iron was mainly covered with a brown layer with several yellow regions (Figs. 11 and 12). After 21 h immersion in 0.5 mol/L Na_2SO_4 solution, the un-charged iron was partly bright and partly covered with a yellow rust layer, and the hydrogen-charged iron was fully covered with a yellow rust layer (Figs. 16 and 17). The effect of hydrogen on the surface morphology of iron after the immersion was more significant in pure water or in dilute Na_2SO_4 solutions.

The results of Raman spectra and XRD patterns for the surface films on iron electrodes after immersion tests are summarized in Table 1. Published XRD and Raman spectroscopy data were referred [6-11]. It should be noted that Raman spectra reflected mainly the near-surface film information, and XRD pattern could reflect the information deeper into the oxide film. Raman spectra data in Fig. 7, 14 and showed that near-surface films formed on un-charged iron in 10^{-4}, 10^{-2} and 0.5 mol/L Na_2SO_4 solutions belonged to the same type, a kind of ferric oxide like γ-FeOOH. In 0.5 mol/L Na_2SO_4 solution, the type of the near-surface film formed on hydrogen-charged iron was similar to that formed on un-charged iron. The type of the near-surface oxide formed on hydrogen-charged iron in 10^{-4} mol/L Na_2SO_4 solution was similar to that in 10^{-2} Na_2SO_4 solution, which was likely magnetite. XRD results showed that the types of oxide films formed on un-charged iron and hydrogen-charged iron in 10^{-4} mol/L Na_2SO_4 solution were different, where a strong peak at for the oxide film on hydrogen-charged iron was observed (Fig. 8). The XRD patterns in Figs. 15 and 20 showed that the oxide films formed on un-charged and hydrogen-charged iron specimens in 0.5 mol/L Na_2SO_4 solution were a similar type that was close to γ-Fe_2O_3.

TABLE 1 RAMAN SPECTRA AND XRD DATA FOR THE SURFACE FILMS ON IRON AFTER IMMERSION TESTS

Immersion solution	Types of measurements	Characteristic peaks for surface films on	
		Un-charged iron	Hydrogen-charged iron
10^{-4} mol/L Na_2SO_4	Raman shit (cm^{-1})	250(I), 374(II), 525(IV), 644(III)	215(III), 282(II), 390(I), 591(IV)
	XRD (degree)	44.6(I*),64.8(III*), 82.4(II*)	35.3(II), 43.0, 44.5(I), 57, 62.5, 64.9(IV*), 82.4(III)
10^{-2} mol/L Na_2SO_4	Raman shift (cm^{-1})	216, 251(I), 378(II), 527(III), 653(IV)	221(II), 250(IV), 290(I), 394(I), 608, 668(III)
	XRD (degree)	35.4(III), 44.6(I),82.4(II)	35.3(III), 36.6, 44.5(I), 65(IV), 82.4(II)
0.5 mol/L Na_2SO_4	Raman shift (cm^{-1})	218, 251(I), 308, 351, 380(II), 528(III), 650	218, 251(I), 308, 351, 380(II), 528(III), 650
	XRD (degree)	44.5(I), 64.8(III), 82.3(II)	36.2(III), 44.6(I), 64.9(IV), 82.4(II)

Peak intensity decreased with increasing number I, II, III and IV. Some peaks with similar intensities are assigned the same number. The XRD peak at 44.5° corresponded to iron.

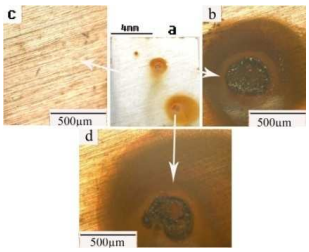


Fig. 1 The surface of the non-charged iron electrode after immersion in pure water for 21 h at 25 ℃.

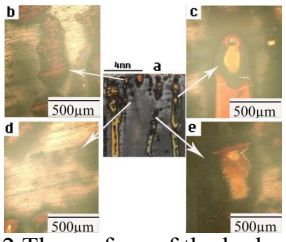


Fig. 2 The surface of the hydrogen-charged iron electrode after immersion in pure water for 21 h at 25 ℃.

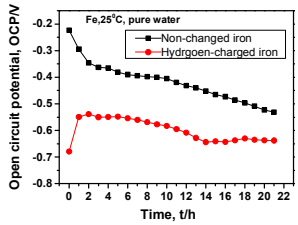


Fig. 3. Open circuit potential vs. immersion time for non-charged and hydrogen-charged iron in pure water at 25 ℃.

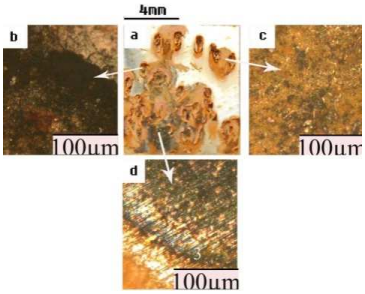


Fig. 4 The surface of the un-charged iron after immersion in 10-4 mol/L Na2SO4 solution for 21 h at 25 ℃

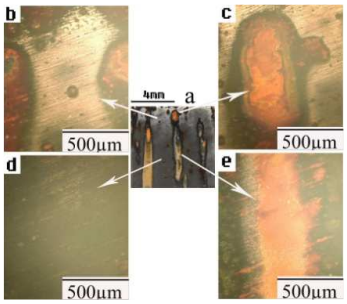


Fig. 5 The surface of the hydrogen-charged iron after immersion in 10-4 mol/L Na2SO4 solution for 21 h at 25 ℃

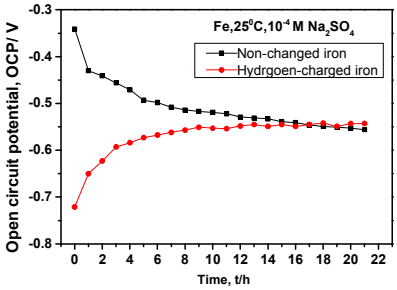


Fig. 6 OCP versus time for non-charge and hydrogen charged iron in 10-4 mol/L Na2SO4 solution at 25 ℃.

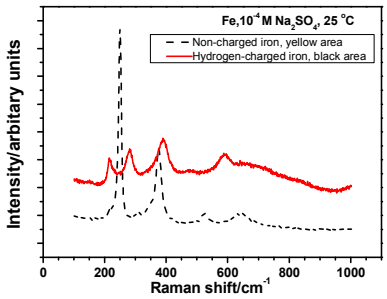


Fig. 7 Raman spectra of the un-charged and hydrogen-charged iron electrodes after immersion in 10-4 mol/L Na2SO4 solution for 21 h at 25 ℃.

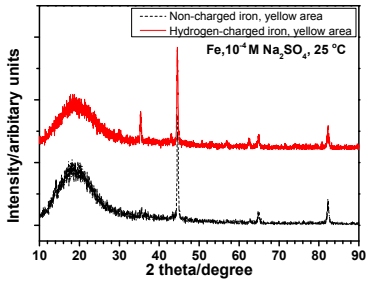


Fig. 8 XRD data of the surface on the un-charged and hydrogen-charged iron electrodes after immersion in 10-4 mol/L Na2SO4 solution for 21 h at 25 ℃.

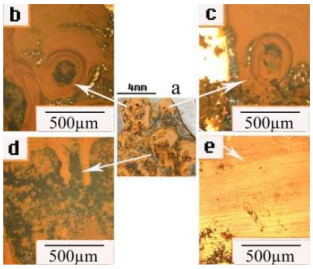


Fig. 9 The surface of the un-charged iron electrode after immersion in 10-3 mol/L Na2SO4 solution for 21 h at 25 ℃.

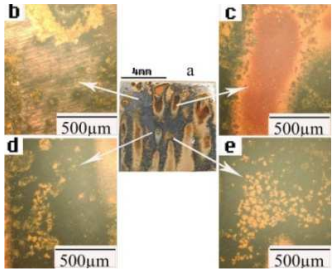


Fig. 10 The surface of the hydrogen-charged iron electrode after immersion in 10-3 mol/L Na2SO4 solution for 21 h at 25 ℃.

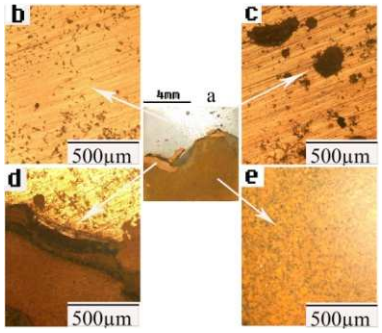


Fig. 11 The surface of the non-charged iron electrode after immersion in 10-2 mol/L Na2SO4 solution for 21 h at 25 ℃.

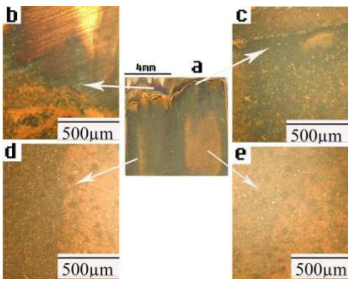


Fig. 12 The surface of the hydrogen-charged iron electrode after immersion in 10-2 mol/L Na2SO4 solution for 21 h at 25 ℃.

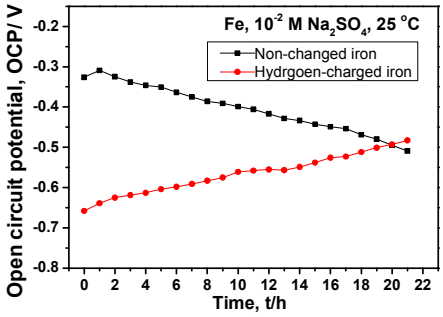


Fig.13 OCP versus time for uncharged and hydrogen-charged iron in 10-2 mol/L Na2SO4 solution at 25 ℃.

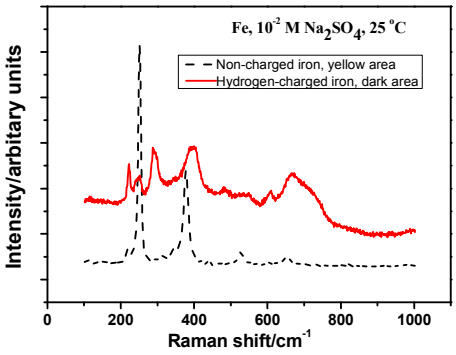


Fig. 14. Raman spectra of the un-charged and hydrogen-charged iron electrodes after immersion in 10-2 mol/L Na2SO4 solution for 21 h at 25 ℃.

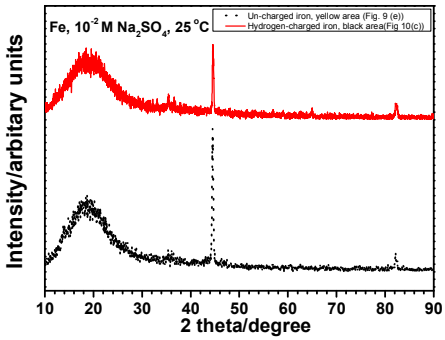


Fig. 15 XRD data of the un-charged and hydrogen-charged iron electrodes after immersion in 10-2 mol/L Na2SO4 solution for 21 h at 25 ℃.

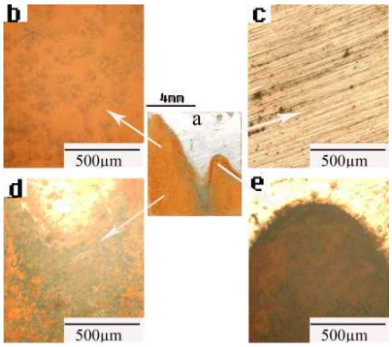


Fig. 16 The surface of the un-charged iron electrode after immersion in 0.5 mol/L Na_2SO_4 solution for 21 h at 25 ℃.

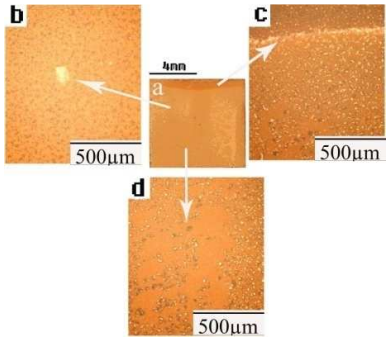


Fig. 17. The surface of the hydrogen-charged iron electrode after immersion in 0.5 mol/L Na2SO4 solution for 21 h at 25 ℃.

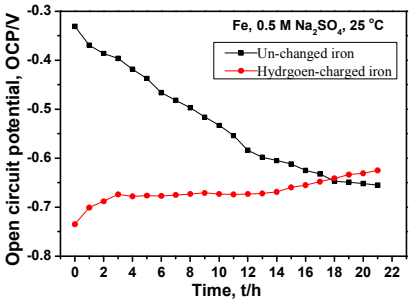


Fig. 18 OCP versus time for uncharged and hydrogen-charged iron in 0.5 mol/L Na2SO4 solution at 25 ℃.

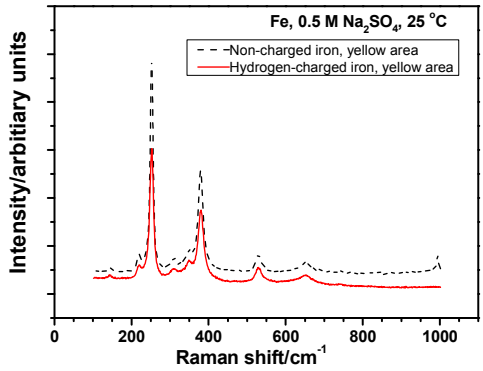


Fig. 19 Raman spectra of un-charged and hydrogen-charged iron electrodes after immersion in 0.5 mol/L Na2SO4 solution for 21 h at 25 ℃.

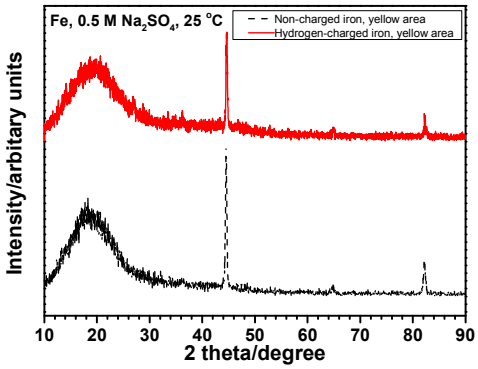


Fig. 20 XRD data of the un-charged and hydrogen-charged iron electrodes after immersion in 0.5 mol/L Na2SO4 solution for 21 h at 25 ℃.

Conclusions

Hydrogen decreased the open circuit potential of iron in sulfate solutions. Hydrogen accelerated the corrosion of iron in pure water and sulfate solutions at 25 °C. Hydrogen changed the types of near-surface oxide films formed on iron dilute sulfate solutions. In concentrated sulfate solutions, the oxide formed on uncharged and hydrogen-charged iron electrodes were close. The effect of hydrgon on corrosion varied with the solution compositions.

Acknowledgements

This work was supported by Shanghai Pujiang Project No. 12PJ1403600, the Ph.D. Programs Foundation of Ministry of Education of China No. 20123108110021, and the National Key Laboratory Fund by Science and Technology on Reactor Fuel and Materials Laboratory.

References

[1] L. Qiao, X. Mao . Acta Metall. Mater., 43(1995) 4001-4006.
[2] Y.M. Zeng, L.J. Qiao, M.Z. Yang, W.Y. Chu. J. Chinese Soc. Corros. Prot., 20 (2000) 74-80.
[3] J.G. Yu, C.S. Zhang, J.L. Luo, P.R. Norton. J. Electrochem. Soc., 150 (2003) B68-B75.
[4] J.G. Yu, J.L. Luo, P.R. Norton., Electrochimica Acta., 47 (2002) 1527-1536.
[5] J.G. Yu, J.L. Luo, P.R. Norton., Electrochimica Acta., 47 (2002) 4019-4025.
[6] D.L.A. De Faria, S. Venâncio Silva, M. De Oliveira, J. Raman Spectroscopy, 28 (1997) 873-878.
[7] D.L.A. De Faria, F.N.Lopes. Vibrational Spectroscopy, 28 (2007) 117-121.
[8] C. Re′mazeilles, Ph. Refait, Corros. Sci., 49 (2007) 844-857.
[9] D. Fu, P.G. Keech, X.L. Sun, J.C. Wren. Phys. Chem. Chem. Phys., 2011, DOI:10.1039/c1cp20188c.
[10] D. Chicot, J. Mendoza, A. Zaoui, G. Louis, V. Lepingle, F. Roudet, J. Lesage. Mater. Chem. Phys. 129 (2011) 862-870.
[11] C. Re'mazeilles, Ph. Refait. Corrosion 49(2007)844-857.

Advanced Materials Research Vol. 936 (2014) pp 1125-1131
© (2014) Trans Tech Publications, Switzerland
doi:10.4028/www.scientific.net/AMR.936.1125

Corrosion Inhibition of Gemini Surfactant for Copper in 3.5% NaCl

Kun Cao[1,a], Huyuan Sun[1,b], Baorong Hou[1,c],

([1] Institute of Oceanology, Chinese Academy of Sciences, Qingdao 266071, China)

[a]E-mail: kevin_cao0811@126.com

[b]E-mail: sun@qdio.ac.cn

[c]E-mail: brhou@qdio.ac.cn

Keywords: Copper; Corrosion; Gemini surfactant; Electrochemical; XPS

Abstract: A new gemini surfactant containing long chain alkyl ammonium headgroups have been used as corrosion inhinbitor for copper in 3.5% NaCl solution. The weight loss and electrochemical methods results showed that presence of inhibitor greatly decrease corrosion rate, gemini surfactant acted as an excellent corrosion inhibitor with inhibition efficiency greater than 96% at an optimum concentration of 30 $mg \cdot L^{-1}$. X-ray photoelectron spectroscopy reveals that the gemini surfactant molecules adsorb onto the copper surface through the two ammonium head groups (N^{+}).

Introduction

Copper has been one of more important materials in industry owing to its plenty of favourable properties, such as high electrical and thermal conductivities, mechanical workability and its relatively noble properties. It is widely used in many applications in electronic industries and communications as a conductor in electrical power lines, pipelines for domestic and industrial water utilities including sea water, heat conductors, heat exchangers, etc. Therefore, corrosion of copper and its inhibition in a wide variety of media, particularly when containing chloride ions, have attracted the attention of many investigators [1–4]. So far, the use of organic inhibitors to protect copper is one of the most important methods. Organic compounds containing polar groups including nitrogen, sulfur, oxygen [5–7] and heterocyclic compounds with polar functional groups and conjugated double bonds [8,9] have been reported to inhibit copper corrosion. The inhibiting action of these organic compounds is usually attributed to their interactions with the copper surface via their adsorption.

Different from conventional inhibitors, gemini surfactant is composed of two hydrophilic head groups and two hydrophobic chains, separated by rigid and flexible aromatic or aliphatic spacers. Due to the special chemical structure of these components, it has been demonstrated that the novel surfactants are more efficient at reducing surface tension and forming micelles than inconventional ways and have lower critical micelle concentration (CMC) [10]. In recent years, gemini surfactants have become the focus of study [11,12]. In most of the available literature, gemini surfactants have been studied as corrosion inhibitors for carbon steel in hydrochloric acid and sulphuric acid solutions [13]. Those works showed that they were excellent corrosion inhibitors.

The purpose of the present research is to prove the hypothesis that cationic gemini surfactant with long chain alkyl ammonium headgroups, which was synthesized by us as shown in Fig. 1, inhibit corrosion of copper when immersing in 3.5% NaCl solutions. The study has been carried out by using potentiodynamic polarization measurement, electrochemical impedance spectroscopy (EIS), weight loss measurements and XPS.

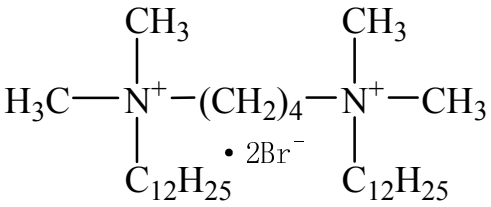


Fig. 1 The structure of gemini surfactant

Experiment

Gemini surfactant was dissolved in 3.5% NaCl solution at various concentrations from 10 mg/L to 100 mg/L, and the solution without gemini surfactant was taken as blank for comparison.

Specimens were mechanically cut into 5.00 cm × 2.50 cm × 0.4 cm (used in the weight loss experiment) and 1.0 cm × 1.0 cm × 1.0 cm (used in the electrochemical experiment) dimensions, abraded with SiC abrasive papers up to 800 grade, washed in distilled water, degreased ultrasonically in acetone, and dried at room temperature.

Electrochemical experiments

Electrochemical experiments were performed in a conventional three electrodes system, copper sealed by epoxy resin with exposure surface of 1 cm^2 as working electrodes, a platinum foil of 1.0 cm×1.0 cm as counter electrode, and a saturated calomel electrode (SCE) provided with a Luggin capillary as reference electrode.

EIS measurement was carried out on steady state open circuit potential (OCP) disturbed with amplitude of 10 mV a.c. sine wave at frequencies from 100 kHz to 10 mHz. The inhibition efficiency (η_R%) obtained from EIS measurement was calculated by

$$\eta_R\% = \frac{R_{ct} - R_{ct}^0}{R_{ct}} \times 100 \quad (1)$$

R_{ct} and R^0_{ct} are polarization resistances in the presence and absence of different gemini surfactant, respectively.

The potentiodynamic polarization curves were obtained from −250 mV (SCE) versus OCP to +250 mV (SCE) versus OCP with a scan rate of 0.5 mV/s. The obtained inhibition efficiency was calculated by

$$\eta_i\% = \frac{i_{corr}^0 - i_{corr}}{i_{corr}^0} \times 100 \quad (2)$$

Where i_{corr} and i^0_{corr} are the corrosion current with and without different gemini surfactant, respectively.

Weight loss experiment

Copper specimens in triplicate for each inhibitor concentration were immersed in the test solutions for 14 d at 298 K. After that, the specimens were scraped, rinsed in water and acetone，and dried in a desiccator. Finally, the loss in weight was determined with analytic balance.

XPS analysis

XPS measurement was carried out on a Thermo ESCALAB 250 photoelectron spectrometer equipped with an Al-anode at a total power dissipation of 150 W (15 kV, 10 mA).

Results and Discussion

Weight loss measurements

Table 1 shows the weight loss values of copper in the test solution in the absence and presence of gemini surfactant.

TABLE 1 THE RESULTS OF WEIGHT LOSS EXPERIMENT

	Concentration [mg L^{-1}]	Corrosion rate [mg cm^{-2} h^{-1}]	η_w%	Θ
Blank	0	1.1071	—	—
Inhibitor	10	0.0713	93.6	0.936
	20	0.0548	95.1	0.951
	30	0.0415	96.3	0.963
	50	0.0443	96.0	0.960
	100	0.0489	95.6	0.956

It can be clearly noticed from Table 1 that gemini surfactant can prevent copper from corrosion efficiently in 3.5% NaCl solution. Their inhibition efficiencies (η_w%) were higher than 96% at the concentration of 30 mg·L^{-1}.

The results in Table 1 also show that inhibition efficiency increases along with the additive concentration of gemini surfactant rising when the gemini surfactant concentration is lower than 30 mg·L^{-1}. However, such increase of concentration does not affect inhibition efficiency significantly, suggesting that a saturated adsorption of surfactant molecules on copper surface is achieved.

Electrochemical impedance spectroscopy (EIS)

The inhibitive performance of gemini surfactant on copper immersed in 3.5% NaCl solution was studied via EIS at 298K. The impedance results were plotted in Fig. 2.

The EIS parameters were calculated by analyzing the impedance plots fitting the equivalent circuit as mentioned in Fig. 3, where R_s is the solution resistance, R_f is the film resistance, R_{ct} presents the charge transfer resistance, CPE_1 and CPE_2 represent the constant phase elementsused to replace the film capacitance (C_f) and double layer capacitance (C_{dl}), respectively, and n shows the phase shift that can be explained as the degree of surface in-homogeneity. The value of the parameters was tabulated in Table 2.

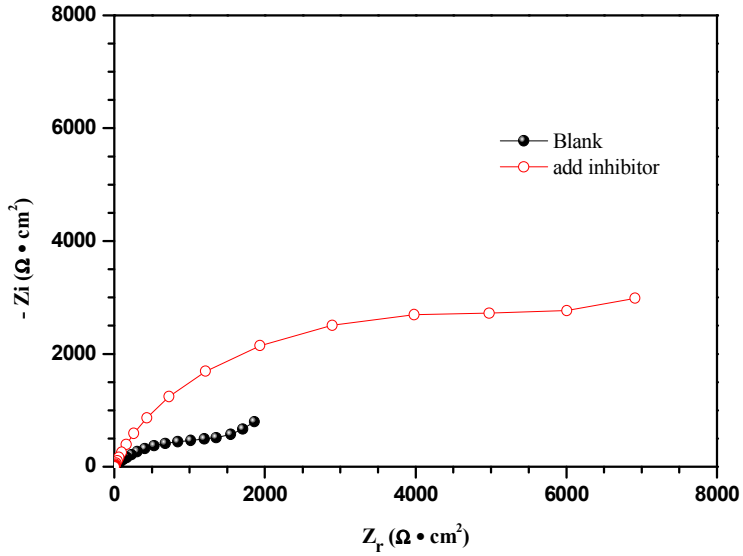


Fig. 2 EIS plots of copper in 3.5% NaCl with gemini surfactant at 30 mg/L

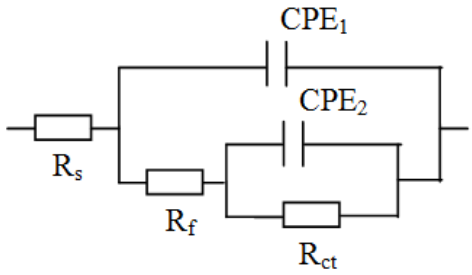


Fig. 3 The equivalent circuit of the Nyquist plot

TABLE 2 IMPEDANCE DATA OF COPPER IN 3.5% NACL WITH GEMINI SURFACTANT AT 30 MG·L-1

Inhibitor	R_s [Ω cm^2]	R_{ct} [Ω cm^2]	C_{dl} [μF·cm^{-2}]	n_1	R_f [Ω cm^2]	C_f [μF·cm^{-2}]	n_2	η_R%
Blank	2.041	1109	475	0.92	87.2	148	0.26	—
Inhibitor	2.256	11840	57.2	0.97	794.3	11.2	0.62	90.6

It can be seen that the values C_f and C_{dl} exhibit a decreasing tendency with adding the inhibitor, which can result from a decrease in local dielectric constant and/or an increase in the thickness of the electrical double layer, suggesting that the surfactant molecules act by adsorption at the metal/solution interface [14]. As a result, the diffusion process of ions from the interface to the solution involved in active corrosion is probably to be retarded.

Polarization curve

Fig. 4 shows the typical polarization curves for the inhibition characteristics of gemini surfactant at the optimum concentration of 30 mg·L^{-1} in 3.5% NaCl solution. The electrochemical parameters E_{corr}, i_{corr}, anodic and cathodic Tafel slopes (β_a, β_c) obtained from polarization measurements are listed in Table 3.

Table 3 and Fig. 4 reveals that: (i) the values of E_{corr} shift toward more negative potential and the values of i_{corr} decreases sharply after adding the gemini surfactant. Such decreas indicates the inhibiting effect of the gemini surfactant, (ii) compared with the blank, the values of Tafel slopes

(β_c and β_a) become larger. This means that the gemini surfactant are mixed type inhibitor which preferentially reretard the anodic process of corrosion.

TABLE 3 POLARIZATION PARAMETERS FOR COPPER IN 3.5% NACL SOLUTION WITH GEMINI SURFACTANT AT THE OPTIMUM CONCENTRATION OF 30 MG·L-1

Inhibitor	E_{corr} [mV/SCE]	i_{corr} [μA·cm^{-2}]	β_c [mV·dec^{-1}]	β_a [mV·dec^{-1}]	η_i%
Blank	-218	4.52	177.2	47.6	—
Inhibitor	-265	0.25	220.1	119.1	94.5

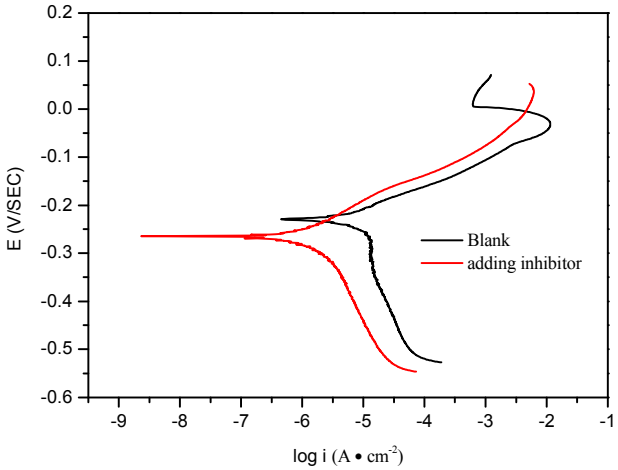


Fig. 4 Polarization curves for copper in 3.5% NaCl with gemini surfactant at 30 mg/L

XPS analysis

In order to find out the adsorption activity area and adsorption mechanism of gemini surfactant, high resolution of XPS spectra of N1s (Fig. 5) regions was recorded to reveal its chemical states. Gemini surfactant located at 399.8, 400.81 eV were used to fit the spectrum. The peaks of the gemini surfactant appeared at higher position than the above values because the coordination bonds between functional group with copper surface brought out the peak shifts to higher binding energy appeared at 399.8 eV [15]. The peak located at binding energy of 400.81 eV has the highest contribution and is mainly attributed to nitrogen in the ammonium group [15].

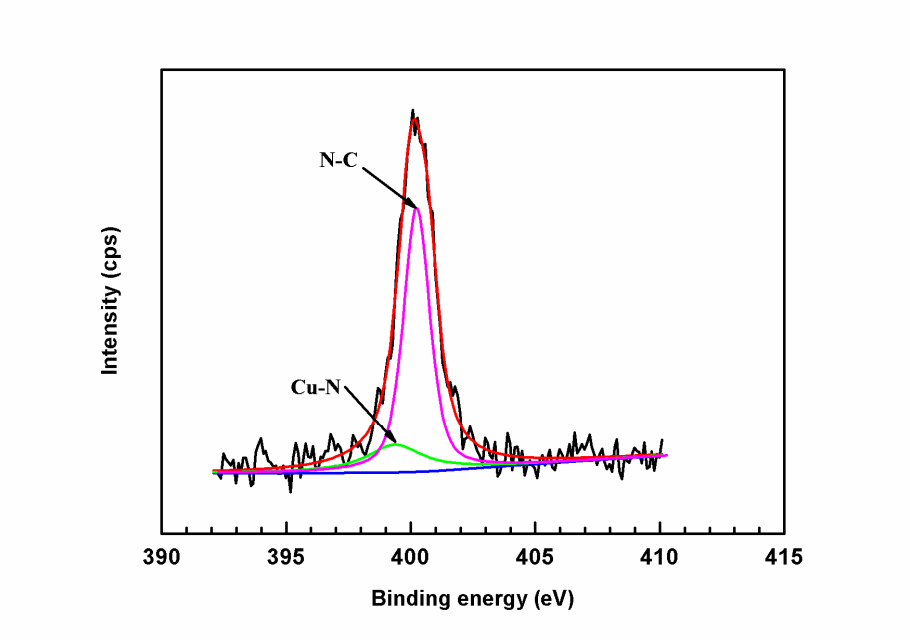


Fig. 5 High-resolution XPS spectra of N1s of copper obtained after 3 h immersion in 3.5% NaCl solution.

Inhibition mechanism

Although the adsorption of gemini surfactant on the copper surface is complicated because the gemini surfactant contain two hydrophilic groups and two hydrophobic groups, the above results enable the authors to propose a relatively simple inhibition mechanism, as Fig. 6 shows.

In 3.5% NaCl solution, Cl^- or $CuCl_2^-$ ions may be preferentially adsorbed on copper surface thereby, making the surface negatively charged. Then, the two quaternary ammonium headgroups (N+) of gemini surfactant molecules could be absorbed on the layer of adsorbed anions by an electrostatic interaction. Subsequently, chemisorption may take place. As a result, the tight adsorbed layer of gemini surfactant on the copper surface can isolate the corrosive media and retard the corrosion reaction.

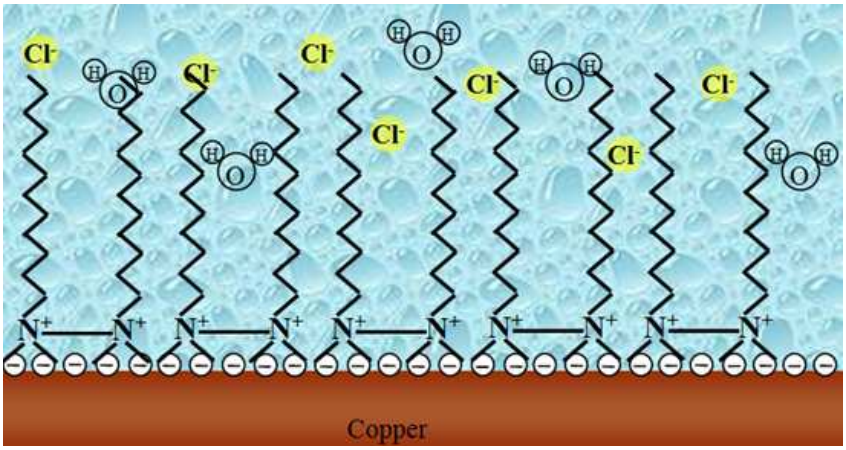


Fig. 6 Proposed adsorption model for the inhibition mechanism of gemini surfactant.

Conclusion

The inhibiting efficiency of the gemini surfactant for copper in 3.5% NaCl solution is higher than 96% at 30 $mg \cdot L^{-1}$ additive concentration. The electrochemical measurements indicate that the gemini surfactant is mixed type inhibitor which preferentially restrain the anodic process of corrosion. XPS analysis revealed that the effect of gemini surfactant is due to adsorption of the two quaternary ammonium headgroups (N+) of gemini surfactant molecules.

References

[1] E.M. Sherif, S.-M. Park, Inhibition of copper corrosion in 3.0% NaCl solution by *N*-Phenyl-1,4-phenylenediamine, J. Electrochem. Soc. 152 (2005) B428-B433.

[2] H.O. Curkovic, E.S. Lisac, H. Takenouti, The influence of pH value on the efficiency of imidazole based corrosion inhibitors of copper, Corros. Sci. 52 (2010) 398–405.

[3] T. Hoepner, S. Lattemann, Chemical impacts from seawater desalination plants --- a case study of the northern Red Sea, Desalination 152 (2003) 133-140.

[4] A.L. Bacarella, J.C. Griess, The anodic dissolution of copper in flowing sodium chloride solutions between 25° and 175°, J. Electrochem. Soc. 120 (1973) 459-465.

[5] S. Issaadi, T. Douadi, A. Zouaoui, S. Chafaa, Novel thiophene symmetrical Schiff base compounds as corrosion inhibitor for mild steel in acidic media, Corros. Sci. 53 (2011) 1484–1488.

[6] H. Ashassi-Sorkhabi, E. Asghari, Effect of hydrodynamic conditions on the inhibition performance of L-methionine as a "green" inhibitor, Electrochim. Acta 54 (2008) 162–167.

[7] E.M. Sherif, R.M. Erasmus, J.D. Comins, Corrosion of copper in aerated synthetic sea water solutions and its inhibition by 3-amino-1,2,4-triazole, J. Colloid Interface Sci. 309 (2007) 470–477.

[8] H.W. Tian, W.H. Li, K. Cao, B.R. Hou, Potent inhibition of copper corrosion in neutral chloride media by novel non-toxic thiadiazole derivatives, Corros. Sci. 73 (2013) 281-291.

[9] M.A. Elmorsi, A.M. Hassanein, Corrosion inhibition of copper by heterocyclic compounds, Corros. Sci. 41 (1999) 2337-2352.

[10] D. Asefi, M. Arami, N.M. Mahmoodi, Electrochemical effect of cationic gemini surfactant and halide salts on corrosion inhibition of low carbon steel in acid medium, Corros. Sci. 52 (2010) 794-800.

[11] L.G. Qiu, A.J. Xie, Y.H. Shen, Understanding the effect of the spacer length on adsorption of gemini surfactants onto steel surface in acid medium, Appl. Surf. Sci. 246 (2005) 1-5.

[12] M.A. Hegazy, M. Abdallah, H. Ahmed, Novel cationic gemini surfactants as corrosion inhibitors for carbon steel pipelines, Corros. Sci. 52 (2010) 2897-2904.

[13] M.A. Hegazy, A novel Schiff base-based cationic gemini surfactants: Synthesis and effect on corrosion inhibition of carbon steel in hydrochloric acid solution, Corros. Sci. 51 (2009) 2610-2616.

[14] M.A. Quraishi, J. Rawat, Influence of iodide ions on inhibitive performance of tetraphenyl-dithia-octaaza-cyclotetradeca-hexaene (PTAT) during pickling of mild steel in hot sulfuric acid, Mater. Chem. Phys. 70 (2001) 95-99.

[15] O. Olivares, N.V. Likhanova, B. Gomez, J. Navarrete, M.E. Llanos-Serrano, E. Arce, J.M. Hallen, Electrochemical and XPS studies of decylamides of a-amino acids adsorption on carbon steel in acidic environment, Appl. Surf. Sci. 252 (2006) 2894–2909.

Advanced Materials Research Vol. 936 (2014) pp 1132-1137
© (2014) Trans Tech Publications, Switzerland
doi:10.4028/www.scientific.net/AMR.936.1132

A Study of the corrosion resistance of M50NiL bearing steel by ion implantation

J. Jin[1, a], Y.B. Chen[2,b], K.W. Gao[3,c], X.L. Huang[4,d]

[1]School of Materials Science and Engineering, University of Science and Technology Beijing, Beijing 100083, PR China

[2]China Academy of Machinery Science and Technology, Beijing 100120, PR China

[A]ion_techonlogy@163.com, [b]webmaster@ht.org.cn

[c]kwgao@mater.ustb.edu.cn, [d]hihxl@qq.com

Keywords: Ion implantation, M50NiL, Corrosion resistance

Abstract. The corrosion resistance of metal-N double-element alternate implanted M50NiL bearing steel was investigated by potentiodynamic polarization and detection methods of SEM, XPS, AES and TEM. The results showed that ion implanted M50NiL can increase the corrosion potential of substrate, reduce the corrosion active points and inhibit the corrosion reaction induced at the grain boundaries. The formed amorphous layer and strengthening phases take main roles in improving the corrosion resistance of M50NiL bearing steel.

Introduction

As a novel bearing material, M50NiL can exhibit higher structure strength [1]. However, the preservation and operation of aero bearings are often in water, oil and corrosive environment containing S^{2-} and Cl^{-}. Corrosion failure becomes one of the main failure forms of bearings under marine environment.

Ion implantation is an effective technique to improve the surface properties of metal materials. Many elements have been applied as implanted ions in increasing the corrosion resistance [2-5]. Previous studies show that N/Zr and N/Ti ions co-implantations could significantly improve the wear resistance and contact fatigue strength properties of M50NiL materials. However, to our knowledge, the reports of improving the corrosion resistance property by using ion implantation on M50NiL materials are few.

Therefore, in this paper, M50NiL steel was respectively co-implanted with N/Zr and N/Ti ions by using double-element alternate implantation. The potentiodynamic polarization test was performed to investigate the effect of ion implantation on the corrosion resistance. To analyze the corrosion resistance mechanism, SEM, AES, GXRD, XPS and TEM tests were carried out.

Experimental

The chemical composition of M50NiL steel is shown in Table 1. The M50NiL specimens were prepared as cylindrical piece with about 20mm in diameter and 8mm thick. Specimens were polished and ultrasonically cleaned before implantation. The original M50NiL material is composed of fine dispersed granular carbides and super fine martensite phases.

TABLE 1 ELEMENTS COMPOSITIONS OF M50NIL STEEL

Elements	C	Cr	Ni	Mo	V	Mn	Si	P	S
Weight percentage/%	0.12	4.00	3.75	4.25	1.10	0.18	0.12	0.15	0.001

During ion implantations, the base vacuum degree was 3.0×10^{-4} Pa. The educed voltage for metal elements (Zr/Ti) was 45 kV, 40 kV, 30 kV and 20 kV. For Nitrogen implantation, the educed voltage was 80 kV. The detailed implanted process and parameters are as follows: firstly, 80 kV for N ion

implantation, then 45kV for metal ion implantation; secondly, 80 kV for N ion implantation, then 40kV for metal ion implantation; thirdly, 80 kV for N ion implantation, then 30kV for metal ion implantation; finally, 80 kV for N ion implantation, then 20kV for metal ion implantation. The total dose was 4×10^{17} ion/cm^2 and the dose in each step was average.

Electrochemical test was carried out in a equipment using a three-electrode cell system (CHI660D) containing a saturated calomel reference electrode, an assistant Pt electrode (20mm×20mm), and the implanted and non-implanted M50NiL specimens (10mm×10mm) as the working electrode. Specimens were cleaned by anhydrous ethanol and air dried before test. The test solution is adopted as 5wt.% NaCl.

Open-circuit potential (OCP) test was firstly performed and the potentiodynamic polarization was measured when the potential was getting stable (the potential undulation is smaller than 3mV in 120s). Three parallel specimens used for each measurement were polarized at a rate of 20mV/min. The scanning potential range varied from -266mV vs. OCP to 800mV vs. OCP.

Surface morphologies of the test specimens were observed by scanning electron microscopy HITACHI S4800. GXRD was performed by D-MAX-2500 diffraction instrument with the CuKα1 (k =0.154 nm) radiation to analyze phase composition of the specimen. The angle between the sample surface and incident X-ray was set 0.5° and the detector scanned from 10° to 90° at 3°/s. AES was carried out on ULVAC-PHI-700 equipment with the Si sputtering rate of 38nm/min. TEM test was performed using JEOL JEM 2010. Cross section sample was used to observe the structure character at different depths. XPS was conducted using AXIS ULTRADLD instrument with the X-ray source of monochromatic Al target, Al Kα=1486.6eV.

Results and Discussion

Corrosion Results

Fig. 1 and Table 2 show the fitting data of potentiodynamic polarization curves and corrosion parameters for M50NiL substrate and N/Ti, N/Zr double-element implanted specimens (The given value is the mean of three measurements). It is obvious that the corrosion potential of implanted specimen moves toward the anode. It indicates that the thermodynamic trend of corrosion reaction under the system weakens. The average corrosion current density of non-implanted specimen is 5μA/cm^2, while those of implanted specimens are lower, 3~4μA/cm^2. The corrosion resistances of the implanted specimens increase. The polarization current density of implanted specimens with the same anode electrode potential is lower, showing that the implanted specimens exhibit higher anti-solubility in the process of acceleration of anodic dissolution.

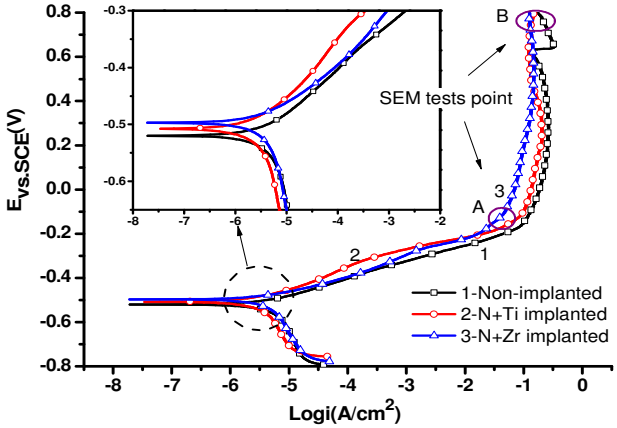


Fig. 1 Potentiodynamic Polarization Curves Of M50nil Implanted With Different Ions, The Upper Graph Shows The Details Of The Polarization Curves At Corrosion Potential.

TABLE2. FITTING PARAMETERS BASED ON POTENTIODYNAMIC POLARIZATION

Samples	E_{corr}/V	I_{corr}/μAcm^{-2}	Cathodic slope	Anthodic slope
Non-implanted	-0.5220	5.0095	2.8805	12.235
N+Ti implanted	-0.5065	3.4370	2.6385	10.330
N+Zr implanted	-0.4945	3.7938	2.6010	13.289

From the corrosion morphologies (Fig. 2a) of corroded M50NiL samples after electrochemical test, the corrosion of M50NiL substrate occurs mainly in the surrounding of grain boundaries and carbide. The corrosion of implanted samples is mainly pits whose distribution density and size increase with increasing anodic polarization time, as shown in Fig. 2b and 2c. The corrosion products expand and accumulate from the pit inside to outside (Fig. 2d). With the increase of the corrosion products, large cracks occur (Fig. 2e). Similar corrosion process is found in N/Zr co-implanted samples. The implanted elements in the corrosion products are analyzed by XPS. It is found that the implanted elements are mainly in form of TiO_2 and ZrO_2 in the corrosion products Fe_2O_3 or FeOOH, as shown in Fig. 3. Due to the low content of N and organic matter pollution, it is failed to get the information about Ti-N, Fe-N and other substances in the corrosion product. For N/Zr implanted specimen, the Zr element exists in the corrosion product in the form of ZrO_2 from XPS results.

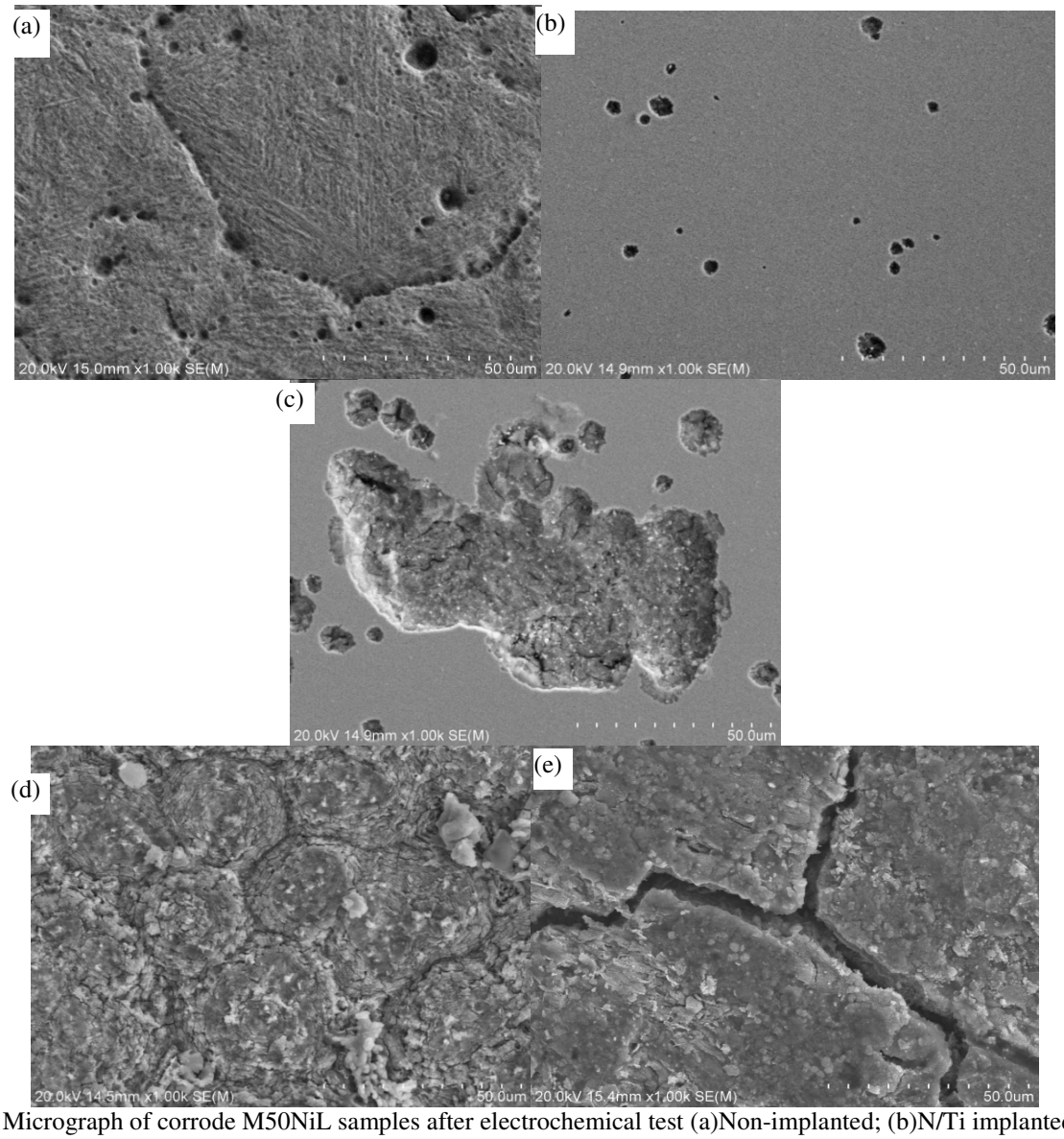


Fig. 2 Micrograph of corrode M50NiL samples after electrochemical test (a)Non-implanted; (b)N/Ti implanted, SEM tests at A point of Fig.1.; (c)N/Ti implanted, SEM tests at B point of Fig.1.; Corrosion product on the N/Ti implanted specimen by SEM test at A(d) and B(e) point of Fig.1.

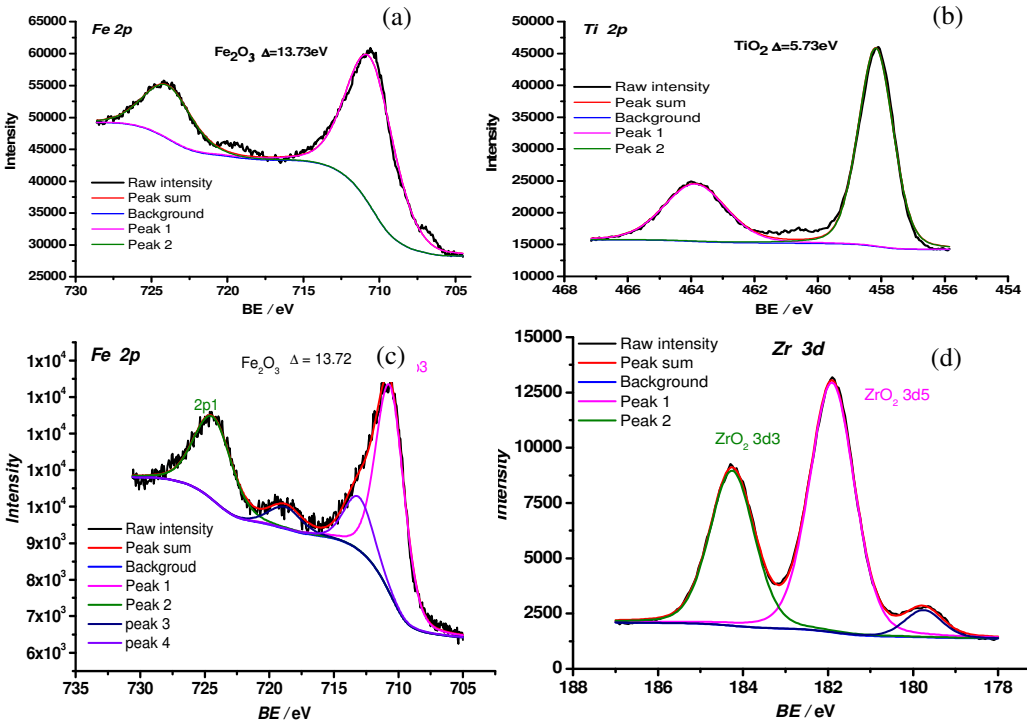


Fig. 3 X-ray Photoemission Spectra Of Corrosion Products On N/Ti (A,B) And N/Zr Co-Implanted Samples(C,D), Respectively

Surface Characterization

Fig. 4 shows the GXRD results for the substrate and implanted samples. Ti_zN compounds are formed on the N/Ti co-implanted specimens. Concerning N/Zr co-implanted samples, Zr-N and Zr-Fe-N form. Fig. 5 shows the concentration-depth distribution of implanted elements in the substrate by using AES technique. The basic elements such as Fe, C, Cr and Mo exhibit similar distribution in the three kinds of M50NiL steels. The concentration peak value of Zr and Ti is consistent, but the Ti concentration peak position for N/Ti implanted sample is obviously deeper than Zr concentration peak position for N/Zr implanted sample. The concentration peak positions of N ions are close to those of metal elements[6]. Under the same N implantation, the concentration exhibits larger difference due to the difference of metal elements, which was consistent with the GXRD peak intensity.

The implantation depth is affected by differences energy and ion radius of ionized state. The concentration-depth profile of N atoms is susceptible to strong nitride forming elements [7-8]. Thus, N atom concentration distribution is mainly affected by the capture of N when forming compounds with Zr/Ti. It further proves that Zr-N and Ti-N compounds form in the concentration distribution region. The same distribution depth of N and Zr is 50nm, while that of N and Ti reaches 250 nm.

In the study of Zr ion implantation into Fe-5%Cr, the zirconium oxide and iron carbide on the implanted substrate are the main factors to improve its corrosion resistance properties [9-10]. In the present study, the corrosion products of implanted metal elements are in form of TiO_2 and ZrO_2. Moreover, after implantation, new corrosion resistant alloy phases, such as various metal nitrides, enrich on the surface structure and can form dense passive film in the corrosive medium to prevent the damage of corrosion medium to the substrate.

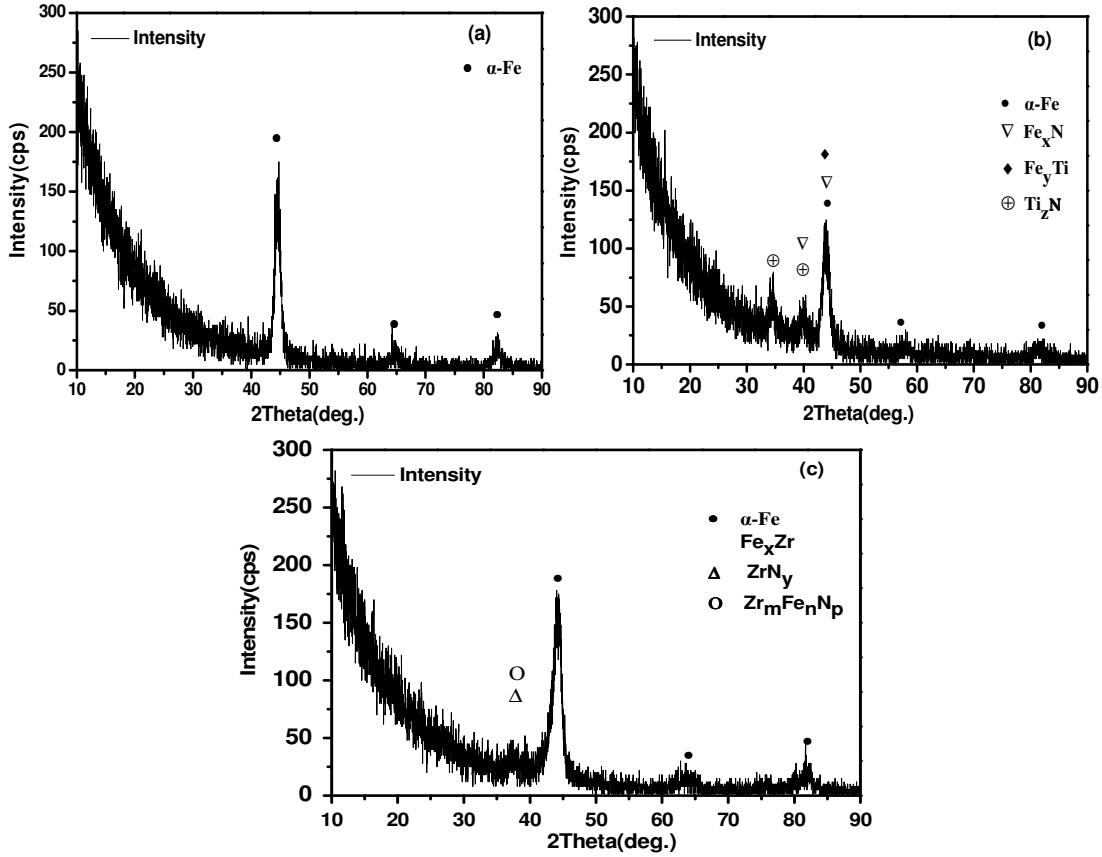


Fig. 4 GXRD Spectra of (a) Non-implanted, (b) N/Ti Implanted,

and (c) N/Zr Implanted M50NiL Steels

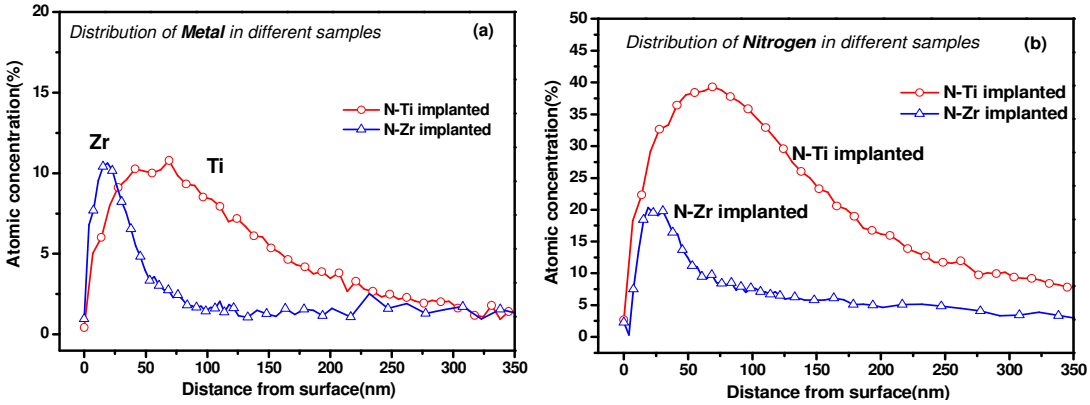


Fig.5 Concentration Profiles of Implanted Elements on M50NiL Specimen by AES

(a) Metal, (b) Nitrogen

Fig. 6 shows high resolution TEM graph of N/Zr implanted sample. An amorphous layer with the thickness of several nanometers appears on the surface. At the same time, certain disturbance of atoms (atom group) with regular arrangement appears in the certain depth, making the arrangement irregular. The implanted particles have the energy of 10~100keV after high speed acceleration. Collision cascades repeatedly occur between the particles with high energy and the substrate surface atoms. Then, energy is transmitted and finally rests in the gap or vacancy of some lattice, even the atoms in the replacement lattice. As the surface is bombarded by large dose or high energy particles, the atoms (atom group) become disordered and ultimately amorphous structure forms.

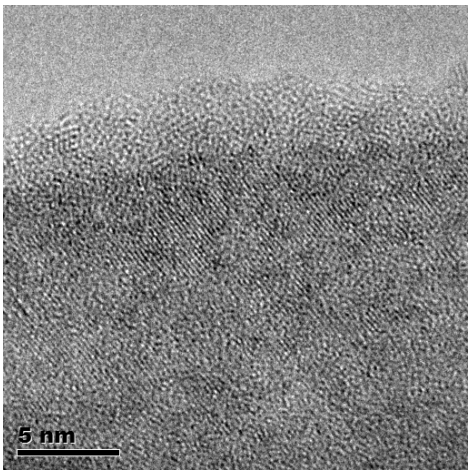


Fig. 6 High Resolution TEM graph of N/Zr Implanted Sample

In terms of surface structure, a layer with amorphous structure[10] is formed in the implanted M50NiL surface. Concerning surface phases, ceramic phases containing nitrogen generate after implantation. In the sense of the rust occurrence time, thermodynamics stability parameters, resistance to anodic corrosion current density and corrosion morphology of grain boundary microstructure, ion implantation improves the overall corrosion resistance of M50NiL substrate by reducing the initiation number of corrosion points, inhibiting grain boundary corrosion and decreasing the corrosion current. It is believed that surface amorphous layer plays the significant role of reducing the number of active sites on the surface and surface energy, while the alloy phases weakening the corrosion strength.

Conclusions

N/Ti and N/Zr ions co-implanted M50NiL can increase the corrosion potential of substrate, reduced the corrosion active points and inhibit the corrosion reaction induced at the grain boundaries to finally enhance the corrosion resistance of substrate.

Amorphous layer and alloy phases are formed on the implantation samples. The surface amorphous layer can reduce the number of active sites on the surface, while the alloy phases can weaken the corrosion strength of substrate.

References

[1] H.J. Böhmer, F.J. Ebert, W.Trojahn. J. Lubr Eng. 48(1992)28–35.

[2] T.A. Harris, J.Skiller, R.F. Spitzer. J. Tribol Trans. 35 (1992)731–737.

[3] A.P. Bond. J. Electrochem Soc. 120 (1973)603–606.

[4] L.D. Yu, T. Vilaithong, B. Yotsombat. J. SURF COAT TECH. 103–104 (1998) 328–333.

[5] Y. Wang, P.K. Chu, B.Y. Tang. J. Nucl instrum meth B. 127/128 (1997)1000-1003.

[6] W. Zhang, J. Ji, Y.H. Zhang. Applied surface science, 253(2007): 8981-8985.

[7] I. Nakatsugawa, R. Martin, E. J. Knystautas. J. Corrosion. 52 (1996) 921-926.

[8] M.Ueda, M. M.Silva, C.Otani. J. Surface and Coatings Technology. 35 (2003)169–170,408-410.

[9] Masaya Iwaki, Katsuo Takahashi. J. SURF COAT TECH, 51(1992) 1–5.

[10] R.S. Bhattacharyaa, A.K. Raia, V. Aronovb. Tribology Transactions, 43(1991): 472-477.

CHAPTER 12:

Alloys and Steels, Metallurgical Technologies

Advanced Materials Research Vol. 936 (2014) pp 1141-1145
© (2014) Trans Tech Publications, Switzerland
doi:10.4028/www.scientific.net/AMR.936.1141

Microstructure Evolution Characterization of Multi-pass Hot Rolling Simulation of Nb-Ti Microalloyed Steel

Bin Shen[1,a], Song-he Zhu[1,b], Heng-hua Zhang[1,c,*]

School of Materials Science and Engineering, Shanghai University, Shanghai 200072,China
[a]shenbin2011@shu.edu.cn, [b]zhusonghe@shu.edu.cn, [c]hhzhang@shu.edu.cn,
[*]Corresponding author

Keywords: Flow Stress; Microstructure Evolution; Hot Rolling Simulation; Microalloyed Steel

Abstract: In this study, a improved mathematical model was developed for Nb-Ti microalloyed steel during hot rolling simulation. Using the compression test, the dynamic and static recrystallization characteristics of Nb-Ti microalloyed steel were studied. Though multi-pass hot rolling simulation, it is found that the recrystallization during hot rolling can play an important role, it can make the mean flow stress lower and refine the grains. And respective comparison between calculated and measured data of microstructure showed some of the validation of the built model. Meanwhile, the evolution characteristic of average austenite grain size during hot rolling can be achieved by theoretical model and experiment.

Introduction

Achieving good mechanical properties of the product is important in hot rolling. However, hot rolling is a very complex process, which requires a strict control over a number of different parameters. Meanwhile, there are different complex metallurgical phenomena, such as strain hardening, static and dynamic recovery, static and dynamic recrystallization. Therefore, many workers have studied these complex metallurgical phenomena and have developed equations relating their kinetics to the processing parameters.

Intensive studies recently were carried on simulating multi-pass hot rolling behavior by hot deformation test. Sang Hun Cho[1] established model of flow stress during hot rolling by hot torsion test. M.Umemoto[2] found that the microstructure of austenite just before cooling to room temperature has a major influence on final ferrite microstructure. Therefore, the accurate understand of microstructure evolution in each pass during hot rolling is one of the most important aspects. Manuel Gomez[3] carried out multi-pass continuous cooling hot torsion test observing microstructure evolution during hot rolling. However, the studies did not make us further accurately understand microstructure evolution during hot rolling.

In this work, a improved mathematical model was developed for Nb-Ti microalloyed steel during hot rolling simulation. Multi-pass hot compression tests were used to simulate hot rolling according to the rolling schedule. The flow stress is analyzed and the metallographic each pass is characterized to study microstructure evolution.

Experimental Procedure

Chemical Composition of Experimental Steels

The steel studied was from billet. As Table 1 shows, the steel has 0.06% carbon content and 0.04% niobium and contains 0.013% titanium content. One-pass compression tests were carried out to determine the effects of the deformation variables on dynamic recrystallization. Double-pass compression tests were then conducted over the temperature range 1000-1150℃, inter-pass time range 1-100s, and pass strain range 0.1-0.4. This was done to evaluate the effects of deformation variables on softening.

Table 1 CHEMICAL COMPOSITION OF EXPERIMENTAL STEELS (wt%)

C	Mn	P	S	Si	Al	Nb	Ti
0.06	1.53	0.009	0.002	0.20	0.036	0.04	0.013

Multi-pass hot simulation tests were carried out in a computer-controlled hot compression machine (Gleeble-3500), on specimens with a gauge length of 15mm and a diameter of 10mm. Prior to the compression tests the specimens were austenitized during 5min at 1250℃, a temperature high enough to completely dissolve the Nb precipitates. After reheating, the temperature was lowered to that corresponding to the first deformation pass in each test at cooling rate 5℃/s. Table2 shows resume of the experimental conditions for multi-pass compression testing. After each pass deformation, the sample was immediately quenched to observe the microstructure.

Table2 RESUME OF THE EXPERIMENTAL CONDITIONS FOR MULTI-PASS COMPRESSION TESTING (t inter-pass time)

Pass	1	2	3	4	5	6	7
T(℃)	1130	1125	1119	1108	1101	1092	1083
ε (%)	12.7	13.2	13.7	13.3	13.7	14.1	14.3
$\dot{\varepsilon}$ (s-1)	1.43	1.57	1.72	2.13	2.33	2.55	3.17
t(s)	4.36	6.6	23.73	8.16	12.6	8.71	/

Results and Discussion

Microstructure Evolution Modeling

For better study of microstructure evolution, the improved mathematical model of microstructure evolution for Nb-Ti microalloyed steel was developed based on Avrami model by one-pass compression test and double-pass compression test.

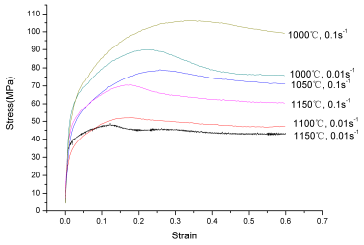


Fig.1.The Typical Stress-Strain Curves for the One-Pass Compression

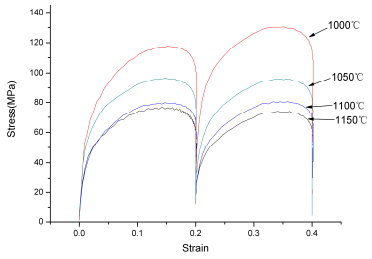


Fig.2 Typical Stress-Strain Curves for the Double-Pass Compression

(t=50s, ε=0.2, $\dot{\varepsilon}$ =1s-1)

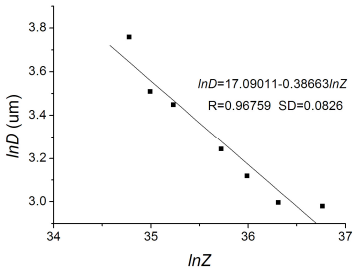


Fig.3 Evolution of Average Austenite Grain Size During Rolling

A)dynamic recrystallization (DRX)

The effect of deformation variables on the flow curves of the one-pass compression test is shown in Fig.1. This was further confirmed by an analysis of the effect of the deformation conditions on peak stress using the hyperbolic sine function and the recrystallization fractional attributable to DRX as follows:

$$Z=\dot{\varepsilon}\exp(\frac{401473}{\mathrm{RT}})=1.94\times10^{14}\left[\sinh(0.012\sigma_p)\right]^{5.4389} \quad (1)$$

$$X_{DRX}=1-\exp\left[-0.5104\left(\frac{\varepsilon-\varepsilon_c}{\varepsilon_p}\right)^n\right] \qquad n=0.01627Z^{0.1489} \quad (2)$$

$$\varepsilon_c = -1.02 + 0.037 \ln Z \qquad \varepsilon_c / \varepsilon_p = 0.717 \tag{3}$$

Here, X_{DRX} is the recrystallization fractional attributable to DRX, ε_c is the critical strain for the initiation of DRX, ε_p is the peak strain, Z is Zener-Holloman parameter, σ_p is peak stress.

n of X_{DRX} is not a constant, but a parameter related with *Z*.

B) Simulation of the double-pass compression test

The effect of deformation variables on the flow curves of the double-pass compression is shown in Fig.2. The model of fractional softening could be obtained by Avrami kinetics, in which the kinetics of recrystallization fractional is given by

$$X_{SRX} = 1 - \exp[-0.694(t / t_{0.5})^{0.2}] \tag{4}$$

$$t_{0.5} = 1.98 \times 10^{-14} \varepsilon^{-1.94203} \dot{\varepsilon}^{-0.4315} \exp\left(\frac{328246}{RT}\right) \tag{5}$$

Here, X_{SRX} is the recrystallization fractional to SRX, $t_{0.5}$ is the time for 50% softening to SRX.

C)Recrystallized grain size.

Fig.3 shows evolution of average austenite grain size during rolling. This does not greatly differ from several equations proposed for austenite recrystallized grain size and inter-pass grain growth C-Mn and microalloyed steels. The evolution of average austenite grain size during rolling could be given by the following expression.

$$D = 26432635.56 Z^{-0.38663} \tag{6}$$

Multi-pass Hot Compression Simulation and Analysis

The flow curves of multi-pass are shown in Fig.4. From the flow curves, it could determine the values of the fractional softening that takes place between passes. The fractional softening was calculated by means of the following expression [3,4].

$$X(\%) = \frac{\sigma_m^i - \sigma_y^{i+1}\left(\sigma_0^i / \sigma_0^{i+1}\right)}{\sigma_m^i - \sigma_0^i} \times 100 \tag{7}$$

$\sigma^i{}_m$ is the maximum stress for the *i*th (at temperature T_i) pass. $\sigma^{i+1}{}_y$ is the yield stress for $(i+1)$th pass. $\sigma^i{}_0$ is the yield stress of a fully restoration material for the *i*th pass. $\sigma^i{}_0$ and $\sigma^{i+1}{}_0$ are determined by the one-pass compression test.

When softening is only partial, some strain is retained into the next pass. Under these conditions the accumulated strain (ε_a) can be calculated from the following relation [5]:

$$\varepsilon_a = \varepsilon_i + (1 - X_{i-1})\varepsilon_{a-1} \tag{8}$$

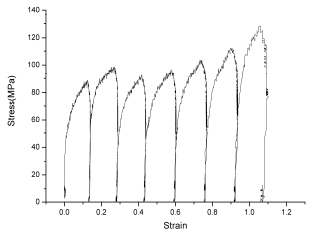


Fig.4 The True Stress-Strain Curves for the Simulation of Multi-Pass Hot Rolling Schedule

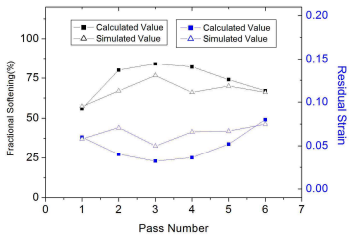


Fig.5 Fractional Softening and Residual Strain for the Simulation of Multi-Pass Hot Rolling Schedule

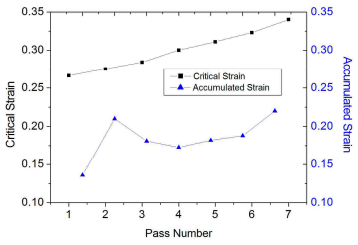
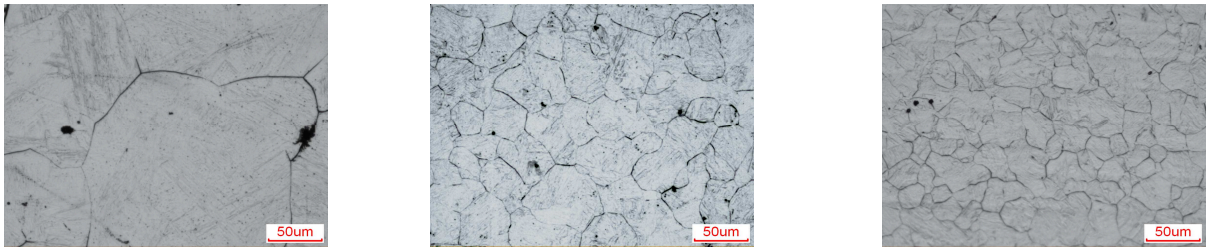


Fig.6 Critical Strain and Accumulated Strain for the Simulation of Multi-Pass Hot Rolling Schedule

It is interesting to note that there is an extreme point in the Fig.5. It accounts for that the fractional softening(X) after the first pass is only 56%, in which the progress of a restoration process happens incompletely, the stress is not fully relaxed, it produces the more accumulated stress. Then, the value of fractional softening(X) reaches about more than 80% after the second, third and fourth pass. With the strain and the time between neighboring pass become more, the stress has been relaxed more, and there is less accumulated stress.

The critical strain for DRX calculated from Eq.3 and the accumulated strain obtained from Eq.6 are compared in Fig.8. As the pass number is increased, the critical strain increases. Accumulated strain of each passes is lower than critical strain. It shows that the passes occurs the static recrystallization.



(a)initial grain size (b) the third pass (d) the seventh pass

Fig.7 Microstructures Obtained at Different Stages of Hot Rolling Simulation

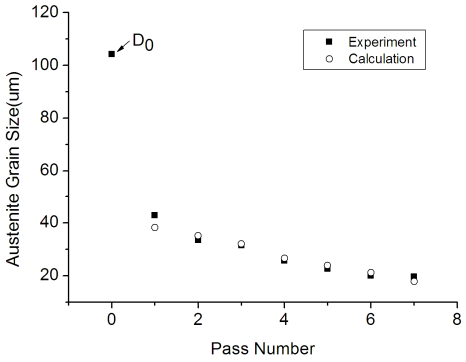


Fig.8 Evolution of Average Austenite Grain Size During Hot Rolling Simulation

Fig.7. shows the microstructure evolution of austenite along the hot rolling schedule. Grain is significantly refined during hot compression deformation. Starting from an initial grain size of 106μm (Fig.7a), grain is significantly refined by successive recrystallization. In Fig.7b, large grains characteristic of the deformed, unrecrystallized austenite are apparent with a few smaller recrystallized grains often located at three grain intersections on prior austenite grain boundaries. The grain size of the last pass (Fig.7c) is almost 20μm.The curve of Fig.8 has been obtained from analysis of Eq.6. In this figure, the evolution of average austenite grain size during rolling is graphically represented against pass number. The results of expression accord with the experimental results. The improved mathematical model could be used for austenite evolution study and it could guide the actual production of the factory.

Conclusion

The improved mathematical model was developed for Nb-Ti microalloyed steel during hot rolling simulation by compression test in this study. It was found that n of X_{DRX} is not a constant, but a parameter related with Z.

According to the simulation results, the predicted microstructure were in good agreement with the measured data. The microstructure evolution model established in this work possessed favorable practicability and accuracy and could be used for austenite evolution study. And it could guide the actual production of the factory.

References

[1] Sang Hun Cho, Yeon Chul Yoo, Hot rolling simulations of austenitic stainless steel, J. Mater. Sci. 36 (2001) 4267-4272.

[2] M Umemoto, A Hiramatsu, A Moriya, et al. Computer modeling of phase transformation from work hardened Austenite, ISIJ Int, 32 (1992) 306-315.

[3] Manuel Gomez, Lucia Rancel, Bernardo J, et al. Evolution of austenite static recrystallization and grain size during hot rolling of a V-microalloyed steel, Mater. Sci. Eng. A, 501 (2009) 188-196.

[4] A Bapari, A Najafizadeh, M Moazeny, et al. Simulation of radial forging conditions by third hits hot compression tests, Mater. Sci. Eng. A, 491 (2008) 258-265.

[5] Hodgson P D, Gibbs R K. A Mathematical Model to Predict Mechanical Properties of Hot Rolled C-Mn and Microalloyed Steels. ISIJ Int, 32 (1992): 1329-1338.

Advanced Materials Research Vol. 936 (2014) pp 1146-1152
© (2014) Trans Tech Publications, Switzerland
doi:10.4028/www.scientific.net/AMR.936.1146

Grade E550 Heavy Steel Plate by TMCP for Offshore Energy Exploration

Weihua Sun[1, a], Zhichao Bi[1,b]

[1] Jigang Group Co., Ltd, Jinan, China 250101

[a]wsun@jigang.com.cn, [b]bizhch@jigang.com.cn

Keywords: TMCP, tempering, high strength steel, offshore infrastructure, welding, CTOD

Abstract: This paper introduces the study and production on steel plate of Grade E550 in 60mm thick by Thermo-mechanical processing (TMCP) and tempering for offshore infrastructure purpose. The steel plate obtained high strength and good toughness in both the base materials and the weld joints. Microstructure and precipitation characteristics were examined in the plate is comprised of bainite with a small amount of pre-eutectoid ferrite. Parallel arranged lath bainite characterizes the bainitic structure with high density of dislocations and precipitates. Carbides MxCy averaging 200nm in dimension and MC type Carbonitrides in several nano to a dozen nano carbides distribute in the bainite ferrite and the bainte lath interfaces. Compatible mechanical properties were achieved at welded joint. Microstructures were analysed in the welding heat affected zone (HAZ).

Introduction

In recent years, world energy consumption keeps continuously growing. This tendency drives the requirement of steel constructions, especially for offshore oil and gas discovery and drilling. Nowadays, offshore oil and gas drilling is extending to a sea depth up to 3000 meters and extremely low temperature area. In the meantime, offshore windy energy exploration is a blooming form of energy generation which is becoming an important part of the total energy consumption [1-2]. There are two key issues that should concern in offshore steel structure design and fabrication. One is the safety and reliability and the other is the economical efficiency. High strength and low alloy steel plates are most common and steel materials to efficiently manufacture the offshore structures. To meet these requirements, steels for the offshore structure fabrication characterized as higher strength and heavier gauges under strict quality control.

Steel plates for offshore structure fabrication have undergone great progresses in the past three decades. Early oil and gas drilling platforms were fabricated by using the as rolled steel plates up to grade 355MPa yield strength, which the steel plate processing are also named as normal rolling without any further heat treatment. To obtain polygonal ferrite and pearlite microstructures and better Charpy V-notch Impact energy, the as rolled steel plates are processed by normalizing heat treatment where the steel are reheated at the austenitization temperature and then cooling in the air. Steel plates by normalizing rolling which the final deformation temperature is controlled in the normalizing temperature range may achieve an equivalent effect of normalizing. However, with oil and gas drilling performance going deeper into the sea, the above processing technology proved to be many limits to produce higher strength and thicker steel plate. Quenching and tempering process are applied in steel plate production to obtain high strength and toughness. In the 1980's, the critical value of crack tip opening displacement (CTOD) was introduced in evaluating fracture toughness in the welding joint of the steel plate to avoid fabricating risks. The advances in steel industry have made it possible to produce steel plates by thermal mechanical controlled processing (TMCP), which benefit for fine grain structure and favorable mechanical properties. As a result, the first -10^{o}C CTOD proof steel plate at a yielding strength of 355MPa by TMCP was available for offshore oil and gas drilling platform fabrication in the 1980's. Since then, yielding strength from 420MPa up to 550MPa steel plate have been developed for offshore structures.

Thermo-mechanical control process (TMCP) is currently used in producing steel products for a variety of purposes to obtain high strength, excellent toughness and good weldability etc[1, 3-4]. In practice, people sometimes encounter problems such as microstructure control, especially for steel plates with a heavy gauge, 50mm and above for example[5]. In this paper, the authors introduced a

60mm thick steel plate of Grade E550 by TMCP for offshore purpose. In this study, tempering heat treatment was suggested to obtain positive mechanical properties. The performance and characteristics of the steel plate were studied.

Study on the TMCP of E550

The chemical analysis (wt%) of steel in the present study is C 0.07, Si 0.25, Mn 1.65, P 0.008, S 0.003. Nb, V, Ti and Mo are added less than 0.050 (wt%) respectively. Thermo-mechanical simulation and laboratory hot rolling experiments were carried out in the similar steps described in the author's previous works [5-6]. Static and dynamic continuous cooling transformation (CCT) curves are displayed in Fig. 1.

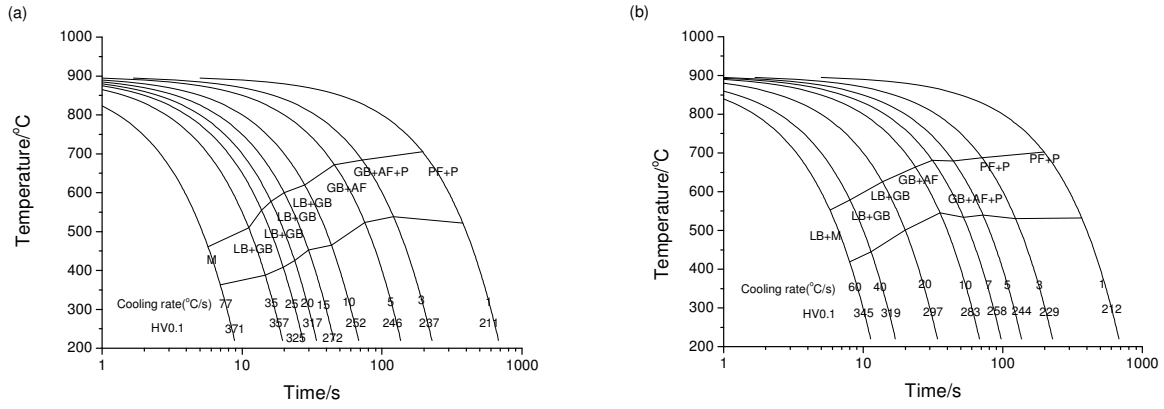


Fig. 1 Schematic of thermal mechanical simulation. (a) Static simulation; (b) Dynamic simulation.

Continuous Cooling Transformation (CCT). The steel is composed of pro-eutectoid ferrite and pearlite when the cooling rate is between 1-3℃/s, as shown in Fig. 1. Lath bainite microstructure may be obtained at cooling rate of 10℃/s when in static CCT curve but at 20℃/s in the dynamic CCT curve. In comparison with the static CCT curve, the dynamic CCT curve shifts to the left, implying an enlargement of the acicular ferrite and granular bainite areas. Lath bainite transformation shifts to the left when in dynamic CCT curve. According to microstructure examination, fine lath bainite is obtained when cooling rate is 40℃/s in the dynamic CCT. Martensite may be obtained when the cooling rate reaches 60℃/s when in dynamic CCT.

Effect of Tempering on Precipitation. Tempering plays a critical role in obtaining propitious mechanical properties and welding performance, as revealed in the author previous study [3, 6-7]. In fact, precipitation behavior in tempering is one of the most important factors in strengthening and/or softening of the steel microstructure.6 The effect of tempering temperature on precipitation was investigated by transmission electron microscope (TEM). Steel plates of 860℃ finish rolling temperature at a 20℃/s cooling rate were tempered respectively from 530 to 650℃ at a holding period of 2min/mm.

Analysis on typical precipitates shows that tempering gives rise to less amounts and small size precipitates in the steel at a lower temperature than at a higher temperature. TEM examinations prove that the precipitates in the steel are comprised of titanium and niobium carbonitrides (MC) in square shape and carbides M_xC_y in irregular shapes that contain iron and manganese. When the steel was tempered at 650℃, large sized M_xC_y about 300nm and MC from 50 to 100nm were found. When temperied at 620℃, the steel was enriched with precipitates, in which the 300nm precipitates were M_xC_y and precipitates from 50 to 100nm were MC. In the meantime, abundant super-fine particles from several to a dozen nano carbides characterized the tempered precipitates at 620℃. The precipitates at 620℃ are studied by selected area diffraction (SAD), as shown in Fig. 2. Analysis on an irregular precipitates confirmed that the precipitate type was $M_{23}C_6$, demonstrating an orientation relationship [011] $M_{23}C_6$ // [721] between the carbides and the base microstructure, as exhibited in

Fig. 2 (a) and Fig. 2 (b). Carbonitrides are characterized in small sizes from 15 to 50nm with a large amount of fine titanium carbinitrides less than 20 nm, in which most of them are titanium nitrides (TiN) in square shape. Diffraction analysis on a typical TiN was carried out along the [001] axis, revealing its Face-centered cubic (FCC) lattice whose constant is approximately 0.43nm, as shown in Fig. 2 (c) and Fig. 2 (d). These small particles play an important role in pinning the dislocations and grain boundaries, which makes the after tempering steel plate characterized with high density of dislocation and fine grains. When tempering at 590 and 530℃, less carbides were found and enriched at grain boundaries. At both 590 and 530℃, the carbides were principally Ti(CN) in square shape with niobium carbonitrides adhesion to the Ti-particles. The tempered precipitates are from 100 to 200nm in size at 590℃. Smaller size particles from 50 to 100nm characterized the carbides at 530℃
.

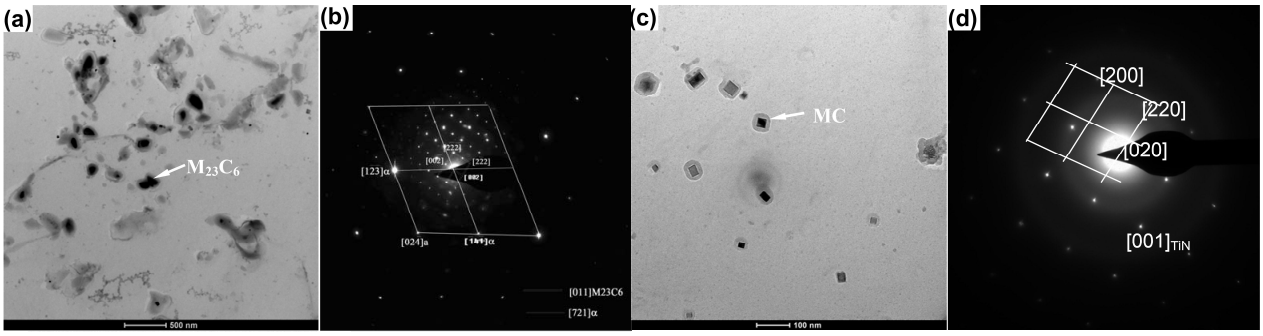


Fig. 2 SAD analysis of typical precipitates. (a) $M_{23}C_6$, (b) SAD pattern of $M_{23}C_6$, (c) TiN, (d) SAD pattern of TiN

Effect of Tempering on Mechanical Properties. The effects of tempering on the steel mechanical properties were also tested, shown in Fig. 3. The tempering experiments were carried out at 630ºC and 650℃ respectively given 1 to 4min/mm holding time on steel plates of 860℃ finish rolling temperature at a 20℃/s cooling rate.

In Fig. 3(a), the tempering temperatures of 630℃ and 650℃ do not obviously affect the steel strength, neither does the Charpy V-notch impact energy. However, as tempering period grows longer, both yield strength and tensile strength decrease while Charpy V-notch impact energy increases. At 2 and 3 min/mm, the steel obtains better toughness. A 2min/mm tempering period at 630ºC is recommended in plate production.

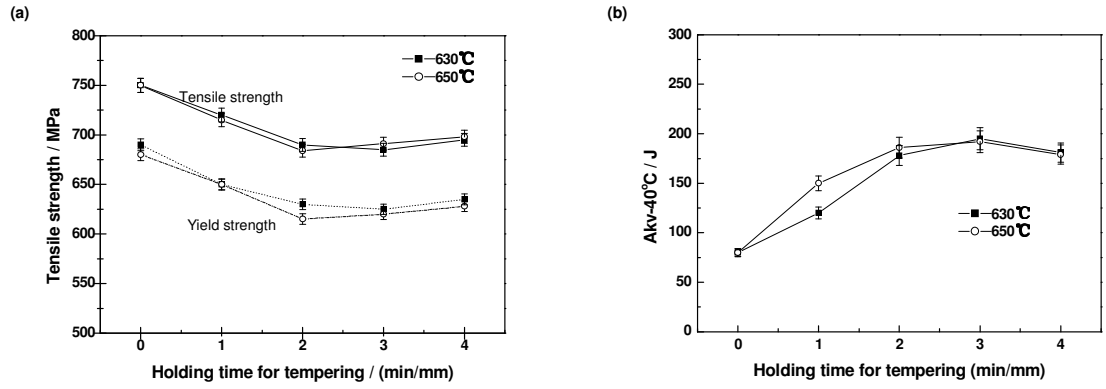


Fig. 3 Effect of tempering on steel strength and toughness.(a) yield and tensile strength; (b) AKv-40℃

Performance of the E550 Steel Plate

Mechanical Properties. A finishing rolling temperature from 850 to 860℃ at a cooling rate of 20 ℃/s was applied in 60mm thick E550 steel plate production. The plates were further processed by tempering heat treatment after the parameters discussed in the previous section. Two pieces of the

plates were examined respectively from both the top end and the bottom end of the top heat from one casting. The examinations included strength and Charpy V-notch impact tests at -40℃ in the top end, the middle and the bottom end respectively at 1/4 and 1/2 thickness of the plate. The above evaluation was also performed at different positions along the plate at 1/4, 1/2, 3/4 of the width from the left and the right edge and both edges. The results of the top end plate are shown in Table 1 and Table 2.

Table 1 Longitudinal and transversal mechanical properties of 60mm plate E550 at 1/4 thickness

Position along width	Direction	Top end					Middle					Tail end				
		$Rp_{0.2}$ [MPa]	Rm [MPa]	A [%]	Akv [J]	FA [%]	Rp0.2 [MPa]	Rm [MPa]	A [%]	Akv [J]	FA [%]	Rp0.2 [MPa]	Rm [MPa]	A [%]	Akv [J]	FA [%]
Left edge	Long.	660	735	22	246	100	640	720	22	240	100	635	710	21	252	100
	Trans.	655	740	21.5	248	100	635	715	21.5	246	95	640	705	21	248	100
1/4	Long.	660	720	21	247	100	640	715	22	234	100	635	700	22	261	100
	Trans.	650	720	20.5	242	95	630	700	21	231	100	630	700	21	239	95
2/4	Long.	655	710	22	237	100	625	715	21	239	100	630	700	21	249	100
	Trans.	650	715	21	226	100	630	700	21	244	100	620	690	22	231	100
3/4	Long.	630	695	22	252	100	615	685	22	228	100	610	680	22	251	100
	Trans.	640	715	22	244	100	620	700	21	236	100	620	690	21	247	100
Right edge	Long.	650	735	21	240	100	620	700	22	247	100	620	690	22	251	100
	Trans.	660	720	22	237	100	635	710	21.5	244	100	630	710	21	247	100

Table 2 Longitudinal and transversal mechanical properties of 60mm plate E550 at 1/2 thickness

Position along width	Direction	Top end			middle			Tail end		
		$Rp_{0.2}$ [MPa]	Rm [MPa]	A [%]	$Rp_{0.2}$ [MPa]	Rm [MPa]	A [%]	$Rp_{0.2}$ [MPa]	Rm [MPa]	A [%]
Left edge	Long.	645	725	23	630	715	22	630	720	23
	Trans.	660	720	23	620	720	23	620	710	23.5
1/4	Long.	645	710	23	615	705	23	615	705	23
	Trans.	635	710	22.5	615	700	22.5	605	710	23
2/4	Long.	645	715	23.5	615	700	23.5	610	710	23
	Trans.	640	710	23	605	690	23	600	700	23
3/4	Long.	620	690	22.5	600	680	22.5	590	685	22
	Trans.	630	710	22	610	690	23	595	695	23
Right edge	Long.	640	710	23	610	705	22	600	705	22
	Trans.	640	720	23	615	710	23	620	715	23

The steel plate demonstrates good Charpy impact energy values. At the 1/4 thickness position, yield strength and tensile strength displays 30MPa and 35MPa difference respectively in the whole plate and, 40MPa and 20 MPa difference at 1/2 thickness position. A maximum difference of 25MPa for both the yield and tensile strength respectively has been found between the 1/4 thickness and the 1/2 thickness in the whole plate. The tensile testing results also indicate larger strength values at the 1/4 thickness position than at the 1/2 and, larger values in the top end than in the middle and the bottom end of the steel plate.

Microstructure. Microstructure of steel plate is comprised of fine grain bainite with a small amount of pre-eutectoid ferrite. Fig. 4 shows the sub-structure whose size is approximately 1 to 2μm. The lath structure in Fig.4 (a) and Fig.4 (b) is bainite, in which high density of dislocation structures were found. Detailed examinations on the high density dislocations and grain boundaries show that many small precipitates in less than 300nm size distribute inside the substructure and at the grain boundary, as shown in Fig.4 (c) and Fig.4 (d).

Welding Performance. Multi-pass submerged arc welding (SAW) tests were conducted under both 7kJ/cm and 50kJ/cm heat input respectively on K-groove and X-groove butt welding according to BS7448. A CHW-SG type welding wire of 4.0mm in diameter was used to accomplish the welding. No pre-heating was implemented and the inter-pass temperatures were controlled under 200 ℃.

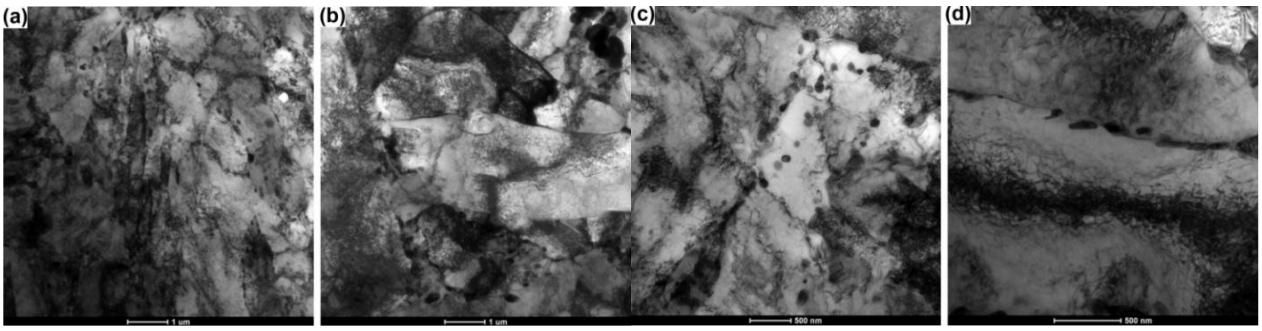


Fig. 4 Microstructure of E550 steel plate. (a) structure, (b) sub-structure, (c) inner-grain precipitates, (d) precipitates at grain boundary

The X-groove welding assemblies were stress released (SR) at 580℃ with 4 hours holding. A Vickers hardness test using a test load of 5kg was performed on both the as weld (AW) and SR specimens taken from the test assembly. The distance between indents is 1.0 mm at 1 to 2mm respectively from both the plate surfaces. Fig.5 shows the hardness distribution across the welding joints, demonstrating small softening in the heat affected zone (HAZ). Charpy V-notch impact at -40℃ tests were also carried out at 2mm from the top surface at both the AS and SR conditions. The absorbed energy after SR heat treatment in the HAZ decreased less than 50J at 7kJ/cm heat input and 100J at 50J/cm heat input. In all tests, the absorbed energy exceeded 100J, as shown in Fig. 5.

In the K-groove welding, Charpy V-notch impact tests at -40℃ were carried out for both the heat input welds in both the square edge and bevel edge side materials with the notch respectively at the fusion line (FL) and at 2mm, 5mm and 20mm from the fusion line (FL+2, FL+5 and FL+20 respectively). The above absorbed energy tests were respectively implemented at 2mm from the top surface, the middle thickness of the plate and 2mm from the bottom surface. The test results are shown in Fig. 6. The average absorbed energy exceeded 110J at each tested position and the minimum value 100J, demonstrating good toughness.

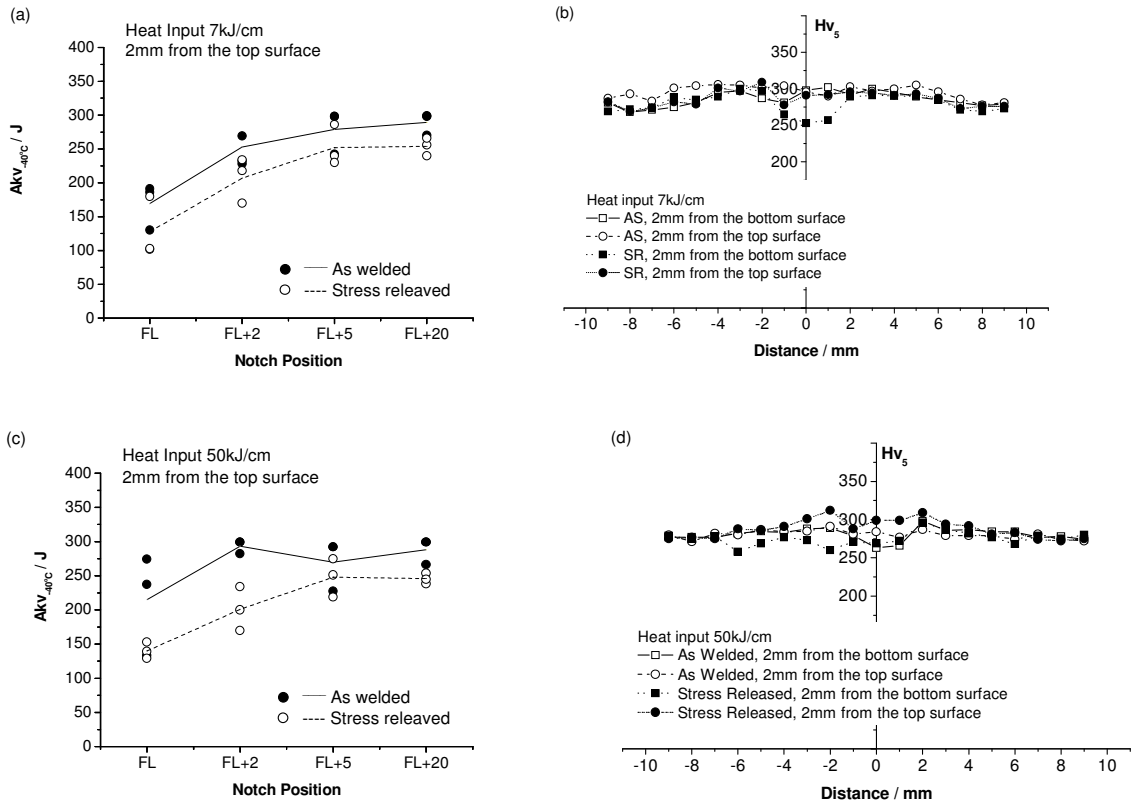


Fig. 5 X-groove SAW testing results

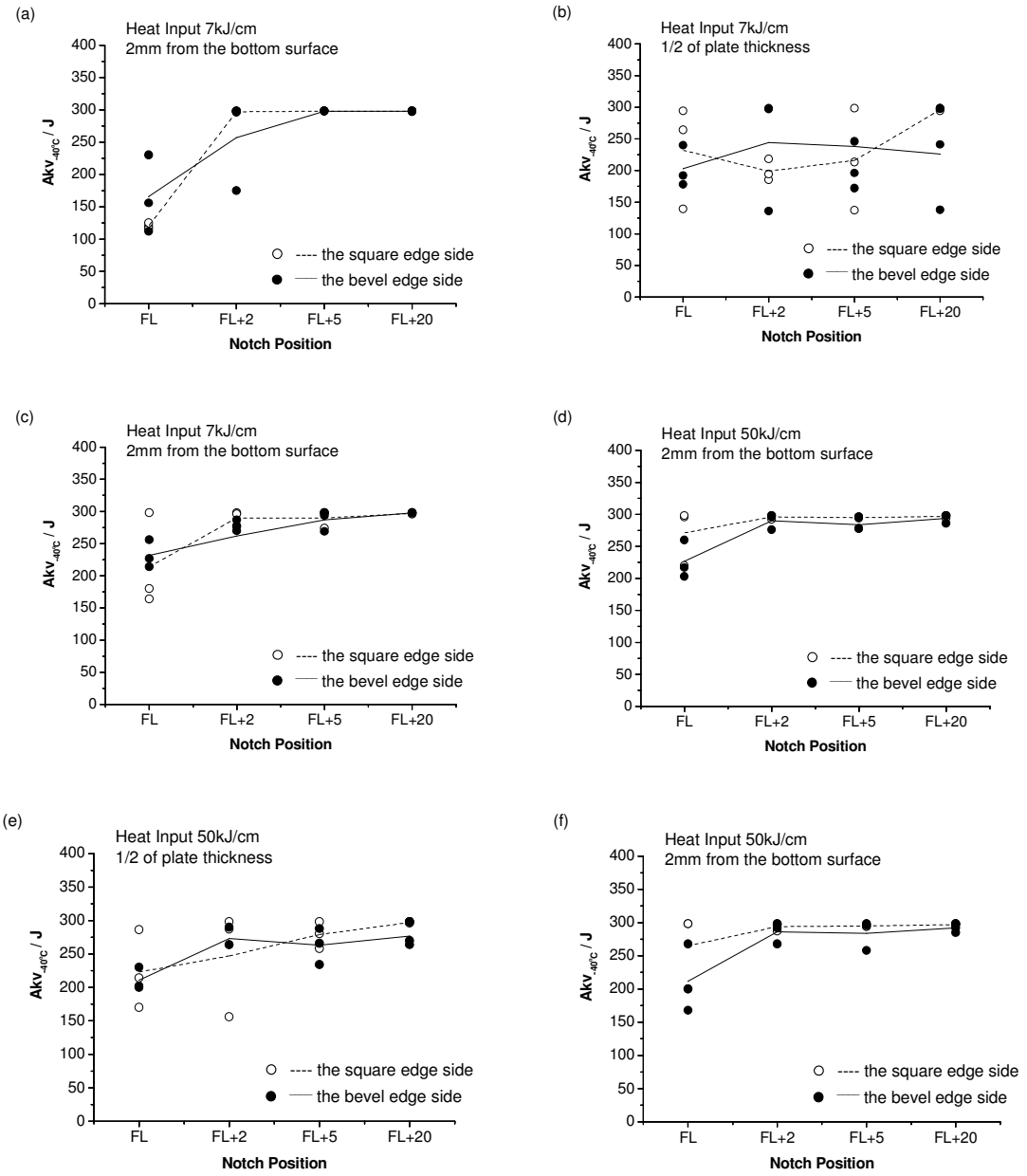


Fig. 6 K-groove SAW testing results

Crack Tip Opening Displacement Tests. Table3 shows the testing results of CTOD tests at -10 ℃for the welded joints in accordance with BS7448. The dimensions of the testing sample were 58×58×400mm and 7kJ/cm and 50kJ/cm heat input were respectively applied when making the welds. The crack orientation were along the weld direction and were located at 2mm inner the weld metal (WM) from straight edge of the fusion line (FL), grain coarsened HAZ (GCHAZ) and the subcritical HAZ/intercritical HAZ boundary (SCHAZ+ICHAC). The CTOD δ c values obtain for both welding conditions prove to be well competent with the requirement.

TABLE 3 The CTOD testing results

Crack position	δ_c /mm	
	7kJ/cm heat input	50kJ/cm heat input
WM-2mm	0.46, 0.43, 0.42	0.35, 0.32, 0.30
GCHAZ	0.43, 0.40, 0.37	0.35, 0.38, 0.33
SCHAZ+ICHAC	0.38, 0.42, 0.40	0.31, 0.37, 0.36

Conclusion

The 60mm thick E550 steel plate processed by TMCP and tempering heat treated was successfully developed with good mechanical properties, weldability and CTOD performance. The steel plate is characterized with fine bainite structures. Carbides and cabonitrides together play an important role in fine grain structure and high density dislocations which are in turn propitious to the plate strength and toughness. Precipitates in nano size that distribute inside the substructure and at the grain boundary are benefit to improve the steel plate weldability and CTOD property.

Acknowledge

The first author is grateful to the Taishan Scholarship by Shandong Province, China.

References

[1] N.Shikanai, S.Mitao and S.Endo: JFE Technical Report. 11 (2008), p77
[2] F.Schroter, in: http://www.dillinger.de/dh/produkte/sparte/index.shtml.en
[3] W.Sun andd G.D.Wang: J. of Mater. Sci. and Techn. Vol 25 (2009), p857
[4] J.M.Zang, W.H.Sun and H.Sun: J. of Iron and Steel Research International Vol 17 (2010), p63
[5] L.J.Zhou, W. H. Sun, H. Sun and Q.B.Han in: Proceedings of the 10th International Conference on Steel Rolling, edited by S.L.Cao Publications/Metallurgy Industry Publishers, Beijing (2010) W.Sun, G.D.Wang and H.Sun: J. of Iron and Steel Research International Vol. 17 (2010), p48
[6] W. H. Sun: PhD Thesis, Shengyang, China (2010)

Advanced Materials Research Vol. 936 (2014) pp 1153-1157
© (2014) Trans Tech Publications, Switzerland
doi:10.4028/www.scientific.net/AMR.936.1153

Preparation of crystalline hematite from bauxite

Juan Liu [1,a], QianQian Jiang[2,b], Jing Wang[1,c], Li Chen[1,d], XingYao Wang[1,*e]

[1]Department of Chemistry, School of Science, Tianjin University, Tianjin, China

[2]Department of Applied chemistry, School of Chemical Engineering, Tianjin University, Tianjin, China

[a]Email liujuansd@163.com ,[b]Email kaiqian2008@163.com, [c]Email wjjcc1984@163.com, [d]Email wshrcn@163.com, [e]Email wxyghw@tju.edu.cn

Keywords: Ferric oxide, nanoparticles, hydrothermal stripping, bauxite

Abstract. A novel of hydrothermal stripping technique is developed to synthesize nano-particles of ferric oxide from iron-loaded organic phase by ammonia. The iron-loaded organic phase was prepared by extracting simulated bauxite hydrochloric acid leaching liquors with N235 and then the iron is stripped by heating the organic phase up to 180°C to precipitate as ferric oxide. XRD patterns exhibits that the ferric oxide is composed of α-Fe_2O_3 and TEM images reveals that the particles of crystalline hematite powders are homogenous with quasi-spherical fine crystallites and its primary particles are about 150 nm. This process is a proof of concept for the removal and precipitation of iron from bauxite hydrochloric acid leaching liquors.

Introduction

To recover aluminium hydrometallurgically from bauxite, which contains Al, Fe and Ca and requires a step to separation iron–aluminium .Many processes are known for the removal of Fe^{3+} from aqueous solutions [1, 2]. The processes generally are comprised of precipitation, solvent extraction, ion exchange, and other techniques. Solvent extraction is one of the most widely methods that is used to the separation of metal ions from different sources [3-5]. Ferric oxide (Fe_2O_3) is functional materials for various applications (magnetic materials, catalytic materials, pigments, coatings, gas sensors, etc.) [6-8]. The hydrothermal stripping process [9,10], in which metal-containing species are hydrolyzed and precipitated directly from the loaded cation exchange solvent extractants, is still differ from hydrolysis, and clearly shows promise for synthesizing oxide ceramic powders for high-performance applications [11-16] .In this study, we developed a method for synthesizing Fe_2O_3 nanoparticles by stripping from iron-loaded organic phase which was prepared by extracting simulated bauxite hydrochloric acid leaching liquors with N235.

Experimental

A typical simulated liquor, which contained 15 g/L Fe^{3+}, 32 g/L Al^{3+}, 75 g/L Ca^{2+} and 3 M HCl (free acid, M: mol/L), was prepared. The simulated bauxite hydrochloric acid leaching liquors were used to prepare the aqueous phases. All other chemicals were of reagent grade. The various volume ratios of N235 and simulated liquor were taken in a reagent bottle and stirred with fixed speed (200 r/min) at room temperature. After mechanical stirring, the phases were separated to obtain iron-loaded organic phase. In each stripping experiment, at first put 40 mL of organic phase, 20 mL of ammoniacal water into the autoclave of 100 mL capacity, seal it, heat to the experimental

temperature, and take this instant as the starting time, then take a series of samples at timed intervals. The content of iron in the organic phase was determined by chemical titration method. The whole Process for Fe recovery (A) and preparation of crystalline hematite (B) was illustrated as follows (Fig.1). The crystal phase structure of ferric oxide was investigated using an X-ray diffractometer (XRD) (BDX-3300 made by Peking University Instrument Co., China). A Transmission Electron Microscope (TEM) (100CX-II made by JEOL, Tokyo, Japan) was used to characterize the ferric oxide powders with respect to their particle size and shape.

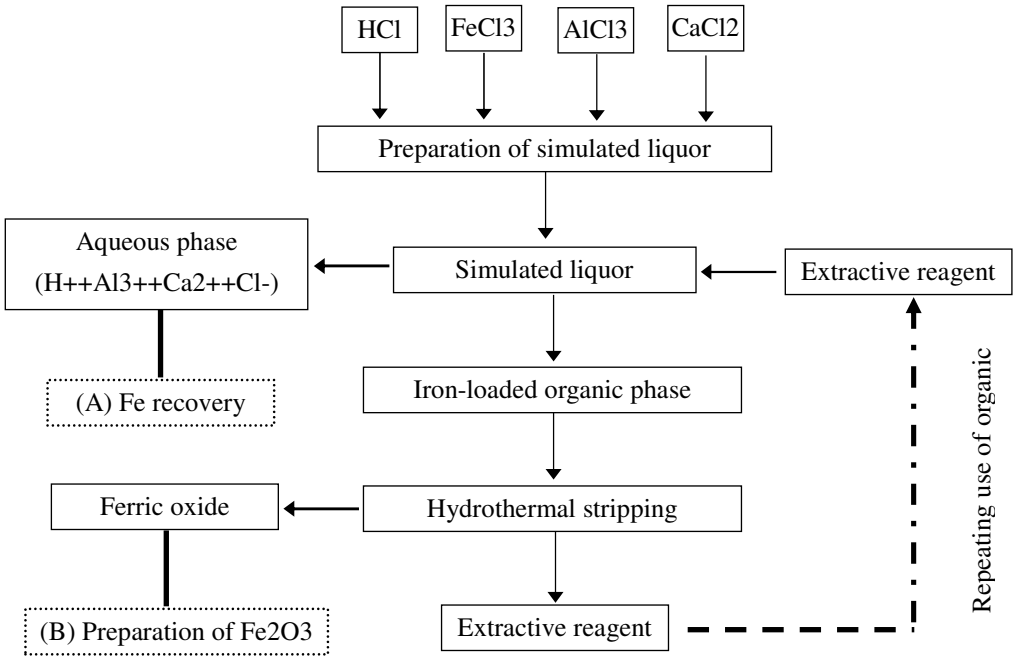


Fig.1 The whole experimental programme

Results and Discussion

Preparation of Crystalline Hematite Powder

The experimental results of stripping iron-loaded organic phase with ammoniacal water are given in Tables 1. It can be seen from Table 1 that the pure crystalline hematite was obtained with ammoniac water phase and at higher temperature (180°C or 200°C).

The percentage of stripping Fe is over 90% after hydrothermal stripping of 40 minutes at 180°C. There is hardly any Fe in the organic phase after hydrothermal stripping of 1.0 hour at 180°C.The size of α-Fe_2O_3 powders will large with the time on the extent of stripping in the same conditions.

Table 1 EXPERIMENTAL RESULTS OF STRIPPING IRON-LOADED ORGANIC PHASE BY AMMONIAC WATER

Ammoniac Water phase*	ratio O:W	Stripping Temperature[°C]	Stripping Time[h]	Sample		
				Color	Component	
Pure water	2:1	130	1.0	No hematite		
Pure water	2:1	180	1.0	Green	Mixture	
1:10	2:1	180	1.0	Red	α-Fe2O3	1#
1:5	2:1	180	1.0	Red	α-Fe2O3	2#
1:1	2:1	180	2.0	Red	α-Fe2O3	3#
1:1	2:1	200	2.0	Red	α-Fe2O3	4#

*The different ratio of ammoniac water phase was obtained by mixing NH3·H2O with water.

XRD of Crystalline Hematite Powder

X-ray diffraction analysis (XRD) of powders was conducted on a Rigaku Dmax X-ray diffractometer. The XRD shown in Fig.2 reveals the crystalline hematite powder obtained by the technique of hydrothermal stripping was well crystallized and composed of α-Fe_2O_3.

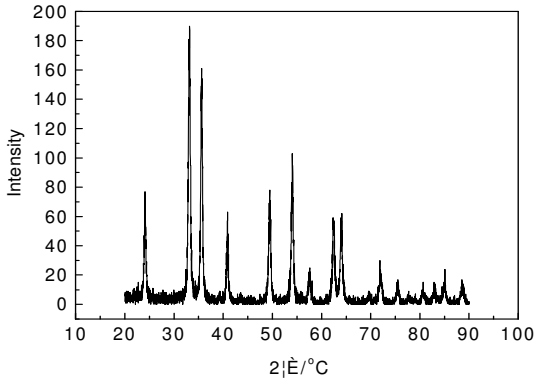


Fig.2 X-ray powder diffraction patterns for the samples 2# in Table 1.

TEM of Crystalline Hematite Powder

A transmission electron microscope (TEM) model H-8100IV was employed to characterize the morphology and the particle size of the powders. Some TEM images at different conditions are shown in Fig.3 reveal that the particles of crystalline hematite powders are homogenous in their shape, with quasi-spherical fine crystallites with an average diameter of sub-micron grade. It can be seen from Fig.3 that the Fe_2O_3 particles sizes were influenced by stripping temperature and time.

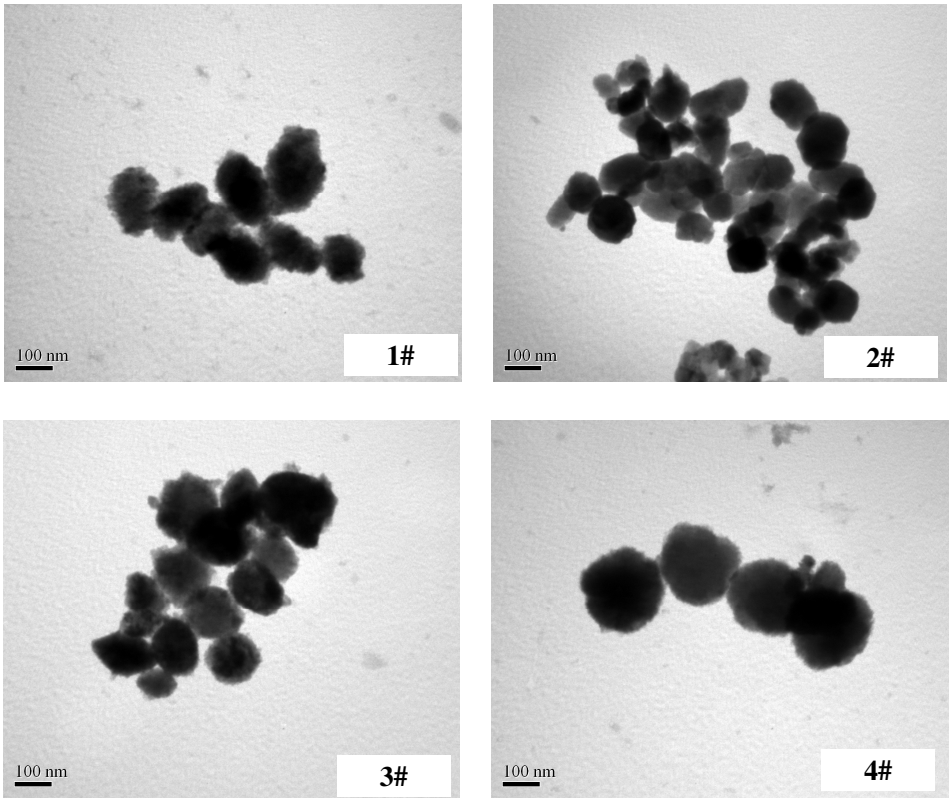


Fig.3 TEM Images of Oxide Particle Prepared by Hydrothermal Stripping

Analysis of the Composition of Crystalline Hematite Powder

The composition of crystalline hematite powder was shown in Table 2. It is can be seen from Table 2 that the iron oxide powder synthesized by hydrothermal stripping route has higher purity.

Table 2 ANALYSIS OF THE COMPOSITION OF THE IRON OXIDE POWDER

Composition of powder, w%			
Fe2O3	Al2O3	Ca	Cl and others
98.97	0.862	0.1615	0.0065

Conclusion

N235 can effectively remove Fe from Al + Fe + Ca liquors. Moreover, The iron-loaded organic phase can be prepared by extracting simulated bauxite hydrochloric acid leaching liquors with N235. The ferric oxide nanoparticles were successfully synthesized via a hydrothermal stripping route which strip ferric ion from iron-loaded organic phase by ammoniacal water. The XRD patterns and TEM images of ferric oxide reveal that the powders are composed of spherical a-Fe_2O_3 with a narrow and uniform size distribution. The experimental results indicated that the Fe_2O_3 nanoparticles sizes were influenced by the stripping temperature and time. The fact that the organic phase and water phase can be reused here means that this route is a green synthesis method.

Acknowledgments

This work was supported by a grant from Alcoa of Australia Limited.

References

[1] Melani Sooriyaarachchi and Jurgen Gailer, Removal of Fe^{3+} and Zn^{2+} from plasma metalloproteins by iron chelating therapeutics depicted with SEC-ICP-AES. Dalton Trans. 39 (2010) 7466-7473

[2] Mohammed A. and Al-Anber, Removal of high-level Fe^{3+} from aqueous solution using natural inorganic materials: Bentonite (NB) and quartz (NQ). Desalination 250 (2010) 885-891

[3] Biswas, R.K., Begum, D.A., Solvent extraction of Fe^{3+} from chloride solution by D2EHPA in kerosene. Hydrometallurgy 50 (1998) 153-168

[4] Anna Parusa, Karolina Wieszczyckaa, Andrzej Olszanowskia ,Solvent Extraction of Iron(III) From Chloride Solutions in the Presence of Copper(II) and Zinc(II) Using Hydrophobic Pyridyl Ketoximes. Separation Science and Technology 46 (2011) 87-93

[5] Sun, P.P., Lee, M.S., Separation of Ir(IV) and Rh(III) from mixed chloride solutions by solvent extraction. Hydrometallurgy 105 (2011) 334-340

[6] Qian X, Zhang X, Bai Y, Li T, Tang X,Wang E,Dong S, Photoelectrochemical characteristics of a-Fe_2O_3 nanocrystalline semiconductor thin film. J Nanopart Res 2(2) (2000) 191-198

[7] Deb P, Biswas T, Sen D, Basumallick A, Mazumder S, Characteristics of Fe_2O_3 nanoparticles prepared by heat treatment of a nonaqueous powder precipitate. J Nanopart Res 4(1-2) (2002) 91-97

[8] Demianets LN, Pouchko SV, Gaynutdinov RV Fe_2O_3 single crystals: hydrothermal growth, crystal chemistry and growth morphology. J Cryst Growth 259(1-2) (2003) 165-178

[9] Konish Y, Kawamura T, Asai S, Preparation and characterization of ultrafine nickel ferrite powders by hydrolysis of iron(III)-nickel carboxylate dissolved in organic solvent. Ind Eng Chem Res 35(1) (1996) 320-325

[10] Adschiri T, Hakuta Y, Arai K, Hydrothermal synthesis of metal oxide fine particles at supercritical conditions. Ind Eng Chem Res 39(12) (2000) 4901-4907

[11] Wang XY, Kang XH, Xie HQ, Lu LZ, Studies of heterogeneous hydrothermal stripping fromiron-loaded naphthenic acid-alcohol-kerosen. Chin J Process Eng 3(2) (2003) 109-115

[12] Wang XY, Kang XH, Xie HQ, Lu LZ, Preparation of nanosized a-Fe_2O_3 by hydrothermal stripping process. Chin J Appl Chem 21(7) (2004b) 655-659

[13] Wang XY, Han JY, Yang GQ, Qin X, Study on synthesis and doped lanthanum of $NiFe_2O_4$ nanoparticles by hydrothermal stripping. J Funct Mater 38 (2007a) 1282-1284

[14] Wang XY, Han JY, Yang GQ, Lu LZ, Xie HQ, Kinetic study of hydrothermal stripping from iron–loaded organic phase. Trans TJU 13(2) (2007b) 113-116

[15] Wang XY, Han JY, Wang J, Yang GQ, Synthesis of spinel $MgFe_2O_4$ nano-powder by hydrothermal stripping. J Mater Eng 10 (2008) 98-100

[16] Wang XY, Miao C, Zhou J, Ma C, Wang HF, Sun SQ, A novel synthesis of spherical $LiFePO_4$ nanoparticles. Mater Lett 65 (2011) 2096-2099

Advanced Materials Research Vol. 936 (2014) pp 1158-1162
© (2014) Trans Tech Publications, Switzerland
doi:10.4028/www.scientific.net/AMR.936.1158

The effect of heat treatment of gray and nodular cast iron with ferrite matrix on mechanical properties and corrosion rate compared with medium carbon steel

Mohamed A. Gebril[1,a], M. S. Aldlemey[2,b], Farag I. Haider[3,c]

[1] Mechanical department, Engineering Faculty, Benghazi University, Benghazi-Libya
[2] Technical collage of Mechanical Engineering, Benghazi-Libya

[3] Mechanical department, Engineering Faculty, Benghazi University, Benghazi-Libya

[a]magmalki@yahoo.com, [b]maldleme@yahoo.com, fah1232003@yaoo.com

Keywords: Heat treatment, gray and nodular cast iron, dissolution of graphite, corrosion rate

Abstract: In this work, the influence of heat treatment process and quenching in different quenchant media of medium carbon steel, gray and nodular cast iron with ferrite matrix on the hardness, ductility and corrosion rate of has been investigated. During this type of operations, the specimens were Austenizing at 900ºC for one hour. Therefore, the specimens were quenched in different kind of oil as quenched medium (oil 20-50, oil 40, oil 90, and water as reference). The hardness , impact energy to measure the ductility, corrosion rate and microstructures were studied. From result of steel 0.47% carbon was clear increasing in hardness and decreasing in ductility with close varying values in oil quenchant kind comparing with as received specimen and water quenched one, corrosion rate decreased with heat treatment and quenching process due to formation of single face instead of double phase before heat treatment process which created galvanic cell. For gray and nodular cast iron it is noticeable that no changing in microstructure within heating for one hour at 900ºC because the matrix in both cast iron types is ferrite, therefore no changing in mechanical properties under heat treatment process with time of one hour which is not sufficient to decomposition of graphite, but with comparison the hardness of gray cast iron is more than nodular one due to distribution of graphite flacks which increase the hardness and decrease the ductility as well as increasesing the corrosion rate compared with nodular cast iron. Microstructure of both types of cast iron have been studied after subjected the specimens to heat treatment at 1000ºC and for 10 hours, the microstructures shown clear diffusion of some carbon in ferrite matrix around the graphite phase and under quenched some of martensite formed.

Introduction

One reason for the versatility of metallic materials lies in the wide range of mechanical properties they possess, which are accessible to management by various means. Steel is an alloy of iron and carbon. Steel with low carbon content has the same properties as iron, soft but easily formed. As carbon content increases, the metal becomes harder and stronger but less ductile and more difficult to weld. Higher carbon content lowers steel melting point and its temperature resistance in general[1]. Medium carbon steel is steel with 0.3 to 0.7%C and approximately 0.8%Mn which are used in the production of machinery parts such as nuts and bolts, shafts and gears[2]. Plain-carbon steels and cast irons are heated to austenitizing temperatures and then rapidly cooled (quenched) in water, brine, or oil to the critical temperature [3-4]. The critical temperature is dependent on the carbon content, but as a general rule is lower as the carbon content increases [3-5]. This results in a martensitic structure; a form of steel or cast iron that possesses a super-saturated carbon content in a deformed body-centered cubic (bcc) crystalline structure, properly termed body-centered tetragonal (bct). This crystalline structure has a very high amount of internal stress [6]. Due to internal stress quenched steel and ductile cast iron is extremely hard but brittle, usually too brittle for practical purposes [6-7]. These internal stresses cause stress cracks on the surface [7].

Experimental Procedure

Materials

Materials use in this study are medium carbon steel, gray and nodular cast iron with ferrite matrix, oil 20-50, oil 40, oil 90,olive oil and water as quenchant medium. The chemical composition of steel and two types of cast iron is shown in Table 1.

Table 1, Chemical compositions of materials specimens samples.

Element	*%C*	*%Si*	*%Mn*	*%P*	*%S*	*%Mg*	*%Al*	*%V*	*%Ti*
Medium carbon steel	0.47	0.26	0.145	0.017	0.012	-	0.012	0.035	0.32
Gray cast iron	2.7-4	1.8-3	0.2	0.07	0.2	0.09	-	-	-
Nodular cast iron	3.79	2.1	0.3	0.1	0.043	0.044	-	-	-

Hardening process

The specimens were initially normalized, followed by austenizing at 900ºC for 60 minutes and then quenched in oil 20-50, oil 40, oil 90, and water.

Result and Discussion

Hardness Result

Hardness values for medium carbon steel and two types of cast iron are shown in Fig. 1.

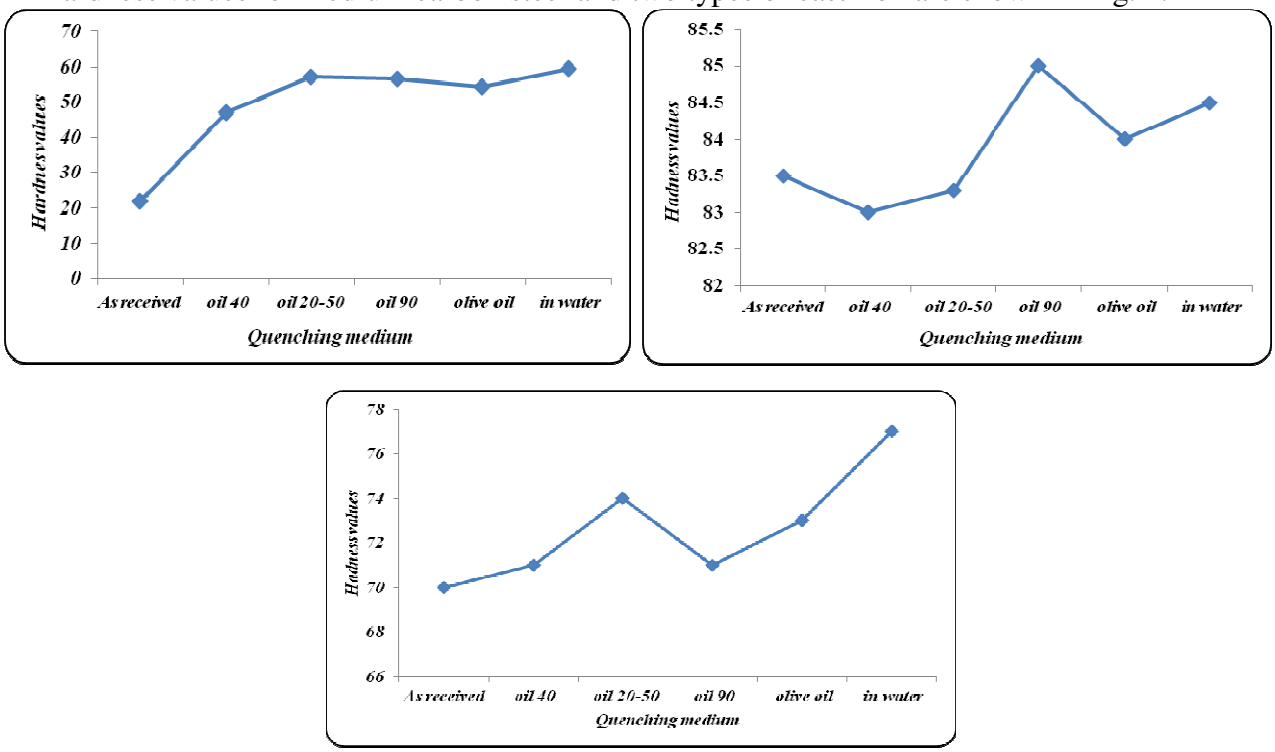


Fig. 1, Show the hardness of 0.47% carbon, gray and nodular cast iron steel respectively in quenching mediums

Corrosion rate values

Corrosion rate values for medium carbon steel and two types of cast iron are shown in Fig. 2.

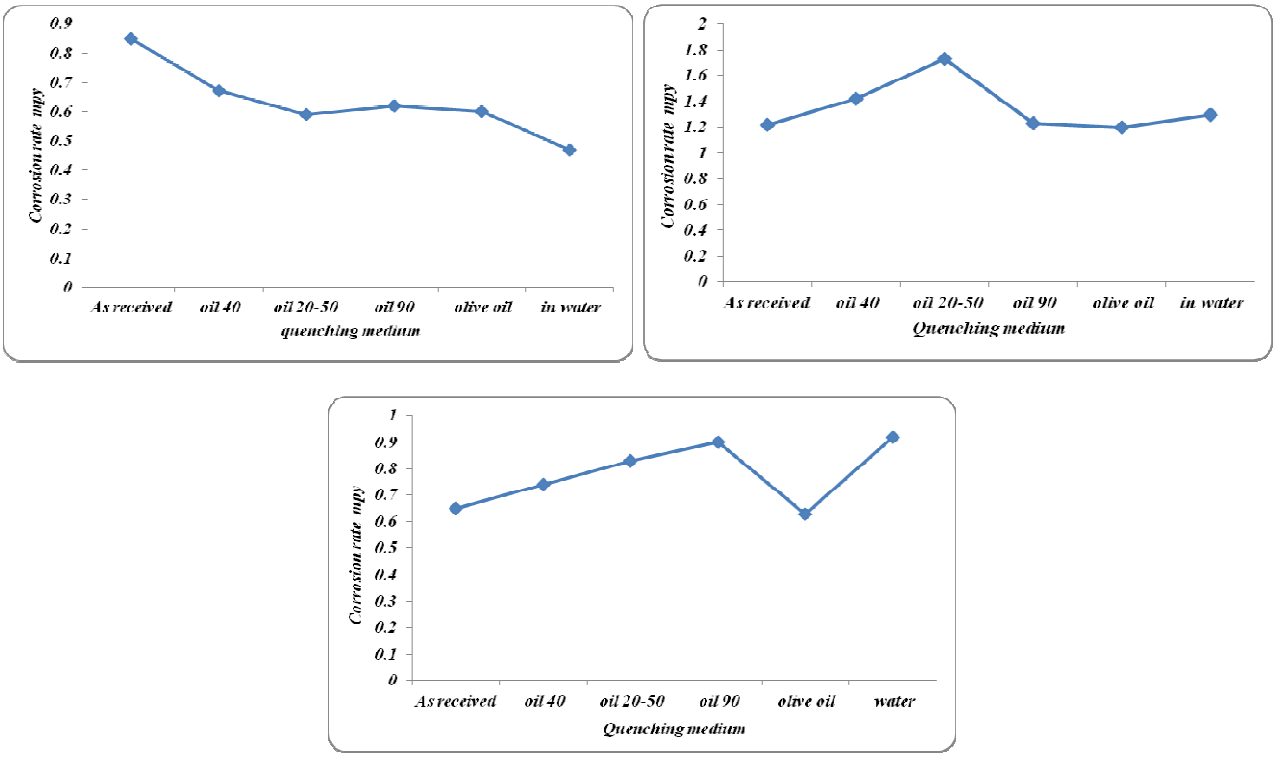


Fig. 2, Show the corrosion rate of 0.47% carbon, gray and nodular cast iron steel respectively

Microstructure

Microstructures of steel 0.47%C, gray cast iron and nodular cast iron respectively.



Fig. 3,Microstructure of 0.47%C, gray and nodular cast iron quenched in water quenching respectively

Microstructure of gray cast iron after 10 hours at 1000^0C then quenching in water

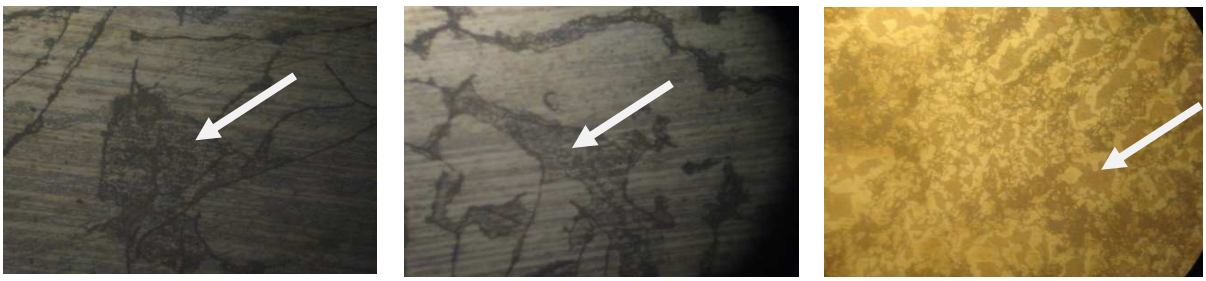


Fig. 4, Microstructure gray cast iron after 10 hour in austenite area at 1000oC and quenched in water

Microstructure of nodular cast iron after 10 hours at 1000^0C then quenching oil and water



Fig. 5, Microstructure nodular cast iron after ten hour in austenite area at 1000oC and quenched in water

Discussion

Fig. 1, Shows the affect of hardening of steel 0.47% carbon, gray and nodular cast iron in different quenched medium, from the results obtained, the hardness value of medium carbon steel specimens increased after quenching in all the mediums. The quenched specimens in the different oils types have a lower hardness values as compared to water. This may be attributed to the fact that water have higher cooling rate than different oil types. Water quenched produced the highest hardness value and most oil kinds or degrees looks get close hardness values. The hardness values for gray cast iron, hardness values obtained looks in same range its between 83.5 to 85 R/B because the microstructure is graphite flacks and ferrite matrix, so heating up to 900ºC for one hour then quenching doesn't change the microstructure also the hardness values of nodular cast iron have hardness in range close about 70 to 74.5 R/B, there is no big changing in hardness value because the microstructure doesn't change after quenching from one hour heating at 900ºC, but it's clear the hardness value of gray cast iron higher than in nodular cast iron do to different in microstructure in both case and area of ferrite which is bigger in nodular that make it more ductile than gray cast iron. Fig. 2, Shows the corrosion rate of steel 0.47% carbon , from result obtained the as received sample have higher corrosion rate due to galvanic corrosion between pearlite and ferrite which acts as cathode and anode respectively, also due to ratio of area for pearlite and ferrite. Corrosion rate will be increased with increases of cathodic and decreases of anodic area, with martensite structure obtained the corrosion rate will be decreased due to one phase martensite structure even thought stresses present. The corrosion rate for both gray and nodular cast iron respectively, shown the rate of corrosion rate of gray is higher than in nodular cast iron because the distribution of graphite with ferrite matrix, in gray cast iron the distribution of flaks that is acting as cathode to ferrite make galvanic cell is higher than shape of graphite as nodular with more big area of anode which is ferrite. Fig. 3, Shows the microstructure of steel 0.47% carbon , as received, oil quenching and water quenching, the microstructure changed from ferrite and pearlite as received sample to martensite structure after quenching which is improve the hardness value but decreases the ductile, for gray and nodular cast iron quenching in water after one hour austenizing doesn't affect in microstructure. Fig. 4 and 5, Shows the graphite decomposition process in both gray and nodular cast iron after ten hour austenizing time at 1000^0C, as arrow shown in the Figures also martensite can be seen near the flakes and nodular graphite's with ferrite matrix .

Conclusion

- Medium carbon steel can be heat treated to improved strength and hardness with sacrificed of ductility .
- Water quenching steel will produced higher hardness than different kinds of oil quenched medium.
- Medium carbon steel exposed to corrosion under many factors specially due to multiphase at room temperature more than after heat treatment and quenching even with stressed martensite structure which produced after quenching.
- Improvement of mechanical properties of both gray and nodular cast iron with ferrite matrix couldn't be achieved with heating at austenite area for one hour then quenching but have to give more time to allow some decomposition of graphite .
- Decomposition of graphite will be around graphite itself with more austenizing time, the ferrite matrix couldn't be changed to pearlite one within 1ten hours treated.
- Strength and hardness in gray cast iron is more than nodular cast iron but the ductility is opposite due to ferrite area.
- The corrosion rate in gray cast iron with ferrite matrix is higher than nodular cast iron with ferrite matrix due to galvanic cell which created from layer structure in gray cast iron.

References

[1] Smith WF and Hashemi J. Foundations of Materials Science and Engineering. 4th ed. Boston: McGraw - Hill Book; 2006. p. 28-36

[2] Ashby MF and Jones DRH. *Engineering Material* 2: An Introduction to Microstructure, Processing and Design. London: Elsevier Science Ltd; 1994. 352 p.

[3] Morrogh, H. (1948): Anew Engineering Materials Production of Nodular Graphite Structures in grey cast irons. AASM pp. 72-90.

[4] Larry Olson (2001): Proper Quenching Option yields Heat Treating Results. pp 1-5.

[5] Rajan T. V. and C. P. Sharma (1988): Heat Treatment, Principles and Techniques. Prentice-Hall of New Delhi-India. pp. 143-150, 236-380.

[6] Gulyaev A. (1980): Physical Metallurgy. Vol 1, Mir Pubilshers Moscow. pp 154-198.

[7] Higgins R.A. (1995): Engineering Metallurgy. Edward Arnold UK, pp 218-257, 285-354.

Advanced Materials Research Vol. 936 (2014) pp 1163-1167
© (2014) Trans Tech Publications, Switzerland
doi:10.4028/www.scientific.net/AMR.936.1163

Microstructure and tensile behavior of Ti-rich Ti-Ni-Cu melt-spun ribbon

Wenjun He[1, 2, a], Guanghui Min[1,b] and Oleg Tolochko[3,c]

[1]Key Laboratory of Liquid Structure and Heredity of Materials (Ministry of Education), Shandong University, Ji'nan 250061, China

[2] Shandong Key Laboratory of Metrology and Measurement, Shandong Institute of Metrology, Ji'nan 250014, China

[3]Department of Material Science, Saint-Petersburg State Polytechnic University, Polytechnicheskaya Str., 29, St. Petersburg, 195251, Russia

[a]hbhwj@163.com, [b]ghmin@sdu.edu.cn, [c]oleg@ftim.spbstu.ru

Keywords: Ti-Ni-Cu alloy; melt spinning; fracture morphology; tensile curve.

Abstract. Microstructure and mechanical properties of $Ti_{51.5}Ni_{25}Cu_{23.5}$ ribbon fabricated by melt spinning were investigated by X-ray diffraction (XRD), transmission electron microscopy (TEM) and tensile tests. Some B19 martensite crystalline with (011) compound twin was embedded in the mainly amorphous ribbon, while the ribbon annealed at 450℃ for 1 h is at fully martensitic state. Annealing process alter the preferential orientation from (022)-B19 to (111)-B19. Tensile fracture stresses of as-spun ribbon and the annealed ribbon are 1257 MPa and 250 MPa, respectively. The tensile fracture morphology of as-spun ribbon shows typical vein fringe while that of the annealed ribbon reveals fine but depth-inhomogeneous dimples. After tensile deformation, the annealed ribbon exhibits typical martensitic detwinning behavior accompanying with the strain contrast.

Introduction

TiNi-based shape memory alloys is well known for the unique nature such as shape memory properties and superelasticity. Addition of Cu substituting Ni decreases the transformation hysteresis as well as reducing the sensitivity of the transformation temperatures to composition changes [1-2]. Besides for Ti-Ni-Cu sputtered thin film, Ti-Ni-Cu ribbons fabricated by melt spinning technique can be as candidate materials for sensors or actuators in micro-miniature systems [3]. The unique microstructure, transformation characteristics and mechanical properties of Ti-Ni-Cu ribbons can be introduced by the technique compared with that in a bulk Ti-Ni-Cu alloy [4]. The above-mentioned properties are affected not only by annealing condition but also by the composition of the alloys [5]. Previous work [6] shows the effect of annealing process on the transformation characteristics of Ti-rich Ti-Ni-Cu ribbon. However, no systematic experimental has been performed on the microstructure and mechanical properties of Ti-rich Ti-Ni-Cu ribbon. In the present study, the microstructure and tensile behavior of Ti-rich Ti-Ni-Cu ribbon were investigated by using X-ray diffraction (XRD), transmission electron microscope (TEM) and tensile test.

Experimental

Initially mainly amorphous $Ti_{51.5}Ni_{25}Cu_{23.5}$ ribbons were prepared by single-roller melt-spinning technique. The surface speed of the wheel is 37 m/s. The ribbon is about 35 μm in thickness and 1.7 mm in width. In order to be fully crystallized, the ribbon was heated at 450℃ for 1 h followed by water quenching to room temperature (RT). The martensitic transformation finish temperature (M_f) of the annealed ribbon measured by DSC (TA-Q100) is 50℃. The tensile test was performed at RGD-5 type electronical tensile testing machine. The gauge length is 50 mm and the tensile rate is 2 mm/min. Crystal structure was characterized by using XRD with Cu Kα radiation. TEM studies have been

carried out on Hitachi H-800 microscope operated at 150 kV. Fracture morphology of the ribbon was characterized by EMPA of a JCXA-733 instrument.

Microstructure of $Ti_{51.5}Ni_{25}Cu_{23.5}$ ribbon

Fig. 1 shows the XRD pattern of as-spun ribbon. A diffuse and low intensity was observed revealing that as-spun ribbon is mainly amorphous. Only a few weak diffraction peaks can be found, being indexed as (022) reflections from B19 martensite. Typical TEM bright field micrograph of $Ti_{51.5}Ni_{25}Cu_{23.5}$ as-spun ribbon in Fig. 2(a) and its corresponding SAD pattern (Fig. 2b) confirms amorphous microstructure of the ribbon. The microstructures of the as-spun ribbons consist of mainly amorphous and a small amount of crystalline particles.

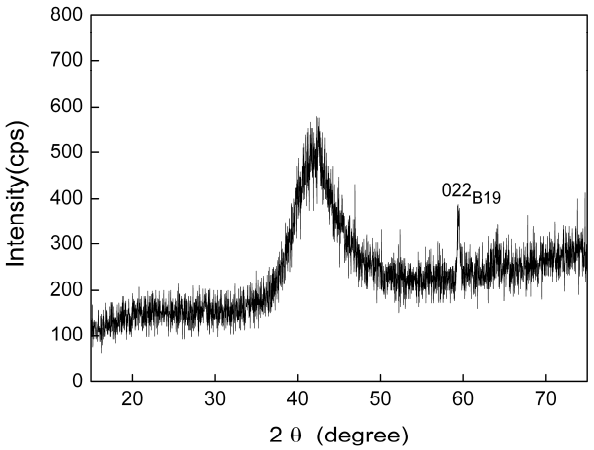


Fig. 1. X-ray diffraction pattern of $Ti_{51.5}Ni_{25}Cu_{23.5}$ as-spun ribbon.

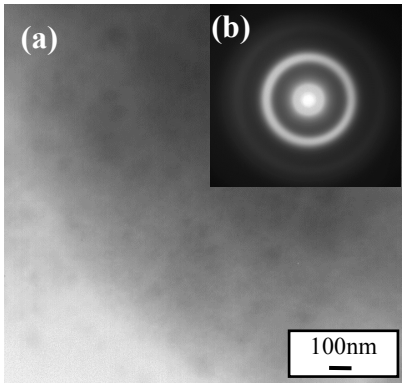


Fig. 2. TEM image (a) and a corresponding SAD pattern (b) of the as-spun ribbon.

Fig. 3 shows bright field micrographs of the B19 martensite in the as-spun ribbon and the corresponding SAD patterns. Fig. 3(a) shows the martensite morphology with preferential orientation. Electron diffraction pattern (Fig. 3b) indicates that the substructures of the martensite variants are dominantly (011) compound twin. The incident electron beam parallels to the $[100]_{M,T}$ zone orientation. Here M and T represent matrix and twin, respectively. TEM observations (Fig. 2 and Fig. 3) indicate non-equilibrium characteristics of as-spun ribbon [7].

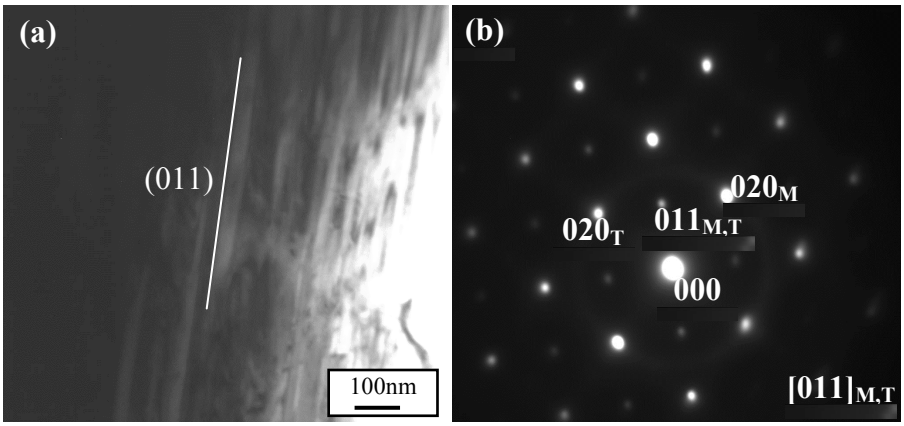


Fig. 3. TEM micrograph of B19 martensite (a) and its corresponding SAD patterns (b) in $Ti_{51.5}Ni_{25}Cu_{23.5}$ as-spun ribbon. Subscripts M and T indicate matrix and twin for martensite, respectively.

Fig. 4 shows the XRD pattern of the ribbon annealed at 450℃ for 1 h. All diffraction peaks only corresponding to B19 martensite are found, indicating the ribbon is fully crystallized. The lattice parameters of the B19 martensite are found to be: a = 0.2903 nm, b = 0.4296 nm and c = 0.4518 nm. Comparing the intensity of (111)-B19 with that of other crystal planes in B19 martensite, it is found

that a strong (111)-B19 texture is developed in the annealed ribbon. From Fig. 1 and Fig. 4, it indicated that annealing process can alter the preferential orientation from (022)-B19 to (111)-B19.

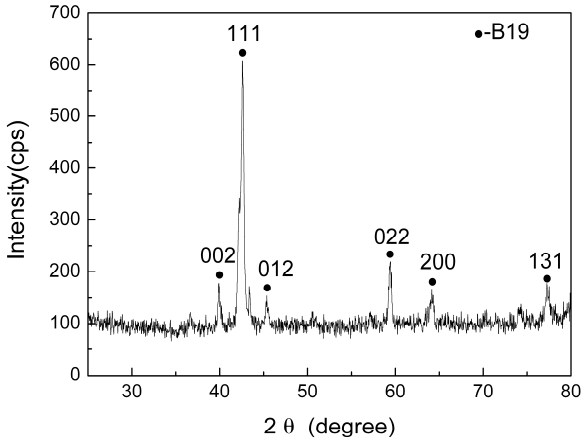


Fig. 4. XRD pattern of the $Ti_{51.5}Ni_{25}Cu_{23.5}$ ribbon annealed at 450℃ for 1 h.

Fig. 5 shows TEM micrographs of the annealed ribbons at 450℃ for 1 h before and after tensile test. Fig. 5(a) is a bright field image, in which the size of the grains varies from about 600 nm to 1.3 μm. Only one pair of twinned martensite variants can be seen in most of these grains and the twin boundaries are straight and well-defined. The characteristics of Ti-Ni-Cu ribbon is different from that of a triangular self-accommodated microstructure with several martensite plates coexisting in one grain in the binary Ti-Ni alloy and Ti-Ni-Cu ternary bulk materials [8-9].

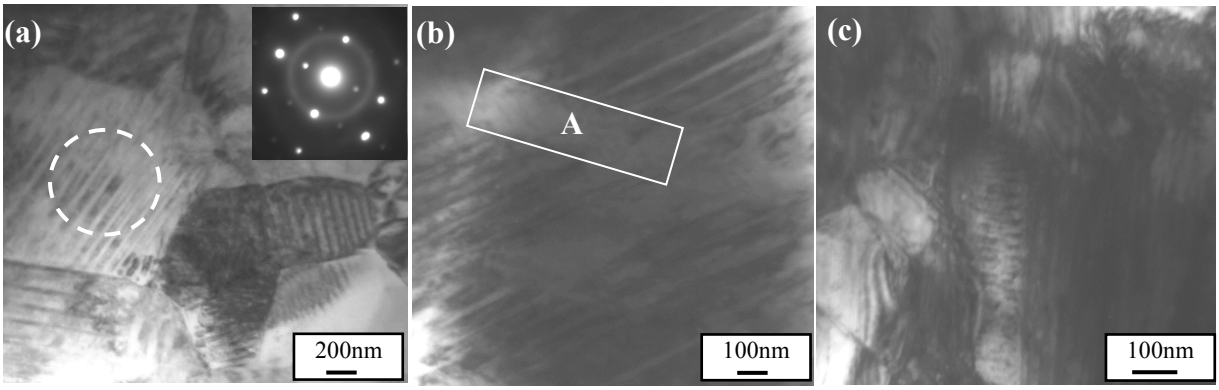


Fig. 5. Typical BF micrographs in TEM observations of $Ti_{51.5}Ni_{25}Cu_{23.5}$ ribbon annealed at 450℃ for 1 h before (a) and after (b-c) tensile tests.

After the tensile deformation, the martensite morphology is still single-pair marentsite mostly. XRD analysis (Fig. 4) and the value of M_f (50℃) indicated that the annealed ribbon before tensile test is in the fully martensitic state at RT. It may exhibit the reorientation behavior or detwinning behavior of martensite variants when applied with tensile stress. Fig. 5(b) shows the detwinning behavior in one martensite variant. The substructural boundaries of the martensite variant are not well-defined, being destroyed or blurred as marked by area A. It is due to the detwinning behavior of martensite variants induced by local severe plastic deformation under the applied tensile stress. The width of rectangle is about 200 nm and the previous preferential orientation of martensite is vanishing. Clear strain contrast is observed between the parts of twinning and detwinning inside one martensite variant. Fig. 5(c) shows the complex contrast and high density of irregular structured grain boundaries resulting from the overlapping of martensite orientation, strain and moiré fringe contrast [10].

Tensile behavior of $Ti_{51.5}Ni_{25}Cu_{23.5}$ ribbon

Fig. 6 shows the stress-strain curves of $Ti_{51.5}Ni_{25}Cu_{23.5}$ ribbon at RT. The curve of the as-spun ribbon (Fig. 6a) shows the fully elastic until fracture without plastically deformation. Its ultimate fracture stress and strain are 1068 MPa and 3.7%, respectively. The tensile response of the ribbon annealed at 450℃ for 1 h is shown in Fig. 6(b). This curve can be divided into three stages. The first linear stage corresponds to the elastic deformation of the martensite phase. The Young's modulus of the annealed ribbon is about 12.5 GPa, being much smaller than that of Ti-Ni wire [11]. The large difference in elastic modulus between binary Ti-Ni and ternary Ti-Ni-Cu is likely due to Cu addition leading to a reduction in the atomic binding force [12]. The second stage corresponds to the rearrangement of the martensite variants. The third linear stage corresponds to the elastic deformation of the reoriented martensite. The fracture stress and fracture strain of the annealed sample are about 216 MPa and 2.7% respectively, which is smaller than that of as-spun ribbon.

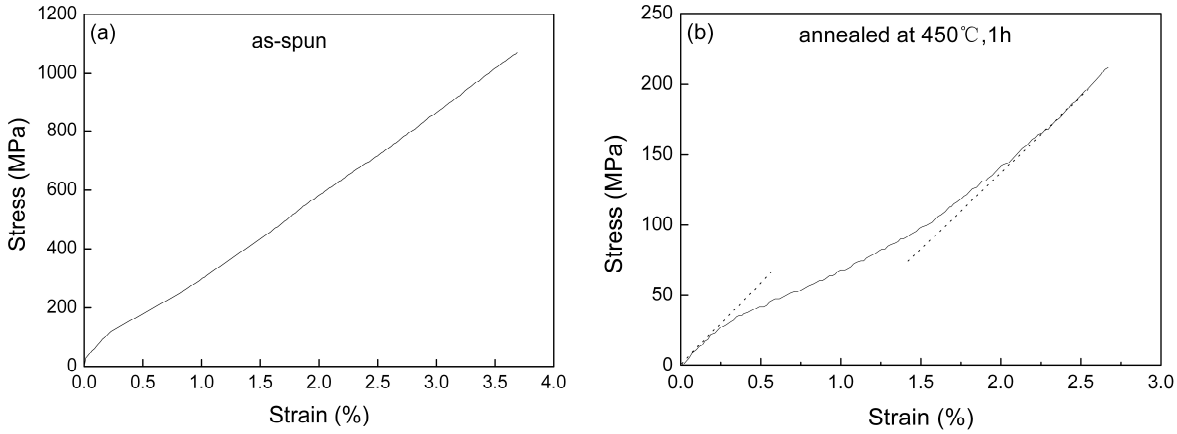


Fig. 6. Stress-strain curves of $Ti_{51.5}Ni_{25}Cu_{23.5}$ ribbon (a) as-spun (b) annealed at 450℃ for 1 h.

Fig. 7 shows the typical fracture morphology for $Ti_{51.5}Ni_{25}Cu_{23.5}$ ribbon. The typical vein fringes and smooth amorphous featureless zone as shown in Fig. 7(a) indicated that the as-spun ribbon is mainly amorphous. The observation is consistent with that of TEM micrograph in Fig. 2 and tensile curve in Fig. 6(a). The vein fringe is generally regarded as an indication that local shear bands expanded in softening fracture surface [13]. A small amount of particles resulting from the melting liquid drop were embedded among the vein fringes. When the ribbon is annealed at 450℃ for 1 h, the fracture morphology as shown in Fig. 7(b) is greatly different from that of as-spun ribbon. The tensile fracture surface is composed of fine but depth-inhomogeneous dimples originating from the nucleation, growth and aggregation up to the fracture of micro-holes.
aggregation up to the fracture of micro-holes.

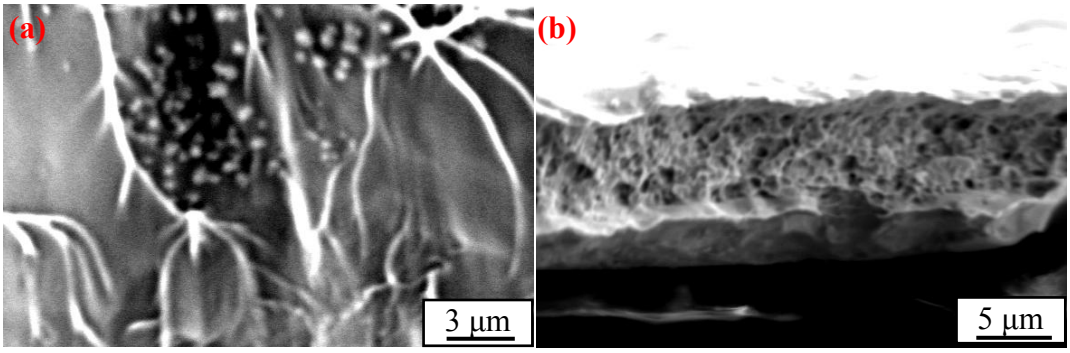


Fig. 7. Tensile fracture morphologies of $Ti_{51.5}Ni_{25}Cu_{23.5}$ ribbon: (a) as-spun, (b) annealed at 450℃ for 1 h.

Summary

As-spun $Ti_{51.5}Ni_{25}Cu_{23.5}$ alloy ribbon is mainly amorphous with the fracture morphology of vein fringe. Some B19 martensite crystalline grains with (011) compound twin were embedded in the ribbon. The ribbon annealed at 450℃ for 1 h is at fully martensitic state and its fracture morphology shows fine and depth-inhomogeneous dimple. Annealing process alter the martensite preferential orientation from (022)-B19 to (111)-B19. Tensile fracture stresses of as-spun ribbon and the annealed ribbon are 1257 MPa and 250 MPa respectively, while the fracture strains of them are 3.7% and 2.7%, respectively. Stress-strain curve of the as-spun ribbon is simple elastic deformation, while that of the annealed ribbon was composed of three stages. TEM observations of the annealed ribbon after tensile test show typical martensitic detwinning behavior.

References

[1] T.H. Nam, T. Saburi and K. Shimizu, Mater. Trans. JIM Vol. 31 (1990), p. 959.
[2] O. Mericier and K.N. Melton, Metall. Trans. A Vol. 10 (1979), p. 387.
[3] D.Reynaerts, J.Peirs and H.Van Brussel, J. Micromech. Microeng. Vol. 5 (1995), p. 150.
[4] T.H. Nam, J.P. Noh, D.W. Jung, Y.W. Kim, H.J. Im, J.S. Ahn and T. Mitani, J. Mater. Sci. Lett. Vol. 21 (2002), p. 685.
[5] A. Ishida, M. Sato, K. Ogawa and K. Yamada, Mater. Sci. Eng. A Vol. 438-440 (2006), p. 683.
[6] W.J. He, O.V. Tolochko, G.H. Min and H. Yu, Metallofiz. Nov. Tekh+. Vol. 29 (2007), p. 1167.
[7] K. Otsuka and X. Ren, Prog. Mater. Sci. Vol. 50 (2005), p. 511.
[8] Y. Liu, Z.L. Xie, J. Van Humbeeck and L. Delaey, Acta Mater. Vol. 47 (1999), p. 645.
[9] T. Saburi, Y. Watanbe and S. Nenno, ISIJ International. Vol. 29 (1989), p. 405.
[10] H.P. Karnthaler, T. Waitz, C. Rentenberger and B. Mingler, Mater. Sci. Eng. A Vol. 387-389 (2004), p. 777.
[11] Y. Liu, Mater. Sci. Eng. A Vol. 354 (2003), p. 286.
[12] J.Z. Chen and S.K. Wu, J. Non-Cryst. Solids Vol. 288 (2001), p. 159.
[13] V. Bengus, E. Tabachnikova, K. Csach, J. Miskuf and V. Ocelik, Scripta Mater. Vol. 35 (1996), p. 781.

Advanced Materials Research Vol. 936 (2014) pp 1168-1172
© (2014) Trans Tech Publications, Switzerland
doi:10.4028/www.scientific.net/AMR.936.1168

The Oxide Defect of C70250 Alloy

Zhongping Chen, Chaojian Xiang, Huaqing Li [a]

Suzhou Research Institute for Nonferrous Metal, Suzhou 215026, China

[a]lihuaqing2008@163.com

Keywords: C70250 alloy; Copper alloy strip; Oxide skin defects

Abstract. The oxide skin defect during hot rolling process for Cu-Ni-Si alloy strip was investigated. Oxide skin defects were analyzed by means of alloy elements detection and microstructures characterization. The characterization and test results showed that high temperature oxidation and silicon segregation are the main causes of the oxide skin defect. Pilot scale tests indicated that hot processing temperature for C70250 alloy should be lower than 950°C. Reducing atmosphere is recommended during the thermal treatment of Cu-Ni-Si alloys.

Introduction

As the second generation of lead frame material [1,2], the consumption demand of Cu-Ni-Si alloy strip keep growth steadily. Plenty of theoretical researches on Cu-Ni-Si alloy have been done in colleges and research institutes [3-11]. However, few works has been carried out in industrial production. Many domestic copper processing enterprises [12], such as Chinalco Luoyang Copper Co., Ltd, Xingye Copper Co., Ltd, et al, have carried out a series of researches, and are developing their abilities of Cu-Ni-Si alloy strip production.

In the present work, Oxide skin defects after hot rolled process were investigated. Helped by alloy elements measuring and microstructures characterization, the main cause of oxide skin defect was analyzed. The heating process of hot rolling was also optimized. A technical problem of strip processing was solved.

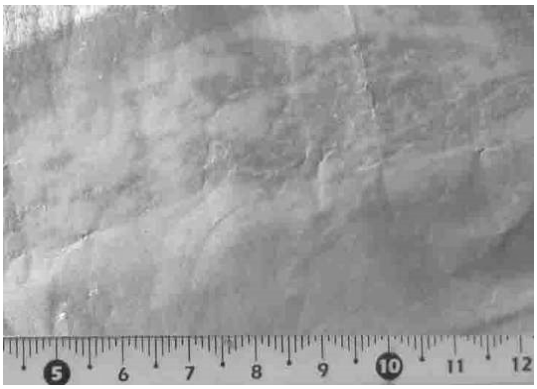
Experimental

The C70250 alloy ingot was heated up to 950±20°C for 3~5h in the chamber resistance furnace, hot rolled to 5mm and cold rolled to 1.5mm. Hot rolling was carried out on the three-roller irreversible rolling mill. The roller size is Φ250×500mm and the draught pressure is 200t. The maximum size of nip cross-section is 75×300mm^2. Cold rolling was carried out on the four-roller reversible cold-rolling mill, and the roller size is Φ200 × 500 mm. Draught pressure is 300t. The cross-section ranges of the strip sizes are 75~0.15×400mm^2.

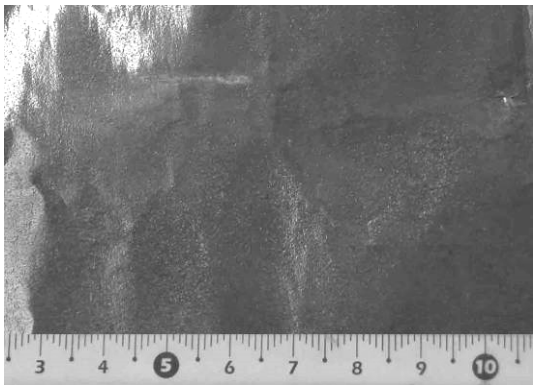
Microstructure and energy dispersive spectrometer (EDS) were analyzed by JEOL scanning electron microscope. The composition of the casting alloy was tested by Inductively Coupled Plasma (ICP) analysis instrument.

Microstructures Characterization and Composition Detection of Oxide Skin

Oxide skin defects appear on the strip surface in the pilot scale test. Local area of the alloy plate slab appeared oxide skin defects during hot rolling, and the oxide skin defects became more obvious after solution treatment. Large scale oxide skin defects appeared on the C70250 strip surface after the first pass rolling. The oxide skin defects could be striped homogeneously, the morphology of oxide skin is shown in Fig.1.



(a) Inner surface of oxide skin defect is wine



(b) Outer surface of oxide skin defect is purple brown

Fig. 1 Macro-morphology of Oxide Skin Defect for C70250 Rolled Strips

The thickness of oxide skin defects is about 0.3~0.4mm. Inner surface of the oxide skin appears dull red color (fig 1(a)), and the outer surface is purple brown (fig 1(b)).

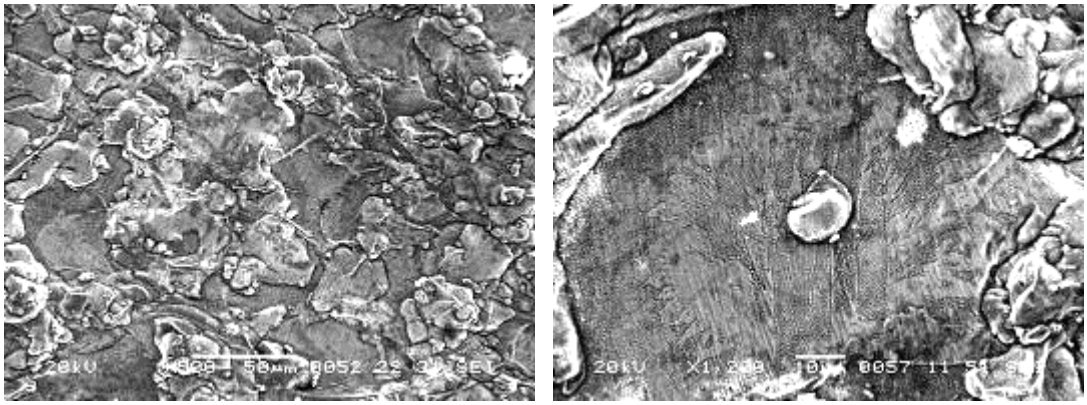
Microstructure Characterization

Microstructure of the oxide skin defects on the Cu-Ni-Si alloy strip after hot rolled is shown in Fig.2. Scanning electron microscopy experiments indicated that the surface distribution of oxide skin defects is no-uniform (Fig.2 (a)). According to the test result, the oxide and precipitated phases tend to appear on the salient area, the flat area is the matrix (Fig.2 (b)).

Selected Area Energy Spectrum Analysis

The micro-topography and selected area energy spectrum analysis results in different parts of oxide skin defect are shown in Fig.3 and table 1.

Energy spectrum analysis results indicated that there were silicon segregations in local area of oxide skin defects. The content of silicon is between 2.2%~5.3%, which is between five to ten times higher than the average content of silicon (0.5%). Qualitative data results indicated that oxide skin defects were very serious.

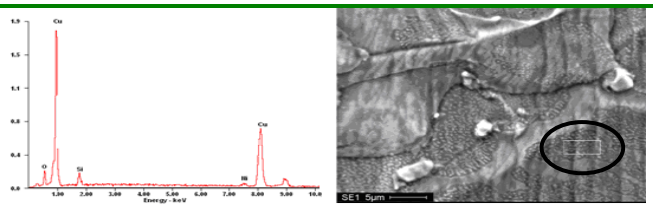


(a)The surface distribution of oxide skin defects (b) The morphology of matrix

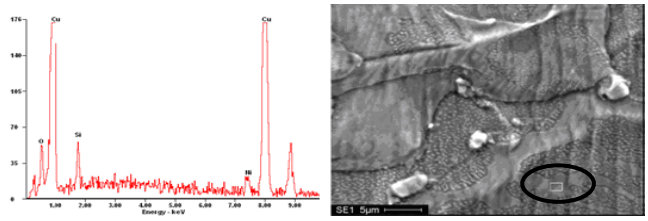
Fig. 2 Microstructure of the Oxide Skin Defects on the Cu-Ni-Si Alloy Strip after Hot Rolled

TABLE 1 CHEMICAL COMPOSITION OF OXIDE SKIN FOR ROLLED STRIP OF CU-NI-SI ALLOY

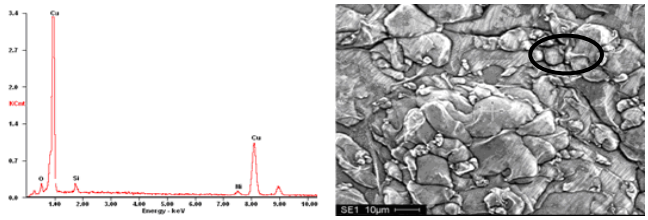
Element	O	Si	Ni	Cu
Wt [%]	$4.5^{+1.67}_{-1.69}$	$3.7^{+1.52}_{-1.53}$	$3.8^{+1.15}_{-0.55}$	$86.0^{+4.7}_{-14.3}$



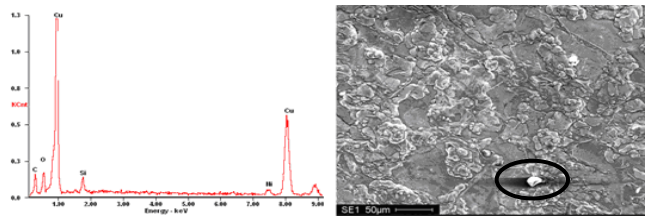
(a) Morphology of local oxide area and EDS



(b) Morphology of local oxide and silicon segregation and EDS



(c) Morphology of local oxide area and EDS



(d) Morphology of local oxide, silicon segregation and carbon segregation and EDS

Fig. 3 Energy Spectrum Analysis of Oxide Skin for Rolled Strip of Cu-Ni-Si Alloy

ICP Results

Alloy composition of the oxide skin was then analyzed carefully. ICP results indicated that nickel content is 2.69 wt. % and the silicon content is 0.45wt. %. The content of nickel and silicon was close to the matrix content. No silicon segregation was found between matrix and the oxide skin itself.

Analysis and Discussions

Qualitative data results indicated that no silicon segregation was found between matrix and the oxide skin surface, but the silicon segregation happened in some local area of the matrix surface. The silicon segregation was relatively serious, and its content is up to 2.2%~5.3%. Overburning evidence was found in the local area by the microstructure observation measure. The characterization and test results showed that high temperature oxidation and silicon segregation are the main reasons leading to the oxide skin defect.

Excessive heating temperature leads to silicon segregation on the surface of Cu-Ni-Si alloy strip. High heating-up temperature also cause oxidation. Meanwhile, the breaking of the precipitated phases, during the deformation process, weakens the bonding force between the surface and the matrix.

Due to unbefitting high temperature, the surface of Cu-Ni-Si alloy strip was seriously oxidated (EDS qualitative data results shown that oxygen content is about 10~20%), which weakens the bonding strength between the oxide skin and the matrix. Oxide skin could be peeled off with the increase of the plastic deformation rate. Carbon content was relatively high in some local area. It's because that high holding temperature lead to carbon diffusion under carbon protection. Pilot scale tests indicated that employing proper holding temperature (≤950°C) could avoid oxide skin defects during rolling process.

Conclusions

The characterization and test results indicate that high temperature oxidation and silicon segregation are the main reasons of oxide skin defects of Cu-Ni-Si alloy strip.

Heating temperature of C70250 alloy should be lower than 950°C during hot rolling and solution treatment.

Pilot scale tests indicated that proper holding temperature and reducing atmosphere could effectively prevent the oxidation of Cu-Ni-Si strip, which can avoid large-scale oxide skin defects during rolling process.

References

[1] Y. Yamamoto, G. Sasaki, K.Yamakawa, et al. Hitachi Cable Review, 2000. 19: 65-70.

[2] Y. Q. Long, P. Liu, Y. Liu, et al. Materials Review, 2008, 22(3): 48-52.

[3] D.M. Zhao, Q.M. Dong, P. Liu, et al. Trans.Nonfen'ous Met. Soc. China, 2003. 13(2): 258-261.

[4] D.P. Lu, J. Wang, L. Lu, et al. Trans.Nonferrous Met.Soc China, 2007: s12-s15.

[5] L. Wang, Y.S. Sun, X.Q. Fu, et al. Journal of Southeast University (Natural Science Edition), 2005. 35(5): 729-732.

[6] J.J. Bao, H.L. Wang. Hot Working Technology, 2005. 7: 14-16.

[7] Pan Zhi-yong, Wang Ming-pu, Li Zhou, et al. Trans.Nonferrous Met.Soc.China 17, 2007: s1076-s1080.

[8] D.M. Zhao, Q.M. Dong, P. Liu, et al. The Chinese Journal of Nonferrous Metals, 2002. 12(6): 1167-1171.

[9] Q.L. Yong, L. Ping, L.Yong, et al. Materials Letters 2008. 62(7-8): 3039-3042.

[10] Y. Zhang, P. Liu, B.H. Tian, et al. The Chinese Journal of N Nonferrous Metals 2013.24(4):970-976.

[11] L. Jia, H. Xie, X. Wang, et al. Foundry technology, 2011. 32(11):1553-1556.

[12] S.M. Wang, H. Li, T. Wang, et al. Shanghai Nonferrous Metals, 1999. 20(2): 66-69.

Advanced Materials Research Vol. 936 (2014) pp 1173-1178
© (2014) Trans Tech Publications, Switzerland
doi:10.4028/www.scientific.net/AMR.936.1173

A Study on Austenite Catalytic Cryogenic Treatment of Cr-W-Mo-V High Alloy Medium-Upper Carbon Steel

MA Yong Qing[1,a *], ZHANG Xiao Jing[2,b], LIANG Yu Fen[2,c], LIU Guo Fang[2,d]

[1]Department of Materials Science, Dalian Maritime University, Dalian, Liaoning116026, China

[2]Changzhou Machinery Blade CO.LTD, Changzhou, Jiangsu 213119, China

[a]myq_dlmu@163.com, [b]jing267@163.com, [c]yufenliang57@163.com,[d]guo_fang@163.com

Keywords: High alloy medium-upper carbon steel, Austenite catalytic, Catalytic temperature, Transformation, Cryogenic treatment, Precipitation hardening, Tempering hardness

Abstract: The processing of austenite catalytic cryogenic treatment of two components of Cr-W-Mo-V high alloy medium-upper carbon steels and the effect on the retained austenite transformation and tempering hardness were studied in this paper. The results show that, the effect of austenite catalytic cryogenic treatment of Cr-W-Mo-V high alloy medium-upper carbon steel is better than that of direct cryogenic treatment after quenching, and the content of residual austenite reduced to below 5%, and the hardness improved by 1.5HRC than that of conventional quenching and tempering. The retained austenite catalytic temperature of Cr-W-Mo-V high alloy medium-upper carbon steel merely is higher than 10℃~20℃ of the temperature for the highest tempering hardness. Catalytic temperature Tc can be determined by experimental method of conventional quenching and tempering of the steel, in which the microstructure feature is precipitation of M_3C carbide particle of 0.01μm～0.03μm in martensite matrix, and the content of retained austenite decreases evidently. By cryogenic treatment after the austenite catalyzed the retained austenite of quenching are transformed into more martensite, and in the subsequent tempering processing the original quenching martensite and the martensite from retained austenite transformation almost will form synchronous precipitation hardening. Thus the tempering hardness improves evidently as well.

Introduction

Has showed that, conventional quenching and cryogenic treatment of tool and die steels can promote the decomposition of retained austenite to martensite transformation and precipitation of ultrafine carbides on large amount of dispersed carbides in the martensite matrix[1-3]. It has become an advanced technology of quality guarantee and upgrade for the tool and die of traditional products. However, in the actual production the tool and die often occurs brittle fracture by direct cryogenic treatment after conventional quenching. And the cryogenic treatment is must in good time after quenching as to avoiding stabilization of the retained austenite for long time stopping, so that is resulting in frequent startup and shutdown of cryogenic processing equipment and resulting in energy waste. Earlier studies have found, the tempering of high speed steel at higher temperatures for short time after quenching, which takes catalytic effect on the quenching retained austenite decomposition[4]. We envision using this principle, the austenitic catalytic treatment of high alloy steel after conventional quenching and then cryogenic treatment can overcome the drawbacks of directly cryogenic treatment after conventional quenching. In this paper the processing of austenite catalytic cryogenic treatment of two components of Cr-W-Mo-V high alloy medium-upper carbon steels and the effect on the retained austenite transformation and tempering hardness are studied, at the same time, in which is contrasted to that of direct cryogenic treatment after quenching and conventional quenching and tempering. And by analysis of phase structure and microstructure the outcome of effect and the mechanism of the phase transformation are discussed.

Experimental materials and method

The composition of two experimental materials was shown in Table 1, which are two kinds of new steels for making tool with thin edge. Experimental materials were melted in 0.5t variable frequency induction furnace adding electro-dregs remelting furnace. After forging and rolling, the steels were processed to 58mm ×11 mm×11 mm samples by incision machining.

TABLE 1 CHEMICAL COMPOSITION OF TWO EXPERIMENTAL STEELS (WT.%)

	C	Si	Mn	Cr	W	Mo	V	Ni
7S	0.69	0.52	0.45	6.98	3.22	1.53	1.45	0.32
6S	0.66	0.62	0.55	6.34	2.26	1.04	0.75	0.25

The experiments of conventional quenching and tempering treatment were performed using KSJ-5kw electric furnace, and the temperatures of conventional heat treatment are reasonable in the light of production process[5]. Cryogenic treatment is using cryogenic tank of the self-made liquid nitrogen vaporization together with the workpieces, and after quickly cooling to -60℃ from room temperature the cryogenic rate is 2℃/min and the returning rate to room temperature is 10℃/min. The hardness was mensurated using 150DT-HR sclerometer, and an average value of the hardness was accounted adopting six testing points or more. The phases present and retained austenite were analyzed using X-ray diffractometer D/max-3A, and carbide phases were analyzed by extraction powder. The microstructure was investigated using scanning electron microscope XL30.

Experimental processes and results

Processes and technical parameters

The experimental processes of two steels and the temperature and holding time of their technics are listed in Table 2. No.1 process is containing of austenitic catalytic cryogenic treatment, the whole process is consist of heating at high temperature and quenching cooling to room temperature and to conducting an austenitic catalytic treatment, and then in conducting the cryogenic treatment and finally tempering treatment 2 times. No.2 process is the quenching cooling to room temperature and then in conducting the cryogenic treatment, and last tempering treatment 2 times. No.3 process is the conventional quenching and tempering treatment. No.2 and No.3 processes are used as contrasting with No.1. And the temperatures of annealing and quenching are the best values of two steels commonly used[5]. The temperature of austenitic catalytic is higher than 20℃ comparing to temperature of the highest hardness of secondary hardening, and the cryogenic treatment at -120℃ is used currently in our production. Final tempering temperature of No1 process is the temperature of highest hardness during secondary hardening. But final tempering temperatures of No2 and No3 processes are higher than 20℃ comparing to corresponding temperatures of the highest hardness, which are commonly used of temperatures in production for the sake to reduce the amount of residual austenite. All values of holding time are correct not only by the study proved and also commonly used in the production.

TABLE 2 EXPERIMENTAL PROCESSES AND TEMPERATURE (℃) AND HOLDING TIME(HOUR) OF TWO STEELS

	No	Annealing	Quenching	Catalytic	Cryogenic	Tempering	Tempering
7S	1	840×4	1080×0.4	540×0.8	-120×0.5	520×2.5	520×2.5
	2	840×4	1080×0.4	not	-120×0.5	540×2.5	540×2.5
	3	840×4	1080×0.4	not	not	540×2.5	540×2.5
6S	1	840×4	1050×0.4	530×0.8	-120×0.5	510×2.5	510×2.5
	2	840×4	1050×0.4	not	-120×0.5	520×2.5	520×2.5
	3	840×4	1050×0.4	not	not	520×2.5	520×2.5

Selection of austenitic catalytic temperature and holding time

Catalytic temperature is related with both the steel composition and quenching temperature. The higher temperature will reduce the subsequent tempering hardness during secondary hardening. The lower than catalytic temperature not only to pall on the catalytic role, and will enhance the thermal stability of retained austenite. The method for determining the catalytic temperature Tc is through the conventional quenching and tempering experiments with cryogenic treatment effect on retained austenite. The experiments show that, the retained austenite catalytic temperature of Cr-W-Mo-V high alloy medium-upper carbon steel is higher than 10℃~20℃ of temperature of the highest tempering hardness. And retained austenite catalytic temperature of high speed steel is higher than 30℃~40℃ of temperature corresponding to the highest tempering hardness[4], which may be related to higher thermal stability of retained austenite with high carbon and alloys. Figure 1 shows selection of the retained austenite catalytic temperatures Tc by tempering curves of two steels, and two temperatures were severally selected 20℃ higher then temperatures Th of the maximum hardness. Namely, Th of 7S steel is 520℃ so Tc is 540℃, and Th of 6S steel is 510℃ so Tc is 530℃. Holding 1.5 hours at the tempering temperature, the tempering hardness is not less than 1HRC of highest hardness, and the microstructure features are appearing precipitation particle of M_3C type of carbides in size of about 0.01μm～0.03μm on martensite matrix and the amount of retained austenite reduced obviously. Hence these criterions can be used as catalytic temperature selection.

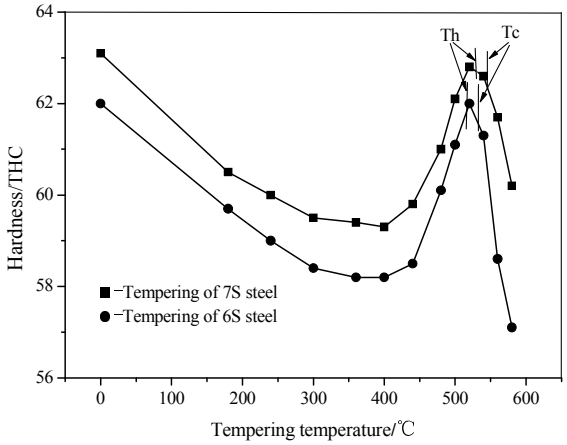


Fig.1 Temperature selection of austenitic catalytic by tempering curve

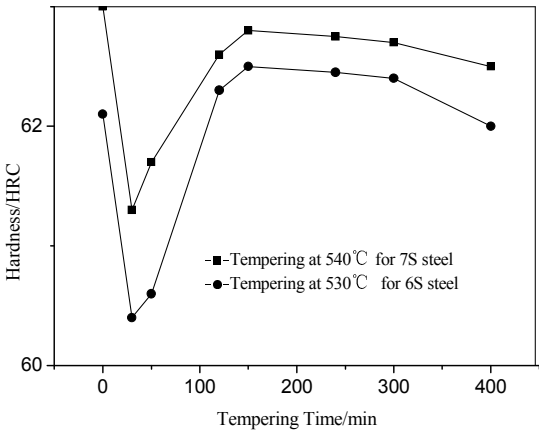


Fig.2 Tempering hardness change with tempering time

Figure 2 is isothermal tempering hardness change of two steels at Tc with tempering time. Figure 2 shows, in tempering for 30 minutes at the austenite catalytic temperature the hardness reduces to lowest. The main reason for the hardness decline in this stage is separating of C atoms oneself from the martensite rapidly. The hardness only slightly elevates until holding 1 hour, at the moment the precipitation of initial M_3C type of dispersed carbide with phase relationship of the matrix begins, and at the same time the transformation of retained austenite into martensite begins as well as beginning of precipitation of M_3C type carbide[6]. When more than 1 hour the dispersed alloy carbides will precipitate to cause precipitation hardening and hardness increased sharply, that in final tempering for longer times there is too large of size difference of precipitated carbides of new martensite from the retained austenite transformation and precipitated carbides of the original martensite by the continued to grow up. Accordingly, the precipitation hardening is not synchronous, It will not help improve the final tempering hardness, therefore, in the actual austenite catalytic processing the holding time is 0.8 hours.

Experimental results and comparison

The effect of austenite catalytic cryogenic treatment on retained austenite and hardness and their contrasts are listed in Table 3. Can be seen from table 3, the amount of retained austenite of two steel after quenching is ~ 40.3 and ~ 36.2 and hardness is HRC63.1 and 62.1 respectively. By No1

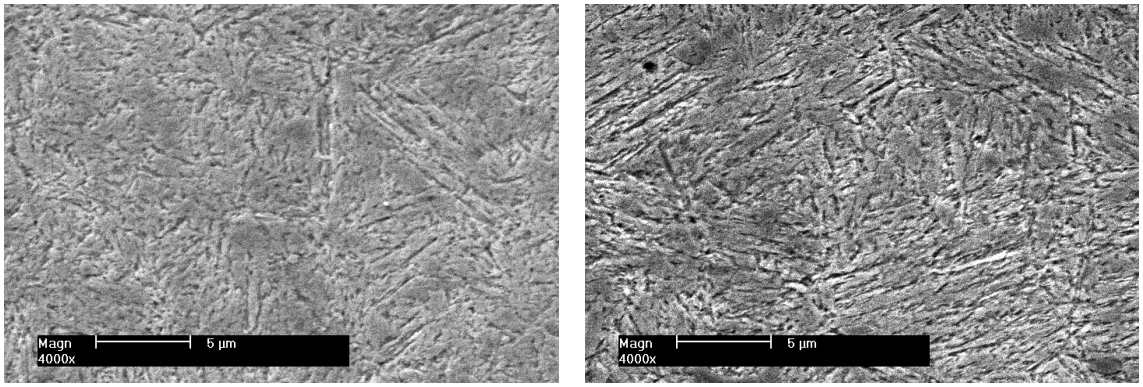
processing the amount of retained austenite of austenitic catalytic is ~ 28.6 and ~ 25.3, and the amount of retained austenite continuing cryogenic treatment is ~ 8.6 and ~ 7.5, and then after final tempering for 2 times the amount of residual austenite is ~ 4.7 and ~ 4.2 and hardness is HRC64.3 and 63.7 respectively. The contrast to results of the tempering for 2 times, the amount of residual austenite of No.1 processing is lowest and the hardness is highest. The effect is better than that of No.2 processing, the amount of residual austenite is reduced to close to 1/2 and the hardness is increased by 0.5HRC, and the effect is a lot of improving than that of No.3 processing obviously, and the amount of residual austenite is reduced to about 1/3 and hardness is increased by about 1.5HRC.

TABLE 3 EFFECT OF AUSTENITE CATALYTIC CRYOGENIC TREATMENT ON RETAINED AUSTENITE* AND HARDNESS

	No	Quenched		Catalytic	Cryogenic	Tempered in twice	
		retained γ′/%	hardness/HRC	retained γ′/%	retained γ′/%	residual γ′/%	hardness/HRC
7S	1	～40.3	63.1	～28.6	～8.6	～4.7	64.3
	2	～40.3	63.1	—	～19.5	～8.8	63.5
	3	～40.3	63.1	—	—	～15.8	62.8
6S	1	～36.2	62.1	～25.3	～7.5	～4.2	63.7
	2	～36.2	62.1	—	～16.7	～7.8	63.2
	3	～36.2	62.1	—	—	～12.6	62.5

* Here symbol ~ is show of error ± 1.5%

Microstructure of two steels tempered by austenite catalytic cryogenic treatment and after tempering 2 times is shown in Figure 3. Although the microstructure of study with transmission electron microscopy after cryogenic treatment has a lot of microscopic characteristics[3,7], and by scanning electron microscopy and optical microscopy those microscopic features are not seen nearly. However, the specimen in the erosion under the same conditions, the microstructure after austenite catalytic cryogenic treatment to observe using scanning electron microscope is etched deeper than that of without cryogenic treatment.



(a) 7S steel at 520℃ (b) 6S steel at 510℃

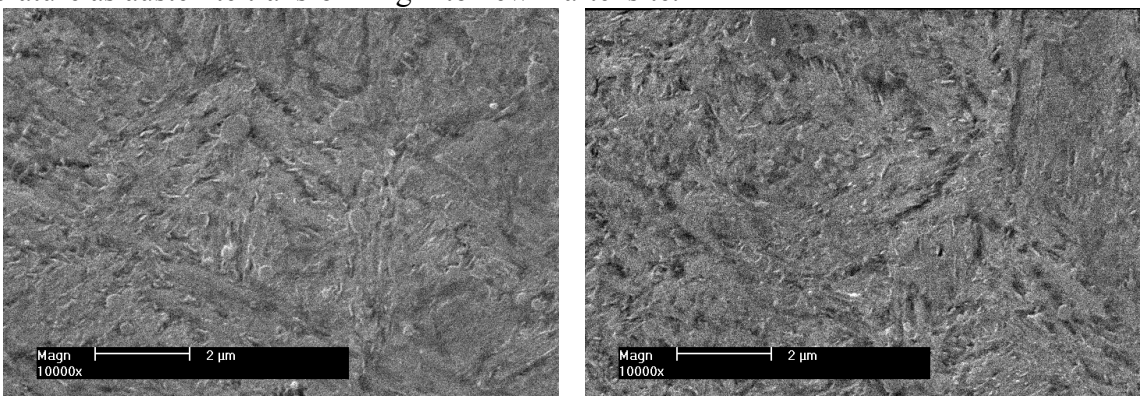
Fig.3 Microstructure of two steels tempered by catalytic cryogenic treatment

Analysis and discussion

Austenite catalytic treatment is tempering processing for short time. In order to analyze the effect on transformation, the samples of austenitic catalytic treatment for 1.5 hours were studied owing to observe clearly using scanning electron microscope and X ray phase analysis, it can estimate the transformation and precipitation of the earlier stage. Figure 4 is the microstructure of two steels treated at catalytic temperature for 1.5 hours. Figure 4 shows, in the quenched martensite the precipitation of more dot and tiny strip carbides is observed, which size is about 0.01μm～0.03μm and the precipitation of tiny dot carbides in primary austenite is observed too.

Table 4 is carbide phase analysis of two steels and calculated equilibrium phases of their tempered, and Figure 5 is the result of analysis carbides phase of two steels by carbides extraction. Can see, in addition to the existence of stable carbides the metastable phase of M_3C type also

appears, which is agreement with tempering precipitation regularity[8]. Figure 6 shows the variation of the amount of retained austenite of two steels tempered at different temperature for 1.5 hours, can see, the amount of retained austenite decreases sharply during tempering at austenite catalytic temperature as austenite transforming into new martensite.

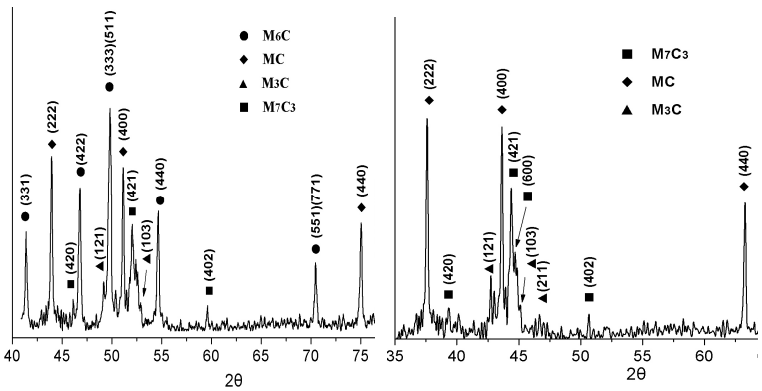


(a)7S steel at 540℃ (b) 6S steel at 530℃

Fig.4 Microstructure of two steels treated at catalytic temperature for 1.5 hours

TABLE 4 CARBIDE PHASE ANALYSIS OF TWO STEELS AND CALCULATED EQUILIBRIUM PHASES OF THEIR TEMPERED

	Annealed phase	Quenched phase	Tempered phase	T/℃	Equilibrium phases of carbide Mass- fraction/% at T/℃
7S	MC,M_6C,$M_{23}C_6$	MC,M_6C	M_6C,MC,M_7C_3,M_3C	540	7.9$M_{23}C_6$, 2.9M_6C, 2.5MC
6S	M_6C,MC, $M_{23}C_6$,M_7C_3	MC,M_6C	MC, M_7C_3,M_3C	530	10.2$M_{23}C_6$, 1.4M_6C, 1.5MC



(a) 7S steel at 540℃1.5h (b) 6S steel at 530℃1.5h

Fig.5 X-ray spectrum of carbides of two steels tempered

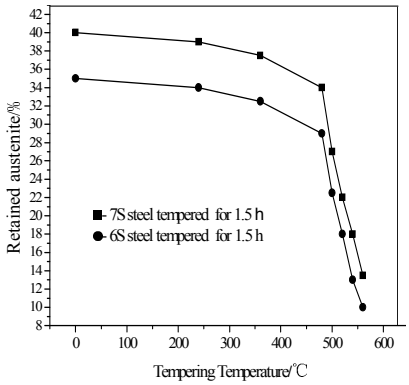


Fig.6 Retained austenite with tempering temperature

In the catalytic temperature the disordered distribution of dislocations by rearranging will become to effective distribution of nucleation, the vacancies and the air mass of solute atoms formation also are removed. The C content in retained austenite is reduced as a result of a small amount of precipitation of dot carbide at this temperature and the temperature of retained austenite transformation to martensite rises as well, it is easy of the retained austenite to transform into martensite[4]. Can be inferred, the tempering transformation at austenite catalytic temperature from 0.8 hours to 1.5 hours is continuous processing, in tempering at the austenite catalytic temperature for short time the precipitation size of carbide particle merely is more fine. Therefore, it can effectively promote the transformation of retained austenite after joining the cryogenic treatment, and the effect of final tempering is better than that of direct cryogenic after quenching. Of course, the experimental method and result also are determining of suitable catalytic temperature for Tc.

The carbides type of this kind of steels after annealing or quenching is agreement with equilibrium phase form, but the metastable phase appears after tempering, i.e.during tempering the first precipitation of M_3C type carbide from quenching martensitic or martensite of retained austenite transformation appears in early. Similarly, in austenite catalytic treatment the first precipitation of M_3C type carbide occurs as well, subsequently, in the continuous tempering or

secondary tempering the M_3C type carbide will anew dissolve and change direction to M_6C and $M_{23}C_6$ forming usually in the M_3C boundary or in situ, that is beginning of precipitation hardening acutely(see Fig.2). Accordingly, in pre catalytic processing the transformation of retained austenite has been made much into martensite, and sequentially in cryogenic processing the transformation of retained austenite has been made more into martensite. In the last tempering processing the original quenching martensite and the martensite from retained austenite transformation almost will synchronously form the precipitation hardening. In other words, the precipitation hardening will be increases as more of particles at the tempering temperature, so it can remarkably improve the tempering hardness[9]. And tempering temperature of the highest hardness is slightly lower, that or called secondary hardening peak left shift[7]. The final tempering hardness of direct cryogenic treatment after quenching increases only 0.5~ 0.8HRC in the same tempering conditions, this is because of the microstructure characteristics of cryogenic treatment by largely eliminated in final tempering processing at high temperature for high alloy steel.

Conclusion

(1) The effect of austenite catalytic cryogenic treatment of Cr-W-Mo-V high alloy medium-upper carbon steel is better than that of direct cryogenic treatment after quenching. The content of residual austenite reduced to below 5% and hardness is increased by 0.5HRC. And the effect is obviously improved much compared to that of the conventional quenching and tempering and the hardness is increased by about 1.5HRC.

(2) The temperature of retained austenite catalytic of Cr-W-Mo-V high alloy medium-upper carbon steel is merely higher than 10℃~20℃ of temperature of the highest tempering hardness. Catalytic temperature Tc can be determined by experimental method of conventional quenching and tempering, and the microstructure feature appears 0.01μm～0.03μm M_3C type carbide in martensite matrix precipitation, and the amount of retained austenite decreases evidently.

(3) As the retained austenite are transformed more into martensite by austenitic cryogenic cryogenic treatment after quenching, so original quenching martensite and martensitic of retained austenite transformation can form almost synchronous precipitation hardening.

References

[1] D Mohan, S Renganarayanan, A Kalanidhi, Cryogenic treatment to augment wear resistant of tool and die steels[J], Cryogenics, Vol.41,Issues 3, March 2001, p149-155

[2] A Mlinan, M Pellizzan, S Gidanella, el, Effect of deep cryogenic treatment on the mechanical properties of tool steels[J], Journal of Materials Processing Technology, Vol.118,Issues 1-3, 3 December 2001, p350-365

[3] J. Y Huang, Y. T Zhu, X. Z Liao, el, T. E Mitchell, Microstructure of cryogenic treated M2 tool steel[J], Materials Science and Engineering:A,Vol.339, Issues 1-2, 3 January 2003, p241-244

[4] Hsu Tzu-yao, Martensitic Transformation and Martensite[M], Beijing, Science Press, 1999, p593-623 (in Chinese)

[5] Zhang Xiaojing, LiuGuofang, Ma Yongqing, Material and heat treatment of knives of rotary and plane cutting for wood working[J], Heat Treatment of Metals, 2012,37(7):114-117(in Chinese)

[6] G. Ghosh, G. B Olson, Simulation of paraequilibrium growth in multicomponent systems[J], Metallurgical and Materials: A, 2001, 32(3): 455-467

[7] CHEN Ying, CHEN Zai-zhi, DONG Han, el, Microstructure and mechanical properties of tempered deep cryogenic treated 4Cr5MoSiV1 steel[J], Journal of Iron and Steel Research, Vol.18 No5, 2006, p29-32 (in Chinese)

[8] D. V. Shtansky, G. Inden, Phase transfomation in Fe-Mo-C and Fe-W-C steels--I. The structural evolution during tempering at 700℃[J], Acta Materialia, 1997,45(7):2861-2878

[9] Yongqing Ma, Hongtao Gao, Yufen Liang, Xiaojing Zhang，Secondary hardening during tempering of Cr-W-Mo-V high alloy medium-upper carbon steel and its hardness forecast[J], Advanced Materials Research, 2012, Vols,415-417, 813-818

Advanced Materials Research Vol. 936 (2014) pp 1179-1183
© (2014) Trans Tech Publications, Switzerland
doi:10.4028/www.scientific.net/AMR.936.1179

Effect Of Forging Process On V-Nb-Ti Microalloyed Non-Quenched And Tempered Steels

Man Ting-hui[1,2], Gao Peng[1],He Yi-gui[1,2], Zhan Zhao-lin[1],Tan Li [3], Bao Yao-zong[2]

[1] Kunming University of Science and Technology, Kunming Yunnan,650093, China

[2] Central Iron & Steel Research Institute, Beijing,100081, China

[3] Jiangsu Suzhou Steel Group Co., Ltd, Jiangsu, 215151, China

[*]email:mantinghuilove@163.com

Key words: non-quenched and tempered steel; dynamic recrystallization; forging technology;

Abstract: The effect of forging process on microstructure and performance of V-Ti, V-Nb-Ti non-quenched and tempered microalloying steel was investigated in this study. By comparing thecharacteristics between V-Ti and V-Nb-Ti microalloyed non-quenched and tempered steels by the forging process,the machinsm of micro-alloy technology and forging process for dynamic recrystallization and microstructure refinement was investigated. It revealed that addition of Nb in micro-alloying steel can increase significantly non-recrystallization temperature during forging process, and enhance the V (C, N) precipitation strengthening effect of V-Ti microalloyed non-quenched and tempered steels. V-Nb-Ti microalloying technology and controlling forging temperature in non-recrystallization region, can refine grain size, promote proeutectoid ferrite emerging and pearlite morphology alienating. By controlling final forging temperature in non-recrystallization region, the strength and toughness of V-Nb-Ti micro-alloy non-quenched and tempered steels can be improved.

Introduction

Microalloyed non-quenched and tempered steel developed with worldwilde energy shortage is an energy efficient steel. Comparing to the traditional alloy structural steel which needs high temperature quenching and tempering heat treatment, it have some advantages such as simple production process, higher material utilization rate, enhanced quality of parts, lower energy consumption and manufacturing cost, so it obtains a wide range of applications. At present, this kind of steel is widely used from the car industry to construction, heavy machinery, high pressure pipelines, bridges, and other fields [1,2].

Non-quenched and tempered steel is essential a kind of mechanical structural steel, requiring a good mechanical property as quenched and tempered steel. For the quenched state of the mechanical structural steel, its rolling (forging) process is only an intermediate product, so it has little effect on the performance of products. The final mechanical properties of parts mainly depend on quenching and tempering process. For non-quenched and tempered steel, the rolling (forging) and cooling is the final production process, so the heating temperature, final rolling (forging) temperature and cooling after deformation have a significant influence on the mechanical properties of final product. Microalloying technology, controlled forging and cooling process are the key way to achieve high strength and toughness [3-5]. Generally, the non-quenched and tempered steel supplied by the domestic market have poor impact resistance. Therefore, in this paper, the V-Nb microalloying non-quenched and tempered steel was investigated, with a view to improving the strength level greatly and enhance the impact properties simultaneously.

Experimental Materials and Methods

The tested material is a rod of non-quenched and tempered steel with diameter of 80mm, belonging to ferrite-pearlite type forging non-quenched and tempered steel, main chemical composition of which is shown in Table 1. The rod of non-quenched and tempered steel for experiments was prepared by controlled rolling and cooling in forging workshop. The controlled rolling and cooling process are as follows: the work-piece was reheated at 1130℃, followed by initial forging at 1050℃, and the final forging was carried out at 850℃, 900℃, 950℃ and 1000℃, and bars with final size of Φ25×500mm were obtained. After forging, the bars were air cooled with rate of about 1.5℃/s to 650℃, followed by air cooling to room temperature.

The tensile specimens (5mm diameter and 65mm gauge length) and U-notch impact test specimens (10mm width, 55mm length and 10 thickness) were machined from the rods according to the GB6397-1986, GB/T229-1994. The mechanical tests was used to determine tensile strength (Rm), yield strength (Rp0.2), percentage elongation (A) after fracture, the percentage reduction (Z) of fracture section and impact absorbed energy (AKU2). Microstructure analysis of the tested material was performed by employing optical microscopy, scanning electron microscopy and transmission electron microscopy.

TABLE 1 CHEMICAL COMPOSITIONS OF THE EXPERIMENTAL V-TI, V-TI-NB STEELS (WT,%)

Steels	C	Si	Mn	S	P	V
V-Ti	0.39	0.60	1.45	≤0.03	≤0.03	0.12
V -Nb-Ti	0.38	0.62	1.44	≤0.03	≤0.03	0.078
Steels	Cr	Ni	Ti	Nb	O	N
V-Ti	0.3	--	0.016	--	--	0.0058
V -Nb-Ti	0.3	--	0.016	0.025	--	0.0092

Results and Discussion

Mechanical Properties

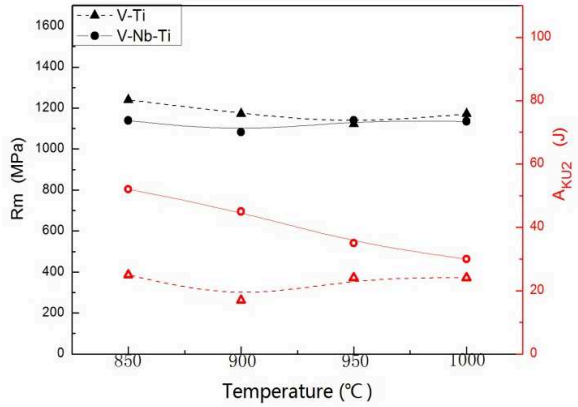


Fig. 1 Mechanical properties of steels with different final forging temperature

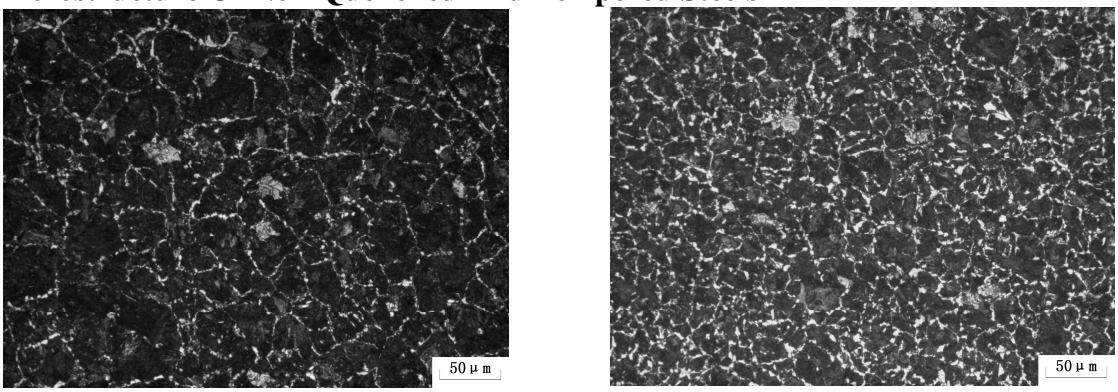
TABLE 2 THE MECHANICAL PROPERTIES OF V-TI AND V-NB-TI MICROALLOYING STEELS AT 850℃

steels	Rm/(MPa)	Rp0.2/（MPa）	A/(%)	Z/(%)	AKU2/(J)
V-Ti	1240	695	14	19	25
V-Nb-Ti	1139	655	13.5	31	52

The mechanical properties of the V-Ti microalloyed steel exhibits a slight change with decreasing of final forging temperature, as indicated in Figure1 and Table2. Their tensile strength fluctuated at about 1150 Mpa, and impact energy at about 20J. The tensile strength of V-Nb-Ti micro-alloy steel went up and down a little with the final forging temperature dropping, indicating an inconspicuous

change. But the impact absorbing energy increased from 30J to 52J with the final forging temperature decreasing, and reached the highest value at 850℃. It is suggested that the strength of the V-Nb-Ti micro-alloy steel reached 1100 MPa level that is close to V-Ti microalloyed steel, and the impact toughness was also promoted greatly. At the same time it can be found that rolling at low temperature in non-recrystallization zone would improve the toughness of the V-Nb-Ti micro alloyed steel.

The Microstructure Of Non-Quenched And Tempered Steels



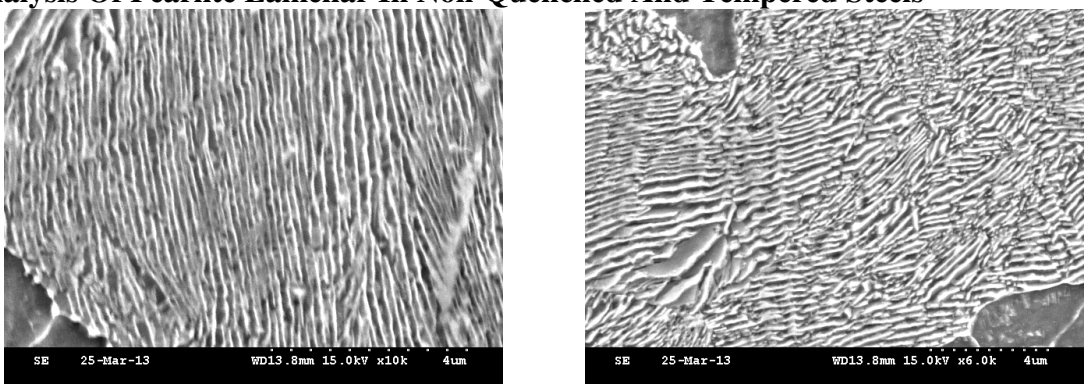
（a）V-Ti (b) V-Nb-Ti

Fig.2 Microstructure of non-quenched and tempered steels at 850℃

It can be observed from Figure 2 that the pearlite structure of V-Nb-Ti microalloyed steels after forging is tinier than that of the V-Ti microalloyed steel. And ferrite content reached 19%, which is the main reason that V-Nb-Ti microalloyed non-quenched and tempered steel has high impact toughness. Because the NbC precipitation in V-Nb microalloyed steel can prevented the austenite recrystallization at final forging stage, and raise obviously finish recrystallization temperature (950 ℃), shorten the time of dynamic recrystallization [6]. V-Nb-Ti microalloyed technology reduces the transformation temperature of austenite to ferrite, and the effect of grain refining can be achieved. The steel were rolled at the temperature range (850℃~900℃)of non-recrystallization region, and the austenite grains were elongated and refined after deformation. Warm rolling increases significantly the dislocation density and stored energy of deformation in the non-quenched and tempered steel. The V-Nb-Ti composite technology promoted the formation of the V(C, N) particles which precipitated along the grain boundary and dislocation line, and promote nucleation and growth of proeutectoid ferrite on VN particles [7, 8].

Rolling at non-recrystallization region of V-Nb non-quenched and tempered steel can promote effectively the homogeneous distributing and refinement of proeutectoid ferrite grain. Therefore, in the V-Nb micro alloyed steel there is a lot of intra-granular ferrite, which break up bulky pearlite group and refined grain. The formations of sufficient intra-granular ferrite form and microstructure refinement are main reasons that V-Nb microalloyed steel has high impact toughness [9, 10].

The Analysis Of Pearlite Lamellar In Non-Quenched And Tempered Steels

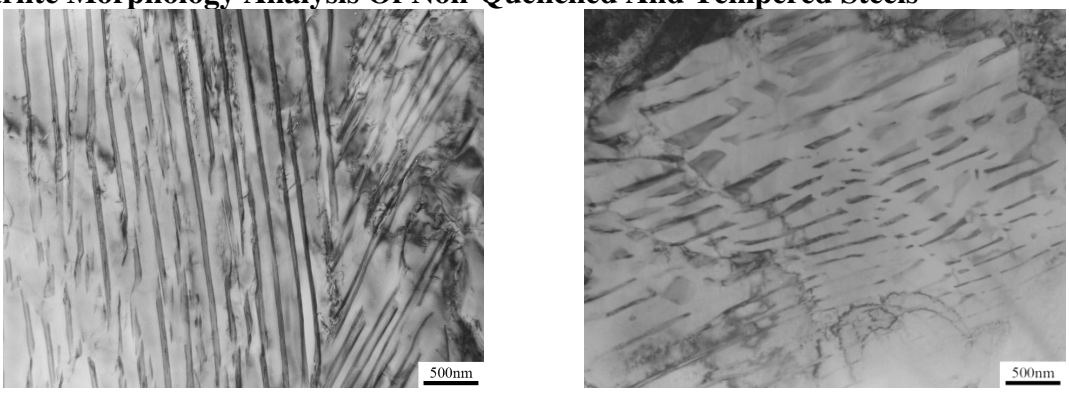


（a）V-Ti (b) V-Nb-Ti

Fig.3 Pearlite morphology of non-quenched and tempered steels at 850℃

Figure 3 shows the influence of forging process on the pearlite morphology of the V-Ti and V-Nb-Ti non-quenched and tempered steel. The figure clearly shows the distinction of pearlite layer between V-Ti and V-Nb-Ti microalloyed steels. The pearlite lamellar of V-Ti steels parallelly arranged, while the V-Nb microalloyed pearlitic arranged as short broken and disorders crowding, and part of them granulated spherically. Because V-Nb-Ti composite microalloying technology reduces the ferrite-pearlite phase transformation temperature and finer pearlite lamella can be obtained at low temperature. The average thickness of cementite layer of V-Ti steels was reduced from 42nm to 27nm, and the lamellar spacing was refined from 110nm to 85nm. The fine and blunt pearlite which disorderly distributed in the V-Nb-Ti steels can improve the toughness and strength [11].

The Pearlite Morphology Analysis Of Non-Quenched And Tempered Steels



（a）V-Ti (b) V-Nb-Ti

Fig.4 TEM micrograph of pearlite

The TEM micrograph of pearlite lamella in the V-Ti, V-Nb-Ti microalloyed steels after forging at 850℃ was presented in figure 4. It shows that the niobium has four effects for steel that preventing recrystallization, grain refinement, reducing pearlite lamellar spacing by the controlling phase transition and precipitation strengthening [12-15]. By using the V-Nb-Ti microalloying technology and taking full advantage of the low temperature forging at non-recrystallization zone, grain refinement can be achieved. Through V-Nb-Ti microalloying technology and controlled rolling technology, the long cementite lamellar during cooling transition process was broken. And the micrograph of short flake or abnormal globurizing, order-disorder transformation and narrow lamellar spacing can be obtained, which improve the toughness of non-quenched and tempered steel without the loss of strength.

The V-Nb composite microalloying steel after rolling exhibit bent, broken and spheroidizing cementite lamellae. At the same time, pearlite appear abnormal form, neat microstructure was arranged into chaos, the aspect ratio of cementite decreased significantly and cementite lamellar nodulizing for non-quenched and tempered steel, and good strength and toughness was obtained.

Conclusions

（1）V-Nb microalloying technology raised the dynamic recrystallization finish temperature, and expanded the recrystallization region of V-Ti non-quenched and tempered steel.The steel was firstly rolled in the dynamic recrystallization region, followed by rolling at low temperature (850℃) in the non-dynamic recrystallization region. And thus the boundaries of fine austenite were elongated, which increased the total effect area of the austenite grain boundary, increasing deformation energy storage and the nucleation position of ferrite phase transformation after deformation. So fine ferrite-pearlite structure can be obtained.

(2) The pearlite obtained after rolling at low temperature in non-recrystallization region, its micrograph changed significantly. Unlike V-Ti microalloyed steels, the cementite piece in pearlite of V-Nb steel is not parallelly arranged, but disordered obviously. Bent, broken and spherical pearlite lamella was observed. The aspect ratio of cementite decreased significantly and granulated, which improves strength and toughness of the V-Nb microalloyed steels.

(3) A small amount addition of Nb in V-Ti non-quenched and tempered steel can promote the precipitation of V, by which grain refinement, wide non-recrystallization region, precipitation strengthening and organization refinement can be achieved. Through V-Nb microalloying technology and rolling at low temperature in non-recrystallization zone, globular pearlite lamella was obtained. The aspect ratio of cementite reduced significantly, which improves the strength and impact toughness of non-quenched and tempered steel. V-Nb microalloying technology optimized the performance of non-quenched and tempered steel, and overcomes the shortcoming of V-Ti non-quenched and tempered steel that strength is high, bu toughness is insufficient.

References

[1] YANG Hong-gen, CUI Qing-hong. Application and evaluation of non quenched and tempered steel in engineering machinery field[J].Journal of Engineering Design,2004,8(4) : 228-230.

[2] Yang Caifu, Zhang Yongquan,Wang Ruizhen. Metallurgical principles and applications of Vanadium steel. Beijing: Metallurgical Industry Press, 2012, 6.

[3] Radovic N. Effect of interpass time and cooling rate on apparent activation energy for hot working and critical recrystallization temperature of Nb microalloyed steel [J].ISIJ Int, 1999, 39(6):575.

[4] Yi Hai-long, Du Lin-xiu, Wang Guodong, etal. High-temperature deformation behavior of Nb-V-Ti bearing and Ti-bearing HSLA rolled steels [J].Journal of Northeastern University: Natural Science, 2007, 28(10):1369-1373.

[5] Ali Reza K hodabandeh, Mohammad Jahazl, Steve Yue. Impact toughness and tensile properties improvement through icrostructure control in hot forged Nb-V microalloyed steel [J]. ISIJ Int, 2005,45(2):272.

[6] Yigui, Zhan Zhaolin, Tan Li, Effect of Niobium On The Microstructure of Microalloyed Steel During Hot Deformation Process, Heat Treatment of Metals,2013,38(6):30.

[7] Rainforth W M,Black M P,Higginson R L,etal. Precipitation of NbC in a model austentic steel. Acta Mater, 2002, 50:735.

[8] Hou Huoran, Chen Qipan, Liu Qingyou, Dong Han.Grain refinement of a Nb-Ti microalloyed steel through heavy deformation controlled cooling [J] . Journal of Materials Processing Technology, 2003, 137:173- 176.

[9] shanban,eghbali.b Characterization of austenite dynamic recrystallization under different Z parameters in a microalloyed steel[J].J Mater Sci Technol,2011,27(4):359-363.

[10] Ishikawa F.Takahashi T.The Formation of Intragranular Ferrite Plates in Medium-carbon Steels for Hot-forging and its Effect on the Toughness[J]. ISU International. 1995,35(9):1128.

[11] Pandita A, Murugaiyana A, Poddera A S, et al. Strain induced precipitation of complex carbonitrides in Nb-V and Ti-V microalloyed steels [J]. Scripta Mater, 2005, 53(11):1309.

[12] HongSC,Lim S H, Hong H S, etal.Effects of Nb on strsin induced ferrite transformation in C-Mn steel, Mater Sci Eng,2003,A355:241.

[13] Cao Jianchun, Liu Qingyou,Yong Qilong. Effect of niobiumon microstructure and strengthening mechanism of HSLA steel [J]. J Iron Steel Res, 2006, 41(8):61.

[14] Cota A B, Lacerda C A, et al. Effect of the austenitizing temperature on the kinetics of ferritic grain growth under continuous cooling of a Nb microalloyed steel[J]. Scripta Mater, 2004, 51:721.

[15] Zhang Zhengyan,Yong Qilong, etal. The effect of niobium in pearlite phase transformation in the eutectoid steel[J] .Iron&steel, 2012,4（4）:79-83.

Advanced Materials Research Vol. 936 (2014) pp 1184-1188
© (2014) Trans Tech Publications, Switzerland
doi:10.4028/www.scientific.net/AMR.936.1184

Experimental Study and Calculation of the Precipitation Behavior of Carbides in Fe-5.78Cr-0.35C Alloy During High-Temperature Aging

Wang Mingyue[a], Wang Jingjing, He Yanlin[b], Lu Xiaogang, Li Lin

Department of Materials Science and Engineering, Shanghai University, Shanghai 200072, China

[a]email: wangmingyue0908@126.com [b]email: ylhe@staff.shu.edu.com

Key words: Aging; Precipitation; M_7C_3 Carbide; Coarsening

Abstract: The precipitation behavior of carbides in Fe-5.78Cr-0.35C (wt.%) alloy during aging at 850℃ was studied. The type, particle size and distribution of carbides were determined and measured by the combination of HRTEM (High Resolution Transmission Electron Microscope), XRD (X-Ray Diffraction) and quantitative metallography technique. Results show that the type of carbides was M_7C_3 and the obvious coarsening of carbides was observed during aging. In addition, the thermodynamic and kinetic calculation using Thermo-Calc software was conducted to study the precipitation of carbides. The stable phase in the alloy aging at 850℃ was M_7C_3 carbide and austenite which is in accordance with experimental results. According to Ostwald coarsening mechanism, the average interfacial energy between γ phase and M_7C_3 carbide was calculated as 0.7 $J \cdot m^{-2}$. Then the precipitation behavior of carbides in Fe-5.78Cr-0.35C alloy during aging was well predicted.

Introduction

To understand the evolution of morphology, size, distribution and volume fraction of precipitates which have strong effects on the mechanical properties of steel materials during aging is quite important[1,2]. The precipitation behavior of carbides in a ternary Fe-Cr-C alloy during aging was experimentally studied in the present work. In addition, thermodynamic and kinetic calculations were also conducted using Thermo-Calc software. With the combination of experimental study and calculation, the precipitation behavior of carbides during aging can be predicted.

Experimental Material and Method

99.98wt.% Cr, 99.998wt.% Fe and Fe-1wt.% C alloy was electric arc and induction melted into the ingot. The composition of the ingot was measured to be Fe-5.78 wt.%Cr-0.35 wt.%C. The ingot was capsuled in a vacuum quartz tube under the pressure below 10^{-2}Pa and homogenized at 1000 ℃ for 100h. The specimens with size of 10mm×10mm×3mm were cut from the ingot and capsuled in a vacuum quartz tube. The specimens were solid-solution treated at 1100℃ for 20h before quenching into water. Then the specimens were capsuled respectively and aged at 850 ℃ for 10min, 1h, 5h, 30h and 100h.

The heat-treated specimens were mechanically polished and etched in 4% nitric acid alcohol to observe the metallographic microstructure.

The carbides precipitating during aging were obtained by chemical extraction in phosphoric acid (2:1) at room temperature[3]. Carbides powder was filtered using micro-porous membrane with 0.15 μm aperture and dried. A D/MAX-2500 X-ray diffractometer using Cu Kα radiation, at a

scanning speed of 5° /min, with scanning angle of 20°~100°(2θ) and operating at 40kV and 40mA was used to determine the type of precipitates.

Samples for TEM observation were obtained by carbon replica technique. Heat-treated specimens were mechanically polished and etched. A layer of carbon was deposited on the etched specimen and then etched in 8% nitric acid alcohol for seconds until the replica began to lift. The specimen was slid into distilled water and the replicas were collected by a copper net. The microscopy work was performed with the JEM-2010F instrument and operating at 200kV accelerating voltage. Precipitates were identified by a combination of electron diffraction patterns and EDS analysis. Morphology of carbides[4] were also observed,.

To determine the size distribution of precipitates, about 300 particles were photographed and measured for each sample. Measurements were conducted by using Image J analysis software.

Experimental Results

XRD results as shown in Fig.1 indicate that the precipitates are all M_7C_3 type carbide when aged for 10min, 1h, 5h, 30h and 100 h.

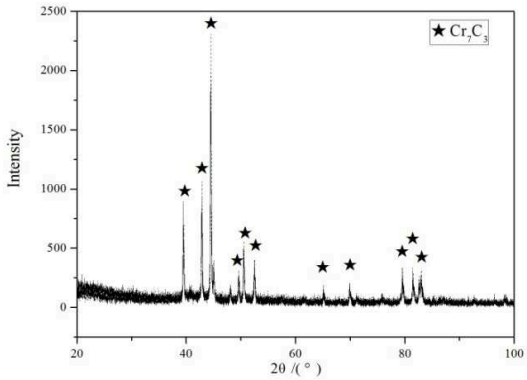


Fig.1 XRD patterns of precipitates in specimens aged at 850℃ for 10min, 1h, 5h, 30h and 100 h

TEM images of precipitates with diffraction pattern and EDS analysis in Fe-5.78 wt.%Cr-0.35 wt.%C (wt.%) alloy after aging at 850℃ for 100h was shown in Fig.2. Diffraction pattern of spherical and rod-like precipitates shows the type of carbides as M_7C_3.

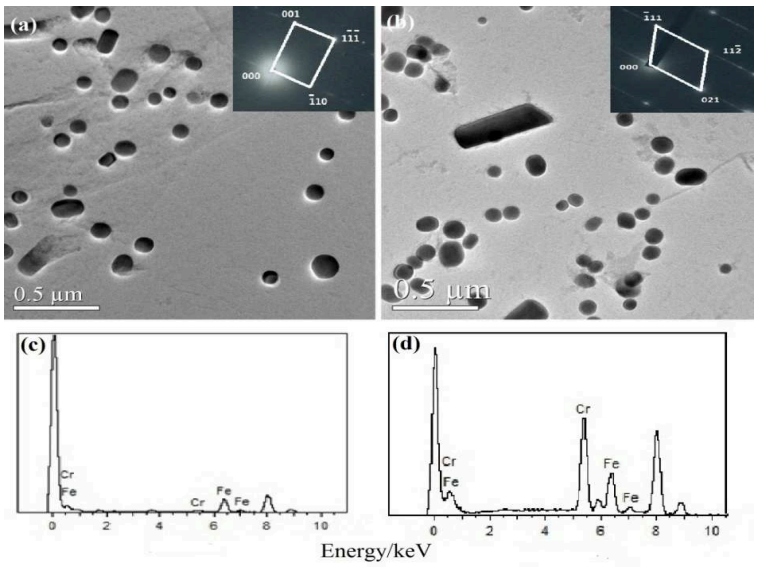


Fig.2 TEM micrographs with diffraction patterns and EDS analyais of (a,c) spherical precipitates and (b,d)rod-shaped precipitates

The analytical process to determine the size and distribution of precipitates was shown in Fig.3. Incomplete particles on the boundaries were not counted. 300 particles were counted to obtain the average particle size of precipitates. Mean radius of carbides after aging at 850℃ for 10min, 1h, 5h, 30h and 100h was 31.79nm, 34.18nm, 42.25nm, 48.36nm and 57.82nm respectively. The size distribution under each heat-treatment condition was shown in Fig.4.

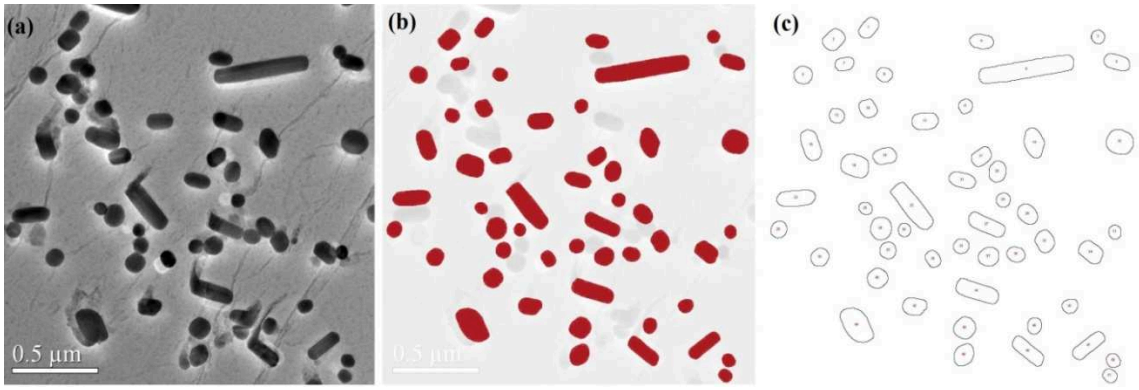


Fig.3 Schematic diagrams of the analytical process to determine the size and distribution of M_7C_3 carbides

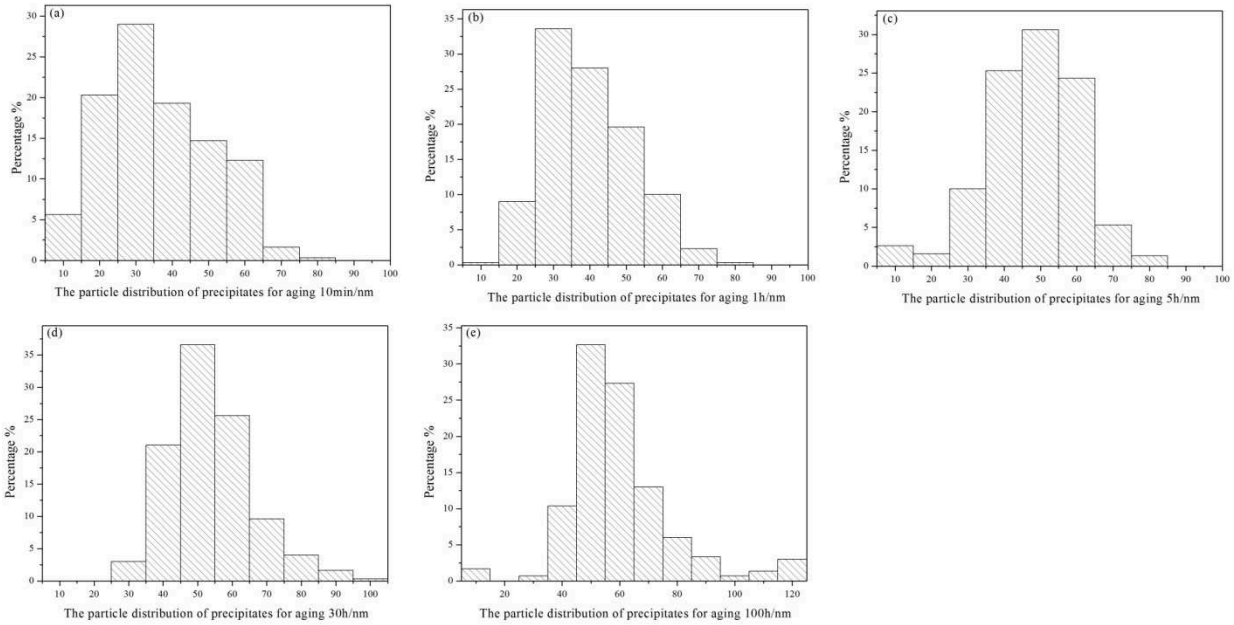


Fig.4 Size distribution of M_7C_3 carbides in specimens aged at 850℃ for (a) 10min, (b) 1h, (c) 5h, (d) 30h and (e) 100h, respectively

Discussion

The equilibrium phases of the Fe-5.78Cr-0.35C alloy aged at 850℃ consist of austenitic(denoted as FCC_A1#1) and M_7C_3 carbide according to the phase diagram calculated by Thermo-Calc Ⓢ [5] software as shown in Fig.5(a). Thus the carbide type precipitated in Fe-5.78Cr-0.35C alloy during aging at 850℃ was well predicted.

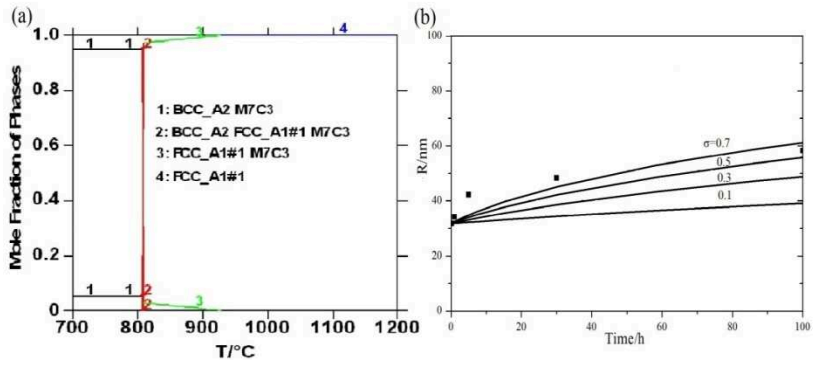


Fig.5 (a)Mole fraction of equilibrium phases as a function of aging time and (b) comparison between the experimental data with calculated coarsening of M_7C_3 carbides in Fe-5.78Cr-0.35C alloy aged at 850 ℃

As well known, the coarsening model Oswald ripening was adopted in DICTRA[5]. It uses the assumption that coarsening of a system can be described by performing calculations on a single particle of maximum size at the centre of a spherical cell. It is assumed that the particle size distribution obeys the Lifshitz-Slyozov-Wagner distribution, i. e.the maximum particle size is 1. 5 times the average size of the precipitates. Based on coarsening model, simulations were performed with thermodynamic database TCFE6 and the mobility database MOB2. Results were shown in Fig.5(b) in comparison with the measured average radius represented by symbols. Since the interfacial energy varies between 0.1 -1.0 $J.m^{-2}$ as a rule of thumb[6,7], value of σ changing from 0.1 to 0.7 $J.m^{-2}$ with a step of 0.2 $J.m^{-2}$ is used for simulation. Simulation of coarsening of M_7C_3 carbides in austenite at 850 °C with the interfacial energy of 0.7 $J.m^{-2}$fits the experimental data well.

Conclusions

(1) The equilibrium phases of Fe-5.78Cr-0.35C alloy aged at 850℃ consist of austenite and M_7C_3 carbide.

(2) The obvious coarsening of carbides was observed during aging at 850℃. The average particle radius of M_7C_3 carbides was equivalent to 31.79nm, 34.18nm, 42.25nm, 48.36nm, 57.82nm when aged at 850℃ for 10min, 1h, 5h, 30h, 100h, respectively.

(3) Precipitation behavior of M_7C_3 carbides in an Fe-5.78Cr-0.35C alloy can be simulated by Thermo-Calc software. Interfacial energy of M_7C_3/austenite interface is 0.7$J.m^{-2}$ for the coarsening of M_7C_3 carbide at 850℃.

Acknowledgements

This study is funded by the National Natural Science Foundation of China (No. 50934011) and National Basic Research Program of China (No. 2010CB630802).

References

[1] Yong Qi-long, The theoretical calculation of semi-coherent interface energy of micro-alloy carbonitrides and ferritic, Chinese Science Bulletin. 34 (1989) : 707.

[2] Mohsen Asadi Asadabad, Shahram Kheirandish, Abdul Javad Novinrooz, Microstructual and Mechanical Behavior of 4.5Cr2W0.25V0.1C Steel[J]. Materials Science and Engineering. 52,1612.(2010)

[3] Compiled by CISRI, Physical and chemical phase analysis in steel and iron-nickel based alloy. Shanghai Science and Technology Press, 1981,205-209.

[4] Lu li, Zhu Na-qiong, He Yan-lin, The Coarsening behavior study on Fe-Cr-C alloy at high temperature aging treatment, Materials and Heat Treatment. 32 (2011) 62-67.

[5] J-O Anderssond, Thomas Helander, Lars Hdghmd,et al. THERMO-CALC & DICTRA, computational tools for material science [J]. Calphad. 28 (2002): 273-312.

[6] Zhu Na-qiong, Lu li, He Yan-lin. Coarsening of M23C6 Precipitates in Fe-Cr-C Ternary Alloy. Journal of Iron and Steel Research, International. 19 (2012):62-67.

[7] Åsa Gustafson, Mats Hättestrand. Coarsening of Precipitates in an Advanced Creep Resistant 9% Chromium Steel-Quantitative Microscopy and Simulations[J]. Materials Science and Engineering, 2002, 333A(1/2):279.

Advanced Materials Research Vol. 936 (2014) pp 1189-1194
© (2014) Trans Tech Publications, Switzerland
doi:10.4028/www.scientific.net/AMR.936.1189

Effect of Temperature on the Ti-Fe Alloy Prepared by Molten Salt Electrolysis

Ruimeng Shi [1, a], Longfei Bao[1,b] and Bo Zhang[1,c]

[1] Metallurgical Engineering College of Xi'an University Of Architecture And Technology, China, Xi'an

[a]shiruimeng@live.cn, [b]blf918279@126.com, [c]love-luckboy@163.com

Keywords: Titanium concentrate; Molten salt electrolysis; Temperature; TiFe; $TiFe_2$; Diffusion

Abstract. Ti-Fe alloy was prepared by electroanalysis using titanium concentrate as the cathode at 3.1V in $CaCl_2$ molten salt. The temperature is respectively 850℃ and 900℃. The comparison of the results under different temperature shows that the temperature has a significant influence on the diffusion process and the electrolytic products. At 850 ℃, the final electrolytic product is the $TiFe_2$ and Ti discrete ball-type structure with the particle size of 1 μm, while at 900 ℃ the final product is the TiFe space net structure with the particle size of 3 μm.

Introduction

Titanium alloy, as a kind of important functional material, has received the widespread attention. In recent years, there are studies and reports about the performance and magnetism of hydrogen storage of the ferro-titanium [1-5]. The method of preparing the ferro-titanium with the mixture of TiO_2 and Fe_2O_3 by electrolytic method is a kind of green metallurgy technology, which has advantages of short process, low energy consumption and low pollution. This method has been reported a lot [6, 7], but little research about the influence of temperature on electrochemical results has not been reported. This paper takes titanium concentrate's cathode as the cathode, with electrolysis voltage of 3.1V, the electrolytic experiments was carried out respectively under the condition of 850℃ and 900 ℃ , and the phase and structure of the electrolytic products are analyzed.

Experiments

Titanium concentrate, the starting material, was separated from tailings, which was the product from beneficiation of vanadium-bearing titanomagnetite. The main phase is $FeTiO_3$ and there is also a small amount of Si, Ca, Al, Mn, V, S, P and other elements. Table 1 is the element analysis of titanium concentrate

Titanium concentrate cathode was prepared by melting method under the protection of the Ar gas. $CaCl_2$ molten salt was used as the electrolyte, which was dried in an oven at 150 ℃. To reduce its moisture content and impurities, $CaCl_2$ was needed to pre-electrolysed at 600℃ for 2 h. The electro-deoxidation experiments were carried out in graphite crucible at atmosphere pressure, and the crucible was dried at 150℃ before the experiments. $FeTiO_3$ was used as the working electrode, a graphite rod was used as the counter electrode, and the graphite crucible was used as the reference electrode. The electrolytic temperature is respectively 850℃ and 900℃and the voltage was increased to 3.1 V.

After electrolysis, the pellet and the graphite rod were removed from the electrolyte and cooled to room temperature in the furnace. The pellet sample was put into distilled water for 12 h and then cleaned by Q2200E ultrasonic cleaner to remove the electrolyte. The morphology and elements distribution were observed by SEM (scanning electron microscopy) and phase composition was analyzed by XRD (Rigak D/Max-2500). Diffraction parameters were as follows: Scanning angle 2 θ was 20°~90°. Scanning speed was 1.2 °/min. Tube voltage was 40 KV. Tube current was 150 mA.

TABLE 1 ELEMENT ANALYSIS OF TITANIUM CONCENTRATE

Element	O	Fe	Ti	Mg	Si	Ca	Al	Mn	S	P
Mass%	34.01	28.90	26.93	3.44	3.31	1.35	1.20	0.56	0.27	0.03

Results and Discussion

Phase and Appearance of the Cathode of the Titanium Concentrate

Fig. 1 and 2 is the XRD pattern and SEM of titanium concentrate cathode, respectively. Fig. 2 shows that the titanium concentrate cathode has a compact structure after solidification by melting. The phase composition of titanium concentrate cathode is the same as the raw ore after melting, showed by XRD, which is $FeTiO_3$.

At the same time, the presence of $CaSiO_3$ is detected and the diffraction peak of compounds of other elements is not obvious.

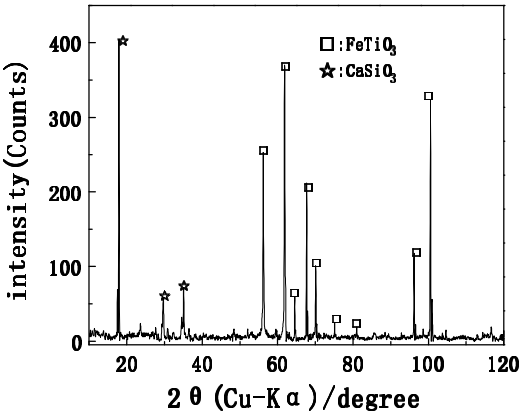


Fig. 1 XRD pattern of molten-solidified cathode

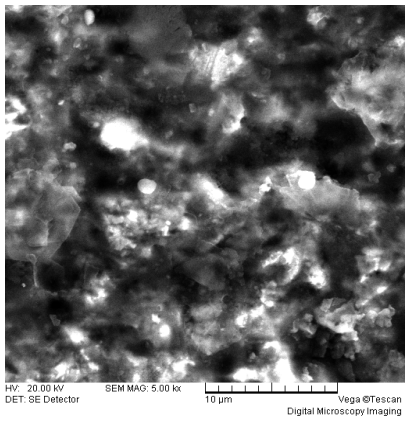


Fig. 2 SEM image of sample

The Analysis of the Electrolytic Product at 850℃

The titanium concentrate cathode was electrolysed in $CaCl_2$ molten salt at 850 °C for 0.5h, 10h and 48h, respectively. Fig. 3-5 are XRD pattern for the titanium concentrate at different electrolytic timescathode. It can be seen that the electrolytic products on cathode has a distinct difference. The main phases are Fe, $CaTiO_3$, $Ti2O_3$ and TiO when the electrolytic time is 0.5 h. when the electrolytic time is extend to 10 h, the phases are mainly $TiFe_2$ and Ti, the diffraction peak of TiFe is not obvious. With increasing the electrolytic time to 48 h, the main reaction product is TiFe and the diffraction peaks of $TiFe_2$ and Ti decrease significantly. It can also be seen that from Fig. 6 that there is an obvious change for the morphology of electrolytic product. The appearance of the cathode changes from the compact structure at the beginning into the discrete spherical structure of the particle size of 1 μm.

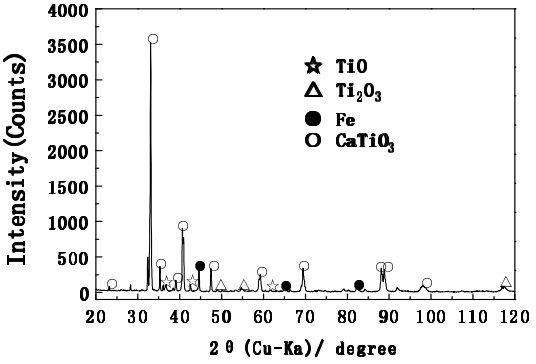


Fig. 3 XRD pattern of sample electrolyzed after 0.5h at 850℃

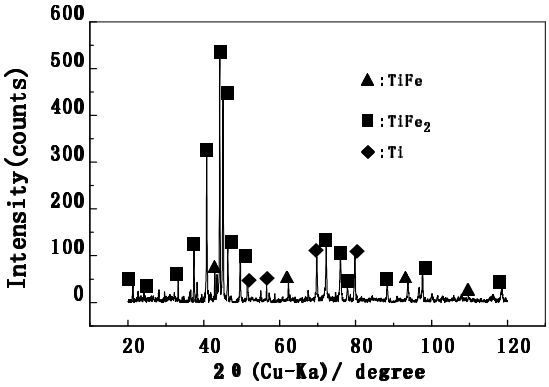


Fig. 4 XRD pattern of sample electrolyzed after 10h at 850℃

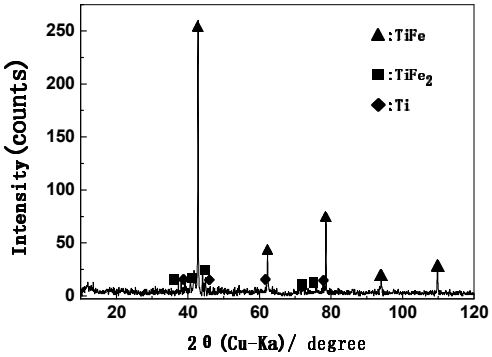


Fig. 5 XRD pattern of sample electrolyzed after 48h at 850℃

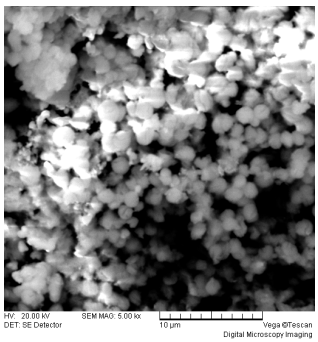


Fig. 6 SEM image of sample electrolyzed after 48h at 850℃（×5000）

The Analysis Of The Electrolytic Product At 900℃

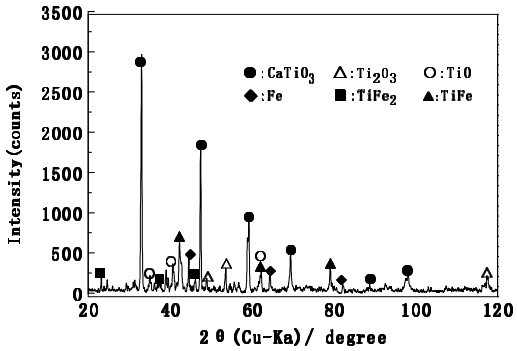


Fig. 7 XRD pattern of sample electrolyzed after 0.5h at 900℃

Under the same conditions, the electrolysis experiment for different electrolytic time at 900℃ is carried out. Fig. 7-9 are XRD pattern for the titanium concentrate at different electrolytic times at 900 ℃ It can be seen that the morphology of the electrolytic product at 900℃ is obviously different from that at 850℃.The particle size increases from 1 μm at 850℃ to 3 μm at 900℃. The appearanceof product changes from discrete spherical structure at 850℃ to spatial reticulated structure and there is significant consolidation phenomenon between particles. By XRD analysis, it can be seen that there are also Fe, $CaTiO_3$, Ti_2O_3, TiO and other intermediates in the electrolytic specimen reacting for 0.5h and there is also existence of $TiFe_2$ and TiFe phase. When the electrolytic time is 10h, the main product is TiFe and a certain amount of $TiFe_2$ at the same time. With increasing the electrolytic time to 48h, the main phases in the electrolytic sample is TiFe and the diffraction peak of $TiFe_2$ is weak. Because the TiFe alloy is formed by mutual diffusion process of $TiFe_2$ and Ti, thusthe existence of $TiFe_2$ is a intermediate process.

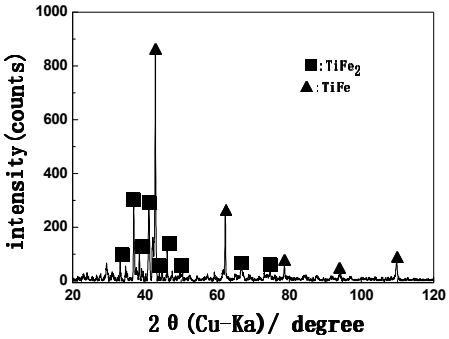


Fig. 8 XRD pattern of sample electrolyzed after 10hours

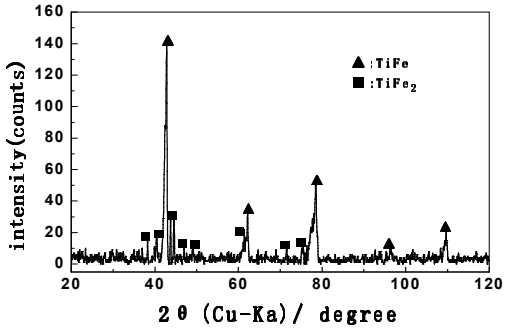


Fig. 9 XRD pattern of sample electrolyzed after 48hours

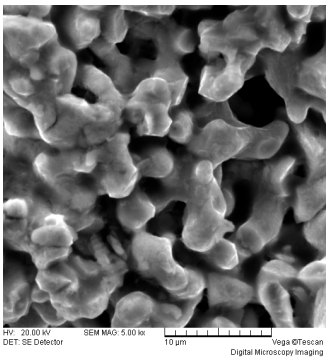


Fig. 10 SEM image of sample electrolyzed after 48h at 900℃（×5000）

Analysis On The Influence Of Temperature On The Electrolytic Product

Relevant electrode reactions in the electrolytic process are as follows:

$$FeTiO_3 + 2e = Fe + TiO_2 + O^{2-} \quad (1)$$

$$Ca^{2+} + TiO_2 + O^{2-} = CaTiO_3 \quad (2)$$

$$2CaTiO_3 + 2e = Ti_2O_3 + 2Ca^{2+} + 3O^{2-} \quad (3)$$

$$2TiO_2 + 2e = Ti_2O_3 + O^{2-} \quad (4)$$

$$2Ti_2O_3 + 2e = 2TiO + O^{2-} \quad (5)$$

$$TiO + 2e = Ti + O^{2-} \quad (6)$$

$$2Fe + TiO + 2e = TiFe_2 + O^{2-} \quad (7)$$

$$Fe + TiO + 2e = TiFe + O^{2-} \quad (8)$$

$$TiFe_2 + TiO + 2e = 2TiFe + O^{2-} \quad (9)$$

The thermodynamics for the electrolytic process is calculated by calculation. The gibbs free energy ΔG within the range of 0~1000℃ for different reactions can be obtained. According to the chemical thermodynamics ($\triangle_r G_m = -zFE$), the theory decomposition voltage of each reaction can be calculated, showed in Fig. 11. It is shown that the theoretical decomposition voltage of FeO is lower than TiO_2, so the Fe is prior to be reduced. The XRD analysis results of 0.5 h after electrolysis under the condition of 850℃ shows that there is the existence of the elemental Fe, and Ti exists in the form of suboxide of perovskite and titanium. The reduction of Ti is from + 4 to + 3 and then to + 2 and finally reduce to reduction process step by step of Ti. Perovskite only exists in the reaction area on the surface of cathode, the compact cathode structure prevents the diffusion of Ca_2+ in the molten salt inside the cathode, so there is no intermediate of $CaTiO_3$ in the electroreduction process inside the cathode.

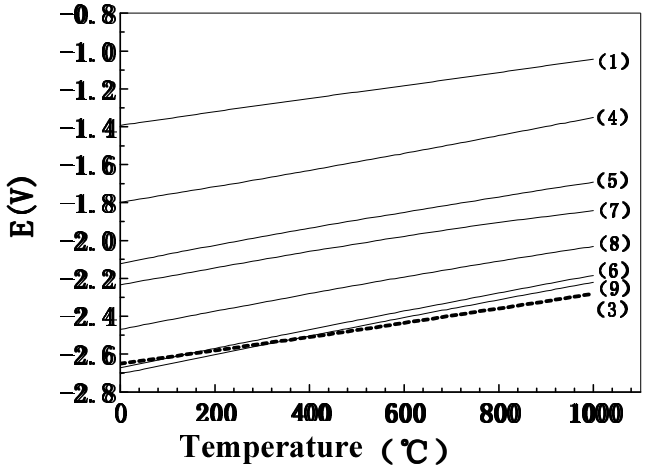


Fig.11 Theoretical decomposition voltage of electrode reaction at 0~1000℃

At the high temperature, the formation of $TiFe_2$ and TiFe alloy by Ti and Fe is a spontaneous process. It can be found from Fig. 11 that the theoretical decomposition voltage of forming $TiFe_2$ and TiFe is lower than that of Ti. Therefore, in thermodynamics, the process of forming $TiFe_2$ and TiFe is more easily than reduction to metallic titanium, thus, there is no simple substance Ti in the early stage of the reaction.

And the electrolysis voltage to form $TiFe_2$ is lower than to form TiFe and the structure is more stable, so in the alloying process, $TiFe_2$ is given priority to produce. However, the process of reduction and alloying of Ti in the $TiFe_2$ particles needs higher electrolytic voltage than that for directly producing the elemental Ti and through thermodynamic calculation, it can be known that the process where Ti combines with $TiFe_2$ to generate TiFe is a spontaneous process. Therefore, when Fe to produce $TiFe_2$ is exhausted, Ti will be electrolyzed and reduced in the elemental form, this result is same as the analysis result of XRD produced by electrolysis for 10 h under the condition of 850℃, with the extension of reaction time, the diffusion is further strengthened and this is same as the electrolytic products after 48h.

Compared with the result at 850℃, the phase and structure of the electrolytic product under the condition of 900℃ is obviously different, indicating the temperature has a significant influence on the process of preparation of titanium alloy by electrolytic titanium concentrate. Under this experimental condition, the priority of each electrode reaction has not changed, so the electrolytic mechanism has not changed. However, the increasing of temperature improves the electrolytic speed and the diffusion ability of Fe, Ti, O and other atoms. Under the condition of 850℃, after electrolysis for 0.5h, t Fe is reducted partially. When temperature is 900℃, after electrolysis for 0.5h, the phase of $TiFe_2$ and TiFe are also existed, which indicating the improvement of temperature is advantageous to the electrolytic process. In the comparison of feature of the product under different temperatures, it can be found that, from the discrete spherical structure at 850℃ to the space mesh structure at 900℃, the increase of electrolytic temperature significantly improves the diffusion ability of Fe and Ti atoms. As under the experimental condition, the process where Ti and TiFe2 combine to generate TiFe is a spontaneous process, combining the results of electrolysis for 48h at 850℃ and 900℃, it shows the mutual diffusion of Ti and $TiFe_2$ eventually generates the TiFe alloy and the temperature is very important for the mutual diffusion of alloying process.

$$FeTiO_3 \Rightarrow Fe+TiO_x \Rightarrow TiFe_2+TiO_x \Rightarrow TiFe_2+Ti \Rightarrow TiFe$$

Fig. 12 Schematic of electro-deoxidization process of titanium concentrates

Conclusions

1) Ti-Fe alloy can be prepared by electroanalysis using titanium concentrate as the cathode at 3.1V in $CaCl_2$ molten salt when the electrolytic time above 850℃. the direct electrolytic products are $TiFe_2$ and Ti.

2) The formation of TiFe alloy by Ti and $TiFe_2$ is a non-spontaneous process in thermodynamics. TiFe alloy is produced by the mutual diffusion between $TiFe_2$ and Ti.

3) The increasing of temperature promotes the mutual diffusion process of $TiFe_2$ and Ti and is favorable for the formation of TiFe alloy.

References

[1] A. Kinaei, M. KAydinol. AB Initio Investigation of Feti—Hsystem[J]. International journal of hydro energy, 2007,32 (13):2466.

[2] B. Singh, H. Ryu. Development of New Hydrogen Storage Material Feti(Ni) for Improved Hydrogenation Characteristics [J]. IEEE transactions on electrical and electronic engineering，2006, 24 (l):1

[3] L., Zhan GM, Pan F. Magnetic Properties and Miro Structure of Fe/Ti Nano2 Seale multilayers [J], 1998, 9 (12):182

[4] X. Yan, X. Chen, A. Grytsiva, et al. Site Preference, Hemodynamic, and Magnetic Properties of the Ternary Laves Phase Ti (Fel—Xalx) (2) with the Crystal Structure of the Mgzn2—TyPe[J].International journal of materials research, 2006, 97(4):450.

[5] J. Koeble, M. Huth. Field Induced Unidirectional Magnetic Anisotropy in Fe2Ti Thin Films [J]. European magnetic materials and applications，2001, 173 (3): 373.

[6] X. Guo, Z. Guo, Z. Wang. Direct Preparation of Tife Alloy by Electrolytic Reduction from TiO2and Fe_2O_3[J]. Journal of University of Science and Technology Beijing, 2008, 30(6): 620-624.

[7] J. Du, Z. Xi, Q. Li, et al. Preparation of TiFe Alloy by Electro-Deoxidization in Molten Salt[J]. Rare Metal Materials and Engineering. 2008, 37(12):2240~2243.

Advanced Materials Research Vol. 936 (2014) pp 1195-1200
© (2014) Trans Tech Publications, Switzerland
doi:10.4028/www.scientific.net/AMR.936.1195

Preparation of Ti-Fe Alloy From Titanium Concentrate by Electro-deoxidization in $CaCl_2$

Ruimeng Shi [1, a], Longfei Bao[1,b] and Bo Zhang[1,c]

[1] Metallurgical Engineering College of Xi'an University Of Architecture And Technology, China, Xi'an

[a]shiruimeng@live.cn, [b]blf918279@126.com, [c]love-luckboy@163.com

Keywords: Molten salt electrolysis; Ilmenite concentrate; Ferro-titanium; TiFe; $TiFe_2$

Abstract. Ti-Fe alloy is prepared by the electrolytic reduction of titanium concentrate in molten $CaCl_2$ under argon atmosphere. The formation mechanism of Ti-Fe alloy is discussed. The impact of electrolytic time on product is studied when electrolytic voltage is 3.1V and electrolytic temperature is 900℃. Results show that Ti-Fe alloy with uniform composition can be obtained by this method. The deoxidize product is iron and TiFe alloy by order. The reduction of Ti is a multi-step process and the intermediate products include $CaTiO_3$,TiO_2, Ti_2O_3, TiO,Fe, $TiFe_2$.

Introduction

Titanium ore resources in China are mainly distributed in Guangdong, Guangxi, Hainan, Hebei and Panzhihua. The TiO_2 grade of titanium concentrate is generally 45%~60%. As a typical hydrogen storage material, Ti-Fe alloy has attracted more attention [1] and how to directly use Chinese rich resources to prepare ferrotitanium is an exploratory work with vital significance.

Since the preparation of metallic titanium can be carried out through the technology of molten salt electrolysis deoxidization [2,3] with TiO_2, this technology has aroused extensive attention in the industry. The researchers have extracted metals or alloys successfully by FFC technology,such as Nb_3Sn[4], Ti-10W [5], Nb [6], Tb_2Fe_{17} [7], Cr [8], Ni-Ti [9], Mg-Zr [10], Co-Cr [11], V-Ti [12], TiFe [13-14] , and also built model of molten salt electrolysis oxide [15] etc.. The cathode reported in literature is mainly metal oxide. The little research on preparing metal or alloy is directly from ore. The author directly adopted the titanium concentrate from Panzhihua region in China as the materials to prepare Ti-Fe alloy through molten salt electrolysis, which possessing the certain significance in the aspects of economic cost and environmental pollution.

Experiments

Titanium concentrate with an average 75 μm particle size was selected as the starting material. The main phase is $FeTiO_3$. Table 1 is the element analysis of titanium concentrate

Titanium concentrate cathode was prepared by melting method under the protection of the Ar gas. $CaCl_2$ molten salt was used as the electrolyte, which was dried in an oven at 150℃. To reduce its moisture content and impurities, $CaCl_2$ was needed to pre-electrolysed at 600℃ for 2h. The electro-deoxidation experiments were carried out in graphite crucible at atmosphere pressure, and the crucible was dried at 150℃ before the experiments. $FeTiO_3$ was used as the working electrode, a graphite rod was used as the counter electrode, and the graphite crucible was used as the reference electrode. The electrolytic temperature is respectively 850℃ and 900℃and the voltage was increased to 3.1 V.

After electrolysis, the pellet and the graphite rod were removed from the electrolyte and cooled to room temperature in the furnace. The pellet sample was put into distilled water for 12 h and then cleaned by Q2200E ultrasonic cleaner to remove the electrolyte. The morphology and elements distribution were observed by SEM (scanning electron microscopy) and phase composition was analyzed by XRD (Rigak D/Max-2500). Diffraction parameters were as follows: Scanning angle 2 θ was 20°~90°. Scanning speed was 1.2 ° /min. Tube voltage was 40 KV. Tube current was 150 m A.

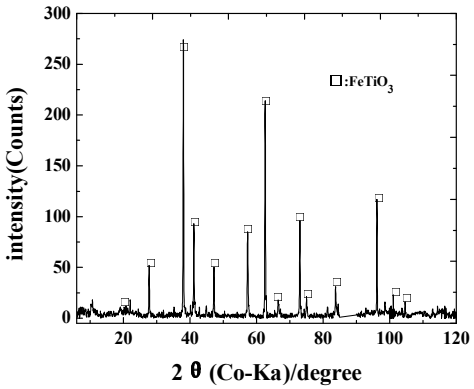


Fig. 1 X-ray diffraction profile of titanium concentrate

Table 1 Elemental analysis of titanium concentrate

Element	O	Fe	Ti	Mg	Si	Ca	Al	Mn	S	P
Mass%	34.01	28.90	26.93	3.44	3.31	1.35	1.20	0.56	0.27	0.03

Results and discussion

A. Morphology and phase composition of titanium concentrate before and after electrolysis

Fig. 2 and 3 are SEM of the sample before and after electrolysis. Before electrolysis, the titanium concentrate presents a compact crystalline state structure. When cathode was electrolyzed at $CaCl_2$ molten salt 48 h, the cathode forms space reticular structure with 3 μm particles. The morphology of the sample changed significantly after electrolysis. Fig. 4 and 5 are XRD profile of the sample before and after electrolysis. We can see from Fig. 4 that the key composition of cathode phase of the preparative titanium concentrate through fusion and solidification is $FeTiO_3$. The oxidization of titanium concentrate can be avoided with protection of Ar. While $CaSiO_3$ detected in the phase may be the result of beneficiation of fusion and solidification of calcium metasilicate contained in the raw ores. XRD and EDS analysis has been conducted for the samples through 48-hour electrolysis. The XRD analysis found that ferrotitanium and a small quantity of elemental titanium and $TiFe_2$ alloy. EDS analysis reveals Ti:Fe (atomic ratio)=1.09 (table 2), showing that ferrotitanium can be prepared through molten salt electrolysis titanium concentrate and atomic ratio of Ti and Fe stays the same as that of raw materials. As ferrotitanium generates through inter-diffusion of $TiFe_2$ and Ti, the main product is TiFe after complete electrolytic reduction of titanium concentrate and alloy phase is very homogeneous and there are a few $TiFe_2$ and elemental Ti.

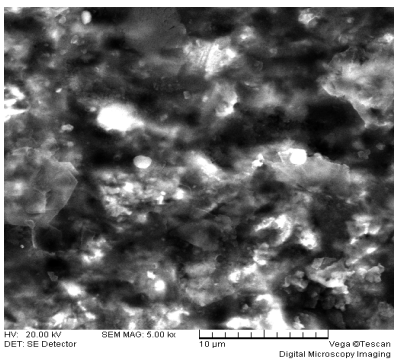


Fig. 2 Morphology of titanium concentrate sample

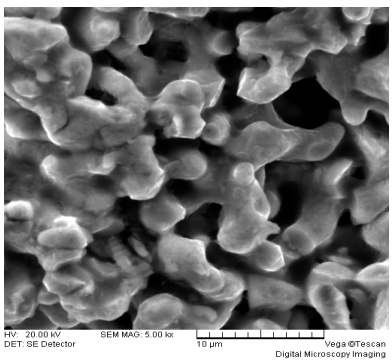


Fig. 3 SEM image of sample 48-h electrolysis

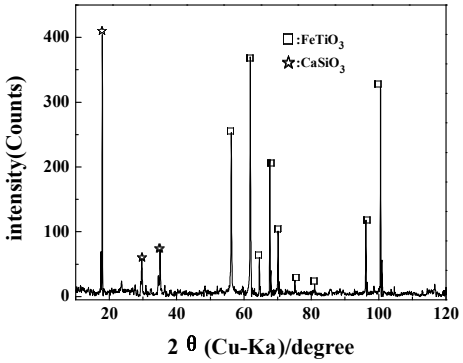


Fig. 4 Cathode X-ray spectrum prepared through fusion and solidification

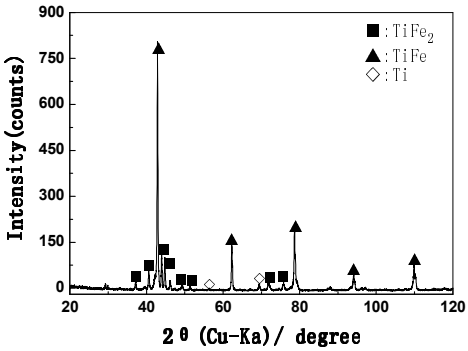


Fig. 5 Sample phase composition after 48-h electrolysis

Table 2 Component analysis of sample after 48-h electrolysis

Element	O	Ti	Fe	Si	Ca	Mg	Al	Mn	Cl
Mass%	8.57	40.67	43.46	0.52	1.42	2.23	1.41	0.70	1.02

B. Phase analysis on cathode surface at earlier stage of electrolysis

In order to deeply analyze the electrolytic reduction of titanium concentrate, under the condition of 3.1V voltage and 900℃ electrolysis temperature, XRD analysis on the surface of samples with 10 min and 30 min of electrolytic time and diffraction profile is shown in Fig. 6. As shown in the Fig., new phases including Fe, $CaTiO_3$, Ti_2O_3 and TiO were generated on the cathode surface and the original phase $FeTiO_3$ disappeared. Due to the reduction potential of Fe is lower than that of Ti, metallic iron and TiO_2 and O^{2-}. TiO_2 were generated on cathode surface and then combined with CaO in the fused salt to produce the intermediate product $CaTiO_3$. $CaCl_2$ has extremely strong hydroscopicity and CaO are formed by the hydrolyzation of $CaCl_2$. With the processing of reaction, the intermediate product $CaTiO_3$ will generate suboxides Ti_2O_3 and TiO of Ti after further electroreduction and Ti and Fe will combine to generate $TiFe_2$ and TiFe. O^{2-} moves toward the anode through electric field action and performs electrode reaction on the anode to emit O^{2-} The involved electrode reactions are as follows.The thoretical electrolytic voltage of the related reaction are also listed when the temperature is 900℃.

$$FeTiO_3 + 2e = Fe + TiO_2 + O^{2-} \quad (1)$$

E1=-1.07813V

$$Ca^{2+} + TiO_2 + O^{2-} = CaTiO_3 \quad (2)$$

$$2CaTiO_3 + 2e = Ti_2O_3 + 2Ca^{2+} + 3O^{2-} \quad (3)$$

E3=-2.32034V

$$2Ti_2O_3 + 2e = 2TiO + O^{2-} \quad (4)$$

E4=-1.73098V

$$TiO + 2e = Ti + O^{2-} \quad (5)$$

E5=-2.23089V

$$2Fe + Ti = TiFe_2 \quad (6)$$

$$TiFe_2 + Ti = 2TiFe \quad (7)$$

$$2O^{2-} + 4e = O_2 \quad (8)$$

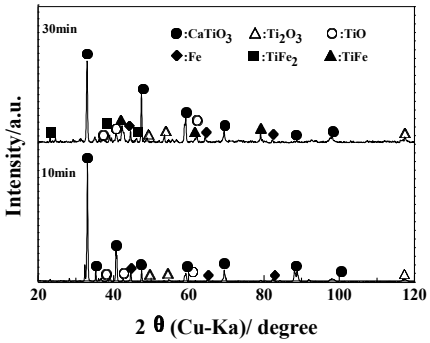


Fig. 6 Surface XRD after 10-min and 30-min electrolysis

C. Phase analysis of cathode at metaphase of electrolysis

Under the same experiment conditions, the sample section with 1h, 8h and 20h electrolytic time were analyzed. it is found that there are obvious reduzate layers between the interior of cathode and the exterior contacted with $CaCl_2$ molten salt(Fig. 7). XRD pattern of cathode section is shown in Fig. 8, which showing that the main product are TiO_2, Ti_2O_3, TiO, $TiFe_2$ With the processing of electrolysis, the reaction region moves toward the center of sample and the mass of intermediate products decrease as well until disappear. With increasing of electrolytic time, mass of TiFe product increases continuously. It can be found from Fig. 8 that X-ray diffraction peak of TiFe phase strengthens increasingly. However, the unreacted $FeTiO_3$ phase does not exist in the sample center at different reaction times. Therefore, there is strong X-ray diffraction peak of $FeTiO_3$ phase in the result of XRD analysis. $CaTiO_3$ phase does not exist in the phase because the compact cathode structure restrict the diffusion of Ca^{2+} inward the cathode in $CaCl_2$ molten salt. The intermediate product $CaTiO_3$ does not formed during electrolytic reduction inside the cathode, which resulting in difference of intermediate products inside the cathode and its surface as the reactions described in formula (2) and (3) do not happened and the chemical reaction described in (9) happens:

$$2TiO_2 + 2e = Ti_2O_3 + O^{2-} \tag{9}$$

E9=-1.39893

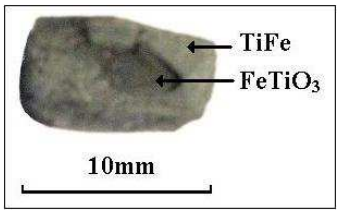


Fig. 7 Center section Fig. of sample after 20-hour electrolysis

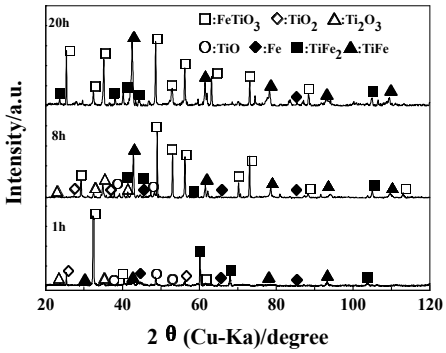


Fig. 8 XRD of cathode section of sample after 1-hour, 8-hour and 20-hour electrolysis

D. Mechanism analysis of process of electrolysis and deoxidization and alloying of titanium concentrate

Due to the complicated compositions of titanium concentrate, the deoxidization is a complex reaction process which not only refers to electrochemical reduction process and chemical reaction but also involves diffusion course of oxygen ion in solid phase and the diffusion and migration of oxygen ion in fused salt. The electrolysis reaction starts from cathode surface. $CaTiO_3$ was formed from Fe, O^{2-} , TiO_2 and CaO. $CaCl_2$ has strong hydroscopicity and the CaO contained in molten salt is mainly due to the hydrolysate of $CaCl_2$. With proceeding of electrolytic reaction, $CaTiO_3$ is electrolyzed to generate the suboxides of Ti, which are Ti_2O_3 and TiO. TiO is further electrolyzed and reduced and to generate TiFe and $TiFe_2$ alloy with Fe through alloying process. O^{2-} moves toward the anode through

molten salt and emits oxygen in anode. The compact cathode structure stops the diffusion of $CaCl_2$ toward inside. Due to the electrode reaction inside the cathode turns into the gradual reduction and alloying of $FeTiO_3$, so the intermediate product $CaTiO_3$ does not exist. According to the thermodynamics calculation, due to the deposition potential of Fe is lower than that of Ti, it will deposit firstly and the results of XRD analysis prove that Fe deposits at the beginning and Ti is reduced gradually, therefore reduction amount of Fe at reaction site will be higher than that of Ti. it can be seen from Fe-Ti phase diag that it is easy to form $TiFe_2$ alloy when the content of Fe is high. Formation of $TiFe_2$ alloy under high temperature is a spontaneous process, so it is easier to perform reduction of suboxide of Ti on Fe atom to form alloy than to form metal Ti. With proceeding of the reaction, Ti will be reduced continually and form TiFe alloy with $TiFe_2$ generated at earlier stage through interdiffusion. The structure of $FeTiO_3$ determines that the atomic ratio of Ti and Fe is 1:1 at micro level which will reduce the difficulty of interdiffusion greatly and avail formation of TiFe. As TiFe alloy generates through interdiffusion of $TiFe_2$ and Ti, the main product will be TiFe after complete electrolytic reduction of titanium concentrate and a small amount of elemental Ti and TiFe2 also exist.

The speed of preparation of TiFe alloy through electrolysis of titanium concentrate is generally decided by the following aspects: ① speed of migration of oxygen from reaction site to the cathode surface through product layer; ② speed of migration of oxygen ion from cathode outer layer surface to anode through electrolyte; ③ speed of electrolytic reduction on cathode; ④ reaction speed of Ti, Fe to form alloy. At the beginning of reaction, the cathode is a non-conductor, seriously impacting movement of electrons in cathode. The reaction will be hard to proceed without participance of electrons and electrolytic reaction is controlled by step ③. With proceeding of reaction, the thickness of product layer increases continually to improve the speed of electrolytic reduction. But the increasing of product layer thickness will increase the difficulty of oxygen migration at product layer. The homogeneity of Ti atom and Fe atom will cause high speed of diffusion and alloying process and the electrolytic reaction is controlled by step ① in fact.

$$FeTiO_3 \rightarrow \begin{matrix} Fe \\ + \\ TiO_{x(x=0\sim2)} \end{matrix} \rightarrow \begin{matrix} TiFe_2 \\ + \\ TiO_{x(x=0\sim2)} \end{matrix} \rightarrow TiFe$$

Fig. 9 Schematic diagram of electrolytic reduction of iron ore concentrate Conclusions

Conclusions

1) Ti-Fe alloy can be prepared by electroanalysis using titanium concentrate as the cathode at 3.1V in CaCl2 molten salt when the electrolytic time above 850℃. the direct electrolytic products are TiFe2 and Ti.

2) The formation of TiFe alloy by Ti and TiFe2 is a non-spontaneous process in thermodynamics. TiFe alloy is produced by the mutual diffusion between TiFe2 and Ti.

3) The increasing of temperature promotes the mutual diffusion process of TiFe2 and Ti and is favorable for the formation of TiFe alloy.

References

[1] L. Yan, et al. Research Progress in the Preparation Techniques of TiFe System Hydrogen Storage Alloy [J]. Materials Review, 2008, 22(11):111-114

[2] G. Chen, D. Fray, T. Farthing. Direct electrochemical reduction of titanium dioxide to titanium molten Calcium Chloride [J]. Nature, 2000 ,407 : 361~364

[3] Ryosuke O.. Suzuki. Calciothermic reduction of TiO2 and in situ electrolysis of CaO in the molten $CaCl_2$ [J]. Journal of Physics and Chemistry of Solids, 2005, 66: 461-465.

[4] B. Glowacki, D. Fray, X. Yan, et al. Superconducting Nb3Sn intermetallics made by electrochemical reduction of Nb2O5-SnO2 oxides[J]. Physical C, Superconductivity. 2003, 387(1-2):242

[5] K. Dring, R. Bhagat, M. Jackson, et al. Direct electrochemical production of Ti-10W alloys from mixed oxide pre-form precursors [J]. Alloys. Compd., 2006, 419: 103

[6] X. Yan, D. Fray. Electrochemical studies on reduction of solid Nb2O5 in molten CaCl2-NaCl eutectic [J]. Electrochem. Soc. 2005, 152 (1) : D12~D21

[7] G. Qiu, D. Wang, X. Jin, et al. Preparation of Tb2Fe17 by direct electrochemical reduction of Tb4O7-Fe2O3 pellet in molten calcium chloride [J]. Acta Metallurgica Sinica, 2008,44(7):859-862.

[8] B. Zhao, L. Wang, L. Dai, et al. Research of preparation of Cr by electrode oxidation in molten salt[J]. Powder Metallurgy Industry, 2008, 18(2):23-27.

[9] X. Liao, H. Xie, Y. Zhai, et al. Preparation of Ni-Ti alloy by direct electrochemical deoxidation in low temperature molten salt[J]. Light Metal, 2009(2):53-57.

[10] Z. Chen, M. Zhang, W. Han, et.al. Electrodeposition of Zr and electrochemical formation of Mg–Zr alloys from the eutectic LiCl–KCl. Journal of Alloys and Compounds. 2007.

[11] D. Hyslop, A. Abdelkader, A. Cox, et al. Electrochemical synthesis of a biomedically important Co–Cr alloy[J]. Acta Materialia, 2010, 58(8):3124-3130.

[12] Ryosuke O. Suzuki, Kai Tatemoto, Hitoshi Kitagawa.Direct synthesis of the hydrogen storage V–Ti alloy powder from the oxides by calcium co-reduction[J]. Journal of Alloys and Compounds 385 (2004) 173–180..

[13] J. Du, Z. Xi, Q. Li, et al. Preparation of TiFe Alloy by Electro-Deoxidization in Molten Salt[J]. Rare Metal Materials and Engineering. 2008, 37(12):2240~2243.

[14] Serdar Tan, et al. Synthesis of FeTi from mixed oxide precursors[J]. Alloys and Compounds (2008): 1–5.

[15] Pritish Kar, James W. Evans. A model for the electrochemical reduction of metal oxides in molten salt electrolytes [J]. Electrochimica Acta 54 (2008):835–843.

Advanced Materials Research Vol. 936 (2014) pp 1201-1208
© (2014) Trans Tech Publications, Switzerland
doi:10.4028/www.scientific.net/AMR.936.1201

Study on Atomic Mobility and Molar Volume for FCC Fe-Co Phase

Xiumian Gong[a], Xiao-Gang Lu[b], YanLin He[c]

School of Materials Science and Engineering, Shanghai University, Shanghai, China.

[a]gxiumian@163.com, [b]xglu@shu.edu.cn, [c]ylhe@staff.shu.edu.cn

Keywords: atomic mobility; molar volume; Fe-Co alloy; fcc phase; EPMA; CALPHAD

Abstract: The diffusion-couple experiments have been performed at 1273 K and 1423 K in order to verify and bias the controversial interdiffusion data in the literature. In the meantime, the literature data on the lattice parameter have been assessed to obtain the molar volume of fcc Fe-Co phase, which was in turn fed into the Sauer-Freise equation to retrieve the interdiffusion coefficients from the EPMA (Electron Probe Micro-Analysis) measured diffusion profiles. The reliable experimental data on the diffusion coefficients for fcc Fe-Co phase have finally been used to assess the atomic mobility. A general agreement has been reached between the calculated and experimentally measured data.

Introduction

As well-known that the Fe-Co alloy is a kind of soft magnetic materials, and the Curie temperature and saturation magnetic flux density are the highest in all magnetic materials [1]. Moreover, Co-base alloys are found to offer great promise as candidates for the next-generation high-temperature materials [2].

In the study and design of these materials, diffusion analysis plays an important role in explaining the mechanisms of various reactions occurring in the condensed states. Various diffusion coefficients (i.e. self-, impurity-, intrinsic-, and inter-diffusion coefficients) are basic parameters when detailed analyses and simulations of complex diffusion-controlled transformations are performed. The quality of these simulations is largely dependents on the precision of both thermodynamic and diffusion data. The present work is a part of the efforts to systematically measure the diffusivities and establish an accurate diffusional mobility database.

The reason to choose the Fe-Co system in the present study is not only because of its technological importance, but also due to the controversial measurements of the diffusion coefficients for the fcc Fe-Co alloys in the literature. Accordingly, the aim of the present work is to verify the diffusion coefficient data by conducting diffusion couple experiments and the CALPHAD-type assessments.

Experimental Procedure

Diffusion Couple

Bulk Fe pieces (purity 99.999 wt.%) and Co plates (purity 99.99 wt.%) were used to fabricate the Fe-Co binary samples containing 58 at.% Co. It was prepared in an arc melting furnace under an argon atmosphere. The arc melting was repeated 5 times to attain a homogeneous composition. The

alloy ingots were hot-rolled into 6mm at 1373 K, and then the alloy ingots were solid-solution treated under vacuum in quartz tubes at 1273 K for 8 days followed by water-quenching. They were cut into bulk with approximate dimension of 7×7×6 mm^3. After grinding and polishing, two of them were bound together to form well-contacted diffusion couples. Then the couples were sealed in quartz tubes and placed in the furnace with specified temperature. Both diffusion couples made in this work and their diffusion conditions are listed in Table 1. After annealing, the couples were quenched in water to maintain the high-temperature microstructures and concentration. The diffusion couples were then cut parallel to the diffusion direction, grinded, and polished by standard metallographic techniques. The microstructure of diffusion zone was observed by scanning electron microscopy (SEM) and the local concentration was analyzed by electron probe microanalysis (EPMA, JXA-8530F, JEOL, Japan).

Table1. Diffusion couples and diffusion conditions involved in this work.

Phase	Diffusion-couple	Temperature (K)	Diffusion time
FCC	Pure Fe/pure Co	1423	23 hours
	Pure Fe/Fe-58 at.% Co	1273	7 days

Interdiffusion Coefficient

The interdiffusion coefficient $\tilde{D}$ was determined by using the Sauer-Freise method [3], i.e.

$$\tilde{D}\left(Y^*\right)=\frac{1}{2t\dfrac{d\left(Y/V_m\right)^*}{dz}}\left[\left(1-Y^*\right)\int_{-\infty}^{z^*}\frac{Y}{V_m}dz+Y^*\int_{z^*}^{\infty}\frac{\left(1-Y\right)}{V_m}dz\right] \tag{1}$$

where the normalized composition variable is $Y=\left(x_{Co}-x_{Co}^{-}\right)\Big/\left(x_{Co}^{+}-x_{Co}\right)$, x_{Co}^{-} and x_{Co}^{+} are the Co compositions of the left and right ends of the diffusion couple, z^* is the location of interest with the normalized composition Y^*, V_m is the molar volume of the alloys and t is the time for the diffusion experiment.

Modeling

Molar Volume

From Eq.1, it is evident that the molar volume of fcc Fe-Co phase is an important parameter. Usually the relation of the volume and composition is assumed to be linear, i.e. Vegard law. However, this is not the case for fcc Fe-Co alloys.

For a solid solution Fe_xCo_{1-x}, the molar volume V_m can be expressed as:

$$\begin{aligned} V_{\mathrm{m}} &= xV_{Fe}+\left(1-x\right)V_{Co}+V_m^E \\ &= xV_{Fe}+\left(1-x\right)V_{Co}+x\left(1-x\right)L \end{aligned} \tag{2}$$

where V_{Fe} and V_{Co} are the molar volume of pure Fe and pure Co. Their values have been assessed by Lu et al. [4] as a function of temperature. x is the mole fraction of Fe. V_m^E is the excess molar volume and the related L is regarded as the interaction parameter for the volume, and can be evaluated by fitting the experimental values of the lattice parameter. In the present work, L is assumed as a constant so the temperature variation of V_m is accounted for by the temperature dependences of V_{Fe} and V_{Co}.

Most experimental data related to volume are lattice parameters. For cubic crystals, the molar volume V_m can be computed from the lattice parameter by $V_m = N_A \frac{a^3}{\eta}$, where N_A is the Avogadro number, a is the lattice parameter, η equals to 4 for fcc phase.

Atomic Mobility and Diffusion Coefficient

According to Anderson and Ågren [5] and Jönsson [6], the atomic mobility of species B, i.e. M_B can be expressed as follows:

$$M_B = M_B^0 \exp\left(\frac{-Q_B}{RT}\right)\frac{1}{RT}{}^{mg}\Gamma = \exp\left(\frac{RT\ln M_B^0}{RT}\right)\exp\left(\frac{-Q_B}{RT}\right)\frac{1}{RT}{}^{mg}\Gamma \tag{3}$$

where M_B^0 is a frequency factor and Q_B is the activation energy. R is the gas constant, and ${}^{mg}\Gamma$ is a factor taken into consideration the ferromagnetic contribution to the diffusion coefficient. For non-bcc phases, the effect of ferromagnetic on diffusion can be ignored [7].

Following the phenomenological CALPHAD technique, a parameter Φ_B is composition dependent [6] and expressed by a Redlich-Kister polynomial,

$$\Phi_B = \sum_i x_i \Phi_B^i + \sum_i \sum_{j>i} x_i x_j \left[\sum_{r=0,1,2} {}^r\Phi_B^{i,j}\left(x_i - x_j\right)^r\right] \tag{4}$$

where Φ_B represents either the activation energy $-Q_B$ or the rescaled frequency factor $RT\ln M_B^0$, x_i and x_j are the mole fraction of species i and j, Φ_B^i is the value Φ_B of species B in pure species i, and ${}^r\Phi_B^{i,j}$ is the binary interaction parameters.

Assuming the mono-vacancy mechanism for diffusion and neglecting correlation factors [5], the tracer diffusivity D_B^* is related to the mobility M_B by the Einstein relation:

$$D_B^* = RTM_B \tag{5}$$

For a system of n members, the interdiffusion coefficient $\tilde{D}_{kj}^{n}$ can be expressed as:

$$\tilde{D}_{kj}^{n} = \sum_{i=1}^{n-1} (\delta_{ki} - x_k) x_i M_i \left(\frac{\partial \mu_i}{\partial x_j} - \frac{\partial \mu_i}{\partial x_n} \right) \quad (6)$$

where μ_i is the chemical potential of species i, the kronecker delta $\delta_{ki} = 1$ when $i = k$, and otherwise equal to 0.

The mobility parameters Φ_B^i and ${}^r\Phi_B^{i,j}$ can be evaluated by fitting the experimental values of the diffusion coefficients. When M_B is obtained, all diffusion coefficients can be calculated by, for example, Eq.5 and 6.

Optimization and Discussion

All the assessments of atomic mobility and molar volume were performed by using the PARROT module [8] in the thermodynamic-kinetic software package Thermo-Calc/DICTRA [9]. This module allows simultaneous numeric fittings of atomic mobility from experimentally determined diffusion coefficients.

Optimization of Molar Volume

The molar volume for pure fcc Fe and fcc Co were taken from the work by Lu et al [4]. In this work, the available lattice parameters from Ohnuma et al. [10] and Ellis and Greiner [11] were used to access the L parameter in Eq.2, which is 0.57 cm^3/mol. The variation of molar volume with the temperature is accounted for by the temperature dependent of pure Fe and Co. The Calculated V_m of fcc Fe-Co alloys are in fair agreement with the available experimental data, as shown in Fig. 1. The values of molar volume at 1423 K and 1273 K were used in retrieving the interdiffusion coefficients described from Eq.1.

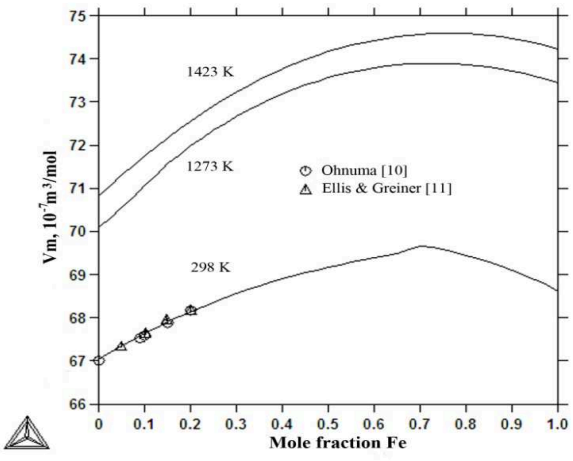


Fig. 1 The calculated V_m of fcc Fe-Co alloys compared with experimental data [10,11] at 298 K, 1273 K and 1423 K.

Optimization of Atomic Mobility

Cui et al. [12] have evaluated the atomic mobility for fcc phase of the Fe-Co system, and the thermodynamic data assessed by Guillermet [13] have been adopted. Recently the thermodynamic property of the Fe-Co system has been carefully reassessed by Ohnuma et al [10]. Therefore it is necessary to reassess the mobilities of the system.

The atomic mobilities for the self-diffusion of fcc Fe and fcc Co have been assessed by Jönsson [6] and Cui et al. [12], respectively. They were adopted in the present work. The impurity diffusion of Co was taken from the work by Badia and Vignes [14]. The assessments of other mobility parameters were carried out based on the measured diffusivities including impurity diffusivity and interdiffusion diffusivity. The results of the assessed mobilities are listed in Table 2.

In the section of follow, the results of the present assessment are discussed compared with experimental information.

TABLE 2. ASSESSED ATOMIC MOBILITIES FOR THE FCC PHASE OF FE-CO SYSTEM.

Mobility	Parameter (J/mol)	reference
Mobility of Fe		
Φ_{Fe}^{Fe}	$-286000-79.55\cdot T$	[6]
Φ_{Fe}^{Co}	$-259074-91.76\cdot T$	Present work
$\Phi_{Fe}^{Fe,Co}$	$-61000+48.96\cdot T$	Present work
Mobility of Co		
Φ_{Co}^{Co}	$-301654-70.10\cdot T$	[12]
Φ_{Co}^{Fe}	$-301900-76.58\cdot T$	[14]
$\Phi_{Co}^{Fe,Co}$	$+370000-255.08\cdot T$	Present work

Fig. 2 shows the calculated impurity diffusivity coefficient of Fe in fcc Co as a function of inverse temperature, compared with the experimental data from Badia and Vignes [15]. Fig. 3 shows the calculated tracer diffusivities of Co and Fe in the fcc Fe-Co alloys compared with the experimental data [16-18].

There are two sets of experimental data about the interdiffusion coefficients of fcc phase of Fe-Co system in the lecture, i.e. data from Badia and Vignes [15] and Hirano et al [19]. Cui et al. [12] has noticed that the data from Hirano et al. [19] were inconsistent with self- or impurity diffusion data and thus resulted an over complex variation of interdiffusion coefficients with composition. Therefore they have only used the data from Badia and Vignes [15] and obtained the mobilities satisfactorily. The experimental results in the present work confirm the bias of Cui et al. A comparison of the interdiffusion coefficients measured at about 1423 K by Badia and Vignes [15], Hirano et al. [19] and the present work is shown in Fig. 4. Data from Hirano et al. [19] are apparently too high and not used in the present assessment. As seen from Fig. 5, the calculated interdiffusion coefficients compare favorably with the selected experimental data.

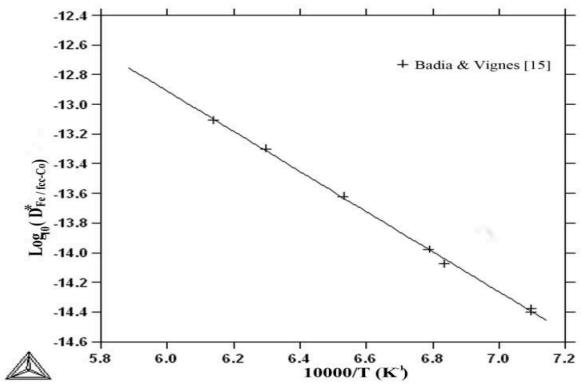


Fig. 2 Arrhenius plot of impurity diffusion coefficients of Fe in fcc Co in comparison with the experiment data [15].

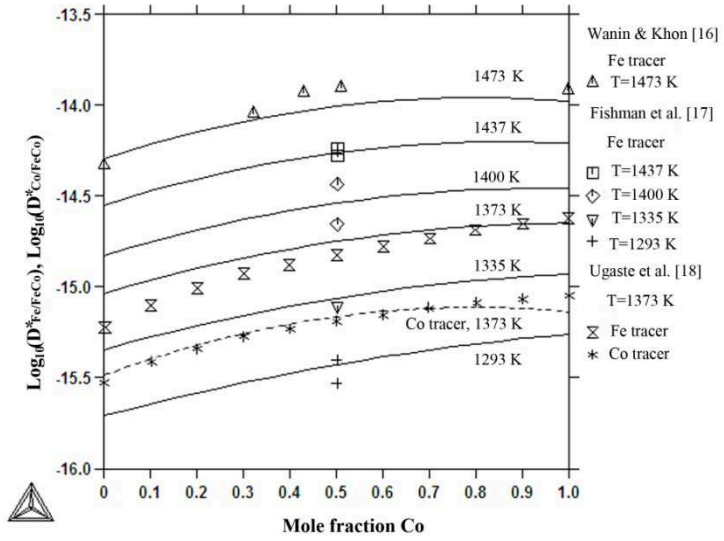


Fig. 3 Calculated tracer diffusivities of Fe (solid line) and Co (dashed line) for the fcc Fe-Co alloys compared with the experimental data [16-18].

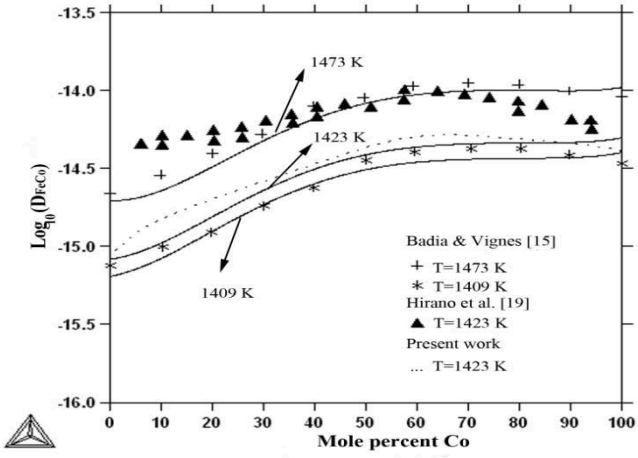


Fig. 4 Calculated interdiffusion coefficients compared with the data from Badia and Vignes [15], Hirano et al. [19] and the present work.

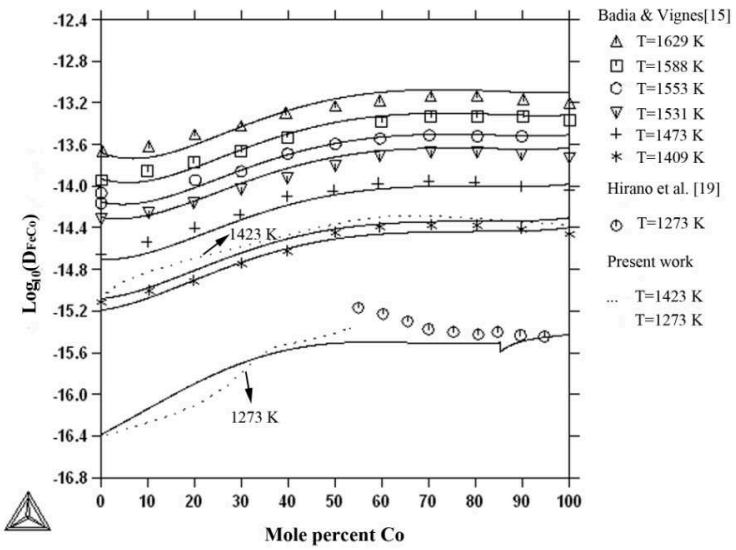


Fig. 5 Calculated interdiffusion coefficients for fcc Fe-Co phase at various experiment temperatures along with the experimental data from Badia and Vignes [15], Hirano et al. [19] and present work. Data from Hirano et al. [19] at high temperatures are proved to be doubtful and are thus not shown, while at 1273K and high Co compositions their data are acceptable.

Calculated Concentration Profile and EPMA Measurements

In order to verify the assessed atomic mobility, concentration profiles were simulated by the software package Thermo-Calc/DICTRA with the mobilities and diffusion-couple conditions as inputs. Fig. 6 shows the calculated concentration profiles compared with the present EPMA measurements. The agreement is fairly good.

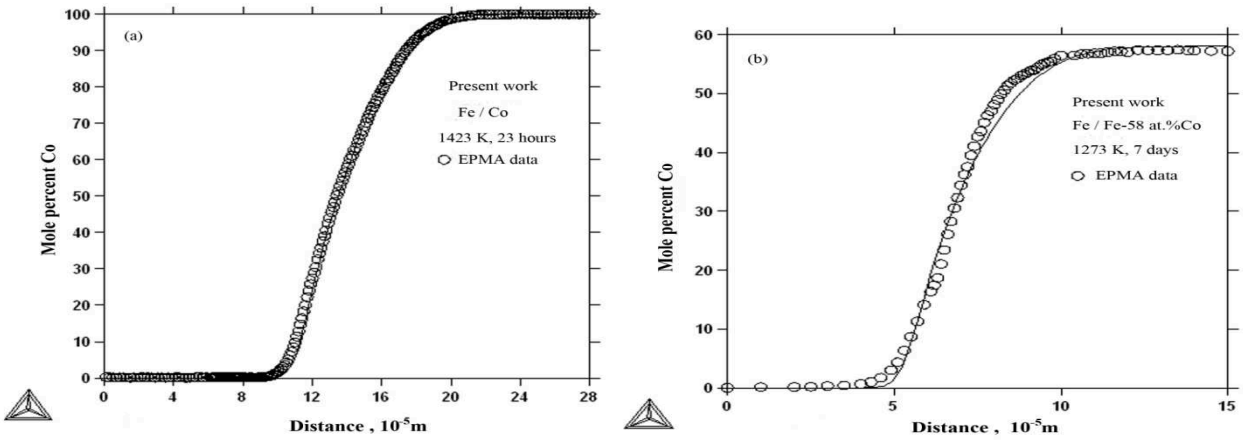


Fig. 6 Calculated concentration profiles of (a) the Fe/Co diffusion couple annealed at 1423 K for 23 hours (b) the Fe/Fe-58 at.% Co diffusion couple annealed at 1273 K for 7 days, compared with the present experimental data.

Summary

Experiments on the bulk Fe/Co and Fe/Fe-58 at.% Co diffusion couples at 1423 K and 1273 K have been performed, respectively. The experimental results have clarified the different interdiffusion data which are controversial in the literature. The molar volume has been assessed by using the available lattice parameter data. A general agreement has been reached between the

calculated and experimentally determined data. On the basis of the reliable data from the literature and the present work, a set of self-consistent atomic mobility of both Fe and Co for the fcc phase has been obtained. Its reliability has been varified by simulating the concentration profiles for the diffusion couples.

Acknowledgements

The financial support from the National Key Project of Science and Technology (Grant number: 2012ZX06004-012) is gratefully acknowledged.

Reference

[1] W.C. Liu, Study on the workability of Fe-Co alloy, Research on Iron & Steel 36 (2008) 34-36, in Chinese.

[2] J. Sato, T. Ohmori, I. Ohnuma, R. Kainuma, K. Ishida, Cobalt-base high-temperature alloys, Science 312 (2006) 90-91.

[3] F. Sauer, V. Freise, Diffusion in Binaren Gemischen Mit Volumenanderung, Z. Elektrochem. 66 (1962) 353-363.

[4] X.-G. Lu, M. Selleby, B. Sundman, Assessments of molar volume and thermal expansion for selected bcc, fcc and hcp metallic elements, CALPHAD 29 (2005) 68-89.

[5] J.O. Andersson, J. Agren, Models for numerical treatment of multicomponent diffusion in simple phases, J. Appl. Phys. 72(1992) 1350-1355.

[6] B. Jönsson, Ferromagnetic ordering and diffusion of carbon and nitrogen in bcc Cr-Fe-Ni alloys, Z. Metallkd. 85 (1994) 498-501.

[7] B. Jönsson, On ferromagnetic ordering and lattice diffusion-a simple model, Z. Metallkd. 83 (1992) 349-355.

[8] B. Jansson, TRITA-MAC 0234, Royal Institute of Technology, Stockholm, Sweden, 1984.

[9] J.-O. Andersson, T. Helander, L. Höglund, P. Shi, B. Sundman, Thermo-Calc & DICTRA, computational tools for materials science, CALPHAD 26 (2002) 273.

[10] I. Ohnuma, H. Enoki, O. Ikeda, R. Kainuma, H. Ohtani, B. Sundman, K. Ishida, Phase equilibria in the Fe-Co binary system, Acta Mater. 50 (2002) 379-393.

[11] W.C. Ellis, E.S. Greiner, Equilibrium relations in the solid state of the Iron-Cobalt system Trans. ASM. 29 (1941) 415-432.

[12] Y.W. Cui, M. Jiang, I. Ohnuma, K. Oikawa, R. Kainuma, K. Ishida, Computational study of atomic mobility for fcc phase of Co-Fe and Co-Ni binaries, J. Phase Equilib. Diff. 29 (2008) 2-10.

[13] A.F. Guillermet, Critical evaluation of the thermodynamic properties of the Fe-Co system, High Temp-High Press. 19 (1987) 477-499.

[14] [14] M. Badia, A. Vignes, Iron, Nickel and Cobalt Diffusion in transition metals of iron group, Acta Met. 17 (1969) 177-187, in French

[15] M. Badia, A. Vignes, Influence of structure changes produced by interdiffusion on interdiffusion coefficient and kirkendall effect, Rev. Met. 66 (1969) 915-927, in French.

[16] M. Wanin, A. Khon, Determination by tracer technics of iron and nickel diffusion coefficients in iron-nickel alloys and of iron and cobalt in Iron-Cobalt alloys, C.R. Acad. Sci. C. 267 (1968) 1558-1561, in French.

[17] S.G. Fishman, D. Gupta, D.S. Lieberman, Diffusivity and isotope-effect measurements in equiatomic Fe-Co, Phys. Rev. B. 2 (1970) 1451-1460.

[18] Y.E. Ugaste, A.A. Kodentsov, F. van Loo, Compositional dependence of diffusion coefficients in the Co-Ni, Fe-Ni, and Co-Fe systems, Phys. Met. Metallogr. 88 (1999) 598-604.

[19] K. Hirano, Y. Iijima, K. Araki, H. Homma, Interdiffusion in Iron-Cobalt alloys, Trans. ISIJ. 17 (1977) 194-203.

Advanced Materials Research Vol. 936 (2014) pp 1209-1215
© (2014) Trans Tech Publications, Switzerland
doi:10.4028/www.scientific.net/AMR.936.1209

Molar Volume of Fcc Phase in the Ni-Cr-Mo System

Jincai Li[a], Xiao-Gang Lu[b] and Yanlin He[c]

School of Materials Science and Engineering, Shanghai University, China

[a]ljc1513875@163.com, [b]xglu@shu.edu.cn, [c]ylhe@staff.shu.edu.cn

Keywords: molar volume; Ni-Cr-Mo; fcc phase; CALPHAD; first-principles calculations

Abstract: The molar volume of fcc phase in the Ni-Cr-Mo system has been evaluated by means of the CALPHAD approach based on experimental data from the literature. The molar volumes of the non-stable fcc Cr and Mo were determined by extrapolating volume data from several stable solid solutions combined with the first-principles calculation results. A set of parameters has been obtained and can give a reasonable description of most experimental data on molar volume.

Introduction

Ni-based alloys have remarkable high strength, high oxidation and corrosion resistance ability at high temperatures and have been used as ideal materials in many kinds of severe environments, such as jet engines, gas turbines, etc. The Ni-Cr-Mo ternary system has close relationship with many Ni-based alloys such as Alloy 22, Alloy 59 and C-4 and the thermodynamic data of this system have been studied by several investigators previous. The CALPHAD method is widely used to develop thermodynamic databases, while the volume data at atmospheric pressure are rarely obtained in a form of database for multicomponent systems. Volume, as a function of chemical composition, temperature and pressure, is a fundamental physical property and volume data has many practical applications. Volume databases can also be established by means of the CALPHAD approach.

In this work, the molar volume of fcc phase in the Ni-Cr-Mo system was assessed by means of the CALPHAD approach and the first-principles calculations. The required experimental data of lattice parameters were collected from the literature and converted to molar volumes.

Methodology

Volume Model for Solution Phases

Similar to the modeling of thermodynamics, the volume model can also be established by means of the CALPHAD method. In this work, we consider only the model and experimental data at the atmospheric pressure.

The molar volume of solution phases in A-B binary system can be expressed as:

$$V_m = (1-x)V_A + xV_B + x(1-x)L \tag{1}$$

where V_A and V_B are molar volumes of pure A and B, respectively. Their values for stable structures have been assessed by Lu et al. as a function of temperature and the elements related to this work are listed in Table 1 [1]. x is the mole fraction of B, and L is the binary interaction parameter which is usually a constant capable of describing most experimental data [2]. The ternary

interaction parameters can be added to fit experimental data when extending from binary to multi-component systems.

First-Principles Calculations (SQS-VASP)

At atmospheric pressure, both Cr and Mo are stable with bcc structure and non-stable in fcc structure. In the CALPHAD approach, the values of the molar volume for fcc Cr and Mo must be obtained in order to describe the volume for the fcc Ni-Cr-Mo phase. However, these values cannot be measured experimentally and it may not be feasible to use the first-principles calculated data for pure elements directly. So a conventional method is adopted by extrapolating linearly from the volume data of stable fcc solution phases to pure Cr or Mo. The problem is that the linear extrapolation may not be correct. To assist the extrapolation, the first-principles special quasirandom structure (SQS) calculations were performed for disordered fcc phases containing 50 at.% Cr or Mo.

We used a 16-atom SQS [3, 4] to represent the randomly disordered fcc structure. The advantage of the SQS approach is that it can adequately reproduce the statistics of a random alloy in a relatively small and thus computationally feasible supercell. For the generated SQS structures, first-principles calculations were performed using the plane wave method with projector augmented wave (PAW) pseudo-potentials [5], as implemented in the Vienna ab initio simulation package (VASP) [6]. We used the exchange-correlation functional within the generalized gradient approximation (GGA), as parameterized by Perdew, Burke, and Ernzerhof (PBE) [7]. The k-point meshes (10*8*6) for Brillouin zone sampling were constructed using the Monkhorst-Pack scheme.

The calculated volume data, together with the molar volumes of pure elements calculated by Wang et al. [8] (listed in Table 1) were assessed to obtain the L parameter in Eq.1. These data present a theoretical view of the relationship between volume and composition. If a linear relation holds, the extrapolation from the volume data of stable fcc solution phases to pure Cr or Mo is straightforward. Otherwise, the L parameter should be assessed by these theoretical data to fit the experimental data.

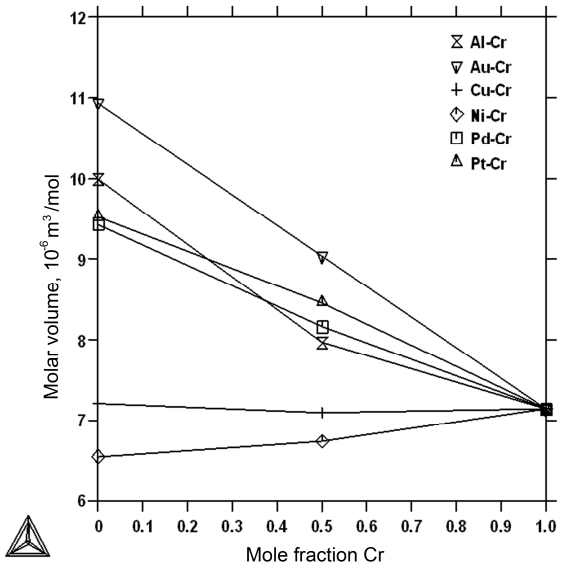
TABLE 1LATTICE PARAMETERS AND MOLAR VOLUMES OF PURE ELEMENTS IN THE FCC STRUCTURE.

Element	a (Å)		Vm (10^{-6} m^3 / mol) at T=298 K [1][a]
	First-principles calculations at T = 0 K [8]	Assessments at T = 298 K [1][a]	
Al	4.048	4.049	9.996
Au	4.173	4.078	10.214
Cu	3.631	3.615	7.112
Ir	3.880	3.839	8.519
Ni	3.517	3.524	6.590
Pd	3.972	3.891	8.866
Pt	3.985	3.924	9.098
Cr	3.619	3.680[b]	7.500[b]
Mo	4.014	3.981[b]	9.500[b]

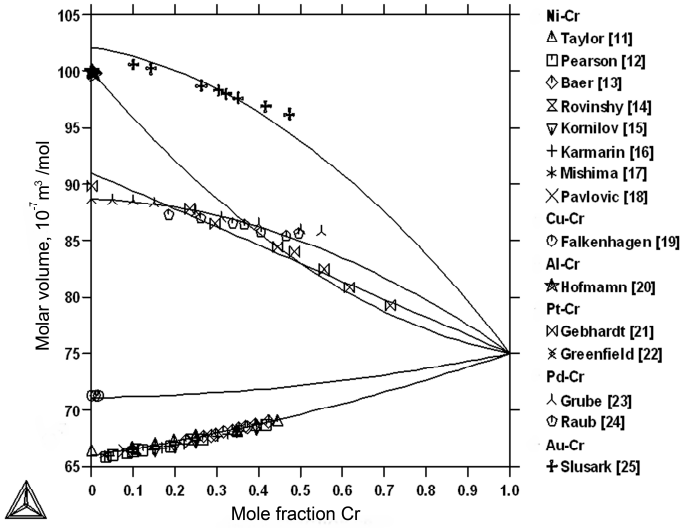
a: data used in this work; b: data assessed in this work

Results and Discussion

After collecting the experimental data extensively from the literature, and guided by the first-principles results, we used the PARROT module [9] in the Thermo-Calc software package [10] to assess the L parameters in Eq.1 as well as the molar volumes of fcc Cr and Mo. A set of model parameters which can represent most of the experimental data was obtained and listed in Table 2.



(a)



(b)

Fig. 1. Molar volume of the fcc X-Cr (X = Al, Au, Cu, Ni, Pd, Pt) phases. (a) First-principles calculated results. (b) Experimental data at 298.15 K.

Molar Volume of Fcc Cr

In the work, six binary systems related to fcc X-Cr phase were chosen, i.e. X = Al, Au, Cu, Ni, Pd and Pt. Their experimental data are shown in Fig. 1b. The fcc Pt-Cr solid solution shows linear behaviour up to about $x_{Cr} = 0.72$ and Ni-Cr up to about $x_{Cr} = 0.45$. The linear extrapolations lead to different values for fcc Cr. Considering the small theoretical value of L and the large composition extension of fcc Pt-Cr, the linear extrapolation is reasonable and the molar volume of fcc Cr is fixed to 7.5×10^{-6} m^3/mol. All parameters for other binary systems are assessed accordingly and listed in Table 2. It deserves mentioning that the theoretical L value for Au-Cr suggests a linear behavior which is consistent with the experimental data. However, due to the large deviation of volume for fcc Au between the first-principles calculations and experimental results, this linear relation for fcc Au-Cr is questionable.

TABLE 2 ASSESSED PARAMETERS (L IN EQ.1) FOR X-CR (X = AL, AU, CU, NI, PD, PT), X-MO(X = AU, IR, NI, PD, PT) BINARY SYSTEMS, AND THE NON-STABLE FCC CR-MO PHASE COMPARED WITH THOSE EVALUATED BASED ON THE FIRST-PRINCIPLES CALCULATION RESULTS.

System	L (10^{-6} m^3 / mol)	
	Based on the first-principles calculations	Based on the experimental data
Al-Cr	-2.40	-1.80
Au-Cr	-0.01[a]	2.10
Cu-Cr	-0.31	-0.35
Ni-Cr	-0.43	-0.32
Pd-Cr	-0.49[a]	1.25
Pt-Cr	0.53	0.00
Au-Mo	-1.27	-1.00
Ir-Mo	-0.62	-0.55
Ni-Mo	0.00	-0.65
Pd-Mo	-1.23	-0.85
Pt-Mo	-0.93	-0.80
Cr-Mo	0.30	-

a: The relatively large deviations are considered to be the deviation between the first-principles calculations and experimental results for fcc Au and Pd. These data were not considered in the assessments.

Molar Volume of Fcc Mo

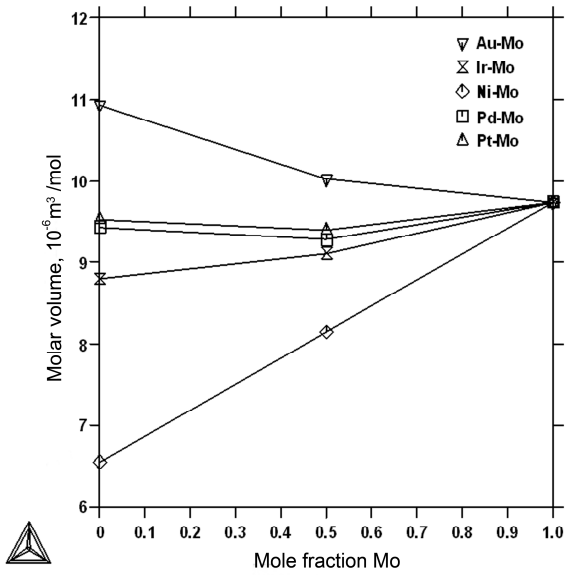
Five binary systems related to fcc X-Mo phase were chosen, i.e. X = Au, Ir, Ni, Pd, Pt. The experimental data are shown in Fig. 2b. For fcc Ni-Mo, the theoretical value of L is zero. The linear extrapolation Ni-Mo and Ir-Mo leads to 9.3×10^{-6} m^3/mol for fcc Mo. However, the experimental data of fcc Pt-Mo and Pd-Mo reveal non-linear behaviors and their distribution trends suggest the molar volume of fcc Mo should be larger than 9.3×10^{-6} m^3/mol. Considering the overall agreement between the theoretical data in Table 2 and the experimental data a value of 9.5×10^{-6} m^3/mol was finally fixed for fcc Mo.

Molar Volume of Fcc Phase in Ni-Cr-Mo System

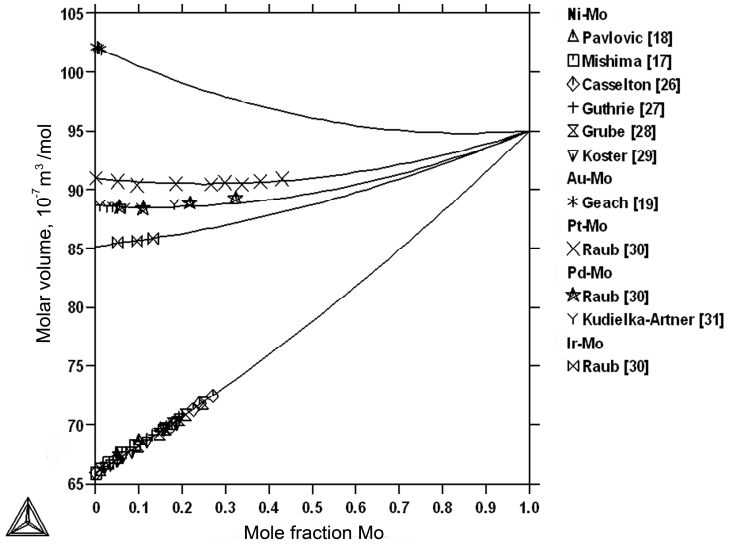
After fixing the value of molar volume for fcc Cr and Mo, the volume of non-stable fcc Cr-Mo was determined by using the theoretical value of L directly. Then the ternary interaction parameter of the fcc Ni-Cr-Mo phase was assessed to be -2.0×10^{-6} m^3/mol based on the experimental data. The molar volume of the fcc phase in the Ni-Cr-Mo ternary system are shown in Fig. 3.

Summary

The values of molar volume for fcc Cr and fcc Mo have been determined and the molar volumes of several Cr or Mo relating fcc binary phases have been evaluated as well. The model parameters for molar volume of fcc phases in the Ni-Cr and Ni-Mo binary systems and Ni-Cr-Mo ternary system have been assessed and the obtained parameters can best describe the collected experimental data from the literature on molar volume. The first-principles calculations play an important role in the assessments.

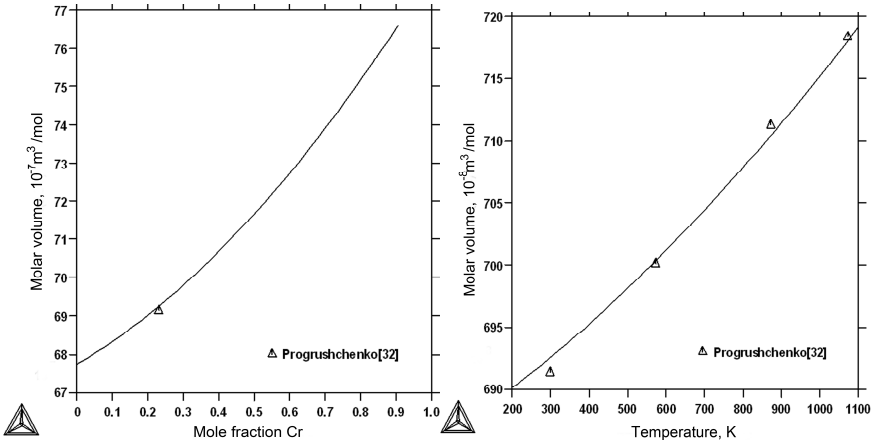


(a)



(b)

Fig. 2. Molar volume of the fcc X-Mo (X = Au, Ir, Ni, Pd, Pt) phases. (a) First-principles calculated results. (b) Experimental data at 298.15 K.



(a) (b)

Fig. 3. Calculated molar volume of the fcc Ni-Cr-Mo phase compared with the experimental data for an alloy with $x_{Mo} = 0.08$ and $x_{Cr} = 0.23$. (a) Variation of volume with the mole fraction of Cr; (b) Variation of volume with the temperature.

Acknowledgements

The financial support from the National Key Project of Science and Technology (Grant number: 2012ZX06004-012) is gratefully acknowledged.

Reference

[1] X.G. Lu, M. Selleby, B. Sundman, Assessments of molar volume and thermal expansion for selected bcc, fcc and hcp metallic elements, CALPHAD 29 (2005) 68-89.

[2] Y.L. He, X.G. Lu, N.Q. Zhu, B. Sundman, CALPHAD Modeling of Molar Volume, Chin. Sci. Bull. 58 (2013) 3642-3646.

[3] C. Wolverton, Crystal structure and stability of complex precipitate phases in Al-Cu-Mg-(Si) and Al-Zn-Mg alloys, Acta Mater. 49 (2001) 3129-3142.

[4] C. Jiang, First-principles study of ternary bcc alloys using special quasi-random structures, Acta Mater. 57 (2009) 4716-4726.

[5] G. Kresse, D. Joubert, From ultrasoft pseudopotentials to the projector augmented-wave method, Phys. Rev. B 59 (1999) 1758-1775.

[6] G. Kresse, J. Furthmüller, Efficient iterative schemes for ab initio total-energy calculations using a plane-wave basis set, Phys. Rev. B 54 (1996) 11169-11186.

[7] J.P. Perdew, K. Burke, M. Ernzerhof, Generalized gradient approximation made simple, Phys. Rev. Lett. 77 (1996) 3865-3368.

[8] Y. Wang, S. Curtarolo, C. Jiang, R. Arroyave, T. Wang, G. Ceder, L.-Q. Chen, Z.-K. Liu, Ab initio lattice stability in comparison with CALPHAD lattice stability, CALPHAD 28 (2004) 79-90.

[9] B. Jansson, TRITA-MAC 0234, Royal Institute of Technology, Stockholm, Sweden.(1984)

[10] J.-O. Andersson, T. Helander, L. Höglund, P. Shi, B. Sundman, Thermo-Calc and DICTRA, computational tools for materials science, CALPHAD 26 (2002) 273-312.

[11] A. Taylor, R.W. Floyd, The constitution of nickel-rich alloys of the Ni-Cr-Ti system, Inst. Met. 80 (1952) 577-587.

[12] W.B. Pearson, L.T. Thompson, The lattice spacings of nickel solid solutions, Can. J. Phys. 35 (1957) 349-357.

[13] H. G. Baer, Superstruture and K-state in the Cr-Ni system, Z. Metallkd. 49 (1958) 614-622.

[14] B.M. Rovinsky, A.I. Samoilov, G.M. Rovensky, Distortions in the crystal lattice in nickel-base alloys at temperatures of 25-500 Celsius, Fiz. Met. Metallogr. 7 (1959) 73-83.

[15] I.I. Kornilov, A.Y. Snetkov, The lattice constants of limited solid solutions of some elements in nickel, Issled. Zharoproch. Splavam, Akad. Nauk SSSR, Inst., Met. Im. A.A Baikova 7 (1961) 106-111.

[16] L. Karmazin, M. Svoboda, New lattice parameter measurement of the homogeneous Ni-Cr solid solution, Kovove Mater. 17 (1979) 355-362.

[17] Y. Mishima, S. Ochiai, T. Suzuki, Lattice parameters of Ni(γ), Ni3Al (γ') and Ni3Ga (γ') solid solutions with additions of transition and B-subgroup elements, Acta Metall. 33 (1985) 1161-1169.

[18] A.S. Pavlovic, V.S. Babu, High-temperature thermal expansion of binary alloys of Ni with Cr, Mo and Re: a comparison with molecular dynamics simulations, J. Phys. 8 (1996) 3139-3149.

[19] W.B. Pearson, A hand book of lattice spacings and structures of metals and alloys, fourth ed., Pergamon, London, 1979.

[20] W. Hofmann, H. Wiehr, Kristallographische und röntgenographische Studien an Aluminium-Chrom-Legierungen, Z. Metallkde. 33 (1941) 369-372.

[21] E. Gebhardt, W. Köster, Contribution to the system platinum-chromium, Z. Metallkd. 32 (1940) 262-264.

[22] P. Greenfield, P.A. Beck, Intermediate phases in binary systems of certain transition elements, Trans. AIME. 206 (1956) 265-276.

[23] G. Grube, R. Knabe, Electrical conductivity and phase diagram of binary alloys. 21: The system palladium-chromium. Z. Elektrochem. 42 (1936) 793-804.

[24] E. Raub, W. Mahler, Die palladium-chrom legierungen, Z. Metallkd. 45 (1954) 567-568.

[25] W. Slusark, B. Lalevic, N. Fuschillo, Structure and electrical conductivity of cosputtered gold-chromium alloy films, J. Aappl. Phys. 44 (1973) 2891-2892.

[26] R.E.W. Casselton, W. Hume-Rothery, The equilibrium diagram of the system Mo-Ni, J. Less-Common Met. 7 (1964) 212-221.

[27] P.W. Guthrie, E.E. Stansbury: Report No. ORNL-3078, Oak Ridge National Laboratory, Oak Ridge, TN, 1961.

[28] G. Grube, H. Schlecht, Elektrische Leitfähigkeit und Zustandsdiagramm bei binären Legierungen. 23. Mitteilung. Das System Nickel-Molybdän, Z. Elektrochem. 44 (1938) 413-422.

[29] W. Koster, W. Schmidt. Correlation Between Lattice Parameter and Ferromagnetism. Arch. Eiscnhuttenwe. 8 (1934) 25-27.

[30] E. Raub, Die Legierungen der Platinmetalle mit Molybdaen, Z. Metallkd. 45 (1954) 23-30.

[31] E. Kudielka-Artner, B.B. Argent, Magnetic and other Properties of some Binary Palladium Alloys, Proc. Phys. Soc. 80 (1962) 1143-1148.

[32] A.V. Progrushchenko, Yu. M. Lebedev, X-ray study of heat expansion of nickel-chromium alloys, Ukrains'kii Fizichnii Zhurna 14 (1969) 282-286.

Advanced Materials Research Vol. 936 (2014) pp 1216-1223
© (2014) Trans Tech Publications, Switzerland
doi:10.4028/www.scientific.net/AMR.936.1216

EFFECT OF AGING TREATMENT ON PHASE TRANSFORMATION OF a PSEUDOELASTIC NiTi ALLOY

Palloma Viera Muterlle[1,a], Eduard Benavides Villamarin[1,b], Paulo Herrera[1,c] and Edson Paulo da Silva[1,d]

[1]Mechanical Engineering Department of University of Brasilia, Brasilia, DF, Brazil

[a] pmuterlle@gmail.com, [b]eduben9@gmail.com, [c] pauloherrera7@gmail.com,

[d] dasilvaunb@gmail.com

Keywords: NiTi, pseudoelasticity, R-phase, phase transformation, heat treatment, shape memory alloy

Abstract: The pseudoelasticity (PE) and shape memory effect (SME) are the two main behaviors presented by the shape memory alloys (SMA's) and are associated respectively to mechanical and thermally induced martensitic transformations. The aim of this work is to investigate the effects of heat treatment temperature on the microstructure properties and phase transformation temperatures of a NiTi alloy with 57 w.t. % Ni. The X-ray diffraction (XRD) was carried out to obtain the phases present. The phase transformation temperatures were measured by differential scanning calorimetry (DSC). The alloy chemical composition and hardness were obtained by X-ray fluorescence (XRF), hardness (HRC) and microhardness (HV) tests, respectively. The analysis were performed in the state as received and after aging treatment at different temperatures between 350 °C and 600°C. The samples as received contained a fully austenitic microstructure at room temperature and the DSC analysis showed the presence of a phase transformation in multiple steps (B19'-R -B2). After aging at 350 °C the R phase was observed at room temperature with the austenite. With the aging treatment at 600 °C the R phase was solubilized and the alloy phase transformation occurred in a single step, ie, direct transformation ~~of~~ from austenite to martensite and vice versa. The transformation temperatures Af, As, Ms and Mf changed with the aging treatment temperatures.

INTRODUCTION

The Shape Memory Alloys (SMA's) are a group of metallic materials that are able to recover their original shapes (or develop considerable restitution forces when you restrict their recovery) through a field of temperature and/or stress, due to martensitic phase transformations

The SMA has the unique property of pseudoelasticity and/or shape memory effect. Both properties are directly associated to the martensite - austenite phase transformation. There are many alloys that have these properties (CuZnAl, CuAlNi, AuCd, NiTiNb and others), but the NiTi alloy exhibits excellent mechanical properties that have been used and investigatedfor decades [1].

The R phase is considered as a martensitic transformation because happens with the same mechanisms of this transformation [4]. The R phase could occur by three different forms: at first, when a specific concentration of Ni equiatomic is substituted for Fe or Al, or, when the Ni-Ti alloy with more than 50,5 at-% of Ni is aged at determined temperatures, where the Ni_4Ti_3 precipitates are formed, and at last, after cold work and subsequently heat treatment due to the reoriented dislocations structure [5].

In the case of a NiTi alloy the type of heat treatment chosen can change the transformation temperatures and the thermal hysteresis [6]. Another important effect of this kind of treatment is the possibility of solubilization of the R phase present in most of the NiTi alloys. The R phase occurs due to the presence of Ti_3Ni_4 precipitate in Ni rich alloys and can increase the size of the thermal hysteresis and the alloy hardness [4,7].

The aim of the present work is to investigate the influence of aging treatment in NiTi alloy in the transformation temperatures and thermal hysteresis and their effect on microstructure properties.

The aging temperatures considered are 350°C, 450°C, 550°C and 600°C followed ~~with~~ by quenching in water.

EXPERIMENTAL PROCEDURES

~~For~~ In the present study the samples were obtained of a NiTi bar with a diameter of 8mm and a nominal composition ranging from 54.5% to 57% of Ni. In order to know the correct composition of the received alloy, x-ray fluorescence procedure was carried out using an EDX-720. The Table 1 shows the acronym for each sample.

To perform the heat treatments a Nabertherm GmbH LHT 04/17 oven was used. The samples were heat treated at 350°C, 450°C, 550°C and 600°C for 30 minutes using a 7°C/min heating rate, and then all samples were water quenched at room temperature.

TABLE 1 - SAMPLES ACRONYM

Samples	
Acronym	**Treatment**
AR	As Received
Ag350	Aged at 350°C
Ag450	Aged at 450°C
Ag550	Aged at 550°C
Ag600	Aged at 600°C

The samples were cut in smaller sizes using a Struers Secotom 15 precision cut-off. To prevent any undesirable transformation or deformation, all the cutting procedures were done using a coolant and performed at a low velocity of 0,005mm/min. To prepare the samples for the metallographic analysis, the procedures described in the ASTM E-384 were used, and the procedures on ASTM E3 were selected in order to prepare them for the micro hardness (HV0,5) tests. Every sample was flattened, grinded and polished according to its own normative process. The Rockwell C (HRC) hardness tests were performed on an Identec Zwickroell durometer.

In order to obtain the phase transformation temperatures, the differential scanning calorimetry (DSC) method was carried out. The heating and cooling rates were of 10°C/min, going from the initial temperature of -100°C to the final temperature of 100°C. Before cooling to -100°C the samples were heated up to 100°C to guarantee full transformations. To perform the differential scanning calorimetry a Netzsch 200 F3 Maia was used. To determine the phases present on the alloy an Ultima IV X-ray diffractometer was usued.

RESULTS

X-ray Fluorescence

The chemical composition of the as received material is presented in the Table 2.

TABLE 2–CHEMICAL COMPOSITION OF AS RECEIVED NITI ALLOY.

	Component Elements (w.t.%)
Element	**XFR**
Ni	57.446
Ti	42.235
Ca	0.159
Fe	0.1
Ac	0.059

As seen on the Tab. 2, the studied material is rich in Ni element, this element tends to stabilized the austenitic phase and to introduce a R phase in it microstructure [5].

Hardness (HRC) and Microhardness (HV0,5)

Hardnes (HRC) and microhardness (HV0,5) were performed in the samples as received and after heat treatment, the results are showed in Figure 1.

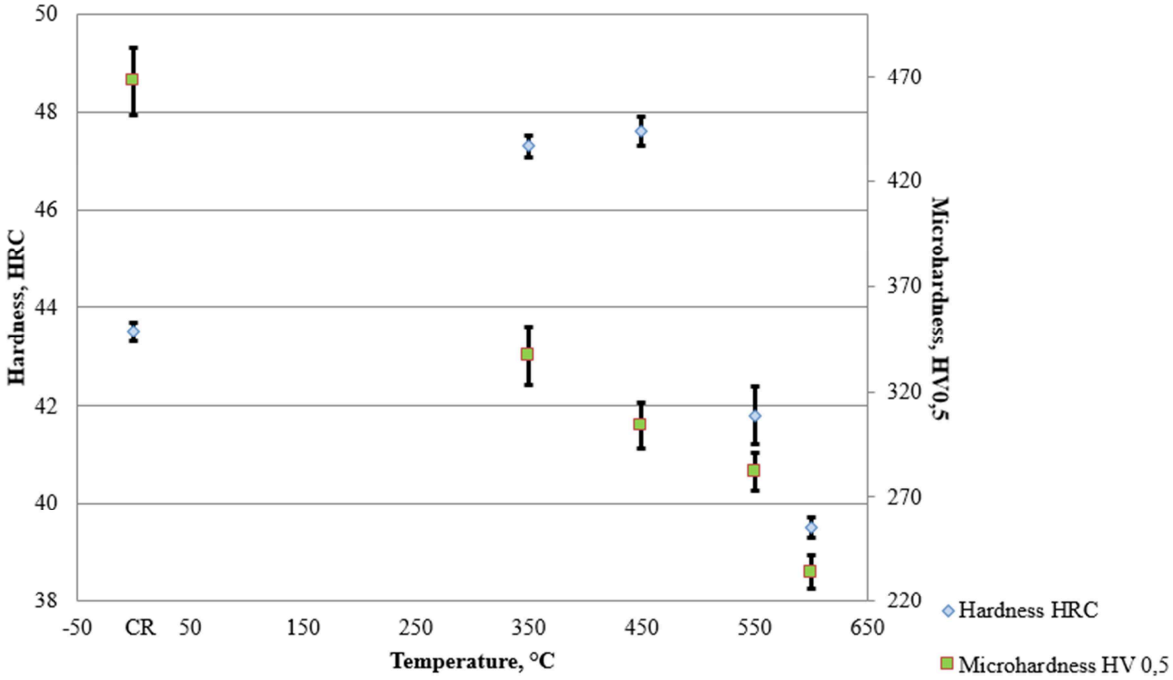


Figure 1: Hardness and microhardness results

The increased hardness found on the Ag350 and Ag450 is probably due to the increased amount of Ti_3Ni_4 precipitate and consequently the presence of R phase. The heat treatments at higher temperatures decrease the hardness, possibly due to the solubilization of precipitates and grain growth.

On the other hand, the microhardness values decreases with the increase of heat treatment temperature.

Themal analysis (DSC)

The Figure 2 shows the transformation temperatures of the sample as received. Upon heating there are two exothermic peaks between As (-41.2°C) and Af (-6.6°C). These peaks could be the transformation from the phase B19' (martensite) to phase R and from phase R to the final phase B2 (austenite). Upon cooling there are also two peaks, in this case endothermic peaks, the bigger one is the martensite start (-74.7°C) and martensite finish (-98°C) and the smaller peak is the R phase that starts at 11.5°C and ends at -60.2°C. So, looking at the temperature of phase transformations, Figure 2, is possible to say that the as received material is probably fully austenitic at room temperature.

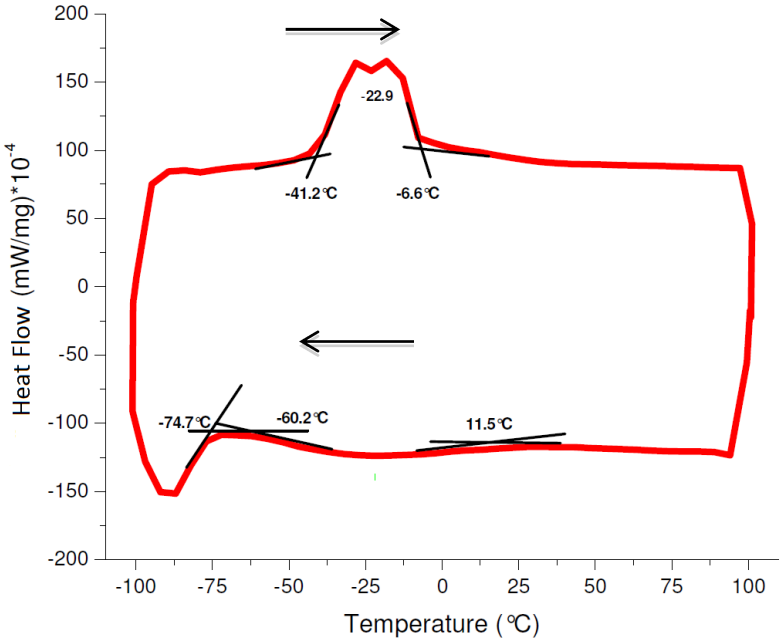


Figure 2 - Sample as received DSC

Figure 3 shows the transformation temperatures of the HT350 sample. In this case the total austenitic and martensitic transformations are again composed by two peaks. The austenite transformation goes from a martensitic phase to an R phase and later to an austenite phase, and the reverse transformation goes from an austenite phase to an R phase and later to a martensitic phase. Upon heating the R phase transformation starts at 5.6°C and ends at 49.53°C; upon cooling the transformation from austenite to the R phase starts at 42.35°C and ends at 23.75°C, and later the martensite transformation starts at -44.95°C and ends at -83.73°C. So, the HT350 sample presents an austenite and R phases at room temperature.

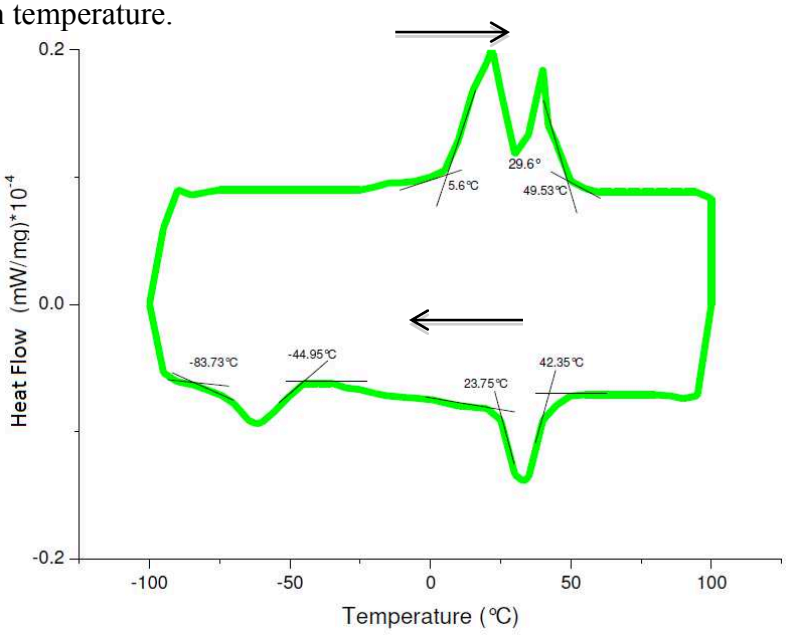


Figure 3 - HT350 sample DSC

Figure 4 shows the martensite to austenite transformation in a single stage for the HT600 sample. So, the R phase was probably solubilized during the heat treatment. From the DSC curve it is possible to find the As (-39.5°C) and Af (-0.9°C) temperatures and the martensite start (-35.4°C) and finish (-79.4°C) temperatures.

In aged Ni rich alloys the appearance of Ti_3Ni_4 precipitate [7] is expected. The R phase transformation appears due to the Ti_3Ni_4 precipitate formed in the B2 phase. Thus, one may state that the

HT350 samples had an increased amount of precipitate and the HT600 samples had most of this precipitate solubilized and the microstructure is fully austenitic at room temperature.

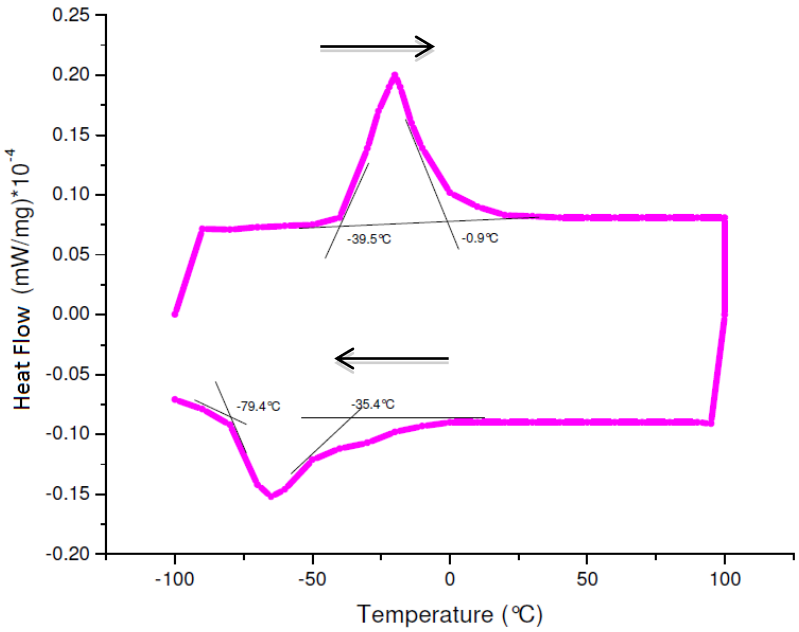


Figure 4 - HT600 sample DSC

To analyze the temperature range of transformation a thermal hysteresis was calculated for each sample, shown in Fig. 5. The thermal hysteresis is obtained calculating the difference between the medium point of the Af and As and the medium point of the Ms and Mf. The samples with 600°C heat treatment showed the lowest thermal hysteresis.

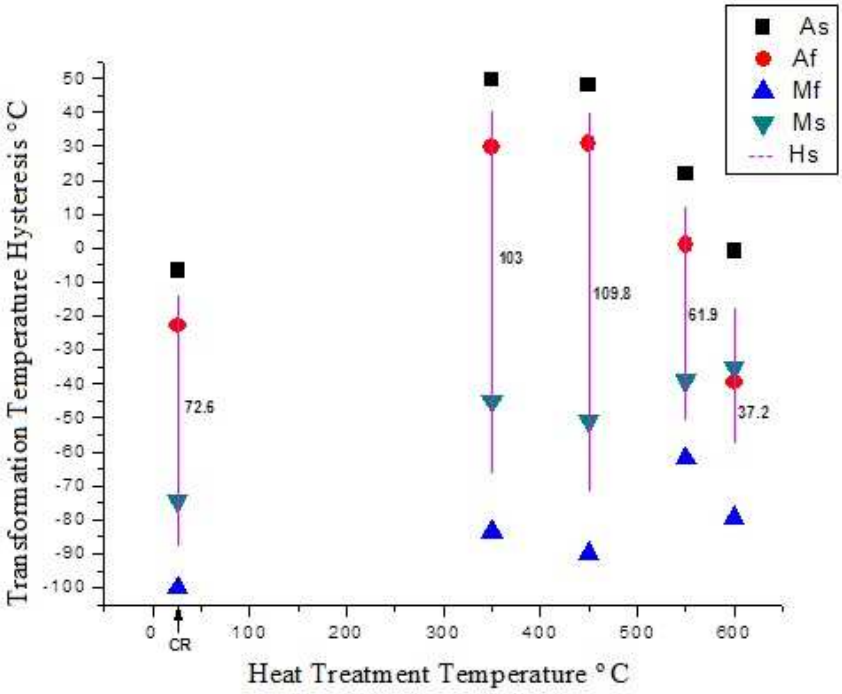


Figure 5 - Transformation temperatures hysteresis for tested samples

X- Microstructural analysis (XRD)

The microstructural analysis was based on a XRD measurement carried out to confirm the phases present at room temperature. The spectrums reported in Fig. 6 presented a high quantity of austenitic phase with B2 structure. It is confirmed by the more intensity diffraction picks that for the austenitic phase are around 42°, 60°, 92° and 108°. So, is possible to state the absence of martensitic phase induced for cut or sample preparation.

Comparing the results with both software Crystallographica Search Math and Crystallographic Data Bases of ICDD (The International Centre For Diffraction Data), the same picks are identified concluding that the main picks are the cubic system of B2 austenitic phase.

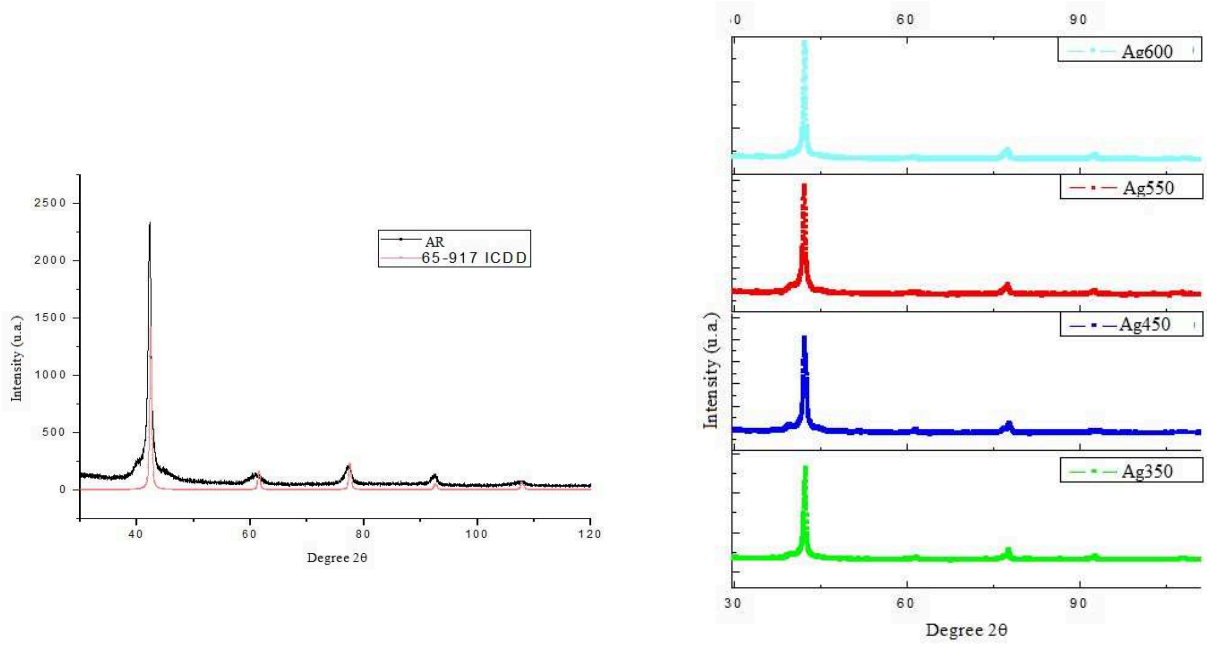


Figure 6 – XRD spectrum of the as received sample (a), and heat-treated samples (b).

Apparently, the XRD results showed in Fig. 6 do not present any variation due to heat treatment. However, if the main pick are zoomed (Fig. 7) one can observe the variations of the intensity as function of the heat treatments.

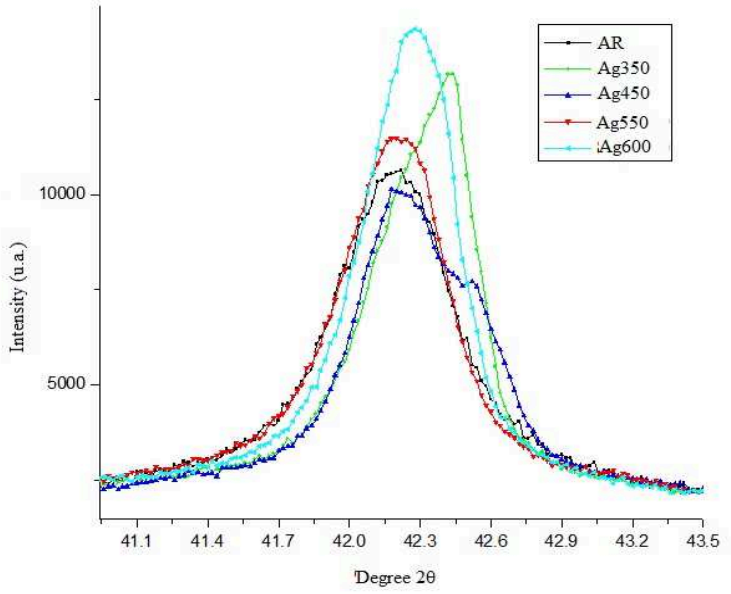


Figure 7 – Zoomed main diffraction pick for as received and heat-treated samples.

The trend of main diffraction picks indicates the presence of another phase that can be attributed to precipitates. According MAGELA (2010) the aging treatments induced the formation of R phase on NiTi alloys due to the heterogeneous composition in B2 matrix caused by the Ni_4Ti_3 precipitates. So, the R phase is a solution of precipitates in the matrix.

To identify the presence of other phase beyond the austenitic phase the deconvolution of the main pick (around 42 degree) are carried out for all samples and showed in Fig. 8. The deconvolution curves are obtained with the Fityk program using the Gaussian fitting.

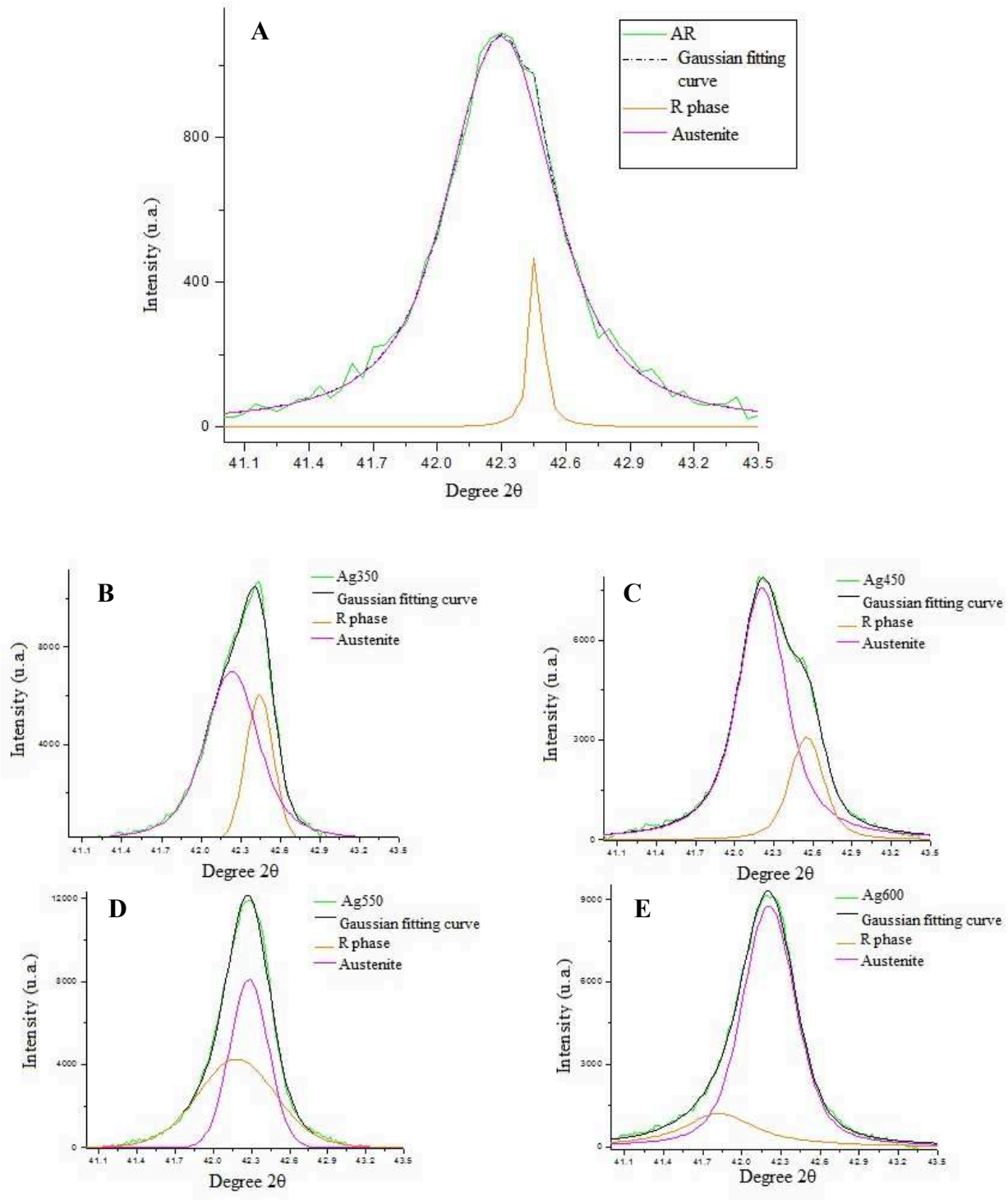


Figure 8 – Diffraction main pick deconvolution for: as received sample (a), Ag350 (b), Ag450 (c), Ag550 (d) and Ag600 (e).

The analysis of the pick deconvolution indicates the presence of R phase and its evolution with the heat treatment temperature. For the as received sample, Fig. 8a, it was observed a small amount of R phase with austenite B2 phase at room temperature. For the heat-treated samples, Fig. 8b to 8e, the R phase quantity changed with the heat treatment temperatures due to the variation of Ni_4Ti_3 precipitates. The pick intensity of this phase decreases with the increase of heat treatment temperature, at 350°C (Fig. 8b) the R phase is in more quantity that at 600°C (Fig. 8e) where this phase is almost totally solubilized.

CONCLUSIONS

From the analysis presented in this study it is possible to realize the influence of the aging at different temperatures on the microstructure of a NiTi shape memory alloys.

The DSC curves showed that different aging temperatures cause changing on phase transformation temperatures and different thermal hysteresis range. The heat treatment at 600°C didn't have an R phase and had a lower thermal hysteresis when compared to the samples as received and the samples treated at 300°C. The DSC also showed the difference found in the hardness tests, indicating that the R phase is present on the samples with more Ti_3Ni_4 precipitate. The deconvolution of XRD picks revealed the presence of R phase and austenite in all studied samples.

Comparing the results obtained by XRD and DSC analyzes it was possible to identify that both methods showed the phase presents in the matrix of the alloy. However, in the case of the as received and Ag600 conditions the DSC analyzes showed only the austenitic phase at room temperature, and the XRD analyzes identified a few quantity of R phase too.

ACKNOWLEDGEMENTS

The authors acknowledge CNPq and FINEP for the financial support, the laboratories of acoustic and vibrations (Mechanical Engineering Department) and the laboratory of Mechanical Properties (Metallurgy and Materials Department) of the Universidade Federal do Rio de Janeiro (UFRJ) for the technical support by the experimental analysis.

REFERENCES

[1] Otsuka, K. and Wayman, C.M., (1998). Shape memory materials, Cambridge University Press. Cambridge.

[2] Moringa, M., KATO, M., Kamimura, T., Fukumoto, M., Harada, I. and Kubu, K. Theoretical design of ß type titanium alloys, Titanium ’92, Science and Technology, The Minerals, Metals & Material Society, 1993.

[3] Gil, F.J. and Pl, J.A. Shape memory alloys for medical applications, Proc Instn Mech Engr Vol 212 Part H, 1998.

[4] Otsuka, K. and Ren, X., Physical Metallurgy of NiTi-based Shape Memory Alloys, Progress in Materials Science, 50 (2005)511.

[5] MATHEUS, T.C. Efeito do teor de carbono e da qualidade superficial na vida em fadiga de fios de Ni-Ti visando aplicações endodônticas. 139p -Tese de doutorado, Instituto Militar de Engenharia, Rio de Janeiro, 2008

[6] Magela , J.O.; Silva, M.I.N.; Ribeiro, G.M. and AndradeE, M.S. Electrical Resistivity and DSC measurements of phase transformation temperatures in Ni-Ti shape memory alloys. In: 11th International Conference on Advanced Materials, 2009, Rio de Janeiro. 11th ICAM, 2009.

[7] MAGELA, J.O. Influência de tratamentos térmicos e mecânicos nas temperaturas de transformação martensítica em ligas Ni-Ti com efeito memória de forma. 126p –Dissertação Mestrado, Universidade Federal de Ouro Preto, Ouro Preto, 2010.

[8] Santos, C.M.L, Ligas Ni-Ti ricas em Ni Tratamento térmico, Termomecânico e Efeito de micromemória de forma,2006,156p. Tese (Doutorado em Ciência dos Materiais) - Instituto Militar de Engenharia, Rio de Janeiro.

Advanced Materials Research Vol. 936 (2014) pp 1224-1228
© (2014) Trans Tech Publications, Switzerland
doi:10.4028/www.scientific.net/AMR.936.1224

Improvement of Paint Hardening Response of a Novel Al-Mg-Si Alloy for Automotive Panel by Adding Zn and Pre-Ageing Matching

Zhihui Li[1,a], Lizhen Yan[1,b], Yongan Zhang[1,c,] Xiwu Li[1], Feng Wang[1], Hongwei Li[1], Shuhui Huang[1], Baiqing Xiong[1]

[1]State Key Laboratory of Nonferrous Metals and Processes, General Research Institute for Nonferrous Metals, Beijing 100088, China

[a] lzh@grinm.com, [b] yanlizhenttnm@163.com, [c] zhangyongan@grinm.com

Keywords: Al-Mg-Si-Zn alloy, pre-ageing, paint baking response, automotive panels

Abstract: In the present work, the microstructure and properties of a novel Al-0.90Mg-0.78Si alloy with Zn addition were investigated by electron back scattering diffraction (EBSD), high transmission electron microscopy (HREM), mechanical properties and Erichsen tests. The average grain size of the alloy after pre-ageing was about 20 μm. The yield strength and elongation of pre-aged alloy was 137 MPa and 30% respectively. The I_E value of the alloy was 8.6 mm. After paint baking at 170 °C for 30 min, the increment of yield strength was about 100 MPa. GP(II) zones were formed in the alloy during paint baking process through adding Zn, which should play a very important role for improving paint hardening response. GP(II) zones and η´ phases were formed after artificial ageing at 170 °C for 10 h.

Introduction

The growing demand for more fuel-efficient vehicles to reduce energy consumption and air pollution is a challenge for the automotive industry, aluminum usage in automobiles will be increased significantly in the near future. The characteristics of 6000 (Al-Mg-Si) series aluminum alloys, high strength stiffness to weight ratio, good formability, good corrosion resistance, recycling, and age-hardenable make it the ideal candidate to replace steel sheet in the car to respond the weight reduction demand within automotive industry [1,2]. Currently, the widely used 6000 series aluminum alloy was AA6016, AA6111 and AA6022 alloy. The formability of AA6016 alloy was excellent, yield strength of AA6111 alloy was higher after baking hardening with high Cu content. Corrosion resistance and formability of AA6022 alloy was good, the 6022-T4E29 was developed by Alcoa, and applied for a patent in 2000 [3], which was used in Ford Crow Victoria, Crand Marquis and Taurus/Sable.

Although 6000 series aluminum alloy was widely used in automotive skin panels, the formability of the alloys still does not meet the requirements of actual stamping, and bake hardening response exhibits inadequately after paint baking. Such as AA6016 alloy, yield strength was less than 200 MPa after paint baking, the formability of AA6111 alloy was bad with high Cu content, meanwhile the corrosion resistance was poor. The overall performances of AA6022 alloy was better, compared with AA6016 and AA6111 alloy. However, yield strength of the alloy was about 220 MPa after paint baking, the dent resistance was insufficient. Consequently, the present work investigated a novel Al-Mg-Si alloy used in automotive skin panels with Zn addition. The alloy shows excellent mechanical properties after ageing.

Experimental

The alloy was prepared from high-purity aluminum, magnesium, copper, Al-10Mn, Mg-30Zr and Al-14Si master alloys. The chemical composition of the ingots was 0.90wt% Mg, 0.78wt% Si, 0.20wt% Cu, 0.60wt% Zn, 0.098wt% Mn, 0.12wt% Zr, <0.01wt% Fe and balance Al. The ingot was homogenized at 430 °C for 10 h plus at 550 °C for 18 h, then hot-rolled and cold-rolled to 1-mm thick sheet, solution treated at 545 °C for 30 min, and immediately water quenched. The sheet was pre-aged at 140 °C for 5 min. In order to simulate the stamping of the sheet, the alloy was prestretched 2% after pre-ageing. The pre-stretched and without pre-stretched sheets were aged at 170 °C for 30 min, corresponding to paint baking process of automotive panels. The alloy was artificial aged at 170 °C for 10 h in order to further investigate the strengthening mechanism.

The microstructure of the alloy was investigated by electron back scattering diffraction (EBSD) and high resolution electron microscopy (HREM). EBSD measurements were performed on a field emission gun (FEG) scanning electron microscopy (SEM) JEOL JSM 7001 using a tilt of 70°, accelerating voltage of 20 kV and a step size of 1.5 μm. Samples for EBSD were electropolished in a 10% perchloric acid solution, at a voltage of 30 V for 15 s at room temperature. The precipitates were investigated by JEOL JEM-2010 high resolution electron microscope operated at 200 kV. The mechanical properties of the alloy were tested by WD 3100 testing machine. The I_E value of the alloy was measured by Zwick/Roell Bup600 Erichsen machine, and the size of samples was 90×90 mm.

Results and Discussions

Bake Hardening Response of the Alloy

The alloy used for automotive skin panels, should be easily deformed during stamping, and very difficult to deform after paint baking. Before stamping, the alloy was required low yield strength, preferably less than 140 MPa, and high formability (δ>25%) for obtaining complex automotive panels with high accuracy [4]. After paint baking, the alloy was required high yield strength for in-service dent resistance. The mechanical properties of the alloy are shown in Table 1. The increment of yield strength without pre-stretching is about 100 MPa, while the increment of yield strength with 2%+pre-stretching is about 130 MPa. Before stamping, elongation of the alloy was more than 25%, and yield strength is less than 140 MPa, and the I_E is 8.6 mm. After paint baking, the alloy exhibits high yield strength, namely excellent in-service dent resistance.

TABLE 1 MECHANICAL PROPERTIES OF THE ALLOY AFTER AGEING

Temper	R_m/MPa	$R_{p0.2}$/MPa	A/%	I_E/mm
T4P	256	137	30	8.6
PB	324	235	28.5	-
2% prestretch + PB	337	270	27	-

EBSD Analysis of the Alloy after Pre-Ageing

The microstructure of the alloy after pre-ageing was investigated by EBSD. The measurement was on the TS plane of the alloy, the results are shown in Fig. 1. The size of grains is very small, and most of grains are equiaxed. The average grain size of the alloy is 20 μm. After pre-ageing, most of grain boundary is high-angle boundary, the fraction is 91.9%. The main grain orientation is cubic, which is useful for the alloy to stamping. The results indicate that perfect recrystallization is occurred after solution treated.

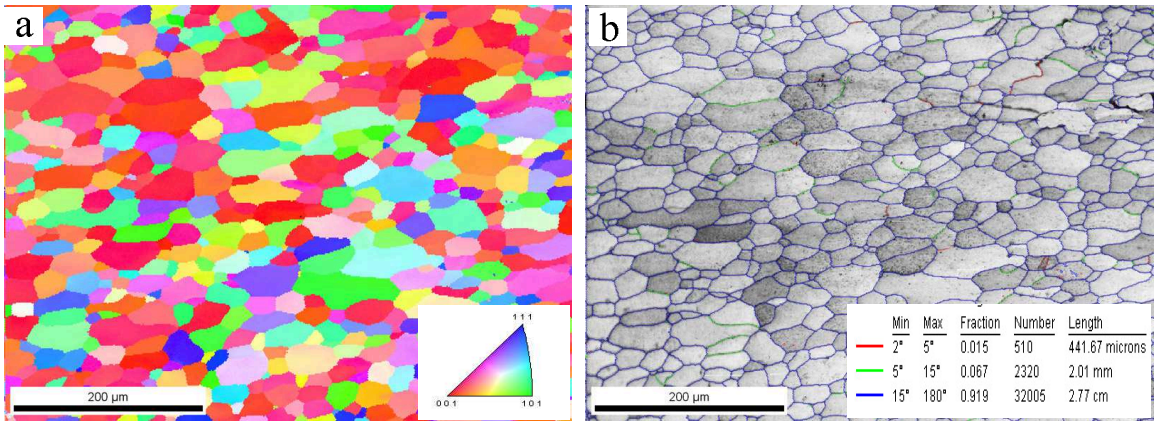


Fig.1 EBSD maps of the alloy after pre-ageing (a) grains orientation distribution and (b) image quality

Microstructure of the Alloy after Ageing

Fig. 2 shows HREM image and selected area electron diffraction (SAED) of the alloy after pre-ageing. HREM image indicates that the precipitates are approximately 2~4 nm and coherent with the matrix, justifying that the phase is GP zones, as shown in Fig. 2(a). SAED pattern shows neither extra reflection nor diffuse scattering, which suggests that the precipitates are fully coherent with matrix and do not have any distinct structure, the result obtained from SAED pattern was the same as the HREM image. GP zones make contributions to yield strength of the alloy, according to the Orowan strengthening mechanism [5]. There is on other phases are found after pre-ageing.

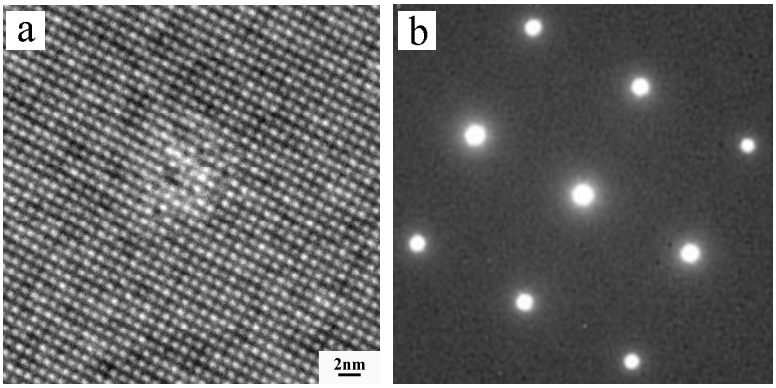


Fig. 2 HREM image (a) and SAED pattern (b) in $<001>_{Al}$ direction of the alloy after pre-ageing

Fig. 3 shows HREM images of the alloy after paint baking. In addition to GP zones, the other phase is precipitated, as observed in Fig. 3(a). The selected area diffraction pattern shows faint streaks along $[010]_{Al}$ and $[100]_{Al}$ due to the precipitates, called β" phases. In Al-Mg-Si alloys, the strengthening effect of β" phase was the best, more volume fraction of β" phase were needed, in order to improve bake hardening response of the alloy [6,7].

HREM image in $<011>_{Al}$ direction are shown in Fig. 3(b), the precipitates are identified as GP(II) zones, formed by adding Zn. The phase is 1-3 atom thick, about 6 nm wide, the habit plane is $\{111\}_{Al}$ [8]. In Al-Mg-Si-Zn alloys, Si postponed the formation of Mg/Zn clusters or GP zones at the early stage of artificial ageing, but the interaction between Mg, Si and Zn atoms was so weak, that Si atom unchanged the evolution of Mg/Zn clusters or GP zones. At the initial stage of artificial ageing, the precipitates including Mg and Si formed firstly, as observed in Fig. 2. After paint baking, GP(II) zones were formed. With the precipitation of GP zones, β" phases and GP(II) zones, the yield strength of the alloy increased apparently, seen in Table 1. The alloy exhibited rapid bake hardening response after artificial ageing at 170 °C for 30 min.

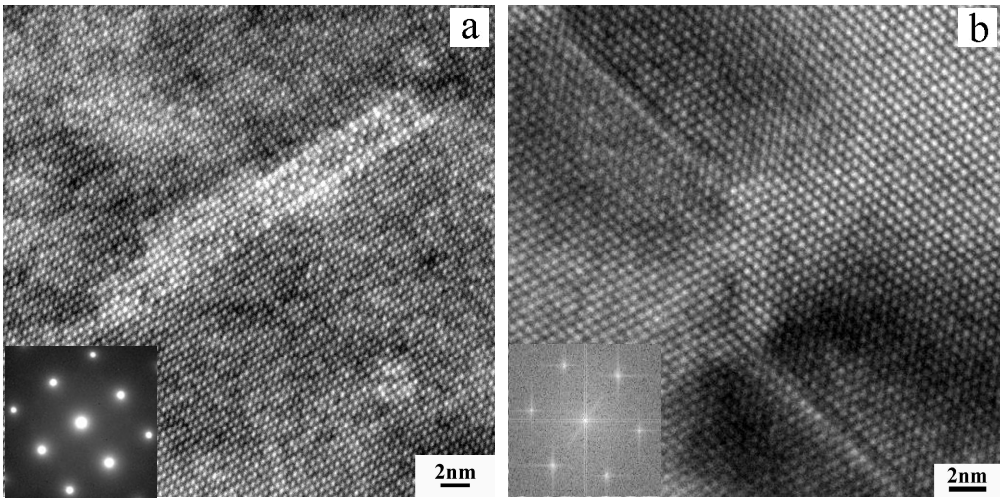


Fig. 4 HREM images in <001>$_{Al}$ (a) and <011>$_{Al}$ (b) directions of the alloy after paint baking

Microstructure in a Sample Aged for 10 h at 170 °C

In order to further investigate the precipitates that were formed owing to Zn addition, the alloy was artificial aged at 170 °C for 10 h, Fig. 5 shows the TEM micrograph of a sample aged at 170 °C for 10 h. The bright field image reveals strain contrast of needle-like precipitates oriented along $[100]_{Al}$ and $[010]_{Al}$ directions together with some fine dots. The needles are typically 20~60 nm long. Most of the dots should be the end-on sections of the needles along $[001]_{Al}$. The selected area electron diffraction pattern showed faint streaks along $[010]_{Al}$ and $[100]_{Al}$ due to the needle-like precipitates, this indicates that the precipitates are mainly β" phases.

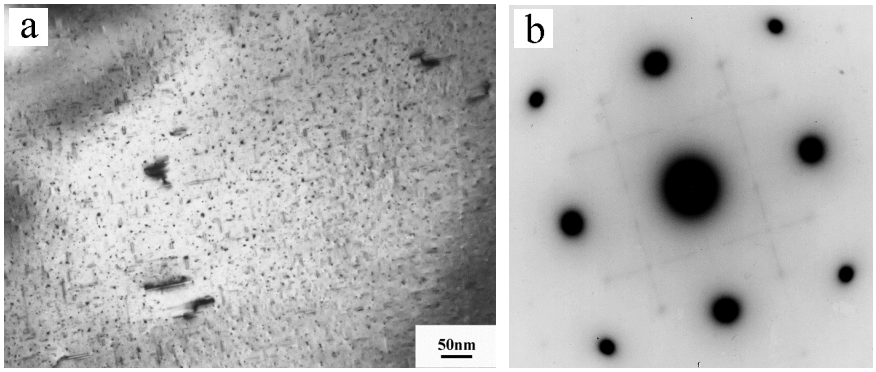


Fig. 5 BF image (a) and SAED pattern (b) in <001>Al direction of the alloy aged at 170 °C for 10 h

Fig. 6 reveals a different set of strong spots in <111>$_{Al}$ and <112>$_{Al}$ directions. The diffraction spots in Fig. 6(a) is slightly outside the $(\bar{4}22)/3$ positions, which indicates the phases is the GP(II) zones. The GP(II) zones are parallel to $\{111\}_{Al}$ plane of the alloy and fully coherent with matrix. The diffraction spots of η´ phases is at 1/3{220} and 2/3{220}, seen in Fig. 6(b), which is the same as the literature reported [9]. The η´ phases are semi-coherent with matrix, and compared with GP(II) zones, the size is larger.

As a result, only GP zones including Mg and Si atoms were formed after pre-ageing. β" phases were observed after paint baking, and GP(II) zones were also precipitated owing to Zn addition. After ageing at 170 ºC for 10 h, in addition to GP zones and β" phases, GP(II) zones η' phases were found.

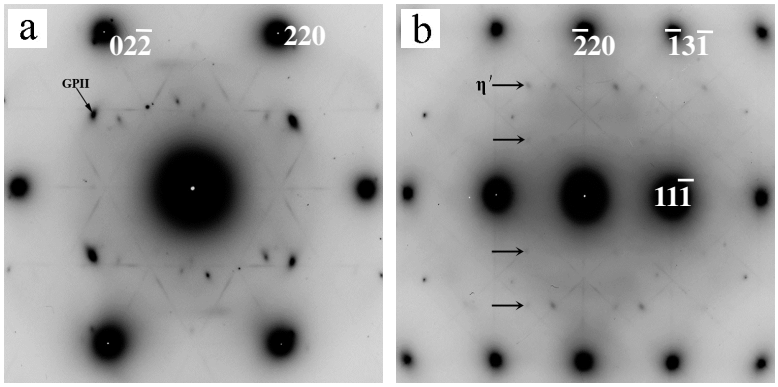


Fig.6 SAED pattern in $<111>_{Al}$ (a) and $<112>_{Al}$ (b) directions of the alloy aged at 170℃ for 10 h

Summary

(1) The average grain size of pre-aged alloy was about 20 μm. The yield strength and elongation was 137 MPa and 30% respectively. The I_E value of the alloy was 8.6 mm.

(2) After paint baking, the increment of yield strength achieved about 100 MPa. The GP(II) zones were formed during paint baking process through adding Zn. Improved paint baking response of the alloy was obtained by precipitation of GP zones, β" phases and GP(II) zones.

(3) The GP(II) zones and η´ phases were formed after the alloy ageing at 170 °C for 10 h.

Acknowledgements

The present work was supported by the National Basic Research Program of China (2012CB723903). The authors wish to thank Dr. Zhiwei Du for the TEM work.

References

[1] W. S. Miller, L. Zhuang, J. Bottema, et al. Mater. Sci. Eng., A 280 (2000) 37-49.

[2] J. Hirsch, T. Al-Samman. Acta Mater. 61 (2013) 818-843.

[3] S. J. Murtha, USA patent No. 6,129,792, 2000.

[4] J. E. Janse, L. Zhuang, J. Mooi, et al. Mater. Sci. Forum, 396/402 (2002) 607-612.

[5] M. J. Starink, L. F. Cao, P.A. Rometsch. Acta Mater. 60 (2012) 4194-4207.

[6] S. J. ANDERSEN, H. W. ZANDBERGEN, J. JANSE, et al. Acta Mater. 46 (1998) 3283-3298.

[7] C.D. Marioara, J. Nakamura, K. Matsuda, et al. Philos. Mag. 92 (2012) 1149-1158.

[8] L. K. BERG, J. GJONNES, V. HANSEN, et al. Acta Mater. 49 (2001) 3443-3451.

[9] J. Z. Chen, L. Zhen, S. J. Yang, et al. Mater. Sci. Eng., A 500 (2009) 34-42.

Advanced Materials Research Vol. 936 (2014) pp 1229-1233
© (2014) Trans Tech Publications, Switzerland
doi:10.4028/www.scientific.net/AMR.936.1229

Effect of Mn and Si on the Microstructure and Mechanical Properties of Bearing Steel

Min Wang [1,a], Guang Xu[1,b*], Zhengliang Xue[1,c], Tao Xiong[1,d] and Mingxing Zhou[1,e]

[1]Key Laboratory for Ferrous Metallurgy and Resources Utilization of Ministry of Education, Wuhan University of Science and Technology, Wuhan 430081, China;

[a]1163850854@qq.com, [b]xuguang@wust.edu.cn, [c]xuezhengliang@wust.edu.cn, [d]taoxiong@163.com, [e]kdmingxing@sina.com

KeyWords: GCrl5 bearing steel; Mn; Si; Hardness; Property

Abstract: Two bearing steels, with higher Mn and Si content than GCr15, were refined in 50kg vacuum induction furnace followed by multi-pass rolling to 12mm thick flat on two-high mill. Mechanical properties and microstructures were measured and observed. The results show that higher content of Mn and Si decreases the martensite starting temperature (Ms), which is beneficial to the forming of martensite. The microstructure changes from martensite plus troostite to martensite, leading to higher hardness of steel and improvement of wear resistance. However, the band microstructure is easily formed by increase of Mn and Si, which is harmful to transverse property.

Introduction

Bearing is one of the important basic parts of mechanical equipment. Considering the structure characteristic and working condition of bearings, the materials for bearings must have high fatigue strength, high yield strength, good toughness, better wear resistance and certain corrosion resistance[1]. Bearing steel includes high carbon chromium bearing steel, carburizing bearing steel and stainless bearing steel, etc, among which high carbon chromium bearing steel is the most commonly used. Many scholars have made a lot of research on GCrl5, a representative chromium bearing steel, which accounts for the majority use of bearing steel in many countries for its high hardness, good wear resistance and better anti-fatigue performance[2-7]. However, with the development of industries, the proprieties of GCrl5 bearing steel can hardly meet some industrial requirements. Researches have shown that the appropriate increase of Mn and Si content can improve the hardenability and elastic limit of GCrl5[8]. In this paper, the effects of Mn and Si on the microstructure and proprieties of bearing steels are studied by comparing the microstructure, hardness and mechanical property of two new steels, with higher Mn and Si content than GCr15 and being treated with multi-pass rolling process and quenching.

Experimental Scheme

The experimental steels in this research were refined in 50kg vacuum induction furnace. To study the effects of Mn and Si on high carbon chromium bearing steel, different contents of Mn and

Si were added in the test steels. The chemical compositions of the test steels are shown in Table 1. Ingots of 120 mm thickness were heated to 1250℃ at a rate of 5℃/s and held for 30min, followed by multi-pass rolling to 12mm thick flat. The rolling process is given in Fig. 1. The initial rolling temperature of steel 1 was 1074℃ and the final rolling temperature was 870℃. After rolling, steel 1 was cooled to 535℃ at a cooling rate of 15℃/s, followed by final air cooling to room temperature. While the initial and final rolling temperature of steel 2 were 1050℃ and 860℃, respectively. After rolling, it was cooled to 574℃ at a cooling rate of 15℃/s, followed by air cooling to room temperature.

TABLE 1 THE CHEMICAL COMPOSITION OF TEST STEELS(WT.%)

Steel	C	Cr	Mn	Si	Mo	P	S
1	0.965	1.495	0.428	0.341	0.050	0.008	0.009
2	1.053	1.553	1.134	0.612	0.058	0.0089	0.018

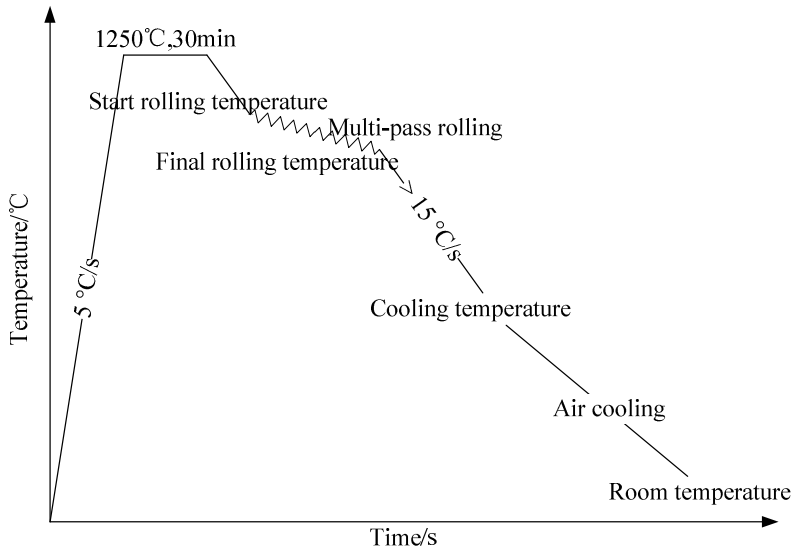


Fig. 1 Experimental Scheme

Experimental Results

Rockwell Hardness and Mechanical Property

The hardness of each experimental plate was measured for three times on a HR-150A Rockwell hardness tester. The average value of steel 2 is 57.5.5HRC, significantly higher than that of stee1 1 (45.5HRC). Then the plates were machined to standard tensile samples according to GBT228-2002. Since the high hardness of steel 2 made it difficult to be machined to standard tensile samples, the performance test both transverse and longitudinal property test were carried out only for steel 1. Table 2 gives the average value of the mechanical properties of steel 1, indicating that the longitudinal property is obviously better than transverse property.

TABLE 2 THE MECHANICAL PROPERTY OF STEEL 1

Steel 1	Yield strength /MPa	Tensile strength /MPa	Yield ratio	Uniform elongation /%	Total elongation /%
Longitudinal property	1120	1582	0.71	5.2	15
Transverse property	1009	1392	0.72	2.5	2.8

Microstructure

Metallographic samples were sampled along the rolling direction. The microstructure of the test steels were observed on Zeiss optical microscope, shown in Fig. 2 and 3, respectively. From Fig. 2 and Fig. 3, it can be seen that the microstructure of steel 1 consists of martensite and troostite, while the microstructure of steel 2 is martensite.

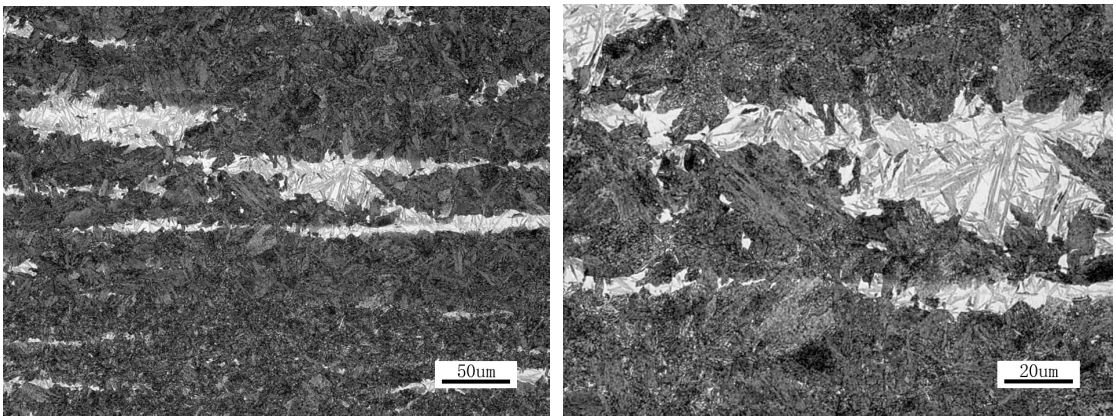


Fig. 2 Microstructure of Steel 1

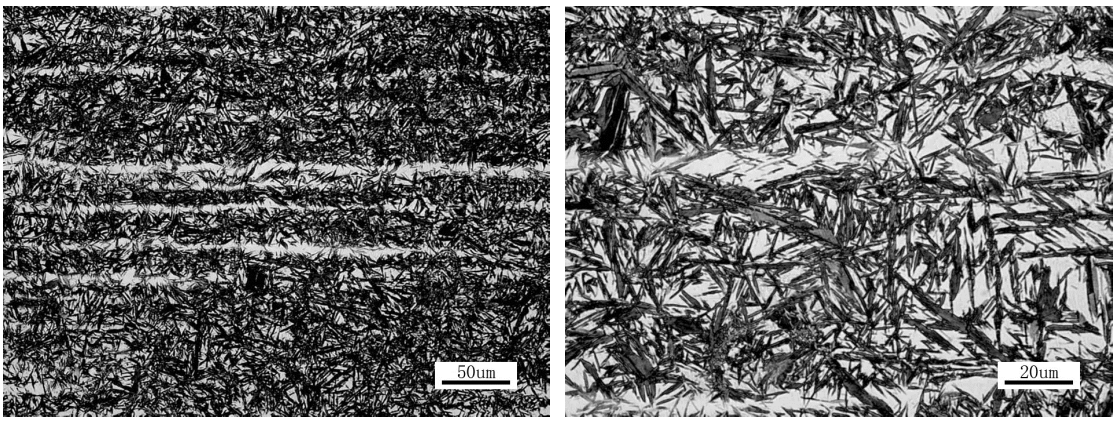


Fig. 3 Microstructure of Steel 2

Discussion

As shown in Table 1, the content of Si and Mn in steel 2 are both higher than steel 1. Silicon plays an important role in improving the stability of austenite by strongly delaying or suppressing the decomposition of cementite in overcooled austenite. Moreover, continuous carbon-riched residual austenite or martensite-austenite island can be found within the bainitic ferrite with the addition of Si. These two aspects result in crack blunting or strain-induced plasticity, thus improving the toughness effectively. However, it should be noticed that the hardness of steel is affected if the content of Si is too high. A certain amount of Mn has great strengthening effects on steel, improving the strength, hardness and wear resistance. Manganese is one of the alloy elements that can significantly enhance the stability of austenite and decrease the decomposition of austenite. Then the hardenability of steel can be increased with the appearance of bay platform on austenite transformation curve.

It can be seen from Fig. 2 that the microstructure of steel 1 is martensite and troostite with some black and white structure. The inhomogeneous distribution of Cr in alloying cementite can lead to the diversity of carbide stability. During the quenching heating process, C and Cr distributes uniformly in austenite base. After quenching, the microstructure of GCrl5 shows black and white

martensite[2,9]. The black region, low carbon martensite, appears in Cr-riched cementite, while the white region of high carbon martensite appears in low Cr cementite. Meanwhile, no martensite can be observed in the black and white martensite structure, which belongs to cover up martensite(fine martensite)[10]. As for steel 1, longitudinal property is obviously better than transverse property, that can be explained by band distribution of nonmetallic inclusions and carbide along the rolling direction. Under the function of maximum normal stress on the surface, longitudinal crack often appears in steel 1 along the distribution direction of nonmetallic inclusions and carbide. Meanwhile, band structure formed from inclusion-riched area is parallel to the rolling direction, causing the direction of mechanical properties. Transverse plasticity and toughness decrease significantly.

As shown in Fig. 3, the microstructure of steel 2 is martensite. The Si and Mn content in steel 2 is higher than steel 1, whereas other elements contents are similar. Martensite starting temperature(Ms) can be calculated according to Eq. 1. Si and Mn are beneficial for the stability of austenite and lowering the Ms, making the hardness of steel 2 (57.5HRC) obviously higher than steel 1(45.5HRC).

$$Ms=525-350(C-0.005)-45Mn-35(V+Nb+Zr+Ti)-30Cr-20Ni-16Mo-8W-5Si+6Co+15Al. \quad (1)$$

Conclusions

Two bearing steels with higher Mn and Si content than GCr15, were refined in 50kg vacuum induction furnace followed by multi-pass rolling to flat of 12mm thickness. The effect of Mn and Si on the microstructure and mechanical properties of bearing steel is investigated. The following conclusions can be obtained:

(1) Higher content of Mn and Si decreases the martensite transformation temperature (Ms), which is beneficial to the forming of martensite and changes the microstructure from martensite plus troostite to martensite, leading to higher hardness . However, the band microstructure is easily formed by increase of Mn and Si, which is harmful to transverse property;

(2) Higher content of Mn and Si can increase the hardness of steel and improve the wear resistance;

(3) The band microstructure is easily formed by increase of Mn and Si, which is harmful to transverse property.

Acknowledgment

This work is financially supported by the National Natural Science Foundation of China (No. 51274154), the National High Technology Research and Development Program of China (No. 2012AA03A504), the State Key Laboratory of Development and Application Technology of Automotive Steels (Baosteel Group) and the key project of Hubei Education Committee (No.20121101).

References

[1] S. S. Zhong, C. S. Wang, Bearing Steel[M]. Metallurgical Industry Press, Beijing, 2002, 414-443.

[2] B. Zong, J. Z. Wei, G. H. Wang, Analysis of Quenching Martensite of GCr15 Bearing Steel[J]. Physical testing and chemical analysis part A: physical testing, 2004, 40(11): 581-588.

[3] H. B. Yang, B. G. Ma, F. X. Zhu, X. H. Liu, The Effects of Controlled Rolling and Controlled Cooling on the Microstructure of GCr15 Beating Steel[J]. China Science and Technology Information , 2008(21): 138-139.

[4] D. X. Wang, Y. Y. Xiao, Controlled Rolling and Cooling Technology of GCr15 Bearing Steel in Continuous Rolling[J]. Speal Steel, 2004, 25(3): 48-49.

[5] Y. H. Kong, D. L. Song, L. X. Xie, S. G. Zhu, Contrast and Analysis of Structure and Performance on Ring of Bearing Steel GCr15[J]. Hot Working Technology, 2012, 41(10): 55-60.

[6] Z. Q. Wang, S. Z. Wang, Analysis on Strength and Toughness of Steel GCr15 M/B Composite Structure[J]. Hot Working Technology, 2013, 42(8): 199-201.

[7] Y. J. Chou,Y. L. Mei, J. Y. Ye, Y. A. Gao, L. X. Liang, Experimental Analysis of High Performance Bearing Steel[J]. Bearing, 2006(10): 28-30.

[8] J. Y. Ye, Y. Z. Li, Z. Y. Wang, Process and Performance Comparison among three kinds of Bearing Steel with High Quench-hardening Ability[J]. MW Metal Forming, 2010(15): 16-21.

[9] Z. F. Qi, Principle of Metal Heat Treatment[M]. Chain Machine Press, Beijing, 1989.

[10][10] X. T. Wang, Metal Material Science [M], Chain Machine Press, Beijing, 1991.

Advanced Materials Research Vol. 936 (2014) pp 1234-1238
© (2014) Trans Tech Publications, Switzerland
doi:10.4028/www.scientific.net/AMR.936.1234

Influence of Nitrogen Atmosphere Annealing on Structural and Transport Properties of $Fe_{1.125}Te$

Yujiang Li[1], Zhenping Wu[1], Yuehua An[1], Guofeng Wang[1,2], Changlong Sun[1], Yaoting Huang[1], Peigang Li[1,2], Linghong Li[3], and Weihua Tang[1,a]

[1] School of Science, State Key Laboratory of Information Photonics & Optical Communication, Beijing University Posts and Telecommunications, Beijing, 100876, CHINA

[2] Center for Optoelectronics Materials and Devices, Zhejiang Sci-Tech University, Hangzhou, 310018, CHINA

[3] Physics Department, The State University of New York at Potsdam, Potsdam, New York 13676-2294, USA

[a] whtang@bupt.edu.cn

Keywords: Alloy; Magnetic properties; Superconducting.

Abstract. $Fe_{1.125}Te$ alloys had been synthesized by solid state reaction methods. The effects of nitrogen annealing on $Fe_{1.125}Te$ lattice structure and physical properties had been studied. It was found that the lattice constants *a* and *c* increased after annealed at temperature 400~600 °C. When the temperature is above 850 °C, the size of the unit cell returns to the similar size of original samples. The step-like magnetic-thermal curves were observed after annealed at 900 °C, which is associated with two magnetic transitions. In vacuum, the transition temperatures are 122 K and 128 K, while in the nitrogen, they are 122 K and 138 K. The resistance-temperature curves indicate a semiconductor to metal transition around 69 K for N_2 atmosphere.

Introduction

Recently, Fe-based superconducting families have received wide attentions since the discovery of superconductivity in LaOFeP [1-7]. Among these materials, $Fe_{1+x}(Te,Se)$ has the simplest crystal structure. It consists of vertically stacked, tetrahedrally coordinated Fe-Te(Se) sheets which are isostructural to the Fe-As sheets in the pnictides. The same structural features may be associated with superconductivity, so compounds with the similar structure may become a new platform to explore new superconductors.

Hsu *et al* first discovered superconductivity in the tetragonal FeSe system, the transition temperature (T_C) is ~8 K [8]. The T_c could be greatly enhanced to 36.7 K under high pressure of 8.9 GPa [9]. Density functional calculations for iron chalcogenides (FeS, FeSe, FeTe) indicated a strong stability of spin density wave for FeTe [10], which could lead to a higher T_c than FeSe. $Fe_{1+x}Te$ adopts the tetragonal PbO structure with the excess Fe atoms occupying an additional Fe(2) site in the Te plane, which is equivalent to the site occupied by Li in LiFeAs [11]. The value of *x* can be determined by the stoichiometric ratio of sample, these excess Fe atoms have a significant effect in the $Fe_{1+x}Te$ lattice structure. Density-functional calculations suggest that the excess Fe is electronically active-acting as an electron donor, and has a large magnetic moment (~2.4 μ_B), which couples to the Fe in the FeTe layers [12]. W. Bao *et al.* suggested that the antiferromagnetic (AF) ordering temperature may be turned by varying the excess Fe concentration [13]. Also, it has been shown that excess Fe is correlated to the suppression of superconductivity [14]. Actually, although FeTe has the similar crystal structure with FeSe, no superconductivity is found in the bulk FeTe material [15,16]. However, epitaxial FeTe films grown on the LSAT, MgO, $SrTiO_3$ and $LaAlO_3$ substrates demonstrate superconducting transition at ~13 K [17]. It is concluded that tensile strain could lead to the superconductivity in FeTe film. However, the relationship between the vacancies at Fe(2) site of FeTe as well as the lattice strain effect on the magnetic and electronic transport properties are still unclear. In this work, we use $Fe_{1.125}Te$ as the original sample, and study the effect of electrical and magnetic properties of $Fe_{1.125}Te$ through a nitrogen atmosphere annealing.

Experimental

$Fe_{1.125}Te$ samples were prepared using a solid state reaction method, as the original samples of the subsequent experiments. Stoichiometric quantities of Fe powders (99.98%) and Te shots (99.999%) were thoroughly ground, pressed into pellets (7mm in diameter), sealed in evacuated quartz tubes under vacuum (at a residual pressure of ca. 3×10^{-4} Pa), and heated at 860 °C for 12 h followed by quenched in brine. Powder X-ray diffraction data were collected using CuK_{α} radiation. The lattice constants for original samples are a=3.8231 Å, c=6.2808 Å. The prepared $Fe_{1.125}Te$ samples were divided into several parts and inserted into quartz tubes respectively. These tubes were evacuated (about 3×10^{-4} Pa), filled with nitrogen to a pressure of 0.5×10^{5} Pa, 0.6×10^{5} Pa, 0.7×10^{5} Pa, and 0.8×10^{5} Pa, respectively. Then, all these samples were sealed and annealed at different temperatures for different times (because of the little impact, we adopt only a pressure of 0.8×10^{5} Pa). Four-probe method was employed to investigate the transport properties. Magnetic measurements were performed using Physical Property Measurement System (PPMS).

Result and Discussion

Fig. 1(a) displays the X-ray diffraction pattern of $Fe_{1.125}Te$ samples annealed at different temperatures in N_2 (550 °C, 600 °C, 850 °C, 900 °C). The pattern appears to be similar to that reported by D. Frunchart *et al*. It is fitted to the tetragonal space group *P4/nmm* of the $Fe_{1.125}Te$ phase and indexed. Fig. 1(b) shows the partial enlarged region of peak (103) in Fig. 1(a). After N_2 annealing process, the peaks of samples shift to lower degree when the temperature is below 600 °C.This might attributed to the nitrogen atoms doping, which could increase the lattice constants and broaden the inter-planar crystal spacing. As the temperature increases, the peaks shift slightly to a higher 2θ compared to the peak of 600 °C annealed sample. It indicates a decrease in the lattice parameters.

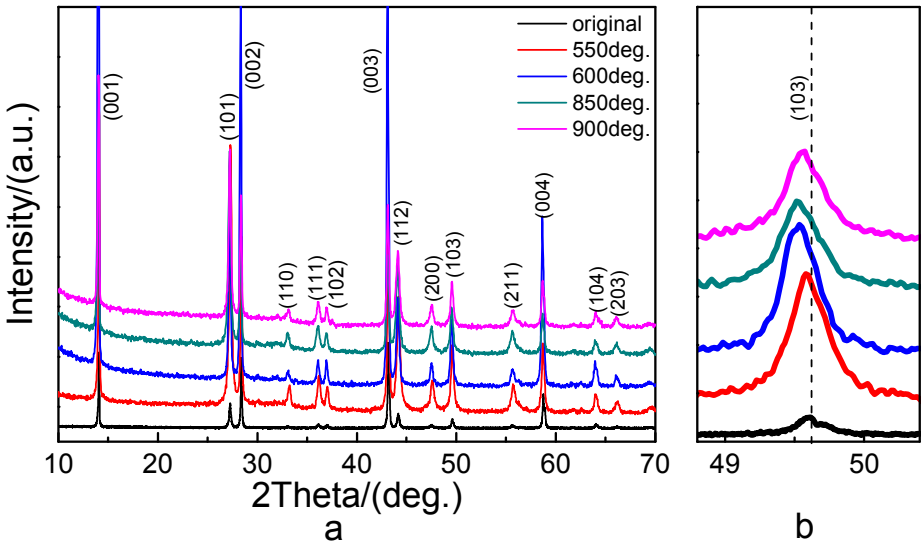


Fig. 1: (a) The XRD Patterns of $Fe_{1.125}Te$ alloys Annealed at Different Temperatures in N_2, (b) Partial Enlarged View of Lines in (103).

Table1 lists the refined lattice constants in different annealing temperatures. The a and c increases with the raising temperature when it is below 850 °C, accompanied by a unit cell volume expansion (~0.7%), which indicates the N atoms entering the lattice. When the temperature is above 850 °C, the size of the lattice contracts to the original size of unannealed samples, which indicates that N atoms can get rid of the lattice during annealing in high temperature. We also found that the value of c/a stays in a restricted range and it means that N effects lattice isotropically.

TABLE1: LATTICE CONSTANTS OF $FE_{1.125}TE$

Anneling T [℃]	*a* [Å]	*c* [Å]	*c*/*a*	*V* [Å^3]
Unannealed	3.8231	6.2808	1.6429	91.80
400	3.8269	6.2910	1.6439	92.13
550	3.8254	6.2943	1.6454	92.11
600	3.8326	6.2959	1.6427	92.48
850	3.8221	6.2859	1.6446	91.83
900	3.8259	6.2802	1.6415	91.92

Fig. 2 displays the scan electron microscope (SEM) patterns of $Fe_{1.125}Te$ samples. The left image indicates the sample is layered structure. To analyze the composition ratio of Fe and Te atoms in the $Fe_{1.125}Te$ sample, a small piece of the sample as shown in the little rectangle of the left image is picked and computed. The right image shows the EDX spectrogram and confirms the actual composition ratio of nearly 1:1.

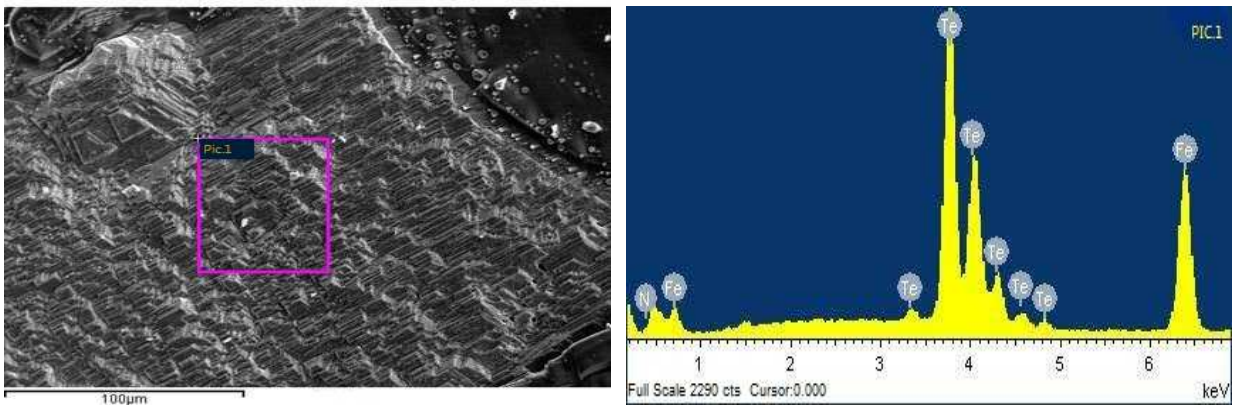


Fig. 2: SEM Images of Fe1.125Te Alloy.

Fig. 3 illustrates the initial sample's mass and heat flow curves measured in a wide temperature range (0~600 ℃). The green curve in fig. 3 shows the thermogravimetric curve of the original sample. It has a maximum increment value of 39.8 μg at 560 ℃. It corresponds with the result of XRD refining. The lattice contracts to the similar size of unannealed samples. The blue curve is the heat flow curve, which indicates that the sample is absorbing the heat during the temperature-rise period except for a slightly releasing of the heat at 527 ℃.

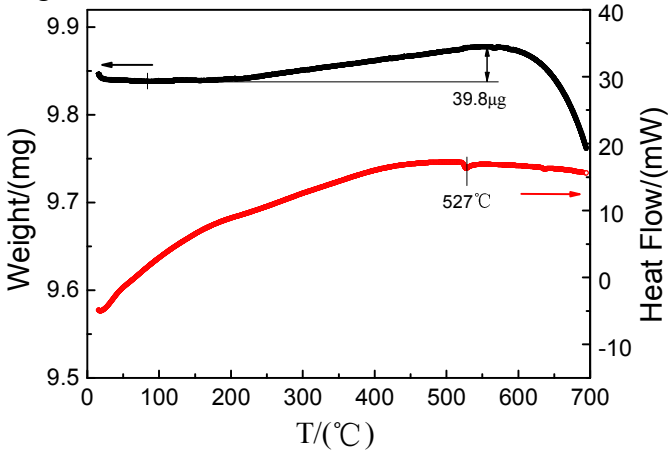


Fig. 3: Thermo#Gravimetric and Heat Flow Curves of Unannealed Fe1.125Te Alloy.

Fig. 4 shows the zero field cooled (ZFC) and field cooled (FC) magnetization (M) vs temperature (T) curves for samples annealed at different temperatures. Both samples annealed in vacuum and N_2 atmosphere have the same magnetic transition at 128 K. It indicates that N_2 takes little effect on the

sample at 600 °C annealing. The step-like curves in Fig. 4(b) are corresponding to two magnetic transitions. The critical temperatures in vacuum are 122 K and 128 K, while in nitrogen are 122 K and 138 K. Although there has no proof for the existence of two lattice structures is found in the XRD patterns, the magnetic transition points in M-T curves confirmed the magnetic phase separation caused by annealing in high temperature. As the magnetic transition temperature increases about 10 K, it indicates a remarkable effect on high-temperature magnetism with the existence of N_2. No overlap of magnetic-thermal curves in high-temperature region is observed under FC condition or ZFC condition, which indicates the impurities in the sample. For XRD shows no impurity phase, it should be caused by the low-level of the impurities, grain refinement or non-crystallizing. The magnetic material in the sample is probably α-Fe impurity.

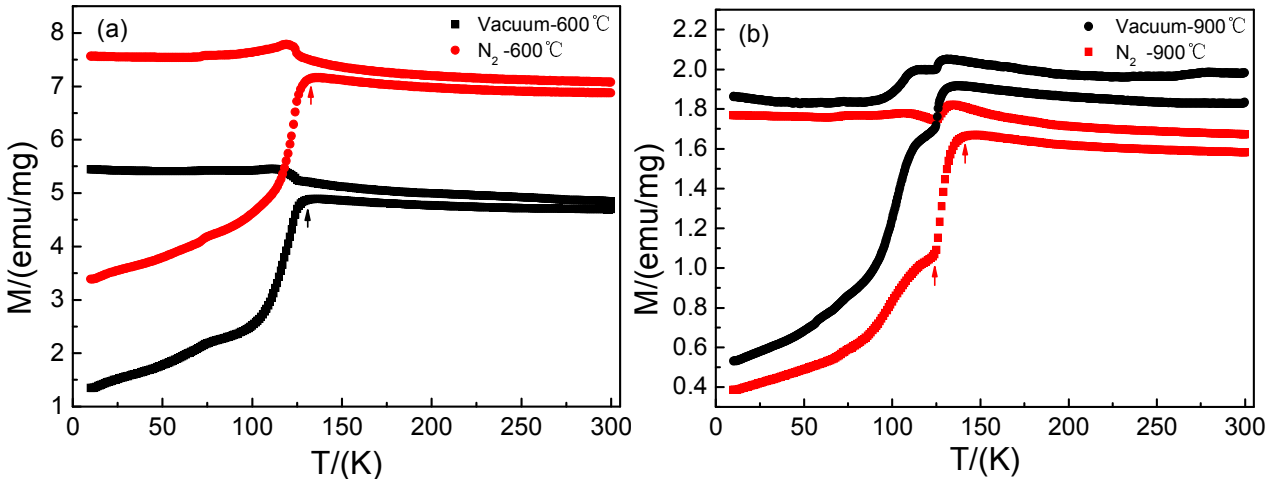


Fig. 4: (a) ZFC and FC (M) vs (T) Curves for $Fe_{1.125}Te$ in Vacuum and N_2 at the Temperature of 600 ºC. (b) ZFC and FC (M) vs (T) Curves for $Fe_{1.125}Te$ in Vacuum and N_2 at the Temperature of 900 ºC.

Conclusion

$Fe_{1.125}Te$ alloys were fabricated and annealed under N_2 atmosphere. The structural and transport properties were investigated by XRD, magnetization, resistance measurements. The lattice constants of $Fe_{1.125}Te$ were elongated after annealing in N_2. A magnetic phase separation and a shift of magnetic transition for samples annealed at 900 °C in N_2 were observed. Our results suggest that N atoms could enter the lattice of $Fe_{1.125}Te$ with a little influence on the structure of lattice and physical properties.

Acknowledgement

This work was supported by Fund of State Key Laboratory of Information Photonics and Optical Communications (Beijing University of Posts and Telecommunications), the National Natural Science Foundation of China (51072182, 51172208) and National Basic Research Program of China (973 Program) (2010CB933501)

References

[1] Y. Kamihara, H. Hiramatsu, M. Hirano, R. Kawamura, H. Yanagi, T. Kamiya, and H. Hosono, Iron-Based Layered Superconductor: LaOFeP. J. Am. Chem. Soc. 128 (2006) 10012.

[2] Y. Kamihara, T. Watanabe, M. Hirano, H. Hosono, Iron-Based Layered Superconductor $La[O_{1-x}F_x]FeAs$ (x = 0.05−0.12) with T_c = 26 K. J. Am. Chem. Soc. 130 (2008) 3296.

[3] Z. A. Ren, W. Lu, J. Yang, W. Yi, X. L. Shen, Z. C. Li, G. C.Che, X. L. Dong, L. L. Sun, F. Zhou, and Z. X. Zhao, Superconductivity at 55 K in Iron-Based F-Doped Layered Quaternary Compound $Sm[O_{1-x}F_x]FeAs$. Chin. Phys. Lett. 25 (2008) 2215.

[4] Z. A. Ren, G. C. Che, X. L. Dong, J. Yang, W. Lu, W. Yi, X. L.Shen, Z. C. Li, L. L. Sun, F. Zhou, and Z. X. Zhao, Superconductivity and phase diagram in iron-based arsenic-oxides $ReFeAsO_{1-\delta}$ (Re=rare-earth metal) without fluorine doping. Europhys. Lett. 83 (2008) 17002.

[5] C. Wang, Y. K. Li, Z. W. Zhu, S. Jiang, X. Lin, Y. K. Luo, S. Chi, L. J. Li, Z. Ren, M. He, H. Chen, Y. T. Wang, Q. Tao, G. H. Cao, and Z. A. Xu, Effects of cobalt doping and phase diagrams of $LFe_{1-x}Co_xAsO$ (L=La and Sm). Phys. Rev. B 79 (2009) 054521.

[6] A. S. Sefat, M. A. McGuire, B. C. Sales, R. Jin, J. Y. Howe, and D. Mandrus, Electronic correlations in the superconductor $LaFeAsO_{0.89}F_{0.11}$ with low carrier density. Phys. Rev. B 77 (2008) 174503.

[7] H. Kito,H. Eisaki, and A. Iyo, Superconductivity at 54 K in F-Free $NdFeAsO_{1-y}$. J. Phys. Soc. Jpn. 77 (2008) 063707.

[8] F. C. Hsu, J. Y. Luo, K. W. Yeh, T. K. Chen,T. W. Huang, P. M. Wu, Y. C. Lee, Y. L. Huang, Y. Y. Chu, D. C. Yan, M. K. Wu, Superconductivity in the PbO-type structure α-FeSe. Natl.Acad. Sci. USA 105 (2008) 14262.

[9] S. Medvedev, T.M. McQueen, I.A. Troyan,T. Palasyuk, M.I. Eremets, R.J. Cava,S. Naghavi, F.Casper, V. Ksenofontov,G. Wortmann, C. Felser, Electronic and magnetic phase diagram of bold italic beta-$Fe_{1.01}Se$ with superconductivity at 36.7 K under pressure. Nat. Mater. 8 (2008) 630.

[10] Alaska Subedi, Lijun Zhang, D. J. Singh, M. H. Du, Density functional study of FeS, FeSe, and FeTe: Electronic structure, magnetism, phonons, and superconductivity. Phys. Rev. B 78 (2008) 134514.

[11] D. Fruchart, P. Convert, P. Wolfers, R. Madar, J.P. Senateur, R. Fruchart, Structure antiferroma gnetique de $Fe_{1.125}Te$ accompagnee d'une deformation monoclinique. Mater. Res. Bull.10 (1975) 169.

[12] Lijun Zhang, D. J. Singh, and M. H. Du, Density functional study of excess Fe in $Fe_{1+x}Te$: Magnetism and doping. Phys. Rev. B 79 (2009) 012506.

[13] W. Bao, Y. Qiu, Q. Huang, M. A. Green, P. Zajdel, M. R.Fitzsimmons, M. Zhernenkov, S. Chang, M. H.Fang, B. Qian,E. K. Vehstedt, J. H. Yang, H. M. Pham, L. Spinu, and Z. Q. Mao, Tunable (δπ, δπ)-Type Antiferromagnetic Order in α-Fe(Te,Se) Superconductors. Phys. Rev. Lett. 102 (2009) 247001.

[14] Zhijun Xu, Jinsheng Wen, Guangyong Xu, Qing Jie, Zhiwei Lin, Qiang Li, Songxue Chi, D. K. Singh, Genda Gu, J. M. Tranquada, Disappearance of static magnetic order and evolution of spin fluctuations in $Fe_{1+\delta}Se_xTe_{1-x}$. Phys. Rev. B 82 (2010) 104525.

[15] Shiliang Li, Clarina de la Cruz, Q. Huang, Y. Chen, J. W. Lynn, Jiangping Hu, Yi-Lin Huang, Fong-Chi Hsu, Kuo-Wei Yeh, Maw-Kuen Wu, and Pengcheng Dai, Firs t-order magnetic and structural phase transitions in $Fe_{1+y}Se_xTe_{1-x}$. Phys. Rev. B 79 (2009) 054503.

[16] Y Mizuguchi, F Tomioka, S Tsuda, T Yamaguchi,Y. Takano: FeTe as a candidate material for new iron-based superconductor. Physica C 469 (2009) 1027.

[17] Y. Han, W. Y. Li, L. X. Cao, X. Y. Wang, B. Xu, B. R. Zhao, Y. Q. Guo, and J. L. Yang, Superconductivity in Iron Telluride Thin Films under Tensile Stress. Phys. Rev. Lett. 104 (2010) 017003.

Advanced Materials Research Vol. 936 (2014) pp 1239-1246
© (2014) Trans Tech Publications, Switzerland
doi:10.4028/www.scientific.net/AMR.936.1239

Interface Reaction Thermodynamics of AgCuTi Brazing Filler Metal and Alumina Ceramic

Honglong Ning[1, a], Linfeng Lan [1,b], Lei Wang [1,c], Junbiao Peng [1,d], Zhijian Peng [2,e*] and Jusheng Ma [3,f]

[1] State Key Laboratory of Luminescent Materials and Devices, Department of Materials Science and Engineering School, South China University of Technology, Guangzhou 510640, P. R. China

[2] School of Engineering and Technology, China University of Geosciences at Beijing, Beijing 100083, P. R. China

[3] Department of Materials Science and Engineering School, Tsinghua University, Beijing 10084, P. R. China

[a]ninghl@scut.edu.cn, [b] lanlinfeng@scut.edu.cn, [c]mslwang@scut.edu.cn, [d]psjbpeng@scut.edu.cn, [e*]pengzhijian@cugb.edu.cn

Keywords: Interface reaction; Thermodynamics; Alumina; AgCuTi brazing filler metal

Abstract: In this work, the interface reaction between Al_2O_3 ceramic and $Ag_{70.5}Cu_{27.5}Ti_2$ brazing filler metal at 845-860℃ was investigated. Based on the data of thermodynamics and kinetics, the Gibbs free energies of the main interface reactions in the real brazing system condition were calculated. But the values of normal equilibrium reaction condition and the real interface reaction brazing system were different; and the main influential factor was the brazing temperature, and the system vacuum of brazing condition can lead the change of equilibrium constant (Kα). The results revealed that the high temperature and vacuum active brazing is a non-equilibrium interface reaction especially to titanium alloy, the vacuum and alloy liquid solution are beneficial to the brazing process, and the by-product formation of titanium-oxygen are affected by the diffusion process.

Introduction

It was well-known that alumina ceramic played an important role in electronic industry because of its superior physical, chemical, mechanical and optical properties. Titanium as an active metal component of brazing alloys had been used on most occasions[1-11]; and Ag-Cu alloy eutectic filler metal owned the advantages of low braze temperature, low stress and simply process; So Ag-Cu-Ti alloy metal were popularly used active brazing metal.

In this research, $Ag_{70.5}Cu_{27.5}Ti_2$ eutectic alloy was used to braze hot-pressed sintered alumina ceramic. The interface reaction and thermodynamics behavior between $Ag_{70.5}Cu_{27.5}Ti_2$ alloy and alumina ceramic were investigated.

Experimental details

Materials preparation

The hot-pressed sintered 99.9% alumina used in this study was obtained from the State Key Laboratory of New Ceramics and Fine Processing, Tsinghua University, China; the alumina faying face was polished by sand paper with diamond paste. $Ag_{70.5}Cu_{27.5}Ti_2$ brazing filler metal was rolled into 500 μm strip and cut into an appropriate size for brazing. The brazing filler metal and 99% alumina ceramic were carefully cleaned with acetone in ultrasonic cleaners and baked before brazing.

Brazing tests

The test sample was fixed in an iron jig. The jig was heated in a vacuum furnace to brazing temperature and then held for a few minutes. The heating rate below 750℃ was 20℃/min, and the heating rate above 750℃ was 10℃/min to the brazing temperature (845-860℃). The cooling rate

after brazing was 5℃/min above 600℃ and then held for a while at this temperature, then about 2℃ /min to room temperature. The pressure of the furnace chamber was kept between 1×10^{-3} and 1×10^{-5} Pa during the heating and the cooling. Fig.1 showed the brazing cure of time with temperature and vacuum in process.

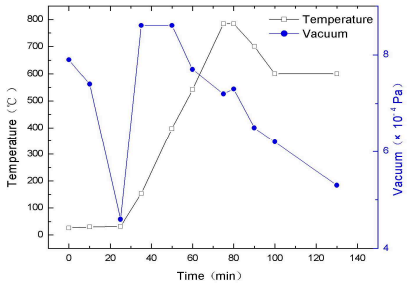


Fig. 1 Brazing cure of time with temperature and vacuum

Sample characterization

The resultant interface reaction was examined with an optical microscope and a scanning electron microscopy (SEM) equipped with energy dispersive X-ray spectroscopy (EDS), and the quantitative analysis of elemental concentration for each phase was made with the electron beam characteristic at 15 kV, life time 60.0 s and take-off angle 34.22 º.

Results and discussion

Metalloscopy and SEM analysis

Fig.2 was the elemental analysis of $Ag_{70.5}Cu_{27.5}Ti_2$ brazing filler metal with SEM EDS; it revealed that the main elements include Ag, Cu and Ti. Fig.3 showed the optical image of the brazing filler metal and alumina ceramic interface, there is an intermetallic compound (IMC) layer between $Ag_{70.5}Cu_{27.5}Ti_2$ brazing filler metal and alumina ceramic, which was sharply contrast with the original layers, confirming that some interface reactions between the filler metal and alumina ceramic happened.

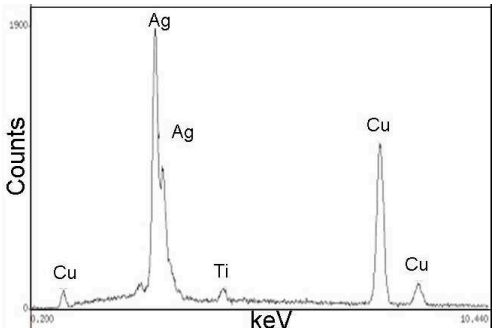


Fig. 2 EDS of elemental analysis of $Ag_{70.5}Cu_{27.5}Ti_2$

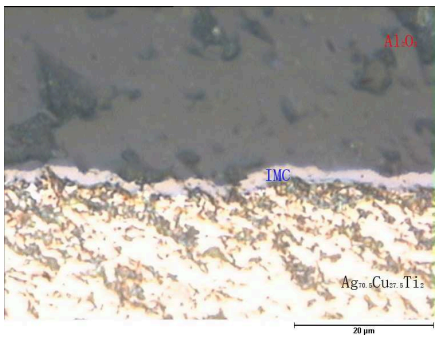


Fig. 3 Optical image of $Ag_{70.5}Cu_{27.5}Ti_2/Al_2O_3$ interface

Fig. 4 illustrated the transverse cross-sectional SEM image of typical $Ag_{70.5}Cu_{27.5}Ti_2$/alumina ceramic brazing interface, there was a nanometer layer in IMC and near to the side of alumina ceramic; EDS indicated that this nanometer layer mainly composed of Ti and O, and the ratio of O to Ti is 2:1. this nanometer layer would be TiO_2 [10]. Fig.5 showed the elemental line scanning results by EDS from $Ag_{70.5}Cu_{27.5}Ti_2$ filler metal intermetallic compound layer nearby the alumina ceramic side, and it revealed that this layer is consisted of Ag, Cu, Ti, O, Al and Ca.

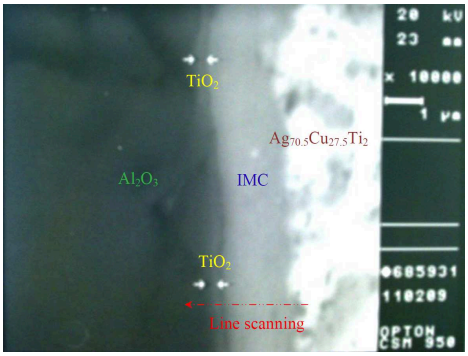
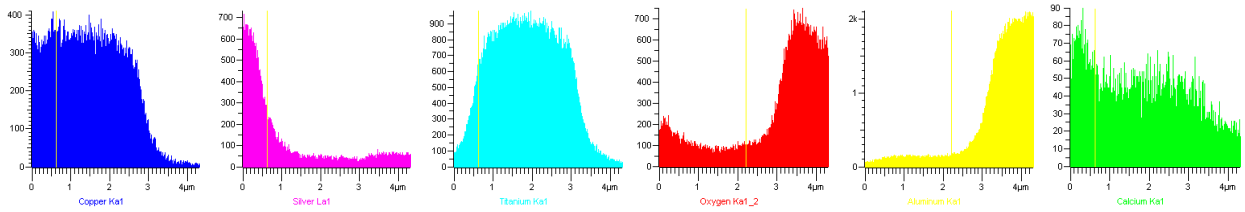


Fig. 4 Cross-sectional SEM image of typical $Ag_{70.5}Cu_{27.5}Ti_2/Al_2O_3$ brazing sample



a) Cu b) Ag c) Ti d) O e) Al f) Ca

Fig. 5 Elemental line scanning results by EDS from $Ag_{70.5}Cu_{27.5}Ti_2$ IMC nearby Al_2O_3 side

In Fig.5a, the concentration of copper kept a high level in IMC layers, indicating that Cu atoms were difficult to diffuse into Al_2O_3. In Fig.5b, the concentration of Ag decreased greatly in IMC layers, revealing that Ag atoms were less correlated to the interface reaction directly. In Fig.5c, the concentration of Ti increased greatly in IMC layers, implying that there was a Ti atom enriching zone. In Fig.5d, the concentration of oxygen kept a low level in IMC layers, but the interface between Al_2O_3 and $Ag_{70.5}Cu_{27.5}Ti_2$ kept a high level, indicating that the oxygen atoms were highly correlated to the interface reaction directly. In Fig.5e, Al atoms could diffuse from alumina into the filler metal slightly. In Fig.5f, the calcium atoms were just the background. Fig.6 was the sketch map of different elements in the line scanning from $Ag_{70.5}Cu_{27.5}Ti_2$ to Al_2O_3.

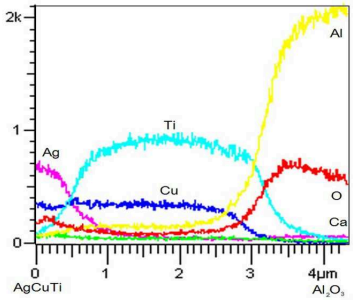


Fig. 6 Sketch map of different elements in the line scanning

Thermodynamics analysis

There were many kinds of feasibility to interface reactions between $Ag_{70.5}Cu_{27.5}Ti_2$ and Al_2O_3. If we want to get high-quality brazing between them, we need know and control the active brazing interface reactions between the main products of $Ag_{70.5}Cu_{27.5}Ti_2$ and Al_2O_3, for example, TiO_2, TiO, Cu_2Ti_4O and so on [10-11].The brazing reaction between Ti and Al_2O_3 could be described by

$$\text{Eq.1: } (Ti) + xAl_2O_3(s) \rightarrow Ti(O)_{3x}(s) + 2x(Al) \quad (1)$$

If the main product was TiO [12], Eq. 1 can be changed to Eq.2:

$$3(Ti) + Al_2O_3(s) \rightarrow 3TiO\ (s) + 2(Al) \quad (2)$$

As we know, Al_2O_3 and TiO were solid phase at 845-860℃, but Ti and Al would be dissolved in liquid alloy welding flux at that temperature; So the Gibbs free energy of this reaction could be described by Eq.3and Eq.4:

$$\Delta G_T^0 = -RT\ln K_\alpha \tag{3}$$

$$\Delta G_T^0 = \Delta H_T^0 - T\Delta S_T^0 \tag{4}$$

where R was the universal gas constant, ΔH_T^0 was the reaction enthalpy change, and ΔS_T^0 was the reaction entropy change. Maybe there were phase changes for Ti and Al from room temperature to brazing reaction temperature, so we also need consider the contribution of these changes. But there was no phase change for Al_2O_3 and TiO in this reaction temperature zone. The reaction could be calculated by Eq.5 and Eq.6:

$$\Delta H = \int_{T_1}^{T_2} C_P dT \tag{5}$$

$$C_P = A_1 + A_2 10^{-3} T + A_3 10^5 T^{-2} \tag{6}$$

where CP was the molar heat capacity at constant pressure, According to Eq.5, Eq.6 could be changed to Eq.7; and the entropy change could be described by Eq.8:

$$\Delta H = A_1 \bullet (T_2 - T_1) + \frac{1}{2} A_2 \bullet 10^{-3}(T_2^2 - T_1^2) + A_3 \bullet 10^5 (\frac{1}{T_1} - \frac{1}{T_2}) \tag{7}$$

$$\Delta S = C_1 \bullet \ln\frac{T_2}{T_1} + C_2 \bullet 10^{-3}(T_2 - T_1) + C_3 \bullet 10^5 (\frac{1}{T_2^2} - \frac{1}{T_1^2}) \tag{8}$$

For Ti and Al, it need add the enthalpy and entropy changes of phase transformation. At 1155K, Ti would change from β phase to α phase; Al would change from liquid to solid at 932 K, so Ti and Al could be described by Eq.9 and Eq.10:

$$\Delta H = \Delta H_{\text{Transformation}}(\Delta H_m) \tag{9}$$

$$\Delta S = \Delta S_{\text{Transformation}}(\Delta S_m) \tag{10}$$

The standard enthalpy and entropy changes of Al_2O_3 reduction reaction could be described by Eq. 11 and 12:

$$\Delta H_{298}^0 = (\sum n_i \Delta H_i^0)_{\text{Re}sul\tan t} - (\sum n_i \Delta H_i^0)_{\text{Re}ac\tan t} \tag{11}$$

$$\Delta \text{S}_{298}^0 = (\sum n_i \Delta \text{S}_i^0)_{\text{Re}sul\tan t} - (\sum n_i \Delta \text{S}_i^0)_{\text{Re}ac\tan t} \tag{12}$$

Table 1 listed the reference data of thermodynamic [12-14]. If we introduced these data to Eq.3 and 4, we could get the reaction equilibrium constant of TiO (Kα) [15]. After that, we could get the reaction equilibrium constant of TiO, and the detail was shown in Eq.13 and Eq.14:

$$K_1 = \exp\left(23.19 + 1.948\times10^{-3}T + 0.73\times10^5 T^{-2} - 3.03\ln T - 11260T^{-1}\right) \tag{13}$$

$$K_2 = \exp(29.61 + 0.51\times10^{-3}T + 2.45\times10^{5}T^{-2} - 2.42\ln T - 61997T^{-1}) \quad (14)$$

TABLE 1 THERMO CHEMICAL DATA BASE OF THE REACTANTS AND RESULTANTS [12-14]

Constituents	State	Parameters			Temperature	Value
Al_2O_3		A_1	A_2	A_3		ΔH^0_{298K}=-400
	Solid	27.43	3.06	-8.47	298-1800K	
		C_1	C_2	C_3		S^0_{298K}=12.2
		27.43	3.06	4.23		
TiO		A_1	A_2	A_3		ΔH^0_{298K} =-124.19
	Liquid	10.57	3.06	-1.86	—	
		C_1	C_2	C_3		S^0_{298K} =8.31
		10.57	3.06	0.93		
TiO_2		A_1	A_2	A_3		ΔH^0_{298K} =-218.21
	Solid	17.99	0.28	4.35	298-1800	
		C_1	C_2	C_3		S^0_{298K} =12.02
		17.99	0.28	-2.18		
Al						S^0_{298K} =6.77
		A_1	A_2	A_3		ΔH_m =2562
						ΔS_m =2.75
	Solid	4.93	2.96	0	298-932K	
	Liquid	7.60	0	0	932-1650K	
		C_1	C_2	C_3		
	Solid	4.93	2.96	0		
	Liquid	7.60	0	0		
Ti						$\Delta H_{\text{Transform}}$ =990
						$\Delta S_{\text{Transform}}$ =0.85
		A_1	A_2	A_3		ΔH_m =4450
						ΔS_m =2.30
						S^0_{298K} =7.32
					298-1155K	
	α	5.29	2.45	0	1155-1933K	
	β	4.74	1.89	0	1933-3574K	
	Liquid	8.5	0	0		
		C_1	C_2	C_3		
	α	5.29	2.45	0		
	β	4.74	1.89	0		
	Liquid	8.50	0	0		

Remarks: ΔH_m and $\Delta H_{\text{Transform}}$: cal/mol; $\Delta S_{\text{Transform}}$, ΔS_m and S^0_{298K}: cal/mol; ΔH^0_{298K}: Kcal/mol.

where K_1 was the reaction equilibrium constant of TiO, and K_2 was the reaction equilibrium constant of TiO_2. From Eq.13 and 14, the value of Kα would be enlarged with the brazing temperature

increased, and the reaction equilibrium would also lead the resultant increasing direction; if the brazing temperature decreased, the value of Kα would decrease, and the process of interface reaction would be restrained too.

In some paper, Eq.15 was used to calculate Gibbs free energy between Ti and Al_2O_3 [16]:

$$\Delta G_T^0 = \Delta H_0 + 2.303aT\log T + b\times10^{-3}T^2 + c\times10^5 T^{-1} + I\bullet T \tag{15}$$

where ΔH_0 was -407950; 2.303a was -6.19; b was -0.78; c was +3.935; and I was +102.37. At 830℃, ΔG_{830}^0 was +19899 cal/mol. Here, we need consider the thermodynamic correction term ($\Delta G_{Correction}^0$). For example, Ti was liquid phase at brazing temperature (lower than its melting point). We need add it with the solid entropy change from brazing temperature to Ti melting point ($\Delta S_{(s)} = \int_{T(Bracing)}^{2000} C_S \frac{dT}{T}$) and the liquid entropy change from Ti melting point to brazing temperature ($\Delta S_{(l)} = \int_{2000}^{T(Bracing)} C_L \frac{dT}{T}$). So $\Delta G_{Correction}^0$ could be described by Eq.16:

$$\Delta G_{Correction}^0 = \Delta H - T(\Delta S_{(L)} + \Delta S_{(S)}) \tag{16}$$

If the brazing temperature was 830℃, $\Delta G_{Correction}^0 = 20457$ cal/mol; the real Gibbs free energy change of Al_2O_3 reduction reaction ($\Delta G_{\text{Real}}^0 = \Delta G_T^0 - \Delta G_{Correction}^0$) was -558 cal/mol, indicating that this reaction could decrease the system energy, so this reaction could occur spontaneously. If Ti was in solid state ($\Delta G_{Correction}^0 > 0$), this reaction could not occur spontaneously. Otherwise, the reaction system temperature need be increased. Ti active atom dissolved in Ag-Cu alloy liquid solution; it not only lowered the required brazing reaction temperature, but also released the stress in brazing process. From Fig.4, there was a very narrow nanometer TiO_2 layer near to Al_2O_3 surface. Based on the thermodynamic theory without correction, the resultant product of TiO_2 was difficult to be formed at 845-860 ℃ because Ti could not reduce Al_2O_3 in equilibrium system. But TiO_2 layer really existed in the reaction zone; the main reason was that the brazing process was in a high vacuum (1×10^{-4} Pa) and metal alloy liquid solution system; the resultant (for example, Al) can be evaporated or dissolved in alloy liquid [17], and it could help the resultant to be removed, so the atoms of titanium and oxygen could be easily combined to TiO_2; it would lead the different resultant products other than that of equilibrium reaction. The binary phase diagram of Ti-O presented in Ref. [18] predicted that if the oxygen concentration was above 37 wt% at brazing temperature, the resultant would be TiO_2; if the oxygen concentration was about 18-37 wt% at brazing temperature, the resultant would be TiO; and this experimental phenomena in this work was a direct proofs for their predictions.

In the real reaction layer, there were Cu_2Ti_4O, Ti and $AlAg_3$, and the brazing reaction between Al and Ag could be described by Eq.17 [10]:

$$(Al) + 3(Ag) \rightarrow AlAg_3 \tag{17}$$

Near to the side of Al_2O_3, TiO_2 (high valence compound) could be easily formed because of the richness of oxygen. When the distance to reaction interface increased, TiO (low valence compound) could be popularly formed because of the difficulty of oxygen atom diffusing. Near to the side of AgCuTi filler metal, partial of TiO would dissolve into Cu-Ti to form IMC. Ref. [18] reported the phase diagram of TiO in Cu-Ti. According to Ref. [19], if the titanium concentration in reaction zone was higher than 30%, there were two kinds of $(Cu,Ti)_6O$ ternary complex oxides, Cu2Ti4O and Cu_3Ti_3O, and the resultant product of Cu_3Ti_3O could be formed through Eq.18:

$$3Ti_4Cu_2O + 5O_{(Al_2O_3)} \rightarrow 2Ti_3Cu_3O + 6TiO \quad (18)$$

In this experiment, the element concentrations of IMC layer (Cu, Ti and O) was near to the chemical composition of Cu_2Ti_4O, maybe the feasibility of reaction would be restrained by reaction kinetics or the shortage of reactant. Based on the research of G. P. Kelkar [20], $\Delta G_f^0(Ti_4Cu_2O)$ was -120 kcal/mol at 945 ℃, and $\Delta G_f^0(Ti_3Cu_3O)$ was -122 kcal/mol at 945 ℃. So these two kinds of ternary complex oxides were stable thermodynamically, and the real resultant was depended on the reaction kinetics. Ti would cluster in the reaction interface, and it was favorable to the formation of Cu_2Ti_4O.

Conclusions

The interface reaction between Al_2O_3 and $Ag_{70.5}Cu_{27.5}Ti_2$ was confirmed by SEM and EDS, and TiO_2 nanometer layer was also detected near to the Al_2O_3 side. Based on the thermo-chemical data of reactant and resultant, the resultant enthalpy was calculated, and the entropy change after the brazing condition correction items was introduced. It was found that the vacuum and alloy liquid solution were beneficial to the brazing process. The formation of TiO_2 and TiO were calculated according to the binary phase diagram of Ti-O. The result showed that the oxygen concentration played an important role in interface reaction, and Ag could not directly react with Al_2O_3, but it decreased the resultant concentration (Al). Finally, the reason for the formation of Cu_2Ti_4O was analyzed.

Acknowledgement

This work was supported by National High Technology Research and Development Program of China (Grant no. 2011AA03A110), National Basic Research Program of China (Grant no. 2009CB623600, 2009CB930604 and2014CB643500), National Natural Science Foundation of China (Grant no. 61204087, 51173049, U0634003, 61036007, 60937001 and U1301243), the Flat Display Foundation of Guangdong Province, China (Grant no. 20081202), Guangdong Innovative Research Team Program (Grant no. 201101C0105067115).

References

[1] R. Soltani Tashi, S. A. A. Akbari Mousavi, M. Mazar Atabaki, Diffusion brazing of Ti–6Al–4V and austenitic stainless steel using silver-based interlayer, Materials and Design. 54 (2014) 161-167.

[2] Tuan Zaharinie, Raza Moshwan, Farazila Yusof, M. Hamdi, Tadashi Ariga, Vacuum brazing of sapphire with Inconel 600 using Cu/Ni porous composite interlayer for gas pressure sensor application, Materials and Design. 54 (2014) 375-381.

[3] Qiaoli Lin, Ran Sui; Wetting of B4C by molten Ni–Ti alloys at 1753 K, Journal of Alloys and Compounds. 577 (2013) 37-43.

[4] W. J. Zhu, J. Wang, H.S. Liu, Z. P. Jin, C. Leinenbach, Modeling and simulation of the TiC reaction layer growth during active brazing of diamond using DICTRA, Computational Materials Science. 78 (2013) 74-82.

[5] K. L. Lin, Mrityunjay Singh, Rajiv Asthana, C. H. Lin, Interfacial and mechanical characterization of yttria-stabilized zirconia (YSZ) to stainless steel joints fabricated using Ag–Cu–Ti interlayers, Ceramics International. 40 (2014) 2063-2071.

[6] Z. W. Yang, L. X. Zhang, Y. C. Chen, J. L. Qi, P. He, J. C. Feng, Interlayer design to control interfacial microstructure and improve mechanical properties of active brazed Invar/SiO_2–BN joint, Materials Science and Engineering: A. 575 (2013) 199-205.

[7] L. C. Tsao, Microstructural characterization and mechanical properties of microplasma oxidized TiO_2/Ti joints soldered using $Sn_{3.5}Ag_4Ti(Ce)$ active filler; Journal of Materials Science, Materials in Electronics. 25 (2014) 233-243.
[8] M. X. Yang, P. He, T. S. Lin, Effect of Brazing Conditions on Microstructure and Mechanical Properties of Al_2O_3/Ti–6Al–4V Alloy Joints Reinforced by TiB Whiskers, Journal of Materials Science & Technology. 29 (2013) 961-970.
[9] W. F. Ding, Q. Miao, J. H. Xu, Z. Z. Chen, C. Y. Yang, Y. C. Fu, Preparation mechanism and grinding performance of single-layer self-lubrication brazed CBN abrasive wheels, The International Journal of Advanced Manufacturing Technology. 68 (2013) 249-255.
[10] H. L. Ning, Z. T. Geng, J. S. Ma, F. X. Huang, Z. D. Han, J. Y. Cui, Research of alumina and brazing filler metal interface, Materials Science Forum. 423-425 (2003) 495-500.
[11] H. L. Ning, Z. T. Geng, J. S. Ma, F. X. Huang, Z. Y. Qian, Z. D. Han, Joining of sapphire and hot pressed Al_2O_3 using $Ag_{70.5}Cu_{27.5}Ti_2$ filler metal, Ceramics international. 29 (2003),689-694.
[12] H. Q. Hao, Ph. D. dissertation, Xi'an Jiaotong University, April (1995).
[13] D. L. Ye, Practical handbook of thermodynamic data of inorganic, Beijing, Metallurgical Industry Press (1981).
[14] L. Z. Chen, Physical chemistry, Shanghai, Shanghai Scientific &Technical Publishers (1988).
[15] D. C. Liu, The alumina ceramics and its sintering, China Ceram. 34 (1998) 13-15.
[16] L. Q. Gao, The art for practical technology of ceramic to metal seal, Beijing, Chemical industry press (2005).
[17] H. Lu, C. L. Bao, D. H. Shen, X. J. Zhang, Y. D. Cui, Z. D. Lin, Study of the Ti/Al_2O_3 interface, Journal of Materials Science. 30 (1995) 339-346.
[18] S. Yamaguchi, K. Hiraga, M. Hirabayashi, Interstitial Order-Disorder Transformation in the Ti-O Solid Solution IV: A Neutron Diffraction Study, Journal of the physical society of Japan. 28 (1970) 1014-1023.
[19] J. L. Murray, Phase Diagrams of Binary Titanium Alloys, ASM International, Materials Park, OH, (1987).
[20] G. P. Kelkar, K. E. Spear, A. H. Carim, Thermodynamic evaluation of reaction products and layering in brazed alumina joints, Journal of Materials Research. 9 (1994) 2244-2250.

Advanced Materials Research Vol. 936 (2014) pp 1247-1251
© (2014) Trans Tech Publications, Switzerland
doi:10.4028/www.scientific.net/AMR.936.1247

Influence of deformation on aging precipitation behavior of anAl-Cu-Mg-Si alloy

Xiwu Li[a], Baiqing Xiong[b], Yongan Zhang[c], Yanqi Zeng, Feng Wang, Zhihui Li, Hongwei Liu, Huang Shuhui

State Key Laboratory of Nonferrous Metals and Processes, General Research Institute for Nonferrous Metals, No.2 Xinjiekou Wai Street, Beijing, China

[a] lixiwu@grinm.com, [b] xiongbq@grinm.com, [c] zhangyongan@grinm.com

Keywords: Al-Cu-Mg-Si alloy, precipitation, deformation, σ phase, S' phase.

Abstract. To meet the stringent requirements of heat-resistance products for aerospace applications, an Al-4.0Cu-1.3Mg-0.6Si alloy containing a cubic σ phase ($Al_5Cu_6Mg_2$) with excellent high temperature stability was developed. Influence of deformation on aging precipitation behavior of the alloy was investigated by transmission electron microscope (TEM) and differential scanning calorimetry (DSC). The results indicated that cold deformation had great effect on aging precipitation behavior in the alloy. When the alloy was processed a pre-stretching deformation before aging, the precipitation of σ phase was restrained while the S′ phase (Al_2CuMg) was promoted. And the nucleation sites played an important role on them.

Introduction

Al-Cu-Mg (2xxx series) alloys are light materials widely used in aerospace applications because their hardness, ductility and superior creep strength at elevated temperatures [1]. The precipitation sequence of Al-Cu-Mg alloys could become very complex depending on the Cu/Mg ratio and trace alloy additions. Many studies have been carried out in order to examine and predict the influence of suitable trace alloy additions on the nucleation of desired precipitates in age-hardenable Al alloys. Several secondary phases have been found in Al-Cu-Mg alloys, including θ, S, Ω and σ phases [2~6]. Among them the cubic σ phase ($Al_5Cu_6Mg_2$) has a simple cube-on-cube orientation relationship with the aluminum matrix. It precipitates as the semi-coherent or coherent phase with a high solvus (above 700°C), which makes it quite stable at high temperatures, above 200°C. So σ phase is known as a very promising new heat-resistant strengthening phase. And some reviews show that small additions of Si to Al-Cu-Mg alloys can induce the formation of σ phase during artificial aging at commercial aging temperature [7~9]. With the rapid development of the new generation of aerospace vehicles, new Al-Cu-Mg series heat-resistance alloys that can be used at a higher service temperature are urgently required. Therefore, to make sure the precipitation behavior of σ phases becomes a concern. To meet the stringent requirements of heat-resistance products for aerospace applications, an novel Al-Cu-Mg-Si alloy containing a cubic σ phase with excellent high temperature stability was developed [10,11].

Moreover, recent demand for weight reduction in aircraft structural component calls for further enhancement in strength of commercial structural alloys. So, it may be of interest to examine the possibility of enhancing the strength of age hardenable aluminum alloys [12]. Therefore, in addition to control the suitable type of precipitation strengthening phase, cold deformation prior to aging is applied widely in the industry to increase the aging response particularly for the strength of 2xxx series alloys. The objective of this study was to investigate the effect of cold pre-deformation on aging precipitation behavior of an novel Al-4.0Cu-1.3Mg-0.6Si alloy.

Experimental Procedures

Additions of 0.6 wt% Si was made to a base alloy composition of Al-4.0Cu-1.3Mg (wt%), as shown in Table 1. Ingots of approximately Φ210 mm were produced by mold casting. After casting,

the billets were homogenized at 490°C for 24 h, and subsequently at 520°C for 12 h, followed by air cooling to room temperature. The billets were then scalped to 190 mm diameter and extruded at 420 °C into plates of 102 mm ×25 mm in cross-section (extrusion ratio 12.6:1). Specimens were solution heat treated at 500~520°C for 1~3h and then water quenched to room temperature. In order to contrast the influence of deformation on the precipitation of the A1 alloy, a 3% pre-stretch deformation was applied. And finally the A1 alloy both of with deformation and without deformation aged for appropriate time at 190°C.

The quenched as well as pre-stretched deformation samples were subjected to DSC to study the precipitation using the heating rate at 10°C/min up to a temperature of 500°C. DSC studies were carried out in a NETZSCH STA 409C/CD instrument using high purity argon gas atmosphere. The specimens for DSC studies were mechanically thinned and the thin slice weighing about 18mg was cut out of the sample strip. Specimens for TEM were thinned by electropolishing using a twin-jet polisher with a 25% nitric acid solution in methanol at -30°C and 15~20 V. The specimens were examined in selected area electron diffraction (SAED) and bright field (BF) imaging modes in a JEOL 2010FX microscope, operating at 200 kV.

Table 1 Composition of the alloys used in the present study (wt%)

Alloy Designation	Cu	Mg	Si	Al
A0	4.0	1.3	-	Bal.
A1	4.0	1.3	0.6	Bal.

Results and Discussion

DSC Curves. The Fig.1 shows the DSC thermogram of A0 alloy (Al-4.0Cu-1.3Mg) in quenching state, the A1 alloy (Al-4.0Cu-1.3Mg-0.6Si) in quenching state and A1 in 3% pre-stretch deformation state after quenching. It can be seen from Fig.1, in the process of heating up, for both of the A0 and A1 alloy in the DSC curve appeared an obvious exothermic peak in 265~300°C (mark A). The difference is that there appeared another exothermic peak between 240~260°C (mark B) in the DSC curve of the A1 alloy. Combined with the previous result, exothermic peak A is corresponding to the precipitation of S (S′) phase. Here a preliminary inference can be obtained that exothermic peak B should correspond to σ phase. For the A1 alloy with 3% pre-stretching deformation, exothermic peak A corresponding to S phase became wider, the area of the exothermic peak increases slightly, and exothermic peak B area corresponding to σ phase significantly decreased. Thus, it can be inferred that cold deformation has great effect on aging precipitation behavior in the alloy.

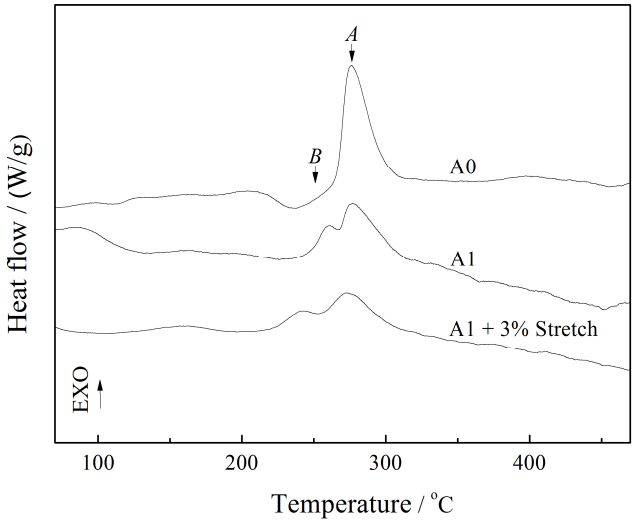


Fig.1 DSC thermogram of A0 and A1 alloy in different condition

Microstructure. Al-Cu-Mg alloys with a Cu:Mg ratio in the range 1.5:1 to 4:1 are strengthened the S′ phase. Therefore, S′ phase was the dominant precipitate in the A0 alloy (Al-4.0Cu-1.3Mg). Si addition can promote the precipitation of σ phase in the alloys. Representative TEM micrographs and corresponding $[100]_{Al}$ selected area electron diffraction (SAED) patterns of the A1 alloy (Al-4.0Cu-1.3Mg-0.6Si) without deformation in aged condition are presented in Fig.2. Fig. 2(a) and (b) shows the typical bright field (BF) image and corresponding SAED pattern, respectively, it can be seen that there are two shapes of precipitate existed in the alloy, including cubic-shaped and lath-shaped precipitate which are matching to σ phase and S′ phase ,respectively. A detailed analysis of the FFT image (shown in Fig.2(d)) indicates that the cubic-shaped precipitate is in agreement with σ phase. Diffuse spots near n/2 {100} positions associated with σ phase were clearly observed; the σ phase was showed to be a semi-coherent or coherent and coplanar phase with the Al matrix, i.e.,$\{100\}_{\sigma}//\{100\}_{Al}$ and $<100>_{\sigma}//<100>_{Al}$.

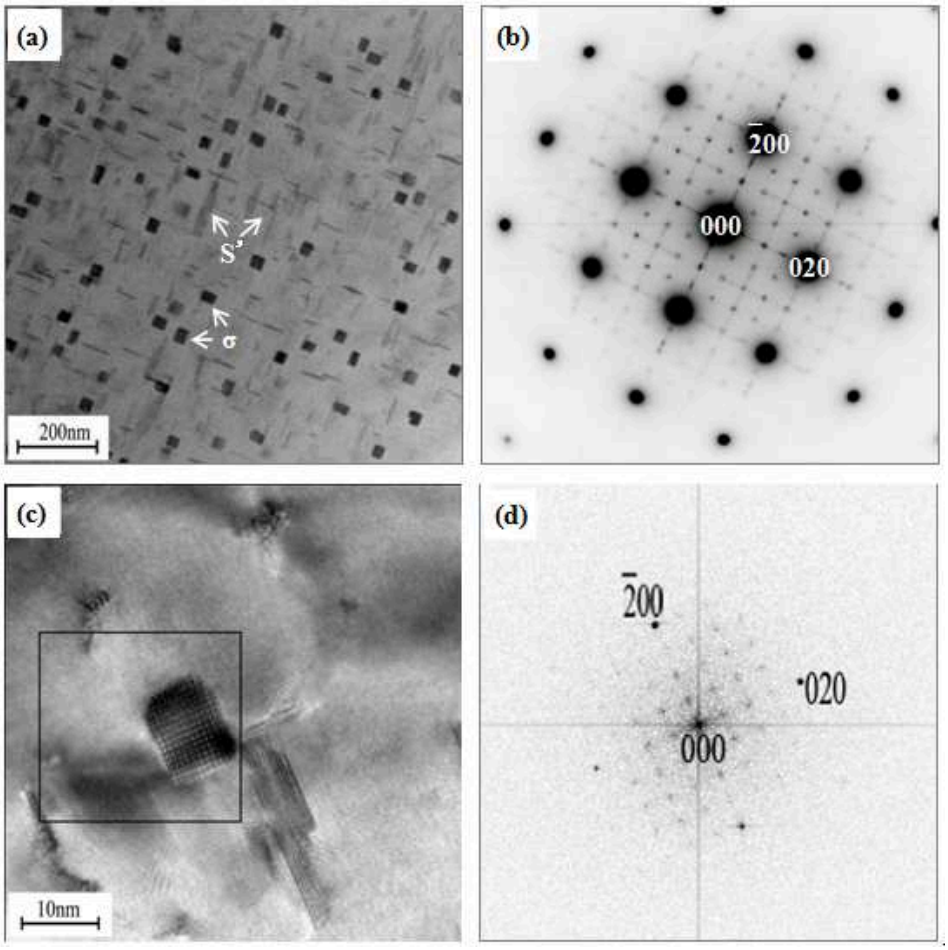


Fig.2 TEM BF images and SAED pattern near the $[001]_{Al}$ of the A1 alloy without deformation in aged condition a,c) BF images; c) SAED pattern in $[110]_{Al}$; (d) the corresponding FFT diffractogram

Fig.3. provides TEM micrographs and corresponding $[100]_{Al}$ SAED pattern of the A1 alloy (Al-4.0Cu-1.3Mg-0.6Si) with 3% pre-stretching deformation in aged condition. Fig. 3(a) shows the typical BF image, comparing to Fig.2(a), it can be found that with deformation, σ phase almost disappeared. And S′ phase is dominant, which can be validated by the corresponding SAED pattern as shown in Fig.3(b). By all appearances, there appear amounts of dislocation in the matrix after deformation. This suggests that the S′ phase precipitation occurs easily by heterogeneous nucleation at dislocations, and σ phase is prone to precipitation of homogeneous nucleation. Presence of dislocation was helpful for heterogeneous nucleation of the S′ phase, but not conducive to homogeneous nucleation of σ phase. Therefore, in the case of the alloy, to precipitate a large amount

of σ phase in order to obtain a good heat resistance property, the traditional pre-deformation technology for 2xxx series aluminum alloy is not suitable.

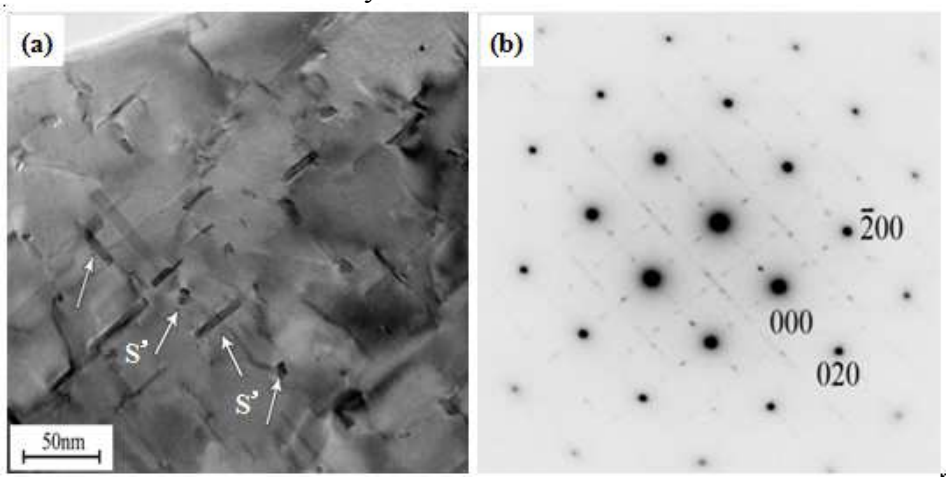


Fig.3 TEM BF images and SAED pattern near the $[001]_{Al}$ of the A1 alloy with 3% pre-stretching deformation in aged condition

a) BF images; b) SAED pattern in $[110]_{Al}$

Summary

Cold deformation had great effect on aging precipitation behavior in the Al-4.0Cu-1.3Mg-0.6Si alloy. In the alloy, in addition to the S′ phase, a cubic phase previously designated σ phase ($Al_5Cu_6Mg_2$) was appeared in large quantities. When the alloy was processed a pre-stretching deformation before aging, the precipitation of σ phase was restrained while the S′ (Al_2CuMg) phase was promoted. And the nucleation sites played an important role on them. Large numbers of dislocation were helpful for heterogeneous nucleation of the S′ phase, but not conducive to homogeneous nucleation of σ phase. In the case of the alloy, the traditional pre-deformation technology for 2xxx series aluminum alloy is not suitable.

Acknowledgement

This work was supported by the National Natural Science Foundation of China (Grants No. 51004018). The authors are also grateful to Dr. Zhiwei Du and Dr. Xin Fu for the TEM work.

References

[1] I.J. Polmear. Light alloys: Metallurgy of the Light Metals. New York: John Wiley, 1995.

[2] L. Kovarik, P.I. Bouma, C. Kisielowski, et al. A HRTEM Study of Metastable Phase Formation in Al-Mg-Cu Alloys During Artificial Aging. Acta Mate. 52 (2004) 2509-2520.

[3] S.P. Ringer, B.T. Sofyan, K.S. Prasad, et al. Precipitation Reactions in Al-4.0Cu-0.3Mg (wt.%) Alloy. Acta Mater. 56 (2008) 2147-2160.

[4] R.N. Lumley, A.J. Morton, I.J. Polmear. Enhanced Creep Performance in an Al-Cu-Mg-Ag Alloy Through Underageing. Acta Mater. 50 (2002) 3597-3608.

[5] S.C. Wang, M.J. Starink. Two Types of S Phase Precipitates in Al-Cu-Mg Alloys. Acta Mater. 55 (2007) 933-941.

[6] R.D. Schueller, F.E. Wawner. Nucleation Mechanism of the Cubic σ Phase in Squeeze-cast Aluminium Matrix Composites. J. Mater. Sci. 29 (1994) 424-435.

[7] I.C. Barlow, W.M. Rainforth, H.J. Jones. The Role of Silicon in the Formation of the (Al5Cu6Mg2) σ Phase in Al-Cu-Mg Alloys. J. Mater. Sci. 35 (2000) 1413-1418.

[8] A.K. Mukhopadhyay. Coprecipitation of Ω and σ Phases in Al-Cu-Mg-Mn Alloys Containing Ag and Si. Metall. Mater. Trans. 33A (2002) 3635-3648.

[9] P. Rodrigo, P.Poza, M.V. Utrilla, et al. Identification of σ and Ω Phases in AA2009/SiC Composites. J. Alloys Compounds. 482 (2009) 187-195.

[10] Xiwu Li, Baiqing Xiong, Yongan Zhang, et al. Influence of Silicon Addition on Precipitqtion Behavior in an Al-Cu-Mg alloy. Proceeding of ICAA13, 2012, pp1289-1294.

[11] Wang Feng, Zeng Yanqi, Xiong Baiqing, et al. Effect of Si addition on the microstructure and mechanical properties of Al-Cu-Mg alloy. J. Alloys Compounds. 585 (2014) 474-478.

[12] S. K. Ghosh. Influence of Cold Deformation on the Aging Behaviour of Al-Cu-Si-Mg alloy. J. Mater. Sci. Technol. 27 (2011) 193-198.

Advanced Materials Research Vol. 936 (2014) pp 1252-1257
© (2014) Trans Tech Publications, Switzerland
doi:10.4028/www.scientific.net/AMR.936.1252

Workpiece surface integrity of GH4169 Nickel-based Superalloy when employing abrasive belt grinding method

Guijian Xiao[1,2,a], Yun Huang[1,2,b], Yuhang Yang[1,2,c], Hao Yi[1,2,d],

[1]College of Mechanical Engineering, Chongqing University, Chongqing 400030, China;

[2]Chongqing material surface precision processing and equipment engineering technology research center, Chongqing 400021, China

[a]xiaoguijian@126.com, [b]yunhuang@samhida.com, [c]394500821@qq.com, [d]1515556950@qq.com

Keywords: Nickel-based Superalloy; Belt grinding; Grinding ratio; Surface integrity; Surface roughness

Abstract: The use of GH4169 nickel-based superalloy for the manufacture of gas turbine engines components for aerospace/energy applications has become a routine exercise. However, components with complex designs specifications might pose manufacturing challenges especially when grinding processes are needed to enable their compliance with tight industrial standards for workpiece surface integrity. Information on grinding processes for such sensitive industrial applications is scarce. The paper reports on the influence of grinding methods/strategies on the quality and integrity of workpiece surfaces obtained after abrasive belt grinding methods on GH4169 nickel-based superalloy. The influences of grinding speed, contact pressure and oscillation frequency on surface roughness were discussed. The performance of the abrasive belt and surface topography were discussed. As a result, the maximum surface roughness of Ra is 0.072μm, and have a good performance of the abrasive belt, it could be concluded that abrasive belt grinding might be considered as a viable process for grinding aero-engine components.

Introduction

Superalloy, also called heat-resistant alloy, has high strength, excellent thermal stability and thermal fatigue resistance. Because of it can be long-term reliable working under complex stress with oxidation and gas corrosion in 600℃~1100℃, widely be used in aviation, aerospace, marine and chemical industry[1]. It also was used for the hot end components for the engine in the aviation industry, such as turbine blade, turbine, afterburner, turbine shaft and so on. Usually, the aero-engine components worked in the corrosive medium and alternating load environment, so the service life of parts were reduced by the poor surface integrity which would accelerate the fatigue destruction. Therefore, investigating and mastering the grinding performance of superalloy is very important for the safety of aero-engine components[2-3].

Due to the especially characteristics of superalloy, including multi component alloy, low thermal conductivity, high temperature and hardness, and containing a large amount of carbides, nitrides, oxides, intermetallic compounds, making its grinding performance poorly, mainly reflected in:①the grinding ratio is very low(ordinary the grinding ratio of grinding wheel is G=1~2), due to the more serious abrasion wear and adhesion blocking when grinding the superalloy;②easily produce strong plastic deformation, so the force is much larger than ordinary steel material;③the heat induced into the workpiece is relatively low, so the heat is concentrated in the thin surface layer, leading to the grinding temperature is very high;④due to the comprehensive effect of grinding force and temperature, the surface quality is difficult to be guaranteed. Therefore, the development of grinding tool which having higher performance and improving grinding efficiency and quality for the superalloy, becoming a very urgent request[4-5].

Some attempts to implement abrasive belt grinding as a grinding process for the refurbished aero-space components have been reported. Axinte et al.[6] reported on belt polishing of heat-resistant titanium alloys. The work proved that belt polishing could fulfil both economical and

part quality requirements for finishing critical aero-engine components made of heat-resistant alloys such as Ti-6-4. High surface finish was achieved after belt polishing (Ra < 0.35μm). No evidence of thermally affected layers was found on the final polished workpiece surfaces. Particularly, Zhang et al. [7]reported on the topic of simulation involving acting force, depth of cut and tool path. Additionally, Nakayamaet al.[8] published the data on the use of the cooling media when using belt grinding.

Despite the report on the surface integrity of ti-6-4 heat-resistant alloy for the critical aero-engine components, no information has been reported on the properties (e.g. surface texture, sureface raughness) of the workpiece surface obtained after belt grinding/polishing especially to the GH4169 Nickel-based Superalloy. These properties are of paramount importance for the acceptance of belt grinding as a final grinding process by the aero-engine manufacturers.

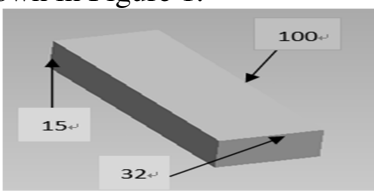
Equipment and methodology

Materials. The experiment material is nickel-based superalloy GH4169, which widely used in aero engines, and has superior performance in high wage environment, its performance parameters are shown in Table 1.

Table 1 Performance parameters of GH4169 nickel-based superalloy

Performance	Elasticity E/Gpa	Thermal λ/W.m	Elongation δ/%	Hardness HB	Impact a_K/(J.cm-2)	Shrinkage ψ/%	Melting /ºC
Parameters	205	14.65	15	346-450	573	41	1260-1320

The experiment specimen size of nickel-based superalloy GH4169 is 100mm×32mm× 15mm, as shown in Figure 1.



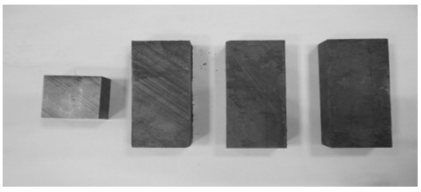


Figure 1 Experiment specimen

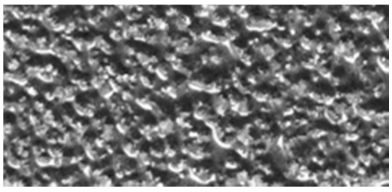


Figure 2 Abrasive belt

Abrasive belt: The abrasive belt CK918X, which is produced by German company VSM, is adopted in this experiment, belt size is 1950mm×50mm, 89#, as shown in Figure 2.

Equipment: The equipment, which is developed by the joint of the chongqing university and the chongqing three grinding Haida machine, is used in this experiment, with constant pressure in the grinding process, as shown in Figure 3. It is made of belt grinding head, driving device, tooling and fixture, the electric control system and other parts, and also equipped with frequency converter, which could achieve stepless speed regulation, is corresponding to the driving wheel of vector variable frequency speed regulation.



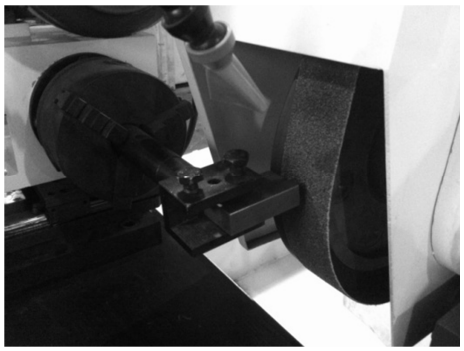


Figure 3 Constant pressure belt grinding machine

Methodology: The experiment methodology for the nickel-based superalloy specimen with abrasive belt grinding is carried out by the method of orthogonal experiment, orthogonal test table as shown in Table 2.

Table 2 Orthogonal test table

Factor	Level		
	1	2	3
Grinding speed（m/s）	18	26	34
Contact pressure（N）	30	60	90
Oscillation frequency（Hz）	0	2	1

The electronic scale is used for measuring the workpiece quality, its measurement accuracy is 0.1g; the stopwatch is used for recording the time of grinding; the roughness instrument TR200 is used for determination of surface roughness Ra by stylus method, which manufactured in Beijing times group.

Results and discussions

Performance of abrasive belt: The grinding ratio, *G*, is a measure of how much material is removed from the workpiece per unit volume of wheel wear.

$$G = \frac{V_w}{V_s} \quad (1)$$

Based on the (1) type derivation, can use the material removal rate to represent the grinding ratio, i.e.:

$$G = \frac{dV_w}{dV_s} = \frac{Q_w}{Q_s} \quad (2)$$

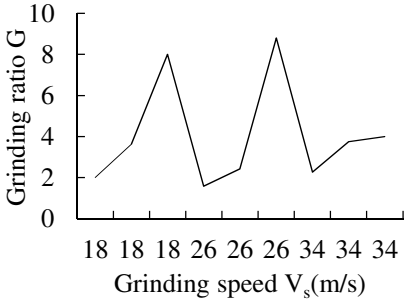


Figure 4 Grinding speed

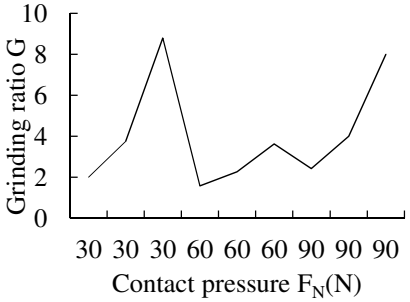


Figure 5 Contact pressure

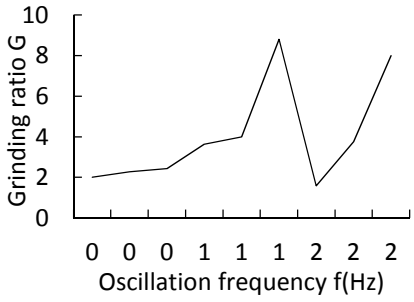


Figure 6 Oscillation frequency

A value of a grinding ratio of $G = 1$ is very low and implies that the abrasive is not hard enough for the task. A grinding ratio of $G = 1{,}000$ is high and may sometimes correspond to a wheel that is too hard for the task. For example, if the abrasive tool wears by a slow glazing of the grains, the machining forces will rise and may lead to various problems such as poor size-holding, vibrations, and poor surface texture. According to the figure 4-6, than G>2 abrasion abrasive belt grinding, its maximum value can reach 8.8, and the grinding wheel wear than G=1~2, so it can confirm the superiority of abrasive belt grinding.

Surface roughness: According to the orthogonal range analysis of surface roughness to the belt grinding of nickel-based superalloy GH4169, as shown in Figure 7, the largest effect of grinding parameter on surface roughness is oscillation frequency, followed by the contact pressure, and then is the grinding speed. At the same time, the optimal combination of process parameters were obtained on the surface roughness, including grinding speed is 26m/s, contact pressure is 30N and oscillation frequency is 2Hz.

(1) Influence of grinding speed to the surface roughness

As shown in Figure 8, with the more increase of belt speed, the better of surface roughness, combined with range analysis in the Figure 7, the best surface roughness is in the middle grinding speed. This is mainly because, on the one hand, easy to burn in condition of high grinding speed; on the other hand, the grinding zone which cutting into workpiece is increased with the lower grinding speed, so the roughness is poorly.

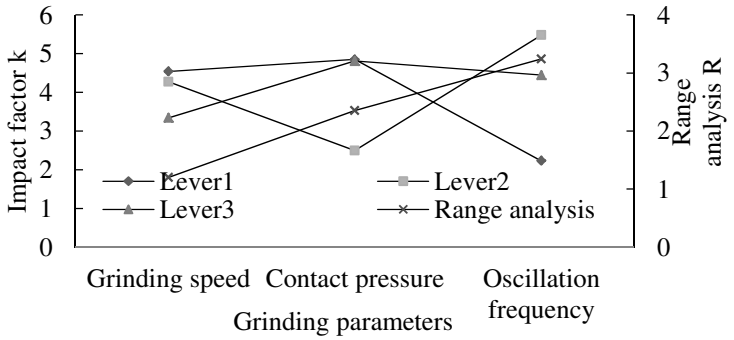


Figure 7 Orthogonal range analysis of surface roughness

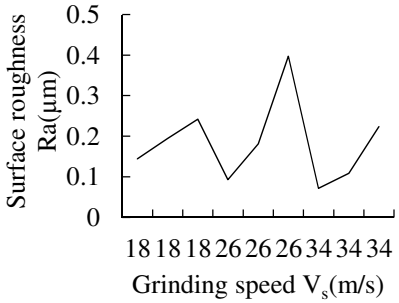


Figure 8 Grinding speed

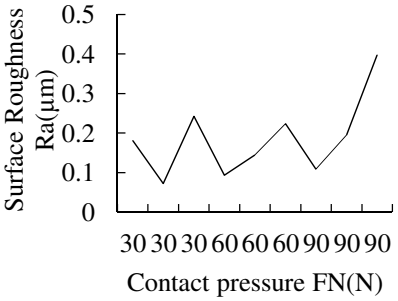


Figure 9 Contact pressure

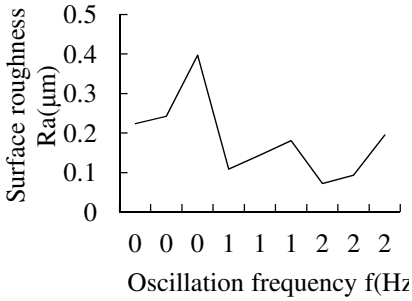


Figure 10 Oscillation frequency

(2) Influence of contact force to the surface roughness

As shown in Figure 9, the surface roughness changed poorly with the increase of contact pressure, the better of surface roughness, combined with range analysis in the Figure 7, the best surface roughness is in the middle grinding speed. This is mainly because, on the one hand, easy to burn in condition of high grinding speed; on the other hand, the grinding zone which cutting into workpiece is increased with the lower grinding speed, so the roughness is poorly. This is because that, the surface roughness is directly to the particle number Ng and the particle shape which participated in the grinding process. The particle number Ng is increased with the increase of contact pressure under lower contact pressure, so the amount of grinding surface roughness decreases uniformly. But under the higher grinding pressure, the surface roughness is increased slowly with the particle fast wear.

(3) Influence of oscillation frequency to the surface roughness

As shown in Figure 10, the surface roughness as oscillation frequency increased, of the rapid rise in. This is because thetransverse vibration of the belt grinding surface grinding trackis complex and is not repeated, i.e. the mesh lines, to reduce the surface roughness.

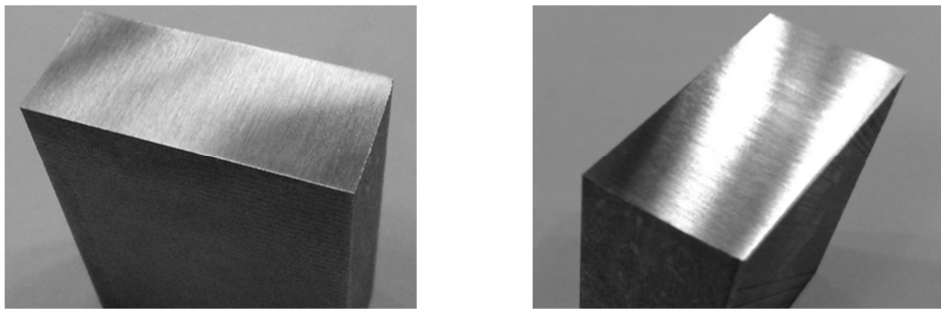


Figure 11 Surface quality of GH4169 nickel-based superalloy after belt grinding

As shown in Figure 11, the surface quality of GH4169 nickel-based superalloy after belt grinding is very good, for the surface quality, surface roughness can reach 0.072μm, more rather than 0.35μm, so it also can confirm the superiority of abrasive belt grinding.

Surface topography: The high precision and material removal processing is achieved through the analysis of the surface topography, combined with the discussion of surface roughness and grinding ratio.

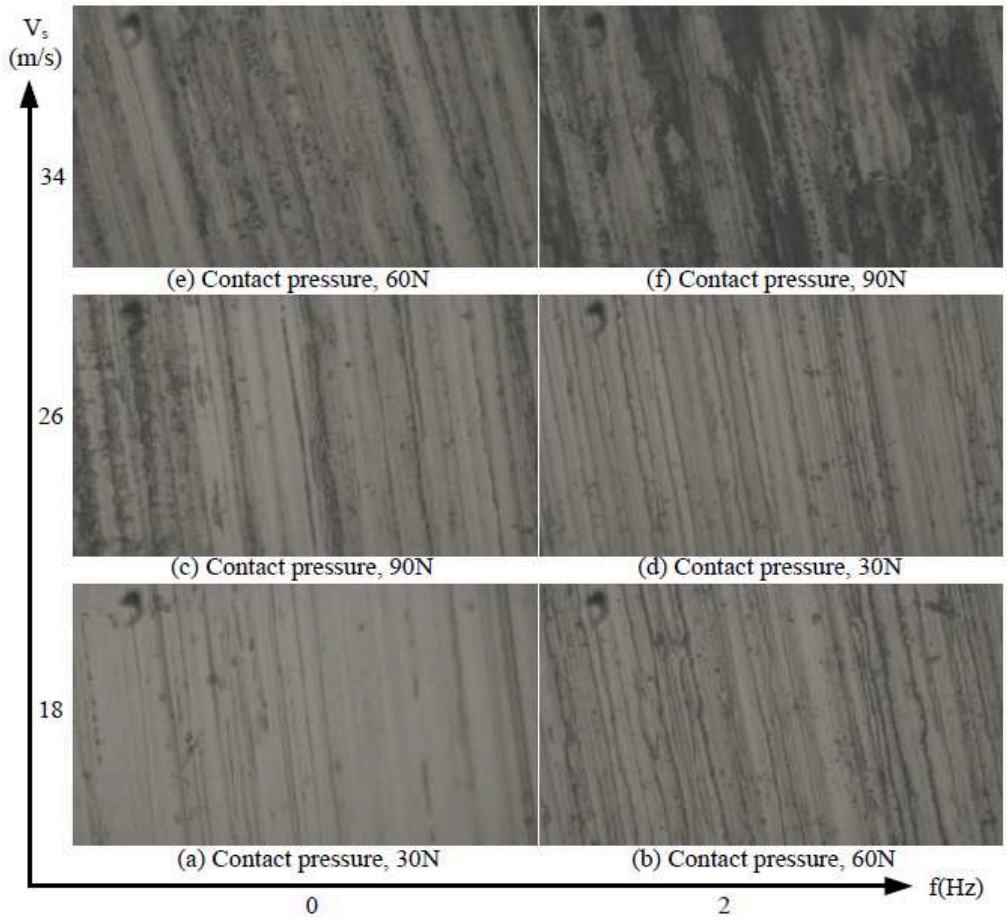


Figure 12 Analysis of surface topography

(1) Influence of grinding speed to the surface topography

As shown in Figure 12(a, d), the grinding depth is improved with the increase of grinding speed, which is useful to remove the surface texture of milling. But As shown in Figure 12(b, e) and (c, f), the grinding depth decreased as the grinding speed is too high, and also having negative effect on material removal, even easily causing workepiece surface burn. The workpiece burn is avoided by increasing the oscillation frequency as the higher grinding speed for the cutting ability to the surface texture of milling, as shown in Figure 12d. This is mainly because, with the increase of grinding speed, the cutting heat and the cutting ability is increased at the same time, and also leading to the temperature of the workpiece surface layer is difficult to dissemination timely, the temperature is distributed by increasing the oscillation frequency, and the high material removal and high precision are obtained. But if the grinding speed is too high, as shown in Figure 12(e, f), the surface is burned very serious.

(2) Influence of contact force to the surface topography

As shown in Figure 12, combining the analysis of grinding ratio, the grinding ratio is wear is relatively large as the higher or lower contact pressure, but the workpiece surface is burned as the contact pressure is too high, as shown in Figure 12(c, f). The high material removal and high precision are obtained by increasing the belt speed and oscillation frequency under low pressure. This is mainly because, the material removal is increased as the contact pressure is too large, but the plastic deformation of the workpiece surface is easy to increased, and then the abrasive belt wear serious, at the same time, the surface of workpiece is burned seriously.

(3) Influence of oscillation frequency to the surface topography

As shown in Figure 12(a, d) and (c, f), the oscillation frequency is improved not only help to improve the material removal, but also can increase the removal ability of milling mark, at the same time ensuring the surface quality.

This is mainly because, with the increase of oscillation frequency, on the one hand, the debris is removed, and the grit removal ability is increased; on the other hand, the temperature is distributed

easily, avoiding the contact pressure is too concentrated, which is resulting in the workpiece surface plastic deformation.

Therefore, in order to achieve efficient, high quality grinding the GH4169 nickel-based superalloy, the lower contact pressure, moderate grinding speed and higher oscillation frequency should be chosen.

Summary

In this paper, the grinding characteristics of the process is optimized by using the technology of abrasive belt grinding, which could reduce the impact of grinding force variation, caused by the plastic deformation. And then reduced the comprehensive effects of the grinding force and temperature, the project of high efficiency and high precision grinding are achieved.

(1) The experiment for the nickel-based superalloy specimen with abrasive belt grinding is carried out by the method of orthogonal experiment, combining with the range analysis, the optimal processes are obtained for the surface integrity: the contact pressure is 30N, the oscillation frequency is 2Hz, the grinding speed is 26m/s.

(2) The regular effect pattern of grinding process parameters to the surface roughness, surface topography and grinding ratio is obtained. The result shows that, in order to obtaining larger material removal and good surface quality, at the same time having lower abrasive belt wear, the lower contact pressure, moderate grinding speed and higher oscillation frequency should be chosen.

(3) The grinding ratio G would reach to 8.8, which much more than the grinding ratio G=1~2 of grinding wheel, by using the method of constant pressure abrasive belt grinding for the nickel-based superalloy GH4169, and the surface quality of GH4169 nickel-based superalloy after belt grinding is very good, for the surface quality, surface roughness can reach 0.072μm, more rather than 0.35μm, it could be concluded that belt grinding might be considered as a viable process for grinding aero-engine components.

Acknowledgment

This research is supported by the national natural science foundation of China(NO.51275545)

References

[1] D.L. Wang, J.P. Chen, et al: Tool Engineering, 38(2004)10-13

[2] P.H. Shen, Y.C. Fu, et al: Diamond & Abrasives Engineering, 32(2012)30-34

[3] P.K. Saha: Wear 258 (2005) 13–17

[4] Y. Huang, Z. Huang: Modern abrasive belt grinding technology and engineering applications, Chongqing, Chongqing University Press, 2009

[5] G.J. Xiao, Y. Huang, Z. Huang, et al: Mechanical Science and Technology for Aerospace Engineerding, 30(2011)92-97

[6] D.A. Axinte, J. Kwong, et al: Journal of materials processing technology, 209(2009)1843-1852

[7] X. Zhang, et al: International Journal of Advanced Robotic Systems, 1(2)109–114

[8] D.Novovic, R.C. Dewes, et al: International Journal of Machine Tools and Manufacture, 44,125–134.

Advanced Materials Research Vol. 936 (2014) pp 1258-1261
© (2014) Trans Tech Publications, Switzerland
doi:10.4028/www.scientific.net/AMR.936.1258

Studies on Refining Effect and Process Optimization about LF

Cheng Silong[1, a*]， Qi Xinxia[2, b]and Jia Qi[3, c]

[1] Railway administration of Zhengzhou,Zhengzhou 450000, China

[2]Zhuhai Campus Beijing Institute of Technology,Zhuhai 519088,China

[3]China Railway Construction Corporation Limited, Beijing 100855, China

[a]80773870@qq.com,[b]qixinxia@126.com, [c]jiaq07@qq.com

Keywords: LF furnace refining process metallurgy's effect.

Abstract: The refining process was investigated, it is the refining process about 100t LF refining furnace of an iron and steel group company, the refining effect was researched and systematic analyzed, by Through systematic sampling and detection to composition, slag, gas and inclusion of different refining period on LF furnace, the measures of process improvement have been proposed, to Optimization of production process and improve the quality of products.

Forewords

A firm has set up a 100t EAF-LF-CC production line, after few years of manufacture, the technology has been stabilized and productivity has been improved. This study is based on that production line, focused on perfect process, develop new product, and bring the ladle furnace refining ability into full play. This experimental program is: using specially made samplers to take slag sample, composition sample, air sample and inclusion sample when the furnace is production same type of steel under a stable working condition; then, take these samples to test and analysis trying to table a proposal of improve production process.

General Technologies

The 100t EAF furnace is using the so called "remaining slag and remaining steel" technology, eccentric bottom tapping and controlling the amount of slag outflow furnace, steel ladles will undergoing precipitation deoxidization and alloying process when the electric furnace is tapping. The ladle furnace is using CaO-Al_2O_3-SiO_2 slag system, major slag making materials are limes and bauxite which will be added separately, approximately 60% of these materials will become bedding material and added into steel ladle,The pre-desulfurization of self-fluxing slag system. The main component of molten slag is listed in Table 1.

TABLE 1 MAJOR CONTENT OF WHIT SLAGS

Slab grade	SiO/ %	Al_2O_3/ %	CaO/ %	MgO/ %	MnO/ %	FeO/ %	R(CaO/SiO_2)
A	16～18	19～23	49～52	3.74～4.86	0.33～0.54	0.36～1.24	2.75～3.16
B	13～18	23～27	49～53	3.91～5.11	0.22～0.48	0.38～2.17	2.76～4.25
C	14～21	21～26	47～53	2.47～5.03	0.33～1.34	0.35～1.24	2.18～3.80

Study of Ladle Furnace's Desulfurization Effet

As showed in reference [1], the desulfurization capacity and rate are influenced by factors such as basicity of slag (R), (FeO) content, quantity of slag, liquidity of molten slag, molten bath temperature and rabbling method. Based on the result of testing samples of this very ladle furnace under normal working condition, major influencing factors are analyzed below.

Desulfurization Capacity of Ladle Furnace's Refined Slag

Desulfurization capacity of molten slag is usually represented by the sulfur content in molten slag divide by sulfur content in molten steel, which is partition coefficient of sulfur (Ls= (%S) / [%S]). Reference [3] indicate that the Ls value could be as high as 235 with a high desulfurization capacity ladle furnace. According to the batch sampling analysis of this study, Ls value of this furnace could be as high as 250, the test result are showed below as Fig.1.

Fig.1 illustrated that Ls value would increase as refining time extend; after it reached 40min, the uptrend would slow down.

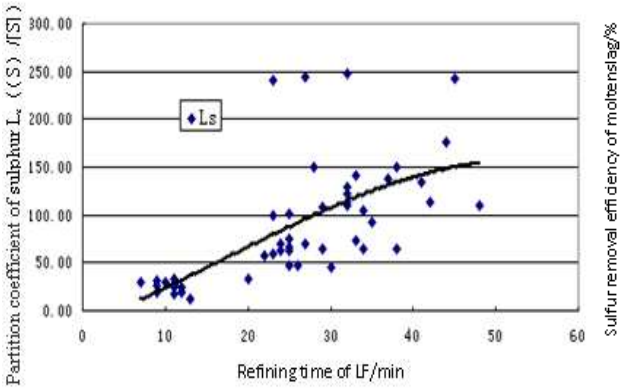


Fig.1 Relationship of refining time and Ls Value

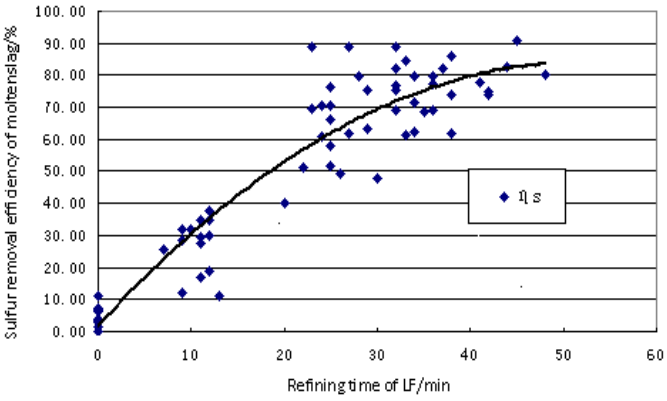


Fig.2 Relationship of refining time and Desulfurization Efficiency of slag

Desulfurization Efficiency

According to this study's batch sample analysis, the Desulfurization efficiency of molten slag during the refining process is showed as Fig.2.

Fig.2 demonstrated that desulfurization efficiency would increase as refining time extend； after it reached 40min, the uptrend would slow down.

According to the experimental result above, the refining time of normal steel types arerecommended to be controlled between 30~40min; the refining time of high grade steels are recommended to be controlled between 40~60min. This paper suggests that these recommendations shouldbe write in to operation instruction.

Influence of Basicity of Ladle Furnace's Slag on Desulfurization

Increasing of free calcium oxide's effective concentration in molten slag would increase the basicity and drive the desulfurization reaction to decrease sulfur concentration. However, basicity isnot higher the better; there is a range for that. According to batch sample analysis, the result is showed as Fig.3.

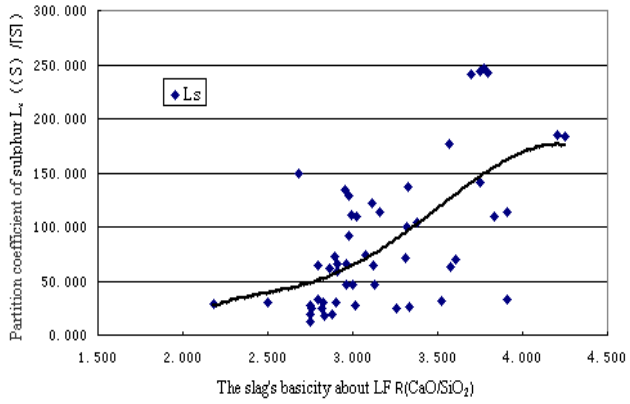


Fig.3 Relationship of slag's basicity and Ls value

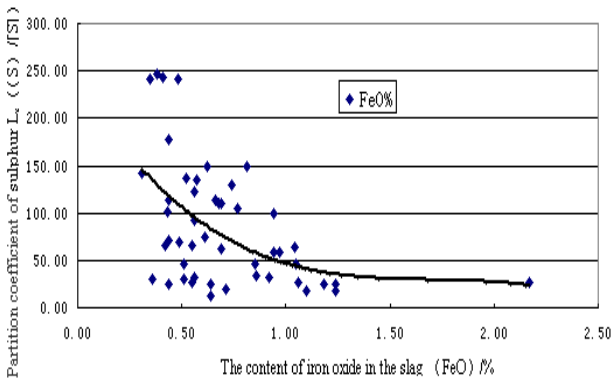


Fig.4 Relationship of (FeO) content and Ls value

What Fig.3 showed is that sulfur's partition coefficient would increase as the slag's basicity increase; it is saying that increase the effective concentration of (Cao) would benefit desulfurization. When the basicity of slag is between 3.5-4.0 desulfurization capacities is highest; after 4.0, the content of (Cao) in slag would slow down molten slag's mobility, in this way slow down the diffusion of (CaS) or (S^{2-}) and then decrease desulfurization. As indicated in Fig.3, the best basicity range of this furnace is 3.5-4.0.

Influence of (FeO) Content in Ladle Furnace's Slag on Desulfurization

According to batch sample analysis, influence of (FeO) content in ladle furnace's slag on desulfurization is showed as Fig.4.

Fig.4 illustrate that (FeO) content in slag is adverse to liquid steel's desulfurization. When the (FeO) content is less than 2.5%, desulfurization capacity of molten slag will increase as (FeO) content drops; especially when (FeO) content is less than 1%, surfer's partition coefficient will rise sharply as (FeO) content drops.

Influence of Ladle Furnace's Refining Time on Desulfurization

Refining time is defined by liquid steel's initial quality, target point and refining technics. All things equal, the rising of sulfur content and reducing of target point will lengthen refining time.

Fig.5 state that when refining time is longer than 40min, sulfur content's dropping trend will slow down in liquid steel, at that time, sulfur content in steel will be less than 0.010%. In commercial steel manufacture S≤0.020% could already meets the requirement, so this paper suggest that refining time for commercial steel could be as short as 30min.

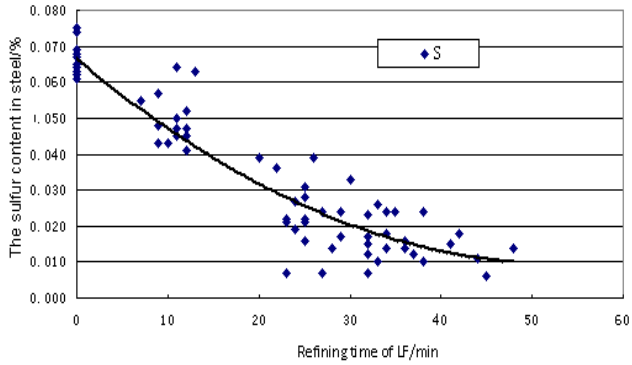


Fig.5 Relationship of refining time and sulfur content in steel

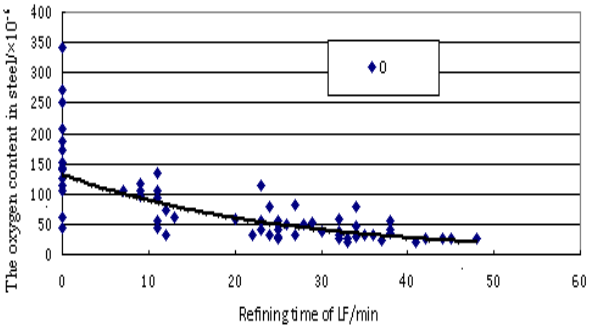


Fig.6 Relationship of refining time and total oxygen content in steel

Influence of Ladle Furnace's Finish Point Week Agitation on Desulfurization

Feed liquid steel with Ca-Si wire (3m/t) at the end point of ladle refining process and conduct argon blowing with week agitation, the argon pressure and rate of flow are controlled to keep the liquid steel sharking slightly but not boiling. Reasonably controlled wire feeding and argon blowing could not only homogenize temperature and contents, but also benefit deoxidization desulfurization and decontamination. According to batch sample analysis, when the argon blowing time is longer than 5min, desulfurization through agitation could result obviously.

Study on Deoxidization Effort of Ladle Furnace

According to batch sample analysis, total oxygen content variation during the refining process is showed as Fig.6.

As what is showed in Fig.6, oxygen content in steel drops as refining time extended; after it reached 40min, the trend of oxygen dropping in steel would
slow down.

Batch sample analysis shows that finish point week agitation would benefit to deoxidization when it last longer than 5min,

According to the result above, ladle furnace's finish point agitation of ladle refining process should be longer than 5min, and it should be listed.

Study on Control Level of Inclusion in Steel

During this study, researchers use fractional electrolytic method to exam bulk sample, steel samples before and after finish point week agitation was tested and inclusion grain was collected and elutriated. Scanning electron microscopy (SEM) and energy analysis of X ray was conducted and results are listed in Table 2.

TABLE 2 BASIC STATUE OF INCLUSL ON GRAIN OF FRACTIONAL ELECTROLYTIC

project	average of before Stirring	average of after stirring	project	average of before Stirring	average of after stirring
Sample weight/g	2352.3	2505.5	100～365μm inclusion heavy / mg	8.9	2.1
residual weight of electrolytic/g	358.8	346.3	50～100μminclusion heavy / mg	1.5	0
Weightlessness of electrolytic/g	1993.5	2159.2	inclusion of 10kg steel/ mg	65.7	12.5
Inclusion heavy of Washing/ mg	13.1	2.7	refining time / min	31.4	39.5
＞365μm inclusion heavy/mg	2.7	0.6			

According to the test result, surface wears of inclusion are majorly irregular, with some spheroid; major content is composite silicon aluminate. As showed in Table 2, inclusion content dropped by 53.2mg/10kg on average after agitation; as the finish point week agitation time of ladle furnace gets longer, the removal rate of inclusion gets higher.

Based on the ladle furnace refining technology research above, conclusions can be concluded as 1) the slag producing system is reasonable; 2) with a 30-40min refining time, sulfur content in steel could reaches 0.010%-0.020%; 3) by applying reasonable finish point week agitation, steel quality could be further improved. So effective agitation time should be longer than 5min; 4) when refining time is longer than 30min, oxygen content in steel could be less than 35×10^{-6}.

References

[1] Zhang qian.The theory and practice of refining outside furnace.beijing，1993.The Press of Metallurgical. pp.14～539.

[2] He Huanyu,Ni Hongwei,Zeng Jing. Phase compositions and formation mechanism of spent slag in ladle furnace.Journal of Wuhan University of Science and Technology.Vo1.31,No.5 (oct.2008).

[3] Li hong. The refining outside furnace. The Press of Metallurgical. 2002.PP206.

Advanced Materials Research Vol. 936 (2014) pp 1262-1266
© (2014) Trans Tech Publications, Switzerland
doi:10.4028/www.scientific.net/AMR.936.1262

Influence of RE Addition on Ferro-matrix Friction Material by In-situ Carbothermal Reduction from Vanadium-bearing Titanomagnetite

LI Ying[1], FENG Keqin[1, a *], DENG Weilin[1], ZHANG Guangming[1, 2], ZHOU Yu[1]

[1] School of Manufacturing Sci. and Eng., Sichuan Univ., Chengdu 610065,China;

[2] Sichuan Eng. Technical College, Deyang 618000,China

[a *] corresponding author: kqfeng@scu.edu.cn

Keywords: vanadium-bearing titanomagnetite; ferro-matrix friction material; RE; TiC

Abstract. Ferro-matrix friction material was obtained by in-situ carbothermal reduction from vanadium-bearing titanomagnetite in vacuum environment. The effect of RE addition (0 ~0.3 wt.%) on the microstructure and properties of ferro-matrix friction material was investigated. As a result, compared with the specimen without RE, those with RE has better connection of substrates and smaller pores size. It results the porosity decreases and, the increase of density, micro-hardness and frictional coefficient. When the adding RE is 0.1 wt.%, the connection of substrates is best, that is to say, the pores distribution is most even and pores size is minimum. Meanwhile, the highest density, hardness and frictional coefficient are obtained with 0.1 wt.% RE addition. However, there is little influence on the properties with excessive RE addition. In addition, the morphology of vanadium-titanium carbide varies with different RE addition.

Introduction

As TiC and VC particles are high strength, inoxidizability, corrosion resistance, good wettability with Fe [1] etc., which are the optimal abrasive in ferro-matrix materials. At present, adding pure powder in metallurgy-process is the conventional method to prepare ferro-matrix friction materials, in which mechanical alloying is not taken place. As a result, it makes interface peel and effect the wear resistant. In addition, it will increase the cost of raw material.

Panzhihua vanadium-bearing titanomagnetite contains iron oxide, TiO_2, V_2O_5, SiO_2, $A1_2O_3$, Ni, S, etc. In terms of blast furnace smelting iron, some associated oxides are regarded as impurities. However, the SiO_2, $A1_2O_3$, Ni, S, etc. are the components of the ferro-matrix friction materials. In order to avoid the problem of smelting blast furnace, especially make the best use of Ti and V elements, it is very necessary to explore a new way of using natural mineral as the main primary material to obtain low cost ferro-matrix friction material. In previous studies, our group had obtained general performance ferro-matrix friction material by in-situ carbothermal reduction from vanadium-bearing titanomagnetite in vacuum environment. Recently, the relevant studies on RE in powder metallurgy are widely concerned because RE can accelerate sintering process, grain refinement, solution strength, improve hardness, decrease porosity and regulate carbonization [2-4]. To improve performances of the material, in this study, ferro-matrix friction material was obtained by in-situ carbothermal reduction, and the effect of RE addition (0 ~0.3 wt.%) on the microstructure and properties of the ferro-matrix friction material was investigated.

Experimental

Panzhihua vanadium-bearing titanomagnetite and graphite (+99.85%) powders were used to prepare the reduced powders, which are the main component of the materials investigated in this study. The constituents of vanadium-bearing titanomagnetite show in Table 1. Firstly, the vanadium-bearing titanomagnetite and graphite powders (100: 20.03 wt.%) were mixed in the planet ball mill at 400 r/min for 3 h. Subsequently, according to the thermodynamic analysis in our previous studies [5], the mixed powders were at 1290 ℃ for 3 h in vacuum furnace to reduce vanadium-bearing titanomagnetite. Table 2 lists the chemical compositions of the reduced powders. Secondly, according to the characteristic of ferro-matrix friction material, different proportional powders were prepared as given in Table 3. It is worth nothing that the RE (La and Ce) were added in the form of $FeSiMg_9RE_9$. The addition of graphite powders is not only used as lubricant of the material, but also to further

reduce surplus iron oxide, TiO_2 and V_2O_5 of reduced powders. And Ni can activate sintering in the ferro-matrix alloys [6]. Finally, the powders of materials investigated were mixed in the ball mill at 400 r/min for 0.5 h. After the mixture powders were pressed to green using uniaxial press at 400 MPa, and then sintered at 1250 ℃ for 3 h.

The microstructures and phase distribution of specimens were characterized by optical microscopy and scanning electron microscopy (SEM), which are prepared for porosity testing as the quantitative metallography image processing system [4]. The chemical compositions of phases were determined with an energy dispersive spectrometer (EDS). The density was tested according to Archimedes' method. Vickers hardness testing was conducted on a Micro-hardness Tester with a loading force of 1000 g. At least five tests were carried out on each specimen and the mean values of the results were reported. The frictional coefficient was tested in friction wear testing machine (MM-1000).

TABLE 1 CHEMICAL COMPOSITION OF THE VANADIUM-BEARING TITANOMAGNETITE (WT.%)

Fe_xO_y	Al_2O_3	V_2O_5	TiO_2	SiO_2	CaO	MgO	Others
59.84	4.89	0.56	2.73	3.89	1.07	1.03	25.99

TABLE 2 CHEMICAL COMPOSITION OF THE REDUCTION POWDERS (WT.%)

Fe	FeO	V_2O_5	TiC	SiO_2	Al_2O_3	CaO	MgO	free C	Others
73.59	1.07	0.29	10.32	4.71	5.90	1.23	1.25	0.10	1.54

TABLE 3 CONTENTS OF THE SPECIMENS INVESTIGATED (WT.%)

	Reduction powder	Fe	Cu	Graphite	Ni	MoS_2	RE
NO.0	59.1	30.7	2	2	3.1	3.1	0
NO.1	59.1	30.7	2	2	3.1	3.1	0.1
NO.2	59.1	30.7	2	2	3.1	3.1	0.2
NO.3	59.1	30.7	2	2	3.1	3.1	0.3

Results and Discussion

Influence of RE addition on the microstructures

Figure 1 shows the microstructures of specimens with different RE sintered at 1250 ℃ for 3 h. It can be seen from Fig.1 (a-1) that the as-sintered materials are mainly composed of light gray, gray and black regions. Table 4 lists the EDS result of the regions A, B and C of the specimen with 0.1 wt% RE. The region A (light gray area) contains Fe, Ni, C, Si and O elements, and the mass ratio of Fe to C is 99.24: 0.76. According to the Fe-C phase diagram, the region A (substrate) belongs to the ingredient of hypoeutectoid steel. Therefore, it should contain amounts of pearlites and bits of ferrites, which are necessary for the ferro-matrix friction material. The region B (black area) mainly composes of C element and a small number of Si, O and Fe elements, this region should be lubricant C and a little of abrasive SiO_2. In the region C (gray area), however, all the atomic number of C, Ti, V is about 85%. Because reinforced phase TiC and VC are stable at 1250 ℃, and Ti and V will not react with Mo, Fe and S. So it can be inferred that TiC, VC or $(Ti/V)_XC$ phases exist in the shape "Y" (C region). In the previous study [7], TiC phases generally presented granulate, featheriness, dendrite and clavate, without the shape "Y". Because of the elements of RE (La, Ce) are distributed in the gray area, whereas there are no RE elements in the light gray and black area, as presented in Table 4. This indicates that the shape "Y" may be related to RE addition.

In addition, RE also influences the connection of substrates, which is related to the density of the specimens. Form Fig. 1 (a-1), (b-1), (c-1) and (d), it is seen that the connection of substrates of specimens NO.1, NO.2 and NO.3 is greatly improved. While most of substrates without RE are surrounded by different sizes of holes and graphites. Because the oxidations RE formed under the room temperatureare are hard grains, which will grind and incise other grains during the grinding

process, resulting in rupture of the pre-existing oxidation film. Hence, decreasing the diffusion resistance between atoms in sintering process [8] and providing convenience for heterogeneous nucleation, are beneficial to the homogeneity of structure and the decrease of holes. However, the tendency doesn't increase continuously with the increase of RE. As can be seen from Fig. 1 (a-1), (b-1) and (c-1), the size of holes and graphites increase with the increase of RE addition. Meanwhile, the distribution of substrates with 0.1 wt.% RE addition are more even and the sizes of holes are less. Since MoS_2 resolves into Mo and S after adding excessive RE (0.2 wt.% and 0.3 wt.%) in sintering process, the S easily combines with Fe into FeS, which impedes the connection of substrates. Therefore, moderate RE addition can improve the connection of substrates, whereas the connection is violated with excessive RE addition.

TABLE 4 THE PERCENTAGE OF ATOM CONCENTRATION OF THE SPECIMEN WITH 0.1WT% RE ADDITION (AT.%)

	Fe	Ti	V	C	Ni	Si	Mo	S	O	Ce	La
A Region	84.12	0	0	3.09	6.09	4.24	0	0	2.46	0	0
B Region	8.84	0	0	90.44	0	0.36	0	0	0.36	0	0
C Region	4.38	20.99	4.81	59.25	0	0	8.28	1.62	0	0.10	0.57

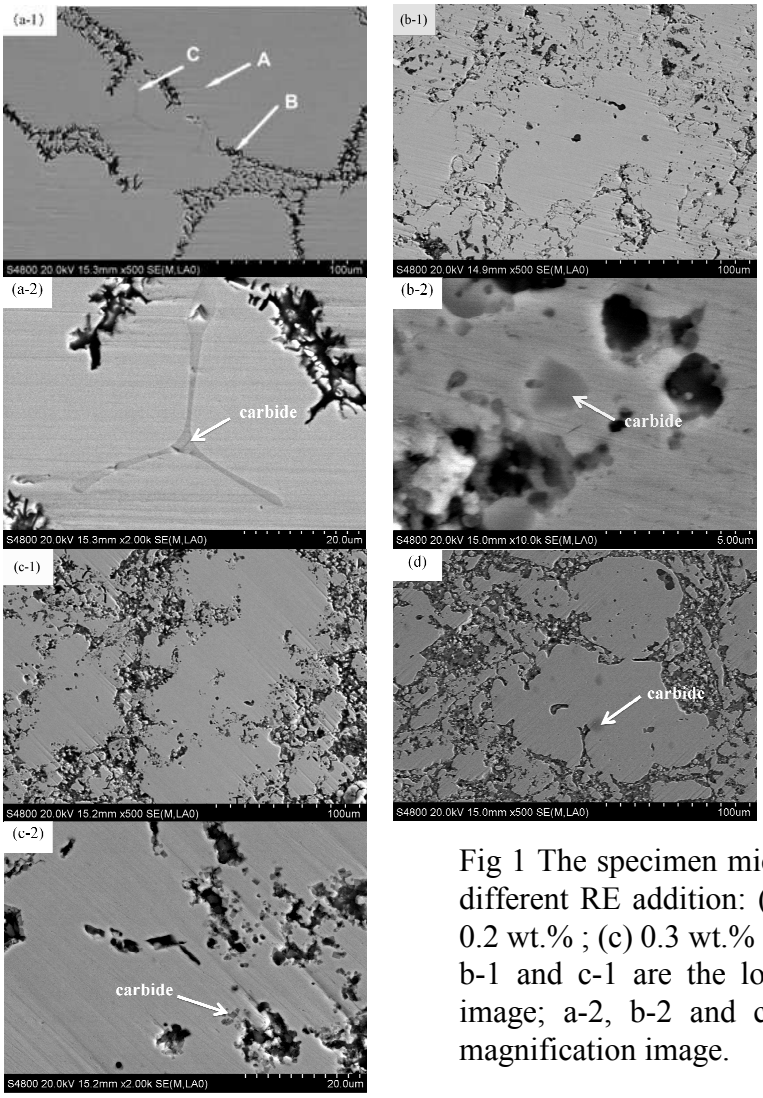


Fig 1 The specimen microstructure with different RE addition: (a) 0.1 wt.%; (b) 0.2 wt.% ; (c) 0.3 wt.% ; (d) 0 wt.%. a-1, b-1 and c-1 are the low magnification image; a-2, b-2 and c-3 are the high magnification image.

Furthermore, with increasing of RE elements (0 ~0.3 wt.%), the shape of the gray area changes from "Spherical particle" to "Y", "approximate spherical particle" and "rectangle particle", which are shown in Fig. 1 (d), (a-2), (b-2) and (c-2). As discussed above, the grey area is mainly composed of

TiC, VC or $(Ti/V)_XC$ and a small number of RE. As it well known, RE can activate and catalyze atomics[9], hence RE could prompt Ti, V and C atomics diffusion greatly during the process of sintering. Moreover, RE also has solid solubility in steel [4, 10]. With the content of RE increases to 0.1 wt%, RE can be completely absorbed in the substrate, strengthen substrates and prompt carbide to form the shape "Y". Whereas, when the adding RE is 0.2 wt.% and 0.3 wt.%, RE can't completely dissolved and the non-dissolved RE makes carbides to form "approximate spherical particle" and "rectangle particle", respectively. So, it can be concluded that the different addition of RE can affect the morphology of carbides in the ferro-matrix friction material.

Effects of RE addition on properties

The density and porosity of the specimens are shown in Fig. 2. It is clear that the densities of all the RE-containing materials are higher than that without RE addition. The density is the highest, when RE addition is 0.1 wt.%. It is known from these results that there is an optimum RE addition, at which the specimen can obtain the highest density. Since when the amount of RE was 0.1 wt.%, RE would completely dissolve in the substrates, improve the connection of substrates and therefore, increase the density of the specimens. In addition, as described in previous study [4], the porosity could affect the micro-hardness and the frictional coefficient of specimens.

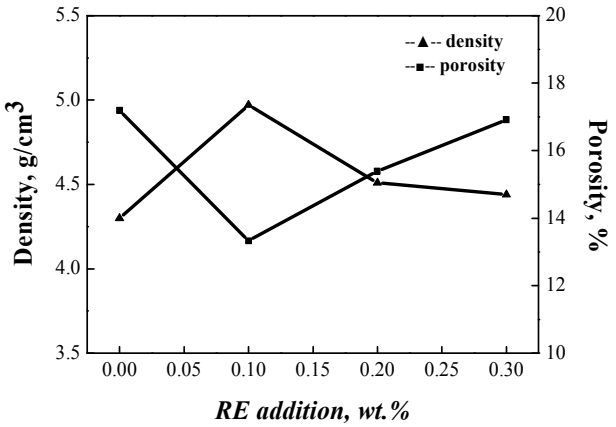


Fig 2 Density and porosity of Ferro-matrix friction material with different RE addition

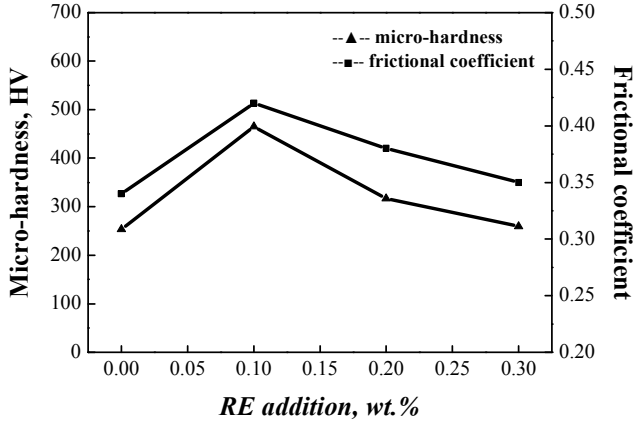


Fig 3 The micro-hardness and frictional coefficient of material with different RE addition

Fig. 3 shows the micro-hardness and average frictional coefficient of the specimens with different RE addition. The micro-hardness and average frictional coefficient of the specimens firstly increased and then decreased with the increase of RE addition. These may be caused by the following reasons: The optimum RE can improve the density and hardness. When the amount of RE was excessive, non-dissolve RE decreases the mechanical performance. Since the MoS_2 could create atomic S combining with Fe to turn into FeS that act as inclusion, which will decrease the specimens frictional coefficient. The morphology of carbides in the gray area is proposed to be a reason for this phenomenon.

Conclusion

(1) RE addition can be beneficial to the connection between the substrates, reduce the size of pores, homogenize the distribution of holes, and improve the properties (density, porosity, micro-hardness and frictional coefficient) of the ferro-matrix friction materials.

(2) The amount of RE addition can affect the morphology of carbides, which change from "Spherical particle" to "Y", "approximate spherical particle", and "rectangle particle" with the increase of RE addition.

(3) When the addition of RE is 0.1 wt.%, the density, hardness and frictional coefficient of specimens improve obviously and the percentage of pores decreases.

Acknowledgments

This research was financially supported by the Science and Technology Supporting Program of Sichuan Province (No. 2012GZX0089). This work was also supported by the Applied Technology R&D Plan of Panzhihua (No. 2012CY-C-1).

References

[1] Z. Mei, Y.W. Yan, K. Cui. Effect of matrix composition on the microstructure of in situ synthesized TiC particulate reinforced iron-based composites [J]. Materials Letters, 2003, 57(21): 3175-3181.

[2] Zhang Hong, Song Ziqian. Summary of Role of Rare Earths in the Ferro-matrix Powder Metallurgical Materials [J].Chinese Rare Earths, 2004, 25(4):67-69.

[3] Yong Zhihua, Wang Shiyuan, et al. The influence of minor rare earth on WC-18Ni cemented carbide [J].Rare Metal Materials and Engineering, 1997, 26(2):40-44.

[4] Zhang Hong. The study on mechanism of rear earth elements in ferro-matrix powder metallurgical friction material [D].Beijing: China Academy of Railway Seiences, 2003.

[5] Zhang Guangming, Feng Keqin, et al. Thermodynamic analysis on ferro-matrix composites by in-situ carbothermal reduction from vanadium- titanium magnetite [J]. Journal of Sichuan University (Engineering Science Edition), 2012, 44(4):191-196.

[6] Lin Wensong, Li Yuanyuan, Chen Weiping. Shrinkage effect in sintering of Fe-Ni alloys [J]. Materials for Mechanical Engineering, 2003, 27(10): 11-13.

[7] Gai Pengtao. The meehanism of Changing and Control of MorPhology of TiC in TiC/Ti6A14V composites [D].Harbin: Harbin Engineering University, 2008.

[8] Wu Yansheng, Liu Yingcai, et al. Influence of Ce addition on the properties of Fe-2.4C-17Cr-1.8Mo-1.0Cu alloy [J]. Powder Metallurgy Technology, 2000, 18(3):200-203.

[9] Jiang Xuezhi, Wang Baofeng, et al. The effect of La on the high temperature oxidation of purity steel [J].Journal of Baotou University of Iron and Steel Technology, 2006, 25(1):40-42.

[10] Long Xiang, Liang Shijin. X-ray preliminary determination of the boundary of Fe -α solid solution phase in the Fe-La phase diagram [J].Journal of Jilin University, 1960, 2: 93-96.

Advanced Materials Research Vol. 936 (2014) pp 1267-1272
© (2014) Trans Tech Publications, Switzerland
doi:10.4028/www.scientific.net/AMR.936.1267

Influence of The Mo and V Contents on Microstructure and Secondary Hardening of 6Cr6W2MoV Steel

ZHANG Xiao Jing[1,a *], MA Yong Qing[2,b], LIANG Yu Fen[1,c], LIU Guo Fang[1,d]

[1]Changzhou Machinery Blade CO.LTD, Changzhou, Jiangsu 213119, China

[2]Department of Materials Science, Dalian Maritime University, Dalian, Liaoning116026, China

[a]jing267@163.com, [b]myq_dlmu@163.com, [c]yufenliang57@163.com,[d]guo_fang@163.com

Keywords: 6Cr6W2MoV steel, The Mo and V contents, Ultra-fine carbide, transformation, Carbide composing, Secondary hardening, Tempering hardness, Temperature decentralization

Abstract. The influence of Mo and V contents on the microstructure and secondary hardening of 6Cr6W2MoV steel was studied in this paper, and the process factors and the transformation mechanism of the influence results were discussed by phase equilibrium thermodynamic analysis. The results show that, the microstructure of 6Cr6W2MoV steel is uniform and thin, in which the undissolved carbide size after quenching is 0.23μm. In the heating and cooling process of the annealing, the dissolution and precipitation of $M_{23}C_6 \leftrightarrow M_6C$ carbides transformation can be used to carbides distributing uniform refinement. Adding an overmany Mo content will lead to coarsening of carbide particles due to small amplitude of $M_{23}C_6 \leftrightarrow M_6C$ transformation. Adding an overmany V content will appear a small of the bulk MC carbide on the crystallization, so the heterogeneity of carbides is increasing. The tempering hardness of 6Cr6W2MoV steel is 63.5HRC, and when adding an overmany Mo content the maximal hardness arrives to 65HRC. Adding Mo changes the carbide composing, it is conducive to the variety of carbides precipitation strengthening near intermediate temperature and the tempering hardness increasing. When adding an overmany V content the more MC carbide well occupy more amount of C, the tempering temperature dispersion increases too, so the tempering hardness debases deservedly and the highest hardness only reaches HRC60.5.

Introduction

A kind of high alloy tool steel 6Cr6W2MoV was successfully developed according to alloy design calculation and experiment result, which is applicable to an edge steel of machinery knives by hot roll-jointing[1]. The microstructure of 6Cr6W2MoV steel is uniform and thin, in which the undissolved carbide size after quenching is less than 0.35μm having ultra-fine characteristic. Although the contents of C and alloy elements in the steel are opposite lowly, also that steel is capable of having high tempering hardniss HRC62-64 and has good rolling welding performance at high temperature, and is suitable for manufacturing the machinery knife by hot roll-jointing. This machinery knife has be obtained Chinese invention patent, which is applies to the slicer cutting pretty good and same as the rotary cutting better for wood working[1,2].The alloy design of the high alloy tool steel as edge steel of machinery knives is mainly using the phase equilibrium thermodynamic method to solve the relationship between carbide refinement and tempered high hardness and the steel composition[3]. And at the same time, the effect of several elements on carbide refining and secondary hardening also was studied with the experimental method. This paper was report the experimental results of the effect of Mo and V contents on the microstructure and secondary hardening, and the process factors and the phase transformation mechanism of the influence results were discussed.

Experimental Materials and Method

The chemical composition of 6Cr6W2MoV high alloy tool steel by alloy design calculation was listed in Table 1, thereinto the Mo and V contents are 1.4/1.7 and 0.4/0.5 respectively. The chemical composition of three experimental steels was listed in Table 2, in which the composition of 6S1 steel

is agreement with composition of 6Cr6W2MoV steel, but the Mo and V contents of 6S2 and 6S3 steels are evidently deviated from the contens of alloy design in order to their experimental results against that of 6S1 steel easily. The Mo content in 6S2 steel is 4.23 and the Mo and V contents in 6S3 steel are 0.87 and 1.65 respectively. The Si and Mn contents in 6S2 steel and the Si content in 6S3 steel are lower than that of alloy design composition, but the effect of their change on carbide transformation and secondary hardening of 6Cr6W2MoV steel is too tinier[3].

Table 1 The composition of 6Cr6W2MoV steel by alloy design calculation(*wt%*)

C	Si	Mn	Cr	W	Mo	V	NiCo
0.52/0.62	0.4/0.6	0.25/0.5	5.2/6.2	2.2/2.7	1.4/1.7	0.4/0.5	0.18/0.3

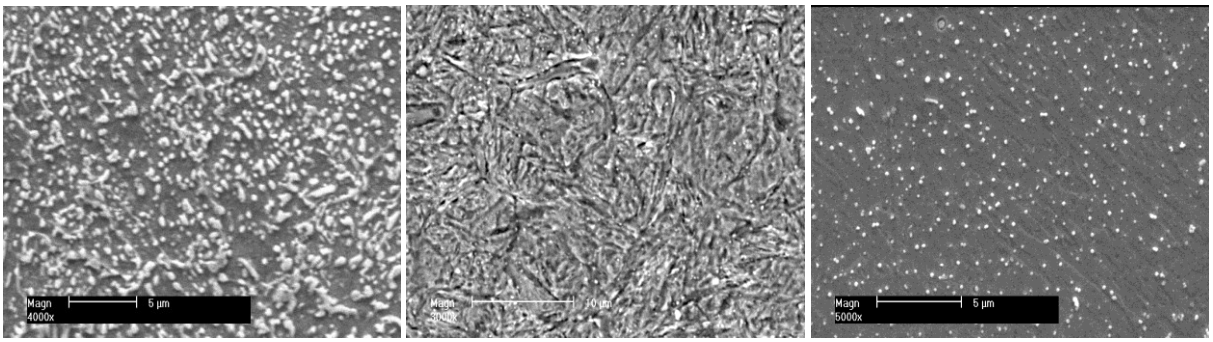
Table 2 Chemical composition of experimental steels (wt.%)

	C	Si	Mn	Cr	W	Mo	V	Ni
6S1	0.58	0.60	0.50	5.45	2.25	1.52	0.50	0.20
6S2	0.61	0.18	0.30	6.22	2.36	4.23	0.47	0.27
6S3	0.62	0.36	0.40	6.22	2.35	0.87	1.65	0.21

Experimental materials were melted in 0.5t variable frequency induction furnace adding electro-dregs remelting furnace. After forging and rolling, the steels were processed to 58mm ×11 mm×11 mm samples by incision machining. The heat treatment was investigated using KSJ-5kw electric furnace, and tempering holding time is 2.5h×2. The hardness was mensurated using 150DT-HR sclerometer, and an average value of the hardness was accounted adopting six testing points or more. The microstructure was investigated using scanning electron microscope XL30.

The Experimental Results

Microstructure The microstructure of 6S1 steel is shown in fig.1. Fig.1(a) for the microstructure of 6S1 steel annealing at 840℃the carbide particle uniformly refined, its size is mainly distributed in a range of 0.2~0.8μm almost no massive primary granular carbide. Fig.1(b) for the microstructure of 1050℃quenching of 6S1 steel the dislocation and twin martensites formed in grain each about 10μm, in which a little of very finely granular carbides distributed uniformly. Fig.1(c) for the microstructure of 6S1 steel tempered at 540℃after quenching at 1050℃the average size of uniform and fine carbide particle is 0.23μm amounting to volume fraction of～3%.

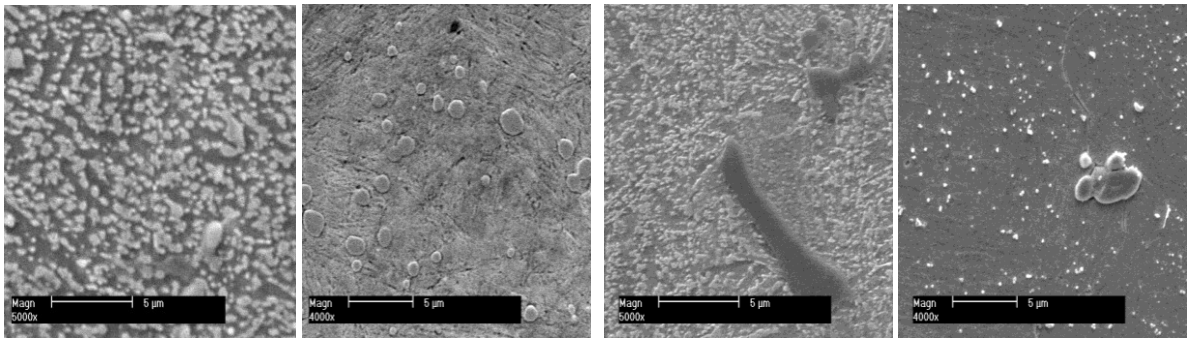


(a) (b) (c)

Fig.1 The microstructure of 6S1 steel
(a) annealed at 840℃, (b) quenched at 1050℃, (c) tempered at 540℃

Fig.2 is the microstructure of 6S2 steel, and fig.3 is the microstructure of 6S3 steel. Fig.2 shows the distribution of the annealing carbide size of 6S2 is uniform in between 0.5～2μm (Fig.2a), the quenching undissolved carbide distribution size is between 0.5～1.5μm amounting to volume fraction of ~ 4% (Fig. 2b). From Fig.3 can be seen, annealing carbide distribution of 6S3 steel is not uniform, the size of a lot of fine carbide uniform distribution is between 0.2～0.5μm, but also the size

of a small decentral of bulk primary carbide is between 2～5μm and individually or even more than 10μm(Fig.3a). The undissolved carbide distribution after quenching is not homogeneous thereinto the fine carbide size 0.2～0.5μm and inside the big size of individual ~5μm(Fig.3b).

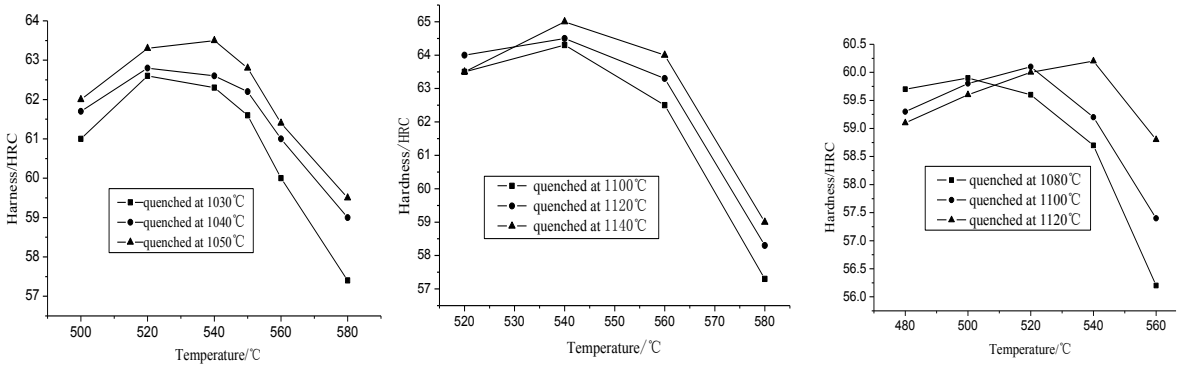


(a) (b) (a) (b)

Fig.2 The microstructure of 6S2 steel (a) annealed at 840℃, (b) quenched at 1120℃

Fig.3 The microstructure of 6S3 steel (a) annealed at 840℃, (b) quenched at 1100℃

Secondary Hardening The tempering hardness curves of secondary hardening of three experimental steels are shown in Fig.4. Fig.4a shows, the highest hardness during tempering secondary hardening of 6S1 steel is HRC62~ 63.5, and the tempering temperature is corresponding to 520～540℃ and the tempering hardness decreases sharply over 550℃. Fig.4b shows, the highest hardness during tempering secondary hardening of 6S2 steel containing high Mo content is HRC63~65, the tempering temperature is corresponding to 520～550℃ and tempering hardness decreases sharply over 560℃. Fig.4c shows, the highest hardness during tempering secondary hardening of 6S3 steel containing high V content is only HRC59.5~60.5, and with increasing of quenching temperature the tempering temperature corresponding to the highest hardness increases as well. For example, the tempering temperature of highest hardness HRC60 corresponding to quenching temperature at 1100℃ is 520℃, and the tempering hardness decreased sharply over 540℃. The tempering temperature of highest hardness HRC60.5 corresponding to quenching temperature at 1120℃ is 540℃, and the tempering hardness decreased sharply over 550℃.



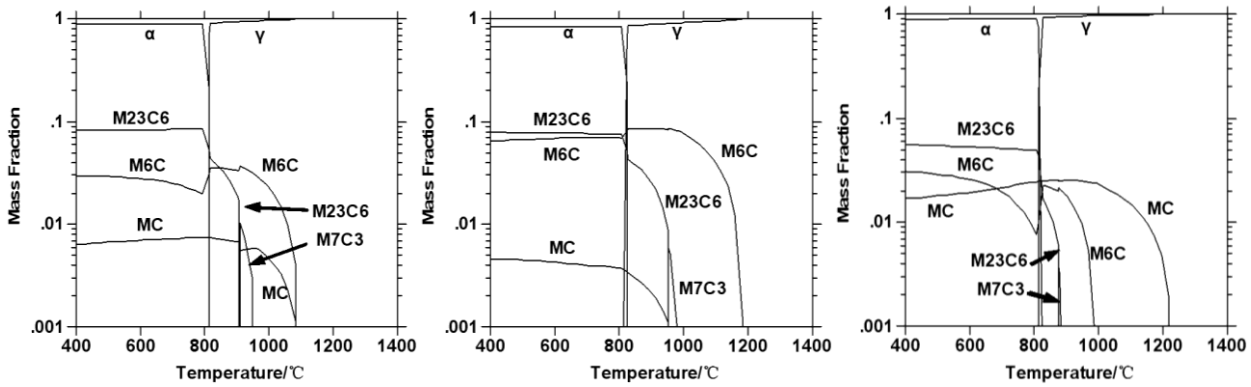
(a) 6S1 (b) 6S2 (c) 6S3

Fig.4 Tempering hardness of secondary hardening of three experimental steels

Analysis and Discussion

Carbide Transformation and Morphology Fig.5 is the equilibrium phase diagram with temperature changes calculated according to the experimental steels. Fig.5a shows, $M_{23}C_6 \leftrightarrow M_6C$ transformation of the heating and cooling process during annealing of 6S1 steel happens substantially, the dissolution and precipitation process for carbides distributing newly lead to uniform refinement[5,6]. The quenching residual carbides are M_6C and MC, and the M_6C in quenching heating process is refined sequentially and the MC after hot working and heat treatment essential is more refinement, therefore, the residual carbide of 6S1 steel quenched is ultra-fine[7]. Moreover, the

initial precipitation of MC begins from lower temperature (< 1100 ℃) during melting solidification, it is difficult to occur in the early stage of MC crystallization and blocky carbide also is eliminated. Fig.5b shows, there is more M_6C in 6S2 steel containing overmany Mo content, and the amplitude of $M_{23}C_6 \leftrightarrow M_6C$ transformation during heating and cooling process of annealing is smaller, therefore, annealing carbide size is large, and in the quenching process the first solution of carbides is $M_{23}C_6$, the larger size of undissolved M_6C still is retained. Fig.5c shows, there is more MC in 6S3 steel containing an overmany V content, and the amplitude of $M_{23}C_6 \leftrightarrow M_6C$ transformation during heating and cooling process of annealing also is greater, therefore, the size of most carbides is very small but the size of a small amount of bulk MC still is very big. In the quenching process the undissolved M_6C and the original fine MC further will be refined, but the larger size of a small amount of bulk MC still is retained although after heating partial dissolution. The bulk MC carbide is occurred at the beginning crystallization of melting solidification. Although MC precipitation start temperature is in the solid region by equilibrium phase diagram but at higher temperature (1230℃), consequently, when adding V iron during melting process at lower temperature in order to reducing the loss rate of melting, the partial segregation can lead to its crystallization in early.



(a) 6S1 (b) 6S2 (c) 6S3

Fig.5 Equilibrium phase diagram with changing temperature

Precipitation Hardening and Tempering Hardness Tempering carbide appeared the metastable phase (M_2C, M_3C), and some stable phase does not appear, this is because of the phase transformation process of hysteretic transition of retained austenite to delay in sectional martensite decomposition[8]. Although the precipitation hardening process is very complicated, but the calculation of stable phase M_6C, $M_{23}C_6$ and MC in 500℃～600℃ has certain universality of review value. And the tempering temperature of highest hardness can be estimated according to phase ratio of mass fractions of the carbides equilibrium at tempering temperature[4]. The highest tempering hardness and tempering temperature are relational to the carbide type and number of the corresponding precipitation strengthening. In a nutshell, when relatively more $M_{23}C_6$ (or M_7C_3) the tempering temperature is lower of 480℃~520℃, and when relatively more M_6C it is moderate in the tempering temperature of 520℃~540℃, and when relatively more MC the tempering temperature is high at 540℃~560℃[4]. Obviously, the separating out amount of some carbide in the precipitation hardening temperature is more, the ability of precipitation hardening is stronger. If the temperatures of all sorts of carbides precipitation hardening are close to tempering temperature, the highest hardness will be higher, and when the more dispersed precipitation hardening the highest tempering hardness will be lower. In addition, research has shown that the alloy elements in steel can alter the precipitation temperature and speed of carbide precipitation[9]. Can reasoning, carbide composing also can affect on the precipitation temperature and precipitation velocity, and also will affect on the highest tempering hardness and tempering temperature.

Table 3 is the carbides composing and mole number of equilibrium carbides according to the calculation of experimental steels. Can be seen from table 3, the adding Mo modified the carbides composing, and the ratio of Mo content in $M_{23}C_6$ of three experimental steel is very high, thereinto, the Mo content in $M_{23}C_6$ carbide of 6S2 steel containing most high Mo reached 18.5%. Furthermore,

the ratio of Mo content in the MC and M_6C is higher, and the ratio is respectively 10.5% and 8.92% in 6S2 and 6S1 steel, thus it is conducive to precipitation strengthening of all kinds of carbide close to the middle temperature. On the other hand, when adding appropriate ratio of W and Mo is of result in a large number of Mo into the M_6C, the Mo content in M_6C of 6S2 steel reached 38% and the relative ratio of M_6C in the steel as well as increased, and then it is conducive to the precipitation focus at intermediate temperature, which can be see from difference values(D-value) of mole fraction at 540℃ and that at quenching temperature. Therefore, the tempering hardness of 6S2 steel is highest and as well as the tempering hardness of 6S1 steel also is higher. Nevertheless, the more MC amount as very high V content of 6S3 steel can occupy the more amount of C, and so it is reducing amount of $M_{23}C_6$ and M_6C. And more MC increases the tempering temperature and leads to disperse temperatures of the precipitation strengthening, therefore, the highest tempering hardness during secondary hardening of 6S3 is lower as well.

Table 3 Carbide composing(wt%)and mole number (%)by equilibrium phase of experimental steels

	Type	Carbide composing at 540℃						Mole 540℃	Quenching (℃)	Quenching mole	D-value of mole
		C	Fe	Cr	W	Mo	V				
6S1	MC	15.2	0.01	0.77	9.81	8.92	65.2	1.02	1040	0.42	0.60
	M_6C	1.92	27.4	2.63	60.9	6.05	0.83	1.78		1.05	0.73
	$M_{23}C_6$	5.04	25.5	49.2	3.69	14.8	0.03	9.37		0	9.37
6S2	MC	15.5	0.01	0.43	3.05	10.5	70.5	0.78	1120	0	0.78
	M_6C	2.16	23.3	3.82	31.7	38.0	0.82	4.78		2.48	2.30
	$M_{23}C_6$	5.08	19.4	55.1	0.95	18.5	0.05	8.93		0	8.93
6S3	MC	15.8	0.01	0.54	5.01	2.28	76.4	2.92	1100	2.11	0.81
	M_6C	1.93	27.6	3.13	62.3	2.62	2.34	1.74		0	1.74
	$M_{23}C_6$	5.09	16.0	59.8	4.58	13.1	0.11	6.11		0	6.11

According to the quenching austenite matrix composition of the steel, can be used to calculate the highest hardness of secondary hardening[4]. Actually, the stable carbides at tempering temperature are $M_{23}C_6$, M_6C and MC carbides basically, thus the balanced carbon formula of matrix can be writed as

$$C_p = 0.011W + 0.02Mo + 0.057Cr + 0.19V \quad (1)$$

here the coefficients are carbon contents of W_6C, Mo_6C, $Cr_{23}C_6$ and VC carbides respectively, and alloy elements are from the matrix composition. The saturation level of carbon Cs in the matrix is C_s/C_p, the tempering hardness value can be obtained from

$$H_S = a(1+b)/(0.0127a + 0.00297k) \quad (2)$$

in which a is the square root of the saturation level of carbon in the matrix, and k is temperature decentralization coefficient and takes 1～1.2, and carbide precipitation correction factor b is as

$$b = 0.00374(Cr-6.6877) + 0.00907(W-2.7554) + 0.01521(Mo-1.3777) + 0.04194(V-0.5961) \quad (3)$$

Table 4 shows the calculational value and the testing result of the hardness of experimental steels, and the calculational results are agreement with testing values.

Table 4 Calculation value and testing result of tempering hardness of experimental steels

	Quench T/℃	Matrix composition(*wt%*)					Calcul-parameter			Calculat /HRC	Testing /HRC
		C	Cr	W	Mo	V	a	$1+b$	k		
6S1	1050	0.515	5.47	1.63	1.25	0.32	1.1121	0.972	1	63.24	63.5
6S2	1140	0.552	6.28	1.58	3.38	0.42	1.0262	1.011	1	64.84	64.9
6S3	1120	0.420	6.20	2.17	0.79	0.82	0.8740	0.993	1.1	60.43	60.5

Conclusion

(1) The microstructure of 6Cr6W2MoV steel is uniform and thin, in which the undissolved carbide size after quenching is 0.23μm. An overmany Mo content will lead to coarsening of carbide particles, and An overmany V content will lead to appear a small of the bulk MC carbide during the crystallizing process, so the heterogeneity of carbides is increasing.

(2) The tempering hardness of 6Cr6W2MoV steel is 63.5HRC and the maximal hardness arrives to 65HRC when an added high Mo content. Whereas, the tempering hardness is decreasing when adding an overmany V content and the maximal hardness arrives barely to 60.5HRC.

(3) When adding an overmany Mo content the M_6C carbide amount is biggish and the range of $M_{23}C_6 \leftrightarrow M_6C$ transformation is less, so the carbide size becomes bigger. When adding a overmany V content, there is being very big MC carbide during crystallizing process after steel melting, so the asymmetric distribution well became badly as inequality of size of carbide particles.

(4) The reason of high tempering hardness is due to the temperature convergence of precipitation strengthening and the amount increasing of carbide precipitation as a result of the change of various carbides composing of the steels containing Mo. When adding an overmany V content the more MC carbide well occupy more amount of C, the tempering temperature dispersion increases too, so the tempering hardness debases deservedly.

References

[1] Ma Yongqing, Liu Guofang, Zhang Xiaojing, The machinery knife of the high alloy tool steel with ultra-fine carbide by hot roll-jointing[P], Changzhou Machinery Blade CO.LTD, November 2010, CN201010538547(in Chinese)

[2] Zhang Xiaojing, LiuGuofang, Ma Yongqing, Material and heat treatment of knives of rotary and plane cutting for wood working[J], Heat Treatment of Metals, 2012,37(7):114-117(in Chinese)

[3] Yongqing Ma, Yang Zhang, Yumei Dai, Alloy design and practice of high carbon alloy steels with ultra-fine carbide[J], Advanced Materials Research, 2011, Vols. 295-297, 1479-1484

[4] Yongqing Ma, Hongtao Gao, Yufen Liang, Xiaojing Zhang， Secondary hardening during tempering of Cr-W-Mo-V high alloy medium-upper carbon steel and its hardness forecast[J], Advanced Materials Research, 2012, Vols,415-417, 813-818

[5] D. V. Shtansky and G. Inden, Phase transformation in Fe-Mo-C and Fe-W-C Steels--I. The structuctural evolution during temerring at 700℃[J], Acta Materialia Vol. 45 n.7(1997), p.2861-2878.

[6] D. V. Shtansky and G. Inden, Phase transformation in Fe-Mo-C and Fe-W-C steels--II. Eutectoid reaction of $M_{23}C_6$ carbide decomposition during austenitization [J], Acta Materialia Vol. 45 n.7(1997), p.2879-2895.

[7] F. A. Khalid, D. V. Edmonds, Effet of vanadium on the grain boundary carbide nucleeation of pearlite in high-carbon steels[J], Scripta Metallurgica et Materialia, 1994,30(10), p1251-1255

[8] Yang Zhang, Application of phase equilibrium thermodynamic method in alloy design for high carbon alloy steel with ultra fine Carbides[D], Dalian Maritime University, 2007,6(in Chinese)

[9] Lee K B, Yang H R, Kwon H, Effects of alloying additions and austenitizing treatments on secondary hardening and fracture behavior for martensitic steels containing both Mo and W[J], Metallurgical and Materials Transactions A:2001,32(7):1659-1670

Advanced Materials Research Vol. 936 (2014) pp 1273-1282
© (2014) Trans Tech Publications, Switzerland
doi:10.4028/www.scientific.net/AMR.936.1273

Study On Wear Behaviors Of Ni_3al/ Cr-Carbides Cladding Layer On High Strength Steel Substrate

Karin Gong[a1], An Tongbang[b], Zhifeng Zhou[c], Zhiling Tian[b], Changhai Li[a]

[a] Department of Materials and Manufacturing Technology, Chalmers University of Technology, SE-412 96 Gothenburg, Sweden

[b] China Iron and Steel Research Institute Group (CISRI), Beijing 10081, P. R. China

[c] Department of Manufacturing Engineering and Engineering Management (MEEM), City University of Hong Kong, Kowloon, Hong Kong

[a]karin.gong@chalmers.se, [b] tianzhl@cisri.com.cn, [c] mezfzhou@cityu.edu.hk

[1] Corresponding author: Tel.: +46 31 7721261 ; Fax: +46 772 1313

E-mail address: karin.gong@chalmers.se

Keywords: Friction coefficient; Specific wear rate; Intermetallics; Sliding wear; Cladding

Abstract:A cladding layer of Ni_3Al matrix composite reinforced with 18 vol. % Cr-carbides was applied by using tungsten inert gas (TIG) welding process on high strength steel substrate. The filler metal as welding wire prepared by horizontal continuous casting process with a composition of Ni-2.5C-30Cr-9Al-0.02B (in wt. %) is used. A bulk material of NAC-alloy composite with 18 vol. % Cr_3C_2-particles produced by Hot Isostatic Pressing (HIP) was also investigated as a reference material. The composition of NAC-alloy is Ni-9.87Al-11.63Fe-0.50Mn-0.50Ti-0.2B in weight percentage. The pin-on-disk (POD) tribometer tests were carried out at room temperature in dry sliding condition at a pressure of 2.83 MPa (20N). The results revealed that Ni_3Al/ Cr-carbides cladded layer by TIG process improved wear properties significantly with very low values of the friction coefficient (0.13 ± 0.02) and the specific wear rate (0.162 x 10^{-5} $mm^3/N{\cdot}m$) as compared to the reference HIP processed composite with the friction coefficient (0.68 ± 0.02) and the specific wear rate (0.908 x10^{-5} $mm^3/N{\cdot}m$) under the same testing conditions.

Introduction

High-temperature wear-resistant intermetallic materials have attracted recently material researchers' attention, especially the Ni_3Al-based materials. Ni_3Al-based alloys exhibit increased yield strength with increase of temperature to about 650-750 ºC, which made them an attractive engineering materials with good wear resistance. Due to these properties, Ni_3Al-based alloys have significant potential in wear critical applications at temperature range between 400 ºC and 650 ºC [1-6]. Intermetallic matrix composites (IMC) with hard particles reinforcements are considered for wear applications in severe, i.e. chemically aggressive environments. For instance, chromium carbide reinforced Ni_3Al matrix composite was developed as candidate wear resistant material under elevated temperatures [7]. Chromium carbides have very high hardness and good wetting ability with the Ni_3Al matrix, and also excellent oxidation resistance [8]. Karin et al. [9] illustrated that the addition of 6 vol. % Cr_3C_2 particles reduced wear rates of the pin and the disk up to 50 %. Clearly, the characteristics of worn surfaces were recognized that the hard Cr_3C_2-asperities supported a couple of sliding surfaces apart during the sliding wear process, then reduced the specific wear rates of the pin and the disk. A surface modification by forming wear resistant layer on steel substrate is a useful technical method to produce components to resist against wear damages under severe wear condition. Therefore, chromium carbides reinforced Ni_3Al composite cladded layer produced by tungsten inert gas (TIG) welding process was investigated in this study. A HIP processed bulk material of NAC-alloy composite with 18 vol. % Cr_3C_2-particles was also investigated as a reference material.

Experimental Methods and Results

Testing Materials and Preparation

The chemical composition of the steel substrate is Fe-0.35C-24Cr-8.5Ni-1.6Si-1.2Mn-0.24N-0.25Re in weight percentage. The welding wire with composition of Ni-2.5C-30Cr-9Al-0.02B in weight percentage was used for TIG welding process, which was prepared by means of horizontal continuous casting process. A vermicular graphite cast iron, a monolithic NAC-alloy and its composites prepared by HIP process were selected as reference materials. The vermicular graphite cast iron is usually used as piston ring material in engines. A grey cast iron was applied as counterpart disk material for tribo-test in this study. The designation of the tested samples is summarized in Table 1.

TABLE 1 DESIGNATIONS OF THE TESTED SAMPLES

Designation	Composition (wt. %)	Process
Pin 1	Ni-2.5 C-30 Cr-9Al-0.02 B	TIG
Pin 2	Ni-9.87Al-11.63Fe-0.50Mn-0.50Ti-0.2B +18 vol.% Cr3C2	HIP
Pin 3	Ni-9.87Al-11.63Fe-0.50Mn-0.50Ti-0.2B	HIP
Pin 4	Fe-3.05C-1.20Si-0.85Mn-0.10±0.05P-0.05S-0.65±0.05Mo-0.9±0.05Cu-0.02V-0.03Ti	as-cast
Disk	Fe-3.20C-1.1Si-0.8Mn-0.2P-0.1S-0.02B-1.0Cu-0.22V	as-cast

During the TIG welding process, it was assumed that all of the C-content in the welding wire reacted with Cr and formed chromium carbides. Afterwards residual Cr-content ~11 wt. % will be dissolved in the Ni_3Al alloy matrix and formed Cr-rich Ni_3Al phase. By taking the densities of the Ni_3Al-matrix and chromium carbides as 7.25 g/cm^3 and 6.68 g/cm^3 from the previous study into consideration, the volume percentage of Cr-carbides formed in the welding wire alloy was calculated ~ 18 vol.%. Therefore, 18 vol. % Cr_3C_2-particles were added to obtain HIP processed bulk Ni_3Al-matrix composite and selected as reference material for studying the influence of the microstructure on tribological behavior. Table 2 showed three different welding parameters were applied in TIG process.

TABLE 2 WELDING PARAMETERS IN TIG PROCESS

	Voltage [V]	Current [A]	Argon flow rates [L/min]	Welding speed [mm/s]	Cooling
1#	10～12	50	8	0.4	air
2#	10～12	70	10	0.8	air
3#	10～12	90	10	0.8	air



Fig. 1 Top Views of the Cladded Layer Prepared by Three Different TIG Process Parameters

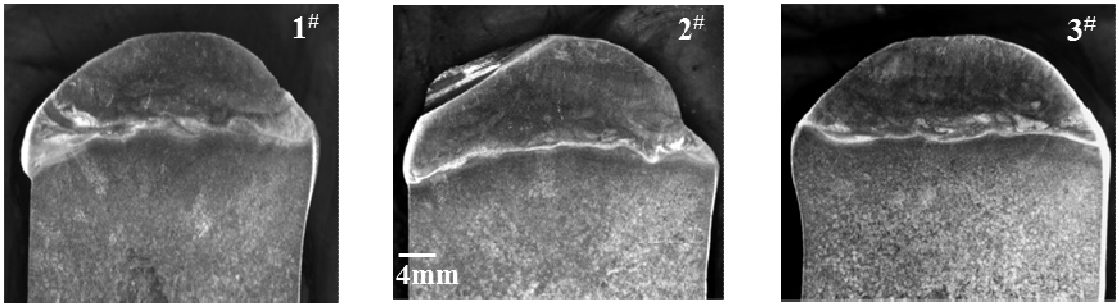


Fig. 2 Cross-section Photographs of the Cladded Layers for Three Different TIG Process Parameters

Figure 1 and Figure 2 show that each cladding area formed is about 80 mm x 40 mm and the thickness of each cladded layer is around 8 mm. The cladded layer of the number 2# shows a uniform thickness (Fig 1b) which was produced with stable TIG process parameters. So the welding parameter of the number 2# was selected to prepare a qualified cladding layer for tribo-test investigation. Two intermetallic reference materials of NAC-alloy and its composite were produced by HIP process. The powders of NAC-alloy for HIP process were prepared by using Plasma Rotating Electrode Process (PREP). The PREP system was evacuated to 0.1 bars to minimize oxidation of the powders formed. The chamber was then filled with argon to attain a clean atmosphere. The electrode rod of the master NAC-alloy is accelerated up to the desired speed of rotation, 14500±500 rpm. An argon plasma arc is then ignited and the plasma jet melts tip of the rotating rod. A fusion film is formed on the front end of rod, which disintegrates into small liquid metal droplets as a consequence of action of centrifugal force. Due to surface tension effects and enough time for spheroidisation, the droplets are spherical. On their trajectories towards the chamber wall, the droplets solidify rapidly in the inert atmosphere and form spherical solid particles. The powder sizes of NAC-alloy and Cr_3C_2 particles applied for HIP processed are in a range of 45µm-120µm, respectively. The density of NAC-alloy and Cr_3C_2 particles used for calculating volume composition of the composites are 7.25 g/cm^3 and 6.68 g/cm^3, respectively. The HIP process data are 1130 -1160 °C as heating temperature under 140 MPa for 3 hours. Dimension of the HIP processed material is Φ70 mm x 150 mm.

Characterization of the Cladded Layer

Chemical analysis of the cladded layer shows Ni-2.33C-29.50Cr-7.46Al -7.99Fe (in wt. %) composition. Comparing to the initial composition of the welding wire Ni-2.5C-30Cr-9Al-0.02B (wt. %), the cladded layer clearly shows less contents of Ni, Al, Cr and C elements, but higher Fe content. Cladding process may result in loss of C and Al by oxidation [7]. It is obvious that the content deviations of Cr and Fe were initiated due to dilution during welding process.

The cladded layer was analyzed by means of Holland Panalytical X'per Pro MPD X-ray diffraction spectrometer to identify phase constitution of the material. The Cu-Kα X-ray radiation with wavelength of 1.5406Å was used to get the diffraction patterns. The XRD pattern (Figure 3) reveals that there are four phases existed in the cladded layer which is Ni_3Al- NiAl-, M_3C_2-, and M_7C_3-types.

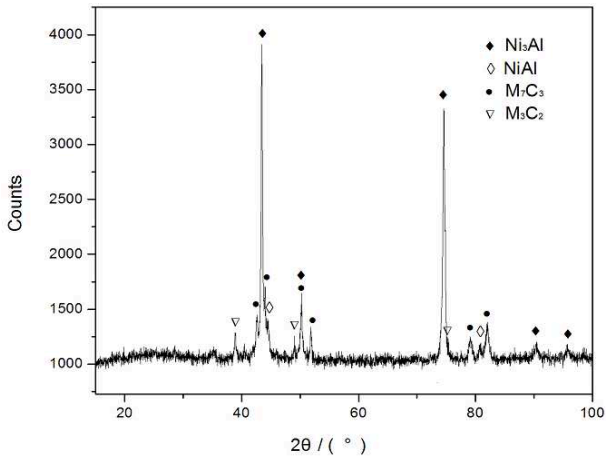


Fig. 3 XRD-spectrum of the Cladded Layer Prepared by Parameter of the Number 2#

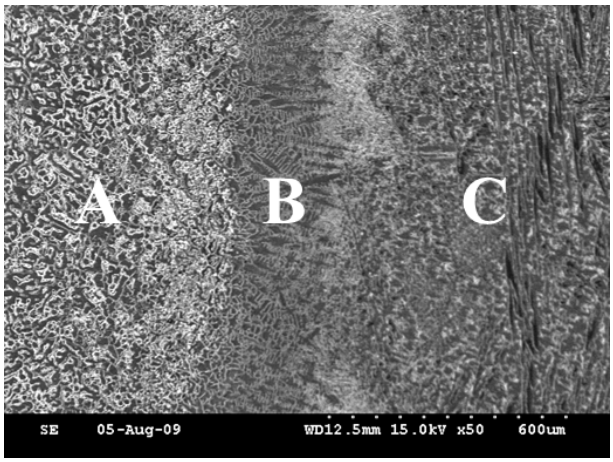


Fig.4 BEI from a Cross-section of the Cladded Layer on (A) Based Material, (B) Fusion Layer and (C) Welding Material

A scanning electron microscope (SEM) equipped with energy dispersive spectrometer (EDS) was utilized to evaluate quality of the testing sample and perform the microstructure analysis. Figure 4 is a backscattering electron image (BEI) from a cross-section of the cladded layer. Three different morphology zones were observed which are based material (A), fusion layer (B) and welding material (C). Furthermore, a good metallurgical bonding can also be observed in the microstructure.

Figure 5 (a) and (b) show backscattering electron images of the HIP processed Ni_3Al/Cr_3C_2 composite and the cladding layer, respectively. It is clearly observed that the morphology of the carbides in these two microstructures is diverse.

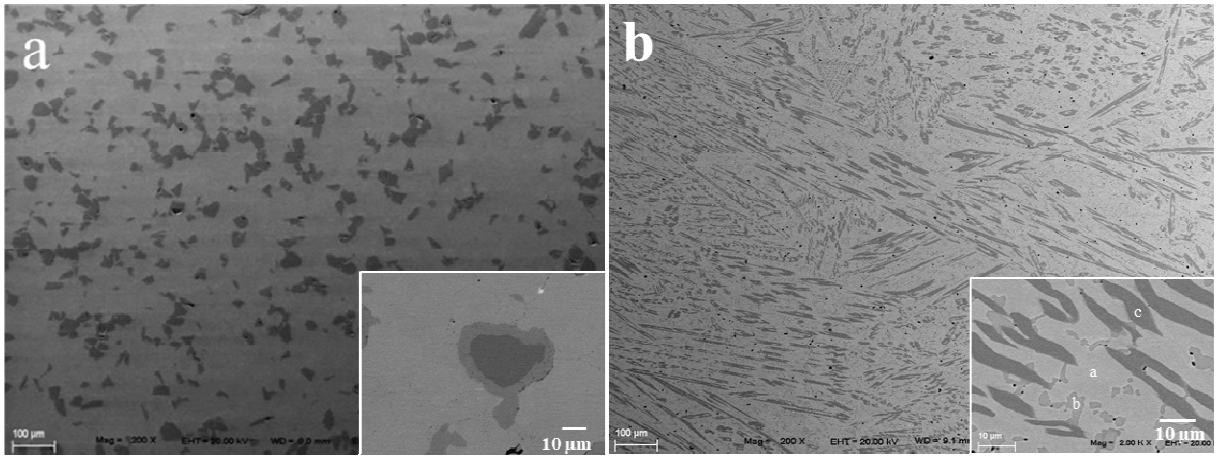


Fig. 5 BEI of (a) HIP Ni_3Al/Cr_3C_2 Composite from Pin 2 and (b) the Cladded Layer from Pin1.

The Cr_3C_2-particles in the HIP bulk composite reacted with Ni_3Al-matrix and formed a good metallurgical bonding with a light grayish boundary area as shown in the inset Figure 5a. From our previous study [10], EDS analysis revealed that the grey reaction zones have higher content of Cr as compared to the matrix, but lower Ni- and Fe-contents. This reaction zone is formed due to the diffusion process during HIP process. The composition of the matrix was same as the Ni_3Al-based alloy. Figure 5b is a backscattering electron image of the cladded layer and the inset figure shows three different phases which were identified by EDS analysis as Ni_3Al-, NiAl-phases and carbides represented by a, b and c respectively. The in-situ formed carbides (Figure 5b) are distributed in the Ni_3Al-matrix with as lamella-like carbides. A secondary phase was also formed in the specimen and the Al content (25.09 at. %) in this secondary phase was much higher than the Al content (12.44 at. %) of the matrix. Fe-content was detected as 14.55 at. % in the matrix and 8.80 at. % in the secondary phase. The Cr content in Ni_3Al-matrix and NiAl-phase were also recorded as 16.52 at. % and 7.01 at. % , respectively. Considering Fe- and Cr-elements with equivalent opportunity to replace Ni- and Al- position in crystals of Ni_3Al and NiAl, the matrix should be specified as Ni_3Al-phase, and the secondary phase as NiAl-type. The reason to form NiAl phase in the cladded layer is due to fast cooling rate during the TIG process, resulting in the non-equilibrium microstructure. The results from the analytical study can be coupled to the experimental data of tribological tests for understanding and evaluating wear behavior of the studied materials.

Hardness Measurement

Vickers hardness on the cross section of cladded layer was measured by using FM-300; the results were referred to a Chinese standard of GB/T 4340.1-1999. The applied load was 200 g and loading time was 10 seconds. The measurement was applied on three different areas along the cross section of the cladded sample; they are the regions of Welding materials (WM), Fusion layer (FL) and Based materials (BM), see Figure.6 and also referred to Figure.4. In the middle of fusion layer, a central line was selected as an initial position for performing indentation. Therefore, the measured indentations were perpendicular from the central fusion layer (FL) towards the WM and BM. The collected data from two tested specimens $2^{\#}$ and $3^{\#}$ were summarized in Fig.6.

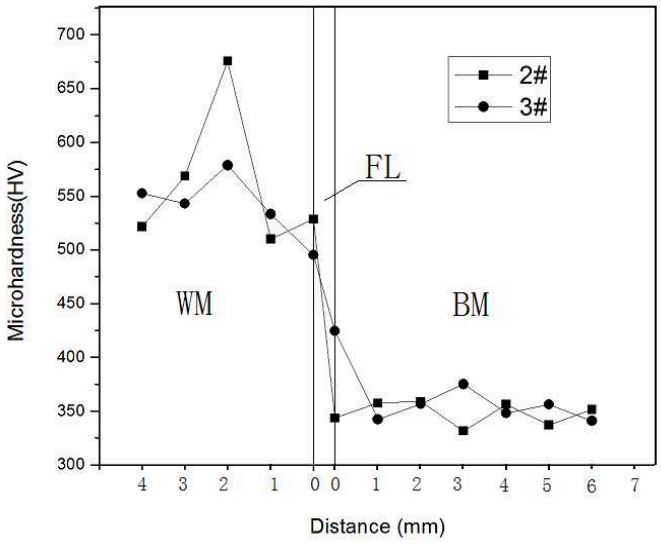


Fig.6 Vickers Hardness Profile on the Cross-section of Two Tested Cladding Layers.

Vickers hardness measurement was also applied on the reference bulk materials and the disk which were used in this investigation. In order to obtain the hardness measurements statistically, 10 indentations on each tested sample were performed. And then, the average Vickers hardness of the tested samples were obtained and listed in table 3.

TABLE 3 MICROHARDNESS OF THE TESTED SAMPLES

Tested samples	Pin 1	Pin 2	Pin 3	Pin 4	disk
HV200	558	560	420	240	237

Hardness results reveal that carbide addition obviously increased hardness of Pin1 and Pin2, as compared to the monolithic Ni_3Al-based alloy Pin3. But, the composites of Pin1 and Pin2 which were reinforced by the same volume percentage of carbide addition exhibited the same average hardness, even though Pin1 contains the in-situ formed carbides in its microstructure.

Pin-on-Disk (POD) Test

To evaluate friction coefficient and wear resistance of the cladded layer and the reference bulk materials, a conventional pin-on-disk tribometer was used. The measurements were performed at room temperature in laboratory with relative humidity of about 45 %. The disks with dimension of Ø30 mm x 4 mm and the pins with dimension of Ø3 mm x16 mm were machined to the surface roughness (Ra) less than 0.2 μm. The tests were performed under the normal load of 20 N, corresponding to contact pressure of 2.83 MPa. For each specified test, three pin-samples of the tested material were investigated in POD test in order to obtain statistical results. The sliding speed of $8cms^{-1}$ was applied as constant value by adjusting the rotation speed (200 rpm) of the disk and the diameter (Ø8 mm) of the wear tracks. The duration of sliding time was 6 hours. Wear volumes of the pin-samples were calculated from weight loss during the test by assuming density of 7.25 g/cm^3 of the cladded layer and HIP processed bulk composite. Wear volumes of the disks were measured accurately by using computerized three-axis profilometer (Taylor-Hobson). Wear tracks of the disks in 3D profiles were also mapped. The results on sliding wear in this study are demonstrated in terms of Archard`s specific wear rate (mm3/N·m) by the following formula.

$$\text{Specific wear rate} = V/ F\times S. \quad (1)$$

where V is the worn volume in mm^3, F is the applied normal load in Newton and S is the total sliding distance in meter.

Friction Coefficient

The friction coefficients of the testing cladded layer and the reference composite were investigated under the load of 20 N. The measured friction coefficients of the cladded layer and the HIP processed Ni_3Al/Cr_3C_2 composite were 0.13±0.02 and 0.68±0.02, respectively, see Figure 7. The friction coefficient of the HIP processed monolithic NAC-alloy (0.45±0.02) and the commercial vermicular graphite cast iron (0.48±0.02) from our previous investigation [9] were also given in the figure, as evaluation references.

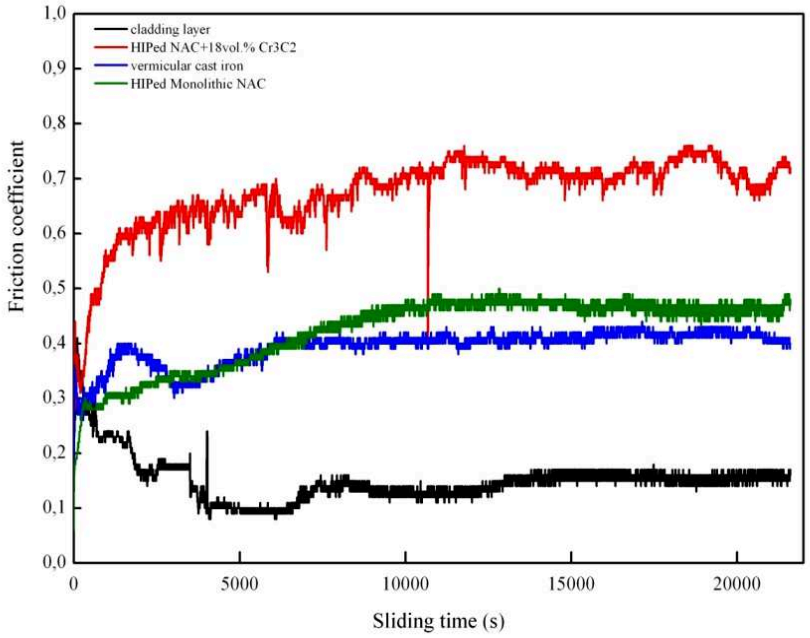


Fig. 7 Friction Coefficients of the Cladded Layer from Pin1, the References Ni_3Al/Cr_3C_2 Composite from Pin2, Monolithic NAC-alloy from Pin3 and the Commercial Vermicular Graphite Cast Iron from Pin4.

Specific Wear Rate

The specific wear rates of the pins and disks were also measured under the normal load of 20 N. The calculated values were illustrated in Figure 8. The specific wear rates of HIP monolithic NAC-alloy and the vermicular cast iron from our previous study [9] were also collected in the Figure 8.

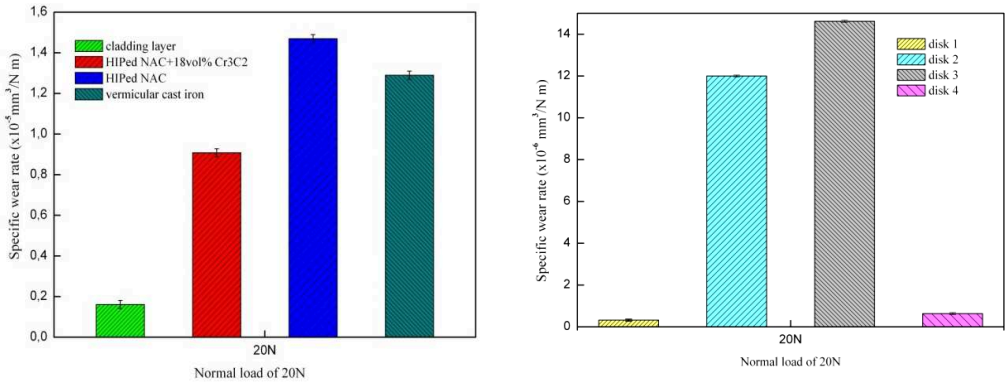
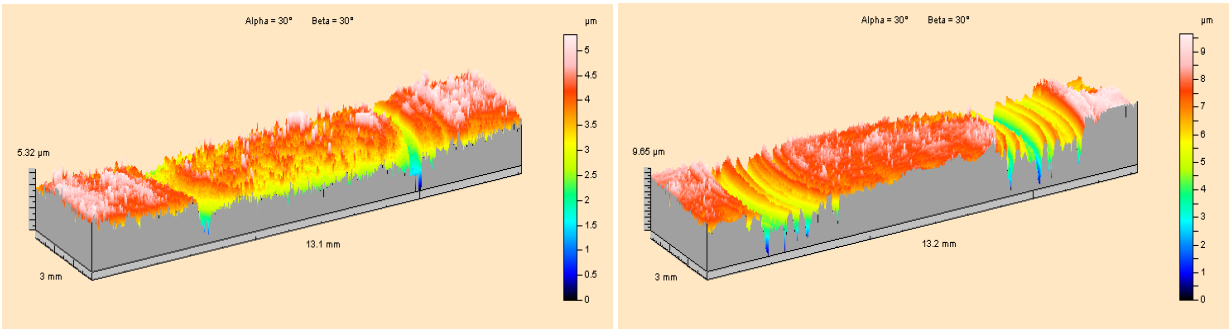


Fig. 8 Shows Specific Wear Rates of the Cladded layer, HIP Ni3Al/Cr3C2 Composite, Monolithic HIP NAC-alloy and Vermicular Cast Iron from (a), and Specific Wear Rates of the Corresponding Disks from (b).

The cladded layer clearly exhibited lower specific wear rate 0.162 x 10^{-5} $mm^3/N \cdot m$ as compared to the commercial cast iron 1.29 x 10^{-5} $mm^3/N \cdot m$ in the same working condition. The specific wear rate (0.91 x 10^{-5} $mm^3/N \cdot m$) of the HIP processed Ni_3Al+18 vol. % Cr_3C_2 composite was reduced as compared to the specific wear rate (1.47 x 10^{-5} mm^3/N) of the monolithic NAC-alloy. Meanwhile, the counterpart disk against to cladded layer showed lower specific wear rate (0.319 x 10^{-6} $mm^3/N \cdot m$) as compared to the specific wear rate (0.633 x 10^{-6} $mm^3/N \cdot m$) of the disk against to vermicular cast iron. The disk worn off by the HIP processed Ni_3Al-18 vol.%Cr_3C_2 composite showed the high specific wear rate of 12 x 10^{-6} $mm^3/N \cdot m$. Clearly, the HIP processed Ni_3Al+18 vol. % Cr_3C_2 composite were working inadequately with its disk. Figure 9 (a and b) illustrated the 3-D images of the disks worn off by the cladded layer and the HIP processed Ni_3Al+18 vol. % Cr_3C_2 composite, which revealed that the disk worn off by the HIP processed Ni_3Al+Cr_3C_2 composite had severe and deeper wear tracks on the surface as compared to the disk worn off by the cladded layer. It indicates that the artificially added coarse hard particles Cr_3C_2 induced mostly the asperities on the worn surface which caused the severe wear tracks on the counterpart disk. In contrast, in-situ formed Cr-carbides from the cladded layer were coupled to smooth worn surface of the disk.



(a) (b)

Fig.9 3-D Images Profiles of the Disk Worn Surface Against to (a) the Cladded Layer and (b) HIP Processed Ni3Al/Cr3C2 Composite.

Discussion

It is well known that the mechanical properties of a MMC (Metal-matrix composites) are important in determining their tribological behavior. During tibological interaction between two surfaces, temperature rises significantly at and near the surface, and the mechanical properties of the composites at elevated temperatures may be of direct relevance. The dispersed hard particles such as chromium carbides are helpful in retaining the high temperature strength of the matrix. During TIG process, chromium and carbon are partially dissolved in the Ni_3Al matrix and resulted in solid-solution strengthening. Then, the dispersed Cr-carbides were formed which increased hardness of the cladded layer. In our previous study, it indicated that the wear rate of metal-matrix composites decreased with an increase in volume fraction, if the bonding between the matrix and the particles is adequate.

Karin et al. [9] investigated previously the sliding wear behavior of the Ni_3Al-based NAC-alloy and its composites reinforced by 6 vol. % Cr_3C_2-particles under unlubricated condition. The experimental results revealed that the bulk monolithic NAC-alloy has similar friction coefficient and specific wear rate to commercial vermicular cast iron used in ship engines under same testing condition. Definitely, the addition of Cr_3C_2 hard particles reduced wear on both sides of pin and disk. The phenomenon was more obvious under the high applied load of 40 N testing conditions. Furthermore, considering other excellent physical, chemical and mechanical properties of the Ni_3Al-based intermetallic materials, the investigation has indicated that it could be meaningful and possible to develop Ni_3Al-matrix composites, reinforced by the hard Cr_3C_2-particles for tribological applications. Therefore, the high contents of Cr-carbides (18 vol. %) composites were prepared by both HIP and cladding process in this study. Clearly, the Ni_3Al/Cr_3C_2 intermetallic cladded layer on

the steel substrate performed superior wear behavior as compared to the wear-resistant vermicular cast iron and the other Ni_3Al-based materials. The Ni_3Al/Cr_3C_2 intermetallic cladded layer exhibited the lowest friction coefficient (0.13±0.02) in this group. It was considered that the superior wear behaviors of the Ni_3Al/Cr_3C_2 intermetallic cladded layer were connected to its unique microstructure. Two types of carbides with different sizes were in-situ formed in the Ni_3Al-matrix during solidification of the TIG process. They are distributed homogeneously with less spacing in the layer material compared to the interval distance of the artificially added carbide in the HIP processed Ni_3Al/Cr_3C_2 composite. Furthermore, the in-situ formed hard NiAl-particles will also be beneficial to the wear properties of the layer material. It should be noticed that the secondary NiAl-phase increased the total volume percentage of the hard phase in the microstructure, although the amounts of the chromium carbides in both of the Ni_3Al/Cr_3C_2 intermetallic cladded layer and the HIP processed composite are in the same range of 18 vol. %. Therefore, it is reasonable to consider that the material with hard particles with less spacing will protect the matrix more effectively and resulting in low friction coefficient with low specific wear rate at same wear conditions.

The present study suggests that such cladded intermetallic layer worked adequately with its grey cast iron disk during sliding wear and obtained the specific wear rate as 0.319×10^{-6} $mm^3/N \cdot m$. This value is only about 50 % the wear rate (0.633×10^{-6} $mm^3/N \cdot m$) induced by the reference vermicular cast iron under the same wear testing conditions. The HIP processed Ni_3Al+18 vol. % Cr_3C_2 composite worked with its counterpart disk shows low wear resistance and induced high specific wear rate of 12×10^{-6} $mm^3/N \cdot m$. This reveals that the microstructure of the composite played a key role and influenced the wear properties. Hence, the fine microstructure is preferable in all aspects. Furthermore, the composition of the matrix in the HIP processed Ni_3Al/Cr_3C_2 composite was maintained invariant during the heating process. In contrast, the added Cr-element in the welding wire was partially dissolved in the solid Ni_3Al-matrix which strengthened and hardened the material resulted in improved the wear-resistance.

Conclusions

From the study, several points can be concluded as follows:

The Ni_3Al-18 vol. % Cr-carbides intermetallic cladded layer on the high strength steel substrate worn off against the grey cast iron disk exhibited less friction coefficient 0.13±0.02 which is one quarter in magnitude of the friction coefficient (0.48±0.02) from the vermicular cast iron under the same testing condition.

The specific wear rate of the Ni_3Al/Cr_3C_2 composite cladded layer is 0.162×10^{-5} $mm^3/N \cdot m$, which is almost equal to one tenth in magnitude of wear rate (1.29×10^{-5}) of the vermicular cast iron under the load of 20 N.

The intermetallic Ni_3Al/Cr_3C_2 cladded layer worked more adequately with its grey cast iron disk, comparing to the reference vermicular cast iron and other tested intermetallic matrix composites. A specific wear rate 0.319×10^{-6} $mm^3/N \cdot m$ of the disk was obtained under the testing condition.

The outstanding properties of the Ni_3Al/Cr_3C_2 intermetallic cladded layer on wear were related to its unique microstructure. The in-situ formed hard Cr-carbides of various sizes with the small spacing may play a key role on the tribological properties of the cladded layer.

The wear behavior of the Ni_3Al/Cr_3C_2 intermetallic cladded layer may also respond to the in-situ formed un-equilibrium hard NiAl-particles and Cr-alloyed Ni_3Al-matrix. Therefore, the cladding process is promising selection to produce wear-resistant layer of Ni_3A-matrix composites in further investigation.

Acknowledgements

The authors are grateful for the financial support given by the Swedish VINNOVA and Chinese MOST for the international collaborative research projects P32737-1 and P32737-2 and appreciate the Department of Manufacturing Engineering and Engineering Management, City University of Hong Kong for allowance to use the facilities for tribological evaluation. Here authors also would

greatly appreciate Li Jikang, the senior of nercast in CISRI, Beijing for her guidance and encouragement through this work. The authors would like to thank Dr. Kumar Babu Surreddi reviewer for his careful polish and insightful comments that helped us improve this paper.

References

[1] Marquardt B. J., Wert J. J., Wear Induced Deformation of Ni3Al, (Fe,Co)3Al and (FeNi)3V [J]. Proc. Mater. Res. Soc.1985, 39:247

[2] Blau P. J., DeVore C. E.Sliding Behaviour of Alumina/Nickel and Alumina/Nickel Aluminide Coule at Room and Elevated Temperature [J]. J Tribology, 1988, 110: 646.

[3] Bonda N. R., Rigney D. A., Unlubricated Sliding Wear of Nickel Aluminides at Room Temperature and 400 °C [J].Proc. Mater. Res. 1989, 133: 585.

[4] Blau P. J., DeVore C. E., Temperature Effects on the Break-in of Nickel Aluminide Alloys [C] Proc. 1989 Wear of Materials Conference, American Society of Mechanical Engineers, 1989: 305.

[5] Blau P. J., DeVore C. E.,Sliding Friction and Wear Behaviour of Several Nickel Aluminide Alloys under Dry and Lubricated Condition [J]. Tribol. Ins., Oct. 1990: 226.

[6] Johnson M., Mikkola D. E., March P. A. et al, The Resistance of Nickel and Iron Aluminides to Cavitation Erosion and Abrasive Wear [J]. Wear (1990) 140:279.

[7] Shangping Li, Di Feng, Heli Luo, Microstructure and Abrasive Wear Performance of Chromium carbide Reinforced Ni3Al Mareix Composite Coating, Surf. Coat. Tech. 201 (2007), 4542:4546.

[8] Compilatory group of machine-producing technology and material (Ed.), Handbook of machine producing technology and material (second part), Machine Industry Press, 1993, 674:xxx.

[9] Karin Gong, Zhifeng Zhou, P.W.Shum, et al, Tribological Evaluation on Ni3Al-based Alloy and Its Composites Under Unlubricated Wear Condition [J] Wear, (2011) 270, 195:203

[10] Karin Gong, Heli Luo, D. Feng, et.al, Wear of Ni3Al-based Materials and Its Chromium-Carbide Reinforced Composites [J] Wear, (2008) 265, 1751:1755.

Advanced Materials Research Vol. 936 (2014) pp 1283-1289
© (2014) Trans Tech Publications, Switzerland
doi:10.4028/www.scientific.net/AMR.936.1283

Study On the Mechanical Stability of Retained Austenite in Cold-Rolled Medium-Mn Steel

HU Jun[1,2,a *], CAO Wen-quan[2], SHI Jie[2], DONG Han[2]

[1.] College of Materials Science and Engineering，Huazhong University of Science and Technology, Wuhan Hubei, 430074,China

[2.] Institute for Special Steels, Central Iron and Steel Research Institute, Beijing 100081, China

[a]hujun-jay2004@163.com

Keywords: volume fraction; retained austenite; tensile test; mechanicl stability; TRIP effect

Abstract: The mechanical stability of the retained austenite in the cold-rolled medium-Mn steel was studied. Tensile tests were carried out to measure the mechanical properties of the annealed steel. Scanning electron microscopy was applied to characterize the microstructure evolution during the tensile process; X-ray diffraction analysis was used to determine the residual austenite content in the deformed steel. It was found that the volume fraction of retained austenite gradually decreases with strain .The value of the stability coefficient of retained austenite *k* was small in the test steel, which indicated high mechanical stability of retained austenite. Due to TRIP effect, the high mechanical stability of the retained austenite strongly delays the onset of necking, which resulted in good comprehensive mechanical properties with ultrahigh strength and plasticity.

Introduction

The TRIP (transformation induced plasticity)-effect was observed in high alloyed austenitic steels already 30 years ago [1]. The excellent combination of strength and ductility of these steels was attributable to the irreversible strain-induced austenite-to-martensite phase transformation during plastic straining. Since the TRIP effect contributes to the high work-hardening rate of the microstructure and delays the onset of necking [2], they have been received increasing attention as new high-formability cold-rolled steel sheets for automobile bodies [3-6]. Nowadays the studies on the development of a new generation of steel with high strength and high ductility at reasonable cost have been promoted worldwide. In light of the high ductility contributed from metastable austenite in TRIP steel and stable austenite in TWIP steel [7-9], together with the high strength from grain refinement by severe plastic-deformed materials [10], increasing the volume fraction of retained austenite and refining the grain size into the submicron region in high-strength low-alloyed steel is a promising approach to design a new type of steel with both ultrahigh strength and high ductility [11].

Previous studies [12-14] confirmed that the volume fraction, the distribution of various phases, especially the stability of retained austenite is of great importance to the mechanical properties of transformation induced plasticity (TRIP) steels. In this study, the medium-Mn steel was produced by intercritical annealing after cold rolling to obtain a certain amount stable retained austenite. The main purpose is to determine the mechanical stability of the retained austenite in the steel and study the relationship between the mechanical stability and mechanical properties, which will provide a theoretical basis for the production of cold-rolled sheet with high strength and high ductility.

Experimental procedure

The chemical composition of the test steel investigated in the present work was shown in Table 1. The vacuum melted material was first made as a hot rolled strip with a thickness of 4 mm through the conventional hot rolling process. Then, the strip was cold rolled to a thickness of 1.2 mm. In order to obtain the TRIP behavior, the cold rolled strip was further processed by austenite reverted annealing, which is bell-type annealing at 650℃for 18h.

TABLE 1 CHEMICAL COMPOSITION OF THE TESTED ALLOY [WT %]

C	Mn	P	S	N
0.1	5	0.008	0.002	30ppm

After annealing, the sheet steel was machined into a tensile specimen shown in Fig.1. And the uniaxial tensile test was carried out on the WE300B tensile testing machine. The microstructure observation of each different tensile strain was conducted in the cross section of the specimen. The sample was treated by means of cold mounting, grinding and polishing, corrosion for 30s with 2% nitric acid alcohol solution, and observation of the microstructure with S-4300 cold field emission scanning electron microscopy (SEM).The X-ray diffraction was used to determine the residual austenite content (volume fraction) on the rolling surface after grinding and polishing. After mechanical polishing the rolling surface was electrolyzed for about 50s with 10% chromic acid electrolysis (voltage 5V) to remove the surface stress, then the residual austenite content was determined by PHILIPS APD-10 X-ray diffraction measurements. The Co target was used in the X-ray diffraction, and tube current and voltage were 30mA and 30kV. The graphite crystal monochromatic was used get to the diffraction patterns with the step scan mode in which scanning 2θ ranged 45-115°, step was 0.02° and integration time was 0.4s.Then X-ray diffraction analysis software was used to search the peaks and compute the angle of diffraction peaks, the FWHM and integral intensity. The amount of retained austenite was derived by comparing the integral intensities of Ferrite (200) and (211) and Austenitic (200) (220) and (311) crystal surface and the retained austenite content is calculated by equation [15] (1):

$$V_i=1/[1+G(I_\alpha/ I_\gamma)]. \quad (1)$$

In the equation, V_i is the amount of retained austenite (volume fraction), G is the parameters of some crystal surface in the austenite and martensite,I_α， I_γ was the integral intensity of the peak in the martensite and austenite. The carbon content of the austenite was calculated by equation (2) using of the austenite lattice constant [16]:

$$a_0=3.555+0.044x. \quad (2)$$

Where a_0 was the austenite lattice constant by actual measurement, x was the mass percentage of carbon in the retained austenite.

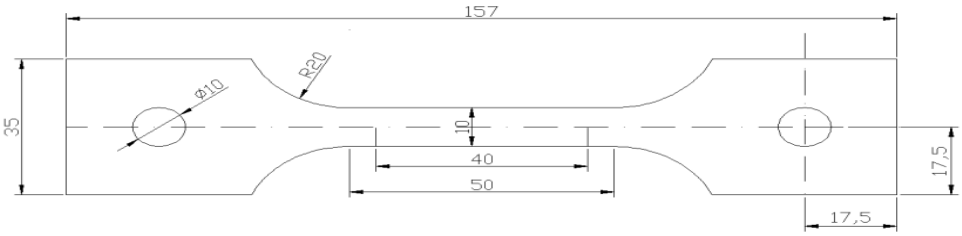


Fig.1 Tensile specimen size chart

Results and discussion

The microstructures before and after tensile test of the steel

The microstructure of the start and deformed steel was characterized by the SEM as shown in Fig.2 (a-d).The microstructures in the four states were quite similar and they all consisted of the convex and concave grains. After annealing the austenite reverted transformation took place [17], so the microstructure was composed by slightly recovered ferrite grains, some precipitated carbides and a few of austenite grains. As the austenite grain was easy to be etched and the ferrite grain was difficult to be etched, the concave grains were identified as the austenite grains. The grain size of the recovered ferrite phase was about 1.5μm.It can be seen that the volume fraction of retained austenite decreased and the grain size of the ferrite was refined with strain increasing.

As the driving force of the applied stress, the transformation from the metstable austenite to martensite occurred during the tensile process which is called “stress-induced martensitic transformation”, which resulted in reduction of the retained austenite. There was another interesting phenomena that the change of the austenite and the grain size of ferrite vary in their pace which implied that the deformation behaviors of different phase were different due to the different interaction behaviors among phases and thus results in the heterogeneous deformation structure.

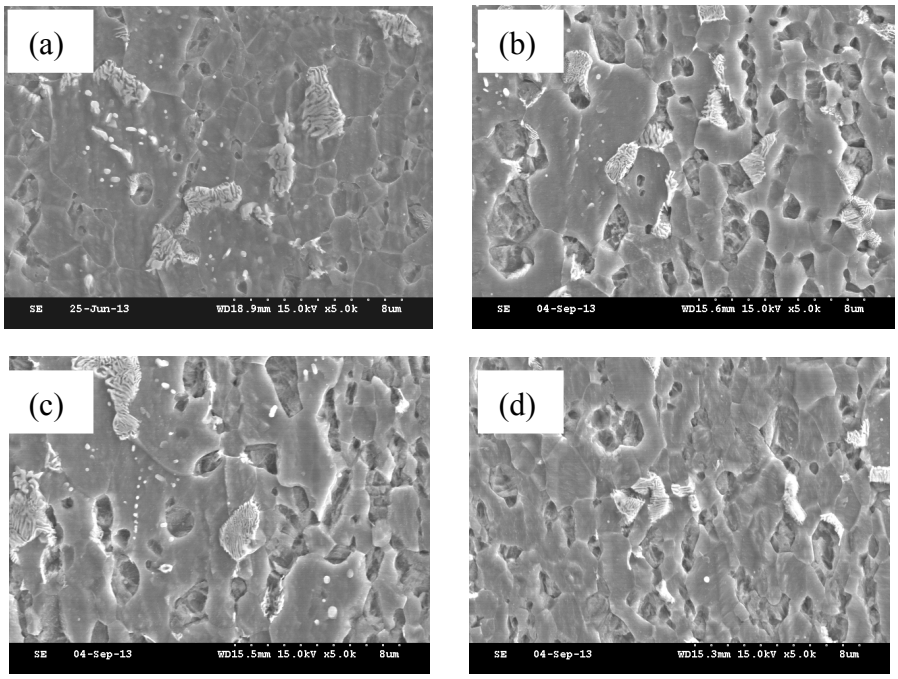


Fig.2 The starting and deformation microstructure of test steel deformed at room temperature characterized by SEM, (a) As-received, (b) 7% elongation, (c) 20% elongation and (d) 30% elongation.

The tensile curve of the steel

The mechanical properties of the steel were measured by the tensile test and the results were shown in Table 2. It can be seen that there is little difference in the mechanical properties between the specimens in the RD (rolling direction) and TD (transverse direction).The ultra tensile strength was about 700MPa and the total elongation was 40% in both of these two direction. The product of the ultra tensile strength (UTS) and total elongation (A) was applied to evaluate the combined mechanical properties of the medium-Mn steels, which intuitively express the forming ability and the deformation energy absorbed in the collision. The product was about 28GPa%, which was higher than that of the traditional TRIP steel and DP steel (normally about 20-24GPa% for TRIP and DP steel).

TABLE 2 MECHANICAL PROPERTIES OF THE TEST STEELS IN DIFFERENT DIRECTION

Direction	UTS[MPa]	YS[MPa]	A[%]	Agt[%]	UTS*A[GPa%]
RD	685	400	40.3	26.0	27.6
TD	704	453	40.0	23.0	28.2

The true stress-strain curves of the tensile test at room temperature with different direction are shown in Fig.3 (a and b). It can be seen the stress increase with strain increasing but the work hardening rate decrease with strain increasing. As we know, the formation of matensite under stress produces more effective “strain hardening” than the ordinary slip mechanism in fcc austenite. From the above analysis, it is suggested that martensitic transformation in TRIP steel has “strain hardening” effect and “uniform elongation” effect due to martensitic transformation causing the redistribution of stress, as a consequence, TRIP steels exhibit greater tensile strength and ductility than many commercial steels currently used in the manufacture of automobiles.

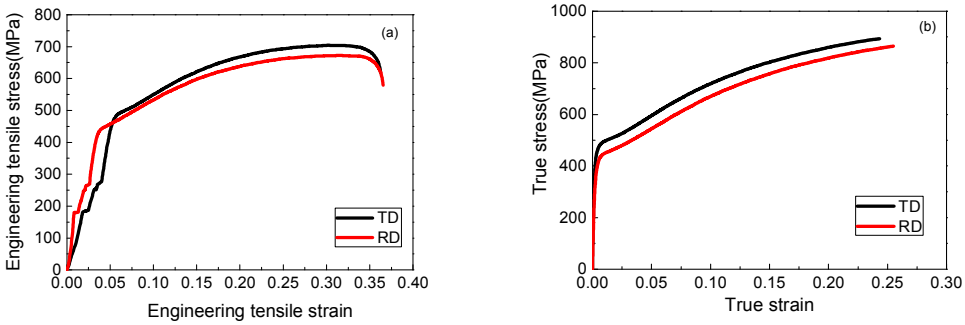


Fig.3 The stress-strain curves during tensile test at room temperature (a) the engineering stress-strain curve (b) the true stress-strain curve

The stability of retained austenite

It can be seen qualitatively from Fig.2 (a-d), the retained austenite fraction decreases with strain increasing during deformation process. In order to describe the changing rate quantitatively, the volume fractions at different strain are given in Fig.4. It can be seen clearly in Fig.4 (a) that the volume fraction of retained austenite gradually decreased with strain increasing. The exponent decreasing trends of retained austenite fraction with strain were clearly indicated in Fig.4 (b), which results were similar to the formula suggested by Chung and Chang et al. as described in equation(3) are already used by researchers [18]. However, in our study, the value of $f_{\gamma,\,u}$ is 0, which means there are no “dead retained austenite” as proposed by these authors. Thus the changing formula of retained austenite can be rewritten as in equation (4).

$$\log\{\ln[(f_{\gamma,0}-f_{\gamma,u})/(f_{\gamma,0}-f_{\gamma,\varepsilon})]\}=\log k+\log \varepsilon. \quad (3)$$

where, $f_{\gamma,0}$, $f_{\gamma,u}$ and $f_{\gamma,\varepsilon}$ refer to the austenite volume fraction in the starting materials, the volume fraction of retained austenite after broken during tensile and the volume fraction of retained austenite at given strain (ε), respectively. k is defined as the stability coefficient of retained austenite, and the larger k value indicates the lower stability of retained austenite and the faster martensitic transformation.

$$f_{\gamma,\varepsilon}=f_{\gamma,0}\exp(-k\varepsilon). \quad (4)$$

Where the parameters assume same meaning as described in equation (3).

In the range where the true strain is lower than 0.11, the retained austenite fraction drops dramatically with increasing strain, indicating very fast strain-induced transformation. Even the true strain rises over 0.17; the austenite fraction of the steel still decreases very slowly, indicating that the strain-induced transformation still continues.

The slope of straight line in Fig. 4 corresponded to the k in equation (4). In general, lower k value indicates higher stability of retained austenite [18]. This stability of retained austenite is closely related with the mechanical properties of cold-rolled steel sheets, with uniform elongation in particular. This is because necking is delayed as the strain-induced transformation lasts up to the higher strain region when the stability of retained austenite is high. The mechanical stability value of k under tensile test at room temperature is 12.9, which is a little lower than the k (from 16.20 to 20.99) in the TRIP steel [12].

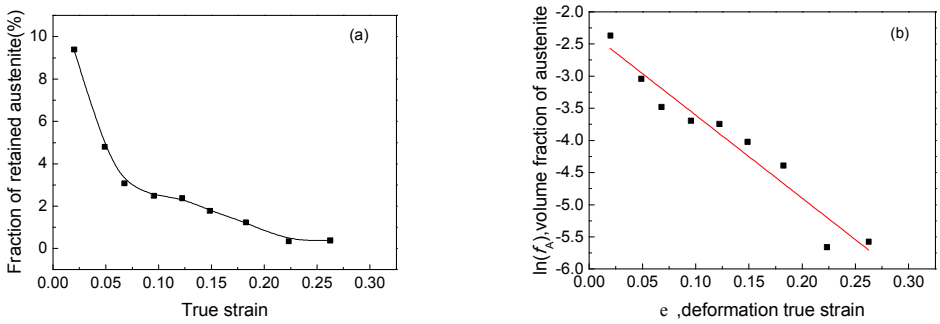


Fig.4 The volume fraction of retained austenite at different tensile strain of the steel deformed at room temperature (a) in the normal scale and (b) in the natural logarithm scale.

Conclusions

The microstructure of the cold-rolled medium-Mn steel was investigated by means of SEM. In addition, the mechanical stability of retained austenite was evaluated by tensile tests through the evolution of the volume fraction of the retained austenite. Main conclusions can be drawn as follows:

(a) It was demonstrated that the recovery and austenite reverted transformation took place during the annealing process in the cold-rolled medium-Mn steel. The duplex ferrite and austenite microstructure was obtained in the steel.

(b) It revealed a very good comprehensive mechanical property with the tensile strength 700MPa and the total elongation 40% in the test steel. Moreover the product of the tensile strength to the total elongation was 28GPa*%, which is higher than that of the conventional TRIP steel.

(c) The TRIP effect of the austenite phase plays an important role in the high strength and high plasticity of the cold-rolled medium-Mn steel. At the same time the stability coefficient of retained austenite *k* was 12.9, which implied the retained austenite was rather stable during the tensile test, so that the high strength and high plasticity was obtained in the test steel.

Acknowledgements

This research is supported by the National Natural Science Foundation of China (no. 51371057) and National Basic Research Program of China (973 Program, no. 2010CB630803).

References

[1] H.K.D.H.Bhadeshia and D.V.Edmonds, The bainite transformation in a silicon steel, Metall.Trans. A. 10(1997)895-907.

[2] T.Yokoi, K.Kawasaki, M.Takahashi, K.Koyoma and M.Mizui, Fatigue properties of high strength steels containing retained austenite. JSAE Review. 17.2(1996)210-212.

[3] K.Sugimoto, N. Ushi, M.Kobayashi and S. Hashimoto, Effects of Volume Fraction and Stability of Retained Austenite on Ductility of TRIP-aided Dual-phase Steels, ISIJ. 32(1992)1311-1318.

[4] K.Sugimoto, N. Ushi, M.Kobayashi and S. Hashimoto, Ductility and strain-induced transformation in a high-strength transformation-induced plasticity-aided dual-phase steel, Metall. Trans.A. 23(1992)3085-3091.

[5] H.C. Chen, H. Era and M. Shimizu, Effect of phosphorus on the formation of retained austenite and mechanical properties in Si-containing low-carbon steel sheet, Metall. Trans.A.20(1989)437-445.

[6] C.G. Lee and S.J. Kim, Microstructures and mechanical properties of high strength hot-rolled steel plates containing tramp elements, J. Kor. Inst. Met. Mater. 1998; 36.7(1998) 1024-1031.

[7] G.Frommeyer, U.Brux, P.Neumann, Supra-Ductile and High-Strength Manganese-TRIP/TWIP Steels for High Energy Absorption Purposes, ISIJ. 43(2003)438-446.

[8] K. Sugimoto, B. Yu, Y. Mukai, S. Ikeda, Microstructure and Formability of Aluminum Bearing TRIP-Aided Steels with Annealed Martensite Matrix, ISIJ. 45(2005)1194-1200.

[9] L.Bracke, K.Verbeken, L.Kestens andJ.Penning, Microstructure and texture evolution during cold rolling and annealing of a high Mn TWIP steel, Acta Mater. 57(2009)1512-1524.

[10] A. A. Gazder, W. Q. Cao, C. H. J. Davies, E. V. Pereloma, An EBSD investigation of interstitial-free steel subjected to equal channel angular extrusion, Mater.Sci.Eng.A. 497(2008)341-352.

[11] K.X. Tao, H. Choo, and H.Q. Li, Transformation-induced plasticity in an ultrafine-grained steel: An in situ neutron diffraction study, Appl. Phys. Let. 90(2007)101911 - 101911-3.

[12] Chang Gil Lee, Sung-Joon Kim, Tae-Ho Lee, Sunghak Lee, Effects of volume fraction and stability of retained austenite on formability in a 0.1C–1.5Si–1.5Mn–0.5Cu TRIP-aided cold-rolled steel sheet, Mater.Sci.Eng.A. 371(2004)16-23.

[13] X.D. Wang a, B.X. Huang, Y.H. Rong, L. Wang, Microstructures and stability of retained austenite in TRIP steels, Mater.Sci.Eng.A. 438-440(2006)300-305.

[14] Arif Basuki, Etienne Aernoudt, Influence of rolling of TRIP steel in the intercritical region on the stability of retained austenite, Journal of Materials Processing Technology. 89-90(1999)37-43.

[15] N. H. van Dijk, A. M. Butt, L. Zhao, J. Sietsma, S. E. Offerman, J. P. Wright, S. van der Zwaag, Thermal stability of retained austenite in TRIP steels studied by synchrotron X-ray diffraction during cooling, Acta Mater. 53(2005)5439-5447.

[16] V. F. Zackay, E. R. Parker, D. Fahr, R. Busch, The enhancement of ductility in high-strength steels, ASM Trans Quart. 60(1967)252-259.

[17] W.Q. Cao, C. Wang, J. Shi, M.Q. Wang, W.J. Hui, H. Dong, Microstructure and mechanical properties of Fe–0.2C–5Mn steel processed by ART-annealing, Mater.Sci.Eng.A, 528(2011) 6661-6666.

[18] H.C. Shin, T.K. Ha and Y.W. Chang, A study on the deformation induced martensitic transformation of 304 stainless steel, J. Kor. Inst. Met. Mater. 34.12(1996)1550-1557.

Advanced Materials Research Vol. 936 (2014) pp 1290-1297
© (2014) Trans Tech Publications, Switzerland
doi:10.4028/www.scientific.net/AMR.936.1290

Influence of Heat Treatment on Fatigue Resistance of Sintered Ti 35Nb 7Zr 5Ta β Alloy

A. H. Franco[1, a], C. R. M. Silva [1, b], P. V. Muterlle [1,c], J. L. A. Ferreira [1, d], J. A. Araujo[1, e].

[1] Department of Mechanical Engineering, University of Brasília, 70910-900 Brasília, DF – Brazil
[a] pacific721031@yahoo.com, [b] cosmeroberto@gmail.com, [c]pmuterlle@yahoo.com.br, [d]jorge@unb.br, [e]alex07@unb.br

Keywords: TI -35Nb-7Zr-5Ta, four point bending fatigue, Powder metallurgy

Abstract: Mean stress on fatigue strength of Ti-35Nb-7Zr-5Ta, used in the manufacture of orthopedic prosthesis, was evaluated. Samples of Ti-35Nb-7Zr-5Ta were pressureless sintered and tested using microhardness (Vickers) and four point bending fatigue apparatus. Characterization was carried out using optical microscopy, scanning electron microscopy, EDS analysis, oxygen analysis and density. The density analysis shows almost 98% of density and microscopy reveals some precipitates of α phase and presumably ω phase at the grain and grain boundaries. The bending fatigue resistance limit reached ($Se(10^6) \approx 88$ MPa), due to, presumably, the influence of coarse α phase precipitates at grain boundaries as well as the high oxygen content in the material after sintering (0.96 %). In this study, Kwofie model best explains the influence of mean stress on fatigue strength of this alloy.

Introduction

The use of Powder Metallurgy (P/M) aims to obtain orthopedic implants with almost net-shaping and adequate mechanical properties and surface porosity. The surface porosity is necessary to improve an efficient interaction between the implant and the bone [1].

The control and quantification of porosity is very important because its size and morphology are essential to the cellular adhesion. It is necessary to obtain a high porosity to improve bone-formation inside the pores [2].

Sintering is irreversible, so a perfect control during the process is necessary. After the sintering, alternative technologies are used to modify some properties, to improve the shape or dimensional accuracy so as to extend the range of application [3].

The lower modulus of β Ti alloys have been developed recently because they exhibit a elasticity modulus near of bone modulus and those alloys have other desired properties like ideal bio-alloy. Biomedical alloys needs a good relation between low modulus and enough strength and alloying additions that are biocompatible [4]. The P/M Ti 35Nb 7Zr 5Ta alloy (TNZT) with 55 GPa modulus is considered one of the best to be used as a orthopedic implant. This TNZT has excellent non-toxic components with good mechanical properties and workability [5 - 7].

The recent trend in research and development of titanium alloys for biomedical applications is to develop low rigidity β type titanium alloys composed of non-toxic and non-allergic elements with excellent mechanical properties and workability [8]. According to this concept, different new β type have been developed like Ti–29Nb–13Ta–4.6Zr [9 - 12] and Ti 35Nb 7Zr 5Ta obtained just by P/M [13] alloy composed of elements like Nb, Ta, and Zr [14, 15] for biomedical applications. It is still necessary to evaluate various performances of Ti–35Nb–7Zr-5Ta for practical use.

Fatigue performance is one of the most important mechanical properties for biomaterials because, in general, these materials are used under cyclic loading. Fatigue performance of titanium alloy varies according to mean stress applied. The influence of mean stress on fatigue strength of the new β type titanium alloy M/P obtained, Ti 35Nb 7Zr 5Ta, were investigated in relation with microstructures in this study.

Basic Relations of Load Characterization

The fatigue life is described by the Wöhler curve or *S-N* curve, Stress-Life, where the number of cycles to failure, *N*, is correlated with the alternating stress, S_a. This method is a relation that can be well used to adjust appropriately experimental data in the sense to correlate the alternate stress and the number of cycles to failure between 10^3 and 10^6 cycles.

Some practical applications and also fatigue tests in materials involve maximum and minimum level stresses that characterize the amplitude loads. The stress range, ΔS, is the difference between the maximum value and minimum value. The mean stress, S_m, is the average between maximum value and minimum value. The half of the range stress is called amplitude stress, S_a. These are basic relations that characterize one load cycle.

And to describe the mean stress, a factor used to characterize the degree of symmetry of the load, is load ratio, *R*. The relation between S_a, S_m and *R* is expressed in the Eq. 1.

$$S_a = (1+R / 1-R) \times S_m \quad (1)$$

Mean Stress Effect Prediction Models

Initially, empiric models were proposed by Gerber (1874), Goodman (1899), Haigh (1917) and Soderberg (1930) to compensate the effect of mean stress in the high cycle fatigue strength. Gerber proposed a parabolic representation of the Wöhler's limit fatigue data on the graphic S_{max}/S_u *versus* S_{min}/S_u , Eq. 5. Goodman introduced a theoretical line to represent the evaluated fatigue data, Eq. 4. Haigh was the first to plot the fatigue data in the graphic S_a *versus* S_m. Starting around 1960, some models to determine the effect of mean stress have been proposed as improvements of the previous models. Fatigue tests indicate that the tensile normal mean stress should reduce the fatigue strength coefficient and that the compressive normal mean stress should increase it [16].

In order to overcome the failure prediction's problem under load conditions with relatively low amplitude and relatively high mean stresses, Smith, Watson and Topper - SWT [17] proposed a model in which the equivalent stress to the endurance limit for the load ratio, $R = -1$, S_{ar}. On this same year, Walker [18] presented a criteria similar to SWT, however using a factor γ that makes possible an adjustment of the curve in relation to the experimental data, Eq. 6. According to empiric data, Berkovits and Fang [19] and more recently Kwofie [20] proposed widespread mathematical relations to describe the effect of mean stress on the fatigue behavior of endurance limit. Such model consists in the substitution of the Basquin's equation's constant, for a function that will depend on the mean stress, S_m, on the limit of fatigue strength for the reverse load condition, S_{rt}, and on the ultimate strength, or yield strength, S_y. According to this model, the stress-life relation can be presented by Eq. 2.

$$\sigma_a = S_{ar} \times e(-\alpha(\sigma_m/Srt)) \quad (2)$$

Expressed in form of power series, the Eq. 2 can be expressed by Eq. 3:

$$\sigma_a = S_{ar} \, X \, e^{(-\alpha(\sigma_m/S_{rt}))} \approx \Sigma^{N}_{i=0} \, X \, 1/i! \, X \, (-\alpha \, \sigma_m/S_{rt})^i \quad (3)$$

Admitting that the argument of the exponential function tends to zero, $\alpha(\sigma_m/S_{rt}) \rightarrow 0$, the consequence is that the terms of superior order converge quickly to zero.

Materials and Methods

For the preparation of the alloy, the blended elemental method followed by a sequence of uniaxial and cold isostatic pressing with subsequent densification by sintering was chosen. All the powders were obtained by hydriding method and sintered in hydride state. The starting powders were weighed and dried for one hour in stove and blended for 30 minutes in a planetary mill. After blending, the powders were cold uniaxially pressed under pressure of 60 MPa. Afterwards, samples were encapsulated under vacuum in flexible rubber molds and cold isostatically pressed (CIP) at 350 MPa during 30 seconds in an isostatic press. Sintering was carried out in niobium crucible in high vacuum condition (10^{-7} Torr), at 1500 °C. Metallographic preparation was carried out using conventional techniques. Specimens were etched with a Kroll solution: 1.5 ml HF: 2.5 ml HNO_3: 100 ml H_2O, for 50 seconds, to reveal its microstructure. Microhardness measurements were carried out with a load of 200g for 20 seconds (15 indentations). The micrographs were obtained using a SEM Philips Quanta model 200 3D and optic microscope "OLYMPUS BX51. The porosity was

determined by the Arquimedes method. The analysis of oxygen and nitrogen was made in the Material's Lab at University of Trento. Bending fatigue at four points was developed in a universal testing machine MTS 810.

The material used in the development of this research was the Ti 35Nb 7Zr 5Ta alloy, a β titanium alloy. This is a new biocompatible alloy used in the production of orthopedic implants. The mechanical properties (Young modulus, E, tensile strength, S_{rt}, and yield strength, S_y), oxygen and nitrogen content, density and densification of the alloy are summarized in Table 1.

TABLE 1 MECHANICAL PROPERTIES OF TI 35NB 7ZR 5TA.

Alloy	kind	Srt* [MPa]	Sy* [MPa]	E* [MPa]	O** [%]	N** [%]	Density** [g/cm^3]	Densification** [%]
Ti35Nb7Zr5Ta	β	596.5	547.1	55	0.96	0.0111	5.60±0.05	97.9

* Theoretical values. **Experimentally Determined Values

Results and Discussion

In the microstructure presented in Fig. 1 one can see a β-homogeneous microstructure with relative high porosity. Due to the complete dissolution of the alloys elements in the titanium matrix, a good combination of microstructure, mechanical properties and desired densification could be reached.

The samples sintered at 1500°C presented a β-homogeneous microstructure with medium porosity. The alloy presented microhardness values around 340 HV, next to the observed in samples produced by the melting conventional method [22]. The microstructure of the TNZT alloy in the sintered condition, observed in optical and scanning electron microscope, are shown in the Figure 1 and Figure 2. The microstructure consists of relatively large grains of phase β with grain boundary α precipitates. In addition, some amount of intra-granular α precipitation is also visible within β grains. These intra-granular primaries α precipitates often exhibit rather different morphologies (plates and needles).

The Figure 2 allows to see α and β areas (sintered at 1500^{o}C) where the analyses for EDS were carried out. Areas 1 and 2 are, preferably, β and α region respectively.

The medium porosity presence, area 3 (observed in Figure 2a) is an important feature for osseointegration, when aiming for surgical implants application, where a medium-high porosity is necessary. An efficient route to control the pore content in TNZT samples is selecting an adequate space holder. This sintering method in order to manufacture highly porous metallic materials was investigated in other research [13]. In Figure 2b are signalized (region 4) the probably ω phase. These precipitates will be certainly identified through the Transmission Electron Microscopy and will be published in future papers. It is possible that the same precipitate would be formed into the grain boundary.

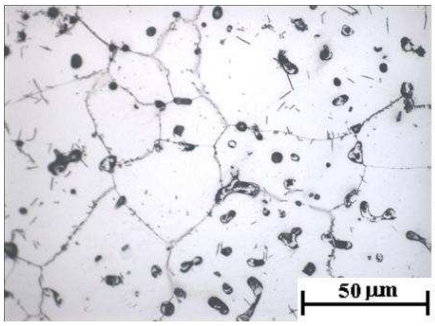
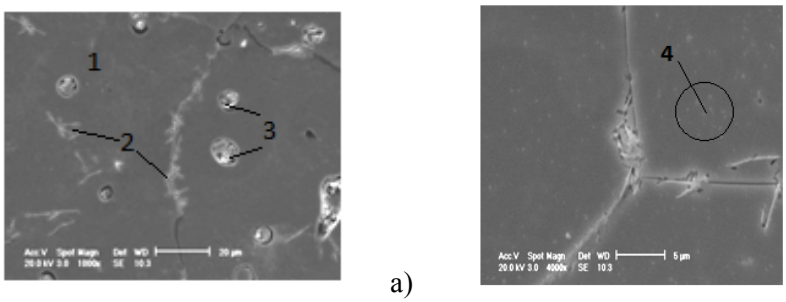


Figure 1. Optic microstructure of sintered Ti 35Nb 7Zr 5Ta alloy a)200x b) 500x



a) b)

Figure 2. Scanning Electron Microstructure of sintered Ti 35Nb 7Zr 5Ta alloy a)1000x b) 4000x

Figure 3 shows the S-N log-log linearization obtained through the Grapher 7 software, based on the experimental data of fatigue test in alternated stress. Figure 4 shows the adjustment of the experimental data considering a Mono-log linearization. Based on test result the fatigue strength of this alloy for the sintered and aged condition is approximately S'_e = 78MPa and approximately S'_e = 88MPa for solubilized samples.

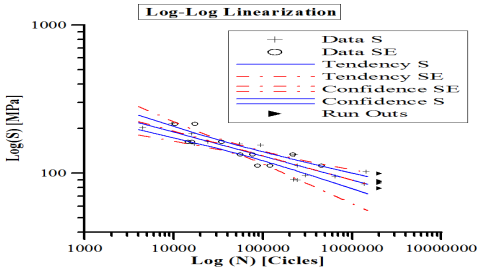


Figure 3. S-N Log-log Linearization

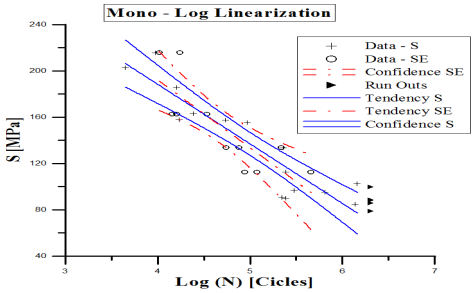


Figure 4. S-N Mono-log Linearization

Considering the goal of this work, it is necessary check the adherence of the Goodman, Gerber, Kwofie and Walker´s models making a comparison between the results and obtained graphics with the results of the S-N linearization results. Since the S-N graphics do not include the mean stress effect it is necessary standardization of the equivalent alternated stress, for Goodman:

$$\sigma a = \sigma alt / 1 - (\sigma med / Srt) \quad (4)$$

Once found, the equivalent alternated stress using Eq. 4 takes in consideration the experimental mean stress. For each point, the S_{ar}-N relation was obtained for Goodman model, considering the adherence of log-log. The Eq.5 was used to calculate equivalent alternated stress at the Gerber Model and the associated graphics were constructed.

$$S_{ar} = \sigma_{alt} / 1 - (\sigma_{med} / S_{rt})^2 \quad (5)$$

The Eq. 6 was used to calculate equivalent alternated stress for the Walker Model and the associated graphics were plotted.

$$S_{ar} = \sigma_a * (2/1-R)^{1-\gamma} \quad (6)$$

Using the Eq. 7 the equivalent alternated stress was calculated for Kwofie Model and the associated graphics were plotted.

$$S_{ar} = \sigma_a / 1 - \alpha(\sigma_m / S_{rt}) \quad (7)$$

From Figure 5 to Figure 8 is showed both the just sintered (S) and sintered and aged (SE) conditions tendency and its confidence curves. Figure 5 shows the log-log linearization obtained for Goodman model. Figure 6 shows the log-log linearization obtained for the Gerber model. Figure 7 shows the log-log linearization obtained for the Walker model. Figure 8 shows the log-log linearization obtained for the Kwofie model. All log-log linearization were obtained using the experimental data.

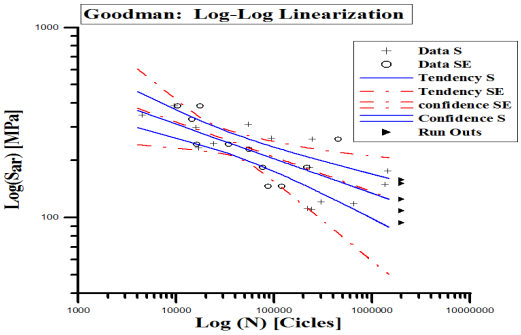


Figure 5. Goodman model adjustment log-log

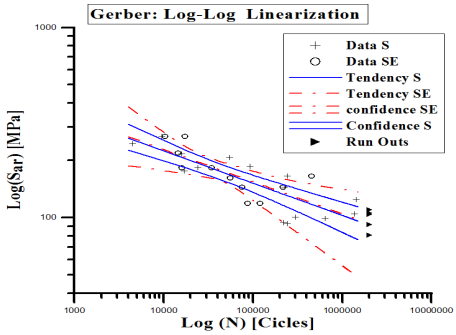


Figure 6. Gerber model adjustment log-log

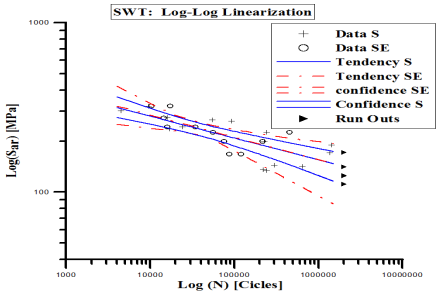


Figure 7.Walker model adjustment log-log

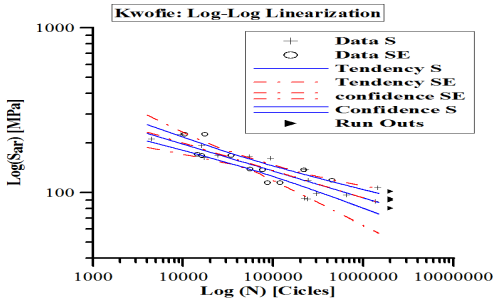


Figure 8. Kwofie model adjustment log-log

Models Comparison

It is possible, with the aid of Table 2, visualize the adhesion for both treatments: sintered (S) and sintered and aged (SE).

TABLE 2 DETERMINATION COEFFICIENTS AND FATIGUE RESISTANCE OF STUDIED MODELS FOR LOG-LOG LINEARIZATION.

Treatment		S-N	Goodman	Gerber	Walker	Kwofie
S	R^2	0.844	0.638	0.741	0.753	0.834
	S_e	88	129	98	121	88
SE	R^2	0.672	0.448	0.545	0.616	0.668
	S_e	78	107	87	109	77

The line S-N shows the analysis done without mean stress influence and, apparently, represents a better grip to the material behavior. Considering also that, according to Kwofie, the closer to zero (0) the parameter α is, the lower the sensitivity of the material to the mean stress. The material (depending on tested samples) is not much sensitive to the mean stress. The coefficient of determination for both the log-log and mono-log curves, show little fit of the experimental data. In all cases, the curves have a better adjustment when analyzed in Log-log linearization.

The diagrams obtained by applying the procedures of ASTM E 739 [23] to the experimental data also reveal that the material has narrow confidence bands; for both the S-N curves (without main stress) and for the Kwofie model, even when some points appear with some scattering. This behavior of the confidence bands reinforces the above statement about the influence of mean stresses in the material. It was also observed that most dynamic models, such as Kwofie tend to have the better fit to the data.

Soderberg model may be considered to be the most conservative of the analyzed criteria, knowing that a safety factor is included in the mathematical model used by him. However, this method is not widely used by engineers in projects. Goodman would be the following more conservative criteria, depending on tested material and levels of loads used in the study. Goodman

has a more conservative behavior when used for analysis of the influence of mean stresses values higher than those studied in this thesis, which are considered low.

The analysis of the influence of thermal treatment applied on the fatigue strength of the alloy showed not improvement or worsening. The trend curves for both analyzed conditions are virtually superimposed, indicating that the material behavior was similar for each heat treatment. Nevertheless, is important to note that the analysis of 10^5 cycles life in solubilized and aged material has a better behavior, keeping trend curve always approximately 10 - 15% above the sintered material.

High values of fatigue strength in titanium alloys obtained by melting electric arc, associated with mechanical forming reported in literature [24], are linked to the formation of cracks beneath surface of material in a more stable phase β, favored by the refinement of precipitates. In the alloy studied in this work, metastable β phase is associated with the presence of coarse precipitates of alpha phase, favoring the formation of internal cracks in the material. These cracks facilitate the advancement of the fracture and consequently causes lower values of fatigue resistance [25].

The value of Se (fatigue resistance) obtained for the Ti-35Nb-5Ta-7zr in this work was 89 MPa. Taylor [26] reported values in the region of 23-30 MPa for human long bones and 32-43MPa for bovine compact bone. Niinomi et al. [27] reported values of fatigue resistance in cattle bones compact 40-50 MPa. Taylor et al. [28] have reported fatigue resistance values of 70-80Mpa to bovine bone. After performing analysis of all these results, it was considered that the material under consideration provides consistent resistance values for use which has been designed.

It is considered that microstructure obtained combined with the level of porosity of the alloy is mainly responsible for mechanical behavior of studied alloy. If necessary, to achieve higher strength values for any other design requirements, one may add to the manufacturing process a rolling step as well as a high cooling rate (quenching water) after the aging treatment as described in other studies that have been achieved fatigue resistance values of 700 MPa [5]. Those high ´Se´ values were also described in other studies [29, 30].

In Table 2, S-N column represents the analysis without the influence of the mean stress effect; apparently it is who better explain the material behavior. Based in Kwofie criteria, when $\alpha \rightarrow 0$, the material mean stress sensibility tend to be lower. Considering the experimental results Ti 35Nb 7Zr 5Ta alloy showed big mean stress insensibility. Mono-log linearizations show us a better adherence to the experimental data and hence, are the models who offer us a better analysis of the statistical test results. Results analysis using ASTM E739 [23] show that S-N curve without incidence of mean stress and Kwofie model presents better confidence rate even in more dispersed points.

Conclusions

The aim of this research was to evaluate the effect of solubilization and aging treatment and mean stress on the fatigue behavior of Ti 35Nb 7Zr 5Ta alloy. In that sense, *S-N* curves were experimentally determined for different stress values. Results obtained allow only for a qualitative study, being this an exploratory research. The results were used to determine the endurance limit of the material and to evaluate the predictions of such models. The Goodman, Gerber, Walker and Kwofie's models were used to predict the mean stress effects. Through the analysis of the test results it is possible to conclude that:
a) Through the micrograph analysis, porosity was determined. These surface porosities are necessary for a good osseointegration [31]. Nevertheless, those pores could affect the mechanical properties, hence, should be controlled. At β matrix, and even at grain boundary, precipitates were found, presumably α and/or ω phase.

b) The fatigue strength limit for this sintered TNZT alloy is approximately $S_e(10E6) = 88$ MPa for solubilized material and $S_e(10E6) = 78$ MPa for solubilized and aged, analytically obtained. Probably the coarse precipitation of α phase as well as the possibility of ω phase precipitation had influenced S_e value; the fatigue strength identified in this research is compatible with some results shown in the literature for different kind of bones [26 - 28]

c) The fatigue strength was not strongly influenced by the presence of mean stresses. ;

d) Goodman model was shown inadequate to describe the statistical test results of mean stress effect on the fatigue strength;

e) Gerber and Walker's model presents a reasonable prediction for the presence of mean stress;

f) Kwofie's model was the model that best describe the effect of the mean stress on the fatigue strength of Ti 35Nb 7Zr 5Ta alloy.

References

[1] Medeiros, W. S., Oliveira, M. V., Pereira, L. C., Cairo, C. A. A., Calixto, M. A., 2005. Calcium Phosphate Deposition on Porous Titanium Samples. In Fifth International Latin-American Conference on Powder Technology, 2005, Costa do Sauipe. Procedings of Fifth International Latin-American Conference on Powder Technology; Metallum Eventos Técnicos Científicos, Bahia, Brazil, v. CD.

[2] Oliveira, M. V., Moreira, A. C., Appoloni, C. R., Lopes, R. T., Pereira, L. C., Cairo, C. A. A., 2005. Porosity Study of Sintered Titanium Foams. In Fifth International Latin-American Conference on Powder Technology, Costa do Sauipe. Procedings of Fifth International Latin-American Conference on Powder Technology; Metallum Eventos Técnicos Científicos, Bahia, Brazil.

[3] German, M. R., 1996. Sintering Theory and practice. By Jhon Wiley & sons, inc.

[4] Banerjee, R., Nag, S., Fraser, H., 2005. A novel combinatorial approach to the development of beta titanium alloys for orthopaedic implants. Materials Science and Engineering C; 25:282-289.

[5] Niinomi, M., 2003. Fatigue performance and cytotoxicity of low rigidity titanium alloy, Ti-29Nb-13Ta-4.6Zr. Biomaterials. 24 (16):2673-2683.

[6] Katti, K. S., 2004. Biomaterials in total joint replacement, Colloids and Surfaces B. Biointerfaces 39 (3):133-142.

[7] Geetha, M., Kamachi, M. U., Gogia, A. K., Asokamani, R., Raj, B., 2004. Influence of microstructure and alloying elements on corrosion behavior of Ti–13Nb–13Zr alloy. Corrosion Science; 46(4):877-892.

[8] Niinomi, M., 2002. Recent metallic materials for biomedical applications. Metal Mater. Trans. A; 33A:477–86.

[9] Kuroda, D., Niinomi, M., Morinaga, M., Kato, Y., Yashiro, T. 1998. Design and mechanical properties of new β type titanium alloys for implant materials. Mat. Sci. Eng. A; A 243:244–9.

[10] Kuroda, D., Niinomi, M., Fukui, H., Suzuki, A., Hasegawa, S., 2001. Mechanical performance of newly developed β -type titanium alloy, Ti–29Nb–13Ta–4.6Zr, for biomedical applications. In: Niinomi, M., Okabe, T., Taleff, E. M., Lesure, D. R., Lippard, H. E., editors. Structural biomaterials for the 21st century. Warrendale: TMS, p. 99–106.

[11] Niinomi, M., Kuroda, D., Fukunaga, K., Morinaga, M., Kato, Y., Yashiro, T., Suzuki, A., 1999. Corrosion wear fracture of new β type biomedical titanium alloys. Mat. Sci. Eng. A; A263: 193–9.

[12] Akahori, T., Niinomi, M., Yabunaka, T., Kuroda, D., Fukui, H., Suzuki, A., Hasegawa, J., 2001. Fretting fatigue characteristics of biomedical new b titanium alloy, Ti–29Nb–13Ta–4.6Zr.In: Hanada, S., Zhong, Z., Nam, S. W., Wright, R. N., editors. Proceedings of the PRICM 4: The Jpn. Inst. Metals, p. 209–12.

[13] Taddei, E. B., 2007. Obtenção da liga Ti 35Nb 7Zr 5Ta por metalurgia do pó para utilização em próteses ortopédicas. Tesis de Doutorado. Campo Montenegro, São José dos Campos, SP-Brasil.

[14] Steinemann, S. G., 1980. Corrosion of surgical implants in vivo and in vitro tests. In: Winter, G. D., Leray, J. L., De Groot K, editors. Evaluation of biomaterials. NewYork: Wiley, p. 1–34.

[15] Kawahara, H., Ochi, S., Tanetani, K., Kato, K., Isogai, M., Mizuno, Y., Yamamoto, H., Yamaguchi, A., 1963. Biological test of dental materials, Effect of pure metals upon the mouse subcutaneous fibroblast, strain L cell in tissue culture. J. Jpn. Soc. Dent. Apparat. Mater; 4:65–75.

[16] Lee, Y-L., Pan, J., Hathaway, R., Barkey, M. E., 2005. "Fatigue Testing and Analysis (Theory and Practice)", Elsevier Butterworth-Heinemann, USA.

[17] Smith, K. N., Watson, P., Topper, T. H., 1970. "A Stress Strain Function for the Fatigue of Metals", Journal of Materials, ASTM, Vol. 5, No. 4, 99. 767 – 778.

[18] Walker, K., 1970. "The Effect of Stress Ratio During Crack Propagation and Fatigue for 2024-T3 and 7075-T6 Aluminum", Effect of Environment and Complex Load History on Fatigue Life, ASTM STP 462, Am. Soc. For Testing and Materials, West Conshohocken, PA, pp. 1-14.

[19] Berkovits, A., Fang, D., 1981. "An analytical master curve for Goodman diagram data", Int. J. Fatigue, 15, pp. 173-80.

[20] Kwofie, S., 2001. "An exponential stress function for predicting fatigue strength and life due to mean stresss", Int. J. Fatigue, 23, pp. 829-836.

[21] Oliveira, F., Ferreira, J. L. A., Araújo, J. A., 2009. Determinação da Resistência à Fadiga do Aço ASTM A743 - CA6NM - Tomo 3 - Efeito da Presença da Tensão Média Sobre a Vida em Fadiga. Universidade de Brasília.

[22] Allvac, 2002. An Allegheny Technologies Company, Catalogue.

[23] American society for testing and materials. ASTM 739 E. 2004. Standard practice for statistical analysis of linear or linearized stress-life (S-N) and strain-life (e-N) fatigue data. s.l.: ASTM International.

[24] Gunawarman, Niinomi, M., Akahori, T., Souma, T., Ikeda, M., Toda, H., Terashima, K. 2005. Fatigue Characteristics of Low Cost beta Titanium Alloys for Healthcare and Medical Applications. Materials Transactions, Vol. 46, pp. 1570 - 1577. n. 7.

[25] [25] Ruppen, J., Bhowal, P., Eylon, D., Macevely, A. J. 1979. ASTM STP. On the process of subsurface fatigue crack initiation in Ti–6Al–4V. pp. 47–68.

[26] Taylor, D. march of 1998. Fatigue of bone and bones: An analysis based on stressed volume. Journal of Bone and Joint Surgery, Inc. Jornal of orthopaedic research, Vol. 16, pp. 163-9. 2.

[27] Niinomi, M., Kim, J. H., Akahori, T., Takeda, J., Toda, H. 2005. Effect of microstructure on fatigue of bovine compacts bone. Japan Society of Mechanical Engineers International Journal, Vol. 48, pp. 472-480. n. 4.

[28] Taylor, D., O'Reilly, P., Vallet, L., Lee, T. C. 6 de march of 2003. The fatigue strength of compact bone in torsion. Journal of biomechanics, Vol. 36, pp. 1103-1109.

[29] Sakaguchi, N., Niinomi, M., Akahori, T., Takeda, J., Toda, H. 12 de maio de 2005. Relationships between tensile deformation behavior and microstructure in Ti–Nb–Ta–Zr system alloys. Materials Science and Engineering C, Vol. 25, pp. 363-369.

[30] Li, S. J., Cui, T. C., Hao, Y. L. , Yang, R. October 7 of 2008. Fatigue properties of a metastable beta-type titanium alloy with reversible phase transformation. Acta Biomaterialia, Vol. 4, pp. 305-317.

[31] Lia, J. P., Habibovic, P., Doel, M. V. D. C., Wilson, E., Wijn, J. R., Blitterswijk, C. A., Groot, K. 16 de Fevereiro de 2007. Bone ingrowth in porous titanium implants produced by 3D fiber deposition. Biomaterials, Vol. 28, pp. 2810-20.

Advanced Materials Research Vol. 936 (2014) pp 1298-1302
© (2014) Trans Tech Publications, Switzerland
doi:10.4028/www.scientific.net/AMR.936.1298

Effect of Hydrogen on the Micro- and Macro-Strain Near the Surface of Austenitic Stainless Steel

Osamu Takakuwa[1, a], Yuta Mano[1,b] and Hitoshi Soyama[1,c]

[1]6-6-01, Aoba, Aramaki, Aoba-ku, Sendai, Japan

[a]o_takakuwa@mm.mech.tohoku.ac.jp, [b]mano@mm.mech.tohoku.ac.jp,

[c]soyama@mm.mech.tohoku.ac.jp

Keywords: Hydrogen, Micro strain, Macro strain, Phase transformation, Austenitic stainless steel

Abstract. The objective of this study is to evaluate the effect of hydrogen on the micro- and macro-strain of austenitic stainless steel using X-ray diffraction. When hydrogen is trapped in lattice sites, it can affect both the micro- and macro-strain. The micro-strain was evaluated through fitting profiles to measured X-ray diffraction profile using a fundamental parameter method. The macro-strain, i.e., the residual stress, was evaluated by a 2D method using a two-dimensional PSPC. The experimental samples were charged with hydrogen by a cathodic charging method. The results revealed that the induced residual stress was equi-biaxial and compressive, and that the micro-strain increased. Both of these varied rapidly with increasing hydrogen charging time. Saturation occurred at a compressive stress of around 130 MPa. On reaching saturation, the hydrogen charging was terminated and desorption of hydrogen began at room temperature. Then, the strains decreased and the compressive stress reverted, ultimately, to a tensile stress of 180 MPa. Martensitic transformation occurred due to hydrogen charging and this had a significant effect on the X-ray diffraction profile.

Introduction

It is well known that hydrogen has an effect on several of the properties of metals, e.g., it can cause embrittlement. Due to its complexity, the mechanism for this is not yet clearly understood. Hydrogen invades the surface of metals, and becomes trapped in the lattice. When hydrogen is trapped at lattice sites, it can lead to changes in both the micro- and macro-strains. The micro-strain refers to the strain between adjacent grains and the random strain within grains. Hydrogen trapped at lattice sites can increase the strain in the lattice. The macro-strain is a more homogeneous quantity and is on a larger scale involving many grains, i.e., the residual stress. In this case, the hydrostatic stress may be affected by hydrogen. In this study, the variations in these strains with the time for which the metal had been charged with hydrogen were evaluated using an X-ray diffraction method.

Hydrogen trapped in the lattice can diffuse freely in the metal and concentrates around inclusions, grain boundaries, dislocations and at the tips of cracks [1]. It can become a trigger for the initiation of micro-cracks around an inclusion and/or accelerate the propagation of cracks due to hydrogen-dislocation interactions. In order to safely use metals in hydrogen environments, the effect of hydrogen on the mechanical properties, i.e., the micro- and macro-strain, yield stress, Young's modulus and the hardness etc., should be examined. It is interesting to note that hydrogen significantly hardens the surface of austenitic stainless steel, as has been demonstrated by indentation tests [2]. In the case of austenitic stainless steel, the effect of hydrogen is more remarkable near the surface because of its low rate of diffusion. Because of the low diffusion rate, austenitic stainless steel, especially type 316L stainless steel, appears to have a high resistance to the effects due to hydrogen. However, in a recent study it was found that hydrogen caused the unstable propagation of fatigue cracks in type 316L stainless steel [3]. In this case, it was found that

cavitation peening, a technique used to modify the surface, could suppress it. For type 304 stainless steel, austenite can be transformed into martensite with relative ease, not only by work hardening, i.e., strain-induced martensitic transformation, but also by the incorporation of hydrogen at lattice sites, i.e., hydrogen-induced martensitic transformation. This transformation enhances the diffusion and concentration of hydrogen. Although type 316L stainless steel has a higher resistance to martensitic transformation than type 304 stainless steel due to its phase stability, there is a possibility that martensitic transformation can occur in type 316L stainless steel when a large amount of hydrogen is absorbed in the austenite lattice. Since the martensitic transformation might be caused by large increases in the micro- and macro-strains, these should be examined in order to understand the effects hydrogen has on the mechanical properties of metals.

Since hydrogen desorbs rapidly from metals, observations have to be made quickly in order to examine the effects it has on the micro- and macro-strains and the martensitic transformation. Therefore X-ray diffraction methods were utilized in this study. The micro-strain was evaluated through fitting profiles to the measured X-ray diffraction profiles using a fundamental parameter method. The macro-strain was evaluated by a 2D method using a two-dimensional position sensitive proportional counter (2D-PSPC).

Experimental Apparatus and Procedures

The material under test was Japanese Industrial Standards JIS SUS316L which has a higher resistance to hydrogen embrittlement than both ferritic and martensitic steel. The specimens used were square, 25 mm on each side, and 4 mm thick. They were thermally refined to remove any pre-strain. The yield stress defined as a 0.2 % offset stress and the tensile strength were 304 MPa and 576 MPa, respectively.

Hydrogen absorption was carried out by employing a cathodic charging method. The solution used for this was 0.5 mol/l sulfuric acid at a temperature of 50oC, and charging was done by controlling the current at a current density of 0.8 mA/mm2. The cathodic and anodic electrodes were the specimen and a platinum wire, respectively. Hydrogen was generated at the cathode, i.e., on the specimen. Thus, the specimen surface was exposed to hydrogen during the cathodic hydrogen charging. For each specimen, the area exposed to hydrogen was 20 mm in diameter. X-ray diffraction measurements were done on specimens that had been charged with hydrogen for various times ranging from 0 to 48 hours. After being charged for 48 hours, the charging was stopped and X-ray diffraction measurements were done continuously for 144 hours during the hydrogen desorption process.

Measurements of the micro-strain were made using an X-ray tube with a Cu target, producing Kα X-rays. Bragg-Brentano geometry was used. The operating voltage and current were 40 kV and 40 mA, respectively. The measurements were focused on the γ-Fe (1 1 1) plane, for which the maximum intensity of diffracted X-rays is at an angle (2θ) of 43.6 deg. The measurements were made from 42 to 45 degrees in steps of 0.001 deg, with the diffracted X-rays being counted for 0.5 sec in each step. The micro-strain was calculated through fitting a profile based on a fundamental parameter method [4]. Furthermore, in order to investigate whether or not the martensitic transformation had been induced, the X-ray diffraction profile was also obtained after hydrogen charging for 48 hours. For this, 2θ was varied from 40 to 95 degrees in steps of 0.005 degree, and the diffracted X-rays were counted for 0.2 sec in each step.

The macro-strain, i.e., the residual stress, was measured by a 2D method using a 2D detector [5]. The method focuses on the direct relationship between the stress tensor and the distortion of the diffracted Debye ring and can measure the biaxial stress, including the shear stress, in one

measurement. The analysis was done using Cr Kα X-rays from a tube operated at 35 kV and 40 mA with a 0.8 mm diameter collimator. The measurements focused on the γ-Fe (2 2 0) plane which has a diffractive angle (2θ) of 128 deg.

Results and Discussion

Figure 1 shows the X-ray diffraction profiles from the γ-Fe (1 1 1) plane for hydrogen charging times of t = 0 (Uncharged), 12, 24 and 48 hours, and 96 hours after termination of the hydrogen charging (t = 144 h). Figures 2, 3 and 4 plot the full width at half maximum of the profile, FWHM, the micro-strain, ε, and the biaxial residual stress, σR, respectively, as functions of the time, t. As shown in Fig. 1, the intensity of the diffracted X-rays decreases significantly and broadens due to hydrogen charging. As shown in Fig. 2, FWHM increases steadily until t = 16 h, and then changes rapidly. The intensity is almost 17,000 before hydrogen charging and decreases to less than 10,000 for a hydrogen charging time of 12 h. At t = 24 and 48 h, the X-ray diffraction profiles have anomalous shapes and it seems that other peaks appear at around 2θ = 43.2 deg due to phase transformation. It is questionable whether the phase transformation, i.e., hydrogen-induced martensitic transformation has occurred, since the peak is close to the γ-Fe (1 1 1) peak. The phase transformation is discussed in more depth later. Interestingly, long after termination of the hydrogen charging (t = 144 h), the sharp profile is restored as a result of hydrogen desorption from the surface.

As shown in Fig. 3, the micro-strain is ε = 0.0003 before hydrogen charging and increases with time until t = 12 h. At t = 12 h, the micro-strain is ε = 0.1853. After that, it was not possible to evaluate it due to the X-ray diffraction anomalies. After terminating the hydrogen charging, it decreases as a result of hydrogen desorption, similar to FWHM. At t = 144 h (96 h after terminating the hydrogen charging), it is ε = 0.1442. Fig. 4 shows that an equi-biaxial compressive stress was introduced by the hydrogen charging. Before charging, the residual stresses in the orthogonal x and y-directions were σRx = -65 MPa and σRy = -110 MPa and these increased to σRx = -147 MPa and σRy = -183 MPa after 8 h of charging. Beyond this, X-ray diffraction anomalies were generated. After termination of the hydrogen charging, the residual stress was rapidly restored, but reverted ultimately to tensile stress, with σRx = 140 MPa and σRy = 127 MPa at t = 144 h (96 h after terminating the hydrogen charging). It is likely that constriction due to a rapid decrease in the concentration of hydrogen as a result of the hydrogen desorption process had occurred. It has been reported that constriction due to hydrogen desorption sometimes causes tensile stress and micro-cracks at the metal surface [6].

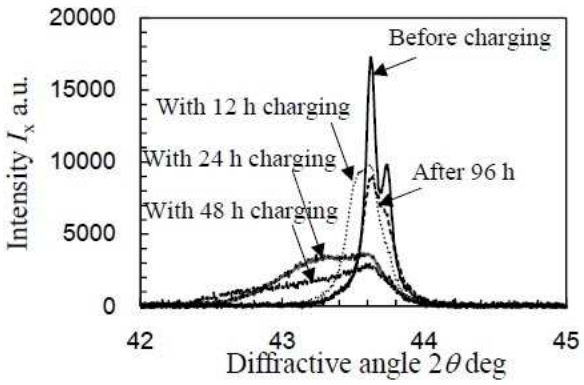


Fig.1 X-ray diffraction profiles from the γ-Fe (1 1 1) plane with and without hydrogen charging

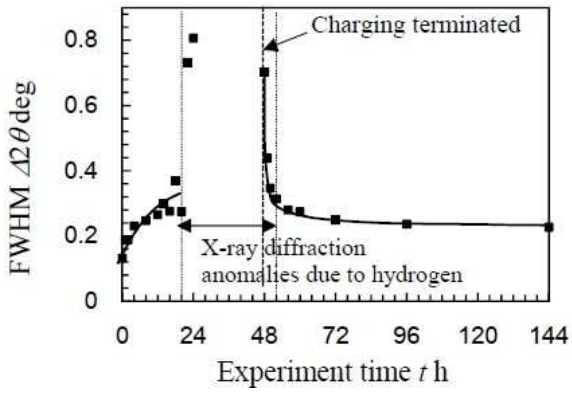


Fig.2 Increase and decrease in the FWHM of the XRD pattern from the γ-Fe (1 1 1) plane due to hydrogen absorption and desorption

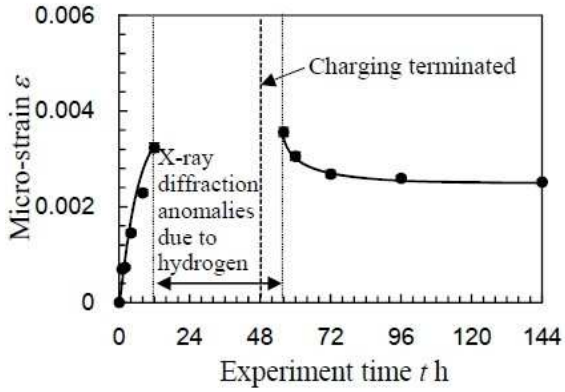


Fig.3 Increase and decrease in the micro-strain due to hydrogen absorption and desorption estimated using a fundamental parameter method

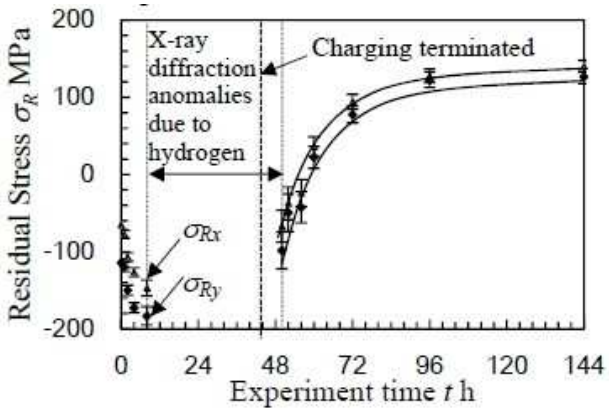


Fig.4 Introduction of compressive and tensile stress due to hydrogen absorption and desorption

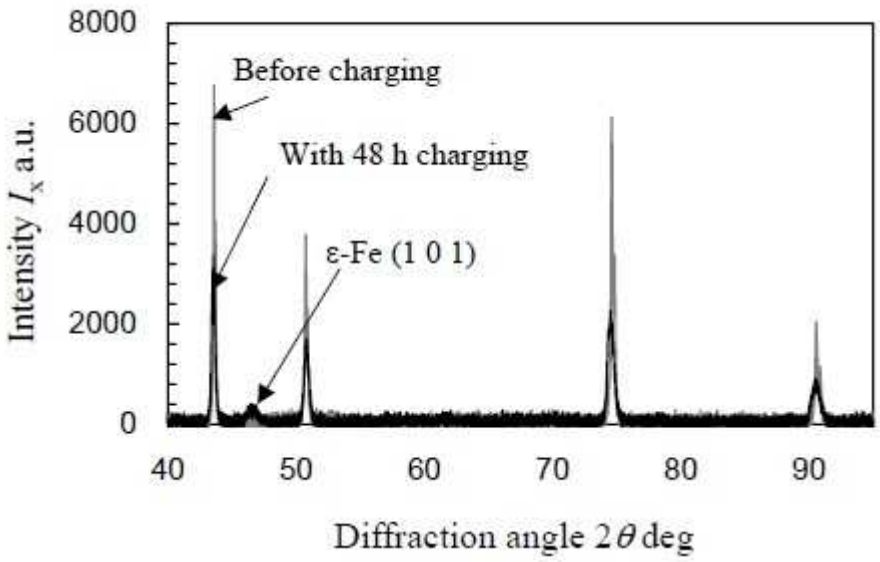


Fig.5 X-ray diffraction profiles before and after hydrogen charging

Figure 5 shows X-ray diffraction profiles (2θ = 40 ~ 95 deg) before and after hydrogen charging (t = 48 h). As shown in the figure, a diffraction peak for the ε-Fe (1 0 1) plane at around 2θ = 46 deg has appeared after 48 hours hydrogen charging. This shows that hydrogen-induced martensitic transformation occurs, not only in type 304 stainless steel, but also in type 316L stainless steel. Moreover, the X-ray diffraction anomalies may be due to the hydrogen-induced martensitic transformation. It is quite likely that the hydrogen-induced martensitic transformation occurs when the micro-strain has increased beyond a certain threshold level.

Summary

In order to investigate the effect of hydrogen on the micro- and macro-strain near the surface of austenitic stainless steel, the micro-strain was evaluated through fitting profiles to measured X-ray diffraction profiles using a fundamental parameter method and the macro-strain was evaluated by a 2D method using a 2D-PSPC. The conclusions obtained from this study are summarized below.

1. The micro-strain, ε, increases significantly from ε = 0.0003 to 0.1853 and an equi-biaxial compressive macro-strain of 80 MPa is introduced by hydrogen charging. After termination of the hydrogen charging, the compressive macro-strain reverts to a tensile strain due to hydrogen desorption.

2. Hydrogen-induced martensitic transformation occurs in type 316L stainless steel. It is quite likely that it occurs when the micro- and/or macro-strain increases beyond a certain threshold level.

This work was partly supported by JSPS KAKENHI Grant Number 24360040, 25820001 and JFE21st Century Foundation.

References

[1] R.A. Oriani and P.H. Josephic, Equilibrium aspects of hydrogen-induced cracking of steels, Acta Metall. 22 (1974) 1065-1074.

[2] Takakuwa and H. Soyama, Using an indentation test to evaluate the effect of cavitation peening on the invasion of the surface of austenitic stainless steel by hydrogen, Surf. Coat. Technol. 206 (2012) 3747-3750.

[3] Takakuwa and H. Soyama, Suppression of hydrogen-assisted fatigue crack growth in austenitic stainless steel by cavitation peening, Int. J. Hydrogen Energy 37 (2012) 5268-5276.

[4] H.P. Klug et al, X-ray diffraction procedure -2nd ed., (1974).

[5] B.B. He, Two-dimensional X-ray diffraction, John Wiley &Sons, Inc., New Jersey, (2009)

[6] N. Narita et al, Hydrogen-related phase transformations in austenitic stainless steel, Metall. Trans. A 13 (1982) 1355-1365.

Advanced Materials Research Vol. 936 (2014) pp 1303-1311
© (2014) Trans Tech Publications, Switzerland
doi:10.4028/www.scientific.net/AMR.936.1303

Thermographic and Microstructural Analysis of Martensitic Stainless Steel ASTM A743 CA6NM Arising Out of Layered GMA Welding Process Using AWS 410 NiMo Welding Wire

Matheus Tabata Santos[1,a], Palloma Vieira Muterlle[2,b]

and Guilherme Caribé de Carvalho[3,c]

[1]UnB - Bloco SG9, Campus Universitário Darcy Ribeiro, Brasília - Brazil

[2]UnB - Bloco SG9, Campus Universitário Darcy Ribeiro, Brasília - Brazil

[3] UnB - Faculdade de Tecnologia, Campus Universitário Darcy Ribeiro, Brasília - Brazil

[a]mateustabata@gmail.com, [b]palloma@unb.br, [c]gccarval@unb.br

Keywords: ASTM A743 CA6NM, AWS 410 NiMo, GMA welding multiple steps, thermographic analysis, microstructural changes.

Abstract. The martensitic stainless steel ASTM A743 CA6NM is typically used in the production of hydroelectric turbines due to its known high resistance to cavitation induced surface damages. Despite the fact the material presents a high resistance to cavitation, depending on the loading condition to which the turbine runner is subjected and on its geometry, fatigue cracks can develop, thus requiring repair by means of removing material around the crack, up to its complete elimination, and by depositing weld metal in the cavity followed by a grinding process, in order to recover the original runner geometry. Such a repair process is normally done on site, which means that it is not possible to carry out the post weld heat treatment necessary to bring the newly deposited weld metal and the base metal to the same microstructure encountered in the runner when it comes out of manufacture. In order to study the effect that a layered welding has on the base material and on the weld metal, this work aims at studying the microstructural changes that occur in the CA6NM stainless steel welded in multiple layers with a AWS 410 NiMo welding wire. In order to attain such an objective, several 410 NiMo weld beads were deposited in successive layers on the border of a 5mm thick sheet while the resulting temperature fields were monitored by a thermographic camera. After the welding process, the samples cut from the welded sheet were examined in the perpendicular direction of deposition and their resulting microstructures where analyzed and correlated with the temperature history recorded during the welding process. Hardness tests were also carried out.

Introduction

Martensitic Stainless Steels belong to a category of high alloy stainless steels which exhibit lower carbon content and higher concentrations of alloying elements such as nickel. They were developed in the 1960s in order to increase the limited weldability of martensitic stainless steels for the construction and repair of hydraulic turbines and their components. Among the alloys belonging to this class of steels, the CA6NM grade presents attractive mechanical properties and solidification characteristics that enable casting of large sections, maintaining an almost uniform martensitic microstructure, even at very slow cooling rates. It facilitates the processes of construction and, also, the repair by welding[1] Due to these characteristics, the CA6NM has been typically used in the production of hydroelectric turbines due to its known high resistance to cavitation induced surface damages. Such turbines are normally manufactured in separate casting processes followed by heat treatment and surface finishing with subsequent coupling via a welding process, in which a similar filler material is used, normally the AWS 410 NiMo grade. Since the turbine runners parts have large thicknesses, typically the welding takes place in several layers in order to fill the joint cavity. After the welding process, normally the whole runner is taken to a final heat treatment, which takes place in big furnaces that provide a means to attain a uniform temperature over the entire part. Despite having

a higher cost compared to carbon steels, the CA6NM facilitated the repair operations during maintenance and reduced their frequency, thus decreasing the downtime of the machine.

The chemical composition of the alloy is shown in Table 1 and the typical mechanical properties of ASTM A743 CA6NM in the most usual condition of hardened and tempered is illustrated in Table 2.

Table 1: Chemical composition of the ASTM A743 CA6NM alloy [2].

Element	%wp
C	$0{,}06_{máx.}$
Mn	$1{,}00_{máx.}$
Si	$1{,}00_{máx.}$
P	$0{,}04_{máx.}$
S	$0{,}03_{máx.}$
Cr	11,50 – 14,00
Ni	3,50 – 4,50
Mo	0,40 – 1,00

Table 2: Mechanical properties of the CA6NM alloy in molten condition, hardened above 955 °C, cooled in air, and tempered [2].

Tensile strength (MPa)	Yield Strength (MPa)	Stretching on 50 mm (%)	Area Reduction (%)	Hardness (HV)	Charpy "V" (J)
827	689	24	60	284	94,9

Despite its higher resistance to cavitation surface damages, the CA6NM is still prone to fatigue cracks, which may result from the cyclic loading conditions at which the runner is subjected during operation. The cavitation erosion and the fatigue crack damages normally require the removal of material from the damaged area and the recovering of the original runner geometry by means of metal deposition using arc welding processes. Fig. 1 shows a crack caused in a turbine blade at ITAIPU hydroelectric power plant[3].



Figure 1: Damaged turbine from ITAIPU hydroelectric powerplant [3].

As outlined before, since the hydraulic turbine components involve large sections, the welds carried out for filling the joints, whether for repair or construction, are made in several layers. Note, therefore, the importance of investigating the behavior of these alloys and the deposited weld metals when they are subjected to multiple temperature cycles.

Therefore, this paper aims at investigating, through an experimental methodology, the effects of sequencial thermal cycles on the microstructure of the CA6NM stainless steel welded in multiple

layers with an 410 NiMo welding wire, in order to study the effect that a layered welding has on the base material and on the weld metal it self.

Methodology

The experiments involving the welding of the base metal CA6NM and 410 NiMo deposition were carried out in an experimental apparatus illustrated in Fig. 2, together with an ABB IRB 2000 welding robot, for controlling the welding torch movement. The experimental apparatus was developed for the study of the transient heat and mass flow involved in the welding of flat plates with small thicknesses, applied to the problem of fast prototyping by metal deposition in successive layers [4]

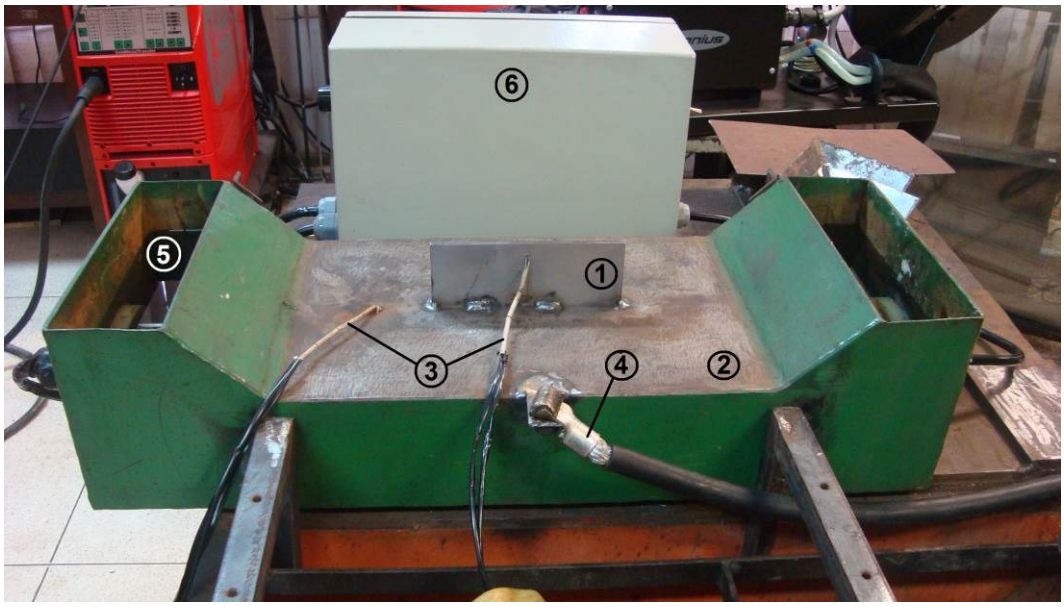


Figure 2: Experimental apparatus for the experiments of metal deposition welding in multiple layers.

In Fig. 2, it is possible to observe the experimental apparatus parts, indicated by numbers and described below:

1. Sample to be tested;
2. Warmed base;
3. K-type thermocouples, being the left one welded at the base and the right in the sample;
4. Ground connection of the welding equipment;
5. Water tank containing two electric resistances for heating;
6. Heating System Control panel.

The experimental apparatus consists horizontal flat surface (2) that is kept at an approximately constant temperature, provided by its permanent heat exchange with a temperature controlled water bath (5). A low thickness sample plate (1) is then spot welded vertically on the top of heated surface and the robot is programmed to move the torch forward along the upper border of the spot welded sample plate, such that it deposits one weld bead. After finishing it, the torch position is increased vertically (direction “y” in Fig. 3) by the amount corresponding to the height of the bead just deposited. The robot then waits for an input signal from the operator to proceed with a new weld deposition, moving the torch in the backwards direction. Such an input signal was issued every time the just deposited material reached 150 ºC (the interpass temperature indicated for layered welding with CA6NM and 410NiMo grades). This cicles is repeated until the desired number of weld runs is attained. Care was taken in the spot welding of the sample plate to provide good electrical and thermal contact with the heated base, were the power source negative connection was located (4). The procedure is showed in Fig. 3:

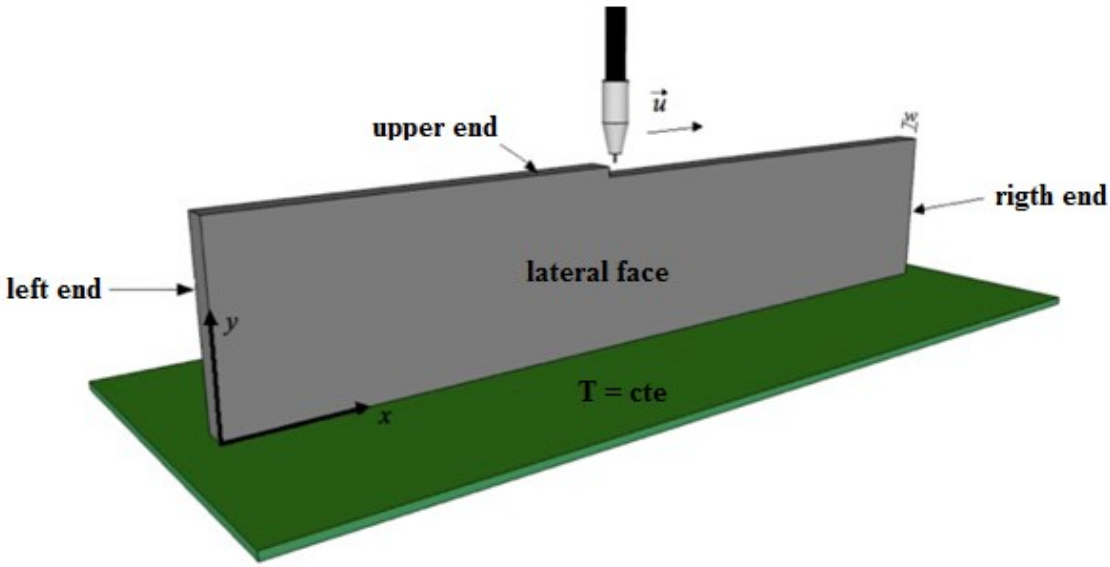


Figure 3: Illustration of the procedure used for the welding experiments [4]

To monitoring the temperature of the whole process, it was accepted that the weld interpass temperature dropped to 150°C, in order to avoid the stress concentration in the welding, facilitate the diffusion of hydrogen out of the weld process and promote tempering of the last weld layer. Twenty-two (22) weld layers were performed; being the location of the end of a step is the same as the beginning of the next step. Fig. 4 shows the equipment used to promote the thermographic monitoring.

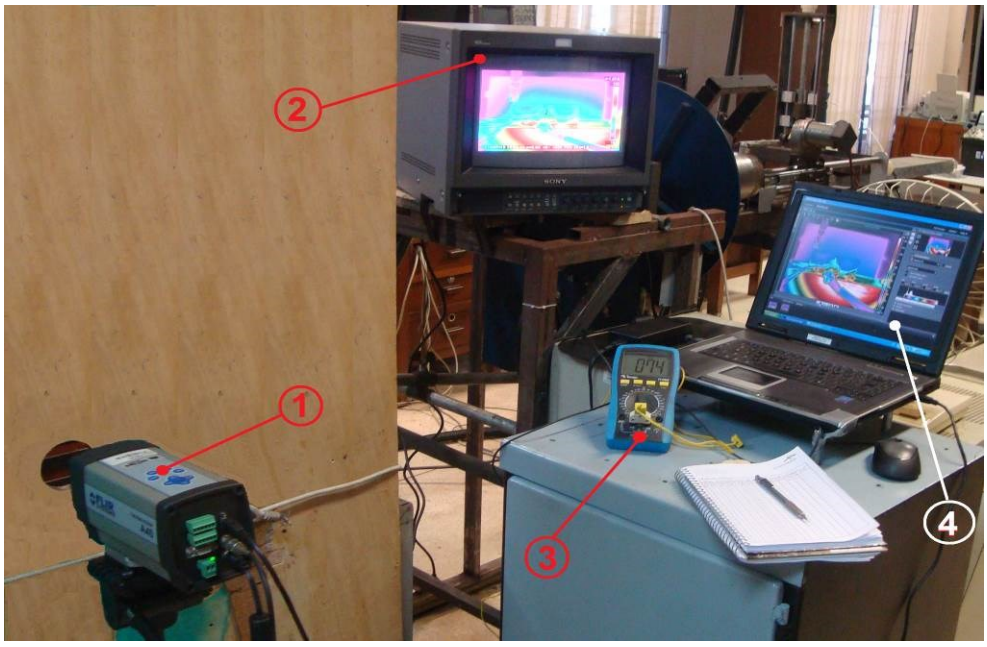


Figure 4: Used equipment for the thermographic monitoring of the welding.

Figure 4 shows the following equipments: (1) InfraRed Camera model ThermoVision A40 M, brand FLIR SYSTEMS™, firewire connection; (2) Sony™ 14" Monitor connected to the camera to control the camera parameters; (3) Digital Multimeter Model 187, brand FLUKE™, 180 series, for controlling the base and sample temperature; (4) Notebook brand ASUS with 3,07 GHz and 1,87 GB RAM memory.

Parameters required for the use of thermography as focal length, emissivity surfaces analyzed, relative humidity, temperature and temperature range to be analyzed, were allocated through measurements and parameters provided in the previous works. In order to investigate the microstructure of the base material (CA6NM) and the joint base material/addition material (410

NiMo) was chosen a sample for the study approximately with 64 mm in height, in the Y-Z plane. Choose the section to be analyzed, were realized consequent steps, such as cutting the sample in the required dimensions; Embed the sample in an appropriate acrylic resin for easy sanding; Realization of sanding the surface with sandpaper grain size from 180 to 1200; Polishing surface finishing, using Alumina 1μm; chemical etching using a Kalling n˚1 reagent, for identifying the phases presents; and microstructural analysis with an optical microscope. Fig. 5 presents the Y-Z section, chosen to be analyzed in the optical microscope.

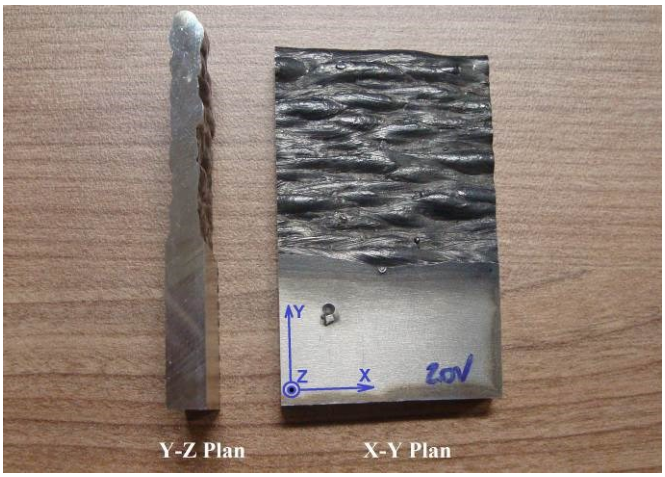


Figure 5: Y-Z Sections to be analyzed

Results and Discussion

The quality of the weld obtained by GMAW process is influenced by some parameters such as current intensity, voltage and arc length, welding speed, shielding gas, electrode type and position of the torch, their types and flow. The welding parameters found that provided better homogeneity, lower sparks, a suitable thickness for the base plate, increment close to the value determined as standard and less welding energy, are shown in Table 3.

Table 3: Defined parameters for the welding trials.

Welding Process: GMAW Short Circuit - Multiple Steps						
Interpass Temperature: 150˚C						
Base Material: ASTM A743 CA6NM						
Added Material: AWS 410 NiMo						
Sample Positioning	Number of Weld Beads	Speed of Wire Feed (m/min)	Speed of Torch Translatory (mm/s)	Tension (V)	Stand Off (mm)	Gas Flow (l/min)
Vertical	22	5,6	12,0	18,0	12,0	15,0

In the process of GMA welding, type short-circuit performed in this work it, was observed that the electrical contact is extremely important to the effectiveness of the welding process, i.e., if there is a contact resistance, the quality result of the weld bead and the process stability are compromised. Due to this fact it was adequate to use the ground connection in the experimental apparatus, in a manner that facilitates the passage of electrical current.

Throughout the time of the experiment happened the thermographic filming of the welding process (Fig. 6), being attentive to the temperature of the base (this always kept around 90°C) and the interpass temperature (that around 150°C as a condition for the beginning of the next step).

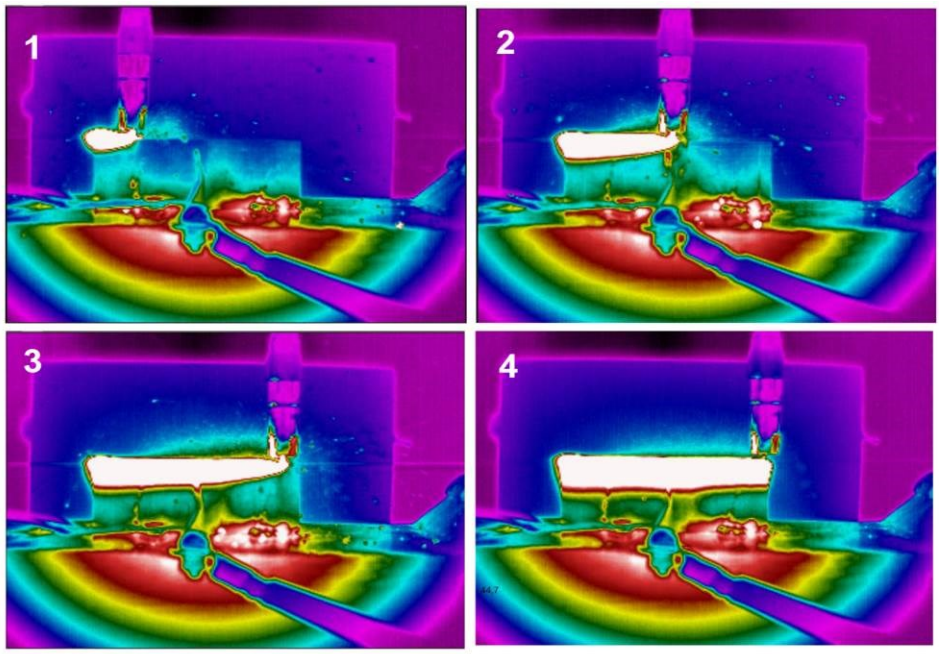


Figure 6: Thermographic monitoring of the GMA welding process.

The interpass temperatures expected, in course of time, can be evaluated in the graph of Fig. 7, together with an indication of each one of the 22 steps made in the weld tested sample.

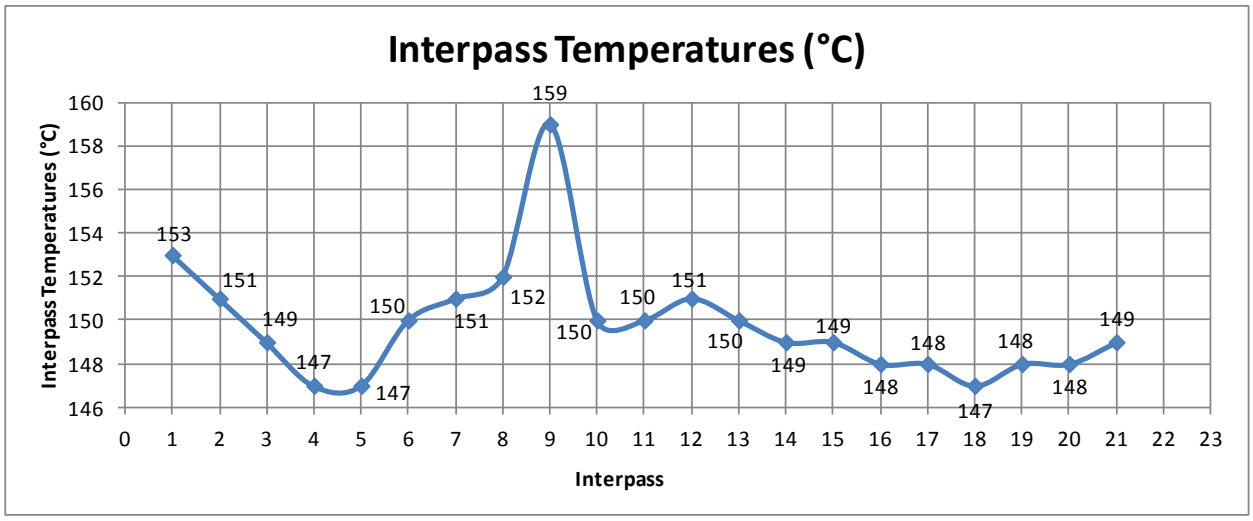


Figure 7: Interpass vs Interpass Temperature during the welding test.

Interpass temperatures varied a little around the 150°C, but remained in the expected value, with an average of 149,6°C. The average real increment was slightly higher than expected, and needed to be adjusted in the next tests. With the use of water as the fluid of the experimental apparatus, it can be seen that the maximum temperature obtained at base was 91,0°C.

It can be noted that in vertical welding condition requires the first 15 mm to equalize and stabilize their dimensions. This fact does not cause problems, since the repairs on the turbine blades require larger fillers and the sample taken for this study is located in the central region.

The metalography of the Y-Z plane, with chemically attacked and polished conditions of the sample, indicating areas of sampling, their microstructures with increased 500X, time attack by chemical reagent Kalling n°1, and their respective Vickers hardness HV10, can be enjoyed in Fig. 8.

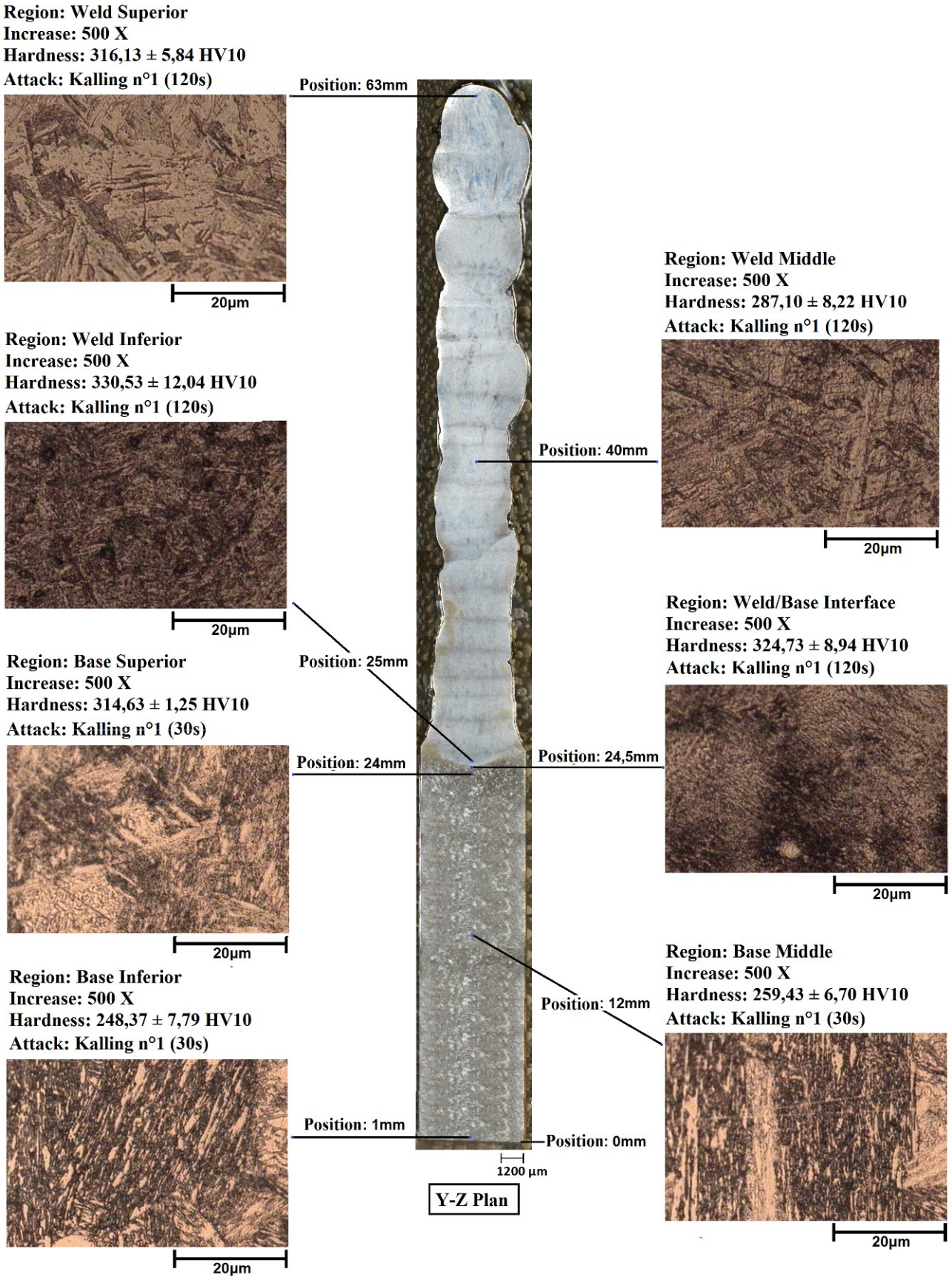


Figure 8: Metallography of the Y-Z plane of the tested sample with their respective hardnesses.

By analysis of the macrostructure above, it can be observed that each weld bead have the appearance of a heat affected zone as evidenced by a dark boundary of steps and provided from the different thermal cycles in which the sample has been subjected. There was found no defect welding

as lack of fusion, inclusions, cracks for retaining hydrogen, pores or cracks during phases of welding and metallographic analysis. The cooling rate low, outdoor, contributed to this fact.

The use of the of GMA welding process, short-circuit type, resulted in a weld bead with height ratio (amount of material added) and heat input proportional to the tests performed by Gouveia, 2008 [5]

The microstructure of the median and lower region of the base material, as evidenced by chemical attack is characteristic of a hardened and tempered material, consisting of a martensitic matrix and is consistent with the microstructure expected for the martensitic stainless steel ASTM A743 CA6NM according to literature [6]

The presence of inclusions - black spots - probably from gas welding [7]or from even their own alloy may be noted in the median region of the addition material in Fig. 8.

Conclusions

Through the micrographic analysis it was observed that the microstructure of the tested sample is predominantly martensitic. In the superior region of the base material, located on the heat affected zone, it can be found refined martensite from a tempering heat treatment. By the conducted analyzes, it wasn't possible to find in any of the regions the presence of ferrite, which would be evidenced by colored pieces. The microstructure of the interface, inferior and middle regions of the filler metal have a characteristic appearance of a weld bead heat-treated [8], as shown in Fig. 8. Based on the same micrographs, it can be concluded that after the 17th step of welding, the microstructure no longer has the appearance of heat-treated. After this welding pass, it is possible to determine a microstructure more dendritic and coarser, unlike the microstructures observed in the literature [8]

The resistance values of Vickers hardness found in the superior region of the base material, at the interface of the base material with the addition material, in the inferior region of the additional material, in the median region of the additional material and the superior region of the material addition are slightly higher compared to the values from the literature [1] [2] [9] (11:11%, 14.73%, 16.78%, 1.45% and 11.66% higher, respectively).

The results of hardness tests on the substrate is 18.78% lower than in deposition metal and in the interface region material has a hardness significantly increased (24.62%) compared to the substrate. This hardness increase in the interface region and in the bottom of the weld metal can be due to precipitation of carbides, requiring further investigation to confirm this fact. A reduction of impact toughness in additional material may also have occurred. Subsequent tests of resistance to fatigue and impact will be required to verify the occurrence of embrittlement of the heat affected zone.

The shield gases containing fractions of CO and CO_2 can lead to incorporation of increasing amounts of carbon in the weld metal, increasing its hardness. This fact can also be responsible for the increased hardness at the interface and in the lower portion of the additional material.

References

[1] Allenstein, Â. N. Estudo da resistência à cavitação do aço inoxidável martensítico CA6NM nitretado por plasma - Universidade Federal do Paraná. Dissertação de Mestrado. Curitiba-BR, 2007.

[2] ASTM - Standard Specification for Castings, Iron-Chromium, Iron-Chromium-Nickel, Corrosion Resistant, for General Application, Designation A743, A743M-06, 2006.

[3] Information on http://www.gazetadopovo.com.br/economia/conteudo.phtml?id=1092579&tit=Reparo-de-turbina-custara-US-8-mi

[4] Fraga, F. F. Estudo numérico e experimental dos processos de transferência de calor em prototipagem rápida por soldagem a arco. 2013. 130 p. Dissertation (Master Degree in Mechatronic Systems), Universidade de Brasília, Brasília, 2013.

[5] Gouveia, R. R de. A influência da temperatura de interpasse na tenacidade do metal de solda na soldagem multipasse do aço inoxidável martensítico CA6NM pelo processo TIG - Universidade Federal do Paraná. Dissertação de Mestrado, 2008.

[6] ASM International. ASM Handbook: Metallography and Microstructure, 2004.

[7] Acesita, S.A. - Soldagem dos Aços Inoxidáveis - Acesita S.A. Associada a USINOR, 2011.

[8] VAZ, C. T. - Avaliação da resistência à erosão por cavitação do metal de soldas produzidas com consumíveis tipo 13% Cr - 4% Ni - 0,4% Mo - Universidade Federal de Minas Gerais, Belo Horizonte. Dissertação de Mestrado, 2004.

[9] FERREIRA et al. - Identificação das Condições de Falha por Fadiga em Materiais Usados na Fabricação de Pás de Turbinas Hidráulicas: Metodologia, Caracterização dos Ensaios e Resultados - Programa Eletronorte de Pesquisa e Desenvolvimento Tecnológico Ciclo 2004/2005, 2013.

Advanced Materials Research Vol. 936 (2014) pp 1312-1316
© (2014) Trans Tech Publications, Switzerland
doi:10.4028/www.scientific.net/AMR.936.1312

Two High Strength Low Alloy Steels for Offshore Application

Tze-Ching Yang[1,a], Ching-Yuan Huang[1,b], Ta-Chien Cheng[2,c], Chieh Yu[2,d], Ren-Kae Shiue[2,e]

[1]China Steel Corporation, Hsiao Kang, Kaohsiung 812, Taiwan

[2]Department of Materials Science and Engineering, National Taiwan University, Taipei 106, Taiwan

[a]166199@mail.csc.com.tw, [b]148023@mail.csc.com.tw, [c]d99527018@ntu.edu.tw, [d] r00527038@ntu.edu.tw, [e]rkshiue@ntu.edu.tw

Keywords: Offshore Steel, Martensite, Bainite, Microstructure, CCT

Abstract. The purpose of this investigation is focused on two high strength low alloy steels for offshore application. TTT, CCT curves, Vickers depth profiles and microstructures of direct water quenched steels are evaluated in the experiment. Microhardness of the direct quenched surface is as high as 400 Hv, and the central region hardness of water quenched specimen is above 250 Hv. Martensite dominates the microstructure of quenched surface. In contrast, the mixture of martensite, bainite and ferrite is widely observed from the center of quenched specimen.

Introduction

Offshore steels belong to the category of high strength low alloy steel (HSLA) [1-3]. They are featured with high strength, better toughness and good weldability as compared with traditional low carbon steels. They have been widely applied in construction of bridge, pressure vessel, oil piping and the offshore wind power foundation [4]. The demand from clean energy such as wind power has been rapidly increased in recent years. For example, the floating turbine foundation is made of high strength low alloy steel, and the weight of each foundation is as high as 200 tons. Therefore, it is important to develop high-performance offshore steel applied in next generation.

Based on the NORSOK standard, S690Q steel is featured with high yield strength (> 690 MPa) and excellent low-temperature toughness (> 100 J at – 40 ºC) for the offshore application [5]. The chemical composition in weight percent of S690Q specification is 0.16 C (max.), (0.2-0.4) Si, (0.9-1.0) Mn, 0.015P (max), 0.005 S (max), (0.8-1.0) Ni, 0.65 Cr (max.), 0.5 Mo (max.), 0.4 Cu (max.), 0.08 Al (max.), 0.009 N (max.), 0.06 V (max.), 0.02 Nb (max.), 0.02 Ti (max.), 0.003 B (max.) and Fe balance [5]. Because the weldability of such a steel is crucial for offshore application, the carbon equilibrium content, C_{eq}, defined by International Institute of Welding (IIW) provides a standard for its chemical composition in weight percent as displayed in equation (1). Additionally, the critical metal parameter for weld cracking, P_{cm}, has been defined by Japanese Welding Engineering Society included in equation (2).

$$C_{eq}\,(IIW) = \%C + \%Mn/6 + (\%Cu + \%Ni)/15 + (\%Cr + \%Mo + \%V)/5 \quad (1)$$

$$P_{cm} = \%C + \%Si/30 + (\%Mn + \%Cu + \%Cr)/20 + \%Ni/60 + \%Mo/15 + \%V/10 + 5B \quad (2)$$

The chemical composition of designed S690Q grade steel should meet the requirements of C_{eq} (IIW) < 0.66 % and P_{cm} < 0.32 % [5].

Experimental Procedures

Chemical compositions in weight percent of two offshore steels designed as OS-A and OS-B are illustrated in Table 1. Chemical compositions of both OS-A and OS-B steels meet the NORSOK S690Q standard. There is a minor difference between these two alloys due to V addition. According

to equations (1) and (2), C_{eq} (IIW) and P_{cm} of the above steels are 0.45 (< 0.66) and 0.22 (< 0.32), respectively. Two steel plates were experienced direct water quench from 900 ºC after hot rolling. Dimension of two steel plates was 200 mm in width, 1000 mm in length and 50 mm in thickness. Specimens were machined perpendicular to rolling direction in order to perform metallographic examination and microhardness test. The specimens were cut, mounted and etched by 2% nital prior to metallographic inspection. Metallographic specimens were examined by using a Nova 450 field emission scanning electron microscope (FESEM). Its operation voltage was 15 kV, and the minimum spot size was set at 1 μm. Vickers microhardness tests of cross sections of OS-A and OS-B steels after direct water quench were performed using Mitutoyo HM microhardness tester with the load of 500 g and duration time of 15 s. CCT and TTT curves are simulated by JMatPro software for comparison's purpose.

TABLE 1 CHEMICAL COMPOSITIONS IN WT% OF TWO DESIGNED OFFSHORE STEELS

Alloy	C	Si	Mn	P	S	V	Fe	others	Ceq (IIW)/Pcm
OS-A	0.1	0.3	0.9	0.01	0.001	0.0	balance	< 1.75	0.45 / 0.22
OS-B	0.1	0.3	0.9	0.01	0.001	0.03	balance	< 1.75	0.45 / 0.22

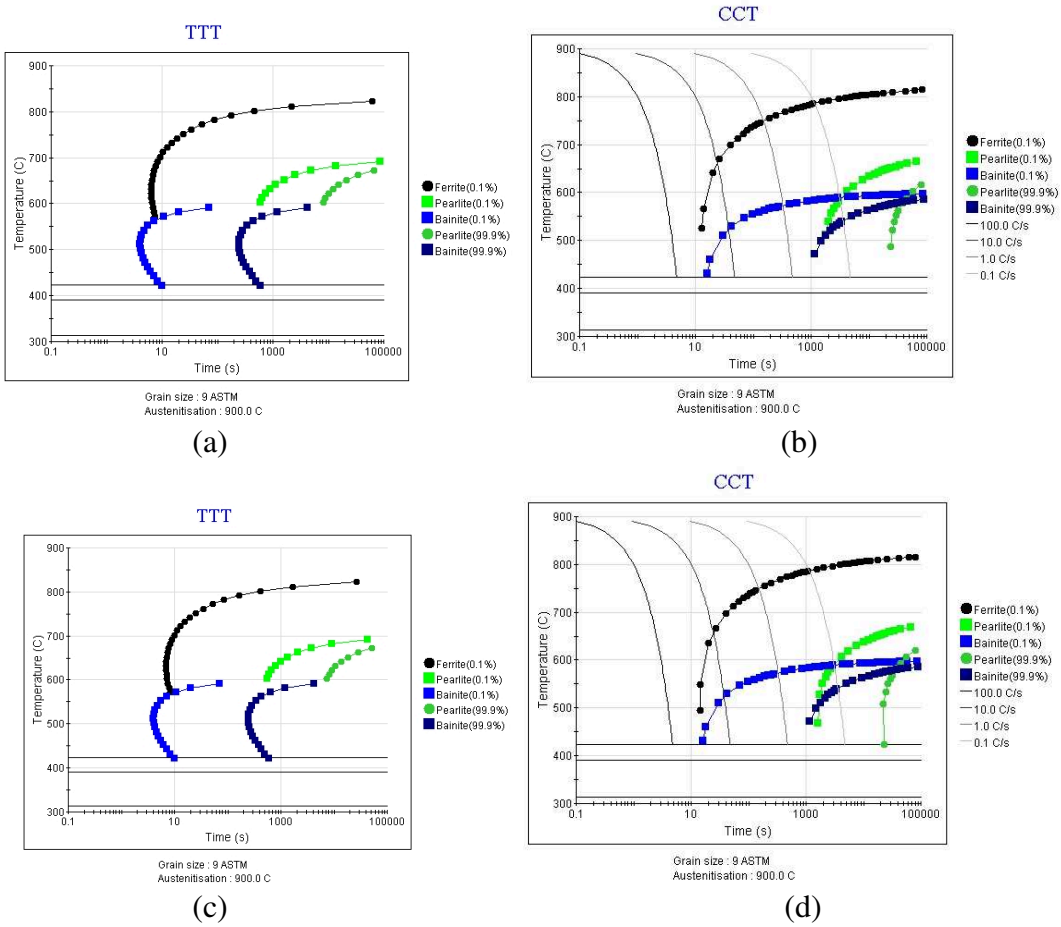


Fig. 1 (a) TTT, (b) CCT Curves of OS-A and (c) TTT, (d) CCT Curves of OS-B Steels Based on JMatPro Software Simulations.

Results and Discussion

Fig, 1 shows TTT and CCT diagrams of two steels based on JMatPro simulation results. Similar TTT and CCT diagrams of two steels are observed from the figure. According to the figure, pearlite will not formed in the specimen direct water quenched from 900 °C. Martensite will be formed on the quenched surface, and proeutectoid ferrite and bainite are formed in the center of specimen due to slower cooling rate.

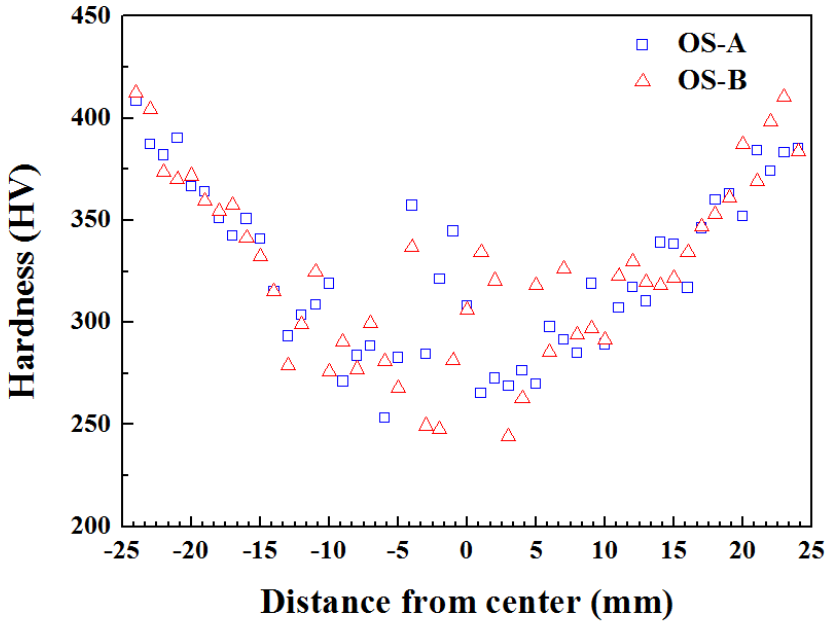


Fig. 2 Microhardness Depth Profiles of OS-A and OS-B Steels after Direct Water Quench.

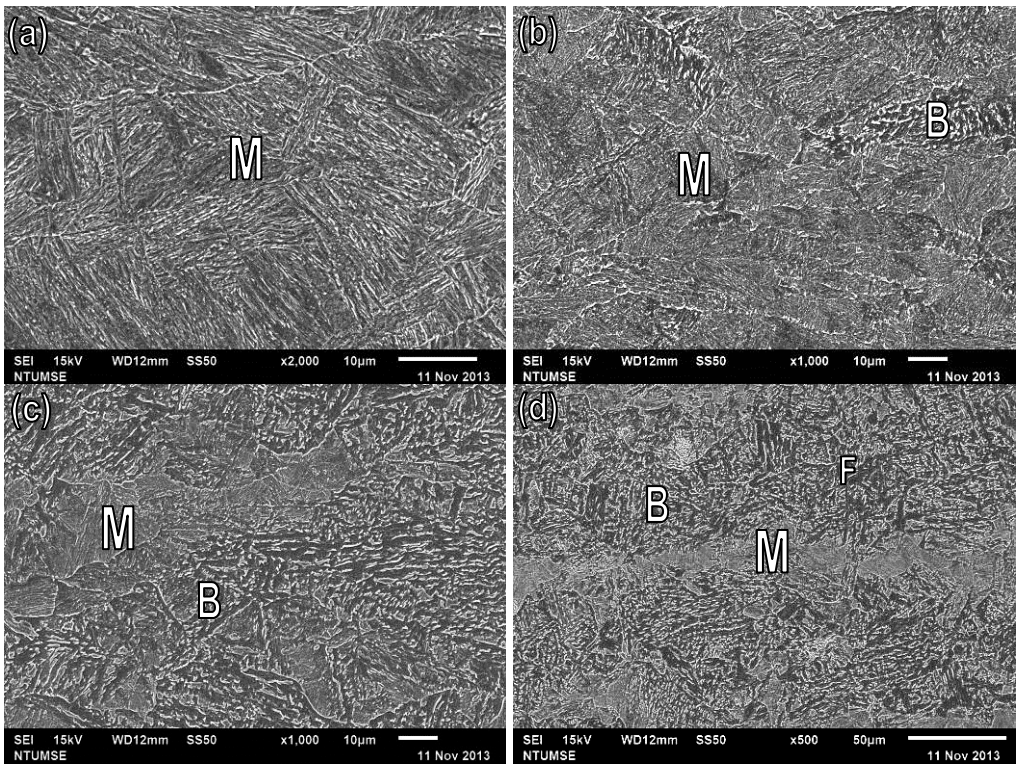


Fig. 3 Metallographic Examination of OS-A Steel at Depths of (a) 5 mm, (b) 10 mm, (c) 20 mm, (d) 25 mm (center) from the Direct Water Quenched Surface. (M: Martensite, B: Bainite, F: Ferrite)

Fig. 2 shows microhardness depth profiles of OS-A and OS-B steels after direct water quench. The microhardness of OS-B specimen at surface is slightly higher than that of OS-A specimen. Minor V addition, 0.03 wt%, slightly increases the hardenability of OS-B steel. The hardness of specimen's surface is approximately 400 Hv. In contrast, the lowest hardness in the central region of steels is 250 Hv. It is worth mentioned that measured microhardness data are scattered in the central region of the specimen as illustrated in Fig. 2. The scattered hardness data are resulted from multiple phases in the center of specimen.

Fig. 3 displays FESEM SEIs (secondary electron images) of OS-A steel after direct water quench from 900 ºC at various depths below the quenched surface. The microstructure of 5 mm below the quenched surface is primarily dominated by martensite as shown in Fig. 3(a). Increasing the depth below the quenched surface results in increasing the amount of bainite and ferrite as illustrated in Figs. 3(b) - 3(d). The amount of martensite at center of specimen is below 50 %, and its microstructure is dominated by bainite and ferrite (Fig. 3(d). Because the hardness of martensite, bainite and ferrite is quite different, microhardness of these multiple phases is scattered in the center of specimen. It is consistent with the aforementioned results (Fig. 1 and Fig. 2). Fig. 4 displays FESEM SEIs (secondary electron images) of OS-B steel after direct water quench from 900 ºC at various depths. Microstructures of OS-B at different depths below the water quenched surface are very similar to those of OS-A specimen.

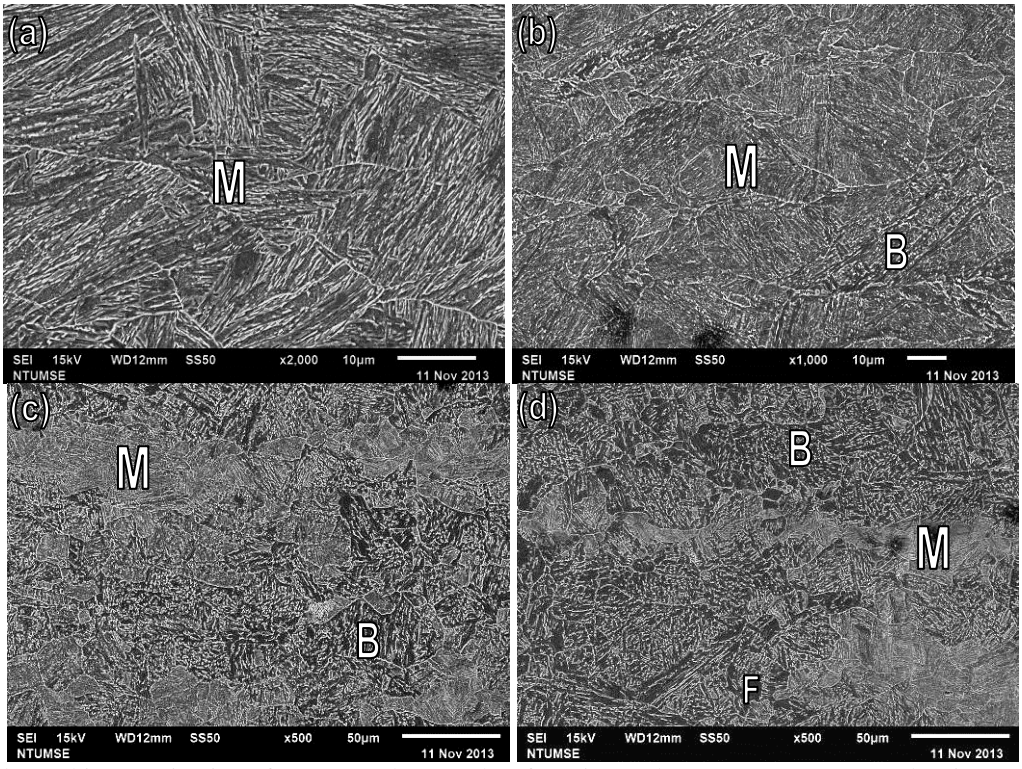


Fig. 4 Metallographic Examination of OS-B Steel at Depths of (a) 5 mm, (b) 10 mm, (c) 20 mm, (d) 25 mm (center) from the Direct Water Quenched Surface. (M: Martensite, B: Bainite, F: Ferrite)

Summary

TTT, CCT curves, Vickers depth profiles and microstructures of two direct water quenched steels for offshore application are evaluated in the experiment. Martensite is observed from the quenched surface. Increasing the depth below the quenched surface results in increasing the amount of bainite and ferrite due to insufficient hardenability of the steels and slower cooling rate at center of specimen. The scattered microhardness depth profiles are resulted from multiple phases in the center of specimen. The experimental results are consistent with TTT and CCT curves simulated by JMatPro software.

Acknowledgements

Authors gratefully acknowledge the financial support of this research by National Science Council and China Steel Corporation, Taiwan (Contract number NSC 102-2622-E-006-032).

References

[1] B. K. Show, R. Veerababu, R. Balamuralikrishnan, G. Malakondaiah, Effect of vanadium and titanium modification on the microstructure and mechanical properties of a microalloyed HSLA steel, Mater. Sci. Eng. A 527 (6) (2010) 1595-1604.

[2] J. Fernández, S. Illescas, J. M. Guilemany, Effect of microalloying elements on the austenitic grain growth in a low carbon HSLA steel, Mater. Lett. 61 (11-12) (2007) 2389-2392.

[3] Z. Wang, X. Mao, Z. Yang, X. Sun, Q. Yong, Z. Li, Y. Weng, Strain-induced precipitation in a Ti micro-alloyed HSLA steel, Mater. Sci. Eng. A 529 (2011) 459-467.

[4] M. Kapsali, J.K. Kaldellis, Offshore Wind Power Basics, Technological Education Institute of Piraeus, Athens, Greece, 2012.

[5] NORSOK Standfard, Material data sheets for structural steel, Norway Technology Center, N-0306 Oslo, Norway, 2000.

Advanced Materials Research Vol. 936 (2014) pp 1317-1322
© (2014) Trans Tech Publications, Switzerland
doi:10.4028/www.scientific.net/AMR.936.1317

Numerical Simulation on Influence of Water-cooled Stool in the Process of Unidirectional Solidification

LI Xiaodong[1,a]*, SHEN Minggang[2,b],WU Chao[3,c]

[1.2.3] School of Materials and Metallurgy, University of Science and Technology Liaoning,Anshan114051, China

[a]402610152@qq.com, [b]lnassmg@163.com, [c]417032886@qq.com

Keywords: water-cooled stool; finite element; unidirectional solidification; temperature field; numerical simulation

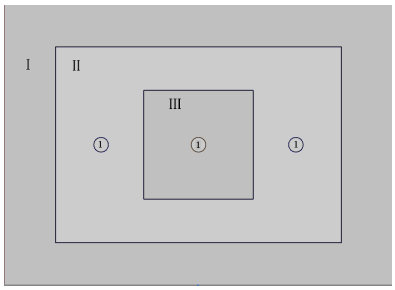
Abstract: To strengthen the bottom cooling is one of the key technologies of directionally solidified ingot process. Stool cooling scheme has a significant impact on the solidification process of the ingot. The study optimizes chassis cooling scheme according to the air gap between the ingot and the stool. With multiple sets of cooling system, water-cooled stool makes the basal water cooling adapt to air gap distribution through subregional cooling of different intensity control, and be uniform with it in the longitudinal direction solidification. The paper establishes mathematical model of unidirectional solidified ingot on temperature field of conventional water-cooled stool and improved one respectively. By the aid of finite element analysis method, numerical simulation of 45t ingot with algebraic model is carried out. In order to optimize parameters of ingot unidirectional solidification, temperature fields influenced by conventional water-cooled stool and improved one in the process of unidirectional solidification are simulated. The numerical results show that the optimized chassis cooling can result in the ingot in a longitudinal uniform solidification. The numerical simulation results can provide important reference for the optimization of unidirectional solidification process.

The solidification process of casting in which most of shrinkage, dispersed shrinkage and crack are produced is one of the most important processes in the production of casting [1]. There is a consistent request of lowering the manufacturing cost in industry. In the past, process improvement was achieved by trial and errors. The experiments demand a high effort and large resources. Using numerical simulation not only would allow for more economical and efficient operations. But also predictions on microstructure changes with respect to change in operation conditions can be easily made. This would help to reduce the formation of defects in a cast and thus improve quality of the finished product [2].

Production technology of directional solidified ingot is mainly reflected in three aspects which include stool cooling, lateral wall and surface insulation above the liquid. Among them, the inhibition of lateral wall heat transfer is the principal symbol which distincts from ordinary steel ingot, guarantees the heat flow and significantly reduces the ingot segregation; stool cooling scheme has a significant impact on the solidification process of the ingot. The rational chassis cooling can make the initial solidified shell unbroken contact with the chassis and improve the cooling rate of solidification process; the ingot can be in a uniform longitudinal solidification. A common practice is to use the thick and large chassis. The other is forced cooling, usually with water. YAMAGUCHI Toshiyuki et al. thinks that whole thick stool in the past had to be changed after the use of certain times, so the cost was too high, but if it is divided into two parts, only the upper one needs to be changed after damage so that the cost can be decreased, but the combination of upper and lower between the two plates is not tight and will form a heat insulation layer. Therefore, inventors set the cooling water loop on the upper part of the lower plate, and control the cooling intensity by the flow of cooling water. Only the upper part which is easier to be damaged needs to be replaced normally. In this way, not only the cost is reduced but also the cooling intensity

is ensured. Therefore, the inventors open groove or inclination on the insulation material which in the side wall, thereby limiting the reverse curls, strengthens the cooling, and increasing the directional solidification of ingot height, with a relative reduction in the volume. However, this approach may have the problem of forging [3].

This paper presents a new improved cooling chassis for directional solidification (geometric model of optimized water-cooled stool and the finite element model as shown in Fig.1 and Fig.2); the water cooling chassis consists of three blocks, laid inside the snake-shaped cooling pipe. Specific measure is to cool for subregion with different strength from the center to the periphery direction by adopting multiple sets of cooling system, hence has a greater effect cooling intensity in the center of the chassis and minor effect one around the chassis. At the same time, the study establishes the mathematical model on the temperature field of heavy steel ingot and compares with conventional water-cooled stool and simulates numerically in order to optimize the chassis cooling parameters.



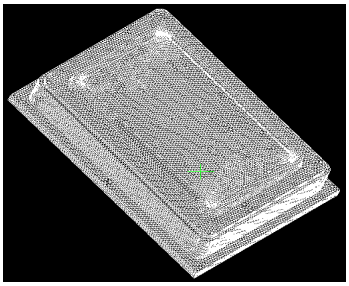


Fig.1 Geometric diagram of optimized water-cooled stool: Ⅰ the outside cooling system； Ⅱ the middle cooling system；Ⅲthe centered cooling system；1 the bottom gating Fig.2 mesh generation diagram of the FEM model

Mmathematical Model for the Heat Transfer in The Solidification

Basic Assumptions

The simulation process needs to be set as close as possible to the actual conditions, but it is impossible to simulate all the phenomena and behavior considering the characteristics of heavy plate ingot solidification during the solidification process. Therefore, the following hypotheses for the computing model on the temperature field of a large ingot solidification process are made [4-7]:

1. The liquid metal starts to coagulate after instantaneous filling the cast. This assumption underlies some initial conditions. Regarding the generous plate steel spindle, this supposition will not cause too much error, because its solidification time is much longer than the casting time;

2. This paper adopts the view of E A Mizikar, without considering the liquid, solid phase flow, heat transfer can be compensated by ignoring internal convection through appropriate amplification liquid metal thermal conductivity;

3. As constant, density does not change with temperature;

4. The metal heat and the thermal conductivity use the effective specific heat and the effective thermal conductivity separately;

5. Calculations involving materials are isotropic;

6. Solidification is in equilibrium conditions;

7. The ingot deformation and volume changes can be ignored.

Controlling Equation

Mass conservation equation：

$$\frac{\partial \rho}{\partial \mathrm{t}}+\frac{\partial(\rho_{\mathrm{u}})}{\partial x}+\frac{\partial(\rho_{\mathrm{v}})}{\partial y}+\frac{\partial(\rho_{\mathrm{w}})}{\partial z}=0 \tag{1}$$

Energy conservation equation：

$$\rho \frac{\partial(\partial H)}{\partial t}+\rho \frac{\partial H}{\partial T}\left[u \frac{\partial T}{\partial x}+v \frac{\partial T}{\partial y}+w \frac{\partial T}{\partial z}\right]=\frac{\partial}{\partial x}(k \frac{\partial T}{\partial x})+\frac{\partial}{\partial y}(k \frac{\partial T}{\partial y})+\frac{\partial}{\partial z}(k \frac{\partial T}{\partial z}) \tag{2}$$

Changes of a specific position in casting can be defined as

$$H(T)=\int_0^T C_P dT+L[1-f_S] \tag{3}$$

Where ρ is the density(Kg · m^{-3})， t is the time(*s*)， *u*, *v* and *w* are velocity component in the direction of the *x*, *y* and *z* (m · s^{-1})，*H* is enthalpy (J · mol^{-1})，*T* is temperature(k)；*k* is permeability (W · m^{-1} · ℃$^{-1}$)； C_p is specific heat (J · Kg^{-1} · K^{-1})， *L* is latent heat(J · kg^{-1})， f_s is fraction solid.

Boundary Conditions and Initial Conditions

The determination of boundary conditions

For this study on 45t heavy plate ingot, ingot bottom surface in contact with water-cooled stool is transformed into the third boundary condition, while centrosymmetric surface of ingot and outside insulation are transformed into the second [8-10].

Upper surface of ingot： $$K\frac{\partial T}{\partial x}=q \tag{4}$$

Downward surface of ingot： $$q=h(T_b-T_f) \tag{5}$$

Ingot around: $$\frac{\partial T}{\partial x}=0 \tag{6}$$

Ingot centre： $$\frac{\partial T}{\partial x}\Big|_{x=d/2}=0 \tag{7}$$

x = d / 2 is half thickness of ingot.

Where： K —Thermal Conductivity Coefficient，W/m℃,

q —Heat Density，W/m2,

h —Heat Exchange Coefficient，W/m2℃,

T_b —Downward Surface Temperature of Ingot，℃,

T_f —Temperature of Cooling Water，℃.

Heavy plate ingot solidification process belongs to the one-dimension unsteady state heat conduction problem, for the initial conditions and three kinds of boundary conditions can be treated with the following form

$$A_T T+B_T Q=C_T \tag{8}$$

In the equation：

T —Temperature of side（wall），K,

Q —Heat flow density through the wall，W/m^2,

A_T， B_T， C_T —Constants according to the boundary conditions.

The determination of initial conditions

For casting process, the study ignores the influence of the filling process on the initial temperature field because the solidification time is considerably longer than the casting time of casting. So take

$$T\,(x,0)=T_C \tag{9}$$

$$T\ \text{Environment}=0 \tag{10}$$

In the equation： T_C — pouring temperature，℃.

Selected steel components for simulation are shown as Table 1, the solid–phase in temperature of 1393℃, the liquids in temperature of 1520℃, and thermo physical parameters curve of steel for calculation are shown in Fig.3. In the simulation process, the heat transfer coefficient of conventional water-cooled stool is set to 5000W/m**2/K, and the improved one which is divided into three parts are set to 20000W/m**2/K，10000W/m**2/K，5000W/m**2/K respectivly from inside to outside.

Table 1 Chemical Composition Of Calculation

C	Si	Mn	P	S	Ti	Ni	Cu	Mo
0.06	0.30	1.60	0.01	0.003	0.017	0.40	0.15	0.025

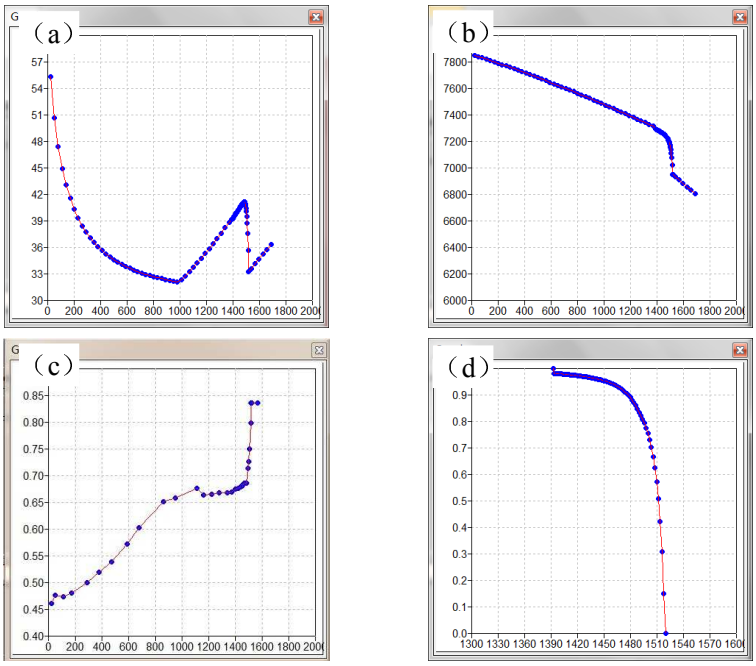


Fig.3 Thermo physical parameters curve of steel for calculation: a) conductivity b)density c) specific heat d)fraction solid

Temperature Field of Directional Solidification

Studying temperature field is a research interesting in casting and solidification processing. These results can provide guidance for production and further investigation. There are experimental methods and computer simulation methods in temperature field investigation. Among them, computer simulation is a very good, helpful and timesaving method. The ultimate goal of numerical simulation on casting solidification process is to optimize the process design and to realize the casting quality prediction. By using finite software ProCAST, temperature field influenced by conventional water-cooled stool and improved one in the process of unidirectional solidification is analyzed.

Fig.4 and Fig.5 show temperature field distribution on 45t directionally solidified ingot solidification with conventional water-cooled stool and improved one when simulation time is 8000s, 13000s, 20000s and 30000s respectively.

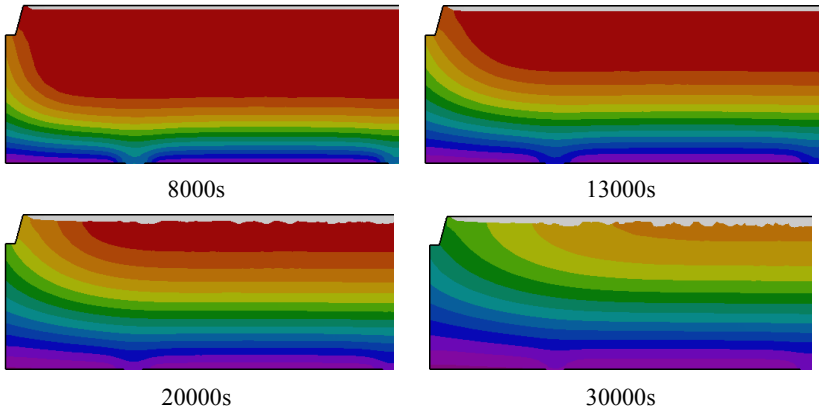


Fig.4 Temperature field distribution of directionally solidified ingot with conventional water-cooled stool

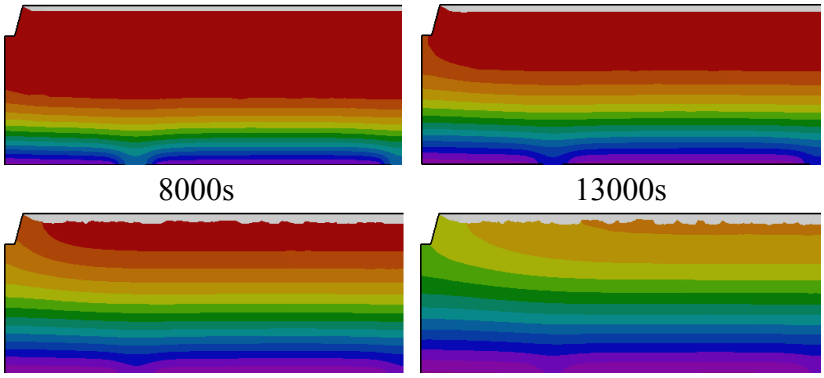


Fig.5 Temperature field distribution of directionally solidified ingot with improved water-cooled stool

From Fig.4 and Fig.5, we can see that the axial active heated temperature region gradually extends to the top from bottom of ingot along with the extension of solidification time. But solidification speeds of different parts are not identical, the bottom of ingot solidified firstly and finally the riser. Lower parts of ingot have a larger vertical temperature gradient at the initial stage of solidification. As time goes on, cooling effect decline obviously and vertical temperature gradient descends. While in the middle section, the liquid phase keeps invariant and then vertical temperature gradient increases but changes a little with temperature fall. The upper of ingot began at liquids, and temperature decreases as time goes by, and temperature gradient near the top increases. Directionally solidified ingot solidification with conventional water-cooled stool causes edge curve heavily. While improved one makes solidification front pushed smoothly and evenly to the top of the ingot with the solidification and promotes the directional solidification.

Conclusions

By subregional cooling of different intensity control with water-cooled stool which adopts multiple sets of cooling system, basal water cooling and air gap distribution are adapted to each other, and uniform solidification in the longitudinal direction is promoted. The two-phase zone between the solidified part and liquid steel is limited at the same time. The solidification front is pushed smoothly and evenly to the top of the ingot with the solidification. Solidification process becomes a natural refining process. The chemical composition of the body which is below the top is homogenized and inclusions can be refined and homogenized.

References

[1] LU Wen-hua, LI Long-sheng, HUANG Liang-yu. Casting alloy and its smelt [M].China Machine Press.1996.

[2] TSAI De-chang，HWANG W eng-sing. Numerical simulation of solidification morphologies of Cu-0.6Cr casting alloy using modified cellular automaton model [J]. Trans．Nonferrous Met．Soc．China 20(2010)1072-1077.

[3] GU Jiang-ping, ZHAO Yong, LIU Zhuang. A Summary of L iterature on Techniques of Unidirectional Solidification Ingots [J]. Heavy Castings and Forgings. 1995,(2):5-8 (in chinese)

[4] H.P. Jin, J.R. Li, J. Yu and S.Z. Liu. Study of Heat Transfer Coefficient Used in the Unidirectional Solidification Simulation Based on Orthogonal Design [J]. Rare Meterial and Engineering. 2010, (39): 767-770．(in Chinese)

[5] YANG Zhi-un，ZHAO Xiao-hua，KOU Hong-chao et al. Numerical simulation of temperature distribution and heat transfer during solidification of titanium alloy ingots in vacuum arc remelting process [J]. Trans．Nonferrous Met．Soc．China 20(20 1 01 1 957-1 962．

[6] Y.H. Shin, C.S. Kang and K.H. Oh. A Mathematical Model of unidirectional Solidification in Cooled Mold [J]. Metals and Materials International. 2000, (6): 189-194．

[7] E.N. Pan, C.S. Lim, C.R. Loper, Effects of solidification parameters on the feeding efficiency of Aluminum alloys [J]. Trans. Am. Foundry men's Soc. 1990. (98): 735-746．

[8] T.R. Vijayaram, S.Sulaiman, A.M.S.Hamouda, M.H.M.Ahmad. Numerical simulation of casting solidification in permanent metallic molds [J]. Journal of Materials Processing Technology.2006, 29-33．

[9] LIU Jing-feng, LI Hong-you, JIANG Kai-yong. Numerical Simulation on Solidification Process of Large Sized Steel Casting [J].Foundry Technology.2011,(32):443-445．(in Chinese)

[10] Lü Nan, Jin Yonglong, Li Shengli, et al. Numerical simulation on gradient cooling behavior of jumbo slab ingot plate. China Foundry, 2013, 10(02): 87-91.

Advanced Materials Research Vol. 936 (2014) pp 1323-1328
© (2014) Trans Tech Publications, Switzerland
doi:10.4028/www.scientific.net/AMR.936.1323

Application of Calcium Treatment to Sulfur Gear Steel 20CrMo

Wu Xiaodong[a], Zhang Daoxin[b], Chen Ruilong[c]

School of Material Science & Engineering, Jiangsu University, Jiangsu Zhenjiang, China 212013

[a:]wuxd@ujs.edu.cn, [b:]417569039@qq.com, [c:]starsmote@sina.com,

Wu Xiaodong, associate professor, Tel:13511697130, E-mail:wuxd@ujs.edu.cn

Keywords: Thermodynamics calculation, Calcium treatment, Sulfide inclusions, Gear steel

Abstract: Based on the thermodynamic calculation, the conditions of calcium treatment to sulfur gear steel are analyzed and the samples of rolled steel are studied. Results show that Calcium treatment to melting steel after RH refining can make the sulfide inclusions and calcium aluminates bind together and form the spindle shaped low melting compound inclusions. In the meanwhile, controlling of w(O) in steel below 0.0012% before calcium treatment is more beneficial to modify the Al_2O_3 and sulfide by the added calcium and to form the oxide-sulfide compound inclusions only if w(Al_S) in steel is adjusted to 0.015%~0.025% before continuous casting. The Ca wire should also be fed at higher temperature.

Introduction

High strength and good mechanical properties are two main characteristics of gear steel[1]. The mechanical properties can be improved by adding sulfur in gear steel. But the sulfide inclusions rating cannot exceed level 3 by the requirements in 20CrMo sulfur gear steel. So the shape of MnS should be modified by calcium treatment and MnS can also be bound together with Al2O3 or CaS to form spindle shaped with low melting point compound inclusions[2]. This type of inclusion is beneficial to the properties of steel[3]. In order to reduce the content of [O] in 20CrMo gear steel, the aluminum is used for deoxidization during tapping. Calcium treatment is used to modify the remained Al2O3. But improper calcium treatment will affect the casting properties of steel. In this paper, the controlling technology of calcium treatment of sulfur 20CrMo gear steel is analyzed and studied comprehensively by thermodynamic calculations.

Analysis on Thermodynamic of Calcium Treatment

The production process of 20CrMo gear steel is Converter, LF refine, RH refine and Continuous casting. The total content of [O] in 20CrMo sulfur gear steel should be controlled less than 12×10-6 and the aluminum is used for deoxidization in the production process. The calcium wire is fed after RH process and the sulfur wire is fed after the calcium treatment. The chemical composition of the steel is shown in Table1.

TABLE 1 CHEMICAL COMPOSITION OF STEEL %

Element	ω（C）	ω（Si）	ω（Mn）	ω（Cr）	ω（P）	ω（S）	ω（Mo）	ω（Al）
Mass fraction	0.16	0.27	0.56	0.94	0.022	0.021	0.1742	0.015

Element interaction coefficient is consulted to Refer 4 and activity coefficient of elements is calculated by formula of Refer 5.

TABLE 2 ACTIVITY COEFFICIENT OF ELEMENTS IN 1873K

Element	Mn	S	Ca	Al	O
Activity coefficient	1.25	0.85	0.000147	1.09	0.24

Thermodynamic of the Modification of Al2O3 by Calcium Treatment

Calcium is used mainly for improving castability of steel and the castability is improved by the reaction between calcium and Al_2O_3 particles in the steel. The Al_2O_3 would be modified into different types of calcium aluminates by adding calcium according to the different Ca content.

Al_2O_3 $CaO{\cdot}6Al_2O_3$ $CaO{\cdot}2Al_2O_3$ $CaO{\cdot}Al_2O_3$ $12CaO{\cdot}7Al_2O_3$ $3CaO{\cdot}Al_2O_3$ CaO

The chemical reaction can be expressed as follows.

$$3[Ca]+Al_2O_3=3CaO+2[Al] \qquad \Delta G^{\theta} = -706200 + 60.6T$$

$$K = \frac{([Al\%]f_{[Al]})^2 a^3_{CaO}}{([Ca\%]f_{[Ca]})^3 a_{Al_2O_3}}$$

In order to avoiding nozzle clogging, the low melting calcium aluminates is the aim inclusion to be expected. The characteristic of each calcium aluminates is showed in Table 3.

TABLE 3 CHARACTERISTICS OF CALCIUM ALUMINATES

Inclusion	Density（$g{\cdot}cm^3$）	Melting point（K）
$CaO{\cdot}Al_2O_3$	2.98	1878
$CaO{\cdot}2Al_2O_3$	2.91	2023
$CaO{\cdot}6Al_2O_3$	3.28	2123
$3CaO{\cdot}Al_2O_3$	3.04	1808
$12CaO{\cdot}7Al_2O_3$	2.83	1728

The activity value of CaO and Al_2O_3 in CaO-Al_2O_3 system of different models and experimental measurements are not uniform and showed in Refer 2. The Korousic classic theoretical model is more applicable for aluminum killed steel[6]. The relationship of [Ca] and [Al] in $CaO{\cdot}Al_2O_3$, $3CaO{\cdot}Al_2O_3$, $12CaO{\cdot}7Al_2O_3$ in 1873K are calculated with Korousic classic theoretical model.

TABLE 4 ACTIVITY VALUE OF CAO AND AL2O3 IN 1873K BY KOROUSIC MODEL

Calcium aluminate	a_{CaO}	a_{Al2O3}
$CaO{\cdot}Al_2O_3$	0.08	0.039
$3CaO{\cdot}Al_2O_3$	1	0.0050
$12CaO{\cdot}7Al_2O_3$	0.36	0.038

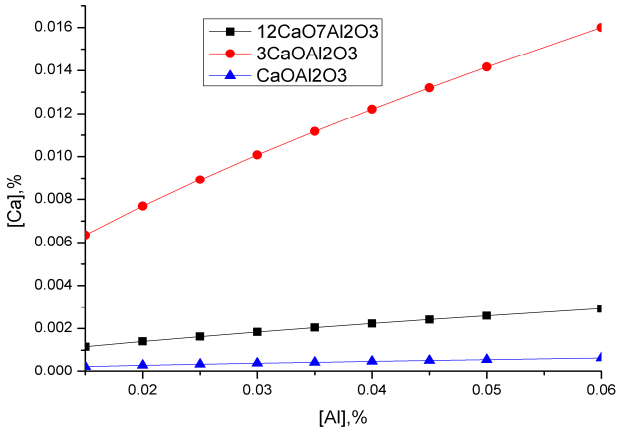


Fig. 1 Relationship Between [Ca] And [Al] In Different Calcium Aluminates In 1873k

To change the Al_2O_3 into $12CaO{\cdot}7Al_2O_3$ and $3CaO{\cdot}Al_2O_3$, the content of [Ca] should be controlled about 0.002% and 0.01% separately while the content of [Al] is 0.03%. The results also show that the Al_2O_3 can be changed into $CaO{\cdot}Al_2O_3$ only if the content of [Ca] is low. In order to get more low melting point inclusion($12CaO{\cdot}7Al_2O_3$), the content of [Ca] after the calcium treatment should be adjusted about 0.002% during the process.

Relationship between [O] and [S] by Calcium Treatment

Calcium is used mainly for improving castability of steel and it can also be used to change the sulfides. Ca is an element with extremely high affinity to oxygen and sulfur. And the content of [S] in 20CrMo gear steel is about 0.021%. In order to avoid the appearance of CaS, the S wires should be fed 5minutes late after Ca wires fed. The following reaction will occur while the calcium is fed into steel.

$$[Ca]+[O]=(CaO) \qquad \Delta G^{\theta}=-645421+146T$$

$$[Ca]+[S]=(CaS) \qquad \Delta G^{\theta}=-530312+118.63T$$

Because of the high melting point of CaO and CaS, the activity of them is 1. The average temperature of steel after RH process is about 1893K. So the equilibrium between the [Ca]-[O]-[S] at 1893K is shown in Fig.1.

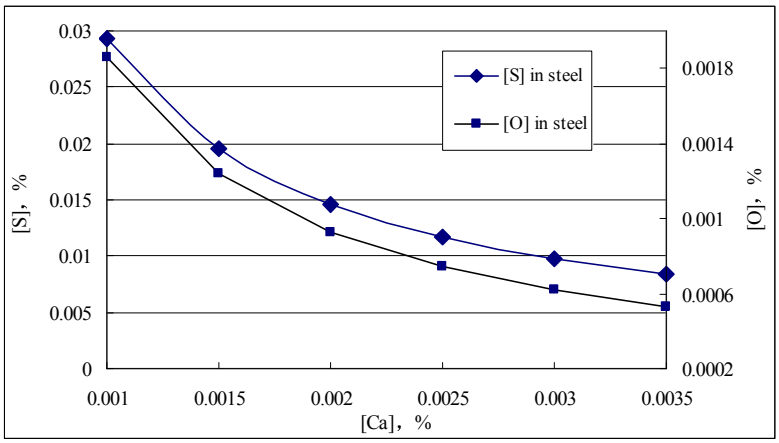


Fig.2 The Equilibrium between [S] and [O] and [Ca] at 1893K

According Fig.2, in order to avoid the simple CaS particle after calcium treatment, the content of [Ca] should be controlled less than 0.0015% before the S wire is fed. And in order to avoid the CaO after calcium treatment, the content of [O] should be controlled less than 0.0012%.

The Equilibrium of [Al] and [S] by Calcium Treatment

Since Ca has such a strong affinity to sulfur, it can react and transform sulfur existing in the melting steel to CaS. The reaction of [Al] and [S] in $CaO\text{-}Al_2O_3$ compound inclusion in aluminum killed steels after calcium treatment is shown below[6].

$$3CaO + 2[Al] + 3[S] = 3CaS + Al_2O_3 \qquad \Delta G^{\Theta} = -907104 + 317.7T$$

$$K = \frac{a_{Al_2O_3} a^3_{CaS}}{a^3_{CaO}([Al\%]f_{[Al]})^2([S\%]f_{[S]})^3}$$

The chemical reaction is carried on continuously by large amount of [Als] in steels. In order to reduce the number of high melting point inclusions, the content of [Als] should meet the demands of thermodynamics conditions to modify Al_2O_3 into $12CaO\cdot 7Al_2O_3$ while calcium treatment. The relationship is shown in Fig 3.

According to Fig.3, the reaction is influenced by temperature and the content of [Al] in steel. When the temperature is 1923K, 1873K, 1823K and the [Al] content is 0.02%, the balance content of [S] is separately 0.023%, 0.017% and 0.009%. The relationship shows that the balance content of [S] reduces with the temperature. In order to reduce the content of [S] and modify more low melting-point inclusions, the Ca treatment must be taken in high temperature. For the reason that MnS can not produce when the temperature is high, reaction in high temperature is beneficial for the combination between CaS and Al2O3. In the meanwhile, the segregation of S is reduced and the production of the reaction can also provide core for MnS to modify into spindle shaped inclusions. The average temperature in the product process after RH refining is 1893K and the temperature meet the demands of Ca treatment. According to the required content of [S] and the thermodynamics condition of $12CaO\cdot 7Al_2O_3$, the content of [Al] must be adjusted to 0.015%~0.025%.

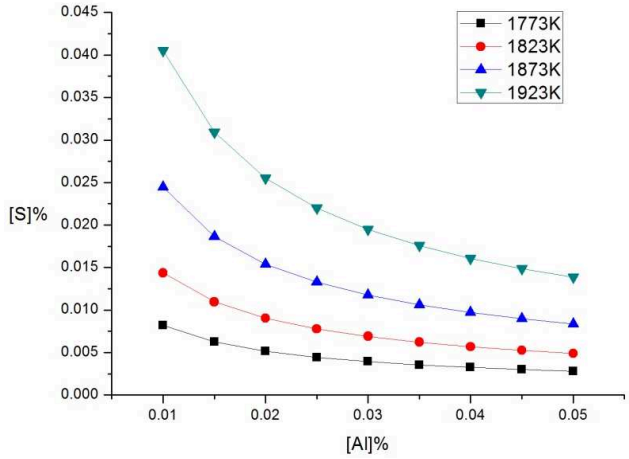


Fig 3. Relationship between [Al] and [S] in 12CaO·7Al2O3

Effect of the Inclusion Control in Rolled steel Using Calcium Treatment

The morphology of the inclusions is well controlled after the process and the number of inclusion is few and the inclusions are well distribution. There are also little long strip of MnS

inclusions to be found. But for the smelting conditions and other factors, a small amount of long strip inclusions can be found in some rolled steels. The samples of rolled steels are collected randomly and the inclusions are determined. The results of the test of rolled steels are showed in Table 5.

TABLE 5 THE TEST RESULTS OF 20CRMO ROLLED STEELS

No.	A type		B type		C type		D type	
	thick	thin	thick	thin	thick	thin	thick	thin
1	1.0	2.5	0.5	0.5	0	0	0	1.0
2	1.5	2.5	1.5	2.0	0	0	0	1.0
3	1.0	1.0	1.0	1.0	0	0	0	0.5
4	2.5	2.0	2.5	2.0	0	0	0	1.0
5	1.5	1.0	2.0	2.0	0	0	0	0.5
6	1.0	0.5	1.0	1.5	0	0	0	0.5

According to the requirements, the sulfide inclusions in 20CrMo rolled steels can't exceed 3 level. And the results show that the inclusions in steels are less that 2.5 level. Above all, the calcium treatment has been able to achieve good results on 20CrMo gear steel. And the occurrence of nozzle blocking has been decreased and the quality of the steel has been improved since calcium treatment. The morphology and composition of the compound inclusions are show in Fig.4.

Most of the inclusions in rolled steels are calcium aluminates compound inclusions with MnS around them. The results show that calcium treatment is more beneficial to modify the inclusions of Al_2O_3 and sulfide by adding calcium and to combine the oxide and sulfide into compound inclusion with oxide as its nucleus.

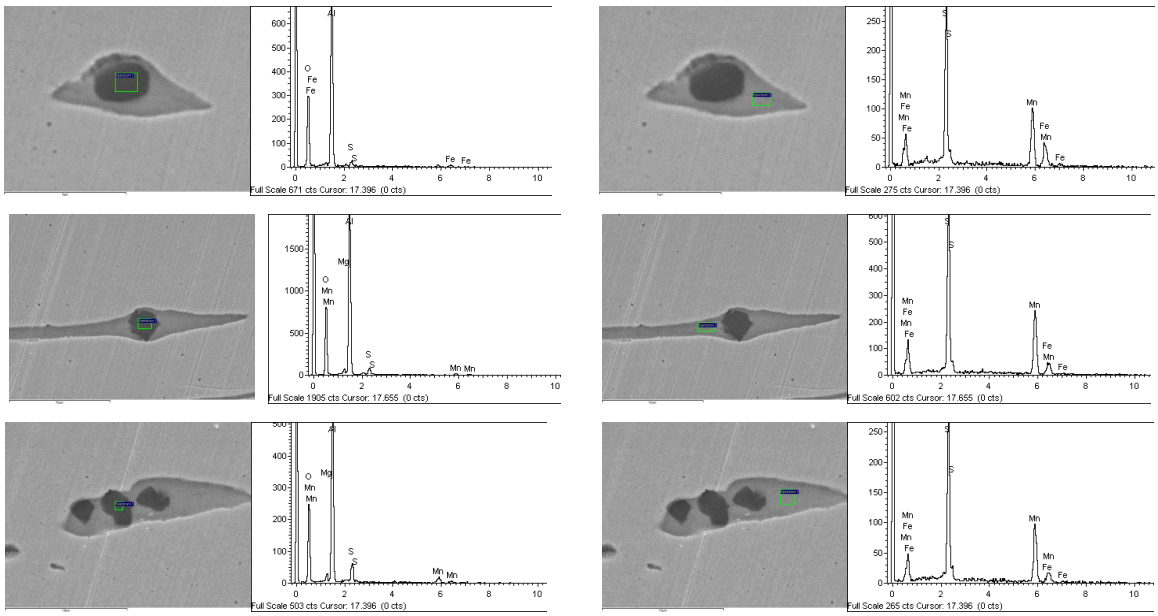


Fig.4 SEM and EDS of Compound Inclusions in Rolled Steels

Summary

To get $12CaO \cdot 7Al_2O_3$, the content of [Ca] should be adjusted about 0.002% during the process while the content of [Al] is 0.03%.

The content of [Ca] should be controlled less than 0.0015% before the S wire is fed.

The [Al] should also be controlled about 0.015%~0.025% to avoid nozzle blocking.

The sulfide inclusions in steel are well modified by calcium and the test results are meet the requirements.

References

[1] Yan Guoan，Qin Zhe etc. Inclusion morphology control in medium-carbon calcium sulphur free-cut ting steel[J]. Journal of University of Science and Technology Beijing，2007. 29(7):685-688

[2] Han Zhijun，Lin Ping，Liu Liu etc. Thermodynamics of Calcium Treatment for 20CrMnTiH1 [J]. Iron and Steel，2007. 42 (9):32-36

[3] Li Guozhong，Jian Long，C. Effect of Ca-Treatment on Sulphide Inclusions in 0.048%～0.065%S Medium-Carbon Structure Steel[J]. SPECIAL STEEL，2006. 27 (3):23-25

[4] Chen Jiaxiang.Chart data of steelmaking[M]. First Edition,Beijing：Metallurgical Industry Press，1984，510-517

[5] Huang Xigu. Iron and steel metallurgy principle [M].Third Edition.Beijing：Metallurgical Industry Press，2002，104-113

[6] Presern V. Thermodynamic Conditions for Inclusions Modification in Calcium Treated Steel[J].Steel Reserch，1991.62(7):289-295

CHAPTER 13:

Building Materials and Technologies in Construction

Advanced Materials Research Vol. 936 (2014) pp 1331-1335
© (2014) Trans Tech Publications, Switzerland
doi:10.4028/www.scientific.net/AMR.936.1331

Nonlinear Dynamic Finite Analysis of BFRP-strengthened Masonry Structure Based on ABAQUS

Lei Zhen[1, a], Wang Yong[2,b] and Qu Jun-tong[1,c]

[1]School of Urban Construction and management, Yunnan University, Kunming 650091, China

[2]Chengdu JZFZ Architectural Design Co. Ltd., Chengdu 610015, China

[a]leizhen0916@163.com, [b]ivvfy@126.com, [c]qujuntong@126.com

Keywords: BFRP (Basalt Fiber Reinforced Polymer); Masonry structure; Strengthening; Time-history analysis; Finite element method.

Abstract: The externally bonded FRP is an effective strengthening technique, which is mainly verified through laboratory tests. In this paper, numerical analysis models were established in ABAQUS respectively based on an experimental scaled three-story confined masonry structures before and after strengthened with BFRP. Then dynamical analysis considering material nonlinearity, geometric nonlinearity and contact nonlinearity was carried out on these two models. Here, representative volume element method was used to simplify the simulation of masonry. Besides, concrete damage plasticity model was adopted to simulate the structural damage and failure process. The reliability and accuracy of nonlinear dynamic finite analysis were validated by comparing the numerical simulation results and experimental results in terms of dynamic property, displacement and acceleration response and the maximum base shear.

Introduction

Externally bonded FRP for strengthening masonry buildings has been widely aroused many researchers' interest for its advantage of low weight-strength ratio, short installation periods, and low intervention on the structures. However, those researches on FRP strengthening technique mainly focus on laboratory experiments [1-3], and their primary strengthening object are masonry members (such as masonry units, walls, columns, arches and so on) [1-6], and the commonly used strengthening fibers are CFRP (carbon fiber reinforced polymer) , GFRP (glass fiber reinforced polymer) and AFRP (aramid fiber reinforced polymer) which are still not the best appropriate strengthening materials when it comes to strength action rate, thermal stability, heat-resistance and alkali resistance. BFRP (Basalt Fiber Reinforced Polymer) used in this paper is a new inorganic continuous fiber, which is much cheaper than the CFRP and has excellent physical and mechanical properties [7,8], while the application of FRP to masonry structures is still in its infancy and needs a thorough study urgently.

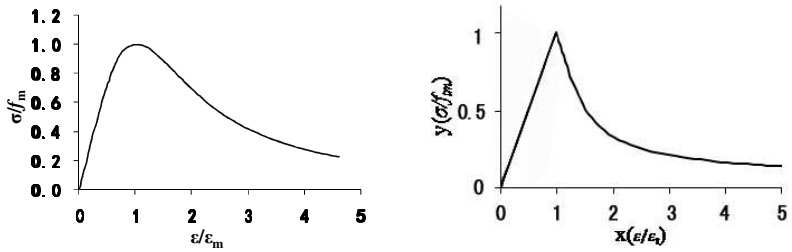
Numerical analysis and modeling are effective and convenient methods on the research of seismic performance of structure. Due to the complicity and difficulty of modeling brick and mortar as well as their contact interaction, it has been only used to analyze the strengthening effect of FRP on masonry members [9,10]. This paper establishes two numerical analysis models in ABAQUS respectively based on a experimental scaled three-story confined masonry structures before and after strengthened with BFRP[8], simplifying the modeling of masonry structure using representative volume element method which takes the brick and mortar as a whole. And then the numerical simulation results of dynamical analysis are compared with the experimental results in terms of dynamic property, displacement and acceleration response and the maximum base shear to verify the reliability and accuracy of nonlinear dynamic finite analysis.

Numerical modeling for (BFRP-strengthened) masonry structure

The detail structural specification of this (BFRP-strengthened) masonry structure refers to the shaking table tests in [8]. In the ABAQUS software, the modeling of masonry walls, structural columns and floor slabs are solid element using C3D8R, and the modeling of BFRP strips are membrane element using M3D4R. Through comparative analysis of various constitutive models, concrete damage plasticity model is chosen for masonry, which can be used for a good simulation of structural damage and failure process. For the masonry, the compression constitutive model in [11] is adopted, and the tensile stress-strain relationship is listed as follows:

$$\begin{cases} D=0 & 0\le\dfrac{\varepsilon}{\varepsilon_t}\le 1 \\ D=1-\sqrt{\dfrac{1}{\alpha_t(x-1)^{1.7}+x}} & \dfrac{\varepsilon}{\varepsilon_t}\ge 1 \end{cases}. \tag{1}$$

The constitutive curves of masonry compression and tensile relationship are shown in Fig.1.

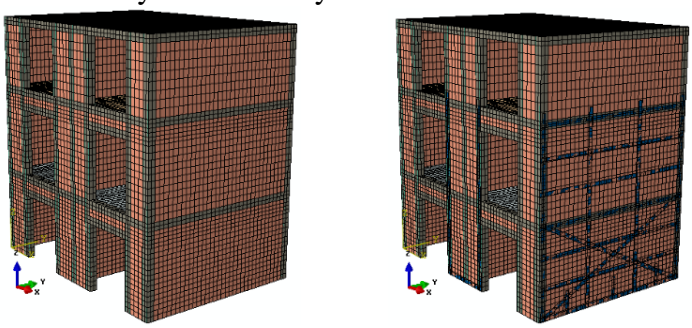


(a) compression relationship (a) tensile relationship

Fig.1 Constitutive model for masonry

According to the principle of energy equivalence, the compression and tensile damage curve for masonry can be obtained.

For the structural columns, concrete damage plasticity model is also chosen, and relative material parameters are decided according to the GB/T 50010-2010 [12]. The rebars embedded in the structural columns and ring beams are idealized as linear elastic model. The BFRP strips are taken as anisotropic linear elastic model. Tie constraint is applied to the interface between masonry walls and fiber strips. The meshed models are shown in Fig.2. The seismic waves (MYG004 removed) and input direction are the same as the laboratory test program [8]. Three seismic series (basic 7, rare 7 and rare 8) are considered in the dynamical analysis.



(a) pre-damaged model(A_{FEM}) (b) BFRP-strengthened model(B_{FEM})

Fig.2 Finite element analytical model

Results and discussion

Dynamic property

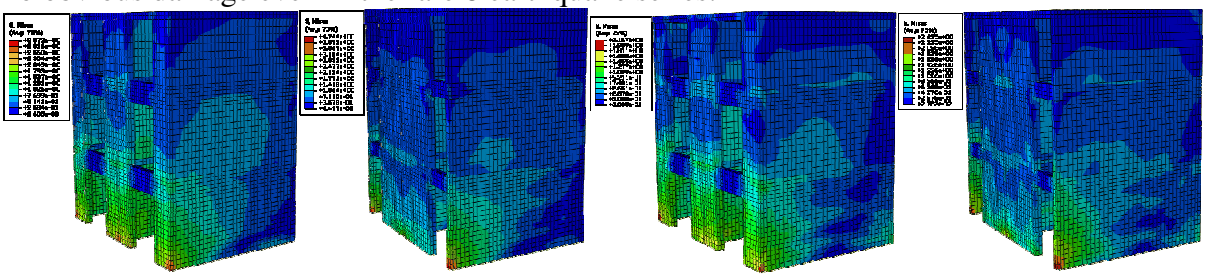
Mode analysis was carried out to these two finite element models. The natural frequencies of the first 9 modes can be obtained and compared to the experimental results (Table 1). The natural frequencies of the fist 3 modes agree well with the test results, and the relative standard deviation within 5%. The deviation increases with the mode. Due to the flexible feature and light self-weight of BFRP strips, the structural model strengthened with BFRP almost gets the same natural frequency as the pre-damaged model.

Table 1 Comparison of natural frequencies (Hz)

model	1st	2nd	3rd	4th	5th	6th	7th	8th	9th
A_{FEM}	6.428	8.607	14.768	23.370	26.203	34.196	36.107	48.134	54.129
$A_{experiment}$	6.445	8.105	15.332	25.563	/	/	/	/	/
B_{FEM}	6.451	8.641	14.791	23.432	26.279	34.259	36.197	48.236	54.155
$B_{experiment}$	6.250	8.105	14.551	26.563	/	/	/	/	/

Stress distribution of walls

Take El-Centro wave in rare 8 series for example, the stress distribution of these two models are shown in Fig.3. The pre-damaged model subjects to damaged at the place where principal compressional and tensile stress are lager. The damage mainly focuses on the horizontal crack on the wall and the crush of structural columns in the first floor, which agrees with the experimental damage phenomena. The BFRP strips cooperate with the masonry structure to resist earthquake, changing the stress distribution of the masonry wall. At the same earthquake moment, the maximum principle stress of B_{FEM} is 2.425MPa, which is 43% smaller than A_{FEM}. The BFRP-strengthened model shows no obvious damage even in the rare 8 earthquake series.



(a) A & 3 axis in A_{FEM} (b) B & 1 axis in A_{FEM} (c) A & 3 axis in B_{FEM} (d) B & 1 axis in B_{FEM}

Fig.2 Comparison of the maximum Mises stress distribution

Displacement response

The maximum displacement at each floor of these two models exhibits a trend of increase as the input acceleration increases. The maximum displacement is always obtained at the top floor. Models show different displacement response at different site waves, especially at the Ⅲ and Ⅳsite waves. Compared to the pre-damaged model, the BFRP-strengthened model shows the increase of 1.4%, 3.2% and 11.3%, respectively, in basic 7, rare 7 and rare 8 series. The simulation results are smaller than the experimental results due the effect of accumulative damage in the laboratory tests. In the rare 8 series (El-Centro), the displacement-time curves of these two models are shown in Fig.3, and Table.2 lists the detailed displacement value at each floor in the rare 8 series.

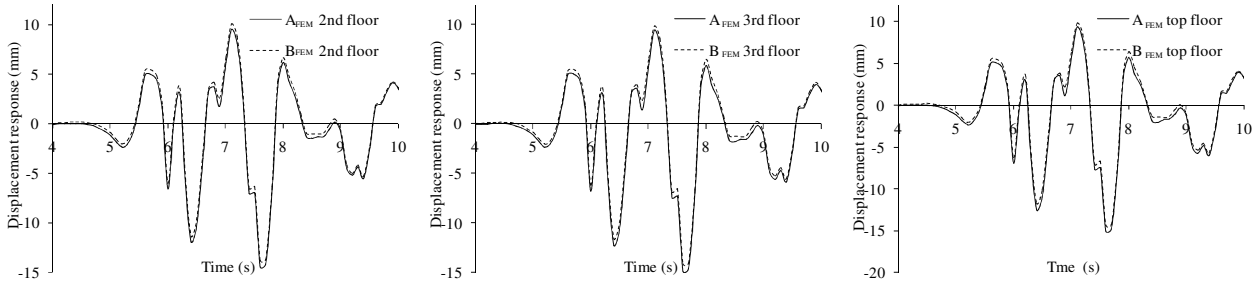


Fig.3 Displacement-time curve (El-Centro in rare 8 series)

Table 2 Comparison of displacement response (mm)

Input signal	Cases	Pre-damaged structure			BFRP-strengthened structure		
		2nd floor	3rd floor	Top floor	2nd floor	3rd floor	Top floor
EI-Centro	S	1.473	2.544	3.222	1.662	2.916	3.591
	E	2.860	2.964	4.120	2.798	3.330	4.648
Wenchuan	S	0.832	1.744	2.392	1.125	2.106	2.886
	E	2.082	3.369	4.468	1.650	2.869	3.999
Pasadena	S	2.408	5.481	7.539	2.443	5.558	7.651
	E	5.159	5.621	7.946	5.330	6.101	8.518
SHW2	S	2.037	2.989	4.228	2.204	3.080	4.396
	E	3.540	3.529	4.840	3.969	3.337	4.427

Note: S=simulation, E=experiment.

Acceleration response

Due to different spectral characteristics of seismic waves, models have not the same response rule under different seismic wave input, while models show the same response rule under the same input with different peak accelerations. When the peak value of input acceleration is 0.10g or 0.22g, the models have no obvious crack and the numerical simulation results agree well with experimental results. After the input of rare 8 series, accumulative damage become predominant, so it makes the simulation results higher than experimental results. In the rare 8 series (El-Centro), the acceleration-time curves of these two models are shown in Fig.4, and Table.3 lists the detailed acceleration-amplifying coefficient at each floor in the rare 8series.

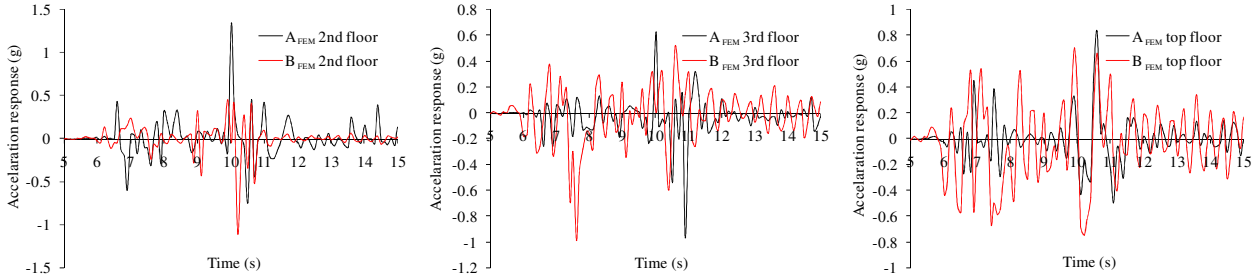


Fig.4 Acceleration-time curve (El-Centro in rare 8 series)

Table 3 Comparison of acceleration-amplifying coefficient

Input signal	Cases	Pre-damaged structure			BFRP-strengthened structure		
		2nd floor	3rd floor	Top floor	2nd floor	3rd floor	Top floor
EI-Centro	S	3.360	2.417	2.085	2.764	2.369	1.868
	E	0.912	0.861	1.143	1.005	0.917	1.254
Wenchuan	S	1.084	1.641	1.721	1.431	1.655	1.969
	E	1.093	1.074	1.426	1.047	1.065	1.552
Pasadena	S	2.854	1.460	1.769	2.259	1.432	1.491
	E	0.985	1.004	1.159	1.024	0.967	1.144
SHW2	S	3.766	3.235	2.851	3.524	2.933	2.623
	E	1.054	0.930	1.034	0.867	0.792	1.108

Maximum base shear

The value of the base shear reflects objectively the level of the earthquake action under certain seismic wave. Fig. 5 presents the maximum base shears of these two simulation models in the rare 8 series (El-Centro). The comparison of the maximum base shear in the rare 8 series is listed in Table 4. The simulation results in the maximum base shear are slightly smaller than the experiment results in most input cases. The base shear of B_{FEM} at other input moment is generally higher than that of A_{FRM}, verifying that BFRP-strengthening technique can obviously postpone the stiffness degradation and improve the energy-dissipating capacity.

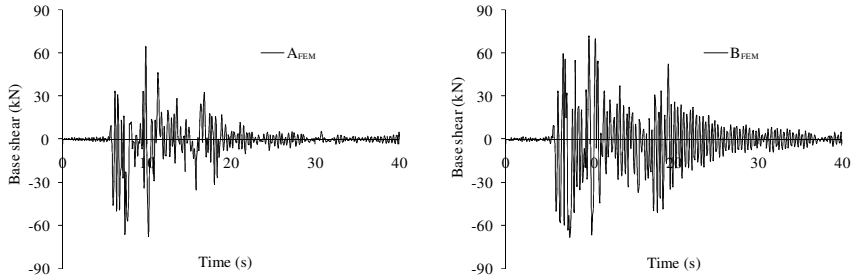


Fig.5 Base shear-time curve (El-Centro in rare 8 series)

Table 4 Comparison of the maximum base shear (kN)

Input signal	Pre-damaged structure		BFRP-strengthened structure	
	E	S	E	S
EI-Centro	98.525	82.247	97.411	83.475
Wenchuan	81.848	70.442	82.758	73.755
Pasadena	92.213	82.206	99.997	79.266
SHW2	81.928	88.047	80.041	88.545

Summary

BFRP-strengthening technique can significantly improve the energy-dissipating capacity and seismic performance due to the co-working action of BFRP strips and masonry structure. The strengthened model shows no obvious damage even in the rare 8 series, which agrees with experiment phenomena. The dynamic property, displacement and acceleration response and the maximum base shear of the numerical analysis models generally consistent with the laboratory results. Representative volume element method can effectively solve the complexity of masonry modeling and reasonably reflect the seismic response and phenomena, and verify the conclusions drawn from laboratory tests.

References

[1] M. A. ElGawady, P. Lestuzzi, M. Badoux, Aseismic retrofitting of unreinforced masonry walls using FRP. Compos. Part B: Engng., 2006, 37(2): 148-162.

[2] P. Alcaino, H. Santa-Maria, Experimental response of externally retrofitted masonry walls subjected to shear loading. Journal of Composites for Construction, ASCE, 2008, 12(5): 489-498.

[3] G. Marcari, G. Manfredi, A. Prota, M. Pecce, In-plane shear performance of masonry panels strengthened with FRP. Composites, Part B, 2007, 38, 887-901.

[4] M. A. Aiello, F. Micelli, L. V. Valente, Masonry confinement with fiber-reinforced polymers. Journal of Composites for Construction, ASCE, 2009, 13(2): 148-158.

[5] S. B. Bati, L. Rovero, U. Tonietti, Strengthening masonry arches with composite materials. Journal of Composites for Construction, ASCE, 2007, 11(1): 33-41.

[6] P. Roca, G. Araiza, Shear response of brick masonry small assemblages strengthened with bonded FRP laminates for in-plane reinforcement. Construction and Building Materials, 2010, 24(8): 1372-1384.

[7] D. Zhou, Z. Lei, J. Wang, In-plane behavior of seismically damaged masonry walls repaired with external BFRP. Composite Structures , 2013, 102: 9-19.

[8] Z. Lei, D. Zhou, Y. Li, Shaking table test of earthquake-damaged masonry structure strengthened with external BFRP. IABSE Symposium Report, Rotterdam 2013, 942-949(8).

[9] B. Luccioni, V. C. Rouhier, Numerical analysis of fiber reinforced polymer retrofitted masonry panels. Engineering Structures, 2013, 49, 360-372.

[10] E. Grande, M. Imbimbo, E. Sacco, Finite element analysis of masonry panels strengthened with FRPs. Composites: Part B, 2013, 45(1), 1296-1309.

[11] W. Z. Yang, Constitutive relationship model for masonry materials in compression. Building structures, 2008, 38(10), 80-82. (In Chinese)

[12] GB50010-2010. Code for design of concrete structures. Ministry of Housing and Urban-Rural development. China; 2010. (In Chinese)

Advanced Materials Research Vol. 936 (2014) pp 1336-1341
© (2014) Trans Tech Publications, Switzerland
doi:10.4028/www.scientific.net/AMR.936.1336

Crystal Structure and Hydration Characteristics of Tricalcium Silicate Doped with Magnesium Oxide

Lin Chen[1,a], Xu Wang[1,b], Xiaodong Shen[2,c], Suhua Ma[2,d], Weiqiang Zhou[2,e]

[1]Department of Civil Engineering, Nanjing Technical Vocational College, Nanjing 210019, PR China;

[2]State key Laboratory of Materials-oriented Chemical Engineering, College of Materials Science and Engineering, Nanjing University of Technology, Nanjing 210009, PR China

[a*]email:Lchen816@126.com, [b]email:wangxulism@126.com, [c]email:xdshen@njut.edu.cn, [d]email:yc982@163.com, [e]email:lch210019@126.com

Key words: tricalcium silicate; MgO; structure; hydration

Abstract: The research investigates various methods to identify magnesium oxide influences on the crystal structure and hydration properties of tricalcium silicate. The f-CaO content of the clinkers were analyzed by chemical analysis. The complex disordered superstructure of the tricalcium silicate has been studied by a joint XRD, NMR and TEM. The results show that MgO exerts a remarkable influence on the polymorphisms of C_3S. Mg is not only substitutional atom but also interstitial atom in the crystal lattice of tricalcium silicate. The HRTEM pattern of C_3S doped with MgO is covered by the various irregular lattice. The addition of appropriate amount of MgO in raw meal can change the formation kinetic of C_3S, slightly perturb the environment of SiO_4^{4-} tetrahedral, modify the crystal structure of C_3S and affect the hydration activity. Doped with MgO in the raw meal can slow down the hydration rate of alite slightly in early stage.

Introduction

The major component of ordinary Portland cement (OPC) is a 50–75 wt. % solid solution of tricalcium silicate ($3CaO{\cdot}SiO_2$ =C_3S) with MgO, Al_2O_3 and Fe_2O_3 [1,2]. Seven structural modifications of C_3S have been identified [3-4]. The most common modifications are M1 or M3, and T2 occurs only rarely in cement clinker.

It is well known that the strength of cement from different localities differs a lot in spite of a high similarity of the contents of alite and other phases. Almost always, such differences are looked upon as a result of different concentrations of the minor oxides, especially MgO, SO_3 and alkali oxides. Alite is the principal hydraulic phase of clinker, having the decisive impact on the strength of Portland cement. Ca_3SiO_5 is characterized by an extensive polymorphism. The hydration activity of clinker is closely related with the different polymorphism of C_3S.

Many investigations[5-7] have been reported the effect of the addition of MgO on the formation of Ca_3SiO_5 minerals, but the results are inconsistent and even contradictory. In this study, the influence of MgO on the crystal structure and hydration characteristics of tricalcium silicate was investigated. The aim of the study was to investigate the influence of MgO on the synthesis, lattice parameters of the clinker phase and the effect on the hydration characteristics of dopped C_3S.

Experimental Procedure

Preparation of Specimen

Pure tricalcium silicate and its solid solutions with magnesium were made by solid-state reaction at 1500℃.The starting materials were analytical reagent grade calcium carbonate and quartz and magnesium oxide. Calcium carbonate and quartz in the stoichiometric ratio of 3:1 were ground to a fine powder and homogenized with MgO. The raw mixtures were mixed with 8% water and pressed into discs using a mould with the size of 25mm in diameter and 40mm in thickness. The discs were dried in an oven and burned at 1500℃ for 6 h in a platinum dish in the Nabertherm resistance furnace. The sintered pellets were ground to pass a 0.08mm sieve and reformed into pellets and fired at 1500C for 6 h again. The samples were all cooled rapidly by a electric fan. The final products were all powdered to pass the 0.08mm sieve. The concentration of MgO in raw meal and the abbreviation of samples are shown in table 1.

Table1 Concentration of MgO and abbreviation of samples[%]

Samples	C_{M0}	C_{M1}	C_{M2}	C_{M3}	C_{M4}	C_{M5}
w(MgO)	0	1	2	3	4	5

Results and discussion

The Content of F-CaO

As seen from Fig.1, the content of free lime in C_{M0} is 0.42%. The content of free lime in alite greatly rises along with the increase of the concentration of MgO up to 3.0%, the content of more than 3.0% MgO except. When the content of MgO exceeds 3.0%, the content of free lime in the alite remains approximately 1.3%. According to the molecular weight of CaO and MgO, Mg^{2+} could substitute for Ca^{2+} in the Ca_3SiO_5. Noticeably, Mg is not only substitutional atom but also interstitial atom.

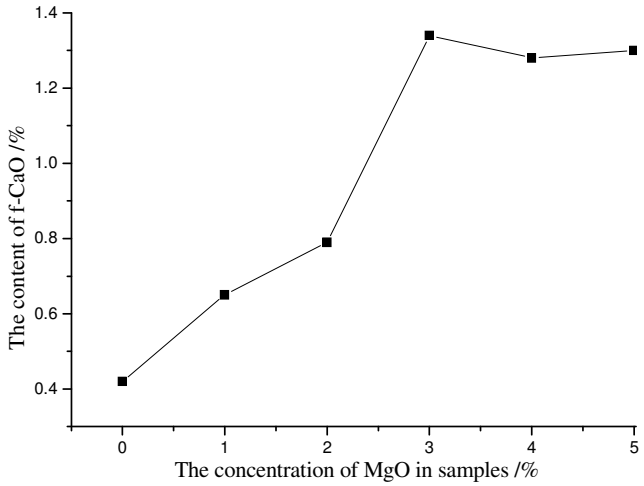


Fig.1 Effect of amount of MgO added on the content free lime of in samples

Mg^{2+} is known to substitute directly for Ca^{2+} in the Ca_3SiO_5 crystal lattice. According to J.Bensted [8], the limiting solid dissolved quantity of MgO in Ca_3SiO_5 was up to 2.2% at 1550℃. It is indicated that the free lime is released in clinker due to Mg^{2+} substitute for Ca^{2+} in the Ca_3SiO_5. When the amount of MgO added is over 3.0%, the solid dissolved MgO in Ca_3SiO_5 maintains a constant value.

Effect of MgO Added on C_3S Formation

Fig.2 presents the X-ray diffraction patterns for the pure tricalcium silicate and its solid solutions with magnesium sintered at 1500℃ for 6h twice. The diffraction peaks of $CaCO_3$ as well as SiO_2 in the patterns are not observed. This denotes that $CaCO_3$ has decomposed completely and the Si-O-Si bonds in SiO_2 have broken down. The primary diffraction peaks are C_3S mineral which have been marked out. The diffraction peaks of f-CaO(d= 0.2403 nm) are rather low, so the content of free CaO is little, the diffraction peak of free lime is visible in the specimen containing 3.0% MgO, which is in agreement with the results in Fig.1.

Seen from Fig.2, the XRD diffraction peaks with d values of 0.243nm and 0.2097nm belong to MgO, the peak of alite solid solutions with magnesium is all shifted toward the angles, it is shown that Mg substitute for Ca in Ca_3SiO_5 lead to decreasing the cell volume of Ca_3SiO_5. Apparently, the addition of MgO can affect the crystal structure of Ca_3SiO_5.

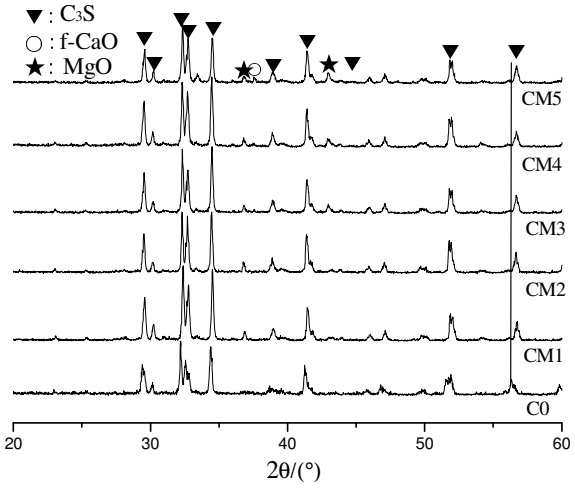


Fig.2.XRD pattern of the pure tricalcium silicate and its solid solutions with MgO

On the basis of the experiment, it is concluded that the addition of MgO can influence on the cell volume of Ca_3SiO_5.When the amount of MgO added is over 3.0%, Mg^{2+} may substitute for Ca^{2+} in Ca_3SiO_5 to release f-CaO. Doped with MgO in the raw meal can affect the structrue of Ca_3SiO_5.

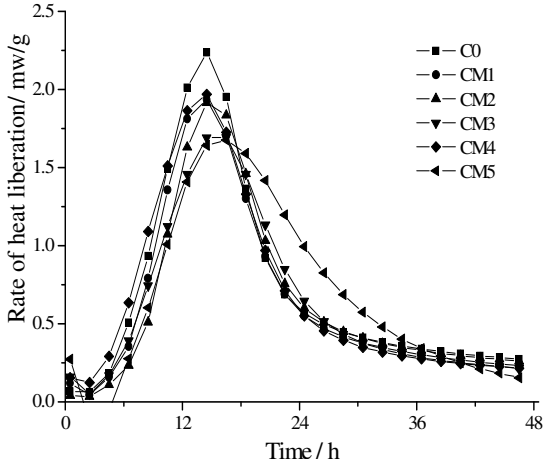


Fig. 3 Heat evolution curves of samples

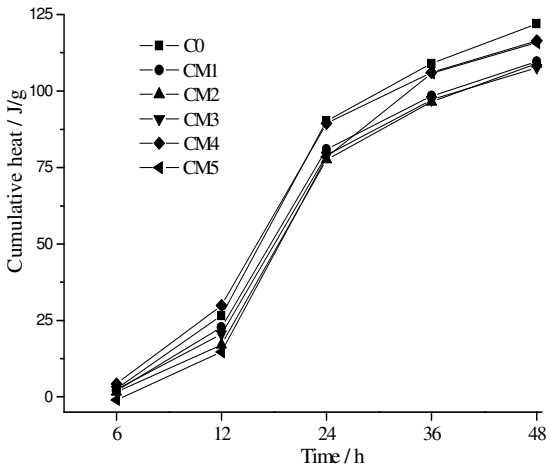


Fig. 4 Cumulative heat of hydration of samples

Heat of hydration

For pure C_3S and solid solutions, the heat evolution during the first 48 h of hydration is shown together with the cumulation heat of hydration over a period of 48 h in Fig.3 and 4, respectively.

Seen from Fig.3 and Fig.4, the effect of MgO added on the hydration behavior of C_3S is remarkable.The hydration rate shows that MgO slows down the hydration of C_3S slightly druing the first 48 h，but the cumulative heat of hydration is nearly the same in 48 h. This is in agreement with the result of Abdul-Maula and Dietmar Stephan[9].

Mechanisms

^{29}Si NMR Spectra of Pure C_3S and Solid Solution

By means of ^{29}Si solid-state NMR it is possible to detect all Si atoms in a sample, regardless of whether the atoms are part of a crystalline or amorphous compound. Furthermore, different chemical shifts make it possible to distinguish Si in the calcium silicates.

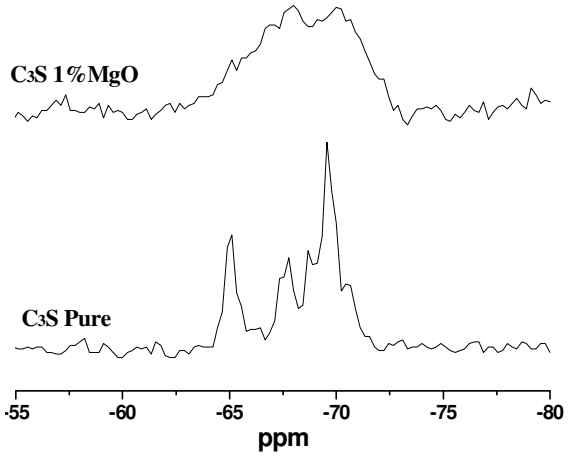


Fig. 5 ^{29}Si NMR of pure C_3S and C_3S doped with 1% MgO

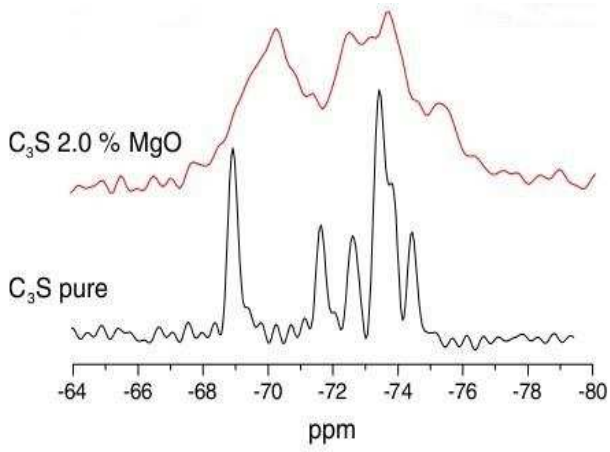
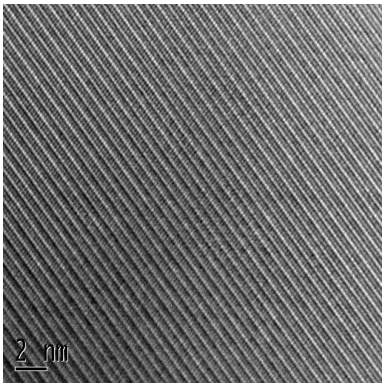


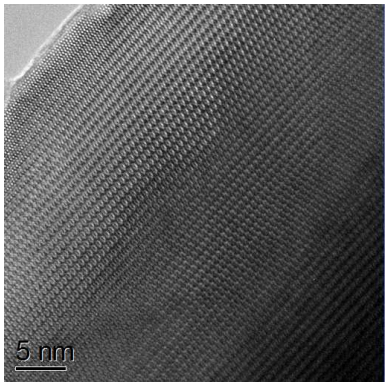
Fig.6 ^{29}Si NMR spectra of pure C_3S and C_3S doped with 2% MgO

Fig. 5 shows that the ^{29}Si MAS NMR spectra of undoped C_3S is compared to the spectra of C_3S with 1.0wt. % MgO. In Fig.6, the ^{29}Si MAS NMR spectra of undoped C_3S is compared with the spectra of C_3S with 2.0 wt.% MgO, which is synthesized using an innovative sol–gel process as precursor[10]. Seen from Fig.5 and Fig.6, the spectra of NMR are very similar, the C_3S doped with MgO give broad signals with complex line shape for the overlapping ^{29}Si resonances. The spectras of C_3S doped with MgO synthesized using solid-state or sol–gel process as precursor all shift to right to compare with the spectra of undoped C_3S. Seen from Fig.5, the area of the peaks at -65.0 and -69.6ppm is twice compared to the other peaks, which shows that these peaks belong to various Si with very different positions.

From the line broadening of the NMR spectra it can be presumed, that the doped elements slightly perturb the environment of SiO_4^{4-} tetrahedral. The sample containing an appropriate amount MgO is the only one with a monoclinic and not a triclinic structure[10]. The line broadening does not only occur for the monoclinic C_3S but also is a result of the incorporation of foreign ions already below the critical concentration for the phase transformation.



a: pure C_3S



b: C_3S doped with 1% MgO

Fig. 7 HRTEM of C_3S and C_3S doped with 1% MgO

TEM. The HRTEM pattern of pure C_3S and C_3S doped with 1% MgO are shown in Fig.7. Seen from Fig.7.a, the crystal lattice of pure C_3S is orderly and regular in the whole region, while the HRTEM pattern of C_3S doped with MgO covers the various irregular lattice in Fig.7.b, indicating several crystal defects, the crystal defect belong to modulated structure, which is consequent on the Mg^{2+} subsitiute for Ca^{2+} in C_3S to lead to vacancy of oxygen ion, as expressed by the following formula: $MgO \xrightarrow{C_3S} Mg_{Ca}+O_O$. It is concluded that the addition of appropriate amount of MgO in raw meal can change the formation kinetic of C_3S, affect the crystal structure of C_3S and alter the hydration activity.

Summary

The following conclusions can be drawn, concerning the crystal structure and hydration properties of tricalcium silicate doped with magnesium oxide:

(1) MgO exerts a remarkable influence on the polymorphism of C_3S. A slight Mg solid solution in the cement clinker is not only substitutional atom but also interstitial atom.

(2) MgO slows down the hydration rate of C_3S slightly during the early stage，but the cumulative heat of hydration is nearly the same in the early ages. The influence of magnesium on hydration properties of cement clinker mineral is significant.

(3) The addition of appropriate amount of MgO in raw meal can change the formation kinetic of C_3S, slightly perturb the environment of SiO_4^{4-} tetrahedral, modify the crystal structure of C_3S and affect the hydration activity.

References

[1] H.F.W.Taylor. Cement Chemistry. Academic Press, London, 1990.

[2] J. Bensted, P. Barnes. Structure and Performance of Cements, Spon Press, London, 2002.

[3] A.M.Bigare, C. Guinier, M. Mazieres et al. Polymorphism of tricalcium silicate and its solid solution, J. Am. Ceram.Soc. 50 (1967) 609-619.

[4] I. MAKI, K. KATO. Phase identification of alite in Portland cement clinker, Cem Concr Res, 12(1982)93-99.

[5] D. Stephan, S. Wistuba. Crystal structure refinement and hydration behaviour of $3CaO \cdot SiO_2$ solid solutions with MgO, Al_2O_3 and Fe_2O_3, J. Eur. Ceram. Soc., 26(2006)141-148.

[6] I. A. Altun. Effect of CaF_2 and MgO on sintering of cement clinker, Cement and Concrete Research, 29(1999)1847-1850.

[7] Wang Chunfang, Zhou zonghui, Liu Caixia.Formation Kintics Of Portland Cement Clinker Containing With Magnesium Oxide, Journal of the Chinese Ceramic Society. 39(2011)714-717.

[8] J. Bensted, P. barnes. Structure and performance of cements. 2nd edition. Spon Press, London, 2002.

[9] D. Stephan, S. Dikoundou, G. Raudaschl-Sieber. Hydration characteristics and hydration products of tricalcium silicate doped with a combination of MgO, Al_2O_3 and Fe_2O_3.Thermochimica Acta. 472 (2008)64-73.

[10] D. Stephan, S. N. Dikoundou, G. Raudaschl-Sieber. Influence of combined doping of tricalcium silicate with MgO, Al_2O_3 and Fe_2O_3: synthesis, grindability, X-ray diffraction and Si-^{29}NMR. Materials and Structures, 41(2008)1729-1740.

Advanced Materials Research Vol. 936 (2014) pp 1342-1350
© (2014) Trans Tech Publications, Switzerland
doi:10.4028/www.scientific.net/AMR.936.1342

Mechanical Damage Model of Concrete Subject to Freeze-thaw Cycles Coupled with Bending Stress and Chloride Attack

DU Peng[a], YAO Yan[b], WANG Ling and CAO Yin

State Key Laboratory of Green Building Materials, China Building Materials Academy, Beijing 100024, China

[a]dupengcbma@gmail.com

[b]yaoyan@cbmamail.com.cn

Keywords: concrete; strain; multiple factors; damage model; mechanical analysis

Abstract. As the action mechanisms of various factors affecting concrete durability are different, it is difficult to understand the durability of concrete exposed to multiple factors using only mechanism analysis. Converting each action mechanism to an appropriate macroscopic mechanical effect can simplify complicated durability problems. Here we study concrete beams exposed to common environmental factors: cyclic freezing and thawing, bending stress and chloride attack. By converting each mechanism into a mechanical process and analyzing its effect on concrete, a damage model based on strain was established. Freezing-induced tensile stress is essentially a low-cycle fatigue tensile stress, as represented by a saw-tooth model. The maximum strains when the maximum freezing-induced tensile stress coupled with the four-point bending stress in every freeze-thaw cycle were measured, and found to increase with freeze-thaw cycling. Our damage model provides a new approach to predict the service life of concrete, and guidance for durability design of concrete.

Introduction

It is well known that the service life of concrete is largely determined by its durability in its environment. Research on concrete durability over the years has focused mainly on materials science, analyzing the physical and chemical mechanism of the degradation process. Results of this research have helped us understand the mechanisms responsible for many losses of concrete structure and function [1]. However, studying the mechanism of concrete durability only from the materials science viewpoint is not a full-scale approach, because concrete in practical engineering situations normally suffers from multiple environmental factors, each with its own action mechanism. Mechanism analysis is not an effective way to investigate the durability of concrete subjected to multiple factors. Converting the action mechanism to a mechanical effect, and then analyzing these mechanical effects at a macroscopic scale, is one way of dealing with this problem. Research on concrete durability should be based on practical engineering considerations, and the best progress will be made by combining materials science and mechanical analysis [2].

Concrete failure caused by non-mechanical factors is similar to that caused by loading. In freeze-thaw cycles, for example, a porous concrete matrix consisting of cement paste and aggregates is widely accepted to generate hydrostatic pressure [3] and crystallization pressure [4] resulting from the ~9 vol.% expansion of water upon freezing. Hydrostatic pressure and crystallization pressure may be considered as an 'inner tensile stress', which, together with the thermal stress, make up a freezing-induced tensile stress that will cause cracking and strain variations once it exceeds the tensile strength that concrete can bear. In this way, the freezing process can be considered as 'loading' and the thaw process as 'unloading' [1]. After long-term cyclic freeze-thaw action, concrete will suffer accumulated damage, causing larger connectivity of microcracks and, eventually, destruction. Based on the above, the mechanism of freeze-thaw damage is converted into mechanical actions. This conversion allows us to establish a mechanical model for the durability degradation process of concrete exposed to multiple factors.

In recent years, strain has increasingly been monitored as a measure of internal damage [5-9], and shown to increase progressively with the progress of deterioration. In this study we used strain to characterize the degree of deterioration in concrete beams in service, exposed to cyclic freeze-thaw, bending stress and chloride attack. We then converted each deterioration mechanism to a mechanical effect on the concrete, and analyzed the strain behavior of the concrete under the synergistic effects of multiple factors, in an attempt to establish a universal damage model of concrete (which could be used to predict the service life of concrete beams), and also to provide reference data for durability design of concrete.

Experimental Program

As well as the results described below, results from a previous paper [8] are examined in this work.

Raw Materials

The raw materials were a Reference Portland cement (strength grade P.I 42.5, composition given in Table 1) with specific surface area of 347 m3/kg and volume density of 3.10 g/cm3, fly ash (FA) with water demand ratio of 91% and ignition loss of 2.2%, blast-furnace slag (BFS) with density of 2.89 g/cm3, specific surface area of 439 m2/kg and activation index of 99%, river sand with the fineness modulus of 2.8 and silt content less than 1 wt.%, crushed gravel with particle sizes of 5–10 mm and 10–20 mm in a ratio of 4:6, polycarboxylate superplasticizer (water reducer) with 40 wt.% solids content, and triterpenoid-saponin air entraining agent (dosed at 0.01 wt.% of the cementitious material content).

Table 1 CHEMICAL COMPOSITION OF CEMENT, wt.%

Raw material	Chemical composition									
	SiO_2	Al_2O_3	Fe_2O_3	CaO	MgO	SO_3	NaO_2eq	Loss	f-CaO	Cl^-
Cement	22.02	4.00	3.48	62.12	2.58	2.72	0.53	1.75	0.87	0.011

Preparation of Specimens

The mix proportions and the physical properties of the concrete are listed in Tables 2 and 3, respectively. Prismatic concrete specimens with dimensions of 100×100×400 mm were employed. Electrical resistance strain gauges, as shown in Figure 1(a), and made as described in reference [9] were located at a depth of 0.5 cm on both sides of the concrete specimens, as shown in Figure 1(b). The specimens were demolded after 24 h, and were then put in a curing room at 20 ± 2 °C and ≥ 90% relative humidity. After 24 d of curing, the specimens were moved into the vacuum salt-saturation equipment, and were saturated with 3.5 wt.% sodium chloride solution saturating for periods between 24 and 28 d.

Table 2 MIX PROPORTIONS OF CONCRETE [kg·m-3]

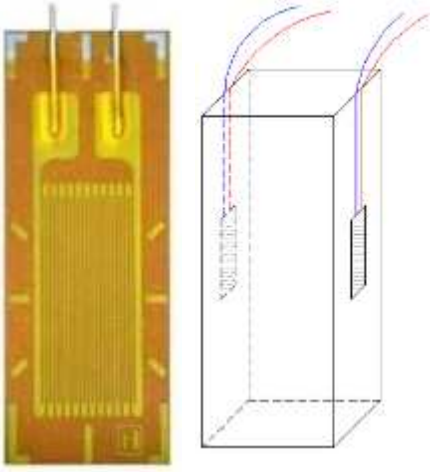
Name.	Cement	Water	FA	BFS	Sand	Stone	WR	AEA
Cao's C30	225	170	79	66	817	1040	4.45	-
Cao's C50	350	160	85	65	702	1053	8.5	-
BI	330	198	-	-	733	1120	-	0.033
BII	330	198	-	-	733	1120	-	0.033

Note: FA – Fly Ash, BFS – Blast-furnace Slag, WR – Water Reducer, AEA – Air Entraining Agent.

Table 3 PHYSICAL PROPERTIES OF CONCRETE AND LOADING STRESS LEVELS DURING FREEZE-THAW CYCLES

Name.	Slump (mm)	Air content (%)	28d compressive strength (MPa)	28d bending strength (MPa)	Stress level
Cao's C30	200	3.7	44.3	4.94	0.35
Cao's C50	200	3.8	63.6	6.39	0.35
BI	105	4.5	27.4	3.25	0.35
BII	105	4.5	27.4	3.25	0.5

Test Method



(a) (b)

Fig. 1 Concrete Specimen with Strain Gauges

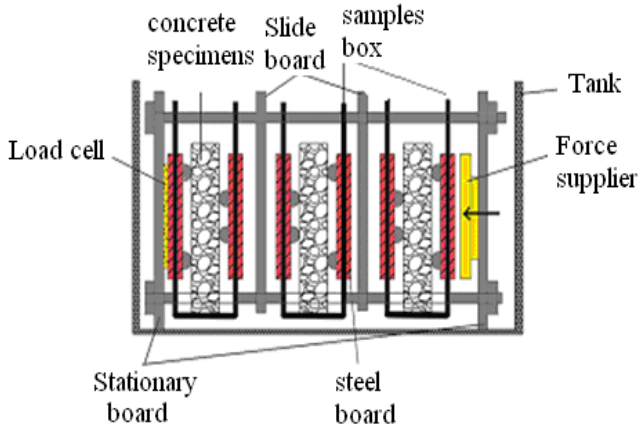


Fig. 2 Schematic of Test Samples in the Vertical Position

The concrete specimens were moved to the test chamber and placed in rubber sleeves filled with NaCl solution (3.5 wt.%) to a level 1–2 cm above the tops of the specimens. This concentration was selected because, according to reference [10], the greatest concrete damage under freeze-thaw cycles occurs in 3.5wt.% NaCl solution (which is also close to seawater concentration). Then the strain gauges were connected to a JC-4A automatic static strain data-logger. The concrete specimens were loaded a static constant four-point bending stress at a level of 0.35 or 0.5 by the force supplier, and the two sides of the concrete that contained the embedded strain gauges were placed next to the steel boards, as shown in Figure 2 and Table 3. Next, the freeze-thaw cycles were started, and strain variations were measured and recorded using a data-logger and computer. The freeze-thaw cycling was carried out according to Standard for test methods of long-term performance and durability of ordinary concrete GB/T50082-2009. The highest and lowest temperatures of the specimen centers were controlled to (-18±2) and (5±2) °C, respectively. An example of the actual measured temperatures of the thermal exchange fluid and specimen centers is shown in Figure 3.

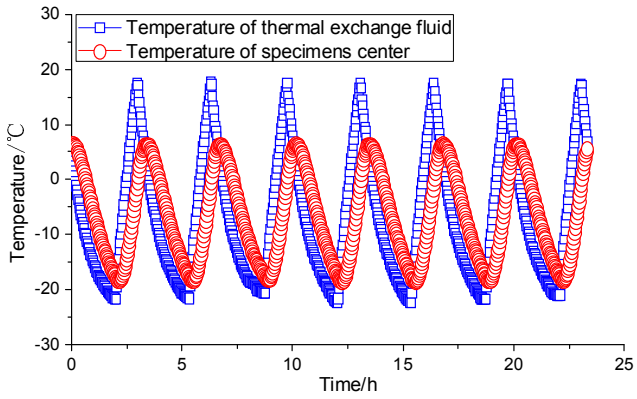


Fig. 3 Temperature Profile for Freeze-thaw Cycles

Experimental Results

Taking concrete specimen BI, for example, the maximum strains all appear near the lowest temperature (-18 °C) in every freeze-thaw cycle. Using the maximum strain in the first cycle as the initial value, Figure 4 shows that the maximum strains on the compression zone edge and the tension

zone edge both increase with the progress of freeze-thaw cycles, and that there is part of the curve where the rate of increase is constant. The increasing maximum strains are caused by the generation of residual strains. The strains at the tension zone edge are all larger in the same cycle and increase faster than those on the compression zone edge, because the tension zone of concrete is stretched by the maximum freezing-induced tensile stress coupled with the bending stress, while the compression zone edge is compressed by the bending stress, which partly counteracts the stretching from the maximum freezing-induced tensile stress. Freezing-induced tensile stress σF is a macroscopic overall stress, which includes stresses caused by hydraulic pressure, crystallization pressure, thermal expansion, thermal contraction, thermal gradients and so on (shown as Equation (1)), and, macroscopically, concrete is elongated by this overall force.

$$\sigma_F=\sigma_P+\sigma_T+\sigma_G+\ldots \quad (1)$$

where σP is the stress caused by hydraulic pressure and crystallization pressure; σT is the thermal-expansion and thermal-contraction-induced stress; and σG is the stress caused by thermal gradients. The values of εTm0 and εCm0 listed in Table 4 can be obtained from Figure 4. εTm0 is the initial maximum strain at the tension zone edge when the four-point bending stress is coupled with the maximum freezing-induced tensile stress (N = 0); εCm0 is the initial maximum strain of the compression zone edge when the four-point bending stress is coupled with the maximum freezing-induced tensile stress (N = 0).

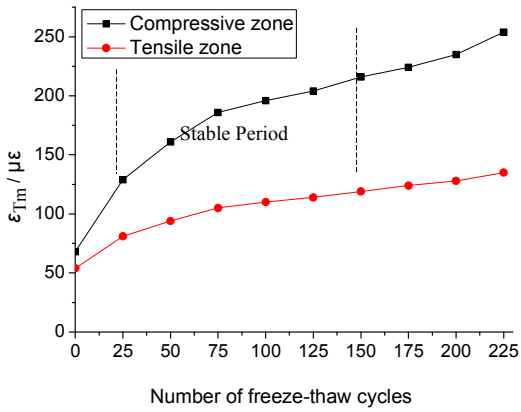


Fig. 4 Relationship Between Maximum Strain of BI and the Number of Cycles

The freeze-thaw damage mechanism of concrete involves several specific stages: the acceleration period, slow growth period and accelerated destruction period. Each stage is discussed in more detail below.

Acceleration period: The maximum strains increase rapidly because of the generation of new microcracks, the propagation of the tips of the original microcracks and the increasing water saturation, which can increase the freezing-induced tensile stress in concrete.

Slow growth period: The maximum strains seem to increase at a lower speed. Because of the damage accumulated during the acceleration period, the microcracks in concrete start to connect, and their connectivity can relieve some of the effects of the freezing-induced tensile stress. The major driving force for the increasing deformation during this period may be moisture migration in the concrete. This period occupies a large part of the whole process, and corresponds to the linear portion of the strain-cycling curve.

Accelerated destruction period: The connectivity of the cracks in the concrete increases greatly, allowing a large amount of the external solution to enter into the looser concrete and thus to generate a more destructive freezing-induced tensile stress. In this stage, the maximum strains again increase rapidly, until the concrete is completely destroyed.

The figures showing the experimental results of samples BII and Cao's C30 and C50 samples are not included here, but the values obtained from analysis of this other data are also listed in Table 4.

Establishment of Damage Model

Proposed Model for Maximum Freezing-induced Tensile Stress

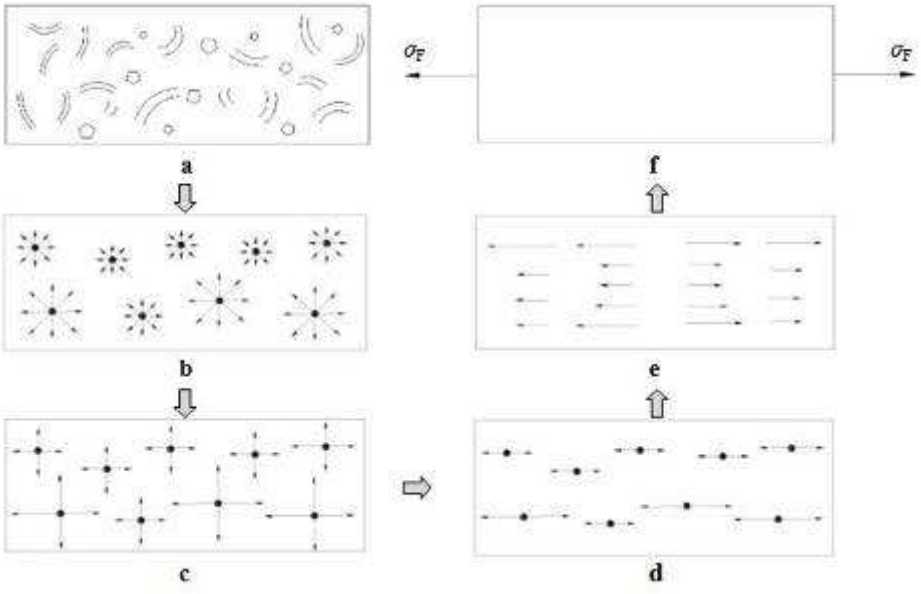


Fig. 5 Model Showing Horizontal Axial Maximum Freezing-Induced Tensile Stress on a Cross-section of Concrete

Figure 5 shows a schematic of the model where the maximum freeze-induced tensile stress is regarded as a horizontal axial stress. This model applies to particular points in time, whenever the freezing-induced tensile stress reaches its maximum value in every freeze-thaw cycle. The strains at these particular moments are the peak strains measured in every freeze-thaw cycle and all appear near the lowest temperature (-18 °C). There are some pores in concrete (Figure 5a), and every pore can be considered as a mass point. These pores each experience the maximum freezing-induced tensile stress in all directions (Figure 5b) during the progress of the freeze-thaw cycles, and this maximum freezing-induced tensile stress can be decomposed into a horizontal axial stress and a vertical axial stress (Figure 5c). Because we are measuring only the horizontal axial stress, we can neglect vertical stresses, as shown in Figure 5d. The increasing maximum strain of the concrete is largely due to variations in the pores, and has little to do with the compacted concrete matrix. Considering all the pores on the cross-section of concrete as a whole, no matter how the positions of these stresses change, provided that these stresses equivalently act on the cross-section of concrete, the degree of damage for this whole will be constant, according to the damage-equivalent hypothesis in the rain-flow counting method [11]. Therefore the maximum freezing-induced tensile stresses can be separated, forming tensile stress as shown in Figure 5e. For the whole piece of concrete, this is equivalent to applying a tensile stress to both ends of concrete in the horizontal axial direction (Figure 5f).

Maximum Freezing-induced Tensile Stress Coupled with Static Constant Four-point Bending Stress

In concrete, the freezing process is equivalent to loading, and the thawing process equivalent to unloading, so freezing-induced tensile stress is similar to a low-cycle fatigue tensile stress, and we can assume that it can be simply represented by a saw-tooth model [1], as shown in Figure 6. We have chosen to couple the freezing-induced tensile stress with a static four-point bending stress applied from above, so that damage will be localized in the central portion of the concrete specimen. The maximum in freezing-induced tensile stress σFm coupled with the four-point bending stress occurs at the tension zone edge, and the maximum compressive stress is at the compression zone edge of the concrete, as shown in Figure 7; we assume that their magnitudes are constant.

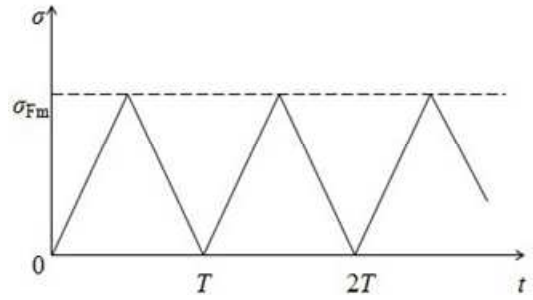


Fig.6 Model of Freezing-induced Tensile Stress

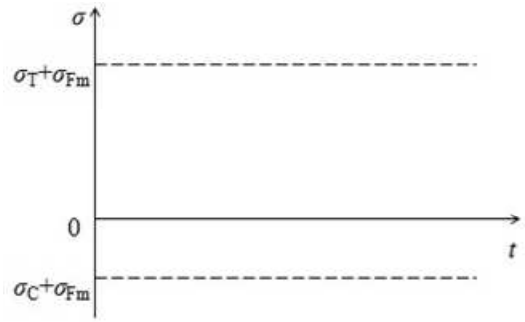


Fig. 7 Maximum Freezing-Induced Tensile Stress σFm Coupled with Four-point Bending Stress

Proposed Model

To apply these ideas to establish a damage model for concrete under synergistic effects of multiple factors, we modify the simple damage mechanics model for the fatigue of concrete proposed by Alliche and Francois [12] , according to Bernouilli's hypothesis. First, we assume that thermal gradients are not created between the center and the surface of the concrete. The elastic modulus of concrete changes with temperature, but in the present paper, since the minimum temperature for each cycle is essentially the same (near -18 °C), we can assume that these slight differences can be ignored. As shown in Figure 8, it is clear that the absolute value of the strain on the abscissa axis is equal to that on the compression zone edge, so the abscissa axis can be regarded as an equivalent compression stress line. When the four-point bending stress is coupled with the maximum freezing-induced tensile stress, the compression zone of concrete is above the axis, and the tension zone is below. We can also assume that damage appears only in the tension zone. The vertical coordinate of any point on the cross-section of the concrete can be expressed by ζ:

$$\zeta = \frac{z}{h\text{-}k} \tag{2}$$

where h is the height of the concrete; k is the distance between the equivalent compression stress line and the bottom of the concrete, and is related to the magnitude of the maximum freezing-induced tensile stress and bending stress; and z is the distance from the bottom of the concrete to the point. The initial value of ζn = 0.5, and then the neutral axis will move up with increasing freeze-thaw cycles, meaning that ζn > 0.5. The equilibrium equations for the normal stress and for the moment are:

$$\int_0^1 \sigma_{\mathrm{T+Fm}}(\zeta) b(h-k)\,\mathrm{d}\zeta = 0 \tag{3}$$

$$\int_0^1 \sigma_{\mathrm{T+Fm}}(\zeta) b(h-k)^2 \zeta\,\mathrm{d}\zeta = M \tag{4}$$

$$M = -\frac{Eb(h-k)^2}{6}\varepsilon'_{\mathrm{Tm0}} \tag{5}$$

where b is the thickness of the concrete; E is its elastic modulus; ε'Tm0 is the initial maximum strain (ζ = 0) of the equivalent compression stress line when the four-point bending stress is first coupled with the maximum freezing-induced tensile stress (N = 0), and can be calculated by the following formula, according to Figure 8:

$$\varepsilon'_{\mathrm{Tm0}} = \left|\varepsilon_{\mathrm{Cm0}}\right| = K_1 \varepsilon_{\mathrm{Tm0}} \tag{6}$$

where K1 is an undetermined constant; εTm0 is the initial maximum strain (ζ = 0) at the tension zone edge when the four-point bending stress is coupled with the maximum freezing-induced tensile stress (N = 0); and εCm0 is the initial maximum strain of the compression zone edge when the four-point bending stress is coupled with the maximum freezing-induced tensile stress (N = 0).

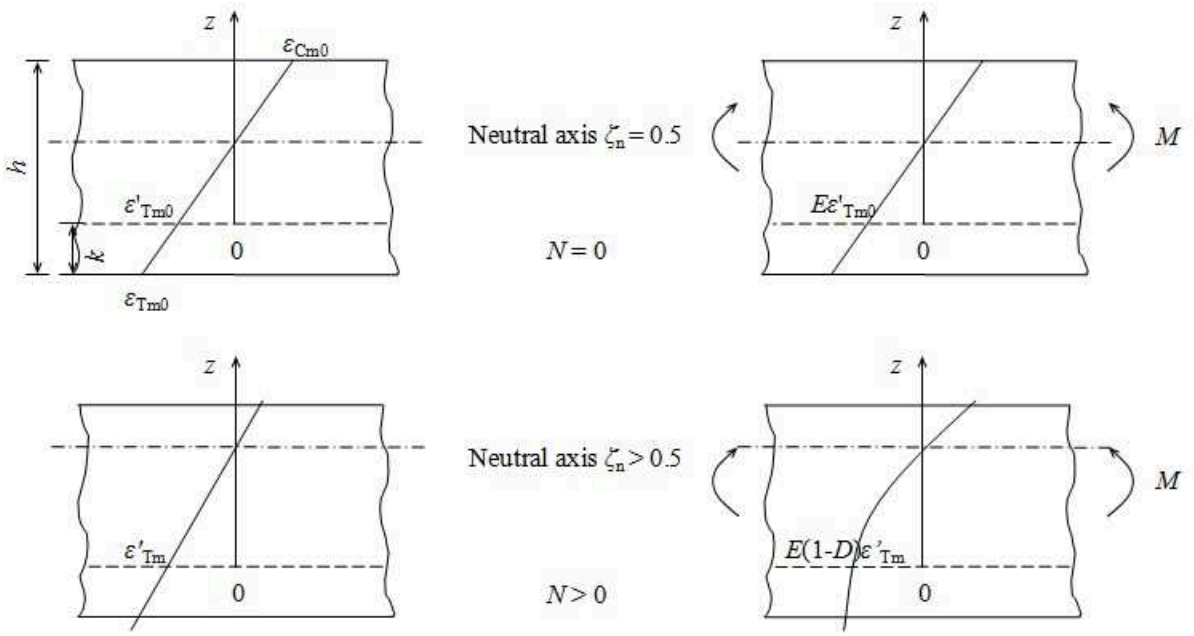


Fig. 8 Schematic of Evolution of Strain and Stress Under Freeze-Thaw Cycles Coupled with Bending Stress

The theoretical derivation shown here is similar to that in reference [12]. Finally, we obtain the relationship between strain and number of cycles N:

$$\frac{24}{13}\left(\frac{\Delta\varepsilon_{\mathrm{Tm}}}{\Delta N}\right)_0 \frac{N}{\varepsilon_{\mathrm{Tm0}}} = -\frac{9}{2}\ln 2\zeta_{\mathrm{n}} - \frac{63}{4\zeta_{\mathrm{n}}} + \frac{69}{8\zeta_{\mathrm{n}}^2} - \frac{2}{\zeta_{\mathrm{n}}^3} + 13 \tag{7}$$

$$\frac{1}{3}D'_{\mathrm{m}} = \frac{1}{\zeta_{\mathrm{n}}} - \frac{1}{2\zeta_{\mathrm{n}}^2} \tag{8}$$

$$D'_{\mathrm{m}} = K_1 D_{\mathrm{m}} \tag{9}$$

$$K_1 = \left|\frac{\varepsilon_{\mathrm{Cm0}}}{\varepsilon_{\mathrm{Tm0}}}\right| \tag{10}$$

where Dm is the maximum damage degree at the tension zone edge; D'm is the maximum damage degree at the equivalent compression stress line. In fact, the magnitude of the maximum freezing-induced tensile stress is not constant. In each cycle, the maximum measured strain occurs near the lowest temperature. The elastic modulus at this point may vary slightly from cycle to cycle, because of differences in temperature and thermal gradients. Thermal gradients are created between the center and the surface of concrete, which influence the freezing-induced tensile stress and the elastic modulus under freeze-thaw cycles. Therefore, we should introduce some correction factors to modify Equation (7):

$$\frac{24}{13}k_\sigma k_{\mathrm{E}} k_{\mathrm{G}} k_{\mathrm{u}}\left(\frac{\Delta\varepsilon_{\mathrm{Tm}}}{\Delta N}\right)_0 \frac{N}{\varepsilon_{\mathrm{Tm0}}} = -\frac{9}{2}\ln 2\zeta_{\mathrm{n}} - \frac{63}{4\zeta_{\mathrm{n}}} + \frac{69}{8\zeta_{\mathrm{n}}^2} - \frac{2}{\zeta_{\mathrm{n}}^3} + 13 \tag{11}$$

where kσ, kE, kG and ku are the correction factors: kσ is used to correct the magnitude of the maximum freezing-induced tensile stress; kE is used to correct the elastic modulus for the effects of slight changes in temperature; kσ is used to correct for thermal gradients; and ku is used to correct for the influence of other unknown factors. $\left(\frac{\Delta\varepsilon_{\mathrm{Tm}}}{\Delta N}\right)_0$ is the initial rate of variation of εTm and this value

must be obtained from the stable period of the experimental results. If Dm is given, D'm can be calculated by Eq. (10) and Eq. (9), and then we can obtain ζn from Eq. (8). The concrete that was loaded in bending experiences brittle fracture starting at the tension zone, so Dm is usually assigned a value of 1. $\left(\frac{\Delta\varepsilon_{\mathrm{Tm}}}{\Delta N}\right)_0$, εTm0 and εCm0 can all be obtained from the experimental measurements. Finally, we can predict the final number of freeze-thaw cycles required for failure, NF.

Verification of Model

Table 4 shows the experimental results from the concrete specimens, the computed results and the values of kσkEkGku. We can conclude that the deformation of the concrete specimens with higher strength grades is smaller than that of those with lower strength grades, when the concretes are made from the same raw materials. For concrete specimens with the same mix proportions but different loading stress levels, the specimens with the larger loading stress level experience larger deformations in the tension zone and smaller deformations in the compression zone.

Table 4 Measured results and comparison with computed life

NO.	$\varepsilon_{\mathrm{Tm0}}$ (με)	$\varepsilon_{\mathrm{Cm0}}$ (με)	$\left(\frac{\Delta\varepsilon_{\mathrm{Tm}}}{\Delta N}\right)_0$ (10^{-6})	N_{F} Measured	N_{F} in Eq. (7) Computed	$k_\sigma k_{\mathrm{E}} k_{\mathrm{G}} k_{\mathrm{u}}$	N_{F} in Eq. (12) Computed
Cao's C30	113.2	-75.2	0.73	175	40	0.229	160
Cao's C50	84.7	-61.0	0.44	225	59	0.262	236
BI	68.1	-54.5	0.40	225	57	0.253	228
BII	73.9	-50.4	0.52	175	43	0.246	172

The computed values of kσkEkGku are almost the same for all samples, so we can determine an overall value of 0.25, and then obtain Eq. (12) from Eq. (11):

$$\frac{6}{13}\left(\frac{\Delta\varepsilon_{\mathrm{Tm}}}{\Delta N}\right)_0 \frac{N}{\varepsilon_{\mathrm{Tm0}}} = -\frac{9}{2}\ln 2\zeta_{\mathrm{n}} - \frac{63}{4\zeta_{\mathrm{n}}} + \frac{69}{8\zeta_{\mathrm{n}}^2} - \frac{2}{\zeta_{\mathrm{n}}^3} + 13 \tag{12}$$

This verification of the damage model shows that there is good agreement between the values of NF computed using Eq. (12) and the measured results. Therefore, the damage model can accurately characterize the degree of damage resulting from freeze-thaw cycling coupled with a constant four-point bending stress and chloride attack.

Conclusions

The combined effects of freeze-thaw cycling, bending stress and salt exposure on concrete beams were evaluated in this study. By converting the freeze-thaw mechanism into mechanical effects on the concrete and then evaluating the synergistic effects of multiple factors, a multiple-factor damage model was proposed to characterize the relationship between strain and freeze-thaw cycles. The damage to concrete under freeze-thaw cycles and salt exposure was converted into a freezing-induced tensile stress action, which is a macroscopic overall stress. The freezing process is equivalent to loading and thawing equivalent to unloading, so freezing-induced tensile stress is similar to a low-cycle fatigue tensile stress and could be simply represented by a saw-tooth model.

Our mechanical analysis targeted the times where the maximum freezing-induced tensile stress was coupled with four-point bending stress in every freeze-thaw cycle. These times are where the peaks of the measured strains in every freeze-thaw cycle occur, and appear near the lowest temperature (-18 °C) in every cycle. The measured maximum strains on the compression zone edge and the tension zone edge of concrete both increase with the progress of freeze-thaw cycles. A

multiple-factor mechanical damage model based on strain, which more closely resembles the complicated situations found in engineering practice, was established. We showed that the model is suitable for predicting the life of concrete exposed to a combination of freeze-thaw damage, bending stress and chloride attack.

Acknowledgements

The authors would like to acknowledge the financial support from China National Program on Key Basic Research Project (973 Program, Nos. 2009CB623106 and 2012CB724602).

References

[1] J. Wei, X.H. Wu, X.L. Zhao, A model for concrete durability degradation in freeze-thawing cycles, Acta Mech. Solida Sin. 2003 16(4) 353-358.

[2] J. Wei, X.H. Wu, Concrete structure durability in geo-technical engineering, Chin. J. Rock Mech. Eng. 2002 21(1) 140-142. (in Chinese)

[3] T.C. Powers, A working hypothesis for further studies of frost resistance of concrete, J. Am. Concr. Inst. 1945 16(1945) 245-272.

[4] G.W. Scherer, Crystallization in pores, Cem. Conc. Res. 1999 29(8) 1347-1358.

[5] T.C. Powers, R.A. Helmuth, Theory of volume changes in hardened portland-cement paste during freezing, Proc. Highway Res. Board 32(1953) 285-297.

[6] C. MacInnis, J.D. Whiting, The frost resistance of concrete subjected to a deicing agent, Cem. Conc. Res. 1979 9(3) 325-336.

[7] J. Kaufmann, Experimental identification of ice formation in small concrete pores, Cem. Conc. Res. 2004, 34(8): 1421-1427.

[8] L. Wang, Y. Cao, Z.D. Wang, et al, Evolution and characterization of damage of concrete under freeze-thaw cycles, J. Wuhan Univ. Tech. – Mater. Sci. 2013 710-714.

[9] Z.D. Wang, Y. Yao, L. Wang, Deformation and deterioration analysis of concrete exposed to freeze-thaw cycles and chloride salt attack, J. Chin. Ceram. Soc. 2012 40(8) 1133-1138. (in Chinese)

[10] G.J. Verbeck, P. Klieger, Study of "salt" scaling of concrete, Highway Res. Board Bull. 150(1957) 1-13.

[11] C. Amazallag, J.P. Gerey, J.L. Robert, et al, Standardization of the rainflow counting method for fatigue analysis, Int. J. Fatigue 1994 16(4) 287-293.

[12] A. Alliche, D. Francois, Damage of concrete in fatigue, J. Eng. Mech. 1992 118(11) 2176-2190.

Advanced Materials Research Vol. 936 (2014) pp 1351-1355
© (2014) Trans Tech Publications, Switzerland
doi:10.4028/www.scientific.net/AMR.936.1351

Numerical Investigation on Fatigue Problem of Cable Net Structure of Five-hundred-meter Aperture Spherical Radio Telescope

Peng Jiang*

National Astronomical Observatories, Chinese Academy of Sciences, Beijing 100012, China

pjiang@bao.ac.cn

Keywords: FAST engineering, cable net structure, active reflector, mechanical analysis

Abstract: The reflector of Five-hundred-meter Aperture Spherical radio Telescope (FAST) is supported by cable-net structure, so that to enable its reflector surface to form a paraboloid from a sphere in real time through active control. However, such form-changing operation would lead to about 500MPa stress range for the cable-net structure. Such stress range is nearly twice as much of that defined by the relative standard. So the cable-net structure is the most critical and expendable part of FAST reflector system. So, the service life of FAST would directly depend on the residual fatigue life of its cable-net structure. The present paper would make an effort to find a more appropriate deformation strategy to decrease the stress amplitude of the cable during form-changing operation.

Introduction

The project of Five-hundred-meter Aperture Spherical radio Telescope (abbreviated as FAST), belongs to the national "11th Five-Year Plan" Key scientific projects, has been approved for construction by the National Development and Reform Commission in July 10, 2007.[1] FAST working frequency can cover the range of 70MHz to 3GHz. The design resolution and point accuracy are respectively 2.9′ and 8″.[1,2] In order to achieve such technical specifications, the root mean square value of the out plane error of its reflector shape should be no more than 5mm.

According to the geometric optical principle of FAST (illustrated as Figure. 1), the supporting structure of its reflector system should be capable of formation of a paraboloid surface from a sphere in real time through active control, that is the most prominent special requirement beyond those of conventional structures. The crossed nodes of the cable-net are used as control points(see Fig.2). Each of them is tied to a control actuator by down tied cable. By controlling the actuator using the feedback from the measurement and control system, the position of these cross nodes can be adjusted to form an illuminated aperture with 300m diameters. And this illuminated aperture can move along spherical surface according to the zenith angle of the target objects (see S1 and S2 in Figure 1). Later, an extensive numerical comparative analysis has been performed among several different grid types, such as three-dimensional grids, kiewitt grids and geodesic triangle grids. Finally, the last one is determined because of its more uniform of cable stress and cable length.[3,4]

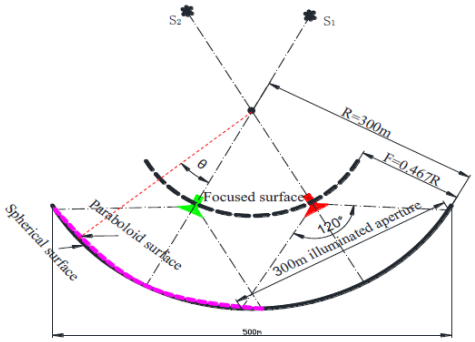


Fig. 1. The geometric optical principle of FAST

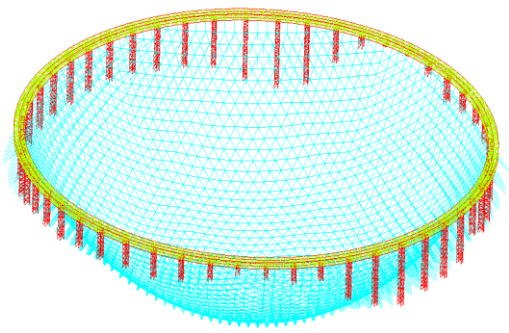


Fig. 2. Concept of the adaptive cable-net structure

From above-mentioned description, it can be easily seen that the long-term observation process of FAST would lead to long-term frequent shape-changing operation of cable-net structure. Previous research results have shown that such shape-changing operation would lead to about 500MPa stress

range[4]. Such stress range is nearly twice as that required by the relative standard.[5] So, the cable-net structure would be the most critical and expendable part of the FAST reflector system. Thus, the service life of FAST would be directly related to fatigue life of its cable-net structure.

In order to improve the reliability of FAST and to extend its service life, the present work, based on the preliminary design, would make an effort to decrease the stress range of the cable caused by shape-changing operation.

The stress range optimization

The main influence factor analysis

There are about 4600 triangular elements supported by the cable-net. The cable-net is consisting of about 7000 steel cables and about 2300 cross nodes. Each cross node is tied to one actuator on the ground. The length of cables is from 10.3m to 12.3m. All cables are disconnected with each other, which enable us to adjust their cross sections according to their loads.

In general, the illuminated aperture is a paraboloid surface, whose profile can be expressed by

$$x^2 = 2py + c \tag{1}$$

The variables and parameters of this problem can be summarized as follow: the weight of reflector element w, the density of the cable ρ, the elastic modulus of cable E, the area of cable cross section A_i, the geometric parameters of illuminated aperture p and c, the diameter of the illuminated aperture d, the radius of the cable-net structure R, the diameter of the ring beam D. So, the stress amplitude can be expressed by

$$\Delta\sigma = f\left(w, E, \rho, A_i, p, c, D, d, R\right) \tag{2}$$

In our preliminary design, w, d, R, D, A_i have already been determined as a certain value. The weight of reflector element w is about $17Kg/m^2$, the diameter of the illuminated aperture d is 300m, the radius of the cable-net R is 300m, and the diameter of the ring beam D is 500m, and all cable's cross section A_i have also been determined according its load. For steel cable, ρ is about 7850Kg/m3. Thus, Eq(2) can be simplified as

$$\Delta\sigma = f\left(E, p, c, d\right) \tag{3}$$

Among these four governing parameters, two of them, namely E and d have independent dimensions. By applying the π theorem in dimensional analysis (Barenblatt 1996), we obtain

$$\frac{\Delta\sigma}{E} = f\left(\frac{p}{d}, \frac{c}{d^2}\right) \tag{4}$$

Furthermore, the nodes of the outer edge of the cable-net are fixed to the ring beam, and their position cannot be adjusted by the actuator like other cross nodes can do (See Fig. 2). In order to expand the observation zenith angle of FAST as large as possible, outer edge of illuminated aperture should coincide with basic spherical surface. Only then can outer edge of illuminated aperture arrive at the outer edge of the cable-net. With such constraint, we can derive that

$$c = 22500 + 2p\sqrt{67500} \tag{5}$$

Then, the Eq(3) can be further simplified as

$$\frac{\Delta\sigma}{E} = f\left(\frac{p}{d}\right) \tag{6}$$

For the steel cable, the elastic modulus is about 200GPa, thus the only variable remained in this implicit function is *p/d*, which is the focal ratio of this telescope.

From Eq(6) we can know that the fatigue stress range of FAST cable is most dependent on the focal ratio of this telescope. The different focal ratio would lead to the different relative position between the illuminated aperture and the base plane, which is directly related to internal forces of cable-net and stroke of actuator.

In our early work, three kinds of deformation strategies, namely the strategy Ⅰ, the strategy Ⅱ, and strategy Ⅲ, have been proposed. The relative positions of these three strategies to the spherical base plane are shown in Figure. 3. Among of these strategies, the strategy Ⅰ and Ⅱ are respectively corresponding to the shortest actuator stroke and the minimum deviation from the illuminate aperture to the base spherical surface. The actuator stroke of the strategy Ⅰ is about 0.67m, and the maximum deviation distance of the strategy Ⅱ is about 0.47m. As for the strategy Ⅲ, it is derived based on equal arclength principle, in which the profile arclength of the illuminated aperture is equal to that of the spherical base plane within the 300m diameters of the illuminated aperture. The focal ratios corresponded to these three strategies are respectively 0.4665, 0.4611, and 0.4613.

In the preliminary design of FAST cable-net structure, the deformation strategy Ⅰ was recommended as the prefer control scheme just because of its shortest actuator stroke. Obviously, it is unreasonable to omit the fatigue problem in the deformation strategy optimization, especially for the present case of about 500MPa stress range.

So the present work would make an effort in establishing the relation between the focal ratio and the deformation stress range. And then, by considering both factors of the actuator stroke and the stress range of the cable, we would re-recommend deformation strategy for FAST future observation.

Numerical analysis

In the present paper, ANSYS software is applied for simulation, and link10 is used to simulate the response of the cable. When it does not work, the FAST cable-net should hold spherical shape under combined loads of gravity, initial stress, and down tied cable. In order to derive such state, the inverse iteration method is applied. As for the observation state, the deformation procedure of forming the illuminated aperture from spherical shape can be simulated by the conventional iteration method.

For the FAST condition, the maxmium distance between the spherical and the paraboloid surface is no more than 1m. As we known, the angular velocity of celestial body is about 15 degrees per hour. Accodingly, the radial velocity of the cross node during FAST tracking observation is less than 1mm/s. So, the deformation procedure of the reflecter system in the tracking observation can be taken as quasi-static state procedure. Base on this conclusion, we can replace a continuous observation procedure with a set of sequential discrete observation states. By comparing with the time history analysis method, this method would be capable of saving a lot of calculation time.

For FAST observation, the illuminated aperture is restricted within the scope of the cable-net. Consequently, we can easily deduce the movement range of the illuminated aperture center, which has been illustrated by Fig. 4. This region contains 550 cross nodes, the interval of any two adjacent ones is no more than 13m which corresponds about only one degree-center angle of 300m radius of reflector.

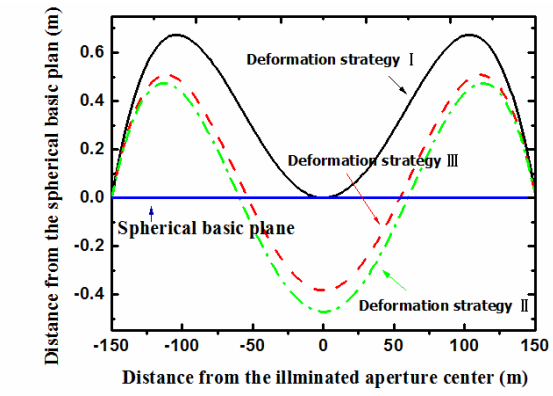


Fig. 3. The relative positions between the paraboloid and base spherical surface for three previous proposed deformation strategies.

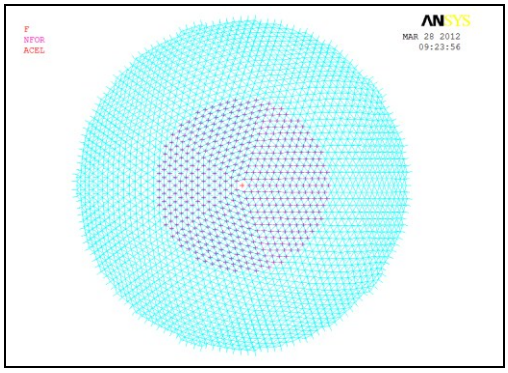


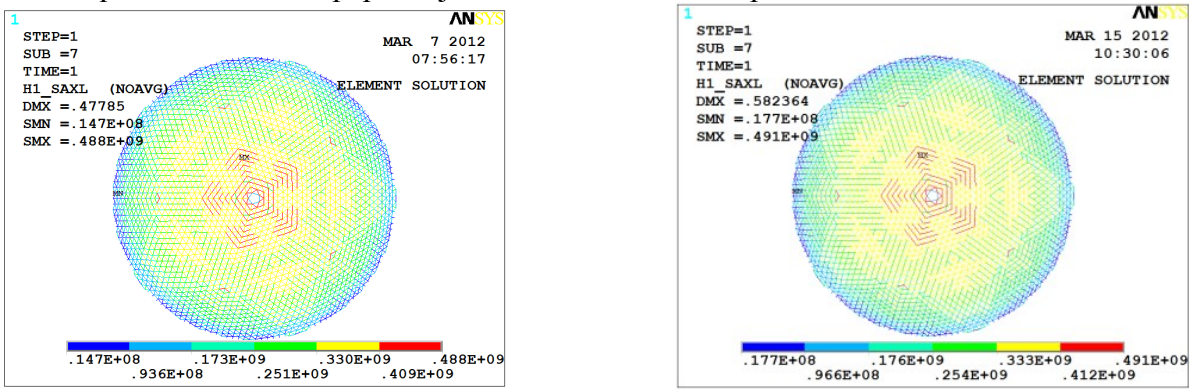
Fig. 4. Illustration of range of cross nodes used as discrete points to describe continuous trajectory path of the center of the illuminated aperture

In the present work, these 550 cross nodes are taken as the discrete points, which is used to describe the continuous trajectory path of the center of the illuminated aperture. Thus, any possible observation state during FAST observation can be approximately recognized as one of 550

observation states, whose centers are corresponding to these 550 cross nodes. By using the finite element analysis method, we can simulate these 550 observation states. With the simulation results, stress data of all cables under those 550 cases can be saved as two-dimensional array data. By processing this two-dimensional array data, the maximum stress range of each cable during FAST observation can be easily derived.

However, using the discrete observation states to describe the continuous observation procedure would bring errors in our evaluation. Magnitude of these errors would be directly depended on how dense discrete points used. Obviously, more dense discrete points would lead to more accurate estimated result. So, comparative analysis has been performed on the deformation strategy Ⅱ respectively by using above 550 discrete points and more dense discrete points. For the later, the discrete points contains not only the cross-nodes but also the mid-points of the cables and median-points of the triangle elements, thus there are more than 2200 deformation states need to be simulated for one deformation strategy.

The calculation results derived by above two sets of the discrete points are respectively shown in Fig. 5 a and b. It is can be readily seen that the peak stress ranges derived by using 550 discrete points and 2200 discrete points are respectively 488MPa and 491MPa, difference between them is no more than 1%. So, we can assume that using 550 cross nodes has enough accuracy for engineering design. The subsequent work of this paper is just based on this assumption.



a) Simulation result achieved by 550 discrete points b) Simulation result achieved by 2200 discrete points

Fig. 5. Comparison of the simulation results of the deformation strategy Ⅱ respectively derived by using 550 discrete points and 2200 discrete points

Utilizing the same procedure, the distribution of the stress range for other two types of deformation strategies can be derived. The peak stress range of the strategy Ⅰ and strategy Ⅲ are respectively 547MPa and 482MPa. By using the least square method, the relation of the focal ratio and the peak stress range can be fitted by quadratic polynomial, from which we can predict that the focal ratio value corresponding to the minimum stress range is about 0.4633. The corresponding profile shape of the illuminated aperture can be determined by Eq(1) and Eq(5).

We input this new deformation strategy into the above analysis procedure, we can derive that the maximum stress range of this deformation strategy is 488MPa, which is same to that of the focal ratio of 0.4613. Then, by repeating the above steps with interpolation of this new data point, the focal ratio of 0.4621 can be further determined. The further simulation result has shown that the maximum stress range corresponding to the focal ratio of 0.4621 is 459MPa, which is about 90MPa beneath that of deformation strategy Ⅰ and 30MPa beneath that of the strategy Ⅱ.

However, it is difficult to say whether 0.4621 is the optimum focal ratio for the fatigue problem of the cable-net. For this reason, other two strategies with 0.4620 and 0.4622 of focal ratios have also been investigated in the present work. And the simulation results have shown that the peak stress ranges leaded by these two deformation strategies are respectively 462MPa and 460MPa, both of them are slightly higher than that caused by the deformation strategy with focal ratio of 0.4621. So, we have reasons to believe that the deformation strategy with focal ratio of 0.4621 is very close to the deformation strategy corresponding to the minimum stress range.

It also should be noted that the actuator stroke of this strategy is 0.89m, which is also 50mm beneath the strategy Ⅱ. By comparing the stress range and actuator stroke of these deformation strategies (see Table. 1), we would recommend the strategy with focal ratio of 0.4621 for FAST application.

TABLE. 1. COMPARISON OF THE FATIGUE STRESS RANGE OF THE CABLE AND THE STROKE OF THE ACTUATOR CAUSED BY DIFFERENT DEFORMATION STRATEGIES.

Focal ratio	0.4603	0.4611	0.4613	0.4620	0.4621	0.4622	0.4633	0.4665
Stress range (MPa)	12	488	482	462	459	460	488	547
Actuator stroke (m)	0.9890	0.9450	0.9341	0.8966	0.8914	0.8861	0.8291	0. 6741

Conclusion

During FAST observation procedure, the stress range borne by its cable is more than twice as that provided by the relative standard. In order to improve the reliability of FAST, the present work has performed an extensive numerical and experimental investigation to decrease the stress range of the cable caused by shape-changing operation. Then, the focal ratio is the key influence factor of the stress range of FAST cable-net structure caused by shape changing operation. And 0.4621 is suggested as the most appropriate focal ratio, which would lead to about 30MPa reduction of the stress range and 50mm reduction of actuator stroke.

Acknowledgment

We acknowledge the support of the National Natural Science Foundation of China (Grant Nos. 11303059) and theYouth Innovation Promotion Association, Chinese Academy of Sciences.

Reference

[1] Nan, R.D., Ren, G.X., Zhu, W.B. et al., 2003. Adaptive cable mesh reflector for the FAST. Acta Astron Sin 44, 13-18

[2] Qiu, Y.H., 1998. A novel design for giant radio telescopes with an active spherical main reflector. Chinese J Astron Ast 22(3), 361-368

[3] Qian, H.L., 2007. Theoretical and experimental research on supporting stucture of FAST reflector. Harbin: School of Civil Engneering, Harbin Institute of Technology

[4] Jiang, P., Wang, Q.M., Zhao, Q., 2011. Optimization and analysis on cable net structure supporting the reflector of the large radio telescope FAST. Appl Mech Mater 94-96, 979-982

[5] ISO15630-3, 2002, Steel for Reinforcement and Pre-stressing of Concrete—Test Methods—Part 3: Pre-stressing Steel, Int. Org. for Standardization, Geneva, Switzerland

Advanced Materials Research Vol. 936 (2014) pp 1356-1360
© (2014) Trans Tech Publications, Switzerland
doi:10.4028/www.scientific.net/AMR.936.1356

Study on compressive performances of fiber reinforced mortar with the application of jute and PP

Junfei Yin[1, a *], Yu Zhang[1,b], Tingting Yan[1,c] and He Qiu[1,d]

[1]School of Textile and clothing, Nantong University, Nantong, Jiangsu, 226019, China

[a]yinjunfei2007@126.com, [b]z.yu@ntu.edu.cn, [c]ytt@ntu.edu.cn, [d]1025582673@qq.com

Key words: jute fiber; compressive strength; pull-out force; saturated alkali treatment

Abstract: In this study, jute fibers and polypropylene fiber (PP) were added into cement-based mortar to improve their compressive strength. Results obtained have shown that the compressive strength of the motar was perfect with jute fiber of 19mm length at the fiber contents of 0.8 $kg \cdot m^{-3}$. The reinforcing mechanism of fiber in the motar was analyzed by means of comparing of the mortar compressive properties under different circumstances, and the testing results of scanning electron microscope (SEM) and the addition of filament in experiments.

Introduction

Fibers have the potential to be used as reinforcement to overcome the inherent deficiencies in cementitious materials. In recent years, there has been sustained interest in utilizing natural fibers in cement composites and in manufacturing products based on them with a view to have alternate building materials, which are energy-efficient, economical and eco-friendly.

It has been recognized that fiber reinforcement is an effective way to enhance the performance of cement-based materials in many ways [1]. Mortar is a kind of quasi brittle material which is easy to be crack and has very low crack resistance [2]. However, jute fibers could be added to improve its compressive strength, flexural strength and early-age crack resistance [3]. The degree of the improvement depends upon both the volume and the type of fibers used [4]. In this study, the mechanical properties such as crack resistance of fiber- reinforced mortar based on the change of length and volumes of jute and PP fibers were studied and discussed.

Experimental materials and equipment

Materials

"Conch" brand PO32.5 cement, sand fineness modulus of 2.5, Running water, Gypsum powder, Dispersibility powder. The needed fiber in the experiment was tested by electronic single fiber strength machines. Each sample was tested 20 times, and the average data was finally obtained. The mechanism of the fiber specimen was carried out on a LLY - 06 B/PC electronic single fiber strength machines, the results in Table 1.

TABLE 1 THE MECHANICAL PROPERTIES OF FIBER

Sample	designation	lineal weight [dtex]	breaking strength [cN/dtex]	breaking elongation [%]	initial modulus [cN/dtex]
Untreated jute	Jute A	29.73	3.95	6.35	15.71
Saturated alkali treatment 12h	Jute B	26.72	2.83	14.42	10.54
PP fiber	PP	3.45	1.91	84.48	1.95

The experimental parameters and experimental steps

Fiber length in the test is chosen according to the market application.The selected length of jute fiber was 10 mm, 19 mm and 30 mm. And the selected length of the pp was 10 mm and 12 mm. The fiber content in the mortar was 0.4 $kg \cdot m^{-3}$, 0.8 $kg \cdot m^{-3}$ and 1.2 $kg \cdot m^{-3}$. In this experiment, mortar strength grade was designed with reference to JGJT plastering mortar, 220-2010 technical regulations. The cube moulds with dimensions of 70.7 mm ×70.7 mm ×70.7 mm were used. Pull-out force tesing of single fiber was carried out in accordance with the self-designed experimental platform. During the mortar manufactured process, the demoulding time of specimen should be completely same, and the mortar specimen should be conserved to avoid being effected by other objective factors.

First of all, the specified size of the compression casting mold should be prepared during the trial production of mortar specimen, and daub on the inner wall of the mold with a layer of lubricating oil, in order to prevent the specimen from accounting for the wall. Then, pour plenty of water into the mixer, and weighed fibers, stired them well. Add cement, yellow sand and dispersibility powder in the mortar mixer, according to the designed proportion . Start the machine to dry mixing for 1-2 minutes, then add stirred water and fiber and stir for another 2-3 minutes. Pour mixed mortar into the prepared triple mold and vibrate it on shaking table, in order to reduce bubbles of mortar. The specimens were stored in the laboratory for 24 hours with the storage temperature 20 ± 1 ℃. After stripping mortar specimens, maintenance them in the 101 B constant temperature and humidity curing box for 7 days, curing temperature 20 ± 1 ℃.

Test results and performance analysis

Fiber reinforced cement compressive strength performance test

The mortar specimens were tested which has reached standard curing time with the JYE-200 type compression testing machine manufactured in the city of WuXi. Each set of the sample was tested for three times[5]. And take the average of the final result. Convert the measured results for strength. The intensity of conversion calculation formula is shown below:

$$f_{cc} = F / A$$

where, fcc was the compressive strength(MPa), F was the maximum crushing load (N), A was the area

of the compression face(mm^2). The change trend of the compressive strength was shown in the Figure.1, Figure.2, and Figure.3 .

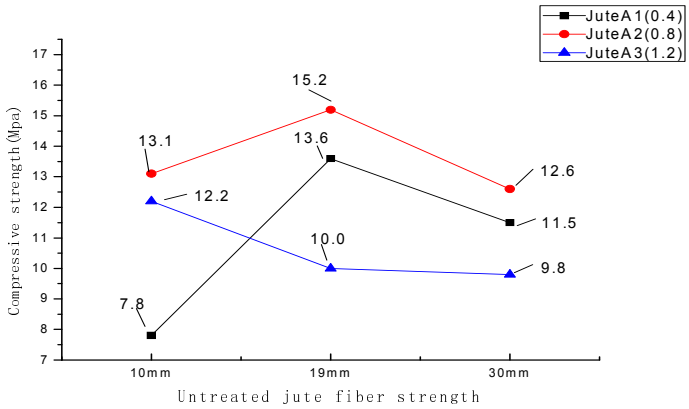


Figure.1 The Compressive Strength of Untreated Jute with Different Lengths, Different Content

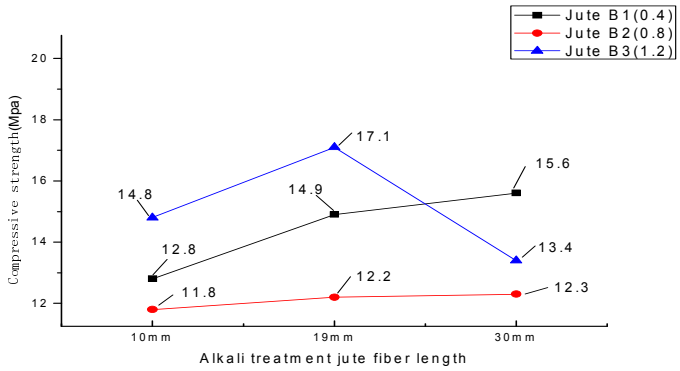


Figure.2 The Compressive Strength of Jute Saturated Alkali Treatment of 12h with Different Lengths, Different Content

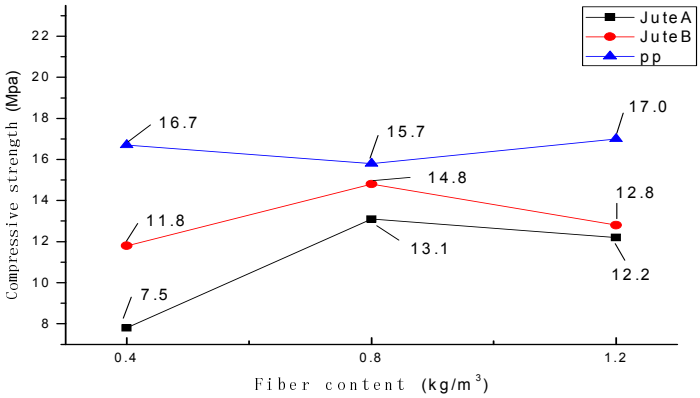


Figure.3 The Compressive Strength of Different Fiber with 10mm

According to the graph, it was recognized that the compressive strength of the specimen as the fiber length changed when the untreated jute (Figure.1) content is 0.4 kg·m^{-3}or 0.8 kg·m^{-3}. And the specimen reached the highest compressive strength when the fiber length was 19mm. When the fiber content was 1.2 kg·m^{-3} and the fiber length was 30mm, the specimen reached the highest compressive strength. When Jute was treated with saturated alkali for 12 hours (Figure.2), as the fiber length increases, the compressive strength increased and then decreased in the case of high content. On the other hand, the compressive strength showed a gradual upward trend in the case of low content. The reasons why mortar intensity changes was that the length of untreated jute fiber was appropriate. Appropriate length may be contribute to increasing in the strength when the content was a certain value. However, the fibers would hold together because of uneven dispersion as the fiber length increased. And some areas under the action of the force would be very brittle due to mortar internal porosity increases when the fiber content was 1.2 kg·m^{-3}. The fibers ,which were treated with saturated alkaline solute ,added to the mortar. It made the strength to get some improvement relative to the untreated jute fibers. However, when the fiber length was 30mm, the strength would be greatly decreased. The reason was that the fiber and the cementitious material in the mortar bonded better. It was caused by a certain degree of degumming of fiber's surface after alkaline treatment. The compressive strength of mortar was improved by jute fiber which owned the role of bridging. However, the phenomenon of fibers hold together was further deteriorated because fiber length was constantly on the rise and friction of fibers was increased . The compressive strength was decreased sharply. When the length of fiber was 10mm (Figure.3), the compressive

strength of the mortar which mixed PP fiber showed a greater advantage .Compared with different fibers, the critical point of compressive strength had been found when the fiber content was 0.8 $kg \cdot m^{-3}$ .This found provided a good reference to the practical application of several fibers .

TABLE 2 THE COMPRESSIVE STRENGTH OF MORTAR REINFORCED BY FIBER WITH 19MM LENGTH UNDER DIFFERENT DOSING CONTENT

Sample	Dosing content [$kg \cdot m^{-3}$]	Fiber Length [mm]	Crushing load [KN]	compressive strength [Mpa]	strength growth rate [%]
Sample 1	-	-	57.5	11.5	-
Sample 2	0.8	19	75.98	15.2	32.17
Sample 3	0.8	19	60.98	12.2	6.09
Sample 4	0.8	12	111.97	22.4	94.78

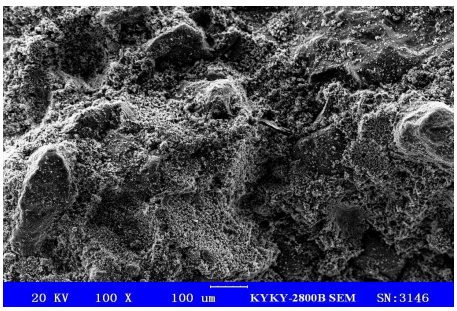
The strength of the specimen growth rate compared with the plain cement mortar strength

Sample 1-plain mortar, sample 2-mortar reinforced by untreated jute, sample 3-mortar reinforced by jute saturated alkali treatment,sample 4-mortar reinforced by PP fiber.

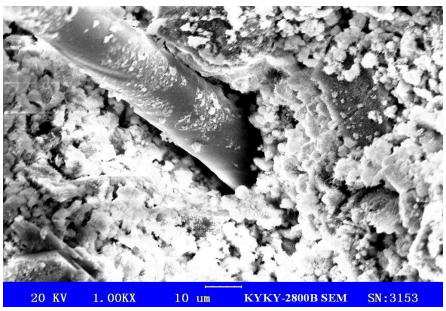
According to pre-experimental research, it was found that when the dosing content of fiber is 0.8 $kg \cdot m^{-3}$, the compressive strength of mortar changes obviously. Considering the PP fiber dosing content in mortar on the current market, the compressive strength of mortar before and after adding fiber is compared. The results are shown in Table 2. Comparing with the plain mortar, the compressive strength of mortar reinforced by fibers has increased. But after adding the fibers treated by saturated alkali solution, it would result in the lower growth rate since there is some loss of fiber strength.

Mortar specimens fracture surface

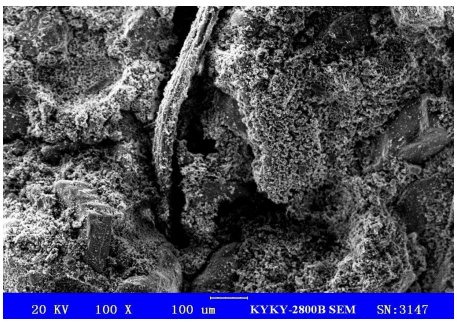
For further description of the fiber's form existence in mortar, we pick up a number of pieces of the fractured specimens are soaked in absolute ethanol for 1h, then placing them in 101 AB thermostatic drum wind drying oven. Finally, the small pieces of specimens were observed under the KYKY2800 type B scanning electron microscope (SEM). The results were show in Figure.4.



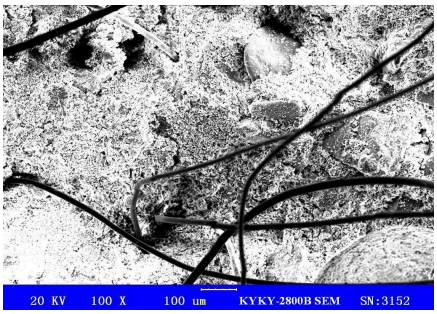
（a）plain mortar



（b）mortar with untreated jute



（c） mortar with jute saturated alkali treatment



（d）mortar with pp fiber

Figure 4 The SEM images of Mortar specimen fracture

Pull experiment of single fiber

Combined with results of compressive strength test, one experiment platform is simulated which can be used to show the role of fiber during the process of fracture in the experiment. ALD spiral frame and SH-500 digital force gauge were chose to compose the platform. In order to explore the effect of the fiber in the mortar, the fiber pull-out force under the same mortar mix ratio, different fiber length and fiber volume of 0.8 $kg \cdot m^{-3}$ is tested to explore the effect of the fiber in the mortar. Several fibers mixed with cement mortar is selected, the pull-out force of single fiber after 5h solidification under normal temperature and pressure is tested. The experimental results are shown in table 3. It was found that the fiber length has a strong influence on the fiber pull-out force required in the experiment. The suitable length of jute fiber is 19mm, while suitable length of PP fiber is 12mm.

TABLE 3 THE TEST OF DIFFERENT FIBER PULL-OUT FORCE

Sample	Fiber pull-out force（N）		
	10mm	19mm	30mm
Untreated jute	0.417	0.511	0.307
Saturated alkali treatment jute	0.215	0.330	0.288
PP fiber	0.205	0.299	-

Conclusions

(1)The compressive strength of mortar were discreteness, but a certain tendency could be obtained. The compressive strength of mortar specimens was largely influenced by the content and length of fiber. In terms of jute fiber, when the volume for 0.8 $kg/m^3$and the fiber length for 19 mm, the compressive strength of reached highest.

(2)For untreated jute with different fiber length, the specimen compressive strength declined after rising, when the fiber volumes were 0.4 $kg \cdot m^{-3}$ and 0.8 $kg \cdot m^{-3}$.But it showed larger variation when the fiber volume is 1.2 $kg \cdot m^{-3}$,while the saturated alkaline treatment of 12h jute showed a slowly increasing trend.

(3) The bonding effect of jute fiber and mortar base material was better than the bonding effect of untreated jute and mortar.

(4)The pull force of single fiber was consistent with compressive strength. The pull force was relatively high when fiber length was 19 mm. But the test standard should be further perfect.

Acknowledgements

This work was financially supported by the projects of Nantong applied research (BK2013040).

References

[1] Bei Liu,Lizhe Zhang,Qixia Liu,Tao Ji,Study on behaviors of jute fiber reinforced cement based materials，Applied Mechanics and Materials Vols. 253-255 (2013) pp 508-511

[2] Tan Hai-tao,Dong Shuai,Chen Yi Song Xiao-ming,The Mechanic Research of Steel-fiber Reinforced Mortar，FLY ASH COMPREHENSIVE UTILIZATION,（2012）p：18-21.

[3] An HQ,Li JX． Iron-coated TiO2 nanotubes and their photocatalytic performance.Journal of Materials Chemistry，2010，20: 603-610．

[4] Suji D, Natesan S. C, Murugesan R: Experimental study on behaviors of polypropylene fibrous concrete beams. Journal of Zhejiang University Science A, Vol. 8 (2007), p. 1101-1109

[5] Mohamed Rabehi , Bouzidi Mezghiche , Salim Guettala, Correlation between initial absorption of the cover concrete, Construction and Building Materials, 45 (2013) 123–129

Advanced Materials Research Vol. 936 (2014) pp 1361-1365
© (2014) Trans Tech Publications, Switzerland
doi:10.4028/www.scientific.net/AMR.936.1361

Study on low-cycle fatigue life of base metal of the shock absorber

Li Aili[1, a], Gao Ri[1,b], Sun Mingde[1,c] and Meng Xi[1]

[1] School of Civil Engineering, Beijing Jiaotong University, Beijing 100044, China

[a]ailili2007@163.com, [b]rigao@center.njtu.edu.cn, [c]mingdesun@163.com

Keywords: shock absorber; low-cycle fatigue; fatigue test; life prediction

Abstract: In this paper, by experiments on the low-cycle fatigue life of groups of base metal test specimens under constant total strain control, the number of cycles to fracture failure are obtained. The measured S-N curve of base metal is established and the fitted formulas based on three low cycle fatigue life prediction models are caculated according to the test data. The relationship between the low-cycle fatigue life and strain amplitude are concluded. The results of observation show that the elastic strain effect can be negligible in the range of strain amplitudes used for the study of low-cycle fatigue (0.01-0.08). In addition, the calculation suggests that the three-parameter power function is suitable for the low-cycle fatigue life prediction of the base metal because its prediction accuracy is higher than other methods. The research provides technology supports for life prediction and engineering application of the shock absorber.

Introduction

Seismic design and technique can be divided into two aspects: isolation techniques and ductility design. The two methods have been used in seismic design code of bridge in Japan, United States and New Zealand.[1-2] The study and application of isolation technology in our country start later especially in bridge engineering.[3] In the counstruction of the high speed railway, the stiffness of the bridge pier improves greatly and the design horizontal seismic force increases further. So it is imperative to find new way to solve the problem of aseismatic design in railway bridge.

Based on the idea of bearing function separation and according to the demand of the seismic design of high speed railway bridge, a new type of shock absorber which possesses the stable hysteretic capacity and sufficient plastic deformation capacity has been proposed by Professor Li Chenggen and Gao Ri in China recently. The design idea is to change the fixed bearing into the movable so that the vertical and horizontal function can be separated.In the serviceability state, the vertical support reaction and rotation at beam ends are still realized by the bearing, but the horizontal force and horizontal displacement, which transferred from the beam, are supported and controlled by the shock absorber. When earthquake occurs,the horizontal force of the beam will be transferred via the absorber to the piers. From the Fig.1 it can be seen that the absorber is a typical of cantilever beam structure, which belongs to bending-shear member statically.

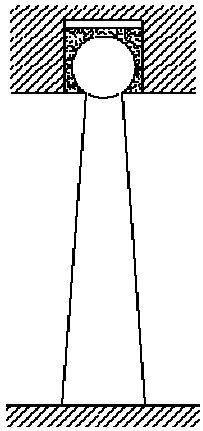


Fig.1 Structure of the shock absorber

Under the earthquake and strong wind effect, due to the low ultimate strength and small maximum ductility, parts of structure destroy quickly at the early stage while the majority fail for the low cycle fatigue. The current study on the fatigue failure of civil engineering are concentrated in high cycle fatigue such as the cumulative damage and fatigue life evaluation. However, little work has been carried out for the low cycle fatigue failure under the earthquake effect. The shock absorber that fabricates entirely from a new type of metal has not yet been thoroughly investigated and the relative literatures are few in China and foreign countries, let alone the study on low cycle fatigue. The subject is concerned chiefly with the study of the low cycle fatigue life of the shock absorber base metal.

Through the experiments on some specimens, the number of cycles to fracture failure are obtained and the measured S -N curve of the base metal is established. Combined with experimental data, we creat fitted curves based on three low cycle fatigue life prediction models and compare the prediction accuracy of three prediction models by caculating the fitting parameter determination coefficient square R^2 and the sum of squares due to error (SSE).

Unidirectional Tensile Test

The cylindrical specimens with gauge length of 20 mm and diameter of 8 mm were used (Fig.2). Three specimens were employed to carry out the unidirectional tensile test. The stress-strain curve is obtained from the experiment, as shown in Fig.3.It can been seen that the stress increases rapidly with the increasing of deformation, but the increased stress value decreases gradually with the increment of the deformation. When the stress reaches its maximum, the stress decreases with the deformation increasing. In addition, the mechanical properties of the base metal are given in Table 1.

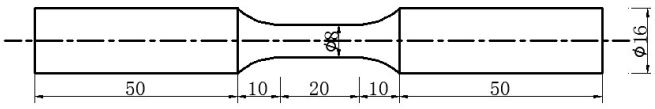


Fig.2 Geometry of test specimen(Unit:mm)

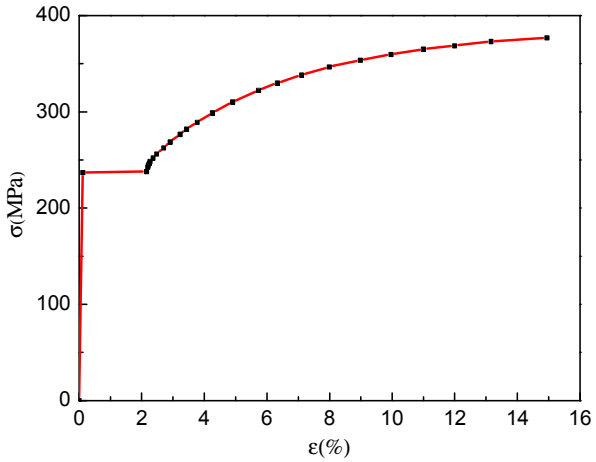


Fig.3 The stress-strain curve

TABLE 1 MECHANICAL PROPERTIES OF TEST MATERIAL

yield strain	ultimate strain	yield strength/MPa	ultimate strength /MPa	elastic modulus/MPa
0.022	0.132	240	375	2.06E5

Low Cycle Fatigue Test Condition

The fatigue tests were conducted on the MTS Hydraulic Servo Fatigue Machine in ambient air at room temperature according to the "GB/T15248-2008: The test method for axial loading constant amplitude low-cycle fatigue of matallic materials". Triangular waveform was used for all the fatigue tests and the frequency was 0.2 Hz. The tests were carried out under uniaxial tension loading with total strain control at given strain amplitudes of 0.01, 0.02, 0.04, 0.06, 0.08 and a strain ratio of 0. The failure criterion of low-cycle fatigue was based on the specimen's fracture. The number of specimens corresponding to different total strains are shown in the Table 2.

TABLE 2 NUMBER OF SPECIMENS

0.01	0.02	0.04	0.06	0.08
7	5	5	3	3

Results and Discussion

The measured S-N curve

According to the experimental conditions above, we obtained the number of cycles to fracture failure. The experimental data choice was based on the Grubbs criterion and the significance level was 0.05. The final measured sresults are shown in the Table 3.

TABLE 3 CYCLES-TO-FAILURE

	1	2	3	4	5	6	7	measured results
0.01	902	782	968	916	303	267	900	376
0.02	95	94	129	71	68			58
0.04	28	--	24	32	16			14
0.06	11	18	17					8
0.08	7	10	14					4

Note:" --" means that the datum is rejected.

It is necessary to put forward feasible analytical method for the computation of the fatigue life. The S-N curve can reflect the fatigue strength property of the material and it is the foundation for fatigue design. So, we must establish S-N curve for estimating the low-cylce fatigue life of the base metal. According to the determination method of S-N curve that provided by Zhang Guodong[4], the measured S-N curve is shown in Fig.4 .

Under the constant total strain effect, the relationship between the low-cycle fatigue life and total strain are concluded as follows:

(1)In the small range of strain amplitud(0-0.02), the fatigue life reduce rapidly with the increasing strain amplitude;

(2)the fatigue life decreases slowly in the large range of strain amplitud (>0.04);

(3)when the strain amplitud is between 0.07 and 0.08, the fatigue life is almost the same.

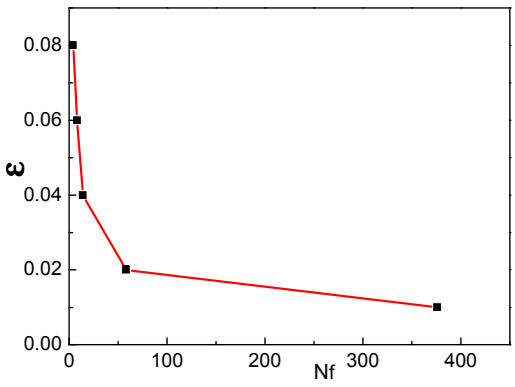


Fig.4 The measured S-N curve

The low-cycle fatigue life prediction models and analysis

In this section,test results are analyzed by considering the applicability of several various predictive strain fatigue life models. Each model can be plotted in a from with the values of model coefficients being obtained from a least-squares regression analysis. By comparing the fitting parameter determination coefficient square R^2 and the sum of squares due to error (SSE), the best prediction model can be determined. N_f and $2N_f$ mean the number of cycles and reversals, respectively.

(1) Manson-Coffin prediction formula

In the basic low-cycle fatigue life prediction models,the initial Manson-Coffin equation is widely applicable.[5] At high strain amplitudes (>0.01), where plastic stains are significant, elastic strain effects are negligible. Eqn.(1) shows the relation between plastic strain $\Delta\varepsilon_p$ and low-cycle fatigue life data.

$$\Delta\varepsilon_p = \varepsilon_f^{'} N_f^c \tag{1}$$

Where $\varepsilon_f^{'}$ and c represent the fatigue ductility coefficient and the fatigue ductility index, respectively. It is merely suitable for the short life span areas.

Many scholars' study show that the total strain amplitude can describe the fatigue properties of material on a larger and wider scope, even including the high cylce fatigue.[6] The total strain consisting of elastic strain and plastic strain is represented by the following equation:

$$\Delta\varepsilon_t/2 = \Delta\varepsilon_e/2 + \Delta\varepsilon_p/2 \tag{2}$$

Where, $\Delta\varepsilon_t$ means the total strain, $\Delta\varepsilon_e$ means the elastic strain. In addition, $\Delta\varepsilon_e$ and $\Delta\varepsilon_p$ can be obtained by the hysteresis loops at half life.

$$\Delta\varepsilon_t/2 = \frac{\sigma_f'}{E}(2N_f)^b \tag{3}$$

Where, σ_f' refers to fatigue strength coefficient, b refers to fatigue strength index, E refers to elastic modulus.

So the fatigue life of a material subjiected to a given strain range could be estimated by superposition of the elastic and plastic strain components given by another variation of Manson-Coffin relationship as:

$$\Delta\varepsilon_t/2 = \frac{\sigma_f'}{E}(2N_f)^b + \varepsilon_f'(2N_f)^c \tag{4}$$

The total strain-fatigue life curve, approaches the plastic-strain life cure at large strain amplitudes and approches the elastic-strain life at low strain amplitudes.

Based on the formula (1) and (4), the fitted curves combined with the experimental data are represented as the Fig.5 and Fig.6, respectively.

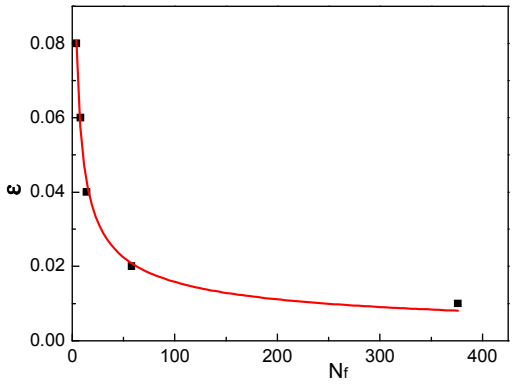


Fig.5 The fitted S-N curve based on Eqn.(1)

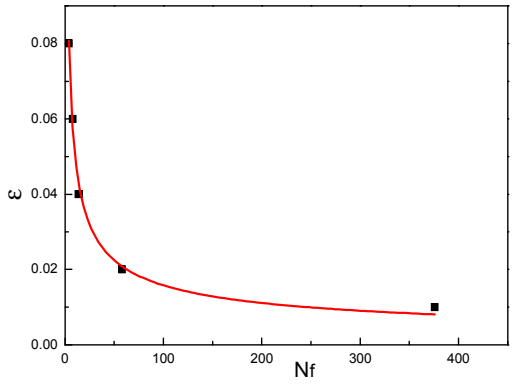


Fig.6 The fitted S-N curve based on Eqn.(4)

It can be seen that the two fitted curves are very close to the experimental data, suggesting that the predicted fatigue life coincides well with the experimental data. Through the optimum fitting, there are two equations can be obtained as followings:

$$\Delta\varepsilon_p = 0.16297\left(N_f\right)^{-0.50669} \tag{5}$$

$$\Delta\varepsilon_t/2 = 4.8544E(-17)(2N_f)^{-0.50669} + 0.29715(2N_f)^{-0.50669} \tag{6}$$

The results are reported along with the the fitting parameter determination coefficient square R^2 and the sum of squares due to error (SSE) in Table 4.

TABLE 4 COEFFICIENT OF MULTIPLE DETERMINATION AND SUM OF SQUARES DUE TO ERROR IN THE FITTING FORMULATIONS

	R^2	SSE
Eqn. (5)	0.99073	2.28125E-5
Eqn. (6)	0.99304	2.28125E-5

From the Table 4, although the SSE of two equtaions are the same, the R^2 of Eqn.(6) is better than that (5). So the modified Manson-Coffin formula prediction accuracy is higher than the later. Through analsis of the Eqn.(6), the first term is so small that it can be negligible compared with the second. This provides further evidence that the elastic strain can be ignored for the range of strain amplitudes used for the study of low-cycle fatigue (0.01-0.08).

(2) Three-parameter power function for low-cycle fatigue

By analysising and studying for a lot of $\varepsilon - N$ curve experimental data, Fu Huimin proposed three-parameter power function, as represented in Eqn.(7). MIL-HDBK-5J has adopted this method in dealing with low-cycle fatigue recently.[7]

$$N_f\left(\Delta\varepsilon_t-\Delta\varepsilon_0\right)^m=C \tag{7}$$

Where, $\Delta\varepsilon_0$, m and C are undetermined consants.

The fitted curve and equation of this model to the experimental data are shown as followings.

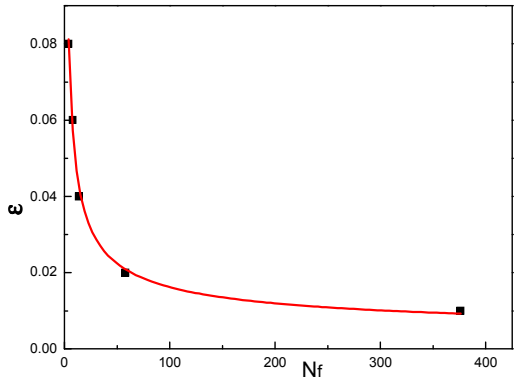


Fig.6 The fitted S-N curve based on Eqn.(8)

$$N_f\left(\Delta\varepsilon_t-0.00273\right)^{1.82786}=0.03814 \tag{8}$$

In this plot, the predicted fatigue life coincides perfectly with the test data. The value of R^2 is 0.9874 and SSE is 2.06562E-5. Compared with the initial Manson-Coffin model, the sum of squares due to error (SSE) is much less than the later although the R^2 is lower. It is indicated that the three-parameter power function is more suitable for the low-cycle life prediction of the base metal.

Conclusion

Through the unidirectional tensile test and low-cycle fatigue experiment, the mechanical properties of the base metal and the count loops to failure are obatained. The measured S-N curve is established according to the experimental data. At the low strain range, the low-cycle fatigue life decreases significantly with sharper gradient with increasing the strain amplitude in the range from 0 to 0.04. However, for the strain amplitude higher than 0.06, the low-cycle fatigue life decreases gradually with increase in the strain amplitude.

There is satisfactory agreement between the three fatigue life prediction models and the experimental life. It is evident that the effect of elastic strain can be neglected compared with the effect of plastic strain in low-cycle fatigue life (0.01-0.08). With the comparison of these three kinds of forecasting methods, the fitting parameter determination coefficient square of modified Manson-Coffin formula is higher than other two methods. But taking account of the sum of squares due to error, the three-parameter power function is more suitable for the low-cycle life prediction of the base metal. Furthermore, the research provides technology supports for life prediction and engineering application of the shock absorber.

Acknowledgements

This paper is supported by the Fundamental Research Funds for the Central Universities of China (Grant No. 2014YJS094).

References

[1] Li Chenggen, Gao Ri. Study on the shock absorbing technique of high speed railway bridges. Engineering Sciences. Vol.11(2009), p.82

[2] Sun Limin, Fan Lichu. Revisions of seismic design codes on bridges in Japan after Kobe Earthquake. Journa Of Tongji University. Vol.29(2001), p.61

[3] Zhu Dongsheng, Lao Yuanchang. et al. Research on some design of seismically & isolated bridges. China Civil Engineering Journal. Vol.33(2000), p.52

[4] Li Guodong, Xu Yongfeng. et al. A method for reducing strain-life curve of low cycle fatigue. Journal of Aerospace Power. Vol.21(2006), p.868

[5] Yang Gongxian, Su Bin. et al. Low cycle fatigue behavior of a new nickle-base superalloy. Transactions of Materials and Heat Treatment. Vol.33(2011), p.47

[6] Sun Jihong, Yang Zichun. low cycle fatigue life prediction of Nickle-based superalloy K435 at high temperature. Proceedings of the CSEE. Vol.30(2010), p.106

[7] Zhang Guodong, Su Bin. A method based on energy and three-parameter power function for low cycle fatigue. ACTA Aeronautica ET Astronautica Sinica. Vol.28(2007), p.315

Advanced Materials Research Vol. 936 (2014) pp 1366-1372
© (2014) Trans Tech Publications, Switzerland
doi:10.4028/www.scientific.net/AMR.936.1366

Corrosion Behavior Of F30s30 Concrete Under Wet–Dry Cycles In Simulated Seawater With Magnesium Salt And Sulfate

Guanguo Liu [1,a*], Aibin Ma[1,b*], Chaoming Pang [3], Ping Zhang[3], Honggen Qin [3], Lun Wang[2]

[1] College of Mechanics and Materials, Hohai University, Nanjing 210098, PR China

[2] Jiangsu Transportation Institute Co., Ltd., Key Laboratory of Large-span Bridge Health Inspection & Diagnosis Technology Ministry of Communications, Nanjing 211112, PR China

[3] School of Materials Science and Engineering, Jiangsu Key Laboratory of Civil Engineering Material, Southeast University, Nanjing, 211189, PR China

[a] lgg@jstri.com (Guanguo Liu); [b]aibin-ma@hhu.edu.cn (Aibin Ma);

Keywords: wet–dry cycles; pore structure; simulated seawater environment; performance deterioration

Abstract: In this paper, we present the corrosion behavior of F30S30 concrete used for a bridge cap which was investigated in simulated seawater with 2.0% NaCl, 0.35% $MgCl_2$, and 0.25% Na_2SO_4 under wet–dry cycles. This behavior was compared with those in 3.5% NaCl, 5.0% Na_2SO_4, and 3.5% NaCl + 5% Na_2SO_4 solutions. Results show that the change in pore structure obtained through X-ray computed tomography could reflect the amount of corrosion products and the degree of destruction. The variety and quantity of corrosion products varied with the corrosive environment. The damage mechanisms of concrete also changed according to the corrosive environment. The effects of Mg^{2+} and SO_4^{2-} were superimposed on each other for the simulated seawater environment, thereby posing a serious threat to the structure, primarily through damage and coarsening of the pore structure caused by Mg^{2+}.

Introduction

In the field of concrete research, corrosion is an important problem when concrete components are operating in seawater, particularly in the splash zone or in water-level change areas **[1].** Seawater normally includes chlorides, sulfates, and magnesium salts. Concrete components working in the splash zone or water-level change areas often undergo corrosion and seawater erosion with wet–dry cycles.

Wet–dry alternation with high chlorine salt content threatened the durability of concrete. Sosa [2] analyzed the concrete contour and steel–concrete interface of samples exposed to the atmospheric zone, alternate drying–wetting, and underwater area. Tittarelli [3] exposed specimens to wet–dry cycles in a 10% NaCl aqueous solution, and then, analyzed the effect of silane-based hydrophobic admixture on the corrosion of galvanized reinforcing steel in concrete. Santiago [4] presented two models that deal with chloride-induced corrosion and subsequent cracking of the concrete cover in reinforced concrete structures. Espinosa [5] analyzed mechanical stress during the crystallization of KNO_3 and Na_2SO_4 in the pores of two bricks with different porosities using strain measurements. Yigiter [6] studied investigative factors, such as cement type, water-cement ratio, and cement

content, on seawater resistance of concrete using mechanical strength tests, chloride penetration depth measurements, and scanning electron microscopy–energy-dispersive X-ray spectroscopy (SEM–EDS). Oh [7] conducted comprehensive tests using variables that include water-binder ratio, cement type, type and amount of mineral admixtures (silica fume, fly ash, and blast-furnace slag), and maximum size of aggregates and air entrainment, to develop a high-performance concrete with high resistance to chloride penetration and high durability. Gruber [8] discussed laboratory evaluations to assess long-term performance of concrete with high-reactivity metakaolin produced in North America in resisting chloride penetration and expansion reduction caused by alkali–silica reactivity.

Although the law of concrete with different dosages of mineral admixture, durability under different environments, variation of concrete permeability under different load conditions, and size effect of concrete on chloride resistance have been studied, their specific applications in engineering have not been reported. Chongqi Bridge is located at the Yangtze River estuary, which intersects with the Yellow Sea. The pier cap and the lower part of the bridge undergo alternating wet–dry cycles, and the maximum salinity in the water reaches 25 g/L. The present study investigates the corrosion behavior of F30S30 concrete in the complex environment described earlier.

Experiments

The specimen size was 100 mm × 100 mm × 400 mm. F30S30 concrete specimens were composed of 30 mass% fly ash and 30 mass% ground slags. The ratio of water to cement was 0.35, and the ratio of cement to sand was 2.90. The specimens were allowed to dry naturally for 12 h to 15 h after 28 d of standard curing. Afterward, four surfaces of the specimen, except for two opposite sides, were coated with epoxy resin. As a result, chloride ions could only enter through the two opposite sides in corrosive solutions.

The wet–dry cycle tests for the specimens were conducted using different corrosive solutions. In accordance with the wet–dry cycles of high-performance concrete [9,10] and the highest salinity of an engineering environment during dry season, the following corrosive solutions were selected: (1) 3.5% sodium chloride (NaCl) solution (C), (2) 5.0% sodium sulfate (Na_2SO_4) solution (S), (3) 3.5% NaCl + 5% Na_2SO_4 solution (CS), and (4) 2.0% NaCl + 0.35% $MgCl_2$ + 0.25% Na_2SO_4 simulated seawater solution (CQ). The specific implementation of the wet–dry cycle test was as follows: soaking for 8 h in one solution, followed by drying for 1 h in natural environment, then drying at 60 ± 2 °C in an oven for 38 h, and finally cooling for 1 h in natural environment. These wet–dry cycles were repeated for 360 d.

The deterioration of concrete after every seven cycles was analyzed by testing the ultrasonic propagation velocity of the specimens. Chloride ion content after the wet–dry cycles was measured using the chemical titration method based on SL352-2006 hydraulic concrete testing procedures.

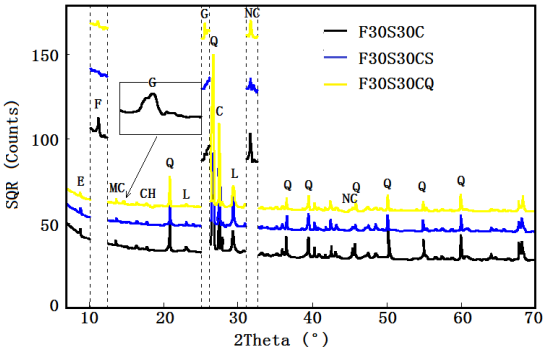
In addition, all specimens were examined using Y.CT Precision system (YXLON International, Germany). The detector of the computed tomography (CT) system was a flat-panel type with 1 024 × 1 024 detector elements and 1 080 projections. The voltage and current of the X-ray tube were set to 185 kV and 0.33 mA, respectively, and the object rotation angle was 360°. For the specimens in this study, the 3D voxel size was 0.063 mm × 0.063 mm × 0.063 mm. Phase structures were analyzed by X-ray diffraction (XRD, D8, Germany), and the experimental samples used were 40 μm powder in diameter. The surface morphology and chemical elements of the corrosion products after a certain number of cycles were obtained by SEM.

Results and Discussion

Analysis and morphology of corrosion products

The XRD patterns of F30S30 concrete specimens after 360 d of wet–dry cycles in three different solutions (C, CS, and CQ) are shown in Fig. 1. Ettringite ($C_3A{\cdot}3CaSO_4{\cdot}32H_2O$) and $MgCO_3{\cdot}3H_2O$ were found in all samples. The former is the product of the hydration reaction between C_3A and sulfate. Friedel salts (F salt: $C_3A{\cdot}CaCl_2{\cdot}10H_2O$) was detected in the samples immersed in C solution but not in the samples immersed in CS solution. This result showed that the presence of sulfate salt hindered the formation of F salt. However, an extremely low peak of F salt appeared in CQ simulated seawater solution. This result indicates that sulfate is more active than chloride and hydroxide ions in C_3A, and that the obstruction of sulfate salts in generating F salt is only effective under certain conditions.

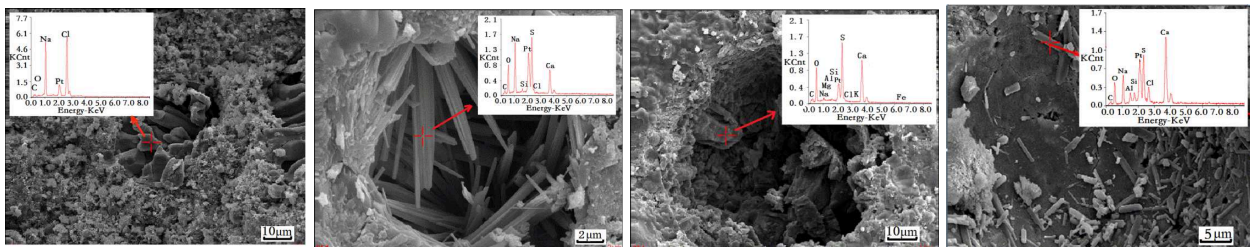
By contrast, chloride, sulfate, and magnesium were detected in the sample immersed in CQ simulated seawater solution. Furthermore, $CaSO_4{\cdot}0.5H_2O$ (d = 3.009Å/100, 2.804 Å/85, 6.010 Å/70, 3.480 Å/55, and 1.850/55) was obtained from the sample immersed in CQ simulated seawater solution.



E：Ettringite; F: Friedel's salts; G: $CaSO_4{\cdot}0.5H_2O$; MC: $MgCO_3{\cdot}3H_2O$; CH: $Ca(OH)_2$; Q: α-SiO_2; L: $CaCO_3$; C: α-C_2SH; NC: NaCl, NS:Na_2SO_4

Fig. 1 XRD patterns of the F30S30 concrete samples after 360 days in three different solutions (C, CS and CQ)

The SEM images and EDS patterns of the samples after 360 d of wet–dry cycles in C, CS, and CQ solutions are shown in Fig. 2. The morphology of NaCl crystals in the sample tested in C solution is presented in Fig. 2a. The figure shows that several holes appeared in F30S30 concrete, and that NaCl crystals filled these holes. The crystallization of NaCl crystals could also be predicted to lead to extremely high pressure in the concrete, which might cause it to crack as crystallization continues to a certain degree. The morphology of the needle-like Na_2SO_4 crystals found in the sample tested in CS solution is presented in Fig. 2b. Under this condition, Na_2SO_4 crystals grew intertwined and almost filled the holes completely. The EDS patterns showed that the short and thick stubs (Fig. 2c) were $CaSO_4$ crystals. Furthermore, several ettringite crystals were found in the sample after 360 d of wet–dry cycles in CQ simulated seawater (Fig. 2d) based on XRD results. Daimond [11] believed that ettringite appears as thin rods 3 μm to 4 μm long, whereas the morphology of the secondary ettringite generated by the external sulfate attack is related to growth conditions. The crystallization speed was significantly faster in a complex environment, thus causing the secondary ettringite to form into slender rods with unobvious edges.



(a) in C solution (b) in CS solution (c) and (d) in CQ simulated seawater

Fig. 2 SEM images and EDS patterns of the F30S30 concrete samples after 360d of wet–dry cycles in the three different solutions

Penetration content of Cl^{-1} and Deterioration Degree

The content distribution of Cl^{-1} along the depth of the samples tested in different solutions for 28, 90, 180, and 360 d of wet–dry cycles is shown in Fig. 3. Cl^{-1} contents in the surface area were highest in all three tested conditions, and they clearly decreased with increasing depth. In particular, when testing time was more than 90 d, Cl^{-1} content distribution at the depth of 14 mm to 18 mm of the samples in CS and CQ solutions tended to exhibit an immobile tendency and its value was approximately 0.2%. Cl^{-1} content in the sample tested in C solution for 360 d wet–dry cycles had a relatively high value but only reached a limited value of 0.8% at the region more than 20 mm from the surface. These data are consistent with the results of the reference [4].

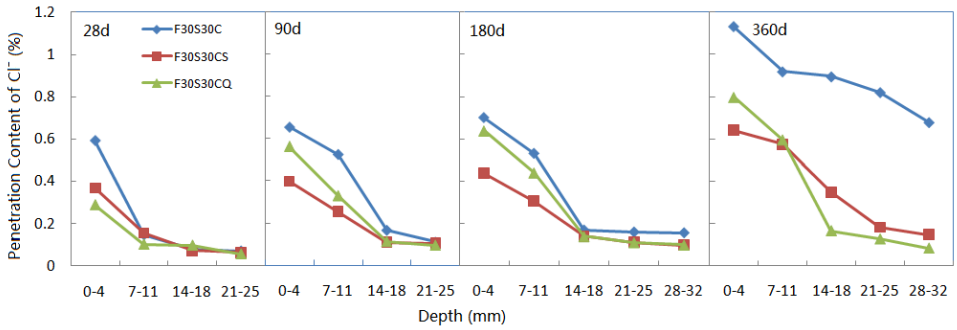


Fig. 3 Cl^- concentration versus depth and ages curve

Cl^- content in the concrete samples was unsaturated under the conditions of wet–dry cycles in the present study. The capillary action introduced by unsaturated concrete accelerated the migration of Cl^- to the internal areas of the concrete. However, when SO_4^{2-} was also present and diffused into concrete, SO_4^{2-} would decrease the concentration of free Cl^- on the concrete surface and hinder the natural diffusion of Cl^-. This result explains why Cl^- content was clearly lower in samples tested in CS and CQ solutions than that in C solution after 360 d of wet–dry cycles.

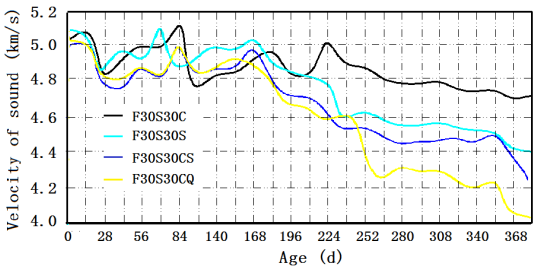
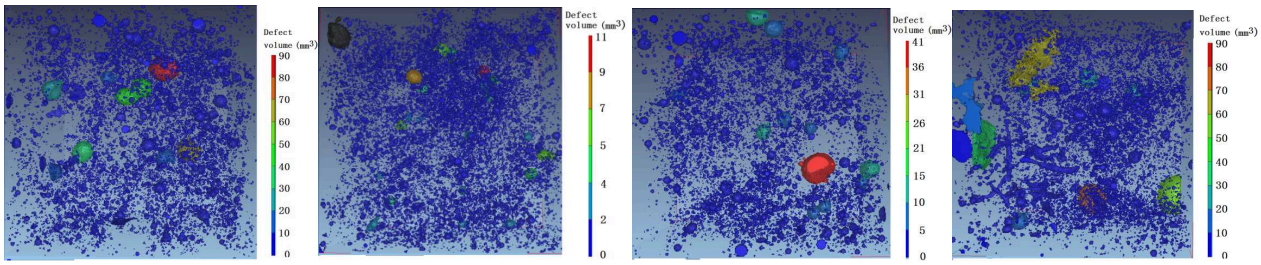


Fig. 4 Effect of time on the ultrasonic velocity in different solutions

The changes in ultrasonic velocity of F30S30 concrete samples after various numbers of wet–dry cycles in four different solutions are presented in Fig. 4. The data show that the velocities of sound clearly declined in the three samples tested in S, CS, and CQ solutions after approximately 200 h. The CQ solution exhibited the most serious result.

Changes in Pore Structures

The 3D renderings of holes in the original F30S30 concrete and that in the sample after 360 d of wet–dry cycles in three different solutions are shown in Fig. 5. Numerous holes were found within the original concrete, including a small number of big holes (Fig. 5a). After 360 d of wet–dry cycles in C or CS solution, the size of the holes within the concrete did not change significantly (Figs. 5b and 5c). However, the shape of the holes changed significantly after 360 d of wet–dry cycles in CQ simulated seawater, as shown in Fig. 5d. In addition, adjacent holes clearly joined and became large irregular holes, whereas several small holes connected to each other and formed long pipelines (Fig. 5d).



(a) Before testing (b) In C solution (c) In CS solution (d) In CQ simulated seawater

Fig. 5 3D renderings of holes

The porosity of the initial sample and the samples tested in C, CS, and CQ solutions after 360 d were 1.76%, 1.19%, 1.20%, and 2.19%, respectively, based on the X-ray CT (X-CT) scan results. Porosity slightly decreased in samples tested in C and CS solutions after 360 d. By contrast, porosity slightly increased in CQ simulated seawater solution. The distributions of pore size in F30S30 concrete before and after the tests are shown in Fig. 6. After the wet–dry cycles in C environment, the number of pores smaller than 0.2 mm markedly increased, whereas the number of pores larger than 0.2 mm decreased. For the specimen tested in CQ simulated seawater, 0.007 mm was the dividing point in the increasing and decreasing trends. For the specimen tested in CS solution, the pore number significantly decreased.

For an individual hole, the pore volume decreased when the corrosion products attached to the pore walls; whereas the pore volume increased when the corrosion products peeled off. After corrosion occurred in C environment for a certain period, the corrosion products attached to the pore walls caused certain pores to become smaller. Thus, the number of smaller pores increased. For large holes, the products peeled off or several pores joined together, thus causing a decrease in the number of holes or an increase in porosity. A high degree of peeling of corrosion products and increase in porosity both occurred in the samples after 360 d of wet–dry cycles in CQ simulated seawater (Figs. 5d and 6).

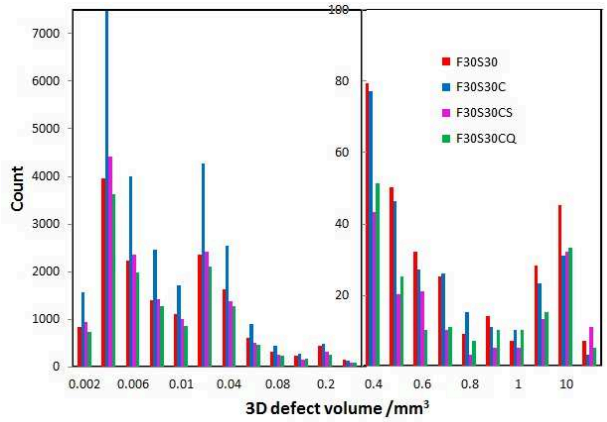


Fig. 6 Distributions of the pore size

In summary, the erosion mechanisms of Cl^- and its damage to the concrete were as follows: (1) the dissolution of $Ca(OH)_2$ and precipitation of calcium; (2) the formation of expansion compounds, such as calcium chloride and magnesium chloride; and (3) Ettringite could be generated under a sulfate environment in concrete, and its volume expanded with age. Shrinkage and tensile stress occurred under dry conditions, thus causing microcracks that allow sulfate ions to penetrate more easily into the concrete.

In CQ simulated seawater, Cl^- and SO_4^{2-} diffused together inside the concrete and reacted with aluminum to generate Friedl and Aft salts, respectively [12]. Meanwhile, Mg^{2+} and SO_4^{2-} superimposed on each other, thus resulting in serious complex erosion. $Mg(OH)_2$ formed on the surface of the concrete, whereas the dense layer was destroyed after the formation, and a new reaction was repeated. The wet–dry cycle accelerated the corrosion reaction rate described earlier. SO_4^{2-} diffused inside the concrete and reacted with the hydration product to generate ettringite or gypsum. These products initially attached to the pore walls and peeled off later. The spalling caused by Mg^{2+} in concrete was more severe than the spalling caused by SO_4^{2-}. Hence, Mg^{2+} caused major deterioration of concrete in the form of spalling.

Conclusions

The following conclusions can be drawn based on the extensive and careful examination of F30S30 concrete used in the Chongqi Bridge cap.

(1) The SEM images and EDS results show that corrosion products emerged from the holes. Crystal pressure potentially causes microcracks. Hence, the change in pore structure can reflect the amount of corrosion products and the degree of destruction.
(2) In the present study, the X-CT test method was used to study the changes in pore structures. The resulting data are consistent with other test results. Pore volume decreased when corrosion products attached to the pore walls. By contrast, individual pore volume and total porosity both increased when corrosion products peeled off.
(3) The effects of Mg^{2+} and SO_4^{2-} were superimposed on each other for CQ simulated seawater solution. These two factors pose a serious threat to the concrete structure, primarily in the form of spalling and coarsening of pore structures caused by Mg^{2+}.

Acknowledgements

This project was supported by the National Natural Science Foundation of China (No. 51108077 and 51308112).

References

[1] W. Chaleea, P. Ausapanitb, C. Jaturapitakkul. Utilization of fly ash concrete in marine environment for long term design life analysis. Mater Des 2010; 31(3):1242-1249.

[2] Sosa. M, T Perez-Lopez, J Reyes ,et.al, Influence of the Marine Environment on Reinforced Concrete Degradation Depending on Exposure Conditions. Int J Electrochem Sc 2011; 6(12):6300-6318.

[3] Tittarelli. F, Moriconi. G, The effect of silane-based hydrophobic admixture on corrosion of galvanized reinforcing steel in concrete. Corros Sci 2010; 52(9):2958-2963.

[4] Santiago. G, Jaime.C G, Jose.M S, Cover cracking of reinforced concrete due to rebar corrosion induced by chloride penetration. Cem Concr Res 2011; 41: 893-902.

[5] Espinosa. R M, Franke. L, Deckelmann. G, Model for the mechanical stress due to the salt crystallization in porous materials. Constr Build Mater, 2008; 22(9): 1305-1367.

[6] Yigiter. H, Yazici. H, Aydin. S, Effects of cement type, Water/ Cement ratio and Cement content on sea water resistance of concrete. Build Environ 2007; 42(4): 1770-1776.

[7] Oh. B H, SW Cha, BS Jang, et.al, Development of high performance concrete having high resistance to chloride penetration. Nucl Eng Des 2002; 212(1-3):221-231.

[8] Gruber. K A, Terry Ramlochan, Andrea Boddy ,et.al, Increasing concrete durability with higher activity metakaolin. Cement Concrete Comp 2001; 23(6): 479-484.

[9] Jin. Z Q, et.al, Study on damage of HPC under the corrosion of chloride and sulfate. Industrial Construction 2005; 35(1): 5-7.

[10] Fan. Y H, Yu. H F, Zhang. Y Q, Effect of drying-wetting cycles on chloride diffusion in concrete exposed to high concentration brine. Journal of Salt Lake Research 2007; 15(1): 49-54.

[11] Lian. H Z, Dong. L, Chen. E Y, Study foundation of construction materials phase. Beijing: Tsinghua University Press; 1996.

[12] Jin. Z Q, et.al, Chloride binding in concrete exposed to corrosive solutions. Journal of the Chinese ceramic society 2009; 37(7):1068-1073.

Advanced Materials Research Vol. 936 (2014) pp 1373-1377
© (2014) Trans Tech Publications, Switzerland
doi:10.4028/www.scientific.net/AMR.936.1373

Different Salt Solution on the Deterioration of Marine Engineering Concrete Under the Action of Chemical- Mechanical Coupling

Honggen Qin[a], Jiajun Deng[b], Ping Zhang[c], Chaoming Pang[d], Yikun Hou[e]

School of Materials Science and Engineering, Southeast University Nanjing, 211189, PR China.

[a]qinhonggen@126.com,[b]djj0068@163.com,[c]zhangpingseu@163.com,[d]pangchao@seu.edu.cn, [e]daniao891108@sina.com.

Keywords: Marine engineering concrete; bending stress; NaCl solution; Na_2SO_4 solution; Simulated seawater; Damage and degradation

Abstract: The loaded specimens were put in fresh water, 3.5%NaCl solution, 5.0%Na_2SO_4 solution, and simulated sea water with different concentrations respectively, and then the damage process under wetting and drying cycle was investigated. The ultrasonic non-metal testing technology, X-CT scanned image, free chloride and sulfate ions chemical titration were used to investigate the degradation of the marine concrete under the coupling effect of Chemistry and Mechanics. The effect of solutions, wetting and drying cycle and bending stress to the durability of marine concrete were further studied. The results indicate that different salt solution affects marine concrete at different degrees: sulfate salt is more corrosive than chloride salt, simulated seawater is similar to 5.0%Na_2SO_4 solution, while five-time simulated seawater is the most corrosive; wetting and drying cycle remarkably accelerates the penetration of corrosive ions, which results in the concrete damage, compared to the corrosive environment, concrete is damaged violently under the coupling effect of Chemistry-Mechanics and tensile stress has greater influence on the damage.

Introduction

The durability of the concrete generally refers to the property or ability to resist physical, chemical or mechanical factors. It directly decides the service life of the concrete structure. In decades, researches showed that marine concrete, especially in marine splash zone and tide zone, were damaged seriously with service life far shorter than expected [1,2]. It can be explained by the complex environment, not only concrete is corroded by the soluble salt rich in the seawater such as chloride and sulfate salt [3,4], but also the corrosion is accelerated by the wetting and drying cycle severely in the tide zone [5,6]. The amount of the internal micro cracks will increase when concrete is loaded, and these micro cracks will expand and connect the cracks which already existed so that attacking medium would transport into the concrete structure easily [7,8]. Coupling of all above factors could accelerate the damage process of concrete remarkably. Therefore, it is significant and practical study the damage mechanism of concrete under coupling effect of chemistry-mechanics.

Experimental Detail

Raw Materials and Mix Proportions

Chinese standard 52.5 R (I) Portland cement equivalent to ASTM Type I Ordinary Portland cement supplied by Wuhan huaxin Cement Corporation in China was used. type I low calcium fly ash; type S95 blast furnace slag grounded to fine powder; river sand with fineness modulus of 2.6 and coarse aggregate of crushed limestone with particle size of 5 ~20 mm were used; Water-reducing rate of polycarboxylic acid type water-reducer JM-PCA(Ⅳ) was 35%; Ordinary tap water. The main chemical compositions of cement and mineral admixtures are shown in Table 1.

Marine concrete need to endure the corrosion of seawater, so mix 30% fly ash and 30% slag powder to replace cement of equivalent quantity. Details are shown in Table 2.

TABLE1 THE MAIN CHEMICAL COMPOSITIONS OF RAW MATERIALS

Parameters	ω（CaO)	ω（SiO2)	ω（Al2O3)	ω（Fe2O3)	ω（MgO)	ω（SO3)
Cement	65.03	21.38	4.71	3.68	2.53	0.53
Fly ash	3.49	52.42	33.25	4.53	1.07	/
Slag	36.35	33.48	12.21	1.41	10.60	0.66

TABLE 2 PROPORTION OF CONCRETE MIXTURE PREPARED

Group	C	FA	SL	W	S	G	JM-PCA	ρ_{co}[kg/m^3]
C50FS	0.40	0.30	0.30	0.33	1.50	2.50	0.51	2390

Test mechanical properties of the specimens after standard curing for 90 days: the compressive strength was 57.6MPa and the flexural strength was 8.7MPa.

Experiment Methods

Concrete specimens were cast in molds of 70 mm×70 mm×280mm, with a Φ10 rebar in center. Then removed from the molds after 24 h, and cured in the condition of 20 ± 3 ℃ and 95% of relative humidity for 90d. Two opposing sides were set as the exposed surface, and the remaining sides brushing epoxy resin before the test. Four sets of salt solution were chosen to compare with fresh water, as listed in Table 3. Simulated seawater, which was made according to 25 g/L high salinity and contained main ingredients of seawater, consisted of 2.00%NaCl, 0.25%Na_2SO_4 and 0.35%$MgCl_2$, five-time simulated seawater consisted of 10.00%NaCl, 1.25%Na_2SO_4 and 1.75%$MgCl_2$. The specimen was immerged in solution for 8h, followed by drying for 38h in an oven under 60±2℃, and then cooled in natural condition for 2h. A whole wetting and drying cycle needs 48h.

TABLE 3 THE SALT SOLUTION USED IN THE EXPERIMENT

Label	A	B	C	D	E
Solution type	Fresh water	3.5%NaCl	5.0%Na_2SO_4	Simulated seawater	Five-time simulated seawater

Use a four-point bending spring-loaded device for long-term constant load on concrete specimens (as shown in Fig.1), the bending stress ratio was 0.35 and every 3 specimens as a group under the same loading device. Specimens were taken out every 20 cycles and tested by NMB-4A nonmetallic ultrasonic detector to detect the speed changes of ultrasonic wave, and then converted these data into dynamic elastic modulus (Fig.2).

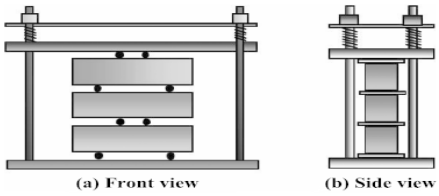


Fig.1 Schematic Diagram of Loading Equipment

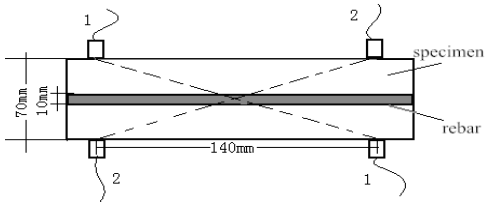


Fig. 2 Schematic Diagram of Ultrasonic Testing

Cut along the vertical direction of the exposed surface, remove the coarse aggregate, and then ground the samples with a mortar and pestle until the powder could pass through the Φ0.63mm square hole sieve. The chloride ion content of the concrete specimens was analyzed according to the "Hydraulic concrete testing procedures" (JTJ270-98) as well as the sulfate ion content of the

concrete specimens was analyzed according to the "Gravimetric method of sulfate content in water" (GB11899-89). The specimens were divided into five layers to cut: 0-3mm, 6-9mm, 12-15mm, 18-21mm, 24-27mm.

Results and Discussion

The Impact of Different Salt Solutions on the Degradation of Concrete

The dynamic elastic modulus of concrete specimens under the action of wetting and drying cycle with bending load in different salt solutions was tested every 20 cycles, and the results are shown in Fig.3.

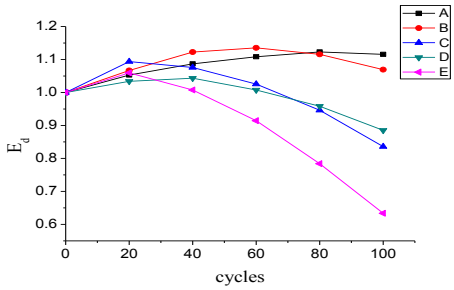


Fig.3 The Relative Dynamic Elastic Modulus of Concrete in Different Salt Solution

Following conclusions could be given from the results:

1) The relative dynamic modulus of elasticity of the specimens in fresh water gradually increased at first, and tended to be stable after 80 cycles;

2) The indicator in 3.5%NaCl solution increased during the first 60 cycles, and declined after that;

3) In 5.0% Na_2SO_4 solution, the dynamic modulus of elasticity of tested-piece increased rapidly during the first 20 circulations and then declined violently after that, So it was 40 circulations earlier than that in 3.5%NaCl solution. It is because the chloride ion damages ferroconcrete by swelling and rusting the surface of rebar and it takes a long time before it gets inside the concrete and accumulates to a certain concentration. However, sulfate and hydration products of cement can react to produce swelling materials such as ettringite and gypsum, which is a fast process. That explains why the specimen in 3.5%NaCl solution damaged more slowly than in 5.0% Na_2SO_4 solution;

4) In five-time simulated seawater, the indicator declined fastest, this is mainly resulted from Mg^{2+} in the simulated seawater. The Mg^{2+} may transform to $Mg(OH)_2$ on the surface of concrete, but the wetting and drying cycle promoted the corrosion reaction, so the compact layer would be damaged soon after it is formed. The reaction, producing not-sticky gel S_2H and MSH, could happened quickly, which resulted in the concrete surface peeling off constantly, thus the damage becoming more and more seriously;

5) Relatively, the specimen of concrete was most damaged in the five-time simulated seawater, followed by 5.0% Na_2SO_4 solution, simulated seawater, 3.5%NaCl solution and the fresh water.

X-CT images of the concrete specimens after 100 wetting and drying cycles are shown in Fig.4. The images show the inside of the concrete after it had been corroded 100 times under the effect of wetting and drying cycle in the simulated seawater. It can be seen that the surface and inside of the concrete already have micro cracks, most of which are existed along tiny openings, and expanding gradually. At last they interconnect and then damage will be produced.

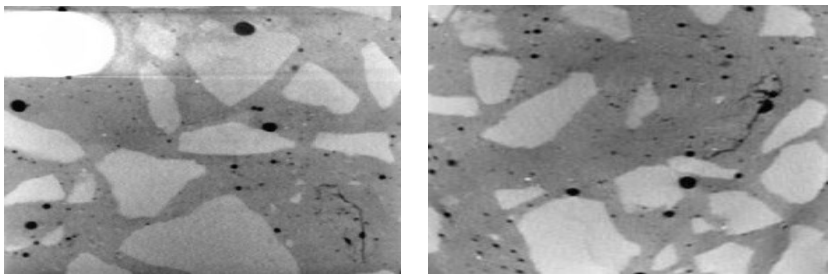
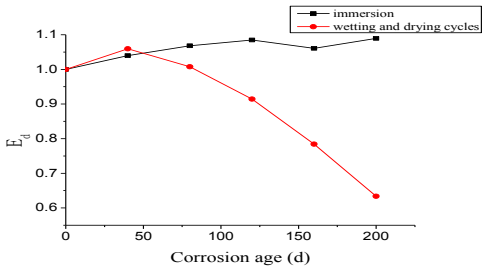


Fig.4 X-Ct Images of the Concrete Specimens after 100 Wetting and Drying Cycles

The Impact of Different Corrosive Environment on the Degradation of Concrete

The specimens of concrete were immerged or under wetting and drying cycles in five-time simulated seawater. The dynamic modulus of elasticity of them were tested every 40d and the result is shown in Fig.5. Meanwhile, the content of free chloride ion after 200d's corrosion was also tested, result of which is listed in Fig.6.



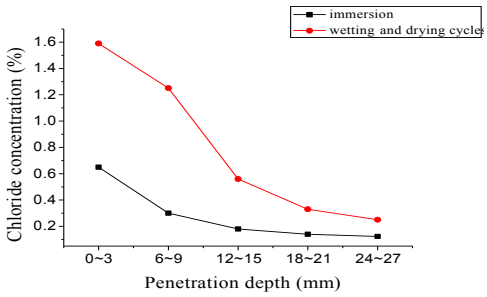


Fig.5 The Relative Dynamic Elastic Modulus of Concrete Fig.6 The Distribution of Chloride Concentration

It can be concluded from the Fig.5 that the relative dynamic modulus of elasticity of the immerged specimens rises gradually at first, and tends to be steady at the 120th day, while the data of specimens under wetting and drying cycle declined violently after 40 days. At the 120th day, the relative dynamic modulus of elasticity decreased by 36.6%. Fig.6 shows that the chloride ion in both environments declined gradually from surface to inside of the concrete as chloride ion invades concrete from surface. However, the surface of specimens under wetting and drying cycle contains more chloride ion than that being immerged. That is because chloride ion on concrete surface in wetting and drying cycle works with great complexity. In the surface, it was mainly because of the absorption of capillaries to accelerate transmission. But inside the concrete, the transmission was still dominated by diffusion. The wetting and drying cycle accelerated the declining of the dynamic modulus of elasticity of the concrete and invasion of chloride ion inside it.

The Impact of Different Load Stress on the Degradation of Concrete

Bending load test under the condition of the five-time simulated seawater was applied in the concrete's specimen and chloride ion in different stress zones was tested every 100 wetting and drying cycles (as showed in Fig.7). Distribution of sulfate ion in different stress zones is listed in Fig.8.

The graphics indicate that, the content of chloride ion and sulfate ion declined with the depth into the concrete and finally became steady. There were more chloride ion and sulfate ion, and their penetration ability was better in tension zone than that in compression zone. That is because the tensile stress produced by the stress area brought quicker expansion of micro cracks, which accelerated the penetration of chloride ion and sulfate ion. On the contrary, the pressure stress in the compression zone limited micro cracks so that the two ions had difficulties in penetrating the concrete and their transmission was restrained.

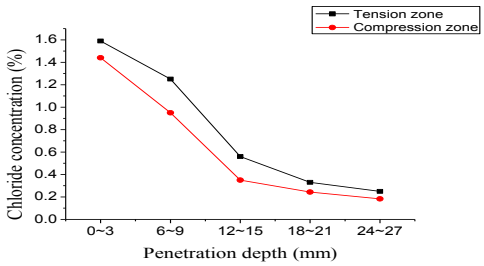


Fig.7 The Concentration of the Chloride Ion

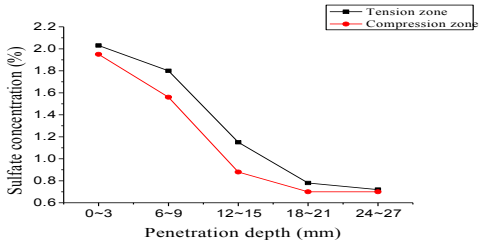


Fig.8 The Concentration of the Sulfate Ion

Conclusions

(1) Under the coupling effect of wetting and drying cycle and bending load, different salt solution affects the durability of marine concrete at different degrees: sulfate salt is more corrosive than chloride salt, simulated seawater is similar to 5.0%Na_2SO_4 solution, while five-time simulated seawater is the most corrosive.

(2) Compared with the immersion corrosive environment, wetting and drying cycle formed capillary suction, which greatly accelerated the diffusion speed of the chloride and sulfate ion.

(3) When under the bending load, there is more chloride and sulfate ion and a deeper penetration depth in tension region than in compression zone, which indicates that the concrete take more damage and degradation under the coupling effect of chemistry-mechanics and the tensile stress has greater influence on the damage.

Acknowledgments

This work was supported by Chinese national key basic research and development plans (No. 2009CB623203) and national Natural Science Foundation of China (No. 51108077 and 51308112).

Reference

[1] Jing Fang, Yanchi Zhang, Yaxian Zhu, et al. The conditions of high-pile wharf harbor and the suggestions to its durability. The Sixth National Symposium on Durability of Concrete, 2004.05.

[2] Weiliang Jin, Yuxi Zhao. Durability of concrete structures Beijing: Science Press, 2002.

[3] Metha P K .Durability of concrete—fifty years of progress Durability of Concrete—G.M.Idom International Symposium SP-126, American Concrete International, Detroit, 1991, 80(3): 120-132.

[4] Neville A. The confused world of sulfate attack on concrete [J]. Cement and Concrete Research, 2004, 34(8): 1275-1296.

[5] Yong Zhang, Hu Zhang. The preventive measures of the deterioration of concrete structures exposed to marine environment and develop of the high performance concrete [Z]. Shenzhen, China: 2004, 06.

[6] POUPARD O, HOSTIS V L, CATINAUD S, et al. Corrosion damage diagnosis of a reinforced concrete beam after 40 years natural exposure in marine environment [J]. Cement and Concrete Research, 2006, 36(3):504-520.

[7] Hui Zhang, Pengcheng Ren, Zuquan Jin, et al. The Law of chloride ion transmission in air entrained concrete under load [J]. Fly Ash, 2013 (04): 40-43.

[8] Jiangang Niu, Ditao Niu. Durability Study of concrete under load [J]. Concrete, 2008(08): 30-33.

Advanced Materials Research Vol. 936 (2014) pp 1378-1381
© (2014) Trans Tech Publications, Switzerland
doi:10.4028/www.scientific.net/AMR.936.1378

Polymer Modified Cementitious Waterproofing Coatings: Application and Problems

Yao Wei[a], Hu Qianqian[b,1], Mu Yan[a], Chen Jianbo[a] and Zhao Fengqing[b, c]

[a]Design and Research Institute of Hebei Construction and Building Material Shijiazhuang 050051, PR China

[b]Chemical Dept. of Hebei University of Science & Technology, Shijiazhuang 050018, PR China

[c]Hebei Engineering Research Center of Solid Wastes Utilization

Shijiazhuang 050018, PR China

[1]516997523@qq.com (corresponding author)

Keywords: Polymer; Waterproof coating; Cement

Abstract: Polymer modified cementitious waterproof coating is an important construction material. In this paper, starting from the classification and choice of waterproof coatings, the importance, advantages and application prospects of the polymer cement waterproof coatings were discussed. The approaches for solving the existing problems and limitations of polymer modified cementitious waterproof coatings were put forward.

Introduction

In accordance with the Outline of the China's 12th Five-year Plan, during the 12th Five-Year Plan period, the country's population will be controlled within 1.39 billion, and China's urbanization rate will increase 1% each year. Large population keeps continuous demand for housing, and the increasing per capita net income can transform the hidden housing into real demand, and thus activating development of waterproof material industry. With the fast-paced urbanization, 450 million farmers enter the cities and towns, the government will make good efforts to build guaranteed house.

During the 12th Five-Year Plan period, asphalt based waterproof membrane will be eliminated. The average annual growth rate of major waterproof materials will remain increase at the rate of over 10 %, and the output of major waterproof materials is expected to reach 1,600 million square meters by 2015 to meet the ballooning waterproof market demand. It is predicted that at the end of the 12th five-year, the enterprises on waterproof materials with the sales revenue over 5,000 million yuan will appear, dozens of which will be more than 10,00 million yuan.

In 2012, production of Chinese waterproof building materials reached 1,356 million square meters, rose by 12.70% compared with 2011, in which new waterproof materials accounted for 90% , and the share will continuously increases. Among them, SBS/APP modified asphalt waterproof coiled material has the largest proportion, 26.37%. Waterproof coating and polymer waterproof coiled material ranked second and third, 22.77% and 15.58% respectively. The main reason is the pull from the real estate market in the first half and affordable housing construction in the second half.

Based on years of experience on waterproof material development, this paper mainly introduced the performance and characteristics of polymer waterproof coatings and put forward the strategies for application and research of this materials.

Classification of Build Waterproof Coatings [1-4]

In the field of construction engineering, waterproof coatings are generally divided into the following four categories:

(1) Synthetic polymer waterproof coatings: polyurethane waterproof coatings, silicon rubber waterproof coatings, acrylic waterproof coating, polyvinyl chloride elastic waterproof coating, PVC waterproof coating, polyurea elastic coatings and methyl methacrylate coatings.

(2) Polymer modified asphalt waterproof coatings: solvent-based rubber asphalt waterproof coatings, butyl rubber modified asphalt waterproof coatings, styrene-butadiene rubber modified asphalt waterproof coatings, APP modified asphalt waterproof coatings, emulsion / solvent type SBS modified asphalt waterproof coatings, water soluble neoprene asphalt waterproof coatings and solvent neoprene asphalt waterproof coatings.

(3) Polymer modified cementitious waterproof coatings: polymer emulsions modified build waterproof coatings, polymer modified cementitious waterproof coatings. Polymer modified cementitious waterproof coatings are divided into type I (polymer) and type II (cement) (Type I is used for non long-term immersion environment / type II for long-term immersion environment building waterproof engineering).

Inorganic waterproof coatings: cement-based capillary crystalline waterproof coatings and mineral admixture or admixture cement-based waterproof coatings.

Among these four kinds of waterproof coatings, synthetic polymer coating has excellent waterproof performance. Because of its strict requirement on the surface moisture content, moisture ratio should be less than 7%, so the yield decreased. Market share of polymer modified asphalt waterproof coating and inorganic waterproof coating are low. The market share of polymer modified cementitious waterproof coatings have been in increase these years.

Selection of Waterproof Coatings

The following requirements should be met in selection of different types of waterproof coatings in application.

(1) Chooses appropriate inorganic coatings or organic coatings with excellent binding force with wet inter-area for wet base, or adopts composite coating which was first coated with cement-based inorganic coatings and than with organic coating.

(2) Corrosive underground environment need organic waterproof coatings with good corrosion resistance as rigid preventive layer.

(3) Polymer modified cementitious waterproof coatings type II is often used in underground waterproof engineering.

Polymer modified cementitious waterproof coating is a kind of two-component waterborne waterproof coating, which is developed by mixing polymer emulsion such as acrylate, cement and additives. The coating consists of two-component composition, polymer and cement. Therefore it has the dual characteristic of rigid and flexible materials, the good elongation and waterproof performance of polymer coating, and high strength and excellent binding force with wet interarea of hydraulic binding material. It meets the requirements of different engineering on flexibility and strength by adjusting the proportion of polymer emulsion and cement. The coating uses water as the dispersant, there is no problem of environmental pollution and human health problems.

Characteristics of Polymer Modified Cementitious Waterproof Coatings

Polymer modified cementitious waterproof coatings have the following advantages.

Non-Toxic, Tasteless and Environmental Friendly

Polymer modified cementitious waterproof coatings do no harm to the construction workers and has no pollution to the environment. In 2012, China's total housing construction area was 5734 millions square meters, and completed 990 millions square meters, of which 790 million square meters for residential (National Bureau of Statistics report 20130118). In residential construction decoration, about 70% of families choose the balcony, kitchen, basement floor to perform waterproof again. The area of kitchen and toilet is generally small, and most of them exists negative and positive angles and pipelines. The choice of waterproof materials should consider the size of kitchen and toilet, the number of negative and positive angles, tube piercing and sanitation, the wet base, etc., as well as the connection structure of floor and wall. Polymer modified cementitious waterproof coating has significant advantages: one is suitable for the change of primary shapes and benefit for pipeline laying, the other is excellent water resistance and the overall coating without seam.

Two-Component, Easy For Use

Unlike reactive two-component synthetic polymer waterproof coating, most of them use thinner, which will evaporate in the construction and curing process and do damage to the environment and human health. With the enhancing awareness of environment protection, the workers, site administrators, designer and users gradually realized environmental advantage of polymer modified cementitious waterproof coating.

Low Cost and High Performance

Polymer modified cementitious waterproof coating can be used for wet inter-area, the total construction period can be shortened effectively and the construction costs be reduced significantly. Synthetic polymer coating has strict requirements for the base. When the content of water in interarea is more than 7%, in the case of the waterproof layer completed before the next procedure finished, it will produce bulge in the sunlight. In such case, the subsequent construction could pierce the waterproof layer, thus waterproof layer lost integrity and waterproof function. When using polymer modified cementitious waterproof coating, it can be done only after the former procedure. Compared with other materials, one waterproof engineering item can save construction time of about 5 days with polymer modified cementitious waterproof coatings.

Obvious Synergistic Effect of Polymer Emulsion and Cement

There exists synergetic effect between polymer emulsion and cement film forming process, which has good aging resistance and mechanical performance. The cost of product protection of later stage is low. Organic polymer emulsion lost water to be elastic film with adhesivity and continuity after using of polymer modified cementitious waterproof coating. Cement, grading quartz powder, coarse whiting absorbed the water in the emulsion and hardened, flexible polymer film layer and the cement inter-fingered each other, forming solid elastic three-dimensional network structure waterproof layer. Flexible polymer filled in the gap of cement stone, which made the cement stone more compact and elastic. The film has good elongation. Cement stone filled in the polymer, which made the polymer possess better durability. Polymer modified cementitious waterproof coating is a kind of coating waterproof layer with high strength, toughness, high durability. With the existence of net structure of cement stone and polymer film, the coating don't need protective layer during the construction of small area, the thickness of the protective layer can be decreased during the construction of large area, thereby reduces the construction cost.

Lower Construction Cost

The price difference between polyurethane waterproof coating and polymer modified cementitious waterproof coating is about 3300 yuan per ton. By using the later, every square meter can save 6.6-10 yuan, which includes no thinner expense of synthetic polymer coating. Thus, the owners and the contractors give more and more attention on polymer cement waterproof coating.

Existing Problems of Polymer Modified Cementitious Waterproof Coatings

(1) There are two major types of polymer modified cementitious waterproof coatings on the market, acrylic emulsion and poly (ethylene-vinyl acetate) copolymer emulsion (EVA). However, there is no water resistance test of the material in routine testing, causing a lot chaos and the low-end development trend. A fast detection method for such materials should be set up as soon as possible.

(2) Compared with synthetic polymer coatings, the extension rate of polymer modified cementitious waterproof coatings are lower and deformability higher. It should necessary to develop new coatings, improving the elongation and broadening the application range.

(3) High-end additional functions and value are low. It should consider adding the root resistance agent, flame retardant etc. to the materials, broadening the application in planting roof, fireproof and waterproof coating fields.

(4) Construction temperature is relatively strict for polymer modified cementitious waterproof coatings, usually above 5℃. It is imperative to break through the inherent thinking on cement, and explore the new coating could be used at lower temperature.

Conclusion

It can be estimated that waterproof coatings are developing from solvent type to emulsion and reaction type, from low-end products to products of high elasticity, high durability and functionality. That is to say, waterproof coatings will play more and more important role in the construction industry and show good prospects for the future. With the increasing concern on environmental protection and construction operation quality, polymer modified cementitious waterproofing coatings will draw much more attention and find more application in construction and building industry.

References

[1] Shen Chunlin, Su Lirong, Li Fang, et al, Waterproof Coatings in Buildings, China, 2003.

[2] Hu Qian-qian, Zhao Feng-qing, Development of the Waterproof Coating Material in China, Advanced Materials Research. 746 (2013) 262-265.

[3] Zhao FQ, Li H, Liu SJ, Chen JB, Preparation and properties of an environment friendly polymer-modified waterproof mortar, Construction and Building Materials. 25 (2011) 2635-2638.

[4] Shao-jie Liu, Hao Li, et al, Preparation of a new polymer-modified adhesive mortar using fine iron tailings as aggregate, Journal of Adhesion Science and Technology. 27 (2013) 951-962.

Advanced Materials Research Vol. 936 (2014) pp 1382-1386
© (2014) Trans Tech Publications, Switzerland
doi:10.4028/www.scientific.net/AMR.936.1382

Analysis of Curing Agent on the Strength of Lightweight Soil Using Recycled Sludge

Guocai Wang[1,a], Linchun Yu[1, b] and Ling Sha[2,c]

[1]Department of Civil Engineering, Zhejiang University of Technology, Hangzhou, 310032, China

[2]Department of Civil Engineering, Zhejiang College of Construction, Hangzhou 311231, China

[a]wgc@zjut.edu.cn, [b]702039135@qq.com, [c]congcong99225@126.com

Keywords: EPS mixed lightweight soil; optimum proportion; unconfined compressive strength; SEM test

Abstract. In order to study the inorganic composite curing agents of lime, gypsum, fly ash on the strength properties of EPS lightweight soil using recycled sludge, the unconfined compressive strength test and scanning electron microscope test are done to investigate the strength properties of EPS lightweight soil. The effect and scope of each curing agent is investigated and determined by means of single-doped unconfined compressive strength test, and the optimum proportion of the curing agent is further determined by the method of orthogonal unconfined compressive strength test, of which the stabilized effectiveness of the lightweight soil is compared with those only using cement as curing agent. Finally, the SEM test is done to study the microstructure and pore characteristics of the lightweight soil mixed with EPS adding with or without curing agent. The test results and curing agent can be used as conference when stabilizing soft soil and treatment of discarded clay.

Introduction

Currently, with the rapid economic growth, China is in the rapid developing period. The development of urban real estate, construction of ocean and coastal projects, expansion of roads and bridges projects, etc., is requiring a lot of engineering soil. Generally, the source of engineering soil is from farmland's excavation, sand and stones of ocean, exploitation of mines, etc., which led to many negative effects, such as soil erosion, landslides and reduction of farmland. Meanwhile, the process of infrastructure and Canal dredging projects will generate a lot of wasted soil and silt, which pollute the environment and land resources again. How to use engineering discarded soil and silt and to make it meet the requirements of engineering soil, has become a popular and urgent issue.

EPS mixed lightweight soil is a kind of lightweight soil which is composed of raw material soil, EPS granules, curing agent and water, etc., and stirred and solidified to form curtain strength. Its research and development can not only reduce environmental pollution, but also can make the project discarded soil and canal silt be converted into a renewable civil resource and reused again. With the growing shortage of consuming resources and the increase of environmental protection awareness, lightweight technology of soil is gaining more and more attention and recognition. However, the strength and deformation of EPS mixed lightweight soil, is still far from the level of wide range of practical engineering applications, as well as construction period, which needs further investigation.

Many scholars and engineers pay more attention on the strength and deformation of lightweight soil at home and abroad. For example, Zhang[1], Huang[2] and Zhang[3], etc. analyzed the influence of the composition and dosage of inorganic curing agents to the strength of solidified soil. Ji[4], Wang[5] and Fan[6], etc. studied the microstructure of cement stabilized soil and lightweight soil by means of XRD and SEM microscopic experiments. Based on the previous research work, this paper use Hangzhou Canal silt as raw soil and study characteristics of EPS mixed lightweight soil and investigated the effect of inorganic curing agent of lime, gypsum and fly ash on the strength of lightweight soil by means of unconfined compressive strength test and scanning electron microscope test.

Curing materials

Soil samples The main raw curing material used in the test is soil samples, EPS spherical particles, curing agents and water. The soil samples are taken from the canal of Hangzhou, of which the main physical and mechanical indexes are shown in table 1.

Table 1 The basic physical and mechanical indexes of canal silt

natural density ρ/(g/cm^3)	water content w/%	specific gravity d_s	void ratio e	liquid limit w_L/%	plastic limit w_P/%
1.62	57.5	2.60	1.489	53.0	28.3

EPS spherical particles The lightweight material used is a in the test is spherical EPS beads produced by Hangzhou Plastic Packaging Material Co. Ltd. , with the density and bulk density of 0.030g/cm^3 and 0.016g/cm^3, respectively. EPS particle content is quantified by the volume fraction α_{eps} of EPS particle in the sample, which is the ratio between the volume of EPS particles in the sample (V_{eps}) and the total sample volume (V):

$$\alpha_{eps} = \frac{V_{eps}}{V} \times 100\% \tag{1}$$

The content of EPS particle used in this test is 15%, 25% and 35%, respectively.

Curing agent The cement, lime, gypsum and fly ash are chosen as curing agent. The cement is chosen from the 42.5# ordinary portland cement produced by Qianchao Cement Plant, Hangzhou.

The cement content(β_c) is the ratio between the quality of cement (m_c)and the quality of canal silt(m_s):

$$\beta_c = \frac{m_c}{m_s} \times 100\% \tag{2}$$

The gypsum is produced by Shanghai Baoping Building Materials Co. Ltd. The lime is produced by Yongfu County of Guangxi Jin Yingtai Co. Ltd. The fly ash is produced by Jiaxing Power Plant, Zhejiang. The content of lime, gypsum and fly ash used in the test is:

$$\beta_b = \frac{m_b}{m_s} \times 100\% \tag{3}$$

where β_b is the content of lime, gypsum and fly ash, m_b is the quality of lime, gypsum and fly ash and ms is the quality of canal silt.

Experimental results

Single-doped test Firstly, the test is taken by only adding cement to the lightweight soil for Hangzhou Canal silt. Then, using soil sample of 15% cement content as the reference volume in the single-doped test, of which the content of lime, gypsum and fly ash is selected as five levels, and the content of EPS particle is chosen as 15%, 25% and 35%. A total of 45 groups, each group prepared three parallel samples, a total of 135 specimens are prepared. Taken the average intensity of the sample curing for 28 days of each factor as Y-coordinate, and the content level of each factor as X-coordinate, the relationship between sample intensity index and changes in the level of each factor is shown in Fig. 1-2.

Fig. 1 is the relationship between the unconfined compressive strength and lime content of lightweight soil under different volume fraction of EPS particles. From Fig. 1, it can be seen that: at certain lime content, the compressive strength of the sample decreases with the increase of EPS particle volume fraction. At certain EPS particle volume fraction, the strength of the sample increases with the increase of lime content, then begins to decrease after passing the peak value. When the lime content is 5%, the compressive strength of the sample reaches the maximum value.

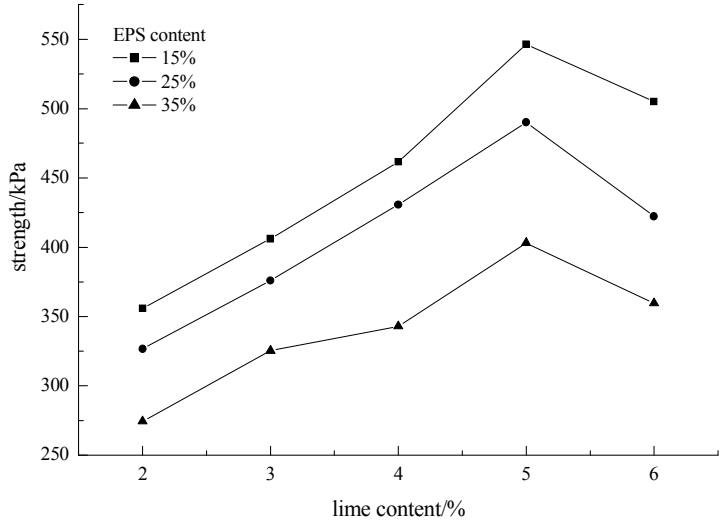


Fig. 1 The relationship between strength and lime content for different EPS content

Fig. 2 is the relationship between the unconfined compressive strength and fly ash content of the lightweight soil. From the figure, it can be seen that the confined compressive strength of the lightweight soil increases with the increase of the fly ash content and decreases with the increase of EPS particle volume fraction. When the fly ash content is 12%, the compressive strength of the sample reaches the maximum value.

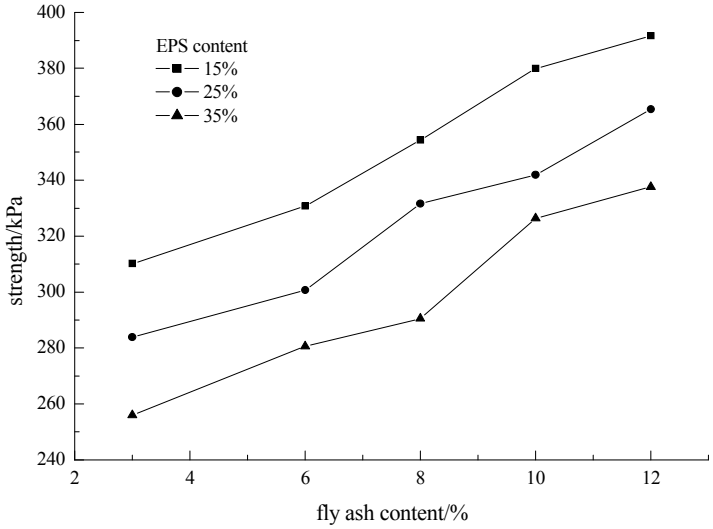


Fig. 2 The relationship between strength and fly ash content for different EPS content

Orthogonal test Based on the single-doped test, the test uses pure soil sample as a reference volume of orthogonal test, and four factors and three levels of the content of lime, gypsum and fly ash are selected, a total of 9 groups, 28 days of curing age, each group preparing three parallel samples, and with the content of EPS particle of 15%, 25% and 35%, a total of 81 specimens are prepared and tested.

The optimal level and the best combination of experimental factors must be determined firstly, of which the optimal level means the level of each factor which makes the strength index to achieve the best. To determine the optimal level of factors, each level's impact of this factor on strength index must be determined. The orthogonal experiment compressive strength is shown in table 2. The 4 number in K_1 line respectively means 1 level of four factors corresponding to the sum of the unconfined compressive strength in the test. Using the same method, it can obtain K_2 and K_3. The 4 number in each line of k_1, k_2 and k_3, respectively, are K_1, K_2 and K_3 corresponding to each number divided by 3, which is the average value of each level. Dosage level with maximum average value is the optimal level of this factor. Taken lime as example, the k_2 is maximum, so 2 level is the best for

lime, and lime content is 15%. Similarly, the optimum dosage level of cement is 18%, the optimum dosage of lime is 5%, the optimum dosage of gypsum is 2%, and the optimum dosage level of fly ash is 12%.

To Determine the primary and secondary order for each factor, the impact of various factors on strength index is different and its importance varies each other. In the same column, the maximum number of k_1, k_2 and k_3 minus the minimum number of the k_1, k_2 and k_3, and the value is called range (R_j). According to the size range of R, the factors' influence of importance on experimental index can be determined. The larger the gap between each data of range R, indicating that the differences between levels of the factor is bigger, which plays more important role in the test, otherwise the factor plays the secondary influence. According to the data of table 2, it can get the sequence of 4 factors from the main influence to the secondary influence. The order is cement, fly ash, gypsum and finally lime.

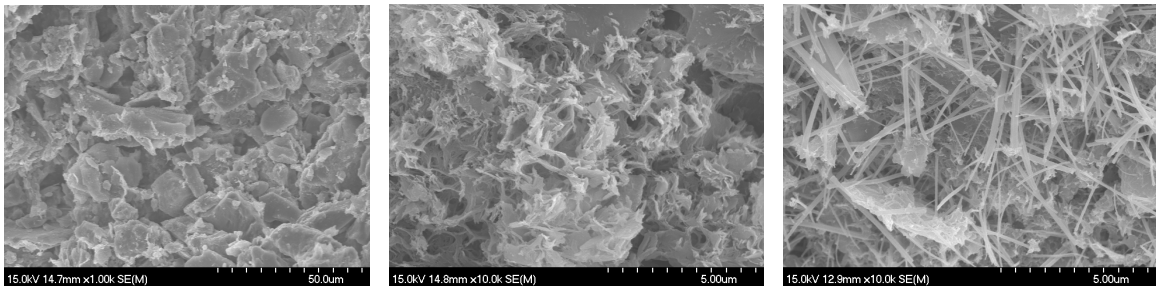
Table 2 Analysis of orthogonal test results (35% EPS)

	cement	lime	gypsum	fly ash
K_1	1218	1648	2137	1352
K_2	1879	1905	1662	1836
K_3	2345	1889	1568	2254
k_1	406	549	712	451
k_2	626	635	554	612
k_3	782	630	523	751
R	376	86	190	301

The maximum value and change trends of R are consistent when the content of EPS particle changes in the range of 15%, 25%, 35%, indicating that the factors' impact on the role of strength index has nothing to do with EPS particle content.

Microstructure of lightweight soil In the SEM test, the lightweight soil with 25% EPS particle content is set as reference volume, and three kinds of soil samples are prepared to investigate the similarities and differences from the microstructure viewpoint: original soil samples, lightweight soil samples of 15% cement content, and lightweight soil samples of optimal combination curing agent and 15% cement content. The results are shown in Fig. 3.

From Fig. 3(a), it can be seen that the blocky and platy aggregates are the elementary cells of Canal silt microstructure. These aggregates are connected by surface contact or edge-to-surface contact. Voids in undisturbed soil are dense and widely distributed. Generally, there are two kinds of voids: big voids which are formed between clay aggregates and small voids between mineral particles inside of clay aggregates. Features of the microstructure are small contact area, poor stability and large void ratio.



(a) (b) (c)

Fig. 3 SEM photos of raw soil and solidified soil
(a) undisturbed soil; (b) without optimal curing agent; (c) with optimal curing agent

Fig. 3(b) and 3(c) is the SEM photos of solidified soil. From the figure, it can be seen that: if the lightweight soil is stabilized without optimal combination curing agent, the clay aggregates are connected by cement hydration products of C-S-H and Aft with fibrous, hexagonal plate lap to form a

network structure. Cement hydration products filling or inserting the voids of soil aggregates, wrapping clay aggregates or bonding clay aggregates nearby together. Therefore, cement hydration products' effects of filling, wraping, bonding can improve strength properties of Canal silt. But there are still a lot of voids among clay aggregates which is caused by unhydrated cement, and hence exists faulty.

If the samples of lightweight soil is stabilized with optimal combination curing agent, there not only exists additional strengthen structure caused by cement hydration products, but also produce a lot of network shaped beam fiber among internal voids and gaps where cement hydration products cannot act, which makes the structure of soil samples further improved, so that the ability to resist damage and deformation of the samples increased.

Summary

By means of unconfined compressive strength test and scanning electron microscope test, the characteristics of EPS mixed lightweight soil is investigated and the effect of curing agent on the strength of stabilized soil is analyzed. From the analysis, the conclusions can be drawn as follows:

(a) Under the same EPS particle volume fraction, the unconfined compressive strength of lightweight soils increases with the increasing content of cement. The compressive strength of the sample decreases with the increasing volume fraction of EPS particle for same cement content.

(b) For 15% cement content, when the content of lime, gypsum and fly ash is same, the unconfined compressive strength of the sample decreases with increasing volume fraction of EPS particle. If the content of lime, gypsum and fly ash is 5%, 2%, 12% respectively, the compressive strength of the sample reaches maximum value for same EPS particle volume fraction.

(c) The best combination of experimental factors is obtained through orthogonal experiment: cement content is 18%, lime content is 5%, gypsum content is 2% and fly ash content is 12%. The sequence of 4 factors from the main influence to the secondary influence is cement, fly ash, gypsum, lime.

(d) From the view point of microstructure, the lightweight soil with optimal curing agent, the internal voids and gaps between voids are appearing a large number of network shaped beam fiber, which makes the network structure of soil samples further improved, so that the ability of anti damage and deformation of the samples is increased.

Acknowledgement

This work was financially supported by the Science Technology Department of Zhejiang Province (2012C31007). The support is gratefully acknowledged.

References

[1] Zhang Huiling, Huang Xin, Xu Shihong, etc. The enhancement effect of fly ash in cement[J]. Journal of Wuhan University of Technology, 2009, 23(9): 14-18

[2] Huang Yu, Zhou Zizhou, Bai Jiong, etc. Analysis of micro test for gypsum additive in cement mixing method reinforcement effect of soft soil foundation[J]. Journal of Geotechnical Engineering, 2010, 32(8): 1179-1183

[3] Zhang Xiaoping, Si Bin, Lu Xiancai. Experimental study on micro-pore structure of expansive soil improved by lime[J]. Chinese Journal of Geotechnical Engineering. 2003, 25(6): 761-763.

[4] Ji Fengling, Lv Qinfeng, Ma Dianguang. Experimental study on microstrueture of lightweight EPS-bead -treated soil mechanical behavior[J]. Journal of Lan zhou University, 2007, 43(1): 19-23.

[5] Ma Mei, Bai Xiaohong, Liang Renwang, Chen Pingan. Microstudy on soft foundations reinforcement with time-fly ash piles. Rock and Soil Mechanics, 2001, 22(1): 67-70.

[6] Fan Henghui, Wu Pute, Gao Jianen, etc. Microstructure Characteristics of Soil Stabilized with Cement-based Soil Stabilizer[J]. Journal of Building Materials.2010, 13(5): 671-674.

Advanced Materials Research Vol. 936 (2014) pp 1387-1392
© (2014) Trans Tech Publications, Switzerland
doi:10.4028/www.scientific.net/AMR.936.1387

Study on Engineering Characteristics of Coarse-Grained Soil based on Large-Scale Triaxial Test

Fu-yong Chu[1, a]

[1]School of Civil Engineering, Lishui University, Lishui, Zhejiang 323000, China

[a]cfy1976@hhu.edu.cn

Keywords：coarse-grained soil; triaxial tests; engineering characteristics; strength and deformat

Abstract：Using large-scale shearing device, isotropiclly consolidated-drained triaxial test under different confining pressures are performed for overburden material of ShuangJiangKou earthdam which relative density is 0.9. The engineering characteristics of coarse-grained soil such as strength and deformation is studied. The results show the peak strength of coarse-grained soil under isotropically increase with the confining pressure and there is a relationship of linear between the peak strength of coarse-grained soil and initial modulus. The volume strain value of isotropically consolidated-drained triaxial shear test increase with increase of confining pressure, and the dilatancy decrease increase with increase of confining pressure. The secant modulus E_{s1} and the tangent modulus E_{t1} obtained by the tests both increase with increase with increase of confining pressure, and the values of E_{s1}/E_i and E_{t1}/E_i are all smaller than one. The failure poisson ratio v_{if} obtained by the tests both decrease with increase with increase of confining pressure, and there is a relationship of power function between vif and σ_3/P_a .

Introduce

Coarse-grained soil usually refers to cohesionless mixed soil composed by coarse particles such as rubble, gravel, stone chip and stone power, etc and the mixed soil which is mixed by cohesive soil and many coarse particles[1]. The engineering properties of Coarse-grained soil behave with good compacting effect, strong perviousness, large packing density, high shear strength, small settlement deformation, high bearing power etc[1]. So it is widely used in hydraulic engineering, traffic engineering and civil engineering.

During the past few decades, A Large number of research on engineering characteristics of coarse-grained soil have been carried out by many scholars abroad, and have obtained certain achievements[2-12].

However, Because the engineering characteristics of coarse-grained soil is more complicated. Research on strength and deformation of coarse-grained soil under many complex stress state need fully be studied.

Therefore, Using large-scale shearing device, Isotropic consolidated-drained triaxial tests under different confining pressures are performed for overburden material of Shuangjiangkou earth dam whose relative density is 0.9. The dissertation studied on the engineering characteristics of coarse-grained soil such as strength and deformation. The result of research will provide the base of tests and theoretical basis for the similar projects.

Test Equipment and Test Soil

Isotropic consolidated-drained triaxial tests is performed for overburden material of Shuangjiangkou earth dam on Dadu River whose relative density is 0.9. Large-scale shearing device

is adopted, which is 300 mm in diameter and 600 mm in height and 60 mm in the most major granular diameter.

The overburden material of Shuangjiangkou earth dam on Dadu River is sand gravel, whose particle is tact, angularity is less, strength is high and permeability is strong. The nature grading is reduced scale by the hybrid method of the document [13] and the size grading curve is showed as the figure 1. The biggest dry density is obtained by the vibratory compaction experiment of surface and the least dry density is obtained by the loose-filled experiment. The biggest dry density is 2.29g/cm3 and the least dry density is 1.93g/cm3. The dry density of sample preparation is 2.25g/cm3, and the initial void ratio is 0.251.

The samples are made by the compaction test and is compacted in five layers. The saturating samples are made by the water head saturated and pumping saturated method. The loading is controlled by the method of radial strain control in loading stage and the shear rate is 0.9mm/min. The confining pressure of different test are all respectively 200, 500, 1200, 2000and 2500kPa.

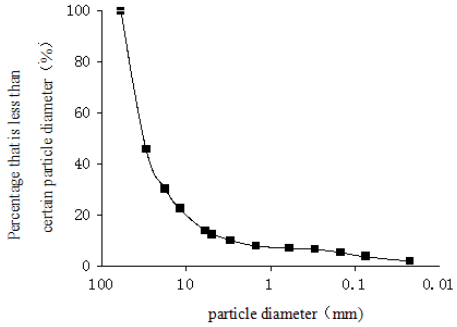


Figure 1 Size grading curve of coarse-grained soil

Test Result Analysis

Stress-strain-strength Characteristics

The curves of $(\sigma_1-\sigma_3)\sim\varepsilon_a$ of consolidated-drained triaxial test in different confining pressure are given in figure 2. Figure 2 shows that the curves of $(\sigma_1-\sigma_3)\sim\varepsilon_a$ of consolidated-drained triaxial test shows hyperbola type and slight strain softening. Figure 2 also shows that there are obvious peak of strength in the curve of consolidated-drained triaxial test, and the peak of strength increases with the increase of confining pressure. he peak strengths under different confining pressure are arranged and listed in the table 1. .

Table 1 shows that the peak strength is 9727kPa when confining pressure is 2500kPa, which has increase amplitude of 8609kPa than when confining pressure is 200kPa, has increase amplitude of 7294kPa than when confining pressure is 500kkPa, has increase amplitude of 4670kPa than when confining pressure is 1200kPa and has increase amplitude of 1600kPa than when confining pressure is 2000kPa.

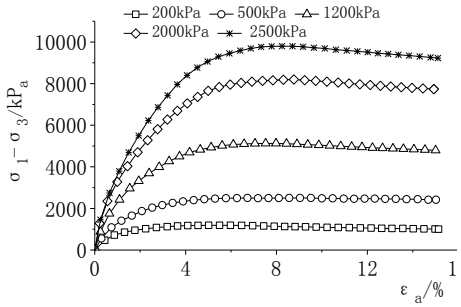


Figure 2 Curves of $\sigma_1-\sigma_3\sim\varepsilon_a$ of consolidated-drained triaxial test

Table 1 The peak strengths under different confining pressure

peak strength	200 /kPa	500 /kPa	1200 /kPa	2000 /kPa	2500 /kPa
$(\sigma_1-\sigma_3)_f$	1188	2503	5127	8197	9797

The initial modulus E_i is sorted out and the curve of $E_i \sim (\sigma_1-\sigma_3)_f$ is accumulated as the figure 3. The figure 3 shows that the E_i increase with the increase of $(\sigma_1-\sigma_3)_f$, and there is a relationship of linear between the peak strength of coarse-grained soil and initial modulus, which may be formulated by the expression

$$(\sigma_1-\sigma_3)_f = aE_i + b \tag{1}$$

Where a and b are both parameters of material. In this experiment, the parameters obtained by fitted is respectively 0.0599 and 41.59. The relative coefficient R^2 is 0.98.

Volume Strain Characteristics

The curves of $\varepsilon_v \sim \varepsilon_a$ of consolidated-drained triaxial test in different confining pressure are given in figure 4. Figure 4 shows that the volume deformation value(volume compression) under lower confining pressure is more bigger than that under higher confining pressure. For example, the volume deformation value(volume compression) when the confining pressure is 2500kP$_a$ is more bigger percentage 1.72 than the volume deformation value when the confining pressure is 200kP$_a$.

Figure 5 also shows that dilatancy of sample increase with the decrease of confining pressure. One point is worth mentioning, that is, the axial strain ε_a from volume compression to volume expansion increase with the increase of confining pressure. For example, the axial strain ε_a from volume compression to volume expansion when confining pressure is 2500kP$_a$ is more bigger percentage 4.47 than that when the confining pressure is 200kP$_a$.

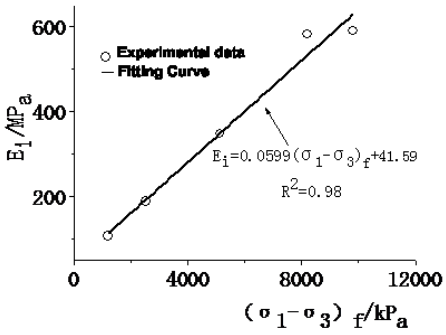


Figure 3 Relationship of $E_i \sim (\sigma_1-\sigma_3)_f$

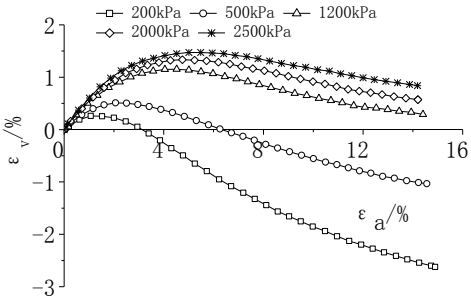


Figure 4 Curves of $\varepsilon_v \sim \varepsilon_a$ of consolidated-drained triaxial test

In order to study the characteristics of deformation of coarse-grained soil, The secant modulus E_{s1} and the tangent modulus E_{t1} under different confining pressure are sorted out and the curves of $E_{s1} \sim \sigma_3/P_a$ and $E_{t1} \sim \sigma_3/P_a$ are accumulated as the figure 5～figure 6. Which E_{s1} is the $(\sigma_1-\sigma_3)/\varepsilon_a$ ratio when ε_a is one percentage and E_{t1} is the slope of tangent when ε_a is one percentage.

figure 5 and figure 6 both show that E_{s1} and E_{t1} both increase with the increase of σ_3/P_a. they show the linear characteristics, which may be formulated by the expression

$$E_{s1} = m(\sigma_3/P_a) + n \tag{1}$$

Where m and n are both parameters of material. In this experiment, the parameters obtained by fitted is respectively 12.32 and 66.91. The relative coefficient R^2 is 0.98.

$$E_{t1} = l(\sigma_3 / P_a) + f \tag{2}$$

Where l and f are both parameters of material. In this experiment, the parameters obtained by fitted is respectively 7.66 and 41.26. The relative coefficient R^2 is 0.97.

The values of E_{s1}/E_i and E_{t1}/E_i are sorted out and listed in the table 2. The table 2 shows that the values of E_{s1}/E_i and E_{t1}/E_i are all smaller than one. That is, there is some attenuation and the attenuation gradually increase with the increase of confining pressure. This shows that particle crush increase and fine particle increase. Then, fine particles of coarse-grained soil fully fill into the pore between the large particles of coarse-grained soil. Therefor, the deformation of coarse-grained soil decrease with increase of the confining pressure

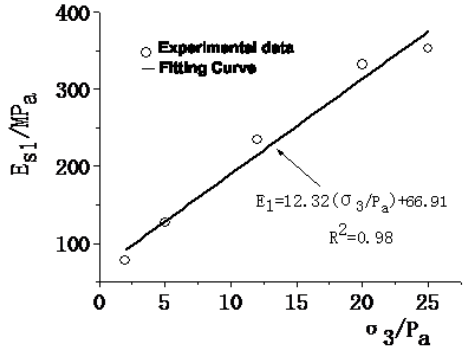


Figure 4 Relationship of $E_{s_1} \sim \sigma_3 / P_a$

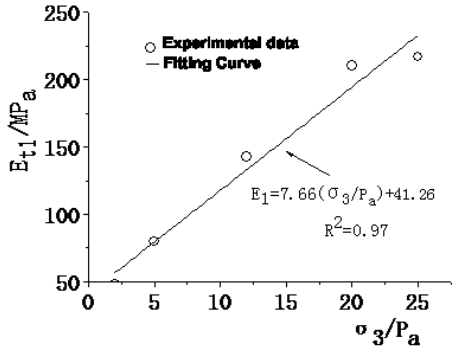


Figure 5 Relationship of $E_{t1} \sim \sigma_3 / P_a$

Table 1 Attenuation of deformation modulus

Confining pressure/kPa	secant modulus		tangent modulus	
	Es_1/E_i	attenuation	Et_1/E_i	attenuation
200	0.73	27.3	0.4465868922	55.4
500	0.685	31.5	0.423519206	58.7
1200	0.673	32.7	0.410416547	59.0
2000	0.598	40.2	0.370482302	63.0
2500	0.570	43	0.361214936	63.9

In order to comprehensively study on the characteristics of deformation of coarse-grained soil, The the failure poisson ratio v_{if} under different confining pressure are sorted out and the curves of $v_{if} \sim \sigma_3 / P_a$ is accumulated as the figure 7. The figure 7 shows that the failure poisson ratio v_{if} decrease with increase of confining pressure, and there is a relationship of power function between v_{if} and σ_3 / P_a which may be formulated by the expression

$$v_{if} = h(\sigma_3 / P_a)^g \tag{3}$$

Where h and g are both parameters of material. In this experiment, the parameters obtained by fitted is respectively 0.69 and -0.083. The relative coefficient R^2 is 0.96.

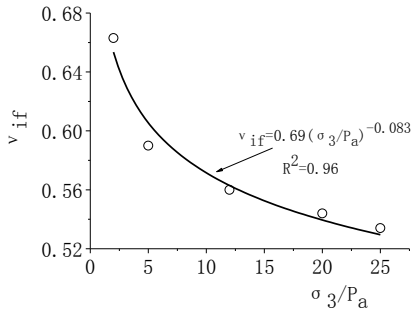


Figure 5 Relationship of $v_{if} \sim \sigma_3/P_a$

Conclusion

Isotropiclly consolidated-drained triaxial test under different confining pressures is performed for overburden material of ShuangJiangKou earth dam which relative density is 0.9 using large-scale shearing device. The engineering characteristics of coarse-grained soil such as strength and deformation is studied. Some preliminary conclusion ise obtained as follows:

(1) The peak strength of coarse-grained soil under isotropically increase with the confining pressure and there is a relationship of linear between the peak strength of coarse-grained soil and initial modulus.

(2) The volume strain value of isotropically consolidated-drained triaxial shear test increase with increase of confining pressure, and the dilatancy decrease increase with increase of confining pressure.

(3) The secant modulus E_{s1} and the tangent modulus E_{t1} obtained by the tests both increase with increase with increase of confining pressure, and the values of E_{s1}/E_i and E_{t1}/E_i are all smaller than one .

(4) The failure poisson ratio v_{if} obtained by the tests both decrease with increase with increase of confining pressure, and there is a relationship of power function between v_{if} and σ_3/P_a .

References

[1] Association of Geotechnique of Japan. In-situ compaction of coarse-grained materials[M]. GUO Xi-ling, WEN Dan, translators. Beijing:China Water Power Press, 1999:2-56.

[2] SI Hong-yang. Characteristic of dilatation of several kinds of grained soils[J]. **Journal of nanjing hydraulic research institute**, 1984, (2): 45-51.

[3] HUANG Hao-ran, ZHU Jun-gao, FANG Zhi-rong, etc al. Triaxial test study of deformation and strength behavior of sand-gravel materials[J]. **Water Resources and Power,** 2012, 30(7): 87-89. in Chinese

[4] MIURA N, O'HARA S. Particle crushing of a decomposed grained soil under shear stress[J].. **Soils and Foundation**, 1979, 19(3): 61-76.

[5] CHEN Xiao-bing. Study of dilatancy effect of red stone coarse grained soil by large scale triaxial tests[J]. **Chinese Journal of Rock Mechanics and Engineering**, 2010，29(supp 1)：3145-3149. in Chinese

[6] INDRARATNA B, IONESCU D, CHRISTIE H D. Shear behavior of railway ballast based on large-scale triaxial tests[J]. **Journal of Geotechnical and Geoenvironmental** Engineering, ASCE, 1998, 124(5) : 439-449.

[7] CHU Fu-yong, ZHU Jun-gao, WANG Ping, etc al. Engineering properties and applications of coarse grained soil[J]. **Rock and Soil Mechanics**, , 2012, 33(6): 1625-1631. in Chinese

[8] QIN Hong-yu, LIU Han-long, GAO Yu-feng, etc al. Research on strength and deformation behavior of coarse aggregates based on large-scale triaxial tests[J]. **Rock and Soil Mechanics**, 2004, 25(10):1575-1580. in Chinese

[9] JIANG Jing-shan, LIU Han-long, CHENG Zhan-lin, etc al. AN Shu-hong. Influences of density and confining pressure on mechanical properties fro coarse-grained soils[J]. **Journal of Yangtze River Scientific Research Institute**, 2009, 26(8): 46-50. in Chinese

[10] ZHANG Qi-yue. Shear strength and stress-strain properties of sand-gravel materials [J]. **Journal of Nanjing Hydraulic Research Institute** , 1985(3)：133-145. in Chinese

[11] MENG Xian-ling, SHI Yan-wen. Shear strength of sandy-gravels in Shitouhe River Dam [J]. **Chinese Journal of Geotechnical Engineering**, 1983, 5(1)：90-101. in Chinese

[12] WEI Song, ZHU Jun-gao. Study on wettig behavior of coarse grained soil in triaxial test[J]. **Rock and Soil Mechanics**, 2007, 28(8):1609-1615. in Chinese

[13] Soil test procedures SL237-1999[S]. Beijing: China Water Power Press. 1999.

Advanced Materials Research Vol. 936 (2014) pp 1393-1398
© (2014) Trans Tech Publications, Switzerland
doi:10.4028/www.scientific.net/AMR.936.1393

Copolymerization Kinetics of Polyetyhylenglycol Allylether Type Polycarboxylate Superplasticizer

Yingfeng Tian[1,a], Xiaping Zhu[2,b,*], Yating Deng[3,c], Kui Wang[4,d]

[1,2,4]College of Materials and Chemistry and Chemical Engineering, Chengdu University of Technology, Mineral Resources Chemistry Key Laboratory of Sichuan Higher Education Institutions, Chengdu 610059,China. [3]COFCO Huaxia Great Wall Red Wine Co. Ltd. Yinchuan 750000,China.

[a]Email: xxsctyf2013@163.com, [b]Email: zhuxiaping@cdut.edu.cn *Corresponding author,

[c]Email: xingruyu223@163.com, [d]Email: 1083102889@qq.com

Keywords: Kinetics of polymerization, Polyethylenglycol allylether, Polycarboxylate superplasticizer

Abstract: The free radical copolymerization kinetics of polyethylenglycol allylether (APEG) with acrylic acid(AA) had been studied in aqueous solution through using ammonium persulfate(APS) and 30% hydrogen peroxide(H_2O_2) as initiators. The structure of polycarboxylate superplasticizer had been characterized by IR and ^{1}H-NMR. The rate of copolymerization was proportional to the molar ratio of monomers (AA:APEG) to the power of 0.4405, and to the amount of initiator (1.5%APS-2%H_2O_2, mass ratio to monomers) to the power of 0.7819, respectively. The overall observed activation energy of copolymerization was 45.048 kJ/mol. The kinetic relationship of copolymerization reaction of APEG with AA had been established as follow: $Rp \propto [\text{APEG/AA}]^{0.4405}[\text{APS-30\%}H_2O_2]^{0.7819}e^{-5418/T}$. The temperature and initiator were main influencing factors on polymerization reaction.

Introduction

The polycarboxylate concrete superplasticizer(PCS) has the advantages of high water reducing rate, low slump loss, good compatibility with cement and friendly to environment, which becomes the focus of concrete research[1,2]. The properties of polycarboxylate superplasticizer are obviously superior to naphthylene or melamin type superplasticizer, its application has increased in construction industry[3,4] such as preparing high-volume fly ash concrete, high-flowing concrete, high-strength concrete and high-durability concrete, etc..

Currently, there were some literatures [5,6]which had reported the synthesis of PCS, those mainly had discussed the synthesis conditions in order to improve the application performance of PCS. Some studies of binary or ternary dispersion polymerization kinetics had mainly aimed the polymerization such as biological, pharmaceutical separated materials and solid-phase supporting materials[7,8]. The study of polymerization kinetics of PCS mainly concentrated on the esterification reaction of monomers. Mehmet R. Altiokka[9] had discussed esterification reaction kinetics of acrylic acid with propylene glycol in the presence of amberlyst-15 as a heterogeneous catalyst, and developed the kinetic equations corresponding to reaction mechanism. The results of Sun[10] showed that the esterification reaction of polyethylene glycol with acrylic acid was typical two grade reaction. Xu[11] had studied the copolymerization kinetics of PCS which used the maleic anhydride, acrylic acid and sodium allylsulfonate as monomers. The relationship between the polymerization rate and the amount of initiator as well as the molar ratio of monomer had been gotten, the apparent activation energy of polymerization was 37.604 kJ/mol.

There were various types of process studies about ether-type polycarboxylate superplasticizer, however, kinetic information had not been given in those studies. Now, there are many problems in the production process of ether-type polycarboxylate superplasticizer, the water reducing effect of some industrialized products are not ideal. The polymerization kinetics study of ether type polycarboxylate superplasticizer is very important to optimizing its production process. This study had discussed the polymerization reaction kinetic of polyethylenglycol allylether with acrylic acid.

The structure of product had also been characterized. The results might provide theoretical and actual reference for production process of ether-type polycarboxylate concrete superplasticizer.

Experimental

Materials

Polyethylenglycol allylether（APEG, Hunan shida chemical engineering factory, industrial grade）. Acrylic acid（AA）, Thioglycolic acid, $(NH_4)_2S_2O_8$（APS）, H_2O_2（30%）, $KBrO_3$, KBr, $Na_2S_2O_3$, HCl, NaOH. The reagents except APEG were of analytical grade, and were of Chengdu kelong chemical reagent factory.

Experimental methods

Polymerization Reaction

A certain amount of deionized water and thioglycolic acid were first added to a 250-mL three-necked flask, then the temperature was raised to 80 °C. APEG, AA and a small amount of deionized water were mixed into a constant pressure dropping funnel. H_2O_2 (30%), APS and a small amount of deionized water were mixed to another constant pressure dropping funnel. The initiator and monomer mixture were added to the three-necked flask simultaneously. The polymerization reaction was continued for 6 hours, then cooled to room temperature. The impurities were removed by rotary distillation. Finally, the purified ether-type polycarboxylate superplasticizer(PS) was obtained.

Determination of the double bond

A certain amount of sample was taken from the three-necked flask at intervals, and placed in iodine flask, 15mL mixed reagent (357 mL of glacial acetic acid, 67 mL of carbon tetrachloride, 58 mL of methanol, 9 mL of dilute sulfuric acid and 35 mL of 100 g/L mercuric chloride-methanol solution) was added, then 20 mL $KBrO_3$-KBr solution (0.05 mol/L) and 5 mL HCl solution (2 mol/L) were added. The mixture was sealed, placed in the dark and often shaken. After 20 minutes, 10 mL of 100 g/L potassium iodide solution was added, the mixture was stood for another 10 minutes. The amount of double bonds was determined through using starch solution as indicator and 0.1 mol/L sodium thiosulfate as titrant.

Calculation of conversion rate and polymerization reaction rate

The conversion rate was calculated according with the concentration of double bond before (c_0) and after (c_i) reaction:

$$\text{Eq. 1: } \eta=(c_i-c_0)/c_0 \quad (1)$$

The linear regression between conversion rate and reaction time of constant speed phase was performed, then the slope of regression curve (dc/dt) and the correlation coefficient(R) were calculated, respectively. The polymerization reaction rate (Rp) of constant speed phase was calculated:

$$\text{Eq. 2: } Rp=(dc/dt) \ (\%/minute) \quad (2)$$

Characterization of PS

Structural characterization of the PS were done by TENSOR27 Fourier transform infrared spectrometer (Germany bruker company) and Avance 600MHz nuclear magnetic resonance spectrometer (Germany bruker company).

Results and Discussion

IR and ^{1}H-NMR spectrum analysis

IR spectrums of APEG and PS were shown in Fig.1. In addition to the common absorption peaks of APEG, such as C-H stretching vibration (2890 cm^{-1}), C-H bending vibration (1341 cm^{-1}), C-O stretching vibration (1102 cm^{-1}), C=C bending vibration (958 cm^{-1}) , PS had some characteristic peaks. The absorption band at 3380 cm^{-1} was attributed to stretching vibration of O-H. The absorption bands at 1642 cm^{-1} was ascribed to stretching vibration of C=O. The absorption bands at 1252 cm^{-1} and 947 cm^{-1} were due to stretching vibration of O=C-O and bending vibration of O-H, respectively.

Fig.2 exhibited the ^{1}H-NMR spectrums of APEG and PS. The solvent peak of deuterated chloroform was 7.26. The multiplet which the chemical shift value was about 5.90 and 3.6 were the methylene hydrogen in the side of long-chain of APEG. The chemical shift 5.2 and 2.0 were methylene and methine hydrogen in the main chain of APEG.

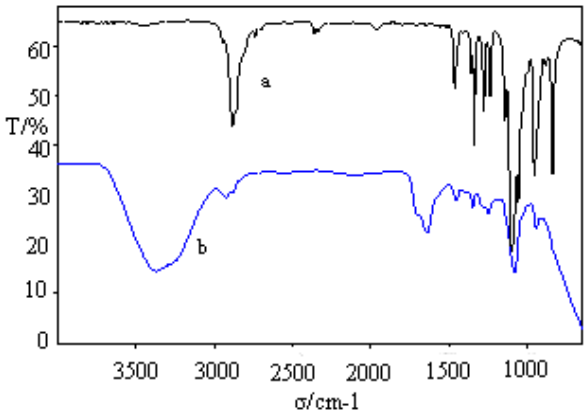


Fig. 1. IR spectrums of APEG（a）and PS(b)

The chemical shift 4.0 was the hydrogen of hydroxyl group. Compared to Fig.2a, it could be seen from Fig.2b, chemical shift at 2.7 and 1.9 were the hydrogen peak of methine and methylene which were connected to the -COOH of AA. Due to the disconnected of double bond of APEG in the polymerization reaction, the chemical shift of methine hydrogen that connected to the double bond changed, so the peaks 2.0 disappeared. The results of IR and ^{1}H-NMR showed that the copolymerization reaction had been occurred successfully.

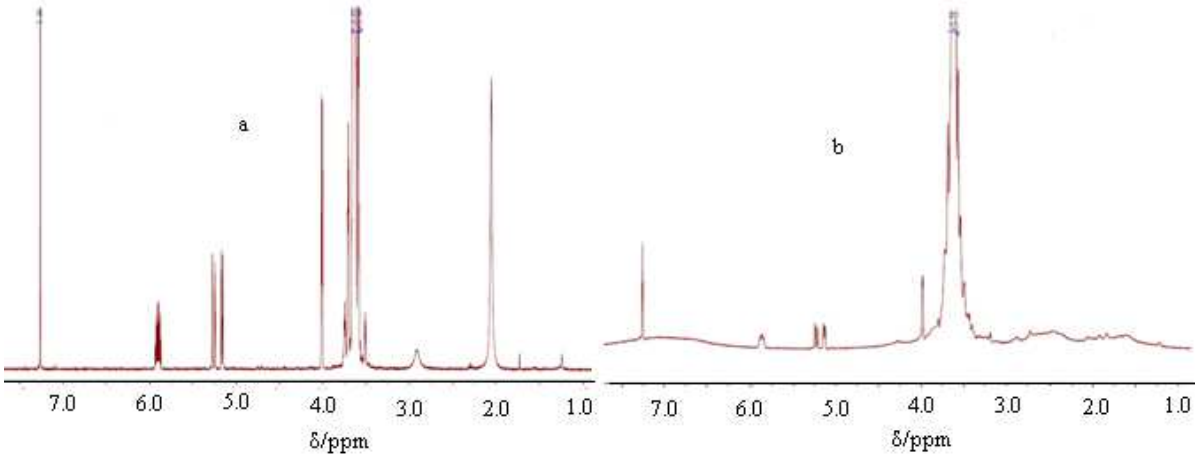


Fig. 2. ^{1}H-NMR spectrums of APEG(a) and PS(b)

The Kinetics of Polymerization Reaction

Effect of temperature on the polymerization reaction rate

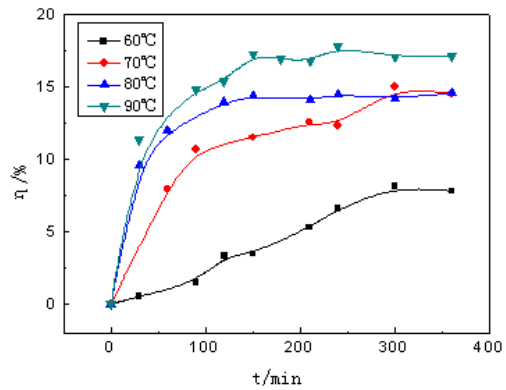


Fig. 3. Polymerization conversion rate at different temperature

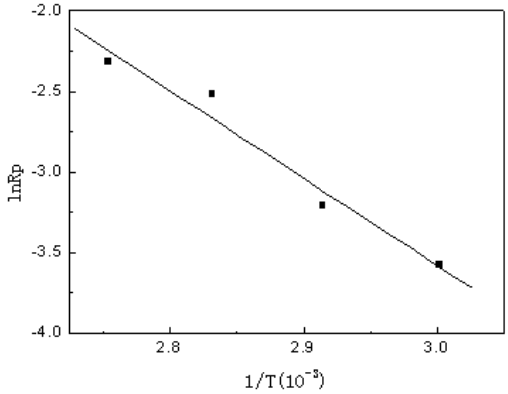


Fig. 4. Relation of lnRp and T-1(10-3)

The mixture of APS and H_2O_2 were used as initiator, the amount were 1.5% and 2.0% of the total mass of monomers, respectively. The thioglycolic acid chain was used as transfer agent, the amount was 1.6% of the total mass of monomers. The monomer molar ratio of APEG: AA was 1:4. The reaction rate curves under different temperatures were shown in Fig.3. The polymerization conversion rate increased with the time prolong, then reached balance. The polymerization conversion rate increased with the temperature increasing from 60℃ to 90℃, the equilibrium time at different temperatures were different with the shorter time under the higher temperature. The temperature raising accelerated decomposition speed of initiator, the generation rate of free radical increased, the concentration of free radical in the polymerization system increased, so the conversion rate increased. Linear regression between conversion rate and reaction time on the constant speed phase of curve was performed, and the polymerization rate（*Rp*）of constant speed phase under different temperatures were obtained, logarithm of the polymerization rate had the linear relation to T^{-1}, as shown in Fig.4. The slope（*K*）of the regression curve was -5.4183, and the correlation coefficients was -0.9824. The total apparent activation energy (*Ea*) of copolymerization was 45.048 kJ/mol calculated according to the Arrhenius equation[9]. The activation energy of polymerization was greater than 40 kJ/mol, it was a typical chemical reaction.

3.2.2 Effect of amount of initiator on the polymerization reaction rate

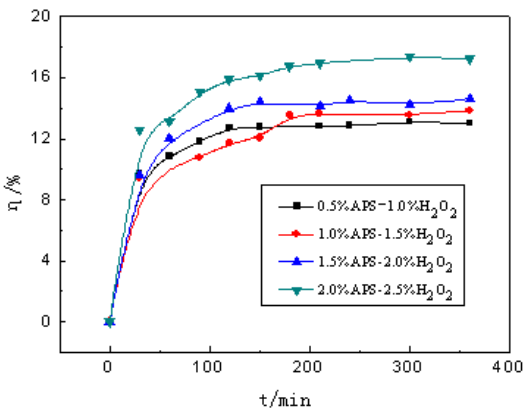


Fig. 5. Polymerization conversion rate at different concentration of initiator

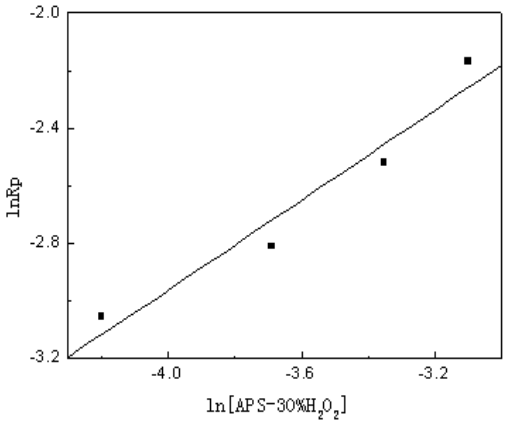


Fig. 6. Relation of lnRp and ln[APS-30%H_2O_2]

At the temperature of 80 ℃, the amount of thioglycolic acid was 1.6% of the total mass of monomers, and monomer molar ratio of APEG/AA was 1:4, the effect of initiator on the polymerization rate was measured. With the mass fraction of initiator growing from 1.5% to 4.5% (0.5%APS-1%H_2O_2,1% APS -1.5% H_2O_2,1.5% APS -2% H_2O_2, 2% APS -2.5% H_2O_2）, the concentration of free radical increased, initiator efficiency raised, and conversion rate increased gradually. In addition, the balanced time of polymerization increased with the increase of initiator amount. The polymerization reaction rate (*Rp*) could be got from the constant speed phase of conversion rate and polymerization reaction time curve under different amount of initiator by linear regression. There was good linearity between ln*Rp* and ln[APS-30% H_2O_2], as shown in Fig.6. The slope was 0.7819, the correlation coefficient was 0.9716. The relationship was showed between polymerization rate and amount of initiator: $Rp \propto [\text{APS-30\%}H_2O_2]^{0.7819}$.

Effect of molar ratio of monomer on the polymerization reaction rate

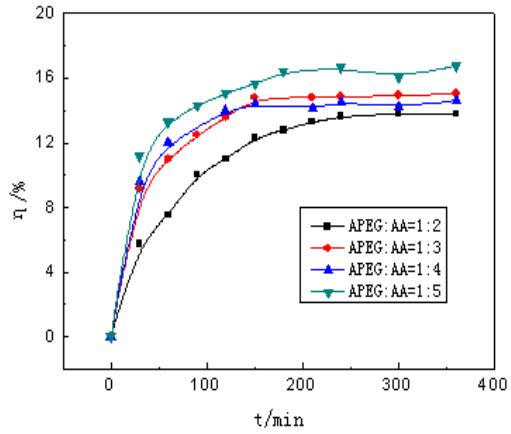


Fig. 7. Polymerization conversion rate at different molar ratio of monomers

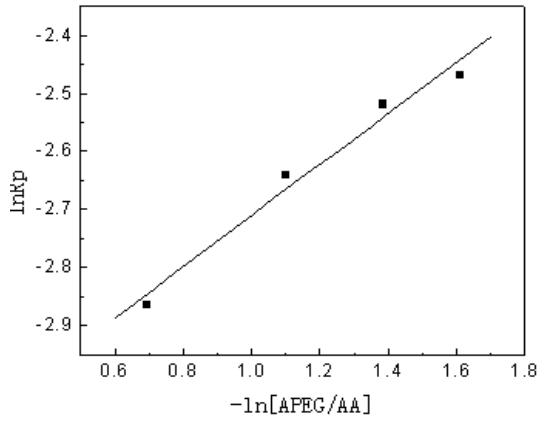


Fig. 8. Relation of lnRp and ln[APE G / AA]

The amount of initiator was 1.5% APS-2.0% H_2O_2, the thioglycolic acid was 1.6%, the kinetics curves of polymerization conversion rate under different molar ratio of monomers were measured at 80℃. The conversion rate increased with the molar ratio of APEG/AA decreasing. The activity of AA was more than that of APEG, the more content of AA, the higher activity of polymerization system and the greater of conversion rate. The molar ratio of APEG / AA had little effect to the polymerization reaction equilibrium time than temperature and initiator. It could be seen that temperature and amount and kinds of initiator could affect the polymerization equilibrium time seriously. Linear regression of conversion rate and polymerization time of the constant speed phase was performed. The polymerization reaction rate(*Rp*) of constant speed phase under different molar ratio of monomers were got. It showed good linearity between ln*Rp* and ln[APEG/AA], the slope was 0.4405, the correlation coefficient was 0.9874. So the relationship of polymerization rate and molar ratio of monomers could be expressed: $Rp \propto [\text{APEG} / \text{AA}]^{0.4405}$.

According to the dynamics results of above discussion, the kinetic relationship could be established as follow: $Rp \propto [\text{APEG/AA}]^{0.4405}[\text{APS-30\%H}_2\text{O}_2]^{0.7819} e^{-5418/T}$.

Conclusions

The overall observed activation energy of copolymerization reaction of APEG with AA was 45.048 kJ/mol. It was a typical chemical reaction. The copolymerization mechanism could be described that the self-polymerization reaction was occurred inside AA monomers firstly, and many polymeric long chain monomer was formed, then APEG opened the internal double bond under the role of initiator, copolymerization reaction with polymeric long chain monomer happened, the network polymer formed, that was the ether-type polycarboxylate superplasticizer.

Acknowledgements

Authors wish to acknowledge financial support from the Quality of higher education projects of Sichuan Province, China(SHZ1106CX05).

References

[1] Z.M.Wang, Polycarboxylate superplasticizer-preparation, properties and application. Beijing, China Building Industry Press, 2009.

[2] X.Zhang, L.Y.Gu, H.T. Zhang, Synthesizes and research status of the high performance water reducing agent of polycarboxylates in china. Chinese Journal of Colloid & polymer,25(2007)45-47.

[3] Y.Su, H Pang., B.Y. Jiang, et al., Research progress and developm ent trend of polycarboxylate type superplasticizers. Modern Chemical Industry, 31(2011)14-17.

[4] C.Z.Li, N.Q. Feng, Q.L. Niu, Model for Molecular Structure of Polycarboxylic Acid Type Superplasticizer and Its High Performance Designing. Journal of Building Materials, 7(2004)194-201.
[5] B. Arzu, T.Gözde, A.Leyla, Synthesis of copolymers of methoxy polyethylene glycol acrylate and 2-acrylamido-2-methyl-1-propanesulfonic acid: Its characterization and application as superplasticizer in concrete. Cement and Concrete Research, 39 (2009) 629-635.
[6] K J.Plank, N. Z. Pöllmann, Synthesis and performance of methacrylic ester based polycarboxylate superplasticizers possessing hydroxy terminated poly(ethylene glycol) side chains. Cement and Concrete Research , 38 (2008)1210-1216.
[7] X. Zhang, Z.L Xuan, L.Cheng, et al., Kinetic of Styrene-Butylacrylate Dispersion Copolymerization. Polymer Materials Science and Engineering, 4(2011)13-16.
[8] H.T. Zhang, R. Lv, M. Chen, Studies on Dispersion Copolymerization of St-AA-EGDMA for Preparing Monodisperse Micron-size Functional Microspheres. Chemical Journal of Chinese Univers It Ies, 25(2004)366-371.
[9] R.Mehmet Altiokka, Elif Odes. Reaction kinetics of the catalytic esterification of acrylic acid with propylene glycol. Applied Catalysis A: General , 362 (2009)115-120.
[10] Y.S. Sun, Y.J Ou, Y. Wu, et al., Study on the Esterifying Process and Kinetics of Polythylene-glycol and Methacrylic Acid. Journal of Nanchang University, 2(2006) 122-125.
[11] Z.N. Xu, G.M. Xiao, J.N. Zhou, Kinerics of Carboxylic Acid Terpolymer High Performance Water-Reducing Agent. Polymer Materials Science and Engineering, 1(2010)26-28.

Advanced Materials Research Vol. 936 (2014) pp 1399-1403
© (2014) Trans Tech Publications, Switzerland
doi:10.4028/www.scientific.net/AMR.936.1399

Improving the Volume Stability of Steel Slag for Construction and building Materials

Li Peng-guan [1,2,a], Zhao Feng-qing[2,3,b*],Ma Zhao[1,c]

[1] Hebei University of Science & Technology, Shijiazhuang 050018, PR China

[2]Hebei Engineering Research Center of Solid Wastes Utilization

Shijiazhuang 050018, PR China

[3]Hebei Engineering Research Center of Pharmaceutical and Chemical Engineering
Shijiazhuang 050018, PR China

[a]564663554@qq.com , [b]zhaofq3366@126.com, [c] mazhao728@163.com

Keywords: Steel slag, Volume stability, Free calcium oxide, Free magnesium oxide

Abstract. Steel slag is a solid waste produced in the process of steelmaking, and applying it to the field of building materials is the main utilization approach at present. However, steel slag contains free calcium oxide and magnesium oxide, existing serious stability problem. The purpose of this work is to discuss the approaches to solve volume stability problem of steel slag through mechanical modification, chemical modification and other methods. Two successful cases we completed recently were presented to illustrate the combined use of several modifying methods for volume stability treatment of steel slag.

Introduction

Steel slag is a solid waste produced in the process of steelmaking, which production accounted for about 11% ~ 15% of the crude steel production. The storage of a large amount of steel slag not only occupies the land, but also pollutes the surrounding environment. Due to steel slag is a kind of potentially active cementing material with the similar chemical composition to cement clinker, applying it to the field of building materials is the main way of recycling at present. But steel slag contains a great amount of free calcium oxide and magnesium oxide which may produce volume expansion in the process of hydration, existing serious stability problem which is the key factor for influencing the comprehensive utilization of steel slag.

It is necessary to modify steel slag before used for building material. The purpose of this work is to discuss various modifying method and modifiers for steel slag, hence giving the guidance and strategies for the development and application of modifying process for steel slag.

Factors for influencing the stability of steel slag

The volume stability is one of the important characteristics to measure whether it is qualified or not while steel slag was used in building materials field as a kind of cementitious materials. The volume stability problem of steel slag is mainly due to that it contains some chemical materials which produce volume expansion in the process of hydration, such as the volume of free CaO increased 1.98 times while generating $Ca(OH)_2$ in the process of hydration, the volume of free MgO increased 2.48 times while generating $Mg(OH)_2$, the volume of FeS and MnS increased 1.4 and 1.3 times respectively while generating $Fe(OH)_2$ and $Mn(OH)_2$ [1,2,3]. Among them, free CaO experiences the high temperature calcination of about 1600℃in the process of generation. As it

coating with the dense protective layer, the hydration rate is slow. It is well known that this is the main cause of resulting in the bad volume stability of steel slag. Free MgO mainly reacts with FeO and MgO and generates the RO phase of the matrix of MgO. The MgO/FeO ratio has effects on the stability of steel slag. The lower the ratio, the better the stability of RO phase. When the content of MgO contained in steel slag exceeds a certain threshold, it will seriously affect the stability of steel slag in the autoclaving conditions [4]. The content of FeS and MnS has little influence on the stability generally. Another study founds that [5], the metallic iron particles contained in the steel slag also affect the stability of autoclave test if the content is over 2.2%.

Treatment technology of stability

Aging treatment by stacking is a common method to solve the stability of steel slag and also is the most simple and effective method to eliminate the volume expansion of steel slag. It not only reduces the content of free CaO, but also makes sulfur ions oxidized which generated in the hydrating process of CaS. But this approach pollutes the environment and damages the ecological because of the long aging time and occupies the large storage area. Therefore we must study the new method to solve the stability problems of steel slag and accelerate the hydrating degradation of free CaO and MgO.

Mechanical modification

Mechanical modification of steel slag is to make ultrafine steel slag under the strong mechanical force, increase the specific surface area of steel slag, making large amounts of free CaO and MgO exposed and hydrated fast. Sun Jiaying's [6] studies showed that the finely ground power of steel slag has no stability problems using in cement mortar or concrete. This is because the dense protective layer in the surface of free CaO and MgO damaged in the grinding process, which makes more free CaO and MgO activated. As the specific surface area of steel slag increased and the hydration rate accelerated, the stability of steel slag improved effectively [7]. Xu Guangliang etc [8] pointed out that the dosage of steel slag can be improved by about 15% through increasing the grinding time of steel slag through the way of grinding respectively before mixing of steel slag and clinker. This is because some iron grain contained in the steel slag is still not clear in the process of smashing and magnetic separation, resulting in bad grindability of steel slag. Mixed grinding of steel slag and clinker fills the gaps between particles and improves the grindability. The fineness of steel slag increases gradually while the grinding time increased. Feng Chunhua etc [9] showed that using triethanolamine as grinding aid can increase the specific surface area of steel slag greatly and improve grinding efficiency. This is due to that the specific surface area of steel slag increases with the grinding time increases. The specific surface energy improves significantly and the force between particles increases gradually. The fine particles get together again. The larger particles increased gradually again and resulting in the specific surface area declined. Adding the grinding aid can make the surface active substances adsorb on the surface of particles, forming a layer of film, reduce the surface energy, decrease the attraction between material particles，preventing the fine particles reunited again. At the same time it increases the hydrophilic on the surface of particles, accelerating the hydration reaction of free CaO and MgO and thus improving the volume stability of steel slag effectively. Hou Xinkai etc [10] observed the microstructure characteristics of f-CaO and RO phase. The results showed that the most of f-CaO contained in the steel slag are strip or dendritic with bad degree of particles and low degree of aggregation. The space distribution is scattered and sparse. Therefore it is difficult to participate in the early time of hydration reaction. When f-CaO produces hydration reaction gradually later, it results in volume expansion and damages the structure of the building materials seriously. The result is accordance with the

conclusion that grinding of the steel slag, enhancing the specific surface area of particles and accelerating the hydration reaction of free CaO and MgO can solve volume stability problem.

Curing treatment

The Curing treatment is to make the free CaO and MgO contained in the steel slag further digestion with the good volume stability, ensuring the safety use of the steel slag for construction materials. Japanese steel-making company used warm water for curing treatment, the hydration expansion rate of steel slag is less than 1.5% [11]. Xu Kuijun [12] showed that using high temperature water for curing treatment can enhance the hydration process of the steel slag and fly ash mixed system obviously. This is due to some of the unsintering f-CaO participate in the hydration reaction by the excitation effect of the high temperature hydrothermal. This way can increase the alkalinity in the slurry system, stimulate the activity of fly ash and accelerate the hydration. The swelter treatment is a complex physical and chemical reaction. Firstly pour the large pieces of steel slag into the swelter tank when they cool to 300 ~ 600℃. Secondly spray the water intermittently on the hot slag through the automatic rotating sprinkler systems below the tank cover. The large amount of steam from tank makes the steel slag produce a complex physical and chemical reaction. The free CaO engenders volume expansion while generating $Ca(OH)_2$ in the process of hydration. It makes the steel slag further disintegrated. This process can improve the recovery rate of scrap steel. The separation effect of steel and slag is good, but it needs a larger area. Steam curing is to put the steel slag in the steam curing equipment and use the steam treating the steel slag. The free CaO and MgO contained in the steel slag digested before use. Japanese Kawasaki steel company cured the steel slag for 2h with 500℃ steam. It is clearly that the high temperature steam can accelerate the hydration reaction of f-CaO significantly and shorten the treating time greatly [13].

Chemical modification

Chemical modification of the steel slag is to solve the volume expansion problems in the process of hydration by adding a small amount of chemical aids. It can destroy the vitreum on the surface of the particles and react with the active components of steel slag. Wang yue [14] showed that adding the blast furnace slag more than 7% or the quartz sand greater than 5% into molten steel slag can solve the stability of steel slag effectively. This is due to the blast furnace slag and quartz sand contains SiO_2 which can react with the f-CaO contained in the steel slag generating silicates. At the same time it lowers the volume expansion of steel slag. Zhang Zuoshun etc [15] showed that the high temperature modification of steel slag using iron tailings as modifier can reduce the content of f-CaO significantly and improve the stability of steel slag. The mass fraction of f-CaO contained in the steel slag reduced from 4.84% to 1.82% while adding the mass fraction of iron tailings 20% at 1250℃. This is due to iron tailings contains a large amount of SiO_2 which can react with the f-CaO contained in the steel slag generating dicalcium silicates and tricalcium silicates. At the same time it promoted the RO phase's decomposition in the process. Part of them changes into $MgFe_2O_4$ and further into Fe_3O_4 under higher temperature. It solves the volume expansion problem of the f-CaO and RO phase in the process of hydration effectively. Wu Fuzhong etc [16] studied the fly ash dosage containing high silicon and temperature effects on the content of f-CaO. The results showed that fly ash can reduce the content of f-CaO. The more the dosages of fly ash, the higher the temperature is, and the lower the content of f-CaO. The turning point for f-CaO absorption is 1100℃. The absorption rate of modifier for the f-CaO increases sharply at this temperature. This is also due to the SiO_2 contained in the fly ash of high silicon react with the f-CaO contained in the steel slag generating the calcium silicate salt. At the same time fly ash begins to melt at 1300℃. It produces the liquid - solid reaction with the steel slag promoting the reaction further.

Typical cases

In 2013, we proposed two methods to improve volume stability of steel slag for construction and building materials: one is the combined use of chemical modification and physical modification, the other is the combined of three method of chemical modification, physical modification and thermal modification.

The combination of chemical modification and physical modification[17]

Firstly get the crude steel slag powder by grinding the steel slag and magnetic separation. Secondly add the digestive agent, dispersing agent and water into the steel slag powder, stir evenly then maintain the mix for 48 ~ 72 hours at 50 ~ 60℃. The highest dosage of slag can reach 50%. The cement products have good stability and the strength fits Chinese national standards. This invention combining the characteristics of steel slag strengthen the process of hydration of the free CaO and MgO through fine grinding, adding the digestive agent and dispersing agent, controlling the temperature and humidity. At the same time, controlling the processing time to form the calcium carbonate as little as possible can solve the stability problem of steel slag and maintain high gelling activity in uses.

The combination of chemical modification, physical modification and thermal modification [18]

Also in 2013, we proposed a method which can prepare the autoclaved aerated concrete block by iron tailings and steel slag. Firstly prepare the wet mixture by grinding the iron tailings, steel slag, water and water reducing agent. Secondly pour the wet mixture into the digestion tank through eliminating the iron after flotation, then add the activator and inflow the waste heat steam keeping 3 ~ 5h at 45 ~ 60℃. Lastly add the crude lime, cement and aluminum powder into the slurry of digestion. The slurry became embryonic body by casting, foaming, aging and cutting. The autoclaved aerated concrete block is produced through autoclave curing the for 8h at 1.2 MPa. This technology solves the stability problem of steel slag and improves the activity of steel slag. .

Conclusion

The stability problem of steel slag is the main obstacle of its utilization in construction and building materials. It is imperative to solve the stability problems of steel slag in the process of application. It can improve the stability of steel slag effectively and expand the safety use through mechanical modification, curing treatment and chemical modification. The combined use of the three methods can improve the stability of steel slag more effectively because each of them exists its own advantages and of course, the corresponding disadvantages. More important, there exist synergistic effects among these methods.

References

[1] T.S. Zhang, F.T. Liu, et al, The research progress of the stability and active excitation of steel slag, J. Journal of the Chinese Ceramic Society. 26 (2007) 981-984.

[2] F.Q. Zhao, J. Zhao, et al, Autoclaved brick from low silicon tailings, C. & B. Materials. 23(2009) 539-541.

[3] Y.L. Fu, Y. Mu, et al, Semi-dry desulfurization ash modification and application in autoclaved brick, Advanced Materials Research. 549 (2012) 762-765.

[4] G.R. Qian, D.D. Sun, et al, Hydrothermal reaction and autoclave stability of Mg bearing RO phase in steel slag, J. British Ceramic Transactions, 101(2002) 159-164.

[5] Y.X. Li, The study of structure and performance of the admixture of cement and concrete Containing steel slag powder, D. Beijing: China building materials science research institute. 2003.
[6] G.Y. Sun, The effect of grinding fine steel slag on the mechanical properties and stability of the admixture of cement and concrete, J. Journal of fly ash. 5(2003) 7-9.
[7] H. Li, F.Q. Zhao, et al, Autoclaved brick from semi-dry desulfuration ash, Advanced Materials Research. 846 (2010) 217-218.
[8] G.L. Xu, J.X. Chen, et al, Increasing the fineness and dosage of steel slag by separately grinding, J. Journal of Shandong Institute of Building Materials. 6(1998) 3-5.
[9] C.H. Feng, D.X. Li, et al, The effect of grinding agent on the fineness and activity of steel slag, J. Journal of the Chinese Ceramic Society. 38 (2010) 1161-1166.
[10] X.K. Hou, D.L. Xu, et al, The discussion of the volume stability problem of the cement from the steel slag, J. Journal of Building Materials. 15 (2012) 589-594.
[11] G.T. Xu, Y. Wang, et al, the discussion of technique and process of steel slag stability, J. Journal of Iron and Steel Research. 5 (2009) 54-56.
[12] K.J. Xu, The research of hydration properties of steel slag powder as auxiliary cementitious materials under the different water heat conditions, D. Hunan: Hunan University of science and technology. 2012.
[13] R.H. Chen, L. Shi, et al, the introduction of the processing and using of converter steel slag, C. Shanghai: baosteel association for science and technology, environmental protection society. (2006)41-46.
[14] Y. Wang, The research of modified steel slag used as cement admixture, J. Technology Wind. 18(2011)174-178.
[15] Z.S. Zhang, F. Lian, et al, The property of iron tailings of high temperature used as modified steel slag, J. Journal of Beijing university of science and technology. 12 (2012)1380-1384.
[16] F.Z. Ma, K.K. Wang, The research of the modification of converter steel slag, J. Journal of Guizhou Science. 31 (2013)35-38.
[17] Hebei university of science and technology, The method of improving the steel slag stability and maintain high gelling activity, P. China, CN 103265189 A. 2013-08-28.
[18] Zunhua central comprehensive utilization of solid waste company, The method of preparation of autoclaved aerated concrete block utilization of iron tailings and steel slag, P. China.

Advanced Materials Research Vol. 936 (2014) pp 1404-1408
© (2014) Trans Tech Publications, Switzerland
doi:10.4028/www.scientific.net/AMR.936.1404

Effect of Grinding Aids on the Particles Characteristics of Cement and Analysis of Action Mechanism

Jihui Zhao[a], Dongmin Wang[b], Xueguang Wang[c], Shucong Liao[d], Hui Lin[e]

China University of Mining & Technology, Beijing, 100083, China

[a]zhaojihui324@163.com, [b]wangdongmin-2008@163.com, [c]243812705@qq.com, [d]liaoshucong2008@163.com, [e]543817339@qq.com

Keywords: cement particles; grinding aids; grinding; particle size distribution; adsorption; dispersion; action mechanism

Abstract. Effects of triethanolamine grinding aids on the angle of repose, fineness, particle morphology and particle size distribution of cement are studied, and the action mechanism of grinding aids is discussed by surface tension and Zeta potential. The results show that the powder fluidity and particle circularity of cement are improved and the particle size and grinding time of cement are effectively reduced by grinding aids. And Grinding aids improve the particles content in the range of 3-32μm particle size by 6.63% and promote destruction of the chemical bonds and lattice distortion of cement mineral during the grinding process. The dispersion grinding mechanism of grinding aids is that they can reduce the surface free energy of powder to prevent fine particles from closing each other and shield or neutralize the particles surface partial charge to prevent facture surface from healing and promoting the cracks to extend easily.

Introduction

Grinding process of cement is a dry grinding process with air as medium. When grinding to certain fineness, cement fine particles have a strong tendency to agglomerate. Thus the fine particles easily mutual adhesion, and particle fracture surface easy to heal, so that the small particles will re-combine to form larger particles [1-3], which can seriously affect the grinding efficiency of cement and miniaturization of particles and particles can not be further ground. In recent years, trace grinding aids are used in the cement grinding can improve the characteristics of cement particles and play a role in the dispersion grinding, then grinding aids have become an important means to improve cement grinding efficiency [4,5]. Currently, the chemicals used as cement grinding aids include triethanolamine, triisopropanolamine, ethylene glycol, glycerol and other organic matter, and triethanolamine is most widely used, so the effect of triethanolamine on cement particles is very important. In this paper, the effect of organic grinding aids on the characteristics of cement particle group is discussed from the angle of repose, fineness, particle morphology, particle size distribution, uniformity coefficient, etc. And the action mechanism of grinding aids in the miniaturization process of cement is analyzed by infrared spectroscopy and adsorption characteristics of ground fine particles.

Materials and Methods

Raw Materials: (1) Cement clinker, slag and limestone are provided from a cement plant in Chongqing city of China, and their chemical compositions are shown in Table 1; (2) Organic grinding aid is triethanolamine (abbreviated TEA) which is diluted with water to the concentration of 48wt%.

Table 1 Chemical composition of raw materials / wt %

Sample	CaO	SiO_2	Al_2O_3	Fe_2O_3	MgO	K_2O	Na_2O	SO_3	Loss
Clinker	66.05	22.28	4.79	2.87	1.84	0.97	0.25	0.63	0.40
Slag	36.12	30.30	13.82	0.66	8.31	0.51	0.28	0.12	9.75
Limestone	50.35	3.29	1.05	0.30	1.51	0.29	0.07	0.21	

Grinding Experiment Methods: Mixing ratio of cement in the grinding experiment is shown in Table 2. The grinding aids are uniformly dropped on the surface of materials which are to be grinding, and the dosage of grinding aids is 0.06wt% of the total mass of materials. The weight of materials for each grinding experiment is 3kg and the grinding time is 15min, 20min and 25min respectively. And cement is sieved by 0.9mm square mesh sieve after grinding, and then the characteristics of cement particles group are tested.

Table 2 Mixing ratio of cement / wt%

Clinker	Slag	Limestone	Gypsum
80	10	5	5

Testing Methods: ① The angle of repose is tested according to GB/T11986-1989, and cement powders is poured into funnel by the injection method, and then samples fall within the disc below the funnel, so the angle of repose for powders is obtained according to the formula ($\tan\theta=h/R$) by measuring the height of powder layer and the radius of the disc; ② The fineness, specific surface are and particle size distribution of cement are tested respectively according to GB/T1345-2005, GB/T8074-2008 and JC/T721-2006; ③ The particles morphology of ground fine cement is observed by Hitachi S-3400 scanning electron microscope and IR is analyzed by Nicoletis 10 Fourier transform infrared spectrometer; ④ The testing method of surface tension is as follows: cement and water are mixed according to 1:200 and the mixture is filtered by suction flask, and then the surface tension of cement filtrate is tested by JK99B type full-automatic tensiometer; ⑤ Zeta potential is tested by electrophoresis, and cement and water is prepared into suspension, then Zeta potential of suspension is tested by Zeta potential meter after stirring suspension 1-3min.

Results and Discussion

Effect of Grinding Aids on the Fluidity of Cement Powder

In this paper, the fluidity of cement powder is characterized by the angle of repose which reflects the friction characteristics between the particles of powder in loose accumulation condition. The relationship of the angel of repose and the fluidity of powder is that the angle of repose is bigger, the fluidity of powder worse, and the repeatability of testing is poor. It can be seen from Table 3 that the angle of repose for cement with grinding aids is smaller than that of blank cement without grinding aids at the same time of grinding, which the angle of repose for cement decrease respectively 9°, 6° and 7° at the grinding time for 15min, 20min and 25min respectively. It is due to the molecules of grinding aids adsorbed on the surface of cement particles form mono-molecular adsorption layer or thin firm, which reducing the contact area, friction and attractive force between particles, and then cement powder are easy to slip between particles, so the fluidity of cement is increased and the grinding efficiency of cement is improved.

Table 3 Repose angle of cement powder

Grinding time / min		15	20	25
Repose angle / °	Blank	65	53	43
	With grinding aids	56	47	36

Effect of Grinding Aids on the Fineness and Particle Morphology of Cement

It can be seen from Fig.1 that both the sieve margin of cement with grinding aids is smaller than that of blank cement sample at the same time of grinding, while both the specific surface area of sample with grinding aids is larger than blank sample. It shows that the content of coarse particles is increased and the content of fine particles is reduced after adding the grinding aids into cement in the grinding process of cement, so the cement particles are effectively refined. In addition, it can be found from Fig.1 that the sieve margin and specific surface area of the cement with grinding aids at the grinding time for 15min and the blank cement without grinding aids are respectively close at the grinding time for 20min, and the sieve margin and specific surface area of the cement with grinding aids at the grinding time for 20min also respectively reach to the level of blank cement. It also shows

that the grinding aids added in the grinding process of cement can reduce the grinding time and power consumption for grinding and improve efficiency of grinding.

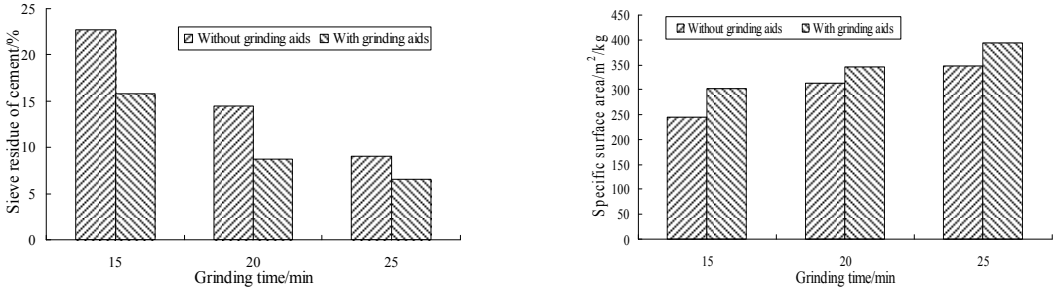
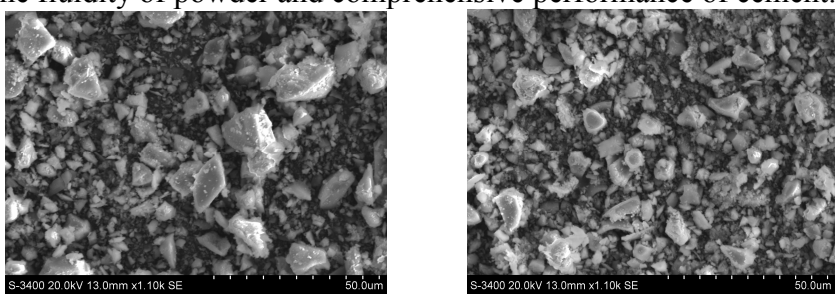


Fig.1 Effect of grinding aids on sieve margin and specific surface area of cement

The morphology of cement particles is shown in Fig.2 which shows that the particles of cement with grinding aids are more uniform and dispersion and the shape of particle more tend to sophericity. Thus it indicates that the circularity of cement particle is increased, which is conducive to improvement of the fluidity of powder and comprehensive performance of cement.



(a) Cement without grinding aids (b) Cement with grinding aids

Fig.2 Effect of grinding aids on the morphology of cement particles

(Note: grinding times of the cement particles is 25min, below)

Effect of Grinding Aids on the Particle Size Distribution of Cement Particles

It can be seen from Fig.3 that the particle size distribution of cement with grinding aids is more narrow than blank cement. And it can be seen from Table 4 that the content of less than 3μm and more than 65μm particles of cement with grinding aids is less by 1.04% and 1.92% respectively than the blank cement, while the content of 3-32μm particles of cement with grinding aids is more by 6.63% than the blank cement, and the 3-32μm particles play a major role on the strength of cement. And the median diameter of cement particles is less than the blank. So the results show that cement particles are effectively refined after adding grinding aids in the grinding process, and the particle size distribution become narrow by reducing over-grinding of cement and the content of large-size particles of cement, especially the particles concentrate in the range of 3-32μm, So grinding aids play a optimal role on particle size distribution.

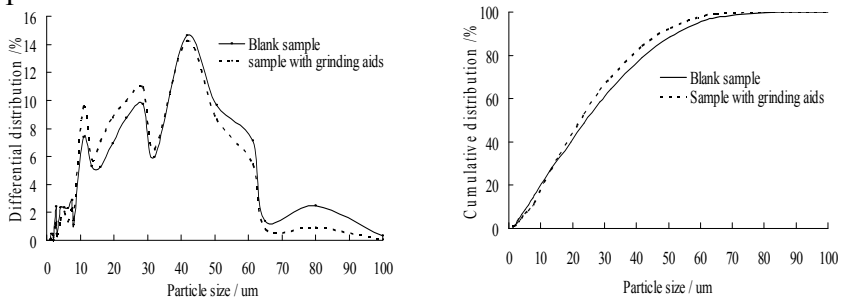


Fig.3 The particle size distribution of cement

Table 4 Particle size distribution of cement powder

Sample	Particles size distribution of cement / %				D50 (Median diameter)/ μm
	≤3μm	3-32μm	32-65μm	≥65μm	
Blank	4.17	60.23	32.82	2.78	24.23
With grinding aids	3.03	66.86	29.05	1.06	22.48

IR Analysis of the Ground Fine Cement

The changes of the order degree and chemical bond of crystal structure for the composition of solid materials in the process of grinding can be investigated by IR [6,7]. It can be seen from Fig.4 that the bands shape of characteristic absorption peaks in the IR chart of cement with grinding aids tends to blunt compare with the blank cement. It shows that grinding aids can reduce the symmetry of crystal structure of cement minerals and promote it to no qualitative of cement surface. The absorption peak [8] of [AlO_6], [SiO_4] in C_3S, [SO_4] in gypsum and [CO_3] respectively appear at about 551cm^{-1}, 925cm^{-1}, 1115cm^{-1} and 1425cm^{-1}, and the absorption peak of [H_2O] in gypsum appear at about 1625 cm^{-1}, 3400 cm^{-1}and 3542cm^{-1}. By comparing the IR of cement with grinding aids with the IR of the blank cement, it can be seen that the wave number of [AlO_6] band is reduced from 551.0 cm^{-1} of blank sample to 550.8 cm^{-1} of sample with grinding aids, and the waves numbers of [SiO_4] band, [SiO_4] band and [CO_3] band are respectively reduced from 926.5 cm^{-1} of blank sample to 925.1 cm^{-1}, from 1115.4 cm^{-1} to 1114.3 cm^{-1} and from 1425.3 cm^{-1} to 1424.5 cm^{-1}. The decrease of wave number for absorption peak of these groups indicates that the damage of crystal structure and chemical bond of cement minerals are accelerated in the process of grinding by adding grinding aids, which increasing lattice distortion of cement minerals.

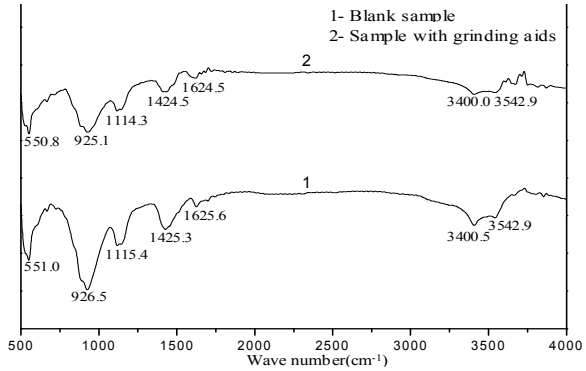


Fig.4 IR of the ground fine cement

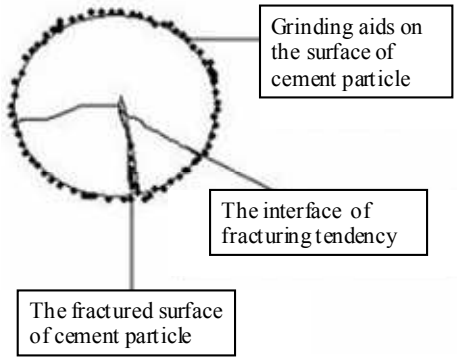


Fig.5 Adsorption of grinding aids in cement particle

Mechanism Analysis of Grinding Aids

It can be seen form the Table 5 that the surface tension of cement with grinding aids is less than the blank, it shows that triethanolamine grinding aids has good surface activity and can reduce the surface free energy of cement particles. In addition, it can be seen from Table 5 that the absolute value of Zeta potentials of cement with grinding aids is less than the blank, this may be due to grinding aids adsorbed in the surface of cement shield or neutralization the partial charge of particles, thus the negative charges of cement particles is reduced, And it shows that grinding aids can change the surface charge distribution of cement particles.

Table 5 Surface tension and Zeta potential of cement

Sample	Surface tension / mN/m^2	Zeta potential / mV
Blank	82	-10.34
With grinding aids	63	-6.02

Triethanolamine is a kind of polar organic compound with amino, hydroxyl and other groups, which has a strong adsorption. In the grinding miniaturization process of cement, the functional groups of grinding aids adsorbed in the surface, fracture surface and cracks of cement particle (as shown in Fig.5), thus play the role of dispersion and grinding. The possible mechanism of grinding aids is as follow: 1) Grinding aids adsorb between micro-crakes of particles and provide the foreign ions or molecules to balance out or shield unsaturated charges of crack section, which preventing facture surface to healing, thus the cracks become easier to extend; 2) grinding aids molecules adsorb in the surface of cement particles and form adsorption film, thus the free energy and interfacial tension of powder surface are reduced and particles to close each other are prevented, and then it plays the role of dispersion and prevents the fine particles agglomeration, so the dispersion of powder and grinding efficiency are improved. Furthermore, the more compact grinding aids form the adsorption film in the particle, the better grinding aids play dispersion action.

Conclusions

(1) In the process of grinding, grinding aids can effectively reduce the sieve margin of particles and grinding time of cement. And the fluidity of powder, specific surface area and sophericity of particle are also improved. Grinding aids play an optimal role on cement particles size distribution by improving the particles content in the range of 3-32μm particle size.

(2) Destruction of the crystal structure and chemical bond of cement minerals are accelerated in the grinding process by adding grinding aids, which increasing lattice distortion.

(3) Grinding aids can reduce the surface free energy of powder and prevent fine particles from closing each other. And they change the surface charge distribution by shielding or neutralizing the particles surface partial charge and prevent facture surface from healing and promoting the cracks to extend easily.

References

[1] H. Choi, W. Lee, D.U. Kim, et al. Effect of grinding aids on the grinding energy consumed during grinding of calcite in a stirred ball mill. Minerals Engineering, 23(2010):54-57.

[2] X.J. Gao, Y.G. Yang, H.W. Deng. Utilization of beet molasses as a grinding aid in blended cements. Construstion and Building Materials, 25(2011):3782-3789.

[3] X.Q. Ding, S. Zhao, J. Ling, et al. A survey on study and application of cement grinding aids. Material Review, 18(2004):61-63.

[4] L.B. DU, W.L. Zhou, J.P. Liu, et al. Research progress of cement grinding aids. Materials Review, 23(2009):80-84.

[5] M. Katsioti, P.E. Tsakiridis, P. Giannatos, et al. Characterization of various cement grinding aids and their impact on grindability and cement performance. Construstion and Building Materials, 23(2009):1954-1959.

[6] N.R. Yang. Test methods of inorganic non-metallic materials. Wuhan University of Industry Press, Wuhan, 1993, pp. 233-64.

[7] C.H. Jiang, J.D Zhou, S. Yan. Study on mochanochomistry of the size reduction process of fly ash with grinding aids. Chongqing Environmental Science, 25(2003):68-70.

[8] Q. Feng, P.M. Wang. Infra-red spectrum analysis of thermal activation of coal-gangue and hydration of cement. Journal of Building Materials, 8(2005):215-221.

Advanced Materials Research Vol. 936 (2014) pp 1409-1413
© (2014) Trans Tech Publications, Switzerland
doi:10.4028/www.scientific.net/AMR.936.1409

Effect of Mineral Admixtures on Rheological Properties of Cement Paste

Linchun Zhang, Ailian Zhang

School of Civil Engineering, Sichuan College of Architectural Technology, Deyang 618000, China

zhanglinchun1980@126.com

Keywords: rheological properties; mineral admixtures; cement paste; Marsh cone method; rotary viscosimeter

Abstract: The Marsh cone method and rotary viscosimeter are used to study the effect of mineral admixtures such as ultra-fine fly ash, ultra-fine slag, zeolite powder and silica fume on rheological properties of cement paste. Test results show that the optimal ratio of ultra-fine fly ash, ultra-fine slag, zeolite powder and silica fume are respectively 20%, 20%, 10% and 8%. And the optimized mix proportion is the composition of 8% silica fume and 12% slag. By using water reducing agent and mineral admixtures we could get the cement paste which has good liquidity and no bleeding.

Introduction

Today concrete is one of the most widely used building materials in the world [1], and it is increasingly used in civil engineering. It is especially important when producing the concrete we must consider its use performance [2]. Rheological property is one of major factors influence on concrete working performance [3, 4]. So it is obviously that it is very important to prepare the concrete which has good liquidity and no bleeding.

Most research so far had focused on controlling superplasticizer, thickener and the dosage of mineral admixtures to achieve great success in improving the rheological properties of concrete [5-10]. The industrial waste residue such as ultra-fine fly ash, ultra-fine slag, zeolite powder and silica fume is the main raw material sources of mineral admixtures [11]. Studying the effect of the single and compound mineral admixtures on the rheological properties of concrete has the vital significance regarding the modern civil engineering construction. The Marsh cone method and rotary viscosimeter are used to study the effect of mineral admixtures such as ultra-fine fly ash, ultra-fine slag, zeolite powder and silica fume on rheological properties of cement paste.

General Situation of Test Area

Raw Material

Cement

P·O 42.5 ordinary portland cement is produced in Harbin cement plant and ordinary medium sand whose fineness modulus is 2.3. Its physical properties and chemical component is respectively shown in Table 1 and Table 2.

TABLE 1 ELEMENTARY PHYSICAL AND MECHANICAL PROPERTIES OF CEMENT

Density (g/cm^3)	BET (m^2/k g)	Setting time (min)		Setting time (min)		compressive strength (MPa)	
		Initial set	Initial set	3d	28d	3d	28d
3.06	334	163	315	5.8	9.5	29.2	52.0

TABLE 2 CHEMICAL COMPOSITIONS OF CEMENT

(wt %)

SiO_2	Al_2O_3	Fe_2O_3	CaO	MgO	SO_3	R_2O	LOI
21.08	5.47	3.96	62.28	1.73	2.63	0.50	1.61

Other Raw Materials

The test uses mineral admixtures are as follows, ultra-fine fly ash which is produced in Harbin cement plant, ultra-fine slag which is produced in Anshan Iron and Steel Factory, zeolite powder which is produced in Neijiang, and silica fume which is produced in Elkem Company. And the additives are as follows, Mighter 100 naphthalene superplasticizer produced by Japan Kao whose quantity is 1% of the cement and whose water reducing ratio is 20%, MICRO-AIR202 concrete air-entraining agent produced by Master Builder Technoloy in Shanghai, and the running water in Harbin.

Mix Proportion

The sum of the quality of cement and mineral admixtures is respectively identically equal to 1000g and 1400g. The water-binder ratio is 0.4. And the cementitious system respectively contains 1% and 0.1‰ of naphthalene superplasticizer and air-entraining agent in accord with weight.

The effects of ultra-fine fly ash, ultra-fine slag, zeolite powder and silica fume composite admixture of them on the rheological properties of cement paste is also studied in this paper. The mix proportion is influenced by the result of every single mineral admixture. So it will be taken on later in this article.

Experimental Programme

First, weigh the raw material according to the above mix proportion. Then, pour the mixture of mineral admixture, water reducer and cement into beaker and mix for one minute. Add the prepared air-entraining agent water into the beaker, and stir for five minutes. After this, pour the new paste into recogizer of NDJ-79 type cylinder rotational viscometer, read the data after stirring for ten seconds. In this way, plastic viscosity and shear stress of new paste could be respectively got by the big rotor and the small rotor.

Measure the time how long it would take for 1725 milliliters pure cement paste five milliliters, plus or minus have all come out the Marsh cone. Then pour the cement paste into the small cone which is used to measure the fluidity of cement paste. Take away the small cone. Five seconds later, measure the diameter using vernier caliper.

Conclusions and Prozspects

Single Mineral Admixture

Slag

Influence of replacement of slag on rheology is shown in Table 3.

TAB. 3 INFLUENCE OF REPLACEMENT OF SLAG ON RHEOLOGY

Replacement (%)	Plastic viscosity (Pa·s)	Shear stress (Pa)	Diameter (cm)	Marsh Time (s)
10	0.02434	122.34797	23.10	24.69
20	0.02300	140.85207	26.90	22.95
30	0.02259	142.70945	28.10	20.47
40	0.01807	148.58512	37.85	17.29

Results show that plastic viscosity of new cement paste and Marsh time reduced gradually with the increase of slag dosage. As slag dosage increases, shear stress and diameter measured by the small cone becomes larger gradually.

The surface of cement particles gets high surface charge when high efficiency water reducing agent molecules are adsorbed on the surface of cement particles after cement is mixed with high efficiency water reducing agent. The same charge cause repulsion between particles. The repulsion has

important roles to play in deflocculating and dispersing the paste, so that the free water wrapped in flocculating constituent could be released. So it has a significant increase in the flow of slurry.

It is particularly gratifying that when high efficiency water reducing agent and slag are both added into the cement, the flow of slurry is further heightened. That's because the free water wrapped in flocculating constituent could be further released due to the electric double layer produced by high efficiency water reducing agent adsorbed by the surface of slag particles.

The best slag dosage is 20% only from view the influence on the rheological properties of cement paste.

Fly Ash

Influence of replacement of fly ash on rheology is shown in Table 4.

TAB. 4 INFLUENCE OF REPLACEMENT OF FLY ASH ON RHEOLOGY

Replacement (%)	Plastic viscosity (Pa·s)	Shear stress (Pa)	Diameter (cm)	Marsh Time (s)
10	0.02319	136.50222	27.75	26.94
15	0.01797	148.61964	28.00	22.40
20	0.01133	162.08344	29.15	20.19
25	0.00689	171.92238	30.05	18.00
30	0.00244	176.89362	30.40	17.60

Results show that plastic viscosity of new cement paste and Marsh time reduced gradually with the increase of fly ash dosage. As fly ash dosage increases, shear stress and diameter measured by the small cone becomes larger gradually.

The influence of fly ash on the rheological properties of cement paste was influenced by its particle morphology. Spherical Vitreous surface of the fly ash is very smooth. Fly ash is filled in cement particles which has the effect of ball bearing so that it has a significant increase in the flow of slurry. At the same time, fly ash surface potential is very big which could adsorb part of water reducing agent. So that, fly ash surface could generate rejection itself which could give rise to the increasement of the flow property.

The best fly ash dosage is 20% only from view the influence on the rheological properties of cement paste.

Silica Fume

Influence of replacement of silica fume on rheology is shown in Table 5.

TAB. 5 INFLUENCE OF REPLACEMENT OF SILICA FUME ON RHEOLOGY

Replacement (%)	Plastic viscosity (Pa·s)	Shear stress (Pa)	Diameter (cm)	Marsh Time (s)
4	0.02264	103.15343	24.95	21.59
6	0.01956	120.55280	25.00	20.06
8	0.01853	122.62415	26.70	19.66
10	0.03446	91.346710	20.30	33.94

The plastic viscosity and Marsh time of the cement paste will go down with the gain of silica fume's dosage at first, and the plastic viscosity will reach a minimum value when the dosage of the silica fume is 8%, and then it will enhance with the increment of the dosage of the silica fume again. As slag dosage increases, shear stress and diameter measured by the small cone have the opposite trend.

The influence of silica fume on the rheological properties of cement paste was influenced by its large specific surface and high water requirement. Silica fume particle surface water raised with the

increment of the dosage of the silica fume. So the plastic viscosity will increase when the silica fume dosage is too much.

The best silica fume dosage is 8% only from view the influence on the rheological properties of cement paste.

Zeolite Powder

Influence of replacement of zeolite powder on rheology is shown in Table 6.

TAB. 6 INFLUENCE OF REPLACEMENT OF ZEOLITE POWDER ON RHEOLOGY

Replacement (%)	Plastic viscosity (Pa·s)	Shear stress (Pa)	Diameter (cm)	Marsh Time (s)
5	0.01274	160.73710	29.05	17.10
10	0.01992	143.86696	28.70	21.82
15	0.02739	133.59078	27.30	22.25
20	0.02929	126.66329	24.00	29.88

Results show that plastic viscosity of new cement paste and Marsh time increased gradually with the increase of zeolite powder dosage. As zeolite powder dosage increases, shear stress and diameter measured by the small cone becomes smaller gradually. We can see that, viscosity of new cement paste increased with the increase of zeolite powder dosage.

Natural zeolite powder itself is lattice structure whose inside is full of uniform pores and channels. At the same time, there is a lot of openness for lattice structure. After being levigated, zeolite powder gets high specific surface area. It can absorb a large number of water molecules and gases with the equilibrium relative humidity in the atmosphere in its natural state.

The zeolite powder mixed with cement paste could absorb the extra mixing water of cement paste so as to overcome the cement's bleeding. Meantime it could increase the cement's viscosity and the amount of wrapped slurry of aggregate.

In the process of condensation hardening of concrete, cement hydration continue to need water. Right now the water absorbed by zeolite powder could release gradually until its inside has the effect of vacuum. That makes the gel in the cement more closely to condense into a whole. So the viscosity of new cement paste increased with the increase of zeolite powder dosage.

The best zeolite powder dosage is 10% only from view the influence on the rheological properties of cement paste.

Composite Mineral Admixtures

By the preceding content, we can conclude that the optimal ratio of fly ash, slag, zeolite powder and silica fume are respectively 20%, 20%, 10% and 8%. For comparison, composite mineral admixtures are as follows, 8% silica fume and 12% slag, 8% silica fume and 12% fly ash, 10% fly ash and 10% slag. A represents 8% silica fume, B represents 20% slag, C represents 20% fly ash, D represents 10% fly ash and 10% slag, E represents 8% silica fume and 12% fly ash, F represents 8% silica fume and 12% slag. Influence of these six groups on rheology is shown in Table 7. The results of ABC are taken from single mineral admixture.

TAB. 7 RHEOLOGY OF NEW CEMENT MORTAR

	plastic viscosity (Pa·s)	shear stress (Pa)	Diameter (cm)	Marsh Time (s)
A	0.01853	122.62415	26.7	19.66
B	0.02300	140.85207	37.9	17.29
C	0.01133	162.08344	28.0	18.00
D	0.01903	120.56842	25.8	20.28
E	0.02856	63.36952	22.7	34.57
F	0.03482	63.56925	22.7	38.63

The rank of the rheological properties of new cement paste with different mineral admixture is: F>E>D>A>C>B.

Summary

In this paper, we choose study the effect of mineral admixtures such as ultra-fine fly ash, ultra-fine slag, zeolite powder and silica fume on rheological properties of cement paste. We can draw the following conclusions:

The plastic viscosity of the cement paste will decrease with the increase of slag or fly ash, but the yield shearing strength will increase gradually with the increase of slag or fly ash. The best slag and fly ash dosage is both 20%.

The plastic viscosity of the cement paste will go down with the gain of silica fume's dosage at first, and the plastic viscosity will reach a minimum value when the dosage of the silica fume is 8%, and then it will enhance with the increment of the dosage of the silica fume again. The best silica fume dosage is 8%.

The plastic viscosity of the cement paste will go up and yield shearing strength will go down with the increase of the ratio of the zeolite powder either the zeolite powder is added as a single agent or combined with silica fume. The best zeolite powder dosage is 10%.

The rank of the rheological properties of new cement paste with different mineral admixture is: F>E>D>A>C>B. silica fume and slag> silica fume and fly ash>slag and fly ash>silica fume>fly ash>slag. The rheological properties of the double mixing mineral admixtures is superior to single doped the rheological properties of mineral admixtures.

References

[1] Ellis W E.For durable concrete, fly ash does not "replace" cement [C]. Concrete International, 1992(7) 47–51.

[2] Sharma R L, Pandey S P. Influence of mineral additives on the hydration characteristics of ordinary Portland cement [J]. Cement and Concrete Reasearch, 1999, 29:1525-1529.

[3] SHI Shuai, DENG Min, MO Liwu, "Effect of super-fine mineral admixtures and chemical admixtures on rheological property of super-fine cement grouts," Concrete, pp. 65–68, Oct. 2011 (in Chinese).

[4] MA Baoguo, Fu Haobing, WANG Huixian, WANG Yingbin, TIAN Zhen, LU Siwen, "Influence of Mineral Admixture Double Mixing on the Cement base Material Rheological Properties," New Building Materials, vol. 40, pp. 1–4, Aug 2013 (in Chinese).

[5] KIM Jong-sun. Groutability of cement-based grout with consideration of viscosity and filtration phenomenon [J]. International Journal For Numerical And Analytical Methods In Geomechanics, 2009, 33 (16): 1171-1797.

[6] SONEBI M. Rheological properties of grouts with viscosity modifying agents as diutan gum and welan gum incorporating pulverised fly ash[J]. Cement and Concrete Research, 2006, 36(9): 1609-1618.

[7] SVERMIVA L. Infiuence of mix proportions on rheology of cement grouts containing limestone powder [J]. Cement and Concrete Research, 2003, 25 (6) : 737-749

[8] MARKOU I N. Development of a pulverized fly ash suspension grout[J]. Geotechnical and Geological Engineering, 2002, 20(7) : 123-147.

[9] PARK C K, NOH M H.Rheological properties of cementitious materials containing mineral admixtures[J].Cement and Concrete Research,2005, 35 (5) : 842-849.

[10] ERIKSSON M.Variations in the rheology and penetrability of cement based grouts-an experimental study[J].Cement and Concrete Research, 2004,34(7) : 1111-1119.

[11] KAMAL H.Khayat.Viscosity-enhancing admixtures for cement-based materials-an overview [J]. Cement and Concrete Composites, 1998, 20(2) : 171-18

Advanced Materials Research Vol. 936 (2014) pp 1414-1418
© (2014) Trans Tech Publications, Switzerland
doi:10.4028/www.scientific.net/AMR.936.1414

Theoretical Study on Seismic Behavior of LYTAG Concrete

Linchun Zhang

School of Civil Engineering, Sichuan College of Architectural Technology, Deyang 618000, China

zhanglinchun1980@126.com

Keywords: LYTAG concrete; seismic; ANSYS; ductility

Abstract: In order to estimate seismic behavior of LYTAG concrete, the seismic behavior of ordinary concrete have been studied in comparison with LYTAG concrete in this article. At first it discusses the advantages of LYTAG concrete, and then it draws following conclusions through the contrast tests of LYTAG concrete and ordinary concrete and the method of finite element analysis. The seismic performance of Lytag concrete is better than that of ordinary concrete. LYTAG concrete has better social and economic benefits than ordinary concrete from the aspects of seismic fortification.

Introduction

It is generally known that the ordinary concrete itself has significant shortcomings in some respects, for example, big weight, easy to produce cracks, poor fire resistance, poor seismic performance, and poor heat insulation performance[1, 2]. These shortcomings limit the application of common concrete in some special engineering. At present, we are in the age whose building technology renew day by day. The buildings have to be more and more weight[3, 4]. Therefore, in the current big weight, how to minimize the weight while improving the seismic performance of buildings has become a pressing question. And it has become one of the important topics which the domestic and foreign scholars are concerned about. We need materials that have the characteristics of light weight and good seismic performance. Therefore, lightweight aggregate concrete rises in response to the proper time and conditions.

There are many pores which can meet the characteristics of light weight in lightweight aggregate concrete. But we don't know how its seismic performance is. Because of our country in the implementation of the strategy of sustainable development, and rich fly ash haydite resources, production of low energy consumption, so it can be recycled and returning in line with the basic national policy of our country. Therefore, this paper focuses on the study of the seismic performance of LYTAG concrete.

Advantage of LYTAG Concrete

Light weight and high strength

There are lots of pores in LYTAG concrete, who can reduce the weight of the lightweight concrete, so as to realize the characteristics of light. LYTAG concrete unit weight is generally 800~1950kg/m^3. But when it is used for structure, its density is generally 1400~1950kg/m^3. And LYTAG concrete used for structure weighed about from 20 percent to 30 percent less than normal concrete, while its intensity can reach of ordinary concrete strength grade (C15~C50). When it is used for wall thermal insulation structure, its density is generally 800~1200kg/m3, while its intensity can reach CL5~CL15. And it weighed about from 30 percent to 50 percent less than normal concrete.

Good temperature preservation and heat insulation performance

There are many voids in the fly ash haydite. These pores not only reduce the weight, but also reduce its coefficient of thermal conductivity to a certain extent, and improve its thermal insulation performance. The data makes clear, coefficient of thermal conductivity of LYTAG concrete can reduce the thermal conductivity of about 50%~60% than ordinary concrete. Especially as wall

materials, the advantage is more prominent. Data show that, as the wall materials, the ratio of coefficient thermal conductivity of LYTAG concrete to ordinary concrete is only about 1/6~ 2/3.

Good fireproof performance

Lytag is made from being baked at the centigrade of 1200~1300. Its main chemical composition is SiO_2, $A1_2O_3$ and so on. Its coefficient of thermal conductivity is low, that is to say, under high temperature, the heat flow from the inside of the LYTAG concrete to the outside is slow compared to the speed of common concrete. So its fire resistant performance is good.

Others

In addition to the above advantages, LYTAG concrete also has other advantages such as good impermeability, good frost resistance, strong corrosion resistance, good anti shock proof performance and low elastic modulus. In addition, its production process is simple, and its strong adaptability, so it is a new building material with good economic and social benefits. There are also data indicate that Lytag concrete seismic performance is good, so this article focuses on its seismic performance. Analysis on seismic performance will be introduced next.

General Situation of Test Area

Raw material

The test uses P·O 42.5 ordinary portland cement produced in Harbin cement plant and ordinary medium sand whose fineness modulus is 2.3, LYTAG produced in Daqing, ultra-fine slag which is produced in Anshan Iron and Steel Factory and silica fume which is produced in Elkem Company.. The chemical component is shown in Table 1.And the additives are as follows, Mighter 100 naphthalene superplasticizer produced by Japan Kao whose quantity is 1% of the cement and whose water reducing ratio is 20%, MICRO-AIR202 concrete air-entraining agent produced by Master Builder Technoloy in Shanghai, and the running water in Harbin.

Tab. 1 Chemical compositions of main raw materails

(wt %)

	SiO_2	Al_2O_3	Fe_2O_3	CaO	MgO	SO_3	R_2O
cement	21.08	5.47	3.96	62.28	1.73	2.63	0.50
slag	38.61	7.27	0.4	42.49	6.71	0.9	0.70
Silica fume	93.7	0.3	0.8	0.2	0.2	0.5	0.30

Mix proportion

According to the relevant requirements of concrete workability, cohesiveness, high strength and large liquidity, the optimum mixture ratio, as shown in table 2 is based on large numbers of experiments. The optimum mixture ratio is to comply with the design and construction requirements. In table 2, NC stands for normal concrete, and LC stands for LYTAG concrete. Water in table 2 is the sum of pure water and the water absorbed by the LYTAG. The water reducer dose used is 5.3kg, and air-entraining agent dose used is 0.053kg in one cubic meter of concrete. And the material dose in Table 2 is in one cubic meter of concrete.

Tab. 2 Mix proportion of LYTAG concrete and normal concrete

	cement	slag	Silica fume	water	sand	LYTAG	stone
NC	330.0	0	0	181.5	765	0	1016
LC	424.0	63.6	42.4	244.0	556	568	0

Table 2 demonstrates that aggregate in Lytag concrete is much lighter than in ordinary concrete. The ratio of aggregate in Lytag concrete to in ordinary concrete is about 0.5.Therefore, the LYTAG concrete can greatly reduce the bulk density of concrete.

Conclusions and Prospects

Strength

The cubic specimens size of cube compressive strength was 150mm×150mm×150mm. The compressive strength was tested by hydraulic universal testing machine. The LYTAG concrete were vibrated forming according to the best ratio shown in Table 3. And the forms are removed after 24 hours. Then put the concrete into the standard curing room to cure 3d, 7d and 28d respectively. Take out the specimens from the standard curing room. And test the compressive strength of each specimen at 3d, 7d and 28d respectively. Each group adopts the average of three pieces as the final result, as shown in table 3.

Tab. 3 Performance of LYTAG concrete and normal concrete

	density/ kg·m^{-3}	Slumps /mm	Compressive strength/MPa		
			3d	7d	28d
NC	2389	195	35.8	57.9	65.7
LC	1835	180	25.9	41.2	52.8

From table 3 we can learn that, slump had little difference between LYTAG concrete and ordinary concrete that can be able to meet the liquidity requirements. It has reached the requirement of concrete structure, although compressive strength of LYTAG concrete of 3d, 7d and 28d is small than ordinary concrete. And the late strength of Lytag concrete growth momentum was sound.

Anti-seismic property

After the 1976 Tangshan earthquake researchers have found that the earthquake-stricken brick structure houses collapsed or were almost completely destroyed in the earthquake area, but dozens of buildings built by the use of lightweight aggregate concrete building is almost intact. This fact proves that the earthquake resistance of lightweight aggregate concrete building is very good. As followed, research the seismic performance of LYTAG concrete.

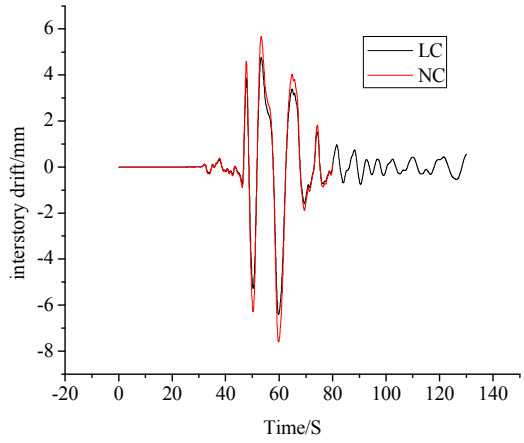
In this paper, the seismic performance of the two buildings of architectural models which were built by the mix proportion shown in Table 2 were compared and analyzed, adopt the Chi-Chi earthquake in Taiwan tcu052 waves recorded. The two buildings are the frame structure model which is located at the earthquake zone of intensity 7. Then, a time history analysis method for the two building model is proposed. To be specific, the seismic performance of the interstory drift and acceleration of the first floor, the third floor, the fifth floor and the seventh floor of the two buildings were analyzed as shown in Table 4 and figure 1.

Tab. 4 The seismic performance of LYTAG concrete and normal concrete

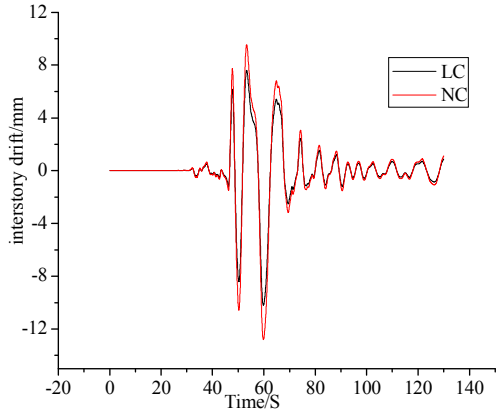
		interstory drift/mm	acceleration/gal
NC	**1**	7.6	192
	3	12.8	273
	5	15.9	362
	7	18.5	469
LC	**1**	6.4(18.8%)	175(9.7%)
	3	10.2(25.5%)	261(5.0%)
	5	13.8(15.2%)	351(3.0%)
	7	15.9(16.4%)	492(-4.9%)

Notes: Figures in brackets denote Damping ratio.

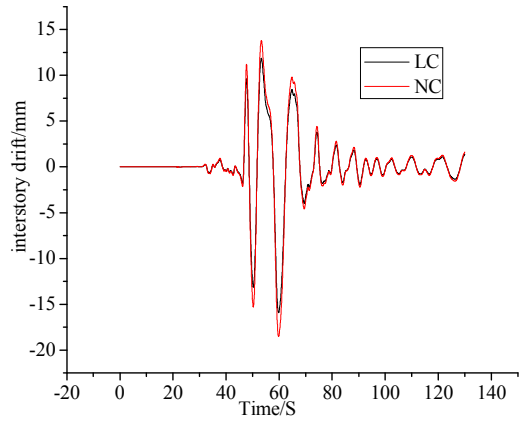
We can learn from Table 3 and Figure 1 that seismic acceleration of Lytag concrete and ordinary concrete frame structure model under the action of waves tcu052 Taiwan Chi-Chi earthquake records is not much difference. But the displacement decreased significantly. Reducing layer displacement has a powerful effect on the seismic performance of buildings. Reducing layer displacement has a powerful effect on the seismic performance of buildings.Therefore, the seismic performance of the seismic performance of Lytag concrete is much better than that of ordinary concrete.



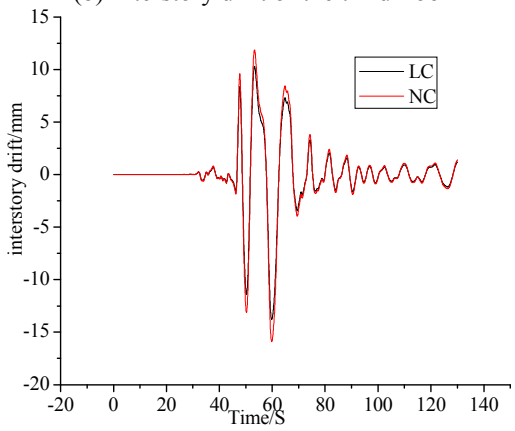
(a) Interstory drift of the first floor



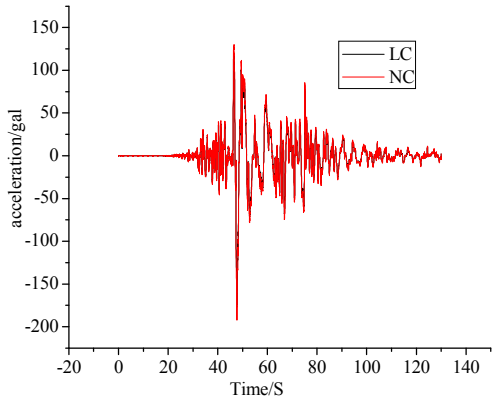
(b) Interstory drift of the third floor



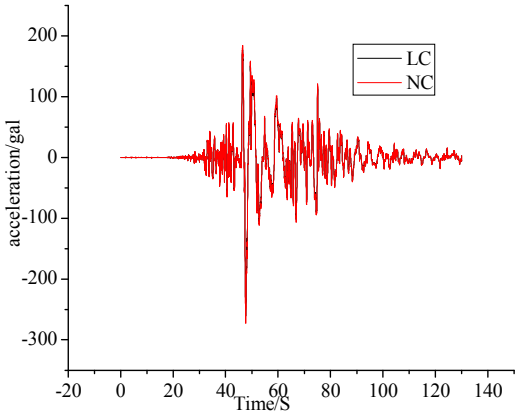
(c) Interstory drift of the fifth floor



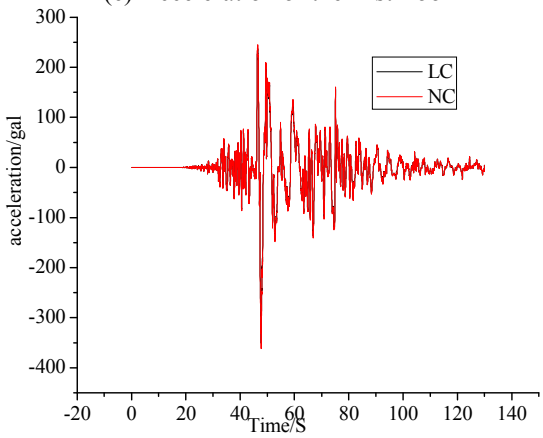
(d) Interstory drift of the seventh floor



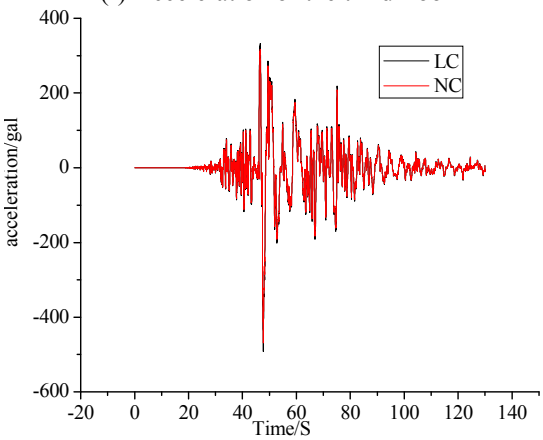
(e) Acceleration of the first floor



(f) Acceleration of the third floor



(g) Acceleration of the fifth floor



(h) Acceleration of the seventh floor

Fig. 1 Reaction curve of LYTAG concrete and normal concrete

Summary

When an earthquake occurs, light weight, low elastic modulus of LYTAG concrete and good deformation performance make the seismic wave velocity performance slow, and it can quickly absorb the impact energy of earthquake. Therefore, the damage of LYTAG concrete with long auto-oscillation period is light under the same load of earthquake. Damping effect is significant when the aggregate is LYTAG. Damping effect will be more significant if both of the bearing structure and maintenance structure adopt LYTAG concrete.

Acknowledgments

The author gratefully acknowledges Wen-I Liao who offers the ground motions records using in this paper!

References

[1] REN Hong-tao, ZU Ya-li, REN Ze-min, LIU Ping, "Experimental Study on Seismic Behaviour of Lightweight Concrete Shear Wall," Journal of Hebei University of Technology, vol. 36, pp. 94–98, Aug 2007 (in Chinese).
[2] N.A. Abrahamson, "Near-Fault Ground Motions from the 1999 Chi-Chi Earthquake," in Proc. of U.S.-Japan Workshop on the Effects of Near-Field Earthquake Shaking. San Francisco, CA, pp.11-13,2000.
[3] Alavi B and Krawinkler H, "Effects of near-field ground motion on building structures," 2001.
[4] Wen-I Liao, Chin-Hsiung Loh, etc, "Comparison of dynamic response of isolated and non-isolated continuous girder bridges subjected to near-fault ground motions," Engineering Structures, vol. 6, pp.2173-2183, 2004.

Advanced Materials Research Vol. 936 (2014) pp 1419-1422
© (2014) Trans Tech Publications, Switzerland
doi:10.4028/www.scientific.net/AMR.936.1419

The Frost Resistance of LYTAG Concrete

Ailian Zhang, Linchun Zhang

School of Civil Engineering, Sichuan College of Architectural Technology, Deyang 618000, China

zhangailian1980@163.com

Keywords: frost resistance; LYTAG concrete; mineral admixture

Abstract: This article studies the frost resistance of LYTAG concrete and ordinary concrete respectively used the RILEM recommended test method (CIF) about frost resistance of concrete. The results indicate that the single surface's frost resistance of Lytag concrete with mineral admixture is much better than normal density concrete's. And the rank of the single surface's frost resistance at 56 cycles of Lytag concrete with different mineral admixture is: silica fume and slag> silica fume and fly ash>slag and fly ash>silica fume>fly ash>slag. The important reasons why LYTAG concrete has good frost resistance is that the scope of blending interfacial transition zone of LYTAG concrete between aggregate ceramsite and cement stone was significantly smaller than ordinary concrete.

Introduction

The lower density and higher insulating capacity and better durability are the most obvious characteristics of Lytag-based lightweight aggregate concrete (Lytag concrete) by which it distinguishes itself from ordinary normal density concrete [1, 2]. But how the frost resistance of LYTAG concrete is. This article studies the frost resistance of LYTAG concrete and ordinary concrete respectively used the RILEM recommended test method (CIF) about frost resistance of concrete.

There are problems in engineering concrete freeze-thaw damage at the area of cold and hot alternate. In general, freeze-thaw conditions including freezing and thawing medium, freezing and thawing temperature and annual cycles of freezing and thawing [3] . By comparison of domestic and foreign specifications, we can find that it is more concise for foreign environment division. It is divided into non freezing, frost damage but no salt freezing, frost damage and salts contact (deicing salt and seawater) three categories.

CIF is one of the RILEM recommended test methods about frost resistance of concrete[4, 5]. CIF has the following advantages: single side test and cooling rate is closer to the actual cold region climate on concrete spalling. CIF adopts the weight and internal damage at the same time as the evaluation index about frost damage[6, 7]. Its test cycle is short. The test results are with high accuracy, repeatability, reproducibility. But its disadvantages are high cost experimental equipment.

General Situation of Test Area

Raw Material

LYTAG

The test uses Lytag with density grade of 800 produced in Daqing whose main raw material is fly ash. Lytag is a special material which is achieved through fining, balling, sintering at high temperature. Its basic properties and particle size distribution are respectively supported for specification compliance. The index is all accorded with the technical requirements of Lytag whose diameters are between 5 and 16 mm in Lightweight aggregates and its test methods.

Other Raw Materials

P·O 42.5 ordinary portland cement is produced in Harbin cement plant and ordinary medium sand whose fineness modulus is 2.81.The test uses mineral admixtures are as follows, ultra-fine fly ash which is produced in Harbin cement plant, ultra-fine slag which is produced in Anshan Iron and Steel Factory, zeolite powder which is produced in Neijiang, and silica fume which is produced in Elkem Company. And the additives are as follows, Mighter 100 naphthalene superplasticizer produced by Japan Kao whose quantity is 1% of the cement and whose water reducing ratio is 20%, MICRO-AIR202 concrete air-entraining agent produced by Master Builder Technoloy in Shanghai, and the running water in Harbin.

Mix Proportion

In this test, Standard cube specimens of 100mm× 100mm× 100mm is used to determine the cubic compressive strength. And 150mm× 150mm× 55mm is used to determine the frost resistance of concrete. The mix proportion is shown in Table 1. And the material dose (in kg) in Table 1 is in one cubic meter of concrete. The slumps (in mm) and 28d compressive strength (in MPa) represented by σ_{28} is measured value in Table 1. O represents ordinary concrte. A represents 8% silica fume, B represents 20% slag, C represents 20% fly ash, D represents 10% fly ash and 10% slag, E represents 8% silica fume and 12% fly ash, F represents 8% silica fume and 12% slag.

TAB. 1 THE MIX PROPORTION AND COMPRESSIVE STRENGTH OF LYTAG CONCRETE

	cement	slag	Fly ash	Silica fume	water	sand	LYTAG	Slumps	compressive strength
O	530.0	0	0	0	244.0	565	568	175	39.0
A	487.6	0	0	42.4	271.0	565	568	175	42.2
B	424	106.0	0	0	244.0	565	568	165	38.1
C	424	0	106.0	0	244.0	565	568	170	37.8
D	424	53.0	53.0	0	244.0	565	568	165	39.1
E	424	0	63.6	42.4	244.0	565	568	170	39.8
F	424	63.6	0	42.4	244.0	565	568	165	41.2

Experimental Programme

Concrete specimens are treated by pre-saturated processing by the way of capillary suction in 3% NaCl solution in the CIF method. At first, determine the initial quality and dynamic modulus of elasticity. Then, the experiment is conducted in the freeze-thaw cycle test machine with the 3% NaCl solution as the freezing and thawing medium. The 12h freeze-thaw cycle is used in the CIF method. The highest temperature for each freeze-thaw cycle test is 20 degree Centigrade and holding one hour at 20 degree Centigrade. While the lowest temperature for each freeze-thaw cycle test is minus 20 degree Centigrade and holding three hours at minus 20 degree Centigrade. It lasts for four hours from 20 degree Centigrade to minus 20 degree Centigrade, so does the time from minus 20 degree Centigrade to 20 degree Centigrade. Temperature cycle of monitoring will be subject to the temperature of the reference point. Reference point for measuring temperature deviation in the low temperature should not exceed 0.5 degree Centigrade, and 1 degree Centigrade for other degrees. The constant time drift between test containers is acceptable. In the CIF method, it takes advantage of the relative dynamic modulus of elasticity under different times of freeze-thaw changes and the mass loss per unit area to evaluate the salt scaling resistance of concrete.

Conclusions and Prospects

There are three blocks for each mix proportion. Specimens are cured in the standard curing room for 28 days. Then put the blocks into 3% salt solution for six days. Freezing and thawing test is conducted. There are two freezing and thawing cycles every day. Test the coming off amount of concretes and sound respectively after 14, 28, 42 and 56 times, and at the same time watch out the surface of scaling of concretes. Coming off amount of concretes is shown in Fig. 1. Loss percentage of

dynamic elastic modulus is shown in Fig. 2. Surface of scaling of concretes is shown in Fig. 3. As shown in Fig. 1, the least of coming off amount of concretes is F, which is about less than 75% than the most B.

According to Fig. 3, the surface of the crack expanding quickly after 56 cycles of freezing and thawing, and at last it leads to faster damage. With the further damage, the aggregate of concrete is exposed, and the exposed aggregate develop step by step. The formation of porous layer makes the surface uneven. The uneven surface creates a good opportunity for NaCl entering into the internal part of concrete. When concrete is in damp environment, NaCl will dissolve and enter into the internal part of concrete. When concrete is in dry environment, NaCl will recrystallize. Recrystallization pressure is larger than interface bond of aggregate and cement paste. Under the action of wet-dry cycling, the concrete bear freezing and thawing is destroyed step by step.

The same result can be gained in surface of scaling of concretes, coming off amount of concretes and loss percentage of dynamic elastic modulus. The rank of frost resistance of LYTAG concrete with single-doped mineral admixture after 56 cycles is silica fume>fly ash>slag. The rank of frost resistance of LYTAG concrete with multiple-doped mineral admixture after 56 cycles is silica fume and slag> silica fume and fly ash>slag and fly ash. The frost resistance of LYTAG concrete with multiple-doped mineral admixture is much better than that of LYTAG concrete with single-doped mineral admixture.

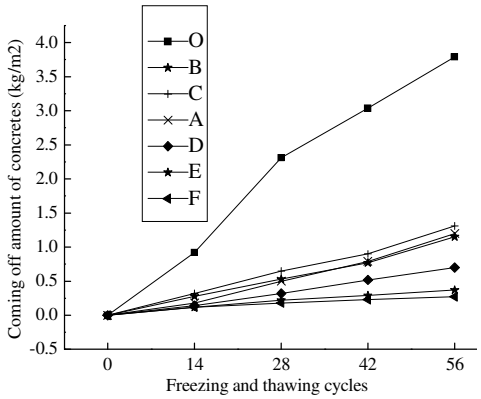


Fig.1 Coming off Amount of Concretes

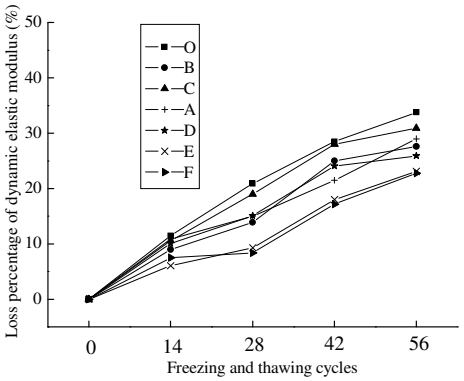
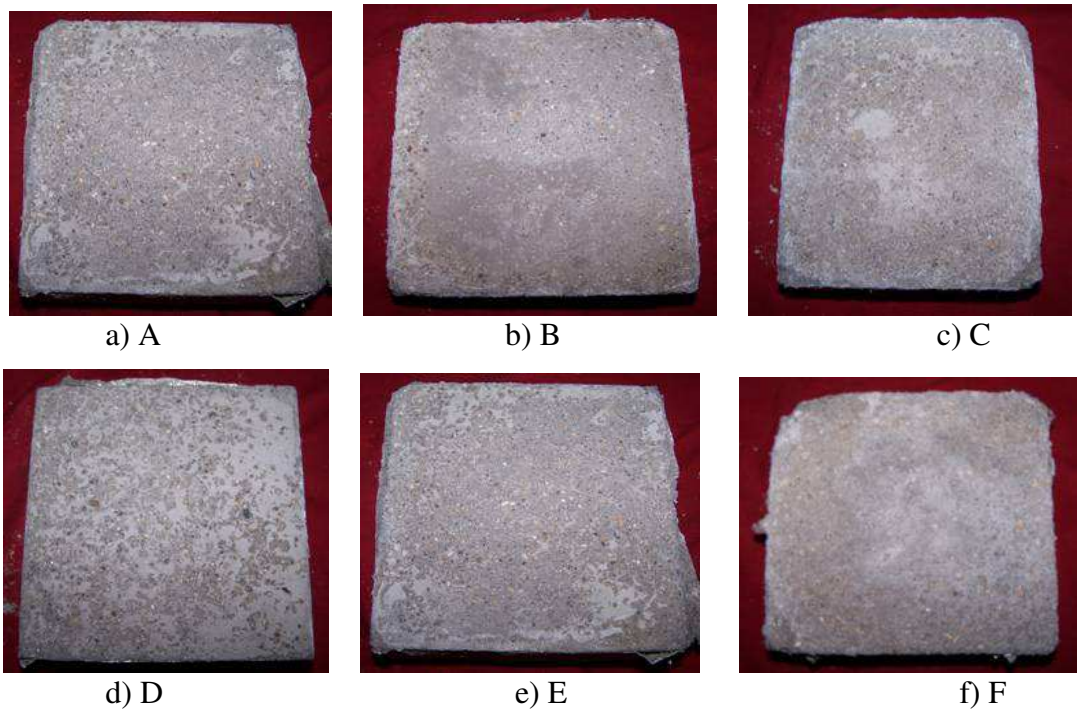


Fig.2 Loss Percentage of Dynamic Elastic Modulus



a) A b) B c) C

d) D e) E f) F

Fig.3 Surface of Scaling of Concretes

Mechanism Analysis

Lightweight aggregate contains many closed pores, and the pore is not easy to be saturated with water. Frozen concrete, lightweight aggregate within the closed pores can play a buffer role on ice pressure water freezes, thereby reducing the expansion pressure and the internal stress of concrete. Therefore, the lightweight aggregate concrete can be obtained a good frost resistance.

Mineral admixtures have differences in particle size distribution, particle morphology and reactivity. When mineral admixtures are mixed with cement particles, the strength of hardened cement paste could sustainably develop because the reaction of cement particles composition and mineral admixtures is based on a certain hydration speed and sequence. The hydration of cement clinker is the fastest, and the hydration of slag powder comes second. The hydration of fly ash is the slowest in the calcium hydroxide excitation conditions. They can be used together to ensure concrete hydration carrying on in order. That is, cement hydration carries on first, and then the secondary hydration of slag powder followed. Finally, the secondary hydration of fly ash carries on. Cement structure becomes denser and the strength is continuous development along with the ongoing hydration. Such as cement composite functional superposition effect of fly ash and silica fume, effectively regulate the hydration process of cement, cement stone structure is optimized. Therefore, single frost resistance of concrete incorporated with mineral admixtures single freeze-thaw resistance is better than the single doped mineral admixture concrete.

Summary

The single surface's frost resistance of LYTAG concrete with mineral admixture is much better than normal density concrete's. The frost resistance of LYTAG concrete with multiple-doped mineral admixture is much better than that of LYTAG concrete with single-doped mineral admixture. And the rank of the single surface's frost resistance at 56 cycles of Lytag concrete with different mineral admixture is: silica fume and slag> silica fume and fly ash>slag and fly ash>silica fume>fly ash>slag.

References

[1] G. Carette, A. Bilodeau, R.L. Chevrier, V.M. Malhotra, Mechanical properties of concrete incorporating high volumes of fly ash from sources in the U.S., ACI Mater J 90 (1993) 535-544.

[2] XU Ding-hua, XU Min. Generality of concrete material [M]. Beijing: Standards Press of China, 2002. (in Chinese)

[3] M.J.Setzer, R.Auberg. Frost Resistance of Concrete. Cement&Concrete, 1997(5):25~29

[4] MA Baoguo, Fu Haobing, WANG Huixian, WANG Yingbin, TIAN Zhen, LU Siwen, “Influence of Mineral Admixture Double Mixing on the Cement base Material Rheological Properties,” New Building Materials, vol. 40, pp. 1–4, Aug 2013 (in Chinese).

[5] L. Lam, Y.L. Wong, C.S. Poon, Effect of fly ash and silica fume on compressive and fracture behaviors of concrete, Cem Concr Res 28 (1998) 271-283.

[6] SETZER M J, FAGETLUND G, JANSSEN D J. CDF test-Test method for the freeze-thaw resistance of concrete tests with sodium chloride solution(CDF)[J]. Materials and Structures, 1996, 29: 523-528.

[7] Dinakar P, Babu KG, Santhanam M. Durability properties of high volume fly ash self compacting concretes. Cem Concr Compos 2008; 30: 880–886.

Advanced Materials Research Vol. 936 (2014) pp 1423-1427
© (2014) Trans Tech Publications, Switzerland
doi:10.4028/www.scientific.net/AMR.936.1423

Recombinant Materials and Contemporary Energy Efficient Architecture

Mohammadjavad Mahdavinejad[1,a], Setareh Ghanavati[2,b], Narjes Elmi[3,c], Airya Norouzi Iarki[2,d], Arash Zia[4,e]

[1]Faculty of Art and Architecture, Tarbiat Modares University, Tehran, Iran

[2]Faculty of Architecture, University of Tehran, Kish international campus,Iran

[3]Faculty of Architecture and Planning, Imam Khomeini International University, Qazvin, Iran

[4]Faculty of Architecture, University of Tehran, Alborz campus, Iran

[a]Mahdavinejad@modares.ac.ir, [b]setare.qanavati@ut.ac.ir, [c]elmi_narjes@yahoo.com, [d]airya.norouzi@ut.ac.ir,[e] zia.arash@ut.ac.ir

Keywords: energy efficient building, material science, net-zero building, recombinant material

Abstract: Nowadays, reducing energy consumption, using clean resources and the aim of creating net-zero building are going to be more and more important. It seems that use of recombinant materials may be a way to reach a more energy efficient architecture. There are considerable advances in development of new material, while the use of these materials is limited in architecture. Regarding to hypothesis of the research, identification of new materials, their performance and their properties, which cause decrease in energy consumption may be helpful for development a more energy efficient architecture. The results of the paper show that architects may incorporate recombinant material to reach energy efficient buildings, however they can play a crucial role in saving natural energy resources through adoption of recombinant materials in architecture and planning

Introduction

The relationship between architecture and materials had been fairly straightforward until the Industrial Revolution. Interaction of building and architecture determined the material choice, and as such, we can consider the pre-19th century use of materials in design to have been subordinate to issues in function and form. The role of materials changed dramatically with the advent industrial revolution. Rather than depending on an intuitive and empirical understanding of material properties and performance, architects began to be confronted with engineered materials. [1] This study is to find material properties, functions and how they reduce energy consumption to recognize when their implementation is appropriate. Renewable energy such as wind energy, and solar source, are known as valuable resources to replace with convention sources, because of the large impact in reducing energy crisis.

Literature Review

Materials play important roles in building stability and construction [2] therefore those are very important in architectural design [3] especially when interaction of tradition and contemporary architecture is needed. [4] Usage of indigenous architectural patterns [5] and modeling traditional achievements [6] are suitable ways to fulfill helpful strategies and tactics [7] for contemporary architecture [8] which roots in traditional architecture of hot and dry climate. [9] Theoretical framework of the paper focuses on challenges regarding old parts of historic cities of developing countries especially Iran. Interaction of energy and materials for sustainability in architecture and planning [8] and focus on social issues [9] is to guarantee comprehensive approach toward environmental sustainability [10] and meet eco-friendly design and planning [11]. Developing countries such as Iran are in need of this comprehensive approach [12, 13] more than other parts of the world. [14, 15] It seems that redevelopment plans in formal documents are more eco-friendly than it is in real perspectives. [16, 17] This article is to present how to reduce the usage of energy

through materials and investigate that recombinant materials are capable of producing desirable behavior to achieve energy efficient architecture. [18, 19] Recent materials can play a crucial role in optimization of energy consumption, and using renewable energy in order to deal with global warming and energy crisis. Hence, utilization of recombinant materials like smart materials and nanostructured materials can help to generate and store energy. Smart material [9, 20] can be categorized in following branches: 1- Immediacy – they respond in real-time. 2- Transiency – they respond to more than one environmental state. 3- Self-actuation – intelligence is internal to rather than external to the material. 4- Selectivity – their response is discrete and predictable. And 5- Directness – the response is local to the 'activating' event.

Discussion

The results of the paper show that [21, 22] there are lots of new adoption of recombinant materials and nanotechnology in contemporary architecture of developed countries as well as developing societies. [23, 24] It is so important to clarify that usage of ultra-fine grains and nano structured materials may result in more energy efficient architecture as adoption process follows proposed method. (Table 1)

TABLE 1- RECOMBINANT MATERIALS AND SOPHISTICATED ARCHITECTURAL CHARACTERISTICS

Materials	Combination	Properties	Sample
Shape memory Alloy	Ni-Ti, Ni-Ti-Fe, Zn-Cu, Au-Cd, Ti-Mb, Ti-Nb-Sn, Ti-Nb-Al, Ti-Nb-Ta, Ti-Nb-Zr, Ti-Nb-O, Ti-Nb-Pt, Ti-Mo-Ca, Ta-Mo-Sn	shape changing	A thermal actuator for ventilators Rock breaker Sensor to operate radiator fan Water purifier
Phasechange material(PCM)	CnH2n+2,CnH2n+2,COOH,N-alkanes C10-C18, CH3(CH2)2NCOOH, CH_3COONa,H_2O $MnH_2O,(SiO_{2n+2})^{2n-}$	CnH2n+2,CnH2n+2, COOH,N-alkanes C10-C18, CH3(CH2)2NCOOH, CH_3COONa,H_2O $MnH_2O,(SiO_{2n+2})^{2n-}$	-Latent heat or latent cold storage -volume changing -Heating thermostat -Building technical service actuator Ventilation system - decentralized ventilation system phase change slurry -Gypsum plaster boar -aluminum foil bags in dry wall -radiant floor systems in concrete slabs
Electroactive	$(C_4H_2NH)_n$ $(C_6H_4NH)_n$	Shape Changing Intrinsically Conductive	Anti-Corrosion for Steel
Photochromics	Spyropyranes Naphtopyranes AgBr, AgCl	Color Change Switch Between the Reflectively and Absorbtively	Photochromic Plastic Photochromic Glass Paint Dyes Made From PC
Thermochromic and thermotropic	Hydrogel Choleterylesters Spiropyranes TiO_2, ZnO,In_2O_3 ,V_2O, V_2O_5 Lyotropic liquid crystal	Color Change, Best Operation in the Near Infrared Region Operates More Reflectively	Thermochromic Glass Thermochromic Plastic Reflective Glass
Electrochromics	Wo3,Moo,Moo_3,IrO_2,MnO_2,Nb_2O_5,V_2O, V_2O_5, B_2O_5, In_2O_3.Sn,NiO, $(CH2CHC6H4SO3H)_n$ Polyaniline, Polythiophence	Color Change Molecular Change Through Oxidation-Reduction.	Glass

Thermoelectric	Bi_2Te_3,$FeSi_2$,SiGe, Sb_2Te_3,Bi_2Te_3,$FeSiO_2$,Mg_2Si, Boron Carbid Nano wire: Bi_2Te_3, Sb_2Te_3,Zn_4Sb_3,PbTe	Absorbing Heat Generating Electricity	Photovoltaic Photo Transistor Solar Cell
Photoelectric	Ruthenium Complex	React to Visible Light, UV Light Electricity Generation	Dye Solar Cells
Piezoelectric	$Pb[Zr_xTi_{1-x}]O_3$ $(C_2H_2F_2)_n$	Electricity Generation	Piezoelectric Ceramics

Level of energy efficiency depends on the process in which ultra-fine grains and nano structured materials are going to be adopted in architectural design process especially in sustecture – sustainable energy efficient contemporary architecture – (Table 2) which enjoys high performance and characteristics.

TABLE 2- RECOMBINANT MATERIALS AND LEVEL OF ENERGY EFFICIENCY

Materials	**Reduction of energy usage**	**Level of energy efficiency**
Shape Memory Alloy	Control the amount of light Control air ventilation	3/4
Phase-Change Material (PCM)	changing heat capacity and density -Open and close in certain temperature-ventilates if it is necessary-Heat storage-Controlling gasses and liquid -Generate and store energy	4/4
Photochromics	Control of solar radiation Controlling light transmittance Controlling solar direct transmittance	1/4
Thermochromic and thermotropic	Controlling light transmittance Controlling solar direct transmittance	2/4
Electrochromics	Conversion of ambient energy to electrical energy Controlling light transmittance Controlling solar direct transmittance	3/4
Thermoelectric	Conversion of ambient energy to electrical energy Controlling solar direct transmittance	4/4
Photoelectric	Day light sensing	4/4
Piezoelectric	turn compression to generate electricity	2/4

Summery

Concern of global warming, reducing energy consumption and using clean sources, which architects play a significant role to achieve, became more and more significant. Therefore recognition and development of new materials and their features and know how to optimum their properties or by integration of the systems they can provide significant solution for architectural demand. In architecture the use of new materials is limited, despite the fact that new materials are capable of wide range of applications. Proper selection of the materials can effectively increase the level of energy efficiency of buildings. Integration of recombinant materials with building systems will provide a great potential for innovation in architectural field. It can result in providing desirable condition for inhabitant. Solar selective glasses such as electrochromic and thermochromic manage both of the solar heat gain and adequate day light .integrate suitable coatings with the glasses enhance the performance. Thermoelectric integrated with solar cells will be more efficient and can

be applied on roof and building facade. The purpose of using thermoelectric film on glass louver is the potential of producing energy from solar source; in addition, heat waste could be convert to electricity. The glass louvers mentioned above are able to change their position based on solar radiation and ambient temperature by using SMA as an actuator. Using PCM in roof, wall, and integrate them with solar cell and glasses such as thermoelectric glasses and the suggestion which was mentioned above lead architects to create energy efficient building. Thus it may be concluded that recombinant materials may bridge contemporary architecture of the world to a more green and energy efficient states.

References

[1] M. Addington, D. Schodek, smart materials and new technologies, Oxford: Elsevier, 2005.

[2] M. Mahdavinejad, M. Bemanian, G. Abolvardi, S. M. Elhamian: Analyzing the state of seismic consideration of architectural non-structural components (ANSCs) in design process (based on IBC). International Journal of Disaster Resilience in the Built Environment, Vol. 3, Iss: 2 (2012) 133 – 147.

[3] M. Mahdavinejad, A. Moradchelleh: Problems and Tendencies of the Development of the Architectural Sciences: Culture Research Aspect, Middle-East J. Sci. Res., 10 (6) (2011) 677-682.

[4] M. Mahdavinejad, A. Doroodgar, A. Moradchelleh: The Impacts of Revivalist Trends on the Contemporary Architecture of Iran (1977-2011), Middle-East J. Sci. Res., 11 (2) (2012) 176-183.

[5] M. Mahdavinejad, M. Bemanian, M. Hajian, N. Pilechiha: Usage of Indigenous Architectural Patterns for Manufacturing Industrial Housing, Case: Renovation Project of Odlajan of Tehran, Iran, Advanced Materials Research, Vol. 548 (2012) 875-879.

[6] M. Mahdavinejad, S. Ahmadzadeh Siyahrood, M. Ghasempourabadi, M. Poulad, M.: Development of Intelligent Pattern for Modeling a Parametric Program for Public Space (Case study: Isfahan, Mosalla, Iran), Applied Mechanics and Materials, Vols. 220-223 (2012) 2930-2935.

[7] M. Mahdavinejad, A. Moradchelleh: The Impact of Family and Social Class on Efficiency of Arts Education and Learning, Middle-East J. Sci. Res., 11 (8) (2012) 1068-1077.

[8] M. Mahdavinejad, A. Moradchelleh: Family-Led Method in Art Education and Learning, Case: Tehran, Iran, Middle-East J. Sci. Res., 9 (4) (2011) 554-560.

[9] M. Mahdavinejad, S. Matoor, N. Feyzmand, A. Doroodgar: Horizontal Distribution of Illuminance with Reference to Window Wall Ratio (WWR) in Office Buildings in Hot and Dry Climate, Case of Iran, Tehran, Applied Mechanics and Materials, Vols. 110-116 (2012) 72-76.

[10] M. Mahdavinejad, A. Moradchelleh, Family-Led Method in Art Education and Learning, Case: Tehran, Iran, Middle-East J. Sci. Res., 9 (4) (2011) 554-560.

[11] M. Mahdavinejad, M. Rezaei Ashtiani, S., Ebrahimi, M., Shamshirband, M. Proposing a Flexible Approach to Architectural Design as a Tool for Achievement Eco-Friendly Multi-Purpose Buildings, Advanced Materials Research, 622-623, (2012) 1856-1859.

[12] M. Nazari, M. Mahdavinejad, M. Bemanian: Protection of High-Tech Buildings Facades and Envelopes with One Sided Nano-Coatings, Advanced Materials Research, 829 (2014) 857-861.

[13] M. Mahdavinejad, M. Mashayekhi, A. Ghaedi, Designing Communal Spaces in Residential Complexes, Procedia - Social and Behavioral Sciences, 51 (2012) 533 – 539.

[14] M. Mahdavinejad, S. R. Ashtiani, Dilemma of Energy Efficiency and Moisture Condensation Damages in Eco-Friendly Buildings, Case: Great Mosque of Saveh, European Journal of Scientific Research, 107 (4) (2013) 46 – 552.

[15] M. Mahdavinejad, L. H. Rafsanjani, M. Rasoolzadeh, M. Nazari: Challenges Regarding to Usage of Nanostructured Materials in Contemporary Building Construction, Advanced Materials Research, 829 (2014) 426-430.

[16] M. Mahdavinejad, M. Nazari, S. Khazforoosh: Commercialization Strategies for Industrial Applications of Nanomaterials in Building Construction, Advanced Materials Research, 829 (2014) 879-883.

[17] M. Mahdavinejad, M. Amini, Public participation for sustainable urban planning In case of Iran, Procedia Engineering (2011) 405-413.

[18] M. Mahdavinejad, M. Abedi, Community-oriented landscape design for sustainability in architecture and planning. Procedia Engineering, 21 (2011) 337-344.

[19] M. Mahdavinejad, S. Mansoori, Architectural design criteria of socio-behavioral approach toward healthy model. Procedia-Social and Behavioral Sciences, 35 (2012), 475-482.

[20] M. Moulaii, M. Mahdavinejad, M. Gheisar, The status of energy efficient usage of smart materials in sustainable, International Conference on Intelligent Building and Management Singapore: IACSIT Press (2011) 6.

[21] M. Mahdavinejad, K. Javanroodi, L. H. Rafsanjani, Investigating condensation role in defects and moisture problems in historic buildings. Case study Varamin Friday mosque in Iran, World Journal of Science, Technology and Sustainable Development, 10 (4) (2013) 308-324.

[22] Antonino Salvatore Aricò1, P. B.-M, Nanostructured materials for advanced energy conversion and storage devices. Nature Materials, (2005) 366-377.

[23] K.Yamauchi., I.Ohkata, K.Fsuchiya, and S.Miyazaki, Shape memory and superlastic alloys technologies and applications 2011.

[24] S.Selkowits, E.Lee, M.Lafrance, Dynamic Building Facades for Zero Energy Building 2009

Advanced Materials Research Vol. 936 (2014) pp 1428-1432
© (2014) Trans Tech Publications, Switzerland
doi:10.4028/www.scientific.net/AMR.936.1428

Effect of the Composite of Fly Ash and Slag on Alkali-Silica Reaction

Tongchao Liu[1,a], Bo Xiao[2,b],Guhua Li[1,c], Nianhong Luo[3,d], Longsheng Zhang[1,e]

[1]School of civil engineering, Southwest Jiaotong University, Chengdu, Sichuan,China,610031

[2]Sichuan Ba Shan expressway co.,Ltd,2nd ring road N.O.90,Chengdu,Sichuan,China,610031

[3]School of foreign language, Southwest Jiaotong University, Chengdu ,Sichuan,China,610031

[a.]1223955681@qq.com [b.]1045748775@qq.com

[c.]LGH-100@vip.163.com [d.]429030833@qq.com [e.]1050335450@qq.com

Keywords: alkali aggregate reaction; fly ash; slag; admixtures

Abstract: The study used the method of accelerated mortar bar test to study alkali aggregate reaction(ASR) with sandstone aggregate. Both fly ash and slag can inhibit the expansion of mortar bar. Results show that 50% slag can inhibit ASR reluctantly, but 10% fly ash and 20% slag can inhibit ASR very well, and the inhibitory effect of fly ash is far better than slag. Because of the high content of CaO in slag, it has inhibit and promote aspects, when the ASR is fierce, slag can inhibit ASR, otherwise slag can promote ASR.

Introduction

Alkali silica reaction (ASR) is a deleterious chemical reaction between alkalis in portland cement paste and certain amorphous silica in a variety of nature aggregate. Numerous concrete structures, such as dams and bridges, have been suffering from ASR[1].

There are so many ways to inhibit the deleterious expansion, but the most effective method is add admixtures, such as fly ash, slag, silica fume, natural zeolite，metakaolin and so on[2].

Papers[2,3] hold the opinion that when the cement is replaced by fly ash by 20%, the deleterious expansion can be constrained availably. And the more the fly ash added, the lower the expansion rate is. Studies[4,5] also indicate that it is an effective mean for controlling expansion due to AAR by blending with steel slag powder. And the amount of slag is always more than 50%.

But if the admixture mix fly ash with slag, can it suppress alkali aggregate reaction better? This is the purpose we design and operate the experiment.

Raw Materials

The cement we used is P Ⅱ 42.5, which brand is lafarge and is made in Dujiangyan city, sichuan province, china. The property is corresponds to the standard *common portland cement* (GB175-2007)[**6**],and alkalinity is 0.56%.

The fly ash and slag are used, the chemical composition is shown in table 1.

Table 1 The chemical composition of fly ash and slag[%]

	SiO_2	Al_2O_3	Fe_2O_3	CaO	MgO	K_2O	Na_2O	Loss
Fly Ash	57.31	32.5	4.89	2.45	0.55	0.76	0.47	2.32
Slag	36.33	10.64	0.79	38.51	8.11	0.51	0.26	

The aggregate is sandstone, which is produced by Ba river, sichuan province, china. Sandstone has potential alkali activity, the activity mainly come from chalcedonic microcrystalline quartz and undulated extinction quartz, the 14d expansion rate is about 0.3% with the test method of accelerate mortar-bar test(AMBT)[7].

Test Methodology

The standard Technical Code for Preventing of Alkali-aggregate Reaction in Concrete (GB/T 50733-2011)[8] is selected and demonstrated. Which operation is almost the same as standard ASTM C1567 test procedure[9].

The size of the specimens are 25mm*25mm*280mm with gage studs at ends, in which the water-to-glue ratio is 0.47, and the aggregate-to-glue ratio is 2.25,by mass. The specimens are cured in 1mol/L sodium hydroxide solution, which is preheated to 80℃.

According to the standard, if the 14d expansion is no more than 0.03%, the suppress is available, the expansion can be calculated by the formulae below:

$$\varepsilon_t = \frac{L_t - L_0}{L_0 - 2\Delta} . \quad (1)$$

There into: ε_t is the expansion ratio of the specimen in the first t days; L_t is the length of the specimen in the first t days; L_0 is the length of the specimen in the first day; Δis the length of the measuring head.

Experiment and Discussion

The inhibition effect of slag on the AAR expansion is shown in Table.2.

Table 2 The effect of different amount of slag on ASR[%]

	3d	7d	10d	14d	21d	28d
30S	0.017452	0.046056	0.075494	0.100921	0.134874	0.163076
40S	0.009948	0.026414	0.047868	0.062767	0.086611	0.105745
50S	0.005083	0.015347	0.027962	0.037023	0.05646	0.073536

S: slag, -30: replacement percentage is 30% by mass.

Figure 1 shows the expansion with the admixture of slag in broken line graphs.

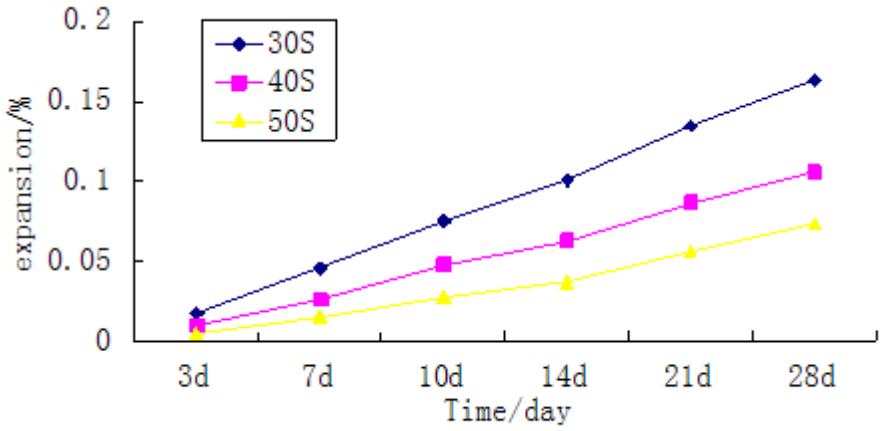


Fig 1 The expansion add slag

It can be seem from Fig.1 that slag can suppress alkali silica reaction. The expansion is decreasing with the increase of slag content., so the slag can restrain ASR.

When the dosages of slag are 30%,40%,50%,the 14d expansions are 0.101%， 0.063 and 0.037% ， although the expansion is decreasing, both of them are greater than 0.03, according to The standard Technical Code for Preventing of Alkali-aggregate Reaction in Concrete (GB/T 50733-2011)[8],the suppress is of no avail, but if we refer to The Standard for Construction Quality Acceptance of Railway Concrete Engineering(TB 10424-2010)[10]， if the 28d expansion is no more than 0.1%,the inhibition is available. Because the 28d expansions are 0.163%, 0.106% and 0.074%, so when the slag replacement ratio is 50%, slag can restrain alkali silica reaction. And conclusion also can be

drawn that the former standard is stricter. It can be forecasted that if the replacement ratio become large, the effect will be better, but study[11] points that when the slag replacement ratio is more than 50%, the concrete strength will decrease significantly, the reason is that the cement content is too low so that the slag can not hydration completely.

No matter how much we replaced, it warn us that, the expansion trend is almost linear, after 28d, the expansion still has a sharp rising trend.

In a word, slag can't restrain ASR very well with the sandstone aggregate. And its effect is far worse than other admixture, such as silica fume, metakaolin[12].

But how does the gel work when it contains fly ash and slag? Table 3 shows the expansion data.

Table 3 The effect of different amount of slag and fly ash on ASR[%]

	1d	3d	7d	10d	14d	21d	28d
10F20S	0.0019	-0.0007	0.0042	0.0059	0.0118	0.0147	0.0128
10F30S	0.0039	0.0009	0.0079	0.0097	0.0181	0.0209	0.0216
20F10S	0.0047	0.0032	0.0103	0.0131	0.0201	0.0264	0.0261
20F20S	-0.0030	-0.0056	0.0008	0.0056	0.0100	0.0128	0.0142

1 S: slag; F: fly ash

To present the result visually, broken line graphs are drawn in figure 2.

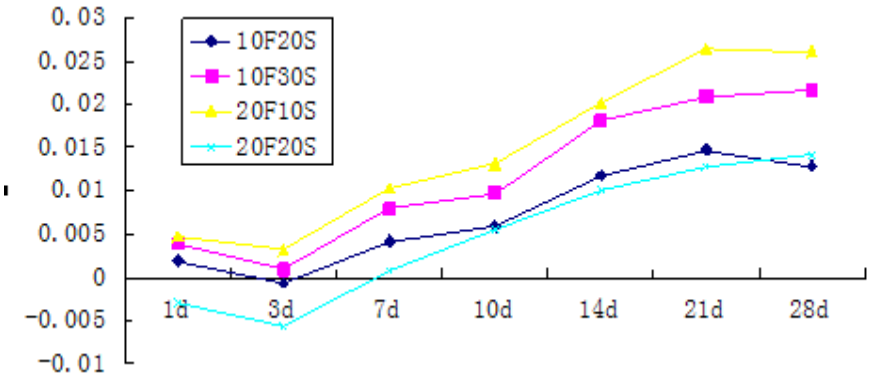


Fig 2 The expansion result add slag and fly ash

The figure above shows that both of the specimens' 14d expansions are less than0.3%,and 28d expansion are less that 0.1%. So no matter standard GB/T 50733-2011[8]or standard TB 10424-2010[10] be refered to, the inhibition is available.

What's more, the expansion rate is slower and slower with the increasing curing age. And the 21d expansions are almost equal to the 28d expansions, it indicates that the specimens' expansion is very slowly, and the suppress effect is very well.

Contrasting to the 1d expansion data and 3d expansion data, the specimens are getting shorter, the reason has 2 respects: the first one is that there have so many cracks in the mortar bars, and the gel produced by ASR can fill into them firstly, this phenomenon will not lead to expansion. The second one is that the cement gel will shrink after its hydration[13].

In the four combinations, the best one is 20% fly ash and 20% slag, and the worst one is 20% fly ash and 10%. But the expansion isn't always decrease with the increase of the dosage of slag. It means sometimes slag has opposite effect.

The reason is stated below.

Slag has large numbers of CaO, which can promote ASR. The low Ca calcium fly ash，has 2%~4% CaO, but the slag has 38%-46% CaO [14].And $Ca(OH)_2$ is harmful to the problem of ASR[15]. The amount of Na^+, K^+ in C-S-H is relate to its Ca/Si，the lower the Ca/Si is, the more the C-S-H absorbed[16].The more the slag is, the more the $Ca(OH)_2$ is, and the absorbing capacity is lower, and more Na^+, K^+ be released to the pores beside the aggregate, so the ASR is fiercer. When the expansion is large, slag's inhibit effect plays a major role, but when the expansion is small, slag's promote effect plays a major role.

To contrast the inhibit effect between fly ash and slag, Fig.1 and Fig.2 can be put together.Fig.3 shows the result.

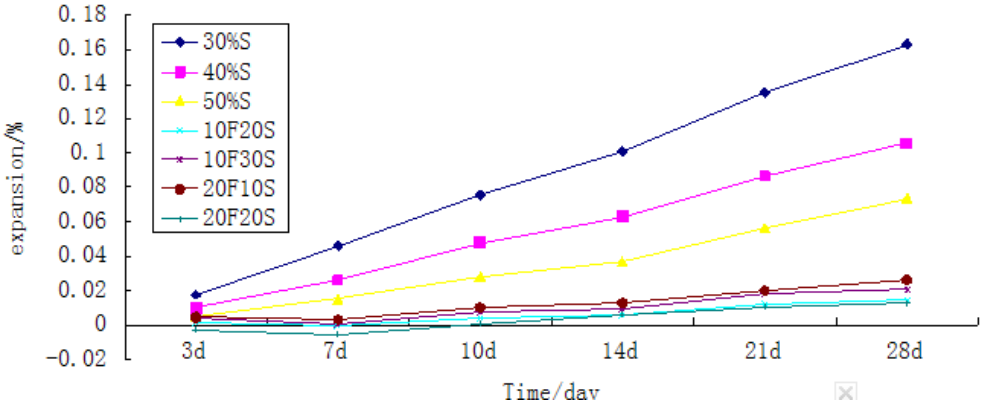


Fig 3 the expansion with slag and fly ash

From Fig.3 above, conclusion can be drawn that the fly ash's inhibit effect is much better than the slag's, even the fly ash's dosage is only 10%, the expansion decrease significantly. The conclusion is accord with former studies[17,18]

Mechanism

The mechanism of fly ash and slag inhibiting ASR are alike, as below shows.[19,20,21].
(1).The admixture can react with $Ca(OH)_2$,which is harmful.
(2).The admixture can fill into the pores around aggregates, and lead to the motar bar compact.
(3).The pozzolanic reaction products C-S-H gel which has low Ca/Si.
(4).The acidic particles in fly ash or slag can absorb K^+,Na^+, and lower PH value in pores.

Summary

(1).50% slag can inhibit ASR reluctantly with the aggregate of sandstone, and the inhibitory effect of fly ash is far better than slag.
(2)When the ASR is fierce, slag can inhibit ASR, otherwise slag can promote ASR.

Acknowledgements

The project is supported by the applied research of mechanical sand on Ba Shan highway program.

Reference

[1] D.R.J.OWEN. Modeling of alkali-silica reaction in concrete: a review[J]. Frontiers of Structural and Civil Engineering,2012,01:1-18.

[2] v, s, Ramachandran. Alkali-aggregate expansion inhibiting admixtures[J]. cement and concrete composites, 1998, (20): 149-161

[3] FENG, Xiao-xin, FENG, Nai-qian, HAN, Dong. Effect of the composite of Natural Zeolite and Fly Ash on Alkali-Silica Reaction[J]. Journal of Wuhan University of Technology, 2003, 18(4): 93-96

[4] Zhu, Yeran. study on the inhibiting effect of GGBS on the alkali-silica reaction in concrete[J]. Concrete, 2010, (1): 94-103(in Chinese)

[5] Li, Yunfeng. Effectivenss of steel slag powder on suppressing alkali aggregate reaction of concrete[J]. advanced materials research , 2009, 79(82): 179-182

[6] GB175-2007, common portland cement[S]

[7] LI Beixing, HU Xiaoman,WEN Ziyun,LI shuangyan. Test of detection and inhibition of alkali aggregate reactivity for sanstone[J]. Engineering journal of wuhan university 2006,01:67-71.

[8] GB/T 50733-2011, the standard technical code for preenting of alkali-aggregate reaction in concrete[S].

[9] ASTM C1567, accelerated mortar bar tests[S].

[10] TB 10424-2010, The Standard for Construction Quality Acceptance of Railway Concrete Engineering[S]

[11] Liu jie,influence of levigate slag to the microstructure of cement-based composite material (IN CHINESE)

[12] Tongchao, Liu, Guhua, li. the study on metakakaolin's effect of restraining the alkali-silica reaction of slate aggregate[J]. applied mechanics and materials, 2013, (1): 732-736

[13] Xianxiao Peng. Study on effect of slate powder on alkali activity of slate aggregate[D].southwest jiaotong university,2013

[14] Yanke, Yang. buinding material[M]. southwest jiaotong university:Yuanning Tang, 2005. 56-57

[15] WU, Ding-yan. Research on alkali activity and inhibition with fly ash of aggregate[J]. concrete, 2008, (1): 69-72

[16] Ramachandram V S. concrete[M]. Shiyuan Huang translet. Beijing: China building industry press,1986（in chinese）

[17] NIU, Quan-lin. Suppresing effect of superfine mineral powder on alkali-aggregate reaction[J]. cement engineering, 2004, (5): 12-15(in chinese)

[18] HU, Rui-quan. the study of the mineral inhibi alkali-aggregate reaction[J]. the journal of engineering and technology of nation defense, 2009, (3): 34-37(in chinese)

[19] Tang, Xiu-sheng. the inhibition of levigated slag to alkali-silica reaction of activity aggregate[J]. Journal of yangtze river scientific research institute, 2011, (2): 56-59(in chinese)

[20] LIU Bin. The summarize of fly ash’s inhibit mechanism to alkali silica reaction[J]. concrete world,2012（33）:85-87.(in Chinese)

[21] Zong, Yong-hong. the study of the inhibit effective of admixture to concrete alkali-aggregate reaction[J]. Journal ofxinjiang university, 2002, (19): 76-79

Advanced Materials Research Vol. 936 (2014) pp 1433-1437
© (2014) Trans Tech Publications, Switzerland
doi:10.4028/www.scientific.net/AMR.936.1433

Analysis of the Influence of Clay Dosage and Curing Age On the Strength of Plastic Concrete

Liangming Hu[1, a], Xueliang Lv[1, b *], Danying Gao[1], Kebing Yan[1], Shuaiqi Song[1]

[1]College of Water Conservancy & Environmental Engineering, Zhengzhou University, Henan, Zhengzhou, 450001, China

[a] liangmingh@zzu. edu. Cn, [b] lxl3344148@163.com

Keywords: plastic concrete; clay dosage; proportion of mixture; strength, analysis of the influence

Abstract: This test is sand coarse aggregate ratio, ratio of water to cementitious material, cement dosage, bentonite dosage, type of sand and type of bentonite in certain cases, studied the influence of clay dosage and curing age on the basic mechanical properties of plastic concrete, it is concluded that the best clay dosage; the clay dosage has a great influence on all the strength of plastic concrete (compressive strength, splitting tensile strength, rupture strength), with the increase of clay dosage and all kinds of strength decreased; when clay dosage is certain, various strengths of plastic concrete are increased with the increase of curing age, curing age has a great influence on various strengths of plastic concrete. If the long curing age (540d) intensity values as the actual strength of plastic concrete, growth rate of strength of 540d long age relative to the 28d age about 120%, this shows that plastic concrete has a higher late strength, plastic concrete curing age longer than concrete curing age.

Introduction

Plastic concrete is a kind of flexible engineering composite materials that between ordinary concrete and clay, by using bentonite or clay replace partial cement in ordinary concrete to form, sometimes in order to improve the performance of plastic concrete, cement savings, reduce investment, but also mixed with fly ash and admixtures. According to the different composition of cementitious materials plastic concrete can be divided into three types of concrete: clay plastic concrete, bentonite plastic concrete, clay and bentonite plastic concrete [1].

Our country is an agricultural country and water is the lifeblood of agriculture. 2011 Central Document No. 1 emphasized the water conservancy as priority areas of national infrastructure construction, the irrigation as a key task in rural infrastructure and develop the people's livelihood and water conservancy, So water conservancy construction is the main focus of China's Twelfth Five-Year Period [2]. With the development of China's water conservancy and hydropower utilities, plastic concrete investment scale of several hundred billion yuan a year for water and soil conservation, harnessing of rivers, reservoirs reinforcement and dam seepage, large construction pit seepage and protection of ancient buildings and other underground seepage control project, and engineering of plastic concrete cutoff wall increased year by year. In the large water conservancy hub project (Three Gorges Project, The Yellow River Xiaolangdi Dam project , Ertan Hydropower Station and so on), cutoff wall technology of plastic concrete has been successfully applied and promotion. For water conservancy engineering and underground engineering have higher seepage control requirements, it very broad application prospects for using plastic concrete seepage instead of the past curtain grouting. With the continuous expansion of the plastic concrete engineering applications, in the practical application of the plastic concrete, clay amount more, will greatly reduce the strength of plastic concrete, and with less, the performance of plasticity concrete does not fully reflect, a large number of scientific issues about performance and applications plastic of concrete need to be studied and resolved as soon as possible; therefore, study of the influence of clay dosage and curing age on the strength of plastic concrete has important theoretical significance and application value.

Experiments

Experimental Design

The purpose of this test is in sand coarse aggregate ratio, ratio of water to cementitious material, cement dosage, bentonite dosage, type of sand and type of bentonite certain cases, studied the influence of clay dosage and curing age on the basic mechanical properties of plastic concrete, it is concluded that the best clay dosage; the results will provide research based for further enrich the theoretical of plastic concrete, formulate norms protocols of plastic concrete and promotion of engineering of plastic concrete.

Varying parameters of test are sand coarse aggregate ratio, ratio of water to cementitious material, cement dosage, clay dosage, bentonite dosage, type of sand, type of bentonite and curing age etc., as shown in Table 1.

TABLE 1 TEST PARAMETERS

Study on factors	Variation of parameters			
Sand coarse aggregate ratio	0.4	0.5	0.6	
Ratio of water to cementitious material	0.75	0.87	1	
Cement dosage(kg/m^3)	90	120	150	
Clay dosage(kg/m^3)	180	220	260	
Bentonite dosage(kg/m^3)	40	70	100	
Type of sand	Coarse sand, fineness module 3.3		Medium sand, fineness module 2.7	
Type of bentonite	Calcium bentonite		Sodium bentonite	
Curing age(d)	28	90	180	540

Experimental Raw Material

Cement

Test uses ordinary portland cement of 42.5 #, the indicators are in line with regulations of Common portland cement (GB175~2007) [3], detailed data see ref [2].

Clay and Bentonite

The silty clay that the test using from Longzihu Lake Zhengdong New District of Zhengzhou. After drying the sample, ground to a powder with standard of 350 mesh particle size. Test using calcium bentonite and sodium bentonite, the main physical and chemical indicators of calcium bentonite and sodium bentonite see ref [2].

Coarse Aggregate and Fine Aggregate

Coarse aggregate used in the test is gravel that particle size of 5 ~ 20mm. According to regulations of Specification of pebble and crushed stone for building (GB/T14685~2011) [4], the stone used for size distribution testing, particle gradation of 5 ~ 20mm gravel meets the requirements of the standard. Experiment uses two kinds of different thickness of sand. The sand used for particle screening, according to requirements of Sand for construction (GB/T14684~2011) [5] and Specifications for hydraulic concrete construction (DL/T5144~2001) [6], and results see ref [2].

Analysis of Test Results

When the ratio of water to cementitious material was 0.87 and the sand coarse aggregate ratio was 0.5, analysis of influence of different clay dosages and curing ages on compressive strength, splitting tensile strength and rupture strength of plastic concrete.

Influence of Clay Dosage and Curing Age on Compressive Strength of Plastic Concrete

To examine influence of clay dosage and curing age on compressive strength of plastic concrete, analysis of the relationship between increment of clay dosage and growth rate of compressive strength of plastic concrete, and the results are shown in Table 2. In the three kinds of clay dosage, the relations between the growth rate of compressive strength and curing age are shown in Table 3.

TABLE 2 RELATIONSHIP BETWEEN CHANGE OF CLAY DOSAGE AND GROWTH OF COMPRESSIVE STRENGTH OF PLASTIC CONCRETE

Change of clay dosage	Rate of change of clay dosage (%)	100mm growth rate of cubic compressive strength (%)		150mm growth rate of cubic compressive strength (%)	
		28d	90d	28d	90d
180~220	22.22	-16.01	-3.31	-8.08	-7.72
220~260	18.18	-34.53	-19.77	-27.47	-21.51

As can be seen from Table 2, the change on clay dosage have a bigger influence compressive strength of concrete, compressive strength of plastic concrete cube of curing age 28d and 90d are accelerated to reduce with increases of clay dosage, the greater the amount the more significant effect. Plastic concrete has the best clay dosage. In this experiment, when clay dosage in 180kg/m3 to 220kg/m3, the cubic compressive strength is reduced slightly, and when clay dosage is more than 220kg/m3, cubic compressive strength drastically reduced. Under the conditions of this experiment, the best clay dosage of one cubic metres of plastic concrete is 220kg.

TABLE 3 RELATIONSHIP BETWEEN CLAY DOSAGE AND COMPRESSIVE STRENGTH GROWTH RATE OF PLASTIC CONCRETE

Clay dosage (kg)	100mm cubic compressive strength (MPa)			150mm cubic compressive strength (MPa)		
	28d	90d	Growth rate of strength	28d	540d	Growth rate of strength
180	2.31	2.72	17.7%	1.98	4.4	122.22%
220	1.94	2.63	35.6%	1.82	4.0	119.78%
260	1.27	2.11	66.1%	1.32	2.9	119.70%

It is seen from Table 3, curing age has great influence on the compressive strength of plastic concrete cube, 90d age relative to the 28d age growth rate of strength with increasing clay dosage increased, growth rate of strength of 540d long age relative to the 28d age about 120%. With the increase of the clay dosage, growth rate of compressive strength of plastic concrete cube caused by curing age acceleration increases, indicating that the more the clay dosage the slower growth of plastic concrete strength, the higher strength relative to the late 28d age.

Influence of Clay Dosage and Curing Age on Splitting Tensile Strength of Plastic Concrete Cube

Changes in the clay dosage, the growth rate results of curing age changes and plastic concrete splitting tensile strength are show in Table 4.

TABLE 4 RELATIONSHIP BETWEEN CLAY DOSAGE AND SPLITTING TENSILE STRENGTH GROWTH RATE OF PLASTIC CONCRETE

Clay dosage(kg)	100mm cubic splitting tensile strength (MPa)			150mm cubic splitting tensile strength (MPa)		
	28d	90d	Growth rate (%)	28d	90d	Growth rate (%)
180	0.35	0.40	14.3%	0.27	0.38	40.7%
220	0.32	0.36	12.5%	0.24	0.35	45.8%
260	0.23	0.33	43.5%	0.18	0.29	61.1%

It is seen from Table 4, the effect of curing age on splitting tensile strength of plastic concrete is larger, growth rate of plastic concrete splitting tensile strength of 90d curing age relative to the 28d age above 10%, the highest reached 61.1%. With the increase of the clay dosage, growth rate of splitting tensile strength of plastic concrete cube increased with curing age increases, which indicates that the more the clay dosage, the longer its curing age. Meanwhile, the effects of curing age on splitting tensile strength of plastic concrete 150mm cube is much larger than splitting tensile strength of 100mm cube, which may be the role of the size effect.

Influence of Clay Dosage and Curing Age on Rupture Strength of Plastic Concrete

Growth rates of rupture strength and difference of rupture strength between the different of clay dosage plasticity concrete are show in Table 5.

TABLE 5 RELATIONSHIP BETWEEN CLAY DOSAGE AND RUPTURE STRENGTH GROWTH RATE OF PLASTIC CONCRETE

Curing age	Clay dosage 180~220 difference of rupture strength (MPa)	Growth rate of strength (%)	Clay dosage 220~260 difference of rupture strength (MPa)	Growth rate of strength (%)
28d	-0.15	-20.0%	-0.09	-15.0%
90d	-0.08	-10.7%	-0.06	-9.0%

It can be seen from table 5, with the increase of clay dosage, rupture strength of 28d curing age plastic concrete decreased, the rupture strength decrease above 15%; rupture strength of 90d curing age plastic concrete decreased also, the rupture strength decrease about 10%, below the decrease of flexural strength of 28d age.

Conclusion

This test is in sand coarse aggregate ratio, ratio of water to cementitious material, cement dosage, bentonite dosage, type of sand and type of bentonite certain cases, studied the influence of clay dosage and curing age on the basic mechanical properties of plastic concrete, the main conclusions are as follows:

(1) The clay dosage has a great influence on all the strength of plastic concrete (compressive strength, splitting tensile strength, rupture strength), with the increase of clay dosage and the all kinds of strength of decrease.

(2) When clay dosage is certain, various strength of plastic concrete are increased with the increase of curing age, curing age has a great influence on various strength of plastic concrete. If the long curing age (540d) intensity values as the actual strength of plastic concrete, the compressive strength of plastic concrete on 90d reached only about 65% of the actual strength [7], this shows that plastic concrete has a higher late strength, plastic concrete curing age longer than the concrete curing age.

(3) Changes of clay dosage have a great impact on compressive strength of plastic concrete cube, compressive strength of plastic concrete cube of curing age 28d and 90d are accelerated to reduce with increases of clay dosage, the greater the amount the more significant effect. Plastic concrete has the best clay dosage. Under the conditions of this experiment, the best clay dosage of one cubic metres of plastic concrete is 220kg.

References

[1] Danying Gao, Liangming Hu, Kebing Yan, Shuaiqi Song, Influence of cement content on strength of plastic concrete [J]. Water Resources and Hydropower Engineering, 2009, 39(9): 57-58.

[2] Liangming Hu, Stress-strain relation model and failure criterion of plastic concrete under compression [D].Zhengzhou: Zhengzhou University, 2012

[3] General Administration of Quality Supervision, Inspection and Quarantine of the People's Republic of China, Standardization Administration of the Peoples Republic of China, GB175-2007. Common portland cement [S], Beijing: China Zhijian Publishing House, 2008.

[4] General Administration of Quality Supervision, Inspection and Quarantine of the People's Republic of China, GB/T14685-2011.Specification of pebble and crushed stone for building [S], Beijing: China Zhijian Publishing House, 2011.

[5] General Administration of Quality Supervision, Inspection and Quarantine of the People's Republic of China, Standardization Administration of the Peoples Republic of China, GB/T14684-2011. Sand for construction [S], Beijing: China Zhijian Publishing House, 2011.

[6] State Economic and Trade Commission of the People's Republic of China, DL/T5144-2001. Specifications for hydraulic concrete construction [S], Beijing: China Electric Power Press, 2002

[7] Liangming Hu, Danying Gao, Yizhi Li, Analysis of the Influence of Long Curing Age on the Compressive Strength of Plastic Concrete[M]. Advanced Resench on Advanced Structure Materials and Engineering, 2012, 382(1): 200-203

Advanced Materials Research Vol. 936 (2014) pp 1438-1441
© (2014) Trans Tech Publications, Switzerland
doi:10.4028/www.scientific.net/AMR.936.1438

The Experimental Study on Bearing Capacity of Reinforced Concrete Structure with Different Reinforce Methods

Qingyi Liu[1,a] Xiaomei Liu[2,b]

[1,2] Xuchang Vocational Technical College,East Section of Xinxing Road,Xuchang City,Henan,461000,China

[a]lyoung@163.com , [b]94189451@qq.com

Keywords： Reinforcement Technology, Concrete structure, Bearing capacity

Abstract: Three reinforcement materials with steel plate, epoxies resin sheet, and glass fiber sheet adhering to failed reinforced concrete beams (RC beams) were used to improve the bearing capacity of Reinforced Concrete beams in the paper. The test results shows all the three materials were proved satisfied with bearing capacity increasing request. Strengthening effects with steel plate and epoxies resin sheet were more obvious.

Introduction

At present, the reinforced concrete structure is widely applied in civil engineering in the world. The structural functions will gradually decline in the influence of erosion, natural environment condition, even unable to satisfy the requirements of normal use[1,2,3]. Therefore, we must take some measures to reinforce the structure, otherwise , the structure will be prematurely terminated. The mature reinforcement methods used today are structure member strengthenting with R.C , structure member strengthenting with R.C ,structure member strengthening with externally bonded reinforced materials,compression member confined by reinforcing wire,structure member strengthening with externally applied prestressing,etc.[4,5,6].Three reinforcement materials with steel plate, epoxies resin sheet, and glass fiber sheet adhering to failed RC beams were compared by experiments in this paper.

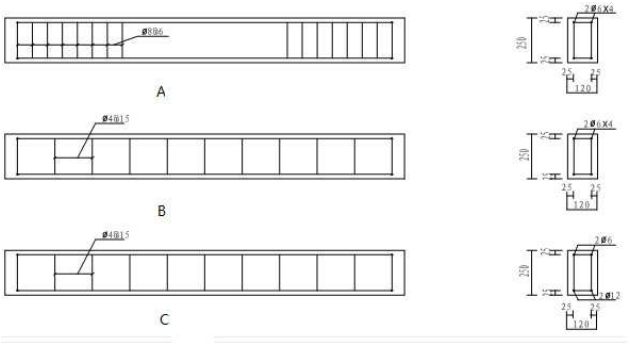


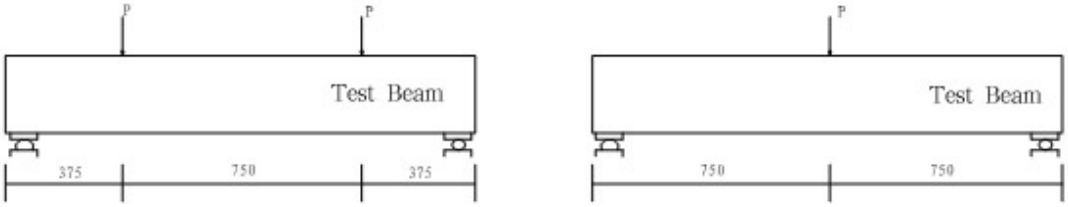
Fig.1 The Different Reinforcement Drawing of Test Beams

Brief Introduction of Test

The size of the test beams is 1500mm × 250mm × 120mm, the concrete grade is C25, with three kinds of reinforcement marked A, B and C .The reinforcement drawing is shown in Fig.1. In order to accelerate the steel corrosion, the main bar is connected to external wire before concreting.

The test is designed like this: the RC beams prepared will be damaged by loading. Loading system is shown in Fig.2. There are two types of loading system: double concentrated forces and single concentrated force. The loading point of the symmetrical loading mode from each end is

375mm, single concentrated force directly loaded at mid-span. The load is applied step by step through hydraulic jack and force transmitting frame.



a double concentrated forces b single concentrated force

Fig.2 The Schematic Diagram of Loading System

Reinforcement treatments are conducted on the failed reinforced concrete beams by adhering steel plate, epoxies resin sheet and multilayer glass fiber sheet respectively. Through experimental comparison, the optimum scheme will be selected.

Reinforcement Materials and Scheme

The type of reinforcement plate is Q235, 3mm thickness, the bottom area of the reinforcement beam increases 3.0cm2; the thickness of epoxies resin sheet is 5mm, 4 cloth 5 glue boards; the width of glass fiber sheet is 50cm. Adhesive glue used is epoxy structural adhesive .The reinforcement scheme of various materials is shown in Tab. 1.

TAB.1 THE COMBINATION OF SAMPLE REINFORCED

Beam category	steel plate bonded to beam bottom	Epoxies resin sheet bonded to beam bottom	Glass fiber sheet bonded to beam bottom	Glass fiber sheet bonded to beam side
A1	√			
A2		√		
A3			3 layer	
A4		√		
A5			3 layer	
B1	√			
B2		√		1layer
B3		√		2 layer
B4			3 layer	
B5			3 layer	
B6			3 layer	2 layer
B7			3 layer	2 layer
B8			3 layer	3 layer
B9			3 layer	3 layer
B10		√		
B11		√		
B12			4 layer	
B13			4 layer	
B14			4 layer	2 layer
B15			4 layer	2 layer
B16			4 layer	3 layer
C2		√		
C3			4 layer	1 layer
C4		√		
C5			2 layer	1 layer

Analysis of Experimental Results

The experimental results are shown in Tab.2. The consolidation just improves the flexural strength of reinforced beams, but the stiffness is decreased.

TAB.2 EXPERIMENTAL RESULTS BEFORE AND AFTER REINFORCEMENT

Beam label	Ultimate bearing capacity[kN]		Loading mode	Crack load[kN]	
	Before reinforcement	After reinforcement		Before reinforcement	After reinforcement
A1	137.3	More than 148	D	58.9	36.0
A2	147.16	158	D	58.9	98.2
A3	135.8	More than145	D	98.2	103.5
A4	142.0	/	D	39.3	
A5	135.5	More than145	D	58.9	91.0
B1	69.3	92	S	27.8	58.7
B2	69.4	100	S	27.8	48.7
B3	74.8	105	S	27.8	48.7
B4	73.0	74.8	S	27.8	48.7
B5	64.6	/	D	39.1	
B6	71	84	S	27.8	6.5
B7	69.4	72	S	27.8	58.7
B8	71	80.1	S	27.8	12.9
B9	69.4	/	S	27.8	
B10	65.1	69.0	S	27.8	42.8
B11	70.5	73.3	S	22.5	38.5
B12	69.4	78	S	18.6	64.1
B13	70.0	80.1	S	27.3	58.7
B14	68.0	80.1	S	27.8	58.7
B15	68.4	More than 85	S	35.5	68.4
B16	64.7	69.0	S	59.2	36.0
C2	61.6	76.9	S	17.8	35.5
C3	63.0	71.5	S	17.8	46.6
C4	60.6	85	S	26.6	46.6
C5	58.7	65	S	17.8	35.5

Note: D-double concentrated forces

S-single concentrated force

In the process of test, when the load increases to a certain extent, the original cracks of the beam will expand again, or new cracks emergence .The load value is greater than the cracking load before reinforcement (shown in Tab. 3).

TAB.3 STATISTICAL TABLES OF LOAD CAPACITY IMPROVEMENT

	category	A（double concentrated forces）	B（single concentrated force）	C（single concentrated force）
Glass Fiber sheet	Steel plate	More than 7.79	32.76 More than 24.27	
	Epoxies resin sheet	7.37	44.09 40.37 5.99	24.84 40.26
	Bottom 2 layer Side 1 layer	6.77 7.01		10.73
	Bottom 3 layer		2.47	
	Bottom 3 layer Side 2 layer		18.31 3.75	
	Bottom 3 layer Side 3 layer		12.82	
	Bottom 4 layer		12.39 14.43	

Bottom 4 layer Side 1 layer		13.49
Bottom 4 layer Side 2 layer	17.79	
Bottom 4 layer Side 3 layer	6.62	

The beams labeled A4,B5 and B9 don't be reinforced because of serious damage. The bearing capacity of the beams after reinforcement increase by 2.47 ~ 44.09%. The increase rate under double concentrated force is inefficiency, less than 10%. Under the same loading mode (single concentrated force or double concentrated force)under the same conditions, the reinforcement effect of using steel plate or epoxy resin board is better than that of the glass fiber steel. The contribution to improve the bearing capacity of using steel plate or epoxy resin board is basic equivalent.

Conclusion

(1)Overall,various reinforcement material used basically meet the requirements of strengthening the bearing capacity, bearing capacity after strengthening are improved to different degrees, but the use of steel plate and epoxies resin sheet increase more.

(2)Scheme selection in practical engineering should be based on different components and site situation. In principle, epoxies resin sheet and glass fiber sheet can be considered while security is guaranteed. Especially in the narrow operation space, the first choice is glass cloth as reinforcement material.

(3)In general, all three kinds of reinforcement material above can meet the requirements of the bearing capacity, but the durability remains to be study further ,especially the anti-corrosion of the steel plate. Besides, the age resistance of the epoxies resin sheet, glass fiber sheet and binder is worth further study.

References

[1] Zhao Rongwei. Experimental study on Corroded RC Flexural Members Reinforced with Grouting Material[D].Zhejiang University, Zhejiang,2012

[2] Li Chunxi.The reinforcement technology of concrete structure[J].Science & Technology Information,2012(19):373,380

[3] Zhang Yiduo, Liu Ronggui.Survey on Research and Application of Strengthening Techniques[J].Journal of JiangSu UniverSity(NaturaI science Edition).2003,Vol24 No.6:14-16, 76:91-94

[4] Bencardino F，Spadea G，Swamy R N．Strength and Ductility of Reinforced Concrete Beams Extemally Reinforced with Carbon Fiber Fabric[J]．Alci StructIlral Journal，2002，99(2)：163—171

[5] Technical Specification for Strengthening Concrete Structures(CECS26:90).China Association for Engineering Construction Standardization

[6] Designcode for strengthening concrete structure(GB50367-2006)[S].Beijing:China Architecture &Building Press,2006.

Advanced Materials Research Vol. 936 (2014) pp 1442-1445
© (2014) Trans Tech Publications, Switzerland
doi:10.4028/www.scientific.net/AMR.936.1442

Mechanical properties of crumb rubber concrete

Jun Cai

Department of Urban and Rural Development & Management Engineering, Shangluo University, Shangluo, China

deyi2665@126.com

Keywords: crumb rubber concrete, mechanical property, flexural toughness

Abstract: Crumb rubber concrete (CRC) has been widely used in many countries because of its good performance. This paper presents the results of a study on mechanical properties of crumb rubber concrete (CRC). The compressive strength, splitting tensile strength and flexural toughness of CRC were investigated. The effect of crumb rubber proportion on the mechanical properties was experimentally analyzed. The test results indicate that the addition of crumb rubber can significantly improve the ductility and flexural toughness of CRC.

Introduction

Crumb rubber concrete (CRC) is known as a promising material because of its better performance and the utilization of crumb rubber from discarded scrap tyres. The properties of fresh and hardened CRC were investigated in previous papers. CRC showed lower density, better sound insulation and acoustic absorption compared with conventional concrete[1-4]. In this paper, the mechanical properties of CRC were experimentally studied. The effect of crumb rubber proportion on the mechanical properties (compressive strength, splitting tensile strength and flexural toughness) of CRC was experimentally investigated.

Experimental program

Materials and mixture proportions

Ordinary Portland cement was used in this study. The coarse aggregate was crushed stone with diameter of 5-20 mm. The fine aggregate was natural sand with a maximum size of 5 mm. Fly ash was used as mineral addition. A polycarboxylic superplasticizer was used in all concrete mixtures. Crumb rubber content used was 25 kg/m^3, 50 kg/m^3 and 75 kg/m^3. The details of the mixture proportions are shown in Table 1.

TABLE 1. MIXTURE PROPORTIONS OF CONCRETE.

Mixture	Rubber (kg/m^3)	Cement (kg/m^3)	Water (kg/m^3)	Coarse aggregate (kg/m^3)	Fine aggregate (kg/m^3)	Fly ash (kg/m^3)	Superplasticizer (kg/m^3)
C	-	375	160	980	420	160	32
CRC 25	25	375	160	980	420	160	32
CRC 50	50	375	160	980	420	160	32
CRC 75	75	375	160	980	420	160	32

Test procedure

Cubes (100 × 100 × 100 mm) were used to evaluate the compressive strength and splitting tensile strength in accordance with Chinese Standard GB/T 50081-2002.

The four-point loading flexural tests were carried out on the beams (100 × 100 × 400 mm) with a closed-loop arrangement in accordance with ASTM C1018. The loading was displacement control at a rate of 0.05 mm/min. Both the applied load and the specimen midspan deflection were recorded

throughout the test. The flexural toughness of all the mixtures were evaluated by measuring the load-deflection curves in accordance with JSCE SF-4 standard [5].

In accordance with the JSCE method, the flexural toughness factor (σ_b) is defined as:

$$\sigma_b = \frac{\tau_b}{\delta_{tb}} \times \left(\frac{l}{b \times h^2} \right) \quad (1)$$

Where l is beam span (300 mm in this study), b is beam width (100 mm in this study), h is beam depth (100 mm in this study), $\delta_{tb} = l/150$ (2 mm in this study), τ_b is the area under the load-deflection curve up to a midspan deflection of δ_{tb}.

Results and discussion

Compressive strength and Splitting tensile strength

The compressive strength and splitting tensile strength values of all the mixtures are illustrated in Fig. 1and Fig. 2, respectively. The test results show that compressive strength and splitting tensile strength decreased with the increase of crumb rubber content. The decrease in compressive strength and splitting tensile strength is due to the increase of porosity caused by the incorporation of crumb rubber.

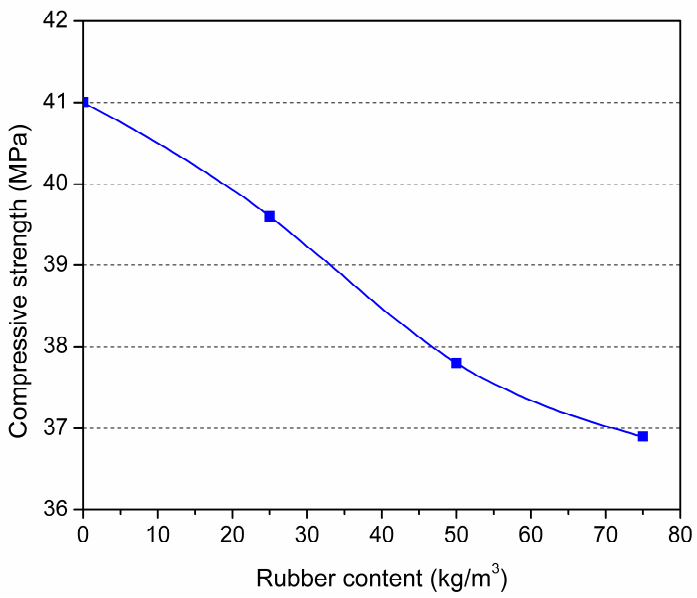


Fig. 1. Effect of rubber content on compressive strength.

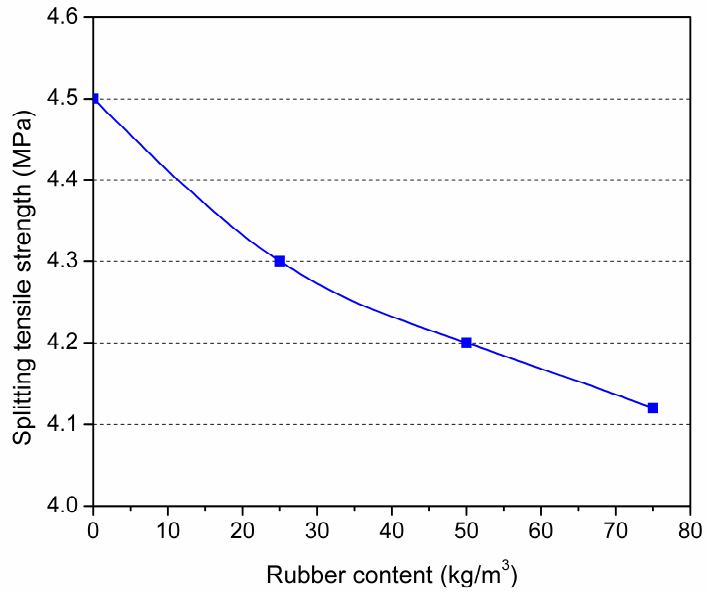


Fig. 2. Effect of rubber content on splitting tensile strength.

Flexural toughness

The flexural load-deflection curve of CRC is shown in Fig. 3. It can be observed that the crumb rubber has great effect on the flexural properties of CRC. The beams show better post-peak behaviour with the increase of crumb rubber content. The load-carrying capacity of CRC improve significantly.

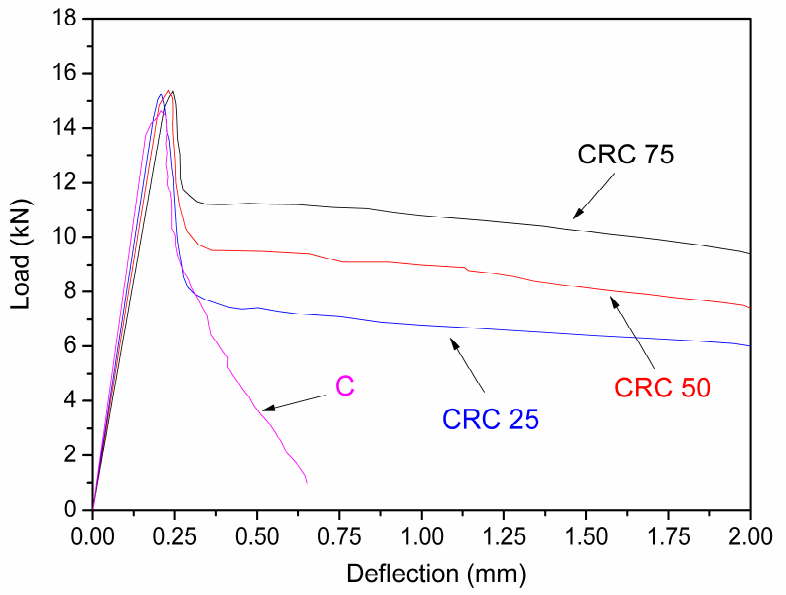


Fig. 3. Flexural load-deflection curve of CRC.

The flexural toughness factor of CRC at various rubber contents is shown in Fig. 4. The results indicate that flexural toughness factor increased with the increase of rubber content. Crumb rubber content has significant effect on the flexural properties of CRC. The flexural toughness improvement of CRC enhanced with the addition of crumb rubber.

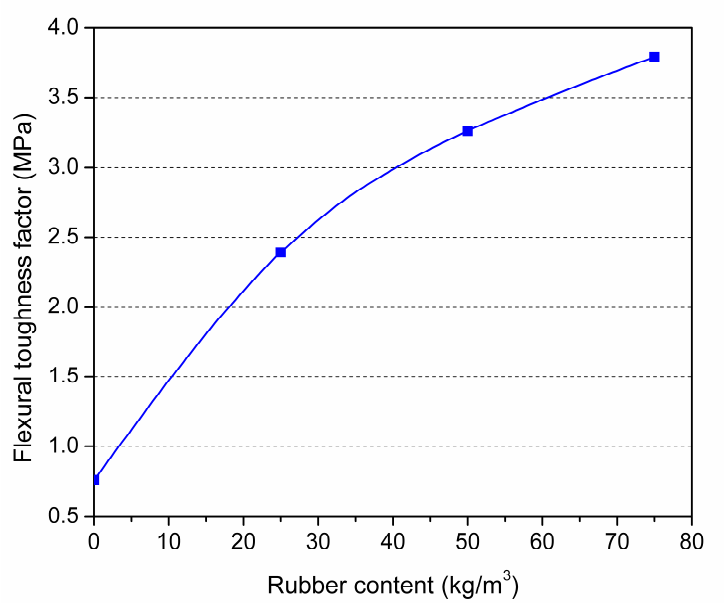


Fig. 4. Effect of rubber content on flexural toughness factor.

Conclusions

This paper studies the effect of crumb rubber on the mechanical properties of CRC. Compared to control concrete without crumb rubber, compressive strength and splitting tensile strength of CRC decreased with the increase of rubber content. The crumb rubber has significant effect on the flexural properties of CRC. The flexural toughness factor of CRC increased with the increase of rubber content. The ductility and flexural toughness of CRC were significantly improved by the addition of crumb rubber.

Acknowledgement

The financial help of the Projects of Shangluo University（13SKY001）is gratefully acknowledged.

References

[1] Anh Cuong Ho, Anaclet Turatsinze, Rashid Hameed, Duc Chinh Vu, Journal of Cleaner Production 23(2012) 209-215.

[2] Bashar S. Mohammed, Khandaker M. Anwar Hossain, Jackson Ting Eng Swee, Grace Wong, M. Abdulla, Journal of Cleaner Production 23 (2012)57-67.

[3] Osama Youssf, Mohamed A. ElGawady, Julie E. Mills, Xing Ma, Construction and Building Materials 53 (2014)522-532.

[4] Mustafa Maher Al-Tayeb, B.H. Abu Bakar, Hanafi Ismail, Hazizan Md Akil, Journal of Cleaner Production 59(2013) 284-293.

[5] JSCE SF-4, Method of Test for Flexural Strength and Flexural Toughness of Fiber Reinforced Concrete, Japan (1984)

[6] Rafat Siddique, Tarun R. Naik, Waste Management 24(2004)563-572.

[7] Camille A. Issa, George Salem, Construction and Building Materials 42(2013) 48-52.

Advanced Materials Research Vol. 936 (2014) pp 1446-1450
© (2014) Trans Tech Publications, Switzerland
doi:10.4028/www.scientific.net/AMR.936.1446

Research on Improving Shrinkage Performance of Cement Stabilized Gravel with Waste Rubber Particles

LIU Qiyang[1, a], HE Min[2,b] and WANG Jue[3,c]

[1, 2]Faculty of Transportation, Kunming University of Science and Technology, Kunming 650500,Yunnan Province, China

[3]School of Transportation, Southeast University, Nanjing 210096,China

[3]List all distinct addresses in the same way

[a]lliuqqiyyang@163.com, [b]Corresponding author: 252419553@qq.com, [c]1050874464@qq.com

Keywords: Cement stabilized gravel; rubber particles; dry shrinkage performance

Abstract: Cement stabilized gravel has good characters like high strength, good stability, anti-erosion properties and better anti-fatigue property, but it is easy to produce desiccation cracks when humidity changes (caused by evaporation), resulting in reflection crack on the bituminous pavement surface, and then influences performance and the service life of the pavement. Along with the changes in traffic conditions, semi-rigid asphalt concrete pavement meets the two major challenges as early damage and heavy traffic. It has significant economic and social significance that support a method of construction and conserve of semi-rigid pavement which accommodate heavy traffic highway and has guidance and reference value in other conditions. It is analyzed by comparison between the performances of mixture with best amount of admixture which obtained by shrinkage test and mixture without admixture.

Introduction

Semi-rigid type base is base that paved by inorganic binder stabilized soil can form a plate and have certain flexural strength. It is helpful to improve the carrying capacity of the road that about 95% of high-grade asphalt concrete pavement base or subbase are semi-rigid material with increasing strength, considered highway pavement which has been built in China.[1,2] However, it is widespread that shrinkage cracking of semi-rigid base and reflective crack of asphalt pavement exist. It is generally taken for cracks sealing but it is difficult on highway or heavy traffic road.

Cement stabilized crushed stone is a semi-rigid pavement structure type emerging in recent years for highway subbase, base construction. It is gradually favoring the design and construct department because of good plate body, water stability, frost resistance, adjustable mechanical strength and good carrying capacity as the bearing layer of asphalt concrete. It is hard to control the material grading, cement dose, paving compaction, segregation treatment, survival time and maintenance so that even the slightest mistake will cause the defect as cracks or thickness, strength that does not meet the design requirements, causing immeasurable losses which the construction companies always spoke of with horror.

Use of waste rubber has far-reaching practical significance. Recycling and treatment technology of scrap tires, called 'black' pollution, is a worldwide problem. The most common practice is to bury or dump waste tires. It not only cause a lot of land expropriation, but the accumulation of a large number of waste tires can easily cause a fire, causing second pollution.[3]

Design of aggregate particles consisting

Coarse aggregate in the mixture of cement stabilized crushed stone play the skeleton role mainly while fine aggregate play the filling role. Aggregate particles directly affect the mechanical properties of the mixture. Reasonable mix of coarse and fine aggregates can make the base more dense, better overall performance and higher compressive strength. To achieve higher density and larger friction, various size aggregates are matched up according to a certain proportion. There are two graded and

this study uses a continuous gradation.[4,5]Synthetic aggregate gradation(Particles) is shown in Table 1 and Fig. 1.

TABLE 1 GRADING DESIGN OF ALL NATURAL AGGREGATES AC-20 MINERAL AGGREGATE

Items	Data											
Particle size(mm)	26.5	19.0	16.0	13.2	9.5	4.75	2.36	1.18	0.6	0.3	0.15	0.075
Pass rate of 1#(%)	100	77.5	64.0	42.6	16.9	1.5	0.2	0	0	0	0	0
Pass rate of 2#(%)	100	100	99.0	91.6	56.0	5.6	2.4	2.0	1.5	1.3	1.1	0.6
Pass rate of 3#(%)	100	100	100	100	99.6	78.6	22.1	15.8	10.2	7.1	5.2	3.3
Pass rate of 4#(%)	100	100	100	100	100	97.2	69.2	48.1	31.1	15.0	10.0	5.0
Ore pass rate (%)	100	100	100	100	100	100	100	100	100	100	100	93.8
Material1#：40%	40.0	31.0	25.6	17.0	6.8	0.6	0.1	0.0	0.0	0.0	0.0	0.0
Material 2#：18%	18.0	18.0	17.8	16.5	10.1	1.0	0.4	0.4	0.3	0.2	0.2	0.1
Material 3#：6%	6.0	6.0	6.0	6.0	6.0	4.7	1.3	0.9	0.6	0.4	0.3	0.2
Material 4#：32%	32.0	32.0	32.0	32.0	32.0	31.1	22.1	15.4	10.0	4.8	3.2	1.6
Ore：4%	4.0	4.0	4.0	4.0	4.0	4.0	4.0	4.0	4.0	4.0	4.0	3.8

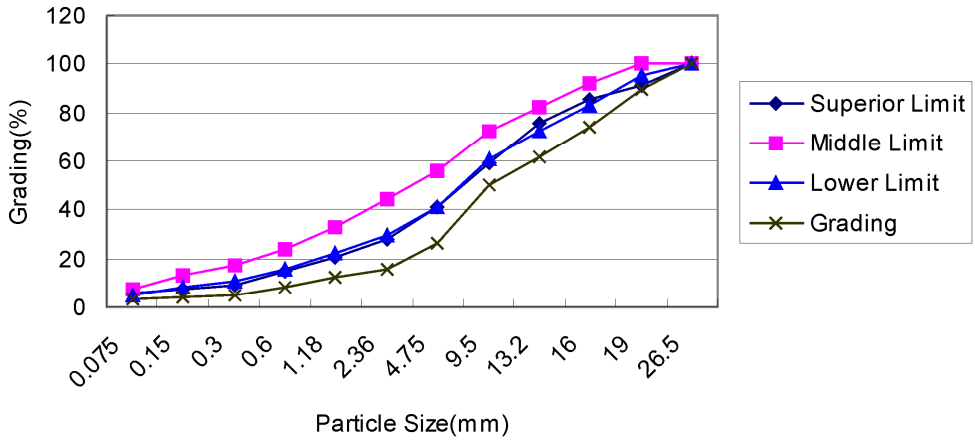


Fig. 1 Grading design of all natural aggregates AC-20 mineral aggregate

Rubber cement stabilized macadam base contraction performance test

Drying shrinkage mechanism

Volume reduction caused by water evaporation, hydration, temperature decreases and other factors in the base of stable inorganic binder material is called shrink of stable inorganic binder material base. Large elastic stress caused by base shrinkage deformation climb with the increase of elastic modulus and shrinkage of base. Creep caused by contraction can reduce such stress to some extent, but if the tensile stress growth after creep relaxation exceeds the tensile strength of the base, it will cause cracking base and seriously affect the performance of the road after reflecting the pavement surface.

Water mixture will continue to decrease after the stable inorganic binder material mixed and compacted because of the internal hydration and water evaporation. Capillary action , adsorption , the role of intermolecular forces , the role of water and Carbonation contraction of mineral crystal material between layers or gel will cause volume shrinkage of stable inorganic binder material. This phenomenon is called drying shrinkage.

Production and conservation of specimens

Hydrostatic press molding method was used to product beam specimens of 100mm×100mm×515mm. Those 24 specimens are divided into 8 groups, and ingredient content of specimens in each group are shown in Table 2.

TABLE 2 INGREDIENT CONTENT OF SPECIMENS

Group 3	**60 mesh rubber powder 0.25%replace0.15**						
Particle size	31.5	26.5	19	9.5	4.75	2.36	0.6
Proportion	0	5	14.5	23.5	18	13	11
Amount of 5%	0	459	1332	2158	1653	1194	1010
Particle size	0.3	0.15	60 mesh rubber	0.075	<0.075	Total	
Proportion	6.5	3.25	0.25	1.5	3.5	100	
Amount of 5%	597	298	12	138	321	9172	
	Amount of cement	Water					
Amount of 5%	459	443					
		.....					
Group 7	**80mesh rubber powder0.25%replace0.075**						
Particle size	31.5	26.5	19	9.5	4.75	2.36	0.6
Proportion	0	5	14.5	23.5	19	13	11
Amount of 5%	0	459	1332	2158	1653	1194	1010
Particle size	0.3	0.15	0.075	80 mesh rubber	<0.075	Total	
Proportion	6.5	3.5	1.25	0.25	3.5	100	
Amount of 5%	597	321	115	12	321	9172	
	Amount of cement	Water					
Amount of 5%	459	443					

Produced specimens are placed in 20±2ºC RH90% conditions and are placed vertically above the shrinkage instrument to dry naturally after it has been removed after 7 days conserve.

Results and analysis of shrinkage test

Shrinkage strain variation with time

Fig.2 and Fig.3 are made to analyze by taking the same time interval (1day) and excluding the test data of last day.

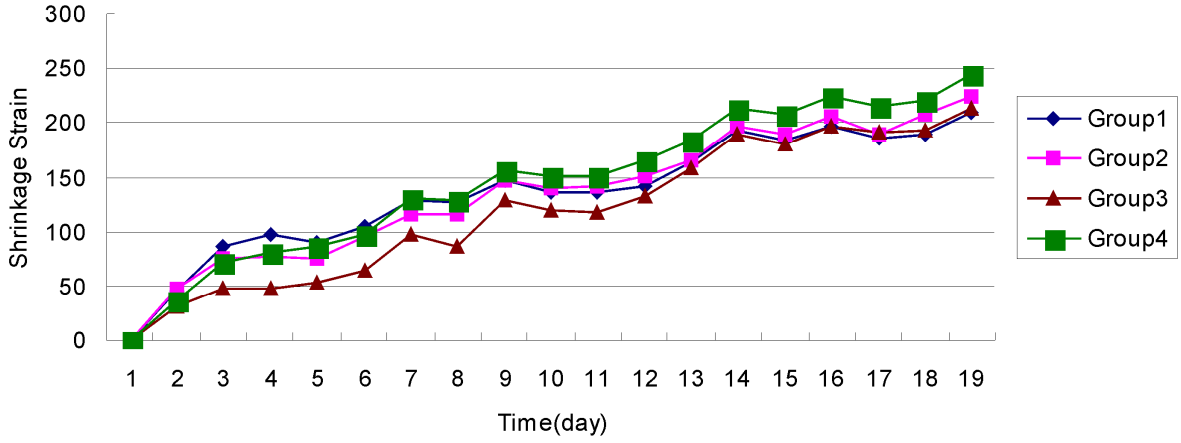


Fig.2(60 mesh) Relationship between shrinkage strain and the time

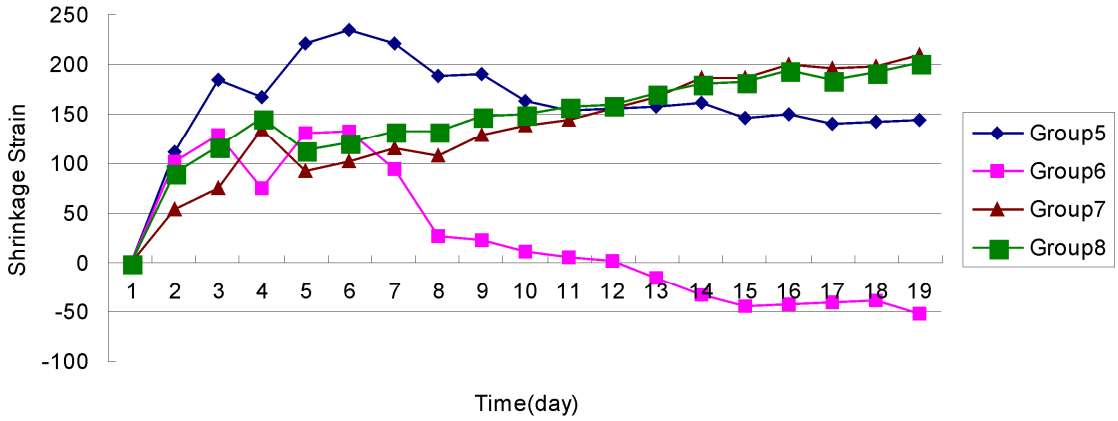


Fig.3 (80 mesh) Relationship between shrinkage strain and the time

As it can be seen from Figures 3 and 4, along with the time, shrinkage strain are gradually climbing (except group 6)and easing in the end. In Fig.3 Shrinkage strain of all-natural solutions essentially maintain a higher level in shrinkage strain than others, but taking a panoramic view of the situation, group 3 has the best improvement of shrinkage performance while the all natural group is the worst.

When mixed with 80 mesh rubber powder, shrinkage strain of cement stabilized gravel changes larger in the first two days and it is significantly easing from the third day and shrinkage strain changes little in the end. Group 6 manifest strange characteristic that is the same with other groups during the first 6 days, but swelling phenomenon whose reason is unknown because that all groups are set in the same cultivating conditions occurred since the 6th day. So this program is invalid. Excluded group 6, from the performance of the other three groups, group 7 is the best while the all natural group is the worst.

In order to optimize when the same dosage (0.25%) of rubber powder (60 mesh or 80 mesh), group 3&7 are compared individually the result is shown as Fig.4.

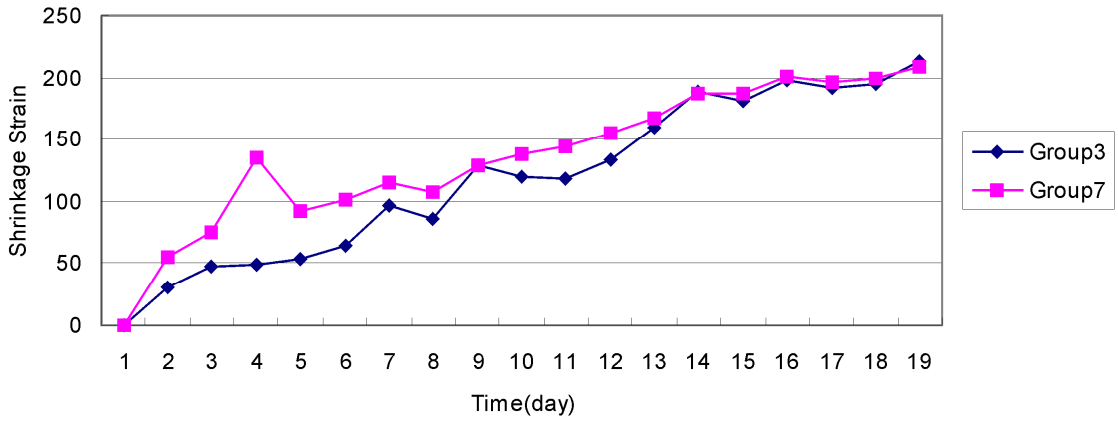


Fig.4 Shrinkage strain contrast of group 3&7

It is easy to find by contrast, shrinkage strain of group 3 is smaller so 60 mesh rubber powder 0.25%replace0.15 is selected to make the greatest improvement in shrinkage performance of cement stabilized crushed stone.

All-natural cement stabilized mixture specimens (group 4&8) basically maintained a high growth trend compared to other groups while incorporation of rubber particles slow down the growth of shrinkage strain from growth trend. The reason might be that cement hydration reaction occurs first by adsorbing water from the surrounding because of the good absorption capacity of rubber particles and then capture previously absorbed moisture of rubber particles to recover a part of their shrinkage. On the other hand, to a certain extent, due to the larger flexibility abate capillary tension caused by water evaporation, the role of intermolecular forces and the role of adsorbed water. Thereby the shrinkage is reduced.

Although the shrinkage characteristics of cement stabilized macadam improved after mixed with rubber powder, but it's not very obvious especially in the latter of observation. We can make nothing of that shrinkage strain versus time curve will remain stable or the difference will expand because of various aspects condition.

Water loss rate variation with time

Similarly, we take the same time interval (1day) and exclude the test data of the last day. Figure 5 is made for analysis.

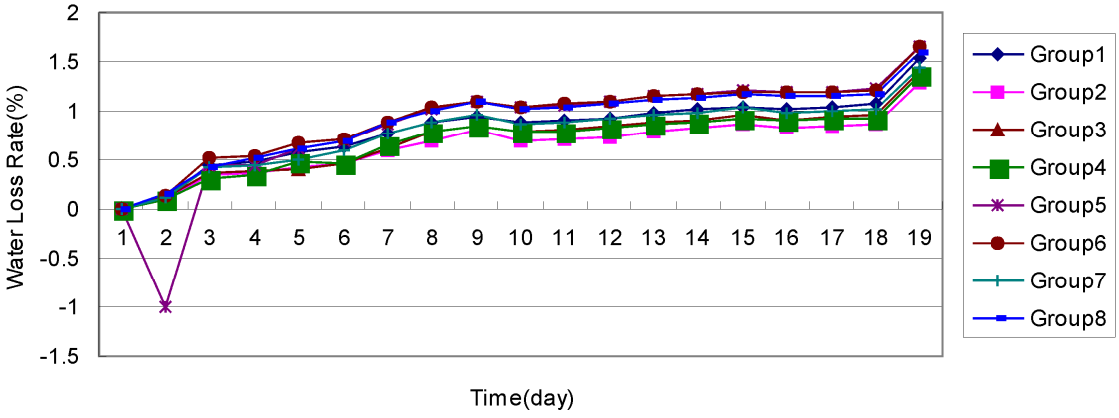


Fig.5 Water loss rate changes with time

It is shown in Fig.5 that specimen loss rate increases with the increase of time. Dehydration is rapid early and it star slowing down from the 8th day which point out the essentiality of the 7th day after cement stabilized macadam compaction ended.

Water loss rate of each group stabilized at about 9th day include that the dehydration is basically the same period after incorporation of rubber powder.

Conclusion

After mixed with a certain amount of rubber particles, shrinkage strain decreases. Shrinkage strain of specimen incorporated within rubber particles is slackening in growth. We should choose 60 mesh rubber powder 0.25% replace0.15 to make the prominent improvement of shrinkage strain of Cement stabilized crushed stone.

Water loss rate rise with increasing time and eventually stabilized and there is no significant relationship between water boss rate and the type or dosage of rubber powder.

References

[1] QIN Feng: Experimental study on shrinkage properties of cement-stabilized macadam base course with rubber powder. New building material, Vol.36 No.12 (2009) , pp.32-35.

[2] SUN Zhaohui, XU Zhihong, WU Meifa: Study on gradation design of cement-stabilized macadam considering shrinkage deformation factors. Journal of Highway and Transportation Research and Development,Vol.6 No.3(2006) , pp.15-19.

[3] YANG Honghui, WANG Jianxun, HAO Peiwen: Utilization of fibre in cement-stabilized aggregate mixture. Journal of Chang'an University (Natural Science Edition), Vol.26 No.3 (2006), pp.14-16

[4] HE Yong: Research on the characteristics of the cement-stabilized macadam with waste rubber particles (2007).

[5] Hernardez-olivers F, Barluenga G: Fire Performance of recycled rubber filled high-strength concrete. Cement and Concrete Research,Vol.34 No.1(2004), pp.109-117.

Advanced Materials Research Vol. 936 (2014) pp 1451-1455
© (2014) Trans Tech Publications, Switzerland
doi:10.4028/www.scientific.net/AMR.936.1451

Bending Properties of Laser Welded Web-core Steel Sandwich Plates

Xiao-Xia JIANG [1,a], Liang ZHU [1,b*], Ji-Sen QIAO [1,c],
Yi-Xiong WU [2,d], Zhu-Guo Li [2,e], Jian-Hong CHEN [1,f]

[1] State Key Laboratory of Advanced Processing and Recycling of Non-ferrous Metals,
Lanzhou University of Technology, Lanzhou 730050, China

[2] Shanghai Key Laboratory of Materials Laser Processing and Modification,
Shanghai Jiao Tong University, Shanghai 201100, China

[a]jiangxiaoxia402@126.com, [b]zhul@lut.cn, [c]jisenqiao@lut.cn

Keywords: Bending properties, Laser welded, Web-core steel sandwich plate, Weld width

Abstract：This paper presents a detailed discussion of the bending properties of laser welded web-core steel sandwich plates and the influence of weld width on stiffness and strength. The over-hanging three point bending test was conducted on the laser welded web-core steel sandwich plates with various welds width by self-designed device, together with the finite element simulations. A good agreement is obtained between the 2D FE analyses and experiment results. The stiffness and strength of the sandwich plates increased with the increasing of weld width, especially for the weld width lower than 60% thickness of the core plate. It is necessary to consider the weld width in the design and evaluation of the stiffness and strength of the laser welded web-core sandwich plate. Base on the results, the FEM is the priority to analysis bending properties of laser welded web-core steel sandwich plates.

Introduction

All steel sandwich plates were found to be 30-50% lighter than traditional stiffened plates due to the thin face plates located away from the neutral axis [1]. Applications of steel sandwich plates in marine structures range from decks, bulkheads, antenna platform to hoistable ramps. Contemporary interest in steel sandwich plates has been awakened by the developments in laser welding technology which enables the efficient production of these plates. Elevated pre-fabrication accuracy of the components, high welding speed and the possibility to connect internal stiffeners with the face sheets from outside has led to a wide application of laser welding in the construction of steel sandwich plates [2].

Web-core steel sandwich plate has the simplest core structure, as showed in Fig.1. This plate has been under active investigations during the last 15 years. Romanoff studied the bending response of web-core sandwich plate using analytical and FEM methods, and the analytical formulations for stiffness and strength of web-core sandwich were exposed [3]. A lot work of the buckling strength of laser welded web-core sandwich plate has been done through the analytical method, finite element method and experiment, as reported in Ref. [4-6]. In these studies, the bending response is evaluated by transforming an originally discrete structure into an equivalent homogenous continuum giving a sandwich plate, and the T-joints of web-core sandwich plate was assumed as continuous features. Actually, the T-joint has a discontinuous features, i.e., there are root gap and inevitable weld offset, weld width is less than the thickness of the face or core plate, as be shown in Fig.1. Besides, the weld width was changes with the different welding parameters and the thickness

of face plates. Ref. [7] reported the ultimate strength of corroded web-core steel sandwich beams both by the experiments and the finite element simulation research, and the weld width may reduce the strength of the plates.

This paper presents a series of bending properties tests on web-core steel sandwich plates in over –hanging three point bending. In order to support and extend the experimental investigation, finite element simulations were performed to analyze the effect of weld width on stiffness and strength of the sandwich plate. Additionally, the bending and shear stiffness and bending strength of sandwich plate obtained by analytical formulation were compared with experimental and FEM results, to ensure the weld width has an important role in the design and evaluation of the stiffness and strength of the laser welded web-core sandwich plate.

Experimental and finite element simulation

The Dimensions of laser welded web-core steel sandwich plate and details of T-joint

The web-core sandwich plate consists of web and face plates, which are connected by laser weld, as be shown in Fig. 1. Two kinds of welding speeds were designed to achieve various laser welds dimensions. The welding parameters and weld width are listed in Table 1. The base metal used in this paper is high strength steel SPFH780. Tensile tests were conducted to determine the material properties. Yield strength of the base material is 631MPa.The tensile strength is 730MPa.

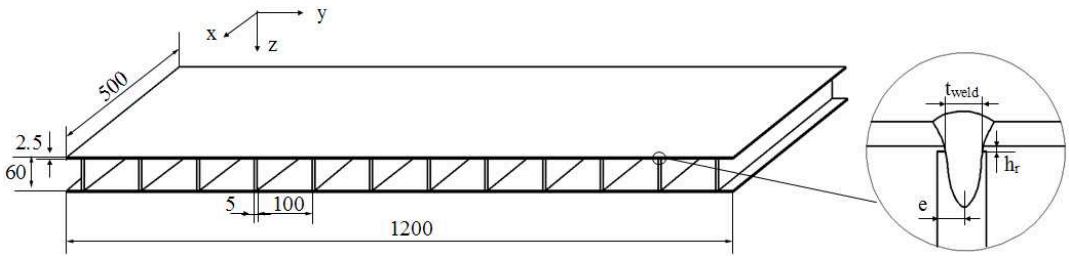


Fig. 1 Dimension of laser welded steel sandwich plate and details of T-joint

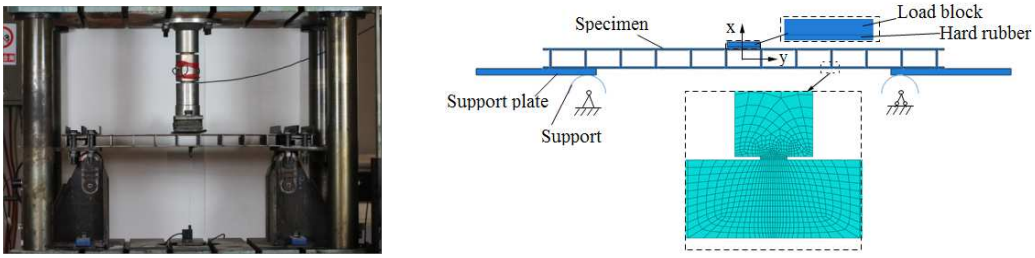
TABLE 1 THE WELDING PARAMETERS AND THE WELD WIDTH OF T-JOINT

Specimen number	1#	2#	3#	4#
V/(mm/min)	1200	1200	800	800
t_{weld}/(mm)	3.25	3.26	4.92	4.95

Three point bending test and finite element modeling

According to ASTM C393-00 standard test method for flexural properties of sandwich structures and GB/T 1456-2005 Performance test methods for sandwich structures, a special test setup which is suitable for simply support, as be shown in Fig. 2(a), was developed to measure the bending properties of sandwich plates by over-hanging three point bending test. The experiments were carried on a 3150kN column hydraulic machine. The span is 936mm, and loading speed is 5mm/min. The load and deflection were recorded by the load and displacement sensor.

The Abaqus6.11 standard solver was employed to analyze bending response of sandwich plates with various weld width, the weld width is varied between 1mm, 2mm, 3mm, 4mm and 5mm, and the root gap is 0.1mm for all models. Fig. 2(b) shows one of the 2D models. In the modeling of sandwich plate, the welds are all at the middle of each core plate. The elements used are CPE8R. In general the aspect ratio in rectangular elements is kept close to 1:2 and the angle in quadrangular between 45°-135° to avoid problems in accuracy of solution.



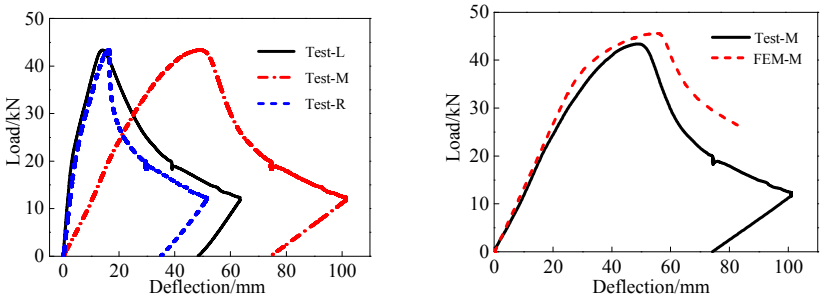
(a) The test setup of three point bending (b) FEM model

Fig. 2 The test setup of three point bending and FEM model

Result and discussion

The deformation of sandwich plate

Fig. 3 displays the typical load-deflection curves. The middle span load-deflection curve was denoted Test-M, and the left and right over-hanging load-deflection curves were denoted Test-L and Test-R, respectively. As can be seen from Fig. 3(a), when the load is larger than 18 kN, the relationship load and deflection are not be linear, and then the larger load, the more gentle the curve. Additionally, Test-L and Test-R curves separated after the load over 18kN. When the load reached the maximum 43kN, the load- deflection curves start to fall. In Fig. 3(b), the FEM load-deflection curve is almost agree with the results in test, especially in the linear segment which will be selected to calculate the bending and shear stiffness. And the strength will be obtained by the max load.



(a) Load-deflection curves from testing (b) FEM result compares with the test curve

Fig.3 Load-deflection curves

The relationship between weld width and stiffness

Bending stiffness and shear stiffness are two important elastic parameters. They were calculated from the elastic segment of the load-deflection curve. The formula is as follows:

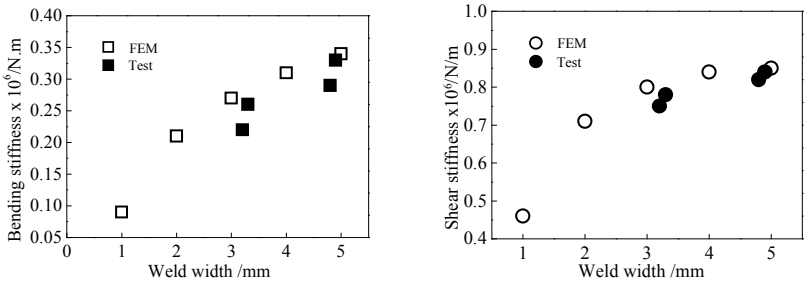
$$D_y = \frac{\Delta P \cdot l^3}{48 \cdot B \cdot \omega_b} \tag{1}$$

$$D_{Qy} = \frac{\Delta P \cdot l}{4 \cdot B \cdot (\omega - \omega_b)} \tag{2}$$

*where D_y is bending stiffness, in N.m; D_{Qy} is shear stiffness, N/m; ΔP is load increment, in N; l is span, in m; B is the width of specimen, in m; ω is the increment of mid span deflection corresponding increment of load, which is caused by the shear deformation of sandwich plate, in m; ω_b is the increment of lest or right over-hanging deflection corresponding increment of load is the deflection caused by the bending deformation, in m; which is caused by the shear deformation of sandwich plate, and $\omega_s = \omega - \omega_b$, in m.

Fig. 4 indicates the relationship between weld width and bending and shear stiffness of web-core sandwich plate. It can be seen that the larger weld width, the greater bending rigidity, as was shown in Fig. 4(a). As the weld width increases from 1mm to 2mm, the bending stiffness increased

0.12×10^6 N.m, while increased 0.03×10^6 N.m as the weld width increases from 4mm to 5mm. Similarly, shear stiffness increases obviously as the weld width lower 3mm (60% thickness of the core plate), see Fig. 4(b). Apparently, the weld width has a great impact on the stiffness of the sandwich plate, especially for the weld width is far less than the thickness of the core plate. However, there exist several publications related to the bending and transverse shear stiffness formulations for web-core sandwich plates all did not consider the weld width (Lok & Cheng, 2000, Kujala & Klanac, 2002, Kolaters, 2002) [8-10], this can lead to overestimates of the stiffness. Therefore, it should be to consider the influence of weld width on the stiffness in the process of design and optimization of laser welded web-core sandwich plate. As a result, the finite element method is the best choice for the stiffness analysis of the laser welded web-core sandwich plates.



(a) Weld width-bending stiffness (b) Weld width-shear stiffness

Fig. 4 The relationship between weld width and stiffness

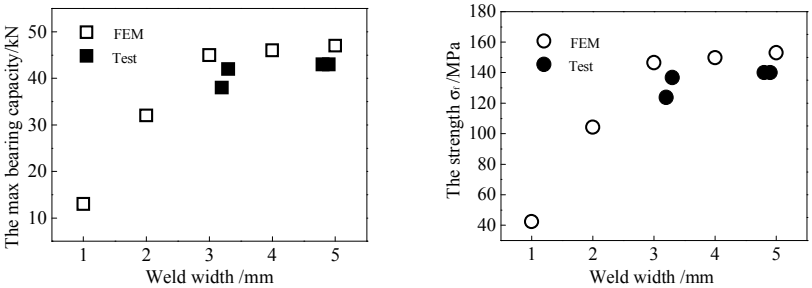
The relationship between weld width and strength

Strength of sandwich plate is another measure of performance parameters. The strength of face plates was calculated from the maximum load, the formulation is

$$\sigma_f = \frac{P_{\max} \cdot l}{4 \cdot B \cdot t_f \cdot \left(h - t_f\right)^2} \tag{3}$$

*where σ_f is the strength face plates, in MPa; $P_{\max}$ is the maximum load, in N; l is the span, in m; t_f is the thickness of face plate; B is the width of specimen, in m; h is the height of specimen, in m.

Fig. 5(a) indicates the relationship between weld width and the max bearing capacity of web-core sandwich plate. In Fig. 5(a), it can be seen that with the increase of weld width, the max bearing capacity and the bending strength are increased. And when the weld width is greater than 3mm (60% thickness of the core plate), the bending strength can break the restriction of weld width. According to the formula (3), the strength of the face plate can be obtained, see Fig. 5(b). As the weld width increases from 1mm to 5mm, the max strength is lower 160MPa, which is far less than the yield strength of the face plate. It is recognized that a big error will occur in the strength design of the sandwich plate by the analytical techniques. Hence, the finite element analysis is a relatively better way to solve problems.



(a) Weld width-the max bearing capacity (b) Weld width-the face strength

Fig. 5 The relationship between weld width and strength

Conclusion

Base on the investigation into the bending properties of laser welded web-core sandwich plates. The following conclusions can be drawn:

(1) With the increasing of weld width, the bending and shear stiffness is increased, especially when the weld width is less than 3mm (60% thickness of core plate), this effect is more significant. In other words, weld width is greater than 3mm at least in the stiffness design for this kind of sandwich plates.

(2) It is quite clear that the maximum load capacity is increased with the increasing of weld width. When the weld width is greater than 3mm (60% thickness of the core plate), and then the bending strength can break the restriction of weld width.

(3) It is necessary to consider the effect of weld width on bending properties in the stiffness and strength design of laser welded web-core sandwich plate. The finite element method is an excellent choice for the stiffness and strength analysis of the laser welded web-core sandwich plates.

Acknowledgement

This research work was funded by the National Nature Science Foundation of China (No. 51035004). The authors wish to thank the editors and reviewers for their comments and suggestions.

References

[1] P. Kujala, A. Klanac, Steel sandwich panels in marine applications, Brodo Gradnja. 56 (2005) 305-314.

[2] J. Kozak. Selected problems on application of steel sandwich plates to marine structures, Pol. Marit. Res. 16 (2009) 9-15.

[3] J. Romanoff. Bending response of laser-welded web-core sandwich plates, Helsinki University of Technology. Doctoral Dissertation, 2007.

[4] H. Kolsters, D. Zenkert, Buckling of laser-welded sandwich panels. Part 1: Elastic buckling parallel to the webs. J. Eng. Marit. Environ. 220 (2006) 67-79.

[5] H. Kolsters, D. Zenkert, Buckling of laser-welded sandwich panels. Part 2: elastic buckling normal to the webs. J. Eng. Mari.t Environ. 220 (2006) 81-94.

[6] H. Kolsters, D. Zenkert, Buckling of laser-welded sandwich panels: Ultimate strength and experiments. J. Eng. Mari.t Environ. 224 (2010) 29-41.

[7] J. Jelovica, J. Romanoff, S. Ehlers, et al, Ultimate strength of corroded web-core sandwich beams. Marine Structures. 31 (2013) 1-14.

[8] Lok T S, Cheng Q H. Elastic stiffness properties and behavior of truss-core sandwich panel. J. Struc. Eng. 126 (2000) 552-559.

[9] Kolsters H. Stiffness and strength of laser-welded sandwich panels. Karlstad University, 2002.

[10] Kujala P, Klanac A. Analytical and numerical analysis of non–symmetrical all steel sandwich panels under uniform pressure load.7th international design conference, Dubrovnik: Scientific Publishing Services, (2002) 1205-1210.

Advanced Materials Research Vol. 936 (2014) pp 1456-1462
© (2014) Trans Tech Publications, Switzerland
doi:10.4028/www.scientific.net/AMR.936.1456

Effect of Rubber particles on properties of Pseudo-ductile cementitious composites

Chaoming Pang [1, 2, a], Christopher K.Y. Leung [2,b] and Wei Sun[1,c]

[1]College of Materials Science and Engineering, Southeast University, Jiangsu Key laboratory of Construction Materials, Nanjing, China

[2]Department of Civil Engineering, Hong Kong University of Science and Technology, Hong Kong, China SAR

[a]pangchao@seu.edu.cn, [b]ckleung@ust.hk, [c]sunwei@seu.edu.cn

Keywords: Pseudo ductile cementitious composites Fiber concrete Ductility Rubber particles Tensile properties Compressive strength Water permeability Shrinkage

Abstract: Pseudo-ductile cementitious composites (PDCC) are a new type of special discontinuous random-fibers reinforced cementitious composites with high tensile ductility achieved by the uniform formation of multiple cracks along the length of the specimen. In the present study, rubber particle was introduced into the cementitious composites as the artificial flaw. The tensile properties, compressive strength, water permeability and shrinkage of PDCC with various volume contents and size of rubber particles were measured. The test results show that incorporation of rubber particle will reduce the compressive strength and first cracking strength of PDCC. With increased size and volume of rubber particles, the compressive strength is increased. To achieve maximum tensile ductility, optimum rubber content and size should be employed. Water permeability is found to be similar for various PDCC mixes with or without rubber addition. The content of rubber particle plays a significant role on the dry shrinkage of PDCC, while the particle size only has a slight effect.

Introduction

Traditional concrete, whether classified as normal concrete, high strength concrete or high performance concrete, is generally brittle in nature. The ease of cracking limits the application of cementitious materials and affects the long-term durability of structures. Over the years, many research studies have been performed to modify the brittle behavior of cementitious composites, and the incorporation of fibers to increase the strain capacity is the most common approach. In traditional plain concrete, tensile failure is usually accompanied by the formation of a single crack, with the post-cracking tensile stress dropping to zero at a very small crack opening. In comparison to plain concrete, fiber reinforced concrete (FRC) exhibits significant post-cracking tensile resistance due to the bridging effects of fibers. However, as the residual stress is decreasing with crack opening, only a single crack will form under direct tension. Although the incorporation of fibers can improve various properties of the material, including flexural and shear capacity, energy absorption, ductility of failure, etc, failure still occurs through the formation of discrete cracks with significant openings. In the early 1990's, Li, Leung and Wu[1-4] investigated the mechanics of crack bridging and proposed the fundamental theory for the development of pseudo-ductile cementitious composites (PDCC), which are composites exhibiting strain-hardening behavior in tension, with the formation of closely-spaced multiple fine cracks rather than widely opened discrete cracks. The design of PDCC is based on two physical conditions: (1) the energy-absorption rate G_r in the fiber-bridging zone behind the crack tip is at least 10 times the value of G_{tip}, which is the energy absorbed at the crack tip, and (2) the flaw size in the material is greater than a certain critical value governed by microscopic material parameters. The first condition ensures that the fracture failure process is governed by the bridging fibers while the second condition ensures subsequent formation of closely-spaced cracks after the first crack is formed. Hereafter, Li and co-workers further developed the theories [5,6] and came up with practical approaches for the making of PDCC, such as tailoring of interfacial properties [7], reduction of matrix

toughness by limiting the particle size in the cementitious matrix [8] and the incorporation of uniformly distributed artificial flaws [9]. Specifically, artificial flaws are introduced in the matrix by the incorporation of bubbles, glass or plastic beads, lightweight aggregates, etc. This will result in reductions in matrix toughness and first-cracking strength as well as making the cracking strength more uniform in different parts of the material, which facilitates the formation of closely-spaced cracks. With low stiffness and weak bonding to the cementitious matrix, rubber particles should be useful for the making of PDCC as the artificial flaws.

Rubber is not biodegradable and its burning can result in the production of carcinogenic gas. With the growing use of automobiles in China, the rapidly increasing amount of waste rubber from tyres has become a big environmental problem. Now rubber particles produced from waste rubber have been used for making concrete, and results in the literature show that concrete with rubber particles exhibits improved flexibility, ductility, energy absorption [10, 11], impact resistance and dissipation under dynamic loading [12], Mortar with 5% or 10% fine rubber ash was also found to exhibit improved resistance to freezing and thawing and chloride diffusion [13]. Due to these excellent properties of cementitious composites with rubber particle, PDCC with rubber particles are expected to combine high tensile performance, dynamic properties and resistance to freezing and thawing etc.

In the present study, PDCC specimens were prepared to study the effect of rubber incorporation on various properties. Control specimen without rubber particles was first prepared and tested. In other specimens, part of sand or filler was replaced by fine rubber particles as the artificial flaws. To identify the appropriate content and size of rubber particles for optimal performance, rubber particles of different particle size distribution were added at different contents. Due to relative low water permeability and high dry shrinkage to PDCC, properties including compressive strength, tensile performance, water permeability and dry shrinkage were measured to obtain a comprehensive understanding on the effect of rubber particles.

Properties of Raw Materials

Portland cement P·II52.5 and the high activity fly ash was employed in this study. The particle size of fly ash is mainly within 2~10μm and the content of major active components (including SiO_2, Al_2O_3 and Fe_2O_3) reaches 76.1%. According to ASTM C311-04, the active index of compressive strength at 7 days, 28 days and 90 days are 86%, 84% and 96% respectively, and the content of calcium silicates and the ratio of Ca/Si is 79% and 3.0 respectively. Silica fume, silica filler and silica sand were also employed and their respective range of particle size are 1~20μm, 1~15μm and 50~200μm. To provide pseudo-ductility, polyvinyl alcohol fiber (PVAF) (Kuraray Limited Corporation, Japan) was used. Its density, length and diameter are 1.3g/cm^3， 12mm and 38μm respectively. Superplasticizer (Sp) with 23% solid content and rubber particles (R) with various maximum particle sizes of 0.4mm, 0.2mm and 2mm were also used in the specimens.

Test Procedure

The tensile performance and compressive performance are obtained respectively from specimens 350×50×15mm and 40×40×40mm in size. Note that the size of cast members may not be exact so the actual dimensions of each specimen were measured by vernier caliper before testing to obtain accurate values for the calculation of material parameters. The specimen was demoulded after 24 hours of wet curing in the laboratory, where the temperature was about 20±2℃, and then cured in water at temperature of about 26 ℃。

Before the performance of tensile testing, four 100x50mm CFRP sheets were bonded to both surfaces at the ends of the tensile specimens. Then, four 70x50mm aluminum plates were also glued to the ends. Testing was performed under displacement control in the MTS810 system and the displacement rate was 0.15mm/min. During testing, the parts covered with aluminum plates were gripped, and strain was measured within the middle 150mm (which was not reinforced). The first

crack strain ε_{Tfc} and the ultimate strain ε_{Tu} were taken to be the strain values corresponding to the first crack stress σ_{Tc} (where the stress vs strain shows a sudden deviation from linearity) and ultimate stress σ_{Tu} (which is the maximum stress reached by the specimen), respectively. In many specimens, after the ultimate stress is reached, softening occurred at a very slow rate. The post-peak stress vs strain behavior can contribute to significant energy absorption and toughness improvement of the material. Moreover, under other kinds of loading (e.g., bending), the slow decrease in post-peak tensile stress can result in hardening behavior in the moment vs curvature relation. As the rate of softening is of practical significance, we defined the maximum strain ε_{Tm} as the strain when the ultimate stress descends up to 90%, and measured it for each of the tested specimen. A high value of ε_{Tm} implies slow softening.

Water permeability test was conducted using the falling head setup, which was originally developed by Ludirdja[14]. With this set-up, the specimen is sandwiched between two water reservoirs and pressure is generated by water in a long vertical tube placed above the upper reservoir. Assuming laminar flow after the specimen is saturated with water, and Darcy's law can be applied to derive an equation for calculating the coefficient of water permeability (k_w). During the test, the height of water in the tube was measured as a function of time (t).

The drying shrinkage was measured according to ASTM C596-01. Members 25mm×25mm×280mm in size were cast and kept wet in the molds for one day. After demoulding, the specimens were cured in water for two additional days. The initial length was then obtained and the specimens was placed in a room with controlled environment, where the temperature and relative humidity were kept at about 27±2^{O}C and 50±5% respectively. The change of specimen length was accurately measured at specific times for the calculation of drying shrinkage.

To study the effect of rubber particle size and content on the performance of PDCC, PDCC with various compositions as shown in table 1 were prepared and tested. In all cases, an appropriate amount of super-plasticizer was added to achieve the required workability; and 2 volume percent of PVAF was added to achieve high ductility. CON is the control PDCC, and in SR3.5, SR7 and SR11, rubber particles including 3.5%, 7% and 11% in volume of the cementitious composites was employed by the decrease of sand content, respectively. For SR16, the sand content is the same as that of SR11, but the filler is also replaced by rubber particles.

In the mixes in Table 1 with rubber particles, the maximum particle size was 0.4mm. In addition to these mixes, two additional mixes were prepared to study the effect of particle size. These mixes, which had the same composition as SR11, were denoted as S2R11 and S0.2R11 and the maximum particle size was 2mm and 0.2mm respectively.

Table1 MIX PROPORTION OF PDCCS WITH VARIOUS CONTENTS OF RUBBER PARTICLES (kg/m^3)

	Cement	FA	Filler	Rubber	Sand	Water	Sp	PVAF
CON	460	690	115	0	460	291	6.98	26
SR3.5	460	690	115	39	391	291	9.20	26
SR7	472	708	118	77	307	274	9.40	26
SR11	472	708	118	121	189	274	9.40	26
SR16	472	708	0	176	189	264	8.08	26

Test Results and Discussions

Mechanical Properties of PDCCs with Various Fractions of Rubber Particles

The test results are showed in table2. To obtain the tensile behavior and compressive strength, at least three specimens were tested at each specified age. The control PDCC specimens were tested at 7, 28 and 90 days. Long-term curing was found to have a significant effect on the tensile ductility. For the specimens with rubber particles, testing was performed at 7 days and 28 days.

It can be observed from Table2 that incorporation of rubber particle will reduce the compressive strength and tensile strength of cementitious composites. With increasing content of rubber particles from 3.5% to 16%, the 28-day compressive strength decreases by 17% to 80% while the tensile

strength decreases by 16% to 56%. With increasing rubber content, the ultimate strain does not exhibit a clear trend. The highest tensile strain at 28 days (2.15%) was achieved with 11% of rubber particles. Fig.3 shows the typical stress vs. strain curves of PDCC with 3.5 % and 11% of rubber particles with different curing conditions.

Table2 MECHANICAL PROPERTIES OF PDCCS WITH DIFFERENT VOLUME FRACTION OF RUBBER POWDER

		σ_{Tfc}(MPa)	σ_{Tu}(MPa)	ε_{Tfc}(%)	ε_{Tu}(%)	ε_{Tm}(%)	σ_{com} (MPa)
	7-day	3.58	4.30	0.050	1.33	1.59	49.6
CON	28-day	3.81	4.53	0.042	0.84	0.98	66.2
	90-day	4.61	5.05	0.027	0.29	0.39	/
	7-day	3.60	3.62	0.022	0.02	0.99	30.2
SR3.5	28-day	3.40	3.83	0.065	0.42	0.74	55.1
	H3d	5.14	5.72	0.032	0.36	0.44	/
	7-day	2.31	2.49	0.036	0.31	0.54	29.7
SR7	28-day	2.60	3.00	0.022	0.58	1.07	35.7
	H3d	3.63	3.81	0.039	0.16	0.71	40.5
	7-day	2.19	2.72	0.034	1.04	1.40	24.8
SR11	28-day	2.31	3.18	0.051	2.15	2.49	31.4
	H3d	3.28	3.57	0.041	0.20	0.34	37.0
	7-day	1.45	1.61	0.041	0.32	1.00	11.8
SR16	28-day	1.88	1.99	0.043	0.25	1.04	13.2
	H3d	1.68	2.14	0.045	0.31	0.56	17.0

Fig1 shows the stress vs. strain curves of SR3.5 at different age and SR11, SR7 at 28 days. It can be observed from Fig.1 that for some specimens, such as SR3.5 and SR7-28, high tensile stress can still be maintained up to a strain far beyond the ultimate strain corresponding to peak stress. For example, for the specimen SR3.5-7 shown in Fig.1, the strain ε_{Tu} corresponds to the ultimate strength is only 0.02, which is equal to the first cracking strain, as maximum stress occurs at first cracking in this case. However, the maximum strain ε_{Tm} (when the post-peak stress is 90% that at the peak) reaches value of 0.99. During the test, although the stress was dropping slowly after first cracking, it is interesting that some fine cracks were found to form away from the main crack which became visible after the peak stress was reached. Specimens within the same group may have different degrees of variation. The three SR11 specimens exhibit similar ultimate failure strain and tensile strength. However, for the SR7 specimens, despite the similarity in tensile strength, there is a large scatter in the ductility. In fact, the control specimens also show a high variation in the ultimate strain, with a high value of 1.66% for one specimen, and much lower values of 0.49% and 0.38% for the other two.

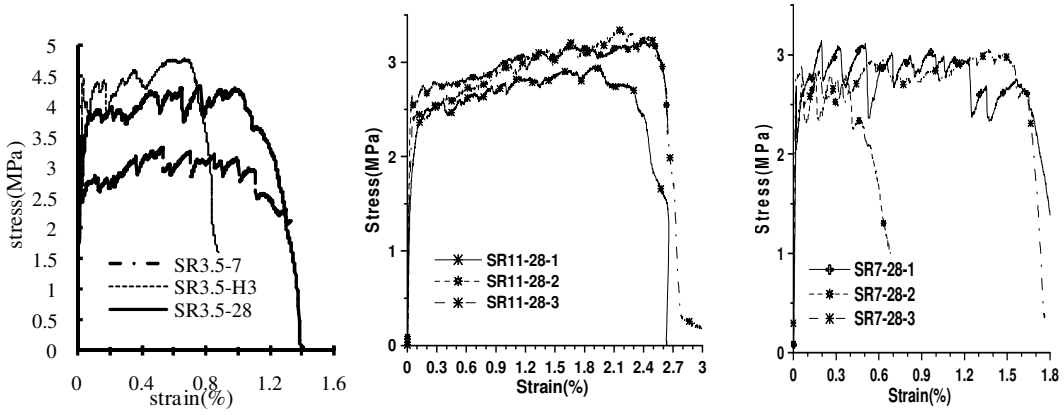


Fig.1 Typical Stress vs. Strain Curves of SR3.5 at Different Age and SR11, SR7 at 28 days

In order for PDCC to have high ductility, a large number of transverse cracks should be able to form under tension. In the ideal situation where the first cracking strength is uniform in every section along the length of the specimen, and is lower than the maximum stress provided by fiber bridging, closely spaced cracks will form, with the crack spacing limited by the distance required for fibers to transmit stresses back into the matrix. In reality, however, flaws of different sizes exist in different

parts of a member. Since first-cracking strength is governed by the initial flaw size, it varies along the length of the specimen. In this case, only the sections with relatively large flaws are able to crack. With a significantly smaller number of cracks than the ideal case, the ductility is greatly reduced. Also, because the uniformity of strength can vary from one specimen to the next, a large variation in the test results is often observed.

The incorporation of small rubber particles serve to introduce artificial flaws in the cementitious matrix. A uniform distribution of rubber particles over the specimen can homogenize the first-cracking strength along the length. It is obvious that a certain minimum volume fraction of rubber particles is required to ensure the presence of artificial flaw in every section of the member. However, when the volume fraction is too high, some particles may get very close to one another and induce the formation of large cracks in certain sections. The first-cracking strength then becomes less uniform again. Based on the above arguments, an intermediate volume of rubber particles is optimal for ductility. Also, when the particles are distributed in such a way to give similar strength in all sections, the variability in test results (for specimens with the same composition) is reduced.

Mechanical Properties of PDCCs with Various Sizes of Rubber Particles

The test results for PDCC with different sizes of rubber particles are listed in Table3.

Table3 Mechanical Properties of PDCCs with different particle size of rubber

		σ_{Tfc}(MPa)	σ_{Tu}(MPa)	ε_{Tfc}(%)	ε_{Tu}(%)	ε_{Tm}(%)	σ_{com} (MPa)
S2R11	7-day	1.82	2.22	0.027	0.29	0.67	27.2
	28-day	1.62	1.93	0.048	0.24	0.41	35.5
	H3d	3.00	3.08	0.032	0.05	0.28	42.0
SR11	7-day	2.19	2.72	0.034	1.04	1.4	24.8
	28-day	2.31	3.18	0.051	2.15	2.49	31.4
	H3d	3.28	3.57	0.041	0.20	0.34	37.0
S0.2R11	7-day	1.31	1.85	0.043	0.77	1.18	21.5
	28-day	1.88	2.69	0.023	0.86	1.37	28.9
	H3d	2.67	3.11	0.055	0.38	0.71	30.1

Comparing the compressive strength of S2R11, SR11 and S0.2R11 at the same age, it can be observed that a larger size of rubber particle gives rise to a higher strength. However, the first cracking strength does not follow the same trend – it is highest when rubber particles with maximum size of 0.4mm were employed. A plausible explanation lies in the different failure modes of cementitious materials in compression and tension. Under compression, many cracks will form in the member and final failure is caused by coalescence of the cracks. As individual cracks are likely to be arrested by rubber particles, the cracks can only link together after they have propagated around the particle. With larger particles, the applied compression for this happen is also higher. Tensile failure occurs in the weakest section and the first cracking strength increases with the toughness of the material but decreases with the maximum flaw size. With small rubber particles, the inherent flaw size is small but so is the fracture toughness. With large particles, the toughness is higher (Note: this has been shown by test results on specimens containing rubber particles but no fibers) but the flaw size is also large. The first cracking is hence highest with an intermediate particle size.

The tensile ductility of PDCC is found to be highest with the 0.4mm rubber particles. When the rubber particle size is too small, it may be even smaller than the air voids inside the cementitious matrix. In this case, the flaws resulted from the incorporation of rubber particles do not dominate fracture failure. The incorporation of small particles will hence have little effect on the ductility. When very large particles are used, there are two unfavorable effects on tensile ductility. Firstly, with the same volume fraction, larger particle size implies a smaller number of particles, which may affect the uniformity of particle distribution. Secondly, with a larger particle size, the fracture toughness (and hence the energy absorption) at the crack tip is also increased. As multiple crack formation and the corresponding ductility is favored by a high ratio of energy absorption behind the crack tip and that at the crack tip, high crack tip toughness will result in reduced ductility. With the above arguments, one can explain the achievement of maximum tensile ductility at an intermediate rubber particle size.

Water Permeability

Water permeability of a particular composition of PDCC has been reported by Lepech and Li [15] to be around $1x10^{-11}$ m/s, which is on the high side of values for normal concrete, which ranges from 10^{-12} to 10^{-11} m/s [16]. As rubber particles have smooth surfaces and do not have strong bond with the hydration products of cement, there is a concern that the particle/cement interface may serve as a preferential path for water permeation. If this is indeed the case, the incorporation of rubber particles will further increase the water permeability of PDCC, and make the material more permeable than normal concrete. To see if this is indeed a problem or not, the water permeability of SR3.5, SR7, SR11 and SR16 after 28 days of curing was also measured, and the test results were 4.72, 4.04, 4.92 and 4.06 $x10^{-12}$m/s respectively. It can be seen that the coefficient of water permeability for various PDCC mixes is close to one another, with values between 4 to 5×10^{-12} m/s. These values are lower than that given in [15] and within the range of normal concrete. According to our results, the incorporation of rubber particles does not necessarily produce a composite with high water permeability.

Shrinkage of PDCCs with Rubber Particles

Fig.2 shows the effect of rubber particle volume on dry shrinkage. Due to the absence of coarse aggregates, the ultimate dry shrinkage strains of all mixes (with or without rubber) are very high and exceed 10×10^{-4}. As expected, the dry shrinkage increases rapidly in the first 14 days, and slowly approaching an asymptotic value. The dry shrinkage strains of specimen SR7, SR11, SR16 at 28 days are 11.17×10^{-4}, 14.61×10^{-4} and 19.85×10^{-4}, respectively, while the corresponding values at 91 days are 13.36×10^{-4}, 16.61×10^{-4} and 23.66×10^{-4}. According to the test results, drying shrinkage of PDCC increases rapidly with content of rubber particle in the mix. For SR11 with S0.2R11, their drying shrinkage strains at 28 days are 14.61×10^{-4} and 13.95×10^{-4}, respectively, and the values at 91 days are respectively 16.61×10^{-4} and 16.02×10^{-4}. The results indicate that the particle size has only a slight effect on the dry shrinkage of PDCC. In summary, when rubber particles are added to PDCC for the generation of artificial flaws, drying shrinkage may be significantly increased. In future work, the combined use of rubber particles with shrinkage-compensating cement should be studied.

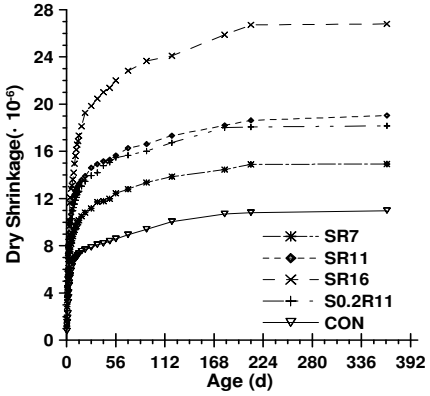


Fig.2 Effect of Rubber Particle on Dry Shrinkage of PDCCs

Conclusion

Pseudo-ductile cementitious composites (PDCC) are composites showing strain hardening behavior under direct tensile loading. Its ductility (defined as the strain corresponding to maximum stress) depends on the spacing of multiple cracks that can form in the hardening regime. Incorporation of artificial flaws in the composite can facilitate the formation of closely spaced multiple crack. In the present study, rubber particles were added in PDCC mixes for the generation of artificial flaws. Specimens were prepared with different volume fractions and sizes of particles were employed, and tested for mechanicals properties, water permeability and dry shrinkage. The following findings from the test results can be highlighted:

(1) The compressive strength and first cracking strength of PDCC generally decreases with increasing content of rubber particles. The tensile ductility, however, is maximal at an intermediate volume fraction of rubber particles. With increasing rubber particle size under fixed particle content,

the compressive strength is increased but the first-cracking strength and tensile ductility attain maximum values at an intermediate particle size. In the design of PDCC, maximizing of material ductility is often the major goal, and rubber particles of optimal volume and size should be employed. In the present study, the 11% rubber particles with particle sizes of 0.4mm are optimal.

(2) Water permeability for various PDCC mixes with rubber particles is close to the value for normal concrete.

(3) The dry shrinkage of PDCC increases greatly with the volume content of rubber particles but is insensitive to rubber particle size.

Acknowledgement

All experiments for this paper are finished in Hong Kong Science and Technology University. This work is financially supported by HongKong research grant, National natural science foundation (51108077) and Jiangsu provincial natural science foundation (BK2011612).

References

[1] Li, V.C. and C.K.Y.Leung, Steady-state and multiple cracking of short random fiber composites. Journal of engineering mechanics, 118(1992) 2246-2264.

[2] Li, V.C. and H.C. Wu, Conditions for pseudo strain-hardening in fiber reinforced brittle matrix composites. Applied mechanics revolution, 45(1992) 390-398.

[3] Li, V.C., From micromechanics to structural engineering-the design of cementitious composites for civil engineering applications. Journal of structure mechanical earthquake engineering, 10(1993) 37-48.

[4] Leung, C.K.Y., Design criteria for pseudo-ductile fiber composites. ASCE Journal of engineering mechanics, 122(1995) 10-18.

[5] Lin, Z. and V.C. Li, Crack Bridging In Fiber Reinforced Cementitious Composites With Slip-Hardening Interfaces. J. Mechanical Physics Solids, 45(1997) l63-181.

[6] Kanda, T., V.C. Li, and M. ASCE, New Micromechanics design theory for pseudostrain hardness cementitious composite. Journal of engineering mechanics, 125(1999) 373-381.

[7] Li, V.C., H.C. Wu, and Y.W. Chan. Interfacial property tailoring for pseudo strain-hardening cementitious composites. In proceedings of advanced technology on design and fabrication of composite materials and structures, 1995. Netherlands.

[8] Li, V.C., D. K.Mishra, and H.-C. Wu, Matrix design for pseudo-strain-hardening fiber reinforced cementitious composites. Materials and structures, 28(1995)586-595.

[9] Wang, S. and V.C. Li. Tailoring of Pre-existing flaw in ECC matrix for saturated strain hardening. In proceedings of the fifth International Conference on Fracture Mechanics of Concrete and Concrete Structures. 2004. Vail, Colorado, USA.

[10] Li, Z., F.Li, and J.S.L.Li, Properties of concrete incorporating rubber type particles. Magazine of concrete research, 50(1998) 297-304.

[11] Topcu, I.B. and N. Avcular, Collision behaviours of rubberized concrete. Cement and concrete research, 27(1997)1893-1898.

[12] Hernandez-Olivares, F., et al., Static and dynamic behaviour of recycled tyre rubber-filled concrete. Cement and Concrete Research, 32(2002) 1587-1596.

[13] Al-Akhras, N.M. and M.M. Smadi, Properties of tire rubber ash mortar. Cement and concrete composites, 26(2004) 821-826.

[14] Ludirdja, D., R.L. Berger, and F. Young, Simple method for measuring water permeability of concrete. ACI materials Journal, 86(1990) 433-439.

[15] Lepech, M. and Li, V.C., Water permeability of cracked cementitious composites, Proceedings of ICF11, Turin, Italy

[16] Wang, K.J., et al., Permeability study of cracked concrete. Cement and concrete research, 27(1997) 381-393.

Advanced Materials Research Vol. 936 (2014) pp 1463-1467
© (2014) Trans Tech Publications, Switzerland
doi:10.4028/www.scientific.net/AMR.936.1463

Back Analysis of Thermal Parameters of Mass Concrete and Its Application Based on Micro-genetic Algorithm

Guo Rong CHEN[1],Bei YANG[2,a]

Department of Engineering Mechanics , Hohai University, Nanjing, 210098, China

[a] beibeibinbin0416@163.com

Keywords: concrete; thermal parameter; back-analysis; simulating calculation; micro-genetic algorithm

Abstract: The value of thermal parameter is very crucial in simulating analysis on temperature control for mass concrete. The inverse analysis on some practical project is done by genetic algorithm and finite element method on the basis of observational data of temperature on the site. The temperature control simulation calculation is performed based on parameters obtained from inverse analysis on this project, so that the temperature distribution is consistent basically with the practical one. With improvement of micro-genetic algorithm, the genetic algorithm becomes globally-optimal by changing the optimal reserving and re-starting strategies. The results show this method is very practical in high precision of calculation in mass concrete parametric inversion.

Introduction

Concrete cracks easily to imperil the structure safety and normal use at a certain temperature as a brittle material with low tensile strength. So the temperature calculation for mass concrete is very indispensable, and the correct selection of concrete thermal parameters is crucial to temperature calculation and control measures for crack prevention[1, 2]. However, the thermal parameters of concrete cannot reflect practical situation as they are usually obtained on site, laboratory or experience. For this, the inverse analysis on these parameters is performed. This is conducive to avoiding complex outside conditions and limited experiments, so that parameters reflecting concrete thermal properties are obtained. However, because of extreme non-linearity and complexity in question, the traditional optimization algorithm often gets into the locally optimal solution by inverse analysis, with a too slow rate of convergence even without convergence. For above reasons, it is the key how to select an effective searching method in analysis.

The genetic algorithm put forth by Professor J.H. Holland is applied soon in inverse problem as it is global and not easy to fall into local optimum. In particular, it is applicable to handle the complex non-linearity which is hard to be dealt with by the traditional searching method. Eiben A.E et al. proved convergence of genetic algorithm[3]. Charles established the retrieval method of initial-value and boundary-value problems [4]. Zhang Yuxin proposed the universal methods such as main thermal parameters and thermal exchange coefficient for inverse steady-state temperature field of concrete[5]. For complex engineering problems, the frequency of positive calculation increases because the rate of its convergence is too slow or the scale of population is oversized. In addition, it is weak in the local searching of algorithm and poorer in stability of variables to be optimized. Krishnakumar K. [7] improved basic genetic algorithm, and proposed the micro-genetic algorithm (MGA) which is applicable for solution of complex engineering—reducing number of individuals of population to some extent. Liu Yinfang et al. improved the micro-genetic algorithm to ensue population diversity by designing restarting function [8]. Li Yi et al. improved the micro-genetic

algorithm to avoid local optimum by the optimal reserving strategy [9]. I compiled the inverse analytical procedures of parameters of the three-dimensional unstable temperature field, retaining optimal individuals instead of mutation operation by binary coding, roulette selection, single-point cross and optimal reserving strategy.

Principles

Temperature filed finite element method

When the transient temperature field satisfies requirements of all possible temperature fields in the coercive boundary condition $T = f(t), x \in s_1$ and the initial condition $(T)_{t=0} = f(x, y, z), x \in V$, the true temperature field can meet the $\delta\Pi = 0$, where the functional is expressed as follows:

$$\Pi = \int_V \left\{ \frac{\alpha}{2} \left[\left(\frac{\partial T}{\partial x} \right)^2 + \left(\frac{\partial T}{\partial y} \right)^2 + \left(\frac{\partial T}{\partial z} \right)^2 \right] + \left(\frac{\partial T}{\partial t} - \frac{\partial \theta}{\partial t} \right) T \right\} dv + \int_{s_2} \frac{1}{c\rho} T \overline{q}_n ds - \int_{s_3} \overline{\beta} T \left(T_a - \frac{1}{2} T \right) ds \quad (1)$$

The transient temperature field is a function of space and time, and its solution domain is divided into finite element gridding. The temperature function for each element is obtained by the interpolation of the node temperature value of this element. The functional after convergence of finite element is equal to the sum of element functionals, i.e.

$$\begin{aligned} \Pi &= \int_V \left\{ \frac{\alpha}{2} \left[\left(\frac{\partial T}{\partial x} \right)^2 + \left(\frac{\partial T}{\partial y} \right)^2 + \left(\frac{\partial T}{\partial z} \right)^2 \right] + \left(\frac{\partial T}{\partial t} - \frac{\partial \theta}{\partial t} \right) T \right\} dv + \int_{s_3} \overline{\beta} \left(\frac{1}{2} T^2 - T_a T \right) ds \\ &= \sum_e \int_V \left\{ \frac{\alpha}{2} \left[\left(\frac{\partial T}{\partial x} \right)^2 + \left(\frac{\partial T}{\partial y} \right)^2 + \left(\frac{\partial T}{\partial z} \right)^2 \right] + \left(\frac{\partial T}{\partial t} - \frac{\partial \theta}{\partial t} \right) T \right\} dv + \sum_e \int_{s_3} \overline{\beta} \left(\frac{1}{2} T^2 - T_a T \right) ds \end{aligned} \quad (2)$$

Where, $\alpha = \frac{\lambda}{c\rho}$, $\overline{\beta} = \frac{\beta}{c\rho}$, and thermal rising math model is Index II:

$$\theta(\tau) = \theta_0 \times \left(1 - e^{-a\tau^b} \right) \quad (3)$$

Genetic algorithm principle

The genetic algorithm is essentially a searching method based on natural selection mechanism and genetics[12]. The MGA is improved greatly in algorithm structure so as to ensure GA global searching ability. The basic operation strategy for genetic algorithm contains crossover and variation, where, the crossover operation is uppermost genetic one in genetic algorithm. Based on crossover probability, each pair of individuals exchange some individual chromosomes each other at this point, forming two new individuals. Some variation operations are cancelled and some GA operations are added in MGA, for example, the optimal reservation. There is a smaller scale of populations in MGA, and its number of populations may be taken as 5-10 (20 populations at least for GA). As a result, the calculated quantity decreases greatly.

Improvement of micro-genetic algorithm

Theoretical analysis

I improved the optimal reserving strategy in MGA, that is, reserving the best or optimal individuals fully and storing them to form the optimal reserved individuals in order for selection of the next generation. By this way, fast convergence is available in case of forming the locally-optimal solution. The setting temporary storage part is used to store the best individuals for comparison, and setting optimal reserved individuals are used to store all the best individuals. By this way, the best individuals selected in each generation of cycle can be stored integrally in the end.

The restarting operation is set in MGA so as to keep the population diversity. The restarting strategy is performed in calculation of some generations. By confining the restarting distance, not only can all excellent genes be reserved by the restarting strategy, but also diversity of superior genes can be realized. By this way, interference of the individuals with the most distinct local superiority in the population can be avoided to diversity of the population.

Inverse analysis model

The temperature inverse analysis model is applied because the thermal parameters are strongly related to temperature in the calculation of temperature field and temperature is measured easily. Supposing inverse parameters used in simulation calculation are the same as the actual ones of the material, then $T_{ij} = T_{ij}^0$, ignoring the errors of numerical calculation and measurement of the model. Generally speaking, the square root of square difference is taken as the inverse objective function as the calculated and measured values of temperature field are not strictly equal, i.e.

$$F = \sum_{i=1}^{m}\sum_{j=1}^{n} \omega_{ij} \sqrt{\left(T_{ij}(X) - T_{ij}^0\right)^2}$$

Where, ω_{ij} stands for weighting coefficient, T_{ij} is the calculated temperature value, T_{ij}^0 is the measured temperature value, i is the serial number of observing point, and j is the serial number of observing time, X is inverse parameter vector; $X(x_1, x_2, x_3, \cdots) = X(a, b, \theta_0, \cdots)$. There is a certain estimated range based on experience or experimental inverse parameter, i.e. the constraint condition is:

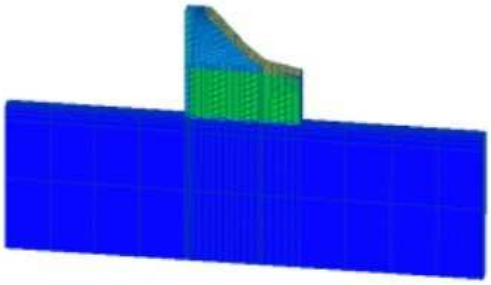
$$x_i^l \le x_i \le x_i^m \qquad (i = 1,2,3, \ldots)$$

The calculation process is shown:

Step 1 Determine initial population quantity and initial value space, and generate the initial population within the initial value space. Each individual is expressed as the gene coding of chromosome. Step 2 Determine the fitness function, obtain the temperature value and fitness value of each individual by calculating the temperature field finite element, and select individuals based on fitness values. The individual selected probability is greater than that of small fitness individual. Step 3 Generate new individual and select the optimal reserving value generated from best individuals in the population based on a certain crossover probability and crossover operation method. Step 4 Judge whether the condition of convergence is satisfied or not. If yes, turn to Step 5;

if no, return to Step 2. Step 5 Judge whether it is local convergence or not, and perform the comparison of distance. If it is local convergence, restart it, then turn to Step 2; otherwise, perform Step 6. Step 6 Store the optimal reserving value into the temporary memory, and judge the terminal condition is satisfied or not. If yes, output best individuals and their optimal solution, and end the calculation; otherwise, write the optimal value in the temporary memory into the optimal reserved part, and turn to Step 2 after the optimal reserved part and stochastic part generate the population together.

Numerical example



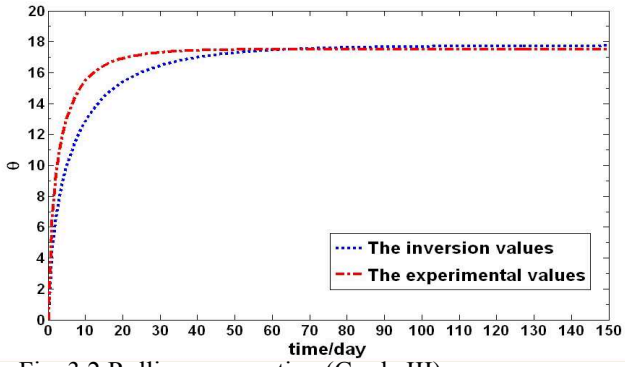
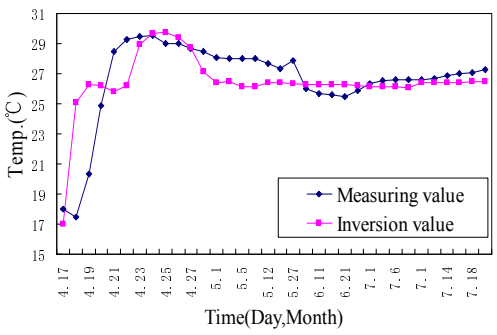


Fig. 3.1 Grid chart of overflow dam section Fig. 3.2 Rolling compaction (Grade III)

The adiabatic temperature rise curve obtained by inversion is shown in Fig. 3.2 The initial phase of inverse adiabatic temperature rise curve is gentler than the experimental curve, and the peak temperature rise is 0.53℃ higher than the experimental value. Figure 3.3and3.4 shows two randomly selected temperature measuring point comparison chart.



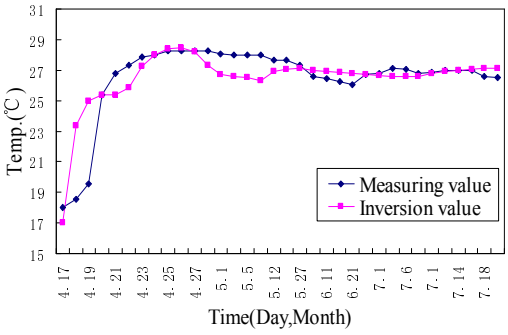


Fig. 3.3 Inverse temperature value at 06 Fig. 3.4 Inverse temperature value at 31

Conclusions

The thermodynamic parameter inversion optimization is performed for the project by improving micro-genetic algorithm and combining three-dimensional unstable temperature field, and the results show as follows:

1. This algorithm can be well applied to finish parameter optimization quickly to converge to the optimal solution. So the local optimum can be avoided, and calculation time and accuracy are improved greatly. It has ability to solve engineering cases, is worth popularizing and applying.

2. The inverse analysis is performed for the engineering project and feedback analysis to enable computer feedback work more realistic to reflect the practice, so that play a more reliable and guiding significance role. The method are economically reasonable and technically feasible, which can be widely applied to the engineering of temperature control in similar in the future.

References

[1] Zhang Ziming，Zhang Yan，Song Zhitong. Analysis of hydration heat induced temperature rise in massive concrete walls [J]. Journal of Hohai University （ Natural Sciences）,2002,30(4):22_27.

[2] Zhang Ziming，Guo Xingwen，Du Rongqiang. Analysis of hydration heat-induced stresses and cracks in massive concrete walls [J]. Journal of Hohai University （ Natural Sciences）,2002,30(5):12_16.

[3] Eiben A E, Arts E H, Van H EE KM. Global convergence of genetic algorithms: an infinite markov chain analysis [C]. Proceedings of the 1st conference on Parallel Problem Solving from Nature. Berlin: Springer Ver- lag,1991: 4 — 12.

[4] Charles L. Karr, Igor Yakushin, Keith Nicolosi. Solving inverse initial-value, boundary-value problems via genetic algorithm [J]. Engineering Applications of Artificial Intelligence 13 (2000) 625–633.

[5] Zhang Xinyu, Song Yupu, Wang Denggang. Inverse analysis of three dimensional unsteady temperature field with genetic algorithms [J]. Chinese Journal of Computational Mechanics.2004, 21(3):338-342.

[6] Zhu Yueming, Wang Hong, Shan Li. Genetic computation method of inverse problem solution of concrete thermo dynamical parameter [J]. Yangtze River.2004,(35)11:55-57.

[7] KRISHNAKUMAR K. Micro-genetic algo-rithms for stationary and non-stationary function optimization [J]. SPIE: Intelligent Control and Adaptive Systems, Society of Photo-Optical Instrumentation Engineers，Philadelphia， 1989， 1196: 289 — 296．

[8] Liu Yinfang, Chen Guorong, You Guoying, Jing Chao. Back Analysis for Thermal Parameters of Concrete Dam with Micro Genetic Algorithm and Finite Element Method [J]. Journal of Zhengzhou University (Engineering Science).2011,32(6):63-66.

[9] Liu Yi, Tan Lei, Cao Shuliang. The Micro Genetic Algorithm and its Usage in the Optimization Design of Mixed-Flow Pump [J]. Machinery Design & Manufacture.2012,9:1-3..

Advanced Materials Research Vol. 936 (2014) pp 1468-1472
© (2014) Trans Tech Publications, Switzerland
doi:10.4028/www.scientific.net/AMR.936.1468

A Effective Solution Method Based on Bayesian Rule for Prediction of Long-term Tensile Strength of GFRP Bars in Concrete Beams

Li DAI [1] Xiongjun HE [2] Feng SHEN[3]

[1,2] School of Transportation, Wuhan University of Technology, Wuhan 430063, China.

[3] Nanjing Fenghui Composite Material Co., Ltd, Nanjing 210004, China.

[a]Email:466583972@qq.com [b]Email: hxjwhut@163.com

Key words: GFRP bars; tensile strength; prediction; concrete beams; solution method

Abstract: It is necessary to research on the long term structural behavior of GFRP bars in concrete by limited samples. The two models, Arrhenius Equation and Fick's Law were compared to form a long-term durability prediction thinking. Based on the work and ideas of the prior researchers, a detailed derivation of the iterative equation on the Bayesian prediction was conducted. Especially, a new likelihood function was set up to solve the long term behavior prediction of GFRP bars in concrete with less information. Then a new and effective solution method was developed. The residual strength behavior of GFRP bars in concrete beams after seven years' environmental exposure was analyzed. The results showed that the theoretical predictions and experimental data were very close and theoretical prediction model was reasonable.

INTRODUCTION

Considerable research has been conducted in the past thirty years to assess the durability of GFRP bars in reinforced concrete structures. It was recognized that GFRP bars were susceptible to moisture, alkaline solutions and elevated temperature. In particular, the durability of GFRP bars could be affected by the alkaline environment of concrete. The material aging may occur in the fiber, matrix, and their interface individually or simultaneously. Much work was highlighted on the short-term performance of GFRP reinforced concrete structures.

Homman studied the durability of GFRP bars under different moisture and temperature environments. The results showed that the above all kinds of environmental factors could reduce the GFRP's mechanics properties more or less (Homam S M. 2005). Chen, Davalos and Ray (2005,2006) and Yousef (2013) presented the short-term test results of a durability study on GFRP reinforcing concrete structures by accelerated test methods. GFRP reinforcing bars were exposed to different solutions at elevated temperature combined with wetting and drying, and freezing and thawing cycling, which were designed to simulate the adverse conditions in the field.

The researchers pointed out that the application of the Fick's law and the Arrhenius equation were of limitations. In order to explain the two theories, we have a further theoretical discussion.

(1) Prediction model based on Fick's Law

Fick-type model has been used to predict the residual strength of GFRP bars embedded in concrete. Shen and Springer (1986) recommended that the diffusion coefficient needed in Fick's law be obtained by using the following equation.

$$D = \frac{\pi r^2}{16}\left(\frac{M_2 - M_1}{M_m}\right)^2\left(\frac{1}{\sqrt{t_2} - \sqrt{t_1}}\right)^2 \quad (1)$$

Where D is the diffusion coefficient in the composite material; M_1, M_2 and M_m are the moisture content of the bar (in percent) at time t_1, t_2, and at saturation, respectively.

Katsuki and Uomoto (1995) proposed a prediction model based on Fick's Law. The authors assumed that the tensile strength of GFRP bars could be determined quantitatively by the amount of alkali penetration area into the bars and recommended that the depth of penetration be calculated by using the following equation:

$$X = \sqrt{2 \cdot D \cdot C \cdot t} \quad (2)$$

Where X is the depth of penetration, C is the alkaline concentration (percent), t is the curing time, and D is the diffusion coefficient.

The authors assumed that as glass fibers were exposed to the diffusing solution these fibers exhibited complete failure and no longer contributed to the bar's capacity. By using this assumption the authors proposed the following equation for estimating the residual strength:

$$\sigma_t = \left(1 - \frac{\sqrt{2 \cdot D \cdot C \cdot t}}{R_0}\right)^2 \cdot \sigma_0 \quad (3)$$

Where σ_o and σ_t are the tensile strength before and after exposure (stress units), respectively, and R_0 is the radius of the GFRP bars.

Trejo et al (2009) reported that the assumption of complete loss of glass fiber capacity probably overestimated the loss of bar capacity and proposed an exposure factor λ, to account for this time-dependent deterioration of the bond between the glass and resin. The equation (3) was rewritten as follows:

$$\sigma_t = \left(1 - \frac{\sqrt{2 \cdot D \cdot \lambda \cdot t}}{R_0}\right)^2 \cdot \sigma_0 \quad (4)$$

Although the model that based on Fick's law satisfied the durability prediction of the GFRP composites to a certain extent, the assumption that the matrix and the glass fibers in the aggressive area would completely fail deviated from the fact (Dejke 2001).

(2) Prediction model based on the Arrhenius law

Arrhenius equation has been widely used to establish correlation between degradation data from laboratory accelerated aging tests and service-life of field structures. The Arrhenius equation reveals a good correlation between the temperature and the rate of diffusivity and chemical reaction. The Arrhenius equation is shown as follows (Litherland 1981, Nelson1990) :

$$k = A \exp\left(-\frac{\Delta E_a}{RT}\right) \quad (5)$$

Where k is the degradation rate (1/time), A is a constant of the material and degradation process, E_a is the activation energy; R is the universal gas constant and T is the Kelvin temperature. The equation (5) can be transformed into:

$$\frac{1}{k} = \frac{1}{A} \exp\left(-\frac{RT}{\Delta E_a}\right) \quad (6)$$

$$\ln\left(\frac{1}{k}\right) = \frac{E_a}{R} \cdot \frac{1}{T} - \ln(A) \quad (7)$$

It is supposed that aging mechanism is not changeable with time and temperature in Arrhenius equation. In practice, new aging mechanism may be produced with temperature becoming higher and higher. So there is error for this method.

Reliability theory equation of long-term performance prediction of GFRP bars

Trejo et al (2009) introduced exposure factor λ in prediction model (4) to make the model more flexible to fit the experimental data, which was modified as follows.

$$\sigma_t = \left[1 - \lambda\left(\frac{D \cdot t}{R_0^2}\right)^{\alpha}\right] \cdot \sigma_0 \quad (8)$$

Where each term has the same definition as in Eq. (4). To account for the uncertainty of σ_0 and σ_t, Eq. (8) was then modified as follows.

$$\sigma_t(D,R_0,\lambda,\alpha,s,s_0)=\left[(1+s_0\varepsilon_0)-(1+s\varepsilon)\lambda\left(\frac{D\cdot t}{R_0^2}\right)^{\alpha}\right]\mu_{\sigma_0} \quad (9)$$

Where stochastic error ε and ε_0 obey N~(0,1) distribution statistically. Because ε and ε_0 are mutual independent, the covariance is 0. $s_0\ \varepsilon_0$ obeys $(0, s_0^2)$ distribution. $s\ \varepsilon$ obeys $(0, s^2)$ distribution. $s\varepsilon\lambda\left(Dt/R_0^2\right)^{\alpha}$ obeys $\left(0, s^2\lambda^2\left(Dt/R_0^2\right)^{2\alpha}\right)$ distribution. In equation (9), $s_0\varepsilon_0 - s\varepsilon\lambda\left(Dt/R_0^2\right)^{\alpha}$ is error term. Because ε and ε_0 are mutual independent with 0 covariance, the standard deviation is $\sqrt{s_0^2+s^2\lambda^2\left(Dt/R_0^2\right)^{2\alpha}}$. Let $x=(D, R_0)$ as a basic variable, $\Theta = (\lambda, \alpha, S_0, S)$ as a vector of unknown empirical model parameters. Based on these, equation (9) can be transformed as:

$$\frac{\sigma_t(x,\Theta)}{\mu_{\sigma 0}}=\left[1-\lambda\left(\frac{D\cdot t}{R_0^2}\right)^{\alpha}\right]+\sqrt{S_0^2+S^2\cdot\lambda^2\left(\frac{D\cdot t}{R_0^2}\right)^{2\alpha}}\cdot\varepsilon \quad (10)$$

The key of using the prediction equation is to determine the unknown parameter λ, α, S_0, S. Therefore, the objective of this paper is to determine the parameters based on a small number of long-term tensile strength empirical data of GFRP bars.

A effective solving method based on Bayesian rule

The unknown model parameters λ, α, S_0, S are empirical and have no direct physical meaning. These parameters are used to fit the experimental data. The parameters are estimated using the Bayesian rule.

$$f(\Theta)=\gamma L(\Theta)p(\Theta) \quad (11)$$

Where $p(\Theta)$ is the priori distribution of unknown parameter Θ, $L(\Theta)$ is the likelihood function that represents the information on the parameter Θ from the tensile strength data y. $f(\Theta)$ is the posterior distribution of Θ. γ is a normalizing factor:

$$\gamma=\frac{1}{\int L(\Theta)p(\Theta)d\Theta} \quad (12)$$

It is difficult to form an effective distribution without enough long term tested tensile strength values. In this case, we can assume it obeys even distribution on a certain interval if the unknown parameters are continuous random variables. Therefore, it is assumed the priori distribution $p(\Theta)$ obeys (0-1) distribution. In this way, Likelihood function can be derived as follows:

$$L(\Theta)=\prod_{i=1}^{n}P\left\{\frac{\sigma_{t_i}(x,\Theta)}{\mu_{\sigma_0}}=\left[1-\lambda\left(\frac{D\cdot t_i}{R_0^2}\right)^{\alpha}\right]+\sqrt{S_0^2+S^2\cdot\lambda^2\left(\frac{D\cdot t_i}{R_0^2}\right)^{2\alpha}}\cdot\varepsilon\right\} \quad (13)$$

Based on (11)-(13), then

$$y=\frac{\sigma_{t_i}(x,\Theta)}{\mu_{\sigma 0}} \quad (14)$$

$$\mathrm{f}(\lambda,\ \alpha,\ S_0,\ S)=\left[1-\lambda\left(\frac{D\cdot t_i}{R_0^2}\right)^{\alpha}\right] \quad (15)$$

$$A_1\cdot\varepsilon=\sqrt{S_0^2+S^2\cdot\lambda^2\left(\frac{D\cdot t_i}{R_0^2}\right)^{2\alpha}}\cdot\varepsilon \quad (16)$$

So equation (10) can be transformed as below.

$$y=\mathrm{f}(\lambda,\ \alpha,\ S_0,\ S)+A_1\cdot\varepsilon \quad (17)$$

Based on the equation (17), an analysis program can be developed to determine the unknown parameters in the long-term value prediction equation of GFRP bars tensile strength.

Numerical examples

Trejo et al.(2009) exposed GFRP bars to seven years outdoor exposure with nearly no stress which is one of the few long-term research results. The V1 type GFRP bars with radius of 16mm were used to predict the long term tensile strength. The V1 type GFRP bars contained E-glass fibers embedded in a vinyl ester resin. These bars were made with external helical fiber wrapping and were coated with fine sand in the surface. The test temperature was room temperature 21.11℃. The diffusion coefficients are different under different environments for different types of GFRP bars. Trejo et al reported a range of diffusion coefficient for the different GFRP bars from 4.47×10-10 in2/sec (2.88×10-13 m2/sec) to 2.39×10-9 in2/sec (1.54×10-12 m2/sec), with a mean value of 1.38×10-9 in2/sec (8.9×10-13 m2/sec). The mean value was used for the modeling.

The historical observations and the approximate density function of unknown parameters Θ (λ, α, S_0, S) are shown in Fig. 1-2.

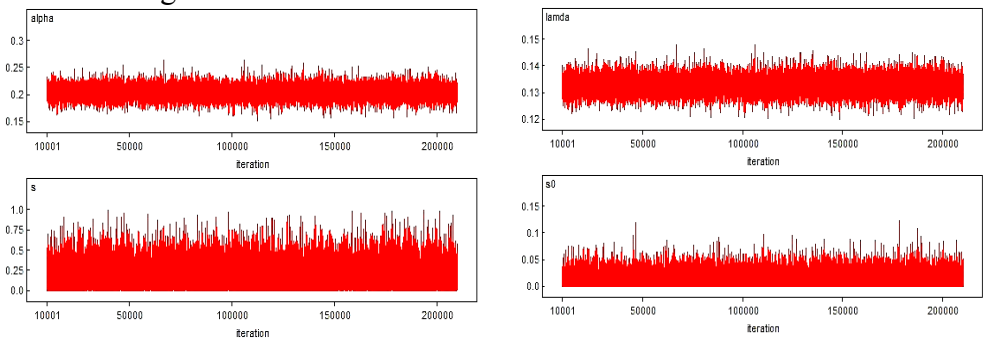


Fig. 1. The historical observations of unknown parameters

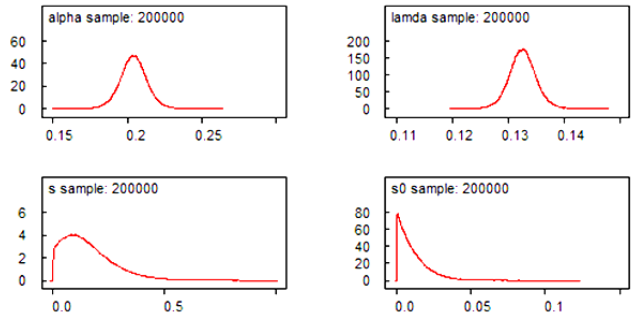


Fig. 2. The approximate density function of unknown parameters

The values of unknown parameters Θ (λ, α, S_0, S) were substituted into the prediction model equation (11), and the time t=7years=22903200 sec was set to obtain tensile strength σ_t=533.24MPa. From the literature (Trejo al 2009) the tensile strength mean value was 537.21MPa and standard deviation was 75.23 MPa after 7 years. The error of tensile strength retention after 7 years is 2.6% based on comparison between the test value and the predicted value under the same environment and materials. Therefore, the prediction model can reasonably predict the tensile strength of GFRP bars as an indicator of the durability after a long time.

Conclusions

The less information likelihood function method based on the results of previous studies was proposed in this paper. A simple and workable prediction model solution was presented which fit the development trend on basis of probability or reliability to set up structural design theory. The residual strength behavior of GFRP bars in concrete beams in environmental exposure of seven years was analyzed. Namely, the tensile strength values of the prior 150 weeks, almost 3 years, were used to set up the model, the tensile strength retention after 7 years' environmental exposure was predicted through the model. The results showed that the theoretical predictions and experimental data were close, which demonstrated that the theoretical prediction model and corresponding solution method was reasonable.

Acknowledgments

The authors would like to acknowledge financial support from the National Natural Science Foundation of China (No. 51178361).

References

[1] Homam S M.(2005). “Fiber reinforced polymers (FRP) and FRP-concrete composites subjected to various loads and environmental exposures.” Ph.D. dissertation，University of Toronto, Canada.

[2] Yi Chen, Julio F. Davalos, Indrajit Ray.(2005). “Critical short-term data on durability of FRP reinforcing bars for long-term prediction models.” American Society for Composites, DES tech Publications, 73-88.

[3] Yi Chen, Julio F. Davalos, Indrajit Ray.(2006). “Durability prediction for GFRP reinforcing bars using short-term data of accelerated aging tests.” Journal of Composites for Construction, 10(4): 279-286.

[4] Shen C. H., and Springer G. S.(1986). “Moisture absorption and desorption of composite materials.” Journal of Composite Materials, 10: 2-20.

[5] Yousef A. Al-Salloum, Sherif El-Gamal, Tarek H. Almusallam, Saleh H. Alsayed, Mohammed Aqel. (2013). “Effect of harsh environmental conditions on the tensile properties of GFRP bars.” Compos. Part B: Engineering, 45(1), 835-844.

[6] Katsuki F., and Uomoto T.(1995). “Prediction of deterioration of FRP rods due to alkali attack.” Proceedings of the Second International RILEM Symposium (FRPRCS-2), Non-Metallic (FRP) Reinforcement for Concrete Structures, 83-89.

[7] Dejke V.(2001). “Durability of FRP reinforcement in concrete-Literature review and experiments.” Licentiate of engineering thesis Dept. of Building Materials, Chalmers Univ. of Technology, Goteborg, Sweden.

[8] Litherland K. L., Okley D. R, and Proctor B. A.(1981). “The use of accelerated aging procedures to predict the long term strength of GRC composites.” Cement Concrete Research, 11, 455–466.

[9] Nelson W.(1990). “Accelerated Testing-Statistical Models, Test Plans, and Data Analyses”, Construction and Building Materials, 18(7):491-503.

[10] David Trejo, Paolo Gardoni, Jeong Joo Kim, and Jason Zidek.(2009). “Long-term performance of GFRP of reinforcement: technical report.” Texas Transportation Institute，The Texas A&M University System.

Advanced Materials Research Vol. 936 (2014) pp 1473-1478
© (2014) Trans Tech Publications, Switzerland
doi:10.4028/www.scientific.net/AMR.936.1473

Seismic Fragility Analysis of RC Isolated Continuous Girder Bridge Using Radial Basis Function Neural Network

Bei Lei Chen[1, a *], Xiao Hong Long[1, 2, b], Jian Jun Li[3, c]

[1]School of Civil Engineering & Mechanics, HuaZhong University of Sci. & Technology, Wuhan 430074, China;

[2]Hubei Key Laboratory of Control Structure, HuaZhong University of Science & Technology, Wuhan 430074, China;

[3]China Railway Siyuan Survey and Design Group Co. Ltd.

[a]cbl-0304516@163.com, [b]xhlong@hust.edu.cn, [c]bambooli127@gmail.com

Keywords: RBFNN; IDA; isolated continuous girder bridge; fragility analysis

Abstract: To approximate the correlating mathematical relationship between many earthquake records' PGA and the responses of bridge structures with minimum efforts and without loss of accuracy, an artificial neural network-based method is proposed in combination with LHS and IDA method. This method is employed to conduct the seismic fragility analysis of RC isolated continuous girder bridge. To investigate the suitability of this approach, the results of the new approach are compared to those obtained by the Cloud method. The comparison shows that the new method is more efficient and reliable.

Introduction

Bridge structures are important hub structures of transportation lifeline engineering. The seismic fragility analysis of RC isolated continuous bridge is comparatively few, as a relatively new bridge type. Fragility curves are often used to express seismic fragility. The curves represent the conditional probability of each damage state's occurrence under different seismic intensities. When the seismic fragility analysis of bridge structures is carried out, the nonlinear time history analysis needs a large amount of calculation, thus the high consumption of computer work and time cost. In addition, the input of seismic earthquake intensities is often limited and fixed and cannot cover all the possible conditions. Former seismic fragility analyses of bridge structures ignored these influential factors.

ANN (Artificial Neural Network, ANN) is an important branch of artificial intelligence, which is able to simulate the structure and function of the human brain system and establish good the appropriate network, through scientific study finding the corresponding input and output mapping relationship [1]. Therefore, it has the ability of processing nonlinear and adaptive information, thus suitable for nonlinear reasoning and predictions in structural engineering. So far, dozens or even hundreds of different types of ANN have been proposed. This paper select RBFNN (Radial Basis Function Neural Network, RBFNN) to train the sample, test the network and predict the seismic response of bridge structures, because of its strength of function approximation ability, learning speed and the good generalization capability.

In view of this, this paper proposes the RBFNN-based seismic fragility analysis method for RC isolated continuous girder bridge. After the trained and tested sample points using RBFNN method are got, the approximation to response values of bridge structure under different PGA horizontal

seismic actions can be conducted, using intelligent reliability algorithms based on RBFNN, indirectly the real limit state equations of the bridge can be achieved. After the bridge seismic fragility curves are obtained, the results are compared to those obtained by the Cloud method.

RBFNN

Fundamentals of RBFNN

An RBFNN structure consists of the input layer, hidden layer and output layer, which is a three-layer feed-forward neural network [2]. The general activation function of the RBFNN hidden layer is Gaussian function, and the activation function of the output layer is completely linear function which can achieve the linear combination of the neurons in the hidden layer. It's crucial that the RBFNN hidden layer is designed appropriately. In the hidden layer the selection of the function center c_j, width b and weight w_j can fundamentally affect the ability of learning and prediction. To build and train a EBFNN, the core is to find a proper neural network mapping function to denote the relationship between input space and output space, which also means to design the parameters of the function center c_j, width b and weight w_j [3].

Realization of RBFNN

To start the RBFNN training the variable and function values of a number of sample points need to be known. Sample points consist of training sample points and test sample points which are used to train RBFNN and test the prediction ability of RBFNN respectively. This paper use Latin Hypercube Sampling (Latin hypercube sampling, LHS) as the sampling method. LHS was first proposed by McKay , and then was given a mathematical formulation by Stein. LHS is a good variance reduction technique and can serve as an alternative to the Monte Carlo method, which is widely applied in simulation, optimization and reliability calculation.

The procedure to realize RBFNN is as follows:

(a) non-guided learning. The parameters of each neuron in the hidden layer, such as c_j, σ_j and the weight between the hidden layer and input layer, are defined according to all input samples;

(b) guided learning. The weight between the hidden layer and output layer is defined based on the input sample data using the least square method. This paper employs the newrb function in matlab to establish, train and test RBFNN. The call of newrb function is as follows: net=newrb (X, T, GOAL,SPREAD,MN,DF) [4].

RBFNN-based seismic fragility analysis for RC isolated continuous girder bridge

Procedures.

(a) Use IDA analysis to provide enough random samples for FBFNN training and test;

(b) Approximate the relationship between some response values of the bridge and PGAs using RBFNN;

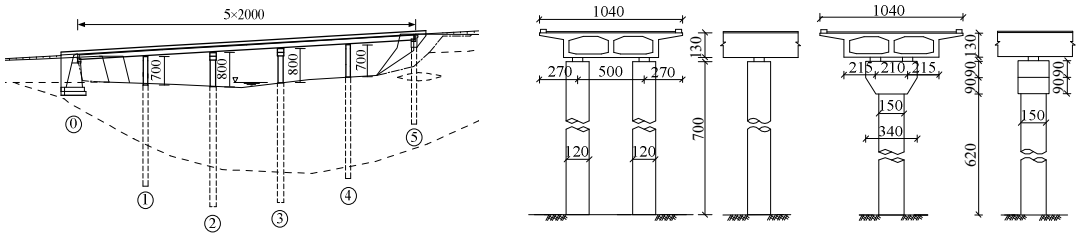
(c) Use RBFNN to predict the seismic response values under every PGA.

(d) Draw seismic fragility curves based on the data obtained through former steps using the Frequency method.

Introduction and formation of the bridge

The bridge this paper studied is on a second class highway located in western part of China. It's a RC isolated continuous bridge with five equal spans and 100-meter overall length. The bridge's

layouts and sections are plotted in Figs.1-(a) and 1-(b) respectively. The seismic isolation bearing LRB500 is used to collect the main beam and the top of the piers. For further information regarding the finite model, refer to Xiao Hong Long et al. [5].



(a) Elevation view (b) Cross-sections of box girder and pier

Fig.1 Elevation and cross-sections of the bridge

Probabilistic seismic demand analysis

(a) Considering uncertainties of earthquake ground motion. Based on Pacific Earthquake Engineering Research Center ground motion database, 100 natural ground motion records are selected correspondent to the site condition (second-class site) where the structure is located. The selected earthquakes are all far-field earthquakes, with the earthquake magnitude ranging from 5.5-8.0, PGA widely distributed, which also satisfy the site conditions demand.

(b) Considering uncertainties of structure. Taking the sensitivity of structure's seismic response to material parameter into consideration, the steel's yield strength f_y, the steel's elastic modulus E_s, the concrete's compressive strength f_c, the seismic isolation bearing's stiffness before yielding K_1, and the seismic isolation bearing's yielding shear force are selected as random variables. The random variables' distributions are shown in Table 1.

100 structure samples can be obtained through random sampling based on the LHS method, and each bridge sample matches one record of ground motion randomly. Each ground motion record includes deformation values of isolator bearings under 30 PGAs ranging from 0.02g to 1.0g uniformly.

Definition of damage states

Displacement ductility is used as piers' demand parameters, while a bearing's displacement based on the relative shear strain is isolation bearings' demand parameters. According to Liu [6] and Zhang [7], the definition of damage states is shown in Table 1.

TABLE 1SUMMARY OF DAMAGE INDEXES AND CORRESPONDING DAMAGE STATES FOR PIER COLUMNS AND BEARINGS

Bridge component	Basically intact	Slight	Moderate	Extensive	Collapse
1# pier column	$\mu_d \le 1$	$\mu_d > 1$	$\mu_d > 1.436$	$\mu_d > 2.302$	$\mu_d > 5.302$
2# pier column	$\mu_d \le 1$	$\mu_d > 1$	$\mu_d > 1.439$	$\mu_d > 2.361$	$\mu_d > 5.361$
isolation bearing[δ/mm]	$\delta \le 75$	$\delta > 75$	$\delta > 112.5$	$\delta > 150$	$\delta > 187.5$

RBFNN-based seismic fragility analysis

After the sample points (training samples and test samples, 5000 samples in longitudinal or lateral direction) are obtained, the building, training and test of RBFNN can be achieved using newrb function in matlab. Take 1# isolator bearing's deformation with No.1 bridge sample under No.54 ground motion as an example. Thirty deformation values are used as training samples under each PGA varying from 0.02g to 1g with the tolerance 0.04g. After RBFNN model is trained, the

deformation under these 20 PGAs (0.04g to 0.98g, tolerance 0.04g) can be predicted, thus the rest 50 PGAs (0.01g to 0.99g) can be predicted further. The data under 20 PGAs (0.04g to 0.98g) are used as the test samples, and the errors of training samples and test samples can be seen in Table3 and Table 4. This paper assumes that the pier's probability of failure is 0, so the seismic fragility of pier is not considered.

TABLE 2 1# ISOLATOR BEARING DEFORMATIONS AND RBFNN TRAINING RESULTS

Sample number	PGA [g]	Real value [m]	Predicted value [m]	Relative error [%]	Sample number	PGA [g]	Real value [m]	Predicted value [m]	Relative error [%]
1	0.02	0.005	0.005	-2.00	16	0.52	0.1124	0.1123	0.00
2	0.06	0.0107	0.0106	0.00	17	0.56	0.122	0.1219	-0.08
3	0.1	0.0165	0.0166	-1.06	18	0.6	0.132	0.1319	-0.04
4	0.12	0.0217	0.0221	0.61	19	0.62	0.1422	0.1421	0.11
5	0.16	0.0282	0.0273	0.44	20	0.66	0.1526	0.1525	0.00
…	…	…	…	…	…	…			
15	0.5	0.1031	0.103	0.00	30	1	0.2593	0.2593	0.02

Relative error = (predicted value-real value) / real value×100%.

TABLE 3 DEFORMATION OF 1# ISOLATION BEARING DEFORMATIONS AND RBFNN TESTING RESULTS

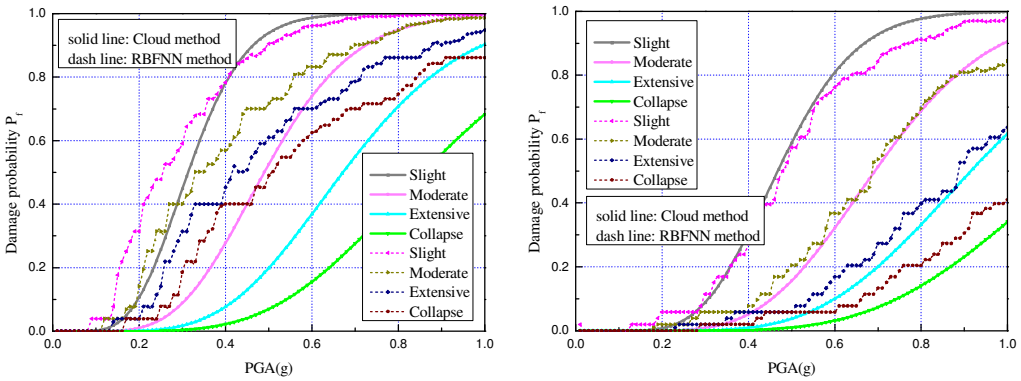
Sample number	PGA [g]	Real value [m]	Predicted value [m]	Relative error [%]	Sample number	PGA [g]	Real value [m]	Predicted value [m]	Relative error [%]
1	0.04	0.0107	0.0099	-7.48	11	0.54	0.227	0.2268	-0.09
2	0.08	0.0217	0.0226	4.15	12	0.58	0.2485	0.2484	-0.04
3	0.14	0.0375	0.039	4.00	13	0.64	0.2808	0.2808	0.00
4	0.18	0.0529	0.0527	-0.38	14	0.68	0.3025	0.3024	-0.03
5	0.24	0.077	0.077	0.00	15	0.74	0.3349	0.3348	-0.03
…	…	…	…	…	…	…			
10	0.48	0.1948	0.1949	0.05	20	0.98	0.4639	0.4634	-0.11

Relative error= (predicted value-real value) / real value×100%.

It can be seen from Table 3 and Table 4 that the maximum absolute value of training samples' relative error is 2%,and the others are also quite small. The maximum absolute value of test samples' relative error is 7.48%, and its maximum value is under the PGA of 0.04g because RBFNN tends to have more errors at the edge (a possible sollution is to select more sample points at the edg), while the absolute value of other test samples' relative error is below 5%. It proves that RBFNN has a good prediction ability. The mean square error of the trained model is 4.35753e-005.

In accordance with the Freqency method [8], the sample points obtained by RBFNN can be directly used to make statistical analysis. The limit state function of the structure can be defined as follows: (a) slight damage: Z=D-0.075; (b) moderate damage: Z=D-0.1125; (c) extensive damage: Z=D-0.15; (d) collapse damage: Z=D-0.1875. D represents the deformation of the isolation bearing. After the training of RBFNN, totally 100 PGAs with 100 samples correspondent to each PGA can be obtained. According to the Frequency method, the sample number N_f of each damage state under each PGA can be counted, and then N_f is divided by the total sample number N_t, hence the

probability of failure corresponding to its damage state can be derived. In this paper, the value of N_t is 100. Based on the results of the matlab calculation, the comparison of seismic fragility curves by the SVM and Cloud method can be seen in Fig.3



(a) In the longitudinal direction (b) In the lateral direction

Fig.3 Fragility curves of bridge system

Conclusion

This paper conducts the seismic fragility analysis of the RC continuous girder bridge based on RBFNN, LHS and IDA method with the thinking of Frequency method. The comparison results of RBFNN and the Cloud method can draw the conclusions as follows.

(a) Compared to the proposed method, the Cloud method has smaller results in the longitudinal direction, and so is it with the situation in the lateral direction except for the results of slight damage. So the seismic fragility analysis of Cloud method is comparatively small.

(b) RBFNN-based seismic fragility analysis method for RC continuous girder bridges can efficiently save some computational work and the results are reliable.

Acknowledgements

The financial support from the National Natural Science Foundation of China (Project 51278213) is greatly acknowledged. The authors appreciate the valuable comments from the anonymous reviewers.

References

[1]. Feng Qinghai, Yuan Wancheng. Comparative study on BP neural network and RBF neural network in performance evaluation of seismic resistance for pier columns. *Structural Engineers*, 2007, 23(5)

[2]. Bi Weihua, Tan Xiaohui, Hou Xiaoliang, WangWei. Reliability analysis of slope based on RBF neural network. *Chinese Journal of Underground Space and Engineering*, 2010, 6(2): 423-428

[3]. Feng Qinghai.Safety evaluation for the concrete filled steel tube arch bridge on RBF neural network. *Wuhan University of Technology*, 2005.

[4]. Bi Weihua. Research on the method of intelligent response surface reliability analysis of slope stability. *Hefei University of Technology*, 2010.

[5]. Xiao Hong Long, Bei Lei Chen, Jian Jun Li. SVM based seismic fragility analysis for RC isolated continuous girder bridge. *Advanced Materials Research*,2013,800:229-235

[6]. H·Hwang, Liu Jingbo. Seismic fragility analysis of reinforced concrete bridges. *China Civil Engineering Journal*, 2004: 37(6).

[7]. Jian Zhang, Yili Huo. Evaluating effectiveness and optimum design of isolation devices for highway bridges using the fragility function method. *Engineering Structures*, 2009, 31: 1648-1660

[8]. Liu Jingbo, Liu Yangbing, Yan Qiushi, Han Qiang. Performance-based seismic fragility analysis of CFST frame structures. *Engineering Structures*, 2010, 43(2) :39-4

Advanced Materials Research Vol. 936 (2014) pp 1479-1484
© (2014) Trans Tech Publications, Switzerland
doi:10.4028/www.scientific.net/AMR.936.1479

Robust Design of Structures with Uncertain Parameters and Frequency Constraints Using Non-probabilistic Methods

Chen Jiyun[1, a], Luo Yan[2, b], Liu Donghuan[3, c]

[1]Patent Examination Cooperation Center of the Patent Office, SIPO, Beijing 100088, P. R. China

[2]AVIC General Aircraft Research Institute, Zhuhai 519040, P. R. China

[3] Department of Applied Mechanics, University of Science and Technology Beijing, Beijing 100083, P. R. China

[a]chenjiyun@sipo.gov.cn, [b]emc201102@163.com, [c]liudh@ustb.edu.cn

Keywords: Optimization design; robust design; uncertain parameters; frequency constraint; Taylor's series

Abstract. The structural physical properties are often uncertain due to manufacture errors, measurement errors and other factors. Consequently, the vibration frequencies and corresponding eigenvectors are also uncertain. Robust design selects suitable design variables so that structural performance is insensitive to the various causes of variation without eliminating possible variations of variables. In practice robust design methods can be classified into probabilistic methods and non-probabilistic methods respectively. A new non-probabilistic robust design method based on the set theoretical convex method is presented in the present paper. The method not only inherits the advantages of existing non-stochastic methods, but also conquers the disadvantages of these methods.

Introduction

Modal analysis of structures plays an important role in structure design. However, due to the manufacturing errors, measurement errors and other factors, structural geometric properties and mechanical properties are usually uncertain. As a result, structural vibration frequency, i.e. eigenvalue, and corresponding eigenvector are also uncertain.

The structural dynamic optimization problems have been gradually focused on since the 1970s. Zarghamee [1], Lin [2], Wang [3] and Grandhi [4] conducted their research on the structural optimization design with constraint conditions having fundamental frequency or frequency restricted area. However, due to the presence of uncertain factors, classical optimization method cannot solve structural design problems effectively. Researchers propose some probabilistic optimization design methods on the basis of probability statistics. Rao [5] discussed probabilistic optimization of design parameters for a mechanical system under random vibration circumstances. Chen et al. [6] chose the mean values and standard derivations of stochastic design parameters as design variables, and converted the probabilistic optimization problem to certain optimization problem using probabilistic approaches, and solved the optimization design problem of MDOF linear torsion vibration system having uncertain parameters. Zang et al. [7] solved a two-DOF vibration damper design problem using the robust property of object functions in a review concerning the robust optimization, and decreased the vibration amplitude of the damper on condition that external excitation frequency and spring stiffness are uncertain.

In this paper, a non-probabilistic robust design method using both first-order and second-order Taylor's series to evaluate the intervals of eigenvalues and eigenvectors is presented on the basis of the parameter perturbation method and interval mathematics. Friswell's method [8] will be utilized to calculate the first-order and the second-order derivatives of eigenvalues and eigenvectors. A spatial 4-bar truss structure is optimized when material modulus and density are uncertain. Comparison among the non-probabilistic and probabilistic methods and the conventional optimization method is performed. Although the weight of the structure obtained from the non-probabilistic method is

heavier than the results generated by the probabilistic method and conventional method, the reliability and robustness of structures have been improved obviously.

Problem Statement

Generally undamped vibration analysis leads to an eigenproblem of the type

$$\boldsymbol{K}\boldsymbol{u} = \lambda \boldsymbol{M}\boldsymbol{u} . \tag{1}$$

where $\boldsymbol{K}$ and $\boldsymbol{M}$ are n-dimensional stiffness matrix and mass matrix respectively; λ is the eigenvalue which is the square of the frequency ω of free vibration, i.e. $\lambda = \omega^2$, and $\boldsymbol{u}$ is the corresponding n-dimensional eigenvector or the mode shape. The eigenvector is often normalized with the mass matrix and stiffness matrix such that

$$\boldsymbol{u}^T \boldsymbol{M}\boldsymbol{u} = 1 \ , \ \boldsymbol{u}^T \boldsymbol{K}\boldsymbol{u} = \lambda . \tag{2}$$

When structural parameters such as physical properties and geometric variables are considered, stiffness matrix $\boldsymbol{K}$, mass matrix $\boldsymbol{M}$, eigenvector $\boldsymbol{u}$ and eigenvalue λ are functions of the structural parameter vector $\boldsymbol{b}$, that is

$$\boldsymbol{K}(\boldsymbol{b})\boldsymbol{u}_i(\boldsymbol{b}) = \lambda_i(\boldsymbol{b})\boldsymbol{M}(\boldsymbol{b})\boldsymbol{u}_i(\boldsymbol{b}) . \tag{3}$$

Differentiating the ith-order eigenvalue in Eq. 3 with respect to the structural parameter b_k, and then expanding it we have

$$(\boldsymbol{K} - \lambda_i \boldsymbol{M})\frac{\partial \boldsymbol{u}_i}{\partial b_k} + \left(\frac{\partial \boldsymbol{K}}{\partial b_k} - \lambda_i \frac{\partial \boldsymbol{M}}{\partial b_k}\right)\boldsymbol{u}_i - \frac{\partial \lambda_i}{\partial b_k}\boldsymbol{M}\boldsymbol{u}_i = 0 . \tag{4}$$

Premultiplying Eq. 4 by $\boldsymbol{u}_i^T$, rearranging and using mass normalization of the ith eigenvector give the first-order derivative of the ith eigenvalue as

$$\frac{\partial \lambda_i}{\partial b_k} = \boldsymbol{u}_i^T \left(\frac{\partial \boldsymbol{K}}{\partial b_k} - \lambda_i \frac{\partial \boldsymbol{M}}{\partial b_k}\right)\boldsymbol{u}_i . \tag{5}$$

In order to calculate the first-order derivatives of eigenvectors, we suppose

$$\boldsymbol{G}_i = \boldsymbol{K} - \lambda_i \boldsymbol{M} \quad , \quad \boldsymbol{p}_{ik} = \frac{\partial \lambda_i}{\partial b_k}\boldsymbol{M}\boldsymbol{u}_i - \left(\frac{\partial \boldsymbol{K}}{\partial b_k} - \lambda_i \frac{\partial \boldsymbol{M}}{\partial b_k}\right)\boldsymbol{u}_i . \tag{6}$$

Thus, from Eq. 4, by making some arrangements, we have

$$\boldsymbol{G}_i \frac{\partial \boldsymbol{u}_i}{\partial b_k} = \boldsymbol{p}_{ik} . \tag{7}$$

Obviously, the first-order derivatives of eigenvectors cannot directly be calculated from Eq. 7 since $\boldsymbol{G}_i = \boldsymbol{K} - \lambda_i \boldsymbol{M}$ is singular with rank n-1. To overcome the difficulty, Nelson [9] proposed that the derivatives be written in the following form

$$\frac{\partial \boldsymbol{u}_i}{\partial b_k} = \sum_{\substack{j=1 \\ j \neq i}}^{n} c_{jk}\boldsymbol{u}_j + c_{ik}\boldsymbol{u}_i = \boldsymbol{v}_{ik} + c_{ik}\boldsymbol{u}_i . \tag{8}$$

where $\boldsymbol{v}_{ik}$ and c_{ik} are vector and scalar respectively. Thus, in terms of vector $\boldsymbol{v}_{ik}$, Eq. 7 becomes

$$\boldsymbol{G}_i \boldsymbol{v}_{ik} = \boldsymbol{p}_{ik} . \tag{9}$$

where vector $\boldsymbol{v}_{ik}$ is not unique. If all the eigenvectors are included in the sum, Eq. 8 is exact. For most problems it is not practical to calculate all the eigenvectors, so that only a few of the eigenvectors associated with the lowest eigenvalues are included. To produce a unique vector $\boldsymbol{v}_{ik}$, Nelson proposed that *m*th element of $\boldsymbol{v}_{ik}$, which corresponds to the element of highest magnitude in the eigenvector $\boldsymbol{u}_i$, be set to zero. The remaining *n*-1 elements can be obtained from Eqs. 7 and 8. We can solve the following equivalent problem to retain the sparse nature of the problem

$$\begin{pmatrix} (\boldsymbol{G}_i)_{11} & 0 & (\boldsymbol{G}_i)_{13} \\ 0 & 1 & 0 \\ (\boldsymbol{G}_i)_{31} & 0 & (\boldsymbol{G}_i)_{33} \end{pmatrix} v_{ik} = \begin{pmatrix} (\boldsymbol{p}_{ik})_1 \\ 0 \\ (\boldsymbol{p}_{ik})_3 \end{pmatrix}. \tag{10}$$

in which the *m*th row and column of the matrix have been replaced by the corresponding row and column from the identity matrix and the *m*th component of the vector $\boldsymbol{p}_{ik}$ has been set to zero. This will produce the zero required in the *m*th component of and also yield a full-rank matrix in Eq. 10.

Once $\boldsymbol{v}_{ik}$ has uniquely been obtained from Eq. 10, the scalar c_{ik} is found by using the derivative of the mass normalization condition in Eq. 2. Differentiating the *i*th-order eigenvector in Eq. 2 with respect to the structural parameter b_k, gives

$$\boldsymbol{u}_i^T \frac{\partial \boldsymbol{M}}{\partial b_k} \boldsymbol{u}_i + 2\boldsymbol{u}_i^T \boldsymbol{M} \frac{\partial \boldsymbol{u}_i}{\partial b_k} = 0. \tag{11}$$

Since all the terms are scalar. Substituting the expression for the eigenvector derivative Eq. 6 into Eq. 12 and using mass normalization condition Eq. 2 provide the solution for c_{ik} as

$$c_{ik} = -\boldsymbol{u}_i^T \boldsymbol{M} \boldsymbol{v}_{ik} - \frac{1}{2} \boldsymbol{u}_i^T \frac{\partial \boldsymbol{M}}{\partial b_k} \boldsymbol{u}_i. \tag{12}$$

Numerical Example

A 4-bar spatial truss structure shown in Fig. 2 is used to demonstrate the present method. The nominal values of structural parameters used are elastic modulus of material E=70 GPa and density ρ=2700 kg/m^3. It is assumed that elastic modulus E and diameter ρ involving perturbations in manufacturing process are uncertain-but-bounded parameters. The variations of each parameter are ΔE=10 MPa and $\Delta\rho$=27 kg/m^3, which can be rewritten as E^I=[E^0- ΔE, E^0+ ΔE] and ρ^I=[ρ^0 - $\Delta\rho$, $\rho^0 + \Delta\rho$] using interval analysis [11].

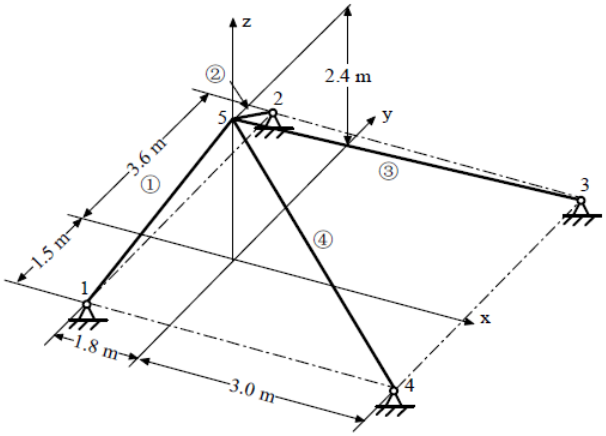


Fig. 2 4-bar spatial truss structure

Assume the lower and upper bounds of the bar cross-sectional area are 6.45E-5 m^2 and 6.45E-3 m^2 respectively, the structural frequency restricted area [$\underline{\omega}$, $\overline{\omega}$]=[110, 180]Hz. According to the approach for determining the concerning frequency mentioned in previous section, the first-order and second-order frequency of the structure are concerning frequencies, i.e. i=1, j=2. The equation of probabilistic and non-probabilistic robust design are given in Eq. 13 and Eq. 14 respectively.

$$\min \quad w \equiv \rho \sum_{i=1}^{4} L_i A_i; \ \text{s.t.} \quad \mu_{g_j} + z_{\alpha_j} \sigma_{g_j} \le 0 \ \ (j = 1,2); \quad A_i^L \le A_i \le A_i^U \ \ (i = 1,2,3,4). \tag{13}$$

where $\mu_{g_1} = \omega_1^2\left(\boldsymbol{A}^0\right) - \underline{\omega}^2$, $\mu_{g_2} = -\omega_2^2\left(\boldsymbol{A}^0\right) + \overline{\omega}^2$, $\sigma_{g_j} = \sqrt{\left(\frac{\partial \omega_j^2}{\partial E}\right)^2 \sigma_E^2 + \left(\frac{\partial \omega_j^2}{\partial \rho}\right)^2 \sigma_\rho^2}$, ($j$=1,2).

$$\begin{aligned} &\min \ w \equiv \rho \sum_{i=1}^{4} L_i A_i \\ &\text{s.t.} \quad g_1 = \omega_1^2\left(\boldsymbol{A}\right) - \underline{\omega}^2 + \Delta g_1 \le 0; \ g_2 = -\omega_2^2\left(\boldsymbol{A}\right) + \overline{\omega}^2 + \Delta g_2 \le 0; \ A_i^L \le A_i \le A_i^U \quad (i = 1,2,3,4) \end{aligned} \tag{14}$$

where $\Delta g_j = \sqrt{2}\sqrt{\left(\frac{\partial \omega_j^2}{\partial E}\right)^2 \left(\Delta E\right)^2 + \left(\frac{\partial \omega_j^2}{\partial \rho}\right)^2 \left(\Delta \rho\right)^2}$ (j=1,2).

Numerical Results for the structure using optimization design methods mentioned before show that, when the elastic modulus and density of material varies for 0.0143% and 1% respectively, the structural weight generated by non-probabilistic robust optimization is heavier by 214.5% than that obtained by traditional optimization method，while the results of probabilistic optimization with reliability 97.5％ and 99.87% are heavier than the result of traditional optimization method by 115.6% and 166.2%. The structural fundamental frequency derived from non-probabilistic method is smaller than that derived from the traditional method by 5.46%. The results of probabilistic method is smaller than the result of the traditional method by 3.71% and 4.62% respectively.

The variance amplitude of the structure weight using different optimization methods is large. Minor varieties of structural parameters, i.e. elastic modulus and density of the material lead to great difference among the structural design results. We can find the reason that, on one hand, the frequency constraints are overall constrains so that any change in structural parameters will affect the optimization result. On the other hand, the structural frequencies are highly non-linear function of the parameters. Define uncertain degree $\beta \in [0, 1]$ as the scale of the variation of uncertain parameters. The weight of the 4-bar truss with respect to β derived from the non-probabilistic and probabilistic methods are shown in Fig.3. The starting point of the curve is the structural weight derived from traditional method when β=0. When β is small, the increasing range of the structural weight is small, which means the result is less influenced by the varieties of the uncertain parameters. When β increased gradually, the increasing range of the structural weight becomes larger, and the trend is the most obvious in the non-probabilistic method. The same trend can be seen in the probabilistic method.

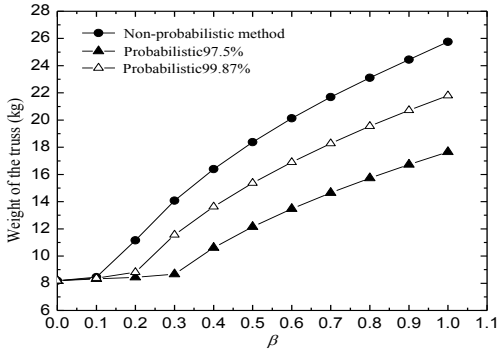


Fig.3 Weight of 4-bar truss with respect to β

Since both non-probabilistic and probabilistic methods need to calculate the first-order derivatives to the uncertain parameters, and the feasible region also depends on the derivatives, the relationship between the first-order derivatives to uncertain parameters and β needs to be considered. The first-order derivatives of the structural fundamental frequency with respect to β are shown in Fig. 4. While β is small such as $\beta \leqslant 0.1$, the value of the derivatives changes slowly, and the value changes

remarkably when β is getting larger. We can see that the value of the derivatives derived from the non-probabilistic method is smaller than that derived from the probabilistic method. The result means the fundamental frequency of non-probabilistic method is the least affected by uncertain parameters.

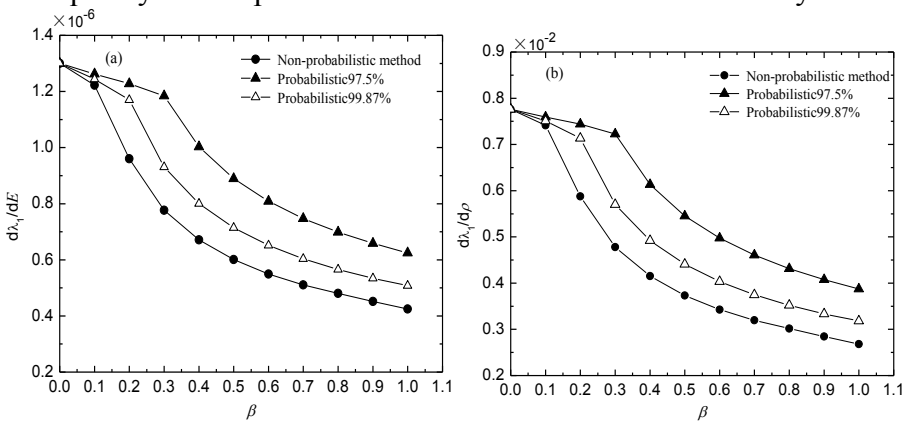


Fig.4 First-order derivatives of fundamental frequency to structural parameters with respect to β: (a) elastic modulus; (b) density

Conclusions

A non-probabilistic robust design method is presented in this paper. When uncertain structural parameters vary in a certain range, the vibration frequencies of the structure will have fluctuation around the nominal values. A numerical example of a spatial 4-bar truss structure with uncertain elastic modulus and density is utilized to demonstrate the method. Comparison among the non-probabilistic, probabilistic methods and the conventional optimization method is performed. Although the weight of the structure obtained from the non-probabilistic method is heavier than the results generated by the probabilistic method and conventional method, the reliability and robustness of structures have been improved obviously.

Acknowledgement

Project was supported by the Natural Science Foundation of China (No. 11302023) and the Fundamental Research Funds for the Central Universities (No. FRF-BR-13-003).

References

[1] M.S. Zarghamee, Optimum frequency of structures, AIAA J. 6 (1968) 749-750.

[2] J.H. Lin, Optimum design of structures with specified non-frequency-band, J. Dalian Univ. Techno. 20 (1981) 27-36.

[3] S.H. Wang, Structural optimization with frequency constraints, Acta Mech. Solida Sin. 2 (1982) 165-175.

[4] R. Grandhi, Structural optimization with frequency constraints-a review, AIAA J. 31 (1993) 2296-2303.

[5] S.S. Rao, Reliability based optimization under random vibration environment, Comput. Struct. 14 (1981) 345-355.

[6] S.H. Chen, D.T. Song and W.Z. Han, Stochastic optimization for vibration systems of mutil-degrees of freedom, Acta Mech. Sin. 26 (1994) 432-439.

[7] C. Zang, M.I. Friswell and J.E. Mottershead, A review of robust optimal design and its application in dynamics, Comput. Struct. 83 (2005) 315-326.

[8] M.I. Friswell, Calculation of second and higher order eigenvector derivatives, J. Guid Control Dyn. 17 (1994) 136-144.

[9] R.B. Nelson, Simplified calculation of eigenvector derivatives, AIAA J. 14 (1976) 1201-1205.
[10] L.X. Qian, Optimum Design of Engineering Structure, China WaterPower Press, Beijing, 1983.
[11] R.E. Moore, Methods and Applications of Interval Analysis, Prentice-Hall, London, 1979.

Advanced Materials Research Vol. 936 (2014) pp 1485-1489
© (2014) Trans Tech Publications, Switzerland
doi:10.4028/www.scientific.net/AMR.936.1485

Research based on scanning electron microscopy to determine original water-cement ratio of hardened concrete

Li Yue[1,2.a], Tong Huan[1,2.b] ,Yang Jinbo[3.c]andDong Wanguo[1,2.d]

[1]The Key Laboratory of Urban Security and Disaster Engineering, MOE, Beijing University of Technology ,Beijing, 100124,China

[2]Beijing Key Lab of Earthquake Engineering and Structural Retrofit, Beijing University of Technology, Beijing, 100124, China

[3]Beijing Shunyi Commission of Housing and Urban-Rural Development, Beijing, 101300, China

[a]liyue@bjut.edu.cn,[b]tonghuan21121@aliyun.com,[c]jinboyang@bjut.edu.cn,[d]471174900@qq.com

Keywords: w/c, BEI, capillary porosity, age, function fitting

Abstract. In order to detect the influence of age on the experiment that use scanning electron microscopy (SEM) to determinate the original water-cement ratio (w/c) of hardened concrete, a series of concrete mixes are tested. Experimental results show that early ages do have an effect on the water-cement ratio of hardened concrete that determined from scanning electron microscopy, this effect will decrease while age increases. The relationship between capillary porosity, w/c and age is analyzed and a calculation equation is given.

Introduction

Water-cement ratio is the primary factor of concrete strength, a direct impact on the properties of concrete and the economic effect, whether the w/c is too large or too small, it will be an adverse effect on the performance of concrete [1]. Internal pore will be formed in the concrete during fresh concrete in the process of hardening [2], different water-cement ratio of hardened concrete result in different final internal porosity, literature [3] pointed out that the porosity of concrete is mainly decided by w/c. The greater the w/c, the greater the capillary porosity of concrete. Even if the w/c of hardened concrete is the same, its internal capillary porosity is not the same in different age, with the growth of the age，its capillary porosity is also increasing, and in different age stages of growth rate is not the same, This brought a great disturbance on the results of scanning electron microscopy test, therefore it is necessary to study the age influence on the results from scanning electron microscopy to determine the original w/c hardened concrete.

Recently, the main theoretical method that determines the water-cement ratio of hardened concrete is: Firstly, sanding the small cubic concrete section , then inset the cubic concrete into epoxyresin with Vacuum Mosaic instrument[4], capillary porosity can be completely filled with epoxy resin, after drying and polishing, pore in the scanning electron microscopy (SEM) to carry on the back scattering model (BEI) [5] ,the shown in the photo is black. However, the other solid phase is bright color, through the image analysis procedure，the capillary porosity of concrete can be quantitatively calculated. Then try to establish a function relationship and the function curve between w/c and capillary porosity. However, in the actual situation, even if the same w/c of hardened concrete, its internal capillary porosity is not the same along with the age which is not at

the same time, it brings great influence on the accuracy of the test results. Literature [5] does not mention the age factor upon the result of the experiment, becauseof the difference on the domestic and foreign cement manufacturing
technique, chemical species, content and quality, the results of same experiment at home and abroad may also have big difference.

This study is based on different age of hardened concrete experiment research to determine the age influence on scanning electron microscopy that determines the original w/c of hardening concrete and try to estimate a function relationship among capillary porosity, w/c and date . This article has carried on the experiment, provides the theoretical methods and technical support for such research.

Materials

Use standard sand and artificial stone（the particle size of 10 to 40 mm），which is the raw materials of hardened concrete ，use benchmark cement as the cement of concrete ，The chemical composition is shown in table 1:

Table 1Chemical composition of benchmark cement

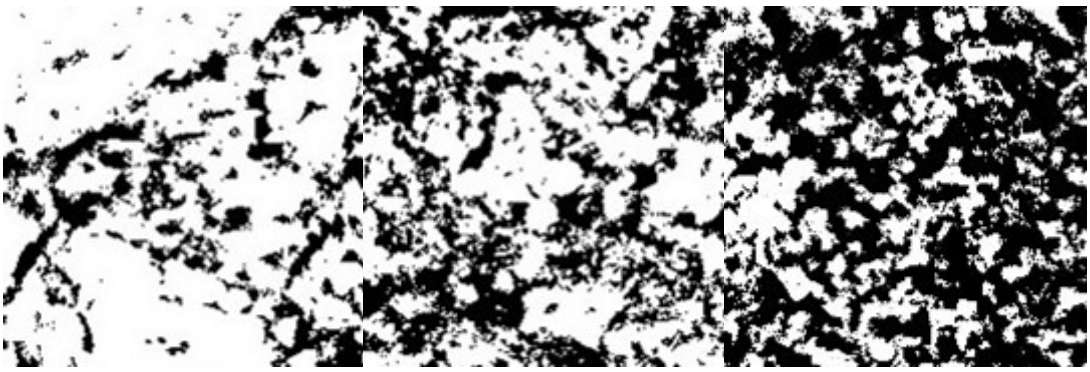
SiO_2	Al_2O_3	Fe_2O_3	CaO	MgO	SO_3
21.96	4.73	3.68	65.3	2.59	0.3
NaO_{eq}	f-CaO	C_3S	C_2S	C_3A	C_4AF
0.56	0.9	57.4	20.3	6.32	11.19

Experimental Methods

Known as the preparation of w/c of hardened concrete :0.3,0.35,0.4,0.45,0.5, removed 3 in its reach 3d, 7d, 28d and 90d of the age respectively, the hardened concrete is cut into a cube of side length which is not more than 1cm with concrete cutting machines, after sanding on concrete sections in small cubes resin saturated with resin inlay instrument , the pores may be completely filled with epoxy resin ,after drying and polishing, the capillary in the resin saturated backscattered SEM photograph mode are displayed as black ,while other solid phases are bright. By image analysis procedures, the capillary porosity of concrete can be quantitatively calculated. Next is to gain data about capillary porosity of different ages to get function fitting, Check whether can get more suitable function ,so as to test the effect of the age for scanning electron microscopy to determine the original w/c of the hardened concrete . If the influence exists，try to build a function relationship among porosity rate, w/c and date.

Results and Discussion

Figure 2 is the picture of hardened concrete section that obtained from the experiment scheme, the following w/c is 0.3, 0.4, 0.5, it can be seen that the greater water-cement ratio, the greater porosity of the section.



w/c=0.3 w/c=0.4 w/c=0.5

Fig2. Photos of hardened concrete section whose w/c are 0.3, 0.4 and 0.5

Figure 3 is about the images of the hardened concrete whose w/c is 0.4 in 3d, 7d, 28d and 90d.

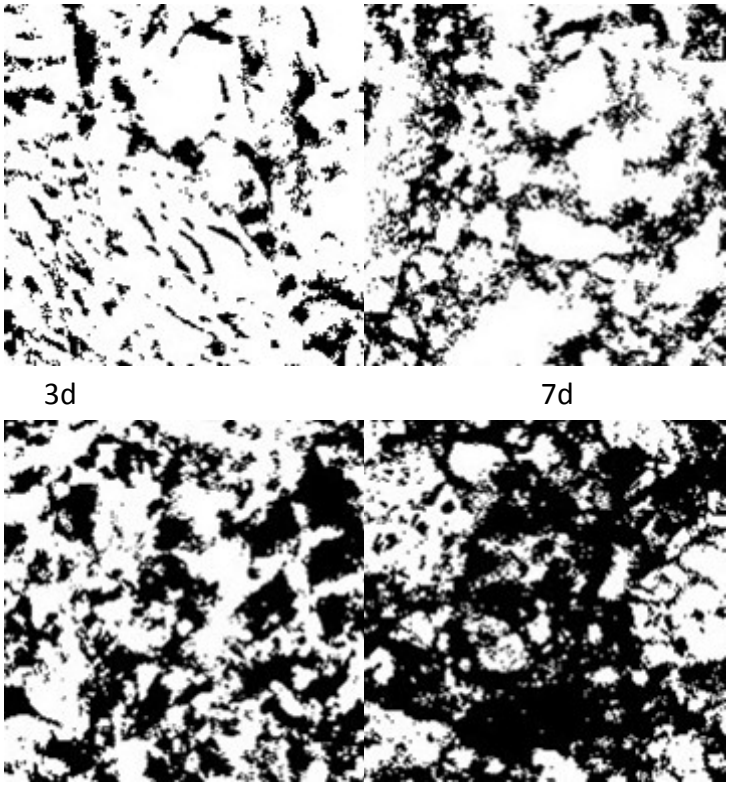


Fig3. Images of the hardened concrete whose w/c is 0.4 in 3d,7d,28d and 90d

Using the image pro plus 6.0 software to analyze the images, three groups of capillary porosity can be got ， the average is in table 2.

Table 2 Capillary porosity under different w/c and ages

age \ w/c	0.3	0.35	0.4	0.45	0.5
3d	27.7	33.6	33.9	38.6	43.5
7d	37.4	39.4	41.3	48.7	52.3
28d	39.2	44.6	49.8	50.1	57.3
90d	41.2	45.8	49.3	52.6	57.9

Take the average of three groups of data to make function fitting, the relationship between w/c of hardened concrete in different ages and the capillary porosity is shown in figure 4.

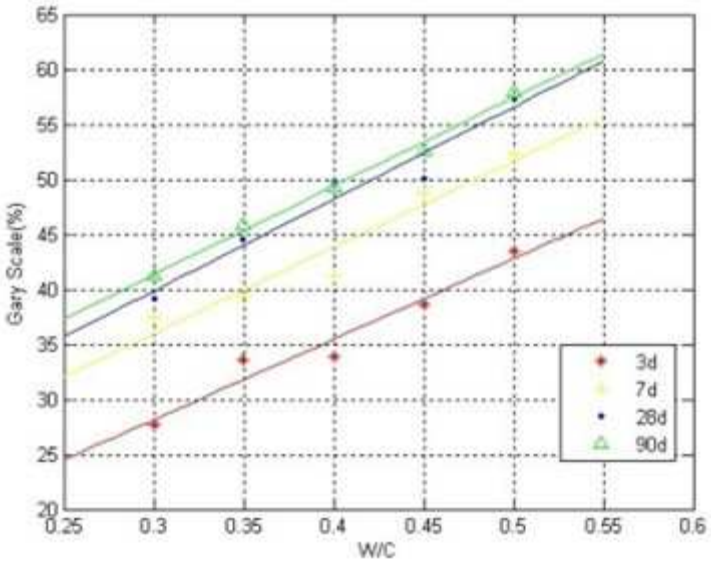


Fig 4 Relationship between w/c and the capillary porosity in different ages

Analytic functions corresponding to the four curves in Fig 4 are：

3d：y=73.200x +6.180 (1)

7d：y=78.200x+12.540 (2)

28d：y=83.400x+14.840 (3)

90d：y=80.400x+17.200 (4)

Formula (1)-(4)suggests that the age did affect on the result from scanning electron microscopy that determines the original w/c of hardened concrete. Using the mat lab software to establish the function relationship between the capillary porosity, w/c and the age , their function relationship is as formula (5)：

$$y=75.6062x_1-328.8918/x_2^3+17.3131 \quad (5)$$

Where y is the capillary porosity, x1 is w/c, x2 is the age of the concrete.

If the types of raw material of this experiment change , it may need to use this test method to simulation analysis again.

Conclusion

Known from the analysis of the above test, early ages do have an effect on the w/c ratio of hardened concrete that determined from scanning electron microscopy , with the increase of age, function fitting is better; with the increase of age ,the results of scanning electron microscopy that determines the w/c of hardened are higher accurate, and relation among capillary porosity ,w/c ratio and ages can be synthesized to a function form, so it is suggested to use a long age sample in the engineering practice .

Acknowledgements

This work was financially supported by the National Natural Science Foundation of China（No. 51208013; 51278014）.

References

[1] Hong Jiang，YihuChen，Effects of too large and too small water cement ratio on concrete performance，China Water Transport，7（10）：132-133. (in Chinese))

[2] ZhongjunBi ,Zhenhui Yang , Weijie Chen Yue Cao ,YongqingJiang,MingqingLi.Concrete pores,Concrete,2008,226(8):43-44. (in Chinese))

[3] Wei Liu ，FengXing，YoujunXie， Effect of water to cement ratio and mineral admixture on the porosity of concrete，Low temperature architecture technology，2006,1:9-11.

[4] PeiminWang， ShuxiaFeng， XianpingLiu.JOURNAL OF THE CHINESE CERAMIC SOCIETY,2013,41(2):211-217.(in Chinese))

[5] SAHU S, BADGER S, THAULOW N, et al. Determination of water/cement ratio of hardened concrete by scanning electron microscopy. CemConcr Compos, 2004,(26):987-992.

Advanced Materials Research Vol. 936 (2014) pp 1490-1495
© (2014) Trans Tech Publications, Switzerland
doi:10.4028/www.scientific.net/AMR.936.1490

Numerical Simulation for the Damping Effect of Empty Holes on Blasting Vibration

BIAN Kaifang[1, a], LI Haibo[1,b] and LIU Yaqun[1,c]

[1] Institute of Rock and Soil Mechanics, The Chinese Academy of Sciences, Wuhan China

[a]junlintianxiabian@163.com, [b]hbli@whrsm.ac.cn, [c]yqliu@whrsm.ac.cn

Keywords: Empty holes; Damping effect; Blasting vibration; Influencing factors

Abstract. The two-dimensional discrete element program (UDEC) is applied to simulate the damping effect of empty holes on blasting vibration. The results show that the peak particle velocity of monitoring point on the condition that there are empty holes between monitoring point and blast hole is less than that without empty holes. The factors which have impact on cushioning effect, such as the depth of empty hole, the diameter of empty hole, the distance between empty hole and blast hole and the rows of empty hole, are investigated numerically. It is found that the depth of empty hole has dominated influence on the damping effect and the damping effect on blasting vibration strengthens with the increment of the depth. The diameter of empty hole and the distance between empty hole and blast hole have slight influence on the damping effect. The increment of rows of empty hole can enhance the damping effect on blasting vibration as well. The results in the present study may provide a reference for the application of empty hole to reduce the blasting vibration in practical engineering.

Introduction

In foundation and slope blasting excavation, the stress waves induced by explosion can have a significant influence upon the engineering safety and even destroy the constructions. Measures should be taken to reduce the stress waves to protect the constructions and keep the engineering safe. Presplitting blasting can be used to reduce the damage on the reserved rock mass and improve the stability of slope in the excavation of rock slope[1]. In foundation excavation of a nuclear power station, the blasting vibration should be controlled strictly in order to ensure the safety of bedrock, buildings and structures around the blasting zone. The empty hole is adopted to reduce the blasting vibration[2]. The in-situ blasting tests reveal that shock absorption holes can reduce the blasting vibration and the peak particle velocity of monitoring points decreases obviously. The excavation of damping slots is an effective measure to reduce the blasting seismic effect. The damping effect of vibration-isolating ditches and influencing factors were researched by numerical simulation [3,4,5]. The length and depth of vibration-isolating slot have a significant influence upon the damping effect.

In this research, UDEC is employed to simulate the damping effect of empty holes on the blasting vibration[6,7]. By comparing the peak particle velocity of the same monitoring point on the condition that there are empty holes between monitoring point and blast hole with that without empty holes, it is revealed that the empty holes can reduce the blasting vibration obviously. The distance between empty hole and blast hole, the depth and diameter of empty hole are changed to study the influencing factors on vibration-isolating effect. The impact of rows of empty hole on vibration-isolating effect is investigated as well by comparison.

Numerical Model

The numerical model is shown in Fig.1. The air in the empty hole can connect with the atmosphere and the hole is shallow, so the effect of air on the blasting vibration is neglected in this study. Physico-mechanical parameters of rock material are shown in table 1.

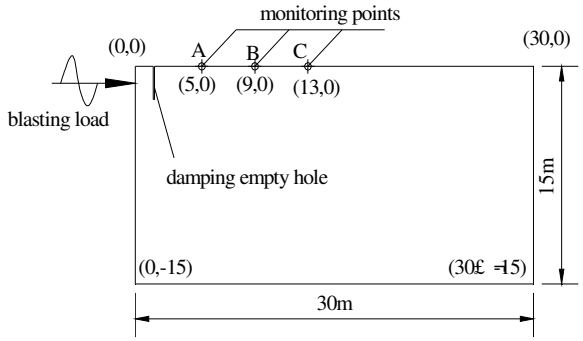


Fig.1 Numerical model

Table 1 Properties of rock material

Property	Value
Density[kg/m^3]	2606
Young's Modulus[GPa]	52.77
Poisson's Ratio	0.28
Cohesion[MPa]	26.83
Friction angle[°]	43.37

Two stages are involved in the UDEC modeling: (a) static modeling to determine the pre-existing stress in the rock mass before the explosion, and, (b) dynamic modeling to investigate the rock mass response due to the explosion [7]. Sine velocity waves are adopted to simulate the blasting load that the peak value is 5cm/s, the frequency is 30Hz, and the duration is 0.1s. The time history of velocity is translated to time history of stress to be the explosion input. To reduce the influence of the reflections of blasting vibration, viscous boundaries are employed.

The peak particle velocity (PPV) is the most appropriate motion parameter to correlate damage. It can be related directly to peak transient stress in the ground wave, and the second power of velocity is related to dynamic strain energy [8]. Three measurement points are placed at 5, 9 and 13m on the x-axis to record the peak particle velocity of the rock mass. A large number of numerical simulations are conducted by changing the model parameters and a lot of PPVs are obtained from the modeling.

Numerical Results

The Damping Effect of Empty Hole

As it is shown in Fig.2, the peak particle velocity of the same monitoring point on the condition that there are empty holes between monitoring point and blast hole decreases evidently when compared with that without empty holes. The horizontal peak particle velocities of monitoring point A, B, C without damping empty hole are 3.31cm/s,2.22cm/s,
1.53cm/s and they are only 1.99cm/s,1.47cm/s,1.02cm/s with damping empty hole, decreasing 39.9%,33.9%, 33.3%, respectively . The results show that the empty hole can have damping effect on the blasting vibration.

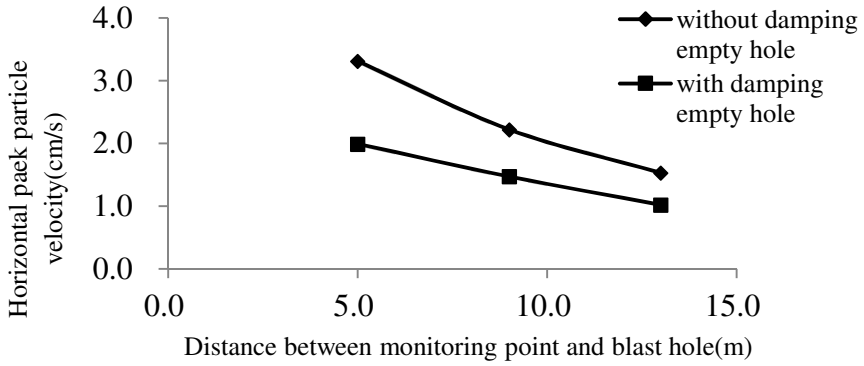


Fig.2 Comparison of horizontal peak particle velocity

The Influence of the Depth of Empty Hole on Damping Effect

Keeping the distance between empty hole and blast hole and the diameter of empty hole unchanged, the depth of empty hole is changed to study the influence of the depth on damping effect.

TABLE 2 PEAK PARTICLE VELOCITY AND DAMPING COEFFICIENT OF MONITORING POINT A WITH DIFFERENT DEPTH EMPTY HOLE

Depth of damping empty hole[m]	0.00	0.50	0.80	1.00	1.20	1.50	1.80	2.00	2.20	2.50	3.00
Horizontal peak particle velocity[cm/s]	3.31	2.76	2.37	1.99	1.61	1.13	0.74	0.56	0.42	0.34	0.33
Vertical peak particle velocity[cm/s]	4.24	4.20	4.07	3.35	2.17	1.14	0.35	0.37	0.38	0.35	0.35
Horizontal damping coefficient	/	0.17	0.28	0.40	0.51	0.66	0.78	0.83	0.87	0.90	0.90
Vertical damping coefficient	/	0.01	0.04	0.21	0.49	0.73	0.92	0.91	0.91	0.92	0.92

Remarks: The depth of blast hole is 2m.

Damping coefficient is defined as

$$\eta = \frac{v_1 - v_2}{v_1} \quad . \tag{1}$$

where v_1 is the peak particle velocity of monitoring point on the condition that there is no empty hole between blast hole and monitoring point, v_2 is the peak particle velocity of monitoring point on the condition that there is empty hole between blast hole and monitoring point.

The peak particle velocity and damping coefficient of monitoring point A with different depth empty hole are listed in table 2. When the depth of empty hole is less than 2.2m, it is shown in Fig.3 that the peak particle velocity decreases obviously with the increment of the depth of empty hole; the peak particle velocity almost keep constant with the increment of the depth of empty hole when it is more than 2.2m. It has the similar law as it is shown in Fig.4. The damping coefficient increases evidently with the increment of the depth of empty hole when it is less than 2.2m and nearly maintain unchanged when it is more than 2.2m. It is proposed that the reasonable depth of damping empty hole is 2.2m.

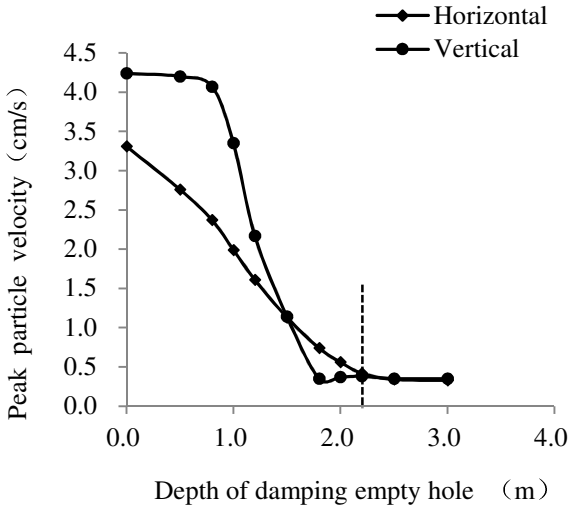


Fig.3 The relationship curves between peak particle velocity and depth of damping empty hole

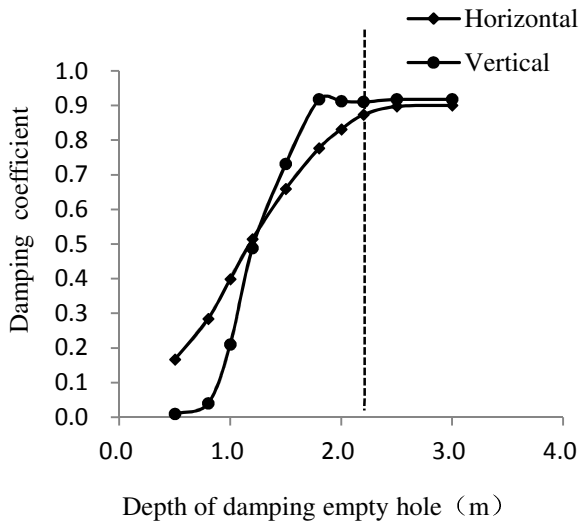


Fig.4 The relationship curves between damping coefficient and depth of damping empty hole

The Influence of the Diameter of Empty Hole on Damping Effect

Keeping the distance between empty hole and blast hole and the depth of empty hole constant, the diameter of empty hole is changed to study the influence of the diameter on damping effect. It is presented in Fig.5 that the horizontal damping coefficient almost keeps unchanged and the vertical damping coefficients fluctuate slightly with the increment of the diameter of empty hole.

The diameter of damping empty hole has slight impact on the damping effect.

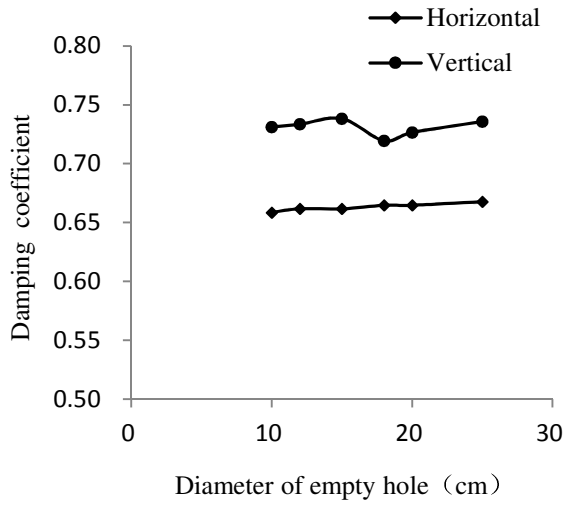


Fig.5 The relationship curves between the damping coefficient of monitoring point A and the diameter of empty hole

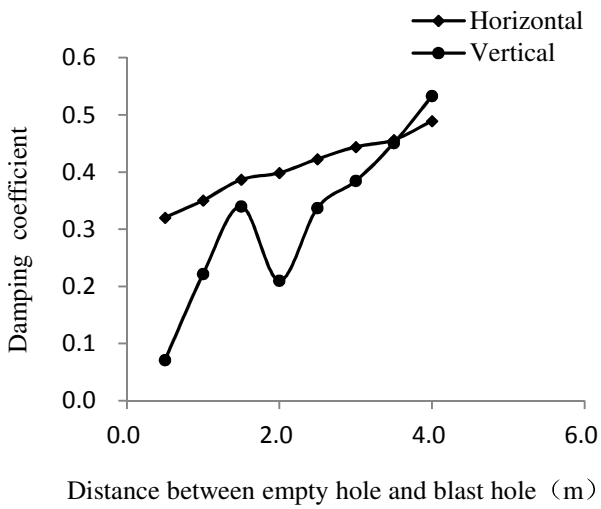


Fig.6 The relationship curves between the damping coefficient of monitoring point A and the distance between empty hole and blast hole

The Influence of the Distance between Empty Hole and Blast Hole on Damping Effect

Maintaining the depth and diameter of empty hole unchanged, the distance between empty hole and blast hole is changed to study the distance between empty hole and blast hole on damping effect.

The damping coefficient will increase with the increment of the distance between empty hole and blast hole on the whole as it is shown in Fig.6. The horizontal damping coefficient almost increases equably from 0.32 to 0.49, and the vertical damping coefficient increases inconsistently from 0.07 to 0.53 and fluctuates on the local scale.

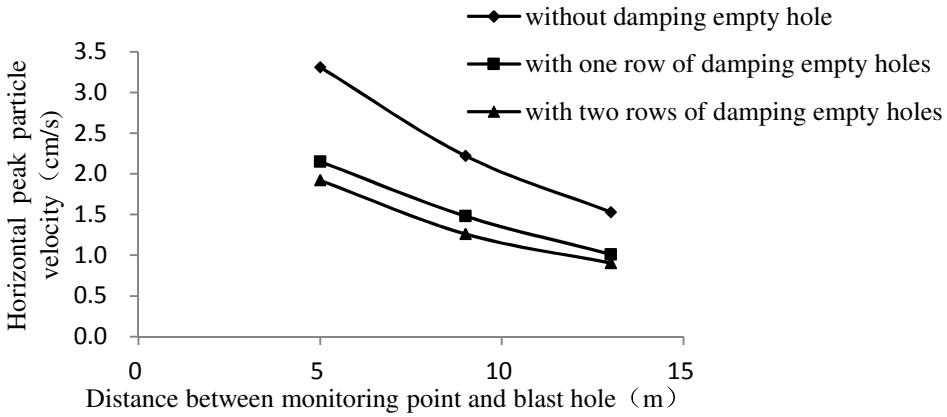


Fig.7 Horizontal peak particle velocity of monitoring point A, B, C with different rows of empty holes

The Influence of Rows of Empty Hole on Damping Effect

With the rows of empty holes increasing, the horizontal peak particle velocity decreases. As it is shown in Fig.7, the horizontal peak particle vibration velocity of monitoring point A is 3.31cm/s without damping empty hole and it is 2.15cm/s, 1.92cm/s with one row and two rows of damping empty hole, respectively. The peak particle velocity of monitoring point decreases with the increment of rows of empty hole, and the rate of decrease becomes slight gradually.

Summary

UDEC is employed to simulate the damping effect of empty holes on blasting vibration and the factors which have impact upon the damping effect are proposed. Some conclusions are reached as follows:

1. By comparing the peak particle velocity of the same monitoring point on the condition that there are empty holes between monitoring point and blast hole with that without empty holes, it is revealed that the empty holes can reduce the blasting vibration obviously. The empty holes can increase the propagation path and consume more energy of blasting waves, so the blasting vibration will decrease when passing through the empty holes.

2. The depth of empty hole has dominating influence upon the damping effect and the damping effect enhances with the increment of the depth of the empty hole. When the depth of empty hole is more than the depth of blast hole, the increment of damping coefficient is very slight. It is proposed that the depth of damping empty hole is 1.1～1.2 H, and H is the depth of blast hole.

3. The diameter of empty hole has slight influence on the damping effect and the damping coefficient almost maintain unchanged with the increment of the diameter of empty hole. The damping coefficient increases with the increment of the distance between empty hole and blast holes, and the increment of damping coefficient is much less than that caused by the increment of the depth of empty hole.

4. The increment of rows of empty hole strengthens the damping effect, and the rate of increasing becomes slight gradually. It is proposed that the rows of damping empty hole should be 2～3. Furthermore, the damping empty holes can be filled with vibration-absorptive material to have better damping effect in practical engineering.

References

[1] V.K.SINGH, D.P.SINGH, Controlled blasting in an open-pit mine for improved slope stability, Geotechnical and Geological Engineering. 13(1995) 51-57.

[2] HUANG Fuqiang, ZHANG Dayan, XIA Xiang, Blasting vibration control of foundation pit excavation in nuclear unit at a nuclear power plant, Soil Engineering and Foundation. 26(2012) 30-32. (in Chinese)

[3] LIANG Kaishui, CHEN Tianzhu, YI Changping, Numerical simulation for vibration-isolating effect of vibration-isolating slot, Blasting. 23(2006) 18-21. (in Chinese)

[4] GU Hongwei, ZHAO Yanming, LI Xiudi, Numerical simulation for vibration-isolating effect of two vibration-isolating slots, Blasting. 24(2007) 21-251. (in Chinese)

[5] WANG Chenlong, ZHANG Shiping, ZHANG Changsuo, Determination of damping ditch size in slope blasting excavation, Blasting. 30(2013) 50-53. (in Chinese)

[6] Itasca Consulting Group, Inc, UDEC (Universal Distinct Element Code) user's manual, Version 4.0, 2005.

[7] S.G. Chen, J.Zhao, Y.X. Zhou, UDEC modeling of a field explosion test, International Journal of Blasting and Fragmentation. 4(2000) 149–163.

[8] Brady, B.H.G, Dynamic behavior of rock, In: J.A. Hudson (ed.), Comprehensive Rock Engineering 1, 1993, pp. 611-624.

Advanced Materials Research Vol. 936 (2014) pp 1496-1501
© (2014) Trans Tech Publications, Switzerland
doi:10.4028/www.scientific.net/AMR.936.1496

Analysis on the Effect of External-wall Insulation on Energy Consumption of Residential Building in Lanzhou

Chune Li [1,a*], Gang Wang [2,b] and Yajun Wang [3,c]

[1]School of Civil Engineering, Lanzhou University of Technology, Lanzhou 730050, China

[2]PetroChina Lanzhou Petrochemical Company Ethylene Factory,Lanzhou,China

[3]School of Civil Engineering, Lanzhou University of Technology, Lanzhou 730050, China

[a]sophie_lce@163.com, [b]wanggang@petrochina.com.cn, [c]wyj79626@lut.cn

Keywords: DeST-h, energy consumption, economical insulation layer residential building

Abstract: Based on the comparison of external wall with different insulation thicknesses and without insulation, residential buildings energy consumption was simulated by using DeST-h in Lanzhou. The effects of external wall insulation on building energy consumption were analyzed. The result shows that the total annual load can be reduced to 42% ~ 72% with the insulation thicknesses vary from 10mm to 80mm. But With the increase of the thickness of the insulation layer, the amount of fluctuation of building load reduces gradually. The insulation layer is thicker the energy saving effect is more distinct and there is should be the thickness is the most economical thickness. So the economic insulation thickness is determined as 40mm by using a life-cycle cost analysis.

Introduction

Since Design standard for energy efficiency of residential buildings in severe cold and cold zones was promulgated and implemented, The 65% energy-saving design standards has been implemented for residential buildings in Lanzhou. This put forward higher requirements of thermal performance standards for residential building envelopes. Reasonable residential building must ensure that the room is not only comfortable but also is energy - efficient. Residential building energy conservation is an important part of building energy saving, energy consumption ratio of residential building has increased year by year

Factors affecting the energy consumption are the building shape coefficient, retaining structure, natural ventilation and natural lighting levels, and the effect of the enclosure structure on energy consumption is the influence of maximum. In order to analyze energy consumption of Exterior wall of residential buildings quantitatively in Lanzhou, the energy consumption simulation software DeST-h [1] was used to simulate heating and air conditioning load. Annual total energy consumption rate was showed by comparing the different thickness of thermal insulation layer of wall. The economic insulation thickness was determined by using a life-cycle cost analysis method.

Construction survey and Establishment of model building

Taking a residential building in Lanzhou city as the simulation object, the area of residential building is 2520 square meters, shape coefficient is 0.342, and comprehensive window wall ratio is 0.16, the building has six floors, it is 2.9 meters high, the top floor is 3 meters high. Building toward the southern and Northern, the building model of plane and DeST geometry model as shown in Fig. 1, Fig. 2, structure and heat transfer coefficient of each part of retaining structure is shown in Table 1. The main part of the external wall insulation thickness is 200 reinforced concrete wall, insulation material are made of extruded polystyrene board [2]

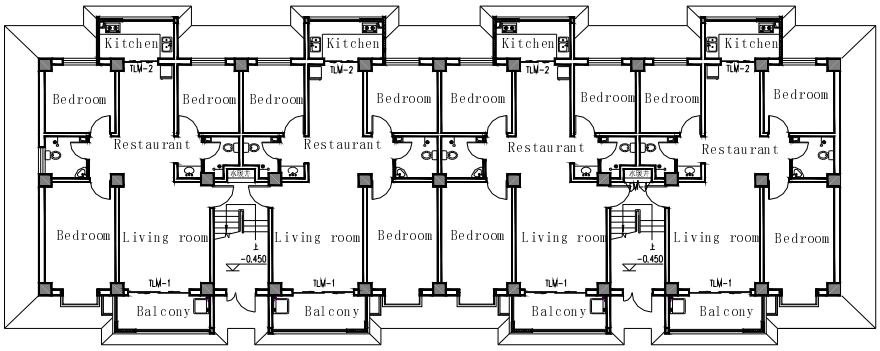


Fig. 1 Architecture model of plan

TABLE 1. THE THERMAL PHYSICAL PARAMETERS OF STRUCTURE

Category	Component	Heat transfer coefficient
Exterior wall	Cement mortar(20mm) +XPS(25mm)+ Cement mortar(20mm)+Reinforced concrete(200mm)	0.83
Inner wall	Cement mortar(20mm)＋Ceramist concrete(180mm)＋Cement mortar(20mm)	1.52
Roof	Cement mortar(20mm)＋XPS(55mm)+ Cement mortar(20mm)+Cement cinder(30mm)＋Reinforced concrete(150mm)＋Cement mortar(25mm)	0.34
Floor	Cement mortar(25mm)＋Reinforced concrete(80mm)＋Cement mortar(20mm)	3.05
Exterior window	Inert gas + Low-E coated hollow	2.0(SC＝0.56)

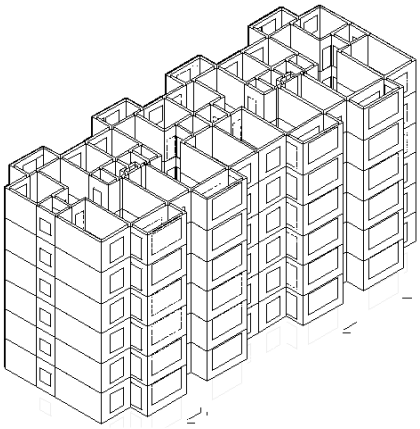


Fig. 2 DeST building model

Simulation results analysis

Calculation parameters of indoor was stetted according to Design standard for energy efficiency of residential buildings in severe cold and cold zones and Design code for heating ventilation and air conditioning of civil buildings . The meteorological data used in the simulation are come from typical meteorological year data issued by Technology Department of Tsinghai University and Meteorological Information Center Meteorological data of China Meteorological Administration. Lanzhou's 8760 hourly meteorological parameters were calculated by using DeST-h as shown in Fig. 3.

The room functions of residential building is simplified as the bedroom, living room. The bedroom, the living room is air-conditioned room. The empty room is not air-conditioned room, including the

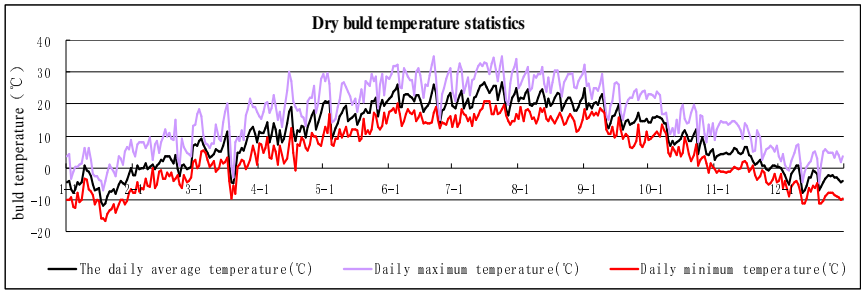


Fig. 3 The dry bulb temperature of every day in Lanzhou

bathroom, kitchen etc. The living room is able to hold a maximum of 3 people and the bedroom is able to hold a maximum of 2 people. Personnel heat divided into sensible heat and latent heat, the sensible heat is 61 Watt apiece and the latent heat is 73 Watt apiece. The maximum lighting heat is 5 Watt per square in the living room and 4 Watt in bedroom.

In order to facilitate comparison of Impact on building energy consumption in deferent thickness of external wall insulation layer, take the building without insulation as reference architecture. The annual Heating and air-conditioning energy consumption were simulated in deferent thickness of external wall insulation layer, from 10mm to 80mm, by using the DeST-h software. As well as the annual Heating and air-conditioning energy consumption was simulated in case of the building without insulation. The simulation results are shown in Table 3 and Fig. 4.

TABLE 3. THE ANNUAL TOTAL LOAD AND THE RELATIVE ENERGY SAVING RATIO

The thickness of the insulation layer/mm	Annual total load （kWh）			Relative energy saving ratio （%）	
	Heat load	Cooling load	Total load	Heat load	Cooling load
0	161458	11073	172529	0	0
10	85891	14060	99951	46.8	42.1
20	57707	17607	75314	64.2	56.3
30	43532	20246	63778	73.0	63.0
40	35011	22256	57267	78.3	66.8
50	29353	23872	53225	81.8	69.1
60	25515	25222	50737	84.1	70.6
70	22717	26307	49024	85.9	71.6
80	20641	27171	47812	87.2	72.2

From Table 3 and Fig. 4, we can see that heat load had decreased obviously when the exterior wall was insulated using extruded polystyrene board, and the insulation layer is thicker and the reduction of energy consumption is more. When the insulation layer thickness is up to 80mm, energy-saving

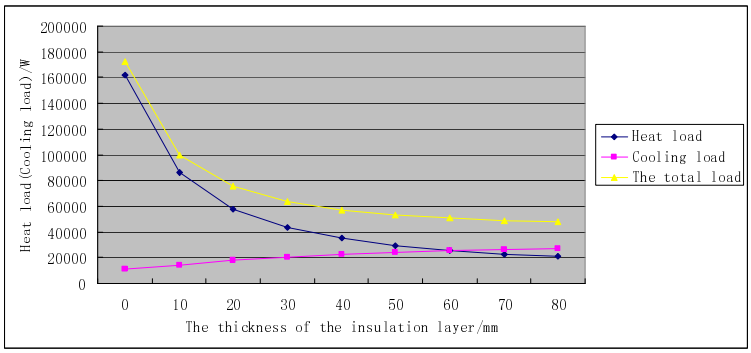


Fig. 4 Variation of load with insulation layer thickness

rate is 87.2% relative to the wall without thermal insulation. From above we can see that the energy saving effect is very obvious. But the cooling load is not reduced but increased when taking measures to insulate the wall. the reason is that the decrease of the heat transfer coefficient is advantageous to prevent that energy transfer from the high-temperature region to the low-temperature region; there the outdoor temperature is higher than the indoor temperature in summer daytime. But in the summer night or over season, the outdoor temperature is lower than indoor temperature; there is an energy transfer from the outdoor to indoor. Therefore the cooling loads of increased with the decreasing of the heat transfer coefficient.

Determination of economical insulation thickness

The thickness of the insulation layer is the main parameter of exterior wall thermal insulation performance in case that the thermal insulation material is determined. Also what can be seen from table 3, the percentage increases of energy saving is respectively 14.2%, 6.7%, 3.8%, 2.2%, 1.5%, 1%, 0.6% when he thickness of the insulation layer changes from 10 to 80mm and relative energy saving ratio tend to moderate. That is to say too much of the increase in the thickness of the insulation layer, the cost will increase, but energy-saving ratio will be reduce relatively. And then there is the total minimum cost of a certain insulation thickness of the wall. This particular thickness is the economic thickness of thermal insulation layer. Therefore, the optimal thickness of insulation will be determined through the economic analysis. At present the life cycle cost analysis on building is usually used as a kind of method of the total cost of economic analysis in foreign. Economical insulation thickness can be calculated with [3].

$$\delta_{op} = \sqrt{\frac{24ZPWF\varepsilon C_f(t_i - t_e)\lambda}{H_c C_i \eta_1 \eta_2}} - \lambda(R_i + R_e + R_w) \tag{1}$$

Where δ_{op} is the economical insulation thickness and the units is millimeter, PWF is The discount coefficient, η is the total efficiency of the heating system, $\eta = \eta_1\eta_2$， η_1 is transmission efficiency of outdoor pipe network, the value is 0.92. η_2 is the boiler efficiency， the value of the Coal fired boiler is between 0.73 and 0.82, the value of the Gas fired boiler is between 0.86 and 0.90[4]. H_c is Calorific value of fuel and it has units of kilojoules per kilogram or kilojoules per cubic meters. C_f is the price of fuel and the units is Yuan per kilogram or Yuan per cubic meters. C_i is heat preservation material cost, the units is Yuan per cubic meter. Z is Heating period, The heating period in Lanzhou for 126 days, R_i is heat resistance of inner surface and the value is 0.11 R_e is heat resistance of outer surface and the value is 0.043 (m^2·K)/W[4]. R_w is the thermal resistance of retaining structure, (m^2·K)/W; λ is thermal conductivity of thermal insulation layer, W/ (m·K) 。 t_i is indoor temperature and the value is 18 Celsius system. t_e is outdoor mean air temperature during heating and the value is 0.6 Celsius system below zero[5]

The life cycle present value factor PWF is not only determined by inflation rate i and the bank interest rate, but also determined by life cycle years N of the insulating layer[3].

$$PWF = \frac{1-(1+I)^{-N}}{I} \tag{2}$$

$$I = \frac{i-g}{i+g} \tag{3}$$

The current state loan interest rates i is 6.55%, the rate of inflation is 2.4%, use fixed of year is 10 years,The resultant for PWF is 8.09 by Formula (2) and (3)

The Equation of economical insulation thickness Can be simplified as followings on the condition of different fuel and Insulation materials (Different fuel calorific value, price and efficiency are shown in Table 4)

$$\delta_{op} = 852\sqrt{\frac{C_f \lambda}{H_c C_i}} - \lambda(0.153 + R_w) \tag{4}$$

TABLE 4 CALORIFIC VALUE, PRICE AND EFFICIENCY DIFFERENT FUEL

Fuel	Calorific value of fuel (MJ/m^3 or MJ/kg)	Price (yuan/kg or yuan/m^3)	Efficiency
Natural gas	9.92x103	2.21	0.9
Oil	10.94 x103	3.69	0.85
Coal	6.97 x103	0.3	0.65

When the residential buildings were heated using gas boiler ,The Equation of economical insulation thickness Can be simplified furthermore as followings

$$\delta_{op} = 12.7\sqrt{\frac{\lambda}{C_i}} - \lambda(0.153 + R_w) = 12.7\sqrt{\frac{0.03}{1800}} - 0.03(0.153 + 0.157)$$
$$= 0.04254\text{m}$$

From the above result of calculation, the economic insulating layer thickness is 40mm when the thermal insulation material is extruded polystyrene board, and from the above equation we can see that the economic insulating layer thickness determined by fuel and insulation materials in special area. So it should not be performed by the construction of energy-efficient design standards and recommended value experience value but it should be calculated according to the concrete conditions of the building. Which makes the building to achieve its economical and energy-saving character.

Summary

Heating, air conditioning load of the residential buildings were calculated by using the building energy simulation software DeST-h in Lanzhou city Based on the comparison of external wall with different insulation thicknesses and without insulation, the result shows that the total annual load can be reduced to 42% ~ 72%. But With the increase of the thickness of the insulation layer, the building load decrease slowly. Therefore the optimal thickness of insulation is determined by using the life cycle cost analysis. The economic insulating layer thickness is 40mm when the thermal insulation material is extruded polystyrene board and the heat source is the gas boiler in Lanzhou. The determination of the economy insulation layer thickness avoids blindly pursuing the insulation effect and ignoring the investment cost increases. Using of life cycle cost analysis method considering the entire life cycle energy consumption of the buildings during the construction and dismantling. This method is more scientific and reasonable. the result of analysis has the reference value for the actual engineering.

Acknowledgements

This research is financially supported by Lanzhou University of Technology (No. 1212RJZA005) and the Fundamental Research Funds for Lanzhou University of Technology (No. TM-TJ-1003). These supports are gratefully acknowledged.

References

[1] Tsinghai University DeST development group. Simulation and analysis method of building environmental system-DeST[M]. Beijing: China Architecture & Building Press, 2005

[2] GB50176-93Thermal design code for civil building[S]. Beijing: China Architecture & Building Press, 1993

[3] Jinfeng Shi, Angui Li.Research on the the thickness of economical insulation layer of external wall in Xian[J]. Architectuer Technology & Design，2008（9）:78-83

[4] JGJ26-2010 Design standard for energy efficiency of residential buildings in severe cold and cold zones [S]. Beijing: The people's Republic of China Ministry of housing and urban rural development，2010

[5] GB50736-2012 Design code for heating ventilation and air conditioning of civil buildings Beijing: The people's Republic of China Ministry of housing and urban rural development,，The people's Republic of ChinaState Administration of Quality Supervision Inspection and quarantine, 2012

Advanced Materials Research Vol. 936 (2014) pp 1502-1505
© (2014) Trans Tech Publications, Switzerland
doi:10.4028/www.scientific.net/AMR.936.1502

Energy Consumption for Heating Residential building from Implementing Deferent Energy-Saving Standard

Chune Li [1,a*], Yajun Wang [2,b] and Ying Cai [3,c]

[1] School of Civil Engineering, Lanzhou University of Technology, Lanzhou 730050, China

[2] School of Civil Engineering, Lanzhou University of Technology, Lanzhou 730050, China

[3] School of Civil Engineering, Lanzhou University of Technology, Lanzhou 730050, China

[a]sophie_lce@163.com, [b]wyj79626@lut.cn, [c]blue9801@163.com

Keywords: Energy-Saving Standard, DeST-h, energy consumption, residential building

Abstract. This paper uses energy consumption stimulation software DeST-h to carry out stimulation study on annual energy consumption for heating of a typical residential building in Lanzhou city, a city in cold zones. We respectively calculated energy consumption under conditions of implementing "50% energy-saving standard" and "65% energy-saving standard", calculated the energy-saving rate, and did research on energy-saving ability, economy, emission-reducing ability of different energy-saving standards.

Introduction

Since《Design standard for energy efficiency of heating residential buildings》 was promulgated and implemented in 2006, The 65% energy-saving design standards has been implemented for residential buildings in Lanzhou. With《Design standard for energy efficiency of residential buildings in severe cold and cold zones》 [1] comprehensive implementing which put forward higher requirements of thermal performance standards for envelopes of residential building. This standard is the supplement to the 《Energy conservation design standard for new heating residential buildings》. Two standards were developed to putting forward different Residential buildings heating energy consumption were reduced to 65% and 50% respectively in new and old standard. According to energy-saving targets, it put forward measures of energy saving requirements for building heating design and building thermal. Nationally, the energy-saving effect for different energy efficiency standards in a specific area of specific simulation calculation is of rare occurrence. Jian Yao [2] did research in Ningbo area and Li Bai [3] made economic analysis under different energy saving standards in Changchun. Lanzhou city is located in cold (A) region and its climate is different from hot summer and cold winter zone and severe cold zone. Therefore this paper simulated the relative energy saving ratio under performing different energy saving standards, this study further analyzed economy, energy saving and emission reduction.

The ratio of energy-saving and emission reduction of the implementation of the "65% energy-saving standards compared with the implementation of the "50% energy saving standards" and how about the economy, witch is unable to draw by the theoretical analysis or experiment. So the simulation method is the best choice under the current conditions. Building simulation analysis software DeST[4] can analyze the energy consumption dynamically throughout the year under the hot and cold conditions. The dynamical simulation for a typical residential building is in accordance with the actual heating conditions. Analyzing the heating consumption at above two energy saving target. Because Lanzhou city is located in cold regions, there is not air conditioning in summer; the air conditioning energy consumption will be analyzed quantitatively.

Building model

Taking a residential building in Lanzhou city as the simulation object ,the area of residential building is 4676 square meters, shape coefficient is 0.342, and comprehensive window wall ratio is 0.16, the building has eleven floors, it is 2.9 meters high, the top floor is 3 meters high. Building toward the southern and Northern, the building model of DeST geometry model as shown in Fig. 1, The performance parameters of retaining structure are settled in accordance with the different energy-saving standard. For the sake of convenience, the residential building of "50% energy-saving standard" was taken as the benchmark residential. The parameters of benchmark residential are settled according to 《Energy conservation design standard for new heating residential buildings》 as shown in Table 1.

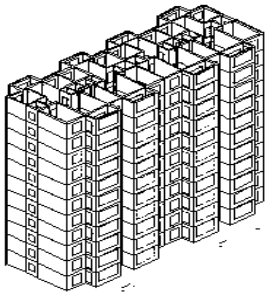


Fig. 1 DeST building model

Table 1. The thermal physical parameters of structure

Component name	50% energy-saving		65% energy-saving	
	Retaining structure material	Heat transfer coefficient	Retaining structure material	Heat transfer coefficient
Exterior wall	Expanded polystyrene board Concrete perforated brick	0.849	Extruded polystyrene board Concrete perforated brick	0.697
Inner wall	Ceramist concrete	1.52	Concrete air brick	1.2
Roof	Aerated concrete thermal insulation	0.68	Light steel structure	0.427
Floor	Reinforced concrete	3.05	Extruded polystyrene board	1.11
Exterior window	Standard Windows	4.7	Standard Windows	2.5

Simulation under different Energy-saving standard

The setting of indoor calculation parameters. Calculation parameters of indoor was stetted according to 《Design standard for energy efficiency of residential buildings in severe cold and cold zones》 and 《Design code for heating ventilation and air conditioning of civil buildings》 [5]. The meteorological data used in the simulation are come from typical meteorological year data issued by Technology Department of Tsinghai University and Meteorological Information Center Meteorological data of China Meteorological Administration. Lanzhou's 8760 hourly meteorological parameters were calculated by using DeST-h as shown in Fig. 2

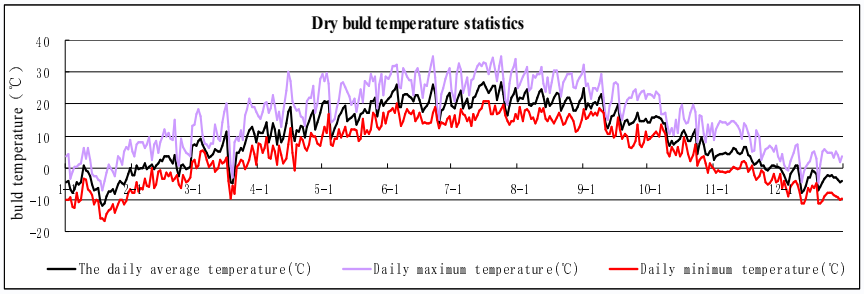


Fig. 2 The dry bulb temperature of every day in Lanzhou

The room functions of residential building is simplified as the bedroom, living room,. The bedroom, the living room is air-conditioned room. The empty room is not air-conditioned room, including the bathroom, kitchen etc. The living room is able to hold a maximum of 3 people and the bedroom is able to hold a maximum of 2 people. Personnel heat divided into sensible heat and latent heat, the sensible heat is 61 Watt apiece and the latent heat is 73 Watt apiece. The maximum lighting heat is 5 Watt per square in the living room and 4 Watt in bedroom.

Energy-saving analysis

Simulation results under different energy saving standards are shown as following Table 2.

Table 2. The annual total load and the relative energy saving ratio

Category	50% energy-saving	65% energy-saving	Savings	Energy saving ratio
Area	4676	4676	-	-
The maximum heat load	58.3	35.8	22.5	38.6
Annual total load (kW·h/ m^2)	63.1	42.1	21	33.3
The average consumption of gas (kgce·m-2)	7.73	5.17	2.56	33.3

From Table 2, we can see that heat load had decreased obviously when the "65% energy-saving standards implemented comparing with the "50% energy saving standards". The maximum heat load is reduced by 38.6% and annual total load is reduced by 33.3%.which means that Heating energy consumption value is reduced by 33.3%.From Table 2, we can see that annual heating gas consumption of residential buildings reduced from 7.73 kgce/m^2 to 5.17 kgce/m^2 when performing different standards, This residential building could be saved gas 9857Nm annually. By the end of 2011 statistics shows that residential area is 10450×10^4 m^2 and performing "65% energy-saving standards will save gas 22109×10^4 Nm in Lanzhou. That is to say energy saving potential of heating is very great

Emission reduction analysis

According to the emission quota of pollutants in China [5], the amount of pollutants produced by burning 1kgce can be calculated. the quota of pollutants are as following Table 3

Table 3 Pollutants produced by 1kgce kg

Contaminants	Emission index
CO_2	33.7
SO_2	0.237
NO_2	0.0126

Energy conservation and emissions under different energy-saving standards is shown in Table 4

Table 4 Energy conservation and emission analysis

Category	50% energy-saving	65% energy-saving	Emission reduction of the building	Emission reduction of Lanzhou
area（m^2）	4676	4676	-	300×10^4
The average consumption of gas ($kgce\cdot m^{-2}$)	7.73	5.17	-	-
CO_2 emissions（t）	1203.64	805.02	398.62	25×10^4
SO_2 emissions（t）	8.4	5.6	2.8	1800
NO_2 emissions（t）	0.44	0.29	0.14	90

The above analysis presented that harmful emissions decreased by 33.3% year-on-year when there are no taking other environmental protection measures, only considering the implementation of different energy saving standards. One building annual reduction of CO_2 emissions is 398.6t per year, SO_2 emissions is 2.8t per year and NO_2 emissions is 0.14t per year. Fatherly, reductions of CO_2 emissions is 25×10^4t per year, SO_2 emissions is1800t per year and NO_2 emissions is 90t per year in the entire city of Lanzhou. Thus it can be seen, the implementation of the "65% energy saving standards", can significantly reduce the emissions of harmful substances, environmental protection is of great significance.

Summary

Residential buildings energy consumption was simulated by using hourly energy consumption simulation software DeST-h in Lanzhou and The analysis result presented that the "65% energy-saving standards implemented comparing with the "50% energy saving standards". The maximum heat load is reduced by 38.6% and annual total load is reduced by 33.3%.which means that heating energy consumption value is reduced by 33.3%. reductions of CO_2 emissions is 25×10^4t per year, SO_2 emissions is1800t per year and NO_2 emissions is 90t per year in the entire city of Lanzhou. This study further shows that the implementation of"65% energy saving standards" can not only save energy, but also can reduce the emissions of harmful substances. On the other hand, the initial investment, operating costs and heating system will decrease.

Acknowledgements

This research is financially supported by Lanzhou University of Technology (No. 1212RJZA005) and the Fundamental Research Funds for Lanzhou University of Technology (No. TM-TJ-1003). These supports are gratefully acknowledged.

References

[1] JGJ26-2010 Design standard for energy efficiency of residential buildings in severe cold and cold zones [S]. Beijing: The people's Republic of China Ministry of housing and urban rural development,2010

[2] Li Bai, Zhao Cheng. Economic analysis of the residential buildings in cold area implementing different energy saving standard[J]. Power demand side management, 2009(5) :38-40

[3] Jian Yao. Residential building for energy saving by 65 % a case study of Ningbo[J]. Heating ventilating Air-conditioning, 2009(10):79-81

[4] Tsinghai University DeST development gr

[5] oup. Simulation and analysis method of building environmental System-DeST [M]. Beijing: China Architecture & Building Press, 2005

[6] GB50736-2012 Design code for heating ventilation and air conditioning of civil buildings [S].Beijing: The people's Republic of China Ministry of housing and urban rural development, Thepeople's Republic of China State Administration of Quality Supervision Inspection and quarantine,2012

Advanced Materials Research Vol. 936 (2014) pp 1506-1510
© (2014) Trans Tech Publications, Switzerland
doi:10.4028/www.scientific.net/AMR.936.1506

The scheme comparison of integral structure after adding steel storey to concrete frame

Sun Ning[1, a *], Shu Ganping[1], Wang Zhiming[1]

[1]Department of Civil Engineering, Southeast University, China

[a]230079099@seu.edu.cn

Keywords: steel adding storey, equivalent damp ratio; selecting models

Abstract: Characteristics and applying conditions of lightweight steel structures in adding buildings are introduced, and the correlative calculating methods in designing are also discussed. The optimal layers in adding are proposed by using bottom storey shear as target parameters. The reactions of structure adding optimal layers are analyzed to judge the adding capacity of original structure. The economy comparison of different materials in adding is also discussed by the parameter of material cost. Using an adding project as an example, an appropriate adding scheme is chosen by this method.

Introduction

With the development of Chinese urbanization, the conflict between increasing population and limits of city land has become sharper and sharper. Meanwhile, it is definitely forbidden to use cultivated land as housing land. Undoubtedly, retrofitting of existing buildings is both the best way to solve these problems and an important means to ease the population pressure.[1]

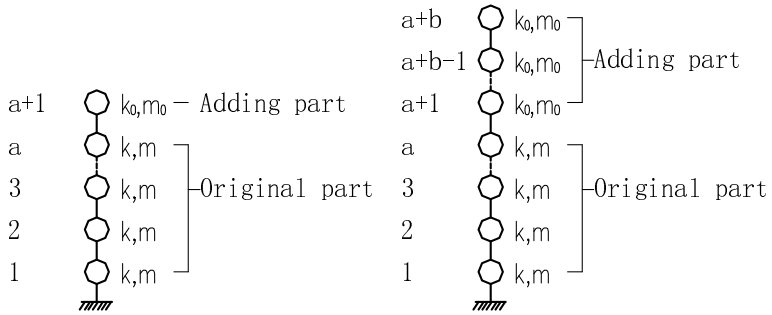
The traditional materials used in storey-adding are brick masonry; concrete; steel and etc., concrete structure is especially common used in adding project. Using the same materials as the original structures to add storey, the structure models are mature, and there're lots of corresponding specifications or guidelines for designers to follow, such as "Technical code for adding stories of brick-concrete structures of building" "Design code for strengthening concrete structure" and etc. Steel structure is a kind of structure with good seismic performances, high strength, and large energy dissipation. Concrete frames using steel as storey-adding material is a composite structure, which has a stiffness mutation vertically. The connection of different materials leads to the appearance of weak layer.

Structural system & Calculation model

The structure system after storey-adding is a composite structure, which has frame or brick structure as bottom frame and has steel frame or bent as the upper frame. The calculation model diagram must be consistent with the actual structure and connections. Meanwhile, the definite force transmission routes, reasonable structure calculation methods, and reliable measures should be adapted. As to concrete frame structure using steel to add storeys, the connection between the upper part and the lower part is so important that the upper steel system and the connection should be designed carefully, in order to avoid steel column base's failure caused to structure's geometric instability.

Seismic calculation

The magnitude of the earthquake effect is proportional to the mass of buildings. So light steel can effectively reduce the earthquake effect of the lower part of the structure which caused by storey-adding. It is worthwhile to note that both the mass and the stiffness between the enhancement layer and the original construction have a great difference. Due to the suppleness of the upper structure, high modes of steel have a significant effect, resulting in different vibration periods and different vibration acceleration of the original structure and the adding structures. In the bottom shear method, every storey is considered as a single degree of freedom, assuming vibration as linear form which ignores the influence of higher modes of vibration. Therefore, dynamic magnification factors should be multiplied to consider the effect of the high mode. In mode decomposition method, enough mode number should be selected which made the mass participation ratio close to 1. Only in this way, the effects of the high modes are considered enough. The damping ratio of concrete and steel is different, the material damping ratio of concrete is 0.05, while the steel 0.02. The damping ratio of the composite structure using different materials is not a constant, but a equivalent damping ratio ranged from 0.02 to 0.05 in various modes of vibration[5-8], which stands for damping and energy dissipation capacity of the structure system, and also affects the calculation results of whole structure analysis, especially for a more-adding-storey building, or a building located in the high intensity region. Under these situations, equivalent modal damping ratio is averaged by using the strain energy.



（a）One storey adding （b）b storeys adding

Fig 1 Mechanical model of composite structure adding by steel structure

$$[K]=\begin{bmatrix} 2k & -k & & & & & \\ -k & 2k & -k & & & & \\ & \cdots & \cdots & \cdots & & & \\ & & -k & k+k_0 & -k_0 & & \\ & & & \cdots & \cdots & \cdots & \\ & & & & -k_0 & k_0 & \end{bmatrix}=\left[\begin{array}{cccc|c} 2k & -k & & & \\ -k & 2k & -k & & \\ & \cdots & \cdots & \cdots & \\ & & -k & k & \\ \hline & & & & 0 \end{array}\right]+\left[\begin{array}{c|ccc} [0] & [0] & & \\ \hline [0] & k_0 & -k_0 & \\ & -k_0 & 2k_0 & -k_0 \\ & & \cdots & \cdots \\ & & -k_0 & k_0 \end{array}\right]$$

$$=\begin{bmatrix} [K_a] & [0] \\ [0] & [0] \end{bmatrix}+\begin{bmatrix} [0] & [0] \\ [0] & [K_b] \end{bmatrix}=[K_1]+[K_2]$$

Among them，$[K_a]$ is a matrix with $a\times a$ order，$[K_b]$ is a matrix with $(b+1)\times(b+1)$ order. Assuming the mode vector of the i th order vibration mode as ϕ_i, the mode vector relevant to structure 1(original structure) as ϕ_{i1}, the mode vector relevant to structure 2(adding structure) as ϕ_{i2},

mode damping ratio of the composite structure can be averaged by material's strain energy [7,9]:

$$\xi_i = \frac{\xi_1 \phi_{i1}^T K_1 \phi_{i1} + \xi_2 \phi_{i2}^T K_2 \phi_{i2}}{\phi_i^T K \phi_i}.$$

Rayleigh damping of different frequency may has certain effects on the calculation results, but the difference is small (within 5%), and it can be accepted in practical project. So using the former 2 natural frequencies to determine the Rayleigh damping is feasible in engineering.[10]

Different damping ratio causes different seismic response. The modifier formula is shown as follows[11]:

$$\alpha(T,\xi) = \alpha(T,\xi = 0.05) \cdot \beta(\xi,T), \text{ while } \beta(\xi,T) = \sqrt[3]{16.6\xi + 0.16}\left(\frac{0.8}{T}\right)^{\frac{0.05-\xi}{0.156+3.38\xi}}.$$

Put every equivalent damping ratio of each mode into the formula, and horizontal maximum affecting coefficient can be figured out.

Preliminary judgments of the number of adding storeys

Number of adding storeys is influenced by many factors: needs, planning requirements, the carrying capacity of the original structure (vertical bearing capacity, horizontal bearing capacity), the total cost of investment (adding & reinforcement), time limit for a project etc.

Using $F_{Ek} = \alpha_1 G_{eq}$ as the target parameters, assuming seismic intensity, the storey mass, loads, the original stiffness, and the adding-storey stiffness are all known, the optimal number of adding storeys can be found out. The larger the number of adding storeys is, the heavier the parameter" G_{eq} " is. In the description of parameter" α " in "code for seismic design of buildings[2]", there's a huge decline when the vibration period is in the range between T_g and $5T_g$. With the increasing of adding storeys" b ", the composite structure becomes more flexible, the vibration period increases rapidly, meanwhile, equivalent damping ratio ξ becomes smaller(approaching to the steel damping ratio). After comprehensive evaluation of the formula $\alpha = \left(\frac{T_g}{T}\right)^{0.9+\frac{0.05-\xi}{0.3+6\xi}}\left(1+\frac{0.05-\xi}{0.08+1.6\xi}\right)\alpha_{\max}$, it can be showed that in a certain range, with the increasing of " b ", the smaller " α " is. Further, there is an extreme point of" b ", so that made the target parameters be the critical point. It also can explain several examples in some literature[12 - 15] that the steel adding causes a smaller bottom shear.

An engineering example

Project overview

A reinforced concrete frame structure with two ground floors and one underground floor, located in the District of 7 degrees of earthquake intensity, second type of site. The construction designed in 2003 has been employed less than 10 years. The original construction area is 6480m^2 (not including the underground area). Adding storey is chosen to meet the requirements of the owner considering the construction period and investment scale.

According to the inspection report, the structural component basically meets the relevant requirements of "code for seismic design of buildings" and "code for design of concrete structures", reinforcement and reconstruction are practicable.

Calculation & Scheme Analysis

Seeking for the optimal number of adding-storeys

The original structure is two story concrete frames, assuming that the stiffness of the beam is infinite. Inter-story shear stiffness of every concrete floor is $k_1 = k_2 = 1.0\times10^7 KN/m$, mass of every concrete floor is $360t$; while inter-story shear stiffness of every steel floor is $k_3 = 3.2\times10^6 KN/m$, mass of every steel floor is $255t$. The damping ratio of concrete and steel are 0.05and 0.02. On the basis of former theory, a procedure is programmed by MATLAB to figure out the equivalent damping ratio of composite structure, which can modify the seismic spectrum. The target parameter presented under the premise of less than 40-meters-tall, the shear deformation takes an important role. Taller the structures are, more effect the high modes take on the bottom shear force, so the assumption does not exist any longer. The first critical point was selected as the optimal point. The result shows: it is 3floors that has the less bottom shear force.

Using design program to calculate, the result shows vertical capacity can bear the adding loads. It is practical to add three floors. To respect owner's idea, we take the scheme of adding two floors.

Economy comparison of concrete and steel adding storey

The computation and analysis shows: In the condition of using concrete structure to add, almost 30% of the columns need to be reinforced, 30% of planar member of the second floor need to be reinforced because of the increasing load and function changes. In the condition of using steel structure to add, only 4% of the columns need to be reinforced, 25% of planar member of the second floor need to be reinforced because of the increasing load and functional changes.

Steel is worth 5800 Y/t, and concrete is worth 300 Y/m^3. The material costs of steel-adding part are 290000; while the material costs of concrete-adding part are 814600. From the sight of reinforcement, the material costs of reinforcement under steel-adding are 800000 less than the costs under concrete-adding. Of course, reinforcement costs are far more than the material itself.

The function of this project after alteration is for the commercial use. In consideration of the construction character, the duration, costs, disturbance to the surroundings, and the economic interests bring by early finished, steel structure takes certain advantages of concrete.

Conclusion

Using steel structure to add can reduce the earthquake effect brought by the increasing storey. A reasonable structure should be chosen by comparing characteristics of all kinds of light steel structure, and considering the actual construction conditions. The connections between adding-storey and original structures should be paid enough attentions on avoiding steel column base's failure caused to structure's geometric instability. Light steel must be designed according to the seismic code; the lower structure can only meet the standard for seismic appraiser. Through economic analysis and comparison, the light steel costs are lightly higher than concrete. Meanwhile, steel structure disturbs less; constructs assembly; can effectively shorten the construction period. After all, steel structure has a better comprehensive benefit. The seismic response of the entire structure is affected by adding-storeys, adding mass and stiffness. There are no clear provisions or instructions to this composite structure, which limits development of the light steel reinforcement in a certain extent. Too much details still need to be researched.

Reference

[1] LvFengwei. STUDY ON THE DESIGN METHOD AND SEISMIC PERFORMANCE OF LIGHT STEEL ADDING STOREY STRUCTURE [D]. China: Southeast University, 2009.

[2] CuiYanqiu, LiuFeng, Some problems in designing and applying of lightweight steel structure in added buildings, J. Journal of Shandong Institute of Architecture and Engineering , 2001(03): 30 - 33.

[3] GB50023-2009. Standard for seismic appraisal of buildings, China Building Industry Press, BeiJing, 2009.

[4] GB50011-2010. Code for seismic design of buildings, China Building Industry Press, BeiJing, 2010.

[5] XieJingjing, MaLu, YangYong, Discussion on confirming method of the light steel adding storey structure damping ratio, J. Shanxi building, 2010(03): 83 - 85.

[6] LiuYang, The discussion of damping ratio in mixed structure about storey-adding, J. Friend of Science Amateurs, 2011(09): 50 - 52.

[7] LvFengwei, CaoShuangyin,ZongZongling, Solution to the Damping Ratio of the Building Added with Light-gauge Steel with Energy Method , J. Earthquake Resistant Engineering and Retrofitting, 2008(05): 100 - 102+106.

[8] YangYofa,WangLifu, ON CALCULATION OF THE NON-PROPORTIONAL DAMPING EFFECT FOR THE INTERLAYER ISOLATION MASONRY BUILDING WITH FRAME STRUCTURE IN THE FIRST STOREY, J, Industrial Building, 2003(12): 47 - 48+76.

[9] XueYantao, WeiChengji, SunR.F., Calculation Method for Damping Ration of Different Story Added Structures (Strain Energy Method), J. Earthquake Resistant Engineering and Retrofitting, 2008(02): 91 - 95.

[10] WangQi, GuZhengwei, The discuss of method of steel adding structure's damping ratio, J, Low temperature construction technology, 2012(11): 32 - 34.

[11] HuYuxian, Earthquake Engineering (Second Edition), Seismological Press, BeiJing,2006.

[12] MaJianSuo, ZhangTao, etc., Analysis of seismic resistance of integral structure after adding steel storeys on top of concrete frame, J, Earthquake Engineering and Engineering Vibration, 2006(03): 118 - 120.

[13] ZhangTao, WangYuanQing, ShiYongJiu, MaJiansuo, Analysis of Response Spectrum on the Seismic Properties of the Integral Structure after Adding Steel Storeys on Top of the Concrete Frame, J. Earthquake Resistant Engineering and Retrofitting, 2006(03): 95 - 100+105.

[14] ZhangTao, WangYuanQing, ShiYongJiu, MaJiansuo, Analysis of time-history on the seismic properties of the integral structure after adding steel storeys on top of the concrete frame, J, Scientific research in Sichuan building, 2006(05): 140 - 143.

[15] LiuYu,GaoXiaowang,ZhangTao, Analysis of Seismic Performance of the Storey-adding Structures of Light-weight Steel Based on SAP2000, J, Earthquake Resistant Engineering and Retrofitting, 2008(06): 100 - 104.

Advanced Materials Research Vol. 936 (2014) pp 1511-1517
© (2014) Trans Tech Publications, Switzerland
doi:10.4028/www.scientific.net/AMR.936.1511

Finite Element Analysis of Rainfall Infiltration in A Compacted Loess Embankment

Qing-feng Lv[1, a], Peng-fei Liu [1,b] and Yan-xu Zhao [2,c]

[1] Key Laboratory of Mechanics on Western Disaster and Environment Mechanics, Lanzhou University, Lanzhou City, Gansu Province, China,730000

[2] China Railway 21st Bureau Group Co., Lanzhou City, Gansu Province, China,730000

[a]lvqf@lzu.edu.cn, [b]lpf313@126.com, [c]zhaoyx822@sina.com

Keywords: Compacted loess; Finite element analysis; Rainfall; Infiltration; Moisture content

Abstract: Because of evapo-transpiration, compacted loess road embankments were considered to be in a partially saturated state in both arid and semi-arid regions. Based on previous studies and the theory of unsaturated soil mechanics, a numerical analysis of rainfall infiltration in a compacted loess road embankment was conducted. The transient seepage characteristics and moisture migration patterns of the moisture in the embankment were analysed. The results showed that after precipitation, the moisture profile of the compacted loess could be separated into three zones .The data also showed that: under the effect of gravity, the water continued to migrate into the embankment after the rainfall had ended. In time, the saturated zone became partially saturated as the moisture content decreased, whereas the moisture content in the conducting and humid zones increased and the wetting front moved downward. The data also showed that the depth of the conducting and humid zones increased in time, but that the moisture content in the conducting zone increased along a linear gradient with depth, while the moisture content in the humid zone decreased in a similar manner.

Introduction

Analysis of seepage within soil zones having different saturation ratios is a common objective for those investigating groundwater movement. The analysis of such problems is complex and the frequency of occurrence of landslides in natural ground, earth dams, railway and highway embankments makes the study of rainfall infiltration on compacted loess in unsaturated seepage conditions significant. Green and Ampt (1911)[1] were the first to describe the process of saturated soil infiltration accurately when they suggested their analytical solution for horizontal infiltration in a homogeneous, dry soil; Richards (1931) [2] uses the law of conservation of mass in his analysis of unsaturated seepage, Rubin (1968)[3] proposed a 2-dimensional finite difference numerical solution of Richards's control equation; Freeze (1971)[4] studied transient seepage flow in a mixed (saturated/unsaturated) underground aquifer, elaborating and summarising the numerical solution of his finite difference method; Remson (1971) [5]undertook a comprehensive evaluation of the finite difference method as applied to saturation-unsaturated seepage. Nenman (1973, 1974, 1977)[6,7,8] was the first to simulate the problem of unsaturated seepage by the use of the finite element (FE) method. Wu (1999, 2000)[9,10] and Peng (2002)[11] studied the FE numerical simulation of transient seepage in an saturated-unsaturated soil and improved upon the transient unsaturated seepage finite element approach developed by Nenman. Based on the theory of unsaturated soil mechanics, and by using the FE method to analyse the transient seepage in a typical loess railway embankment under rainfall infiltration, this research explored the seepage characteristics and moisture migration patterns in the process of humidifying deformation in compacted loess.

The Finite Element Method

The FE method, in which the basic concept is that the area under evaluation is discretised into inter-connected finite units (the elements), can simulate the geometrical shape of complex evaluation areas. The unknown field function over the evaluation area expresses each of its sub-regions by

approximation function which is assumed to apply to each unit. Because of the non-linearity of the saturated-unsaturated seepage equation, Galerkin's method of weighted residuals is applied: this method requires the substitution of an approximate solution into the governing general differential equation and the subsequent elimination of the weighted average over the whole problem. The gap between the premise and the approximate solution is called the margin of the equation which is minimised en route to a solution.

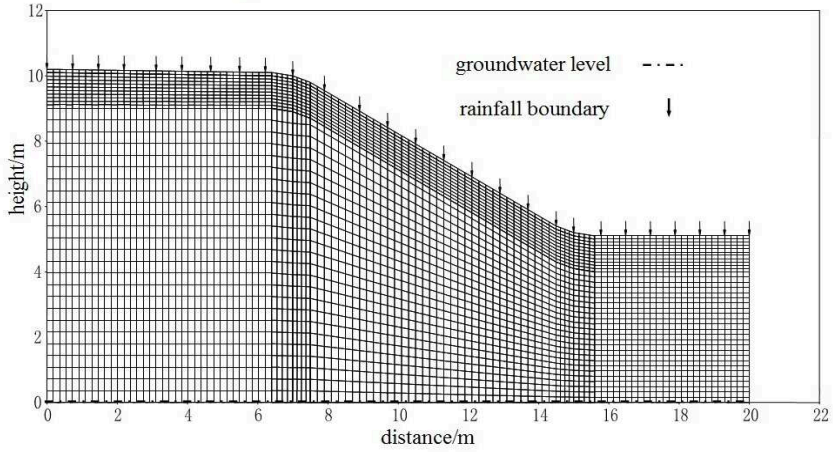
Under complicated boundary conditions, the seepage characteristic of unsaturated soils can be calculated by such a numerical method. Two main elements must be taken into account with regards the unsaturated seepage caused by rainfall infiltration: the first is the varying infiltration rate, which results from changing the external conditions during precipitation; the second is the migration and distribution of the infiltrated water within the soil mass. The calculation of unsaturated seepage deals with the first of these issues as a boundary condition problem and the second as a transient seepage field problem.

The solution method for problems incorporating a raining boundary condition influences the infiltration and distribution of the water in the soil mass: this affects the simulated results of the unsaturated seepage. Under the present unsaturated transient seepage simulation, there were three methods for handling the rainfall infiltration as a boundary condition: the first took the surface nodes as the known flow boundary, so the value was the infiltration rate or the rainfall intensity (i.e. it was assumed that all the rainfall had infiltrated the soil mass); the second defined the surface nodes as a known water head boundary (i.e. it was assumed that the suction of the surface nodes was zero during precipitation) and then calculated the amount of the water infiltrating the soil according to its unsaturated seepage coefficient and hydraulic gradient under negative pressure; the third was to transfer the surface nodes onto the boundary. When the rainfall intensity was less than the saturated seepage coefficient, the entire rainfall volume infiltrated the soil, so the boundary conditions became equivalent to the first category. When the permeability coefficient of the surface nodes was equal to that pertaining to saturated seepage, the surface nodes were converted to a known head boundary. In other words, this method took the saturated seepage coefficient as the infiltration capacity, which was then used as the factor by which the authors judged the conversion of the boundary. The third category of boundary condition was applied here to simulate the distribution and migration of infiltration moisture in the loess filled embankment slope beneath a railway.

Determination of Parameters and Geometry

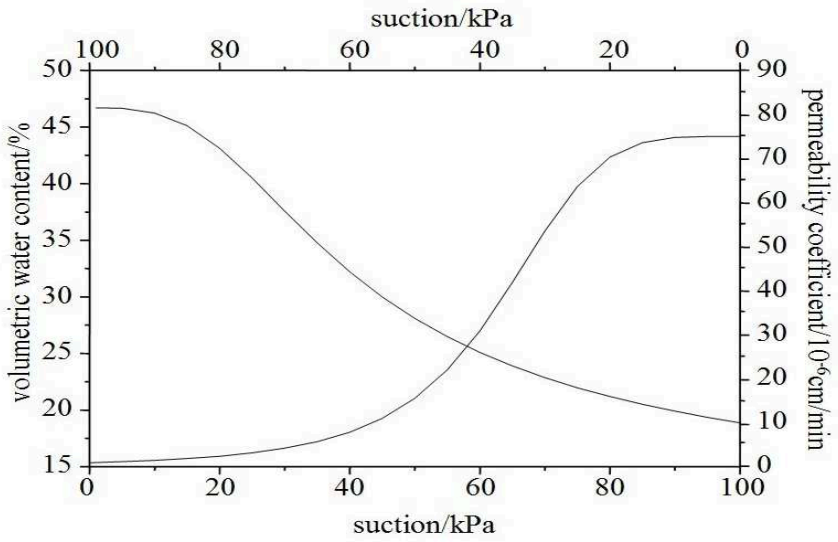
The loess railway embankment analysed here as a semi-infinite symmetrical half-space is shown in Fig. 1. The height of the embankment was 5 m, the width of the pavement was 7 m, and the slope was 1H:1.5V. The mesh incorporated the ground at up to 5 m from toe of the slope and some 5.1 m depth below original, natural ground level. The shoulder and toe of slope were smoothed to eliminate boundary discontinuity effects. The upper surface, shoulder, slope, and its toe had an applied rainfall boundary condition: the base and other two sides were set to zero flux conditions under a static phreatic surface assumed to lie at 0 m as indicated in Fig. 1.

Fig. 1 Geometrical model and FE mesh



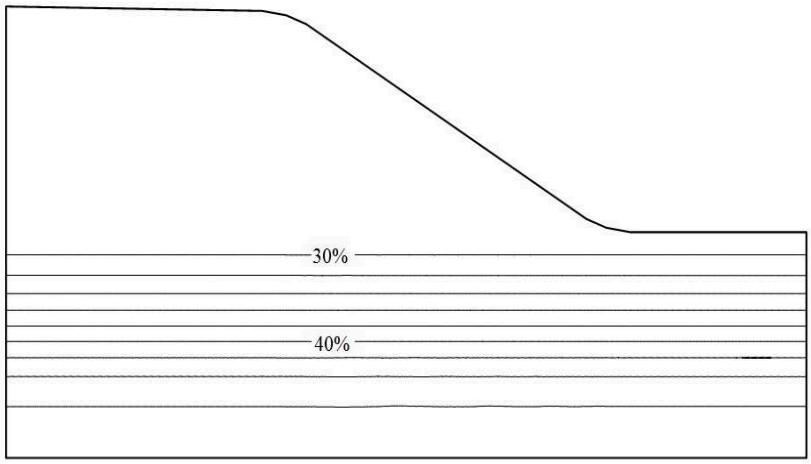
The dry density of the subgrade fill was 1610 kgm^{-3} (equivalent to 93 % relative density), the SWCC and unsaturated penetration coefficient curves are shown in Fig. 2.

Fig. 2 SWCC and penetration coefficient curve (ρ_d = 1610 kgm^{-3})



The initial volumetric moisture content of the slope, as shown in Fig. 3, was 28 %, which was the optimum moisture content of the subgrade.

Fig. 3 Section of initial volumetric water content



A rainfall intensity of 3.4 × 10^{-3} cm/min for 24 h was chosen as the rainfall boundary condition. Also, nine days after cessation of precipitation, the cloudy conditions were deemed to have prevented evaporation so the water migrated under the action of gravity alone. The author's analysis started from the distribution and migration of the moisture within the embankment at cessation of precipitation and continued for s further 10 days.

Discussion

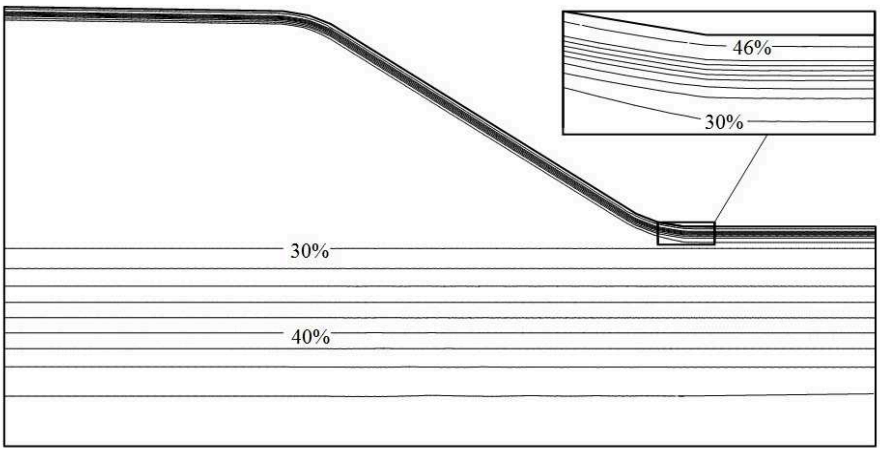
Analysis of Transient Seepage During Precipitation

The volumetric water content contour map of rainfall migration in one day is shown in Fig. 4 where it can be seen that the infiltration was lower in the compacted loess and that it reached a depth of infiltration of approximately 0.5 m, which placed the wetting front within the region typifying shallow unsaturated infiltration.

According to this research, the water content in a uniform soil under the influence of rainfall can be divided into four zones: a saturated zone, a transition zone, a conduction zone, and a humid zone. The leading edge of the humid zone represented the wetting front. Each zone had the following

characteristics: a saturated region of only a few millimetres depth which was relevant to the ponding time, a transition region, generally several centimetres in depth wherein the moisture content decreased rapidly with depth, a conduction region which was typically a thicker, unsaturated zone of high moisture content that remained little changed with depth, and a humid region in which the moisture content differed from that in the conduction zone and was locally higher than the initial water content. The wetting front was a steep front formed between that soil still at its initial moisture content and that affected by the unsaturated hydraulic gradient.

Fig. 4 Section of volumetric water content for one day's rainfall



The moisture content of the slope and its toe varied with depth as shown in Fig. 5. There was no obvious transition but the rainfall induced volumetric water content could itself be further sub-divided into: a saturated zone, suffused with water to a depth of approximately 10 cm; a conduction zone, about 20 cm thick and subject to smaller variations in moisture content as well as a smaller equivalent linear rate of change with depth; and a humid zone, some 20 cm thick, in which the moisture content differed significantly from that in the conduction zone which was itself also at a greater moisture content than at the outset.

Fig. 5 Variation of moisture content with depth after rainfall

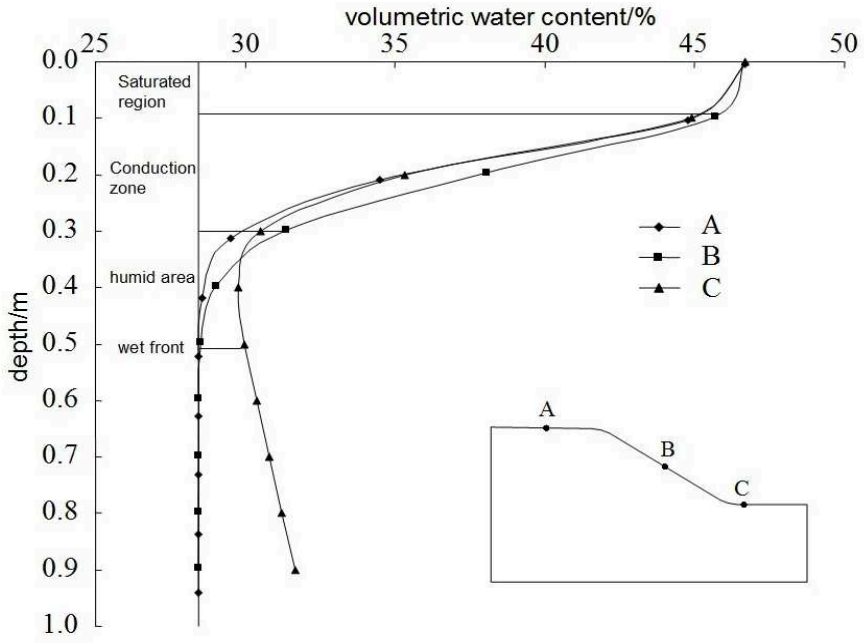
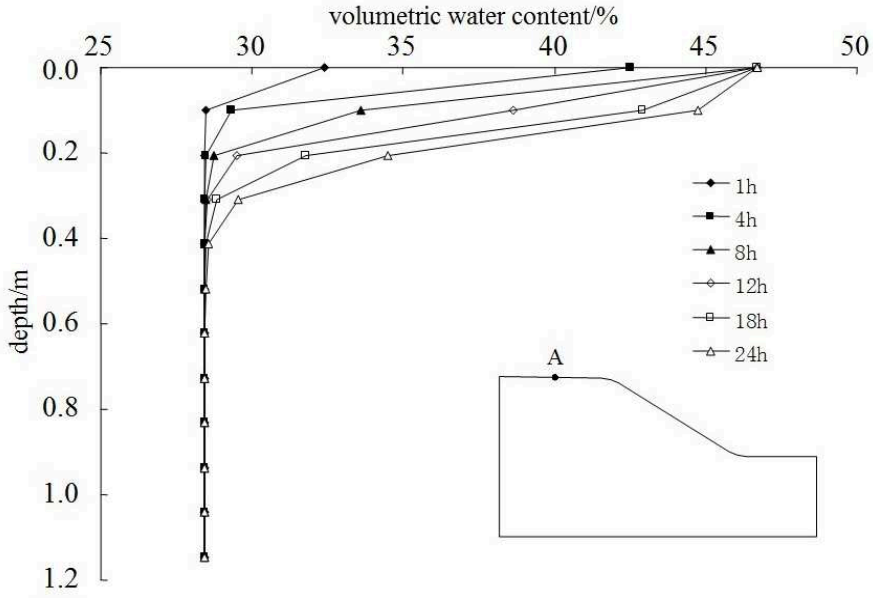


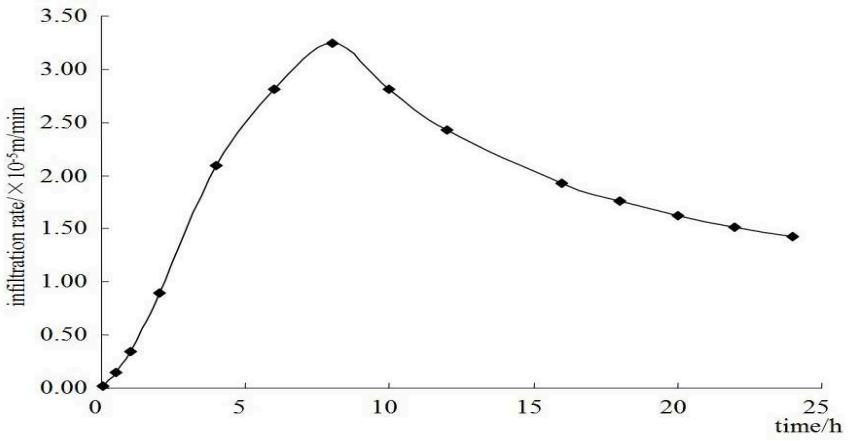
Fig. 6 shows the change of moisture content with depth and time: the upper surface became saturated and the wetting front propagated as the rainfall increased.

Fig. 6 Change of moisture content with the depth at different time



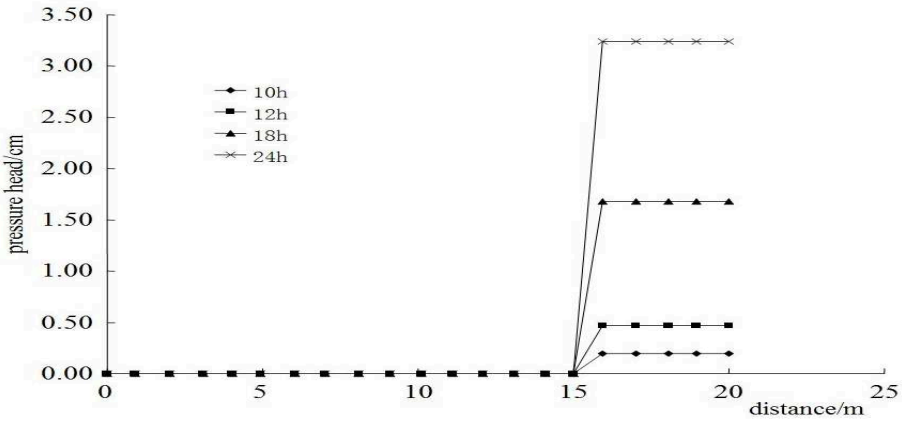
The infiltration rate variation curve at the rainfall boundary is shown in Fig. 7. There were three stages in the development of the equilibrium moisture content: initially, the moisture content was low and the infiltration rate started to increase with the wetting of the surface (Fig. 6).The surface moisture load increased during precipitation and indeed for up to 8 hours thereafter, the infiltration rate was equal to the rainfall intensity, then the soil became saturated (Fig. 6). The infiltration rate then decreased as it tended to an eventual equilibrium, stable, state: the steady state infiltration rate was also dependent on the properties of the soil.

Fig. 7 Change of infiltration rate during the rainfall



The accumulation of moisture at the bottom of the mesh during rainfall is shown in Fig. 8. There were surface stream-flows, slope run-off, and the surface began to pond after 8 hours' precipitation. The pressure head at both the upper surface and down the slope were held at zero throughout, while the pressure head at the bottom increased with time and the seepage reached a depth of 3.24 cm after one day's rain.

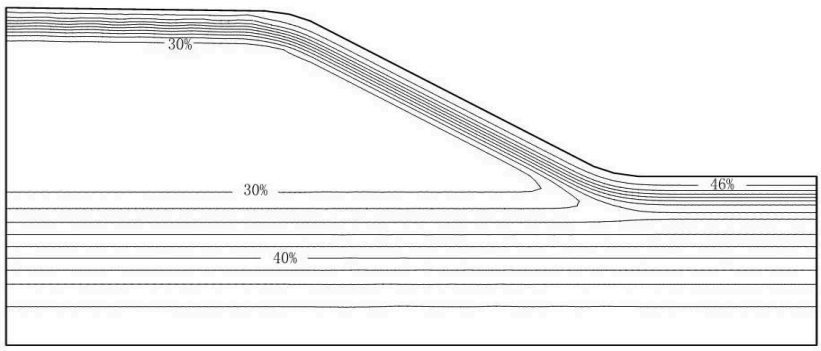
Fig.8 Variation of the accumulation of water at the base of the mesh



Migration of Embankment Moisture after Rainfall

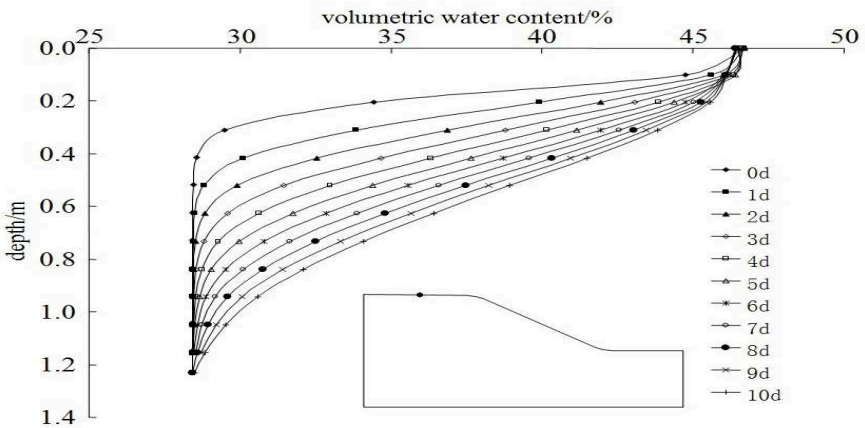
The distribution of volumetric moisture content 10 days after the cessation of precipitation is shown in Fig. 9. compared to the conditions shown in Fig. 4, the moisture had continued to migrate into the embankment under gravity, the thickness of the zone nearest to the surface was thicker at approximately 120 cm and its volumetric moisture content exceeded 28 %. As a result of bottom infiltration, the thickness of this moisture content zone within the slope area increased significantly.

Fig. 9 Volumetric moisture content 10 days after the cessation of precipitation



The variation in moisture content with depth upon cessation of precipitation and onwards for a 10 day period is shown in Fig. 10: the saturated area became partially saturated which implied that the moisture content decreased, the wetting front propagated downwards carrying additional moisture into the conduction, and humid, zones whose extents widened over time. The rate of change of moisture content with depth increased in the humid zone and decreased in the conduction zone.

Fig. 10 Variation of moisture content with depth upon cessation of precipitation



Conclusions

After the rain, the compacted loess moisture profile could be sub-divided into three zones according to infiltration rate: a saturated zone, a conducting zone, and a humid zone. The saturated zone was approximately 10 cm thick. The conducting zone had a thickness of approximately 20 cm and its moisture content decreased linearly with depth. The humid zone had a thickness of approximately 20 cm and its moisture content reverted to the original moisture content after the rainfall.

At the onset of precipitation, the surface of the soil became wetter, but with a low moisture content and an increased seepage rate. By the end of the rainfall event, the moisture content had increased until the eighth hour, whereupon the seepage rate balanced the rainfall intensity, and the soil surface had become saturated. From then on, the seepage rate decreased and stabilised: thereafter the steady state seepage rate was governed by the properties of the soil.

Under gravity, the water migrated into the embankment after the cessation of precipitation; eventually the saturated zone at the end of the rainfall event had become partially saturated as the moisture content decreased. While the moisture content in the conducting and humid zones increased, the wetting front moved downwards. The size (depth extent) of both the conducting and humid zones expanded over time. The moisture content in the conducting zone increased linearly with depth, while the moisture content in the humid zone decreased linearly with depth.

References

[1] Green W H, Ampt G. A.Studies on soil physics, Part I. Flow of air and water through soils[J]. Journal of Agricultural Science, 1911, 4:1–24.

[2] Richards L A. Capillary conduction of liquids in porous mediums[J]. Physics, 1931, 1:318~333

[3] Rubin J. Theoretical analysis of two-dimensional transient flow of water in unsaturated and partly unsaturated soils[J]. Pros. Soil Sci. Soc. Am., 1968,.32:929-941.

[4] Freeze R A. Three-dimensional transient saturated-unsaturated flow in a groundwater basin[J]. Water Resources Res. 1971(7):929-941.

[5] Remson I, Hornberger G M, Molz F J. Numerical methods in sub surface hydrology[M]. Wiley-Interscience, 1971.

[6] Neuman S P. Saturated-Unsaturated Seepage by Finite Elements[J] Journal of the Hydraulics, Division, ASCE, Dec, 1973:2233-2250.

[7] Neuman S P. Galerkin approach to saturated-unsaturated flow in porous media. Finite elements in fluids[J], Viscous Flow and Hydrodynamical, 1974:201-217.

[8] Neuman S P. Narasimhan T N. Witherspoon P A. A plication of mixed explicit-implicit finite element method to nonliner diffusion-type problems [J]. Finite Elements in Water Resources, Pentech Press, London, Plymouth, 1977.

[9] Wu Meng-xi,Gao Lian-shi.Unsteady seepage numerical analysis saturated-unsaturated soil [J].Journal Of Water Conservancy，1999(12):38-42.

[10] Wu Meng-xi.Unsaturated soil seepage and deformation analysis method and the application of the heart wall dam [D]. Tsinghua University 2000.

[11] Peng Hua, Chen Sheng-hua, An unsteady seepage finite element analysis of saturated unsaturated soil [J]. Water Dynamics Research And Progress, 2002, 17(6):253-259.

Advanced Materials Research Vol. 936 (2014) pp 1518-1521
© (2014) Trans Tech Publications, Switzerland
doi:10.4028/www.scientific.net/AMR.936.1518

Numerical Analysis on Synergetic Behaviors of AE in Concrete Failure Process

Li hua Wei

College of Architecture, Linyi University, Linyi, Shandong 276005

35809831@qq.com

Keywords: Concrete failure; AE; Synergetic effect

Abstract: The AE phenomenon can show the laws of concrete break well. In virtue of researching the relationship between inner structure state change and AE characteristic, the synergetic characteristic of AE in the concrete failure process was analyzed. Opened out the laws of concrete failure on high levels, and beneficially discussed the synergetic characteristic of AE. It is value to forecast the trend of concrete stability before failure and nondestructive testing.

Introduction

AE signal in the concrete failure progress will be emitted. Although AE technology is potential in concrete failure mechanism analysis and practical engineering, its theoretical basis still falls behind its technology development. A great deal of results of examination and scene are lack of rational theory analysis and the relationship between AE rule and patulous cracks also can not be described validly. As a result, the auspice of concrete failure has not been mastered accurately yet. The monitoring and forecast in application mostly depend on experience judge. The reliable criterion and theory foundation are absent. Those lead to low success ratio and unexpected effect. Restrict AE technology application. So the relationship between AE signal and cracks spread are confirmed and AE will be an important monitoring technology of failure.

In order to make concrete failure process clear, we should start with the whole propagation of the crack occurrence and its development, then study the inherent law of the failure character transform systematically.

Because of the complexity, fuzziness, nonlinear and indeterminacy of the character, the traditional mechanics can not be used commendably[1]. The nonlinear science, such as synergetics, catastrophic theory, chaos and fractal, have already been put into application [2~4].

Description on Synergetic Effect of Concrete AE Parameters

Establishment of Theorder Parameter Evolutionary Master Equation of Concrete Failure

Assume that the order parameter of the whole system is *Y*, which is AE counts rate. The order parameter of the subsystem parameter is *X*, which is the event counts rate. The change of the AE time counts rate can represent the whole process of concrete failure.

For the change of order parameter *Y*, assume that attenuation l is direct proportional to *Y*, and attenuation velocity $k_1 > 0$, then $l = -k_1 Y$.

For increase *m*, assume that s_1 is the rate of increase, and $s_1 > 0$. Because rather big crack propagation will lead to secondary crack' development, the influence of the subsystem must be considered. [5] indicated that the rate of increase of bifurcate affairs is direct proportional to the square of the former event counts. The increase *m* can be expressed as $m = h_1 X^2 + s_1 Y$.

So the variable equation of order parameter *Y* can be written as

$$\frac{dY}{dt} = -k_1 Y + h_1 X^2 + s_1 Y \tag{1}$$

And the variable equation of sub system *X* is

$$\frac{dX}{dt} = -k_2 X + h_2 Y + s_2 Y \tag{2}$$

Where k_2 is the attenuation of velocity, s_2 is the increase of velocity, and $s_2 > 0$.The change of the order parameter of the whole system represents evolution process of concrete failure. Because there are associated items in equation (1), the expected solution can not be gained. It can be simplified by the slaving principle of synergetics.

From Eq.2, we also find that

$$X = \frac{h_2 Y}{k_2 - s_2} \tag{3}$$

Put into Eq.1, we will have

$$\frac{dY}{dt} = -mY + nY^2 \tag{4}$$

Where $m = k_1 - s_2, n = \frac{h_1 h_2^2}{(k_2 - s_2)^2}$,From Eq.4 we can find that the coupling action between system and subsystem also restrict and is associate with the change of order parameters. The interaction is realized by positive and negative feedback.When $h_1 < 0$, $n < 0$, it is a negative feedback; $h_1 > 0$, $n > 0$, it is a positive feedback.

The Solution of Order Parameter Evolution Equation

(1) Analysis on the stable solution of order parameter evolution equation

In Eq.4, set $dY / dt = 0$, the stable solution will be gotten.

$$Y_1 = 0, Y_2 = m / n \tag{5}$$

When $Y_1 = 0$, it is a disorder state. Corresponding to the unloaded concrete it is a stable balance state and there is no AE.

Make linear stability analysis on $Y_2 = m / n$. Assume that μ is the perturbation near the steady state.

$$Y = Y_2 + \mu \tag{6}$$

Put Eq.6 into Eq.4 and ignore quadratic term of μ.

$$d\mu / dt = m\mu \tag{7}$$

The solution of this linear equation is

$$\mu(t) = \mu(0)e^{mt} \tag{8}$$

The stability of stable solution Y_2 depends on the sign of m. When $m < 0$ ($k_1 < s_2$), the stationary state is stable. In physical meaning, when the increase of the counts rate is bigger than that of attenuation, the AE order is stable.

(2) Analysis on the unstable solution of order parameter evolution equation

The unstable solution of nonlinear differential equation of Eq.4 is

$$Y(t) = \frac{1}{a + be^{mt}} \tag{9}$$

Where $a = \frac{m}{n}, b = \frac{m - nY(0)}{mY(0)}$,When $m < 0$ ($k_1 < s_2$), the increase of AE counts rate is bigger than that of attenuation. It is an active stage. From Eq.9, we can see that the AE counts rate increase by time.

When $m = 0$, it is corresponding to the phase that the counts rate changes relatively steady. The unstable solution is

$$Y(t) = \frac{Y(0)}{1 - Y(0)nt} \tag{10}$$

If $n < 0$, the order parameter will decreases by time. That contributed to the frequent generation of big ruptures results in the distribution of concrete stress. The AE counts rate in unit time is reduced. But if $n > 0$, the order parameter will increases by time. When reduce $Y(0)nt$ to 1, the total AE time will be infinite. Obviously this is corresponding to the catastrophic state.

Numerical Simulation on AE Phenomena in Concrete Failure Process

Simulation test was performed on the failure process of concrete specimen by RFPA2D. The size of specimen is 100mm×100mm, poisson ratio is 0.2, compressive strength is 40Mpa, and elastic modulus is 32.5Gpa. The specimens are loaded by displacement and the increase is 0.001mm in one step.

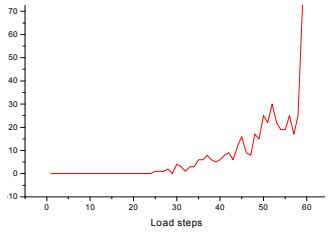


Fig.1 The 1st to 82th steps of AE counts

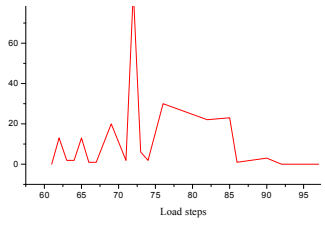


Fig.2 The 84th to 97th steps of AE counts

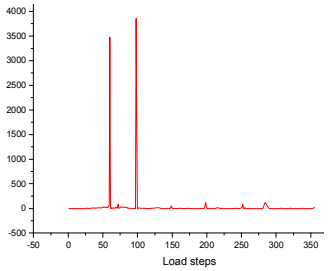


Fig.3 Whole failure propagation

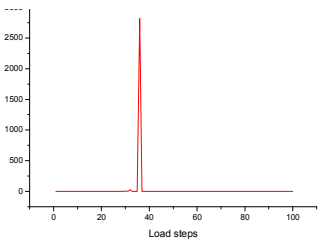


Fig.4 100 times of the 83th step

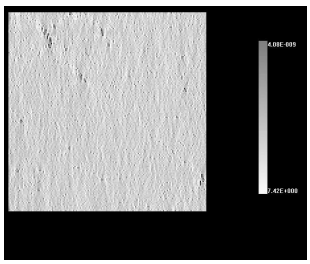


Fig.5 Failure figure of the 59th step

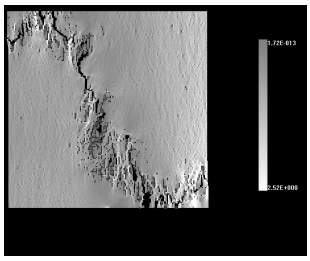


Fig.6 Failure figure of the 60th step

Synergetic Description on AE of Concrete Failure Process

According to the synergetic analysis and numerical simulation results, crack generates and develops gradually at the initial stages of load, and the AE counts increase. Here the complexity is also enhanced. When the load achieves a certain level, crack propagates quickly and induces to the AE crack increases sharply. The system is catastrophic. After this stage, the stress will be distributed again and the propagation action goes release. The AE count descends accordingly. So the whole load process is a cycle process that the AE counts rate undergoes relatively calm increase- catastrophic- attenuation- calm increase- catastrophic.

Conclusions

Due to dynamic, real-time, and the advantages of small influence on the structure of AE, the concrete nondestructive testing technology in engineering application will more and more widely. Because acoustic emission signal itself is complicated, effective feature extraction is difficulty, and acoustic emission parameters is disunion, all will influence acoustic emission directly to apply into the theory research and engineering application. In this case, the introduction of new theories, new methods to carry on the research to this problem are very necessary. Based on the study of numerical simulation method, and the combination of concrete from a new perspective, the failure process of the phenomenon of acoustic emission preliminarily analyzed. Provide new idea for concrete acoustic emission theory research and application.

Referrences

[1] Yin, G. Z., Dai, G. F., and Wan, L., Characteristics of bifurcation, chaos and self-organization of evolution of micro-cracks in concrete: Chinese Journal of Concrete Mechanics and Engineering, 2002 , 21(5), pp. 635-639.

[2] Li, X. B., and Liu, Z. X., Research on chaos and intelligent identification of acoustic emission in concrete mass: Chinese Journal of Concrete Mechanics and Engineering, 2005, 24(8), pp.1296-1300.

[3] Yin, X. G., Li, S. L., and Tang, H. Y., Study on strength fractal features of acoustic emission in process of concrete failure: Chinese Journal of Concrete Mechanics and Engineering, 2005, 24(19), pp. 3512-3516.

[4] Zhang, H.Q., Tang, C.A., and He Y.N., Discussion on selforganized criticality in concrete failure progress: Northwestern seismological journal, 2006, 28(1), pp. 1-5.

[5] Yu, G. M., Wei, Y., and Pan Y. Z., Synergetic Study and Eyeable Simulation of AE Laws in the course of concrete Break: Journal of Qingdao institute of architecture and engineering, 2005, 26(4), pp. 1-16.

Advanced Materials Research Vol. 936 (2014) pp 1522-1526
© (2014) Trans Tech Publications, Switzerland
doi:10.4028/www.scientific.net/AMR.936.1522

Simulation and Analysis of Energy Consumption Transformation in Office Buildings' Envelopes of Lanzhou

Xilian Han[1, a],Huimin Wang[1, b]and Chune Li[1,c]

School of Civil Engineering, Lanzhou University of Technology, Lanzhou, Gansu, China 730050

[a]342620786@qq.com, [b]jhjys@lut.cn, [c] xl_han77@163.com

Keywords: Dest-c; office building; energy consumption

Abstract: Taking Lanzhou meteorological condition as the background, this article simulates the energy consumption of heating system in an office building of Lanzhou using simulative software Dest-c under different building envelopes, and attained the load distributed curves and the detailed energy consumption about the system of heating and air conditioning in two different conditions, and supplied the new idea to validate the construct ion of energy consume guideline in this area.

In our country, Heat preservation and insulation performance of building envelope is very poor in cold regions. Generally, the energy consumption of the per unit building area is about 3 times than the developed countries under similar climate conditions[1]. Heating energy consumption of office building occupies a large proportion in the energy consumption of public buildings, so it is very important to research on energy conservation in office buildings [2]. This paper adopts an office building in Lanzhou as a model of this heating system. Using a simulation tool package that is developed by Ting—Hua University (Dest) for designing the building hot environment, the currently heating load of the building modeled during heating season can be calculated. The values of the maximal load and the currently maximal load can be obtained from the simulation results.

Geography and climate conditions in Lanzhou area

It is very long, cold and dry in winter in Lanzhou city, range, large diurnal, there is large different temperature between day and night. Table 1 is the coldest month outdoor temperature change curve, It shows, the minimum temperature in one day is -16.86℃, the maximum temperature is 3.7℃, the average temperature of the month is -5.53℃. The Number of days that the average daily temperature is less than or equal to 5 ℃ are 25% of the days, the Number of days that the average daily temperature is less than or equal to 5 ℃ are 25% of the days, so it need more days for heating.

The Theoretical Study

The Building Thermal Load

The thermal loads is made up of convection heat consumption, radiation heat consumption and interference heat consumption, heat passes from the outside surface to the inner surface of the enclosure structure and then pass to the indoor air. The heat load is made up of heat consumption of structure heat transfer and heat consumption which heating ventilation generated. And the second one is decided by the air circulation ratio, the first one is according to the type of calculation:

$$Q = \alpha KF(t_n - t_w) \quad (1)$$

Among them： K —Heat transfer coefficient of envelopes structure, W/m^2•℃; F —The area of the retaining structure,m^2； α —The correction temperature factor of different envelopes structure；

t_n—indoor calculation temperature in winter，℃； t_w—The outdoor calculated temperature of heating in winter,℃。

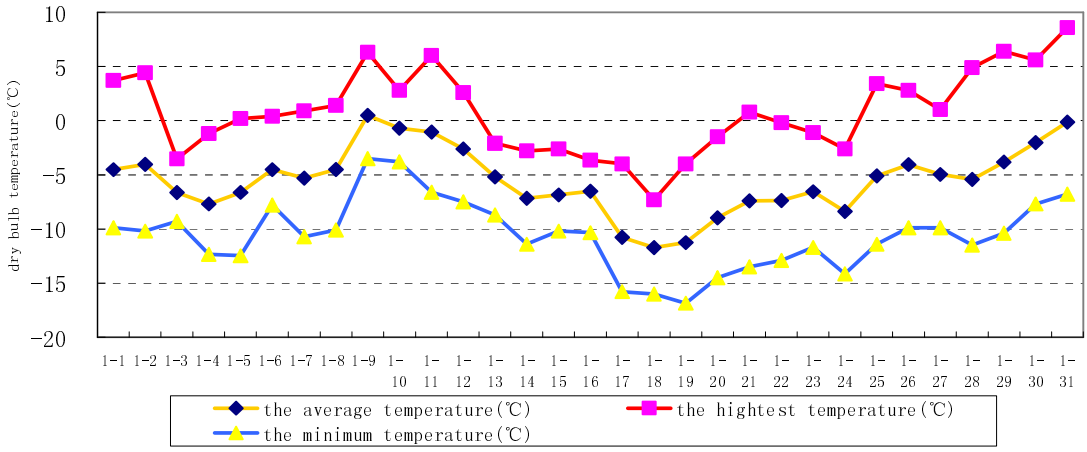


Figure 1 The Coldest Month Outdoor Temperature Change Curve

General Situation Of Building

The building models is a office buildings in Lanzhou city, and it has three layers, the height of each layer is 3.6 m, the building's area is 1580 m^2, the shape coefficient is 0.22, the area of window than wall is: east to 0.03, south 0.12, west 0.03 and north 0.17, the thermal parameters of envelopes structure are shown in table 1. Architectural appearance as shown in figure 3.1. The building including hall, office, office, stair, corridor and toilet etc. the generated building of modeling shows as Figure 2. The building includes hall, office, office, stair, corridor and toilet etc.

TABLE 1 THE THERMAL PARAMETERS OF ENVELOPES STRUCTURE

building envelope	*structure*	*Heat transfer coefficient* $W/(m^2 \cdot K)$
wall	20mm Cement mortar+240mm Hollow brick + 20mm lime mortar	1.37
window	6 mm Ordinary glass	5.7
roof	5mm mixed mortar+100mm ceramsite concrete +95mm reinforced concrete + 5 mm plaster	1.05

The Building Model

The Establishment Of Building Geometric Model

According to construction drawings to build a model in the Dest, it mainly includes the architectural appearance size, the building envelops structure parameters such as heat input, room internal interference, setting of operating time, heating operation conditions, such as figure 2.

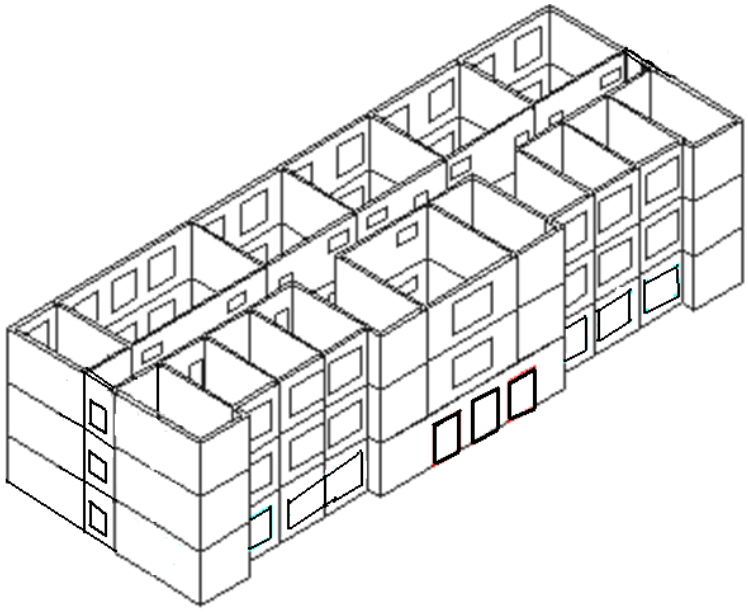


Figure 2 The Generated Building By Dest Modeling

The Results of the Simulation By Dest

By the building thermal environment simulation software Dest, We get the all-year hourly office building energy saving heat load of 134.5 kW h, the building heating season heat load index is 85.13 W/m^2. According to the design experience, such office buildings' heat load estimate index for 65 W/m^2 in Lanzhou. The office building heating load index is a little bigger, it is mainly because the building is located in cold areas, according to the requirement of《public building energy efficiency design standard》, the office buildings are not up to standard, high heat transfer coefficient leads to higher energy consumption, so the energy-saving renovation must be done.

The DeST Simulation Results and Analysis

Analysis For Different Thermal Insulation Thickness Of The Wall On Building Energy Consumption

The most simple and effective way is to remove the outside wall surface mortar , and then add thermal insulation layer in the surface of palisade structure, according to the ministry of public security fire rating requirements for the wall heat preservation material, this article selects EPS expansion of polystyrene board, as well as the popularization and application of the ministry of construction of the wall exterior insulation materials [3]. This paper selected thickness of 20 mm, 30 mm, 40 mm, 50 mm and 60 mm, after transforming the outer wall heat transfer coefficients are shown in table 2.

TABLE2 EXTERNAL WALL THERMAL PARAMETERS

thickness（mm） / name	0	20	30	40	50	60
Heat transfer coefficient	1.37	1.02	0.87	0.79	0.65	0.53

In the other condition is constant, only change the wall under the condition of different thickness of wall in the same heat preservation material, analysis the impacton on the construction of cold and heat treatment of annual accumulative total load by simulation calculation. Results such as3～4.

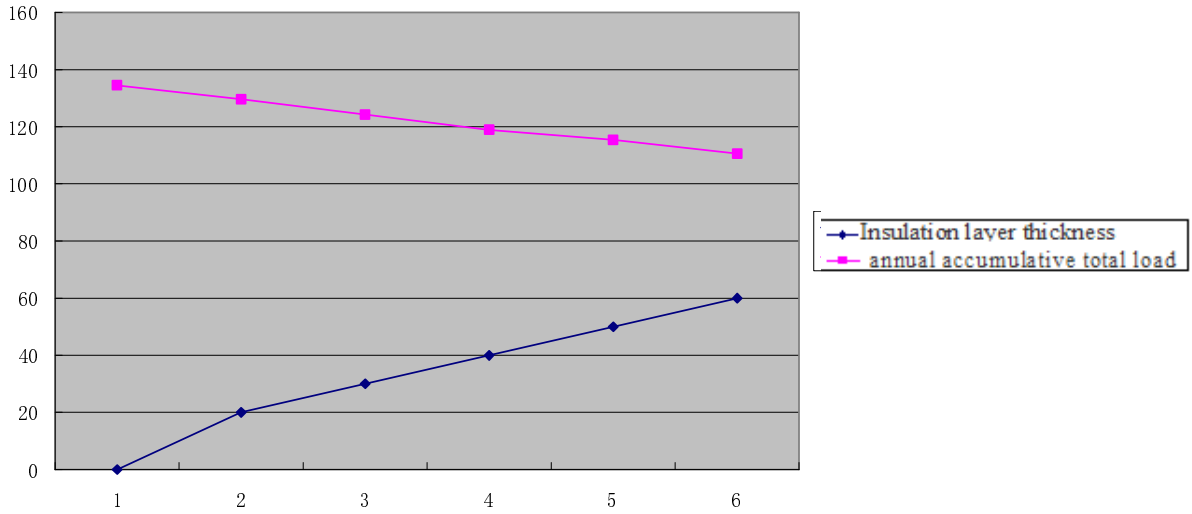


Figure 3 Different thickness of building thermal load

Analysis

Figure 3 shows that both public buildings of the main structure of hollow brick add wall thermal insulation materials have bigger influence on the building thermal load throughout the year, mainly due to lanzhou winter indoor and outdoor temperature difference is bigger, increase the thermal insulation layer thickness in order to reduce the wall heat transfer, heat transfer coefficient can effectively prevent the indoor to outdoor, to improve building thermal treatment of annual accumulative total load effect is obvious. But with the increase of the insulation layer thickness, the effects on the heat load gradually reduce, add 20 mm less insulation heat load effect was most pronounced; Add insulation layer thickness of 20 ~ 40 mm, with thermal insulation layer of heat treatment of annual accumulative total load rate approximately 1.98 x 10^3, and add the insulation layer thickness of 40 ~ 60 mm, with thermal insulation layer of heat treatment of annual accumulative total load rate approximately 1.04 x 10^3, so when a thermal insulation layer thickness of 30 mm or increase the insulation layer thickness to reduce the effect of the building throughout the year the total heat load is not obvious.

4.2 Change the outside window and analysis of impact on building energy consumption

Windows modification measures can be based on the original outside the window with a layer of the window, also can be replaced the original window for energy-saving window, literature [4] to simulate the energy saving effect of different types of Windows, this paper would not be in white.

4.3 Conclusion

Lanzhou city public building exterior wall thermal insulation at least 35 mm thick increase EPS insulation board into a more optimal solution.

Lanzhou city public building retrofit design of the window, in order to double hollow Low radiation low-e glass is the best, the limited economic conditions can consider double hollow glass window.

Acknowledgements

This research is financially supported by the National Science Supported Planning Foundation(2011BAJ03B08）and the Fundamental Research Funds for Lanzhou University of Technology (No. TM-TJ-1003). This support is gratefully acknowledged.

References:

[1] Zhang jun, YanQing etc. Cold area residential exterior energy-saving effect analysis [J]. Journal of northeast forestry university. 2009, 5 (6) : 62-63.

[2] Zhang Haijun Ding Yunfei. Guangzhou office building air conditioning energy consumption analysis and evaluation [J]. Energy saving technology. 2007, 25 (6) : 523-534.

[3] Yao Jian Zhou Yan, Lin Yun, Zhang Wenhong. Exterior wall construction of residential energy consumption in hot summer and cold winter region [J]. The influence of new building materials, 2006.

[4] Liu Yuning, Chen, etc. Glass Windows in the building energy conservation function and its characteristic analysis [J]. Journal of architectural ventilation and air conditioning heat. 2006, 25 (6), 80-84.

Advanced Materials Research Vol. 936 (2014) pp 1527-1530
© (2014) Trans Tech Publications, Switzerland
doi:10.4028/www.scientific.net/AMR.936.1527

Study on the Key Technology of Hot Regeneration of Plant-mixed Asphalt Material

Qing Jin[1,a] , Xinzhuang Cui, Junjie Lou, Weize Tang, Wei Sui, Zhijun Gao

[1]School of Civil Engineering, Shandong University, No. 17922, Jingshi Road, Jinan, Shandong Province, PR China

[a]262970068@qq.com

Keywords: Asphalt Pavement; Plant-mixed Hot Regeneration; Mix Design

Abstract: It is necessary to mend the shattering process and heating technique in order to improve the technology of hot regeneration of plant-mixed old asphalt. The temperature and the reactivation of old asphalt material is supposed to be better controlled as well as the process of mixing and paving roadways as a result of technological improvement. With the reconstruction works of the highway G205 from the Yellow River Bridge to the Liuqiao roundabouts, research of old asphalt mixture has been carried out and all the products turned out to meet the design requirements, according to the results of thimble test, water stability test and tension test in low temperature of Marshall specimen.

Introduction

An increasing number of distresses with varying degrees of damage appear in the high grade roads in China, especially the ones constructed in early 1990s. These appearances severely impact the traffic safety and riding comfort. Pavement maintenance, as a measure tackling the problems, also brings lots of old asphalt materials and, as a result, environmental pollution and economic problems. Therefore, it is significant for the whole society to research on the technology of asphalt regeneration.

The technology, as mentioned above, actually has experienced a huge development since 1980s. In situ cold regeneration, hot regeneration and plant-mixed hot regeneration are the three mature techniques nowadays. Among them, the plant-mixed hot regeneration technology is a kind of practical, flexible and convenient method also with some drawbacks, such as low consumption of materials and inadequate heating of old asphalt. In 2007, the Highway Administration of Binzhou, Shandong invested 800 million yuan to introduce the technology and facilities from Japan and reform the existing craft of plant-mixed hot regeneration. This improvement has been successfully applied in the reconstruction project of G205.

Improvement of technological process

As to reform the asphalt mix plant, more than 800 thousand yuan has been invested to introduce an impact crusher, to crush the old asphalt blocks into a suitable gradation. After crushing the mixture, all the materials should be sieved and stored respectively, in order to restrict the variation of gradation. Unlike the traditional method, asphalt particles should be heated in an indirect downstream furnace with a long combustion chamber (the second dryer) successively. This device makes the materials not exposed to fire and heated by hot air current, effectively prevents the asphalt from burning and aging. The old material gets mixed with the regenerant and after that new asphalt should be put into the mixture. The process above ensures the regeneration of old asphalt in

old material. In comparison with the traditional technology, the demand of old asphalt mixture increases to 30% and the heating temperature becomes 160℃. In the reconstruction project of G205, the whole asphalt pavement (about 12cm) is excavated and recycled for regeneration. The process flowchart shows in Fg.1.

Temperature control

Temperature-control goes throughout the whole process of hot regeneration. In another word, temperature-control, along with the regeneration craft, makes up the core of this technique.Firstly, when heating the old mixture, an appropriate temperature is needed in order to create conditions for further malaxation and reactivation. Since the aging phenomenon under high temperature (>180℃) and oxidation in aerobic environment, the preheat process of old asphalt mixture should be located in a cooler situation. On the other hand, there should be sufficient heat permeating into the mixture while being heated as a result of low electric conductivity of asphalt. Therefore, it is supposed to raise the temperature with a certain heating time or lengthen the time with a certain temperature. Longer heating time lowers the efficiency of construction. The optimum point of temperature and heating time should be identified according to an actual project. Secondly, it's also needed to offer suitable operating temperature for the regeneration of old asphalt and the mixing of new material through temperature control. That is because the asphalt binder in the old material must be in softening state when regenerating. Difference between the temperatures of the old and new material makes it necessary to provide such a heating environment for the sake of final products.At last, as well as the process of paving with new asphalt mixture, the products require an adequate paving temperature in order to obtain enough time for compaction, meeting the design requirements and demands of structure. In addition, cracks could be effectively avoided with less temperature difference.

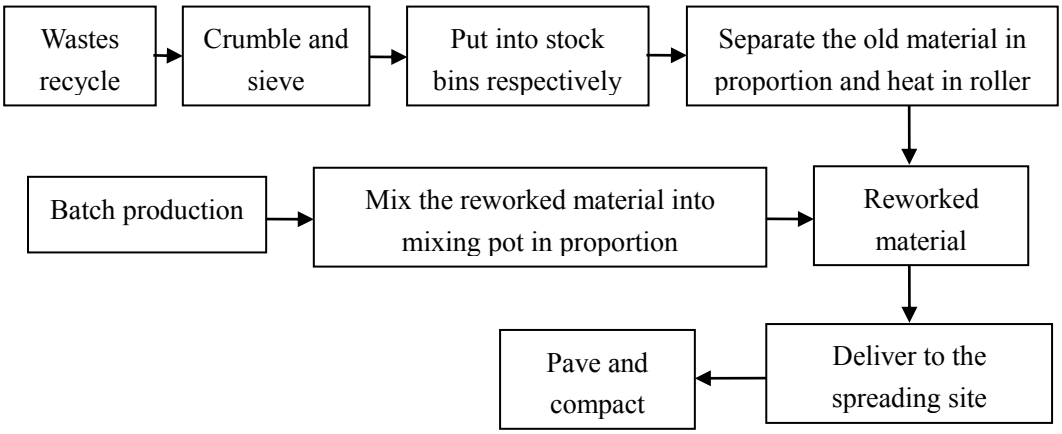


Fig. 1. Flow chart of the technology of Plant-mixed Hot Regeneration

TABLE 1. TEMPERATURE CONTROL REQUIREMENTS OF THERMAL REGENERATION [℃]

procedure	Preheating phase of crumbles		Before delivering	New materials	Recycled materials	Paving temperature
	Temperature at the fan entrance	Storage temperature of crumbles				
requirement	160~180	150~160	>150	>150	>150,<170	>140

Mixture design

The quality of old asphalt materials is the foundation of the whole regeneration project. Thus it is necessary to evaluate these raw materials. The result of the asphalt content test, which was executed at the Highway G205 from the Yellow River bridge to the Liuqiao roundabouts, shows that the content of milling scraps between 10-20mm is 2.9%, and 4.9% for between 0-10mm. The following experiment of sieve test (water washing) with raw materials is listed in Table 2.

TABLE 2. RESULT OF THE SIEVE TEST WITH OLD ASPHALT MIXTURE CRUMBLES

Mesh size [mm]	19	16	13.2	9.5	4.75	2.36	1.18	0.6	0.3	0.15	0.075
Quality percentage through the sieve pore [%]	100	100	100	95	68.8	41.7	30.0	22.2	16.5	12.6	9.4

Grading test was executed in the grading range (Hot regeneration AC-20) recommended by Shandong Transportation Construction Testing Center, according to the experimental results in Table 2. By controlling the major pore sizes (4.75mm; 2.36mm; 0.075mm), the optimal curve could be selected as the target proportion. The proportion is: 10-20mm: 0-10mm: 10-20mm: 5-10mm: 3-5mm: 0-3mm: mineral powder = 10:10:28:23:6:20:3.

Quantity of new asphalt materials was calculated according to the proportion and the content of asphalt in the scrap. After conducting the Marshall test at the asphalt content of 3.5%, 4.0%, 4.5%, 5.0%, 5.5%, the optimum volume was confirmed at 4.4% (3.6% for new asphalt material). Marshall void fraction was 4.6%. Percent voids in mineral aggregate (VMA) was 13.3%. Asphalt saturation was 65.7%. Stability value was 10.16kN. Flow value was 3.14mm. Density was 2.422g/cm^3. All the values above meet the design requirement perfectly.

Performance test for the reclaimed mixture

Performance test for the reclaimed mixture was carried out in the selected asphalt content according to the Marshall test before. High-temperature stability, water stability and low-temperature tension test are the major items. Water stability and anti-rutting performance was evaluated by Hamburg Wheel-tracking Test.

High-temperature stability

The high-temperature stability was evaluated by the rutting test according to the standard JTJ052-200. Dynamic stability of the regenerating specimens forming with the optimal asphalt content was measured in order to evaluate the mixture's anti-rutting performance. As a result, the maximum deflection was 2.34mm, dynamic stability value was 1380 times/mm. The anti-rutting performance of regenerating asphalt mixture turns out to meet the minimum requirements (800times/mm) in this climate zone.

Water stability

Water is able to separate asphalt from mineral aggregate and dissolve soluble compounds, which reduces the strength of the product. The water permeating into the mixture could expand the pavement while after that the pavement is going to shrink again. The circulation above will ultimately crack the pavement.

This project used the freeze-thaw split test for examining the water stability and the result showed that TSR=85.3% (meet the requirement: TSR=75%).

Low-temperature tensile property

When temperature decreases, asphalt mixture should be constricted by the base course and then lead to stress. When the stress exceeds the ultimate tensile strength, cracks occur. Therefore, a great low-temperature crack resistance and deflection performance is necessary for the product.
The tensile property was evaluated under -10℃ and the loading rate of 50mm/min and the result was 2357μm, which meets the requirements in the climate zone.

Hamburg Wheel-tracking Test

Hamburg wheel-tracking test is used for asphalt water stability and anti-rutting performance evaluation.

The test was executed according to the test procedure and the criterion in Texas (50℃, soaking in water). The result evidently showed that the mixture with 20% scraps possesses the best property for both. This result is consistent with the test by the standard of China. An inflection point appears in the mixture with 30% scraps after 12500 times of the test, which means the shortage of new asphalt material leads to the deficiency of asphalt film and weaken the water stability and anti-rutting performance as well.

Conclusion

The technology of plant-mixed hot regeneration has been improved in favor of temperature control and old asphalt mixture recycling. Depending on the practical project of G205 and laboratory tests, the grading curve and proportion of new asphalt was successfully determined and all indexes met the stipulations appropriately. In conclusion, the maximum volume of old asphalt mixture was 20% of the total, amounts to 4.4% of the regenerating material, including 3.6% for new asphalt.

Acknowledgments

This work was supported by the Chinese Natural Science Foundations (Nos.51279094, 51078222 and 50708056), the Independent Innovation Foundation of Shandong University (IIFSDU) (No.2010JQ001) and the Natural Science Foundations of Shandong Province, China (No.ZR2011EEM012).

References

[1] X. Yi, G.D. Zhao, X.M. Chen, The key technology of bituminous pavement hot regeneration in situ, Journal of highway and transportation research and development. 2009，1: 39-42.

[2] J.G. Geng, J.L. Dai, Z.D. Chen, Low-temperature crack resistance of hot regenerating asphalt mixture evaluation, Journal of Wuhan University of Technology, 2008，32(6): 1029-1032.

[3] J. Xie, J.H. Fan, S.S.Wu, Bitulith factory hot regenerating mixture design and regenerant research, Highway, 2008, 9(9). 368-372

Advanced Materials Research Vol. 936 (2014) pp 1531-1538
© (2014) Trans Tech Publications, Switzerland
doi:10.4028/www.scientific.net/AMR.936.1531

Analyses of the Protective Effect of Polyethylene-triethoxysilane and Triethoxysilane Emulsion Coatings on Concrete Substrate

Zhang Xinyuan[1, a], Li Shaochun[2, b], Zhao Tiejun[3,c] and Jin Zuquan[4,d]

[1,2,3,4]Collaborative Innovation Center of Engineering Construction and Safety in Shandong Blue Economic Zone, Qingdao 266033, China; Qingdao Technological University, Qingdao 266033, China

[a]15165214457@163.com, [b]seaman0294@126.com, [c]ztjgp@263.net, [d]jinzuquan@126.com

Keywords: Silane coating; Durability; Waterproof; Service life

Abstract: Water could transport aggressive substances such as carbon-dioxide, sulfates and chloride ions in reinforced concrete structures. By penetration, the stability of the whole structure is influenced. This paper deals about waterproof effect and chloride resistance of two kinds of silane coatings, polyethylene-triethoxysilane and triethoxysilane emulsions on concrete substrate along with the mechanism of the hydrophobic action. The results, in terms of visual observations, chloride test and water absorption test, showed that the two silane coatings could reduce the chloride penetration and the water absorption efficiently. The comparison between the two indicates that polyethylene-triethoxysilane penetrates little when applied on the substrate, but it performs better waterproof effect and is more efficient to chloride penetration.

Introduction

Nowadays low durability of concrete structures has become a serious problem. The demand for longer service life leads people to focus more on the function materials. The surface tension in capillary pores in concretes pulls in water because of capillary suction[1’2]. In this process, the penetration of deleterious dissolved substances such as carbon-dioxide, sulfates and chloride ions is allowed and the freeze-thaw damage is harmful to the durability as well. Surface treatment is commonly used to improve the resistance of concrete against the penetration and freeze-thaw damage. In general, protective surface treatment can be attained though surface coating, sealing, and impregnation. [3-9]. As a kind of wonderful protective material, silane materials have good permeability and waterproof effect, they function by penetrating concrete pores, forming a transparent thin layer on the surface of the inner capillary pores of the concrete. Because the pores are left open, the water evaporation of concrete is allowed which is essential for massive concrete structures. The advantages make them an potential protective material as isolators and they are widely used in different engineerings to increase the service life of reinforced concrete structures.

This article is to compare and analyze the waterproof effect, permeability, workability and chloride resistance of two different types of silane coatings for concretes, polyethylene-triethoxysilane and silane emulsions. The corrosion process, the protective effect and the relative mechanisms are mentioned as well.

Mode of Action

Concrete, even of high quality, contains capillaries and micro cracks in nature. In the capillary absorption process is irresistible unless the surface state is changed. Hydrophobic agents always result in chemical reactions on the concrete substrate. Currently, the silanes, silanes polymers and a mixture of these two components are widely used. [10] The small structure of silane materials allows them to easily penetrate in dense substrates. Although the molecular structure is relatively large compared to silanes', silane polymers and silane emulsions also can penetrate in the concrete substrate efficiently. [11-13] In this paper, the silicon-oxygen bonds are relatively quick formed as the silanol groups contact the concrete substrate. The major difference between the radical polymer and emulsion is the carbon chain is formed before the Si-O-Si bonding, so the substrate is protected by a double chain structure, this structure is more durable and the hydrophobic effect still remains. For emulsions, the alkyl-groups bonded to the silicon atom are not linked together and spread out the concrete surface, so the hydrophobic groups can function. The preparation and protective mode of polyethylene-triethoxysilane are illustrated in Fig.1. Through free-radical polymerization, carbon chain is formed, then ethanol molecules are released and silanol structures are formed, polycondensation leads to polysilane, which can be reacted to the hydroxyls on the concrete substrate, forming a stable bond with two surface layers.

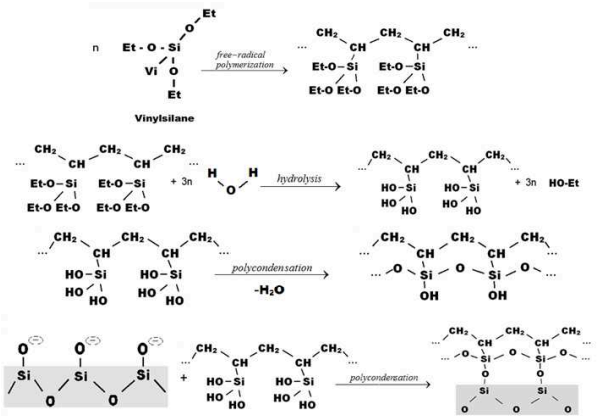


Fig.1: Mechanism Preparation and Reaction of Polyethylene-triethoxysilane on Concrete

It should be noted that, depending on the service conditions, concrete structures absorb liquids (such as water) by capillary forces following the Washburn equation, $\rho=(2\gamma/r_c)\cos\sigma$, where γ represents the liquid surface tension, r_c is the radius of capillary pore, and σ is the contact angle as it is showed in Fig.2. In the condition of constant pore structure and water viscosity, the contact angle is the main factor of capillary force. When the low-surface-tensioned silane coati ng is applied on the concrete structure, it spreads quickly on the concrete and the surface energy of concrete is changed. The low surface energy effect determines that the silane coated concretes show good hydrophobic effect. The molecular attraction between water and the pore walls is decreased and the contact angle becomes more than 90°, ρ becomes negative and the liquid won't fill the pore spontaneously, but remains as sphere water drops on the concrete surface.

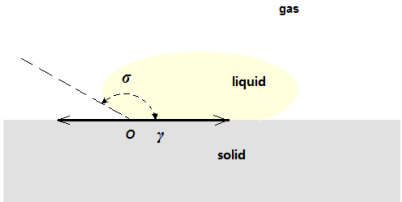


Fig.2: Illustration of Water and Silane Coated Concrete Surface

Experimental Methods and Materials

Materials

Standard concrete (water-cement ratio 0.4 and 0.5) have been prepared as the substrates for the experiments. The compositions of concretes are given in Table.1. According to the amount of mixing water, 1% and 0.8% polycarboxylate superplasticizer were added respectively,

TABLE. 1: CONCRETE COMPOSITION GIVEN AS KG/M^3

Components	Cement	Sand	Gravel	Water	Superplasticizer	W/C
A	380.0	579.0	1269.0	152.0	1%	0.4
B	320.0	653.0	1267.0	160.0	0.8%	0.5

The concretes were added in cubes with an edge length of 100mm and have been cast in steel forms without release agent in order not to disrupt the surface waterproof effect. After 48 hours curing under wet burlap, the cubes were formed and placed in a humid maintenance room (T=20±3℃, RH≥90%) until the age of 14 days. At the age of 14, the cubes were cut into two halves with a diamond saw, then, these half cubes were put back in the maintenance room until the age of 28 days. The half cubes were then dried in a ventilated oven at 50℃ until constant weight had been reached. Then the side surfaces (50×100mm) were sealed with wax, then the blocks were ready for coating, the surface which was in contact with water and steel form during hardening has been coated with polyethylene-triethoxysilane and silane emulsions respectively with the amount of 400 g/m^2. After a static duration of 7 days of penetration, the blocks were ready for the water absorption tests and chloride penetration test. The coated surface has been put in contact with water and the weights were measured in the regular intervals for 72 hours. In the chloride penetration test, the same half cubes have been put in contact in 3% aqueous NaCl solution for 28 days. Then thin layers of concrete have been milled off and the chloride content of collected powder has been determined by means of ion chromatography.

Preparation of Silane Coating

Dicumyl peroxide was selected as initiator. Firstly, vinyl-triethoxysilane was added to the flask, the air was eliminated from the flask by nitrogen, dicumyl peroxide was added into the flask, then the system was heated to 95℃ with stirring speed of 500 r/min until the reaction time for 12 hours, finally the desired polyethylene-triethoxysilane was obtained after cooling. Special attention should be paid to the time and temperature during the synthesis since high degree of polymerization is not required in this study, the synthesis time could be determined by half-life of dicumyl peroxide when the temperature changes.

Two kinds of emulsion were prepared, namely methyl-triethoxysilane emulsion and octyl-triethoxysilane emulsion. Since there is no particular emulsifier for silane, a series of tests have been done to get a steady emulsifier for the silane system. Eventually a compound emulsifier with good emulsification and significant stabilization has been chosen to be the emulsifier for silanes. The mixture contained a proportion of deionized water, silane and a compound emulsifier of Emulsifier S-80, peregal and polyethylene glycol 2000. All these materials were added in the reactor, then stirred evenly with temperature of 55℃and stirring speed of 1200r/min until they were all completely dissolved. Then the emulsion was kept stirring for 5 hours, then the stable emulsion was obtained after cooling. Though the change of proportion, the balance of water, silane and emulsifier assures the emulsion could be function effectively.

Results

Capillary Absorption and Water Repellency

The capillary water absorption by reference concretes and polyethylene-triethoxysilane coated concretes have been determined experimentally. The amount of absorbed water has been plotted. Results are shown in Fig. 3. During the initial phrase of capillary absorption the mass gain can be approximated by a linear function. The inclinations of the straight line is called capillary absorption coefficient.

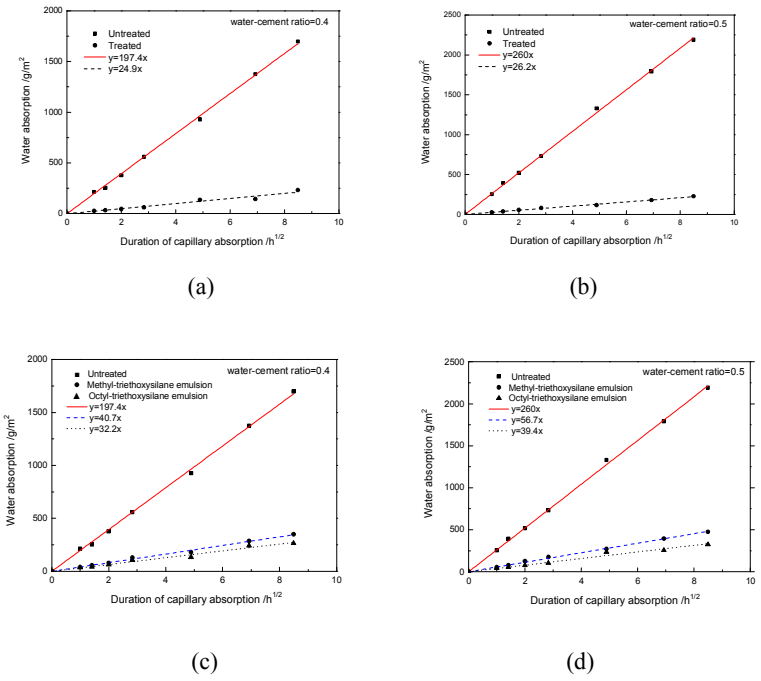


Fig. 3 Effect of Polyethylene-triethoxysilane(a,b) and Silane Emulsion(c,d) on Properties of Concrete Capillary Water Absorption (W/C=0.4(a,c);0.5(b,d))

The results showed in Fig. 3(a,b) indicates that polyethylene-triethoxysilane has significant waterproof effect as concrete coating. When the water-cement ratio is 0.4, the capillary absorption coefficient of the untreated concrete is 197.4 g/(m^2•$h^{0.5}$), but it is only 24.9g/(m^2•$h^{0.5}$) after the coating, the coefficient reduces approximately to 1/8; and when concrete cement ratio is 0.5, the capillary absorption coefficient of the untreated concrete is 260.0g/(m^2•$h^{0.5}$), but it is only 26.2g/(m^2•$h^{0.5}$) after coating, reduces approximately to 1/10. Comparison between the different water-cement ratio concretes with polyethylene-triethoxysilane coating, it is shown that in the case of higher water-cement ratio, the absorption coefficient is relatively larger though, the reduction of water absorption coefficient is great, which indicates that polyethylene-triethoxysilane, as a concrete coating, is more suitable for the waterproof treatment in high water-cement ratio concrete.

The results of two silane emulsions are shown in Fig. 3(c,d). As is shown, when water-cement ratio is 0.4, the capillary water absorption coefficient of methyl-triethoxysilane emulsion treated concrete is 40.7g/(m^2•$h^{0.5}$), and is 32.2g/(m^2•$h^{0.5}$) of octyl-triethoxysilane emulsion treated one. When the water-cement ratio is 0.5, the capillary absorption coefficient increased to 56.7g/(m^2•$h^{0.5}$) of methyl-triethoxysilane emulsion treated concrete, and 39.4g/(m^2•$h^{0.5}$) of octyl-triethoxysilane emulsion treated one. The results indicate that the octyl-triethoxysilane emulsion has better waterproof effect than methyl-triethoxysilane, especially for concrete of W/C=0.5. From another perspective, the change of water-cement ratio had little effect (capillary water absorption coefficient

increased by 18.3%) for the results of octyl-triethoxysilane emulsion, while for methyl triethoxysilane emulsion, the effect is relatively greater (capillary water absorption coefficient increased by 28.2%).

Chloride Penetration

The results of chloride penetration are shown in Fig. 4 of different water-cement ratio (0.4, 0.5) and different silane coatings.

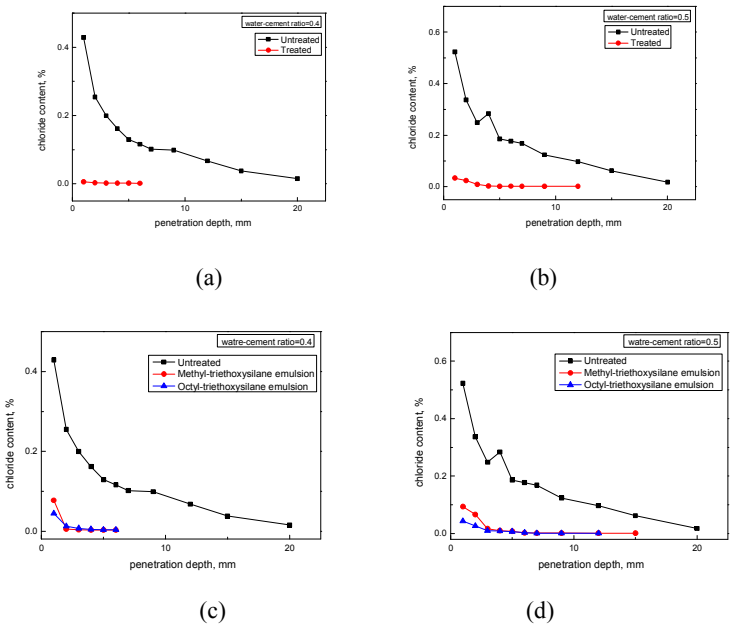


Fig. 4 Effect of Polyethylene-triethoxysilane(a,b) and Silane Emulsion(c,d) on Chloride Penetration in Concrete (Water-cement ratio=0.4(a,c);0.5(b,d)).

It can be seen clearly that silane coatings can efficiently prevent chloride penetration into the concrete when the surface is in contact with NaCl solution. A significant reduction of chloride penetration is observed. As we can see, polyethylene-triethoxysilane has a very good ability to resistance chloride ion invasion. The chloride penetration depth can reach to 20mm of the untreated concrete with high content, but there is little content when the polyethylene-triethoxysilane is applied, especially when the water-cement ratio is 0.4, the content is too low to measure; even when the water-cement ratio is 0.5, the penetration depth of chloride ions is existed in a thin surface layer of only 1~2 mm with a minimum content. After silane emulsions' treatment, the chloride ion content of concrete is still very low, penetration depth is only 1~2mm; when water-cement ratio is 0.5, penetration depth ranges from 1mm to 5mm, but with low content too. In addition, the octyl-triethoxysilane emulsion has better resistance to chloride penetration than the methyl-triethoxysilane emulsion.

Penetration Depth

The results of penetration depth in concrete of all the coatings mentioned above are shown in Table. 2.

TABLE. 2 PENETRATION DEPTH OF SILANE COATING IN CONCRETE(MM)

	Silane coating types		
W/C	Silane coating types	Methyl-triethoxysilane emulsion	Octyl-triethoxysilane emulsion
0.4	1.5	4.7	3.7
0.5	1.3	6.8	5.4

From the table above, it is obvious that penetration depth of different silane coatings varies. When the water-cement ratio is 0.4, methyl-triethoxysilane emulsion has deeper penetration depth of 4.7mm than the others, and 6.8mm when the water-cement ratio is 0.5. The results indicate that methyl-triethoxysilane emulsion has the best penetration among these coatings. Besides, from the penetration depth of 1.5mm and 1.3mm, it could be seen the polyethylene-triethoxysilane of high viscosity is prevented of penetrating into the concrete, which makes it only function in the very thin surface layer of concrete. Moreover, the emulsion penetrate quickly into the substrate, while polyethylene-triethoxysilane seems to have a little penetration difficulty.

Discussion

If the high molecular polyethylene-triethoxysilane is obtained, it can significantly improve the waterproof effect of concrete surface as a protective coating. However, because of the high polymerization degree, its penetration depth is low. The water spray test shows that it is about only 1mm penetration depth of polyethylene-triethoxysilane, which means the protection is effective within very thin depth of concrete. If the upper surface of concrete is pilled off by the external force, the protection can not be guaranteed.

When water-cement ratio gets higher, the porosity of the concrete gets higher too, and this allows silane emulsion to penetrate deeper. In addition, the particle size results in the degree of coating itself penetration into concrete in the same condition. Methyl-triethoxysilane emulsion has deeper penetration depth than the others; this is because the particle size of methyl-triethoxysilane is relatively small compared to octyl-triethoxysilane emulsion. This results in the variation of penetration depth in the same condition. Besides, because of the large molecular structure of polyethylene-triethoxysilane, it is prevented from penetrating into the concrete, which makes it very difficult to get to the inner concrete to function. Although its penetration ability is not desirable, it is still efficient as an isolator to water absorption and chloride penetration.

As higher concrete porosity could allow deeper penetration of silane materials, the resistance ability improves. Therefore, it can be considered that high water-cement ratio concrete is more suitable for surface treatment of concrete.

It can be indicated that the penetration depth of coating is directly related to the molecular structure of the silane material itself. As a macro-characteristic of molecular weight and molecular structure, viscosity could be used to determine the penetration ability of silane coating. From the prepared coatings, it can be observed that the molecule complicated polyethylene-triethoxysilane, which has the highest viscosity, showed the poorest penetration ability. The less viscosity ones, methyl-triethoxysilane emulsion and octyl-triethoxysilane emulsion shows very good penetration ability, so viscosity could be considered as the penetration ability indicator of the silane materials.

Conclusions

Through radical polymerization, stable polyethylene-triethoxysilane of low evaporation rate and high content can be obtained.

Polyethylene-triethoxysilane has significant waterproofing effect. When the water-cement ratio is 0.4, the capillary water absorption coefficient for treated concrete is about 1/8 of the untreated concrete; when the water-cement ratio is 0.5, the capillary water absorption coefficient decreased to 1/10. It is more suitable for the protection of high water-cement ratio concrete.

Polyethylene-triethoxysilane coated concrete has good resistance to chloride intrusion. The chloride ion content in concrete is very low after 28 days' soaking, and depth of chloride ions invasion is only 1~2mm.

The stable silane emulsions could be prepared compounded of Emulsifier S-80, peregal and polyethylene glycol 2000.

The silane emulsion can effectively prevent water from entering into the inner concrete, octyl-triethoxysilane emulsion has better waterproof performance than methyl-triethoxysilane emulsion, but water-cement ratio has great influence on the waterproof ability of the emulsions.

The silane emulsion can obviously resist chloride intrusion. The chloride content of silane emulsion treated concrete is very low with chloride ions only existed in a depth of 1~2mm(W/C=0.4) and 1~5mm(W/C=0.5) of the surface. Octyl-triethoxysilane emulsion's ability to resist chloride ion penetration is better than that of the methyl-triethoxysilane emulsion, because of the involvement of its excellent waterproof effect of the silane itself.

Acknowledgment

This study was supported by the National Natural Science Foundation of China (Grant No. 51178230), the National Natural Science Foundation of China (Grant No. 51308316), the State Key Laboratory Open Foundation of High Performance Civil Engineering Materials (Grant No.2011CEM007), the Joint Fund Project of Qingdao Basic Research and Science and Technology Bureau of Qingdao and the Research and innovation teams in university of Shandong Province.

References

[1] C. Feng, Y. Kong, G. Jiang, J. Yang, Y. Zhang and Y. Li: 'Effect of Silane-Acrylic Emulsion Treatment on Wettability of Porous Media',Transp Porous Med. ,2012, 92,(3), 619-631.

[2] A. Geetha and P. Perumal: 'Effect of Waterproofing Admixtures on the Flexural Strength and Corrosion Resistance of Concrete', J. Inst. Eng. India Ser. A ,2012, 93, (1), 73-78.

[3] M. Medeiros and P. Helene: 'Efficacy of surface hydrophobic agents in reducing water and chloride ion penetration in concrete', Mater. Struct., 2008, 41, (1), 59-71.

[4] M. A. Kargol, U. Müller, A. Gardei: 'Properties and performance of silane: blended cement systems', Mater. Struct., 2012, Nov.,27

[5] W. J. van Ooij, D. Zhu, M. Stacy, A. Seth, T. Mugada, J. Gandhi and P. Puomi: 'Corrosion Protection Properties of Organofunctional Silanes - An Overvie', Tsinghua Sci. Tech., 2005, 10, (6), 639-664.

[6] L. Schueremans, D. V. Gemert and S. Giessler: 'Chloride penetration in RC-structures in marine environment-Long term assessment of a preventive hydrophobic treatment', Constr. Build. Mater., 2007, 21, (6), 1238–1249.

[7] Y. Xu and D.D.L. Chung: 'Improving the workability and strength of silica fume concrete by using silane-treated silica fume', Cement Concrete Res., 1999, 29, (3), 451-453.

[8] P. A. M. Basheer, L. Basheer, D. J. Cleland and A. E. Long: 'Surface treatments for concrete: assessment methods and reported performance', Constr. Build. Mater., 1999, 29, (3), 451-453.

[9] F. Tittarelli and G. Moriconi: 'The effect of silane-based hydrophobic admixture on corrosion of galvanized reinforcing steel in concrete', Corros. Sci., 2012, 52, (9), 2958-2963.

[10] F. Tittarelli , G. Moriconi: 'The effect of silane-based hydrophobic admixture on corrosion of reinforcing steel in concrete', Cement Concrete Res., 2008, 38, (11), 1354-1357.

[11] J. Dai, Y. Akira, F.H. Wittmann, H. Yokota and Peng Zhang: 'Water repellent surface impregnation for extension of service life of reinforced concrete structures in marine environments: The role of cracks', Cement Concrete Comp. 2010, 32, (2) , 101-109.

[12] F.H Wittmann, R. Jiang, R. Wolfseher and T. Zhao: 'Application of Natural Products to make Integral Water Repellent Concrete', Proc. 6th Int. Conf. On 'Water Repellent Treatment of Building Materials', Italy, May 2011, Istituto Superiore per la Conservazione ed il Restauro, Paper 11.

[13] T. Zhao, F.H Wittmann, R. Jiang and W. Li: 'Application of Silane-based Compounds for the Production of Integral Water Repellent Concrete',Proc. 6th Int. Conf. On 'Water Repellent Treatment of Building Materials', Italy, May 2011, Istituto Superiore per la Conservazione ed il Restauro, Paper 13.

CHAPTER 14:

Technologies and Materials in Oil Industry

Advanced Materials Research Vol. 936 (2014) pp 1541-1548
© (2014) Trans Tech Publications, Switzerland
doi:10.4028/www.scientific.net/AMR.936.1541

Research Progress of Thickening Agents for Supercritical CO_2

Sun Wenchao[1,a], Sun Baojiang*[1,b], Fan Zhi[1,c]

[1]School of Petroleum Engineering, China University of Petroleum（East China）,Qingdao, Shandong, China, 266580

[a]sunwenchao8306@163.com, [b]sunbj1128@126.com, [c]fanzhi.2009@163.com

Keywords: Shale gas, Supercritical CO_2, Thickening agents, Polymer, Small molecular, Surfactant

Abstract. Although supercritical CO_2 fracturing has incomparable advantages compared to hydraulic fracturing as a new recreating technology of shale gas reservoir, the application of this technology has been limited by the low viscosity and weak carrying capacity of proppant. It's critical to enhance the viscosity of supercritical CO_2 by adding thickening agents. Thickening agents for supercritical CO_2 that have been studied by researchers mainly contained polymers, small molecular compounds and surfactants. Thickening agents that match with CO_2 are characterized by low cohesive energy density, low polarity, high free volume and Lewis base. It's necessary to study the interaction between thickening agents and CO_2 by molecular simulation to design inexpensive, green thickening agents which could increase the viscosity of supercritical CO_2 remarkably under low concentration.

Introduction

Compared to conventional natural gas reservoirs, shale gas reservoirs are hard to be exploitated. It is uneconomic to exploit shale gas without well stimulation such as fracturing. Hydraulic fracturing technology has been appiled effectively in shale gas exploitation in the United States, but also introduced some significant problems at the same time, such as reservoior damage, large water consumption, and the pollution of groundwater[1]. The shale gas reservoirs in China mainly distribute over unwatered interior area.Compared to the United States, the water sensitivity of the shale gas reservoirs in China is stronger.So hydraulic fracturing can not adapt to the need of massive commercial production[2,3]. Therefore new fracturing technology should be researched in accordance with characteristics of shale gas reservoirs in China.

Supercritical CO_2 fracturing has incomparable advantages compared to hydraulic fracturing [4].However, the application of this technology was limited by it's low viscosity and weak carrying capacity for proppant.One way of overcoming this problem is adding thickening agents to CO2 to increase it's viscosity. If the viscosity of CO_2 is effectively increased,the stimulation results of supercritical CO_2 fracturing could be improved greatly [5].

To track new technology trends and provide reference, the research progress of thickening agents for CO_2 has been introduced and analyzed in three aspects,including polymers, small molecular compounds and surfactants.

Polymer Thickening Agents

Supercritical CO_2 is weak solvent for polar or high-molecular compounds because of it's nonpolarity. Heller *et al.*[7,28] summarized the characters of polymers that dissolved in CO_2, and proposed that polymers that dissolved in CO_2 should be amorphous and atactic.Desimone and Guan[8,9] found that fluoropolymer and siloxane polymer can dissolve in CO_2 at lower pressure than other polymers under certain temperature.

Siloxane Polymer. Bae and Williams *et al.* [10,11] found that poly (dimethylsiloxane) can increase the viscosity of CO_2 effectively with the addition of toluene as cosolvent.Measurement results of capillary viscometer indicated that the lowest dissolving pressure of siloxane polymer in CO_2 decreased after adding cosolvent. The viscosity of CO_2 was increased to 3.48mPa•S,about 90 times

greater than the viscosity of pure CO_2,by adding 6wt% polymer and 20wt% cosolvent at 130F and 2500Psi.This kind of thickening agent wasn't available because of the high cost and the high concentration required.

Fluoropolymer. Fluorinated groups were used to design and synthesize thickening agents for supercritical CO_2 due to their low cohesive energy density and CO_2-philic property. McClain *et al.*[12] reported the breakthrough that polymer can dissolve in CO_2 without cosolvent under proper pressure. They found that poly(1-,1-,dihydroperfluorooty arcylate)-PFOA can dissolve in CO_2 and increase the viscosity of CO_2 apparently. At 323K and 4500Psi, the addition of 6.7wt% PFOA increased the CO_2 viscosity by a factor of 6 relative to pure CO_2.

Enick *et al.*[13,14] synthesized fluoropolyurethane disulfate.The fluoride telechelic ionomer can dissolve in CO_2 without cosolvent, and increase the solution viscosity by 2.7 times at a concentration as low as 4 wt % at 298K and 25MPa.

DeSimone and Guan *et al.*[8,9] found that the addition of 5-10wt% fluorinated acrylate homopolymer increased the CO_2 viscosity by a factor of 3-6. Huang and Xu *et al.*[15,17] synthetized styrene-fluoroacrylate random copolymer as thickening agent and found that this copolymer can increase the viscosity of CO_2 sharply,thickening effect was the best when the molar volume ratio of CO_2-phobic styrene and CO_2-philic fluoroacrylate was 29:71.At 3.4wt% styrene-fluoroacrylate random copolymer in CO_2,the solution viscosity was about 400 times greater than the viscosity of pure CO_2 at the same condition.They attributed the increase of viscosity of CO_2 to π-π stack of CO_2-phobic tyrene aromatic ring functional groups in side chain.

So far, styrene-fluoroacrylate random copolymer was the only thickener that can make the viscosity of CO_2 increase by two orders of magnitude without cosolvent. However, because of the expensive cost and environmental issues, fluoropolymer thickener was just a proof of concept,not a feasible proposal. Therefore,more and more researchers focused attentions on hydrocarbon polymers.

Hydrocarbon Polymer. Heller *et al.*[7,28] evaluated solubility and thickening property of a series of polymers in liquid and supercritical CO_2, and found that polymers that dissolved in CO_2 can't increase CO_2 viscosity effectively. They also synthesized amorphous, random polymer and hydrocarbon telechelic ionomer with ion groups in the end of chain, but those polymers didn't dissolve in CO_2.

Terry *et al.*[18] measured the solubility of a series of organic compounds in supercritical CO_2, and put forward that n-alkanes,isoparaffin below C_{12}, n-alkanol,etherification phenol below C_6, aliphatic carboxylic acid, polyesters below C_9 and aliphatic aldehyde can be miscible with supercritical CO_2. Lancaster *et al.*[19,20] implemented in-situ polymerization through the reaction of organic titanate with organic matrix, but the reaction product was almost insolube in CO_2.

Enick *et al.*[21] researched solubility of some hydrocarbon polymer in CO_2, and found that Poly(vinyl acetate)-PVAc had the highest solubility among those polymers. PVAc can dissolve in CO_2 at 298K and 13.6-67.6Mpa.They attributed CO_2-philic property of PVAc to the the high free volume from ample side chain and interaction between acetate group and CO_2.

Beckman *et al.*[22] found the hydrocarbon polymer that was solube in CO_2 should be composed of two monomer, M1 and M2. M1 provided high flexibility,high free volume and weak solvent/solvent interaction to polymer;M2， which contained lewis base groups,provided favorable solute/solvent interactions between the polymer and CO_2. Proportion adjustment between M1 and M2 can balance solubility and thickening capacity.His work provided direction for the development of hydrocarbon polymer thickening agents.

Small Molecular Compounds

The second strategy that has been explored for CO_2 thickeners is the design of small molecules that have the capability to associate and form viscosity-enhancing networks in solution[23].

Hydrogen Bonding Compound. Enick *et al.*[24,25]synthesized fluorinated aspartate bisureas and ureas for CO_2 thickening. All the samples could dissolve in CO_2 at 7000 Psi and below 373K.

Although both fluoroalkyl and fluoroether were CO_2-philic, fluoroether was more CO_2-philic and therefore was able to impart higher solubility in CO_2 if the other molecular structures are the same.However, all the fluorinated bisureas and ureas couldn't enhance CO_2 viscosity effectively.

In an attempt to design a non-fluorous analog to fluorinated diurea[23,26], CO_2-philic hydrocarbon groups and carbonyl groups were incorprated into the structure. It was hoped that these compounds might also dissolve in CO_2 and self-assemble into long cylinders to thicken CO_2.However,as the molecules began to self-assemble,they came out of solution and formed fibers. Enick *et al.*[24] designed three kinds of triurea compounds which contained polypropylene glycol monomethyl ether tails, dipropylene glycol monomethyl ether tails and di(ethylene glycol)n-butyl ether tails respectively.These compounds did't dissolve in CO_2 at 7000Psi and 373K.

Gullapalli *et al.*[27] reported the gelling result of 12-Hydroxystearic Acid in supercritical CO_2.HAS molecules could interact with each other through hydrogen bond and formed gel networks. At 294-307K and 1800Psi, HSA did't dissolve in CO_2.But HSA could completely dissolve in CO_2 after adding 10% ethyl alcohol or 20% trichloromethane as cosolvent, and formed white fibrous gels. Measuring result of capillary viscometer indicated that the thickening effect of HAS was slight.For example ,the addition of 3wt% HAS and 15% ethyl alcohol just increased CO_2 viscosity by 58% at 307K and 1800Psi.

Organometallic Compound. Heller and coworkers considered organometallic compounds as CO_2 thickeners[28-31].They studied the solubility of organotin fluorides in various solvents including dense CO_2.The trialkyltin fluorides have structure R_3SnF,R represents alkyl, alkylaryl, or aryl group. Because of electronegativity differences between tin and fluorine atoms, there exist dipole moment in these molecules, which causes weak dipole-dipole interactions in neighboring molecules. Even at low concentrations (less than 1wt%), this transient polymer could increase the viscosity of non-polar solvents by several orders of magnitude. For example, tributyltin fluorides could dissolve in n-hexane, and increase solvent viscosity by three orders of magnitude with a concentration of 10g/L. But trialkyltin fluorides could not thicken CO_2 due to their low CO_2 solubility.

Chunmei Shi et al.[32,33] synthesized semi-fluorided trialkyl fluorides to thicken CO_2, and found that CO_2 solubility was enhanced by introducing the fluoroalkyl functionality into the trialkyltin fluoride molecular structure. The solution viscosity was raised by only 3.3 times at a concentration of 4wt% with this low molecular weight compound at 10-18MPa, however.

Surfactants

Appropriate surfactants can assemble and form linear or cylindrical reverse micelle to increase CO_2 viscosity[35]. Consani *et al.*[36] researched more than 130 kinds of commercial surfactants, and found that only a few non-ionic surfactants can dissolve in CO_2. Hoefling et al.[37-41] tried to produce surfactant for supercritical CO_2 by incorprating functional groups ,which were characterized by low solubility parameter, low polarizability or Lewis base,such as fluorinated ether, fluorine and alkyl siloxane,into surfactant tail. Now the researched supercritical CO_2 surfactants mainly were fluorosurfactant, siloxane surfactant and hydrocarbon surfactant.

Fluorosurfactant. Johnston *et al.*[42]produced W/C microemulsion by ammonium carboxylate perfluoropolyether surfactant,and brought surfactant into supercritical CO_2 system successfully.Hoefling *et al.*[37] designed fluoroalkyl surfactants and proved that the fluorinated analogue to AOT surfactant can dissolve in CO_2. Trickett *et al.*[35] replaced hydrocarbon with fluorocarbon and designed fluoroalkyl analogues to AOT,which could form thickening cylindrical micelles in CO_2. At 298K and 35MPa, the addition of 6wt% Na(di-HCF_4), Co(di-HCF_4)$_2$, i(di-HCF_4)$_2$ increased CO_2 viscosity by 15%, 20%,40%,respectively.

Harrison *et al.*[43]reported the first double chain hybrid surfactant comprising of fluororocarbon chain and hydrocarbon chain-F_7H_7.Water up W of 32 could be stabilized in W/C microemulsion at 208K, 26.2 MPa, and surfactant concentration of 1.9 wt%. Cummings and Eastoe et al.[44,45] evaluated

the thickening effect of semi-fluorinated F_7H_4 surfactant in surpercritical CO_2,the addition of 4.4wt% K-F_7H_4, Li-F_7H_4, Na-F_7H_4 increased the viscosity by 10%, 23%, 100% respectively,at 313K and 40MPa.

Siloxane Surfactant. Siloxane surfactant is cheaper than fluorosurfactant,but needs higher critical pressure to form reverse micelle.Fink *et al.*[46] researched siloxane ionic surfactants, and claimed that siloxane analogue to AOT could dissolve in CO_2 when the concentration was below 1wt%,at 338K and below 31MPa. Psathas *et al.*[47] produced W/C or C/W emulsion by segmented copolymer which was made up of CO_2-philic poly (dimethylsiloxane) and CO_2-phobic poly(methyl acrylate) or poly(acrylic acid).

Optimization and adjustment of siloxane surfactant structure could improve it‘s property and lower it’s critical micellar pressure. Fink *et al.*[48] added propyl acetate functional groups to side chain of siloxane oligomers, and found it‘s cloud point pressure fell by 17.2MPa. Rocha et al. [49] found that short and thick tail structure of trisioxanes surfactant could reduce free volume fraction and separate CO_2 and water more efficiently,thus offered stronger capacity of forming reverse micelle in CO_2.

Hydrocarbon Surfactant. Siloxane surfactant and fluorosurfactant aren’t available because of cost and environmental problems.So the researchers tried to develop cheap hydrocarbon surfactants which could dissolve in CO_2. Hutton *et al.*[50] found that AOT could dissolve in CO_2 and form stable reversed microemulsion by adding cosurfactants, such as F-pentanol, alcohol and 1-Pentanol.The required amount of F-pentanol that made a certain amount of AOT dissolve in CO_2 was significantly less than ethanol and 1-Pentanol.Fulton *et al.*[51] found that PFPE-PO_4 and AOT couldn‘t form stable reversed microemulsion lonely，but they could form stable reversed microemulsion when they were mixed together in supercritical CO_2.

Eastoe *et al.*[52,53]provided new idea for the research of hydrocarbon surfactant.By modification of AOT,they produced branching analogue to AOT,AOT3 and AOT4,which contained tertiary butyl in the tail. AOT3 and AOT4 could dissolve in CO_2, but couldn’t form reverse micelle. Whereafter, they designed and synthesized AOK surfactant that contained both tertiary butyl and carbonyl, and proved it can form W/C microemulsion[54]. Ryoo *et al.*[55] researched methylated branched hydrocarbon surfactant,poly(ethylene glycol) 2,6,8-trimethyl-4-nonyl ethers,which had strong capacity of reducing interfacial tension. At 308K-338K and 24MPa, 1.0wt% surfactant and 1.1wt% water,it could form stable microemulsion in CO_2.Methylated branched chains lowered the interaction among tails,which played important role in the formation of microemulsion.

Liu *et al.*[56,57] reported the solubility and phase behavior of alkynol surfactant in supercritical CO_2, such as Dynol-604,Ls-36 and Ls-45.At 208-333K and 26 MPa, Dynol-604 that contained polyether structure could dissolve in supercritical CO_2 and form W/C microemulsion,the hightest solubility was 5wt%.At the same condition,the solubility of Ls-36 in supercritical CO_2 was higher than Ls-45, this was because the ratio of CO_2-philic propenyl oxygen(PO) to CO_2-phobic ethenyl oxygen(EO) was bigger in Ls-36.So we can improve the property of surfactant by adjusting the quantity CO_2-philic groups.

Conclusions

At present, the research of supercritical CO_2 thickeners is still in testing phase.There is no complete and unified theory about this technology. The most significant barrier that continues to impede progress in the development of CO_2-thickening agents is the low solubility of candidate compounds in CO_2.The compounds that dissolve in CO_2 may have properties of low cohesive energy density, low solubilty parameter, low polarizability,high free volume and Lewis base. The solubility may be increased by incorprating functional groups which have above mentioned properties into thickener molecules to promote the interaction with CO_2.Meanwhile, CO_2-phobic functional groups should be incorprated to increase the thickenging capability.

In conclusion, a lot of research work about thickening agents for supercritical CO_2 has been carried out in recent years.The thickening mechanisms and molecular structure design of thickening agents

should be studied in further research.The combination of theory methods such as molecular simulation and experimental means is required to research the thickening mechanism of thickening agents. The ultimate objective should be to produce thickener composed solely of carbon, oxygen and hydrogen that is soluble in supercritical CO_2 and can increase the viscosity of supercritical CO_2 by two orders of magnitude at concentrations less than 1 wt%.

Acknowledgements

This work is supported by the National Natural Science Foundation of China (Grant No. U1262202, No.51034007, No.5121006, No.51104172).

References

[1] Qian Bozhang, Li Guangwu, Research about Technologic And Envirmental Problems of Shale Gas Hydraulic Fracturing,J. Nature Gas and Petroleum. 31 (2013) 48-53.

[2] Li Qinghui, Chen Mian, Jin Yan, Wang Mingyuan, Jiang Hailong, Application of New Fracturing Technics in Shale Gas Exploitation, Special Oil & Gas Reserviors. 19 (2012) 1-7.

[3] Nie Haikuang, He Faqi, Bao Shujing, Special Geologic Characteristic and its Exploitary Countermeasures, Natural Gas Industry. 31 (2011) 111-116.

[4] Wang Haizhu, Shen Zhonghou, Li Gensheng, Fesibility Analysis on Shale Gas Exploitation with Supercritical CO_2, Petroleum Drilling Techniques. 39 (2011) 30-35.

[5] Jianhang Xu, CO_2 thickening agent for reduced CO_2 mobility, Pittsburgh:University of Pittsburgh,2003.

[6] Harris T V, Irani C A, Pretzer W R.Enhanced Oil Recovery Using CO_2 Flooding, U.S. Patent,4913235,1990.

[7] Heller J P, Martin F D. Improvement of CO_2 Flood Performance, New Mexico Petroleum Recovery Research Center Report, 1990.

[8] J R Combes , Z Guan, J M DeSimone. Homogeneous free radical polymerizations in supercritical CO_2:3. Telomerization of1,1-Difluoroethylene in Supercritical CO_2, Macromolecules. 27 (1994) 865-867.

[9] Guan Z B. Homogeneous free radical polymerization in supercritical CO_2:2. Thermal Decomposition of 2,2'-Azobis(isobutyronitri1e), Macromolecules. 26 (1993) 2663-2669.

[10] J H Bae and C A Irani, A Laboratory Investigation of Viscosified CO_2 Process: The thickened CO_2 process utilizing a commercial silicon polymer and toluene as cosolvent is technically viable , SPE Advanced Technology Series. 1(1993)166-171.

[11] Williams L L, Rubin J B, Edwards H W. Calculation of solubility values for a range of pressure and temperature conditions, including the supercritical region, Industrial & Engineering Chemistry Research. 43 (2004) 4967- 4972.

[12] McClain J B,Betts D E,Canelas D A, *et al.*, Characterization of polymers and Amphiphiles in supercritical CO_2 using small angle neutron scattering and Viscometry, Spring meeting of the ACS, Division of Polymer Material,New Orleans La:Science and Engineering. 74(1996)234-235.

[13] Enick R M,Beckman E,Yazdi A,et al.Phase behavior of CO_2-perfluoropolyether oil mixtures and CO_2-perfluoropolyether chelating agent mixtures, Supercritical Fluids. 13 (1998) 121-126.

[14] Enick R M.A literature review of attempts to increase the viscosity of dense CO_2,University of Pittsburgh Report,1998.

[15] Jianhang Xu, CO_2 thicking agent for reduced CO_2 mobility, Pittsburgh:University of Pittsburgh,2003.

[16] Huang Z,Shi C,Xu J, *et al.*, Enhancement of the viscosity of CO_2 using styrene/fluoroacrylate Copolymers, J. Macromolecules. 33 (2000) 5437- 5442.

[17] Jianhang Xu, Aron Wlaschin, R M Enick.Thickening CO_2 with the fluoroacrylate-styrene copolymer. SPE71497, 2001.

[18] R E Terry, A Zaid, C Angelos, D L Whitman, Polymerization in Supercritical CO_2 To Improve CO2/Oil Mobility Ratios. SPE 16270,1987.

[19] G W Lancaster, C Barrientos, E Li, R C Greenhorn, High phase volume liquid CO_2 fracturing fluids. CIM 87-38- 71,1987.

[20] G W Lancaster, M Sinal, Liquid CO_2 Fracturing: Advantages and Limitations, The Journal of Canadian Petroleum Technology. 26(1986)26-30.

[21] R M Enick, E J Beckman, Andrew Hamilton, Report: Inexpensive CO_2 Thickening Agents for Improved Mobility Control of CO_2 Floods. 2009.

[22] Sarbu T, T Styranec, E J Beckman, Non-Fluorous Polymers with very High Solubility in Supercritical CO_2 down to Low Pressures, Nature. 405(2000)165-168.

[23] R M Enick,D Olsen, *et al.*, Mobility and Conformance Control for CO_2 EOR via Thickeners, Foams and Gels—A Literature Review of 40 Years of Research and Pilot Tests. SPE154122, 2012.

[24] R M Enick, E J Beckman, Andrew Hamilton, Report:Novel CO_2-Thickeners for Improved Mobility Control, 2001.

[25] Shi C, Huang Z,Xu J, *et al.*, The gelation of CO_2:A sustainable route to the creation Of miscrocellular materials, Science. 19 (1999) 1540-1543.

[26] Paik I H, Tapriyal D, Enick R,Hamilton, A Fiber formation by highly CO_2-soluble bis-ureas based on peracetylated carbonhydrate groups, Angewandte chemic international edition. 46(2007)3284-3287.

[27] Gullapalli P, Tsau J S, Heller J P, Gelling behavior of 12 hydroxystearic acid in organic fluids and dense CO_2. SPE 28979,1995.

[28] Heller J P, Dandge D K, Card R J, Donaruma L G. Direct thickeners for mobility control of CO_2 floods,Society of Petroleum Engineers Journal. 25(1985) 679-686.

[29] Dandge D K,Taylor C,Heller J P,Wilson K V, Brumley N, Associative Organotin Polymers. 2. Solution Properties of Symmetric Trialkyltin Fluorides, Journal of Macromolecular Science. 26(1989)1451-1464.

[30] Heller J, Dandge D, Topical Viscosity Control for Light Hydrocarbon Displacing Fluids in Petroleum Recovery and in Fracturing Fluids for Well Stimulation, U.S. Patent: 4607696(1986).

[31] Heller J, Kovarik F, Improvement of CO_2 Flood Performance, Petroleum Recovery Research Center Report, 1987.

[32] R M Enick, E J Beckman, Chunmei Shi, *et al.*, Direct Thickeners for CO_2. SPE59325,2000.

[33] Chunmei Shi, Zhihua Huang, E J Beckman, *et al.*, Semi-Fluorinated Trialkyltin Fluorides and Fluorinated Telechelic Ionomers as Viscosity-Enhancing Agents for CO_2, Industrial & Engineering Chemistry Research. 40(2001)908-913.

[34] Liave F M, Chung F T, Burchfield T E, Use of entrainers in improving mobility control of supercritical CO_2, SPE Reservoir Engineering. 5(1990)47-51.

[35] Trickett K, Xing D, Enick R,*et al.*, Rod-like micelles thicken CO_2, Langmuir. 26(2010)83-88.

[36] Consani K A, R D Smith, Observations on the Solubility of Surfactants and Related Molecules in CO2 at 50°C, Journal of Supercritical Fluids. 3(1990)51-65.

[37] Hoefling T A, R M Enick, E J Beckman, Microemulsions in Near-Critical and Supercritical CO_2, J. Phys.Chem. 95 (1991) 7127-7129.

[38] Newman D A, *et al.*, Phase-Behavior of Fluoroether-Functional Amphiphiles in Supercritical CO2, Journal of Supercritical Fluids. 6 (1993) 205-210.

[39] Desimone J M, Z Guan, and C S Elsbernd, Synthesis of Fluoropolymers in Supercritical CO_2, Science. 257 (1992) 945-947.

[40] Hoefling T A, *et al.*, Effect of Structure on the Cloud-Point Curves of Silicone Based Amphiphiles in Supercritical CO_2, Journal of Supercritical Fluids. 6 (1993) 165-171.

[41] Hoefling T A, *et al.*, Design and Synthesis of Highly CO_2 Soluble Surfactants and Chelating-Agents, Fluid Phase Equilibria. 83 (1993) 203-212.

[42] Heitz M P, *et al.*, Water Core within Perfluopolyether-based Microemulsions formed in Supercritical CO_2, J. Phys. Chem. B. 101(1997)6707.

[43] Harrison K , *et al.*, Water-in-CO_2 Microemulsions with a Fluorocarbon-Hydrocarbon Hybrid surfactant,Langmuir. 10(1994)3536-3541.

[44] Stephen Cummings, Dazun Xing, Robert Enick,*et al.*, Design principles for supercritical CO_2 viscosifiers, Soft Matter. 8 (2012) 7044-7055.

[45] Audrey Dupont, Julian Eastoe, Laura Martin, *et al.*, Hybrid fluorocarbon hydrocarbon CO_2-philic surfactants, Langmuir. 20 (2004) 9960-9967.

[46] Fink R, E J Beckman, Phase Behavior of Siloxane-based Amphiphiles in Supercritical CO_2, Journal of Supercritical Fluids. 18 (2000) 101-110.

[47] Psathas P A, *et al.*,Water-in-CO_2 Emulsions with Poly(dimethylsiloxane)-based Block Copolymer Ionomers. Industrial & Engineering Chemistry Research. 39 (2000) 2655-2664.

[48] R Fink, E J Beckman, R Valentine, *et.al.*, Toward the development of "CO_2-philic" hydrocarbons.1.Use of side-chain functionalization to lower the miscibility pressure of polydimethylsiloxanes in CO_2, J. Phys.Chem.B. 103 (1999) 6441-6444.

[49] SRP da Rocha, J Dickson, D Cho, PJ Rossky, *et al.*, Stubby surfactants for stabilization of water and CO_2 emulsions: Trisiloxanes,Langmuir. 19 (2003)3114-3120

[50] Hutton B H, Pcrera J M, Gricser F, *et a1.*, AOT reverse,micro-emulsions in SC-CO_2—a further investigation, Colloids and Surfaces A:Physicochemical and Engineering Aspects. 189 (2001) 177-181.

[51] Ji M, Chen X, Wai C M, Fulton J L J, Synthesizing and dispersing silver nanoparticles in A water-in-supercritical CO_2 microemulsion, J. Am.Chem. Soc. 121 (1999) 2631- 2632.

[52] Eastoe J, Paul A, Nave S, *et al.*, Highly Efficient and Thermally Stable Nonlinear Optical Dendrimer for Electro-optics, Journal of American Chemical Society 123 (2001) 988-989.

[53] Eastoe J,Dupont A,Steytler C D, *et al.*, Micellization of economically viable surfactants in CO_2, Journal of Colloid and Interface Science. 258 (2003) 367-373.

[54] Eastoe J, Gold S, Rogers S, et al.Designed CO_2-philes stabilize water-in-CO_2 microemulsions, J. Angewandte Chemie,International Edition. 45 (2006) 3675 -3677.

[55] Ryoo W, Wobber S E, Johnston K P, Water-in-CO_2 micromulsions with methylated branched hydrocarbon surfactants, Industrial & Engineering Chemistry Research. 42 (2003) 6348-6358.

[56] Liu J, Han B, Li G, *et al.*, Investigation of nonionic surfactant Dynol-604 based microemulsion formed in Supercritical CO_2. Langmuir. 17 (2001) 8040-8043.

[57] Juncheng Liu, Buxing Han, Zhengwu Wang, *et al.*, Solubility of Ls-36 and Ls-45 Surfactants in Supercritical CO_2 and Loading Water in the CO_2/Water/Surfactant Systems, Langmuir. 18 (2002) 3086-3089.

Advanced Materials Research Vol. 936 (2014) pp 1549-1552
© (2014) Trans Tech Publications, Switzerland
doi:10.4028/www.scientific.net/AMR.936.1549

Study on the Crosslinkers Used in Gelling Agents

Qianru Sun[1, a], Rongwei Liu[1, a]

[1] Drilling & Production Technology Research Institute of Liaohe Oilfield Company, Petrochina Panjin, Liaoning , 124010, China.

[a]Liurongwei007@163.com

Keywords: Crosslinkers, Gel, Mechanism, Profile Control Agent, plugging

Abstract: This paper is closely related to the crosslinkers used in gelling agents. Both physical crosslinking and chemical crosslinking are discussed. Crosslinkers are added to form intermolecular linkages in between the primary polymer chains to form a stable gel. Both gelling and plugging agents have similar aims---to minimize the permeability of a formation. With the producing water is becoming the big problem, crosslinkers are becoming more important.

Introduction

With the exploitation of the oilfield, excessive water production is a serious issue in maturing oil and gas reservoirs. It leads to additional costs in terms of constructing larger gas/oil separation plants. Additionally, scale formation, emulsion, bacteria and corrosion problems may arise because of high water cut. The oil industry worldwide spends USD billions every year to address the problem of excess water production[1]. Various water-control techniques exist. They include mechanical and chemical means. Among the available chemical water-control techniques, polymer gels have been used widely for lowering water relative permeability while keeping oil relative permeability unaffected through disproportionate permeability reduction or for completely blocking water flow from water-producing zones[2]. For a given well candidate, several factors, including reservoir temperature, lithology, and salinity of the formation water, affect the selection of the required polymer-gel treatment. PAM-based polymers have been used in most water control gels. Depending upon the crosslinker used, gelling systems can be classified into two categories- inorganically and organically crosslinked gels. The term gel can refer to a crosslinked polymer or to a polymer solution that is sufficiently viscous to appear as a gel. This paper is closely related to the crosslinkers used in gelling agents. Both physical crosslinking and chemical crosslinking are discussed.

Physical Crosslinking

Modified PAM which carry negative charges on their backbone can form gels by addition of multivalent positive ions, such as chromium salts. The gel consists of a physical network, which is similar to an ionomer. A single multivalent ion shares a salt with the charges of different polymer chains. The gelation time depends on the molecular weight of the primary polymer, the concentration of ions on the primary polymer chains, and the concentration of the multivalent cations in the solution.

Crosslinker formulations based on iron (III), such as ferric acetylacetonate or ammonium ferric oxalate have been described[3]. 2,4-Pentanedione can adjust the gel strength in such formulations. Zirconium acetylacetonate is also a suitable crosslinker, which have been proposed for physical crosslinking. Chromium (III) salts are used mainly for physical crosslinking. These are not as toxic as chromium(VI) salts, but they are not environmentally desirable compounds, and their use causes additional costs to avoid the contamination of surface waters. Efforts to develop other methods of crosslinking have been therefore undertaken. There are some commercially available salts for physical crosslinking, such as Chromium chloride, Chromium propionate, Chromium acetate, Zirconium lactate, Tetrakis triethanol amine zirconate, Zirconium tartarate and so on.

Chemical Crosslinking

Besides of physical crosslinking, chemical crosslinking systems have been also described. A combination of hydroquinone and hexamethylenetetramine can be used. Sodium bicarbonate in a concentration of 2% serves as buffer and it softens the water by precipitating certain divalent cations present in the sea water. Other chemical crosslinking systems include terephthalaldehyde, terephthalic acid, dihydroxy-naphthalene, glutaric acid, gallic acid, and dibasic esters. The chemical crosslinkings are divided into primary and secondary crosslinkers. Primary crosslinkers are those that produce gels with the polymer, although the gels may be unstable. Secondary crosslinkers stabilize the gels produced by primary crosslinking.

Polyethyleneimine Crosslinker. Polyethyleneimine has been used as anorganic crosslinker for polyacrylamide tertiary butyl acrylate copolymer. Literature reported that polyethyleneimine can also form ringing gels with polyacrylamide (PAM) copolymers in addition to simple PAM homopolymers. For copolymers of AAm, and of AAm and methyl acrylate (5%), polyethyleneimine can be used as crosslinker[4]. Polyethyleneimine has been used as the organic crosslinker to form gels with polyacrylamide tertiary butyl acrylate and mixtures of acrylamide and acrylamido-2-methylpropane sulfonic acid and N,N-dimethyl acrylamide[5]. Someone have reported that polyethyleneimine can form gels with polyacrylamide at room temperature. A recent study has indicated the possibility of crosslinking a simple PAM with polyacrylamide at high temperatures.

Phenol-formaldehyde Type Crosslinkers. The amide groups on PAM can be crosslinked with formaldehyde or a mixture of formaldehyde and phenol, but these small molecules are toxic, and hard to dispose of higher molecular weight reagents, such as hexanal and heptanal, which are not classed as toxic. These are suitable crosslinking agents but they are not sufficiently soluble in water to crosslink normal hydrophilic polymers such as the PAM/polyacrylate copolymer. However, they can be readily solubilized in aqueous solutions by hydrophobically modified PAM polymers, and can then crosslink them. Hexamethylenetetramine hydrolyzes slowly into ammonia and formaldehyde, and can be used in place of formaldehyde[6]. Hexamethylenetetramine with an aminobenzoic acid compound produces better gels than those produced with phenol and formaldehyde, and this gelling system is more environmentally acceptable.

Aluminum Phosphate Ester Salts. Organic liquid gels are used for temporary plugging during fracturing operations. This type of gelling agent permits on-the-fly gelling of hydrocarbons, especially those used in this type of operation. A gel of an organic liquid, such as diesel or crude oil, can be formed using an aluminum phosphate diester in which all of the reagents are free of water and pH-affecting substances. The diester may be prepared by the reaction of a trimester with phosphorous pentoxide to produce a polyphosphate, which is then reacted with an alcohol to produce a phosphate diester. The latter diester is then added to the organic liquid along with a nonaqueous source of aluminum, such as aluminum isopropoxide in diesel oil, to produce the metal phosphate diester. The conditions in the two preceding reaction steps are controlled, in order to provide a gel with good viscosity versus temperature and time characteristics. A similar process involves the reaction of triethyl phosphate and phosphorous pentoxide to form a polyphosphate in an organic solvent. Aluminum sulfate is used as a crosslinker. Hexanol results in hightemperature viscosity of the gel, while maintaining a pumpable viscosity at ambient temperatures.

Aluminum Citrate. Aluminum citrate can be used as a crosslinker for many polymers. In particular, this crosslinker provides a valuable tool for in-depth blockage of highpermeability regions of rock in heterogeneous reservoirs. PHPAs, CMC, polysaccharides, and acrylamido methylpropane sulfonate have been screened in an investigation of the performance of aluminum citrate as a chelate-type crosslinker. The performance of the colloidal dispersion gels depends strongly on the type and the quality of the polymer used. The gels were mixed with the polymers in concentrations at three polymer-to-aluminum ratios. The gels were quantitatively tested 1, 7, 15, and 30days after preparation.

Aluminum Trichloride. Aluminum trichloride is a waste product in chemical industry, and it can react with polymer, form a gel under certain conditions with carbonates and on mixing with alkalies. Laboratory and field tests have shown that aluminum trichloride can be used as a crosslinker agent, for reducing the permeability of water-conducting channels. Because of its low price, and abundant, aluminum trichloride is widely applied in the field.

Crosslinker used in Gelling System

An gelling system has been made of a polymer, a crosslinking agent, a gel stabilizer, and oxygen scavengers. The crosslinking agent is activated at elevated temperatures and the system forms a gel. And portions of oil producing or water injecting reservoir can be temporarily sealed. All the components are selective, so the system does not leave residues that can cause formation damage in the more permeable zones. The polymer is preferably polyacrylamide polymer. The crosslinker are physical crosslinking and chemical crosslinking. Chemical crosslinking used widely at present. The gel stabilizer is ammonium chloride. As known, the most effective oxygen scavengers contained thiourea as the radical transfer agent, isopropyl alcohol as the sacrificial oxidizable alcohol, sodium sulfite as the oxygen scavenger, either tri- or pentachloro- phenol, and a sufficient brine concentration.The initial mixture contains the non-crosslinked polymer chains. When exposed to proper temperatures, typically temperatures of 35-90°C, the crosslinking agent reacts with polymer, and a polymeric gel results.

Special Applications

Chromium acetate-partially hydrolyzed polyacrylamide gel systems have also been applied in fractured reservoirs for conformance control. A wide variety of polymers create flexible gels: polyvinyl alcohol or polyvinyl acetate, PAMs, AAm copolymers, acrylic acid methacrylamide copolymers, and PHPAs, as well as polymethacryl-amides, several natural and modified polysaccharides, lignosulfonates, and polyalkylene oxides[7],[8].

The crosslinking of polysodium 4-styrenesulfonate using Al^{3+} ions to form a gel is described by Keller and Narh. The concentration of the high molecular weight hydrophilic polymers used to form hydrogels is typically in the range 3-10 gl^{-1}, and diverting agents can be added, to improve the penetration of a sand consolidating fluid into areas of lower permeability[9].

Conclusions

From the present study, excessive water production is a serious issue in maturing oil and gas reservoirs. So polymer gels have been used widely for lowering water relative permeability while keeping oil relative permeability unaffected through disproportionate permeability reduction or for completely blocking water flow from water-producing zones. Depending upon the crosslinker used, with the continuous development of environmental protection, the development direction of crosslinking agent is non-toxic, selectivity. Efforts to develop such crosslinkings have been therefore undertaken.

References

[1] Bailey, B., Crabtree, M., Tyrie, J. , Elphick, J., Kuchuk, F., Romano, C., and Roodhart, L.2000. Water Control. Oilfield Review 12(1):30-51.

[2] Rongwei Liu, 2011, Study and application of in-depth profile modification and flooding technology in water-flooding reservoir, Advances in Fine Petrochemicals, 12-15.

[3] Moradi-Araghi, A., Daasvatn, K., Hamouda, A.A., 2002. Compositions and processes for oil field applications. US Patent 6 387 986, May 14, 2002.

[4] Al-Muntasheri, G. A., Nasr-El-Din, H.A., and Zitha, P.L.J.2008.Gelation Kinetics and Performance Evaluation of an Organically Crosslinked Gel at High Temperature and Pressure. SPEJ. 13(3):337-345.
[5] Vasquez, J. ,Dalrymple, E.D. ,Eoff, L., Reddy, B.R., and Civan, F.2005. Development and Evaluation of High-Temperature Conformance Polymer Systems. Paper SPE 93156 presented at the SPE International Symposiumon Oilfield Chemistry, The Woodlands, Texas, USA, 2-4 February. doi: 10.2118/93156-MS.
[6] Jones, T.G.J., Tustin, G.J., 2001. Gelling composition for wellbore service fluids. US Patent 6 194 356, assigned to Schlumberger Technology Corporation (Sugar Land, TX), February 27, 2001.
[7] Ganguly, S., Willhite, G.P., Green, D.W., McCool, C.S., 2002. The effect of fluid leakoff on gel placement and gel stability in fractures. SPE J. 7 (3), 309-315.
[8] James, S.G., Nelson, E.B., Guinot, F.J., 2002. Sand consolidation with flexible gel system. US Patent 6 450 260, assigned to Schlumberger Technology Corporation (Sugar Land, TX), September 17, 2002.
[9] Robert, J.A., Rosen, J.W., 2002. Fluid placement and pumping strategy. In: Economides, M.J., Nolte, K.G. (Eds.), Reservoir Stimulation, chap. 19-3.

Advanced Materials Research Vol. 936 (2014) pp 1553-1555
© (2014) Trans Tech Publications, Switzerland
doi:10.4028/www.scientific.net/AMR.936.1553

Oil, Water, Slag Three Phases Separation Technology of Heavy Aging Oil

Meng Zheng[1, a]

[1]Drilling & Oil Production Technology Research Institute of Liaohe

Oilfield Company, Petrochina, Panjin, Liaoning, 124010, China

[a]zhengmeng@petrochina.com.cn

Keywords: aging oil, centrifugal separation, dehydration, slag

Abstract. The technology was used for handling heavy aging oil by demulsifier and three phases horizontal scrow centrifuge. Through laboratory and field test, it showed that the water content of the processed aging oil dropped from 50% to 5% below, purity oil recovery rate reached more than 95%, meeting export quality requirements. The technology improved the effective storage capacity of flow station, is of great significance to the safe and steady operation of flow station.

Preface

Usually, The crude oil which is difficult to deal with the existing technical means is known as aging oil, including in the process of oilfield production, oily sewage went through sewage settling tanks, deoiling tanks, flotation tanks and formed a significant number of waste oil; slops in sewage recycling pool; the oil-water emulsion and the falling oil formed during drilling, operation and transportation of crude oil [1 ~ 3]. Aging oil is complicated, the water content is often more than 30%, it is a very stable oil emulsion system [4 ~ 6], so it is difficult to handle using common means of gathering dehydration. Aging oil problem is a worldwide problem because of its complicated components, high viscosity and difficult demulsification. There are typically the following three kinds of approaches to handle aging oil in oil field gathering systems: one is mixing it to crude oil transportation system directly, which make the water content of Oil Transmission overtake standard, affecting the quality of oil products. Two is dropping the water content to10% below, but the existing crude oil dehydration process can't achieve. Three is taking it as tank waste, so it is not selled as qualified goods, of low economic efficiency.

Operating Principle

The separation principle of demulsifier and three phases horizontal scrow centrifuge is based on the demulsifier making oil-water interfacial film damage, when aging oil go into the centrifuge, centrifugal field makes the desity differences of oil, water and solid particles extend a few thousand times, solid phase is settled under the centrifugal force, two kinds of liquid are separated to form two liquid layers to achieve the solid / liquid / liquid three-phase separation and are discharged separately. The feeding and separation process is continuous, closed and automatic.

Results and Discussions

Test oil is the aging oil returned from Liaohe Oilfield Leng Yi flow station sewage treatment system, it is heavy oil, of high viscosity, oil-water density difference is small, emulsion breaking and the centrifugal separation is difficult. The physical property of Leng Yi flow station aging oil is shown in Table 1.

TABLE 1 THE PHYSICAL PROPERTIES OF LENG YI FLOW STATION AGING OIL

Source	Aging oil viscosity （mPa•s，80℃ ）	Crude density （g/ml，80℃ ）	Water content （%）	Solid particles （%）
Leng Yi flow station	428.9	0.9254	50.02	4.37

Considering the peculiarity of aging oil, after research and laborary test, demulsifiers are developed for Liaohe oil field aging oil dehydration. And a series of demulsifier are synthesized for screening. To Leng Yi flow station aging oil, demulsifier A2 is the best from Table 2.Experimental temperature: 90 ℃.

TABLE 2 DEMULSIFIER EVALUATION EXPERIMENT

No.	Drug name	Dosage （ppm）	Dehydration volume（ml,min）				
			15	30	60	90	120
1	A1	600	3.5	3.5	17	18	19
2	YP1	600	3	3.5	20	20	20.5
3	A2	600	3	3.5	20	21	22
4	A3	600	3	3	14	16	17
5	SP1	600	3	3	13	15	18.5
6	Ap1	600	2	2	18.5	18.5	19.5
7	YP2	600	2.5	3	15	16	16

Since 2009, demulsifier and three phases horizontal scrow centrifuge technology, the accumulate treatment amount in Leng Yi flow station, Shu Si flow station, Shu Wu flow station, Huan Er flow station of Liaohe oilfield is 100 thousand ton, the average water content of processed aging oil dropped from around 50% to below 3%.

Taking Leng Yi flow station aging oil as an example, the processing temperature is 90 ℃, dosing of dehydration demulsifier concentration is 600 ppm. Thermochemical settling time is 2 hours. The water content of aging oil before and after processing is shown in Figure 1.

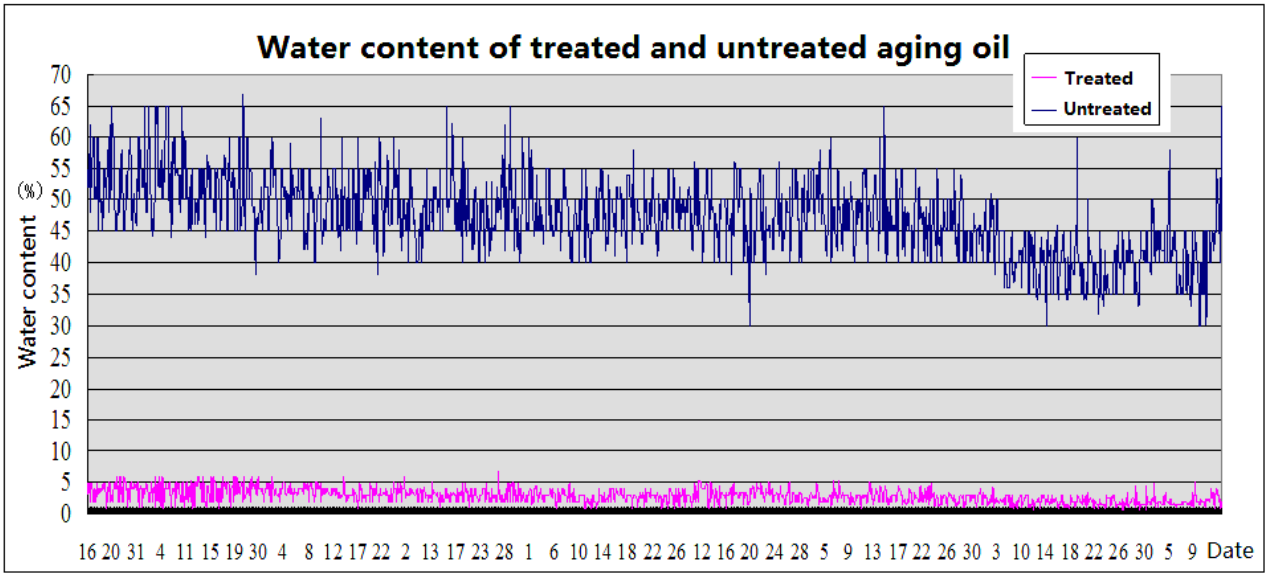


Figure 1 The Water Content Of Treated And Untreated Aging Oil

From the Figure 1, we can see the average water content of processed aging oil dropped from around 50% to below 5%.the aging oil processed by thermochemical settling and centrifuge dewatering, oil and water had been completely separated, achieving the aging oil dehydration, to meet the normal production of Leng Yi flow station requirements.

Conclusions

Demulsifier combined with centrifugal formed processing heavy aging oil technology, which solved the problem of aging oil demulsification and dehydration of heavy oil in Liaohe Oilfield, satisfy the need of production.

The water content of the processed aging oil dropped to 5% below to meet export quality requirements. Previsely unsellable heavy aging oil has reached the required standard , thus improving the rate of oil products and its cost effectiveness.

The technology improved the effective storage capacity of flow station, is of great significance to the safe and steady operation of flow station.

References

[1] Yumei Zhang, Study of Ultrasonic Demulsification and Dehydration of Refinery Waste Oil, Nanjing, 2003.

[2] M. Danuta, Sztukow ski, W. Harvey, Yarranton Oilfield solids and water-in-oil emulsion stability, Journal of Colloid and Interface Science, 285(2005): 821- 833.

[3] Mohammad A. Khadim, Mohammad A. Sarbar, Role of asphaltene and resin in oil field emulsions, Journal of Petroleum Science and Engineering, 23(1999): 213-221.

[4] Yongmei Pan, Hongyuan Wang and Xuejun Wang, Swirl separation technology of dealing with the aging oil adaptability analysis. Journal of oil and gas, 27(2005) : 414- 416.

[5] Xiulian Wang, Application of hydrocyclone in the aging oil treatment, Daqing, 2006.

[6] Fujun Xia etal., Containing ferrous sulfide particles oil recycling technology, Petroleum Planning & Engineering, 17(2006): 13- 16.

Advanced Materials Research Vol. 936 (2014) pp 1556-1559
© (2014) Trans Tech Publications, Switzerland
doi:10.4028/www.scientific.net/AMR.936.1556

Research on Chemical Degradation of PAM in Oil Recovery Application

Rongwei Liu[1, a]

[1]Drilling & Production Technology Research Institute of Liaohe Oilfield Company, Petrochina

Panjin, Liaoning , 124010, China.

[a]Liurongwei007@163.com

Keywords: Polyacrylamide, Chemical Degradation, Mechanism, Iron ion

Abstract. This paper is closely related to chemical degradation of PAM. The degradation refers to any process that breaks down the molecular structure of macromolecules. The most important degradation pathways in oil recovery applications are oxidation reduction, ironic ions and divalents. The influences of each factor is discussed, and preventive measures are also put forward. It is beneficial to provide the degradation of the polymer, and it can largely improve the utilization rate of PAM.

Introduction

Excessive water production is a serious issue in all oilfield worldwide. It leads to additional costs in terms of constructing larger gas/oil separation plants. Various water control techniques exist. Among the available chemical techniques, polymer flooding has been used for lowering water relative permeability and improving sweep efficiency. The polyacrylamide is widely used, polymer degradation problems could not be ignored. Polymer degradation refers to any process that breaks down the molecular structure of macromolecules. The main degradation pathways in oil recovery applications are chemical, mechanical, and biological[1]. The research is mainly worked on chemical degradation. Chemical degradation refers to the breakdown of polymer molecules, either through short-term attacking by oxygen and iron, or through longer-term attacking to the molecular backbone by processes such as hydrolysis. In other words, polymer chemical stability is mainly controlled by oxidation reduction reactions and hydrolysis.

Oxidation Reduction

For polyacrylamide polymer, the presence of oxygen always leads to oxidative degradation. However, at a low temperature, the effect of dissolved oxygen on HPAM solution viscosity is not significant, and the polymer solution could be stable for a long time. As the temperature increases, even if a small amount of oxygen exists, HPAM solution viscosity quickly decreases with time. For example, the half-lives for a polymer at 50°C, 70°C, and 90°C are respectively 115, 21, and 3 hours.

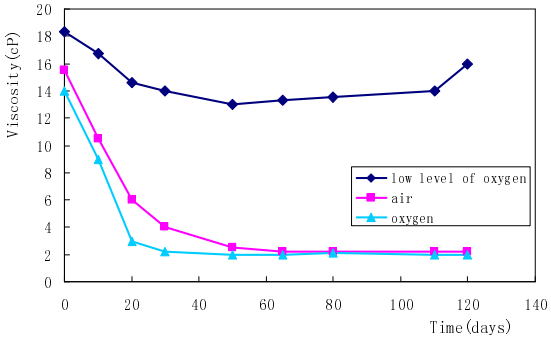


Fig.1 Oxygen's effect on HPAM stability at 90°C

As the oxygen concentration increases, the viscosity decreases faster[2]. Through researching on the chemical stability of PAM solution under simulated field conditions, the rate and extent of polymer degradation were governed mainly by the oxygen content of the solution and temperature. At low oxygen levels (1ppb), the polyacrylamides were stable over 100 days up to 90°C.

The degradation is serious as shown in Figure 1 when air or oxygen presents. When the oxygen was completely consumed, the degradation reaction stopped. This behavior is opposite to the general suspect that after the reaction is initiated by oxygen, it will proceed without further oxygen supply. Therefore, the amount of oxygen in the solution should be minimized by using oxygen scavengers. We can put some methanol or thiourea to protect the polymer from any further oxygen into the solution. The most effective way contained thiourea as the radical transfer agent, isopropyl alcohol as the sacrificial oxidizable alcohol, sodium sulfite as the oxygen scavenger, either tri- or pentachloro-phenol, and a sufficient brine concentration.

Effects of Ironic Ions

In the process of preparing PAM solution, the water usually contains much iron ion. And water conveying pipelines have been used for many years, which coatings have been aging, iron ion soluting in water when it flows through. They are the main source of iron ions. The influence of iron ions are making the PAM degradation, destroying the structure of PAM, lowing the viscosity of PAM[3]. Iron ions mainly exist in the form of Fe^{3+} and Fe^{2+}. Research on the influence of iron ions was carried on.

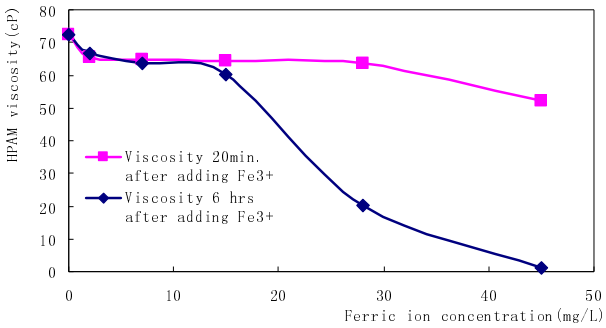


Fig.2 Effect of Fe3+ concentration on HPAM viscosity

Figure 2 shows the ferric ion (Fe^{3+}) effect on an HPAM viscosity at room temperature. The primary viscosity was 72.2 mPa·s. We can see that when the Fe^{3+} concentration was low, the viscosity loss was not significant. The viscosity loss was caused by the salinity effect. When the Fe^{3+} concentration was increasing (>15 mg/L), a brown precipitate was observed. Because the amount of precipitate was little, the viscosity loss was not significant. When the Fe^{3+} concentration was high enough, Fe^{3+} crosslinked with HPAM, and formed a type of gel. The viscosity loss was significant.

In order to give a comparison, we use Fe^{2+} to do the same experiment.

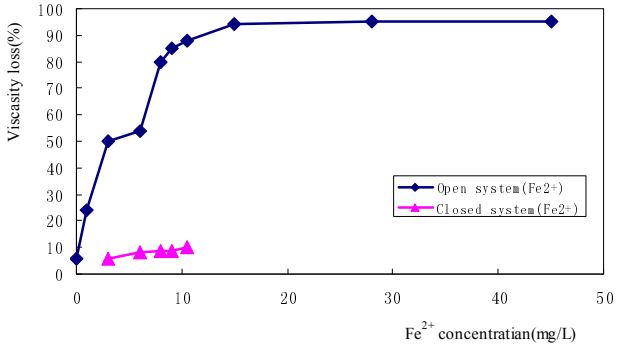


Fig. 3 Effect of Fe2+ concentration on HPAM viscosity

Figure 3 shows the 1200 mg/L HPAM viscosity in a closed system without oxygen at 35°C and 3 hours after adding Fe^{2+}. When Fe^{2+} concentration was lower than 10 mg/L, the viscosity loss was less than 10% owing to the salinity effect. However, when the HPAM solution was put in an open system,

the viscosity was significantly lost, as shown in Figure 3. In the open system, Fe^{2+} was oxidized to Fe^{3+}. We can see that the viscosity loss caused by oxidized Fe^{3+}. The reason is that when Fe^{2+} is oxidized to Fe^{3+}, the free radical O^{2-} is produced. O^{2-} reacts with HPAM to produce peroxide and break the backbones of HPAM. The free radical produced from the reaction further reacts with Fe^{3+} to generate Fe^{2+}, which is further oxidized to produce Fe^{3+} and O^{2-}. A chain reaction occurs, and the polymer viscosity is significantly reduced. In this chain reaction, Fe^{2+} virtually works as a catalyst. Fe^{2+} concentration should be controlled below 0.5 mg/L.

Effect of Temperature

The backbone chain of polymers is quite thermally stable to temperatures as high as 120°C, If there is no oxidative degradation. Indeed, PAM was stable at 90°C for at least 20 months under controlled conditions. At high temperatures, the PAM tend to hydrolyze, therefore increasing the total carboxylate content of the polymer. Thermal stability tests performed showed that the dissolved salts had just a little effect on the hydrolysis rate, and the temperature was the main determining factor. The higher the temperature, the faster the rate of hydrolysis. Hydrolysis was significantly affected by temperature.

In alkaline conditions, initially hydrolysis is fast. As the hydrolysis reaches a certain level, the electrostatic repulsion between carboxyl group and OH- limits further hydrolysis at pH > 13. Finally, hydrolysis is stopped. Therefore, pH has been found to have a minimum effect. At a high temperature, acrylamide is progressively hydrolyzed into acrylic acid; thus, hydrolysis is increased.

In the beginning, hydrolysis increased almost linearly with aging time. After hydrolysis of 44%, the rate of increase slowed down. One of the HPAM characteristics is that hydrolysis quickly increases at high temperatures. Consequently, hydrolysis directly affects HPAM stability. The effect of initial hydrolysis is that the rate of hydrolysis was higher at a higher initial hydrolysis[4]. Therefore, a higher initial hydrolysis is needed in a low-temperature (e.g, 55°C) reservoir so that high viscosity can be quickly reached. In a high-temperature reservoir, the HPAM viscosity near the wellbore will be lower if a polymer with a lower initial hydrolysis is used[5]~[6]. The polymer would be more stable if it is under thermal degradation when the temperature is gradually increased so that the oxygen is consumed at low temperatures.

Divalent Effect

In the low salinities solution, the viscosity of PAM solution increases as hydrolysis increases. In the presence of divalents, the viscosity behavior will be determined largely by the divalent metal ion concentrations. When hydrolysis increases, more acrylic acid produces in the solution. Hydrolyzed polyacrylamides interact with divalent metal cations such as Ca^{2+} and Mg^{2+}. This phenomenon is commonly associated with reduction solution viscosity, which may be formed gels or precipitates.

Through tests we observed the HPAM solution viscosity remained stable until the PAM was hydrolyzed to about 60 mol%, when the Ca^{2+} concentration was below 200 ppm. When the hydrolysis is up to 60~80 mol%, polymer solutions lost almost one half of viscosity. When hydrolysis is limited to less than about 60 mol%, excellent long-term stability can be achieved. Increasing the Ca^{2+} concentration to 500 ppm had a largely effect on viscosity retention.

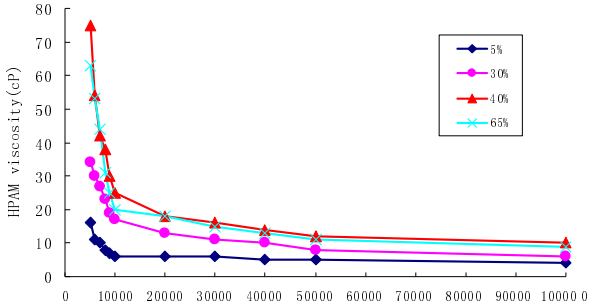


Fig. 4 Effect of CaCl2 concentration on HPAM viscosity with different hydrolysis.

Figures 4 shows an HPAM solution viscosity versus an $CaCl_2$ concentration. In a $CaCl_2$ solution, as the concentration of $CaCl_2$ was increased, the HPAM viscosity decreased rapidly at different levels of hydrolysis. At high $CaCl_2$ concentrations, the viscosity at a lower hydrolysis was higher. The reason is that the divalent Ca^{2+} crosslinks with the acrylic group in HPAM, resulting in coagulation of the molecules. Mg^{2+} is similar but less effect than Ca^{2+}. Davison and Mentzer (1980) found that the precipitation time for the HPAM in seawater at 90°C depended on the primary degree of the polymer's hydrolysis; the higher the initial hydrolysis, the shorter the time before precipitation was observed[7]. Thus, the central role of divalent ions (Ca^{2+} and Mg^{2+}) and the primary degree of hydrolysis of the PAM are known to affect and limit the stability of HPAM in solution at elevated temperatures, even under anaerobic conditions.

Conclusions

From the present research, polymer degradation is serious issue. It refers to any process in oil recovery applications. Chemical degradation refers to the breakdown of polymer molecules. In other words, polymer chemical stability is mainly controlled by oxidation reduction, ironic ions and divalents. They can easily destroy the structure of PAM, or interact with the acrylic group in HPAM. The solution viscosity is largely reducted. Both of them affect HPAM stability.

References

[1] Rongwei Liu, 2010, Study on the Mechanism of PAM-Degradation in the oily wastewater, Petrochemical Industry Application, 1-5.

[2] Luo, J.-H., Liu, Y.-Z., Zhu, P., 2006. Polymer solution properties and displacement mechanisms. In: Shen, P.-P., Liu, Y.-Z., Liu, H.-R. (Eds.), Enhanced Oil Recovery-Polymer Flooding. Petroleum Industry Press, pp. 1-72.

[3] Rongwei Liu, 2013, Study on the effect and controling methods of deep profile control technology due to Iron ion, Advances in Fine Petrochemicals, 27-29.

[4] Han, J., Kong, B.L., Lu, X.H., 2006a. Study on changes of hydrolysis degree and solution viscosity of HPAM at different reservoir temperatures. Oilfield Chemistry 23 (3), 235-238, 255.

[5] Kong, B.-L.,1996. Aging effect at high temperature on HPAM solution behavior. Oil and Gas Recovery Technology 3 (4), 7-12.

[6] Levitt, D.B., Jackson, A.C., Heinson, C., Britton, L.N. Malik, T., Dwarakanath, V., Pope, G.A., 2006. Identification and evaluation of high performance EOR surfactants. Paper SPE 100089 presented at the SPE/DOE Symposium on Improved Oil Recovery, Tulsa, 22-26 April.

[7] Davison, P., Mentzer, E., 1980. Polymer flooding in North Sea reservoirs. Paper SPE 9300 presented at the SPE 55th Annual Fall Conference, Dallas, 21-24 September; SPEJ (June 1982), 353-362.

Advanced Materials Research Vol. 936 (2014) pp 1560-1564
© (2014) Trans Tech Publications, Switzerland
doi:10.4028/www.scientific.net/AMR.936.1560

The Application of Based on Case-based Reasoning for drilling parameter optimization in HaiTa Oilfield

Lei Chang[1,2,a],Tie Yan[1,b],Shan Li[2,c],Hong-ming Fei[2,d]

[1]Key laboratory of Enhanced Oil and Gas of Education Ministry. Northeast Petroleum university,Daqing Heilongjiang 163318,P.R.China

[2]Da Qing Oilfield Production Engineering & Research Institute, Daqing Heilongjiang 163453,P.R.China

[a]changlei@petrochina.com.cn,[b]yant@nepu.edu.cn,

[c]lishan1@petrochina.com.cn,[d]feihongming@petrochina.com.cn

Keywords: case-based reasoning; drilling speed; drilling parameter; optimization

Abstract: In the view of the complex influence factor, simplified research method and structural or partial structural application model a drilling parameter selection optimization method based on case-based reasoning is provided in this paper. The goal of the research is to build up a drilling parameter selection optimization method which has great applicability. Based on the field drilling data and parameters a case base is built up. Afterward data discovery is used to deal with the case selection problem and select case from case base. Combining with field situation, drilling parameters selection is optimized and drilling speed could be predicted.

Introduction

Drilling parameter optimization called optimized drilling. Optimized drilling is a drilling technology in jet drilling and balance drilling developed. Is the combination of the optimization mathematical theory and the drilling of scientific experiments. Is the study of drilling pressure, rotating speed, hydraulic parameters, drilling combination drilling parameters and mechanical drilling rate, and so on. The increase rate of penetration is learned for reducing the cost and increasing economic benefits[1]. However, In the drilling operation, affect the rate of penetration is very complex, factors affecting is very various. Although the drilling rate equation was established, but practicality is not strong, General equation is not necessarily on a different block, it is difficult to use the exact model to simulate and forecast. Because Case-based Reasoning in processing semi-structured and unstructured problems have excellent ability, thus the drilling parameter optimization model based on Case-based Reasoning for drilling rate prediction is established having realistic and important meaning.

In this paper, drilling parameter optimization is researched using the theory of Case-based Reasoning. Case-based Reasoning will achieve two functions in the drilling parameter optimization by two aspects of research work. The first function is that according to drilling parameters of the case base for Haita oilfield data analysis, using the theory of Case-based Reasoning for drilling parameter optimization. It play a direction role for drilling parameter optimization and drilling rate forecasting in the area. The second function, according to drilling parameters data case base of Haita oilfield being used by the drilling parameters, the seismic data and logging data of, using the

theory of Case-based Reasoning, according to the geological characteristics of block and regional similarities were simulated and matched, for different strata in different areas of the drilling parameter optimization and forecasting of rate of penetration, the new blocks has a applicability.

Based on Case-based Reasoning Drilling Parameter Optimization Model

The Basic Principle of Drilling Parameter Optimization Based on CBR

Drilling parameter optimization based on Case-based Reasoning is a kind of use in the past a lot of actual drilling parameters to establish the parameters of case base, dig out many useful information and knowledge, based on previous actual drilling parameters to analysis and forecast the trend of the drilling rate of penetration under the new situation and the new conditions, so as to improve the rate of penetration and save drilling cost, increase the economic benefits. The basic idea is: in the solution of the problem, first of all, retrieve the most similar cases with the issue in the case base for drilling parameters, if we can find an exact match, as solving the output, if can't find, a similar case be seek and be revised according to the requirements of the problem, and the correction results be saved in the case base. Fig.1 is drilling parameter optimization system structure diagram base on the example of reasoning[2,3].

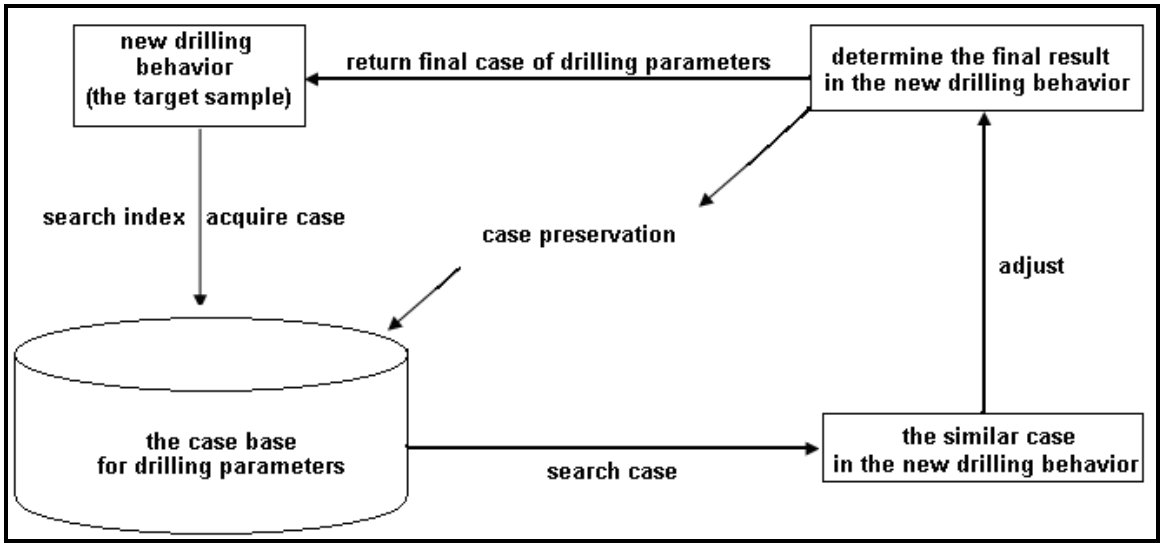


Fig.1 Drilling Parameter Optimization System Structure Diagram Base On Case-Based Reasoning

The Pretreatment of the Drilling Data

In Case-based Reasoning, the establishment of drilling parameters of the case base is the primary work. In the process of the construction of case base, a reasonable and consistent case representation method is indispensable. an appropriate expression way of he scenario, the answer, the result is a question of fundamental importance of construct a sample based on Case-based Reasoning. In drilling parameter optimization system based on Case-based Reasoning, using object-oriented technology show affect the penetration rate of drilling parameters, the object of each instance and background database record is one-to-one correspondence and them will be Dynamic Structured by the system in running[4].

Because of the complexity and accuracy of the actual drilling parameters, the actual drilling data will be calculated by Case-based Reasoning model. Firstly, make the data into use the data of the model can make. Drilling parameters of the original data include stratigraphic composition description, the drilling strata, segment, bit type and bit size, footage, rate of penetration, penetration time, actual drilling time, round trip time, drilling pressure, rotating speed ,

displacement, the stand pipe pressure, the pressure drop of the bit, annular pressure loss, impact, injection speed, bit specific hydraulic horsepower, upward velocity, tooth wear, diameter wear and bearing wear, etc. The formation components described are based on textual descriptions, so for example reasoning model application has the certain difficulty. This paper prepared to take lithological types description into a comparative value of digital type description or letters type description. The other drilling parameters are a digital type data, So as long as the actual drilling data is dealt for unification and tidy.

The Establishment of the Drilling Parameters Case Base

Case base on Case-based Reasoning plays a decisive role, the realization of the case base sample directly affect the success of reasoning. Drilling parameter optimization method based on Case-based Reasoning, therefore, is to establish the priorities for drilling parameters of case base[5,6]. Processing method according to the actual drilling parameters and requirements, turn drilling parameters, establish drilling parameters case base suitable for Case-based Reasoning.

The drilling parameters case base is established by SQL server in this study. The case base have some function is more significant which in addition to the drilling parameters input, find and keep the basic functions, such as network sharing, it can directly share the enterprise database and remote calls. Using the Delphi form software platform, for case base calls, implemented with platform operation ability and visual oriented practical examples based on case-based reasoning of drilling parameter optimization software.

Similarity Measure and Retrieval Technology of Drilling Parameter Optimization System

Assumptions, n set of drilling parameter data, constitute n dimension data, one group of drilling parameter data is X, X characteristic parameters——drilling parameters of the stratigraphic composition description written by X_1, drill for drilling period by X_2, interval remember to X_3, type of bit for X_4. and so on, Mathematical expressions has the following form, $X=\{X_1,X_2,\cdots,X_n\}, X_i(1\le i\le n)$ is characteristic value, W_i is weight. X is a point of n dimension characteristic space $D=(D_1,D_2,\cdots,D_n)$, $X_i\in D_i$.

$$Dist(X,Y)=\left(\sum_{i=1}^{n}D(X_i,Y_i)^r\right)^{1/r} \tag{1}$$

$$D(X_i,Y_i)=\begin{cases}|X_i-Y_i| & \text{If } D_i \text{ is continuous}\\ 0 & \text{If } D_i \text{ is discrete, and } X_i=Y_i\\ 1 & \text{If } D_i \text{ is discrete, and } X_i\neq Y_i\end{cases} \tag{2}$$

When r is equal to 2,and $Dis(X,Y)$ is Euler distance.The similarity measure function between the goal case of this model and the source case using euler distance.

$$Sim(X,Y)=1-Dist(X,Y)=1-\sqrt{\sum_{i=1}^{n}D(X_i,Y_i)^2}\ (Dist(X,Y)\in[0,1]) \tag{3}$$

$$Sim(X,Y)=\frac{1}{1+Dist(X,Y)}=\frac{1}{1+\sqrt{\sum_{i=1}^{n}D(X_i,Y_i)^2}}\left(Dist(X,Y)\in[0,\infty)\right) \quad (4)$$

Although examples based on the reasoning of drilling parameter optimization algorithm of comparability measurement function has been established, but the sample reasoning retrieval strategy is also very important. An example of how to retrieve the as less as possible, an example of retrieved as far as possible with the target sample related or similar is the key retrieval examples. This system adopts the nearest neighbor retrieval method and retrieval method based on knowledge, the core of the nearest neighbor retrieval method is to calculate the similarity between example, identify one or more examples of the maximum similarity retrieval results for its. And deep retrieval method based on knowledge is according to the characteristics of attribute importance in question given properties of different weights, usually combined with the nearest neighbor method is used.

The Drilling Parameter Optimization System Based on Case-based Reasoning Correction Technology

The old paradigm which is similar to the drilling parameter optimization problem is found and then the sample drilling parameters is corrected if there is no old paradigm matched the new sample completely in drilling parameter optimization system based on model reasoning[9]. Correction technique is the key technology of drilling parameter optimization system, it affects directly ,the success of drilling parameter optimization system based on model reasoning, but it is difficult to access, correct knowledge compared with capture, because its lack of methodology ,which is accessed and used rules in the correction techniques.

This system takes advantage of a repeat method based on the example, this method records the process of solving and preserves, drilling parameters as the instance then reasoning new problems based on the corrected instance, and complete correction of the new problems of drilling parameter correction phase.

Application

122 Wells Field data is collected for the establishment of case base. The Field application is carried out according to the drilling parameter optimization model based on Case-based Reasoning. The haita oilfield drilling parameter optimization results are obtained. The table 1 is the drilling parameter optimization results.

TABLE1 DRILLING PARAMETER OPTIMIZATION RESULTS

block	Formation	rotate speed of the optimization	WOB of the optimization	delivery capacity
19 block	U.Zuun bayan	135~170	150~170	29~32
	L.Zuun bayan	130~155	155~180	28~32
21 block	U.Zuun bayan	135~172	150~175	29~32
	L.Zuun bayan	130~154	155~178	29~32
Wudong block	U.Zuun bayan	140~185	150~182	28~32
	L.Zuun bayan	130~162	175~192	28~32
Bei block	U.Zuun bayan	140~181	150~188	29~32
	L.Zuun bayan	130~165	175~200	28~32

Through the field test, the drilling speed after parameter optimization is very good. The average rate of penetration is 15.32 m/h in 2011, the average rate of penetration after optimization is 21.35 m/h in 2012, after optimizing the mechanical drilling rate increased by 39.36% than before optimization.

Conclusions

(1) The drilling parameter optimization based on Case-based Reasoning optimize the drilling parameter from a unique Angle, has the advantages of simulate human reasoning process, has excellent ability in the treatment of the semi-structured and unstructured problems.

(2) The characteristics of case base organization, sample selection and retrieval, similarity measure method and the correction of sample characteristics directly affect the quality and quantity of drilling parameters, and directly affect the credibility and fidelity of drilling parameter optimization.

(3) The drilling parameter optimization method based on Case-based Reasoning is built on the basis of case base. the accuracy of the sample must be improved for the preferences credibility.

References

[1] Shi Zhongzhi. Knowledge Discovery [M]. Tsinghua University Press, 2004.

[2] Tom M. Mitchell.Machine Learning[M].Computer Science Series,2003.

[3] Yan Tie. Theory and Practice of Optimizing Drilling Parameters [M]. Harbin Industrial University Press, 1994.

[4] Tu Xuyan. Intelligent Management [M]. Tsinghua University Press, 1995.

[5] Ni Zhiwei, Cai Qingsheng, Jia Ruiyu. the Knowledge Discovery on Case Base [J]. Journal of Nankai University (natural science). 2002, 35 (4) : 45-49.

[6] Zhao peng, Ni ZhiWei, Jia Zhaohong. Establish Case Base Using Data Mining Technology from The Meteorological Database [J]. Microcomputer Development, 2002 (03) : 67-70.

[7] Geng Huantong, Xiao MingJun, Zou Xiang, etc. The Application of Clustering Algorithm in Case Base Maintenance [J]. Computer Engineering, 2005, 31 (12) : 166-168.

[8] Yang Aijun, Jiang Jingzhuo, Zhang Junxue. Command Decisions Based on Case-based Reasoning [J]. Journal of Military Strategy and System Engineering, 2003 (01) : 10-14.

[9] xia Hong, Liu Qun, Zhang Zhihua. Machinery Fault Diagnosis Method Based on Case-based Reasoning [J]. Journal of Harbin Engineering University, 1999, 20 (5) : 43-50.

CHAPTER 15:

Methods and Devices of Measurements in Materials Engineering

Advanced Materials Research Vol. 936 (2014) pp 1567-1570
© (2014) Trans Tech Publications, Switzerland
doi:10.4028/www.scientific.net/AMR.936.1567

Evaluation of Uncertainty of Hydrogen's Consistency in Transformer oil by Gas Chromatography

SHEN Han-lin [1, a] and LUO Hai-yan [1, b]

[1] Civil Aviation Flight University of China, Guanghan, China

[a] shenhanlin@163.com, [b] 122562354@qq.com

Keywords: Gas Chromatography, Metrology, Uncertainty, On-line Monitoring , Transformer

Abstract. According to the Evaluation and Expression of Uncertainty in Measurements, the author establishes the mathematical model for measuring the purity of hydrogen in transformer oil by means of Gas Chromatography. Meanwhile the author analyses resources of uncertainty and deduces formulas of uncertainty measurement. By calculating uncertainties of the components, the author obtains the synthesis uncertainty.

Introduction

As one of the important equipments in the power industry, the transformer plays a critical role in economical power transportation and flexible power distribution. As an effective method to maintain and monitor the transformer, Gas chromatography, a way of on-line analyzing Hydrogen content dissolved in transformer oil and deducing potential problems in the transformer has been widely applied and developed.

The Process of Test

Instruments and Materials

The instruments and materials include GC-900AD Gas-Phase chromatographic instrument produced by Zhongfen Instrument, Chromatography column filled with Hayesep-D, Hayesep-S, GDX-502 filling materials, Electric six-way valve Port produced by VICI Corporation SWISS, TGS813 Semiconductor gas transducer produced by Figaro JAPAN, High-purity air, High-purity oxygen and High-purity nitrogen (Nominal value is 99.9%±0.05%).

Chromatographic Conditions

Head pressure: 10MPa; Column Temperature: 40℃initially, 10minites later, raise to 60℃at speed of 5℃/min; Carrier Gas Flow Rate: 10ml/min; Injection Volume: 1ml in quantitative tube.

Procedures

According to GB/T 5274-2008 Gas Analysis - Preparation of Calibration Standard Gas Mixture, H2 is the raw material made of high-purity H2, N2. H2 are prepared at the purity of 21, 66, 142, 203, ppm respectively.

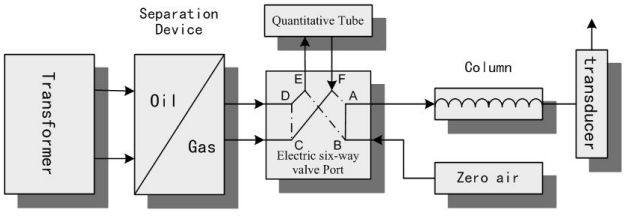


Fig. 1. Flow chart of oil and gas analysis

Evaluation of Uncertainty

According to the experiment methodology, experiment process and Modern Error Theory, The uncertainty of H2 purity is tested by Gas Chromatography and has the following uncertain resources:

(1) Uncertainty caused by quantitative tube capacity error
(2) Uncertainty caused by repetitive operation
(3) Uncertainty caused by standard curve regression
(4) Uncertainty caused by measuring the standard gas

Uncertainty Caused by Quantitative Tube Capacity Error

The author uses SL1KUW stainless quantitative tube made from VICI, Swiss. The standard error is ±0.05ml according to the manufacturer. This uncertainty is classified into B-level uncertainty.

The standard uncertainty is in (1).

$$u(v)=\frac{0.05}{\sqrt{3}}=0.0289 \tag{1}$$

Relative uncertainty is in (2).

$$u(V)=\frac{u(v)}{V}=\frac{0.0289}{1}=0.0289 \tag{2}$$

Standard uncertainty is in (3).

$$u(v)=\frac{0.05}{\sqrt{3}}=0.0289 \tag{3}$$

Relative uncertainty is in (4).

$$u(V)=\frac{u(v)}{V}=\frac{0.0289}{1}=0.0289 \tag{4}$$

Uncertainty Caused by Repetitive Operation

Due to the variety of stuff's familiarity with the operation and instability of the instruments, uncertainty caused by repetitive operation belongs to A-level uncertainty. Table-1 is the H2 purity after repetitive tests.

TABLE I. Repetitive Tests（unit: ppm）

No.	1	2	3	4	5	6	7
Purity of H_2	62.8	62.9	62.9	62.8	62.9	62.8	62.8

Standard error is in (5).

$$s(m)=\sqrt{\frac{\sum_{i=1}^{n}(x_i-\bar{x})^2}{n-1}}=0.000251 \tag{5}$$

Standard uncertainty is in (6).

$$u(m)=\frac{s}{\sqrt{n}}=\frac{0.000251}{2.646}=0.0000945 \tag{6}$$

Relative uncertainty is in (7).

$$u(M)=\frac{u(m)}{\bar{\rho}}=\frac{0.0000945}{0.998957}=0.0000946 \tag{7}$$

Uncertainty Caused by Standard Curve Regression

The H2 with 9 different Purities are tested for four times by Gas chromatography for the maxim of the gas purity, and the results are bellow after 36(n) times of testing.

TABLE II. The result of repetitive testing

H_2 purity in standard gas /ppm	Maxim No.1	Maxim No.2	Maxim No.3	Maxim No.4	AVERAGE Maxim
21	5.2401	5.5960	5.4524	5.1773	5.3664
66	8.5025	8.8574	8.7661	8.6428	8.6922
142	15.9825	16.2332	15.6636	15.2033	15.7706
203	24.0192	24.1774	25.8811	26.1741	25.0629

Suppose the mathematic model of linear fitting standard curve is

Where

H_i ——The maximum of standard gas i

ρ_i ——Purity of H2 in gas i

And the slope of the fitting line is in (8).

$$k=\frac{S_{xy}}{S_{xx}}=\frac{\sum_{i=1}^{36}(\rho_i-\overline{\rho})(H_i-\overline{H})}{\sum_{i=1}^{36}(\rho_i-\overline{\rho})^2}=\frac{1994743}{3557768}=0.0561 \tag{8}$$

Intercept b is in (9).

$$b=\overline{H}-k\cdot\overline{\rho}=30.2665-0.056\times374=9.2973 \tag{9}$$

So the linear fitting regression curve is in (10).

$$H_i=0.0561\rho_i+9.2973 \tag{10}$$

The standard deviation of H2 purity is in (11).

$$s(H)=\sqrt{\frac{\sum_{i=1}^{n}v_i^2}{n-2}}=\sqrt{\frac{\sum_{i=1}^{n}(H_i-k\rho_i-b)}{n-2}}=4.0431 \tag{11}$$

Now certain transformer oil is under test for 3 times and its H2 purity is 68.4 ppm. Its standard uncertainty is in (12).

$$\begin{aligned}u(x)&=\frac{s(H)}{k}\sqrt{\frac{1}{p}+\frac{1}{n}+\frac{(\rho_0-\overline{\rho})^2}{S_{xx}}}\\&=\frac{4.0431}{0.0561}\times\sqrt{\frac{1}{3}+\frac{1}{36}+\frac{(68.4-374)^2}{3557768}}\\&=44.8549\end{aligned} \tag{12}$$

And relative uncertainty is in (13).

$$u(X)=\frac{u(x)}{\rho_0}=\frac{44.8549}{68.4}=0.6558 \tag{13}$$

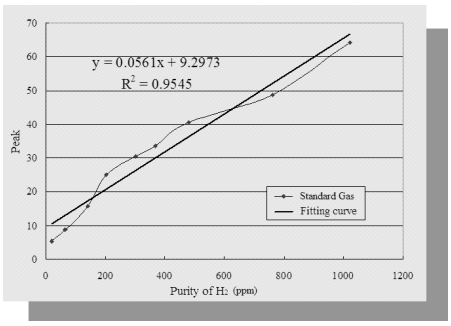


Fig. 2. Linear regression fitting curve.

Uncertainty Caused by Measuring Standard Gas

The gas bottle should be cleaned with N2 and vacuum pressure should reach 0.1kPa before it is filled. Retained N2 quantity can be calculated by (14).

$$m = \frac{x_i \cdot p_f \cdot V_{cyl} \cdot M_i}{R \cdot T \cdot Z_f} \tag{14}$$

Where

mi ——quantity of component i in mixture gas, in grams

xi ——expected concentration of component i in mixture gas, in ppm

T ——environmental temperature, in K

Zf ——compressibility at T and pf

The quantity of retained N2 is in (15).

$$m = \frac{x_i \cdot p_f \cdot V_{cyl} \cdot M_i}{R \cdot T \cdot Z_f} = \frac{0.9 \times 1.04 \times 10^{5} \times 5 \times 10^{-6}}{294 \times 8 \times 1} = 5.3mg \tag{15}$$

Because of even distribution of retained gas quantity, standard uncertainty is in (16).

$$u_r = \frac{5.3}{1.732} = 3.06005 \tag{16}$$

Comparative uncertainty is in (17).

$$u_R = \frac{u_R}{M} = \frac{3.06005}{773.5} = 0.00396 \tag{17}$$

Combined Uncertainty

Relatively combined uncertainty of H2 concentration in transformer oil is in (18).

$$u = \sqrt{u^2(V) + u^2(M) + u^2(X) + u^2{}_M + u^2{}_R} = 0.6564 \tag{18}$$

Conclusion

Relative synthesis uncertainty of H2 purity in oil transformer is 0.6564, tested by Gas chromatography, and H2 purity in a certain type of transformer oil is 62.89 ppm, and Relative synthesis uncertainty is 0.6564.

References

[1] BAO De jun, "An Evaluation of the Uncertainty of Standard Reference Material of Anti oxidant D by HPLC" *ACTA METROLOGICA SINICA*, vol. 28, pp. 175-177, Apr. 2007.

[2] Li Song, "Uncertainty Evaluation of Measurement Results for the Determination of BTEXs in Groundwater Samples by Purge and Trap-Gas Chromatography-Mass Spectrometry" *Chinese Journal of Spectroscopy Laboratory.* vol. 27, pp. 423-425, Mar. 2010.

[3] Zhang Song, "Evaluation of Uncertainty of Methods of Determination for Benzoyl Peroxide in Wheat Flour" *ANALYSIS AND TESTING TECHNOLOGY AND INSTRUMENTS.* vol. 13, pp. 259-262, Dec. 2007.

[4] ZHANG Pan, "Analysis of Trace Pentachlorophenol in Cotton Textiles by Liquid Chromatography-Isotope Dilution Mass Spectrometry and Its Uncertainty Evaluation" *Journal of Instrumental Analysis.* vol. 29, pp. 953-957, Sep. 2010.

Advanced Materials Research Vol. 936 (2014) pp 1571-1575
© (2014) Trans Tech Publications, Switzerland
doi:10.4028/www.scientific.net/AMR.936.1571

Dissolution of Zirconium Power and Detection of Zirconium Powder Content by ICP-AES Method

Zhang Xiao Lian[1, a *], Zhu Wei Hua[1,b], Zheng Xin[1,c], Liu Hong Xia[1,d]

[1]College of Chemistry and Chemical Engineering, Gannan Normal University, Ganzhou 341000, China

[a]zhlxyzw@126.com, [b]zhuweihuameinv@163.com, [c]lixishziji@163.com, [d]hongxia19838486@yeah.net

Keywords: zirconium powder；plasma-atomic emission spectrometer；dissolution；zirconium content

Abstract: Instrument analysis method is used in this experiment, which detecting the zirconium content of zirconium powder by using plasma-atomic emission spectrometer. In this experiment, the instrumental detective conditions were determined, and analyzed several main factors affecting the experimental results, concluded the effects of temperature, hydrofluoric acid and deionized water on dissolving zirconium powder, summarized the method to detect zirconium powder content directly by ICP.

Introduction

Zirconium and zirconium alloys possess outstanding nuclear performance, beside it have excellent corrosion resistance and mechanical performance, have been applied extensively in civilian area of energy, petroleum, chemical industry, pharmacy, medical equipments and light industry and so on, also as an important additional element of high property magnesium alloys [1], the additive of medium temperature nuclear materials [2], armament industry and aerospace new materials [3]. Zirconium and zirconium alloys have been praised as "one of the most promising materials in 21 century". Zirconium powder is the important product of zirconium series products, has great surface free energy and strong liveness. For different areas, the demand of zirconium content is also different. As alloying additive and powder metallurgy, etc, the zirconium content should more than 97%; as fireworks and ordnance industry, etc, the zirconium content should more than 90%; as nuclear industry, the zirconium content should more than 99% [4-6]. As a result of the higher zirconium content in general products, it will have a bigger deviation by chemical analysis method, and detect zirconium content is different, mainly detect impurities content in zirconium powder in all kinds of documents, so in order to detect zirconium content quickly and conveniently, deciding to use ICP-AES to detect zirconium content directly in this paper through continuous experiments.

In this experiment, mainly detect zirconium powder that produced by metal calcium deoxidate zirconium dioxide, the content of zirconium powder is more than 97%.

Experiment

Main reagents

Hydrofluoric acid; nitric acid; standard zirconium reagent. The reagents in this experiment are AR, water is secondary distilled deionized water（ultrapure water）. The standard sample solutions which content 0.1 mg/L，1 mg/L，10 mg/L，100 mg/L were prepared for build work curve.

Experimental process

Taking 0.01g zirconium powder accurately into 100 ml beaker which made by teflon, then add 10 ml nitric acid to ensure the sample fully soaked in acid, heating solution until about 60 ℃ and shake beaker gently to make sure uniformity of temperature, then add 4 ml hydrofluoric acid slowly by using one-time dropper, the reaction is drastic and solution turns yellow with smoke, when the color up-to the most yellow, add 15 ml deionized water to control reacting rate in order to getting more thorough of the reaction, and the standard volume of deionized water is till to the color of solution become limpid[7]. Until the reaction is complete, adjusting temperature of electric furnace to about 100 ℃ for evaporate and concentrate, when the solution volume become 2-3 ml, then stop heat, chill, finally allow the solution into 100 ml volumetric flask through constant volume.

Inductively coupled plasma atomic emission spectrometry (Prodigy XP, Lee man Company, USA) was used to detect.

Work conditions of instrument:

RF 1:1.2 kw，high frequency generator: 40.68 MHz, cooling air: 18 LPM, atomizer: 35 PST, observation way: bidi-rection, optical system: high resolution echelle, wavelength range: 175-900 nm, detector temperature: - 16 ℃, lifting capacity of sample: 1.5 ml/min, integral time: 20 s.

Firstly, according to work conditions of instrument, establishing proper work curve by using standard sample of zirconium which prepared already, spectral line of zirconium generally choose in 339.198 nm, then shake un-test solution until uniform and detect by instrument.

Results and analysis

This experiment is trace experiment, some microelements in acid and some trace elements in deionized water are influential to the experimental results, so every experiment requires blank experiment, try to reduce the effects of dissolving process. Generally, the main impurities in zirconium powder which made by metal calcium thermal reduction is calcium, the emission line of calcium is 317.933 nm, while detecting the elements of different emission signal values has less effects by using plasma atomic emission spectrometer[8]. Detective results and influence factors as shown in the Tab. 1.

Tab. 1. Detective results of zirconium powder under different conditions

Sample weight/g	Temperature/℃	HNO_3: HF/ml	Deionized water/ml	Concentration/ppm	Zirconium content/%
0.0112				71.2383	63.61
0.0108				75.7520	70.15
0.0103	30	6:3	10	62.8229	60.99
0.0100				51.4422	51.44
0.0104				52.3679	50.35
0.0101				82.5064	81.68
0.0110				83.9743	76.34
0.0100	60-70	6:3	10	89.2372	89.24
0.0103				71.4831	72.65
0.0113				84.1253	74.45
0.0100				98.0280	98.02
0.0103				100.8654	97.93
0.0106	60-70	10:4	15	104.1725	98.27
0.0099				97.3071	98.29
0.0113				110.9729	98.21

The average of detective sample content in this study is 98.144%, a same batch of samples will be send to national nonferrous metals and electronic materials analysis inspection center (assay is detect the content of impurities in zirconium powder) , the zirconium content was 97.6573%, and the error of the test results which using this instrument is less than 0.5%, detective error of overall content is between plus or minus 0.4%, basically meet the test requirements.

The influence of solution temperature on the test results

ICP-AES plasma test method belongs to trace test, so pay attention to eliminate all influential factors for the experiment is needed. During the process of sample dissolution, founding that the temperature has much effects on the dissolution process, dissolving in the condition that around 30 ℃,for the rest of the solution, we can obviously see some residues have not been dissolved completely in the bottom of the beaker. Also, the test solution is stable at around 60-70 ℃ for reaction, the clear solution is obtained, which sample completely dissolved. Comparing the results of the samples which reaction in same quality and different temperatures, as shown in Fig. 1.

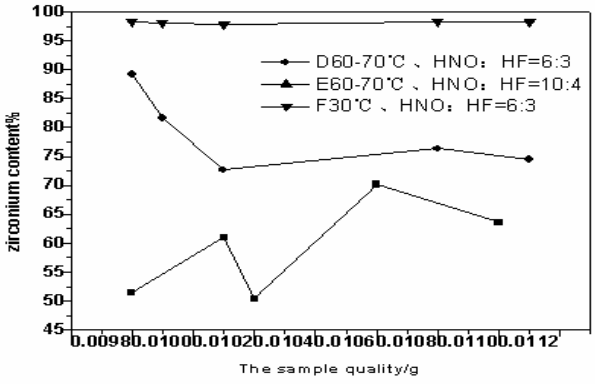


Fig. 1. The contrastive chart of the influence of temperature on the content

From Fig. 1, We can see that the influence of thermal control on dissolution results and product content is very big in the process of dissolution, especially before joining hydrofluoric acid, the influence of thermal control of nitric acid on dissolution process and test results.

The influence of acid on test results

The chemical nature of zirconium is not active and not reacts with hydrochloric acid, while sulfuric acid can heighten the activity of partial active zirconium in zirconium powder, then produce a lot of heat and dissolve active zirconium, but cannot dissolve other substances in zirconium powder completely. Partial active zirconium will dissolve in nitric acid by adding nitric acid, and produce less heat that not enough to dissolve the zirconium powder completely, most of samples are still stable. So choose hydrofluoric acid as the initiator when dissolving samples, on the basis of dissolving use nitric acid, enhancing the activity of zirconium powder and make sure the reaction can proceed smoothly and the samples can be completely dissolved. For different acid ratios, contents of zirconium powders were compared, and the results are shown in Fig. 2.

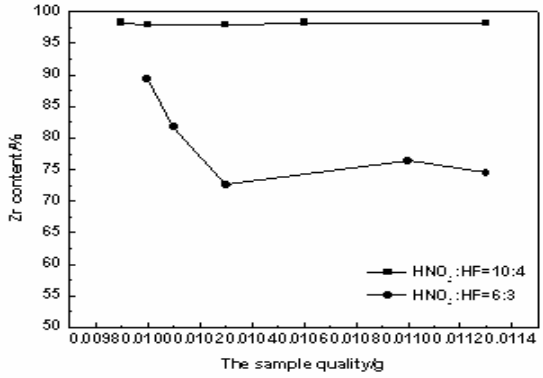


Fig. 2. The contrastive figure of zirconium content in the detective zirconium powder under different acids

From Fig. 2, We can see that the influence of the nitric acid proportion and hydrofluoric acid on the content of zirconium powder is also very big.

The influence of deionized water on test results

The reaction will be intense when add hydrofluoric acid, while in the initial stage of reaction, reactive speed is over fast that can lead to some powders which deposited on the bottom of the beaker are too late to participate in the reaction, the subsequent activity is not enough to make the reaction thoroughly. It can control the reaction rate firstly by adding deionized water, and also can float the samples which have settled at the bottom of the beaker , try to speed up the fluidity of samples inside test solution, let all samples can be dissolved in hydrofluoric acid and react completely.

Conclusions

The method by using ICP-AES is simple and more intuitive, accurate, and the operation is simple, the data is more intuitive, also shortens the time of testing and further ensure the accuracy of analysis results than the traditional method of testing zirconium content through impure content.

Acknowledgments

This work was financially supported by the National Natural Science Foundation of China (51064001) and Science and Technology Project of Jiangxi Municipal Education Department (GJJ11723).

References

[1] Chen Bin, Lu Chen, Lin Dong-liang, Effect of zirconium addition on microstructure and mechanical properties of $Mg_{97}Y_2Zn_1$ alloy [J]. Trans. Nonferrous Met. Soc. China 22 (2012) 773-778.

[2] Wang Feng, Wang Kuaishe, Ma Linsheng,et al. The research status and develop prospect of nuclear grade zirconium and zirconium alloys [J]. Ordnance Material Science and Engineering, 2012, 35(1).

[3] Huang Lin, Yuan Xiaoli, Cui Shouxin,et al. Compressive behavior of mew aerospace material metal zirconium [J]. Physical journal of atomic and molecular , 2012, 29 (6).

[4] Xiong Bingkun, Wen Wangguang, Yang Xinmin, et al. Zirconium and hafnium metallurgy [M]. Beijing: Metallurgical Industry Press, 2010.

[5] Xiong Bingkun, Wen Wangguang, Yang Xinmin, et al. Zirconium and hafnium metallurgy [M]. Beijing: Metallurgical Industry Press, 2002.

[6] Xiong Bingkun,Wen Wangguang, Luo Fangcheng, et al. Application of zirconium and hafnium compounds [M]. Beijing: Metallurgical Industry Press, 2002.

[7] Ning Jiabao. Dissolution methods of titanium and zirconium metal, China, 1090521A[P]. 1994-08-10.

[8] Hou Lieqi, Wang Shuan, Li Jie. The research of detecting 17 impurity elements in nuclear pure zirconium sponge by ICP-AES [J]. Spectrographic laboratory, 13 (5), 42-46.

Advanced Materials Research Vol. 936 (2014) pp 1576-1581
© (2014) Trans Tech Publications, Switzerland
doi:10.4028/www.scientific.net/AMR.936.1576

Application of Magnetic Barkhausen noise in the Evaluation of Heat Treatment Process

Yin Hechi[1,a], Zhou Lan[2,b], Wang Zhensheng[1,c], Cai Chunbo[3,d]

[1] School of Electromechanical Engineering, Hunan Univ. of Sci. & Tech., Xiangtan, China

[2] School of Information&Electrical Engineering, Hunan Univ. of Sci. & Tech., Xiangtan, China

[3] Norinco Group Jianglu Machinery&Electronics Group Co., Ltd., Xiangtan, China

[a]hcyin@hnust.edu.cn,[b]lzhou@hnust.edu.cn,[c]58282675@qq.com,[d]66958015@qq.com

Keywords: Barkhausen noise, magnetic domain, residual stress, Root Mean Square, Power Spectrum.

Abstract: Magnetic Barkhausen noise(MBN) is a new technique on non-destructive testing of residual stress. The testing system based on virtual instrument was explored. It can achieve the MBN and deal with it in time. The technique is applied to analyze residual stress in the welding line of iron materials back and forth the heat treatment. Through comparing with the data of blind-hole method, the corresponding change between Barkhausen signals and residual stress is verified.

Introduction

At present, the methods which detect the residual stress of welding components are commonly used x-ray, strain gage method and acoustic emission. Moreover, magnetic Barkhausen noise on measurement of residual stresses in the nondestructive testing is a new technology. In 1919, the German physicist Barkhausen the first time discovered the Barkhausen effect. He observed ferromagnetic hysteresis loop of materials and found: curve is not smooth, see changes which jitter level amplified, known as the Barkhausen transition. This is the magnetization in the ferromagnetic material in the process of rapid changes of the local emergencies when using this detection coil to feel continuous changes. Which use headphones and listening, you can hear a noise form, it's known as the Barkhausen Noise(BN). MBN on the main signal analysis was used to determine the residual stress in ferromagnetic materials. Its advantage is to conduct nondestructive stress analysis, can be fully automated, can be a permanent record.

Labview software platform based on virtual instrument technology in recent years is an emerging discipline, mainly for building a computer analysis of test systems and automatic control system. Its softwares replace the traditional electronic devices, and give full play to a new generation of computer potential of big capacity and high-speed. It is an important signal acquisition and analysis tools. Virtual instrument technology is the use of high-performance modular hardware with highly efficient and flexible software to complete all kinds of test, measurement and automation applications. By MBN Virtual instrument technology for measurement of residual stress, realized the acquisition and real-time processing of the Barkhausen noise, and applied to residual stress analysis after heat treatment in the ferromagnetic material weld. The entire measurement process is a high degree of automation, high speed, high accuracy.

MBN Measurement Mechanism

During magnetization in the ferromagnetic materials, magnetic domain wall will happen mobile magnetic moment and the overall rotation within magnetic domains, which is a re-orientation of magnetic domain changes. A number of factors of the material structure that would impede and restrict magnetic domain wall motion and happen changes in the block, and in the irreversible magnetization of the back line hysteresis due to magnetic domain wall displacement and irreversible direction from a stable mutation to another stable direction, therefore, the magnetization in the region is composed of many irregular discontinuous jump, which will in the specimen surface of the receiving coils produce a series of chaotic electrical pulse signal, that is MBN signal [1], see Fig.1.

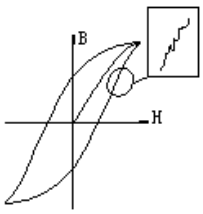


Fig. 1 Barkhausen noise

The size, direction distribution, jump on the instant process and the mutual relations of magnetization upspring, and the mechanical stress state of detected materials are closely linked[2]. Through processing and amplifying for observed MBN noise by the use of electronic methods, which usually displayed as noise pulse of amplitude, width and time interval without the rules. Combined with the virtual instrument technology, MBN noise is changed into residual stress values.

Testing Techniques and Instruments

The instruments required to detect Barkhausen signals are shown in Fig.2. To produce Barkhausen noise, a magnetizing field is generated and applied to a ferromagnetic material through an electromagnet[3,4]. The material reacts to the magnetic field and emits Barkhausen bursts, which are captured by a sensor consisting of a coil of conducting wire. The signal is then amplified and filtered. The amplitude is calculated by an RMS equation and Power Spectrum analysis and the data is digitized for display and output to a computer.

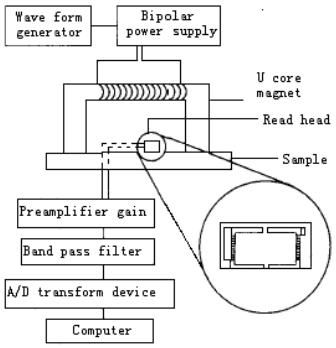


Fig.2 Testing instruments of MBN

The composition of the entire hardware system is divided into four parts: ① Excitation: input sensor excitation source of 20 Hz , 4V after the power amplifier by PCI1712 data acquisition cards. ② Sensors: compose a magnetic circuit with testing board, and then collect MBN signal by the receiver coil. ③ Receivers: integrated operational amplifier CA3140 is composed of preamp, qualcomm, analog low-pass filtering and postmagnification. MBN signals pass through PCI1712 data acquisition card into the PC. ④ PC: signal processing and display [5].

Software development is the core of virtual instrument. Labview provides a powerful data collection, processing and analysis functions. Graphical combination of functional modules achieves various functions required [6,7]. Through channel signal acquisition module, and then a noise signal analysis and processing, mainly through the processing RMS of time domain and Power Spectrum analysis of frequency domain, shows the micro-structural changes of the plate weld before and after heat treatment and MBN's changes caused by the residual stress changes.

Testing material

Testing material is plate, and its type is SM570. Size of the sample is 700mm×299mm ×45mm. Two plates have been used during the testing. Each has two states of heat treatment after welding or no.

Testing data of blind-hole method

Testing data of residual stress of the weld in blind-hole method is shown in tab.1.

Table 1 The most value of principal residual stress (σ_{max})(mpa) in blind-hole method

Testing place	No heat treatment after welding	Heat treatment after welding
1	168	118
2	180	84
3	173	40
4	236	96
5	167	94
Average	185	87

Results indicate the most average value of principal residual stress (σ_{max}) is 185MPa when the plate has not been treated by heating after welding. Whereas the average value is 87MPa when the plate has been treated by heating after welding. The fall ratio of residual stress is 53%. It shows residual stress of the weld has been released in a certain degree. The right effect of principal residual stress before and after heat treatment is show in Fig.3.

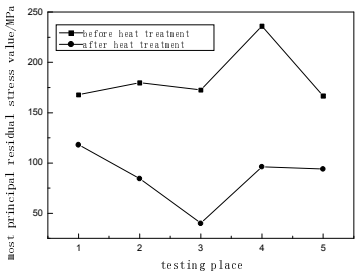


Fig.3 The distribution of principal residual stress

Testing data of magnetic Barkhausen noise method

Magnetic Barkhausen noise (MBN) is rather complicated. It was measured by self-made instrument. Data processing means, such as RMS equation and Power Spectrum analysis, was adopted to process the results of measurement [8].

Data analysis of RMS equation

The statistic analysis was done after sampling signal in a certain period. Eq. (1) of RMS follows:

$$\psi_x = \sqrt{\frac{1}{n}\sum_{i=0}^{n-1} x_i^2} \tag{1}$$

Sampling signal and RMS value of a certain signal is shown in Fig.4.

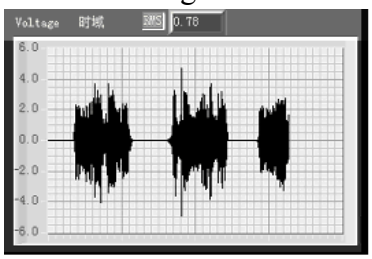


Fig.4 MBN sampling signal and its *RMS* value

Tab.2 shows testing data of RMS equation before and after the heat treatment. It is the average value of four measuring data in every testing place. We can find the signals' intensity before and after the heat treatment in X and Y direction has the dropping trend in whole, though some is increased. The dropping ratio is 26% in X direction and 17% in Y direction. It indicates that the intensity of MBN signal comes to drop with the release of residual stress.

Table 2 Testing data of rms (v)

Testing place	Before the heat treatment		After the heat treatment	
	X	Y	X	Y
1	0.728	1. 064	0. 596	0. 952
2	1.080	1. 190	0. 594	0. 708
3	0.766	0. 948	0. 482	0. 790
4	0.898	0. 746	0. 912	0. 836
Average	0.868	0. 987	0. 646	0. 822

Testing Data of Power Spectrum Analysis

On the basis of programming by Labview software, the MBN signal is transformed from time field to frequency field. Furthermore, it is analyzed by Power Spectrum to explain its change before and after the heat treatment. The distribution and analysis of Power Spectrum of a certain MBN signal is shown in Fig.5. It gives its maximum and corresponding frequency [9].

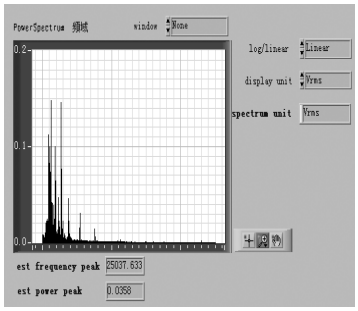


Fig.5 The distribution and analysis of Power Spectrum

Tab.3 is the testing data of Power Spectrum analysis in four testing place. It shows the frequency is about 25 kHz when the maximum of MBN signal and keeps in accordance with the sampling process before and after the heat treatment. But the maximum of Power Spectrum has been changed obviously whether X direction or Y direction. The dropping ratio of the maximum reaches 48% in X direction and 26% in Y direction in whole.

Table 3 Testing data of *power spectrum* analysis

Testing place	X direction before the heat treatment		Y direction before the heat treatment		X direction after the heat treatment		Y direction after the heat treatment	
	Frequency (Hz)	Maximum (V)	Frequency (Hz)	Maximum (V)	Frequency (Hz)	Maximum (V)	Frequency (Hz)	Maximum (V)
1	25032	0．0279	25151	0．0318	25104	0．0199	25035	0．0163
2	25090	0．0403	25034	0．0363	25247	0．0112	25105	0．0324
3	25089	0．0295	25149	0．0243	25175	0．0168	25322	0．0153
4	25205	0．0264	25103	0．0323	25174	0．0166	25177	0．0229
Average	25104	0．0310	25109	0．0310	25175	0．0160	25159	0．0230

Conclusions

Testing system of MBN signal has been constructed，which is made up of self-made MBN sensor and signal process circuit and PCI1712 and Labview software. The system becomes the basis of developing new non-destructive testing technique.

Indicates that the intensity of MBN signal comes to drop with the release of residual stress. We can find the MBN's intensity before and after the heat treatment in X and Y direction has the dropping trend in whole whether RMS or Power Spectrum analysis.

This technique can illuminate qualitatively the effect of the heat treatment on releasing residual stress, but it cannot analyze their relations quantitatively.

Acknowledgement

This work was supported by the National Natural Science Foundation（No.61203010, No. 51101055）and the Science and Technology Department of Hunan Province（No.2012FJ4111）and the Natural Science Foundation of Hunan Province（No.13JJ8015）.

References

[1] W. Zhong. Ferromagnetism[M]. Beijing: Science Press, 1987.

[2] Zhu B, Johnson MJ, Lo CCH, et al. Multifunctional magnetic Barkhausen emission measurement system[J]. IEEE Trans on Magnetics, 2001,37(3):20-22.

[3] Qi Xin, Chen Juan, Liu Diankui. Testing magneto-elasticity noise of local magnetization method on residual stress of welding frame[J]. Transaction of the China Welding Institution, 2000,21(3):1-4.

[4] Zhu B., Johnson M.J.. Multifunctional magnetic Barkhausen emission measurement system[J]. IEEE Transaction on Magnetics, 2001,37(3):20-22.

[5] Qi Xin，Hou Zhiling，Tian Jianlong. Relationship between magnetic Barkhausen noise and the stresses, the hardness and the phase content of ferromagnetic materials[J]. Journal of Harbin Institute of Technology, 2005, 12(1):67-70.

[6] Jiles D. C., Garikepati P., Palmer D. D.. Evaluation of residual stress in 300MPa steels using magnetization, Barkhausen effect and X-ray diffraction techniques[C]. Proceedings of the 15th Annual Review of Progress in Quantitative Nondestructive Evaluation, La Jolla, California (USA), 31 Jul. – 5 Aug. 1988.

[7] Yin Hechi, Zhang Guangye, et al.. Application of magnetic Barkhausen noise in non-destructive testing fields of residual stress[J]. China Welding, 2007,16(2):22-26.

[8] Zhang Yizhi. Design and Realization of Virtual Instrument[M], Xi'an: Xidian University Press, 2002.

[9] Virtual Instrument Laboratory of Tsinghua University Electrical Engineering Department. User Manual of Labview[Z]. Beijing:Beijing Zhong Ke Fan Hua Measurement&Control Technology Co. Ltd., 2000.

Advanced Materials Research Vol. 936 (2014) pp 1582-1586
© (2014) Trans Tech Publications, Switzerland
doi:10.4028/www.scientific.net/AMR.936.1582

Stress-stain Response of PVC Geomembrane under Uniaxial Tension Test

WU Haimin[1, 2, a], SHU Yiming[1, 2, b]

[1]State Key Laboratory of Hydrology-Water Resources and Hydraulic Engineering, Hohai University Nanjing 210098, China;

[2]College of Water Conservancy and Hydropower Engineering, Hohai University, Nanjing 210098, China

[a]wuhaimin@hhu.edu.cn, [b]shym@hhu.edu.cn

Keywords: PVC geomembrane; uniaxial tension test; mechanical response; stress-strain relationship

Abstract: The mechanical property of polyvinyl chloride (PVC) geomembrane was usually expressed using engineering stress-strain response in traditional uniaxial tension test. By failing to account for deformation of specimen during the test, the deviation of true stress and strain maybe caused from the test results. In this paper, the true stress-strain response of PVC geomembrane was investigated using uniaxial tension test. The photographic analysis method was used to measure axial and lateral true strain of specimen. The Poisson's ratio and true stress were also acquired based on measured true strain in the test. Then the true stress-strain relationship was obtained from the test results. By comparing with the engineering stress-strain results expressed by traditional method, it can be found that the engineering stress-strain result is unreasonable. The engineering stress-strain expression easily leads to the underestimation of the true stress.

Introduction

Evaluation of mechanical response of geomembrane by laboratory testing is very important for engineering structures involving geomembrane. Especially the stress-strain relationship is the key theoretical basis and foundation for engineering design and safety assessment[1]. But the traditional method of expressing the strain and stress does not consider the deformation of specimen during tension test[2][3]. That may lead to mistakes of test results. In current paper, the uniaxial tension test was performed to evaluate the stress-strain response of PVC geomembrane. The two method of expressing the stress-strain response of PVC geomembrane were examined and compared. The photographic analysis method was used to measure the axial and lateral true strain of specimen. And then, the true stress-strain relationship was obtained based on measured true strain during in the test. The differences between true stress-strain and engineering stress-strain responses were compared and analyzed in this paper.

Uniaxial Tension Test

Test Apparatus

The uniaxial tension test was conducted using the Multi-functional mechanical test system in geosynthetic laboratory of Research Institute of Hydraulic structures, Hohai University. The apparatus was controlled by electro-servo system. The tension force and displacement were automatically collected by sensors and computer. The test was conducted using strain-controlling mode. A strain rate of 1%/minute was desired and the crosshead speed for the test was 1.25 mm/minutes as required in ASTM D 4885-06[4]. The laboratory air was maintained at relative humidity of 50 to 70 % and a temperature of 25±2℃.

Test Specimens

In this paper, the uniaxial tension mechanical response of a 0.75 mm polyvinyl chloride PVC geomembrane was investigated. According to the results presented by Merry and Bray (1996)[5], there is no systematic variation in the stress-strain response of PVC geomembranes due to specimen width to length aspect ratio variations over a range of 0.1 to 5.5. So the specimens of PVC geomembrane with length of 200mm and width of 100mm were used in the experiments.

Measurement of Tension Force and Strain

The axial tension force of specimen was measured by a tension transducer which connected to the end of clamps. The minimum resolution and maximum capacity of transducer are 0.01kN and 10kN, respectively. The axial displacement of clamp was measured by Linear Variable Differential Transformer (LVDT) with minimum resolution and maximum capacity of 0.01mm and 800mm, respectively. The tension force and displacement were all automatically gathered by the acquiring system. And tension force-displacement curve can be shown on the software interface in time.

In order to acquire the true strain of the specimen, the CCD camera was employed to tracking the deformation of marking points on the surface of specimen. Then the true axial and lateral strains of specimen were all calculated by photographic analysis method[6]. To aid with the photographic analyses, a reference line was placed on the clamps, and a reference grid was drawn on the surface of specimens. The reference grid on the surface of specimen (10mm×10mm)was centered vertically and horizontally. Prior to the load application, both the grid lines on the specimen and the vertical edges of the specimen formed straight lines.

Expression of Stress and Strain

Axial Strain

Axial Engineering Strain

According to ASTM[3][4] and Specification for test and measurement of geosynthetics (SL 235-2012) [2], the axial strain of geomembrane specimen of uniaxial test is typically formulated as an axial engineering strain, ε_{aE}, as follows:

$$\varepsilon_{aE} = \frac{\Delta L}{L_0} = \frac{L_f - L_0}{L_0} \tag{1}$$

where L_0 is the original length of PVC geomembrane specimen between the clamps, ΔL is the specimen elongation, L_f is the separation between the clamps.

Engineering strains are usually used due to its simplicity and for the sake of consistency with normal design practice. The engineering strain definition is most appropriate at small strains. When larger strains are of interest, there maybe significant difference between the engineering strain and the true strain of specimen.

Axial and Lateral True Strain

The axial true stain ε_{aT} and lateral true strain ε_{lT} can be measured using photographic analysis method. Through analyzing the deformation of the marking points in the central of the specimen, axial and lateral true strains were obtained at any time during tests.

Poisson's Ratio

As presented by Giroud (2004) [7], the Poisson's ratio can be theoretically deduced. The relative volume change of PVC specimen throughout the test can be expressed as:

$$\frac{V}{V_0} = (1+\varepsilon_{aT})(1+\varepsilon_{lT})(1+\varepsilon_{tT}) \tag{2}$$

where V is volume of the specimen that corresponds to strain ε_{aT}, V_0 is the original volume of specimen at the beginning of test, ε_{tT} is true stain in thickness direction.

And the true stain in thickness direction can be calculated by:

$$\varepsilon_{tT} = -\nu\varepsilon_{aT} \tag{3}$$

where ν is Poisson's ratio.

For incompressible material, the relative volume change is equivalent to 0. As a result, Eq. (2) and Eq. (3) become:

$$(1+\varepsilon_{aT})(1-\nu\varepsilon_{aT})^2 = 1 \tag{4}$$

So the Poisson's ratio derived from Eq. (4) can be expressed as:

$$\nu = \frac{1}{\varepsilon_{aT}}\left(1-\frac{1}{\sqrt{1+\varepsilon_{aT}}}\right) \tag{5}$$

Cross Section Area

The cross section area on the centre of specimen corresponds to strain ε_{aT} can be expressed as:

$$A_\varepsilon = W_{\varepsilon=0}(1-\nu\varepsilon_{aT})\cdot T_{\varepsilon=0}(1-\nu\varepsilon_{aT})_\varepsilon = W_{\varepsilon=0}T_{\varepsilon=0}(1-\nu\varepsilon_{aT})^2 \tag{6}$$

where $W_{\varepsilon=0}$ is the original width of specimen, $T_{\varepsilon=0}$ is the original thickness of specimen.

Axial Stress

The axial engineering stress is defined on the assumption of constant cross section area of specimen. It can be calculated by dividing the observed tension force at each strain by the original cross sectional area:

$$\sigma_{aE} = \frac{F}{A} = \frac{F}{W_{\varepsilon=0}T_{\varepsilon=0}} \tag{7}$$

where σ_{aE} is the axial engineering stress, F is the measured axial tension force, A is the original cross section area of the specimen.

The axial true stress on the centre cross section of specimen corresponds to strain ε_{aT} can be calculated as:

$$\sigma_{aT} = \frac{F}{A_\varepsilon} = \frac{F}{W_{\varepsilon=0}T_{\varepsilon=0}(1-\nu\varepsilon_{aT})^2} \tag{8}$$

Results and Discussion

Axial True Strain

The comparison between axial true strain and engineering strain is presented in Fig. 1. The axial true strain was measured by photographic analysis method. The axial engineering strain was calculated by Eq. (1). It can be shown that the difference between axial true strain and axial engineering strain is not obvious when axial strain is less than 60%. The results show a good agreement with the data presented by previous studies performed by Wesseloo et al. (2004) [6]. For practical

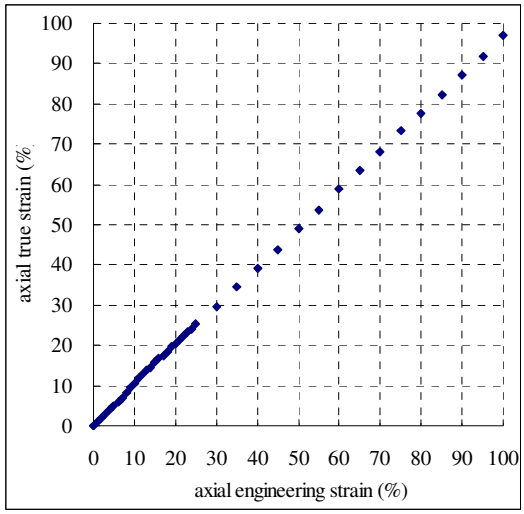


Fig. 1 Axial true strain-engineering strain relationship for PVC geomembrane

engineering application, difference between the two stains calculated by different methods can be ignored. When strain is greater than 60%, the axial true strain in the centre area of PVC geomembrane specimen is a little smaller than engineering axial strain. The test results reported by Merry and Bray (1996) [5]supported this conclusion.

Poisson's Ratio

The relationship between Poisson's ratio and axial engineering strain is presented in Fig. 2. The Poisson's ratio was calculated by Eq. (5) based on the measured axial true strain. The plots show that the Poisson's ratio of PVC geomembrane is not a constant and decrease with the increase of axial strain. So the Poisson's ratio is dependent on the strain state for PVC geomembrane.

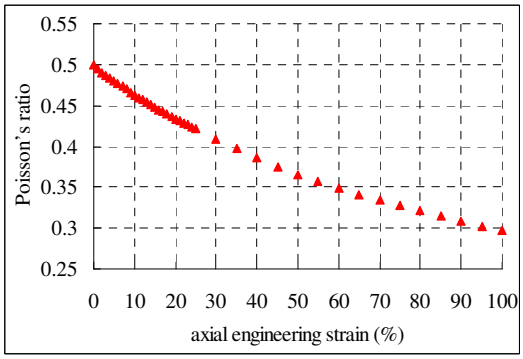


Fig. 2 Poisson's ratio - axial engineering strain relationship for PVC geomembrane

Cross Section Area

Fig. 2 shows the values of cross sectional area calculated by Eq. (6) based on the measured axial true strain, versus the axial engineering strain for the PVC specimen. It can be observed that the cross section area decrease with the increase of axial strain. So the traditional method of calculating engineering stress based on the constant cross section area for PVC geomembrane is not responsible.

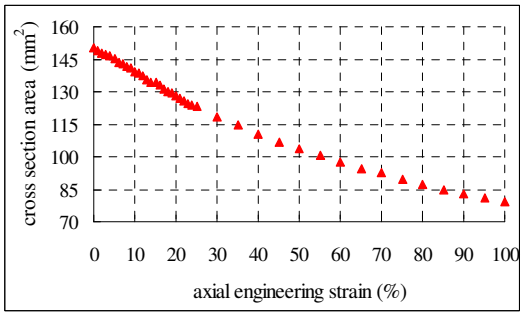


Fig. 3 Cross section area- axial engineering strain relationship for PVC geomembrane

True Stress-strain Relationship

The relationships between axial stresses and strains are shown in Fig.4. The engineering stress-strain and true stress-strain responses are compared in the same figure. The axial engineering strain and stress were calculated by Eq. (1) and Eq. (7), respectively. The axial true strain was directly measured using photographic analysis method. The axial true stress was calculated by Eq. (8) based on the measured axial true strain. As shown in Fig.4, both the engineering stress-strain and true stress-strain responses express approximate linear

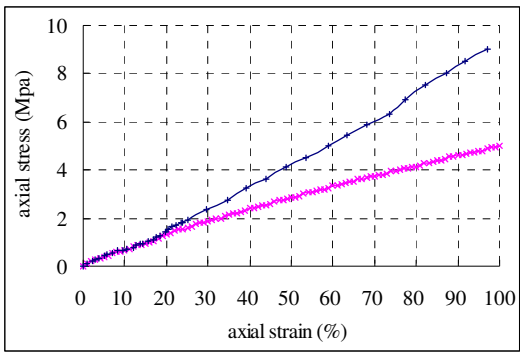


Fig. 4 Relationship of axial tension stress – strain for PVC geomembrane

relationship. An obvious difference can be observed between the engineering stress and true stress. For the same axial strain, the axial engineering stress is less than axial true stress. It is because that the axial engineering stress did not considering the decrease of the cross section area with the increase of axial strain. So the engineering stress-strain expression easily leads to the underestimation of the axial true stress of PVC geomembrane in uniaxial test. That may bring unsafe risk for engineering design.

Conclusions

In this study, the stress-strain response of PVC geomembrane was investigated with uniaxial tension test. The photographic analysis method was used to measure the true strain in axial and lateral direction of specimen during the test. The cross section area and true stress on the center of specimen were calculated based on the measured true strain. The following conclusions can be drawn from the test results:

(1) The difference between axial true strain and engineering strain of PVC geomembrane is not obvious when axial strain is less than 60%. For practical engineering application, the axial engineering strain can be used based on traditional uniaxial tension test method.

(2) Poisson's ratio of PVC geomembrane is not a constant. It is dependent on the strain state and decrease with the increase of axial strain.

(3) The cross section area of the centr of specimen decrease with the increase of axial strain. So the traditional method of calculating engineering stress based on the constant cross section area is not responsible.

(4) The stress-strain response of PVC geomembrane express approximate linear relationship. For the same axial strain, the axial engineering stress is less than axial true stress. So the engineering stress-strain expression easily leads to the underestimation of the axial true stress.

Acknowledgements

The project is supported by National Natural Science Foundation of China (No. 51079047, No. 51379069). Authors would like to thank the anonymous referees whose comments helped us improve the presentation of this paper.

References

[1] Ministry of Water Resources of the People's Republic of China, 1998. Standard for applications of geosynthetics in hydraulic and hydro-power engineering(SL/T225-98). Beijing: China WaterPower Press. (in Chinese).

[2] Ministry of Water Resources of the People's Republic of China, 2012. Specification for test and measurement of geosynthetics (SL 235-2012). Beijing: China WaterPower Press. (in Chinese).

[3] ASTM, 2001. Standard Test Method for Tensile Properties of Plastics, D638-01.

[4] ASTM, 2006. Standard Test Method for Determining Performance Strength of Geomembranes by the Wide Strip Tensile Method, D4885-06.

[5] Merry, S.M. and Bray, J.D.. Geomembrane Response in the Wide Strip Tension Test, Geosynthetics International, 1996, 3(4): 517-536.

[6] J. Wesseloo, A.T. Visser, E. Rust. A mathematical model for the strain-rate dependent stress-strain response of HDPE geomembranes. Geotextiles and Geomembranes, 2004, 22(4): 273-295.

[7] J.P. Giroud. Poisson's ratio of unreinforced geomembranes and nonwoven geotextiles subjected to large strains. Geotextiles and Geomembranes, 2004, 22(4): 297-305.

Advanced Materials Research Vol. 936 (2014) pp 1587-1591
© (2014) Trans Tech Publications, Switzerland
doi:10.4028/www.scientific.net/AMR.936.1587

Design of the EMF-PF and Error Correction

Kai-xia WEI

School of physics and electronic, Nanjin Xiaozhuang College, 211171, China

wkx@xznu.edu.cn

Keywords: Electromagnetic flowmeter; Partially-filled pipes flow measurement, Error correction.

Abstract. This paper designs the electromagnetic flowmeter in partially filled pipes (EMF-PF), which sensor alternate duties, sensing both the fluid velocity and fill height signals in order to get the flow in the partially filled pipes. Because the errors caused by two parameters measured, different sensitivities and zero-shifts reduce the accuracy of the EMF-PF, therefore calibration is needed. The repeated tests show that the third-order correction of the errors achieved good results.

Introduction

The flow measurement needs to measure flow velocity and fill cross-section to obtain the flow in partially filled pipes because the fill cross-section of fluid is changing[1]. The fill cross-section of fluid can be calculated by fill height in partially filled pipe. Based on this principle, the flow measurement of EMF-PF needs to measure both flow velocity and fill height. Thus the functional requirements of multi-parameter measurement are put forward for EMF-PF. At present, the fill height is obtained mostly by additional level sensor in EMF-PF, such as capacitive height gauge[2] and micromanometer[3]. However, there are the complex structure to EMF-PF using additional level gauge. This paper designs an EMF-PF sensor for measuring both flow velocity and fill height without additional level sensor. Because the errors caused by two parameters measured, different sensitivities and zero-shifts reduce the accuracy of the EMF-PF, therefore calibration is needed.

Principle

System architecture

The schematic diagram of the designed EMF-PF is shown in figure 1.

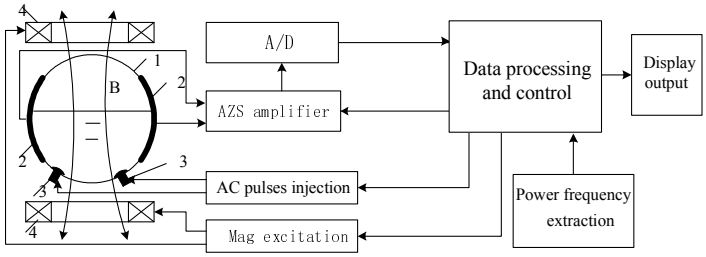


Figure 1 The schematic diagram of the EMF-PF architecture

In figure 1, 1 denotes the insulation pipes, 2 denotes the long-arc multi-electrodes, 3 denotes the signal injection electrodes, 4 denotes the coil.

One pair of long-arc electrodes is set on the pipe wall as the measurement electrodes. On the pipe bottom, one of pair of the electrodes is set as the signal injection electrodes that inject the AC pulses used to determine liquid fill height. Coils are used to produce the magnetic field necessary for flow measurement. The raw signals are transmitted via an interconnection cable to a converter, where the data are used to calculate the desired flow and height. The hardware composing of converter mainly includes the module of power frequency extraction, the magnetic field excitation module, the AC

pulse signal injection module, auto-zero signal amplification module, analog-digital conversion module, data processing module and display output module.

Measurement principle

A narrow pulses for measuring fill height is applied through the signal injection electrodes, and operates between the AC wide pulses to the coils. The measurement electrodes alternate duties, sensing both the flow and fill height signals. Both the flow and fill height raw signals are alternately disposed in different time period by the same signal processing channels in order to avoid the impact of electrical signal between them. System working timing is shown in figure2.

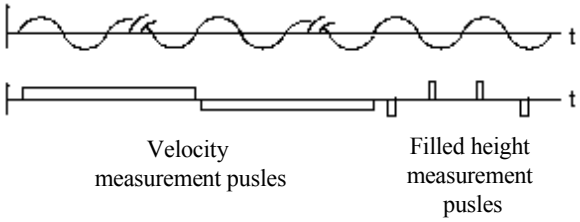


Figure 2 The EMF-PF flow measurement working timing

In the flow velocity measurement cycle, the AC wide pulses inject to the coils, and the AC narrow pulses to determine fill height are turned off. The measurement electrodes sense flow velocity signal.

In the fill height measurement cycle, the AC narrow pulses inject to the electrodes that set at the pipe bottom, and the AC wide pulses to the coils are turned off. The measurement electrodes sense fill height signal.

When the AC pulses inject to the electrodes that set at the pipe bottom, A stable electric field is formed within the liquid in partially filled pipes.Based on Ohm's law, the current density vector $\vec{j}$ is

$$\vec{j} = \sigma \vec{E} \tag{1}$$

where σ is the liquid conductivity, the electric field vector $\vec{E}$ is

$$\vec{E} = -\nabla \psi \tag{2}$$

If the conductivity of the liquid is homogeneous, isotropic, the electric field distribution within the liquid is associated with the distance from the electrodes to which the AC pulses inject[4]. Hence, the fill height signal Vo that is sensed by the measurement electrodes has a single-valued correspondence with the fill height H. The relation between H and Vo may be expressed as follow:

$$H = k f\left(\frac{V_i}{V_O}\right) \tag{3}$$

Where, k is a coefficient that can be calibrated by experiment, and Vi is input voltage value. We can use the equation (3) to calculate the desired fill height.

According to the measurement electrodes sensing flow velocity and fill height data, the volume flow Q in partially filled pipe can be obtained[5]:

$$Q = \frac{D^2}{4}[Arc\cos(1-2\alpha) - (1-2\alpha)\sqrt{1-(1-2\alpha)^2}]v \tag{4}$$

where, v is flow velocity, and α is flow fill degree, and $\alpha = \frac{H}{D}$. D is pipe diameter, and H is fill height.

Error correction

When the EFM-PF is employed to measure the flow in the partially pipes, both of the flow velocity and the fill cross-section needs to be measured. Because the errors caused by two parameters measured, different sensitivities and zero-shifts reduce the accuracy of the EMF-PF, therefore calibration is needed. The repeated tests show that the third-order correction of the errors achieved good results.

Established error correction curve of third-order parameter matrix equation is as follow:

$$E(\lambda)=\begin{bmatrix}\lambda^3 & \lambda^2 & \lambda^1 & 1\end{bmatrix}\begin{bmatrix}a\\b\\c\\d\end{bmatrix} \quad (5)$$

Where, *a, b, c, d* is constant matrix.

$a=\begin{bmatrix}a_x\\a_y\end{bmatrix}$, $b=\begin{bmatrix}b_x\\b_y\end{bmatrix}$, $c=\begin{bmatrix}c_x\\c_y\end{bmatrix}$, $d=\begin{bmatrix}d_x\\d_y\end{bmatrix}$

$E(\lambda)=\begin{bmatrix}x(\lambda)\\y(\lambda)\end{bmatrix}$, λ is intermediate parameter, $0\le\lambda\le 1$

On the equation (2) for first order derivative, we obtain

$$E'(\lambda)=\begin{bmatrix}3\lambda^2 & 2\lambda^1 & 1 & 0\end{bmatrix}\begin{bmatrix}a\\b\\c\\d\end{bmatrix} \quad (6)$$

For collected sample of n point $P_i(i=1,\cdots,n)$, it need to express in n cubic curve segment. The cubic sample curve is shown in figure 3.

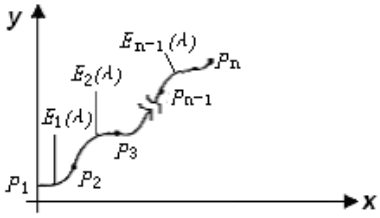


Figure 3 The cubic sample curve

In figure 3, the boundary condition of each cubic curve segment is

$E_i(0)=P_i$, $E_i(1)=P_{i+1}$

$E_i'(0)=P_i'=kP_i$, $E_i'(1)=P_{i+1}'=kP_{i+1}$

Where, *k* is constant matrix. λ =0,1 are respectively substituted in equation (2) and equation (3), we obtain

$$\begin{bmatrix}P_i\\P_{i+1}\\P_i'\\P_{i+1}'\end{bmatrix}=\begin{bmatrix}0&0&0&1\\1&1&1&1\\0&0&1&0\\3&2&1&0\end{bmatrix}\begin{bmatrix}a\\b\\c\\d\end{bmatrix} \quad (7)$$

The inverse matrix of matrix 7 is

$$\begin{bmatrix}a\\b\\c\\d\end{bmatrix}=\begin{bmatrix}2&-2&1&1\\-3&-3&-2&-2\\0&0&1&0\\1&0&0&0\end{bmatrix}\begin{bmatrix}P_i\\P_{i+1}\\P_i'\\P_{i+1}'\end{bmatrix} \quad (8)$$

By equation (8), the value of *a, b, c, d* can be obtained. Hence, error correction equation *E*(λ) can be obtained by sample point $P_i(x_i,y_i)(i=1,\cdots n)$.

According to given error limit, the system continuously implements error correction to *E*(λ). The software algorithm steps is as follow:

I. Collected data of sample point (x_i,y_i) is entered.

II. Compared (x_i,y_i) with $(x_i,E(x_i))$, if $|y_i-E(x_i)|<\varepsilon$, then go to 5, ε is error limit.

III. Point (x_i,y_i) is used to replace next sample point (x_k,y_k)

IV. Determining whether (x_k, y_k) is the first point, if it is then re-fit $E_1(x)$ .if it is not then re-fit $E_{n-1}(x)$

V. If continuing to correct, then go to 1. If not, then over.

The algorithm is embedded into the flow measure -ment program to achieve measurement error dynamic correction and compensation

Experiments

The schematic diagram of the EMF-PF experiment system is shown in figure 6.

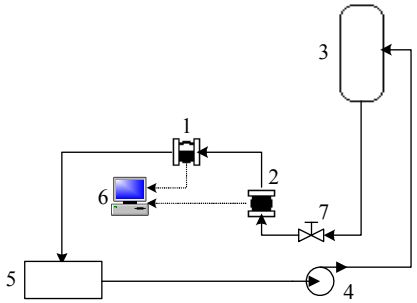


Figure 4 The experiment system of the EMF-PF

In figure 4, 1 denotes the EMF-PF, 2 denotes the standard EMF, 3 denotes stable pressure watertower, 4 denotes the pump, 6 denotes upper PC, and 7 denotes water valve.

The experiment prototype of EMF-PF is installed in horizontal straight pipe. ADMACSE standard flowmeter is installed in vertical pipe. The experiment results of EMF-PF prototype is shown in figure 5.

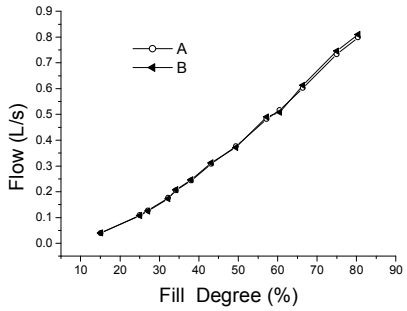


Figure 5 The EMF-PF experimental results

The experiment results show the flow measurement relative error of EMF-PF prototype is less than 2% except flow measurement below 15.1%fill degree.

Summary

This paper designs an EMF-PF for the flow measurement of partially filled pipe without additional level sensor. Experiment result shows that the measurement accuracy of this EMF-PF meets the actual requirements by software correction.

Acknowledgement

This research was financially supported by the Jiangsu Higher Education Reform Research Fund, NO: 2013JSJG211

References

[1] Richard W. Miller. Flow Measurement Engineering Handbook [M], Cambridge University Press ,2000,11

[2] John Flood. Single-Sensor Measurement of Flow in Filled or Partially Filled Process Pipes[J]. Sensors Magazine online,1997.

[3] Zhang Tao, Xu Ling an. Investigation on Measurement of flow in part-filled pipes based on calculation method. Chinese journal of scientific instrument.Vol.17,No.1,Jan, 1996

[4] Wei kaixia. Research on the sensor technologies of electro- magnetic flow measurement in partially filled pipes[D], Shanghai University, Ph.D thesis,2009,6

[5] Cai Wuchang, Ma Zhongyuan. The Electromagnetic flow- meter. China Petroleum & Chemical Press,2005

Advanced Materials Research Vol. 936 (2014) pp 1592-1596
© (2014) Trans Tech Publications, Switzerland
doi:10.4028/www.scientific.net/AMR.936.1592

TURBISCAN: History, Development, Application to Colloids and Dispersions

LIU Zequan[1, a], YANG Xue[1, b], ZHANG Qiang[1, c,*]

[1]School of Chemistry, Beijing Institute of Technology, Beijing 100081, China

[a]liuzq1988@foxmail.com, [b]yangxue901222@126.com,[c]zhangqiang6299@bit.edu.cn

Keywords: Turbiscan, emulsion stabilization ,sedimentation behavior

Abstract: Turbiscan is a new rapid and non-destructive method that has found increasing use in detecting physical destabilisation of concentrated and liquid dispersions. This review introduces the history and development of Tubiscan and focuses on applications of Turbiscan. The applications of Tubican were wildly used in dispersion stability of drug, carbon nanotubes dispersion, alumina suspension, emulsion stabilization and sedimentation behavior studying.

Introduction

Colloids and dispersions are inherently unstable systems which can be considered as kinetically stable if the destabilization rate is enough small compared with the expected lifespan[1]. The analysis of the dispersion instability is prime importance. The currrent techniques used to detect physical destabilisation are either simply the naked eye or optical analytical methods, such as microscopy, particle size and zeta potential. The accuracy and scope of these methods are reduced by sample dilution, due to most colloidal systems and dispersions are quite concentrated and opaque.

In this review, we describe a relatively new non-destructive method (no sample dilution) that was developed for detecting physical destabilisation of concentrated and liquid dispersions (emulsions, suspensions, foams, etc.). The method is based on measurement of particle migration (creaming or sedimentation) and particle-size variation (coalescence)[2]; it was called TURBISCAN.

TURBISCAN History and Development

The history and development of the TURBISCAN technique dates back to the invention of the Le TURBISCAN by G. Meunier in the early 1990's[3]. Then the TURBISCAN MA 1000 and TURBISCAN MA 2000 were developed[14]. A pulsed near infrared (λ = 850 nm) was used as light source and the sample concentrated could reach 50%. The next development of TURBISCAN was TURBISCAN LAB which using the pulsed near infrared (λ=880 nm) as light source. The TURBISCAN LAB could change the temperature of sample and detect high concentrated sample(up to 95%).

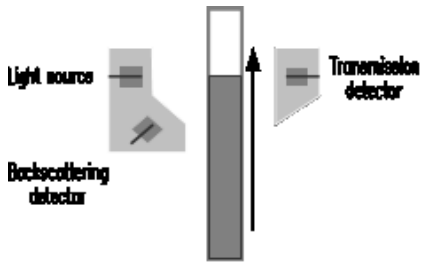


Fig.1

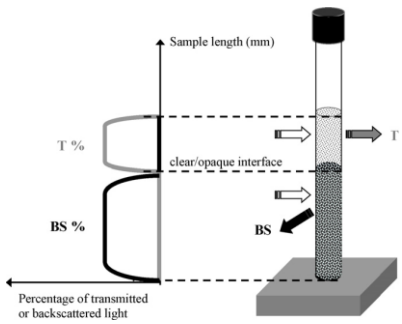


Fig.2

Measurement principle.

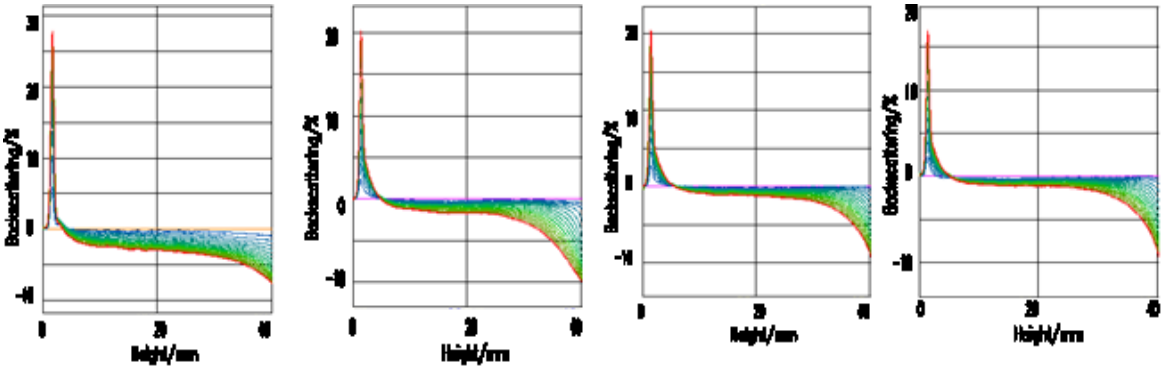
The TURBISCAN head is composed of a pulsed near infrared light source (λ = 850/880nm) and two synchronous detectors: a transmission detector which receives the light going across the sample (at 0° from the incident beam) and a back scattering detector which receives the light scattered

backward by the sample (at 135° from the incident beam(Fig.1). The detection head scanned the entire length of the sample acquiring transmission (T) and backscattering (BS) data(Fig.2)[5].

TURBISCAN Applications

The dispersion stability of Drug.

We firstly use TURBISCAN LAB to study the stability of pesticide WDG[6]. The sedimentation thickness of WDG suspension decrease as the contents of polymer dispersant increased(Fig.3). The particle diameter of WDG reach minimum as the Mw=12000. The results show that the stability of WDG suspension related with content and molecular weight of dispersant[3]. The effect of surfactant, polymer and dilution on dispersion stability of aqueous suspensions of drug particles was ivestgated by mesuring the sedimentation rate of drug particles by using Turbiscan MA2000[6,7]. he results suggest that a combination of surfactant and polymer provides more stable aqueous dispersion of drug particles than surfactant alone or polymer alone. The drug particles gradually sediment before dilution, while after the dilution they sediment a slightly faster.



(a) (b) (c) (d)

Fig.3 Backscattering profile of WDG suspension system containing different content of dispersant

Carbon nanotubes(CNTs) dispresion.

The dispresion of CNTs in solvents by either modifying the CNT surface chemistry or by the addition of surfactants has attracted an enormous amount of attention of reachers. Hyoung-Joon Jin et al have studied the stability of the multiwalled carbon nanotubes(MWCNTs) dispersions with various surfactants by using Turbiscan Lab. By comparing the delta transmittances and average transmission rates of the MWCNTs dispersions,they found the aqueous MWCNT dispersions with surfactants were more stable than that without surfactants[8]. In the other hand, the alkylated MWCNTs could disperse in common organic solvents without the use of surfactants[9]. The dispersion stability poly(4-vinylpyridine)-encapsulatedMWNTs is better in alcoholic medium than other solvents due to the chemical affinity of P4VP with alcohol[10].

Alumina suspension.

Małgorzata Wiśniewska et al studied the temperature effect on the stabilization – destabilization propertiesof the alumina (Al2O3) – polyacrylic acid (PAA) systems.The data obtained by the use of Turbiscan LabExpert and the calculated values of Turbiscan Stability Indexes (TSI) indicate that the addition of PAA causes lowering of the alumina suspension stability towards settling at both 15 and 35 °C. On the other hand, at 25 °C the polymer adsorption improves insignificantly the stability of Al2O3 suspension[11].They also investigated the influence of solution pH on the adsorption mechanism of polyacrylamide (PAM) on the alumina surface and stability of its suspension in the presence of polymer. The results indicate that the stability of suspensions depends on the molecular weight of the polymer and the pH of the solution. The suspension of alumina in the absence of polymer at pH 9 has much lower stability compared to the systems at pH 3 and pH 6 (electrostatic stabilization). The addition of polymer to the alumina suspension results in a drastic reduction of its stability at pH6 (close to pHIEP of PAM, bridging flocculation) and slight deterioration in the pH values 3 and 9[12]. The influence of solution pH and polymer molecular weight on the stability of

mixed alumina-silica oxide suspension in the absence and presence of polyacrylic acid (PAA) was shown in Tab.1[13]. The composition of the adsorbent was: Al2O3 (96%) and SiO2 (3%). To obtain changes in the stability of the investigated systems as a function of time the turbidimetry method was applied. It was shown that the suspension without the polymer was characterized by the smallest stability at pH 9, whereas at pH 3 and 6 the systems are successively stable. PAA with the molecular weighs 2000 at pH 3 (large deterioration of system stability conditions) and PAA (all molecular weights) at pH 9 (considerable improvement of suspension stability) have a great effect on the alumina-silica stability. The specific conformation of PAA chains on the solid surface which depends on solution pH and polymer molecular weight is responsible for the stabilization – flocculation properties of polyacrylic acid in the colloidal suspension.

Table 1 The TSI indexes for SA 96 suspension in the absence and presence of polyacrylic acid.

System	TSI		
	pH=3	pH=6	pH=9
SA 96	7.52	7.55	63.20
SA 96–PAA 2000	64.30	6.36	8.82
SA 96–PAA 100000	5.80	4.41	5.35
SA 96–PAA 240000	2.22	5.61	6.45

Suspension mechanism study.

Settling properties of barium sulphate suspensions have been examined by turbiscan measurement. The settling results show a sharp transition between the behaviour of aggregating and well-dispersed suspension. For the two polyelectrolyte dispersants used (PAA and PSS), at the transition the adsorbed amounts correspond to a samevalue of the electrokinetic potential, avalue that agrees well with DLVO theory predictions[14].

A better understanding of sedimentation behaviours of mineral suspensions has been investigated by three complementary optical methods of dispersed systems analysis: laser granulometry, electrophoresis measurements, and concentrated dispersion analyser. Only the study of sediment formation by Turbiscan MA 2000 has shown that before this limit of stabilisation, nascent agglomeration phenomena occurs although the suspension seems globally stabilised. In addition, by this approach, two destabilisation behaviours have been identified: one corresponding to the global migration of particles without sediment formation which corresponds to compression settling[15]. Physico-chemical stability of mineral suspensions , studied by optical dispersion analysis (Turbiscan MA 2000) enables the clarification rate to be measured and to propose a new global parameter, the "phase separation index"[16]. In J. Bongono's work,[17] the multiple light-scattering model through the optical analyzer, Turbiscan MA 2000 is used to determine the mean settling velocities of monodisperse glass beads and two polydisperse samples of powders, kaolin D and alumina, differing by their particle size distribution, their shape and their surface properties.

Emulsion stabilization.

Caroline Lemarchand et al. [18] prepared oil-in-water nanoemulsions by using graft copolymers with dextran(DEX) and poly-ε-caprolactone(PCL) and studied the emulsion stabilizing abilities by using the Turbiscan. They found that PCL-DEX copolymers successfully stabilized ethyl acetate-in-water emulsions, even in the absence of additional surfactants. This stabilizing ability of PCL-DEX related to the localization of their blocks with regard to the oil–water interface .The optical characterization of the stability by means of the Turbiscan gives interesting information about the global stability of the emulsions. I. Roland et al [19]used Turbiscan to characterize oil-in-water emulsions with difference surfactant concentration. All the emulsions exhibit a tendency to creaming. The creaming kinetics calculated from the backscattering differential profiles obtained. L. Day et al [20] found that fish oil emulsions, stabilized using sodium caseinate (25% w/w oil and 0.1–1.0% w/w sodium caseinate giving oil-to-protein ratios of 250–25), were either homogeneous or exhibited depletion or bridging flocculation, depending on the concentration of protein in the formulation.

Summary

In this paper we have presented an overview of the history, theory, and practice of the Turbiscan technique, with emphasis on the fundamentals principles underlying the technique and practical examples. As Turbiscan is a relatively new technique, it is likely to become more widely used in the years to come. We hope that this paper facilitates such further development

Acknowledgement

This work was financially supported by the National Science and Technology Pillar Program in the 12th Five Year Plan Period (No. 2011BAE06B06-2)

References

[1] O. Mengual, G. Meunier, I. Cayre, K. Puech and P. Snabre, 'Characterisation of instability of concentrated dispersions by a new optical analyser: the TURBISCAN MA 1000', Colloids and Surfaces A: Physicochemical and Engineering Aspects 152 (1999), 111-23.

[2] C. Celia, E. Trapasso, D. Cosco, D. Paolino and M. Fresta, 'Turbiscan Lab® Expert analysis of the stability of ethosomes® and ultradeformable liposomes containing a bilayer fluidizing agent', Colloids and Surfaces B: Biointerfaces 72 (2009), 155-60.

[3] M. Gr., Le TURBISCAN: un nouvel instrument de mesure de phe´nome`nes naissants de de´mixtion dans lese´mulsions et les suspensions (1994), pp. 53-8.

[4] O. Mengual, G. Meunier, I. Cayré, K. Puech and P. Snabre, 'TURBISCAN MA 2000: multiple light scattering measurement for concentrated emulsion and suspension instability analysis', Talanta 50 (1999), 445-56.

[5] S. Daoud-Mahammed, P. Couvreur and R. Gref, 'Novel self-assembling nanogels: Stability and lyophilisation studies', Int J Pharm 332 (2007), 185-91.

[6] Q. Zhang, Y. Chen, W. J. Fu and S. Y. Sun. Study on the stability of pesticide WDG suspension by TURBISCAN LAB. 2008. 28, 4. 843-846

[7] H. Terayama, K. Okumura, K. Sakai, K. Torigoe and K. Esumi, 'Aqueous dispersion behavior of drug particles by addition of surfactant and polymer', Colloids and Surfaces B: Biointerfaces 20 (2001), 73-7.

[8] H. Kim, W. Park, M. Kang and H. Jin, 'Multiple light scattering measurement and stability analysis of aqueous carbon nanotube dispersions', J Phys Chem Solids 69 (2008), 1209-12.

[9] Y. Kim, S. Kwon, D. Kim, H. Kim and H. Jin, 'Dispersity and stability measurements of functionalized multiwalled carbon nanotubes in organic solvents', Current Applied Physics 9 (2009), e100-3.

[10] S. Hong, M. Kim, C. K. Hong, D. Jung and S. E. Shim, 'Encapsulation of multi-walled carbon nanotubes by poly(4-vinylpyridine) and its dispersion stability in various solvent media', Synthetic Met 158 (2008), 900-7.

[11] M. Wiśniewska, 'Influences of polyacrylic acid adsorption and temperature on the alumina suspension stability', Powder Technol 198 (2010), 258-66.

[12] M. Wiśniewska, S. Chibowski and T. Urban, 'Investigation of the stability of an alumina suspension in the presence of ionic polyacrylamide', Thin Solid Films 520 (2012), 6158-64.

[13] M. Wiśniewska, K. Terpiłowski, S. Chibowski, T. Urban, V. I. Zarko and V. M. Gun'Ko, 'Effect of polyacrylic acid (PAA) adsorption on stability of mixed alumina-silica oxide suspension', Powder Technol 233 (2013), 190-200.

[14] M. Balastre, J. F. Argillier, C. Allain and A. Foissy, 'Role of polyelectrolyte dispersant in the settling behaviour of barium sulphate suspension', Colloids and Surfaces A: Physicochemical and Engineering Aspects 211 (2002), 145-56.

[15] N. Azema, 'Sedimentation behaviour study by three optical methods — granulometric and electrophoresis measurements, dispersion optical analyser', Powder Technol 165 (2006), 133-9.

[16] R. Vie, N. Azema, J. C. Quantin, E. Touraud and M. Fouletier, 'Study of suspension settling: A approach to determine suspension classification and particle interactions', Colloids and Surfaces A: Physicochemical and Engineering Aspects 298 (2007), 192-200.

[17] J. Bongono, N. Azema, A. Johannet and P. Gaudon, 'Determination of the characteristics of agglomerates in aqueous suspensions using nonlinear optimization', Powder Technol 208 (2011), 271-8.

[18] C. Lemarchand, P. Couvreur, C. Vauthier, D. Costantini and R. Gref, 'Study of emulsion stabilization by graft copolymers using the optical analyzer Turbiscan', Int J Pharm 254 (2003), 77-82.

[19] I. Roland, G. Piel, L. Delattre and B. Evrard, 'Systematic characterization of oil-in-water emulsions for formulation design', Int J Pharm 263 (2003), 85-94.

[20] L. Day, M. Xu, P. Hoobin, I. Burgar and M. A. Augustin, 'Characterisation of fish oil emulsions stabilised by sodium caseinate', Food Chem 105 (2007), 469-79.

Advanced Materials Research Vol. 936 (2014) pp 1597-1602
© (2014) Trans Tech Publications, Switzerland
doi:10.4028/www.scientific.net/AMR.936.1597

A progress in development and application of size exclusion chromatograph/multi-angle laser light scattering

YANG Xue [1, a], LIU Zequan[1,b] and ZHANG Qiang[1,c *]

[1]School of Chemistry, Beijing Institute of Technology, Beijing 100081, China

[a]yangxue901222@126.com, [b]liuzq1988@foxmail.com, [c]zhangqiang6299@bit.edu.cn

Keywords:SEC-MALLS, molecular weight, molecular weight distribution, macromolecular polymer

Abstract: This paper reveals the development and significance of size exclusion chromatograph/multi-angle laser light scattering(SEC-MALLS) for determination of the molecular weight and characterization of the molecular weight distribution. This technique has been applied in many aspects, such as biology, polymer and carboxylate surfactant. It has made a big contribution to study the property of macromolecular substances.

Introduction

There are something, which are very crucial for product properties, such as molecular weight, molecular weight distributions, size and branching of polymer. These directly influence many polymer physical properties, such as, tensile strength, chemical resistance viscosity and solubility [1], especially the molecular weight, which can affect polymer physical properties. Therefore, the accurate determination of polymer molecular weight is essential to reveal the properties and activities of a kind of materials.

A lot of methods have been applied to determine polymer molecular weight, such as Vapor-pressure Osmometry, Gel-permeation Chromatograph and Light-scattering [2], but they have some drawbacks, respectively. Recent years, a new technique, SEC-MALLS has been used for determination of molecular weight and molecular weight distribution of polymers, especially for branched ones [3]. This allows the computation of the weight-average molecular weight (Mw). Various other molecular weight averages [number-average molecular weight (Mn) and z-average molecular weight (Mz)] are then computed from the distribution curve. Mw is the most accurate average that can be obtained by SEC-MALLS [4] .

Device and Principle

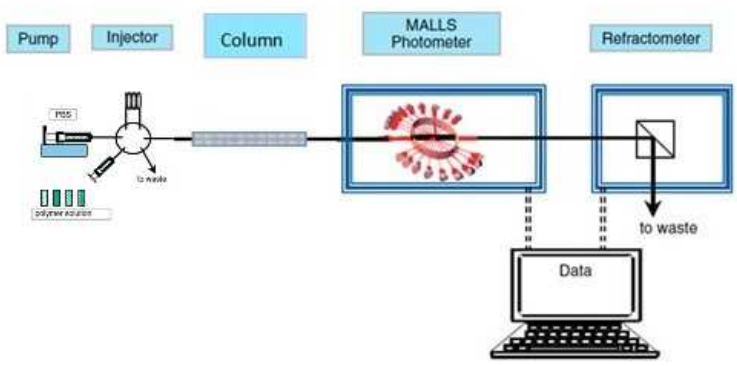


Fig. 1 Schematic of the SEC-MALLS system

The system consists of a syringe pump, an injector with a sample loop, a column, a MALLS photometer and a refractometer, as shown in Fig.1. The polymer samples are prepared at an accurate concentration and keep 24h for dissolution. The solution is filtered by using a 0.22 μm syringe filter. In each experiment, samples continuously flow through the system at a rate of about 0.5 mL • min–

1 by using a syringe pump. The known samples responses of the MALLS photometer and refractometer are used as baselines. An amount of 2 mL of each polymer solution is injected into the sample loop and infuse through the flow cells of MALLS and RI detectors. The MALLS and RI data are collected simultaneously by using a computer ASTRA software [5].

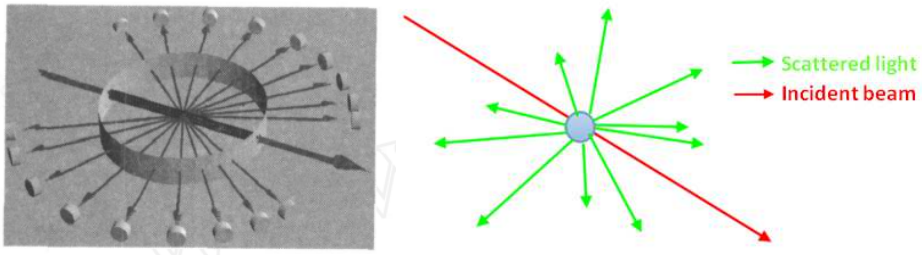


Fig. 2 Light scattering and collecting light

SEC-MALLS online determine the molecular weight and molecular weight distribution of polymers, which apply that light scattering intensity is in proportion to relative molecular mass and concentration, and light scattering intensity in different angles is relative to molecular size [6,7]. When light source shines a laser on to the polymers, incident beam will occur scattering, then scattered light will be collected and detected by 18 multi-angle laser light scattering, Fig. 2 shows that.

So the molecular weight for polymers can be calculated according to the following equations:

$$K^{*}C/R(\theta)=1/[MwP(\theta)]+2A_2C \quad (1)$$

Where: R(θ) is the excess Rayleigh ratio; P(θ) is the particle scattering factor; C is the concentration of the polymer particles (g/mol); Mw is the weight-average molecular weight; A2 is the second virial coefficient (ml • mol/g2); θ is scattering angle and K* is a constant.

For vertically polarized incident light with a wavelength $\lambda 0$ in vacuum, K* is given by:

$$K^{*}=4\pi^{2}n2\ 0/\lambda_0\ 4N_A(dn/dc)^2 \quad (2)$$

Where: n0 is the refractive index of the solvent at wavelength $\lambda 0$; NA is Avogadro's number and dn/dc is the specific refractive index increment of the polymer [3]. Using the obtained data make a plot of K*C/R(θ) vs. Sin2(θ/2), and the slope is the mean square radius, while Mw can be directly determined from the intercept at zero angle [8].

The application of SEC-MALLS

Biological

Light scattering is almost the few method for the determination of the molar mass and the structure of polymer [9]. Because of the limitation of this approach: polydispersity of the sample, nonideal thermodynamic behavior of many polymers, unknown conformation in solution of some molecules and possible interactions between the polymers studied. But these limitations can be overcome by SEC-MALLS.

TAB. 1 THE ACCURACY OF SEC-MALLS

Sample	declared values Mw	Measured value Mw	D	Relative deviation(%)
PS-1	5900	6050	1.005	2.54
PS-2	11800	11460	1.002	-2.88
PS-3	47300	47000	1.004	-0.634
PS-4	112000	112300	1.008	0.268
PS-5	212000	216900	1.006	2.31

In the aspect of biological, SEC-MALLS has been employed to characterize the mass-average molar mass, z-average radius of gyration and second virial coefficient of biological macromolecules [5]. Through the SEC-MALLS technique, the molecular weight or the structure of natural polysaccharide [8,10], hydroxyethyl starch [11], protein aggregates [9,12], hyaluronic acid [13], cationic hydroxyethyl cellulose derivatives [5] and the plasma substitute succinylated gelatin [14] has been obtained. For instance, Determination of Molecular Weight and Its Distribution of Hyaluronic Acid by Combination of Multi-angle Laser Light Scattering Instrument and Size Exclusion Chromatography [13]. It is known by principle of measurement that macromolecular compound Mw is its absolute molecular weight by this method, and its error is caused by the instrument detection. SEC-MALLS detect the Mw of Polysaccharide standards, then they compared measured value with the declared values, the conclusion showed that accuracy of the method was very well representated in Tab. 1.

This method was also used in food additives and drug formulations to determine the molar mass and molecular weight distribution. The retention time of drug in the body is very important and the drug’s structure depends on the molar mass and molecular weight distribution, so the determination the molecular weight and the characteristics of molecular weight distribution are meaningful to the study of biological macromolecules. The results of the usage of SEC-MALLS technique demonstrate that the method is simple, accurate, reproducible and high separation and can be applied to test the molecular weight, molecular weight distribution and structure of biological macromolecules [11,15].

Polymer

Molecular weight is a key, fundamental property of a polymer, thus the use of SEC-MALLS has been established as an effective method for the direct determination of molecular weigh [16]. This technique was used to characterize several fluoroalkyl acrylic, fluoroalkyl methacrylic polymers, perfluoropolyethers and hydrocarbon polymers. To yield accurate results, the concentration detector must be carefully calibrated and it is essential that the refractive index increment (dn/dc) be known for the polymer being analyzed-in the mobile phase employed. It is best if dn/dc is determined at the same wavelength employed by the light scattering detector and that it is relatively constant across the sample being characterized. They have successfully characterized fluoroalkyl acrylic samples with molecular weights (Mn) in excess of 1 000 000 g/mol. An overlay of elution chromatograms for an extended series of primary polystyrene standards ranging from 1100 g/mol to 1 600 000 g/mol is shown in Fig. 3.

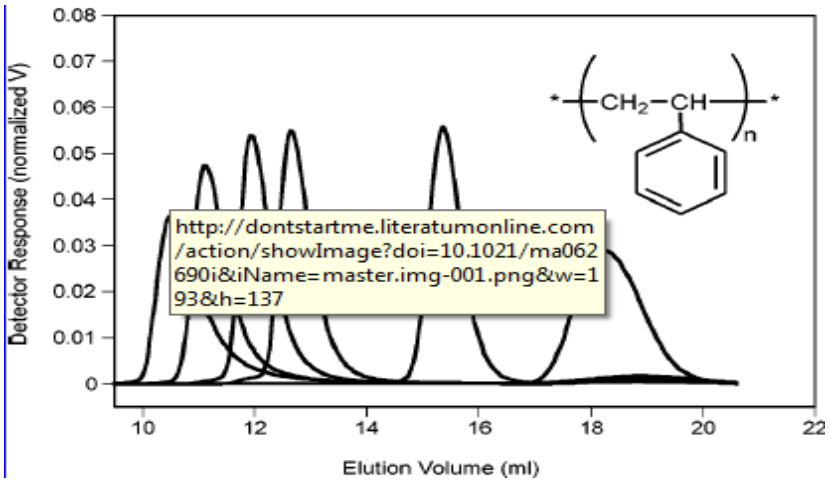


Fig. 3 GPC-MALS data for a representative series of pol

y(1,1,2,2-tetrahydroperfluorodecyl acrylate) macroinitiators made using ATRP

Finally, they concluded, SEC-MALS in α, α, α-trifluorotoluene mobile phase has been employed successfully to determine molecular weight and molecular weight distribution for highly fluorinated (hydrocarbon insoluble) fluoroalkyl acrylic polymers and hydrocarbon polymers. It is the mainstay technique for determination of molecular weight and molecular weight distribution of synthetic polymers [17].

The series of PAM [18] samples was characterized with SEC-MALLS and its data is correlated well with the previously reported literature values. At the same time, information about the radius of gyration and molecular structure was obtained. Furthermore, differences in polymer structure can be observed depending on the polymerization conditions [19].

Carboxylate surfactant

The MALLS method have begun to use since 1980s [20,21], coupled with revolution in computer and with development of SEC, which makes SEC-MALLS a perfect technique for determining polymer absolute molecular weight and molecular weight distribution. Raymond et al. [22] have reported their effort to develop and validate a SEC-MALLS method to directly determine absolute molecular weight and molecular weight distribution of HPMCAS(hypromellose acetate succinate). Due to the properties of HPMCAS, they use a mixed solvent to create a challenging condition for the SEC-MALLS method that uses refractive index detector. Finally, their results and the design of experiments indicate that the method is accurate and robust for determining HPMCAS absolute molecular weight and molecular weight distribution.

Recently, we are studying the SEC-MALLS method to directly determine absolute molecular weight and molecular weight distributions of carboxylate surfactant. The sample solution of carboxylate surfactant at 2 mg/ml were prepared by adding a weighed amount of polymer into a vial and dissolving it with a measured volume of mobile phase. Then the MALLS data were collected and processed by Wyatt ASTRA software. Representative chromatograms of the sample polymer are shown in Fig. 4. We use measured light scattering signals, refractive index signal, sample concentration and injection volume to calculate the dn/dc values in software to gain the molecular weight of Carboxylate surfactant. The statistics of these measurements are listed in Tab. 2.

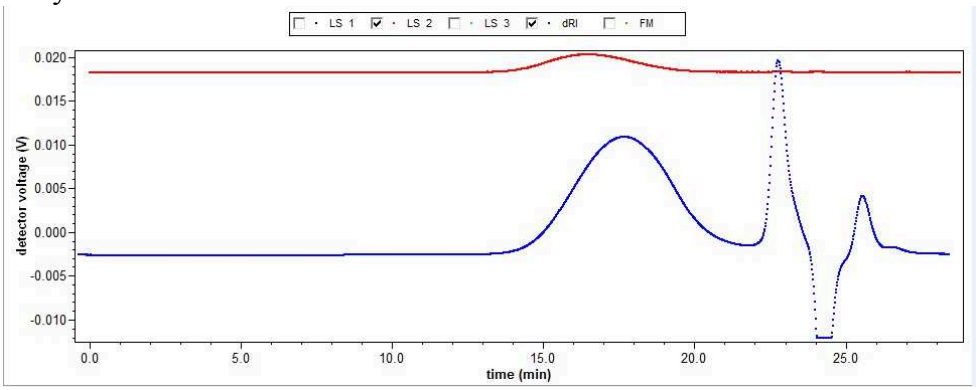


Fig. 4 Elution volume of sample

TAB. 2 STATISTICS OF THESE MEASUREMENTS

Sample	dn/dc	Mn	Mw	Mw/Mn
Sample-1	0.1591	8684	14490	1.622
Sample-2	0.1594	11050	15560	1.408
Sample-3	0.1594	8062	14490	1.797
Sample-4	0.1589	9874	14710	1.49
Sample-5	0.1591	8385	14390	1.716
Sample-6	0.1589	9672	15140	1.565

The above result and experiment prove that the method is accurate and robust for determining carboxylate surfactant absolute molecular weight distribution.

Summary

A simple, rapid, precise method was developed and validated for determination of molecular weight. As is concluded in this review, this approach is very significant to study the property of polymer and has a wide application. However, the reach method for polymer are needed to develop.

Acknowledgments

This work was financially supported by the National Science and Technology Pillar Program in the 12th Five Year Plan Period (No. 2011BAE06B06-2)

References

[1] Cheng, G., Fan, X., Liu, G., Liu, Y., Determination of molecular weight of polyethylene glycol using size-exclusion chromatography with multi-angle laser light scattering and acid-base titration, J. Polymer Testing 2009, 28 (2), 145-149.

[2] Wang, M., Yao, S., Determination of Molecular Weight of Sodium Cellulose Sulfate by Low Angle Laser Light Scattering, J. The Chinese Journal of Process Engineering 2009, 9 (6), 1159-1163.

[3] Grcev, S., Schoenmakers, P., Iedema, P., Determination of molecular weight and size distribution and branching characteristics of PVAc by means of size exclusion chromatography/multi- angle laser light scattering (SEC/MALLS). J. Polymer 2004, 45 (1), 39-48.

[4] Puskas, J. E., Chen, Y. H., Kulbaba, K., Kaszas, G., Comparison of the molecular weight and size measurement of polyisobutylenes by size exclusion chromatography/multi-angle laser light scattering and viscometry. J. Journal of Polymer Science Part a-Polymer Chemistry 2006, 44 (5), 1777-1783.

[5] Gao, W., Liu, X. M., Gross, R. A., Determination of molar mass and solution properties of cationic hydroxyethyl cellulose derivatives by multi-angle laser light scattering with simultaneous refractive index detection. J. Polymer International 2009, 58 (10), 1115-1119.

[6] Li, C., Zhang, H.,Wang, N.,Yan, Z., Determination of the Relative Molecular Weight of Grape Seed Proanthocyanidin by Laser Light Scattering with GPC. Jiangsu Journal of Agricultural Sciences 2009, 25 (6), 1354-1359.

[7] Wu, Y., Wang, Y., Yang, Y., Wang, X., Li, K., Luo, Y., Xu, S., Niu, X., The Determination of Molecular Weight and its Distribution of Polylactid with GPC Eighteen Angles Light Scattering Method. J. Modern Scientific Instruments 2007, (02), 78-81.

[8] Zhong, X., Huang, Q., Xi, Y., Determination of molecular weight and molecular weight distribution of chitosan by malls in conjunction with refractive index detector. J. Chinese Journal of Pharmaceutical Analysis 2006, (09), 1258-1260.

[9] Beaulieu, M., Corredig, M., Turgeon, S. L., Wicker, L., Doublier, J. L., The formation of heat-induced protein aggregates in whey protein/pectin mixtures studied by size exclusion chromatography coupled with multi-angle laser light scattering detection. J. Food Hydrocolloids 2005, 19 (5), 803-812.

[10] Girod, S., Baldet-Dupy, P., Maillols, H., Devoisselle, J. M., On-line direct determination of the second virial coefficient of a natural polysaccharide using size-exclusion chromatography and multi-angle laser light scattering. J. Journal of Chromatography A 2002, 943 (1), 147-152.

[11] Song, Y., Du, Z., Yu ,P., Ren ,C., Yuan, H., Determination of weight average molecular weight and molecular weight distribution of hydroxyethyl starch 130/0.4 by SEC-MALLS. J. Qilu Pharmaceutical Affairs 2012, (03), 155-157.

[12] Li, X., Hua, Y., Wang, Z., Qiu, A., Steve Cui, Studies of Heat-induced Soy Protein Aggregates by High Performance Size Exclusion Chromatography and Laser Light Scattering. J. Chinese Jounmal of Analytical Chemistry 2007, (02), 251-254.

[13] Ding, H., Wang, H., Guo, X., Determination of Molecular Weight and Its Distribution of Hyaluronic Acid by Combination of Multi-angle Laser Light Scattering Instrument and Size Exclusion Chromatography. J. Food and Drug 2009, (03), 24-26.

[14] Kaur, M., Jumel, K., Hardie, K. R., Hardman, A.; Meadows, J., Melia, C. D., Determining the molar mass of a plasma substitute succinylated gelatin by size exclusion chromatography–multi-angle laser light scattering, sedimentation equilibrium and conventional size exclusion chromatography. J. Journal of Chromatography A 2002, 957 (2).

[15] Wu, C., Li ,P., Ma, Y., Li, A., Qiao, J., Ren, C., Determination of macromolecular in Shuanghuanglian injection by combination of multiangle laser light scattering instrument and size exclusion chromatography . J. Chinese Journal of Pharmaceutical Analysis 2011, (10), 1954-1956.

[16] Romack, T. J., Harrison, Z. J., French, D. V., Amin, D. H., Hartsell, J. L., Meyer, J. D., GPC-MALS characterization of fluoropolymers in a alpha,alpha,alpha-trifluorotoluene mobile phase: An enabling step in the syntheses of well-defined fluoropolymer-based self-assembling materials. J. Macromolecules 2007,40(20), 7180-7183.

[17] Odian, G. G. Principles of Polymerization, 3rd ed., J. Wiley-Interscience:New York, 1991; p 768.

[18] Fevola, M. J., Hester, R. D., McCormick, C. L., Molecular weight control of polyacrylamide with sodium formate as a chain-transfer agent: Characterization via size exclusion chromatography/multi-angle laser light scattering and determination of chain-transfer constant. J. Journal of Polymer Science Part a-Polymer Chemistry 2003, 41 (4), 560-568.

[19] Tackx, P., Tacx, J., Chain architecture of LDPE as a function of molar mass using size exclusion chromatography and multi-angle laser light scattering (SEC-MALLS). J. Polymer 1998, 39 (14), 3109-3113.

[20] P.J. Wyatt, C. Jackson, G.K. Wyatt, Part 1. Absolute GPC determinations of molecular weights and sizes from light scattering, J. Am. Lab. 20 (1988), 86, 88–91.

[21] P.J. Wyatt, D.L. Hicks, C. Jackson, G.K. Wyatt, Part 2. Absolute GPC [gelpermeation chromatographic] determinations of molecular weights and sizes. Incorporation of light scattering techniques into GPC-SEC measurements, J. Am.Lab. 20 (1988) 108, 110, 112–113.

[22] Chen, R., Ilasi, N., Sekulic, S. S., Absolute molecular weight determination of hypromellose acetate succinate by size exclusion chromatography: Use of a multi angle laser light scattering detector and a mixed solvent. J. Journal of Pharmaceutical and Biomedical Analysis 2011, 56 (4), 743-748.

CHAPTER 16:

Technologies and Equipment for Manufacturing and Processing of Materials

Advanced Materials Research Vol. 936 (2014) pp 1605-1608
© (2014) Trans Tech Publications, Switzerland
doi:10.4028/www.scientific.net/AMR.936.1605

Application of Polycarboxylic Acid Anti-Crease Finishing Agent for Silk

Xulei[1,a]

[1]No. 287, Xuefu Road, Suzhou Institute of Trade & Commerce,Shi-hu International Education Park, Suzhou city, Jiangsu Privince, CHINA

[a]1981_xl@163.com

Keywords: polycarboxylic acid; silk; anti-crease finish

Abstract: Polycarboxylic acid anti-crease finishing agent is used to finish silk. The optimal finishing process was selected through orthogonal experiment. The optimal process conditions were as follows. The optimal concentration of both finishing agent Y and magnesium chloride was 100g/L. The optimal baking temperature and baking time were 160 ℃ and 3min, respectively. The results show that the silk fabrics treated by finishing agent Y had high strength retention and washing fastness. In addition, the effect of ant-crease finishing on the whiteness of fabrics was small.

Introduction

Silk fabric is characterized with gentle gloss, soft feeling, moisture absorption, ventilation, lightness and nature. The garment made from silk is not only artistic and comfortable but also possesses a multi-healthcare function.However the poor rebound resilience and easy-wrinkle have restraint the application of the garment. Therefore, it will bring new chance to the silk industry to improve the wrinkle resistance and the level of the silk fabric. 2D resin (DMDHEU, dihydroxy methyl two hydroxy ethylene urea) is one kind of traditional anti-crease finishing agents.Though it has received a confirmed wrinkle-resistance ability applied in natural fabrics and blended fabrics, there exists a problem of the release of formaldehyde on fabrics.[1] Four carboxylic acid (BTCA) is an excellent and special no formaldehyde anti-crease finishing agent for silk which can provide silk fabrics with good wrinkle-resistance ability, protect their original characteristics (such as whiteness, strength and drapability) and improve its dyeing property.[2] But the application of BTCA is limited for its high cost. So it is important to find an easy-using and eco-friendly anti-crease agent with a relative low price and high properties to meet the needs of customers and producers.

Experiment

Materials & Instruments

Material: silk habotai.

1)Drugs: anti crease finishing agent Y (citric acid and maleic acid molar ratio of 1:2 mixture), magnesium chloride (CP), JY08 (industrial grade), peregal O (industrial grade).

2)Instruments: HM-450 type pneumatic electric rolling vehicle, YG541B fabric crease recovery tester, DSBD-1 digital whiteness meter, YG026 fabric strength tester, SW-12A type washing fastness tester ， LA-250 type test for heat setting machine.

Experimental methods

Finishing process[3]

The silk was immersed in the bath ratio 1:30, temperature 30 ℃ finishing solution, two dipping and rolling, pick-up 90%. Then the silk at 90 ℃ drying 4min, baking in a condition, fully washed in hot water of 50 ℃, cold water washing, drying.

Test Method

1) Whiteness:

The samples were folded into four layers, the DSBD-1 tested on both sides of the instrument and taking the average value of whiteness.

2) The wet crease recovery angle (anelastic):

Sample was immersed in 0.2% peregal O solution, removed after soaking 5min, Silk is placed between two layers of filter paper and absorbed the water.According to (GB/T 3819-1997 Textile fabrics Determination of the recovery) in the vertical method.

3) Breaking strength

According to “GB/T 3923.1 - 1997 textile fabric tensile properties of first parts: the breaking strength and elongation at break were determined", Taking the average value in warp and weft fabrics after 3 times test. Silk breaking strength retention rate is calculated as:

Breaking strength retention (%) = (After finishing silk breaking strength/ Before finishing silk breaking strength) ×100％

4) Soaping fastness

According to “GB/T 3921-2008 textile color fastness resistance soaping fastness" Test.

Results and discussion

Finishing conditions selection

Select the finishing agent Y dosage, magnesium chloride dosage, baking time of 3 factors, Because the catalyst and anti-crease agent dosage ratio of 1:1 is better, so the test was used to maintain this ratio.Orthogonal test results as shown in table 1.

Table 1 Results of orthogonal test of anti-crease finishing

Serial number	Anti wrinkle agent dosage of Y (g/L)	Baking temperature （℃）	Baking time （min）	DWRA （°）	WWRA （°）	Breaking strength retention （%）	whiteness
Untreated	—	—	—	203	184	100	84.3
1	80	150	2	233	211	94.1	82.6
2	80	160	3	240	218	91.5	81.5
3	80	170	4	252	235	89.4	81.2
4	100	150	3	268	252	91.2	81.4
5	100	160	4	270	253	89.6	80.8
6	100	170	2	258	244	89.7	79.2
7	120	150	4	270	258	89.4	80.5
8	120	160	2	267	249	91.6	82.1
9	120	170	3	274	257	87.7	77.4

The result of orthogonal test is analyzed, considering the dry, wet recovery angle, whiteness and breaking strength retention can be optimized finishing condition: The optimal concentration of both finishing agent Y and magnesium chloride was 100g/L. The optimal baking temperature and baking time were 160 ℃ and 3min, respectively.

Application performance comparison

The optimum process for silk habotai finishing, Y and JY08 (the main composition is BTCA)) anti-crease finishing agent were compared, The optimal concentration of both finishing agent JY08 and magnesium chloride was 100g/L. The optimal baking temperature and baking time were 160 ℃ and 3min, respectively.

Table 2 Comparison of application performance of finishing agent Y

finishing agent	DWRA（°）	WWRA（°）	Breaking strength retention（%）	whiteness
Untreated	203	184	100	84.3
finishing agent Y	270	253	89.6	80.8
JY08（BTCA）	283	262	82.5	81.7

It is shown in table 2 that anti-crease finishing agent Y dry, wet anti-crease performance is slightly lower than the JY08, but the breaking strength retention rate is better than the JY08.The Y is a kind of polycarboxylic acid anti-crease finishing agent, the silk fabrics treated by finishing agent Y had high strength retention and washing fastness. In addition, the effect of ant-crease finishing on the whiteness of fabrics was small.

Finishing agent Y washing fastness test

After finishing of silk fabric washing fastness test results are shown in table 3.

Table 3 Finishing agent Y washing fastness test

Washing times (time)	DWRA（°）	WWRA（°）	whiteness
0	270	253	80.8
10	272	254	80.6
20	268	249	81.0
30	265	245	80.9
50	261	242	80.5

We can see from table 3, After finishing of silk fabrics, washed 50 times with water, dry and wet recovery angle decreases a little. Silk habotai still has good performance of anti-crease, whiteness has a little change, so it is a durable anti-crease finishing agent.

Conclusion

1) The Y is a kind of polycarboxylic acid anti-crease finishing agent, the optimum process conditions were as follows: The optimal concentration of both finishing agent Y and magnesium chloride was 100g/L. The optimal baking temperature and baking time were 160 ℃ and 3min, respectively.

2) compared with JY08, anti-crease finishing agent Y dry, wet anti-crease performance is slightly lower than the JY08, But the results show that the silk fabrics treated by finishing agent Y had high strength retention and washing fastness. In addition, the effect of ant-crease finishing on the whiteness of fabrics was small.

3) After finishing of silk fabrics, washed 50 times with water, dry, wet recovery angle decreases a little. Silk habotai still has good performance of anti-crease, whiteness has a little change, so it is a durable anti-crease finishing agent.

Reference

[1] Wang Haifeng,Tang Ju.DP finish of silk fabric with fibroin/citric acid[J]. Printing and dyeing,2010，(15)：8～10.

[2] Gao Xiaohong,Zhang Ruiping,Wang Haifeng,etc.The crease-resistant finishing of silk fabrics with silk fibroin and polycarboxylic acid mixtures[J]. Silk,2009，10：22～25.

[3] Xing Tieling, Chen Guoqiang.studies on synthesis of polycarboxylic acid and its application to crease-proofing finish of tussah silk[J]. Dyeing auxiliaries,2002,19（6）:24～27.

Advanced Materials Research Vol. 936 (2014) pp 1609-1613
© (2014) Trans Tech Publications, Switzerland
doi:10.4028/www.scientific.net/AMR.936.1609

A same area method used to calculate the strain in forming for an axisymmetric workpiece

Zhiren Han[1,a], Qiang Xu[1,b], Zebing Yuan[1,c]

[1]Aeronautical Manufacturing Technology Digitization National Key Discipline Laboratory，Shenyang Aerospace University, Shenyang, 110136, Liaoning, P. R. China

[a]hanren888@163.com,[b]xuqiangf22@126.com,[c]75722279@qq.com

Keywords: sheet metal forming; strain analysis; thickness reduction rate; forming limited diagram

Abstract. An experimental study is conducted to explore a new method to calculate the strain in axisymmetric workpiece forming. When designing deep drawing die for an axisymmetric workpiece, the principal strain during the forming is needed to estimate formability and to decide whether the forming is finished in one pass. Strain calculation is a difficult task, so an ideal same area method used to calculate the strain for an axisymmetric workpiece along with a correction same area method considered thickness reduction rate is proposed here. The deep drawing test for an axisymmetric workpiece is used to obtain the strain along circumference and generatrix direction. The strain along the two directions calculated by the ideal same area method and correction same area method is compared with experimental results. The results show that ideal same area method can be used to calculate the strain during the forming process for an axisymmetric workpiece and the result from correction same area method is close to the experiment.

Introduction

Sheet metal forming operations having high productivity are generally employed in the production of aircraft parts, automotive workpieces, electric appliances, etc. For sheet metal products with complex geometry, if the deformation in single stage forming is larger than the maximum allowable deformation of the material, the product needs to be manufactured by multi-pass forming process to prevent the occurrence of defects such as necking, wrinkling and cracking [1, 2].

The forming limit diagram (FLD) is used in sheet metal forming to determine how susceptible sheet metal is to tearing when it is formed into a product shape in a stamping process. The concept of the FLD was found by Keeler and Backofen and Goodwin to research the formability of sheet metals [3, 4]. Both the strain-based FLD and the stress-based FLD are forming limit diagrams and the strain-based FLD is often used in sheet metal forming. The path of the forming limit is called the forming limit curve (FLC) and is the key feature of FLD [5, 6]. The distance between the FLC and all of the measured or predicted strain throughout the forming part characterize the degree of safety. The concept of FLD is widely applied to metal forming process [7, 8]. It is important to get the FLC of material and strain throughout the forming part. The principal strain in sheet plane is used to decide its forming state through FLD. The two kinds of principal strain in a position of forming part taken as two coordinates of a point in FLD. For an axisymmetric workpiece, the principal strain is the strain in the circumference direction and the generatrix direction. The relative position between strain point and the FLC determines the formability in this position of the forming part. Strain calculation and analysis is a difficult task. For half a century, considerable efforts have been devoted to explore new methods for determining strain. Among these methods, experimental method and simulation method are the mainstream. Grid method is popularly used in experiment

processes, and the circle grid is widely applied for its simpleness and convenience. With the development of computer technology, finite element simulation becomes an important method to calculate and analyze strain during forming process. For instance, Mohebbi used the finite element simulation method to analyze strain in flow forming of tubes [9]. Additionally, Tszeng investigated ring rolling process by strain finite element method analysis [10]. A modified method to obtain the principal strain for an axisymmetric workpiece is discussed in this paper.

Strain Calculation

Ideal Same Area Method

Before the possibility of multi-pass deep drawing process is assessed, we must determine whether the degree of deformation that parts require is larger than the maximum allowable degree of deformation of the material during the forming process of the axisymmetric workpiece. The situation of deformation degree in sheet metal forming can be expressed by three kinds of principal strain—circumference direction strain, generatrix direction strain, and thickness direction strain, and all of them have to be calculated before making the forming scheme and designing the die.

Fig.1 is an axisymmetric workpiece and Fig.2 is the blank used to form the axisymmetric workpiece. The workpiece has same volume with the blank in sheet metal forming according to the plasticity theory. If the workpiece thickness does not change during forming, it will have the same outside surface area as the blank. The axisymmetric workpiece surface is divided into n portions as shown by Fig.1， and the distance along generatrix direction for every portion is same. The area of every portion can be determined using CAD. Similarly, the blank is divided into the same number of sections. The portions are numbered by 1 to n from center to the outside boundary in axisymmetric workpiece and blank. The same number portions in axisymmetric workpiece and blank have same area.

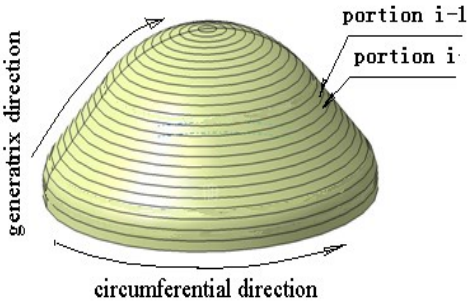


Fig.1 Workpiece

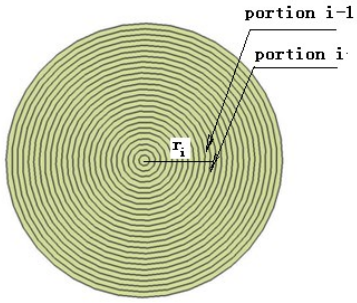


Fig.2 Blank

Here

i is a serial number, A_{w_i} is the area of portion i in workpiece and A_{b_i} is the area of portion i in blank. Then

$$A_{w_i} = A_{b_i}. \quad (1)$$

$$A_{w_1} + A_{w_2} + ... + A_{w_{i-1}} + A_{w_i} = A_{b_1} + A_{b_2} + ... + A_{b_{i-1}} + A_{b_i}. \quad (2)$$

The A_{w_1}, A_{w_2},..., A_{w_i},... can be obtained from the workpiece CAD model, and from that $A_{b_1}, A_{b_2},..., A_{b_i},...$ are known quantities. The radius used to express boundary line in blank can be calculated by the below formula.

$$r_i = \sqrt{(A_{b_1} + A_{b_2} + ... + A_{b_{i-1}} + A_{b_i})/\pi}. \quad (3)$$

To calculate circumferential direction strain and generatrix direction strain, we use the equation below.

$$\varepsilon_{g_i} = (\Delta L - (r_i - r_{i-1}))/(r_i - r_{i-1}). \quad (4)$$

$$\varepsilon_{c_i} = (a_{1_l} - 2\times 3.14159\times r_i)/(2\times 3.14159\times r_i). \quad (5)$$

Here,

ΔL is the distance along generatrix direction for per portion in axisymmetric workpiece. It is given before dividing workpiece.

a_{1_l} is the maximum boundary circumference of portion i in axisymmetric workpiece. It can be obtained from the CAD model of workpiece .

Correction Same Area Method

There is some change in thickness during sheet metal forming. The change in thickness can have an influence on ε_{g_i}, ε_{c_i} calculated in same area method. The volume of sheet metal workpiece keeps constant during forming.

Then

$$A_{w_i} \times t_{w_i} = A_{b_i} \times t_{b_i}. \quad (6)$$

Here,

A_{w_i} is the area of outside surface in portion i for axisymmetric workpiece. A_{b_i} is the area of outside surface in portion i for blank. t_{w_i} is thickness in portion i for axisymmetric workpiece. t_{b_i} is thickness in portion i for blank.

Then,

$$A_0 = At/t_0 = A[1-(t_0 - t)/t_0]. \quad (7)$$

Here,

$(t_0 - t)/t_0$ is thickness reduction rate.

If the average thickness reduction rate η_i in per portion is considered, then the correction radius used to express boundary line in blank can be calculated using the below formula

$$r_{c_i} = \sqrt{A_{b_1}(1-\eta_1) + A_{b_2}(1-\eta_2) + ... + A_{b_{i-1}}(1-\eta_{i-1}) + A_{b_i}(1-\eta_i)/\pi}. \quad (8)$$

When the average thickness reduction rate η_i per portion is taken into account, the circumference direction strain and generatrix direction strain can be calculated using the following equations.

$$\varepsilon_{cg_i} = [\Delta L - (r_{c_i} - r_{c_{i-1}})]/(r_{c_i} - r_{c_{i-1}}). \quad (9)$$

$$\varepsilon_{cc_i} = (a_{1_i} - 2\times 3.14159\times r_{c_i})/(2\times 3.14159\times r_{c_i}). \quad (10)$$

Experiment

The workpieces shown as Fig.3 are formed by deep drawing. Six test pieces are used in each experiment and the average value is obtained. Grid method is used in this experiment to study the distribution. Grid printed on the blank was done using the circle grid analysis technique [11]. Then

the strain level and distribution is obtained by measuring and analyzing the change after the deformation. The grid on the blank is a circular shape having diameter of 3 mm as shown in Fig.4. After the deformation, the grid turns to ellipse shape, and the strain in two principal directions can be calculated by measuring the strain along the major and minor axes of the ellipse.

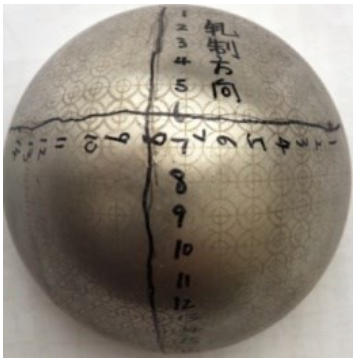


Fig.3The Arc intermediate shape test piece

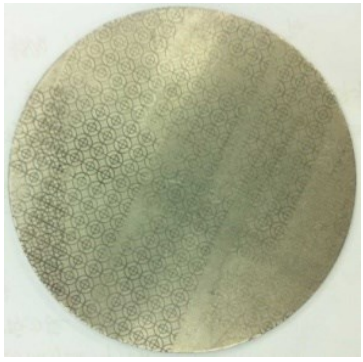


Fig.4 The blank with grid

Results

The generatrix and circumferential direction strain distribution for the workpiece shown as Fig.1 are calculated by ideal same area method and correction same area method respectively. The average thickness reduction rate η_i in each portion is used in correction same area method come from finite element analysis for the workpiece. The calculated and experimental strain results are plotted in Fig.5 and Fig.6. The blue curve is the strain form experiment. The red curve is the strain form ideal same area method. The yellow curve is the strain form correction same area method. The strain curves from ideal same area method, correction same area method, and experiment have the same trend， and the results from correction same area method are close to the experimental results. The results far from the center of the workpiece have larger differences between ideal same area method and experiment.

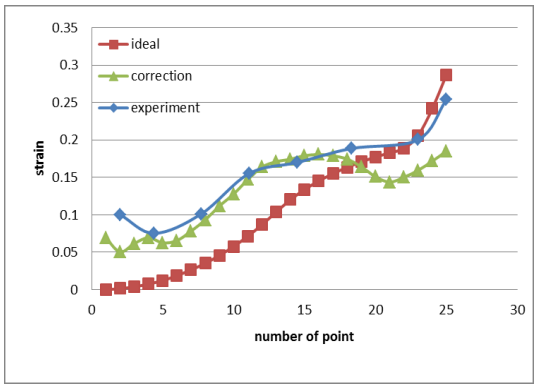


Fig.5 The generatrix direction strain distribution

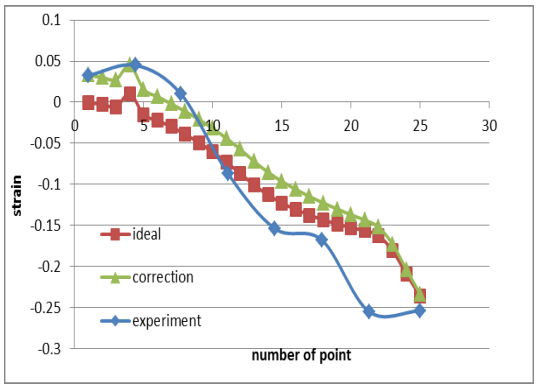


Fig.6 The circumference direction strain distribution

Conclusions

The ideal same area method and correction same area method have been put forward. The results calculated by the ideal same area method and correction same method compared with experiment. The conclusions are as follow:

1) An ideal same area method is proposed for the calculation of the principal strain along circumferential direction and generatrix direction. The strain can be used to forecast formability when we design deep drawing die.

2) A correction same area method is proposed for the calculation of the principal strain along circumferential direction and generatrix direction. The average thickness reduction rate η_i in each portion is taken into account in the strain calculation. We can obtain the average thickness reduction rate η_i in each portion through finite element analysis or experiments.

3) The data on strain obtained from the deep drawing forming experiment show that the strain curve from correction same area method is close to the experimental strain curve.

References

[1] C.S.Park, T.W.Ku, Process design and blank modification in the multistage rectangular deep drawing of an extreme aspect ratio, J. Journal of Materials Processing Technology. 153–154 (2004) 778–784.

[2] M.A.Hassan, K.I.E.Ahmeda, N.A.Takakurac, A developed process for deep drawing of metal foil square cups, J. Journal of Materials Processing Technology. 212(2012) 295–307.

[3] S.P.Keeler, W.A.Backofen, Plastic instability and fracture in sheets stretched over rigid punches, J. Trans ASM. 56(1963) 25–48.

[4] G.M.Goodwin, Application of strain analysis to sheet metal forming problems in the press shop, J. Trans Soc Automot Eng. 77(1968) 380–387.

[5] T.B.Stoughton, X.H.Zhu, Review of theoretical models of the strain-based FLD and their relevance to the stress-based FLD, J. International Journal of Plasticity. 20(2004) 1463-1486.

[6] G.Fang, Q.J.Liu et al, Comparative analysis between stress- and strain-based forming limit diagrams for aluminum alloy sheet 1060, J. Transactions of Nonferrous Metals Society of China. 22(2012) 343−349.

[7] C.Vallellano, D.Morales, F.García-Lomas, A Study to Predict Failure in Biaxially Stretched Sheets of Aluminum Alloy 2024-T3, J. Materials and Manufacturing Processes. 23(2008) 303-310.

[8] S.B.Kim,H.Huh et al, Forming limit diagram of auto-body gsteel sheets for high-speed sheet metal forming, J.Journal of Materials Processing Technology. 211(2011) 851-862.

[9] M.S.Mohebbi, A. Akbarzadeh, Experimental study and FEM analysis of redundant strains in flow forming of tubes, J. Journal of Materials Processing Technology. 210(2010) 389–395.

[10] T.C.Tszeng, T.Altan, Investigation of ring rolling by pseudo plane-strain FEM analysis, J. Journal of Materials Processing Technology. 27(1991) 151-161.

[11] M.P.Sklad, Aspects of automated measurement of proportional and non-proportional deformation in sheet metal forming, J. Journal of Materials Processing Technology. 3(2004) 377-384.

Advanced Materials Research Vol. 936 (2014) pp 1614-1619
© (2014) Trans Tech Publications, Switzerland
doi:10.4028/www.scientific.net/AMR.936.1614

Applying BP Neural Network Model to Forecast the Largest Coiling Torque of Down Coilers

Ke Zhao[1], Zhigang Wang[2*], Changming Liu[2]

[1]College of Machinery and Automation, Wuhan University of Science and Technology, Wuhan, China

[2]Ministry of Education Key Lab of Metallurgical Equipment and Control, Wuhan University of Science and Technology, Wuhan, China

Keywords: Down Coiler; BP Neural Network; Coiling Torque; Forecast

Abstract: Down coiler is an important equipment of hot rolling mill. The coiling torque is changing constantly in the process of strip steel coiling, and the largest coiling torque depends on several factors, such as the material and specification of coiling strip, the coiling temperature and the process parameters and so on. Only when the largest coiling torque is less than the carrying capacity could the coiler work in security. A topology relationship of the largest coiling torque among the materials, the specification of the strip and the coiling temperature is established. Based on the BP(backward propagation of errors) artificial neural network, a predicted formula model of the largest coiling torque in coiling high strength strip is built, which provides a theoretical basis for the development and utilization of the largest working potential of the down coiler.

Introduction

The down coiler, usually used for coiling strips extracted from a finishing mill, is consists of side guides, a pinch roll, a mandrel, and wrapper rolls, as illustrated in Fig.1.

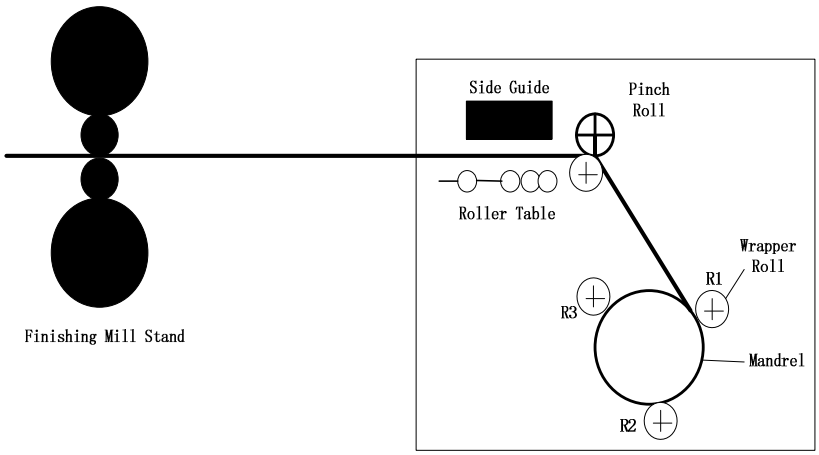


Fig.1 Diagram of a down coiler

The down coiler plays an important role in the hot strip mill lines. And the coiling torque of down coiler will affect the quality of the strip steel directly[1]. But it is affected by many complicated and non-linear factors such as coiling temperature, material and specification of strip steel, which often make the largest coiling torque difficult to forecast. As there is no method for forecasting the largest coiling torque accurately and effectively at the moment, scientists have done a lot of calculation, mostly based on empirical formula[2].

The successful application of artificial neural network in many fields provides a good method for the forecast of the largest coiling torque of down coiler recently. The artificial neural network model, with the good nonlinear fitting ability and efficient method of learning, has been more widely used in the field of data prediction. In this paper, BP neural network is used for forecasting

the largest coiling torque of down coiler. The accuracy of forecasts will be largely improved and it will ensure the safety of the down coiler as well as the quality of strip steel.

The establishment of BP neural network model

An artificial neural network is consisted of an interconnected group of artificial neurons, and it processes information using a connectionist approach. ANN(artificial neural network)is an adaptive system and non-linear statistical data modeling tool, which could exactly reflect characteristics of a system[3].

Determination of influencing factors of coiling torque

In order to derive a dynamic equation for strip coiling, it is important to ensure the required load torques for activating the mandrel. There are three kinds of torque: M_T for the strip tension, Mw for bending the strips, M_d for the rotational deceleration of the mandrel resulting from the increasing outside diameter of the coil[4].

$$M_T = \frac{1}{2} \times U_T \times h \times b \times D(t) \tag{1}$$

Where U_T is the unit tension of strip, h is the thickness of strip, b is the width of strip, D(t) is the coil diameter of strip.

$$M_w = \frac{1}{4} \times \sigma_s \times b \times h^2 + \frac{1}{60 \times D(t)} \times \sigma_s \times b \times h^3 \tag{2}$$

Where σ_s is the hot yield stress.

$$M_d = I \times \frac{C_{RPM}(t)}{T_i} \left\{ C_{RPM} = \frac{d}{dt} \left(\frac{\pi}{60} \times D(t) \right) \right\} \tag{3}$$

Where $C_{RPM}(t)$ is the rotate speed of the mandrel, T_i is the coiling time, I is the total inertia.

The total load torques M for strip coiling is shown as following：

$$M = M_T + M_w + M_d \tag{4}$$

As the above formula shown, coiling torque is mainly influenced by the thickness, the width, and the yield strength of the strip steel. In addition, the performance of strip steel is related to the temperature of coiling steel. Therefore the coiling torque is mainly determined by the four above factors.

BP neural network model

Neural network, as a nonlinear complex system, is composed of a large number of simple processing units (or neurons) which extensively interconnect[5]. BP neural network with three layers and sigmoid activation function is used for the model.[6].

In the system of forecasting coiling torque, there are four input parameters, which are the most affecting factors of the largest coiling torque. The principle of forecast of neural network is described by a 4-4-1 ANN with the hidden layer composed four units. The structure of the artificial neuron model is shown in Fig 2.

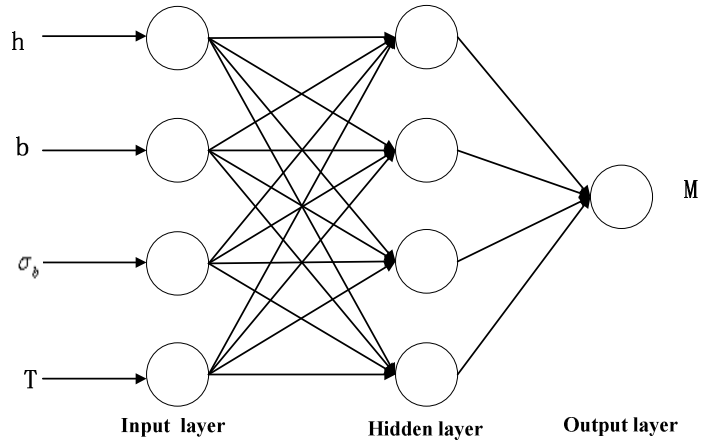


Fig.2. The structure of the artificial neuron model

The input of the input layer:

$$\{x_r\} = \begin{Bmatrix} x_r(1) \\ x_r(2) \\ x_r(3) \\ x_r(4) \end{Bmatrix} = \begin{Bmatrix} h \\ b \\ \sigma_b \\ T \end{Bmatrix} \tag{5}$$

Where X_r is the unit value of the input layer, h is the thickness of the strip, b is the width of the strip, σ_b is the tensile strength of the strip, T is the temperature of the strip.

The output of the output layer:

$$\{ y \} = \{ M \} \tag{6}$$

Where y is the predictive value of output layer, M is the largest coiling torque.

Selection of transition function

BP Network is able to access any curve,which requires the transition functions tobe differentiable all the time.The hidden layer of this paper adopts hyperbolic tangent function of the S type transmission function—Tansig. Meanwhile, the output layer adopts a linear transfer function--Purelin.

Obtainment of the training sample

By collating and analyzing the testing data, the largest coiling torque is recorded in different coiling temperature and different strips in thickness, width and yield stress for BP network testing samples. A total number of 28 groups of testing samples was used. The coiling temperature of which is between 500 and 700 Celsius, and the thickness of strips ranges from 3.5 to 16 mm, the width is 1043 to 2065mm, while the yield stress is from 280 to 920MPa.Generally speaking, various types of strip steel are covered in the 28 groups testing sample.

Realization of the neural network model

Normalization of the training sample

A unipolar Sigmoid function is used for the activation function, which needs to unify dimension of different parameters in each sample. Single node data mapping mode (SNDM) is taken to normalize the input data of the neural network. The normalized conversion formula is shown as follow:

$$x_{ri}=(x_{si}-\min(x_{si}))/(\max(x_{si})-\min(x_{si})) \quad (7)$$

Where x_{ri} is sample value of i-th unit in the input layer, x_{si} is the normalized scaled value

Initialization of the input value

Quantification of conjugate gradient method is adopted for training function; The initial vector of each connection weight in hidden layer as well as output layer should be protocol selected as 0.05;the largest times of training is set to 2000;the accuracy requirement of training is set to 0.009.

Training results of BP neural network model

28 samples of measured value are input into the BP Neural Network model. The comparison of the 28 samples between measured value and the predicted value are showed in Fig 3.The error of training process is showed in Fig 4.Parts of the sample value and predicted value are showed in Table1.As the Fig 4 shows, when the number of training times reaches to 400, the predictive value could reach the expected target. Fig 3 shows that predicted value are nearly the same as the measured value after training, and further calculation shows that the error ranges from 0.01%to 5.60%, only 2 samples are out of the range. This shows that the trained BP neural network model reaches the expect effect and the built model could be used to predict the largest coiling torque of down coilers accurately and effectively.

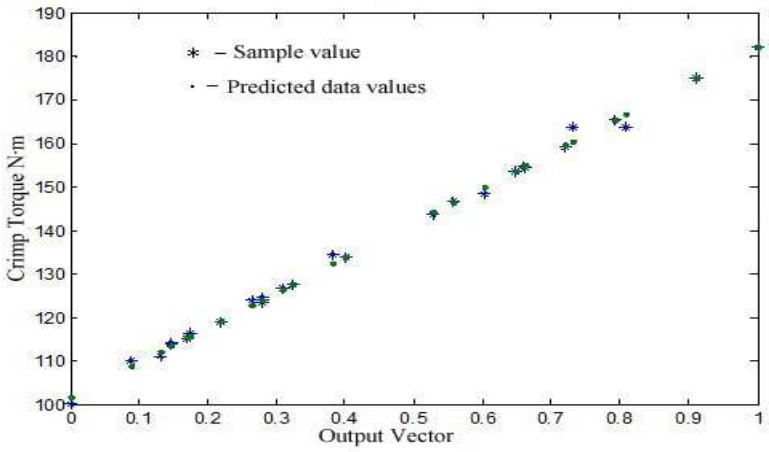


Fig. 3. Linear regression of torque

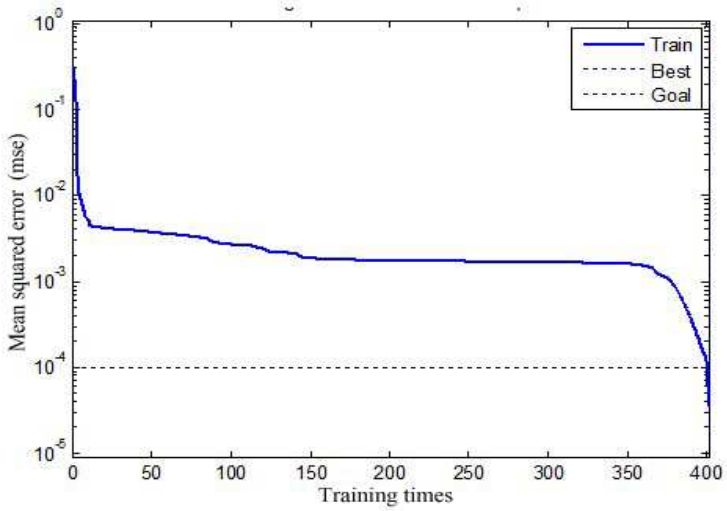


Fig. 4. The training error curve

TABLE 1. RESULTS OF NETWORK PREDICT

No	Thickness h(mm)	Width b(mm)	yield stress σ_b (Mpa)	tempe-rature T(℃)	Measured value (kNm)	Predicted value (kNm)	Error (%)
1	4.07	1527.4	305	650	132.4	136.4	2.98
2	4.03	1514.3	365	645	126.5	125.3	0.97
3	4.07	1486.9	310	645	150.1	141.7	5.60
4	3.57	1497.0	315	650	119.4	122.9	2.89
5	4.07	1400.9	315	650	115.4	123.7	7.21
6	5.59	1099.9	280	600	154.9	153.1	1.15
7	5.59	1099.9	320	600	146.6	150.1	2.40
8	4.58	1188.4	320	600	124.1	121.6	2.03
9	5.08	1147.3	360	700	123.0	123.4	0.32

The result of the BP neural network model prediction

When the training was completed, the weigh value and the threshold value in each layer could be got, as shown in Table 2 to Table 5.

TABLE 2. THE WEIGH VALUE FROM INPUT LAYER TO HIDDEN LAYER

w_{ij}	j=1	j=2	j=3	j=4
i=1	1.0877799	3.0733752	0.4209466	2.2076918
i=2	-2.1797475	2.0555984	-2.5888778	-0.0304502
i=3	-1.8312260	1.7691505	-2.3690986	-1.8931690
i=4	-0.8835241	-1.7232298	-3.4536379	-0.0474229

TABLE 3. THE WEIGH VALUE FROM HIDDEN LAYER TO OUTPUT LAYER

w_{cj}	j=1	j=2	j=3	j=4
	-0.7047835	-0.8900517	0.7014253	0.1211190

TABLE 3. THE THRESHOLD VALUE IN THE HIDDEN LAYER

θ_{ri}	j=1	j=2	j=3	j=4
	-5.3747958	2.03170495	1.50220523	1.0740084

TABLE 4. THE THRESHOLD VALUE IN THE OUTPUT LAYER

θ_c	j=1
	0.8592177

The relationship between the various units in the hidden layer and the input layer:

$$x_{cj}=\mathrm{tansig}\left(\sum_{i=1}^{4} w_{ij}x_{ri}-q_{ri}\right) \tag{8}$$

$$\mathrm{tansig}(x) = \frac{2}{(1+e^{-2x})}-1 \tag{9}$$

The relationship between the various units in the hidden layer and the output layer:

$$y=\mathrm{purelin}\left(\sum_{j=1}^{4} w_{cj}x_{cj}-\theta_c\right) \tag{10}$$

$$\mathrm{purelin}\ (x) = x \tag{11}$$

The largest coiling torque is obtained from the equation:

$$M = y \times (182.1 - 101.7) + 101.7 \tag{12}$$

A part of the predicted value is shown in Table 6:

TABLE 3. PREDICTED VALUE TABLE OF THE LARGEST COILING TORQUE

No	h(mm)	b(mm)	σ_b (Mpa)	T(℃)	M (kN·m)
1	5.5	1100	280	600	152.4
2	13	1830	920	550	160.2
3	6	1280	280	695	114.4
4	8	1600	510	600	153.9
5	18.4	1550	910	500	204.4

Conclusion

In this paper, a neural network model for forecasting the largest coiling torque of down coilers was established based on back propagation algorithm. Compared with the measured value and predicted value, the relative error is in the 5.60%.The errors satisfy the requirement of practical application. The results demonstrated that the forecast of the largest coiling torque was accurate and effective. The largest coiling torque of different kinds of strip steels could be forecasted. Moreover, the accuracy of forecasts will be largely improved and it will ensure the safety work of the down coiler as well as the quality of strip steel.

Acknowledgments

The authors would like to thank the National Natural Science Foundation of China (51075310), the Research Fund for the Doctoral Program of Higher Education of China (20114219110003), the Hubei Province Natural Science Fund Project (2012FFA022), Program for New Century Excellent Talents in University of Ministry of Education of China (NCET-12-0715) and the Postdoctoral Science Foundation of China(2013M542072)for the financial support.

References

[1] Yong Lv,YouRong Li,ZhiGang Wang. Carrying Capacity Analysis of Main Driver System of Coiler [J]. Wuhan University Of Science &Technology, vol.4.no.26,pp.380-382(2003).

[2] Alberto Hernandez, Neto Fla´vio, Augusto Sanzovo Fiorelli. Comparison between detailed model simulation and artificial neural network for forecasting building energy consumption[J]. Energy and Buildings, vol.40,pp.2169-2176 (2008).

[3] Lv Shuran,Lv Shujin.Applying BP Neural Network Model to Forecast Peak Velocity of Blasting Ground Vibration[J]. Procedia Engineering, vol.26,pp.257-263 (2011).

[4] Yong-Joon Choi,Min-Cheol Lee.A Downcoiler Simulator for High Performance Coiling in Hot Strip Mill Lines[J], International Journal of Precision Engineering and Manufacturing.vol.10,no.2,pp.53-61(2009).

[5] Zhenhua Xie, Yu Zhang, Cai Jin. Prediction of Coal Spontaneous Combustion in Goaf Based on the BP Neural Network[J]. Procedia Engineering, vol.43,pp.88-92(2012).

[6] Xiaomin Wang, Xiyu Liu, Fen Dai. Improvement and Application of BP Neural Network Forecasting Algorithm[J], Computer Technology and Development, pp.64-67(2009).

Advanced Materials Research Vol. 936 (2014) pp 1620-1623
© (2014) Trans Tech Publications, Switzerland
doi:10.4028/www.scientific.net/AMR.936.1620

Brazing Incoloy 800 Using the MBF-51 Filler Foil

Wen-Shiang Chen[1,a], Ren-Kae Shiue[1,b]

[1]Department of Materials Science and Engineering, National Taiwan University, Taipei 106, Taiwan

[a]d99527002@ntu.edu.tw, [b]rkshiue@ntu.edu.tw

Keywords: Brazing, Incoloy 800, Nickel Base Filler, Microstructure, Shear Strength

Abstract: The purpose of this research is focused on developing a reliable plate heat exchanger made by Incoloy 800 (IN-800) alloy featured with high corrosion resistance in order to replace the current Cu brazed plate heat exchanger made by the 316 stainless steel. A Ni-based filler, MBF-51, was applied to braze the plate heat exchanger made by IN-800. According to the brazing optimizing experiments, the successful brazed joint was made by brazing at 1170 ^{o}C for 1800 s. Better shear strength is achieved from the specimen brazed at 1120 ^{o}C for 1800 s.

Introduction

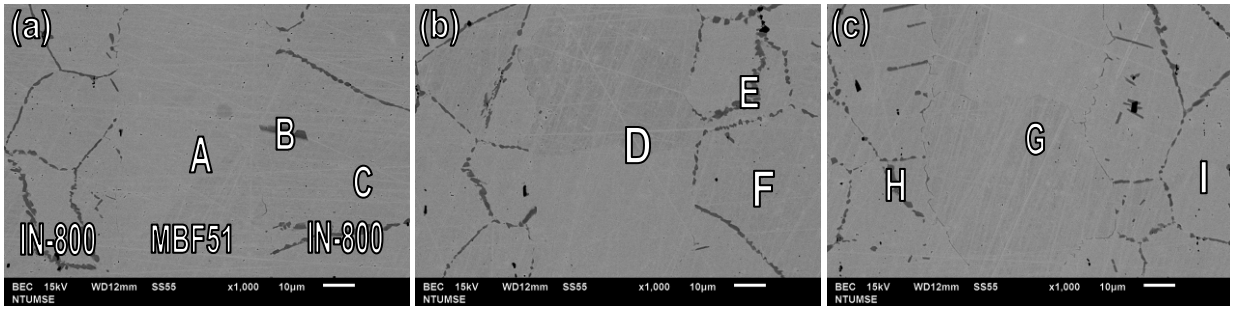
The technology of manufacturing plate heat exchanger is much more difficult than that of making traditional heat exchanger. The plate heat exchanger is currently made by Cu brazed 304/316 stainless steel(s) for most major heat exchanger manufacturer in the world [1]. Stable brazing process and inexpensive filler alloy are primary advantages of Cu brazing. However, requirements of increased corrosion resistance, avoiding Cu ion contamination, resisting to high temperature and pressure resulting from various users make the Cu brazed stainless steel plate heat exchanger failed to satisfy all demands. Other materials such as Inconel 625 and commercially pure Ti currently applied in manufacturing plate heat exchangers for special purpose are suffered from high cost and/or insufficient pressure resistance [2-4]. Therefore, it is crucial to develop high-performance plate heat exchangers applied in next generation.

Incoloy 800 (IN-800) is a Fe/Ni-based alloy, and its chemical composition in weight percent is 44.5 % Fe, 21 % Cr, 0.4 % Al, 0.4 % Ti, 0.8 % Mn, 0.5 % Si, 0.4 % Cu and Ni balance [5]. It is widely used in furnace and heat exchanger parts due to its high corrosion resistance and moderate creep strength [5]. Additionally, its price is much cheaper than that of Inconel 625 alloy. IN-800 alloy is a good choice to produce the plate heat exchanger. The MBF-51 foil is a modified Ni-based braze alloy, and its chemical composition in weight percent is 15 % Cr, 7.3 % Si, 1.4 % B and Ni balance [2]. Compared to traditional Ni-based braze alloys, the boron content in MBF-51 filler has been greatly decreased in order to diminish the amount of brittle boride precipitates in the brazed joint [2, 6-9]. Therefore, it has been selected as the brazing filler metal in the experiment.

Experimental Procedures

IN-800 alloy is used as the base metal with the dimension of 15 mm in length, 6 mm in width and 3 mm in thickness. All IN-800 plates were ground by SiC papers up to grit 600 and subsequently cleaned in ultrasonic bath using acetone solution prior to brazing. The thickness of MBF-51 filler foil is 40 μm. Because liquidus temperature of MBF-51 foils is 1126 ^{o}C, vacuum furnace brazing under the vacuum of 5×10^{-5} mbar was performed at 1170, 1185, 1200 ^{o}C for 900, 1800, and 3600 s, respectively. The heating rate was set at 0.33 ^{o}C/s, and all specimens were preheated at 1000 ^{o}C for 600 s prior to brazing. Cross-sections of brazed joints were cut by a low-speed diamond saw and examined by using a JEOL JSM 6510 scanning electron microscope (SEM). A JEOL 8600SX electron probe microanalyzer (EPMA) equipped with the wavelength dispersive spectroscopy (WDS) was utilized for quantitative chemical analyses of various phases in the brazed joint. Its operation voltage was 15 kV, and the minimum spot size was set at 1 μm.

Shear tests were performed to evaluate the bonding strength of the brazed joint [2,10]. The specimen was compressed by a Shimadzu AG-10 universal testing machine with a constant speed of 0.0167 mm/s. There are at least three specimens were measured for each brazing condition. Failure analyses of fractured surfaces after shear tests were conducted using the SEM secondary electron images (SEIs). Cross-sections of brazed joints after shear tests were inspected using SEM backscattered electron images (BEIs) in order to locate fracture locations of the joints.



Location / Phase	Al	B	C	Cr	Cu	Fe	Mn	Ni	Si	Ti
A (Cr/Fe/Ni-rich matrix)	0.5	0.4	0.1	19.1	0.1	16.6	0.4	54.3	8.2	0.2
B (boride)	0.1	22.1	0.5	48.1	0.0	21.8	0.6	6.6	0.2	0.1
C (Cr/Fe/Ni-rich matrix)	0.9	1.4	0.3	22.3	0.1	45.5	0.8	27.8	0.6	0.3
D (Cr/Fe/Ni-rich matrix)	0.5	0.8	0.2	18.9	0.1	19.3	0.4	51.8	7.9	0.2
E (boride)	0.1	22.4	0.4	47.7	0.0	21.8	0.6	6.8	0.2	0.1
F (Cr/Fe/Ni-rich matrix)	0.7	0.6	0.3	22.8	0.1	45.8	0.7	28.1	0.7	0.3
G (Cr/Fe/Ni-rich matrix)	0.4	0.1	0.2	19.8	0.0	20.3	0.5	51.1	7.3	0.2
H (boride)	0.1	20.5	1.3	47	0.0	22.4	0.6	7.8	0.1	0.2
I (Cr/Fe/Ni-rich matrix)	0.6	0.2	0.4	23.2	0.1	45.3	0.8	28.3	0.7	0.4

Fig. 1 EPMA BEIs and WDS chemical analysis results of IN-800/MBF-51/IN-800 joints brazed at (a) 1170, (b) 1185, and (c) 1200 ^{o}C for 1800 s.

Results and Discussion

Fig. 1 displays EPMA BEI and WDS chemical analysis results in atomic percent of IN-800/MBF-51/IN-800 joints brazed at 1170, 1185, and 1200 ^{o}C for 1800 s. At least two phases are readily observed from the brazed joint, including Cr/Fe/Ni-rich matrix as marked by A, C, D, F, G, I and boride mainly containing B, Cr, Fe as marked by B, E, H. The Cr/Fe/Ni-rich matrix is alloyed with approximately 20 % Cr. It is expected that the brazed joint is corrosion resistant. Based on the Fig. 1, the interfacial reaction between the molten braze and IN-800 substrate is primarily along grain boundaries of IN-800 alloy. It is difficult to quantify interfacial lengths based on SEM images. Because the growth of interfacial thickness is diffusion controlled, especially along grain boundaries, there is no sharp interface between the braze and IN-800 substrate. The fact of borides primarily existing along grain boundaries is consistent with previous studies using Ni-based braze alloys [2,7,11].

Fig. 2 displays microstructural evolution of IN-800/MBF-51/IN-800 joints under various brazing conditions. The width of MBF-51 brazed joint is slightly increased with increasing the brazing temperature. Increasing the brazing temperatures and/or time also enhance the penetration depth of grain boundary borides. However, higher brazing temperature and/or longer brazing time cannot remove grain boundary borides from the joint. On the contrary, grain boundary borides are slightly coarsened with increasing the brazing temperature and/or time.

TABLE 1 AVERAGE SHEAR STRENGTHS OF SELECTED BRAZED JOINTS

Filler Metal	Brazing Temperature (K)	Brazing Time (s)	Average Shear Strength (MPa)
MBF-51	1170 ^{o}C	1800	366
MBF-51	1200 ^{o}C	1800	Yielding of IN-800 Substrate

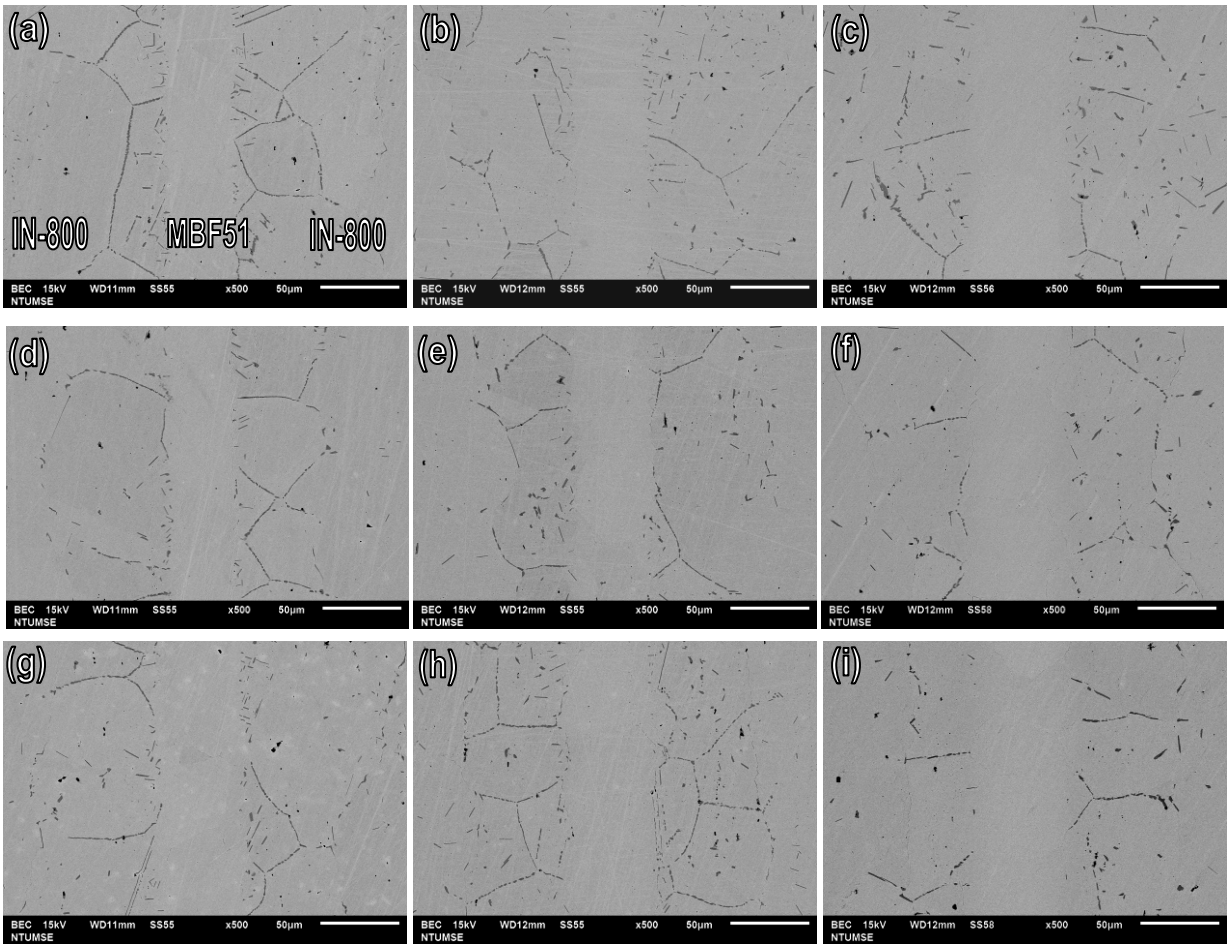


Fig. 2 EPMA BEIs of IN-800/MBF-51/IN-800 joints brazed at (a) 1170 ^{o}C for 600 s, (b) 1170 ^{o}C for 1800 s, (c) 1170 ^{o}C for 3600 s, (d) 1185 ^{o}C for 600 s, (e) 1185 ^{o}C for 1800 s, (f) 1185 ^{o}C for 3600 s, (g) 1200 ^{o}C for 600 s, (h) 1200 ^{o}C for 1800 s, (i) 1200 ^{o}C for 3600 s.

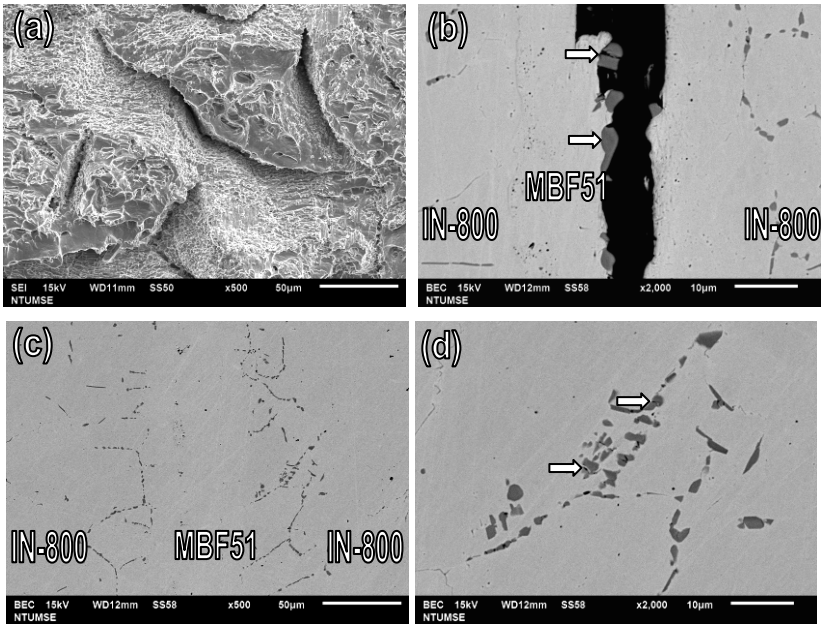


Fig. 3 SEM failure analyses of fractured IN-800/MBF-51/IN-800 joints after shear tests: (a) SEI fractograph, (b) BEI of fracture location brazed at 1170 ^{o}C for 1800 s; (c, d) BEIs of the cross section brazed at 1200 ^{o}C for 1800 s.

Table 1 displays average shear strengths of selected IN800/MBF-51/IN-800 brazed joints. The joint brazed at 1170 ^{o}C for 1800 s has the average shear strength of 336 MPa. In contrast, the brazed joint is not fractured even yielding of the IN-800 substrate for the specimen brazed at 1200 ^{o}C for

1800 s. Fig. 3 shows SEM failure analysis results of fractured IN-800/MBF-51/IN-800 joints after shear tests. For the specimen brazed at 1170 ^{o}C for 1800 s, quasi-cleavage dominated fractograph is observed from Fig. 3(a). The crack is initiated from the grain boundary boride as demonstrated by arrows in Fig. 3(b). The presence of continuous grain boundary boride is detrimental to bonding strength of the brazed joint. For the specimen brazed at 1200 ^{o}C for 1800 s, grains of the brazed joint is distorted (Fig. 3(c)), and a few grain boundary borides are fractured as indicated by arrows in Fig. 3(d).

Summary

Furnace brazing IN-800 alloy using the MBF-51 foil has been investigated in the experiment. The brazed joint mainly comprised of grain boundary borides and Cr/Fe/Ni-rich matrix. The Cr/Fe/Ni-rich matrix is ductile as compared with grain boundary borides. The presence of continuous grain boundary borides deteriorates bonding strength of the joint. The average shear strength of IN-800/MBF-51/IN-800 joint brazed at 1170 ^{o}C for 1800 s is 366 MPa. Increasing the brazing temperature to 1200 ^{o}C is beneficial to its shear strength. Because wide brazing process window is achieved, it shows the potential for industrial application.

Acknowledgements

Authors gratefully acknowledge the financial support of this research by National Science Council, Taiwan (Contract number NSC 102-2221-E-002-148).

References

[1] W.S. Chen, R.K. Shiue, Microstructural evolution of brazing 304 stainless steel using an amorphous (Ni,Fe)-based foil, ISIJ Inter. 52 (5) (2012) 939-941.

[2] W.S. Chen, R.K. Shiue, Brazing Inconel 625 using two Ni/(Fe)-based amorphous filler foils, Metall. Mater. Trans. 43A (2012) 2177-2182.

[3] T.Y. Yeh, R.K. Shiue, C. S. Chang, Microstructural evolution of brazed CP-Ti using the clad Ti-20Zr-20Cu-20Ni foil, Metall. Mater. Trans. 44A (2013) 9-14.

[4] W.S. Chen, R.K. Shiue, Microstructural evolution of brazed Inconel 625 using amorphous VZ-2106 foil, ISIJ Inter. 53 (5) (2013) 923-925. (SCI/EI)

[5] W.F. Smith, Structure and Properties of Engineering Alloys, McGraw-Hill Inc, New York, 1993.

[6] D.L. Olson, Metals Handbook, Vol. 6 Welding Brazing and Soldering, ASM International, Materials Park, 1990.

[7] R. K. Shiue, S.K. Wu, C.M. Hung, Infrared repair brazing of 403 stainless steel with a nickel based braze alloy, Metall. Mater. Trans. 33A (2002) 1765-1773.

[8] M. Schwartz, Brazing: For the Engineering Technologist, ASM International, Materials Park, 1995.

[9] G. Humpston, D.M. Jacobson, Principles of Soldering and Brazing, ASM International, Materials Park, 1993.

[10] C.H. Lee, R.K. Shiue, Infrared brazing zirconium using two silver based foils, J. Mater. Sci. Tech. 29 (3) (2013) 283-286.

[11] C.L. Ou, D.W. Liaw, Y.C. Du, R.K. Shiue, Brazing of 422 stainless steel using the AWS classification BNi-2 braze alloy, J. Mater. Sci. 41 (19) (2006) 6353-6361.

Advanced Materials Research Vol. 936 (2014) pp 1624-1629
© (2014) Trans Tech Publications, Switzerland
doi:10.4028/www.scientific.net/AMR.936.1624

Activating of Nickel Slag and Preparing of Cementitious Materials for Backfilling

Li Keqing[a*], Zhang Yangyi[b], Zhao Peng[c] and Feng Lin[d]

Key Laboratory of the Ministry of Education of China for High-Efficient Mining and Safety of Metal Mines, University of Science and Technology Beijing, Beijing 100083, China

[a]lkqing2003@163.com, [b]Yangyi@126.com, [c]18810750076@163.com, [d]linfeng@126.com

Keywords: water-granulated nickel slag; cementitious materials; back-filling method; chemical activation

Abstract. The back-filling method is distinguished from other mining methods by its higher cost. In order to solve this problem and utilize water-granulated nickel slag as much as possible, nickel slag from flash smelting operation was used to prepare cementitious materials for backfilling. Approaches including mechanical activation and chemical activation were adopted to improve the cementitious activity of the slag. By taking the strength of the backfill materials as the evaluation standards, the hydration activity and cementitious performance of the slag were investigated under different activation conditions, and the mechanism of chemical activation was analyzed. The results shows that cementing agent prepared by using mainly the slag (occupying 85% of the total raw materials) can be used to replace cement and meet the production requirements for backfilling materials.

Introduction

The increasingly more attention to the environmental pollution, the greatly improved mining and cementing agent technology, help foster the cemented backfilling mining to become a modernized mining technology characterized with its high efficiency, high strength and high recovery rate[1]. Traditionally, cemented filling generally uses Portland cement as cementitious materials (cementing agent). According to the statistics of the mines using back-filling method in China[1], cemented filling accounts for 25%~40% of the total cost of mining, and cementing agent accounts for 70%~80% of the cemented filling cost. Therefore, taking suitable measures and developing proper cement substitute will have important meaning to reduce the filling cost and extend the application field of the filling mining technology [2, 3].

At present, lots of work has been done on the research of cement substitute, for instance, fly-ash was used to replace cement directly through adding partially based on its volcano ash activity [4-7], and slag was used to partially or completely replace cement after grinding and chemical activating [8-10]. As a kind of granular material with latent hydraulic activity, slag is somewhat similar to Portland cement in the chemical and mineral composition, therefore, it has a great potential to be used as cementitious material. The research on slag cement has a history of thirty years, and slag cement has been widely used in China. However, because of the peculiarity of the mine filling operation, less research on using slag as the main component of cementing agent has been done.

Since the late 90's of the last century, the Jinchuan Group Co. Ltd. (JGCL, Gansu Province, China) began to apply paste filling technology which backfill materials was produced by using cement as cementing agent, which means large amounts of cement has to be bought every year. Practice in JGCL has proved that the cement dosage and slurry concentration of the filling material are the main factors affecting the filling cost and the strength of the filling materials [11]. Therefore, if the slag of JGCL could be used to produce cementitious material, quite amount of money used to buy the cement would be saved. It could not only improve the economic efficiency of the enterprise, but also alleviate the land occupation and environmental pollution caused by slag discharge. This paper mainly focuses on the methods of using the water-granulated nickel slag of JGCL as the main raw material to produce exclusive cementitious material and the cementing mechanism of the slag.

Experiment

Experimental materials.

Water-granulated nickel slag: the slag whose chemical constituents mainly include SiO_2, CaO, MgO, etc. (Table 1) was fromJGCL. It is a second water-granulated slag produced by the technology extracting iron from the flash smelting slag (original slag). In addition to a small amount of pyroxene, $2CaO \cdot SiO_2$ and olivine, 80%~90% of the slag is glass phase, so it has a certain degree of potential activity. However, compared with the ordinary Portland cement, it cannot be directly used as cementitious material because of its low CaO content, high SiO_2 content, and relatively low activity coefficient (Al_2O_3/ SiO_2). It has to be activated by mechanical or chemical activation.

Activating agent: including natural gypsum, calcium carbide slag, anhydrous sodium sulfate, cement clinker. The composition of the activating agents is shown in Table 1.

Rod-milling sand: a kind of sang from the neighbourhood of JGCL, having -3mm granular size, used as filling aggregate.

Table 1 Chemical composition of water-granulated nickel slag and activating agents [wt%]

Raw materials	SiO_2	Al_2O_3	CaO	MgO	Fe_2O_3	FeO	K_2O	Na_2O	SO_3	Other	Loss
Water-quenched nickel slag	36.62	6.97	22.69	28.81	0.27	3.01	0.15	0.16	0.35	0.33	-0.38
Carbide slag	4.09	2.16	67.09		0.04	0.36		0.28	0.14		25.84
Desulfurized gypsum	3.16	1.35	33.38	7.49	0.47	0.09			45.70	0.08	8.28
Cement clinker	22.50	4.86	66.30	0.83	3.43	0.02			0.31	0.79	0.96
Sodium sulfate								43.23	55.77	0.008	0.002

Experimental methods.

The dried water-granulated nickel slag was milled by using Φ500×500 test mill (mechanical activation), then it was mixed with activating agents according to pre-designed mixing ratio. The mixture and rod-milling sand were poured into a mortar stirring pot at a ratio of 1:4, and enough water was added to guarantee that the materials were under standard consistence. The materials were stirred for reasonable time according to the standards of GB/T50080-2002, then poured into a standard cement mortar mold (40mm×40mm×160mm). The mold was placed on cement mortar shaking table and the materials was compacted and molded by tamping vibration, then they were put into curing box and steam-cured under the temperature of 45±1℃ and relative humidity of 97±1%. When the curing time reached 24 hours, the specimen was demoulded. The demoulded specimen was continuously cured for 7 days and 28 days respectively in standard curing box, and then its strength was tested.

Results and discussion

Effect of mechanical activation on backfill materials strength.

Precious research showed that the hydration activity of cementitious material can be improved by increasing the specific surface area through mechanical grinding [10]. After the water-granulated nickel slag was ball-milled 40, 60, 80, 100, 120, 140, 160 and 180 min respectively, the specific surface area was 215, 320, 490, 565, 620, 705, 770 and 800 $m^2 \cdot kg^{-1}$. The milled slag was used as cementing agent and mixed with rod-milling sand at ratio of 1:4, then the mixture was made into backfill materials with slurry concentration of 79%. The backfill material was steam-cured for 24 hours and then cured for 7 days and 28 days in curing box. The strength of the backfill material was tested respectively and the results are shown in the Fig. 1.

Fig. 1 shows that the strength of the backfill material increases with the growth of the specific surface area. When the specific surface area of the slag increases from 490 $m^2 \cdot kg^{-1}$ to 620 $m^2 \cdot kg^{-1}$, the compression strength exhibits fastest growing. When the specific surface area is over 620 $m^2 \cdot kg^{-1}$, the compression strength grows slowly. Considering comprehensively strength of backfill material and grinding cost of the slag, the best grinding time should be 120 min (accordingly, the specific surface area is 620 $m^2 \cdot kg^{-1}$), and at that time the corresponding compression strength of the backfill material cured for 7d and 28d is 2.2 MPa and 3.3 MPa respectively.

Effect of chemical activity on the performance of backfill material.

The above grinding experiment shows that mechanical activity can activate the potential activity of water-granulated nickel slag to a certain extent, but not distinctively, and the strength of the backfill material can't meet the requirement of backfill operation. Therefore, further experiment on chemical activating was carried out. In order to explore the effect of activating agent on nickel slag backfill material, desulfurized gypsum and carbide slag were selected as the main activating agents and sodium sulfate and cement clinker as the supplementary activating agents.

Effect of the main activating agents on the strength of backfill material.

To determine the best ratio of desulfurized gypsum and carbide slag, the mass ratio of mechanical-activated slag, desulfuized gypsum and carbide slag, sodium sulfate, and cement clinker was set as 85:10:3:2 firstly, then classifying the ratio of desulfurized gypsum in main activating agent (desulfurized gypsum+carbide slag) into 0%, 20%, 50%, 80%, 100%. As shown in Fig. 2, when the ratio of the desulfurized gypsum in the main activating agent is 50%, that is, the quantity of the desulfurized gypsum and the carbide slag is the same, the strength of the backfill material reaches the highest point, and the compression strength of 7d and 28d is 2.2 MPa and 3.3 MPa respectively.

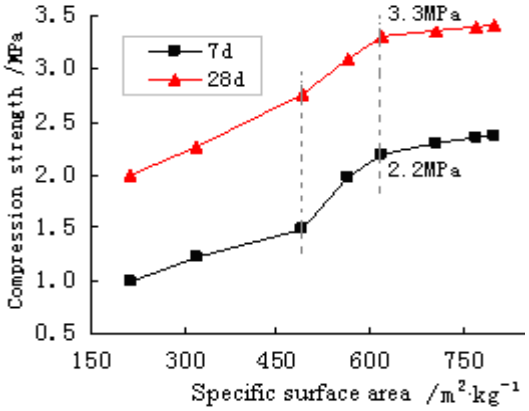


Fig. 1 Effect of specific surface area on compression strength of backfill materials

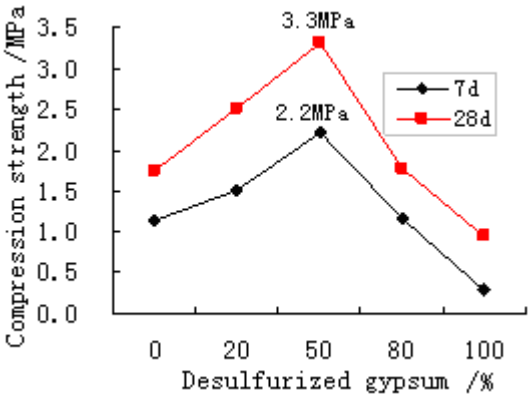


Fig.2 Effect of main activated agents on compression strength of backfill material

Effect of the supplementary activating agent on the strength of backfill material.

Based on abovementioned result that the best ratio of desulfuized gypsum and carbide slag is 1:1, further experiment was carried out to compare the effect of supplementary activating agent. Table 2 shows the proportions of the raw materials in each test scheme and the test result of the strength for each specimen is shown in Fig. 3, which shows that adding of Na_2SO_4 can apparently improve the strength of backfill material, and when the content of the slag is 81~85 wt%, the strength of the backfill materials reaches relatively higher point. From the viewpoint of making full use of water-granulated nickel slag, 85 wt% should be selected as the best proportion.

Table 2 Proportions of raw materials in each scheme [wt%]

Scheme No.	1	2	3	4	5	6	7	8	9
Mechanical-activated slag	85	81	77	73	69	81	77	73	69
Sodium sulfate	3	3	3	3	3				
Cement clinker	2	2	2	2	2	2	2	2	2
Desulfurized gypsum	5	7	9	11	13	7	9	11	13
Carbide slag	5	7	9	11	13	7	9	11	13

To examine the effect of cement clinker on the strength of backfill material, experiments were carried out that the proportions of the cement clinker in cementing raw materials was 2%, 3%, 4%, 5% and 6% respectively. The result shows that the compression and flexural strength of backfill material fluctuate with the increase of the dosage of cement clinker. In the aspect of saving cost by using less cement, the proper proportion of cement clinker in backfill material should be 2%.

Effect of slurry concentration on the strength of backfill material.

Based on the requirement that the flurry concentration of backfill material used in JGCL is 77%~79%, the mass ratio of mechanical-activated nickel slag, Na_2SO_4, cement clinker, desulfurized gypsum and carbide slag in cementing raw materials was set as 85:3:2:5:5, and backfill material with slurry concentration being 88%, 85%, 82%, 79%, 76% and 73% respectively were prepared. The test result of the strength of each backfill specimen is shown in Fig. 4.

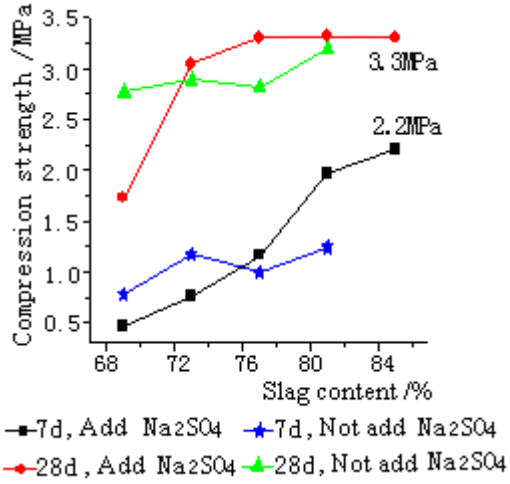


Fig.3 Effect of Na_2SO_4 on the strength of backfill material

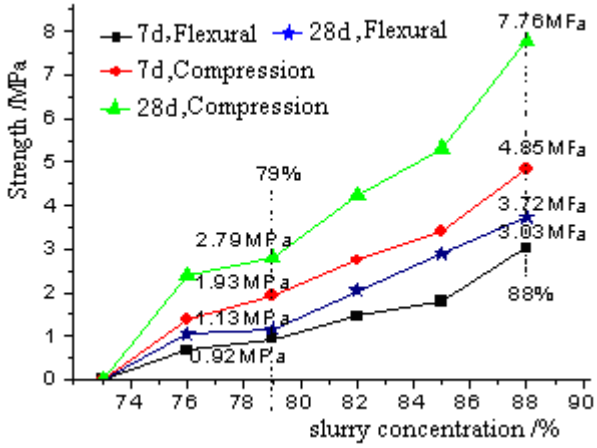


Fig.4 Effect of slurry concentration on strength of backfill material

It is shown in Fig. 4 that the strength of the backfill specimen increases with the growth of the slurry concentration, and when the slurry concentration reaches 79%, the highest point that was required, the flexural strength of the specimen cured for 7d and 28d reaches 0.92 MPa and 1.93 MPa respectively, and the compression strength reaches 1.13 MPa and 2.79 MPa respectively.

Effect of the fluidity of backfill material on its strength.

Backfill materials was prepared from raw materials whose mass ratio of the mechanical-activated nickel slag, Na_2SO_4, cement clinker, desulfurized gypsum and carbide slag was set as 85:3:2:5:5. The fluidity and strength were measured and then compared with the backfill material prepared by using Portland cement as cementitious material. Considering that water-reducing agent has an effect of improving slurry fluidity, a contrast experiment was carried out by adding high efficiency water-reducing agent which accounts for 0.156% of the total cementitious material. The comparison result is shown in Fig. 5.

Fig.5 shows that when the slurry concentration is 79~80%, the fluidity of the backfill material prepared by using mechanical-activated nickel slag is apparently higher than that of the backfill material using cement as cementitious agent. While the addition of high-efficiency water-reducing agent has greatly increased the fluidity of slag-based backfill materials, and the fluidity of slag-based backfill materials with slurry concentration of 82% is similar to that of the cement-based backfill materials. This method not only improves fluidity of the slurry, but also helps to improve the strength of the backfill material. The test results of strength show that among three backfill materials with same fluidity (390mm), the strength of the cement-based backfill material is the highest, the slag-based backfill material

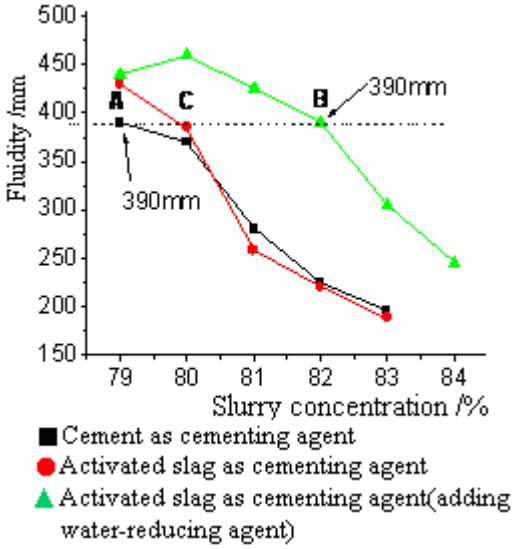


Fig. 5 Relation between slurry concentration and fluidity

with addition of high efficiency water-reducing agent takes the second place, and the strength of slag-based backfill material is the lowest. Although the strength of the slag-based backfill material prepared by adding high efficiency water-reducing agent is lower than that of the cement-based backfill material, its compression strength cured for 7d and 28d has reaches 3.93 MPa and 7.94 MPa respectively, which already meets the requirement of backfill operation [11].

Hydration products and hydration mechanism.

Fig. 6 is the SEM images of the slag-based backfill material that was hydrated for 28d. It can be seen that lots of floccular hydrated products have generated on and around the calcium-magnesium olivine crystals. In the hydration process, these substances lapped and adhered with each other to form irregular cementitious structure. The EDS spectrum of the B section in Fig.6b shows that the cementitious material consists of $CaO{\cdot}MgO{\cdot}SiO_2$ and little amount of Al_2O_3 and Na_2O, etc. These calcium silicates (aluminates) or magnesium silicates (aluminates) are the hydrated product of the water-granulated nickel slag under the action of activators.

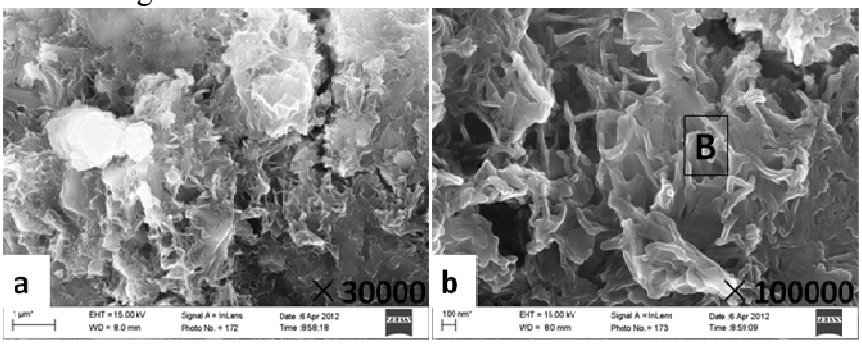


Fig.6 SEM images of water-granulated slag cementitious material hydrated for 28d

At the early stage of hydration, the C_3A and C_4AF from cement clinker reacted with gypsum ($CaSO_4{\cdot}2H_2O$) to form ettringite (AFt) and $Ca(OH)_2$. Due to the small amount of cement clinker, only little amount of AFt was produced in the reaction. Together with activating agents such as carbide slag, Na_2SO_4, and desulfurized gypsum, the $Ca(OH)_2$ produced in the reaction would have further reaction with the water-granulated nickel slag.

Carbide slag provided sufficient $Ca(OH)_2$ at the early stage of the hydrated reaction, which guaranteed the high concentration of OH^- in the system. The addition of sodium sulfate greatly affected dissolution of carbide slag, which was exhibited by the formation of gypsum after the reaction of sodium sulfate with calcium ion from carbide slag. Thus, the carbide slag was dissolved and the OH^- concentration in the system increased quickly, and as a result, silicate or aluminosilicate glass was dissolved steadily under the erosion of OH^-. Firstly, due to the absorption of OH^- by the Ca^{2+} and Mg^{2+} distributing on the surface of the silicate glass, some hydroxides formed and the surface structure of water-granulated nickel slag was destroyed. Secondly, because the chemical bonds such as Ca-O, Mg-O in the glass network were much weaker than that of Si-O, Al-O, the OH^- could have replacement reaction with Ca^{2+} and Mg^{2+}, which would destroy the network structure of the glass dominated by oxygen-silicon tetrahedron and oxygen-aluminum tetrahedron. Finally, with continuous depolymerization of the glass structure, complex reaction between various kinds of ions took place and the hydrated products formed. These products gradually nucleated, grew up, and eventually lapped with each other to form irregular network. In addition, under the erosion of OH^-, the Si-O-Al and Al-O-Al in the glass structure would gradually release Al ions, which would react with Ca^{2+} and SO_4^{2-} ions coming from sulfate activators to form ettringite ($3CaO{\cdot}Al_2O_3{\cdot}3CaSO_4{\cdot}32H_2O$). In the forming process of ettringite, the irons such as Na, Mg, Si would also participate in the reaction and form quasi-ettringite phase. Due to the participation of large amount of Mg in the reaction system, the final structure of hydrated calcium silicate would have large amount of Mg ions. Since the radius of the Mg ion is nearly equal to that of Ca ion, it is believed that the cementing performance of this kind of hydrated product is similar to that of hydrated calcium silicate, which would mainly affect the later strength of the slag-based cementitious material.

Conclusions

Mechanical activation result shows that the best specific surface area of the water-granulated nickel slag should be 620 $m^2 \cdot kg^{-1}$, and the effect of excessive grinding is not so distinctively. Activators such as desulfurized gypsum, carbide slag, sodium sulfate and cement clinker help to activate the activity of the water-granulated nickel slag. Under the condition that the dosage of nickel slag accounts for 85% in the cementitious material, the best mass ratio of these activators is 5%, 5%, 3% and 2% respectively. Adding of PC high efficiency water-reducing agent which accounts for 0.156% of the total cementitious material helps to improve performance of backfill slurry. Backfill material prepared by using activated-slag as cementitious material can meet not only the fluidity requirement under special slurry concentration, but also the strength indexes required by JGCL.

Acknowledgements

This work was financially supported by the National High Technology Research and Development Program of China (No. 2012AA062406).

References

[1] Li W, Zhou X, Liao M Q, et al. Research and practice on replacement materials for cementing backfilling. Mining technology, 2011, 11(3): 19-23.

[2] Zhu L P, Ni W, Huang D, et al. Whole-tailings backfilling materials with fly ash. J Univ Sci Technol Beijing, 2011, 33(10): 1190-1194.

[3] Zhao C Q, Hu N L. Development and application of cementing filling materials. Gold, 2008, 29(1): 25-28.

[4] Sun Junmin, Chen Ping. Resourcing utilization of high alumina fly ash. Advanced Materials Research, 2013, 652-654: 2570-2573.

[5] Sadique Monower, Al-Nageim Hassan, Atherton William, et al. A laboratory study for full cement replacement by fly ash and silica fume. Magazine of Concrete Research, 2012, 64(12): 1135-1139.

[6] Ahmaruzzaman M. A review on utilization of fly ash. Prog Energy Combust Sci, 2010,36: 327.

[7] Donatello Shane, Fernández-Jimenez Ana. Very high volume fly ash cements. Early age hydration study using Na 2SO4 as an activator. J Am Ceram Soc, 2013, 96(3): 900-904.

[8] Yi Z L, Sun H H, Wei X Q, et al. Iron ore tailings used for the preparation of cementitious material by compound thermal activation. Int J Min Met Mater, 2009, 16(3): 355-358.

[9] Siddique Rafat, Bennacer Rachid. Use of iron and steel industry by-product (GGBS) in cement paste and mortar. Resources, Conservation and Recycling, 2012, 69(12): 29-31.

[10] Ki Yong Ann, Jaeh Wan Kim，Development of cement-free concrete using finely grained slag for portland cement，Applied Mechanics and Materials, 2013, 316-317: 1063-1067.

[11] Zhang H J, Li Y, Zhao Y X. Study on paste filling using fly ash to replace few cement. Nonferrous Metals(Mining Section), 2009, 61(3): 1-4.

Advanced Materials Research Vol. 936 (2014) pp 1630-1634
© (2014) Trans Tech Publications, Switzerland
doi:10.4028/www.scientific.net/AMR.936.1630

Preparation and Characterization of Plasma Treated Melt-blown Polypropylene Nonwovens Grafted with Acrylic Acid

Wang Dan[1,a], Xu Qing-Yan[1,b], Chen Yue-Jun[1,c], Xu Hua-Jun[1,d], Wang Yi-Min[2,e], Wang Yan-Ping[2,f]

[1]College of Material Science and Engineering, Donghua University, Shanghai 201620, China

[2]State Key Laboratory for Modification of Chemical Fibers and Polymer Materials, Shanghai 201620, China

[a]wangdan0211@126.com, [b]albeexu@hotmail.com, [c]chyj897@163.com, [d]huajun87@hotmail.com, [e]ymw@dhu.edu.cn, [f]wyp@dhu.edu.cn

Keywords: polypropylene; melt-blown nonwoven fabric; plasma; hydrophilicity

Abstract: The melt-blown polypropylene nonwoven fabric plasma treated to graft with acrylic acid has been investigated by FTIR, SEM and Contact Angle Determinator respectively. It was found that after grafting with acrylic acid the wettability of the PP nonwoven fabric could be significantly improved from 140.9°to almost 0°in a short period of time by plasma treatment and increased to 110.6° and 133.2° after 20 days and 40 days respectively. However, the wettability of acrylic acid grafted PP nonwoven fabric could be improved to 72.9°with a permanent hydrophilic behavior.

Introduction

Recently, polypropylene fiber has drawn great attention from the scientific research and industry for its light, high strength, good flexibility, corrosion resistance, good filtering performance, low cost, and has become one of the most developing products in the field of non-woven fabric[1,2]. Polypropylene fiber has not only certain characteristics of high crystallization rate, none-hydrophilic group, but also the shape of circular, dense structure, lacking of microporous and crannies, which limit the scope of application of the polypropylene fibers. Since the hydrophilicity of untreated melt-blown PP nonwoven fabric is poor and difficult to be infiltrated by an aqueous solution, the effective area of the filter material is reduced, which results in slowing filtration rate, extending the filtration time and reducing the efficiency[3]. Therefore, the surface modification, for example, the introduction of a hydrophilic group, etc., is a effective way to permanently alter the wetting properties of the fibers[4]. In different surface modification techniques, plasma treatment is considered the most effective method[5-7]. In this article, the surface of PP nonwoven fabric was grafted with acrylic acid using the method of He plasma to change its surface properties. The surface structure, morphology and surface properties of the PP nonwoven fabric before and after grafting were investigated systematically.

Experimental

Materials and Equipments

The raw material is melt-blown PP nonwoven fabric with a planar density of 45-55g/m^2 (laboratory preparation). The chemical reagent is acrylic acid (type Q/CYD2848-2007) from Sinopharm Chemical Reagent Co., Ltd. The equipments are the Cold plasma modification treatment Instrument(SY-I type 500W RF power source from ChangZhou ZhongKe ChangTai Plasma Technology Co., Ltd), Contact angle determinator(type OCA40Micro from German Dataphysics Co.), Scanning electron microscopy(type JSM-5600LV from Japan JEOL Co.), Fourier transform infrared-Raman spectrometer(type Nicolet Nexus 670+Raman Module from USA Thermo Fisher Co.).

Plasma Treating

The PP nonwoven fabric was grafted with acrylic acid in a method of atmospheric liquid phase in this article. Before starting the plasma treating, the PP nonwoven fabric was firstly cleaned with distilled water, placed in 70% ethanol for 24 hours, then cleaned with distilled water three times and dried for back up. After that, the PP nonwoven fabric was cut into 4×7(cm) rectangular cloth strips to hang in the cold plasma processing instrument, and then maintained the chamber pressure at about 20Pa with the high frequency power of 100w to supply the plasma treatment for 8min. The treated samples were left to stand in air for 30min, so that the free radical on the PP nonwoven fabric surface was reacted with oxygen, converted to a relatively stable peroxide group.

Graft Polymerization

The activated PP nonwoven fabric was immersed in 40% concentration of the acrylic acid monomer solution, heated to the 50℃ using water bath for 6 hours. Grafted PP nonwoven fabric was ultrasonic cleaned several times with distilled water, and then washed in 60℃ distilled water for 6 hours. The purified samples were natural dried in room temperature and stored for further analysis.

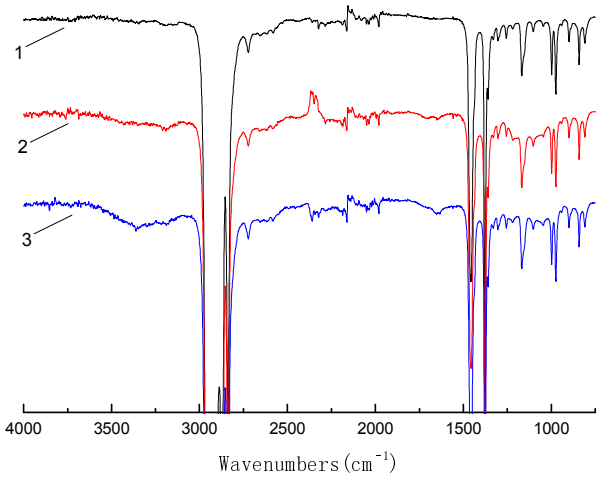
Characterization

The PP nonwoven fabric was cut into 1×5(cm) and fixed on the German Dataphysics company OCA40Micro video contact angle tester. Each sample was measured 15 points derived by software, the average value of them was the contact angle of the samples. The PP nonwoven fabric surface was observed by scanning electron microscopy. The study of the molecular structure and chemical bonding change of the PP nonwoven fabric before and after the plasma treatment can be characted by Fourier transform infrared spectroscopy with the ATR analysis within scanning range of 4000-400cm^{-1} .

Results and Discussions

Ftir Analysis of the PP Nonwoven Fabric

The surface structure of PP nonwoven fabric was observed by infrared spectroscopy before and after plasma treatment, as shown in Fig. 3. The C=O characteristic absorption peak was located at 1750cm^{-1} in curve 2 for plasma treated PP nonwoven fabric. There was also a wide absorption band in 3500~3000 cm^{-1} region corresponding to the -OH stretching vibration peak, because the active groups reacted with the oxygen in the air to form groups such as -OH, C=O. In curve 3, it appeared a characteristic absorption peak of the ester bond at 1800~1600 cm^{-1} and a wide absorption peak in the region of 3500~3000 cm^{-1} corresponding to the -OH stretching vibration. However, the untreated PP non-woven fabric on the infrared spectra did not show any above absorption peak in curve 1. The experimental results show that the PP nonwoven fabric has been successfully grafted with acrylic acid.

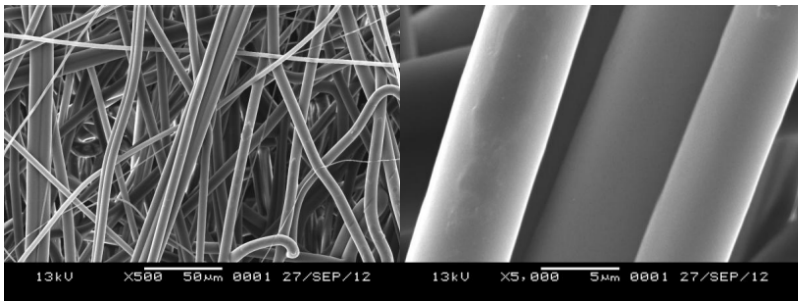


1-Untreated; 2-Plasma Treated; 3-Acrylic Graft Treated

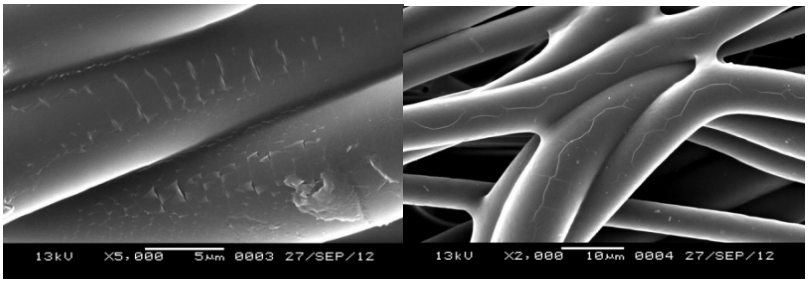
Fig. 1 Ftir Spectra of PP Nonwoven Fabric

Sem Analysis of the PP Nonwoven Fabric

The surface morphology of the PP nonwoven fabric was shown in Fig. 2. Before helium plasma treatment, the original sample of the PP nonwoven fabric was smooth, as presented in Fig. 2 (a) and (b). However, after helium plasma activation etching, the surface of the PP nonwoven fabric fibers was etched and cracked, and as shown in Fig.2 (c) , this is formed because the surface effect by the physical and chemical reactions. The etching of the fiber surface played a positive role in improving the hydrophilicity of the PP nonwoven fabric. The surface morphology of the PP nonwoven fabric grafted acrylic acid was shown in Fig.2 (d). It was no longer smooth and just liked coating with a layer covering. The mutual adhesion between the fibers appearing the "bridging" phenomenon indicated that the PP nonwoven fabric surface was successfully grafted acrylic.



a. The Original Sample (X500) b. The Original Sample (X5000)



c. The Plasma Treated Sample (X5000) d. The Grafted Sample (X2000)

Fig. 2 The Sem Image of The PP Nonwoven Fabric

Changes of the PP Nonwoven Fabric Hydrophilicity

The surface contact angles of PP nonwoven fabric before and after modification were shown in Fig. 1.The surface contact angle of the untreated sample was 140.9° (Fig.1(a)), plasma treated sample was almost 0° (Fig. 1(b)) , and acrylic acid grafted sample was 72.9° (Fig.1(c)). After plasma treatment, PP nonwoven fabric surface was rich in a number of reactive groups, so that the surface contact angle changed to almost 0° . In the grafting process, the activated surface of the PP nonwoven fabric had only a small amount of effective group grafting with acrylic monomer and most of the groups were disappeared. Thereby, the contact angle of the grafting sample was larger than the one only plasma treated sample.

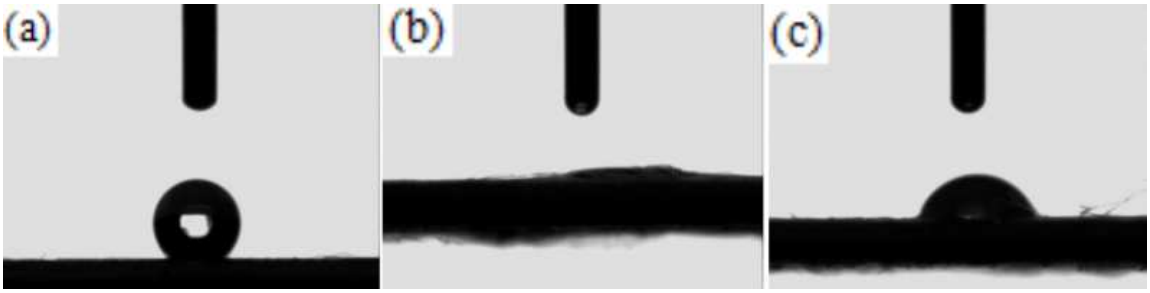


Fig. 3 The Surface Contact Angles of PP Nonwoven Fabric Before And After Modification

(a) Untreated; (b) Plasma Treated; (c) Acrylic Acid Grafted

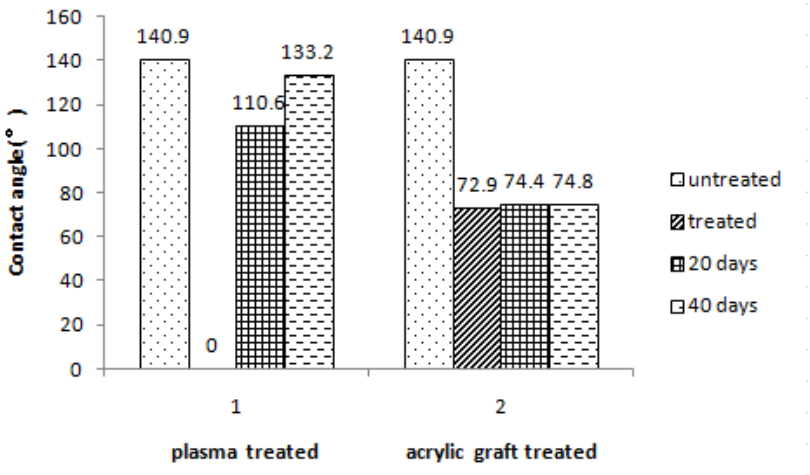


Fig. 4 The Changes Of Contact Angles Before And After Modification

Although the plasma treatment can increase material hydrophilicity, but after a period of time, the hydrophilicity of PP nonwoven fabric will deteriorate, as shown in Fig. 4. After the plasma treatment, PP non-woven fabric reduced the contact angle to 0°, it increased to 110.6° and 133.2° after 20 days and 40 days respectively. But the hydrophilicity of acrylic acid grafted PP nonwoven fabric was stable and non-aging. This is because the volume of the molecular chains of polyacrylic acid is much greater than the one introducing polar groups by the plasma treatment on the surface. They are difficult to flip and migrate in the PP nonwoven fabric but reside on the nonwoven fabric surface stably to achieve a permanent hydrophilic.

Conclusion

(1) After plasma treatment modification, the surface structure of PP nonwoven fabric has been changed and the surface morphology of the PP nonwoven fabric appeared the "bridging" phenomenon. The results indicated that the PP nonwoven fabric surface was successfully grafted with acrylic.

(2) The surface contact angles of PP nonwoven fabric were significantly improved from 140.9°to almost 0°in a short period of time after plasma treatment and the grafting sample was larger than the one only plasma treated sample. However, the hydrophilicity of grafted PP nonwoven fabric was stable and the contact angle of the surface did not change with time.

References

[1] R.R. Hegde, G.S. Bhat. Nanopartical effects on structure and properties of polypropylene meltblown webs. Journal of Applied Polymer Science, 2010, 115 (2): 1062-1063

[2] R.G. Zhao, L.C. Wadsworth. Attenuating PP/PET bicomponent melt-blown microfibers. Polymer Engineering and Science, 2003, 43(2): 463-496

[3] J.N. Lai, B. Sunderland, J.M. Xue, et al. Study on hydrophilicity of polymer surfaces improved by plasma treatment. Applied Surface Science, 2006, 252: 3375-3379

[4] C.L. Li, C.Y. Tu. Surface modification and adhesion improvement of expanded poly(tetrafluoroethylene) films by plasma graft polymerization. Surface and Coatings Technology, 2005: 10-17

[5] L. Carrino, W. Polini, L. Sorrentino. Ageing time of wettability on polypropylene surfaces processed by cold plasma. Journal of Materials Processing Technology, 2004(153 /154): 519-525

[6] B. Jaleh., P. Parvin., P. Wanichapichart., et al. Induced super hydrophilicity due to surface modification of polypropylene membrane treated by O_2 plasma. Applied Surface Science, 2010, 257(5): 1655-1659

[7] K.N. Pandiyaraj, V. Selvarajan, R.R. Deshmukh. Modification of surface properties of polypropylene (PP) film using DC glow discharge air plasma. Applied Surface Science, 2009, 255(7): 3965-3971

Advanced Materials Research Vol. 936 (2014) pp 1635-1640
© (2014) Trans Tech Publications, Switzerland
doi:10.4028/www.scientific.net/AMR.936.1635

Microstructure and Mechanical Properties of High-entropy Alloys CoCrFeNiAl by Welding

Lang Cui [1,a *], Bing Ma [1,b], Shengqiang Feng [1,c] and Xiuling Wang[1,d]

[1]Ningbo Branch of China Academy of Ordnance Science, Ningbo 315103, China

[a]cl040903@sina.com, [b]mabing_008@hotmail.com, [c]fsq7980@hotmail.com, [d]xlwang@163.com

Keyword: Multiple principal elements, High entropy alloy, Microstructure, Mechanical properties

Abstract: Five common elements Co, Cr, Fe, Ni and Al were selected, and CoCrFeNiAl was prepared by arc-melting. The microstructure and mechanical properties after spot welding were studied. The results show that the cast microstructure of high entropy alloy CoCrFeNiAl is relatively uniform with a dendritic morphology. The heat is inversely proportional with the alloy grain sizes. The greater the heat is, the smaller the grain size is, which leads to the higher hardness and more uniform tissue. But there is a critical value of the heat(H_{crit}) in spot welding. When H_{actu}(actual heat) exceeds H_{crit}, it will adversely affect the performance, resulting in crack, splash and other defects.

Introduction

For thousands of years the development of practical alloy systems has been based mainly on one principal element as the matrix, as in iron-based, copper-based, and aluminum-based alloys, limiting the number of applicable alloy systems, even though a substantial amount of other elements is incorporated for property/processing enhancement [1,2]. Since the 1970s, metal-matrix composites and intermetallic compounds have attracted much attention [3-4]. During this time, new processing technologies such as rapid solidification and mechanical alloying have become popular [5-7]. In 1995, Taiwan scholar Ye Wei, etc. [8] were the first to break the traditional concept of the material design, a new alloy design concept, namely high entropy alloys. Due to the high entropy alloy has many traditional alloys do not have the excellent characteristics, such as through appropriate alloy formulation design, availability of high hardness, high work hardening, softening temperature, high temperature oxidation resistance, corrosion resistance and other characteristics of high portfolio therefore have great potential[9-12].

Spot welding is the method of assembled the welded into the lap joints, pressed between the two electrodes, using the thermal of resistance melt base metal, forming solder joints. With high structural strength, joint good sealing, saving material, reduce the structural weight, production efficiency, therefore, the applications of spot welding in the material increasingly have been important. Previous studies were based on microstructure, mechanical properties of six element or more main element of high entropy alloys, while the research of five element of high entropy alloy welding properties was few, so in this article through the spot welding two identical high-entropy alloys, the spot welding heat was changed to study the microstructure and mechanical properties.

Experimental

Alloys with high purity Al, Co, Cr, Fe, Ni were taken as a raw material in an argon atmosphere. The vacuum arc was employed to melting alloy. The alloy was cut into 9 equal parts, each spot welding 2 equal parts, the remaining parts of a 1 reference, each specification is 30mm × 5mm × 1.5mm, spot welding parameters are shown in table 1. Optional DN-16 type spot welder for spot

welding, spot welds by grinding, polishing, etching, the morphology was observed under the microscope, and then microhardness was measured by the A-200-type hardness meter GALILEO , with applied load of 300N.

TABLE 1 WELDING PARAMETERS

Sample	heat	pressing time(s)	power on time(s)	cooling time(s)	maintenance time(s)	off time(s)
1	0	0	0	0	0	0
2	0.052Q	1	0.6	0.4	0.4	1
3	0.069Q	1	0.6	0.4	0.4	1
4	0.101Q	1	0.6	0.4	0.4	1
5	0.153Q	1	0.6	0.4	0.4	1

Results

Microstructure

Fig.1 is the microstructure photograph of sample 1 (unwelded). It can be seen that alloys original tissue is uniform, a single structure, and a typical dendritic phase can be observed.

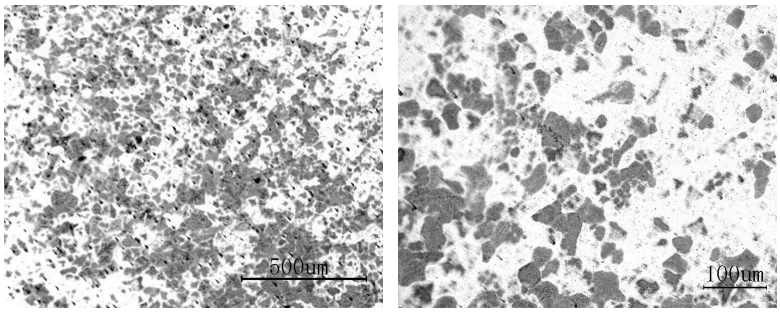
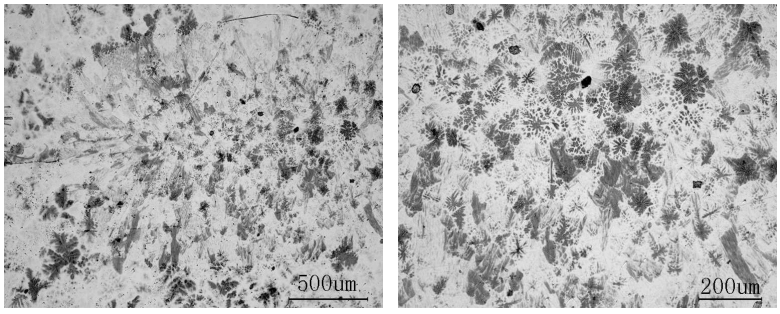
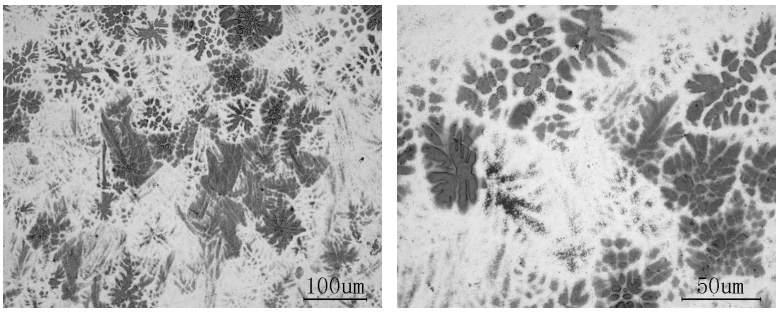


Fig.1 Microstructure of Sample 1

Fig.2, Fig.3 and Fig.4 are the photomicrograph of the sample 2, 3 and 4 after welding, respectively. Fig.2(a) and Fig.3(a) indicate the tissue of weld and fusion zone. (b), (c) and (d) represent the fusion zone tissue. The fusion zone grain size is less than elsewhere, from the Fig.(a), respectively. It can be seen that welding can refine the grains, enabling organizations to be more uniform, and has a certain size circular heat-affected zone, so the heat is the heir round outward diffusion of heat.



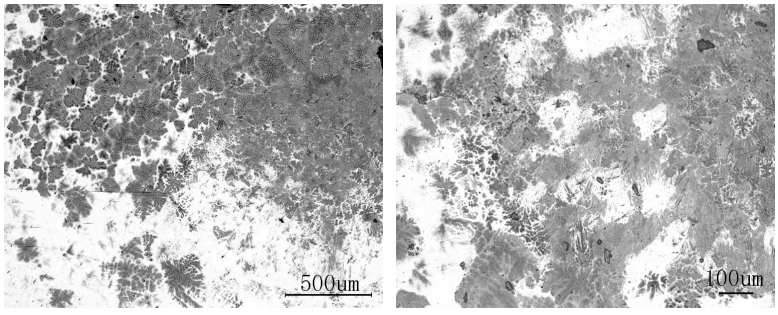
(a) 50X (b) 100X



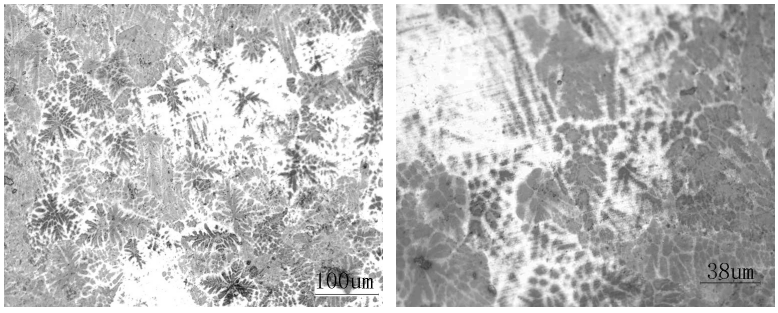
(c) 200X (d) 500X

Fig.2 Photomicrograph of Sample 2 after Welding

The alloy cracks in the nugget from Fig.4 (a). The deformations of welded joints under the action of thermal result in non-uniform stress and strain fields are uneven. In the welding process, the welding heat is too large, resulting in metal melting and excessive expansion. Nugget will be under pressure, in the influence of low temperature base material near the electrode and the molten metal b and d shows an image fusion zone, c shows the grain around the weld. It can be seen dendritic grain in all figures, and grain size of the fusion zone is much smaller than elsewhere, which can be drawn, welded produce a certain size heat-affected zone, the closer the weld, the greater the intensity and the smaller size of grains.

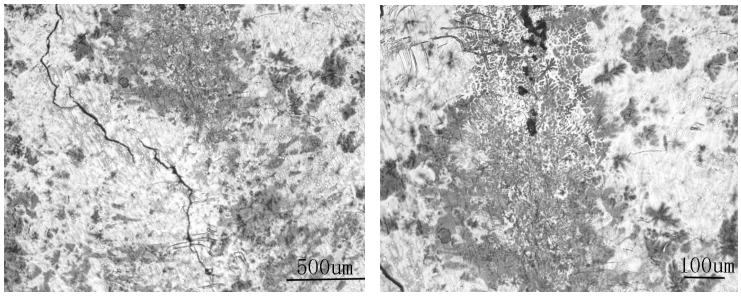


(a) 50X (b) 100X

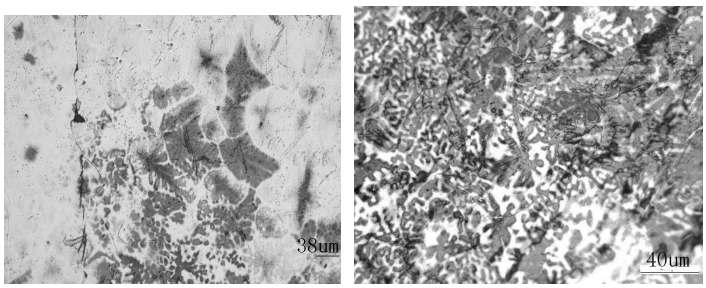


(c) 200X (d) 500X

Fig.3 Photomicrograph of Sample 3 after welding



(a) 50X (b) 100X



(c) 200X (d) 500X

Fig.4 Photomicrograph of Sample 4 after Welding

Fig.5 is the image of sample 5 after welding. The welding heat is too high, causing splashing, which illustrates there is a critical value of the heat(H_{crit}) in spot welding. When H_{actu}(actual heat) exceeds H_{crit}, it will adversely affect the performance.



Fig.5 Sample 5 after Welding

Dendritic grain size is shown in Fig.6. a and b are the grain size of horizontal and vertical, respectively. Four samples grain size were measured and draw the diagram of grain size versus heat, as shown in Fig.7(a) and Fig7(b). That is to say, the grain size reduces with the increase of heat.

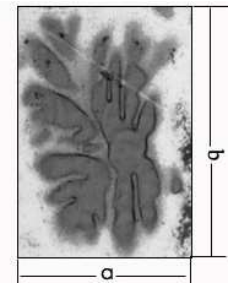
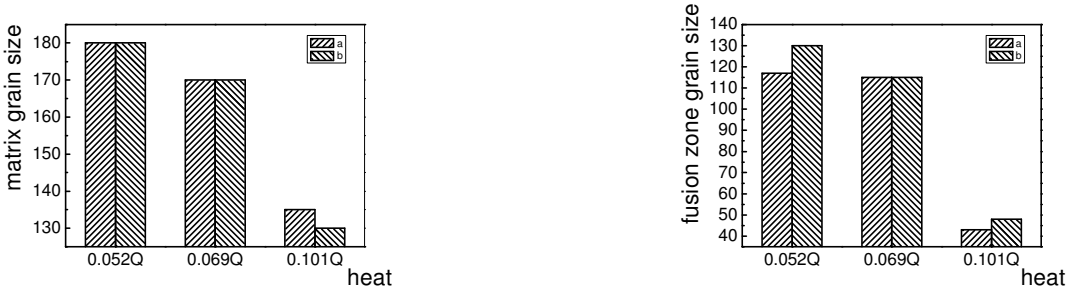


Fig.6 Grain size



(a) matrix grain size versus heat (b) fusion zone grain size versus heat

Fig.7 Grain Size Versus Heat

Mechanical Properties

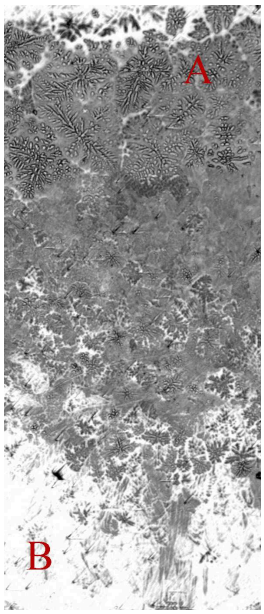


Fig.8 Photomicrograph of Sample after welding

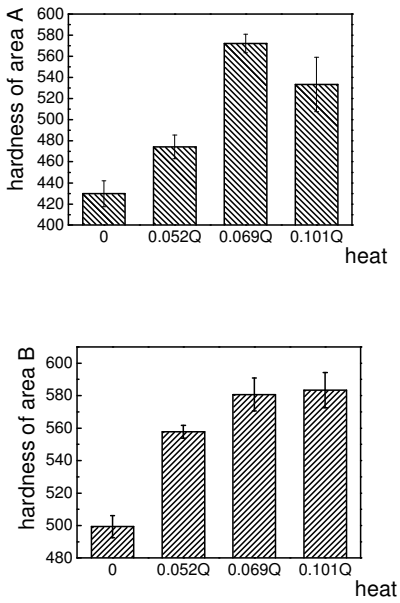


Fig.9 Hardness versus heat

As is show in the Fig.8, A is a branched grain of gray body region, and B is the matrix white region. A and B regions between the hardness of the heat are shown in fig9. Alloy weld zone hardness and heat relationship was shown in Fig.10. The hardness is inversely proportional with the heat.

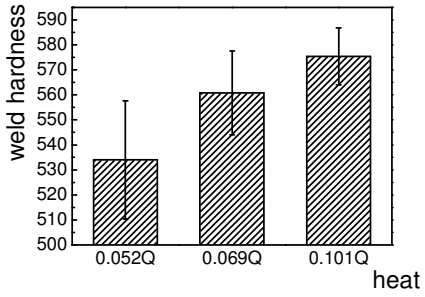


Fig.10 Weld Hardness Versus Heat

Spot welding is a typical transient heat transfer with internal heat source problems, dominated by thermal conduction when weldments obtained thermal. Transient nonlinear heat conduction equation is:

$$cp\frac{\partial T}{\partial t}=\frac{\partial}{\partial x}\left(k_x\frac{\partial T}{\partial x}\right)+\frac{\partial}{\partial y}\left(k_y\frac{\partial T}{\partial y}\right)+\frac{\partial}{\partial z}\left(k_z\frac{\partial T}{\partial z}\right)+Q$$

c --specific heat capacity of the material(J/Kg·K);
p--density;
T --temperature field distribution function;
t--time;
k_x, k_y, k_z--thermal conductivity of x, y, z,in this experiment k_z is 0;
Q--internal heat source

Cooling rate V($\frac{\partial T}{\partial t}$) is as Q increases by the formula, the cooling rate is greater, the smaller the grain size,so the grain size is decreased with the increase of Q.

According to Hall Page formula：

$б_S=б_0+Kd^{-1/2}$

Where $б_s$ represents the yield strength;$б_0$ expressed intragranular resistance to deformation, the equivalent of a great single crystal yield strength; K reflects the impact of grain boundaries on the deformation coefficient is the average grain diameter. Conclusions it can be concluded that the smaller the grain size, the greater the yield strength, corresponding to the higher hardness of the alloy from the formula, and consistent with experimental data.

Conclusions

CoCrFeNiAl was prepared by arc-melting, the microstructure and mechanical properties after spot welding were studied. The results are as follows:

(1) The cast microstructure of high entropy alloy CoCrFeNiAl is relatively uniform，with a dendritic morphology.

(2) The hardness of the alloy is proportional with the welding heat, because the heat is inversely proportional with the alloy grain sizes, the greater the heat, the grain size is smaller, the higher the hardness and more uniform tissue.

(3) There is a critical value of the heat(H_{crit}) in spot welding. When H_{actu}(actual heat) exceeds H_{crit}, it will adversely affect the performance, resulting in crack, splash and other defects.

References

[1] J. R. Davis (Ed.), Metals Handbook, 10th edn., Vol. 1,ASM International, Metals Park, OH, 1990.

[2] J. R. Davis (Ed.), Metals Handbook, 10th edn., Vol. 2,ASM International, Metals Park, OH, 1990.

[3] D. J. Lloyd, Ch. 13 in Composites Engineering Handbook(Ed: P. K. Mallick), Marcel Dekker, Inc., NY 1997.

[4] J. H. Westbrook, in Intermetallic Compounds: Principles and Practice (Eds: J. H. Westbrook, R. L. Fleischer),Wiley, NY 1995.

[5] J. R. Davis (Ed.), Metals Handbook, 10th edn., Vol. 7,ASM International, Metals Park, OH, 1990.

[6] G. He, J. Eckert, W. G. L ser, L. Schultz, Nature 2003, 2,33.

[7] A. Takeuchi, A. Inoue, Mater. Trans.: JIM 2000, 41, 1372.

[8] Yeh J W, Chen S K , Lin S J. Advanced Engineering Materials, J. 2004, 6(5): 299

[9] Liu Yuan , Li Yanxiang, Chen Xiang et al. Materials Review, J. 2006, 20(4): 4

[10] Jien-Wei YEH.Recent Progress in High Entropy Alloys.Ann.Chim.Sci.Mat.2006，31(6):633-648.

[11] Chin-You HSU, Jien-Wei Yeh,Swe-Kai Chen and Tao-Tsung Shun. Wear Resistance and High-Temperature Compression Strength of fcc CuCoNICrAl$_{0.5}$Fe Alloy with Boron Addition. Metall and Mater Trans A. 2004，35A:1465-1469.

[12] Jien-Wei Yeh, Swe-Kai Chen, Jon-YIew Gan et al. Formation of Simple Crystal Structures in Cu-Co-Ni-Cr-AI-Fe-Ti-V Alloys with Multiprincipal Metallic Elements. Metall and Mater TransA.2004，35A:2533-2536.

Advanced Materials Research Vol. 936 (2014) pp 1641-1646
© (2014) Trans Tech Publications, Switzerland
doi:10.4028/www.scientific.net/AMR.936.1641

Microstructure Refinement and Crack Initiation in the Forging Process

Wenlong Zhao[1, a], Qingxian Ma[1, b]

[1]Department of Mechanical Engineering, Tsinghua University, Beijing, 100084, China

[a]zwl2007010475@163.com, [b]maqxdme@mail.tsinghua.edu.cn

Keywords: Heavy forging, Forging, Microstructure refinement, Crack.

Abstract. In this paper, the type and morphology of defects in heavy ingots were detected mainly on the basis of experimental results, which were obtained by metallographic analysis of the materials dissected from one 380 ton 30Cr2Ni4MoV ingot. Then the evolution of typical defects in the forging process was investigated at temperatures ranging from 900˚C to 1200˚C and reduction ratios ranging from 0% to 50%. It was shown that coarse grains and inclusions were the main types of defects. In the forging process, the refinement of coarse grains and crack initiation at inclusions were summarized respectively with respect to temperature, reduction ratio and multi-pass forging. The microstructure evolution of 30Cr2Ni4MoV steel is accompanied by the formation of fine grains on condition that multi-pass forging or an optimal reduction ratio of 10% is adopted at temperatures lower than 1000˚C, while temperatures higher than 1100˚C can lead up to coarse grains. Besides, cracks originate from CaO and FeS inclusions at 900˚C and 1000˚C related to intense shear stress and melting of the FeS-Fe eutectics distributing along grain boundaries.

Introduction

In spite of the high strength and good ductility, 30Cr2Ni4MoV steel is widely used as the turbine rotor material in China due to its ductile-brittle transition temperature below the room temperature when compared with other structural steel [1,2]. However, as the volume and weight of a steel ingot increase gradually, more and more attention is turned to the elimination of casting defects existing in heavy ingots instead of the improvement of material itself in the technical field of heavy forgings. Although the quantity, distribution and size of casting defects are kept within a certain range by the advanced casting technology, they cannot be removed completely. Therefore, forging becomes the effective material processing method to control casting defects, such as coarse grain, non-metallic inclusion, segregation, shrinkage and loose et al. to meet the required standard, which ensures the service performance of a heavy forging not to be seriously affected [3,4].

In order to prevent casting defects from being the potential hazards affecting the mechanical properties of a heavy forging, details on the types and morphology of casting defects were discussed firstly in this paper by dissecting one 380 ton ingot. Then the evolution in the forging process of the typical defects was investigated by means of thermal experiment and numerical simulation conducted on the platform of Deform-3D. This research aimed at providing a theoretical framework for the microstructure control and property improvement of heavy forgings.

Experimental Material and Procedures

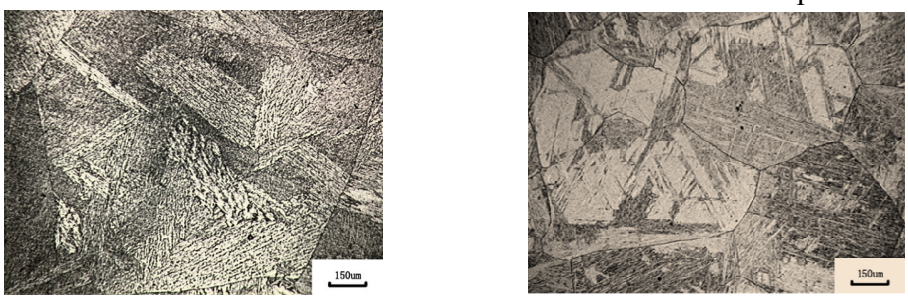
The material used in the experiment was 30Cr2Ni4MoV steel, which was dissected from the nozzle of one heavy ingot for a 1000MW low-pressure turbine rotor. The main chemical compositions and contents are (wt. %) C 0.280, Cr 1.720, Ni 3.630, Mo 0.410, V 0.110, Mn 0.020, Si 0.010, P 0.003, S 0.003 and Fe (balance).

To detect the defects of cast ingots, a large number of specimens along different orientations of the ingot were prepared after grinding and polishing, and then etched with the saturated picric acid solution for recording the optical micrographs. To explore the evolution of casting defects in the forging process, some cylindrical specimens were machined with a diameter of 30mm and a height of 45mm. Then the specimens were heated to 900˚C, 1000˚C, 1100˚C, 1200˚C and compressed at the reduction ratio of 0%, 10%, 20%, 30%, 40%, 50% respectively. After deformation, the specimens were quenched into cold water immediately to keep the austenite structure. Finally, all the specimens were sliced along the axial section and followed by grinding, polishing and etching.

The types and Morphology of Typical Casting Defects

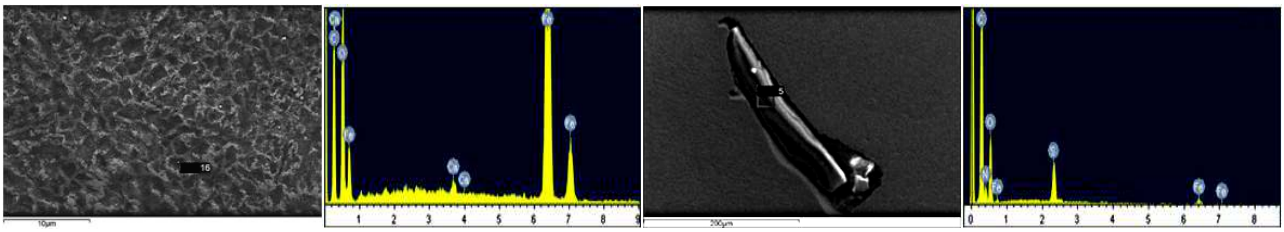
Optical microscopic observations of the dissected specimens show that coarse grains and non-metallic inclusions are the typical defects in the 30Cr2Ni4MoV steel ingot. Coarse grains primarily consist of columnar and equiaxed grains, as shown in Fig. 1. Foreign inclusion CaO and endogenous inclusion FeS are the main types of non-metallic inclusions, as shown in Fig. 2.

The mechanical properties of heavy forgings can be seriously affected by coarse grains. In addition, the dendritic segregation which deteriorates the performance of steel usually appears in the columnar zone of a casting. Cracks originating from inclusions are one of the main causes of forging scrap. In case the forging conditions are not controlled properly, the size of coarse grains may be beyond the normal size and the non-metallic inclusions cannot be dispersed.



(a) columnar grain (b) equiaxed grains

Fig. 1 Coarse Grains



(a) CaO inclusion (b) FeS inclusion

Fig. 2 Non-metallic Inclusions

Refining Law of Coarse Grains

Effects of Temperature and Deformation on Grain Refinement

The average grain size in the primary deformation zone of the specimen was measured after deformation at different experimental conditions, and the grain size grade was also calculated (see Table 1).

After deformation, fine grains can be formed at 900˚C and 1000˚C, while the grain size increases obviously when the temperature is higher than 1000˚C. Fig. 3 illustrates that the lower the temperature, the finer the grains. The main reason for the tendency can be discovered from the grain

growth curve of 30Cr2Ni4MoV steel in Fig. 4 which demonstrates that grain coarsening occurs at about 950˚C, and after that the grain size rises from 40um to 180um rapidly. Therefore, in the forging process, the recrystallized grains will grow fast to a larger size corresponding to each temperature, especially for the grains formed at temperatures higher than 1000˚C.

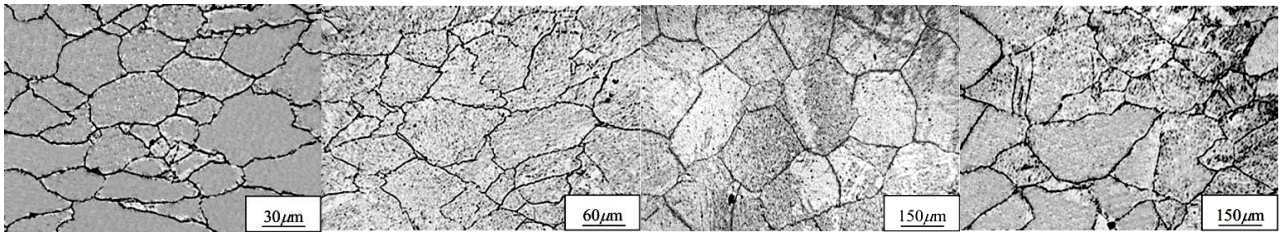
Table 1 Average grain size and grain size scale

[T—temperature, R—reduction ratio, d—average grain size, G—grain size grade]

NO.	C1	C2	C3	C4	C5	C6	C7	C8	C9
T/˚C	900			1000					
R/%	0	10	20	0	10	20	30	40	50
d/um	20.5	15.9	15.7	73.8	51.9	54.8	58.8	50.2	49.1
G/deg	8.0	8.5	8.5	4.0	5.0	5.0	5.0	5.5	5.5

NO.	C10	C11	C12	C13	C14	C15	C16	C17	C18	C19	C20	C21
T/˚C	1100						1200					
R/%	0	10	20	30	40	50	0	10	20	30	40	50
d/um	102.3	97.0	108.9	105.2	96.5	83.6	166.7	123.0	128.5	134.3	120.1	107.6
G/deg	3.5	3.5	3.0	3.0	3.5	4.0	2.0	3.0	2.5	2.5	3.0	3.0

The reduction ratio has a complex effect on the grain size due to the occurrence of dynamic recrystallization, grain growth and grain elongated with the deformation proceeding. However, a comprehensive analysis of the grain size at 900˚C, 1000˚C, 1100˚C and 1200˚C has found that there exists an optimal reduction ratio at which microstructure gets refined furthest and the grain size is more uniform than the as-cast. The optimal reduction ratio is 10%, independent of temperature.



(a) 900˚C (b) 1000˚C (c) 1100˚C (d) 1200˚C

Fig.3 Microstructure at Different Temperatures and the Reduction Ratio of 10%

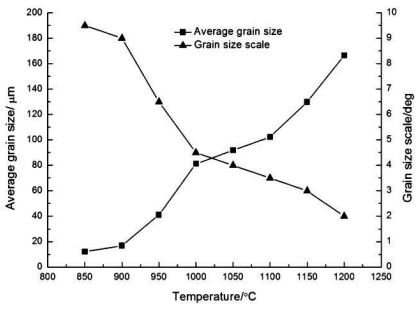
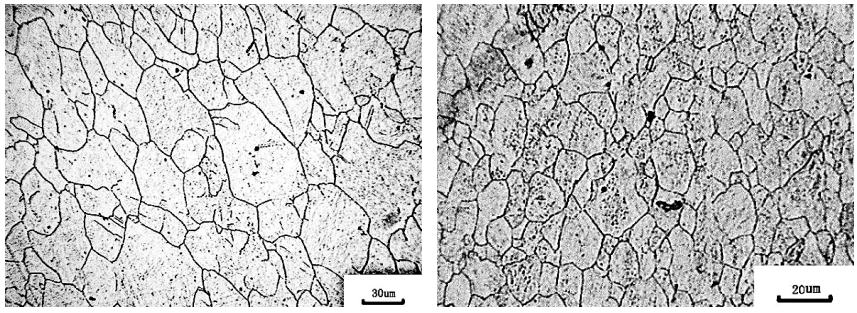


Fig.4 Grain growth curve of 30Cr2Ni4MoV steel

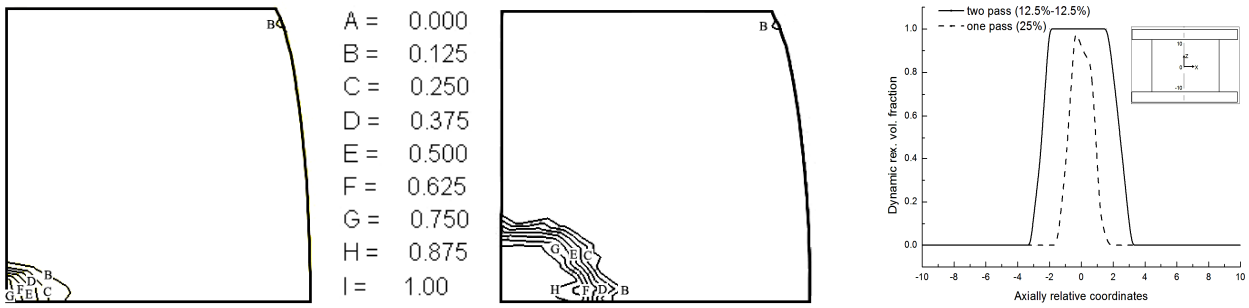


(a) one-pass (25%) (b) two-pass (12.5%-12.5%)

Fig.5 Microstructure at 900˚C and the Total Reduction Ratio of 25%

Effect of Multi-pass Forging on Grain Refinement

The multi-pass forging has a significant impact on the microstructure refinement of 30Cr2Ni4MoV steel. Compared with one-pass forging at the reduction ratio of 25%, two-pass forging with each reduction ratio of 12.5% makes more contributions to the refinement of microstructure and uniformity of grain size. What is more, two-pass forging increases the area of the region where dynamic recrystallization occurs and the volume fraction of dynamic recrystallization at the same position of the ingot. After two-pass forging, the average grain size is refined to 6.50um, which ensures heavy forgings to have more excellent mechanical properties. Comparison of the two microstructure formed in one-pass and two-pass forging is shown in Fig. 5. Numerical simulation illustrating two-pass forging raise the volume fraction of dynamic recrystallization is shown in Fig. 6.



(a) one-pass (25%) (b) two-pass (12.5%-12.5%) (c) dynamic rex. vol. fraction

Fig.6 Distribution of Dynamic Recrystallization Volume Fraction in the Vertical Section

Crack Initiation in the Forging Process

Cracks Originating from CaO Inclusion

Three cracks originated in the outer wall of the specimen deformed at 900˚C, as shown in Fig. 7. The intermediate crack connects the upper and lower cracks, leading the three cracks to be joined with an axial angle of about 45°. The fracture is smooth, dark black and similar to the surface of the CaO inclusion shown in Fig.1 (a). CaO is brittle inclusion which has low intensity, poor plasticity and is easy to generate a concentration area of large strain and stress in the forging process.

Fig.8 indicates that a reduction ratio of 30% can make the intense shear strain generated in the axial section of the ingot and the angle between the large strain zone and the axis is about 45°. Due to its poor deformation capacity, the CaO inclusion separates from the metal matrix gradually with the deformation proceeding in virtue of shear stress generated in the upsetting process, so that micro cracks originate from the interface between the inclusion and the matrix. Meanwhile, low temperature such as 900˚C is not conducive to the diffusion of metal atoms. Therefore, micro cracks continue to expand and ultimately bigger faults are formed.

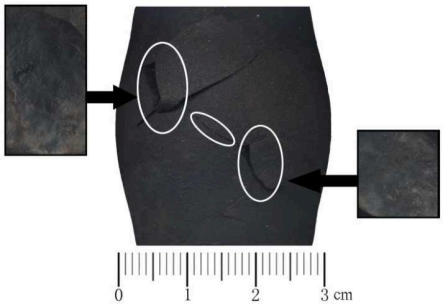


Fig. 7 Cracks after Deformation at 900˚C

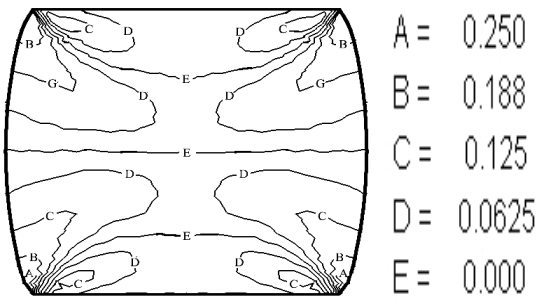


Fig. 8 Distribution of Shear Strain in the Vertical Section

Cracks Originating from FeS Inclusion

Cracks along the grain boundaries originated both in the outer wall of the specimen and inside the specimen deformed at 1000˚C. The fracture is characterized by a rough and torn texture containing many deep furrows, and the tip of the crack inside the specimen disperses into several micro cracks, as shown in Fig. 9.

FeS can initiate the formation of the eutectics distributing in the grain boundaries with Fe, and the melting point of this eutectic is only 985˚C. The eutectics can weaken the strength of grain boundaries due to melting at temperatures higher than 985˚C and cracking along grain boundaries follows. The optical microscopic illustration in Fig. 9 shows that the eutectics are located in many grain boundaries instead of one, so several cracks are formed along the grain boundaries. The role of deformation on the behavior of cracks distributing densely at inclusions can be grouped into two aspects: On the one hand, small deformation has limited influence on the behavior of cracks, e.g. the tips of cracks inside the specimen are just in the rigid region, existing separately. On the other hand, large deformation can make cracks extend into metal matrix and joined with each other, e.g. several cracks in the outer wall of the specimen are just in the concentration area of stress, joined to be a bigger fault. In addition, when the deformation is large enough, the hydrostatic stress along the outer wall of the ingot will turn into tensile stress, as shown in Fig. 10, which further increases the tendency of cracking.

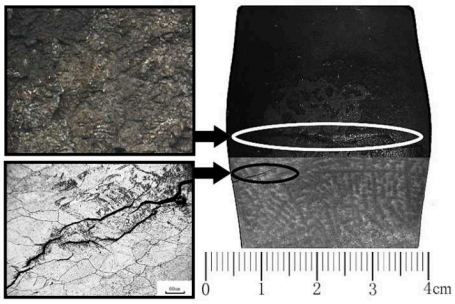


Fig. 9 Cracks after Deformation at 1000˚C

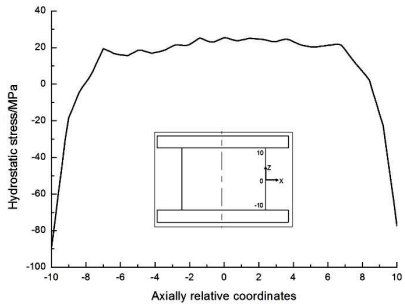


Fig. 10 Distribution of Hydrostatic Stress

Conclusions

Coarse grains and inclusions which are comprised of columnar grains, equiaxed grains, CaO and FeS inclusions are the typical defects of 30Cr2Ni4MoV steel ingot. It is shown that small deformation with temperatures below 1000˚C is conducive for fine grains to be formed. Additionally, multi-pass forging can reduce the grain size significantly at the same reduction ratio. Cracks originating from CaO and FeS inclusions are one of the main faults at low temperatures such as 900˚C and 1000˚C. CaO is brittle inclusion, and intense shear stress further leads up to such cracks. FeS-Fe eutectics enriched at the grain boundaries weaken the strength of grain boundaries due to melting at high temperatures, so FeS cracks originate easily affected by tensile stress.

Acknowledgements

This work was financially supported by National Science and Technology Major Project of China (2011ZX04014-051) and National Basic Research Program of China (2011CB012903).

References

[1] F. Chen, Z.S. Cui, S.J. Chen, Recrystallization of 30Cr2Ni4MoV ultra-super-critical rotor steel during hot deformation. Part I: Dynamic recrystallization, Mater. Sci. Eng. A. 528 (2001) 5073-5080.

[2] R.F. Li, Y. Zhang, J. Chen, M.Y. Wang, Fatigue and fracture property of turbine rotor steel-30Cr2Ni4MoV, Power Syst. Eng. 19 (2003) 29-30.

[3] Q.X. Ma, Z.C. Wang, Y.X. Zhong, The mechanism of faults originating from inclusions in the plastic deformation processes of heavy forging, J. Mater. Process. Technol. 123 (2002) 61-66.

[4] C.Y. Zhang, S. Yang, Smelting of ultrapure rotor steel 30Cr2Ni4MoV, Cfhi. Technol. 2 (2008) 40-41.

Advanced Materials Research Vol. 936 (2014) pp 1647-1652
© (2014) Trans Tech Publications, Switzerland
doi:10.4028/www.scientific.net/AMR.936.1647

Effect of Aging on Microstructure and Performance after superplastic deformation of fine grained 1420 Al-Li alloy

Yanling Zhang[a], Hongliang Hou[b *], Yaoqi Wang[c]

Beijing Aeronautical Manufacturing Technology Research Institute, Beijing, P.R.China

[a] zhangyanling205@163.com, [b] hou_hl@163.com, [c] xiaoqigh@sina.com

Keywords：Fine grained 1420 Al-Li alloy, Superplastic forming, aging, strengthening mechanism

Abstract: Superplastic forming (SPF) is an important process for forming fine grained 1420 Al-Li alloy. However, the mechanical properties will be decreased after deforming at high temperature. How to obtain the optimize relationship of strength and ductility after SPF is one of the key problems for the process. In this paper, a set of artificial aging tests including single and two-step aging were carried out, which are the typical strengthening process for Al-Li alloy. Based on experimental results, strength and elongation were studied by means of tensile tests at room temperature, and the effect of aging processes on mechanical properties was analyzed. Finally, the microstructures fore and after aging were examined by OM and TEM, and the strengthening mechanism of 1420 Al-Li alloy was further studied. It is found that artificial aging especially two-step aging can increase mechanical properties of post-SPF material obviously, and δ'（Al_3Li）is the primary strengthening phase.

Introduction

Aluminum-lithium (Al-Li) alloys have been receiving a great deal of attention for application in aerospace industry because of their low density, high specific strength and stiffness, and good weldability. If Al-Li alloys are used in aircraft structures in place of convention aluminum alloys, the component quality can be reduced 10%~15% and the stiffness increased 15%~20%[1~3]. However, Al-Li alloys exhibit lower ductility and higher notch sensitivity at room temperature, which make the fabrication of useful thin-wall components difficult.

Superplastic forming (SPF) is a special processing, which is developed by superplastity of certain material under specific conditions of temperature and strain rate. It can form complex thin-wall components for Al-Li alloy. The advantages of the process include saving in machining and fastening time, and improved damage tolerance in the produced components[4][5]. The SPF also has several limitations; such as the material experiences long time at high temperature and the cavity formation will have a deleterious effect on any post-forming applications. For the aerospace industry, where it is desired to manufacture light weight stiff structures composed of few parts. Parts that are superplastically formed should be structurally stable in order to withstand the operational static and dynamic loading. Thus, post forming heat treatment, of the superplastically formed parts, is essential in enhancing their strength[6]. However, there are far fewer reports in the literature concerning precipitate control through different aging processes, especially by a two-step aging treatment on post forming 1420 Al–Mg–Li alloy.

Taking into account the aging strengthening of 1420 Al-Li alloy, the present work aims to investigate the effect of aging treatment on tensile performance and microstructure after SPF, and gain proper treatment process for increasing performance of formed parts.

Experimental procedure

The chemical composition of 8.5 mm thick 1420 Al-Li alloy hot rolled plate is listed in table 1. Thermomechanical processing(TMP) based on hot rolled plate is used in producing a fine grained structure, and the detail procedures of TMP are as following: solution-treated at 475℃ for 2h, quenched in water and then over-aging at 300℃/48h+400℃/4h. Subsequently preheated at 300~400℃for 1h, and then rolled to the final thickness of about 2mm, the rolling reduction per pass is 10%~20% and a rolling speed is about 0.427m/s. Finally, rapid recrystallization process is conducted at 510℃ for 30 min. The microstructure of the plates is shown in Fig 1 and the average grain size is about 12μm.

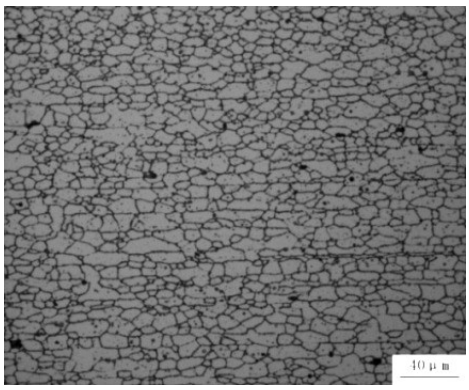


Fig.1 Microstructure of fine grained 1420 Al-Li alloy

Table 1 Chemical composition of 1420 Al-Li alloy (wt %)

Mg	Li	Zr	Ti	Cu	Fe	Si	Al
5.30	2.12	0.11	0.1	0.05	0.07	0.03	Bal

Rectangular pans with a dimension of approximately 250*250*40mm (Fig2) are fabricated on 150t SPF machine. Each is formed at 480 ℃, and the forming pressure is 0.8MPa with the rate of 0.02 MPa per miniute, and then keep pressure for 30 min. Tensile specimens are cut along the rolling direction from the bottom of rectangular pans, and then divided into five groups: (ⅰ) post-SPF without heat treatment; (ⅱ) aged at 170℃/12h; (ⅲ) solution-treated at 510℃ for 30min, quenched in water and then aged at 170℃/12h； (ⅳ) two-step aging at 120℃/4h+150℃/24h; (ⅴ) solution-treated at 510℃ for 30min, quenched in water and then aged at 120℃/4h+150℃/24h. Effects of heat treatment on mechanical properties and microstructure are studied by means of tension experiment and OM, TEM.

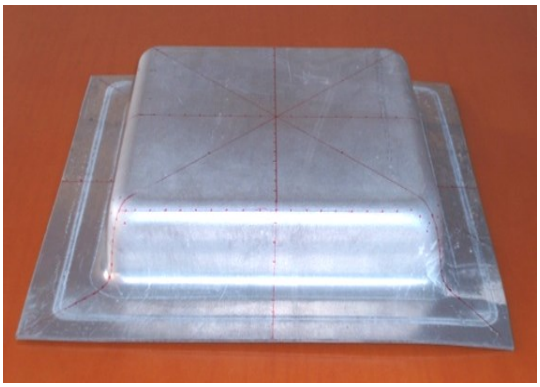


Fig.2 Rectangular pan of SPF

Results and Discussion

Microstructure and mechanical properties of post-SPF

Fig.3 shows the tensile properties of fine grained 1420 Al-Li alloy at room temperature before and after SPF. The results of the tensile tests indicate that there is a significant loss of tensile strength after SPF, ultimate strength is decreased 44.5% ,from 513MPa to 279.5MPa, and the yield strength is decreased 43%, from 323MPa to 184MPa.

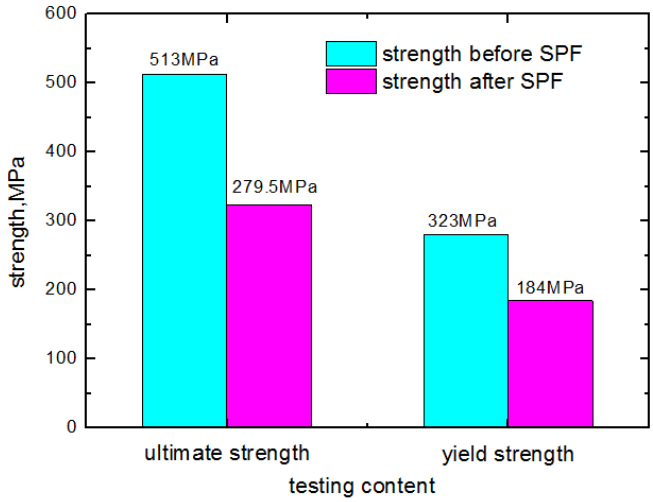


Fig.3 Tensile properties at room temperature of fine grained 1420 Al-Li alloy

The microstructure of post-SPF which is obtained from the rectangular pan is shown in Fig.4. It is found that a large number of cavities are existed in post-SPF materials. Superplastic deformation is carried out at high temperature, and the evolution of microstructure plays very important role in the tensile properties of SPF materials. Dynamic grain growth and cavitation are the major result in the decreasing of mechanical properties for post-SPF materials [7-9].

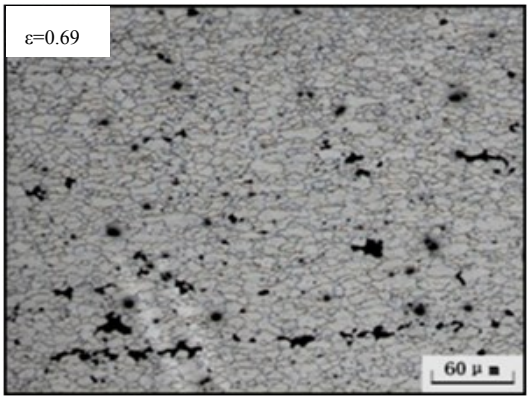
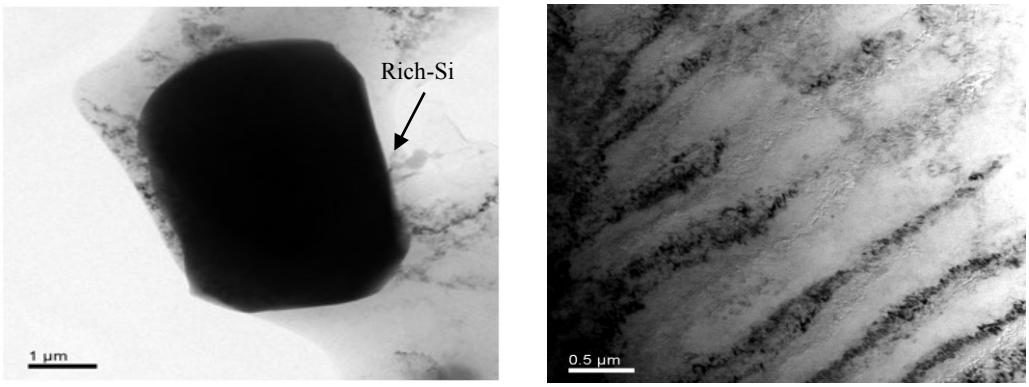


Fig.4 Microstructure of rectangular pan after SPF

Furthermore, the results of TEM are shown in Fig.5. Superplastic deformation temperature is usually higher than 0.5Tm (melting point) which is similar to solution treatment of Al-Li alloy. So most of second-phase particles are melted at that temperature, only rich-Si etal impurity particles (Fig.5(a)) are existed in the materials after SPF. In addition, materials experience to a certainty deformation, dislocation movement is an important deformation mechanism. There are a great deal of dislocations in post-SPF materials, as shown in (Fig.5 (b)).



（a）rich-Si particle (b) dislocation morphological

Fig.5 The results of TEM after SPF

The effect of artificial aging on tensile properties for post-SPF

The effect of several aging treatment systems on post-SPF tensile properties are shown in Fig 6. It is noted that aging treatment can improve the strength of post-SPF 1420 Al-Li alloy. For example, solution treatment at 510℃/ 30min and then aging at 170℃/12h, ultimate strength can be increased from 279.51MPa to 433.85MPa and the yield strength be increased from 184MPa to 238.7MPa. The ultimate and yield strength are individually increased 55% and 30%.

At the same condition, tensile strength with solution treatment are higher than the results without solution for post-SPF specimens. In comparison with single aging, it is discovered that the higher strength can be obtained after two-step aging. Such as the specimens are solution treatment at 510℃/30min, and then aging at 120℃/4h+ 150℃/24h, the ultimate and yield strength are separately reached to 482 MPa and 246MPa, which are similar to the materials before SPF.

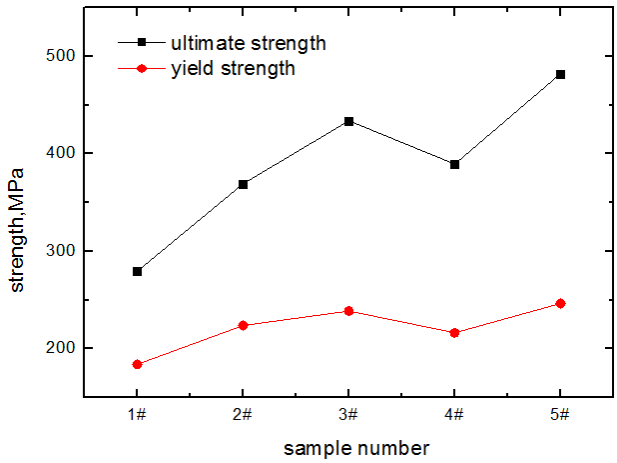


Fig.6 The effect of aging on tensile strength at room temperature after SPF

（1#：post-SPF without aging；2#：170℃/12h；3#：510℃/30min +170℃/12h；4#：120℃/4h+150℃/24h；5#：510℃/30min+120℃/4h + 150℃/24h）

Fig.7 shows the elongations at different aging parameters. Compared to post-SPF, all the elongations are increased after aging. For example, the elongation is increased from 6.64% to 9.09% after aging at 170℃/12h. The tensile strength is not only increased but also elongation is improved when artificial aging treatments are conducted after SPF.

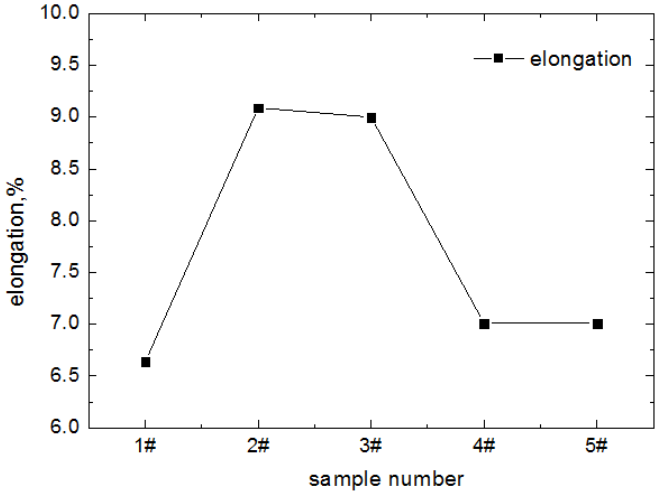
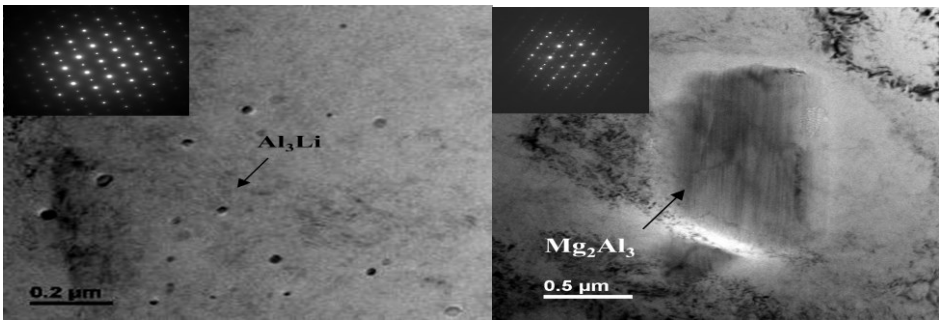


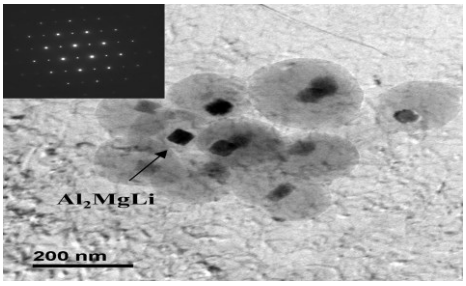
Fig.7 The effect of aging on tensile elongation at room temperature after SPF

The effect of aging on microstructure for post-SPF

Fine grained 1420 Al-Li alloy exhibits aging strengthening characteristic obviously, and which is owe to δ'（Al_3Li）precipitation and growth. To further investigate the strengthening mechanism of 1420 Al-Li alloy, precipitated phases are examined through TEM after aging at 510℃/30min+120℃/4h +150℃/24h, as shown in Fig.8. A large number of δ' phase (Fig.8(a)) which is the major strengthening phase are existed and distributed homogeneously in material after two-step aging. In addition, β（Mg_2Al_3）and S（Al_2MgLi）phases are precipitated, and S phase can improve coplanar slipping which is created by δ'. In consequence, stress concentration occurred in grain boundary will be weakening, and the strength and plasticity are increased after two-step aging for post-SPF products.



(a) δ'(Al_3Li) phase (b) β(Mg_2Al_3) phase



(c) S（Al_2MgLi）phase

Fig. 8 The precipited phases after two-step aging at 510℃/30min+120℃/4h +150℃/24h

Conclusion

According to the experiment on the artificial aging for post-SPF 1420 Al-Li alloy, the following conclusions can be obtained:

a) The mechanical properties of material are decreased obviously after superplastic deformation. Compared to the original plate without deformation, ultimate strength is decreased 44.5% from 513MPa to 279.5MPa, and the yield strength is decreased 43% from 323MPa to 184MPa.

b) Artificial aging can improve the strength of post-SPF. Compared to single aging, the strength is increased higher after two-step aging treatment, such as aging at 510℃/30min +120℃/4h +150℃/24h, the ultimate and yield strength are separately reached to 482 MPa and 246MPa, which are similar to the materials before SPF.

c) δ'(Al_3Li) phase is the major strengthening phase for 1420 Al-Li alloy. A large number of δ' phase are precipitated and distributed homogeneously in material after two-step aging for post-SPF. β（Mg_2Al_3）and S（Al_2MgLi）phases are also exsited, and S phase can improve coplanar slipping which is created by δ'.

Acknowledge

This work was supported by the Major State Basic Research Development Program of China (2011CB012803) and National Natural Science Foundation of China (51334006).

References

[1] Y. W. Xun, Y. Y. Zhu, W. F. Mao, etal. Materials Processing Technology, Vol.72(1992), p.183-187.

[2] H. Imamura, N. Ridley, in: S. Hori, M. Tokizane, N. Furushiro. The Japan Society for Research on superplasticity, 1991, p.453-458.

[3] R Kaibyshev; O Osipova. Materials Science and Technology, Vol.21 (2005), p. 1209-1216.

[4] T. Y. M. Al-Naib, J. L. Duncan, International Journal of Mechanical Sciences 12 (1970) 463.

[5] G. C. Cornfield, R. H. Johnson, International Journal of Mechanical Sciences 12 (1970) 479.

[6] Bao-Tong Ma, Joseph R. Pickens. NASA Contractor Report 4367,1991,ρ.

[7] T. G. Langdon, Met. Sci. 16 (1982) 175.

[8] B.P. Kashyap, A.K. Mukherjee, Res, Mechanica 17 (1986)293.

[9]X. Jiang, J. C. Earthman, F.A.Mohamed, J.Mater. Sci.29(1994) 5499.

Advanced Materials Research Vol. 936 (2014) pp 1653-1656
© (2014) Trans Tech Publications, Switzerland
doi:10.4028/www.scientific.net/AMR.936.1653

Numerical Simulation of One Pulse Power Laser shock Peening

Lei Chen [1, a]

[1]Institute of Mechanical Engineering, Hangzhou Dianzi University, 310018, China

[a] ujs_cl@qq.com

Keywords: Laser shock peening, Shock wave, Residual stress, FEM

Abstract. Laser shock peening (LSP) is a novel technology of surface treatment. LSP utilizes a short laser pulse with high energy density, which induced a high pressure stress wave propagation and residual compressive stress on material surface. The effects of LSP of SAE9310 steel with a laser pulse of 14.2J at 2.9mm square beam have been studied by finite element method. The underlying formulation is based on Lagangian elastoplastic materials model. The propagation of shock wave, residual stress and plastic strain are simulated. The simulations show that the residual stress is mainly in the radial direction of the workpiece, and nearly zero in the longitudinal direction. The plastic strain remains on the processed surface dominantly. Divergences between theoretical and experimental residual stress occur due to the simplification of shock peening conditions.

Introduction

Laser shock peening (LSP), as shown in Fig.1, is a promising surface treatment technique similar to shock peening and has been shown to be effective in improving the fatigue properties of a number of metals and alloys by imparting compressive residual stresses in materials. LSP utilizes a high-energy, pulsed laser to vaporize an opaque overlay (i.e. black paint) applied to the surface of the sample. The ensuing vapor created by the ablation process is trapped between the sample and a transparent overlay (i.e. water), generating an extremely high localized pressure pulse of short time duration (~10 ns) which in turn causes a shock wave to propagate into material. Since the amplitude of this pressure pulse is much greater than the dynamic yield strength of the material, yielding occurs and the material is plastically deformed. The process was originally developed at the Battelle Columbus Laboratory in the 1970s [1]. Since then considerable attention has been paid to potential application of LSP in the aerospace and automotive industries. The beneficial effects of LSP on static, cyclic, fretting fatigue and stress corrosion performance of aluminum alloys, steels and nickel-based alloys have been demonstrated [2-5]. Laser shock waves are much more preferable than other sources (explosion, electron and ion accelerators) since they provide better experimental opportunities, allow more flexible control of their parameters, and have a more significant effect upon materials. Thus far investigation of laser shock waves, taking into consideration their similarity with other types of actions, allows the technological scope of application to be extended.

Much experimental work has been done to analyze LSP [6], but relatively little effort has been spent in studying the shock wave of LSP with analytical methods. Arif [7] used a finite difference algorithm to simulate propagation of stress wave in the material, and a finite element model to predict deformation and stresses. William [8] used a commercial software Abaqus/Explicit to analyze the one-sided and double-sided LSP.

Fig.2 shows the typical optical graph of dented region produced by LSP. The clearance d between two dented regions, as shown in Fig.2, is very important to the efficiency of the LSP. The objective of this work was to examine the effect region of laser shock peening on the workpiece. The residual stress acquired from simulation was compared with experiment.

FE Model

An elastoplastic FEM was used to simulate the one-sided LSP of a semi-infinite solid. The analysis was conducted by using MSC.Marc based on the Updated Lagrangian formulation. The pressure

pulse with duration of 40ns is modeled as a triangular ramp pressure [8], as shown in Fig.3. The pressure rises linearly to the max plasma pressure in a span of 10ns, and then decays linearly during the following 30ns. The max plasma pressure is given by:

$$P(GPa) = 0.01\sqrt{\frac{\alpha}{2\alpha+3}}\sqrt{Z(g\cdot cm^{-2}\cdot s^{-1})\cdot I_0(GW/cm^2)} \quad (1)$$

Where α represents the ionization energy of the plasma. $\alpha=1$ for a perfect gas. Here α was estimated to be 0.2 . Z is a reduced acoustic impedance ($2/Z=1/Z_1+1/Z_2$) of the confining (Z_1) and the target (Z_2) materials. I_0 is the laser intensity.

The material used in this study was SAE9310 alloy with chemical composition as listed in Table 1. Young's modulus and yield strength for SAE9310 were determined to be $2.16\times10^5\,MPa$ and $570MPa$, respectively. Poisson's ratio was assumed to be 0.28. The test sample is a cylinder with a height of 12mm and a diameter of 95mm. The geometries of the specimens are shown in Fig.1. The laser beam spot size was maintained at $2.9mm\times2.9mm$. The Laser power density used was $5GW/cm^2$. The residual stress generated by LSP was measured using the X-ray diffraction technique.

A section is adopted to analyze in agreement with the experiment. The finite element model of the section is shown in Fig. 4. The section is subdivided into 6000 elements.

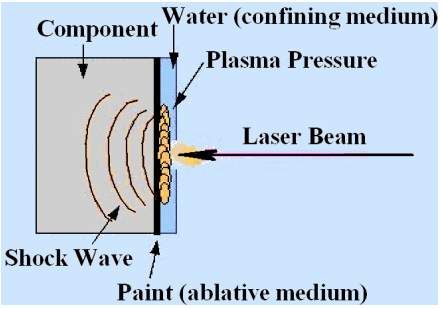


Fig.1 One Dimensional Model of LSP

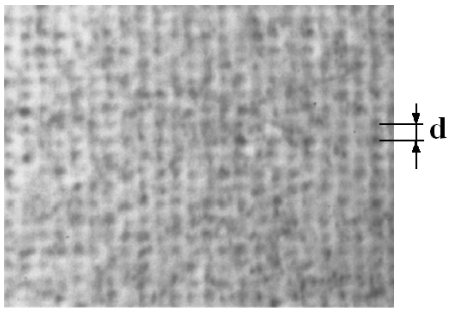


Fig. 2 Typical Optical Graph of Dented Region

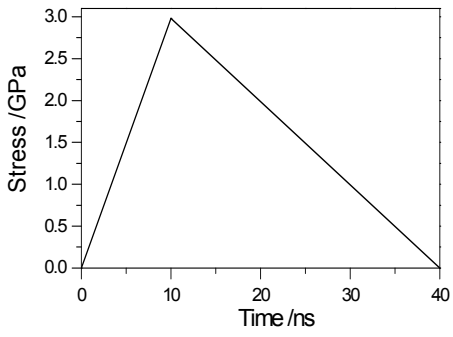


Fig.3 Pressure of Laser-induced Plasma

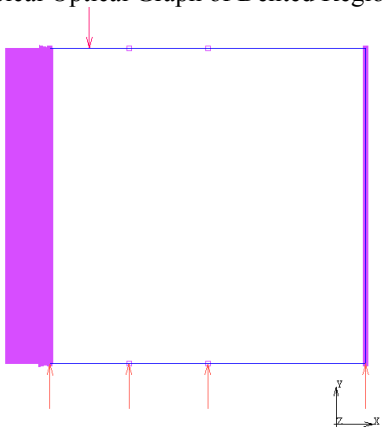


Fig.4 FEM Model

TABLE 1 COMPOSITION OF SAE9310 (WT.%)

C	Mn	Pmax	Smax	Cr	Ni	Mo	Si
0.08-0.13	0.45-0.65	0.025	0.025	1.00-1.40	3.00-3.50	0.08-0.15	0.15-0.35

Results and Discussion

Fig.5 shows the propagation of shock wave. It can be found that the wave front reach 0.3mm, 0.6mm, 0.9mm at 50ns, 100ns, 150ns, the velocity is about 6000m/s. This is equal to the velocity of sound transmitting in the steel. The residual stress is acquired and becomes larger with the development of the propagation, as shown in Fig.5 (a), (c) and (e), whilst no residual stress is acquired in Y direction, as shown in Fig.5(b), (d) and (f).

Total equivalent plastic strain distribution after one pulse laser shock peening is shown in Fig.6. The region of the largest strain is the surface. The total strain is small, and the depth of the strain is about 0.6mm. The strain region area is equal to the laser spot. And the strain in other region is 0.

Fig.7 shows the comparison of the simulation results and experimental results of residual stress of SAE9310 after one pulse LSP. It can be found that the residual stress is decreasing first, and then increasing to 0 with the augmentation of the depth. From the surface to 0.2mm, the simulation results agree well with the experiment. The simulation residual stress is increasing to 0 abruptly when the depth is larger than 0.2mm. The largest depth is about 0.6mm, whilst the depth of experiment is about 3.5mm. The divergence between the simulation and experiment may be caused by the shock waves. In the simulation, the computation is stopped when the shock wave transmits from the surface to bottom of the specimen, and the effect of the carburized layer on the residual stress is not considered. This is the future work. Otherwise, the laser shock waves may transmit several times in the steel, whilst the one pulse LSP in the experiment is harder to perform. Owing to the limitation of the CPU time, the divergence is large between the simulation and experiment.

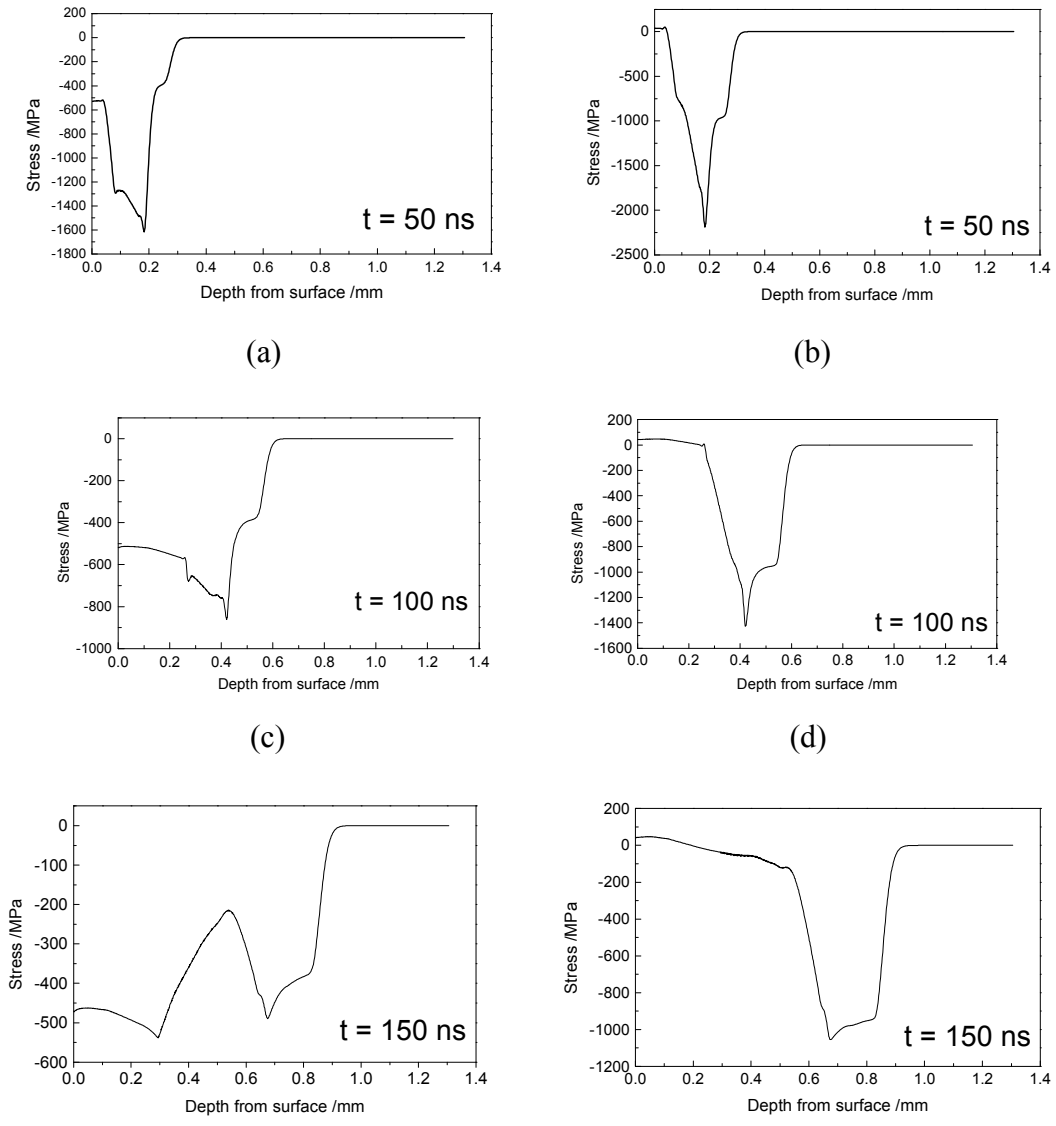


Fig.5 Propagation of Shock Wave Induced by one Laser Pulse

a, c, e—Comp11 of Stress b, d, f—Comp22 of Stress

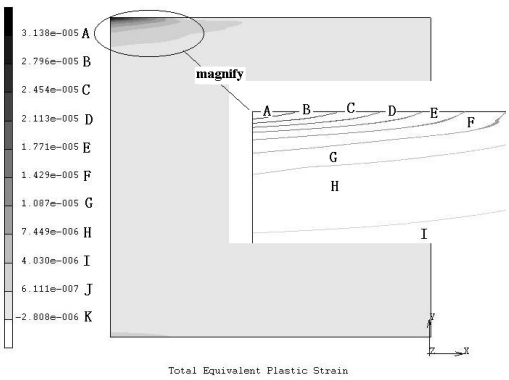


Fig. 6 Total Equivalent Plastic Strain Distribution

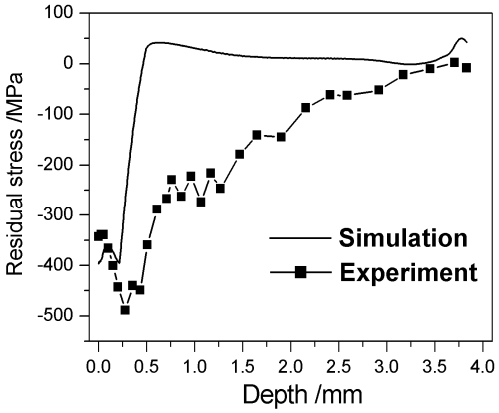


Fig.7 Comparison between Simulation and Experimental Residual Stress

Summary

The FE model of pulse laser shock peening is erected preliminarily. The FE model has been shown to forecast the residual stress and shock wave propagation. From the model it can be found that the residual compressive stress is mainly in X direction, whilst nearly 0 in Y direction. The largest strain is in the surface. With the increase of the depth, the strain becomes weaker. The strain region area is equal to the LSP spot. The residual stress is decreasing first, and then increasing with the increase of the depth from the surface. The divergence between the simulation and the experiment is due to the simplicity of the LSP conditions.

Acknowledgement

The financial support for this work is from Foundation of Hangzhou Dianzi University (No. KYS015613011) and is greatly appreciated.

References

[1] P. Peyre, X. Scherpereel, L. Berthe, Current Trends in Laser Shock Processing, Surf. Eng., 14 (1998) 377-380.

[2] J.M. Yang, Y.C. Her, Nanlin Han, Laser shock peening on fatigue behavior of 2024-T3 Al alloy with fastener holes and stopholes, Mater. Sci. Eng. A, 298(2001) 296–299.

[3] P. Peyre, R. Fabbro, P. Merrien, Laser shock processing of aluminium alloys. Application to high cycle fatigue behaviour, Mater. Sci. Eng. A, 210(1996)102-113.

[4] B.S.Yilbas, S.Z.Shuja, A.Arif, Laser-shock processing of steel, J. Mater. Processing Technol. 135(2003)6-17.

[5] H. Zhang, Y.K. Zhang, C.Y. Yu, Surface treatment of aluminum alloy by laser shock processing, Surf. Eng. 15(1999) 454-456.

[6] P. Peyre, R. Fabbro, L. Berthe, Laser shock processing of materials, physical processes involved and examples of applications, J. Laser Appl. 8(1996) 135-141.

[7] A. Arif, Numerical prediction of plastic deformation and residual stresses induced by laser shock processing, J. Mater. Processing Technol. 136(2003) 120-138.

[8] B. William, B. Robert, Finite element simulation of laser shock peening, Inter. J. Fatigue, 21(1999) 719-724.

Advanced Materials Research Vol. 936 (2014) pp 1657-1661
© (2014) Trans Tech Publications, Switzerland
doi:10.4028/www.scientific.net/AMR.936.1657

Analysis of Hydraulic Prop High Frequency Induction Cladding Temperature Field

Fudong ZHu[1, a], Biyun Zhu[2,b] and Bin Liu[3,c]

[1]ORDOS Vocational College, Kangbashi district, ORDOS China

[2] ORDOS Vocational College, Kangbashi district, ORDOS China

[3] 23th floor,In-Do Mansion A,NO.48 Zhichun Road A, Haidian District, Beijing China

[a]pb701@163.com, [b]danawinner@126.com, [c]liubin@hnceri.com

Keywords: hydraulic prop High frequency cladding temperature field

Abstract: The temperature field of mobile column is simulated, with the theory of high frequency induction heating and fourier heat conduction law , to analyze the change law of the temperature field with time, with different cladding parameters. The results show that the induction heating speed is mainly affected by power frequency of high frequency induction heating and cladding current. The higher frequency induction heating power is or the larger the cladding current is, the the faster the surface temperature of hydraulic prop is rising, the lower the inside-wall termperature and the less influenced the matrix is. The effect and the efficiency of cladding is comparatively superior when cladding frequency is 250KHz and current is 1160A.

Introduction

In mines, the environment is wretched, the air humidity is large, and operational equipments are in the corrosive environment for a long time. The mobile column of single hydraulic prop is exposed on the external surface of the upper part of oil cylinder, which can be corroded, crushed and damaged partially very easily in moist and corrosive environments. The traditional method is surface chromium plating [1-4], but electroplating production, with complicated technology and high cost will pollute the environment seriously, which is not accord with sustainable development policy in our country.

High frequency induction cladding has characteristics of averaged thickness of cladding layers, high strength and abrasive resistance and low production costs, becoming the hotspot of domestic and foreign researches gradually [5-8]. The author of this paper builds mobile column high frequency induction cladding tube wall temperature filed heat conduction model in accordance with induction heating principles, analyze the temperature distribution of mobile column matrix and alloy layers in different frequencies and cladding currents with Fluent6.3.

Mathematical Analysis of Mobile Column High Frequency Cladding Temperature Field

Mathematical model of temperature field analysis

The mobile column of hydraulic prop can be hollow cylinder work piece, its effective power in high frequency cladding P is [9-11]:

$$P = \pi\mu f L_2 F H_0^2 A = 4\pi^2 \times 10^{-9} \mu_r f H_0^2 L_0 F A \tag{1}$$

In the equation: μr is the relative magnetic conductivity of work piece, H/cm; f is high frequency induction heating power supply frequency, Hz; L0 is the length of work piece in high frequency cladding work head, cm; F is the cross section area of the outside-wall of work piece（cm2）, F=πR2（R is the outside radius of work piece, cm）; A is the function of hollow cylinder work piece; H0 is the magnetic strength of the surface of work piece, A/cm, which can be given by the following equation:

$$H_0 = \frac{B}{\mu_r \mu_0} \tag{2}$$

In the equation, μ_0 is vacuum magnetic permeability; B is work piece surface magnetic response strength, T, determined by equation (3):

$$B = 0.3nI\mu_0 \tag{3}$$

In the equation: n is the coil number of work heads of high frequency in unit length, r/m; I is the output current sent by high frequency induction heating power supply, A; μ_0 is vacuum magnetic permeability.

Value Calculation

In the process of high frequency cladding of mobile column, high frequency induction eddy layer is distributed on the surface of the matrix of mobile column firstly. With the progress of induction heating, alloy powders on the matrix surface melt, after the eddy layer reaches the surface of the alloy layer as the thermal source, it conducts in the inside-wall direction of mobile column by heat conduction until the surface layer of the matrix of mobile column melts and forms metallurgical combination with alloy so as to complete the entire high frequency cladding process. In the analysis of temperature field, the material of alloy powder is Ni45, the material of mobile column is 27SiMn（ ingredients of 2 materials are shown in Table 1）.

TABLE1 CHEMICAL COMPOSITION OF ALLOY POWDER AND MOBILE COLUMN[12] (MASS FRACTION,%)

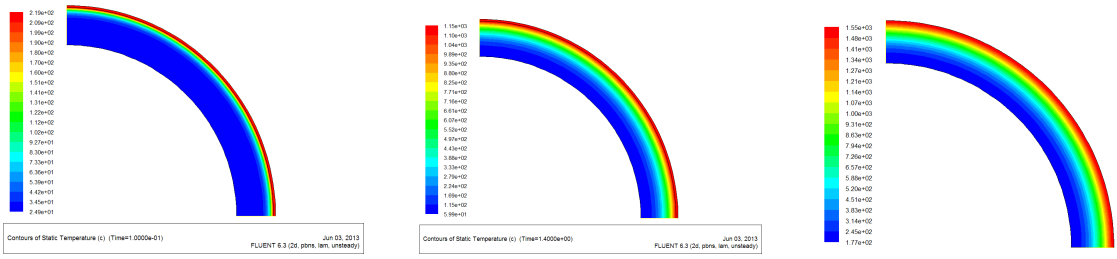
	Ni	Cr	B	Si	Fe	C	Mn	S	P
Ni45 alloy layer	Bal.	12.5	1.9	4.1	6.6	0.34	—	—	—
27SiMn	≤0.03	≤0.03	—	1.1~1.4	Bal.	0.2~0.3	1.1~1.4	≤0.04	≤0.04

Considering that the mobile column is a revolution, distributed in the surrounding of eddy layer in high frequency cladding in average, mobile column and alloy layer are heated evenly. Therefore, we pick 1/4 for analysis to divide with simplified gridding and fasten the speed of analysis. At the same time, make following assumptions in the calculation and analysis of the temperature field:(1)Assume that alloy layer and matrix material is averaged, magnetic inductivity and heat inductivity of the material in each layer are the same; (2)ignore the heat lost by radiation between mobile column and alloy layer tube wall or air convection;(3)neglect the heat brought by water.

Value Simulation Calculation Results and Analysis

The temperature field of mobile column in high frequency cladding at different moments

Fig. 1 shows the tube-wall temperature distribution cloud figure of mobile column with high frequency induction heating power supply f is 250 kHz and cladding I is 1160A, diameter is 76mm, tube-wall thickness is 5mm and surface coating thickness is 0.5mm. Fig.1(a) shows the beginning of cladding, the eddy layer moves outside to the alloy layer from the surface of mobile column, large quantities of heat produces at the interface between the surface of mobile column and alloy layer and alloy powders near the eddy layer melt. Fig. 1(b) reveals that the eddy layer just moves to the most outermost layer of the alloy layer, at this time, the alloy powder layer has melted entirely (the outermost layer of alloy powders has reached 1150℃, the temperature at the interface between alloy and matrix has been 1100℃)，the eddy layer moving to the outermost surface of eddy layer continues to produce heat and conduct the heat to the inside matrix, alloy layer surface, tube-inside wall. Until the moment Fig. 1(c) shows, the thin layer of matrix forms the metallurgical combination with Ni45 alloy at this time, the cladding of the tube reaches the stability and the cladding of this segment of mobile column is completed. From the Figure, the outsourcing stage of the eddy layer takes approximately 1.4s, nearly occupying 60% of the total time of cladding.



(a) 0.1s (b)1.4 (c)2.3s

Fig.1 Temperature field at different moments during high frequency induction cladding

By simulation, we know that at the beginning moment, the temperature increases very rapidly, with the constant heating, the temperature rise becomes slow; in the latter period, for the limited thermal volume of mobile column, the heat absorbed by tube-walls starts to accumulate, the partial heating at the interface starts to be used to heat the material at the interface to make the interface temperature increases a little more rapidly. We also see from the Figure that, the temperature of the interface has been always over 1000℃ in 1.4-2.3s and as high as over than 1500 degrees in the heating later period, making the alloy and matrix at the interface have enough time to diffuse, permeate and form metallurgical combination.



(a)t_1=6.4s (b)t_2=8.9s

Fig. 2 Temperature field distribution cloud figure at t_1 and t_2 moment when f=10KHz and I=1160A



(a)t_1'=2.8s (b)t_2'=4.2s

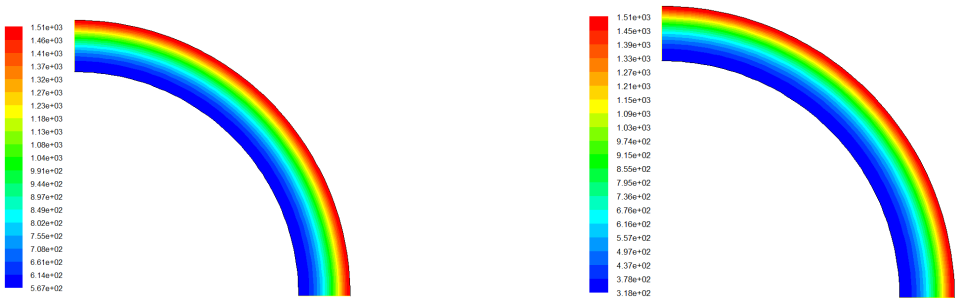
Fig. 3 Temperature field distribution cloud figure at t_1' and t_2' moment when f=50KHz and I=1160A

With the increase of frequency, the surface temperature of mobile column increases more rapidly, the time of high frequency cladding decreases and cladding efficiency becomes higher. The higher the efficiency is, the shorter the induction heating time is, the lower the inside-wall temperature of mobile column is when cladding is over. By contrasts, we can find that: the higher the frequency is, the more rapidly the surface temperature of work piece is rising, the tube inside-wall temperature cannot catch up to reach the high temperature within the short time, metallurgical combination has occurred at the interface between alloy layer and matrix, which are characteristics of high frequency induction heating; when using low frequency, the power density of skin layer is low, the surface temperature of work piece increases slowly, the surface heat gradually conducts to the mobile column wall, the temperature of tube wall gradually increases, the tube temperature has reached over a thousand degree when the cladding is over (or almost the same with the surface temperature), which would cause serious thermal destruction, deformation on the matrix and the flowing of alloy powder of melting status.

Effects of High Frequency Cladding Currents

Select f=250KHz，I=850, 1000, 1160A to calculate and simulate separately and obtain the work piece temperature field distribution cloud chart in different cladding currents when high frequency induction heating is over（as Fig. 4 and Fig. 1（c））. We can know from the Figure that: when cladding

current are chosen 850, 1000 and 1160A separately, induction heating time are 5.5s, 3.5s and 2.3s separately, the inside-wall temperature of mobile column when induction heating is over is 567℃, 318℃ and 177℃ separately.



（a）I_1=850A，T_1=5.5s (b)I_2=1000A，T_2=3.5s

Fig. 4 Work piece temperature field distribution cloud figure in different cladding currents when heating is over

With the increase of cladding current, the surface temperature of work piece raises more rapidly, cladding efficiency improves; when induction heating is done, the inside-wall temperature of mobile column reduces with the increase of cladding current. When using higher cladding current, power density of skin layer is high in unit volume, mobile alloy layer can reach the high temperature within the short time, but the inside-wall temperature inside the mobile column cannot catch up to reach the high temperature, making the structure and mechanical performance of the matrix basically not change at all; when using lower cladding current, the induction current density of skin layer is low in unit volume, the surface temperature of mobile column increases slowly, the quantity of heat in the alloy layer gradually conducts to the matrix layer, making the inside-wall temperature in the mobile column increases to 567 degree when induction heating ends, which seriously damages matrix materials and even causes the flowing of alloy in the coating.

Conclusion

(1) In mobile column high frequency cladding, high frequency heating power efficiency mainly affects cladding efficiency and effect. With the rise of frequency, the surface temperature of mobile column raises more rapidly, the temperature difference between tube surface and inside-wall increases and the thermal effect on the matrix reduces.

(2) In mobile column high frequency cladding, cladding current mainly influences cladding efficiency. In certain ranges, with the increase of the current, the surface temperature of mobile column rises more rapidly, the temperature of inside-wall tube reduces when induction heating ends and the thermal effect of induction heating on the matrix reduces.

(3) When frequency is 250KHz, cladding current is 1160A, cladding efficiency and effect is good.

References

[1] ZHAO Wenqiang,MIAO Hongbin et al.Study on laser cladding strengthening technology for mine hydraulic props. mining machinery, 2011,12:18-20.

[2] WANG Lichu,Cteate Problems of Hydraulic Prop Analysis.Coal Mine machinery,2010,08,145-146.

[3] YU Shanqi,Research on Remanufacturability of Mine Hydraulic Prop.Coal Mine machinery, 2012,03,49-51.

[4] WANG Chao,LYU Zhi,XIAO Hongbing,Coal Mine Hydraulic Pillar Surface Treatment Process Innovation.Coal Mine machinery,2013,02,122-124.

[5] LIU Xiangqing, GUOZhimeng, GAO Kewei et al. Microstructure and corrosion resistance of Ni60 coating prepared by induction cladding. Transactions of Materials and Heat Treatment, 2012, 33(supplement)：309-312.

[6] HE Dingyong, XU Jing, MA Ran et al. Properties of WC reinforced Ni60 coating prepared by high frequency induction cladding. Transactions of Materials and Heat Treatment, 2008, 29(3)：138-141.

[7] T. Umeda, P. Thirathipviwat, M. Supradist et al. Microsegregation development of heavily electromagnetically stirred melt of super high strength Al-10Zn-2.5Mg-2.3Cu alloy. International Journal of Cast Metals Research, 2011, 24(3)：184-189.

[8] M. Hazra, A.K. Mondal, S. Kumar et al. Laser surface cladding of MR1 153M magnesium alloy with (Al+Al2O3). Surface & Coatings Technology, 2009, 203(16)：2292-2299.

[9] FU Zheng-bo. Induction Heating and Energy Conservation—the Design and Application of Induction Heater. Beijing: Mechanical Industry Press, 2008: 11-97.

[10] JIN Xiao-shu, YANG Xi-chen, FENG Li-wei et al. Numerical simulation of coaxial powder flow with carrying gas in laser manufacturing. Chinese Journal of Mechanical Engineering, 2007, 43(5):161-166.

[11] J.P.Park, M.G. kim, U.S.Yoon, W.J.Kim. Microstructures and mechanical properties of Mg-Al-Zn-Ca alloys fabricated by high frequency electromagnetic casting method. Journal of Materials Science, 2009, 44: 47-54.

[12] The Compiling Group of Mechanical Manufacturing Process Materials Technic Directory. Mechanical Manufacturing Process Materials Technic Directory. Beijing: Mechanical Industry Press, 1992: 265-269.

Advanced Materials Research Vol. 936 (2014) pp 1662-1665
© (2014) Trans Tech Publications, Switzerland
doi:10.4028/www.scientific.net/AMR.936.1662

Cfd Simulation On Hydrodynamics Of Liquid-Liquid Slug Flow In Microchannel

Wang Yi[1,a]

Department of Pharmacy, Tianjin Medical College, Tianjin 300222, China

[a]wangyii_2013@163.com

Keywords: CFD simulation; liquid-liquid; slug flow; microchannel.

Abstract: Hydrodynamics in a liquid-liquid slug flow in a T-junction microchannel of 600μm diameter, operated under a squeezing regime, was simulated with the computational fluid dynamics method. The slug flow generation simulated shows very good agreement with experimental snapshots where the clear slug formation takes place in the vicinity of the T-junction. The internal circulation within each slug was also obtained, which could make us better understand the hydrodynamics of liquid-liquid slug flow in microchannel.

Introduction

Liquid–liquid slug flow is a flow of two immiscible liquids, characterized by a series of liquid slugs of one phase separated by the other. Since both phases move alternatively, each slug serves as an individual processing sub volume which is highly regular and guarantees well defined interfacial area for transfer processes. The liquid–liquid slug flow microreactor has been demonstrated to be a useful instrument for the enhancement of heat and mass transfer limited reactions[1]. The mass transfer arises by two mechanisms: convection through the internal circulations within each slug and diffusion between two adjacent slugs. The internal circulations within both slugs resulted from the shear between the wall surface and the slug axis renew the interface and enhance the diffusive penetration.

Several liquid-liquid slug flow microreactors with different types of two-phase mixing elements such as T-type[2] and Y-type[3] have been used for experimentation in the laboratory. Garstecki et al. (2006)[4] used a T-type mixing element where the dispersed phase was introduced in the continuous flow channel at a right angle and proposed a correlation for slug length as a function of the ratio of dispersed to continuous phase flow, which was found to be independent of flow velocity. Recently, Dessimoz et al. (2008)[5] used both types of mixing elements (T and Y) and reported the effect of mixing element on the two-phase flow patterns. In the case of Y-type element the pressure drop is less when compared with T-type mixing elements as frictional losses are lower in the former case. Thus, to understand the slug flow generation mechanism, more work is needed.

The numerical method can provide information that might not be available directly by experiments, such as pressure fluctuation in a very short time, flow fields in any profile without the influence of tracers, etc. Several CFD studies are available on the behavior of liquid-liquid two-phase slug flow in the microreactor. Kashid et al.[6] performed two-dimensional (2-D) simulations of liquid-liquid slug flow in a microchannel to investigate liquid recirculation in the slugs. In their simulations, the shape of the slug was assumed to be fixed and the slugs were modeled to be stationary with a moving wall boundary condition. Wu et al.[7] performed 2-D

simulations of a liquid-liquid flow in a cross-junction rectangular microchannel using the lattice-Boltzmann method. They investigated the effects of Capillary number (Ca) and Weber number (We) on the slug formation mechanism. Kashid et al.[8] performed 2-D VOF simulations of liquid-liquid slug flow through a T-junction microchannel for Ca < 0.01 and validated the results using the experiments of Tice et al.[9].

In view of the above summary, detailed work on the process occurring in the two-phase contacting zone of microchannels is still inadequate. Therefore, in this paper, we designed a 2D T-junction microchannel with water and oil inlets located head-to-head and investigated the slug formation process. A VOF based CFD methodology is developed to investigate the slug flow generation in a T-type mixing element considering the wall film.

Numerical methods

In immiscible liquids, the movement of interface is important in evaluating the performance of the reactor, and therefore, free-surface modeling is necessary. Different methods are available to model immiscible fluids such as level set, volume of fluid (VOF), Lattice Boltzmann and so on[10]. VOF and level-set approaches belong to the most common implicit free-surface reconstruction methods, while, particularly, VOF is relatively simple to treat topological changes of the interface and is naturally conservative. The finite volume calculus in the commercial computational fluid dynamics (CFD) package of FLUENT 6.3.26 was used for the numerical simulations. The VOF model provided by FLUENT was employed to track the interface of water and oil, and the continuum surface force (CSF) was adopted to include the surface tension in the momentum equation. The governing equations for the present simulations are as follows:

equation of continuity:

$$\frac{\partial \rho}{\partial t} + \nabla \cdot (\rho \vec{v}) = 0 \tag{1}$$

equation of motion:

$$\frac{\partial (\rho \vec{v})}{\partial t} + \nabla \cdot (\rho \vec{v} \vec{v}) = -\nabla p + \nabla \cdot [\mu (\nabla \vec{v} + \nabla \vec{v}^{T})] + \rho \vec{g} + \vec{F} \tag{2}$$

volume fraction equation:

$$\frac{\partial \alpha_k}{\partial t} + \vec{v} \cdot \alpha_k = 0 \tag{3}$$

where

$$\rho = \alpha_1 \rho_1 + \alpha_2 \rho_2, \quad \mu = \alpha_1 \mu_1 + \alpha_2 \mu_2$$

The model geometry is illustrated in Fig. 1, where d = 600μm, and the lengths of the water and oil inlets, the contacting zone and the main channel are 2d, 2d, d and 10d, respectively. It was meshed with the preprocessor GAMBIT. A grid independence study was performed by varying the number of grid cells in the model geometry. Based on this study, the number of grid cells was determined to be 15,340. The gravity effect was neglected in the whole process. The boundary conditions were velocity inlet for the water and oil inlets, outflow for the outlet, and no-slip condition for all walls. The PISO scheme was chosen for pressure-velocity coupling. In the simulations, time step and relaxation factors were adjusted to ensure convergence.

Two-phase fluids are n-butyl acetate and 0.4M NaOH aqueous solution, whose densities are 877 and 1015kg/m^3, respectively. The interfacial tension σ between two phases was set to 0.25N/m and the contacting angle was set to 60 degree according to the snapshots acquired by experimental method.

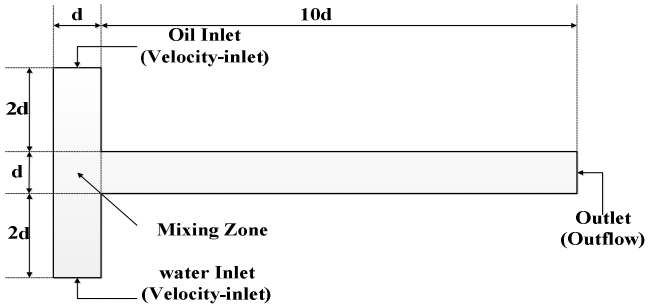


Fig. 1 - Schematic of geometry and boundary conditions used in present work.

Results and discussion

In the simulation method, two immiscible liquids were introduced into the mixing element considering that the microreactor is initially filled with the continuous phase. The interpenetration of two streams in the vicinity of the junction generates the characteristic alternating slug flow structure.

In general, two different mechanisms for slug formation in microchannel are proposed: dripping and squeezing regime. The capillary number Ca is the criterion to distinguish the two phenomena. When the capillary number is larger than 0.01, shear stress plays a leading role and the dripping regime arises. In this case, the dispersed fluid occupies only part of the cross-section when it enters the main channel. If Ca is smaller than 0.01, the interfacial force dominates the shear stress and the squeezing regime appears; then, the dispersed fluid fills almost the entire cross-section and blocks the continuous phase until it breaks off. The squeezing regime is considered to be specific to microdevice and becomes the focus of our present studies.

A typical process of slug formation with squeezing regime we studied can be described in four stages (Fig. 2) as explained as follows:

(a) Initially, The two immiscible fluids form an interface at the junction of the inlet and main channel. The stream of the dispersed phase penetrates into the main channel and a droplet begins to grow.

(b) As the tip of the dispersed phase grows, it blocks almost the entire cross-section of the main channel. The continuous phase then flows through the space between the wall and the dispersed phase droplet with high velocity.

(c) The pressure gradient along the length of the channel and the shear exerted by the continuous fluid distort the droplet in the downstream direction. The drop elongates and grows downstream. When the interface approaches the downstream edge of the inlet for the dispersed phase, the neck connecting the inlet channel with the droplet breaks and a slug is formed in the main channel.

(d) The disconnected slug flows downstream along the main channel, while the tip of the stream of dispersed phase retracts to the end of the inlet and the process repeats.

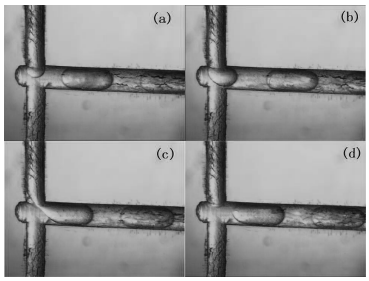


Fig. 2 - Four steps of slug flow generation with laboratory experiment.

The simulated snapshots corresponding to the experimental operating conditions of Fig. 2 are depicted in Fig. 3. The results show very good agreement with experimental snapshots where the clear slug formation takes place in the vicinity of the T-junction.

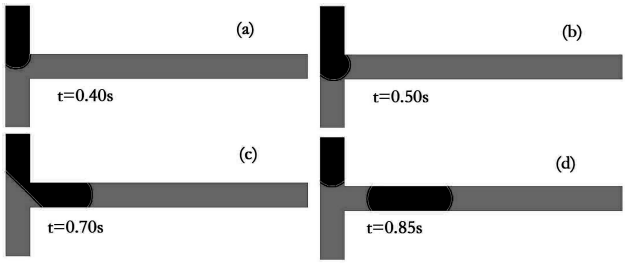


Fig. 3 - CFD simulated snapshots for the operating conditions corresponding to Fig. 2.

Conclusion

Simulations were conducted in a liquid-liquid two-phase microchannel to investigate the hydrodynamics of slug flow with computational fluid dynamics method. The slug flow generation with squeezing regime in the T-junction geometries studied was described in four stages. The simulated results was compared with experimental snapshots and showed good agreement. The internal circulation within slugs was also presented, which can intensify mass transfer.

References

[1] Dummann, G., et al.: Catal. Today. 2003, 79–80(0), 433-439.
[2] Burns, J.R. and C. Ramshaw: Lab Chip. 2001, 1(1), 10-15.
[3] Kashid, M.N. and D.W. Agar: Chem. Eng. J. 2007, 131(1-3), 1-13.
[4] Garstecki, P., et al:. Lab.Chip. 2006, 6(3), 437-446.
[5] Dessimoz, A.-L., et al.: Chem. Eng. Sci. 2008, 63(16), 4035-4044.
[6] Kashid, M.N., et al.: J. Comput. Appl. Math. 2007, 203(2), 487-497.
[7] Wu, L., et al.: Int. J. Numer. Meth. Fl. 2008, 57(6), 793-810.
[8] Kashid, M.N., A. Renken, and L. Kiwi-Minsker.:Chem. Eng. Res. Des. 2010, 88(3), 362-368.
[9] Tice, J.D., A.D. Lyon, and R.F. Ismagilov: Anal. Chim. Acta. 2004, 507(1), 73-77.
[10] van Sint Annaland, M., et al.: AIChE Journal. 2006, 52(1), 99-110.
[11] Kashid, M.N., et al.: Ind. Eng. Chem. Res. 2005, 44(14), 5003-5010.

Advanced Materials Research Vol. 936 (2014) pp 1666-1670
© (2014) Trans Tech Publications, Switzerland
doi:10.4028/www.scientific.net/AMR.936.1666

Characterization of Local Cavity Pressures in Squeeze Casting of Magnesium Alloy AM50

Xuezhi Zhang[1], Alfred Yu, and Henry Hu[2]

Mechanical, Automotive & Materials Engineering

University of Windsor

401 Sunset Ave.

Windsor, Ontario, Canada N9B 3P4

E-mail: [1] zhang11w@uwindsor.ca, and [2] huh@uwindsor.ca

Keywords: Squeeze casting, magnesium, cavity, pressure, solidification process, numerical simulation.

Abstract: In this study, the experimental measurement of the pressure distribution in a cylindrical die cavity for squeeze casting of magnesium alloy AM50A was carried out. Piezo-electric quartz pressure transducers were integrated into a die cavity for real-time pressure measurements. The experimental results revealed that local cavity pressures at various locations changed with time in the duration of squeeze casting solidification and cooling. The pressure transfer rate varied considerably within the casting geometry. The distribution of local cavity pressures was inhomogeneous in the cavity.

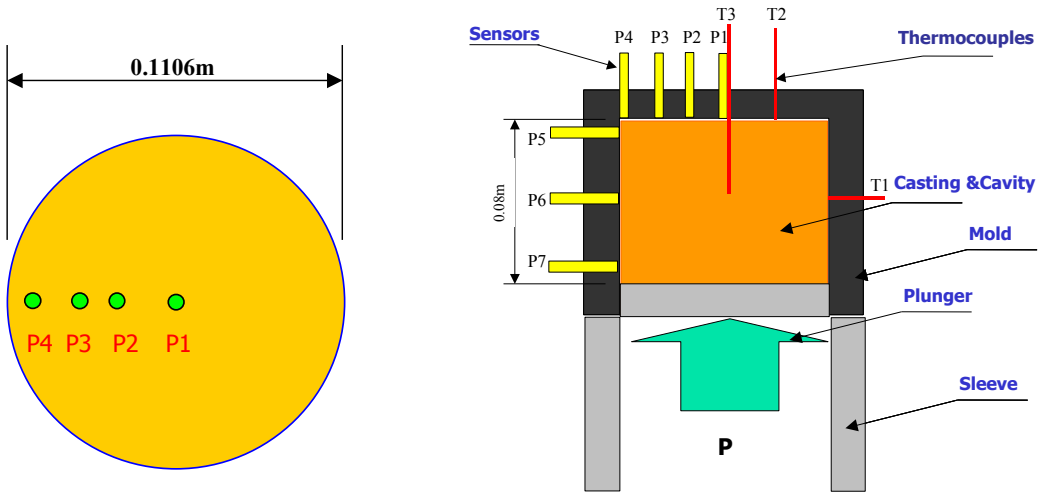
Introduction

During squeeze casting, the cavity pressure usually is not considered as the first process parameter. Instead, the hydraulic pressure is measured and used as specific pressure, or the cavity pressure is even eliminated as a quality control variable by simply using large machine which provide as high press load more than that required [1]. The main reason is that the real characteristics of the cavity pressure in squeeze casting had yet to be fully understood.

Due to the extreme hostile environment of squeeze casting cavity (thermal, mechanical and chemical conditions in the die), there are few reliable pressure sensors which can withstand such conditions. Hence, measuring local cavity pressures directly inside the die becomes an extremely challenging task. It is not surprised that, despite of the presence of numerous publications [1-8] on squeeze casting, very few of them are related to the characterization of cavity pressures. Thus, the principal objective of this study is to elucidate a fundamental understanding of pressure distribution in die cavities during squeeze casting of magnesium alloys AM50A due to its potential application in automotive components.

Experimental setup and procedures

A squeeze casting setup utilized in this study consisting of A 75 tons laboratory hydraulic press, a die, an electric resistance furnace and a data acquisition system, which includes the press and mold assembly consisting of the die, sleeve and plunger. The mold assembly was composed of two parts, i.e., the upper die of casting cavity with a diameter of 0.102 m and a height of 0.097 m; and the bottom sleeve with a diameter of 0.102 m and a height of 0.127 m. This combination enables to make a cylindrical coupon with a diameter of 0.102 m and a height of 0.080 m (Fig. 1). Both the upper die and the bottom sleeve were heated by Acrolab (Acrolab Ltd. in Windsor, Ontario, Canada) ceramic band heaters, of which temperatures were separately controlled by Shinko (Shinko Electric Industries Co., Ltd. in Tokyo, Japan) Temperature Controllers. The detailed description of the setup are given in reference 9.



(a) (b)

Figure 1. Scheme diagram showing the locations in which pressure transducers and thermal couples are embedded in the system, (a) top view, and (b) cross-section view.

Kistler pressure transducers Type 6175A2 were employed to directly measure in-cavity pressures. As show in Fig. 1, four pressure transducers (P1, P2, P3 and P4) were inserted into the cavity through the top wall of the die. The sensing tips of the transducers were flush to the inner top die surface. Transducer P1 was positioned at the center of the inner top die surface. In the radial direction, transducers P2, P3 and P4 were arranged 0.020, 0.030 and 0.040 m away from the centerline of the casting, respectively. Along the inner side die surface, three transducers (P5, P6 and P7) were placed 0.010, 0.040 and 0.070 m downward from the inner top die surface. Due to the contour shape of the inner side die surface, an extension pin with a diameter of 0.011m and a length of 0.025 m was placed in front of the tip of each transducer for preventing potential damage resulting from melt cavity filling. The front surfaces of the pins were machined to accommodate the contour shape of the inner side die surface for the accuracy of pressure measurements. Real-time pressure data were recorded at regular intervals of 100ms over the entire user-defined period of measurement during the pressurized solidification stage of squeeze casting.

A Lindberg electric resistance furnace was employed to melt magnesium alloy AM50A held in a mild steel crucible with a maximum holding capacity of 4 kilogram. The melt temperature was regularly monitored by a digital thermometer (Omega HH509) during melting. The molten metal was poured directly from the crucible into the sleeve to minimize the loss of melt superheat once it reached a desired temperature. Protection gas (Sulfur Hexafluoride SF_6 0.5% + carbon dioxide CO_2) was used during both melting and casting magnesium alloys to protect the melt from any excessive oxidation or possible burning. A data acquisition system (DAS) containing a National Instruments PCI-6033E processor with eight temperature (K type) channels and eight sensor channels was employed.

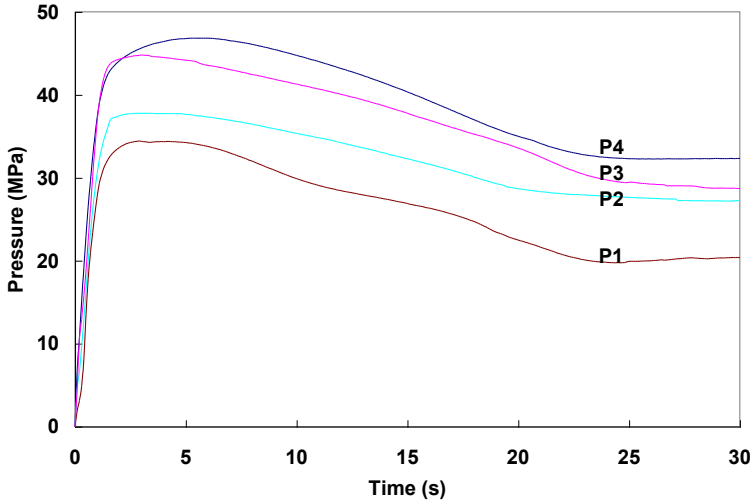
The squeeze casting operation procedures are summarized as follows: (a) preheating and the graphite-lubricated die to 275 ^{0}C, and selecting the operating parameters; (b) pouring molten magnesium alloy AM50A into the shot sleeve until it reached 695 ^{0}C; (c) injecting the melt into the die cavity by the plunger with an upward velocity of 0.055m/s once the die was closed by moving up the lower platen with the sleeve; (d) applying a predetermined pressure to the solidifying melt for a preset dwell time upon the completion of; and (e) retracting the plunger and the lower platen to its original position, and ejecting the cast coupon.

Results and discussion

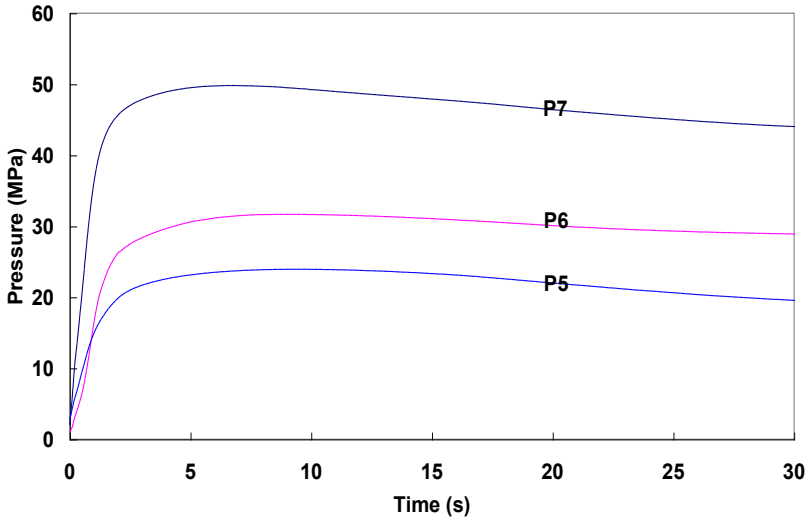
Local Pressure Change with Time

Fig. 2(a) presents the local in-cavity pressure change with time at four locations along the top surface of the casting during the pressurized solidification step of squeeze casting when the external

pressure was applied. P1, P2, P3, and P4 represent the pressure histories at the transducer-embedded locations. It is evident from Fig. 2(b) that the local cavity pressures at all the sampling locations built up very rapidly after the cavity filling completed once the external force was applied. Then, at each location, the local pressure reached its own peak before starting to decrease. It took less than 5 seconds for P1, P2, P3 and P4 increased to their peak values of 47, 43, 38 and 34 MPa from 0 MPa, respectively. Along the top surface, the peak values of the local pressures increased as the distance of the sampling locations away from the centerline of the casting extended. Around 25 seconds after the applied pressure set in, the individual local pressures decreased to its own stable plateau.



(a)



(b)

Figure 2. Typical experimental results of local pressure measurements on the (a) top surface, and (b) the side surface of a cylindrical squeeze casting of magnesium alloy AM50A under applied pressure of 70MPa.

The variation of the local pressure with time along the side surface of the casting is shown in Fig. 2(b). As can be seen from Fig. 2(b), the local pressures at locations P5, P6 and P7 increased quickly to the highest points, 23, 37 and 50 MPa respectively after the external force was applied. This indicates that the individual local pressure along the side surface decreased when the casting height increases. All the local pressures decreased slowly afterward.

Variation of Pressure Transfer Rate and Temperature

Examination of Fig. 2(a) and 2(b) manifests that, at the beginning of the external force application, the local pressures increased up to 95% of its peak value along the top surface in a much faster pace than that at the side surface of the casting despite that the local pressures along the top surface decrease considerably faster than those at the side surface after a certain period of time. For the clarification of discussion, the increasing rate of the local pressures up to 95% of its peak

value is defined as an initial local pressure transfer rate thereafter in the text. Fig.3 compares the initial pressure transfer rates on the top surface to those at the side. The pressure transfer rate on the top surface varies from 19 to 30 MPa/s with an average of 23 MPa/s. But, at the side surface, the average pressure transfer rate is only around 12 MPa/s.This observation suggests that the pressure transfer in a direction perpendicular to the external force is faster than that in a parallel direction.

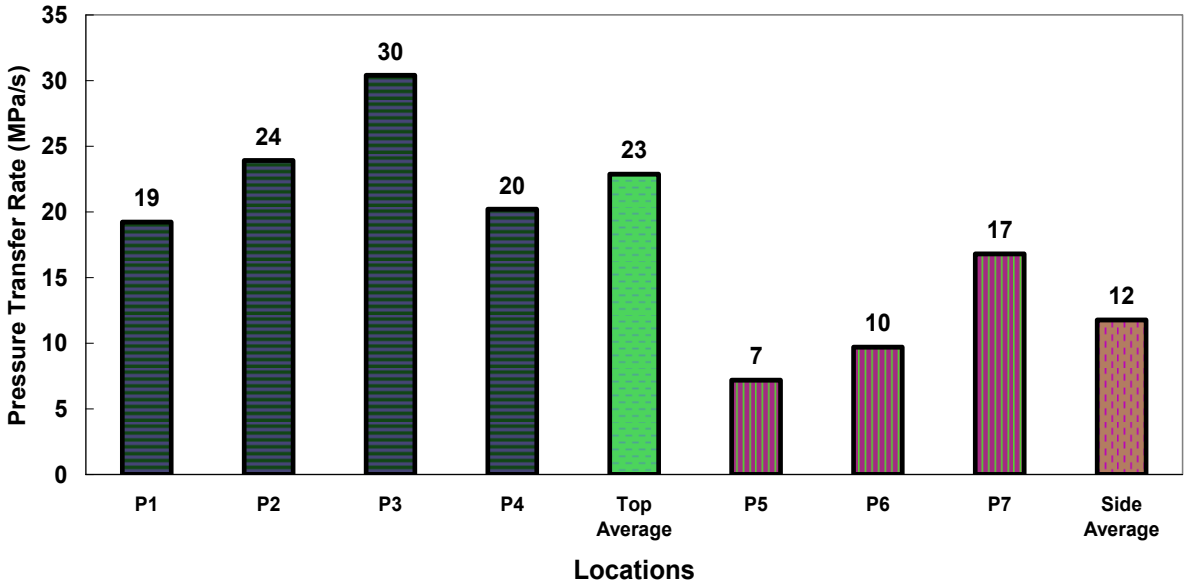


Figure 3. Initial local pressure transfer rates on the top and side surfaces of a cylindrical squeeze casting of magnesium alloy AM50A.

Pressure Distribution on Casting Surfaces

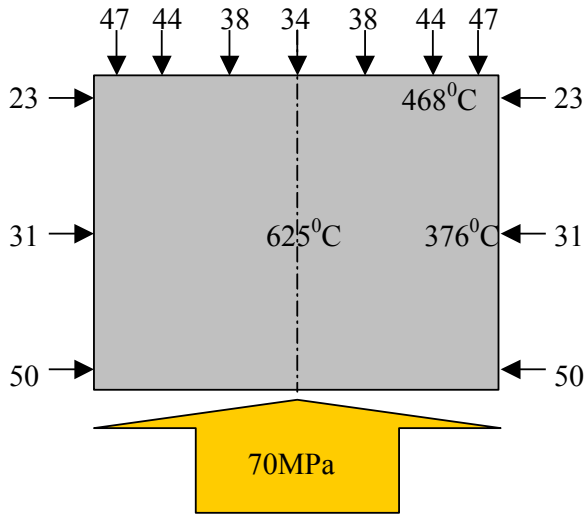


Figure 4. Initial pressure distributions 5 seconds after an external pressure of 70 MPa being applied.

A pressure distribution along the top and side surfaces of the cylindrical casting 5 seconds after the completion of the cavity filling under the applied pressures of 70 MPa with three instantaneous temperature measurements at the top, side and center of the casting is shown in Fig. 4. There was an increase in the pressure from 34 to 47 MPa as the distance from the center increases on the top surface. All the measured pressures were much lower than the original applied pressure of 70 MPa. Along the casting side, the pressure decreased considerably to 23 from the original applied pressure of 70 MPa with increasing the height from the bottom to the top of the casting. It is evident that the pressure distribution was inhomogeneous on either the side or top surfaces of the casting. This finding contradicts the existing viewpoint about squeeze casting, i.e., “molten metal is solidified under applied hydrostatic pressure” [10, 11].

Summary

The experimental investigation has been undertaken to obtain an understanding of transient pressure behavior in squeeze casting of magnesium alloy AM50A. The in-cavity pressures were directly measured. The results showed that that local cavity pressures at various locations changed with time in the duration of casting solidification and cooling. The pressure transfer rate varies considerably within the cylindrical geometry of the casting. The pressure transfer in a direction perpendicular to the external force is faster than that in a parallel direction.

Acknowledgements

The authors would like to take this opportunity to thank the Natural Sciences and Engineering Research Council of Canada and the University of Windsor for supporting this work.

References

[1] H. Hu, "Squeeze Casting of Magnesium Alloys and Their Composites", Journal of Materials Science, Vol. 33, 1998, 1579-1589.
[2] Y. Rolland, "Squeeze Casting: a Literature Review. (Report Review)" Gov. Res. Announc. Index. PB94-124575/XAB, 1993, ISSN 0097-9007,58.
[3] J. R. Franklin and A. A.Das, "Squeeze Casting--a Review of the Status. British Foundryman" Vol. 77, No. 3, Apr.1984, 150-158.
[4] S. Rajagopal, "Squeeze Casting: a Review and Update", J. Appl. Metalwork. Vol. 1, No. 4, Jan. 1981, 3-14.
[5] H.Matsubara,Y.Nishida, and S. Suzuki, "Measurement of Load Loss in Squeeze Casting" Rep. Gov. Ind. Res. Inst., Nagoya, Japan, Vol. 27, No. 7, July 1978,211-215.
[6] I.Yasushi, S.Yoshio, H. Iwahori and Y. Awano, "Transferred Pressure and Shrinkage Cavity of Aluminum Alloys on Squeeze Casting", Casting Engineering, Vol. 72, No. 4, 2000,263-267 (in Japanese).
[7] P. Krishna and R.D. Pehlke, "Theoretical and Experimental Investigation of Indirect Squeeze Casting of A356 Alloys", Light Metals 2001, 377-390.
[8] V.K. Venkatasamy, "Analysis of In-Cavity Thermal and Pressure Characteristics in Aluminum Alloy Die Casting", Master Thesis, The Ohio State University, Columbus, Ohio, 1996.
[9] Alfred Yu, "Mathematical Modeling and Experimental Study of Squeeze Casting of Magnesium and Aluminum Alloys", PhD Dissertation, University of Windsor, Windsor, Ontario, Canada, 2006.
[10] A.A. Das, B. Zantout and A.J. Clegg, "Solidification Processing by Squeeze Casting", Con. Proc. in Solidification Processing, Inst. of Metals, London, 1988. 472-475.
[11] M.R. Ghomashchi, A. Vikhrov, "A. Squeeze Casting: an Overview", Journal of Materials Processing Technology, Vol. 101, No. 1, 2000, 1-9.

Advanced Materials Research Vol. 936 (2014) pp 1671-1675
© (2014) Trans Tech Publications, Switzerland
doi:10.4028/www.scientific.net/AMR.936.1671

Microstructure and Mechanical Properties of Brazed Joints Used in Electronic Devices

Xuerui Wu[1,a *], Wenqing Qu[2,b], Haitao Li[3,c]

[1]XueYuan Road No.37,HaiDian District,Beijing, BeiHang University, China

[2]XueYuan Road No.37,HaiDian District,Beijing, BeiHang University, China

[3]No. 19, North 4th Ring Road West, Haidian District,

Institute of Electronics, Chinese Academy of Sciences P. R. China

[a]wuxuerui0745@163.com，[b]quwenqing@buaa.edu.cn，[c]442079679@qq.com

Keywords: AgCu28, AuCu20, oxygen-free copper, microstructure, mechanical properties

Abstract：The microstructure and mechanical properties of brazed joints of oxygen-free copper and oxygen-free copper, nickel-plated kovar, monel, nickel-plated stainless steel were respectively studied by using AgCu28 and AuCu20 filler metal. Effects of different filler metal on microstructure of the brazed joints were analyzed through metallurgical microscope, SEM, EPMA. The brazed joints tensile strengths were analyzed through tensile test. The results indicate that the brazing process of oxygen-free copper and nickel content alloy used AgCu28 filler metal, nickel element is easy to diffused into AgCu28, AgCu28 filler metal with nickel element wetting spreadability along grain boundary of the oxygen - free copper, resulting in the penetration of the grain boundary of the oxygen-free copper. The joints brazed by AuCu20 filler metal have the better performance than the joints brazed by AgCu28 filler metal.

Introduction

Electronic devices, such as multi-beam klystron, space traveling wave tube, high power klystron, are widely used in the field of basic research in physics, chemistry, information and the field of technical in communications, radar, medical diagnosis and treatment. There are nearly one hundred processes in the production of electronic devices, including metal brazing, welding, electronic spot welding.

Materials currently used in electronic devices are copper and copper alloys, nickel and nickel alloy, iron and steel, tungsten and molybdenum, tantalum and niobium, zirconium titanium and beryllium expansion alloy. These materials usually bonding by brazing. So far, there are few data on the microstructure and mechanical properties of brazed joints of oxygen-free copper, nickel-plated kovar, monel, nickel-plated stainless steel used in electronic devices.

The microstructure and mechanical properties of brazed joints of oxygen-free copper and oxygen-free copper, nickel-plated kovar, monel, nickel-plated stainless steel were respectively studied by using AgCu28 and AuCu20 filler metal. Through the analysis of the brazed joints performance, provide data support and technical guidance for production of electronic devices.

Experimental Procedures

The base metal used in the experiments were oxygen-free copper, nickel-plated kovar, monel and nickel-plated stainless steel. The base metals were brazed by butt. AgCu28 and AuCu20 were used

as filler metal.OlympusBX51M metallurgical microscope and JSM-5800 scanning electron microscope was used to observe and detect the microstructure and major element content distribution of the brazed joints. Joints tensile strength of each sample is the average of the five joints tensile strength. Table1 gives the major chemical composition of oxygen-free copper, nickel-plated kovar, monel and nickel-plated stainless steel.

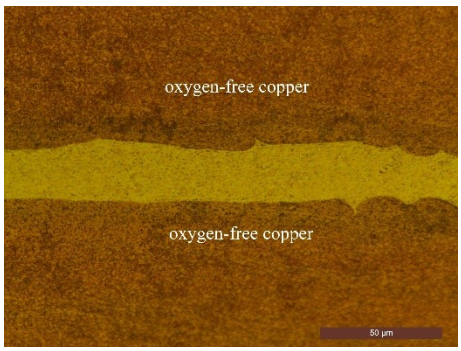
TABLE1 MAJOR CHEMICAL COMPOSITION OF BASE METALS (WT%)

base metal	Cu	Fe	Ni	Mn	C	Co	Si	Cr
oxygen-free copper	≥99.97	0.005	0.002	-	-	-		-
kovar	-	rest	32.1～33.6	0.05	-	14.0～15.2	0.30	-
monel	38.0～42.0	≤1.0	rest	1.25～2.25	0.3	rest	0.75	-
stainless steel	-	-	8.25～10.50	≤2.00	≤0.08		≤1.00	18.00～20.00

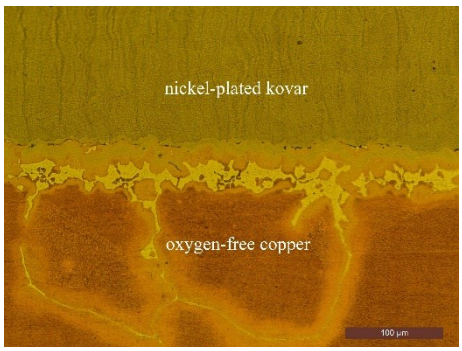
Results and Discussion

Microstructure of joints brazed by AgCu28 filler metal

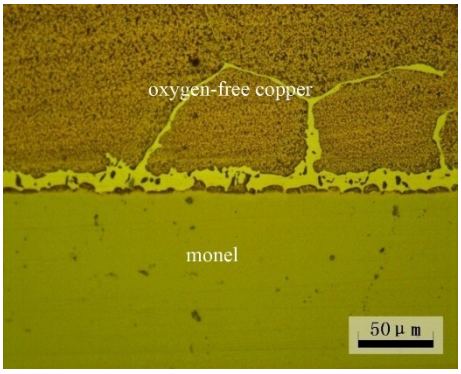
Figure 1 shows the microstructure of joints brazed by AgCu28 filler metal. As shown in Fig.1(a), the brazing seam is completely filled with AgCu28 filler metal. AgCu28 filler metal melts uniformity, having good wetting effect with oxygen-free copper. No defects existed in the brazing seam. Fig.1(b)-(d) show the microstructure of brazed joints of oxygen-free copper and nickel-plated kovar, oxygen-free copper and monel, oxygen-free copper and nickel stainless steel. In joints of oxygen-free copper and nickel content alloy brazed by AgCu28 filler metal, grain boundary penetration was occurred in oxygen-free copper after brazing. The depth of AgCu28 eutectic liquid penetrating into oxygen-free copper grain boundaries is about 100μm.



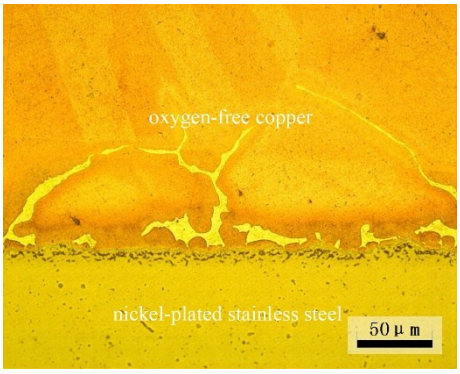
（a）oxygen-free copper and oxygen-free copper



（b）oxygen-free copper and nickel plated kovar



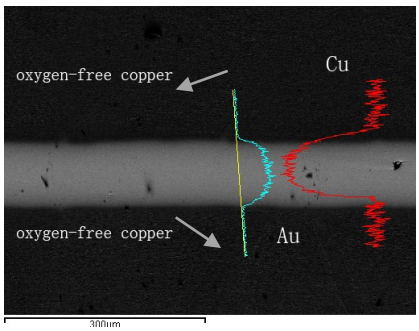
（c）oxygen-free copper and monel



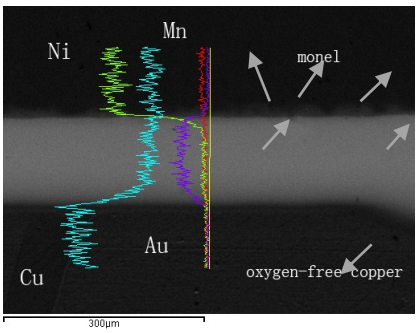
（d）oxygen-free copper and nickel-plated stainless steel

Fig.1 Microstructure of joints brazed by AgCu28 filler metal

As shown in Fig.2(a),the brazing seam of oxygen-free copper and oxygen-free copper distributed Ag (Cu) solid solution. Fig.2(b) shows the result of major element content distribution of the brazed joints of oxygen-free copper and nickel-plated kovar. Nickel element in the base metal was observed to be diffused into AgCu28 filler metal. Nickel element distribution in other joints brazed by AgCu28 filler metal are similar with that of the brazed joint of oxygen-free copper and nickel-plated stainless steel.



（a）oxygen-free copper and oxygen-free copper

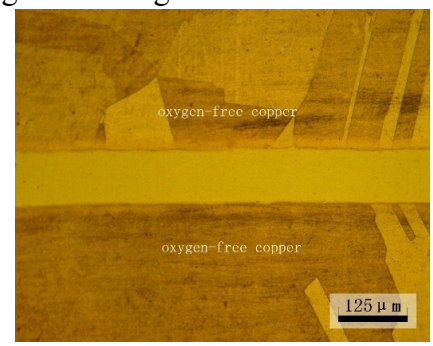


（b）oxygen-free copper and nickel-plated stainless steel

Fig.2 Major Element Content Distribution of Joints Brazed by AgCu28 Filler Metal

Microstructure of joints brazed by AuCu20 filler metal

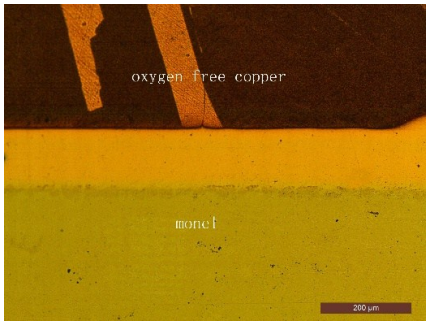
As shown in Fig.3，the microstructure of the joints brazed by AuCu20 filler metal are significantly different from that of the joints brazed by AgCu28 filler metal. The brazed joints of oxygen-free copper and oxygen-free copper, oxygen-free copper and nickel-plated kovar, oxygen-free copper and monel, oxygen-free copper and nickel-plated stainless steel obtained nearly best microstructure . AuCu20 filler metal melts uniformity, having obvious boundary with base metal and good wetting to surface of the base metal, no defects existed in the brazing seam.



（a）Oxygen-free Copper and Oxygen-Free Copper



（b）Oxygen-free Copper and Nickel Plated Kova



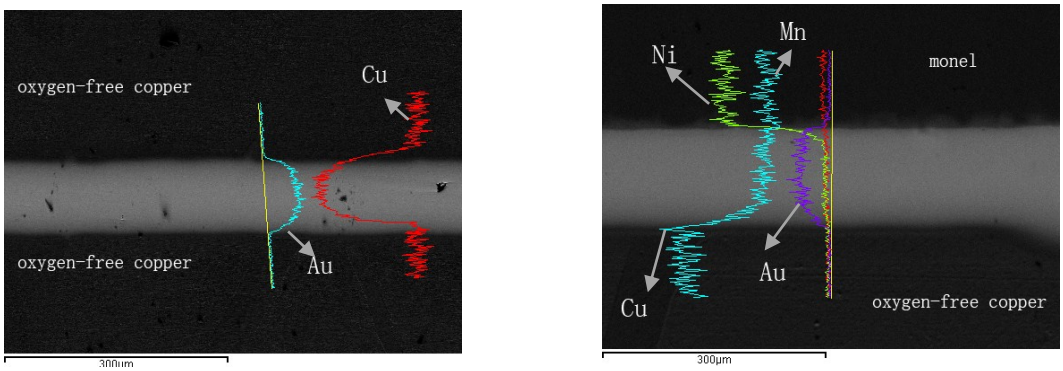
（c）Oxygen-free Copper and Monel



（d）Oxygen-free Copper and Nickel-plated Stainless Steel

Fig.3 Microstructure of Joints Brazed by AuCu20 Filler Metal

As shown in Fig.4(a), the boundary oxygen-free copper slightly dissolved and copper element was observed to be dissolved into AuCu20 filler metal. The more close to the oxygen-free copper base metal, the mass fraction of copper element is higher. This kind of phenomenon exists in all joints brazed by AuCu20 filler metal.



(a) oxygen-free copper and oxygen-free coppe

(b) oxygen-free copper and monel

Fig.4 Major Element Content Distribution of Joints Brazed byAuCu20 Filler Metal

Strength of brazed joints

Fig.5 shows the tensile strength test result of the brazed joints. Tensile testing specimens using AgCu28 as filler metal fractured at the base metal with the joint strength over 220MPa, expect for the testing specimens of oxygen-free copper and nickel-plated stainless steel. Tensile testing specimens using AuCu20 as filler metal fractured at the base metal with the joint strength over 215MPa.

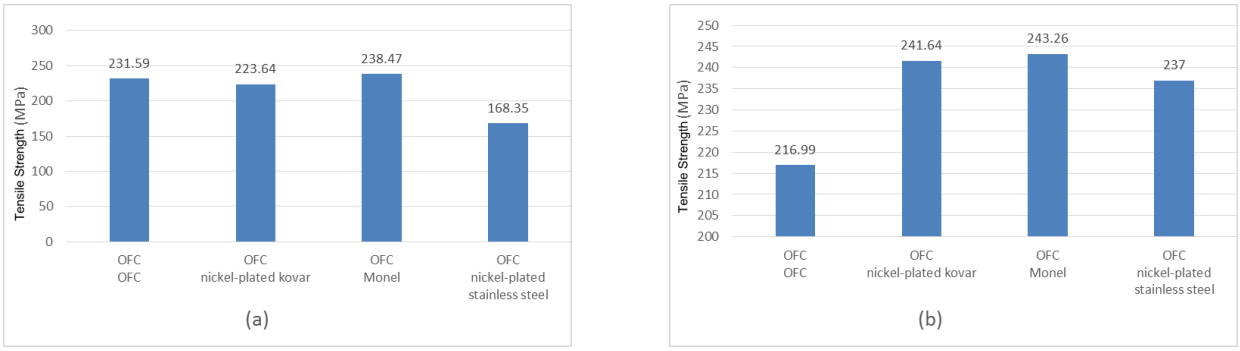


Fig.5 Tensile Test Results of Specimens Brazed by AgCu28 Filler Metal（a），AuCu20 Filler Metal（b）

Discussion

The experimental results show that the microstructure of joints brazed by AgCu28 filler metal vary along with the base metal. The joint of oxygen-free copper and oxygen-free copper brazed by AgCu28 filler metal has good performance, however, the other joints brazed by AgCu28 filler metal are found that filler metal penetrates along the grain boundaries of oxygen-free copper. The joints brazed by AuCu20 filler metal obtained nearly best microstructure.

The joint of oxygen-free copper and nickel-plated stainless steel brazed by AgCu28 filler metal fractured at the brazing seam, and the other brazed joints fractured at oxygen-free copper in tension test.

Comprehensively, the joints brazed by AuCu20 filler metal have the better performance than the joints brazed by AgCu28 filler metal.

Summary

(1) The microstructure of joints brazed by AgCu28 filler metal vary along with the base metal. The brazed joint of oxygen-free copper and oxygen-free copper has good performance, however, the other brazed joints brazed by AgCu28 filler metal are found that filler metal penetrates along the grain boundaries of oxygen-free copper.

(2) Nickel elements which base metal contains diffuse into AgCu28 filler metal, however, no obvious diffuse occurred at the joints brazed by AuCu20 filler metal in tension test.

(3) The joint of oxygen-free copper and nickel-plated stainless steel brazed by AgCu28 filler metal fractured at the brazing seam, and the other brazed joints fractured at oxygen-free copper.

References

[1] DING Yao-gen The Trend of High Power Microwave Vacuum Devices,2006,03:37-40.

[2] Wang Ming-hong，Xue Qian-zhong，Liu Pu-kun，Review of THz Vacuum Electronic Devices and Development,2008,07:1766-1771.

[3] DING Yao-gen, The application of High Power Microwave Vacuum Devices,2011,08: 1989-1994.

[4] Shi Xiu-mei, Development Situation and Prospect of Filler Metal used in Vacuum Devices,2012,1:16-19.

[5] LI Yine,JIANG Ting,SUN Xiaoliang，MA Guang, Brazing Material Used for Common Metal Materials in Vacuum Electron Devices,2010,12:203-205.

Advanced Materials Research Vol. 936 (2014) pp 1676-1680
© (2014) Trans Tech Publications, Switzerland
doi:10.4028/www.scientific.net/AMR.936.1676

Structure and Performance of Chemical Duplex Plating Ti Metal Layer on Diamond Surface by Hydrothermal Method

Xiang Dong[1,a*], Jia Li-qun[1,b], Liu Ke-gao[1,c]

[1] School of Material Science and Engineering, Shandong Jianzhu University, Jinan 250101,China
[a] e-mail: xiangd1015@163.com, [b] e-mail: jialiqun@sdjzu.edu.cn, [c] e-mail: liukg163@163.com

Keywords: Diamond; Hydrothermal method; Chemical duplex plating; Electorless plating; Surface metallization; Heat treatment

Abstract: As a surface of diamond has a higher interfacial energy and worse binding force, the diamond shed from matrix easily. For solving this, the microstructures and properties of the metallic coating on diamond surface were studied. The different temperatures, such as 110, 120, and 130 ℃ for 6 h, were used for coating diamond in the high-pressure reactor respectively. The structure and performance of the metallic coating on diamond surface were tested by Scanning Electron Microscopy (SEM), X-ray Diffraction (XRD) and diamond compressive strength instrument. The results showed that a continuous and compact coating of Ni, W and Ti on the diamond surface is obtained by the hydrothermal coating technology (chemical duplex plating) at 120 ℃. After heat treatment at 850 ℃ for 1 h, the better layer coatings form for protecting diamonds and reducing the trend of oxidize. Because the carbides of W and Ti present at the boundries between the coating and diamond surface, the combination of chemistry and metallurgy is gotten. The compress strength of diamonds after hydrothermal and heat treatment is higher than that of uncoated particles (those are 54.40% and 85.48%, respectively).

Introduction

A reaction environment which can make of less soluble or insoluble material dissolved and crystallized is created at high-temperature (100-1000 ℃) and at high-pressure (1-100 MPa) by using aqueous solution and heating reaction container [1]. The high purity, good homogeneity and strong combination substrates of a thin film are gained at lower temperatures by hydrothermal method [2, 3]. The method of hydrothermal is low cost, simple equipment and the grain size controlled in the forming thin film [4, 5].

The problem of diamond shedding from diamond tools has not been completely solved by far, it makes the efficiency and life of diamond tools reduce [6]. The metallization can be adopted for the metal layers which contain carbide forming elements coating on the diamond surface. The metallurgical binding between coating and diamond is formed by heat treatment, which metallic carbides are presented by the carbide forming elements reacting with carbon in the diamond. This lessens the shedding tendency of diamond [7, 8]. The coating layers of Ni-W-P are formed on the diamond surface by electroless plating [9], but the contents of strong carbide forming elements W is fewer, and the effects of metallurgical binding is limited. The layers contain Ti powders are deposited on the layer of Ni-W-P by chemical duplex plating (hydrothermal). When Ti and W react with carbon on diamond surface, the chance of forming carbide increase, the binding strength and wear resistance of diamond improves, and their cutting performance and the life of the product enhance [10-12].

Experiment

Experimental Methods

In this experiment, MBD50/60 diamond particles were used for electroless plating Ni-W-P. Then we put them into the reactor with reaction medium, and hydrothermal reaction carried out in IOIB-2 thermostats. Heat treatment performed in the experimental box-type resistance furnace. The surface morphology and composition distribution of diamonds were tested by JSM-6380LA scanning electron microscope and JXA-8800R electron probe. The produced phases studied by XRD (Rigaku D/MAX-Ra, CuK_{α}, 40kV×50mA, λ=1.54184 Å). The compressive strength of diamonds was tested by ZMC-Ⅱ diamond using hydrostatic strength meter.

Experimental Process

The technologic process of chemical duplex plating showed in Fig.1.

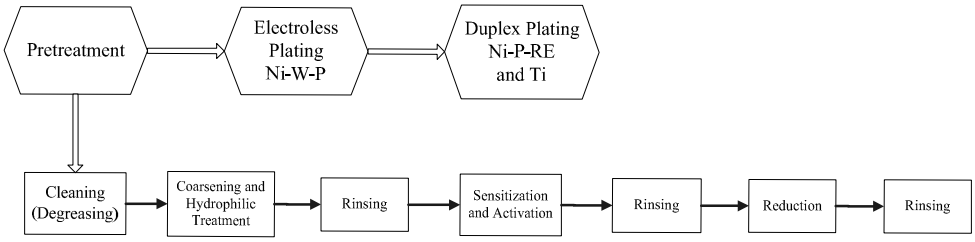


Fig.1 The technologic process of chemical duplex plating.

Pretreatment

Because the diamond belongs to nonmetallic crystals, its chemical properties are so stable. Therefore, it does not have the role of the surface catalytic activity. The catalytic center of palladium on diamond surface can be form by pretreatment including sensitization and activation (Fig.1), and the center can make Ni and W plasma deposite on diamond surface. For this, we adopted the salt-based colloid palladium.

Electroless Plating

Ni is elected as inducing metal to reduce the dissolving erosion of the diamond coating layer [13]. In diamond tools, W, which has good chemical binding affinity with the carbon atoms in diamond and does not damage diamond, considered the best binding metal of diamond. The solution made of $NiSO_4 \cdot 6H_2O$ 6～10g/L, $Na_2WO_4 \cdot 7H_2O$ 32～38g/L, $NaH_2PO_2 \cdot H_2O$ 8～12g/L, $Na_3(C_6H_5O_7) \cdot 2H_2O$ 4～10g/L, $C_3H_6O_3$15～20mL/L, trace stabilizer and pH 8.0~8.4. The temperature of electroless plating Ni-W-P is 90~95℃, and the plating time is 1h. The speed of stirring is moderate.

Chemical Duplex Plating (Hydrothermal)

If chemical duplex plating brought into effect after sensitization and activation, the catalytic activity on diamond surface would be destroyed because of metal Ti powders adsorbed on the layer of sensitization and activation [13]. Therefore, the technology of hydrothermal duplex plating Ti must be used after electroless plating. The solution made of $NiSO_4 \cdot 6H_2O$ 27g/L, $NaH_2PO_2 \cdot H_2O$ 30g/L, $Na_3C_6H_5O_7 \cdot 2H_2O$ 8~12g/L, $C_3H_6O_3$ 28~30mL/L, $C_4H_6O_4$ 1~4 g/L, $C_4H_6O_6$ 2~4 g/L, Rare Earth 0.5~1.0 g/L, Titanium 2~5 g/L, trace stabilizer and pH 4.0~5.0. The temperature of hydrothermal duplex plating is 110~130℃, and the plating time is 6h.

Heat Treatment

The heat treatment can make carbides (such as WC, TiC) form. The chemical and metallurgy combination between coating layer and diamond surface was achieved. According to the literature [14], the composition, structure and formation conditions of compounds is Ti/diamond:＞873K(600℃), TiC; W/diamond:＞973K(700℃), WC. The heat temperature must be above 700℃to forming carbide, and it may be below 900℃ for avoiding thermal damage. The heat treatment process was selected for 1h at 850℃.

Results and discussion

Surface Morphology and Composition Analysis

Surface Morphology and Composition Analysis after Electroless Plating Ni-W-P

The surface morphology of diamond particles after electroless plating by SEM shows in Fig.2(a). The coating which is complete, uniform and dense on diamond surface is observed. When the coating is enlarged, the particles (see Fig.2(b)) which are more uniform size, round cellular on the coating are observed. The composites of coating are analyzed by EPMA. It presentes in Fig.2(c) the main element is Ni and then is W, P.

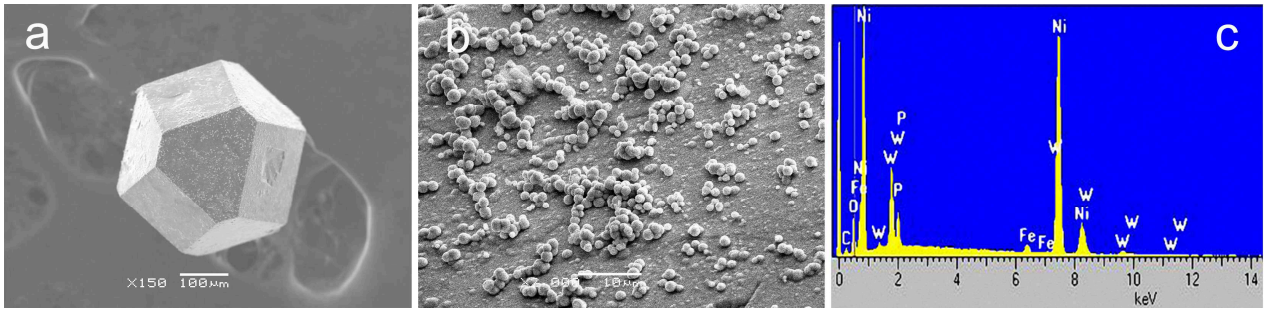


Fig.2 Surface morphologies and EDS of electroless plating Ni-W-P of diamond:
(a) surface morphology, (b) micro-morphology, and (c) EDS.

Hydrothermal Coating Surface Morphology and Composition Analysis

Fig.3 shows particle morphology at different hydrothermal temperatures. The coating on diamond surface at 120℃ is relatively complete and fully coated diamond particles, which surface are formation, uniform, dense and rarely shedding. The diamond surface coating sheds in varying degree at the other temperatures, of which shedding coating is the most serious at about 110℃. Therefore, diamond particles which treated at 120℃ by the hydrothermal method take as the main research object.

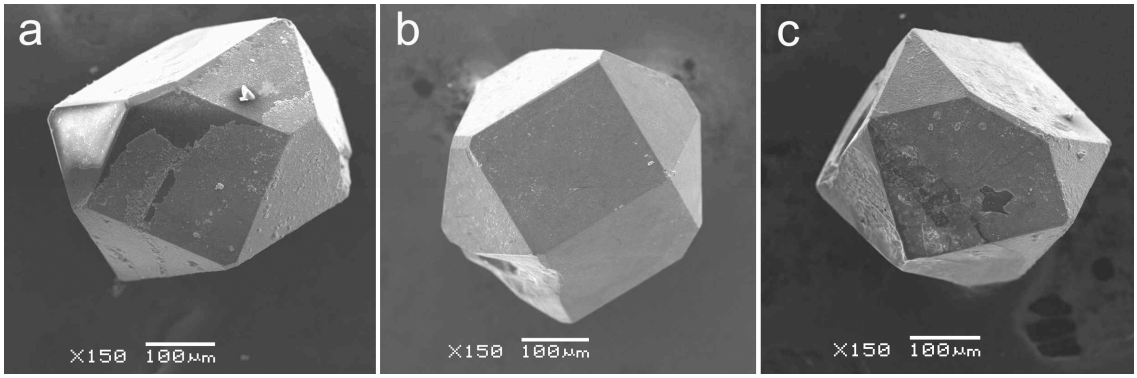


Fig.3 Surface morphology of hydrothermal of diamond at different temperatures.
(a)110℃, (b) 120℃, (c) 130℃

The Coating Surface Morphology after Heat Treatment and XRD Analysis

Fig.4(a) shows the particle morphology and the micromorphology of the coating diagram respectively after surface plating and heat treatment at 850℃. The coatings cauterize to form a large or small cellular layer at a high temperature. The coating surface is rough but more dense comparing with that before heat treatment. Fig.4(b) points out the thickness of coating after electroless plating, hydrothermal duplex plating and heat treatment is about 5-10 μm. The sediment particles formed a dense coating, and the coatings of electroless plating and hydrothermal method have mixed up after heat treatment. However, the internal layer can keep completely in order that the carbide forming elements have enough time to react with the diamond, and this will reduce the oxidation tendency.

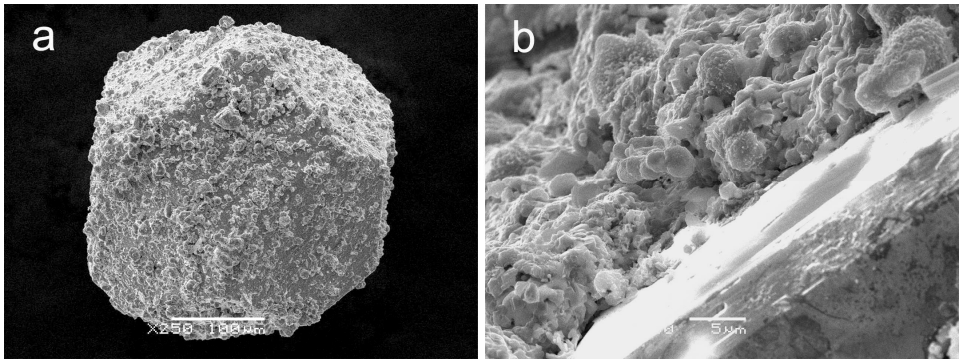


Fig.4 Surface morphology of diamond after plating and heat treatment at 850℃

(a) Diamond particle morphology, and (b) The cross-section morphology of the coating.

XRD analysis can be seen (Fig.5) that the WC and TiC diffraction peaks lines are more sharply after heat treatment. With the temperature raising, the diffusing of W and Ti from high concentration to be low in coating produces. It proves that the carbide WC and TiC created by carbon on the diamond surface and metal W, Ti after heat treatment, and increase binding force between diamond and the coating.

Determination of Compressive Strength

It can be seen from Fig.6 that the compressive strength of diamond improves with temperature increasing. It is because that the boundaries of each solution increased and the rate of coating improves. When the deposition amont of elements increases, the thickness of coating layer will increase. It makes the compressive strength increase similarly. However, when the temperature is 130℃, the Ni compound layer on the reactor's wall would be difficult to clean, and the coating easily shatters. So the compressive strength would decrease. Therefore, the hydrothermal coating temperature should select for 120℃. The carbide forming elements diffuse to the diamond surface under thermal stress between the coating and the diamond after hydrothermal and heat treatment, and the strengthening, hardening and toughening produces at the location area of join parts enhances. That makes the compressive strength increased. The carbide WC and TiC formed with carbon on diamond and carbide forming elements in coating can create greater binding strength and improve the compressive strength of diamond. The compressive strength of hydrothermal treatment at 120℃ is 755MPa, while that after plating and heat treatment is 907MPa. Compared with original uncoated particles, the compressive strength of them can improved to 54.40% and 85.48%, respectively.

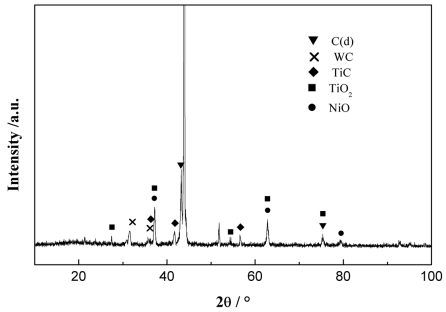


Fig.5 XRD pattern of diamond after plating and heat treatment at 850℃.

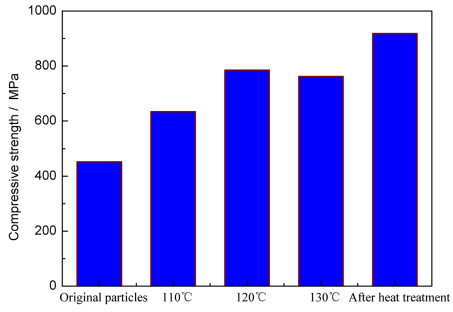


Fig.6 The comparison of compressive strength of diamond.

Conclusion

According to discuss experimental results, the following results are summarized:

(1) The reasonable process of electroless plating and hydrothermal method on diamond surface was studied. The metal coatings on diamond surface which are an uniform, dense and containing Ni, W, Ti after a certain technological, have been gained.

(2) The morphology of coating after hydrothermal at 120℃ for 6h and heat treatment at 850℃ for 1h which is dense and complete was observed by SEM. Such structure is helpful to combing between diamond and coating, and oxidation tendency decreases.

(3) Carbides WC and TiC in coating after hydrothermal and heat treatment were tested by XRD. This can improves the binding force between the diamond and coating, and the chemical combination of diamond has realized.

(4) After hydrothermal and heat treatment, the compressive strength of diamond can be increased. Comparing with the original diamond, the compressive strength of diamond at 120℃ increase to 54.40%, and while that after hydrothermal and heat treatment increases to 85.48 %.

References

[1] K. Byrappa, T. Adschiri, Prog. Hydrothermal technology for nanotechnology, Cryst. Growth Ch. Mater. 53 (2007) 117-166.

[2] A. T. Chien, J. S. Speck, F. F. Lange, A. C. Daykin, C. G. Levi, Low temperature/Low pressure hydeothermal synthesis of Barium Titanate: Powder and heteroepitaxial thin films, J. Mater. Res. 10 (1995) 1784-1789.

[3] H. Huang, H. Gong, H. J. Luo, The affecting factors of nanocrystalline titanium dioxide powdersrerived by hydrothermal precipitation, Chi. Ceram. 38 (2002) 11-14.

[4] Y. Q. Song, Z. Z. Kong, Y. Gao, Study on interface of diamond and metal matrix, J. Syn. Cryst. 28 (1999) 404-408.

[5] F. F. Lange, Chemical solution routes to single-crystal thin films, Science. 273 (1996) 903-909.

[6] M. Hayashi, N. Ishizawa, S. E. Yoo, Preparation of barium titanate thin film on titanium-deposited glass substrate by hydrothermal electrochemical method, J. Am. Ceram. Soc. 73 (1990) 930-933.

[7] Z. W. Huang, H. Y. Lu, L. B. Li, Y. D. Li, Methods to enhance bonding strength between diamond and matrix in diamond tools, Diamond & Abrasives Engineering. 28 (2007) 15-17.

[8] D. Xiang, M. S. Li, B. Xu, K. G. Liu, Research progress of techniques of coated diamond, Superhard Material Engineering.18 (2006) 44-49.

[9] D. Xiang, L. W. Yin, K. G. Liu, L. Q. Jia, Study of W metallic coating layer on diamond surface by hydrothermal, Adv. Mater. Res. 79-80 (2009) 699-703.

[10] W. W. Steven, Diamond retention in sintered cobalt bonds for stone cutting and drilling, Diam. Relat. Mater. 8 (1999) 2043-2052.

[11] X. L. Shi, G. Q. Shao, X. L. Duan, Z. Xiong, H. Yang, The effect of tungsten buffer layer on the stability of diamond with tungsten carbide–cobalt nanocomposite powder during spark plasma sintering, Diam. Relat. Mater. 15 (2006) 1643-1649.

[12] R.C.Agarwala, V. Agrawala, Electroless alloy/composite coatings: A review, Sadhana. 28 (2003) 475-493.

[13] E. Breval, J. P. Cheng, D. K. Agrawal, Development of titanium coatings on particulate diamond, J. Am. Ceram. Soc. 83 (2000) 2106-2108.

[14] Y. H. Wu, G. B. Li, C. L. Li, C. F. Wang, Cladding on diamond, J. Tianjin Instit. Tech. 18 (2002) 62-65.

Advanced Materials Research Vol. 936 (2014) pp 1681-1686
© (2014) Trans Tech Publications, Switzerland
doi:10.4028/www.scientific.net/AMR.936.1681

Numerical simulation and optimization technology of Lost foam casting

Hong-ze CHEN [1,a], Hong-zhao DONG [2, b], Zhong-de SHAN [3, c]

[1,2]College of Mechanical Engineering, Zhejiang University of Technology, Hangzhou, 310014, China

[3] China academy of machinery science and technology, Beijing, 100044, China

[a] chenhongze110@sina.com, [b] its@zjut.edu.cn (Corresponding author)

[c] shanzd@cam.com.cn,

Keywords: Numerical Simulation, Lost Foam Casting (LFC), Defect Analysis, Process Optimization

Abstract: The filling and solidification process of casting that is closely related to lots of casting defects and has significant effect on the mechanical properties of castings. In this paper, the research status and development direction of numerical simulation technology of casting, especially of lost foam casting were reviewed and discussed. Also a brief introduction of the basic situations and product characteristics of several outstanding cast filling and solidification simulation softwares were summarized. In addition, the actual domestic application status of numerical simulation technology of lost foam casting in the foundry enterprises was analyzed and some suggestions were given as well.

Introduction

In the LFC process, liquid metal is poured directly onto a refractory-coated, foamed polymer pattern which is buried in loose sand, the polymer pattern undergoes thermal degradation and is gradually replaced by the molten metal, which solidifies and produces the casting. Compared with the traditional way of casting, LFC is more green and efficient, its advantages are as follows [1]: (1) High quality of the castings, particularly for the complicated parts. (2) The flexible design. (3) The clean processing. (4) The low cost of investment. LFC has been very successful in areas such as automobile manufacturing and is widely applied to cast iron and cast steel, but the development of LFC of AI alloy and Mg alloy was relatively slower [2]. The application prospect of LFC will be more extensive as the technology continues to be more mature and innovative.

Due to the gasification of the foam pattern and the gas's interaction with the molten metal, the filling process of LFC is quite complex and very different from the traditional casting in flow field, temperature field, filling capacity, etc. Although it has many advantages, casting defect is more easily generated in the LFC process, thus its further development is cramped. The filling and solidification process can be studied qualitatively and semi quantitatively by computer numerical simulation technology without restriction on the experimental condition, various influencing factors of the casting defect can be found and analyzed, it is significant to both the development of LFC process theory and the guidance of practical production [3, 4, 5].

Numerical simulation technology of casting

A two-dimensional fluid flow software MAC was applied to the filling process of casting for the very first time by R.A.Stoehr et al. in 1983 [6]. Fruitful developments in model description, algorithm optimization, experimental verification and the development of simulation software of

numerical simulation technology of casting which were mainly conducted by American, European, Japanese research workers were witnessed soon afterwards[7, 8, 9]. The tenth International Conference on Modeling of Casting, Welding and Advanced Solidification Processes was held at Destin city of Florida, United States in 2003, the progress in numerical modeling of solidification was briefly reviewed on structure simulation, segregation & microporosity simulation, shaped casting simulation, database and critical experiments[10]. Plenty of studies focused on alloy materials simulation and even some experimental investigations of the flow in continuous-casting mold under the influence of the magnetic field in recent years [11, 12, 13]. Domestic development of numerical simulation of casting is relatively slower, still some important work have been conducted, such as a mathematical model was developed for simulating the fluid flow and heat transfer phenomena during mold filling for die casting using the finite difference method by several scholars at Tsinghua University[14].

Numerical simulation technology of LFC

Numerical simulation technology had been applied to the filling and solidification process of LFC for the prediction of casting defect by Wang et al. in 1993[11]. Abundant research findings of numerical simulation technology of casting have been gradually applied to LFC because of its numerous advantages compared to the traditional way of casting though the craft process is far more complicated. The general flow chart of numerical simulation of LFC is shown in figure 1: (1) The establishment of a reasonable 3-D model of the castings. (2) Generating 2-D and 3-D finite element meshes of the model. (3) Check the grid. (4) Set the corresponding simulation parameters if the meshes are proper, or rezoning the meshes. (5) Simulation calculation. (6) Analyzing the simulation results. The mainly influencing factors of filling and solidification process of LFC are given in figure 2: (1) The gas evolution and chemical reaction of different density of the foam pattern materials are diverse. (2) The air permeability and strength of the coating is vital. (3) The quality of the castings would be affected by different pouring way, sprue-runner-gate area ratio, pouring rate and pouring temperature. (4) Also the vacuum degree, the breathability of the molding sand and the molten metal material are crucial.

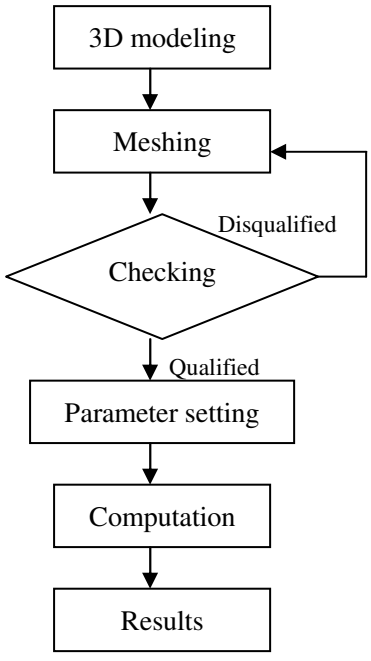


Fig. 1 Simulation flow chart

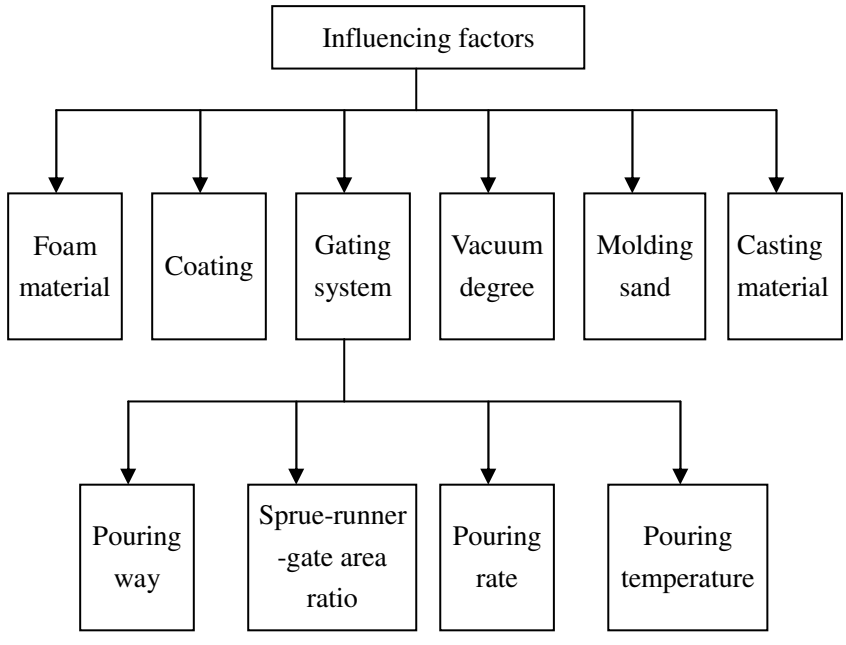


Fig. 2 Influencing factors of LFC simulation

The fundamental key points of an effective numerical simulation of LFC are as follows: (1) The establishment of a reasonable 3-D model, the mesh division and the data transmission problem between them must be solved properly. (2) Lucubrate the mathematical and physical model of the simulation software. (3) Having adequate craft knowledge of LFC. As shown in table 1, these are some major soft wares that have been widely adopted by foundry enterprises of different countries, they have achieved significant economic benefits especially in the western countries. Filling and solidification simulation, residual stress and deformation analyzing can be done by almost all of these softwares though each of them has their own features and focuses. Even some of them can make a predictive analysis of the casting defect and the mechanical performance of the castings and the microstructure analysis is the development direction.

Table 1 Major simulation softwares of different countries

Name	Country	Arithmetic	Main Function	Application
Flow 3D	USA	FVM/FDM	Automatic mesh division; Solidification shrinkage; Binary segregation; Surface defects tracking; Microstructure analysis	Sand mould casting; Die-casting; LFC; Centrifugal casting; Continuous casting
MAGMA Soft	Germany	FDM/FEM	Analysis of flow and heat transfer, stress and microstructure; Strong pre processing and post processing functions	Sand mold casting; Shell mold casting; Pressure casting; Investment casting; Metal mould casting
Procast	France	FEM	Free surface flow, stress and deformation calculation; Simulation of the microstructure formation	Sand mold casting; Shell mold casting; Low pressure permanent casting; LFC; Investment casting; Centrifugal casting
ADSTEFAN	Japan	FEM	Large mesh model; Predict shrinkage, thixomolding, defects, temperature; Stress and structural deformation calculation	Pressure casting; Sand mold casting; Thixomolding casting
InteCAST	China	FDM	Flow mold filling & solidification process; Mold filling heat transfer coupling	Sand mold casting; Shell mold casting; Pressure casting; Investment casting; Metal mould casting

Lots of foreign scholars focused on the establishment of the mathematical model of the LFC process in recent years. A computational fluid dynamics model has been developed by S.H. Bhavnani et al. to simulate the fluid flow of molten aluminum and the heat transfer involved at the interfacial gap between the metal and the foam pattern [15].A 2D model was developed by J. Shayegh et al. for heat transfer, foam degradation and gas diffusion at the interfaces of the liquid metal, foam pattern and gaseous gap in between, for EPS lost foam casting process [16]. Appropriate physical and kinetic models of thermal degradation of EPS foam applicable to LFC were reviewed by Pravin Kannan et al [17].

Domestically, the hydrodynamics characteristic of foam degradation of LFC was studied by Z.L. Zhang et al. and they also predicted the remnants of the foam pattern and its impact to the casting quality [18]. How different alloy materials, pouring system affect the filling and solidification process of LFC and how to choose the optimum casting parameters were given by J.H. Zhao by using Procast [19]. Y.L. Ma proposed to optimize craft from the perspective of defect prediction and

the analyzing of the causes of the formation of the defects [20].On the basis of production experience, the characteristics of LFC and the actual production conditions, X.SH. Li designed a kind of LFC craft of connecting cylinder and the causes of foundry defects were analyzed [21]. J. Peng researched the variations in vacuum degree during the filling process of LFC and analyzed the wall attachment effect and the gas trapping and regurgitating process [22]. Also numerical simulation for filling process of EPS beads in LFC is one of the hotspots [23].

Domestic application Status

Table 2 Domestic application status of numerical simulation technology of LFC

Actuality	Major cause	Suggestions
1. Perfunctory with the customer 2. Popularisation means 3. Good earning performance	1. Technological base is poor 2. Lack of consciousness in application of new techniques 3. Improper use of the technology 4. The limitations of the software itself	1. Change some technicists's backward perception 2. Enhance training specialized talents 3. Having a correct view of the technology and utilize it rationally

Numerical simulation technology of casting is having a widespread use in the western countries, particularly almost all of the car castings manufacturers are equipped with simulation system, but the popularization rate of numerical simulation technology of LFC of our country is very low, of course there are some but rare enterprises which have successfully applied this technology and have a good earning performance. The domestic application status is shown in table 2, since small and medium-sized enterprises dominate the domestic LFC industry, the technological base is poor and even some senior technicists thought that problems could be solved based on their experience.

Conclusions and Outlook

The numerical simulation of filling and solidification process, stress and microstructure analysis of solidification process, the prediction of shrinkage cavity and porosity are the main current research and application fields. Because of the coexistent of liquid and solid metal, the mechanical property of the castings is hard to measure during the simulation process and still the proper mechanical model can't be completely established. The simulation of microstructure is far more complicated than the filling and solidification process, whereas the simulation technological conditions are generally set in a too simplistic and idealized way, besides, the scale of majority domestic foundry enterprises are small, the production equipment is lag behind and the technical strength is weak, it is difficult for them to provide the rigorous actual production process conditions and the technicians are lack of systematic professional training, thus domestically there is still some way to go to apply this technology to the actual production efficiently and broadly.

Acknowledgements

The financial support of the National High Technology Research and Development Program of China, Grant NO. 2012AA040201, is gratefully acknowledged.

References

[1] Z.T. Fan. Advanced material forming technology and theory. Chemical Industry Press, 2006.

[2] Z.T. Fan, WM Jiang. Development Trend and Status of Lost Foam Casting Technology. Casting, 2012, v.61; No.42706:583-591.

[3] H.T. Zhao, G. F. Mi, K. F. Wang. Status of filling and solidification process simulation of casting. Aerospace Manufacturing Technology,2007,01:28-33.

[4] B.Y.Yao,H.K.Mao,H.Xu,X.B.Meng. Status and Development Trend of Numerical Simulation of Flow Field in Casting Process. Foundry Technology,2012,10:1211-1214.

[5] Y. Li. Application of Foundry Numerical Simulation Software on the Foundry Practice. Foundry Technology, 2011, 04:572-574.

[6] Hwang W S, Stoehr R A. Fluid now modeling for computer aided design of castings. Journal of Metals, 1983, 35.

[7] Hang J D, Tsai H T, Lin H J, et a1. Modeling of fluid flow and heat transfer phenomena during the thin-plate casting process for Fe-4.5wt%Si alloy. Modeling of Casting, Welding and Advanced So1idification Processes, 1993.

[8] Frayce D, Loong C A. Mathematical modeling of the die casting process. Light Metals, 199l.

[9] Ilinca F, Hetu J F, Audet M, Bramley R. Simulation of 3-Dmold-filling and solidification processes on distributed memory parallel architectures. ASME Fluids Eng DiV Publ FED, 1997.

[10] M.F.Zhu, J.Yu, T.Dai. Recent progress in Numerical Modeling of Solidification Processes. Foundry, 2005, Vol.54, NO.2.

[11] Iwona Nowak, Jacek Smolka, Andrzej J. Nowak. An effective 3-D inverse procedure to retrieve cooling conditions in an aluminium alloy continuous casting problem.Applied Thermal Engineering, Volume 30, Issue 10, July 2010, Pages 1140-1151.

[12] Timmel K, Eckert S, Gerbeth G. Experimental Investigation of the Flow in a Continuous Casting Mold under the Influence of a Transverse, Direct Current Magnetic Field. Metallurgical and Materials Transactions B-Process Metallurgy and Materials Processing Science. Vol: 42 Pages: 68-80, FEB 2011.

[13] Fagerholt E, Dorum C, Borvik T. Experimental and numerical investigation of fracture in a cast aluminum alloy. International Journal of Solids and Structures. Vol: 47, P: 3352-3365, DEC 1 2010.

[14] L.G. Jia, S.M. Xiong, W.M. Feng, B.CH. Liu. Numerical simulation of fluid flow and heat transfer during mold filling for die casting. Journal of Tsinghua university, 2001,(02):8-11.

[15] X.J. Liu, S.H. Bhavnani, R.A. Overfelt. Simulation of EPS foam decomposition in the lost foam casting process. Journal of Materials Processing Technology, V 182, 2 Feb 2007, P: 333-342.

[16] J. Shayegh, S. Hossainpour, M. Rezaei, A. Charchi.Developing a new 2D model for heat transfer and foam degradation in EPS lost foam casting process.International Communications in Heat and Mass Transfer, Volume 37, Issue 9, N 2010, P 1396-1402.

[17] Pravin Kannan, Joseph J. Biernacki, Donald P. Visco Jr.A review of physical and kinetic models of thermal degradation of expanded polystyrene foam and their application to the lost foam casting process. Journal of Analytical and Applied Pyrolysis, Volume 78, Issue 1, J 2007, P: 162-171.

[18] Z.L.Zhang et al.Three-Dimensional Simulation of EPS Evaporation Process for Lost Foam Casti. Foundry, 2010, 59(10).

[19] J. H. Zhao et al. The Research on the Numerical Simulation Technology of EPC Based on Procast. The 22th Chongqing Annual meeting of the casting, 2012.

[20] Y. L. Ma et al. Application of Simulation of Filling and Solidification in LFC Process Based on ProCAST. Hot Working Technology, 2012, 41(01).

[21] X. S. Li et al. EPC Casting Process and Numerical Simulation of Connection Cylinder. Hot Working Technology,2012,41(11).

[22] J. Peng et al. Numerical Simulation Analysis on Filling Process of Lost Foam Casting. Journal of Chengdu Textile College, 2012,29(3).

[23] Y.J.Chen et al.Numerical simulation on filling process of expendable polystyrene beads and its application in LFC. The 7th international conference of China casting factory director,2006.

Advanced Materials Research Vol. 936 (2014) pp 1687-1693
© (2014) Trans Tech Publications, Switzerland
doi:10.4028/www.scientific.net/AMR.936.1687

A Research on Optimization of Cutting Parameters Based on NSGA-II

Liang Xiaozhen[1, a], Yan Guangrong[2, b], Chu Hongzhen[3,c]

[1,2]School of Mechanical Engineering and Automation, Beijing University of Aeronautics and Astronautics, Beijing 100191, China

[3]Shenyang AircraftCorporation [a]liangxz3116@foxmail.com

[b]yangr@buaa.edu.cn [c]Chu_hz@126.com

Keywords: cutting parameters; NSGA-II; optimization

Abstract: In this paper, we take the CNC milling on as the object of the research and establish an optimized model of cutting parameters by using algorithms based on NSGA-II. Taking the machining time and the surface roughness as target function, and the rotational speed and cutting power as constraint condition, the optimization of a CNC milling case is realized, and is verified by simulation of cutting using CAXA ME and Vericut. The outcome confirms the truth that NSGA-II is a useful technique in the optimization of cutting parameters.

Introduction

Choosing cutting parameters is one of the most important steps in a machining process. Using appropriate cutting parameters is the guarantee of machining quality, it also lowers the production cost and increases the productivity in a machining process [1]. However, choosing cutting parameters is constrained by many factors among which there exists interaction and restriction with each other. The core problem to be solved in the optimization of machining process is to make an appropriate choice of cutting parameters and find the optimum combination of them.

Genetic algorithms have been applied in optimization of machining process, but they have their disadvantages respectively. In reference [2] there is only one production target considered, while although in reference [3] and reference [4] multiple goals are taken into consideration, we have to set weight for different production targets, which is subjective and lacks of flexibility when responding to changes in actual production, because we can't decide the weight of one production target when unknown variant involves and production changes.

MOGA (multiple-objective genetic algorithms), which evolves from GA, has been focused on methods based on Pareto-optimal in recent years [5]. Research on MOGA has produced SPEA (strength-Pareto evolutionary algorithm), PAES (Pareto-archived evolutionary strategy), NSGA-II (non-dominated sorting genetic algorithms II), etc. NSGA-II, one of the mature algorithm of MOGA, approaches the Pareto-optimal front by using a fast non-dominated sorting approach [6] and presents a new selection operator. The NSGA-II has also been widely studied because of its good performance in multi-objective optimization.

In this paper, we build an optimized mathematical model, using t_w (machining time of each work piece) and Ra (surface roughness) as the optimization target, v_c (milling speed), f (feed rate), a_p

(milling depth) and a_e (milling width) as design variables, and spindle rotation speed and cutting power as the constraint condition. By using NSGA-II, we make a pilot study of applying this method to optimize machining process and attempt to get an optimal set of values when the condition of multiple production targets are considered and give relative quantitative production targets values, which is for technologists' reference in production practice.

NSGA-II

Introduction to NSGA-II

Non-dominated sorting genetic algorithm, which was first proposed by Srinivas and Deb in 1994, is a multi-objective genetic algorithm based on Pareto-optimal. It's flexible in choosing the number of objectivities to be optimized and can give the non-inferior solution which is even distributed, hence in the field of multi-objective optimization it shows strong superiority. However the defects emerges as deeper researches are taken, mainly in the following three aspects: a) computational complexity, b) elitism approach is lacking, c) the need for specifying a sharing parameter. Against these defects, Deb improved the core algorithm in NSGA [7], as well as introduced elitism approach and computation for congestion degree, which alleviated all the three difficulties mentioned above.

As experiment already presented [8], NSGA-II shows a better functionality in contrast with other representative algorithms like PAES, SPEA, etc.

The non-dominated sorting algorithm is shown in Fig. 1:

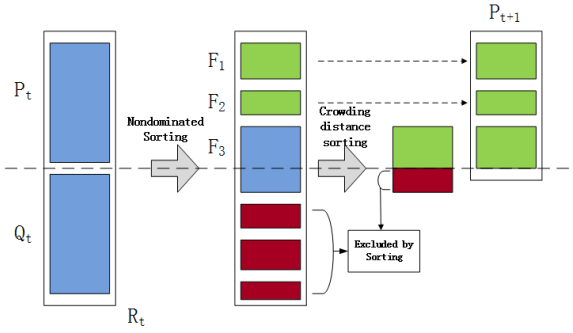


Fig. 1. Non-dominated Sorting

Calculation Process of NSGA-II

The calculation process of Non-dominated Sorting Genetic Algorithm based on Pareto solution can be described as follow (also shown in Fig.3):

(a). Randomly generate the initial parents population P_0 with population size N;

(b). Apply non-dominated sorting on population P_0, assign adapted value for each individual correspondingly;

(c). Manipulate P_n using genetic operators (selection, intersection, variation) to get population Q_n;

(d). Get a synthetic population R_n of size $2N$ which composes of parents population P_n and offspring population Q_n, apply non-dominated quick sorting, delaminate R_n anew through non-dominated hierarchy and get hierarchy F_1, F_2, F_3 ……;

(e). Empty P_n and put F_1, F_2, F_3……in P_{n+1} seriatim until the number of elements in $\{P_{n+1} + F_t\}$ is bigger than N and the individual number of P_{n+1} is less than N;

(f). Compute the crowding degree of hierarchy F_t and sort on it, put the first $N - |P_{n+1}|$ individuals in P_{n+1}.Now the individual number of P_{n+1} is N;

Repeat step (c) to step (f) until the iteration stops.

The whole process is shown in Fig.2 as follows.

Mathematical Model of Optimization in Machining Process

Multi-objective Optimization

Problems on multi-objective optimization can be described in a mathematical model as Eq.1, Eq.2 and Eq.3.

$$\text{Design variables: } X = [x_1, \ldots, x_n]^T \tag{1}$$

$$\text{Target Functions: } f(X) = [f_1(X), f_2(X), \ldots, f_n(X)] \tag{2}$$

$$\text{Constraint conditions: } \begin{matrix} g_i(X) \geq 0 (i = 1, 2, \ldots, n) \\ h_i(X) = 0 (i = 1, 2, \ldots, n) \end{matrix} \tag{1}$$

Target functions described above are always optimization targets which conflict with each other. Optimization of each target function maybe either maximum or minimum. But since transformation between them can be realized, we can take minimum as the optimization target of each function uniformly.

In this paper, we consider minimum as the optimization target.

Design Variables

We reference the four elements of milling dosage [9] as design variables, which includes: milling speed v_c, feed rate f, milling depth a_p, milling width a_e.

The relation between milling dosage and related parameters are:

$$v_c = nD\pi / 100 \tag{2}$$

$$v_f = fn = f_z zn \tag{3}$$

In above equations Eq.4 and Eq.5, n is milling speed, D is cutter diameter, f_z is feed rate per tooth, and v_f is feed speed.

Objective Functions

In production practice, the following objective functions are in common use: maximum production rate, the minimum production cost, the maximum profit rate, metal removal rate and surface roughness. Here we use the maximum production rate (the shortest time to produce a singleton) and the minimum surface roughness as our objective functions.

Production Time Function

Referring to MINFRE, the method to calculate time of machining a singleton [10, 11] is:

$$t_w = t_m + t_c \frac{t_m}{T} + t_0 \tag{4}$$

$$T = \left(\frac{C_v d_0 q_v}{v_c a_p^{x_v} f_z^{y_v} a_e^{u_v} z^{p_v}} \right)^{\frac{1}{m}} \tag{5}$$

In above equations Eq.6 and Eq.7, t_w is time of machining a singleton, t_m is cutting time of a single process, t_c is tool change time, T is tool life, t_0 is auxiliary time besides tool change time; and $C_v, q_v, x_v, y_v, u_v, p_v, m$ are correlation coefficients related to tool life T, which are bound up with cutting parameters and cutting conditions.

Surface Roughness

The calculation of surface roughness [10] is:

$$Ra = 318 \frac{f_z^2}{4 d_0} \tag{6}$$

In the above equation Eq.8, f_z is feed rate per tooth and d_0 is cutter diameter.

Constraint Conditions

Machine Tool Speed Constraint

Constrained by machine tools, the rotating speed must be controlled within the limits of spindle speed

$$v_{\min} \le v \le v_{\max} \tag{7}$$

In the above equation Eq.9, $V_{\min}$ is the minimum spindle speed while $V_{\max}$ is the maximum.

Machine Tool Power Constraint

The actual cutting power P_m is supposed to be less than the product of rated power P_E and total efficiency η, that is [10]

$$P_m \le P_E \bullet \eta \tag{8}$$

$$P_m = \frac{F_c \bullet v}{1000} (kw) \tag{9}$$

$$F_c = C_{F_c} a_p^{x_{F_c}} f_z^{y_{F_c}} a_e^{z_{F_c}} d_0^{m_{F_c}} Z n^{p_{F_c}} K_{F_c} (N) \tag{10}$$

In the above equations Eq.10, Eq.11, Eq.12, F_c is main cutting force, C_{F_c} is influence coefficient which is related to experiment conditions; $x_{F_c}, y_{F_c}, z_{F_c}, m_{F_c}, n_{F_c}$ are impact indexes on

cutting force; d_0 is cutter diameter, Z is the number of cutter teeth and K_{F_c} is the correction factor of cutting force when calculation conditions are different from experimental conditions.

Other Machine Tool Constraint

In actual production, the choose of cutting dosage is limited by the constraint of machine tool system, it need to satisfy the following conditions shown as Eq.10 and Eq.11:

$$f_{\min} \le f \le f_{\max} \tag{11}$$

$$a_{p\min} \le a_p \le a_{p\max} \tag{12}$$

Cutting Experiment Simulation

Experiment Process

a). Consult with the manual to get each coefficient and a recommended range of cutting dosage for reference; b). Implement the NSGA-II through programming language, input each parameters and get a set of optimum values after computing; c). Establish the geometry model and generate NC machining code in CAXA ME; d). Operate the simulative cutting test in Vericut and analyze the experimental results we get.

Machining Environment

The size of machining part: 230*120*35, mm as its unit of measurement (which is illustrated by Fig. 4).

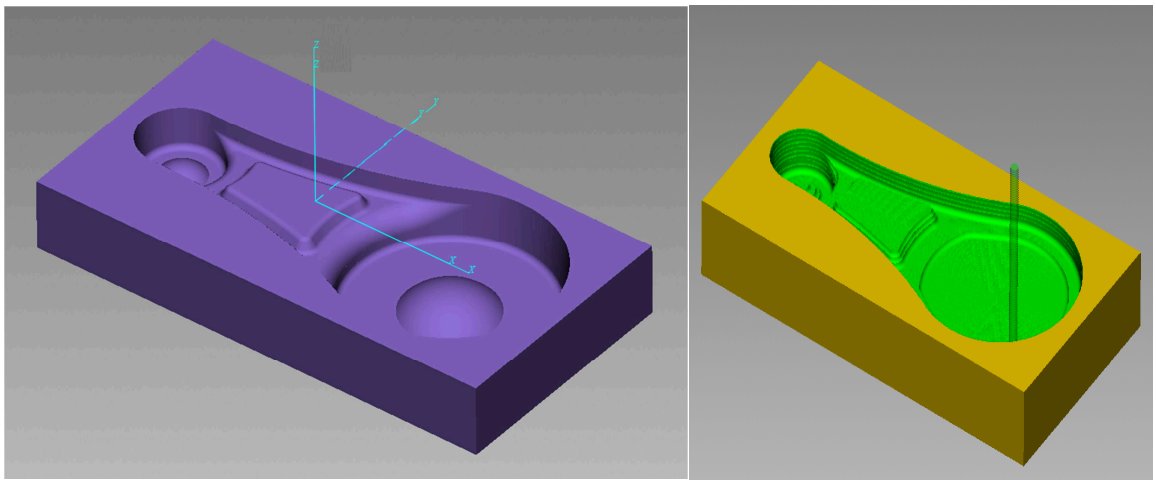


Fig. 4. Part design and machine Simulation

Material of machining part: carbon structural steel, σ_b=650MPa.

Machining tool: ball end cutter with diameter 10mm and material cemented carbide.

Table 1 shows the type of machine tool for use: XK5032, consulting with manual for relevant information [12].

TABLE 1.MACHINING TOOL INFORMATION

Type	Machine size(mm)	Table travel (mm)	Spindle speed (r/min)	Main electric power(kw)
XK5032	320×1120	760×350×400	80~4500	5.5

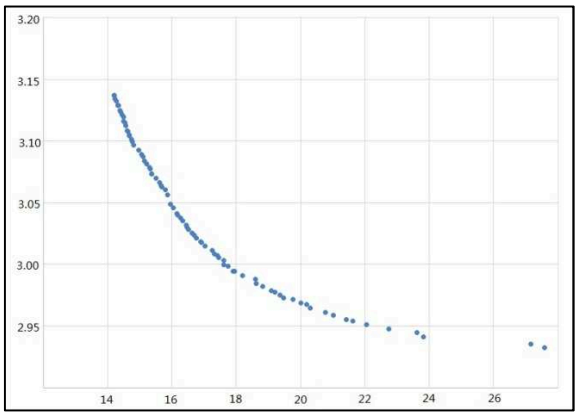


Fig. 5. Computation result

Experimental results

By applying the non-dominated sorting in the calculation process of NSGA-II, we eventually get the datum which belongs to the same non-sorting degree after calculation. The distribution of the outcome shown in Fig.5 can be considered as the Pareto front of the calculation.

In the following table we choose a set of datum in the medium of the result as optimized parameters to compare with empirical parameters:

TABLE 2. EXPERIMENTAL RESULTS

Parameters	n(r/min)	v_f (m/min)	a_p (mm)	a_e (mm)	Ra (μm)	t_w (s)
Empirical parameter[9]	1900	0.95	3	3	3.15	23.57
Optimized parameter	2763	1.10	3	3	3.01	17.13

From the experimental results shown in Table 2, we come to the conclusion that after we use the optimized cutting parameters not only has the surface quality been improved but also the machining time reduces substantially. Hence we draw the conclusion that this algorithm is effective in optimizing cutting parameters. Referring to related theories of metal-cutting, a higher cutting speed can produce a better surface, which proves the correctness of the result in another aspect.

Conclusion

In this paper we introduce the NSGA-II algorithm into cutting parameters optimization. Optimize the cutting dosage by establishing optimal mathematical model and realize the optimization by programming language. Then we validate the optimized results using CAXA ME, generating the NC code, and Vericut, simulating the machining process. By the verification and analysis of the simulative machining results, we could draw the conclusion that the algorithm we have used in this paper can meet the demand for parameters optimization and it can be valuable when applied in engineering.

Acknowledgements

This work was financially supported by the Important National Science & Technology Specific Projects (2013ZX04012021).

References

[1] Hua Chen, Hai-xia Zhao. Multi-objective optimal model of cutting parameters based on linear goal programming. Journal of Xi'an Institute of Technology [J]. 2007(01): 24-28.

[2] Xiufen Xu. Based on genetic algorithm for CNC gear milling machine for cutting parameter optimization [J]. Journal of Chinese Agricultural Mechanization. 2013(01): 214-216.

[3] Xiaogang Sun. A research on CNC milling machining parameter optimization and simulation based on genetic algorithms [D]. Southwest Jiaotong University, 2008.

[4] Hao Huang. Cutting parameters optimization based on improved genetic algorithm [D]. Huazhong University of Science and Technology, 2009.

[5] Xundi Diao. A study on project scheduling problem and its simulation based on multi-objective genetic algorithm [D]. Shanghai Jiao Tong University, 2010.

[6] Yuan Gao. Non-dominated sorting genetic algorithm and its application [D]. Zhejiang University, 2006.

[7] Deb K, Pratap A, Agarwal S, et al. A fast and elitist multiobjective genetic algorithm: NSGA-II [J]. IEEE TRANSACTIONS ON EVOLUTIONARY COMPUTATION. 2002, 6(2): 182-197.

[8] Mao-Guo GONG, Li-Cheng JIAO, Dong-Dong YANG, Wen-Ping MA. Research on Evolutionary Multi-Objective Optimization Algorithms [J]. Journal of Software, Vol.20, No.2, February 2009, pp.271−289.

[9] Zhang Chen, Zhan Zhi-hui. Comparisons of selection strategy in genetic algorithm [J]. Computer Engineering and Design, 2009, 30(23): 5471-5478.

[10] Wen Shi-hua, Zheng Jin-hua, Li Mi-qing. Comparison and research of mutation operators in multi-objective evolutionary algorithms [J]. Computer Engineering and Application, 2009, 45(2): 74-78.

[11] Wanshang Wang, Min Xing. Mechnical Manufacture Manual [M]. Shenyang: Liaoning Science and Technology Press, 2002.

[12] Rongdi Han. Metal Cutting Theory and Tools [M]. Harbin: Harbin Institute of Technology Press, 2007: p94.

[13] Xing Ai, Shigang Xiao. Concise Cutting Manual [M]. Beijing: China Machine Press, 2002: p107.

[14] Xianzhi Ma. Practical Handbook of mechanical processing [M]. Shenyang: Liaoning Science and Technology Press, 2002: p654-655.

Advanced Materials Research Vol. 936 (2014) pp 1694-1700
© (2014) Trans Tech Publications, Switzerland
doi:10.4028/www.scientific.net/AMR.936.1694

Behavior of Microwave Heating of 316 Stainless Steel Green Body

Zhiwei Li[1, a], Kaiyong Jiang[1,b *], Fei Wang[1,c] and Jiliang Zhang[1,d]

[1]Xiamen Key Laboratory of Digital Vision Measurement, Huaqiao University, Xiamen, 361021, China

[a]lzw_lee@163.com, [b]jiangky@hqu.edu.cn, [c]wangfei@hqu.edu.cn, [d]mikeswell@hqu.edu.cn

Keywords: microwave heating; 316 stainless steel; heating behavior

Abstract. This paper mainly introduces the mechanism of microwave heating: electric conduction loss, eddy current loss and arc discharge. The microwave heating behavior of 316 stainless steel powder body which made by gel casting was investigated in the paper. Experiments on different microwave power, powder particle size, and the content of auxiliary heating material showed that the smaller the powder particle size, the larger microwave power and auxiliary heating materials help 316 stainless steel body for sintering.

Introduction

Microwave sintering began in the 1960s when Tinga. W. R [1] proposed the microwave sintering of ceramics materials. The microwave sintering of metal materials was proposed 30 years later. Metals do not absorb microwaves and reflect it totally in the traditional view, until the Professor R. Roy [2] proved that stainless steel, copper alloy, nickel base alloy powder parts can be sintered by microwave heating. The report caused the wide attention of microwave sintering of metals. Then, K. Saito [3] sintered Fe, Co, Ni, Cu and stainless steel powder compact successfully by microwave sintering, and found that microwave can promotes sintering process except Fe. A. Upadhyaya [4] et al using both conventional sintering and microwave sintering way to sintered 316L stainless steel and 434L stainless steel powder compacts, and found that heating rate reached 45℃/min, the sintering time reduced by 90% by using microwave sintering.

In China, microwave sintering technology was proposed by Wuhan University of Technology in 1988. Then comes to Shenyang Metal Research Institute of Chinese academy of sciences, Shanghai Silicate Research Institute of Chinese academy of sciences, Tsinghua University [5]. Huang [6] analyzed the theory model of microwave heating mechanism, proposed the calculation method of absorbing properties. Peng [7] studied the heating properties of metal powder compact with different elements, different compacting pressure and different output power, and drew a conclusion: the temperature curve of microwave heating is a function of metal powder particle size. The smaller the particle size, the faster the heating rate and the higher the heating temperature obtained. Heating rate depends on the porosity of metal powder compact. Under the same power output, the higher the porosity gets faster heating rate, while the temperature eventually achieved has nothing to do with the initial porosity. Zhou [8] used the microwave sintering sintered WC-Co alloy, found that magnetic loss dominates in low temperature area (below 1100℃), while in high temperature (above 1100℃), Co changes from ferromagnetism to paramagnetism with the collapse of the magnetic domain. The magnetic contribution to the energy dissipation is very weak, WC-10Co alloy absorbs microwave energy mainly in the form of dielectric loss.

Microwave heating technology, with its unique advantages in metallic materials applications, has broad prospects. In this paper, the characteristics of microwave heating 316 stainless steel(316SS) is studied with a series of experiments, and microwave sintering process of 316SS are discussed.

Microwave Heating Mechanism of Powdered-metal Body

When a metallic metal conductor in the electromagnetic field, its internal free charge will quickly gather to the surface under the effect of electromagnetic field. Relaxation time is used to characterize the speed of free charge response to electromagnetic field change. It is far shorter than

electromagnetic vibration period, so in the beginning of every vibration cycle, free charges had already gathered on the conductor surface, and internal free charge density is zero. Since there is no free charge inside the bulk metal, bulk metal cannot be effectively heated. Electric current exists on the surface of the metal conductor within the electromagnetic field, which results ohmic losses. Decreasing the size of metal conductor, to make it exactly couple with microwave electromagnetic field, causes effectively heating [9 ~ 11].

The mechanism of interaction between microwave and material are free charge movement loss, bound charge polarization loss and non-uniform interface loss [12 ~ 13]. For powdered-metal body, Yi [6] considered that the dielectric loss, the eddy current loss and powder particles of microwave multiple scattering lead to energy transformation. In the process of sintering microwave energy will be converted to heat energy.

Conductance Loss

Interaction between electromagnetic wave and material varies with wavelength, microwave mainly affects the rotation of the free molecule and bound molecule. The mechanism of interaction between microwave and materials is closely related to the external electromagnetic field, and it can be described using Maxwell's equations.

For nonmagnetic material, the microwave propagation law in the material submits to the differential forms of Maxwell's equations. The power absorbed per unit area of the conductive surface, P, is expressed as

$$P = \frac{R_s}{2}\int_v |H_t|\,\mathrm{d}V = \frac{2R_s|E_0|^2}{\eta_0^2} \tag{1}$$

Where Rs is the surface resistivity ($Rs = 1/\delta\sigma$, σ is electrical conductivity, and δ is the skin depth); E_0 is the electric field amplitude at the surface; and η_0 is the impedance of free space (377Ω). Assuming the radius of spherical metal powder particle is r_p, the electromagnetic power density (PEM) can be expressed as

$$P_{EM} = \frac{3P}{r_p} = \frac{6R_s|E_0|^2}{\eta_0^2 \cdot r_p} \tag{2}$$

If all the microwave energy is converted into heat energy, the change of temperature can be expressed as

$$\frac{\Delta T}{\Delta t} = \frac{P_{EM}}{\rho C_p} = \frac{6R_s|E_0|^2}{\eta_0^2 r_p \rho C_p} \tag{3}$$

Where T is the temperature; t is the time; ρ is the density of powder; and C_p is the specific heat capacity.

Eddy-current Loss

Initially, particles are loose contact in the green body, electric contact and heat transfer are very weak. When the green body is put in the microwave field, electrons on the metal surface move directionally under the effect of microwave electromagnetic field, which produce the so-called eddy current [16].

The eddy-current loss is one of the microwave sintering mechanisms of powdered-metal [11, 14]. Free charges in metal conductor have a very fast speed under the effect of electric field force. Relaxation time is 1e(-18)s orders of magnitude, while microwave vibration period is between 1e(12)~1e(9)s. There is a great difference between them. It is assumed that microwaves' component of electric and magnetic field are constants to the movement of free charge, which means microwave can be described as the uniform plane wave which is a simple superposition of orthogonal

electrostatic field and static magnetic field. Before charges move to the surface of the particle, the particle is not an equipotential body, it still exists the electric field intensity (E_x) inside. As shown in Fig. 1, motion electron is forced by electric field force (F_E) and Lorentz force (F_B) at the same time, their circular motion in plane OXZ forms eddy current. If lower the intensity of electric field and magnetic field, the induced current could not breakdown the particle interface with certain resistance, free electrons are bound in the respective of particles, no accumulation of charge on the surface. There are eddy current inside each particle, and produce joule heat, thus heating the body as a whole.

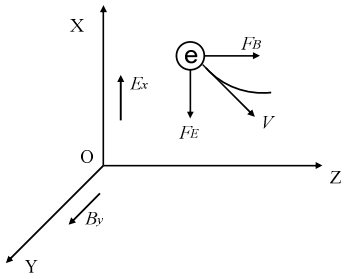


Fig. 1. The Movement of Free Electron in the Metal Particles in Microwave Field

Arc Discharge

Arc discharge also makes contribution to the microwave heating. Powered-metal body is porous, there are lots of gaps between particles. The clearance between the powder particles produce arc discharge in the microwave field, so as to heating the body. Residual gas in the body fuelled the arc discharge phenomenon. Arc discharge was promoted by increasing the microwave power. On one hand, it is propitious to promote the sintering, on the other hand, too much of arc discharge will lead to "thermal runaway", and there will be a larger reflected power into the magnetron, reduce the service life of magnetron.

Experiment

Powders used in the experiments were gas-atomized 316(C: 0.053; Si: 0.611; Mn: 0.757; Ni: 10.49; Cr: 17.99; Mo: 2.197; S: 0.0085; P: 0.033; and Fe: bal.) stainless steel (Shandong Zhongtai alloy co., LTD.). The mean particle size is 12.71μm. Powders were graded to four levels (<25μm, 25~38μm, 38~50μm, >50μm) according to size by using vibration test sieve.

Green bodies were obtained by gel casting; gelatin was selected as binder, sodium alginate as dispersant. A slurry made from metal powder and a water-based monomer solution is poured into a mold, polymerized in-situ to immobilize the particles in a gelled part, removed from the mold while still wet, then dried. Green bodies were heated in a vacuum tube furnace (Yixing Qianjin Furnace Industry Equipment Co., Ltd., KTF1400) to eliminate moisture at 600℃. The body is about 8g. Microwave vacuum sintering furnace (Changsha Synotherm co., LTD., HAMiLab - HV3) with a frequency of 2.45GHz was used for Microwave sintering. Bodies were placed in a quartz crucible, alumina was selected as thermal insulation material, and silicon carbide as auxiliary heating material. The temperature of specimen was measured using an infrared pyrometer (American Raytek MM2MH). The heating equipment is shown in Fig. 2.

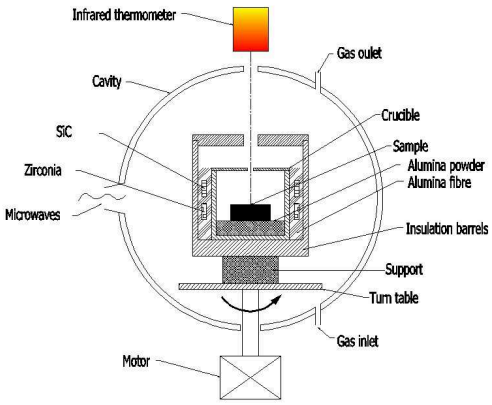


Fig. 2. Microwave Heating Experiment Device

Parametric Comparative Experiments and Discussion

As compare to conventional sintering, microwave sintering is expected to be more uniform and energy-saving. The microwave heating behavior is influenced by many factors, three of them were studied in this paper. Experiments with different microwave power: 600w, 800w, 1000w, and 1200w were carried out on microwave heating characteristics of the gelcast body, and powder size is 0~25μm. Experiments with different powder size: <25μm, 25~38μm, 38~50μm, >50μm under the microwave heating power of 1000w were carried out. Experiments with different content of auxiliary heating materials (SiC): 0g, 25g, 50g, and 100g were performed, and powder size is 0~25μm.

Microwave Heating Power

Microwave power has great effect on the heating behavior of 316SS. As shown in the Fig. 3, the temperature curve can be divided into four stages. In the initial stage, the body temperature rises quickly (300~400℃/min) until to a turning point (600~800℃). This is because the body is the source of heat, it absorbs a lot of microwaves and converts them into heat energy. The second stage: body temperature maintains a balance or decrease, mainly because heat dissipation is more than heat absorption. A lot of heat conduction and radiation, cause the decrease of body temperature. The third stage: heat absorption is greater than the heat dissipation the body temperature rise gradually. Stage 4: when the temperature reaches a certain value, the heating rate decreases, temperature curve flatten out, until the body reach thermal equilibrium, the sintering temperature reach the maximum.

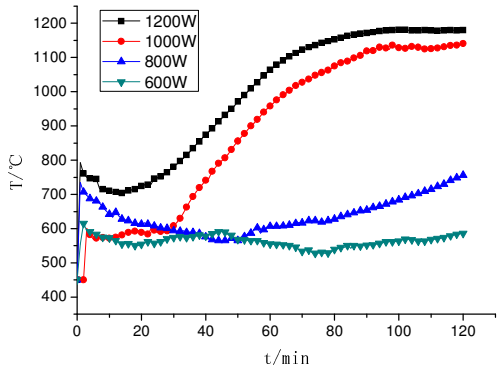


Fig. 3.Thermal Profiles of 316SS Powdered-metal Body as a Function of Microwave Heating Power.

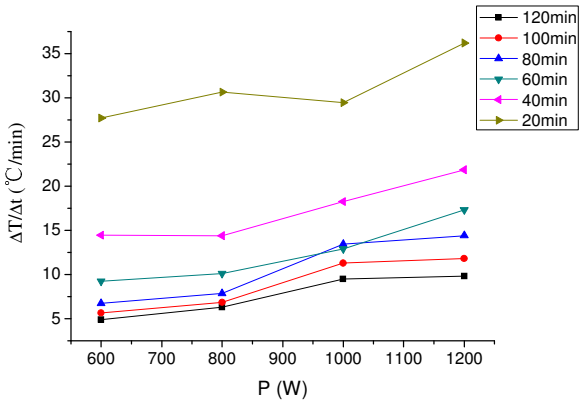


Fig. 4.The Heating Rate of 316SS Powdered-metal Body During the Different Time Period

Fig.4 shows a linear relationship between heating rate and the microwave power approximately. As mentioned in formula (3), $\Delta T/\Delta t$ is in direct proportion to P_{EM}/C_p. When increasing the input power, the power density will increase, so does the heating rate. But too high microwave power has adverse effects on the sintering. First, it may lead to "thermal runaway". Local sample absorbs a large amount of microwaves, then the temperature rises rapidly, resulting in a burnt body and grain

boundary oxidation. Second, higher power means more microwaves, the body cannot absorb all of them, plenty of them are reflected back, not only cause the waste of energy, but also shorten the service life of the magnetron microwave generator.

Powder Particle Size

Fig. 5 shows that bodies with smaller powder particle size have higher heating rate. For 316SS, the magnetic permeability is μ=1.008, resistivity is σ=7.4×10-7Ω·m, and microwave frequency is f = 2.45GHz. According to the penetration depth formula, the penetration depth of 316SS is about 3μm. For spherical powder, those radius less than 3μm undergo volumetric heating when subjected to microwaves. However, for relatively coarse powders (r_p >3μm), the heating may be conductive from the outside (skin) to the interior of the powder. The volume fraction of the coupled zone can be calculated.

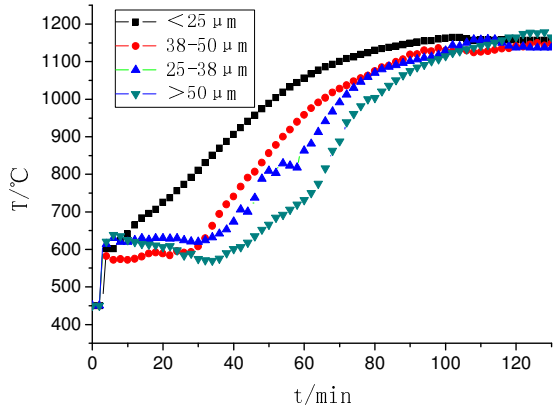


Fig. 5. Thermal Profiles of 316SS Powdered-metal Body as a Function of Particle Size under the Microwave Heating Power of 1000w.

As presented in Fig. 6, assumes that the powder radius is r_p, the penetration depth is δ. The shadow part is the area of interaction with microwaves.

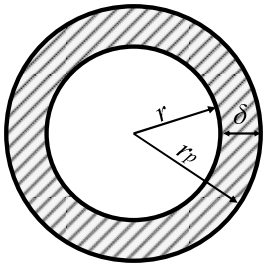


Fig. 6. The Spherical Powder

The volume of powder is

$$V = \frac{4}{3}\pi r_p^{\,3} \tag{4}$$

The interaction volume is

$$V_e = \frac{4}{3}\pi\left(r_p^{\,3} - r^3\right) \tag{5}$$

The interaction volume fraction is

$$\frac{V_e}{V} = \frac{r_p^{\,3} - r^3}{r_p^{\,3}} = \frac{r_p^{\,3} - \left(r_p - \delta\right)^3}{r_p^{\,3}} = 1 - \left(1 - \frac{\delta}{r_p}\right)^3 \tag{6}$$

It indicates that the larger powder size results in the smaller interaction volume fraction. The interaction volume fraction of four powder sizes are calculated in table 1.

TABLE 1. THE INTERACTION VOLUME FRACTION OF DIFFERENT POWDER SIZES.

Powder size	0~25μm	25~38μm	38~50μm	>50μm
Volume fraction	0.56~1	0.40~0.56	0.32~0.40	0~0.32

The Content of Auxiliary Heating Materials

Auxiliary heating materials also have influences on the microwave heating behavior. As presented in Fig. 7, surrounded by SiC, the body obtains lower temperature at first stage. The main reason is that at the beginning of sintering both bodies and SiC absorb microwaves, the body surrounded by SiC absorbs less microwaves. The Fig. also suggests that heating rate and sintering temperature increase with the increase of the SiC content. When the content of SiC reaches a certain value, more SiC have little influence on microwave heating. To compare temperature cure of 50g of SiC and 100g of SiC, they are almost the same.

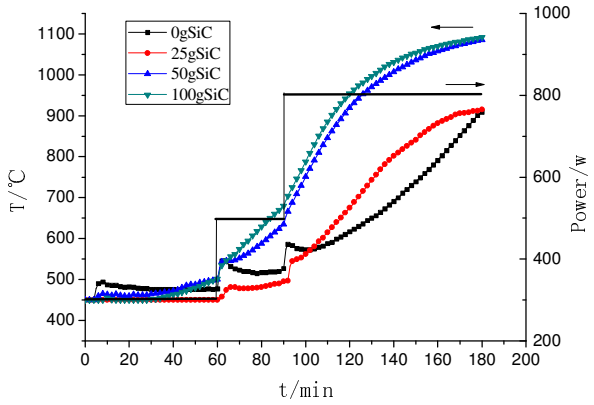


Fig. 7. Thermal Profiles of 316SS Powdered-metal Body as a Function of the Content of SiC.

As shown in Fig. 8 after adding SiC, the body with different powder particle size show the familiar heating properties and their temperature curve almost coincide. Power of 300W, 500W and 800W result in the heating rate of 3℃/min, 5℃/min and 7℃/min respectively. To sum up, SiC help microwave rapid heating, promote the effect of sintering. Both SiC and green body absorb microwaves, the body could be volumetric heating. However, excess SiC is not conducive to the uniformity of temperature field. Excess SiC absorb more microwaves than the body, thus the temperature of the edge of the crucible is higher than the center.

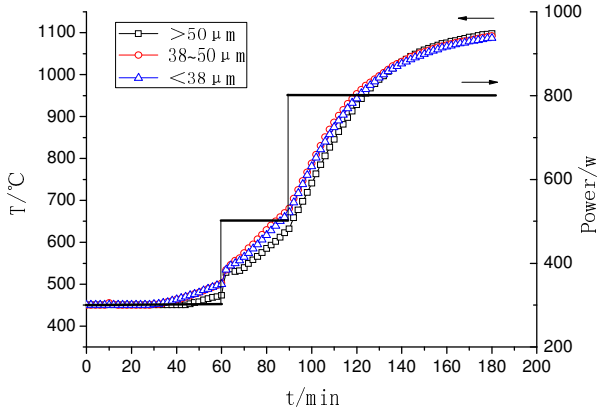


Fig. 8. Thermal Profiles of 316SS Powdered-metal Body as a Function of Particle Size after Adding 50g of SiC.

Conclusions

Experiments on heating of 316SS green bodies in microwave oven with 2.45GHz indicated that 316SS powders with varying mean size can effectively couple with microwaves and be heated to high temperatures. Compare to the conventional sintering, microwave sintering exhibits different remarkably heating behavior. Sintering process is influenced by the microwave power, powder particle size and the thermal insulation installation. The results show that the heating rate is increased by the increase of the microwave power, which approach a linear relationship. The smaller the powder size, the higher the heating rate. The auxiliary heating material (SiC) also has great effect on the heating behavior. It is helpful to achieve fast and uniform heating in green body.

Acknowledgements

This work was financially supported by the National Natural Science Foundation of China (50975100), Project of Fujian Science and Technology Innovation Platform (2011H2003), and The Natural Science Foundation of Fujian Province Youth Innovation (2012J05093).

References

[1] Tinga W R, Voss W A G. Microwave power engineering, Academic Press, New York, 1968, pp. 73-78.
[2] R. Roy, D. Agrawal, J. Cheng, et al. Full sintering of powdered-metal bodies in a microwave field, Nature, 1999, 399(6737), pp. 668-670.
[3] K. Saitou, Microwave sintering of iron, cobalt, nickel, copper and stainless steel powders, Scripta Materialia, 2006, 54(5), pp. 875-879.
[4] S. S. Panda, V. Singh, A. Upadhyaya, et al. Sintering response of austenitic (316L) and ferritic (434L) stainless steel consolidated in conventional and microwave furnaces, Scripta Materialia, 2006, 54(12), pp. 2179–2183.
[5] Ma Jinlong, Tong Xuefeng, Peng Hu, A revolution of sintering technology, Advance Materials Industry, 2001, 11(6), pp. 30-32.
[6] Huang Ming, Peng Jinhui, Wang Jiaqiang, et al. Theoretical study on heating mechanisms of interaction between microwave and material, Journal of Kunming University of Science and Technology(Natural Science Edition), 2005, 30(6), pp. 15-17.
[7] Peng Yuandong, Studies on microwave heating mechanism and sintering behavior of powder metallurgy materials, Central South University, 2011.
[8] Zhou Jian, Quan Feng, Liu Weibo, et al. Research on microwave sintering WC-10Co cemented carbide in a single- mode cavity, Journal of Wuhan University of Technology, 2007(12), pp. 1-4.
[9] Fang Ke, The research advance of microwave sintering metal powder, Metal Materials and Metallurgy Engineering, 2011(02), pp.48-53.
[10] Fang Ke, Fang Li, The principle and development of microwave sintering technology, Value Engineering, 2011(14), pp. 53-55.
[11] Yi Jianhong, Lu Shudong, Tang Xinwen, et al. On mechanism of microwave sintering of P/M parts, Powder Metallurgy Industry, 2003(02), pp. 22-25.
[12]]Hedvig P, Dielectric Spectroscopy of Polymem, Akademiai Kiado, Budapest, 1977, pp. 34-37.
[13] Jin Qinhan, Microwave Chemistry. Science Press, Beijing, 1999, pp. 13-15.
[14] Yi Jianhong, Lu Shudong, Tang Xinwen, et al. Mechanism of microwave sintering of powder metallic part, Materials Science and Engineering of Powder Metallurgy, 2002(03), pp. 180-184.
[15] P. Mishra, G. Sethi, A. UPadhyaya, Modeling of microwave heating of particulate metals, Metallurgical and Materials Transaction B, 37(2006)839-845.
[16] Zhu Fengxia, Yi Jianhong, Peng Yuandong, Sintering response of copper powder metal compact in microwave field, Journal of Central South University (Science and Technology), 2009(01), pp.106-111.

Advanced Materials Research Vol. 936 (2014) pp 1701-1706
© (2014) Trans Tech Publications, Switzerland
doi:10.4028/www.scientific.net/AMR.936.1701

Effects of Environment Temperatures on the Microstructures and Mechanical Properties for Welding Joints of A5083-H111 Alloy

Chuangang Wang[1,a], Yan Liu[2,b], Xiaomin Wang[2,c], Guoqing Gou[2,d], Hui Chen[2,e]

[1] CSR SIFANG Co.,Ltd, Qingdao 266111,China

[2] Institute of Materials Science and Engineering, Southwest Jiaotong University, Chengdu, 610031, P.R China

[a] wangchuangang@cqsf.com, [b] liuyanzt@163.com, [c] xmwang991011@163.com

[d] gouguoqing1001@163.com, [e] xnrpt@163.com

Keywords: A5083-H111 Al alloy; Environment Welding; Temperature; Microstructure; Mechanical Properties

Abstract: In this paper, A5083-H111 aluminum alloy was welded under different environment temperatures. Microstructures and mechanical properties were analyzed. The results show that the grain size of precipitated phase in welded seam deceased and the content increased with the increase of environment temperature. The hardness was the lowest in welded seam. The hardness increased with the distance away from welded centre. The hardness of welding zone of welded joint was generally low below 0 ℃. The strength and toughness were higher at welding temperature above 0℃ than that welded below 0℃. If the welding parameters were well controlled, A5083-H111 Al alloy can be welded at temperature ranging from -20℃ to 40℃ with relative humidity of 50%.

Introduction

With the development of transportation, light weight for transportation vehicles was an important factor to improve train speed. At present, as a light weight material,aluminum alloy was applied more and more widely in high speed train. At the same time, A5083 was one kind of aluminum alloy which was widely used in high speed train. Most of the train structures were connected by welding. Aluminum alloys were generally difficult to fusion weld because mechanical properties can be seriously degraded as a result of heat-induced changes to their precipitate structure and dentritic structures formed during the fusion welding process [1]. The quality of welding joints was not only influenced by welding parameters, but also by the environmental conditions in the process of welding. Welding temperature, humidity and wind speed are all likely to have underestimated influence on the quality of welding joints.

Chen Li [2] et al. researched performance of pipeline steel welding under low temperature of -28 ℃ ~ - 15 ℃. The result showed that the effect of welding temperature on tension strength, surface bending, back bending, slot breaking and hardness was not obvious, while the effect was higher on low temperature impacting stiffness value.

Yang Wu [3] et al. have researched the influence of construction site on thick steel plate welding stress. The results showed that the welding residual stress declined with the increasing of air temperature in construction site. The increasing rate of stress was 6%-32% when temperature decreased per 10 ℃.

Meng Qing li [4] et al. investigated the welding procedure for petroleum-natural gas X65 pipeline steel in 90%-95% humidity environment. The results showed that if joints was good designed and the welding process parameters was made to control heat input during welding, good properties of welding joints can be obtained.

In order to keep the welding quality, factories had to keep the environment at constant temperature and humidity, which leaded to high cost of manufacturing. Thus, A5083-H111 aluminum alloy was welded under different environment temperature in this paper to research effects of environment temperature on the microstructures and mechanical properties.

Experimental Details

Welding process

The A5083-H111 aluminum alloy was used as base metal. The chemical composition of A5083-H111 aluminum alloy was listed in Table 1. The welding wire used was ER5356，whose chemical composition was listed in Table 2.

TABLE 1 CHEMICAL COMPOSITION OF A5083-H111 ALUMINUM ALLOY（WT%）

Element	Si	Fe	Cu	Mn	Mg	Cr	Zn	Ti	Al
A5083-H111	≤0.40	≤0.40	≤0.10	0.40-1.0	4.0-4.9	0.05-0.25	≤0.25	≤0.15	

TABLE 2 CHEMICAL COMPOSITION OF ER5356 WELDING WIRE（WT%）

Element	Si	Fe	Cu	Mn	Mg	Cr	Zn	Ti	Al
ER5356	≤0.25	≤0.10	≤0.10	0.05-0.20	4.5-5.5	0.05-0.20	≤0.10	≤0.15	

The aluminum alloys were welded using the PHOENIX series 421 EXPERT forceArc MIG welding equipment (EWM Co.Ltd). The welding processes were finished in an environmental simulation laboratory which can simulate temperature, humidity and wind speed in real circumstance. The entire environment simulation laboratory consists of refrigeration systems, heating systems, humidifiers, dehumidifiers, blower machine and so on. The combination of two-stage low temperature refrigeration units and stainless steel single straight tube heat pipe can control the temperature varied from -30 ℃ to +50 ° C. The range of 20 % to 95% relative humidity can be realized by the combination of ultrasonic humidifier and dehumidifier. The low noise fan can make the wind speed achieve 0m/s-12m/s to simulate wind. The whole system can basically achieve a variety of environmental regulation. The welding parameters are showed in Table 3.

TABLE 3 WELDING PARAMETERS OF A5083-H111 ALUMINUM ALLOY

temperature（℃）	humidity	Wind speed	Plate thickness（mm）	Current (A)	Voltage（V）	Welding speed (cm/min)	Gas flow (L/min)
-20	50%	calm	10	240～260	25～26	300	25
-10	50%	calm	10	240～260	25～26	300	25
20	50%	calm	10	230～260	25～26	330	25
40	50%	calm	10	230～260	25～26	330	25

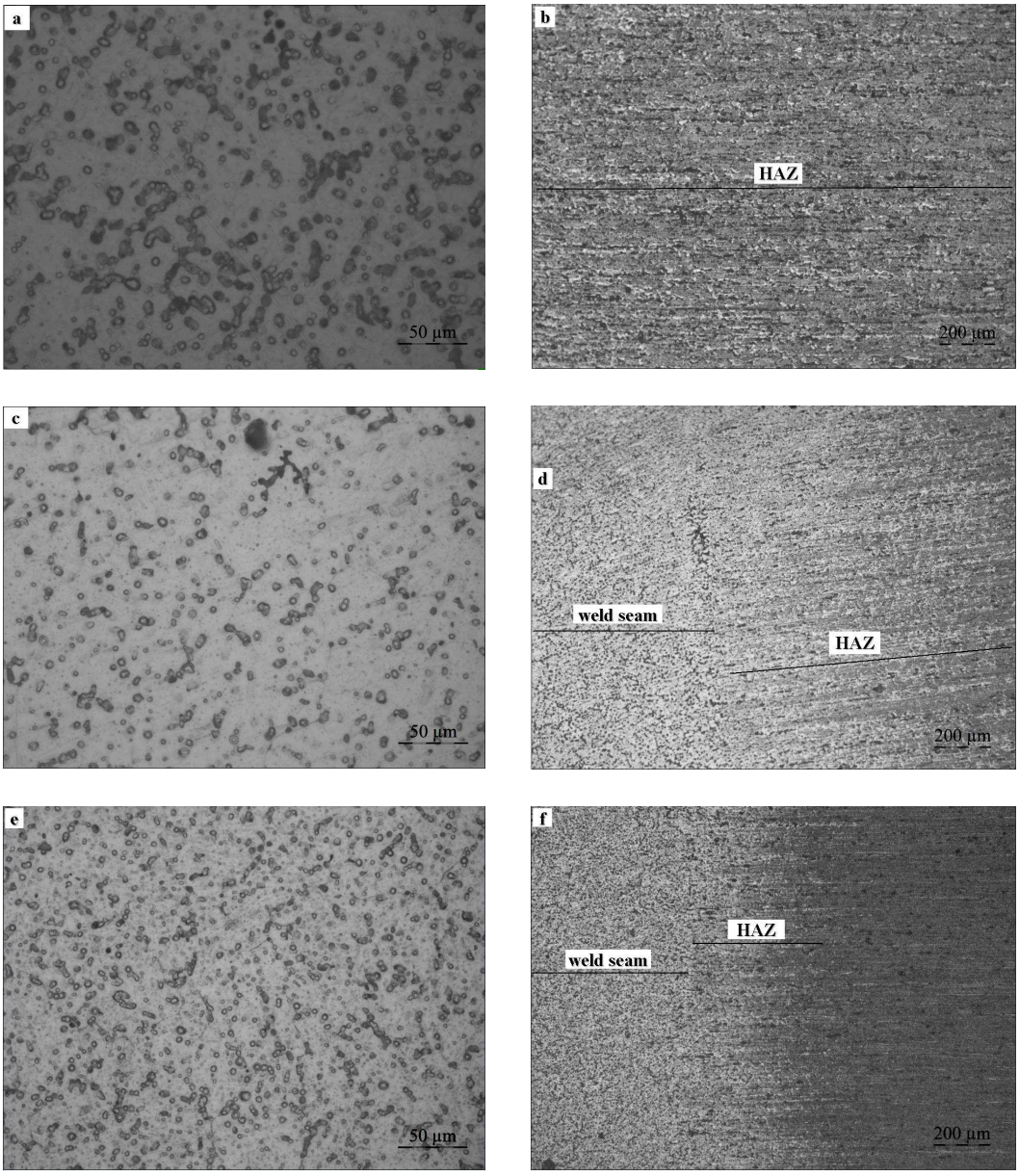
The cross-section specimens were grounded by sand paper from mesh size 80 to 2000, and then polished. The specimens were etched by mixed acid solution. The composition of corrosive liquid is 1% HF+1.5%HCl+2.5% HNO_3. The microstructures were observed by optical microscope.

The hardness of the welding joint was measured using HVS-30 digital hardness tester with a 29.4N load with dwelling time of 10s. The spacing between hardness points was 1mm.

The tension test was done according to GB/T2651-2008. The test was finished in WDW 3100 computer control electronic universal testing tensile machine. The stretching rate was 1mm/min. The test machine automatically records the load displacement curve. The impact test was carried out according to the GB/T2650-2008. The test was done at room temperature. The gap shape was V-shaped gap. The test machine was JBN -300, which was manufactured by Wztongli Material Testing Machine Co. The absorbed energy value was recorded.

Experiment Results

Microstructure



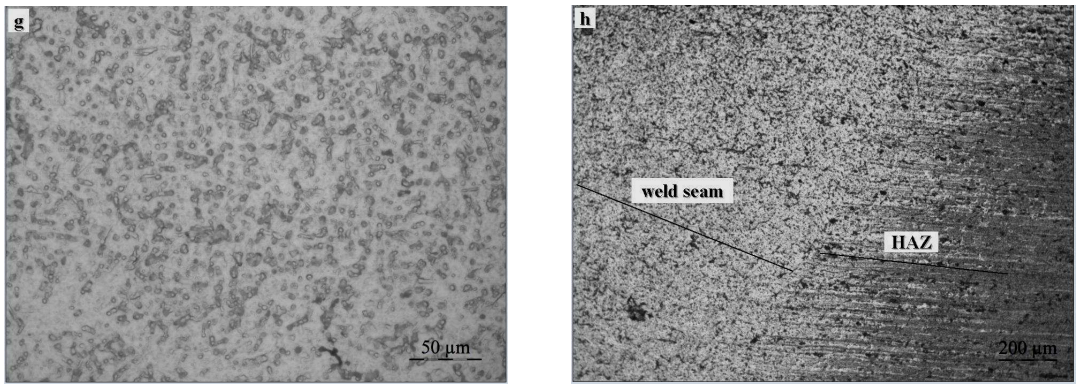


Fig.1 Microstructure of A5083-H111 aluminum alloy welded under different temperature:(a)weld seam at -20 ℃;(b)HAZ at -20 ℃; (c)weld seam at -10 ℃;(d)HAZ at -10 ℃; (e)weld seam at 20 ℃;(f)HAZ at 20 ℃; (g)weld seam at 40 ℃;(h)HAZ at 40 ℃

The microstructures of A5083-H111 aluminum alloy welded under different temperature were shown in Fig.1. It can be seen that the grain size of precipitated phase in welded seam deceased and the content increased with the increase of environment temperature. The width of HAZ decreased with the increase of temperature. The width of HAZ at -20℃ was about 1.5mm, while it was only about 500μm for the welding joint at 40℃.

From the welding parameters listed in Table 3, it showed that the welding velocity at temperature above 0℃was higher than that at temperature below 0℃. Therefore, the cooling velocity after welding was higher and the time precipitated phase stayed at higher temperature was short, which leaded to fine precipitated phase and narrow HAZ.

Mechanical Properties

Hardness test

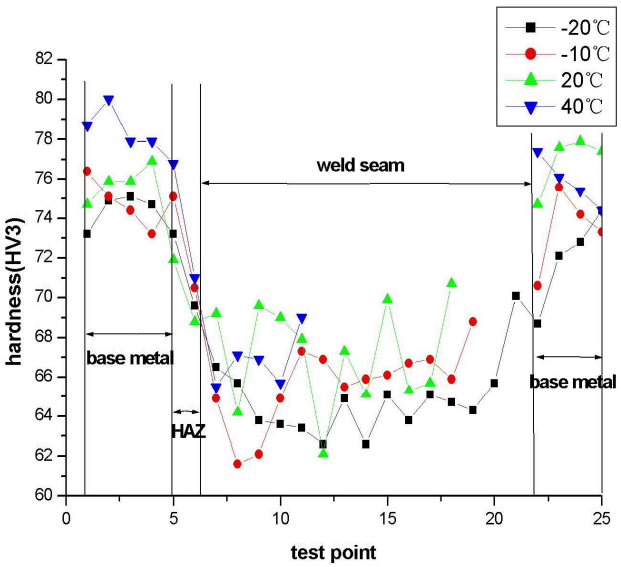


Fig.2 Hardness Distribution Curve Under Different Temperature

The hardness distribution of A5083-H111 aluminum alloy welding joint under different temperature was shown in Fig.2. The points in welded seam were discontinuous at 20℃ and 40℃, because the welded seam was narrower than that at -20℃ and -10℃. It can be seen that the hardness was the lowest in welded seam. The hardness increased with the distance away from

welded centre. The hardness of welding zone of welded joint was generally low below 0 ℃.The A5083-H111 aluminum alloys were annealed condition before welded. The original metallurgical structures were α-Al solid solution and full precipitation of β（Al8Mg5）phase. However, precipitation strengthening effect was not obvious, though the compound can be dissolved in solid solution or precipitated from solid solution in the process of heating and cooling experienced in welding. Therefore, the hardness of HAZ was only slightly lower than the base metal.

Tensile test

Table 4 shows the results of tensile test. It can be clearly seen that most of the specimens welded below 0℃ fractured at welded seam, while most of the specimens welded above 0℃ fractured at HAZ. This indicated that the weak position of joints welded below 0℃ was welded seam. The weak position of joints welded above 0℃ was HAZ. The tensile strength and elongation differed little under different welding temperatures; all of them were in the range of standard requirement.

TABLE 4 RESULTS OF TENSILE TEST FOR WELDING JOINTS UNDER DIFFERENT TEMPERATURE

Welding temperature（℃）	-20	-10	20	40
Average of tensile strength (Mpa)	299	297	310	310

Impact test

Table 6 shows the results of impact test on weld seam. It can be found that the impact energy was slightly higher when the temperature was up to 20℃. .

TABLE 6 RESULTS OF IMPACT TEST UNDER DIFFERENT TEMPERATURE

Welding temperature（℃）	-20	-10	20	40
Average of impact energy /Aku（J）	30.3	28	34	33.8

Discussion

From the mechanical properties of A5083-H111 Al alloy welding joints, it can be found that the strength and plasticity of aluminum alloy welding joints welded at 20℃ and 40℃were both higher than that below 0℃. This may related to the welding thermal cycle experienced. The air temperature directly influenced thermal cycle process, welding pool metallurgy action degree, phase transformation of weld seam and HAZ and alloy element and stress distribution [5].At lower temperature, the heat output velocity was quicker, which can not always promised the aluminum alloy temperature reaching to the requirement of welding process. From Fig.3, the precipitated phase in welded seam below 0℃ was larger and fewer than that welded above 0℃. The improvement in such properties can be explained by the fact that as the size of precipitated phase decreased, the strength and toughness increased according to the Hall-Patch [6] relationship. Thus, the strength and toughness were higher at welding temperature above 0℃ than that welded below 0℃.

Though the mechanical properties of the welding joints welded under different temperatures had slight difference, they all met the standard requirement of A5083-H111 Al alloy welding joints. Literature [2] indicated that low temperature had little effects on the room temperature mechanical of pipeline, but had influence on the low temperature impact toughness. However, it was considered

that little effect on low temperature impact toughness for A5083-H111 Al alloy. It was thought that as an aluminum alloy has a face centered cubic (fcc) crystal lattice, there was no low temperature toughness effect as observed in alloy [7].

Therefore, if the welding parameters were well controlled, A5083-H111 Al alloy can be welded at temperature ranging from -20℃ to 40℃ with relative humidity of 50%.

Conclusions

(1) The grain size of precipitated phase in welded seam deceased and the content increased with the increase of environment temperature. The width of HAZ decreased with the increase of temperature.

(2) The mechanical properties of the welding joints welded under different temperatures all met the standard requirement of A5083-H111 Al alloy. The hardness increased with the distance away from welded centre. The hardness of welding zone of welded joint was generally low below 0 ℃.The strength and toughness were higher at welding temperature above 0℃ than that welded below 0℃. If the welding parameters were well controlled, Al alloy can be welded at temperature ranging from -20℃ to 40℃ with relative humidity of 50%.

Acknowledgements

This work was financially supported by the pillar projects in the national science & technology (Grant No. 2009BAG12A04-D02).

Reference

[1] C. Rhodes, M. Mahoney, W. Bingel, R. Spurling, W. Bampton. Effects of friction stir welding on microstructure of 7075 aluminum [J]. Scripta Mater. 1997, 36(1): 69-75.

[2] CHEN Li, GUO Rui. Performance Test on Pipeline Steel Welding under Low Temperature. Journal of Oil and Gas Technology, 2008, 30(6):158-160

[3] Yang Wu. The research of influence of construction site on thick steel plate welding stress. Master's thesis. Chongqing Jiaotong University, 2010

[4] MENG Qing li, WANG Yi, ZHANG Lin-lin. Welding Procedure for Petroleum-natural Gas X65 in Humidity Environment [J]. Welding pipe, 2007,30(5):39-41

[5] Zhang Zhen. Steel structure environment welding distortion and prevention measures analysis [J]. Science and Technology Innovation Herald.2012.01:83

[6] Zhao Pin, Xie Fuzhou, Sun Zhengguo, etc, Materials science Essentials, Harbin Institute of Technology Press, Harbin, 2003, in Chinese

[7] K.C. Moon, N.W. Kang, J.H. Lee, The dynamic fracture toughness of aluminum alloy weld zone by instrumented Charpy test [J]. J. Korean Weld. Soc. 1985,3 (2): 43-51.

Advanced Materials Research Vol. 936 (2014) pp 1707-1715
© (2014) Trans Tech Publications, Switzerland
doi:10.4028/www.scientific.net/AMR.936.1707

Experimental Research on Grinding Surface Layer Behavior and Process Parameter Optimization of Spiral Bevel Gears

Xingzu Ming[1, a], Zhongqun Li[1,b], Xianwen Xiong[1, c] and Jing Zhou[1,d]

[1]Hunan industry university, Zhuzhou city, Hunan provincial, China

[a]mxz9036@126.com,[b]zhqunli@163.com,[c]xiongxianwen9633@sina.com,[d]coolrainjing@21cn.com

Keywords: Surface layer behavior; Process parameters optimization; Experiment research; Grinding; Spiral bevel gears.

Abstract. Based on the test analyses of grinding surface layer behavior of spiral bevel gears, many conclusions are gotten. Compressive residual stresses are occurred on grinding tooth surface, tensile residual stresses are located in tooth layer, and change laws of grinding residual stresses are different from ones of grinding surface roughness R_a as the grinding process parameters. A temper layer is occurred in tooth layer after normal grinding, and the micro-hardness of grinding surface is lower. When arriving at the critical condition, namely grinding temperature is above 600 degree Celsius, and metamorphic layer depth is greater than 0.2mm, different degree of grinding burn is produced, and their microstructures are changed. Based on grinding orthogonal test $L_{16}(4^5)$, the optimizing configuration of grinding process parameters of spiral bevel gear is obtained by using a mean variance analysis of integrated balance method. Based on the test optimization of grinding surface layer behavior, the comprehensive performances of grinding surface, such as grinding residual stresses, surface roughness, micro-hardness and structure, metamorphic layer depth et al, are better. These provide a basis for improvement of grinding surface quality of spiral bevel gears.

Introduction

Spiral bevel gears are crucial components achieved the motion transmission of intersectant axes, and they are used widely in energy sources, traffic, military industry and so on. Its precision finishing method is generally the multi axis NC grinding. The grinding surface layer behavior is affected by grinding process parameters, and the transmission performance and usage safety of spiral bevel gears are restricted seriously by grinding surface layer behavior.

The grinding surface layer behavior is comprised of a grinding surface residual stresses, surface roughness, surface hardness and metamorphic layer depth, grinding burn and so on. Foreign scholars NABIL et al. compared with the grinding quality of austenitic stainless steel under different grinding conditions by test, the results showed that the grinding surface quality had been improved when the low temperature cooling grinding [1]. Based on the grinding test data, SAHIN established the prediction model of surface roughness by using response surface method [2]. By means of test data, CHEOL et al built up the intelligent models of material removal rate, surface roughness, grinding residual stress and so on for the grinding of cylindrical insert type [3]. Domestic scholars Tian etc obtained the optimal test results of ceramic grinding based on orthogonal test design [4]. Du made a fuzzy comprehensive evaluation of grinding process by using the theory of fuzzy mathematics [5].

The above researches object were mainly grinding ones of simple parts, such as plane, cylinder parts, and so on, but it is rarely reported for the research of grinding surface layer behavior and process parameter optimization of spiral bevel gears with space shape and complex processing.

Grinding Experiment Conditions of Spiral Bevel Gears

Gear Material and Machining Process

Here 20CrMnTi of spiral bevel gears was commonly selected in automobile gear material. The machining processes and technical requirements in experiment of spiral bevel gear pair were expressed as: Baiting → Blank forging → normalizing → milling teeth → carburizing, quenching and tempering →grinding tooth. Effective hardening layer depth was 0.80~1.20mm,surface hardness was 58~62 HRC,and centre hardness was 30~42 HRC.

Grinding Process Conditions

Specimen was processing in PHOENIX450PG grinding machine with the straight cup wheel SG60-JV. Grinding way was out-cut inverse grinding, and the oil-base extreme pressure grinding fluid was used. Small gear was processed in generative grinding with single-sided method, and big gear was grinded with double-sided method [6].Basic parameters of spiral bevel gear pair were listed in table 1, and their adjusted parameters of grinding machine were listed in table 2.

TABLE 1 BASIC PARAMETERS OF THE SPIRAL BEVEL GEAR PAIR

Item	Parameters		Item	Parameters	
	Small gear	Big gear		Small gear	Big gear
Teeth Number	z_1=15,right spin	z_2=46,left spin	Pitch cone angle(°)	δ_1=18.0605	δ_2=71.939 5
Module m(mm)	8.22	8.22	Root cone angle(°)	δ_{f1}=16.427 3	δ_{f2}=68.658 5
Pitch circle diameter (mm)	d_1=123.3	d_2=378.12	Body cone angle(°)	δ_{a1}=21.341 5	
Spiral Angle β(°)	35	35	Tooth face width(mm)		b_2=57.15
Pressure angle α(°)	20	20	Tooth dedendum(mm)	h_{ef1}=5.67	h_{ef2}=11.4
External cone distance R_e(mm)	198.857 8	198.857 8	Tooth addendum(mm)	h_{ea1}=9.85	h_{ea2}=4.12
Pitch cone distance R (mm)	170.282 8	170.282 8			

TABLE 2 ADJUSTED PARAMETERS OF GRINDING MACHINE OF THE SPIRAL BEVEL GEAR PAIR

Item	Parameters		
	Concave of small gear	Convexity of small gear	Big gear
Nominal cutter diameter r_0(mm)	152.4	152.4	152.4
Cutter tooth profile angle α_p(°)	14	-31	22
Tooth blank setting angle(°)	γ_1=358.2094	γ_1=355.5921	γ_2=68.658 5
Radial cutter spacing(mm)	S_{r1}=136.775	S_{r1}=149.682	S_{r2}=149.83
Angular cutter spacing(°)	q_1=61.9167	q_1=54.5336	q_2=56.42
Bed position(mm)	X_{B1}=35.6273	X_{B1}=59.6701	X_{B2}=0
Perpendicular gear position(mm)	E_{01}=-4.190 9	E_{01}=5.079	E_{02}=0
Axial gear position(mm)	X_{g1}=-6.6309	X_{g1}=9.7967	X_{g2}=0
Ratio of roll	i_{o1}=2.8545	i_{o1}=3.2252	i_{o2}=0.95

Experimental Analysis of Grinding Surface Layer Behavior of Spiral Bevel Gears

Experimental Analysis of Grinding Residual Stress

Grinding surface residual stress was measured by X-ray diffraction method, a text equipment was Japanese D/Max 2550 18KW turn target X-ray diffractometer.

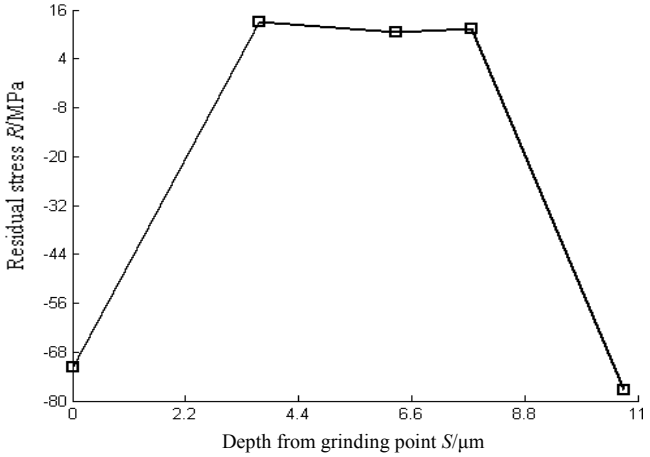


Fig. 1 Test distribution curve of grinding residual stresses of big gear

On the condition of grinding dosage of big gear concave, grinding depth a=0.03 mm, wheel speed v_s =30 m/s and gear generating speed v_w=4 m/min, the residual stresses of five depth node from big gear grinding point were measured by test after grinding, and the test distribution curve of grinding residual stress was shown in Fig. 1. The first and the fifth node were respectively the one on concave and convex.

Further experimental results showed that the residual stresses on grinding tooth surface of spiral bevel gears were residual compressive stresses, and the ones in tooth layer were residual tensile stresses. The residual stresses of grinding layer would be increased rapidly as magnifying v_s, and when a was greater than 0.03 mm, grinding surface residual stresses were increased rapidly as increasing a, but the ones would be decreased as increasing v_w.

Experimental Analysis of Grinding Surface Roughness

The surface profiler instrumentation Hommel Werke T8000 made in German was used in the measurement of grinding surface roughness. The R_a of tooth surface was measured three times each, and its average value was the experimental measuring one of R_a.

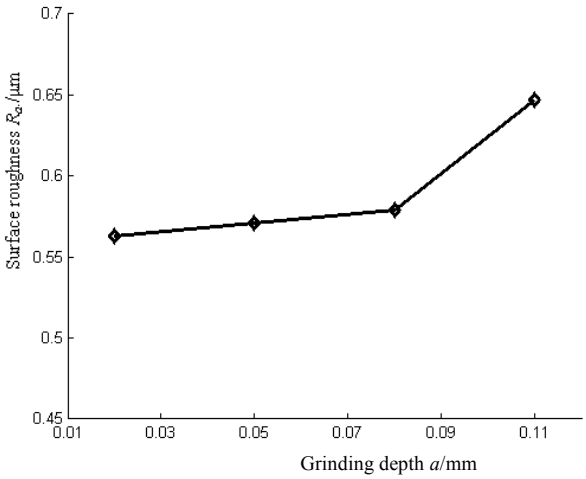


Fig. 2 Test Distribution Curve of *Ra* and *a* When Grinding Big Gear Concave

On the condition of grinding dosage of big gear concave, v_s=20.6 m/s and v_w=3.1 m/min, when grinding depth a was respectively taken for 0.02, 0.08 and 0.11mm, the test distribution curve of R_a and a was shown in Fig. 2. The results indicated that when a was less than 0.08 mm, the value R_a was increased slightly with the enhance of a; but when a was greater than or equal to 0.08 mm, the value

R_a was increased significantly with improvement of a. This showed that the smaller a had little impact on R_a, and on the normal grinding stage without passivation, grinding efficiency was improved by increasing a appropriately.

The experiment also showed that the value R_a was decreased significantly as increasing v_s, but the one was increased slightly as enhancing v_w. With the increase of grinding granularity, the value R_a was decreased gradually, and smaller granularity would make the roughness change slowly.

Experimental Analysis of Grinding Layer Micro-hardness and Metamorphic Depth

When measuring of grinding layer micro-hardness and metamorphic depth, grinding layer micro-hardness was measured by automatic micro-hardness tester Lecd AMH2000.While grinding concave of big spiral bevel gear, v_s=52.1m/s, v_2=3.1m/min,grinding depth a are respectively taken for 0.02, 0.08 and 0.11mm, the distribution curves of layer micro-hardness and a were shown in Fig. 3.

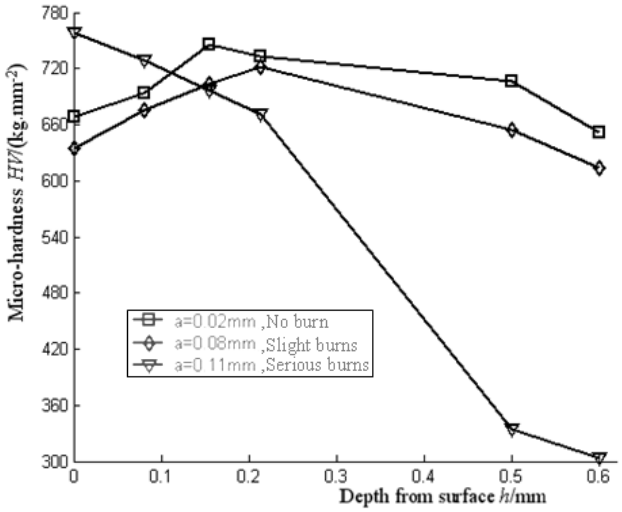


Fig. 3 Distribution curves of layer micro-hardness and a when grinding big gear concave

As shown in Fig. 3, when a=0.02mm, burn in layer was not produced, and a tempering softening layer was produced. The layer mcro-hardness HV was 669HV (equivalently 59 HRC), thus grinding surface hardness requirement was satisfied. The highest hardness of inner layer was 745HV, tempering layer depth h, 0.155mm, was shallow. When a was 0.08mm and grinding temperature was more than 600 degree Celsius, slight tempering burns in layer were produced, surface micro-hardness was 635HV (equivalently 57.4 HRC), and it was inferior to one of grinding surface hardness requirement. The highest hardness of tempering layer was 722HV, and tempering layer depth h, 0.213mm, was increasing. When a was 0.11mm, serious quenching burns in layer were produced, and surface micro-hardness was 758HV (equivalently 63.1 HRC), it was greater than one of grinding surface hardness requirement, and burns layer depth h was 0.5mm.

The experiment also showed that h increased with the enhance of v_s, but slightly reduced with the increase of v_w in the same other grinding conditions.

Experimental Results and Analysis of Grinding Microstructure

The microstructure of grinding hardening layer was observed and analyzed through the metallographic microscope. Before the observation tooth was firstly cut into specimens by wire-electrode cutting. The specimens were eroded with 4% nitric acid alcohol solution after polishing, and their structure were observed by German Leica-DM IRM metallographic microscope.

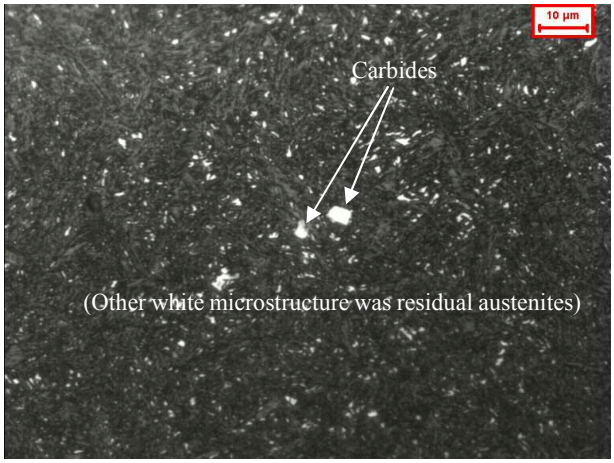


Fig. 4 Surface microstructure of no burn when grinding big gear concave (1000×)

1) Grinding unburned microstructures

When grinding concave of big spiral bevel gear, grinding dosage a =0.02 mm, v_s =52.1 m/s, v_2 =3.1 m/min, burn was not taken place in grinding tooth surface, tooth surface microstructures were acicular martensites + residual austenites + a small amount of carbides, their microstructures were shown in Fig. 4. While The microstructures of central tooth were lath martensites + bainites + a small amount of ferrolites. The bainites were mainly feathered upper ones, and were a small amount of granular ones.

2)Microstructures of grinding burn

When a was 0.11mm,v_s was 52.1m/s and v_2 was 3.1m/min, severe quenching burns were took place in grinding concave of big spiral bevel gear, and they were line form with steel-gray. Maximum depth of burns was 0.5mm approximately; the cementite layer distribution was shown in Fig. 5, and the crescent-shaped area with blanch color was martensite one formed by quenching burns. The layer microstructure was shown in Fig. 6, the area from surface to inner was divided into quenching burn and temper burn area.

The burn layer microstructures near surface of quenching burn area (place A in Fig. 6) were acicular martensites + residual austenites + a small amount of carbides, and there were more martensites in this area. This showed that grinding temperature in this area already achieved A_{Ccm} of material or overtaked A_{C3}. The microstructures beneath quenching burn area(near the temper burn area, namely place B in Fig. 6) were martensites + ferrolites + residual austenites, and the microstructures from top to bottom of in temper burn area were deep black troostite and temper sorbite.

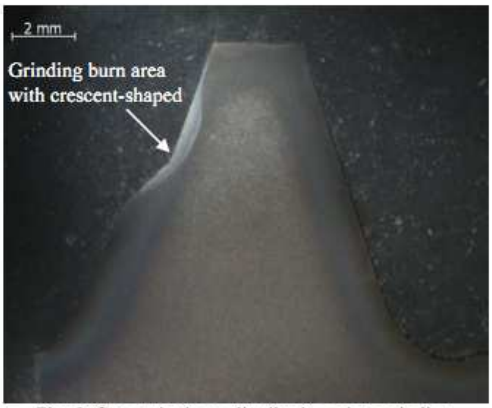


Fig. 5 Cementite layer distribution when grinding big gear concave

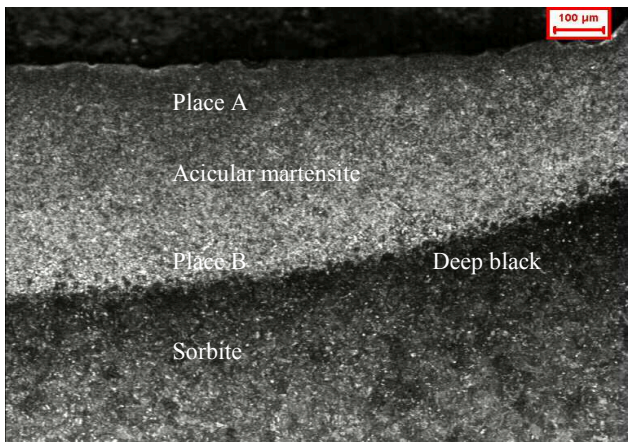


Fig. 6 Burn layer microstructure when grinding big gear concave (100×)

Further studies showed that, when reaching a critical condition, namely the grinding temperature was higher than 600 degree Celsius, metamorphic layer depth was greater than 0.2mm, different degree grinding burns were produced, and the surface micro-hardness was higher while severe burns.

Grinding Orthogonal Test Analysis and Process Parameter Optimization of Spiral Bevel Gear

Grinding Orthogonal Experimental Design and Results

1) Grinding orthogonal experimental design

Grinding process and parameters had a greater impact on the grinding surface layer behavior and productivity. When designing orthogonal experiment and considering four variational factors, such as grinding depth a, wheel speed v_s, grinding wheel granularity M and gear generative speed v_w, these factors were chosen as orthogonal factors [5]. According to the grinding experience value, four different level values were taken in each factor, and these factors and levels of grinding orthogonal experiment were listed in table 3.

TABLE 3 FACTORS AND LEVELS OF GRINDING ORTHOGONAL EXPERIMENT

level	Grinding depth A(mm) A	Wheel speed v_s(m·s^{-1}) B	Wheel granularity M(#) C	Generative speed v_w(m·min^{-1}) D
1	0.02	16.5	46	2.7
2	0.05	26.5	60	3.6
3	0.08	35.2	80	4.4
4	0.11	52.6	120	7.2

2) Grinding orthogonal experimental results

To consider the grinding surface layer behavior and productivity, three index of grinding experimental evaluation, such as surface roughness R_a, metamorphic layer depth h and grinding removal rate Z_w, could be chosen. According to four certain factors and levels, orthogonal table L_{16} (4^5) was used [3], and a blank column 5(e) was put apart in the table to use in variance analysis [6].16 set of experiments were done, and the orthogonal experimental results of grinding concave of small spiral bevel gear were listed in table 4 (except comprehensive evaluation index value).

TABLE 4 GRINDING ORTHOGONAL EXPERIMENT RESULTS OF SMALL GEAR CONCAVE

Experiment No.	1 A	2 B	3 C	4 D	5 e	Surface roughness R_a(μm)	Deterioration depth h(mm)	Removal rate Z_w(mm^3·s^{-1})	comprehensive evaluation indexs
1	1	1	1	1	1	0.543	0.041	0.185	6.4380
2	1	2	2	2	2	0.524	0.048	0.197	6.6153
3	1	3	3	3	3	0.417	0.058	0.248	7.9934
4	1	4	4	4	4	0.425	0.061	0.314	8.1117
5	2	1	2	3	4	0.554	0.073	0.362	6.5220
6	2	2	1	4	3	0.581	0.069	0.479	6.7140
7	2	3	4	1	2	0.526	0.083	0.357	6.6977
8	2	4	3	2	1	0.567	0.089	0.413	6.3216
9	3	1	3	4	2	0.756	0.087	0.495	4.3356
10	3	2	4	3	1	0.729	0.112	0.482	4.2397
11	3	3	1	2	4	0.732	0.129	0.611	4.4589
12	3	4	2	1	3	0.728	0.132	0.544	4.1961
13	4	1	4	2	3	0.871	0.135	0.569	2.4775
14	4	2	3	1	4	0.801	0.146	0.643	3.4735
15	4	3	2	4	1	0.901	0.155	0.651	2.1293
16	4	4	1	3	2	0.851	0.173	0.687	2.6198

Because different levels of four factors in experiment have different impact on three experimental evaluation index, the gotten optimal scheme of each index was not consistent. In order to obtain the final solution of optimal grinding process parameters taken compatibly into account R_a, h and Z_w index, integrated balance method could be used to analyze [5]. Let single factor evaluation index set U be $\{ y_{mn} \}$, which y_{mn} was respectively three evaluation index in table 4,and m was 1,2,3,also n was 1,2,⋯,16.The influence function set Π of experimental index was $\{ \eta_{mn}\}$, which η_{mn} was between 0 and 10. Assuming that the impact function value η_{mn} of the best experiment index was 10,all impact function values were determined proportionally by the difference between other experimental values and the best index.

Let comprehensive evaluation index set be V gotten by comprehensive balance method. In order to find the relationship between U and V, the weight distribution set γ was determined to be $\{\gamma_1, \gamma_2, \gamma_3\}$, and it reflected the importance of each index. According to grinding process technology requirements of spiral bevel gears, the weight distribution set γ could be determined to be {0.4,0.2,0.4}. All comprehensive evaluation index v_n in set V of $\{v_n\}$ was

$$v_n = \sum_{i=1}^{m} \gamma_i \eta_{in} \qquad (m = 1,2,3; n = 1,2,\cdots,16) \tag{1}$$

Based on the equation (1), the evaluation index of three single factor in table 4 was calculated, comprehensive evaluation index obtained were listed as the last column in table 4.

Grinding Orthogonal Experimental Analysis and Process Parameter Optimization

Range analysis and variance analysis method was usually used in process optimal analysis of orthogonal experimental results, and range analysis method was mainly to estimate the effect strength of all factors. In order to further analyze the significance and accuracy that process parameters impacted on the experimental results, the variance analysis of integrated balance method was used in grinding orthogonal experiment of small gear concave, and the analytic results were listed in table 5.

TABLE 5 VARIANCE ANALYSIS OF INTEGRATED BALANCE METHOD

Variation soruce	Deviation of square sum S	Freedom degree f	Sum of mean square $MS(S/f)$	F value (MS/MS_e)	Critical value	Significance
A	53.5920	3	17.8640	32.8402		▲▲▲
B$^{\triangle}$	0.3849	3	0.1283			
C$^{\triangle}$	1.0971	3	0.3657		$F_{0.01}(3,12)=5.95$	
D$^{\triangle}$	0.3562	3	0.1187		$F_{0.05}(3,12)=3.49$	
Error e	1.6319	3	0.5440		$F_{0.1}(3,12)=2.61$	
$e^{\triangle}$	3.4701	12	0.2892			
Total T	57.0621	15				

Known from table 5, factor a have highly significant effects on the experimental results. According to the bigger value k, level A_1 was chosen. The influencing degree of other three factors was not significant, level B_3,C_3 and D_3 could be selected separately. Thus the optimal scheme determined was $A_1B_3C_3D_3$, namely a=0.02mm, v_s=35.2 m/s, M=80$^{\#}$, v_w=4.4 m/min.

Experimental Optimization Analysis of Grinding Surface Layer Behavior of Spiral Bevel Gear

The experimental results of grinding surface layer behavior of small gear concave were listed in table 6 by test in general process parameters and the optimal process $A_1B_3C_3D_3$.

TABLE 6 TEST RESULTS OF GRINDING SURFACE LAYER BEHAVIOR OF SMALL GEAR CONCAVE UNDER GENERAL AND OPTIMAL PROCESS PARAMETERS

Grinding scheme	Grinding process parameters				Experimental values of grinding surface layer behavior			
	a (mm)	v_s ($m \cdot s^{-1}$)	M ($^{\#}$)	v_w ($m \cdot min^{-1}$)	Surface residual stress(MPa)	Surface roughness R_a(μm)	Surface hardness (HRC)	Deterioration depth h(mm)
General process	0.02	16.5	46	2.7	-49.52	0.543	61.1	0.041
	0.05	16.5	60	4.4	-60.73	0.554	59.7	0.073
	0.08	52.6	60	2.7	-65.87	0.728	57.5	0.132
	0.11	26.5	80	2.7	-70.14	0.801	58.3	0.146
Optimal process	0.02	35.2	80	4.4	-65.41	0.417	60.2	0.058

Comparing with the grinding surface layer behavior under general process parameters in table 6, the grinding surface residual stress under optimal process parameters was better of residual compressive stress (-65.41 MPa), grinding surface roughness values were smaller, grinding surface hardness was of satisfying the requirement (58~62 HRC), and grinding metamorphic layer depth was shallower(0.058 mm). In addition, known from grinding orthogonal experiment results in table 4, removal rate Z_w was reached 0.248 mm^3/s, comprehensive evaluation index was higher (7.9934). This showed that the comprehensive performance of grinding surface quality was better under the grinding process optimization.

Conclusions

(1) Grinding experiment shows that the residual stresses of grinding surface of spiral bevel gear are residual compressive stresses, and the ones in tooth layer are residual tensile stresses. The residual stresses of grinding layer are increased markedly as magnifying v_s, but the ones are decreased as increasing v_w. When a is greater than 0.03 mm, grinding layer residual stresses are increased obviously as increasing a. The value R_a of grinding surface roughness is decreased significantly as increasing v_s, but the one was increased slightly as enhancing v_w. When a is greater than or equal to 0.08 mm, the value R_a is increased significantly with improvement of a. A temper layer is occurred in tooth layer after normal grinding, and the micro-hardness of grinding surface is lower. When arriving at the critical condition, namely grinding temperature is above 600 degree Celsius, and metamorphic layer depth is greater than 0.2mm,different degree of grinding burn is produced, and their microstructures are changed. The microstructure of quenching burn area is different from one of temper burn area, the micro-hardness of tooth surface while quenching burn is increased obviously while quenching burns.

(2)Based on the results of grinding orthogonal experiment $L_{16}(4^5)$, the variance analyses is made by the integrated balance method, and optimal combination of grinding process parameters of spiral bevel gear is $A_1B_3C_3D_3$, namely the grinding depth a is 0.02mm, wheel speed v_s is 35.2 m/s, wheel size M is $80^{\#}$, gear generative speed v_w is 4.4m/min.

(3)Comparing with the grinding surface layer behavior under general process parameters, the value R_a of grinding surface roughness under optimal process parameters is more less 0.1μm, the surface residual stress is -65.41MPa, surface hardness is of satisfying the requirement, grinding metamorphic layer depth is shallower (0.058 mm), and the grinding surface comprehensive performance is better.

Acknowledgements

This project is supported by National Natural Science Foundation of China (Grant No. 51375161 and 51375160) , and Hunan Provincial Natural Science Foundation of China (Grant No. 13JJ6064).

References

[1] B.F. Nabil, S. Habib, B. Chedly, Ground surface improvement of the austenitic stainless steel AISI 304 using cryogenic cooling. Surface & Coatings Technology,2006,200:4846-4860.

[2] Y. Sahin, A.R. Motorcu, Surface roughness model in machining hardened steel with cubic boron nitride cutting tool. International Journal of Refractory Metals & Hard Materials,2008,26:84-90.

[3] W.L. Cheol, Intelligent modeling and optimization of grinding processes. Ann Arbor:Purdue University, 2000:188-191.

[4] X.L. Tian, A.b. Yu, B. Lin, The Effect of the grinding temperature on ceramic surface residual stresses. China Mechanical Engineering, 2002,18(9):1600-1601.

[5] J.P. Du, Research about Optimization of Grinding Process Based on Fuzzy Synthetic Evaluation. Coal Mining Machinery, 2008,29(7):55-57.

[6] F.L. Litvin, A.G. Wang, R.F. Handschuh, Computerized design and analysis of face-milled, uniform tooth height spiral bevel gear drives. Mech. Design, 2006, 118:573-579.

Advanced Materials Research Vol. 936 (2014) pp 1716-1719
© (2014) Trans Tech Publications, Switzerland
doi:10.4028/www.scientific.net/AMR.936.1716

Development of Permanent Magnet Generator Used for Magnetic Field Assisted Micro Electroforming Technology

Huijuan Li, Pingmei Ming[a], Xiaohui Bao, Xiaodong Zhang, Xiangyang Bi

Henan Polytechnic University, Jiaozuo 454003, P.R. China

[a]pmming@hotmail.com

Keywords: Permanent magnet generator, Magnetic field, Micro electroforming, Magnetic circuit structure

Abstract. To provide appropriately high and uniform magnetic field for micro electroforming process, a permanent magnet generator was specially developed which based on the fundamental process requirements. On the basis of determining the number of permanent magnet combinations numerically. Mainly, the geometrical shape of the permanent magnet blocks and magnetic circuit structure were optimized, and then the working gap regulating mechanism for this generator was designed. Utilizations indicated that the developed generator met the requirements well.

Introduction

As one of the main processes of forming metal microstructures and microcomponents, micro electroforming technique has some unique advantages including high replication precision, low process temperature, favorable flexibility, and low cost, etc..It has been widely employed in the field of micro-and nano-manufacturing. However, the micro electroformed articles usually feature some defects, such as pinholes, nodules, and hydrogen embrittlement, due to serious mass transfer limitation during the deposition. Since the deposition articles electrodeposited under the magnetic field have been found to show good surface quality and/or interesting microstructures and properties owing to some magnetic field effects (i.e., MHD effect, magnetic force effect, magnetizing force effect), the studies of magnetic field assisted electrochemical deposition technique has been an attractive topic in the academia and industry field. Ming et al. [1] discussed the mechanism of electrodeposition within high-aspect-ratio micro holes exposed to magnetic field, and analyzed the influence of process parameters on surface morphology and performances of nickel layer. The research by Coey et al. [2] showed that the use of magnetic field in the electrodeposition can enhance deposition rate of magnetic or non-magnetic species resulting from the induced turbulence. At present, the magnetic fields generally used in the electrodeposition processes are mainly electromagnetic field and permanent magnetic field. Electromagnetic field can easily achieve high strength and is easy to adjust in terms of magnitude and direction. In addition, it can provide suitably high intensity magnetic field for the electrodeposition process with a big interelectrode gap. But it has some limitations in the industrial applications because the generation of electromagnetic field needs costly and complex devices as well as various cooling apparatuses, leading to high process and maintenance cost. Although the permanent magnetic field is very difficult to obtain a magnetic field with an intensity of more than 1T in the interelectrode gap, it can offer favorably high value for the electrodeposition process at a very low cost and with almost no maintenance. In contrast, permanent magnetic field is more attractive for the conventional electrodeposition practices. However, it is not easy to get uniform high-intensity magnetic field in the entire working-area at a relatively wide gap due to inherent limitations of permanent magnet materials. Thus, it still needs further research to explore more effective generator that can meet the requirements of magnetic field assisted micro-electroforming process. Although some papers [3-5] reported some permanent magnet generators employed for the electrodeposition process, but they were still not satisfactory. To this end, this paper specifically introduces a novel permanent magnet generator for the micro electroforming process.

Overall Design and Requirements

The system of magnetic field assisted micro-electroforming process was mainly composed of magnetic field generator, electrodeposition cell unit and electrolyte circulation unit, etc..The electrodeposition cell unit was located in the gap between the N pole and S pole of permanent magnets. Taking into consideration of the fundamental requirements, cost and practicability of the micro-electroforming process, the permanent magnet generator should have the following functions: (1) it can provide uniform constant magnetic field in the entire gap space, and the magnetic field intensity in the central region is over 0.8T; (2) the magnetic field intensity can be changed uniformly with the variation of the working gap; (3)the effective area that is subjected to uniform constant magnetic field is not less than 100 mm×100 mm; And (4) it is significantly easy to make with a high throughput efficiency and an extremely small magnetic leakage, as well as a low cost. To achieve the above requirements, the key is the optimization design of magnetic circuit structures and regulation mechanism of interelectrode gap.

Optimization Design of Magnetic Circuit Structure

The core tasks of magnetic circuit structure design include selection of permanent magnet and aggregation magnet material and determination of magnetic circuit structure. In terms of practicability and economy, we chosen commonly-used rubidium iron boron magnet (50M: 1400mt<Br<1450mt) and industrial pure iron (DT4:$\mu'_{max}\geq 6000\mu m$) as the material of permanent magnet and aggregation magnet respectively. At the same time, as described above, in order to meet the basic requirements of magnetic field assisted micro electroforming process, uniform magnetic field area is not less than 100 mm×100 mm and NS interpole distance is not less than 30 mm. Obviously, under the given conditions, how to achieve as high as possible (at least 0.8 T) uniform magnetic field in the gap is the goal of optimization design of magnetic circuit structures.

According to the Kirchhoff's first and second law, in order to obtain desired magnetic gathering effect, the magnetic circuit structure is expected to be closed and have a good symmetry. The ideal structure of magnetic circuit was shown in Figure 1. Since different magnetic fields are required during the electrodeposition, the working gap between magnetic poles should be adjustable. Therefore, we divided the aggregation magnet into two parts: inner [-shaped part and outer]-shaped part (shown in Figure 2).The inner [-shaped part and outer]-shaped part were assembled through the alignment of the rabbets which were respectively configurated in the two side-arms of the above aggregation magnets. Two magnet combinations containing the same number of magnet blocks were stalled at the center of the bottoms of the inner [-shaped part and the outer]-shaped part respectively, with the surfaces of the combination being parallel. According to design experiences and analysis

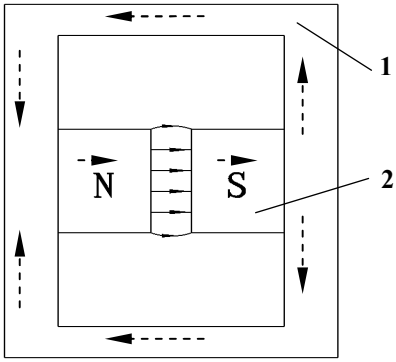


Fig.1 Schematic Diagram of the Permanent Magnet Structure
1. Aggregation Magnet; 2. Permanent Magnet

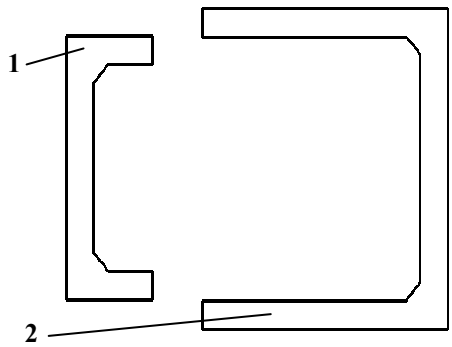


Fig.2 Schematic Representation of Assembled Magnetic Structures
1. Inner [-shaped part; 2. Outer]-Shaped Part

results, the thickness of the side arms of the two aggregation magnet parts was selected to be30 mm, and that of the bottom sides was designed to be 40 mm. In addition, the width between the two side-arms of the outer]-shaped part was 300mm. Because the resulting magnetic field strength of the magnet combinations is, to some extent, dependent on cross section shape of permanent magnet

involved, the cross section shape was specially studied numerically using the magnetic mirror image method [6] based on Matlab software. Eventually rectangle cross section was adopted as it was proved to have the capability of achieving higher magnetic field intensity. On the other hand, previous research indicated that the surface residual magnetization of the magnet combinations increases with increasing of stacking number, and then becomes almost unchanged when the stacking number reaches the limitation[7].To meet the requirements for conventional applications, we chose 7 pieces of permanent magnet blocks (cross section100 mm×100 mm and thickness 10mm) to form the magnet combinations.

For the sake of simplicity and accurate analysis, a three-dimensional physical model on the basis of the simplified magnetic circuit structures was established. The calculation results obtained by using Ansys software was illustrated in Figure 3. Almost all high intensity magnetic fields was

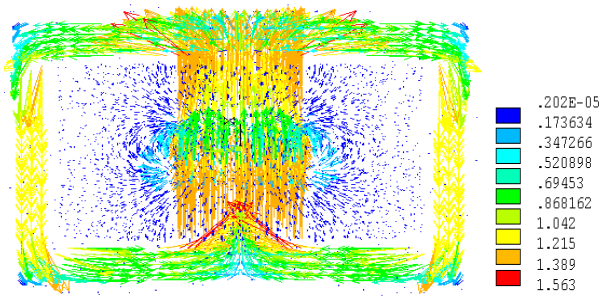
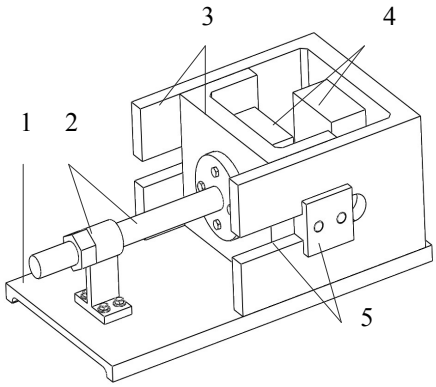


Fig.3 Distribution of Magnetic Field Obtained from Numerical Analysis

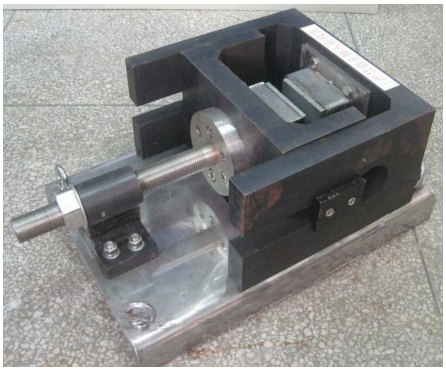
gathered in the space of the working gap with the intensity of 0.868162T, and the other regions showed extremely little magnetic field. These findings verified that the design totally realized the goal.

Design of Working Gap Regulating Mechanism

To realize the adjustment of the working gap between N and S pole, we designed a nut-screw mechanism which linked the bottom arm of the inner [-shaped part to drive one of the permanent magnet assemblies to move linearly. In addition, a chute-slider was installed into each side-arm of the inner [-shaped part and the outer]-shaped part to facilitate to make the working gap change uniformly and stably. In order to remarkably reduce the loss of magnetic field from the working gap during the adjustment, T-shaped slider was adopted with the alignment between the inner wall of slider head and the outer wall of the side-arm in the outer]-shaped part. The schematic of adjusting mechanism was shown in Figure 4.



(a) 3D schematical drawing



(b) Photo of permanent magnet generator

Fig.4 The Resulting Permanent Magnet Generator Designed
1. Baseboard; 2. Regulating Mechanism; 3. Assembled Magnetic Parts; 4. Permanent Magnet Poles; 5 .chute-Slider

Conclusions

Based on the fundamental process requirements as well as practicality, we explored a magnetic field generator for the magnetic field assisted micro electroforming technique. After choosing the materials of permanent magnets and aggregation magnet, we optimized the geometrical shape of the permanent magnet blocks and magnetic circuit structure, and then determined the number of permanent magnet combinations numerically. Furthermore, we designed the working gap regulating mechanism for this generator. Measurements showed that magnetic field intensity of the central region was 0.867T, the generator worked well.

Acknowledgment

This work was supported financially by National Natural Science Foundation of China (No. 50805077).

References

[1] P.M. Ming, Y.D. Lv, Y. Zhang, W. Li and S.Z. Li: J. Henan Polytech. Uni. Vol. 30(2011), P. 571 (in Chinese)

[2] J.M.D. Coey and G. Hinds: J. Alloy Compound Vol.326(2001), P.238

[3] P.M. Ming, Y.D. Lv, W. Li and Z.S. Li：CN Patent 201020670105.5. (2011)

[4] A. Masaaki: JP Patent 2002177243. (2002)

[5] J.J. Chen, C. Ni and T.Q. Xue: US Patent 2007257758. (2007)

[6] L.L. Tian, R. Jia, G.Q. Yang, Q. Tian, Z. H. Li and H. Li: Transact.China Electrotech. Soc. Vol.23(2008), P.7 (in Chinese)

[7] X.F. Gou,Y.Yang and X.J. Zheng: J. Appl. Math. Mech. Vol.25(2004), P.271 (in Chinese)

Advanced Materials Research Vol. 936 (2014) pp 1720-1724
© (2014) Trans Tech Publications, Switzerland
doi:10.4028/www.scientific.net/AMR.936.1720

Spray Cooling Unit for Heat Treatment of Stainless Steel Sheets

Hnizdil Milan [1,a], Chabicovsky Martin [1,b], Raudensky Miroslav[1,c],
Magadoux Eric[2,d], Code Florent[2,e]

[1]Brno University of Technology, Technicka 2, 616 69 Brno, Czech Republic

[2]Fives Stein, 108-112 avenue de la Liberté, 947 00 Maisons-Alfort, France

[a]hnizdil@fme.vutbr.cz, [b]chabicovsky@lptap.fme.vutbr.cz, [c]raudensky@fme.vutbr.cz,
[d]eric.magadoux@fivesgroup.com, [e]florent.code@fivesgroup.com

Keywords: Heat treatment, heat transfer coefficient, strip cooling, cooling intensity, sheet cooling, spray, water cooling, stainless steel

Abstract: Stainless steel sheets are successively heated to a temperature of 1150°C and cooled until ambient temperature during the production process. Requirements for high cooling rates of stainless steel sheets producers lead to use water as a cooling medium. The information about cooling intensity (heat transfer coefficient) of different nozzles configurations is necessary for designing cooling sections. Although many researchers deal with water spray cooling, actually a general correlation for predicting heat transfer coefficient for wide range of nozzles configurations does not exists. That is the reason why heat transfer coefficient for different nozzles configurations can be only obtained by laboratory measurements. Heat transfer coefficient is mostly influenced by water impingement density and impact velocity. However other factors e.g. water temperature and velocity of the sheet can influence the heat transfer coefficient. Optimized design of the cooling unit with high cooling intensity and low water consumption was achieved by appropriate choice of these parameters. The moving experimental sheet was cooled from a temperature of 900°C to a temperature of 50°C with various configurations of nozzles. The tests shown that heat transfer coefficient was increasing with water impingement density and impact velocity. Increasing water temperature from 20 °C to 80 °C caused a decrease of the heat transfer coefficient and Leidenfrost temperature. The effect of velocity is negligible when velocities are between 25 and 100 m/min. The cooling unit was designed according to laboratory measurements to fulfill the stainless steel producer's requirements. The measurements which were done in an industrial plant confirmed the accuracy of heat transfer coefficient obtained in the laboratory. The maximum difference between laboratory and plant measurements was 15%.

Introduction

Water is used as a cooling medium during the annealing of stainless steel strips because the producers require high cooling rates and cooling homogeneity to avoid thermal distortions [1]. The cooling intensity has to be known to design the cooling unit. Although many researchers are focused on water spray cooling, general correlation which predicts the cooling intensity for wide range of nozzles and spray parameters does not exist. The cooling intensity is often represented by heat transfer coefficient. Formulas described in papers usually use only water impingement density to compute the heat transfer coefficient [2]. Heat transfer coefficient is mostly influenced by water impingement density but it is also influenced by impact velocities and many other factors. They can be for example: water temperature, strip velocity, surface quality, etc [3][4]. This is the reason why the laboratory measurements of heat transfer coefficient for various cooling parameters are necessary to predict the cooling intensity.

Fives Stein company is concerned with designing of cooling sections for carbon and stainless steel annealing. Their object was to design a cooling section of stainless steel strips where stainless strips of thickness between 1 and 6 mm will be cooled rapidly to avoid precipitation of carbides without thermal distortions of the strip and with low consumption of water. They cooperate with the Heat Transfer and Fluid Flow Laboratory where the tests were done to obtain heat transfer coefficient for

various cooling unit set. This knowledge gives possibility to simulate cooling of the strip for various parameters and find optimal design of cooling section. The sizing part and final design was done by Fives Stein company.

Experimental Part – Experimental Equipment and Procedure

Heat Transfer and Fluid Flow Laboratory is equipped by testing devices to simulate cooling during continuous casting, hot rolling and heat treatment. The objective of the experimental part was a description of the influence of five parameters on the cooling intensity - water pressure (flow rate), nozzle span, gravity, velocity of the strip and water temperature.

Experimental Equipment

A special cooling unit was built for laboratory measurements. It was compound of eight rows of nozzles. This system allowed changing nozzle span very easily. It was mounted under and below the linear stand to simulate upper and bottom cooling. The Linear stand is six meters long rotatable girder with a trolley on which was installed experimental sheet. Trolley moved the tested sheet reversibly through the cooling section with defined velocity. An austenitic, 1.5 mm thin sheet was used as an experimental plate (Fig. **1** – hot surface) because of its resistance to material oxidation and because phase changes do not occur in this material. Five thermocouples were welded to the bottom side of the sheet (the front side of the sheet is sprayed by water). The data-logger was positioned also on the trolley and it was moving together with the sheet and it recorded measured data with very high frequency of 320 Hz. These data represented the temperatures from the bottom side of the tested sheet. So the surface temperature, the heat flux and the heat transfer coefficient were computed by inverse task.

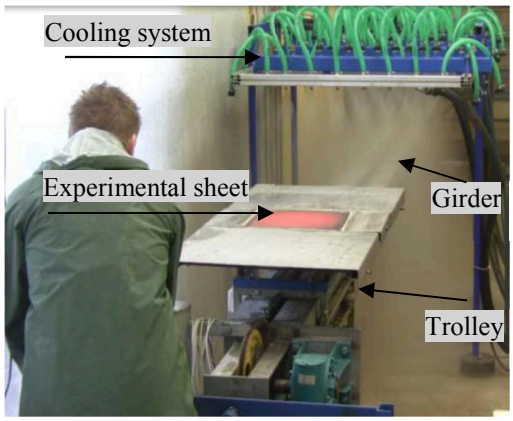


Fig. 1 Experimental device with hot experimental sheet – upper cooling with cluster of nozzles

Experimental Procedure

Each experiment started by heating of the sheet to the initial temperature (900 °C). The tested plate was oriented by surface down and it was inserted into the electrical furnace. The temperature regulator controlled heating and the furnace power. The inert atmosphere protected the surface of the sheet against oxidation. The water pump was switched on when the initial temperature was reached. The required water pressure and flow rate was set and the sheet was moved out from the furnace. Then the surface orientation was set. The surface was oriented down for bottom cooling and by rotating the girder of 180° the surface was oriented up for upper cooling. The trolley moved reversibly the tested sheet through the cooling section until the temperature of the sheet was lower than 50 °C. The data recorded by the data-logger were downloaded to the computer as soon as the experiment ended.

Data Processing

The temperatures were measured on the non-sprayed side of the test plate. A value of Biot number shows that the heat conduction inside the sheet is much faster than heat convection on the surface. When the Biot number is lower than 0.1 the temperature gradients in material are negligible [5]. The Biot number in this case is grater then 0.1 so the inverse task has to be used for data processing. A difference between surface and measured temperature is shown in Fig. 2 (on the left). The Beck's sequential algorithm was used to compute the heat fluxes. The surface temperature and heat transfer coefficient were easily computed by using standard formulas. The graph in Fig. 2 (on the right) shows an example of heat transfer coefficient dependence on the surface temperature in the area ± 150 mm around a single row of nozzles.

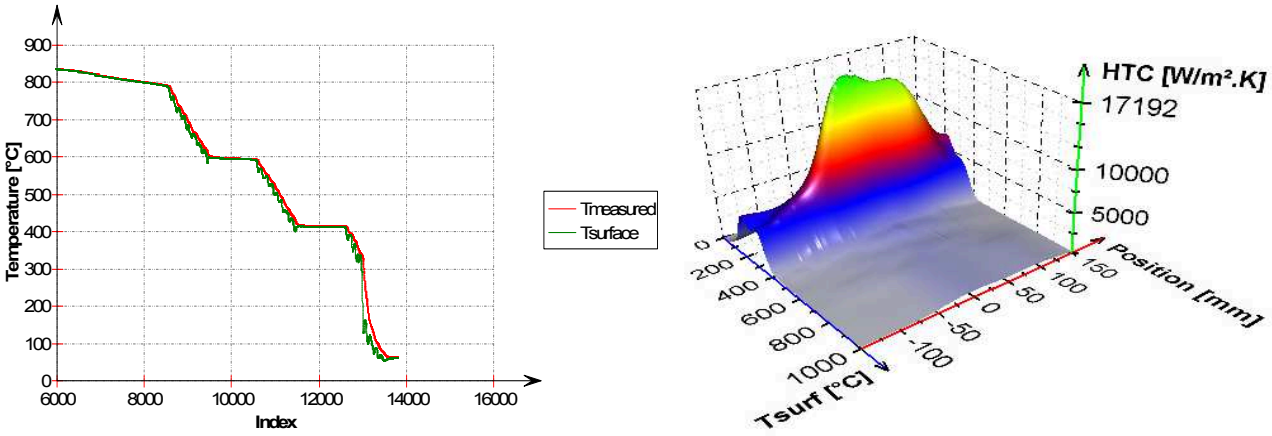


Fig. 2 Example of difference between measured temperature and computed surface temperature (on the left), computed heat transfer coefficient dependence on the surface temperature and position of sheet in cooling section, zero represents the center of the single row of nozzles.

The Influence of Various Parameters on the Heat Transfer Coefficient

The influence of five parameters on the cooling intensity was tested. The first parameter was water pressure. It was tested in a range from one to five bar. The heat transfer coefficient increases with increasing water pressure (Fig. 3 on the right). It is caused by the higher kinetic energy for higher water pressures. Very interesting results were obtained for the second tested parameter. It was found out the water temperature has a significant influence on the Leidenfrost temperature. Increase of the water temperature of 60°C caused the decrease of Leidenfrost point by 200°C. This finding can explain some problems with cooling during different seasons.

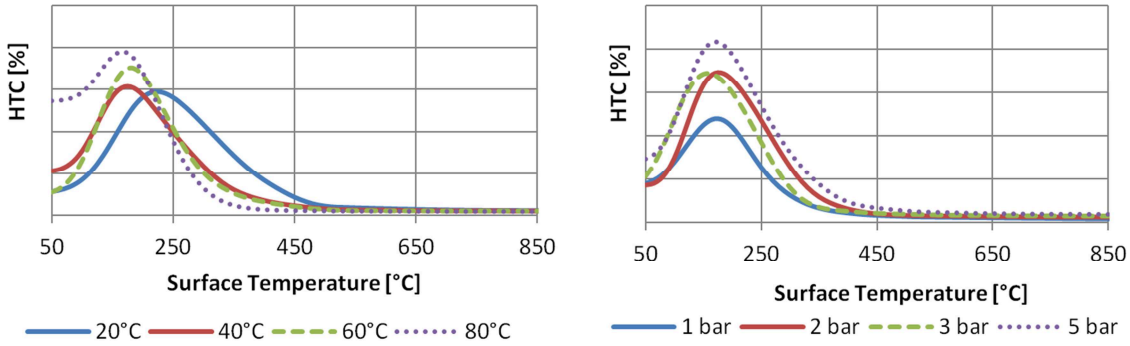


Fig. 3 Example of influence of water temperature on the heat transfer coefficient (HTC) (on the left) and dependence of heat transfer coefficient on the surface temperature for different water pressures and flow rates.

Next tested parameters were strip velocity and surface orientation. For both parameters, it was found out that they have negligible influence on the heat transfer coefficient for tested conditions (Fig. 4).

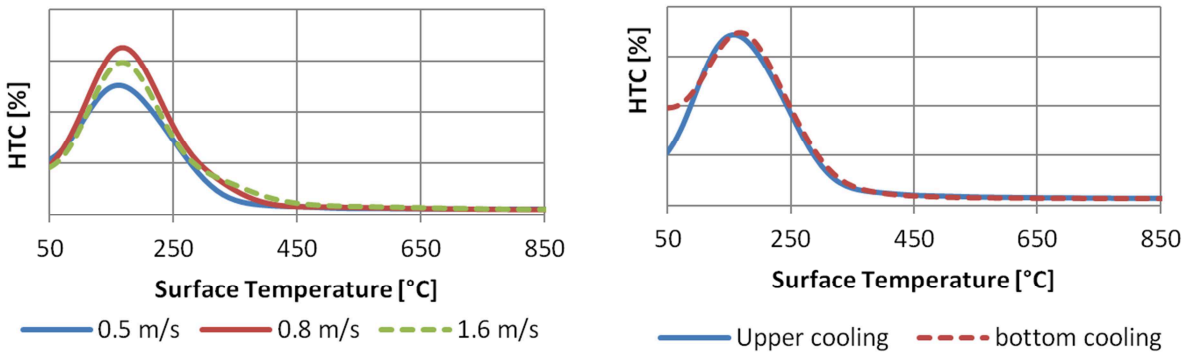


Fig. 4 Example of influence of strip movement velocity (on the left) and of the surface orientation (on the right) on the heat transfer coefficient

The last tested parameter was a nozzle span. This parameter was tested for optimization of the cooling section with respect to the homogeneity. The non-homogeneity of cooling was increased with increasing nozzle span.

Simulation and Cooling Section Sizing

Fives Stein used the curves of measured heat transfer coefficients depending on the surface temperature to size and to design its cooling section for stainless steel annealing. Fives Stein has made a measurements campaign on an industrial plant to compare laboratory measurements and plant measurements. It appeared that these measurements are in good agreement.

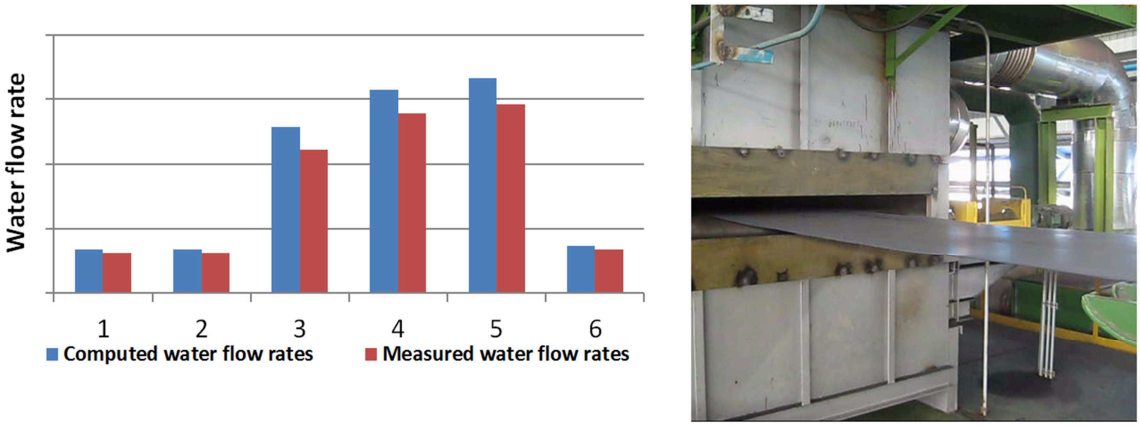


Fig. 5 Differences between predicted and measured flow rates which are necessary to cool down the strip for various cooling sections (on the left) and picture of the strip after annealing

Conclusion

The Fives stein company had to design a new cooling section for heat treatment of stainless steel. The sheet is heated to 1150 °C and cooled until ambient temperature. High cooling rates are required to produce the stainless steel to avoid the precipitation of carbides. The cooling intensity is essential information for designing cooling sections. Laboratory measurements are very important to obtain heat transfer coefficient. Heat Transfer and Fluid Flow Laboratory is fully equipped to test influence of different parameters on the cooling intensity. They were water pressure (water flow rate), water temperature, strip velocity and surface orientation (bottom and upper cooling). It was found out that water pressure has a significant influence on the cooling intensity. Increasing water pressure increases also the kinetic energy of droplets and also heat transfer coefficient. Second tested parameter was water temperature. It was found out a very interesting result that the water temperature

has a significant influence on the heat transfer coefficient. Increasing water temperature decreases the Leidenfrost temperature. Last two tested parameters were the velocity of moving strip and different surface orientations. These two parameters did not influenced heat transfer coefficient significantly for tested conditions. Obtained results were used by Fives stein company for sizing a cooling section with respect to required high cooling rates, homogenous cooling and low consumption of water. The cooling section was mounted in a real annealing line and a measurements campaign has been done on the real annealing line. This measurements campaign gave a very good result. The maximum difference between computed and measured flow rates which are necessary to cool down the strip was 15%. It is a great result in the field of a very complicated problem such as heat treatment.

Acknowledgement

The present work has been supported by the European Regional Development Fund within the framework of the research project NETME Centre, CZ. 1.05/2.1.00/01.0002, under the Operational Programme Research and Development for Innovation.

The research in the presented paper has been supported by the project No. CZ.1.07/2.3.00/20.0188, HEATEAM - Multidisciplinary Team for Research and Development of Heat Processes.

References

[1] M. Chabicovsky, M. Raudensky: Experimental investigation of spray cooling of horizontally and vertically oriented surfaces, In Conference proceedings of 22nd Conference on metallurgy and materials. 1. Ostrava, Tanger, s.r.o. 2013. p. 102 - 107. ISBN 978-80-87294-39-0.

[2] J. Wendelstorf, K. H. Spitzer, R. Wendelstorf: Spray water cooling heat transfer at high temperatures and liquid mass fluxes, International Journal of Heat and Mass Transfer, 2008.

[3] J. Hrabovsky, M. Raudensky, J. Horsky: Influence of the oxide scale on spray cooling intensity. In Rolling 2013. 1. Venice, AIM Italy. 2013. p. 1 - 7. ISBN 9788885298958.

[4] M. Raudensky; M. Hnizdil; J. Hwang. S. Lee, S. KIM: Influence of water temperature on cooling intensity of mist nozzles in continuous casting. Materiali in tehnologije, 2012, vol. 46, no. 3, p. 311-315. ISSN: 1580-2949.

[5] A. Sprock, M. Peretic, J. Speer: Compact cooling of as an alternative to alloying for production of DP/TRIP steel grades. AISTECH 2010 conference and exposition review, 2010, p. 170 - 177

Advanced Materials Research Vol. 936 (2014) pp 1725-1729
© (2014) Trans Tech Publications, Switzerland
doi:10.4028/www.scientific.net/AMR.936.1725

Research on Forming Accuracy of Two Point Incremental Forming for Aluminum 1060

Qiucheng Wang[1, a], Haihan Hu[1,b] , Jinhan Wu[1,c], Jiang Cao[1,d]

[1]School of Mechanical Engineering, Zhejiang University of Technology, Hangzhou, China

[a]wqc@zjut.edu.cn, [b]huhaihan@aliyun.com,[c]wjhkimi@163.com,[d]cjnhky90@163.com

Keywords: Two point incremental forming; Tool-path; Forming accuracy

Abstract. Two point incremental forming is proposed to form the thin sheet into the desired shape in this paper. The forming accuracy of two point incremental forming is compared with single point incremental forming for Aluminum 1060. Then the forming accuracy is measured by FARO three coordinates measuring instrument. And a new method is proposed to analyze forming accuracy quantificationally. The experimental results show that the forming accuracy of two point incremental forming is obviously higher than single point incremental forming.

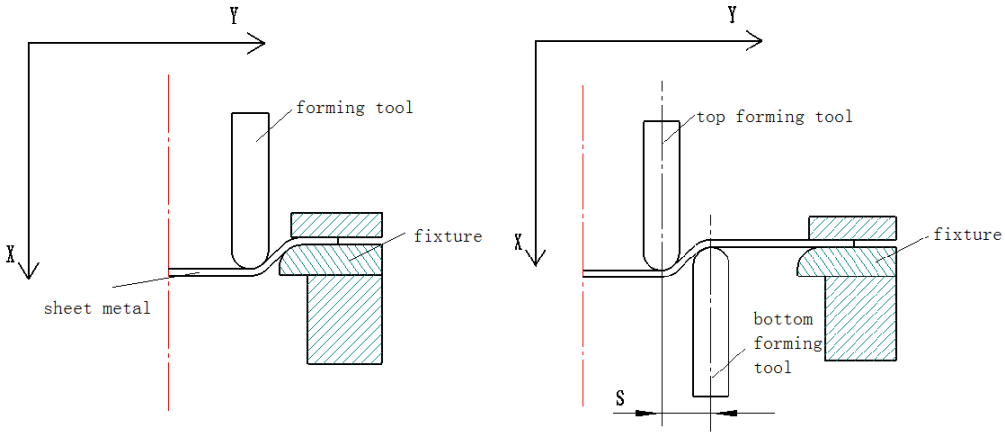
Introduction

The sheet metal incremental forming technology is based on layered progressive plastic deformation. Through the accumulation of plastic deformation, the shape of the component will be made. Following the development of sheet metal incremental forming technology, it is applied for different kinds of industrial production. Because of the characteristics of dieless forming, programmable control and flexible manufacturing, it has been gradually applied to some parts of small batch production [1]. Compared with the traditional sheet metal forming technology, it does not need special design die. The product development cycle will be shortened by using this technology. A lot of research subjects is studied, such as forming equipment, forming mechanism, forming process, tool-path.

Compared with single point incremental forming, the forming accuracy of two point incremental forming was quantificationally studied by experiment study. Before the experiment, the tool-path, the measuring method and the date analysis was prepared.

The Principle of Incremental Forming and the Forming Equipment

The principle of incremental forming includes single point incremental forming (SPIF) and two point incremental forming (TPIF). The equipment is spacial for sheet metal incremental forming.



(a) SPIF (b) TPIF

Fig.1 The Principle of Incremental Forming

Fig.1 (a) schematically presents the structure of single point incremental forming. The structure is very simple , including a machine, which can control the tool-path of the forming tool, a fixture and a forming tool [2]. The fixture is used to fix the sheet metal and define the processing area. The forming tool has no blade and the shape of the head is hemispherical. The plastic deformation will be accumulated by the forming tool working along the tool-path. Finally the shape of the sample will be made.

Fig.1 (b) schematically presents the structure of two point incremental forming [3]. Compared with the structure of single point incremental forming, the structure of two point incremental forming has two forming tools, including top forming tool and bottom forming tool. The top forming tool is used to form the sheet and the bottom forming tool is used to support the sheet. There is a predetermined distance between two of them. Two forming tools are controlled separately [4]. Through numerical control programming, two forming tools have different tool-paths. But the tool-path of the bottom forming tool follows the tool-path of the top forming tool [5].

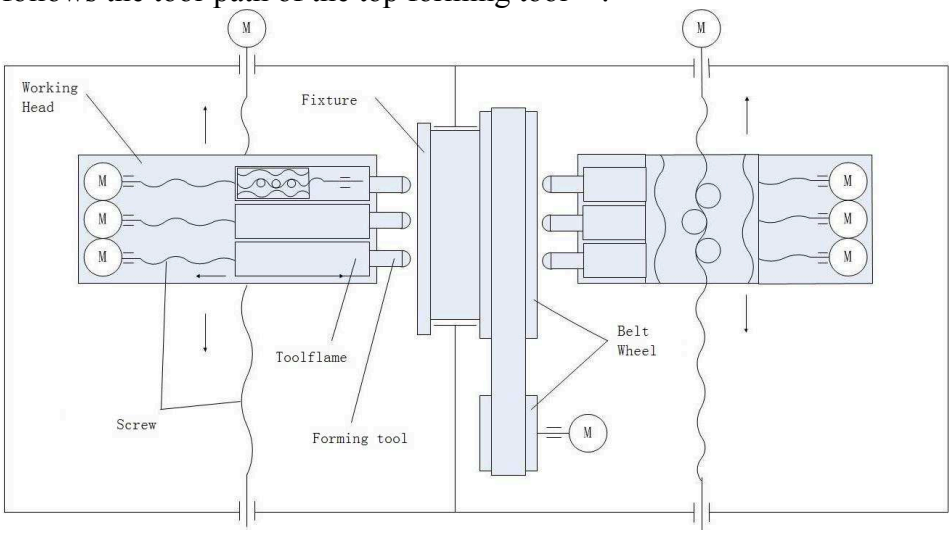


Fig.2 The Schematic Diagram of Sheet Metal Incremental Forming Equipment

This equipment is specially designed for the experiment of sheet metal incremental forming. Both of SPIF and TPIF can be done by this machine. Fig.2 presents the schematic diagram of this equipment. There are two working heads on each side. Through the screw, the working head is controlled by servo motor. There are three forming tools on each working head. All of them are controlled by servo motor, through the screw. The fixture is fixed on the rolling bearings. So the fixture can rotate and the power is supported by servo motor, through the bell wheel [6].

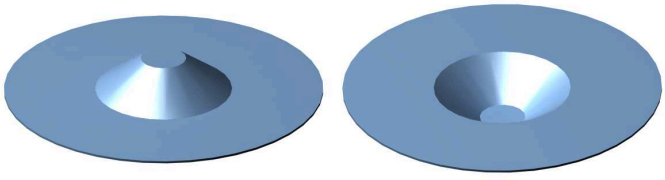


Fig.3 The Schematic Diagram of the Designed Geometry

The Designed Geometry and Tool-Path

Before the experiment, a designed geometry should be determined. Then, based on the designed geometry, the tool-path can be determined. Aluminum 1060 is chosen as sample material, diameter $D = 160mm$, thickness $T = 1mm$.

The designed geometry is determined by two requirements: (1) Because the forming limit will not be studied in this paper, forming angle should be lower than the forming limit. (2)The forming angle also should not be too low, otherwise the result of the experiment would not be obvious.

Above the two requirement, after referring to a lot of the reference on forming limit, the designed geometry is determined as Fig.3: the top diameter is 60mm, the bottom diameter is 2omm, the depth is 15mm and the forming angle is 53.2° .

About the tool-path of SPIF, the conventional contour line and out-to-in tool-path is chosen. Fig.4 (a) schematically presents the too-path of SPIF. The feeding in every step is smaller than 1mm to ensure the surface quality. Based on the designed geometry ,the feeding is determined: $\Delta X = 0.75mm$, $\Delta Y = 1mm$. After 20 step, the forming consequence is completed.

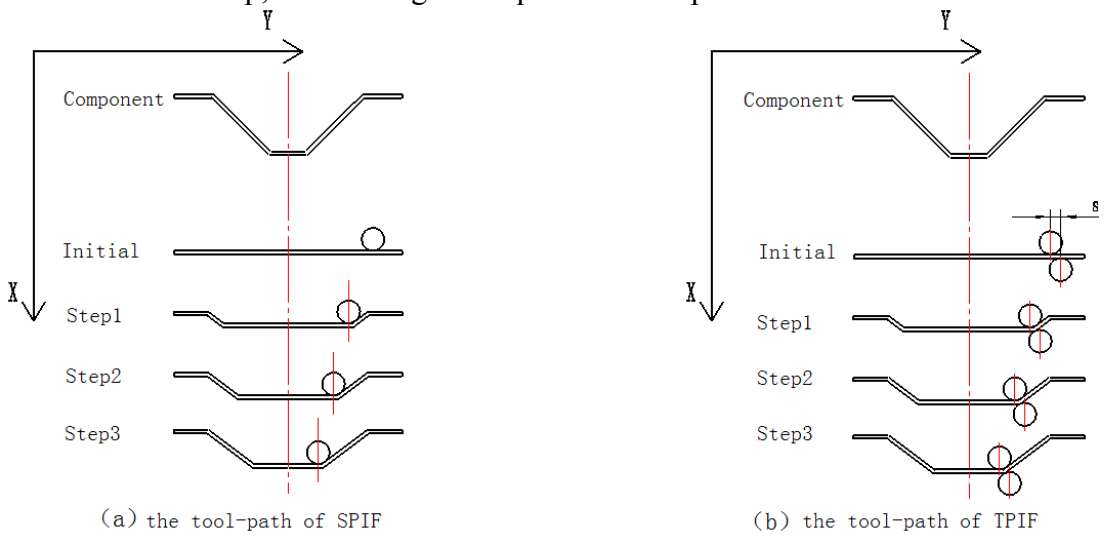


Fig.4 The Tool-path of SPIF and TPIF

About the tool-path of TPIF, the same as SPIF, the conventional contour line and out-to-in tool-path is chosen too. Fig.4 (b) schematically presents the too-path of TPIF. The tool-path of bottom tool is determined by the tool-path of top tool, but the feeding in each step is in common except for the first step. Based on the designed geometry ,the feeding is determined: $\Delta X = 0.75mm$, $\Delta Y = 1mm$. After 20 step, the forming consequence is completed [7].

Experiment and Results

Based on the tool-path, CNC Programming was completed and the sample was made by the equipment. Fig.5 presents the pictures of the samples.



Fig.5 The Formed Samples

The coordinates of the discrete points on the generatrix were measured by FARO three coordinates measuring instrument. The steps are as follows: (1) Clear the surface strains and spray imaging agent. (2) Scan the component by FARO three coordinates measuring instrument. (3) Based on geometric projection principle, the geometry of the generatrix was obtained on CATIA. (4) Obtain the coordinates of the discrete points on MATLAB. (5) Draw the curve on the origin.

Three parameters were presented to analyze the date quantificationally: Δ_{max}, $\varepsilon_{0.5\sim1}$, ε_1. Fig.6 presents comparison of designed geometry with practical geometry. In this graph, 70 points were picked on the curve, and the coordinates were (-1, y_1), (-2, y_2), (-3, y_3)... (k , y_k)... (-70, y_{70}),

$k=-1,-2,-3...-70$. The corresponding points on the designed geometry were (-1，Y_1), (-2,Y_2), (-3,Y_3)... (-k,Y_k)... (-70,Y_{70}). So the springback in each point was

$$\Delta_k = \left| y_k - Y_k \right| \tag{1}$$

When $x=-30mm$, the springback was max. So three parameters could be presented as

$$\Delta_{\max} = \left| y_{-30} - Y_{-30} \right| \tag{2}$$

$$\varepsilon_{0.5\sim1} = \frac{\sum(0.5mm \le \Delta_k < 1mm)}{70} \tag{3}$$

$$\varepsilon_1 = \frac{\sum(\Delta_k > 1mm)}{70} \tag{4}$$

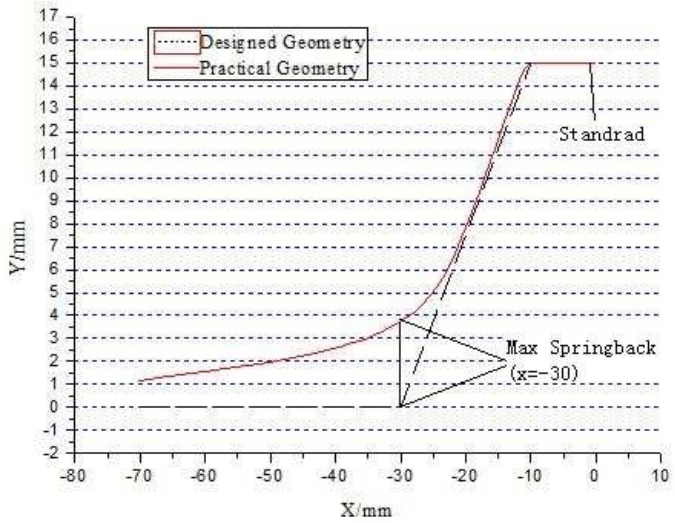


Fig.6 Comparison of Designed Geometry with Practical Geometry

Fig.7 presents comparison of the practical geometries from SPIF and TPIF with the designed geometry. Based on the formulas (1~4), three parameters were obtained in Table 1. The maximum springback of SPIF was 2.58mm, higher than TPIF. The $\varepsilon_{0.5\sim1}$ of SPIF was 5.7%, more than TPIF. And the ε_1 of SPIF was 48.6%, more than TPIF.

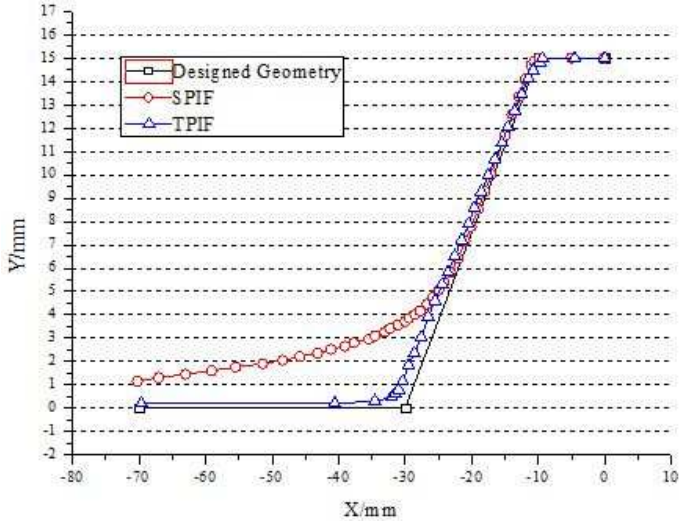


Fig.7 Comparison of the Practical Geometries from SPIF and TPIF with the Designed Geometry

TABLE 1 THE PARAMETERS OF SPIF AND TPIF

	SPIF	TPIF
Δ_{max}	3.71mm	1.13mm
$\varepsilon_{0.5\sim1}$	2.9%	8.6%
ε_1	65.7%	17.1%
$\varepsilon_{0.5\sim1}+\varepsilon_1$	68.6%	25.7%

Conclusions

This paper compared the forming accuracy of TPIF with SPIF quantificationally. A kind of method for measurement and analysis was presented. The experimental result shows that with the same process parameters, the forming accuracy of two point incremental forming is obviously higher than single point incremental forming.

In the future work, the influence of tool-path in TPIF on geometric accuracy and the influence of feeding on surface accuracy will be researched.

Acknowledgments

Authors would like to thank Zhejiang Provincial Natural Science Foundation for financial support (No. LZ12E05003)

References

[1] Yushan Deng. Research on Single point incremental forming device. Forging Equipment and Manufacturing Techniques, 2011,1(2):44-48.

[2] Martins PAF, Bayn,Skjoedt M, et al. Theory of Single Point Incremental Forming. Annals of CIRP, 2008,57(2008): 277- 280.

[3] Rajiv Malhotra, Jian Cao. Improvement of Geometric Accuracy in Incremental Forming by Using a Squeezing Toolpath Strategy With Two Forming Tools. MSEC2011,1-9.

[4] Silva MB, Skjoedt M, Atkins AG, Bay N, Martins PAF. Single Point Incremental Forming & Formability/Failure Diagrams. Journal of Strain Analysis for Engineering Design, 2008,43(1):15-36.

[5] M.B. Silva, P.A.F. Martins. Two-Point Incremental Forming with Partial Die Theory and Experimentation. Journal of Materials Engineering and Performance. 2013,22(4):1018-1027.

[6] Qiaogang Wang, Chunyan Yao, Wei Peng, Minghuan Wang. Research on Experimental Equipment for Three Point Incremental Forming. Light Industry Machinery, 2012,30(5):13-15.

[7] A.Attanasio,E.Ceretti,C.Giardini, L.Mazzoni. Asymmetric two points incremental forming: Improving surface quality and geometric accuracy by tool path optimization. Journal of materials processing technology 2007,197 (2008) :59-67.

Advanced Materials Research Vol. 936 (2014) pp 1730-1734
© (2014) Trans Tech Publications, Switzerland
doi:10.4028/www.scientific.net/AMR.936.1730

A Servo Control System Based on Fuzzy PI Method for Transverse Flux Machine in Mechanical Press

Jia Xie[1,a], Ailin Gao[1,b], Yanxiang Wu[1,c] and Zhongyong Gao[1,d]

[1]College of Engineering Science and Technology, Shanghai Ocean University, Shanghai, China

[a]jiaxie@shou.edu.cn, [b]aileen91417@126.com, [c]yxwu@shou.edu.cn, [d]gaozhongyonggood@126.com

Keywords: Servo control system, Fuzzy PI, ACPTFM, Mechanical press

Abstract. A control method for servo control system of Assembled Claw Pole Stator Transverse Flux Machine(ACPTFM) by controlling the armature current Root-Mean-Square (RMS) and the angle between armature current and no-load EMF is proposed in this paper. The servo control system of ACPTFM is composed of a series of closed-loop controllers, and the most complexity design of speed controller is described in detail. Fuzzy adaptive PI control method which integrates the advantages of fuzzy control and PI control is adopted to design the speed controller. Experimental results show that it can improve the system dynamic response and steady state accuracy.

Introduction

Comparing with the conventional mechanical press, mechanical press driven by AC servo motor is hailed as the third-generation mechanical press,which has the advantages of simple structure, high quality of product, good flexibility of slider movement, energy saving and noise reduction[1]. The performance of the servo mechanical press depends on the high performance of servo motor, which must be able to achieve low speed, high torque operation and have wide speed range. Transverse flux machine can meet the requirements quite well due to its special structure[2,3]. However, the effective servo control system and its control strategy of TFM has not been fully researched and discussed in this field.

In this paper, the Assembled Claw Pole Stator Transverse Flux Machine(ACPTFM)[4] is applied to servo press JS21-36 as its power plant, innovatively. Based on the analysis of ACPTFM electrical characteristics the servo control system is designed. The control method for speed loop is the main subject in this paper. Because fuzzy control has better robustness, meanwhile PI control can speed up the dynamic response and eliminate the steady-state error. So combine the advantages of both control methods, using fuzzy adaptive PI control strategy to design the speed loop in servo control system. Experimental results show that the servo control system and the control strategy is feasible to establish.

Servo Control System of ACPTFM

Servo system is one of the automatic control system, it generally takes mechanical position(angle) or speed as the controlled object. The main task of servo control system is let the position(angle) or speed commands quickly and accurately achieved by executive mechanism. In this way, the system can automatically, continuously and accurately reproduce the input changes of the given. Servo control system is usually a closed-loop control system with negative feedback. For the motor servo control system, it takes the rotor angle and speed as the controlled object, including the controllers and detection devices.

In this paper, the researcher creatively uses ACPTFM as the drive of the mechanical press. The single-phase average electromagnetic torque of ACPTFM is expressed as

$$\mathrm{T_m} = p[\psi_f I\cos\varepsilon + \frac{1}{2}(L_q - L_d)I^2\sin 2\varepsilon]. \quad (1)$$

where p, L_q and L_d are the number of pole pairs, cross-axis inductance and direct-axis inductance respectively. I, ε and Ψ_f are the armature current, the angle between armature current and no-load EMF (armature current initial phase) and the flux produced by permanent magnet. After the motor have been produced, the permanent magnet flux linkage Ψ_f is a constant. Within the rated current the quadrature-axis inductance L_q and direct-axis inductance L_d can also be regarded as constants. So, actually, the torque control of ACPTFM is the controlling of the armature current Root-Mean-Square (RMS) and the angle between armature current and no-load EMF. After researched the electrical characteristics of the ACPTFM, the servo control system of ACPTFM is designed. Fig.1 shows the system chart.

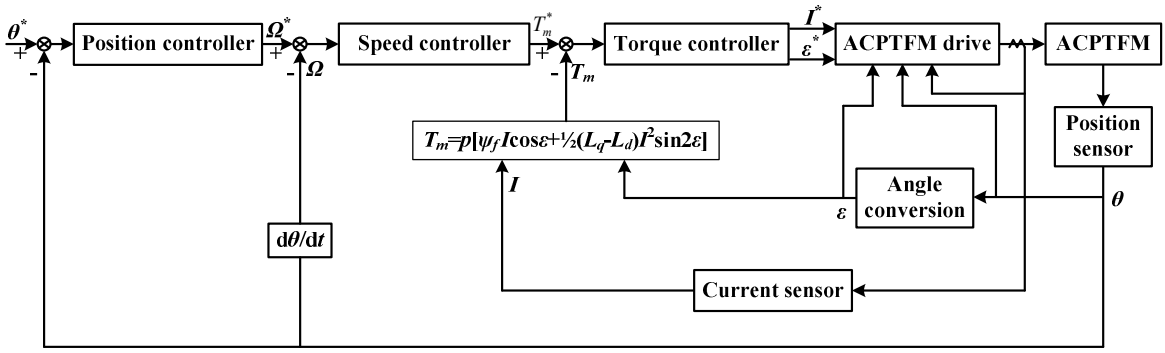


Fig.1 Servo Control System of ACPTFM

In Fig.1, θ and Ω represent the ACPTFM angle spatial displacement and angular speed. In order to control the armature current initial phase ε, change the ACPTFM angle spatial displacement θ into actual current initial phase by angle conversion. I presents the RMS of armature current. The servo control system of ACPTFM use a series of four closed-loop to achieve the controlling task which is the control of the ACPTFM position, speed, torque and current, and the current loop is included in the internal of drive. The signal flow is as follow: the input signal of position controller is the difference value of rotor position given value subtract its actual value, the output signal of position controller subtracts the actual speed value and the result uses as the given signal of speed controller. Then the speed controller's output is as the given signal of the torque controller. The practical torque value can be acquired by Eq.1. The difference value which the torque given value subtracts the actual torque value inputs into the torque controller, after computing, the RMS of single phase armature current and the given signal of initial current phase are gotten, thus, the sinusoidal signal of armature current can be acquired. Consequently, input the signal into the ACPTFM drive as the current given. Finally, through the current loop and a series of calculation processing, the ACPTFM drive outputs the actual armature current, so as to achieve controlling of the machine.

Control Strategy of Servo Control System of ACPTFM

The servo control system of mechanical press can take slider position as its control object, but the whole system from servo motor to slider exist nonlinear and inertial seriously, so the design of entirety closed-loop position controller is very difficult. Often needs to add a lot of compensation control strategies, but the result still does not meet the accuracy requirement. On the other hand, there are many detection taches in the system, it needs plenty of time to handle the detection and sampling, and the complex algorithms of position controller also need time to run. Because of the serious delay of the system, the real time performance of this kind control system needs to be considered.

Researches have studied the kinetic characteristic of mechanical press and built its mathematical model of Bezier curve. The process characteristic parameters of crank input and slider output have gotten as well. In this paper, these characteristic parameters are applied to the servo control system of mechanical press, which will greatly simplify the entire control system and the rapidity of system will be improved to a great extent.

In the mechanical press driven by ACPTFM, the motor output drives the slider movement through some intermediate synchronous conversion links, directly. The Bezier curve mathematical model of the process for servo mechanical press is already known, which determines the input of the servo control system of ACPTFM. In the servo control system, control strategy is the main issue. Wherein the functional relationship between input and output of the position controller and the torque controller is clear, not described in detail here. A simple incremental PI regulator can be added to meet the control requirements. But for the speed controller, the input is speed value and the output is torque value, because of the frequent change of load torque and the relationship between speed and torque is complex, moreover, the inconsistency of the workpiece, it is prone to large disturbance. By the previous analysis, the range of motor speed requirement for position servo control is relatively wide and have higher demands on the accuracy of response curve. Therefor, simple PID speed controller cannot meet the requirements of control.

Currently, the fuzzy control is a more mature intelligent control strategy, the control characteristics of which is change the expert knowledge and experience into language control rules. And use these rules to control the system, so fuzzy control has strong robustness. However, compared with traditional PID control, fuzzy control has some shortcomings and deficiencies. For example, the control action is less delicate, the stability of system is less precision and the system is under the influence of the subjective. In addition, fuzzy control generally use two-dimensional structure, in this case, using speed deviation e and the rate of change e_c as input variables. This two-dimensional fuzzy controller has a similar role like the conventional PD controller, it can obtain good dynamic characteristics, but its stability is poor. And consider the function of PI controller, the proportional control accelerates the dynamic response speed; the integral control eliminates static errors but the dynamic response is slow. The combination of fuzzy control and PI control strategy can compensate the shortcomings of each other, this will enhance the control system dynamic and static performance. In this article, the speed controller uses fuzzy adaptive PI control method as its control strategy. This method combines the fuzzy logic control and adaptive strategies together, it is able to get a good control effect.

Fig.2 shows the block diagram of fuzzy adaptive PI speed controller. Fuzzy variables E and E_c are the fuzzy output, then through fuzzy reasoning and defuzzification acquire correction value which can adjust the parameters of PI controller. With the motor running state changes, parameter P and I in the PI controller are changing as well, so good dynamic and static control effect can be obtained.

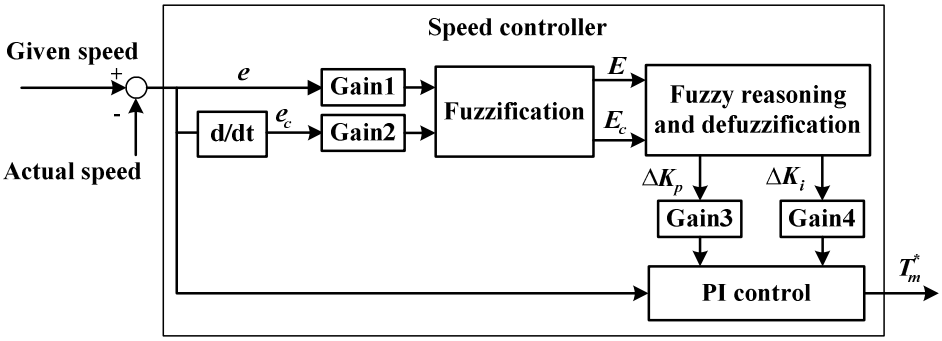


Fig.2 Speed Controller of ACPTFM

Fuzzy reasoning calculation bases on the experience and expertise, it needs to define the language variable. This article defines the variable range of language as follow: positive largest (PL), positive middle (PM), positive small (PS), zero (ZO), negative small (NS), negative medium (NM) and negative largest (NL). Seven triangular membership functions are used to definite the input and output variables, the range of the abscissa of membership function is (-1,1), and the input and output using the same membership function. The amplitude of input and output variables are controlled by adjusting their switches Gain1, Gain2, Gain3 and Gain4.

The fuzzy controller uses fuzzy language control rate to describe the control features, the fuzzy control rate is a set of language-based rules, it is a refined process of forming human reasoning and

inference knowledge. Fuzzy control rate, membership function and reasoning method determine the transfer characteristics of fuzzy controller, they also are called the transfer function. When establish the fuzzy control rate its integrity should be ensured, which means all input states need to be covered, so under each of the input state system has a corresponding control rule to work. According to the actual situation of speed controller in servo control system of ACPTFM, the fuzzy control rate of the speed controller is as shown in Table 1.

TABLE 1 FUZZY CONTROL RULE

		deviation e						
		NL	NM	NS	ZO	PS	PM	PL
Deviation rate of change e_c	NL	NL	NL	NL	NL	NM	NS	ZO
	NM	NL	NL	NM	NM	NS	ZO	PS
	NS	NL	NM	NM	NS	ZO	PS	PM
	ZO	NL	NM	NS	ZO	PS	PM	PL
	PS	NM	NS	ZO	PS	PM	PM	PL
	PM	NS	ZO	PS	PM	PM	PL	PL
	PL	ZO	PS	PM	PL	PL	PL	PL

Fig.3 shows the flow diagram of adaptive fuzzy PI control system. From the controlling flow start, the knowledge base of fuzzy control is initialized firstly. The initialization includes the determination of fuzzy control rates and membership functions. Secondly, the speed deviation e and the deviation rate of change e_c and their membership are calculated. Fuzzy reasoning usually uses the minimum and maximum method and defuzzification adopts the area of the center of gravity method. Finally, the output parameters and participate are fixed in PI controller operation.

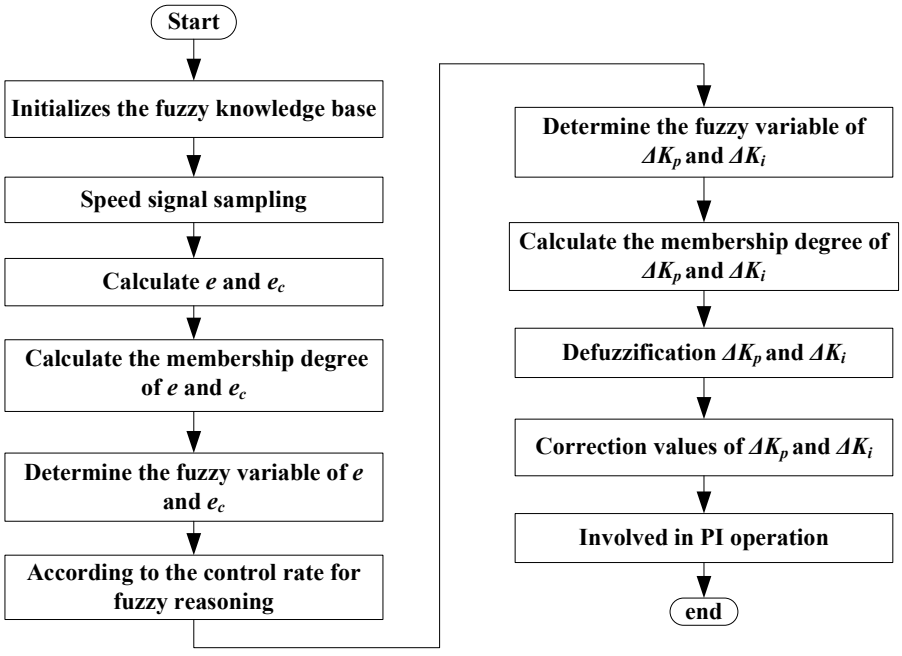
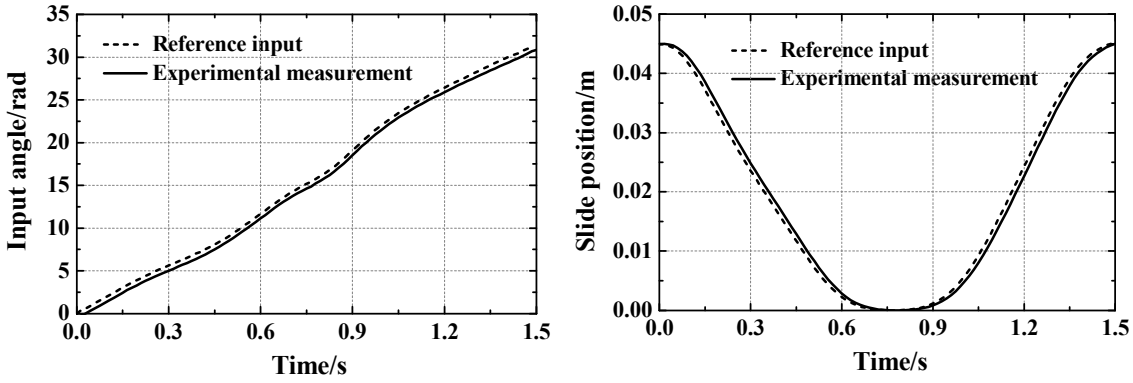


Fig.3 The flow diagram of adaptive fuzzy PI control system

Results and Discussion

The test results of the drawing process movement characteristics are shown in Fig.4. It can be seen that the servo mechanical press operation characteristic curve (reference input) of experiment and optimized are the same. In Fig.4(a), the motor input angle curve shows that the change of motor angle is non uniform. This is a servo operation status, which is to meet the requirements of drawing process

in press. Fig.4(b) shows that within the design range of the drawing processing of 0.03~0.01mm, the displacement curve is nearly a straight line. This will ensure a good processing quality of drawing process. The servo operation status illustrate that within the drawing processing interval, the motor is running at rated speed. This interval is the constant torque operation of motor which means low speed, high torque range, and motor outputs rate torque. Without the drawing processing interval, the motor is working above the rate speed, which is the constant power range.



(a) (b)

Fig.4 Experimental Results of Drawing Process Under Servo Control. (a) Input Angle. (b) Slider Position

Conclusions

In this paper, the servo control system of ACPTFM is established and its control strategy is discussed. Particularly, the control strategy of speed loop is presented. Because the rapidity, accuracy and stability of fuzzy adaptive PI control system is better than the traditional control method, the speed loop uses fuzzy adaptive PI control strategy as its control method. The fuzzy control rules are established and they cover all input states effectively. Based on the analysis of speed loop, a flow diagram of fuzzy adaptive PI control system is presented. The slide position output curves show that the servo control system based on fuzzy adaptive PI control method is effective to achieve high performance for the press.

Acknowledgements

This work was financially supported by Dr. Scientific Research Foundation of Shanghai Ocean University (A-0209-13-0105376) and Significant Scientific Foundation of State Oceanic Administration of China (SHME2011GD01).

References

[1] Z. Azpilgain, R. Ortubay, A. Blanco, et al, ervomechanical press: A new press concept for semisolid forging, Diffusion and Defect Data Part B (Solid State Phenomena), Vol. 141–143 (2008), 261-166.

[2] J. Xie, S. D. Zhao, and J. X. Li, Research on key techniques of green mechanical press directly driven by transverse flux machine, Proc. IEEE Int. Conf. Mechatronics and Automation, Xi'an, China, (2010), 1381-1386.

[3] J. Pippuri, A. Manninen, J. Keränen, et al, Torque density of radial, axial and transverse flux permanent magnet machine topologies, IEEE Trans. Magn., Vol. 49 (2013), 2339-2342.

[4] J. Xie, D.H. Kang, B.C. Woo, et al, Optimum design of transverse flux machine for high contribution of permanent magnet to torque using response surface methodology, J. Electr. Eng. Technol., Vol. 7 (2012), 745-752.

Advanced Materials Research Vol. 936 (2014) pp 1735-1741
© (2014) Trans Tech Publications, Switzerland
doi:10.4028/www.scientific.net/AMR.936.1735

Effect of Traverse Speed on the Microstructure and Mechanical Properties in Friction Stir Welded Dissimilar Barrier Butt Joints of AA2024 to AA6061/SiC/55p Composite

SONG Xue Cheng[1, a], GUO Li Jie[1,b], FENG Xiao Song[1,c],
YIN Yu Huan[1,d] and CUI Fan[1,e]

[1] Shanghai Aerospace Equipments Manufacturer, Shanghai, China 200245

[a]songxcaff@hotmail.com, [b]guolijie149@163.com, [c]fxsupc@nuaa.edu.cn

[d]yinyuhuan@hotmail.com, [e]cuifan2004@126.com

Keywords: Friction stir welding, Dissimilar barrier butt joints, AA2024, AA6061/SiC/55p composite, Microstructure, Mechanical properties

Abstract. Dissimilar barrier butt joints of AA2024 to AA6061/SiC/55p composite were fabricated by friction stir welding. Effect of the traverse speed on interface bonding, joint microstructure and tensile properties was investigated. Results revealed that, all joints possessed a tensile strength stronger than 80% that of the composite base materials, and the highest strength value was 178MPa. Macro interface can be readily identified in the weld zone between AA2024 and AA6061/SiC/55p composite, of which the area decreased and then increased as the traverse speed increased. The size and shape of SiC particles in the interface zone varied a lot due to different stirring effect and forward impact of the pin in different traverse speeds. Increasingly impairment of the composite base material near the interface was also detected with the traverse speed increasing.

Introduction

Aluminum alloys and SiC particles reinforced aluminum matrix composites (AMCs) are widely applied in aerospace, automotive and many other applications due to their superior physical and mechanical properties[1-3]. Among them, AMCs with high volume SiC particles, possessed higher thermal conductivity, lower thermal expansion coefficients and well wear resistance, has been an important material for some components in recent years[4,5]. However, application of AMCs with high volume SiC particles is limited for its poor weldability and high cost[6,7], which illuminates its joining to aluminum alloys. Nonetheless, due to the presence of SiC particles, it is difficult to join AMCs by using conventional fusion welding techniques[8-10], which always give rise to defects such as voids and cracks and deleterious chemical reactions of aluminum matrix with the reinforcement particles.

As a relatively novel solid-state joining process, friction stir welding (FSW) was invented by TWI in 1990s[11], and shows a great capability to join aluminum alloys and dissimilar materials[12-15]. It is also considered as one desirable joining method for AMCs because of no material melting in the process and so avoiding the presence of voids and other defects[16-18]. Xiao et al[19] investigated the FSW of AA2009/SiC/15p composites to AA2024 and examined the microstructure and mechanical properties of the joints. They found that complicated microstructure evolution occurred in the weld nugget zone during welding and the ultimate tensile strength of the joint was 85% that of AA2024 base materials. NASA [20]also studied the feasibility of FSW of AMCs with 50vol.% SiC particles to AA2195 and found that the pin broke off after only 38mm of weld and concluded the two materials can not be joined by FSW. As many difficulties have been encountered in joining similar or dissimilar AMCs with high volume SiC particles, researches on it are very limited[21,22].

In this study, an attempt was made to join 2mm thick AMCs with 55vol.% SiC particles and AA2024 using FSW and investigation on the influence of the traverse speed on the microstructure and tensile properties of the dissimilar joints was also studied.

Experimental Procedure

AA6061/SiC/55p AMCs plates produced by non-pressure infiltration methods and extruded plates of AA2024 in a T4 temper condition were used in this study. The nominal median particle size of silicon carbide in the AMCs is 40μm and the matrix is a standard AA6061. The chemical composition of the AA2024 extruded plate and composite matrix AA6061 are given in Table 1. A h-13 tool with a concave shoulder 19mm in diameter and an unthreaded tapered cylindrical pin 6mm in diameter and 3mm in length with a spherical tip was used.

TABLE 1. CHEMICAL COMPOSITION OF AA2024 AND AA6061 (WT.%).

Materials	Si	Fe	Cu	Mn	Mg	Cr	Zn	Ti	Al
AA2024	0.5	0.5	3.9	0.6	1.6	0.10	0.25	0.15	Bal.
AA6061	0.48	0.7	0.25	0.15	1.0	0.25	0.25	0.15	Bal.

The weld assembly is shown in Fig. 1, where AMCs with 100mm in length and 50mm in width is placed on the advancing side of the weld, and the butted AA2024 is on the retreating side with the same size as the AMC plates. A barrier, having the same constitution and heat treated condition as the composite matrix, is placed on the butt joint to avoid wear of tool shoulder, with a length of 90mm, width 80mm and thickness 0.8mm. Also a back plate, as same as the barrier, is used to avoid insufficient joining near the bottom of the butted plates. Aiming at reducing the pin wear and enlarging the plastic zone size of the weld, pin-offset of 1.5mm to AA2024 side was also employed.

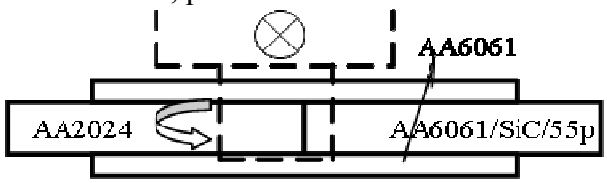


Fig. 1. Schematic of the Welding Process

All plates were carefully degreased with liquid acetone and air dried. A steel brush was used on the plate and its edges to remove residual smudges and oxide films before the actual welding. The rotational speed was set 750rpm, and the traverse speed was varied from 10mm·min^{-1} to 80 mm·min^{-1} in the welding process.

After FSW, the specimens were cross-sectioned perpendicular to the weld direction for microstructural examination and were prepared by mechanical grinding, polishing and etching using Keller's reagent. The microstructures were examined using optical microscopy(OM, Observer10) and scanning electron microscopy(SEM, Hitachi-S4800). After the barrier and the back-plate alloy being milled away, tensile tests were carried out at a test speed of 1 mm·min^{-1} at room temperature, and three specimens were tested for each group. The fracture surfaces were then examined using SEM.

Results and Discussion

Macroscopic Structure

Fig. 2 shows the macroscopic images of dissimilar joints produced in different traverse speeds. It was observed that sound welds can be obtained for all the welding conditions investigated. A macro interface between the AMC and AA2024 can be readily identified. It is evident that the two materials were not completely blended for all four welding conditions. This can be attributed to the unthreaded feature of the FSW tool designed to reduce the tool wear. It was reported[23]that the macro- interface can also be easily identified in dissimilar FSW of AA6063 alloy and B_4C/Al MMC when using a cylindrical tool with no threads, which is similar to the results in the present study. It was also

observed that FSW tools without threads could not fully mix the materials macroscopically because the materials experienced a weak vertical flow movement[24,25].

As the traverse speed increased from 10 mm·min^{-1} to 40 mm·min^{-1}, the contour of the macro-interface changed a little, but all possessed a feature of a relatively smooth and moderate transition from the upper to the lower side of the interface, as shown in Fig. 2(a) to Fig. 2(c). When the traverse speed increased to 80 mm·min^{-1}, the macro-interface became sharper in transition, which may result in a weaker load-transfer near the interface and a higher stress-concentration. Because its segregation from the interface can be detected in magnified views, the composite material adjacent to the top of the macro-interface in Fig. 2(b) was not taken as part of the contour.

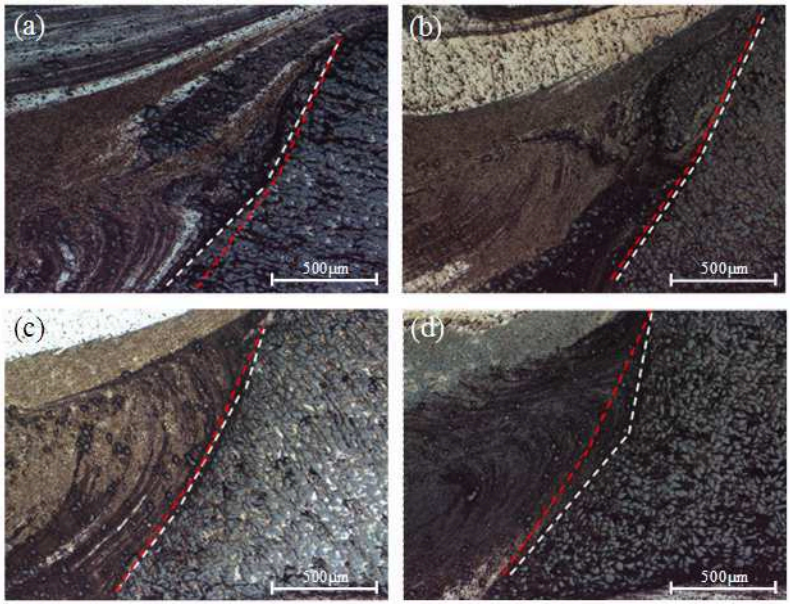


Fig. 2. Macrographs Of Welds In Traverse Speed Of (a) 10 mm·min^{-1}, (b) 20 mm·min^{-1}, (c) 40 mm·min^{-1} and (d) 80 mm·min^{-1}.

To facilitate discussion, the macro-interface contour in 20 mm·min^{-1} was used as a reference, and was painted red. It can be seen that the slope of upper side of the interface in 10 mm·min^{-1} is similar to that of the reference, while slope of the lower side is a little smaller, so a larger interface area in 10 mm·min^{-1} can be concluded. And the overall slope of the interface in 20 mm·min^{-1} and that in 40 mm·min^{-1} are similar, suggesting their interface areas are nearly the same. When the traverse speed increased to 80 mm·min^{-1}, the interface area increased again with a lower slope compared to that of 20 mm·min^{-1}. This may be explained by a higher traverse speed induced stronger impact of the pin to the composite material. Furthermore, the higher traverse speed caused a lower heat input which reduced the tendency of the composite materials to be plastically deformed[26,27].

Microstructure Characteristics

Fig. 3 shows the SEM microstructures of the joint interface and composite base material (CBM) adjacent to it. As can be seen, when the traverse speed is 10 mm·min^{-1}, particles in small sizes, with blunt edges, can be found in the interface zone, which indicates the particles were refined as a result of the stirring effect of the tool pin in low traverse speed. Meanwhile, the CBM kept its original features due to a low impact to it of the pin in low traverse speed.

As the traverse speed increasing, the size of the SiC particles increased and their edges became sharper, probably leading to high stress-concentration around the sharp edges and cause crack initiation under load condition. However, when the traverse speed increases to 80 mm·min^{-1}, size of SiC particles became smaller again. This may result from the fact that the impact to the SiC particles from the pin and collisions between the particles themselves became more severe in higher traverse speed. However, it can be observed in Fig. 4 that impairment of the CBM became more severe and microcracks in it is much more. This may result from the stronger impact to the CBM and a lower plasticity due to lower heat input as the traverse speed increased.

Tensile Properties

The effect of the traverse speed on the tensile strength of the joints is depicted in Fig. 5. It is evident from the curve that the joints fabricated in 10 mm·min^{-1} of traverse speed exhibit the highest tensile strength, which is 178MPa and 98% of that of CBM. As the traverse speed increases, a decrease in tensile strength occurred, reaching a lowest tensile strength of 146MPa, i.e., 80.7% that of CBM, when the traverse speed is 80 mm·min^{-1}. Thus, all joints fabricated in range of 10 mm·min^{-1} to 80 mm·min^{-1} possessed a strength higher than 80% that of CBM, indicating that good joint strength can be obtained in such welding parameters. The fracture location of the joint is shown in Fig. 6 with the cross-section view inserted below. It can be seen that the joint failed in the interface of the two materials, implying it's the weakest part of the joint.

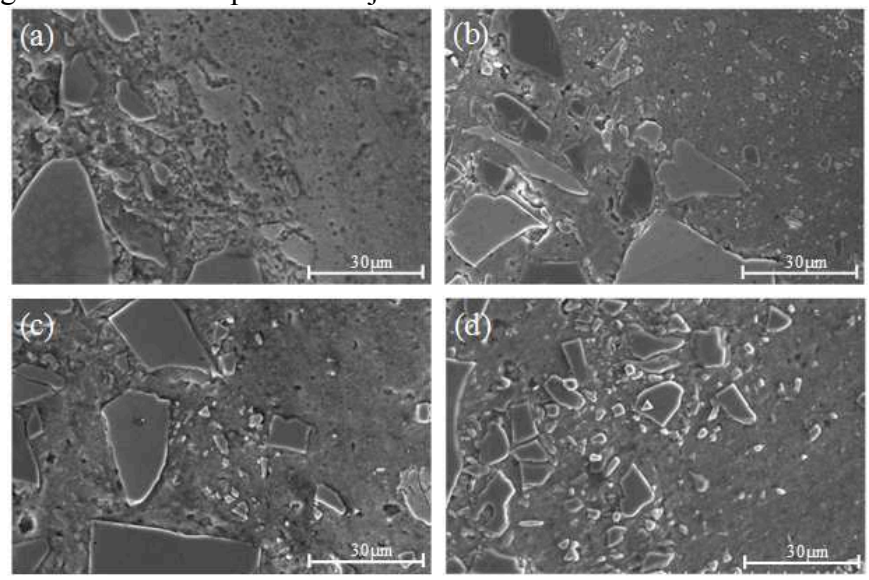


Fig. 3. Micrographs of the Joint Interfaces in Traverse Speed of (a) 10 mm·min^{-1}, (b) 20 mm·min^{-1}, (c) 40 mm·min^{-1} and (d) 80 mm·min^{-1}.

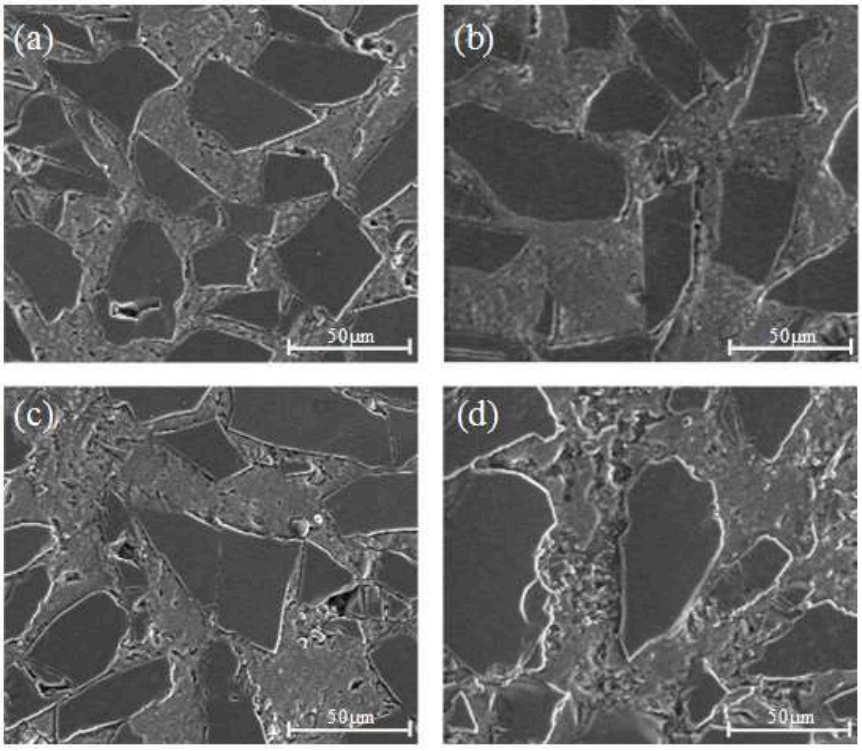


Fig. 4. Micrographs of the Composite Base Material Near The Joint Interface In Traverse Speed of (a) 10 mm·min^{-1}, (b) 20 mm·min^{-1}, (c) 40 mm·min^{-1} and (d) 80 mm·min^{-1}.

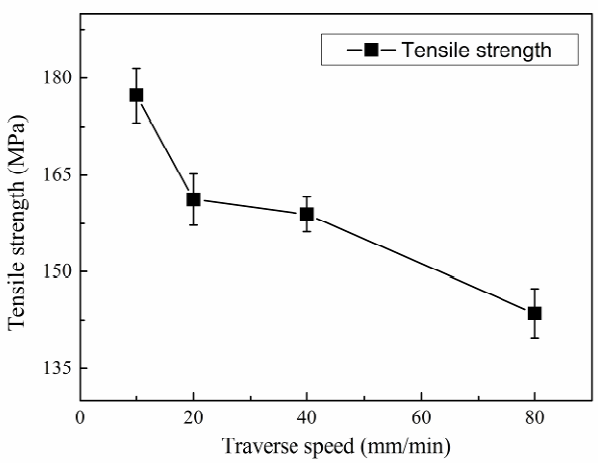


Fig. 5. Tensile Strength of the Joint in Different Traverse Speeds.

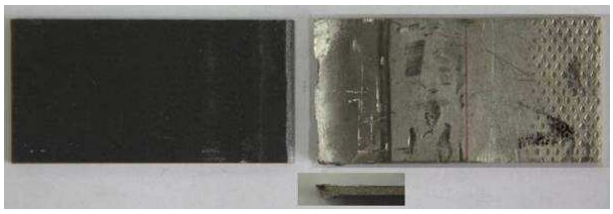


Fig. 6. Fracture Location of the Tested Specimen.

The factors which determine the tensile strength of the joints are: (i) presence of macroscopic defects in weld zone, (ii) impairment of the CBM adjacent to the interface, (iii) degree of plastic flow and amount of mixing of both materials, (iv) stress-concentration in interface deriving from sharp edges of the SiC particles. The defect-free joints can be achieved for all parameters, so all the joints experienced an intact macrostructures. Joints fabricated in 10 $mm \cdot min^{-1}$ yielded the highest tensile strength due to an relatively intact feature of CBM and intense plastic flow and mixing of the two materials, as well as the bluntness of SiC particles edges. In 20 $mm \cdot min^{-1}$ and 40 $mm \cdot min^{-1}$ the tensile strength of joints became lower as a result of insufficient mixing of the two materials and the sharp edges of ceramic particles in the interface zone. And in highest traverse speed of 80 $mm \cdot min^{-1}$, severe impairment took place on the CBM and finally reduced the tensile strength of the joint to a large extent.

The fracture surface, which is shown in Fig. 7, was characterized by some Al dimples and large amount of SiC particles, and microcracks were also observed. The Al dimples derived from fracture of the composite matrix are small and shallow. And the SiC particles in different size and shape all looks smooth. This may be explained by the fact that high stress-concentration was induced by the sharp edges of the particles, from which cracks initiated and propagated by the particles surfaces[28]. Thus, the failure mode is brittle domained brittle-ductile fracture, due to the segregation of SiC particles to composite matrix and fracture of composite matrix itself.

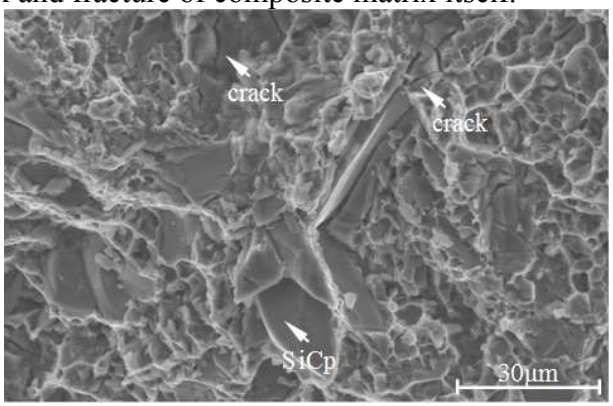


Fig. 7. Fractography of the Joint

Conclusions

In summary, the following conclusions are drawn:

1. Defect-free dissimilar barrier butt joints of 2mm thick AA2024 to AA6061/SiC/55p composite can be obtained under all welding conditions investigated.

2. With the increase of the traverse speed, the area of the interface increases first and then decreases, vise versa the size of the SiC particles in the interface zone, while impairment of the composite matrix near the interface increases all through. This may be a result of the reinforcement particles and the composite base material suffering stronger impact from the stirring pin and the material's lower plasticity in higher traverse speed.

3. The tensile strength of the joints decreases with the increasing of traverse speed. The highest tensile strength obtained is 178MPa with a 10 $mm \cdot min^{-1}$traverse speed, while the lowest is 146MPa when the traverse speed is 80 $mm \cdot min^{-1}$. All joints possessed a tensile strength higher than 80% that of the composite base material.

4. Failure mode of the joints is brittle domained brittle-ductile fracture, which is the result of the segregation of SiC particles to composite matrix and fracture of composite matrix itself.

References

[1] B. Li, Y. Shen, A feasibility research on friction stir welding of a new-typed lap–butt joint of dissimilar Al alloys, J. Mater. Des. 34 (2012) 725-731.

[2] D. Wang, B.L. Xiao, Q.Z. Wang and Z.Y. Ma, Friction stir welding of SiCp/2009Al composite plate, J. Mater. Des. 47 (2013) 243-247.

[3] F. Cioffi, R. Fernández, D. Gesto, P. Rey, D. Verdera and G. González-Doncel, Friction stir welding of thick plates of aluminum alloy matrix composite with a high volume fraction of ceramic reinforcement, J. Composites Part A 54 (2013) 117-123.

[4] H.S. Lee, K.Y. Jeon, H.Y. Kim and S.H. Hong, Fabrication process and thermal properties of SiCp/Al metal matrix composites for electronic packaging applications, J. J. Mater. Sci. 35 (2000) 6231-6236.

[5] J. Sadanandam, G. Bhikshamaiah, B. Gopalakrishna, S.V. Suryanarayana, Y.R. Mahajan and M.K. Jain, Effect of different reinforcements on the thermal expansion of 2124 aluminium metal-matrix composites, J. J. Mater. Sci. Lett. 11 (1992) 1518-1520.

[6] Y. Katoh, L.L. Snead, C.H. Henager Jr., A. Hasegawa, A. Kohyama, B, Riccardi and H. Hegeman, Current status and critical issues for development of SiC composites for fusion applications, J. J. Nucl. Mater. 367 (2007) 659-671.

[7] R.H. Jones, L. Giancarli, A. Hasegawa, Y. Katoh, A. Kohyama, B. Riccardi, L.L. Snead and W.J. Weber, Promise and challenges of SiCf/SiC composites for fusion energy applications, J. J. Nucl. Mater. 307 (2002) 1057-1072.

[8] D. Storjohann, O.M. Barabash, S.A. David, P.S. Sklad, E.E. Bloom and S.S. Babu. Fusion and Friction Stir Welding of Aluminum Metal Matrix Composites, J. Metall. Mater. Trans. A 36 (2005) 3237-3247.

[9] R. García, V.H. López, A.R. Kennedy and G. Arias, Welding of Al-359/20% SiCp metal matrix composites by the novel MIG process with indirect electric arc (IEA), J. J. Mater. Sci. 42 (2007) 7794-7800.

[10] H.Z. Ye, X.Y. Liu, Review of recent studies in magnesium matrix composites, J. J. Mater. Sci. 39 (2004) 6153-6171.

[11] W.M. Thomas, E.D. Nicholas, J.C. Needham, M.G. Murch, P. Temple-Smith and C.J. Dawes, G.B. Patent 9125978.8. (1991)

[12] H. Bisadi, A. Tavakoli, M.T. Sangsaraki and K.T. Sangsaraki, The influences of rotational and welding speeds on microstructures and mechanical properties of friction stir welded Al5083 and commercially pure copper sheets lap joints, J. Mater. Des. 43 (2013) 80-88.

[13] M.A. Mofid, A. Abdollah-Zadeh and F. Malek Ghaini, The effect of water cooling during dissimilar friction stir welding of Al alloy to Mg alloy, J. Mater. Des. 36 (2012) 161-167.

[14] M. Koilraj, V. Sundareswaran, S. Vijayan and S.R. Koteswara, Friction stir welding of dissimilar aluminum alloys AA2219 to AA5083–Optimization of process parameters using Taguchi technique, J. Mater. Des. 42 (2012) 1-7.

[15] P. Dong, H. Li, D. Sun, W.B. Gong and J. Liu, Effects of welding speed on the microstructure and hardness in friction stir welding joints of 6005A-T6 aluminum alloy, J. Mater. Des. 45 (2013) 524-531.

[16] T. Prater, Friction stir welding of metal matrix composites for use in aerospace structures, J. Acta Astronaut. 93 (2014) 366-373.

[17] M. Bahrami, K. Dehghani, M.K.B. Givi, A novel approach to develop aluminum matrix nano-composite employing friction stir welding technique, J. Mater. Des. 53 (2014) 217-225.

[18] U. Patthi, M. Awang, F. Ahmad, AMA Rani and N. Ezinger, Study of physical and mechanical properties of aluminum 6092/SiC 25p/t6 friction Stir welded plate, J. Asian J. Scientific Research 6 (2013) 555-563.

[19] B.L. Xiao, D. Wang, J. Bi, Z. Zhang and Z.Y. Ma, Friction stir welding of SiCp/Al composite and 2024 Al alloy, J. Mater. Sci. Forum 638 (2010) 1500-1505.

[20] J.A. Lee, R.W. Carter, J. Ding, Friction stir welding for aluminum metal matrix composites (MMC's), J. NASA MSFC Alabama USA December1999 (1999).

[21] Diwan R, Investigation of Friction Stir Welding of Al Metal Matrix Composite Materials, J. NASA (2002).

[22] T. Prater, An investigation into the friction stir welding of Al 6061 and Al 6061/SiC/17.5p using diamond coatings, D. Vanderbilt University (2008) 1-180.

[23] J. Guo, P. Gougeon, X.G. Chen, Microstructure evolution and mechanical properties of dissimilar friction stir welded joints between AA1100-B_4C MMC and AA6063 alloy, J. Mater. Sci. Eng. A 553 (2012) 149-156.

[24] K.N. Krishnan, On the formation of onion rings in friction stir welds, J. Mater. Sci. Eng. A 327 (2002) 246–251.

[25] K. Kumar, S.V. Kailas, The role of friction stir welding tool on material flow and weld formation, J. Mater. Sci. Eng. A 485 (2008) 367–374.

[26] O. Lorrain, V. Favier, H. Zahrouni and D. Lawrjaniec, Understanding the material flow path of friction stir welding process using unthreaded tools, J. J. Mater. Process. Technol. 210 (2010) 603-609.

[27] F. Gratecap, M. Girard, S. Marya and G. Racineux, Exploring material flow in friction stir welding: tool eccentricity and formation of banded structures, J. Int. J. Mater. Form 5 (2012) 99-107.

[28] B.L. Xiao, J. Bi, M.J. Zhao and Z.Y. Ma. Effects of SiCp size on tensile property of aluminum matrix composites fabricated by powder metallurgical method, J. Acta. Mech. Sinica 38 (2002) 1006-1008.

Advanced Materials Research Vol. 936 (2014) pp 1742-1746
© (2014) Trans Tech Publications, Switzerland
doi:10.4028/www.scientific.net/AMR.936.1742

Deformation Behavior of Aluminum Alloy Tube in Semi-Dieless Metal Bellows Forming Process with Local Heating Technique

ZHANG Zicheng [1, 2, a*], MANABE Ken-ichi [2, b], FURUSHIMA Tsuyoshi [2, c], TADA Kazuo [2, d] and SASAKI Osamu [3, f]

[1]School of Mechanical Engineering and Automation, P.O. Box 319, Northeastern University, No. 11 Lane 3, Wenhua Rd, Heping District, Shenyang 110819, Liaoning Province, PR China

[2]Department of Mechanical Engineering, Tokyo Metropolitan University, 1-1 Minami-Osawa, Hachioji-shi, Tokyo, Japan

[3]Showarasenkan Seisakusyo Co., Ltd, 2-26-10 Azusawa Itabashi-ku, Tokyo 174-0051, Japan

[a]zhangzicheng2004@126.com, [b]manabe@tmu.ac.jp, [c]furushima-tsuyoshi@tmu.ac.jp, [d]tada-kazuo@jmj.tmu.ac.jp, [f]sasaki_o@showarasen.co.jp

Keywords: aluminum alloy bellows, semi-dieless metal bellows forming process, compression, local heating technique, bellows shape.

Abstract: The metal bellows are used in a large number of industrial applications for their flexile and elastic properties. For the traditional manufacturing methods for metal bellows, the dies and (or) tools are required. It is inconvenient to change the shape of metal bellows and also leads to the high cost. To reduce the manufacturing cost and produce the metal bellows with various shapes, the semi-dieless metal bellows forming process was proposed. The deformation behavior of aluminum alloy tube in semi-dieless bellows forming process was investigated in the study. The effects of compression ratio, heating length on the convolution height, pitch of bellows during the semi-dieless bellows forming process were studied. The results showed that the deformation conditions of semi-dieless forming process have significant influences on the shape of aluminum alloy bellows and deformation behavior of aluminum alloy tube in the forming process. The increase of compression ratio, heating temperature and heating length resulted in the increase of pitch and decrease convolution height of aluminum alloy metal bellows.

Introduction

Metal bellows are one kind of special tube whose wall with the convolution shape. The shape of convolution of the metal bellows can be changed easily by the external force along the axial direction of metal bellows. The expansion and shrinkage caused by heating and cooling, as well as mechanical vibrations can be absorbed by the metal bellows for their special properties [1]. The metal bellows are used in a large number of industrial applications for their airtight and elastic properties, such as piping systems, automotive industries, aerospace and micro-electromechanical systems etc. [2]. The metal bellows are divided into two main types - formed and welded. The formed metal bellows are produced by reworking tubes, with a variety of processes, including cold tube bulging [3], cold forming (rolling) [4], electroforming, hydroforming[5], combination process of bulging and upsetting [6] and gas bulging at elevated temperature [7]. This kind of metal bellows are also called convoluted bellows or sylphons.

To reduce the cost and manufacture the metal bellows with various shapes, the semi-dieless metal bellows forming process with local heating technique tube was proposed. For this new semi-dieless metal forming process, only the mandrel was used to prevent the bending and buckling of long tube due to the compressive force during the forming process. The metal bellows with a material of SUS 304 has been successfully manufactured with the new semi-dieless bellows forming process with local heating technique [2]. The forming process is easy to be realized with the tubular material which has a low thermal conductive coefficient because it is easy to control the length of heating zone. In the

present study, to confirm the applicability of the new semi-dieless bellows forming process with local heating technique for the tubular materials with high thermal conductive coefficient, the aluminum alloy tube was chosen to manufacture the bellows with the new method. The deformation behavior of aluminum alloy tube in the semi-dieless forming process was investigated. The effects of compression ratio, heating temperature and heating length on the convolution height, pitch of bellows and deformation behavior of aluminum alloy tube during the semi-dieless bellows forming process were studied. The results showed that the semi-dieless forming process with local heating techneque can be used to manufacture the metal bellows with tubular materials which have a high thermal conductive coefficient. The deformation conditions of semi-dieless forming process have significant influences on the shape of aluminum alloy bellows and deformation behavior of aluminum alloy tube in the forming process. The increase of compression ratio, heating temperature and heating length resulted in the increase of pitch and decrease convolution height of aluminum alloy metal bellows.

Material and Experimental Method

The Aluminum alloy (A6061) tubes with a dimension of 25(outside diameter) × 2 (wall thickness) ×800 (length) mm were used in the present study. It is known that at the action of compression force in the axial direction of tube, the axisymmetric buckling phenomenon will occur sequentially if there is a mandrel in the tube. In the current study, the continuous buckling phenomenon was used to manufacture the metal bellows. The principle of semi-dieless metal bellows forming process is given in Fig. 1. The experimental equipment was developed according to this principle. To control the location of the buckling appeared, the local heating technique and water cooling method were utilized. A high-frequency induction heating device was used to heat the metal tubes. The circulating water with a constant temperature of 20°C was used. The different heating temperatures of 300°C, 350°C, 400°C and 450°C were used to study the effect of heating temperature on the bellows shape and deformation behavior of aluminum alloy tube in the forming process. The compression ratios ($C=V_1/V_2$) of 1.3, 1.5, 1.6 and 1.7 were chosen.

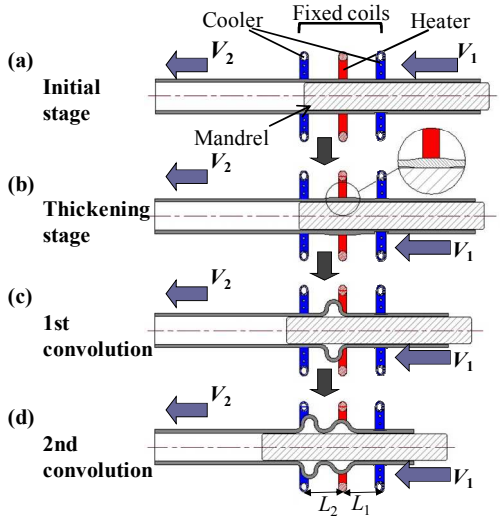


Fig. 1: Schematic illustration of principle of semi-dieless metal bellows forming process (a) initial stage (b) thickening stage (c) 1st convolution (d) 2nd convolution.

The semi-dieless forming process of the metal bellows can be divided into four stages. In the first stage, when the metal tube is heated to the certain temperature the drive plates start to move with different speeds of V_1 and V_2 ($V_1 > V_2$). In the second stage, at the compression force caused by the speed difference of tube ends, the heated part of tube started to deform and become thicker. With the continuous action of compression the first convolution was formed, as shown in Fig. 1(c). The water coiling was adjacent to the heating zone. The metal bellows was cooled by the water and then became hard enough to prevent the further deformation when the metal bellows moved to the cooling region.

So its shape was fixed by the cooling process. At the same time, the second convolution was formed, as shown in Fig. 1(d). The metal bellows were formed with the forming process continuing.

Results and Discussion

Forming process of aluminum alloy bellows. The aluminum alloy bellows with a uniform shape were successfully obtained by the semi-dieless forming process with local heating technique, as shown in Fig. 2. In the experiment, the forming process can be divided into two stages, initial stage and stable stage. In the present study, the two drive plates started to move when the tube was heated to a certain temperature accompanied by water cooling process in the initial stage. In this stage, the first convolution was formed due to the different speeds of the two drive plates. Because the water cooling was realized with two nozzles, the contact area between water and tube surface was changed when the tube started to move driven by the two drive plates. It resulted in the instability of convolution forming process in the initial stage. However, the instability can be alleviated by adjusting the initial heating temperature and cooling intensity. In the stable stage, the convolutions were formed continuously as the stable heating and cooling processes. The shapes of the convolutions which formed in the stable stage are the same.

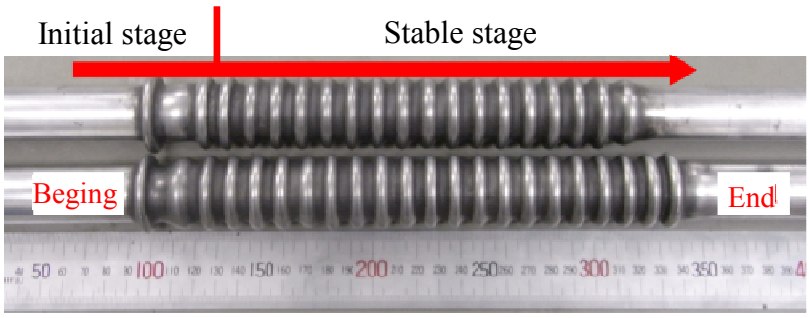


Fig. 2 Aluminum alloy bellows manufactured by semi-dieless forming process with local heating technique (Temperature, 400°C; Compression ratio, C=1.7).

Effect of compression ratio on the convolution shape. The compression ratio has a significant influence on the convolution shape of bellows manufactured with semi-dieless forming process. The lateral section of a convolution of aluminum alloy bellows is shown in Fig. 3. The thickness and shape of convolution of aluminum alloy metal bellows manufactured with different compression ratios were also given in Fig. 3. The tangent lines of the convolution were drawn from the given point which located on the center line of the convolution and with a distance of 500μm from the out surface of convolution. The included angles of the tangent lines of convolution were used to study the bending deformation of tube wall during the manufacturing process of aluminum alloy bellows. The included angles become smaller ($\alpha_1 > \alpha_2 > \alpha_3 > \alpha_4$) with the increase of compression ratio from 1.3 to 1.7, as shown in Fig. 3.

The measured thicknesses of the convolution peak of aluminum bellows obtained with different compression ratios are presented in Fig. 4. The original wall thickness of the aluminum alloy tube is 2mm. After the forming process, the wall thickness in the peak point of the convolution became thicker comparing to the tube original thickness of 2mm. However, the compression ratio did not show significant influence on the thickening of wall thickness during semi-dieless bellows forming process. By analyzing the semi-dieless bellows forming process, it was known that the tube wall of the heating part was thickened by the compression deformation, as shown in Fig. 1(b). For the semi-dieless bellows forming process with different compression ratios, the tube wall thickening process is almost the same. But the duration of the thickening stage is different with that at the same V_1. The duration of the thickening stage became shorter with the compression ratio increasing from 1.3 to 1.7. So, it can be conjectured that for the same tubular material, the compression ratio does not have a significant influence on the amount of thickening when the heating temperature is the same.

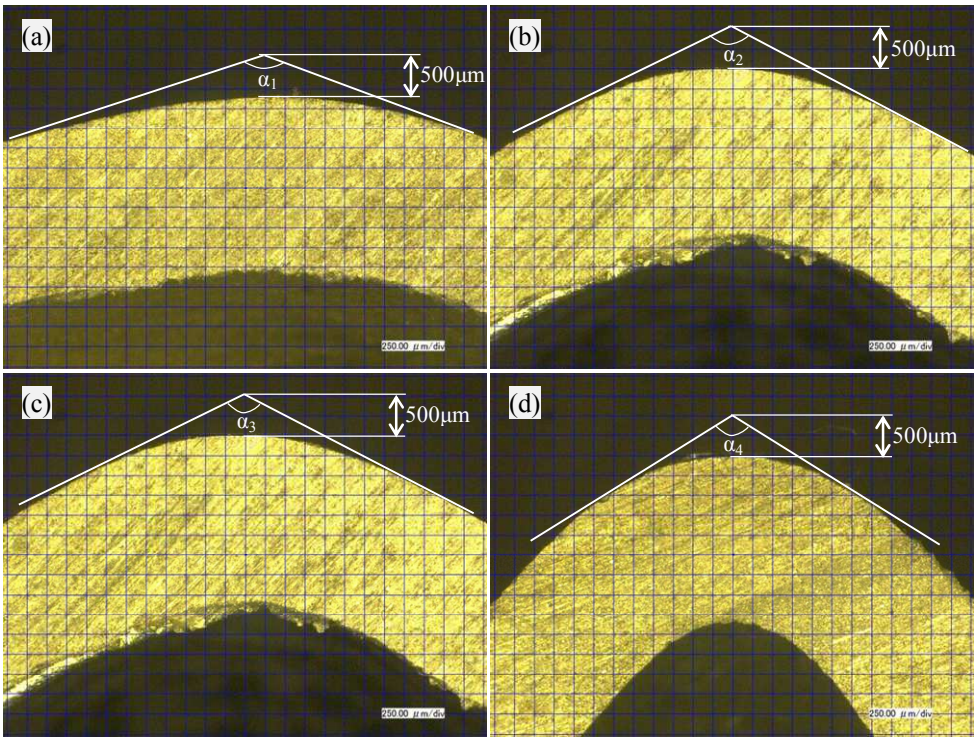


Fig. 3 Convolution shape of Al bellows obtained with different compression ratios. ((a) *C*=1.3; (b) *C*=1.5; (c) *C*=1.6; (d) *C*=1.7)

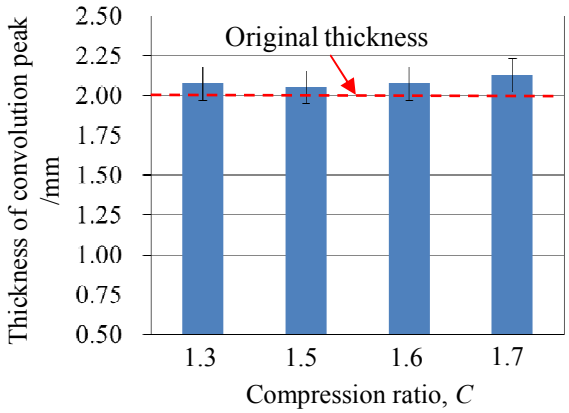


Fig. 4 Effect of compression ratio on thickness of the convolution peak.

Effect of compression ratio on the convolution height and pitch. How to obtain the expected convolution height and pitch of the metal bellows is one crucial technique in the bellows manufacturing process. In the new proposed semi-dieless metal bellows forming process, the convolution height and pitch can be controlled by the compression ratio. The effect of compression ratio on the convolution height and pitch of aluminum alloy bellows are presented in Fig. 5. It can be observed that the convolution height increased with the increase of compression ratio in the range from 1.3 to 1.7. The compression ratio also showed a significant influence on the pitch (distance between the adjacent crests) of the metal bellows manufactured with semi-dieless metal bellows forming process, as shown in Fig. 5. The pitch became smaller with the increase of compression ratio in the range from 1.3 to 1.7. With the increase of compression ratio, the reduction rate of pitch became small. When the compression ratio increases to the limit value, the pitch will also decreases to the smallest.

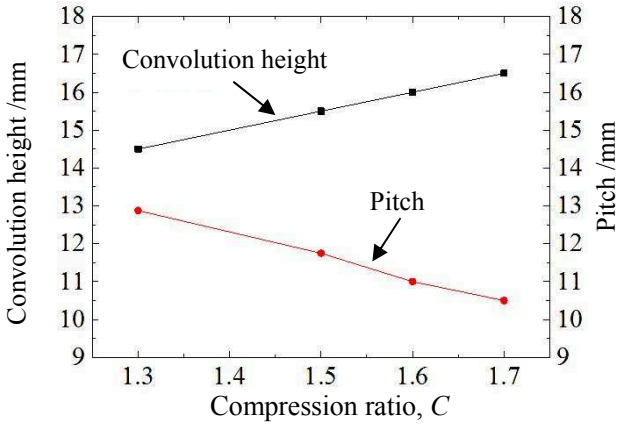


Fig. 5 Effect of compression ratio on the convolution height and pitch.

Summary

In the present paper the deformation behavior of aluminum alloy tube in semi-dieless metal bellows forming process with local heating technique was studied. The effect of the compression ratio on the convolution shape, convolution height and pitch were investigated. The main conclusions were summarized as follows.

1) Even the aluminum alloy tube with high coefficient of thermal conductivity was successfully used to manufacture the bellows with a uniform shape by the semi-dieless forming process with local heating technique.

2) For the semi-dieless bellows forming process with different compression ratios, the tube wall thickening process is almost the same.

3) The convolution height increased and the pitch decreased with the increase of compression ratio in the range from 1.3 to 1.7.

Acknowledgement

This work was supported by the Light Metal Educational Foundation, Inc. of Japan and the Scientific Research Starting Foundation for Introduced Talents of Northeastern University, PR China (Grant No. 02080021233061).

References

[1] C. Becht, Fatigue of bellows, a new design approach, Int. J. of Pressure Vessels and Piping. 77 (2000) 843-850.

[2] T. Furushima, N.Q. Hung, K. Manabe, O. Sasaki, Development of semi-dieless metal bellows forming process, J. Mater. Process. Technol. 213 (2013) 1406-1411.

[3] S.W. Lee, Study on the forming parameters of the metal bellows, J. Mater. Process. Technol. 130-131 (2002) 47-53.

[4] H. Koyama, T. Aoyagi, Development of pinch roll type incremental forming equipment, in: Proceedings of 59th Japanese Joint Conference for the Technology of Plasticity. 2008, pp. 275-276.

[5] B.H. Kang, M.Y. Lee, S.M. Shon, Y.H. Moon, Forming various shapes of tubular bellows using a single-step hydroforming process, J. Mater. Process. Technol. 194 (2007) 1-6.

[6] T. Teramae, K. Nakamura, K. Ueno, O. Takahashi, S. Shirota, Effects of hydrostatic forming conditions on shape accuracy of large bellows, J. Japan Society for Technol. of Plasticity. 41 (2000) 1118-1122.

[7] G. Faraji, M.M. Mashhadi, V. Norouzifard, Evaluation of effective parameters in metal bellows forming process, J. Mater. Process. Technol. 209 (2009) 3431-3437.

Advanced Materials Research Vol. 936 (2014) pp 1747-1753
© (2014) Trans Tech Publications, Switzerland
doi:10.4028/www.scientific.net/AMR.936.1747

Properties of X80 Pipeline Girth Welds For Different Welding Procedures

Xiaodong He[1, a], Ke Tong[1, b], Minghua Liang[1, c], Lixia Zhu[1, d], Weiping Lin[1, e]

[1]CNPC Tubular Goods Research Institute, China

[a]hexiaodong002@cnpc.com.cn, [b]tongk@cnpc.com.cn , [c]liangmh@cnpc.com.cn,

[d]zhulx@cnpc.com.cn, [e]linwp@cnpc.com.cn

Keywords: X80; pipeline; girth welds; welding procedures; structures and properties

Abstract: The X80 girth welds were produced by solid-wire gas metal arc welding (GMAW) and shield metal arc welding (SMAW) using two welding consumables respectively, which contained different mass fraction of C, Mo and Ni. The tensile properties, notch toughness, hardness, and microstructures of welded joints were evaluated. The results indicate that high strength and good toughness of welded joints can be achieved. But the tensile properties of all weld metal of GMAW and SMAW process were evidently different because of the difference of mass fraction of C, Mo, Ni. The strength reduced slightly in softening zone of HAZ. Using welding consumable which contain higher Mo additions, the microstructure in filler weld and fusion zones were IAF+GB and GB+M respectively. Furthermore, the mechanical properties of X80 pipeline welded by single wire welding and double wire welding respectively have been compared. The double wire welds exhibited lower yield strength but higher toughness compared to the corresponding single wire welds.

Introduction

With the increasing demand for energy source and the declining output from existing reserve, the petroleum and natural gas were developed from more remote and harsh regions such as desert, polar region and blue water. So the gas or oil must be transmitted by large diameter and high strength pipeline to reduce the operation costs. The Canada pipeline industry has demonstrate that pipe wall thickness can be reduced by 14% by using X70 compared to X60 and further 12.5% by using grade X80 compared to X70[[1],[2]]. At the present time, API Spec. 5L X80 has become accepted practice in Canada and Europe. In China, X80 has been used on a large scale in the 2nd West-East Pipeline Project. And the use of X100 and X120 in pipeline systems has been widely investigated to increase economic advantages.

However, the metallurgical properties of high grade linepipe and potential weld metals are such that consumable selection, welding procedure development and production welding controls will require comprehensive testing to ascertain their feasibility in the field. The incremental change in technology between X70 and X80 is significantly more complex than it was between X60 and X70, with markedly different microstructures present in both linepipe and potential weld metals. One of the major challenges in high strength pipeline construction is producing girth welds that both possess enough tensile strength and also exhibit excellent toughness. In order to control grain size and microstructure morphology lower heat input and suitable preheated temperature should be adopted [3]. In addition, as strength increases, so does the risk of weld metal hydrogen-assisted cracking (HAC). This is particularly important for pipeline construction since pipeline girth welds are inspected shortly after welding and, as results; there can be no risk of delayed cracking. In the harsh conditions, the high productivity with minimum intervention by the welder should be also taken into account for the welding of large diameter gas transmission pipelines to shorten the construction time limit for a project [4].

To fully realize the economic benefits associated with application of high strength pipeline steels, welding processes and procedures must be developed and assessed to ensure the requirement

for overmatch strength, combined with excellent toughness, are achievable in field girth welds. The work presented in this paper was focused on the mechanical properties and microstructure of girth welds of grade X80 pipeline.

Experimental Material and Methods

Experimental Material

The welding trials were performed using X80 Longitudinal seams submerged-arc welded pipe (SAWL pipe). The pipe sizes were 1016.0mm diameter, 22.0mm wall thickness. The bulk composition of the base metal is 0.069C-1.91Mn-0.18Cr-0.27Ni -0.26Cu. The quantities of other microalloying element, such as Mo (0.022wt %), Nb (0.036wt %), V (0.049wt %), and Ti (0.015wt %) were small. The microstructure of the pipe body was bainitic ferrite (B), polygonal ferrite (PF) and pearlite (P). The tensile properties in the longitudinal and transverse directions of the X80 pipe body were measured by extracting standard ASTM E8 round tensile specimens (0.500-in diameter). Yield strengths of 598 and 676 MPa were measured in L-T and T-L tensile specimens. Similarly, tensile strengths were respectively 670 and 716 MPa giving Y/T ratios of 0.89 and 0.94. The tensile strength of the welded joints of pipe was 730 MPa, and the fracture location at base metal. The full-size (10-×10-×55-mm) standard CVN specimens were machined and tested at 20℃. The average impact energy of pipe body and welds and HAZ were respectively 271J, 162J, and 215J.

Welding Procedures

A series of X80 pipeline girth welds were prepared by semi-automatic gas metal arc welding (GMAW), manual shield-metal arc weld (SMAW) and automatic gas metal arc welding (GMAW) using single wire and double wire. The girth seams were welded by using vertical down on full-scale pipe sections in the horizontal (5G) position. For GMAW, two solid C-Mn-Si electrode wires with Mo-Cu-Ti, and Ni- Mo-Ti alloy additions were selected for this evaluation. The electrode wires were classified as ER80S-G and ER90S-G respectively. GMAW was carried out using the short circuit transfer mode with shielding gases; 85%Ar-15%CO2 for the root and cap passes, and 100%CO2 for all fill passes. For SMAW, the filler welding and cap welding utilized C-Mn-Si electrodes alloyed by Ni-Mo-Ti (classified E11016-G) and Ni-Ti (E10018-G), bur the root welding used the same electrode E8018-G. The welding consumables are given in Table 1. The pipes were initially preheated to 150°C. And the Precise control of preheat interpass temperatures were controlled precisely.

TABLE 1. WELD IDENTIFICATION AND CONSUMABLE FOR X80 PIPELINE GIRTH WELDS

Weld	Welding consumable		
	Root pass	Fill pass	Cap pass
GMAW-B	Bohler NiMo 1-1G, 0.9 diameter (ER 90S-G, Ni-Mo-Ti)	Bohler NiMo 1-1G, 0.9 diameter (ER 90S-G, Ni-Mo-Ti)	Bohler NiMo 1-1G, 0.9 diameter (ER 90S-G, Ni-Mo-Ti)
GMAW-N	YM-60A, 1.2 diameter (ER 80S-G, Mo-Ti)	YM-60A, 1.2 diameter (ER 80S-G, Mo-Ti)	YM-60A, 1.2 diameter (ER 80S-G, Mo-Ti)
SMAW-B	BVD RP, 3.2 diameter (E8018-G)	Fox BVD100, 4.0 diameter (E10018-G, Ni-Ti)	Fox BVD100, 4.0 diameter (E10018-G, Ni-Ti)
SMAW-N	BVD RP, 3.2 diameter (E8018-G)	L-80SN, 4.0 diameter (E11016-G, Ni-Mo-Ti)	L-80SN, 4.0 diameter (E11016-G, Ni-Mo-Ti)

Mechanical Testing and Metallographic Analysis

A series of tensile tests were conducted on X80 girth welds using round and strip tensile specimens. Round and strip tensile specimens of welded joints were cut parallel to the pipe axis welds. The strip tensile specimens of welded joints were cut at the major clock positions, i.e., near 1:00-2:00, 4:00-5:00, 7:00-8:00, 10:00-11:00. The round specimens were machined from the mid-thickness of welded joints near 4:00-5:00 and 9:00-10:00. To further understand the all-weld-metal properties of different welding procedures, the tensile tests using round specimens that were cut from 5:00-6:00 and 9:00-10:00. All tensile testing was carried out at room temperature using a

universal testing machine. The round specimens utilized a 25.4 mm gauge length and appropriate extensometer to allow full stress-strain curves to be obtained. Subsequent plotting and analysis of the data allowed the engineering yield strengths (0.5 % extension), and ultimate tensile strength to be determined, along with the percent elongation.

To evaluate the weld metal and heat affected zone (HAZ) notch toughness properties a series of full-size (10×10×55 mm) Charpy specimens were cut transverse to the girth weld from major clock position 12:00 and 3:00 and notched through-thickness at the weld centerline and fusion line. Triplicate tests were conducted at 20℃. To further assist with characterization of the weld joints, a series of Vickers hardness surveys were conducted along the through thickness centerline, as well as across the entire weldment to provide a relative indication of the strength variation between the pipe base material, heat-affected zone and weld metal regions. The cross-weld surveys were made at positions near the subsurface OD, mid-thickness, and sub-surface ID (root region) locations.

The full-thickness weld sections were cut transverse to the weld and prepared using standard metallographic techniques. The samples were assessed by optical microscopy to characterize the microstructure of weld metal and HAZ.

Results and Discussion

Weld Metal Chemical Composition

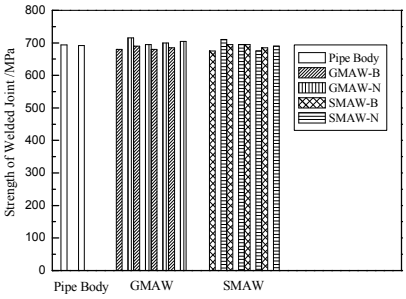
The chemical compositions of weld metal are given in Table 2. There are obvious differences in chemistry between the welds produced by GMAW using ER 90S-G and ER 80S-G. The most notable being the higher Mo and Cu but lower C, Cr, Ni for the GMAW-N weld. In the same way, the carbon contents of SMAW-N welds is lower but the Mn, Mo, Ni are higher than the contents of GMAW-B welds.

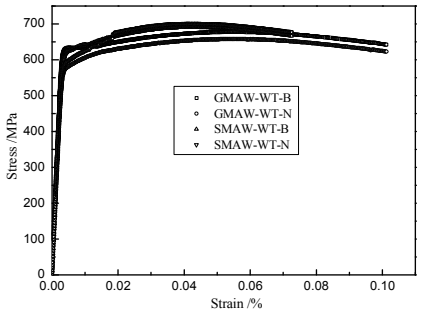
TABLE 2. CHEMICAL COMPOSITIONS OF X80 PIPELINE GIRTH WELDS (MASS FRACTION / %)

Element	C	Si	Mn	P	S	Cr	Mo	Ni	Nb	V	Ti	Cu
GMAW-B	0.066	0.55	1.52	0.006	0.010	0.088	0.26	0.82	0.010	0.009	0.028	0.14
GMAW-N	0.040	0.40	1.62	0.011	0.0061	0.015	0.38	0.012	0.007	0.006	0.023	0.25
SMAW-B	0.070	0.45	1.39	0.008	0.008	0.038	0.031	2.08	0.011	0.024	0.016	0.06
SMAW-N	0.034	0.42	1.60	0.014	0.0040	0.029	0.50	4.39	0.012	0.015	0.011	0.03

Mechanical Properties of Welded Joints and all Weld Metal

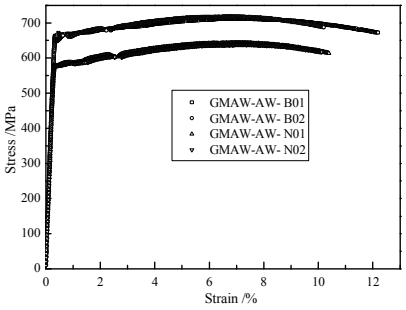
The tensile properties measured in welded joints specimens are shown in Figure 1. The data from figure 1(a) shows that the tensile strength of welded joints produced by GMAW and SMAW can be achieved the strength level of pipe body although the carbon contents are lower for the GMAW-N and SMAW-N welds. So the Mo contents have significant effect on the strength of welded joints, Fig. 2. However, the figure 1 shows distinctly that the strengths of joints welded by GMAW using ER 90S-G are a bit higher than that of joints welded using ER 80S-G. An important observation is the similar forms of stress-strain curves for the round specimens of welded joints, which exhibited continuous or roundhouse yielding behavior, Fig. 1 (b). These data demonstrate that the tensile results from round tensile specimens equally detect the yielding behavior of pipe material because the strengths of joints are higher than that of pipe body.

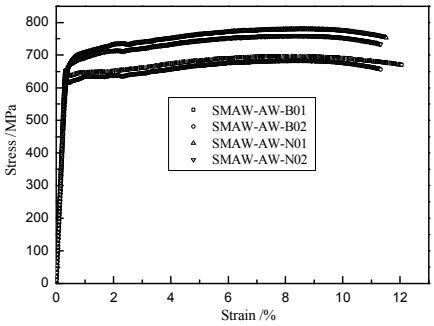




(a) Tensile strength of pipe body and welded joints (b) Stress-strain curve obtained from round specimens

Figure 1. Tensile properties of X80 pipeline girth welds



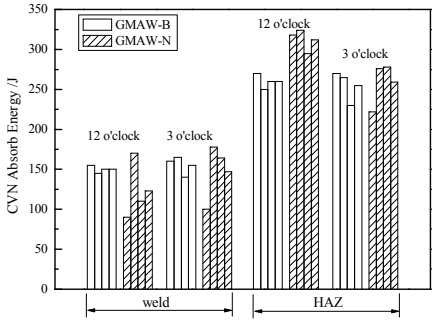


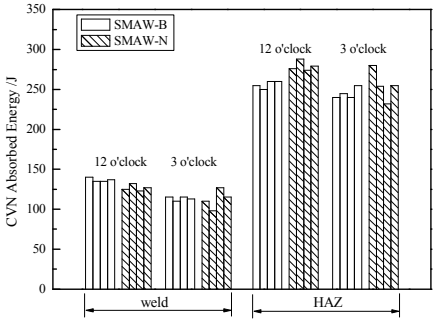
(a) GMAW (b) SMAW

Figure 2. Stress-strain curve obtained from round specimens of all-weld metal for (a) GMAW and (b) SMAW

The Charpy impact test results of welded joints for GMAW and SMAW are summarized in Figure 3. The average CVN impact energies measured in weld metal and HAZ welding were above 110J and 240J at 20℃ respectively. But the CVN absorbed energy values of welded joints for GMAW-N and SMAW-N are more dispersive than that of welded joints for GMAW-B and SMAW-B. Whether GMAW-B or SMAW-B, the Charpy impact energies are higher in welds but lower in HAZ. The very high levels of single impact value measured in GMAW-N weld are very encouraging with respect to finding a robust welding process/welding procedure that will allow a balance of high strength and good temperature toughness to be consistently achieved.

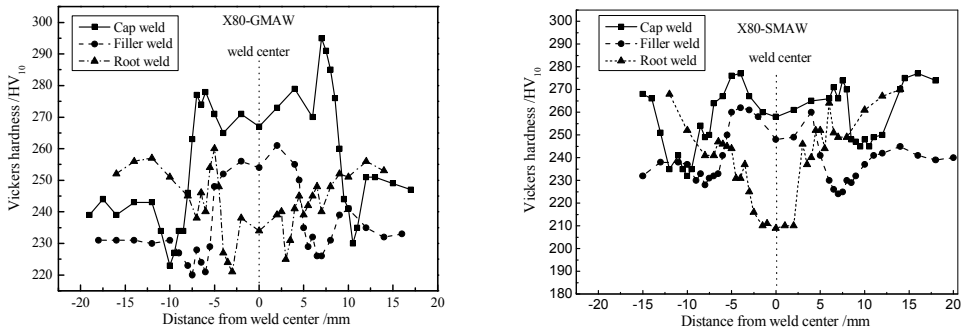
Figure 4 shows the distribution of Vickers hardness of welded joints for GMAW-B and SMAW-B. It was found that hardness would range from 210 HV10 to 300 HV10. The data demonstrate that the hardnesses of cap pass are higher than the values at fill pass and root pass. Furthermore, the maximum hardness is at the fusion line location with minimum value in softening zone of HAZ. So the strength in softening zone for X80 pipeline girth welds will reduce slightly than the base metal.





(a) GMAW (b) SMAW

Figure 3. CVN test results measured in weld and HAZ



(a) GMAW-B (b) SMAW-B

Figure 4. Hardness measured in welded joints

Comparison of Mechanical Properties of Welded Joints for Double and Single Wire Welding

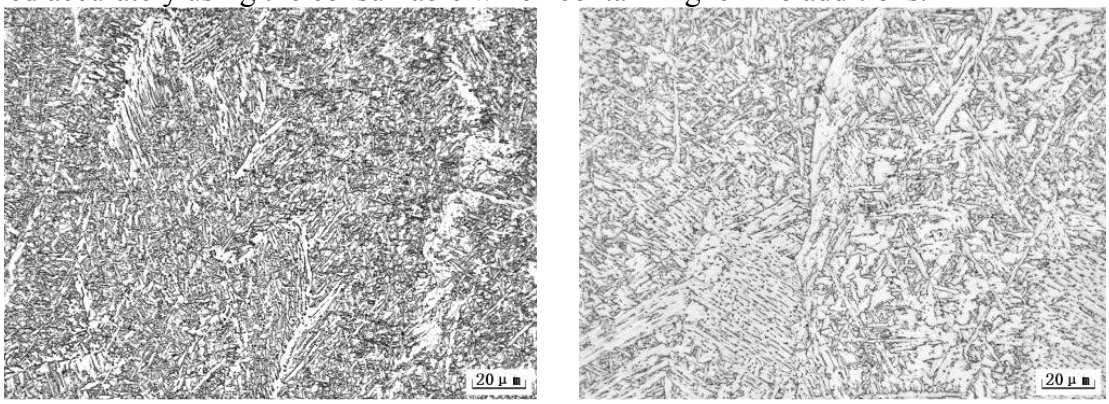
The tensile results, Charpy and CTOD results from tests for double and single wire welding are listed in Tables 3. There were slightly lower yield strengths and ultimate strength observed for the double wire welds. The data also show a trend of increasing impact toughness and generally higher fracture resistance for the welds of double wire welding as compared to the corresponding single wire welding.

Table 3. Mechanical Properties of welded joints of double and single wire welding for X80 pipeline

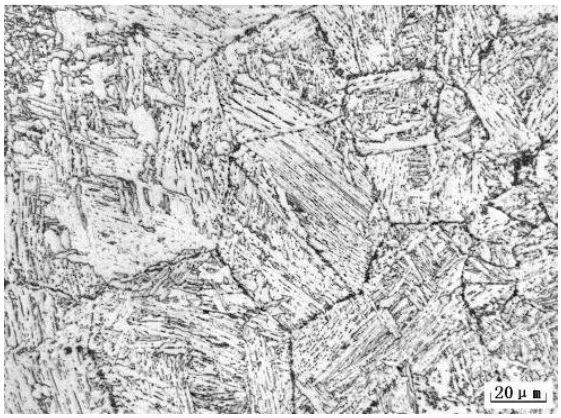
Weld consumable	Welding process	Tensile properties /MPa		CVN absorbed energy /J		CTOD（－10℃）/mm		
		$R_{t0.5}$	R_m	-40℃	-10℃	Min.	Max.	Avg.
Bohler NiMo1-1G (C-Mn-Si-Ni-Mo-Ti)	Single wire	704	755	72	98	0.22	0.29	0.26
	Double wire	662	729	95	122	0.23	0.39	0.33

Microstructure of Welded Joints

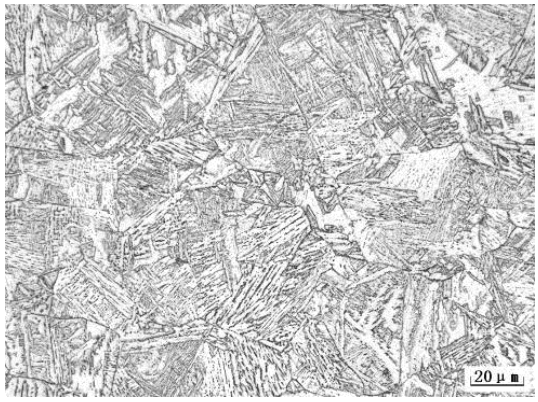
The representative micrographs of X80 pipeline girth weld are shown in Figure 5 and Figure 6. The optical micrographs reveal the predominantly columnar as deposited weld metal structure. As can be seen a relatively high proportion of intra-granular nucleated acicular ferrite (IAF) with bainite (B), polygonal ferrite (PF) and pearlite (P) was formed in GMAW-B and SMAW-B welds. But the microstructures of GMAW-G and SMAW-N welds are IAF and grain boundary ferrite (GBF). And the IAF structures formed in the GMAW-N and SMAW-N welds were generally coarser compared to the GMAW-B and SMAW-N welds. Furthermore, martensite (M) is observed in fusion zone of GMAW-N and SMAW-N. So, it is worth noting that the heat input should be controlled accurately using the consumable which contain higher Mo additions.



(a) Microstructure of Weld for GMAW-B (b) Microstructure of Weld for GMAW-N

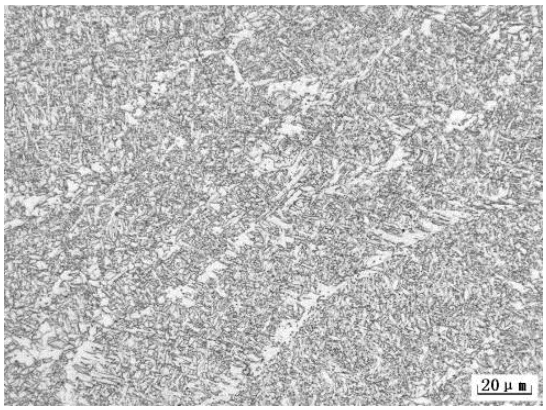


(c) Microstructure of fusion zone for GMAW-B

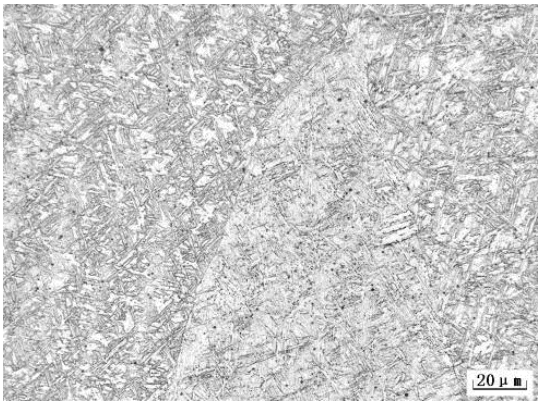


(d) Microstructure of fusion zone for GMAW-N

Figure 5. Micrographs of welds and fusion zones for GMAW



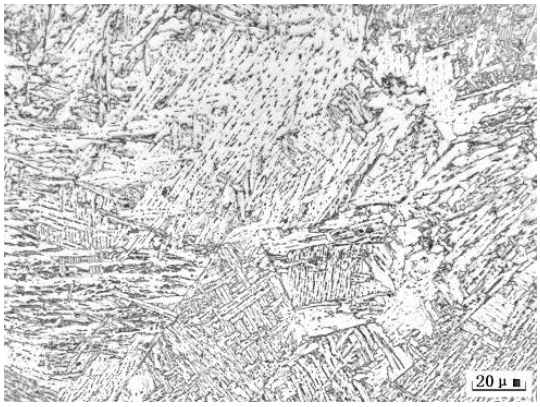
(a) Microstructure of Weld for SMAW-B



(b) Microstructure of Weld for SMAW-N



(c) Microstructure of fusion zone for SMAW-B



(d) Microstructure of fusion zone for SMAW-N

Figure 6. Micrographs of welds and fusion zones for SMAW

Conclusions

This experimental investigation provides data on the mechanical and structure properties of X80 pipeline girth welds produced by GMAW and SMAW. The results indicated that high strength and good toughness of welded joints can be achieved. But some precision is required in the control of welding parameters to avoid the forming of martensite (M) using the welding consumable which contain higher Mo additions. For X80 pipeline, the hardnesses in softening zone are lower than base material, so the strength reduces slightly. The double wire welds exhibited lower yield strength but higher toughness compared to the corresponding single wire welds. The application of double wire welding in high grade pipeline girth welding not only can improve the mechanical performance of the welded joints, but also can raise the welding efficiency.

References

[1] D. V. Dorling, A. Loyer, A. N. Rusell and T. S. Thompson: Welding Journal, May (1992): 55-61.

[2] J. Hammond, N. A. Millwood: Proceedings, 3rd International Conference, Brugge, Belgium (2000): 21-24.

[3] Chen Cuixin, Li Wushen, Wang Qingpen. Research on influencing factor of impact toughness in coarse grain heat-affected zone for X80 pipeline steel. Journal of Materials Engineering. May (2005):22-26 (in Chinese).

[4] J.A. Gianetto, J.T.Bowker, R. Bouchard. Tensile and Toughness Properties of Pipeline Girth Welds. Proceedings of IPC 2006, Alberta, Canada (2006).

Advanced Materials Research Vol. 936 (2014) pp 1754-1758
© (2014) Trans Tech Publications, Switzerland
doi:10.4028/www.scientific.net/AMR.936.1754

Investigation Of Porous Defects In Spray Formed 7xxx Aluminum Alloy

Yibin Yin[1,2,a], Yongan Zhang[1,b], Baiqing Xiong[1,c], Feng Wang[1,d], Hongwei Liu[1,e], Zhihui Li[1,f], Xiwu Li[1,g]

[1]State Key Laboratory of Nonferrous Metals and Processes, General Research Institute for Nonferrous Metals, Beijing 100088, China

[2]College of Material Science and Technology, Liaocheng University, Liaocheng 252059, China

[a]sdyyb@163.com, [b]zhangyongan@grinm.com, [c]xiongbq@grinm.com, [d]wangfeng@grinm.com, [e]liuhongwei@grinm.com, [f]lzh@grinm.com, [g]xiwulee@126.com

Keywords: Spray formed, 7XXX aluminum alloys, Porous defects

Abstract: In this work, Al-10.8Zn-2.8Mg-1.9Cu alloy was manufactured by the spray forming technique. The microstructure of the spray-formed alloy was investigated by optical microscopy and field emission scanning electron microscopy. The results indicated that the porosity in the spray-deposited alloy was mainly composed of interstices, interconnected pores and gas pores. The distribution and types of porous defects were different, responding to position of the preform.

Introduction

Spray forming introduced by Singer at the University College of Swansea during 1970s, has been applied to manufacture high strength 7XXX Al alloys [1, 2]. Compared with conventional metallurgy, spray forming presents several advantages, however, porous defects cannot be avoided in as-deposited materials with the accomplishment of inert gas atomizing liquid alloy into droplets and depositing solidification on the collected substrate [3]. The presence of porosity especially gas pores and interconnected pores will greatly reduce the high strength and high resistance to cyclic deformation [4-6]. The inherent porosity in deposited alloys may reduce the mechanical properties at high temperature.

All the time, little considerable attention is paid to porous defects [7], owing to the difficulty of characterization methods and numerous influence factors. The smooth industry application of spray forming is restricted by the fundamental mechanisms controlling porosity formation and evolution. The previous reports have no systematic summary of porous defects in spray-deposited 7XXX alloys, which restricted the densification and industry application of spray-deposited 7XXX alloys.

In this paper, Al-10.8Zn-2.8Mg-1.9Cu alloy was produced by the spray formed technique. The present work was aimed at classifying porosity at different position in as-deposited 7XXX aluminum alloys and studying formation of porous defects.

Experimental

The composition of the studied alloy was Al-10.8Zn-2.8Mg-1.9Cu (mass fraction, %). The spray-deposition experiments were conducted with a SF-200 type environmental chamber.

The microstructures of the alloy were characterized with OM (Zeiss Axiovert 200MAT), and FESEM (JEOL JSM 7001F), operated at 15 kV. The investigated alloys were abraded and polished

without etching. The amount of nitrogen in the alloy preform was conducted using LECO TC436 Nitrogen/Oxygen Determinator through inert gas pulse infrared thermal conductivity method. The photo and sample positions are shown in Fig. 1. The investigated preform bars have dimensions of 10 mm × 10 mm × 10 mm.

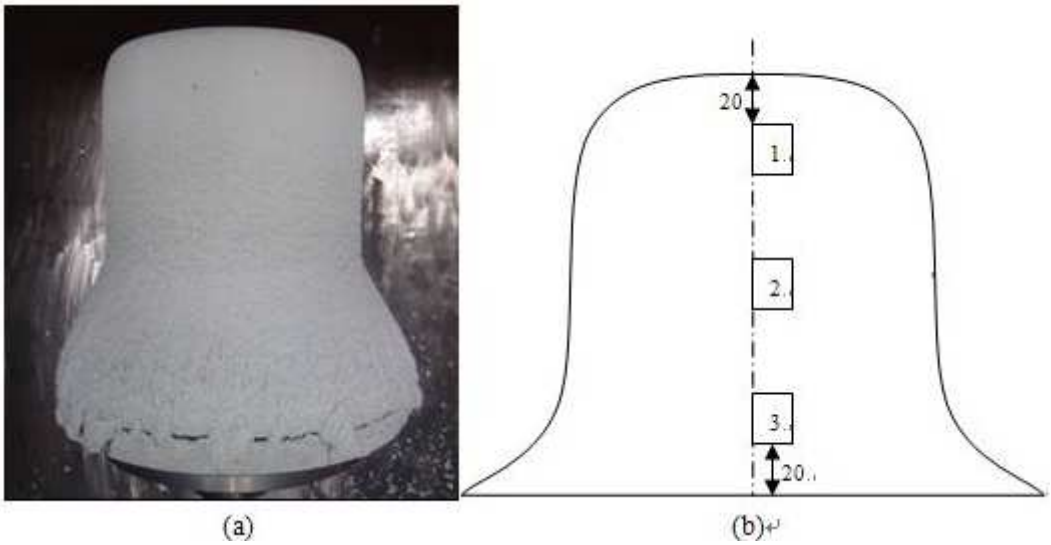


Fig. 1 Position of samples in spray-formed alloy (a) Spray formed deposit; (b) sampling location

Results and discussion

The nitrogen content and density of samples at different positions of spray formed 7XXX alloy are shown in Table. 1. It indicates that nitrogen content in the deposited alloy center is lower than that of the top and the bottom. Owing to high cooling rate, the density in the edge of the preform is higher. And the nitrogen in the preform has nothing to do with the density distribution.

TABLE 1 NITROGEN CONTENT AND DENSITY OF SAMPLES AT DIFFERENT POSITIONS

samples	1	2	3
N wt.%	70ppm	58ppm	70ppm
density %	90.4	90.9	91.3

Fig. 2 shows the microstructures on the preform topside, which contains several kinds of porous defects. Interstices with size less than 30μm, which exhibit irregular morphology, are easier to be found (Fig. 2a). The spherical inward gas pores with size of about 10 μm can be seen in Fig. 2c. Inside spherical pores, the pore wall is smooth, grain boundaries are coarser than outside, the number of secondary phases in the grains is increased and the size is larger. When there is an excessive amount of liquid present in the atomized droplets during deposition, liquid alloy droplets may entrain inert N_2 to bring into gas pores, which have smooth walls because of gas pressure. Single interstices distribute along grain boundaries with size of several microns to tens of microns (Fig. 2d). The morphology of interstices is anomalous and pore wall is

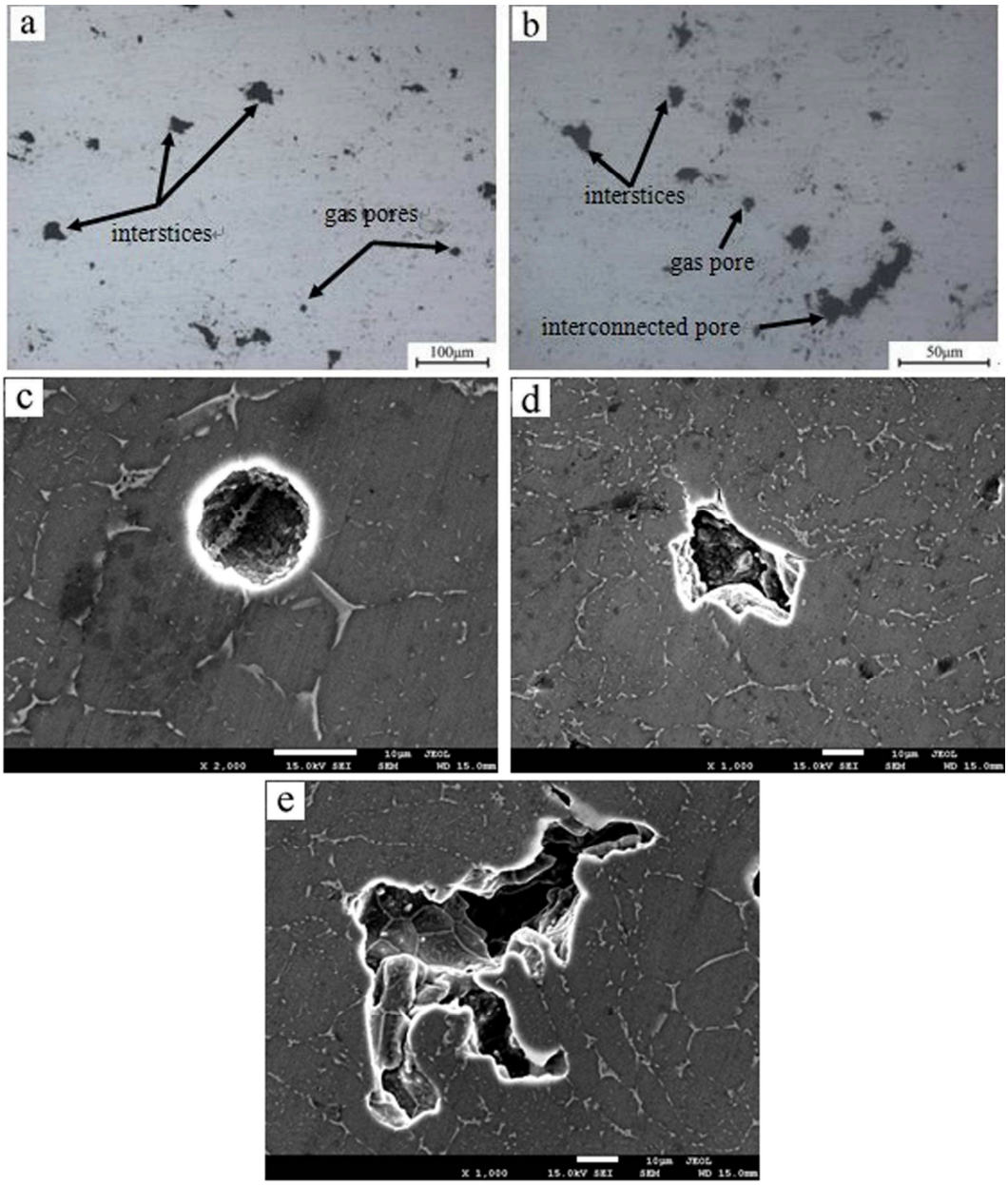


Fig.2 Microstructures of spray-deposited alloy (1# position)

very coarse. This type of porosity is generated as a result of the incomplete filling of the voids between solid or partially solidified droplets. One important difference between gas pores and interstices lies in the morphology, which is dented and smooth because of gas pressure for gas pores. Interconnected pores can be obviously observed from Fig. 2e, which have bigger size and interconnected channels.

The microstructures in the center of the alloy have been shown in Fig. 3. The porous defects in this area consist of single gas pores, interstices and a few interconnected pores with little size. Single gas pores have sizes about 10μm (Fig. 3c), the size of interstices is mostly less than 20μm (Fig. 3a, b), and interconnected pores are also restricted within 40μm (Fig. 3b). Both the size and amount of pores in the center of as-deposited alloy are smaller than that in the topside. Interconnected pores arise along grain boundaries with long and thin morphology (Fig. 3d).

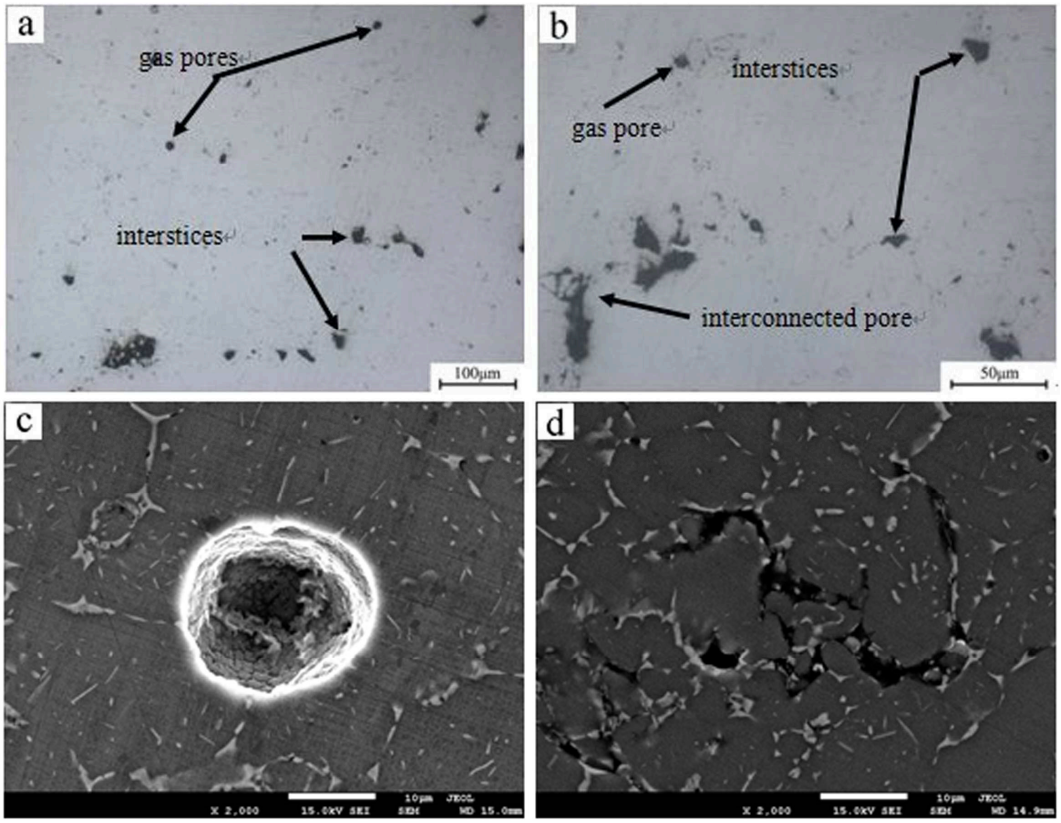


Fig. 3 Microstructures of spray-deposited alloy (2# position)

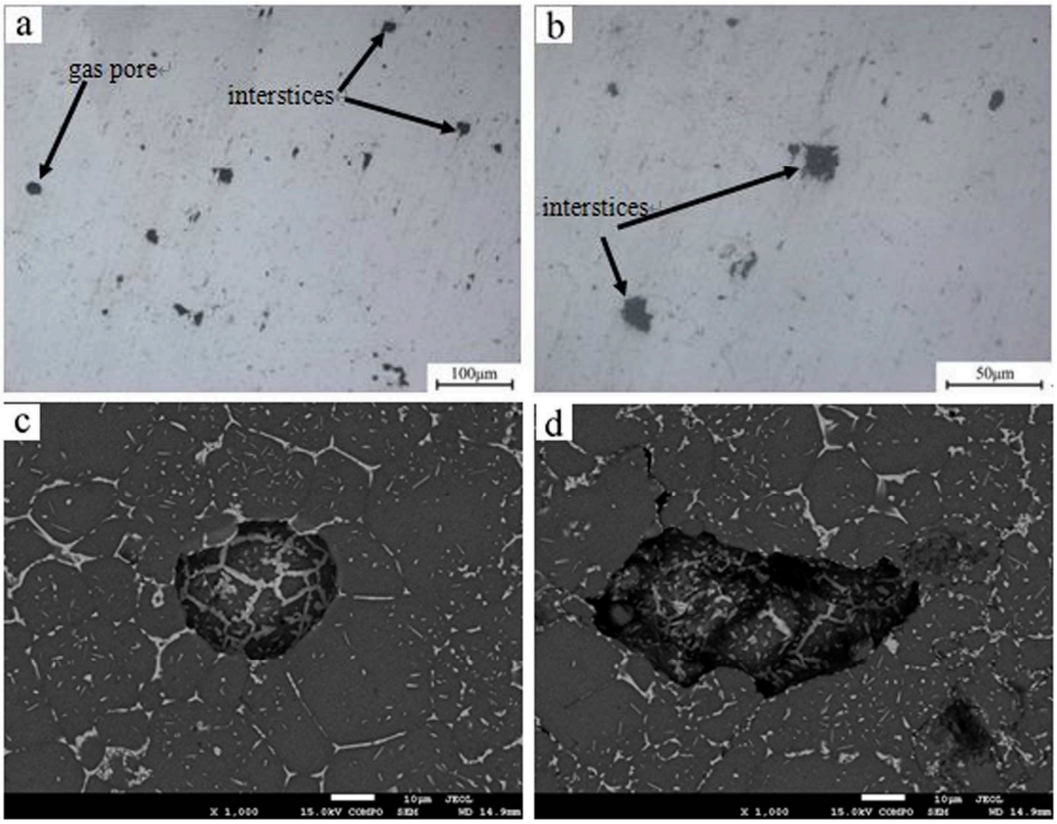


Fig.4 Microstructures of spray-deposited alloy (3# position)

Fig. 4 shows the microstructures of 3# position in spray-deposited alloy, with the defects of single interstices and a few gas pores. There are short of large interconnected pores here. 3# position locates closer to the substrate where the coming droplets have already solidified, so the interstices will come into being as the body after droplets impinging with the surface. The

interstices with size of about 30μm are partly filled with particles (Fig. 4d). The gas pores in this area have spherical morphology with size of about 30μm (Fig. 4c). And grain boundaries inside the gas pores are broader than outside.

In summary, there are several types of porous defects in spray-deposited alloy, which are different with the position of the preform. The final microstructure is strongly related to the cooling of droplets and deposited materials [3]. Plenty of droplets in atomizing cone experience complicated procedures during spray forming, so the porosities in the preform have several morphologies and distribute unevenly.

Conclusion

The porous defects of spray-deposited Al-10.8Zn-2.8Mg-1.9Cu alloy are composed of single interstices, gas pores and interconnected pores. The porosity expresses mainly single and interconnected pores in the upper of as-deposited billet, single interstices and gas pores in the center and single interstices on the base of deposition billet. There are more interconnected pores on the side of as-deposited billet. The grains and intragranular precipitates around gas pores are bigger than that of interstices. The walls inside gas pores are smooth and concave and the morphology of gas pores remains near spherical.

References

[1] Zhang Yongan, Xiong Baiqing, Shi Likai, Research on spray forming technology and products. Materials Review. 16(2002)11-14.

[2] Malavika M Sharma-Judd, Investigation of the structure/property relationship of spray formed 7xxx series high strength aluminum alloys and their metal matrix composites, University of Pennsylvania, Pennsylvania, 2000.

[3] Enrique J Lavernia, Yue Wu, Spray Atomization and Deposition, John Wiley & Sons Ltd., Chichester, 1996, 343-360.

[4] A. Zyska, Z. Konopka, M. Lagiewka, M. Nadolski. Characteristics of squeeze cast AlZn5Mg alloy castings, Archives of Metallurgy and Materials. 55 (2010)969-975.

[5] H. Paul, T. Baudin, F. Brisset, The effect of the strain path and the second phase particles on the microstructures and the texture evolution of the AA3104 alloy processed by ECAP. Archives of Metallurgy and Materials. 56(2011)245-261.

[6] D. Lesniak, Weldability investigation of AlCuMg alloys for extrusion welding. Archives of Metallurgy and Materials. 57(2012)7-17.

[7] Nadimpalli Raghukiran, Ravi Kumar, Processing and dry sliding wear performance of spray deposited hyper-eutectic aluminum-silicon alloys. Journal of Materials Processing Technology. 213(2013)401-410.

Advanced Materials Research Vol. 936 (2014) pp 1759-1763
© (2014) Trans Tech Publications, Switzerland
doi:10.4028/www.scientific.net/AMR.936.1759

A study on development of the optimal neural network in GMA welding process

Qian-Qian Wu[1, a], Ji-Hye Lee[1, b], Jong-Pyo Lee[1, c],
Min-Ho Park[1, d], Young-Su Kim[1, e] and Ill-Soo Kim[1, f]

[1]Department of Mechanical Engineering, Mokpo National University 61, Dorimri, Chungkye-myun, Muan-gun, Chonnam, 534-729, South Korea

[a]wuqianqian@mokpo.ac.kr, [b]jihyelee@mokpo.ac.kr,

[c]jplee@mokpo.ac.kr, [d]parkminho21@mokpo.ac.kr, [e]kimyoungsu@mokpo.ac.kr, [f]ilsookim@mokpo.ac.kr

Keywords: GMA Welding Process, Mahalanobis Distance, Neural Network, Error Backpropagation Algorithm

Abstract. Gas Metal Arc (GMA) welding is considered as a multi-parameter process that it's hard to find optimal parameters for good welding. To overcome the problem, an artificial neural network based on the backpropagation algorithm was built to realize the relationships between process parameters and welding quality as output parameter. In this study, Mahalanobis Distance (MD) was employed to evaluate the availability of a given welding parameters which was proved to performance well in multivariate statistics. Input parameters such as welding current and arc voltage were chosen due to their significant influence on the welding quality. To improve the precision of given parameters' evaluation, neural networks with different configurations were verified. The analyses on the measured and predicted MD by the proposed neural network were conducted. The proposed neural network based on the error backpropogation algorithm was proved to have high reliability to evaluate process parameters, which further makes it available in on-line monitoring system.

Introduction

For the automated welding system, optimal welding parameters for the GMA welding process should be well established and categorized. Thus, it is necessary to develop an intelligent algorithm to obtain suitable process parameters in the automatic GMA welding process. However, the waveform of welding current and arc voltage obtained from the on-line monitoring system differ slightly from the fault weld and good weld [1]. It is very difficult to find the good and fault waveform. Therefore MD is applied to character the welding quality. If the distance between the test point and the centre of mass is less than one standard deviation, then we might conclude that it is highly probable that the test point belongs to the set.

With the development of computational technology, the neural networks appear to constitute a workable model for predicting the bead geometry under given set of welding conditions according to the work done by Nagesh and Datta [2]. Srikanthan and Chandel [3] proposed the steps adopted to construct the neural network model for GMA welding process and evaluated the proposed neural network model. Kim et al. [4] used the backpropagation neural network to predict bead geometry for GMA welding process and proved that the proposed neural network model can predict bead geometry with reasonable accuracy. However, the accuracy of the prediction depends on the algorithm employed in the neural network. Backpropagation learning algorithm is the most widely applied neural network model [5, 6]. To achieve a high level of welding performance and quality, a suitable algorithm is required to fully understand the influence of welding parameters on MD in the GMA welding process.

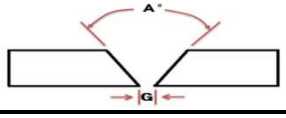
This study attempts to develop an optimal neural network to establish relationships between the input and output parameters for applying the robotic GMA welding process. The neural network with the error backpropagation algorithm is firstly established. Secondly, the averaged RMS error is

calculated. Finally, comparison of the qualitative and quantitative analysis of GMA welding faults based on MD by the error backpropagation algorithm with different numbers of neurons is presented. Results indicate that the error backpropagation algorithm is the preferred algorithm for building neural network in the prediction of MD in GMA welding process.

Description of GMA Welding of Steel

To perform GMA robotic welding on SM490A steel which is mainly used in marine pressure vessel requires specification on the manual welding condition. Table 1 represents details of GMA welding process based on standard Welding Specification Procedure (WPS) and manual welding conditions based on preliminary experiments to drive a stable bead area.

Table 1 The details of robotic GMA welding process

	Details		Details
Joint Type		Welding Wire	AWS ER70S-3
		Shielding Gas	CO_2 99%
Groove Angle	60°	Root Gap	1[mm]
Base Metal Grade	SM490A	Welding Length	400[mm]
Thickness	12[mm]	Evaluation Item	Welding Condition (Amp/Volt/Speed/Weaving)

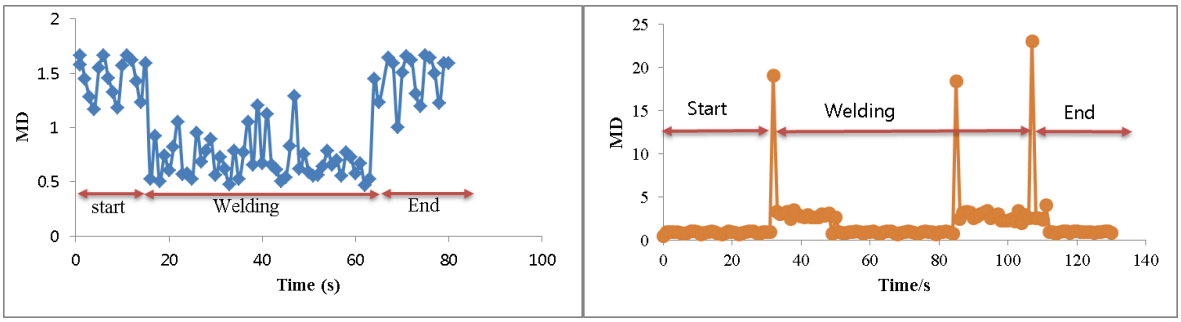
The MD is a descriptive statistic that provides a relative measure of a data point's distance (residual) from a common point. It is a unities introduced by Mahalanobis in 1936 [7]. Similarly, the welding quality whether it fault or good could be determined by the observated MD space of the multivariate outliers for the input parameters such as welding current and arc voltage in the GMA welding process. If the magnitude of MD derived from a welding current C_i and arc voltage V_i is smaller than a certain value, the parameter of (C_i, V_i) can be considered as a suitable value and good weld will be produced. The smaller the MD is, the better the weld quality will be [8].

To provide reliable data for recognition of welding current and arc voltage on welding quality, the MD equation is transformed by means of robust procedure complied in MATLAB software. The transformed equation is defined below:

$$M_d = \frac{V_i'^2 - 2rV_i' + C_i'^2}{1 - r^2} \tag{1}$$

Where V' and C' indicate the normalized value of arc voltage and welding current, and r is the correlation coefficient after normalization.

As shown in Fig. 1, the welding quality can be easily identified by MD. According to MD concept, a longer data space existence between each other indicates the fault weld. Therefore, Fig. 1(a) is found to be good weld, whereas Fig. 1(b) is found to a fault weld. The start and end welding current and arc voltage are also recorded on the on-line monitoring system, and presented on transformed current verse transformed voltage. The result shows that current and voltage are very low and unstable during start and end welding process but as moves along process, it gets stable. In addition, Fig. 1(b) shows unstable normalized MD results through welding process. The MD values are big during the welding process results to fault weld quality, which is also the results of artificial increase of arc length.



(a) Good quality welding (b) Fault quality welding

Fig. 1 MD distributions with respect to time variations

Modeling of GMA welding process using neural network

The process parameters of the robotic GMA welding process are inter-dependent and constantly in conflict in a complex way. Therefore a structure of feed-forward neural network is adapted to this work. A one-layer feed-forward network is constructed with two input neurons in the input layer and a neuron in the output layer to map the output parameters of MD to two input parameters of welding current and arc voltage. And the schematic representation of the multi-layer neural network architecture employed in this research is shown in Fig. 2.

Modeling of the GMA welding process with neural networks is composed of two phases: training and testing of the neural networks with experimental welding data. The convergence criterion for the developed networks is determined by the average RMS error between the desired output value y_i and predicted output value y_i' for the i th prediction, i.e.:

$$E_{RMS} = \sqrt{\frac{1}{n}\sum_{i=1}^{n}(y_i - y_i')^2} \tag{2}$$

Where i is the number of training data or testing data. In this study, a specific training algorithm has been employed to train the neural network, and the development architecture of the network is carried out on a Pentium PC using MATLAB.

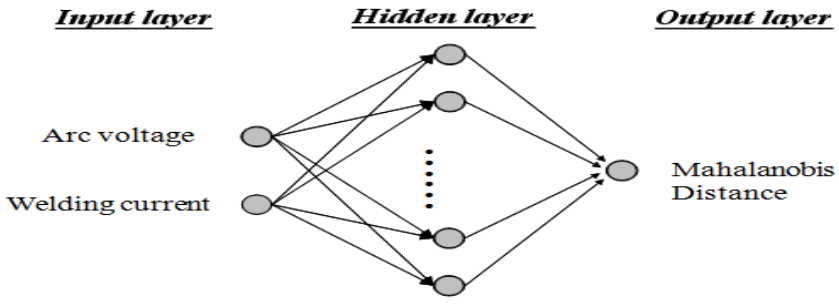


Fig. 2 Optimal neural network architecture for MD

Results and Discussion

To get an effective neural network, a large amount of training examples as much as 12500 are employed. And the trained neutral network is tested by 100 collections of arc voltage and welding current. By simulation, it was found that one hidden layer can provide better convergence in the modeling of the robotic GMA welding process. Network configurations with different numbers of neurons in the hidden layer are studied. The performance of the neural networks could be shown in Table 2. It is found that increase of the number of neurons in the hidden layer does not ensure the

decrease of the average RMS error. For the testing phase, the average RMS error of the testing set is almost the same as that of the training set, which means that the network has good generalization ability for the modeling of the GMA welding process. Furthermore, during the training process, the average RMS error can be reduced to about 0.4059 when the number of neurons in the hidden layer is increased to 16. In other words, this network configuration of 2-16-1 seems to be best for the prediction of the MD with the lowest RMS error. Accordingly, the error backpropagation algorithm provides a good learning ability for the robotic GMA welding process as the training MD presents high consistency with testing ones.

Table 2 The results of various network configurations with the error backpropagation algorithm

Configuration	Training RMS error	Testing RMS error	CPU time for training [min]
2-2-1	0.7500	0.6426	2.23
2-4-1	0.8332	0.6823	2.30
2-6-1	0.5516	0.5150	2.33
2-8-1	0.5213	0.4765	2.35
2-10-1	0.5143	0.4900	2.35
2-12-1	0.5200	0.4920	2.40
2-14-1	0.5019	0.4658	2.40
2-16-1	0.4059	0.3745	2.37
2-18-1	0.5202	0.4925	1.95

Fig. 3 indicates the absolute error between the measured and predicted MD. The lower the values of error are, the better the correlations of the measured MD and predicted MD of separating percentage will be. It can be found that the error of the MD is within 1.2 and the data are mainly distributed within the absolute value of error of 0.4, which indicates that the accuracy of the predicted MD by this method is acceptable.

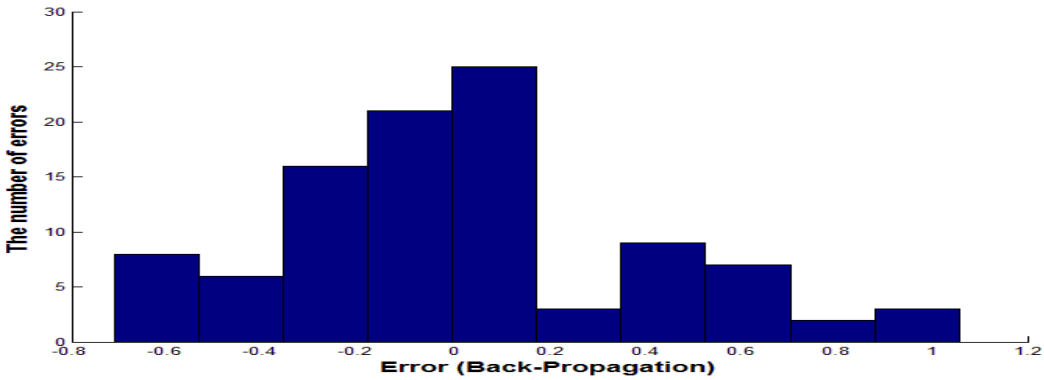


Fig. 3 The error of the predicted MD with error backpropagation algorithm

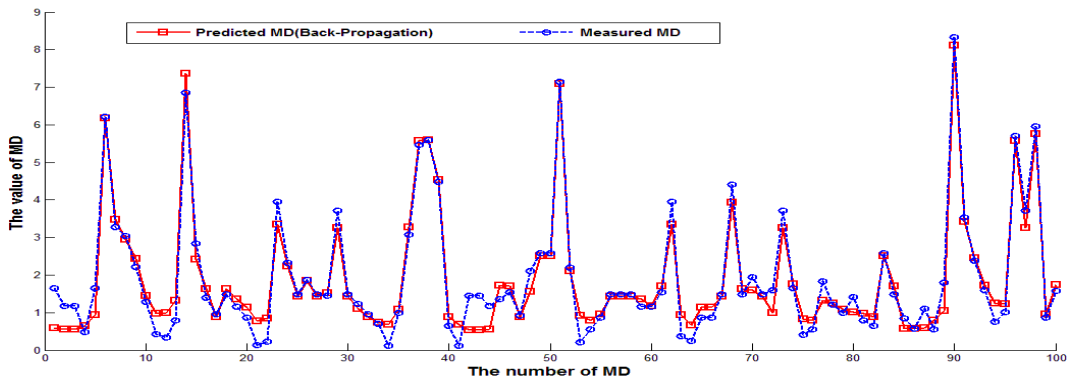


Fig. 4 Performance of the error backpropagation algorithm

The results of the study in the performance with the error backpropagation algorithm are plotted in Fig. 4. In the figure, the solid line with red square represents the predicted MD using the error backpropagation algorithm and the dash line with blue circle represents the measured MD obtained from the developed equation. It is easily observed that the calculated values obtained using the error backpropagation algorithm shows a good accuracy. The worst accuracy point locates at the MD number of 1 and the deviation is the largest with a value of 1.05, while the best one locates at the MD number of 38 with a very small deviation. Therefore, it might be concluded that the amount of the errors generated from the error backpropagation algorithm is still reasonably small to be accepted in most cases of practical applications.

Summary

This study investigates the application of statistical method for quantifying the welding quality in robotic GMA welding. Neural network with the error backpropagation algorithm is established and the one-hidden-layer neural network with configuration of 2-16-1 is found to be the best fit for this application. Not only high consistency between the measured and predicted MD, but also the low value of the error of predicted MD away from the zero point in configuration of 2-16-1 indicate that this developed neural network performs quite well in prediction of MD in GMA welding process. Therefore, the developed models shows a reasonable reliability to predict the on-line process parameters to obtain the desired MD as welding quality, to establish guidelines and criteria for the most effective joint design and further to help the development of automatic control system of arc welding robot.

Acknowledgements

This research was financially supported by the Ministry of Education (MOE) and National Research Foundation of Korea (NRF) through the Human Resource Training Project for Regional Innovation (No. 2013H1B8A2032082).

References

[1] T. Melfi, New code requirements for calculating heat input, J. Welding 89(2010) 61-63.

[2] D.E. Rumelhart, G.E. Hinton and R.J. Williams, Learning representations by back-propagating errors, J. Nature 323 (1986) 533-536.

[3] A.J. Torija, D.P. Ruiz and A.F. Ramos-Ridao, Use of back-propagation neural networks to predict both level and temporal-spectral composition of sound pressure in urban sound environments, J. Building and Environment 52 (2012) 45-56.

[4] Jiří Šíma, Back-propagation is not efficient, J. Neural Networks 9 (1996) 1017-1023.

[5] H.B. Kim, S.H. Jung, T.G. Kim and K.H. Park, Fast learning method for back-propagation neural network by evolutionary adaptation of learning rates, J. Neurocomputing 11 (1996) 101-106.

[6] Y. Fukuoka, H. Matsuki, H. Minamitani and A. Ishida, A modified back-propagation method to avoid false local minima, J.Neural Networks 11 (1998) 1059-1072.

[7] S.Q. Feng, Off-line Programming of arc welding robot based on UG and welding qualification based on statistic methods, Ph.D., Tianjin University, 2010.

[8] S.Q. Feng, O. Hiroyuki, T. Hidennori, K. Yuichi and S.S. Hu, Qualitative and quantitative analysis of gmaw welding fault based on Mahalanobis distance, Int. J. Precision Engineering and Manufacturing 12 (2011) 949-955.

Advanced Materials Research Vol. 936 (2014) pp 1764-1768
© (2014) Trans Tech Publications, Switzerland
doi:10.4028/www.scientific.net/AMR.936.1764

Potential Spark Erosion Approaches to Silicon Nanoparticles Production

Ahmad Farooq[a*], Wei Wang[a]

[a]College of Mechanical and Electrical Engineering, Nanjing University of Aeronautics and Astronautics (NUAA), 29 Yudao St., Nanjing, 210016, China
* Corresponding author. Tel.: +86-158-0518-7394; .E-mail address: ahmf239@yahoo.com.

Keywords: Silicon nanoparticles, nontraditional machining, spark erosion

Abstract: This article demonstrates potential approaches to the production of Silicon Nanoparticles (SiNPs) using spark erosion in forms of Wire-EDM (WEDM), Die-sink and Micro -EDM. Utilizing the data from research work on such commercialized spark erosion approaches, a novel method of nanoparticle production by spark erosion under high pressure flushing has been introduced in this paper. This system is a crossbreed of Die-sink and Small Hole-EDM that comprises deionized water sprayed @ 0.8 MPa through a rotating copper tube as an electrode, boring on boron doped silicon ingot workpiece, under submerged conditions. SiNPs constituting an average diameter of 50nm were generated with approximate productivity of 1.5g/hr from the high pressure flushing system. The productivity of the nanoparticles for every system was calculated after post-process purification. The results demonstrate that SiNPs production from spark erosion, in terms of size and productivity, is least affected by electrical parameters, rather is much dependant on other aspects, such as pressure of dielectric flushing as well as dielectric type. The results also show that high pressure flushing spark erosion process holds excellent potential as an industrialized SiNPs preparation method in terms of size and productivity.

Introduction

SiNPs can be produced via physical and chemical approaches. From the chemical approaches, Stöber Process is perhaps the most popular method for metal coating with silica [1] [2], producing SiO_2 spheres with diameters ranging from 200 to 800 nm [3]. There is also Chemical Vapor Deposition (CVD)[4], which can produce very fine single crystal spherical particles under decomposition of silane/disilane gas [5], with varying distribution from 40nm to 100nm [6]. Additionally inductively coupled plasma (ICP) has reported to produce well-defined highly crystalline SiNPs [7], with an average diameter of 13nm.

Along with chemical approaches, non-traditional physical approaches for silicon nanoparticle production potentially higher production capability over chemical approach such as Sol gel [8]. Laser ablation (LA) is a nontraditional nano production technique [9], that produces pure SiNPs in gaseous medium having a distribution of 60 to120nm & 25 to 100nm in liquid [10].

Spark erosion is another nontraditional physical approach could very well be one of the most resourceful non-traditional techniques for generation of NPs. Similar to laser ablation, spark erosion has similar mechanism of material removal, i.e. to completely vaporize workpiece material as method of erosion. However spark erosion has the potential to produce NPs at large quantities, an area which laser ablation lacks due to its low productivity, especially in liquid mediums [11]. Commercial spark erosion by electro discharge machines (EDM) in forms of Wire-EDM (WEDM), Die-sink and Micro-EDM were used as potential approaches to SiNPs production in this paper. Along with experimental data of SiNPs production concerning WEDM, Die-sink and Micro-EDM, a potential novel method of producing SiNPs using high pressure flushing spark erosion is also being introduced in this paper. The new method holds great potential size and productivity compared to other spark erosion nanoparticle production approaches.

SiNPs production using spark erosion

Debris produced from spark erosion was identified as a viable process of fine powder production typically at micro scale range during 1980s [12]. Application of voltage pulse on 2 electrodes at close proximity in a dielectric fluid produces a spark discharge between them. The electrodes are heated in highly localized regions above their melting temperatures, ejecting molten and vaporized materials from them. These are solidified due to rapid quenching from the dielectric fluid, forcing the debris to solidify into spherical shape due to surface tension [13]. Characteristic aspects of these debris normally attribute with large micro particles mixed with nano sized ones. Larger particles are produced from molten material being re-solidified, while the particles from nanoscale region are assumed to be re-solidified from vapor state.

Commercialized EDM should not be mistaken with experiments related to spark discharge in gaseous environment[8]. Although both use spark discharge as the mechanism of material removal, their setups are vastly different, specifically on dielectric and electrodes. These are near-dry gas-dielectric based discharge processes that have proved to produce NPs of high purity and ultrafine size (5-50nm). However they are not good at processing semiconductors. This is due to high resistance of semiconductor electrodes and processing is hampered if semiconductor electrodes of same types are used. Even by using boron doped samples, the maximum productivity rate of SiNPs shown for Si-Si electrode setup is very low, approximately 1mg/h [8]. With low productivity as well as complexity of the set-up, this method is not suitable when it comes to industrial scale productivity.

Experimental

There are several methods of spark erosion based EDM processes, such as Wire-EDM (WEDM), Die-sink EDM, Micro-EDM and every one of them has ability to produce NPs in debris form. However size distribution differs vastly from one another, as well as energy consumption and extraction purification processes. The machining centre in NUAA consists of all these 3 types of EDM machines, which were used to machine heavily doped Si ingot in order to produce respective samples of debris particles. The working parameters of machining processes are given below in table 1.

TABLE1 WORKING CONDITIONS FOR SPARK EROSION PROCESSES

Type	Tool electrode	Working fluid	Open voltage(V)	Peak current(A)	Pulse duration(μs)	Flush Pressure (MPa)
WEDM	Copper wire	Kerosene(mix)	120	30	30	0.1
Die-sink	Copper electrode	Kerosene	120	30	30	0.05
Micro-EDM	Copper electrode	Kerosene	90	5	0.5	0.01
High Pressure	Copper tube	Deionized Water	100	30	1	0.8

Since the debris particles consists of both micro and nano sized constituents, as well as the tool and workpiece electrodes being different, second part of this experimental consists of separating impurities from the NP. This is done with the combination of KQ3200B Megahertz ultrasonic bath and 6 pocket ANKE-TGL-10B Centrifugal separator. The raw debris sample produced from kerosene based dielectric consists of the following impurities: (i) carbon produced from pyrolysed kerosene (ii) Tool material solidified from vapor state (iii) Solidified tool material from molten state (iv) Solidified workpiece material from molten state.. In case of (i), attempt was made to remove the carbon impurities by use of suspension method, using $ZnBr_2$ and separating lamella structured carbon impurities from the spherical shaped residue. However some of the ultra fine SiNPs that might have agglomerated on the carbon particles may also got removed from the test sample. As for (ii) it is extremely difficult to remove such nanoscale impurities using centrifuge from other SiNP (by physical means). For (iii) and (iv) an attempt was made to physically separate the larger particles from the smaller using centrifuge.

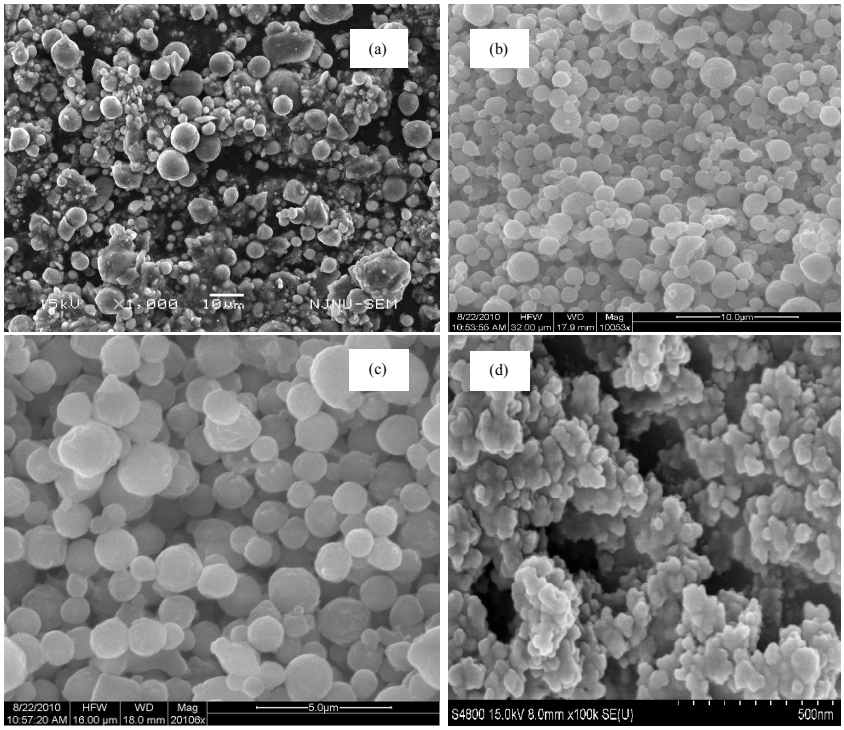


Fig. 1 SEM images showing samples from (a) WEDM (b) Die-sink (c) Micro -EDM and (d) High pressure flush spark erosion

The process of centrifugation is carried out after suspension method, the sample is dispersed using ultrasonic vibrating machine, after which it is mounted on a centrifugal machine. Spun at 4000rpm, the large debris were separated from the smaller ones. The smaller particles floating in the test tubes were all then transferred to a new container and left for 24hrs to settle down. After that the excess liquid was siphoned off and the sediment was extracted by centrifuging once again at 10000rpm and treated to ethanol for SEM testing. For SEM tests, the samples were sputter coated using Baltech SCD 500 sputter coater, and were mounted on Hitachi S-4800 SEM machine.

Result and Discussion

Size distribution for the debris produced by WEDM (Fig 1a) is very uneven, with too many large (5-10μm above) spreading around smaller particles of 800-900 nm. Extraction and purification of debris particles is very difficult for WEDM due to the fact that the dielectric is a special liquid made from mixture of different solvents, most of which are insoluble. Hence during centrifugal separation there is a strong chance of ultra nanosized particles to get washed away along with impurities, suggesting this is not good mechanism for nano production.

For Die-sink EDM (Fig 1b), size and shape distribution improves compared to WEDM. Size distribution is still very uneven, containing large spheres of around 1.5-2 μm while smaller ones range between 500-700nm. Equating E=VIt (V= open voltage, I= current, t= pulse duration), the spark energy for the process can be calculated, using voltage 120V, peak current 30A, time is 1 micro seconds. Hence energy dissipated during discharge is 3.6μJ, while productivity is 0.1g/hr. For the Micro-EDM (Fig 1c), the size and shape distribution doesn't differ much, compared to Die-sink. The size distribution was between 500-600nm and the shape distribution was evenly spherical. The spark energy for this system was (V=90V, A=5A, t = 0.5μs) 0.2 μJ. The productivity was approx 0.02g/hr. Hence the samples produced from these 3 systems are not in accordance with the general nanoparticle dimension of less than 100nm and hence cannot be termed as nanoparticles. In comparison to the research works that has been undertaken on various types of spark discharge/erosion approach to NPs generation, a new system with PLC automated spark erosion machine has been developed in our labs at NUAA. This system is a cross breed between Die-sink and Small Hole-EDM that consists of a copper hollow tube of 1mm and dielectric used is deionized

water. When the machine is initiated the tool rotates and sprays deionized water at 0.8MPa pressure on the machining region, sinking in and initiated spark to erode the silicon ingot. Processing conditions were Voltage 100V, Current 30A; pulse 1µs duty cycle of 2, hence average spark energy calculated is 3µJ. The system is submerged in deionized in order to engage both pouring and submerged flushing, increasing machinability.

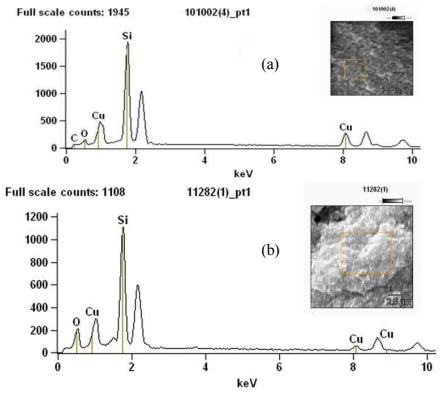


Fig 2 EDS of sample from (a) Micro EDM (b) High pressure flush spark erosion. Notice that the sample produced from kerosene based dielectric contains carbon and copper impurity while deionized water contains only copper oxide.

Due to the high flushing rate of this system, the name given to this prototype machine is High Pressure Flush Spark Erosion. SiNPs comprising an average size of 50nm (Fig 1d) were generated with an average productivity of 1.5g/hr, while EDS (Fig 2b) scanning indicated high Si-based material purity. The size of the nanoparticles achieved was 10-15 times smaller than that of Micro/Die-sinking EDM and with higher productivity. The size is with accordance with the general dimension of nanoparticles (i.e. within 100nm). However the NPs are highly agglomerated, hence research is underway on dispersing the particles by introducing in the system megahertz ultrasonics machine as a source of additional energy during the machining. [14] Also according to EDS results, amount of copper(II)oxide (CuO) impurity seems to be on the higher side, hence further research is required on acquiring a suitable purification process, which is still a semi automated process with combination of ultrasonics and centrifugation.

Conclusion

A comprehensive outlook has been undertaken in this paper to discuss various SiNPs production processes in form of spark erosion. EDM processes such as WEDM, Die-sink and Micro -EDM were carried out on boron doped silicon ingot and corresponding samples were produced and tested under SEM. Additionally a new form of spark erosion process namely High Pressure Flush Spark Erosion has also been introduced which is a cross-breed between Die-sink and Small Hole-EDM. SEM images show SiNPs diameter of 50nm formed from the new system, as well as productivity of 1.5g/hr. Experiments indicated that Die-sink, having higher pulse rate, gave higher productivity however it also consists of similar size distribution with lower pulse rate process (Micro-EDM). This hints that controlling size at nano-scale may not be possible by controlling electrical parameters. Whereas using pressure flush rate with deionized water, the new system was the only liquid dielectric based spark erosion approach that achieved to produce particles in accordance to general nanoparticle dimensions (less than 100nm). This denotes that controlling the flushing pressure of dielectric fluid may be the key to control resultant particle size. Note that although WEDM also consists of fairly high flush pressure, due to cumbersome purification process the resultant sample hardly show any debris at nanoparticle range. However major drawbacks of the high pressure system consist of agglomeration and semi-automated purification process, hence further research is needed for improvement.

Acknowledgements

Many thanks go to Jiangsu Key Laboratory of Precision & Micro-engineering, China Electric Equipment Group and Nanjing Worthwind Optoelectric Company limited.

References

[1] Wang, Sea-Fue, et al. "Silica coating on ultrafine α-alumina particles." Materials Science and Engineering: A 395.1 (2005): 148-152.

[2] Zhang, Yingchao, et al. "Preparation and characterization of aluminum pigments coated with silica for corrosion protection." Corrosion Science 53.5 (2011): 1694-1699.

[3] Ibrahim, Ismail AM, A. A. F. Zikry, and Mohamed A. Sharaf. "Preparation of spherical silica nanoparticles: Stöber silica." J. Am. Sci 6.11 (2010): 985-989.

[4] Rao, Rajesh A., Ramachandran Muralidhar, and Tushar P. Merchant. "Method of forming Nanocrystals in a memory device." U.S. Patent No. 6,808,986. 26 Oct. 2004.

[5] Pierson, Hugh O. Handbook of chemical vapor deposition: principles, technology and applications. William Andrew, 1999.

[6] Woo D.K., N.K.T., Kim, Y.G., Kim K.S., Kang Y. H. and Kim T, Formation of silicon Particles Using Silane Pyrolysis. European Aerosol Conference 2007

[7] Jang, Y., Lee, J.C., and Ko, C.H, Microstructures of Silicon Nanoparticles Synthesized Using Double Tube Reactor with Inductively Coupled Plasma. Journal of the Korean Physical Society, 2010. 57(4): p. 1029-1032

[8] Vons, Vincent A., et al. "Silicon nanoparticles produced by spark discharge."Journal of Nanoparticle Research 13.10 (2011): 4867-4879.

[9] Hashida, M., et al. "Non-thermal ablation of expanded polytetrafluoroethylene with an intense femtosecond-pulse laser." Optics express 17.15 (2009): 13116-13121.

[10] Csanadi, Ozzie, et al. "Formation of microspheres through laser irradiation of a surface." U.S. Patent No. 7,700,032. 20 Apr. 2010.

[11] Hahn, Anne, Stephan Barcikowski, and Boris N. Chichkov. "Influences on nanoparticle production during pulsed laser ablation." Pulse 40.45 (2008): 50.

[12] Berkowitz, A. E., and J. L. Walter. "Spark erosion: A method for producing rapidly quenched fine powders." Journal of Materials Research 2.02 (1987): 277-288.

[13] Kunieda, M., et al. "Advancing EDM through fundamental insight into the process." CIRP Annals-Manufacturing Technology 54.2 (2005): 64-87.

[14] Wang W., Z.W., Zhao E. J., Hong. J., Method of preparation of nano particles by using shockwave assisted ultra short pulsed spark erosion. China Patent, 201210222341.4

Advanced Materials Research Vol. 936 (2014) pp 1769-1774
© (2014) Trans Tech Publications, Switzerland
doi:10.4028/www.scientific.net/AMR.936.1769

Study on CMT Welding of Stainless Steel Railway Vehicle Body

Wenquan Wang[1,a],Qingliang Meng[1,b] and Liyuan Niu[2]

[1] College of Materials Science and Engineering,Jilin University

No.5988 Renmen Road,Changchun,Jilin Province,130022 P.R.China

[2]Zhejiang Industry and Trade Vocational College

No.717 Fudong Road,Wenzhou,Zhejiang Province,325003 P.R.China

[a]wwq@jlu.edu.cn,[b]mengql12@126.com

Keywords: Stainless steel sheet,Cold metal transfer,Welding parameters,Microstructure

Abstract: Cold metal transfer (CMT) process is a modified inert gas metal welding process,which characterrizes of low heat input and no spatter welding comparing with traditional GMAW process.In this paper,research of the CMT welding features of stainless steel sheet has been conducted.The effects of welding parameters including wire feed rate,welding speed and arc-length modification coefficient on mechanical properties and surface morphology were investigated.In addition,optical micrograph(OM) and scanning electron microscope(SEM) were used to analyze the weld microstructure,and microstructural characteristics were discussed as well.In the end,the optimum welding parameters which were used in real production and achieved good effect were obtained by means of orthogonal experiment.

Introduction

With the rapid development of rail transportation in recent years, Stainless steel have been used in the manufacture of railway vehicle widely[1].Stainless steel vehicle bodies with its advantages such as light weight,low energy consumption and good corrosion resistant have been the first choice for railway passenger vehicles[2].In order to reduce pollusion and save energy,it is attractive to make vehicle bodies lighter though using stainless steel sheet with thin thickness [3].Due to stainless steel sheet is easy to bum through,some especial welding process were required to reduce heat input such as AC pulsed MIG,spot welding and laser welding[4].B. Gulenc etc have studied 304L stainless steel with MIG process in different parameters,and its conclusion that though MIG process has many advantages,the negative effects were the HAZ grain coarsening and smooth transitional droplet is hard to obtain[5].

In this article,research was conducted to weld in corrugated sheet on the top of vehicle body to side roof.The thickness of corrugated sheet is 0.6mm and the thickness of side roof is 1.5mm.To achieve to weld the lap of longitudinal seam successfully,many efforts have been made[6].

Currently,tradition methods in the industry were using gas metal arc welding process with the shielding gas including 97%Argon and 3%Oxygen to make the weld joint.GMAW actual welding surface morphology of stainless steel vehicle body is shown in Fig. 1.

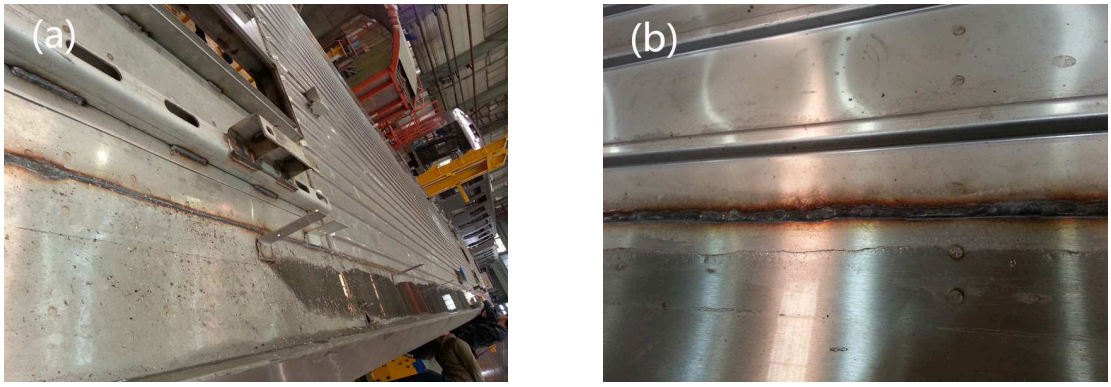


Fig. 1 Surface morphology of stainless steel vehicle body with traditional process

Apparently,GMAW welding surface morphology showed that the welding quality is not ideal.Defects including air hole and overheat were found in welded joint.So it is difficult to achieve the sound weld with acceptable weld strength of the welded joints and smooth surface morphology.Welding quality become a key problem which should be resolved.To the problem,Welding process have to be improved.By a large number of investigation and study,GMAW process is replaced by cold metal transfer(CMT) process.

The arc characteristics of the CMT process

The CMT process is a modified metal inert gas welding process which was invented by Fronius company[8].CMT was developed on the basis of research on joining steel to aluminum alloy,SFI and micro-connection technology.R.Cao andZ.Feng etc have made titanium-copper lap welded joints by cold metal transfer technology[9].CMT is wildly applied to join the dissimilar metals and also used to weld thin metal sheet.

The arc shape variation of the CMT process as shown in Fig. 2 .In one cycle,the brightness of the arc in the picture is low except two frames at the beginning of the cycle.The wire retraction motion assists droplet detachment during the short circuit, thus the metal can transfer into the welding pool without the aid of the electromagnetic force.CMT process has three differences comparing to traditional metal inert gas welding process[10]:

(1)The motions of the wire have been integrated into the welding process and into the overall control of the process in the first time.

(2) The current of short circuit is close to zero during the short circuit.

(3)The wire retraction motion assists droplet detachment from parent metal.

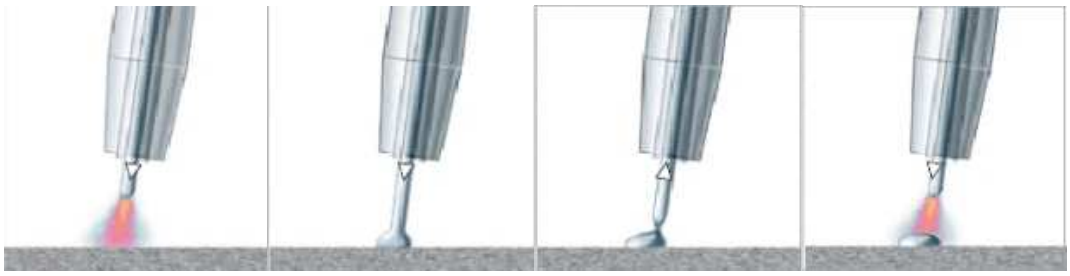


Fig.2 Arc shape variation of the CMT process

The wire retraction motion helps droplet detachment during the short circuit,thus the metal can transfer into the welding pool without the aid of the electromagnetic force.Then the heat input is decreased greatly and the welding process could almost without spatter[11].Thereby the joint can deduce welding deformation to achieve the mechanical performance.

Experimental set-up

The selected materials was A304 stainless steel which is a kind of austenite stainless steel.The welding wire was selected 308LØ1.Table 1 shows material and filler wire specified composition values.The sheets in thickness of 1.5mm were cut into blanks with dimensions of 100×200mm and the corrugated sheets with thickness of 0.6mm were cut into blanks with dimensions of 100mm×200mm.Fig. 3 shows the schematic of the welding configuration.

Table 1 Material and filler wire specified composition values

Material	C	Mn	P	S	Si	Cr	Ni
A304	0.08	2.00	0.045	0.030	1.00	18.0-20.0	8.0-11.0
ER308L	0.03	1.80	0.015	0.008	0.60	20.0	10.0

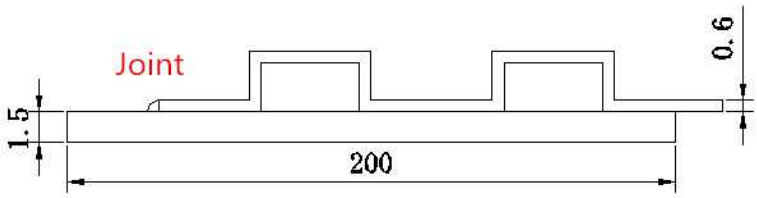


Fig. 3 Schematic of the welding configuration

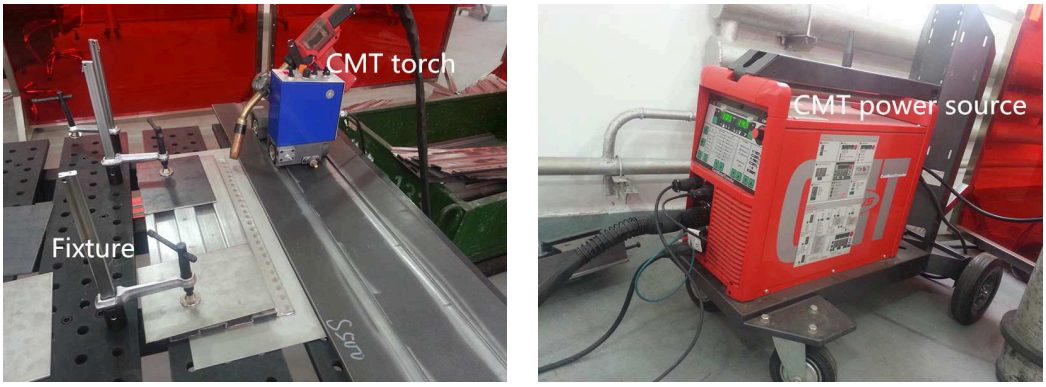


Fig. 4 Experimental set-up

The CMT equipment model used in this study is TransPuls Synergic 2700.As shown in Fig. 4 ,It is the environment of experimental set-up.When the leftward welding method was adopted,97.5%Argon and 2.5%carbon dioxide was used as the shielding gas at a flow rate of 28.5L/min.

Considering the CMT process parameters of welding equipment with expert system,welding current and welding voltage were directly controlled by wire feed rate.Hence,three factors were investigated included wire fee speed,welding speed and arc-length modification coefficient[12].

The wire feed rate ranged from 6m/min.to 11m/min.,in 1m/min. step.and the welding speed was in the range of 360mm/min.-680mm/min.,every step is 80mm/min.Then arc-length modification ranged from－25% to 25% in step of 5%[13].

Results and discussion

Microstructural examination. After the welding, the welds were sectioned into blanks with dimensions of 10mm×20mm,polished and etched for microstructure analysis.Optical microscopy(OM) and scanning electron microscope(SEM) were used investigate the weld microstructure.

Due to a very small heat input from the CMT welding,the distortion was not observed in the weld,and the HAZ zone was narrow comparing with traditional fusion welding.In the macroscopic view,as shown in Fig. 5(a) .The welding line of weld metal and base metal was a stretch of v-shaped contour.The crystallizing morphology on the weld seam was equiaxed grains and dendrites and that on the fusion area were columnar crystals.Crystals on the weld appeared in growth to the weld center,and coarse grain size of austenite in HAZ was relatively uniform.

Further studies on CMT welding joint microstructure morphology by using SEM.As shown in Fig. 5(b),Microstructure morphology is more distinct and the heterogeneity of grain size nearby the fusion line is obvious.Base metal grain with dimensions of 20 microns to 40 microns.The fusion zone is only about 150 microns width due to small heat input from the CMT welding.

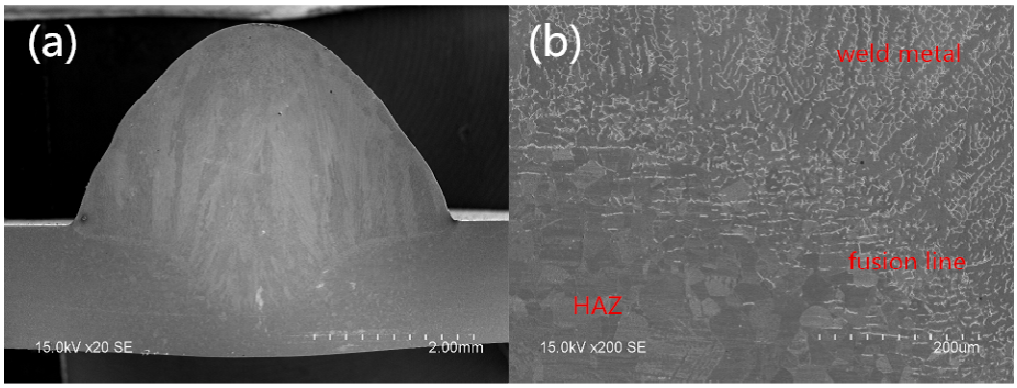


Fig. 5 Microstructure characteristics of joint

Effect of wire feed rate. According to the actual needs,wire feed rate selected ranged from 6mm/min.to 11mm/min,in step of 1mm/min.As shown in Fig. 6 ,the cross-sectional views of the welds obtained in different wire feed rate.When wire feed speed is low,such as 6mm/min.Weld bead presents the characteristic of the high reinforcement and the narrow weld width.But With the improvement of wire feed rate,the weld width and reinforcement increase gradually.It is need to explain that if wire feed rate is further improved,especially exceed 9m/min.,variation of CMT weld appearance is not very obvious.Analysis the reason,when wire feed rate exceeds a certain value,welding current growth begin to play a major role in weld appearance morphology.

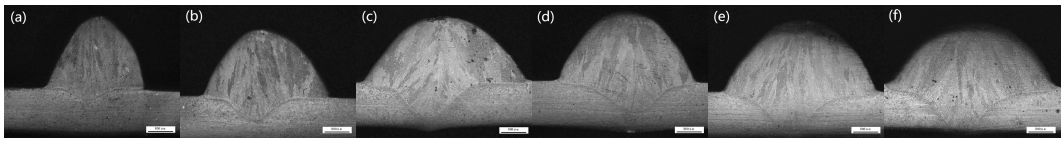


Fig. 6 Cross-sectional views of the welds obtained in different wire feed rate
(a:6m/min.b:7m/min.c:8m/min.d:9m/min.e:10m/min.f:11m/min.)

Effect of welding speed. For cold metal transfer (CMT) welding process,welding speed is a influencing factor corresponding to the welded quality and appearance.Six wire feed rate parametersincluding360mm/min.,440mm/min.,520mm/min.,600mm/min.,680mm/min.,760mm/min .were selected.As shown in Fig. 7 ,the cross-sectional views of the welds obtained in different welding speed.With the improvement of welding speed,it means that decrease of the deposited metal mass per second.Hence,the weld width of weld deposited metal showed a trend of gradual decline.With the increase of welding speed,weld reinforcement and weld penetration is smaller while increased welding speed.

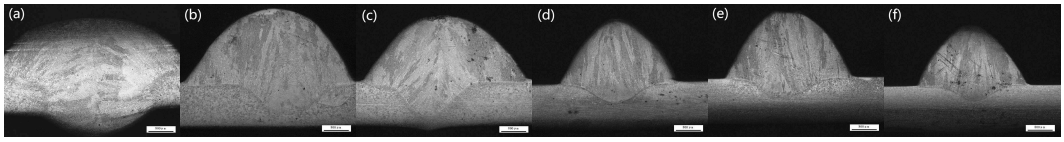


Fig. 7 Cross-sectional views of the welds obtained in different welding speed (a:360mm/min.b:440mm/min.c:520mm/min.d:600mm/min.e:680mm/min.f:760mm)

Effect of arc-length modification coefficient. As shown in Fig. 8 ,cross-sectional views of the welds obtained in different arc-length modification parameters.We selected five parameters including－25%,－15%,－5%,＋5%,＋15%and＋25%.The CMT welding quality and appearance morphology was investigated while different arc-length modification parameters.With arc-length modification changed from small to large,weld width presented a gradually increasing trend,But variation of weld reinforcement was not evident.Due to adjust arc-length modification parameter,there were no significant changed in current and greatly changed in voltage.therefore,The current is the main factor of weld penetration,while the voltage is the main factor affecting weld width.

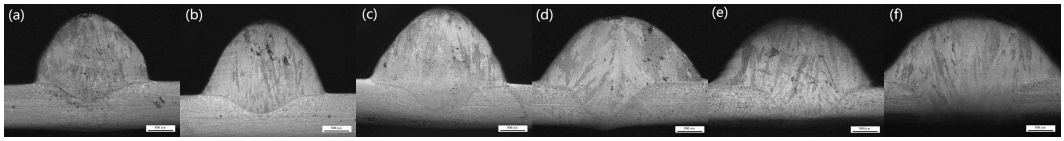


Fig. 8 Cross-sectional views of the welds obtained in different arc-length modification (a:－25% b:－15% c:－5% d:5% e:15% f:25%)

Conclusions

Based on the experimental results and discussions,conclusions were drawn as follows:

(1)The stainless steel sheet was successfully welded by cold metal transfer (CMT) process. Experiment achieved the sound weld with acceptable weld strength of the welded joints and smooth appearance.

(2)Cold metal transfer (CMT) has many potential applications due to its advantages, such as limited heat-affected zone and welding process with no spatter.Practical application shows that the characteristics of CMT make itself feasible in stainless steel railway vehicle manufacture.

(3)By single factor and multifactor orthogonal experiment,it is concluded that the fine weld bead can be obtained under the following parameters: welding current was 99A,welding voltage was 10.5V,wire feed rate was 8m/min,welding speed was 520mm/min,the arc-length modification coefficient is 5%.

References

[1] M. Zhao, Y. Liu, Research and Development of Stainless Steel Car Body for UMT, J. Urban Mass Transit, 7(2007) 76-80.(In Chinese)

[2] K. Xue. Selection of Car Body Materials for Urban Railway Vehicles, J.Urban Mass Transit, 1(2001) 14-19.(In Chinese)

[3] Y. Li, J Zhou. Lightening Design and Research on Steel Trailer Car bodies of High Speed Trains, J. Rolling stock, 6(2002) 23-25.(In Chinese)

[4] G. Li, X. Han.The welding technology for stainless steel car body and its development. Locomotive and Rolling Stock Technology, 1(2004) 1-4.(In Chinese)
[5] B. Gulenc, K. Develi, N. Kahraman et al. Experimental study of the effect of hydrogen in argon as a shielding gas in MIG welding of austenitic stainless steel, J. International Journal of Hydrogen Energy, 30(2005) 1475-1481.
[6] Z. Sun. Laser beam welding of austenitic/ferrite dissimilar steel joints using nickel based filler wire , J. Materials Science and Technology, 19(1993) 603-608.
[7] H. Zhang, J. Feng. The arc characteristics and metal transfer behavior of cold metal transfer and its use in joining aluminum to zinc-coated steel, J. Materials Science and Engineering A , 499 (2009) 111–113.
[8] C.G. Pickina, S.W. Williams. Characterization of the cold metal transfer (CMT) process and its application for low dilution cladding, J. Journal of Materials Processing Technology, 211(2011) 496–502.
[9] R. Cao, Z. Feng. Microstructures and properties of titanium-copper lap welded joints by cold metal transfer technology, J. Materials and Design , 53(2014) 192–201.
[10] J. Shang, KH. Wang. Microstructure Characteristics and Properties of Mg/Al Dissimilar Metals Made by Cold Metal Transfer Welding with ER4043 Filler Metal, J. Rare Metal Materials and Engineering, 2013, 42(7) 1337–1341.
[11] P. liu, F. Lu. Study on fatigue property and microstructure characteristics of welded nuclear power rotor with heavy section, J.Journal of Alloys and Compounds, 584 (2014) 430–437.
[12] P. Bhargava, C.P. Paul. Study on weld bead surface profile and angular distortion in 6 mm thick butt weld joints of SS304 using fiber laser, J. Optics and Lasers in Engineering, 53(2014) 152–157.
[13] L. Cui, X. Yang. Process parameter influence on defects and tensile properties of friction stir welded T-joints on AA6061-T4 sheets, J. Materials and Design , 51(2013) 161–174.

Advanced Materials Research Vol. 936 (2014) pp 1775-1779
© (2014) Trans Tech Publications, Switzerland
doi:10.4028/www.scientific.net/AMR.936.1775

Energy Consumption Discussions of Porcelain Produce with Operating Conditions in a Simplified Model

Junliang Yu[1,2,a]

[1]School of Energy and Power Engineering, Jiangsu University, Zhenjiang, 212013, China

[2]ISUT, Otto-von-Guericke-University, Magdeburg, 39104, Germany

[a]Yu_Jun_Liang@163.com

Keywords: Energy consumption, Porcelain, Modeling, Operating condition

Abstract. Porcelain produce is a very high energy consumption process. According to total energy balance analysis, a variety of operating conditions are analyzed for effect of net energy consumption. One real porcelain plate produce process is introduced as the reference case. Operating conditions are defined in three parameters, which are air excess number, fuel distribution and solid mass ratio. A simplified model based on finite difference method (FDM) is solved to calculate axial gas and solid temperature profiles and net energy consumption. The net energy consumption in porcelain produce is calculated and discussed in quantity with three operating conditions above separately. Finally, it is concluded that net energy consumption is higher with bigger air excess number and solid mass ratio, while fuel distribution will have no influence on net energy consumption.

Introduction

Porcelain is one of materials commonly seen in our daily life. According to the material properties differences, the porcelain is one kind of ceramic product. Generally, the energy consumption range of ceramic produce process is from 2.3 MJ/Kg to 50 MJ/Kg. Especially; the thermal efficiency of whole process is also very low, which are about from 33% to 46%. The tunnel kiln is one of main devices to produce porcelain products. More than half percentage of energy is lost to ambient and absorbed by furniture in tunnel kiln. Therefore, energy consumption analysis is a very hot topic these days [1]. Due to the limitation of experimental conditions in the real porcelain factory, the simulation and modeling is the only validated method to predict energy consumption with different operating situations.

In order to produce different porcelain products according to different sintering temperatures and temperature gradient, the real factories also do it by adjust operating conditions. The operating conditions are meanly about burner group operation. However, different operating conditions may cause energy consumption difference. In the following subsections, the simplified model and operating conditions on energy consumption will be discussed.

Total Energy Balance

According to total energy balance analysis, the factors which will affect net energy consumption can be analyzed theoretically. The whole porcelain produce process is assumed as a closed energy system. The mass and energy flows in this system are shown in Fig. 1.

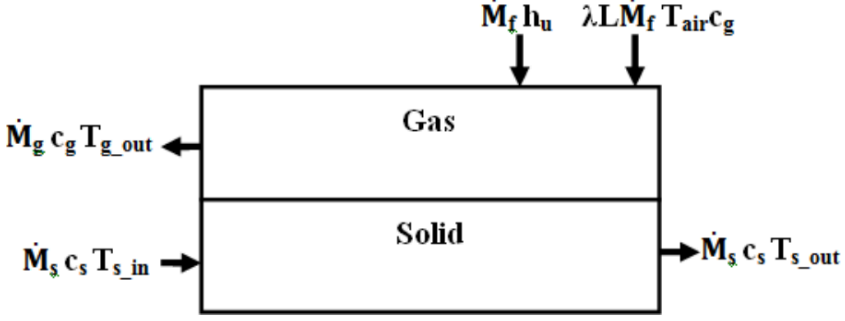


Fig. 1 Simplified energy flows in porcelain produce process

In the graph representation of energy flows, there are gas and solid flows are in parallel and opposite directions. The hot gas flow is from fuel combustion. The net energy from fuel is $\dot{M}_f h_u$ and the energy of air used for combustion is $\lambda L \dot{M}_f T_{air} c_g$. While $\dot{M}_f$ is mass flux of fuel, T_{air} is ambient air temperature, λ is air excess number, L is mass related air demand with Kg_{air}/Kg_{fuel} and c_g is heat capacity of ambient air. After heat transfer from hot gas to cold porcelain products, the gas with energy $\dot{M}_g c_g T_{g_out}$ is sucked out from tunnel kiln with T_{g_out} is gas temperature out from kiln and $\dot{M}_g$ is mass flux of flue gas. For solid, green porcelain products with energy $\dot{M}_s c_s T_{s_in}$, the product with energy after thermal process is $\dot{M}_s c_s T_{s_out}$. With $\dot{M}_s$ is mass flux of porcelain product which is assumed still a constant in whole process. T_{s_in} is temperature of green porcelain product when entering the tunnel kiln and T_{s_out} is temperature of porcelain products out of the tunnel kiln. Due to the simplification, only preheating and firing zones are considered for energy consumption, the T_{s_out} is the sintering temperature.

From the total mass and energy analysis, the energy flows pushed in E_{in} and pushed out E_{out} are defined in Eq.1 and Eq.2

$$E_{in} = \lambda L \dot{M}_f T_{air} c_g + \dot{M}_f h_u + \dot{M}_s c_s T_{s_in} \tag{1}$$

$$E_{out} = \dot{M}_g c_g T_{g_out} + \dot{M}_s c_s T_{s_out} \tag{2}$$

Based on mass and energy balance, the E_{in} must be equal with E_{out}, finally the equation to calculate the net energy consumption for porcelain produce process can be defined in Eq.3 with h_u is fuel enthalpy.

$$E = \frac{\dot{M}_f h_u}{\dot{M}_{prod}} = \frac{(c_s T_{s_{out}} - c_s T_{s_{in}})\dot{M}_s h_u}{[\lambda L T_{air} c_g + h_u - \left(1 + \lambda L\right) c_g T_{g_{out}}]\dot{M}_{prod}} \tag{3}$$

Due to the fuel enthalpy h_u is too much bigger than term $\lambda L T_{air} c_g$ and $(1 + \lambda L)c_g \approx \lambda L c_g$, the whole equation can be simplified as Eq.4

$$E = \frac{\dot{M}_f h_u}{\dot{M}_{prod}} = \frac{(T_{s_out} - T_{s_in})c_s \dot{M}_s h_u}{(h_u - \lambda L c_g T_{g_out})\dot{M}_{prod}} \tag{4}$$

We can conclude which parameters will affect the net energy consumption theoretically from this equation. In real industry, two porcelain product temperatures T_{s_out} and T_{s_in} are fixed, which are sintering temperature and 50℃. The air demand L and energy enthalpy h_u are dependent on fuel. Therefore, two parameters air excess number λ and Solid Mass Ratio (SMR) $\frac{\dot{M}_s}{\dot{M}_{prod}}$ will affect net energy consumption, which is related with operating conditions.

In another way, the fuel distribution (FD) in burner groups can be different in reality. Therefore, the FD can be another operating condition that will be discussed for net energy consumption. Gas temperature in outlet T_{g_out} cannot be known in advance, only modeling and simulation can predict its possible value. Therefore, a simplified model programmed in MATLAB is introduced to adjust operating conditions and calculate T_{g_out}. Finally, the net energy consumption with different cases can be discussed in this simplified model.

Simplified model introduction

The simplified model for porcelain plate production is already developed with finite difference method (FDM) [2]. The differential equations can be solved with two fixed porcelain products temperatures, which are porcelain temperatures before pushing in kiln and sintering temperatures. In the existed model, only preheating zone and firing zone are considered. Because all flue gas is only pushed through these two zones, and no flue gas in cooling zone. It means no energy

consumption in cooling zone. Therefore, this model can be developed further to discuss net energy consumption. The Fig. 2 shows the how the porcelain plate are produced in tunnel kiln.

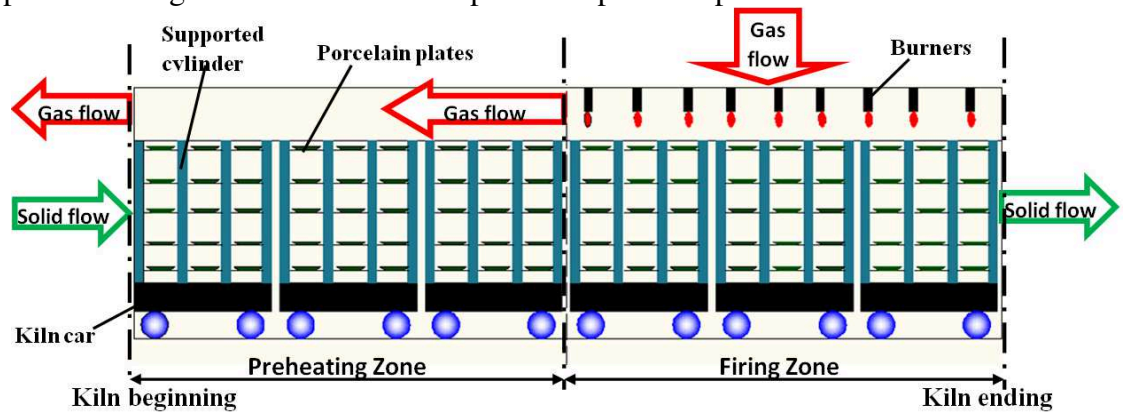


Fig. 2 Brief representation of work principle of porcelain produces

In this model, all porcelain products keep the same temperature with furniture and kiln car. The convective and radiative heat transfers from flue gas to porcelain products are considered. The convection description is from Lorenz's Nusselt function [3]. All constructions of tunnel kiln are the same as the real existed kiln. The detailed construction data are shown in Table 1.

Table 1 Construction data of one real porcelain plate tunnel kiln

Preheating length	8 [m]	Plate diameter	0.26 [m]
Firing length	36 [m]	Sintering temperature	1350 [℃]
Kiln width	1.5 [m]	Net performance	500 [Kg/h]
Kiln height	0.8 [m]	Net energy consumption	14 [MJ/Kg]
Car length	1.9 [m]	Fuel	Natural gas
Plates per car	144 [-]	Burner groups number	9
Solid mass ratio	10 [-]	Gas heat capacity	1100 [J/Kg/K]
Solid heat capacity	880 [J/Kg/K]	Fuel heating value	50.28 [MJ/Kg]

It is already proved this model is available to predict axial flue gas and solid temperature profiles. Therefore, it can also be applied to predict net energy consumption for porcelain produce.

Results and Discussions

According to the energy consumption analysis and model operating condition discussion, there are three main parameters we can discuss. They are air excess number, SMR and FD.

Firstly, the air excess number of nine burner groups can be discussed in four different cases shown in Table 2. Theoretically, air excess numbers of these nine burner groups can be different. In order to make sure all discussions are based on the same standard, only the air excess numbers in the middle three burner groups are variables. From case 1 to case 4, they are varied from 1.2 to 2.4, the mean air excess number is from 1.4 to 1.8. In the first three burner groups, the air excess numbers are exactly one, because oxygen is not allowed in this region. Due to porcelain products temperatures are fixed in the tunnel kiln beginning and ending, only axial flue gas temperature profiles are shown in Fig.3 and net energy consumption are shown in Fig.4.

Table 2 Air excess number in burner groups with four different cases

Burner	9	8	7	6	5	4	3	2	1	**Mean λ**
Case 1	2	2	2	1.2	1.2	1.2	1	1	1	1.4
Case 2	2	2	2	1.6	1.6	1.6	1	1	1	1.53
Case 3	2	2	2	2	2	2	1	1	1	1.67
Case 4	2	2	2	2.4	2.4	2.4	1	1	1	1.8

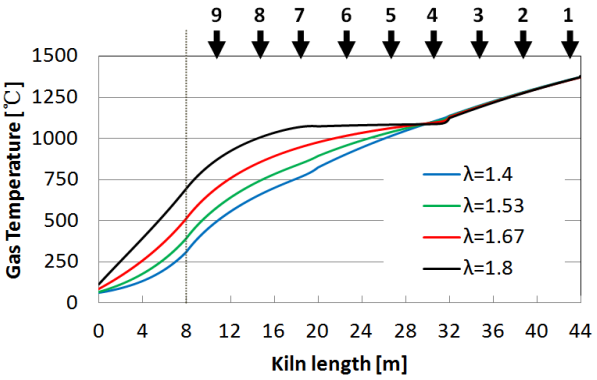


Fig. 3 Gas temperature profiles with different air excess numbers

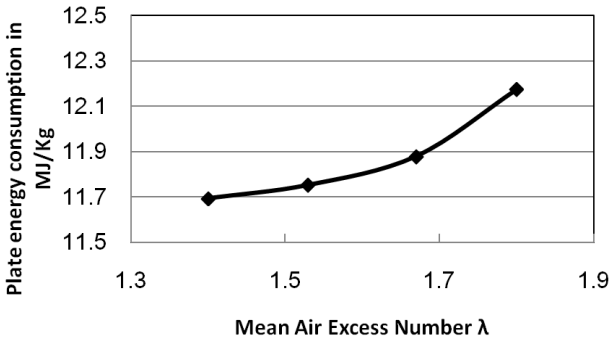


Fig. 4 Net energy consumption curve with different air excess numbers

In gas temperature curves, they are covered absolutely in the first three burner groups region, because the operating conditions are exactly the same. In the following burner groups region, gas temperature profiles are raised higher with bigger air excess number. Because the temperature gradient is related with mass flux of flue gas [4]. Finally, it is shown that net energy consumption increase with bigger air excess number. Because of more energy should be used to heat cold air. However, air excess number does not have a very big effect on energy consumption. There is only about 4% energy consumption increase with about 30% increase of air excess number.

Secondly, different FD is discussed. Fuel is distributed in three different ways shown in Table 3. The sum of fuel percentages in burner groups is 100%. For case 1, less and less fuel is input along gas flow direction. Case 2 distributes fuel in average while case 3 distributes more and more fuel in burner groups. Finally, axial gas temperature profiles are shown in Fig.5 and energy consumption curve is shown in Fig.6.

Table 3 Fuel distribution with different arithmetic progressions

Burner	9	8	7	6	5	4	3	2	1
Case 1 [%]	3.1	5.1	7.1	9.1	11.1	13.1	15.1	17.1	19.1
Case 2 [%]	11.1	11.1	11.1	11.1	11.1	11.1	11.1	11.1	11.1
Case 3 [%]	19.1	17.1	15.1	13.1	11.1	9.1	7.1	5.1	3.1

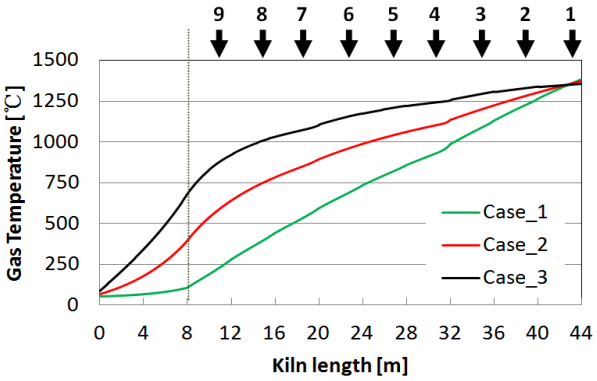


Fig. 5 Gas temperature profiles with different fuel distribution

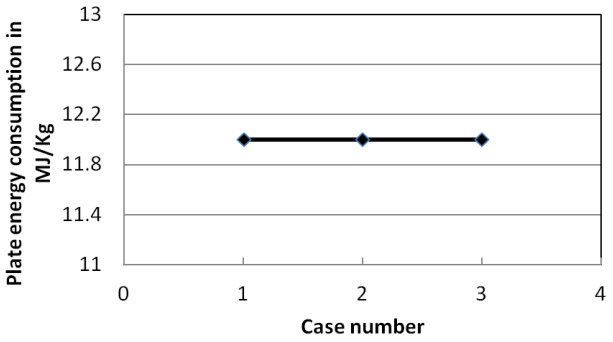


Fig. 6 Net energy consumption curve with different fuel distribution

As seen in Fig.5, gas temperatures in kiln ending and beginning are the same for cases. The flue gas variances during whole process are different with different cases. One important point is shown in preheating zone of case 1 from 0m to 8m, the flue gas temperatures almost keep a constant. It means almost no heat transfer from hot flue gas to cold porcelain products is this region. In reality, the porcelain factories always want more heat transfer in this region and temperature of porcelain product can increase faster. Therefore, the situation of case 3 should be avoided in reality and more fuel should be input in the last burner groups. The net energy consumption profile shows that net

energy consumptions are the same with different fuel distribution. The reason is the same amount of fuel is input in whole process but only with different percentages in burner groups. According to definition in Eq.3, the net energy consumptions must be the same with the same fuel mass flux.

Thirdly, the axial flue gas temperature profiles and net energy consumptions with different SMR are discussed and shown in Fig.7 and Fig.8. The SMR is changed from 4 to 13.

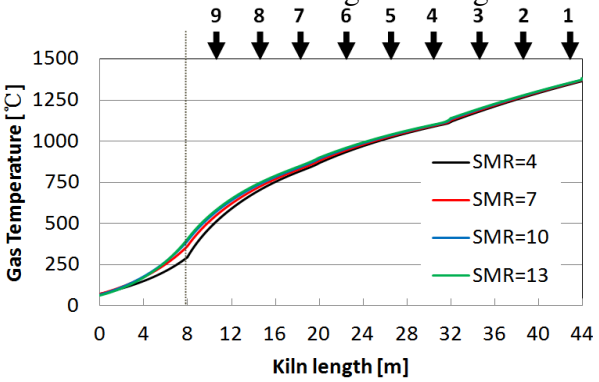


Fig. 7 Gas temperature profiles with different solid mass ratio

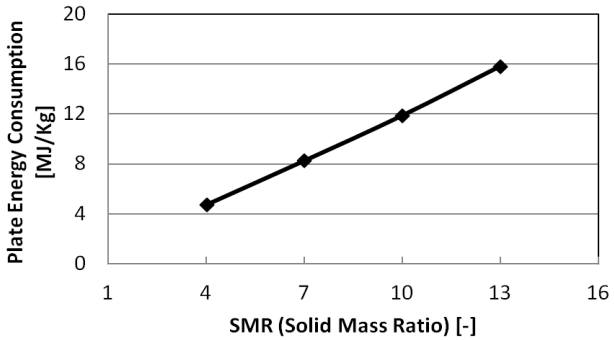


Fig. 8 Net energy consumption curve with different solid mass ratio

As shown in gas temperature profiles, different SMR will have less effect on temperature profiles. As shown in net energy consumption curve, the net energy consumption will be bigger with bigger SMR. According to definition of total solid mass flux, it is the sum of porcelain products, furniture and kiln car. If mass flux of porcelain products is fixed, the mass flux of furniture and kiln car will be bigger with bigger SMR. In these four cases, the mass flux of porcelain product is assumed to be a constant. Therefore, it means more energy is absorbed with heavier furniture and kiln car. The net energy consumption will be three times bigger when SMR is two times bigger [5]. Compared with net energy consumption influence of air excess number, the SMR will dominate the energy consumption influence.

Conclusion

This paper discussed the net energy consumption, which the porcelain plate as an example. The existed model can predict the axial porcelain temperature and calculate net energy consumption. The net energy consumption is discussed with three different operating conditions including air excess numbers, fuel distribution and solid mass ratio. The following conclusions can be obtained:

(1) When porcelain performance is fixed, with bigger air excess number, the net energy consumption will be bigger.

(2) When air excess number and porcelain performance are fixed, different fuel distribution in burner groups will only affect axial porcelain temperature profiles. Moreover, fuel distribution will not affect net energy consumption

(3) When air excess number and fuel distribution are fixed, the net energy consumption will increase with bigger solid mass ratio

(4) In order to produce the certain amount of porcelain products with fixed fuel amount, the lighter furniture and kiln car should be applied.

References

[1] Ring, T.A., 1 - Ceramic Powder Processing History and Discussion of Natural Raw Materials, in Fundamentals of Ceramic Powder Processing and Synthesis. 1996, San Diego. p. 7-41.

[2] J. Yu, Simplified Modeling for Burning of Porcelain Plates in Tunnel Kiln, ICMTM,2014

[3] Lorenz, L., Heat transfer by current superimposed on goods stacked on the example of flatware fire in furnaces, 2007, Dissertation at Technical University of Freiberg (In German)

[4] Mançuhan, E., Analysis and optimization of drying of green bricks in a tunnel dryer. Drying Technology, 2009. 27(5): p. 707-713.

[5] McGinnis and D. Llaguno, Low-Mass Kiln Furniture. Ceramic Industry,2002.152(2): p. 41-45.

Advanced Materials Research Vol. 936 (2014) pp 1780-1785
© (2014) Trans Tech Publications, Switzerland
doi:10.4028/www.scientific.net/AMR.936.1780

Microstructure and Mechanical Properties of Submerged Arc Welding Filled with Ni wire Dissimilar Joints Comprising SUS304 and Q245R

Pengxian Zhang[1,a*], Peng Zhao[1,b], and Yanquan Cui[1,c]

[1]State Key Laboratory of Advanced Processing and Recycling of Non-ferrous Metals,

Lanzhou University of Technology, Lanzhou 730050, PR China

[a]email: pengxzhang@163.com, [b]email: zhaopenglut@163.com,

[c]email: cuiyanquanlut@163.com

Keywords: Dissimilar welded joint, Submerged arc welding filled with Ni wire, Transition width, Peak temperature, Holding time at elevated temperature.

Abstract: Aim at the issue that the bending crack is easy to generate inside dissimilar welded joint of low alloy steel and stainless steel, a new process of submerged arc welding filled with Ni wire is put forward. The influence mechanism of filling quantity of Ni wire to the joint of microstructure evolutions and mechanical properties is mainly explored based on the contrast test of non-filling Ni wire and three different filling speeds of Ni wire. The experiment results indicate that, the filling process of Ni wire supplies austenite forming element, and alters heat allocation process of molten pool. The filling quantity of Ni wire is the quantitative parameter, it is used to control the transition width between low alloy steel and weld metal, also to adjust the peak temperature and holding time at elevated temperature of molten pool. When the value of the filling quantity of Ni wire is determined, the problem of bending crack in the fusion zone of low alloy steel can be solved, and also the overheat damage can be eliminated. At the same time, the grains of weld metal and heat affected zone are refined. And on this basis the plasticity, toughness and microhardness of welded joint can be guaranteed.

Introduction

Dissimilar weldments have been widely used in shipbuilding and chemical industry because of reducing fabrication costs as well as the full advantage of each outstanding physical property, such as stainless steel with corrosion and oxidation resistance[1,2]. Although the welding joints of austenite stainless steel (ASS) and low alloy steel (LAS) are often applied in the manufacture of pressure vessels, some weld defects such as dilutions and cracks will generate in the weld metal (WM) and lead to great decrease of properties of the welded joint[3,4]. This is mainly because austenite forming element deficiencies in the fusion zone close to LAS side leads to develop temporary stabilization structure of austenite and martensite[5]. Submerged arc welding filled with Ni wire is a welding process that inserting another filling wire without power supplying in submerged arc welding molten pool. Filling wire can make WM component uniform and control heat reallocation of molten pool reasonably[6]. Submerged arc welding filled with Ni wire is tried to solve the welding problem about the dissimilar joint of Q245R and SUS304 in this paper.

Materials and Experiment

Base metals employed are LAS (Q245R) and ASS (SUS304), arcing wire adopts 4mm diameter ER309, their chemical composition is given in Table 1. Filling wire adopts 1mm diameter pure Ni wire. All of the plates are machined to the same dimension of 300 mm×100 mm×10 mm. The joints were produced in two passes (front and back) using the following parameters: 530A; 35V; and 30m/h welding speed. The front without groove and the back with 90°single-V edge preparation was followed with a root face of 5 mm. To find out the effect of the filling process of Ni wire on microstructure and properties of the dissimilar joint, four type tests are carried out. Their test condition is different, so we can get four different type joints. Type Ⅰ represents the joint without

filling Ni wire; type Ⅱ, Ⅲ, Ⅳ represent the joints on the condition of filling speed of Ni wire is 130m/h, 194m/h, 266m/h respectively. A series of microanalyses and properties tests on these joints are conducted. The mechanical properties tests of welded joints include bending test, Charpy 'V' notch impact test and microhardness measurement. The microstructure characterizations of the dissimilar joints are analyzed using scanning electron microscopy (SEM). The chemical analysis in different zones of weldments is detected employing Energy-dispersive spectroscopy (EDS).

TABLE 1 CHEMICAL COMPOSITIONS OF BASE METALS AND FILLER METALS (WT.%).

Materials	C	Cr	Ni	Mn	Si	Mo	S	P
SUS304	≤0.07	17.0-19.0	8.0-11.0	≤2.0	≤1.0	-	≤0.03	≤0.035
Q245R	≤0.2	-	-	0.5-1.0	≤0.35	-	≤0.015	≤0.025
ER309	≤0.12	23.0-25.0	12.00-14.00	1.00-2.50	0.30-0.65	≤0.75	≤0.03	≤0.03

Results and Discussion

Microstructure

The difference of thermal physical property and electromagnetic property between ASS and LAS, not only makes different temperature of liquid metal in both sides of the molten pool, but also makes the liquidity of molten pool metal, mechanical agitation and electromagnetic stirring effect relatively weak. So the metal in the edge of Q245R molten pool can't blend with the filling metal from arcing wire intensively, result in forming solidification transition layer with certain width close to LAS side. The layer can be described by EDS spectra at interfaces between Q245R and WM, which is shown in Fig.1. The diluting effect of LAS on WM and the fast cooling of the molten pool leads to alloy element gradients near the fusion line[7]. From Fig. 1, the variations in Cr, Ni content decrease gradually. They present evident gradient variation near the fusion zone, and the content of Cr varies more markedly than that of Ni. The concentration gradient curve of Cr and Ni shows that the interface of LAS and WM with a certain width sudden change zone, it is defined as transition width (TW). Although this zone location overlaps solidification transition layer, it expresses the failure location more accurately than solidification transition layer (the zone between type Ⅱ boundary and fusion line)[8,9]. Fig. 1(a) represents EDS spectra of type Ⅰ, and Fig.1(b), (c) and (d) represent EDS spectra of type Ⅱ, Ⅲ and Ⅳ respectively. The TW is maximum in Fig. 1(a), as is seen in Fig. 1(b), (c), (d), the TW is decreased gradually with the filling speed of Ni wire increasing. It make the weak zone of the joint is improved obviously that the Ni wire provides adequate austenite forming element for the organization transformation of LAS on the action of the heat of molten pool and the force of electromagnetic stirring.

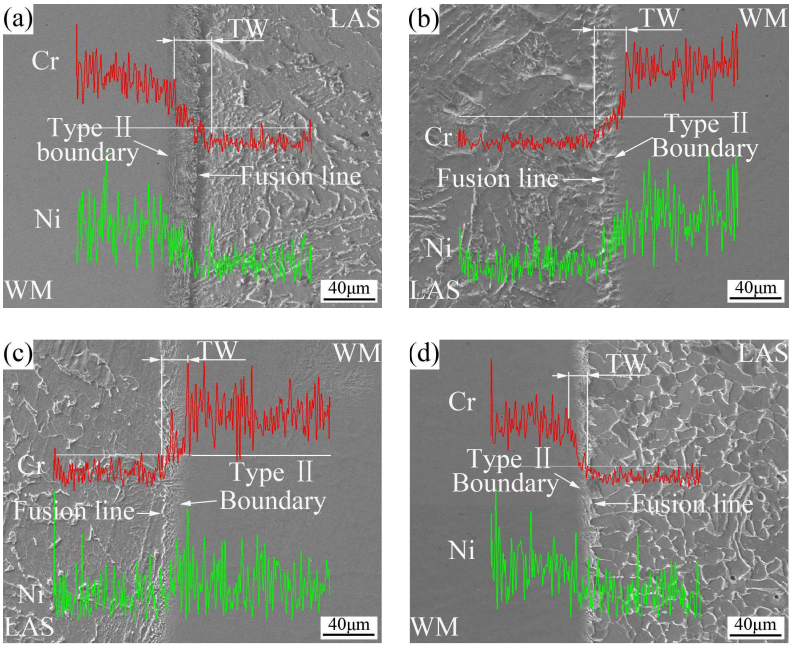


Fig. 1 EDS line scanning across the Q245R-WM interface: (a) type Ⅰ; (b) type Ⅱ; (c) type Ⅲ; (d) type Ⅳ.

The filling process of Ni wire not only provides austenite forming element for the WM, but also changes the heat distribution of molten pool. To reflect its impact on the temperature fields of molten pool, the computer data acquisition system is built. By means of the system, the thermal cycling curve of the center of molten pool is measured, which is shown in Fig.2. NW and FW represents the thermal cycling curve of type Ⅰ and type Ⅳ respectively, the peak temperature of FW is up to 243℃ lower than the NW. t_1 and t_2 represent the holding time at elevated temperature of type Ⅰ and type Ⅳ respectively, the holding time at elevated temperature of FW is 8s shorter than that of NW. This shows that the filling process of Ni wire alters the heat distribution of the molten pool markedly. The change is mainly due to the fact that a part heat of molten pool is used to melt Ni wire. Through controlling the filling quantity of Ni wire, anticipant peak temperature and holding time at elevated temperature can be also obtained.

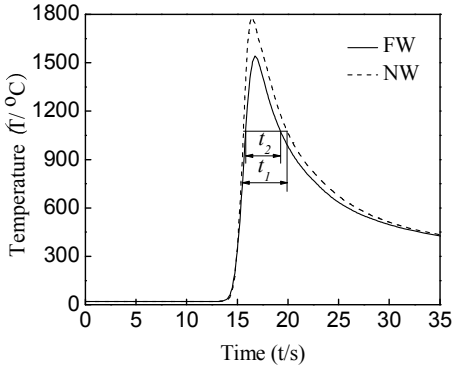


Fig. 2 The thermal cycling curve of type Ⅰ and type Ⅳ.

Reasonable peak temperature and holding time at elevated temperature are the condition precedent of eliminating grain coarsening and obtaining the anticipant microstructure of HAZ. The microstructure of type Ⅰ is shown in Fig.3(a). The HAZ structure mainly is the coarse block ferrites and widmanstatten structures. The HAZ microstructure of type Ⅱ, Ⅲ and Ⅳ is shown in Fig.3(b), (c) and (d) respectively. Apparently, their microstructures are greater improvement than that of type Ⅰ. The difference of the structure between the HAZ and the base metal is decreased, the matrix structure is lamellar pearlite, ferrite distributes uniformly along the grain boundary. And the dimension of grains becomes finer, more homogeneous and rounder with the filling speed of Ni wire increasing. Consequently, the anticipant microstructure of HAZ can be achieved by means of controlling the filling quantity of Ni wire.

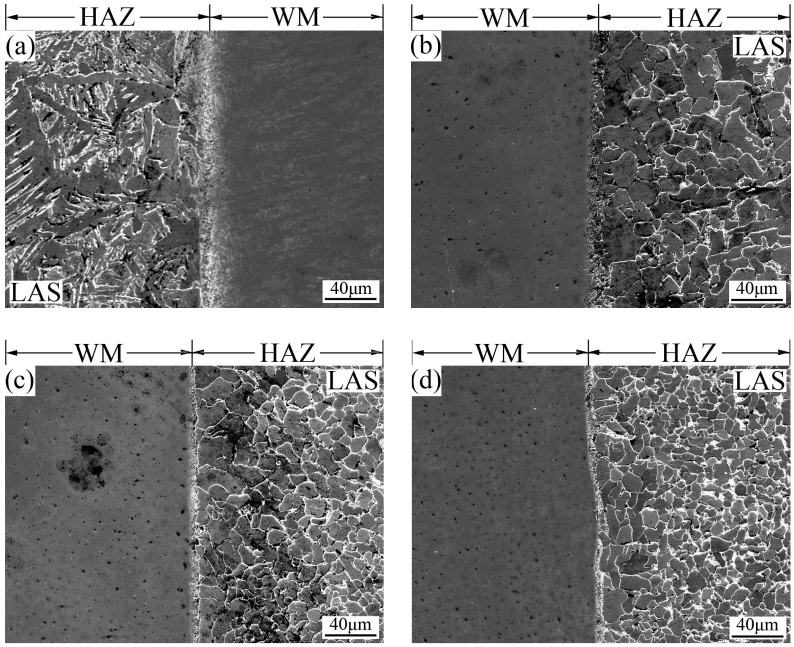


Fig. 3 Microstructures of HAZ in LAS side: (a) type Ⅰ; (b) type Ⅱ; (c) type Ⅲ; (d) type Ⅳ.

Mechanical Properties

Root bending tests are accomplished for the joints of four type tests. In all joints of the test, the cracks with no exception appear in the fusion zone close to LAS side. This indicates that the zone is the weak location of the dissimilar welded joint. In the four type tests, whether generating the crack or not and the length of the crack are selected as evaluation indexes. The two indexes are measured and shown in Table 2 and Fig.4. The joints of type Ⅰ, Ⅱ and Ⅲ almost generate the crack, while only the two of the twenty joints appear the crack for type Ⅳ test. This shows that the joint plasticity of the type Ⅳ is better than the others. The crack length is closely related to the filling speed of Ni wire. In Fig. 4, WE1, WE2 and WE3 represent the number of samples. The crack length of type Ⅰ, Ⅱ, Ⅲ and Ⅳ is contrasted in each sample. The fact observed from Fig. 4, the crack length is obviously shortened with the filling speed of Ni wire increasing. Apparently, the shorter crack length, the better joint plasticity is. The austenite phase increased and the brittle nitrides phase reduced with the filling speed of Ni wire increasing. This is a major reason for the improvement of plasticity and crack resistance. Therefore, the plasticity of welded joint can be guaranteed by means of the filling process of Ni wire.

TABLE 2 THE BENDING TEST RESULTS OF WELDED JOINT.

Test type	Number of joint [pcs]	bending angle [°]	Number of generating the crack [pcs]
Type Ⅰ	20	180	20
Type Ⅱ	20	180	18
Type Ⅲ	20	180	18
Type Ⅳ	20	180	2

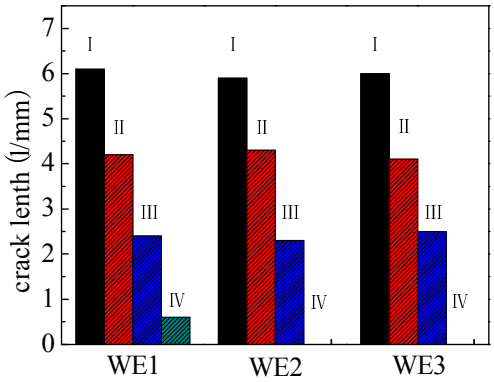


Fig. 4 Crack length of root bending test.

The Charpy impact test of LAS in HAZ is conducted. The relation curve between the filling speed of Ni wire and impact energy is shown in Fig.5. The data point is the mean, which is taken from running each test three times. The value of impact energy increases with the filling speed of Ni wire increasing. The filling process of Ni wire also brings a welcome change to microhardness of the joints. This change can be indicated from the microhardness curve of FW and NW in Fig.6. The filling process of Ni wire not only decreases hardness of HAZ and WM obviously, but also makes the width of HAZ narrow. Furthermore, it is for the filling process of Ni wire that carbon migration near fusion line is availably inhibited. This makes the change range of hardness in fusion zone decrease. These changes are advantage to improve mechanical properties of the dissimilar joints.

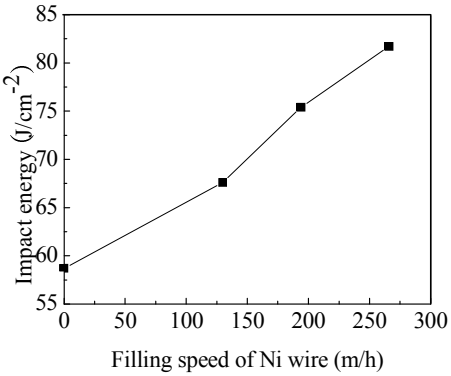


Fig. 5 Relationship between impact energy and filling speed of Ni wire.

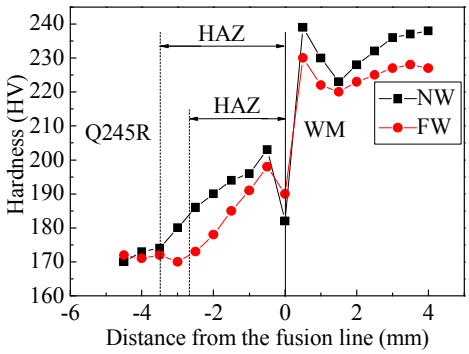


Fig. 6 Microhardness profile across the LAS-WM interface.

Summary

When LAS and ASS are connected by fusion welding, the existence of solidification transition layer is the mainly reason for bending property degradation. The filling of Ni wire supplies austenite forming element when LAS melt to form WM. When the value of the filling quantity of Ni wire is determined, the value of TW can be controlled within the limits of mechanical properties. If so, the problem of bending cracks can be solved.

When the Ni wire inserts molten pool to melt, it will absorb part heat to result in altering temperature fields of molten pool. So, reasonable peak temperature and holding time at elevated temperature of molten pool can be obtained by controlling the filling quantity of Ni wire. On this basis, microstructure and mechanical properties of welded joint can be guaranteed. Submerged arc welding filled with Ni wire puts forward to a new idea for the joint of LAS and ASS.

References

[1] R.S. Chen, F.G. Zhang, D.Y. Liu, Microstructure of Liquid and Solid Diffusion Bonding Region of Carbon Steel-brass Interlayer-stainless Steel, Transactions of the China Welding Institution. 30, No.4 (2009) 61-64.
[2] D. Akbari, I. Sattari-Far, Effect of the welding heat input on residual stresses in butt-welds of dissimilar pipe joints, International Journal of Pressure Vessels and Piping. 190 (2009) 1-8.
[3] C.R. Das, A.K. Bhaduri, G. Srinivasan, et al, Selection of filler wire for and effect of auto tempering on the mechanical properties of dissimilar metal joint between 403 and 304L(N) stainless steels, Journal of Materials Processing Technology. 30, No.2 (2009) 141-144.
[4] C. Pan, Z. Zhang, Morphologies of the transition region in dissimilar austenitic-ferritic welds, Materials Characterization. 36, No.1 (1996) 5-10.
[5] R. Wang, F.H. Wang, H.M. Tian, et al, Analysis of bending property of dissimilar steels welded joints, Transactions of the China Welding Institution. 34, No.2 (2013)58-61.
[6] P.X. Zhang, H. Li, J. Zhang. A GABP optimized algorithm for filler rate of non-heated wire, Transactions of the China Welding Institution. 33,No.12 (2012) 77-80.
[7] P.Bala Srinivsan, V. Muthupandi, W. Dietzel, and V.Sivan, Microstructure and corrosion behavior of shielded metal arc-welded dissimilar joints comprising duplex stainless steel and low alloy steel, J.Mater. Eng. Perform., 15(3006), No.6, p.758.
[8] T.W. Nelson, J.C. Lippold, M.J. Mills, Nature and evolution of the fusion boundary in ferritic-austenitic dissimilar weld metals: Part 1, Nucleation and Growth, Weld. J. 78, No.10 (1999) 329-332.
[9] T. Hattori, T. Fujita, K. Kinoshita, et al, Hydrogen include disbanding of stainless steel overlay weld and its preventive measures, Nippon Kokan Tech. Rep. Overseas.47 (1986) 17-21.

Advanced Materials Research Vol. 936 (2014) pp 1786-1790
© (2014) Trans Tech Publications, Switzerland
doi:10.4028/www.scientific.net/AMR.936.1786

The Behavior of Second Phase Particles in a Ti-Nb Microalloyed Steel During Welding Thermal Cycle

Maoai Chen[1a], Chuansong Wu[1b]

MOE Key Lab for Liquid-Solid Structure Evolution and Materials Processing, Shandong University, Jinan 250061

[a] chenmaoai@sdu.edu.cn, [b]wucs@sdu.edu.cn

Keywords: Second phase particle, Microalloyed steel, Weld thermal cycle

Abstract. The behavior of second-phase particles in a microalloyed steel during weld thermal cycle has been investigated using analytical electron microscopy. All the particles in the base metal contains Nb and Ti, and the Nb weight fraction of the analyzed particles ranged from 0.22 to 0.85. During the heating stage of the weld thermal cycle, the small particles which were rich in Nb disappeared through complete dissolution and the large particles survived the weld thermal cycle with Nb weight fraction decreased. With a high cooling rate ($t_{8/5}$ no greater than 60s), only heterogeneous re-precipitation occurred during cooling. With a low cooling rate ($t_{8/5}$ = 120s), homogenous re-precipitation also occurred, producing a large number of small Nb-rich particles during cooling.

Introduction

During welding of HSLA steel, austenite grain growth will inevitably results in poor toughness of the coarse grained heat-affected zone (CGHAZ).One method of alleviating this problem is to introduce fine dispersed particles, such as TiN, TiNb(C,N) into the steel. These stable second phase particles are expected to pin the grain boundaries, thus restricting austenite grain growth [1-4]. However, the second phase particles in the microalloyed steel can dissolve, coarsen and re-precipitate during welding, which affect the size, quantity and distribution of the particles, and therefore affect the impact toughness in the CGHAZ. Hence, it is important to understand the response behavior of the second phase particles to the welding thermal cycle.

In this paper, the morphology, quantity, size of second phase particle in Nb, Ti and Ti-Nb microalloyed steels and their simulated CGHAZ were investigated so as to understand change of these second phase particles in the weld thermal cycle.

Experimental

The composition of the microalloyed steel used is shown in Table 1. Specimens with dimension of 10.5mm×10.5mm×55mm were cut from the steel plate and subjected to CGHAZ simulation by using a Thermorestor simulator. The peak temperature (T_p) of weld thermal cycle was 1350°C, the heating rate was 96.6°C /s, and the cooling times from 800°C to 500°C ($t_{8/5}$) were 16s-120s.

TABLE 1 THE COMPOSITION OF TI-NB MICROALLOYED STEEL USED/%

C	Mn	Si	Nb	Ti	Al	N	S	P
0.13	1.36	0.35	0.023	0.017	0.030	0.013	0.005	0.016

The procedure described in reference 5 was used to fabricate carbon replica. The samples used in the carbon extraction replica experiment were cut from the center of the simulated specimen.

The morphology, quantity, and size of the particles on the carbon replica were examined by H-800 TEM, the particle compositions were also investigated by the energy dispersive X-ray spectroscopy (EDX). More than 150 fields were examined and the number of particles analyzed was at least 1000 for every specimen.

Results and Discussion

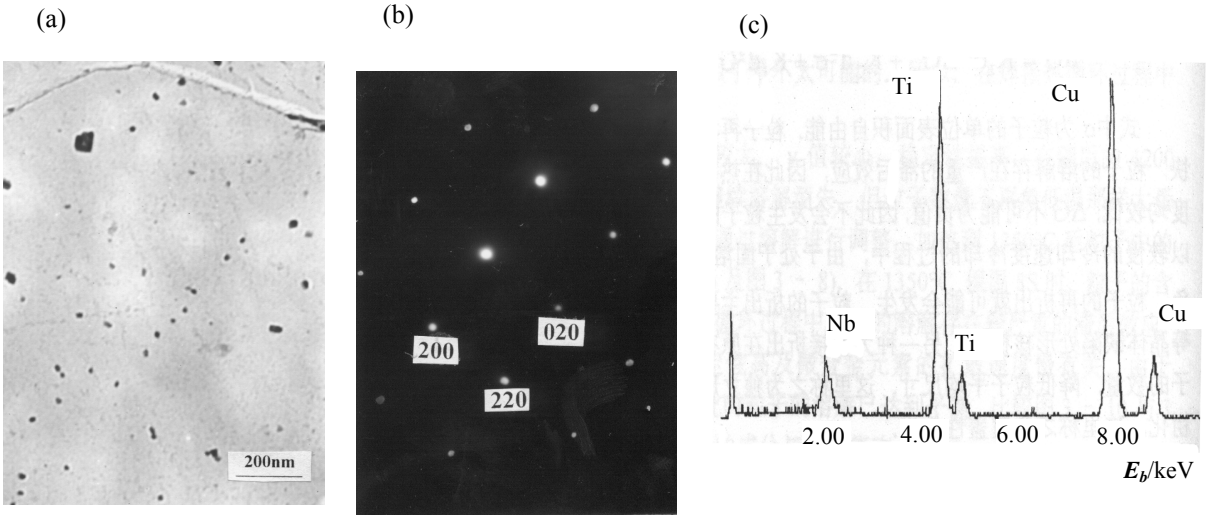


Fig. 1 TEM morphology (a), diffraction pattern (b) and EDX spectrum (c) of particles in Ti-Nb microalloyed steel

Fig.1 shows the typical morphology, diffraction pattern and EDX spectrum of particles in the base metal. Most of the particles are roughly spherical and only a few of them are roughly cubical (see Fig.1a). Electron diffraction analysis revealed that particles possessed a face center cubic structure (see Fig.1b). The lattice constant measured was 0.43502nm, which was closed to those of TiC, TiN, NbC, NbN. EDX analysis indicated that all the particles contains Ti and Nb. These particles are complex carbo-nitrogen compound of the form Ti_xNb_{1-x}, (C_yN_{1-y}).

Fig.2 shows the particle size distribution and composition in the base metal, where D is the average diameter of particles, N is the particle number per unit area (μm^2). Most of the particles is less than 20nm in diameter, the average diameter is just 14.2nm, and the particle number per unit area is about 42.88 /μm^2(Fig.2a). The relative weight fraction of Nb ranges from 0.22 to 0.85(Fig.2b). Small particles less than 50nm tend to be rich in Nb (Nb/(Nb+Ti) >0.5), and large particles greater than 50nm tend to be rich in Ti (Nb/(Nb+Ti) <0.3).The Ti and Nb content of the particle vary with its precipitating temperature[6]. During cooling of the steel, the particles precipitating at high temperature are rich in Ti, and those precipitating at low temperature rich in Nb. The Ti-rich particles precipitating at high temperature have more time to coarsen, thus tending to be larger, the Nb-rich particles precipitating at low temperature have less time to coarsen, thus tending to be smaller.

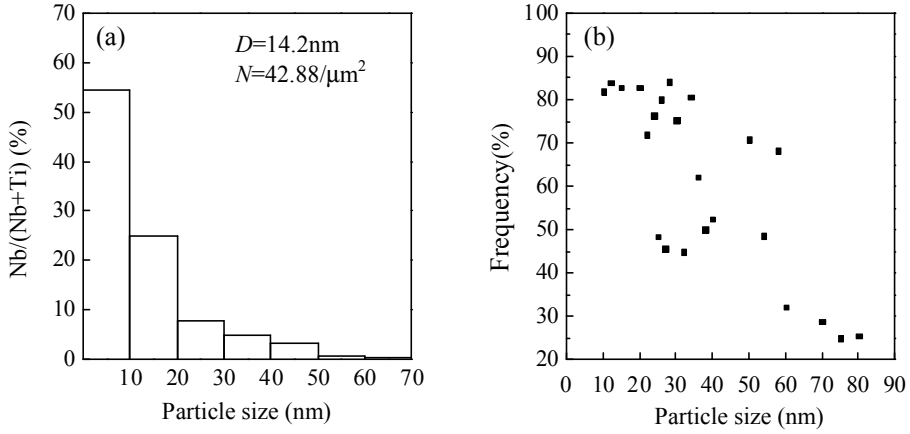


Fig. 2 Size distribution (a) and composition distribution (b) of particles in the base metal

Fig.3 shows particle morphology, size and composition distribution in specimen heated to1350℃ at a heating rate of the weld thermal cycle and then quenched into water after 2s at 1350℃. After heating to 1350℃, all the particles have a cubical morphology, see Fig.3a. The particle number per unit area changes from 42.88 to 3.144, the average particle diameter changes from 14.2nm to 24.6nm,

see Fig.2b. While the Nb weight fraction of the particles decreases considerably, falling in a narrow range from 0.06 to 0. 16. These all suggest that the small Nb-rich particles dissolve completely, the large particles dissolve partially accompanied by a composition change from Nb-rich to Ti-rich during heating stage of the weld thermal cycle.

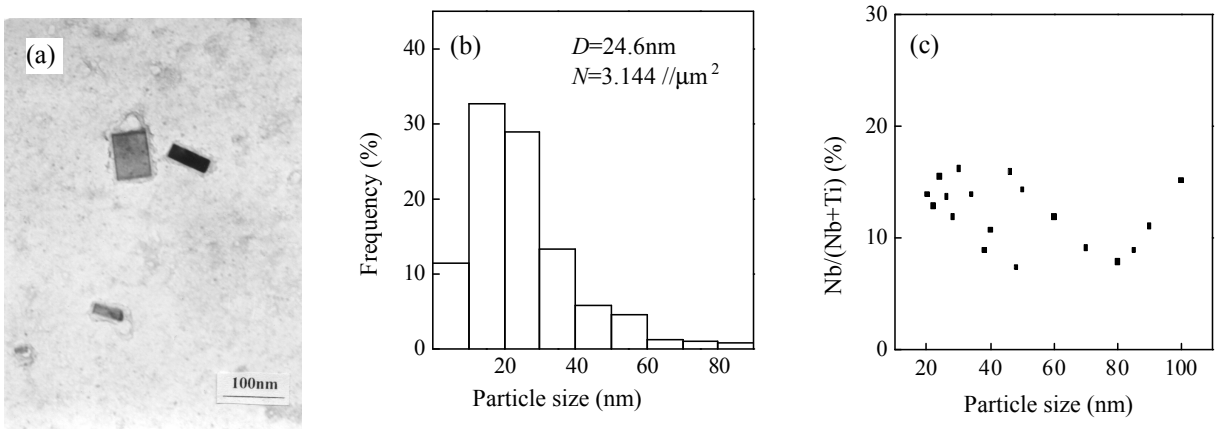


Fig. 3 Particle morphology (a), size distribution (b) and composition distribution (c) in specimen heated to 1350°C and then water quenched

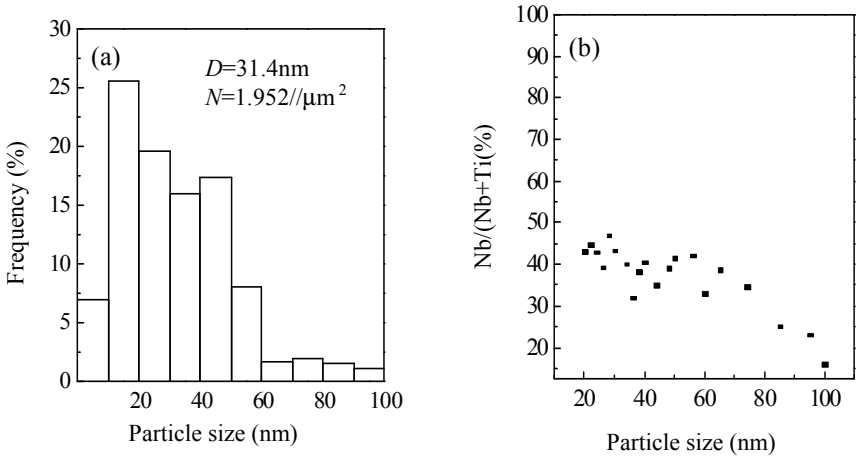


Fig. 4 Particle size distribution (a) and composition distribution (b) after weld thermal cycle with a $t_{8/5}$ of 16s

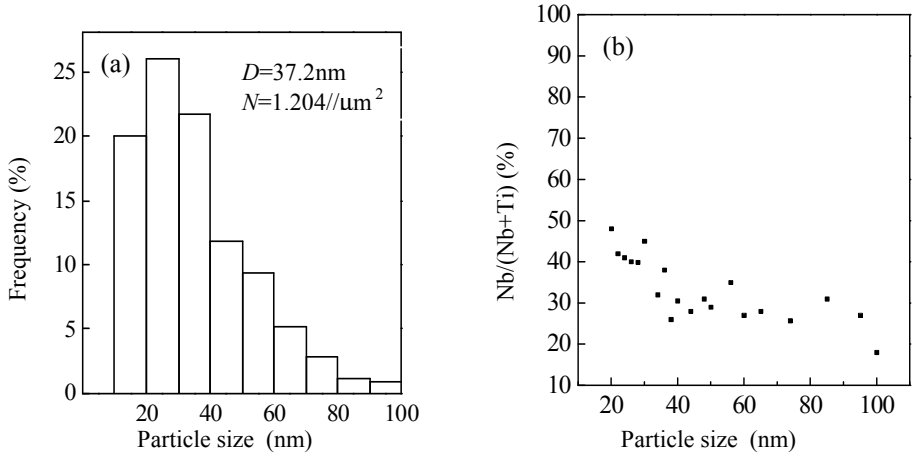


Fig. 5 Particle size distribution (a) composition distribution (b) and after weld thermal cycle with a $t_{8/5}$ of 60s

Fig. 4 shows particle size and composition distribution after weld thermal cycle with $t_{8/5}$=16s. After cooling down from 1350°C at a $t_{8/5}$ of 16s, the mean particle size increases and the particle number per unit area decreases, see Fig. 4 a and Fig. 3b, suggesting that dissolution still occurs during cooling and no homogenous reprecipitation occurs. The slight increase in Nb weight fraction after cooling down (see Fig. 4b and Fig.3c) results from the heterogeneous reprecipitation of Nb-rich particles on the survived particles.

Fig. 5 shows particle size and composition distribution after weld thermal cycle with $t_{8/5}$=60s. With increasing the $t_{8/5}$ from 16s to 60s, the particle number per unit area decreases and the average particle size increases (see Fig.5a and 4a), while the particle composition changes little (see Fig.5b and 4b). It is also noted that the small particle less than 10nm complete disappear through dissolution after weld thermal cycle with $t_{8/5}$=60s, see Fig. 5a .This confirms that dissolution still occurs in the high-temperature stage of cooling.

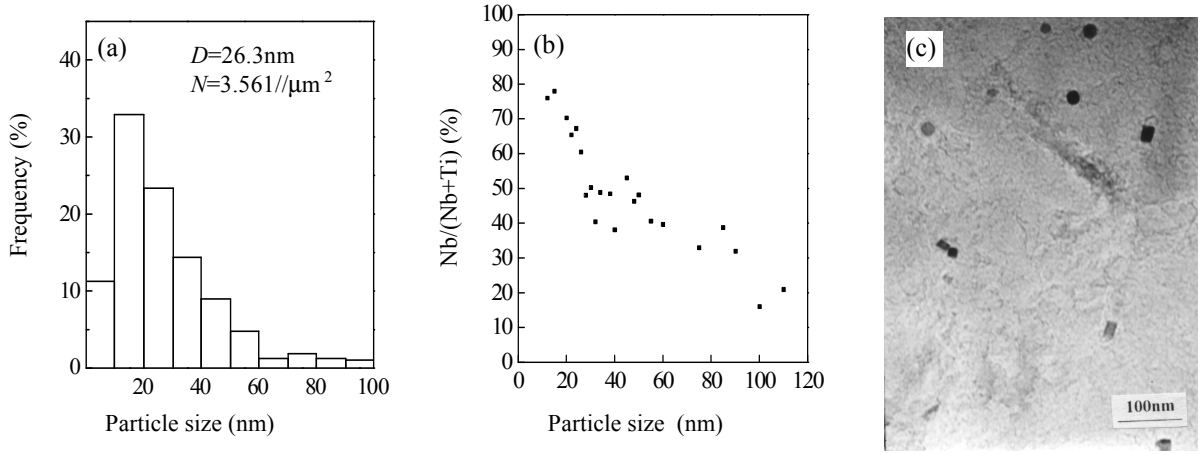


Fig. 6 Particle size distribution (a), composition distribution (b) and morphology after weld thermal cycle with a $t_{8/5}$ of 120s

With the $t_{8/5}$ increasing from 60s to 120s, the particle number per unit area increases, the mean particle size decreases unexpectedly (see Fig.6a and 5a) . It can also be noted that after cooling down from 1350°C at a $t_{8/5}$ of 120s, the mean particle size decreases and the particle number per unit area increases, see Fig. 6a and Fig. 3b; the Nb weight fraction increases and ranges from 0.18 to 0.80. These all suggest that not only heterogenous but also homogenous reprecipitation of Nb-rich partials occur when cooling at a $t_{8/5}$ of 120s. The homogenously reprecipitated particles have a spherical shape, see Fig 6c.

Conclusions

All the particles in the Ti-Nb microalloyed steel contains Nb and Ti, and the Nb weight fraction of analyzed particles ranged from 0.22 to 0.85. The large particles greater than 50nm tend to be rich in Ti (Nb/(Nb+Ti) <0.3), and large particles greater than 50nm tend to be rich in Ti (Nb/(Nb+Ti) <0.3). During the heating stage of the weld thermal cycle, the small particles which were rich in Nb disappeared through complete dissolution and the large particles survived the weld thermal cycle with Nb weight fraction decreased. With a high cooling rate ($t_{8/5}$ no greater than 60s), only heterogeneous re-precipitation occurred during cooling. With a low cooling rate ($t_{8/5}$ = 120s), homogenous re-precipitation also occurred, producing a large number of small Nb-rich particles during cooling.

Acknowledgements

This work is supported by Shandong Natural Science Foundation under contract No. ZR2010EZ005.

References

[1] K.Seifrt and S,Yao, HAZ fracture toughness properties of Ti-microalloyed offshore steel, 11th Int.Conf.OMAE, 1992. Calgary. Alberta, Canada.

[2] S.C.Wang. The effect of trace-Ti content on the solubility of Nb and the consequent properties of Nb-bearing steels, Metall.Trans., 1993; 24A (9): 2127-2130.

[3] M Nakanishi and Yu-ichi komizo. Improvement of welded HAZ toughness by dispersion with nitride particles and oxide particles. J. Jpn. Weld Soc., 1993，52 (2): 117~131.

[4] S Muzuki. Solution of TiN during synthetic weld thermal cycling and HAZ toughness in low carbon steels. Trans.JWS, 1997, 18 (2): 58~68.

[5] J.Stird and K.E. Easterling. On the chemistry and stability of complex carbides and nitride in microalloyed steels. Acta mtall. 1985, 33(11):2057-2074.

[6] H Adrian, F B Pickering. Effect of Ti addition on austenite grain growth kinetics of medium carbon V-Nb steels containing 0.008~0.18%N. Material Science and technology, 1991, 7 (2): 176~182.

Advanced Materials Research Vol. 936 (2014) pp 1791-1795
© (2014) Trans Tech Publications, Switzerland
doi:10.4028/www.scientific.net/AMR.936.1791

Study on the Technology and Defects in Low-pressure Semi-solid Die Casting of Aluminum Alloy Wheel Hub

Rui Wang[1, a], Hui Zhu[2, b], Heng-hua Zhang[3, c *]

[1, 2, 3] School of Materials Science and Engineering, Shanghai University, Shanghai 200072, China

[a]wr.0@163.com, [b]zhuhui0718@163.com, [c *]hhzhang@shu.edu.cn

Keywords: Aluminum alloys, Semi-solid, Low-pressure die casting (LPDC), Wheel, Casting defect

Abstract. Technology and defect in the low-pressure semi-solid die casting of aluminum wheel hub under different process has been studied. The simulation software ADSTEFAN 2012 is used to analyze the solidification in different die temperature. Stereomicroscope, digital camera and optical microscope (OM) are used to study defect in the casting. The result shows that the low slurry temperature (606℃) will result in higher viscosity, and the low preheated die temperature will increase the cooling rate so that shrinkage is formed in the isolate solidification area. In the technology of casting wheels, the optimum temperature of the slurry is 614℃, preheated temperature of die is 400℃.

Introduction

With the increasing attention on the environmental consequences of the burning of fossil fuels and the expected increase in the oil price, there is a growing interest in the automobile lightweight. The lightweight of automotive can be effectively achieved by using aluminum wheels [1-2].Semi-solid metal (SSM) forming has been recognized as a technique offering several potential advantages over casting and solid state forming, such as producing aluminum wheels. On one hand, contrasting with casting processes, an enhanced die life, lower shrinkage and a reduction in macroscopic and microscopic porosities are gained through SSM. On the other hand, the lower forming pressure and higher deformation homogeneity are some advantages of the SSM over traditional solid state forming procedures such as rolling and extrusion [3-6]. Generally, the main technology for casting aluminum alloy wheels is the low-pressure die casting (LPDC), which guarantees to obtain a good compromise between high mechanical properties, high production, cost-effectiveness and design demand. In the process of LPDC, filling and solidification are under a pressure which uses compressed air. Due to the fluidity of slurry will be hindered by the increased viscosity in semi-solid condition, the pressure of low-pressure semi-solid die casting is higher than LPDC [7].In order to aid the optimizing technology of filling system, computer simulation technique is introduced to predict forming process and to reduce defect during trial manufacture of automotive wheels by using low-pressure semi-solid die casting process [8-9].

Experimental Procedure

Materials and Procedures. Commercial aluminum A356 alloy (Al, 7.48 wt.% Si, 0.384 wt.% Mg, 0.132 wt.% Ti, 0.148 wt.% Fe, 0.02 wt.% Cu, 0.0067 wt.% Mn) was used. The alloy liquidus and solidus temperatures are 615℃ and 555℃, respectively [10].

Firstly, A356 alloy was melted in an electric-induction furnace setup at 720±5℃.The melt was refined with HGJ-1 and modified with HGSrB. AlTi5B1 rod type grain refiner was also added to the molten metal. Secondly, the molten metal is transferred to a crucible for low-pressure semi-solid die casting of aluminum alloy wheels. Then, the preheated die is assembled on the forming equipment. Thirdly, open the electromagnetic stirring when the temperature of molten aluminum has been decreased to semi-solid state. When slurry reaches the casting temperature, switch on the pressurized air valve. Open the die and remove the wheels after the process of filling and pressure maintaining.

Three wheels are obtained after casting. Wheel-1 is cast at 606℃ and die is preheated to 500℃, Wheel-2 is cast at 614℃ and die is preheated to 400 ℃, Wheel-3 is cast at 614℃ and die is preheated to 300℃.

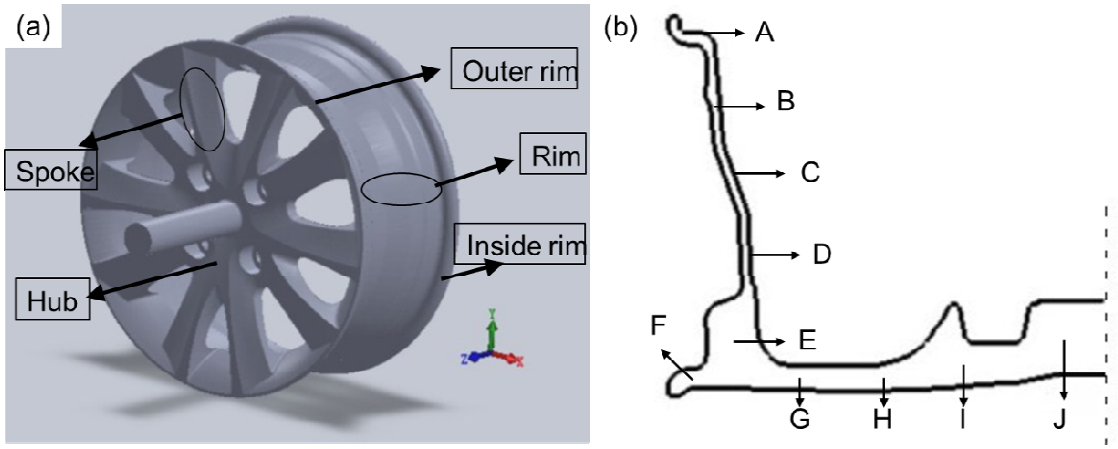


Fig. 1 (a) 3D models of automotive wheel hub, (b) wheels' section number along the XZ plane.

Casting Simulation. The ADSTEFAN2012 software which is based on the finite element method (FEM) published by Hitachi was used for study the solidification process of low-pressure semi-solid die casting. Numerical simulating parameters is that casting temperature at 614℃ and die heated temperature at 300℃and 500℃.

Analysis of Defect and Microstructure. Defect in the specimen drawn from the cross-section of spoke and rim (the position of B, C, D, G, H, I in Fig. 1(b)) region of the wheels (Fig. 1(a)) were studied with stereomicroscope and digital camera. A ruler is used as a measure of the proportion of each scale 1mm. In order to observing the section, three wheels were cut along the XZ plane in rim and XY plane in spoke (Fig. 1(a)). The microstructure and defect of wheels were evaluated by OM, which the metallographic samples come from the position A to J in the wheels.

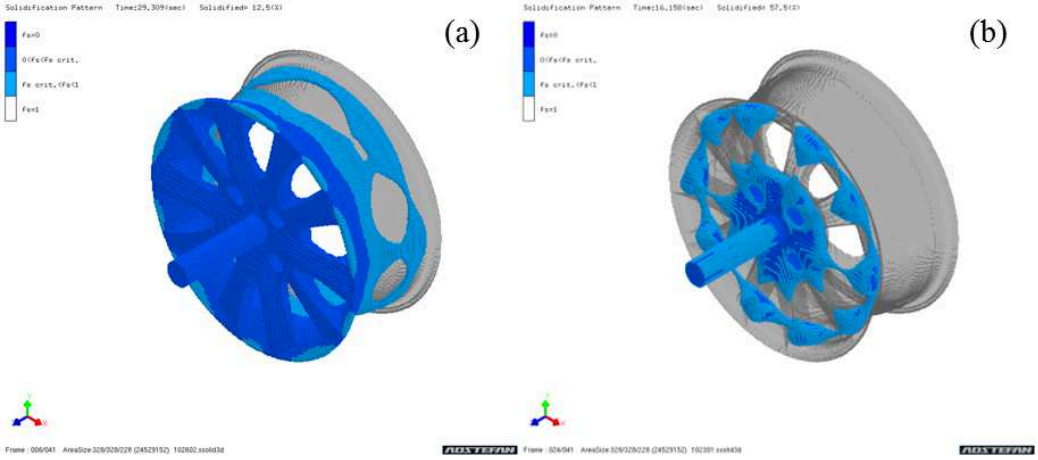


Fig. 2 Simulation results of wheel forming at filling temperature 614℃, blue represent liquid and gray is solid, (a) die preheating temperature 500℃, fs = 12.5% (b) die preheating temperature 300℃, fs = 57.5%

Results and Discussion

Simulation Results. It is easy to find shrinkage and pore at rim and spoke because of rim is thin and large, while spoke is thick and narrow. Therefore, the results of simulation select the solid-phase fraction (fs) of 12.5% to reveal the rim in Fig. 2(a), and fs of 57.5% to reveal the spoke in Fig. 2(b). Isolated solidification can be found in rim and spoke, this is called non-directional solidification. The existing of non-directional solidification result in mass shrinkage and cold shut. The purpose of this study is to decrease the extent of non-directional solidification, so as to reduce the defect.

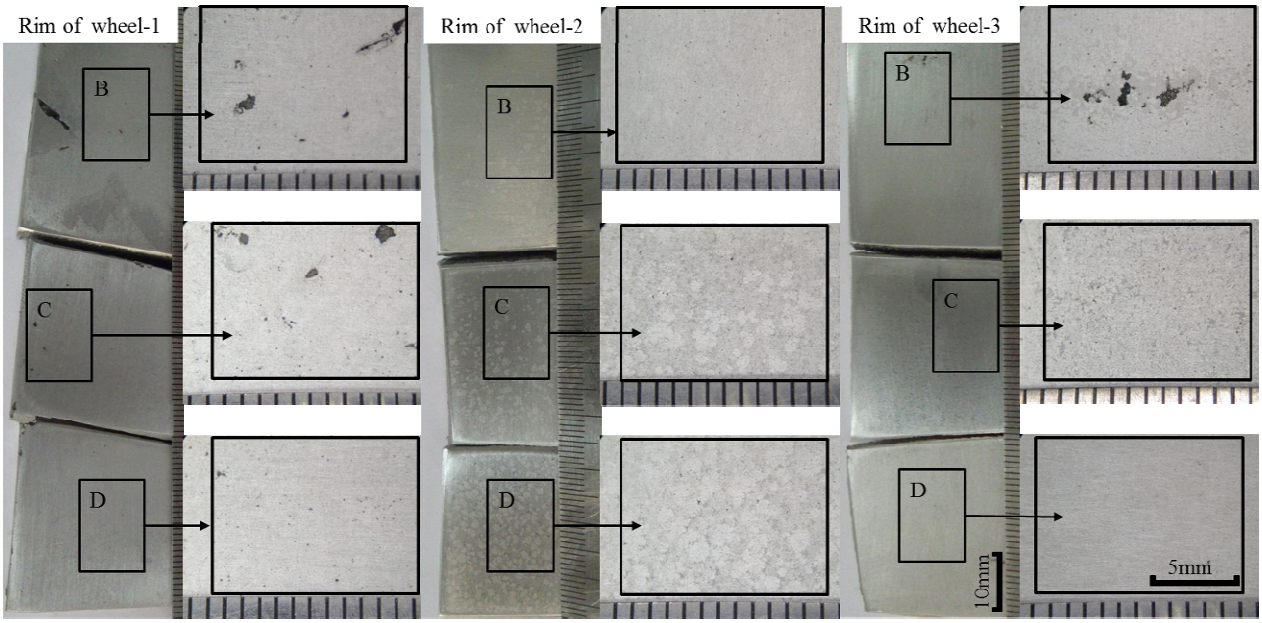


Fig. 3 Macroscopic defect of rim in wheel-1, 2, 3

Solidification Defect in Rim. Three wheels' rim is divided into three regions, respectively, B, C and D (Fig. 1(b)), and macroscopic defect situation is shown in figure 3. As shown in figure 3, there is obvious difference among the wheel-1, 2 and 3, wheel-1 has a maximum of defects, wheel-2 is fewer defects, and wheel-3 is between the two. And the macroscopic figures also show that there is much defect in the direction close to the inside rim (position B), and less defect near to the outer rim (position D), which is corresponding to simulation result (Fig. 2(a)). Solidification that start from position A and C and end with position B makes position B have more defect, on the other hand, position D has a directional solidification started from position D to G makes position D have less defect (Fig. 1(b)). Above all, wheel-1 with too much defect is because of a low slurry temperature (606℃), which results higher alloy viscosity. A low die temperature (300℃) of wheel-3 increases the cooling rate so that shrinkage is formed in the isolate solidification area.

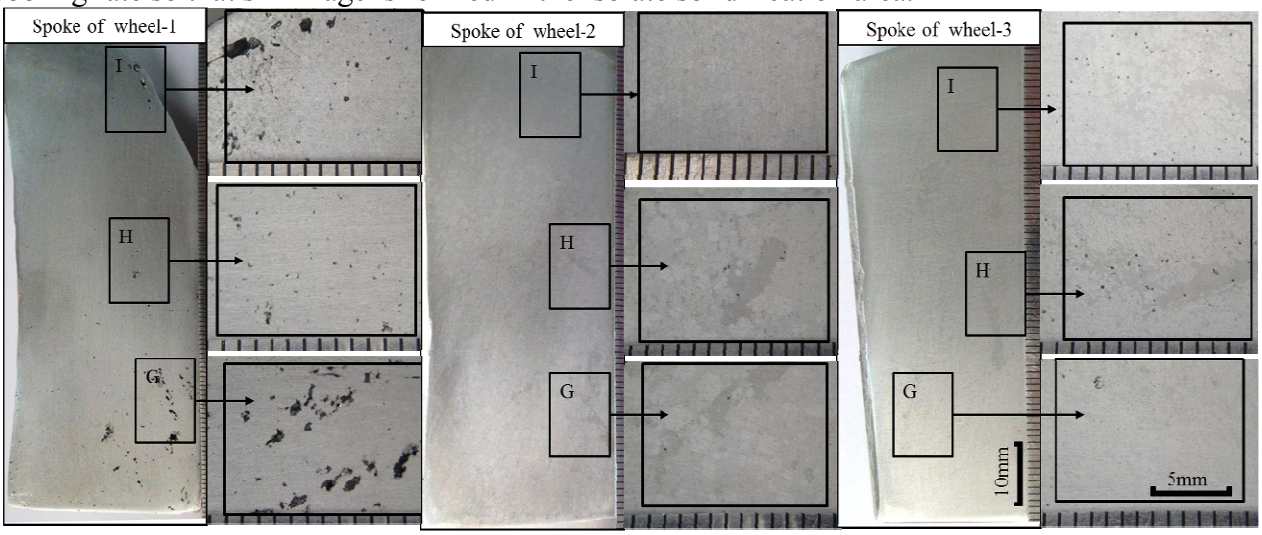


Fig. 4 Macroscopic defect of spoke in wheel-1, 2, 3

Solidification Defect in Spoke. Three wheels' spoke is divided into three regions, respectively, G, H and I (Fig. 1(b)), and macroscopic defect situation is shown in Fig. 4. It is clear to know in wheel-1 that the defect is mainly located in position G and I. In wheel-2 and wheel-3, defect is mainly loceted in position H. A non-directional solidification which start from position H and F and end with position G and J makes G and J become the final solidification areas which can generate defect easily. The defect area is moved from G to H with the die temperature declined from 500℃ (wheel-1) to

300℃ (wheel-3). The die temperature of wheel-3 is 300℃, which results in the fact that the final solidification region can not obtain continuous. Wheel-2 has fewer defect in the three wheels, and it is significant to continue research.

Microstructural Investigations. Wheel-2 shows the minimal defect combine with previous analysis. The microstructure of wheel-2 in different position are very different as illustrated in Fig. 5, where the white is primary α-Al, gray is eutectic silicon. As can be seen from Fig. 5, the direction of the wheel filling is from hub to inside rim (from position J to A), and solidified direction is the opposite order (from position A to J).

The first solidified position of inside rim and rim has a smaller grain size (Fig. 5 A, B, C), but there still exists little dendrites, which is due to higher cooling rate. As the solidification progresses, primary α-Al start to transfer from dendrites to rosette-like because of heat dissipation slows down (Fig. 5 D, E, F). The large and round is shrinkage, small and long is porosity in the gray area of eutectic silicon, which is consistent with previous analysis (Fig. 5 D, G).

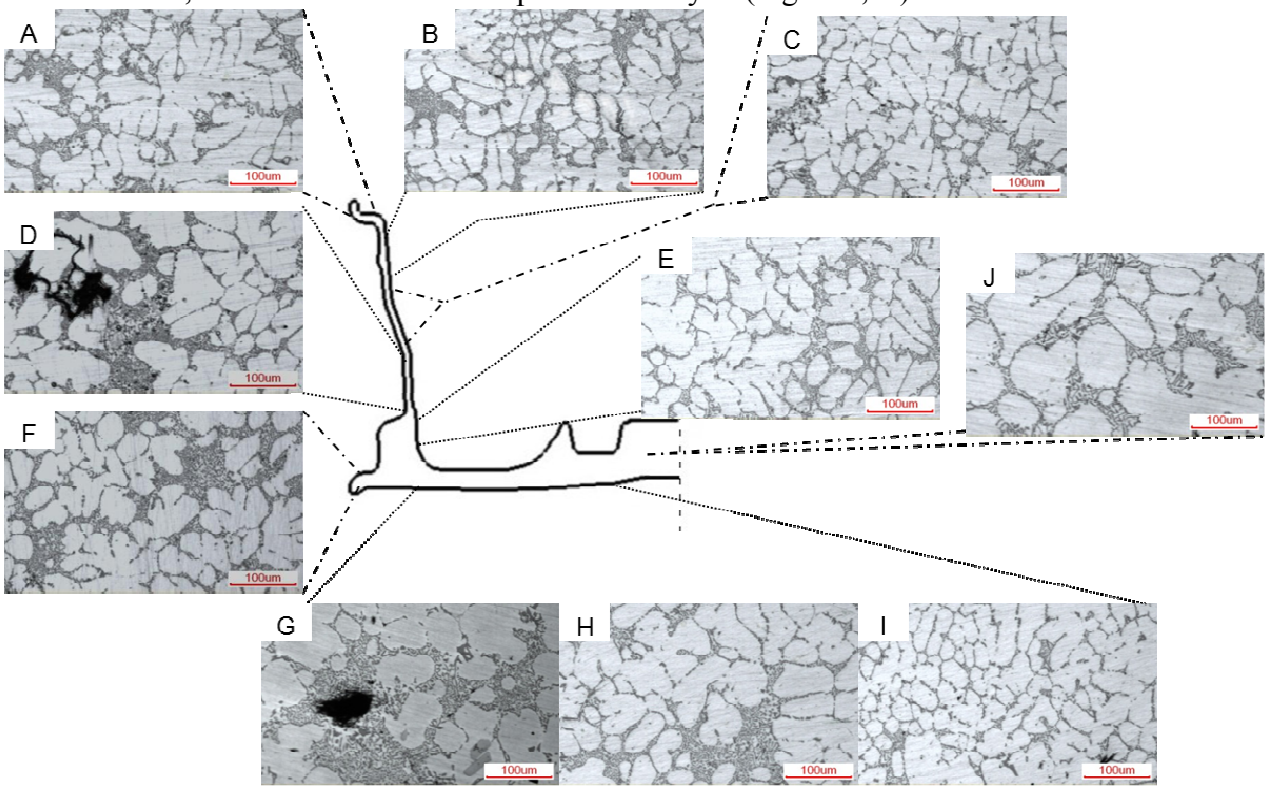


Fig. 5 Microstructure of wheel-2 located in different positions

It can be observed that primary α-Al grains start to become spherical and large slowly in the positions G, H, I, J of Fig. 5). But the grain size has become larger than rim and inside rim because of spoke and hub is massive and thermal dissipation is slow. Therefore, to prevent grain growth need to consider the factor of die design, cooling and filling process.

Summary

The technology and defect of low-pressure semi-solid die casting aluminum wheels are studied. From the simulation results, defect was predicted during the forming process because of the non-directional solidification often occurs at rim and spoken. Wheel-1 with too much defect is because of the slurry temperature is low (606℃). For another, a low die preheated temperature (300℃) will increase the cooling rate so that shrinkage is formed in the isolate solidification area. The factor of casting wheels is die structure, cooling and filling process. The results showed that optimum temperature of the slurry is 614℃, preheated temperature of die is 400℃ to decrease the casting defect.

References

[1] Zhang B, Maijer D M, Cockcroft S L. Development of a 3-D thermal model of the low-pressure die-cast (LPDC) process of A356 aluminum alloy wheels[J]. Materials Science and Engineering: A, 2007, 464(1): 295-305.

[2] Long Wei, Zhou Disheng, Zhang Henghua, et al. Mechanical properties and simulation to the forging process of 6061 aluminum alloy wheel hub[J]. Shanghai Metals, 2012, 34(3): 29-32. (Chinese)

[3] Guo H M, Yang X J, Wang J X. Pressurized solidification of semi-solid aluminum die casting alloy A356[J]. Journal of Alloys and Compounds, 2009, 485(1): 812-816.

[4] Flemings M C. Behavior of metal alloys in the semisolid state[J]. Metallurgical Transactions B, 1991, 22(3): 269-293.

[5] Hassas-Irani S B, Zarei-Hanzaki A, Bazaz B, et al. Microstructure evolution and semi-solid deformation behavior of an A356 aluminum alloy processed by strain induced melt activated method[J]. Materials & Design, 2013, 46: 579-587.

[6] Yang Y T, Yin X L, Sun B L, et al. Reverse design of microstructure and application effectiveness for semi-solid processing of aluminum alloy[J]. Transactions of Nonferrous Metals Society of China, 2010, 20: s973-s980.

[7] Merlin M, Timelli G, Bonollo F, et al. Impact behaviour of A356 alloy for low-pressure die casting automotive wheels[J]. Journal of materials processing technology, 2009, 209(2): 1060-1073.

[8] Yang Y T, Zhang H H, Shao G J. Application of computer simulation in developing automotive parts of Al alloy by using semi-solid die cast process[J]. Solid State Phenomena, 2006, 116: 630-634.

[9] Yang Y T, WANG Jian-fu, Zhang H H, et al. Mensuration and simulation of mold filling process in semi-solid die-cast of aluminum alloy[J]. Transactions of Nonferrous Metals Society of China, 2006, 16: s1402-s1406.

[10] Mao W M, Zheng Q, Zhu D P. Rheo-squeeze casting of semi-solid A356 aluminum alloy slurry[J]. Transactions of Nonferrous Metals Society of China, 2010, 20(9): 1769-1773.

Advanced Materials Research Vol. 936 (2014) pp 1796-1800
© (2014) Trans Tech Publications, Switzerland
doi:10.4028/www.scientific.net/AMR.936.1796

Influence of Heat-treatment on Properties, Microstructure and Corrosion Resistant of Zirconium Sheet

DANG Peng [a], ZHANG Xiao Wei, WANG Yun, ZHANG Qing, LI Chang Liang

Western titanium technologies Co., Ltd, Xi'an 710201, China

[a] dpengg@aliyun.com,

Keywords: R60702; Vacuum annealing; Microstructure; Mechanical properties; Corrosion resistant.

Abstract: The influence of annealing temperature on the microstructure, mechanical properties and corrosion resistant of cold rolling zirconium sheet were studied in the manuscript. The experimental results shown that the tensile strength and yield strength of zirconium sheet were decreased and the elongationwas raised with the raising of annealing temperature from 500 ℃ to 580 ℃. The recrystallization are not happened in zirconium sheet at the annealing temperature of 500 ℃. Zirconium sheet complete recrystallized and the strength and elongation get a well match at the annealing temperature of 540℃. Zirconium sheet also complete recrystallized at the annealing temperature of 580℃ but the crystalline grain has the tendency of growing. The annealing temperature has no effect on the corrosion resistant of zirconium sheet.

Introduction

Zirconium and zirconium alloys are a kind of excellent corrosion resistance of rare metal and an important structural materials in the chemical industry. Zirconium and zirconium alloys show impressive corrosion resistance in harsh corrosive medium such as most of the organic acid, inorganic acid, strong base and a number of the molten salt. Greatly improve the life and reliability of the chemical equipment. In recent years, zirconium and zirconium alloys increasingly widely applied in civil chemical equipment manufacturing field, such as heat exchanger, scrubbing tower, reactor, pump and corrosive medium pipeline and so on[1-4].

However, there are some disadvantage of R60702 zirconium sheet such as instability of mechanical performance, and inconformity of corrosion resisitance, which will limited its application. Thus, the influence of annealing temperature on the microstructure, mechanical properties and corrosion resistant of cold rolling zirconium sheet were studied in the manuscript. The better heat treatment regime is determined and provide a reference for the industrial production of zirconium sheet.

Materials and Methods

The R60702 slab size is 100×1000×1200mm in this experiment. The slab chemical component as shown in table 1. The slab was heated to 650~750℃, lasting 2~2.5 h, and then its thickness was decreased to 30 mm by the first hot rolling. Subsequently, the second heating temperature was 600~700℃, holding 40~50min, and the thickness was reduced to 4.5 mm by the second hot rolling. Finally, the treated slab was dealed with cold rollding, and its thickness was changed to 3mm. After stress relief annealing and surface treatment. The zirconium sheet was disposed by vacuum annealing treatment using three different heat treatment:

Sample1: 500℃, 3h, furnace cooling;

Sample2: 540℃, 3h, furnace cooling;

Sample3: 580℃, 3h, furnace cooling.

The samples were processed 3×20×30mm which was deal with at different heat treatment. Samples successively were burnished with 200 to 800 mesh water sand paper, then were degreased with acetone, then were chemical polished in HF, HNO3 and water volume is 1:3:9 6 chemical

polishing solution, and then were rinsed with water more than 3 times, the last were rinsed with deionized water. The corrosion test were carried out after the samples drying. the samples were put in boiling 70% sulfuric acid solution, for 72 h. The operational approach carried standard GB/T4334-2008, process B. The sample weight before and after corrosion are measured using high precision electronic balance (0.0001 g). Zirconium sheet room temperature mechanical properties are tested by computer control electro-hydraulic servo universal testing machine, Zirconium plate microstructure observe by around OLYMPUS PMG3 metallographic microscope.

Table 1. Chemical compositions of slab

Furnace No.	Mass fraction/%						
	bases		impurities（≤）				
R60702	Zr+Hf	Hf	Fe+Cr	C	N	H	O
1	99.4	2	0.038	0.02	0.008	0.001	0.15
ASTM B551	≥99.2	≤4.5	0.2	0.05	0.025	0.005	0.16

Experimental Results and Analysis

The influence of annealing temperature on the mechanical properties

The room temperature mechanical of zirconium sheet properties under different annealing temperature were shown in table 2. The results shown that the tensile strength and yield strength of zirconium sheet were decreased and the elongation was raised with the raising of annealing temperature from 500 ℃ to 580 ℃. This can be explained by that the atom can be obtained more enough activity with a higher annealing temperature in the same annealing time, which make the density of point defect and dialocation decline and the internal stress gradual eliminate. The tensile strength and yield strength of zirconium sheet were decreased slightly, but the elongation has a little increased at the annealing temperature of 500 ℃. However, because the sheet was at recovery stage, and its internal stress was taken away partly at this condition, the sheet also had a higher strength and lower elongation. When the annealing temperature was raised to 540 ℃, the tensile strength and yield strength of zirconium sheet were decreased signally, while the elongation has a complete crosscurrent. At this moment, the internal stress of sample was eliminated completely, and the strength was matched with its elongation well. When the annealing temperature was 580 ℃, the strength of zirconium sheet went on declining, but the elongation only had a little change.

Table 2. Room-temperature mechanical properties of zirconium sheet annealed at various temperature

Temperature /℃	Direction	σb/MPa	σ0.2/MPa	A/%
Cold-rolled state	C	587	510	15
Cold-rolled state	L	590	517	14
500	C	565	480	17
500	L	575	505	16
540	C	467	380	28
540	L	470	372	30
580	C	420	330	27
580	L	435	340	31

C: Cross; L: Longation.

The influence of annealing temperature on the microstructure

Figure 1 was given the microstructure of zirconium sheet annealed at different temperature. From figure 1(a) and (b), it can be see that the sample does not recrystallization at the annealing temperature of 500 ℃, and both the across organization and vertical organization were processing organization. When the annealing temperature raised from 500 ℃ to 540℃, the perfect recrystallization was grown on zirconium sheet. From figure 1(c) and 1(d), it can be obtained that the grain grown up as novel and orthoscopic equiaxed grain perfectly, and the average size of grain was about 10μm. It can be

explained by that the transmutative metal transformed to a stable state spontaneously with a higher annealing temperature, deu to a higher activity. And then recrystallization core is generated by the driving of deformation energy, because that the grain boundary or subboundary are combined together. The recrystallization core is growing bigger and bigger by the driver. Until primary deformed microstructure disappear completely, the microstructure after recrystallized process present equiaxed grain, according to a lower interfacial energy. The strength of recrystallized zirconium sheet was decreased significantly, on the contrary, its plasticity was increase rapidly, which is in accordance with the teast result of mechanical property. When the annealing temperture added to 580℃, the higher temperature resulted in that the average diameter of recrystallized grain was raised up to 20μm,which can be seen clearly in figure 1(e) and (f). In this situation, the reasons of the grain growth phenomenon were that large grain swallowed small grain and the total system free energy declined after grain boundary migration.

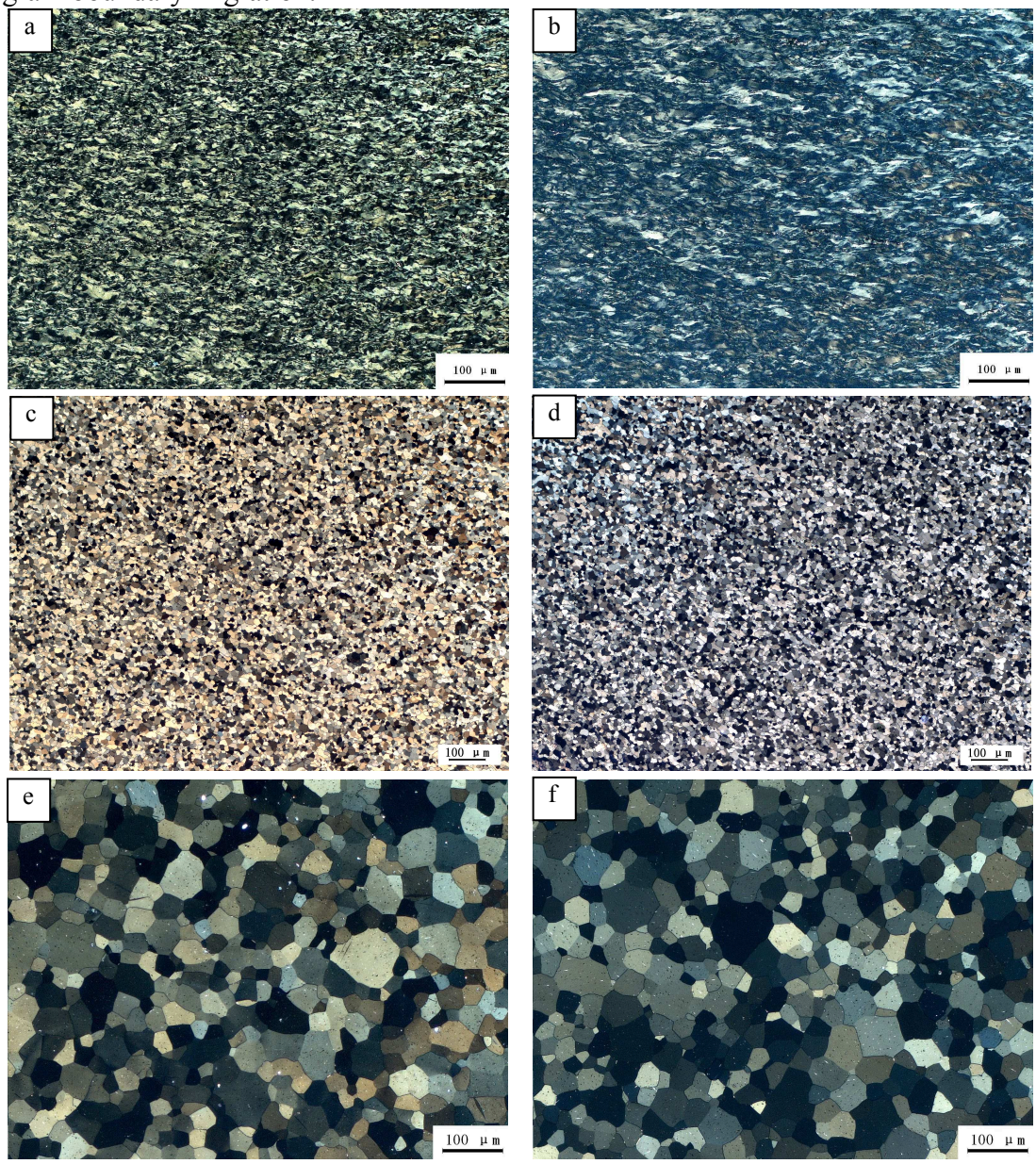


Figure 1. Microstructure of zirconium sheet annealed at various temperature
a: sample1，C，b: sample1，L，c: sample2，C
d: sample2，L，e: sample3，C，f: sample3，L

The corrosion rate of zirconium sheets annealed with different temperatures were listed in table 3. The data in table 3 shown that the corrosion rate of samples changed from 0.19 mm/year to 0.22

mm/year, which is consistent with report [5,6]. This can be explained that the superficial zirconium was oxidized as ZrO_2 in air, which because that zirconium is a reactive metal as many refractory metals. ZrO_2 film is a inert film, which hardly has chemical reaction with O or N in air. Thus zirconium had a perfectly stability. Additionally, ZrO_2 film also can be generated in strong deoxidizing medium. Figure 2 was given to indicate that the corrosion velocity of zirconium R60702 in sulfuric acid media. From this figure, it can be obtained that the zirconium can retain a low corrosion velocity in less than 70% of sulfuric acid solution, and then its corrosion velocity increased with a higher concentration of sulfuric acid solution. When the concentration of sulfuric acid solution was more than 80%, the corrosion velocity is large. The reason was that zirconium sheet was oxidized as ZrS in more than 80% sulfuric acid solution. Thus, it can be said that the corrosion resistance of zirconium closely related to the dense passive film on the surface of zirconium sheet, but not internal microstructure.

Table 3. The corrosion rate of zirconium sheets annealed at various temperature

Temperature /℃	corrosion rate/year
500	0.19mm
540	0.21mm
580	0.22mm

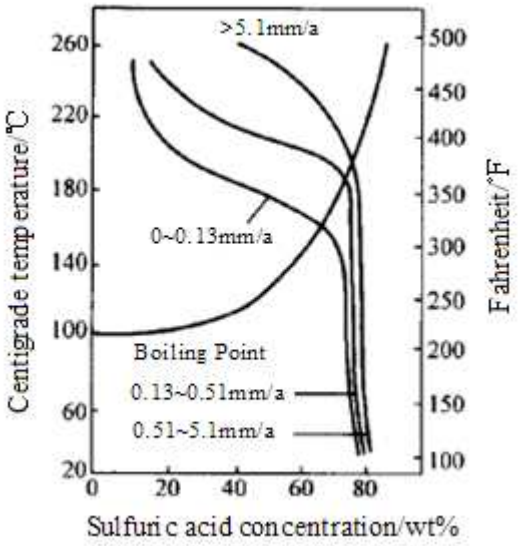


Figure 2. The corrosion rate of zirconium R60702 in sulfuric acid

Summary

The relationship of annealing temperature and the microstructure, mechanical properties and corrosion resistant of cold rolling zirconium sheet were investigated in the manuscript. From the experiment result, it can be come to the conclusion that the tensile strength and yield strength were reduced when the annealing temperature raised from 500 ℃ to 580℃, but elongation was increased. The metallograph shown that recrystallization was not appeared at the annealing temperature of 500 ℃. However, the perfect recrystallization was obtained at 540 ℃, meanwhile, the strength and plasticity cooperated very well. When the annealing temperature was up to 580 ℃, the recrystallization was also acquired, but the difference is that the grain was grown up. Lastly, corrosion experiment indicated that the annealing temperature had no effect on corrosion resistance of zirconium.

References

[1] B.Y. Huang, C.G. Li, L.K. Shi, G.Zh. Qiu, and T. Y. Zuo, China Materials Engineering Canon(Volume Five), Chemical Industry Press, Bei Jing, 2005.

[2] X.J. Li, F. Xia, Zh.G. Wu, J.N.Feng, and F. Chen, Application of industrial grade and corrosion resistance of zirconium in acetic acid industry, Metal World. 6(2009)100-104.

[3] X.J. Li,The performance and application of industrial zirconium products, China Titanium Industry. 4(2011)3-6.

[4] Zh.H.Peng, Rare metal materials processing technology, Central South University press, Chang Sha, 2006.

[5] G.L. Song, The effect of zirconium grain refinement on the corrosion behaviour of magnesium-rare earth alloy MEZ, Journal of Light Metals 2 (2002), 1-16.

[6] T.L. Yau, Corrosion of Zirconium and its Alloys, Corrosion and Degradation of Engineering Materials, 2(2010)2094 – 2134.

Advanced Materials Research Vol. 936 (2014) pp 1801-1808
© (2014) Trans Tech Publications, Switzerland
doi:10.4028/www.scientific.net/AMR.936.1801

Multi Response Optimization of Carbon- Carbon(c/c) Drilling Parameters by Using Grey Theory Technique

K.V.Krishnasastry[1,a*], V.Seshagirirao[2,b]

[1]Sathyabama University &Dept.of Mech.Engg, AVIT, Chennai, India.

[2]Department of Mech.Engg. St. Joseph's college of engineering, Chennai, India.

[a]kvkrishnasastry@gmail.com, [b]raosvaddi@hotmail.com,

Keywords: Orthogonal Array, Taguchi method, Carbon-Carbon composites, Design of experiments, GRA, CFRC

Abstract: The objective of this paper is to determine the optimum values of drilling parameters of carbon fibre reinforced carbon (CFRC) composite material with the help of an experimental investigation, which includes the application of unique Grey theory method. The growing application of CFRC composites, which are popularly known as 'carbon-carbon' composites in Aerospace, Automobile, Defence and other advanced industries has prompted research studies to develop drilling technology of these special materials. The present work demonstrates the optimization process of multiple responses.The optimum values of drilling characteristics of these composites are calculated by the application of Taguchi method in combination with Grey Relational Analysis technique. The drilling experiments were carried with a High speed steel tool on a plate of carbon-carbon composite material on a CNC Drilling vertical Machining centre.

Introduction

Drilling is probably the most frequently used metal cutting process operation and it is one of the major complicated machining processes. This process further becomes more complicated, when the work piece is a composite material. But much attention was not given on the drilling process of the most advanced and promising engineering material called 'carbon fiber reinforced carbon (CFRC)' composite. The use of CFRC composites in Aerospace, Automobile, Defence, Bio and other related industries has grown recently, due to their low weight and high strength properties. Drilling of Carbon Fibre Reinforced Carbon composites may generate several kinds of damage, which can lead to the degradation of quality of holes. Hence care should be taken in selecting the parameters of drilling process. Hence an experimental investigation of drilling of Carbon-Carbon composites has been considered for study.

CFRC composites-Fabrication and uses

CFRC or C-C composites are the materials, in which Carbon/Graphite fibres are reinforced in a Carbon Matrix. The Carbon fibre preform, which is woven, is impregnated under heat and pressure with pitch. This is followed by pyrolysis of the pitch to obtain a carbonaceous matrix. .This cycle may be repeated to obtain the desired densification. This is also obtained by chemical vapour deposition method from a gaseous phase [1]. CFRC seems to be a promising material for use in orthopedic surgery due to its good biocompatibility and low stiffness. The replacement of knee and hip joints with metallic prosthetic devices has provided mobility to many elderly patients suffering from bone diseases. Heart valves have been produced with isotropic pyrolitic carbon and they have been implanted in more than two lakh patients [2].Most notable applications of this special material are Heat shields for re entry vehicles, hot pressing dies, nozzles, and nose cones of intercontinental ballistic missiles and leading edges of the space shuttles. Carbon/Carbon brakes are used in subsonic aircrafts, supersonic aircrafts and racing cars. Tooling, Racing Helmets, Race car seats, sports equipment etc., are built entirely from carbon-carbon composites. Agni missile, a reentry structure has used this advanced material for its production. CVRDE has developed high performance Carbon fibre reinforced carbon Brake discs for Main Brake assembly of MBT Arjun [3.4,5].

Taguchi method and Grey theory method

Design of Experiment is a powerful statistical tool suggested by Mr. Taguchi is used to design and conduct the experiments with minimum resources. Orthogonal Array is a statistical method of defining parameters that convert test areas into factors and levels. In this work, an L_{27} orthogonal array table was chosen for the experiments based on Taguchi's quality design technique as shown in fig.1 [6].

Experiment	P1	P2	P3	P4	P5	P6	P7	P8	P9	P10	P11	P12	P13
1	1	1	1	1	1	1	1	1	1	1	1	1	1
2	1	1	1	1	2	2	2	2	2	2	2	2	2
3	1	1	1	1	3	3	3	3	3	3	3	3	3
4	1	2	2	2	1	1	1	2	2	2	3	3	3
5	1	2	2	2	2	2	2	3	3	3	1	1	1
6	1	2	2	2	3	3	3	1	1	1	2	2	2
7	1	3	3	3	1	1	1	3	3	3	2	2	2
8	1	3	3	3	2	2	2	1	1	1	3	3	3
9	1	3	3	3	3	3	3	2	2	2	1	1	1
10	2	1	2	3	1	2	3	1	2	3	1	2	3
11	2	1	2	3	2	3	1	2	3	1	2	3	1
12	2	1	2	3	3	1	2	3	1	2	3	1	2
13	2	2	3	1	1	2	3	2	3	1	3	1	2
14	2	2	3	1	2	3	1	3	1	2	1	2	3
15	2	2	3	1	3	1	2	1	2	3	2	3	1
16	2	3	1	2	1	2	3	3	1	2	2	3	1
17	2	3	1	2	2	3	1	1	2	3	3	1	2
18	2	3	1	2	3	1	2	2	3	1	1	2	3
19	3	1	3	2	1	3	2	1	3	2	1	3	2
20	3	1	3	2	2	1	3	2	1	3	2	1	3
21	3	1	3	2	3	2	1	3	2	1	3	2	1
22	3	2	1	3	1	3	2	2	1	3	3	2	1
23	3	2	1	3	2	1	3	3	2	1	1	3	2
24	3	2	1	3	3	2	1	1	3	2	2	1	3
25	3	3	2	1	1	3	2	3	2	1	2	1	3
26	3	3	2	1	2	1	3	1	3	2	3	2	1
27	3	3	2	1	3	2	1	2	1	3	1	3	2

Fig. 1 Orthogonal array (l_{27})

Grey theory, which was introduced by Mr. Deng, provides an efficient solution to uncertain and multi-input problems. By this method, the experimental results are first normalized and then the grey relational coefficients are calculated from data. Then, the grey relational grade was computed by averaging the grey relational coefficients corresponding to each response parameter. The overall evaluation of the multiple responses is based on the grey relational grade. Optimization of a factor is the level with the highest grey relational grade [7].

Experimental Investigation

Drill bit point Angle, Spindle speed and Feed rate were chosen as the controlling drilling parameters and each parameter was designed to have three levels, denoted by 1, 2, and 3 as shown in Table 1.

TABLE 1: EXPERIMENTAL PROCESS PARAMETERS AND THEIR LEVELS

Drilling Parameters	Symbol	Unit	Level (1)	Level (2)	Level (3)
Point Angle	A	degree	100	118	135
Spindle Speed	N	r.p.m	1000	2000	3000
Feed Rate	F	mm/rev	100	300	500

The experiments were carried out on a computer numerical control Vertical Machining centre (VMC100). A Tin coated solid carbide drill bit of 10mm diameter is used for drilling of carbon-carbon composite material plate. The experimental setup is shown in Fig.2.

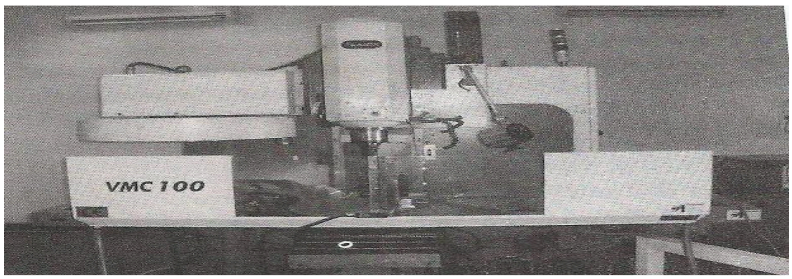


Fig.2 CNC vertical machining centre

The drilling process performance is evaluated by five following response parameters.

Thrust Force

It is the axial force required to drill the work material and is measured in Newtons. The values are obtained by observing through Kistler make piezoelectric dynamometer . Data acquisition and analysis software, Dynoware is used to plot the force signals with respect to time. The typical plot observed in experimental study is shown in Fig.3.

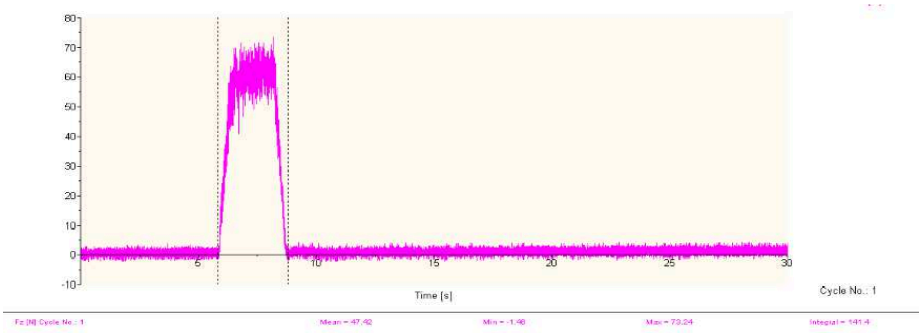


Fig.3 A typical thrust force observed from Kistler Dynamometer

Torque

It is the twisting moment required to drill the work piece and is measured in N-m. The Torque values are obtained by observing through Kistler piezoelectric dynamometer by means of sensors. Dynoware is used to plot the torque signals with respect to time. The typical plot observed in experimental study is shown in Fig. 4.

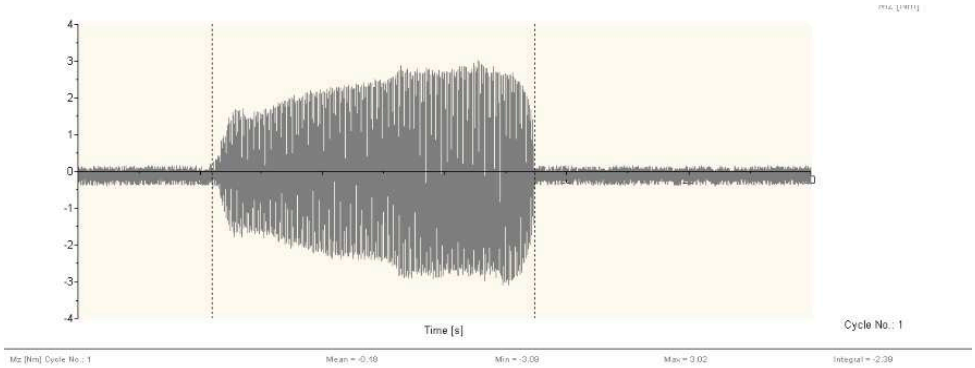


Fig.4 A typical torque observed from Kistler Dynamometer

Surface Roughness {R_a}

It is the roughness of the walls of the drilled hole and is measured in microns. It is measured by using Surface Roughness Tester**.** The setup is shown in fig.5**.** The arithmetic mean average roughness (R_a) is used to indicate the roughness of a drilled surface.

Delamination Factor {D_f}

It is the degree of Delamination and Delamination is a mode of failure in composite materials. It is the separation of layers in a laminate. The most important phases during drilling composite laminates are close to the entry and exit where extensive damage in terms of delamination occur due to peel-up and push-out effects respectively [8].The drilled holes are photographed by using a digital camera and it is measured with the help of Corel Draw image software. The values of diameters of drilled holes are magnified by 5 times and the delamination factor is calculated by using the ratio D_{max}/D.



Fig.5 Surface roughness tester

The experimental values of all five response parameters are given in Table.2.

TABLE 2: EXPERIMENTAL VALUES OF T.F, TORQUE, RA AND DELAMINATION FACTORS (ENTRY &EXIT)

S.No.	A [^{0}]	N[rpm]	F [mm/min]	T F [N]	M [N-m]	R_a [μ m]	Entry-D_f	Exit-D_f
1	100	1000	100	20.48	3.65	7.59	1.013508	1.013228
2	100	1000	300	22.25	2.83	4.42	1.01951	1.033258
3	100	1000	500	33.77	4.15	3.56	1.064578	1.01753
4	100	2000	100	16.3	5.46	4.34	1.075521	1.01708
5	100	2000	300	14.93	5.42	5.59	1.016629	1.044606
6	100	2000	500	24.44	7.71	4.74	1.079932	1.065364
7	100	3000	100	12.18	1.32	3.93	1.009156	1.034754
8	100	3000	300	13.11	2.03	6.49	1.02375	1.04234
9	100	3000	500	13.49	2.69	4.70	1.019844	1.008397
10	118	1000	100	59.81	4.21	3.09	1.066515	1.016654
11	118	1000	300	21.6	9.75	6.42	1.025953	1.043824
12	118	1000	500	98.36	7.76	5.37	1.022189	1.043824
13	118	2000	100	39.25	9.81	7.67	1.022899	1.044606
14	118	2000	300	70.44	10.29	7.30	1.015639	1
15	118	2000	500	104.42	12.01	8.63	1.001659	1.043824
16	118	3000	100	29.07	6.75	6.21	1.006795	1
17	118	3000	300	44.71	7.17	6.73	1.000373	1.045007
18	118	3000	500	63.06	10.3	4.20	1.043323	1.108999
19	135	1000	100	40.67	8.89	4.57	1.050276	1.024774
20	135	1000	300	39.18	2.2	3.74	1.012348	1.009166
21	135	1000	500	78.53	9.14	3.80	1.045766	1.024774
22	135	2000	100	29.29	5.74	5.72	1.009983	1
23	135	2000	300	38.54	7.04	4.45	1.015939	1.013881
24	135	2000	500	66.23	6.8	4.84	1.054045	1.006704
25	135	3000	100	26.49	9.12	4.03	1.091755	1.044849
26	135	3000	300	31.37	8	4.68	1.001879	1.035635
27	135	3000	500	43.05	7.67	3.82	1.01718	1.007137

Data Deprocessing

Generally the normalized value of the data is known as comparable sequence. The range and unit in one data sequence may differ from others, hence normalization is necessary. It is also necessary when the sequence scatter range is too large, or when the directions of the target in the sequences are different.

The normalized value of "higher-the-better" characteristic and it is expressed as,

$$x_i^*(k) = \frac{x_i^0(k) - \min x_i^0(k)}{\max x_i^0(k) - \min x_i^0(k)} \quad (1)$$

The normalized value of "lower-the-better characteristic is expressed as,

$$x_i^*(k) = \frac{max\, x_i^0(k) - x_i^0(k)}{\max x_i^0(k) - \min x_i^0(k)} \quad (2)$$

If the characteristic is "nominal-the-best", then the normalized value is expressed as,

$$x_i^*(k) = 1 - \frac{|x_i^0(k) - x^0|}{\mathrm{Max}\, x_i^0(k) - x^0} \quad (3)$$

Where i=1… m; k=1… n. m is the number of experimental data items and n is the number of parameters. $x_i^0(k)$ is the original sequence, $x_i^*(k)$ is the sequence after the normalization, $max\, x_i^0(k)$ is the largest value and $\min x_i^0(k)$ is the smallest value of $x_i^0(k)$ and x^0 is the desired target value [9].The normalized values of the response parameters are tabulated in Table 3.

Determination of Grey Relational coefficients and Grades

The GRC (grey relational coefficient) value is calculated after the calculation of normalized values. The GRC expresses the relationship between the ideal and the actual normalized experimental results. The Grey Relational Coefficient, $G_{ij\ is}$ expressed as,

$$G_{ij} = \{\Delta_{min} + \zeta\Delta_{max}\} / \{|x_i^0 - x_{ij}| + \zeta\Delta_{max}\} \quad (4)$$

Where x_i^o is the ideal normalized results for the i^{th} performance characteristic and ζ is the distinguishing coefficient, which is defined in the range $0 \leq \zeta \geq 1$. But for practical purposes, ζ is taken as 0.5.

After the calculation of GRC values, the data can be reduced to a single value known as Grey Relational Grade (GRG). The GRG is calculated by the following formula by giving equal importance to the influence of various response parameters. The GRC and GRG values of all 27 trials are entered in Table.4.

$$\mathrm{GRG}\ (\alpha_j) = \frac{1}{N}\sum_{I=1}^{N} G_{ij} \quad (5)$$

TABLE 3: NORMALIZED VALUES OF EXPERIMENTAL RESULTS

Expt.No.	T F	M	R_a	Entry-D factor	Exit-D factor
1	0.9100	0.7820	0.1873	0.85626	0.878645
2	0.8908	0.8587	0.7608	0.790579	0.69488
3	0.7659	0.7353	0.9163	0.297399	0.839177
4	0.9553	0.6127	0.7741	0.177646	0.843297
5	0.9702	0.6165	0.5488	0.822112	0.590768
6	0.8671	0.4022	0.7018	0.129381	0.400326
7	1.0000	1.0000	0.8488	0.903884	0.681148

8	0.9899	0.9336	0.3855	0.744182	0.61156
9	0.9858	0.8718	0.7090	0.786934	0.922964
10	0.4836	0.7297	1.0000	0.276198	0.847211
11	0.8979	0.2114	0.3988	0.720083	0.597941
12	0.0657	0.3976	0.5886	0.761269	0.597941
13	0.7065	0.2058	0.1735	0.753494	0.590768
14	0.3684	0.1609	0.2398	0.832946	1
15	0.0000	0.0000	0.0000	0.985925	0.597941
16	0.8169	0.4920	0.4361	0.929727	1
17	0.6473	0.4528	0.3434	1	0.587084
18	0.4484	0.1600	0.7994	0.53	0
19	0.6911	0.2919	0.7331	0.453905	0.77271
20	0.7073	0.9177	0.8831	0.86896	0.915903
21	0.2807	0.2685	0.8723	0.50326	0.77271
22	0.8145	0.5865	0.5247	0.894838	1
23	0.7142	0.4649	0.7554	0.82966	0.872652
24	0.4140	0.4874	0.6849	0.41267	0.938497
25	0.8449	0.2703	0.8307	0	0.588539
26	0.7920	0.3751	0.7127	0.983518	0.673072
27	0.6653	0.4060	0.8693	0.81608	0.934522

TABLE 4 GRADE RELATIONAL COEFFICIENTS& GREY RELATIONAL GRADES

Expt.No.	GRC-TF	GRC- M	GRC-R_a	GRC-Entry-D_f	GRC-Exit-D_f	GRADE(GRG)
1	0.8164	0.6473	0.1975	0.776711	0.804693	0.648521
2	0.7856	0.7390	0.4554	0.7048	0.621025	0.661165
3	0.6309	0.6017	0.7049	0.415766	0.756632	0.62198
4	0.8996	0.5081	0.4696	0.378114	0.761379	0.603359
5	0.9306	0.5105	0.3071	0.737585	0.549914	0.60714
6	0.7506	0.4009	0.4015	0.364799	0.45468	0.474496
7	1.0000	1.0000	0.5695	0.838762	0.610611	**0.803775**
8	0.9754	0.8576	0.2456	0.661535	0.562784	0.660584
9	0.9657	0.7574	0.4074	0.701197	0.866497	0.739639
10	0.4365	0.5967	1.0000	0.408563	0.765945	0.641542
11	0.7966	0.3365	0.2496	0.641094	0.554288	0.515616
12	0.2998	0.3990	0.3271	0.676837	0.554288	0.451405
13	0.5768	0.3350	0.1948	0.669787	0.549914	0.46526
14	0.3877	0.3228	0.2083	0.749564	1	0.533673
15	0.2857	0.2857	0.1667	0.972622	0.554288	0.453002
16	0.6860	0.4406	0.2618	0.876773	1	0.653035
17	0.5314	0.4223	0.2335	1	0.547695	0.546979

18	0.4203	0.3226	0.4992	0.515464	0.333333	0.418179
19	0.5643	0.3610	0.4284	0.477968	0.687483	0.50383
20	0.5774	0.8293	0.6312	0.792343	0.856022	0.737253
21	0.3574	0.3535	0.6103	0.501635	0.687483	0.502064
22	0.6832	0.4917	0.2962	0.826225	1	0.659465
23	0.5833	0.4278	0.4499	0.74589	0.797006	0.600779
24	0.4057	0.4383	0.3883	0.459842	0.890468	0.516522
25	0.7205	0.3541	0.5416	0.333333	0.54857	0.499621
26	0.6578	0.3903	0.4104	0.968088	0.604648	0.606247
27	0.5445	0.4024	0.6047	0.73108	0.884208	0.633378

The highest grey relational grade will give the optimal combination of various process parameters.i.e. 0.803775 (7th experiment).

Experimental Results Analysis by Using Response Table and Response Graphs.

The average grey relational grade for each level of all input parameters can be computed and the overall mean also calculated and entered in the Table 5.

TABLE 5. RESPONSE TABLE

DRILLING PARAMETER	SYMBOL	GREY RELATIONAL GRADE		
		Level 1	Level 2	Level 3
Point Angle	A	**0.6467**	0.5199	0.5844
Spindle Speed	N	0.5870	0.5460	**0.6179**
Feed Rate	F	**0.6087**	0.6077	0.5345
Overall mean of Grey Relational Grade = 0.5836				

The effect of each drilling parameter can be clearly presented by means of the response graph shown in Fig 5.

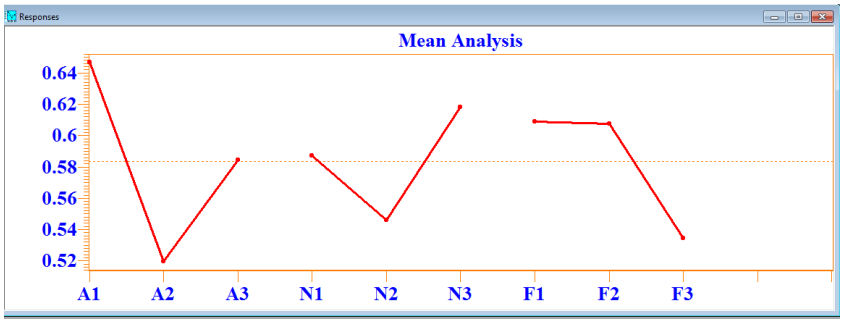


Fig.5 Response Graph

Validation Experiment

After the optimal level has been selected, the final step is to predict and verify the improvement in the response characteristics for the CFRC plate by drilling process with respect to the chosen initial parameter setting.

This validation test is important and last part of the parametric design. The expected mean grey relational grade at the optimal settings is calculated by using the following model.

$$\tilde{\alpha} = \alpha_m + \sum_{i=1}^{n} [\overline{\alpha_1} - \alpha_m] \quad (6)$$

where α is the total mean of grey relational grade, $\bar{\alpha}$ is the mean grey relational grade corresponding to the i^{th} significant factor on the j^{th} level and n is the no. of significant factors that affect the multiple response parameters.

The predicted value of GRG,

$$\tilde{\alpha} = 0.5836 + (0.6467-0.5836) + (0.6179-0.5836) + (0.6087-0.5836) = 0.7061$$

TABLE 6: RESULTS OF VALIDATION EXPERIMENT

Setting Level	Initial Drilling process Parameters	Optimal Drilling process Parameters	
		Prediction	Experiment
Response Parameters	$A_2N_3F_3$	$A_1N_3F_1$	$A_1N_3F_1$
TF [N]	63.06	-	12.18
M[N-m]	10.3	-	1.32
$R_{a[}\mu m]$	4.20	-	3.93
Entry-D_f	1.0433	-	1.0091
Exit-D_f	1.1089	-	1.0347
Grade	0.4181	0.7061	0.8037

Table 6, shows the comparison of the predicted and the actual drilling performance of the Tin coated solid carbide drill for multiple performance characteristics using their optimal cutting parameters. The confirmation experiment results at the optimal level show that Thrust Force is decreased from 63.06 N to 12.18 N, Torque is also decreased from 10.3 N-m to 1.32N-m, Surface finish has improved from 4.2 μm to 3.93 μm and delamination factor has also come down in both the cases, i.e., entry and exit of holes due to the improvement of grade by 0.3856.It is clearly evident from the results that the multiple performance characteristics in the CFRC composite material drilling process are greatly improved through this technique.

Conclusion

1. The predicted results were checked with experimental results and a good agreement was found.
2. A point angle of 100^0, a feed rate of 100mm/rev and a spindle speed of 3000 rpm of 7^{th} experiment is the optimal combination to have good drilling results.
3. A combination of high speed and low values of feed rate and point angle seems to be an appropriate selection for minimizing the delamination.

References

[1] Krishan.K.Chawla. Composite materials Science and Engineering ed.2, Springer (India) pvt.ltd.New Delhi (2008).

[2] J.C Bokros, Carbon- Biomedical devices, Carbon, vol.15, pp355-371(1977).

[3] Krishnasastry ,in:Carbon fibre reinforced CARBON (cfrc) - A SPECIAL material proc.int.conf.& exhibition on Pressure vessels and piping,IGCAR,Kalpakkam, C-086,pp120.

[4] Krishnasastry ,in: Characteristics of Reinforced carbon-carbon proc. int. conf. on frontiers in automobile and mechanical engineering, sathyabama univ, Chennai, pp.12-15 (2010).

[5] Krishnasastry **,** in**:** CFRC- A new millennium composite material, proc. int. conf. on recent advances in mechanical engineering, drmgr univ, Chennai, pp.32-36 (2011).

[6] P. J. Ross, Taguchi Techniques for Quality Engineering , McGraw-Hill, NY , pp 66-71(2004).

[7] S. Balasubramanian, S. Ganapathy, Grey Relational Analysis to determine optimum process parameters for Wire Electro Discharge Machining (WEDM)., International journal of engineering Science and Technology, Vol. 3, pp. 95-101,(2011).

[8] Koenig.W, in:Machining of fibre reinforced plastics, Ann.CIRP,Vol.34,pp 537-548.

[9] k.v.krishnasastry,v.seshagirirao,application of grey relational analysis to determine the optimum drilling parameters of RCC, int.jour.of research in eng. and ad. Tech,vol.1.aug-sept,(2013)

Advanced Materials Research Vol. 936 (2014) pp 1809-1815
© (2014) Trans Tech Publications, Switzerland
doi:10.4028/www.scientific.net/AMR.936.1809

Study On Optimal Condition Of Activated Carbon Prepared By Microwave Heating From Shot Coke

Yingfei Hou[1, a *], Yaya Gu[1, b], Qingping Mou[2, c], Gang Yao[2, d], Jianhui Zhang[3, e]

[1]State Key Laboratory of Heavy Oil Processing, China University of Petroleum (East China), Qingdao 266580, China

[2]Shandong Jingbo Holdings Co., Ltd, Bingzhou 256500, China

[3]China Petroleum Engineering Co., Ltd, Beijing 10085, China

[a]houyf@upc.edu.cn, [b]yayagu1989@gmail.com, [c]mqp926@126.com, [d]ygzlyyf@sohu.com, [e]zhjianhui@cnpc.com.cn

Keywords: Shot coke, Microwave heating, Activated carbon

Abstract. The activated carbon was prepared from the Jing Bo shot coke using KOH as the activation agent by microwave heating. The effect of microwave radiation time, the microwave power and the ratio of activation to shot coke on the properties of the activated carbon were investigated in detail. The result showed that the optimized condition of preparation of activated carbon is as followed: the ratio of activation agent to shot coke is 3:1, the microwave power 900 W and the microwave radiation time is 40 min. In this condition, the BET surface area of the activated carbon is 2668 m^2/g; the iodine adsorption value 2281 mg/g and the benzene adsorption value 1368 mg/g.

Introduction

Activated carbon is the most widely used adsorbent because of its larger porous area which has been commonly used for adsorption separation purification in pharmaceutical, food, environmental, chemical engineering and especially in pollution control applications. The precursor of activated carbon can be coal, wood, fruit shells and coke. During upgrading, a larger amount of petroleum coke is generated as a by-product. And the amount of petroleum coke is rapidly increasing along with the worldwide supply of heavy crude oil continues to increase. Currently most of the petroleum cokes are used as aluminum industrial fuel combustion with low value and low processing depth. While as the precursor of activated carbon, petroleum coke has great advantages of low cost and high carbon content. Shot coke is a kind of petroleum coke, with spherical the shape, smooth and shiny little hole, generally only used for power generation, cement and other industrial fuels [1]. In this article, the shot coke was used to prepare the active carbons.

Microwave heating in the environment applications in recent years has caused considerable attention of researchers which has unique advantages over convention heating method due to its high energy efficiency, fast heating rate, volume and selective heating from the inside to the outside of the heating [2,3]. Most of the carbonaceous material have a high dielectric loss, and can be quickly heated in a microwave oven [4]. The above advantages provide a strong motivation to prepare the activated carbon from shot coke in trough microwave heating. This paper reports a method for the preparation of high surface area active carbon from coke by microwave radiation

using KOH as active regent. Factors affecting the adsorption properties of the products produced with microwave activation were studied as well as the BET surface area and pore volume of the activated carbon. Optimizing the microwave conditions and the KOH/Coke ratio were investigated in the article.

Experimental

Preparation of microporous activated carbons

The shot coke from Shandong Jingbo Holdings Co., Ltd was used as raw material. It was grounded and sieved to 74 μm before use. The Proximate and elemental analysis of shot coke is listed in table 1.

TABLE 1 PROXIMATE AND ELEMENTAL ANALYSIS OF SHOT COKE

Parameter	Proximate analysis (wt %)			Elemental analysis (wt %)				
	A	V	M	C	H	N	S	O[b]
Raw	0.6644	10.60	0.86	88.61	3.57	2.20	2.65	2.97

[b] by difference

Then the shot coke was placed in a drying oven for 24 h and at 120 ℃ and mixed with KOH. A 2.45 GHz microwave oven (MKG-F2-1) with 1400W nominal power output and continuously adjustable microwave power was used for activation the coke samples. The mixture was placed in a microwave tube oven which was purged with 100 cm^3/min nitrogen to provide an inert atmosphere. After activation, the activated carbon was washed with hydrochloric acid and deionized water till neutral. Then, it was dried at120 ℃in an oven for 24 h.

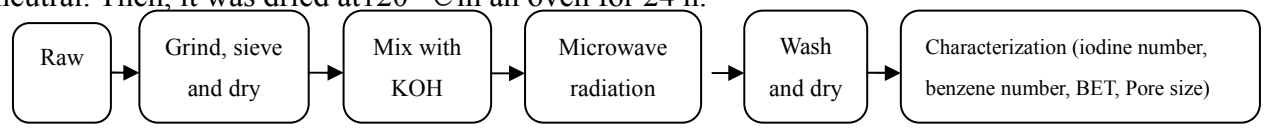


Fig.1 A schematic diagram for the microwave activation process

Characterization of microporous activated carbon

The iodine adsorption value was determined according to the standard test method GB / T 7702.7-2008. The adsorption of benzene was measured by a static Paul drying method, namely: 0.1 g of sample is placed in a desiccator containing benzene for 24 h. Based on the mass changes before and after the adsorption, benzene adsorption value of per gram of activated carbon was obtained.

The specific surface area and pore structure of activated carbon were measured using low temperature (77 K) N_2 adsorption method by a surface area analyzer (Quantachrome Instruments, Autosorb-1). The total surface areas were calculated from the BET formula, the total pore volume were measured when the relative pressure P/P0 = 0.97, and the micropore volume from the t-plot method, pore size distribution from the BJH method. The surface morphology of raw materials and activated carbon was characterized using a scanning electron microscope (Japanese production, JED-2300).

Results and discussion

Effect of microwave radiation time

According to the literature [5-7], in this paper we chose KOH as activating agent. The effect of microwave heating time was studied at a KOH/Coke ratio of 3:1. Fig.2 shows the effect of microwave radiation time on iodine and benzene adsorption properties.

As can be seen from the figure, both of the adsorption values didn't monotonically with the microwave heating time, and the iodine adsorption and benzene adsorption of the activated carbon both reached the maximum at 40 min of microwave heating. When the radiation time was lower than 40 min the adsorption of iodine increased with the increasing activation time, while after 40 min, the iodine value of activated carbon decreased. The benzene adsorption value showed the same trend with microwave heating time. Overall, the Adsorption properties of activated carbon achieved the best conditions in the heating time of 40. This may be due to that the rate of generating new hole of raw material is higher than rate of the sample being ablated, the number of holes presents upward trend, and therefore increases the adsorption performance. With the increase of the activation time, the generation rate is gradually reduced, and is less than the rate of ablation, reducing the overall numbers of the holes, so that the adsorption properties of activated carbon decreased.

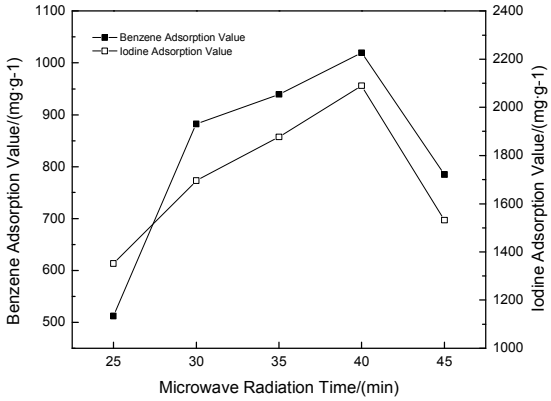


Fig.2 Effect of microwave radiation time on adsorption properties of activated carbon

TABLE 2 BET SURFACE AREA AND PORE STRUCTURE PARAMETERS OF ACS MADE BY DIFFERENT MICROWAVE RADIATION TIME

Microwave radiation time (min)	BET surface area ($m^2 \cdot g^{-1}$)	Total pore volume ($cm^3 \cdot g^{-1}$)	Pore diameter (nm)	Micropore volume (%)
25	1132.8	0.57	2.02	93.2
30	1913.4	0.99	2.08	90.0
35	1903.1	1.00	2.10	93.6
40	1960.8	0.99	2.02	92.9
45	1196.8	0.72	2.42	78.6

Table 2 presents the effect of microwave heating time on the pore structure. It can be found that the BET surface area of activated carbon and total pore volume were increased with the increase of heating time, and then decreased at 40min. This may because most of the holes that the activation produced are micropore. The rising content of microspores determined the BET surface area and total pore volume. While the activation time increasing, the rate of ablation of activated carbon increased and part of the microporous collapsed, which lead to the micropore content gradually reducing along with the BET surface area and pore volume decreased as well.

Effect of microwave power

Fig.3 presents the effect of microwave power on adsorption properties of activated carbon while the microwave heating time was 40min, the KOH/Coke ratio of 3:1.

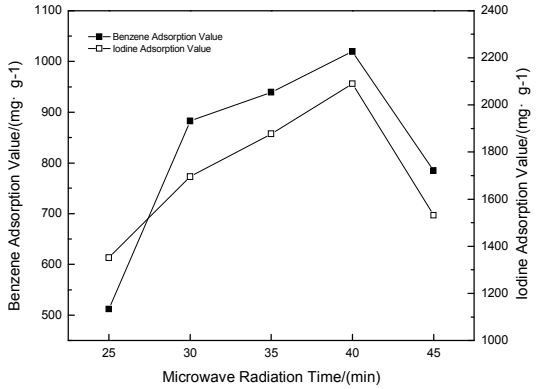


Fig.3 Effect Of Microwave Power On Adsorption Properties Of Activated Carbon

Figure 3 shows that with the increase of microwave power, benzene and iodine adsorption of activated carbon showed a decreasing trend after the first increase. When the microwave power is 900 W, adsorption got maximum properties. This is mainly due to that when the microwave power increased; the material temperature can be raised to promote the activation reaction, accelerating the hole generating speed, thereby improving the adsorption performance of activated carbon. However, higher than 900W, the power increases as well as the ablation of the material increases. The pore structure of the new generation is ablated, collapse, resulting in the decrease of the number and volume of the pores. Thus the adsorption performance of activated carbon degraded [8, 9].

TABLE 3 BET SURFACE AREA AND PORE STRUCTURE PARAMETERS OF ACS MADE BY DIFFERENT MICROWAVE POWER

Microwave power (W)	BET surface area ($m^2 \cdot g^{-1}$)	Total pore volume ($cm^3 \cdot g^{-1}$)	Pore diameter (nm)	Micropore volume (%)
600	2314.8	1.20	2.25	92.16
700	2316.8	1.13	2.10	92.61
900	2668.3	1.39	2.24	92.95
1000	1972.0	0.98	2.15	92.25
1200	1777.5	0.86	2.03	94.63

Table 3 indicated the BET surface area and pore structure parameters of ACs made by different microwave power. With the increasing power the BET area and total pore volume of the activated carbon increases. It can be seen that the increasing of power lead to a fast heating rate thus the activation behavior become obvious reflecting the pore development behavior. When the power was 900 W, the activated carbon surface area and total pore volume reached a maximum. Higher than 900 W, the sample was overreacted with pore collapsing along with the decreasing of the surface area and total pore volume.

Effect of KOH/Coke ratio

The effect of KOH/Coke ratio on the properties of the activated carbon was studied for the coke exposed to 900W microwave power for 40min.

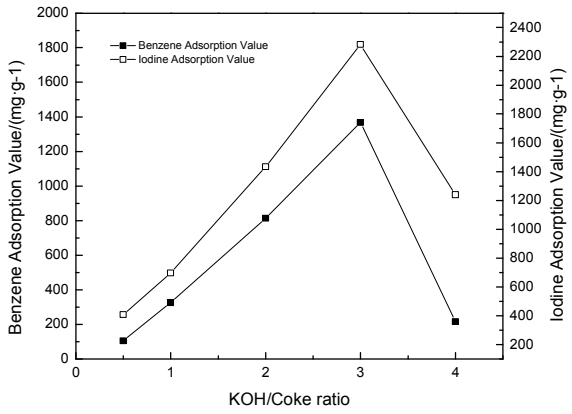


Fig.4 Effect of KOH/Coke ratio on adsorption properties of activated carbon

Fig.4 Shows the iodine and benzene adsorption value of the activated carbon at different KOH/Coke ratio. From the figure, we can see that when the KOH/Coke was 3:1, the activated carbons perform best. In the low range of ratio, the adsorption performance of activated carbon increases significantly as the ratio increased. When the agent coke ratio is higher than 3:1, the adsorption properties of activated carbon decreased. It can considered that with low ratio, the raw material was not fully activated, pore structure formation was not fully developed, so the adsorption performance of activated carbon was poor; As agents coke increases, the reaction between KOH and raw materials got developed, so the degree of porosity increased. Thus the activated carbon's adsorption property was also enhanced. When agents coke was 4:1, some micropore collapsed, resulting in decrease of absorption values.

Table 4 shows that the specific surface area of activated carbon, total pore volume and micropore rate was first increased and downward later when the ratio increased, the optimal KOH/Coke radio was 3:1. This was because when the agent coke ratio is increased, the better the mixing performance of raw material and activator is, the larger the contact area is, and therefore the activation react more fully and the micropore content is large, so the specific surface area and the total pore volume of the activated carbon rise . When the agent to achieve the best focal ratio, as the focal ratio of the agent is increased, because of the excess activating agent, the reaction is too violent and activated ablation rate increase; the new generation of pores continuously burned into collapse, resulting in reduce of micropore content. Thus the surface area and pore volume of activated carbon decreased [10, 11].

TABLE 4 BET SURFACE AREA AND PORE STRUCTURE PARAMETERS OF ACS MADE BY DIFFERENT KOH/COKE RADIO

KOH/Coke radio	BET surface area ($m^2 \cdot g^{-1}$)	Total pore volume ($cm^3 \cdot g^{-1}$)	Pore diameter (nm)	Micropore volume (%)
1:2	130.4	0.08	2.34	79.1
1:1	457.7	0.25	2.17	89.5
2:1	2146.9	1.14	2.13	92.5
3:1	2688.3	1.50	2.24	92.9
4:1	1503.9	0.81	2.16	88.8

SEM images

Figure 5 shows SEM images of samples under different power conditions. In the Figure 5 (a), we can see that in the layered structure of raw petroleum coke is more obvious, but the surface has

almost no gaps. After activation, the surface of petroleum coke is etched, showing varying degrees of crack. In particular, Figure 5 (b) and Fig 5 (c) etching is obvious, this is consistent with a high surface area activated carbon and the developed pore structure under this conditions. These cracks may extend to the very interior of the particle, although these cracks and cavities do not provide greater surface area and adsorption properties, they are able to provide the adsorbate a passage to enter microporous and mesopore of the particles. Figure 5 (d) shows surface pores is more obvious and surface smooth. This may be that in the higher power, the structural order of activated carbon improved and part of the pore collapse. This is more consistent with the aforementioned decrease in the specific surface area.

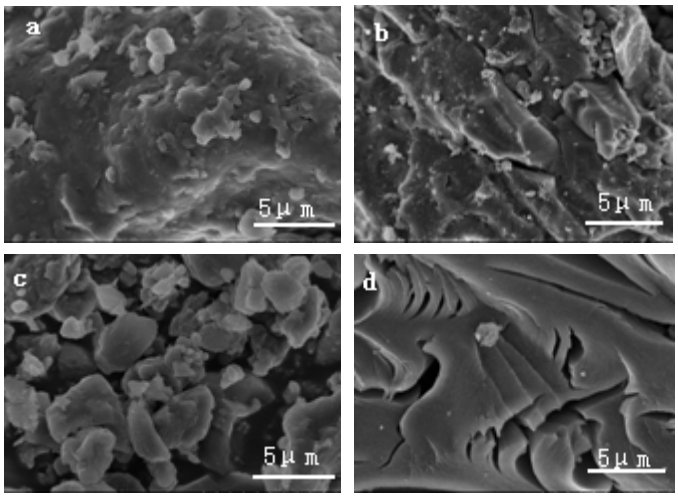


Fig.5 SEM images of different sample treated at different conditions

a .untreated; b. 800 W/40 min; c. 900 W/40 min; d. 1200 W/40 min.

Conclusions

The research determined the effect of different factors on the quality of activated carbon prepared from shot coke using microwave heating and KOH as activation agent. Based on the obtained results, the following conclusion can be made:

(1)The optimum KOH/ coke ratio and microwave power as well as microwave heating time exists due to the adsorption performance of the activated carbon. The optimum conditions of the microwave heating method for the microwave heating activation of activated carbon from shot coke are as follows: KOH as the activation agent, microwave power of 900 W and microwave heating time of 40 min, KOH/coke ratio of 3:1. Under this optimal condition, the BET area of the activated carbon reached 2668.3 $m^2 \cdot g^{-1}$with great iodine and benzene adsorption properties.

(2) Microwave-assisted activation of KOH mainly produce micropore with the microporous rates above 78% and up to 94.6%, with an average pore size distribution of about 2 nm.

Acknowledgements

The study was supported by the Natural Science Foundation of Shandong Province (ZR2012BL15), and the Fundamental Research Funds for the Central Universities.

References

[1] C J Li. Research on the Domestic Petroleum Coke Market, J. China Business Update. 6 (2012): 158. (In Chinese)

[2] D A Jones, T P Lelyveld, S D Mavrofidis, et al, Microwave Heating Applications in Environmental Engineering-A Review, J. Resources, Conservation and Recycling.34.2 (2002): 75-90.

[3] F K Yuen, B H Hameed, Recent Developments in The Preparation and Regeneration of Activated Carbons by Microwaves, J. Advances in colloid and interface science.149.1 (2009): 19-27.

[4] D D L Chung, Electromagnetic Interference Shielding Effectiveness of Carbon Materials, J. Carbon.39.2 (2001): 279-285.

[5] H Chen, Z Hashisho, Fast Preparation of Activated Carbon from Oil Sands Coke Using Microwave-Assisted Activation, J. Fuel. 95 (2012) 178-182.

[6] P H Ling, J J Yao, W D Chen, X J He, Preparation of Porous Carbon for Supercapacitors by Microwave Heating in One Step, J. Electronic Components & Materials. 03(2012)20-24. (In Chinese)

[7] H Yang, M Liang, J Hu, Preparation of Activated Carbon for Electric Double Layer Capacitors from Petroleum Coke by Microwave Radiation, J. Electronic Components & Materials.26.7 (2007): 11-13. (In Chinese)

[8] M Kang, Y S Bae, C H Lee, Effect of Heat Treatment of Activated Carbon Supports on The Loading and Activity of Pt Catalyst, J. Carbon.43.7 (2005): 1512-1516.

[9] N Guo, Z F Li, J M Yan, et al. Optimization of Preparation Conditions of Activated Carbon by Microwave Heating from Petroleum Coke, J. Carbon Techniques.28.3 (2009): 5-9. (In Chinese)

[10] X He, Y Geng, J Qiu, et al. Effect of Activation Time on The Properties of Activated Carbons Prepared by Microwave-Assisted Activation for Electric Double Layer Capacitors, J. Carbon. 48.5 (2010): 1662-1669.

[11] Y Ji, T Li, L Zhu, et al, Preparation of Activated Carbons by Microwave Heating KOH Activation, J. Applied Surface Science. 254.2 (2007): 506-512.

Advanced Materials Research Vol. 936 (2014) pp 1816-1820
© (2014) Trans Tech Publications, Switzerland
doi:10.4028/www.scientific.net/AMR.936.1816

Adhesive Systems for the Production of Multi-Layer Bonded Fabrics for Composite Applications

Iris Käppler[1, a], Ayham Younes[1], Georg Bardl[1] and Chokri Cherif[1]

[1]Institute of Textile Machinery and High Performance Material Technology,

Technische Universität Dresden

Hohe Straße 6, 01062 Dresden, Germany

[a] Iris.Kaeppler@tu-dresden.de

Keywords: Non-Crimp Fabric, Adhesive, Binding Systems, Surface Modification, Composite, Textile Reinforcement

Abstract: Nowadays Non-Crimp Fabrics (NCF) are of substantial use in the field of technical textiles. Due to their lightweight, multilayer set-up, NCF became to an important factor for several technology sectors, i. e. automotive, wind energy and civil engineering. In order to eliminate known drawbacks of current manufacturing technologies, to enhance mechanical properties and to increase production speed of such NCF, a novel technology is proposed. This manufacturing technique is based on the adhesive bonding of layers made of high-performance fibres. Different adhesives were investigated to check their wettability and adhesion properties in relation to the high-performance fibres made of carbon or glass. Furthermore, the interface between the adhesive and a classical matrix for fibre-reinforced plastics was examined.

Introduction

As lightweight materials for fibre-reinforced composites, Non-Crimp Fabrics (NCF) are increasingly used for applications as diverse as automotive, aerospace or civil engineering. Because of the ascending demand of technical textiles, the production process has to be revised as well as limitations of production have to be improved [1].

Issue. In a classic multiaxial warp-knitting machine, several layers of unidirectional high-performance fibres are fastened during a stich-bonding step. The reinforcement yarns are set up in the load direction of the prospective structural element. This technique induces a couple of disadvantages. Single filaments in the high-performance yarn can be damaged, which reduces the load transmission capacity [1]. In addition, the warp-knitting yarn narrows down the cross-section of the yarn and causes ‘fish-eyes’ in a layer of a closed NCF [2]. Such gaps represent a weak point for reinforced materials due to the accumulation of resin and the fact that an accurate position of load bearing fibres is no longer assured.

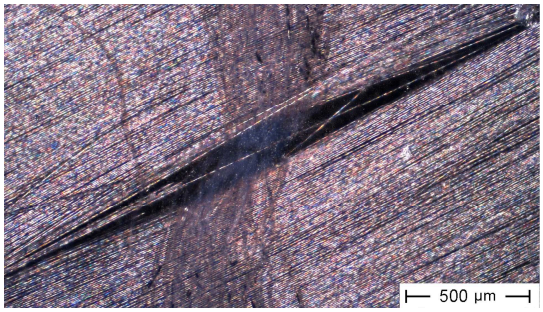


Figure 1: ‚Fish-eyes‘ in a closed NCF made of carbon

Therefore, a non-destructive joining method would be desirable that replaces the warp-knitting yarn in the NCF. The bonding with a adhesive system is proposed. Consequently, a new production technology for NCF has to be developed, which is the aim of the young researcher group SAXOMAX supported by the European Social Fund ESF.

The new process implies different key aspects which have to be clarified. For example, the adhesive system has to be suitable to the used high-performance fibre, to the process conditions and typical reinforcement matrices. Different adhesives were taken into account, i. e. hotmelts and reactive systems as cyanoacrylates. To ensure a good wettability of the binder to the yarn, the surfaces of fibres were modified by oxi-fluorination and plasma treatment. Finally, a method for adhesive application was developed that depends on the mode of action of adhesive corresponding to different chemical and physicochemical conditions.

Novel Production Technology. To a great extent, a warp-knitting unit is used to join at least two layers to an NCF with high-performance yarns made of carbon or glass. For special applications, the 'walking-needle' was invented to preserve the damaging by the stitching needle. In this case, the warp knitting unit moves in the conveying direction of the warp thread.

This work focuses on another approach which is the replacement of the warp-knitting unit by a binder application unit. Here, the adhesive is applied through the multilayer fabric in one step to fix the NCF. This method is defined by the use of a nozzle system for reactive adhesives and for hotmelts that fix a multilayer fabric in one step. To achieve the required draping properties of the fabric, smallest amounts of adhesive and statistically distributed adhesive dots in accordance with the later application are desired (Figure 2, right). These technical demands will be realized in a demonstrator by a jet valve P-jet CT (Liquidyn, Germany) and a Kuka robot KR 6- R900 which enables movements around six axes.

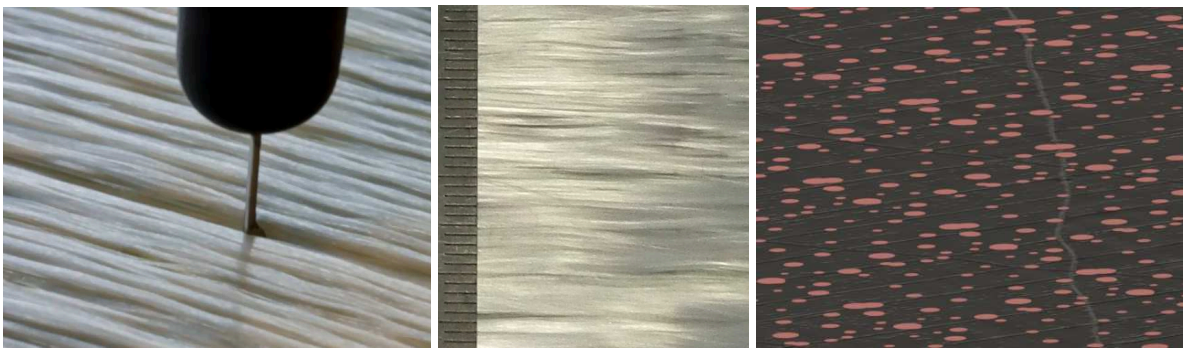


Figure 2: Left, Fixing of a multilayer glass fibres NCF by adhesive application; Middle: Adhesive fastened glass NCF; Right: Adhesive pattern on a carbon fibre NCF

Materials

High-performance fibres. The typical used high-performance fibres for NCF are based on carbon or glass. They exhibit high mechanical load bearing properties [4], especially carbon fibres. Both fibre types differ in the inner structure, glass fibres (GF) are defined by an amorphous structure and carbon fibres (CF) by an anisotropic graphite lattice [3]. In this work, the used CF were HTS 45 E23 (epoxy sizing), HTS 40 F13 (polyurethane sizing) and UMS 40 F23 (polyurethane sizing), all purchased from Toho Tenax, Germany. The used GF types were EC 600 350 and EC 600 354 with different silane sizings supplied by P-D Glasseiden GmbH, Germany. In general, the surface chemistry of CF is often driven by the applied sizing. Without such a sizing, the CF is characterized by acidic surface groups like carboxylic and hydroxylic groups [4, 5]. The mechanical properties of the used yarns are presented in Table 1. The diameter of the single filament of a carbon fibre was determined by a light microscope. The surface energy was measured by single fibres tensiometry as explained below.

Table 1: Properties of used carbon fibres

Typical properties		**Tenax®-E HTS45 E23**	**Tenax®-E HTS40 F13**	**Tenax®-J UMS40 F23**	**EC 600 350**
Sizing		PU-sizing	EP-sizing	PU-sizing	silane sizing
Linear density	[tex]	796.4	800.3	797.6	600
Grade	[K]	12	24	12	9

Diameter of single filament (average)	[µm]	6.19	4.40	6.30	20.6
Surface energy, total	[mN/m]	39.9	43.3	45.9	53.4
Surface energy, polar	[mN/m]	6.5	9.7	10.7	9.3
Surface energy, disperse	[mN/m]	33.4	33.6	35.2	44.1

Adhesives. The existing warp-knitting process gives well and narrowly defined specifications for the binding system and adhesive, respectively. Firstly, the present machine speed determines the potential curing time of the adhesive. Secondly, there are only a few installation options at the multiaxial machine for the application of the adhesive. Additionally, a couple of chemical aspects are important: The adhesive has to be suitable for the surface of the carbon or glass fibres, which are often sized with polyurethane, epoxides or silanes. Furthermore, the adhesive has to be compatible with the reinforcement matrix, i. e. epoxides or polypropylene. For a later forming of NCF in special geometries, it has to be considered to activate the adhesive by wetting or heat. Caused by the capillarity of the high-performance fibres, the viscosity of the used adhesive is of interest.
Different adhesives were investigated: Polyolefines B 42042 and B 41742 (Bühnen, Germany), the cyanoacrylates Delo 2351 and Delo 2219 (Delo, Germany) and Loctite 3090 (Henkel, Germany), 2K-Methylmethacrylate adhesive as 'Carbon Kleber' (Carbon Team), thermoplastic acrylate J 41619 (Bühnen, Germany) and copolyester hotmelt adhesive D 2351 E as granulates and as suspension (EMS Griltex, Switzerland) [6].

Matrix. The adhesives were embedded in a conventional thermosetting matrix based on epoxy resin MGS® RIM 135 (L135i) and the curing agent LARIT RIMH 137 (Lange + Ritter, Germany). The samples were cured out at room temperature.

Methods

Wetting Studies. Two different types of wetting studies were performed. First, the drop shape analyzer DSA 100 (Krüss GmbH, Germany) method was used which operates with a resting drop on an ideally, smooth and solid surface. This method estimates the wetting and adhesion on a solid surface. The contact angles of the high-performance fibres were determined by the single fibre tensiometry, Krüss K100 (Krüss GmbH, Germany) which works in accordance to the Wilhelmy plate principle [7]. In each case, the contact angle is a determining factor of the degree of attraction of the liquid by the substrate. The surface energy (γ) is composed of two components: The polar (^{p}) part is induced by dipol-dipol and acid-base interactions as well as hydrogen bonds. The disperse (^{d}) part is mainly driven by van-der-Waals forces [8].

Surface Modification of High-Performance Fibres. To increase the number of surface functional groups of carbon fibre, several methods were used. Firstly, the carbon fibres were treated with an atmospheric plasma torch (Plamsa Brush® Pb2, Reinhausen GmbH, Germany) fed by different process gases i. e. Argon, compressed air and Nitrogen. Another method to increase the surface energy was the use of oxi-fluorination. The oxi-fluorination was done by 10 Vol% fluor gas in the presence of oxygen (Fluor Technik System GmbH, Lauterbach/ Germany).

Scanning Electron Microscopy (SEM). The SEM was used to observe the fibre surface in the micrometre range. The measurements were performed with a high resolution low-voltage SEM with a field emission cathode Zeiss DSM 982 Gemini.

Results

Surface Morphology of High-Performance Fibres and Surface Modification. To understand the wettability by an adhesive, the morphology of the adherend has to be known. Therefore, the high-performance fibres were investigated via SEM. Exemplary, a single filament of a ultra-modulus carbon (UMS 40 F23) fibre is presented in Figure 3. In general, CF exhibits parallel oriented stripes and striations. These surface morphologies are probably caused by stretching of the fibrous

polyacrylonitrile precursor [4]. Often, this rough texture is filled by the used sizing, i. e. polyurethane (PU) or epoxy (EP). In the case of a surface treatment, the surface morphology changes significantly: Parallel striations and other roughness effects disappear during surface treatment. For example, the surface looks flatter and the sizing seems to be removed, because the irregularities became more substantial after removing the sizing (Figure 4).

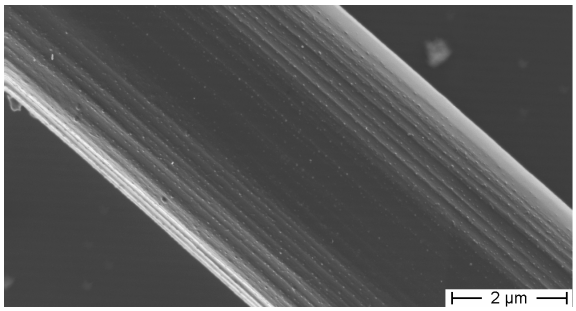


Figure 3: Ultra-modulus carbon fibre (UMS 40 F23)

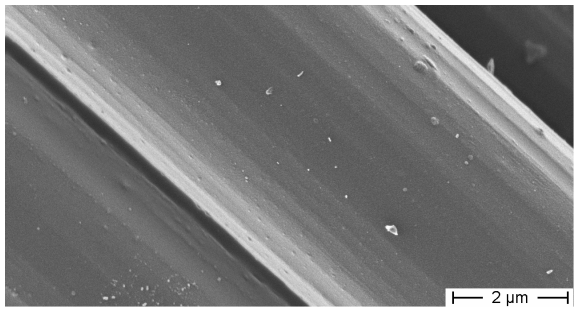


Figure 4: UMS 40 F23 treated with argon plasma

This assumption is supported by the finding of a reduced polar energy after atmospheric argon plasma treatment. The carbon fibre HTS 45 E23 exhibited a polar surface energy of 6.5 mN/m (in Table 1). After a short processing time, the polar energy increased and the sizing was functionalized. With increasing process time, the sizing was removed and the polar surface energy decreased to 6 mN/m. However, with passing time the polar surface energy increased again to 12 mN/m. In this case, the original carbon fibres surface and not the sizing received new functional groups, which were determined by the increase of the surface bound oxygen measured with X-ray photoelectron spectroscopy.

Wettability Studies. A good wettability of components to each other is realized, if the total surface energy (sum of polar and disperse) is comparable or the same, respectively. In regard to Figure 5 and Table 1, the surface energy of carbon fibres is around 40 mN/m to 46 mN/m.

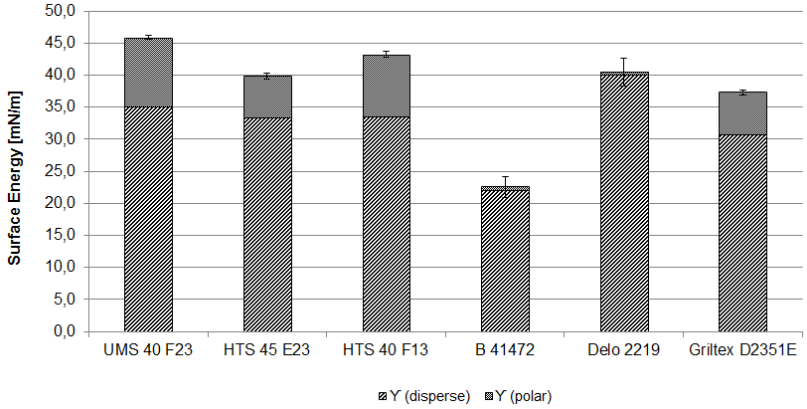


Figure 5: Surface energies of selected carbon fibres and possible adhesives

Furthermore, a selected number of potential adhesives are presented in Figure 5: B 41472 (polyolefin) and Griltex (copolyester) D 2351 E are typical hotmelts. Griltex D 2351 E exhibit a very high polar surface energy of 6.9 mN/m which indicates a high number of polar surface functional groups compared to the polyolefin hotmelt B 41472 with a polar surface energy of 0.6 mN/m. Another promising adhesive is the Delo 2219 (cyanoacrylate) which has a high total surface energy. Both binders, the Griltex D 2351 E and Delo 2219 were investigated successfully by tensile tests of glued high-performance yarns. Moreover, both adhesives are suitable for the used epoxy matrix. Therefore, they will not represent weak points that introduce fractures in a carbon fibres reinforced plastic.

Conclusion and Outlook

This fundamental work was done to achieve the innovative goal of a novel manufacturing technology for NCF. Different adhesive systems were investigated to find the optimal binder system for the non-stitched NCF. Limiting factors of process and chemical properties were considered and two adhesives were sorted out. They exhibit a short curing time and easy handling. The Griltex D 2351 E hotmelt is preferred for realisation of the new type of NCF. This binder can be implemented with the developed technology to achieve the desired structures. To improve the wettability of the fibre by the adhesive, different surface modifications were performed successfully, i. e. plasma treatment and oxi-fluorination.

Acknowledgement

Financial support of this work by the European Social Fund (SAB 10016845, “SAXOMAX”) and the Free State of Saxony is gratefully acknowledged.



References

[1] Mouritz, A. P., Leong, K. H., and Herszberg, I.: A review of the effect of stitching on the in-plane mechanical properties of fibre-reinforced polymer composites, *Composites Part A*, Vol. 28 A (1997), 979-991

[2] Miene, A.: „Bildanalytische Qualitätssicherung in er Preformfertigung“, Carbon Composites e.V., 5. Sitzung der Arbeitsgruppe „Werkstoff- und Bauteilprüfung“, Faserinstitut Bremen, Augsburg, 05.03.2010

[3] Guigon, M., Oberlin, A., and Desarmont, G.: Microtexture and Structure of Some High Tensile Strength, PAN-Base Carbon Fibres, *Fibre Science and Technology*, Vol. 20 (1984), 55-72

[4] Krekel, G., Hüttinger, J., Hoffmann, W. P., and Silver, D. S.: The relevance of the surface structure and surface chemistry of carbon fibres in their adhesion to high –temperature thermoplastics, *Journal of Materials Science, Part I Surface structure and morphology*, Vol. 29 (1994), 2968-2980

[5] Boehm, H.-P., Diehl, E., Heck, W., and Sappok, R.: Surface. Oxides of Carbon, *Angewandte Chemie international Edition*, Vol. 3 (1964), 69-77

[6] Käppler, I., Döbrich, O., Matthäi, P., Schulz, C. Hund, R.-D., and Cherif, Ch.: „Characterisation, Surface Treatment and Adhesion Problematic of Carbon Fibres“, 13th AUTEX World Textile Conference May 22nd to 24th 2013, Dresden, Germany

[7] Hoecker, F. and Karger-Kocsis, J.: Surface Energetics of Carbon Fibers and Its Effects on the Mechanical Performance of CF/EP Composites, *Journal of Applied Polymer Science*, Vol. 59 (1996), 139-153

[8] Schultz, J., Lavielle, L., and Martin, C.: The Role of the Interface in Carbon Fibre-Epoxy Compositest, *Journal Adhesion*, Vol. 23 (1987), 45-60

Advanced Materials Research Vol. 936 (2014) pp 1821-1824
© (2014) Trans Tech Publications, Switzerland
doi:10.4028/www.scientific.net/AMR.936.1821

Development Of A Novel Technology For New Generation Of Non-Crimp Fabrics – Manufacturing And Simulation

Paul Matthäi[1, a], Oliver Döbrich[1], Chokri Cherif[1]

[1]Institute of Textile Machinery and High Performance Material Technology, Technische Universität Dresden, Germany

[a)]paul.matthäi@tu-dresden.de

Keywords: Warp Knit Fabric, Multilayer Fabric, Non-Crimp, Stitch-Free Fabric, Composite

Abstract: In the field of technical textiles, Non-Crimp Fabrics (NCF) are increasingly used as fibre-reinforced polymers in automotive, aircraft and wind power industry. The rising consumption of multi-axial fabrics for fiber reinforcement requires new fabrics and process requirements for the large scale production. The development of a new type of NCF demands a convergence of diverse disciplines namely mechanics, construction design and chemistry. This research includes the manufacturing of novel adhesive bonded NCF. The characterization and of the warp-knitted fabric, selection of binding technology, the development of suitable application system and numerical models for simulation are the major focus areas.

Introduction

Fiber-Reinforced Plastics (FRP) made of high-performance carbon and/or glass fiber textiles are increasingly used in various technical applications like automotive-, aeronautics and aerospace industry, mechanical engineering and civil engineering. Especially NCF produced on multi-axial warp-knitting machines are characterized by an excellent property profile combined with a high production rate and lead to novel developments. In the conventional manufacturing process of NCF, the reinforcement fibers are placed in parallel layers, each with a different specific orientation. In the consecutive step, these yarn layers are fixed by a binding thread during a warp-knitting process [1]. Hereby, the penetration of the material by the stitching needles damages the fiber material of NCF. This causes defects like gaps and fish-eyes which affect the load-bearing properties and creates weak area in the structure by inclusions of resin [2], shown in Figure 3. These defects are highly connected to the inner tension of the binding thread systems. In addition microscopic studies have also shown that these defects represent a weak area in reinforced materials where the resin can accumulate. Such issues lead to a decreasing quality of the final FRP product.

Technological Challenges and Requirements

The development of a new generation increased quality NCF require that some base conditions must be maintained. In addition to a fiber-friendly manufacturing process and associated decrease of fiber damages and deflections, the process must be comparatively productive to the conventional manufacturing process. For this reason new bonding technologies for oriented fiber layers are developed. These are based upon the local applied suited adhesives between the single fiber layers of the NCF. The used binder materials have to be adapted to different fiber materials as well as to their corresponding application system.

For the realization of this adhesive-based production approach, a patent for injection of adhesive into the unbound layers of oriented fibers has been registered. Multiaxial non-crimp fabrics are locally bonded by injecting very small adhesive droplets/microdroplets [3]. This binding system replaces the warp knitting yarn, which usually form loops around the fiber layers in order to fix the different layers. The current approach aims on a localized application and fixation by suitable chemical binders. The substitution of the knit yarn system with adhesive binders improves upon the current disadvantages of the stitch bonding technology. Figure 2 shows a sketch of the novel production technology. The arrangement of the adhesive nozzles is displayed. The adhesive system

can be seen here infiltrating the previously deposited layers by the nozzle-system. For laying the fibers on top of each other the existing system of the warp knitting machines of Karl Mayer (Germany) can be used. Either after the laying process or between every layer, the nozzle-system can induce the binder according to a computational pattern plan as shown in Figure 1.

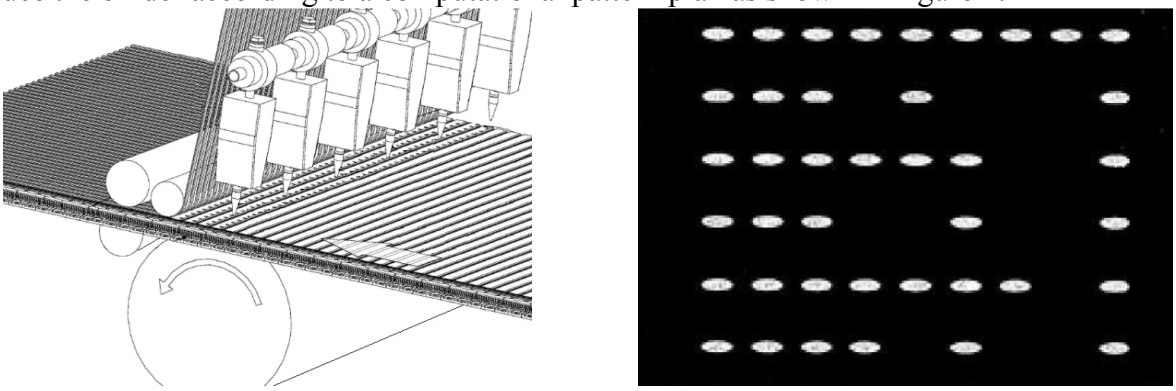


Figure 1: Left: Schematically principle of novel technology for yarnless layer binding by adhesives, Right: Sample pattern plan [2]

Technology Development

The binding of layers with a suitable adhesive system require an understanding of the bonding process, application technology and the surface properties of adhesives and fiber. In order to retain the fiber characteristics, a micro-scale application of the adhesives is essential. This can be only fulfilled using a high frequency application technique. Besides, process stability, durability and maintenance form a decisive factor in the selection of this technology. The modularity and flexibility for the integration with the common fiber laying system on the machine is also needed to be considered. Different systems were tested for upon these requirements to evaluate their suitability.

Studies were carried out on the application system with respect to the speed and their positioning accuracy. The dimension and the mass of the adhesive micro-droplets together with the speed of application were evaluated. It is required that the nozzle injection must ensure a fast and accurate binder infiltration in the fiber and between their layers. These analyses were experimentally carried out using a portal application system. The ability of the nozzle-systems was also investigated with this system in order to create accurate and reproducible samples which are shown in Figure 2.



Figure 2: Left: Portal system; Middle: Nozzle system; Right: Produced samples after binder activation

Manufacturing of Sample Structures

To validate the achieved results on the adhesive binder system and the chosen application technology, samples were manufactured on a laboratory scale. Figure 3 shows two produced specimens with two adhesive dot patterns which vary in their binding dot density. The achieved production speed was sufficient and the quality of the fixation was as expected. At this point of research, data about the mechanical behavior are still pending. Examinations concerning the

influence of the adhesive binder material in a cured composite will be done in addition to the economic analysis concerning the efficiency of this new technology. Figure 3 also shows the proof that some of the disadvantages of the classic production (Figure 3, left) technology can be eliminated by the novel introduced approach. A four layered fabric is fixed by a pattern of adhesive dots. It is clear to see that there is nearly no displacement of the fiber layers and no formation of fish eyes.

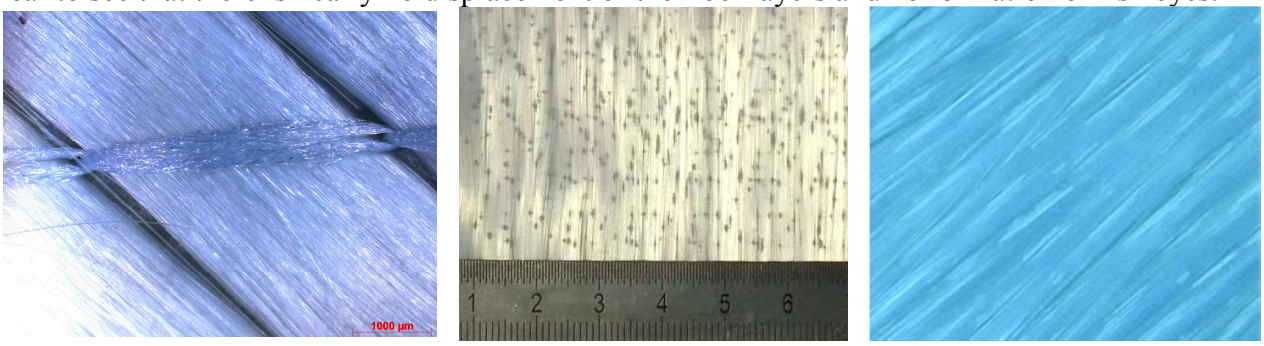


Figure 3: Left: NCF with fish-eye, Middle and Right: Produced multilayer adhesive bonded fabrics

Simulative Development of the Non-Crimp Fabric Structure

To support the development of the introduced production technology, simulative analysis will be done. With the help of numerical finite element models and simulations, knowledge about the structural behavior of fibrous materials interacting with cured adhesive dots will be generated. After successfully implementing a structural model with its characteristics, large scale models of the non-crimp structure with near microscopic resolution will be generated to examine the deformation behavior of the novel textile structure under deforming conditions. Deformation mechanisms on the yarn- and even on the filament-level will be investigated to qualify the novel textile structure with regards to micro- and meso-deformational effects.

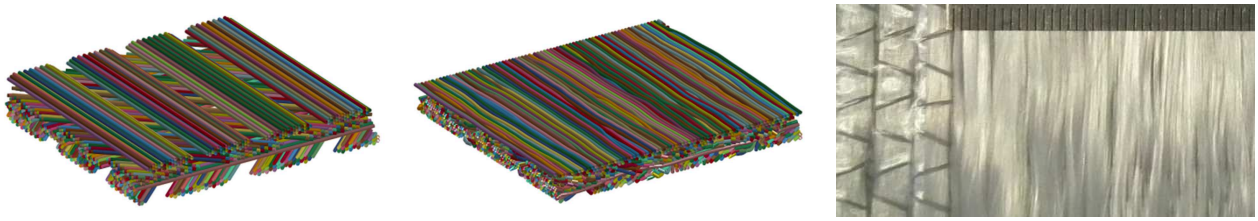


Figure 4:Unit cell model of 4 layered NCF before and after compaction
(right side: real structure without knitting yarns or adhesive dots)

For the model of the yarn layers, a near micro scale resolution was chosen to enable the analysis of inter and intra yarn effects. To handle this model and the accompanying computational costs, some simplifications have to be made. For this purpose, the digital element approach introduced by Wang and Sun [4] was chosen.

It is obvious, that not every single filament of a technical 12K glass-roving can be represented by a single digital element chain but a sufficient large number of these element chains are enough to satisfyingly represent a multifilament yarn [5]. For the introduced simulations, an amount of 39 digital element chains per yarn were chosen. Figure 4 shows the model of a unit cell which represents a four layered fabric. At the beginning of the simulation, the yarns are arranged in four different directions. The result of this simulation shows the alignment of the fiber bundles after compacting the structure without any bonding from knitting yarns or adhesive dots. As seen on the right hand side of Figure 4, the shape of the yarn traces matches the reality when the yarns are not bounded anyhow.

To gain knowledge about effects that occur while forming a textile structure with the introduced properties, a large dimensional model will be assembled. Not only results about effects on the filament level shall be obtained, but statements and suggestions about the adhesive dot pattern shall be created virtually with the help of such a mesoscopic model. The adhesive dots can be placed individually regarding the infiltration depth and the pattern. Variations in adhesive mass and dots per

inch can be made. Obviously, the adhesive dot concentration and the adhesive mass per unit cell have a significant effect on the local forming ability of the structure. Hence the influence of the adhesive injection process and its parameters shall be analyzed virtually to reduce cost intensive production and examinations. With knowledge about the adhesive influencing the deformation behavior, suggestions about local fixation patterns and the local adhesive amount can be made after analyzing the deformational process.

Conclusions

A suitable technology for the fixation of NCF by adhesive was adapted. The solution is based on systems that are available on the market, which enables options for integration in a large scale production technology on any multi-axial warp-knitting machine. Considering the lifetime of the nozzles, this is very important to guarantee a robust implementation of the technology and also to enables a user friendly attendance. Topics for further research will be the implementation in a non-laboratory dimension. Here economic aspects concerning the use of more than one nozzle and their controlling as well as the cost effectiveness of the resulting product has to be investigated.

All the examinations and investigations dealing with the analysis of suitable adhesive binder materials and sufficient application technologies to achieve a competitive reinforcement product for the use in large scale structural parts made out of composite material, done presently, ended in a successful preparation of loop less multilayer fabrics fixed with chemical adhesive binder materials. Disadvantages of the classic NCF production technology were eliminated and the produced samples were suitable for reinforcing thermoset matrices.

Acknowledgement

Financial support of this work by the European Social Fund and the Free State of Saxony is gratefully acknowledged.

We also would like to thank the Center for Information Services & High Performance Computing at TU Dresden for their generous allocation of computing capacity.

References

[1] Cherif Ch.: Textile Werkstoffe für den Leichtbau, Springer-Verlag, ISBN: 978-3-642-17991-4, Berlin Heidelberg, (2011)

[2] Chun H.-J., Kim H.-W., Byun J.-H.: Effects of through-the-thickness stitches on the elastic behavior of multi-axial warp knit fabric composites, Composite Structures, 74(2006)4, pp. 484-494, ISSN 0263-8223

[3] Patent 102013221176.7, Verfahren zur Herstellung von maschenfreien multiaxialen Gelegen, Applied German patent, Technische Universität Dresden (18.10.2013), Cherif C., Schulz C., Bardl G., Döbrich O., Käppler I., Matthäi P.

[4] Wang, Y.; Sun, X.: Digital-element simulation of textile processes, Composites Science and Technology, 61(2001)2, pp. 311-319, ISSN 0266-3538

[5] Miao Y., Zhou E., Wang Y., Cheeseman B. A.: Mechanics of textile composites: Micro-geometry, Composites Science and Technology, 68(2008)7-8, pp. 1671-1678, ISSN 0266-3538

Advanced Materials Research Vol. 936 (2014) pp 1825-1829
© (2014) Trans Tech Publications, Switzerland
doi:10.4028/www.scientific.net/AMR.936.1825

Optimization of Drafting Conditions in the Break Drafting Zone Additional Pressure Bar on INA-V Spinning Frame

Feng Qingguo[a], Ren Jiazhi[b], Zhang Yifeng[c]

College of Textile,Zhongyuan Universy of Technology,Zhengzhou 450007, P.R. China

[a]assiz@163.com, [b]rjzhi@163.com, [c]zckh@sina.com

Keywords: INA-V drafting, Pressure bar, Break drafting ratio, Roving twist factor, Yarn quality.

Abstract: To improve the yarn quality, the pressure bar was installed in the break drafting zone of the INA-V spinning frame. The process parameters were optimized in the break drafting zone with pressure bar of the INA-V spinning frame, the drafting principle in the break drafting zone with pressure bar of INA-V spinning frame was analyzed, and the sliver configuration was observed in the break drafting zone with pressure bar. The result revealed that installed the pressure bar in break drafting zone after, when the roving twist factor was small, CV%, thinness, thickness and neps of the yarn spun decrease as the break drafting ratio increase; when the twist factor of roving was larger, the break draft ratio as 1.3 time was optimum drafting conditions. The yarn quality was improved as roving twist increased.

Introduction

Research shows that, in the break drafting zone additional pressure bar of INA-V spinning frame can improve the yarn evenness, reduce yarn thickness and thinness [1-8]. But, after additional pressure bar in the break drafting zone of INA-V drafting frame, the conditions of spinning changes, in order to further improve the yarn quality, we must optimized parameters. Based on analyzing drafting principle of the break drafting zone with pressure bar of INA-V drafting frame, experimental studied the effect of the different break draft ratio and roving twist factor to the yarn quality. Through defined reasonable spinning process parameters, to obtain the higher quality yarn.

Drafting Principle

The position of the pressure bar and roller center distance shown in Fig. 1.the diameter of the pressure bar is 6 mm ,the distance between the pressure bar center and the roller center is 24 mm, and the vertical distance from the middle roller is 18mm.

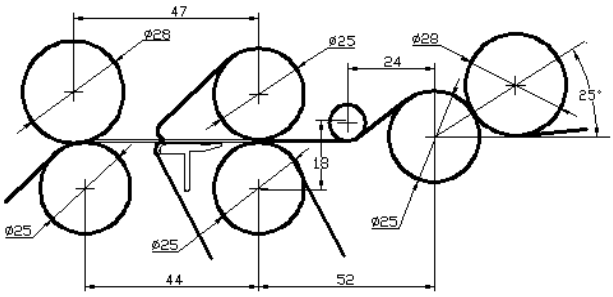


Fig. 1. The position of the pressure bar in break drafting zone

After additional pressure bar in the break drafting zone of INA-V drafting frame, the parameters such as the frictional force field distribution, the drafting force and the roving twist distribution will change.

Variety of Frictional Force Field and Drafting Force

After installing pressure bar in the break drafting zone, not only eliminate the back-surrounded arc on the middle roller, but also further expand the length of surrounded arc on the rear roller. Through calculated we can see: the length of surrounded arc of on the rear roller become 25mm from 20mm; simultaneously, the fiber strand is formed a surrounded arc about 6mm on the surface of the pressure bar, which make the friction force field strengthen and expand into the middle nip. The drafting force and its peak value are augmented, the critical drafting ratio increased too. At the same time, the drafting force wave is decreased, which is benefit to improving and stability of yarn quality.

Twist Distribution

In the break drafting zone, the fiber strands straighten and moved under tension. Thus, the roving strand is untwisted, and the twists transfer to the middle roller nip, it make the twists increase near the middle nip, and the twists decrease near the rear roller, that is the twists redistribution. Twists redistribution phenomenon makes the middle friction force filed weaken, the roving strand become loose, and it is unfavorable for improving yarn quality.

After installing pressure bar in the break drafting zone, the surrounded arc which is formed on the surface of pressure bar prevent the writhe of the roving, and the twists transfer to the middle roller gradually, thus it will decrease the twists redistribution phenomenon. Because the pressure bar has the function that prevent untwist and decrease the twists redistribution, the remaining twists in the break drafting zone can transfer to the front drafting zone, and make the fibers produce centripetal force in the up-down aprons. Thus, the compactedness and friction field are strengthen, and the fiber accelerated point approach to the front roller nip, the yarn quality can be improved.

Making use of the camera to photograph the roving strand in the drafting process, we can see that the stands distribution state with the pressure bar or no shown in Fig. 2 and Fig. 3.

In Fig. 2, when no pressure bar, the twists of the fiber stands almost disappear in the break drafting zone; On the contrary, when installing pressure bar in the break drafting zone in Fig. 3, due to the fiber stand contact with the pressure bar closely, it cannot be untwisted freely in the break drafting zone; According to the actual observation, when the twist factor of roving is 117, there are about 1.5-2 twists.

In a word, after installing pressure bar in break drafting zone of INA-V spinning frame, because the frictional force field, the drafting force and the compactedness of the fibers increase in the front zone, we must optimized parameters such as the break drafting ratio, roving twist factor and so on, otherwise, the drafting force and gripping force discordance and it will produce serious thickness, thinness, unevenness.

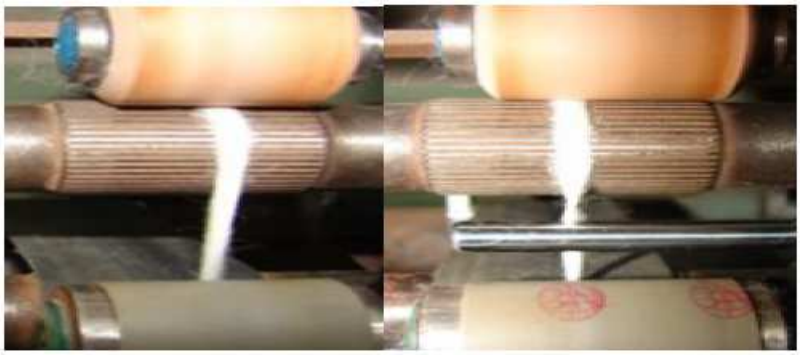


Fig. 2.The roving strand distribution Without t pressure

Fig. 3.The roving strand distribution bar with pressure bar

Experimental

Materials

The cotton we used has the following specifications:0.14tex, 5% of the span length for 35.12 mm, 50% of the span length for 23.43mm, effective length for 30.90mm ,the short fibers content that under the 16mm of 18.73%(n), the roving for 452tex,the neps count for 18 neps /g, CV% of the roving is 7.85%.

Experimental conditions

The SDDA2122P(D) type pneumatic weighting cradle was used in spinning frame. 20.2tex cotton yarn were spun on a laboratory spinning frame with the INA-V drafting system under the following conditions: the front roller center distance for 44mm, the rear roller center distance for 52mm, the apron nip for 3.0mm, the front roller pressure for 180N, the roving twist factor for 97,117, the break drafting ratio1.1, 1.2, 1.3, 1.4, and 1.5 respectively, spinning speed for 13000 rpm, OSS traveler.

Test equipments

Yarn quality such as CV%, thickness (+50%), thinness(-50%), and neps (+200%) was tested with the YG135 tester; Yarn breaking strength (cN/dtex) was tested with the INSTRON5582 strength tester; Yarn hairiness index(3mm)was tested with the YG172 hairiness tester.

Results and Analysis

When the apron nip is 3.0mm, the roving twist factor is respective 97 and 117, and the break drafting ratio is respective 1.1~1.5, the relationship between the roving twist factor and evenness thickness, thinness, hairiness index and strength shown in Fig. 4~Fig. 9.

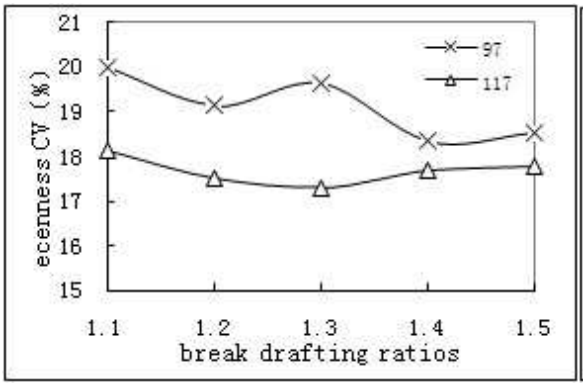


Fig. 4. Evenness CV%

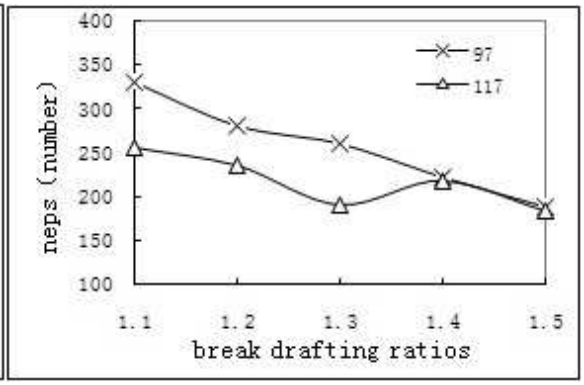


Fig. 5. Neps

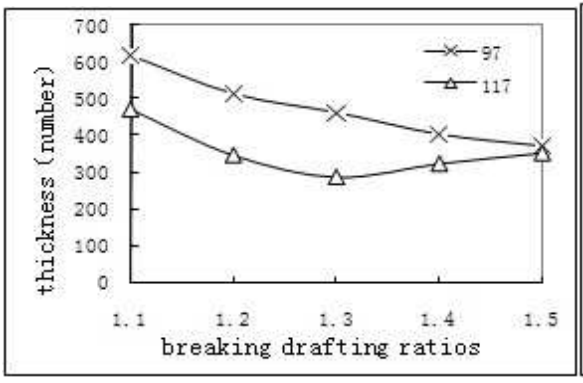


Fig. 6. Thickness

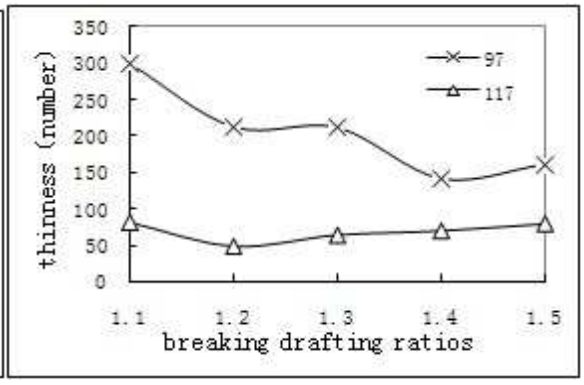


Fig. 7. Thinness

Compared the roving twist factor for 117 with 97, the evenness , thickness, thinness, neps and strength is improved significantly, which shows after installing pressure bar in the break drafting zone of INA-V spinning frame, adopting larger roving twist factor, not only enhances friction force, but also can make partial twists enter the front drafting zone. Thus, the compactedness and friction force of the fiber strands is increased in the front drafting zone, and strengthen the control to the fiber movement.

When the break drafting ratio changes from 1.1 to 1.5 time, the yarn quality is different in the laws of Change with the roving twist factor. When the roving twist factor is 97, CV%, thickness, thinness and neps almost all improve with the breaking drafting ratio increasing. However, when the roving twist factor is 117, CV%, thickness, thinness and neps increase after decrease with the break drafting ratio increasing; at 1.3 time the minimum when it has.

When the roving twist factor is smaller, the larger break drafting ratio is conducive to improve CV%, thickness, thinness and neps. When adopted the larger roving twist factor, the breaking drafting ratio has little effect on the yarn quality. Because after installing pressure bar in break drafting zone, the drafting force and its peak value are augmented, the critical drafting ratio increased also. At the same time, the drafting force wave was decreased, which is benefit to improve the yarn quality. This also shows that after installing pressure bar in break drafting zone of INA-V spinning frame, larger break drafting ratio is feasible.

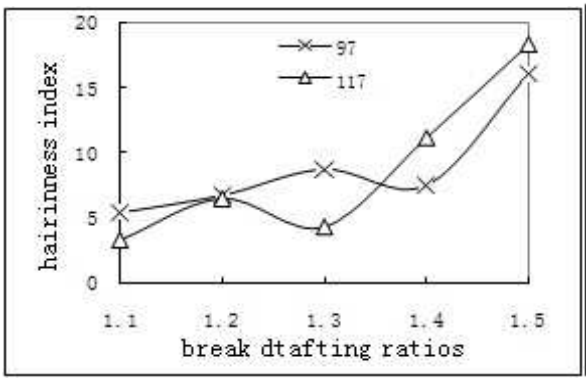


Fig. 8. Hairiness

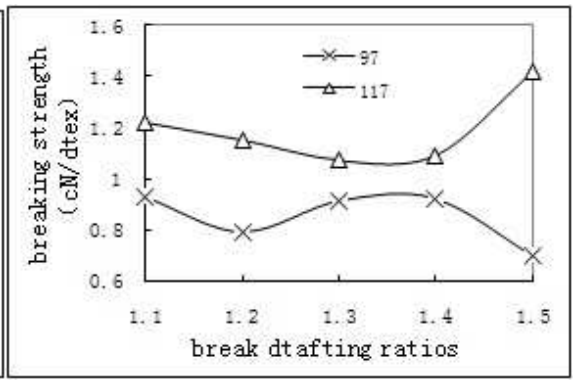


Fig. 9. Breaking strength

The roving twist factor changes in yarn hairiness index of no significant impact. When the break drafting ratio more than 1.4 time, the hairiness index increased significantly.

The larger the roving twist factor, the higher the yarn strength. The yarn strength increase after decrease with the break drafting ratio increasing, at 1.3 time the minimum when it has.

Conclusions

After installing pressure bar in break drafting zone of INA-V spinning frame, there are following characteristics:

Appropriate increase the roving twist factor, enabling improve the yarn quality such as CV%, thickness, thinness and neps and yarn strength.

When adopted smaller roving twist factor, CV%, thickness, thinness and neps almost will decrease with the break drafting ratio increased. When larger roving twist factor, CV%, thickness, thinness and neps increase after decrease with the break drafting ratio increasing, at 1.3 time the minimum when it has. Therefore, after installing the pressure bar in break drafting zone adapt to the larger break drafting ratio.

The effect of roving twist factor is not obvious to yarn hairiness index. When the break drafting ratio is more than 1.4, the yarn hairiness index will be increased significantly.

References

[1] [1] Zhang JF. Shanghai Textile Technology. Vol. 34(2006). p. 115-116

[2] Zhao WC, Cotton Textile Technology. Vol. 35(2007) p. 42-44.

[3] Su XZ, Xie CP, Yang LL. Cotton Textile Technology. Vol. 34(2006) p. 555-557.

[4] Tang WH. Cotton Textile Technology. 35(2007), p. 24-28.

[5] Xue JS. Cotton Textile Technology. 34(2006), p. 112-114.

[6] Ji XX. Cotton Textile Technology. 35(2007), p. 5-8.

[7] John S.G, Charles K.B. Textile Research Journal. 45(1975), p. 515.

[8] Chen KZ, Huang CZ, et al. Textile Research Journal. Vol. 70(2000), p. 154-160.

Advanced Materials Research Vol. 936 (2014) pp 1830-1835
© (2014) Trans Tech Publications, Switzerland
doi:10.4028/www.scientific.net/AMR.936.1830

Non-isothermal Resistance Heating for Hot-stamped Parts with Tailored Properties and Tempering Treatment on Directly Hot-stamped Parts

SUN Caina[1, a] and Zhang Henghua[1,b]

[1]School of Materials Science and Engineering, Shanghai University, Shanghai 200072, China

[a]SCNSHU@163.com, [b]hhZhang@mail.shu.edu.com

Keywords: 22MnB5 steel, Hot stamping, Resistance heating, Tailored properties, Tempering treatment

Abstract. Non-isothermal resistance heating in the hot stamping of quenchable steel sheets was developed to produce ultra-high strength steel formed parts with tailored properties. The heating temperature of parts is related with width of samples heated by resistance heating. With the same input energy, the strength in the narrow portions is high owing to the high energy density and that in the wide portions is low owing to the low energy density. Hat-shaped products having a tensile strength arrange from 600 MPA to 1800 MPa were formed. The tempering treatment on the directly hot-stamped boron steel resulted in better mechanical properties and higher formability index. The SEM figures indicates that the nano-carbide formation during the tempering treatment were suggested as the evident reasons for the occurrence of the mentioned robust properties. Finally the combination of temperature 250 ℃ and holding time 45 min can achieve the best comprehensive mechanical properties.

Introduction

In the hot stamping, a whole body of parts is conventionally quenched with dies, and thus the whole body becomes highly strong. This leads to the limitation of application to high strength body panels having high crash safety for protecting passengers. But an improved crash performance of a vehicle structural component can be achieved by introducing regions which have an increased elongation for improved energy absorption. The manufacturing of a single part with tailored properties can be carried out using different process control strategies or tailor welded blanks[1-2]. In the present study, Non-isothermal resistance heating in the hots tamping of quenchable steel sheets was developed to produce ultra-high strength steel formed parts with tailored properties.

The lower toughness originates from the martensitic microstructure of the hot-stamped parts. XIN Peisen[3] recently managed to enhance the mechanical properties of the indirectly hot-stamped 22MnB5 steel using the quenching and partitioning (Q&P) process. They successfully generated a high product of tensile strength and ductility which is increasing 24% than the traditional hot stamping material. In the current work, in a new attempt, the effects of the tempering process on the microstructure and the mechanical properties of directly hot-stamped parts made of boron-alloyed steel were investigated. The hot stamping process was followed up by the tempering treatment for the various combinations of temperatures and holding times.

Non-isothermal Resistance Heating

Materials and procedures. The quenchable steel sheet 22MnB5 (C: 0.23%, Si: 0.26%, Mn: 1.1%, Cr:0.182%, B: 0.0038%) having 1.5 mm in thickness was employed for this experiment. The Vickers hardness of the as-received sheet was 229 HV.

Resistance heating method is to heating steel sheets by sandwiching with a pair of electrodes and it is sensitive to the sample size (length / cross section ratio)[4]. The heating temperature is related to cross-section, in other words, is related to width as the thickness is given due to per unit volume input energy is different. It is possible to obtain desirable heating temperature of the sample by varying the width of material. So parts with tailored properties followed by hot stamping can be obtained. The relationships between the Vickers hardness and properties versus the hating temperature and width of

samples are illustrated in Figure1. As described above, samples for non-isothermal resistance heating are designed as Figure 2. The length of the sheet is 200 mm and the distance between the two electrodes is 120mm. The width of the left 80 mm part is 10 mm and of the right 80 mm part is 12 mm. The width of the middle 40 mm is continuously changing from 12 mm to 10 mm. Thermocouples are welded on different parts to detect temperature. After hot stamping Vickers hardness are measured. The hardness detective pots on the surface of samples are illustrated in Figure 2.

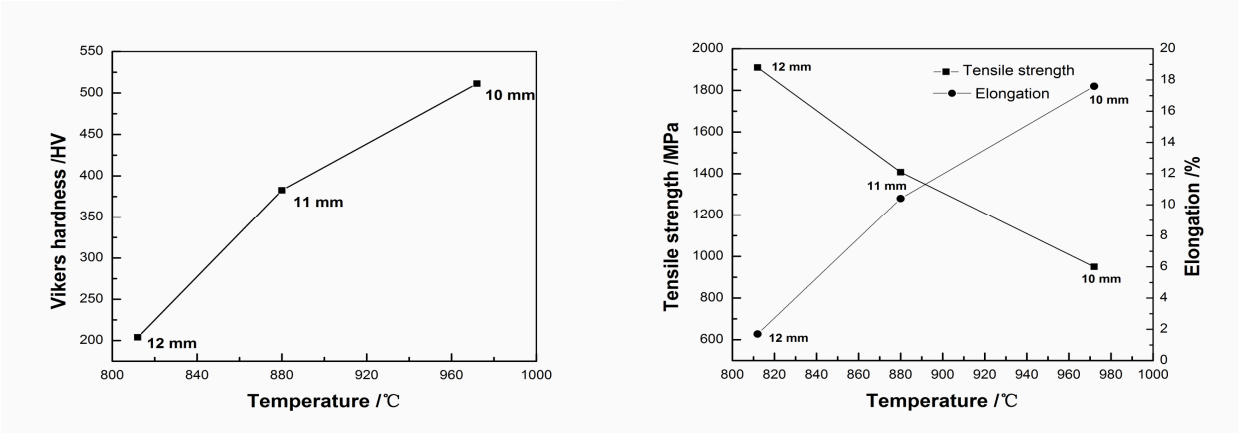


Fig.1 Relationship between Vickers hardness and properties versus the hating temperature and width of samples.

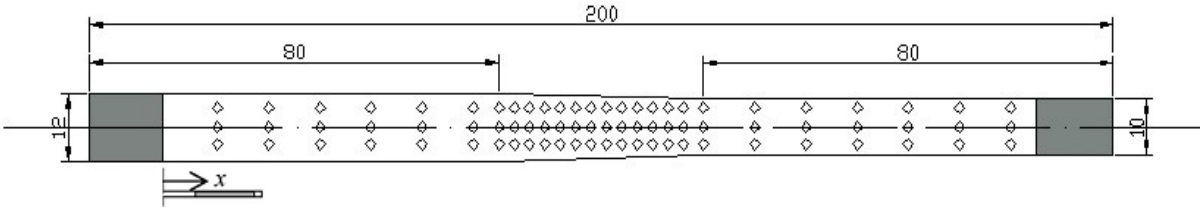


Fig. 2 The size of samples /mm

Results for non-isothermal resistance heating. The distributions of temperature in the longitudinal direction on the surface of the sheet measured by thermocouples are illustrated in Figure 3(a). Heating temperature varies with the changing width transition area of the sample which is about a linear relationship. The distributions of the Vickers hardness and microstructure in the longitudinal direction are shown in Figure 3(b). The hardness increases as the heating temperature increases. Temperature is above 950 ℃ and hardness is about 500 HV with the width 10 mm. And temperature is about 810 ℃ and hardness is about 220 HV for the width of 12 mm. In the transition zone, the hardness is changing slowly and flexibly depending on the changing slope of the temperature. Therefore, the tailored properties of samples can be obtained. When temperature is below the critical transition temperature, the microstructure of sample is same as the sample as-received containing about 75% ferrite and 25% pearlite. With heating temperature increasing, parts of pearlite began to transform into austenite and interface between pearlite and ferrite began to blur until finally completely transformed into austenite. Then martensite attained after quenching. The distributions of tensile strength and elongation of samples are given in Figure 3(c). The tensile strength in the high temperature portion is about 1800 MPa, and elongation is about 5% whereas tensile strength in the low temperature portion is about 600 MPa and elongation can reach 18%. In the intermediate transition zone the tensile strength and elongation of samples must changed continuously according to the change of hardness.

Tempering Treatment

Experimental Process. Some of the direct hot-stamped specimens were selected to undergo the tempering treatment. Tempering treatments at four different temperatures of 200℃, 250 ℃, 300 ℃ and 350 ℃ were performed for different holding times of 5, 15, 30, 45, and 60 minutes. All the tempering treatments were conducted in a furnace with a non-protected atmosphere.

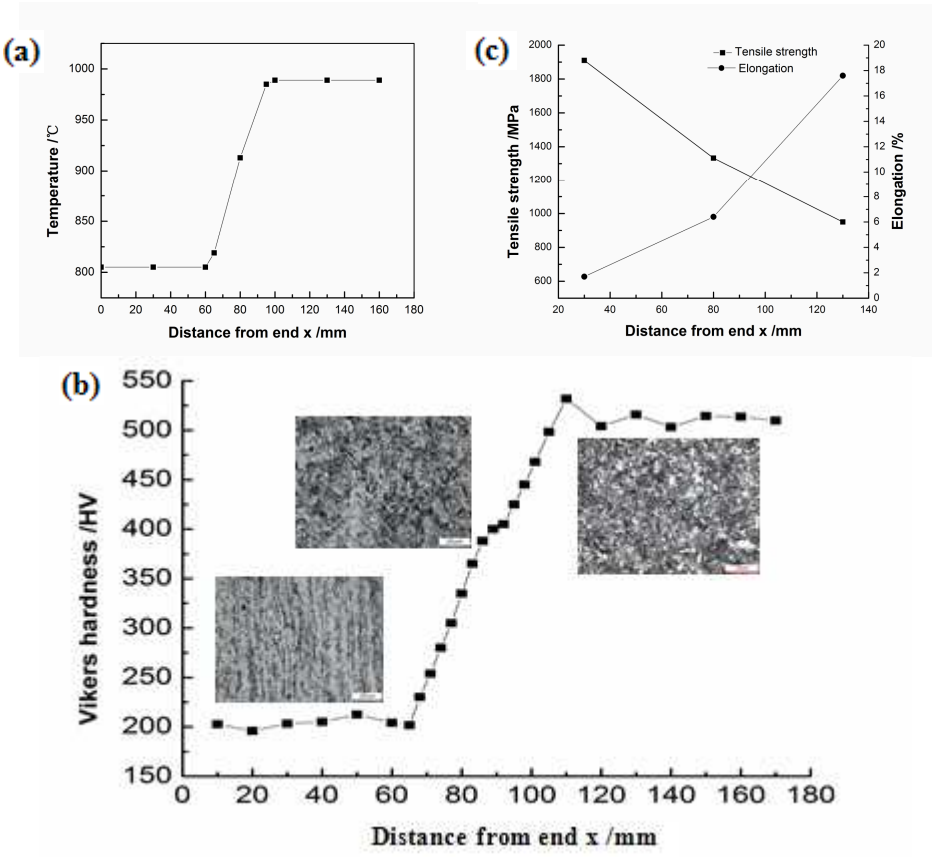


Fig. 3 Temperature, hardness and tensile strength versus distance from end

The microstructure of the samples processed under different conditions, hot-stamped as well as hot-stamped and subsequently tempered, respectively, were evaluated by OM and SEM. For the OM analysis, Nital was used as the etching agent by which ferrite, bainite, and martensite phases can be detected. The microstructure of the steel was characterized by a SEM after the conventional Nital etching. The mechanical properties of the processed samples were determined by tensile testing using disproportional samples due to the resistance heating samples are very small.

Results and Discussions for Tempering Treatment.

Microstructural Investigations. The OM microstructural changes during the tempering treatment are presented in Figure 4. A clear lath martensitic microstructure is representative of the hot-stamped specimen, while this characteristic began to blur in the microstructure of the tempered 5 minutes specimens. The SEM images of hot-stamped as well as hot-stamped and tempered specimens are compared in Figure 5. While the needle-like microstructure is observed for the quenched steel (Figure 5(a)), the micrograph of the quenched and tempered specimen (Figure 5(b,c)) clearly demonstrates the carbides precipitation. This observation agrees with well-known phenomena occurring during the tempering process in which carbides constitute, and a needle-like martensite phase is replaced by equilibrated phases (ferrite and cementite)[5].

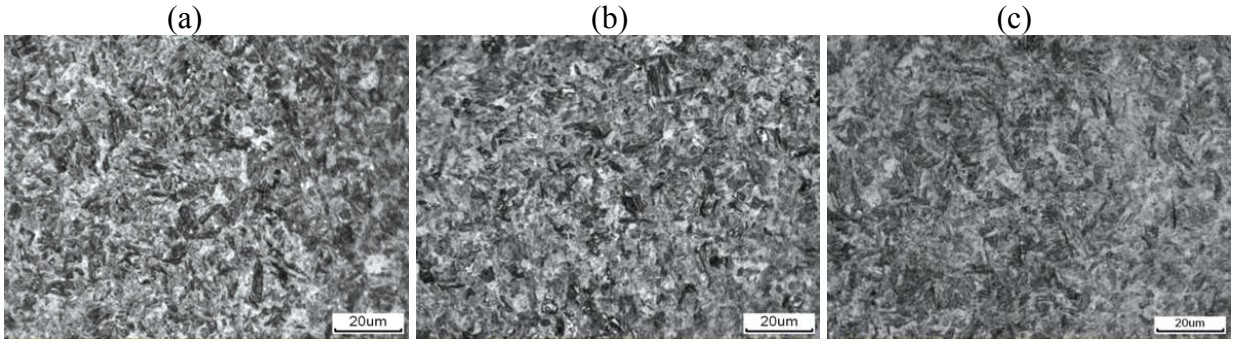


Fig. 4 OM microstructure images of (a) hot-stamped specimen, hot-stamped specimen and tempered at 250 ℃ for (b) 5 min, (c) 60 min

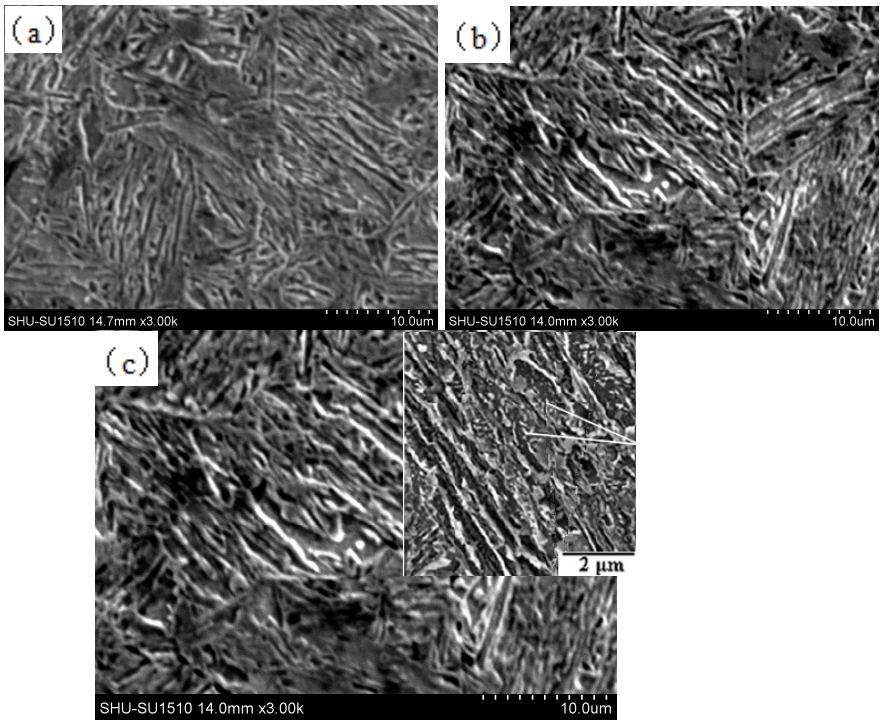


Fig. 5 SEM images after (a) hot stamping, (b, c) hot stamping + tempering at 250 ℃for 15 min.

Mechanical Properties. The mechanical properties of the studied specimens are represented in Figure 6. Tensile strength gradually decreases as the tempering time and temperature increase.While yield strength has a tend that increasing at shorter tempering times and decreasing at longer tempering times. It is well known that the quenching specimens shows a high dislocation density and as well as the hot-stamped specimens[6], while the lower dislocation density, together with the presence of nano-carbides, distinguishes the tempered specimens. The annihilation of dislocations during tempering treatment has been indicated by Gorynin et al. [7]. The increase of yield strength after tempering treatment can be related to the effect of carbide strengthening. The decreased effect of carbide strengthening at long tempering times can be related to the growth of carbides based on the "Ostwald ripening" mechanism[8] which decreases the contribution of carbide strengthening. The low yield strength/tensile strength ratio expresses the capacity of modern high-strength steels' grades to give a reliable behavior in service[9]. As seen in Figure 6 (b), when the tempered temperature at 250 ℃ the yield strength/tensile strength ratio is at a lower level. When holding times are at 5~30 min, the yield strength/tensile strength ratio increases while the yield strength/tensile strength ratio decreases when holding times are at 30~60 min. The product of tensile strength and elongation represents the overall mechanical properties of steel. As seen in Figure 6 (c), the product of tensile strength and elongation is at a high level. Compered with Figure 6 (b) and Figure 6 (c), it is found that the condition of temperature 250 ℃ and holding time 45 min can achieve the best comprehensive mechanical properties.

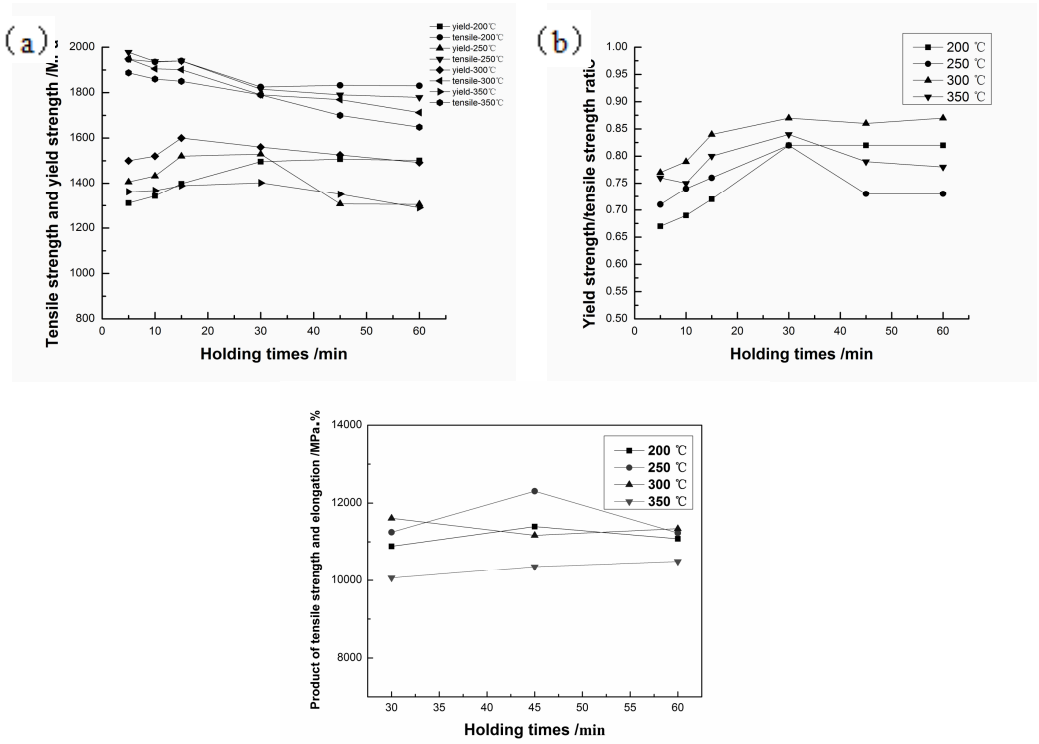


Fig.6 Mechanical properties of the studied steel after hot-stamped and tempered at different temperatures and times.

Summary

Non-isothermal resistance heating in the hot stamping of quenchable steel sheets was developed in order to form ultra-high strength steel products with tailored properties. The formed products can be obtained easily by changing the width of steel sheets and additionally mechanical properties of these products changed slowly and flexibly. The products with tensile strength from 600 MPa to 1800 MPa and elongation from 5 % to 18 % are formed. And mechanical properties can be changed with engineers' intention and special needs.

Hot stamping and tempering process makes it possible that significantly increase the ductility of hot stamping sample without decreasing the tensile strength greatly. By analyzing the different conditions that tempering temperature and holding time on the microstructure and properties of the sample it can be found that the condition of temperature 250 ℃ and holding time 45 min can achieve the best comprehensive mechanical properties.

References

[1] Sun Caina, Zhang Henghua, Effect of high temperature deformation on characteristics of γ→α phase transition of an E36 ship plate steel, Transactions of materials and heat treatment 2013, 34(9): 132-139.

[2] K. Mori, Y. Okuda, Tailor die quenching in hot stamping for producing ultra-high strength steel formed parts having strength distribution, CIRP Annals - Manufacturing Technology 59 (2010) 291–294

[3] XIN Peixin, Investigations on hot stamping technology based on Quenching & Partitioning (Q&P) process. 2013

[4] Seijiro Maki, Yuuki Tanaka and Ken-ichiro Mori, Resistance heating characteristics of high-strength steel sheet blank for hot press forming. (Trans Tech Publications, Switzerland 2007)

[5] W. Bleck: Materials Science of Steel, Textbook for RWTH students, Verlag Mainz, Aachen, 2007.

[6] R.L. Brockenbrough & Associates, Inc, Effect of Yield-Tensile Ratio on Structural Behaviour-High Performance Steels for Bridge Construction, ONR-AISI Agreement No.N00014-94-2-0002,1995.

[7] I.V. Gorynin, V.V. Rybin, V.A. Malyshevskii, T.G. Semicheva, and L.G. Sherokhina: Transformations of dislocation martensite in tempering secondary-hardening steel[J]. Met. Sci. Heat Treat., 1999, vol. 41,pp. 377–83.

[8] R.E. Reed-Hill and R. Abbaschian: Physical Metallurgy Principles, 3rd ed., PWS Publishing Company, Boston, 1991.

[9] A.C. Bannister and S.J. Trail: Structural Integrity Assessment Procedures for European Industry. British steel plc., 1996.

Advanced Materials Research Vol. 936 (2014) pp 1836-1839
© (2014) Trans Tech Publications, Switzerland
doi:10.4028/www.scientific.net/AMR.936.1836

Comparisons of Explicit and Implicit Finite Element Methods for Sheet Metal Forming

Lei Chen[1, a]

[1] Institute of Mechanical Engineering, Hangzhou Dianzi University, 310018, China

[a]ujs_cl@qq.com

Keywords: sheet metal forming, finite element method, simulation, comparison

Abstract: Sheet metal forming is one of the most commonly practiced fabrication processes in industry. Numerical simulations of the complex parts are possible by finite element method in the past thirty years. The most important problem of the simulation is the reliability of the model. Static implicit method (SI) and dynamic explicit method (DE) were used to simulation sheet metal forming process. It was found that simulation speed in dynamic explicit software has large effect on the simulation results. The best simulation speed is 5~10 m/s. Compared with the simulation and experimental results of thickness, draw-in and CPU time, the DE method is preferred.

Introduction

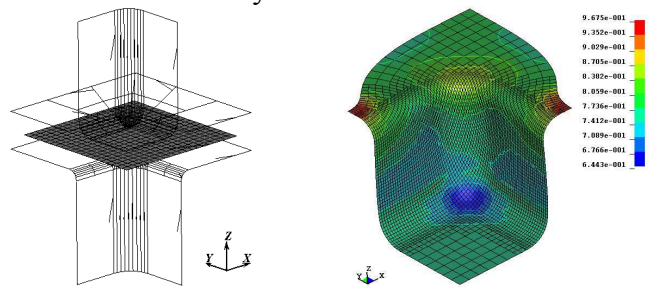
Sheet metal forming is one of the most commonly practiced fabrication processes in industry. Throughout the years, the sheet metal forming industry experienced technological advances that allowed the production of complex parts. However, the advances in die design and fabrication progressed at a much slower rate, and they still depend heavily on trial-and-error and the experiences of skilled workers.

With the development of the mechanical theory, finite element method and computer science, numerical simulation of sheet metal forming have been developed. It allows an early assessment of the part during the design stage, and enables a reduction in the product development time. Numerical simulations of the complex parts are possible by finite element method in the past thirty years. The most important problem of the simulation is the reliability of the model. An inappropriate model can lead to the long computer time and wrong results. There are at least two approaches available to model the sheet forming process. One is static implicit method (SI) and the other is dynamic explicit method (DE). Narkeeran et al. [1] utilized the explicit method to analyze the contact based forming operation of a production stamping process, and then an implicit solution was performed to simulate the springback that develops in a blank after the forming pressure has been removed. Ls-dyna3D and Pamstamp is the typical dynamic explicit software to simulate the sheet metal forming. Silva [2] illustrates the utilization of a dynamic explicit finite element computer program (PAM-STAMP) for evaluating the consequences of possible changes in process parameters and for debugging the causes of undesirable manufacturing occurrences. Firat [3] demonstrated in the stretch drawing process simulation using the Ls-Dyna finite element analysis code. Qiu [4] finishes the simulation of an engine hood panel's forming process with eta/DYNAFORM. Marc, Autoform and Abaqus/Implcit are the typical static implicit software. Taylor [5] used Abaqus to simulation the sheet metal forming. Kubli [6] optimized of sheet metal forming processes using the special purpose program AUTOFORM. Nguyen [7] described an inverse approach (IA) formulation for the analysis of tubes under free hydroforming conditions using the Marc finite element code. In this paper, the Numisheet 93 square benchmark problem was used to analyze the difference between the dynamic software Lsdyna and implicit software Marc. The simulation results were compared with the experiments.

Finite Element Model

Fig.1 shows the finite element model and simulation result. The blank thickness is 0.78 mm. the friction coefficient is 0.144. The blank holding force is 19.6KN. The plastic behavior of the sheet

material was modeled using a power law relation ($\sigma = K(\varepsilon_0 + \varepsilon)^n$), where σ is stress, K is material strength coefficient, ε_0 is initial strain, ε is strain, n is strain hardening coefficient. The material parameters are shown in Table1. The Barlat yield criterion was used.



(a) (b)

Fig.1 The FEM model and result

(a) mesh (b) simulation result

TABLE 1 MATERIALS PARAMETER

	E/GPa	*v*	*r*	Stress-strain relation /MPa
0°			1.79	
45°	206	0.3	1.51	$\sigma = 565.32(0.007117 + \varepsilon_p)^{0.2589}$
90°			2.27	

Results and Discussion

Simulation speed in dynamic explicit software has large effect on the simulation results. So the simulation speed must be optimized firstly. Fig.2 shows the CPU time needed for different simulation speeds (1~100m/s). From the Fig.2, we can arrive that the CPU time decreases quickly with the increase of the simulation speed. When the simulation speed is more than 20 m/s, the CPU time is nearly steady.

Fig.3 shows the blank thickness with the different simulation speeds. From Fig.3, we can see that the largest and smallest thickness of the blank are nearly invariable with the speed of 1~10 m/s, and when the speed is larger than 10 m/s, the largest thickness decrease slowly and the smallest thickness decrease quickly. So the simulation results is unbelievably.

Fig.4 defines the draw-in length of the blank. Fig.5 shows the comparison of the simulation results and experimental results [8]. From Fig.5, we can see that the variations of the simulation results are very small with the simulation speed of 1~10m/s. When the simulation speed is larger than 20 m/s, the simulation results vary largely. Fig.6 shows the punch force with different simulation speeds. From the Fig.6, we can see that the punch force turn fluctuately largely with the increase of the simulation speed. Comparing with the experimental results, the best simulation speed is 5~10 m/s.

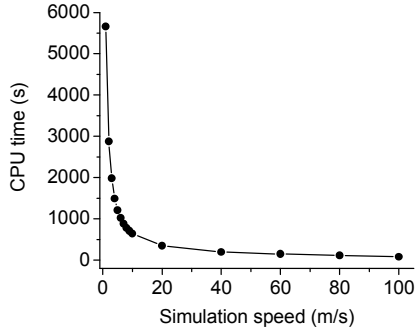


Fig.2 CPU time consumed with varied simulation speeds

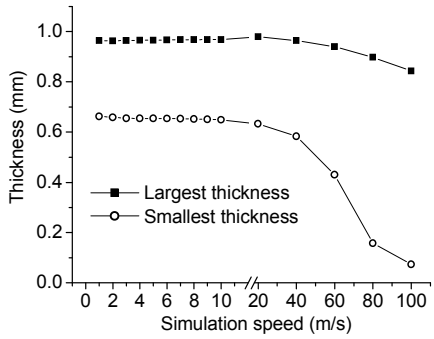


Fig.3 Thickness of element versus different simulation speeds

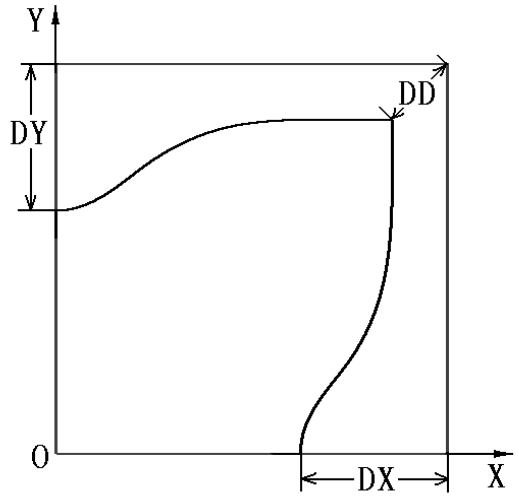


Fig.4 Definition of Draw-in length

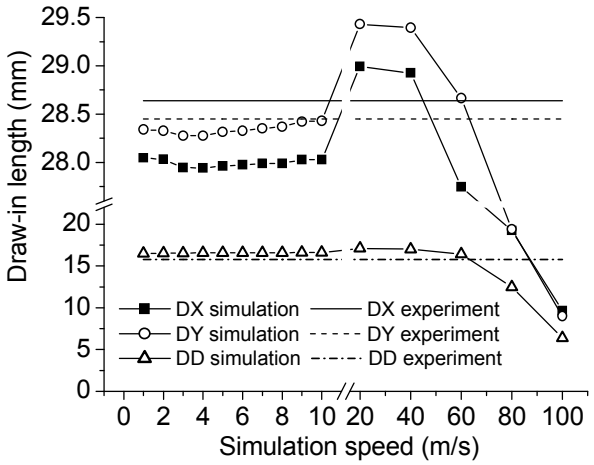
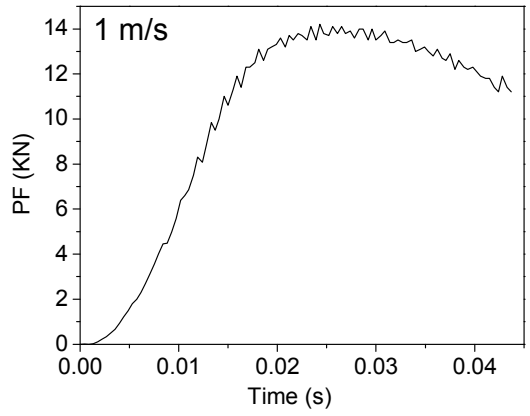
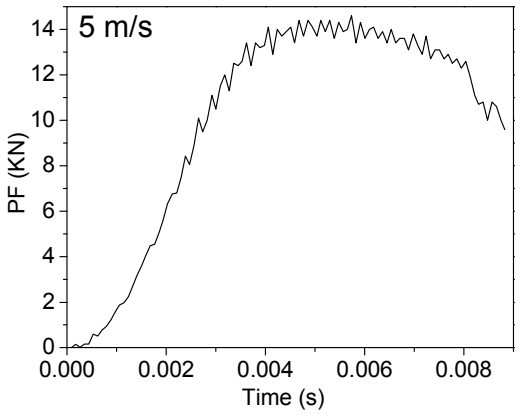


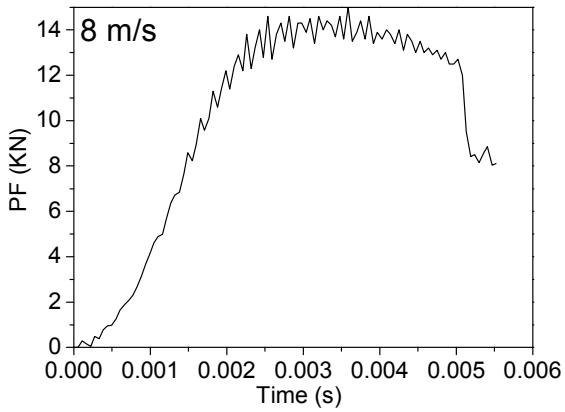
Fig.5 Draw-in length of flange with different simulation speeds



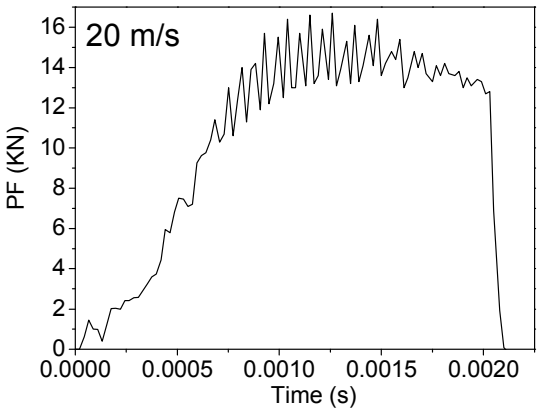
(a)



(b)



(c)



(d)

Fig.6 Punch force versus different simulation speeds

Table 2 shows the simulation results using different methods. The simulation speed in dynamic explicit method is 5 m/s. From the table, we can see that the Max thickness of SI is larger than that of DE, whilst the min thickness of SI is smaller than that of DE. The draw-in of SI is smaller than that of DE. The CPU time of SI is ten times of that of DE. Compared with the experimental and simulation results , the DE method is preferred.

TABLE 2 SIMULATION RESULTS USING DIFFERENT METHODS

		Static implict	Dynamic explicit
Thickness (mm)	Max.	0.994	0.967496
	Min.	0.6233	0.651557
Draw-in (mm)	DX	26.4917	27.98764
	DY	25.9701	28.37004
	DD	15.3011	16.58653
CPU time (s)		8279	782

Summary

Static implicit method (SI) and dynamic explicit method (DE) were used to simulation sheet metal forming process. It was found that simulation speed in dynamic explicit software has large effect on the simulation results. The best simulation speed is 5~10 m/s. Compared with the simulation and experimental results of thickness, draw-in and CPU time, the DE method is preferred.

Acknowledgement

The financial support for this work is from Foundation of Hangzhou Dianzi University (No. KYS015613011) and is greatly appreciated.

References

[1] N. Narkeeran, L.Michael, Predicting springback in sheet metal forming: an explicit to implicit sequential solution procedure, Finite Elements in Analysis and Design 33(1999) 29-42.

[2] M.B. Silva, R.M.S.O. Baptista, Stamping of automotive components: a numerical and experimental investigation, J. Mater. Processing Technol. 155–156 (2004) 1489-1496.

[3] M. Firat, Computer aided analysis and design of sheet metal forming processes: Part II – Deformation response modeling, Mater. Des. 28 (2007) 1304-1310.

[4] Hongyang Qiu, Yajuan Huang, Qiang Liu, The study of engine hood panel forming based on numerical simulation technology, J. Mater. Processing Technol.187–188 (2007) 140-144.

[5] L.Taylor, J. Cao, A.P. Karafillis, Numerical simulation of sheet metal forming, J.Mater. Processing Technol. 50 (1995) 168-179.

[6] W. Kubli, J. Reissner, Optimization of sheet metal forming processes using the special purpose program AUTOFORM, J. Mater. Processing Technol. 50 (1995) 292-305.

[7] B. N. Nguyen, K. I. Johnson, Analysis of Tube Free Hydroforming Using an Inverse Approach with FLD-Based Adjustment of Process Parameters, J. Eng. Mater. Technol. 125(2003), 133-140.

[8] J. Danckert, Experimental investigation of a square cup deep drawing process, J. Mater. Processing Technol. 50(1995) 375-384.

Advanced Materials Research Vol. 936 (2014) pp 1840-1844
© (2014) Trans Tech Publications, Switzerland
doi:10.4028/www.scientific.net/AMR.936.1840

Numerical Simulation Study of the Influence of Turning Depth on the Bending Vibration Mode of Work-piece

Wu Ming-ming[1,a], Li Shun-cai[1,b], Zhang Qiang[2,c]

[1]School of Mechanical and Electrical Engineering, Jiangsu Normal University, Xuzhou 221116, China

[2] Department of Aerospace Ground, Air Force Logistics College, Xuzhou 221000, China

[a]xswumingming@163.com, [b]jnulishuncai@gmail.com (corresponding author),

[c]zhangqiang2000.student@sina.com

Keyword: Turning Work-piece; Bending Vibration; Model; Turning Depth; Numerical Simulation

Abstract: The mechanical models with and without thimble constraints for the turning work-piece are built respectively, applying ABAQUS software to analyze the modes of work-piece, then the law of the influence that different turning depth on the bending modes of work-piece is obtained. The study indicates that each-order natural frequency increase gradually in linear form for the work-piece without thimble constraint, while for the work-piece with thimble constraint, the natural frequency of the first four orders decrease linearly with the increase in the turning depth, but the change of high order frequency is relatively complicated.

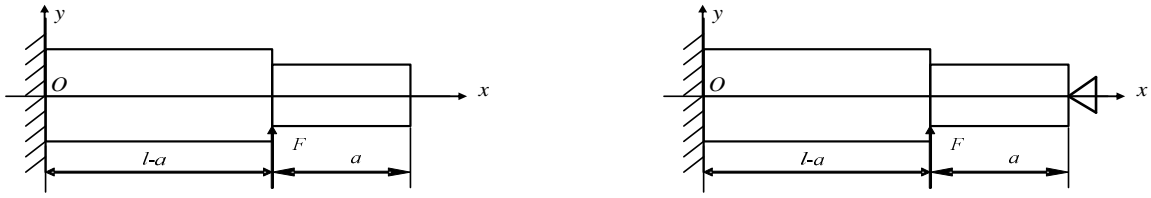
Introduction

The effects of the dynamic characteristics especially the vibration characteristics of the work-piece and the cutting tool on the quality of products in the turning process are more and more concerned. Structural vibration characteristic analysis involves modal analysis, transient dynamic analysis, harmonic response and random spectrum analysis and so on. Modal analysis of structure is the basic of all structure vibrations analysis; it mainly studies the natural frequency and vibration mode of the structure. Modal analysis is the process to get the modal parameters and the parameters can be gained by calculation or experimental analysis [1-2]. The turning process of work-piece is time-variation and nonlinear [3]. At present, many basic researches have been studied; they are mainly about the deformation and vibration of work-piece [4-5], the vibration and wear of cutting tool [6-7], theoretical analysis and experimental test of dynamic characteristics [8]. When we analyze the modal of the work-piece in turning process, it is convenient to grasp the main modal characteristics of the work-piece in the easily effected frequency range at any processing time; it can also provide important reference for dynamic processing design of work-piece and diagnosis of vibration problem in manufacturing process. This article is based on the finite element calculation method, it studies the rule that how the turning depth influence the bending vibration model of the work-piece in the turning process.

Mechanical Model of Turning Work-piece

The work-piece can be simplified to a stepped shaft in turning process, seen as Fig. 1, turn short axis without thimble constraints; when turn long axis, there is thimble constraints on the right side.

As the turning tool moves, the location of the cutting force *F* and length *a* of the axis that has been cut will change along with time; with the material removals, the diameter and inertia moment of axis for the work-piece change with time piece-wisely.



(a) without thimble constraints (b) with thimble constraints

Fig. 1 Mechanical Model of Turning Work-piece

The free vibration equation of the work-piece is showed as follows

$$\frac{\partial^2}{\partial x^2}[EJ(x)\frac{\partial^2 w(x,t)}{\partial x^2}]+m(x)\frac{\partial^2 w(x,t)}{\partial t^2}=0 \quad (1)$$

Among them, $J(x)$ is the moment of inertia of axis on any section of the work-piece, m(x) is the weight of per unit length of the work-piece, $w(x,t)$ is the deflection on section x at time t.

Formula (1) is a time-varying differential equation, it's very difficult to seek out the modal analysis solution of the time-dependent dynamics in a variable boundary by analytical method, we will apply ABAQUS software which is based on finite element method to work out numerical solution.

Numerical Calculation Scheme and Finite Element Model

Set the calculating scheme of the short axis as following:

Select the parameters of the axis as following: Length l=100mm , diameter d=40mm , density ρ=7.8×10^{3}kg/m^3 ,turning speed n=600rpm, calculate the natural frequency and the vibration mode of the work-piece when the turning depth e=0.0, 0.5, 1.0, 1.5, 2.0 and 2.5mm ,respectively ,and the turning length a=50.0mm.

Set the calculating scheme of the long axis as following:

Select the parameters of the axis as following: Length l=600mm , diameter d=30mm,density ρ=7.8×10^{3}kg/m^3 ,turning speed n=600rpm , calculate the natural frequency and the vibration mode of the work-piece when turning depth e=0.0, 0.5, 1.0, 1.5, 2.0 and 2.5mm ,respectively, and the turning length a=300.0mm.

The numerical simulation is conducted by using software ABAQUS ，a large-deformation theory for static analysis is presented , the modal parameters are gained by linear perturbation analysis method , the element birth and death is used to realize the material failure in turning process. Short axis uses solid model, select C3D4 first-order tetrahedral element to mesh it; long axis uses beam element modeling, select BEAM31 to mesh it, Figure 2 is the corresponding finite element mesh figure of Figure 1.

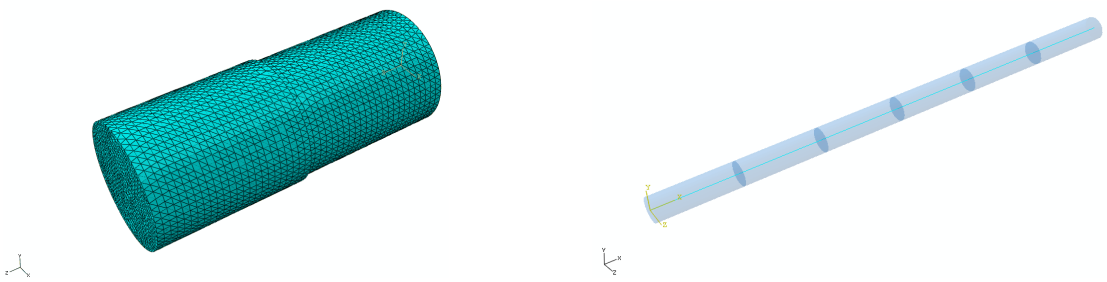
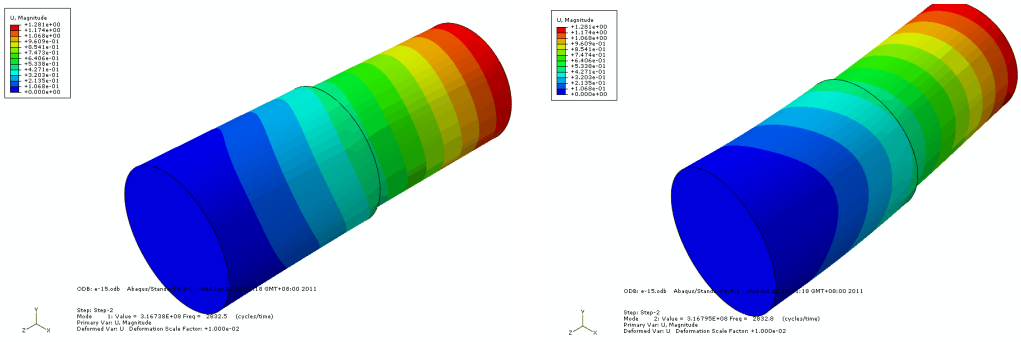


Fig.2 Finite Element Meshing

The Result of the Modal Simulation of the Work-piece in Turning Process

The Simulation Result of the Short Axis

Figure 3 shows the first and the second order bending vibration model of the work-piece when we select the parameters: turning speed n=600rmp, turning depth e=1.5mm, turning length a=50.0mm; table 1 shows the natural frequency f of the work-piece with different turning depth e; figure 4 shows the change curve that the first order natural frequency f_1 of the work-piece change along with turning depth e in turning process.



(a)First order (b) Second order

Fig. 3 The first and the second order vibration mode of the work-piece at e=1.5mm

TABLE 1 BENDING NATURAL FREQUENCY F OF THE WORK-PIECE WITH DIFFERENT TURNING DEPTH

Natural Frequency	Turning Depth [e/mm]					
[f/Hz]	0	0.5	1.0	1.5	2.0	2.5
1st order	2658.4	2716.5	2773.2	2832.5	2892.9	2953.7
2nd order	2658.7	2716.7	2773.4	2832.8	2893.0	2954.3

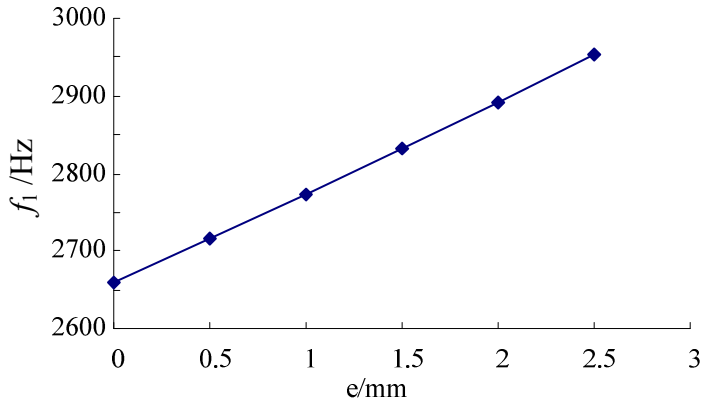
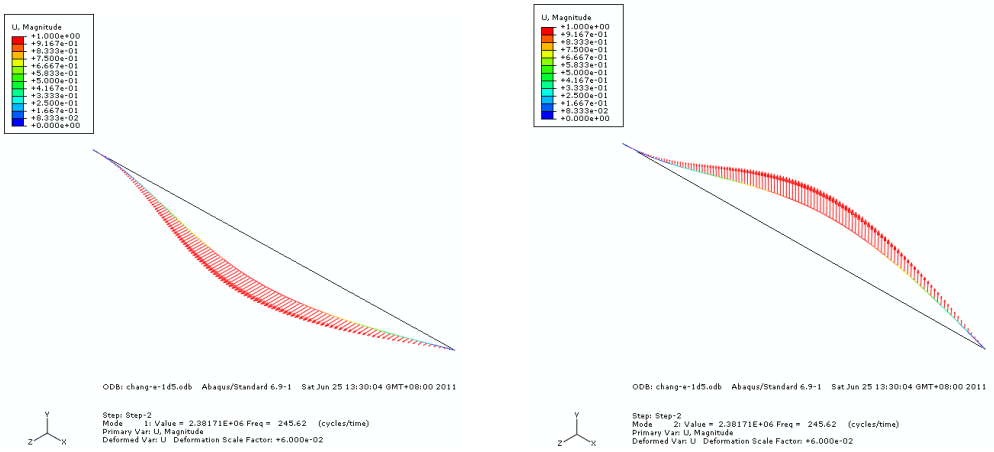


Fig. 4 Change Curve of the First-order Frequency with the Turning Depth e

According to figure 4, we know w that with the turning depth *e* increasing in turning process, each-order natural frequency *f* of the work-piece increases gradually in linear form.

The Simulation Result of the Long Axis

Figure 5 shows the first and the second order bending vibration model of the work-piece when we select the parameters: turning speed n=600rmp, turning depth e=1.5mm, turning length a=300.0mm; table 2 shows the natural frequency f of the work-piece with different turning depth e. Figure 6 shows the change curve that the first order natural frequency f_1 of the work-piece change along with turning depth e in turning process.



(a) First Order (b) Second Order

Fig. 5 The First and Second Order Vibration Mode of the Long Axis at e=1.5mm

TABLE 2 NATURAL FREQUENCY *F* OF LONG AXIS WITH DIFFERENT TURNING DEPTH *E*

Natural Frequency	Turning Depth [*e*/mm]					
[*f*/Hz]	0	0.5	1.0	1.5	2.0	2.5
1st order	256.86	253.41	249.65	245.62	241.36	236.93
2nd order	256.86	253.41	249.65	245.62	241.36	236.93

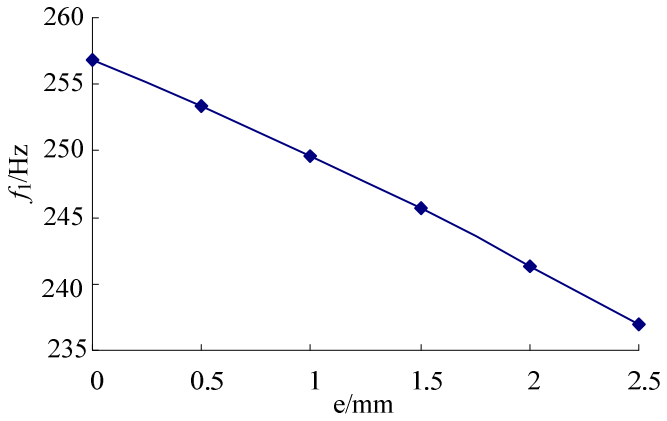


Fig. 6 Change Curve of First-order Natural Frequency f_1 with Different Turning Depth of the Long Axis

According to table 2 we know that with the turning depth e increases in turning process, the first-four-order natural frequency f of the work-piece decreases gradually mainly in linear form ,but the change of high order frequency is relatively complicated, for example the five order natural frequency increases constantly but the sixth order natural frequency decrease constantly. This

mainly because, as the turning depth e increases, the material of work-piece decreases, structure changes and integral rigidity decreases constantly, which cause the low-order natural frequency decreases. But the trend of high order natural frequency is relatively complicated due to the boundary condition and the effect based on nonlinear algorithm.

Conclusions

Mechanical model is built based on turning work-piece with and without thimble constraint , the law of the influence that turning depth of the work-piece on bending modes is studied by using the software ABAQUS to conduct numerical simulation , then we get the low order natural frequency and the vibration curve of the work-piece. Research shows that as the turning depth increases, each-order natural frequency increases gradually in linear form without thimble constraints, while for the work-piece with the thimble constraint, the first four-order natural frequency decreases in linear form, but the higher order frequency are relatively complicated.

Acknowledgements

The authors gratefully acknowledge the financial support from the National Natural Science Foundation of China (Project No.50974107), the Qing Lan Project of Jiangsu Province (10QLD006), “333”project of Jiangsu Province.

References

[1] Ren C., Modal analysis of work-piece in turning operation, Mechanical research & application, 2006, 19(4): 32-33 (in Chinese)

[2] Zheng J., Zhang M., Meng Q., Experimental Modal Analysis and its Application in Structure Dynamic Characters of CNCM machine Tools, Measurement and control technology, 2007,26(12):28-31 (in Chinese)

[3] Li S., Meng H., Time-Varying Characteristics of Bending Deformation of Work-Piece in the Turning Process, Advanced Materials Research, 2011, 337:pp 203-208.

[4] Li S., Zhuo S., Jiang H., Meng Hua. Numerical Simulation of Time-dependent Model of Work-piece During Turning, Noise and vibration control, 2012, 32(4): 60-62 (in Chinese)

[5] Meng H., Li S., Liu Y., Test and analysis of vibration response of turning tool in turning process, The experiment technology and management, 2012.3,29(3):80-83 (in Chinese)

[6] Zhang Q., Li S., Huang C., Cai C., Experimental Study on Turning Vibration Responses of Cutting Tool on Upper and Lower Surface, Coal mine machinery, 2013, 34(10): 63-65. (in Chinese)

[7] Huang S., Chen H., Fu P., Gan J., Dynamic tool wear monitoring in CNC turning. Machinery Design & Manufacture, 2010,(2):191-192. (in Chinese)

[8] Zhang B., Zhang Q.; Li S., Experimental Study on the Vibration Response of the Work-piece during the Numerical Control Milling. Machine Tool & Hydraulics, 2013, 41(5):30-32. (in Chinese)

Advanced Materials Research Vol. 936 (2014) pp 1845-1850
© (2014) Trans Tech Publications, Switzerland
doi:10.4028/www.scientific.net/AMR.936.1845

Application of Multidisciplinary Design Optimization in the Casting Process Optimization

WANG Ming-zhi[1, a], CHEN Gang[1, b], ZHOU Zhi[2, c]

[1]School of Materials Science and Engineering, Jiangsu University, Zhenjiang, China

[2]Jiangsu Zhonglian Aluminum co., LTD, Wuxi, China

[a]wissman@126.com, [b]chengang70@126.com, [c]zlwjs@126.com

Keywords: multidisciplinary design optimization; casting process optimization; iSIGHT; ProCAST

Abstract. Casting process optimization usually includes modifying the mold structure, regulating the pouring temperature, changing pouring time, etc., which involves the mold structure optimization, but also involves optimization of temperature field. In order to get a better process conditions, it will generally make multiple simulation test under the different processes conditions. Many parameters should be set in each simulation test. In order to make casting engineers get liberation from a lot of repetitive work, multidisciplinary design optimization technology is firstly brought into the field of casting, successfully achieved ProCAST integrated into iSIGHT. The method of sample points collected is used in Optimal Latin Hypercube Design, and the building of approximation models is based on Kriging Model. On this basis, the optimization of the objective function is applied to Multi-Island Genetic Algorithm to obtain a global optimal solution. Compared to the verification result of the corresponding simulation, the relative error of the global optimal solution is 0.47%. The result of optimization is ensure average shrinkage rate of casting a smaller value when technological yield of the casting from 54.6% of the existing production case up to 61.1%.

Introduction

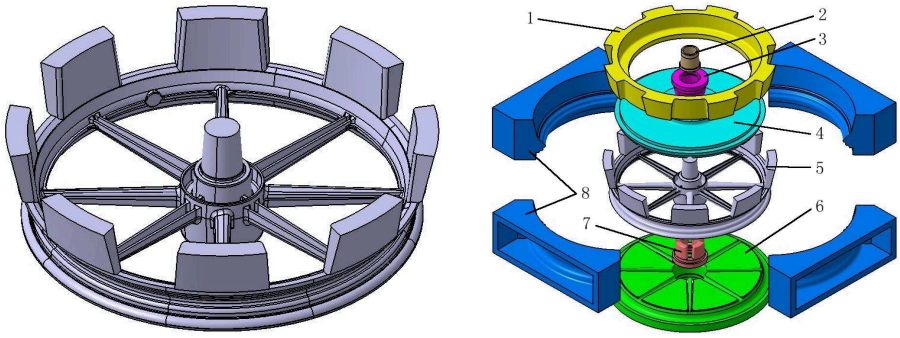
In recent years, the casting process simulation experiment is carried out in the optimization of casting process by a lot of technical personnel. ProCAST is one of the excellent casting process simulation software. The usual steps are: setting up 3D geometric model, grid generation, pre-processing to set parameters, calling the solver, post-processing to obtain the required results. If we want to get a better technological condition, a series of simulation experiment under different conditions are usually carried out. Because each simulation experiment will take a long calculation time, casting technician have to spend many days to constantly modify the geometry, meshing, setting simulation parameters and analyze and compare the results. The engineer usually find out the influence trend of the process parameters based on experience or using orthogonal experimental design and select the relative optimal combination as the process parameters process scheme, which rarely involves the use of optimization methods. Although a relatively good technology program is found out though the traditional optimization process, the optimization process does not guarantee the resulting solution is optimal. Therefore this optimization process, which is lengthy, inefficient, short of optimization method, is unsatisfactory.

Multidisciplinary Design Optimization (MDO) is a new method for engineering design, which takes full advantage of the respective strengths of each sub-discipline part, organize and manage the overall system design variables and optimization goals, finally allowing the system to get the global optimal solution. [1]

The current research about the multidisciplinary design optimization mainly concentrated in the field of aircraft design. [2-4] However, with the gradual development of multidisciplinary design optimization, workers in other fields have also done some research. [5-7] In the paper, we firstly introduce the method of multidisciplinary design optimization into the field of casting, successfully achieve ProCAST and the other software of casting process optimization integrated into iSIGHT. Here, taking casting process optimization of the wheel as an example, we specifically detail the method of multidisciplinary design optimization applied to the casting process optimization.

Optimization Model Building

The research object of this paper is the aluminum alloy wheel, using metal mold gravity casting, pouring way as the top-injection style, with eight risers uniformly distributed at the top position in the circumferential direction. The geometric model of the casting and molds are shown in **Fig. 1**.



(a) (b)

Fig. 1 (a) Casting of the aluminum alloy wheel; (b) Schematic diagram of casting and molds(1-riser mold, 2-gate mold,3-upper die core,4-upper die,5-casting,6-lower die,7-lower die core,8-side mold)

Design Variable

The three main parameters of the riser shape are selected as the design variables in this paper.

$$X=[\text{angle0}, \text{height0}, \text{width0}]^T. \quad (1)$$

Where angle0 is the inclination angle of the riser's side face respecting to the vertical plane, height0 is the riser height, width0 is the riser width. Each parameter is shown in **Fig. 2**.

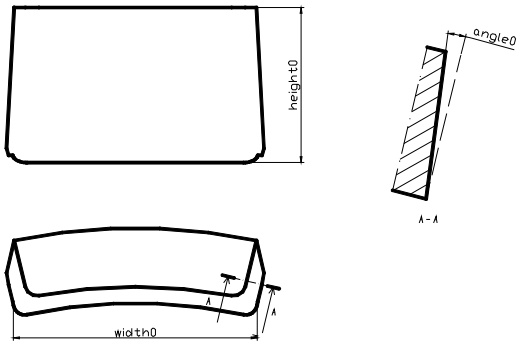


Fig. 2 Schematic diagram of the riser shape

The range of the three design variables about the riser shape are shown in table 1.

Table 1 The range of the design variables

design variables	lower limit	upper limit
angle0 [°]	3	9
height0 [mm]	55	75
width0 [mm]	90	110

Objective Function

There is no doubt that a good casting process is to make the casting shrinkage rate (f_1) as low as possible, at the same time to improve the casting process yield (f_2) as high as possible. Normally the two objectives are conflicting, that is, this is a multi-objective optimization problem. The multi-objective problem is transformed into a single objective problem through constructing a new objective function in this article. Define a new objective function as below,

$$y = w_1 \cdot f_1 + w_2 \cdot \frac{1}{f_2}. \tag{2}$$

Where, f_1 is the average shrinkage rate of the casting removal of the casting system and the riser, f_2 is the casting process yield, w_1 and w_2 are the weight coefficients of the two functions respectively.

According to the simulation result of the current process, it is found that the value of f_1 is about 0.01 and the value of f_2 is about 0.55. Due to the requirement of shrinkage rate is usually more important than the casting process yield, comprehensive considering w_1 =300, w_2=1.

Integration Process

Technological Process

Studied contents in this paper based on the software of iSIGHT integrated optimization platform, the integration process is shown in **Fig. 3**.

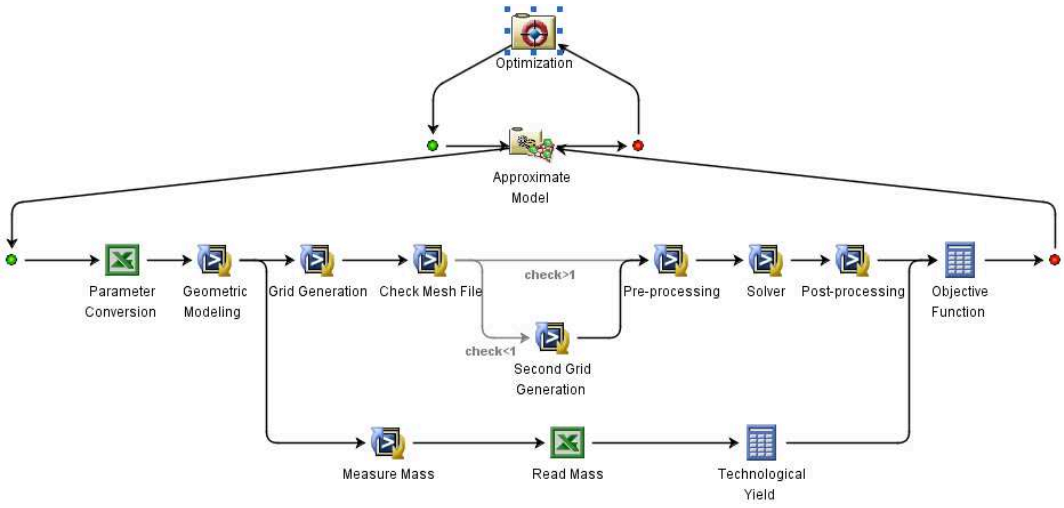


Fig. 3 Integration process

The first excel component "Parameter Conversion" shown in Figure 4 is the role of converting the three riser shape parameters angle0, height0, width0 data into CAD modeling process data. After the component "Geometric Modeling" completing, it is divided into two two processes simultaneously, one flow is meshing and generating the ProCAST simulation, then obtaining the average shrinkage rate of castings which excluding the part of the riser and gating system. The other flow is measuring the mass of the casting etc., then obtaining the casting process yield. Finally, the two processes get together, calculating the value of the objective function.

As the pre-processing of ProCAST software needs high quality tetrahedral mesh, thus to ensure the grid size of the thin-walled parts such as spokes is smaller enough, at the same time the grid size of the large surface on the die molds is bigger enough. While doing so, it reduces the number of the mesh model and decrease the computation time. Meshing model is shown in **Fig. 4**.

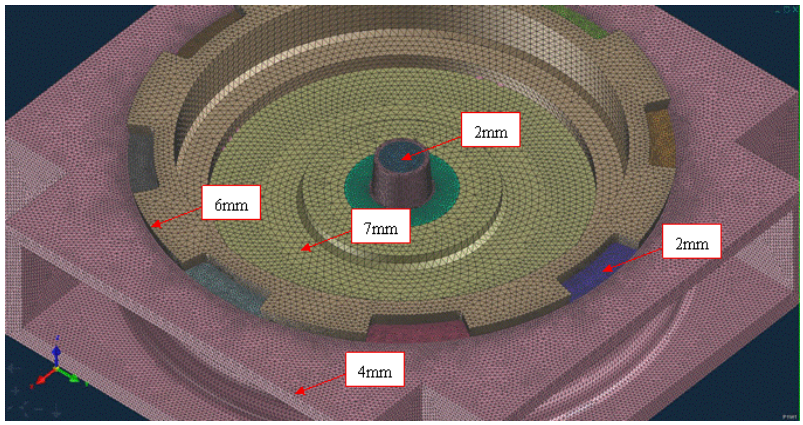


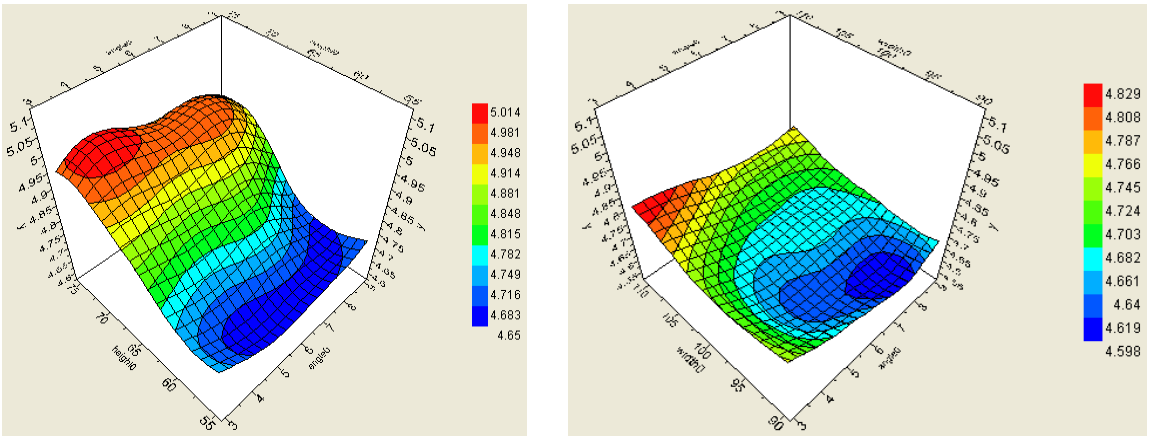
Fig. 4 Meshing model diagram

Building the Approximate Model

For engineering problems requiring casting process simulation, because of the time spent calculating the simulation experiment is usually very long. Therefore, the method of constructing the approximation model is considered in indirect optimization, it can reduce the computational cost and shorten the optimization time [8].

The approximate model is constructed by Kriging model in this article. Kriging Model which did not make any restrictions on the form of unknown function, can adaptively adjust the weights assigned each sample point. As Kriging Model take into account the spatial correlation of the regression error terms, the quality of approximate surface is very high [9].

The approximate model is based on the Optimal Latin hypercube design method in this article, finally it is concluded that the R-squared error value of the approximate model is 0.90721, of special note is on engineering, general requirement of R-squared is greater than 0.9. Therefore, the approximate model constructed in this article has a higher credibility. The approximate surface of angle0 and height0, angle0 and width0 on the value of an objective function diagram are shown in **Fig. 5(a)** and **Fig. 5(b)**, respectively.



(a) **(b)**

Fig. 5 (a) The approximate of angle0 and height0 to the objective function; (b) The approximate of angle0 and width0 to the objective function

Optimization Process

Optimization Methods

On the basis of the approximate model with the high credibility, we use a global optimization algorithm for optimization. There are many global optimization methods. Multi-island Genetic Algorithm (MIGA) is a improved optimization algorithm from the distribution of parallel genetic

algorithm, avoiding the easy premature phenomenon appeared in the traditional genetic algorithm. And MIGA algorithm is a pseudo-parallel genetic algorithm which can effectively improve the computational efficiency [10, 11]. Therefore, Multi-island Genetic Algorithm is employed in this paper. The sub-populations size is set to 10, the number of islands is set to 10, genetic crossover probability is set to 0.9.

Optimization Results

With the deepening of MIGA optimization process, after the end of the 2002 iterations, the last occurrence of "Feasibility=9" solution is the global optimal solution. The global optimal solution which corresponds to the design variables (angle0=7.3879°, height0=58.125mm, width0=91.681mm), achieve the objective function value (y=4.596) for the minimum. The objective function values of the optimization process are shown in **Fig. 6**. From the figure, it can be seen that the objective function value decreases rapidly at the beginning of the optimization, then the value gradually decreases to a minimum. The optimal solution is obtained after 1974 iterations of the optimization process.

Verification Results

In order to verify the optimization results obtained on the basis of the approximate model is accurate or not, The optimal solution (angle0=7.3879°, height0=58.125mm, width0=91.681mm) is used to make the casting process simulation experiment, the calculated value of the objective function is 4.6179. Compared to the objective function value of 4.596 which is the global optimal solution in the optimization process, the relative error is 0.47%, the accuracy of the optimization results is very high.

By means of casting process simulation for the optimal solution, when the critical porosity value is 5%, the distribution of the casting shrinkage porosity is shown in **Fig. 7**. The shrinkage porosity mainly concentrates in the gate and the riser, the shrinkage porosity of the wheel casting under the riser is almost non-existent. After optimization, the casting technological yield increases from 54.6% of the existing production case up to 61.1%, which obtains the good effect.

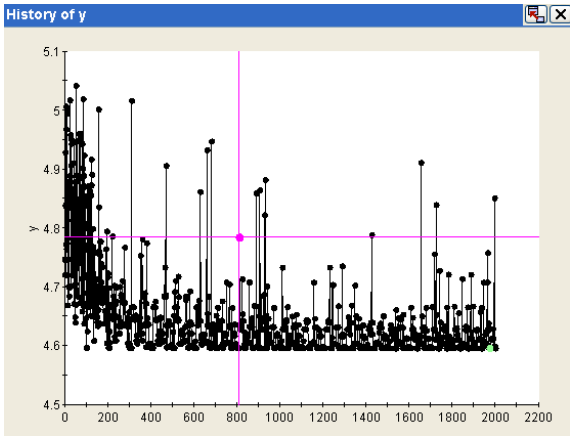


Fig. 6 The optimization process of value y

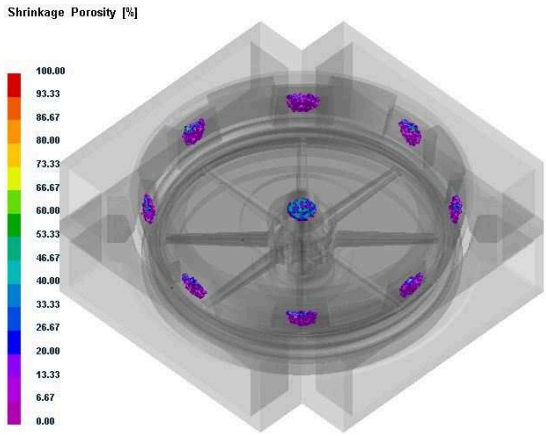


Fig. 7 Distribution of the porosity shrinkage

Summary

1. It is firstly to introduce the method of multidisciplinary design optimization into the field of casting, successfully achieve ProCAST and the other software of casting process optimization integrated into iSIGHT.

2. It realizes to optimize the casting process of the aluminum alloy wheels. Under ensuring the average shrinkage rate of the casting a smaller value, the casting technological yield increases from 54.6% of the existing production case up to 61.1%, which obtains the good effect.

3. Although it only optimize the riser shape of the wheel in this article, the application described in this article of multidisciplinary design optimization in the casting process optimization is not limited to this, such as further considering the pouring temperature, the pouring time, the cooling conditions, the riser shapes, the interfacial heat transfer conditions and the mold opening and closing time as the design variables, and further considering the casting technological yield, the average shrinkage rate of casting and the maximum stress value as objective functions. Therefore, the multidisciplinary design optimization techniques in the field of casting will have a more broad application prospects.

References

[1] X.Q. Yu, W.X. Yao, F. Xue, et al., A study on the requirements for the framework of multidisciplinary design optimization, Mechanical Science and Technology. 23(2004)286-289.

[2] J.S. Sobieski, R.T. Haftka, Multidisciplinary aerospace design optimization: survey of recent developments, Structure Optimization. 14(1997)1-23.

[3] S.H. Wang, L.S. He, Y.Z. Zhang, Flight vehicles multidisciplinary design optimization software system, Journal of Beijing University of Aeronautics and Astronautics. 31(2005)51-55.

[4] C.L. Gong, L.X. Gu, Modeling method for multidisciplinary optimization of hypersonic flight vehicle, Computer Integrated Manufacturing Systems. 14(2008)1690-1695.

[5] L.Y. Zhao, S.X. Yang, Optimization design for thrust project of MLRS, Journal of Projectiles, Rockets, Missiles and Guidance. 26(2006)83-85.

[6] K. Rajesh, P. Ravi, G. Ramana, Multidisciplinary optimization of a light weight torpedo structure subjected to an underwater explosion, Finite Elements in Analysis and Design. 43(2006)103-111.

[7] W.J. Hu, L. Chen, Multidisciplinary design optimization for automobile disk brake based on iSIGHT, Transactions of the Chinese Society of Agriculture Machinery. 41(2010)17-20.

[8] T.W. Simpson, J.D. Peplinski, P.N. Koch, et al., Metamodels for computer-based engineering design: survey and recommendations, Engineering with Computers. 17(2001)129-150.

[9] X. Song, Z.Q. Gu, Q.L. Zhang, et al., Study of the turbulence model optimization based on Multi-island Genetic Algorithm, Journal of Hunan University (Natural Sciences). 38(2011)23-29.

[10] M. Milano, P. Koumoutsakos, A clustering genetic algorithm for cylinder drag optimization, Journal of Computational Physics. 175(2002)79-107.

[11] H. Chen, R. Ooka, S. Kato, Study on optimum design method for pleasant outdoor thermal environment using genetic algorithms (GA) and coupled simulation of convection, radiation and conduction, Building and Environment. 43(2008)18-30.

Advanced Materials Research Vol. 936 (2014) pp 1851-1856
© (2014) Trans Tech Publications, Switzerland
doi:10.4028/www.scientific.net/AMR.936.1851

Analysis of the Common Causes of Papermaking Cast Iron Dryer's Defects and the Study of Test on-line

Wenwei LI [1, a], Qing DU [2,b], Weizhong LI [2,b]

[1]Hangzhou Administration of Quality Control Supervision, Hangzhou China

[2]Hangzhou Special Equipment Inspection Institute, Hangzhou China

[a]liwenwei5460@163.com, [b]hzqts911@163.com

Keywords: Paper, Cast Iron, Dryer, Defects, Causes, Test

Abstract: The existing researches only put forward the stress concentration portion and design improvements from the perspective of stress analysis, or conducts safety assessment on dryers with the methodology of fracture mechanics, without non-destructive testing methods. Based on over 3,400 tests on cast iron dryers in Hangzhou, an ultrasonic testing technology with longitudinal wave double crystal probe is developed in the present investigation. This study illustrates how to identify the volume defects through testing on the air holes, shrinkage cavities and inclusions in the dryer cylinder and small R transition zone with longitudinal wave double crystal probe at a small angle (5°), as well as plane defects with deep cracks through testing on the dryer cylinder and small R transition zone with longitudinal wave double crystal probe at a large angle (42°). It addresses the issues of how to measure the thickness in regular online testing for cast iron dryers, to calculate the intensity or compare with the design value, to identify low hardness value, to determine the key parts in online testing, and how to conduct safety assessment on the cast iron dryers with small cracks. This technique may resolve various problems in cast iron dryer testing.

Introduction

Papermaking cast-iron drying cylinder is the very important component in equipment of papermaking. Since the cast-iron drying cylinder has thick wall, large heat capacity, good thermal insulation property, good abrasive resistance and low relative price, it is common to adopt gray drying cylinder for papermaking drying cylinder, such as HT200, HT250 and HT300, etc. The diameters of the cast-iron drying cylinder are generally 1.0m, 1.5m, 1.8m, 2.5m and 3m, etc, and it is over 4m at the maximum; The designed pressures of cast-iron drying cylinder are generally 0.3MPa, 0.5MPa, and even 0.8MPa; The media are mainly saturated steam or superheated steam and they are used to heat the cast-iron drying cylinder in order to dry the paper tasted in the surface of drying cylinder closely. The gray cast iron of cast-iron drying cylinder belongs to brittle material, and therefore, cast iron is easy to have casting defects in the process of casting. Every place in the whole casting structure may have potential dangerous defects. The inner casting structure is loose, the crystal grain is coarse and it contains a large amount of flake graphites inside, therefore the detection technology has great difficulties and there are very few researches on testing cast-iron drying cylinder in terms of internal defects of cast iron. The experimental research on testing specimen of papermaking cast-iron drying cylinder may use ultrasonic non-destructive testing. The common specifications of cast-iron drying cylinder are 1000mm, 1500mm, 1800mm and 2500mm and 4000mm at the maximum. Cast-iron drying cylinder is different from general structure of steel

pressure vessel. Cylinder block and cylinder cover are connected by bolt and discontinuous area in structure of cylinder block (for example, transition region of cylinder block) is the weakest part in drying cylinder.

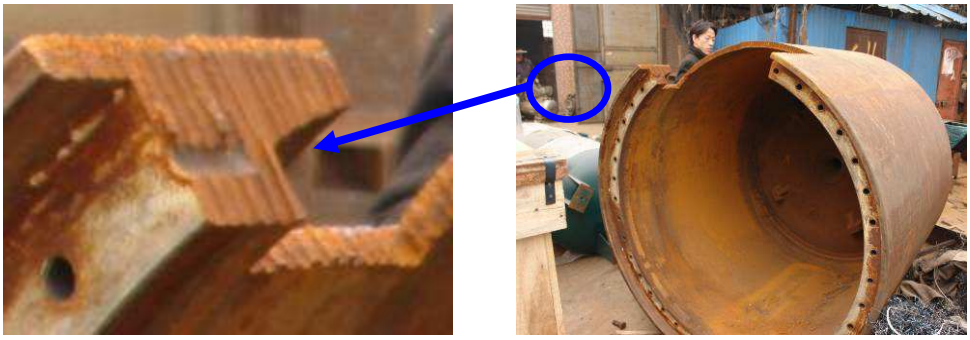


Fig 1 Dryer Cylinder's Internal Structure and Discrete Structure

The characters of ultrasonic testing of papermaking cast-iron drying cylinder

Bad air permeability of papermaking cast-iron drying cylinder

The features of casting of papermaking drying cylinder are that crystal grain is coarse and structure is not tight and even, and permeability to ultrasound is bad. In the process of casting, the cooling speed in each part of casting is different and it leads to the uneven microstructure. Generally, the diewall cools rapidly and has a large amount of solid nuclear particles, and the crystal grain of diewall is fine. When temperature of diewall increases, the cooling speed will be reduced and then it forms column zone in the direction of vertical diewall. When temperature of diewall increases further, the temperature of molten metal decreases, differences in temperature reduces, cooling speed is slown down and the directivity of crystal grain disappears, hence, equi-axed zone forms.

Bad acoustic coupling of papermaking cast-iron drying cylinder

The surface of casting of papermaking drying cylinder is coarse, the acoustic coupling is bad, the flaw sensitivity reduces, the beam directional characteristic is not good and probe wears seriously.

Much interference noise for ultrasonic testing of papermaking cast-iron drying cylinder

There are a lot of interference noises of ultrasonic testing of papermaking cast-iron drying cylinder. Firstly, it is due to that the stray reflection led by uneven property of the coarse crystal grain and structure forms grass echo. As a result, SNR decreases, especially in high frequency. Secondly, it is attributed that the shapes of castings are complex and there are a lot of signals without defect that are led by some outline echos and late strain waves. Besides, the coarse surface of casting will also create some reflection echo to interfere the correct judgment of flaw wave. The thickness of flange of papermaking drying cylinder changes from 20mm to 150mm and inner surface is sloped, therefore, there is no bottom surface to reflect echo in ultrasonic testing. The property of papermaking cast-iron drying cylinder is the reason why it can not be tested by current normal ultrasonic testing.

The block research of online ultrasonic testing of papermaking cast-iron drying cylinder

This is tested by using reflection longitudinal by longitudinal double crystal probe. In the same frequency, the attenuation coefficient is relatively smaller than s-wave, which is favorable for the testing of castings with coarse crystal grain. The detector can be divided into detector with small angle and detector with wide angle according to the angle of wafer. The material of block is gray

cast iron and the ultrasonic attenuation coefficient should be the same as or similar to the attenuation coefficient of tested cast iron drying cylinder. The defect of flat-bottomed hole more than or less thanΦ2 is not allowed to exist. Furthermore, it requires: ① roughness of test surface: the surface of casting Ra≤12.5μm and the surface of mechanical processing Ra≤10μm; ② it has no dirt affecting ultrasonic testing in test surface; ③ coupling agent: coupling agent with high viscosity can be selected, for example, grease, blending agent of machine oil and grease and paste etc.

5 Φ3mm flat-bottom holes, every hole is 25mm apart and the 5 holes are located in the middle of block with width of 50mm. And the distances of 5 flat-bottom holes with 3mm from test surface are respectively 5mm, 10mm, 15mm, 20mm and 25mm.

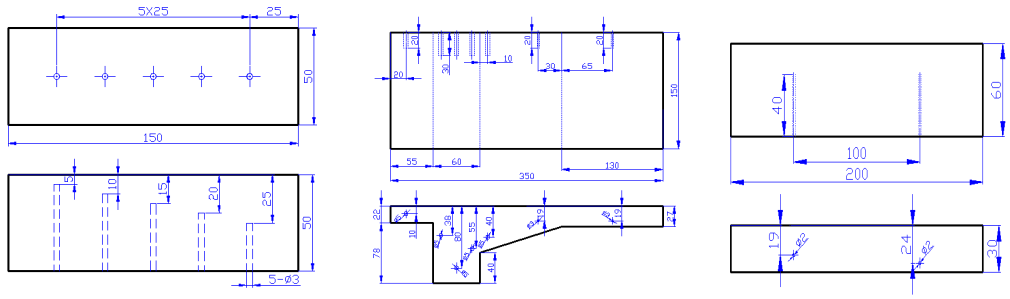


Fig 2 Long Cross-hole Reference

Drill Φ3 long cross-drilled hole at 10mm and 20mm of barrel of drying cylinder and drill four Φ5 long cross-drilled holes at 38mm, 40mm, 55mm and 80mm of small R part. Drill two Φ2×40 long cross-drilled holes at 19mm and 24mm of block with long cross-drilled hole. Make 2 blocks and 30mm length of grooving with depth of 2mm, 4mm, 6mm and 8mm in barrel and small R part respectively.

The online ultrasonic testing of papermaking cast-iron drying cylinder

Testing instrument and probe

The testing instrument is HS616e; the probe is 2.5MHz Φ20mm normal probe which is the specific probe; 1.5MHz longitudinal double crystal normal probe, 1.5MHz longitudinal double crystal probe with small angle and 1.25MHz longitudinal double crystal probe with wide angle.

Testing of permeability to ultrasound

Ultrasonic longitudinal wave is incident vertically on testing surface and non-defective cast-iron materials parallel to its back and the tested difference of wave height of B1 and B2 via longitudinal normal probe is showed by dB. In the area with the same cast-iron thickness, the average value should be obtained at least through testing three points.

Test actually block of long cross-drilled hole and that the difference of wave height of comparing blocks B1 and B2 of drying cylinder with long cross-drilled hole by 2.5MHz Φ20mm normal probe. It can not be tested by the secondary wave but by the primary wave.

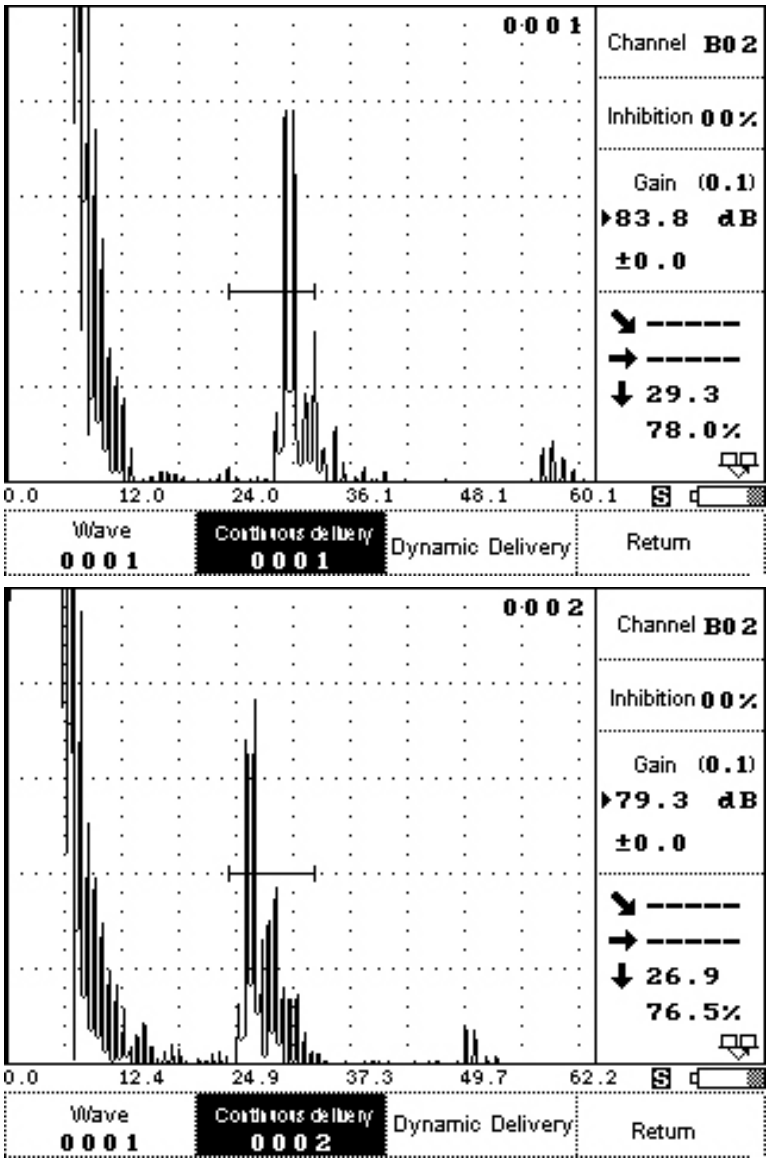


Fig 3 A Wave Detection Test Block Dryer

The sensitivity testing of various probes and comparative analysis of test results

Test flat-bottom hole in 25mm depth of block which is used by ZGZ series of double crystal probe through 2.5MHz Φ20 longitudinal normal probe. Because the frequency is too high and clutter is excessive, the defect can not be distinguished clearly.

Test block of long cross-drilled hole and comparing block of long cross-drilled hole by 1.5MHz longitudinal double crystal normal probe. The sensitivity of bottom wave is obviously higher than that of 2.5MHz Φ20 longitudinal normal probe.

Test flat-bottom hole in 25mm depth of block which is used by ZGZ series of double crystal probe through 1.5MHz longitudinal double crystal normal probe. It is also because the clutter is excessively high, the defect can not be distinguished clearly.

Test flat-bottom hole in 25mm and 20mm depth of block which is used by ZGZ series of double crystal probe through 1.5MHz longitudinal double crystal probe with a small angle, it can be distinguished clearly.

Make DAC curve in standard block of long cross-drilled hole by 1.5MHz longitudinal double crystal probe with a small angle.

Test comparing block of drying cylinder with long cross-drilled hole by 1.5MHz longitudinal double crystal probe with a small angle and the Φ3×25 long cross-drilled hole with 19mm depth can

be distinguished clearly. Test comparing block of grooving drying cylinder by 1.25MHz longitudinal double crystal probe with a wide angle. The waveform of grooving in 4mm and 2mm depth of barrel is shown in Figure 8.

Test comparing block of grooving drying cylinder by 1.25MHz longitudinal double crystal probe with a wide angle.

The research result of online ultrasonic NDT technology of papermaking cast-iron drying cylinder

Regular test scheme of papermaking cast-iron drying cylinder

The cast-iron materials of papermaking cast-iron drying cylinder belong to brittle materials. There is no practical test scheme specific to cast-iron drying cylinder in new "*The Inspection Regulations of Safety Technology of Fixed Pressure Vessel*" (TSG R0004-2009) and in "Design Regulation of Cast-iron Drying C*ylinder Used by Papermaking Machine*" (Q/T2556－2002) and "*Technical Specifications of Cast-iron Drying Cylinder Used by Papermaking Machine*" (Q/T2551－2002), they are only specific to design and manufacturing of cast-iron drying cylinder used by papermaking machine.According to general investigation and research requirement of inspection, the key test projects conducted in online regular test scheme of papermaking cast-iron drying cylinder include: review of original materials, macroexamination, geometry examination, measurement of wall thickness, surface inspection, hardness inspection, ultrasonic inspection, strength checking, pressure test and checking of safe accessories.

Ultrasonic testing method of papermaking cast-iron drying cylinder

According to the features of bad permeability to ultrasound, bad acoustic coupling, much interference noise of papermaking cast-iron drying cylinder, they can be solved via the following six measurements after experimental research:

In terms of bad permeability to ultrasound, it can be improved from detection instrument, probe and testing method. Ultrasonic detection instrument can be the instrument with big launching strength and high surplus sensitivity; the probe selects longitudinal double crystal probe with high sensitivity and they can make specific low-frequency probe. If it is low frequency, the wavelength is long and the ultrasonic penetrability is good as well. The testing method takes primary longitudinal wave method, because the longitudinal wave is of rapid speed and long length.

In terms of bad acoustic coupling, they can make grease with high paste or machine oil as coupling agent. In terms of a lot of interference noises, they can develop specific probe. The double crystal probe with different focal distances can make beam energy concentrate on the tested part, while the probe with a small angle is good to reduce interference noise so as to increase the rate of inspecting defect.

In terms of testing crack in small R part, they can take double crystal longitudinal probe with different focal distances and a wide angle to conduct primary wave test. Test air hole, shrinkage and inclusions of barrel and transaction of small R part through longitudinal double crystal probe with a small angle. Test crack of barrel and transaction of small R part through longitudinal double crystal probe with a wide angle.

The process of online testing defect of papermaking cast-iron drying cylinder

The reduction of wall thickness of papermaking cast-iron drying cylinder and surplus wall thickness are involved in the safety allowance, the reduction of hardness and strength should go through strength check on the basis of online checking. Papermaking cast-iron drying cylinder is

easy to loosen particles and enlarge shrinkage. According to the above defects, they should conduct strength intensity check for drying cylinder. Under this premise of ensuring strength calculation requirements and referring to manufacturing requirements of cast-iron drying cylinder, the surface defects can be repaired by thread plug, but the depth of plug can not be more than 40% of section depth, the diameter of plug can not be more than the depth of plug and widen it to less than 8mm: as for round defect of air hole and shrinkage etc, if the maximum diameter≤4.0mm and the depth is less than 40% of the section depth, they can not be handled; If the maximum diameter ≤10.0mm and the depth is less than 40% of the section depth, the diameter of plug is not more than 10mm, and the level of safety condition of drying cylinder by online regular test is level 3.

Drying cylinders with more air hole can be repaired in some conditions. But if repaired holes increase, the strength of drying cylinder will be weaken. Therefore, the total repaired holes in per square meter of active drying cylinder can not more than 10. It is not allowed to have cracks in the process of online testing of papermaking cast-iron drying cylinder. In case of crack, if it disappears after being polished, the intensity check is qualified and will not influence the normal classification. Otherwise, it is the level 5 of disqualification and must be scrap. As for the crack less than 2mm depth, It is hard to be found in online testing. This kind of crack is basically in the range of safety assessment via research and can be used safely.

References

[1] Zhang Chunliang, Wang Tiesong. Stress Analysis on Flanges with Discontinuous Structure of Dryers [J]. Transactions of China Pulp and Paper, 2002,17(2):87～91.(In Chinese)
[2] Huang Xuekun; Wang Zhiwen. Defect assessment of cast iron drying cylinders in Ser-vice [J]. CHEMICAL ENGINEERING & MACHNERY,1995,22(4):233～237. (In Chinese)
[3] Supervision Regulation on Safety Technology for stationary Pressure Vessel. TSG R0004-2009 (In Chinese)
[4] Designed standard in cast iron dryers used in paper machinery. QB/T2556-2002(In Chinese)
[5] Technological condition of cast iron dryers used in paper machinery. QB2551-2002(In Chinese)
[6] Nondestructive testing of pressure equipments. JB4730-2005(In Chinese)
[7] LI Jie, JIAO Lei. Finite Element Analysis of Large-scale High-Pressure Cast Iron Dryer [J]. Transactions of China Pulp and Paper,2005,20(2): 160～163. (In Chinese)
[8] Li Wei, Feng Bing. The Inspection and Assessment for Cast Iron Oven Used in Papermaking [J]. PRESSURE VESSEL TECHNOLOGY,1998(6):76～80. (In Chinese)
[9] Zhang Chunliang. Design and Calculation of Bolts in Cast Iron Dryer [J]. China Pulp & Paper, 2002(6):39～42. (In Chinese)
[10] XU Li, GANG Tie. Review of Non-destructive Test Methods for Castings Defect [J]. Foundry, 51(9):535～540. (In Chinese)
[11] Zhang Chunliang. Design and Research of The φ1500mm Wide Cast Iron Dryer [J]. Light Industry Machinery, 2001(4):8～10. (In Chinese)
[12] Luo Pei. Strength Calculation of Oven Used in Papermaking [J]. PRESSURE VESSEL TECHNOLOGY, 2000,17(1):51～53. (In Chinese)

Advanced Materials Research Vol. 936 (2014) pp 1857-1861
© (2014) Trans Tech Publications, Switzerland
doi:10.4028/www.scientific.net/AMR.936.1857

Reserch on a NO_X Emission Forecasting Method Based on Naïve Bayesian

Zhang Lin[1,a] ,Wang Xin[2,b]andZhang Qi[1,c],

[1]School of Light Industry and Chemical Engineering, Dalian Polytechnic University, 116034, Dalian, China

[2]Dalian Frontier Defence Police Force,116001,Dalian,China

[a]zhlpopo@126.com,[b]bfddwx@163.com,[c]844183991@qq.com

Keywords: Diesel Engine; naïve Bayesian classifier; NO_x; one-dependence classifier

Abstract. Increasingly serious environmental pollution,trying to find a effective method to control NO_x emission become more importance. Under this background, this paper adopts the naïve Bayesian classifier method which built on the basis of the probability density function to forecasting the NOx emission of diesel engine. This paper proposes a new approach to weight the super-parent one dependence estimators, and uses the UCI datasets to verify the validity of the proposed method. Finally, apply this diagnosis technology to the collected WD615 diesel engine data. The comparison experiments with other algorithms demonstrate the effectiveness of the proposed method.

Introduction

Bayesian forecasting is established based on the probability density function. Compared to the others, it has smaller diagnostic error rates. So it has an extensive application. With the development of information and automation technology, a lot of running data and diagnostic data has been accumulated and it is possible to calculate the prior probabilities of Bayesian method. However, in many practical fields, the independency assumption of naïve Bayes (NB) does not hold. Therefore, many researches are mainly about how to use some technology to find a most favorable topology among all possible network structures. At present, such technologies can be summarized into two categories: heuristic search and correlation analysis. To relax the independency assumption, the researchers have done a lot of work. With the development of modern science technology and the degree of automation, diesel engine fault diagnostic technique has undergone significant changes and Bayesian diagnosis become one of the most efficient diagnosis methods.

Among all these improving approaches, Super-Parent One Dependence Estimators (SPODEs) [1] can be considered a subcategory of ODEs where all attributes depend on the same attribute. L.X. Jiang [2] et al adds the parent node for some attributes in Bayesian network using conditional mutual information. Aggregating One-Dependence Estimators (AODE) ensembles all SPODEs that satisfy a minimum support constraint[3] and estimate class conditional probabilities by averaging across them. This ensemble has demonstrated very high prediction accuracy with modest computational requirements. However, it is based on an implicit assumption that all SPODEs have the same or equivalent learning ability. But the leaning ability of different Bayesian networks is different. Simply averaging all SPODEs may scale up the influence of the bad performance classifiers so as to affect the final classification result. WAODE [4] is an improvement of AODE.

New Approach to Weight SPODE

SPODE

Super-Parent One Dependence Estimators (SPODEs) can be considered a subcategory of ODEs where all attributes depend on the same attribute. A SPODE requires all attributes to depend on the same attribute, namely the superparent, in addition to the class.

A data sample of n attributes can potentially have n SPODEs, each alternatively taking a different attributes as the super parent, as shown in Fig.1. In this paper, we consider the diversity of SPODE and its corresponding NB and propose a new approach to weight SPODE.

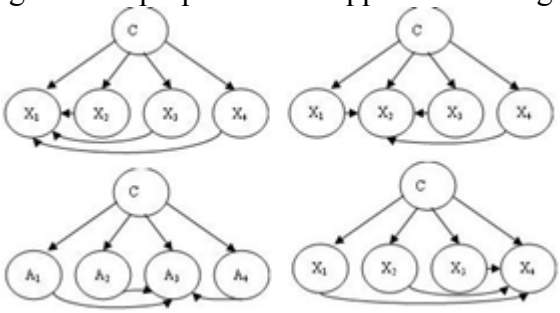


Fig.1 SPODEs with 4 Attributes

Diversity of SPODE and its Corresponding NB

A natural question is that how well a SPODE can perform in predictive tests. If the prediction result for a test instance by using a SPODE is same with that by using NB, we can say that the performance of the SPODE is not very well. We would rather use its corresponding NB than the SPODE since the structure of SPODE is more complex than simple NB and the parameter estimation needs more time while the performance are the same.

Definition 1 if a test instance X is classified to the same class by using SPODE and NB, we say the performance of SPODE and NB is equivalence.

Definition 2 Suppose there are m classes. Let *Diver* ($SPODE_{A_t}$, NB) be a m×m square array such that $Diver_{ij}$ is the number of test examples assigned to class c_j by $SPODE_{A_t}$ with and to class c_i by its corresponding NB. Let |Diver| be the number of all test examples. The diversity of $SPODE_{A_t}$ and its corresponding NB is defined as follows.

$$Diff(A_t) = \frac{1-\alpha}{1-\beta} \tag{1}$$

Where α be the probability that the $SPODE_{A_t}$ and its corresponding NB perform the same, β be the probability that the $SPODE_{A_t}$ and its corresponding NB agree by chance. They are respectively defined as follows.

$$\alpha = \frac{\sum_{i=j=1}^{m} Diver_{ij}}{|Diver|} \tag{2}$$

$$\beta = \sum_{i=1}^{m}(\sum_{j=1}^{m}\frac{Diver_{ij}}{|Diver|}\sum_{j=1}^{m}\frac{Diver_{ji}}{|Diver|}) \tag{3}$$

Further, we have the following discussion.

(1)When $Diff(A_t)$=0, we can get $\alpha=1$. It means that the classification results using $SPODE_{A_t}$ and its corresponding NB are completely same. The two classifiers agree on every example.

(2)When $Diff(A_t)$=1, we can get $\alpha=\beta$. It means that $SPODE_{A_t}$ and its corresponding NB equals that expected by chance.

(3)When $Diff(A_t)$>1, we can get $\alpha<\beta$. It means that agreement is weaker than expected by chance. In another words, the probability of the two classifiers obtain the same classification is little.

(4)If the diversity between the augmented naïve bayes and the simple naïve bayes is small, it has no need to expand the network structure of NB. Because the complexity of probability estimation is closely related to the network structure.

From the above discussion, we can get the conclusion that the diversity between the augmented naïve bayes $SPODE_{A_t}$ and the simple naïve bayes increases with the increase of the value of $Diff(A_t)$. Therefore, we take $Diff(A_t)$ as the weight of $SPODE_{A_t}$.

SPODEs Ensemble

According to the above discussion, firstly we give the definition of the weight of $SPODE_{A_t}$.

Definition 3 Let w_t represents the weight of $SPODE_{A_t}$. w_t is defines as:

$$\omega_t = \frac{Diff(A_t)}{\sum_{i=1}^{n} Diff(A_i)} (\sum_{i=1}^{n} Diff(A_i) \neq 0) \tag{4}$$

Where $Diff(A_t)$ is defined in (4) and $\sum_{t=1}^{n} \omega_t = 1$.

Since (4) holds for every SPODE, we can get our classifier as follows.

$$P(c \mid X) = \begin{cases} \dfrac{\sum_{t=1}^{n} \omega_t P(c, a_t) \prod_{j=1, j \neq t}^{n} P(a_j \mid c, a_t)}{P(X)}, \sum_{t=1}^{n} \omega_t \neq 0 \\ \dfrac{P(c) \prod_{j=1}^{n} P(a_j \mid c)}{P(X)}, else \end{cases} \tag{5}$$

The value of w_t can determine the number of SPODEs used as well as the the importance of every SPODE. For example, if $w_{t=0}$ and $w_j \neq 0 (j \in [1,n], j \neq t)$, we actually only select n-1 SPODEs. In a extreme case when $\sum_{i=1}^{n} Diff(A_i) = 0$, we will use NB to classify all test samples. But this kind of situation is rare. Because it means that all SPODE perform exactly the same with NB. Every SPODE and its corresponding NB agree on every example.

Experiments

Experimental Settings

(1) Test data

In this paper, we choose 16 UCI datasets (shown in table 1) and 3 foul diagnostic datasets of WD615 diesel engine (shown in table 2). All datasets are preprocessed with the help of WEKA software before using. Use the supervised filter Discretize in WEKA to discretize all the numeric attributes; Use the unsupervised filter Remove in WEKA to remove useless attributes.

(2) Validation method

10 runs of 10-folds CV test for comparing the classifier performances. Each datasets are divided into 10 almost equal-sized blocks randomly, and in each validation, one block was used for test data and the remaining blocks were used for training classifiers. Average all 10 runs as the final results.

(3) Measurement

Throughout all the tests, we measured the classification error rate, i.e., the percentage of incorrectly classified instances.

Error rate= number of incorrectly classified instances / the total number of instances of prediction.

(4) Comparison algorithms

This paper compares the proposed method with AODE，WAODE and LODE.

TABLE 1 UCI DATASETS

Id	dataset	size	C#	A#	Id	dataset	size	C#	A#
1	breast_w	699	2	9	9	machine	209	7	7
2	car	1728	4	6	10	promoter	106	2	57
3	diabetes	768	2	6	11	sonar	208	2	21
4	Flags	194	6	30	12	tic_tac_toe	958	2	9
5	flare	1389	2	13	13	vote	435	2	16
6	heart_h	294	5	9	14	vowel	990	11	14
7	iris	150	3	4	15	waveform	5000	3	19
8	lymph	148	4	18	16	zoo	101	7	16

TABLE 2 DIESEL NOX DATASETS

	number	Description
size	1600	When the load is 0Nm, 100 Nm, 200 Nm, 300 Nm and 400 Nm, collect 2000 cycles' data respectively. The datasets are denoted as Diesel1, Diesel2, Diesel3, Diesel4 and Diesel5. Each dataset has 2000 records.
. A#	11	①speed; ②maximum Cylinder Pressure; ③phase of maximum Cylinder Pressure; ④phase of maximum of rising rate of maximum Cylinder Pressure; ⑤phase when energy conversion reaches 50%; ⑥phase of starting burning,; ⑦phase of ending burning; ⑧phase difference between burning start and burning end; ⑨ mean indicating effective pressure; ⑩net mean effective pressure; ⑪indicated power

Experimental Results and Analysis

The experimental results are shown in table 3. Since the average error rates of different classifiers are very close. So we compare each two algorithms A-B via two tailed t-test with a 95 percent confidence level. The results are shown in table 5, where win indicates that algorithm A obtained significantly lower average error rate than algorithm B, draw indicates that A and B haven't significant differences, and loss indicates that A obtained significantly higher average error rate than algorithm B. From table 5, we can see that WSPODE outperforms AODE on 9 datasets, outperforms WAODE on 8 datasets, and outperforms LODE on 8 datasets.

Conclusions

The traditional naïve Bayesian diagnostic model is established under the strict independency assumption. On order to relax the assumption so as to gain smaller classification error rate, the study of one-dependence estimator is receiving more and more attention. This paper proposed a new strategy. It took advantage of the diversity of SPODE and its corresponding NB to weight the super-parent one dependence estimators. Through the comparison experiments with the existing AODE, WAODE and LODE, the results verified the effectiveness of the proposed algorithm.

TABLE 3 DETAILED RESULTS OF ERROR RATE AND STANDARD DEVIATION

dataset	AODE	WAODE	LODE	WSPODE
breast_w	3.02±0.17	2.98±0.11	2.95±0.17	2.92±0.18
car	8.09±0.36	8.92±0.29	8.04±0.35	7.73±0.43
diabetes	21.69±0.28	21.81±0.36	21.60±0.34	21.62±0.37
Flags	39.82±1.20	39.77±1.36	41.04±0.99	39.31±1.24
flare	19.80±0.57	18.20±0.25	19.41±0.68	18.08±0.31
heart_h	14.59±0.38	14.52±0.55	14.55±0.36	14.62±0.37
iris	6.54±0.84	6.88±0.72	6.54±0.84	6.08±0.76
lymph	14.77±0.85	13.41±1.38	14.83±0.97	13.54±1.46
machine	9.48±0.49	9.24±0.50	9.48±0.58	9.43±0.60
promoter	10.93±1.47	10.03±2.13	23.22±2.27	9.77±1.81
sonar	14.22±0.90	13.21±0.78	14.32±0.78	13.84±0.99
tic_tac_toe	25.88±0.39	27.05±0.49	25.73±0.35	25.62±0.36
vote	5.58±0.16	5.70±0.18	5.60±0.16	5.65±0.19
vowel	13.04±0.57	15.94±0.52	10.76±0.61	12.60±0.49
waveform	13.73±0.13	13.64±0.14	15.20±0.40	13.69±0.15
zoo	5.21±0.91	5.21±0.91	5.21±0.91	5.13±0.90
Diesel1	17.52±0.22	17.54±0.29	17.11±0.33	17.33±0.30

Diesel2	14.26±0.29	13.57±0.26	14.09±0.26	13.84±0.31
Diesel3	18.60±0.29	19.01±0.20	18.32±0.32	18.38±0.17
Diesel4	17.05±0.26	17.03±0.28	17.22±0.21	16.95±0.26
Diesel5	8.06±0.15	8.16±0.19	8.13±0.14	7.98±0.12
mean	14.38±0.52	14.37±0.57	14.92±0.57	14.00±0.56

References

[1] N. Friedman, D. Geiger, and M. Goldszmidt, "Bayesian Network Classifiers," Machine Learning, vol. 29, pp. 131-163, 1997.

[2] Jiang, L., Zhang, H., Cai, Z., Su, J.: One Dependence Augmented naïve Bayes.In: Li, X., Wang, S., Dong, Z.Y. (eds.) ADMA 2005. LNCS (LNAI), vol. 3584, pp.186–194. Springer, Heidelberg (2005).

[3] G.I. Webb, J. Boughton, and Z. Wang, "Not So naïve Bayes: Aggregating One-Dependence Estimators," Machine Learning,vol. 58, pp. 5-24, 2005.

[4] Jiang L.,Zhang H..Weightily averaged one-dependence estimators. In: Yang Q.,WebbG.(eds.)PRICAI2006.LNCS(LNAI),vol.4099,pp970-974.Springer,Heidelberg,2006.

Advanced Materials Research Vol. 936 (2014) pp 1862-1867
© (2014) Trans Tech Publications, Switzerland
doi:10.4028/www.scientific.net/AMR.936.1862

Analysis of Grinding Roller Stress Distribution of Vertical Roller Mill

Xiaohong Jiang [a], Ping Ye [b], Zongkai Li [c]

College of Mechanical and Electrical Engineering, China University of Mining and Technology, Xu Zhou city, Jiang Su Province, P. R. China

[a]xh.jiang@126.com, [b]yp@cumt.edu.cn,[c]lizk@cumt.edu.cn

Keywords: Vertical roller mill, roller force, Compaction zone stree, Weibull distribution

Abstract: The quality of powder of non-metal materials directly relates to the force exerted on grinding roller, while the force on grinding roller relates to the thickness of the material layer. The uneven pressure distribution between the roller and material layer is caused by the drum-shaped characteristics of vertical mill grinding roller. This paper studies the pressure distribution of roller in compacted zones, established mathematical models of pressure distribution analysis, and provides a theoretical basis for improving the vertical mill production process as well as yield and quality of the powder.

Introduction

Vertical mill is suitable for middle and high hardness, brittle material crushing processing, mainly used in pharmaceutical, food, daily chemical and other industries and non-metallic mineral areas.

Analyzing the forces on the grinding rollers and the stress on the rolling compaction zone are the foundation for studying the vibration mechanism of the non-steady state of the vertical roller mill. From the published articles, the little research in this area of the vertical roller mill is not yet enough on research depth. This paper attempts to analyze theoretically the grinding roller force and the rolling compaction zone stress distribution, strive to describe the forces acting on grinding rollers and the stress distribution of the compaction zone more accurately, and draw relevant parameters, to provide a basis for follow-up study.

Roll crush is by a heavy grinding rollers rolling over the material layer, the role of static and dynamic pressure is to make the compaction materials layer obtain permanent residual deformation h, shown in Fig.1. As the number of rolling increased, the materials layer become denser, and the residual deformation are accordingly reduced, and finally the residual deformation h is equal to zero, and then the material are crushed[1,2].

During the vertical roller mill in working, the role of the external forces acting on the rollers include: the vertical force G (1/3 the weight of the grinding rollers framework of gravity plus hydraulic loading force); horizontal force T (the framework supporting force in the horizontal direction), as well as the reaction force from the material layer. The reaction force of material layer on the grinding rollers are divided into the vertical pressure N and the friction force F. It is the friction F that driving grinding rollers rotating, as shown in Fig. 1.

In the rolling compaction zone, the vertical component of the joint force of the pressure N and the friction force F balances with the vertical force G, and the horizontal component of the joint force, with the horizontal force from the pressure framework T. Friction F acting on grinding roller drive roller rotation, while the horizontal component of the friction acting on three grinding rollers, combining the horizontal component of the normal pressure N constitute a torque on pressure framework through the rollers, while the overall torque of the pressure framework is ultimately acting on the buffers.

Be discussed later, it is this torque is one of the main reasons for the abnormal vibration of the mill.

Stress Analysis of The Rolling Compaction Zone Between the Roller and the Materials

The mill table rotates initiatively, the roller passive rolling. In the circle view direction of the grinding roller, the contact stress distribution between the roller and the material layer [3, 4], is shown in Fig.2.

Grinding rollers weight, the gravity of the pressure framework and hydraulic loading force are the active external forces, and due to the role of the horizontal component of the active external force T, the maximum compressive stress σ_{max} of material layer is not at the lowest point of grinding roller, but move to the feeding direction for some distance Δa. As pressed material has a certain viscosity, the deformation is often later than the stress changes, resulting in load aftereffect phenomenon, that is, when the stress reaches its maximum and began to decline, the material deformation will remain for some time [5].

Actually, load mainly acts on the first half contact arc between material layer and rollers, the compressive stress was non-symmetrical distribution, the total depth h of the roller indentation can be divided into two parts of elastic deformation h_a and plastic deformation h_H, namely, $h = h_a + h_H$.

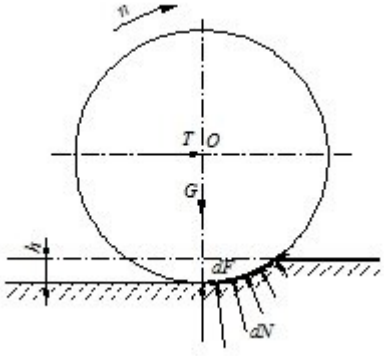
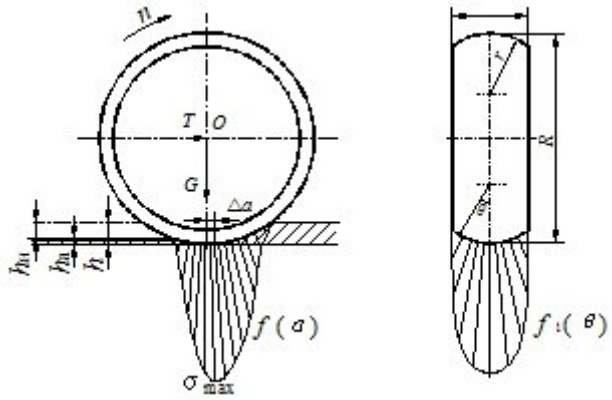


Fig. 1. The residual deformation of the materials layer



(a) The roller circle view direction (b) The roller width direction

Fig. 2. Rolling stress distribution

There had been some formulas to describe the stress distribution of wheel roller compacted material layer[3], such as, the relationship between the material pressure p and indentation depth h under the rigid wheel is expressed as:

$$p = kh^{\mu} \qquad (1)$$

Meanwhile, the outer edge of the roller is grinded more seriously than the inside edge by the materials.

k - material compression coefficient; μ - material condition factor, the range of 0～1.

Formula (1) is very simple, but there are limitations: It could not describe the stress condition on the vicinity of separation point of material away from the wheel; The formula (1) only able to apply to the rolling wheel of a cylinder shape.

The grinding roller in this paper is of a drum-shaped, so it is necessary to investigate the stress distribution from the circle view direction of the grinding roll, from the width view direction of the roller, as well as in three-dimensional rolling compaction region, to find out the normal pressure acting on the grinding roller, the expression of the vertical and the horizontal component of the normal pressure as well as related parameters.

The direction of the grinding roll circle view, district material layer stress distribution curve

To more accurately establish the pressure distribution model between the roller and the materials, according to the information and references provided by the manufacturer, the form of a three-parameter Weibull distribution curve is presented in this paper, to describe the stress distribution pattern from the circle view direction of the grinding roller [6,7].

Determining stress distribution curve form

$$f(\alpha)=\frac{\beta}{\eta}\left(\frac{\alpha-\gamma}{\eta}\right)^{\beta-1}\exp(-\left(\frac{\alpha-\gamma}{\eta}\right)^{\beta}) \quad (2)$$

Where β -shape parameters; γ - positional parameters; η - scale parameter.

Variable α is the central angle of the down the longitudinal axis of the grinding roller radius as starting line, clockwise negative, counterclockwise normal. Show in Fig. 3.

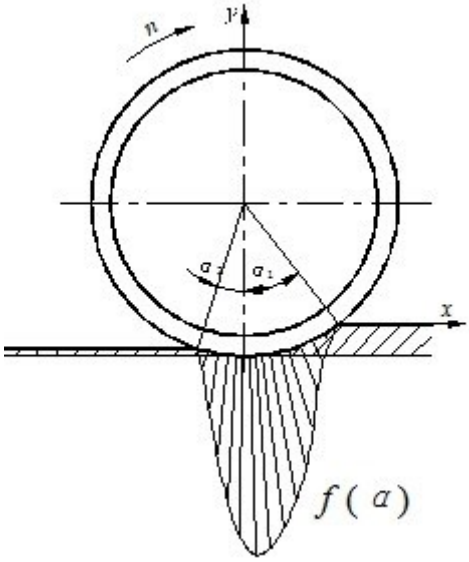


Figure 3 Central angle settings of roller stress zone

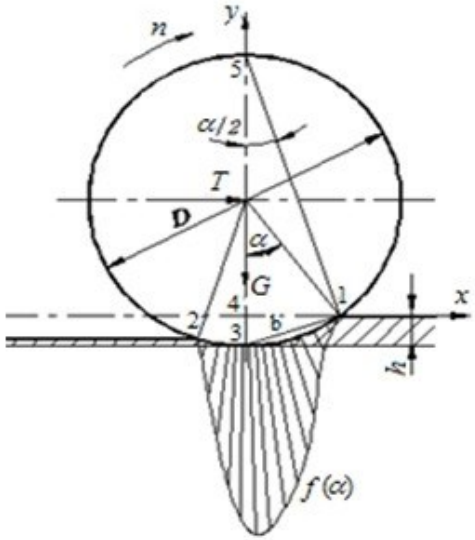


Figure 4 Relations between *b*, *d* and *h* in roller stress zone

Here are just using the probability density function $f(\alpha)$ to describe the distribution pattern of roll grinding stress. Weibull curve $f(\alpha)$ multiplied by an undetermined the constants C_1 to describe the actual stress.

Suppose materials entering the grinding roller from right to left, see Fig. 4, and the material moving from the feed point 1, through the lowest point 3 of grinding roller, and finally to the discharge point 2, to leave the grinding roller. It can be seen from the Fig. 4, that the arc length of grinding roller from the contact point 1 to the lowest point of the roller contains the material stress varied from zero to maximum process, set the chord length from point 1 to point 3 is *b*, the roller diameter is *D*, sag depth (distance between two points 3,4) is h, relationship between the three variables:

$$b=\sqrt{Dh} \quad (3)$$

According to the data given by the factory, the difference of material layer thickness between the material feed inlet of the mill roll and the roller lowest point, h = 42 mm. Roller diameter D = 2.8m, the circumferential angle (α_1/2)=arcsin*(h/b)*.

Central angle α_1 twice in the circumferential angle, equal to 0.2456 radians, is approximately 14.0718 °, from the point of contact of the roller and the material layer to about 14° central angle between the grinding rollers lowest point.

Given the central angle α corresponding with the chord length b, then

$$\frac{b/2}{D/2} = \sin(\frac{\alpha_1}{2}) \quad (4)$$

$$\text{or } \sqrt{\frac{h}{D}} = \sin(\frac{\alpha_1}{2}) \quad (5)$$

The indentation depth h is:

$$h = D\sin^2(\frac{\alpha_1}{2}) \quad (6)$$

It can be seen from equation (6): Once the roller diameter D is given, the deeper the sag, the greater the contact angle.

In the grinding process, the material layer thickness are constantly changing in the range of 80mm~130mm, the size of feeding material is also changing around 70mm, so is the contact angle α and the pressure area of material layer, resulting in the size and the location of the vertical and the horizontal component of the normal pressure changing, which make the torsional angle of the pressure framework change ceaselessly, forming the torsional vibration. Severe, the crash sound of pressure framework against the shell could be heard on-site.

Stress distribution curve parameters

Shape parameter β

The grinding process without elastic deformation of the material layer are described in Fig.1, the material layer height of the roller lowest point is the material thickness at the grinding roller export, that is h_a=0, location parameters γ=0. At this time, the stress distribution between the roller and the material layer can be described by the two-parameter Weibull distribution function:

$$f(\alpha) = \frac{\beta}{\eta}\left(\frac{\alpha}{\eta}\right)^{\beta-1}\exp(-\left(\frac{\alpha}{\eta}\right)^{\beta}) \quad (7)$$

Without loss of the generality and the simplicity, let the scale parameter η = 1, the interval of α among [0, 2.5], the Weibull curve is shown in Fig.5. It can be seen that the Weibull curve of the parameters β = 2 is more appropriate to describe the stress curve between the roller and the material layer.

Scale parameter

The scale parameter η affects the dispersion degree of curves along the abscissa axis. Fig.6 shows the β=2, γ= 0, the influence to the Weibull curve by the scale parameterη changing.

In order to make the starting point and end point of the stress distribution curve is consistent with the contact zone of the grinding roller and the materials, the arc length of the stress curve is needed to adjust, which mainly by modifying the scale parameter η values, and at the same time, location parameters γ also needs to make some adjustments. According to the data provided by the factory: the central angle α of the contact zone between material and roller is about 14 °, refer to fig.3. The central angle α_2 of the discharge interval typically is less than feeding interval angle α_1, α_2 equal approximately 1/3α_1~ 1/10α_1, take α_2 = 1/8 α_1, hence the angle interval is [-1.75°, 14°]

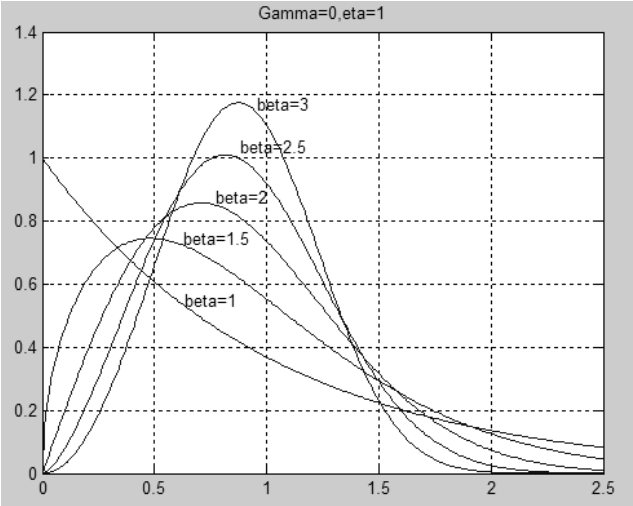


Fig. 5. Influence of shape parameter β on Weibull curve under certain parameters γ and η

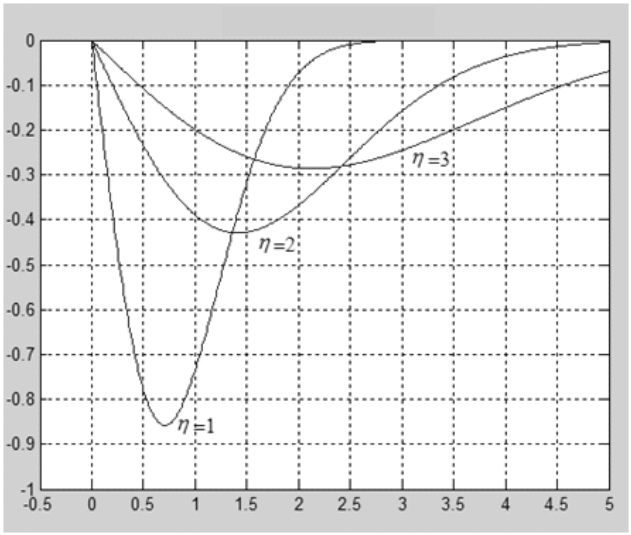


Fig. 6. Influence of shape parameter η on weibull curve under certain parameters β and γ

It can be seen from Fig. 6, when $\eta = 1$, Wilbur curve distribution interval is about 0 ~ 2.5 radian, corresponding to the angle value is about [0°, 143°], in order to adapt [-1.75°, 14°] angle interval, this paper take $\eta = 14°/143° \approx 0.1$, known from the previous discussion, $\beta = 2$， γ=-1.75° = -0.03 radians, the Weibull curve equation to describe the rolling compaction zone the material layer stress distribution is:

$$f(\alpha)=200(\alpha+0.03)\exp(-((\alpha+0.03)/0.1)^2) \tag{8}$$

It can be seen from Fig. 7.

Location parameters

Location parameters γ affect the starting point of the Weibull curve, which is equivalent to move the curve along a coordinates. Fig.8 shows the influence of the location parameters changing to the Weibull curve, when the $\eta = 0.1$, $\beta = 2$.

In fact, after the roller rolling, there is elastic recovery of material layer, that is, passing through the grinding roller lowest point, the materials still has the contact pressure with roller. So the location parameters of the distribution curve, $\gamma \neq 0$. Here for a more accurate representation of the compressive stress, take γ = -0.2, and the preceding discussion shows, $\beta = 2$, and temporarily take $\eta = 1$, according to the actual direction of the compressive stress, add a negative for the curve $f(\alpha)$,get the equation:

$$f(\alpha) = -2(\alpha + 0.2) \cdot \exp(-(\alpha + 0.2)^2) \tag{9}$$

It can be seen from Fig. 9.

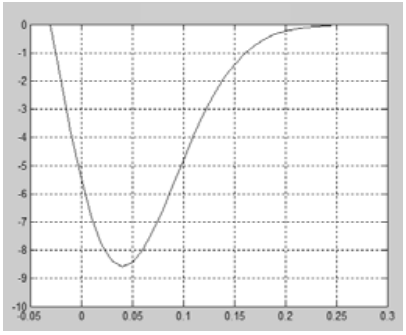


Fig. 7. Weibull curve for describing stress distribution on material layer of roll area

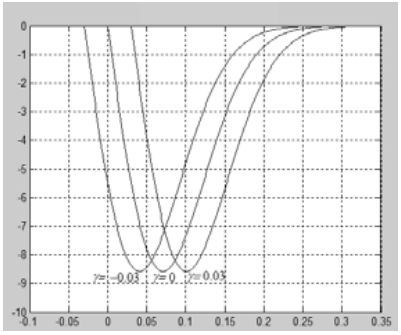


Fig. 8. Influence of shape parameter γ on weibull curve under certain parameters β and η



Fig. 9. Weibull curve, when η=1, β=2, γ=-0.2

Conclusion

1) Theoretically analyzing the force acting on the grinding rollers, and establishing a mechanical model for the grinding roller stress distribution;

2) The form of a three-parameter Weibull distribution curve presented in this paper can better describe the stress distribution in the circle view direction of the roller; the three parameter values of Weibull distribution curve could be got according to the actual mill conditions and operating parameters;

3) Due to the grinding roller having the drum-shaped, so the stress on the rolling compaction zone is more complex, the mathematical equations of the rolling compaction stress and normal pressure are established in this paper, the mathematics equation of the vertical component and horizontal component of the friction acting on the grinding roller surface, as well as the mathematical equation of the vertical force and horizontal force the material role in the grinding roller surface. Making use of MATLAB software, the mathematical model of stress and the force of the roller rolling area of analytical and numerical calculations, and calculate the stress distribution patterns of curve correction coefficient.

This work provides a theoretical basis to study the mill table force and the load conditions.

References

[1] Jia Jianmin, Qi Jiyu, “Research on Wear Mechanism of MPS Type Mill Roll,” Journal of North China Electric Power University, Vol. 25, p. 88-91,(1998).

[2] Zhang Zhifeng, Hao Fei, Feng Zhongxu, "Vertical Stress Distribution in Soil Under the Wheel Vibration," Journal of Wuhan University of Technology (Transportation Science & Engineering), Vol.33, No.6, p.133-135, (2009).

[3] Yang Shimin "Analysis of soil stress and compaction effect under the action of roller"[J]. Road Machinery & Construction Mechanization 1994,11(6): p.10-13.

[4] Li Xin, Wang Guoqiang. "The determination of the roller press main operating parameters" [J]. Chinese cement, Vol. 7, p. 23 -26, (2003).

[5] Li Bing, Jiao Shengjie. "Roller selection and compaction technology.[M].China Communications Press, p.91-105, (2001).

[6] Li Xin. "Mechanism of high-pressure roller mill and the finite element analysis of the roller strength",[D]. Changchun: Jilin University, p.15-16.(2003).

[7] Wang QiGuang, Ye Ping. Modern design theory,[M]. China university of mining and technology press, p. 131-133, (2005).

Advanced Materials Research Vol. 936 (2014) pp 1868-1872
© (2014) Trans Tech Publications, Switzerland
doi:10.4028/www.scientific.net/AMR.936.1868

Establish the Load Distribution Model for Vertical Mill Grinding Roller in Width Direction

Ping Ye[1, a], Shu Ye[2, b]

[1]College of Mechanical and Electrical Engineering, China University of Mining and Technology, Xu Zhou city, Jiang Su Province, P. R. China

[2]School of Electronic Information and Electrical Engineering, Shanghai Jiao Tong University,Shanghai city, P. R. China

[a]yp@cumt.edu.cn, [b]yeshu_sjtu@163.com

Keywords: vertical roller mill, grinding roller, load distribution.

Abstract: The width of the grinding rollers are far greater than the arc length of the compaction zone in the circle view direction of the roller, and the actual wear of the mill roll surface also appear in the width direction. Therefore, it is helpful for analyzing the load distribution in the width direction of the grinding rollers, to clarify the state of mill work, and understand the non-steady-state vibration of the mill.

The Material Layer Stress Distribution Curve of the Compaction Zone in the Roller Width Direction

Vertical mill in nonmetallic ultrafine powder preparation has got more and more application. It is discussed in this paper of the vertical mill pressure distribution that relate directly to production efficiency, equipment wear and tear.

The grinding roller of MPS vertical mill is of the drum-shaped. On both sides of the grinding roller width, there will be materials being squeezed out during working, so the stress distribution is uneven on the roller surface. Experiments show that [1,2], the pressure distribution in the compaction zone of the roller width direction is big in the middle, and little on both sides. In the condition of other parameters remain unchanged, the speed - pressure distribution curve near a steep parabola [3].

Mathematical expression that describes the pressure change rate along the width direction of the roller [4, 5] is as follow:

$$p(z) = C_2\left[1-\left(\frac{2z}{l}\right)^m\right] \tag{1}$$

Where C_2 is the constant to be determined, l for the mill roll width, m is the grinding roller axial coefficient.

Eq. 1 describes the pressure distribution between the cylindrical roller and the material layer in the width direction. The grinding roller of MPS vertical mill has a drum-shaped surface, so this paper uses the Eq. 2 to describe the stress distribution in the width direction of the roller. The drum-shaped surface and the angle θ are shown as in Figure 1.

Set mill roll width direction stress distribution function $C_2 f_1$, stress distribution curve f_1 is in the form of:

$$f_1(\theta) = \left[1-\left(\frac{2\theta}{2\theta_0}\right)^2\right] \tag{2}$$

The stress distribution in both directions of the roller circle view and the width view multiplied by undetermined coefficients and integral, the spatial distribution of roll grinding force could be obtained. The calculation of roll grinding force and the actual external load phase equilibrium, in order to determine the undetermined coefficients.

In order to get the undetermined coefficients, the calculation roller force ought to balance with the actual external load.

As the Weibull stress distribution of compaction zone and the parabolic stress distribution of the width direction, the main operating parameters are provided by the factory, therefore the stress distribution can better describe the actual working conditions, and equilibrium with the external load. The research work of this paper have laid the foundation for the further studying the force of roller and mill table as well as the load conditions.

The Normal Pressure on the Grinding Roller Surface

Rolling zone stress *p* and normal pressure *dP*

Compaction zone stress p obtained by multiplying the stress distribution $f(\alpha)$ of the circular view direction and stress distribution $f_1(\theta)$ of width direction:

$$p(\alpha,\theta) = C f(\alpha) f_1(\theta) \tag{3}$$

Where: C is the stress distribution patterns of curve correction factor, $C = C_1 C_2$, the unit Pa.

Roll grinding the surface of the micro-area dA as follows:

$$dA = Rrd\alpha d\theta \tag{4}$$

The micro-pressure micro-area dA dP as follows:

$$dP = p(\alpha,\theta)Rrd\alpha d\theta$$

$$= C\left[1-\left(\frac{2\theta}{2\theta_0}\right)^2\right](20(\alpha-0.03)/0.1)\exp(-\left(\frac{\alpha-0.03}{0.1}\right)^2)Rrd\alpha d\theta \tag{5}$$

The vertical component of the normal pressure $dP(\alpha,\theta)$

The micro-pressure points to the circle center of arc surface in the roller width direction.

$$dP_y = \cos(\alpha)\cos(\theta)dP = \cos(\alpha)\cos(\theta)Cf(\alpha)f_1(\theta)dA \tag{6}$$

Herefore, the vertical component of the surface stress of the roller and of P_y

$$P_y = \int_{-\frac{\theta_0}{2}}^{\frac{\theta_0}{2}} C\left[1-\left(\frac{2\theta}{2\theta_0}\right)^2\right]\cos(\theta)rd\theta)\int_{\alpha_2}^{\alpha_1}(20(\alpha+0.03/0.1)\exp(-\left(\frac{\alpha+0.03}{0.1}\right)^2)\cos(\alpha)Rd\alpha \tag{7}$$

The variable α and variable θ is independent of each other, so you can calculate the integral respectively.

The following integral the stress distribution patterns function $f(\alpha)$ in the roller round view direction. Try to simplify the calculation in the case meet the requirements of engineering precision. Due to the radius of the grinding rollers is large, and the sag depth h is limited, so the integral angle range of the stress $f(\alpha)$ in the circle view direction is not large, according to the previous calculation, the α value range of [-1.75°, 14°]. In order to facilitate integration, trigonometric function in equation (7) near the origin to expand as the Taylor series, the $\sin(\alpha)\approx\alpha$, and $\cos(\alpha)\approx 1-\alpha/2$.

The following calculated the specific values of the vertical component P_y of the roller surface stress. The specific values of P_y can be obtained by integral Eq. 6 or integral Eq. 7, but it is needed to know the specific values of correction factor C of stress distribution shape curve. (The C value is unknown yet); the specific values of P_y can also be obtained through the mechanical analysis of the grinding rollers.

Vertical external force G acting on the roller shown in Fig.2 is equal to the roller weight + 1/3 the gravity of framework + hydraulic loading force. It is known that the hydraulic loading force is 1.4e+6 N, grinding roller weight is 52000kg, 1/3pressure framework weight = 37000/3 = 12333 kg. So G should be equal to 2.03e+6 N. Because of the vertically downwards external force G acting on the grinding roller should be equal to the vertical component P_y of the grinding roller surface compressive stress, and P_y should be equal to 2.03e+6 N. shown in Figure 2.

The specific value of the stress distribution curve factor C is calculated as -21.126MPa.

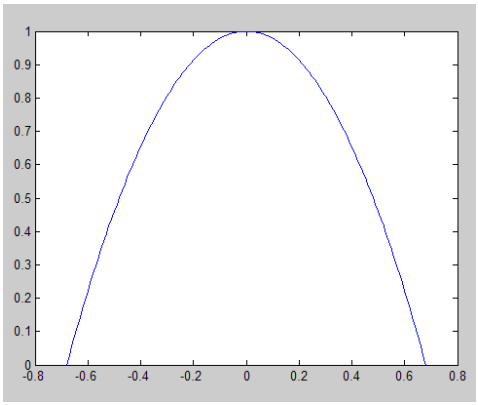


Fig. 1. Stress simulation curve in roll width direction

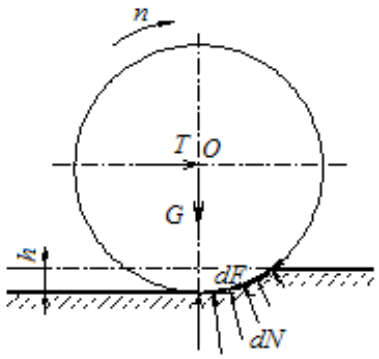


Fig. 2. The residual deformation of the materials layer

D stress distribution

The stress distribution between the roller and the material in the top view direction is shown in Figure 3.

Using MATLAB software to draw the area of the roller rolling three-dimensional stress distribution shown in Figure 4.

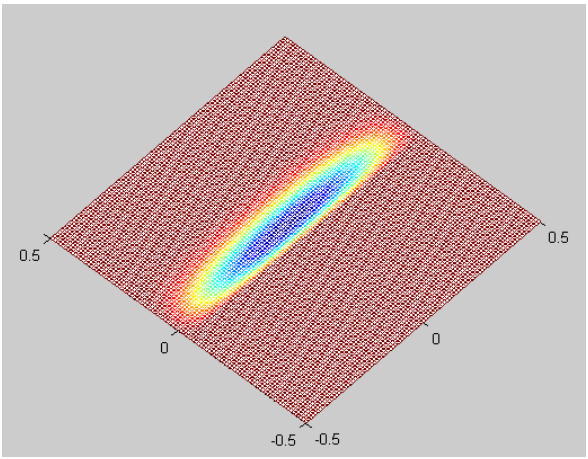


Fig. 3. Stress distribution of rolling area in top view direction

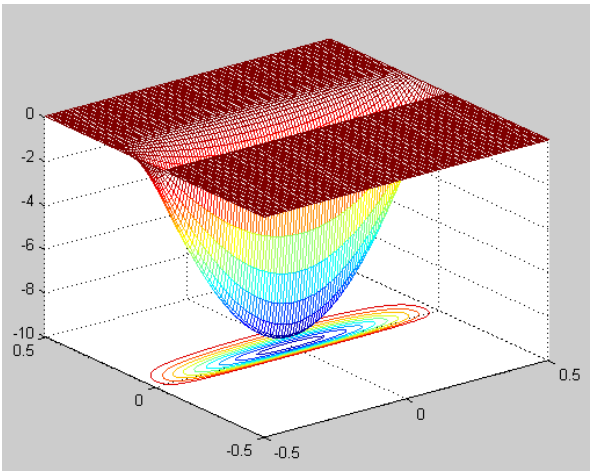


Fig. 4. 3D graph of stress distribution in rolling area

The three-dimensional graphics of the compaction zone stress distribution is shown in Figure 4. Intercepted part of the Weibull curve below the horizontal axis, said that the compressive stress.

It can visually be seen from Figure 4: The stress distribution in the central region is much larger than the stress on the edge region; the distribution range of stress in roller round view direction is much smaller than the distribution range of roller width direction stress, the crushing of the material is mainly due to the compaction of mill roll width direction.

2.4 The horizontal component $dP(\alpha,\theta)$ of the pressure

The horizontal force components of material layer acting on the grinding roller constitute of the normal pressure horizontal component and the friction horizontal component. Among them, the horizontal component dP_x of the normal pressure on the micro-area dA as follows:

$$dP_x=\cos(\theta)\sin(\alpha)dP=\cos(\theta)\sin(\alpha)f(\alpha)f_1(\theta)dA \tag{8}$$

In order to carry out the numerical integration, it is needed to determine the integration upper and lower limits of θ angular.

Known width b = 1002mm grinding roller mill roll width direction of circular surface of radius r = 800mm. Set mill roll circular surface corresponding central angle $2\theta_0$, and from down the y axis to any position of the central angle is set to θ, the range of variation of the angle θ: [- θ_0, θ_0]. Calculated:

$$\theta_0=\arcsin(b/2r_1)=\arcsin(501/800)=0.6767(\text{rad}) \tag{9}$$

It is worth noting that $f_1(\theta)$ in the z-axis projection, symmetry, and therefore cancel each other out.

The Vertical and Horizontal Component of the Friction of Material Role on the Roller Surface

The $dP(\alpha, \theta)$ multiplied by the friction coefficient μ to get the friction of the dF:

$$dF=\mu\, dP(\alpha,\theta) \tag{10}$$

The vertical component dF_y of the friction：

$$dF_y=\mu\sin(\alpha)dP(\alpha,\theta) \tag{11}$$

The horizontal component dF_x of the friction：

$$dF_x=\mu\cos(\alpha)dP(\alpha,\theta) \tag{12}$$

$\mu\sin(\alpha)$ is a higher order, the calculation of the vertical load can ignore the influence of the friction force F_y. Friction force horizontal component F_x in the calculation of pressure framework torsion could not be ignored.

Vertical Force and Horizontal Force of the Material Role in the Surface of the Roller

In order to calculate the pressure on the framework of the role of the grinding rollers horizontal force, the horizontal component of the normal pressure in the dP_x and friction horizontal component dF_x summation:

$$\begin{aligned} dP_x+dF_x &= \cos(\theta)\sin(\alpha)dP(\alpha,\theta)+\mu\cos(\alpha)dP(\alpha,\theta) \\ &= (\cos(\theta)\sin(\alpha)+\mu\cos(\alpha))dP(\alpha,\theta) \\ &= (\cos(\theta)\sin(\alpha)+\mu\cos(\alpha))p(\alpha,\theta)dA \end{aligned} \tag{13}$$

Take $p(\alpha,\theta)=f(\alpha)f_1(\theta)$，$dA=Rrd\alpha d\theta$ into Eq. 12，And integral equation on both sides:

$$\begin{aligned} &P_x+F_x \\ &=\int_{-\frac{\theta_0}{2}}^{\frac{\theta_0}{2}}\int_{\alpha_2}^{\alpha_1}C_1\left[1-\left(\frac{2\theta}{2\theta_0}\right)^2\right][\cos(\theta)\sin(\alpha)+\mu\cos(\alpha)])(20(\alpha+0.03)/0.1)\exp(-\left(\frac{\alpha+0.03}{0.1}\right)^2)Rrd\alpha d\theta \end{aligned} \tag{14}$$

In order to calculate the integral of the right hand side, appropriate to simplify the integrand. Round view of the direction of the angle α in smaller intervals, so the origin near the Taylor series expansion: $\sin(\alpha)\approx\alpha$; $\cos(\alpha)\approx1-\alpha^2/2$; into Eq. 3-23, are:

$$P_x+F_x=200C_1Rr\int_{-\frac{\theta_0}{2}}^{\frac{\theta_0}{2}}\int_{\alpha_2}^{\alpha_1}\left[1-\left(\frac{2\theta}{2\theta_0}\right)^2\right][\cos(\theta)\cdot\alpha+\mu(1-\alpha^2/2)])((\alpha+0.03))\exp(-\left(\frac{\alpha+0.03}{0.1}\right)^2)d\alpha d\theta \tag{15}$$

here

$$P_x = \int_{\alpha_1}^{\alpha_2} \int_{-0.68}^{0.68} (1-(2z/(2\times 1.36)^2)\cos(z)kf(\alpha)(\sin\alpha+\mu\cos\alpha)dzd\alpha \tag{16}$$

The vertical and the horizontal force acting on the roller surface from materials are offset by the force T of the pressure framework.

X-axis components of the normal pressure and the friction acting on the roller are shown in Figure 5.

The vertical force acting on the grinding roller surface by the materials should be equal to $P_y + F_y$, because of the $\mu\sin(\alpha)$ is a higher order, so the influence of friction F_y could ignored, that is, the vertical force of materials acting on the surface of roller approximately equal to P_y.

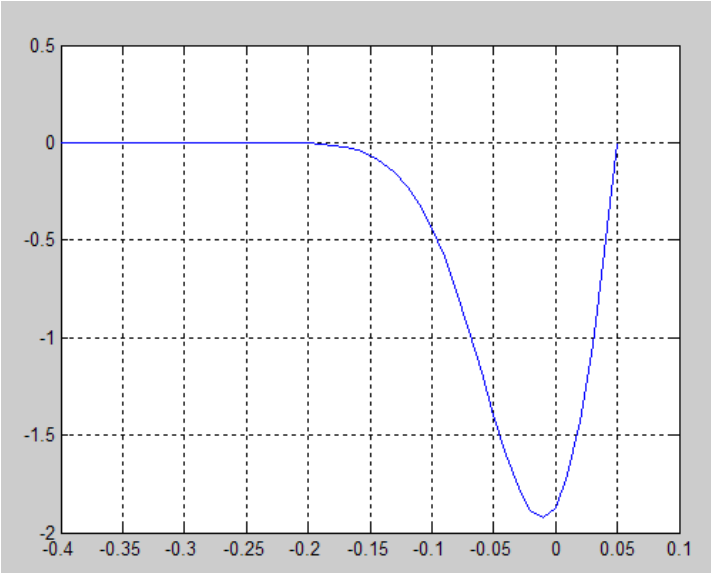


Fig. 5. *X*-axis component of normal pressure and friction force on roller suffered

Conclusion

1) The three-dimensional stress distribution graph in the rolling compaction is obtained. Be intuitively seen from the stress distribution graphic: the stress in central area is much larger than the stress of the edge region; the stress distribution in the circle view direction of the grinding roller is far less than the range of width direction of the mill roll, that means the crushing of the material comes mainly from the rolling of grinding roller in width direction.

2) The horizontal force between the roller and the material layer comes from the horizontal component of the normal pressure *P* and the friction force *F*, ie, P_x+F_x; the vertical force comes from the vertical component of the normal pressure *P* and the friction force *F*, namely $P_y + F_y$.

This work provides a theoretical basis to study the mill table force and the load conditions.

References

[1] Li Xin. "Mechanism of high-pressure roller mill and the finite element analysis of the roller strength" [D]. Changchun: Jilin University, p. 15 -16. (2003)

[2] Yu Chaomin, "Experimental Study of the Dynamic Characteristics of the Subgrade and Pavement Structure," Road Engineering, Vol. 3, p. 50-53, (2010)

[3] Unland,G.,Wang,G."Model of high pressure roller mills-A phenomenological-mathematical approach," ZKG International, Vol. 51, p. 600-617, Nov. (1998)

[4] Li Xin, Wang Guoqiang "The determination of the roller press main operating parameters," Chinese cement, Vol. 7, p. 23 -26, (2003)

[5] Northwestern university. Mechanical design,[M]. Beijing, People's Education Press, p.512-514, (1978)

Advanced Materials Research Vol. 936 (2014) pp 1873-1877
© (2014) Trans Tech Publications, Switzerland
doi:10.4028/www.scientific.net/AMR.936.1873

The Optimal Levenberg-Marquardt Algorithm To Predict Welding Quality Using Mahalanobis Distance Theory

Ill-Soo Kim[1, a], Qian-Qian Wu[1, b], Ji-Hye Lee[1, c], Jong-Pyo Lee[1, d], Min-Ho Park[1, e] and Young-Su Kim[1, f]

[1]Department of Mechanical Engineering, Mokpo National University 61, Dorimri, Chungkye-myun, Muan-gun, Chonnam, 534-729, South Korea

[a]ilsookim@mokpo.ac.kr, [b]wuqianqian@mokpo.ac.kr, [c]jihyelee@mokpo.ac.kr, [d]jplee@mokpo.ac.kr, [e]parkminho21@mokpo.ac.kr, [f]kimyoungsu@mokpo.ac.kr

Keywords: Gas Metal Arc (GMA) Welding, Mahalanobis Distance, Root Mean Square (RMS), Levenberg–Marquardt algorithm, On-line Control

Abstract: With the development of computational technology, neural network has attracted the more and more attentions to reveal the relationships between the process parameters and welding geometry. However, the Gas Metal Arc (GMA) welding is complex and of multiple interactions so that mathematical model for welding parameters has not been achieved. Neural networks have been noted as being particularly advantageous for modeling systems which contain noisy, fuzzy and uncertain elements, while a sufficient algorithm is employed. In this study, Levenberg-Marquardt algorithm was employed into GMA welding process. Mahalanobis Distance (MD) was measured to determine the on-line welding quality to avoid joint failure as welding quality. To get an optimal neural network, cases with different configurations were carried out. The Root of the Mean sum of Squared (RMS) error was adopted to evaluate the accuracy of the prediction by neural networks with LM algorithm. The results presented that the proposed algorithm had the superiority of high accuracy that can be used in the on-line welding process.

Introduction

GMA welding process is a very complex process due to the fact that it involves multiple interaction of solid, liquid, gaseous and plasma-state. This complexity makes the sensing and controlling of the welding parameters in the welding process very difficult to perform real-time. Since measuring, sensing, or monitoring, the welding parameters of a physical system were of primary importance in the application of any automatic control technique. Therefore it is necessary to develop an intelligent neural network to obtain suitable welding parameters in the automatic GMA welding process to achieve the desired MD and weldability.

In recent years, neural network has becomes a very useful tool in the modeling of inter-relationships between input and output variables of many complicated systems. The most being well known of supervised technique is backpropagation neural network, which adjusts initial randomized weights during training according to the steepest gradient along the error surface [1]. However, it was also pointed out that the backpropagation method encountered slow learning progress and convergence to a false local minimum according to works done by JiříŠíma [2], Kim [3], Fukuoka [4], etc. Thus, for a real-time GMA welding process, a better algorithm is required.

Meanwhile, it is hard to identify the quality of input parameters since the waveform of welding current and arc voltage obtained from the on-line monitoring system differ slightly. Thus, a descriptive statistic of MD, which is a unitless measure introduced by Mahalanobis in 1936 [5], is applied to character the quality of the welding parameters. According to the description, a point that has a greater MD from the rest of the sample population of points is said to have bigger difference. In other words, in a group of experimental data which most of them are good, the one with a greater MD can be considered as false one.

This study attempts to use an optimal neural network to establish a prediction system of MD for GMA welding process. And the feed-forward backpropagation neural network with Levenberg-

Marquardt algorithm is firstly established. Secondly, the averaged RMS error is calculated to evaluate the accuracy of the optimal neural network. Finally, comparison of the qualitative and quantitative analysis of GMA welding fault based on MD by Levenberg-Marquardt algorithm with different numbers of neurons is presented. In order to analyze the influences of the input parameters (welding current and arc voltage) on the resulting output parameter (MD). The result shows that the Levenberg-Marquardt algorithm is the preferred algorithm to construct neural network in the prediction of MD for automated GMA welding process.

Experimental procedures

The GMA welding process, sometimes called Metal Inert Gas (MIG) welding, is a welding process that yields coalescence of metals by heating with a welding arc between a continuous filler metal (consumable) electrode and the workpiece. Fig. 1 presents the experimental setup of GMA welding process. In the GMA welding process, the bead geometry is determined by wire feed rate, welding current and welding voltage, which is controlled by the computer controller. Not only, welding current and wire feed rate dominate the penetration for single pass welds, but also arc voltage dominates the bead width and has an influence on the penetration since it controls the arc shape [6].

A steel plate is conducted as a multi-parameters process. The dimensions of welding plate and the direction for butt GMA welding process on a test specimen is shown in Fig. 2.

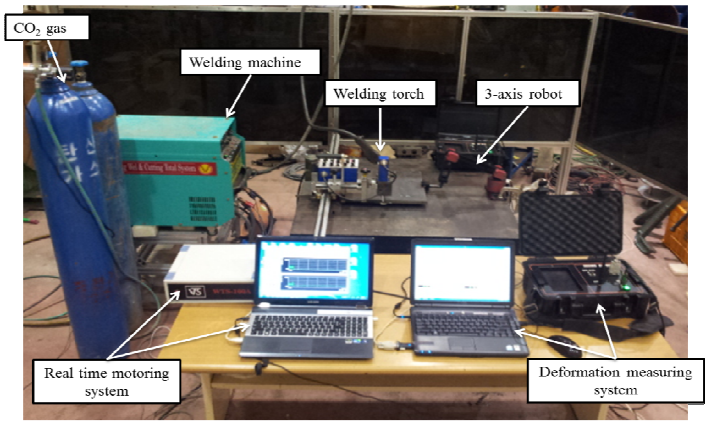


Fig. 1 Experimental setup of GMA welding

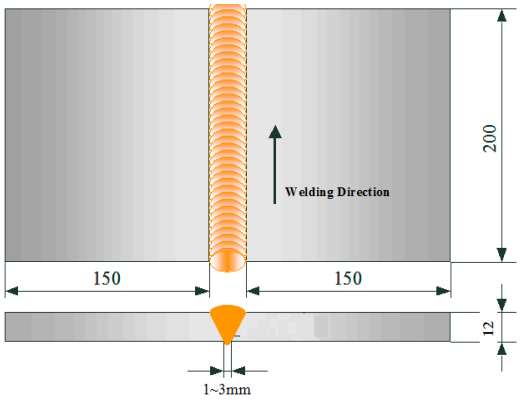


Fig. 2 Overview of GMA butt weld specimen process

Description of Mahalanobis Distance

MD has successfully been applied to a broad range of cases mainly because it is very sensitive to inter-variable changes in data. It is measured in terms of standard deviations from the mean of the samples. It takes into account the correlations of the data set and is scale-invariant to provide a statistical measure of how well an unknown sample matches a known sample set. In other words, if the magnitude of MD derived from a welding current C_i and arc voltage V_i is smaller than a certain value, the parameter of (C_i, V_i) can be considered as a suitable value and good weld will be produced. The smaller the MD is, the better the weld quality will be [7].

The MD takes advantages over classical statistical approaches in several aspects. First, MD considers the variance and covariance of the measured variables rather than just the average value. It weights the differences by the variability range in the sample point direction. Second, it also accounts for the ranges of acceptability between the variables which is useful since most systems are not just comprised of independent variables rather dependent variables are also impacting the system's performance. Besides, it calculates distances in units of standard deviation from the group mean. By using standard deviation, the attribute under consideration is given in the original units, which relates the results to the original data. Using Levenberg-Marquardt algorithm to establish a

neural network for GMA welding process is composed of two phases: training and testing of the neural networks with experimental welding data.

To provide the reliable measures for recognition of welding current and arc voltage on bead geometry as welding quality, the transformed equation is defined below:

$$M_d = \frac{V_i'^2 - 2rV_i' + C_i'^2}{1 - r^2} \tag{1}$$

Where V' and C' indicate the normalized value of arc voltage and welding current, and r is the correlation coefficient after normalization.

Modeling of GMA welding process

In this work, the welding parameters are mapped to the MD through the internal representation of neural network with Levenberg-Marguardt algorithm. Data obtained from the experiments and regression models are provided to a network at the learning stage. During network learning, the network output is compared with the desired output and the connector weights inside the network adjust to minimize the difference. The error is then propagated backwards through the network and weights are changes based on the Levenberg-Marguardt algorithm. This learning process is an iterative process and learning will stop once an acceptable error is achieved. When the trained network is presented with new input (beyond training), the network responds according to the knowledge it has acquired. Fig. 3 shows the major input and output parameters associated with the quality characteristics in robotic GMA welding process.

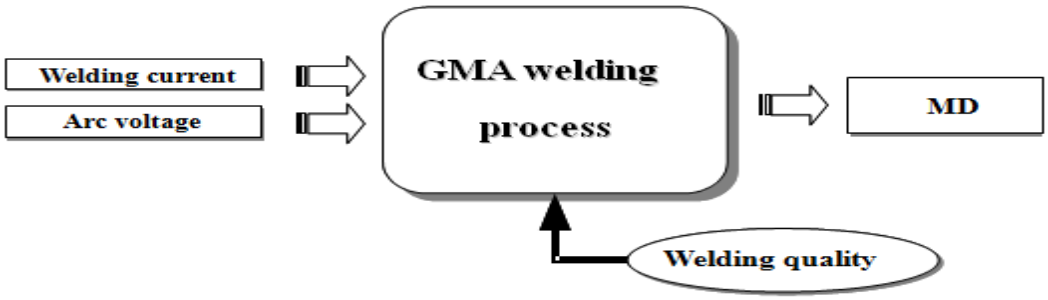


Fig. 3 Input and output parameters of the gma welding process

In this study, a one-layer feed-forward backpropagation neural network is employed as a tool for mapping the complex and highly interactive process parameters such as welding current and arc voltage into the MD to predict the optimal MD in robotic GMA welding process.

The convergence criterion for the developed networks is determined by the average RMS error between the desired output value y_i and predicted output value y'_i for the *ith* prediction, i.e.:

$$RMS_{error} = \sqrt{\frac{1}{n}\sum_{i=1}^{n}(y_i - y_i')^2} \tag{2}$$

Where i is the number of training data or testing data.

In this paper, the Levenberg-Marguardt algorithm is employed because generally this algorithm could provide a faster convergence than the gradient descent algorithm used in the error backpropagation algorithm. Also, the development and the training of the neural network are carried out on a Pentium PC using MATLAB. The training process continues until either the error goal is met or the maximum number of epochs is completed. The neural network configuration setup for the training is shown in Table 1. The neurons of the input and the interpolation layers are employed to accept the welding parameters and then generate the estimated MD.

TABLE 1 NEURAL NETWORK CONFIGURATIONS FOR THE TRAINING WITH THE LEVENBERG-MARQUARTDT ALGORITHM

Four layer network	Four neurons in input layer, one hidden layer, one neuron in output layer
Max._epoch	500
Error goal	1e-6
Learning rate	0.01
Multiplier for increasing MU	10
Multiplier for decreasing MU	0.1
Maximum value for MU	1e+10
No. of neurons in hidden layer	2-16 (in steps of 2)
Number of training sets used	one

Results and Discussion

A series of input variables (12400 examples) are used for training the neural network. Then the trained neutral network is tested by 100 new data. Network configurations with different numbers of neurons in the hidden layer are studied. Many attempts are made to find a result showing the minimum error or the maximum prediction accuracy. The discussion presented here is based only for the case of the optimal results obtained with different configurations. In order to understand the effect of the network parameters on the MD, the number of neurons is intentionally chosen from two to sixteen neurons in a hidden layer. The accuracy of the developed neural network was evaluated by the RMS error between the measured and the predicted values for the training and the testing process (Fig. 4). The histograms indicate the RMS error in the training process is not directly related to the increase of the number of neurons in the competition layer. To the testing phase, the average RMS error of the testing set is almost the same as that of the training set, which means that the network has good generalization ability for the modeling of the GMA welding process. Furthermore, the lowest RMS error obtained by using this algorithm is as low as 0.0014 with 14 neurons in hidden layers in 284 training cycles. It is clear that the 2-14-1 network configuration seems to be best fit for the prediction of the MD with the lowest RMS error. Therefore, the network with this configuration was selected for the good learning ability.

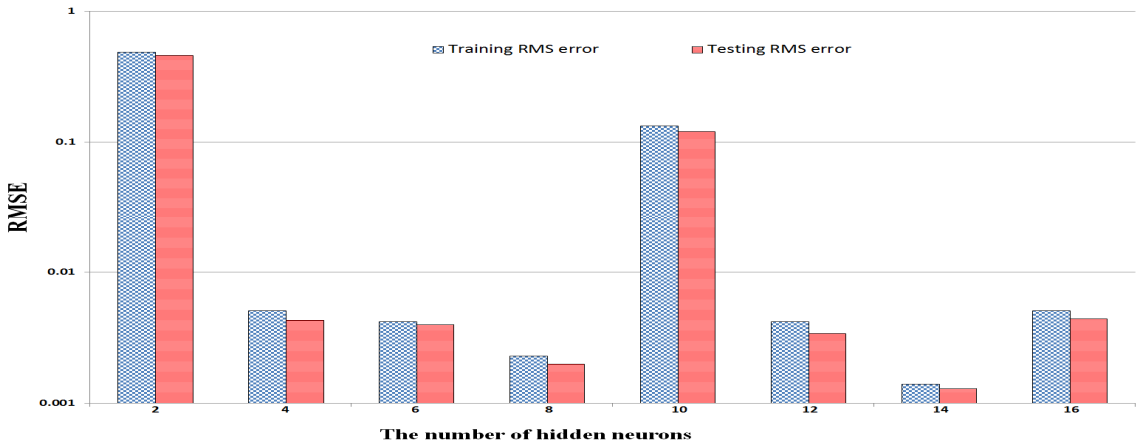


Fig. 4 The value of training and testing RMS error for the developed neural network with a number of neurons between 2 and 16 in the hidden layer

The results of the measured MD and predicted MD using the developed neural network model by the Levenberg-Marquardt algorithm method with the 2-14-1 network configuration are compared and shown in Fig. 5. Where the horizontal ordinate represents the predicted MD, the vertical

ordinate presents the measured MD. The dash line of best fit is drawn using regression computation to get a direct view. It is evident that the predicted MD completely coincides with the measured one

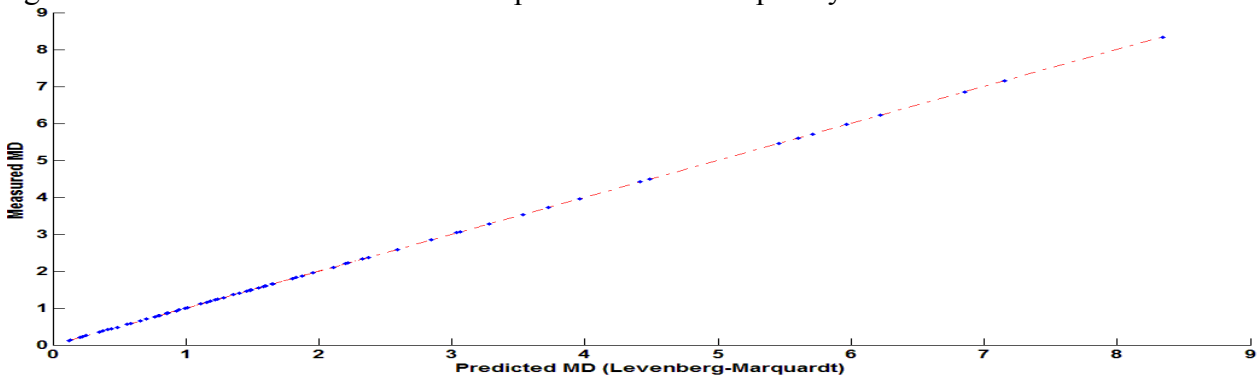


Fig. 5 Comparison between the measured and predicted MD with the developed algorithm

Summary

In this study, we have developed a new approach to predict MD in automatic GMA welding process using the neural network. The Levenberg-Marquardt algorithm neural network with one-hidden-layer in configuration of 2-14-1 is found to be more effective and greater precision than any other structures, as it can provide accurate prediction and reduce the RMS error to a significantly small value. Also the developed algorithm is able to predict that the MD completely coincides with the measured MD and increases reliability of welding quality in GMA welding, which can be proposed for real-time welding quality predetermination on automatic control system of on-line GMA welding process.

Acknowledgements

This research was financially supported by the Ministry of Education (MOE) and National Research Foundation of Korea (NRF) through the Human Resource Training Project for Regional Innovation (No. 2013H1B8A2032082).

References

[1] D.E. Rumelhart, G.E. Hinton and R.J. Williams, Learning internal representations by error propagation, In D.E. Rumelhart, J.L. McClelland and PDP Research Group, J.A. Feldman, P.J. Hayes and D.E. Rumelhart (Eds.), Parallel Distributed Processing: Explorations in the Microstructure of Cognition, MIT Press, Cambridge, MA, 1986, pp. 318-362.

[2] Jiří Šíma, Back-propagation is not efficient, J. Neural Networks 9 (1996) 1017-1023.

[3] H.B. Kim, S.H. Jung, T.G. Kim and K.H. Park, Fast learning method for back-propagation neural network by evolutionary adaptation of learning rates, J. Neurocomputing 11 (1996) 101-106.

[4] Y. Fukuoka, H. Matsuki, H. Minamitani and A. Ishida, A modified back-propagation method to avoid false local minima, J. Neural Networks 11 (1998) 1059-1072.

[5] S.Q. Feng, Off-line Programming of arc welding robot based on UG and welding qualification based on statistic methods, Department of Materials Processing Engineering, Tianjin University, 2010.

[6] R.L. Brien (Ed.), Welding handbook: Welding process, American Welding Society, Vol. 2, pp. 110-155.

[7] S.Q. Feng, O. Hiroyuki, T. Hidennori, K. Yuichi and S.S. Hu, Qualitative and quantitative analysis of GMA welding fault based on Mahalanobis distance, Int. J. Precision Engineering and Manufacturing 12 (2011) 949-955.

Advanced Materials Research Vol. 936 (2014) pp 1878-1881
© (2014) Trans Tech Publications, Switzerland
doi:10.4028/www.scientific.net/AMR.936.1878

Research on the Ni-Cr Alloy Coatings on the Hydraulic Prop by High-Frequency Induction Cladding

Fudong ZHu[1, a], Biyun Zhu[2,b] and Juan Liu[3,c]

[1]ORDOS Vocational College, Kangbashi district, ORDOS China

[2] ORDOS Vocational College, Kangbashi district, ORDOS China

[3] ShouGang QianGang Company, TangShan China

[a]pb701@163.com, [b]danawinner@126.com, [c]773786321@qq.com

Keywords: High frequency cladding Hydraulic prop Component analysis

Abstract. Ni-based cladding coatings are prepared on the surface of hydraulic prop mobile column by high-frequency induction cladding with different current. Microstructures of coatings are analyzed by metallographic microscope as well as SEM, while coatings and matrix elements are analyzed by EDS. The results show that metallurgical bonding is formed among transition regions of matrix and coatings with obvious white band, when cladding frequency is 250KHz and current is 1160A. The microstructures of coatings are eutectics of "austenite + carbide", relatively uniform. During the process of cladding, Fe as well as Mn in matrix permeats to coatings; while Si element in coatings permeats to matrix. As a result, the Fe content of trasition regions is raised, and the contents of Ni and Cr is comparatively reduced.

Introduction

Equipments are chronically exposed to damp and corrosion circumstance with high air moisture under coal mine. A part of mobile column of single hydraulic prop out of cylinder is easily corroded under harsh environment with parts breaking. Chromium plating on the surface of column [1-4] is a traditional way, but electroplating production, with complicated technology and high cost will pollute the environment seriously, which is not accord with sustainable development policy in our country.

High frequency cladding, with coatings uniform thickness, high strength and wear resistance as well as low production cost, is gradually becoming research focus home and abroad. At present, research on this region is basically aiming at such solid specimens as axis, plate and tooth; as thin-walled specimen, mobile column with low heat capacity, has strict demands on parameters, which directly determine the depth of heat-affected zone and performance of cladding coatings. In this paper, high frequency cladding technology on the surface of mobile column, as well as microstructure of specimens, is the research emphasis.

Experimental Materials

The experiment adopts 27SiMn as mobile column material with length 400mm, a diameter of 76mm, pipe wall thickness 5mm; self-fluxing alloy powder N45 is adopted as cladding material.

TABLE1 CHEMICAL COMPOSITION OF ALLOY POWDER AND MOBILE COLUMN[11] (MASS FRACTION,%)

	Ni	Cr	B	Si	Fe	C	Mn	S	P
Ni45 alloy layer	Bal.	12.5	1.9	4.1	6.6	0.34	—	—	—
27SiMn	≤0.03	≤0.03	—	1.1~1.4	Bal.	0.2~0.3	1.1~1.4	≤0.04	≤0.04

Experimental Results and Analysis

Macroscopic Morphology of Metallographic Specimen

Fig. 1 is macrophotograph of the metallographic specimen after cladding, when cladding frequency is 250KHz and current is 1160A. From it, it can be seen that, vaulted silver white part is structure of specimen, in the middle of test block; while upper part of the structure is alloy coating and the black is mosaic powder. Besides, it also can be seen that the coating is uniform. Meanwhile, coating and matrix combine closely.

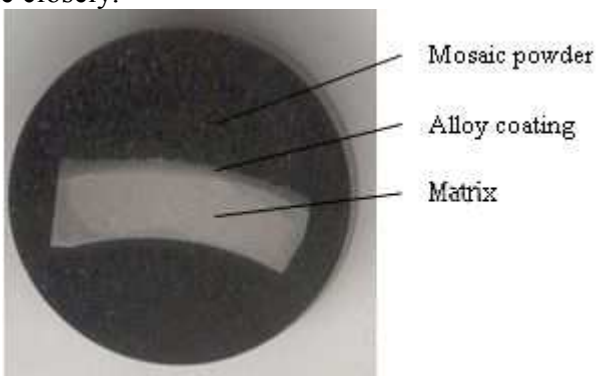


Fig.1 Macrophotograph of the Metallographic Specimen

Microstructure of Cladding Coating

Fig. 2 is the microstructure of claddding coating. From it, it can be seen that, upper side is alloy coating and the lower is matrix. Besides, a white zigzag band can be seen obviously in the juncture of coating and the matrix. Structure of the band is eutectics of "austenite + carbide", coarse and uniform compared with the coating. Dendritic austenite structures increase obviously, near to the transition and the components of the coating and the matrix are completely permeated and diffused. After induction heating, the structure of coating is cooled rapidly, and the alloy elements are left in the obvious white band composed in the matrix. What's more, the zigzag shape of white band has the function of mosaic, which is beneficial to increase the bonding strenth of coating and matrix at the interface.

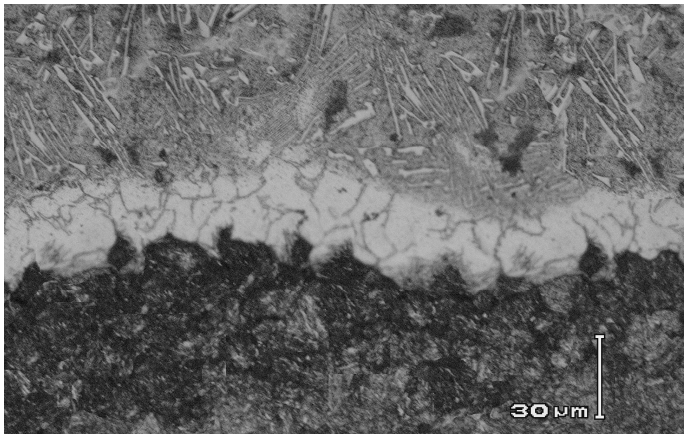
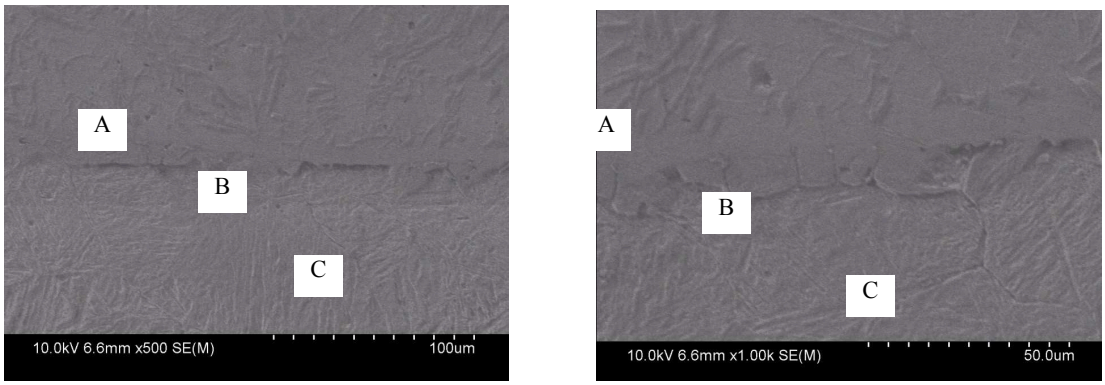


Fig.2 The Microstructure of Cladding Coating

Component Analysis of Cladding Coating and Matrix

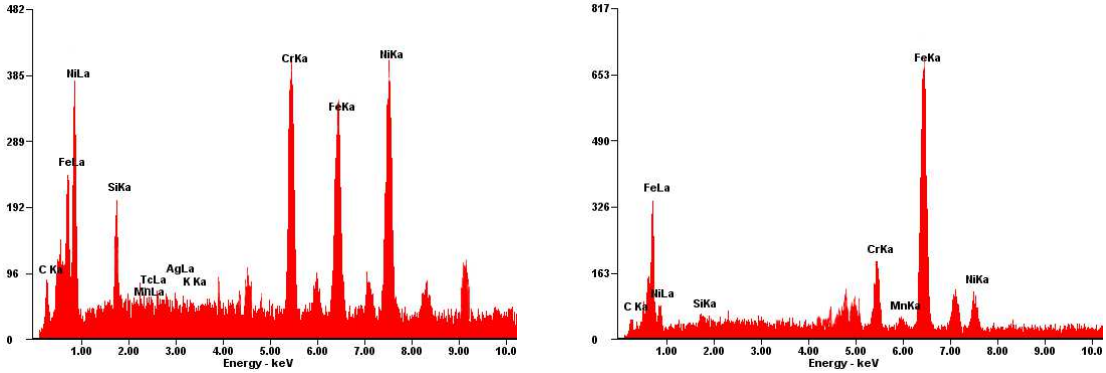
Fig. 3 are SEM micrographs of the cross section for cladding coating. And from Fig. 3(a), it can be seen that coating is composed of compact structures and dendritic one, and the juncture of coating and matrix is basicly combined. From Fig. 3(b) is SEM photo amplified 1000 times, from which, it can be seen that, a small amount of pores apear in the coating and it is because that some air in the alloy can't be eliminated during the process of high frequency cladding.



(a)×500 (b)×1000

Fig.3 SEM Micrograph of the Cross Section for Cladding Coating (A—Cladding Coating；B—Transition Region；C—Matrix)

Fig. 4 are energy spectrum distribution of cladding coating and matrix. And Fig. 4(a) is the spectrum analysis of cladding coating, from which, it can be seen that the coating mainly contains Fe, Cr, Ni, Si, C as well as small amount of Mn. From Tab.1 above, it can be seen that Mn is basicly not existed in the alloy layer but in the matrix material, and obviously, Mn, which belongs to the matrix material, permeats to the cladding layer during the process of high frequency cladding. Fig. 4(b) is the spectrum analysis of transition material, from which it can be seen that transition religion mainly contains Fe, Cr, Ni, Si as well as a small amount of Mn permeating from the matrix. The content of Fe has greatly increased relative to the coating, while the content of Ni, Cr has obviously reduced. And the reason is that the Fe contained in the matrix permeates to the transition religion during the high frequency cladding, with the content of Fe in transition increasing and the Ni, Cr of coating relatively reducing.



(a)—Energy spectrum distribution of cladding coating；(b)—Energy spectrum distribution of Transition region；

Fig.4 Energy Spectrum Distribution of Cladding Coating and Matrix

Conclusion

Metallurgical bonding is formed among transition regions of matrix and coatings with obvious white band, when cladding frequency is 250KHz and current is 1160A.

The microstructures of coatings are eutectics of “austenite + carbide”, relatively uniform. SEM micrographs of the cross section show that the coating, with a small amount of pores is composed of compact structures and dendritic ones.

References

[1] ZHAO Wenqiang,MIAO Hongbin et al.Study on laser cladding strengthening technology for mine hydraulic props. mining machinery, 2011,12:18-20.

[2] WANG Lichu,Cteate Problems of Hydraulic Prop Analysis.Coal Mine machinery, 2010,08, 145-146.

[3] YU Shanqi,Research on Remanufacturability of Mine Hydraulic Prop.Coal Mine machinery, 2012,03,49-51.

[4] WANG Chao,LYU Zhi,XIAO Hongbing,Coal Mine Hydraulic Pillar Surface Treatment Process Innovation.Coal Mine machinery,2013,02,122-124.

[5] LIU Xiangqing, GUOZhimeng, GAO Kewei et al. Microstructure and corrosion resistance of Ni60 coating prepared by induction cladding. Transactions of Materials and Heat Treatment, 2012, 33(supplement)：309-312.

[6] HE Dingyong, XU Jing, MA Ran et al. Properties of WC reinforced Ni60 coating prepared by high frequency induction cladding. Transactions of Materials and Heat Treatment, 2008, 29(3)：138-141.

[7] T. Umeda, P. Thirathipviwat, M. Supradist et al. Microsegregation development of heavily electromagnetically stirred melt of super high strength Al-10Zn-2.5Mg-2.3Cu alloy. International Journal of Cast Metals Research, 2011, 24(3)：184-189.

[8] M. Hazra, A.K. Mondal, S. Kumar et al. Laser surface cladding of MR1 153M magnesium alloy with (Al+Al2O3). Surface & Coatings Technology, 2009, 203(16)：2292-2299.

[9] YANG Hui-long, Sun Yu-fu, ZHAO Jing-yu et al. Study on the Fe-based coating reinforced by WC on cutting pick surface formed by high frequency induction cladding. Surface Technology, 2011, 40(4): 26~29.

[10] YANG Jian-ming, QIN Yi. Numerical Simulation on temperature field of cylinder workpiece in high frequency induction cladding. Foundry Technology, 2012, 33(4): 419-422.

[11] The Compiling Group of Mechanical Manufacturing Process Materials Technic Directory. Mechanical Manufacturing Process Materials Technic Directory. Beijing: Mechanical Industry Press, 1992: 265-269.

Advanced Materials Research Vol. 936 (2014) pp 1882-1885
© (2014) Trans Tech Publications, Switzerland
doi:10.4028/www.scientific.net/AMR.936.1882

Research on Material Structure, Appearance and Color Design and Application of Humidifiers—With Student Consumers as Research Objects

Xiaoli Nie[1, a], Chaoying Ouyang [2,b] and Ning Li[3,c]

[1] Wuhan, hubei province of hubei university of technology

[2] Wuhan, hubei province of hubei university of technology

[3] Wuhan, hubei province of hubei university of technology

[a]124801047@qq.com, [b]849304481@qq.com,[c]313498405@qq.com

Keywords: Humidifier, Material structure, Appearance design, Color design, Student consumer group

Abstract: The winter in northern China is cold and dry. With the centralization and generalization of heating devices, people have become more and more aware that dry environment does not only cause loss of water in the body, but also breeds numerous germs threatening health. In response, humidifiers are created. The widespread use of air-conditioners because of climate has accelerated the development of humidifiers. Although it is expanding, the potential consumer market of humidifiers has not been fully developed as the designers ignore students who are believed to be a big consumption group. This paper touches three aspects of humidifier design: material, appearance and color. According to the research, the humidifier market is believed to be better developed if humidifiers are designed to meet students' consumption concept by taking care of the three aspects.

Introduction

As people nowadays are pursuing life of better qualities, they have higher requirement for living environment. However, heating applied in cold dry winter makes people feel dizzy, thirsty and uncomfortable if they stay indoors for long. A large number of researches have shown that only moderate air humidity can make things full of life. Only when the indoor humidity stays between 45% and 55% RH can furniture be prevented from being deformed or damaged due to excessive dryness or humidity. However, the indoor humidity of the households in northern China in winter is merely 10% to 15% RH. Such a dry environment can generate high-level static electricity. A humidifier can produce humid air to fill a room with negative oxygen ions that can eliminate static electricity. Therefore, controlling air humidity is of great significance to health and life. When preparing for exams, many in-school students are vulnerable to diseases because of the change of humidity as germs are generated and infection sources are spread rapidly. As a result, students often fail to perform well in exams.

With student consumers as its research objects, this paper talks about appearance, material and color designs of humidifiers. In addition, it's suggested in this paper that the circuit design of humidifiers should be improved so as to create lower-powered humidifiers which can work in case of power failure.

Birth and Concept of Humidifiers

Birth of Humidifiers

Because of the dry climate in northern China, people often feel skins dry and throats sour after getting up in the morning. Such discomforts are worsened especially after November 15th when the supply of central heating starts. The discomforts mentioned above are caused by low air humidity. According to medical research, dry air accelerates the loss of water in the body, which can cause wrinkles beyond repair and thus speed up the aging of the body. What's worse, dry air can cause diseases of the respiratory system especially among vulnerable groups such as old people and young children. The first humidifier in China hence came into being in Beijing Yadu Indoor Environment Protection Technology Co., Ltd. in 1987.

Concept of Humidifiers

As a kind of indoor air moistener, a humidifier consists of a water tank, moisture spreading elements, and a moisture outlet valve. The water tank matches the heating bag. Positioned in the water tank, the moisture spreading elements are partially submerged. Water is heated by the heating bag, and evaporates to humidify the in-door air. Changing the number of moisture elements can adjust humidity. It can not only make in-door relative humidity reach the required level, but also provide certain amount of hot non-potable water.

Development State of Humidifiers

In the current market, humidifiers can be classified into two types in terms of service environment: the industrial type and the household type. In terms of technological principles, there are four types: ultrasonic humidifiers, purity degree humidifiers, spray mist humidifiers, and electric heating humidifiers. According to the ways of placement, there are cabinet-type and floor-type. The majority of humidifier consumers are office workers; the number of student consumers is not large. The main reasons for such a phenomenon are as follows. 1. The prices of humidifiers are beyond the students' purchasing power. 2. Electricity supply in school dormitories is restricted and power failure is set to a certain limitation. 3. Humidifiers are oversized, taking up the limited storage space in dormitories. 4. Humidifiers make sounds, disturbing school fellows.

Research on Humidifier Material and Structure Design

Research on External Structural Material of Humidifiers

Most humidifiers in the current market are made of plastics. Some are made of other materials such as ceramic and synthetic wood, and they are of higher prices, which is not easy to be accepted by the potential student consumption group. Therefore, the materials to be studied in this paper are plastics.

The American Society of Testing Materials (ASTM) defines plastics as typically organic polymers of high molecular mass. They are of solid shape when processed. During manufacturing and processing, they are moldable as it flows. Because of its universal use, plastics have produced heavy white pollution, causing great damage to the ecological environment. Now the environmentally-friendly plastics have come into being in response to the wave of green designs around the world. An excellent designer can design humidifiers meeting students' consumption concept only when he or she fully understands material properties and strives to obtain win-win interests for economy and environment. Plastic materials used to make humidifiers can be classified into following types:

(1) Acrylonitrile-Butadiene-Styrene (ABS): As one of the five major synthetic resins, ABS resin has good heat resistance, low-temperature resistance, chemical resistance, easy workability and dimensional stability. Besides, it is not only easy to color, but also useful in secondary processing such as hot-pressing and splicing. With prominent mechanical and thermal properties, ABS resin is widely used in household appliances such as air-conditioners, humidifiers, and so on.

(2) Polypropylene (PP): PP is a thermoplastic resin made from propylene. According to the methyl position arrangement, it can be classified into three types: isotactic polypropylene, atactic polypropylene, and syndiotatic polypropylene. The polypropylene is milk white high-crystallized polymer that is non-toxic, odorless, and flavorless. It has good properties of heat-resistance, flexural fatigue resistance, erosion resistance and electrical insulating. Because of its bad impact resistance and easy-aging, some additives, such as zinc oxide, can be added to remedy its weaknesses.

(3) Polystyrene (PS): PS is of linear structure made from monomer styrene. It is made in the ways of massive polymerization and emulsion polymerization. As a transparent raw material, polystyrene can be widely used when transparency is required in vehicle lampshades, clear parts of daily use, transparent glasses and jars, etc. It has good heat-resistance, low water-absorbing quality and strong radioactivity-resistance.

The three plastics mentioned above are non-toxic by themselves, and have their own advantages and disadvantages. Designers can take advantages of their properties to the fullest by appropriately adding some environmentally-friendly additives to them.

Research on Internal Structural Material of Humidifiers

Considering the facts that electricity supply is restricted and power failure is set in student dormitories, and that all humidifiers available in the current market must be powered on, it is necessary to design a kind of humidifiers that can work with a battery.

An important material named wet film is applied inside humidifiers. Generally, it can be classified into four types: compound type, which is corrosion-resistant, bacterium-proof, repeatedly cleanable, and durable for eight to ten years; fire-proof white compound type, which is fire-proof, water-absorbing, and easy-for-cleaning, and durable for eight to ten years; glass fiber type, whose properties are similar to the former two, but is used less and less because it is fragile and the glass fiber dust is harmful to health; metal hole type, which is greatly fire-proof, but is not recommended because of its bad performance of humidifying.

Through studying and improving the interior material of circuit design and structure, humidifiers can still be used in case of power failure in school dormitories. Currently most humidifiers are powered on by an external power source. If designers want to design humidifiers that can be powered on both internally and externally, they should adopt ultrasonic humidifier theory. By adopting the theory of ultrasonic high frequency oscillation, water can be atomized into ultramicrons of 1 to 5mm, spraying into the air and humidifying it. The ultrasonic humidifiers consist of a power circuit, a control circuit, an oscillating circuit, a draught fan, and a transducer (piezoelectric ceramic piece). It is feasible to use batteries to supply power for the internal circuit as the device is powered with direct current. There are two ways of power-supply if external power source is adopted. One is to use the transformer, which is applied to different types of humidifiers because of its powerful overload capacity, to power the oscillating circuit after it lowers down the rectifier filter. The other is to use a switching power source to supply power, whose features are the evident reduction of weight and high power-supply efficiency. If adopting internal power-supply, designers can use layer-built battery to power the device. Its maximum voltage can generally satisfy it. Therefore, based on the current technology, humidifiers using a direct power source and a built-in battery can be designed. Given this, humidifiers can work normally with an external power supply when power is on, or with a built-in battery when power is off. This design is very practical for students.

Research on Appearance and Color Design of Humidifiers

Research on Humidifier Appearance Design

The appearances of the humidifiers available in the market can be classified into following types: cartoon images, simple geometries, and artworks. To win student consumers, designers should consider saving materials, lowering the cost, and raising water volume. Besides, they should design humidifiers meeting to students' aesthetic standards by creating formal beauty. To school students at different ages, appearance designs can vary accordingly. To junior middle students, for example, designers can make use of popular cartoon images by appropriately making some changes. To senior high school students, however, designers should focus on special styles based on guaranteeing the basic functions of humidifiers as they are more mature than junior middle school students and more rebellious than university ones. While to university students, appearances should merely be simple and fashionable, for example, geometry-shaped ones. Owing to limited space available in school dormitories, designers should design humidifier packing of hang-up type and stickup type according to different appearance designs. Humidifiers can be hung up at bed side or tied to one of the supporting bars on the bed. The external packing of those designs, of course, should be made of environmentally friendly materials with good air permeability and insulating property.

Research on Color Application in Humidifier Design

For its quick acceptance by students, humidifiers should be designed in appearance to satisfy students' beauty-appreciation. In addition, colorific collocation is especially important. When it comes to colors, designers should consider which materials can be colored easily, which pigments are environment-friendly and harmless, and the color and lustre of which materials can last for a long time. Colors have three properties: hue, lightness, and purity. Hues are categorized into 24

types, including red, orange, yellow, blue, green, purple, and intermediate colors. Different hues have different color temperatures. Lightness of colors actually refers to light and shade of colors. Light colors make people feel relaxed and light-hearted; dark colors make people feel pressured and heavy-hearted. With gray is added to a color, its purity changes. For example, when gray is gradually added to yellow in a certain degree, yellow turns to grayish yellow which may provoke nostalgia.

Different colors bring people different feelings, such as coldness and warmness, heaviness and lightness, softness and hardness, strongness and weakness, heavy-heartedness, excitement, quietness, gorgeousness, simplicity and so on. Colors are not emotional. However, influenced by conventional concepts, various colorific collocations, and different textures of differently colored materials, consumers unconsciously associate different colors with different emotions. For example, if a humidifier is designed yellow and table lamp-like, it may make people feel cozy when placed in a bedroom. It can be ornamental, as well as functional, which makes it a perfect combination of appearance and function. Black makes people feel serious, greeny yellow relaxed and light-hearted, and blue calm and gloomy. Different collocations of colors create different visual effects. For example, pink glass material and Sailor Moon images may make a humidifier appear lovely, sweet and dreamlike, and accepted more easily by girl students in junior middle schools. Geometric shapes made of purple-and-white compound type plastic strips may make a humidifier look elegant, simple, but not plain, and accepted more easily by university student consumers. People in different age grades and of different genders may have different preference for colors. Only based on full understanding the colorific preferences of people in different age grades and of different genders, qualitative and quantitative analysis and assessment, can we design humidifiers accordingly to satisfy the needs of student consumers.

Conclusion

As the living standard of Chinese people has been increasingly improving, the market of humidifiers is enlarged gradually with the popularization of electric equipment. However, humidifiers have been accepted only in big cities. The importance of humidifiers is still overlooked in towns and villages in Chinese countryside. Students as a large consumption group have been neglected by businessmen. Humidifiers should be properly designed with various factors taken into consideration such as material, appearance, colors, and the living condition of students. Cheap and high-quality humidifiers that can work in case of power failure are bound to enjoy a better market. Renovated humidifiers will not only be accepted by students, but also become a favorite of people fond of beauty.

References

[1] The Meaning of the Art of Design. Comp. Zhao Jianghong. (Hunan University Press, Changsha 199). (in Chinese)

[2] Du Linying and Liao Chuanshan: The Importance of Humid Environment and Its Implement. HVAC, 1990. (in Chinese)

[3] Information on http://wenku.baidu.com/view/ce60dec7a1c7aa00b52acb2d.html (in Chinese).

[4] Information on http://wenku.baidu.com/view/d4d664dad15abe23482f4d5d.html (in Chinese).

[5] Wang Cheng: On Development and Application of Humidification Technology. Cleaning and Air-conditioning. 1991.

[6] Information on http://baike.baidu.com/view/30598.htm?wtp=tt#2 (in Chinese)

Advanced Materials Research Vol. 936 (2014) pp 1886-1889
© (2014) Trans Tech Publications, Switzerland
doi:10.4028/www.scientific.net/AMR.936.1886

260t Ladle Stress and Deformation Finite Element Analysis

Yanping Sun, Dechen Zhang, Ming Yang, Yuan Li

Mechanical Engineering and Automation, University of Science and Technology Liaoning, Anshan, Liaoning ,China, 114051

Zhangsun6411@163.com

Keywords: iron ladle; finite element method; stress; deformation

Abstract: In this paper, iron ladle stress and deformation has been accurately calculated using finite element analysis software ANSYS based on 260t iron ladle in standing, lifting, tipping working conditions. Distribution of stress field was obtained. The stiffness and strength of the iron ladle has been evaluated. The results show that the iron ladle in the standing, lifting and tipping working conditions, structural deformation is small, the strength and stiffness meet the requirements. This research extends the working life of 260t iron ladle. It provides theoretical basis for producing and using of the iron ladle and further optimal designing.

Introduction

Irom ladle applied to the molten iron of the iron and steel metallurgy field of logistics and transport for iron works, foundry use in blast furnaces, stoves, cast iron blast furnace to undertake the molten iron and blending, transshipment, casting operations, engaged in the transfer of molten iron peak production tasks, is the iron and steel metallurgy a high frequency of necessary equipment. Ladle refractory and shell, in which the refractory insulation from the main payload of the ladle shell suffered: the molten iron, refractory and shell gravity load and temperature load. The shell is the main load-bearing structures need to have sufficient stiffness and strength[1]. Existing large ladle largely based on the mechanical load, the use of elementary mechanics theory and the empirical coefficient for structural design calculations, the calculation accuracy can not meet the requirements of the modern iron and steel production[2]. Accurate 3-D stress and deformation of the structure has become a necessary precondition of large-scale the ladle structure design. 260t large ladle design research, consider the various stages of loading, a comprehensive analysis of the circumstances under load, to determine the most dangerous working conditions, using finite element program ANSYS for 260t iron ladle calculation, calculation of iron pitcher stress and deformation for 260t ladle steel strength and stiffness analysis.

The ladle structure introduced

260t iron ladle assembly ladle was shown in Fig.1. It composed of shell, lining, trunnion, base and so on. Tank shell adopted iron plate welding structure, the top was duckbill structure, the main structure was pyramid, the top outer diameter was 4615 mm, the bottom outer diameter was 4020 mm, wall thickness was 30mm, bottom thickness was 40 mm, height was 4600mm, internal depth was 4560 mm. The top thickness of the refractory material layer was 175.5 mm, the bottom thickness was 403mm, the inner bottom fillet radius was 750mm, and bottom thickness was 560 mm. The maximum volume of iron ladle was 260 t; there are 300 mm between liquid surface and

tank brim. The weight of shell was 33t, the weight of refractory material was 64t, the average temperature of the outer shell was 350°.Shell density was 7800kg/m^3, lined with refractory material density was 2800 kg/m^3, the molten iron density was 6800 kg/m^3, lined with refractory material elastic modulus of 40GPa, and Poisson's ratio was 0.3. The load of shell, the weight of the molten iron and the mechanical properties of the ladle shell were shown in Table 1.

Table.1 Ladle shell mechanical properties

Material	Elasticmodulu-s / GPa	Poisson's ratio	Strength limit / MPa	Yield limit / MPa	Allowable stress / MPa
20 g	203	0.3	410	235	100



Fig.1 Ladle shell structure

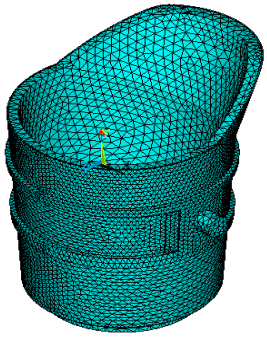


Fig.2 Finite element model of the iron ladle

Finite element mode

3-D model [3]of 260t iron ladle shell and lining were built using SolidWorks according to 2-D engineering drawings ,as shown in Fig.1.

Importing the shell and lining 3-D assembly model file into the finite element software ANSYS, and bonding the shell and lining, share the same side that is used to simulate contact with the inner surface of the shell and the outer surface of the lining. The type of grid was set. Shell, lining, trunnion and base were 3-D physical unit. Structural entity uses the Brick 8 node 45, the shell unit number 41545, the number of nodes 13935; lining unit number 50824, the node number 18949; local grid refining in the shell and trunnion contact area was carried on. Attach a shell and liner material properties and meshing [4,5]. In this paper, 3-D finite element algorithm was adopted to calculate the iron ladle shell and lining. The finite element model was shown in Fig. 2.

Imposed by the finite element model loads and constraints

The applied load.

loading in three conditions [6]:

(1)Working conditions of iron ladle in the hot metal tanker on standing;

(2)Working conditions of iron ladle trunnion lifting operation at full load;

(3)Working conditions of iron ladle pitcher tipping molten iron.

The shell blocked with lining as a whole. The densities of the shell and the lining are given, acceleration of gravity is 9.8m/s2. In variety of working conditions iron ladle shell structure dead weight and refractory material weight as volume force applied on tank.

Gravity reflected the side pressure of refractory layer and base pressure of lining bottom refractory layer. The distribution load of the molten iron weight applied on the tank side and bottom, the molten iron pressure on each inner surface increase with depth. Plane load was used; changing gradient is 66640N/m^2.

Impose constraints.

Iron ladle on vehicle in standing working conditions, trunnion hasn’t outside force, the full constraints applied to the contacting surface of the bottom of the iron ladle and car. Iron ladle operation conditions are, trunnion has tension of hoisting, Y and Z direction constraints were applied to the trunnion. Iron ladle out the hydraulic conditions, ladle tilt, and vertical angle of 30°, the applied load and constraint. Trunnion and turned molten iron rings at the upward lifting of tension therefore exert Y, Z direction constraints [6].

Analysis and Evaluation of calculation results

The equivalent stress of the structure was calculated according to Mises stress that is the fourth strength theory, the specific formula is

$$\sigma_d = \sqrt{\left[\left(\sigma_x-\sigma_y\right)^2+\left(\sigma_y-\sigma_z\right)^2+\left(\sigma_z-\sigma_x\right)^2+6\left(\tau_{xy}^2+\tau_{yz}^2+\tau_{xz}^2\right)\right]/2}$$

The maximum equivalent stress and maximum equivalent deformation of the various working conditions were analyzed by the output of nephogram and numerical analysis.

Working conditions of iron ladle in the hot metal tanker standing.

The load has been calculated considering the molten iron, refractory materials and shell weight. The overall stress of the iron ladle was shown in Fig.3, the deformation shown in Fig.4. The result shows the maximum stress is 28.9MPa in the upper edge of the shell; maximum deformation is 0.973mm in the duckbill.

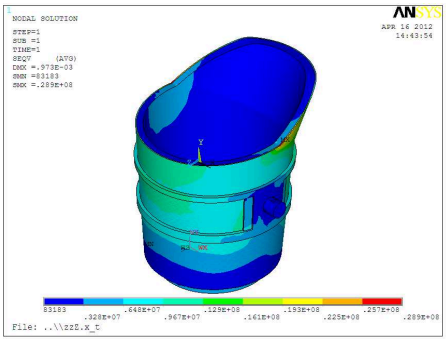


Fig.3 Stress in working condition 1

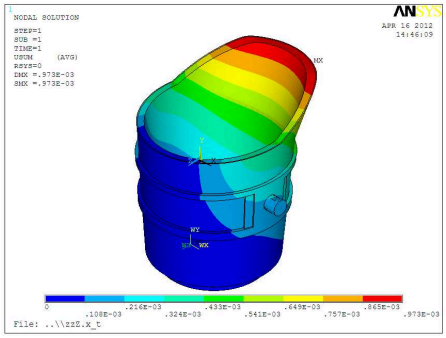


Fig.4 Deformation in working conditions

Working conditions of iron ladle lifting operation.

The overall stress of the iron ladle was shown in Fig.4, the deformation shown in Fig.5. The result shows the maximum stress is 93.4MPa around the trunnion; maximum deformation is 2.328mm in the upper edge of the duckbill.

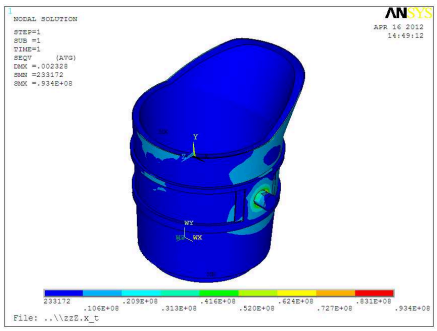


Fig.5 Stress in working condition 2

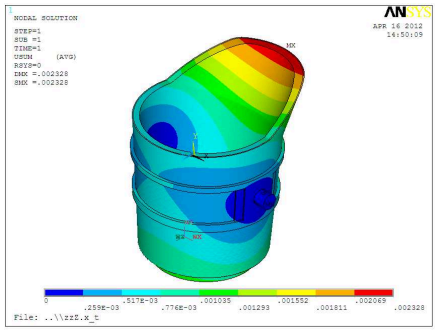


Fig. 6 Deformation in working conditions 2

Working conditions of tipping molten iron from iron tank.

The overall stress of the iron ladle was shown in Fig.7, the deformation shown in Fig.8. The result shows the maximum stress is 32.6MPa in the root of the trunnion; maximum deformation is 0.860mm in the upper brim of the ladle.

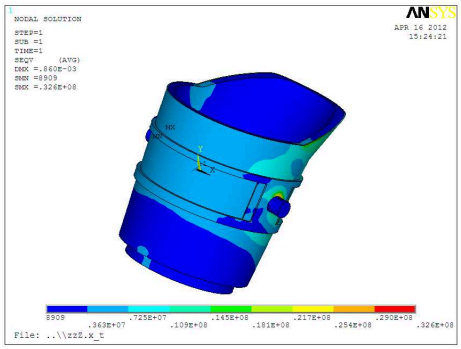


Fig.7 Stress in working condition3

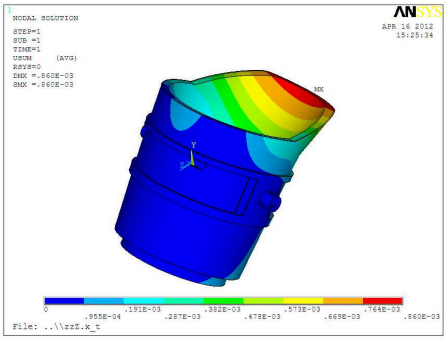


Fig.8 Deformation in working conditions 3

The iron ladle shell stress levels significantly higher than the stress level of the refractory layer from the nephogram of the iron ladle shell and lining surface stress field in Fig.3, Fig.5, Fig.7. The trunnion is the main and complicated loading structure. The higher stress distribution was shown around the trunnion. Ladle on strengthening rib stress, indicating the strengthening ribs strengthen the ladle shell. Analyzing the three cases, the maximum equivalent stress is less than the allowable stress of 100MPa, it meets the strength requirements. The maximum deformation is less than allowable deformation 5 mm; it also meets the stiffness requirements.

The results show that the full load of the iron ladle through the trunnion lifting operation in the most dangerous working conditions, strength and stiffness of the 260t iron ladle was sufficient .

Summary

(1)260t iron ladle has been under good conditions, and the deformation risk factors haven't existed yet through finite element analysis and design using ANSYS.

(2) It proves that the result of the analysis to the iron ladle using ANSYS accord with the actual stress. This method is reasonable and reliable. It will lay a foundation for checking and analyzing the iron ladle.

(3)More accurate calculation has been done to the iron ladle stress and deformation using three-dimensional finite element technique. The results provide a theoretical basis for the production and use of the iron ladle and further optimization of the design.

References

[1] Qianglong Zhang, Naiyuan Tian. Ladle multi-functional technology, Beijing University of Science and Technology. 2007, (4) :424-427

[2] Daliang Shi. Ladle design quick calculation method. Chinese casting machine. 1994, (3) :15-18

[3] Renxi Hu, Shiting Kang, Cunhong Lu. Solid Chinese board in the Works 2008 Standard instance tutorial Mechanical Industrial Press . 2009:69-89

[4] Shihui Li, Furong Chen. element analysis of stress field of the ladle. Steelmaking. 2007, 23 (3):62-37

[5] Zhihua Chen.150Tladle three-dimensional mechanical stress and deformation analysis of metallurgical equipment . 2010, (1): 41-43

[6] Saeed Moaveni. Finite Element Analysis Theory and Application ANSYS, Third Edition. Electronic Industry Press, Beijing. 2008:493-522

Advanced Materials Research Vol. 936 (2014) pp 1890-1893
© (2014) Trans Tech Publications, Switzerland
doi:10.4028/www.scientific.net/AMR.936.1890

1450 cold rolling mill rack finite element modal analysis

Dechen Zhang, Chaowen Dong, Ming Yang, Yanping Sun

Mechanical Engineering and Automation, University of Science and Technology Liaoning, Anshan, Liaoning , China, 114051

ssspppp64@163.com

Keywords：rolling mill; natural frequency; finite element

Abstract：The vibration of the fifth frame mill of 1450 Cold Tandem Rolling Mill in the rolling process was studied using finite element software ANSYS. The dynamic analysis of one-piece frame and two- piece frame on the fifth frame mill were carried on. The natural frequency and mode of vibration were calculated. Through analyzing, we obtained that two- piece frame performed better.

Introduction

In the rolling process, shock vibration of the mill caused by biting steel and taking off the steel often lead to loosening of the anchor bolt，damage of the frame component and oscillation marks and so on, these will cause huge economic losses to enterprises. Therefore, in order to ensure the stability and enhance the plate quality, dynamic analysis of the rolling mill and controlling of their vibration characteristics were carried on in this paper [1, 2, 3].

Abnormal vibration phenomenon of the fifth frame mill of 1450 Cold Tandem Rolling Mill was studied in this paper; the vibration situations of one-piece frame and two-piece frame were analyzed. The natural frequency and mode of vibration were calculated and compared.

Model and Meshing

Some parts of the frame were simplified because calculating of the rolling frame was dynamic analysis rather than stiffness and strength. The finite element modal of one-piece frame and two-piece frame were built in ANSYS10.0 according to structural size of the mill frame [4].In order to ensure the accuracy of the calculating, 8-node solid 45 hexahedral element type of the entire structure was adopted. As the mesh density and mesh ways have small impact on the modal analysis results, free way mesh was used in this paper. Frame meshes were shown in Fig. 1 and Fig. 2.

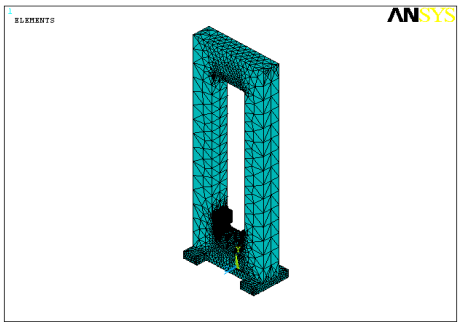


Fig.1 One-Piece Frame

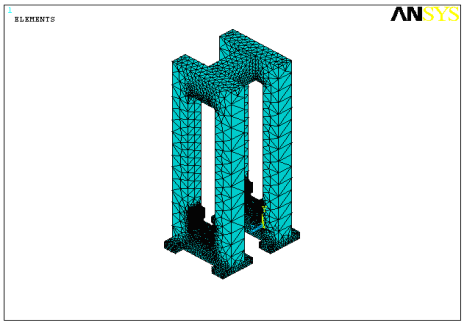


Fig.2 Two-Piece Frame

Modal Analysis

Using the above established frame finite element model, according to installation stress and rolling process stress, rigid constraints were imposed on the anchor bolt. The bottom surface of the left and right foot were imposed zero displacement constraints on X,Y, Z direction, respectively.

One-piece frame and two-piece frame natural frequencies were obtained , shown in Table 1 and Table 2.

TABLE.1 THE ONE-PIECE FRAME NATURAL FREQUENCIES

Order	1	2	3	4	5	6	7
Frequenc f_1 / Hz	8.21	17.02	35.95	55.95	81.56	85.63	96.14
Order	8	9	10	11	12	13	14
Frequenc f_1/ Hz	128.35	149.25	152.43	189.65	205.17	236.00	249.48

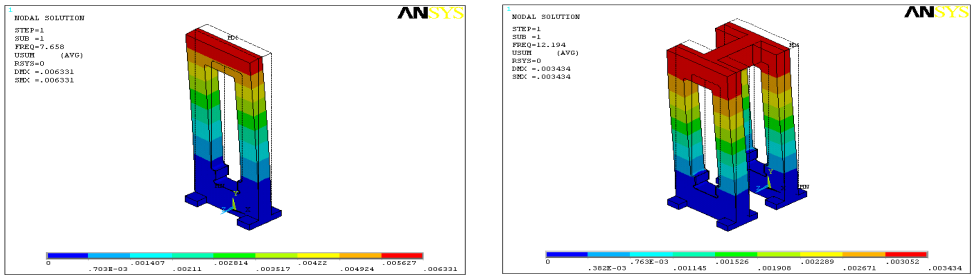
TABLE.2 THE TWO-PIECE FRAME NATURAL FREQUENCIES

Order	1	2	3	4	5	6	7
Frequenc f_2 / Hz	12.19	15.85	27.54	55.70	58.90	68.01	68.25
Order	8	9	10	11	12	13	14
Frequenc f_2/ Hz	80.88	82.55	92.77	94.31	106.69	123.72	133.88

Results Analysis

1st Order Mode

1st order modal shapes of one-piece frame and two-piece frame were shown in Fig.3 (a) and Fig.3 (b), respectively. In this natural frequency of the modal, vibration is most likely to occur. It can be seen from the figures, regardless of one-piece frame and two-piece frame, the vibration modes are rack along the swing before and after the roll axial direction. The top of the rack has the maximum deformation. According to Table 1 and Table 2, the 1st order natural frequency mode shape of one-piece frame is f_{101} = 8.21 Hz, and 1st order natural frequency mode shape of the two-piece frame is f_{201} = 12.19 Hz.



(a) One-Piece Frame (b) Two-Piece Frame

Fig.3 1st Order Mode Shapes

Comparison of two frequencies:

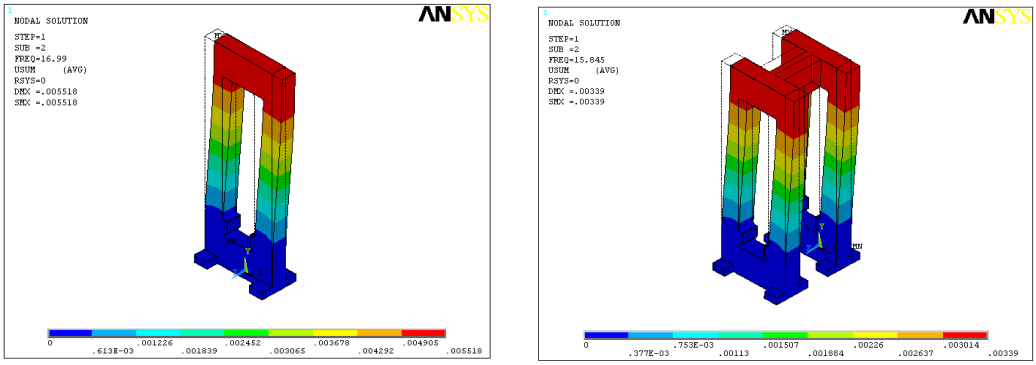
$$\alpha = \frac{8.21}{12.19} \times 100\% = 67.35\%$$

Conclusion: the coincidence rate was 67.35%, consistent with the 1st order natural frequency of the one-piece frame 8.21 Hz and two-piece frame 12.19 Hz. Both frequencies differ large, mainly due to two-piece chassis rigidity improved, leading to the increasing of vibration natural frequency.

2nd Order Modal

2nd order modal shapes of one-piece frame and two-piece frame were shown in Fig.4 (a) and Fig.4 (b), respectively. They are anti-symmetric modes. It can be seen from the figures regardless of one-piece frame or two-piece frame, the vibration modes are swing forward along the strip before and after. At the top of the frame deformation has maximum. However, according to Table 1 and

Table 2, the 2nd order natural frequency mode shapes of one-piece frame is f_{102} = 17.02Hz, and 2nd order natural frequency mode shapes of two-piece frame is f_{202} = 15.85Hz



(a) One-Piece Frame (b) Two-Piece Frame

Fig.4 2nd Order Mode Shapes

Comparison of two frequencies:

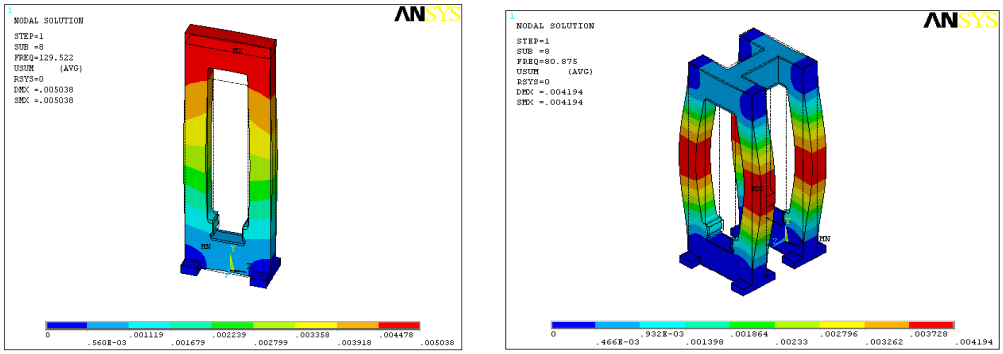
$$\alpha = \frac{15.85}{17.02} \times 100\% = 93.13\%$$

Conclusion: the coincidence rate was 93.13%, consistent with 2nd order natural frequency mode shapes of one-piece frame 17.02 Hz and 2nd order natural frequency mode shapes of two-piece frame 15.85 Hz, both frequencies are closer.

8th Order Modal

8th order modal shapes of one-piece frame and two-piece frame were shown in Fig.5 (a) and Fig.5 (b), respectively. It can be seen from the figures that one-piece frame mode shape is the vertical vibration mode shape; the two-piece frame is the symmetric mode shapes.According to Table 1 and Table 2, the 8th order natural frequency mode shapes of one-piece frame is F_{108} = 128.35Hz, and 8th order natural frequency mode shapes of two-piece frame is f_{208} = 80.88Hz.

Vibration modals are different, so they can not compare the frequencies of the matching rate.



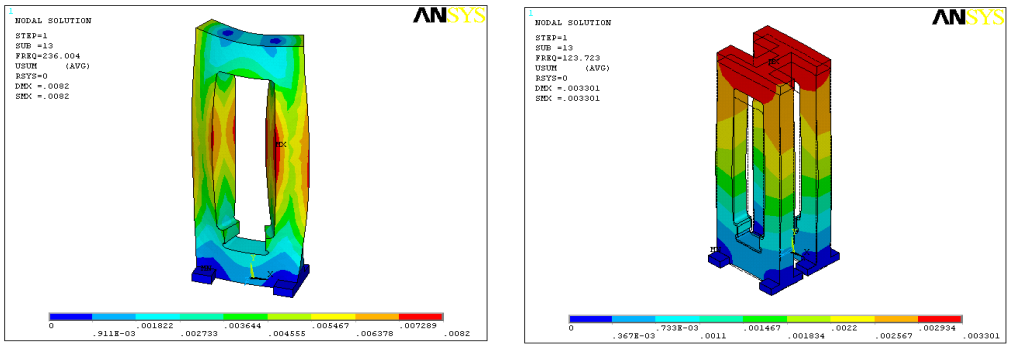
(a) One-Piece Frame (b) Two-Piece Frame

Fig.5 8th Order Mode Shapes

13th Order Modal

13th order modal shapes of one-piece frame and two-piece frame were shown in Fig.6 (a) and Fig.6 (b), respectively. As can be seen from the figures, one-piece frame mode shape bending along the roll axial and two-piece frame is vertical mode. According to Table 1 and Table 2 shows, the 13th order natural frequency mode shapes of one-piece frame is f_{113}=236.00Hz, and 13th order natural frequency mode shapes of two-piece frame is f_{213} =123.72 Hz.

Vibration modes are not same, so they can not compare the frequencies of the coincidence rate.



(a) One-Piece Frame (b) Two-Piece Frame

Fig.6 13th Order Mode Shapes

Vertical Modal

One-piece frame and two-piece frame vertical modals are shown in Fig.5 (a) and Fig.6 (b), respectively. According to Table 1 and Table 2, the natural frequency are f_{108} =128.35 Hz and f_{213} =123.72 Hz.

Comparison of two frequencies:

$$\alpha = \frac{123.73}{128.35} \times 100\% = 96.4\%$$

Conclusion: from the consistent rate, the anastomosis of one-piece frame vertical natural frequency and two-piece frame vertical natural frequency is 96.4%, both frequencies are closer.

Summary

From the above analysis, we can conclude that modal analysis on two-piece frame did better than one-piece frame, and it obtained more real vibration model and more precise vibration frequencies. Therefore, the results of dynamic analysis on two-piece frame are closer to the real situations, it would be easier to solve vibration phenomenon appeared in the process of rolling process.

References

[1] Zou Jiaxiang and Mr. Xu. Cold tandem mill vibration control system [M]. Beijing: Metallurgical Industry Press, 1998

[2] Zou Jiaxiang. Rolling machinery [M].Beijing:Metallurgical Industry Press .2000

[3] YUKIOK, YASUHIROS, NOBUON, et al. Analysis of chatter in tandem cold rolling mill [J]. ISIJ International, 2003, 43:77-84

[4] Li Liming. Practical tutorial ANSYS finite element analysis [M] Beijing: Tsinghua University Press, 2005

Advanced Materials Research Vol. 936 (2014) pp 1894-1899
© (2014) Trans Tech Publications, Switzerland
doi:10.4028/www.scientific.net/AMR.936.1894

Set-up and Application of Thermal Fatigue Knowledge Ontology

Guo Caifen, Dong zhi, Ning Haixia, Wan Changdong

College of Mechano-electronic Engineering, Suzhou Vocational University, Suzhou, Chain, 215104

guocf@jssvc.edu.cn, dongzhi@jssvc.edu.cn, nhx@jssvc.edu.cn, wancd@jssvc.edu.cn

Keywords: thermal fatigue knowledge. ontology. super-hard cutting tools

Abstract: In order to reuse and share thermal fatigue knowledge, the thermal fatigue knowledge ontology is exploited. The basic ontology relationship and characteristics are analyzed and the concept classification and axiom are devised. With the help of Protege3.1.1 software, the thermal fatigue knowledge ontology comes into being. Based on the crack axiom, the intelligent matching of thermal fatigue crack states of super-hard cutting tools is accomplished.

Introduction

Ontology arises from the philosophy that deals with the nature of being. In such fields as knowledge engineering, natural language processing and intelligent information searching, ontology is the basis of formalization description, which may play the role of translation and mapping among different modeling tools, languages and software. When used in knowledge management, ontology is a glossary which is made up of concepts, axioms and rules. As a semantic model efficiently representing concept arrangements, its essence is reusing and sharing of knowledge.

On the other hand, ontology may provide advanced inter-operating utilities among different information systems, that is to say, the greatest contribution of ontology is that it can standardize concepts and terms in certain or many specialized fields, and make their applications easy to realize. Supported by the above mentioned justifications, the ontology application would improve the efficiency of knowledge searching, accumulating and sharing greatly and make it truly possible of knowledge reuse and sharing[1~3].

Concept Classification of Thermal Fatigue Knowledge Ontology

The concept classification is established in order to ascertain the main concepts, perform the collection and classification, and establish structure levels about thermal fatigue knowledge ontology. The first step is to build the thermal fatigue knowledge dictionary, which is a kind of professional one and aims at defining the domain nomenclatures and making clear its form and semantic. The needed knowledge may originate from experts, books, tables, networks, etc. The united domain dictionary would solve various understanding and settle the basis of field knowledge formalization.

The second step is to sum up the above nomenclatures into several super-species and make certain their suitable structure levels. In this paper, five species are gathered, including the component structure information, its material information, its working environment information, its states detecting information and cracks information, which corresponds to five sub-domain ontology separately, as shown in Fig.1.

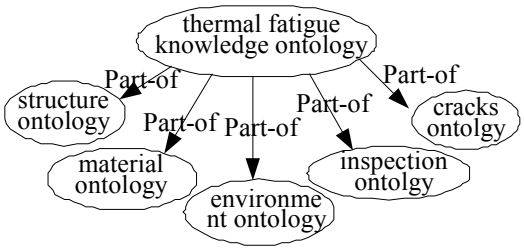


Fig.1 Five Sub-domain Ontology

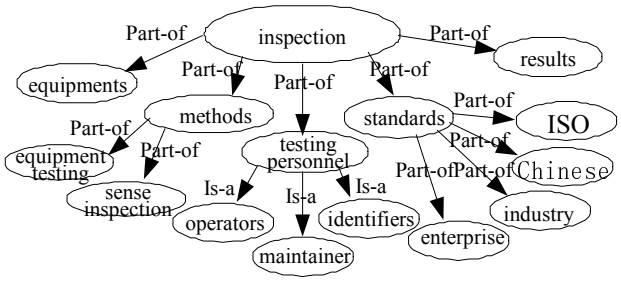


Fig.2 Components Inspection Ontology

Set-up of Sub-domain Ontology

Component Inspection Ontology

This ontology is designed to represent inspecting methods during machining processes, including testing standards, methods, equipments, testing personnel and results, etc. This sub-domain ontology is displayed in Fig.2.

Component Material Ontology

This ontology is applied to describe the component's property information as the material's constitutes and structure, heat treatment requirements, its mechanical and thermal properties, machinability, etc. This sub-domain ontology is indicated in Fig.3.

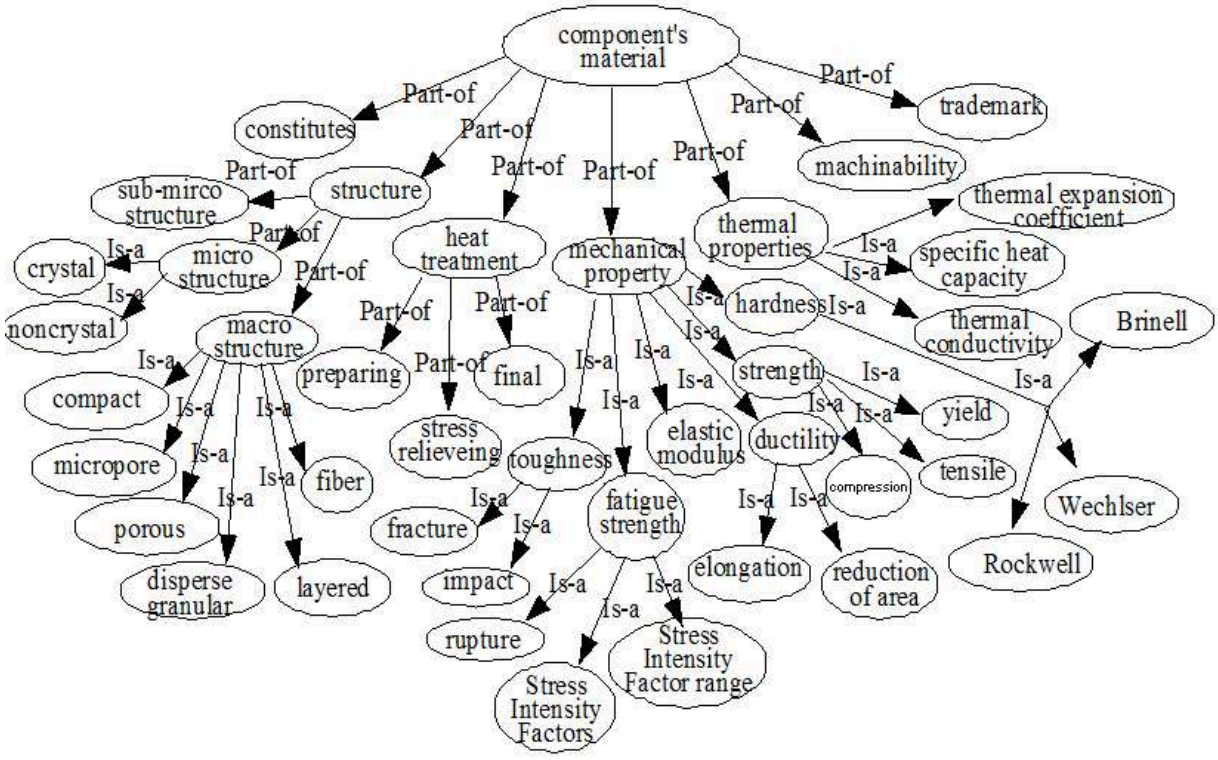


Fig.3 Components Material Ontology

Component Structure Ontology

It is used to depict the component's serial number, its roughcast type, its geometric characteristics, its machining process structure (including chamfer angle, chamfer circle, relief groove and grinding undercut, etc.), structural machinability, machining quality, etc. This sub-domain ontology is represented in Fig.4.

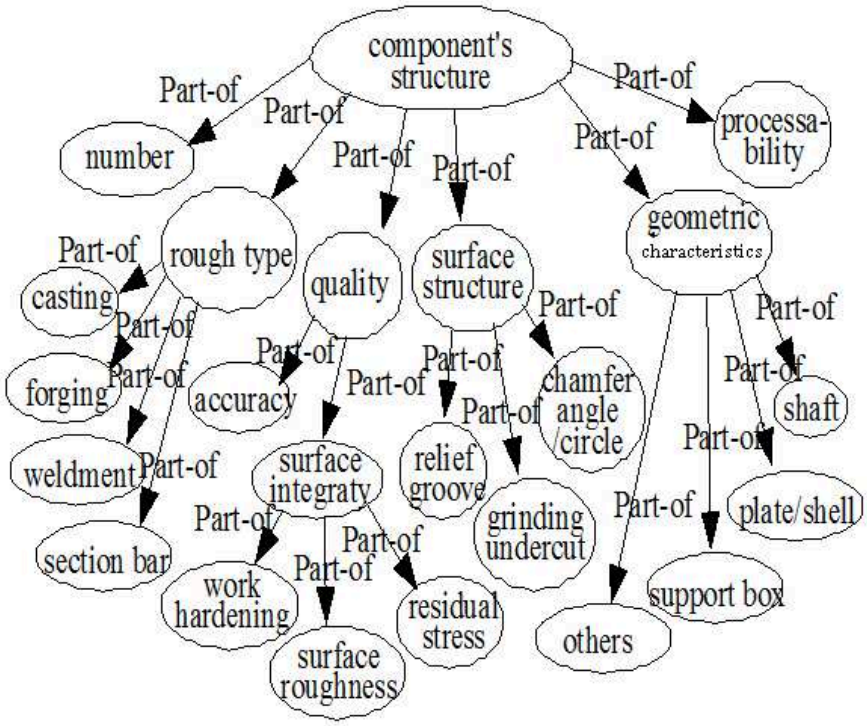


Fig.4 Components Structure Ontology

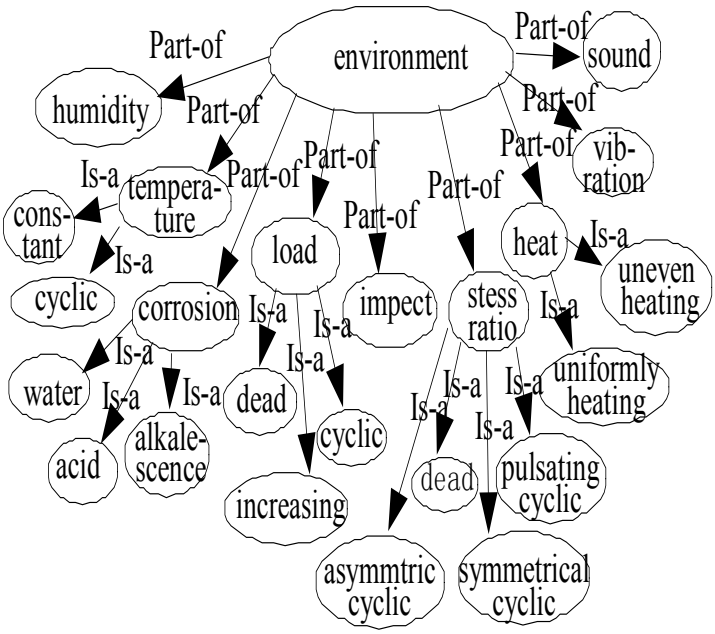


Fig.5 Components Environment Ontology

Component Environment Ontology

It is deployed to represent the component's working environment, including temperature, humidity, corrosion, load conditions, stress ratio, acoustic impulsion, vibration, and heat influence. This sub-domain ontology is displayed in Fig.5.

Component Cracks (Processes) Ontology

In the final analysis, failures of structures or components originated from cracks, which may be clear or obscure. Initiation and development of cracks dominate the failure processes, which may be classed into four phases, 1) changing of microstructures or substructures attributes to the permanent

damage contributing to micro-defects, 2) enlarging of micro-cracks or micro-pores forms dominant cracks, 3) dominant cracks propagate steadily, 4) structures lose stabilization or fail completely. Therefore, initiation, propagation and dominant cracks formation information should be included in the cracks ontology. This sub-domain ontology is shown in Fig.6.

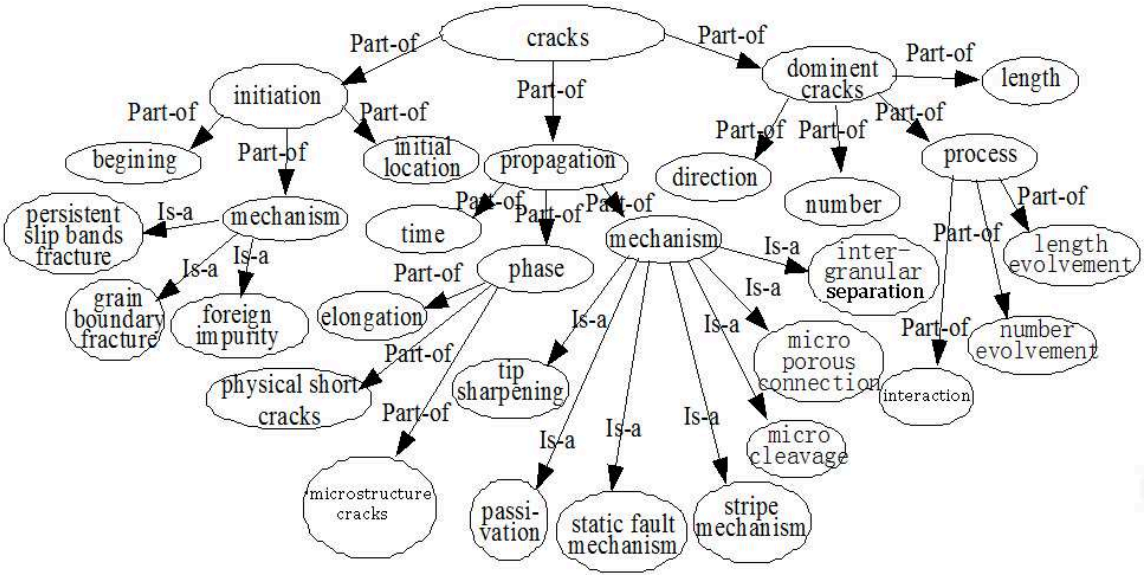


Fig.6 Components Cracks Ontology

Basic Relationships and Axioms Establishment

Some relationships may be applied all over the domain, not limited within certain single ontology, which possess several basic characteristics, as being symmetric, transferable, reverse, etc.

Basic relationships[4]

1) Inherited relationship, is-a.

Axiom 1: Relationship is-a is transferable.

Axiom 2: Relationship is-a is asymmetric.

2) Partial and whole relationship, part-of.

Axiom 3: Relationship part-of is transferable.

Axiom 4: Relationship part-of is asymmetric.

3) Case relationship, instance-of.

This one represents relationship between cases and concepts, similar to that between objects and kinds.

Basic Axioms

Besides some axioms shown above, there also exist axioms between top kinds and those belonging to sub-domains[5].

Temporary Conditions Axiom

$$(\forall a, \sigma_1, \sigma_2)\sigma_1 < do(a, \sigma_2) \rightarrow \sigma_1 \leq \sigma_2$$

$$(\forall a_1, a_2, \sigma)do(a_1, \sigma) = do(a_2, \sigma) \rightarrow a_1 = a_2$$

$$(\forall \sigma_1, \sigma_2)\sigma_1 < \sigma_2 \rightarrow \neg\sigma_2 < \sigma_1$$

Where a_i (i=1,2) stands for activities, σ_i(i=1,2)represents conditions, the function do(a, σ) represents what obtaining from carrying out the activity **a** under the condition $\boldsymbol{\sigma}$.

Axioms Applied in Sub-domains

After establishing axioms between top kinds, axioms used in sub-domains would be defined. For example, the crack axiom would be described as below, if a kind of crack state comes forth easily under certain machining condition, and this kind of condition does be detected in certain

manufacturing process, then it may be reckon that cracks appear in the component during this kind of machining process.

Ontology Realization

The Protege3.0 is a kind of developing tool based on Java designed by American Stanford University [4], supporting OWL(web ontology language), visual plug-in units and Chinese input. It possesses excellent ontology and knowledge base developing environments. With Protege3.1.1, ontology is displayed in tree like hierarchical directory structure and the domain model would be designed on the concept hierarchy, through adding or editing classes, sub-classes, attributes and cases by clicking the corresponding projects.

The crack ontology is set up and displayed in Fig.7.

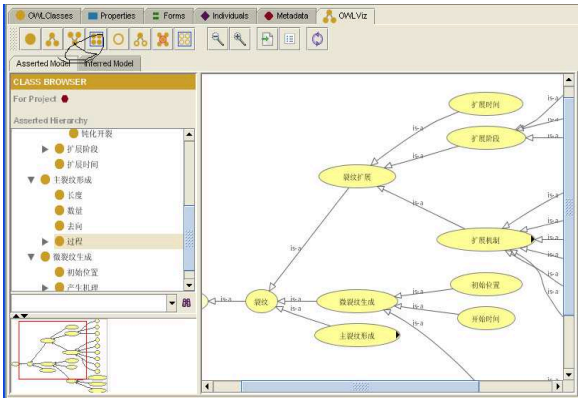


Fig.7 Crack Ontology Developed Through Protege3.1.1

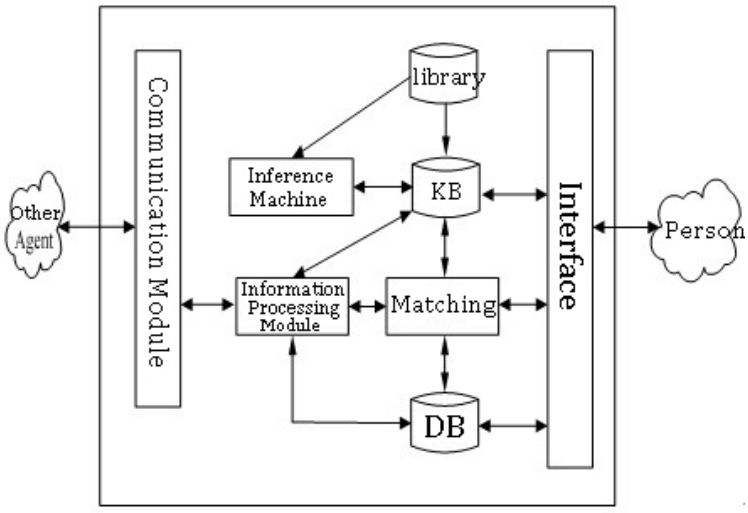


Fig.8 The Agent Structure

Ontology Applications

The Agent Structure

When the Agent technology is applied to thermal fatigue knowledge management, two problems must be solved. The first is how to represent ontology, the other is the disjoining of ontology with the knowledge describing information based on it. The sharing knowledge applied through fields is stored in ontology, which is the general understanding of various concepts and meanings and is hardly modified as soon as its establishment. If its modification is unavoidable, the ontology structure would not be changed as far as possible. While what be put in the knowledge base is practical cases and actual information existed in the present world, which should be changed and updated along with facts, so disjoining of them is necessary. In this paper, the Agent technology is used to realize the thermal fatigue knowledge management. Its schematic structure is shown in

Fig.8. This system consists of the following modules, as an information collecting and processing module, the decision-making module, the database, the ontology base, the learning and evolution module and the users interface.

Crack States Matching Evaluation

During high-speed milling processes, super-hard cutting tools are subjected to a hostile environment, where both heat and fluctuating forces act upon them. To get a full-scale of practical thermal fatigue crack states, multi-signals must be collected and analyzed because different signals have a variety degree of sensitivity. Under normal working conditions, values of all evaluation indexes, obtaining from practical measuring and relevant literatures[6], are displayed in Table 1.

Table 1 EVALUATION INDEX VALUES OF THERMAL CRACK STATES

Evaluation index （characteristic）	thermal fatigue crack rank			
	crack initiation	propagation	dominant crack formation	tools failure
Milling-force signal	80~90	90~100	100~105	105~115
Acoustic-emission signal	0~0.38	0.38~0.5	0.5~0.78	0.78~1.0
Vibration signal	0~0.35	0.35~0.48	0.48~0.83	0.83~1.0
Temperature signal	500~650	650~750	750~820	820~880

If the four evaluation values are 86, 0.28, 0.35, 590 respectively, it is known from Table 1 that this group value corresponds to the range of crack initiation. With the help of crack state evaluation axiom, it would be deduced that crack initiation has come into being in this cutting tool. Therefore, measures would be taken to avoid crack rapid propagation, such as introducing low cutting speed and low feed rate per teeth.

If there doesn't exist certain corresponding crack state in the knowledge base, the inference machine may reason by ontology axioms, then get the knowledge base updated and match using the matching module, finally return the result to users or certain relevant system.

Conclusions

The ontology model is proposed in this paper, together with the agent structure of thermal fatigue knowledge management. The crack state is intelligently evaluated and matched. This paper would help to promote the research on thermal fatigue cracks evaluation of super-hard cutting tools.

References

[1] Arpirez J C, Gomez-Perez A, Lozano-Tello A, et al. Reference ontology and (ONTO)2Agent: the ontology yellow pages[J]. Knowledge and Information Systems, 2(4)(2000)387-412.

[2] Fernandez M, Gomez-Perez A, Pazos J, et al. Ontology of tasks and methods[J]. IEEE intelligent systems and their applications, 14(1)(1999))37-46.

[3] Schreiber A T, Terpstra P. Sisyohus-V(ertical)T(ransportation) : A Common KADS solution[R]. ESPRIT Project 8145 KACTUS, University of Amsterdam, 1995.

[4] Li Xiangquan, Wang Ningsheng. Study on some key Technologies of Multi-Agent based Software Enterprise Human Resource Management System(in Chinese)[D]. Nanjing University of Aeronautical and Astronautical, Nanjing, China, 2007。

[5] Perez A G, Benjamins V R. Overview of Knowledge Sharing and Reuse Components: Ontologies and Problem-Solving Methods. In:Stockholm V R, Benjamins B, Chandrasekaran A,eds. Proceedings of the IJCAI-99 workshop on Ontologies and Problem-Solving Methods (KRR5) 1999 ,1~15.

[6] Wu Dongmin, Rui Yannian. Research on the evaluation of drill wear based on extension theory (in Chinese)[J]. Modern Manufacturing Engineering, 4 (2012) 17-20.

Advanced Materials Research Vol. 936 (2014) pp 1900-1904
© (2014) Trans Tech Publications, Switzerland
doi:10.4028/www.scientific.net/AMR.936.1900

Void Formation and Growth at Solder-bonded Interfaces In HP LEDs

Wei Liu* and Peng Jin*

Peking University Shenzhen Graduate School

Room E-321A, University Town, Nanshan District

Shenzhen, P.R. China

weiliu@pkusz.edu.cn, jinpeng@pkusz.edu.cn

Keywords: high power LED PKG; solder-bonded interfaces; die-attach process; electrical stress; void

Abstract: Heat flux inside the HP LED chip is also increasing with the increasing drive current, integration and miniaturization of LED chips. The junction temperature of LED strongly depended on the heat transmission capacity of die attach layer, which provided the heat dissipation channel between the heat generating LED chips and the heat slug. The voids, interrmetallic compounds or a small delamination would lead to the increasing thermal resistance in the die attach layer. In this paper, the reliability of soldered-bonded interfaces was studied in high-brightness LEDs, which were prepared by Cree and currently available on the market. Results revealed that the higher drive currents would lead to the accelerated degradation or failure of treated LEDs. Additionally, the injection current had an important effect on void formation and growth at the solder-bonded interfaces. The larger drive current would induce the delamination between LED die and heat slug. This study provided some guidance for the end users and a theoretical basis for solder-bonded technologies.

Introduction

Since LED was first available in the 1960s, the efficiency and brightness have been rapidly increased by using new materials and new processes [1]. It is well known that LED has so many superior characteristics such as higher efficiency, lower power consumption, longer life, ultra-high-speed response time, controllable color temperature and so on. Currently, LEDs have acquired wider applications in automotive front lighting, backlighting for large LCD displays and city improvement engineering. And high-power LEDs are expected to substitute the traditional lightings. [2, 3]

However, for power and high-power LED devices, heat flux inside the chip is larger. If the heat generated in the chip could not be transferred instantly to the heat sink, the higher junction temperature would reduce light output, change color temperature and forward voltage, and decrease the service lifetime [4]. As we all know, LED chip is mounted on a heat sink. The die-attach materials and processes played a key role in the heat dissipation of LED chips [5, 6]. Traditionally, LED chip is mounted on a heat sink by silver paste, which has a poor capacity of heat transmission and could not meet the needs of high-power LEDs' heat dissipation [7, 8]. At present, solder alloys have been employed to achieve the solder joint between LED chip and heat sink. Cree, the leader in the LED industry, has declared that the value of thermal resistance was lower to 2.5K/W and the void ratio was even less than 5%. However, few interrelated research achievements about the solder-bonded technologies have been reported in the literature.

In this paper, the reliability of solder-bonded technology was investigated in the high-brightness LED components, which were commercially available in the market and prepared by Cree. The interfacial failure features were revealed and the corresponding failure mechanisms were discussed. This study would provide some basic data as well as a theoretical basis for die-bonding technologies.

Experiments

The treated components were high-brightness white LEDs produced by Cree, as shown in Fig. 1. The product information came from the Cree's official website. The LED chip was attached to a heat slug by solder joint. The value of thermal resistance is less than 5K/W and the void ratio is lower than 5%.

All the tested LED components prepared by Cree have been mounted on the hexagonal aluminum substrate by the manufacturer. The tested samples were aged by using the SSP3516-A high power LED aging test machine from Hangzhou Star Spectrum Photoelectric Technology Co., Ltd. The injection currents of 350mA, 750mA, 1000mA and 2000mA were adopted and the ambient temperature was maintained at 25℃. The luminous flux, luminous efficacy, color temperature and color rendering index were measured by Spec300 LED photoelectric integrated test system. These data were separately recorded after the samples were aged for 30 days, 60 days, 90 days, 120 days, 150 days and 180 days. After aged for 180 days, the tested components were mounted in epoxy and metallurgically polished. The microstructure and voids at solder joints was observed and analyzed by using a scanning electron microscope (SEM).



Fig. 1 Optical picture of the tested LED component prepared by Cree

Results and discussions

Fig. 2 showed the luminous flux changed with the aging time under the different injection currents of 350mA, 750mA, 1000mA with the ambient temperature of 25℃. It was indicated that the average value of luminous flux degraded by about 5% under the injection current of 1000mA after 180 days (4320h). Under electric stresses of 350mA and 750mA, the luminous flux degraded relatively slowly by the average value of about 3%.

Under the injection current of 2000mA, all the tested LED components could not be lit up within 48 hours. In fact, the temperature of the hexagonal aluminum substrate was very high, and the encapsulant became black and the carbonization occurred. Moreover, the optical lens was easy to fell off the heat sink. When the higher drive current of 2000mA was applied, a large amount of heat was generated inside the LED chip. If the generated heat could not be spread out instantly, the junction temperature of LED chip would be very high. Just as reported, the higher electrical stress and extreme thermal shock would induce the catastrophic failure of LEDs [9].

Fig. 3 showed the color temperature of the treated LEDs changed with the aging time under the different injection currents of 350mA, 750mA, 1000mA with the ambient temperature of 25℃. It was indicated that the color temperature almost had no change under the condition of 350mA/25℃. However, the values of color temperature under the injection currents of 750mA and 1000mA had changed even by 10%, far beyond the scope of 50K-100K human eyes could distinguish color difference.

Fig. 4 showed the cross-sectional SEM images of solder joint in the tested components aged with the different injection currents. It was obvious that the voids had been formed at the solder-bonded interface at the injection current of 350mA, as shown in Fig. 4a. With the increasing injection current (700mA and 1000mA), larger voids were observed at the solder-bonded interfaces (Fig. 4b and c). Fig. 4d indicated the cross-sectional SEM images of solder joint in the LED component tested under the injection current of 2000mA, which failed within 24 hours. It was found that even the

delamination had occurred at the solder-bonded interface. From above, it was concluded that the electrical stress played a key role in the void formation and growth.

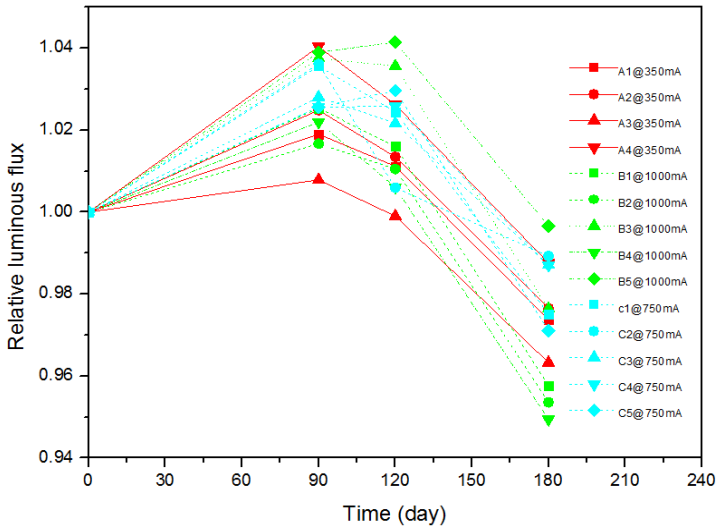


Fig.2. Relative luminous flux as a function of aging time under the various currents

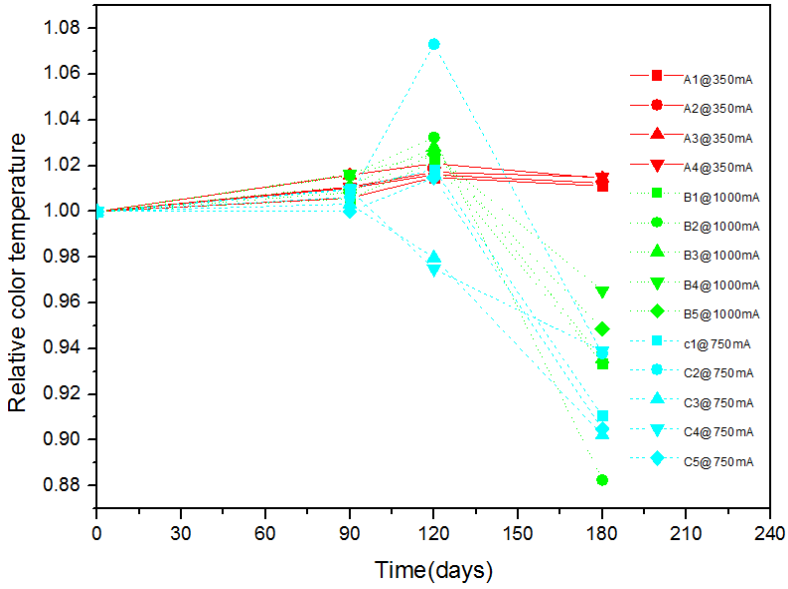


Fig.3 Relative color temperature as a function of aging time

It is well known that Cree has declared that its high-brightness LED component could offer the ultra-low thermal resistance down to 2.5K/W and its solder-bonded interface almost remained void-free. Surprisingly, after the LED components were aged, voids formed and grew at the solder-bonded interfaces and even the delamination occurred between LED die and heat slug.

Just as reported, any void or a small delamination would cause the instant temperature rising in the die, decreasing the internal quantum efficiency of LED chip. Additionally, the higher junction temperature would also deteriorate the conversion efficiency of the phosphor, and light extraction efficiency of silicon lens. [10] So, it was easy to understand why the luminous flux degraded by about 5% under the injection current of 1000mA and the values of color temperature under the injection currents of 750mA and 1000mA had changed even by 10%, just as shown in Fig 2 and 3. Especially, in Fig. 5 the larger delamination had occurred between LED die and heat slug, resulting in that the treated LED components could not be lit up again. It was concluded that under the electrical stress and thermal stress, voids would form and grow at the solder-bonded interfaces. This indicated strong

physical and chemical reactions had happened at the solder joints. Void formation and growth mechanisms would be discussed in another paper.

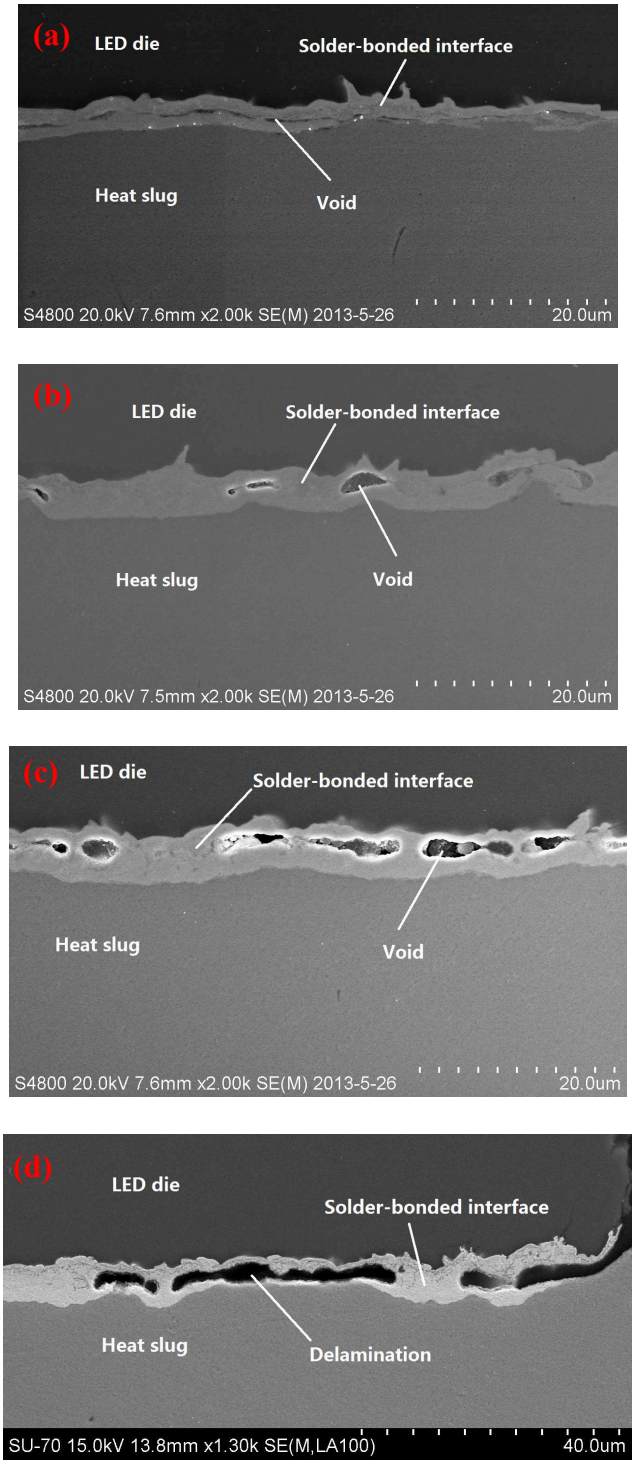


Fig.4 SEM images of solder-bonded interfaces after aging:

(a) 350mA,180days; (b) 750mA,180day; (c) 1000mA,180day; (d) 2000mA,2days.

Summary

In this study, high-brightness white LEDs from Cree were aged under various injection currents. Consequently, at 350mA the tested LEDs had a good performance. However at 750mA &1000mA the tested LEDs had a significant degradation and at 2000mA the treated LEDs could not illuminate within 24 hours. It was concluded that the higher drive current would reduce the reliability of LEDs

and shorten the service lifetime. It was interesting to find that voids would form and grow at the solder-bonded interfaces during aging. Moreover, higher currents would induce the number and size of voids increasing. At 2000mA, the delamination even occurred between LED die and heat slug. The die-attach quality played a key role in the heat transmission of LED. Any void or a small delamination would cause the instant temperature increasing in the die, leading to the degradation or failure of high power LEDs.

Acknowledgments

This work was supported by the National Natural Science Foundation of China (Grant Nos. 51301003) and the Shenzhen new material special fund (JC201105170718A).

References

[1] M.R. Krames, O.B. Shchekin, et al., Status and future of high-power light-emitting diodes for solid-state lighting, J Disp Technol 2007;3:160–175.

[2] M.S. Huang, Optical design and optimization of light emitting diode automotive head light with digital micromirror device light emitting diode, Optik–Int J Light Electron Opt2009:1–9.

[3] Z. Y. Liu, S. Liu, et al. Status and prospects for phosphorbased white LED packaging. Frontier Optoelectronics in China, 2009, 2(2): 119.

[4] R. Johnson, M. Palmer, C, Vang. Packaging materials and approaches for high temperatures SiC power devices. Adv Microelectron 2004;31(1):8-11.

[5] L. Cappola, D. Huff, et al. Survey on high temperature packaging materials for SiC based power electronics modules. In: IEEE power electronics specialists conference, PESC2007; 17-21.

[6] M. Kuramoto and etc. Die Bonding for a Nitride Light-Emitting Diode by Low-Temperature Sintering of Micrometer Size Silver Particles. IEEE Transactions on components and Packaging Technologies. Vol. 33, No. 4, 2010(11).

[7] N. Narendran, and Y. M. Gu, 2005,Life of LED-Based White Light Sources, J. Disp. Technol., 1, pp. 167–171.

[8] G. Lu, S. Yang, Analysis on failure modes and mechanisms of LED. 8th ICRMS; 2009. p. 1237–41.

[9] H.H. Kim, S.H. Choi, S.H. Shin, Y.K. Lee, S.M. Choi, S. Yi, Thermal transient characteristics of die attach in high power LED PKG, Microelectronics Reliability. 48 (2008) 445-454 .

[10] G. Meneghesso, S. Levada, et al. Failure modes and mechanisms of DC-aged GaN LEDs. Phys Status Solidi A2002;194:389-392.

Advanced Materials Research Vol. 936 (2014) pp 1905-1909
© (2014) Trans Tech Publications, Switzerland
doi:10.4028/www.scientific.net/AMR.936.1905

Evaluation of Thermal Fatigue Crack states of Super-hard Cutting Tools Based on the Extension Theory

Guo Caifen, Dongzhi, Wan Changdong, Zhang Yongkang

College of Mechano-electronic Engineering, Suzhou Vocational University, Suzhou, Chain, 215104

guocf@jssvc.edu.cn, dongzhi@jssvc.edu.cn, wancd@jssvc.edu.cn, zyk@jssvc.edu.cn

Keywords: super-hard cutting tools. thermal fatigue cracks. matter-element model

Abstract: A monitoring system is set up to get the machining process where super-hard cutting tools are used under surveillance. Signals such as the milling force signal, the acoustic emission signal, the vibration signal and the temperature signal are all collected to reflect tools practical conditions. Based on the extension theory, the partial-field matter-element, the full-field matter-element and the awaiting one are formed to evaluate the thermal fatigue crack states with the help of the relating function and the relating degree equation. Results show that this method is very reasonable and practical.

Introduction

While milling processes going on, where interrupted cutting takes place, subjecting super-hard cutting tools to a variety of hostile conditions, such as cyclic loading and alternately heating and cooling, all of these factors attribute to fluctuating thermal stress and strain, and finally thermal fatigue fractures, which result in tools failure and shorter tool life.

Small or micro, clear or obscure cracks contributed to thermal fatigue fractures of super-hard cutting tools [1~5]. Researches on variety states of thermal cracks, including its initiation, join or propagation, dominant crack appearance, may help the real-time identifying of thermal fatigue crack conditions of super-hard cutting tools.

A new multi-data quantitative decision-making method, the extension-element evaluation, is used to analyze thermal fatigue crack conditions of super-hard cutting tools, which unites qualitative and quantitative indexes effectively to make results reasonable and applicable.

Set-up of the thermal fatigue cracks identifying system

During machining, super-hard cutting tools are located in a hostile environment, where both heat and fluctuating forces act upon them. To get a full-scale of practical thermal fatigue crack conditions, multi-signals must be collected and analyzed because different signals have a variety of sensitivity degrees. The thermal fatigue cracks identifying system is established, as shown in Fig.1, sensors used including a force sensor, a acoustic emission sensor, a vibration sensor and a temperature recording sensor.

Signal collection is performed using the computer interface card, the infrared temperature measuring instrument, the SR150A acoustic emission sensor and the piezoelectricity acceleration instrument. On the Labview board, a front-panel, schematic programs and Ico /connection ports are deployed to realize virtual measurement. The CIN (Code Interface Node) technology is applied as the interface between Labview and C language to fulfill the following functions, as data collection, storing, evaluation and displaying.

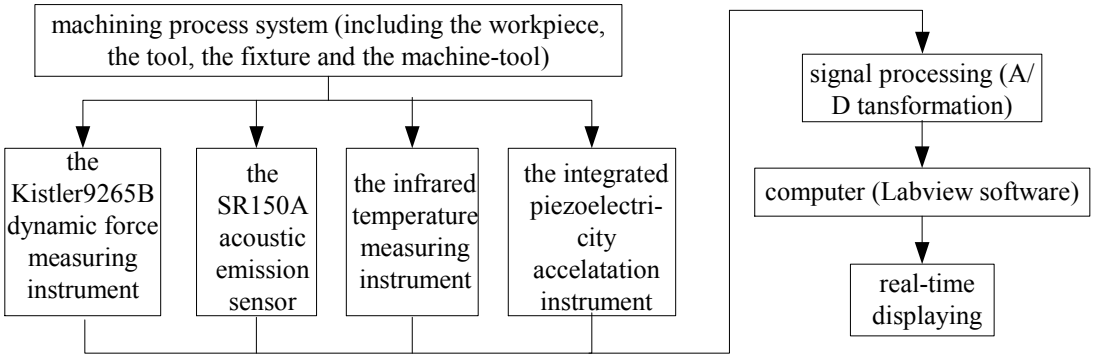


Fig. 1 The super-hard cutting tools thermal fatigue cracks identifying system

Milling-force signals

When milling at high cutting speeds, the milling-force is changeable in a dynamic pattern. In fact, tool teeth strike the workpiece in a cyclic style, corresponding to emergence of periodic impulse force acting upon it, that in turn results in vibration of the cutting tool and the workpiece. The above vibration also influences the milling depth which is what causes changing in the milling force. So the milling-force signal is used to vision the tools' thermal fatigue cracks conditions.

The Kistler9265B dynamic force instrument is used to measure the dynamic milling-force. Experiments indicate that when one of these parameters, the cutting speed, the feed rate per tooth, the radial cutting depth, changes respectively, the axial and perpendicular components of the milling-force, Fy and Fz ,remain almost unchanged, whilst only its radial component, Fx,changes prominently. So Fx is adopted to weigh the milling-force changing range.

Acoustic Emission Signals

Acoustic emission (AE) signal is a kind of elastic-stress wave originated from the release of elastic- transfiguration within materials. It appears from the cutting zone directly and is suitable for monitoring the thermal fatigue crack conditions due to its prominent properties of high frequency, fine sensitivity and rapid response. The SR150A acoustic emission sensor is adopted to measure the emission signals, which later is processed with the Matlab software. Thus the relationship between crack conditions and acoustic emission signals are established.

Vibration signals

Emergence of thermal fatigue cracks may directly affects the dynamic characteristics of machining processes, as well as the system arousing frequency and vibration swing. Therefore, through monitoring vibration signals, tools' thermal fatigue crack conditions would be informed exactly. An ICP (Integrated Circuits Piezoelectric) CA-YD-1182 type sensor is used to get vibration signals as the acceleration measuring is convenient and costless.

Temperature signals

When milling titanium alloys at high cutting speeds, because of small contact area between the cutting tool and the chip, the great stress acted on the tip and very low thermal conductivity of alloys, the cutting heat is too difficult to give out that local high temperature at cutting zone arises. Especially, when thermal fatigue fractures come into being, the attrition area between tools and workpieces enlarges, together with friction force increasing, all of which would result in prominent temperature raising. The manual thermo-electric couple method is applied to measure milling

temperatures and the wavelet transform method is adopted to deal with them. The results conform to regularity.

Evaluation process

Setting up of the matter-element mode

Information reflecting thermal fatigue crack states of super-hard cutting tools is denoted by the matter-element [6]. The following matter-element matrix R is called the awaiting matter-element, expressed as

$$R=\begin{bmatrix} p_0 & c_1 & X_1 \\ & c_2 & X_2 \\ & c_3 & X_3 \\ & c_4 & X_4 \end{bmatrix}$$

Where p_0 stands for a awaiting evaluation cutting tool; c_i（i=1~4）, properties of thermal fatigue crack states (N_{oj}), that is, the main factors affecting tools' thermal fatigue cracks, including milling force, acoustic emission, vibration and temperature; X_i is the practical measuring value of its corresponding affecting factor, c_i.

Partial and full field of matter-element model *R*

The partial field of R is shown below

$$R_{01}=\begin{bmatrix} \text{cracks initiation} & c_1 & 80\sim90 \\ & c_2 & 0\sim0.38 \\ & c_3 & 0\sim0.35 \\ & c_4 & 500\sim650 \end{bmatrix} \qquad R_{02}=\begin{bmatrix} \text{cracks propagation} & c_1 & 90\sim100 \\ & c_2 & 0.38\sim0.5 \\ & c_3 & 0.35\sim0.48 \\ & c_4 & 650\sim750 \end{bmatrix}$$

$$R_{03}=\begin{bmatrix} \text{dominant crack formation} & c_1 & 100\sim105 \\ & c_2 & 0.5\sim0.78 \\ & c_3 & 0.48\sim0.83 \\ & c_4 & 750\sim820 \end{bmatrix} \qquad R_{04}=\begin{bmatrix} \text{tools failure} & c_1 & 105\sim115 \\ & c_2 & 0.78\sim1.0 \\ & c_3 & 0.83\sim1.0 \\ & c_4 & 820\sim880 \end{bmatrix}$$

The full field of R is expressed as

$$R_P=\begin{bmatrix} P & c_1 & X_{P1} \\ & c_2 & X_{P2} \\ & c_3 & X_{P3} \\ & c_4 & X_{P4} \end{bmatrix}=\begin{bmatrix} P & c_1 & 80\sim115 \\ & c_2 & 0\sim1 \\ & c_3 & 0\sim1 \\ & c_4 & 500\sim880 \end{bmatrix}$$

Where P denotes all ranks of tools thermal fatigue crack states; X_{pi} stands for the actual value range corresponding to c_i, that is, the full field of P.

Determination of the awaiting matter-element

Under normal working conditions, measuring values of all characteristic indexes obtained through the thermal cracks monitoring system (Fig.1) are displayed in Table 1

TABLE 1 MEASURING VALUES OF THERMAL CRACK CHARACTERISTIC INDEXES

Evaluation index （characteristic）	thermal fatigue crack rank			
	crack initiation	propagation	dominant crack formation	tools failure
Milling-force signal	80~90	90~100	100~105	105~115
Acoustic-emission signal	0~0.38	0.38~0.5	0.5~0.78	0.78~1.0
Vibration signal	0~0.35	0.35~0.48	0.48~0.83	0.83~1.0
Temperature signal	500~650	650~750	750~820	820~880

The awaiting matter-element R is achieved as

$$R=\begin{bmatrix} p_0 & c_1 & u_1 \\ & c_2 & u_2 \\ & c_3 & u_3 \\ & c_4 & u_4 \end{bmatrix}$$

Where u_i (i=1~4) stands for the practical measuring values of evaluation indexes(milling force signal, acoustic emission signal, vibration signal and temperature signal), as shown in Table 1.

Foundation of the relating function

Based on the matter-element model, the relating degree between the cutting tool and its thermal fatigue crack states is got

$$K_j(u_i)=\begin{cases} \dfrac{-\rho(u_i,V_{0ji})}{|X_{0ji}|} & u_i \in V_{0ji} \\ \dfrac{\rho(u_i,V_{0ji})}{\rho(u_i,V_{pi})-\rho(u_i,V_{0ji})} & u_i \notin V_{0ji} \end{cases} .$$

Where $|V_{0ji}|=b_{0ji}-a_{0ji}$; $\rho(u_i,V_{0ji})=\left|u_i-\dfrac{a_{0ji}+b_{0ji}}{2}\right|-\dfrac{b_{0ji}-a_{0ji}}{2}$

$$\rho(u_i,V_{pi})=\left|u_i-\frac{a_{pi}+b_{pi}}{2}\right|-\frac{b_{pi}-a_{pi}}{2}$$

a_{0ji} is the minimum value of certain evaluation index in its partial field under its corresponding thermal crack condition; b_{0ji} the maximum value of certain evaluation index in its partial field under its corresponding thermal crack condition; a_{pi} the minimum value of certain evaluation index in its full field; b_{pi} the maximum value of certain evaluation index in its full field; α_i the power coefficient of certain selected index (milling force signals, acoustic emission signals, vibration signals and temperature signals), $\alpha=(\alpha_1, \alpha_2, \alpha_3, \alpha_4)=\{0.25,0.2,0.2,0.35\}$, $\alpha_1+\alpha_2+\alpha_3+\alpha_4=1$.

Therefore, the relating degree between the awaiting super-hard cutting tool p_0 and its certain thermal fatigue crack state is obtained. The equation is displayed below

$$K_j(p_0)=\sum_{i=1}^{4}\alpha_i K_j(u_i).$$

The value of relating degree $K_j(p_0)$ accords with certain thermal fatigue crack state. The bigger the higher corresponding degree, that is, $K_{j0}(p_0) = \max_{j0\in 1\sim 4} K_j(p_0)$.

Evaluation processes

Under certain milling conditions, and consulting relevant literature results, the measuring characteristics values are shown in Table 2. With the help of the relating function and the relating degree equation, results are got and displayed in Table 3.

TABLE 2 VALUES OF TESTING EVALUATION INDEXES

tools	milling-force signal	acoustic-emission signal	vibration signal	temperature signal
1	100	0.56	0.53	845
2	65	0.24	0.40	580
3	82	0.42	0.45	650
4	76	0.36	0.43	620

TABLE 3 EVALUATION OF THERMAL FATIGUE CRACK STATES OF SUPER-HARD CUTTING TOOLS

tools	$K_{10}(p_0)$	$K_{20}(p_0)$	$K_{30}(p_0)$	$K_{40}(p_0)$	evaluation results
1	−0.489	−0.299	−0.07	−0.119	normal
2	0.754	0.008	0.153	−1.191	dominant crack formation
3	−0.052	−0.21	−0.539	−0.661	normal
4	0.036	−0.452	−0.613	−0.674	crack initiation

Under normal cutting and testing conditions, the system where the whole evaluation process is embedded would automatically display the tools thermal fatigue crack states with the help of measuring evaluation indexes and distinguishing criteria. Experiments show that this method may be very reasonable and practical.

Conclusion

The tools' thermal fatigue fracture is a united consequence of cutting force and heat, whose evaluation and analysis are very complicated. Among so many affecting factors, some is suitable to be qualitatively analyzed, whilst others need quantitatively settled. Therefore, the extension theory is applied in order to obtain reasonable results through the combination of both qualitative and quantitative evaluation. This paper would provide a new effective method to access the thermal fatigue crack conditions of super-hard cutting tools.

References

[1] A.Jawaid, S.Sharif, S.Koksal. Evaluation of wear mechanisms of coated carbide tools when face milling titanium alloys [J]. Journal of Materials Processing Technology, 99(2000) 266-274.
[2] R.M.Freeman, Ph.D.Thesis, University of Birmingham, UK,1974.
[3] M.Nouari, A.Ginting. Wear characteristics and performance of multi-layer CVD-coated alloyed carbide tools in dry end milling of titanium alloys [J]. Surface & Coatings Technology, 200(18-19) (2006) 5663-5676.
[4] Wand Z G, Rahman M, Wong Y S. Tool wear characteristics of binderless CBN tools used in high-speed milling of titanium alloys [J]. Wear, 258(2005) 752-758.
[5] LI Anhai, ZHAOJun, LUO Hanbing, etc. Wear mechanisms of coated carbide tools in high-speed dry-milling of titanium alloy [J]. Tribology, 32(1)(2012) 40-46.
[6] Cai Wen, Wang Guanghua. A new cross subject-extenics[J].China Science Foundation, 5 (2004) 268-272.

Advanced Materials Research Vol. 936 (2014) pp 1910-1917
© (2014) Trans Tech Publications, Switzerland
doi:10.4028/www.scientific.net/AMR.936.1910

Relationship between the Textures and the Elastic Moduli of Electron Beam Welded Joint in Ti-6al-4v Titanium Alloy

Xing-Zhi Li[1,2a,] Shu-Bing Hu[1,b]

[1.] State Key Laboratory of Material Processing and Die&Mould Technology, Huazhong University of Science & Technology, Wuhan 430074, China

[2.] Department of Materials Engineering, Hubei University of Automotive Technology , Shiyan 442002, China

E-mail: li_xingzhi@163.com, hushubing@163.com

Keywords: titanium alloys, texture, electron back scattered diffraction (EBSD), nanoindentation, electron beam welding, elastic modulus

Abstract: The microstructure, texture and elastic modulus of electron beam welding joint in Ti-6Al-4V titanium alloy were investigated by transmission electron microscopy, X-ray diffraction, electron back scattered diffraction and nanoindentation techniques. The α phase was in the majority, and a $\{0001\}\langle\bar{2}110\rangle$ texture of α phase was observed in the base material. A very weak $\{11\bar{2}3\}\langle\bar{1}\bar{1}22\rangle$ texture of α′ phase was in the fuse zone. Most of the α′ grain boundaries in the fuse zone were high-angle boundaries by electron backscattered diffraction, and it also confirmed that the orientations of α′ phase had a nearly random distribution in the fuse zone. The maximum average elastic modulus value measured by the nanoindentation techniques was in the base material due to the effect of the $\{0001\}\langle\bar{2}110\rangle$ texture. The average elastic moduli of three different zones in the joint were 134.8±3.5Gpa, 125.5±5.8Gpa and 123.0±4.7Gpa, respectively.

Introduction

Titanium alloys have been used in many fields of high performance applications. Hence, the processing of titanium alloys and the resulting microstructures and properties have received considerable attention [1, 2]. The textures or orientations in hexagonal-close-packed (HCP) materials could result in the strong mechanical and physical anisotropy [3–5]. The tensile strength, bend and fatigue responses in the transverse orientation were distinctly different from that in the longitudinal orientation due to the strong α-titanium texture [6]. The developments of microstructure and crystallographic texture were highly dependent on the method of joining the material as well as the subsequent processing steps. Several studies have investigated the evolution of microstructure and crystallographic texture of titanium alloys occurring in friction stir welding [7–10]. However, as an important fusion welding method of processing titanium alloys, electron beam welding (EBW) was distinguished from friction stir welding, which did not form the shear texture in the fuse zone (FZ). The solidification structure and microtexture in the FZ by gas tungsten arc welding were only investigated in two literatures [11, 12], and yet they focused on the effect of the heat input on the microtexture.

Elastic modulus (E) would play a critical role in determining the designs and the applications of the welded structures, so the research on the relation of the texture and elastic modulus was very essential. Nanoindentation provided an effective, non-destructive technique to measure mechanical properties such as elastic modulus or the hardness of local area and small volumes of materials [13, 14]. However, the developments of textures and elastic moduli in the whole joint of Ti-6Al-4V EBW, and as well as the connection between them, have not been examined in detail so far. For these reasons given above, the X-ray diffraction, electron backscattered diffraction (EBSD) techniques were employed in an attempt to provide the textures and orientations evolution in the joint of Ti-6Al-4V EBW. The nanoindentation technique was used to measure the Elastic moduli of different zones in the joint. The present study was also helpful in improving the basic physical understanding of mechanical behaviors of EBW joint in titanium alloys, such as the tensile and fatigue.

Experimental Procedures

The Ti-6Al-4V alloy used in this study was processed by unidirectional hot rolling in the (α+β) region, and it was supplied as a 21mm thick plate with no subsequent heat treatment. The base material (BM) had a chemical composition (wt. %) of 6.06 Al, 3.92 V, 0.3 Fe, 0.15 O, 0.0014 H, and balance Ti. A single pass, full-penetration, electron beam butt welding was performed perpendicular to the hot rolling direction (RD); hence the welded direction (WD) was parallel to the transverse direction (TD). The main welding parameters were an accelerated voltage of 150 kV, a focus current of 332 mA, an EB current of 28 mA, and a welding speed of 200 mm/min. A vacuum annealing at 600 °C for 4h was implemented to release the residual stress after EBW.

The samples were etched with a solution (HF:HNO3:H2O = 1:4:45) after being polished, and then the microstructure of the welded joint was observed by an Olympus optical microscope. After being removed from the FZ, the transmission electron microscopy (TEM) foils were electro-polished in a solution of 94% methanol and 6% perchloric acid at -30℃ with an applied voltage of 10V. The foils were then observed through TEM (Tecnai G2). The textures of the specimens were measured using D5000 x-ray diffraction goniometer based on Schulz reflection geometry. The crystallographic textures of the α phase in the BM and the α′ phase in the FZ were also shown, using three orthogonal pole figures {0002}, $\{11\bar{2}0\}$ and $\{10\bar{1}0\}$. A plan-view section in the FZ (RD-TD plane) was prepared for examination by electron backscatter diffraction (EBSD), and EBSD experiments were conducted in a Nano 400 field-emission scanning electron microscope equipped with the Channel 5 system. Nanoindentation experiments were conducted to evaluate the individual E values of the constituent phases: α and α′. These experiments were performed on a CSM nanoindentation instrument with a Berkovich tip. Maximum load was 10 mN, and the loading/unloading rates were 20 mN/min. The resulting load, P, vs. depth of indentation, h, curves were analyzed with the aid of the Oliver–Pharr method [15] to extract the E values.

Results

Microstructure and Texture

The base metal had a duplex microstructure that consisted of coarse equiaxed primary α grains in a transformed β matrix and secondary α laths separated by a thin layer of β phase (Fig. 1a). The equiaxed primary α grains tended also to be elongated along the hot-rolling direction. The cooling rate in EBW was high, and high cooling rate promoted the martensitic transformation [16–18]. The

coarse column β grains in the FZ were transformed into the aciculate α′ martensite below the transus temperature. Consequently, the FZ was mainly composed of aciculate α′ martensitic phase that formed a basket-weave microstructure, as shown in Fig. 1b. At very high magnification, the very fine β lamellar could be observed between the α′ martensitic laths (Fig. 1d). The heat affected zone (HAZ) showed a continuously transitional microstructure due to the temperature gradient, as shown in Fig. 1c. The HAZ near the BM contained many equiaxed grains, whereas the HAZ near the FZ formed many the aciculate α′ martensitic. The x-ray diffraction patterns of the BM and the FZ were shown in Fig. 2, it was further confirmed that almost the entire α′ martensitic phase was in the FZ.

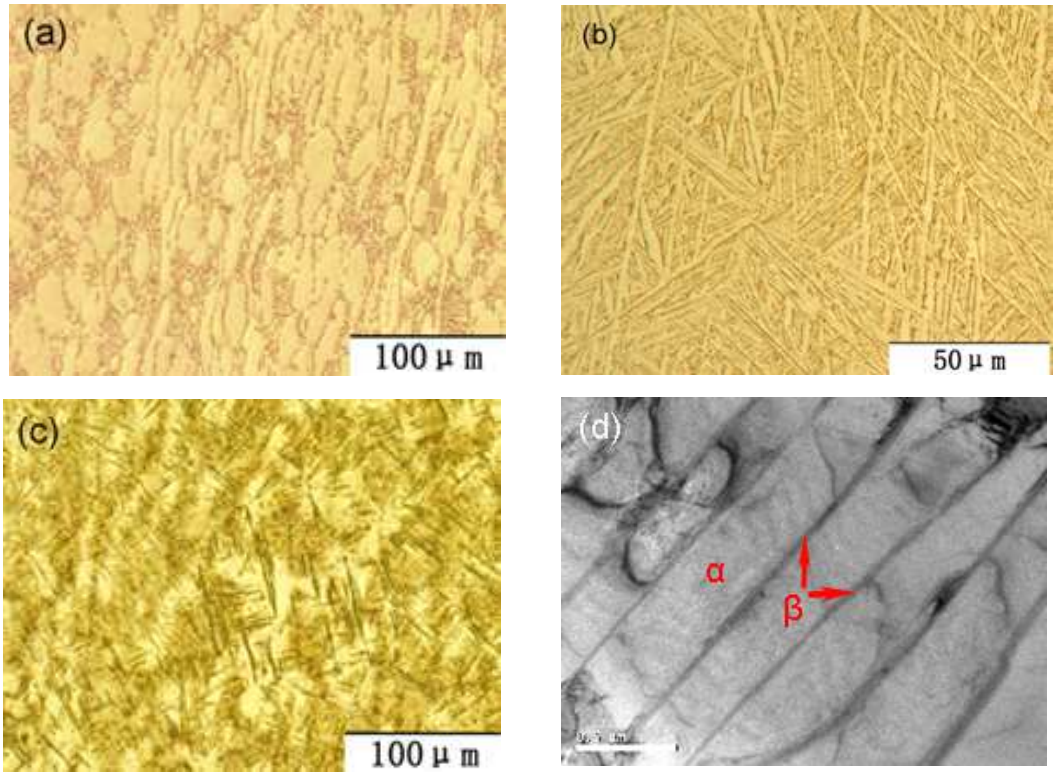


Fig. 1 Optical and TEM micrographs of Ti-6Al-4V EB-welded joint after post-weld vacuum anneal treatment: (**a**) BM, (**b**) FZ, (**c**) HAZ, (**d**) TEM micrograph of the FZ.

The β vol. % was approximately 18.5% in the BM, and the α phase was in the great majority. The microstructure was almost aciculate α′ martensite with a HCP structure in the FZ. For this reason, the textures of the two HCP phases were considered, and their textures were measured in the BM and the FZ. The {0002}, $\{\bar{2}110\}$ and $\{10\bar{1}0\}$ pole figures of the BM were shown in Fig. 3, two pole concentrations were observed in the normal direction (ND) and TD in Fig. 3a& 3b respectively, with the maximum intensity as 6.1 and 4.2. It indicated that a strong $\{0001\}<\bar{2}110>$ basal plane texture existed in the BM. The {0002}, $\{\bar{2}110\}$ and $\{10\bar{1}0\}$ pole figures of the FZ were shown in Fig. 4. The intensity of pole figures (Max: 2.1, 1.7 and 1.4) in the FZ subjected to the welding process was quite less when compared with the BM. It indicated there was a very weak $\{11\bar{2}3\}$ $<\bar{1}\bar{1}22>$ texture in the FZ, and the pole figures showed mainly the random spread of orientations in the FZ.

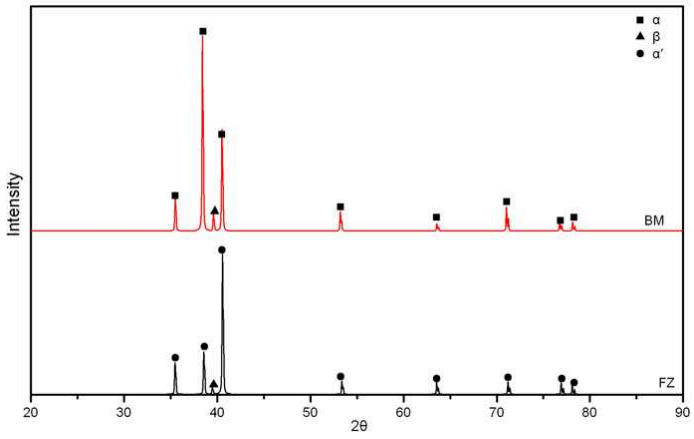


Fig. 2 X-ray diffraction patterns of the BM and the FZ.

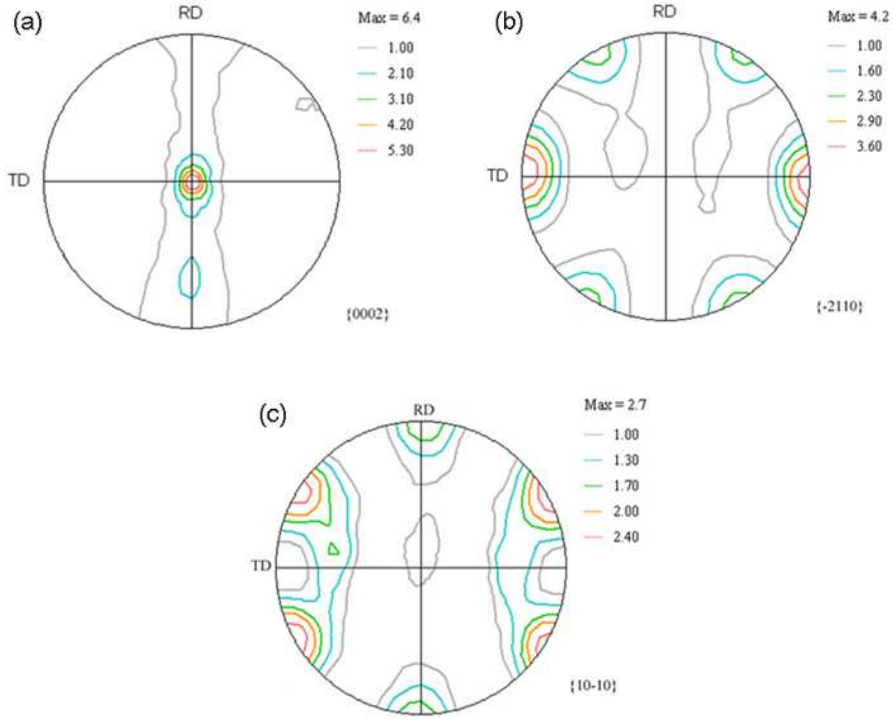
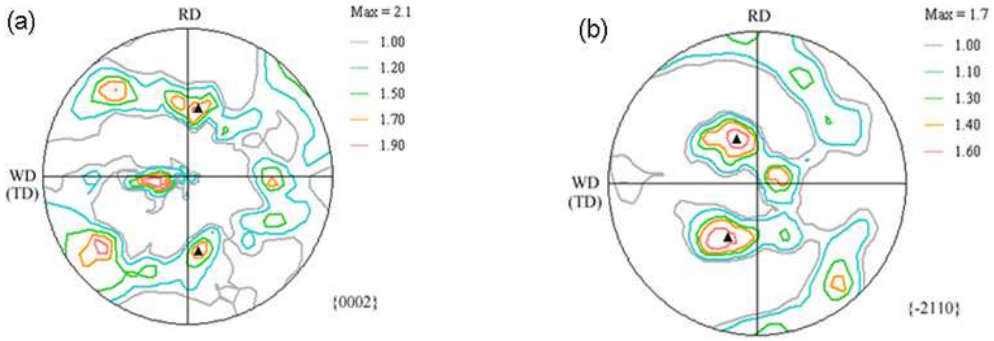


Fig. 3 Texture of the α phase in the BM: (a) {0002} pole figure, (b) { $\bar{2}$ 110} pole figure and (c) {10$\bar{1}$0} pole figure.



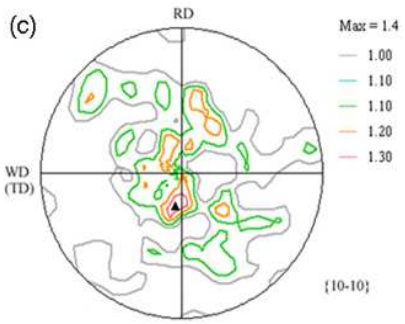
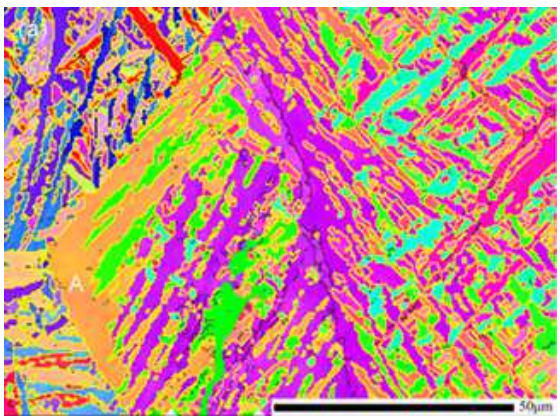


Fig. 4 Texture of the α ′phase in the FZ: (a) {0002} pole figure, (b) { $\bar{2}$ 110} pole figure and (c){10$\bar{1}$0} pole figure.
▲ {11$\bar{2}$3} <$\bar{1}\bar{1}$22>

An EBSD map of the FZ was showed in Fig. 5, colored according to crystal orientations in the inverse pole figure. This EBSD map depicted the types of crystallographic plane that were aligned with the sample surface, i.e., RD-TD plane. The α′ laths were very thin, about 1~3μm; and 10~60μm in the length. Within each column prior β grain, there were a number of α′ laths with various orientations, which were shown in different colors. Some α′ laths within the colony shared a common crystallographic orientation, as indicated by mark A in Fig. 5. Low-angle boundaries (LABs) were depicted as black lines, and high-angle boundaries (HABs) as yellow lines (Fig. 5). Obviously, most of the grain boundaries were HABs and only sporadic LABs were interspersed within some grains.

Elastic Modulus

After the sample was finally prepared by mechanical and chemical polishing, ten indentation points were measured for the HCP phases in each zone. The average E value of α phase was 134.8±3.5Gpa in the BM, and the average E value of α′ phase was 123.0±4.7Gpa in the FZ. It contained two HCP phases in the HAZ: α and α′, and their volume fractions gradually varied in different positions. Consequently, the elastic moduli were composed of the E values of α and α′, and the average E value was 125.5±5.8Gpa in the HAZ. The average E values of HCP phases in three zones were given in the Table 1. The E could be derived from analyzing the load-displacement curve, and representative P–h curves obtained from the HCP phases of three zones in the joint are shown in Figure 6.



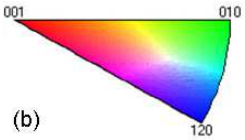


Fig. 5 (a) EBSD analysis of the α′ crystallographic directions (b) the color key was described in the inverse pole figure legend.

TABLE 1 AVERAGE E VALUES OF HCP PHASES IN THREE ZONES

measured position	BM	HAZ	FZ
E value (GPa)	134.8±3.5	125.5±5.8	123.0±4.7

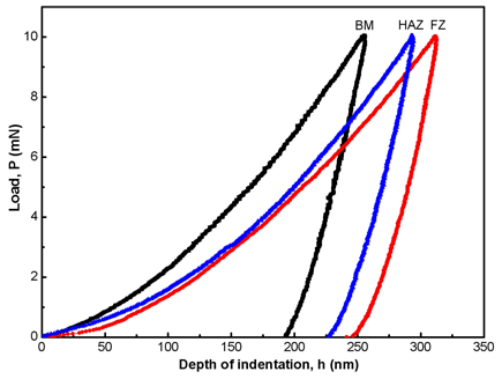


Fig. 6 Representative P vs. h nanoindentation curves of the HCP phase in the BM, HAZ and FZ, respectively.

Discussion

The α laths formed in the β matrix were known to be oriented according to the Burgers orientation relationship: $\{110\}_\beta // \{0001\}_\alpha$, $<111>_\beta // <11\bar{2}0>_\alpha$. So the sharpening α′ texture could be inherited when the material underwent a cold rolling prior to the α→β→α′ transformation sequence, which depended on the deformation texture in the parent phase [19]. However, the α′ inherited orientations were almost randomly distributed in the FZ, because the β texture has been removed in the melted state during the welding process. For cubic β phase, the crystallographic direction favoring fastest growth was <100> direction, and the other two orthogonal axes could exist at any arbitrary rotation about the <100>axis. Hence, the prior β columnar grains in the FZ would be expected to have a $\{h\ k\ l\}$ <100 > fiber texture, and [100] crystal orientation was parallel to the RD. If so, the distribution of the maximum intensity points in $\{110\}_\beta$ pole figure would be shown as Fig. 7. According to the Burgers orientation relationship, so should be the similar maximum intensity distribution of $\{0001\}_\alpha$ pole figure. However, this case did not be observed in Fig. 4a. It suggested that the β grains did not form the strong $\{h\ k\ l\}$ <100> fiber texture during the solidification.

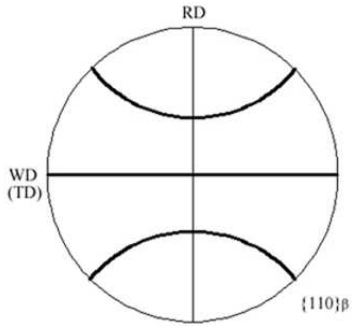


Fig. 7 The deduced distribution of intensity points in $\{110\}_\beta$ pole figure (as black bold lines), if the strong $\{h\ k\ l\}$ <100 > fiber texture could form in the FZ during the solidification

Due to the high cool rate in EBW, the growth of prior β grains were slower, but the nucleation more rapid, and so the preferential growth along <100> direction could not perform very well. Because of crystal symmetry, there were 12 distinct α orientation variants subjected to the Burgers relationship, which could form in a single parent β grain. For EBW, the high cool rate greatly promoted the homogeneous nucleation. As a result, many orientation variants could occur with

equal statistical probability during the β→α′ transformation in the FZ. Furthermore, an increase in the number of variants came with the increasing of the cooling rate [12, 20]. When two α′ laths or colonies with different variants adjoin in a prior β grain, a HAB would be formed, as shown in Fig. 5.

The strong anisotropy existed in the HCP Ti because of its lower crystal symmetry. Viswanathan et al. [21] have reported the hardness varied significantly with orientation. Near the [0001] stress axis, the hardness values were the highest, and the hardness values decrease as the stress axis deviates from near [0001] orientations. The values of indentation modulus measured by employing atomic force acoustic microscopy were 121.1GPa for $\{10\bar{1}0\}$, 142.7GPa for {0001}, and 130.3GPa for $\{10\bar{1}1\}$ [22]. These values matched quite well with the range of E values obtained from the present investigation. The indentation modulus of the α′ martensite is marginally lower than that of the α phase [22]. Hence, the mean E value of α phase in the BM was higher than that of α′ phase in the FZ, due mainly to the existence of the strong $\{0001\}<\bar{2}110>$ texture. The elastic and plastic strain fields around an indentation were very complicated. A given slip system depended on whether the value of the shear stress resolved on the system has exceeded its necessary critical resolved shear stress (CRSS). The CRSS in the basal slip system was much greater than in the prismatic and pyramidal slip systems [23]. Thus, when loading normally to the basal plane texture in the BM, the activation of slip systems was difficult. Consequently, the plastic deformation was difficult in the basal plane. Furthermore, the {0001} crystal plane was the strong close-packed plane. As a result, the maximum E value could be measured in the BM. The texture in the FZ was very weak, so the E was hardly influenced by the crystal orientations, and exhibited the mean value of random orientations. The average E value in the HAZ was between that of the BM and the FZ because of the effect of fractional basal <a> texture.

Conclusions

In this study, microstructure, texture and E developments in the EBW joint were investigated in Ti-6Al-4V titanium alloy. The α phase was in the great majority in the BM. A strong $\{0001\}<\bar{2}110>$ texture existed in the BM, as a result, the mean E value of HCP α phase in the BM was largest among three zones of the joint. Because of the high cool rate during the solidification and β →α′ transformation, the FZ was composed of aciculate α′ martensitic phase. It formed a very weak texture in the FZ, and most of grain boundaries were HABs. So the E value in the FZ represented the average value of random orientations. The HAZ between the BM and the FZ showed the characteristic of the transition zone, and had the moderate average E value.

References

[1] H. Matsumoto, S. Watanabe, S. Hanada, Microstructures and mechanical properties of metastable β TiNbSn alloys cold rolled and heat treated, J. Alloys Compd. 439 (2007) 146-155

[2] A.N. Kalinyuk, N.P. Trigub, V.N. Zamkov, Microstructure, texture, and mechanical properties of electron-beam melted Ti–6Al–4V, Mater. Sci. Eng. A 346 (2003) 178-188

[3] Z.S. Zhu, R.Y. Liu, M.G. Yan, Texture control and the anisotropy of mechanical properties in titanium sheet, J. Mater. Sci. 32 (1997) 5163-5167

[4] L.Yu, K. Nakata, N. Yamamoto, Texture and its effect on mechanical properties in fiber laser weld of a fine-grained Mg alloy, Mater. Lett. 63 (2009) 870-872

[5] W. Chen, C.J. Boehlert, Texture induced anisotropy in extruded Ti–6Al–4V–xB alloys, Mater. Charact. 62 (2011) 333-339

[6] M.R. Bache, W.J. Evans, Impact of texture on mechanical properties in an advanced titanium alloy, Mater. Sci. Eng. A 319-321 (2001) 409-414

[7] A.P. Reynolds, E. Hood, W. Tang, Texture in friction stir welds of Timetal 21S, Scripta. Mater. 52 (2005) 491-494

[8] K.E. Knipling, R.W. Fonda, Texture development in the stir zone of near-α titanium friction stir welds, Scripta. Mater. 60 (2009) 1097-1100

[9] R.W. Fonda, K.E. Knipling, Texture development in near-a Ti friction stir welds, Acta Mater. 58 (2010) 6452-6463

[10] L. Zhou, H.J. Liu, Q.W. Liu, Effect of process parameters on stir zone microstructure in Ti–6Al–4V friction stir welds, J. Mater. Sci. 45 (2010) 39-45

[11] T. Karthikeyan, A. Dasgupta, S. Saroja, Solidification structure in Ti–5Ta–1.8Nb weld, Sci. Technol. Weld. Joining 14 (2009) 597-605

[12] R.K. Leary, E. Merson, K. Birmingham, Microstructural and microtextural analysis of InterPulse GTCAW welds in Cp-Ti and Ti–6Al–4V, Mater. Sci. Eng. A 527 (2010) 7694-7705

[13] Sen Indrani, U. Ramamurty, Elastic modulus of Ti–6Al–4V–xB alloys with B up to 0.55 wt.% , Scripta. Mater. 62 (2010) 37-40

[14] V.H.B. Hernandez, S.K. Panda, Y. Okita, A study on heat affected zone softening in resistance spot welded dual phase steel by nanoindentation, J. Mater. Sci. 45 (2010) 1638-1647

[15] W.C. Oliver, G.M. Pharr, An improved technique for determining hardness and elastic modulus using load and displacement sensing indentation experiments, J. Mater. Res. 7 (1992) 1564-1583

[16] J.M. Manero, F.J. Gil, J.A. Planell, Deformation mechanisms of Ti–6Al–4V alloy with a martensitic microstructure subjected to oligocyclic fatigue, Acta. Mater. 48 (2000) 3353-3359

[17] R. Mythili, V.T. Paul, S. Saroja, Study of transformation behavior in a Ti–4.4 Ta–1.9 Nb alloy, Mater. Sci. Eng. A 390 (2005) 299-312

[18] K.K. Murthy, S. Sundaresan, Phase transformations in a welded near-alpha titanium alloy as a function of weld cooling rate and post-weld heat treatment conditions, J. Mater. Sci. 33 (1998) 817-826

[19] N. Gey, M. Humbert, Characterization of the variant selection occurring during the α→β→α phase transformations of a cold rolled titanium sheet, Acta Mater. 50 (2002) 277-287

[20] T. Karthikeyan, A. Dasgupta, R. Khatirka, Effect of cooling rate on transformation texture and variant selection during β → α transformation in Ti–5Ta–1.8Nb alloy, Mater. Sci. Eng. A 528 (2010) 549-558

[21] G.B. Viswanathan, E. Lee, Direct observations and analyses of dislocation substructures in the α phase of an α/β Ti-alloy formed by nanoindentation Acta Mater. 53 (2005) 5101-5115

[22] A. Kumar, U. Rabe, W. Arnold, Mapping of Elastic Stiffness in an α+β Titanium Alloy using Atomic Force Acoustic Microscopy, Jap. J. Appl. Phys. 47 (2008) 6077-6080

[23] A.F. Gerday, M.B. Bettaieb, L. Duchêne, Material behavior of the hexagonal alpha phase of a titanium alloy identified from nanoindentation tests, Eur. J. Mech. A 30 (2011) 248-255

Advanced Materials Research Vol. 936 (2014) pp 1918-1924
© (2014) Trans Tech Publications, Switzerland
doi:10.4028/www.scientific.net/AMR.936.1918

Investigation of the Influence of Geometric and Technological Factors on the Stress-Strain State of Metal in the Implementation of the Combined Rolling-Pressing Process

Lezhnev Sergey[1, a], Panin Evgeniy[2, b]

[1]Republic avenue, 30; Temirtau, Republic of Kazakhstan

[2]Republic avenue, 30; Temirtau, Republic of Kazakhstan

[a]Sergey_legnev@mail.ru; bcooper802@mail.ru

Keywords: combined process “rolling-pressing”, equal-channel step matrix, grooved rolls, modelling, stress-strain state.

Abstract

In the development of new technology metal forming the main purpose is improvement the quality of the source material. The main aspect of quality improvement is increasing the strength characteristics. Often to increase the strength of deformable metal should be given reduced grain structure, up to subultra and even nano-level. There are several ways to obtain sub-ultra-fine-grain structure of metals, and one of those ways is a method of severe plastic deformation (SPD), implemented in the whole volume of the deformable metal.

In this work computer modeling was performed of the combined process "rolling-pressing" with the use of grooved rolls and equal channel step matrix with varying basic geometric and technological factors which have a significant impact on the process, what was made for the analysis of the impact of various factors on the stress-strain state of the process.

Introduction

In recent years a number of new processes of metal forming to obtain metal with sub-ultra-fine-grain structure were developed. One of the most promising, exceeding the previously known methods of metal forming, is a combined process of "rolling-pressing" with the use of grooved rolls and equal channel step matrix for pressing (Fig. 1), which was developed at the department "Plastic Metal Forming" of Karaganda State Industrial University [1]. The advantage of this process is that the implementation of the combined process ensures the continuity of the process and removes limits of size of initial workpiece.

The essence of this process consists in the fact that the billet pre-heated to the temperature of the beginning of deformation is fed to the rolls which grip it into the roll gap at the cost of contact friction forces and on leaving the roll gap they push it through the channels of the equichanneled step die. When the billet leaves the roll gap completely another billet is fed which having passed through the rolls and entering the die pushes out the previously deformed billet from the die. That means that in – this case the billet extrusion in the equichanneled step die is realized at the cost of using contact friction forces emerging on the surface of the contact of metal with the spinning rolls.

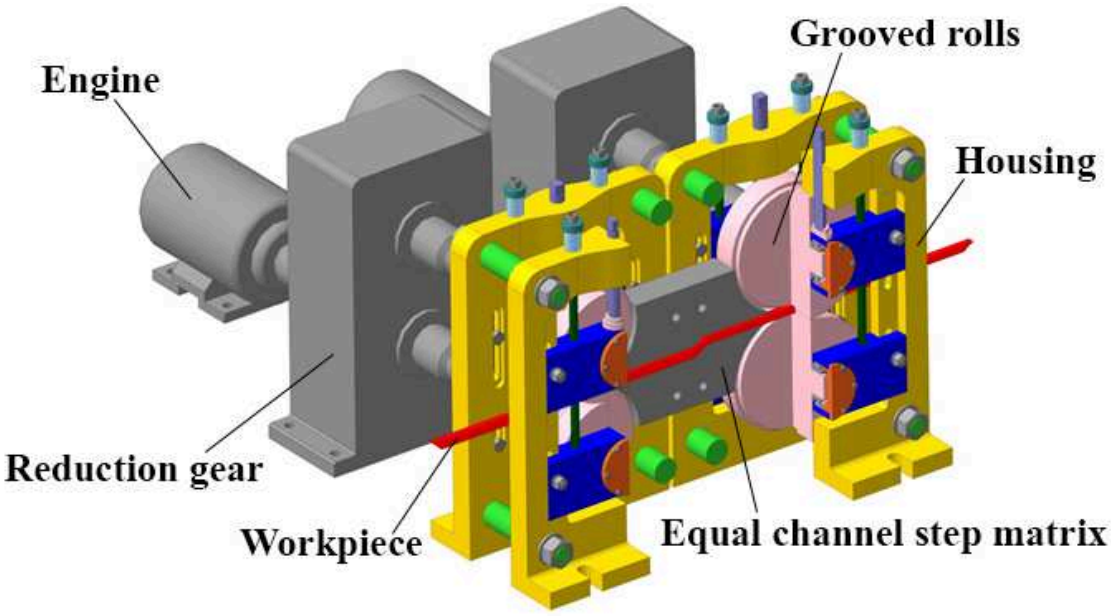


Figure 1 - Combined process of "rolling - pressing"

Investigation of stress-strain state

In the development of any process of metal forming study of stress-strain state is a critical step. The analysis of the strain state allows the examination of accumulated strain distribution throughout the volume of the workpiece during the deformation, to identify the areas that are more susceptible to deformation, and based on this define rational as geometric and technological parameters deformation and stress state of analysis allows to evaluate the voltage occurring at deformation and to identify the most dangerous areas, where possible tool breakage. Therefore, this paper deals with the influence of geometrical and technological factors on the stress-strain state (SSS) of the metal in the implementation of the combined process of rolling - pressing using equal channel step matrix and grooved rolls. To do this, it was decided that the variation of the basic geometrical and technological factors which have a significant impact on the process of rolling - pressing.

Study the impact of major technological and geometrical factors on the implementation of SSS metal combined process of "rolling-compression" using equal channel step matrix and grooved rolls made in the software package DEFORM-3D.

For a thorough study of the stress-strain state the following parameters were considered:

1) Strain Effective.
2) Stress Effective

In the course of previous studies [2], it was discovered that the main geometrical and technological factors that have a significant impact on the combined process of "rolling- pressing ", are following:

- the radii of the first and second pairs of rolls R_1 and R_2, mm;
- Angle of joint channels in the matrix φ, deg;
- absolute reduction Δh, mm;
- length of first and second channels in the matrix L_1 and L_2, mm;
- coefficients of friction in rolls and matrix μ_1 and μ_2;
- temperature of the billet.

However, as noted in work [3], the selection of the optimum geometry and process parameters is critical to the very possibility of the implementation of the "rolling - pressing" in the grooved rolls. And the wrong choice of at least one of the parameters can lead to a denial of the process. Therefore, it was decided to carry out the variation within the acceptable range for each parameter. Also, you need to provide the "reality" of variation, ie, exercise varying the factors which may change the parameters in real terms. Change the values of the radii of the first and a second pair of

rolls is irrational because to install the new roll is necessary to create new designs of stand. Vary the size of the coefficient of friction in the rolls is also unreasonable, because the recommended value for this parameter is the maximum (μ_1 = 0,5). Rotational speeds of the first and second pair of rolls can be varied, but only in a certain ratio, in disassembled [4]. Otherwise, the workpiece will not be captured by the second pair of rolls.

The base model is modeled, constructed in work [3]. The parameters of this model are following:

Table 1 – Parameters of the base model

Cross-section of the billet after deformation $h_1 \times b_1$, [mm]	Parameters								
	R, [mm]	μ_1	l_1, [mm]	l_2, [mm]	Δ h, [mm]	μ_2	φ, [deg]	$\sigma_т$, [MPa]	R_2, [mm]
40 x 60	250	0,1	40	30	15	0,5	140	40	280

The initial billet had its original size h_0 x b_0 x l_0 = 55 x 35 x 200 mm. As the material of the workpiece has been selected steel 35 heated to a temperature of 1100 °C.

Since the implementation of the process necessary for compliance with the conditions $P_{ROLL} > P_{PRESS}$, so for modeling were taken the following coefficients of friction:

- in rolls – 0,5 – for maximum P_{ROLL};
- in matrix – 0,1 – for minimum P_{PRESS}.

For varying the geometry and process parameters have been set up additional models with the following factors changes:

- Angle of joint channels in the matrix φ=145°, φ=150°;
- length of first channel in the matrix L_1=35 mm, L_1=30 mm;
- length of second channel in the matrix L_2=25 mm, L_2=20 mm;
- absolute reduction Δh =18 mm, Δh =20 mm;
- coefficient of friction in matrix μ_2=0,08, μ_2=0,05;
- temperature of the billet t=1200 °C, t=1000 °C.

Since almost all parameters are only to varying matrix, in the study of SSS it was decided to analyze the deformation of the next stage: the workpiece is rolled in the first pair of rolls, passes through the channels of the matrix, and then rolled to the second pair of rolls. At this stage it is possible to study the SSS in the matrix, and both pairs of rolls.

a) Basic model

In the implementation of the "rolling-pressing" billet passes through three stages of accumulation of plastic strain (Fig. 2):

Stage 1 - after rolling billets in the first pair of rollers - the value of equivalent strain ε_{eqv} is 0 ÷ 0,617;

Stage 2 - after overcoming a sloping channel in the matrix - the value of equivalent strain ε_{eqv} is 0,617 ÷ 1,33;

Stage 3 - After rolling billets in the second pair of rolls - the value of equivalent strain ε_{eqv} is 1,33 ÷ 2,0.

Accordingly, when implementing the "rolling-pressing" occurs three zones of deformation (Fig. 3): in the first and second pairs of rolls, and at the junction of the channels in the matrix. The average value of the stress is 70-85 MPa, maximum value is 118 MPa.

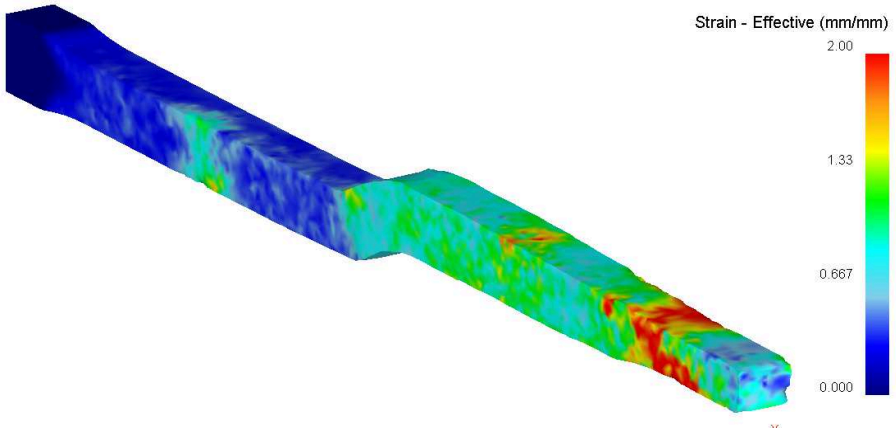


Figure 2 - Distribution of equivalent strain ε_{eqv}

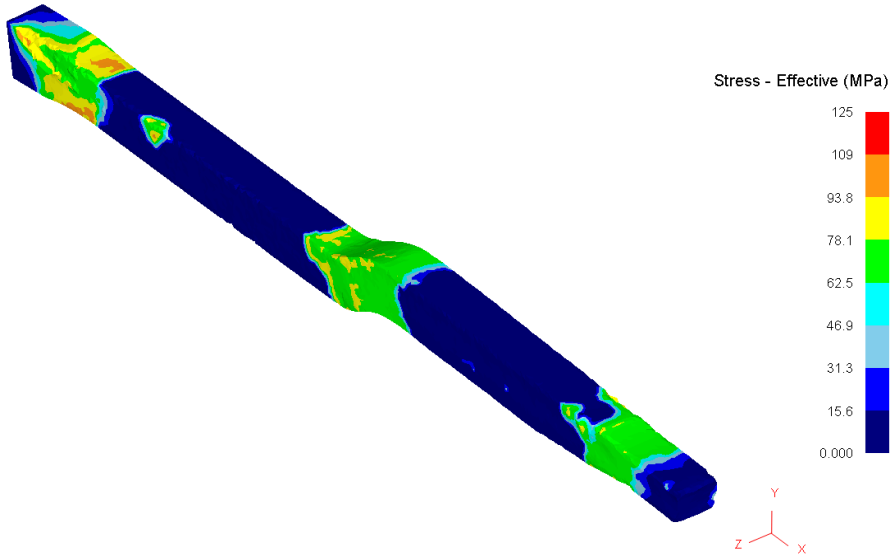


Figure 3 - Distribution of the equivalent stress σ_{eqv}

b) The model with the angle of the junction of channels 145°

When using a speed equal channel matrix with an increased angle of the joint channel intensity of the accumulation of plastic deformation is reduced by reducing the back pressure force. This occurs in the second and third stages, whereas the first stage ε_{eqv} value is not changed.

On the 1st stage the value ε_{eqv} is 0 ÷ 0,617;

On the 2nd stage the value of ε_{eqv} is 0,617 ÷ 1,27;

On the 3rd stage the value of ε_{eqv} is 1,27 ÷ 1,9.

The equivalent stress is also reduced by reducing the back pressure force. The average value of the equivalent stress is 70-75 MPa and 110 MPa maximum.

c) The model with the angle of the junction of channels 150°

Similarly the model with the angle of the junction of channels 145°, using a step equal channel matrix with the angle of the junction of channels 150° rate of accumulation of plastic deformation is reduced by reducing the back pressure force.

On the 1st stage the value ε_{eqv} is 0 ÷ 0,617;

On the 2nd stage the value of ε_{eqv} is 0,617 ÷ 1,21;

On the 3rd stage the value of ε_{eqv} is 1,21 ÷ 1,85.

The equivalent stress as the previous model is also reduced by reducing the counter force. The average value of the equivalent stress is 60-70 MPa and 98 MPa maximum.

d) Models with a length of the first channel in the matrix L_1=35 mm and L_1=30 mm.

In studying these models, it was noted that the distribution of stresses and strains throughout of the workpiece with change of length of the first channel in the matrix is not changed.

e) Models with a length of the second channel in the matrix L_2=25 mm.

When studying the model with the reduced length of the second channel in matrix L_2 = 25 mm, it was noted that the value of the equivalent strain decreases in the 2nd and 3rd stages of the process. At the first stage of the value of ε_{eqv} remains unchanged.

On the 1st stage the value ε_{eqv} is 0 ÷ 0,617;

On the 2nd stage the value of ε_{eqv} is 0,617 ÷ 1,21;

On the 3rd stage the value of ε_{eqv} is 1,21 ÷ 1,82.

The study of equivalent stress showed that when the length of the second channel matrix stress distribution is changed only at the junction of channels, while the deformation of rolls arising stress values are not changed. The average value of the equivalent stress is 140-170 MPa, a maximum of 200 MPa.

f) Models with a length of the second channel in the matrix L_2=20 mm.

Similarly to the previous model, the study of model with a length of second channel of matrix L_2 = 20 mm was noted that the value of the equivalent strain is reduced only to the 2nd and 3rd stages of the process.

On the 1st stage the value ε_{eqv} is 0 ÷ 0,617;

On the 2nd stage the value of ε_{eqv} is 0,617 ÷ 1,17;

On the 3rd stage the value of ε_{eqv} is 1,17 ÷ 1,76.

Similarly the model with a length of the channel matrix L_2 = 25 mm, using a step equal channel matrix with length of the second channel L_2 = 20 mm it was noted that the distribution of stress when the length of the second channel matrix changes only at the junction of channels. The average value of the equivalent stress is 130-160 MPa, 180 MPa maximum.

g) Models with the absolute reduction Δh=18 mm and Δh =20 mm.

The analysis of these models revealed that increasing the absolute reduction in the rolls increases value of equivalent strain sequentially at all three stages (fig. 4). In the model with Δh = 18 mm on 1st stage ε_{eqv} value is 0 ÷ 0,767; on 2nd stage ε_{eqv} value is 0,767 ÷ 1,53; on 3rd stage ε_{eqv} value is 1,53 ÷ 2,3. In the model with Δh = 20 mm on 1st stage ε_{eqv} value is 0 ÷ 0,843; on 2nd stage ε_{eqv} value is 0,843 ÷ 1,69; on 3rd stage ε_{eqv} value is 1,69 ÷ 2,53.

In the analysis of these models, it was found that the stress distribution with an increase of absolute reduction only changes in the deformation zones of rolls (Fig. 5), and the value of the equivalent stress increases. While at the junction channel matrix values of stress are not changed.

In a base model with Δh = 15 mm, the average value of the equivalent voltage power was 70-85 MPa at h = 18 mm it is 85-100 MPa; with Δh = 20 mm it reaches 95-115 MPa.

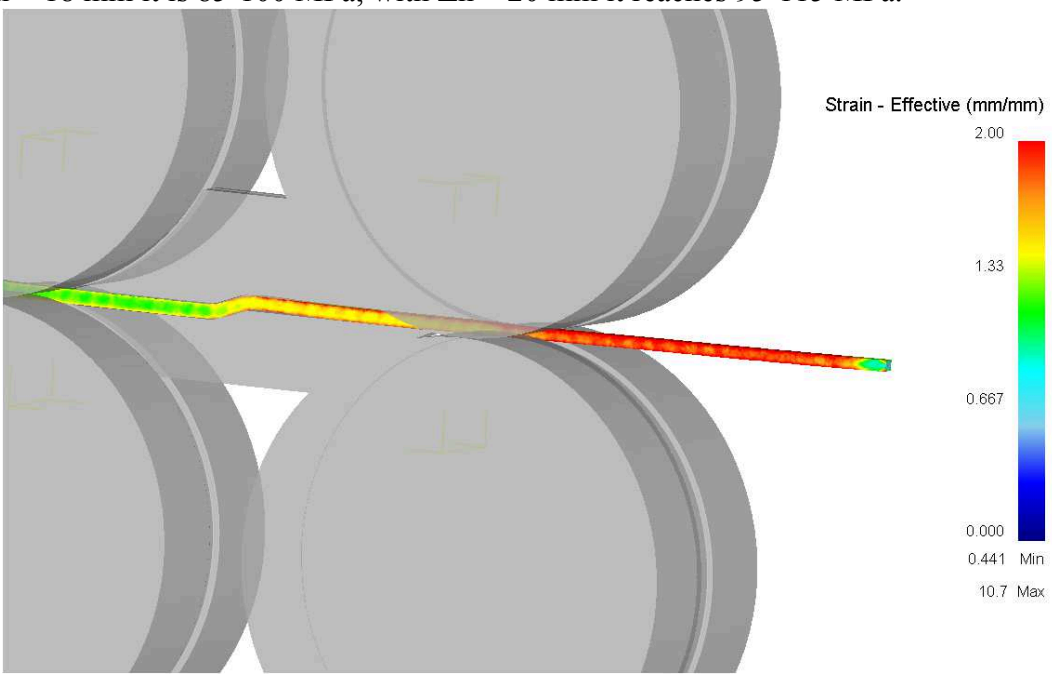


Figure 4 – Increasing of equivalent strain at all three stages

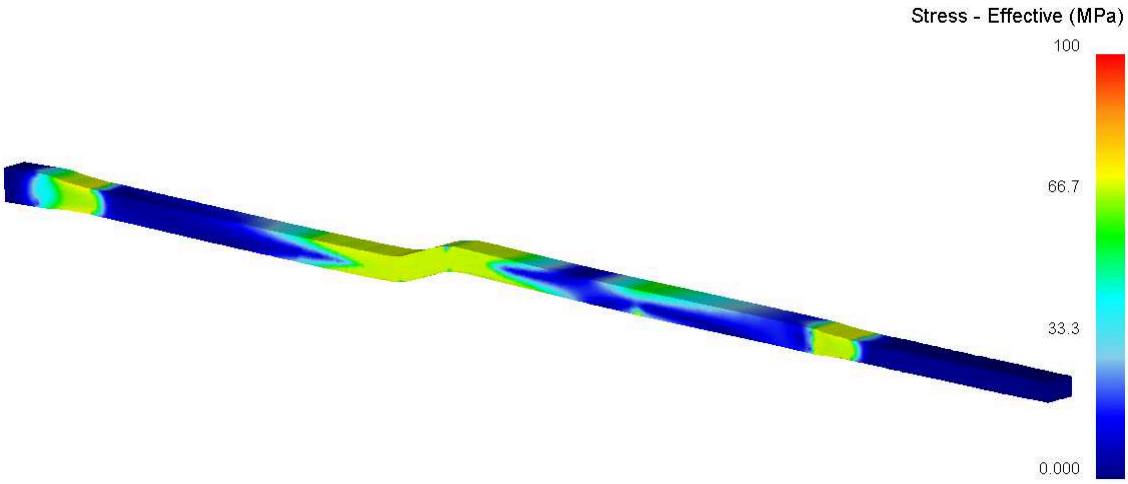


Figure 5 - Zones of deformation

h) Models with value of the friction coefficient in matrix μ_2=0,08 and μ_2=0,05.

Analysis of models with different values of the friction coefficient in the matrix showed that the decline in the value of this parameter contributes to a very slight decrease in the values of equivalent strain in the second and third stages of the process. At the first stage of the value of ε eq remains unchanged.

In the model with the value of the friction coefficient matrix μ_2 = 0,08 maximum equivalent strain ε_{eqv} decreased from 2.0 to 1.97, and in the model with the value of friction coefficient in matrix μ_2 = 0,05 - to 1.94.

Analysis of the stress state showed that the decrease in the coefficient of friction reduces the value of the equivalent stress in all three of the deformation zone. In the basic model for μ_2 = 0,1 average equivalent stress was 70-85 MPa, when μ_2 = 0,08 it is 67-70 MPa and when μ_2 = 0,05 it reaches 55-65 MPa.

i) Models with the value of billet temperature t=1200 °C and t=1000 °C

Analysis of models with different values of the billet temperature has shown that reduction of this parameter reduces the value of equivalent strain at all three stages, and an increase of temperature increases the intensity distribution of equivalent strain in the billet.

In the model with the value of the billet temperature t = 1200 °C on 1st stage ε_{eqv} value is 0 ÷ 0,703; on 2nd stage ε_{eqv} value is 0,703 ÷ 1,41; on 3rd stage ε_{eqv} value is 1,41 ÷ 2,11. In the model with the value of the preform temperature t = 1000 °C on 1st stage ε_{eqv} value is 0 ÷ 0,64; on 2nd stage ε_{eqv} value is 0,64 ÷ 1,28; on 3rd stage ε_{eqv} value is 1,28 ÷ 1,92.

Analysis of the stress state showed that the reduction of temperature increases the value of the equivalent stress in all three of the deformation zone, and an increase in temperature reduces the intensity distribution of the equivalent stress. In the basic model at t = 1100 °C average value of the equivalent stress is equal to 70-85 MPa, at t = 1200 °C it is equal to 67-70 MPa, at t = 1000 °C it reaches 85-95 MPa.

Conclusions

It was used to simulate the process of "rolling-pressing" with the use of grooved rolls and equal channel step matrix with varying basic geometric and technological factors which have a significant impact on the process. Analysis of the impact of various factors on the stress-strain state of the process has shown that factors such as the angle of the joint channel matrix, the coefficient of friction, temperature, length of the channel matrix have a significant impact on the stress-strain state in the whole volume of the workpiece in the implementation of the combined process of "rolling-pressing". And the only rational choice of mode of deformation for a given the profile and size of the workpiece, and consideration of all factors will make this complex process and end up getting a metal with sub-ultra-fine grain.

References

[1] Patent RK №25862 MKI[3] B21 J 5/00., 2013 Bul №6. Device for pressing metals and alloys. Naizabekov A.B., Lezhnev S.N., Panin E.A.

[2] Naizabekov A.B., Lezhnev S.N., Panin E.A. Theoretical studies of the combined process of "rolling-pressing" using an equal channel step matrix.// Proceedings of Higher Education. Black metallurgy, Moscow, 2008, №6. - p. 22-26.

[3] Naizabekov A.B., Lezhnev S.N., Panin E.A. Simulation of the joint 'rolling-extrusion' process using equichanneled step die // 17-th International Conference on metallurgy and materials METAL-2008, Ostrava, Czech Republic, 13. -15. 5. 2008. Hradec nad Moravici.

[4] Naizabekov A.B., Lezhnev S.N., Panin E.A. Kinematic calculation of the combined process of "rolling-pressing", implemented with the use of grooved rolls and equal channel step matrix // Technology of production of metals and recycled materials. Temirtau, 2008, №1. – p. 66-70.

CHAPTER 17:

Research in Area of Applied Materials

Advanced Materials Research Vol. 936 (2014) pp 1927-1932
© (2014) Trans Tech Publications, Switzerland
doi:10.4028/www.scientific.net/AMR.936.1927

Influences of Material Parameters on Terminal Effect of PELE with Tungsten Fiber Composite Jacket

ZHU Jiansheng[1,a *], FAN Zhi[2,b] and GAO Bin[1,c]

[1]Department 5, army officer academy of PLA, China

[2]Department of training, army officer academy of PLA, China

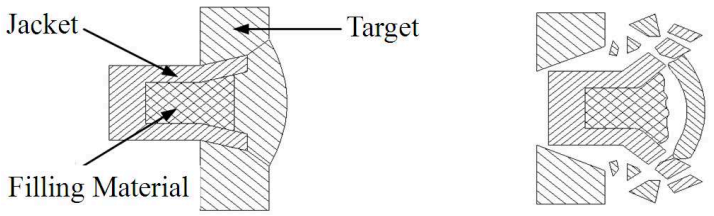
[a]zhujsheng102526@yahoo.com, [b]wisteed@126.com, [c]563321248@qq.com

Keywords: PELE; tungsten fiber composite jacket; material parameters; penetrating performance; lateral damage effect.

Abstract: There are a series of disadvantages in tungsten alloy (TA), which is adopted as the jacket of PELE widely at present, such as inadequate obdurability, uncontrollable shape and amount of fragments, imperfect lateral damage effect, and so on. To solve the problem, tungsten fiber composite (TFC) is brought forward to produce PELE jacket. In order to verify its feasibility, numerical simulations are carried out on PELE impacting armor steel target with TFC jacket. The simulation results are compared with that of PELE with TA jacket and the reasons that the penetrating performance and lateral damage effect of PELE with TFC jacket being superior is discussed. After that, the function mechanism of PELE with TFC jacket is investigated through analyzing the influences of some factors on impacting behavior of PELE projectiles. These results can provide reliable theory and computational bases for future research.

Introduction

PELE (Penetrator with Enhanced Lateral Effect) is new ammunition which consists of a high-density jacket, closed at its rear end and filled with a low-density material. The exterior jacket has good penetration performance if fired against a steel plate, while the inner core has little penetration performance. If the projectile composed with above two materials hits a target the exterior jacket will penetrate successfully while the plastic filler will go forward tardily in the target. In the inner core an extremely high pressure will be generated leading to fragmentation of the outer structure once the projectile leaves the target [1,2]. The phenomenon is illustrated in Figure 1.



(a) At the beginning of penetration (b) Perforation of the target

Fig.1 Sketch map of functional principle of PELE

The exterior jacket, which answers for perforating targets and producing kill elements behind targets. The existing researches show there is an apparent difference in the penetration performance and lateral effect of PELE with distinct jackets [3,4]. For the high density and high strength, TA is adopted to armor-piercing projectiles widely at present, so to exterior jacket of PELE. Nevertheless, the inadequate obdurability of TA weakens the penetration performance of PELE with TA jacket in a certain extent [5], which results in the limited impacting ability of PELE. Moreover, TA jacket tends to fall to pieces naturally, which leads to uncontrollable shape and amount of fragments.

TFC are composed of tungsten fibers and an appropriate matrix. Due to the high density, high strength and big slenderness, tungsten fiber is the reinforcement and the main source of strength while the matrix glues all the fibers together in shape and transfers stresses between the reinforcing fibers. The existing researches show that the matrix sheds gradually during the penetrating process and

tungsten fibers answer for armor-piercing mainly. On account of the advantage of big slenderness, the penetration performance of TFC projectile overmatches that of TA projectile [6-8].

If TFC can be employed to produce jacket of PELE, thanks to the virtue of tungsten fibers, the penetration performance of PELE with TFC jacket would increase more. Furthermore, recurring to perfect matrix, in the inner core an extremely high pressure will be generated leading to disperse and fragmentation of the TFC jacket once the projectile leaves the target. The tungsten fibers and matrix fragments produced during above process would destroy objects behind the target and augment the destroy effect.

Paralleled with experiment, numerical simulation is a much more effective research means, which not only may obtain lots of datum that can't be derived from experiments to support theoretical analysis, but also can be carried out easily with different initialized boundaries, materials and structures and so on. To disclose the mechanism of the penetration performance and the lateral wrecking capability of PELE with TFC jacket, numerical simulations are carried out on the influences of some factors on terminal effect of PELE projectiles in this paper. Forenamed factors involve the diameter and volume fraction of tungsten fibers, and the sort of matrix. The study is put forward to increase the whole damage effect of PELE and further widen its employment scope.

Means of Numerical Simulation

In the paper, numerical simulation about the terminal effect of PELE with tungsten fiber composite jacket has been carried out, in which RHA plate is chosen as target and the impact velocity is 1500m/s.

The existing research indicates PELE will enhance its lateral effect availably when the slenderness ratio is in the range of 3~5 and inside tube radius ratio is between 0.5 and 0.7 [9]. Accordingly, the slenderness ratio is 4 and inside tube radius ratio is 0.6 in this paper. Idiographic dimensions of simulation models are as follows. The outer diameter and length of PELE is 30mm and 120mm apart, and that of inner core is 18mm and 110mm respectively. While the target is a 30mm-thickness quadrate plate, whose length and width is both 100mm. The PELE and target dimensions are quarter of the experiment model due to symmetry. The heat energy loss is ignored during the simulation.

The tungsten fibers and matrix are both simulated with PLASTIC_KINEMATIC material model combined with Von-Mises yield criteria, the inner core with VISCOELASTIC model, and the bottom of PELE and target are characterized with JOHNSON-COOK model and EOS_GRUNEISEN together. During the impacting process, the contact mode of ESTS is adopted between PELE and the target, while ASTS is introduced among constitutes of PELE [10].

Influence of Jacket Materials

The process of PELE with TFC jacket penetrating RHA with impact velocity of 1500m/s is simulated in this paper, in which PELE is composed of 40% tungsten fibers and 60% matrix, and the diameter of tungsten fibers is 1mm and the sort of matrix is ferro nickel alloy. Figure 2 shows the fragmentation and disperse of jacket behind target.

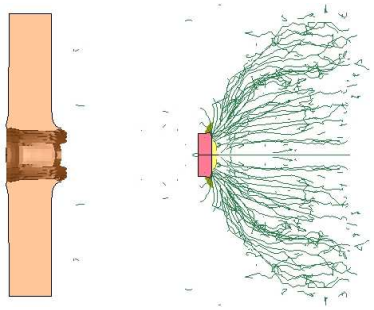


Fig.2 Lateral effect of PELE with TFC jacket

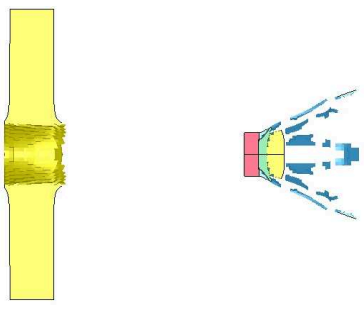


Fig.3 Lateral effect of PELE with TA jacket

To compare the lateral effects of PELE with different jackets, the process of PELE with TA jacket, adopting the same configuration and dimension as forenamed, penetrating RHA target with the same impact velocity is also simulated, and the corresponding result is shown in Figure 3.

Contrasted with Figure 3, some obvious characteristics are shown in Figure 2, such as the diameter of perforation being smaller, the debris being more plentiful and regular, and the lateral disperse angle of fragments being much bigger. Provided with the same impacting speed, the varieties of axial velocity and radial velocity of PELE with different jackets are shown in Figure 4 and Figure 5.

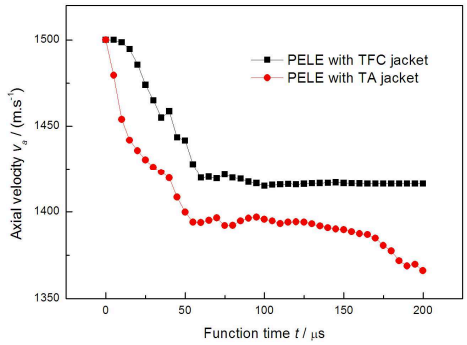


Fig.4 Axial velocity of PELE debris with different jackets

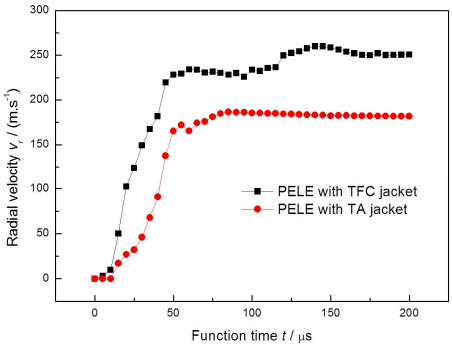


Fig.5 Radial velocity of PELE debris with different jackets

It can be seen from Figure 4 and 5 that the axial velocity and radial velocity of PELE with TFC jacket are both bigger than that of PELE with TA jacket. The underlying reasons for these phenomena lie in that under high strain rate loading there is a great compression of grains in axial orientation and the head of TA jacket will be formed as mushroom-head, shown as Figure 6. With the increasing of penetration depth, the mushroom-head grows up constantly, which widens the perforation further and weakens the penetration performance of PELE with TA jacket. But for PELE with TFC jacket, in the process of penetration the matrix ruptures abruptly as brittle material and tungsten fiber perforates mainly, shown as Figure 7. So the adiabatic shear failure is observed in the head of TFC jacket, which shows self-sharpening behavior and the penetration ability of jacket swells consequently. Because of the low tensile stress of the matrix, in the inner core an extremely high pressure will be generated leading to fragmentation of the outer jacket once PELE leaves the target and a mass of tungsten fibers debris with high radial velocity will be produced.

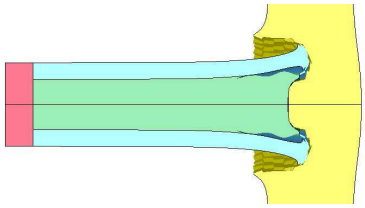


Fig.6 Mushroom-head of PELE with TA jacket

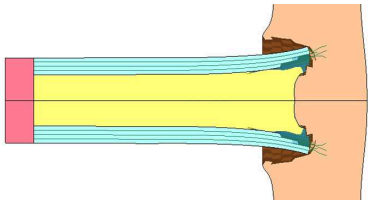


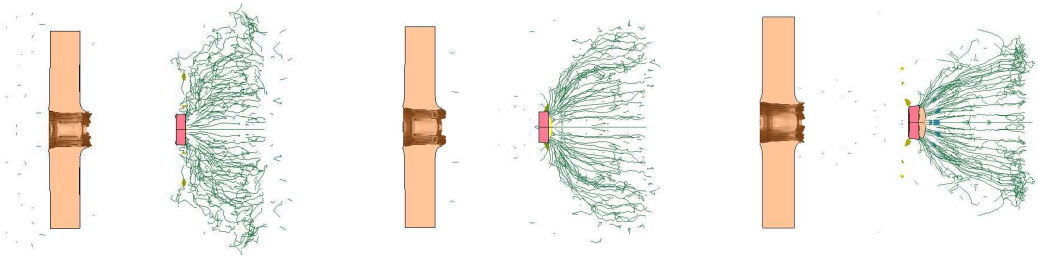
Fig.7 Self-sharpening of PELE with TFC jacket

Influence of Jacket Constitutes

Diameter of tungsten fibers

To investigate the influence of diameter of tungsten fibers on the terminal effect of PELE with TFC jacket, the process of PELE penetrating target perpendicularly with the same impact velocity is simulated, in which the target is 30mm RHA plate and the sort of composites matrix is ferro nickel always, while the diameter of tungsten fibers is 0.25mm, 0.5mm and 1mm respectively.

Figure 8 shows the lateral effect of PELE with TFC jacket adopting distinct diameter tungsten fibers, in which *d* denotes diameter of tungsten fibers. It can be seen that the diameter of tungsten fibers has much to do with the fragmentation and disperse of TFC jacket. That is, the thinner the tungsten fiber, the stronger the swelling during the penetrating process and the bigger the disperse angle of fragments behind target.



(a) d=0.25mm (b) d=0.5mm (c) d=1mm

Fig.8 Lateral effect of PELE with TFC jacket adopting distinct diameter tungsten fibers

During above simulation process, because of the same number and different diameters of tungsten fibers, PELE projectiles have distinct volume fractions of tungsten fibers and unlike density of jacket accordingly. The axial velocity and radial velocity of PELE debris with three different diameter tungsten fibers are shown in Figure 9 and Figure 10.

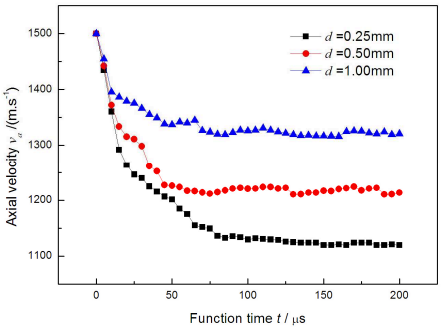


Fig.9 Axial velocity of PELE debris with different diameter tungsten fibers

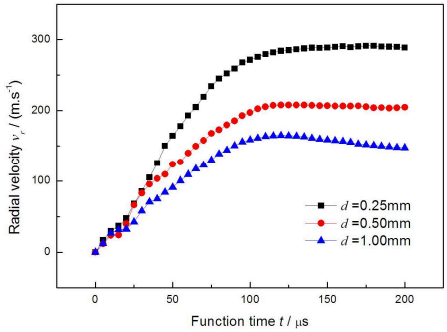


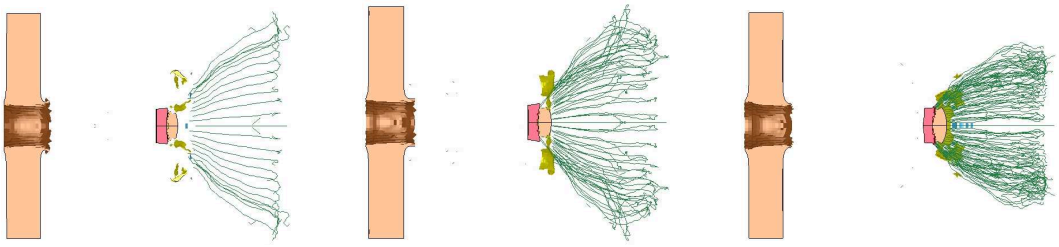
Fig.10 Radial velocity of PELE debris with different diameter tungsten fibers

It can be seen from Figure 9 that provided with same number tungsten fibers, the thicker the tungsten fiber, the bigger the residual axial velocity of PELE with TFC jacket behind target, which means PELE having more adequate penetration ability. The reason lies in that PELE jacket with thicker tungsten fibers has bigger density. While from Figure 10, it can be seen that the thicker the tungsten fiber, the smaller the radial velocity. That means PELE having more feeble penetration ability, which matches with the debris disperse in Figure 8 to the moment. For that matter, the imaginable causation rests with that, because of the more feeble penetration ability, it costs more time for PELE perforating target with thinner tungsten fibers, which leads to more axial kinetic energy turning to radial disperse energy in jacket owing to the swelling of inner core of PELE, thus tungsten fibers are inclined to disperse behind target more easily.

However, due to the limit of dimension, thicker tungsten fiber is not all better for PELE. To take account of the penetration ability and the lateral effect of jacket at the same time, the diameter of tungsten fiber should be in a reasonable range for PELE with a curtain dimension.

Volume fraction of tungsten fibers

To research the influence of volume fraction of tungsten fibers on the functional effect of PELE with TFC jacket, the process of PELE penetrating target is simulated, in which the sort of composites matrix is ferro nickel still and the diameter of tungsten fiber is uniform, while its volume fraction is 20%, 40% and 60% respectively. The lateral effect of PELE with TFC jacket adopting distinct volume fraction of tungsten fibers is shown in Figure 11, in which p denotes volume fraction of tungsten fibers.



(a) p=20% (b) p=40% (c) p=60%

Fig.11 Lateral effect of PELE with TFC jacket adopting distinct volume ratio of tungsten fibers

It can be learned from Figure 11 that the volume ratio of tungsten fibers also has much to do with the fragmentation and disperse of TFC jacket. That is to say, the bigger the volume ratio of tungsten fibers, the smaller the disperse angle of fragments behind target. Further more, study on the simulation results utilizing post processing software indicates that, the bigger the volume ratio of tungsten fibers, the bigger the residual axial velocity and the smaller the radial velocity. That means PELE having adequate penetration ability and feeble lateral disperse performance.

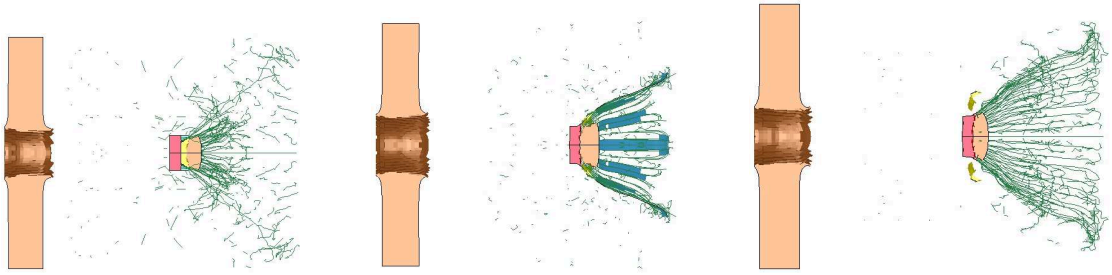
The potential reasons for these phenomena lie in that the irregularity of tungsten fibers in jacket because of its small volume percent, which leads to the difference of stress and strain environment among every tungsten fiber nearby consequentially. Herein, partial stress convergence happens, and rupture and failure come into being thus in some tungsten fibers. Then the strength of composites jacket weakens and its penetration performance reduces finally. With the augment of volume ratio of tungsten fibers, the main rupture manner alters from shearing to ripping gradually. Here, compress stress of jacket improves and the penetration ability swells.

Besides, simulations on PELE with TA jacket penetrating target with same configuration and dimension is also carried out. Comparison analysis shows that the strength of PELE with TA jacket is higher than that of PELE with TFC jacket as the volume ratio of tungsten fiber is on the small side, until it is bigger than a certain value. For the destroy performance of PELE is related to both axial velocity and radial speed, to give consideration to above two factors at the same time, the volume fraction of tungsten fibers should be in a sound range as to PELE.

Sort of bonding phase

Common fiber reinforced composites are composed of fibers and a matrix. Fibers are the reinforcement and the main source of strength while the matrix glues all the fibers together in shape and transfers stresses between the reinforcing fibers. Requirements for a matrix material usually include relatively low cost, easy achieve, and indiscerptible capability each other and so on. At present, aluminum, copper and ferro nickel alloy are the main matrixes used for tungsten fiber reinforced composites.

To study the influence of matrix on the terminal effect of PELE with TFC jacket, the process of PELE penetrating target is simulated, in which the diameter and volume ratio of tungsten fiber are uniform, while the matrix is aluminum, copper and ferro nickel alloy respectively. The lateral effects of PELE with TFC jacket adopting distinct matrixes are shown in Figure 12.



(a) Aluminum alloy (b) Copper alloy (c) Ferro nickel

Fig.12 Lateral effect of PELE with TFC jacket adopting distinct bonding phase

It can be learnt from Figure 12 that PELE jacket falls to pieces badly when its matrix is aluminum alloy and breaks up deficiently with copper alloy bonding phase, and only with ferro nickel alloy matrix can PELE produce perfect debris disperse. The primary functions of the matrix are to transfer stresses between the reinforcing fibers and damage duly to disperse the tungsten fibers. Compared with aluminum alloy bonding phase, ferro nickel has higher compress stress and transfers stresses between the tungsten fibers better, which keeps the uniformity of stress in composites jacket from easy failure of tungsten fibers and improves the penetration performance of PELE thus. On the other hand, contrasted with copper alloy matrix, ferro nickel has lower tensile stress, which would make the bonding phase brittle rupture easily and dismiss the tungsten fibers and then improve the lateral disperse performance.

Summary

It can be learned from numerical simulation results, compared with PELE with TA jacket, PELE with TFC jacket not only has self-sharpening during the penetrating process which improves its penetration ability, but also has the advantage of lower tensile stress and being prone to disperse which improves its lateral disperse performance. So it should be feasible in theory for PELE to produce jacket with tungsten fiber composites.

Farther researches show a series of results. With the same number of tungsten fibers, the thicker the tungsten fiber, the greater the penetration ability and the more difficult to disperse for PELE. The strength of PELE with TA jacket is higher than that of PELE with TFC jacket until the volume ratio of tungsten fiber is bigger than a certain value. Compared with other two matrixes, PELE with ferro nickel alloy matrix can produce perfect penetration performance and debris disperses almost. Above-mentioned analysis results may provide reliable theory and computational bases for future research of PELE with TFC jacket.

References

[1] G Kesberg, V Schirm. PELE – The Future Ammunition Concept. 21st International Symposium on Ballistics. Adelaide, Australia, 2004, pp. 1134-1144.

[2] G Paulus, V Schirm. Impact behavior of PELE projectiles perforating thin target plates. International Journal of Impact Engineering. 33 (2006) 566-579.

[3] J S Zhu, Z Fan, Z H Du. Influence of the Jacket Material on PELE Effect. Ordnance Material Science and Engineering, 2010, 33(6): 14-16.

[4] D Y Huang, J R Wang, Z R Chen, Z G Chen and S L Zhang. Influence of Ceramic Jacket Material on PELE. Explosive Materials, 2011, 40(4): 5-8.

[5] C X Zhang, L B Qin, W Y Mi and Z G Bai. Recent Research Progress and Prospect of Armor-piercing Projectile in China. Materials Science and Engineering of Powder Metallurgy, 2006, 11(3): 125-130.

[6] Z H Zhang, F C Wang, S K Li. Numerical Simulation on Penetrating Process of Tungsten Fiber Composites Penetrators. Rare Metal Materials and Engineering, 2003, 32(6): 440-442.

[7] G Rong, D W Huang. Self-Sharpening Phenomena of Tungsten Fiber Composite Material Penetrators during Penetration. Explosion and Shock Waves, 2009, 29(4): 351-355.

[8] B Lei, D W Huang, M C Yang and G Rong. An Experimental Study on the Self-Sharpening Behavior of Armor Piercer using Tungsten Fiber Composite Material [J]. Transactions of Shenyang Ligong University, 2008, 27(1): 72-76.

[9] J S ZHU. Functional Mechanism of Penetrator with Enhanced Lateral Effect. Ph. D. Dissertation of Nanjing University of Science and Technology, (2008)

[10] LSTC. LS-DYNA Keyword User's Manual (Version 970)-Nonlinear Dynamic Analysis of Structures in Three Dimensions. Livermore: Livermore Software Technology Corporation, (2003)

Advanced Materials Research Vol. 936 (2014) pp 1933-1936
© (2014) Trans Tech Publications, Switzerland
doi:10.4028/www.scientific.net/AMR.936.1933

Analysis and Optimization of Segregators' Structures on Separation Efficiency

Guo Caifen, Li Shaokun, Wan Changdong

College of Mechano-electronic Engineering, Suzhou Vocational University, Suzhou, Chain, 215104

guocf@jssvc.edu.cn, lsk@jssvc.edu.cn, wancd@jssvc.edu.cn

Keywords: oil-gas separator. separation efficiency. response surface methods(RSM). computational fluid dynamics

Abstract: Inside segregators, such as the air compressor, refrigerant and lubricant are mixed together. It is hoped that the lubricant could be reclaimed back to continue to work when it is expelled from the compressor**.** But designing of some kinds of air conditioning compressors has taken no notice of that, or it has lower separation efficiency. RSM (Response Surface Methods) is put forward to optimize the structure parameters so as to improve the separation efficiency. It is a collection of mathematical and statistical techniques, by which fewer experiments are needed to obtain the relationship between its parameters and their influences. Finally, by the use of computational fluid dynamics software, the optimum structure parameters are obtained, through which the better separation efficiency is available.

Introduction

Lubrication is very important to moving structures in machine comportants such as compressors, so that the good condition of machines is guaranteed to promote their life-span. The lubricant in gaseity condition is mixed with cold intermediary and together are expelled out of compressors. The leakage of lubricant would put structures at a disadvantage so a separation cavity is designed at its exit which would disjoin lubricant and intermediary to make lubricant reuse as good as possible. The mechanism of the separation is cyclone by which the big mass would be swung to the wall to go back to the compressor because of their different desity[1].

Separation Simulation of lubricant with cold intermediary is accomplished with the computational fluid dynamics software to obtain some parameters affecting the separation efficiency. In order to get the best results, the parameter optimization is needed with the help of Response Surface Methods (RSM) to ensure the optimum structure parameters with as fewer experiments taking as possible.

The Basic Principle of RSM

Although optimum values may be received through some common optimization means, intuitionistic graphs could not be observed and it is difficult to distinguish the optimum region and points. So RSM emerges as the times require. It is a kind of optimization method, which defines the system response (for example, the extraction rate in extraction chemistry) as the function of one or many factors (e.g., the concentration of extraction agent, its acidity, etc.). RSM reveals this kind of relationship using graphics techniques to let designers choose optimum conditions by instinct observation. RSM may perceive and confirm the response influences to make certain their feedback, and the respond may be the biggest or the smallest value.

RSM is a kind of sequence methods. Generally, when a point is located far from the optimum point, the first-order model is suitable for a little bending existed in the system. Therefore, the experiment is aimed at leading triers to go forward along the route to find the optimum fastly and effectively. Once the optimum region is found, the more refined model (e.g., the second-order one) may be utiliyzed to fix the optimum point. The analysis of RSM would be imagined as to climb a

moutain, with its top representing a maximum point of the reponse. If the true optimum is the smallest point of the reponse, the aforementioned analysis would be thought as falling down into a valley[2].

The conventional optimization may be put forward as[3,4]

$$\left.\begin{array}{l} \text{Seeking} \quad x \in E \\ \text{So that} \quad y_0(x) \to \min \\ s.t \quad y_j(x) \le 0; \quad \underline{x_i} \le x_i \le \overline{x_i} \\ (i = 1, \cdots, n; j = 1, \cdots n_c) \end{array}\right\}. \tag{1}$$

Where n, n_c stand for the number of variables and restricted functions respectively.

RSM is applied to express the objective funtion $y_0(x)$ or restricted funtion $y_i(x)$ as the function of x_i explicitly, which are difficult to do so with other means so as to solve Eq.1 using the optimization settler. For example, the linear equation is listed below

$$\eta(x) = \beta_0 + \beta_1 x_1 + \beta_2 x_2 + \cdots + \beta_n x_n . \tag{2}$$

Then a non-linear restricted optimization model is attained finally

$$\left.\begin{array}{l} y_0(x) = x^T H x + f^T x \to \min \\ s.t \quad \sum_{i=1}^{n} \sum_{r=1}^{n} \beta_{jir} x_i x_r \le b_j \\ \underline{x_i} \le x_i \le \overline{x_i} (i = 1, \cdots, n) \end{array}\right\}. \tag{3}$$

Where y is the response function, x_i stands for a $(k \times 1)$ vector of predicting variables, b represents the coefficient vector, and β_i the linear multi-variables regression analysis estimation (unknown coefficients), n the number of variables; H is a $(k \times k)$ symmetric matrix whose main diagonal elements are the pure quadratic coefficients and whose off-diagonal elements are one-half the mixed quadratic coefficients; f is a $(k \times 1)$ vector of the first –order regression coefficients.

The convergence rule is

$$\Delta y_0^k = \left| (y_0^{k+1} - y_0^k) \Big/ y_0^{k+1} \right| \le \varepsilon . \tag{4}$$

Where y_0^k and y_0^{k+1} are objective function values of the former and later iterating.

Analysis and Optimization of Computational Fluid Dynamics Software

The Computational Fluid Model and Optimization of Structure Parameters

The model of the separation cavity is showed in Fig.1, where D_1 stands for its exit diameter and D_2 its lubrication mouth diameter. Calculation of phase field is performed with the SIMPLE arithmetic and oil dripping is tracted by the dislete phase model. With the initial location, speed, dimensions and temperature predefined according to its physical characteristics, its trajectory is initialized and the amount of heat transfering/mass is performed. When granule moves through fluid, their trajectory and the amount of heat and mass tranfering may be calculated based on various balancing forces, as well as the amount of convection and radialization of heat and mass. The RNGk-ε model is adopted as the onflow model. The oil dripping diameter is 4μm and its entrance speed is 19m/s which is defined as the escaping borderline, altogether with the outflow. The wall-face is defined as “trap” form, by which the oil dripping would be caught when it reaches it[5,6]. The oil dripping moving trajectory is simulated and then showed in Fig. 2.

The structure parameters taken into account in simulation are cold intermediary exit diameter D_1 and lubricant going-back diameter D_2. The optimization objective is the maximum value of separation efficiency μ.

The range of D_1 and D_2 are defined as follows
$2mm \leq D_1 \leq 6mm$, $4mm \leq D_2 \leq 10mm$

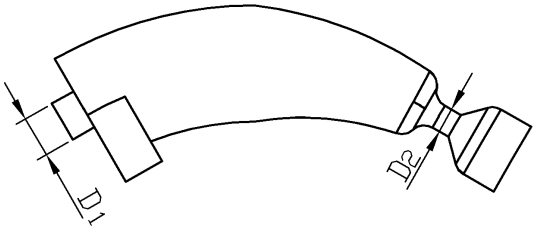
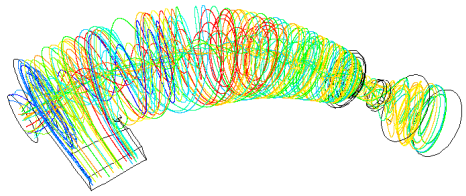


Fig.1 Structure of the separation cavity


Fig.2 Oil dripping moving trajectory during separation

Response Surface Optimization

According to CCD(Central Composite Design) test designing principle, separation efficiency optimization is carried out with the help of Response Surface Analysis. The test diagram and results are listed in Table 1. 13 tests are included, where various values of D_1 and D_2 are tried and a fitting regression(Eq.5) is reached. On the basis of the fitting function, a response surface is made out.

$$\mu=0.22399+0.10247\,D_1+0.083393D_2-1\times10^{-3}D_1D_2-0.011759\times D_1{}^2-6.08750\times10^{-3}D_2{}^2 \quad (5)$$

TABLE 1 TEST DIAGRAM DESIGNING AND DATA PROCESSING

No.	D_1[mm] (cold intermediary exit diameter)	D_2[mm] (lubricant mouth diameter)	**μ (separation efficiency)**
1	4	7	0.70
2	4	7	0.71
3	4	2.76	0.64
4	6.83	7	0.62
5	4	7	0.71
6	6	4	0.61
7	2	10	0.59
8	2	4	0.59
9	6	10	0.58
10	4	7	0.72
11	4	7	0.67
12	1.17	7	0.61
13	4	11.24	0.56

Influence of both parameters D_1 and D_2 on the separation efficiency is showed in Fig.3. When D_1 remains unchanged, the separation efficiency μ increases along with D_2 firstly, then decreases after it arrives at its maximum value. In the samilar way, when D_2 keeping steady, first of all, μ enlarges with D_1, then decreases after it attains to its crest. When D_1=4mm, D_2=7mm, a maximum μ is got, that is, μ_{max}=72%.

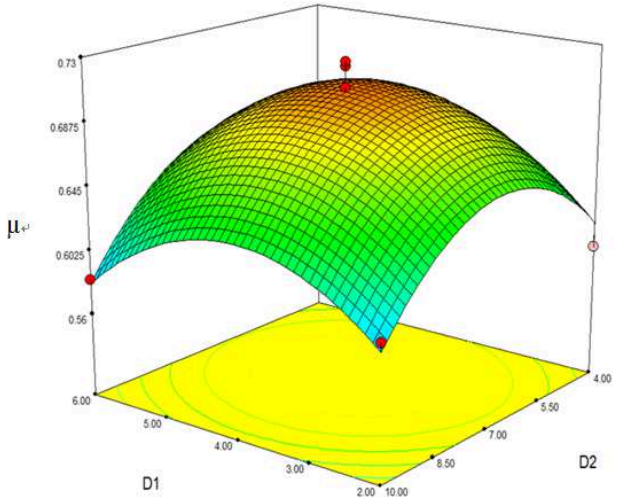


Fig.3 Response surface of both parameters D_1 and D_2 on separation efficiency

Conclusion

Based on the above optimization test, a maximum separation efficiency is achieved, μ_{max}=72%. Then based on the same parameters, the value of μ=72.5% is acquired validated by the hydrodynamics calculation, which proves the reliability of the above method. Based on RSM, the objective function or restriction may be approximately expressed with designing variables so clearly, that complex optimization could be turned into linear or non-linear restricted one and iterated with the advanced settler. Through the set-up of hydrodynamics simulation testing plan and reasonably arranging parameters, the optimum value would be got finally. This method would provide valuable reference to separation cavity structure designing.

Reference

[1] Alex. C. Hoffmann and Louis E. Stein. Gas “cyclones and swirl tubes: principles, design and operation” Springer-Verlag Berlin Heidelberg, 2002, 30-78.

[2] Hill W J, Hunter W G. A review of response surface methodology. Technometrics, (1966) 571-590.

[3] Box, G. E. P., and Behnken, D. W.. Some New Three Level Designs for the Study of Quantitative Variables**,** Technometrics, 2 (1960) 435-475.

[4] Wu, C. F. Jeff, and Hamada, Michael. Experiments: Planning, Analysis and Parameter Design Optimization**,** John Wiley & Sons, Inc., New York, 2000.

[5] Zhu Chuanyu. The numerical simulation research of effects of interior structures deformation on characteristic of cyclone separator(in Chinese)[D]. Dalian, Dalian University of Science and Technology, 2006.

[6] Sui Yunkang, Zhangxuan, Yu Kangping. Improvement and application on response surface methodology in shape optimization(in Chinese)[J]. Journal of Beijing Industrial University, 34(2008) 31-36.

Advanced Materials Research Vol. 936 (2014) pp 1937-1941
© (2014) Trans Tech Publications, Switzerland
doi:10.4028/www.scientific.net/AMR.936.1937

Manufacturing and Analysis of Non-asbestos Sealing Gasket

Meng Zhang[1,a], Meihong Liu[2,b*], Yuxian Li[3,c]

Faculty of Mechanical and Electrical Engineering, Kunming University of Science & Technology, Kunming, 650500, China

[a]782826490@qq.com, [b]64115737@qq.com, [c]2429126569@qq.com

*corresponding author

Keywords: non-asbestos; hybrid fiber; manufacturing

Abstract: Under the fiber hybrid effect, the merits of organic and inorganic fibers were integrated. The appropriate organic and inorganic fibers were chosen to prepare the non-asbestos gasket which meets the usage requirements and has a good cost performance. The ratio of basic craft and materials for industrial production were obtained. Results indicate the new non-asbestos gasket which is made by non-asbestos fibers and enhanced rubber adhesive has reached the performance of similar international products and has formed our unique non-asbestos sealing materials.

Introduction

Preface

Sealing material is widely used in petroleum, chemical industry, machinery, automobile, etc. Because of its high tensile strength, large surface area, good adsorption performance, asbestos fibers are widely used to make the main body of soft sealing packing and gasket materials. However, long-term inhalation of asbestos dust can cause asbestos AD cool-headed disease, asbestosis and cancer. The asbestos fiber causes serious damage to human body health[1]. The developed countries have put forward strictly limits on the use of asbestos[2]. In our country such as asbestosis an occupational disease prevention and control of asbestos are paid more and more attention. Foreign non-asbestos sealing materials research and development have made great progress. Entered the practical stage, the domestic research and developed quickly. At present, fiber including Kevlar fiber, Aramid fibers, cellulose fiber and various inorganic fibers are commonly used. But in known fiber material, there is no a kind of fiber which can completely replace the asbestos fiber, which limits the non-asbestos sealing composites reinforced by a single fiber of popularization and application. Therefore, the author uses fiber hybrid effect, the synthesis of organic and inorganic fiber one's respective advantage. Choosing the right variety of inorganic and organic fiber has a good cost performance of non-asbestos sealing gasket and the development of non-asbestos gasket is analyzed and compared to the level of similar foreign products.

Test Materials And Test Methods

Test Materials

In the early stage of the study[3 ~6], based on choose raw materials as follows: cellulose fiber and mineral fiber, aramid pulp, pulp fiber, aromatic polyamide fiber, rubber adhesive, silica, mica, calcium carbonate, talcum powder, kaolin, diatomite, wollastonite, surface active agent, coupling agent, paper alum, etc.

Test Method

Experimental methods: determining the copy [7] as the basic production process, according to the performance requirements for materials design product formula and production process, for determining the copy without asbestos sealing gasket pilot, have achieved using requirements and a good cost performance of non-asbestos sealing gasket, basic scientific research, and analysis and comparison with similar foreign products.

Test the main equipment: grinding machine, plate mill, taking into a copy machine, vacuum device and so on.

Testing equipment: WE - 30 hydraulic universal material testing machine, CSS44020 tensile tester, TM3000 scanning electron microscope, optical microscope.

The Results Of The Experiment And Analysis

Single Fiber And Hybrid Fiber Structure Analysis

Figure 1 and figure 2 are respectively separate mineral cotton fiber and mineral fiber, cellulose fiber and aramid pulp fibers taking the SEM photo of paper copy. From figure 1, you can see, most of the latex can absorb the fiber, but there are some fibers which failed to absorb on fiber latex. This will lead to the end product is not uniform, and has larger entanglement between fiber, poor dispersibility; Figure 2, the hybrid fiber dispersion is separately using mineral cotton fiber, which has better effect with glue and a winding. Therefore, the strengthen effect is good, which can be lost in rubber matrix effect after the material having some residual strength. Therefore, it has a better performance is with mineral cotton fiber mixed with a certain amount of aramid pulp, cellulose fiber than replace asbestos fiber preparation with single fiber latex copy without asbestos gasket.

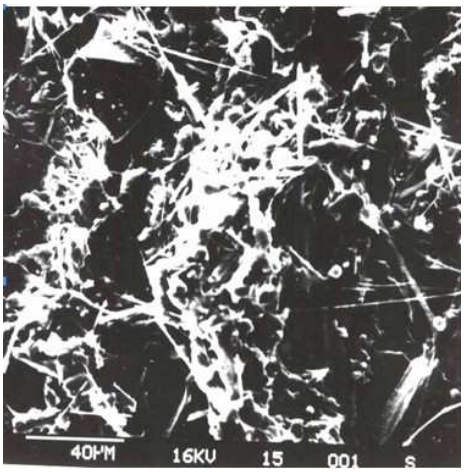


Figure 1 SEM Figure of Mineral Cotton Fiber

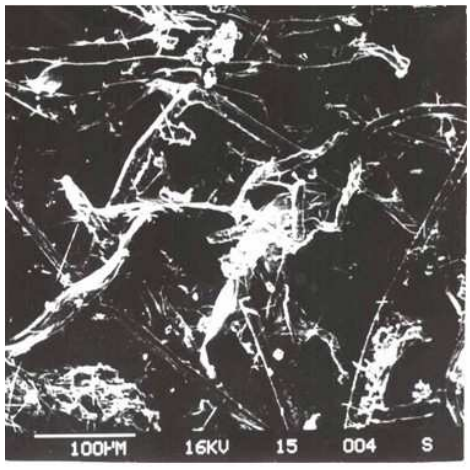


Figure 2 SEM Figure of Hybrid Fiber

Latex - Packing - Fiber Content Of Optimization

Improving the content of latex can make material more elastic, and provide a better sealing. But it lowers the stability under high temperature stress. If using two or more different average particle diameter of packing, the combination of particle will closely unifies together. This will have less space for rubber. Early non-asbestos gasket materials mainly use aramid pulp as reinforcing fiber. This is because the aramid pulp has the obvious advantages such as high strength, large specific surface area. But the cost is high. So, to sum up, the lower content of latex formula mixed aramid pulp, mineral cotton fiber (long fiber and short fiber) and cellulose fiber, and reducing the amount of aramid pulp, chooses different granularity of packing at the same time, to reduce production costs and make products with good comprehensive performance.

The Use Of Other Additives And Processing Aids

(1) To join the right amount of surfactant, improve the composition of surface charge, make the fiber surface with a negative charge, outer rubber latex particles with positive charge, the polymer particles attracted by fiber and polymer particle agglomeration effect and deposited on the fiber surface.

(2) To join the right amount of coupling agent, enhance the cohesive force between packing and latex substance, in the multiphase system formed in the good interface, the material has excellent overall performance.

Performance Analysis Under Different Formula

Picking two formula optimization shows in table 1: the performance of the product shows in table 2 (and compared with foreign interface products).

TABLE 1 SELECTED FORMULA

Composition	Quality percentage (wt ％)	
	A	B
Kaolin	32	33
White carbon black	2	3
Talcum powder	9	11
Mica	3	3
Rubber adhesive	16	18
Mineral cotton fiber	28	23
Cellulose	7	6
Aramid fibers	3	3

Known from table 2: using latex copy process and using without contain asbestos composition of inorganic fibers mixed with organic fiber reinforced rubber adhesive preparation of a new type of sealing gasket and similar foreign products than its tensile strength, compression spring rate, sealing and other major technical indicators have reached the level of similar foreign products, formed with characteristic of our country which has no asbestos sealing plate.

TABLE 2 THE PERFORMANCE OF THE PRODUCT

performance			case 1	case 2	NI-2085
density g/cm3			1.56	1.69	1.44(min))))
The tensile strength Mpa			20.7	18.73	13.79 (min)
The compression ratio %			12.5	11.85	10 - 20
Resilient rate %			62.4	51.51	50 (min.)
The medium resistance	ASTM3＃ oil (150℃5h）	Gain weight %	11.9	14.08	30 (max.)
		Thickenig rate %	0.6	5.89	10 (max.)
	ASTM B oil (21~30℃5h)	Gain weight %	13.7	7.45	30 (max.)
		Thickenig rate %	14.9	6.8	15 (max.)
sealing	Bolt tightening torque 20±2N·m The internal liquid pressure 0.5Mpa 30min		No	No	-

Conclusions

(1) The hybrid aramid pulp, mineral cotton fiber (long fiber and short fiber) and cellulose fiber, and reducing the amount of aramid pulp, and choosing different packing sizes, can reduce the production cost and make products with good comprehensive performance.

(2) To join the right amount of surface active agent, coupling agent and paper making alum can play the role of material to improve overall performance.

(3) Preparing a new type of sealing gasket has been basically achieved the performance of the same products abroad. However, comparing with the similar foreign products remain with poor product density will be improved in future research.

Acknowledgement

The authors would like to thank JinChuan's engineers for their constructive and insightful suggestions for further improving the quality of this paper. This work is supported by National Natural Science Foundation of China（No. 51165014）, Science and technology plan projects of Yunnan Province (No. 2012FB130),and Scientific research funds of Yunnan Province(No. 2012Y540).

References

[1] Tan Xishun, the threat to human health killer - asbestos [J]. Journal of labor protection, 2005 (3) : 96.

[2] Nikolaus Becker, Jurgen Berger, Ulrich Bolm - Audorff. Asbestos exposure and malignant lymphomas - a review of the epidemiological literature [J]. Int the Arch Occup Environ Health, 2001 (2001) : 459 ~ 469.

[3] Liu Meigong Cai Renliang, Xie Sujiang. No asbestos latex copy in sealing material formula research [J], rubber industry, ploidy of 2004 (2) : 83 ~ 86.

[4] Liu Meigong Li Zhenhua, Cai Renliang etc. No asbestos latex copy from the suspension stability of the sealing material research [J]. Journal of mechanical engineering materials, 2005, 29 (12) : 7 ~ 9.

[5] Liu Meigong, Cai Renliang Xie Sujiang, Meng Feng, Tian Dongmei. Non asbestos latex copy in the performance of the sealing material research [J]. Journal of mechanical engineering materials, 2005.29 (1) : 34 ~ 36.

[6] Liu Meihong, Li Zhenhua, Zhou Rong, Yu Cai Renliang. Study on the Assorted Non - Asbestos Fiber Reinforce Composite by Beater - addition Process. Materials Science Forum Vols. 475-479 (2005) : pp1051-1054.

[7] Liu Meigong Cai Renliang, Xie Sujiang. Latex copy took non-asbestos sealing material formulation study [J]. Journal of rubber industry, ploidy of 2004 (2) : 83 ~ 86.

Advanced Materials Research Vol. 936 (2014) pp 1942-1947
© (2014) Trans Tech Publications, Switzerland
doi:10.4028/www.scientific.net/AMR.936.1942

The Swelling Properties of Nitrile Rubber with Different Acrylonitrile Contents in Cyclohexane Medium Research

Huiming Wang[1, a], Xiaoren Lv[1, b] and Shijie Wang[1, c]

[1]School of Mechanic Engineering, Shenyang University of Technology, Shenyang, China, 110870

[a]wanghm118@126.com, [b]xrlvsut@126.com, [c] wang_shijie@263.net

Keywords: Submersible screw pump; Nitrile rubber; Acrylonitrile content; Swelling properties; Mechanical properties.

Abstract. By the research of swelling and mechanical properties of nitrile rubber with different acrylonitrile contents in cyclohexane medium, the influences of physical and mechanical properties with diffrent acrylonitrile contents is analyzed. The results indicated that: the quality of all the nitrile-butadiene rubbers with different acrylonitrile contents is increasing with the increase of soaking time. It increases rapidly in the first 24 hours then gently. With the increase of the acrylonitrile content, the increasing proportions of swilling quality is reduceing. But N40 cyclohexane performance is better relatively. After drying the three kinds of rubber in 110 degrees Celsius, all the qualities is lower than the original value. It means that in swelling process, the material in rubber is pulled out and the distance between the rubber molecules decreases. After swilling the three kinds of rubber, their hardness decreases and the decline proportion is reducing by the increase of acrylonitrile content. With different acrylonitrile contents and swilling times the nitrile rubber shows different mechanical properties. After soaking three kinds of rubber their tensile strengthes are on the decline by swilling time and their rates of permanent deformation are on the rise. It shows that as the swelling time extended, the mechanical properties descends and the corresponding indicators after soaked and dried is lower than the quantitative values after soaked. The study has a certain reference of design of ESPCP stator under certain operating conditions.

Introduction

As a new oil extraction and lifting equipment, the submersible screw pump has a great development and application with its unique advantage [1]. As an important component of screw pump, the material of stators is nitrile rubber mostly and chose different formula according to the different conditions [2,3].Screw pump is often used in high temperature ,high pressure, corrosive medium and periodic extrusion etc conditions, so the stator rubber inevitably appears swelling phenomenon. That makes the stator rubber machinery performance degradation and influence the efficiency of screw pump oil production. So the elastic stator material of screw pump must have a good swelling resistance, corrosion resistance, abrasion resistance and other properties[4—8]. The results indicated that: if the acrylonitrile contention in NBR is changed the performance of the rubber will be change too[9—12].Three kinds of NBR with different content of acrylonitrile were selected for crude oil swelling. As the complicated composition of crude oil, it is difficult to analysis the phenomenon of swelling. So cyclohexane is selected as the medium of swelling which is a representative cycloparaffin in crude oil. By researching the influence of different acrylonitrile content and soaking time to the quality of nitrile rubber, hardness, the volume and mechanical properties ,comparative analysing and revealing the swelling mechanism, it will provide a basis for the research and development of new formula and product a reasonable evaluation system of screw pump rubber.

Experimental

Materials

The three kinds of NBR in this experiment adopt the acrylonitrile content 18%, 26%, 41%and the base formula of NBR contains: zinc oxide, stearic acid, protective agent, carbon black, plasticizer, vulcanizing agent, promoter. For the purposes of comparison, the three kinds of rubber formula try to only change the content of carbon black and the other components remain the same, so as to achieve the shoreA hardness of three rubbers is 70 after vulcanization, and other additives should be optimized according to the general oil resistant seal matching principle of NBR as far as possible. With the opening-style rubber-mixing machine and plant vulcanizing press produced by Qingdao Yadong Machinery Group Company Limited, the temperature, pressure, the time required for sulfide can be measured by the Rheometer which produced in the GOTECH testing machines incorporate .

Experimental Techniques

Firstly, specimens of each NBR is prepared according to the standard GB/T1690-2006 (vulcanized rubber or Liquid-resistant thermoplastic rubber test methods), swelling the three kinds of NBR in cyclohexane with normal temperature and pressure. The size of rubber sample is 40mm×20mm×5mm, and the soak time is 24h, 48h, 72h, 120h and168h for respectively. With 0.1 mg precision weighing electronic balance, weighing the quality of the samples before and after swelling, and using LX - A rubber hardness tester measuring the hardness of rubber sample. Taking some soaking specimens in drying oven, drying experiment is carried out in 100 ℃and9 h.

Secondly, according to the standard GB/T528-1998(vulcanized rubber or thermoplastic rubber determination of tensile stress strain properties), test the three rubber specimens using a tensile testing machine for mechanical performance before and after swelling and drying, cutting the samples as dumbbell shaped II type, the tensile speed is 500mm/min range of 20 mm. All the measured experimental data are the average of three times that resulted from experiments.

The percentage mass change (△m) after soaking and drying of samples are calculated by the following formulas. Three specimens were used and the average value was calculated.

$$\Delta m = \frac{m_2 - m_1}{m_1} \times 100\% \quad (1)$$

Where, m_1 and m_2 are the weight of the specimen in air before and after immersion respectively, g.

Express the permanent deformation rate in R, it was determined as:

$$R = \frac{L_t - L_b}{L_b} \times 100\% \quad (2)$$

Where, Lt is the scale distance after sample fractured and placed up 3 min later,mm; Lb is the scale distance while the sample fractured,mm.

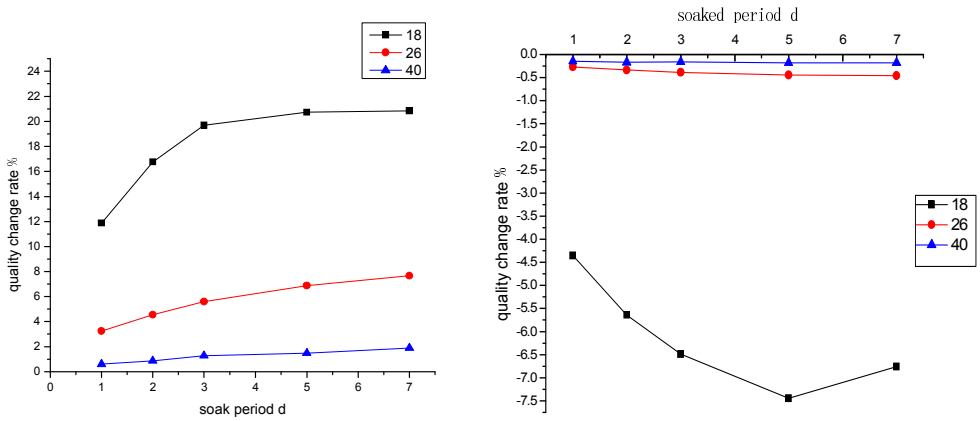
Results and Discussion

Mass Change Rate

In figure 1 (a),it is the quality change curve with immersion time for the different content of acrylonitrile rubber specimen swelling in cyclohexane reagent. From that, over time, the quality of rubber samples are gradually increased, the increase proportion of N18 is the largest, the

quality increase percentage is 20.84% after swelling seven days .In the second place the largest swelling percentage is 7.66% by N26, the N40 has the least quality increase by 1.9%. The swelling quantity of three kinds of NBR increased most rapidly in first 24h, and then the increase becomes gentle gradually, after 72 hours swelling changes are less. The cause of above phenomenon is the imparity of solubility parameters (SP). Due to swelling phenomenon is greatly influenced by SP, the closer between rubber and solvent SP, the greater with rubber swelling. The cyclohexane SP value is 8.3 and the SP of N18, N26, N40 are 8.7～8.8, 9.4～9.9 and10.3～10.5. Because cyclohexane and N18 SP values are most close, the quality of N18 swelling increment is the largest, followed by N26, minimum incremental quality is N40.

Figure 1 (b) is the quality change curve with immersion time for three kinds of different acrylonitrile content NBR specimen that soaked in cyclohexane reagent and dryed. It can be seen from the diagram that the three kinds of rubber is less than the original quality after drying, and the amount of reduced is increase along with the increasing of acrylonitrile content. The reduce proportion of N18 is the largest, the quality reduce percentage is 7.44% after dried .In the second place is1.11% by N26, the N40 has the least quality reduce by 0.18%. N18, N26 shows the quality decrease is increased with the extension swelling time but the quality decrease of N40 is approximate to constant over time .The quality reduced after drying that indicates cyclohexane has entered into rubber mesh structure, but at the same time some additives small molecules in rubber is separated out and spread into the reagent.With the increase of acrylonitrile content, the distance between the molecules is reduced, the intermolecular force increases, which makes a difficult plasticizer migration from the NBR. And after soaking the solvent color changed from colorless to yellow, with the increase of the acrylonitrile content, yellow solvent becomes shallow gradually, shows that the amount of precipitation gradually reduced.



（a）swelled NBR （b）dried NBR

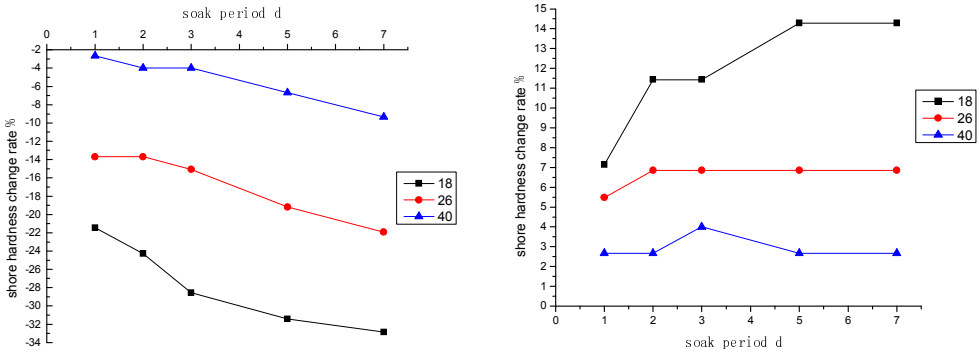
Fig.1 The Quality Change Rate Of Swelled And Dried Nbr In Different Soak Periods

Hardness Change Rate

Figure 2 shows the rubber shaw hardness percentage change curve after swelling and drying in different soaking time. Figure 2 (a) showed that three kinds of rubber hardness decreases obviously after swelling in cyclohexane medium, and there is a approximate linear relationship between the reduce hardness and soak time. In the contact of rubber and cyclohexane the intermolecular force between cyclohexane and rubber molecules is greater than the rubber

molecules internal forces.So cyclohexane molecules can spread into the rubber mesh structure and damage the junction, that results a rubber hardness reduction. With the increase of the acrylonitrile content the rubber hardness decline, in turn, reducesd. The hardness of N18 and N26 decreased most rapidly in first 24h, and then the increase gradually flattened out over time; the change of N40 is approximate uniform decline.With the increase of the acrylonitrile content,the nitrile groupings(-CN) in NBR increases and molecular inter-atomic forces increases. In the process of swelling, the damage of cyclohexane to rubber junction reduced and the proportion of hardness decreased less.

In figure 2 (b), all the rubber hardness increased after drying, with the extension of swelling time, the increasing hardness rate of N18 increased. N26 and N40 hardness changed approximatively as a straight line. Rubber hardness increase after drying, because the plasticizer is pumped out from NBR. As time changes, the plasticizer proportion of N18 which pumped out continuously increased. And the plasticizer proportion of N26 and N40has a poorer correlation to swelling time . With the increase of the acrylonitrile content, the force between plasticizer and rubber matrix get stronger and difficult to be pulled out.



（a） swelled NBR （b）dried NBR

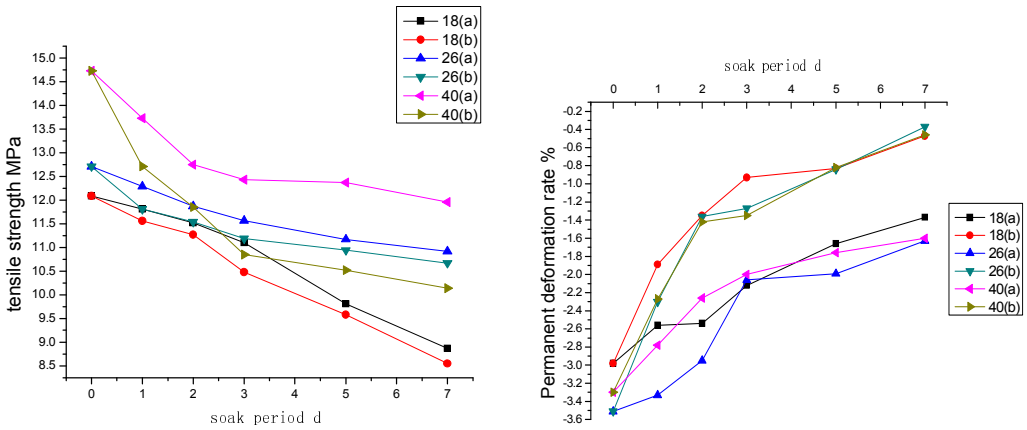
Fig.2 The Shore Hardness Change Rate Of Swelled And Dried Nbr In Different Soak Periods

Mechanical Properties

Tensile properties is one of the most important measure to the physical properties of rubber. Figure 3 shows the samples change rate curve of tensile strength, permanent deformation in different swelling and drying time. From figure 3 (a) it can be seen clearly that with the extension of soaking time the tensile strength of three kinds of rubber after cyclohexane soaked is on the decline by the mechanics performance reduction. According to the theory about the number of net chain that have been put forward by Flory[13], the reason is that the number of effective mesh chain in NBR declined after swelling. After cyclohexane spread into rubber, the rubber net structure has changed; physical junction fractured; net structure appeared cracks and pores, that makes mechanical performance of NBR felled sharply.

To three kinds of rubber the tensile strength is on the decline with the extension of swelling time. But at corresponding time points, with the increase of the acrylonitrile content, the tensile strength increased. With the increase of the acrylonitrile content,the nitrile groupings(-CN) in NBR increases and molecular inter-atomic forces increases it makes the tensile strength increase. After drying three kinds of rubber tensile strength are all lower than the swelling value. On the first two time points the tensile strength increases with the increase of acrylonitrile content; but on the other time points,

N26 has the largest tensile strength, N18 is minimum and N40 is in the middle but has a smaller gap with N26 . It is mainly because after swelled and dried, rubber auxiliaries were pulled out, hardness increased, elasticity and tensile strength decreased. N26, N40 due to acrylonitrile content increases, the cohesive force between the molecules increased; the extract increase less after 48 hours, so the both tensile strength are similar after two days.



（a） （b）

Fig.3 The Mechanical Properties Change Of Swelled And Dried Nbr In Different Soak Periods

In Figure 3 (b) it shows permanent deformation rate of three kinds rubber presents a rising trend with the extension of swelling time, which shows the rubber rebound ability and the ability to resist deformation is poor. There are many factors can influence the rate of the permanent deformation such as rubber net structure between the molecules; molecular force; displacement between the molecules and so on. The springback ability of the original NBR, N18 is the worst, N40 is better and N26 is the best.

With the increase of the acrylonitrile content, nitrile groups (-CN) increases, the molecular spacing decreases, and conducives to the crosslinking reaction.A high degree of crosslinking can reduce the displacement and stress relaxation of rubber molecules .It can also keep a high the deformation recovery capability and a smaller permanent deformation rate.But N40 has a exorbitant acrylonitrile content and polarity is too large. The movement of macromolecular chain is limited.It influenced the crosslinking reaction of free radicals, and the crosslinking density decreased. So the permanent deformation rate will be lower than N26 on the absolute value. With the increase of soaking time, N18 also has a poor resilience, the permanent deformation of N26 and N40 are close to each other. This phenomenon is attributed to the cyclohexane that diffused into the grid structure of NBR ; destroyed the rubber crosslinking structure ; declined the crosslink density of N26.But the macromolecular motion constrained problem of the N40 has been solved. So that the rate of permanent deformation is constantly close to N26 and N40.

After soaked and dried the NBR rates of permanent deformation are on the rise by swilling time. Initially N18 has a poor resilience than other NBR and the permanent deformation rate of N26 is close to N40. On the fifth day, all the NBR specimen after soaked and dried have poor resiliences ,the rates of permanent deformation is approach to each other. The change rate of swelling increases rapidly in the first day then gently, until balance is reached. The grid structure of NBR has the same variation tendency, So in the Figure 4 (b)there has three curves of the dried NBR.

Summary

In this paper we have investigated the Swelling phenomenon of three NBR with different acrylonitrile contents in cyclohexane medium, the influences of physical and mechanical properties with diffrent acrylonitrile contents is analyzed. The results show that the mass, hardness, tensile strength, permanent deformation rate of three kinds NBR are affected obviously by cyclohexane. At the same time, performance differences of the three kinds NBR are related closely to the containing of the acrylonitrile content.

Acknowledgement

It is a project supported by National Natural Science Foundation of China (50875178) and Shenyang municipal science and technology plan projects(F13-077-2-00).

References

[1] Wang Shi-jie, Li Qin compiled. Technology and design for progressing cavity pump system [M].Beijing: Metallurgy Industry Press, 2006.

[2] Wang Zuo-ling, Zhang Zhuo-ya compiled. Test method for rubber[M].Beijing: Chemical Industry Press, 2012.

[3] Yang Qing-zhi. Modern technology of rubber[M]. Beijing:China Petrochemical Press,2007

[4] Wang Shijie,Li Fubao, Sun Shuhui1 et al. Research on the On- line Monitoring Technology for Progressing Cavity Pumping(PCP) Operation[J]. China Mechanical Engineering. 2005. 15(14): 1276-1279

[5] Shi Baoguang,Chen Hui,Zhang Lianshe et al.Application of screw pump and its matching technology to heavy oil production[J].OGRT,1998,5(3):71-74

[6] Wiltse, D J, and B A Weir. Eliminating Sucker Rod Couplings Can Reduce Progressing Cavity Pump Operating Costs[J]. SPE International Heavy Oil Symposium. 1995, 6 : 19- 21.

[7] Chen De-chun, Li Zhao-wen and Wu Xiao-dong .Kinematic Model for Rod Strings of Screw Pump in Surface Drived Pumping System[J].Journal of the Univer sity of Petroleum.1999, 23(1) : 42- 44

[8] Chen Yu-xiang, Wang Xia, Zhou Song et al. Analyses on Improving the Life of the Screw Pump's Stator Rubber[J] . Drainge and Irrigation Machinery, 2005, 23(4):6- 9.

[9] L I Xiao-qiang, Tang Bin. Characteristics of Soft NBR and its Compounding Technique[J]. Special Purpose Rubber Products, 2004, 25(2) : 1- 4.

[10] Wang Zuo-ling. Nitrile Rubber and Hydrogenated Nitrile Rubber [J]. World Rubber Industry, 2005, 32(10) : 17- 22.

[11] Schreib er H P, Ddg endeleC,Bat aill eP. Component interactions and properties of cross linked vinyl systems[J]. Polymer Engineering and Science, 1990, 30 (16) : 981 -988.

[12] C Wang, et al. Study on heat-resist ant property of adhesive/carbon- carbon composites joints[J]. International Journal of Adhesion & Adhesives, 2006, 26: 206- 211.

[13] Flory,p.j. Principles of Polymer Chemistry[M].Ithaca, N.Y.: Cornell Univ. Press, 1953

Advanced Materials Research Vol. 936 (2014) pp 1948-1952
© (2014) Trans Tech Publications, Switzerland
doi:10.4028/www.scientific.net/AMR.936.1948

Effect of Reserved Texture on Mechanical Properties of Cold Drawn Pearlitic Steel Wire

Lichu Zhou, Yufei Zhao, Feng Fang*

School of Materials Science and Engineering, Southeast University, Nanjing, 211189, China

*Fangfeng@seu.edu.cn

Keywords：pearlitic wire, texture, cold drawn

Abstract: In this paper, pearlitic steel wire with/without reserved texture were investigated with the help of mechanical test system, scanning electron microscope (SEM) and XRD. Experimental result shows that: Tensile strength of two wire are almost same. After cold drawn tensile strength of wire with reserved texture are higher than tensile strength of the without one. Before cold drawn, two wires have same microstructure of isometric pearlite and after drawing the wire with reserved texture has less shear deformed pearlitic colony. Intensity of <110> fiber texture in the wire with reserved texture are stronger than the without one at all strains. The stronger <110> texture mean the orientation of α-ferrite lamella were more closely and improve working hardening rate of pearlitic wire

Introduction

High strength steel wire was widely used in many fields, such as wire rope, tire cord, springs and suspension bridge cable[1]. Relative research[2-5] on deformation pearlitic wire focused on controlling microstructure to improve the tensile strength of steel wire have achieved a great deal of success that it have reported the tensile strength of cold drawn pearlitic steel wire have achieved 6.3GPa. Evolution of texture during drawing was also widely investigated[6,7] but there were no research on how the texture affect mechanical properties of steel wire. Recent studies[8,9], texture of α-ferrite in cold drawn steel should be reserved after austenite heat treatment. How is the effect of reserved texture on the cold drawing process should be focus on.

In this paper, deformed pearlitic steel wires with/without reserved texture was investigated. Effect of reserved texture on mechanical properties of cold drawn wire was discussed.

Experimental Procedure

Pearlitic steel wires used were produced by Sha-steel Group Company, PR China. The chemical composition of the wires were shown in Table1.

TABLE 1 COMPOSITION ANALYSIS OF EXPERIMENTAL STEELS (WT%)

C	Si	Mn	Cr	V	S	Fe
0.83	0.3	0.71	0.19	0.07	0.003	Bal.

After pickling and phosphating[10], hot-rolled wire rods (12mm and 5.5mm diameter) were successively drawn to a diameter of 5.1 mm with a total reduction of 82% and 14% (ie., ε=1.7 and 0.15).

Heat treatment of deformed wires were carried out in salt bath of 950℃ for 5 min, Wires were put into salt bath of 550℃ for 5 min at once. After in salt bath wires were cold in air to room temperature. After treatment, the wire drawn from 12mm have reserved texture and wire from 5.5mm have no reserved texture.

Tensile strength of this wires were tested by using a universal testing machine. This test were operating at a constant speed of 2 mm/min. Evolution of microstructure of cold drawn wires was examined using a FEI Siron-400 scanning electron microscope (SEM). Texture tested were used D-Max 2000 to test three pole figures calculated to integral pole figure. Using integral pole figure to calculate the intensity of <110> fiber texture.

Results and Discussion

Mechanical Properties

The tensile strength of wires as a function of true strain was presented in figure 1.

Tensile strength of wires increase with the increase of true strain from 0 to 3. Before drawing, this two steel wires with/without different reserved texture have almost same tensile strength. After cold drawing , tensile strength of steel wire with reserved texture are higher than the without one. Reserved texture improve working hardening rate of pearlitic wire.

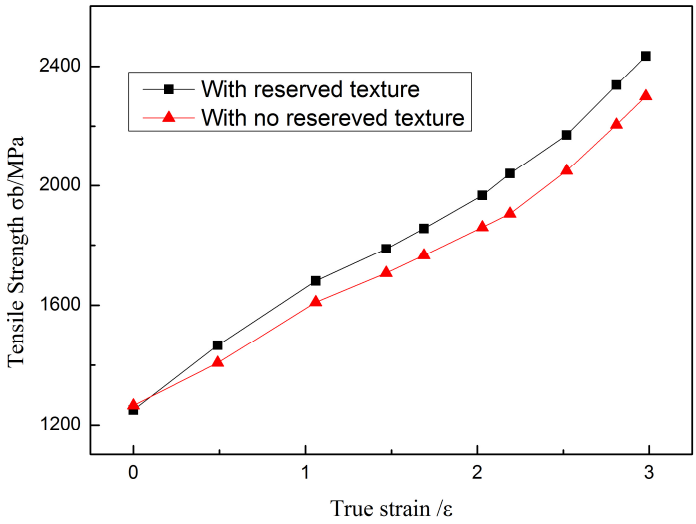
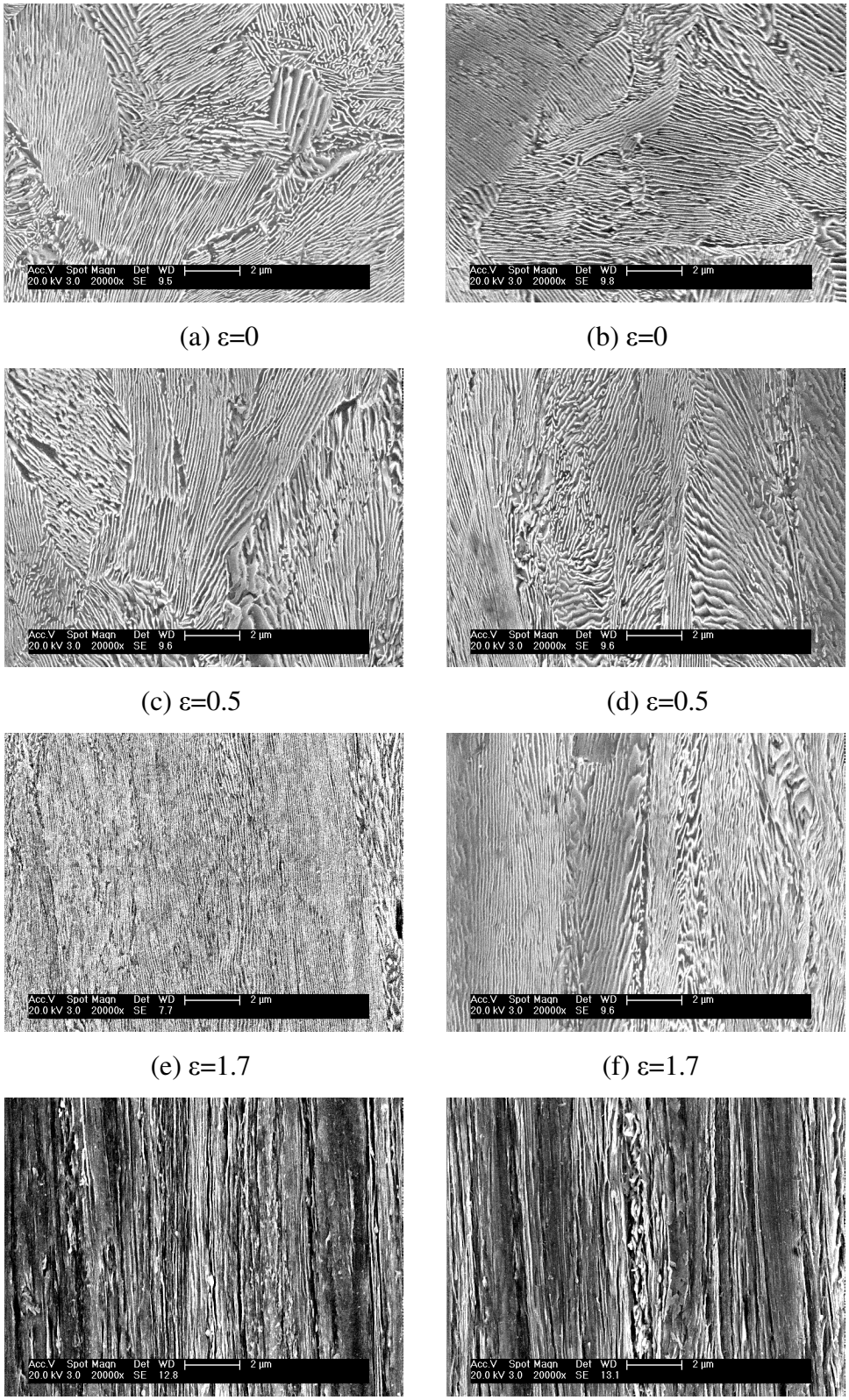


Fig.1. Relationship Between Tensile Strength and True Strain of Two Wires

Microstructure Evolution

Wires were observed from the longitudinal section as figure 2. Figure 2a,2b show before drawing, both of the two pearlitic wires' microstructure are same isometric pearlite. Lamellae of ferrite and cementite is complete and parallel to each other in one colony.

After drawing pearlitic lamella of wires thinned and rotated to be parallel to drawing direction. Pearlite have turned into fibrous microstructure after heavily drawing. Comparing microstructure of wires with and without reserved texture, as figure 2c and 2d show there were no visible different when at ε=0.5. There were more cementite lamella bent or fractured in wire without reserved texture than with one as figure 2e, 2f, 2g and 2h.



(a) ε=0 (b) ε=0

(c) ε=0.5 (d) ε=0.5

(e) ε=1.7 (f) ε=1.7

(g) ε=3 (h) ε=3

Fig.2 Microstructure of steel Wires after Cold Drawing 1st Column: With reserved Texture 2nd Column: Without Reserved Texture

Texture Analysis

Change of intensity of <110> texture in two wires were shown in figure 3. Figure 3 shows that intensity of <110> texture of wires increase with the increase of true strain from 0 to 1.69. Intensity of <110> texture of wire with reserved texture is higher than the without one. The evolution of

α-ferrite's texture in the two wires drawn to different strains was measured by using inverse pole figure measured in the drawn direction corresponding to the true strain of 0,0.49,0.93,1.69 as shown in figure 4. Comparing inverse pole figure of two wires, the α-ferrite's orientation in wire with reserved texture turn into <110> pole more quickly.

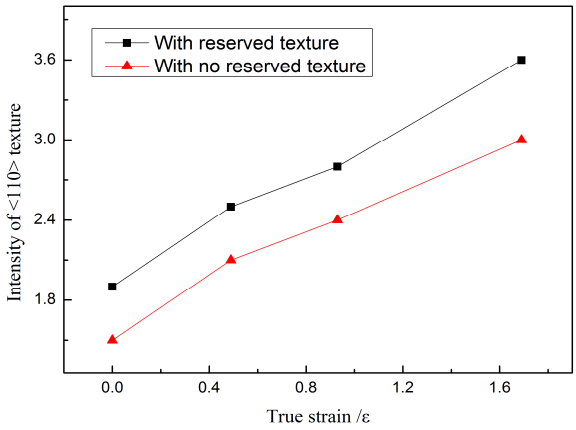
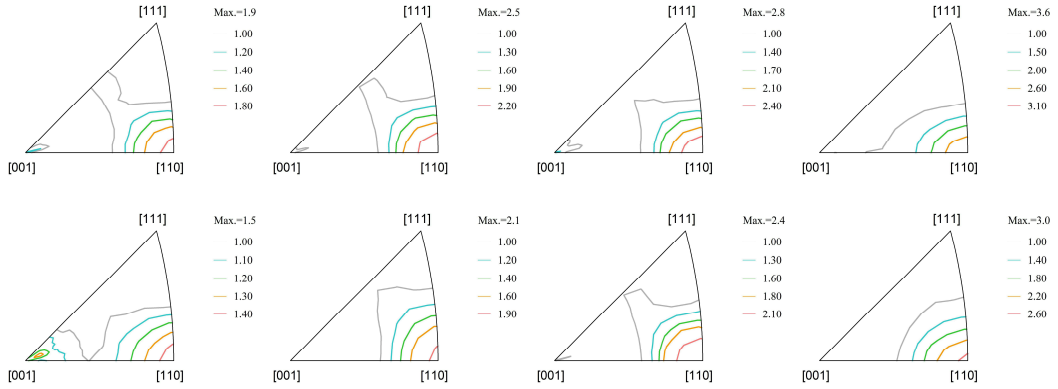


Fig.3. Relationship Between Textural Intensity and True Strain of Two Wires



(a)ε=0 (b) ε=0.49 (c) ε=0.93 (d) ε=1.67

Fig.4 Inverse Pole Figure of Two Wires in Different Strains. The First Line is the Wire With Reserved Texture and Second Line is the Wire with no Reserved Texture

Discussion

Reserved texture improve working hardening rate of pearlitic wire. Intensity of <110> texture in wire with reserved texture are stronger than the without one at all strain. Studies[3,6,11-12] have demonstrated that closely orientation of pearlite improve the mechanical properties. Microstructure of pearlite is composite structures of two phase: α-fe and cementite. Deformation of this two phase are more closely to composite materials of laminate structure. α-fe(soft phase) deform more than cementite(hard phase) when deformation was not heavily. If α-fe's <110> orientation were not in or near to the drawing direction the pearlitic colony must rotate to the direction. When α-fe's <110> orientation were nearly perpendicular to the drawing direction rotation will be difficulty, pearlitic colony were subjected high shear stresses. Cementite lamellae may bent or fracture. Fractured cementite cause stress concentration and become micro-crack resource when wire was subjected stresses.

Reserved texture make intensity of <110> fiber texture higher during drawing. Higher <110> textural intensity means there are more pearlitic α-fe's <110> orientation are closely to drawing direction. Less pearlite need rotate to deform, less cementite lamellae may bent or fracture and more pearlite may get thinning. It reduce shear deformation and improve the hard working rate of pearlitic wire.

Conclusion

1) Reserved <110> texture improve working hardening rate of pearlitic wire. After drawing, tensile strength of wire with reserved texture are higher than the without one at all strains.

2) Intensity of <110> texture of wire with reserved texture is higher than wire without reserved texture at all strains. It indicated orientation of pearlite near to drawing direction and reduce shear deformation of pearlite.

Acknowledgment

The authors would like to thank Prof.Fan Li in the Jiangsu Key Lab for Advanced Metallic Materials,Southeast University and Dr. Xianjun Hu in the Sha-Steel Group for the help of analysis.

This work was supported by Natural Science Foundation of China (grant no. 51371050), Natural Science Foundation of Jiangsu Province, China (grant no. BK2011616) and was partially funded by Jiangsu Province Industry-University strategic Research Project (grant no. BY2011144).

References

[1] M Zelin, Microstructure evolution in pearlitic steels during wire drawing. Acta. Mater. 50(2002) 4431-4447.

[2] F Fang, X.J Hu, B.M Zhang, Deformation of dual-structure medium carbon steel in cold drawing. Mat. Sci. Eng A-Struct. 583(2013) 78-83

[3] X.D Zhang, A Godfrey, N Hansen, X.X Huang, Hierarchical structures in cold-drawn pearlitic steel wire, Acta. Mater, 61 (2013) 4898–4909.

[4] F. Fang, X.J. Hu etc. Revealing microstructural and mechanical characteristics of cold-drawn pearlitic steel wires undergoing simulated galvanization treatment. Mat. Sci. Eng A-Struct. 547(2012) 51-54

[5] Y.J. Li, P. Choi, S. Goto, C. Borchers, D. Raabe, R. Kirchheim, Evolution of strength and microstructure during annealing of heavily cold-drawn 6.3 GPa hypereutectoid pearlitic steel wire. Acta. Mater. 60(2012) 4005-4016.

[6] X.J Hu, F Fang etc. Origin and mechanism of torsion fracture in cold-drawn pearlitic steel wires, J. Mater. Sci. 48(2013) 5528-5535..

[7] Zolotorevskii N Y, Nesterova E V, Rybin V V, et al. Micro-and macrotexture evolution during steel-wire drawing. Phys. Met. Metallorg+. 99(2005) 73-79

[8] I.Lischewski, G.Gottstein, Nucleation and variant selection during the α→γ→α phase transformation in microalloyed steel. Acta. Mater. 59(2011) 1530–1541

[9] X.Y Yao, H.B Huang, F Li, Texture of cold drawn and recrystallized high carbon steel wire. J. Southeast University. 40(2010) 1323.

[10] [10] F Fang, J.H Jiang, S.Y Tan etc, Characteristics of a fast low-temperature zinc phosphating coating accelerated by an ECO-friendly hydroxylamine sulfate. Surf. Coat. Tech. 204(2010) 2381-2385

[11] Y.D Liu, Q.W Jiang, G Wang etc, Influence of microstructures and textures on the torsional behavior of pearlitic wires. Journal of Materials Science and Technology. 21(2005) 357-360

[12] Y. Tomota, T. Suzuki, A. Kanie etc. In situ neutron diffraction of heavily drawn steel wires with ultra-high strength under tensile loading. Acta. Mater. 53(2005) 463-467.

Advanced Materials Research Vol. 936 (2014) pp 1953-1957
© (2014) Trans Tech Publications, Switzerland
doi:10.4028/www.scientific.net/AMR.936.1953

Microstructural and mechanical properties of 9%Ni steels used for the construction of LNG storage tanks.

Sara Hany [a,b,c,h*], Benoit Duponchel [a,d], Christophe Poupin [a,b], Antoine Abou Kais [a,b], Dorothée Dewael [a,e], Jean-Bernard Vogt [a,f], Jeremie Bouquerel [a,f], Hassine Kacem [g], Anne Mouftiez [g], Said Hariri [g], Mariana Milochova [c], Eugène Bychkov [a,c], Edmond Abi Aad [a,b,h]

[a] Université Lille Nord de France, 59000 Lille, France

[b] UCEIV, EA 4492, ULCO, 145 Avenue Maurice Schumann, 59140 Dunkerque, France

[c] LPCA, EA 4493, ULCO, 189A Avenue Maurice Schumann, 59140 Dunkerque, France

[d] UDSMM, EA 4476, ULCO, 145 Avenue Maurice Schumann, 59140 Dunkerque, France

[e] CCM, ULCO, 145 Avenue Maurice Schumann, 59140 Dunkerque, France

[f] UMET, UMR CNRS/USTL/ENSCL 8207, Bâtiment C6, 59655 Villeneuve d'Ascq, France

[g] Dept. Technologie de Polymères et Composites et Ingénierie Mécanique, Ecole des Mines de Douai 941, rue Charles Bourseul, BP 10838, 59508 Douai Cedex, France

[h] INNOCOLD, Institut Technologique du Froid, 145 Avenue Maurice Schumann, 59140 Dunkerque, France

*sara.hany@univ-littoral.fr

Keywords: Cryogenic Steels; 9%Ni Steel; structural studies; mechanical tests.

Abstract: The growing needs for energy combined with the will to reduce CO_2 emissions lead to the increase of the demand for liquefied natural gas (LNG), which will be stably available for many decades to come. Cryogenic materials used for the manufacture of the inner tanks for LNG storage are composed of 9% Ni steel plates with excellent low-temperature toughness, great ductility and crack resistance for a high safety level. To guarantee the reliability and safe operation of large-scale metallic structures exposed to cryogenic temperatures for extended periods, it is important to evaluate structural and mechanical properties of the metal base as well as the welded zone in their own operating conditions in order to prevent damages that could occur.

Introduction

The increase in energy consumption, as well as the predictable lack of oil and the rise of extraction costs, encourage manufacturers to find new energy sources. Liquefied natural gas (LNG) that can replace oil and allow the transition to a low carbon economy is one of them. Thus the use of liquefied natural gas as a clean energy source from the point of view of global environment and installation of LNG terminals are growing rapidly [1].

LNG represents the ideal solution to transport natural gas coming from distant fields towards markets where it is not feasible to construct a pipeline. LNG provides several advantages: It is a relatively clean energy neither toxic and non-corrosive, practical, with a reasonable calorific value, and finally approximately twice lighter than water. The environmental qualities of natural gas make it a fuel of choice. In vehicle fleets where the evaporation of LNG can be controlled appropriately, the LNG storage provides benefits over compressed natural gas in terms of compactness and tanks weight as well as flow of filling [1, 2].

Cryogenic materials used for the manufacture of the tanks for Liquefied Natural Gas (LNG) need to remain tough, ductile and crack resistant with a high level of safety. Steels with specific mechanical properties are required [3]. Thus The 9% Ni steel has been widely used around the

world as a material for the inner walls of LNG-tanks and pipelines because of its excellent cryogenic fracture toughness. The brittle fracture properties of the steel, which are closely related to the safety of structures, among others, has been extensively studied, and as a result, it has been made clear that the steel and its welded joints have sufficiently good brittle fracture properties for application to above-ground LNG tanks[3-7].

In this work, the effects of cyclic fatigue at very low temperature on mechanical and structural properties of 9% Ni steel were investigated. The structure and the chemical composition of the samples were determined by means of several techniques such as: Inductive Coupled Plasma – Atomic Emission Spectroscopy (ICP-AES), X-ray Fluorescence, X-ray Diffraction at low temperature, High Energy Synchrotron X-ray diffraction, ^{57}Fe Mossbauer Spectroscopy and Electron Paramagnetic Resonance. Mechanical tests were carried out at room temperature and at –196°C to evaluate the degradations of the mechanical properties of the 9% Ni steel, and its weld joints. Then, the topography of fractured surfaces was observed by Scanning Electron Microscope to identify the fracture modes. X-ray diffraction analysis was employed to reveal phase changes which could promote the degradation in the mechanical properties of these materials.

Materials and experimental procedures

The studied material is the 9% Ni steel (base and weld metals). This material is commercial grades used for LNG storage tanks supplied by Salzgitter Mannesmann (France).

The chemical compositions of 9% Ni steel base metal established on casting according to the material certification sheets supplied by the manufacturers as well as that on product determined by ICP AES (Inductively coupled plasma Atomic emission spectroscopy), X ray Fluorescence, Inert Gas fusion Infrared and thermal conductivity detection (LECO TC 436 used to determine O_2 and N_2) and (LECO CS 444 used to determine C and S) are given in Table 1.

For the cryogenic 9% Ni steel, the steel plates are processed by Quenching and Tempering (QT) heat treatment X8Ni9_QT640 in its initial state (according to the standard NF EN 10028-4): Hardening at 800°C; Soaking time: 1min. /mm, (minimum 15 minutes) then water Quenching and finally tempering at 600°C; Soaking time: 1min. /mm, (minimum 30 minutes) then air cooling.

The microstructure of the steel is a tempered martensite with residual austenite with high Ni-content. The presence of these phases in this material was confirmed by X-ray diffraction analyses (Fig. 1) (martensite peaks noted as M and austenite peaks noted as A), and ^{57}Fe Mossbauer Spectroscopy (Fig. 2).

Nine percent Ni steel for LNG storage tank are invariably joined by welding. The welding of these materials for LNG applications determines for a great deal the structural integrity.

The 9% Ni steel plates were welded with stick electrodes (SMAW). Consumable is a high nickel alloy ENi–Cr–Mo6 used for its ductility and its thermal expansion capacity.

The X-ray spectrum of 9% Ni steel weld metal (Fig. 1) shows an austenitic microstructure due to the high nickel content alloy used as a filler metal for the welding.

Table 1: Chemical composition of 9% Ni steel base metal.

Material	Mn	Co	Al	Cu	Cr	Ni	Mo	Fe	Ti	P	C	N	H	S	O
Chemical composition on product (Wt %)	0.546 ±0.03	0.044 ±0.002	0.034 ±0.002	0.047 ±0.002	0.029 ±0.001	8.955 ±0.448	0.015 ±0.001	90 ±0.42	0.02 ±0.001	0.003 ±0.0002	0.0499	0.0037	0.025 ±0.0013	0.0002 ±0.00001	0.0145
Chemical composition on cast (Wt %)	0.53	NC	0.048	0.06	0.04	8.99	0.01	NC	0.01	0.006	0.04	0.004	NC	0.001	NC

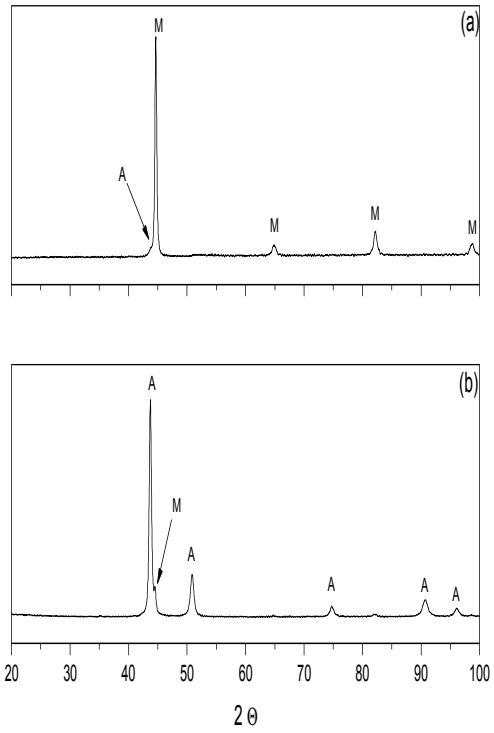


Fig. 1 XRD spectra of 9% Ni steel base metal (a), 9% Ni steel weld metal (b)

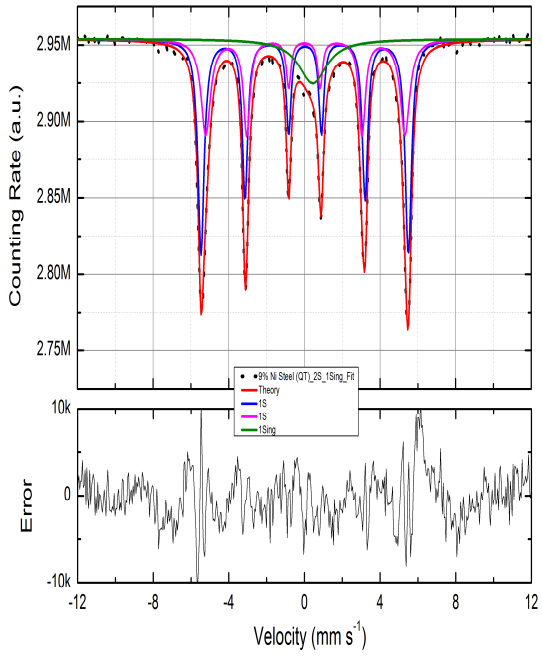


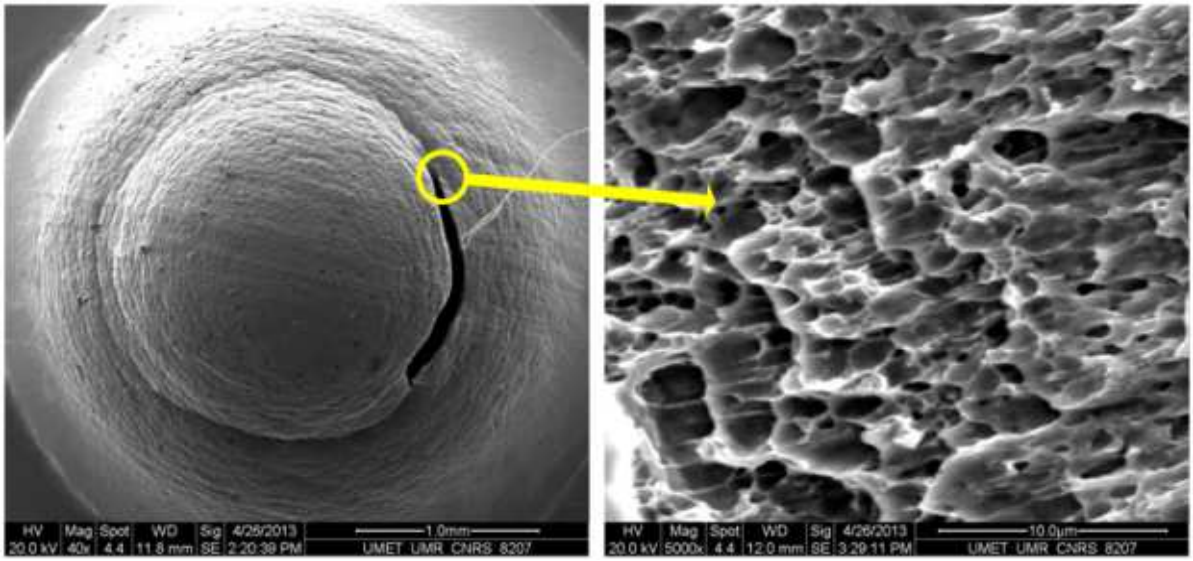
Fig. 2 Mossbauer spectra of 9% Ni steel base metal

The Small Punch Test (SPT) is a non-standard mechanical test. It has been developed to obtain mechanical properties (yield strength, ultimate strength, elongation, fracture energy, and toughness) of small regions, the quantity of which is limited or has been reduced (e.g. irradiated material). This type of test became attractive and provided interesting information on the deformation behavior, on the fracture, as well as on ductile to brittle transition or evolution of the mechanical properties due to the temperature, to an environment or to ageing [8].

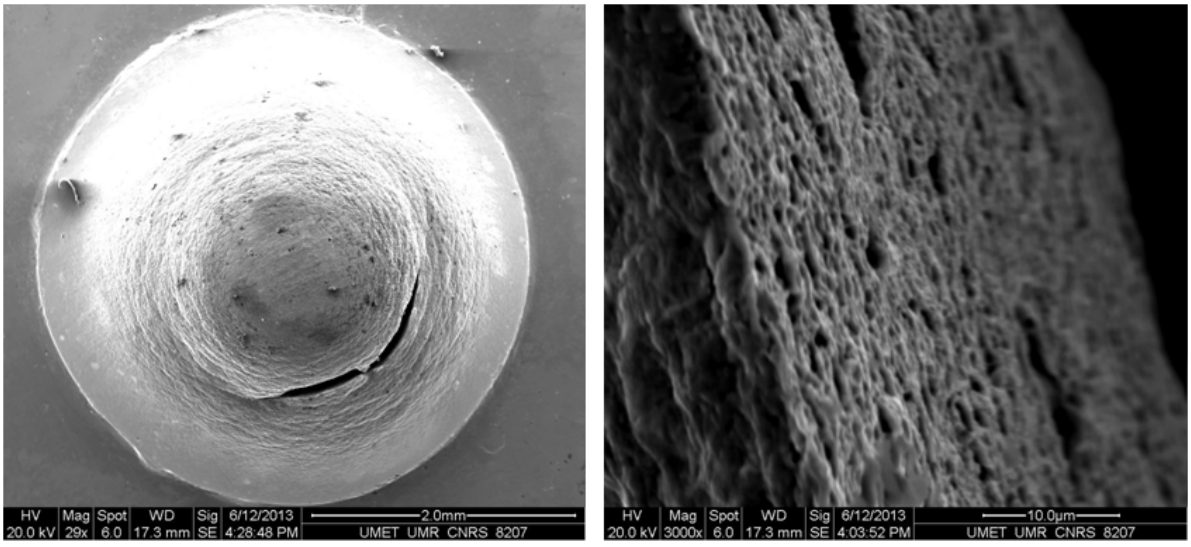
The SPT were performed at room T and at -196°C using an (MTS DY 35) tension / compression electro mechanical machine with a controlled cross-head speed of 0.5 mm/min. Load–cross-head displacement curves were recorded during the tests. The specimen has a squared shape (8mm). Before testing, the sample surfaces were mechanically polished with an automatic polisher (Phoenix 4000) using SiC paper up to 1200 grade until 500 (±20) μm thickness and a diamond suspension in an aqueous solution, in order to avoid effects due to the roughness of the surface. After mechanical tests, scanning electron microscope (SEM) observations were performed on a LEO 438VP SEM to determine the fracture appearance of the specimens. The fracture surfaces contain dimples typical of ductile rupture at room T and -196°C (Fig. 3). Furthermore, for all SPT specimens, cracking is circular or semicircular. These results are in agreement with a cracking mechanism due to the membrane stretching and with the observations mentioned for ductile fracture behavior [9–11].

The temperature decrease from room temperature to -196 ° C provides an improvement in the mechanical properties of the 9% Ni steel, without affecting its ductility.

No changes were observed on the mechanical and structural properties of 9%Ni steels after 6000 cycles of mechanical fatigue with a frequency of 1Hz at room T and at -196°C.



(a)



(b)

Fig. 3 SEM micrographs showing the fracture surfaces of the samples at room T (a) and at -196°C (b)

Summary

The 9% Ni steel is used in the cryogenic applications because of its good toughness at low temperature. Its mechanical properties increase with decreasing temperature, due to a greater consolidation.All tensile tests and small punch tests curves, as well as SEM observations, are in agreement with a ductile fracture behavior at room T as well as at -196°C.

References

[1] The outlook for energy: a view to 2040.Information on http://www.exxonmobil.com

[2] S Kumar, H-T Kwo , K-H Choi, W Lim, J H Cho, K Tak,I Moon , LNG: An eco-friendly cryogenic fuel for sustainable development, Applied Energy 88 (2011) 4264–4273.

[3] H.S. Shin, H.M Lee, M.S. Kim, Impact tensile behaviors of 9% nickel steel at low temperature, International Journal of Impact Engineering, 24 (2000) 571–581

[4] F. Lebel, E. Abi-Aad, B. Duponchel, I. P. Serre, S. Ringot, P. Langry, and A. Aboukaïs, Thermal ageing process at laboratory scale to evaluate the lifetime of Liquefied Natural Gas storage and loading/unloading materials, Materials and Design 44 (2013) 283–290.
[5] S. Wei and S. Lu, Effects of multiple normalizing processes on the microstructure and mechanical properties of low carbon steel weld metal with and without Nb, Material adn Design 35 (2012) 43–54.
[6] J. Hilkes, F. Nessen, Welding 9% nickel steel for liquefied natural gas (LNG) applications, Weld Cut 6 (2007) 103–112.
[7] S. Yoshie, C. Albertini, Y. Mentani, Impact tensile properties of nine percent nickel steel. Journal of the Society of Materials Science (Japan) 46 (1997) 1286–1292.
[8] C. Rodríguez, J. García Cabezas, E. Cárdenas, F.J. Belzunce, C. Betegón, Mechanical properties characterization of heat-affected zone using the small punch test, Welding Journal 88 (2009) 188s-192s.
[9] T. Misawa, T. Adachi, M. Saito, Y. Hamaguchi, Small punch tests for evaluating ductile–brittle transition behaviour of irradiated ferritic steels, Nuclear Materials 150 (1987) 194–202.
[10] M. Abendroth, M. Kuna, Identification of ductile damage and fracture parameters from the small punch test using neural networks, Engineering Fracture Mechanics 73 (2006) 710–725.
[11] I. Serre, J.B. Vogt, Liquid metal embrittlement of T91 martensitic steel evidenced by small punch test, Nuclear Engineering and Design 237 (2007) 677–685.

Advanced Materials Research Vol. 936 (2014) pp 1958-1962
© (2014) Trans Tech Publications, Switzerland
doi:10.4028/www.scientific.net/AMR.936.1958

Influence of Moisture and Temperature on Relaxation Function of Oil-paper Insulation in Traction Transformers

SHEN Han-lin [1, a] and LUO Hai-yan [1, b]

[1] Civil Aviation Flight University of China, Guanghan, China

[a] shenhanlin@163.com, [b] 122562354@qq.com

Keywords: Frequency Domain Spectroscopy, Transformer, Insulation, Relaxation function

Abstract: Relaxation function can well reflect the microscopic polarization mechanism of dielectric. In order to analyze the influence of moisture and temperature on relaxation function of oil-paper insulation, building a physical model of the oil-paper insulation system containing moisture and obtaining the expression of relaxation function. Setting up a testing device for the oil paper insulation dielectric spectroscopy in the laboratory, the parameter values of relaxation function expression were obtained according to test result by Fourier inverse transformation. The results show that the relaxation function containing three relaxation factors are more suited for the relaxation of oil-paper insulation containing moisture content and microscopic polarization mechanism, moisture and temperature have a significant effect on relaxation function.

Introduction

Oil paper insulation is the main insulation systems for traction transformer, and the micro water severely reduces the insulation performance of traction transformer, this will bring huge hidden trouble on rail transportation especially the safe operation of high-speed railway[1]. However, the traditional test method of traction transformer operation process is too complicated, and the measurement result varies. In recent years, using the frequency domain dielectric spectroscopy (FDS, Frequency Domain Spectroscopy) in evaluation of oil paper moisture content has been studied. However, researches focus on the content of moisture, temperature effects on the FDS characteristic parameters, but few reports are about the explanation of influence mechanism [2-4]. To analyze the mechanism of moisture and temperature effects on the dielectric spectrum, the equivalent physical model must be constructed with the micro water in oil paper insulation composite system. At present, the analysis on test results of the dielectric theory of Debye model, Cole-Cole model has been widely used, but it has limitation [5].

For example, the dielectric spectrum of Debye model is mainly applied to the polar liquid and solid medium, and it is only suitable for single phase insulation system [6]. To get general frequency-domain analysis methods, the expression of relaxation function must be first established. However, relaxation function is related to the composition, structure and environmental factors such as temperature and material, so it is not easy to find the general expression of [7] suitable for all occasions. FFT can decompose any real periodic function into the sum of sinusoidal signal with higher and higher frequency domain. Therefore, the mathematical properties of FFT transform could be used to obtain the relaxation function, through the combination of numerical analysis and FFT inverter commutation.

Theoretical basis

Relaxation function

In the flat electrode filled with a dielectric constant of ε, two ends are imposed of a sinusoidal voltage signal E (T), degree of dielectric polarization and loss in different frequency AC electric field can be described with micro relaxation function. Macroscopic representation is a complex dielectric constant (or complex capacitance). Document [6] establishes the relationship between the two, as is shown in the type (1) and (2).

$$\varepsilon'(\omega) = \varepsilon_\infty + (\varepsilon_s - \varepsilon_\infty)\int_0^\infty \varphi(t)\cos\omega t dt \quad (1)$$

$$\varepsilon'(\omega) = (\varepsilon_s - \varepsilon_\infty)\int_0^\infty \varphi(t)\sin\omega t dt \quad (2)$$

In which, ε_s is static relative permittivity, ε_∞ is the optical dielectric constant, ε' is the real part of permittivity, representing polarizability of materials, namely, the relative dielectric constant; ε'' is the imaginary part of complex permittivity, representing dielectric loss of materials. $\varphi(t)$ is the time expression of the relaxation function , ε' and ε'' are dependent on the function. By using the Fourier transform, the test results in the frequency domain can be transformed in time domain, thus the relaxation function can be obtained.

The physical model of oil -water composite system

Head pressure: 10MPa; Column Temperature: 40℃initially, 10minites later, raise to 60℃at speed of 5℃/min; Carrier Gas Flow Rate: 10ml/min; Injection Volume: 1ml in quantitative tube.

Oil paper insulation system is a two-phase insulation system, which can be regarded as combination of a plurality of capacitor and resistor. If the system contains "free water", it can be equivalent to a three-phase heterogeneous model, as shown in figure 1. The physical model consists of equivalent sery-wounded circuit containing three [C-G] loops; it has three relaxations, from which the corresponding relaxation function from the physical model can be concluded as:

$$\varphi(t) = \frac{1}{\tau_1}e^{-k_1 t} + \frac{1}{\tau_2}e^{-k_2 t} + \frac{1}{\tau_3}e^{-k_3 t} \quad (3)$$

In which τ_1, τ_2, τ_3 respectively represent the insulating paper, transformer oil and water relaxation time.

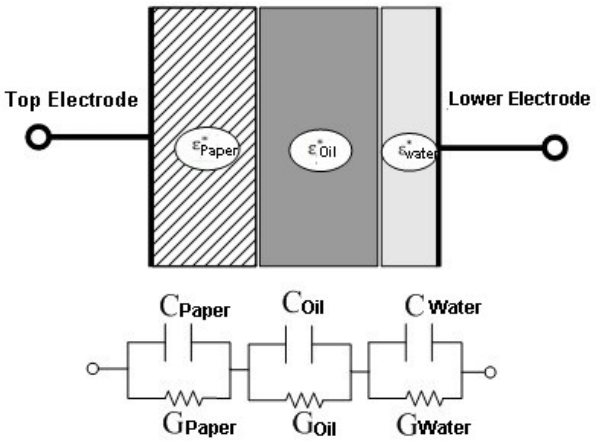


Fig.1The equivalent three-phase insulation system model of oil, paper and water

Experiment

Experimental materials

Insulating paper: 0.3mm ordinary cellulose insulation paper

Insulating oil: 25# naphthenic transformer oil

Experimental procedures

After shaping insulating paper (140mm*140mm), put it in the "WD841-2" type electric blast oven; keep it for 2 to 3 days at constant temperature of 120 ℃and dry it. Then put sample indoors, with the purpose of natural absorption of moisture in the air. By Karl Fisher titration, insulating paper samples with water content 0.98%, 2.03%,3.11% and 4.16%can be obtained, and then place them in transformer oil (12ppm less than the water content in oil). When micro water balance in oil paper combination insulation is reached, conduct FDS test.

Test results and analysis

Effect of micro water on the relaxation function

In order to study the effect of micro water on the relaxation function, oil paper insulation electric frequency spectrum with micro water content 0.98%, 2.03%, of 3.11% and 4.16% are tested below 50 ℃, as shown in Figure 3.

By using the FFT transform, curve fitting of the real and imaginary parts of the complex dielectric constant , and then obtain relaxation function through the FFT transform, the parameters of a value in an expression are shown in table 1. Put the relaxation function into type (1) and (2), get the function expression of frequency domain $\varepsilon'(\omega)$ and $\varepsilon''(\omega)$, as shown in Figure 3 (solid line). As can be seen from the graph $\varepsilon'(\omega)$ and $\varepsilon''(\omega)$ results are agreed with the test value, indicating that the relaxation function expression constructed by physical model can reflect dielectric relaxation in oil paper insulation system containing micro water. As can be seen from table 1, with the increase of water content, three kinds of dielectric relaxation time increase, that is mainly because under applied electric field. There is a close relationship between strength and interfacial water molecules concentration polarization, the higher moisture content is , stronger ability of induced polarization of oil and paper, interfacial polarization strength increases, the corresponding relaxation time is longer. When micro water content is the same, because the water molecules has the advantages of small size, polarization ability is high, under the action of the electric field, polarization is very likely to happen., relaxation time （τ_3） is minimum ; cellulose molecules are polar molecules, but because of large volume, polarization requires a long time, the relaxation time （τ_1） is slightly longer; transformer oil is a weak polar molecules, polarization is less influenced by electric field, therefore, relaxation time （τ_2） is maximum.

Tab.1Parameter values of relaxation function at different moisture content

Water	τ_1	k_1	τ_2	k_2	τ_3	k_3	R^2
0.98%	17.2622	1.401	159.9744	2.372	0.0656	0.0116	0.9836
2.03%	42.2297	1.808	607.1645	2.215	0.0859	0.1427	0.9921
3.11%	853.2423	2.852	17241.379	3.092	0.1289	0.3278	0.9894
4.26%	4545.454	3.257	31250.000	2.938	0.2558	0.2705	0.9833

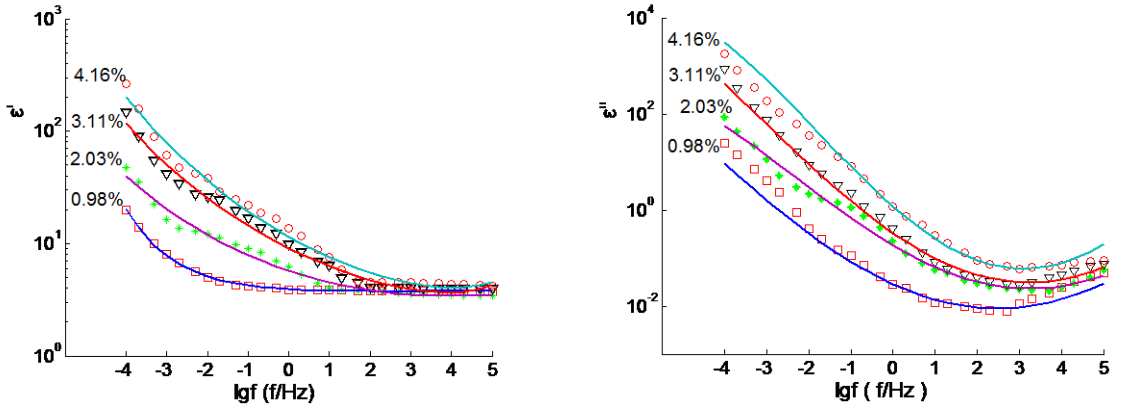


Fig.2Test value and calculated value of ε' and ε'' at different moisture content

Effect of temperature on the relaxation function

In order to study the influence of temperature on the relaxation function, dielectric power spectrum of oil paper insulation is tested under the temperature of 10 ℃, 30 ℃, 50 ℃, 70 ℃,when the micro water content of 2.03%, as shown in Figure 4. Using the same principle in 3.1, the relaxation function values can be obtained at different temperatures (as shown in Table 2) and the function expression the frequency domain $\varepsilon'(\omega)$ and $\varepsilon''(\omega)$ could also be obtained. (As shown in Figure 4 (solid line)). We can see from table 2, oil and paper relaxation time （τ_1 and τ_2） increases

as the temperature raises, the water molecular relaxation time （τ_3） decreases with the increase of temperature. That is mainly because relationship between the dielectric relaxation strength （$\Delta\varepsilon$） and temperature (T) is as shown in formula (4):

$$\Delta\varepsilon=\frac{a}{T}g_r(T)\mu_{eff}^2 \tag{4}$$

In which, A is a parameter independent of temperature, $g_r(T)$ is the strength of molecular interactions, and is related to the temperature, μ eff is the effective dipole moment, the temperature has little influence on it. Transformer oil molecules and cellulose have large volume, in a certain temperature range; we can take B and C as a fixed value. Therefore, with the increase of temperature, the oil molecules and molecules of cellulose transformer dielectric relaxation strength is enhanced, the corresponding relaxation time decreases. Water molecules is with small size, and strong polarization ability, when the temperature increases, thermal motion of molecules intensifies, thus it weakens the interaction forces between molecules, i.e. $g_r(T)$ is reduced, leading to water dielectric relaxation strength weakened, but increased the relaxation time.

Tab.2Parameter values of relaxation function at different temperature

Temp.	τ_1	k_1	τ_2	k_2	τ_3	k_3	R^2
10℃	352.1582	1.296	2710.8326	0.01247	0.0084	0.0239	0.9965
30℃	107.9132	0.4946	1429.4820	0.02085	0.0605	0.0219	0.9863
50℃	42.2297	0.808	607.1645	2.215	0.0859	0.1427	0.9804
70℃	4.6514	0.2126	493.2861	0.3294	0.1036	0.2261	0.9772

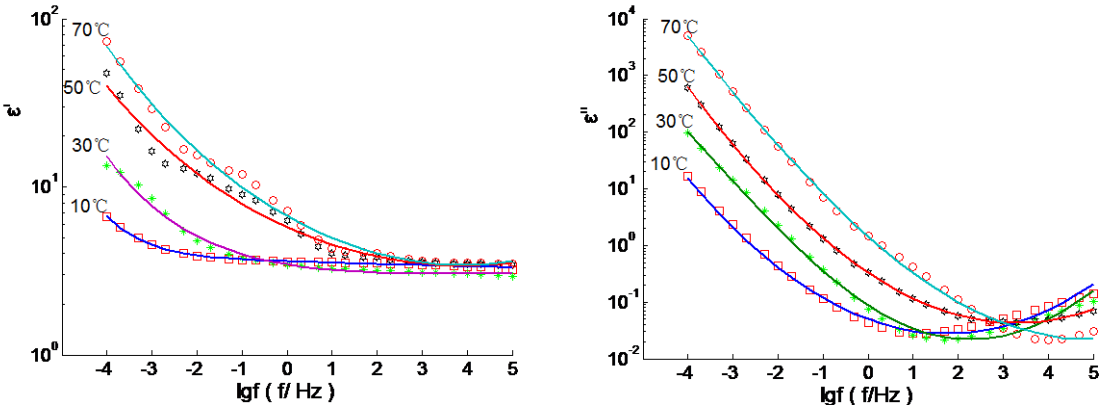


Fig.3 Test value and calculated value of ε' and ε'' at different temperature

Conclusion

(1) The expression of relaxation function established from three relaxations, can reflect the traction transformer oil paper insulation relaxation containing water and microscopic polarization mechanism, an association exists between the relaxation function and the micro water content and temperature.

(2) In the same temperature, insulation paper, transformer oil and water relaxation time gradually increase with increasing water content.

(3) When micro water content in oil paper insulation is the same, insulating paper and transformer oil relaxation time decreases with the increase of temperature, moisture of the relaxation time increases with the increase of temperature.

References

[1] Y.Du，M.Zahn，B.C.Lesieutre，et al．Moisture Equilibrium in Transformer Paper-Oil Systems[J]．IEEE Electrical Insulation Magazine，1999，15(1)：11-20．

[2] Blennow J，Gubanskism．Filed Experiment with Measurement of Dielectric Response in Frequency Domain for Power Transformer Diagnostics[J]．IEEE Transaction on Dielectric and Electrical Insulation，2006，21(2)：681-688．

[3] Liao Ruijin. Frequency domain dielectric spectrum characteristics of simulation and Experiment Study on transformer oil paper insulation [J]．Chinese Journal of Mechanical Engineering，2010，30(22)：113-119．

[4] I.Fofana，H.Hemmatjou，F.Meghnefi，et al．On the Frequency Domain Dielectric Response of Oil-paper Insulation at Low Temperatures [J]．IEEE Transaction on Power Delivery，2010，17(3)：799-807．

[5] Shen Hanlin. Research on the key technology of oil immersed transformer state detection based on recovery voltage method [D]. Southwest Jiaotong University, China，2012.

[6] Zhao Kongshuang．Method of dielectric spectroscopy and its application [M]．Chemical Industry Press, China，2008：49-51．

Advanced Materials Research Vol. 936 (2014) pp 1963-1968
© (2014) Trans Tech Publications, Switzerland
doi:10.4028/www.scientific.net/AMR.936.1963

Influence of Si Content on the Characteristics of Al-Zn-In-Mg-Ti Sacrificial Anode

Shusen Wang[1, a], Chenghao Liang[1,b], Naibao Huang[1,c]

[1]Transportation Equipments and Ocean Engineering College, Dalian Maritime University, Dalian 116026, China

[a]13604118437@139.com,[b]lchenghao@126.com,[c]hnaibao@163.com

Keywords: Aluminum alloy.Sacrificial anode.Microstructure.Electrochemical characteristics.

Abstract: The influence of Si on the corrosion behaviour of Al-Zn-In-Mg-Ti alloy was investigated by the microstructure observation and electrochemical measurements in order to improve its corrosion non-uniform and electrochemical properties. The results show that the current efficiency of Al-5Zn-0.02In-1Mg-0.05Ti-0.09Si (wt.%) alloy corroded uniformly reaches 92%. It presents the property of low resistance and high capacitance. While the Si content exceeds 0.12 wt.%, the resistance of active dissolution increases gradually. The current efficiency decreases obviously. The results indicate that the electrochemical characteristics and corrosion uniformity can be improved significantly after adding 0.09 wt.% Si into Al-Zn-In-Mg-Ti alloy.

Introduction

Nowadays, aluminum alloy sacrificial anode materials have been widely used in anti-corrosion protections for all kinds of ships, oil platforms and subsea pipelines [1], because it is light, cheap and with large capacity. Aluminum ingot usually contains many kinds of impurities, such as iron, silicon and copper, etc. Some researchers hold that these impurity elements have negative influences on the performance of aluminum alloy anode [2,3]. Because of the excellent comprehensive performance in seawater and no need of heat treatment, Al-Zn-In series of alloying became one of the most popular materials for aluminum alloy sacrificial anode [4,5]. And it has become an arrestive research to improve the electrochemical properties of Al-Zn-In-Mg-Ti alloy by adding different elements [6,7]. Si is the most common impurity in Al-Zn-In series anode. The solubility of Si is very small in aluminum and it is nearly zero at room temperature. There is only few Si in the solid solution, most of them exists in the second phases or forms intermetallic compounds with other impurity elements. Si impurities bring cathode phases which aggravate the hydrogen evolution self-corrosion and reduce the current efficiency of aluminum alloy sacrificial anode. So, Ponche, Horst [8] and Sakano [9] have defined a primary limitation on Si impurity content in Al-Zn-In series anode through their study. And some corresponding provisions have been made for Si impurity content in Al-Zn-In series anodes used in seawater [10,11] at home and abroad. But not all impurities are harmful, they also have some advantage. Reduction in density and thermal expansion coefficient, improvement in hardness, ambient temperature mechanical properties and wear resistance along with an excellent castability can be achieved by addition of Si to aluminum alloy [12-14]. The aim of the present work is to improve the corrosion non-uniformity and electrochemical performance of Al-Zn-In-Mg-Ti anode by adding a suitable Si content.

Experimental materials and Methods

According to aluminum ingots' impurity content in the preparation of Al-Zn-In series sacrificial anode, Al-5Zn-0.02In-1Mg-0.05Ti-XSi-0.10Fe-0.01Cu (wt.%) was designed and applied, the values of X in 1#-4# samples were 0.06, 0.09, 0.12, 0.15 (wt.%).

According to DET NORSKE VERITAS (DNV) RP B401 "Cathodic Protection Design" [11], the accelerated experiment that can test and measurement the work potential and the actual capacitance of the sacrificial anode was applied. The corroded samples were observed by scanning electron microscope (SEM) after constant potential corrosion applied -0.9 V at 30 ℃ for 3 h. EIS measurements were carried out with three electrodes system by using VMP3 workstation. Working electrode was aluminum alloy, reference electrode was saturated calomel electrode (SCE), auxiliary electrode was Pt electrode and working area was 1 cm^2. Testing medium was the natural seawater

from Bohai Sea, temperature was 22 ± 1℃. For electrochemical impedance spectroscopy (EIS) measurement, samples were immersed for 48 h and expressed 10 mV disturbances in the frequency range of 10^{-1}-10^{5} Hz.

Results and discussion

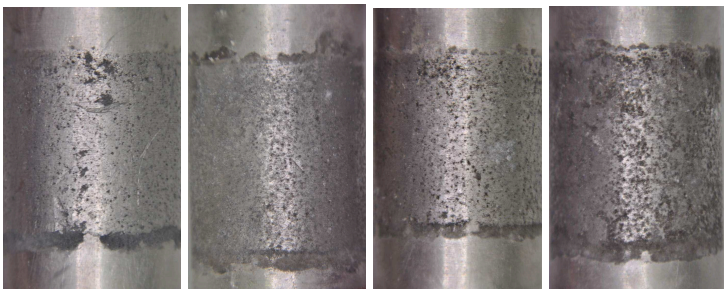
Anode current efficiency

Table 1 presents electrochemical performances of 1#-4# samples. The working potential of sample 1# was negative, but the actual capacitance and current efficiency were only 2364.05 $A \cdot h \cdot kg^{-1}$ and 82.43% because of microstructure non-uniformity. Many shiny particles considered to be aluminum by energy spectrum test were found in sample 1# corrosion products. A mass of mechanical loss leaded to the lowest current efficiency. The potential of sample 2# fluctuated slightly. The actual capacitance was 2640.50 $A \cdot h \cdot kg^{-1}$ and the current efficiency reached 92.05%. While the Si content exceeded 0.12 wt.%, the anode current efficiency decreased obviously. Si can refine grains and trap Fe impurities to form Al_2Fe_3Si which is harmless to anode's potential. Added Si as non-spontaneous nucleations which fine grains in crystallization process can reduce the current efficiency loss caused by grains dropping. The activation is from active elements as solid solution in dissolution process. The finer grains are, the more uniformly active elements can distribute in the alloy, which indicates that the aluminum anode has dissolved more uniformly. The moderate addition of Si is helpful to reduce galvanic corrosion and the anode potential to a certain extent, which means that the cathodic protection property will be improved [15]. Due to the low solubility of Si in aluminum alloy, the excess Si segregates on the grain boundaries is in free status, which causes the grain-boundary attack in the poor Si region near grain boundaries. Besides, the excess Si could form the cathode phase (relative to the aluminum substrate) with Fe impurities. The difference of electrochemical properties lead to alloy self-corrosion, which reduce the anode efficiency [16]. As indicated above, aluminum alloy can achieve high anode current efficiency by adding 0.09 wt.% Si.

The corrosion morphology images of samples are shown in Fig. 1. Corrosion products which adhered to sacrificial anodes almost fell off after acid etching. Sample 1# presented non-uniform corrosion obviously. As Si increases, sample 2# had a general corrosion tendency. The depth and width of pits were uniform and moderate on sample 2# surface which had excellent corrosion feature. There were some deeper pits and a few severe corrosion areas on sample 3# surface. Its integral dissolution morphology was good. The pits of sample 4# whose surface was uneven were further deeper, which indicates that non-uniform corrosion had been intensified. To conclude, a moderate addition of Si can improve the casting property of aluminum alloy and reduce casting defects. Sample 4# presented the excellent dissolution morphology and continuous protection performance by adding 0.09 wt.% Si. Not all impurities are harmful, they also have some advantage. Si can raise the recrystallization temperature and refine grains in high purity aluminum [12,13,17]. It can also improve the mechanical property at high temperature (hot strength) and wear resistance of aluminum alloy [18], etc. The use-type of sacrificial anode material is as-cast that has defects appear usually. These defects lead to the degradation of electrochemical performance and the non-uniform dissolution on alloy surface. Both the crystallization latent heat and the heat release of Si are big. Added Si can bring the excellent alloying liquidity that makes alloying elements having enough time to dissolve into matrix. The small shrinkage and expansion coefficient of Si cause defects such as shrinkage porosity and shrinkage cavity, etc., which indicates the casting property and microstructure uniformity of aluminum alloy are improved. It becomes a practical way to improve the comprehensive mechanical properties of Al-Zn-In-Mg-Ti anode by adding 0.09 wt.% Si.

TABLE 1 ELECTROCHEMICAL PERFORMANCES OF 1#-4# SAMPLES

No.	Working potential ($-V_{SCE}$)	Open circuit potential ($-V_{SCE}$)	Actual capacitance ($A \cdot h \cdot kg^{-1}$)	Current efficiency (%)
1	0.928~0.947	0.942	2364.05	82.43
2	0.918~0.935	0.938	2640.50	92.05
3	0.919~0.933	0.936	2618.15	91.26
4	0.912~0.942	0.933	2580.75	89.94

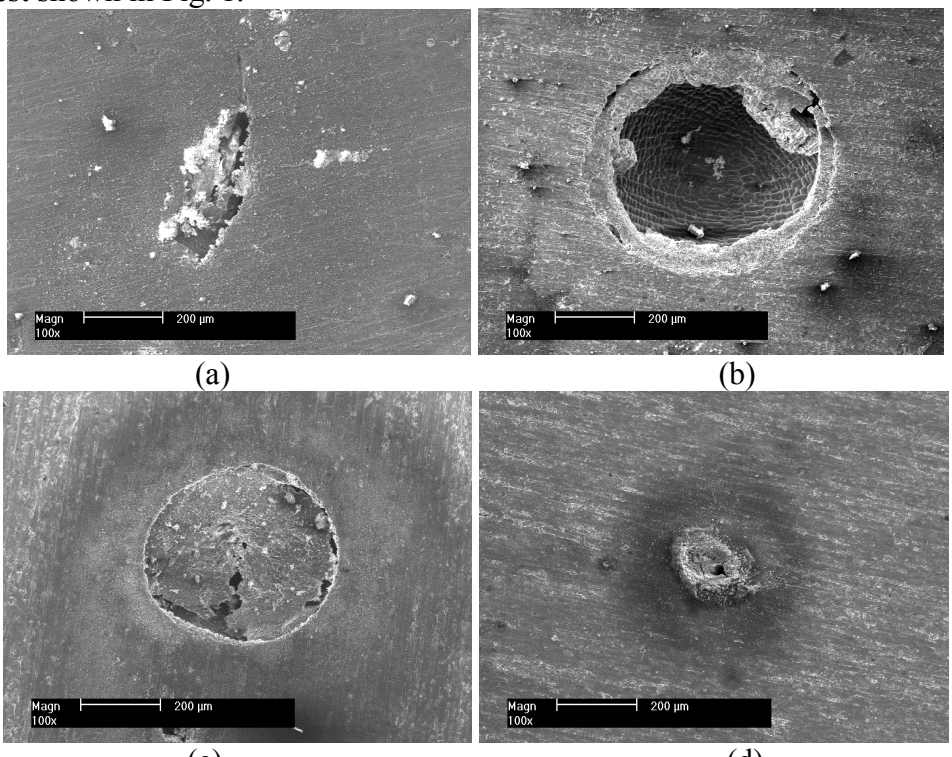


(a) (b) (c) (d)

Fig. 1 Sample 1#-4# macrophotography(a)Sample 1# (b)Sample 2# (c)Sample 3# (d)Sample 4#

Corrosion Morphology analysis

The SEM pictures are shown in Fig. 2. It is found that the crevice corrosion appeared and grains fell off mechanically on the sample 1# surface because of many defects of organization and structure. Owning to the good microstructure uniformity and dissolution-precipitation mechanism, the pit hole of sample 2# expanded to surrounding gradually, which means that the anode has a tendency toward general dissolution by adding 0.09 wt.% Si. Due to the excess Si blocking the formation of amalgam, the pore size of sample 3# decreased slightly with respect to that of sample 2#. And the orifice was covered with the passive film formed by corrosion products and oxide, which indicates that the dissolution of sample 3# tended to inside. However, the deep pit whose orifice was narrow and small appeared on the sample 4# surface. This phenomenon showed that the excess Si impurities stop the dissolution-precipitation proceeding continuously. The pitting corrosion tendency of sample 4# was enhanced, and the ability of uniform corrosion declines. Above results were corresponding to those of accelerated test shown in Fig. 1.



(a) (b)

(c) (d)

Fig. 2 SEM images of 1#-4# samples(×100) (a)Sample 1# (b)Sample 2# (c)Sample 3# (d)Sample 4#

EIS measurements

Nyquist graphs of 1#-4# samples in seawater are shown in Fig. 3. Aluminum alloy anodes in seawater present the single capacitive reactance arcs which are squashed arcs in the high frequency region and linear in the low frequency region. The curves show the change of resistance in the high frequency region and the electrochemical reaction charge transferring resistance's change. As Si content increases, the diameters of capacitive reactance arc turn to long, which indicates that the impedance of electrochemical reaction increases. So the impedances of samples increase and the electrochemical activity of samples are weakened.

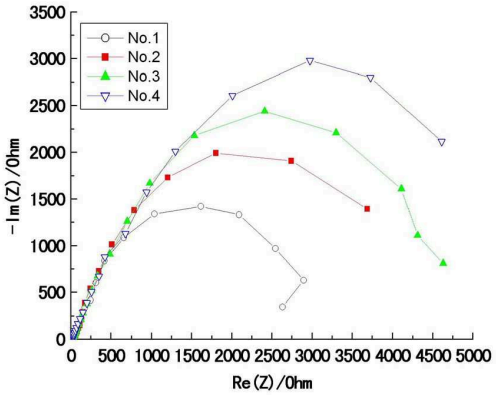


Fig. 3 EIS Nyquist diagram of 1#-4# samples

In order to get more information from these EIS curves, we adopted the equivalent circuit shown in Fig. 4 to imitate the EIS of aluminum alloys [19]. The alloy surface is covered with Al_2O_3 oxide film before being soaked in seawater. R_s is solution resistance, CPE_1 and R_1 represent the capacitance and resistance of electric double layer which are formed by the deposition of Zn and In on the alloy surface, CPE_2 and R_2 represent the capacitance and resistance of electric double layer which are formed by the passivation film on the alloy surface in the solution. Capacitance is replaced by phase components due to the strong dispersion effect of EIS in seawater.

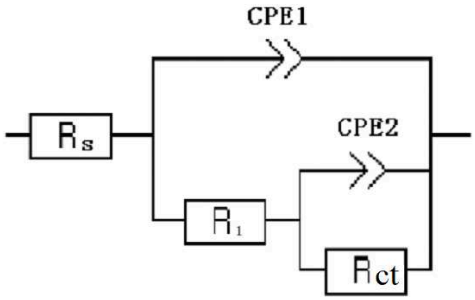


Fig. 4 Fitting equivalent circuit of EIS

The values of CPE, Q and n have the following relation,

$$CPE = [Q(j\omega)^n]^{-1}. \quad (1)$$

The value of Q is interrelated to the state of electrode surface or the species of electric active substance. Jω is the composite variable of sinusoidal disturbances, $j = \sqrt{-1}$, ω=2πf. The value of n (0~1) represents the index of CPE, When n=1, CPE is the ideal pure capacitance.

Table 2 shows the results of fitting parameters in the equivalent circuit. The results show that the value of R_s was between 19.87 $\Omega \cdot cm^2$ and 21.16 $\Omega \cdot cm^2$, the value of R_{ct} increased from 2862 $\Omega \cdot cm^2$ to 5889 $\Omega \cdot cm^2$, while the double-layer capacitance of passive film (Q_2) decreased from 7.435×10^{-5} $F \cdot cm^{-2}$ to 3.274×10^{-5} $F \cdot cm^{-2}$. It is found that along with the increase of Si content, the charge transfer resistances increase and the values of double-layer capacitances decrease clearly. The value of n is close to one which means that the phase angle element is close to capacitance. Due to the low values of Q, the total impedance of equivalent circuit equal to R_{ct} approximately. The resistance of electric double layer formed by the deposition of Zn and In on the alloy surface (R_1) and the capacitance of electric double layer from matrix and solution interface (Q_1) have the same tendency like R_{ct} and Q_2. The results show that when Si content 0.09 wt.%, the anode presents the property of low resistance and high capacitance, which has positive influence on improving the electric capacity of anode.

TABLE 2 COMPONENT VALUES OF FITTING CIRCUIT

No.	R_s $\Omega \cdot cm^2$	R_1 $\Omega \cdot cm^2$	Q_1 $F \cdot cm^{-2}$	n_1	R_{ct} $\Omega \cdot cm^2$	Q_2 $F \cdot cm^{-2}$	n_2
1	21.04	76.38	4.016×10^{-5}	0.956	2862	7.435×10^{-5}	0.9257
2	20.92	118.9	2.127×10^{-5}	0.9887	3722	6.486×10^{-5}	1
3	21.16	124.2	1.415×10^{-5}	0.9568	4586	5.201×10^{-5}	0.9549
4	19.87	194	0.964×10^{-5}	0.9895	5889	3.274×10^{-5}	0.8897

Conclusions

The Al-5Zn-0.02In-1Mg-0.05Ti-0.09Si (wt.%) alloy has excellent anode properties. Its working potentials are between -0.918 V~-0.935 V and current efficiency reaches 92%. It has good dissolution morphology and presents the property of low resistance and high capacitance. While the Si content exceeds 0.12 wt.%, the current efficiency decreases obviously. The results reveal that the microstructure, electrochemical characteristics and corrosion uniformity can be improved significantly after adding 0.09 wt.% Si into Al-Zn-In-Mg-Ti alloy.

Acknowledgements

This work was supported by National High-tech R&D Program of China(Grant No. 2009AA05Z120) and National Nature Science Foundation of China (No. 21276036).

References

[1] J. Xu and W. Yao, Current distribution in reinforced concrete cathodic protection system with conductive mortar overlay anode, J. Constr. Build. Mater. 23 (2009) 2220-2226.

[2] J.C. Norris, J.D. Scantlebury, M.R. Alexander, C.J. Blomfield and R.F. Crundwell, Quantitative analysis of indium and iron at the surface of a commercial Al-Zn-In sacrificial anode, J. Surf. Int. Anal. 30 (2000) 170-175.

[3] A.R. Despic, R.M. Stevanovic and A.M. Vorkapice, A new method of obtaining electrochemically active aluminum, in 35th ISE Meeting, CA, University of Berkely, 1984, pp. A2-19.

[4] I. Gurrappa, Cathodic protection of cooling water systems and selection of appropriate materials, J. Mater. Process. Tech. 166 (2005) 256-267.

[5] J.B. Bessone, D.O. Flamini, Comprehensive model for the activation mechanism of Al-Zn alloys produced by indium, J. Corros. Sci. 47 (2005) 256-261.

[6] W. Xiong, G.T. Qi, X.P. Guo, Z.L. Lu, The effect of tellurium on the Al-Zn-In anode, J. Electrochem. Soc. 158 (2011) 48-54.

[7] J.L. Ma, J.B. Wen, The effects of lanthanum on microstructure and electrochemical properties of Al-Zn-In based sacrificial anode alloys, Corros. Sci. 51 (2009) 2115-2119.

[8] B.M. Ponchel and R. Horst, Performance of Al-Zn-Sn alloy anodes in seawater service, J. Mater. Prot. 7 (1968) 38-41.

[9] T. Sakano, K. Toda and M. Hanada, Tests on the effects of indium for high performance aluminum anodes, J. Mater. Prot. 5 (1966) 45-50.

[10] GB/T 4948-2002, Sacrificial Anode of Al-Zn-In series alloy, China Standard Press, Beijing, 2002.

[11] Det Norske Veritas, Cathodic Protection Desigh, Norway, RP-B401, 2010, section 11 and 12.

[12] H. Ahlatci, Production and corrosion behaviours of the Al-12Si-XMg alloys containing in situ Mg_2Si particles, J. Alloy Compd. 503 (2010) 122-126.

[13] D.K. Xu, N. Birbilis, D. Lashansky, P.A. Rometsch, B.C. Muddle, Effect of solution treatment on the corrosion behaviour of aluminum alloy AA7150: Optimisation for corrosion resistance, Corros. Sci. 53 (2011) 217-225.

[14] X.S. Shen, Q. Wu and J.X. Jiang, Effect of impurity Fe and Si content on the capacitance of anode aluminum foil in low voltage electrolytic capacitor, J. Electron. Compon. Mater. 14 (1995) 1-7.

[15] W.A. Ferrando, Development of a novel composite aluminum anode, J. J. Power. 13 (2004) 309-314.

[16] T.T. Zhao, W. Ran and G.T. Qi, Analysis of Loss in Current Efficiency of Aluminum Alloy Sacrificial Anode in Aqueous Sodium Chloride, J. Mater. Prot. 40 (2007) 58-60.

[17] K. Li, L. Ma, Y. G. Yan, J. H. Wu and G. Z. Chen, Study of Low Voltage Sacrificial Anode Materials, J. Mater. Prot. 4 (2010) 95-97.

[18] J. Ma and J. Wen, The effects of lanthanum on microstructure and electrochemical properties of Al–Zn–In based sacrificial anode alloys, J. Corros. Sci. 51 (2009) 2115-2119.

[19] F. P. Ijsseling, General Guidelines for Cormsion Testing of Materials for Marine APPlieations. Br, J. Corros. J. 24 (1989) 55-78.

Advanced Materials Research Vol. 936 (2014) pp 1969-1972
© (2014) Trans Tech Publications, Switzerland
doi:10.4028/www.scientific.net/AMR.936.1969

The Application of Green Materials in Product Packaging Design

Ouyang Chaoying, Li Lin, Xiong Yajie, Nie Xiaoli

School Of Arts & Design.HuBei University Of Technology,China

oycyen 001@126.com

Keywords: natural, green materials, product packaging design

Abstract. Packaging requirements for products are increasingly high as society advances , the development of logistics. This paper revolves around the green material, through the selection of green materials and design concepts, analyzed the application of green materials in product design and its development trend. Through the knowledge of advanced materials, the better product design that meet market needs could be created, the value of the material could be unfolded, the “Green Life” period, the new style and new material of design could be created.

Introdution

According to "Kao Gong Ji" recorded: design to be harmonious with time, environment, material, and art. We can find the thought that represent beauty with the property and feature of material has already exist since ancient times. Human beings through the stone age, pottery age, bronze age and the iron age, entered the era of contemporary synthetic materials, materials has become an indispensable and important part of human survival and life, has become an important factor to measure the development level of social science and technology.

In the traditional product design, the less consider impact on the environment on the material selection, therefore in the process of production, consumption has certain harm on the environment. So in such an era of rapid development of science and technology , what material is wonderful we think of ?Where is the way of packaging design and product design material?

Green Materials And Design Concepts

Green materials refers to the materials in raw materials taken , product manufacturing use and recycling and waste processing and other aspects which helpful to human health and can harmonious coexistence with ecological environment of the environment. They should have a purifying absorption function and health-promoting functions. Green material was first time proposed on 1988 First International Materials Conference, and was designated as one of the most important materials human to realize in next century.

Materials which are suitable for green product design all be considered as green materials, also including those although have harm to the human and the environment, but can take appropriate measures to reduce or eliminate the materials and manufactured goods. Its main concepts including the advanced nature of the material itself (high quality production of low energy consumption), the safety of the production process, the rationality of the materials used (saving, recycling), and accord with the requirement of modern engineering, etc. Green material is the key point of green product design. Green material require people with environment awareness, on the one hand, reform the existing material, make it has good coordination with environment; on the other hand the development of new materials, which was used to purify the environment, environmental restoration, or has good comprehensive performance and environmental coordination.

Also known as ecological design, green design aims to balance the human demand and the relationship between the supply of the natural environment. The most important methodology of green design is to emphasize the “product life cycle” ideas, make product with recyclability, removable, maintainable, reusable, and other products of environmental attributes. Green design is not only a technical consideration, more importantly it is a change of the concept. It requires stylist to abandon that too much emphasis on product on the appearance of novelty, but focus on innovation with true sense, and with a more responsible approach to create a product form, and use a more concise, lasting modeling make the products as much as possible to prolong its service life.

The Status Of The Domestic Packaging Design

Packaging requirements for products are increasingly high as society advances, the development of logistics. On the one hand to protect goods from damage, easy to transport and storage, on the other hand require beautiful and easy to sell commodity packaging, and even to some extent become the external form of competition of the commodity, and because of the luxury packaging, make commodity packaging gradually become the main performance of commodity value, so the packaging costs rise, prices rise, the vast majority of the packaging has not been spared from the garbage after use. According to data statistics, every year in our country about 16 million ton producing waste, the main is plastic packaging products of waste, which waste each year up to 1 million ton, including plastic lunch box, cup dish, foaming material, plastic bottles, all kinds of candy, food packaging, and all kinds of plastic bags, etc. According to experts, the white garbage will be retained for quite a long time also won't disappear in the earth's surface. So how to reduce waste, how to make good use of waste, this is a status and problems of domestic packaging.

The current domestic market became a hodgepodge of product packaging. They are proud of conceptualization of foreign products mimic, the supermarket full of beautiful things in eyes of different styles of packaging products, but on behalf of the Chinese nation style products and rarely lack of personality.

The Application And Development Trend Of Green Materials In The Product Packaging Design

The Material On Design Return To Nature

First of all, the material on design can choose natural biological material, such as use paper, wood, bamboo weaving materials, hemp, cotton, willow, reed and the stem, rice straw, wheat straw and other crops for packaging. They're very easy to break down in the natural environment, never polluting the ecological environment, renewable, and the cost is low.

For example, a Swiss stylist designed a white gift paper bag, in the process of paper making will join in the seeds of trees which make the paper itself can break down after abandoning, and the seeds inside still have a chance to take root, sprout, grow up in the soil.

Muji clothing material all adopt organic cotton, noil, linen, wool and other natural materials and recycled materials. Organic cotton has no chemical drug residues in the production and process, all natural environmental protection in planting production process. Noil is the falling short fiber in the processing of cotton, is the recycling of natural materials. As shown in figure 1 is the cotton fabric design handbags.

Secondly, we can develop in the direction of the use of edible packaging materials on the material selection. For its abundant raw materials, edible, harmless or even beneficial to human body, the characteristics of a certain intensity, edible packaging materials has rapid development in recent years. It has been widely used in food, medicine packaging. Such as Germany invented a cup made of starch which in the liquid will not melt, and this kind of cup can eat together with the cup beverage, but won't produce too much heat. Another example is the cone we usually eat, the part which pack ice cream is the edible crispy.This is a kind of very promising green packaging materials, is also very active in the field research.



Fig.1 Cotton fabric handbags



Fig.2 Ribbon embroider packing

Thirdly, we can develop in the direction of the using biodegradable packaging materials, biodegradable materials is a kind of plastic that its chemical structure will change in certain circumstances. The development of biodegradable plastic packaging materials, and gradually eliminate non-biodegradable plastic packaging materials is the trend of world science and technology development, and one of the hot spot of materials research and development. Biodegradable plastic packaging materials with both traditional plastic functions and features, and after it is used, through the microbial function of nature or the role of sunshine, it can be divided in the natural environment, and finally to return to nature in the form of non-toxic.

Beauty Of Simplicity On Design Idea

As a whole, the simplicity follow the "subtraction" principle, that minus unnecessary troubles in the largest extent, directly reveal the true nature of things, brief, simple, delicate, pure. "Subtraction" is a process that constantly changing and growing less and simple. "Subtraction" is a standard, a scale in the works of art appreciation and mastery of social life.

Design concept is to save material on the direction of development. In guarantee the basic function of packaging, we need reforming excessive packaging, developing moderate packaging, reducing the use of packaging materials, reducing the packaging cost, saving the packing material resources, reducing the discharge of waste packaging materials. One of the characteristics of this design is pursuitting concise simple materials and packaging frames.

For example, Japanese flavour essence company design of condiment packaging uses white sheet made of corrugated paper, and the label printing is plain.

Muji on the choice of materials pay attention to show the natural material itself unique aesthetic trait. Its products adhere to the principle of simple and durable, and pay attention to the efficiency of material, adopting the processing mode of concise, adhere to the simple packaging, and unified use without bleaching, environmental protection recycling recycled paper as product packaging under guarantee packing basic recognition and protection, abandoned the excess packaging. As advocate green design in the field of product design pioneer, Muji has practical success. As a goods, it abandoned the profiteering in multifarious packaging and precious raw material behavior. As shown in figure 2 ribbon embroider packing, Muji set his sights on reducing unnecessary costs, advocating rational consumption, pay attention to environmental protection and ecological balance, and this is the code of ethics should be follow by each developer, designer, manufacturer's.

Conclusion

A famous German designer had summed up the relationship between design and material, he put forward design directly associated with the new technology and new materials. While there is a new material, the old design will be reassessed. It is easy to find that the design thought is based on material, and the properties of materials is obtained by design. Every discovery, invention and application of a new material, all means that a new form of expression will be created and applied. Different material presents different features by reason of its material, craft. Therefore, in the process

of product design, material selection is extremely important, reasonable material application can not only enrich the content of the product and individual character, but also can make the product more produce new charm.

In a word, the age that only depend on own feelings of formal beauty design is over. Designers should keep up with the demand of times, cooperate with natural science, social science, and many other scientists, master the knowledge of advanced materials, create a better green design which meets the demands of the market, fully display the material itself value and aesthetic feeling and used it into product design, make the product reflect humane use value and aesthetic value. Let us hand in hand to create a new style, new material, "green life" design.

References

[1] Zheng. B. J., Green Packaging Materials and Modern Packaging Design, Applied Mechanics and Materials 271 (2013) 77-80.

[2] Zhang. J., A Study into Green Package Design Practice, Advanced Materials Research. 655 (2013) 2033-2036.

[3] Liu. F, Brief Analysis on Green Design and Manufacture of Furniture Products, Advanced Materials Research. 694 (2013) 3269-3272.

[4] Ji. H. Q., Application of Low Carbon Materials in Packaging, Advanced Materials Research. 651 (2013) 462-465.

[5] Horvath, A., Akos M., Reducing packaging waste by GIS applications, Green Design, Materials and Manufacturing Processes. (2013) 443.

Advanced Materials Research Vol. 936 (2014) pp 1973-1984
© (2014) Trans Tech Publications, Switzerland
doi:10.4028/www.scientific.net/AMR.936.1973

The hand making of radius fillers and the establishment of its evaluative requirements

Hailei Wang[1, a], Meirong Xiong[2, b], Yuexin Duan [3, c*], Jin Yang, Dongxiu Yan, Shaochen Xu

[1, 2, 3] School of Materials Science and Engineering, Beihang University, Beijing 100191, China

[a] wanghailei2012@126.com, [b] xmr040901@126.com,[c] duanyuexin@126.com

Keywords: Composite; Prepreg; Radius filler; Hand-made craft; Evaluative requirement

Abstract. Radius filler is a kind of filling material which is used in triangle gap of the composite girder and rib. To optimize the hand-made craft of radius fillers and specify the evaluative requirements for detecting radius fillers, a research on handcraft parameters of the radius fillers had been conducted; the boundary dimension, microstructure and mechanical property of the R6 radius fillers had been characterized with the use of different detective methods and the microanalysis includes: nondestructive testing; microscope photos; fiber volume fraction and void content. The evaluative requirements to detect the quality of radius fillers have been established and its validity has been confirmed by the R8 radius fillers.

Introduction

With the increasing development of composite, they are widely used for the components of large airplanes such as center wing box, vertical fin and so on with the combined structures of girder and rib with skin panels. [1, 2] Because composite is manufactured by attaching the mold, a large triangle gap will exist at the corner of girder and rib (as shown in the Fig. 1). Problems of crazing along the fibrous layer or destroying fibrous will emerge at the place where gap exists leading to the degradation of component performance under the effect of outside force, which is a big problem facing in engineering practice.

Aiming at the risk caused by this T type of structure, there are many kinds of solutions such as the curvature design of the corner, fixed by mental accessories, filled with resin or glue saluting and so on. With the development of technologies, the method is widely used to fill the gap at the corner of girder and rib with composite radius fillers.

Generally, The so-called composite radius fillers is to choose unidirectional or multi-directional composite pregreg which is made with certain technology applied into body structure in form of cylinder or triangular prism. Composite radius fillers can be put into the triangle gap of girder and bid play the role of filling and bonding after oven heating.

Currently, radius fillers are manufactured through manual operation in most places, but there will be some serious problems: it is hard to control the size of radius fillers for too big a size will cause the bulge while too small will cause the hollow on the surface of components; the performance of radius fillers is not stable so that the homogeneity of covering pregreg will make an influence on the formation of void and structural void and warp and damage of fibrous will weaken the force performance of filling materials; the product of radius fillers is not continuous so that only short radius fillers can be produced as a result that they must be used after jointing to fill large components; it takes a long time to produce radius fillers through manual operation. Meanwhile, there is no evaluation system to test and evaluate radius fillers, so it is very important for further engineering research and application to optimize the hand-made craft of radius fillers and standardize its evaluation system.

Boeing company made great efforts on the hand-made craft of radius fillers used for filling composite girder and rib. As early as the end of last century, Boeing put forward that producing unidirectional fiber reinforced composite laminate plates firstly and then cutting these plates into equilateral strips that are passed through rolling equipment to form radius fillers matched with the

gap in the patent of US4789594[3]. In the patent of US5650229[4], it proposed filling gap with radius fillers made up of unidirectional fiber adding stabilizer (consisting of bismaleimide resin, poly isocyanates and epoxy) at a proportion of 3-5% to get the shape needed to fill the gap and then infiltrating resin through RTM craft. By this mean, the fiber volume fraction can reach 60-70% to avoid transformation of resin-rich area and fiber efficiently. Next, in order to solve the problem of stress concentration in filling area, Boeing proposed the method of filling gap with radius fillers made up of titanium alloy in the patent of US5833786[5].

With the further research in 21st century, Boeing considered various elements including performance, weight and cost together as a whole and proposed a method of manufacturing composite laminate radius fillers in the patent of US6709538[6] that the gap was filled with multi-layer fabric with the layers of [0°/90°] or [±45°] and enough or excess resin. Compared with unidirectional or pure resin adhesive, laminate composite radius fillers can avoid the damage due to internal crack.

In the patent of US7758715[7], it put forward the method of taking thermoplastic material whose curing temperature was lower than that of composite components as radius fillers to fill the gap and taking good control of heating rate and time to get the radius fillers in good performance. Recently, Boeing proposed to produce radius fillers with nanostructure including carbon nanotubes, carbon nanofiber and carbon nanowires in patent of US20120074265[8] in order to strengthen the interface connection of filling materials with composite components. Meanwhile, viscosity of this composite can be controlled in terms of additive amount of nanostructure, radius filler appears to be semi-cured during the production process, and finally cured with other components.

To meet the demands of industrial production, Boeing designed a set of facilities used to produce radius fillers in the patent of US4559005[9] in 1985. However, this facility only can produce radius fillers with the same cross sectional dimensions and if the gap at the corner of girder and rib were changed, radius fillers will become too small or large and the groove of idler wheel needed to replace to change the size of radius fillers. Intelligent facility was created by Boeing in the patent of US4778545Z[10], This facility can measure the radius of circle, store and compute the sectional area of the gap and then cut the composite into strips as same the width as that of the gap and then make them into radius fillers.

In this investigation, technological parameters of hand-made radius fillers were studied and optimized, different detection methods were adopted to characterize the boundary dimensions, microstructure and mechanical properties. In terms of the characterized results chosen, this paper established initially a method of testing and evaluating the quality of radius fillers taking elements such as the cost and reliability into consideration, which paves the path for the engineering practice and further automatic production.

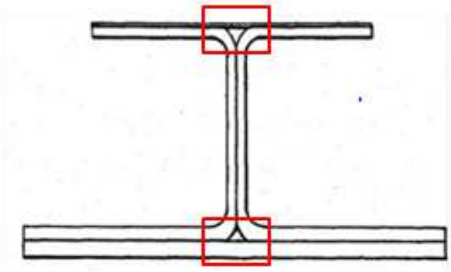


Fig. 1 Triangle gap of composite girder and rib

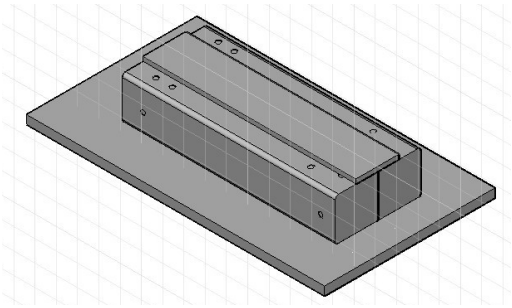


Fig. 2 Design of homemade mould

Experimental Investigation

Specimen fabrication. The material used for the specimen was T300-6k, unidirectional prepregs manufactured by the Jilin Petrochemical Company. This material has a fiber areal density of 150g/m^2, while the resin content is 33%.

A homemade mold which manufactured based on the investigation of the elevator is presented in Fig. 2. Each arris of the rectangle has a special radius of curvature, therefore, radius fillers with the size of R2,R4,R6,R8 can be respectively prepared used the mold.

Theoretical relationships between the Prepreg add volume and the size of radius filler are described in Eq. 1.

$$\frac{A\times(1-R)\times \mathrm{b}}{\rho} = S\times V_f \quad (1)$$

Where A and R is the prepreg areal density and resin content, b is breadth of the additive amount of the radius filler, ρ and V_f is the fiber density and volume fraction. The theoretical sectional area of the cavity, S, can be expressed as a function of the radius of radius filler curvature r:

$$s = 0.43r^2 \quad . \quad (2)$$

However, hollow defects appeared in the Specimen when we applied the dosage calculated by the Eq. 1.So an authentication method had been applied to amend Eq. 1. The cavity filled with gypsum was used to simulate the shape of the mold cavity. Five simulated simple with better section was polished with 180 # sandpaper, and then record the gypsum section with red ink pad. Cross-sectional area and other parameters was measured and calculated with a Ruler. The self-designed R6 cavity average cross-sectional area is 21.1mm^2 that can be obtained from the data in Table 1.

Table 1 Area parameters of mold cavity

Number	Left R [mm]	Right R [mm]	Area of calculation [mm^2]	Area of measurement [mm$^{2]}$	Area of overflowing [mm^2]
1	6.5	6.6	20.4	23	11
2	6.5	6.5	20.2	30	11
3	6.8	6.8	22.6	28	11
Average	6.6	6.6	21.1	27	11

A new equation, Eq. 3, had been put forward. Where S' is the measured sectional area of the cavity, L' is the area of the overflow part.

$$\frac{A\times(1-R)\times b}{\rho} = (\mathrm{S'+L'})\,\mathrm{V}_f \quad (3)$$

Given the fiber volume fraction which you need, the additive amount of the radius filler prepreg can be calculated.

A range of additive amount of the radius filler prepreg had been designed (as shown in table 2) for the investigation refers to Eq. 3. Prepreg was wound into a compact cylindrical, then put into the cavity of the mold. No.1-12 semi-cured and cured 24 radius fillers were made up by the craft of the Vacuum Assisted Resin Infusion (VARI) which is described in Fig. 3.The semi-cured process was 60℃ for 30 minutes, while the cured process was 80℃ for 45 minutes, then 120℃ for 75 minutes.

The quality characterization of the radius filler. Ultrasonic C-scan NDT was applied to characterize the semi-cured radius fillers in the research. The cured radius fillers had been characterized from three aspects: boundary dimension; microstructure; mechanical property. While, microstructure which also includes: non-destructive testing, metallurgical analysis, fiber volume fraction and porosity.

The floating of the radius filler boundary dimension was not so obvious since it was cured in the rigid mold. Five groups of width and thickness (Fig. 4) from appropriate intervals (2mm-3mm) were measured by the caliper, then their average values were calculated.

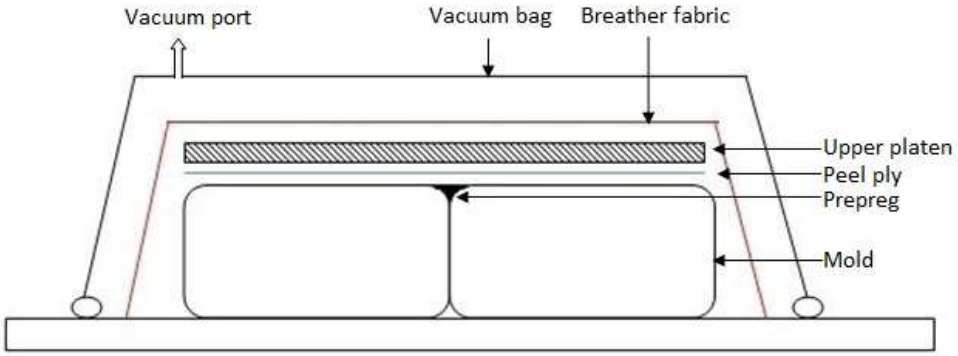


Fig. 3 Schematic diagram of the radius filler craft

Table 2 Additive amount of the radius filler prepreg

Specimen	Breadth [mm]	Specimen	Breadth [mm]	Specimen	Breadth [mm]	Specimen	Breadth [mm]
1	158	4	176	7	194	10	220
2	164	5	182	8	200	11	230
3	170	6	188	9	207	12	240

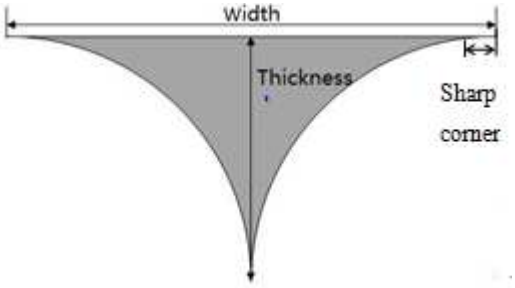


Fig. 4 Size sketch of the radius filler

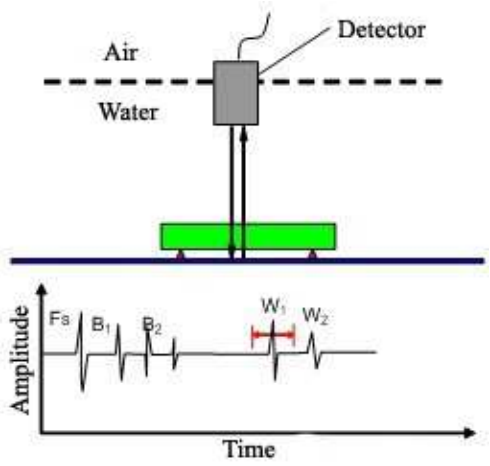


Fig. 5 Propagation path of the ultrasonic wave

Water Immersion Ultrasonic C-scan NDT was used to detect the radius fillers. C-scan images were obtained by utilizing the reflector to detect echo information. Acoustic propagation is described in Fig. 5.

Where F_S is specimen surface echo; B1 and B2 are specimen bottom echo and secondary echo; W1 and W2 are reflector surface echo and bottom echo at the bottom of the container.

Microscope photos of the cured specimens were obtained from two random cross-sections.

Fiber volume fraction and void content of the cured specimens were calculated by using the microscope photos and Sisc IAS refer to standard GB/T 3365-2008.

INSTRON 5982 mechanical testing machine was used for the bending performance test of the cured specimens refer to the standard GB/T 1449-2005. The testing results will be used to detect whether the cured specimens meet the design requirements.

Results and discussion. The added amount of the prepreg will have a greater impact on the curing size. Radius filler will not be closely connected with the product owing to its small size when the added amount of the prepreg is not sufficient. And other defects, e.g. great stratification, hollow filler will appear. However, embossment in the triangular area can be found when the added amount is over sufficient.

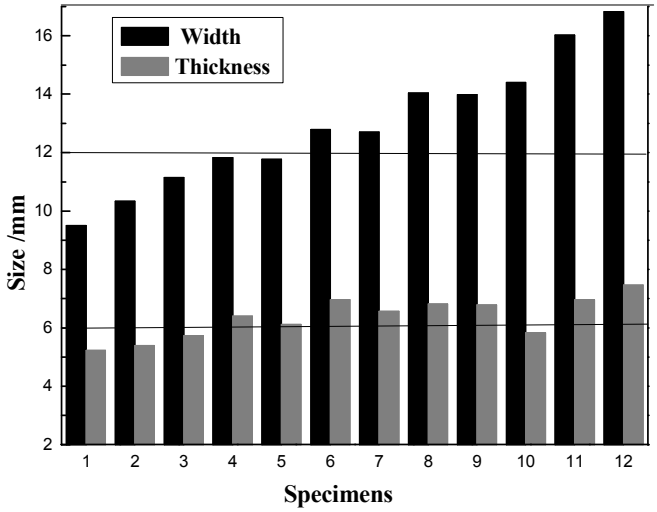


Fig. 6 Size contrast of the cured radius filler

The relationships between the size of the radius filler and the added amount of the prepreg are presented in Fig. 6.As observed in this figure, the width and thickness all rise with the added amount. The size of the radius filler needs to be controlled in a certain range when it is used as filler in the interspace of the stiffened panel structure. Compared to the desired size (width of 12mm, thickness of 6mm), size error of the specimens No.5,6,7,8 are in the range of 15% . And start from No. 6, the size of the specimens is larger than the desired size.

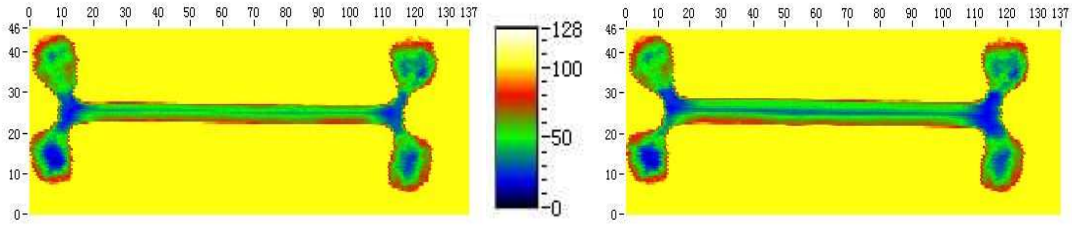
Water Immersion Ultrasonic C-scan NDT was used to detect both the semi-cured and cured radius fillers, at the same time, representative specimens were selected. Test results are presented in Fig. 7 and Fig. 8.

As an uneven thickness and complex part, uniformity of the ultrasound spectrogram color change reflects the uniformity of the fiber arrangement in the radius filler. Theoretically, the thicker and the more compacting of the specimen, the more attenuation of ultrasonic signal, then the darker the spectrogram will be. On the contrary, the shallower the spectrogram will be.

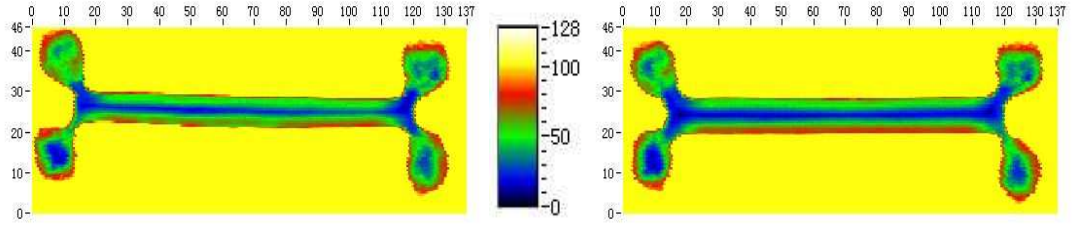
Spectrogram of the semi-cured specimen No. 1 (Fig. 7(a)) is mainly green, a thin blue line appears in the middle, and the edge is faint red. The dark range increases in the spectrogram of the semi-cured specimen No. 5(Fig. 7(b)), however, there are some ups and downs at the interface over blue and green. Therefore, specimen No.5 is poor uniformity, thickness and compaction. The dark range continue to increase in the spectrogram of the semi-cured specimen No. 7(Fig. 7(c)), the interface still be some ups and downs. Then the thickness and density of the No.7 is better, and its uniformity has improved but still is not so good.

The color distribution of the ultrasound spectrogram is related to the shape of the radius filler. As a typical prism, its ultrasound spectrogram turns to shallow from the middle to the edge owing to its different acoustic attenuation. Color difference of different specimens illustrates the difference of their density and uniformity. As observed in Fig. 7, the density of the semi-cured specimens rises with the additive amount of the prepreg at the same pressure. Thickness and density of the specimens are overall good start from the specimen No.7.

The NDT results of the cured specimens are presented in Fig. 8. Large areas with good thickness and density appear from the specimen No.6, in which, more echo attenuation occurs in most areas of the cured specimen No.8, corresponds to the blue area of the Fig. 8 (d), and the degree of attenuation is approximately 80%.Variation of the cured specimens spectrograms is similar to the semi-cured specimens, namely, the density of the cured specimens rises with the additive amount of the prepreg at the same pressure. At the same time, the interface over the different color on the image appears to be a straight line, therefore, the uniformity of the cured specimens dimension and internal structure is better than the semi-cured.

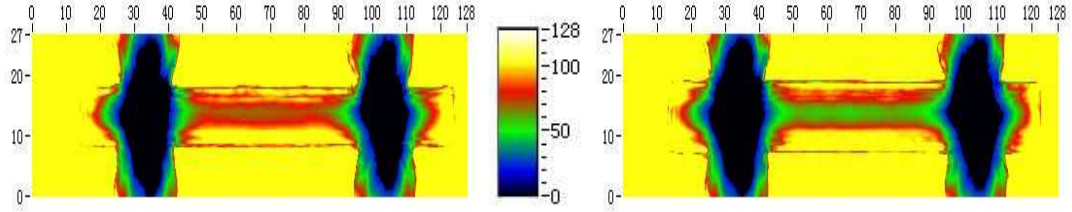


(a) No. 1 (b) No. 5

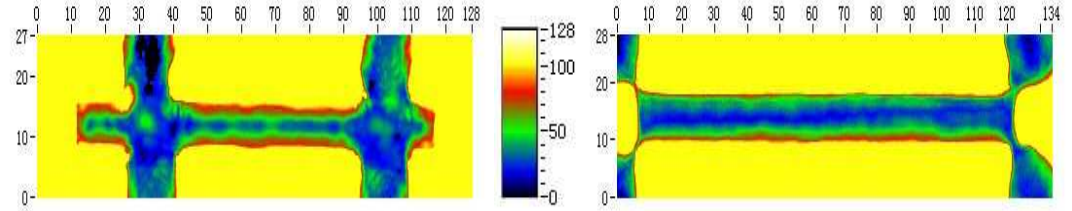


(c) No. 7 (d) No. 11

Fig. 7 Nondestructive testing (NDT) spectrograms of the semi-cured specimens



(a) No. 1 (b) No. 3

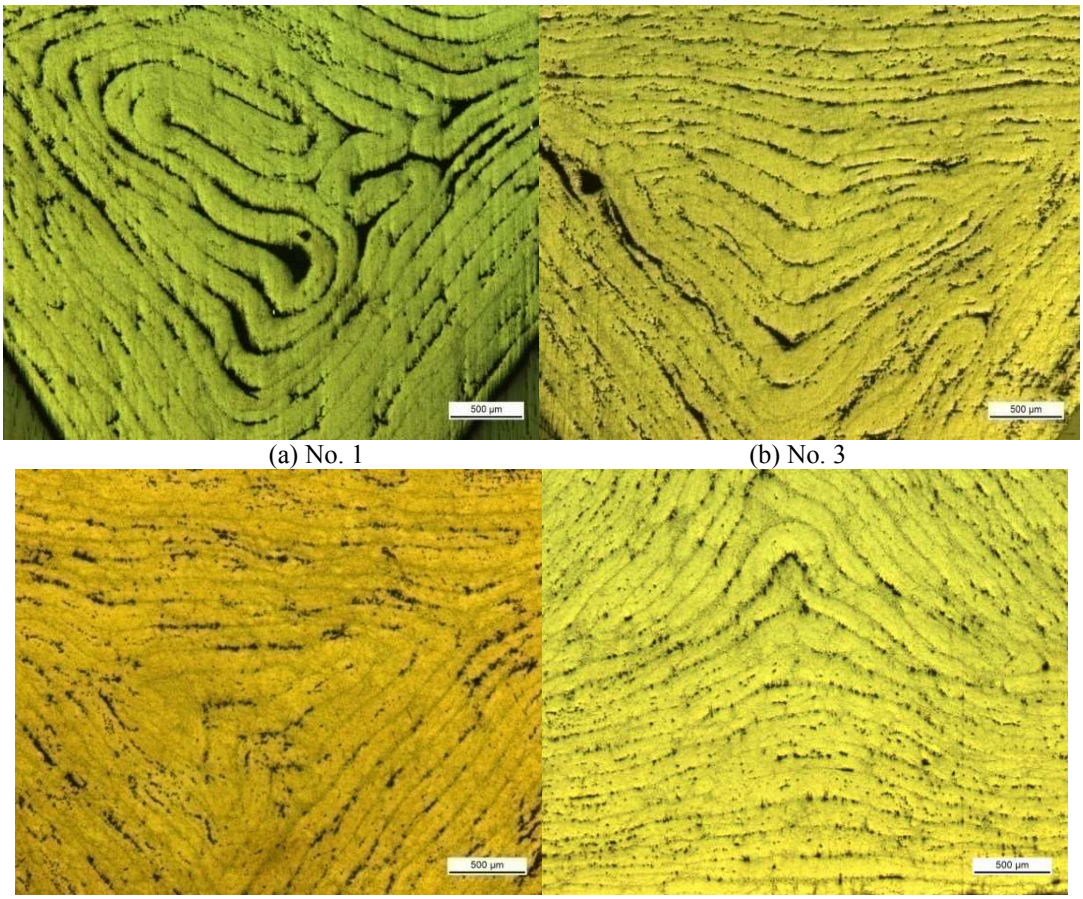


(c) No. 6 (d) No. 8

Fig. 8 NDT spectrograms of the cured specimens

Representative microscope photos of the cured specimens are given in Fig. 9. Internal structure of the specimen No.1 (Fig. 9 (a)) is incompact, numerous voids concentrated in the interlayer, large voids distribute in the core of the triangle, and fibrous layer appears to be disorganized. Void size of the specimen No.3 is smaller than the No.1 as a result of the increase additive amount of the prepreg. Although the core of the triangle is filled with fibers, lots of medium-sized and little large-sized voids still exist, gaps in the interlayer are still obvious. As seen in Fig. 9 (c), gaps and large-sized voids of specimen No.7 have disappeared, Most of the areas get a better density in case of the decrease of the voids. Fiber layer of specimen No.11 arranged neatly, the density has been great improved, the voids appear to be small and uniformly distributed.

As depicted in Fig. 9, all defects occur in the interlayer, moreover, probability and size of the interlayer defects reduce with the increase of the additive amount of the prepreg. However, the defects are inevitable even if the additive amount of the prepreg is sufficient, and it can be explained by four reasons [11]: (1) cavitation and folds produced by hand-folding; (2) blocking of the stomatal channel during pre-compaction; (3) volatilizing of the small molecule volatile components in the resin; (4) bubbles left caused by the bending, deformation and fracture of the fibers. Therefore, defect rate should be controlled within the acceptable range during the actual production process.



(a) No. 1 (b) No. 3

(c) No. 7 (d) No. 11

Fig. 9.Microscope photos of the cured specimens

Fiber volume fraction is around 60% begins with specimen No.6, and increased to about 62% start from the specimen No.8, as seen in Fig. 10. Owing to the requirement of 62% of the fiber volume fraction with autoclave molding in the aerospace field, 60% of the fiber volume fraction as dividing line using VARI craft (a standard atmospheric pressure conditions) is selected in the research to guarantee that the quality of the radius fillers meets the requirements of aerospace in the autoclave conditions. As observed in this figure, fiber volume fraction rises with the increase of the additive amount of the prepreg. Fiber volume fraction of most specimens is more than 60% and meets the design requirements start from the specimen No.6.

The void content of the specimens is large at the beginning, it can be controlled within 3% start from specimen No.7, and it reduced to 1.51% ultimately (specimen No.12) in the case of the increase of the additive amount of the prepreg, shown in Fig. 10. Therefore, the void content decreases with the increase of the additive amount.

Maximum bending load of the cured radius filler linear increases with the increase of the additive amount of the prepreg within the permitted error range, as illustrated in Fig. 11. Moreover, maximum bending load is 1200N, the corresponding additive breadth of the prepreg is 190mm which between the specimen No.6 and No.7 when plotting on the linear fitting curve of Fig. 11. The overall performance of the specimens can meet the design requirements start from the No.6, therefore, maximum bending load of 1200N can be seen as an evaluation requirements of the radius filler mechanical properties.

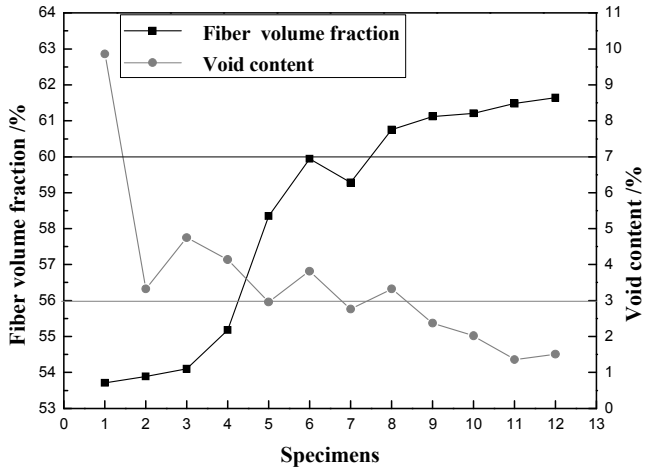


Fig. 10 Fiber volume fraction and void content of the cured specimens

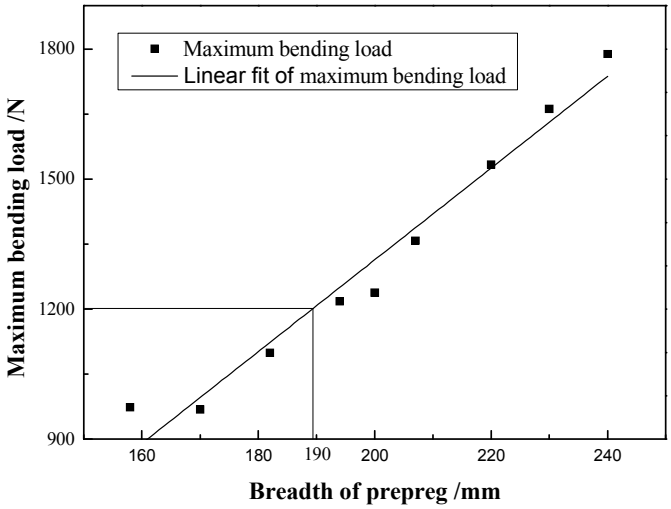


Fig. 11 Bending test results of the specimens

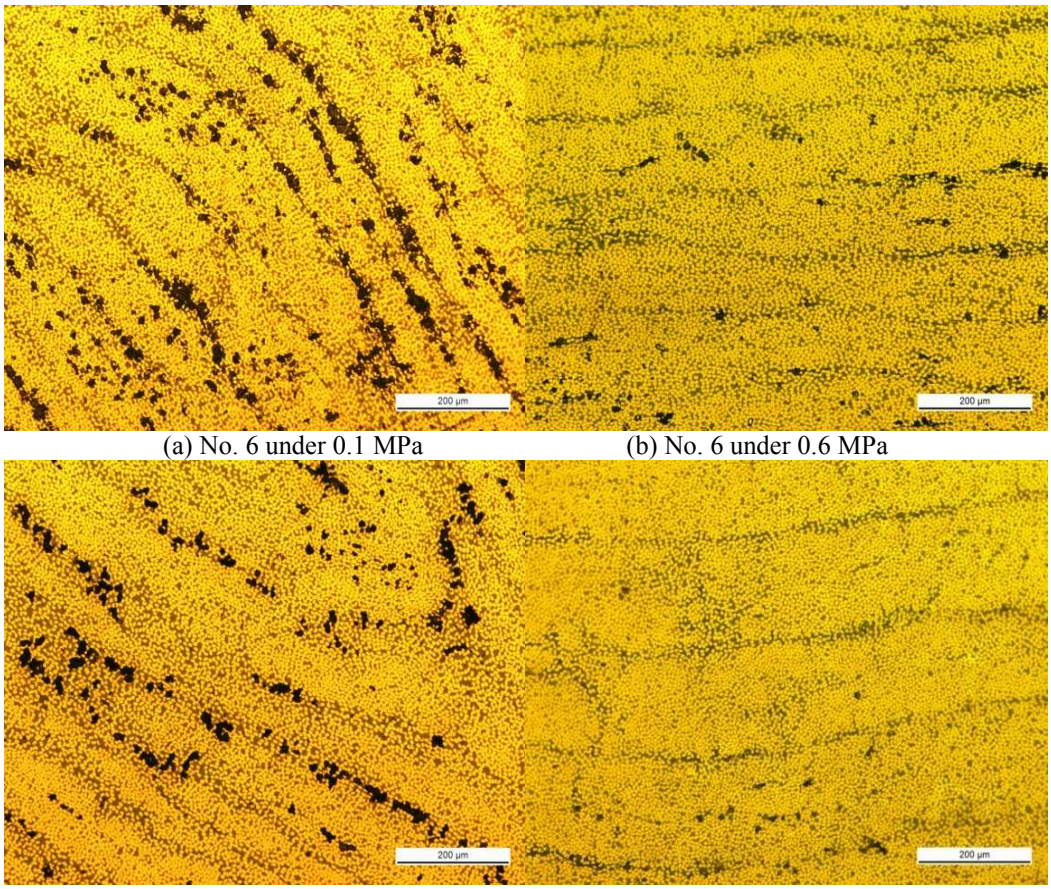
Table 3 Contrast of the radius filler under different pressure

Specimen	Pressure [MPa]	Width [mm]	Thickness [mm]	Void content [%]	V_f [%]
6	0.1	12.79	6.96	3.82	59.94
	0.6	11.90	6.13	2.38	60.27
7	0.1	12.71	6.57	2.76	59.28
	0.6	14.26	6.96	2.12	61.44

In summary, width and thickness of the radius filler increase, internal uniformity, density and fiber volume fraction rise, void content decrease, maximum bending load almost linear increase with the increase of the additive amount of the prepreg.

In order to compare with the cured specimen formed under 0.1MPa pressure, hot compacting was selected to simulate the actual pressing process of the specimen, and its performance was tested for the fact that curing pressure is 0.6MPa in practical aerospace applications. Specimen No.6 and No.7 which are the most representative specimens were chosen to show the differences.

Void content of the two hot compacted specimens is about 2% which has a large degree of decrease, as described in Table 3. The residual air and other volatile components in the interlayer have been dissolved in the resin due to the great pressure [12], therefore, the internal structure of the radius fillers becomes more dense and uniform, there was greater improvement of the fiber volume fraction, and the void content of the specimens appears to be decrease (Fig. 12).



(a) No. 6 under 0.1 MPa (b) No. 6 under 0.6 MPa

(c) No. 7 under 0.1 MPa (d) No. 7 under 0.6 MPa

Fig. 12 Microscope photos of the No. 6 and No. 7 cured specimens under different pressure

Establishment and verification of radius fillers' evaluative requirements. A series of quality evaluative requirements have been established based on the characterization and analysis of the R6 radius fillers. The using state of radius filler is prepreg, it is usually filled in the interstice and cured under the pressure of 0.6 MPa. The size, void content, fiber volume fraction of the radius filler change with the increase of the pressure, therefore, the Dimensions of the hand-made radius filler, semi-cured and cured specimens should meet the following requirements:

(1) Dimensions

The width and thickness error of the prepreg should be controlled in the range of +15% compared to the theoretical size.

(2) Microstructure

a. Standard NDT spectrogram of the semi-cured radius fillers is shown in Fig. 13 (a).

b. Standard NDT spectrogram of the cured radius fillers is shown in Fig. 13 (b).

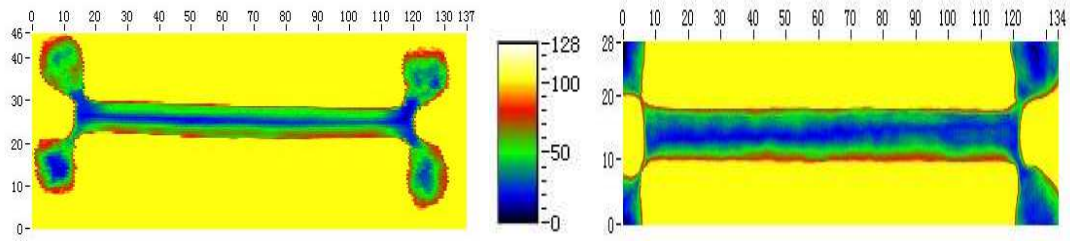
c. Standard microscope photo of the cured radius filler is shown in Fig. 13 (c).

d. Void content of the cured radius filler should be controlled less than 3%.

e. Fiber volume fraction of the cured radius filler should be controlled more than 60%.

(3) Mechanical property

Maximum bending load of the cured radius filler obtained by the three-point bending test should be larger than 1200N.



(a) Semi-cured radius filler (b) Cured radius filler

Fig. 13 Standard NDT spectrogram of the radius fillers

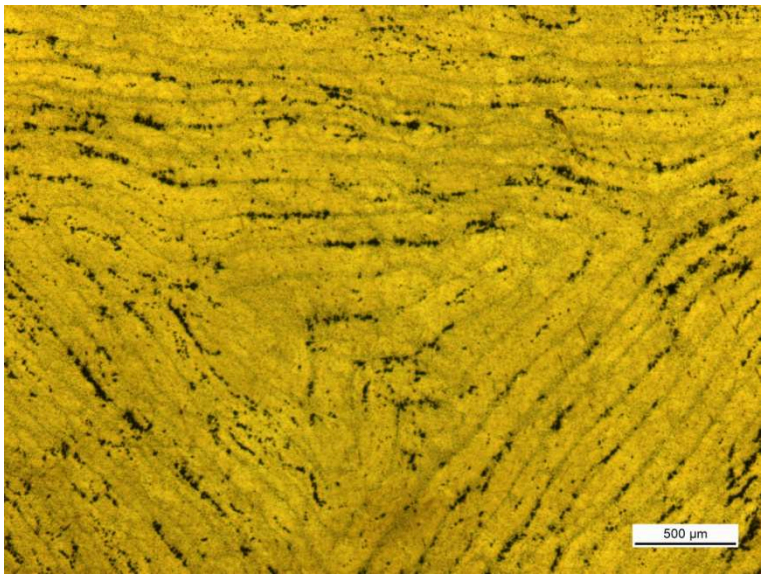


Fig. 14 Standard microscope photo of the cured radius filler

R8 radius filler was selected to verify the validity of the evaluative requirements. The theoretical additive breadth of the radius filler is 300mm calculated by Eq.3. Therefore, two additive amounts are designed, one is 300mm, the other one is 310mm, and the process is the same with R6 radius filler.

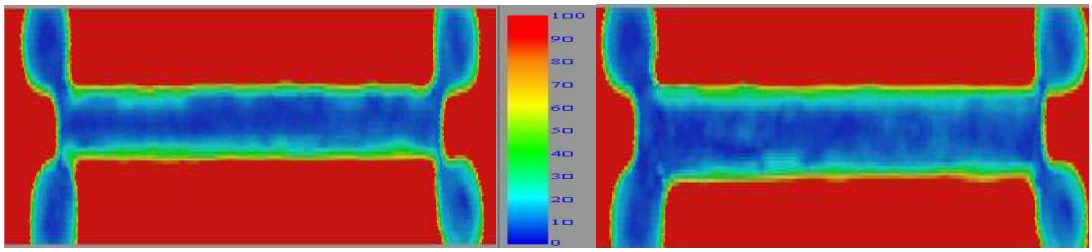
Table 4 Relevant data of the radius filler

Specimen	Width [mm]	Thickness [mm]	Void content [%]	V_f [%]	Maximum bending load [N]
a	16.52	7.90	0.63	58.31	1221.37
b	16.67	7.98	1.47	61.81	1522.58

As described in Table 4, the actual width of the cured specimen (a) is 103.3% of the theoretical width, the actual thickness of it is 98.8% of the theoretical thickness. While the actual width of the cured specimen (b) is 104.2% of the theoretical width, the actual thickness of it is 99.8% of the theoretical thickness. And both of their void contents are less than 3%, their fiber volume fraction is 58.31% and 61.81%, which is very close to or more than 60%. Meanwhile, maximum bending load of the cured radius filler (a) and (b) is larger than 1200N.

Nondestructive testing (NDT) spectrograms of the R8 cured radius fillers are presented in Fig. 15. As observed in this figure, structural uniformity, thickness and density of the R8 specimens have met the evaluative requirements. Small-sized voids with uniform distribution appear in the interlayer, rather than medium-sized and large-sized voids, as shown in Fig. 16.

Therefore, all aspects of the R8 radius fillers can meet the evaluative requirements, and the validity of the evaluative requirements has been verified. The evaluative requirements can be popularized to the hand making of other radius fillers.



(a) (b)

Fig. 15 NDT spectrograms of the R8 specimens

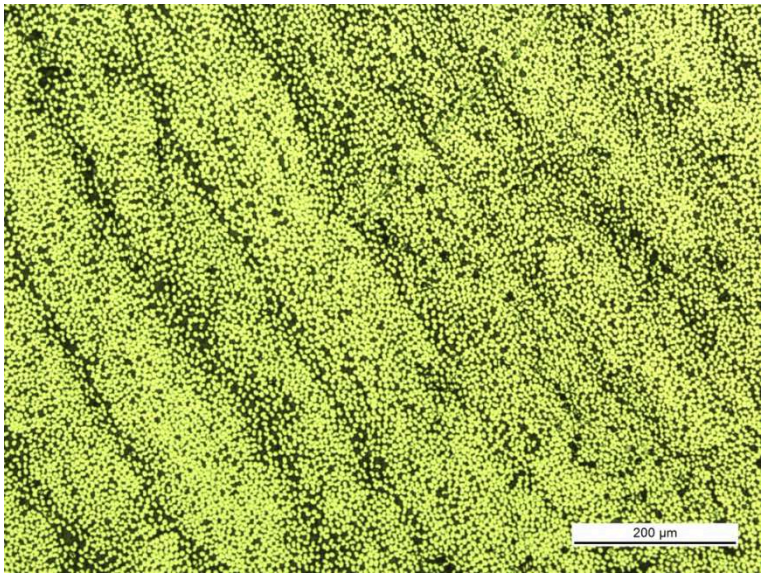


Fig. 16 Microscope photos of the R8 cured specimens

Conclusions

A kind of commonly commercial used prepreg was selected, and a series of hand-made radius fillers had been characterized and evaluated in this study. The achievements can be summarized as follows:

(1) The R6 radius fillers had been manufactured and been characterized from three aspects: boundary dimension; microstructure; mechanical property. While, microstructure which also includes: non-destructive testing, metallurgical analysis, fiber volume fraction and porosity.

(2) A set of systematic quality evaluative requirements had been established by the characterization and analysis of the R6 radius fillers.

(3) R8 radius fillers which meet the dimension requirements had been made owing to the accurate calculation of the additive amount of the prepreg by Eq.3. Meanwhile, the validity of the evaluative requirements had been verified by the analysis of its microstructure and mechanical property.

It is significant to establish a set of systematic evaluative requirements for the quality evaluation of the manual and the future automated radius fillers. Automated production will become the mainstream in the production technology of the radius fillers due to the significant limitations of the hand-made craft. Exploration on the automated production of the radius fillers will be the forthcoming work in our laboratory.

References

[1] J. Feng, Application of Composite Technology in Modern Aircraft Structure, J. Aeronautical Manufacturing Technology, 22 (2009) 40-42, (In Chinese).

[2] J. Xu, C. W. Yin, and M. B. Tong, Research on interface performance of the T reinforced composite structures, J. Jiangsu Aviation, S1 (2012) 111-113, (In Chinese).

[3] S. W. Stawski, U.S. Patent,4,789,594 [P].(1988)

[4] R. D. Gross, B. D. Kushner, U.S. Patent,5,650,229A[P].(1997)

[5] D. A. McCarville, J. S. Howitt, and M. L. Younie, U.S. Patent,5,833,786A.(1998)

[6] P. E. George, K. B. Kajita, and B. P. V. West, U.S. Patent,6,709,538 B2[P].(2004).

[7] M. Petersson, P. Hallander, and B. Weidmann, U.S. Patent,7,758,715B2[P].(2010)

[8] P. Hallander, M. Petersson, and B. Weidmann, et al, U.S. Patent,2012/0,074,265A1[P]. (2012)

[9] W. L. Gants, W. T. Kline, and J. T. Sneddon, U.S. Patent,4,559,005 A[P].(1985)

[10] F. C. V. Derau, M. G. Cavin, U.S. Patent,4,778,545[P].(1988)

[11] Y. F. Luo, G. Q. Peng, and Z. H. Cao, et al, Application of Composites Manufactured With Out-of-Autoclave Prepreg for Aviation Industry, J. Aeronautical Manufacturing Technology, 18 (2012) 26-31, (In Chinese).

[12] L. K. Grunenfelder, S. R. Nutt, Void formation in composite prepregs–Effect of dissolved moisture, J. Composites Science and Technology,70(2010)2304-2309.

Advanced Materials Research Vol. 936 (2014) pp 1985-1988
© (2014) Trans Tech Publications, Switzerland
doi:10.4028/www.scientific.net/AMR.936.1985

Comparative Study Of High-Power White Led'S Lifetime Based On Temperature Accelerated Test

Shi wei, Zou Nianyu, Zhang Yuncui, Li Desheng

Research Institute of Photonics Dalian Polytechnic University

No.1 Qinggongyuan, GanjingziDist, Dalian 116034, China

email: desheng@dlpu.edu.cn

Keywords: LED; lifetime; temperature; Arrhenius model.

Abstract: The lifetimes of two white high-power LEDs were studied based temperature-acceleration life test. the acceleration temperatures were selected as 100°C and 90°C separately in the experiment, and the accelerated time was 800 hours. Based on Arrhenius model, activation energy of the two tested samples are 0.6978 and 0.7014 separately, and lifetime are7.41×10^5h and 1.46×10^5h separately. Our experimental results showed that the quality of the two type LEDs is very different, and lifetime of 50000 hours is recommended as the threshold of entering the market for high power white LEDs.

Introduction

The white LED is considered as one of the most potential and preponderant commodities, which can replace traditional lighting device in the industry. White LEDs gradually enter the field of general lighting with lower cost and the increase of luminous efficiency [1]. But at the moment, the quality of white LEDs is very differently. Take lifetime for example, the lifetime of good quality LEDs can reach tens of thousands of hours, but some products can only own a few thousands hours. Long lifetime ensures LED can be widely used in various areas, so the study on the reliability of LED is very important [2-6].

Recently, there are two main approaches to test high-power LED's lifetime, which are temperature acceleration experiment and current acceleration experiment [7-8].The main mechanism of Accelerated lifetime test (ALT) is to make devices work in higher stress than the actual stress levels, so as to shorten the failure time of the device, and then according to the calculation formula to get the lifetime under normal use conditions. In this paper, the lifetimes of two white high-power LEDs were studied based temperature-accelerate life test, and some recommendations for evaluating white LED's lifetime and establishing related standards were proposed.

Arrhenius model

Arrhenius model is commonly utilized in temperature-accelerated lifetime test, which reflects the connection among product's performance, activation and stress. The luminous power of LED is degenerative with time, and the relationship is expressed in the form of exponent, as following,

$$P_t = P_0 exp(-\beta t) \quad (1)$$

Where, P_t is luminous power (or flux) after time t, P_0 is original value of light efficacy (or flux), β is the attenuation coefficient under certain temperature.

The lifetime of LED is usually defined the time of flux from original to 70%. In accelerated lifetime test, for luminous power attenuate to P_i after t_i , the relationship between them is given by equation (2).

$$L_{(c,i)} = t_i \frac{ln0.7}{ln\frac{P_i}{P_0}} \tag{2}$$

Where, $L_{(c,\,i)}$ is the time of flux from original to 70%.

The attenuation coefficient and junction temperature T_j satisfy Arrhenius model, as showed in equation (3).

$$\beta = \beta_0 I_f \exp(-E_a/kT_j) \tag{3}$$

Where, I_f is operating current of LED, and E_a is activation energy, which is one certain value for certain LED. Combining equation (1) and (3), the lifetime of LED L_c in normal condition could be calculated.

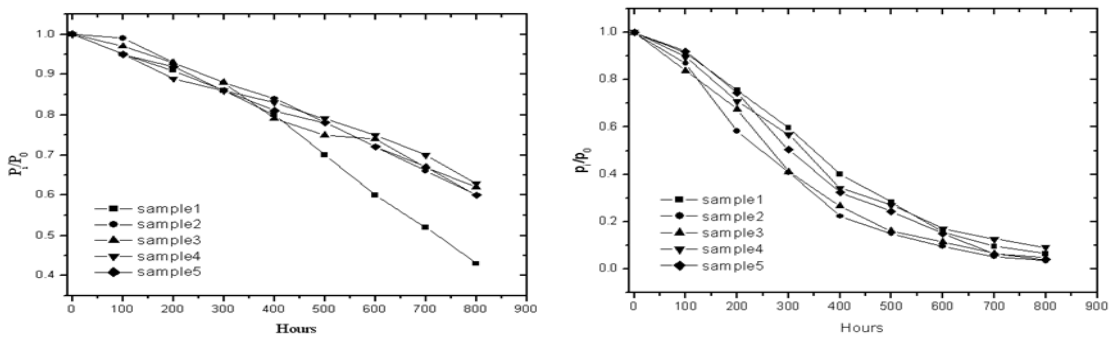
$$L_c = L_{(c,i)} \exp \frac{E_a}{k} \left(\frac{1}{T_{(j,o)}} - \frac{1}{T_{(j,i)}}\right) \tag{4}$$

Where, $T_{(j,i)}$ is the junction temperature of LED under accelerated temperature, $T_{(j,o)}$is the junction temperature of LED under normal operating conditions.

Experiment and result analysis

The tested white LEDs are selected from different manufacturer production, Marked as sample A and sample B, respectively, and ten LEDs were selected randomly for each kind of sample. In the experiment, all the tested LEDs were stressed under two different forward-temperature densities 100°C and 90°C for up to 800 h. The temperature stress is provided by high and low temperature alternating temperature humidity test chamber, which is applicable for the testing of electrical and electronic products, components and parts in high-temperature, low-temperature, humid and heat environment. The samples were tested at intervals of 100 hours at ambient temperature, using an integrating sphere and a silicon photodiode-array fiber-optic spectrometer. To ensure accurate measurements of the changes in light output, the testing setup remained constant during the stress period.

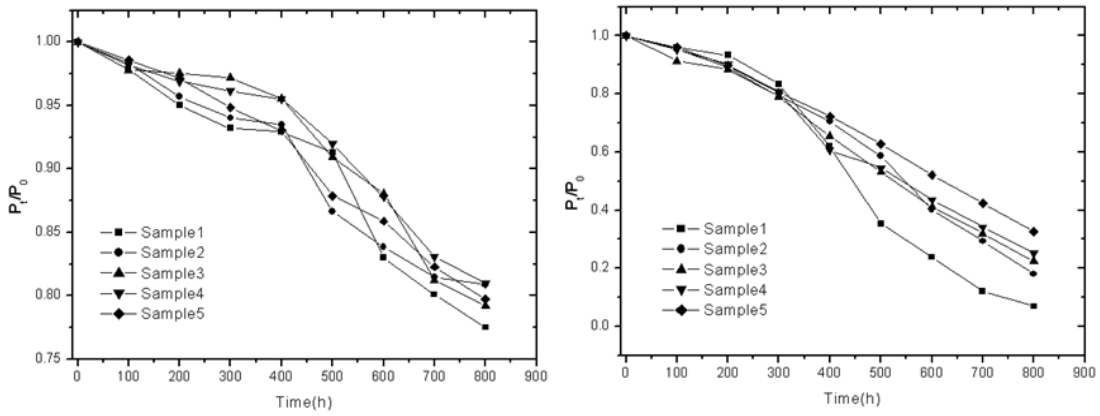
The luminous flux degradation curve for two kind of tested sample sunder 100°C and 90°C were obtained, shown in Figure 1 and Figure 2, respectively.



sample A sample B

Fig.1. Luminous flux curves of tested samples under 100°C

Under the condition of 90°C, Two samples of luminous flux decay curve is shown in figure 2, respectively.



sample A sample B

Fig.2. Luminous flux curves of tested samples under 90°C

The thermal resistances of two kinds of LED samples are about 9°C/W and 15°C/W. Assume using under ideal conditions, that is, the shell temperature is 25°C, thermal resistance temperature of two samples are 9°C and 15°C, respectively. Based on the theory of Arrhenius model, the activation energy of sample A is 0.6978 and sample B is 0.7014. Lifetimes of the two kind of tested LEDs were calculated. And our experimental results showed that the lifetime of the two type LEDs is very different, 7.41×10^5h and 1.46×10^5h separately, which means the quality of sample A is much better than sample B.

Conclusion

The actual lifetime of white LED has become the major concern, whether for LED light source manufacturers or LED light source users, so it is very important to study the lifetime of white LED. In this article, Comparative study of high-power white LED's Lifetime through temperature accelerated test based on the Arrhenius model were demonstrated, and lifetime of two type of tested samples are calculated 7.41×10^5h and 1.46×10^5h respectively. Nowadays, both high quality white LEDs and low quality products are exist on the market, so it is very important to establish relative national standard to constrain the quality of LED products. Here lifetimes of 50000 hours were suggested for high-power white LED as the threshold of entering the market.

ACKNOWLEDGEMENT

This work is supported by the National Technology Support Project for the 12th five-year plan (NO.2011BAE01B00), scientific research project of Liaoning Province (L2012184), excellent talents plan project for universities of Liaoning Province (NO. LR201006), and Youth Fund of Dalian Polytechnic University (NO.QNJJ201219).

References

[1] Hao Luoxi, Yang Xiu. Innovation and Tendency of LED Lighting Based on LED's Feature [J]. China Illuminating Engineering Journal, 2012, 23(1):1-6 (in Chinese).

[2] Li Desheng, Zou Nianyu, He Xiaoyang, et al. Accelerated life test on white LEDs based on flux degradation and color temperature drift [J]. ICIC Express Letters, 2012, 6 (9): 2389-2393.

[3] S. Koh, W.D.vanDriel, Cadmus Yuan, et al. Solid State Lighting System Reliability. [C]. Proceeding ChinaSSL 2011, pp121-126.

[4] E. Suhir. Accelerated Life Testing in Photonics Packaging: Its Objectives, Role, Attributes, Challenges, Pitfalls, Predictive Models, and Interaction with Other Accelerated Stress Categories. Laser Diodes, Optoelectronic Devices, and Heterogenous Integration, 2003, 175-196.

[5] W. Y. Ho, Charles Surya, et al. Studies of High DC Current Induced Degradation in Ⅲ-Ⅴ Nitride Based Heterojunctions. IEEE Trans on Electron Devices, 2000, 47(7):1421-1425.

[6] Li Desheng, Zou Lin, Zhang Yuncui, et al. Evaluation of reliability for LED lamp based on fuzzy algorithm [J]. Optics and Precision Engineering, 2012, 20(12):2661-2666 (in Chinese).

[7] G. Meneghesso, S. Levada, E. Zanooonnni, et al. Failure Modes and Mechanisms of DC-Aged GaN LEDs [J]. Phys. Stat. sol. 2002, 194(2):389-392.

[8] Gao Jinhuan ,PengHao , Wu Hongyu, et al. Evaluation of Power LED Operation Life. [J]. Semiconductor Technology, 2009, 34(5): 452-457. (in Chinese).

Advanced Materials Research Vol. 936 (2014) pp 1989-1993
© (2014) Trans Tech Publications, Switzerland
doi:10.4028/www.scientific.net/AMR.936.1989

Study of surface-enhanced Raman spectroscopy of crystal violet in acid aqueous

Xin Jia[1, a *], Lingling Dong[2, b]

[1]Department of Mathematics and Physics, Shanghai Dianji University, 201306, China

[2]Department of Chemistry, Fudan University, 200433, China

[a] jiaxin@sdju.edu.cn, [b] dongling@fudan.edu.cn

Keywords: surface-enhanced Raman scattering; crystal violet; silver colloid; acid effect

Abstract: We reported the spectra intensity of surface enhanced Raman scattering (SERS) for crystal violet with changing the acid concentration. The SERS signals of crystal violet ascended firstly and then descended with the acid concentration increasing when we put the nitric acid into the crystal violet-silver colloid system. The phenomenon was considered to be associated with the interaction between hydrogen ions and crystal violet, which may influenced the SERS signals.

Introduction

Surface-enhanced Raman scattering (SERS) is a unique surface optical phenomenon for that Raman signals of the molecules adsorbed on some metal surface can be enhanced by a factor of several millions. Surface-enhanced Raman spectroscopy shows high sensitivity for detecting the molecules in sub- and monomolecular layers, and presents plentiful surface informations of the structural change. Therefore, the spectroscopy has been widely used in some scientific and technical fields, such as chemistry, biology, surface science, qualitative and quantitative analysis [1-10]. SERS has become a usefule techinique for the rising monomolicular science [8]. The appropriate substrate is the premises to obtain favorable surface enhancement and metal colloids are widely used as substrates for their low cost, simple preparation and favorable enhancement [4, 5].

Crystal Violet (CV) is a purple dye molecule and also a kind of biological chromosin due to the strong fluorescence [11-15]. CV molecules have the characteristics of typical symmetric structure, belonging to three aryl dye and three dimethyl aniline groups link in the center of carbon atoms. CV molecules can interact with biological macromolecule, such as DNA and protein, so that the signals of CV via spectrophotometric or light scattering methods can be measured to indicate the structural changes of DNA or protein. CV could be used as Raman markers and the structure information of molecules marked by CV molecules could be detected via Raman microscopy. However, there is little work on SERS spectra of CV at different solution acidities. In this manuscript, we study the SERS signals of CV with changing the solution acidity and explain the possible mechanisms.

Materials and Experiments

Reagents: Nitric acid (HNO_3); Sodium citrate ($Na_3C_6H_5O_7 \cdot 2H_2O$); Silver nitrate ($AgNO_3$); CV ($C_{25}H_{30}N_3Cl \cdot 9H_2O$). The reagents were analytically pure and the water was three times distilled deionized water.

Silver colloid was prepared according to Lee's method [1]. 36mg silver nitrate was added into 200 ml deionized water and heated to boilling rapidly. Then, 8 ml sodium citrate solution with a concentration of 1% was added with vigorous stirring. Boiling state was kept for 60 minutes and naturally cooled to room temperature with stable stirring. The dark gray green silver colloid was prepared to be added to CV solution as the suface-enhanced substrate for detection of SERS spectra.

Raman spectra was acquired by a confocal micro-Raman spectrometer (Jobin-Yvon, T64000) equipped with a 514.5 nm diode laser and an integrated Olympus IX81 microscope.

Results and Discussions

Figure 1 shows the typical Raman spectra of CV after incubation with the silver colloids (b) and the normal Raman spectra (a). The SERS spectra show a high signal-to-noise ratio whereas the normal spectra are not oberved at the same experimental conditions.

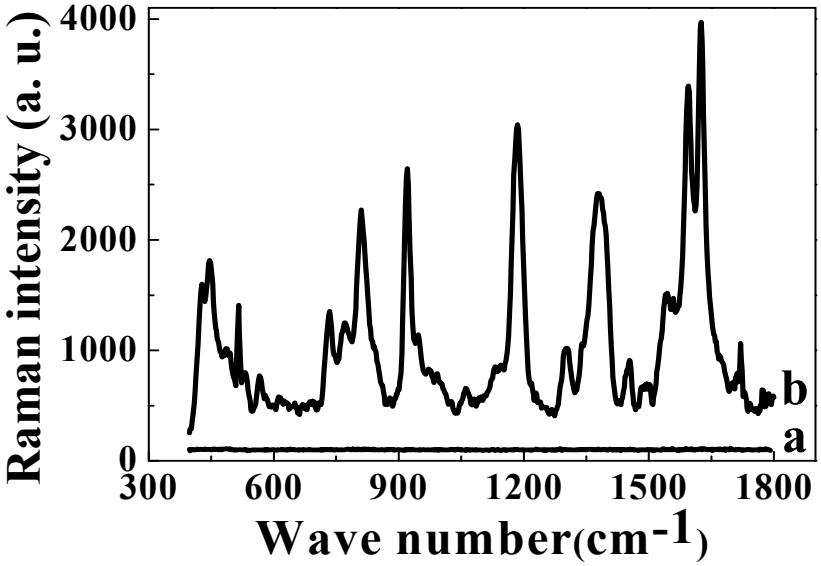


Fig. 1 Raman spectra of CV solution (1×10^{-6} mol/L)：a normal Raman spectra；b SERS spectra.

Most of the Raman bands are observed for the SERS spectra, which indicates the good adsorption between CV molecules and silver nanoparticles. After adding the silver nanoparticles, the fluorescence quenching of dye molecule, change of system colors and increase of resonant scattering may be due to the micelles formation and molecular polarization effects [14]. Nitrogen atoms in CV molecules have lone pair electrons and the benzene ring has π electrons, which results in the charge transfer between the CV molecules and the silver atoms surface as well as a molecular channel of nonradiative attenuation. The fluorescence of CV molecules quenches greatly and the enhanced Raman signals are obtained.

Nitric acid with a concertration of 5×10^{-3} mol/L is added into CV-silver colloid system and the intensity of SERS spectra increase 5-10 times, as shown in Fig. 2.

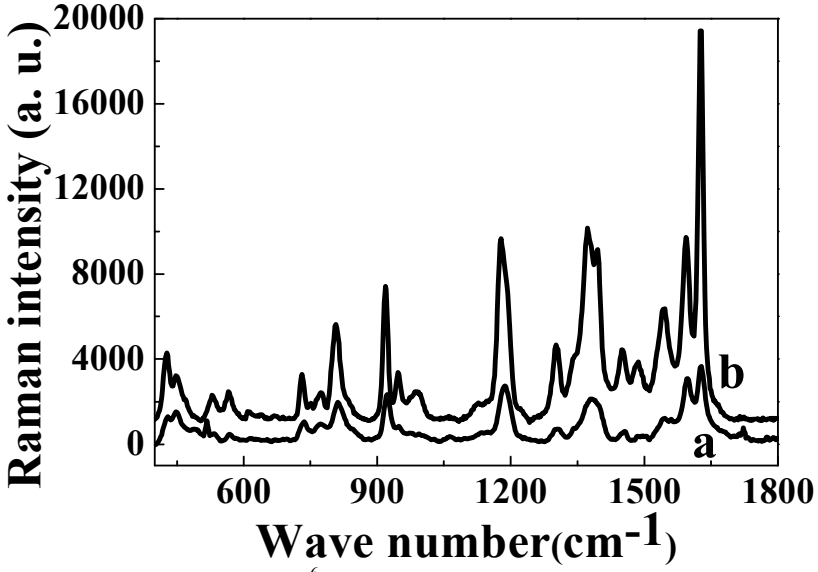


Fig. 2 SERS spectra of CV (1×10^{-6} mol/L) without nitric acid (a) and with nitric acid (b).

The SERS spectra bands corresponding to the information of the molecular structures are shown in Table 1 [14].

Table 1 Assignment of SERS bands for CV with and without nitric acid

SERS bands [cm^{-1}]	SERS bands after nitric acid addition [cm^{-1}]	Assignment of vibration modes
427.8	427.1	Out-plane vibration of Ph-C^{+}-Ph bend
531.8, 567.2, 920.7, 946.7, 1015.3	528.9, 565.6, 609.0, 918.1, 946.7, 988.3, 1016.7	Ring skeletal vibration of radical orientation
734.1, 770.0, 810.0	731.3, 773.9, 807.4	Out-plane vibration of ring C-H bend
1185.0	1178.4	In-plane vibration of ring C-H bend
1303.6	1301.4	Phenyl ring C-C stretching
1379.0	1372.7, 1395.7	N-phenyl stretching
1449.6, 1493.0	1449.6, 1486.8	Phenyl ring C-C stretching + ring deformation
1546.3	1546.3	Phenyl ring C-C stretching + N^{+} = phenyl stretching
1595.2	1593.3	Phenyl ring C-C stretching and bend
1623.6	1625.8	Phenyl ring C-C stretching + N - phenyl stretching

According to the SERS bands of CV in Table 1, when CV molecules are adsorbed on silver colloid surface and mixed with acid solution, most of the bands are enhanced and frequency-shifted, from which the interaction between CV molecules and silver nanoparticles can be infered. Bands at 916.3, 947.6, 527.2 and 566.2 cm^{-1} are assigned to ring skeletal vibration of radical orientation and relative intensity has a large increase in SERS spectra, which indicates that the CV molecules are adsorbed on the surface of silver colloid via a big π bond. Therefore, intense interaction of the nitrogen atoms and carbon atoms with silver ones is produced, which analogously acts as an coordination bond. With regard to the 5-10 times increase of SERS spectra intensity of CV after nitric acid addition, we propose that the combination of hydrogen ions with CV molecules may generate a kind of unstable coordination compond only existing in the acidic condition, which is electropositive and more easily adsorbed on the silver colloid so that better Raman signals are obtained.

We add the nitric acid of different concentrations into CV-silver collide system and measure the respective SERS spectra, as shown in Fig. 3.

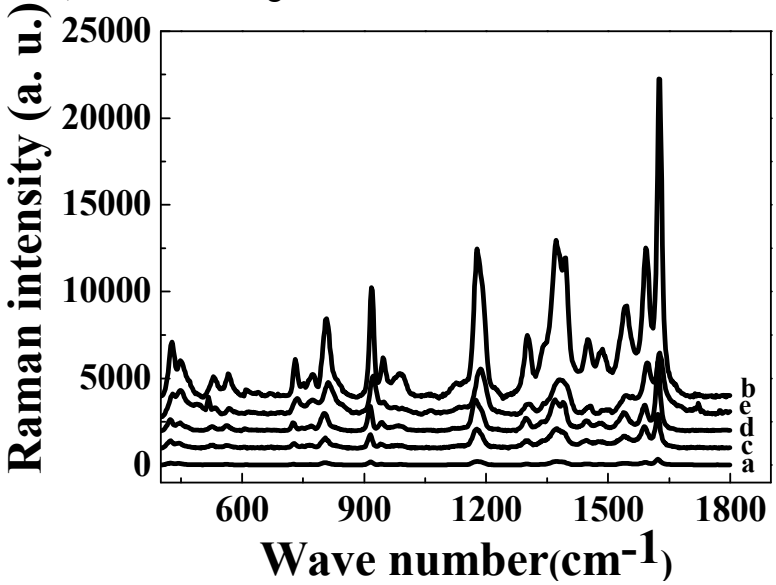


Fig. 3 SERS spectra of CV-silver colloid in nitric acid solution at different concentrations. a 0mol/L; b 0.005mol/L; c 0.0001 mol/L; d 0.01 mol/L; e 0.001mol/L.

Six characteristic SERS bands of CV are chosen to be compared dependent on the concentrations of nitric acid solution, given in Fig. 4. The intensity of SERS bands at 427.1, 918.1, 1176.2, 1301.4, 1593.3, 1625.8 cm^{-1} ascends gradually with the acid concentrations increasing from 0 to 0.005 mol/L and descends with the acid concentrations further increasing, which indicates a maximum value of SERS spectra intensity for CV with the modification of acid concentrations.

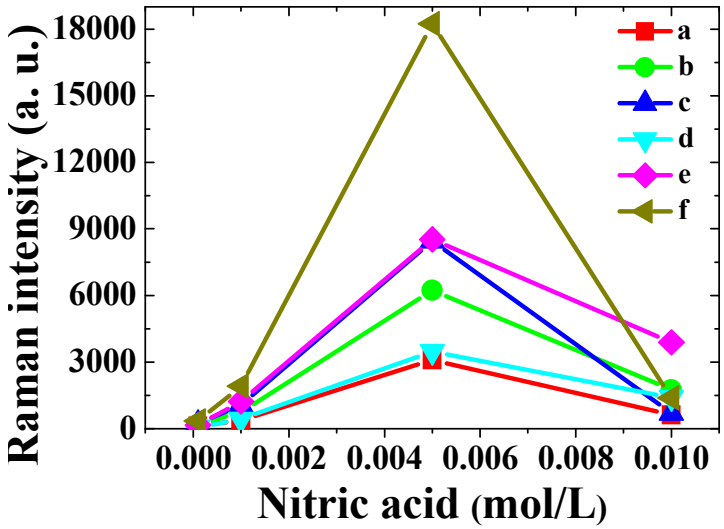


Fig. 4 The intensity of six characteristic SERS bands as a function of concentrations of nitric acid solution. Bands [cm-1]: a 427.1; b 918.1; c 1176.2; d 1301.4; e 1593.3; f 1625.8.

A kind of unstable coordination compond, only existing in the acidic condition, is produced by combination of hydrogen ions of nitrid acid with CV molecules, while it is electropositive and more easily adsorbed on the silver colloid, which leads to better Raman signals. The quantities of the coordination compond increase following the concentration of hydrogen ions (namely acid concentration), so the SERS signals asend in the acid concentration range from 0 to 0.005 mol/L. However, when acid concentration become larger, emerging agglomerate of silver colloid reduce the quantities of enhanced-effect silver atoms, which makes SERS signals of CV decrease.

Summary

The spectra intensity of SERS for CV with changing the acid concentrations was studied. The SERS spectra intensity intially ascended and then descended with the acid concentration increasing in the CV - silver colloid system, which indicated a maximum value of SERS spectra. The phenomenon was considered to be associated with the interaction between hydrogen ions and CV, which may influenced the SERS signals.

Acknowledgements

This work is supported by National Natural Science Foundation of China (11104178), Innovation Program of Shanghai Municipal Education Commission (14YZ156), Young Teacher Program of Shanghai University (shdj006), and Discipline Foundation Project of Shanghai Dianji University (12XKJC01).

References

[1] P. C. Lee, D. Meisel, Absorption and surface-enhanced Raman of dyes on silver and gold sols, J. Phys. Chem. 86(1982) 3391–3395.

[2] S. Nie, S. R Emory, Probing Single Molecules and Single Nanoparticles by Surface-Enhance Raman Scattering, Science 275 (1997) 1102-1106.

[3] K. Kneipp, Y. Wang, H. Kneipp, L. T. Perelman, I. Itzkan, R. R. Dasari, M. S. Feld, Single Molecule Detection Using Surface- Enhanced Raman Scattering (SERS), Phys. Rev. Lett. 78 (1997) 1667-1670.

[4] Y. S. Li, J. C. Cheng, Y. Wang, Surface-enhanced Raman spectra of dyes and organic acids in silver solutions: chloride ion effect, Spectrochimica Acta A 56 (2000) 2067-2072.

[5] L. Guo, X. Zhang, Z. Du , Y. Huang, Y. Mo, The Charge Transfering between Silver Nanoparticles and R6G, Spectrosc. Spect. Anal. 21 (2001) 16-18.

[6] S. L. Kleinman, E. Ringe, N. Valley, K. L. Wustholz, E. Phillips, K. A. Scheidt, G. C. Schatz, R. P. van Duyne, Single-Molecule Surface-Enhanced Raman Spectroscopy of Crystal Violet Isotopologues: Theory and Experiment, J. Am. Chem. Soc. 133 (2011) 4115-4122.

[7] R. Li, Z. Y. Guo, Z. F. Zhuang, K. Xiong, S. J. Chen, S. H. Liu, Quantitative Analysis of Crystal Violet by Raman Spectroscopy, Spectroscopy 27 (2012) 54-57.

[8] B. Sharma, R. R. Frontiera, A. I. Henry, E. Ringe, R. P. Van Duyne, SERS: Materials, applications, and the future, Mater. today 15 (2012) 16-25.

[9] W. Xie, S. Schlücker, Medical applications of surface-enhanced Raman scattering, Phys. Chem. Chem. Phys. 15 (2013) 5329-5344.

[10] P. Negri, K. T. Jacobs, O. O. Dada, Z. D. Schultz, Ultrasensitive Surface-Enhanced Raman Scattering Flow Detector Using Hydrodynamic Focusing, Anal. Chem. 85 (2013) 10159-10166.

[11] L. Angeloni, G. Smulevich, M. P. Marzocchi, Resonance Raman Spectrum of Crystal violet, J. Raman Spectroscopy 8 (1979) 305-310.

[12] J. D. Jiang, E. Burstein, H. Kobayashi, Resonant Raman Scattering by Crystal-Violet Molecules Adsorbed on a Smooth Gold Surface: Evidence for a Charge-Transfer Excitation, Phys. Rev. Lett. 57 (1986) 1793-1796.

[13] E. J. Liang, C. Engert, W. Kiefer, Surface-enhanced Raman scattering of halide ions, pyridine and crystal violet on colloidal silver with near-infrared excitation: low-wavenumber vibrational modes, Vib. Spectrosc. 8 (1995) 435-444.

[14] Y. Du, Y. Fang, NIR-SERS Study on Crystal Violet Molecules at Acidic Conditions, Chin. J. Light Scattering 15 (2003) 131-138.

[15] A. Kudelski, Raman studies of rhodamine 6G and crystal violet sub-monolayers on electrochemically roughened silver substrates: Do dye molecules adsorb preferentially on highly SERS-active sites?, Chem. Phys. Lett. 414 (2005) 271-275.

Advanced Materials Research Vol. 936 (2014) pp 1994-1998
© (2014) Trans Tech Publications, Switzerland
doi:10.4028/www.scientific.net/AMR.936.1994

Evaluation of Sound Absorption Capability from PET Mesh to PET/PU Composite Board

YuCheng Liu[1,a], JinHuang Huang[2,b], ChenHung Huang[1,3,c], MinHon Tsai[1] and YuChun Chuang[4]

[1]Master's Program of Electro-Acoustics, Feng Chia University, Taichung City 407, Taiwan.

[2]Department of Mechanical and Computer-Aided Engineering, Feng Chia University, Taichung City 407, Taiwan.

[3]Department of Aerospace and Systems Engineering, Feng Chia University, Taichung City, 407, Taiwan.

[4]Laboratory of Fiber Application and Manufacturing, Department of Fiber and Composite Materials, Feng Chia University, Taichung City 407, Taiwan.

[a]yucliu@fcu.edu.tw, [b]jhhuang@fcu.edu.tw, [c]chhuang@fcuoa.fcu.edu.tw

Keywords: absorption coefficient, nonwoven, foam, PU composite board, impedance tube.

Abstract: This article completely investigates from nonwoven to PET/PU composite board on the variations of absorption coefficient by using standard impedance tube with four microphones. Recently, PET/PU composite board is becoming one popular and functional material because of the high flexibility in the abilities, such as thermal-protection, chemical-proof, acoustic-resistance and etc.. Thus, it is important to realize the variations of absorption capability from single material to complete composite material, and feedback some suggestions to the designer. Results shows that nonwoven only has a stable increase in absorption coefficient with the frequencies because of the inherent porous characteristics. With the substantial properties, foam has lower absorption coefficient and two peaks occurring in the higher frequencies. Both two peaks are caused by the resonance between wave and foam at specified frequency. With an additional nonwoven in the rear side of composite foam, absorption coefficient of PET/PU composite board will effectively increase. Based on the diverse applications, absorption coefficient of PET/PU composite board can be flexible modulated to consistent with the requirements.

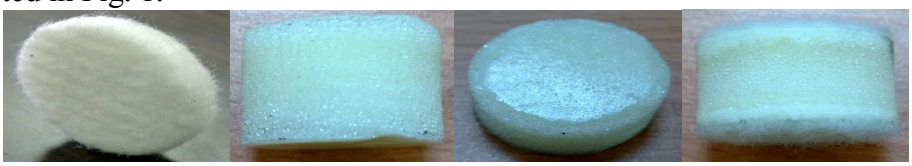
Introduction

With recent rapid advancement of techniques, human life had definitely improved and became more and more convenient. Meanwhile, the situation of some pollution, such as air, water, noise and etc., are more and more serious and emphasized recently, especially in the factories. One of common example is that the noise coming from working machine will jeopardize workman's hearing and cause occupational disease. Thus, the techniques and limitations of noise control is derived and becoming a standard [1]. At present, passive noise control which utilizes the internal structures of composite material and places around the noisy machine to resist or block the noise transmission is one cheaper, useful, and popular method [2]. Plenty researches are focused on the inventions of diverse composite material, such as polyethylene teraphthalate (PET), thermoplastic polyurethane (TPU) honeycomb grid, or polyurethane (PU) foam [3,4]. This article was conducted to explore the sound absorption capabilities beginning from single material of nonwoven and foam to the composite material of nonwoven-foam and nonwoven-foam-nonwoven. The influence of the internal organizations and structures of composite material will also be completely discussed.

Experiments

Material preparations and experiments

All of the experimental materials, such as flame-retardant polyester (PET) fiber and porous-structure Polyurethane (PU), were provided by Far Eastern New Century Corporation and Zhongxing Chemical, Taiwan, respectively. In the part of nonwoven, flame-retardant PET composite nonwoven fabrics were fabricated by 6D flame-retardant PET fibers after the processes of opening, blending, carding, lapping, and needle-punching (100 needles/min). In the part of foam, based on the mixture of Polyol and Isocyanate with the optimal percentage of 1:1, porous-structure Polyurethane foam can be made by the foaming and curing processes. During the foam processing, various bulk density of foam can also be controlled and modulated. PU composite boards, finally, can be completed by the compounds of flame-retardant PET mesh composite fabric and PU foam. All the samples are listed in Fig. 1.

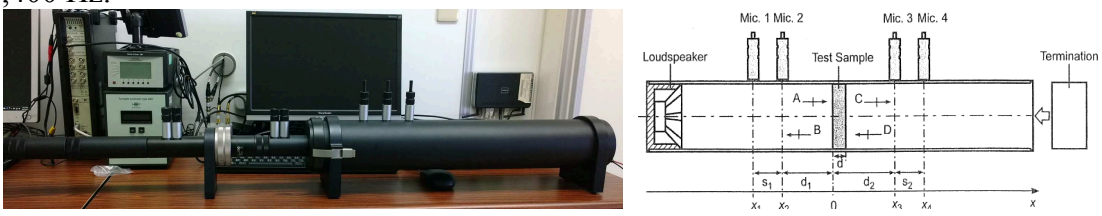


(a) (b) (c) (d)

Fig. 1. Samples; (a) nonwoven only; (b) foam only; (c) foam-nonwoven; (d) nonwoven-foam-nonwoven.

Testing by impedance tube

Absorption coefficient which is often utilized to assess if this material belongs to an absorption material is an important parameter. A useful tool, impedance tube, is not only usually used to obtain absorption coefficient but also serve as standard processes, such as ASTM E 1050-95. Due to the smooth, nonporous, and dusty-free inside the tube, wave energy with low attenuation inside the tube can be guaranteed, and precise results for material characteristics can be obtained. In this article, the impedance tube with 29 mm in diameter, Brüel & Kjær, type 4206T shown in Fig. 2, will be utilized to investigate the variations of absorption coefficient for these five composite material. Based on the geometric limitations of tube, all of the testing results are focused on the frequency range between 500 Hz to 6,400 Hz.



(a) (b)

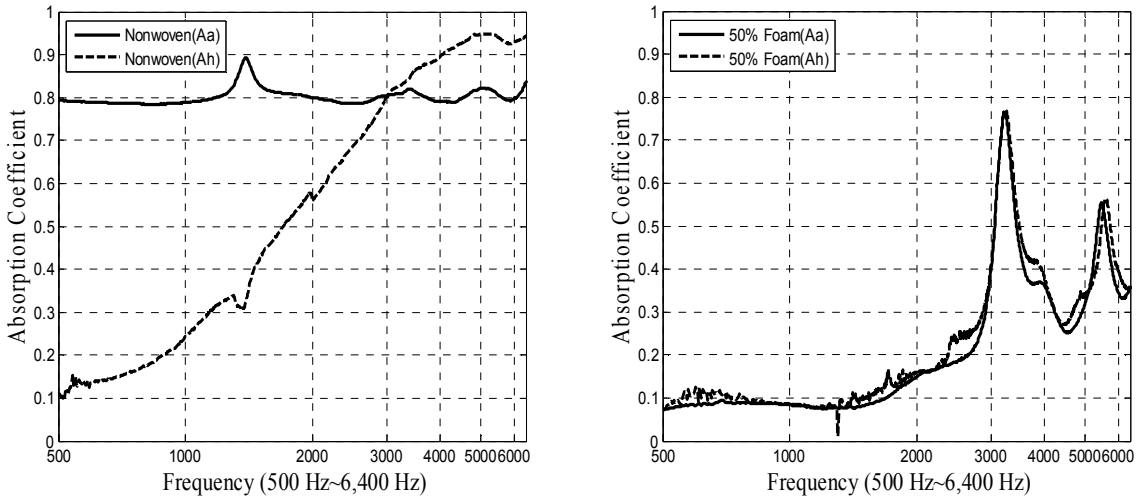
Fig. 2. Brüel & Kjær type 4206; (a) experimental picture; (b) schematic diaphragm inside the tube.

Discussion

Absorption characteristics for single nonwoven and signal foam

With different conditions behind the material in the tube, the absorption coefficient of different material, shown in Fig. 3, will be much different. Based on the condition with reflected board behind the nonwoven shown in Fig. 3(a), the absorption coefficient will increase with the frequencies instead of the constant value (0.8) which can be found under the condition without reflected board. Theoretically, nonwoven which is one of common porous material should belong to an absorption material, and have the capability of absorbing sound. If the reflected board locates closely behind the material, wave or sound passing through the material and immediately reflecting back to the tube, especially for the wave with longer wavelength or lower frequencies. Thus, the absorption coefficient will be much minor in the lower frequencies. With the increase of frequencies(> 1,500 Hz), the respective wavelength will become shorter enough, and its energy can be dissipated by the holes inside the nonwoven itself. Without the reflected board, there is no reflection of wave and dissipation

of energy during the wave passing the nonwoven. The absorption coefficient of nonwoven should be constant in the frequency ranges. However, this situation will not be found in the material with high density or solid construction, such as foam with 50% bulk density shown in Fig. 3(b). Thus, based on the different applications and compositions with porous material, the absorption capability of composite material will be much different and should be carefully paid attention.



(a) (b)

Fig.3. Absorption coefficients for signal material: (a) Nonwoven; (b) Foam with 50% bulk density.
(Note: Both lowercase letter, h and a, attached behind of A represent the conditions behind the material with and without reflected board, respectively.)

With foam only testing in the tube, Fig.3(b) shows that the absorption coefficient will increase slowly with the frequencies. In other words, foam with 50% bulk density can be recognized as the material with the ability of absorption only with the frequency above 3,000 Hz. This absorbing capability is coming from the inherent holes inside the foam in the initial foaming processes. These holes have enough abilities to limit the motions or dissipate the energy of wave in the shorter wavelength(higher frequencies). In addition, two peaks which also represent the higher absorption capability can be observed at 3,100 Hz and 5,600 Hz. The amplitude of peaks will reduce with the frequencies evidently. The phenomenon of both abrupt increments can be conjectured that the wave in the specified frequency have enough ability to enter the foam material, and be just consistent with the internal size and construction of foam. Then, the resonant phenomenon inside the foam occurs, and wave energy further dissipates with the resonance. By the observation of above results, thus, foam with different bulk density is useful to deal with the absorption in the specified frequency.

Absorption coefficient for the both arrangements between nonwoven and foam

Fig. 4 shows the change of absorption coefficients for both arrangements between nonwoven and foam with 50% bulk density. Obviously, absorption coefficient obtained under the arrangement of foam-nonwoven is higher than that under the arrangement of nonwoven-foam, especially above 1,500 Hz. This is because that the adhesive layer existed between foam and nonwoven will form a higher reflected interface to resist the wave propagation. For the nonwoven-foam type, this layer is located in front of the foam-nonwoven type. Thus, most parts of wave energy had been blocked to enter to the foam. In addition, similar to the results for foam only, two peaks possibly resulted from the resonance between foam and specific frequency of wave in the higher frequencies can also be found.

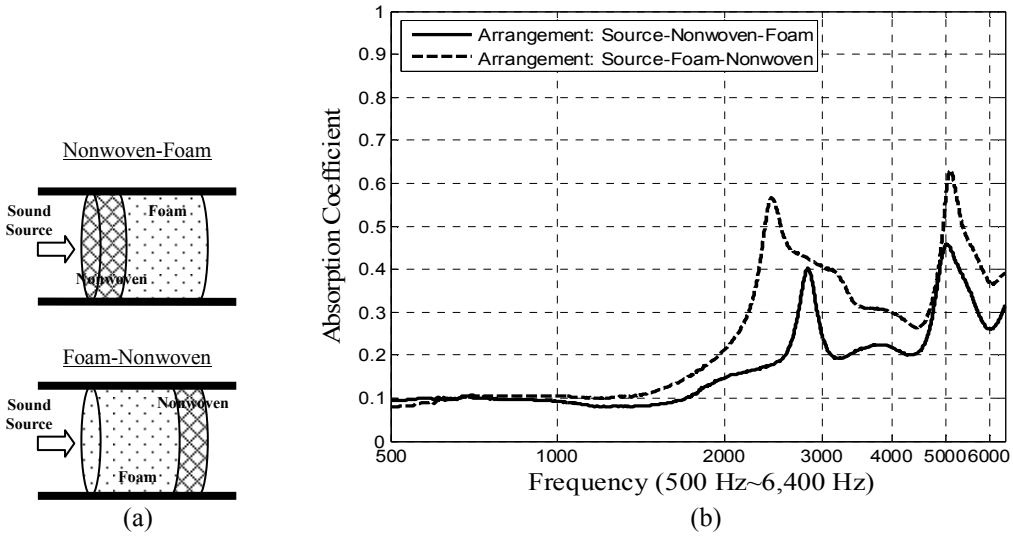


Fig. 4. Absorption coefficient for the composite material with 50 % bulk density in foam; (a) both arrangements; (b) nonwoven-foam(full line) and foam- nonwoven(dashed line).

Absorption coefficient for nonwoven-Foam-Nonwoven with various bulk density

The functional PU composites board with nonwoven layers glued on the both sides of foam can be usually found in the practical applications, especially in the chemical proof, mechanical impact-resistance, thermal protection and etc.. Fig. 5 shows the related performance of absorption coefficient for this composite material with various bulk densities. With the increase of bulk density in foam, the frequency of first peak of absorption coefficient decreases and converges gradually. Because of an additional nonwoven glued on the other side of foam, the level of absorption coefficient will be lower than that in Fig. 4 which only one nonwoven is located on one side of foam. The peak cause by the resonance between propagating wave and foam can also be obtained in this case. After this peak frequency, absorption coefficient abruptly decreases and then increases again until the next resonant frequency coming. Due to the artificial error in the processing and experiment, the variations of absorption coefficient between first and second peak frequency can be found to be irregular instead of the with 60% foam.

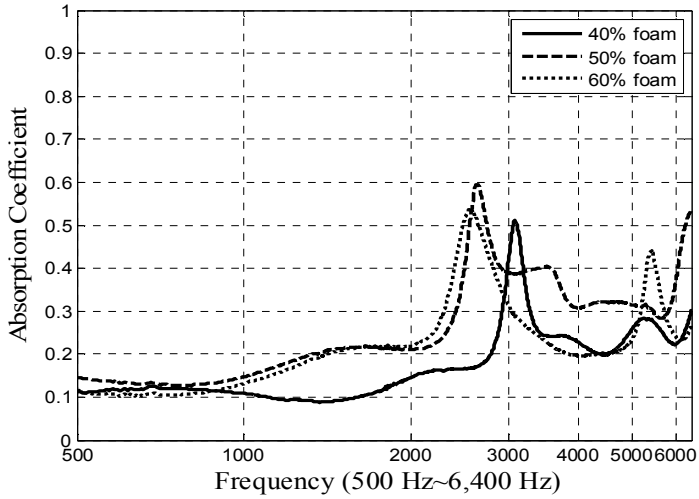


Fig. 5. Absorption coefficient with three kinds of bulk density in foam.

Comparisons

Fig. 6 integrates and collects all the performance of absorption coefficient discussed above. Obviously, Due to the inherent porous characteristics, the level of absorption coefficient of only nonwoven is the highest, and increases dramatically with the frequency. For foam only, absorption coefficient is not only lower than nonwoven but more importantly, two peaks in the higher

frequencies can also be obtained because of the resonance between propagating wave and size of foam inside the impedance tube. Due to the influence of glue layer between nonwoven and foam, absorption coefficient will reduce especially in the case of nonwoven-foam instead of foam-nonwoven. However, when the foam are glued with nonwoven in the both side of foam, the level of absorption coefficient will be increase in evidence. It is conjectured that the additional contribution and increase of absorption coefficient is coming from the rear side of nonwoven.

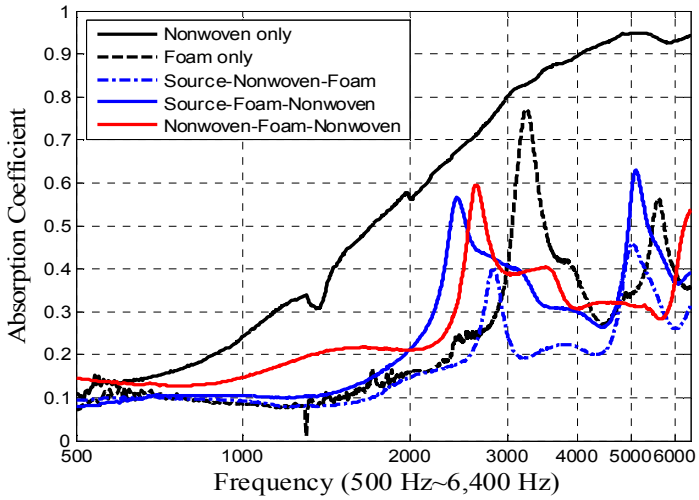


Fig. 6. Comparisons for all composite board

Summary

This article successfully and comprehensively investigates the performance of absorption coefficient from nonwoven to nonwoven-foam-nonwoven. Theoretically, the material such as nonwoven had highest absorption capability because of the porous characteristics in the organization. With the increase of frequency, these porous characteristics inside the material has more possibilities to limit and dissipate these propagating wave. Thus, level will increase with frequencies. Due to the foam processing and bulk density, foam which has more solid properties inside will reduce the absorption capability and caused two abrupt peaks in the higher frequencies because of resonance between structure and wave. With the nonwoven located in the rear side of PU composite board, absorption coefficient will obviously increase. Therefore, based on the diverse applications, the characteristics of functional PU composite such as absorption capability can be controlled and modulated artificially. Of course, some important and potential parameters, such as thickness of foam and nonwoven, which will cause the variations of absorption coefficient should be investigated in the future.

References

[1] H.CL. Shih, C.Y. Chuang, Noise Control Manual, Noise Control Network, 1987.

[2] L.L. Beranek, Noise and Vibration Control, New York, McGraw Hill, 1988.

[3] T.Y. Huang, K.C. Chan, Study of Nonwoven Acoustic, Chinese Culture University of the 5th Department of Textile Engineering Thesis Album, (1993) 365-370.

[4] C.Y. Chu, P.H. Lin, C.H. Lo, Vibration cover acoustic impedance of porous sound absorption material, Republic of China Vibration and Noise Association of Engineering Thesis Album, (2008) 394-496.

[5] J.H. Lin, C.M. Lin, C.C. Huang, C.C. Lin, C.T. Hsieh, Y.C. Liao, Evaluation of the manufacture of sound absorbent sandwich plank made of PET/TPU honeycomb grid/PU foam, J. Compos Mater. 45(13) (2011) 1355-1362.

Advanced Materials Research Vol. 936 (2014) pp 1999-2006
© (2014) Trans Tech Publications, Switzerland
doi:10.4028/www.scientific.net/AMR.936.1999

Mode i Crack Problem for a Functionally Graded Orthotropic COATING-Substrate Structure

Lifang Guo[1, a *], Xing Li[2, b] and Youzheng Yang[3, c]

[1]School of Sciences, Ningxia Medical University, Yinchuan, 750021,China
[1]Department of Mathematics, Shanghai Jiaotong University,Shanghai 200240, China.
[2]School of Mathematics and Computer Science, Ningxia University, Yinchuan, 750021, China
[3]School of physics Electrical Engineering, Ningxia University, Yinchuan, 750021, China

[a]email: glf1998@163.com, [b]email: li_x@nxu.edu.cn, [c]email: 13126330@qq.com

Keywords: Functionally graded orthotropic material, coating-substrate structure, mode I crack problem, singular integral equation

Abstract: In this paper, the Fourier integral transform-singular integral equation method is presented for the Mode I crack problem of the functionally graded orthotropic coating-substrate structure. The elastic property of the material is assumed vary continuously along the thickness direction. The principal directions of orthotropy are parallel and perpendicular to the boundaries of the strip. Numerical examples are presented to illustrate the effects of the crack length, the material nonhomogeneity and the thickness of coating on the stress intensity factors.

Introduction

The analysis of functionally graded materials has become a subject of increasing importance motivated by a number of potential benefits from the use of such novel materials in a wide range of modern technological practices. The major advantages of the graded material, especially in elevated temperature environments stem from the tailoring capability to produce a gradual variation of itsthermo mechanical properties in the spatial domain. A great efforts have been made to study the fracture behavior of FGMs [1-5]. As it is reported in the literature [6, 7], the graded materials are rarely isotropic because of the nature of techniques used in fabricating them. Thus, it is necessary to consider the anisotropic character when studying the failure behaviors of FGMs. Guo et al. [8] investigated the mode I surface crack problem for an orthotropic graded strip. H. M. Xu et al. [9] studied the problems of a power-law orthotropic and half-space functionally graded material (FGM) subjected to a line load. In the paper [10], asymptotic analysis coupled with Westergaard stress function approach is used to develop quasistatic stress fields for a crack oriented along one of the principal axes of inhomogeneous orthotropic medium. Kim and Paulino [11, 12] examined mixed-mode stress intensity factors for cracks arbitrarily oriented in orthotropic FGMs using modified crack closure method and the path-independent J_k -integral, respectively. Though there are lots of papers related to the crack problem of orthotropic functionally graded materials, very few papers on the plane crack problem of a functionally graded strip with a crack perpendicular to the boundary are published. It is very significant to study this kind of crack problem, since the geometry can be used as an approximation to a number of structural components and laboratory specimens, at the same time in line with the result of the Kawasaki and Watanabe[13]'s experiments about the thermal fracture behavior of metal/ceramic functionally graded materials(PSZ/IN 100 FGMS and PSZ/Inco 718 FGMs), the sequence of sapling behavior was found to be: crack vertical to the sample surface formed during cooling, then transverse crack formed in graded layer during heating, and subsequent growth of transverse cracks and their coalescence led eventually the ceramic coating to spall. Therefore, the surface crack problem is a very important issue to be considered during the design of FGMs. In these papers, the Mode I crack problem for a functionally graded orthotropic coating-substrate structure will be presented and the results could be useful in the laboratory test and the design of the orthotropic functionally graded materials.

Formulation of the Problem

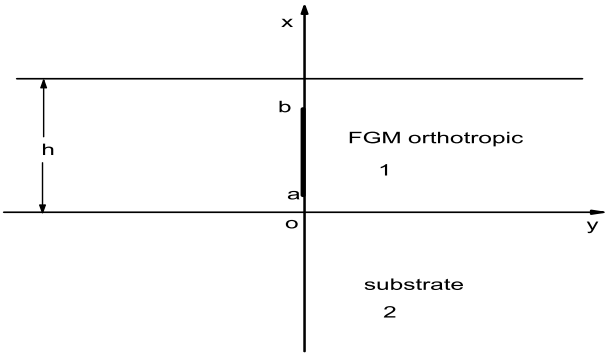


Figure 1: The geometry of the mode I crack problem for the functionally graded orthotropic substrate-coating structure.

As shown in Fig.1: A functionally graded orthotropic strip with properties varying in the x-direction bonded to a half infinite orthotropic elastic substrate. The strip is infinite along the y-axis and has a thickness h along x-axis. The principal directions of orthotropy are parallel and perpendicular to the boundaries of the strip. The material properties are defined as

$$c_{11}(x)=c_{110}e^{\delta x},c_{12}(x)=c_{120}e^{\delta x},c_{22}(x)=c_{220}e^{\delta x},c_{66}(x)=c_{660}e^{\delta x}, \tag{1}$$

Where c_{110}, c_{120}, c_{220}, c_{660} and δ are constants. c_{110}, c_{120}, $c_{220}$and c_{660} are the material parameters of y = 0, δ is the gradient parameters of functionally graded material.

The general constitutive relation can be written as

$$\sigma_{1xx}=c_{11}(x)\frac{\partial u}{\partial x}+c_{12}(x)\frac{\partial v}{\partial y},\ \ \sigma_{1yy}=c_{12}(x)\frac{\partial u}{\partial x}+c_{22}(x)\frac{\partial v}{\partial y},\ \ \sigma_{1xy}=c_{66}(x)(\frac{\partial u}{\partial y}+\frac{\partial v}{\partial x}), \tag{2}$$

The equilibrium equation in terms of the displacements can be given as:

$$\frac{\partial\sigma_{1xx}}{\partial x}+\frac{\partial\sigma_{1xy}}{\partial y},\ \ \frac{\partial\sigma_{1yy}}{\partial y}+c_{22}(x)\frac{\partial\sigma_{1xy}}{\partial x}=0 \tag{3}$$

make use of the equation Eqs. (1), (2) and (3), it can be obtained that

$$\begin{aligned}&c_{11}(x)\frac{\partial^2u}{\partial x^2}+c_{66}(x)\frac{\partial^2u}{\partial y^2}+[c_{11}(x)+c_{66}(x)]\frac{\partial^2v}{\partial x\partial y}+c_{11}(x)\delta\frac{\partial u}{\partial x}+c_{12}(x)\delta\frac{\partial v}{\partial y}=0,\\&c_{22}(x)\frac{\partial^2v}{\partial y^2}+c_{66}(x)\frac{\partial^2v}{\partial x^2}+[c_{12}(x)+c_{66}(x)]\frac{\partial^2u}{\partial x\partial y}+c_{66}(x)\delta\frac{\partial u}{\partial y}+c_{66}(x)\delta\frac{\partial v}{\partial x}=0,\end{aligned} \tag{4}$$

if let the $\delta=0$, then the equations of the elastic substrate can be obtained.

The mixed boundary conditions of the problem in Fig.1 can be written as

$$\begin{aligned}&\sigma_{1xx}(h,y)=0,\sigma_{1xy}(h,y)=0,\sigma_{1xx}(0,y)=\sigma_{2xx}(0,y),\\&\sigma_{1xy}(0,y)=\sigma_{2xy}(0,y)=0,u_1(0,y)=u_2(0,y),v_1(0,y)=v_2(0,y)\end{aligned} \tag{5}$$

$$\begin{aligned}&\sigma_{2xx}(x,y)=0,\sigma_{2xy}(x,y)=0,x\to-\infty,\\&\sigma_{1xy}(x,0)=0,\ \ 0<x<h,\ \sigma_{1yy}(x,0)=-\sigma_0(x),\ \ a<x<b,\end{aligned} \tag{6}$$

$$v_1(x,0)=0,0<x<a,\ b<x<h \tag{7}$$

By use of the Fourier transform method and thinking of the Eq. (6), the following displacement forms can be obtained, for functionally graded coating:

$$u_1=\frac{1}{2\pi}\int_{-\infty}^{\infty}\sum_{j=3}^{4}E_{1j}(s)A_{1j}e^{\lambda_{1j}(s)y-isx}ds+\frac{2}{\pi}\int_0^{\infty}\sum_{j=1}^{4}E_{2j}(\alpha)A_{2j}e^{\lambda_{2j}(\alpha)x}\cos\alpha y d\alpha,$$
$$v_1=\frac{1}{2\pi}\int_{-\infty}^{\infty}\sum_{j=3}^{4}A_{1j}(s)e^{\lambda_{1j}(s)y-isx}ds+\frac{2}{\pi}\int_0^{\infty}\sum_{j=1}^{4}A_{2j}e^{\lambda_{2j}(\alpha)x}\sin\alpha y d\alpha, \quad (8)$$

for elastic substrate:

$$u_2=\frac{2}{\pi}\int_0^{\infty}\sum_{j=1}^{2}A_{3j}(\alpha)E_{3j}e^{\lambda_{3j}(\alpha)x}\cos\alpha y d\alpha,$$
$$v_2=\frac{2}{\pi}\int_0^{\infty}\sum_{j=1}^{2}A_{3j}(\alpha)e^{\lambda_{3j}(\alpha)x}\sin\alpha y d\alpha, \quad (9)$$

where

$$E_{1j}=\frac{\left[c_{660}(s+i\delta)s-c_{220}\lambda_{1j}^2\right]i}{\left[c_{120}s+c_{660}(s+i\delta)\right]\lambda_{1j}},E_{2j}=\frac{c_{660}\lambda_{2j}(\lambda_{2j}+\delta)-\alpha^2c_{220}}{\alpha\left[c_{120}\lambda_{2j}+c_{660}(\lambda_{2j}+\delta)\right]},E_{3j}=\frac{c_{660}\lambda_{3j}^2-\alpha^2c_{220}}{\alpha(c_{120}+c_{660})\lambda_{3j}},$$

$$\lambda_{1j}=-\sqrt{-\frac{\Omega_{11}}{2}\pm\frac{1}{2}\sqrt{\Omega_{11}^2-4\Omega_{12}}},\lambda_{2j}=\frac{-\delta\pm\sqrt{\delta^2-2\Omega_{21}\pm2\sqrt{\Omega_{21}^2-4\Omega_{22}}}}{2},\lambda_{3j}=\frac{\sqrt{2}}{2}\sqrt{-\Omega_{31}^2-4\Omega_{32}},$$

$$(j=1,\cdots4,)\ \Omega_{11}=\frac{\left(c_{120}^2-c_{120}c_{220}\right)s(s+i\delta)+\left(2s^2+2is\delta-\delta^2\right)c_{120}c_{660}}{c_{220}c_{660}},\Omega_{12}=\frac{c_{110}s^2(s+i\delta)^2}{c_{220}},$$

$$\Omega_{21}=\frac{\left(c_{120}^2-c_{120}c_{220}+2c_{120}c_{660}\right)\alpha^2}{c_{110}c_{660}},\Omega_{22}=\left(\frac{c_{220}}{c_{110}}\alpha^2+\frac{c_{120}}{c_{110}}\delta^2\right)\alpha^2,\Omega_{31}=\left(\frac{c_{120}^2}{c_{110}c_{660}}+2\frac{c_{120}}{c_{110}}-\frac{c_{220}}{c_{660}}\right)\alpha^2,$$

$\Omega_{32}=\frac{c_{120}}{c_{110}}\alpha^4$, $A_{ij}\ (i=1,2,3,\ j=1,\cdots,4)$ are unknown functions, which can be solved by the boundary conditions. To obtain the integral equations, let's introduce the following auxiliary function

$$g(x)=\frac{\partial}{\partial x}v_1(x,0), \quad (10)$$

and $g(x)$ subjected to the following single-valuedness conditions

$$\int_a^{vb}g(t)dt=0 \quad (11)$$

By using Eqs. (7), (10) and applying the Fourier transform to Eq. (10), it can be obtained that

$$A_{13}=q_{13}\int_a^b g(u)e^{isu}du,\ A_{14}=q_{14}\int_a^b g(u)e^{isu}du, \quad (12)$$

Where

$$q_{13}=\frac{-i\left(c_{120}s^2+c_{220}\lambda_{14}^2\right)}{c_{220}s\left(\lambda_{13}^2-\lambda_{14}^2\right)},\ q_{14}=\frac{i\left(c_{120}s^2+c_{220}\lambda_{13}^2\right)}{c_{220}s\left(\lambda_{13}^2-\lambda_{14}^2\right)}.$$

Then by residue theorem and the boundary conditions, we can get the following linear algebraic equations

$$\begin{vmatrix} B_{21}e^{\lambda_{21}h} & B_{22}e^{\lambda_{22}h} & B_{23}e^{\lambda_{23}h} & B_{24}e^{\lambda_{24}h} & 0 & 0 \\ F_{21}e^{\lambda_{21}h} & F_{22}e^{\lambda_{22}h} & F_{23}e^{\lambda_{23}h} & F_{24}e^{\lambda_{24}h} & 0 & 0 \\ B_{21} & B_{22} & B_{23} & B_{24} & -B_{31} & -B_{32} \\ F_{21} & F_{22} & F_{23} & F_{24} & -F_{31} & -F_{32} \\ E_{21} & E_{22} & E_{23} & E_{24} & -E_{31} & -E_{32} \\ 1 & 1 & 1 & 1 & 1 & 1 \end{vmatrix} \begin{vmatrix} A_{21} \\ A_{22} \\ A_{23} \\ A_{24} \\ A_{25} \\ A_{26} \end{vmatrix} = \begin{vmatrix} R_1 \\ R_2 \\ R_3 \\ R_4 \\ R_5 \\ R_6 \end{vmatrix}, \tag{13}$$

where

$$R_1(u) = \frac{\left(-c_{120}^2 + c_{110}c_{220}\right)\alpha^2\lambda_{23}}{c_{110}\left(\lambda_{23}-\lambda_{21}\right)\left(\lambda_{23}-\lambda_{22}\right)\left(\lambda_{23}-\lambda_{24}\right)}e^{-\lambda_{23}(u-h)} + \frac{\left(-c_{120}^2 + c_{110}c_{220}\right)\alpha^2\lambda_{24}}{c_{110}\left(\lambda_{24}-\lambda_{21}\right)\left(\lambda_{24}-\lambda_{22}\right)\left(\lambda_{24}-\lambda_{23}\right)}e^{-\lambda_{24}(u-h)},$$

$$R_2(u) = \frac{\left(-c_{120}^2 + c_{110}c_{220}\right)\alpha\lambda_{23}\left(\lambda_{23}+\delta\right)}{c_{110}\left(\lambda_{23}-\lambda_{21}\right)\left(\lambda_{23}-\lambda_{22}\right)\left(\lambda_{23}-\lambda_{24}\right)}e^{\lambda_{23}(h-u)} + c_{110}\left(\lambda_{24}-\lambda_{21}\right)\left(\lambda_{24}-\lambda_{22}\right)\left(\lambda_{24}-\lambda_{23}\right)e^{\lambda_{24}(h-u)},$$

$$R_3(u) = \frac{-\left(-c_{120}^2 + c_{110}c_{220}\right)\alpha^2\lambda_{21}}{c_{110}\left(\lambda_{21}-\lambda_{22}\right)\left(\lambda_{21}-\lambda_{23}\right)\left(\lambda_{21}-\lambda_{24}\right)}e^{-\lambda_{21}u} + \frac{-\left(-c_{120}^2 + c_{110}c_{220}\right)\alpha^2\lambda_{22}}{c_{110}\left(\lambda_{22}-\lambda_{21}\right)\left(\lambda_{22}-\lambda_{23}\right)\left(\lambda_{22}-\lambda_{24}\right)}e^{-\lambda_{22}u},$$

$$R_4(u) = \frac{\left(-c_{120}^2 + c_{110}c_{220}\right)\alpha\lambda_{21}\left(\lambda_{21}+\delta\right)}{c_{110}\left(\lambda_{21}-\lambda_{22}\right)\left(\lambda_{21}-\lambda_{23}\right)\left(\lambda_{21}-\lambda_{24}\right)}e^{-\lambda_{21}u} + \frac{\left(-c_{120}^2 + c_{110}c_{220}\right)\alpha^2\lambda_{22}\left(\lambda_{22}+\delta\right)}{c_{110}\left(\lambda_{22}-\lambda_{21}\right)\left(\lambda_{22}-\lambda_{23}\right)\left(\lambda_{22}-\lambda_{24}\right)}e^{-\lambda_{22}u},$$

$$R_5(u) = \frac{1}{c_{110}}\left[\frac{c_{120}\lambda_{21}^2 + 2\delta c_{120}\lambda_{21} + c_{120}\delta^2 + \alpha^2 c_{220}}{\left(\lambda_{21}-\lambda_{22}\right)\left(\lambda_{21}-\lambda_{23}\right)\left(\lambda_{21}-\lambda_{24}\right)}e^{-\lambda_{21}u} + \frac{c_{120}\lambda_{22}^2 + 2\delta c_{120}\lambda_{22} + c_{120}\delta^2 + \alpha^2 c_{220}}{c_{110}\left(\lambda_{22}-\lambda_{21}\right)\left(\lambda_{22}-\lambda_{23}\right)\left(\lambda_{22}-\lambda_{24}\right)}e^{-\lambda_{22}u}\right],$$

$$R_6(u) = \frac{-\alpha\left(-c_{120}^2 + c_{110}c_{220} - c_{120}c_{660}\right)\lambda_{21}^2}{c_{110}c_{660}\lambda_{21}\left(\lambda_{21}-\lambda_{22}\right)\left(\lambda_{21}-\lambda_{23}\right)\left(\lambda_{21}-\lambda_{24}\right)}e^{-\lambda_{21}u} + \frac{-\alpha\left(-c_{120}^2 + c_{110}c_{220} - c_{120}c_{660}\right)\lambda_{22}^2}{c_{110}c_{660}\lambda_{22}\left(\lambda_{22}-\lambda_{22}\right)\left(\lambda_{22}-\lambda_{23}\right)\left(\lambda_{22}-\lambda_{24}\right)}e^{-\lambda_{22}u}$$

$$+\frac{\alpha\delta\lambda_{21}\left(c_{120}^2 - c_{110}c_{220} + 2c_{120}c_{660}\right) - \alpha c_{660}\left(\delta^2 c_{120} + c_{220}\alpha^2\right)\lambda_{21}^2}{c_{110}c_{660}\lambda_{21}\left(\lambda_{21}-\lambda_{22}\right)\left(\lambda_{21}-\lambda_{23}\right)\left(\lambda_{21}-\lambda_{24}\right)}e^{-\lambda_{21}u} + \frac{\alpha\left(\delta^2 c_{120} + c_{220}\alpha^2\right)}{c_{110}\lambda_{21}\lambda_{22}\lambda_{23}\lambda_{24}}$$

$$+\frac{\alpha\delta\lambda_{22}\left(c_{120}^2 - c_{110}c_{220} + 2c_{120}c_{660}\right) - \alpha c_{660}\left(\delta^2 c_{120} + c_{220}\alpha^2\right)}{c_{110}c_{660}\lambda_{22}\left(\lambda_{22}-\lambda_{21}\right)\left(\lambda_{22}-\lambda_{23}\right)\left(\lambda_{22}-\lambda_{24}\right)}e^{-\lambda_{22}u}$$

During the process of obtaining Eq. (13), the integral identities[14]

$$\begin{aligned} &\int_0^\infty e^{-px}\sin\left(qx+\lambda\right)dx = \frac{1}{p^2+q^2}\left(q\cos\lambda + p\sin\lambda\right), \\ &\int_0^\infty e^{-px}\sin\left(qx+\lambda\right)dx = \frac{1}{p^2+q^2}\left(q\cos\lambda + p\sin\lambda\right), \end{aligned} \qquad p>0, \tag{14}$$

are used. The B_j, C_j and F_j are some expressions of material consistent. Then the solution of the unknown functions can be obtained. Substitute the solution of the above equation and using the conditions of the crack surface, after considering the asymptotic when $s\to\infty$ and $\alpha\to 0$, the following equation can be obtained

$$\frac{1}{\pi}\int_a^b\left[-\frac{\mathrm{Im}\left(\omega_1\right)}{u-x} + h_1\left(u,x\right) + 2K_{2s} + 2h_1\left(u,x\right)\right]g\left(u\right)du = -\sigma_0\left(x\right)e^{-\delta x}\ , \tag{15}$$

Where

$$\omega_1 = \frac{ic_{660}\left(c_{120}+c_{220}p_{11}^2\right)\left(c_{120}+c_{220}p_{12}^2\right)}{c_{220}\left(c_{120}+c_{220}\right)p_{11}p_{12}\left(p_{11}+p_{12}\right)}, h_1\left(u,x\right) = \frac{1}{2}\int_{-\infty}^{\infty}\left(\sum_{j=3}^{4}C_{1j}q_{1j} - \omega_1\right)e^{is(u-x)}ds$$

$$K_{2s} = \left[\frac{\Lambda_1}{p_{21}\left(x+u\right)} + \frac{\Lambda_2}{p_{21}x+p_{22}u} + \frac{\Lambda_3}{p_{22}x+p_{21}u} + \frac{\Lambda_4}{p_{22}\left(x+u\right)}\right], h_2\left(u,x\right) = \int_0^\infty[\sum_{j=3}^{4}C_{2j}e^{\lambda_{2j}x}A_{2j} - \Lambda_1 e^{-p_{21}\alpha(x+u)}$$

$$-\Lambda_2 e^{-\alpha(p_{21}x+p_{22}u)}-\Lambda_3 e^{-\alpha(p_{22}x+p_{21}u)}-\Lambda_4 e^{-p_{22}\alpha(x+u)}]d\alpha,$$

$$\Lambda_1=\frac{1}{4}\left(c_{120}p_{21}^2+c_{220}\right)\left(c_{120}c_{660}+c_{120}^2-c_{110}c_{220}+c_{110}c_{660}p_{22}^2\right)\left[-c_{110}c_{660}p_{21}^4+\left(c_{110}c_{220}-c_{120}^2-2c_{120}c_{660}\right)p_{21}^2-c_{220}c_{660}\right]$$

$$\frac{1}{c_{660}c_{110}^2p_{21}^2\left(c_{660}+c_{120}\right)\left(p_{21}+p_{22}\right)^2\left(p_{21}-p_{22}\right)^2},\ \Lambda_2=\frac{1}{4}\left(c_{120}p_{21}^2+c_{220}\right)[-c_{110}c_{660}p_{22}^4+\left(c_{110}c_{220}-c_{120}^2-2c_{120}c_{660}\right)p_{22}^2$$

$$-c_{220}c_{660}]\left(c_{110}c_{220}-c_{110}c_{660}p_{21}p_{22}-c_{120}^2-c_{120}c_{660}\right)\frac{1}{c_{660}c_{110}^2p_{22}^2\left(c_{660}+c_{120}\right)\left(p_{21}+p_{22}\right)^2\left(p_{21}-p_{22}\right)^2},$$

$$\Lambda_3=\frac{1}{4}\left(c_{120}p_{22}^2+c_{220}\right)\left[-c_{110}c_{660}p_{21}^4+\left(c_{110}c_{220}-c_{120}^2-2c_{120}c_{660}\right)p_{21}^2-c_{220}c_{660}\right]$$

$$\left(c_{110}c_{220}-c_{110}c_{660}p_{21}p_{22}-c_{120}^2-c_{120}c_{660}\right)\frac{1}{c_{660}c_{110}^2p_{21}^2\left(c_{660}+c_{120}\right)\left(p_{21}+p_{22}\right)^2\left(p_{21}-p_{22}\right)^2},$$

$$\Lambda_4=-\frac{1}{4}\left(c_{120}p_{22}^2+c_{220}\right)\left[-c_{110}c_{660}p_{22}^4+\left(c_{110}c_{220}-c_{120}^2-2c_{120}c_{660}\right)p_{22}^2-c_{220}c_{660}\right]$$

$$\left(c_{110}c_{220}-c_{110}c_{660}p_{21}^2-c_{120}^2-c_{120}c_{660}\right)\frac{1}{c_{660}c_{110}^2p_{22}^2\left(c_{660}+c_{120}\right)\left(p_{21}+p_{22}\right)^2\left(p_{21}-p_{22}\right)^2},$$

$$p_{1j}=-\frac{\sqrt{2}}{2}\xi_{11}\sqrt{aa_1\pm bb_1},\ \xi_{1j}=sign\left[\mathrm{Re}\sqrt{aa_1\pm bb_1}\right],\ p_{2j}=\frac{\sqrt{2}}{2}\xi_{21}\sqrt{aa_2\pm bb_2},\ \xi_{2j}=sign\left[\mathrm{Re}\sqrt{aa_2\pm bb_2}\right],$$

$$\left(j=1,2\right),aa_1=\frac{c_{110}c_{220}-c_{120}\left(c_{120}+2c_{660}\right)}{c_{220}c_{660}},aa_2=\frac{c_{110}c_{220}-c_{120}^2-2c_{120}c_{660}}{c_{110}c_{660}},$$

$$bb_1=\frac{\sqrt{\left(c_{120}^2-c_{110}c_{220}\right)\left[\left(c_{120}+2c_{660}\right)^2-c_{110}c_{220}\right]}}{c_{220}c_{660}},bb_2=\frac{\sqrt{\left(c_{120}^2-c_{110}c_{220}\right)\left[\left(c_{120}+2c_{660}\right)^2-c_{110}c_{220}\right]}}{c_{110}c_{660}},$$

the Eq. (15) is the first kind of Fredholm integral equation, which can be solved by the method of [15]. The stress intensity factors of the internal crack tips can be express as

$$\begin{aligned}K_I(a)&=\lim_{x\to a}\sqrt{2(a-x)\sigma_{yy}(x,0)}=-\mathrm{Im}(\omega_{11})e^{\delta a}\sum_{n=1}^{N}a_n,\\ K_I(b)&=\lim_{x\to b}\sqrt{2(x-b)\sigma_{yy}(x,0)}=-\mathrm{Im}(\omega_{11})e^{\delta b}\sum_{n=1}^{N}a_n,\end{aligned}\tag{16}$$

For convenience, the SIFs are normalized by $\kappa_0=\sigma_0\sqrt{a_0h}$, where σ_0 is uniform crack surface pressure.

Numerical Results and Discussion

In the following analysis, we will study the influence of the length of the crack, the location of the crack, the functionally graded strip's width h and the gradient parameters of functionally graded material δ on the normalized stress intensity factors (SIFs) of the crack.

Firstly, the influence of the length of the crack and the gradient parameters of functionally graded material δ on the normalized stress intensity factors (SIFs) of the crack will be discussed. Here $h=5.0,\delta h=-1,0,1,2,c=0.4h$. It can be found in the Fig.2–Fig.3 that the normalized intensity factors of both crack tips $\mathrm{K}_I(a)$ and $\mathrm{K}_I(b)$ increases with the increase of the normalized half crack length a_0 and the gradient parameters of functionally graded material δ. Therefore, to prevent the coating crack from growing toward the interface, the gradient parameters of functionally graded material δ should be chosen as $\delta<0$.

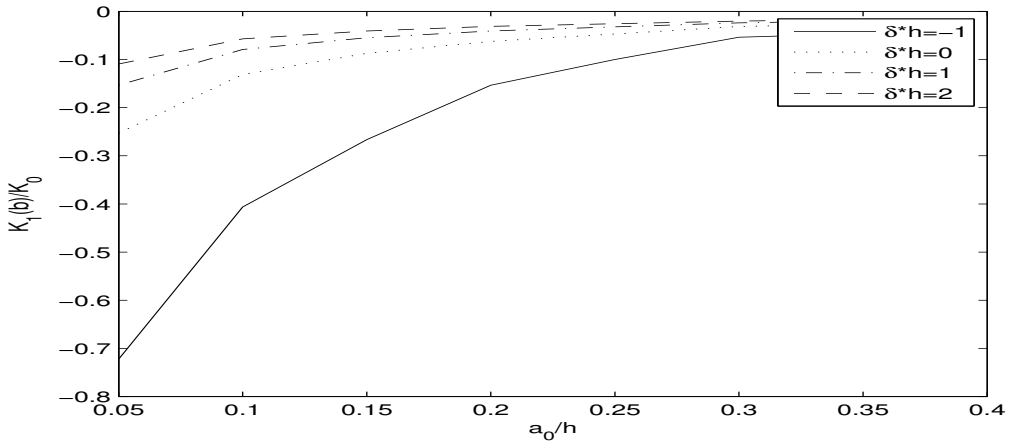


Figure 2: The normalized stress intensity factor $\mathrm{K}_I(b)$ versus $\frac{a_0}{h}$

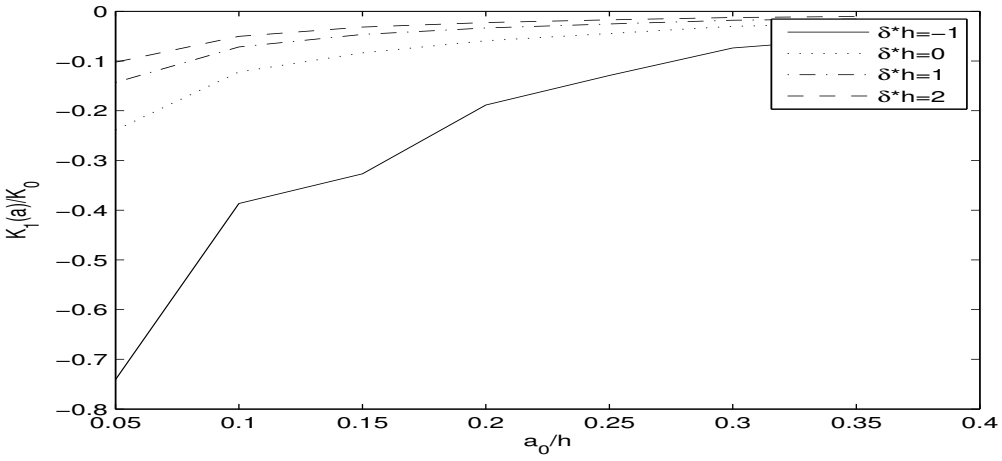


Figure 3: The normalized stress intensity $\mathrm{K}_I(a)$ versus $\frac{a_0}{h}$

Secondly, we will discuss the influence of the location of the crack on the normalized stress intensity factors (SIFs) of the crack. Here δh = 1, c = 0.5, 1, 1.5, 2. It can be found from Fig.4–Fig.5 that the normalized intensity factors of both crack tips $K_I(a)$ and $\mathrm{K}_I(b)$ increases with the increase of the $c=\frac{a+b}{2}$.

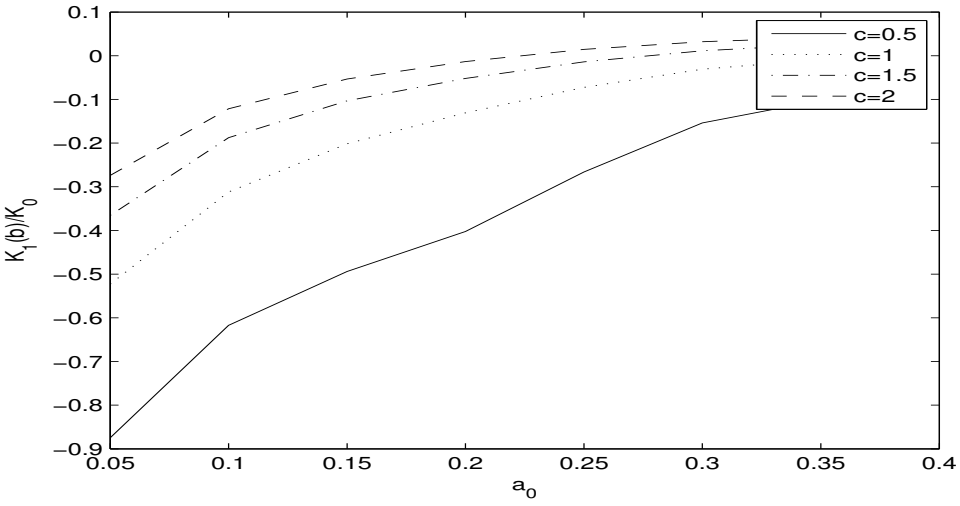


Figure 4: The normalized stress intensity $\mathrm{K}_I(b)$ versus a_0

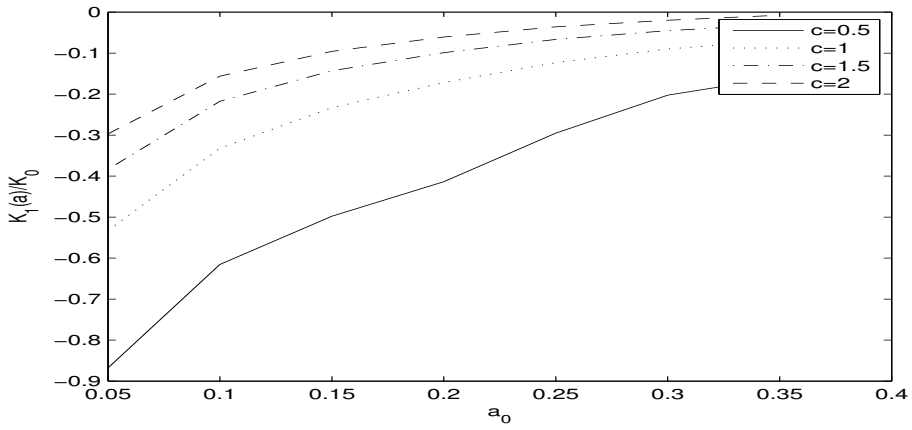


Figure 5: The normalized stress intensity $\mathrm{K}_I(a)$ versus a_0

Finally, we will discuss the influence of the width of the functionally graded orthotropic strip on the normalized stress intensity factors (SIFs) of the crack. Here The normalized stress intensity h= 1, 2, 3, 4, δh = 1, c = 0.5 . It can be found from the Fig.6–Fig.7 that the normalized intensity factors of both crack tips $\mathrm{K}_I(a)$ and $\mathrm{K}_I(b)$ decreases with the increase of the h, but as the increase of the strip width and the increase of the crack length, the effect is not obvious, so increasing the width of coating is not an effective way to restrain the expansion of the crack.

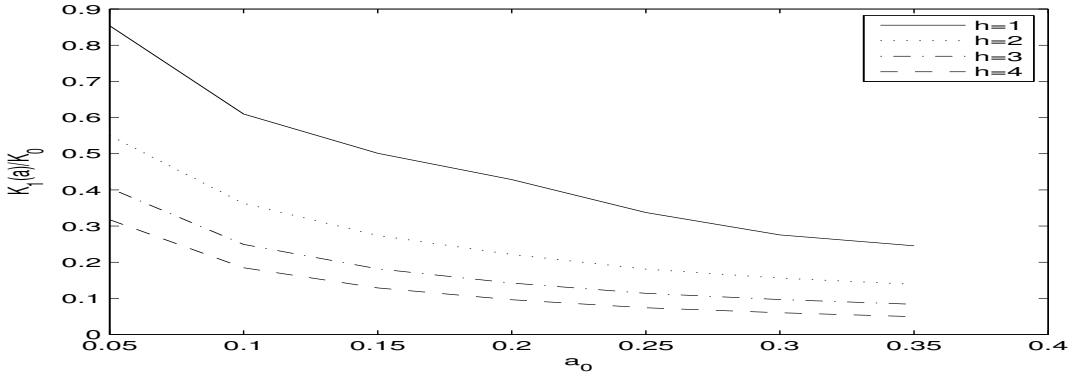


Figure 6: The normalized stress intensity $\mathrm{K}_I(a)$ versus a_0

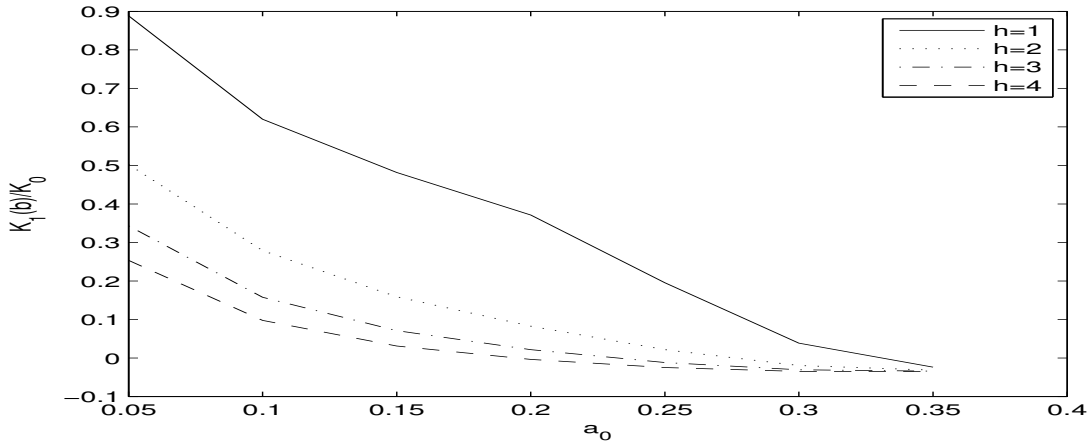


Figure 7: The normalized stress intensity $\mathrm{K}_I(b)$ versus a_0

Conclusion

In this paper, the mode I crack problem for a functionally graded orthotropic strip bonded to orthotropic substrate is studied analytically. The influences of the nonhomogeneity constants and geometric parameters on the stress intensity factors are investigated. The result may be help for the analysis and design of functionally graded orthotropic coating-substrate structures.

References

[1] F. Delale, F. Erdogan: International Journal of Applied Mechanic 55 (1988), p.317
[2] S. Dag, F. Erdogan: Engineering Fracture Mechanics 69 (2002), p.1729
[3] Y. D. Li, W. Tan and H. C. Zhang: International Journal of fracture 142 (2006), p.163
[4] L. C. Guo, L. Z. Wu and L. Ma: Composite structure 63 (2004), p.397
[5] L. C. Guo, L. Z. Wu, L. Ma and T. Zeng: International Journal of fracture 127(2004),p.21
[6] M. Ozturk, F. Erdogan: Journal of Engineering Science 35 (1997), p.869
[7] S. Dag, B. Yildirim and F. Erdogan: International Journal of Fracture 130 (2004),p.471
[8] L. C. Guo, L. Z. Wu, T. Zeng and L. Ma: European Journal of Mechanics A/solids23 (2004), p.219
[9] H. M. Xu, X. F. Yao, X. Q. Feng and H. Y. Yeh: Composites Science and Technology 68 (2008), p.27
[10] Vijaya Bhaskar Chalivendra: Mechanics of Materials 40 (2008), p.293
[11] J. H. Kim, G. H. Paulino: Engineer fracture mechanic 69 (2002), p.1557
[12] J. H. Kim, G. H. Paulino: mechanic material 35 (2003), p.107
[13] A. Kawasaki, R. Watanabe: Engineering Fracture Mechanics 69 (2000), p. 1713
[14] I. S. Gradshteyn, I. M. Ryzhik: Table of integrals, series, and products, Elsevi-er/Academic Press, Amsterdam, 2007.
[15] X. Li, Integral equations, Science Press, Beijing, 2008.

Advanced Materials Research Vol. 936 (2014) pp 2007-2010
© (2014) Trans Tech Publications, Switzerland
doi:10.4028/www.scientific.net/AMR.936.2007

Investigation of the fluorescence spectra of the fluorescent dyes

Saksit Sukprasong[1,2,a], Tanabat Promjun[2,b], Komsanti Chokethawai[1,c] and Athipong Ngamjarurojana[1,d]

[1]Department of Physics and Materials Science, Faculty of Science, Chiang Mai University, Chiang Mai 50200

[2]Faculty of Science at Si Racha, Kasetsart University Si Racha Campus, Chon Buri 20230

[a] saksitsukprasong@yahoo.com, [b] tanabat-promjun.cmu@hotmail.com,

[c] komsanti@gmail.com, [d] ngamjarurojana@yahoo.com

Keyword: Laser-induced fluorescence; temperature effect; solvent effect

Abstract.: The experiment was conducted to study the effects of concentration, temperature and solvent on the luminescence decay curves obtained in laser-induced fluorescence (LIF) experiment from fluorescent orange dye. Sample solutions of fluorescence dye were prepared by mixing with ethanol solvents at different concentration. The sample was illuminated with a radiation of 470 nm using a blue laser excitation source. Luminescence spectra were recorded using a compact fiber coupled CCD spectrometer and the results were analyzed.The results showed that both concentration and temperature affected the luminescence decay of orange dye in the same way. The luminescence decay was decreased when the concentration and temperature were increased.The appearance of peak positions was slighly shifted to higher wavelength (lower photon energy) when concentration were varied. Then the results of concentration effect were analyzed using peak fit, the appearance of peak positions was slightly shifted from 601.51 to 604.12, 607.64, and 618.44 nm at the concentration of 50, 60, 70 and 80 % by volume, respectively.

Introduction

Fluorescent dyes have the unique property of absorbing in the UV range and emitting in the visible range of the color spectrum. Each fluorescent dye has its own unique properties and emission spectrum of fluorescent dyes often vary with environmental conditions. Thus, many fluorescent dyes can be used as sensors to probe their local environments in biological and analytical applications. For example, coumarin [1], rhodamine [2], and oxazine [3] dyes are known to be efficiently quenched by the nucleobase guanosine (dG) and the amino acid tryptophan (Trp). In order to obtain an accurate indicator for fluorescent dyes, an accurate analysis of the color and fluorescence is necessary. Therefore, a system to measure the fluorescence spectra of high quality is needed. The current laser-induced fluorescent (LIF) system is one popular measurement system used [4].

The basic idea of LIF is simple. Light from a tunable laser impinged on the sample is to be investigated. As the frequency of the laser is changed, molecules within the irradiated portion of the sample will be excited to fluorescence whenever the spectral envelope of the laser overlaps an absorption line of the molecule [5]. Since the only excited molecules are those in the specific lower level(s) of the corresponding transition, the excitation is selective for this state or group of states. Hence, the "excitation spectrum" obtained by recording the fluorescent intensity as a function of wavelength reflects the relative populations of these different states. The excitation spectrum depends on the factors of environmental conditions such as concentration, temperature, pH value, molecular structure and solvent effect [6-8].

This experiment aims to study the effect of concentrations, temperature and solvent on the luminescence decays of fluorescence orange dye at different concentrations and temperatures by comparing the fluorescence properties of dye to the level of concentration and temperature in

wavelength-intensity relationship. In the last step all the results were analyzed by peak fitting in order to study the effects of concentration on the fluorescent dye.

Experimental procedure

An orange dye was used in this study. Sample solutions of fluorescence dye were prepared by mixing with ethanol at the concentration of 50, 60, 70 and 80 % by volume to investigate the concentration effect. To study the temperature effect, a mixture of fluorescence dye and ethanol solvents was kept constant at the 50 % by volume. The solutions were allowed to cure under ambient conditions for 1 h before the measurements. The fluorescence dye solution was illuminated with a radiation of 470 nm using a blue laser as an excitation source. Luminescence fluorescence spectra of dye solutions were recorded using a compact fiber coupled CCD spectrometer model BTC-110S and the temperature was increased from 25 to 55^{o}C with a step size of 5^{o}C by temperature control chamber for the study of temperature effect. The experimental setup consists of the blue laser and temperature control chamber as shown in Fig. 1. The effects of concentration and temperature on luminescence decay of fluorescent dye can be investigated and the analysis of the spectrum of orange dye at different concentrations and temperatures was carried out using peak fit analysis method.

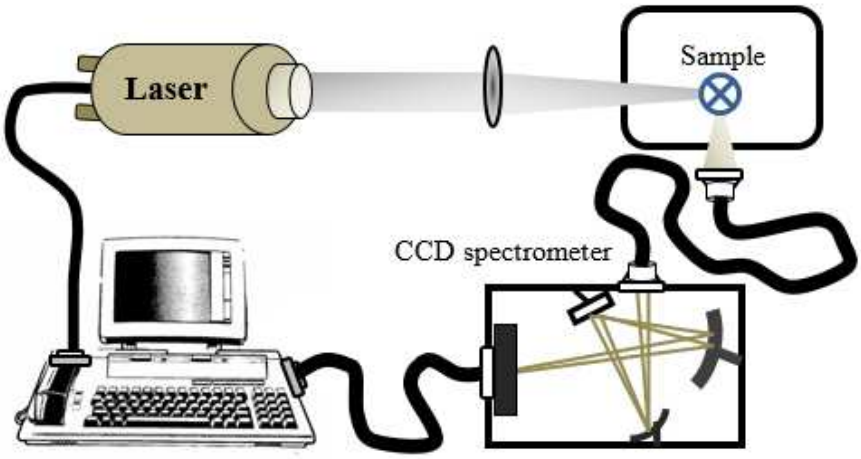


Fig. 1. Schematic diagram of experimental set-up. 470 nm blue laser was utilized as light source. Fluorescence spectra were obtained with the use of a Fiber Optic Spectrometer (model BTC-110S). The system was controlled by a computer.

Results and discussion

When fluorescence dye solutions were excited by the blue laser in the wavelength of 470 nm, the energy was absorbed by the molecule dye. This molecule was excited to exciting state energy level and this energy was transferred to the ground state by the emission at 570-640 nm. The results showed that fluorescence spectra of the orange dye had the same response when the concentration and temperature of the dye solution increased, resulting in a decrease of the maximum emission intensity of the orange dye (Figs. 2-3).The luminescence decays of fluorescence dye decreased as temperature increased. The mechanism of the temperature sensitivity of the fluorescence dye solutions is based on thermal quenching. The effects is a general tendency for fluorescence quantum yields of solute molecules in liquid solutions to decrease slightly with increasing in temperature because non-radiative decay rate increases with increasing temperature [8,9].

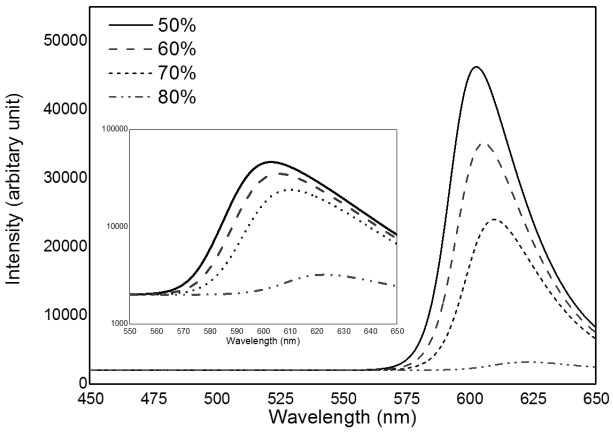


Fig. 2. Relationship between the orange dye wavelength and fluorescence intensity in various concentration at 50, 60, 70 and 80% by volume

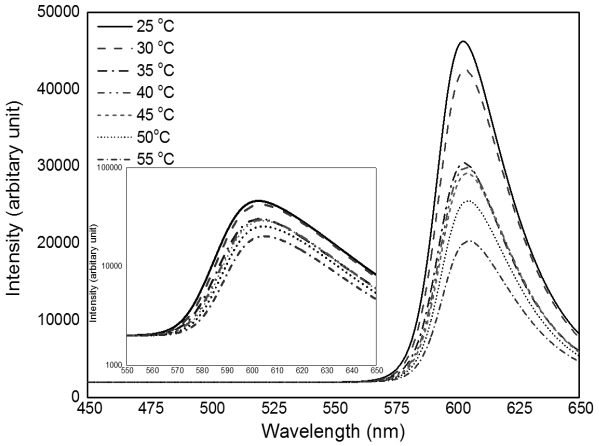


Fig. 3. Relationship between the orange dye wavelength fluorescence intensity at various temperature from 25 to 55°C

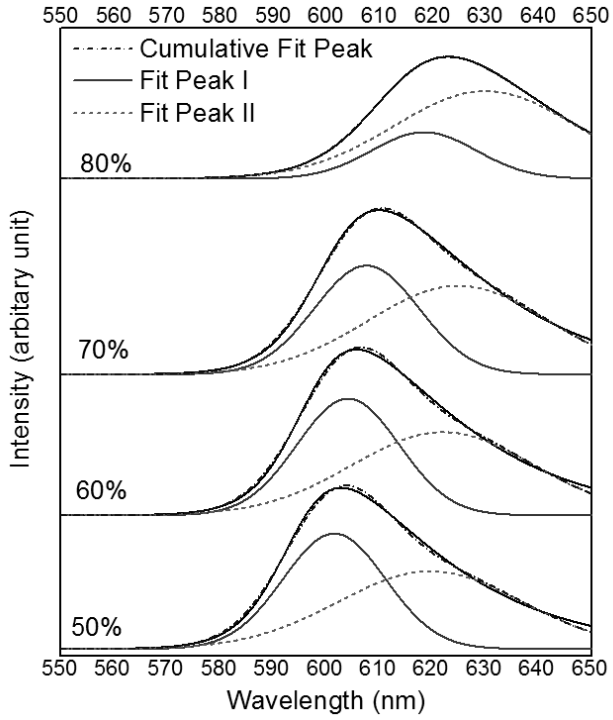


Fig. 4. Effect of concentration on the florescence spectra of the orange dye by using program fit peak analysis

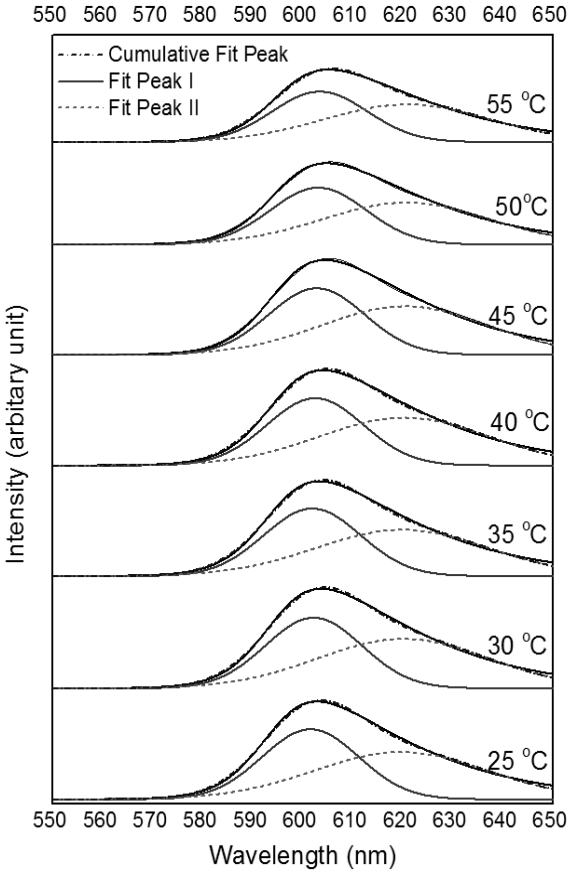


Fig. 5. Effect of temperature on the fluorescence spectra of the orange dye by using program fit peak analysis

The results were analyzed using peak fitting. When the concentration and temperature of the orange dye increased, the fluorescence intensity of the dye was decreased and appearance peak positions was slightly shifted as shown in Figs. 4-5. The appearance of peak positions was slightly shifted from 601.51 to 604.12, 607.64, and 618.44 nm at the concentration of 50, 60, 70, and 80 % by volume respectively as shown in Table 1 (left). The result of interaction between solvent (ethanol) and solute (dye) is probably responsible for the peak shift observed [10]. However, the increase of temperature resulted in only a slight change of peak shift to higher wavelength (Table 1 (right)).

TABLE 1: PEAK FIT ANALYSIS DATA RELATED TO CONCENTRATION AND TEMPERATURE PARAMETERS

Concentration (by volume)	Peak I (nm)	Peak II (nm)
50%	601.51	619.62
60%	604.12	622.01
70%	607.64	624.87
80%	618.44	630.00

Temperature	Peak I (nm)	Peak II (nm)
25°C	601.51	619.62
30°C	601.88	619.88
35°C	602.16	620.06
40°C	602.46	620.27
45°C	602.76	620.41
50°C	603.07	620.63
55°C	603.39	620.87

Conclusions

The results showed that the orange dye gave the same trend of luminescence decay curves for the study of temperature effect and concentration effect. The luminescence decays of fluorescence dye decreased as temperature and concentration increased. In analysis by peak fitting**,** it was found also from the experiment that the peak positions of the luminescence spectra changed with concentration from 601.51 to 604.12, 607.64, and 618.44 nm wavelengths at the concentrations 50, 60, 70, and 80 % by volume, respectively.

Acknowledgments

This work was supported by Laser and Applied Optics Research Laboratory, Department of Physics and Materials Science, Faculty of Science, CMU. The authors are thankful to Faculty of Science at Si Racha**,** Kasetsart University Si Racha Campus and Graduate School, Chiang Mai University for financial support. We also acknowledge Assist. Prof. Drs. Samran Lacharojana and Apichart Limpichaipanit for discussion and technical support.

References

[1] C. A. M. Seidel, A. Schulz and M. Sauer, Nucleobase-specific quenching of fluorescent dyes. 1. Nucleobase one electron redox potentials and their correlation with static and dynamic quenching efficiencies, J. Phys. Chem. 100 (1996) 5541-5553.

[2] M. Sauer, K. T. Han, V. Ebert, R. Müller, A. Schulz, S. Seeger, J. Wolfrum, J. Arden-Jacob, G. Deltau, N. J. Marx, C. Zander and K. H. Drexhage, New fluorescent dyes in the red region for biodiagnostics, J. Fluoresc. 5 (1995) 247-261.

[3] M.Sauer, K. H. Drexhage, U. Lieberwirth, R. Müller, S. Nord and C. Zander, Dynamics of the electron transfer reaction between an oxazine dye and DNA oligonucleotides monitored at the single molecule level, Chem. Phys. Lett. 284 (1998) 153-163.

[4] W. M. Fairbank, Jr., T. W. Hänsch, and A. L. Schawlow, Absolute measurement of very low sodium-vapor densities using laser resonance fluorescence, J. Opt. Soc. Am. 65 (1975) 199-204.

[5] V. Krajicek and M. Vrbova, Laser-induced fluorescence spectra of plants, Remote Sens. Environ. 47 (1994) 51–54.

[6] J. Chen, E.J. Leboeuf and S. Dai, Fluorescence spectroscopic studies of natural organic matter fractions, Chemosphere. 50 (2003) 639–647.

[7] B. Rosen, Selected Constants-Spectroscopic Data Relative to Diatomic Molecules, Pergamon, Oxford, 1970.

[8] G. G. Guilbault, Practical Fluorescence*,* second ed., Marcel Dekker, New York, 1990.

[9] E.R. Pantke and H. Labhart, On the temperature dependence of non-radiative deactivation processes, Chem. Phys. Lett. 16 (1972) 255-259

[10] G. S. Stephen, Fluorescence and phosphorescence spectroscopy, first ed., A. Wheaton & Co. Ltd, Great Britain, 1979.

Advanced Materials Research Vol. 936 (2014) pp 2011-2016
© (2014) Trans Tech Publications, Switzerland
doi:10.4028/www.scientific.net/AMR.936.2011

X-Ray Analysis of Residual Stress in Weld Region of X70 Pipeline Steel

Zakaria Boumerzoug[1,a*], Kelthoum Digheche[2], and Vincent Ji[3]

[1]Laboratory of semiconductor and metallic materials, Biskra University, B.P. 145, Biskra- Algeria.

[2]Department of Chemical Industry, Biskra University, B.P. 145, Biskra- Algeria.

[3] ICMMO/LEMHE, Université Paris-Sud, bat. 410, Orsay-91405- France

[*a] e-mail : zboumerzoug@yahoo.fr

Keywords : Steel ; arc welding ; Stress ; X-Ray Diffraction ; microstructures.

Abstract: X-ray diffraction method has been used to analyze the residual stress distribution in weld region of an X70 pipeline steel before and after heat treatment. The welding process has been realized by industrial arc welding with circular weld seams. The effect of heat treatments on the level and the distribution of residual stresses were investigated. Stress distribution was characterized by relative high compressive stresses in weld seam just after welding. However, residual stress relaxation phenomenon was observed in weld region after heat treatments due to microstructure restoration and recrystalization. Optical microscope observation and Vickers hardness measurements were also realized as complementary microstructure characterization techniques.

Introduction

Welding is a process of joining materials into one piece. Welding is one of the most important technological process used in many branches of industry such as industrial engineering, shipbuilding, pipeline fabrication among others. Generally, welding is the prefered joining method and most common steels are weldable.

However, welding is a complicated process accompanied by shrinkage effects, phase transformations, intensification of corrosion and arising of residual stresses. Residual stresses arising after welding exert a considerable influence on the service characteristics of welded equipment and their control allows to avoid failure of welded joint [1].

In arc welding operations residual stresses are introduced within the welded metal owing to the non-uniform tmerature distribution and severe temperature gradients. These residual stresses may be responsible for brittle fracture, decreasing fatigue life as well as stress corrosion cracking [2]. Consequently, it is very important to understand and quantify the residual stresses.

A wide variety of residual stress measurement techniques exist [3-9]. but one of the important is the X-ray diffraction technique. The aim of the present work is to analyze by X-ray diffraction the residual stress development in the heataffected zone (HAZ) of an X70 pipeline steel. This investigation is a contribution as many scientific works which have been done on welding of low carbon steel [10-13]

Experimental procedure

X70 pipeline steel with single-V preparation joint were welded by arc welding (Fig.1).



Fig. 1 X70 pipeline steel after industrial arc welding.

Figure 2 presents the analysis by EDAX of this steel which indicates the high quantity of Mn.

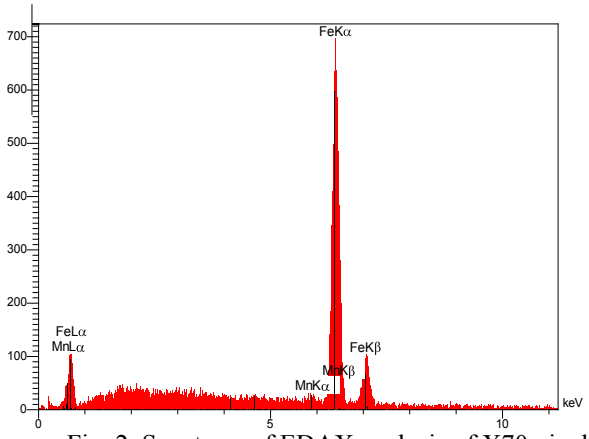


Fig. 2 Spectrum of EDAX analysis of X70 pipeline steel.

The chemical composition of this pipeline steel is given in table 1:

TABLE 1 CHEMICAL COMPOSITION OF PIPELINE STEEL(WT %).

C	Si	Mn	P	S	Cr	Ni	Cu	Al	N	Mo
0.064	0.2047	1.573	0.0154	0.0015	0.0553	0.1922	0.0291	0.0319	0.007	0.1353

The microstructure of this base metal is presented in figure 3. This material is composed of ferrite (85%) with bands of pearlite (15%). The average hardness is 200 HV_{10}. These bands of perlite-rich area (banding) were observed. This macrosegregation phenomenon which called banding is due to the presence of high percentage of Mn in these zones. However, in more alloyed weld metals elements such as chromuim and molybdenum can be found to be segregated in these areas [14].

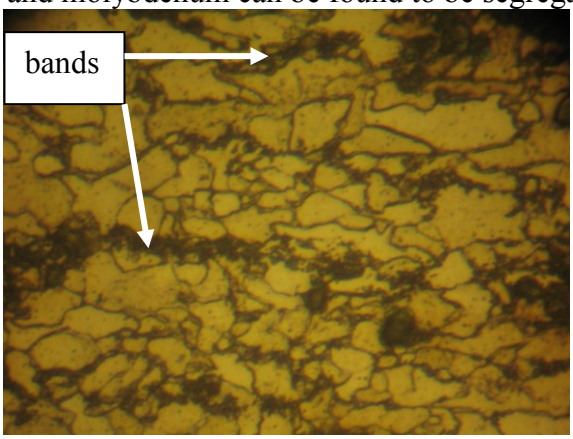


Fig. 3 Microstructure of X70 pipeline steel.

The welds were deposited using steel electrodes by the shielded metal arc welding process. The chemical composition of the weld metal is presented in table 2.

TABLE 2 : CHEMICAL COMPOSITION OF ELECTRODE (WT %).

C	Si	Mn	P	S	Cr	Ni	Cu	V	Mo
0.05	0.32	0.87	0.013	0.006	0.03	0.71	0.039	0.01	0.01

X-ray stress measurements were carried out by SET-X equipment. A general view of this apparatus is shown on figure 4. Cr-Ka radiation and (211) reflections were used to study residual stress distribution in weld region.



Fig. 4 General view of the X-ray apparatus.

For optical microscopy, chemical etchning was used to reveal microstructures ofdifferent zones. The hardness across the weld was measured by microhardness tester using a 2 kg load. Stress measurements were made in the longitudinal and transversal directions (parallel and perpendicular to the weld joint, respectively). In order to remove residual stresses introduced by machining, an electropoloishing technique has been applied. Optical observation after chemical etchning by Nital of the weld material has revealed the microsstructures of different zones, i.e, weld seam, heat affected zone (HAZ) and base metal. Heat treatments were applied on welded specimens by isothermal annealing at 200 and 600 °C during 1 hour in order to study their effects on residual stresses distribution in X70 pipeline steel.

Results and discussion

In order to have a general idea about the effect of heat treatments on microstructural evolution in weld region of X70 pipeline steel, figure 5 reveals microstructural transformation from non-heated to heated specimen at 600°C in weld seam which represents the core of welding region. This zone submits recrystallization reaction after heat treatments.

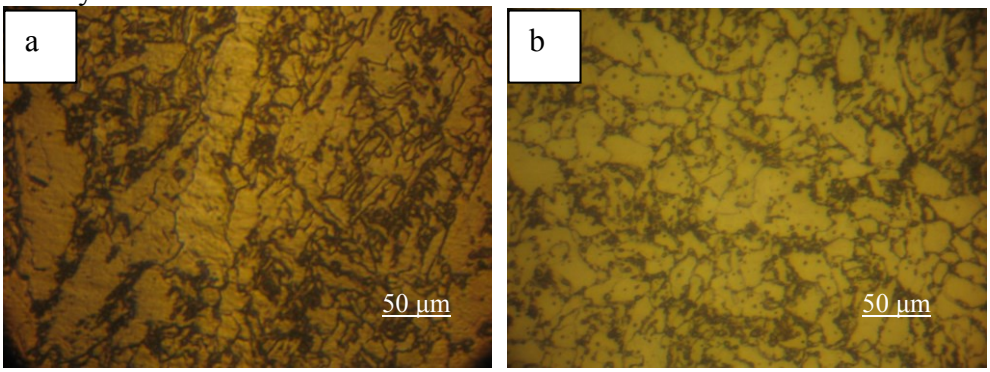


Fig. 5 Microstructures of X70 pipeline steel in weld region:
(a) non-heat treated and (b) heat treated 1h at 600°C.

It was reported that a hardness testing is the usual approach in dilineating the properties of these various zones, but the information obtained is very limited [15]. For other researchers, a simple rapid way to obtain important information is by hardness testing [16]. Concerning our material, the

hardness distribution in different zones is shown in figure 6. The hardness values of 192-214 HV in figure 6 are observed at location within 1 mm from the fusion zone, through the HAZ to the other base metal. Our hardness results are in good agreement with literature. Because, Gul et al [17], have found that maximum hardness values are measured in the area of weld metal (WM). The variation in properties across the weld can be attributed to several factors, mainly to residual stresses just after welding. On the other hand, other factors can contribuate to this hardening like grain size, phase composition, metallic inclusions.

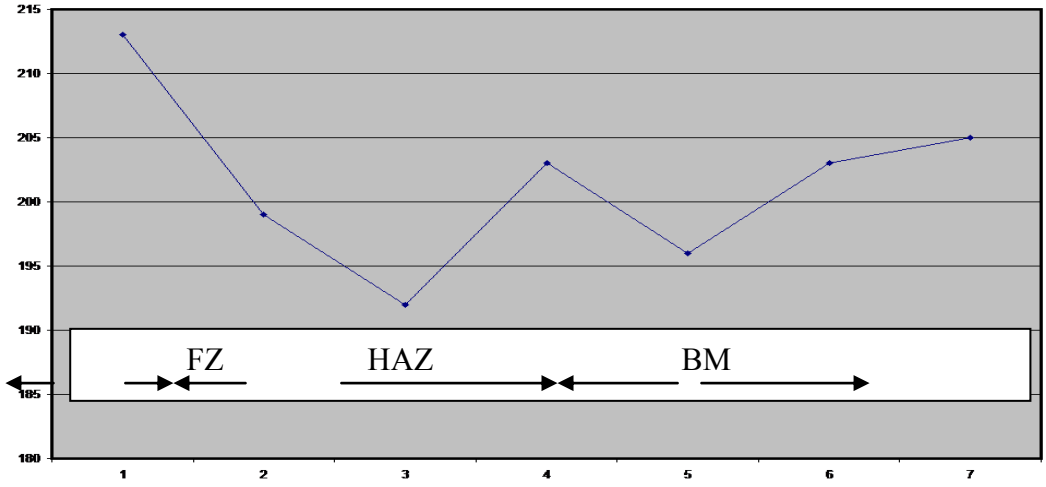


Fig. 6 Microhardness from the fusion zone (FZ) across the weld metal after welding of X70 pipeline steel.

However, figures 7, 8 and 9 present both residual stresses distribution in the weld region of X70 pipeline steel at different states and the peak width evolution in weld region respectively. Concerning the stress distributions, it is clear that all curves have the same shape but not the same magnitude because the the effect of heat treatments is obvious. The magnitude of residual stresses decrease significantly with increasing a temperature.

For example, figure 7 presents the stress distributions in the weld region of X70 pipeline steel. Compressive residual stresses in two directions were observed in weld seam, heat affected zone (HAZ) and base metal. The results indicate that in weld seam the value of stress is -195 in longitudinal direction and – 265 MPa in transversal direction. The maximum of compressive residual stresses are at 2 mm from weld seam (– 265 Mpa and 300 MPa). From 10 mm to weld seam the level of stress becames low compressive in both directions (- 100 MPa). For example, Ranjbarnodeh et al [18] habe been found that when dissimilar metals are joined by fusion process such as TIG welding technique, mixing of the base metals and the filler metal results in the weld region to have different mechanical properties and this phenomenon affects the distribution of residual stress after welding operation.Generally, the predominant cause of welded residual stresses is quenching, because according to Macherauch et al [19] the principal sources of residual stresses after welding are: shrinkage, quenching or phase transformation. Shrinkage causes the appearance of tensile stresses, whereas quenching and phase transformation cause compressive stresses at the weld seam. On the other hand, Prabhat et al [20] considered that the distribution of residual stresses in a girth welded pipe is complex. Weld shrinkage in the circumferential direction induces both shearing and bending that result in stress components in the circumferential direction (hoop stress) and in the axial direction (meridian stress).

However, heat treatments induce a phenomenon of relaxation in the material , because the width peak diminishs with increasing temperature. For example, the heat treated specimen at 200°C, the width peak of diffraction varies from 1,34° to 1,97° which corresponds to high relaxation in all zones (Fig; 8b). The same evolution has been observed in heat treated sample at 600°C (Fig.9). In addition, the level of stresses became nul after the heat treatment at 600°C. There is reasonable agreement between the the stress distributions and width peak of diffraction in weld region.

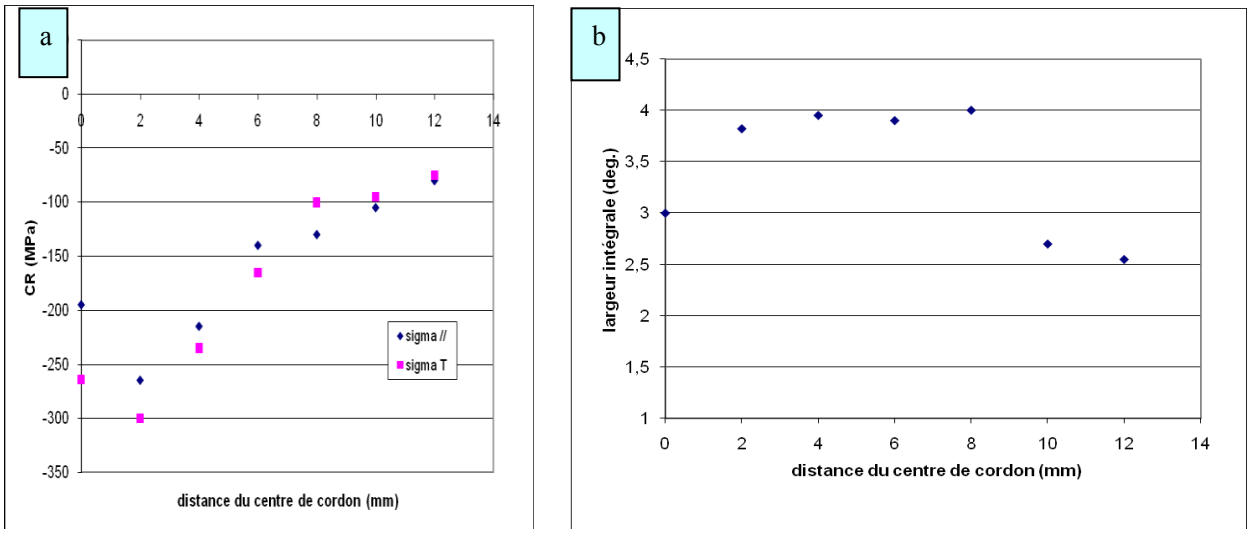


Fig.7 : (a) The stress distributions and (b) width peak evolution in the weld region of X70 pipeline steel

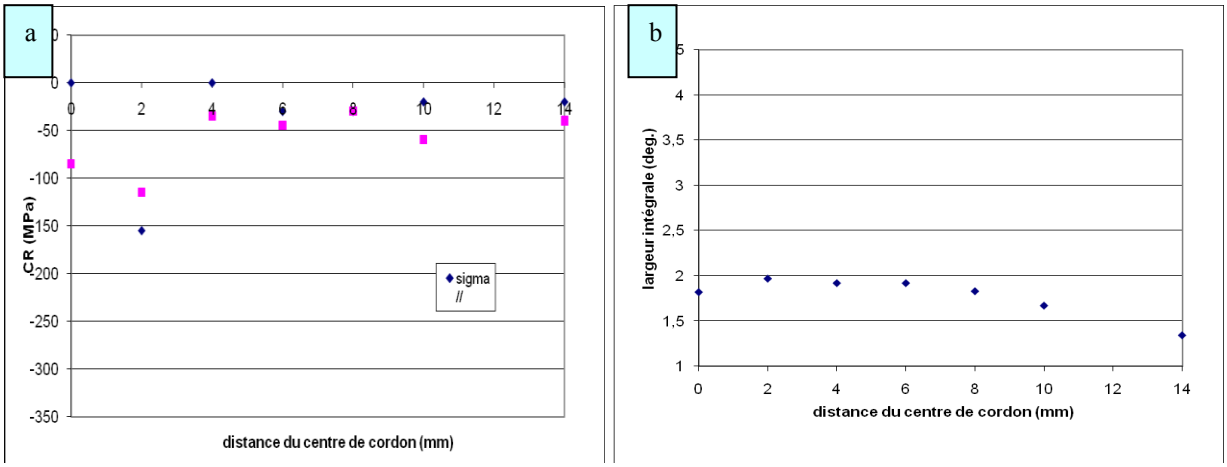


Fig. 8 : (a) The stress distributions and (b) width peak diffraction evolution in the weld region of X70 pipeline steel heat treated 1 h at 200°C.

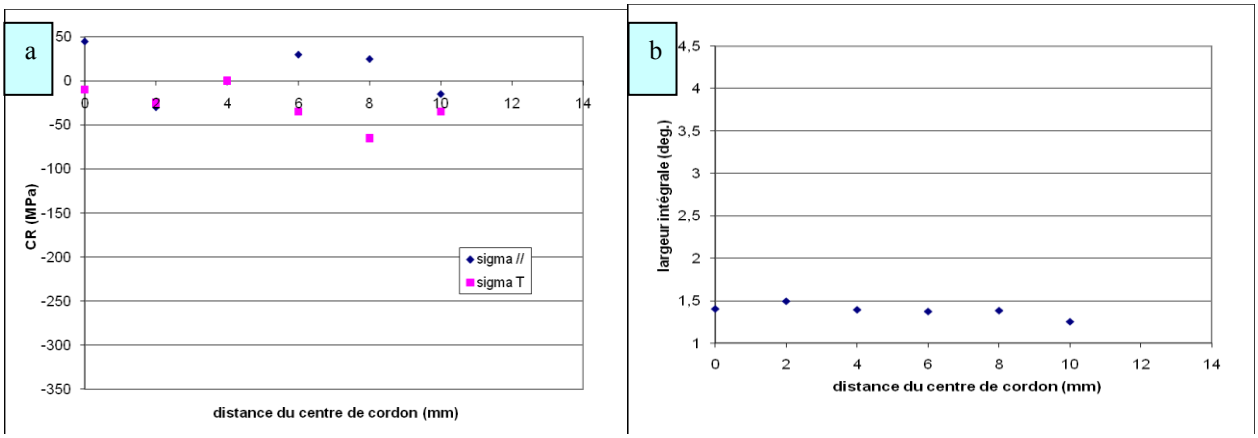


Fig. 9 : The stress distributions and (b) width peak diffraction evolution in the weld region of X70 pipeline steel heat treat 1 h at 600°C.

Conclusion

Our investigation represents a contribution to the study of the distributions of residual stresses on the X70 pipeline steel jointed by industrial arc welding. Stress distribution is characterised by high compressive stresses in weld seam. However, the heat treatments cause relaxation phenomenon in weld region which is due to the recrystalization reaction caused by the heat treatments.

References

[1] J.T. Assis, V Monin1, J.R.Teodosio, T. Gurova, Advances in X-ray Analysis, Volume 45, 2002.
[2] S. Kou, Welding metallurgy, Wiley, New Jersey, 2003.
[3] AS. Maxwell, A. Turnbull, Measurement of residual stress in engineering plastics using the hole-drilling technique,Polym. Test, (2003), 22, 231-3.
[4] S. Chowdhury, MT. Laugier, J. Henry, XRD stress analysis of CVD diamond coatings on SiC substrates,Int. J. Refract Met Hard Mater, 25:39-45, (2007).
[5] JG Kim, J. Yu, Behavior of residual stress on CVD diamond films, Mater Sci. Eng. B, 57:24-7, (1998).
[6] Y. Kang, Y. Qui, Z. Lei, M. Hu, An application of Raman spectroscopy on the measurement of residual stress in porous silicon ,Opt Laser Eng, 43:847-55, (2005).
[7] T. Sasaki, S. Takahashi, Y. Kanematsu, Y. Satoh, K. Iwafuchi, M. Ishida, Y. Moriti, Wear, 265:1402-7, (2008).
[8] D. Devos D, M. Duquennoy, E. Roméro, F. Jenot , D. Lochegnies, M. Ouaftouh, M. Ourak, Ultrasonic evaluation of residual stresses in flat glass tempering by an original double interferometric detection. U Ultrason, 44:923-7, (2006).
[9] D. O'Sullivan, M. Cotterell, S. Cassidy, DA Tanner, I. Meszaros, Magneto-acoustic emission for the characterisation of ferritic stainless steel microstructural state, J. Magn Mater, 271:381-9, (2004).
[10] A. Giraud et X. Boy, ' Géopolitique du pétrole et du gaz', Ed. Technip. 1987.
[11] J.N.H. Tiratsoo, 'Pipeline pigging technology', 2nd Ed. 1992.
[12] Welding Handbook, 7th ed. Vol.4, American Welding Society, Miami,FL, 1982, p.9.
[13] Z.Boumerzoug, C. Derfouf and T. Baudin, Effect of welding on microstructure and mechanical properties of an industrial low carbon steel, Journal of Engineering, 2, (2010) 502-506.
[14] S. Lars-Eric, Control of Microstructures and Properties in Steel Arc Welds, Library of Congress Cataloging-in Published Data, 1994.
[15] G.R. Stewart, A.M. Elwazri, R Varano, N. Pokutylowicz, S. Yue and J.J. Jonas, Testing of Welded Pipeline Steel ,Materials Science and Engineering A420 (2006.) 115-121.
[16] [S. Lars-Eric, Control of Microstructures and Properties in Steel Arc Welds, Library of Congress Cataloging-in Published Data, 1994.
[17] A. Güral, B. Bostan, A.T. Özdemir, Heat treatment in two phase region and its effect on microstructure and mechanical strength after welding of a low carbon steel,Materials and Design 28 (2007) 897-903.
[18] E. Ranjbarnodeh, S. Serajzadeh, A. H. Kokabi, and A Fischer, Effect of welding parameters on residual stresses in dissimilar joint of stainless steel to carbon steel ,J. Mater Sci,46: (2011) 3225-3232,.
[19] Macherauch, E., Kloos, K.H., Origin, Measurements and Evaluation of Residual Stresses, Residual Stresses in Science and Techology. DGM Inform., Verlag, pp. 3-26, 1987
[20] K.S. Prabhat, I. Raisul, P. Chandan, K. Mohd, Analysis of Residual Stresses and Distortions in Girth-Welded Carbon Steel Pipe, IJRTE, Vol.2, Issue-2, (2013) 192-199.

Advanced Materials Research Vol. 936 (2014) pp 2017-2023
© (2014) Trans Tech Publications, Switzerland
doi:10.4028/www.scientific.net/AMR.936.2017

Static Tensile Properties Simulation of Plane Woven-reinforced Laminates with Hole Damage

WEI Wuguo

Aviation Engineering Institute, Civil Aviation Flight University of China, Sichuan Guanghan, 618307, China

weiwuguo@163.com

Keywords: plane woven-reinforced laminates; damage tolerance analysis; 3-D finite element; tensile properties simulation

Abstract: According to the structural difference between the unidirectional and the bidirectional laminate ply, the traditional 3-D (three-dimensional) Hashin failure criteria and the corresponding stiffness degradation rules were amended for damage tolerance simulation analysis of plane woven-reinforced laminates. Based on 3-D finite element technique, a secondary development was carried out on ANSYS software platform, a cumulative damage model was established, and the simulation analysis program for damage tolerance analysis of plane woven-reinforced laminates with hole damage was developed by use of APDL (ANSYS Parametric Design Language). In order to study the influence of different hole diameters on damage tolerance of plane woven-reinforced laminates, two kinds of G803/BMP316 plane woven-reinforced laminates with different hole diameters were selected as the analysis and verification object, and residual tensile strength and damage extension process of the damaged laminates were predicted and analyzed in the simulation. The simulations results are close to the experimental results, and visually present the situation of damage extension in each ply. It provides an effective tool for the damage tolerance analysis of plane woven-reinforced laminates with hole damage.

Forewords

Plane woven-reinforced laminates is one kind of textile composites material, is one kind of composite laminates formed by the combination of plain, twill or satin fabric as reinforced material and resin matrix, and has a widely application in civilian aircraft structure, such as helicopter main blades, tail rotors, et.. In principle, there are repair requirements for all composite structures which applied in engineering field [1]. In the actual operation of civil aircrafts, a variety of damages, for example: hole damage, will be generated inevitably in the composite structures, and there is necessary to repair without delay. But before the repair, damage tolerance analysis for damaged composite structures should be carried out, including residual strength calculation and damage extension analysis. And then, based on the analysis results, the repair tolerance (allowable damage, repairable damage or irreparable damage) of the damaged composite structures should be determined according to flight loads and airworthiness standards. These analyses can reduce the cost of test specimens, shorten the repair cycle and improve the repair design level. For those damage repairs of key parts which unable to test, damage tolerance analysis is particularly important.

Since the 1980s, an advanced composites technology (ACT) project had been launched by NASA. The mechanical properties and test methods of textile composite material had been studied deeply for many years, and a lot of achievements had been summarized. The strength [2-4] and the elastic modulus [5,6] of fabric bidirectional ply had been predicted by use of finite element method on the perspective of mesomechanics in most of existing researches. Compared with the traditional unidirectional ply, the fibers are laying in both warp and weft directions in each ply of plane woven-reinforced laminates. And, warp and weft fibers are interwoven, the interwoven parts of the fibers are slightly bent, lead to some changes on mechanical properties of the fibers itself. So, plane woven-reinforced laminates which laminated by several bidirectional plies in different angles is different from the traditional composite laminates which laminated by several unidirectional plies in different angles on mechanical properties and failure characteristics. The fabric reinforced

composites which applied in helicopter structures had been taken as analysis object by some Chinese researchers [7,8], through the comparison with traditional composite material on mechanical properties and failure characteristics, and based on 2-D (two-dimensional) finite element technique; the damage tolerance of these materials had been analyzed by use of cumulative damage method. But, the influence of interlaminar stress had not been taken into account in the research; there were no delamination failure criteria in the finite element model. And, the influence of different hole diameters on mechanical properties and damage extension process also had not been taken into account.

On the basis of previous studies, a 3-D (three-dimensional) finite element model was established in this paper, which could be applied in damage tolerance analysis of plane woven-reinforced laminates. The delamination failure criteria were added, the stiffness degradation rules were redeveloped, and a material nonlinear factor was introduced in failure criteria. And the simulation program was developed by use of APDL (ANSYS Parametric Design Language) on ANSYS software platform. In order to explore the tensile failure mechanism and study the influence of different hole diameters on damage tolerance of plane woven-reinforced laminates, two kinds of G803/BMP316 plane woven-reinforced laminates with different hole diameters were selected as analysis object. Residual tensile strength and damage extension process of the damaged G803/BMP316 laminates were estimated and analyzed by use of the program, and the analysis results were verified by experiments. Obviously, a feasible method for engineering application for damage tolerance analysis and repair tolerance analysis of damaged composite structures was provided through these analyses.

The Analysis Objects

G803/BMP316 plane woven-reinforced laminates with hole damage was selected as the analysis object in this paper. The reinforced material is satin fabric woven by carbon fibers, and the resin matrix is Polyimide resin. In order to analyze the influence of different damage holes on damage tolerance of plane woven-reinforced laminates, two kinds of laminates with different hole diameters but same material system and same layer way were selected for the simulation analysis and experimental verification. The specimens were prepared according to corresponding national standards. In order to simulate the hole damage, the ϕ5mm and ϕ7mm carbide drills were applied to drill holes on undamaged laminates. The geometrical parameters of specimens are shown in Table 1.

Table 1 Dimension parameters of the analysis objects

Material	Layer way	Number of layers	Physical dimension[mm]			
			Length	Width	Thickness	Hole diameter
G803/BMP316	$[(\pm45)/(0,90)/(\pm45)/(0,90)/(\pm45)]_S$	10	230	25±0.5	2.78	5
		10	230	35±0.5	2.69	7

In addition, the mechanical properties and thickness of G803/BMP316 bidirectional ply are listed in Table 2.

Table 2 Mechanical properties of G803/BMP316 bidirectional ply [9]

Strengths[MPa]						Elastic modulus[GPa]				Poisson's ratio		Thickness of bidirectional ply[mm]
$X_T=Y_T$	$X_C=Y_C$	Z_T	Z_C	S_{12}	$S_{23}=S_{31}$	$E_1=E_2$	E_3	G_{12}	$G_{23}=G_{31}$	μ_{12}	$\mu_{23}=\mu_{31}$	
758.43	380.28	64	185	80.798	39.998	65.208	6.542	4.65	3.725	0.0957	0.0454	0.25

Note: X_T, Y_T, Z_T respectively are tensile strength in direction 1, 2, 3 of bidirectional ply; X_C, Y_C, Z_C respectively are compression strength in direction 1, 2, 3 of bidirectional ply; S_{12}, S_{23}, S_{31} are in-plane shear strength; E_1, E_2, E_3 respectively are tensile modulus in direction 1, 2, 3 of bidirectional ply; G_{12}, G_{23}, G_{31} are in-plane shear modulus; μ_{12}, μ_{23}, μ_{31} are Poisson's ratio.

The Finite Element Simulation Method of Damage Tolerance

The finite element simulation method of composite material gradually accumulated damage, which based on the theory of bidirectional ply, was established in this paper. The damage tolerance of plane woven-reinforced laminates with hole damage could be analyzed by use of the method. There were mainly three problems must to be solved: 3-D finite element modeling and static stress solution; failure determination; stiffness degradation and damage accumulation.

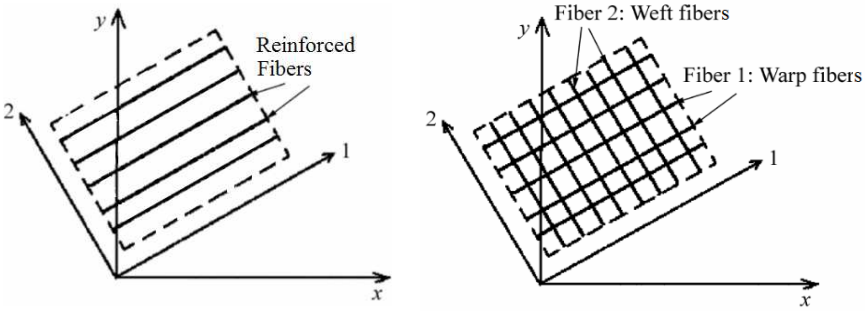
3-D Finite Element Modeling and Static Stress Solution

The static stress analysis of plane woven-reinforced laminates with hole damage was based on 3-D finite element technique. In order to solve the stress accurately, the influence of interlaminar stress must be taken into account. The calculations in theses [10,11] indicate that, there is accurate enough of ANSYS software in the solution of interlaminar stress in composite laminates. So, the software ANSYS10.0 was selected to establish the 3-D finite element model of plane woven-reinforced laminates with hole damage, and to solve the static stress.

A parametric modeling program of damaged laminates with good universality was developed by use of APDL, which could build finite element model of plane woven-reinforced laminates with different hole diameters, layer ways, geometry size or material system. During the simulation in this paper, just the corresponding parameters listed in Table 1 and Table 2 needed to be taken into the program.

Failure Determination

Through the good judgment of strength failure characteristics in direction 1 (fiber direction) and direction 2 (matrix direction) of unidirectional ply, the strength of laminates which laminated by several unidirectional plies at different angles can be well predicted with Hashin failure criteria [12]. But the bidirectional ply in plane woven-reinforced laminates is different from the unidirectional ply on structure, like shown in Figure 1. The mechanical properties of bidirectional ply in direction 1 (warp direction) and direction 2 (weft direction) all are controlled by fibers. So, there is necessary to amend the traditional Hashin failure criteria, and to make it effectively reflect the strength failure characteristics of bidirectional ply.



(a) Unidirectional ply (b) Bidirectional ply

FIG.1 THE DIFFERENCE BETWEEN UNIDIRECTIONAL PLY AND BIDIRECTIONAL PLY

If there is the same percentage of fibers in direction 1 and in direction 2 of bidirectional ply, that means, there are the same strength failure characteristics in direction 1 and in direction 2 of bidirectional ply, then, the Hashin failure criteria can be amended as follows:

(1) Fiber failure criteria in direction 1 (warp direction):

$$\text{Tensile failure } (\sigma_1>0):\ \left(\frac{\sigma_1}{X_T}\right)^2+\left(\frac{\tau_{12}}{S_{12}}\right)^2+\left(\frac{\dfrac{\tau_{31}^2}{2G_{31}}+\dfrac{3}{4}\alpha\tau_{31}^4}{\dfrac{S_{31}^2}{2G_{31}}+\dfrac{3}{4}\alpha S_{31}^4}\right)^2\geq 1 \tag{1}$$

$$\text{Compressive failure } (\sigma_1<0):\ \left(\frac{\sigma_1}{X_C}\right)^2\geq 1 \tag{2}$$

(2) Fiber failure criteria in direction 2 (weft direction):

$$\text{Tensile failure } (\sigma_2>0):\ \left(\frac{\sigma_2}{Y_T}\right)^2+\left(\frac{\tau_{12}}{S_{12}}\right)^2+\left(\frac{\dfrac{\tau_{23}^2}{2G_{23}}+\dfrac{3}{4}\alpha\tau_{23}^4}{\dfrac{S_{23}^2}{2G_{23}}+\dfrac{3}{4}\alpha S_{23}^4}\right)^2\geq 1 \tag{3}$$

$$\text{Compressive failure } (\sigma_2<0):\ \left(\frac{\sigma_2}{Y_C}\right)^2\geq 1 \tag{4}$$

(3) Delamination failure criteria in direction 3 (normal direction):

$$\text{Tensile failure } (\sigma_3 > 0): \left(\frac{\sigma_3}{Z_T}\right)^2 + \left(\frac{\frac{\tau_{31}^2}{2G_{31}} + \frac{3}{4}\alpha\tau_{31}^4}{\frac{S_{31}^2}{2G_{31}} + \frac{3}{4}\alpha S_{31}^4}\right)^2 + \left(\frac{\frac{\tau_{23}^2}{2G_{23}} + \frac{3}{4}\alpha\tau_{23}^4}{\frac{S_{23}^2}{2G_{23}} + \frac{3}{4}\alpha S_{23}^4}\right)^2 \geq 1 \quad (5)$$

$$\text{Compressive failure } (\sigma_3 < 0): \left(\frac{\sigma_3}{Z_C}\right)^2 + \left(\frac{\frac{\tau_{31}^2}{2G_{31}} + \frac{3}{4}\alpha\tau_{31}^4}{\frac{S_{31}^2}{2G_{31}} + \frac{3}{4}\alpha S_{31}^4}\right)^2 + \left(\frac{\frac{\tau_{23}^2}{2G_{23}} + \frac{3}{4}\alpha\tau_{23}^4}{\frac{S_{23}^2}{2G_{23}} + \frac{3}{4}\alpha S_{23}^4}\right)^2 \geq 1 \quad (6)$$

In the formula (1) to (6), σ_1, σ_2, σ_3 respectively are normal stress in direction 1, 2, 3 of the finite element; τ_{12}, τ_{23}, τ_{31} are in-plane shear stress of the finite element; α is the material nonlinearity factor. In failure analysis, as long as one of the inequalities (1) to (6) satisfied by stresses component of one element, then the corresponding failure will be taken place on the element.

Related research in thesis [13] indicates that: the main tensile failure mode of plane woven-reinforced laminates is fiber breakage. The tensile-shear coupling effect on [(±45°)] plies is very small, and the tensile-shear coupling effect on [(0, 90°)] plies basically does not exist. So, the fiber-matrix shear failure criteria were deleted from the amended Hashin criteria.

Stiffness Degradation and Damage Accumulation

If one failure mode taken place on a element in failure analysis, then the mechanical properties of damaged element will be corrected according to the corresponding stiffness degradation rules.

Because there are the same strength failure characteristics in direction 1 and in direction 2 of bidirectional ply, there are the same stiffness degradation rules in direction 1 and in direction 2 of bidirectional ply. And based on the stiffness degradation rules which from theses [14], the new rules could be developed as shown in Table 3:

TABLE 3 STIFFNESS DEGRADATION RULES

No.	Damage forms	Stiffness degradation methods
1	Fiber failure in direction 1	$E_1^*=0.1E_1$; $G_{12}^*=0.1G_{12}$; $G_{31}^*=0.1G_{31}$; $\mu_{12}^*=0.1\mu_{12}$; $\mu_{31}^*=0.1\mu_{31}$;
2	Fiber failure in direction 2	$E_2^*=0.1E_2$; $G_{12}^*=0.1G_{12}$; $G_{23}^*=0.1G_{23}$; $\mu_{12}^*=0.1\mu_{12}$; $\mu_{23}^*=0.1\mu_{23}$;
3	Delamination failure in direction 3	$E_3^*=G_{31}^*=G_{23}^*=\mu_{31}^*=\mu_{23}^*=0$;

Note: E^*, G^*, μ^*, are elastic modulus and Poisson's ratio of damaged element after degradation.

The failure elements gradually accumulate with the increase of load until the laminates can not support. The final destruction criterion of laminates in thesis [15] is: when the elements with fiber failure extended to the edge of laminates along the direction vertical tensile load, the laminates will fracture, cannot support. The rationality of the final destruction criterion was verified by several test results. And, the same final destruction criterion was applied in this paper. That is, for plane woven-reinforced laminates with hole damage, when the elements with fiber failure extended to the edge of laminates along the direction vertical tensile load, the laminates will final fracture.

Analysis Process

According to the failure criteria and stiffness degradation rules, the cumulative damage simulation analysis program was developed by use of APDL on ANSYS software platform, and the specific procedures are as follows:

(1) Determining the size of hole damage and other dimension parameters of damaged laminates according to the actual situation;

(2) Building the 3-D finite element model of the damaged laminates, according to the geometry size of damaged laminates and mechanical properties of bidirectional ply;

(3) Stress solution, and the stress components of each element should be stored in corresponding arrays;

(4) Failure determination of each element according to the amended failure criteria, and stiffness degradation of damaged elements according to the redeveloped stiffness degradation rules;

(5) Increasing load, repeat step (3) and step (4) until the final destruction of laminates, then stop the simulation.

Simulation Results and Experimental Verification

Residual Strength Calculation

The 3-D finite element model of G803/BMP316 laminates with hole damage was established according to the parameters listed in Table 1 and Table 2, and is shown in Figure 2. The boundary conditions are: along the length direction of the model, one end is fixed, and the other end is applied with a tensile load.

The model was meshed with 3-D layered structure 8-nodes solid element SOLID46. In order to analyze the influence of stress concentration in the edge of hole, the edge region of hole was densely meshed by use of grid partial encryption technique. And, in order to analyze the influence of interlaminar stress easily, element thickness was taken as bidirectional ply thickness. According to the above meshing method, the total number of grids of two kinds of laminates models with different hole diameters all are 11200.

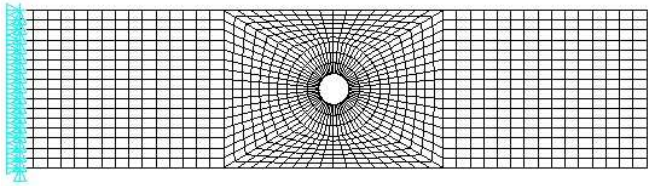


Fig.2 Finite element model of laminates with hole damage

During simulation, the material nonlinearity factor in failure criteria was taken as $\alpha=3.057\times10^{-8}MPa^{-3}$ [16]. And, the calculation results are shown in table 5.

Damage Extension Analysis

The simulation analysis indicates that, there is a same damage extension process of plane woven-reinforced laminates with two kinds of hole diameters under tensile load. So, only the damage extension process of laminates with ϕ5mm hole damage will be analyzed and discussed in this section.

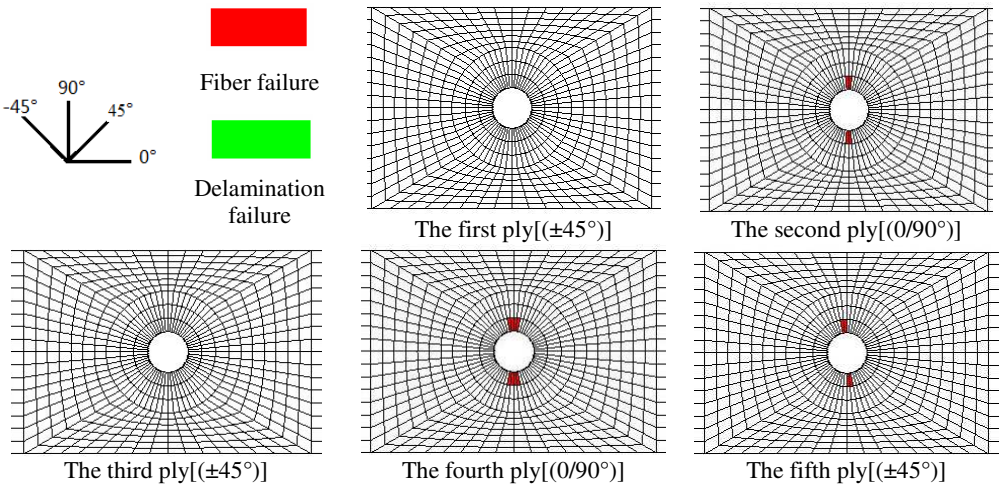


Fig.3 The damage situations of laminates when loading to 325MPa

In the process of simulation, when tensile load is increased to 325MPa, the fiber fracture damage will be found on the second, fourth, fifth, sixth, seventh, ninth ply of laminates model, and all the damages are concentrated in the edge region of hole, as shown in Figure 3. There is no damage found on other plies, and there are no other damage forms only fiber failures. The damage situations of the sixth to the tenth ply are symmetrical with the damage situations of the first to the fifth ply in Figure 3.

With the increase of tensile load, damage quickly extends to other plies, but all of them concentrate in the edge region of hole, and no sign of extension towards the edge of laminates. When the load is increased to 330MPa, damage begins to extend towards the edge of laminates. When the load is increased to 375MPa, eventually damage reaches to the edge of laminates. Then, the laminates model is totally broken, at the same time, the tensile strength of plane woven-reinforced laminates with hole damage is figured out. The damage situations on the first to

the fifth ply of broken laminates are listed in Figure 4, and the damage situations in the sixth to the tenth ply are symmetrical with these failures. Just like the Figure 4, the area and shape of damaged region in each ply of broken laminates are substantially similar, and a little of delamination failures can be found in a few plies.

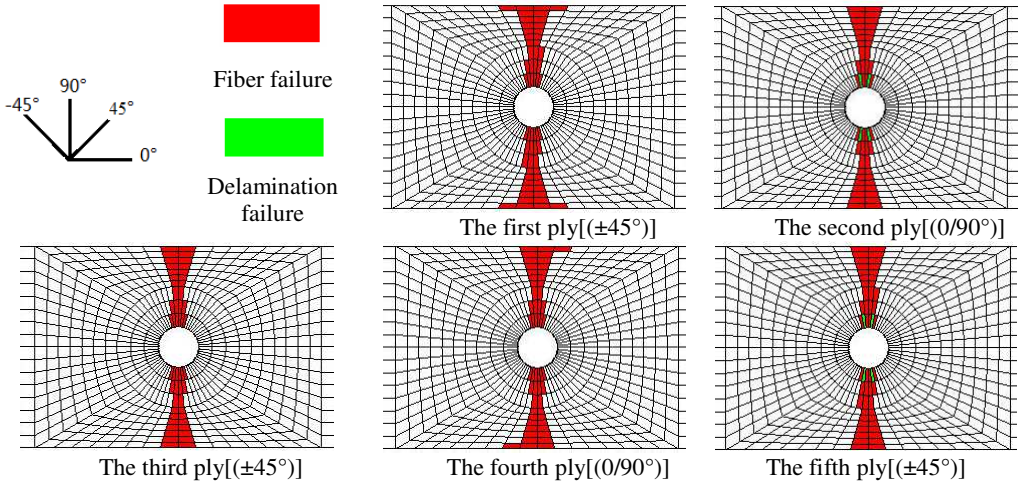


Fig.4 The damage situations of laminates when it finally fractured

Experimental Verification

The specimens for tensile test of plane woven-reinforced laminates with hole damage were prepared according to the size in Table 1. There are five pieces of specimens with ϕ5mm hole, four pieces of specimens with ϕ7mm hole.

Static tensile tests were carried out on WDW-E2000 microcomputer-controlled electronic universal testing machine. The maximum tensile force of testing machine equipped with automatic data acquisition and processing system is up to 200KN, the displacement resolution is 0.01mm, and the test precision is high enough. These tests were carried out in the environment of 18℃ temperature and dry state according to GB/T 3354-1999, and the loading rate was 1mm/min. The test results are shown in Table 4, and the comparison with simulation results is shown in Table 5. The calculated values are close to the experimental values. The maximum error listed in Table 5 is 7.18%, it is enough satisfactory for most engineering applications.

TABLE 4 STATIC TENSILE TEST RESULTS OF G803/BMP316 LAMINATES

Hole Diameter [mm]	Amount of specimens	The average of failure load [KN]	The average of strength [MPa]	Coefficient of Variance of strength [%]
5	5	21.45	387.00	4.79
7	4	29.15	387.84	0.86

Table 5 The comparison of test results and calculated results

Hole diameter [mm]	Strength calculation [MPa]	Strength tests [MPa]	Error [%]
5	375	387.00	3.10
7	360	387.84	7.18

Conclusion

Based on the analysis of mechanical properties and failure characteristics of bidirectional ply, a 3-D finite element model of plane woven-reinforced laminates with hole damage was established, and the simulation program was developed by use of APDL on ANSYS software platform. And then, the damage tolerance of G803/BMP316 laminates with hole damage was analyzed by use of the simulation program and was verified by experiment. The conclusion includes:

(1) The calculated values of residual tensile strength are close to the experimental values. It proves the effectiveness of amended failure criteria and stiffness degradation rules, and provides a convenient engineering approach for damage tolerance analysis of plane woven-reinforced laminates with hole damage.

(2) Most of the failure modes in plane woven-reinforced laminates with hole damage under tensile load are fiber fracture. It is mainly because both direction 1 and direction 2 of bidirectional ply are reinforced by fibers.

(3) There is almost no influence of different hole diameters on mechanical properties and damage extension process of plane woven-reinforced laminates. At first, the damage appears at the edge of hole, with the increase of tensile load, the damage extends mainly along the cross-section stability, rarely along longitudinal.

Supported by: Civil Aviation Flight University of China Research Foundation (J2009-19); National Natural Science Foundation of China (U1233202) .

References

[1] CHEN Shaojie, Composite Structural Repair Guide, first ed., Aviation Industry Press, Beijing, 2001.

[2] Naik N K, Tiwari S I, Kumar R S, An analytical model for compressive strength of plain weave fabric composites, J. Composites Science and Technology. 63 (2003) 609 - 625.

[3] Key C T, Schumacher S C, Hansen A C, Progressive failure modeling of woven fabric composite materials using multicontinuum theory, J. Composites Part B. 38(2007) 247 – 257.

[4] Takeda T, Takano S, Shindo Y, Narita F, Deformation and progressive failure behavior of woven-fabric-reinforced glass/epoxy composite laminates under tensile loading at cryogenic temperatures, J. Composites Science and Technology. 65(2005) 1691 – 1702.

[5] Barbero E J, Lonetti P, Sikkil K K, Finite element continuum damage modeling of plain weave reinforced composites, J. Composites Part B. 37(2006) 137 – 147.

[6] Barbero E J, Trovillion J, Mayugo J A, Sikkil K K, Finite element modeling of plain weave fabrics from photomicrograph measurements, J. Composite Structures. 73(2006) 41 – 52.

[7] ZOU Jian, CHENG Xiaoquan, SHAO Shigang, FAN Jinjuan, ZHANG Weifang, Numerical simulation for plain woven composite laminate based on ANSYS software, J. Acta Materiae Compositae Sinica. 24(2007) 180 – 184.

[8] ZOU Jian, CHENG Xiaoquan, CHEN Hao, SHAO Shigang, Tensile properties simulation of two-dimensional woven reinforced composite laminates after high velocity impact, J. Journal of Beijing University of Aeronautics and Astronautics. 34(2008) 638 – 642.

[9] YANG Ying, Strength Prediction and Optimization of Woven Composite Laminates with Hole, D. Nanjing University of Aeronautics and Astronautics, Nanjing, 2009.

[10] Jose'Sancho, Antonio Miravete, Design of composite structures including delamination studies, J. Composite Structures. 76(2006) 283-290.

[11] CHEN Jianqiao, PENG Wenjie, WEI Junhong, GU Mingkai, Study on the laminates's strength by accounting for internal damage growth, J. Acta Mechanical Solida Sinica. 30(2009) 1-6.

[12] Hashin Z, Failure criteria for unidirectional fiber composites, J. Journal of Applied Mechanics. 47(1980) 329~335.

[13] ZHENG Haiyan, Study on low velocity impact and compression characteristic after impact of woven fabric composite - Test and Numerical Calculation, D. Northwestern Polytechnical University, Xi'an, 2002.

[14] Reddy Y S, Reddy J N, Three – dimensional finite element progressive failure analysis of composite laminates under axial extension, J. Composites Technology and Research. 15(1993) 73 – 87.

[15] Chang F K, Chang K Y, A progressive damage model for laminated composites containing stress concentrations, J. Journal Composites Material. 21(1987) 834~855.

[16] Chang F K, Chang K Y, Post-failure analysis of bolted composite joints in tension or shear-out mode failure, J. Journal of Composite Materials. 21(1987) 809~833.

Advanced Materials Research Vol. 936 (2014) pp 2024-2029
© (2014) Trans Tech Publications, Switzerland
doi:10.4028/www.scientific.net/AMR.936.2024

A Review of Numerical Study on Explosion and Shock Wave Resistance of Metal Foam Material

YI Jian-kun[a] * SHEN Huang YAN Ke-bin GAO Bing

Hefei New Star Applied Technology Institute Hefei China

[a]kjyyjknanjing@126.com

Keywords: Explosion and shock wave Metal foam material Numerical simulation

Abstract: The goal of this research is to understand the status quo and trend of research on numerical simulation of explosion and shock wave resistance of metal foam material. Methods of modelling metal foam material and numerical algorithms of explosion and shock, as well as the current advances in two aspects have been briefly reviewed. Some problems existing in numerical simualtion of explosion and shock wave resistance of metal foam material have also been pointed out. Conclusions of this research will be of benefit to study explosion and shock wave resistance of metal foam material using numerical approach farther.

Introduction

For excellent cushioning performance and energy-absorption characteristics under blast and impact loading, metal foam has been received extensive attention from research on explosion and shock wave resistance of military vehicle, armed helicopter, naval ship, protective works and so on.

Extensive numerical studies on dynamic mechanical behavior and explosion and shock wave resistance of metal foam have been conducted with the convenience of freely seting analysis conditions in compiled program or general commercial software. The key problem in these numerical simulations is how to characterize this material. There are two ways to solve this problem now. One is to construct solid geometry model with continuous and homogeneous equivalent material for simulating macro dynamic mechanical behavior of metal foam. The other is to construct porous geometry model which has equivalent micro-structural characteristics with matrix material of metal foam to simulate macro dynamic performance and meso structure deformation of metal foam. Moreover, using which kind of numerical algorithms to achieve a better balance between computational accuracy, efficiency and hardware configuration requirements is another important problem which should be taken into account. So, in this paper, this two important problems of numerical simulations on metal foam material have been reviewed.

Characterization Model of Metal Foam Material

Macroscopic Characterization of the Material

The numerical investigation on dynamic behavior of metal foam under blast and impact loading always assumes it as a continuous and homogeneous material except meshless material point method which takes it as noncontinuous material. Macrosc-

poic characterization of metal foam is often adopted, such as: constructing abstract 2D or 3D geometric model of metal foam with no consideration of micro porous structures, only describing macroscopic mechanical behavior of metal foam by using a phenomenological constitutive model and experimental stress-strain curve for metal foam material. The method mentioned above can't investigate the material inhomogeneity, evolution processing of meso structure deformation and its'effect on macro dynamic behavior. When it is accepted in numerical simulation by different researchers, the difference only lies in constitutive model of metal foam material.

Honeycomb Material Model

Honeycomb material model is one of the two typical material models usually applied for characterization of material when the explosion and shock wave resistance of metal foam, such as aluminum foam has been numerical studied by general commercial software such as LS-DYNA, AT-

UO-DYNA, ABQUS etc[1-4]. The major use of this material model is for honeycomb and foam materials with real anisotropic behavior. A nonlinear elastoplastic material behavior can be defined separately for all normal and shear stresses .

Modified honeycomb material model is the improvement of honeycomb material model. The major use of it is for aluminum honeycomb crushable foam materials with anisotropic behavior. Three yield surfaces are available. In the first, nonlinear elastoplastic material behavior can be defined separately for all normal and shear stresses. In the second, a yield surface is defined that considers the effects of off-axis loading. The second yield surface is transversely isotropic. In the third option, the model has been modified so that the user can prescribe the shear and hydrostatic resistance in the material without affecting the uniaxial behavior. For the development of the second and third yield surfaces, the modified honeycomb material model can predict mechanical behavior of honeycomb material more accurately than the honeycomb material model.

Crushable Foam Material Model

Crushable foam material model is another typical material model widely applied for characterization of aluminum foam material in general commercial analysis software[5-8]. This material model can modeling crushable foam with optional damping and tension cutoff. Unloading is fully elastic. Tension is treated as elastic-perfectly-plastic at the tension cut-off value. A modified version of this model , Modified Crushable Foam material model includes strain rate effects.

Other Material Models

In numerical calculation of dynamic behavior of aluminum foam by self-compiling program or otherwise, there are some other elastoplastic models applied for aluminum foam material by some researchers. Ramajeyathilagama K. et al.[9] adopted a elastoplasitc material model with Cowper-Symonds strain rate effect to describe behavior of the aluminum foam material and predicte the deformation and rupture of sandwich plates subjected to underwater shock. A elastoplasitc hydrodynamic model was used for aluminum foam material in LIU's numerical investigation[10]. WANG, et al.[11] accepted a isotropic nolinear material for aluminum foam to simulate explosive resistance and deformation and rupture process of composite steel plate with aluminum foam core. While a linear kinematic hardening material model was used to simulate Constitutive Behaviors of aluminum foam by KANG[12].

Micromechanical Characterization of the Material

Developments of mechanics of porous material and some experiments have indicated that mechanical behavior of metal material could be more accurately and comprehensively predicted by establishing the corresponding relationship between macroscopic mechanical properties and micro structure parameters of metal foam material from the views of micromechanics. As for numerical simulation on this problem, there should be a key reconstruction of micro porous structures of material in numerical model and just a material model of matrix metal of metal foam. There are mainly two reconstruction methods, an approximate theoretical reconstruction method and a experimental characterization method. The approximate theoretical reconstruction is divided into two kinds: reconstruction with periodic micro structures and reconstruction with random irregular micro structures, respectively.

Approximate Theoretical Reconstruction with Periodic Microstructures

Considering micro porous structures, earlier numerical simulations of mechanical behavior of metal foam material always construct a geometry model with periodic distributing cellular micro structures to simplify the real structure of material. Some cellular models such as hollow cubic cell[13-15], tetrakaidecahedral cell[16, 17] are often used(Fig.1). To characterize inhomogeneity of the material, geometric or material parameters of cellular microstructure are assumed fitting a certain statistical distribution.

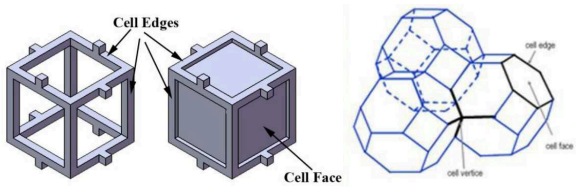


Fig.1 Microstructure model of metal foam(left: cubic cell, right: tetrakaidecahedral cell)

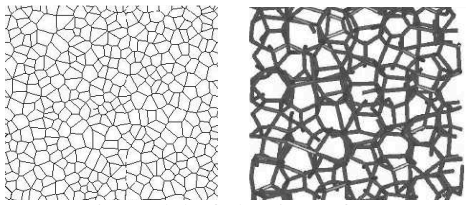


Fig.2 Geometric model of aluminum foam based on voronoi cells (left:2d, right:3d)

Approximate Theoretical Reconstruction with Random and Irregular Microstructures

With improvement of graphic processing ability of computer, finite element analysis of performance of metal foam material by generating geometric model with random microstructures to simulate the real microstructure of material has become a hot research. At present, the dynamic mechanical properties of metal foam are generally numerical calculated with random geometric model based on voronoi spatial distributed algorithm. The voronoi spatial distributed algorithm is a way of dividing space into a number of regions called voronoi cells(Fig.2). The regions are formed by bubbles which grow from each point in a set of points specified beforehand in space.

Finite element simulations of simpler 2d voronoi honeycombs were used by P.J.Tan[18]to illustrate why a greater expenditure of energy accompanied the shock compaction of aluminum foam. The result showed that some macro mechanical performances could be attributed to dynamic deformation in cell edges of 2d voronoi honeycombs. M.Borovinsek, et al. [19] adopted a 3d voronoi lattice model to simulate a open-cell aluminum projectile in Taylor impact test with LS-DYNA. each cell edge of Voronoi model was replaced with three to five beam finite elements of Hughes-Liu type. In order to simulate underwater explosion effects on the deformation behavior of open-cell aluminum foam, M. Vesenjak [20] used 3d voronoi lattice model of aluminum foam to represent the irregularity of the structure. But fluid structure interaction didn't work because of the foam cell edges modeled with beam finite elements in LS-DYNA. For transfering pressure forces to the foam model, a PVC plate was added on the top of aluminum foam and a fluid structure interaction interface was defined between the plate and water.

For limitation of geometry algorithm, 2d voronoi random model can simulate open-cell and close-cell metal foam while 3d voronoi random model can just model open-cell metal foam. In addition voronoi random model embodies randomness of microstructure generating process, but it still can't completely represent inhomogeneity of all mechanical properties of this material.

Another random geometric model carried out by parametric modeling method more easily than that above generally models the closed-cell metal foam material. It consists of a number of hollow spheres (circles for 2d,Fig.3)whose variables including sphere location, size, wall thickness, porosity and number of spheres fit a certain probabilistic distribution in geometry algorithm [21-25].

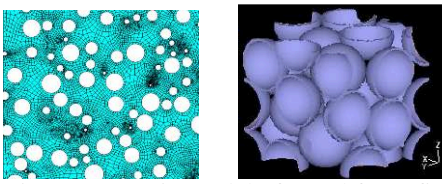


Fig.3 Geometric model of metal foam fitting a probabilistic distribution (left:2d, right:3d)

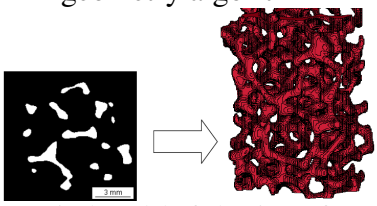


Fig.4 3d numerical model of aluminum foam reconstructed by CT scanning technique

Experimental Reconstruction of Microstructure

Experimental characterization of microstruct-ures of cellular materials reflects characteristics of microstructures of material more accurately than those approximately theoretical reconstructions .Earlier experimental techniques of characterization of microstructure are mainly based on electron microscopy, but only generate two-dimensional image until the focused ion beam technique is applied in forming three-dimensional image.

A better substitute technique has been adopted in recent years [25-27]. It is X-ray microtomography (XRT). The internal microstructures of metal foam material can be imaged by XRT. The 3d numerical model of metal foam material can be reconstructed by the CT scanning pictures of cross sections with certain scanning parameters. Process of reconstruction is as follows: the pictures of cross

sections are replaced with the monochromatic bitmaps. one pixel at the bitmap is assumpted to be the middle layer of one hexagonal finite element in numerical model. A special application that transforms the numbers of pixels into the numbers of finite elements is created. The result of that process is the raster numerical model of an open-cell foam (Fig.4).The experimental reconstruction realistically describes internal structure of metal foam material, but require more resources of computer hardware.

In summary, numerical simulations of mechanical behavior of metal foam material with meso-scale material model mostly focus on quasi static compression, dynamic compact and ballistic impact but a few involve dynamic response of metal foam material under blast loading at present.

Algorithms of Numerical Simulation on Blast and Impact Resistance of Metal Foam Material

Handling capacity for large deformation problem and resolution of different algorithms exist difference in numerical simulation. So it is very important for numerical investigation to select appropriate numerical algorithm. Lagrangian algorithm, Eulerian algorithm, ALE algorithm, et al. can be used to numerically analyze the problem of explosion and shockwave.

Lagrangian Algorithms

Lagrangian algorithms allows an easy tracking of free surfaces and interfaces between different materials but can't follow large distortions of the computational domain without frequent remeshing operations.So it for simulation of blast resistance of aluminum foam material or composite structure filled with aluminum foam will terminate numerical calculateion for mesh large distortion caused by the process of explosion and expansion of detonation products. There are two ways to avoid this phenomenon.

The first one is using lagrangian algorithm to simulate explosion of explosive and interaction between explosion products and structure without air, but manually deleting computational meshes of high explosive model when the contact force between the explosive and structure decreases to nearly zero. This finite element method has been adopted by ZHU[28] in numerical simulation of aluminum foam core sandwich panels with purely Lagrange meshes. Compared with ALE algorithms, this method has the advantage of less calculation time, less computer hardware resources and relatively higher calculating efficiency while has shortcomings of difference between calculating result and actual condition because of omitting air.

The another one is defining blast equations for directly applying blast load to structures without simulation of explosion. For example, to apply blast load to structure in LS-DYNA program, ConWep blast equations is defined. Compared with the first one without considering effects of air, the second method more accurately reflects actual load condition, more simplifies the numerical model, saves more calculating time and hardware resources. So,it has been widely applied in Lagrangian algorithms for simulation of dynamic response of metal foam subjected to blast loading[2, 3, 4, 29].

Arbitrary Lagrangian–Eulerian Algorithms

When the explosion of high explosive and propagation of shock wave should be considered in numerical simulation of blast resistance of metal foam material and composite structure filled with it, the ALE algorithm can be used[5, 7, 8, 10, 20]. To avoid the termination of calculation for large distortion of mesh, the computational meshes of explosive and air medium model are be held fixed but the continuums move with respect to the grids in Eulerian manner. While the computational meshes of metal foam material or composite structure model are be moved in normal Lagrangian fashion to easily tracking deformed surfaces of metal foam material or composite structure.Dynamic data can be transferred with method of fluid-structure coupling among the lagrangian mesh and Eulerian mesh. This ALE algorithms can well cope with explosion of high explosive, propagation of shock wave and large distortion of material or structure in numerical simulation with more resolution than that afforded by a purely Eulerian approach. ALE numerical method can more truly reflect the physical process but at expense of adding complication of numerical model, more calculation time and computing hardware resources. Moreover, the precision of numerical result is dependent on the quality of mesh of numerical model.

Conclusion

How to characterize the metal foam material and which kind of numerical algorithms to be adopted in numerical simulation of blast resistance of metal foam have been discussed in this review. This discussion indicates that numerical simulation has been improved to the level that it can reproduce a truly deformation and failure process of microstructures of metal foam subjected to explosion and shock wave, moreover, can model the whole process of explosion, propagation of shock wave and interaction between shock wave and structure.

Nevertheless, there are still following problems to be solved. Firstly, reconstruction of microstructures of metal foam material whether based on 3d random geometry model or based on CT technique, adds complication and time of numerical calculation and improves the hardware requirements, although more truly describes the internal structures of metal foam. Secondly, numerical simulations of whole physical process of metal foam material under blast loading are still correspondently deficient at present. Thirdly, there isn't a kind of numerical algorithms for simulation can achieve a optimization in truly reflecting of physical process, computational precision, computational efficiency and requirement of hardware resources at the same time.

References

[1] Michael J.Mullin,Brendan J.O.,Simulation of Energy Absorbing Materials in Blast Loaded Structures, 8th International Ls-dyna Users Conference, Dearborn, Michigan ,2004,8-67-80.

[2] Rajan Sriram,Uday K.Vaidya,Blast Impact on Aluminum Foam Composite Sandwich Panels, 8th International LS-DYNA Users Conference, Dearborn, Michigan ,2004,14-29-38.

[3] Bazle A.Gama, Venkat S.Chiravuri, John W.Gillespie Jr.,Modeling Blast Damage of Composite Structures, 11th International Ls-dyna Users Conference, Detorit, 2010,5-13-22.

[4] Marian Klasztorny,Tadeusz Niezgoda,Pawel Dziewulski,Numerical modelling and experimental validation of the protective shield – protected plate –test stand system under a blast shock wave, CMM-2011-Computer Methods in Mechanics, Warsaw, Poland,2011.

[5] SHI Shao-qing,LIU Ren-hui,WANG Min,Shock Wave Reduction Behavior of a New Compound Structure Composed of A Foam Aluminum Layer Between Two Steel Plates, Journal of Virbration and Shock, Vol.27, No.4, 2008, pp. 143-146.

[6] KANG Jian-gong,SHI Shao-qing,LIU Ying-Fang,WANG Min,Finite Element Analysis of Anti-blasting Performance of Aluminum Foam Sandwich Beam, Blasting, Vol.26, No.3, 2009, pp. 10-13.

[7] TIAN Jie, HU Shi-sheng,CHEN Jian,Experimental Study and Numerical Simulation of Secondary Shock Overpressure in Air, Acta Armamentarii, Vol.28, No.12, 2007, pp. 1483-1488.

[8] YAN Shi, LI Wei,Numerical Analysis on Energy-consumption Performance of Foam Aluminum Composite Structures under Blast Loading, Journal of Water Resources and architectural Engineering, Vol.8, 2010, No.1, pp. 12-14.

[9] Ramajeyathilagama K，Vendhan C P. eformation and Rupture of Thin Rectangular Plates Subjected to Under Water Shock, International Journal of Impact Engineering,2004,Vol.30, No.6, pp. 699-719.

[10] LIU Ying-fang, LIU Ren-hui, SHI Shao-qing, WANG Min , ZHAO Yong-bin,Numerical Simulation Analysis of Reducing Blast by Using Foam Aluminum, Chinese Journal of Underground Space and Engineering, Vol.4, No.2,2008, pp. 230-233.

[11] WANG Yu-xin, CHEN zhen, ZHANG Hong-wu, SUN Ming,Response of Multi-layered Structure Due to Impact Load Using Material Point Method, Engineering Mechanics, Vol.24, No.12, 2007, pp. 186-192.

[12] KANG Jian-gong, SHI Shao-qing, Theoretical and numerical analysis for a cladding aluminum foam sandwich panel attenuating blasting wave pressure, Journal of Vibration and Shock, Vol.24, No.12,2010, pp. 199-202.

[13] Gibson L.J.,Ashby M.F.Cellular, Solids:Structure and Properties,2nd edition, Cambridge:Cam-bridge University Press,1997.

[14] PAN Yi, HU Shi-shen, JIANG Jia-qiao, HUANG Xi-chen,Dynamic deformability of cell in aluminum foams, Explosion and Shock Waves, Vol.24, No.5, 2004, pp. 407-412.

[15] HAN ChunGuang, TANG LiQun , HUANG XiaoQing, Meso statistics properties of material constants and constitutive relation of medium or high void ratio metal foams under tension, Scientia Sinica(Physica,Mechanica & Astronomica) , Vol.40, No,10, 2010,pp. 1247-1255.

[16] ZHANG JiaLei, LU ZiXing, Finite Element Analysis for the Elastic Properties of Closed-cell Foams Based on a Tetrakaidecahedron Model, Journal of Mechanical Strength, Vol.29, No.2, 2007, pp. 315-319.

[17] TU Yong-qing,LIU Lin-lin,WAN Jian-fang,YANG Ming ,Improvement of the tetrakaidecahedral model for closed-cell aluminum foams, Chinese Journal of Computational Mechanicas, Vol.27, No.2, 2010, pp. 275-279.

[18] P.J. Tan, S.R. Reid_, J.J. Harrigan, Z. Zou, S. Li. Dynamic compressive strength properties of aluminium foams. Part II-'shock'theory and comparison with experimental data and numerical models,Journal of the Mechanics and Physics of Solids,53 (2005) 2206-2230.

[19] M. Borovinsek, M. Vesenjak, Z. Ren, Computational simulations of aluminum foam projectile behavior, 8th European LS-DYNA Users Conference, Strasbourg, 2011.

[20] M. Vesenjak, M. Borovinšek, Z. Ren, Shock Wave Effect on Aluminium Foam, 8th European LS-DYNA Users Conference, Strasbourg,2011.

[21] SU Hua-bing .HUANG Xiao-qing.TANG Li-qun.LIU Ze-jia.ZHANG Hong, Finite Element Simulation and Analysis of Small Compression of Foam Aluminum Based on the Statistical Hole-diameter,Science Technology and Engineering, Vol.9, No.23, 2009, pp. 6991-6995.

[22] B.H.Smith, S.Szynisze wski, J.F.Hajjar,Material characterization and microstructural simulation of hollow spheres and PCM steel foams, Proceedings of the Annual Stability Conference Structural Stability Research Council, Grapevine, Texas, April 18-21,2012.

[23] K.A. Brown, R. Brooks, O. Awoyemi, Meso-scale Modelling of Shock Wave Propagation in a Cellluar Glass Particle Reinforced Thermoplastic Composite, 18th International Conference on Composite Materials, Jeju, Korea,2011.

[24] L. Filice, F. Gagliardi, D. Umbrello, Simulation of aluminum foam behavior in compression tests, Advanced Manufacturing Processes and Technologies (AMPT) Conference, Bahrain, 2008,pp. 128-137.

[25] N.K.Bourne, K.Bennett, A.M.Milne,The shock response of aluminium foams,Scripta Materialia, Vol.58 2008,pp. 154-157.

[26] Danuta Miedzińska, Tadeusz Niezgoda.Numerical simulations of shock energy absorption mechanisms in metal foam microstructure. 12th Pan-American Congress of Applied Mechanics, Port of Spain, Trinidad, 2012.

[27] Mohammad Irshidat,Physics-Based Simulation and Experiment on Blast Protection of Infill Walls and Sandwich Composites Using New Generation of Nano Particle Reinforced Materials, Ph.D Thesis, The University of Mississippi, Mississippi.2010.8.

[28] Feng Zhu,Impulsive Loading of Sandwich Panels with Cellular Cores, Ph.D Thesis, Philosophy.Swinburne University of Technology, 2008,pp. 63-102.

[29] Wang Hongxin, Zha Xiaoxiong, Dynamic Response of Sandwich Panels Under Blast Loading, Industrial Construction , Vol.41, No.3,2011, pp. 23-28.

Advanced Materials Research Vol. 936 (2014) pp 2030-2034
© (2014) Trans Tech Publications, Switzerland
doi:10.4028/www.scientific.net/AMR.936.2030

Modelling Method for Preventing Thermal Runaway Reaction Accident of Thermal Reactive Material

I-Tien Chu[1,a], Shu-Yao Tsai[1,b], Wan-Tran Huang[1,c], Jo-Ming Tseng[2,d], Jin-Shuh Li[3,e], and Chun-Ping Lin[1,f*]

[1]Asia University, 500, Lioufeng Rd., Wufeng, Taichung, Taiwan 41354, ROC

[2]Central Taiwan University of Science and Technology, 666, Buzih Rd., Beitun District, Taichung, Taiwan 40601, ROC

[3]National Defense University, 75, Shiyuan Rd., Dasi, Taoyuan, Taiwan 33551, ROC

[a]chuitien@asia.edu.tw, [b]sytsai@asia.edu.tw, [c]wthuang@asia.edu.tw, [d]jmtseng@ctust.edu.tw

[e]lijinshuh@gmail.com, [*f]cp.lin@asia.edu.tw

Keywords: Thermal reactive material, Differential scanning calorimetry, Modelling method, Safety parameter

Abstract: Thermally reactive materials have caused many serious accidents involving storage and transportation, due to being thermally reactive. The safe storage and management of these materials still is a critical problem in many countries. We studied the thermal hazard of thermal reactive materials, such as a propellant, by employing differential scanning calorimetry (DSC) non-isothermal tests and isothermal tests, and then comparing the kinetic parameters by isothermal and non-isothermal of kinetics, avoiding the mistaken results of the single thermal analysis model. The chosen approach was to obtain reliable kinetics of thermal decomposition by safety and effective technology by modelling method, which acquired the safety parameters of storage condition that could be applied as thermal reactive materials' safer design during storage safety conditions and relevant operations.

Introduction

The focus of this study is on the thermal hazard of thermal reactive materials, such as the rifle gun propellant (GP). GP is dangerous and should be transported and stored under limited temperature. In terms of storage and transportation management, many serious explosions and high ambient temperature occur because of thermal decomposition. One reason involves the function group and material of nitrate ester, nitrate, chlorate, perchlorate and phosphorus, etc., due to thermal instability and high sensitivity to spark, light, static electricity, or other energy [1–8].

Here, useing differential scanning calorimetric (DSC) non-isothermal tests and isothermal tests, and then compared the kinetic parameters of GP by isothermal and non-isothermal tests, avoiding the mistaken results of thermal analysis. The chosen approach was to obtain reliable thermal decomposition that included the kinetic parameters, such as the mechanism of thermal decomposition, pre-exponential factor ($\ln k_0$), reaction order (n), activation energy (E_a), and heat of decomposition (ΔH_d) [9–11].

The safety parameters of thermal decomposition for storage conditions include parameters, such as isothermal time to maximum rate (TMR_{iso}), total energy release (TER), and time to conversion limit (TCL) [9–11], and in addition, the thermal hazard properties of thermal reactive materials that could be applied as a reduction of loss prevention for safer design during storage lifetime conditions and relevant operations, which all usefully data will be obtained by modelling method.

Reliable Thermokinetic Parameters Evaluation

Evaluation of kinetic models can involve complex multi-stage reactions that may consist of several independent, parallel, and consecutive stages, demonstrated as Eqs. (1) to (5) [9–11]:

Simple single-stage reaction:

$$\frac{d\alpha}{dt} = k_0 e^{\frac{-E_a}{RT}} f(\alpha) \tag{1}$$

Single-stage for *n*-th order reaction:

$$\frac{d\alpha}{dt} = k_0 e^{\frac{-E_a}{RT}} (1-\alpha)^n \tag{2}$$

Multi-stage for autocatalytic reaction:

$$f(\alpha) = (1-\alpha)^{n_1}(\alpha^{n_2} + z) \tag{3}$$

where E_a is the activation energy, k_0 is the pre-exponential factor, z is the autocatalytic constant, and n_1 and n_2 are the reaction orders of a specific stage.

Reactions that include two consecutive stages:

$$\frac{d\alpha}{dt} = k_1 e^{\frac{-E_1}{RT}} (1-\alpha)^{n_1}; \frac{d\gamma}{dt} = k_2 e^{\frac{-E_2}{RT}} (\alpha-\gamma)^{n_2} \tag{4}$$

where α and γ are the conversions of the reactant A and product C, respectively. E_1 and E_2 are the activation energies of the stages.

Two parallel reactions for full autocatalysis:

$$\frac{d\alpha}{dt} = r_1(\alpha) + r_2(\alpha); \quad \begin{matrix} r_1(\alpha) = k_1(T)(1-\alpha)^{n_1} \\ r_2(\alpha) = k_2(T)\alpha^{n_2}(1-\alpha)^{n_3} \end{matrix} \tag{5}$$

where r_1 and r_2 are the rates of each stage, and n_3 is the reaction order of stage three.

Experimental and Method

GP, which was supplied directly from National Defense University of the Republic of China (ROC) in Taiwan, was stored under 15 °C. The test cell was used to carry out the experiment for withstanding relatively high pressure to approximately 10 MPa. ASTM E698 was used to obtain thermal curves for calculating kinetic parameters. Approximately 0.9–1.1 mg of the sample was used to acquire the GP experimental data. Non-isothermal tests of the scanning rate selected for the programmed temperature ramp were 1, 2, and 4 °C/min. The range of temperature rise chosen was from 30–300 °C for each experiment. Isothermal tests of the holding isothermal condition were several at 175, 180, and 185 °C. The results for the thermal decompositions of GP from the non-isothermal and isothermal of DSC tests are listed in Figs. 1 and 2 & Table 1, respectively.

TABLE 1 RESULTS OF GP DSC TESTS.

Sample mass (mg)	Scanning rate (°C/min)	Peak of Temperature T_p (°C)	ΔH_d (kJ/kg)
1.0	1	181.4	2438
0.9	2	186.3	1655
1.0	4	191.8	2818
Sample mass (mg)	Isothermal conditions (°C)	Maximum heat flow (mW)	ΔH_d (kJ/kg)
1.0	175	2.47	2588
1.0	180	4.93	3201
1.1	185	10.14	1814

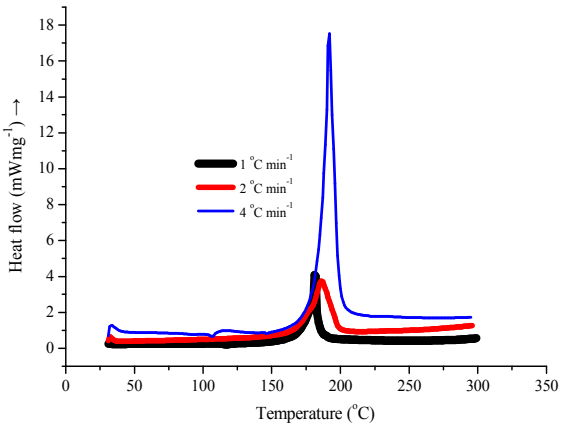


Fig. 1 DSC thermal curves with scanning rate of 1, 2, and 4 °C/min.

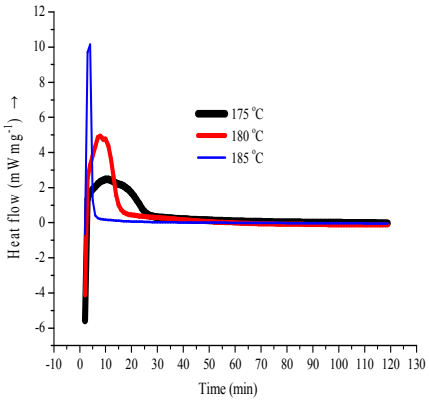


Fig. 2 DSC thermal curves with isothermal temperature at 175, 180 and 185 °C.

Results and Discussion

Determination of Reliable Kinetics by DSC

The thermal decomposition of GP represents an unknown mechanism of reaction, such as an *n*-th order or autocatalytic reaction in this study. Here, using the *n*-th order and autocatalytic simulations to evaluate the thermokinetic parameters and then to compare the results of non-isothermal and isothermal kinetic model simulation, we obtained the mechanism of thermal decomposition for GP. The simulation results are presented in Table 2.

Table 2 show they can be matched very well to the results of the autocatalytic simulations and the *n*-th order simulation for GP, respectively. Clearly, from comparisons of thermokinetic parameters of non-isothermal and isothermal kinetic model simulation, we could observe from the GP kinetic parameters that the mechanism of thermal decomposition belongs to the autocatalytic reaction in this study.

TABLE 2 COMPARISONS OF GP OF THE KINETIC PARAMETERS FOR THE EVALUATION OF *N*-TH ORDER AND AUTOCATALYTIC MODEL SIMULATIONS.

Scanning rate (°C/min)	1		2		4	
Kinetic model	*N*-th order	Autocatalytic	*N*-th order	Autocatalytic	*N*-th order	Autocatalytic
$\ln(k_0)$/ln (1/sec)	60.01	26.04	61.48	24.79	96.17	26.30
E_a (kJ/mol)	249.25	110.97	255.48	113.46	388.59	111.76
Reaction order (n)/nth Reaction order (n_1)/auto	0.57	2.6588	1.14	1.33	1.12	1.96
Reaction order (n_2)	N/A	3.0000	N/A	1.10	N/A	1.83
Autocatalytic constant (z)	N/A	0.0168	N/A	0.08	N/A	0.01
ΔH_d (kJ/kg)	2282.66	2577.39	1733.38	1802.99	2638.97	2770.82
Isothermal temperature (°C)	175		180		185	
Kinetic model	*N*-th order	Autocatalytic	*N*-th order	Autocatalytic	*N*-th order	Autocatalytic
$\ln(k_0)$/ln (1/sec)	27.00	24.61	44.20	24.43	29.60	28.17
E_a (kJ/mol)	127.85	113.04	192.32	110.88	133.86	115.90
Reaction order (n)/nth Reaction order (n_1)/auto	0.14	1.53	0.09	1.80	0.03	2.95
Reaction order (n_2)	N/A	0.65	N/A	0.73	N/A	1.53
Autocatalytic constant (z)	N/A	8.707E-08	N/A	7.051E-06	N/A	3.000E-03

Tables 1 and 2 shows the heat effect of GP at the 2 °C/min scanning rate is smaller than that observed at the other scanning rates. In addition, Tables 1 and 2 also shows the heat effect of GP at holding the isothermal temperature at 185 °C is smaller than that observed at the other isothermal

temperatures. While analyzing the GP's kinetic parameters by simulation, we obtained four values for the autocatalytic thermokinetic parameters by using scanning rates of 1 and 4 °C/min and holding isothermal temperatures under 175 and 180 °C for processing the safety parameters of storage lifetime thermal hazard simulation, respectively.

Storage Lifetime and Safety Parameters Evolution

From above-mentioned results, which were applied to simulate the safety parameters of the thermal decomposition for predicting the TMR_{iso}, TER, and TCL of GP, which can be improved to the actually storage lifetime conditions and relevant operations of thermal reactive materials. The safety parameter assessment of the TMR_{iso}, TER, and TCL of GP was acquired by simulating autocatalytic non-isothermal and isothermal simulation, as displayed in Figs. 3–5.

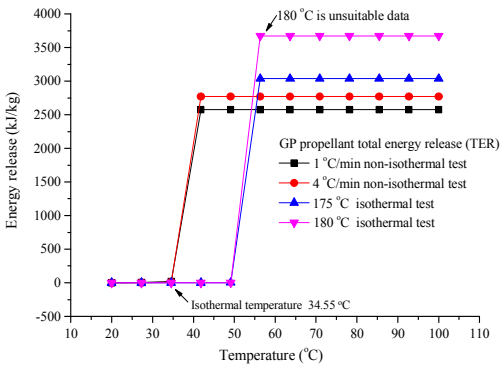


Fig. 3 The storage lifetime and safety parameter assessment of GP total energy release.

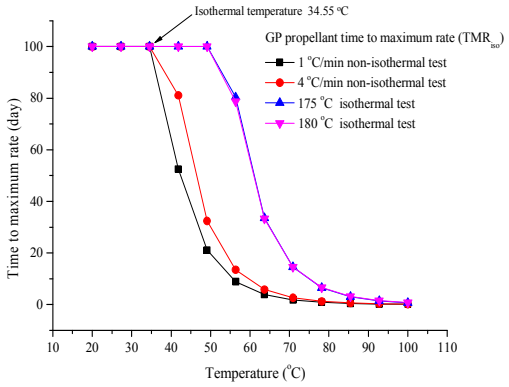


Fig. 4 The storage lifetime and safety parameter assessment of GP time until the maximum rate.

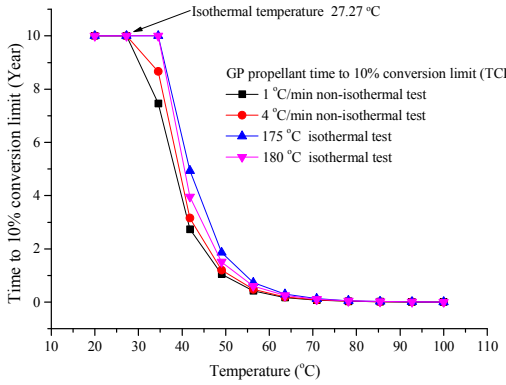


Fig. 5 The storage lifetime and safety parameter assessment of GP time until 10% conversion.

Here, Fig. 3 shows the TER of GP is stored in less than 34.55 °C, and the energy release is under safety condition, and Fig. 4 shows TMR_{iso} of GP obtained, which values were ca. less than 34.55 °C and exceeded the upper limit 100 days. Fig. 5 shows the TCL of GP is less than 27.27 °C, which is beyond the upper limit of 10 years.

Conclusions

These results could be applied toward energy reduction and safer designs for storage of thermal reactive materials. The validity of the results significantly depends on the reliability of the applied kinetic model, which can be confirmed by the proper selection of a kinetic model for a reaction, and the correctness of the modelling methods used for the kinetics and safety parameter evaluation.

Acknowledgments

We are indebted to the donors of Asia University in Taiwan under the contract number 101-asia-44 for financial support. The authors are grateful to National Defense University of ROC in Taiwan.

Nomenclature

E_a	activation energy, kJ/mol	GP	rifle gun propellant
TCL	time to conversion limit, year	TMR_{iso}	time to maximum rate under isothermal conditions, day
TER	total energy release, kJ/kg	ΔH_d	heat of decomposition, kJ/kg

References

[1] M.A. Bohn, Kinetic modeling of the stabilizer consumption and of the consecutive products of the stabilizer in gun propellant , Propellants Explos. Pyrotech. 22 (1997) 125-136.

[2] T.B. Brill, Thermal decomposition of energetic materials 69 analysis of the kinetics of nitrocellulose at 50–500 °C, Propellants Explos. Pyrotech. 22 (1997) 38-44.

[3] M. Chovancová, S. Zeman, Study of initiation reactivity of some plastic explosives by vacuum stability test and non-isothermal differential thermal analysis, Thermochim. Acta. 460 (2007) 67-76.

[4] A.S. Tompa, W.F.B. Jr, Microcalorimetry and DSC study of the compatibility of energetic materials, Thermochim. Acta. 367–368 (2001) 433-441.

[5] G. Singh, D.K. Pandey, Studies on energetic compounds. Part 27: kinetics and mechanism of thermolysis of bis(ethylenediamine) metal nitrates and their role in the burning rate of solid propellants, Propellants Explos. Pyrotech. 28 (5) (2003) 231-239.

[6] G. Singh, S.P. Felix, P. Soni, Studies on energetic compounds part 28: thermolysis of HMX and its plastic bonded explosives containing Estane, Thermochim. Acta. 399 (2003) 153-165.

[7] S. Zeman, Kinetic compensation effect and thermolysis mechanisms of organic polynitroso and polynitro compounds, Thermochim. Acta. 290 (1997) 199-217.

[8] S, Zeman, Z. Friedl, Relationship between electronic charges at nitrogen atoms of nitro groups and thermal reactivity of nitramines, J. Therm. Anal. Calorim. 77 (2004) 199-217.

[9] C.P. Lin, J.M.Tseng, Green technology for improving process manufacturing design and storage management of organic peroxide, Chem. Eng. J. 180 (2012) 284-292.

[10] J.M. Tseng, C.P. Lin, Green thermal analysis technology for evaluating the thermal hazard of di-tert-butyl peroxide, Ind. Eng. Chem. Res. 50(16) (2012) 9487-9494.

[11] J.M. Tseng, J.Z. Lin, C.C. Lee, C.P. Lin, Prediction TMCH thermal hazard with various calorimetric tests by green thermal analysis technolog, AICHE J. 58(12) (2012) 3792-3798.

Advanced Materials Research Vol. 936 (2014) pp 2035-2040
© (2014) Trans Tech Publications, Switzerland
doi:10.4028/www.scientific.net/AMR.936.2035

Thermal-structure Coupling Research and Thermal Fatigue Life Prediction of the Large Mining Machinery Brake

LIU Zhuli [1,a *], ZHAO Minmin [2,b], LI Mengli [3,c]

[1,2]School of Mechanical Engineering, Zhengzhou University，Zhengzhou 450001，China

[3]Henan EPRI High Tech Group Ltd. Co., Zhengzhou 450052, China

[a]zhuli_liu@126.com, [b]zhaominmin25@163.com, [c]limengli163@126.com

Keywords：Brake Disc; Temperature Field; Stress Field; Sequential Coupling Methods; Thermal Fatigue Life

Abstract：This paper analyzed the temperature field of one large mining machinery disc brake during normal braking conditions in ANSYS. Basing on the sequential coupling methods, analyzed the brake disc's thermal stress distribution and changes. According to the analysis results, estimated its thermal fatigue life.

Introduction

Disc brakes are commonly used in large mining machinery. When braking, the huge mechanical energy is almost converted into heat through the interaction of the brake disc and the friction plate except part consumed by the running resistance of the conveyor, which leads to the surface temperature of the brake disk rising sharply, and then causing uneven distribution of the thermal stress. After several brakes, it can lead to thermal fatigue cracking [1]. Therefore, it has important practical engineering significance to the design of the brake disc and to ensure safe operation of the equipment through the temperature and stress fields simulation and thermal fatigue life estimation.

Thermal - structure Coupling Analysis Theory of the Disc Brake[2]

Due to there is no internal heat during braking, and the braking time is short, so the friction heat is mainly redistributed in the form of heat conduction inside the brake disc, and part spreads into the air through the convection heat transfer. In contrast, the proportion of heat radiation is smaller which can be neglected.

Temperature Field Calculation of the Brake Disc

According to the heat transfer theory , the temperature field T satisfies the three-dimensional isotropic transient heat conduction differential equation without internal heat. that is (in the cylindrical coordinate system):

$$\frac{\lambda}{\rho c}\left(\frac{\partial^2 T}{\partial r^2}+\frac{1}{r}\frac{\partial T}{\partial r}+\frac{1}{r^2}\frac{\partial^2 T}{\partial \theta^2}+\frac{\partial^2 T}{\partial z^2}\right)=\frac{\partial T}{\partial t}. \tag{1}$$

In the formula，λ is the thermal conductivity, W/(m·K)；ρ is density, kg/m^3；c is specific heat capacity, J/(kg·K); t is time, s.

Because of the high speed of the brake disc, it causes the convective heat transfer between the ambient air and the brake disc, the heat flux density q of convective heat transfer is:

$$q = h(t_f - t_w) . \tag{2}$$

In the formula, t_f is air temperature(℃); t_w is brake disc surface temperature(℃);h is convective heat transfer coefficient(W/(m^2·K)),changed with the rotational speed, k_a is thermal conductivity of the air, d is the diameter of the friction center, Re is Reynolds Number, $Re=V\rho_a L_c/\mu_a$, V is line speed, ρ_a is air density, L_c is characteristic length, μ_a is air viscosity, then:

$$h = 0.70\left(k_a / d\right)\mathrm{Re}^{0.55} \tag{3}$$

.

Elastic Thermal Stress Calculation

The tremendous friction heat generated during braking lets the temperature distribution in the brake disc uneven, and changing with time, while the brake disc is bound by the supporting shaft and other constraints, so thermal stress is generated. The thermal stress caused by the temperature changing is[3]:

$$\sigma = D(\varepsilon - \varepsilon_0) . \tag{4}$$

σ - stress matrix, MPa; D - elastic matrix, MPa; ε - strain matrix; ε_0 - the initial strain matrix.

Finite Element Model of the Brake Disc

Some related parameters are as follows: Diameter of the brake disc, 2.5m; Disc thickness, 0.1m; Length of the friction plate, 0.36m, Width, 0.25m; Distribution diameter, 2.21m. There are a group of friction plates on both sides of the brake disc, two groups present a 180° distribution. Braking torque and time are respectively 176.8kN·m and 24s, and the initial rotational speed is 60rpm.

Element Selection and Meshing of the Brake Disc

In the temperature field, select the eight node hexahedral elements SOLID70, and use mapped meshing method. In the stress field, convert the SOLID70 elements into SOLID45 elements. The finite element model is shown in Figure 1.

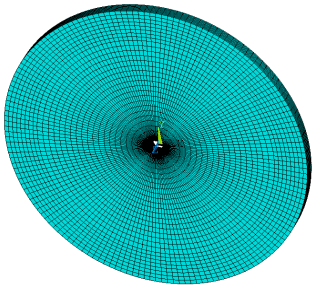


Fig.1Finite Element Model of the Brake Disc

Calculation of Some Relative Data

The material of the brake disc is 16Mn, which density is 7870kg/m^3, poisson ratio is 0.3, the material thermo-physical properties parameters are shown in Table 1[5]:

TABLE 1 THERMO-PHYSICAL PROPERTIES PARAMETERS OF THE BRAKE DISC

temperature [℃]	heat conductivity [W/m·K]	specific heat [J/kg·K]	elasticity modulus [Pa]	coefficient of linear expansion[10^{-6}1/k]
room temperature	53.2	473	2.12E11	0
100	53.2	473	2.08E11	12.8
200	40.9	507	2.03E11	13.4
300	39.4	548	1.97E11	13.9
400	37.8	582	1.85E11	14.5

Assuming that the friction wear between the plate and the brake disc can be neglected, the friction plate clamping pressure in every moment is evenly distributed. According to Fourier's law, heat flux generated by friction $q(r,\theta,t)$ is[6]:

$$q(r,\theta,t) = \mu p(r,\theta,t)\omega(t)r\,. \tag{5}$$

In the formula, μ is friction coefficient, the value is 0.4; p is contact pressure (kN/m^2); ω is angular velocity (rad/s) , assuming the braking is uniform deceleration, in the period of 0 to 24s, the brake disk speed reduced to 0 from 60rpm; r is radius of the brake disc(m).

Temperature Field Analysis under Normal Braking Conditions

In the temperature field analysis, move the thermal load calculated in formula (5) on the friction surface in the form of moving heat.

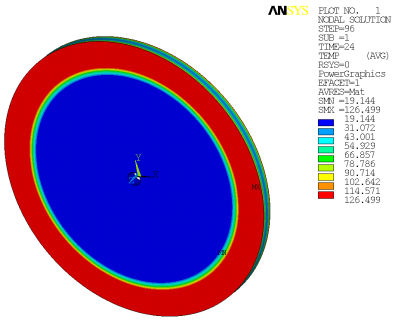


Fig.2 Temperature Contours at the End of Braking

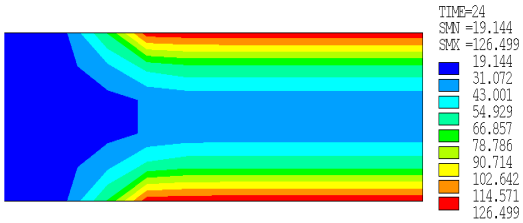


Fig.3 Temperature Contours of a Cross-section

Temperature contours at the end of braking is shown in Figure 2, we can see that along the radial direction , the intermediate region, and along the axial direction, the disc surface ,temperature are all higher . the maximum temperature is 126 ℃ at the end of braking.

Temperature contours of a cross-section at the end of braking is shown in Figure3. the maximum temperature occurs about 0.002m apart from the surface. During the braking, the surface heat not only diffuse from the surface to inside, but also spread into the air through the form of convective heat transfer.

Temperature-time curve of the disc surface in different radius is shown in Figure4. At the beginning of the braking, because of the high rotational speed and huge friction heat, the temperature rises sharply. With braking ,the friction heat decreases, so, after reaching the maximum, the temperature begins to decrease. The temperature of the outermost node is lower than the middle node (r = 1.145m), this is because the outermost node is influenced by the convective heat transfer.

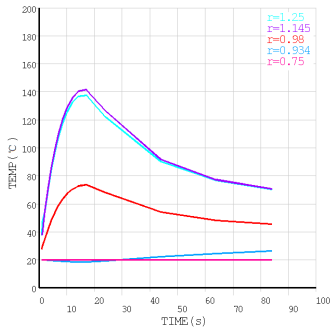


Fig.4 Temp-time Curve in Different Radius

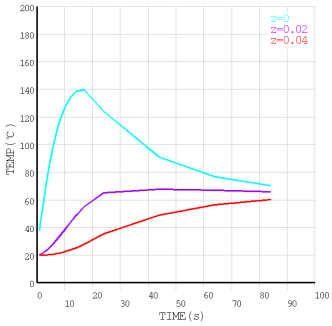


Fig.5 Temp-time Curve at Different Distance from Surface

Figure 5 is the temperature-time curve at different distance(expressed by z)from the surface in the radius of 1.115m. The surface temperature is highest. The farther away from the surface, the lower temperature rise and more smoothly changes. The temperature converged at the end of braking.

Stress Field Simulation Based on the Sequential Coupling Methods

In a braking, the disc experiences alternating heating and cooling cycles. When it brakes more than one time, it will produce thermal fatigue damage. Stress analysis is the gist of the safety assessment and life prediction.

Sequential coupling method, refers to a physical analysis is analyzed in order ,the results of the first physical analysis can be used as the load of the second physical analysis. In this section, we analyze the thermal stress field by using the sequential coupling method. Apply the temperature field analysis results on the stress analysis as body loads, and calculate the brake disc's stress field. Stress contours at the end of braking is shown in Figure 6. The maximum stress is 213MPa.

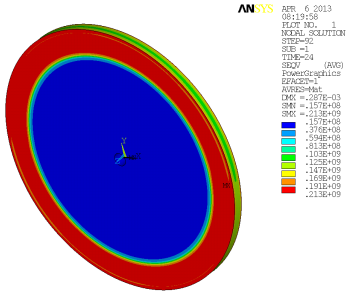


Fig.6 Stress Contours at the End of Braking

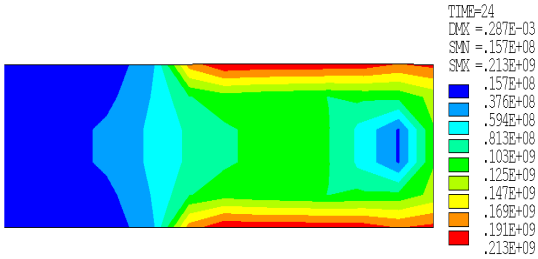


Fig.7 Stress Contours of a Cross-section

Stress contours of a cross-section at the end of braking is shown in Figure 7. The maximum stress occurs in the intermediate region where the brake disc surface contacts with the friction sheet.

Figure 8 is the stress-time curve of the disc node in different radius. With increase of time , the stress value increases firstly and then decreases. The stress curve zigzags during the braking, this is because the alternate function of the input heat and convection heat transfer.

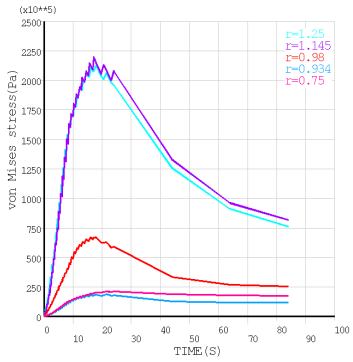


Fig.8 Stress-time Curve in Different Radius.

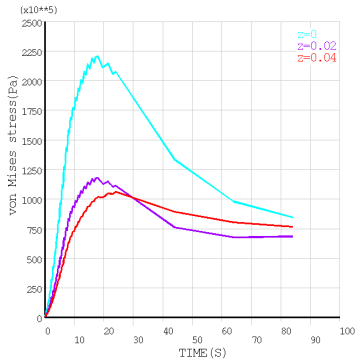


Fig.9Stress-time Curve at Different Distance from Surface.

Figure 9 is the stress-time curve at different distance (expressed by z) from the surface in the radial of 1.115m. The variation of stress in the disc surface is most intense. This is because that the frictional heat can't spread into the inside of the brake disc during the initial period，large amount of frictional heat centered in the surface, so the surface stress rises dramatically.

Thermal Fatigue Life Prediction in Normal Braking Conditions

The brake disc has to endure the alternating load which is shown in Figure 8 in every brake, that is to say the load which the brake disc suffered during its life is unidirectional, unstable and periodic alternating stress，but thinking that the temperature fluctuation is low in one rotation, we can simplify the load to one-way, cyclical and stable alternating stress-pulsating cyclic alternating stress. The minimum stress is 0, and the maximum is 220MPa.

When $N_0 = 10^7$, the pulsation cycle fatigue limit of the 16Mn is 376.4MPa. In accordance with the *S-N* curves, when $N_0 = 10^7$,the survival rate of the sample P=90%, the symmetrical cyclic stress amplitude is, $\sigma_{-1a} = \sigma_{-1\max} = 150$ MPa. The fatigue limit of the structural steel in the pulsation cycle is[7]:

$$\sigma_{0\max} = 1.42\sigma_{-1\max} = 1.42\times 150MPa = 213MPa\,. \tag{6}$$

According to the relevant theories of finite life fatigue calculation, we can estimate the thermal fatigue life N of the brake disc in the normal conditions[8]:

$$\sigma_{0N} = \sigma_0 \sqrt[m]{\frac{N_0}{N}}\,. \tag{7}$$

Material constants m is the negative slope of the *S-N* curve in logarithmic coordinates, that is:

$$m = -\frac{\lg N_0}{\lg \sigma_{0\max}}\,. \tag{8}$$

Hereby, we get the number of braking cycles during its life is: N=5.008×10^7.

Conclusions

This paper analyzes the temperature field of one large mining machinery disc brake during its normal braking conditions in ANSYS. Basing on the sequential coupling methods, we analyze the thermal stress distribution and changes inside the brake disc. The results show that, due to the friction heat, the temperature rises in the braking, and the distribution is uneven, which caused the pulsating cyclic thermal stress during its lifetime. According to the thermal and stress analysis results, we study the thermal fatigue life estimation method, and estimate the brake disc's thermal fatigue life. The simulation methods and analysis results have important reference value and engineering significance to the design and safe operation of the brake disc.

References

[1] Wang Tao, Zhu Wenjian, Friction brake, M, Guangzhou, South China University of Technology press, 1992,1-2.

[2] Yang Shiming, Tao Wenshuan, Heat transfer theory, M, Beijing, Higher education press, 2006,1-213

[3] Wang Xucheng, Shao Min, Basic principles of the finite element method and numerical methods, M, Beijing, Tsinghua university press, 2006,423-440

[4] Li Mengli, Thermal-Structure coupling analysis for brake disc of the large mining belt conveyer, C, Zhengzhou University,2013.

[5] Properties data sheet of mechanical engineering materials Editorial board, Properties data sheet of mechanical engineering materials ,M, Beijing: Mechanical industry press,1995,100

[6] Z-B Kung，S.N.Atluri, Temperature field due to a moving heat source, A moving mesh finite element analysis , J，ASME Journal of Applied Mechanics，1985，52 ,18-24

[7] Xu Hao, Mechanical design handbook ,S, Beijing, Machinery industry press,2004.

[8] Pu Lianggui, Ji Minggang, Mechanical design , M, Beijing, Higher education press, 2006,2

Advanced Materials Research Vol. 936 (2014) pp 2041-2049
© (2014) Trans Tech Publications, Switzerland
doi:10.4028/www.scientific.net/AMR.936.2041

Study On The Response Of Composite Material Cylinder With Metal Liner Under Thermal-Mechanical Impact

XU Ya-dong[1,a], Chen Guang-song[1,b]and Ma Jia[1,c]

[1]Nanjing University of Science and Technology, Nanjing 210094,

People's Republic of China

[a]13601580051@139.com

[b]cgsnjust@163.com

[c]majia_njust@163.com

Keywords: the composite cylinder, metal liner, thermal-mechanical coupling mechanism, finite element method

Abstract: As to the composite cylinder with metal liner under the high temperature and high pressure, thermal-mechanical coupling mechanism and response are studied. On the basis of equations for coupling thermal and mechanical impact load and the non-linear thermoelastic finite element equations, the 3-D analysis model of the composite cylinder is established by using the finite element method. The direct coupling analysis is conducted and the variation regularity of the dynamic stress field is obtained. The results show that the thermal-mechanical impact loads can cause large transient stress, which influences the strength of the metal liner obviously.

Introduction

Metal fiber-reinforced liner structure is a common structure among all the composite cylinders in the engineering field such as pressure vessels, compressors, high pressure pipes, barrels and so on. These structures often work subjected to pressure and temperature loads simultaneously. In some special situations, they are even under transient high pressure and high temperature impact. The most typical one is the composite material cylinder which withstands pressure load more than a few hundred MPa and heat shock more than a thousand degrees within several millisecond during the launch of the gun.

This complex loading condition often results in damage and destruction to the structure of composite material cylinders with metal liner, thus, the relation of coupling mechanism of thermal-mechanical load is very important for the research on damage and destruction of the composite cylindrical structures. Several works have been done by scholars at home and abroad on this topic. Kollár [1] gave a solution of a dynamic response model of fiber-reinforced composite material cylinder withstanding variable mechanical and thermal loads which assumes the material is elastic. Brischetto etal [2] analyzed the coupling effects of composite laminated plates on thermal-mechanical aspect. Considering the hot and humid conditions, Jacquemin et al [3] established a semi-analytical model to calculate the stress field under the internal pressure loads. Mei et al [4]conducted theoretical modeling analysis on the carbon fiber composite materials under the thermal-mechanical cyclic loading, moreover, analytical solutions and experimental values were compared; Adopting the two methods of three-dimensional photoelastic experimental stress analysis and finite element calculation ,Zhao Yanru et al [5] did some research on the interfacial shear stress of a three dimensional freezing slice of single-fiber pullout resin matrix composites under the combined effect of pullout loading and thermal residual stress. Based on microscopic damage

mechanism, Wang Fang et al[6] studied the fatigue life of metal matrix composites under the thermal-mechanical cyclic loading. Few research is on thermal-mechanical shock load in all these studies. This paper focuses on the coupling mechanism and response of thermal- mechanical load for composite material cylinder with metal liner.

Basic equations for coupling thermal and mechanical impact load

The composite material cylinder with metal liner is a kind of special structure which works under extreme conditions and is subjected to strong thermal shock and pressure load. The basic equations of thermal structure coupling problem include heat conduction equation of structural deformation and thermoelastic equation considering the effect of inertia.

Without considering the impact of structural deformation on heat transfer, based on the first law of thermodynamics, the heat conduction fundamental equation of structure can be expressed as ,

$$Q\mathrm{d}t = \mathrm{d}U \,. \tag{1}$$

Where, Q is the heat absorbed per unit time, U is the internal energy .

Considering the impact of structure strain on the thermal conductivity , the first law of thermodynamics is expressed as

$$Q\mathrm{d}t = \mathrm{d}U - (\sigma_x \mathrm{d}\varepsilon_x + \sigma_y \mathrm{d}\varepsilon_y + \sigma_z \mathrm{d}\varepsilon_z) \,. \tag{2}$$

Where, $\sigma_x \mathrm{d}\varepsilon_x + \sigma_y \mathrm{d}\varepsilon_y + \sigma_z \mathrm{d}\varepsilon_z$ is the work of mechanical force to the strain.

According to the relationship of thermodynamics and heat transfer theory, the heat conduction fundamental equation can be derived as

$$\frac{\partial}{\partial x}\left(k_x \frac{\partial \phi}{\partial x}\right)+\frac{\partial}{\partial y}\left(k_y \frac{\partial \phi}{\partial y}\right)+\frac{\partial}{\partial z}\left(k_z \frac{\partial \phi}{\partial z}\right)+\rho Q-\beta\phi_0 \frac{\partial e}{\partial t}=\rho c \frac{\partial \phi}{\partial t} \,. \tag{3}$$

Where, ϕ_0 is the initial temperature, $e = \varepsilon_x + \varepsilon_y + \varepsilon_z$ is the total strain, β is the coefficient of thermal stress.

In which $\beta\phi_0 \dfrac{\partial e}{\partial t}$ is the coupling term describing the relation of the structure and thermal, which performs in the form of strain rate. Thus, it is significant on high-speed deformation.

According to the thermo-elastictheory,we can propose the motion equations, geometric equations and physical equations considering the effect of the temperature. The fundamental equations based on displacement method follows:

$$\left.\begin{aligned}
(\lambda+G)\frac{\partial e}{\partial x}+G\nabla^2 u-\beta\frac{\partial \phi}{\partial x}+X=\rho\frac{\partial^2 u}{\partial t^2}\\
(\lambda+G)\frac{\partial e}{\partial y}+G\nabla^2 v-\beta\frac{\partial \phi}{\partial y}+Y=\rho\frac{\partial^2 v}{\partial t^2}\\
(\lambda+G)\frac{\partial e}{\partial z}+G\nabla^2 w-\beta\frac{\partial \phi}{\partial z}+Z=\rho\frac{\partial^2 w}{\partial t^2}
\end{aligned}\right\} . \tag{4}$$

where, λ and G are lame coefficients.

When we solve the coupled thermo-elastic problems by using direct coupling method, we must solve heat conduction Eq.1 and thermo-elastic fundamental Eq.4 simultaneously. Compared with non-coupled thermo-elastic problem, we must consider the impact of thermal conductivity coupling term and thermo-elastic inertia term for coupled dynamic problems.

The non-linear thermoelastic finite element equations

Composite material cylinder with metal liner withstands transient thermal shock and its temperature changes fairly severely. The elastic constants and thermal parameters of metal material and composite material will change as the temperature changes, which makes the thermal conductivity, heat capacity matrix and elastic matrix in finite element equation all relative with Temperature ϕ .Thus the finite element exhibits a temperature-related material nonlinearity.

Therefore, in the transient heat conduction, the temperature recursive format become

$$\left(\boldsymbol{K}(\phi^*)+\frac{\boldsymbol{C}(\phi^*)}{\Delta t}\right)\phi_{n+1}=\boldsymbol{P}(\phi^*)+\frac{\boldsymbol{C}(\phi^*)}{\Delta t}\phi_n . \tag{5}$$

Where $\phi^*=\phi-\phi_0$ is the temperature change for a moment, ϕ_0 is the reference initial temperature. The corresponding thermal strain caused by the change of temperature i.e.

$$\boldsymbol{\varepsilon}_0=\boldsymbol{\alpha}(\phi^*)(\phi-\phi_0) . \tag{6}$$

Meanwhile, the elastic matrix D in the stress-strain relationship $\boldsymbol{\sigma}=\boldsymbol{D}(\boldsymbol{\varepsilon}-\boldsymbol{\varepsilon}_0)$ is also variable because the elastic modulus and poisson's ratio both change with temperature:

$$\begin{aligned} E&=E(\phi^*)\\ \nu&=\nu(\phi^*) \end{aligned} . \tag{7}$$

Therefore, for composite anisotropic material

$$\boldsymbol{D}=\begin{bmatrix} C_{11}(\phi^*) & C_{12}(\phi^*) & C_{13}(\phi^*) & 0 & 0 & 0\\ C_{12}(\phi^*) & C_{22}(\phi^*) & C_{23}(\phi^*) & 0 & 0 & 0\\ C_{13}(\phi^*) & C_{23}(\phi^*) & C_{33}(\phi^*) & 0 & 0 & 0\\ 0 & 0 & 0 & C_{44}(\phi^*) & 0 & 0\\ 0 & 0 & 0 & 0 & C_{55}(\phi^*) & 0\\ 0 & 0 & 0 & 0 & 0 & C_{66}(\phi^*) \end{bmatrix} . \tag{8}$$

Where,

$$
\begin{aligned}
&C_{11} = (1-\upsilon_{23}\upsilon_{32})VE_1 \\
&C_{22} = C_{33} = (1-\upsilon_{12}\upsilon_{21})VE_2 \\
&C_{12} = C_{13} = \upsilon_{21}(1+\upsilon_{23})VE_2 \\
&C_{23} = (\upsilon_{23}+\upsilon_{21}\upsilon_{12})VE_2 \\
&C_{44} = G_{23} = \frac{(1-\upsilon_{23}-2\upsilon_{21}\upsilon_{12})VE_2}{2} \cdot \\
&C_{55} = C_{66} = G_{12} = E_6 \\
&V = \frac{1}{(1+\upsilon_{23})(1-\upsilon_{23}-2\upsilon_{21}\upsilon_{12})}
\end{aligned}
\tag{9}
$$

All parameters are relative with elastic parameters $E_1(\phi^*), E_2(\phi^*)$, $G_{12}(\phi^*), \nu_{12}(\phi^*), \nu_{21}(\phi^*)$ and $\nu_{23}(\phi^*)$ of unidirectional composites. Thus, they are all expressed as the expressions of temperature ϕ^*, for isotropic material,

$$
\boldsymbol{D} = \frac{E(\phi^*)(1-\nu(\phi^*))}{(1+\nu(\phi^*))(1-2\nu(\phi^*))}
\begin{bmatrix}
1 & \frac{\nu(\phi^*)}{1-\nu(\phi^*)} & \frac{\nu(\phi^*)}{1-\nu(\phi^*)} & 0 & 0 & 0 \\
\frac{\nu(\phi^*)}{1-\nu(\phi^*)} & 1 & \frac{\nu(\phi^*)}{1-\nu(\phi^*)} & 0 & 0 & 0 \\
\frac{\nu(\phi^*)}{1-\nu(\phi^*)} & \frac{\nu(\phi^*)}{1-\nu(\phi^*)} & 1 & 0 & 0 & 0 \\
0 & 0 & 0 & \frac{1-2\nu(\phi^*)}{2(1-\nu(\phi^*))} & 0 & 0 \\
0 & 0 & 0 & 0 & \frac{1-2\nu(\phi^*)}{2(1-\nu(\phi^*))} & 0 \\
0 & 0 & 0 & 0 & 0 & \frac{1-2\nu(\phi^*)}{2(1-\nu(\phi^*))}
\end{bmatrix}.
\tag{10}
$$

So, finite element equation is

$$
\boldsymbol{K}(\phi^*)\boldsymbol{a} = \boldsymbol{P}(\phi^*) . \tag{11}
$$

From the Eq.(5~11),we can see that the finite element equation for thermal shock problem of composite material with metal liner is relative with the temperature ϕ.It is a material nonlinear problem with temperature effect which is independent of the time.

The FEM model of the composite material cylinder with metal liner

The nonlinear finite element method(FEM) is used to investigate the response of the composite material cylinder with metal liner under the transient thermal-mechanical impact load.

The geometry construction is shown in Fig.1. It is a complex structure where there are three layers of composite material ($90^\circ/\pm\alpha^\circ/0^\circ$) outside the metal liner locally.

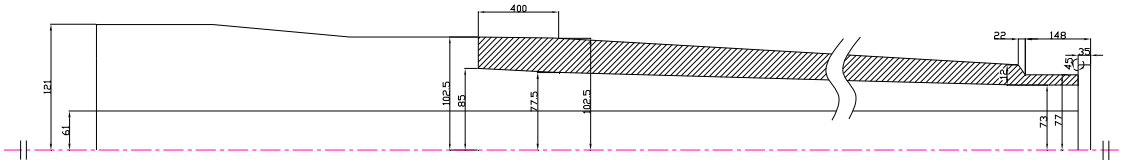


Fig.1 The geometry construction of composite material cylinder with metal liner

The material parameters are shown in Table 1 and 2

TABLE 1 MATERIAL PARAMETERS OF METAL LINER（PCRNI3MO）

E1 [MPa]	υ	σs [MPa]	ρ [Kg·m-3]
210000	0.27	850	7800

TABLE 2 MATERIAL PARAMETERS OF COMPOSITE MATERIAL(T300/EPOXY)

E1 [MPa]	E2 [MPa]	G12 [MPa]	υ12	υ32	ρ [Kg·m-3]	Xt [MPa]	Xc [MPa]	Yt [MPa]	Yc [MPa]	S [MPa]
181000	10300	7170	0.28	0.5	1600	1500	1500	40	246	68

Three-dimensional thermal structure coupled element with 20 nodes is used to mesh the FEM model. The FEM mesh model is as shown in Fig.2.

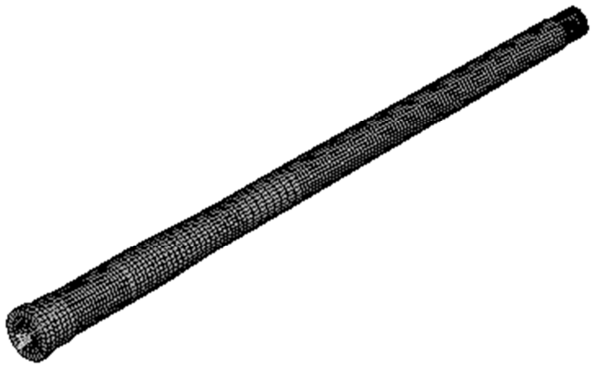


Fig.2 FEM mesh model of the composite material cylinder with metal liner

The loads of the FEM model are thermal shock load and mechanical impact load. They are the high temperature airflow and transient pressure which acted on the inner surface of the hollow cylinder, respectively. In Fig.3, we can easily get the airflow temperature loads curves in different positions. Fig.4 shows the variation range of pressure in the hollow cylinder. The different curves in the figure represent the data of the axis position Z which are from the bottom of the cylinder.

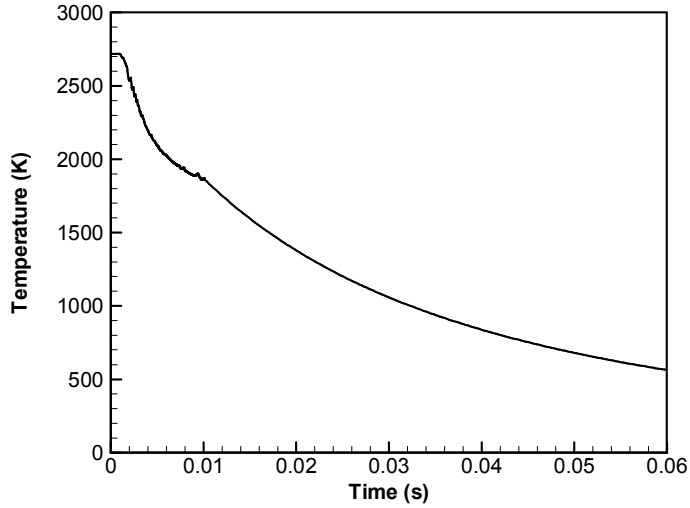


Fig.3 Temperature loads

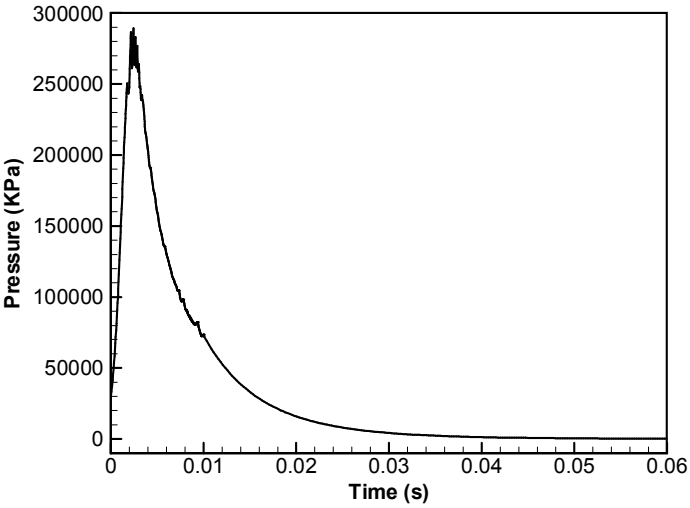


Fig.4 Pressure loads

Result and Analysis

Based on the finite element model, coupling analysis for a three-dimensional composite cylinder subjected to transient thermal-mechanical shock is made by using the direct coupling method which can study the heat conduction equation and stress in the same finite element model. To analyze the thermo-mechanical coupling effects conveniently, two cases are presented. i.e. considering the effect of temperature and without considering the effect of the temperature (only the effect of the pressure is considered). They are presented by the solid and broken lines in the Fig. 5 and Fig.6 respectively.

The equivalent Vonmises stress of the inner wall

The equivalent Vonmises stresses of the inner wall of cylinder are given in Fig.5 and Fig.6. As the figures show that the equivalent Vonmises stress of the inner wall which considers the thermal stress is significantly larger than the one which considers the pressure only, especially for the composite parts . As the poor thermal conductivity of the composite material, a large internal temperature gradients are caused. Thus, the effect of thermal stress must be also considered during the design process as it plays a leading role in the coupled thermal environment.

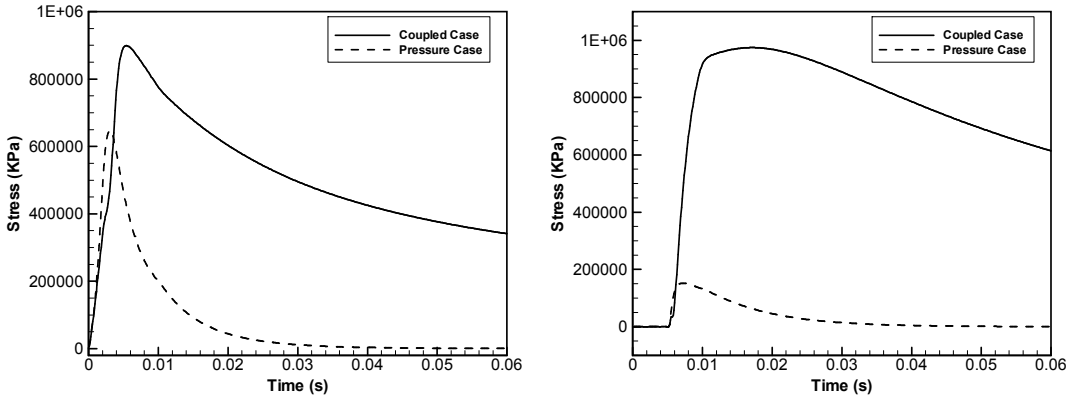


Fig.5 Equivalent Vonmises stress of the inner wall of the metal parts

Fig.6 Equivalent Vonmises stress of the inner wall of the composite parts

The stress of composite part

Fig.7 and Fig. 8 show the radial stress of inner wall and the metal/composite at the interface of the cylindrical composite structure. As we can see from the Fig.7 that the radial stress caused by the pressure is smaller. The radial stress of the metal inner wall is affected by the thermal stress. The three curves are basically the same in Fig.8 as temperature load is transient and the heat has not been conducted only a higher temperature in the wall, thereby causing a higher temperature gradient to a large thermal stress. The same conclusion can be obtained from the result of circumferential stress and axial stress.

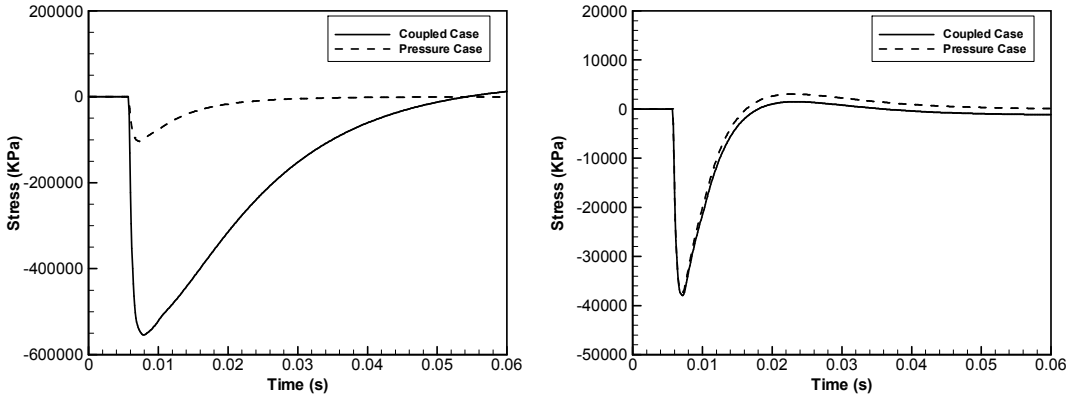


Figure 7 Radial stress of inner wall of metal lining layer

Figure 8 Radial stress of Interface (metal part and composite part)

The results of the circumferential stress are given in Fig. 9 and Fig.10. From the Fig.9, we can find that the circumferential stress is positive in the inner wall of the metal layer lining. While taking into account the effect of temperature, a large stress in the wall as the thermal stress is existed caused by high temperature in the inner wall and the temperature of outer wall is small. With the combined effect of the pressure, the compressive stress caused by heat is large than the tensile stress caused by the pressure. Therefore, it is negative. Fig.10 and Fig.11 shows that the circumferential stress is not affected by temperature for the gradient of temperature is small in the composite material layer. Moreover, the circumferential stress of the metal part and the composite material is not the same since that it must satisfy the continuous strain assumptions in the interface layer between two different materials. Due to the different elastic moduli of the material, the result obtained is no longer equal. The situation exists in the axial stress.

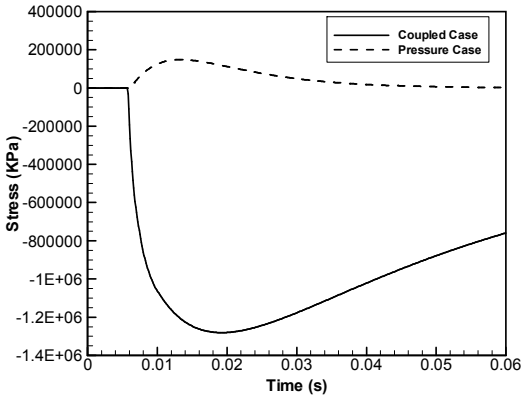


Figure 9 Circumferential stress of inner of metal lining layer

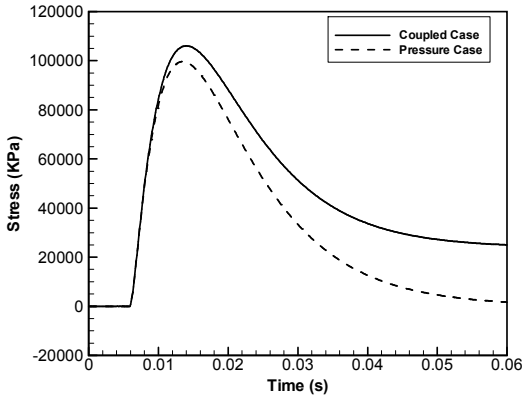


Figure 10 Circumferential stress of Interface wall (metal part)

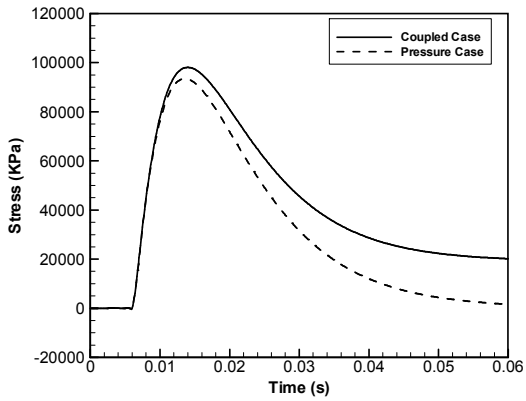
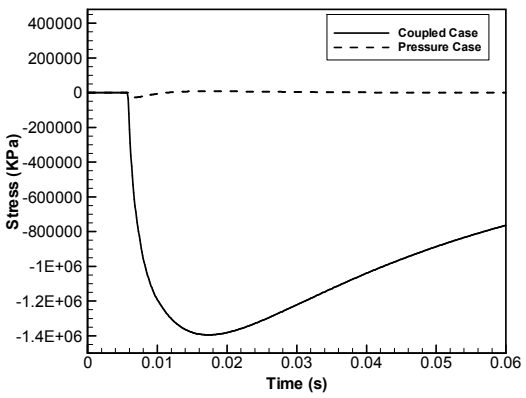


Figure 11 Circumferential stress of Interface (composite part)

The results of the axis stress are given in Figure 12, Figure 13 and Figure 14. The similar conclusion can be obtained through the curves of the axis stress that thermal stress caused by gradient of temperature has a greater contribution to the stress in the inner wall. While in the composite layer, stress doesn't change significantly for the gradient of temperature is small.



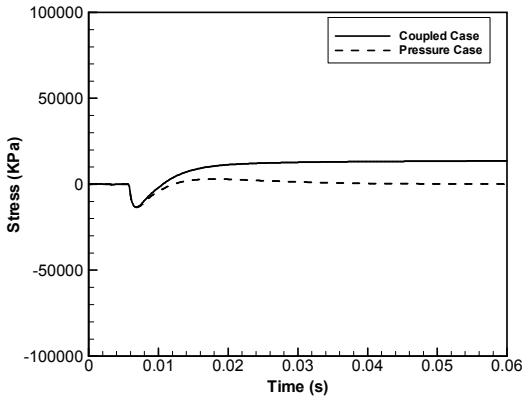


Figure 12 Axial stress of inner wall of metal lining layer

Figure 13 Axial stress of Interface（metal part）

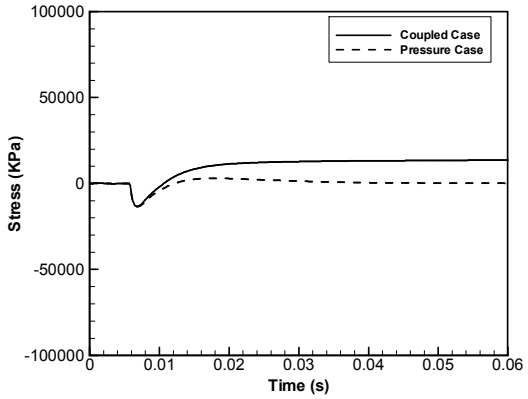


Figure 14 Axial stress of Interface (composite part)

Conclusion

The response of the composite cylinder with metal liner is studied under the thermal-mechanical impact loads by using FEM. The results show that thermal stress can not be ignored as the temperature of the inner wall change fast causing large gradient of temperature. Especially for the composite part, it is more significant because of the poor thermal conductivity of the composite material. Therefore, it should be possible to improve the thermal performance of the composite material and keep the performance of structure when designing the composite structure of the cylinder. For example, adding metal powder or other thermally conductive material in the composite material resin matrix.

References

[1] L.P. Kollár, Three-dimensional analysis of composite cylinders under axially varying hygrothermal and mechanical loads, Computers & Structures, 1994, 50: 525-540.

[2] S. Brischetto, E. Carrera, Coupled thermo-mechanical analysis of one-layered and multilayered plates, Composite Structures, 2010, 92: 1793-1812.

[3] F. Jacquemin, A Vautrin, A closed-form solution for the internal stresses in thick composite cylinders induced by cyclical environmental conditions, Composite Structures, 2002, 58: 1-9.

[4] H. Mei, L.F. Cheng, L.T. Zhang, Y.D. Xu, Modeling the effects of thermal and mechanical load cycling on a C/SiC in oxygen/argon mixtures, Carbon, 2007, 45: 2195-2204.

[5] ZHAO Yanru, XING Yongming,LEI Zhenkun,LANG Fengchao, Interfacial stress transfer behavior of single fiber composite under the effect o mechanical and thermal loading, Acta Materiae Compositae Sinica, 2008, 25(4): 187-93.

[6] WANG Fang,CHEN Zhi-qian,LU Shi-jin, Effects of influential parameters on fatigue life of metal matrix composites under thermo-mechanical loading, Journal of Ship Mechanics, 2010, 14(7): 765-770.

Advanced Materials Research Vol. 936 (2014) pp 2050-2053
© (2014) Trans Tech Publications, Switzerland
doi:10.4028/www.scientific.net/AMR.936.2050

Porous Glass Composite as Diesel Particulate Filter and the Microwave Regeneration

LEE Chang Chuan[1,a *], YOSHIKAWA Noboru [2,b] and TANIGUCHI Shoji [2,c]

[1]School of Manufacturing Engineering, Universiti Malaysia Perlis, Kampus Tetap Ulu Pauh, 02600 Arau, Perlis, Malaysia

[2]Graduate School of Environmental Studies, Tohoku University, 6-6-02 Aramaki-Aza-Aoba, Aoba-ku, Sendai, 980-9879 Japan.

[a]cclee@unimap.edu.my, [b]yoshin@material.tohoku.ac.jp, [c]s-tanig@material.tohoku.ac.jp

Keywords: microwave regeneration, porous composite, diesel particulate filter

Abstract:In this study, porous SiO_2·RO/stainless steel composite body was prepared through the polyurethane sponge replica method. Porous samples obtained through sintering consist of well dispersed and distributed stainless steel particles within the glass matrix. Such microstructure is desired for the purpose as a soot particulate filters (DPF) utilizing microwave rapid and selective heating characteristic, especially during the cold start phase of an engine. Results of microwave heating ability and diesel soot regeneration tests shows that, the fabricated porous composite material is proven to be reliable for rapidly microwave assisted regeneration. Both the regeneration temperature and O_2 composition in the supplied gas played an important role in the regeneration process.

Introduction

Diesel engines are superior to conventional gasoline engines with regard to fuel consumptions, which reduces CO_2 emissions and helps suppress global warming. These engines, however, produce more NO_x as well as particulate matter (PM) [1]. In response to the environmental and health concern from the emission of diesel particulate matter (DPM), governments over the world have continued to impose more stringent regulations restricting its emissions. Among techniques that have been designed to reduce the particulate emission, diesel particulate filters (DPF_s) have been considered as the best option. However, with accumulation of the DPM in the filter media, the pressure drop across the filter increase which in-turn exerts a back pressure on the engine exhaust, resulting in gradually poorer engine performance. Therefore, effective regeneration of the filter by continuously or periodically burning off the trapped DPM is of important.

Self regeneration of DPM is not possible due to high ignition temperature, typically 500 – 650 ^oC [2], and low engine exhaust temperature, generally lower than 400 ^oC. Therefore, an additional measure is needed to get rid of the trapped soot. Few studies utilizing microwave power for the regeneration of trapped filter has been reported in the literature [3-7]. Microwave heating significantly differs from conventional heating, as the energy is strongly concentrated in the material itself. Microwaves penetrate the material at a depth depending on the dielectric permittivity, resulting in a heating from the inside out. Microwave heating is very rapid and selective. With the choice of proper material as filter substrate, it can easily provide high temperature needed for DPM combustion and DPF regeneration [6-8]. In additional, microwave energy can be deposited directly to the DPM which is collected in the DPF. However, microwave assisted DPF regeneration has been experienced with uneven energy distribution which result in hotspots during DPM oxidation reaction [9].

The primary aim of the present work was to fabricate a filter material which can be heated up evenly by microwave for DPM regeneration. A porous glass-metal composite has been developed to serve as the DPF instead of using cordierite honeycomb ceramics. Experiments have been conducted in a 2.45 GHz (2 kW) single mode applicator to measure the efficiency of regeneration of the fabricated filter by varying the regeneration temperature and oxygen content.

Experimental Details

Glass /stainless steel (SS) porous composite bodies were produced by polyurethane sponge replica method using a slurries containing mixture of SiO_2·RO/ 10-30 vol% SS. The slurry was prepared by dispersing the powder mixture with distilled water without any further additives to give a suspension with approximately 40 wt% solids loading. According to Sifontes et al. [10], this weight allowed obtaining adequate viscosities of slurry and proper mechanical strength for ceramic foam.

Microwave heating of the obtained composite filter was conducted prior to regeneration test to evaluate their heating behavior. Subsequently, filter that has been preloaded with artificial soot (carbon black, (PRINTEX from Dagussa Corp.) was placed in the microwave applicator so as to have its axis coincident with the applicator axis. Apparatus for microwave regeneration is illustrated in Fig. 1. Detail of the single mode applicator is reported elsewhere [11]. Temperature was measured by an optical pyrometer which has a lower detection limit of 350 ^{o}C. Temperature-programmed regeneration (oxidation of the soot deposited filter) was performed under pure air condition, O_2/N_2 (21%/79%). In each test, filter temperature was raised from room temperature to 640-680 ^{o}C at a maximum heating rate (attained 600 ^{o}C around 13 s) and maintained at the target temperature for 1 to 3 min. The concentration of O_2, CO_2 and CO gases at the outlet was analyzed using a Hodakatest HT-2700 gas sampling device. In addition, effect of O_2 composition in the inlet gas stream on the regeneration process was also being evaluated.

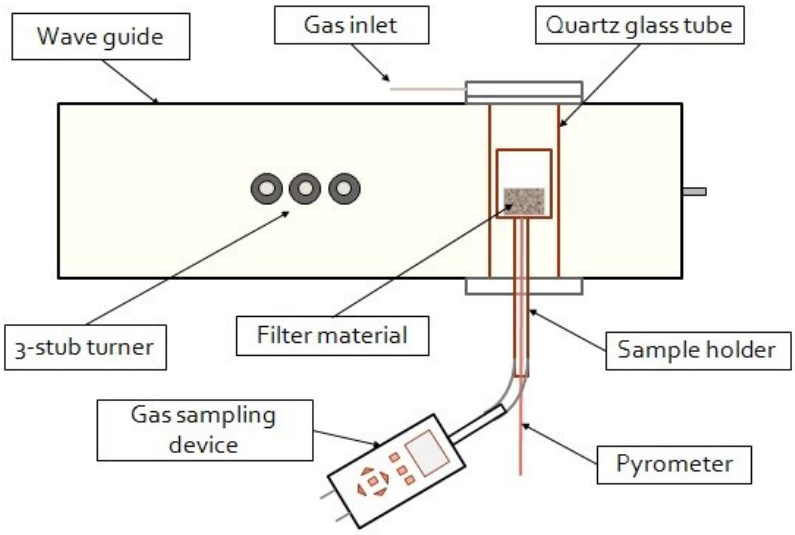


Fig. 1 Scheme of apparatus for microwave regeneration

Results and Discussion

Fig. 2 shows the microstructure of the skeleton surface with different stainless steel fraction. The SiO_2·RO matrix had a grey appearance whereas the stainless steel particles were in light grey. No obvious remnants of the PU sponge were detectable. Stainless steel particles were well dispersed and distributed within the glass matrix, increasing with the increased of stainless steel fraction in the mixtures. This microstructure effect was generated during the impregnation process. Since the stainless steel powder has a higher density compared to SiO_2·RO glass powder, segregation might occur in the slurries which could draw in non-homogeneity that will influence the uniformity of the stainless steel particle distribution within the glass matrix. Hence, uninterrupted stirring is needed during the impregnation step, to minimize the occurrence of segregation.

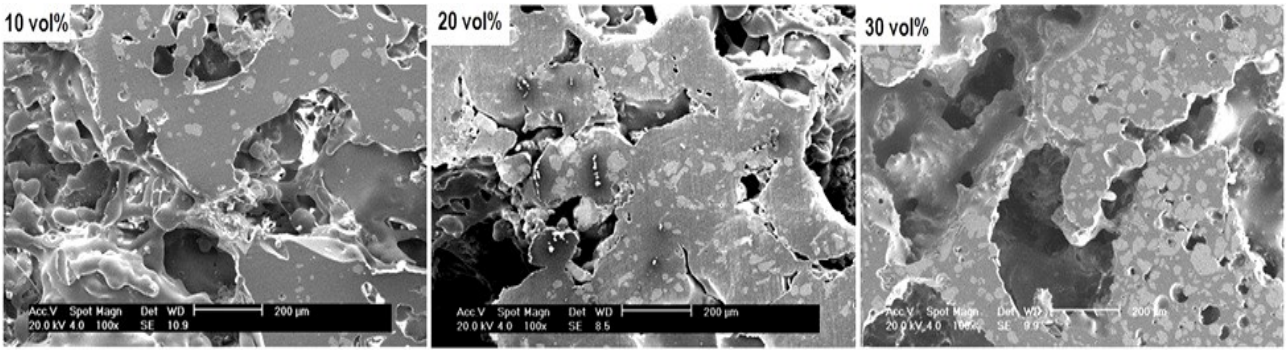


Fig. 2 SEM micrograph of sintered glass-stainless steel porous composite with different stainless steel fraction.

Microwave heating ability of the fabricated porous glass-stainless filter was studied using a 2.45 GHz, 2 kW, single mode applicator. The heating ability of these products is illustrated in Fig. 3. It revealed that, heating rate of the porous composites was fully associated with the amount of stainless steel particle in the sample. As the fraction of stainless steel in the mixtures increased, the heating rate also increased. Samples with higher metal fraction can be heated up rapidly as compared with those of lower metal fraction.

Effect of heating temperature and O_2 concentration in the gas stream on the regeneration of soot loaded filter are presented in Fig. 4. As can seen in Fig. 4, total CO_2 and CO concentration increased as the regeneration temperature keep on increasing (up to 660 ^oC). Above this temperature it shows a steady constant value due to saturation of the carbon oxidation rate. At low regeneration temperature, conversion rate of the soot was mainly determined by the reaction rate, whilst at a higher regeneration temperature, mass transfer rate determines the conversion rate.

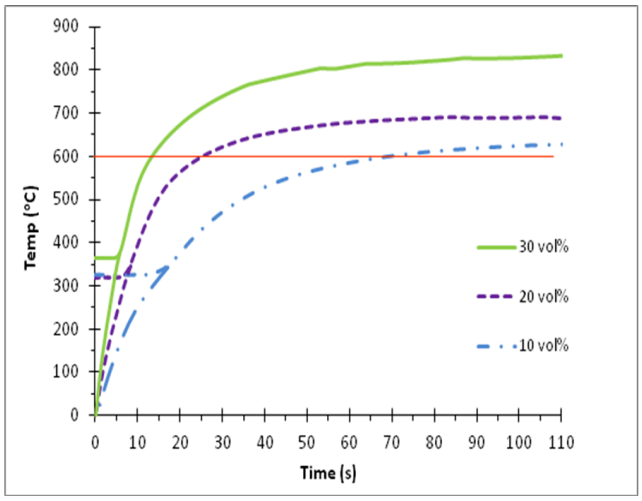


Fig. 3 Heating curve of porous glass-stainless steel with differents stainless steel fraction

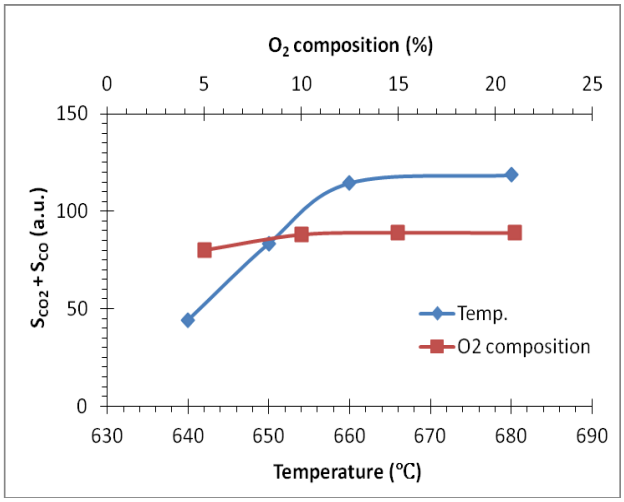


Fig. 4 CO_2 and CO concentration as a function of regeneration temperature and O_2 composition

Completely soot free filter with a regeneration efficiency of as high as 99 % can be achieved. Thus, for the remaining experiments, filter regeneration temperature was set at 680 ^oC. Indicated in the figure also, total CO_2 and CO concentration was gradually increased with the increasing of O_2 composition. As a consequence, it is definite that compositions of O_2 present in the gas stream have a significant effect on the regeneration process, as expected. With higher oxygen composition in the gas stream, more oxygen is supply to the system for combustion, which can promotes the oxidation rate and conversion of carbon to CO_2.

Conclusions

(1) Porous glass-stainless steel composite with interconnected pores and high porosity (65-70%) were obtained by the sponge replica method. The porous SiO_2·RO/SUS composite consist of well dispersed and distributed stainless steel particles within the SiO_2·RO glass matrix. Samples with higher stainless steel volume fraction shows a better and faster heating by microwave.

(2) Both the regeneration temperature and oxygen composition in the supplied gas stream shows a significant effect on the oxidation and conversion rate of carbon. Higher regeneration temperature and oxygen composition is preferable for the full regeneration of soot loaded filter, which is at least or higher than 660 ^{o}C with an O_2 composition of 15 % or higher respectively.

References

[1] S. Pallavkar, T.H. Kim, D. Rutman, J. lin and T. Ho, Active regeneration of diesel particulate filter employing microwave heating, Ind. Eng. Chem. Res. 48 (2009) 69-79.

[2] C.C. Lee, Fabrication of porous composite material for diesel particulate filter and the regeneration by microwave heating, PhD thesis, Tohoku University, Japan, March 2013.

[3] V. Palma, P. Russo, M. D'Amore and P. Ciambelli, Microwave regeneration catalytic foam: a more effective way for PM reduction. Top. Catal. 30/31 (2004) 261-264.

[4] J. Beckers, L.M. Vander Zande and G. Rothenberg, Clean diesel power via microwave susceptible oxidation catalysts, Chem. Phys. Chem. 7 (2006) 747-755.

[5] V. Palme, P. Russo, G. Matarazzo and P. Ciambelli, Microwave improvement of catalyst performance in soot oxidation without additives, Appl. Catal. B: Environ. 70 (2007) 254-260.

[6] Y.Z. Steenwinkel, L.M. Vander Zande, H.L. Cstricum, A. Bliek, R.W. Vanden Brink and G.D. Elizinga, Microwave assisted in-situ regeneration of a perovskite coated diesel soot filter, Chem. Eng. Sci. 60 (2005) 797-804.

[7] Z. Ning and Y. He, Experimental study on microwave regeneration characteristics of diesel particulate after-treatment system, Soc. Auto. Eng. 1999-01-1470 (1999).

[8] J. Ma, M. Fang, P. Li, B. Zhu, X. Lu and N.T Lau, Microwave assisted catalytic combustion of diesel soot, Appl. Catal. 159 (1997) 211-228.

[9] R. Nixidorf, J.G. Green, J.M. Story and R.M. Wagner, Microwave regenerated diesel exhaust particulate filter, Soc. Auto. Eng. 2001-01-0903 (2001).

[10] A.B. Sifontes, M. Urbina, F. Fajardo, L. Melo, L. García, M. Mediavilla, N. Carrión, J.L. Brito, P. Hernandez, R. Solano, G. Mejias and A. Quintero, Preparation of ɣ- Alumina Foams of High Surface Area Employing the Polyurethane Sponge Replica Method. Lat. Am. Appl. Res. 40 (2010) 185-191.

[11] C.C. Lee, N. Yoshikawa and S. Taniguchi, Microwave-induced substitutional combustion reaction of Fe_3O_4/Al ceramic matrix porous composite, J. Mat. Sci., 46 (21) (2011) 7004-7011.

Advanced Materials Research Vol. 936 (2014) pp 2054-2062
© (2014) Trans Tech Publications, Switzerland
doi:10.4028/www.scientific.net/AMR.936.2054

The Fracture Properties of Sandwich Structures Based on a Metal Foam Core

Yiou Shen[1, a], Yan Li[1,b], Wesley Cantwell [2,c] and Yuyuan Zhao[3,d]

[1] School of Aerospace Engineering and Applied Mechanics, Tongji University,

, Shanghai, 200092, P R China

[2]Department of Aerospace Engineering, Khalifa University of Science, Technology and Research (KUSTAR), PO. Box 127788, Abu Dhabi, UAE

[3]Department of Engineering, University of Liverpool, Liverpool, L69 3GH, UK

[a]syoeva@tongji.edu.cn, [b]liyan@tongji.edu.cn, [c]w.cantwell@liv.ac.uk, [d]y.y.zhao@liv.ac.uk

Keywords: Metal foam, sandwich structure, lost carbonate sintering, fracture

Abstract: The fracture properties of a series of metal foam sandwich structures based on glass fiber-reinforced polyamide 6,6 composite (GF/PA6,6) skins have been investigated. The open cell core materials were manufactured using the Lost Carbonate Sintering (LCS) process, a recently-developed technique for manufacturing metal foams. Initially, the effect of varying the compaction pressure used in producing the metal foams as well as the density of the samples were investigated through a series of compression tests. Here, it was shown that the compressive strength and the elastic modulus of the foams varied with density and compaction pressure, in spite of the fact that the average size of the cells in these foams were insensitive to either of these two parameters.
The resistance of sandwich structures to localized loading was investigated through a series of indentation tests. Here, it was shown that the indentation response of sandwich structures could be characterized using a simple indentation law, the parameters of which did not exhibit any clear dependency on the density of the foam. Finally, three point bend tests on the sandwich structures have shown that their loading-bearing properties were sensitive to foam density.

Introduction

Traditional fiber reinforced sandwich structures are based on polymer core materials, however, polymer foams typically offer a relatively low strength and only a moderate energy-absorbing capacity. Recently, a range of lightweight metallic core materials offering higher strength, stiffness and energy absorption characteristics have been developed for applications in the aerospace, land and marine sectors [1-5]. Currently, there are a number of processing technologies used in the manufacture of metal foams. Frequently, a liquid-state foaming route is employed for manufacturing low-melting-point metal systems such as aluminum foam [2]. In contrast, high-melting-point metal cores are usually manufactured by a solid state method such as a powder metallurgy process. However, many commercial aluminum foams offer cell sizes between 2 and 10 mm. Recently, the introduction of the Lost Carbonate Sintering (LCS) process has enabled researchers to manufacture open-cell metal foam structures with well-controlled cell dimensions at very low cost [6-13]. The work presented in this paper investigates the properties of a metal foam-based sandwich structure based on glass fiber-reinforced composite skins. Iron powder was employed to manufacture the metal foams via the LCS process. Iron foam offers several advantages over aluminum foam, including a higher strength and stiffness, lower raw material costs and a higher melting temperature [14]. Initially, the mechanical properties of the foam materials are investigated through a series of compression tests on cylindrical samples. Following this, the indentation and flexural properties of sandwich structures based on glass fiber reinforced polyamide 6,6 composite skins are investigated.

Experimental procedure

The iron foam cores investigated in this study were manufactured using the Lost Carbonate Sintering (LCS) process, a procedure that is described in detail elsewhere [7]. The raw materials used here were based on iron powder (supplied by Pometon Metal Powders), potassium carbonate (K_2CO_3) spheres (supplied by E&E Ltd in Widnes, UK) and glass fiber reinforced polyamide 6,6 (TEPEX) composite skins (supplied by Bond Laminates, Germany). The iron powder used in this study (FERSINT RI 180/3.0) was supplied with a particle size between 25 and 200 μm and the K_2CO_3 spheres used in the LCS process were in the size range of 710 to 1000 μm. The thickness of the glass fiber reinforced polyamide 6,6 composite used in the manufacture of the skins was 0.5 mm. The nominal volume fraction of iron in the Fe-K_2CO_3 mixtures was 0.25, 0.3 and 0.35, yielding metal foam samples with nominal relative densities of 0.2, 0.25 and 0.29, respectively. The Fe-K_2CO_3 mixtures were sealed in cylindrical mild steel tubes by placing iron powder in the two ends. The samples were compacted by a press prior to sintering. Three compaction pressures were used during the manufacture of the foam samples, these being 100, 150 and 200 MPa. Following compaction the samples were sintered in a temperature-controlled electrical furnace. The temperature in the furnace was increased at a rate of 10℃ per minute from room temperature to 850℃ and samples were sintered at this temperature for 4 hours. After the sintering process was complete, the K_2CO_3 particles were dissolved in running water for 90 minutes. The resulting metal foams were subsequently dried in an oven for two hours at a temperature of approximately 100℃. This process yielded high quality foams with an open-cell structure.

A series of mechanical tests were carried on foams manufactured using compaction pressures of 100, 150 and 200 MPa. The iron foam specimens used in these compression tests were based on 20 mm diameter, 10 mm high cylinders. The compression tests were carried out on an Instron 4505 universal test machine at a crosshead displacement rate of 1 mm/min. Following the compression tests on the plain iron foam samples, a series of sandwich structures were manufactured to evaluate the potential offered by such core materials. Here, an Araldite LY5082 epoxy resin combined with an Araldite AY 103 hardener was used to bond the core and glass fiber/polyamide 6,6 skin materials. After the resin was applied, the sandwich beams were placed under a light pressure and left overnight at room temperature to ensure complete curing of the adhesive. Initially, indentation tests were conducted on sandwich beams positioned on a solid base. Samples with dimensions of 120 x 25 x 25 mm (manufactured using a compaction pressure of 100 MPa) were tested on an Instron 4505 mechanical test machine at a crosshead displacement rate of 1 mm/min. The diameter of the indentor was 10 mm and the maximum indentation was approximately one millimeter. Three point bend tests were conducted on samples with dimensions of 120 x 25 x 25mm (a compaction pressure of 100 MPa was used due to limitations in the capacity of the press) on an Instron 4505 universal test machine. The beams were supported on two 10 mm diameter cylinders positioned 100 mm apart. A 10 mm diameter steel indentor was used to load the samples at a crosshead displacement rate of 1 mm/minute.

Results and Discussion

Compressive properties of the core materials

Fig. 1 shows the microstructures of the three densities of iron foam manufactured using compaction pressure of 200 MPa. Fig. 1a, the sample with a relative density of 0.2 indicates that many of the cell walls have not fully formed during the sintering process and a number of cell walls have fractured, possibly during the subsequent grinding process. The microstructures of the foams with relative densities of 0.25 and 0.29, Figs. 1b and 1c, are better defined, with the individual cells being more clearly visible. Closer examination highlights the fact that some cells here effectively merged and the cell wall is missing. This occurs when two potassium carbonate particles are in very close proximity and the metal powder is forced out. The average diameters of cells in the three foams were measured and Fig. 1 shows the variation of the average cell diameter with relative density. Clearly, the

average cell sizes in the three types of foam are similar suggesting that the size of the cells does not vary over the range of densities considered. It is evident from the micrographs and the data in Fig. 1 that the average cell size reflects the size of the potassium carbonate particles used in the manufacture of the foams. Fig. 2 shows the variation of cell size with compaction pressure where it is again evident that the size does not vary over the range of manufacturing conditions studied here. The degree of voiding in the cell walls decreased as the compaction pressure was increased, indicating that the higher manufacturing pressures produced a greater level of contact during the sintering stage. Clearly, the size of the cells in these systems is significantly smaller than those observed in commercially available metal forms where values in the latter can be as large as 10 mm [15].

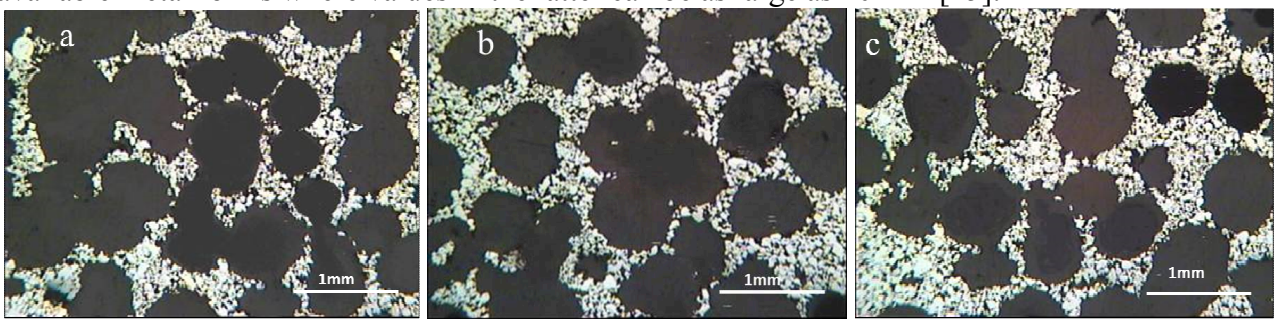


Fig. 1 Microstructure of the foam cell, (a) relative density of the foam was 0.20, (b) relative density of the foam was 0.25, (c) relative density of the foam was 0.29.

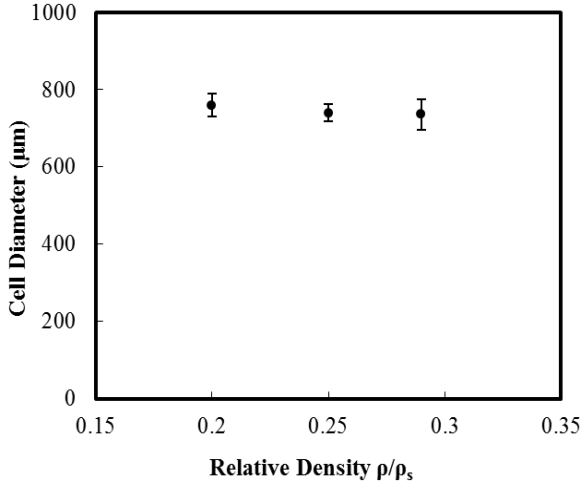


Fig. 2 The variation of cell diameter with relative density for foams manufactured using a compaction pressure of 200 MPa.

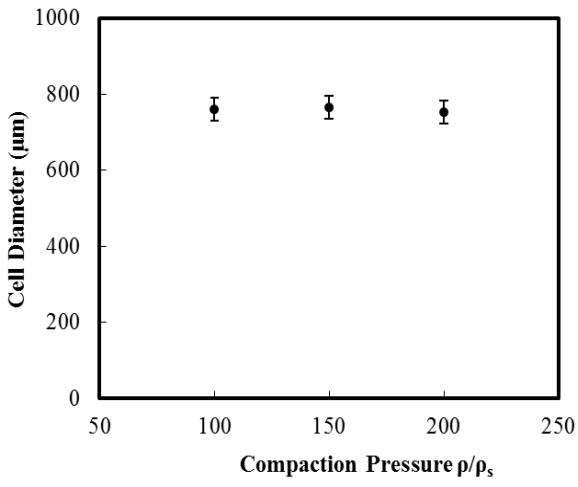


Fig. 3 The variation of cell diameter with compaction pressure for foams with a relative density of 0.25.

Fig. 4 shows typical stress-strain traces following compression tests on samples manufactured using compaction pressures of 100, 150 and 200 MPa. In each case, the relative density of foams was nominally 0.25. The curves in Fig. 4 exhibit a region of linear elasticity at low stresses, followed by a long plateau stress before the stress rises steeply in the regime of densification. Included in the stress-strain trace for the 200 MPa sample is the procedure for determining the plastic collapse stress, σ_{pl}. The figure shows that increasing the compaction pressure serves to increase both the plastic collapse stress and the stress at the onset of densification (the final rise in the stress-strain plot). Fig. 5 shows sections removed from samples that had been subjected to strains ranging from 0.2 to 0.5. An examination of the micrographs indicates that the samples fail due to the cell wall buckling and collapse under the increasing strain. At a strain of 0.2, Fig. 5a, a number of cell walls close to the top of the sample fail causing strain localization. With increasing strain, the regions in which cell wall buckling occurs increase in size, spreading out across the sample. At a strain of 0.5, Fig. 5d, virtually all of the cell walls have collapsed and densification occurs. Fig. 6 shows the variation of the plastic collapse stress of the foams, σ_{pl}, with compaction pressure. Clearly, the plastic collapse stress

increases rapidly with the level of pressure applied during compaction, indicating that this processing parameter has a significant effect on the mechanical properties of the foam. As previously stated, increasing the compaction pressure forces the metal particles into contact during the sintering process, leading to fewer voids in the cell walls following manufacture.

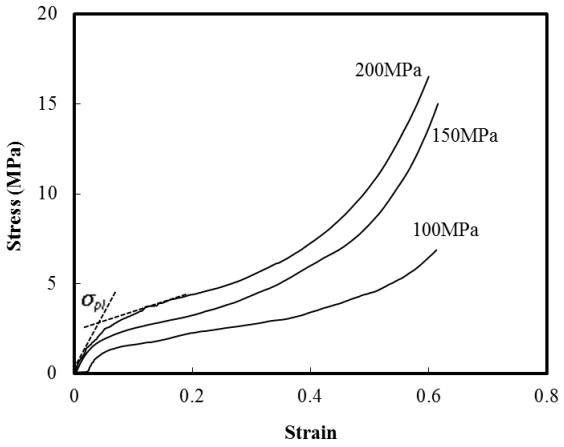


Fig. 4 Typical stress-strain curves following compression tests on samples manufactured using compaction pressures of 100, 150 and 200 MPa. The relative density of the foam was 0.25.

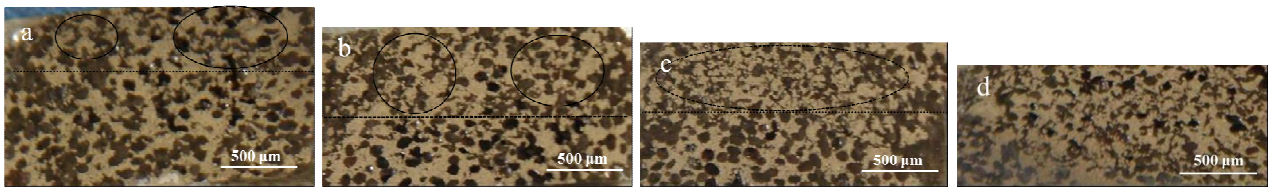


Fig. 5 Deformation banding during a typical compression test: (a) ε=0.2, (b) ε=0.3, (c) ε= 0.4, (d) ε=0.5.

Fig. 7 shows typical compression stress-strain curves following tests on the three different densities (0.20, 0.25 and 0.29) of metal foam manufactured using a compaction pressure of 200 MPa. It is clear from Fig. 7 that the stress-strain response of the foam samples depends on the density of iron foam; this phenomenon was also observed by Park et al [14]. Lowering the density of the foam gives a more pronounced plateau since the structure affords more opportunity for cell walls to deform and collapse during the loading process. The variation of the plastic collapse stress with relative density is shown in Fig. 8. Clearly, the compressive properties of the foam increases rapidly with foam density. The compressive properties of these foams compare favourably with previously published data for an aluminum foam where values of compression strength of approximately 1.5 MPa were recorded [15].

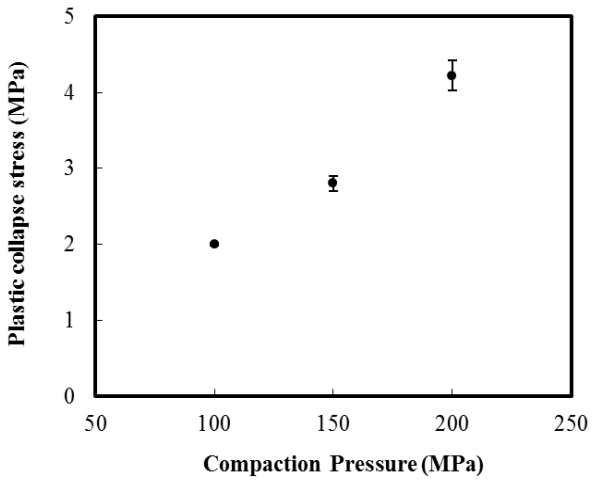


Fig. 6 The variation of compressive stress with compaction pressure. The relative density of the foam was 0.25.

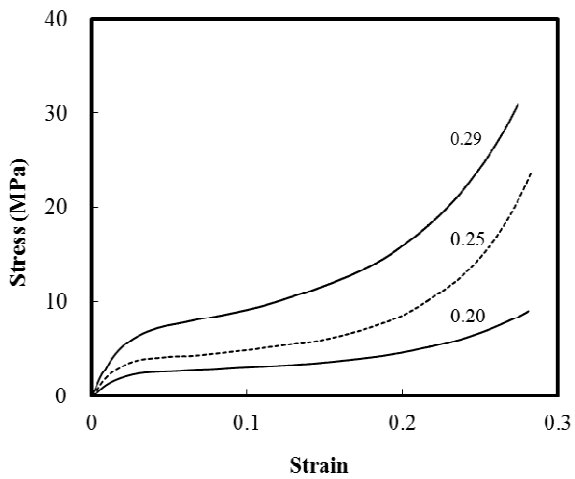


Fig. 7 Typical stress-strain curves following compression tests on samples manufactured using a compaction pressure of 200 MPa.

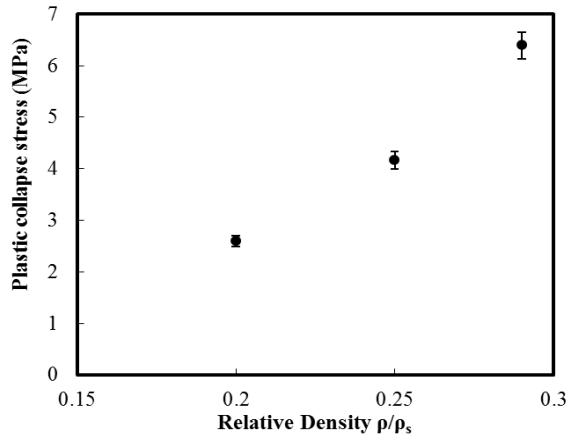


Fig. 8 The variation of compressive stress with relative density for foams manufactured using a compaction pressure of 200 MPa.

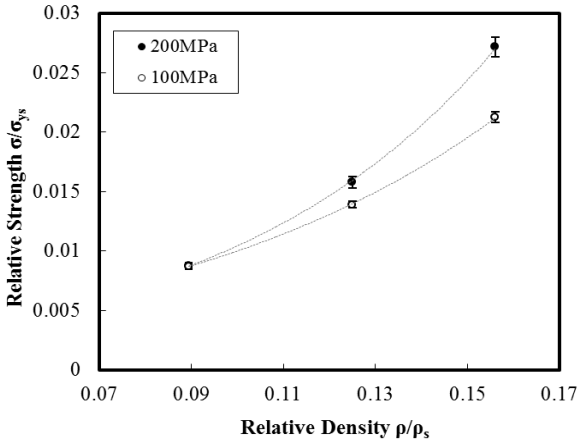


Fig. 9 The variation of relative strength with relative density for foams manufactured using compaction pressures of 100 MPa and 200 MPa.

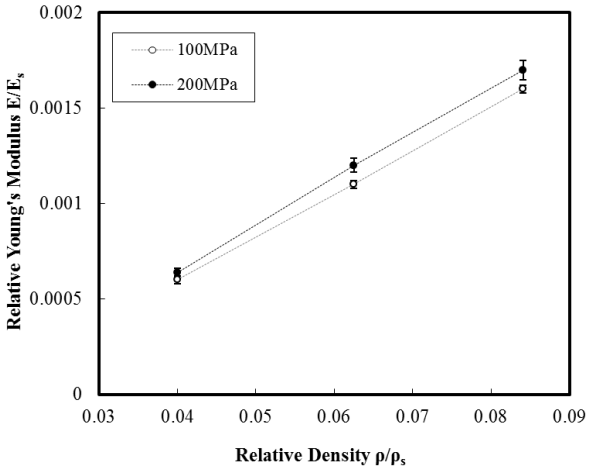


Fig. 10 The variation of the relative Young's modulus with relative density for foams manufactured using compaction pressures of 100 MPa and 200 MPa.

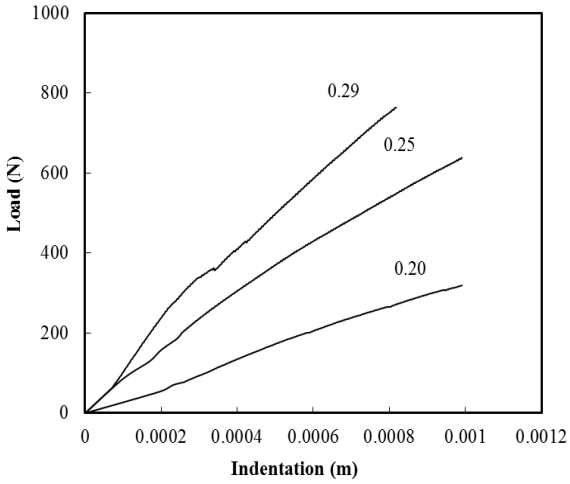


Fig. 11 Typical load-indentation curves for the sandwich structures manufactured using a compaction pressure of 100 MPa.

Table 1 summarises the average plastic collapse stresses of the foams considered here. Clearly, the plastic collapse stress of the foam is sensitive to both density and compaction pressure. The strength data for the iron foam are plotted as a function of relative density in Fig. 9. Previous work [3] investigating the compressive properties of open-cell foam structures has shown that the relative plastic-collapse stress, σ_{ys}, of such a structure can be written in the form:

$$\frac{\sigma_{pl}}{\sigma_{ys}} = \mathrm{M}\left(\frac{\rho}{\rho_s}\right)^{3/2} \tag{1}$$

where ρ/ρ_s is the relative density, σ_{ys} is the yield strength of the solid material and M is a constant with a value equal to approximately 0.3 [3]. In this study, the data from the compression tests were forced to fit this type of relationship, yielding a value for M. The data in Fig. 10 were used to determine the appropriate values of M in Equation 1. Table 2 summarizes the average values of M where it can be seen that the experimentally-determined values are well below the values of 0.3 predicted by a cubic model for open-cell foams [3]. Since the model assumes a cubic cell geometry and the iron foams are clearly more irregular than this, some significant deviation between the measured and predicted behavior is expected.

TABLE 1 SUMMARY OF THE PLASTIC COLLAPSE STRESSES OF THE METAL FOAMS.

Relative density	Compaction Pressure (MPa)		
	200 MPa	150MPa	100 MPa
0.20	2.18		
0.25	4.30	2.80	2.00
0.29	7.24		

TABLE 2 SUMMARY OF THE CONTACT PROPERTIES OF THE METAL FOAMS [3].

	Theoretical value	Compaction Pressure (MPa)	
		100	200
M	0.3	0.144	0.174
C	1	0.018	0.018

The relative Young's modulus properties of the foams are summarized in Fig. 10. Previous work has shown that the relative Young's modulus of a foam, E/E_s, (where E_s is the Young's modulus of the solid material) can be written in terms of its relative density, ρ/ρ_s, as follows [3]:

$$\frac{E}{E_s} = C\left(\frac{\rho}{\rho_s}\right)^2 \tag{2}$$

where C is a constant (approximately equal to unity for an open cell foam [3]). As before, this relationship was applied to the experimental data, yielding a value for the constant C. Table 2 reports the values of C for the systems evaluated here. It is clear that the measured values for this constant are significantly lower than those predicted by the cubic cell geometry.

Indentation characteristics of the sandwich structures

Fig. 11 shows typical load-indentations plots following tests on the three sandwiches manufactured using a compaction pressure of 100 MPa. Clearly, the slope of the load-indentation trace increases with foam density. It can be seen from the figure that the initial portions of the curves were slightly non-linear, and effect that may be due to the compliance of the test machine and a slight lack of fit in the test fixture. The reason for the change of slope in the sandwich structures was explained by Davies et al [16], who attributed it to the initiation of local damage such as core crushing under the point of indentation. The load, P, versus indentation, α, plots were forced to fit a generalized contact law of the form:

$$P = C\alpha^n \tag{3}$$

where n and C are indentation parameters that can be determined from the load-indentation plots. The type of relationship has been successfully used in previous studies investigating the indentation response of sandwich structures [17] and was considered appropriate here. Plots of *log P* versus log α were drawn, to yield the indentation parameter 'n' (from the slope of the graph) and the constant '*C*' (from the intercept with the y-axis).The values of the parameters *n* and *C* in this indentation law are summarized in Table 3, which dictate the shape and slope of the indentation trace [17]. The load-indentation curve should be a straight line when n is equal to unity, the curve will tend upwards when n is greater than one and downwards when n less than one. The value of *C* determines the effective gradient of the curve.

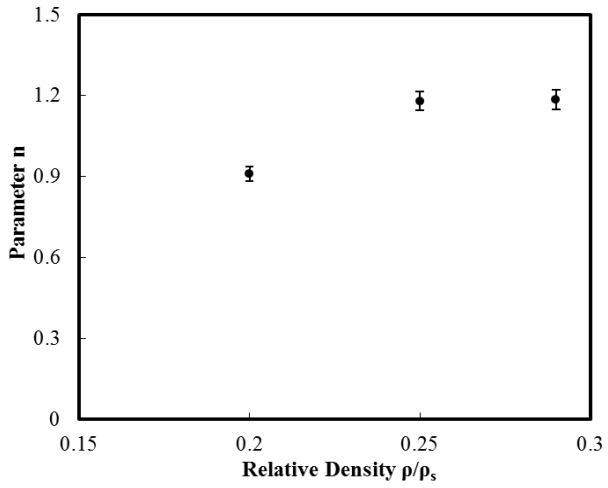


Fig. 12 The variation of the contact parameter, n, with relative density for foams manufactured using a compaction pressure of 100 MPa.

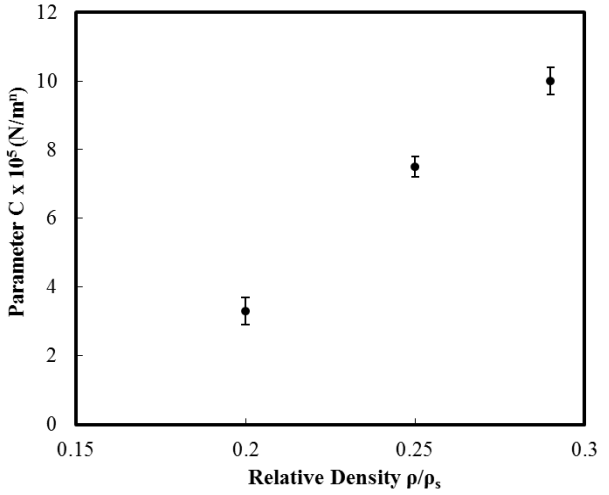


Fig. 13 The variation of the contact parameter, C, with relative density for foams manufactured using a compaction pressure of 100MPa.

TABLE 3 SUMMARY OF THE CONTACT PROPERTIES OF THE SANDWICH STRUCTURES FOLLOWING INDENTATION TESTS.

Relative Density	C (N/m^n)	n
0.2	3.3×10^5	0.91
0.25	7.5×10^5	1.18
0.29	1.0×10^6	1.185

The variation of the parameter 'n' with relative density is shown in Fig. 12; the average values of 'n' for the 100 MPa samples varied between 0.91 and 1.185. It can be seen that for the samples with a relative density of 0.2, the average values of 'n' are lower than unity, approximately 0.91. In contrast, samples with relative densities of 0.25 and 0.29, the average values are clearly greater than unity. Similar results were observed when the parameter 'C' is plotted against relative density as shown in Fig. 13. The average values of 'C' show an increasing trend with increasing relative density. This is expected since increasing the density of the foam increases the stiffness of the sandwich structure, thereby increasing the effective slope of the load vs. indentation curve.

Flexural properties of the sandwich structures

Fig. 14 shows typical load-displacement curves following three-point bending tests on the sandwich structures. Fig. 15 shows a photograph of a fractured sandwich structure following a three-point bend test, the relative density of the foam in this sample was 0.25. From the figure, it can be seen that the core has fractured in shear at one end of the sample leading to debonding of the composite skin along the uppermost interface. Similar failure modes were observed in the samples based on foams with relative densities of 0.2 and 0.29. Clearly, the load-bearing capacity of the sandwich structures is limited by the fracture properties of the core. Similar modes of failure have been observed following three-point bend tests on aluminum foam core sandwich structures based on glass fiber PA 6,6 skins [15].The maximum stress in the lower composite skin at maximum load was determined using sandwich beam theory. Here, the maximum tensile stress in the lower face is given as:

$$\left(\sigma_f\right)_{\max} = \pm \frac{ME_f}{D}\frac{h}{2} \tag{4}$$

where M is the maximum bending moment, E_f is the modulus of the composite skins and D can be approximated as [1]:

$$D = E_f \frac{btd^2}{2} \tag{5}$$

where the dimensions b, t and d are defined in Fig. 16.

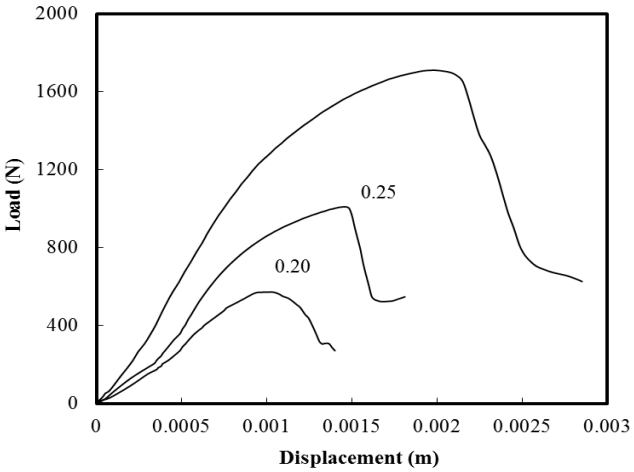


Fig. 14 Typical load-displacement curves following three point bend tests on sandwich structures manufactured using a compaction pressure of 100 MPa.

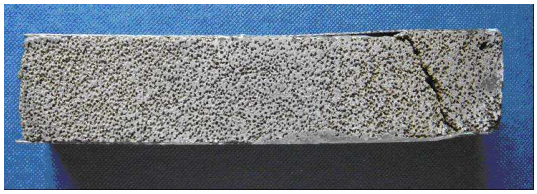


Fig. 15 The photograph of deformed sandwich structure after three point bend testing, relative density of foam was 0.25.

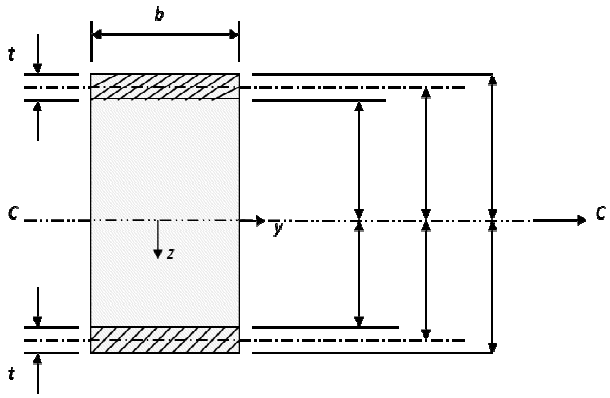


Fig. 16 Schematic of the cross-section of a sandwich beam showing the characteristic dimensions.

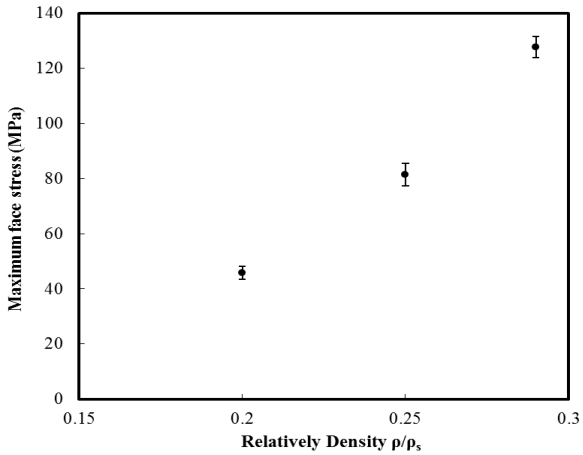


Fig. 17 The variation of the face stress with relative density for sandwich structures manufactured using a compaction pressure of 100 MPa.

The average values of the maximum stress in the face material were calculated using Eqn. 4 and these values are shown in Fig. 17. From the figure, it is clear that the stress in the lower skin at failure increases as the relative density increases. The maximum stress in the skins in the highest density laminate was approximately 130 MPa, this being approximately thirty percent of the tensile strength of the composite skins. Clearly, the strength of the sandwich structures is limited by the shear strength of the core, increasing as the shear strength of the core increases. These findings do suggest, however, that the LCS technique offers potential for manufacturing low cost metal foam cores for use in the manufacture of sandwich structures. The LCS technique is currently being used to manufacture metal cores based on other metal alloys such as steel and nickel-titanium shape memory alloys.

Summary

A range of iron foam core sandwich structures have been manufactured by the LCS process. Initial tests to characterize the mechanical properties of core materials have shown that the compressive strength and the elastic modulus of the systems were sensitive to the relative density of the foam and the compaction pressure used during manufacture. The compressive strength of the foams was also sensitive to the geometry of the foam.

Indentation tests on the sandwich structures have shown that the load-indentation response of these systems can be characterized using a generalized indentation law. Subsequent three point bend tests have shown that the load-bearing properties of these systems are also sensitive to the relative density of the core.

References

[1] Allen H.G., Analysis and Design of Structural Sandwich Panels, Pergamon, London, 1969.

[2] Ashby M.F., Evans A.G., Fleck N.A., Gibson L.J., Hutchinson J.W. and Wadley H.N.G, Metal Foams: A Design Guide. Boston: Butterworth-Heinemann; 2000.

[3] Gibson L.J. and Ashby M.F., Cellular Solids: Structure and Properties, 2nd Ed., Cambridge University Press, Cambridge, 1997.

[4] Banhart J., Ashby M. and Fleck N., Cellular Metals and Metal Foaming Technology, MIT-Verlag, Berlin 2001.

[5] Lenel Fritz V, Powder Metallurgy: Principles and applications, Metal Powder Industries Federation, Princeton (N.J.), 1980.

[6] Zhao Y.Y., Porous metallic materials and method of production thereof, UK Patent Application Number: 0412125.7, 2004.

[7] Zhao Y.Y., Fung T., Zhang L.P., and Zhang F.L., Lost carbonate sintering process for manufacturing metal foams, Scripta Materialia, 52(2005) 295-298.

[8] Zhao Y.Y. and Sun D.X., A novel sintering-dissolution process for manufacturing Al foams, Scripta Materialia, 46(2001), 273-282.

[9] Sun D.X., and Zhao Y.Y., Static and dynamic energy absorption of Al foams produced by the sintering and dissolution process, Metallurgical and Materials Transactions B, 34(2003), 69-74.

[10] Zhao Y.Y., Stochastic modelling of removability of NaCl in sintering and dissolution process to produce Al foams, Journal of Porous Materials, 10(2003), 105-111.

[11] Zhao Y.Y., Han F.S. and Fung T., Optimisation of compaction and liquid-state sintering in sintering and dissolution process for manufacturing Al foams, Materials Science and Engineering A, 364(2004), 118-126

[12] Sun D.X. and Zhao Y.Y., Phase changes in sintering of Al/Mg/NaCl compacts for manufacturing Al foams by the sintering and dissolution process, Materials Letters, 59(2005) 6-10.

[13] Ma X., Peyton A.J. and Zhao Y.Y., Measurement of the electrical conductivity of open-celled aluminium foam using non-contact eddy current techniques, NDT & E International, 38(2005) 295-298.

[14] Park C., Nutt S. R., PM Synthesis and properties of steel foams, Materials Science and Engineering, A288 (2000) 111-118.

[15] Kiratasaevee H., PhD thesis, the University of Liverpool, 2004.

[16] Davies P., Choqueuse D. and Wahab A., Response of composite sandwich panels to impact loading, Revue de l' Institut, Francais du Petrole, 1995.

[17] Hazizan M. K., Cantwell W. J., The low velocity impact response of foam-based sandwich, structures, Composites: Part B 33(2002) 193-204.

Advanced Materials Research Vol. 936 (2014) pp 2063-2067
© (2014) Trans Tech Publications, Switzerland
doi:10.4028/www.scientific.net/AMR.936.2063

Research on Tribological properties of Cast Iron at High-Speed Dry Sliding Condition

CHEN Yue [a], SHANGGUAN Bao [b] and HUANG Ying-yu[c]

School of Material Science and Engineering, Henan University of Science and Technology, Luoyang 471003, China

[a]chenyue@haust.edu.cnl, [b]shanggb@haust.edu.cn, [c]loulan1122@yahoo.com.cn

Keywords: Matrix Microstructure; Cast Iron; High-speed Dry Sliding; Friction and Wear

Abstract: The friction and wear properties of cast iron with different graphite morphologies and matrix microstructure were investigated at high speed dry sliding against GCr15 steel on the MMS-1G high-speed tribometer apparatus. The various wear micro-mechanisms and tribo-metallographic phases were studied by using scanning electron microscopy. The results show that as friction material, vermicular iron exhibits excellent comprehensive tribological properties. The friction coefficient of cast iron sliding against GCr15 decreases while the wear rate increases with the increase of sliding speed, friction coefficient and wear rate decline with the increase of pearlite content. Under the experimental condition, the main wear mechanisms of flake iron are abrasive wear, of vermicular iron are abrasive wear and oxidative wear and of nodular iron are oxidative wear, abrasive wear and fatigue spalling.

Introduction

Above half of world energy was consumed in different forms by the friction of friction pair components of machinery taking place on the rubbing surfaces[1]. Hence, tribologists at home and abroad implemented in succession research on tribological properties of material at high speed dry sliding[2,3]. As one of the commonly used materials, cast iron has a series of virtues such as abundance in resources, low price, simple to produce, etc. Meanwhile graphite morphology and matrix microstructure may produce significant influence on mechanical properties and tribological properties[4-5]. Hence, in this study an attempt has been made to investigate tribological properties of flake iron, vermicular iron, nodular iron with different matrix microstructures sliding against GCr15 bearing steel on MMS-1G high-speed tribometer apparatus, and the objective of present work is to establish the foundation for cast iron in dry sliding frition applications.

Experimental details

Cast Iron Pin Sample Preparation. The compositional details of pin samples with identical chemical composition are presented in Table 1. Through inoculation, spheroidising and vermicularizing flake iron blank, vermicular iron and nodular iron blank tested in this study were obtained. Moreover, green sand casting was employed to produce all the pin samples. Each type of pin sample was subjected to different heat treatments to obtain three matrix, the specific process is as follows:normalizing and 550℃ high temperature tempering were processed to obtain pearlite matrix;The pin sample with ferite matrix was achieved by means of high temperature graphitization and annealing; 880 ℃ normalizing and 550℃ high temperature tempering caused the formation of mixed matrix microstructure, and the holding time is（2.4min/mm）×52.5 mm. The pin samples were obtained in form of Φ14mm ×40mm using wire cutting.

Table 1 Chemical composition of cast iron（mass fraction/%）

C	*Si*	*Mn*	*P<*	*S<*
3.6	*2.5*	*0.6*	*0.07*	*0.03*

Counter-disc Preparation. GCr15 bearing steel used as rotating counter-surface was in the form of 160-mm diameter discs. All the rubbing discs have undergone quenching and low tempering to have surface hardness of 57~60 HRc. The nominal chemical composition of discs is shown in Table 2.

Table 2 Chemical composition of GCr15 bearing steel（mass fraction /%）

C	*Mn*	*Si*	*P≤*	*S≤*	*Cr*
0.95～1.05	*0.25～0.40*	*0.15～0.35*	*0.020*	*0.027*	*1.30～1.65*

Sliding Wear Tests. Sliding wear tests were conducted using MMS-1G high-speed tribometer apparatus allowing maximum sliding speed of 100m/s and maximum load of 3MPa. Sliding speed adopted in the study was 10,30,50,70 and 90m/s, and the variable load was changed from 0.33 to1.67 MPa. Preliminary tests were first conducted on all pins samples to ensure good contact between pin and counter-surface before each test. An average of three observations has been considered in this study.

Dry Tribological Properties. Friction coefficient was determined by recording the friction force with the help of a friction transducer, and computered by the following expression：

$$\mu = \frac{F}{N} \tag{1}$$

μ：friction coefficient; F: frictional force calculated by friction torque/fricton arm; N: normal press. Wear rate is calculated following the expression（2）.

$$W = \frac{\Delta W}{2\pi R t n \mu N} \tag{2}$$

W：Physical significance stands for wear loss of unit friction work.Where R is average friction radius(m), namely, the distance of pin from the center of the disc; t: sliding time(s); n: rotational speed of disc(r/min); N is the normal stress applied on pin(N); μ:friction coefficient;Wear loss ΔW was measured by the weight loss of pin samples measured with the help of BS210S weighing balance of accuracy 0.1mg.The samples were cleaned well with alcohol and then dried prior to and after wear testing.

Microstructure Analysis. Worn surfaces of cast iron were observed by JSM-5610LV scanning electron microscopy to analyze wear mechanism.

Experimental Results

Effect of Graphite Morphology on Tribological Behaviour

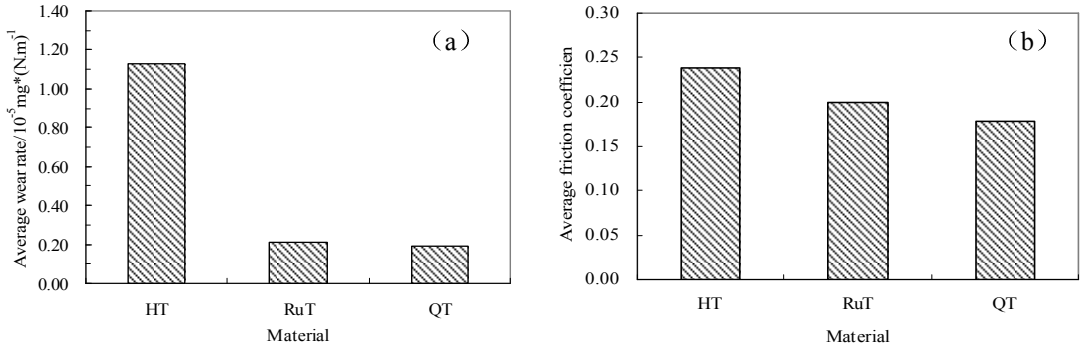


Fig.1 Effect of different graphite morphology on tribological behaviour of cast iron

Average friction coefficient and average wear rate of cast iron with different graphite morphologies are showed in Fig.1 under different conditions. It shows that RnT attained higher friction coefficient than that of QT and significantly less wear rate than that of HT irrespective of test conditions and matrix microstructure.

Wear resistance of the cast iron depends largely on graphite morphology when all the samples attained one type of matrix microstructure. Firstly,graphite morphology may affect strength and toughness of cast iron,and the change of flake graphite converted into to vermicular graphite or

nodular graphite could lead to an increase in strength and toughness of cast iron resulting in superior wear resistance.On the other hand, graphite morphology may also affect thermal conductivity of cast iron.Flake graphite and vermicular graphites may form a bond with each other in one eutectic cell causing an increase in thermal conductivity as compared to QT.Under similar conditions, it is expected that QT achieved the highest friction surface temperature causing severity of surface and subsurface regions damage and the ability of plastic deformation.As a whole,RuT exhibited superior comprehensive tribological properties due to the better thermal conductivity as compared to that of QT and graphite vermicular contributed to more superior strength and toughness in comparison with HT for friction material.

Effect of Matrix Microstructure on Triboligical Behaviour

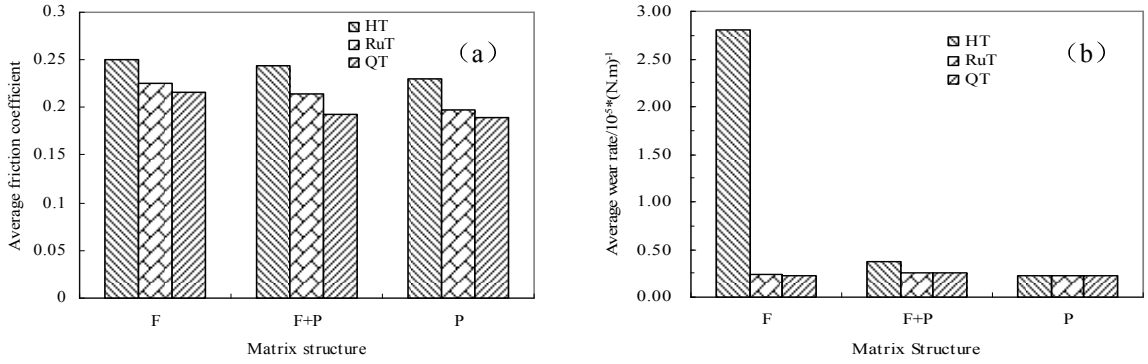


Fig.2 Effect of different matrix microstructures on triboligical behaviour of cast iron

Fig.2(a) represents the average friction coefficient of HT, RuT, QT with different matrix microstructures tested under different conditions.The testing results show that friction coefficient of HT deceased slightly with increasing pearlite content, similar trend occurred for RuT and QT,thereby higher content of pearlite is more beneficial for antifriction material.Higher content of ferite could lead better performance for friction material.

Fig.2(b) represents the average wear rate of HT, RuT, QT with different matrix microstructures tested under different conditions.It can be seen that verage wear rate of HT, Ru T, QT deceased with increasing content of pearlite,moreover HT with ferrite matrix attained significantly higher wear rate than that of all other samples tested,thereby higher content of pearlite generally leads to an increase in wear resistance of cast iron.

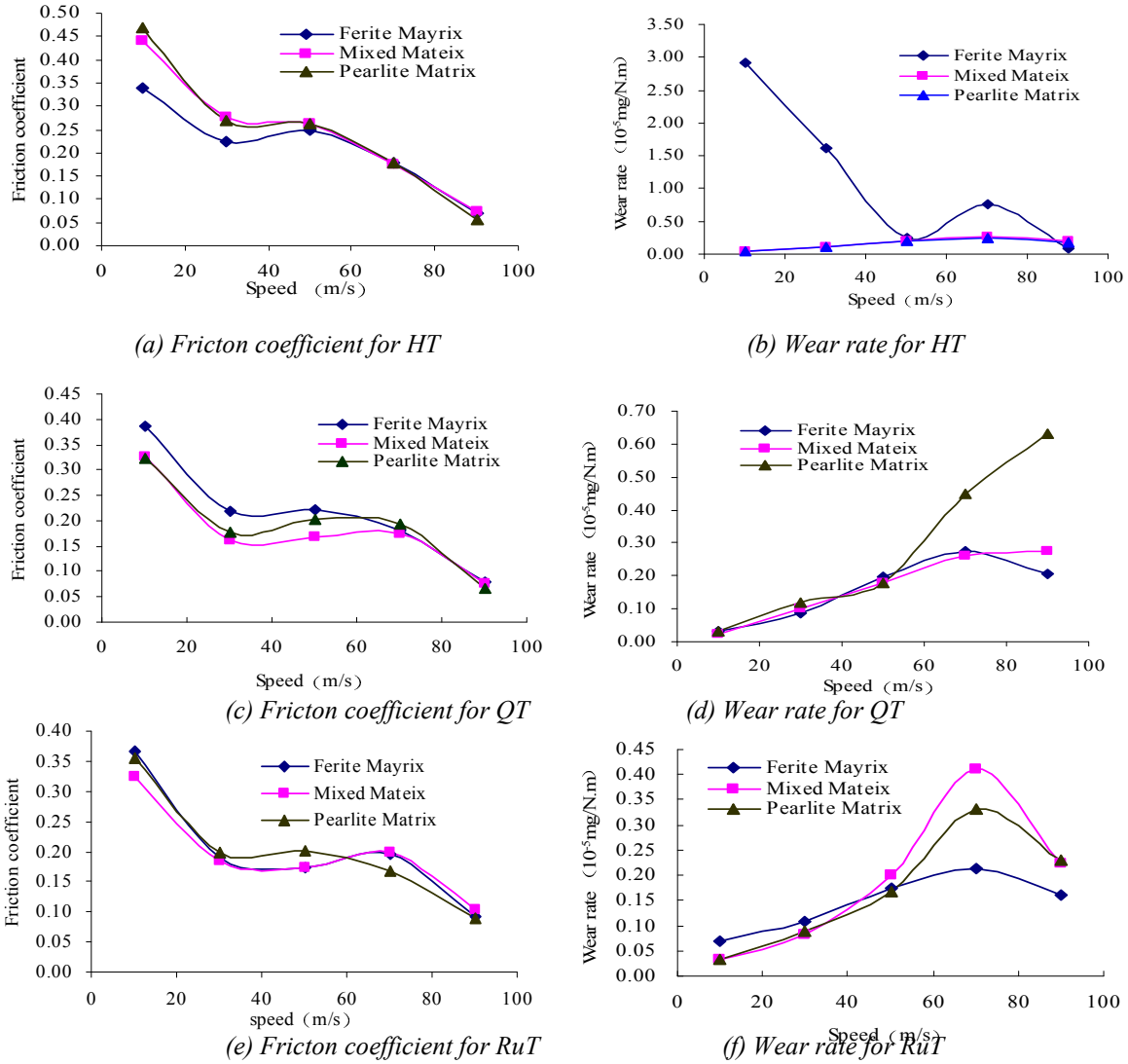
Effect of Sliding Speed on Triboligical Behaviour

The variation of friction coefficient of cast iron with sliding speed are shown in Fig.3(a), (c), (e).The results indicate that friction coefficien deceased with increasing sliding speed on controlled condition.As shown in Fig.3(a), (c), (e), there was a significant decease in friction coefficient of the samples tested with increase in sliding speed from 10m/s to 30m/s, accordingly suggesting that friction coefficient was quitely sensitive to the variation of sliding speed,with further increase in sliding speed to 30 and 70m/s, average friction coefficient recorded stabilised with the varition of sliding speed; At higher sliding speed(70~90m/s), significant decease in friction coefficient was observed with increasing sliding speed.

Fig.3(b), (d), (f) show the wear rate as a function of sliding speed of testing samples at 0.33MPa load. It can be seen that wear rate of cast iron increased in general with increasing sliding speed, in the case of cast iron with ferite matrix opposite, this is possibly due to severe abrasive wear at low sliding speed.

Wear Mechanism

The representative scanning electron micrographs for wear surface of cast iron with varying graphite morphologies at 90m/s speed and 0.33MPa load are shown in Fig.4.It can be observed that worn faces of flake iron showed large amount of microcracks and melt spots,deep and plough-hooked scratch indicating higher spalling probability of wear debris, thereby wear rate of flake iron remained higher than that of the other samples tested, and under act of alternative contact



(a) Fricton coefficient for HT *(b) Wear rate for HT*

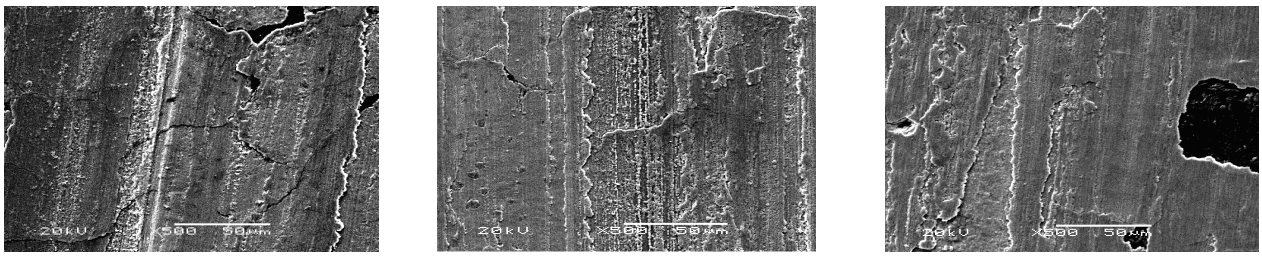
(c) Fricton coefficient for QT *(d) Wear rate for QT*

(e) Fricton coefficient for RuT *(f) Wear rate for RuT*

Fig.3 Effect of sliding speed on triboligical behaviour of cast iron (0.33MPa）

stress,wear mechanism was dominanted by abrasive wear.The presence of oxide adhesion and limited quantity of grooves on the worn surface of RuT suggested abrasive wear and oxidative wear to be the dominant mechanism of material removal.Worn surface of QT showed a limited quantity of grooves, meanwhile the peeling phenomenon induced by stress concentration was also observed around graphite phase,thereby the main wear mechanism was combination of oxidative wear, abrasive wear and fatigue spalling.As a whole, it could be summaried that abrasive wear would lead to higher friction coefficient and wear rate, and oxidative wear could in turn decline friction coefficient due to the rubbing surface covered by oxidation film.

Fig.5 shows the worn surfaces of QT with different matrix microstructures.It can be observed that worn surface of pin sample with ferite matrix showed rough topography containing severe scratch in



(a)HT×500 (b)RuT×500 (c)QT×500

Fig.4 SEM morphology of the worn surfaces on pin sample of different graphite morphologies (at the sliding speed 90m/s and the load 0.33MPa）

form of groove and wear mechanism was dominanted by abrasive wear.Worn surface of pearlite matrix with large amount of particles was relative smoother in contrast with that of pearlite+ferrite matrix containing small amount of grooves.The presence of large amount of particles could be contributed to the increse of friction coefficient and wear rate, which was also in agreement with the trend of friction coefficient and wear rate with the varition of content of pearlite as shown in Fig.2(a),(b).EDS analysis showed that oxidation wear was observed on the worn surface of all the samples tested; Wear mechanism was dominanted by abrasive wear when the content of was higher, increased content of pearlite could lead to the change of wear mechanism varied from abrasive wear to combined action of abrasive wear, oxidative wear due to the severity of oxidation.



(a)Ferite Matrix×500 *(b) Ferite +Pearlite Matrix×500* *(c) Pearlite Matrix×500*

Fig.5 SEM morphology of the worn surfaces on pin sample with different matrix microstructures (QT: at the sliding speed 90m/s and the load 0.33MPa）

Conclusions

(1) In the present work, HT achieved the highest friction coefficient, next was RuT, whereas the lowest wear rate was obtained for QT, and then RuT, HT in order. In the view of above, RuT exhibited superior comprehensive tribological properties used as friction material.

(2) Average friction coefficient of all samples tested decreased slightly sliding against GCr15 steel with the increase in content of pearlite, and as for wear rate also.

(3) The friction coefficient of the tested samples deceased with increasing sliding speed sliding against GCr15 bearing steel. There was a significant decrease in the friction coefficient of the samples tested with sliding speed increased from 10m/s to 30m/s accordingly, suggesting that the friction coefficient is quite sensitive to the variation of sliding speed. With further increase in the sliding speed from 30m/s to 70m/s, friction coefficient recorded stabilised with the variation of sliding speed. At higher sliding speed (70~90m/s), significant decrease in friction coefficient was observed with increasing sliding speed. Wear rate of cast iron increased in general with increasing sliding speed.

(4) Under the test condition, the principal wear mechanism of flake iron was abrasive wear, and the principal wear mechanism of RuT was the combination of abrasive wear, oxidative wear. Moreover, the presence of abrasive wear, oxidative wear and fatigue spalling was observed on the worn surface of QT. Wear mechanism was dominated by abrasive wear when the content of ferite was higher, and increased content of pearlite could lead to the change of wear mechanism from abrasive wear to combined action of abrasive wear and oxidative wear due to the severity of oxidation.

References

[1] Huo Lin. Tribology Theory [M]. Beijing: China Machine Press, 1981.

[2] Y. Guilmard, J. Denape, J.A. Petit. Friction and wear thresholds of alumina-chromium steel pairs sliding at high speeds under dry and wet conditions [J]. Tribology International, 1993, 26(1): 29-39.

[3] Duan Haitao, Du Sanming, Zhang Yongzhen, Wang Guanmin.Study on the Friction Heat Rule under High-speed Dry Sliding Conditions[J]. Lubrication Engineering, 32(10):40~42.

[4] Zhang Yongzhen,et al.Dry Tribology of Material [M]. Beijing:Science Press,2007.

[5] Shen Bailing,Ren Guosheng,Zhang Yongzhen,et al. Effect of matrix on The Tribological Behavior of Ru T[J].Ordnance Material Science and Engineering, 1992,15(9):55-59.

CHAPTER 18:

General Mechanical Engineering

Advanced Materials Research Vol. 936 (2014) pp 2071-2074
© (2014) Trans Tech Publications, Switzerland
doi:10.4028/www.scientific.net/AMR.936.2071

A Semi-analytical and Semi-numerical method for Acoustics Radiation Characteristics of Rotational Shells

Jing Lu[1,2*]

[1]Automotive and Transportation Engineering Institute, Guangxi University of Science and Technology, Liuzhou, 545006, China

[2]Guangxi Key Laboratory of Automobile Components and Vehicle Technology, Guangxi University of Science and Technology, Liuzhou, 545006, China

gxustlj@126.com

Key words: rotational shell, acoustics radiation, semi-analytical method, sound pressure

Abstract: A semi-analytical and semi-numerical method is presented for analyzing the acoustics radiation characteristics of a rotational shell. Combining the dynamics control equation and the sound pressure expression, the vibro-acoustics equation of the rotational shell is formulated firstly. Then, a semi-analytical method is developed based on the superposition principle. The comparisons with the document show that the proposed method is accurate and efficient.

Introduction

Rotational shells are widely used in many engineering fields, such as aircrafts, spacecrafts, submarines and pipelines. The acoustics characteristics of these structures have attracted extensively attention[1]. Because its curvatures are variable in both directions, the dynamic equation of the rotational shell is more complicated than the cylindrical shells. For this reason, the FEM and BEM is the popular method for acoustics radiation analysis of rotational shells. However, it is proved that the numerical method has some disadvantages, i.e., large number of the elements and the poor calculation precision in the higher frequency range, etc. To overcome these shortcomings, this paper attempts to establish the vibro-acoustics equation of the rotational shell and put forward a semi-analytical method to study the acoustics characteristic of rotational shells.

Vibro-acoustics Equation of Rotational Shells

Figure 1 is the geometric scheme of a rotational shell. Under a harmonic external excitation, the displacement and internal force can be expanded with the Fourier series. Performing the dimensionless processions and only taking the symmetric terms for the purpose of simplicities, the displacement and internal force components can be expressed as

$$\xi = \frac{s}{L},\ (u,w) = L\sum_n \left(\overline{u}^{(n)}, \overline{w}^{(n)}\right)\cos(n\theta)\ ,\ v = L\sum_n \overline{v}^{(n)}\sin(n\theta),\ \theta_\varphi = \sum_n \overline{\theta}_\varphi^{(n)}\cos(n\theta),$$

$$S_\varphi = \sum_n K\overline{S}_\varphi^{(n)}\sin(n\theta),\quad M_\varphi = \sum_n (KL)\overline{M}_\varphi^{(n)}\cos(n\theta),\ \left(N_\varphi, V_\varphi\right) = \sum_n K\left(\overline{N}_\varphi^{(n)}, \overline{V}_\varphi^{(n)}\right)\cos(n\theta),$$

where L is the length for dimensionless, K is the membrane stiffness of the rotational shell, n is the circumferential wave number, u, v, w are the displacement amplitudes in φ, θ, z directions at the mid-plane, θ_φ is the rotation of the cross-section in φ direction, $N_\varphi, M_\varphi, S_\varphi, V_\varphi$ are the amplitudes of the membrane internal force, bending internal force, Kelvin-Kirchhoff's equivalent in-plane shear force and transverse shear in unit length of the rotational shell respectively. The variables with "—" stand for relevant dimensionless variables. The superscript n is omitted in the follows for conveniences.

Referring to the approaches in Ref.[2], for a given circumferential wave number n, the dynamics control equation of the rotation shell is

$$\frac{\mathrm{d}\overline{\boldsymbol{y}}}{\mathrm{d}\xi} = \mathbf{g}\overline{\boldsymbol{y}} - \frac{R_\varphi}{K}\boldsymbol{q}, \tag{1}$$

where $\bar{\boldsymbol{y}}=\left\{\bar{u}\ \ \bar{v}\ \ \bar{w}\ \ \bar{\theta}_{\varphi}\ \ \bar{N}_{\varphi}\ \ \bar{S}_{\varphi}\ \ \bar{V}_{\varphi}\ \ \bar{M}_{\varphi}\right\}^{T}$ is the dimensionless state vector of the rotational shell. The coefficient matrix $\mathbf{g}$ is an eight-by-eight matrix, and the expression of each element can be seen in Ref.[3]. $\boldsymbol{q}=\left\{0\ \ 0\ \ 0\ \ 0\ \ \tilde{q}_{\varphi}\ \ \tilde{q}_{\theta}\ \ \tilde{q}_{z}\ \ 0\right\}^{T}$ is the load vector acted on the shell, and R_{φ} is the lame coefficient in the meridian direction.

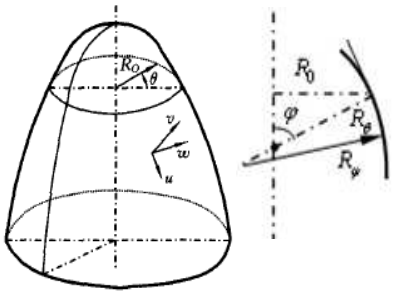


Fig.1 The rotational shell

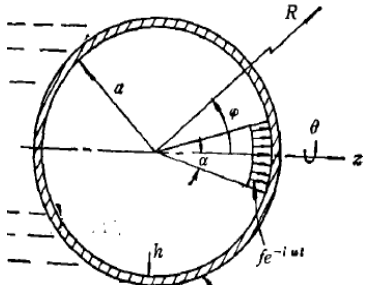


Fig.2 The immersion spherical shell

In Ref.[3], we have derived the expression of the radiation sound pressure as follows:

$$p(P)=\tilde{p}\left(\bar{P}\right)\cos\left(n\theta\right)=\sum_{m=0}^{+\infty}c_{mn}\bar{K}_{mn}\left(\bar{P}\right)\cos\left(n\theta\right),\quad n=\left(0\sim+\infty\right), \tag{2}$$

where c_{mn} denotes unknown coefficients, and the parameter $\bar{K}_{mn}\left(\bar{P}\right)$ is

$$\begin{cases}\bar{K}_{mn}\left(\bar{P}\right)=-\int_{0}^{\pi}\int_{0}^{2\pi}K\left(\bar{P},\varphi_{Q},\theta\right)\cos\left(m\varphi_{Q}\right)\cos\left(n\theta\right)r_{Q}\left(\varphi_{Q}\right)R_{\varphi}\left(\varphi_{Q}\right)d\varphi_{Q}d\theta\\ K\left(\bar{P},\varphi_{Q},\theta\right)=G\left(\bar{P},\bar{Q},\theta\right)=\dfrac{e^{-ik_{0}d\left(\bar{P},\bar{Q},\theta\right)}}{d\left(\bar{P},\bar{Q},\theta\right)}\\ d\left(\bar{P},\bar{Q},\theta\right)=\left[r_{P}^{2}+r_{Q}^{2}-2r_{P}r_{Q}\cos\theta+\left(z_{P}-z_{Q}\right)^{2}\right]^{1/2}\end{cases}, \tag{3}$$

In which, P and Q are coordinates of the field point and source point respectively, $\bar{P}$ and $\bar{Q}$ are the corresponding points on the meridian plane, $d\left(\bar{P},\bar{Q},\theta\right)$ is the distance between point $\bar{P}$ and point $\bar{Q}$.

Substituting Eq.(2) into Eq.(1), the vibro-acoustics equation of a PCLD rotational shell is obtained

$$\frac{\mathrm{d}}{\mathrm{d}\varphi}\begin{Bmatrix}\bar{u}\\ \bar{v}\\ \bar{w}\\ \bar{\theta}_{\varphi}\\ \bar{N}_{\varphi}\\ \bar{S}_{\varphi}\\ V_{\varphi}\\ \bar{M}_{\varphi}\end{Bmatrix}=\boldsymbol{g}\begin{Bmatrix}\bar{u}\\ \bar{v}\\ \bar{w}\\ \bar{\theta}_{\varphi}\\ \bar{N}_{\varphi}\\ \bar{S}_{\varphi}\\ V_{\varphi}\\ \bar{M}_{\varphi}\end{Bmatrix}+\begin{Bmatrix}0\\ 0\\ 0\\ 0\\ \bar{f}_{\varphi}\\ \bar{f}_{\theta}\\ \bar{f}_{z}\\ 0\end{Bmatrix}+\sum_{m=0}^{m_{c}}c_{mn}\begin{Bmatrix}0\\ 0\\ 0\\ 0\\ 0\\ 0\\ \left(R_{\varphi}/K\right)\bar{K}_{mn}\left(\bar{P}\right)\\ 0\end{Bmatrix}, \tag{4a}$$

The above equation can be written as a matrix equation

$$\frac{\mathrm{d}\boldsymbol{y}}{\mathrm{d}\varphi}=\boldsymbol{g}\boldsymbol{y}+\boldsymbol{F}+\sum_{m=-m_{c}}^{+m_{c}}c_{mn}\boldsymbol{p}_{sm}\left(\varphi,m,n\right), \tag{4b}$$

where m_c is the truncated number in the meridian direction, $\overline{f}_\varphi$, $\overline{f}_\theta$, $\overline{f}_z$ are the dimensionless load in φ, θ, z directions respectively, $\boldsymbol{p}_{sm}(\varphi,m,n)=\left\{0 \quad 0 \quad 0 \quad 0 \quad 0 \quad 0 \quad \left(R_\varphi/K\right)\overline{\overline{K}}\left(\overline{P}\right) \quad 0\right\}^T$ is the generalized sound pressure vector.

The coupling equation Eq.(4) can not be solved for the coefficient c_{mn} is unknown.

Numerical Method

On the juncture of the flow and solid, the Neumann boundary condition is

$$\frac{\partial p(\varphi)}{\partial n}=\rho_0\omega^2 w(\varphi), \tag{5}$$

where n is the unit outward normal vector of the boundary, ρ_0 is the mass density of the fluid media, and ω is the circular frequency of the external excitation.

Based on the superposition principle, the radial displacement of an arbitrary point can be obtained from Eq.(4)

$$w(\varphi)=L\overline{w}_F(\varphi)+L\left[\sum_{m=-m_c}^{+m_c} c_{mn}\overline{w}_{sm}(\varphi)\right], \tag{6}$$

where $\overline{w}_F^{(n)}(\varphi)$ is the Fourier expansion coefficient of the dimensionless radial displacement induced by the external load vector $\boldsymbol{F}$, $\overline{w}_{sm}^{(n)}$ is that induced by the generalized sound pressure load vector $\boldsymbol{p}_{sm}$.

Combining Eq.(2), Eq.(5) and Eq.(6), it is obtained

$$\sum_0^{m_c} c_{mn}\left[\overline{\overline{K}}'\left(\overline{P},m,n\right)-\rho_0\omega^2 L\overline{w}_{sm}(\varphi)\right]=\rho_0\omega^2 L\overline{w}_F(\varphi), \quad n=\left(0\sim n_c\right), \tag{7}$$

where the parameter $\overline{K}'_{mn}\left(\overline{P}\right)=-\int_0^\pi\int_0^{2\pi} K'\left(\overline{P},\varphi_Q,\theta\right)\cos(m\varphi_Q)\cos(n\theta)r_Q(\varphi_Q)R_1(\varphi_Q)d\varphi_Q d\theta$, and n_c is the truncated number of the Fourier series.

Setting M_P ($M_P>\left(m_c+1\right)$) distributing points along the meridian of the rotational shell, and calculating the value of $\boldsymbol{p}_{sm}$, $\overline{\overline{K}}'\left(\overline{P},m,n\right)$, $\overline{w}_{sm}(\varphi)$ and $\overline{w}_F(\varphi)$ for each distributing point, M_P equations can be assembled to an algebraic matrix equation as

$$\boldsymbol{A}_n\boldsymbol{c}_n=\boldsymbol{W}_n, \quad n=\left(0\sim+n_c\right) \tag{8}$$

where $\boldsymbol{A}_n$ is the coefficient matrix, $\boldsymbol{c}_n$ is a column vector of the unknown coefficient c_{mn}, and $\boldsymbol{W}_n$ is the displacement vector.

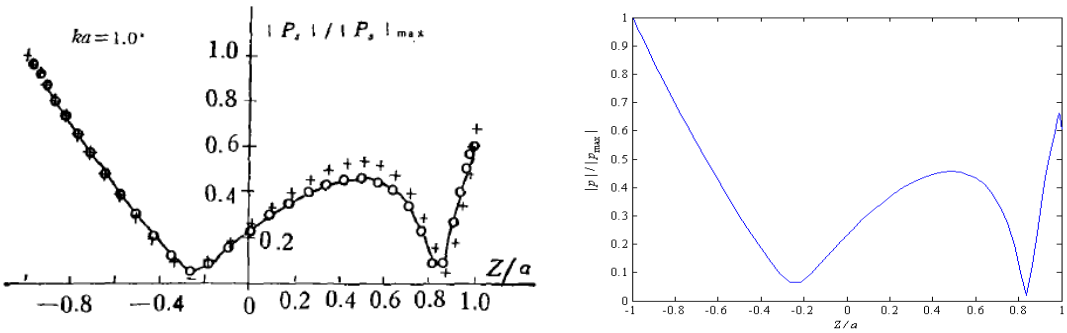
The unknown coefficient c_{mn} can be determined by solving the above equation, then the sound pressure of an arbitrary point is given by substituting c_{mn} into Eq.(2).

Numerical Results and Discussion

In order to invalid the effectiveness of the present method, we consider an immersion spherical shell under a uniform load, as shown in Fig.2. Its geometric and physical parameters are as follows [5]:

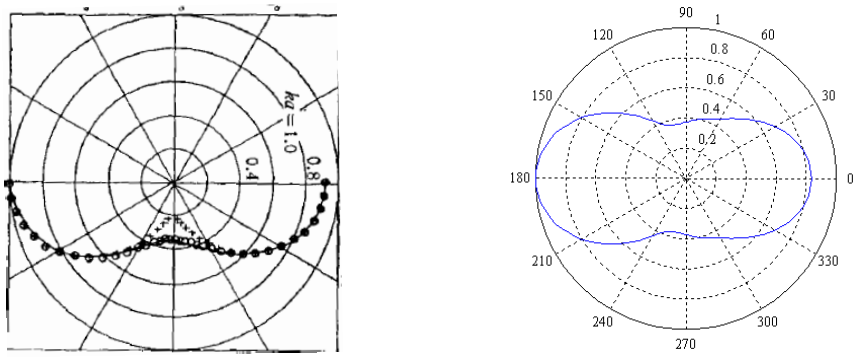
$a=1$ m, $h=0.02$ m, $E=210$ GPa, $\rho=7669$ kg/m^2, $\rho_0=1000$ kg/m^2, $c_0=1524$ m/s, $\alpha=32^0$.

The comparisons of the surface and far-field sound pressure between the present method and those in Ref.[4] are shown in Fig.3 and Fig.4. It is seen from figures that the results of the present method is more agreed with the analyzed solution (solid line in Fig.(a)) , which is better than the numerical method in Ref.[4]



(a) Surface sound pressure in document (b) Surface sound pressure in present

Fig.4 Comparison of the surface sound pressure



(a) Far-field sound pressure in document b) Far-field sound pressure in present

Fig.5 Comparison of the far-field pressure

Conclusions

The vibro-acoustics coupled equation of a rotational shell is derived, and a high precision and wide-used semi-analytical method is established in this paper. The numerical results have proved the effectiveness of the present method, which can be extended to the rotational shell with arbitrary shape conveniently. Because it avoids the numerical discretization, the proposed semi-analytical method is more accurate and efficient, and it can be applied in higher frequency range.

Acknowledgements

This paper is supported by the National Natural Science Foundation of China (11162001, 51105083) and Natural Science Foundation of Guangxi Province of China (2012GXNSFAA053207)

References

[1] B.M. Efimtsov, L.A. Lazarev, Sound pressure in cylindrical shells with regular orthogonal system of stiffeners excited by a random fields of forces, Journal of Sound and Vibration, 330(2011) 3684-3697.

[2] J. Lu, Y. Xiang, Y.Y. Huang, X.N. Li, Q. Ni. A transfer matrix method for analyzing vibration and damping characteristics of a rotation shell with passive constrained layer damping treatment, Acta Mechanica Solida Sinica, 23(2010) 297-311.

[3] J. Lu, Y. Xian, Y.Y. Huang, A virtual boundary spectral method with complex radius vector for acoustic radiation problem of 3-Dimension axisymetric cavity, ACTA. ACUSTICA, 36(2011) 308-317(in Chinese).

[4] J.D. Zhang and Z.Y. He. A finite element +boundary element-modified modal decomposition method for vibration and sound radiation from submerged revolutional shells, ACTA. ACUSTICA, 15(1990) 12-19(in Chinese)

Advanced Materials Research Vol. 936 (2014) pp 2075-2081
© (2014) Trans Tech Publications, Switzerland
doi:10.4028/www.scientific.net/AMR.936.2075

Validation of a Novel Method for Thermal Performance Evaluation of Parabolic Trough Receivers

XIONG Yaxuan[1, a], WU Yuting[2,b*], MA Chongfang [2,c], XU Peng[3d], LI Deying[3e*]

[1]Key lab of HVAC, Beijing University of Civil Engineering and Architecture, Beijing 100044,China

[2]Key Laboratory of Enhanced Heat Transfer and Energy Conservation Ministry of Education, Beijing University of technology, Beijing 100124, China

[3]Key lab of HVAC, Beijing University of Civil Engineering and Architecture, Beijing 100044,China

[a]xiongyaxuan@bucea.edu.cn, [b]wuyuting@bjut.edu.cn, [c]macf@bjut.edu.cn, [d]xupeng@bucea.edu.cn, [e]lideying@bucea.edu.cn

Keywords: parabolic trough receiver, RIH, heat loss, emissivity

Abstract. Parabolic trough receivers are a kind of key components of a solar trough power plant, which absorb and transfer the high flux solar energy to the heat transfer fluid flowing in it. A Receiver Impedance Heating (RIH) method is put forward by analyzing the inadequacies of traditional methods. Voltage is imposed on both ends of the receiver and then the receiver is self-heated via a large electrical current flowing through it based on the Joule Effect. Once the receiver reaches a thermal equilibrium the product of voltage imposed on the receiver and electrical current flowing through the receiver is equal to the heat loss of the receiver to ambient environment at corresponding temperature difference of receiver temperature above ambient. The experiment system is simple, low-cost, and easy to operate. Experiment results show that curve of heat loss is smooth and measurement uncertainty is low, which means accuracy of the experiment results is high, while time period to reach a thermal equilibrium at every absorber temperature reduces to 2-3hours which is one fifth of that needed in traditional methods.

Introduction

Parabolic trough receivers are a kind of key components of a solar trough power plant. Receivers convert the incoming solar radiation into high temperature heat and transfers it to the heat transfer fluid flowing in it while losing thermal energy to ambient in combination of conductive, convective and radiative energy through the vacuum space and support brackets when the collector is on focus. Usually emissivity of selective coating on outer surface of an absorber, geometry of glass envelops and glass-metal sealing, vacuum condition in annular space, and other properties have strong influences on receiver's thermal performance [1][2][3][4][5]. So it is very important for the buyers and sellers to know the thermal performance of a parabolic trough receiver.

Generally there are two principles to quantifying the heat loss of a receiver [1][5]. One is the quasi-steady-state equilibrium. Larger parabolic trough collectors, heat transfer fluid and other devices are necessary according to this principle, which is complicated to operate and costs very much. Another is the steady-state equilibrium. In this way a heat source brings the receiver to a test temperature. The whole receiver ideally has a uniform temperature on the surface of the absorber. The power required to maintain the receiver in steady-state equilibrium is equal to the heat loss at some absorber temperature. DLR employed a 4m long quartz heater to supply thermal energy for the test stand of parabolic trough receivers [5]. The heater is coaxially inserted inside a tubular copper pipe which is used to uniform the temperature field of the quartz heater and then to heat the receiver uniformly as much as possible. 14 thermocouples are employed to measure the temperatures of receiver, glass envelop and ambient respectively. The maximum heating power of the heater is 5.9KW. The time to reach steady state equilibrium is from 5 to 24hours depending on the heating

power, when temperature changes less than 1.0℃ within one hour. NREL erected a similar test system to evaluate the thermal performance of parabolic trough receivers based on the steady state equilibrium and electrical heating, which employ 6 heaters and corresponding temperature controllers [5]. Maximum heating power of the test system is 9.0KW and the time to reach steady state equilibrium is from 12 to 24hours depending on the heating power. Then some tests have been carried out by the test system [7][8]. In addition, there are some similar test systems based on the same principle and electrical heating in China [1].

Due to the existing problems in above test systems a novel test system based on receiver impedance heating (named RIH) and steady state equilibrium is presented to reduce the time period of reach steady state equilibrium and to improve the temperature uniformity on absorber surface.

Experimental Setup

Experiment System Description

Based on the steady state equilibrium and Joule affect of metal an experimental system has been established while receivers serve as impedance, which is named as receiver impedance heating (RIH) method.

The experiment system is made up of three receivers, a regulated power supply, a current transducer, a MCU data acquisition unit, touch screen and several thermocouples. Fig. 1 and Fig. 2 show the schematic diagram and picture of the experimental system based on the RIH method respectively.

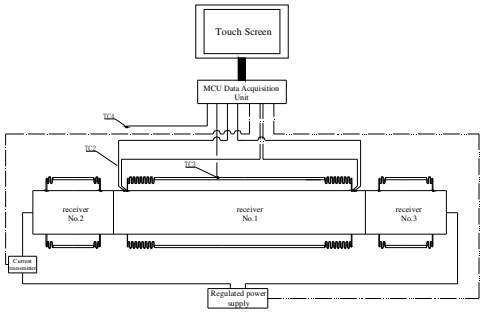


Fig. 1 Schematic Diagram of the Experimental System based on the RIH Method



Fig. 2 Experiment System Established based on the RIH Method

Three receivers are welded in line to form a receiver group via stainless-steel welder protected by argon, where the centered receiver No.1 is the test target. Two power cables with a cross-section of 100mm2 serve to connect two ends of the receiver group respectively with Regulated power supply to form a closed circuit. A current transmitter(typed CHZ 500G, Accuracy: ±0.5%) traversed by one power cable serves to measure the current flowing through the receiver and puts out a analog voltage signal in the range of 0 to 5V collected by MCU data acquisition unit. Voltage imposed on the inner part of receiver No.1 is collected directly by connecting welding locations where the absorber joints with the bellows, and the MCU data acquisition unit connected with data cables. Four thermocouples (Type K, Class II) are used in the test system. Two of them serve to measure absorber temperature,

and the other two serve to measure the glass envelop temperature and ambient temperature. A MCU data acquisition unit and a touch screen serve to acquire, monitor and save the data collected. All the thermocouples are calibrated in advance. Parts of receiver exposed to ambient should be insulated with a mineral wool of 150mm thickness before conducting the experiments.

Experiment Principles

Because of the uniform wall thickness, current flowing through the receiver will generate a uniform temperature field along the axis direction and the circumferential direction on the absorber wall based on the famous Joule affect of current. Temperature gradient does not exist in theory. Therefore, one thermocouple is attached to the outer surface of the absorber of receiver No.1, which is enough for the absorber temperature. Likewise one thermocouple is enough for glass envelop temperature and the ambient temperature respectively. Two thermocouples are fixed on each end joint of the absorber of receiver No.1 by spot welding. The thermocouple for glass envelop temperature is attached to the outer surface of the glass envelop. The thermocouple for ambient temperature is placed in an opened carton which is more than 1.0 meter far away from the receiver group. By setting different output voltage of the power supply in the touch screen the receiver group will reach different steady-state equilibrium of energy. Electric power exhausted depends on absorber temperature and the thermal performance of the receiver. Time period that the receiver group reaches steady state equilibrium of energy is defined by temperature fluctuation of less than ±0.2K within one hour. Experiment results show that average time period is around 2 hours to reach steady state equilibrium of energy.

Data Processing

Absorber temperature, glass envelop temperature, ambient temperature, electrical current, voltage and receiver length inside vacuum space of receiver No.1 are expressed with T_1, T_2, T_0, V, I and Labs, then absorber temperature T_1 minus ambient temperature T_0 is equal to the temperature difference $\Delta T10$ of absorber above ambient, while absorber temperature T_1 minus glass envelop temperature T_2 is equal to Temperature difference ΔT_{12} of absorber above glass envelop. For each steady state equilibrium of energy total heat loss of receiver No.1 is equal to production of the current flowing through the receivers and the voltage exerted. Heat loss per meter q_T can be expressed with eq. 1,

$$q_T = VI / L_{abs} . \tag{1}$$

Assuming that the absorber is a blackbody included in a big closed cavity, the selective coating emissivity ε can be calculated by eq. 2,

$$\varepsilon = q_T / \left[\pi D_{abs} L_{abs} \sigma \left(T_1^4 - T_2^4\right)\right]. \tag{2}$$

Where, Dabs is the outer diameter of absorber and σ is the Stefan-Boltzmann constant.

Via eq. 1 and 2, Heat loss per meter and the selective coating emissivity at different work temperature can be obtained. Then performing polynomial fitting Experimental correlations between q_T and ΔT_{10}, between q_T and ΔT_{12}, and between ε and ΔT_{10} can be correlated. Comparing the heat loss per meter at same temperature difference and selective coating emissivity of different receivers at same absorber temperature you can easily evaluate the thermal performance of difference receivers quantitatively. The lower the heat loss is at the same temperature difference, the better the thermal performance of a receiver is. And the lower the emissivity is the better the thermal performance of the selective coating is.

Results Discussion

Two receivers tested in this paper are from our cooperation. The receiver is 4060mm long, 70mm in absorber diameter and 115mm in glass envelop diameter. Receiver 1# has been working for two year at maximum temperature around 350 ℃ and receiver 2# is a new one, which are chose at random

from the same batch of products. Ambient temperature is around 20 ℃. Absorber temperature is in the range of 150 to 450 ℃ with an interval of 50 ℃.When fluctuation of absorber, glass envelop and ambient temperature is in the range of ±0.2 ℃ while fluctuation of voltage and electrical current is in the range of 0.05 V and 0.25A respectively during one hour, receiver group are thought of reaching a steady-state equilibrium. Experimental results are shown in fig. 3 to fig. 6.

Fig. 3 shows the heat loss change with temperature differenceΔT_{10}. From fig. 1 we know that the heat loss curves from receiver 1# and receiver 2# are very smooth, which indicate precision of the experiment data is very high. Heat loss of receiver 1# is higher than that of receiver 2# apparently, which means thermal performance of receiver 2# is better than that of receiver 1# and thermal performance of a new receiver reduced after a year of operation.

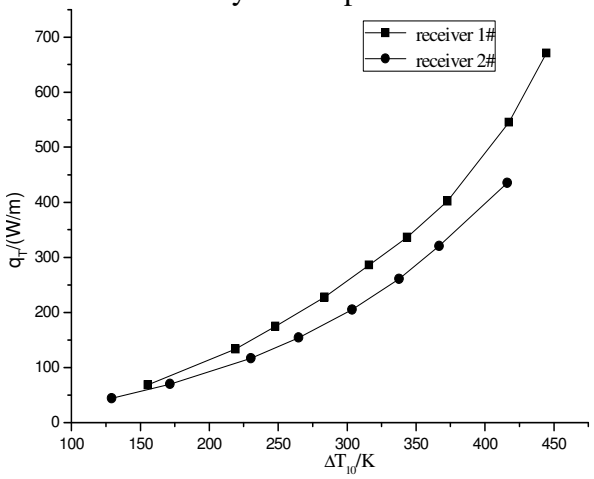


Fig. 3 Heat Loss Change with Temperature Difference ΔT_{10}

After the experiment we find coating became red and getter became white and smaller. We think that aging of selective coating and reduction of vacuum level in annular space cause the thermal performance reduction of receiver 1#.

Experimental correlation of receiver 2# by polynomial fitting is as eq. 3:

$$q_T = -65.04 + 1.3462\Delta T_{10} - 6.13\times10^{-3}\Delta T_{10}^2 + 1.89193\times10^{-5}\Delta T_{10}^3 - 1.20563\times10^{-8}\Delta T_{10}^4 . \quad (3)$$

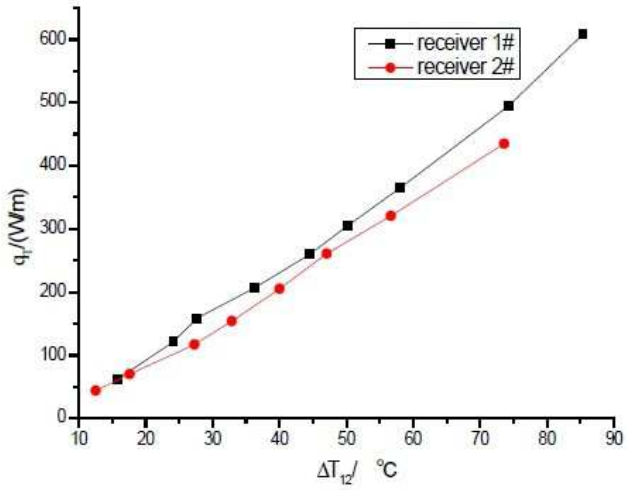


Fig. 4 Heat Loss Change with Temperature Difference ΔT12

Fig. 4 shows the heat loss change of receiver 2# with temperature difference ΔT_{12}. Its experimental correlation by linear fitting is as follows:

$$q_T = -49.65 + 6.513\Delta T_{12} . \quad (4)$$

This correlation is almost a straight line (R^2=0.99539). So as an alternate we can also make evaluation qualitatively by comparing the slop of two straight lines: the larger the slop is, the higher the heat loss is.

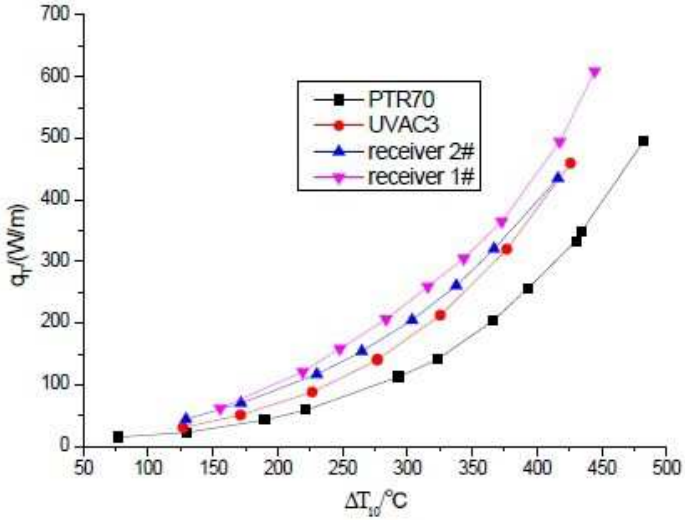


Fig. 5 Comparison of Heat Loss Curves from the Novel System and the Traditional System [7][8]

Fig. 5 shows the comparison of experiment data with that in literature data. Fig. 5 indicates heat loss of receiver 1# and receiver 2# is higher than that of PTR70 and UVAC3, but heat loss curves of receiver 1# and receiver 2# are smoother than that of PTR70 and UVAC3 generally, which validates the feasibility and Reliability of RIH method put out above.

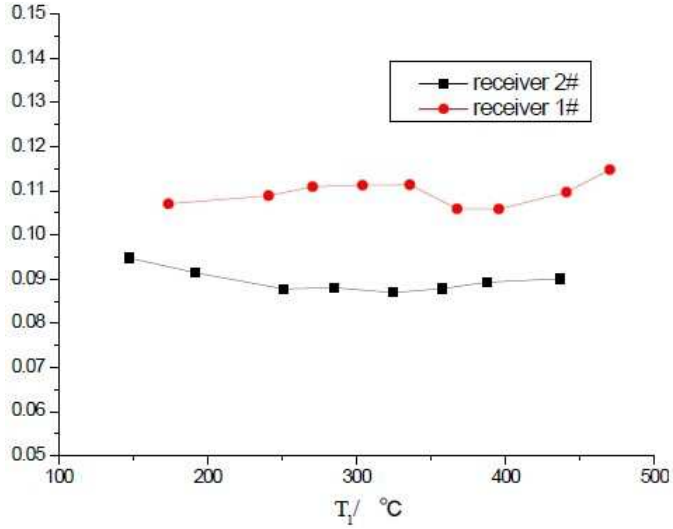


Fig. 6 Emissivity of Solar Selective Coating Change with Receiver Temperature T1

Fig. 6 shows the selective coating emissivity changes of receiver 1# and 2#. We know, from fig. 6, that coating emissivity of receiver 1# is higher than that of receiver2#, which confirms the aging of selective coating and explains the heat loss increase after a year of operation at the temperature over 350 ℃. In addition, coating emissivity reduces first and then increases generally, which are consistent with that in literature [7],[8]. But the curves' trends in fig. 6 don't meet the general law that the selective coating emissivity on outer surface of absorber increases with the increase of absorber temperature. We think it is probably the measurement error of temperature difference ΔT_{12} of receiver above glass envelop that causes a calculation deviation of selective coating emissivity. From eq. 2 we have

$$\varepsilon = q_T / \pi D_{abs} L_{abs} \sigma \left(T_1^2 + T_2^2\right)\left(T_1 + T_2\right)\left(T_1 - T_2\right)^{-1}. \quad (5)$$

In eq. 5 the item (T_1+T_2) and the item (T_{21}+T_{22}) are the sum of absolute temperatures and the sum of square of absolute temperatures respectively. However the item (T_1-T_2) is the temperature difference of absolute temperatures. So a small deviation in item (T_1-T_2) will cause a very large

fluctuation in the value of the selective coating emissivity, especially in lower value of the item (T_1-T_2). Moreover, measurement error of absorber length L and outer diameter will also have some influence on selective coating emissivity. In addition, Thermal contact resistance caused by fixation of temperature sensor on absorber and glass envelop, and fixation locations of temperature sensors on absorber will have influence to some extent. Further work will be done to perfect this experimental system and more receivers will be tested in follow-up experiment.

Uncertainty Analysis

Measurement Uncertainty is the root of sum of squares of total bias uncertainty and total precision uncertainty, while Total bias uncertainty and total precision uncertainty are computed by eq. 6 respectively [9]. Precision uncertainty of each independent variable is expressed in Standard deviation of the mean, expressed as eq. 7, while bias uncertainty of each independent variable is calculated according to the uniform distribution, expressed as eq. 8.

$$U_f = \sqrt{\sum_{i=1}^{n} (\partial f / \partial u_i)^2 \Delta u_i^2} \ . \tag{6}$$

$$u_{pre} = \sigma_x / \sqrt{n} \ . \tag{7}$$

$$u_{bias} = a / \sqrt{3} \ . \tag{8}$$

Where, U_f is the uncertainty of function f, u_{pre} is the uncertainty of random error of variable x, n is the number of measurements, σx is the standard deviation of variable x, the letter a is the systematic errors of equipments, and u_{bias} is the uncertainty of systematic errors of equipments.

For the above experiment system calculation of heat loss of the receiver is independent with temperature, shown as eq. 2. Experiment uncertainty of heat loss and temperature should been computed respectively. For electrical current transmitter the variable a is equal to 0.5% of the measuring value. For thermocouple on the absorber, glass and ambient temperature the variable a is equal to 0.0075 of the measuring value, 2.5 ℃ and 2.5 ℃.

Assuming that Measurement uncertainty of length L of the absorber is neglectable. According to eq. 6-8, the maximum measurement uncertainties of heat loss, temperature difference of absorber above glass envelop, temperature difference of absorber above ambient, and emissiveity of selective coating are shown in table 1.

TABLE 1 MAXIMUM MEASUREMENT UNCERTAINTY

Max uncertainty	Receiver 1#	Receiver 2#
$U_{\Delta T1}$[℃]	4.3	4.1
$U_{\Delta T2}$[℃]	4.3	4.1
$U_{heatloss}$[W/m]	1.9	1.4
U_ε	0.0051	0.0055

Measurement uncertainties of emissivity of selective coating at different temperature respectively are shown in fig. 7.

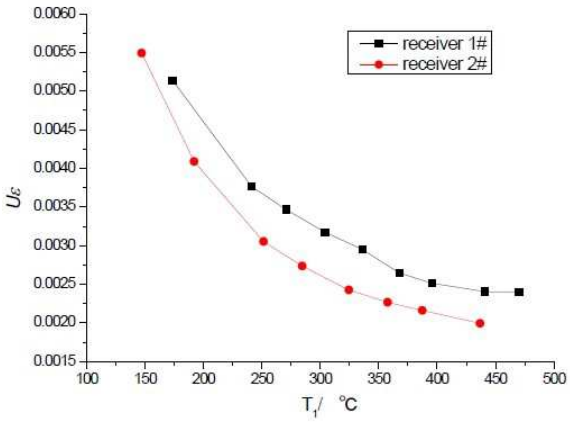


Fig. 7 Selective Coating Emissivity Changes at Different Receiver Temperature

Fig. 7 shows that measurement uncertainty of selective coating reduces with the increase of receiver temperature. Maximum measurement uncertainty of selective coating is up to 0.0055 which causes a high influence on the emissivity of selective coating and so explains why the emissivity curves in fig. 6 reduces first and then increases.

Conclusions

A novel experiment system, named RIH, has been developed to evaluate the thermal performance of parabolic trough receivers, which employs receiver impedance heating based also on the steady state equilibrium. A uniform temperature is formed along both the axial and circumferential directions on receiver surface in this way. Via the novel system RIH developed heat loss of parabolic trough receivers is measured and then the selective coating emissivity is calculated at different absorber temperature levels. Experiment results show that heat loss curves are very good and selective coating emissivity is reasonable. Uncertainty calculation shows that uncertainty of heat loss is very low while uncertainties of temperature and selective coating emissivity at low receiver temperature are very high, which causes high influence on the selective coating emissivity, especially at low receiver temperature.

Acknowledgment

The authors are grateful to acknowledge the financial support for the present work provided by the Key of HVAC, Beijing University of Civil Engineering and Architecture and the National Basic Research Program (also called 973 Program) of China with the grant number 2010CB227103.

References

[1] Y.X. Xiong, Y.T Wu, C.F Ma, et al. Numerical investigation of thermal performance of heat loss of parabolic trough receiver, Science in China Series E: Technological Sciences. 53(2010) 444-452.

[2] M. Roesle, P. Good, V. Coskun, et al. Analysis of conduction heat loss from a parabolic trough solar receiver with active vacuum by direct simulation Monte Carlo, Numerical Heat Transfer Part A-Applications. 62(2012) 432-444.

[3] M. K. Traore, Y.X. Xiong, Y.T Wu, et al. evaluation methods of thermal performance of parabolic trough receivers, Solar Energy. 5 (2009)31-34. (in Chinese)

[4] R. V. Padilla, G. Demirkaya, D. Y. Goswami, et al. Heat transfer analysis of parabolic trough solar receiver, Applied Energy. 88(2011) 5097–5110.

[5] E. Lüpfert, K. J. Riffelmann, H. Price, et al. Experimental analysis of overall thermal properties of parabolic trough receivers, Journal of Solar Energy Engineering. 130(2008) 1-5.

[6] Y.X. Xiong. Development and study of a parabolic trough collector, Beijing University of technology, Beijing., 2010. (in Chinese)

[7] F. Burkholder, C. Kutscher. Heat loss testing of Schott's 2008 PTR70 parabolic trough receiver, NREL, USA, 2009.

[8] F. Burkholder, C. Kutscher. Heat-loss testing of Solel's UVAC3 parabolic trough receiver, NREL, USA, 2008.

[9] Y. T. Fei. Error theory and data processing, sixth ed., China Machine Press, Beijing, 2010.6.

Advanced Materials Research Vol. 936 (2014) pp 2082-2086
© (2014) Trans Tech Publications, Switzerland
doi:10.4028/www.scientific.net/AMR.936.2082

Analysis of Penetration-Explosion Warhead Fragments Distribution and Damage Efficiency

ZHANG Peng-fei[1,a], ZHOU Jian-ping[2,b]

[1,2] New Star Institute of Applied Technology, Hefei, 230031, China

[a]594338413@QQ.com, [b]13956047666@139.com

Keywords: fragments; numerical simulation; LS-DYNA; damage efficiency

Abstract: By means of theoretical calculation and LS-DYNA, fragments weight distribution law, fragments velocity and fragments distribution, fragments motion law and static dispersion range are compared. The two results are basically consistent. Analysis result proves that penetration-explosion warhead can form greater bound of valid fragment cluster.

Introduction

When projectile explodes, the projectile forms plenty of with high velocity fragments which damage martial personnel and equipment and device around. Fragment kill elements demolish targets structure and weaken targets strength by means of high-velocity bump and penetration, which make targets lose partial or all functions. Natural fragments formation is divided into four steps, which connects with the axial expansion of projectile shell.

Projectile explosion is a highly nonlinear course of transient dynamics state, concerned with impact dynamics, structural dynamics, fluid dynamics and fluid-structure interaction etc. It is hard to gain complete result of damage effect by means of purely theoretical calculation. With theoretical calculation and numerical simulation, damage effect is analysed comprehensively, which provide basis for applications of penetration-explosion ammunition.

Theoretical calculation of fragments damage effects

Fragments weight distribution law

Projectile explosion produces detonation outcome which acts on projectile body. Projectile body expands fast. When warping reach certain level, projectile body first forms slight crackle at the most weak link place and enlarge step by step. Because detonation outcome continues on acting, projectile body warping increases gradually, then projectile body produces new slight crackle continuously. After slight crackle intersects each other, projectile body forms fragments. Penetration-explosion warhead produces plenty of fragments with certain weight, fragments weight is controlled by means of shell crystalloid size and thickness, fragility, tenacity as well as dynamite pack type.

（1）Natural fragments total quantity N_0

$$N_0=\frac{m_s}{k^2 t_0^{5/3} d_i^{2/3}(1+t_0/d_i)^2} \quad (1)$$

In formula, m_s shell weight, t_0 shell thickness, d_i shell inner diameter, k rest on detonator coefficient.

（2）Fragments weight distribution $N(m_f)$

$$N(m_f)=N_0\exp[-(\alpha m_f/u)^{\lambda}] \quad (2)$$

In formula, α is constant, λ is experiential constant, thin projectile body λ=1/2 ($\alpha=2$), thick projectile body λ=1/3 ($\alpha=6$).

Fragments velocity and velocity distribution

Penetration-explosion warhead damage effect closely related to the factors of fragments initial velocity, fragment weight, valid fragments quantity, shape of fragments, the dispersion angle and direction angle etc. Warhead expands and warps fast under detonation outcome acting, so fragments have very high velocity. Fragments acceleration reduces gradually as detonation outcome leaks from body crack. When the mutual balance of air resistance and detonation outcome acting on fragments, the velocity of fragments reaches biggest value, this velocity is named of original velocity. Fragments original velocity usually is up to 600~2000 m/s.

The major factors that affect fragments original velocity include detonator pack type, pack restraint and shell material. Now in the point of kinetic energy, various theoretical calculation methods of fragments original velocity have been established in the basic expression of kinetic energy. For warhead in cylindrical detonator pack, the most general formula of fragments original velocity is Gurney formula:

$$v_0=\sqrt{2E}\sqrt{\frac{\beta}{1+\beta}} \quad (3)$$

In formula, $\sqrt{2E}$ is detonator constant, each kind of detonator has certain Gurney constant, it relates to loading density and other factors. $\beta=m/M$, m is detonator weight, M is shell weight. This formula is based on assumption that fragments owned the same original velocity, without consideration of the influence of axial sparse wave in instant detonation. The formula applies to cylindrical warhead original velocity calculation, with the ratio of length to diameter $L/D>2$, the ratio of shell to detonator weight $0.2\le\beta\le0.3$ and the same body thickness. Because of the assumption of instant detonation, the formula only figures out approximation of the biggest velocity, the velocity distribution can not be calculated by virtue of the formula. The calculation result only reflects that the performance of detonator, pack type and the ratio of shell to detonator weight affect fragments original velocity, but the influence of other structural parameter is ignored outright.

About fragments velocity distribution according to detonator pack axis, Randers has studied the influence of end effect on original velocity distribution, and put forward the correction Gurney formula.

$$v_x=\sqrt{2E}\sqrt{\frac{F(x)\beta}{1+0.5F(x)\beta}} \quad (4)$$

Here, $F(x)$ is correction coefficient on end flight and dispersion of Gurney relation, its expression

$$F(x)=1-[1-\min(\frac{x}{2r},1.0,\frac{l-x}{r})]^2 \quad (5)$$

In formula, x is the distance of fragments to benchmark end, priming end is benchmark end (m), r is detonator pack radius (m), l is detonator pack length (m), v_x is fragments original velocity of x position (m/s).

Static flight dispersion range of fragments

The dispersion angle and direction angle are the two most important factors to destroy target among fragments dispersion parameter. Warhead fragments dispersion angle is shown as Fig.1. Compared with fragments fight range, the length and diameter of warhead are very little, which can be neglected. In practice, warhead fragments dispersion angle is defined, shown as Fig.2. Because of the influence of end effect, fragments density of dispersion angle edge is lower. The dispersion angle, used for damage efficiency calculation, is equal to the angle that the effective occupancy space where fragments distribution density accords with requirements. The dispersion angle is accustomed to the angle of space taken by effective 90% fragments.

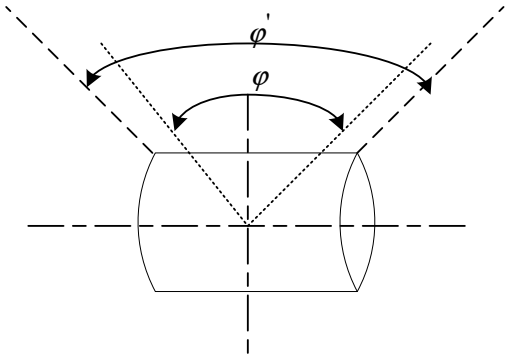


Fig.1 Fragments Dispersion angle

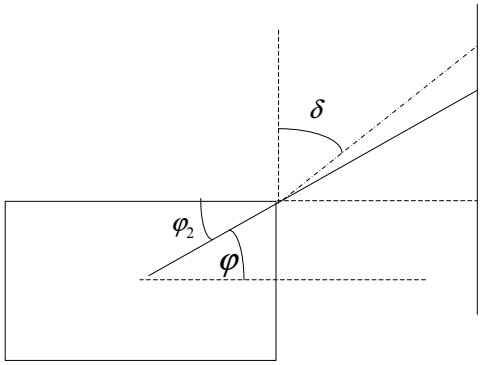


Fig.2 Relation of Angles

The number of penetration-explosion warhead explosion initiation position is limited, fragments will deviate normal direction when thrown out. Taylor formula is a classical formula used for calculation dispersion direction. In 1941 G. E. Taylor put forward experience formula, when Taylor was researching on that metal medium (plain plate or round pipe) is driven by detonator. The Taylor formula extensively applied in project field, its specific form is $\delta=\arcsin\left(\frac{v_0}{2D}\cos\phi_2\right)$.

In formula, δ is the angle between dispersion direction and shell normal, v_0 is fragments original velocity (m/s), D is velocity after detonator explosion (m/s), ϕ_2 is the angle between explosion initiation position to some shell dot shell, the angle between x-axis and the normal of this point on the detonation wave surface. The relation between angles is shown as Fig.2.

δ is converted into the angle between dispersion direction and warhead axis, $\varphi_0=\frac{\pi}{2}-\delta-\gamma$.

In formula, γ is the angle between projectile axis and shell bus, when shell is cylindrical, $\gamma=0$.

Numerical simulation of fragments damage effects based on LS-DYNA

The basic thought of finite element analysis is that the more simple problem replaces complex problem, then solve the more simple problem. Since most actual problems are hard to get accurate solution, nevertheless finite element analysis not only calculate precisely but also apply to complex shapes, so FEA has become an effective project analysis mean. Now, large scale commercial FEA software includes ANSYS, ADINA, DYNA-3D, AUTODYN and CTH etc. LS-DYNA is chosen as research means for numerical simulation of penetration-explosion warhead fragments damage.

Penetration-explosion warhead holds plane symmetrical character, which could be simplified into 1/4 model for calculation. Model is divided with entity unit, symmetrical restraint condition is exerted at symmetrical boundary. The method of fluid-structure interaction is chosen to accurately describe detonation course and the interaction of shell and detonation wave. In model air medium and detonator pack are partitioned into Euler unit, shell and end cover are partitioned into Lagrange unit. In this model, air and detonator grid are partitioned into 987,684 units. After shell breakage, erosion contact algorithm is adopted to control mutual collision between fragments. In the calculation course, numerical model is simplified and installed as follows, gravity role and air stickiness are neglected, initialization of air grid boundary is 1 atm to prevent air weight escape, seepage control is carry out for fluid-structure interaction to maintain conservation of energy.

In calculation model, the major packs dynamite is B dynamite, density is 1.7 g/cm3, explosion velocity is 7900 m/s, CJ pressure is 29 GPa. Shell and end cover material density are 7.8 g/cm3, elastic modulus is 210 Ga, Poisson's ratio is 0.3, yield strength is 245 MPa, all parameters are described by MAT_PLASTIC_KENEMATIC model. As far as the development performance of material change under explosion load, this model has considered the influence of strain rate effect.

Comparison and analysis of the result based on calculation and simulation

Penetration-explosion warhead fragments damage effect is analysed with theoretical calculation and numerical simulation, the result of theoretical calculation and numerical simulation is consistent on the whole. The dispersion angle of fragments is shown as Fig.3. The original velocity distribution of fragments is shown as Fig.4. The quantity dispersion of fragments is shown as Fig.5 according to weight.

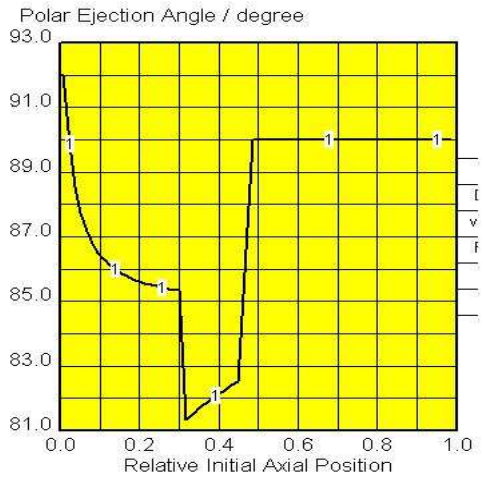


Fig.3 Dispersion angle of fragments

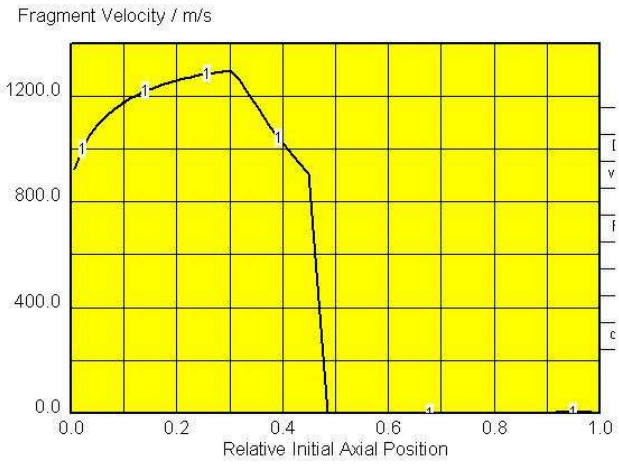
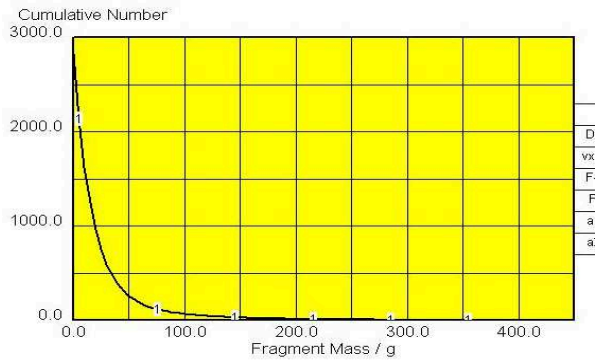


Fig.4 Original velocity distribution of fragments



The summary can be found out from result of calculation and simulation. The dispersion angle of fragments is between 81°and 92°, The original velocity distribution of fragments is from 900m/s to 1300m/s, the velocity at warhead bottom is higher than other part. At warhead peak, Fragments don't exist because of scarcity of detonator. From fragments quantity and weight distribution, the total quantity of fragments is up to 2910 pieces, fragments average weight is about 22g.

Conclusion

The quantity, weight and velocity distribution, dispersion direction and kinetic energy of penetration-explosion warhead fragments are researched based on theoretical calculation and numerical simulation, the analysis result proves that the weight and velocity distribution, dispersion direction of penetration-explosion warhead fragments are efficient to damage targets, which can form larger area of effective fragments.

References

[1] HONG Jian-hua, TAO Jiang-yuan. Study of fragment penetrating and detonate target missile [J]. Journal of Ballistics, 2002, 14(4):60- 65.

[2] ZHANG Hui, QIAN Jian-ping, etc. Simulation and Damage Analysis about Performed Fragments of Axial Forward Projection Fragment Warhead [J]. Computer Simulation, 2011(10)13-17.

[3] SONG Wen-yuan. Modeling analysis of nature fragments of pill warhead [J].Journal of Projectiles, Rockets, Missiles and Guidance, 2008(6)121-122, 130.

[4] YAO Jian-hong, WANG Yong-qing, etc. Calculation of damage effects of natural fragments on armored targets [J]. ACTA ARMAMENTARII, 2009(12): 159-162.

Advanced Materials Research Vol. 936 (2014) pp 2087-2093
© (2014) Trans Tech Publications, Switzerland
doi:10.4028/www.scientific.net/AMR.936.2087

MR Based Brake-by-wire System with Self-energizing Capability

Xuhui Liu[1, a], Liangyao Yu[1, b*] and Liangxu Ma[1, c]

[1] State Key Laboratory of Automotive Safety and Energy, Tsinghua University, Beijing 100084 China

[a]liuxh.allen@googlemail.com, [b]yly@tsinghua.edu.cn, [c]mlx07@mails.tsinghua.edu.cn

Keywords: Brake-by-wire, MR Brakes, Self-energizing, Wedge Mechanism, Torque Analysis

Abstract. Brake-by-wire system is a new concept of brake system using electromechanical actuators instead of conventional hydraulic actuators. It is more compact, more efficient and responses faster than traditional brake systems. Magneto-rheological (MR) fluid is widely used due to its outstanding properties. In this paper, an MR based Brake-by-wire system with self-energizing capability were proposed and designed. It combined a typical single-disk-type MR brake with a wedge mechanism for self-energizing purpose. According to the torque analysis of the proposed MR brakes, the brake torque was significantly amplified. This research work presented a promising brake actuator, which allows MR fluids to be applied in automotive Brake-by-wire systems.

Introduction

MR fluids are suspension of micron sized magnetic particles dispersed in non-magnetic liquids. They behave as Newtonian Fluids in the absence of an external magnetic field. However, when a magnetic field is exerted to the MR fluids, they will turn into Bingham Fluid in milliseconds. This process is reversible, continuous and repeatable. Moreover, the yield shear stress of the MR fluids can be precisely controlled by adjusting the intensity of the magnetic field. Due to these favorable properties, MR fluids are widely used in areas such as dampers, clutches, valves, brakes, biological assistant devices, building constructions etc.

MR brakes are an important branch among these applications. Since they can be precisely controlled by electric signals, they are promising to be adopted as Brake-by-wire system. However, the brake torque generated by MR brakes is normally too small to be applied in vehicles. Recently there are mainly three categories of measures to increase the brake torque. The first category is to change the structure of the rotor. For example, multiple-disk-type MR brakes were widely tested and could generate much larger brake torque than single-disk-type MR brakes [1,2]. Other researchers verified the form of the rotor from disk-type into drum-type, including the so-called T-shape drum-type brake [3,4]. It has also been proved that changing the formation at the end of a brake disk can also increase the brake torque, such as using a wave form disk [5] or a disk with circular cuts at the end [6]. The second category can be summarized as changing the layout or size of the coils [7,8,9]. The last category utilized the property of the MR fluids that its shear yield stress will be significantly enlarged under compression [10]. Therefore, the brake torque can be improved either by the compression from the radial direction or axial direction [11]. For this purpose, extra components which provide the compression force need to be added to the brake device.

The common drawbacks of the first two categories of measures are the complexity of the structure, resulting in the difficulties during manufacturing, assembly and more heat will be generated during braking, which is unfavorable for the working efficiency of MR fluids. In terms of the third category, how to precisely control the desired brake torque coordinated with the

compression force is tough to handle. This paper presented an automotive MR based Brake-by-wire system with a simple structure and easy to be controlled. It combines a single-disk-type MR brake with a self-energizing wedge mechanism, which helps significantly increase the brake torque. Moreover, it can cooperate with regenerative braking, thus to save certain amount of energy.

Operational principle of typical single-disk-type MR brakes

A disk-type or drum-type rotor is common used in MR brakes. In this paper, a single-disk-type MR brake is chosen since it is more compact and thus easier to be combined with the wedge mechanism. As shown in Figure 1, it mainly consists of housing, coil, rotor plate, bearing, shaft and seal rings. The MR fluids fill in the sealed working gap between the housing and the rotor plate.

Under normal driving conditions, when no braking demand is raised, no current will be applied to the coil. The rotor plate as well as the shaft rotates almost freely in the MR fluids, only with a small resistance torque caused by the Newtonian viscosity of the MR fluids. When a braking action is demanded, certain amount of current corresponds to the desired brake torque will be applied to the coil. Then the MR fluids transform promptly into solid-like form thus providing the desired brake torque to the rotor plate. Fig. 2 shows the microstructure of the MR fluids with or without the effect of an external magnetic field. Under the external magnetic field, the MR particles will form promptly chains between the stator and rotor. The resistance torque will mainly caused by the deformation or destruction of these chains due to their relative motions. Since the change of yield shear stress of the MR fluids is corresponding to the intensity of the magnetic field, the generated brake torque can be precisely controlled by adjusting the magnitude of the applied current.

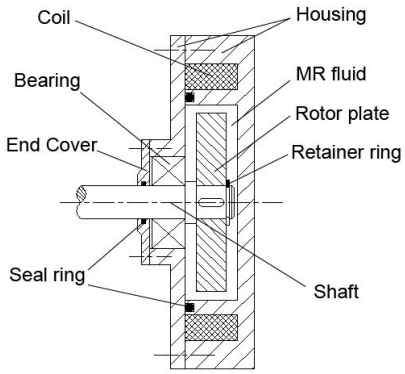


Fig. 1 Structure of single-disk-type MR brakes.

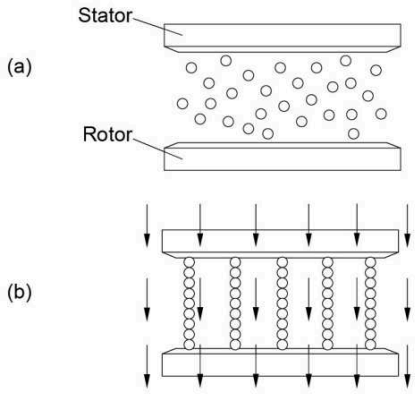


Fig. 2 Microstructure of MR fluids (a) without or (b) with external magnetic field.

Operational Principle of a wedge mechanism with self-energizing capability

Electric Wedge Brakes with self-energizing capability were firstly proposed and several generations of prototypes have been developed by Siemens VDO [12]. The self-energizing is realized by a wedge mechanism. As shown in Fig. 3, operational principles of a conventional brake and a wedge brake are presented on the left and right side, respectively. It is obvious that the normal force to the brake lining of the conventional one is equal to the input force, while in the wedge brake, the normal force will be largely increased due to the wedge mechanism, as expressed by Eq. 1 and Eq.2, respectively.

$$F_b = \mu \cdot F_I \tag{1}$$

$$F_b = F_I \cdot \frac{\mu}{\tan\alpha - \mu} \tag{2}$$

where F_b and F_I are the brake force and input force, respectively, μ is the friction coefficient and α is the angle of wedge.

As can be figured out from Eq. 1 and Eq. 2, no input force will be needed under the optimal condition when $\tan\alpha$ is equal to μ. Nevertheless, since the friction coefficient μ will change during the braking process, the wedge mechanism is not really able to work under an optimal condition. Moreover, an input force from an opposite direction will be required to pull out the moving wedge if the friction coefficient μ changes to a value which is larger than $\tan\alpha$. In principle, a certain amplification factor can be obtained by coordinating the displacement of the wedge and the input force according to the change of friction coefficient. In this way, an amplified brake torque can be achieved as long as a certain input force is exerted to the moving wedge.

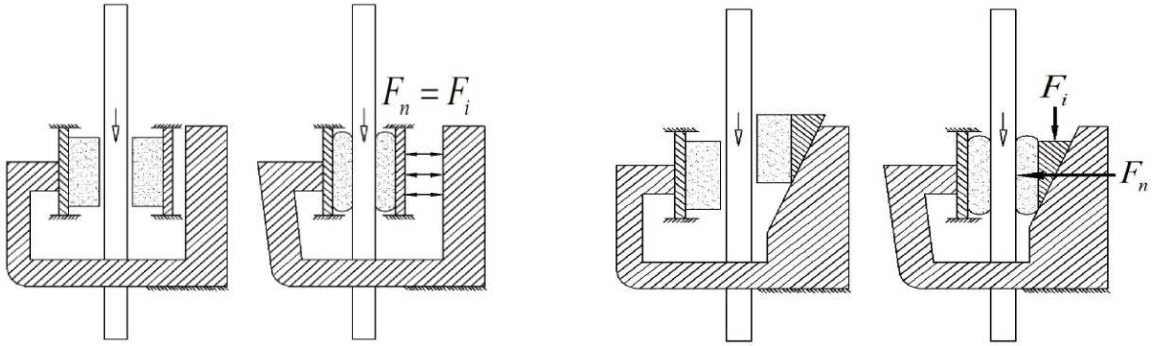


Fig. 3 Schematic of conventional brakes (left) and wedge brakes (right).

Design of MR brakes with self-energizing capability

The configuration of the proposed MR brakes is shown in Fig. 4. In general it combines an MR brake part with a wedge mechanism together. The inner structure of the MR brake part was already presented in the second section of this paper. Unlike typical MR brakes, the rotating shaft of the MR brake part here is not the driving shaft, instead it is parallel to it by applying a gear pair. The rotor plate inside the housing rotates synchronously with the driven gear. The housing of the MR brake part is not fixed and will rotate together with the inner rotor plate when current is applied to the coil and the MR fluids turn into solid-like state. As shown in Fig. 5, the torque of rotation of the housing will be transformed onto the moving wedge via a connecting rod, which connects the housing and the moving wedge on both ends respectively using ball joints. A return spring fixed on the car body is used to provide a counter force to the wedge mechanism. Particularly there are rollers amounted between the moving wedge and the stationary wedge so as to reduce the frictional resistance between them. The brake lining is fixed on the moving wedge and can move together with it towards the brake disk to perform a brake action. Moreover, a flat generator is connected to the driven axle for regenerative braking purpose, which enables regenerative energy recovery, thus electric energy can be saved.

The operational principle is easy to be understood. Under normal driving conditions, no current is applied to the coil and thus there is no displacement of the wedge mechanism. The driving shaft as well as the rotor plate inside the MR brake part rotates almost freely. When a brake action is

demanded, certain amount of current is conducted through the coil according to the brake signal, resulting in the rheological effect of the MR fluids. The housing will then rotate together with the inner rotor plate, pushing the moving wedge via the connecting rod against the stationary wedge, thus exerting the desired brake force onto the brake disk. During this brake process, regenerative braking is involved with the help of the generator, thus certain amount of energy can be saved.

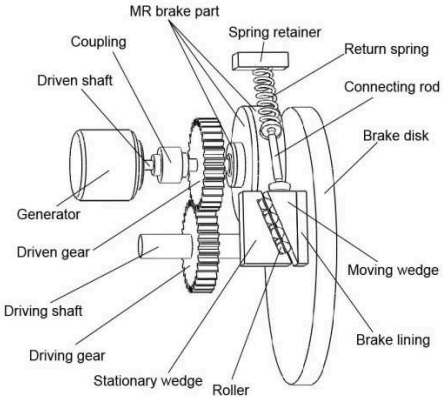


Fig.4 Structure of the proposed MR brakes

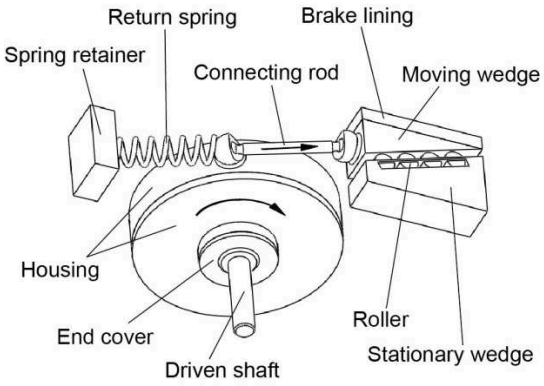


Fig. 5 Structure of the force transform mechanism

Torque analysis of MR brakes with self-energizing capability

Torque analysis of the proposed MR brakes can be separated into the following two parts: (1) relationship between rotating torque of the housing and the input control current, (2) relationship between the rotating torque of the housing and the input force of the wedge mechanism. Moreover, with the Eq.2 above we can easily obtain the amplification of the torque and the relationship of the desired brake torque and input control current.

The brake torque model of a typical single-disk-type MR brake was already established by many researchers [11,13]. Fig. 6 shows the design parameters of such an MR brake. By applying the Bingham Model, the relationship between the brake torque and the yield shear stress of MR fluid can be expressed in Eq. 3:

$$T = \frac{4}{3}\pi\tau_{yd}\left(r_o^{\,3} - r_i^{\,3}\right) + \frac{\pi\eta\omega}{h}\left(r_o^{\,4} - r_i^{\,4}\right) \tag{3}$$

where r_i and r_o are inner and outer radii respectively, τ_{yd} is the yield shear stress, η is the off-state viscosity of MR fluid, ω is the rotational speed of the rotor plate, and h is the gap thickness.

In addition, the relationship between the yield shear stress of MR fluid and the input control current can be derived from Eq. 4 and Eq. 5 as follows[13]:

$$\tau_{yd} = \alpha_1 \cdot H^{\beta} \tag{4}$$

$$H = \frac{NI}{2h} \tag{5}$$

where the proportional coefficient α_1 and the exponent β are intrinsic values of the MR fluid, N is the number of turns of the coil, and I is the input control current.

Therefore, the relationship between the brake torque and input current can be achieved by substituting Eq. 4 and Eq. 5 into Eq. 3, yielding

$$T = \frac{4}{3}\pi\alpha_1\left(r_o^{\ 3} - r_i^{\ 3}\right)\left(\frac{NI}{2h}\right)^{\beta} + \frac{\pi\eta\omega}{h}\left(r_o^{\ 4} - r_i^{\ 4}\right). \tag{6}$$

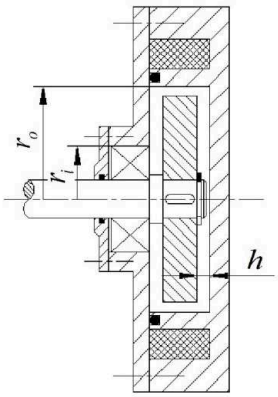


Fig. 6 Schematic of MR brake part

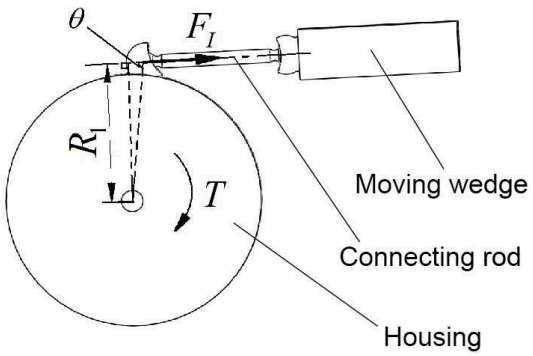


Fig. 7 Schematic of the transform mechanism

Since the amplified component of the input force of wedge mechanism is parallel to the rotating plane of the housing of MR brake part, the calculation of the input force can be simplified with the help of Fig. 7 and it can be expressed in Eq. 7:

$$F_I = \frac{T}{R_1 \sin\theta} \tag{7}$$

where R_1 is the distance between the rotate centers of the MR brake part and the ball joint of the connecting rod, and θ is the angle between the rod and the connecting line of the two above mentioned centers. Here, the tension force of the spring can be neglected during braking since it is quite small compared with the force transformed by the housing.

Combined Eq. 7 with Eq. 2, the brake torque of the proposed MR brake can be expressed as Eq. 8:

$$T_b = \frac{T}{R_1 \sin\theta} \cdot \frac{\mu}{\tan\alpha - \mu} \cdot R_2 \tag{8}$$

where R_2 is the effective radius of the brake disk. In this way, the amplification factor of the brake torque compared with typical single-disk-type MR brakes can be yielded as follows:

$$\gamma = \frac{T_b}{T} = \frac{R_2}{R_1 \sin\theta} \cdot \frac{\mu}{\tan\alpha - \mu} \tag{9}$$

where γ is the amplification factor. Since R_2 is larger than R_1, the self-energizing capability of the proposed MR brakes is higher than that of wedge brakes. Furthermore, different amplification factors γ can be achieved by verifying design parameters such as R_1, R_2, the wedge angle α etc.

Finally, the relationship between the brake torque and the input control current can be obtained by integrating Eq. 6 into Eq. 8, thus yielding

$$T_b = \left\{ \frac{4}{3}\pi\alpha_1 \left(r_o^{\,3} - r_i^{\,3} \right) \left(\frac{NI}{2h} \right)^{\beta} + \frac{\pi\eta\omega}{h} \left(r_o^{\,4} - r_i^{\,4} \right) \right\} \cdot \gamma . \tag{10}$$

To validate results of the above torque analysis in a visible way, numerical calculation should be carried out. Assumption of the parameters is made as follows: $R_2 = 150\,mm$, $R_1 = 60mm$, $\theta = 90°$, $\omega = 100rad/s$. Parameters of the wedge mechanism [14]: $\alpha = 24.2°$, $\mu = 0.35$. Parameters of the MR brake part: $r_o = 40mm$, $r_i = 10mm$, $h = 1mm$, $N = 1200$. Parameters of typical MR fluids [11]: $\alpha_1 = 7.714 \times 10^{-4}\, Pa(m/A)^{1.5}$, $\beta = 1.5$, $\eta = 0.0925\, Pa \cdot s$. The generated brake torque of the proposed MR brakes compared with typical single-disk-type MR brakes, corresponding to different input currents are shown in Fig. 8. The brake torque is significantly amplified, for example, from $2036Nm$ at $I = 2A$ to $17923Nm$ with an amplifying factor $\gamma = 8.8$. Thus its brake torque is large enough for the application as automotive brakes. It is also shown that the brake torque increases with the increasing input currents.

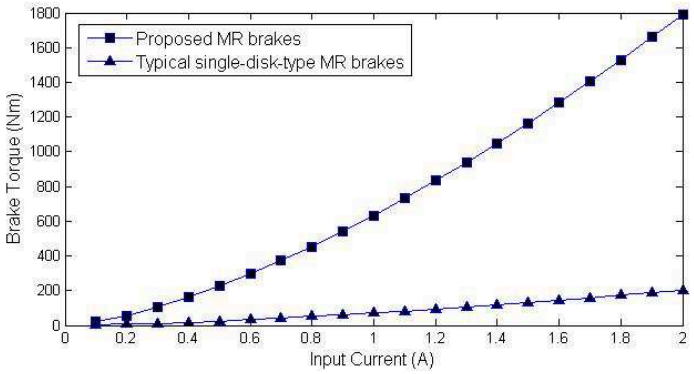


Fig. 8 Comparison of the brake torque under different input currents.

Conclusion

In this paper, an MR based Brake-by-wire system with self-energizing capability was proposed in order to enlarge the brake torque so that it can be adopted as automotive brake system. It combined a typical single-disk-type MR brake with a wedge mechanism. The configuration and operational principle were presented in details. Finally, according to the torque analysis, it was shown that the proposed MR brakes could generate much larger brake torque than conventional MR brakes, thus they can be adopted as automotive Brake-by-wire system.

Acknowledgement

This work was supported by the National Basic Research Program of China (Grant No. 2011CB711205), and the National High Technology Research and Development Program of China (Grant No. 2012AA111204 & No. 2012AA110903).

References

[1] D.M. Wang, Y.F. Hou and Z. Z. Tian, A novel high-torque magnetorheological brake with a water cooling method for heat dissipation, Smart Mater. Struct., 22 (2013) 025019.

[2] R Russo and M Terzo, Design of an adaptive control for a magnetorheological fluid brake with model parameters depending on temperature and speed, Smart Mater. Struct., 20 (2011) 115003.

[3] A. Farjourd, N. Vahdati and Y. F. Fah, Mathematical model of drum-type MR brakes using Herschel-Bulkley shear model, J. Intell. Mater. Syst. Struct., 19 (2008) 565-572.

[4] N. Q. Hung and S. C. Bok, Optimal design of a t-shaped drum-type brake for motorcycle utilizing magnetorheological fluid, Mech. Based Des. Struct. Mech., 40 (2012) 153-162.

[5] T. H. Nam and K. K. Ahn, A new structure of a magnetorheological brake with the waveform boundary of a rotary disk, Smart Mater. Struct., 18 (2009) 115029.

[6] B. Assadsangabi, F. Daneshmand, N. Vahdati, M. Eghtesad and Y. Bazargan-Lari, Optimization and design of disk-type MR brakes, Int. J. Automot. Technol., 12 (2011)921-932.

[7] Q.H. Nguyen and S.B. Choi, Selection of magnetorheological brake types via optimal design considering maximum torque and constrained volume, Smart Mater. Struct., 21 (2012) 015012 .

[8] V. K. Sukhwani and H Hirani, Design, development, and performance evaluation of high-speed magnetorheological brakes, Proc. Inst. Mech. Eng. Pt. L-J. Mater.-Design Appl. 222 (2008) 73-82.

[9] L. X. Ma, L. Y. Yu, Z. Z. Wang and J. Song, Design and Development of an Automotive Magneto-Rheological Brake System, SAE Paper, 2013-01-2061.

[10] H. Y. Wang and H. Q. Zheng, Shear and squeeze rheometry of magnetorheological fluids, Advanced Materials Research, 305 (2011) 344-347.

[11] C Sarkar and H Hirani, Design of a squeeze film magnetorheological brake considering compression enhanced shear yield stress of magnetorheological fluid, Journal of Physics: Conference Series, 412 (2013) 012045.

[12] J Fox, R. Roberts, C. Baier-Welt, L.M. Ho, L.Lacraru and B. Gombert, Modeling and control of a single motor Electronic Wedge Brake, SAE Paper, 2007-01-0866.

[13] W. H. Li and H Du, Design and experimental evaluation of a magnetorheological brake, Int. J. Adv. Manuf. Technol., 21 (2003) 508-515.

[14] H Hartmann, M Schautt, A Pascucci and B. Gombert, eBrake® - The Mechatronic Wedge Brake, SAR Paper, 2002-01-2582.

Advanced Materials Research Vol. 936 (2014) pp 2094-2097
© (2014) Trans Tech Publications, Switzerland
doi:10.4028/www.scientific.net/AMR.936.2094

Design and Optimization of the Bridge Expansion Joints Cleaning Machine

Jiang Jianping[1,a], Zhang Baoxiang[1,b] ,Wang Jibao[1,c],

Zhang Dongyan[1,d],Wang Lei[1,e],Cheng Xiaofeng[1,f] Wu Chengge[2,g]

[1]Ji'nan Highway Administration Bureau, Jinan 250108, China

[2]Shandong Jiaotong University,Jinan 250023,China

[a]jiang1_ping@163.com,[b]zhbx214@sina.com,[c]wangjibao2836@163.com,

[d]86556001@163.com, [e]jinanyanghu@sina.com, [f]jnyhzh@163.com,[g]chgwu2002@163.com

Keywords: Bridges, Expansion joints, Cleaning machine, Optimization, Cyclone dust removal

Abstract. Bridges are hinges of city road and railway, which play an important function in national economy. The changes of temperature affect the length of the highway bridge beams, so the bridge should be equipped with the expansion joint device. When vehicles pass the bridge, dust flies up and clogs the gap of the bridges. The bridge expansion joints should be cleaned in time. The main task of this project is to study a kind of device used to clean the bridge expansion joints, which including two parts: the cleaning system and vacuum dust removal system. First, we use the sweeping wheels to loose dust, then the air-blower to blow away the dust. The optimization of vacuum dust removal system was discussed in this paper. Especially, the Cyclone dust removal device works well. The machine is of higher productivity, wide application, low energy consumption, simple structure compared with similar equipments.

Introduction

With rapid development of the national economy, the highway is becoming longer, but there exist many questions such as complex terrain , complex structures, and the proportion of bridges is incresing. Bridge plays a significant role in the national infrastructural construction, the maintenance of expansion joints become an urgent problem to be solved for Highway Management.

Bridge Expansion Joints and the Maintenance Methods

Temperature changes will affect the length of the highway bridge beam which can cause some tiny displacements at the end of the bridge beam . Therefore, the bridge expansion joint device must be installed to adapt to this displacement of the beam in road and bridge construction to ensure road safety, as shown in Figure.1. Expansion joint inspection and maintenance is an important part of the bridge safety inspection, it must be inspected timely and conveniently. Because of the accumulation of sand and other debris, as shown in Figure.2, resulting in function loss of expansion joints which will cause the damage of bridge when the temperature rises. According to the above statement, it is very important to clean up the expansion joint[1-2]. But the current bridge expansion joints conservation technology is still relatively inferior, mostly restricted to disassemble or manual cleaning, the cleaning efficiency is low and the operating environment is harsh, there are some security risks. Some researchers invented the device to improve conservation efficiency, these studies exists different advantages and disadvantages [3-5].



Fig. 1 Expansion Joints on the Bridge



Fig. 2 The Gravel Accumulation of the Expansion Joints

The Overall Design of the Cleaning Machine

Based on the Science and Technology Innovation Project of Transportation Department of Shandong, we designed structure of the bridge expansion joints cleaning machine and made the optimization of the main vacuum dust removal system.

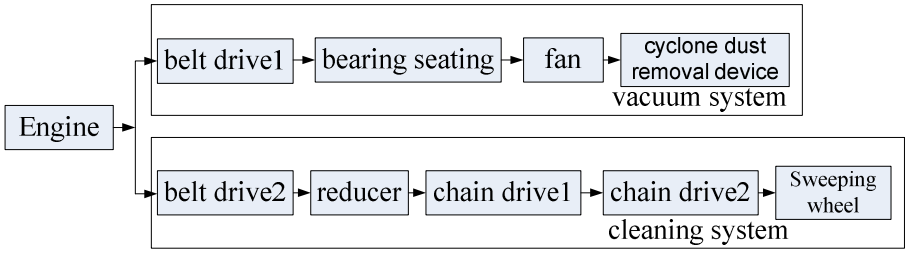


Fig. 3 The Overall Design of the Cleaning Machine

The overall design of the cleaning machine is divided into two systems, as seen in figure.3, cleaning system used to drive the cleaning wheel and the vacuum system to clean up the debris. The debris will become loose when the sweeping wheel rotates and the cyclone dust removal device will remove them in the end.

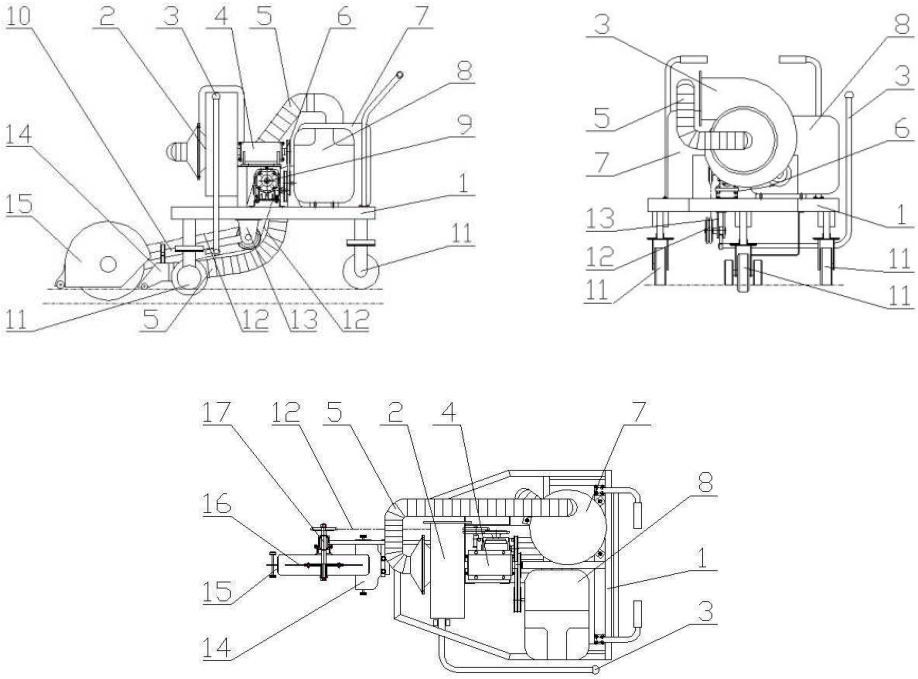
The power of these two systems was transferred by belt drive assembled from engine. The speed of the sweeping wheel can not be too high, so we chose the worm gear reducer to reduce the speed. We chose the belt of SPZ to make the machine more compact, and the worm gear reducer can provide small volume and big speed reduce range. Two chain drives were used to connect the sweeping wheel. The system was optimized to design the adjust seat to adapt complex working environment. Whole structure of the cleaning machine is shown in figure.4.

The Design and Optimization of Vacuum Cleaning Device

The vacuum attraction system was applied to the cleaning machine to clean up the gravel and debris in the joints, so there is a dust collection box in the front of the blower .The volume of traditional dust collection box is very large and it makes use of area change to generate sudden

pressure changes, so the dust was removed by this theory. But this traditional method is less efficient, then the dust removal device has been optimized in this study.

As shown in Figure.5, the dust box entrance was connected to the cleaning device and the air with gravel and debris is pulled into the box, the air flows along screw path under the function of spiral blade and intermediate cylinder which plays a part of cyclone separator, then the air flows into intermediate cylinder, upper strainers can cleaned the air further. The air without dust runs into the blower through the export.



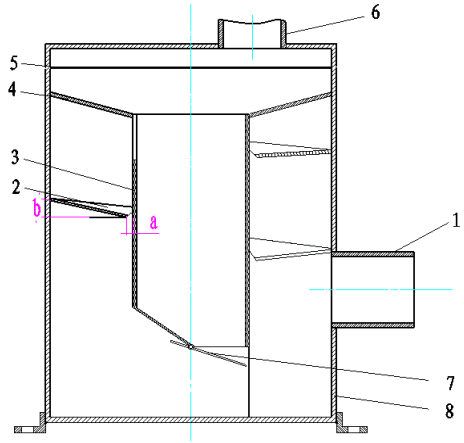
1. mainframe 2.blower 3.lift handle of sweeping wheel 4. bear seat of blower 5. channel 6.belt drives7. dust bin 8.engine 9.reducer 10.oscillating bar 11. guide wheel 12. chain drives 13.fix seat14. Vacuum head 15.cover 16.sweeping wheel 17. transmission shaft

Fig.4 The Structure of the Cleaning Machine

The blade has an inclination angle (we call it “b”) and there is a gap between the cylinder and the blade (we call it “a”) ,the filtered dust drop into the bottom of the box through the gap. Besides, there was a rotary switch under the cylinder, it closed because of the pressure of the wind flow to prevent the un-filtered dust into the box. But it will open freely to assure the dust drop into the bottom of the box. After optimization, the cleaning machine will be more efficient in similar device and it’s structure is more compact.

Summary

In this project we focus on the study of the general structure of cleaning machine used to clean the expansion joint and emphasized on the design and optimization of vacuum cleaning device with cyclone dust removal system which improved the efficiency of the whole device. The machine has characteristics of high productivity, low energy consumption, simple structure compared with similar domestic equipments.



1.entrance 2. spiral blade 3.intermediate cylinder 4.Bulkhead 5. Filter 6.Export 7.Rotary switch 8.Box

Fig.5The Principle of the Structure of the Dust Removal Device

Acknowledgments

The authors greatly appreciate the plan for Science and Technology Innovation Project of Transportation Department of Shandong (Grant No.2013B02) and the financial support(Z201220) from Shandong Jiaotong University.

References

[1] X.W.Jiang: science. Technol. Inf. No.27(2012),p.39

[2] D.K Guo: HLJ. JiaoTong. KeJi No.3(2012),p.108

[3] Y.P.Wang: HLJ. JiaoTong. KeJi No.8(2012),p.89

[4] Y. Cheng, X. Ling, Z.Z. He, Q .Z. Qi, B.T Li and J.R.Xie: patent, 201110154763

[5] D.Y. Wu: patent, CN98245465.1

Advanced Materials Research Vol. 936 (2014) pp 2098-2102
© (2014) Trans Tech Publications, Switzerland
doi:10.4028/www.scientific.net/AMR.936.2098

Research on Tracked Vehicle Suspension Parameter Optimization Based on Surrogate Model Method

Wang Hongyan[1, a], Wang Qinlong[1, b], Rui Qiang[1, c], Ma Weibiao[1, d]

[1]Department of Mechanical Engineering, the Academy of Armored Forces Engineering, Dujiakan 21, Fengtai District of Beijing, 100072, China

[a]why_cvt@263.net, [b]wang_qinlong@126.com, [c]ruiqiang2006@163.com, [d]wy_horse@163.com

Key words: suspension system parameters optimization; ride comfort; surrogate model method; radial basis function method.

Abstract. In this article a surrogate model between suspension system parameters of tracked vehicle and comfort evaluation indices has been built up by using radial basis function method and the dynamic simulation of tracked vehicle. Then the optimization of suspension system parameters has been carried out by using surrogate model and adaptive simulated annealing optimization arithmetic. The results show that the research method is feasible.

Introduction

A lot of efforts have been done to improve the ride comfort of wheeled vehicle [1,2]. However, parameter optimization about the ride comfort is so infrequent in the field of tracked vehicle. In this paper an effective parameter optimization design method is discussed which research object is a certain type of light-duty high-speed tracked vehicle. The multibody dynamic model of the tracked vehicle has been founded and the experimental verification has been carried out. Then the surrogate model between suspension system parameters and comfort evaluation indices has been built up by using radial basis function method and dynamic simulation of tracked vehicle. At last, the suspension system parameters have been optimized using the optimization algorithm about adaptive simulated annealing (ASA).

Dynamic Model of Tracked Vehicle and Experimental Verification

The dynamic model of tracked vehicle which has been founded in the environment of Recurdyn software is shown in Fig. 1.

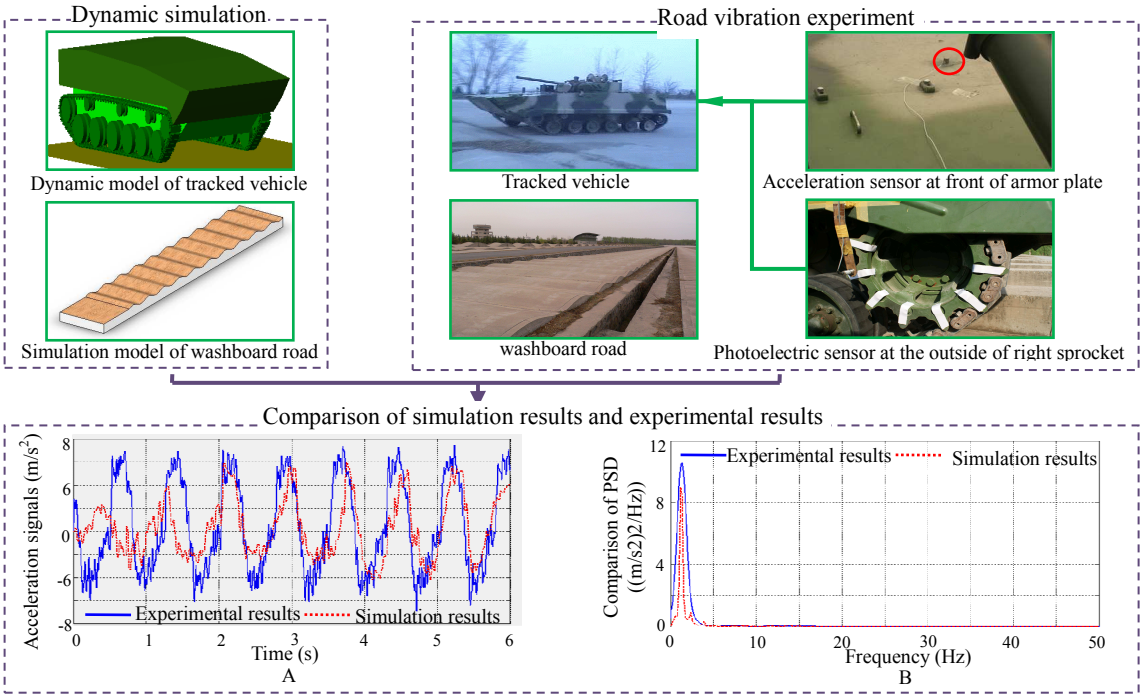


Fig.1 Dynamic Simulation, Road Vibration Experiment and Comparison of Results

A road vibration experiment has been carried out to verify the credibility of the vehicle dynamic simulation model. An acceleration sensor has been installed at front of armor plate in the vehicle to collect the acceleration signals in virtual direction; A photoelectric sensor has been installed at the outside of right sprocket to collect the rotation speed signals, which are shown in Fig. 1. A washboard road which amplitude is 15cm is selected as the experimental road. Comparisons as shown as in Fig. 1 have been made between simulation acceleration signals and actual experimental acceleration signals which are collected and processed from sensor at front of armor plate. It indicates that there is a good consistence between these signals both in time domain (shown in Fig. A) and in frequency domain (shown in Fig. B), that is to say, the dynamic simulation model can meet the need of evaluation of ride comfort.

Basic Theory of Radial Basis Function Surrogate Model Method

Radial basis function (RBF) which is one kind method of Surrogate model Methodology (RMM)[3] has advantages of time saving, simplicity by using least square method to parameter estimation[4]. The basic idea of RBF is the weighted interpolation to primary function of euclidean distance. For N data points where $x_1,\ldots,x_N \in \Omega \subset R^N$, the primary function can be defined as

$$g_j \equiv g(\|x-x_j\|) \in R, \quad j=1,\ldots,N, \tag{1}$$

where $\|x-x_j\|$ is the Euclidean distance space, $g(\|x-x_j\|)$ can be any forms of low-order polynomial. $\|x-x_j\|c$ is selected as RBF where $0.2<c<3$. Consequently, c can be ensured the obtainment of the optimal approximation function results.

Assume that the function values of N data points are $y_1,\ldots,y_N \in R$, then the interpolation function can be determined by RBF as

$$F(x)=\sum_{j=1}^{N}\alpha_j g_j(x)+\alpha_{N+1}, \tag{2}$$

Bringing x_i and y_i which has a number of N groups into Eq. 2, let $\sum_{j=1}^{N}\alpha_j=0$, so N groups of linear equations can be determined as

$$\sum_{j=1}^{N} \alpha_j g_j(x_i) + \alpha_{N+1} = y_i \quad i = 1, \ldots, N, \tag{3}$$

let $p = \begin{bmatrix} 1 \\ \vdots \\ 1 \end{bmatrix} \in R^N$, $G = \begin{bmatrix} g_1(x_1) & \cdots & g_N(x_1) \\ \vdots & \ddots & \vdots \\ g_1(x_N) & \cdots & g_N(x_N) \end{bmatrix} \in R^{N \times N}$, $H = \begin{bmatrix} G & p \\ p^T & 0 \end{bmatrix} \in R^{(N+1)\times(N+1)}$,

$\alpha = (\alpha_1, \ \ldots, \ \alpha_{N+1})^T$ and $y = (y_1, \cdots, y_N, 0)^T \in R^{N+1}$, So Eq. 4 can be transformed into $H\alpha = y$, and

$$\alpha = H^{-1} y, \tag{4}$$

Bringing the value of α from Eq. 4 into Eq. 2, the interpolation functions from $x_1, \ldots, x_N \in \Omega \subset R^N$ to $y_1, \ldots, y_N \in R$ can be obtained.

Suspension System Parameters Optimization of Tracked Vehicle

Design Variable

For the tracked vehicle with torsion bars independent suspensions, what have the biggest effect on the ride comfort are the stiffness of torsion bars and the damping of damper. In this paper variable *K* and *C* are expressed as stiffness coefficient of torsion bars and damping coefficient of torsion spring which belong to the 1st, 2nd, and 6th of road wheel separately at the dynamic model of tracked vehicle. In order to ensure that there is no big change of the hull attitude, the pre-install angle α of road arm is defined as the function of stiffness coefficient of torsion bars *K*

$$\alpha = K_0(\alpha_0 - \alpha_s)/K + \alpha_s, \tag{5}$$

where K_0 is initial value of stiffness coefficient of torsion spring, α_0 is initial value of pre-install angle of road arm and α_s is statical inclination angle of road arm.

Considering the limitations of combining engineering practice and safety factors, α is assumed not more than 80°, therefore, the change range of design variables are shown in Table 1.

TAB1 CHANGE RANGE OF DESIGN VARIABLES

design variables	lower limit	initial value	upper limit
K	5340（-45.2%）	9743	14147（+45.2%）
C	0（-100%）	2187	4375（+100%）

Constraint Conditions and Objective Function

When there is an impact between road arm and stopper during the riding of vehicle, the ride comfort will be badly damaged. In order to minimize the probability of impact, the dynamical inclination angle of road arm should meet the condition

$$[\alpha_d] \geq 3\sigma_f, \tag{6}$$

where, σ_f is the RMS of dynamical inclination angle at the 1st right road arm.

Assuming that $\alpha_{\max}$ is maximum allowing twisting angle of torsion bar and $[a_d] = \alpha_{\max} - \alpha + \alpha_s$, as a result, the constraint condition of optimization design can be determined as

$$s.t. \quad F_{cons} = (\alpha_{\max} - \alpha + \alpha_s)/3 - \sigma_f \geq 0, \tag{7}$$

According to Ref. [5], the total weighted acceleration RMS A_w at the position of driver's seat is selected as the ride comfort evaluation index. So the objective function which is the minimum total weighted acceleration RMS can be shown as,

$$min \quad F_{obj} = A_w, \tag{8}$$

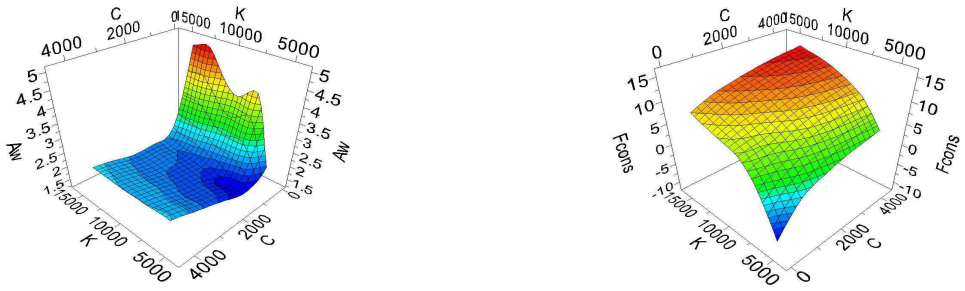
Optimization Results.k

In order to make the optimization results meet the driving requirement of vehicle, a rough road model with rank of F and the speed of 10km/h, 20km/h, 30km/h and 40km/h are selected as the driving condition of dynamic model, then, 36 sample points are get according to the dynamic

simulation and the experimental design of two-factors and six levels. The surrogate models between K, C and evaluations indices A_w , F_{cons} have been built up based on RBF using these sample points. The surrogate models under the speed of 40 km/h are shown in Fig. 2.

TAB.2 THE RESULT OF ERROR ANALYSIS OF SURROGATE MODEL

velocity [km/h]	10	20	30	40
A_w	0.032	0.034	0.023	0.038
F_{cons}	0.003	0.006	0.005	0.004



A surrogate Model between Design Parameters and Aw B surrogate Model between Design Parameters and Fcons

Fig.2 The Surrogate Model when Vehicle Velocity is 40km/h

An error analysis has been given in Table 2 for checking the fitting accuracy of surrogate model. It is proved that the fitting accuracy is acceptable. That is to say, the surrogate models can meet the need of suspension system parameters optimization. Then, the optimal combinations of suspension parameters under four kinds of velocity which are shown in Table 3 has been obtained after about 800 times of iterations using Adaptive simulated annealing (ASA)[6] and surrogate model.

TAB.3 THE RESULT OF PARAMETERS DESIGN OPTIMIZATION

velocity [km/h]	K	C	A_w	F_{cons}
10	7537	1260	0.697	4.423
20	6388	1190	1.058	2.004
30	6078	1232	1.254	2.000
40	6908	1243	1.363	3.276

Comparison between Surrogate Model Optimal Result and Virtual Evaluation Result

To verify the optimal results of suspension system parameters based on surrogate model, an virtual evaluation about ride comfort of tracked vehicle has been made using the optimal combination parameters. The simulation environment of virtual evaluation is as same as the driving condition of building up the surrogate model. The comparison about ride comfort between virtual evaluation result and optimized result based on surrogate model is shown in Table 4 and Fig. 3.

TAB4 COMPARED RESULT BETWEEN VIRTUAL EVALUATION RESULT AND OPTIMIZED RESULT BASED ON SURROGATE MODEL

velocity [km/h]	A_{w1}	F_{cons1}	A_{w2}	F_{cons2}	A_{w0}	F_{cons0}
10	0.696	4.422	0.739	5.346	0.798	10.965
20	1.057	2.004	1.072	2.494	1.167	10.302
30	1.254	2.000	1.301	2.219	1.546	10.239
40	1.363	7.945	1.501	3.386	1.775	9.989

Remarks: Among the evaluation indices of ride comfort in this table, subscript 0 denotes non-optimal result, subscript 1 denotes optimal result based on surrogate model, subscript 2 denotes optimal result based on virtual evaluation result

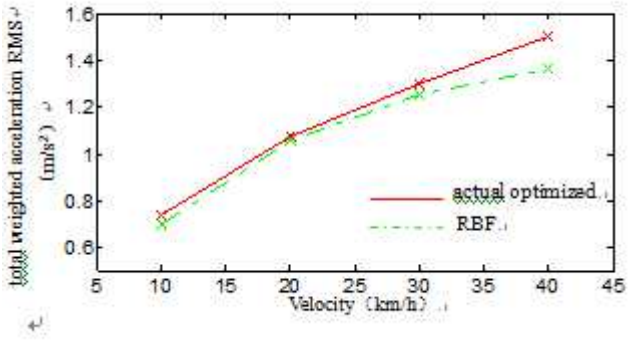


Fig.3 Compared Result Between Virtual Evaluation Result and Optimized Result Based on Surrogate Model

As fitting errors between surrogate model and actual function, there is a little difference between optimal result based on surrogate model and optimal result based on virtual evaluation using the optimal parameters. The maximum difference is 9.2% when the velocity is 40km/h, while the minimum difference is only 1.4% when the velocity is 20 km/h. As a result, surrogate model which are built up based on RBF can meet the need of suspension system parameters optimization of tracked vehicle.

It is shown in Table 4 that the ride comfort of vehicle has been improved after optimization design, especially when the vehicle is driving under a high velocity.

Conclusions

In this paper a dynamic model of high-speed tracked vehicle has been founded which credibility are verified by carrying out a road vibration experiment. The surrogate model between suspension system parameters of tracked vehicle and evaluation indices of ride comfort has been built up based on radial basis function method and dynamic simulation of vehicle. The ride comfort of vehicle has been improved after optimization design by using ASA and surrogate model. The results show that this research method is feasible and can be the basis of vehicle performance improvement.

References

[1] NI Jin-shang, RUAN Mi-qing. Optimization and Simulation of the vehicle comfort. Modern Machinery, 2006, 2.(in Chinese)

[2] WANG Yan-ke, DING Wei-ping and DU Fei-long. Optimal design of the suspension structure of a vehicle using response surface method. Mechanical Science and Technology, 2009, 28(1). (in Chinese)

[3] MYERS R H, MONTGOMERY D C. Response surface methodology, New York: Wiley and Sons, 1995.

[4] DOU Yi-fang, LIU Fei, ZHANG Wei-hua. Research on comparative analysis of response surface methods. Journal of Engineering Design, 2007, 14(5). (In Chinese)

[5] YU Zhi-sheng. Automobile theory, 4thed. Beijing: China Machine Press, 2003. (in Chinese)

[6] LIU Peng, LIU Yu-ling, Yu Fei-hong. Thin film optical parameters determination using adaptive simulated annealing algorithm. Optical Instruments, 2005, 27(4). (In Chinese)

Advanced Materials Research Vol. 936 (2014) pp 2103-2108
© (2014) Trans Tech Publications, Switzerland
doi:10.4028/www.scientific.net/AMR.936.2103

The Simulation of Heat Transfer and Flow Performance for Supercharged Boiler Superheater

Zhang Hongyan[1,a],Xie Haitao[1,b],Jin Xiangdong[1,c]

[1]College of Power and Energy Engineering, Harbin Engineering University, Heilongjiang, China

[b] xht037030@163.com

Keywords:superheater; simulation;heat transfer;flow.

Abstract: According to the basic mechanism of the supercharged boiler superheater, a superheater simulation model was established. The simulation about a whole superheater system including the flue gas,steam and tube wall was conducted according to the simulation model.Therefore, the internal working laws of superheater system are revealed by the simulation results.

Introduction

Superheater is one of the most important parts of a steam power plant. It not only recover energy from the high temperature and highly corrosive flue, but also improving the quality of steam to provide protection for the safe operation of the turbine. Superheater wall subjected to high temperature flue gas erosion and superheated steam flowing inside the superheater, so the working conditions of superheater is very poor. With the improving of modern steam power system parameters, the temperature of superheater tube wall is close to the temperature of the wall material allows. Due to the unreasonable structural design, deviate from the design point run, variable load operation frequently and other reasons, the localized over-temperature and tube rupture frequently occur in the actual operation of the superheater. It is affects the safety and efficient operation of the power plant seriously. Therefore, the simulation study of the structure design and operation of the superheater have important practical significance to forecast the problems that may arise during the superheater design and operation.

Current studies of the superheater are focuses on the numerical simulation of internal field and strength analysis. Purbolaksono J[1]and Pronobis M[2]applied finite element software to calculate the heat flux distribution under different conditions. Madejski Pawel[3]and Taler D[4]had numerical calculation on the superheater tube wall temperature distribution and analyzed the stress in order to study the causes of over-temperature. Wojnar W[5]proposed distribution model of superheater and analyzed the impact of the changes in the specific heat of the steam on temperature distribution. Based on the working mechanism of the superheater, we established the mathematical model of superheater infinitesimal segment in order to learn supercharged boiler superheater heat transfer and flow characteristics in this paper. The heat transfer coefficient of the inner and outer walls has been amended accordingly to consider the impact of the internal wall dirt and the outer wall grime on the temperature distribution. At last, we programmed and debugged the superheater mathematical model simulation procedures using C language in Visual C + +6.0 platforms and simulated the internal transfer and flow field of supercharged boiler superheater.

Mathematical model

The supercharged boiler superheater work process is flue across the metal wall. Superheated steam as the working fluid flow within the pipe and flue gas flow outside. The heat transfer process is a typical cross-flow heat exchanger. The three-dimensional geometric model of experimental platform supercharged boiler superheater as shown in Figure 1.

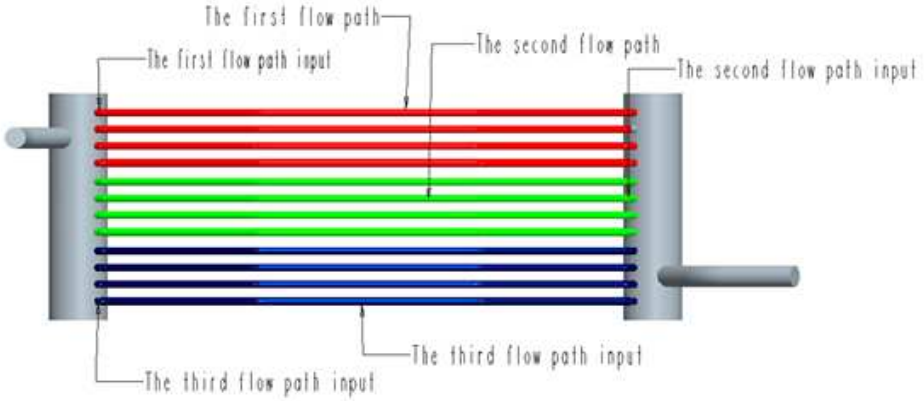


Fig1 Three-dimensional geometric model of superheater

Superheater tubes are arranged in the back of the convection evaporation bundle and occupy the entire width of the flue. It's a counter-flow and cross-flow heat exchanger. The superheater is divided into three passes, consists of 12 rows and each row contain 3 tubes. The specific spatial arrangement as follows:

The first flow path: located in the tail four rows of superheater, steam flows from top to bottom in the inner tube.

The second flow path: located in the middle four rows of superheater, steam flows from bottom to top in the inner tube.

The third flow path: located in the front four rows of superheater, steam flows from top to bottom in the inner tube.

The flue gas laterally scour tube wall of the third, second and first flow path successively and the steam vertical scour tube wall of the first, second and third flow path successively. Specific structural parameters as shown in Table 1.

TAB1 THE MAIN STRUCTURAL PARAMETERS OF THE SUPERHEATER

Number	Name	Unit	Value
1	The number of the first flow pass tubes	—	12
2	The number of the second flow pass tubes	—	12
3	The number of the third flow pass tubes	—	12
4	Outside diameter/d_o	mm	20
5	Inside diameter/d_i	mm	14
6	Wall thickness / δ	mm	3
7	Lateral distance /s_1	mm	32
8	Longitudinal distance /s_2	mm	45
9	Tube length / L	mm	1535

The assumptions of the working fluid

(1) Gas side: flue gas has the uniform physical parameters in the same section along its flow direction, flue gas temperature only changes along the direction of flow.

(2) Steam side and the tube wall: the flow of steam near the plug flow and there is no axial mixing, steam has the uniform physical parameters in the same section along its flow direction, the temperature of the wall only changes in the axial direction.

Mathematical equations

The superheater is discrete into a number of infinitesimal segments along the flue gas flow direction, the axis of Tube bundle direction and the width of flue area direction. Supercharged boiler superheater mainly absorb heat from the flue gas rely on convection heat transfer and the radiant heat exchanger was very small. Therefore, we do not consider the effects of radiation[6]. For the purposes of infinitesimal superheater, it is still a cross-flow heat exchanger. Therefore, the ε -NTU method was used to analysis and calculation. For superheater infinitesimal segment, there are:

$$\varepsilon = \frac{1-\exp\{-Rc[1-\exp(-NTU)]\}}{Rc} \tag{1}$$

$$NTU = [(\frac{1}{K_q \pi d_i dx} + \frac{1}{K_y \pi d_o dx} + k_{wg} + k_{hg}) m_y C_{py}]^{-1} \tag{2}$$

$$Rc = \frac{m_y C_{py}}{m_q C_{pq}} \tag{3}$$

And according to the heat balance equation and the heat transfer equation:

$$\varepsilon m_y C_{py}(T_{yin} - T_{qin}) = m_q C_{pq}(T_q - T_{qin}) = m_y C_{py}(T_{yin} - T_y) \tag{4}$$

$$K_y \pi d_o dx(T_y - T_w) = K_q \pi d_i dx(T_w - T_q) \tag{5}$$

Where:

y, q, w are for flue gas, steam and wall,respectively;

T——temperature, ℃;

di ,do——the inner and outer diameter of the tubes, m;

Cp——specific heat capacity at constant pressure, J/(kg·K);

K——heat transfer coefficient, W/(㎡·K);

k_{wg}——fouling resistance, K/W;

k_{hg}——ash resistance, K/W;

m——mass flow, kg/s.

The temperature of outlet flue gas,steam and tube wall can be obtained by solve the above equations.

The steady-state simulation

The simulation program was written in C language and running on Visual C++6.0 platform.

The calculation of thermo-physical properties

The working fluids of the superheater have larger temperature difference between each pass during the pressurized boiler running, which leads to the physical properties of the working fluid is very different.To make the established model reflect the characteristics of superheater operating more accurately, we call the flue gas properties program which have been compiled[7]and 《IAPWS-IF97/IFC67 water and steam properties calculation package》.So we can always call the working fluid thermal parameters depending on the temperature and pressure.

The initial boundary conditions

The input conditions of the program including:steam flow rate, steam inlet temperature and pressure, fuel consumption, flue gas inlet pressure and temperature.Their values are given based on supercharged boiler experiment platform test data ,as shown in Table 2.

TABE2 SUPERCHARGED BOILER EXPERIMENT PLATFORM TEST DATA

Fuel consumption, kg/h		64.0
Steam	Inlet temperature, ℃	174.1
	Inlet pressure, MPa	0.7012
	Flow rate, t/h	0.6627
Flue gas	Inlet temperature, ℃	491.2
	Pressure, kPa	61.3

The results and analysis of simulation

Fig2 shows the steam temperature change along the flow direction.Along the steam flow, steam continue to receive heat from the tube wall and the temperature gradually increased.It is clear that steam temperature is substantially linear with the distance between location and the entrance. This means that the steam endothermic along the axis of the tube bundle is uniform.

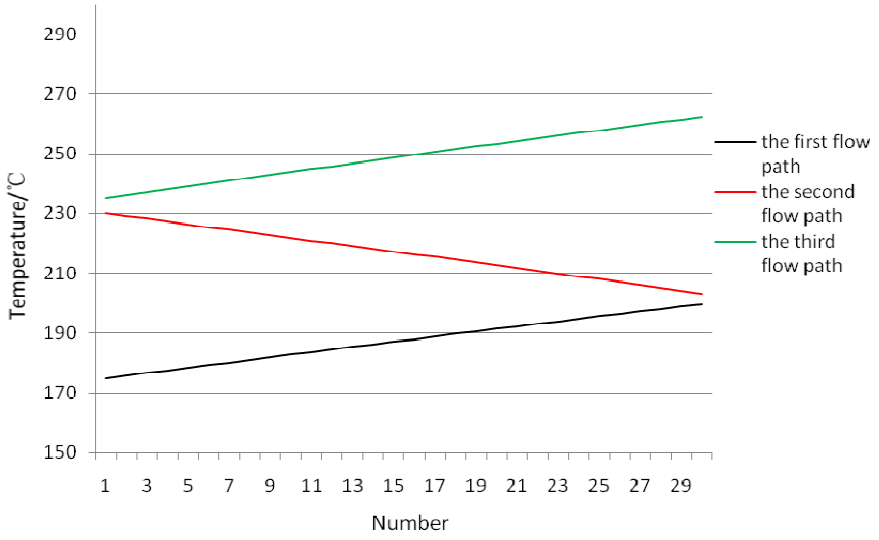


Fig2 Steam temperature change along the flow direction

Fig3 and Fig4 shows steam and flue gas convective heat transfer coefficient values at different tube row, respectively. From the figure we learn that steam heat transfer coefficient gradually decreases after steam flowing through the first,second and third pass.The heat transfer coefficient between steam and the inner tube wall is related to the physical properties and flow rate of the fluid. The steam temperature gradually increasing along the direction of steam flow,this leads to vapor density and Prandtl number decrease while kinematic viscosity, dynamic viscosity and thermal conductivity increase. Although the temperature of steam in the first flow path is lower, the density is large and kinematic viscosity is small, both of them have the combined effects on the Reynolds number. As the vapor density is more sensitive to temperature changes,therefore, the Reynolds number of the first pass is greater than the other passes. Prandtl number decreases with increasing temperature, and less sensitive to temperature changs. These factors lead to a greater heat transfer coefficient in the first flow path. Flue gas heat transfer coefficient decreases with the number of rows increases, which is mainly caused by different degrees of disturbance flue gas. Since the

superheater is a countercurrent and cross flow heat exchanger, so the smaller the number of rows, the farther away from the flue gas inlet, the corresponding disturbance is more intense and flue gas heat transfer coefficient is greater. The 12th row pipe located at the entrance of the flue gas, so the heat transfer coefficient is minimum.



Fig3 Steam heat transfer coefficient

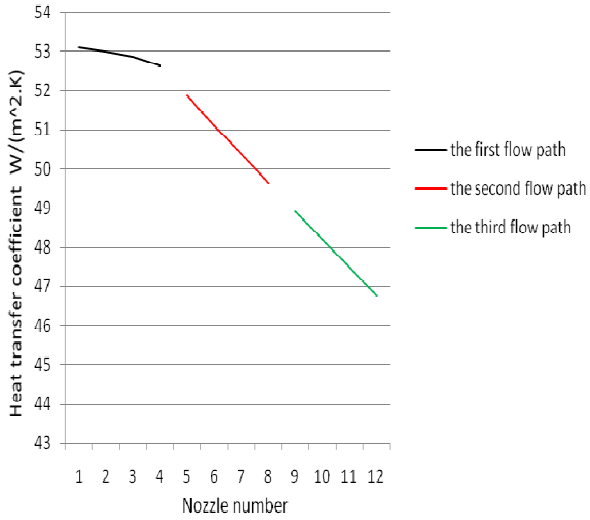


Fig4 Flue gas heat transfer coefficient

Fig 5 shows the heat exchange at different flow path.We can see that heat transfer increased along the flow direction of the flue gas.The factors affected heat transfer in superheater mainly are the total thermal resistance and temperature difference between steam and flue gas.From fig 3 and fig 4 we can see that the first flow path have the minimum total thermal resistance and the third pass is the largest. And the temperature difference is just the opposite. So the heat exchange of each pass is basically the same.

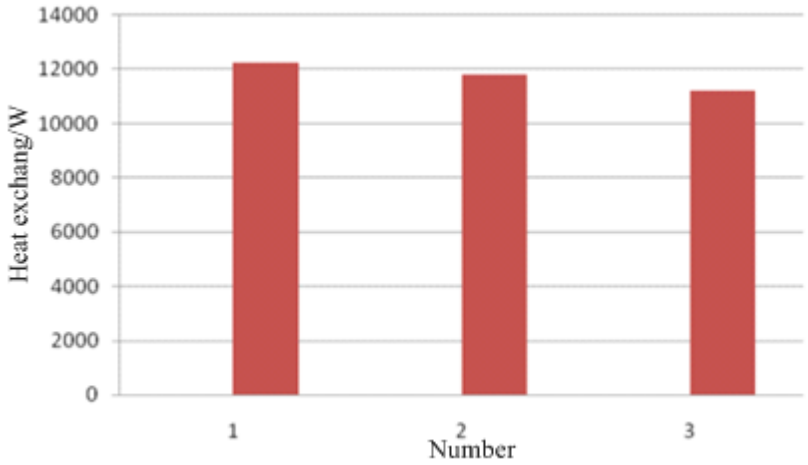


Fig 5 Heat exchange

Conclusion

In this paper, supercharged boiler superheater experimental platform as the research object and a superheater simulation model was established based on the supercharged boiler superheater basic working principle.According to the calculation results it can draw the following conclusions:

(1)The steam temperature changes uniformity along the flow direction and the heat absorption along the axis of the tube bundle is uniform.

(2)The maximum heat transfer coefficient in the first flow path, the third pass has the smallest heat transfer coefficient and the heat exchange of each pass is basically the same.

References

[1] Purbolaksono.J, Khinani.A,Rashid.A.Z, Ali.A.A, Ahmad.J, Nordin,N.F,A new method for estimating heat flux in superheater and reheater tubes,J. NUCLEAR ENGINEERING AND DESIGN.239(2009)1879-1884.

[2] Pronobis.M, Woinar.W, Czepelak, J,Influence of non-uniform heating on the stresses in tubes of superheaters in boilers,J. FORSCHUNG IM INGENIEURWESEN-ENGINEERING RESEARCH.69(2004)29-37.

[3] Madejski Pawel，Taler Dawid,Analysis of temperature and stress distribution of superheater tubes after attemperation or sootblower activation,J. ENERGY CONVERSION AND MANAGEMENT.71(2013)131-137.

[4] Taler.D, Korzen.A, Madejski.P,DETERMINING TUBE TEMPERATER IN PLATEN SUPERHEATER TUBES IN CFB BOILERS,J.RYNEK ENERGⅡ.2(2011)56-60.

[5] Wojnar.W, Pronobis.M,THE MODEL OF FLOW AND TEMPERATURE DISTRIBUTION IN THE SUPERHEATER OF A POWER BOILER,J.RYNEK ENERGⅡ.6(2008)39-46.

[6] Li Yanjun, Jiang Renqiu, Sun Baozhi,The analysis of marine supercharged boiler thermal calculation method,J.Thermal Power Engineering.20(2005)93-96.

[7] Yuan Yichao, Liu Yuzheng, Cheng Zhihang,The study of large utility boiler flue gas temperature deviation and steam temperature deviation,J.Boiler Technology.34(2003)15-20.

Advanced Materials Research Vol. 936 (2014) pp 2109-2113
© (2014) Trans Tech Publications, Switzerland
doi:10.4028/www.scientific.net/AMR.936.2109

The Resistance Performance Influences from Hull Line Variation of V-Shaped Non-Ballast Ship (NoBS)

HESHAM ELKADY[1,a*], Prof. HAN DUANFENG[1],and Prof. GAO LIANGGAO[1]

Harbin Engineering University, College of Shipbuilding Engineering, China, 150001

[a] haklmm@yahoo.com

Keywords: Hull line, Non-Ballast ship, Rise angle, Total resistance, Effective power

Abstract: As a new concept in ship design to be alternative of ballast water system, to emerge that remedy the introduction of invasive marine species and the disadvantages of ballast water treatment systems. The Non-Ballast ship has been studied abroad, but it is rarely mentioned in China. In this paper, the hydrodynamic influences due to hull line variation of this kind of ships were studied, using the method of invariant cross-section area curve under the design draft to change the rise angle at bottom. Then by using numerical calculation, get the resistance and effective power at each angle.

Introduction

The Non-Ballast ship concept was invented and initially investigated at Shipbuilding Research Centre of Japan (SRC) as a way to overcome the introduction of invasive marine species and the disadvantages of ballast water treatment systems.

The paper studies the hydrodynamic effect by changing the rise angle at ship's bottom with a wider breadth, while the major factors such as mid-section area, length, draught, etc. were kept unchanged. In the present research, the hydrodynamic aspects of Non-Ballast concept were further investigated numerically using Maxsurf software to construct the 3D modeling and Hullspeed software to calculate and analyses the resistance performance.

Background

Ships are designed to operate safely while carrying a full load. Ballast water is used to account for situations when vessel has only a partial load or no load at all. The functions of ballast are to maintain a necessary draught to ensure efficient propeller and rudder operation, safe navigation and to avoid bow slamming especially in heavy seas. Ballast water is also used to balance the ship as fuel is used up during a long voyage, or during loading and unloading operations.

The transportation and introduction of invasive marine species into new environments through ships' ballast water, attached to ships' hulls and via other vectors has been identified as one of the four greatest threats to the world's oceans as it cause damage to the environment and impacts on human health, social and economic[1]. Research had targeted technologies that treat ballast water to remove or destroy the living organisms being carried including ballast water exchange, filtration, heat, ultra-violet light, ozone, de-oxygenation, electro ionization and chemical biocides, among others.

However all current treatments techniques would require high cost for installation of sensitive equipment and retrofit on a ship, extra cost of operation, maintenance and training of the ship crew to operate, plus the cost of managing tank sediments. These techniques also require more power which will result in more combustion of fuel and consequently bring more emission gasses and air pollution. In Addition of single treatment method would not provide an effective solution.

Ballast water exchange at sea subject to several serious limitations, including inapplicability on short voyages or when the voyage is mainly in coastal waters, ship safety and stability limitations in rough seas, and highly variable biological effectiveness.

A new concept was invented to be alternative to ballast water system. The concept is based on a V-shaped hull which stems from new thinking about optimal hull shape and buoyancy distribution.

The V-hull alters the vertical distribution of hull buoyancy, causing a deeper draught in the light (unloaded) condition than that of conventional hull as shown in figure (Fig.1). By widening the beam by ~30%, the ship's displacement can be kept at the same full load draught as that of an equivalent deadweight of conventional hull, while hull length is minimally altered.

The V-shape cross-section maintains sufficient unloaded draught and stability and avoid bow slamming and propeller racing without needing any ballast water (BW) for the majority of sea conditions. It also likely provides the potential for better vessel control, reduce hull resistance and improve propulsion efficiency for most speeds and sea conditions.

Overall, the investigation of the Non-Ballast (NoBS) Ship Concept has shown that it provides a viable alternative to the addition of costly ballast water treatment systems in order to meet the evolving performance requirements for ballast water treatment. The concept essentially eliminates the transport of foreign ballast water. This should be more effective than current treatment methods in reducing the potential for the further introduction of nonindigenous aquatic species[2-4]

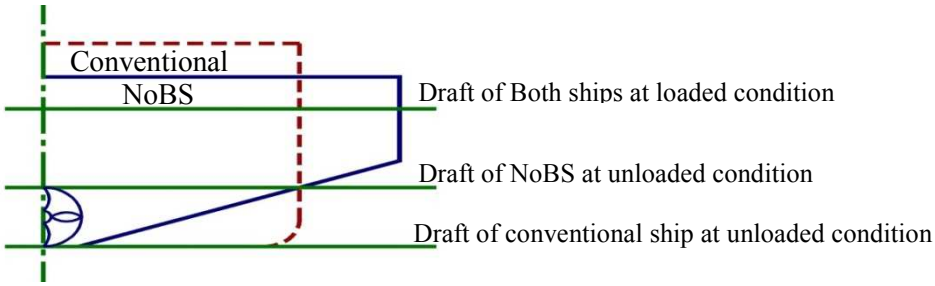


Fig.1Deeper draught of V-hull in its unloaded condition than that of conventional hull

Analysis and Determination of Main Dimensions

In this paper, a 59000 DWT oil tankers selected as the mother ship, which was designed to be V-Hull Non-Ballast ship with principal dimensions shown at table (Table 1).[5] Figure (Fig.2) shown the Maxsurf Pro model for the V-Hull Non-Ballast ship.

TABLE 1 THE V-HULL NON-BALLAST SHIP' MAIN PRINCIPAL DIMENSIONS

Total length L_{OA}	200[m]	Design draft T	12.5[m]
Length between perpendiculars L_{BP}	196[m]	Depth D	19.5[m]
Maximum beam B	32.2[m]	Rise angle at the bottom θ	25°

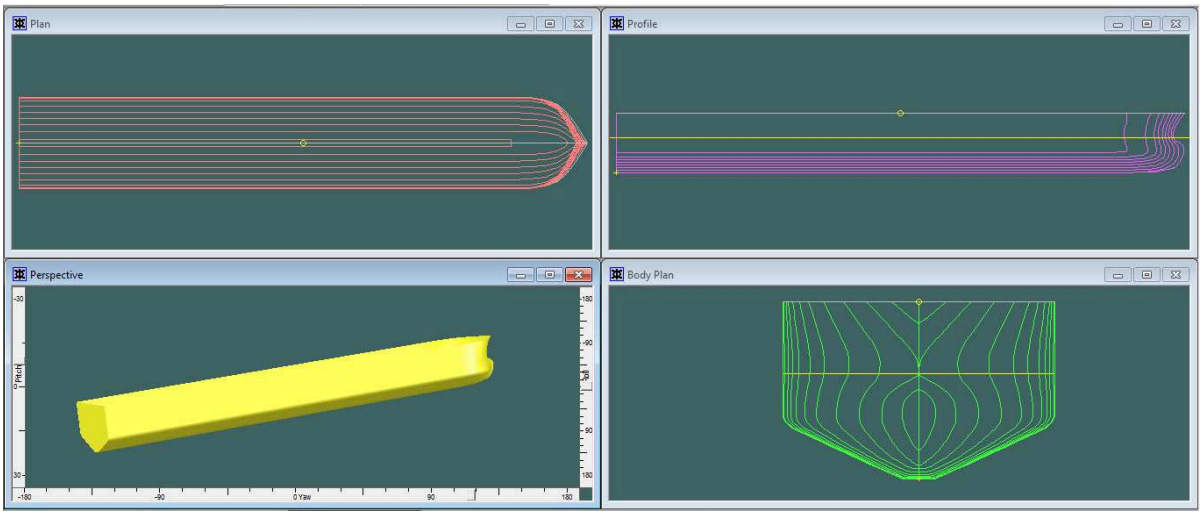


Fig.2 The V- hull Non-Ballast ship Maxsurf Pro model

The rice angle at the bottom θ is altered with the change in beam, while the major factors unchanged according to equation (Eq.1) which base on invariant cross-section area curve under the design draft as shown in figure (Fig.3), The increased area B is equal to the reduced area A.[6]

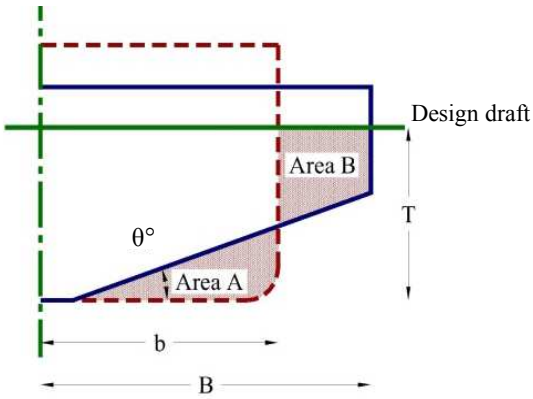


Fig.3 The invariant cross-section area

$$n = \frac{-b(b\tan\theta - T) \pm \sqrt{[2b(b\tan\theta - T)]^2 - 4b^2\tan\theta \times b^2\tan\theta}}{2b^2\tan\theta} \quad (1)$$

Where n is the single coefficient range 0< n <1, b is the half breadth of conventional ship, B= (n+1) b is the half breadth of design ship, and θ is the rise angle. From equation(Eq.1) we can get the half breadth of design ship for changed θ between 10° and 25° as shown in table (Table 2) and figure (Fig 4) with constant draft 12.5 [m]

Table 2 The half breadth of design ship with different θ

θ	T[m]	B[m]	Area A[m^2]	Area B[m^2]
10°	12.5	13.3	9.520277	9.520277
15°	12.5	13.9	14.46716	14.46716
20°	12.5	14.8	19.65156	19.65156
25°	12.5	16.1	25.17696	25.17696

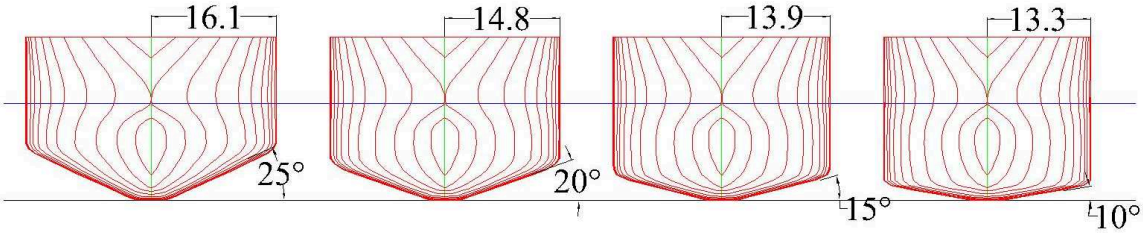


Fig.4 The Maxsurf models

Numerical Investigation

The commercial software Maxsurf is a powerful three-dimensional surface modeling system for use in the field of marine design. Allowing any number of surfaces to be modeled in any given design, offer scope for the creation of a wide range of hull forms. Combined with the built-in hydrostatic calculations, there are a couple of tools to experiment with shapes and explore design parameters. And Hullspeed software provides a means of predicting the resistance of a ship hull. Maxsurf designs may be read in and automatically measured to obtain the required parameters.

In this paper selected the Slender body method from the Hull speed resistance prediction methods, because the models' main principal dimensions achieved the certain limits of hull

dimension, which the resistance prediction algorithms are useful within. The Slender body method calculate the total resistance as equation (Eq.2) and power as equation (Eq.3) [7]

$$R_T = R_W + R_V + R_{Cor} + R_{App} + R_{Air} \quad (2)$$

Where R_T is the total resistance, R_W is wave making resistance; R_V is viscous resistance and equal $(1+k)R_F$ fraction resistance uses the ITTC'57 ship-model correlation line, R_{Cor} is Correlation allowance resistance; R_{App} is Appendage resistance and R_{Air} is wind resistance.

$$P = \frac{R_T V}{\eta} \quad (3)$$

Where P is the power, V is the velocity of ship and η is the efficiency, which is selected to be 75%.

The figure (Fig 5) and figure (Fig 6) shows the result for numerical investigation of total resistance R_T and effective power P respectively, for variation rice angle at bottom θ of model, in range of velocity V from 0 to 17 [kts].

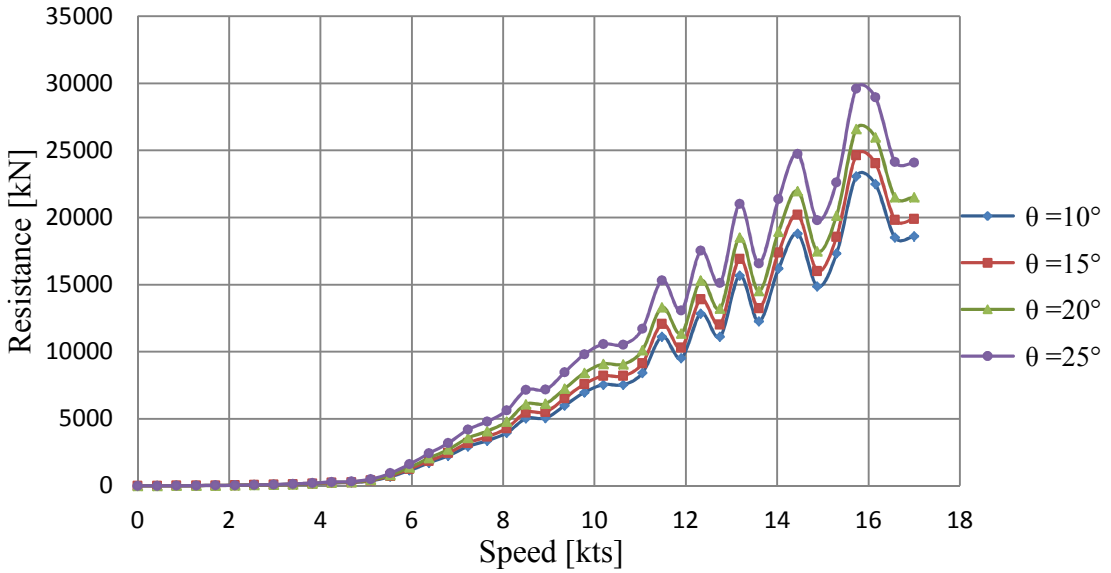


Fig.5 The total resistance

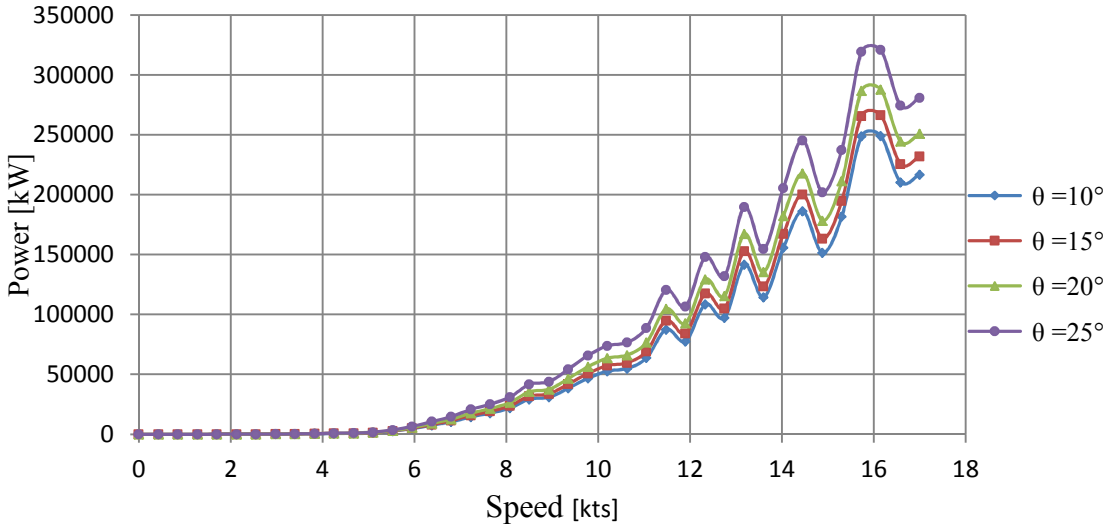


Fig.6 The effective power

Conclusion

From the previous study, the following facts can be deduced. The total resistance will increase with the augment of rise angle at the bottom. Especially under high speed condition, the increate even reach by 22%between the lowest and highest rise angle, due to the broaden breadth, which consequently make the half angle of entrance increase, further affect the wave resistance of ship.

The increase of resistance is not so noticeable at low speed, because the convergence of wet area surface, which not increase than 1.6% between the lowest and highest rice angle. So the frication resistance the main domain resistance at low speed will be approximately the same.

The effective power will increase accordingly as increased total resistance. As a result the fuel oil consumption and the cost of voyage will rise consequently.

The Non-ballast ships as a new concept, from the design to the application there is obviously still a long way to go. But no doubt it is to solve issues of ship ballast water, worth investing more energy to exploration and research.

Reference

[1] Christopher, F. Deacutis, and Richard C. Ribb, "BALLAST WATER AND INTRODUCED SPECIES: Management Options for Narragansett Bay and Rhode Island," Narragansett Bay Estuary Program, R.I. Department of Environmental Management2002.

[2] International Maritime Organisation (IMO), "International Convention for the Control and Management of Ships' Ballast Water and Sediments," 2004.

[3] Japan Ship Technology Research Association, "Research and Development of Non Ballast Water Ship," *Briefing Report of Research Achievements,(in Japanese.),* 2006.

[4] Marine Environment Protection Committee, "55th Session," *Brief description of the technologies presented,* 2006.

[5] L. Yu, "Preliminary Design and Research on NOBS," Master of Engineering, Naval Architecture and Ocean Engineering, Harbin Engineering University, 2013.

[6] We Jun, ka Lin Yah,, "Hull Line Design and Variation for a V-Shape Ballast-Free Ship," *Chinese Journal of Ship Research,* vol. 5, 2010.

[7] Formation Design Systems Pty Ltd, *Hullspeed user manual*, 2004.

Advanced Materials Research Vol. 936 (2014) pp 2114-2119
© (2014) Trans Tech Publications, Switzerland
doi:10.4028/www.scientific.net/AMR.936.2114

A Computational Fluid Dynamics Method for Resistance Prediction of the Floating Hull of Wave Glider

Aladdin Elhadad [1, a*], Duan Wenyang [1, b] and Deng Rui [1, c]

[1] College of Shipbuilding Engineering, Harbin Engineering University, Harbin, China

[a]robyhadad@yahoo.com

Keywords: Wave glider; Wigley hull; Resistance; Computational Fluid Dynamics (CFD).

Abstract: The *wave glider* is a surface vehicle with an attached sub-surface wing system which propels the surface component forward, negating the need for a motor. *Wave glider* could be used for intelligence, surveillance, passive monitoring of marine life, monitoring exclusive economic zones for fishing and other economic resources that are important and useful to coastal countries. Monitoring of coastal waters normally requires large amounts of expensive surveillance. They can be used to find and research resources and fisheries at a fraction of the cost of other methods. Since the *wave glider* can either be programmed for a journey or to keep station, it is looked at as an alternative for expensive moored buoys. In this paper we present a method focused on the mesh generation to predict calm water resistance for the floating part of the *wave glider* (the hull). In this study a *wigley hull* form (4m) used as the floating hull has been investigated in order to predict the fluid flow of the ship using *computational fluid dynamics (CFD)*. Calculations for total resistance are carried out for Froude numbers in the range of 0.10 to 0.40. Commercial *CFD* software fluent is used to investigate the fluid flow of *wigley hull*. Three different mesh sizes are used in this study to calculate the mesh effects. The results obtained from *CFD* calculations for total resistance are compared with the experimental results for accuracy of the solution parameters. The comparison shows a good agreement between experimental and *CFD* results. The method is evaluated by comparing the numerical predictions for *wigley hull* form (2m) with *wigley hull* form (4m) using the same mesh sizes under the same conditions in an attempt to design the floating hull of *wave glider* . The results obtained from *CFD* calculations are compared for accuracy of the solution parameters and the method is useful and acceptable.

Introduction

The *wave glider* is a surface vehicle with an attached sub-surface wing system. The wing system is comprised of six individual wings that adjust to the current, speed, and direction of passing waves as shown in figure (1). This system propels the surface component forward, negating the need for a motor. The *wave glider* can be programmed for travel or to keep station at a certain location which is hopeful in the need for replacement of buoys with expensive mooring systems. The *wave glider* has instruments on the surface component that can be customized for ADCP and CTD measurements, passive monitoring of marine life and other commercial applications. The instruments are powered by solar panels on the surface component, making the *wave glider* a self-sustaining vehicle. The vehicle transmits data to land in real-time sequence, allowing for accurate and easy monitoring of the vehicle's trip and the data collected [1].

In current practice, early stage design studies often use empirical data to estimate the total resistance because more sophisticated numerical methods or physical experiments are too expensive or time consuming for preliminary decision making. Unfortunately, empirical data may be misleading when used for new and exotic hull form types that differ significantly from the conventional hulls from which the experiential data has been collected. The objective of this paper is to bring accurate numerical prediction of ship resistance closer to early stage design using a method that relies minimally on empiricism and is flexible and general for application to new and high-performance hull form types.

The *CFD* technology is always developing, especially in terms of new solution techniques, and these developments are often given in terms suitably applicable to the ship building industry. In recent years, the development of advanced computing technology and numerical tools have made the use of *CFD* techniques much more practical with regards to ship resistance calculations [2].

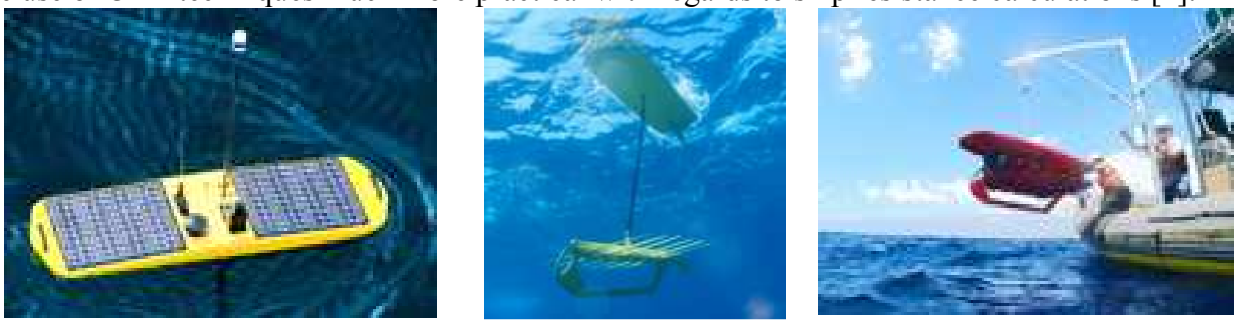


Fig. 1 Wave glider

CFD applications related to ships often concern hydrodynamics problems, which involve the task of computing pressure and velocity components and then further calculating the forces and moments acting on the ship. According to the lake of design information and data for the *wave glider*, the main aim of the study is to investigate the *CFD* capability in solving fluid flow around the *wigley hull* form (2m) compared with *wigley hull* form (4m) using the same mesh sizes under the same conditions by using commercial general-purpose software fluent in an attempt to design the floating hull of *wave glider* [3].

Methodology

Wigley hull model (L=4m) is mathematically defined, simple and has a long history in being used for validation. Although *wigley parabolic hull* is not employed to design actual ships, it is a good test case because of its simple geometrical form and the large amount of experimental and computational data available. These experimental results are compared to *CFD* calculated results to ensure proficiency in *CFD* theory and tools [4].

Mathematical Model used in CFD Calculations

To solve the governing equations for fluid flow, the fluid domain is subdivided into a finite number of cells and these equations are changed into algebraic form via discretion process. Finite volume method is used for the discretion. The coupling between the pressure and velocity fields was achieved using *simple* (semi-implicit methods for pressure- linked equation) algorithm.

The *shear-stress transport* (SST) k − turbulence model is adopted to calculate eddy viscosity in our study; this model is believed to be one of the best choices to simulate turbulence flow around ship hull.

Governing Equations

In this paper, three-dimensional steady, incompressible, two-phase (air and water), and viscous turbulent flow is used. For incompressible flow, well known, continuity and *Navier – Stokes* equation are given by:

$$\frac{\partial ui}{\partial xi} = 0 \tag{1}$$

$$\frac{\partial}{\partial xj}(\rho u_i u_j) = \frac{\partial}{\partial xj}\left[\mu\left(\frac{\partial ui}{\partial xj} + \frac{\partial uj}{\partial xi}\right) - \left(\frac{2}{3}\mu\frac{\partial uj}{\partial xi}\right)\right] - \frac{\partial p}{\partial xi} + \frac{\partial}{\partial xj}(-\rho u_i' u_j') \tag{2}$$

Where u_i and u_j are time-averaged velocity components (i, j=1,2,3), ρ is fluid density, p is pressure and μ is dynamic viscosity. In this equation, additional terms appear that represent the effects of turbulence and $-\rho u_i' u_j'$ is called *Reynolds stress* which must be modeled in order to close the equations. A turbulence model is required here in order to close the system of *RANS* equations.

SST k-ω model is developed by Menter [5]. Transport Equations for the SST k-ω Model

$$\frac{\partial}{\partial t}(\rho k) + \frac{\partial}{\partial xi}(\rho k \mathrm{ui}) = \frac{\partial}{\partial xj}\left(\Gamma k \frac{\partial k}{\partial xj}\right) + G\tilde{}k + Yk + Sk \quad (3)$$

$$\frac{\partial}{\partial t}(\rho \omega) + \frac{\partial}{\partial xi}(\rho \omega \mathrm{ui}) = \frac{\partial}{\partial xj}\left(\Gamma \omega \frac{\partial \omega}{\partial xj}\right) + G\tilde{}\omega - Y\omega + D\omega + Sw \quad (4)$$

In these equations, $G\tilde{}_k$ represents the generation of turbulence kinetic energy due to mean velocity gradients, G_ω represents the generation of ω, Γ_k and Γ_ω represent the effective diffusivity of k and ω respectively. S_k and S_ω are user-defined source terms. Y_k and Y_ω represent the dissipation of k and ω due to turbulence. D_ω represents the cross-diffusion term.

Computational Domain and Grid Generation

The ship model used for this study is *wigley hull* with block coefficient (C_B) of 0.222. *Wigley hull* model is a standard for ship-hydrodynamics research and it is one of the hull forms used by ITTC research program. The characteristics of hull model and the longitudinal profile of the 3D model used for *CFD* calculations are given in table (1).

TABLE 1. CHARACTERISTICS OF HULL MODEL

Description	Units	Dimensions	Description	Units	Dimensions
Length	L (m)	4.00	Wetted Surface Area	S (m2)	3.227908
Beam	b (m)	0.80	Water Density	(Kg.sec2/m4)	101.930
Draft	d (m)	0.25	Kinematic Viscosity	(m2 /sec)	1.2845*10-6
Temperature	c○	10.6	Volume of displacement	∇ (m3)	0.1777

A complete *CFD* solution requires three major steps: preprocessing, analysis of the problem using a solver and post processing the results. Preprocessing of the solution involves geometry creation of the model, and an appropriate mesh generation. In this study, preprocessing of the solution is carried out in *gambit* software. The geometry of the hull is obtained by the use of offset table as shown in figure (2). This offset data is imported into *gambit* in the form of vertices and then 3-D model is generated. The major dimensions of the *wigley hull* are given in table (1). For flow calculations, half of the *wigley hull* is modeled due to the symmetry of hull. The domain volume is taken to be of cylinder shape. The overall size of the cylinder is 5Lx1.5Lx L. The Cartesian coordinate system is setup with x-axis pointing towards the bow, y-axis upwards and z-axis to portside. The length in front of the hull (inlet boundary) is taken as 1.0L (main hull), the length behind the hull (outlet boundary) is taken as 3.0L (main hull). The top, bottom and side boundaries are taken as 1.0L (main hull) each, the domain volume is subdivided into various sub volumes in order to obtain structured multi-block grid as shown in figure (3).

Three different mesh sizes are evaluated in this study, coarse grid of 275,220, medium grid of 400,620 and a find grid of 427,940. Analogous results were obtained for the total resistance R_T as shown in table (2), where the difference $\Delta R_T\% = (R_T^{CFD} - R_T^{exp})/ R_T^{exp}$.

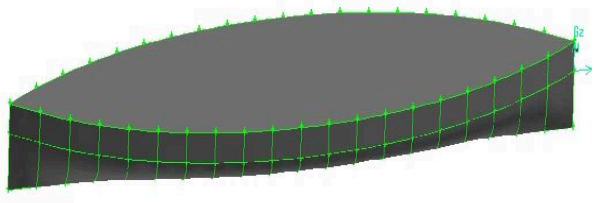


Fig. 2 Geometry of the hull model

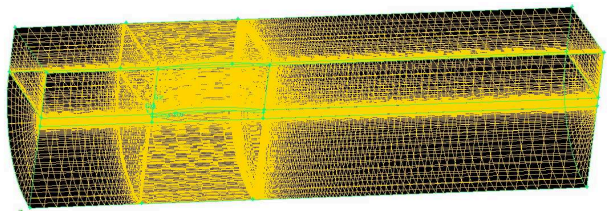


Fig. 3 Meshed domain volume in gambit

The grid generator *gambit* was used for meshing the computational domain with structured hexahedral grid. Unstructured tetrahedral was not chosen since this type of mesh reduces accuracy and increases the computational cost despite the fact that it is easy to handle while dealing with complex geometry [6].

Boundary Conditions and Solution Parameters

Assumed boundary conditions were of pressure inlet and pressure outlet for the inflow and outflow surfaces respectively, while the flow velocity is considered equal to the experimental velocity of the model. The non-slip condition is used on the hull, sides and top of boundary. Symmetry condition is invoked on the symmetric plane.

The commercial finite-volume software *fluent* is used for computations in this study. Since the motion of the free-surface is governed by gravitational and inertial forces, therefore, gravity effects must be taken into account in boundary conditions. Thus the variables and properties in any given cell are either purely representative of one of the phases, or representative of a mixture of the phases, depending upon the volume fraction values. The turbulence models of SST k-ω with standard coefficients are employed in the calculations. Convergence of the solution is assessed by monitoring the residuals of continuity, velocity, turbulence, volume fraction and drag force. The residual convergence criterion is taken as $1e^{-07}$ [7].

Resistance Calculations

The total resistance of the *wigley hull* (4m) is calculated. The calculations are carried out for *Froude number* ranging from 0.10 to 0.40. The calculated drag on the hull is recorded every 100 iterations, in order to judge the convergence of the solution.

TABLE 2. THE COMPARISON OF EXPERIMENTAL AND CFD RESULTS FOR WIGLEY HULL 4M

F_n	R_T (N) (Experimental)	R_T (N) (Software)	ΔR_T (%)	Fn	R_T (N) (Experimental)	R_T (N) (Software)	ΔR_T (%)
0.32	23.3478	22.636	3.048681	0.37	30.44043	31.548	-3.63848
0.32	23.3478	24.808	-6.25412	0.37	30.44043	30.264	0.579591
0.32	23.3478	23.72	-1.59415	0.38	33.19704	31.944	3.774553
0.35	26.55567	25.57	3.711712	0.38	33.19704	33.824	-1.8886
0.35	26.55567	27.546	-3.72926	0.38	33.19704	32.798	1.202035
0.35	26.55567	26.536	0.074071	0.4	40.1229	38.296	4.55326
0.37	30.44043	29.564	2.879164	0.4	40.1229	39.208	2.280244
0.37	30.44043	31.548	-3.63848	0.4	40.1229	38.728	3.476568

The results of the total resistance for *wigley hull* (4m) as a function of the *Froude number* are shown in Figure (4). The experimental results are extracted from the NMRI report [8]. For mesh study, resistance calculations for the three grids are carried out for higher Froude numbers; the turbulence model used in these calculations is SST k-ω. The coarse and medium grid results are in very close agreement. The difference between the medium and fine grid is relatively larger, although still acceptably small.

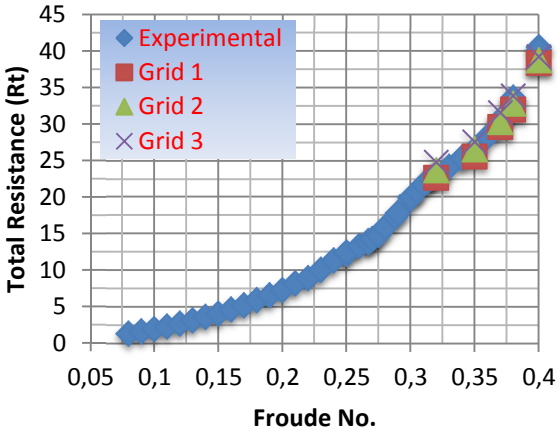


Fig. 4 Resistance curve for wigley hull (4m) comparing three different sized grids

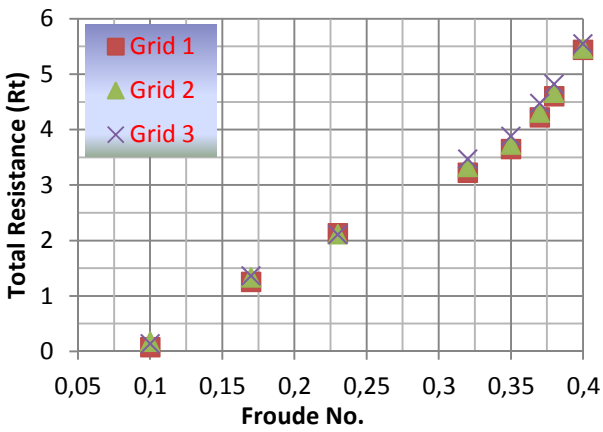


Fig. 5 Resistance curve for wigley hull (2m) comparing three different sized grids

The comparison of results obtained from different mesh sizes indicates that the difference ΔR_T% is too small and acceptable as shown in table (2). Also the difference ε = (medium - coarse) / (fine - medium), where 0< ε <1 is small and acceptable as shown in table (3).

TABLE 3. THE COMPARISON OF EXPERIMENTAL AND CFD RESULTS FOR WIGLEY HULL 4M AND 2M

Fn	R_T (N) (Exp.)	R_T (N) 4 m (Calculated)			ε_{4m}	Fn	R_T (N) 2 m (Calculated)			ε_{2m}
		Grid 1	Grid 2	Grid 3			Grid 1	Grid 2	Grid 3	
0.32	23.3478	22.636	23.72	24.808	0.996324	0.32	3.218	3.324	3.466	0.746479
0.35	26.55567	25.57	26.536	27.546	0.956436	0.35	3.646	3.728	3.876	0.554054
0.37	30.44043	29.564	30.264	31.548	0.545171	0.37	4.22	4.304	4.47	0.506024
0.38	33.19704	31.944	32.798	33.824	0.832359	0.38	4.596	4.66	4.816	0.410256
0.4	40.1229	38.296	38.728	39.208	0.9	0.4	5.438	5.456	5.548	0.195652

The total resistance of the *wigley hull* (2m) is calculated using the same mesh sizes under the same conditions. The calculations are carried out for Froude number ranging from 0.10 to 0.40. The calculated drag on the hull is recorded and plotted as shown in figure (5) in order to judge the convergence of the solution. The close agreements between the numerical predictions show that the overall numerical scheme is suitable for resistance prediction. The difference **ε** is small and acceptable as shown in table (3). Also coefficient of residual resistance (Cr) is calculated for both *wigley hull* and the difference of the predicted resistance coefficient is very small and of the same order of magnitude. This means the linear free-surface boundary conditions adequately describe the flow for this hull form.

Finally Contours for free surface wave and volume fraction (water) for both of *wigley hull* at various *Froude number* are shown in figure (6) and figure (7) respectively.

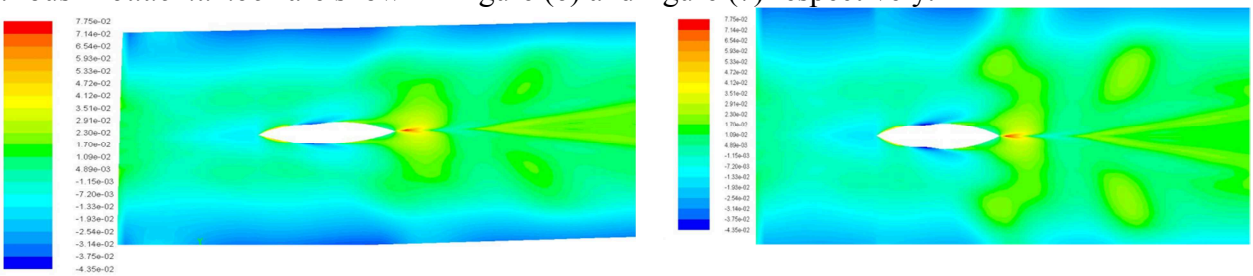


Fig. 6 Free surface wave contours for wigley hull at Fn=0.40 for 2m and 4m respectively

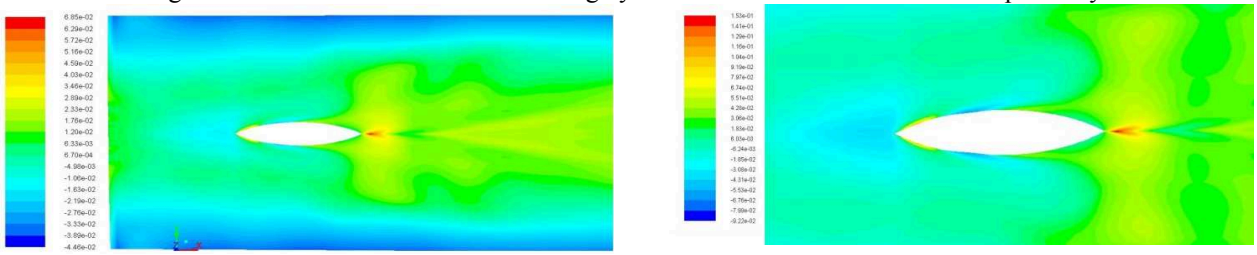


Fig. 7 Free surface wave contours for wigley hull at Fn=0.37 for 2m and 4m respectively

Conclusion

The *wave glider* is a surface vehicle with an attached sub-surface wing system which propels the surface component forward, negating the need for a motor. In this study a *wigley hull* form (4m) used as the floating hull has been investigated in order to predict the fluid flow of the ship using *CFD*. Calculations for total resistance are carried out for Froude numbers in the range of 0.10 to 0.40. *Gambit s*oftware is used for geometry creation and generation of mesh. *Fluent* software is used to calculate the total resistance of *wigley hull*. Three different mesh sizes are used in this study to calculate the mesh effects. The results obtained from *CFD* calculations for total resistance are compared with the experimental results for accuracy of the solution parameters. The comparison shows a good agreement between experimental and *CFD* results for wigley hull (4m).

In this paper we present a new method for computing the flow around a ship based on comparing the numerical predictions for *wigley hull* form (2m) with *wigley hull* form (4m) using the same mesh sizes under the same conditions in an attempt to design the floating hull of *wave glider* . The results obtained from *CFD* calculations are compared for accuracy of the solution parameters and

the method is useful and acceptable. Finally, a good agreement in results is found which shows the importance of CFD applications in calculating fluid flow to design the floating hull of *wave glider*.

References

[1] Hine et al., U. S. Patent 8,287,323 B2, Oct. 16, (2012).
[2] Y. H. Özdemir S. Bayraktar, T. Yılmaz, Computational Investigation of a Hull, 2nd International Conference on Maritime Research and Transportation ICMRT, (2007).
[3] Ansys, Fluent 6.3User's Guide, Fluent Inc. (2006).
[4] Cooperative experiments on Wigley parabolic models in Japan. Technical report, Ishikawajima-Harima Heavy Industries Co., Ltd., Ship Research Institute, University of Tokyo, Dec., (1983).
[5] F. R. Menter, Two-Equation Eddy-Viscosity Turbulence Models for Engineering Applications, AIAA Journal, (1994) vol. 32(8), pp. 1598-1605.
[6] Z. Zhi-rong, L.I. Hui, others, Application of CFD In Ship Engineering Design Practice and Ship Hydrodynamics, Journal of Hydrodynamics, Ser. B, vol. 18(3), Supplement 1, (2006), pp. 315-322.
[7] B.E. Launder, others, Lectures in Mathematical Models of Turbulence, Academic Press, London, England, (1972).
[8] Hiroyuki A., others, Experimental separation of ship resistance for thin ship, National Maritime research Institute, (1997).

Advanced Materials Research Vol. 936 (2014) pp 2120-2124
© (2014) Trans Tech Publications, Switzerland
doi:10.4028/www.scientific.net/AMR.936.2120

Bifurcation And Chaos In Couplings With Clearance

Martin Houfek[1, a], Lubomir Houfek[2,b]

[1]Faculty of Mechanical Engineering, Brno University of Technology, Technická 2896/2, 616 69 Brno, Czech Republic

[2]Faculty of Mechanical Engineering, Brno University of Technology, Technická 2896/2, 616 69 Brno, Czech Republic

[a]houfek.m@fme.vutbr.cz, [b]houfek@fme.vutbr.cz

Keywords: drive systems, bifurcation, chaotic behavior.

Abstract: The paper is focused on analysis of dynamic properties of drive systems. It describes the possible ways of stability analysis and possible ways of analysis of bifurcation of steady states and possible occurrence of chaotic behavior.

Introduction

Stability analysis can not be omitted when examining the dynamic properties of drive systems. In case of nonlinear systems and its models one can also expect occurrence of chaotic movements. The approach towards the analysis of its occurrence possibilities will be different when analyzing models with one or a few degrees of freedom or models of real technical systems. Those problems are addressed in the contribution [1].

Occurrence of chaos in drive systems and its modelling

Dissipative dynamic system can be characterized as systems whose behaviour with increasing time asymptotically approaches steady states if there is no energy added from the outside. Such system description is possible with relatively simple nonlinear equations of motion. For certain values of parameters of those equations the solution does not converge towards expected values, but chaotically oscillates. Strong dependency on small changes of initial conditions occurs as well. When analyzing such phenomena its mathematical essence can be connected with existence of “strange attractor” in phase plane. Possible creation of chaos can be seen in repeated bifurcation of solution, with so called cumulation point behind which the strange attractor is generated. Phase diagram of system solution then transfers from stable set of trajectories towards new, unstable and chaotic set. Creating the global trajectory diagrams is of essential importance. When succesfull, the asymptotic behavior of systems model is described.

Global behaviour of model of dissipative system

The problems of drive systems analysis belong into the most discussed problem of current engineering practice. There is still a number of conceptual and methodical questions which require further and mainly deeper understanding and explanation. One of those is the existence of deterministic chaos. And mainly the problem of deterministic chaos, its identification (and expectation) are described in this contribution [2].

Such system when nonlinear can be extremely sensitive on small changes of initial conditions or certain design parameters. A typical example would be a clearance in drive systems. In the chaotic case the solution becomes unstable and new solution appears, unstable and diametrically different. In the case of the presentation of the computational results in phase plane the transition appears from stable set of trajectories towards new, unstable (chaotic trajectories). It is clear that it is extremely important to understand the parameters areas in which the chaotic phenomena can occur mainly with controlled systems and/or with systems containing subsystems of different physical nature.

The changes in number of solutions of corresponding equation of motion depending on the change of a single variable (when all other variables remain constant) is called bifurcation. The importance of bifurcation diagrams is in the possibility to show the area of dynamic system parameter for which the system behavior is chaotic [3]. On of the possible approaches of bifurcation diagram construction is in following steps:

- select one parameter which is considered bifurcation from the set of technical parameters characterizing the properties and behavior and determine the interval of such parameter change
- perform the solution of system of equations which describe the system under consideration (or its model) depending of the particular value of bifurcation parameter
- change the value of bifurcation parameter for sufficiently low value
- repeat the above described steps until the full interval of bifurcation parameter is fulfilled draw bifurcation diagram where each partial calculation corresponds to a single point.

Sample model of drive system

We selected a simple drive system for verification of theoretical conclusions from last chapter. The model of the system is on Fig. 1. This system represents a machine unit consisting of drive element and a work element coupled to each other by stiff clutch. This clutch does not have linear characteristic. The characteristic is nonlinear and its diagram is on Fig. 1 too.

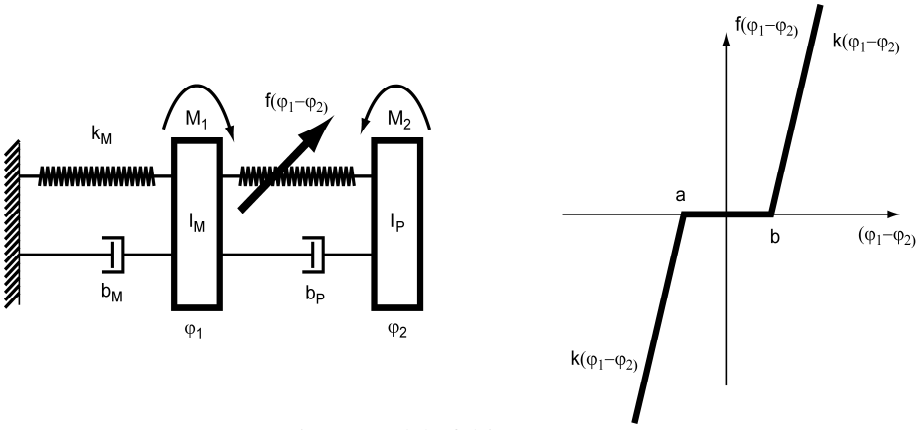


Fig. 1. Model of drive system

System equations of motion can be written in form:

$$\begin{aligned} &I_M \cdot \ddot{\varphi}_1 + k_M \cdot \varphi_1 + f_{(\varphi_1,\varphi_2)} + b_M \cdot \dot{\varphi}_1 + b_p \cdot (\dot{\varphi}_1 - \dot{\varphi}_2) = M_M + M_1^M \cdot \cos(\omega \cdot t) \\ &I_P \cdot \ddot{\varphi}_2 - f_{(\varphi_1,\varphi_2)} + b_P \cdot (\dot{\varphi}_1 - \dot{\varphi}_2) = M_P - M_1^P \cdot \cos(\omega \cdot t - \nu) \end{aligned} \tag{1}$$

where nonlinear function $f_{(\varphi_1,\varphi_2)}$ is defined by

$$\begin{aligned} &f_{(\varphi_1,\varphi_2)} = k \cdot (\varphi_1 - \varphi_2) \quad for \quad (\varphi_1 - \varphi_2) < a \\ &f_{(\varphi_1,\varphi_2)} = 0 \quad for \quad a < (\varphi_1 - \varphi_2) < b \\ &f_{(\varphi_1,\varphi_2)} = k \cdot (\varphi_1 - \varphi_2) \quad for \quad (\varphi_1 - \varphi_2) > b \end{aligned} \tag{2}$$

Lets analyze the case of symmetrical clearance, when $|a| = |b| = a$. Then for $|\varphi_1 - \varphi_2| \le a$ following equations hold

$$\begin{aligned} &I_M \cdot \ddot{\varphi}_1 + k_1 \cdot \varphi_1 + b_M \cdot \dot{\varphi}_1 + b_p \cdot (\dot{\varphi}_1 - \dot{\varphi}_2) = M_M + M_1^M \cdot \cos(\omega \cdot t) \\ &I_P \cdot \ddot{\varphi}_2 + b_P \cdot (\dot{\varphi}_1 - \dot{\varphi}_2) = M_P - M_1^P \cdot \cos(\omega \cdot t - \nu) \end{aligned} \tag{3}$$

and for $|\varphi_1 - \varphi_2| > a$ the following equations hold

$$\begin{aligned} I_M \cdot \ddot{\varphi}_1 + k_1\varphi_1 + k \cdot (\varphi_1 - \varphi_2) + b_M \cdot \dot{\varphi}_1 + b_p \cdot (\dot{\varphi}_1 - \dot{\varphi}_2) &= M_M + M_1^M \cdot \cos(\omega \cdot t) \\ I_P \cdot \ddot{\varphi}_2 + k \cdot (\varphi_1 - \varphi_2) + b_P \cdot (\dot{\varphi}_1 - \dot{\varphi}_2) &= M_P - M_1^P \cdot \cos(\omega \cdot t - \nu) \end{aligned} \quad (4)$$

Results

These parameters were obtained in MAXON MOTOR catalogue. DC motors represent both drive and work element.

The numerical simulations were performed for these parameters. Angular velocity of excitation was selected as parameter to change, in interval from 1 rad/s to 200 rad/s. The angular displacement and angular velocity of the system was calculated for phase plane and attractors projection. The excitation in the clutch must be calculated as well for attractors projection.

The phase plane for both angular displacement and for relative angular displacement is drawn. The Poincarre map and attractor for relative angular displacement were solved and drawn too. Another possibility of system analysis is to transfer angular displacements into frequency domain and perform the analysis in this domain. The FFT from relative angular displacement was calculated and analyzed.

Next pictures show all of earlier discussed schemes for excitation angular velocity ω = 18.93 rad/s, ω = 110 rad/s. These angular velocities were chosen as representative's values. The changes in dynamic system evolution depend on chosen parameter changes. On the spectrum of relative angular displacement you can see it very well. Although the structure of the system does not change and one parameter changes only, in the spectrum you can see many natural frequencies. These frequencies appear and disappear with the changes of angular velocity ω. Phase planes also have different shapes. Poincarre maps are interesting for analysis as well. Here we can discover typical diagrams known from theoretic studies, as stable focus for ω = 110 rad/s, see Fig. 9. The system is closest to the chaotic behavior for ω = 18.93 rad/s. The high dumping in the system protects the creation of fully chaotic behavior, instead relaxation oscillation occurs.

Conclusion

Chaos and other statements of nonlinear systems became phenomenon in variety of engineering problems in last years. Therefore we focused on it also in analysis of drive systems. Based on performed analysis we can state following recommendations:

- when evaluating the properties and behavior of dynamic system it is useful to define such parameters of models, which can influence the occurrence of parasitic motion including chaotic one (fluctuation of initial conditions, links gaps, control parameters),
- to observe the evolution of responses in phase planes based on changes of selected parameters and to identify typical chaos effects,
- if such effect occur then evaluate Fourier spectrum of responses. Chaotic motion corresponds to broadband spectra, even when exciting spectra is narrowband.

With respecting given recommendations it is not difficult to identify the areas of possible occurrence of chaos in technical systems using mathematical modelling. However, we do not want to disvalue the analytical approaches with above described alternative approach.

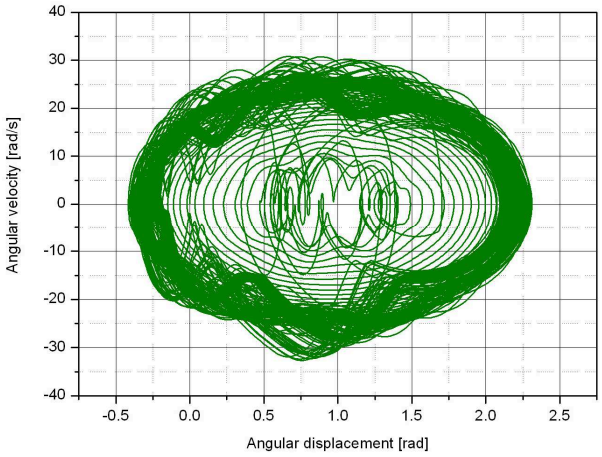


Fig. 2: Phase plane for angular displacement φ1 for ω = 18,93 rad/s

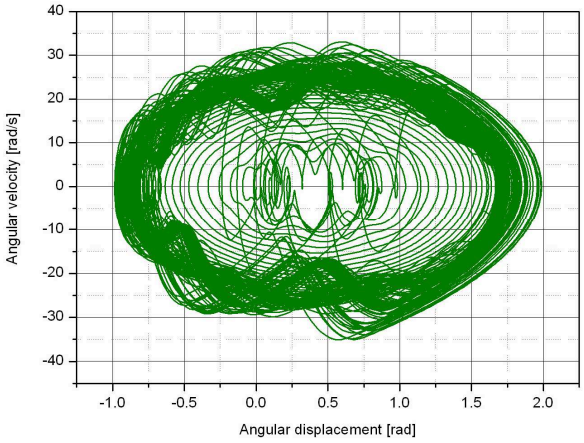


Fig. 3: Phase plane for angular displacement φ 2 for ω = 18,93 rad/s

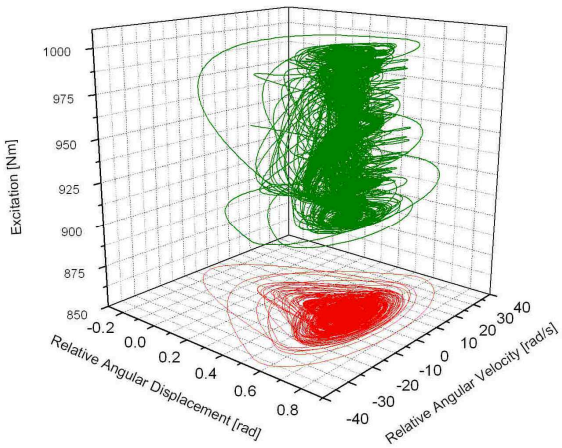


Fig. 4: Attractor for relative angular displacement for ω = 18,93 rad/s

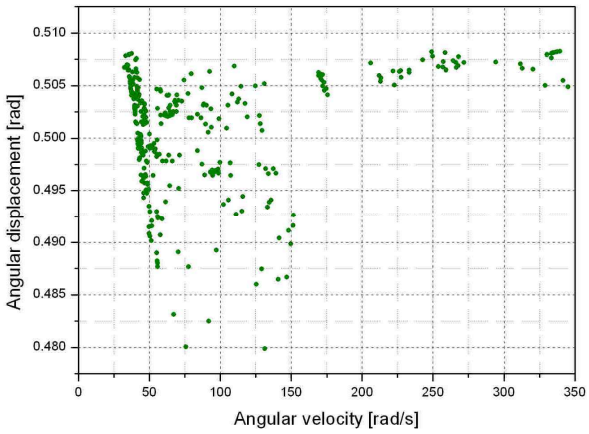


Fig. 5: Poincare map for relative angular displacement for ω = 18,93 rad/s

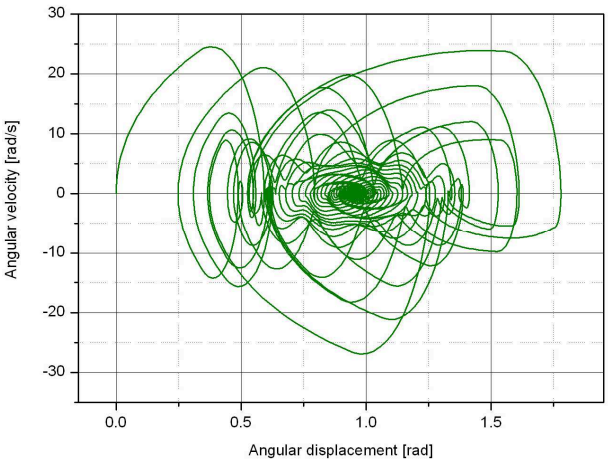


Fig. 6: Phase plane for angular displacement φ 1 for ω = 110 rad/s

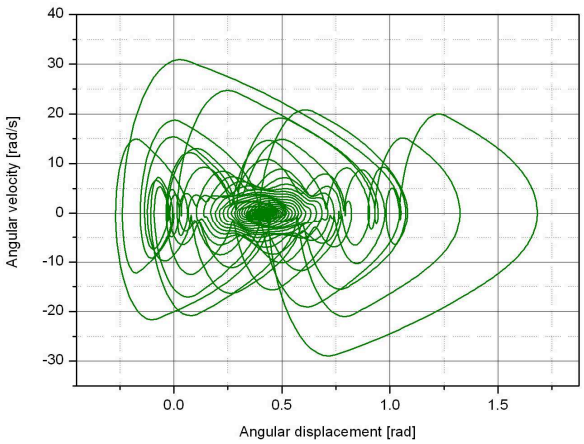


Fig. 7: Phase plane for angular displacement φ 2 for ω = 110 rad/s

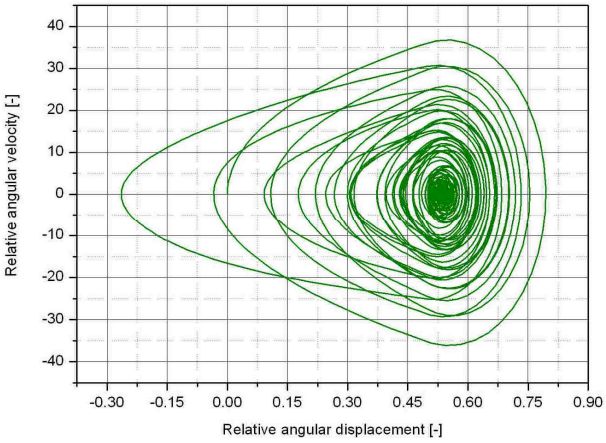


Fig. 8: Phase plane for relative angular displacement for ω = 110 rad/s

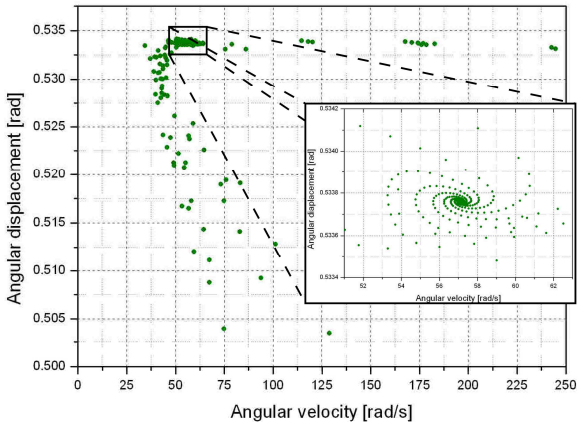


Fig. 9: Poincare map for relative angular displacement for ω = 110 rad/s

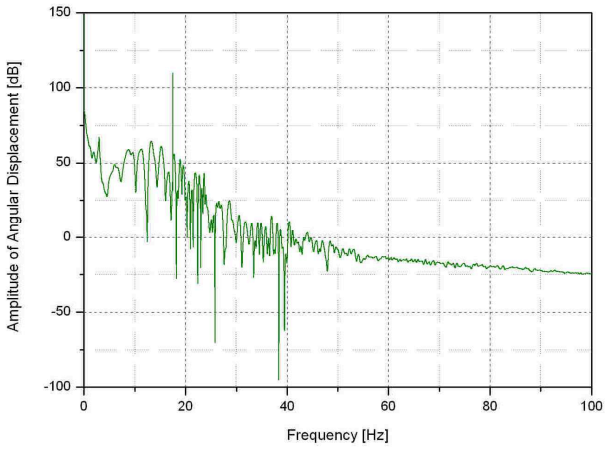


Fig. 10: Spectrum of relative angular displacement for ω = 110 rad/s

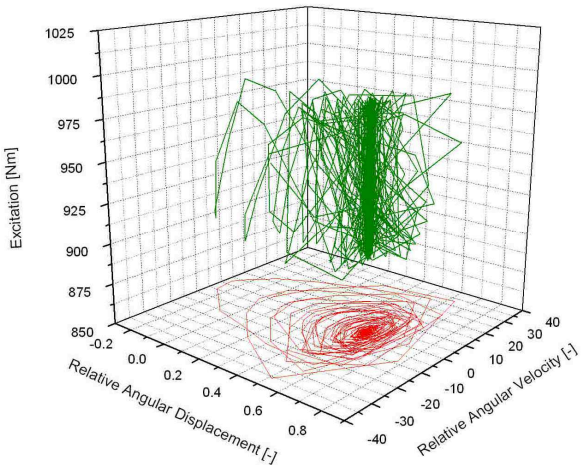


Fig. 11: Attractor for relative angular displacement for ω = 110 rad/s

Acknowledgment

This work is an output of cooperation between XYZ and NETME Centre, regional R&D centre built with the finan-cial support from the Operational Programme Research and Development for Innovations within the project NETME Centre (New Technologies for Mechanical Engineering), Reg. No. CZ.1.05/2.1.00/01.0002 and, in the follow-up sustainability stage, supported through NETME CENTRE PLUS (LO1202) by financial means from the Ministry of Education, Youth and Sports under the „National Sustain-ability Programme I. And FSI-S-14-2311 Strength and dy-namics of modern materials and designs II

References

[1] Procházka, F., Kratochvíl, C.: Úvod do matematického modelování pohonových soustav, CERN, s.r.o., ISBN 80-7204-256-4, Brno 2002 .

[2] Kratochvíl, C., Procházka, F., Pulkrábek, J.: Pohonové soustavy v mechatronických objektech, Int. Conf. Computional Mechanisc 2005, Hrad Nečtiny 2005:

[3] H.J.Korsch, H.J.Jodl, Chaos, ISBN 3-540-57457-3, Springer-Varlag Berlin Heidelberg New York, 1994.

Advanced Materials Research Vol. 936 (2014) pp 2125-2129
© (2014) Trans Tech Publications, Switzerland
doi:10.4028/www.scientific.net/AMR.936.2125

Material Selection and Finite Element Analysis for the Enclosure of Mine Exploration Robot

Zhiying Song[1, a*],Jianyang Zhao[1, b], Ruiqing Jia[2,c]

[1]108, Mechanical Electronic Building, China University of Mining and Technology, Beijing, Ding 11 Xueyuan Road, Hadian District, Beijing, China

[2]102, Mechanical Electronic Building, China University of Mining and Technology, Beijing, Ding 11 Xueyuan Road, Hadian District, Beijing, China

[a]mitsong@126.com, [b]zjycumtb@163.com, [c]Ruiqingjia@yahoo.com

Keywords: mine exploration robot; material selection; flameproof enclosure; finite element analysis

Abstract：This paper focuses on materials selection and finite element analysis for flameproof enclosure of mine exploration robot. The internal environment of abandoned mine is unknown, thus the robot must be designed explosion proof. This research deals with a safe solution to environment exploration for abandoned mines by using mine exploration robot. Modeling by using 3D software and finite element analysis verifies whether enclosure strength satisfies requirements. It will provide a reference for the development of mine exploration robot.

Introduction

In the process of mining, a large number of goaves were formed. The area of coal mine goaves formed each year can be hundreds of millions cubic meters [1]. Comprehensive development and utilization of abandoned mine becomes the new world topic of resources recycle. In the middle of the 20th century, the developed countries began to study on how to handle with abandoned mines, for instance, the Netherlands has built a new type geothermal power station by using geothermal resources in an abundance mine. In China, although there are few applicable examples, it has drawn great attention. Reusing abandoned mines is necessary and useful from the perspective of environmental protection and resources comprehensive utilization [2-4].

For ecological reconstruction and utilization of abandoned mines, it is necessary to work out reasonable measures, and to explore the internal environment of abandoned mines. The underground temperature and the concentration of toxic gases can also cause danger to underground workers or researchers. Thus there is a need to do research on mine exploration robot which can replace workers or researchers into mines to explore mine temperature and gas concentration. This kind of robot will be a powerful tool for researchers, and this research is of great practical significance.

Because of the unknown and dangerous environment underground, in addition to the requirement of flexibility, high reliability and obstacle avoidance ability, mine exploration robot must also have flameproof design. With reference to national standards GB3836.1-2000, it is suitable to adopt flameproof design on the main body of small mine exploration robot. Electrical equipments which may easily generate electrical arc or spark will be placed inside the flameproof enclosure.

This paper introduces the structure design of abandoned mine environment exploration robot based on the Chinese and foreign research status of mine robot. It focuses on the design of flameproof enclosure and finite element analysis.

The Development Status of Mine Exploration Robot

Chinese and foreign research on mine exploration robot has made some achievement, and some robots are designed for flame proof. For example, the rescue and exploration robot of Remotec Co., Ltd., named V2, has the ability of moving in dangerous mine environment. V2 is propelled by explosion-proof motors that drive rubber tracks. V2 has combines overall flameproof design with

partial explosion-proof design [5].CUMT-1, developed by China University of Mining and Technology, is the first coal mine robot for rescuing. It is equipped with low luminous camera, thermometer and toxic gas sensor. CUMT-1 can transmit live information including images, concentrations of gas and dust and temperature at the scene through a wireless network to operator. The main body is designed to adopt flameproof enclosure [6, 7].

The Structure Design of Mine Exploration Robot

Abandoned mine exploration robot mainly consists of three parts: six-wheeled mechanism, synchronous belt transmission and flameproof enclosure, as shown in Fig.1. It has the characteristics of compact structure, good mobility and high transmission efficiency.

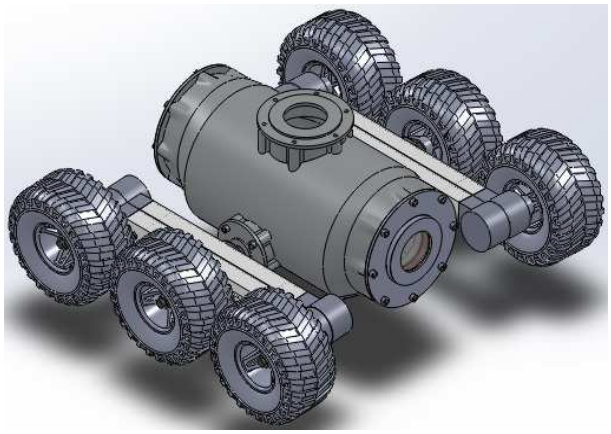


Fig.1 3D Model of Mine Exploration Robot

The flameproof enclosure of mine exploration robot is not only the robot chassis, it also need enough space for installing electrical equipments, such as control and communication module and power module [8]. When the explosive mixture gases, from environment into the enclosure, are ignited by spark or ack in the enclosure, the enclosure should not be destroyed, and the explosive gases from the environment outside the enclosure should not be detonated [9, 10]. Therefore, the robot flameproof enclosure should have enough strength and installation space. In addition, under the circumstance of same volume, volume of different shapes has an effect on explosion pressure [11].

Table 1 shows that the pressure of rectangle container and cylindrical container is small. But cylindrical container has advantages of even stress, simple structure and compact inside, compared with rectangle container [12]. Therefore, this research adopts cylindrical shape for robot body structure, and for the requirement of robot mobile performance, the enclosure bottom is designed as flat. The shape of enclosure is similar to cylindrical.

TABLE 1 THE EXPLOSION PRESSURE UNDER THE SAME VOLUME OF DIFFERENT SHAPE OF PRESSURE VESSEL

Shape	Volume /L	Pressure /Mpa (CH_4 9%-10%)
Cuboid	8	0.51
Cylinder	8	0.55
Cube	8	0.61
Sphere	8	0.71

Enclosure Material Selection

The enclosure of mine exploration robot should not only have enough strength, it should also has light weight to improve robot mobility. Robot flameproof enclosure can be aluminum ally casted. Because dangerous mechanical collision spark and friction spark may be easily generated when aluminum alloy contains large amount of magnesium (Mg), the amount of Mg cannot exceed a certain standard. Chinese standard is less than 0.5%. This research finds out that the tensile strength of the

enclosure material of an electric drill used in coal mine, named ZA1Zn11Si7 (code name: ZL401; Mg 0.1%-0.3%) , is greater than 195Mpa. This kind of alloy has good casting performance, and is suitable for vessels under pressure.

Flameproof Enclosure Finite Element Analysis

The design pressure of flameproof enclosure of mine exploration robot is mainly related to explosion pressure. If the volume of vessels is fixed, the gas pressure after explosion can be expressed in Equation 1： $p_1 = p_0(273 + t_1)/(273 + t_0)$ (1)

In Equation 1:

p_0 refers to the pressure of mixed gas before explosion: generally $1*10^5$pa;

t_0 refers to the temperature before explosion: generally 15-17 ℃;

p_1 refers to the pressure of mixed gas after explosion;

t_1 refers to the temperature after explosion: taking1850-2650 ℃.

The calculation result of Equation 1 suggests that p1 is 0.732-1.015Mpa.

A large number of experiments conclude that the pressure caused by explosive gas explosion is usually at 0.703-1.01Mpa. Thus the design pressure value is made as 1.01Mpa [13, 14]. According to Chinese National Standard GB3836.2-2000, this research carried out enclosure static pressure experiment, and the analysis type is static. In addition, because the minimum thickness of aluminum made cylindrical pressure vessel is 3mm, and in consideration of mine corrosion allowance, the thickness of robot enclosure is made as 5mm.

This research carries on modeling and finite element analyzing by using Solidworks software [15], which is a 3D software. The analysis result comes up after initialization settings and calculation. As shown in Fig.2, the maximum stress appears in the middle of the bottom, and safety coefficient is less than 1.5. Thus it does not meet the requirement. This research increases the thickness of bottom to 8mm. It can be seen in Fig.3, the maximum stress is 130.4Mpa which is less than the tensile strength of materials used, the weakest part of the enclosure is on the border between the enclosure and the above lid. The minimum safety coefficient is 1.5, and it satisfies the requirement.

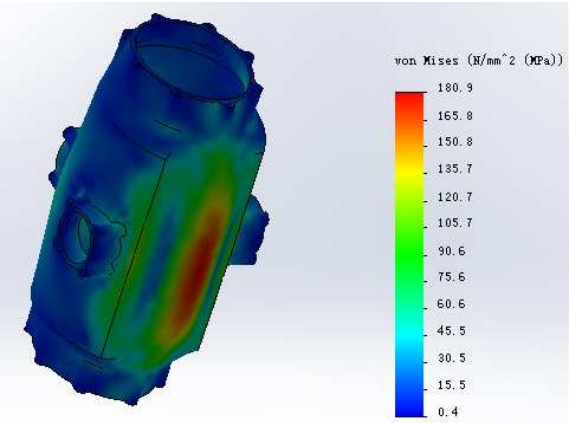


Fig.2 Static Analysis Diagram (a)

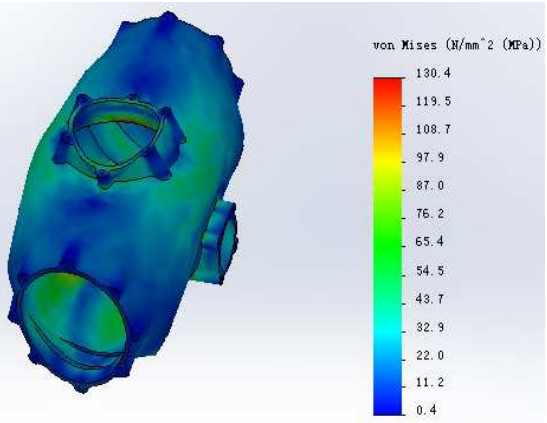


Fig.3 Static Analysis Diagram (b)

Based on the foregoing content of robot structure design, enclosure material selection and finite element analysis, and by adopting electrical explosion-proof standards and assembly requirements, this research made out a prototype of mine exploration robot. Fig.4 shows the prototype.



Fig.4 The Prototype of Mine Exploration Robot

Conclusions

With the development of economy, there are more and more abandoned mines. Therefore, the operation and utilization of abandoned mine is imperative. Firstly, this paper explains the research significance of mine exploration robot. Due to the uncertain mine environment, exploration robot will replace researchers to explore the environment of mines in avoidance of injury. Secondly, this paper designs the robot to be flameproof, and adopts light alloy materials for enclosure. Finally, it carries out static analysis by finite element analysis software, and verifies that the flameproof enclosure satisfies strength requirement. It provides a reference for future mine robot safety design.

References

[1] Pengfei Meng. Study on the Recycling of the Discarded Mine Resources, J. China Mining Magazine. 20(2011)62-65. In Chinese.

[2] Guoliang Xu, Juru Yuan, Zhaoxiu Tu, et al. Utilization of Obsolete Mineral Mines, J. China Population, Resources and Environment. 22(2012)360-362. In Chinese.

[3] Min Zhen, Junwei Zhao. A New Comprehensive Utilization Way of Abolished Mining Pits, J. Conservation and Utilization of Mineral Resources. 3(2003)49-53. In Chinese.

[4] Xiexing Miao, Minggao Qian. Research on Green Mining of Coal Resources in China:Current Status and Future Prospects, J. Journal of Mining & Safety Engineering. 26(2009)1-14. In Chinese.

[5] Information on http://www.msha.gov, 2014.

[6] Yong Wang, Hu Zhu, Yongsheng Wang,et. Current Status and Technical Problems in Research of Coal Mine Rescue Robot, J. Coal Mine Machinery.28(2007)107-109. In Chinese.

[7] Yunwang Li, Shirong Ge, Hua Zhu. Research on Application of Coal Mine Rescue Robots, J.Coal Mine Machinery. 30(2009)164-167. In Chinese.

[8] Dan Zhou, Junjia Zhang, Zhiying Song, et. Modeling and Finite Element Analysis of Flameproof Enclosure of Coal Mine Mobile Mobile Robot. Coal Mine Machinery. 33(2012)84-86. In Chinese.

[9] Yunwang Li, Shirong Ge, Hua Zhu, et. Design and Manufacture of Flameproof Enclosure of Coal Mine Rescue Robot, J. Coal Mine Machinery. 30(2009)104-106. In Chinese.

[10] Song Qian, Chunming Ni. Enclosure Strength Design of Minning Flame Proof Electrical Apparatus, J. Colliery Mechanical & Electrical Technology.6(2006)30-33. In Chinese.

[11] Xiaoe Guo, Jinlu Zhao. Design of Mine Cylindrical Flameproof Enclosure, J. Colliery Mechanical & Electrical Technology. 1(2008)16-20. In Chinese.

[12] Liping Gong, Zhian Song, Yu Wang. Design on Flameproof Cylindrical Enclosure for Coal Mine Based on Finite Element Method, J. Electric Explosion Protection. 3(2008)1-6. In Chinese.

[13] Liping Gong, Zhian Song, Zeyong Liu. Design Method on Mine Cylinder Explosion – resistant Enclosure, J. Coal Mine Machinery. 30(2009)30-33. In Chinese.

[14] Shuanghui Li. On the Explosion Pressure in Flame-proof Enclosures and the Influential Factors, J. Safety In Coal Mines. 34(2003)101-103. In Chinese.

[15] Wenjie Li, Qingliang Zeng, Tao Yu,et. Finite element analysis for steel pressure vessel based on COSMOSWorks, J. Machinery Design & Manufacture. 5(2011)33-35. In Chinese.

Advanced Materials Research Vol. 936 (2014) pp 2130-2134
© (2014) Trans Tech Publications, Switzerland
doi:10.4028/www.scientific.net/AMR.936.2130

Initial Pressure Influence On Explosion Pressures Of Methane–Air Deflagrations In Linked Vessels

Yihu Cui[1,a], Juncheng Jiang[1,b *], Yuan Yu[1,c] and Qingwu Zhang[1,d]

[1]Jiangsu Key Laboratory of Urban and Industrial Safety, Institute of Safety Engineering, Nanjing University of Technology, Mail Box 13, No. 200 North Zhongshan Road, Nanjing 210009, China

[a] yihucui@163.com, [b] jcjiang@njut.edu.cn, [c] yuyuan@njut.edu.cn [d] zhqingwu@163.com

Keywords: linked vessels; gas explosion; closed explosion; vented explosion; initial pressure; peak pressure

Abstract：An experimental study on pressure evolution during closed explosion and venting progress of methane–air mixtures ([CH_4=10%]) in linked vessels was performed, for systems at various initial pressures (P_0=0-0.08MPa). The effects of initial pressure on regularity of pressure variation in vessels were discussed. For the closed explosion in isolated vessel, the higher level of the initial pressure in isolated big vessel is, the larger the peak pressure and rate of pressure rise is, and the peak pressure increases nonlinearly with initial pressure; For closed explosion in linked vessels, the higher initial pressure within the linked vessels system leads to the higher peak pressures in two vessels and there is an approximate linear relationship between them, which is similar to explosion in isolated vessel. For vented explosion in linked vessels at higher initial pressure, venting has poorer effect on protection of the linked vessels.

Introduction

Linked vessel configuration handling or storing flammable gas is very common in industry (linked reactors and tanks, mines, electrical equipment casings, adjacent buildings)[1]. Once explosion takes place in one vessel, it can propagate to other vessels through linked pipes, which leads to higher value of peak pressures and rates of pressure rise in the vessels as compared to the explosion in isolated vessel. The term pressure-piling was often used to describe this phenomenon.

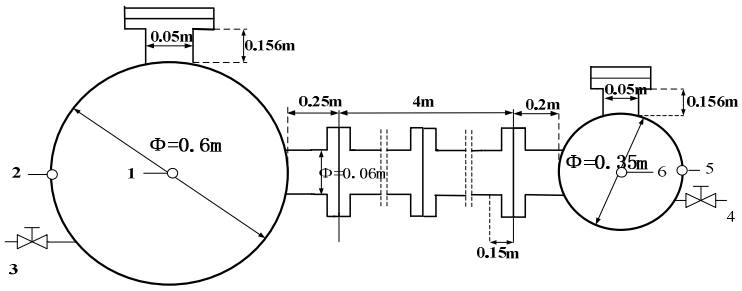
Pressure-piling in linked vessels was first recognized as a special explosion hazard in 1906[2], and then some comprehensive experiments were reported in literatures. These experiments demonstrate that pressure-piling is strongly influenced by ignition position, pipe diameter, volume ratio of the two vessels[3-6]. Some authors[1,7] established and developed CFD model to model gas explosions in linked vessels, aiming at investigating the effect of the ignition position, the pipe diameter and the volume on linked vessel explosion. These efforts have been contributed to guide the protection against explosion hazard in linked vessels. However, some other parameter such as intinal pressure may be significant to safety design of linked vessels. What's more, there are few reports on vented explosion of linked vessels at higher initial pressure.

In this work, the effect of initial pressure on the closed and vented explosion characteristics in a linked vessels experiment system was investigated.

Experimental apparatus

The apparatus used in the present experiments is illustrated in Fig.1. It consists of two spherical vessels: 0.113 $m^3$and 0.022 m^3 (referred as big vessel and small vessel respectively) which were linked by cylindrical pipe of 4 m. The area of each vent is 1.96×10^{-3} m^2 (D=0.05 m).

During the experiments, linked vessels system was filled with 10% methane–air mixture at ambient initial temperature and various initial pressures. The pressure variation was recorded using a series of high-frequency pressure transducers. The position of interface for pressure transducer and gas inlet were shown in Fig.1. Ignition using a standard 6J inductive-capacitive spark was positioned at the two vessels center (see Fig1).The pressure signals were monitored with a data acquisition system DEWE 4.3.



Position 1, 14,——ignition； 3, 4——gas inlet；2, 5——pressure transducer；

Fig.1 Schematic diagram of explosion in linked spherical vessels

Results and discussion

Effect of initial pressure on gas explosion in isolated big vessel

The pressure history and peak explosion pressures of CH_4-air mixtures at various initial pressure is shown in Fig 2 and Fig 3 respectively. As shown in the Fig 2 and Fig 3, the explosion pressure and the rate of pressure rise increase with the increasing initial pressure. And the peak explosion pressure is correlated to initial pressure by the linear equation： $P_{max}=7.6315P_0+0.681$. With regard to closed explosions in isolated vessel, the present data, as well as some previous data[8-10] show a common feature: there is a linear relationship between the peak pressure and the initial pressure. With the increase of the initial pressure, the vessel has more flammable gas, more abundant the energy is released, which leads to the higher peak pressure. And with the increase of the initial pressure, the distance between the molecules is closer, probability of activated molecular collision is bigger, which accelerates the reaction rate and urges the rate of pressure rise to increase

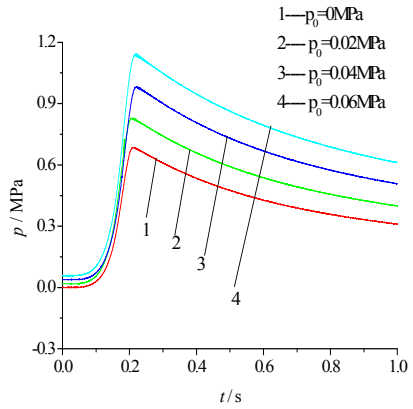


Fig.2 Pressure histories in the vessel at different initial pressure

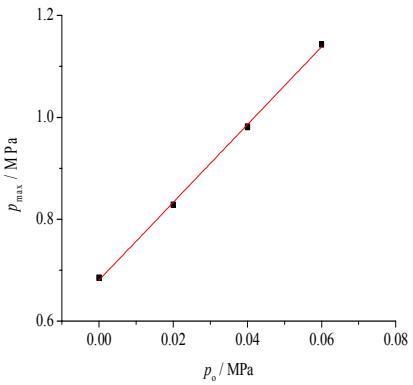
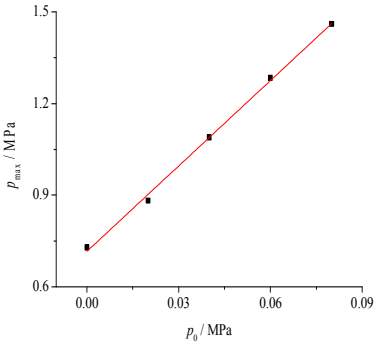


Fig.3 The fitting curve of peak pressure at different initial pressure

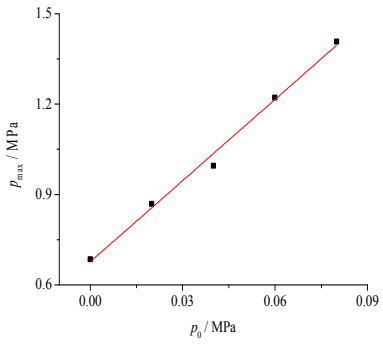
Effect of initial pressure on closed explosion of linked vessels

Fig.4 and Fig.5 illustrate peak pressures in two vessels connected by 4.45 m linked pipe, for ignition in the small vessel center and the big vessel center, respectively, by varying the initial pressure. As displayed in Fig.4 and Fig.5, initial pressure has significant effect on the peak pressures in two vessels; the higher initial pressure within the linked vessels system leads to the higher peak pressures in two vessels. There is an approximate linear relationship between them, which is similar to explosion in isolated vessel.

The linear equations for the peak pressure and initial pressure are listed in Table 1 and Table 2. As presented in Table 1 and Table 2, for ignition in the small vessel center, the slopes of linear relationship between peak explosion pressures in the two vessels and initial pressure is almost the same as that obtained in the isolated vessel. For ignition in the big vessel center, the slope of linear relationship between peak explosion pressure in the big vessel and initial pressure is almost the same as that obtained in the isolated vessel, however, the slope of linear relationship between the peak pressure in the small vessel and initial pressure in linked vessels system is larger as compared to that in isolated vessel, and the former slope is about twice the latter. Therefore, compared to the isolated vessel's explosion, the peak pressure in the small vessel is sensitive to variation within system initial pressure, while igniting in big vessel.

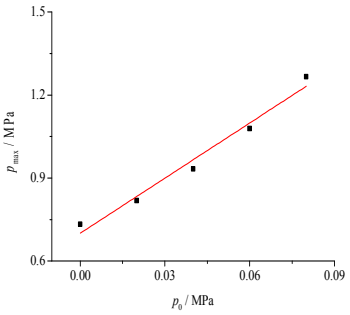


(a) The fitting curve of peak pressure in big vessel

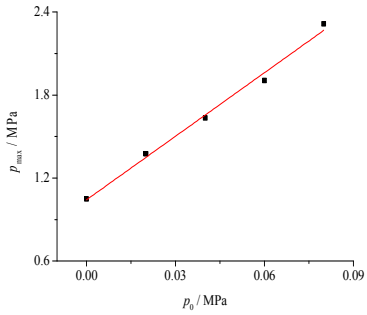


(b) The fitting curve of peak pressure in small vessel

Fig.4 The fitting curve of peak pressure in the two vessels for ignition in small vessel center and different initial pressure



(a) The fitting curve of peak pressure in big vessel



(b) The fitting curve of peak pressure in small vessel

Fig.5 The fitting curve of peak pressure in the two vessels for ignition in big vessel center and different initial pressure

TABLE 1 THE FITTING EQUATION OF PEAK PRESSURE IN THE TWO VESSELS FOR IGNITION IN SMALL VESSEL CENTER AND DIFFERENT INITIAL PRESSURE

Parameter		Fitting equation	Relevance	Instructions
Peak pressure /MPa	113L	P_{max}=9.332P_0+0.235	0.99746	Initial pressure P_0
	22L	P_{max}=8.985P_0+0.415	0.99152	

Table 2 The fitting equation of peak pressure in the two vessels for ignition in big vessel center and different initial pressure

Parameter		Fitting equation	Relevance	Instructions
Peak pressure /MPa	113L	P_{max}=6.641P_0+0.700	0.97124	Initial pressure P_0
	22L	P_{max}=15.314P_0+0.743	0.99065	

Effect of initial pressure on vented explosion of linked vessels

Fig.6 illustrates pressure histories of closed explosion and vented explosion of two vessels connected by 4.45 length linked pipe, for ignition in big vessel center and at 0.06 MPa initial pressure. For vented explosion experiment, safety membranes (the membrane rupture pressure is 0.28 MPa) are used to cover the vents. As compared to closed explosion, the peak pressure in big vessel drops from 1.08 MPa to 0.98 MPa and the peak pressure in small vessel drops from 1.91 MPa to 1.86 MPa, which suggests that there is few difference in peak explosion pressure between closed explosion and vented explosion of linked vessels. In this case, for peak explosion pressure, venting can't get the expected effect for linked vessels system at higher initial pressure. However, as shown in Fig.6, compared to closed explosion, the pressures in the two vessels quickly decrease after reaching peak pressures without oscillation process, so venting can reduce impulse acting on the two vessels. Because of methane–air mixtures in linked vessels burned out and cooling effect of vessel wall, as well as discharging of the high temperature and high pressure products from the vent increase the rate of pressure decline in two vessels.

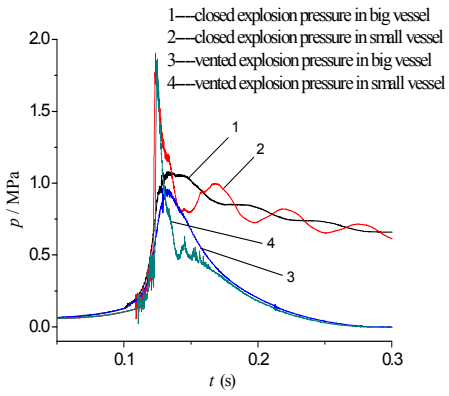


Fig.6 Effect of initial pressure on linked vessels venting process

Conclusions

Through experiments and theoretical analysis, following conclusions about the effects of initial pressure on gas explosion in linked vessels can be drawn.

(1) For closed explosion in isolated vessel: the higher level of the initial pressure in isolated big vessel is, the larger the peak pressure and rate of pressure rise is, and the peak pressure increases nonlinearly with initial pressure

(2) For closed explosion in linked vessels: the higher initial pressure within the linked vessels system leads to the higher peak pressures in two vessels and there is an approximate linear relationship between them; compared to the isolated vessel's explosion, the peak pressure in the small vessel is sensitive to variation within system initial pressure, while igniting in big vessel..

(3) For vented explosion in linked vessels: for linked vessels system at higher initial pressure, there is few difference in peak explosion pressure between closed explosion and vented explosion of linked vessels. However the pressures in the two vessels quickly decrease after reaching peak pressures without oscillation process, so venting can reduce impulse acting on the two vessels

Acknowledgements

The research was supported by National Natural Science Foundation of China (No. 51376088 and No.20976081) and Natural science fund for colleges and universities in Jiangsu Province (No.12KJB620001).

References

[1] Di Benedetto, A., & Salzano, E. (2010). CFD simulation of pressure piling. Journal of Loss Prevention in the Process Industries, 23, 498-506.
[2] Beyling, & Gluckauf, 42, 1906, 97-99 and 129-138.
[3] Phylaktou, H., & Andrews, G. E. (1993). Gas explosions in linked vessels. Journal of Loss Prevention in the Process Industries, 6(1), 15-19.
[4] Abdullin, R. K., Babkin, V. S., & Senachin, P. K. (1988). Combustion of gas in connected vessels. Combustion, Explosions and Shock Waves, 24, 123-132.
[5] Singh, J. (1994). Gas explosions in inter-connected vessels: pressure piling. Transactions of the IChemE, 72B, 220-228.
[6] Razus, D., Oancea, D., Chirila, F., & Ionescu, N. I. (2003). Transmission of an explosion between linked vessels. Fire Safety Journal, 38, 147-163.
[7] Maremonti, M., Russo, G., Salzano, E., & Tufano, V. (1999). Numerical simulation of gas explosions in linked vessels. Journal of Loss Prevention in the Process Industries, 12, 189-194.
[8] Gieras, M., Klemens, R., Rarata, G., & Wolanski, P. (2006). Determination of explosion parameters of methane–air mixtures in the chamber of 40dm^3 at normal and elevated temperature. Journal of Loss Prevention in the Process Industries, 19, 263–270.
[9] Huzayyin, A.S., Moneib, H.A., Shehatta, M.S., & Attia, A.M.A. (2008). Laminar burning velocity and explosion index of LPG–air and propane–air mixtures. Fuel, 87, 39–57.
[10] Razus, D., Brinzea, V., Mitu, M., & Oancea, D. (2009). Explosion characteristics of LPG–air mixtures in closed vessels. Journal of Hazardous Materials, 165, 1248–1252.

Advanced Materials Research Vol. 936 (2014) pp 2135-2139
© (2014) Trans Tech Publications, Switzerland
doi:10.4028/www.scientific.net/AMR.936.2135

Optimization Design of Transverse Flux Permanent Generator Based on Response Surface Method

Gao Zhongyong[1,a], Xie Jia[1,b], Wang Shiming[1,c]

[1]College of Engineering Science and Technology, Shanghai Ocean University, Shanghai 201306, China

[a]gaozhongyonggood@126.com, [b]jiaxie@shou.edu.cn, [c]shmwang@shou.edu.cn

Key words: transverse flux permanent generator; response surface method; center combination design; optimization design

Abstract: To consider the complicated situation fully such as saturation, leakage flux and so on, and to make the generator size to meet the design requirements, we use the methodology of response surface method combined with center combination design to optimize the transverse flux permanent generator. At first, the optimization goals and the optimization design variables are set on the basis of the finite element model in the initial design. Then an optimized design model of the generator is built by the variable sequential combination response surface methodology. Experiment is arranged by the center combination design methodology, and optimal parameters are selected through response surface method. At last, we get all the structural dimensions of transverse flux permanent generator. The optimization makes the output voltage meet the design requirement.

Introduction

Transverse flux permanent generator is a special generator with high torque density. The generator is very promising in the field of direct-drive marine power system and ocean power generation system [1]. The concept of transverse flux permanent generator was raised by professor Herbert Weh, a generator expert of Germany Braunschweig University [2]. The generator uses a unique structure which solves the mutual restraint contradiction between the armature winding section and alveolar width in the traditional generator. At the same time it can improve the generator electromagnetism load, thus improve the ability of magnetoelectric energy conversion and it also has characteristics of small volume, light weight, wide speed range and controllability [3-6]. Resulting from the initial design of the generator often fails to effectively meet the design needs. In order to solve this problem, generator will introduce various correction coefficients based on magnetic circuit design in the traditional design process. Obviously, this method is time-consuming, cost of design is large and difficult to meet the needs of modern generator design. So in the modern generator design, in order to improve the accuracy of calculation, we use the finite element numerical calculation method and use the methodology [7] of response surface method combined with center combination design to optimize the transverse flux permanent generator.

Based on the initial design and practical optimization design requirements of transverse flux permanent generator, we raised the methodology of response surface method combined with center combination design to optimize the transverse flux permanent machine on the basis of the finite element model in the initial design. Eventually, we made the main parameters of generator output voltage is 223.2V.

Determination of the transverse flux permanent generator's optimization goals and optimization variables

We optimize the transverse flux permanent machine on the basis of the finite element model in the initial design. The maximum objective of transverse flux permanent generator is that the generator can provide to enough induction electromotive force. We analyze the generator's torque in terms of electromagnetic chain. Because the generator's each phase are the same, we analyze the condition of single phase.

In case of transverse flux permanent machine loading, a phase armature winding magnetic chain is

$$\Psi = \Psi_{PM} + \Psi_a = \Psi_{PM} + Li \tag{1}$$

Ψ -Total flux linkage of the winding, Ψ_{PM} -Flux linkage of permanent magnet effect, Ψ_a - Flux linkage of armature coils effect, L- The armature coil inductance, i- The armature coil current.

When the generator is running, excluding copper loss of the armature coil, the single-phase instantaneous electromagnetic power of generator can be expressed as:

$$p_m = -ei = \frac{d\Psi}{dt} i = \frac{d}{dt}\left(\frac{1}{2} Li^2\right) + \left(\frac{\partial \Psi_{PM}}{\partial \theta} i + \frac{\partial L}{\partial \theta} i^2\right)\Omega \tag{2}$$

p_m - Single-phase instantaneous electromagnetic power, θ - The mechanical angle of the generator rotor, Ω - The mechanical angular velocity of the generator rotor

In the formula (2), the first term is the inductive energy storage and it does not participate in electromechanical energy conversion of generator, so the instantaneous electromagnetic torque of generator is:

$$t_m = \frac{\partial \Psi_{PM}}{\partial \theta} i + \frac{\partial L}{\partial \theta} i^2 \tag{3}$$

The induced electromotive force is determined according to Faraday's law of electromagnetic induction and its size is proportional to the rate of change of the coil flux linkage, and its direction is determined by Lenz's law. Generator no-load induced electromotive force can be expressed as:

$$e_0 = -\frac{\mathrm{d}\Psi_{PM}}{\mathrm{d}t} = -\frac{\mathrm{d}\Psi_{PM}}{\mathrm{d}\theta}\Omega = -N\frac{\mathrm{d}\Phi_{PM}}{\mathrm{d}\theta}\Omega \tag{4}$$

e_0 - No-load EMF instantaneous value

We obtained some values by using finite element analysis and the no-load electromotive force under different speeds can be calculated by these values. Instantaneous induced electromotive force is close to the flux linkage waveform of generator, and the change of the flux linkage is determined by the change of excitation source and magnetic resistance of the main magnetic circuit. If we can get the appropriate kind of flux linkage waveform, the desired output induced electromotive force would be got. Optimizing tooth shape of rotor and stator can be achieved. So The optimization design variables of the transverse flux permanent generator are:

$$X = [x_1, x_2, x_3, x_4]^T = [h_{PM}, t_{PM}, r, l_e]^T \tag{5}$$

h_{PM} -The length of the permanent magnet magnetization direction.

t_{PM} - The radial length of permanent magnet.

r - The rotor tooth fillet radius.

l_e - Each pole core effective length of generator stator.

Optimal goal of transverse flux permanent generator:

$$E_0 = \sqrt{\frac{1}{T}\int_0^T e_0^2 dt}$$

E_0- No-load induced electromotive force valid values.

Optimization of rotor

The function relationship between the induced electromotive force and three rotor design variables (h_{PM}:x_1, t_{PM}:x_2 and r:x_3) is a curved surface. We use the second order response surface model to approximate it. For three design variables, CCD required fifteen tests. In CCD test, design variable range and level of three generator rotor design variables was shown in Table 1, among α=1.216. We got induced electromotive force data of different combinations of variables by using Ansoft Maxwell software to simulate.

TABLE 1 RANGE AND HORIZONTAL LEVEL OF CCD TEST DESIGN VARIABLES X_7, X_8 AND X_9

design variables of generator	Horizontal level				
	-α	-1	0	+1	-α
x_1 [mm]	3.568	4	6	8	8.432
x_2 [mm]	6.92	8	13	18	19.08
x_3 [mm]	0.96	1.5	4	6.5	7.04

According to the sample data of CCD, the estimated value of β was calculated by the least square method, and we can obtain fitting the response surface models of the induced electromotive force of three rotor design variables x_7, x_8, x_9. Response surface optimization diagram of induced electromotive force can be directly obtained by the response surface model. It is shown in Figure 1. The optimized rotor design variables (x_7, x_8 and x_9) are 6.3685mm, 13mm and 2.3725mm.

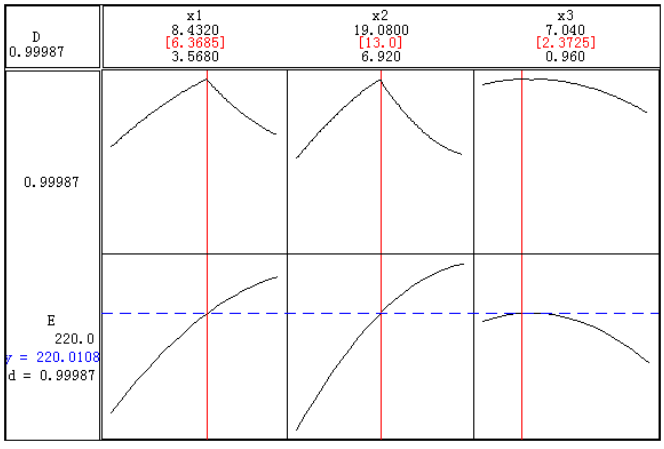


Fig.1 Response surface optimization diagram

The optimization of the stator

After determining the part of the rotor size, we optimized each pole core effective length l_e of generator stator. Figure 2 is corresponding changes of induced electromotive force when l_e is changing. As you can see from figure2, when l_e is extending from the middle position of the generator stator axial length (Stator teeth begin to overlap in axial direction), induced electromotive

force is increasing. However, when l_e reaches a certain length, induced electromotive force would be unchanged. This shows that l_e has no effect on induced electromotive force of the generator. So, optimization objective l_e can be achieved by the induced electromotive force(emf) is 47mm.

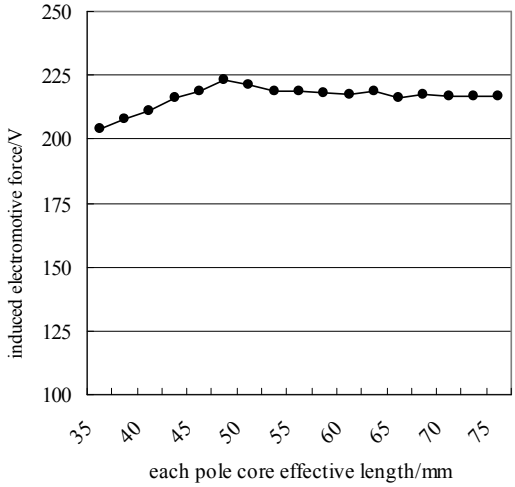


Fig.2 Effect change of each pole core effective length on the induced emf

Conclusion

So far all the structural dimensions of transverse flux permanent generator have been determined. The length of the permanent magnet magnetization direction is 6.3685mm, the radial length of permanent magnet is 13mm, the rotor tooth fillet radius is 2.3725mm and each pole core effective length of generator stator is 47mm. When number of coil is one, valid value of no-load induced electromotive force is 11.16V_{rms}. The figure 3 shows it. Output voltage equal to 20 times 11.16 V_{rms}. Eventually, we made the main parameters of generator output voltage is 223.2V. As the above optimal design process shown, we used electromagnetic field finite element analysis method to analyze, experiment was arranged by the center combination design methodology, and optimal parameters were selected through response surface method in the design of the generator stator and rotor structure size. All the structure sizes of transverse flux permanent generator are reasonable and meet requirements of the generator design.

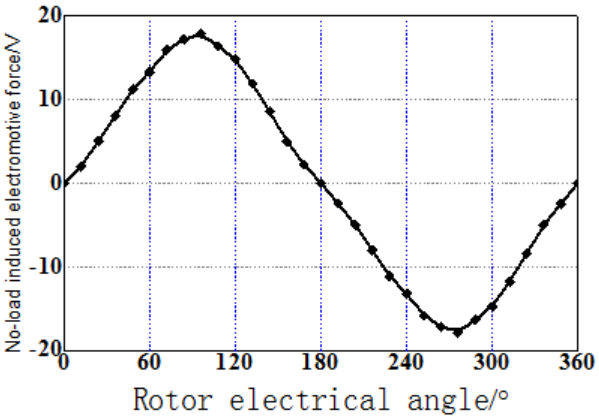


Fig.3 No-load electromotive force of one coil

Acknowledgements

This work was financially supported by Dr. Scientific Research Foundation of Shanghai Ocean University (A-0209-13-0105376) and Significant Scientific Foundation of State Oceanic Administration of China (SHME2011GD01).

References

[1] Chen AY, Nilssen R, Nysveen A: IEEE Transactions on Industry Applications Vol.46 (2010), p.779-789.

[2] Ahn HT, Jang GH, Chang JH, et al: IEEE Transactions on Magnetics Vol.44 (2008), p.4066-4069.

[3] Hoang TK, Kang DH, Lee JY: IEEE Transactions on Magnetics Vol.46(2010), p.3795-3801.

[4] Hong DK, Woo BC, Chang JH, et al: IEEE Transactions on Magnetics Vol..43(2007), p.1613-1616.

[5] Lei G, Guo YG, Zhu JG, et al: IEEE Transactions on Magnetics Vol.48(2012), p.923-926.

[6] Kang DH: IEEE Transactions on Magnetics Vol.41(2005), p.1952-1955.

[7] Xie Jia, Zhao Shengdun, et al: Journal of Xi'an Jiaotong University Vol.46(2012), p.57-62.

Advanced Materials Research Vol. 936 (2014) pp 2140-2146
© (2014) Trans Tech Publications, Switzerland
doi:10.4028/www.scientific.net/AMR.936.2140

Application of the Lumped-parameter Model in concept design phase of Side Impact Safety Development

Chen Tao[1,2,a] Peng Yun[2,b]

[1] State Key Laboratory of Vehicle NVH and Safety Technology, Chongqing, China

[2]State Key Laboratory of Advanced Design and Manufacturing for Vehicle Body, Hunan University, Changsha, China

[a]chentaohndx@gmail.com,[b]pengyun1989@163.com

Keywords: the lumped-parameter model; side impact; concept design phase; optimization

Abstract: In the process of side impact, the door was directly contacted with the chest, abdomen and pelvis of dummy and its movement has a large effect upon dummy injury. A evaluation about dummy injury influenced by the velocity and displacement of chest, abdomen and pelvis in dummy was proposed. A rapid forward development strategy which is applied in forward development was presented. A new type side impact LPM (Lumped-Parameter Model) was established. The stiffness of critical area in vehicle body was optimized by LPM which used the intrusive velocity and displacement of chest, abdomen and pelvis in dummy as design object. The example showed that the safety performance was improved obviously and the development period was shortened in some extent.

Introduction

In the progress of new car forward development, the detail finite model of new car cannot be established in the concept phase because of CAD data absence. However, LPM can be used for rapidly analyzing stiffness of vehicle body for achieving better new car safety performance, which plays a very important role in new car development based on same platform. In 1970, Kamal[1] developed a relatively simple but powerful model for simulating the crashworthiness response of a vehicle in full frontal impact. Lim, Green and Chevad[2-4] used LPM in full frontal impact, side impact and offset frontal impact analysis, the results were proved good. Zhao Kaishen and Shi Yuliang[5] from Qirui Co., Ltd used LPM for optimizing the stiffness of frontal critical area. The movement of door has a large effect upon dummy injury because it directly contacted with the chest, abdomen and pelvis of dummy. The intrusive velocity and displacement on chest, abdomen and pelvis were affected by stiffness of critical area in BIW (Body In White), which did not be researched formerly. In this paper, for improving side impact performance and shortening new car forward development period, a rapid forward development strategy that used new type side impact LPM for optimizing stiffness of critical area in BIW was proposed, which was applied in new car forward design based on same platform.

A rapid forward development strategy

During the concept phase of new car forward development, the traditional method is just put stiffness, modal and mass of BIW as performance assessment target. The crashworthiness

performance was out of consideration because of lacking detail CAD data. The disadvantage is that the potential of safety performance cannot be exploited completely in detail design phase. A rapid forward development strategy was proposed which used new type side impact LPM in new car based on same platform forward development. Take a new car forward development of a company as example, at first, the new type side impact LPM was established based on original platform FE (Finite Element) model. Then, the LPM accuracy was confirmed for optimizing the stiffness of BIW. At last, the optimum stiffness of BIW was outputted which optimized with LPM. The critical area structure of BIW was designed reasonable by this process flow and the development period can be shortened effectively.

Establishment of new type side impact LPM

In the progress of side impact, the injury of dummy was influenced by stiffness of BIW which maintain a sufficient survival space for occupants in crash. Properly side structures and doors design can minimize intrusion effectively. The goal of crashworthiness is an optimized vehicle structure that can absorb the crash energy by controlled vehicle deformations while maintaining adequate space so that the residual crash energy can be managed. Side structures were the main energy absorbed components in side impact. On the base of energy management, the side impact can be divided into six parts, MDB (Moving Deformable Barrier), Front door, Rear door, B pillar, Rocker, Rest of vehicle. For describing the intrusion of chest, abdomen and pelvis in dummy, the Front door was divided into outdoor and four parts of inner door. The detail description was as shown in Figure.1.



Figure.1 The division of Front door

For exploring the relationship between intrusion of chest, abdomen, pelvis in dummy and stiffness of side structure, the new type side LPM based on Ded [6]'s LPM was proposed by analyzing side impact mechanics. The topology of new type side impact LPM was as shown in Figure.2. The detail description of parameters in new type side impact LPM was illustrated in Table 1.

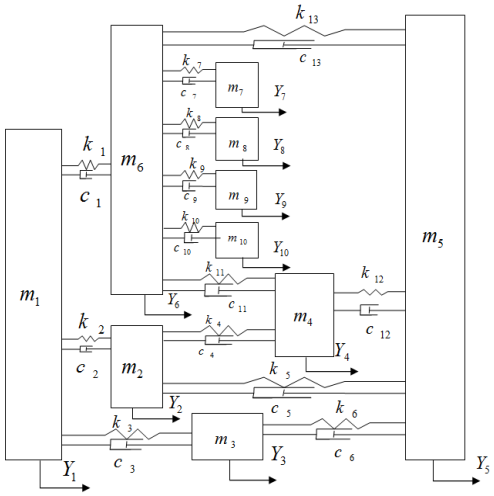


Figure.2 New type side impact LPM

TABLE 1 THE DESCRIPTION OF PARAMETERS IN NEW TYPE SIDE IMPACT LPM

Parameters	Description
m_1	MDB
m_2	Rear door
m_3	Rocker
m_4	B pillar
m_5	Rest of vehicle
m_6	Outdoor
$m_7 \sim m_{10}$	Four parts of inner door
$k_1 \sim k_{13}$	Stiffness
$c_1 \sim c_{13}$	Damping
$Y_1 \sim Y_{13}$	Displacement

The most important parameters in LPM were spring properties, which extracted from the results of FE simulation based on same platform. Take a forward development of new car which as a typical MPV in market as example, the finite element simulation model was developed (Figure.3). The FE model was built based on C-NCAP which includes the vehicle, MDB and dummy. The initial velocity of MDB is 50km/h. The experimental and numerical vehicle deceleration results at B pillar were illustrated in Figure.4.

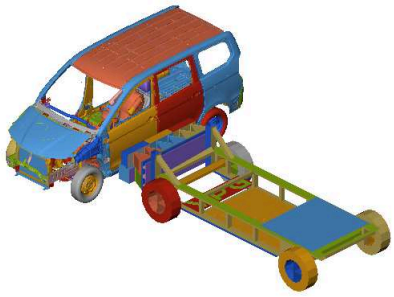


Figure.3 A finite element model of reference vehicle

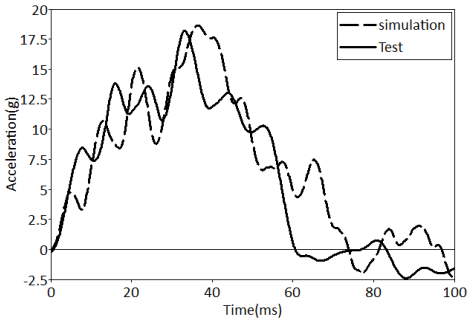


Figure.4 The vehicle deceleration comparison between test and simulation

It is noticed that the spring properties in the LPM in Figure.3 represent interaction between a pair of subsystems. The spring characteristics of LPM were obtained by defining a number of contact and sectional forces in the direction of impact, which based on the least-squares error approximation of FE results. The displacement-time histories of subsystems are obtained by measuring serious points from results of FE model. One principle must be satisfied that the area enclosed between LPM stiffness curve and horizontal axis was equal to the FE's area. The idealized stiffness of MDB to Rocker subsystem was shown in Figure.5. For describing the damping affection between different subsystems, damping coefficients were defined by trial and error. The LPM parameters were summarized in Table 2.

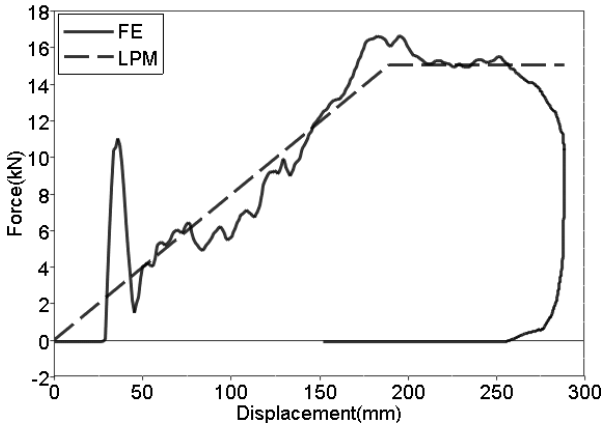


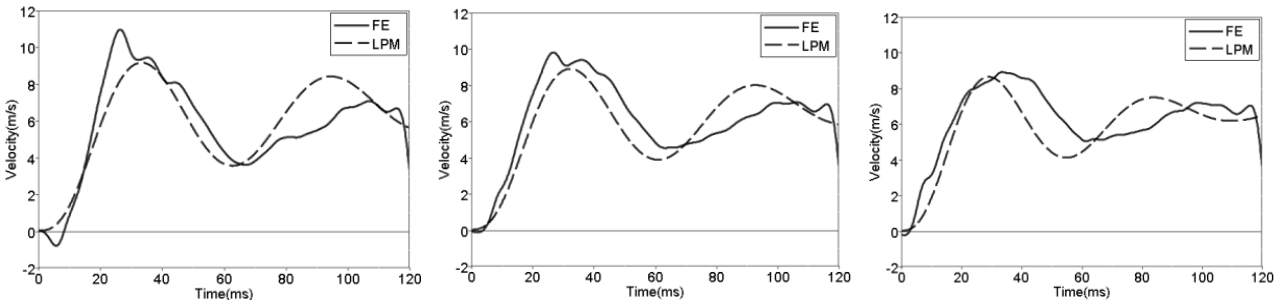
Figure.5 Idealized of behavior of spring between MDB to Rocker

TABLE 2 LPM PARAMETERS

Mass	Value (kg)	Damping	Value (kN.ms/mm)	Stiffness	Intrusion (mm)	Stiffness coefficient (kN/mm)	Yield force (kN)
m_1	960	c_1	0.5	k_1	212	0.2431	30.4
m_2	18	c_2	0.5	k_2	220	0.1207	20
m_3	17	c_3	0.5	k_3	288	0.0793	15
m_4	5.5	c_4	0.1	k_4	37	2.1621	28
m_5	1270	c_5	2.5	k_5	247	0.1336	30.1
m_6	14	c_6	2.5	k_6	154	0.1227	12.6
m_7	1.0	c_7	0.025	k_7	41.4	0.01	0.414
m_8	0.8	c_8	0.025	k_8	40.4	0.0092	0.323
m_9	0.6	c_9	0.025	k_9	35.9	0.0086	0.251
m_{10}	3.0	c_{10}	0.025	k_{10}	47.5	0.006	0.190
		c_{11}	0.1	k_{11}	50	0.3651	5.7
		c_{12}	2.5	k_{12}	230	0.4	60
		c_{13}	2.5	k_{13}	232	0.3073	50.2

Validation of new type side impact LPM

For describing the movement of inner door, the Madymo model was established on the basis of LPM in Figure.4. The comparison of intrusive velocity and displacement of chest, abdomen and pelvis in dummy between LPM and FE were as shown in Figure.6. The relative errors between LPM and FE were given in Table 3 and the max error was not exceeded 20%.



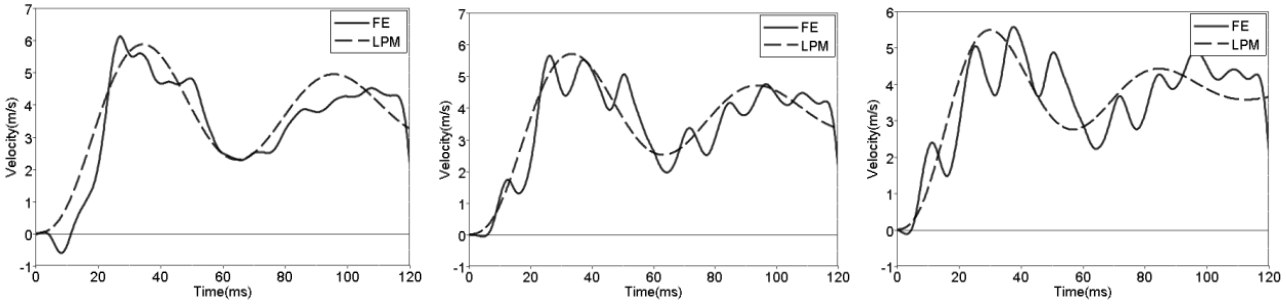
(a) Chest (b) Abdomen (c) Pelvis

Figure.6 Comparison of intrusive velocities between LPM and FE at 50km/h

TABLE 3 RELATIVE ERROR BETWEEN LPM AND FE

	LPM	FE	Relative error (%)
Intrusion at Chest	208(mm)	224(mm)	7.1
Intrusion at Abdomen	203(mm)	223(mm)	9.0
Intrusion at pelvis	191(mm)	208(mm)	8.2
Velocity at Chest	9.1(m/s)	11.0(m/s)	17
Velocity at Abdomen	8.9(m/s)	9.9(m/s)	10
Velocity at pelvis	8.6(m/s)	9.0(m/s)	4.4

For validating the stability of LPM, the intrusive velocity and displacement of chest, abdomen and pelvis in dummy at the condition of MDB initial velocity is 30km/h were exported. The comparison between LPM and FE was as shown in Figure.7.



(a)Chest (b) Abdomen (c) Pelvis

Figure.7 Comparison of intrusive velocities between LPM and FE at 30km/h

Optimization

In the earlier stage of new car development based on same platform, the target of vehicle safety performance should be disintegrated into a series of subsystem targets. The intrusive velocity and displacement of chest, abdomen and pelvis in dummy are always used for assessing the side impact performance [7]. In order to utilize the potential of side structure sufficiently, the stiffness of BIW was optimized by above LPM. The mathematical model of optimization was illustrated in follow formula:

$$\begin{aligned} &\text{Minimize} && U = f\left(x_1, x_2, \ldots x_k\right) \\ &\text{Subject to} && g_i\left(x_1, x_2, \cdots, x_k\right) = 0 \left(i = 1,2, \cdots, m\right) \\ & && h_j\left(x_1, x_2, \cdots, x_k\right) \le 0 \left(j = 1,2, \cdots, n\right) \\ & && x_1, x_2, \ldots x_k \in R \end{aligned} \tag{1}$$

Where U represents the objective function, $g_i\left(x_1, x_2, \cdots, x_k\right)$ represents the equation restrain, $h_j\left(x_1, x_2, \cdots, x_k\right)$ represents the non-equation restrain, $x_1, x_2, \cdots x_k$ represent the design variables.

The yield force scales of Front door, Rear door, B pillar and Rocker were defined as design variables as shown in Table 4, the intrusive velocity and displacement of chest, abdomen and pelvis in dummy were defined as design targets. A comprehensive assessment was defined about dummy injury in follow formula:

$$U=\left(\frac{V_{c1}-V_{c0}}{V_{c\max}-V_{c\min}}\right)^2+\left(\frac{V_{a1}-V_{a0}}{V_{a\max}-V_{a\min}}\right)^2+\left(\frac{V_{p1}-V_{p0}}{V_{p\max}-V_{p\min}}\right)^2+\left(\frac{D_{c1}-D_{c0}}{D_{c\max}-D_{c\min}}\right)^2+\left(\frac{D_{a1}-D_{a0}}{D_{a\max}-D_{a\min}}\right)^2+\left(\frac{D_{p1}-D_{p0}}{D_{p\max}-D_{p\min}}\right)^2 \quad (2)$$

Where $V_{c1}, V_{a1}, V_{p1}, D_{c1}, D_{a1}, D_{p1}$ represent the velocity of chest, abdomen, pelvis and intrusive displacement of chest, abdomen, pelvis respectively. $V_{c0}, V_{a0}, V_{p0}, D_{c0}, D_{a0}, D_{p0}$ represent the design target based on five star standard. $V_{c\max}$ and $V_{c\min}$ represent the max and min velocity of chest in sample points, so as $V_{a\max}, V_{a\min}, V_{p\max}, V_{p\min}, D_{c\max}, D_{c\min}, D_{a\max}, D_{a\min}, D_{p\max}, D_{p\min}$.

TABLE 4 UPPER, LOWER AND OPTIMUM OF VARIABLES UNIT (MM)

Variables	Lower	Initial	Upper	Optimum
Yield force scales of B pillar c_1	0.5	1.0	2.0	1.8722
Yield force scales of Front door c_2	0.5	1.0	2.0	1.4847
Yield force scales of Rear door c_3	0.5	1.0	2.0	1.2723
Yield force scales of Rocker c_4	0.5	1.0	2.0	1.1134

For solving this optimization problem rapidly, One hundred points were created by Latin Hypercube for establishing quadratic order RSM (Response Surface Model) which was validated by error analysis with thirty-three points. The stiffness of BIW was optimized by NLPQL (Sequential Quadratic Programming).The error coefficients R^2 of RSM were shown in table 5. It is indicated that the accuracy of approximate model was good because all error coefficients were exceeded 0.9.

TABLE 5 ERROR COEFFICIENT R^2 OF RSM

Objective function	R^2
Intrusion at Chest	0.92513
Intrusion at Abdomen	0.93455
Intrusion at pelvis	0.95951
Velocity at Chest	0.99823
Velocity at Abdomen	0.99825
Velocity at pelvis	0.99866

The target function based on RSM was optimized by NLPQL though 52 times iteration, the history of iteration was shown in Figure.8. The comparison of optimum results between LPM and approximate model was as shown in Table 6. The relative errors were not exceeded 1% and the performance improved 20%. The results indicated that the intrusive velocity and displacement of chest, abdomen and pelvis in dummy can be optimized by designing stiffness of BIW appropriately.

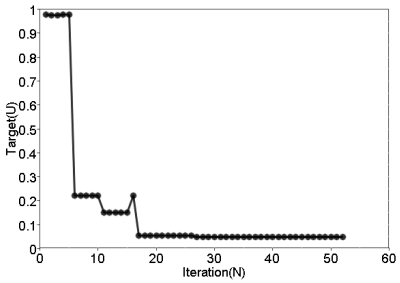


Figure.8 History of iteration

TABLE 6 RESULTS OF OPTIMIZATION

Objective function	Initial value	Optimum of RSM	Optimum of LPM	Relative error (%)	Improvement (%)
Intrusion at Chest	232mm	155.2 mm	155.95 mm	0.48	32.8
Intrusion at Abdomen	227mm	151.47 mm	152.21 mm	0.49	32.9
Intrusion at pelvis	215mm	143.1 mm	143.81 mm	0.49	33.1
Velocity at Chest	9.7m/s	7.4861 m/s	7.5027 m/s	0.22	22.7
Velocity at Abdomen	9.4 m/s	7.2761 m/s	7.2914 m/s	0.21	22.4
Velocity at pelvis	9.1 m/s	7.0981 m/s	7.1101 m/s	0.17	21.9

Conclusion

A rapid forward development strategy was proposed which used new type side impact LPM in new car based on same platform forward development. The example indicated that the intrusive velocity and displacement if chest, abdomen and in dummy can be optimized by designing stiffness of BIW reasonably. The development period can be shortened effectively by this method in new car development early stage. How to realize the stiffness of BIW in detail side structure CAD design stage is the next work.

Acknowledgement

2011 annual Open Fund of the State Key Laboratory of vehicle noise vibration and safety technology (NVHSKL-201103), Science Research and Technical Development Project of Guangxi Province(11107001-10).

References

[1] Kamal, M. M. Analysis and simulation of vehicle to barrier impact. SAE paper 700414, 1970.
[2] Lim, G. G., and Paluszny A., “Side Impact Research,” XXII Fisita Congress- SAE Publication P-211, Paper No. 885055, Sept. 1988.
[3] Green, J. E., “Computer Simulation of Car-To-Car Collisions,” SAE Paper No. 770015, February-March 1977.
[4] Cheva, W., Yasuki, T., Gupta, V., and Mendis, K., “Vehicle Development for Frontal/Offset Crash Using Lumped Parameter Modeling,” SAE Paper No. 960437, 1996.
[5] Zhao Kaishen, Shi Yuliang, Zhang Xiuqin, Wu Shenrong. Application of lumped mass-spring model in vehicle passive safety pre-research stage[J].Computer Aided Engineering,2013.22(2):15-19.
[6] Ded A, Srinivas K C. Development of a New Lumped-parameter Model for Vehicle Side-impact Safety Simulation[J].Proceeding of International Mechanical Engineering Part D:Journal of Automobile Engineering,2008,222:1793-1811.
[7] Zhang Xuerong, Su Qingzu. A research on influencing factors of occupant injury in side impact [J].Automotive Engineering, 2008, 30(2)146-150.

CHAPTER 19:

Mechatronics, Control and Automation

Advanced Materials Research Vol. 936 (2014) pp 2149-2154
© (2014) Trans Tech Publications, Switzerland
doi:10.4028/www.scientific.net/AMR.936.2149

Improved Dynamic Bayesian Networks in Sea-battlefield Situation Assessment

Yongtao Yu [1, a], Ying Ding[2]

[1] Naval Academy of Armament, Beijing, china, 100161

[2]Beijing Sino-Ocean JIYE Propetry Management CO., LTD, Beijing, china, 100038

[a]y_yt128@aliyun.com

Keywords: Dynamic Bayesian;Sea-battlefield;situation assessment

Abstract. How to efficiently evaluate the dynamic and complex the sea-battlefield situation facing the reality of the problem is the operational decision support. According to research sea-battlefield situation assessment based on improved dynamic Bayesian networks. First constructed the sea-battlefield situation assessment Bayesian networks model; second specific assessment task to establish the corresponding dynamic Bayesian networks; again reintroduced extended hidden variables, supplemental situation information to construct improved dynamic Bayesian networks; finally, according to the battlefield event reasoning, complete sea-battlefield situation assessment.

Introduction

Sea-battlefield is a giant complex system. The sea-battlefield situation assessment, both deterministic analysis of current events, or predictions of future events have the distinctive temporality, the time factor must be used as the assessment of the key factors. Dynamic Bayesian networks expansion the timing process modeling Bayesian networks, a collection of random variables can be evolved over time is compressed representation of a complex random processes. Quantitative assessment using dynamic Bayesian networks processing, give full consideration to the impact of timing factors, and the first time situational factors as current time situation assessment part of the evidence, and to predict the trend for the next time; at the same time can show continuity and cumulative characterization of the threat assessment. Therefore, based on the analysis of the characteristics of the sea-battlefield situation, the dynamic Bayesian networks applied to the complex sea-battlefield the sea-battlefield situation assessment reasoning.

Improved Dynamic Bayesian Networks Theory Overview Dynamic Bayesian Networks

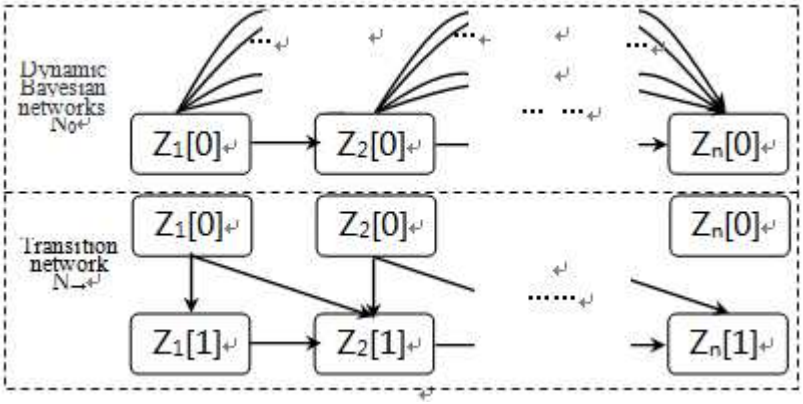


Fig.1 Dynamic Bayesian Networks

Dynamic Bayesian networks processing direction of the time factor on Bayesian networks extends as a knowledge representation and probabilistic reasoning framework. Assuming there is a Bayesian network, a set of variables for the discrete variables set $Z=(Z_1, Z_2, ..., Z_n)$, the set of variables Z sort

network topology, Z[t] for the variable set value of Z in the time t, Z_i[t] is a set of variables Z_i's value at time t. Dynamic Bayesian networks available Z[0]→ Z[1]→ ...→ Z[n] to represent the timing problem. Obvious need to deal with the dynamic Bayesian networks to get all the variables set Z[0] ∪ Z[1] ∪ ... ∪ Z[n], the set of conditional probability, in fact, such conditional probability of solving very difficult, and can cause quite high network inference complexity. In order to simplify the network, usually require dynamic Bayesian networks follows the Markov and time invariance assumption. A dynamic Bayesian network can be of two parts, part of the initial state contains a set of variables Z[0] Bayesian network N_0, another part is set by the variable Z[0] and Z[1] constitute, and give $P_{N\rightarrow}$ (Z[t +1] | Z[t]) the probability distribution of the transition condition of the transition network $N_{\rightarrow}$ two parts, the specific composition is shown in Fig. 1.Therefore, a dynamic Bayesian networks by tuple: DN = <N_0, $N_{\rightarrow}$>., the probability of transition condition of $N_{\rightarrow}$ can be written as Eq. 1:

$$P_{N\rightarrow}(Z[t+1]/Z[t]) = \prod_{0}^{n} P_{N\rightarrow}(Z_i[t+1]/PaZ_i[t+1]) \quad (1)$$

The joint probability of the entire set of variables as Eq. 2:

$$P(Z[0],Z[1],\cdots,Z[T]) = P(Z[0])\prod_{t=0}^{T-1} P_{N\rightarrow}(Z[t+1]/Z[t]) \quad (2)$$

The Introduction of the Extended Hidden Variables

Dynamic Bayesian networks hidden variables introduced the original intention to make the original dynamic Bayesian networks model with Markov properties. On this basis, we can propose the extension of hidden variables. That does not meet the local network, such as a random variable probability distribution specified state or a specified value, do not participate in the probability of network nodes update calculation; when the local probability distribution of the designated state or a specified value, the impact on the global probability distribution of the network, the random variable can be referred to as the expansion of hidden variables.

Be seen from the above analysis, the introduction of dynamic Bayesian networks expansion hidden variables, not only can add some status information to the original dynamic Bayesian networks model, transferred to the additional variable makes the subsequent time slice on the variable dependencies; but also qualitative dependence between the number of makes random variable and can be set and random variable having characteristics change over time. But the introduction of the extended hidden variables Bayesian networks model must first be guaranteed Markov and time invariance assumption. From the literature [2] to prove that the introduction of hidden variables improved dynamic Bayesian networks model is always equal to 4, and therefore not increase the complexity of the original model, improved dynamic Bayesian networks model satisfies the Markov and time invariance assumptions.

The Sea-battlefield Situation Improved Dynamic Bayesian Assessment Model

The sea-battlefield situation assessment application of dynamic Bayesian networks for solving the problem solving process can be divided into three steps; first is to establish the sea-battlefield situation assessment model Bayesian network structure; second is built on the basis of the improved dynamic Bayesian network; finally, based on the evidence obtained information Bayesian networks inference drawn sea-battlefield situation assessment conclusions.

Design Sea-battlefield Situation Assessment Bayesian Networks Structure

Here we have chosen a relatively simple surface ship fleet antiaircraft defense scenario, said sea-battlefield situation assessment of dynamic Bayesian model design, building and reasoning. Specific combat situation is set to: the war environment Open ocean area, Climatic conditions to meet the opposing sides weapons use requirements; in our fleet of surface ships, equipped with SAM(ship to air missiles), electronic countermeasures and radar and other systems; the enemy for the Air Force

fleet, equipped with ASM(air-ship missiles), electronic warfare and radar systems; the enemy tactics intentions for the search to find and assault my surface ships fleet; our tactical intent to carry out the fleet antiaircraft defense operations; the purpose of our sea-battlefield situation assessment is to ensure that our greatest degree seize the control initiative on the battlefield; that infer the enemy's tactics may be used according to the current trend factors we take the most effective measures accordingly.

Surface ship fleet antiaircraft scenarios mainly consider the following three situational factors:

1) Visible distance, i.e., the relative distance between two sides of visible, set two critical distance, assault weapons effective range and detection system effective distance. The value of the Outside (> Max (detection system effective distance & assault weapons effective range)); In(Max (detection system effective distance & assault weapons effective range) ≥ visible distance ≥ Min (detection system effective distance & assault weapons effective range)); Within (<Min (detection system effective distance & assault weapons effective range)).

2) Fighting determination, that the two sides of the implementation of a fighting attitude, value Positive (before finding the target; Finding the target and proactively identify; Confirm the target and attack);General (maintain existing athletic stance);Negative (keep a safe distance from the target, or do not take the initiative to attack).

3)Target identification, that the two sides of assault or incoming targets to identify possible, value is Clear (after finding the target can quickly distinguish the target type);Normal (determine target type target after a period of time);Fuzzy (finding the target, the target type can not be determined).

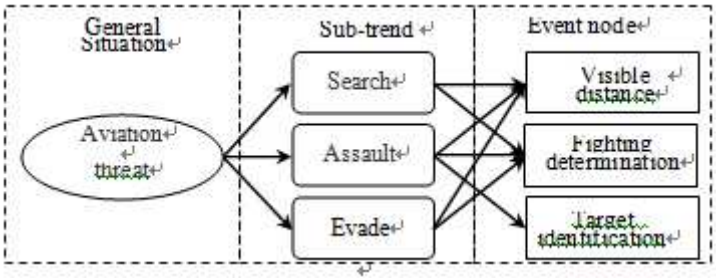


Fig.2 Bayesian Networks Structure Diagram

Select the aviation threat for both sides against the total momentum, which contains three sub-trend; Search, Assault and Evade. Which sub-trend "Search", "Visible distance" and "Fighting determination" associated; Sub-trend "Assault", "Visible distance", "Fighting determination "and "target identification" associated; Sub-trend "Evade", "Visible distance"and "Fighting determination" associated. Based on the above analysis, the sea-battlefield surface ship fleet antiaircraft posture to assess Bayesian networks structure as shown in Fig.2.

Building Sea-battlefield Situation Assessment Model Based on Improved Dynamic Bayesian Networks

Sea-battlefield surface ship antiaircraft operations is obvious dynamic complex process involving the warring parties countermeasures. Each event occurred in the sea-battlefield exists to some extent associated with events that occurred before, and that is the first time the sea-battlefield situation will inevitably impact on sea-battlefield situation to a certain extent on the current moment, and therefore can not ignore the situation assessment time factor. Based on the above analysis, we can building improved dynamic Bayesian networks inference and prediction of sea-battlefield situation any time.

According to the theoretical analysis of Section II, the sea-battlefield surface ship fleet antiaircraft defense posture assessment Bayesian networks N_0 dynamic Bayesian networks model is also by situational factors variable contains the initial state set Z[0] set of variables and situational factors Z[0] and Z[1] constitute the given transition conditional probability distribution $P_{N\rightarrow}(Z[t+1] \mid Z[t])$ of the transition network $N_{\rightarrow}$ two-part, and to follow the Markov and time invariance two assumptions.

Sea-battlefield surface ship antiaircraft defense posture assessment improved dynamic Bayesian networks model complex electromagnetic environment factors introduce extensions hidden variables

sea-battlefield. Introduction of the extended hidden variables, not only for the antiaircraft defense posture assessment supplemental the electromagnetic environmental impact related information, but also enable the antiaircraft defense posture review random variable set of qualitative dependencies between size and variable changes over time, and can guarantee that the dynamic Bayesian networks model satisfies the Markov and time invariance assumption. Extended hidden variables the sea-battlefield complicated electromagnetic environment factors set two key threshold. Guided blocking threshold (I): the sea-battlefield electromagnetic strength of the values of the indicators, lapsed assault weapons guidance systems. The search mask threshold value (II): sea-battlefield electromagnetic strength of the values of the indicators, early warning search system failure.

When the sea-battlefield electromagnetic strength threshold is reached, the expansion of hidden variables (sea-battlefield complex electromagnetic environment factors) involved in antiaircraft defense posture to assess the probability of dynamic Bayesian networks model node update calculation; hen the local probability distribution reach guided blocking threshold value (I) or search mask threshold (II), is involved in target identification model node probability update affect antiaircraft defense posture to assess the probability distribution of dynamic Bayesian networks globally.

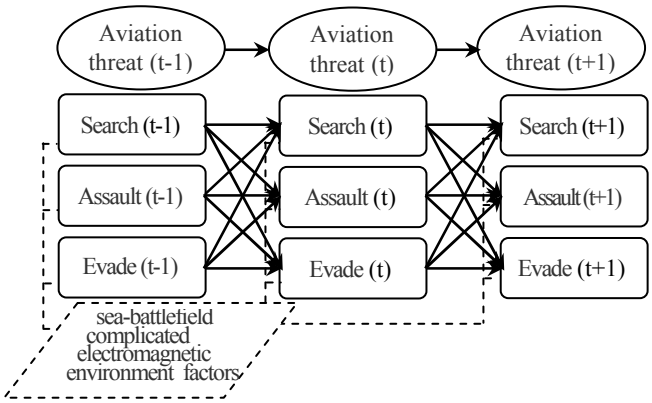


Fig.3 Improved Dynamic Bayesian Networks.

Based on the above analysis, three time slices (the current time slice t, the previous time slice t- and the next time slice t+1), for example, the sea-battlefield surface ship fleet antiaircraft defense posture assessment improved dynamic Bayesian networks model specific configuration shown in Fig.3.

Bayesian Networks Inference Sea-battlefield Situation Assessment

The sea-battlefield surface ship fleet antiaircraft defense posture assessment improved dynamic Bayesian networks model to introduce the extended hidden variables sea-battlefield complicated electromagnetic environment factors dynamic Bayesian networks. Its reasoning process of the first combination of the use of literature [2], the EM algorithm and Bayesian statistics BDE scoring function, cyclical iterative learning dynamic Bayesian networks structure with extended hidden variables, can draw on expertise, given the probability distribution of all the random variables in all the time slice may solve the local optimum problem that may arise; commonly used algorithm of junction tree algorithm, or cut-set conditional methods such as Bayesian network can then use to complete the reasoning.

Sea-battlefield Situation Assessment Example Analysis

Such as t=0 and t=1 time slice of the the sea-battlefield situation factors such as probability distribution data in Table 1 shown below.

TABLE 1 SEA-BATTLEFIELD SITUATIONAL FACTORS PROBABILITY DISTRIBUTION TABLE

Time slice	Visible distance			Fighting determination			Target identification		
	Outside	in	Within	Positive	General	Negative	Clear	Normal	Fuzzy
t=0	0.63	0.22	0.15	0.52	0.25	0.23	0.71	0.15	0.14
t=1	0.28	0.51	0.21	0.61	0.28	0.11	0.75	0.13	0.12

Based on reasoning algorithm, we can obtain t=1 time slice of antiaircraft defense posture, and forecast t=2 time slice of antiaircraft defense posture, specific assessment values in Table 2 below.

TABLE 2 SEA-BATTLEFIELD SITUATION ASSESSMENT TABLE OF VALUES

Time slice	Extended hidden variables	Aviation threat		Assault		Search		Evade	
		True	False	True	False	True	False	True	False
t=1	<Threshold Ⅰ & Ⅱ	0.43	0.57	0.16	0.84	0.76	0.24	0.28	0.72
t=2	<Threshold Ⅰ & Ⅱ	0.69	0.31	0.63	0.37	0.32	0.68	0.13	0.87
	≥Threshold Ⅰ	0.16	0.84	0.42	0.58	0.53	0.47	0.45	0.55
	≥Threshold Ⅱ	0.13	0.87	0.11	0.89	0.41	0.59	0.78	0.22

Analysis improved dynamic Bayesian networks model to assess value available, When t=1 time slice visible distance, the fighting determination is positive, target recognition is clear, judgment at this time uncertain the sea-battlefield surface ship antiaircraft defense posture aviation threat, weak trend in the aviation threat (False distribution probability close to the set threshold value of 65%).

And when t=2 time piece extensions hidden variables sea-battlefield complicated electromagnetic environment factors local probability distribution is not reached guided blocking threshold value (I)or search shielding threshold (II), predicted sea-battlefield water surface warship fleet antiaircraft defense posture of the aviation threat (True distribution probability reaches a set threshold value). Air Force fleet carries out assaults, can achieve effective search and target identification is clear and visible distance continues to decrease, Air Force fleet constantly close to the attack position threat has continued to improve.

When t=2 time piece extensions hidden variables sea-battlefield complicated electromagnetic environment factors local probability distribution to achieve guided blocking threshold value(I), predicted sea-battlefield water surface warship fleet antiaircraft defense posture of the aviation threat weak (False distribution of the probability of exceeding set threshold), Air Force fleet action status is unknown, can achieve effective search, visible distance continues to decrease, the Air Force is constantly approaching surface ship fleet, but the guidance system failure can not be reached surprise necessary condition Threat Reduction.

When t=2 time piece extensions hidden variables sea-battlefield complicated electromagnetic environment factors local probability distribution reach search shielding threshold (II), predicted sea-battlefield water surface warship fleet antiaircraft defense posture of the aviation threat to the weak (False distribution of the probability of exceeding set threshold) and Air Force fleet carry out evasive action, unable to achieve an effective search, resulting in reduced threat.

Reasoning improved dynamic Bayesian networks model to assess sea-battlefield situation can be seen conclusions credible. Predict more complex situation is not ideal, to analyze the main reason is built the sea-battlefield situation assessment model included the representation of the potential link between the amount of information and the factors of the situational factors is not comprehensive, need to be further improved.

Summary

The sea-battlefield situation assessment application improved dynamic Bayesian networks. First can use dynamic Bayesian time series modeling of complex stochastic process scalability to address the problem of the sea-battlefield situation assessment of the impact of the time factor; then by

introducing the extended hidden variables, rich battlefield situation assessment information to solve a large number of sea-battlefield situational factors not fully recognize the description of the potential relationship and deep impact assessment. Future research will also continue to explore the dynamic Bayesian networks structure optimization, in order to improve the efficiency of the operations of the sea-battlefield situation assessment.

References

[1] Lei Yingjie. Based on the intuitive fuzzy decision battlefield situation assessment method [J]. Electronic Journal 2006,34 (12):2175-2179.

[2] Zhang Hongwei. DBNS learning and the approximate reasoning model study [A]. The fourth automatic control theory International Conference, Shanghai, 2002.

[3] Santos E J r. a unified framework for reasoning with time and uncertainty[J].International Journal of Approximate Reasoning,1999,20(3):191-216

[4] Mahoney S M. Constructing Situation Specific Belief Networks[EB/OL].[2008-6-30]

[5] Hall D L. Handbook of multi-sensor data fusion[M], Washington DC:CRC Press,2001.

[6] Tian F. Learning Bayesian networks with hidden variables using the combination of EM algorithm[A].Pacific-Asia Conference on Data Mining,Hongkong,2001.

[7] KILIC R . A practical guide for studying Chua's circuits [M]. [S.l.]: World Scientific，2010.

Advanced Materials Research Vol. 936 (2014) pp 2155-2159
© (2014) Trans Tech Publications, Switzerland
doi:10.4028/www.scientific.net/AMR.936.2155

Energy Control of HEV Based on Fuzzy Controller Optimized by Particle Swarm Optimization

Liyan Zhao [1,a], Niaona Zhang [2,b]

[1]Jilin Teachers Institute of engineering and technology, Changchun, China

[2]Changchun University of Technology, Changchun, China

[a]zly11211121@126.com, [b]zhangniaona@163.com

Keywords: Fuzzy Control Strategy, Particle Swarm Optimization(PSO), Hybrid Electrical Vehicle (HEV), Energy Control.

Abstract: Energy control of HEV plays a very important role in the process of HEV design, which is directly related to the safety and feasibility. Considering the drive system of HEV is nonlinear and complex, a fuzzy control strategy which is combined with particle swarm optimization algorithm is designed to realize the energy control of HEV. Fuzzy control strategy does not need to built accuracy mathematics model and has good robustness, but it mostly depends on engineering experience and has poor ability of self-learning. So particle swarm optimization algorithm has been added to solve these disadvantages of fuzzy control strategy. In conclusion, this method can not only keep the advantage of fuzzy control strategy, but also has ability of self-learning and self-adapt because of particle swarm optimization added. And the simulation proves that this method is feasible and effective.

Introduction

In recent years, the price of oil keep increasing all over the world, the global problem of energy is more and more obvious. As an important part of oil consumption, Automobiles begin to seek for technical innovation. Hybrid electrical vehicle (HEV) and electric vehicle (EV) are emerged under this circumstance.

Energy control of HEV plays a very important role in the process of HEV design. Only appropriate distribution of energy can realize the real value of HEV. At present, the energy strategy of PHEV mainly are steady control strategy based on rules, fuzzy control strategy, instantaneous optimization control strategy, global optimization control strategy[1].

In this article, an energy control strategy which is based on fuzzy control strategy combined with particle swarm optimization(PSO) has been designed aiming at parallel hybrid electric vehicle (PHEV). Simulation proves that it has good actual results.

Structure of Parallel Hybrid Electric Vehicle

Parallel hybrid electric vehicle is mainly composed of engine, battery and generator/motor. The engine and motor are non-coaxial, so the engine and motor can drive cars separately[2], its structure is as follow:

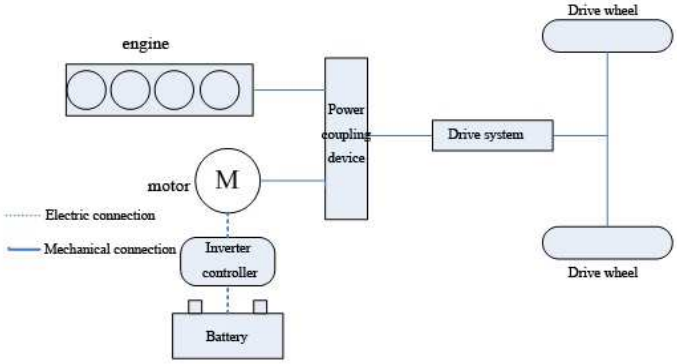


Fig. 1 Structure of PHEV

During the running of PHEV, engine drives gearbox to drive the car, at the same time, the electric drive system can also drive the car through the battery and motor, the power is overlying. When the car is running steadily, it is mainly driven by engine. If the battery power is low, engine can give more power to charge the battery which is based on the engine is working at the optimal state. When the car demands large torque such as quick acceleration or uphill, electric drive system can assist the engine to provide the large torque to ensure the dynamic property of PHEV.

Since the power of two drive systems can be overlaid, it can use the engine and motor of smaller power which can make the power assembly small, light and low cost. But in parallel hybrid electric vehicle, engine is impacted by driving condition, so it is not suitable to the driving condition which varies frequently.

Control Strategy of PHEV

In order to achieve the fuel economy, cancel the idle speed state of the engine and the starting state that the efficiency of the engine is very low. The normal running of the vehicle is mainly driven by engine. If the demand torque is less than the optimal torque of the engine under current speed, redundant torque is used to charge the battery. If the demand torque is more than the optimal torque under current speed, motor is used to provide the insufficient torque so as to keep the engine working under the best working condition[3]. That means to keep the engine always working under the best working condition.

This paper aims to make the reasonable distribution of the demand torque under normal running process. So choose the demand torque of the running process T_{req} as one of the inputs of the fuzzy controller. Because the SOC of the battery must always be known during the running process, choose SOC of the battery as the other input of the fuzzy controller. Then the output of the fuzzy controller is the output torque of the engine T_e the output torque of the motor T_m can be calculated by $T_m = T_{req} - T_e$ (assuming that the torque coupler ratio is 1). In order to ensure the generality of the fuzzy controller, use the following formula to do the field transformation of demand torque T_{req} which can change the actual physical quantity to real number between -1 and 1.

$$\begin{cases} \dfrac{\Delta T}{T_{e_\max} - T_{e_opt}} & \Delta T \geq 0 \\ \dfrac{\Delta T}{T_{e_opt}} & \Delta T \leq 0 \end{cases} \tag{1}$$

Where $T_{e_\max}$ is the maximum torque of the engine, T_{e_opt} is the optimal torque of the engine under current speed, $\Delta T = T_{req} - T_{e_opt}$ is the difference between the demand torque and the optimal torque of the engine[4].

In conclusion, the picture of the structure of the fuzzy controller is as follow.

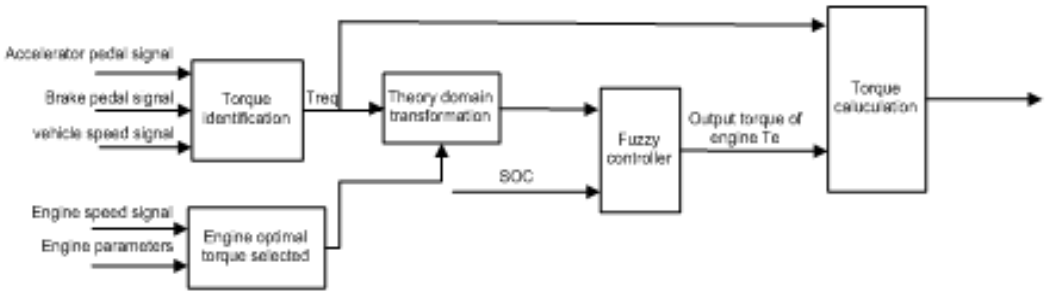


Fig.2 Structure of fuzzy controller

The design of membership functions of input and output of the fuzzy controller is as follow:

Demand torque $T_{req}^{'}$ is divided into $\{MN, N, ZERO, P, MP\}$, theory field is [-1,1]. The SOC of battery is divided into $\{lower, low, opt, high, higher\}$, theory field is [0.4,0.8]. Output torque of the engine T_e is divided into $\{smaller, small, opt, big, bigger\}$, theory field is [0,1]. The forms of membership functions are all trimf combined with trapmf.

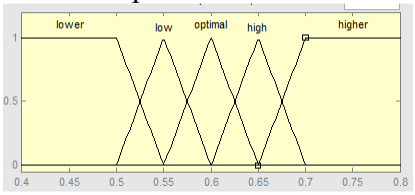


Fig.3 SOC MF

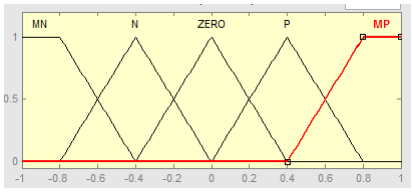


Fig.4 Demand torque MF

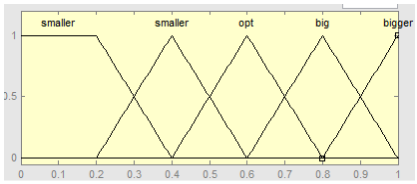


Fig.5 Output torque of engine MF

Fuzzy control rules are as follow：

TABLE3-1 FUZZY CONTROL RULE TABLE

T_e		SOC				
		lower	low	opt	high	higher
$T_{req}^{'}$	MN	opt	opt	smaller	smaller	smaller
	N	big	opt	small	small	Small
	ZERO	Bigger	Big	Opt	Opt	Opt
	P	Bigger	bigger	Big	Big	Opt
	MP	bigger	bigger	bigger	big	big

Basic particle swarm optimization algorithm (PSO) is a new random global optimization algorithm. For a n-dimensional search space, particle is represented as $X=\{x_1, x_2, \cdots, x_m\}$, each particle is a feasible solution in the search space which is going to be optimized. Each particle seeks for optimal solution through cooperation and competition[5]. The position of the i^{th} particle is represented as $x_i=\{x_{i1}, x_{i2}, \cdots, x_{in}\}^T$, the speed of the particle is represented as $v_i=\{v_{i1}, v_{i2}, \cdots, v_{in}\}^T$, individual extremum is represented as $p_i=\{p_{i1}, p_{i2}, \cdots, p_{in}\}^T$, global extremum is represented as $p_g=\{p_{g1}, p_{g2}, \cdots, p_{gn}\}^T$, the speed and position update according to the follow formulas:

$$v_{id}^{k+1}=\omega v_{id}^{k}+c_1\times rand()\times\left(p_{id}-x_{id}^{k}\right)+c_2\times rand()\times\left(p_{gd}-x_{id}^{k}\right) \tag{2}$$

$$x_{id}^{k+1}=x_{id}^{k}+v_{id}^{k+1} \tag{3}$$

Where $i=1,2,\cdots,m$, m is the total number of the particle. K is the current iterations. v_{id}^{k} is the d^{th} weight of the velocity vector of the k^{th} generation particle i. p_{id} is the d^{th} weight of individual optimal position value $pbest$ of current particle i. p_{gd} is the the d^{th} weight of global optimal position value $gbest$ of current swarm. ω is the inertial weight. c_1 and c_2 are the acceleration constants. $rand()$ is random numbers between 0 and 1[6].

Now use variables x_1,x_2,y_1,y_2,z_1,z_2 to encode membership functions as follow:

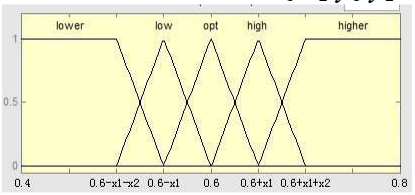


Fig.6 Encoding SOC MF

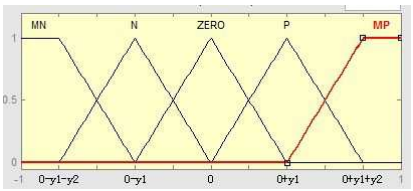


Fig.7 Encoding demand torque MF

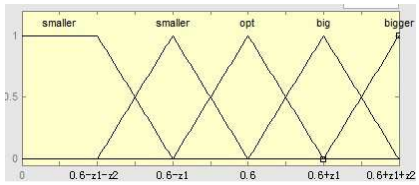


Fig.8 Encoding output torque of the engine MF

In order to make fuel consumption minimum, use PSO algorithm to optimize the fuzzy controller, the algorithm flow chart is as follow[7].

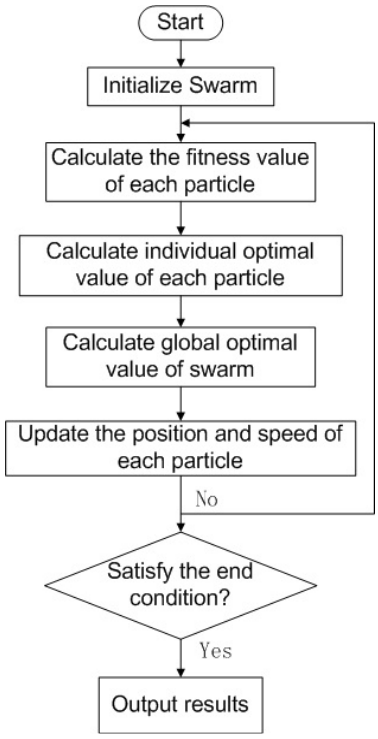


Fig.9 Algorithm flow chart of PSO

Simulation

A forward simulation model has been built on MATLAB/Simulink, it includes diver model, engine model, motor model and vehicle model. Then program in the S-function to realize the simulation. The results of the simulation are as follow.

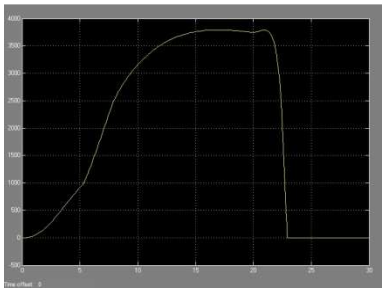


Fig.10 Speed of vehicle

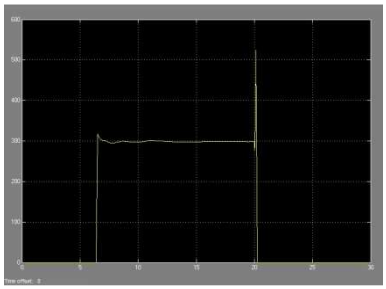


Fig.11 Fuel consumption

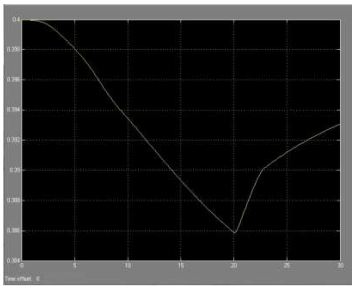


Fig.12 SOC

Figure 10 is the speed of the vehicle, the model simulates a working condition that includes states of starting, accelerating quickly, accelerating slowly, slow down and parking. These states can be recognized from figure 10. Figure 11 is the fuel consumption of the vehicle which is corresponding to these states. From figure 11, it can be tell that the fuel consumption of starting state is zero, which means the fuel consumption of the lowest efficient state is zero. And during the whole accelerating state, the fuel consumption is almost constant, which means the motor works in that state to keep the engine work under higher efficient state, which can also make the fuel consumption less. Also from figure 12, SOC of battery decreases during the accelerating state, so the motor must work to offer some torque which can not only meet the demand of running, but also keep the engine work under higher efficient state. When the car slows down, it entry into regenerative braking state to charge the battery.

From the results, it can be see that idle speed state and the starting state are cancelled, which means motor takes over the lowest efficient states of engine. And with the assist of motor, engine can work under efficient state. From the figure 12, it can be see that regenerative braking state is realized. And during the whole working condition, the SOC of battery does change too much, and the battery is only charged once which can keep the battery a long life.

Summary

In this paper, a fuzzy control strategy based on particle swarm optimization has been designed in order to solve the problem of energy control of HEV. This method designs a fuzzy controller according to the running process of HEV which the inputs are SOC of battery and the demand torque and the output is the output torque of engine. Then use PSO algorithm to optimize the membership functions of inputs and output of the fuzzy controller so as to make the fuel consumption minimum. This method combines the advantages of fuzzy control and particle swarm optimization, has good robustness and precision.

Reference:

[1] Wang Yifei, Zhang Yun, Wu Jian, and Chen Ning, "Energy Management System Based on Fuzzy Control Approach for Hybrid", IEEE, 2009, pp. 3382-3386.

[2] Fu Shunzhu, Hong Wenhe, Yi Lin, Guo Feilin, "Study on Fuzzy Logic Control Strategy of ISG Hybrid System", International Conference on Computer, Mechatronics, Control and Electronic Engineering (CMCE), National Engineering Laboratory of Electric Vehicles, Beijing Institute of Technology,2010,pp.519-522.

[3] Hyeoun-Dong Lee, Euh-Suh Koo, Seung-Ki Sul, and Joohn-Sheok Kim, "Torque Control Strategy for a Parallel-Hybird Vehicle Using Fuzzy Logic", IEEE Industry Applications Magazine, November 2000, pp.33-38.

[4] Laila Majdi, Ali Ghaffari, Nima Fatehi, "Control Strategy in Hybrid Electric Vehicle using Fuzzy Logic Controller", Proceedings of the 2009 IEEE International Conference on Robotics and Biomimetics, December 19-23,2009, pp.842-847. [5] R.J. Ong, J.T. Dawley and P.G. Clem: submitted to Journal of Materials Research (2003)

[5] Hua Rong, "An Adaptive Chaos Embedded Particle Swarm Optimization Algorithm ", Proceedings of International Conference on Computer, Mechatronics, Control and Electronic Engineering (CMCE), Shanghai Institute of Technology, 2010, pp. 314-317.

[6] Xiao Lanwu, Bing Gangcao, Jian Pingwen, Yan Shengbian, "Particle Swarm Optimization for Plug-in Hybird Electric Vehicle Control Strategy Parameter", IEEE Vehicle Power and Propulsion Conference (VPPC), September 3-5,2008, pp.978-983.

[7] Miao Huahuang, Hou Yuyu, "Optimal Control Strategy Based on PSO for Powertrain of Parallel Hybrid Electric Vehicle", IEEE,2006, pp.352-355.

Advanced Materials Research Vol. 936 (2014) pp 2160-2164
© (2014) Trans Tech Publications, Switzerland
doi:10.4028/www.scientific.net/AMR.936.2160

Non-Ideal Excitation Approach for Piezoelectric Vibration Based Energy Harvesting

Douglas da Costa Ferreira[1,a], Fábio Roberto Chavarette[1,b], Cláudio Henrique Cerqueira Costa Basquerotto[1,c] and Nelson José Peruzzi[2,d]

[1]UNESP - Univ. Estadual Paulista, Faculdade de Engenharia de Ilha Solteira, Departamento de Engenharia Mecânica, Ilha Solteira, SP, Brazil

[2]UNESP - Univ. Estadual Paulista, Faculdade de Ciências Agrárias e Veterinárias, Departamento de Ciências Exatas, Jaboticabal, SP, Brazil

[a]dcferreira@ufmt.br, [b]fabioch@mat.feis.unesp.br, [c]cbasquerotto@ymail.com, [d]peruzzi@fcav.unesp.br

Keywords: Non-Ideal behavior, Energy Harvesting, Random Vibration, Efficiency.

Abstract: Common solution for energy harvester device is project design according harmonic excitation around natural frequency matching excitation source. Environment vibration is random and wide band causing short time of resonance in disagreement of project objectives. Control driven of energy harvesting to take advantage of the higher vibration range can results in greater energy converted. This study investigates a non-ideal excitation behavior and their efficiency in convert electricity via piezoelectric direct effect from the available system energy compared to harmonic excitation source. Numeric evaluation was performed based in bimorph piezoelectric beam in dimensionless consideration. Chaos behavior and harvest energy capability were compared from non-ideal to harmonic excitation. Results demonstrate considerable higher quantity of energy available for non-ideal approach compared to harmonic resonant design and encourages advance study to control and enhance energy from random and wide band vibration source.

Introduction

Energy Harvesting is harnessing energy from the environment. The most common sources of environmental energy for harvesting systems are solar, thermal gradients and mechanical and acoustic vibrations [1].

Vibrational energy harvesting technique is considered attractive for low-power devices, for example, wireless sensor [2]. The vibration energy to be harnessed can be from structures motion and acoustic waves [3], for example. The vibration energy can be converted into electrical energy by means of piezoelectric materials, electromagnetic and electrostatic transducers. Using harvesters as power source a device can be in operation for long periods or even indefinitely, without need of any other power source or an energy storage system [4].

Harmonic excitation for energy harvesting investigation normally considers natural frequency for resonance response [5]. It is notable in piezoelectric harvesters devices a vibration amplification when natural frequency matches vibration frequency source. However, the environment offers a wide range of vibration and such project solution is not taken advantage of the broadband [6]. In this direction some solution were proposed, for example bi-stable magnetic cantilever, which can absorb more energy from the system [7]. These designs are known as non-linear solution. Among linear and non-linear approach a harmonic excitation was considered as power source [8]. Nevertheless environment vibration can be considered as a non-ideal power source and cannot be modeled as a harmonic excitation which has constant amplitude and frequency.

According [9], when an excitation is not influenced by system response it is considered an ideal excitation that has origin in an ideal energy source. On the other hand, when the excitation is influenced by the system response the excitation is considered to be non-ideal. Since, non-ideal system presents an equation that describes the interaction between power source and the dynamic system. Therefore, in non-ideal system the dynamics depends directly on excitation properties whose

available energy power, generally, it is limited. The main propose of this study is to investigate a non-ideal behavior of a piezoelectric bimorph cantilever used for energy harvesting. There will be a comparison of energy offered from a harmonic and non-ideal vibrating excitation as power source. The study takes in consideration numeric evaluation.

Considering the paper organization: section 2 presents the harmonic and non-ideal modeling approach. Section 3 presents the evaluation results comparison considering harmonic and non-ideal excitations. Finally, section 4 presents the final remarks from this investigation and acknowledgements.

Harmonic and Non-Ideal Approach

A bimorph cantilever excited by a harmonic [7] or non-ideal vibration [9] is given in Fig. (1), including an electrical load circuit. Previous study performed in [7] compared performance of linear and non-linear approach; however the accomplished study only considered harmonic vibration as excitation source and this present study considers non-ideal excitation.

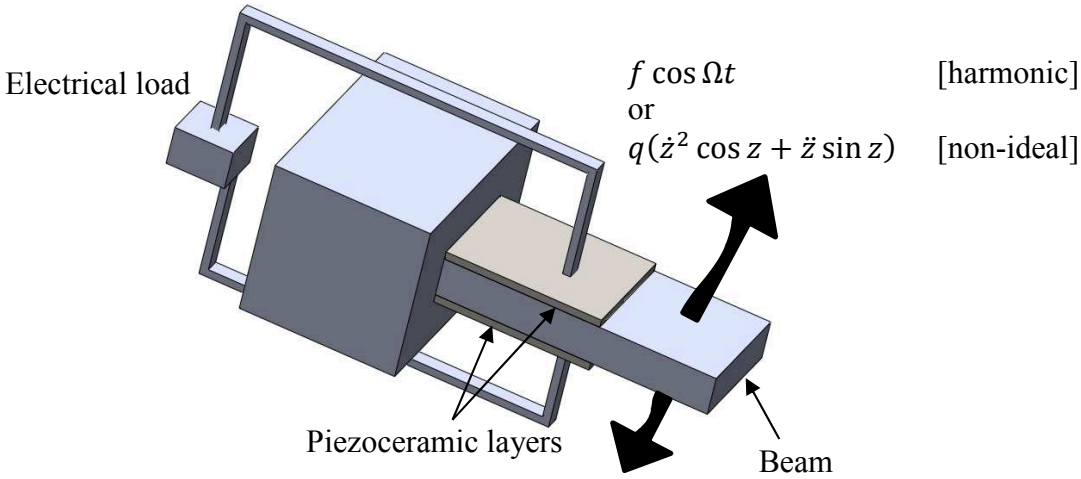


Fig. 1- Bimorph Cantilever [7].

Harmonic Model.

The dynamic model for the proposal energy harvesting subject to a harmonic excitation is given in dimensionless Eq. (1), where ζ is the damping, χ is piezoelectric mechanical coupling, v is the resistance voltage, f is force, Ω is the frequency, Λ is reciprocal of time constant and k is piezoelectric electric coupling. It is a dimensionless dynamic model proposed by [7].

$$\begin{aligned}\ddot{x}+2\zeta\dot{x}+x-\chi v&=f\cos\Omega t\\ \dot{v}+\Lambda v+k\dot{x}&=0\end{aligned} \tag{1}$$

The space-state form of Eq. (1) is given by Eq. (2):

$$\begin{aligned}\dot{x}_1&=x_2\\ \dot{x}_2&=-2\zeta x_2-x_1+\chi x_3+f\cos\Omega t\\ \dot{x}_3&=-\Lambda x_3-\kappa x_2\end{aligned} \tag{2}$$

Non-Ideal Model.

The coupled system excited by non-ideal vibration can be model according Eq. (3), where z is a non-ideal excitation response and the values (a, b, q, r) are positive dimensionless constants [9]. The same coupling presented by [7] is considered in non-ideal model and only the excitation source is replaced for this study. Is important to notice that non-ideal model do not consider resonance because power is limited and the vibration influence his own behavior as can be notice by the z component.

$$\ddot{x}+2\zeta\dot{x}+x-\chi v=q(\dot{z}^2\cos z+\ddot{z}\sin z) \tag{3}$$

$$\ddot{z} + b\dot{z} = r\ddot{x}\sin z + a$$
$$\dot{v} + \Lambda v + k\dot{x} = 0$$

The space-state form of Eq. (3) is given by Eq. (4):

$$\begin{aligned}
\dot{x}_1 &= x_2 \\
\dot{x}_2 &= \frac{-x_1 - 2\zeta x_2 + \chi x_5 + \mathrm{q}x_4{}^2\cos(x_3) + \mathrm{q}\sin(x_3).(\mathrm{a} - \mathrm{b}x_4)}{1 - \mathrm{qr}\sin^2(x_3)} \\
\dot{x}_3 &= x_4 \\
\dot{x}_4 &= \frac{\mathrm{r}\sin(x_3).(-x_1 - 2\zeta x_2 + \chi x_5 + \mathrm{q}x_4{}^2\cos(x_3)) + a - bx_4}{1 - \mathrm{qr}\sin^2(x_3)} \\
\dot{x}_5 &= -\Lambda x_5 - \kappa x_2
\end{aligned} \tag{4}$$

Performance Comparison Analysis

Analysis was performed according Runge-Kutta method for solving ordinary differential equations and the results and discussions are presented.

Harmonic Parameters.

For Harmonic excitation the dimensionless parameters are used according [7] given in Table 1. It is notable the frequency f = 0.083 matches the resonance natural frequency of the bimorph cantilever.

Table 1- Parameters for Harmonic Excitation.

Parameter	ζ	χ	f	Ω	Λ	κ
Value	0.01	0.05	0.083	0.8	0.05	0.5

Non-Ideal Parameters.

For Non-Ideal excitation the dimensionless parameters are used according [9] given in Table 2.

Table 2- Parameters for Non-Ideal Excitation.

Parameter	a	b	r	q
Value	2.3	1.5	0.5	0.5

Stability.

Lyapunov exponents were calculated by Wolf method [10] and can be notice according Fig. 2 that harmonic excitation has negative exponents resulting in stable comportment and the non-ideal excitation has a positive exponent causing chaotic behavior.

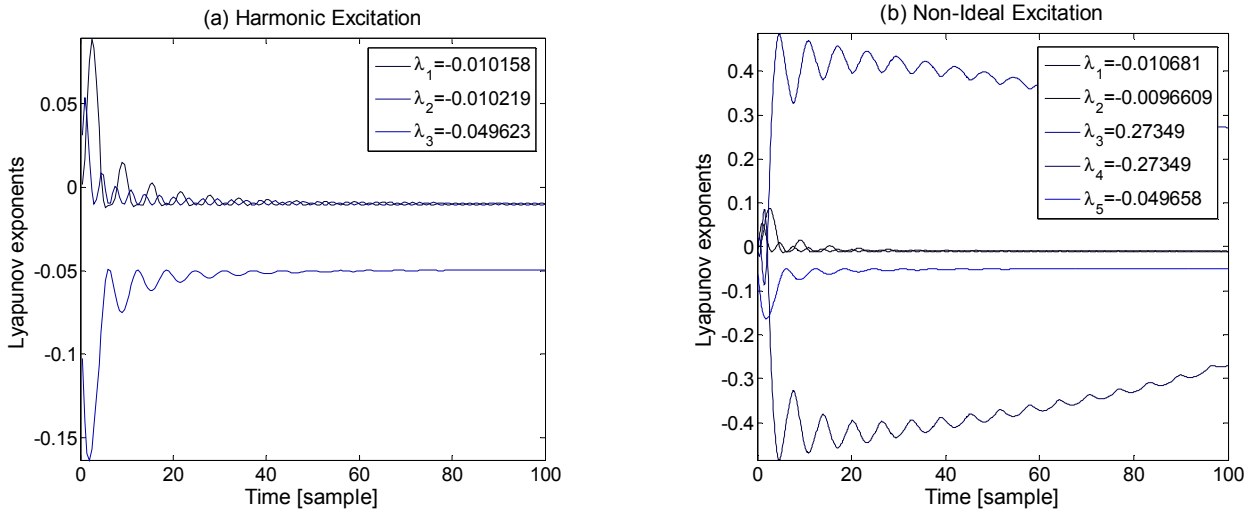


Fig. 2 - Lyapunov Exponents via Wolf method.

The Eigenvalues for harmonic excitation can be seen in Table 3.

Table 3 - Eigenvalues for harmonic excitation.

λ_1	-0.01061 + 1.01235i
λ_2	-0.01061 + 1.01235i
λ_3	-0.0488 + 0.0000i

Time History.

In order to compare harmonic and non-ideal it was computed displacement and velocity considering time history from 100 samples. For displacement time history (Fig. 3) and velocity time history (Fig. 4) it was possible to conclude that non-ideal excitation offers around seven times more amplitude. It can be note that harmonic excitation was chosen according resonance and then the amplitude should be greater from this model, however the non-ideal excitation instead not be aided for resonance effect, has the chaotic effect in his favor.

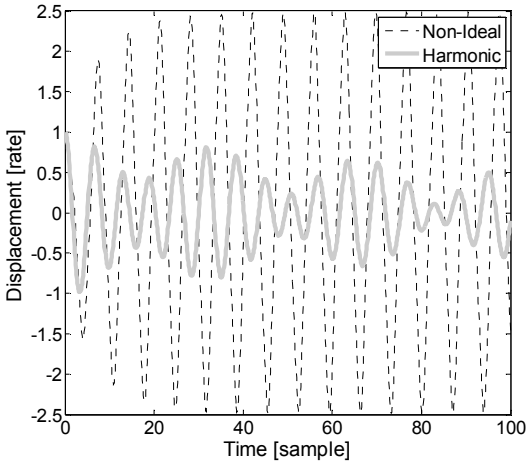


Fig. 3 - Displacement

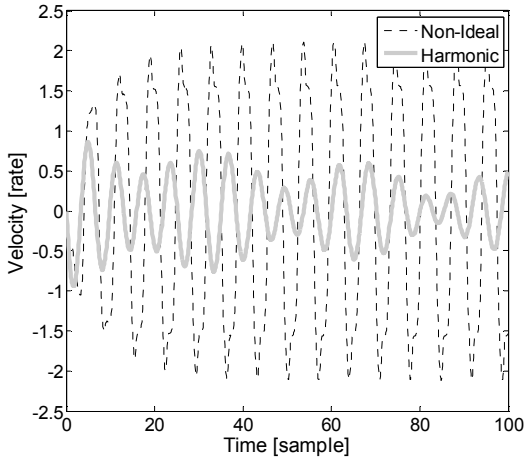


Fig. 4 - Velocity

Since displacement and velocity amplitude has direct relation to energy harvested, than non-ideal system presents a preferable behavior compared to harmonic excitation.

Phase Portrait.

A phase portrait of velocity x displacement (Fig. 5) demonstrates how many kinetic energy is available in the system. It is possible to verify that non-ideal excitation results in expressive more kinetic energy than harmonic excitation.

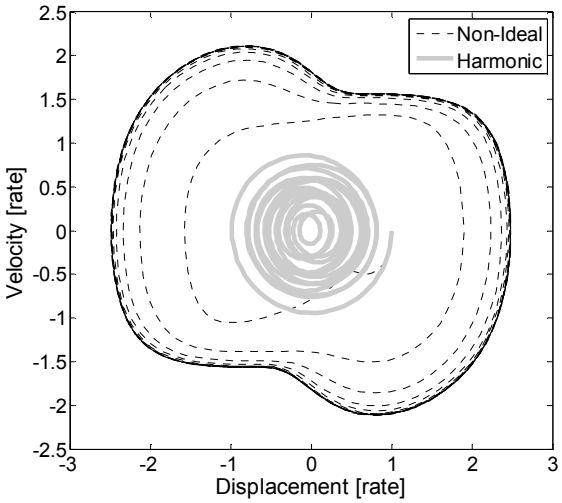


Fig. 5 - Velocity x Displacement

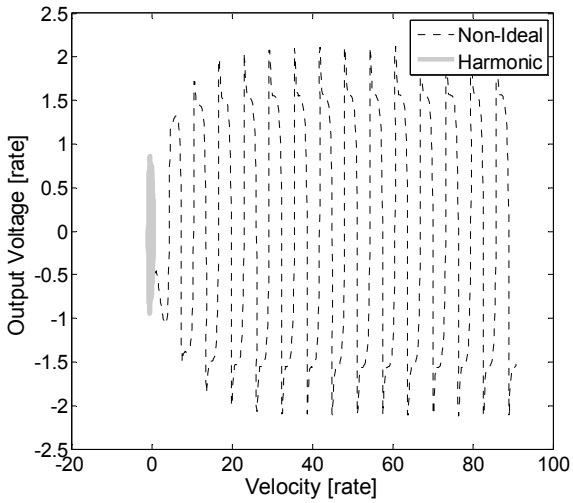


Fig. 6 - Output Voltage x Velocity

The total vibration energy that can be converted in electricity is presented by phase portrait of output voltage x velocity (Fig. 6). It can be seen that non-ideal excitation is more efficient considering

total energy absorbed from the system. Again it is important to emphasize that harmonic excitation match resonance and takes advantage of this condition. As environment vibration has a large range, than resonance will occur only in a certain period of time and non-ideal excitation could have an even more superior behavior.

Final Remarks

Many studies regarding energy harvesting has been outcome in the last few years. The principal propose from these many works is to enhance the harness capability from energy harvesters which conducted to dynamic analysis and project designs proposals. In the same direction, this investigation presented a study of dynamic behavior considering harmonic and non-ideal excitation.

As principal result it was possible to evaluate the promising superiority of non-ideal excitation in harnessing energy from environment. Such results encourage studies focusing in dynamic control to tuning harvesters to a non-ideal instead harmonic behavior.

The authors would like to thank to CNPq (Proc. n.º 301769/2012-5) and Minas Gerais State Research Foundation (FAPEMIG) for funding through the National Institute of Science and Technology in Smart Structures (INCT-EIE).

References

[1] Raghunathan V., Kansal A., Hsu J., Friedman J., Srivastava M. Design Considerations for Solar Energy Harvesting Wireless Embedded Systems. IEEE, 0-7803-9201. (2005)

[2] Challa V. R., Prasad, M. G., Shi Y., Fisher F. T. A vibration energy harvesting device with bidirectional resonance frequency tenability. Smart Materials and Structures, No. 17. (2008)

[3] Sherrit S. The Physical Acoustics of Energy Harvesting. IEEE International Ultrasonics Symposium Proceedings. (2008)

[4] Sodano H. A., Inman D.l J. Comparison of Piezoelectric Energy Harvesting Devices for Recharging Batteries. Journal of Intelligent Material Systems and Structures, 16(10), 799-807. (2005)

[5] Harb, A. Energy harvesting: State-of-the-art. Renewable Energy, 36, 2641-2654. (2011)

[6] Miller, L. M., Halvorsen, E., Dong, T., Wright, P. K. Modeling and experimental verification of low-frequency MEMS energy harvesting from ambient vibrations. Journal of Micromechanics and Microengineering, No. 21, 13p. (2011)

[7] Erturk, A. and Inman, D. Broadband piezoelectric power generation on high-energy orbits of the bistable duffing oscillator with electromechanical coupling. Journal of Sound and Vibration, Vol. 330, No. 10, pp. 2339 – 2353. (2011)

[8] Moehlis, J., DeMartini, B. E., Rogers, J. L., Turner, K. L. Exploiting Nonlinearity to Provide Broadband Energy Harvesting. Proceedings ASME Dynamic Systems and Control Conference, October 12-14, Hollywood, California, USA. (2009)

[9] Chavarette F. R. On an Optimal Linear Control of a Chaotic Non-Ideal Duffing System. Advances in Mechanical Engineering, Vol. 2, No. 3. (2012)

[10] Wolf, A., Swift, J. B., Swinney, H. L. and Vastano, J. A. Determining Lyapunov Exponents from a Time Series. Physica, North-Holland, Amsterdam,16D, 285-317. (1985)

Advanced Materials Research Vol. 936 (2014) pp 2165-2170
© (2014) Trans Tech Publications, Switzerland
doi:10.4028/www.scientific.net/AMR.936.2165

The Study of Water Level Fuzzy Control for Supercharged Boiler Drum

Zhang Hongyan[1,a],Jin Xiangdong[1,b],Xie Haitao[1,c]

[1]Hei Longjiang Province,Harbin City,Nangang District,Nantong Street 145,China

[a]zhangqingkai1989@126.com,[b]jinxiangdong04@163.com,[c]xiehaitao@hrbeu.edu.cn

Keywords: Fuzzy theory; water level controller; supercharged boiler; PID.

Abstract: Based on the application of the fuzzy theory,we designed a state level fuzzy controller for the marine steam power system. Compared with the level PID controller and a single-stage cascade PID level controller about disturbance response, the state level controller is more suitable for marine supercharged boiler level control because of its Smaller overshoot, shorter settling time, and other characteristics.

Introduction

Drum level is an important parameter affecting the safe operation of the boiler,for a lower or higher water level could cause a major accident, therefore, the study of boiler water level control is necessary. PID control is often used as level control method, which has intuitive, simple,good robustness characteristics,the premise of this method is to obtain a mathematical model , while the boiler is a complex objects ,which is nonlinear, multivariable adjustments, large lag and strong interference, and the presence of coupling of multiple variables, it is difficult to establish accurate mathematical model. So it is difficult to achieve the desired control effection just apply a PID control, and it is not ideal for the phenomenon of false water level in the drum level control [1]. To achieve good control effection, it needs to be improved on the basis of PID control.

Deriving fuzzy PID control strategy from the fuzzy PI was proposed by Om Prakash [2], Weeka Meshram et al made a further advance study [3] . AMProkhorenkov, ASSovlukov et al [4] used the fuzzy control strategy in centralized control system of the boiler .Compared with other control strategies rule ,the relative merits of the fuzzy controller is simply accessible, easy to implement, and a better control effection. Many scholars has made a contribution in fuzzy water level control . For example , to settle issues that the PID control parameters can not adapt to errors change , Chen Lin [5] et al make the error range according to the water level PID parameters in the actual operation of the process PID controller to form a cascade three impulse fuzzy PID control system.Huang Ming Zhang [6]adjusted PID control parameters by fuzzy controller , and compared results by controlling the simulation with PID controllers , and gave the method to achieve fuzzy control on hardware. Zhang Yongsheng [7] designed a humanoid combining logic level control strategy which was controlled by PID and fuzzy based on human logic features, the control method composed by PID and fuzzy control channel.

These studies focused on utility boiler drum level control, but less on marine supercharged boiler drum level control. Compared with power plants steam power systems, marine steam systems change conditions frequently in accordance with the requirements of the ship Operating conditions, the interference of the load to the drum level is uncertain,the changes of drum level have large non-linear , load disturbances, uncertain time lag and other features. In this paper, , a drum level fuzzy controller was designed for small marine boiler based on the research of utility boilers.

Designing Fuzzy Controller

Fuzzy controller is the core part of fuzzy control, the design steps of Fuzzy controller is Divided into determining the structure,definiting fuzzy sets, determining the membership function, building fuzzy control rules, and anti-blur.

Building Fuzzy Relationship

In this paper, the fuzzy controller selects two-dimensional structure,the water level errors and water level error changes will be used as input variables,and the control variables (valve) is output. As the state balance point,the valve position Selects 19.02, the steam flow is 0.187kg /s.

According to the demand for automatic control of the experimental level, the water level range is ±20mm,the rate of water level range is ±0.02mm/ms, the control valve range is ±20mm in the vicinity of the equilibrium point , which correspond to the seven fuzzy terms {large negative; middle negative; small negative; zero;small positive;middle positive;large positive},corresponding fuzzy symbols is{NB, NM, NS, O, PS, PM, PB}.

According to experience, choosing Gaussian distribution function as the membership functions for controller input and output fuzzy variables [8]:

$$f(x,\sigma,c)=e^{\frac{(x-c)^2}{2\sigma^2}} \quad . \tag{1}$$

The output fuzzy variableturn into fuzzy controller through anti-blur according to center of gravity method [9] :

$$\mu=\frac{\sum_i f_i\mu_i}{\sum_i f_i} \quad . \tag{2}$$

The fuzzy rules were established according to experience, for example: When the water level is large negative(the actual water level is lower than the normal water level), the water level change is small negative(the actual water level is far from equilibrium point), when the water flow is less than the steam flow, the valve position is below the equilibrium point. In order to restore to normal water level,the flow of feed water should be greater than the flow of superheated steam,for restoring the balance point as soon as possible, the amount of valve opening should be larger (large positive). Therefore, the fuzzy rules was built as shown in tab 2.1.

TAB 2.1 FUZZY RULES

OUT EC E	NB	NM	NS	O	PS	PM	PB
NB	PB	PB	PM	PM	PS	PZ	O
NM	PB	PM	PM	PS	PZ	O	NZ
NS	PM	PM	PS	PZ	O	NZ	NS
O	PM	PS	PZ	O	NZ	NS	NM
PS	PS	PZ	O	NZ	NS	NM	NM
PM	PZ	O	NZ	NS	NM	NM	NB
PB	O	NZ	NS	NM	NM	NB	NB

The Setting of State Point

Because the fuzzy control can directly calculated valve valve position through the error and error rate of change , it is faster than the PID control ,however, the fuzzy control only can be adjusted

near the stable point,so ti is not adaptable for changing stable point and system model structure[10],it will reduce the execution speed and stability if use integral part.In this paper, according to state of the boiler,which is the boiler temperature, pressure and flow parameters, it calculate the current valve position that can make the system stabilize, the valve position was used as a stable point of fuzzy control, it makes up the problem that the traditional fuzzy control is larger outside stable point, the paper accord the stable point as state point.

Assumed that in a fixed steam flow, the water level stabilized at the set value, when the value of feedwater flow is equal to steam flow, the corresponding feedwater valve position is accorded as stable point valve for the steam flow. The stable point valve is determined by water pressure, water temperature ,steam flow rates drum pressure and several other parameters, so we can determine the state point by these state parameters.

$$p_B - p_z = \frac{\xi\left(L_p\right) w_f^2}{2\rho} \quad . \tag{3}$$

$$W_f = W_g \quad . \tag{4}$$

$$\rho = f\left(p,t\right) \quad . \tag{5}$$

$$L_p = f\left(\xi\left(L_p\right)\right) \quad . \tag{6}$$

Where: p_B ——pressure of feedwater main tube,MPa；

$\xi\left(L_p\right)$——Valves and valve flow resistance coefficient linear relationship.

Experiment

In order to verify the superiority of the state fuzzy controller, we compared the control effection with single stage PID controller and cascade three impulses level controller systems.

Water perturbation experiments

Fig 3.1 is the response contrast for large water level fluctuations between a fuzzy controller with state-controller and a fuzzy controller without state-controller. As can be seen from the figure, when there is a large fluctuation in the water level, the adjusting speed of both is the same, but when the water level returns near to setting point,there is obvious steady-state error for the fuzzy controller without state-controller,it shows that the introduction of state controller can improve the control precision for fuzzy controller.

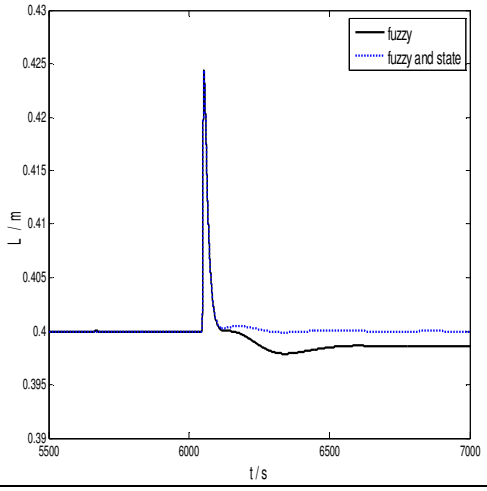


Fig 3.1 The fuzzy controller with state-controller

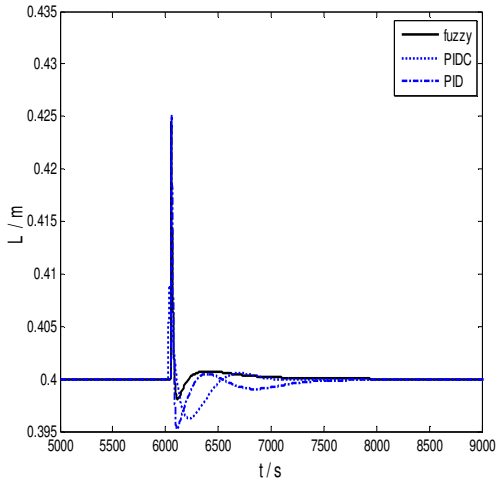


Fig 3.2 The effect of different controller in the same valve opening

The applications of single-stage cascade PID and three impulses level control system is ripe in engineering. Fig 3.2 shows a control effection contrast among single-stage PID controller,three cascade PID controller and fuzzy state controller. As can be seen from the figure, when the water level has great fluctuation, all the three controllers can achieve the setting fast, but from the view of settling time and overshoot, state fuzzy controller was significantly better than the other two groups controller ,which need a shorter regulation time, and at least faster than cascade PID controller 100s, faster than the single-stage PID controller about 300s. This is because the drum control is a non-linear systems, though the PID control response fast in linear system,but fuzzy control more responsive in non-linear systems.

Switching Conditions Experiments

In the marine steam power systems, turbines have three conditions: T1, T2 and T3, supercharged boiler has two conditions: B3 and B4. Tab 3.1 shows the all conditions of marine steam power systems, simulating running station of marine steam power system to inspect the performance of PID and fuzzy controller through changing the gear of boiler and turbine.

TAB 3.1 MARINE STEAM POWER SYSTEM RUNNING STATE

Time t /s	0~ 4000	4000~ 4500	4500~ 5000	5000~ 5500	5500~ 6000	6000~ 6500	6500~ 7000	7000~ 9000
Turbine	T1	T2	T3	T2	T3	T2	T1	T2
Boiler	B3	B4	B4	B4	B4	B4	B3	B4

Fig 3.3 shows the effect of the three controllers to control the water level in different conditions. As can be seen from the simulation results, when steam power system switching conditions,which will have a great disturbance for drum level, state fuzzy controller can rapidly adjust water level to the set value, while the single-stage water level controller PID and Cascade PID controller adjusts the water level slower and have larger overshoot. So,from the perspective of security and stability of the system, only the state fuzzy control system was able to meet the control requirements of supercharged boiler .

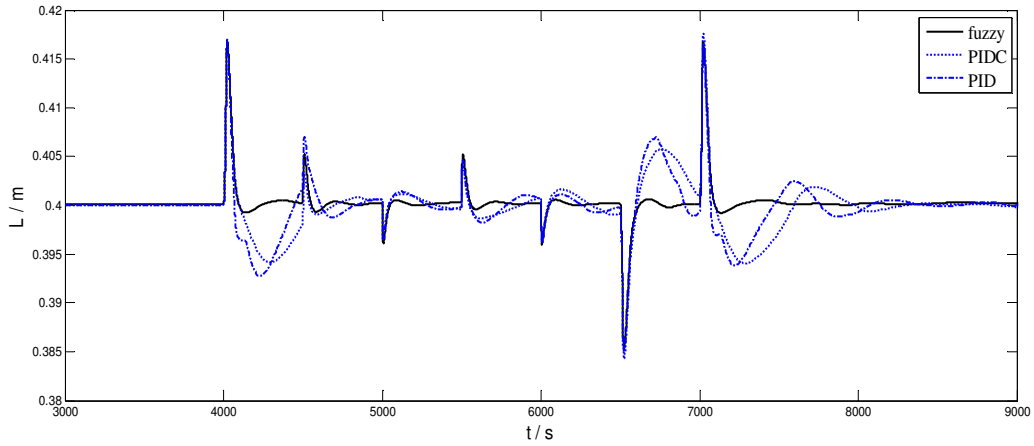


Fig 3.3 The control effection of different controller in running state

Summary

In this paper,a state fuzzy controller was established based on state control theory and fuzzy theory. Compared with single-stage PID controller and cascade PID controller it can draw the following conclusions:

(1)Comparing cascade PID controller with single-stage PID controller, the former has respond faster, shorter time to adjust and better effection of control characteristics.

(2)Comparing the state fuzzy controller with the cascade PID controller,because the state fuzzy controller collects data through the fuzzy processing, which is not too sensitive to changes in water level, smaller overshoot, steady rapidlier, the system better stability.

(3)For the marine steam systems change conditions frequently in accordance with the requirements of the ship Operating conditions,from the perspective of security and stability of the system, only the state fuzzy control system was able to meet the control requirements of supercharged boiler .

References

[1] Liu Min, MA Junshuang, The application of Fuzzy RBF Neural Network in boiler water level control, J. Microcomputer Information. 22(2006)56-58.

[2] Om Prakash, A.N.Sinha, A new design analysis of Fuzzy Proportional Integral controller in Boiler system, J.Proceedings of Int. conf. on Emerging Trends in Electrical. 22 (2007)257-261.

[3] Sweeka Meshram, Omprakash Sahu, Application of ANN In Economic Generation Scheduling In IEEE 6-Bus System, J. International Journal of Engg Science and Tech. 3 (2011)2461-2466.

[4] A.M.Prokhorenkov, A.S.Sovlukov, Fuzzy models in control systems of boiler aggregate technological processes, J. Computer Standards&Interfaces. 01(2002)151-159.

[5] Chen Lin,Gao Hui,Shi guohui, Boiler fuzzy control application and its performance evaluation, J. Instrumentation Customer. 01(2012)91-92.

[6] Huang Zhangming, Li Fangyuan, Boiler Drum Level Fuzzy Control System Design and Simulation, J. Automation Expo. 09(2011)76-78.

[7] Zhang Yongsheng,Ma Yunyi, Boiler drum level humanoid Logic Control Strategy, J. Ship Science and Technology. 04(2011)55-57.

[8] Liu Jinkun, Intelligent Control, third ed., Electronic Industry Press, Beijing, 2005.

[9] Liu Jinkun, MATLAB simulation of advanced PID control, third ed., Electronic Industry Press, Beijing, 2004.

[10] Ping Jingshui, Liu Heng, Ma Xin, Fuzzy Control Features and Simulation of Boiler feed water level, J. Huainan Teachers College Journal. 04(2011)72-75.

Advanced Materials Research Vol. 936 (2014) pp 2171-2176
© (2014) Trans Tech Publications, Switzerland
doi:10.4028/www.scientific.net/AMR.936.2171

The Application of HPWM in Improving Vehicle Lateral Stability

Zhang An-jing[1, a*], Xu Yan-hai[1, b], Lv Xin[1, c]

[1]School of Transportation and Automobile Engineering, Xi Hua University, Chengdu 610039, China

[a]zhanganjing2006@163.com, [b]xuyanhai.cn@gmail.com, [c]laughing629@163.com

Keywords: HPWM; Vehicle lateral stability; high-speed switching valve; Hydraulic control unit

Abstract: The application of the High-frequency pulse width modulation (HPWM) for improving vehicle lateral stability is investigated in the paper. Firstly, a hydraulic control unit (HCU) combined with a high-speed switching valve (HSV) for controlling hydraulic oil pressure by adjusting duty cycle is presented. Then, a typical control strategy is described based on the application of HPWM. Finally, by using a 15dofs vehicle model, a simulation is carried out to investigate the role of HPWM on improving vehicle lateral stability. The results show that HPWM is capable to control the output pressure of HSV accurately and improve vehicle lateral stability effectively.

Introduction

Vehicle dynamic control system used to keep vehicle lateral stability by additional longitudinal forces is an active safety device and developed based on ABS and TCS. Numerous studies focus on the development of control strategy and its implementation [1]. There also exists many literatures on research how to estimate vehicle state parameters such as vehicle speed and side slip angle et al [2, 3]. The effect of hydraulic characteristics on the efficiency of the control system has also been investigated [4]. Currently, low-frequency pulse width modulation (LPWM) makes HSV switch frequently between open and close. Therefore, the procedure can't control braking torque accurately and cause pressure fluctuations and noise. So it deteriorates the efficiency of the control system.

The purpose of the paper is to investigate the application of HPWM in vehicle stability control and the efficiency in improving vehicle lateral stability.

HSV's PWM Control Model

The force acted on the spool of a HSV can be written as

$$m\ddot{x} = F_i(i,x) - F_p(x,\Delta p) - F_k(x) - F_c(\dot{x}) \tag{1}$$

Where m is the spool mass. x is spool displacement. $F_i(i,x)$ is electromagnetic force. $F_p(x,\Delta p)$ is the fluid dynamic force. $F_k(x)$ is the spring force. $F_c(\dot{x})$ is the damping force. Δp is the pressure differential between inlet and outlet. i is the current.

Fig.1 presents the electromagnetic force of solenoid valve along with the change of current and air gap. As the current increases and the air gap decreases, the electromagnetic force becomes increasing. Fig.2 gives the effects of valve opening and pressure difference on steady flow force of HSV.Solenoid valve usually uses LPWM regulation whose frequency is not more than 100Hz and it can't control pressure accurately. But HPWM regulation with a frequency more than 4000Hz is able

to keep spool in any place and control pressure accurately [5]. Figs. 3 and 4 present the valve opening and electromagnetic force of solenoid valve along with duty cycle and time. The frequency of HPWM is 4000Hz and the duty cycle is changed from 20% to 70%. It is obvious that the status of valve opening increases with the increase of duty cycle and the valve is fully opened when the duty cycle is 70% in fig.3. In addition, the valve opening keeps constant at each duty cycle. The electromagnetic force increases with the increase of duty cycle and keeps constant at a given duty cycle.

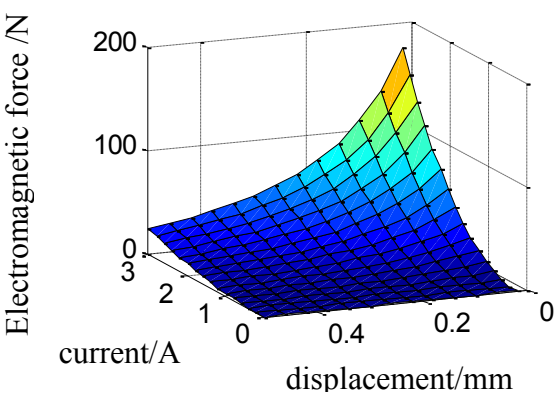


Fig.1 Electromagnetic force

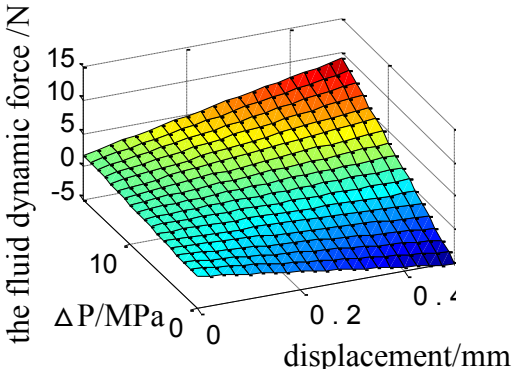


Fig.2 Dynamic forces of fluid

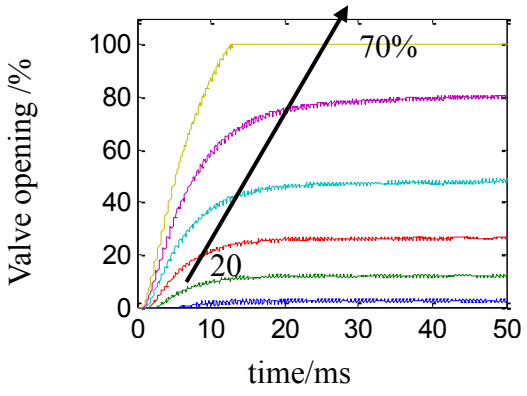


Fig.3 Valve opening with HPWM

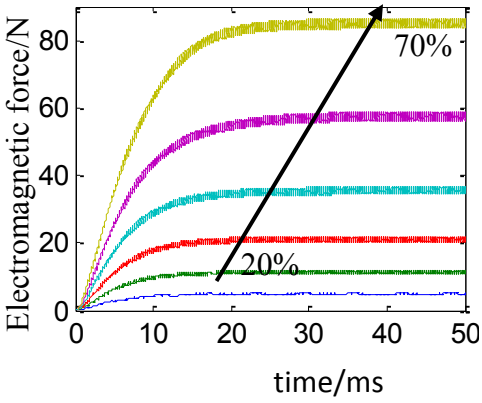


Fig.4 Electromagnetic force with HPWM

Control strategy

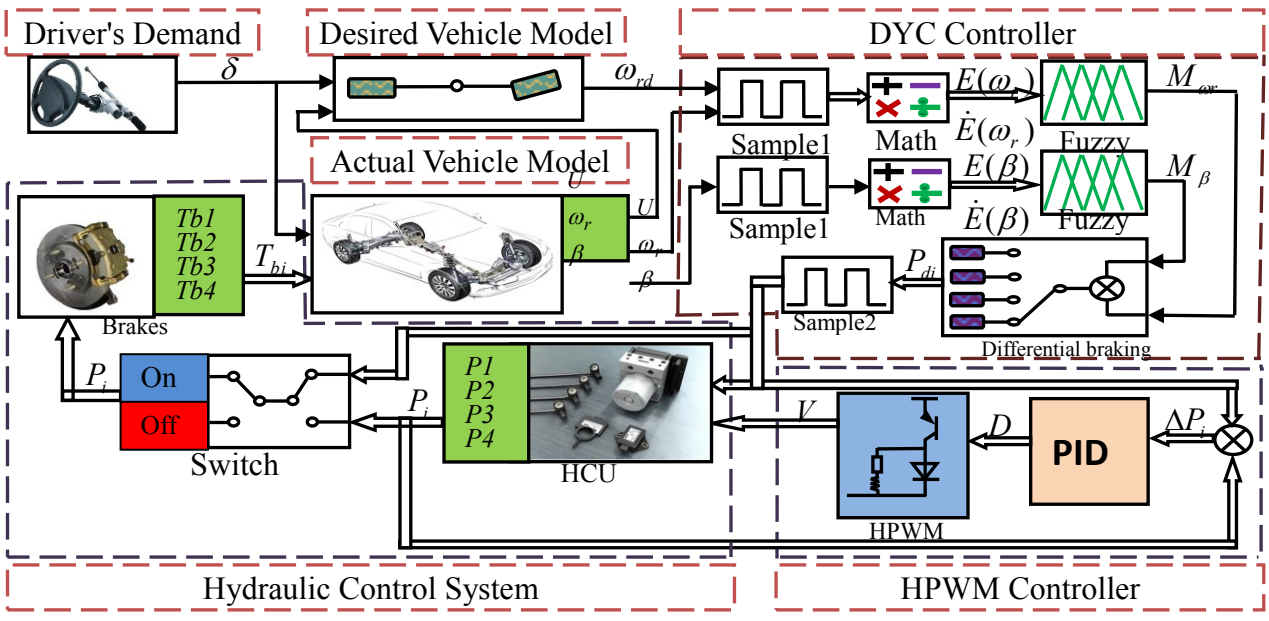


Fig.5 Flowchart of control strategy

The flowchart of control strategy is shown in Fig.5. There are 6 parts in the flowchart. Driver's demand model is used to obtain driver's input. Desired vehicle model is to demonstrate ideal trajectory and output ideal yaw rate ω_{rd}. Actual vehicle model have 15dofs used to present an actual vehicle. The DYC controller with 2 fuzzy controllers is used to control sideslip angle and yaw rate. Sample1 is used to obtain vehicle dynamic parameters as shown in the flowchart with a frequency of 25Hz. The output of DYC controller is corrective moment which is done by differential braking pressure P_{di} in assigned brake system. The high-frequency pulse voltage (4000Hz), whose duty cycle is regulated by PID in HPWM model, is used to make sure that the output pressure P_i close to ideal pressure P_{di} in HCU. Sample2 ensures that the output frequency of P_{di} is 10Hz. Finally, P_i is converted into braking torque which is used to control vehicle lateral stability. Switch is used to debug the control system such as with or without control, with considering the dynamic characteristics of the hydraulic control unit (with HCU) or not.

Simulation and Analysis

The performance of strengthening vehicle lateral stability by using HPWM is evaluated through numerical simulations of vehicle response to a fishhook wheel input. Road coefficient is 0.85. The initial vehicle speed is 80Km/h. The simulation is subjected to without control, with HCU and without HCU in order to compare vehicle lateral stability.

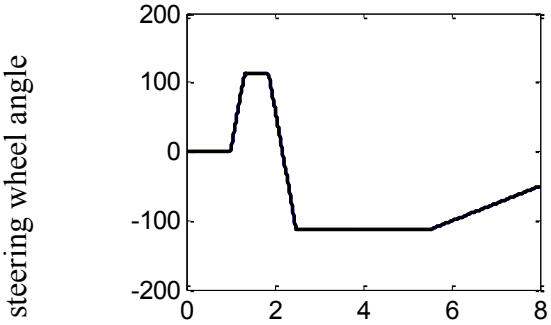


Fig.6 Steering wheel angle

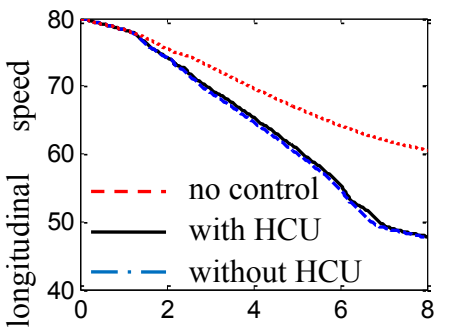


Fig.7 Longitudinal speed

Steering wheel angle is shown in Fig.6. It is zero in the first second, then changes from 115°to -115°in the middle 1.5 seconds and maintains 3 seconds, finally gradually closes to zero. Fig.7 gives the information of vehicle longitudinal speed. Red dashed shows vehicle speed without control. The vehicle speed with HCU control is shown via solid black line. Blue dotted line shows vehicle speed without HCU control. It indicates that the 3 vehicles longitudinal speed with resistance acting is the same and gradually decreases in the first 1 second. The vehicle longitudinal speed without HCU control decreases faster than it with HCU control, but without control decreases the fastest in the remaining time. That because, compared with speed without control, the speeds without HCU control and with HCU control is exerted braking force at an assigned tire and braking force with HCU control is smaller than it without HCU control.

Vehicle tracks are presented in Fig. 12. They are ideal trajectory with green dotted line presented, trajectory without HCU control via blue short dashed, trajectory with HCU control via solid black line and trajectory without control via red long dashed. Trajectory with HCU control and trajectory without HCU control are all could closed to ideal trajectory, but the Trajectory without HCU control is more closer. The maximum difference between trajectory with HCU control and trajectory

without HCU control reaches to 1.5m. The trajectory without control is obviously far away from the ideal trajectory. Fig. 9 gives the information of yaw rate. The yaw rate without control is shown via red long dashed. The solid black line and blue short dashed shows yaw rate with HCU control and without HCU control. The ideal yaw rate is presented by green dotted line. It is obvious that the yaw rate with HCU control and without HCU control is close to ideal yaw rate well, but the yaw rate without control is far away ideal yaw rate.

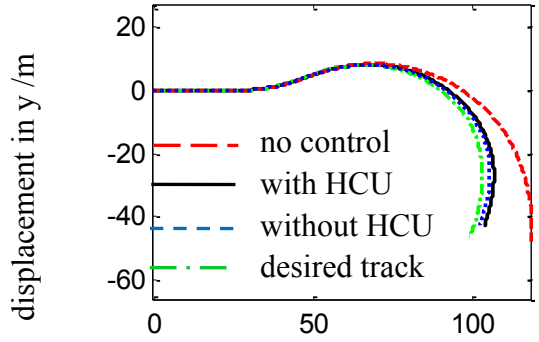


Fig.8 Comparison of tracks

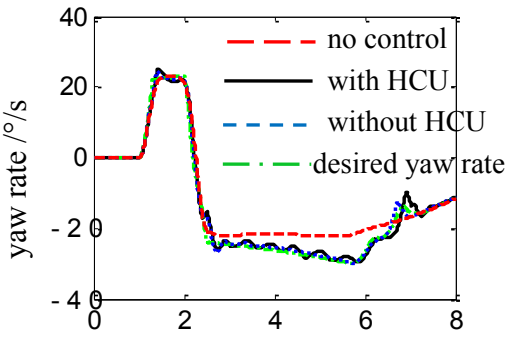


Fig.9 Comparison of Yaw rate

Fig.10-12 give wheel cylinder's brake pressures, braking torques and wheel speeds on each wheel. FL, FR, RL and RR present left tire of front axle, right tire of front axle, left tire of rear axle and right tire of rear axle. Ideal value is shown via green dashed. Solid black line describes the value with HCU control. Blue dotted line presents the value without HCU control. It is shown from Fig.10 that the wheel cylinder pressures follow the tracks of ideal value well, so it proves that HPWM could accurately control output pressure. The normal force translated from inside tire to outside tire in turning in that the resultant force in longitudinal and lateral at inside tire of rear axis gets physical limit, so the peak braking torque without HCU control can't reach ideal peak braking torque as well as the peak braking torque with HCU control. Although the braking torques without HCU control is mostly as the same as the braking torques with HCU control on FL, FR, and RL, it is deferent on RR and the braking torque with HCU has some fluctuations on RR. There are the same tendencies in Fig.12. It indicates that the dynamic characteristics of the hydraulic control unit influence the additional yaw moment with DYC Controller outputting.

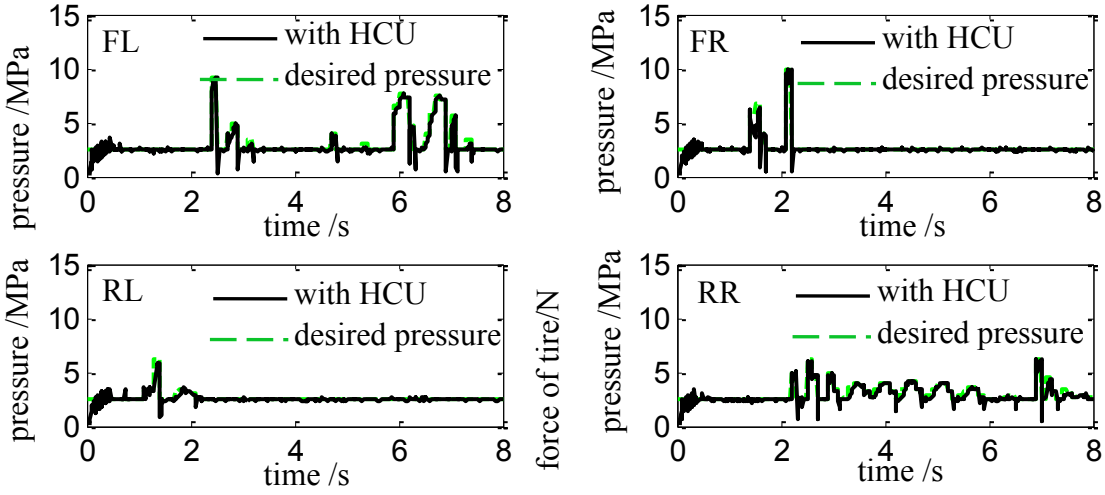


Fig.10 Pressure of brake cylinder

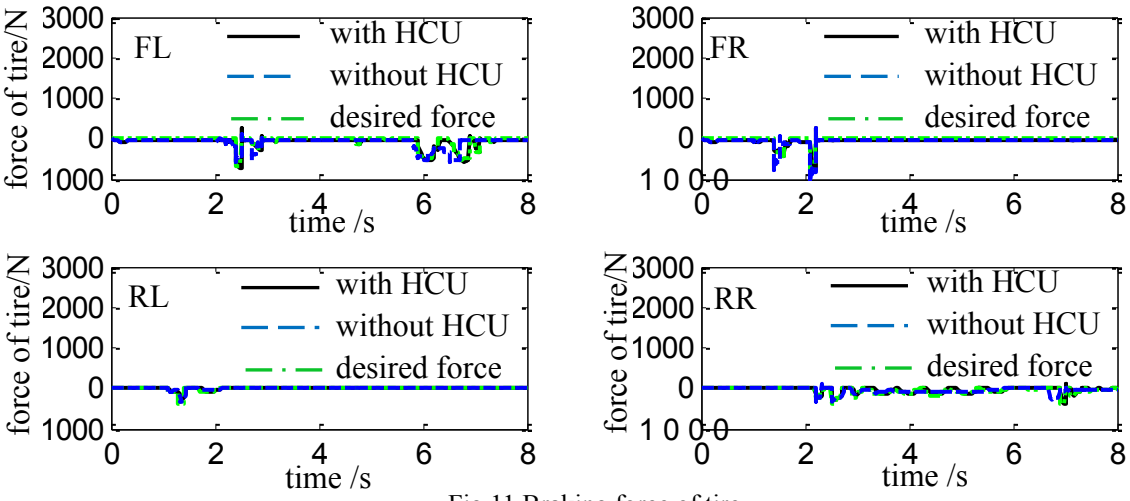


Fig.11 Braking force of tire

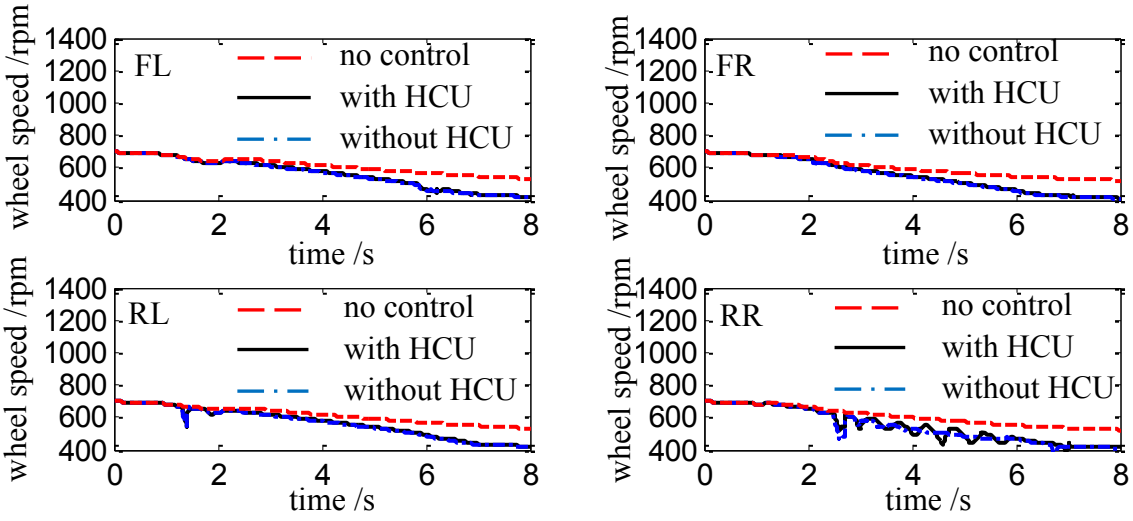


Fig.12 Wheel speed of tire

Summary

(1) The output pressure of HCU can accurately follow the ideal pressure with HPWM control. Compared with LPWM, HPWM not only adjusts the output pressure more accurately and improve vehicle stability efficiently, but also it can reduce the fluctuations of braking pressure.

(2) The entire control system for vehicle lateral stability composed of solenoid valve, HCU and control strategy is close to actual system. Analysis result shows that the dynamic characteristics of HCU have influence on the efficiency of vehicle lateral stability.

Acknowledgments

This work is supported by Science & Technology Department of Sichuan Province, under Grant NO. 2011J00043.

Reference

[1] Liangmo Wang, Li Tan, Li-hua An, et al; Study on the ESP System Based on Fuzzy Logic PID Control and Multibody Dynamics, J. Electrical Systems, 2012, 8(1): 57-75.

[2] Yang Cai, Song Jian. A Research on Algorithms for Calculating Vehicle Reference Speed and Slip Ratio in ABS/TCS/AYC Systems, J. Automotive Engineering, 2009, 31(1): 24-27.

[3] Yu Zhuoping, Gao Xiaojie. Review of Vehicle State Estimation Problem under Driving Situation, J. Journal of Mechanical Engineering, 2009, 45(5):20-32.

[4] Qi Xue 1e，Song Jian，Wang Huiyi，et al. Modeling and Analysis of Vehicle ESP Hydraulic Control Device Using AMESim, J. Machine Tool & Hydraulics，2008,8: 115-116.

[5] Wang Weiwei, Song Jian, Li Liang, et al. High speed on-off solenoid valve with proportional control based on high frequency PWM control, J. Journal of Tsinghua University, 2011, 51(5):715-719.

CHAPTER 20:

Power Engineering

Advanced Materials Research Vol. 936 (2014) pp 2179-2183
© (2014) Trans Tech Publications, Switzerland
doi:10.4028/www.scientific.net/AMR.936.2179

Photovoltaic Power Generation Data Preprocessing Using Wavelet Thresholding

Bai Kai[1], Qu Hongda[13], Zong Jin[1], Li Zhi[1], Zhai Huaxin[2], Zhao Zhou[2]

[1].North China Electric Power Research Institute Co. Ltd. , Beijing 100045, China;
[2]Zhangjiakou Wind and Solar Power Energy Demonstration Station Co. Ltd. , Zhangjiakou 075000, China;
[3].North China Electrical Power University, Beijing 102206

Keywords：power predication, the historical data, photovoltaic power generation, de-noising

ABSTRACT ：The accuracy of power prediction of photovoltaic power generation will be reduced if there are noises in the historical data of photovoltaic power generation. It is necessary to eliminate noises in the historical data. First, the power generation can be arranged in a two-dimensional data set by date. Secondly, the grayscale image matrix will be obtained after data normalized. Thirdly, two-dimensional wavelet based image de-noising method will be used in the matrix de-noising. Finally the real historical data will be obtained through anti-normalization the matrix which is already de-noised. We will analyze its results feasible and effectiveness.

INTRODUCTION

Derived from the data collection and monitoring database data is not only the foundation of photovoltaic power prediction and power characteristics, but also the basis of grid control. As the amount of data, data monitoring process will inevitably be a certain degree of error interference, this will directly affect the photovoltaic power prediction accuracy as well as mastery of the PV output characteristics of a negative impact. Therefore, high-accuracy photovoltaic output data for the future smart grid power system real-time scheduling and planning is very important. After more and more small-scale PV systems such as building-integrated photovoltaic (BIPV), etc. connected into the grid, the challenge of PV output prediction for the next day is getting more and more important[1-2]. Therefore, in order to more accurately predict photovoltaic system generating capacity curve, it is necessary to de-noising the abnormal data to improve data quality and reduce the problem of randomization PV impact on the grid.

Today, the signal processing has become an important part of contemporary science. The ideal tool for the nature which is stable and unchanging over time signal processing is Fourier. However, in practice, most of the signal is unstable, in particular for non-stationary signals is the wavelet analysis tool. Our PV data is discrete data signal is non-stationary. This article will use the wavelet transform of the PV data signal processing.

So far, the data de-noising research focuses on the load forecasting research, mostly one-dimensional de-noising [3-4]. Given a certain degree of de-noising dimensional limitations, this paper made a two-dimensional photovoltaic power data de-noising. The horizontal axis represents the coordinates adjacent to the date, the vertical axis represents the node at different times of the same date. Then the matrix formed through the normalization process, Get each element in the matrix between 0-1. This matrix can be seen as a gray-scale image matrix. Followed by the two-dimensional wavelet-based image de-noising . Finally, anti-normalization, get de-noised PV output data.

Wavelet Transform De-Noising

This is wavelet threshold shrinkage method [5-6]: Wavelet transform of $f(k)$ which contains noise, M represents the number of layers. The k_{th} frequency coefficients of the j_{th} layer is called wavelet coefficients $w_{j,k}$. According to the different nature of the noise and signal, we threshold processing to $w_{j,k}$, then the new wavelet coefficients $\tilde{w}_{j,k}$ is obtained. The de-nosied signal will be obtained by reconstructing $\tilde{w}_{j,k}$.

Determination of the threshold value

Threshold directly affects the denoising results. Smaller threshold is able to retain more of the wavelet coefficients and image information, but retained the noise is greater; While larger threshold value makes the picture in some useful high-frequency information is removed.

Existing threshold selection criteria, including the fixed threshold criterion, mixed threshold criterion, unbiased risk estimation criteria and Minimax threshold criteria, etc. [7]. Compared to the above criteria, a fixed threshold criterion is relatively simple and de-noising better. This article is taken globally fixed threshold de-noising method, The threshold is

$$T = \sigma\sqrt{2\log_2 N} \tag{1}$$

Where σ Is the noise standard; N is the length of the signal.

$$\sigma = \frac{\left|\overline{w}_{j,k}\right|}{0.6475} \tag{2}$$

Where $j = 1,2,\cdots M$; $k = 1,2,\cdots,N_j$, N_j are the high-frequency numbers after the level j resolved, $\overline{w}_{j,k}$ is the arithmetic mean value of the sequence of number $\{w_{j,k}\}$.

The selection of threshold function

Soft threshold function de-noising has some flaws [5-6]. So we use the semi-soft threshold function. Mathematically expressed as follows:

$$\tilde{w}_{j,k} = \begin{cases} (1-\mu)w_{j,k} + \mu\,\mathrm{sgn}(w_{j,k})(|w_{j,k}| - T) & |w_{j,k}| \geq T \\ 0 & |w_{j,k}| < T \end{cases} \tag{3}$$

$$\mu = \frac{T}{|w_{j,k}|}\exp\left(-\frac{|w_{j,k}| - T}{|w_{j,k}| + T}\right) \tag{4}$$

Where μ is the weighting factor.

It can be proved that the formula in both continuous threshold function, and in the threshold greater than the threshold within a continuous wavelet threshold higher order derivatives, it is simply hard threshold or soft threshold values are not available.

PV DATA DE-NOISING PROCESS

In summary, for short-term prediction of photovoltaic output data de-noising wavelet analysis as follows:

Step1：Select the n days before the test and 96 time breakpoint per day as data sample nodes

Step2：This matrix normalization processing, the new matrix is a two-dimensional gray-scale image matrix. Each element in the matrix represents the brightness in the image.

Step3：Wavelet decomposition of the image in step 2 and select the appropriate wavelet for the original signal $f(k)$, for M-layer wavelet decomposition，finally we obtain a series of wavelet coefficients $w_{j,k}$。

Step4：The wavelet decomposition of the high-frequency coefficients thresholding, The $w_{j,k}$ for semi-soft threshold function processing, to obtain the estimated coefficients $\hat{w}_{j,k}$.

Step5：Reconstructing the two-dimensional images using $\hat{w}_{j,k}$ and we get the signal $\hat{f}(k)$ which has already been de-noised.

Step6：Anti-normalize $\hat{f}(k)$ which has been already de-nosing and get de-noised PV output data.

EXAMPLES OF EFFECTIVENESS ANALYSIS

Here we select U.S. Sheldon Village 2010 Years 20 days per 96 time points photovoltaic output data, a total of 1920 sample data. Using matlab wavelet transform data box, decomposition level of M = 3，Wavelet selection db4. The next will be from the de-noising performance and accuracy for the photovoltaic power prediction accuracy to evaluate and analyze.

Analysis of photovoltaic data de-noising

For image de-noising after evaluation of the effectiveness of the indicators, including peak signal to noise ratio (PSNR) and root mean square error (RMSE)[8-10]， $f(x,y)$ as a size of $M \times N$, the quantization level is $0,255$：

$$RMSE = \left(\frac{1}{MN} \sum_{x=0}^{M-1} \sum_{y=0}^{N-1} \left(f(x,y) - \tilde{f}(x,y) \right)^2 \right)^{\frac{1}{2}} \tag{5}$$

$$PSNR(dB) = 10 \log_{10} \frac{255^2}{(RMSE)^2} \tag{6}$$

$\tilde{f}(x,y)$ is the image reconstructed after de-nosing.

Table 1 shows the soft threshold and hard threshold and the actual use of semi-soft wavelet threshold de-noising comparison results. Table 1 shows the results of the indicators can be seen, based on semi-soft thresholding wavelet method is better than the hard threshold and soft threshold method.

TABLE 1 DIFFERENT THRESHOLD FUNCTION DE-NOISING RESULTS

Threshold function	RMSE	PSNR/dB
Hard threshold	3.54×10^{-4}	38.75
Soft thresholding	8.73×10^{-5}	40.24
Semi-soft threshold	5.31×10^{-5}	44.60

Accuracy assessment of daily electricity generation

Sparse Bayesian algorithm proposed theoretical model based on support vector machines by Dr. Michael E. Tipping in 2001. Probabilistic model introduced by artificial intelligence methods can get rid of the vast majority of errors encountered interference. At present, this method has been used in the power load forecasting[11-12]. We will use this method for photovoltaic power generation data preprocessing before and after pretreatment, evaluate the accuracy of using the root mean square error indicators.

Table 2 shows a month in predictions, from which we can see through to the noise after most days, root mean square error will be reduced. From the point of view throughout the month of RMSE, de-noised 0.08 is better than before de-noised 0.088 so that achieve the purpose of improving the prediction accuracy

TABLE 2: BEFORE AND AFTER DE-NOISING PV OUTPUT PREDICTION ACCURACY COMPARISON (RMSE)

TIME	AFTER	BEFORE	+/—
d1	0.05	0.064	-0.014
d2	0.047	0.049	-0.02
d3	0.142	0.142	0
d4	0.092	0.076	+0.016
d5	0.058	0.06	-0.002
d6	0.015	0.014	+0.01
d7	0.046	0.044	+0.002
d8	0.068	0.067	+0.001
d9	0.08	0.088	-0.008
d10	0.095	0.182	-0.087
d11	0.079	0.083	-0.004
d12	0.127	0.208	-0.081
d13	0.165	0.145	+0.021
d14	0.119	0.146	-0.027
d15	0.074	0.068	+0.006
d16	0.049	0.054	-0.005
d17	0.037	0.039	-0.002
d18	0.069	0.074	-0.005
d19	0.028	0.029	-0.001
d20	0.116	0.116	0
d21	0.092	0.095	-0.003
d22	0.048	0.056	-0.008
d23	0.015	0.039	-0.024
d24	0.043	0.04	+0.003
d25	0.044	0.057	-0.013
d26	0.06	0.058	+0.002
d27	0.059	0.081	-0.022
d28	0.051	0.06	-0.009
d29	0.015	0.048	-0.033
d30	0.042	0.049	-0.007

CONCLUSION

We can de-noising PV data while maintaining PV power's vertical and horizontal time on the basis of trends. The original data after de-noising, PV power forecasting can provide higher quality input data in order to reach a higher level of prediction accuracy.

ACKNOLEDGMENT

This work was carried out with the financial support by National Research Program of China. The contract number is 2011BAA07B04

REFERENCES

[1] Zhanglan, ZhangYanxia, GuoChangmin, ZhaoJie, PV systems based on neural network predictive power generation [J]. China Power，2010,43(9)：75-78.

[2] XieLimei, Grid-connected PV system modeling and on the distribution grid voltage and the impact loss of grid[D],Peking：Thesis of North China Electric Power University，2009.

[3] WuYaohua, Based on wavelet soft thresholding Term Load Forecasting [J]. Guangdong Electric Power，2007,12(20)：5-8.

[4] XiongChuanping, CaoJunjie, ChenQian, JuPing, Power load based on wavelet analysis denoising model identification [J]. Journal of Hohai University，2011,39(4)：470-474.

[5] DONOHO D L，JOHNSOTNE I M. Idea spatial adaptation by wavelet shrinkage[J].Biometrika, 1994, 81(3);425-455.

[6] DONOHO D L，De-noising by soft thresholding[J]. IEEE Trans on Information Theory,1995,38(2):613-627.

[7] XieJiecheng, ZhangDali, XuWenli, Image denoising Review [J]. Chinese Journal of Image and Graphics，2002，7（3）：209-217.

[8] ShiHongbo, Based on wavelet transform image denoising [D]，JiLin：Jilin University，2007.

[9] ShiJiachen, Image Denoising Based on Wavelet Transform Algorithm and Its FPGA Implementation [D].NanJing：Nanjing University，2010.

[10] ZhangMing, LiKaicheng, HuYisheng, Neighborhood threshold based on wavelet classification power quality signal denoising algorithm [J]. Power Systems，2010,34(10):84-89.

[11] YangMing, HanXueshan, FanShu, Component based Sparse Bayesian learning probabilistic wind power output prediction method [J]. Power Systems，2012,36(14)：125-130.

[12] DuanQing, Learning method based on Sparse Bayesian regression and classification in the prediction of the power system [D], Shandong：Dissertation of Shandong University，2010.

Advanced Materials Research Vol. 936 (2014) pp 2184-2189
© (2014) Trans Tech Publications, Switzerland
doi:10.4028/www.scientific.net/AMR.936.2184

Transmission Line Insulators Detection based on KAZE Algorithm

Li Dan[1, a], Zhang Meng[2,b] and Tong Zubing[3,c]

[1-3]School of Electrical and Information Engineering, AnHui University of Technology, Maanshan 243000,China

[a]lidan@ahut.edu.cn, [b]15665557006@163.com, [c]772832185@qq.com

Keywords: KAZE algorithm, transmission line, insulators detection

Abstract: Transmission Line obstacle detection technology is one of the hot spots of computer vision and transmission line inspection robot system.As the most common obstacle of inspection robot,correctly identify of insulators can help improve the reliability and accuracy of self-inspection. Low robustness of traditional detection algorithm can not meet the requirements on insulators detection when dealing with complex environment. To solve the above problem, a transmission line insulators detection method based on KAZE algorithm is given. The feature extraction is done in the nonlinear scale space, and feature vectors are formed with M-SURF algorithm, what's more, feature vectors detecting is worked through the nearest neighbor algorithm as matching criteria and RANSC generated algorithm. Experimental results show that the effect of insulators detection algorithm based on KAZE detect faster and also make a good performance on accuracy and robustness.

Introduction

In the study of transmission line inspection robot , the real-time detection and identification of obstacles is a very important technology , which refers to the line inspection robot charged in case of crawling along the ground line to identify shock hammer, insulators , suspension clamps , towers and other obstacles independently, thus improving the reliability and accuracy of the self-inspection[1]. In recent years, transmission line insulators detection has aroused general interest in the field of transmission line insulators detection. Currently, the method of transmission line insulators detection can be divided into three parts: multi-sensor-based detection , machine vision based detection and active learning based detection[2]. Among them, the detection method based on machine vision is simple and effective , which mainly divided into feature detection, structural constraints detection,stereo vision detection. These three methods can give a good detection result , but they are sensitivity of the complex images[3-6]. To solve this , this paper propose a transmission line insulators detection system using KAZE algorithm , which enhance the robustness of the system and help to improve the robot navigation's accuracy and sensitivity .

KAZE feature detection algorithm is based on nonlinear scale-space , it construct stable nonlinear scale space by additive operator splitting algorithm (AOS) and variable conduction diffusion[7]. It has outstanding robustness, high precision and partial match performance compared with Harris, SIFT, SURF and other traditional detection algorithm, what's more,it's insensitive with scale, affine, perspective and illumination invariance which can make it maintain better detection results for insulators detection under complex background.

KAZE Features

KAZE algorithm is based on nonlinear scale space, which detection includes four steps: construction of the nonlinear scale space , feature detection, precise positioning of features , generation of feature vector .

Construction of the Nonlinear Scale Space

Scale-space theory first introduced in the field of computer vision, which aims to simulate multi-scale features of image data, its main idea is to KAZE algorithm construct nonlinear diffusion filtering with additive operator splitting algorithm (AOS) and variable conduction, and you can take any step to construct a stable nonlinear scale space[8]. Eq.1 shows the nonlinear diffusion formulation:

$$\frac{\partial u}{\partial t} = \mathrm{div}(g(|\nabla u_\sigma(x,y,t)|) \bullet \nabla u_\sigma) \quad . \tag{1}$$

Where u is image luminance,div is divergence,time t is scale parameter, ∇u_σ is the gradient of a Gaussian smoothed version of the original image, $g(|\nabla u_\sigma(x,y,t)|)$ is conductivity function which can be shown as Eq.2:

$$g(|\nabla u_\sigma(x,y,t)|) = \exp(-\frac{|\nabla u_\sigma|^2}{k^2}) \quad . \tag{2}$$

The contrast parameter k determines the mount of edge information to be keep.

KAZE algorithm discrete the scale space in logarithmic steps arranged in a series of o octaves and s sub-levels. Make sure that each image has and the the same resolution with original image. The octave and sub-level indexes are mapped to their corresponding scale σ through the following Eq.3:

$$\sigma_i(o,s) = \sigma_0 2^{\sigma+\frac{s}{S}} \qquad o \in [0,\cdots,o-1],\ s \in [0,\cdots,S-1],\ i \in [0,\cdots,N]. \tag{3}$$

Where σ_i is the scale level in pixel,σ_0 is the base scale level and N is the total number of filtered images.

Feature Detection in Nonlinear Scale Space

KAZE features can be achieved by finding normalized Hessian local maximum at different scales.Hessian matrix is calculated as Eq.4:

$$U_{\mathrm{Hessian}} = \sigma^2 (U_{xx} U_{yy} - U_{xy}^2) \tag{4}$$

We should generate Hessian determinant value of each pixel in each level first, and then compare with its adjacent points to find local maximum. As it's shown in Figure 1,the middle point

is compared with its eight adjacent points at same scale and the 9*2 points at scale corresponding vertically :

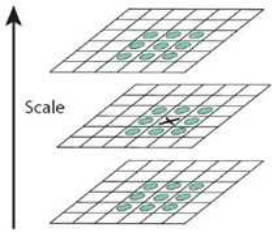


Fig.1 Feature Detection

Precise Positioning of Features

KAZE algorithm determines the location and scale of key points accurately by using Taylor expansion spatial of spatial scales function, while removing the key points with low-contrast edges and unstable response to enhance the matching stability and noise immunity[9]. the Taylor expansion of spatial scales function can be shown as Eq.5:

$$U(x)=U+(\partial u/\partial x)^T x+½\ x^T(\partial^2 U/\partial X^2)x \tag{5}$$

Feature Description

We find the dominant orientation in a circular area of radius $6\sigma_i$ with a sampling step of size σ_i. In order to find the dominant orientation,first order u_x and u_y are weighted with a Gaussian centered at the interest point, make sure that the near feature points with a large contribution and the feature points away with a small contribution. Then,the derivative responses are represented as points in vector space and the dominant orientation is found by summing the responses within a sliding circle segment covering an angle of 60°(Figure 2).From the longest vector the dominant orientation is obtained.

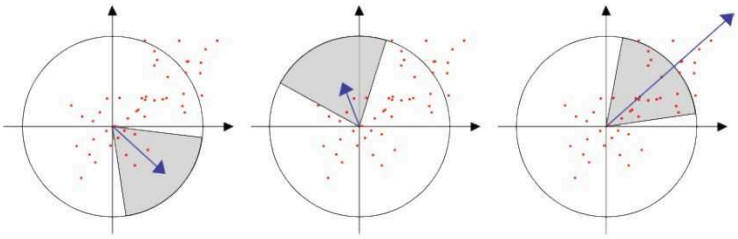


Fig.2 Finding the Dominant Orientation

We use the M-SURF algorithm to get the descriptor. For a detected feature at scale σ_i,we first get a $24\sigma_i \times 24\sigma_i$ rectangular grid centered on the feature, this grid is divided into 4×4 subregions of size $9\sigma_i \times 9\sigma_i$ with an overlap of $2\sigma_i$. Each subregion are weighted with a Gaussian kernel ($\sigma_1=2.5\sigma_i$) and get a descriptor vector dv , dv can be shown as Eq.6:

$$dv = (\Sigma U_x : \Sigma U_y : \Sigma|U_x| : \Sigma|U_y|). \tag{6}$$

Then,each subregion vector is weighted using a Gaussian($\sigma_2=1.5\sigma_i$) defined over a mask of 4×4, and it is normalized to remove the impact of light. In a word,we can get 64-dimensional vector description for each feature point.

Matching Feature Description

Feature description matching can be done after generating KAZE feature vector. For the purposes of transmission line insulators detection, getting more accurate and uniform distribution of key points is important,so that we can reduce the overall error by data fitting. According to Lowe's ideas, for the matching points, if the nearest neighbor and next nearest neighbor Euclidean distance ration is less than a certain threshold, then the matching points can be accepted . Then,false matching points are further eliminated using the feature set of geometric constraint relations by RANSAC algorithm.

Experiment Results and Discussion

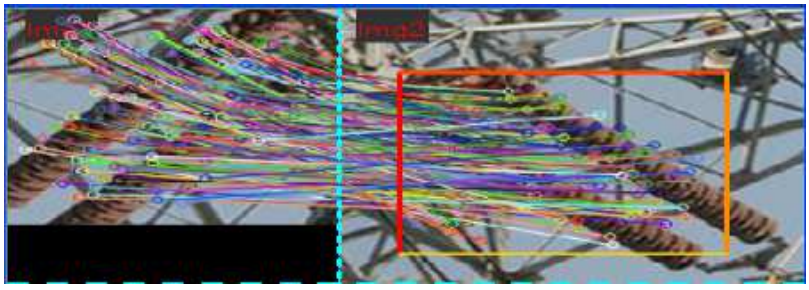
Experimental platform is a personal computer with the frequency 2.8GH z, memory 1.99G, windows XP operating system, experimental environment is VS2010. This paper use 100 different types of insulator images(60 with insulators,40 without insulators)to fully verify the experiment. The images are with size of 265×240 ,and they are under complex background with different geometric and photometric transformations such as image blur, lighting, viewpoint,scale changes,zoom compression. Below is results of two sets among them. The first group includes insulator (Fig. 3), it was rotated 90^{o} counter-clockwise, stretched 1.8 times on the horizontal,the result shows that the insulator can be detected correctly, and can determine the position of insulator(Fig.3(c)). The second group without insulator(Fig.4),it was 1.5 times enlarged, distortion 5^{o} on horizontal,and they are also impacted by light and noise.The result shows that the image does not include the insulator (Fig.4(c)).



(a) Image to be Detected



(b) Reference to Image



(c) Detection Result

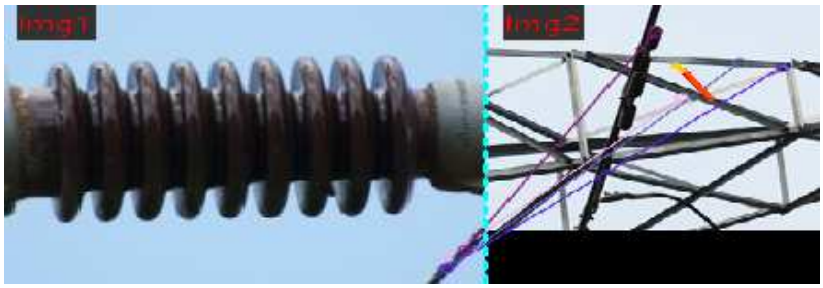
Fig.3 Result of Image with Insulator



(a) Image to be Detected



(b) Reference to Image



(c) Detection Result

Fig.4 Result of Image without Insulator

Experimental results show that KAZE algorithm can extract more feature points under complex background and various distortion in images.With the real-time ensuring,KAZE algorithm can accurately determine whether the image contains insulator, and if the insulator is detected, it can determine the location of the insulator, thereby providing a basis for the inspection robot's autonomous navigation and obstacle avoidance.

TABLE1 DETECTION RESULT OF INSULATORS

	Images with Insulators	Images without Insulators
Total Number	60	40
Correct Number of Detection	59	40
Detection Rate	98.33%	100%
Average Detection Time（ms）	8596	7605

Summary

This paper has presented a novel transmission line insulators detection methods based on KAZE algorithm. It extract insulators feature points based on nonlinear scale space, then use M-SURF algorithm to generate feature descriptor, and finally through the nearest neighbor criteria and RANSC algorithm matching the feature descriptors, thereby we can obtain detection results. The experimental results show that this method can accurately detect whether an image contains insulators, and it has good robustness, high accuracy and high speed, so that it can improve real-time avoidance performance of autonomous inspection robot.

References

[1] Zuo Qi,Xie Zhi,Liang Zize,Development and Application of Transmission Line Inspection Robot,J.Robot Technique and Application.3(2007)37-42.

[2] Zhang Yunchu,Liang Zize,Fu Siyao,Structure Constrained Obstacle Recognition for Transmission Line Inspection Robot,J.Robot.1(2007)1-6.

[3] Guo Weibin,Wang Hongguan, Jiang Yong, Obstacle Navigation Planning for a Power Transmission Line Inspection Robot,J.Robot.34(2010)506-512.

[4] Jaka Katrasnik, Franjo Pernus, Bostjan Likar.A Survey of Mobile Robots for Distribution Power Line Inspection,J.IEEE Transactions On Power Delivery.25(2010)485-493.

[5] Sun Fengjie,Yang Zhenhuan,Li Yuanyuan,Methods of transmission line target recognition, J.Journal of Image and Graphics.17(2012)349-356.

[6] MARTIN H, DE LOPE J, MARAVALLD. The KNN-TD reinforce-ment learning algorithm,in:Proceedings of the 3rd International Work Conference on the Interplay Between Natural and Artificial Computation. Spain: Springer, 2009: 305 – 314.

[7] Pablo F.Alcantarilla, Adrien,Andrew J. Davison,KAZE Feature. ECCV, 2012.

[8] Jiang Murong,Guo Ruilin,Zhang Zexian, Parallel Implementation for AOS Scheme on a Dual-core Cluster,J.International Conference on Intelligent Networks and Intelligent Systems, 3(2010).

[9] Lowe D.Distinctive image features from scale-invariant keypoints,J. Inrl.J.of Computer Vision,60(2004)91-110.

Advanced Materials Research Vol. 936 (2014) pp 2190-2195
© (2014) Trans Tech Publications, Switzerland
doi:10.4028/www.scientific.net/AMR.936.2190

IDENTIFICATION OF LIGHTNING STRIKES ON TRANSMISSION LINES BASED ON INTEGRAL METHOD AND WAVELET ANALYSIS

Hongwei Yan*, Yongli Zhu, Guochen Fan, Xi Xiong

North China Electric Power University, Baoding, Hebei, 071003, China

yanhongwei51@163.com

Keywords: transmission line, lightning strike, integral, wavelet transformation

Abstract: Transient signals caused by lightning strikes on transmission lines may interfere with the distance measuring devices relying on traveling wave. A synthesized method based on the additional components of disturbed current is proposed to distinguish between lightning interference, lightning fault and short-circuit fault. Firstly, since the disturbed current waveform generated by lightning interference and faults are distinct in the time domain, transient current components over and below timeline are respectively integrated to identify lightning interference from faults. And then, due to the distribution differences of current in the frequency domain, multi-scale transformation of wavelet is adopted to analyze the energy spectrum of transient current generated by short-circuit fault and faults of lightning. Numerous PSCAD simulation results demonstrate the proposed method is valid and correct.

Introduction

Based on the transient fault traveling wave, distance measuring devices on transmission lines achieve fault locations by detecting the time at which the traveling wave reaches the bus. Meanwhile they have advantages of rapid location and high accuracy[1-3]. Lightning strikes can have serious interference in the accuracy of those devices. Therefore, it is significant and practical to identify faults and interference accurately in order to take protective and repairable measures correspondingly.

At present, some researchers have started to pay attention to the identification of lightning and achieved certain results. [4] proposes the consistency coefficient of the traveling waveform and utilizes its size to distinguish between interference and faults. It is quite sensitive, but the data window is too long to the traveling wave protection. [5] just analyzes the induced lightning regardless of the direct lightning. [6] takes advantages of the changing trends of zero-mode fault voltage in a period of time to identify shielding and back striking lightning. However, this method aims at identifying lightning strikes on DC transmission lines, the effectiveness of AC system has not been verified.

In this paper, a 220kV electromagnetic transient model is set up and different kinds of disturbances are simulated with the use of PSCAD. Relying on the analyses of the existing identification methods, a hybrid approach is proposed to identify lightning strikes. Lightning interference and faults could be seperated by the integral method of additional current in time domain. Afterwards short-circuit fault and most faults of lightning could be distinguished by the energy ratio which is extracted by multi-scale transformation of wavelet in frequency domain.

Lightning Simulation Model of Transmission Line

Since the induced lightning does not act on the transmission lines directly and generates small over-voltage, it is not considered in this paper. At the same time, back striking lightning interference occurs once in a while and has limited impact on the transmission lines. So it is also not researched[7].

The simulation model of a 220kV power system set up with the application of PSCAD shows in Fig.1 and lightning interference, fault of lightning and short-circuit fault are respectively simulated. The measuring lines last for 100 kilometers and adopt the Marti frequency dependent model.

Meanwhile, the arresters make use of the model approved by IEEE and locate at both sides of the transmission line. Towers in the model utilize the conventional horizontal arrangement, double shielding wire furnished on the top. And the insulators employ the voltage controlled model and flash at 1200 kV. 2.6/50μs double exponential waveform is applied to the lightning current and the wave impedance of lightning channel is 300Ω. In the simulation, the sampling frequency chooses 500 kHz and the simulation period takes 2ms.

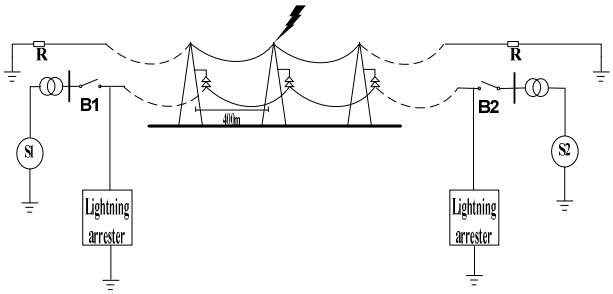


Fig.1 Simulation System of 220kV Transmission Line

Analyses on Transient Characteristics of Lightning Interference and Faults

The transient current measured by CT located at both sides of buses contain rated frequency component and additional component, the former is out of consideration in order to stress the transient characteristics. Because of the electromagnetic coupling between the respective phases, Clarke transformation is applied to decouple the additional current and aerial mode components are studied which is shown in Fig.2~4.

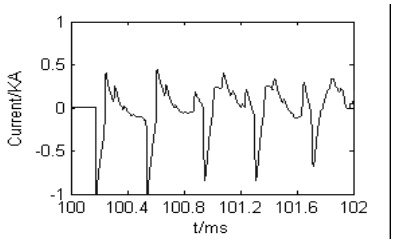


Fig.2 Aerial Mode Current Generated By Lightning Interference

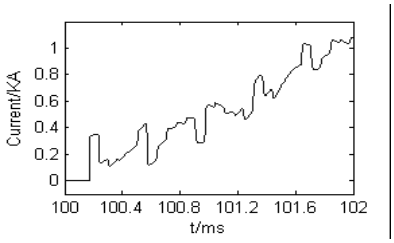


Fig.3 Aerial Mode Current Generated by short-circuit Fault

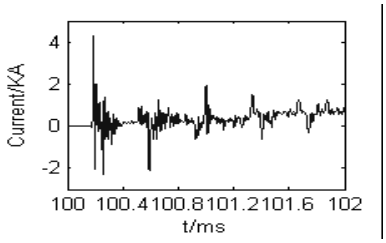


Fig.4 Aerial Mode Current Generated By Lightning Fault

As seen in figures above, the aerial mode current of lightning interference is alternative around the timeline. Furthermore, positive and negative peaks appear alternately. However, the current of short-circuit fault incline to one side of the timeline and can change monotonously overall. Transient signal of lightning fault is similar to that of lightning interference in the beginning stage while presents the characteristics of short-circuit fault in the later stage.

From analyses of the waveform above, it can be seen that the lightning current waveform is shaking because of the constant reduction of the catadioptric lightning current and the little damped coefficient of the transmission line system. While, when the short-circuit fault occurs, it is equivalent to attach a rated frequency power to the fault point which makes the current waveform monotonous.

According to the analyses above[8], an integral identification method is put forward and the identification criterion S is defined. The integral of transient current waveform over and below timeline respectively make up the original signals $I_1$and I_2 which are expressed as

$$I_1 = \int_{t_0}^{t_0+\tau} i_+(t)dt\,, \tag{1}$$

$$I_2 = \int_{t_0}^{t_0+\tau} |i_-(t)|\, dt\,, \tag{2}$$

$$S = \sqrt{(I_1 - \bar{I})^2 + (I_2 - \bar{I})^2}\,, \tag{3}$$

where $i_+(t)$ and $i_-(t)$ are the transient current components over and below timeline. I_1 and I_2 act as the integral of current in τ period. t_0 is the time detecting the mutation of transient current. $\bar{I}$ is the average of I_1 and I_2. Then due to the symmetry in the waveform, I_1 and I_2 should be very approaching and S is small in the lightning interference, but they differ quite a lot and S becomes huge as the faults take place.

Table 1 is the simulating results of lightning interference and faults occur 50 kilometres away from bus B1.

TABLE.1 CHARACTERISTICS IN TRANSMISSION LINE DISTURBANCES

Type of faults	I_1[kA·ms]	I_2[kA·ms]	S
Single-phase ground	179.64	0.0011	127.03
Two-phase fault	509.02	0.0011	113.82
Two-phase ground	421.99	0.0011	298.34
Three-phase fault	271.65	0.0011	192.09
Lightning fault	391.15	51.02	240.51
Lightning interference	86.94	98.03	7.84

Data in the table above apply that identification value of lightning interference is much less than that of faults.The biggest S in the interference is 7.84, while the smallest that of faults is 113.82.

In this way, S_0 which is 50 can be defined as the threshold value. If $S < K_1 S_0$ (K_1 is the reliable coefficient, defined as 1.5) lightning interference must be determined, on the contrary faults can be determined. It should be learnt from the results that this identification criterion is able to effectively distinguish between lightning interference and faults.

Analyses on the Wavelet Energy Spectrum of Lightning and Short-circuit Faults

Researches on the Multi-scale Transformation of Wavelet

Based on the multi-resolution analyses, fast wavelet transformation makes use of the orthogonal wavelets to decompose transient signals into several components at different scales. Assuming transient signal x(n) has been converted, $D_J(k)$ and $A_J(k)$ separately act as coefficients of high-frequency and low-frequency components in time k of scale J. Therefore the frequency range of the signal which is generated after the single branch reconstruction shows as

$$\begin{cases} D_J(k):[2^{-(J+1)}F_s, 2^{-J}F_s] \\ A_J(k):[0, 2^{-(J+1)}F_s] \end{cases}, \tag{4}$$

where F_S is the sampling frequency. And the biggest scale is M. Hence the former signal x(n) may be expressed as the sum of components.

$$x(n) = D_1(n) + A_1(n) = D_1(n) + D_2(n) + A_2(n)$$
$$= \sum_{J=1}^{M} D_J(n) + A_M(n)\,, \tag{5}$$

After the fast wavelet transformation, the sum of squared wavelet coefficients at different scales can be extracted as the signal energy of corresponding frequency range. The formulae display as

$$E_{DJ} = \sum_{K=1}^{N} |d_J(k)|^2\,, \tag{6}$$

$$E_{AJ} = \sum_{K=1}^{N} \left| a_J(k) \right|^2 , \tag{7}$$

where E_{DJ} and E_{AJ} are the energy of high-frequency and low-frequency components at scale J.

According to the theory of Parseval, a correlation between the energy of wavelet transformation at each scale and the original signal energy is built. Therefore the effective identification of varied transient signals can be achieved by the research on the energy distribution feature in distinct frequency bands[9].

Analyses on the Wavelet Energy Spectrum of Various Disturbances

In this paper, wavelet db4 is applied to decompose the aerial mode current components which are 2ms after diverse faults occur to 6 levels. The results show as

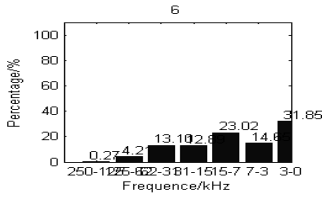


Fig.5 Energy Distribution of Shielding Lightning Fault

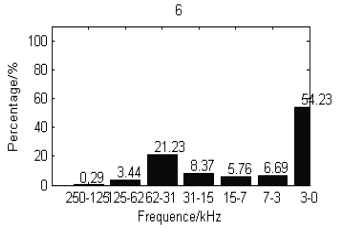


Fig.6 Energy Distribution of Back Striking Lightning Fault

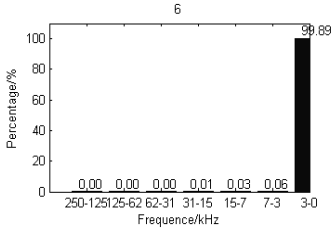


Fig.7 Energy Distribution of Short-circuit Fault.

Comparing Fig.5, 6 and 7, it can be seen that energy distribution of lightning faults and short-circuit fault vary greatly in high and low frequency bands. Therefore energy ratio criterion K can be defined as

$$K = \frac{E_{DJ}}{E_{AJ}} \quad . \tag{8}$$

All things considered, K_0 which is 0.05 can be defined as the threshold value. If $K > K_1 K_0$ lightning faults can be determined, on the contrary is short-circuit fault. Based on the simulation model showed in Figure 1, mass PSCAD simulations are conducted to verify the effectiveness of the criterion. Results list in Table 2-3.

Summarizing the researches above, it is practicable to identify lightning interference, fault of lightning and short-circuit fault through the integral algorithm of time domain and the energy spectrum of frequency domain obviously. The specific process shows as figure 8.

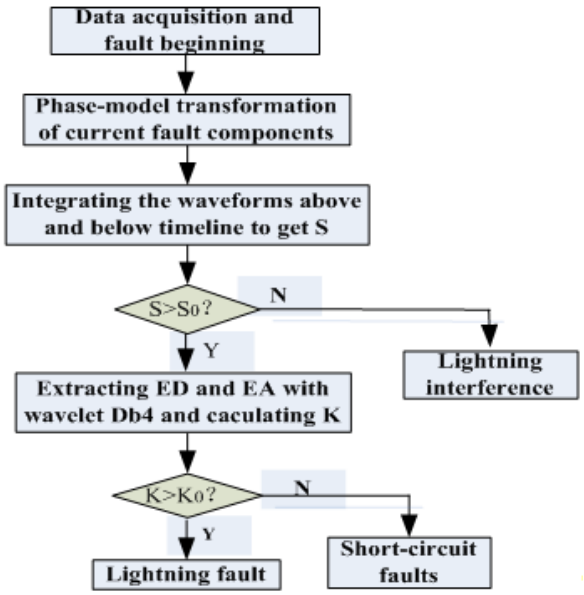


Fig. 8 Flow Chart of the Identification of Lightning Strike Faults

Simulation of Identification and Analyses

Numerous simulations of lightning faults under different current waveform and peaks and short-circuit faults under various transition resistances have been carried out according to the 220kV system shown in Fig1. And part of results are displayed in Table 2-3.

TABLE.2 FEATURES OF LIGHTNING FAULTS

Type	Waveform[us]	Current[kA]	$E_{DJ}[10^6A^2]$	$E_{AJ}[10^6A^2]$	K
shielding	2.6/50	30	423.52	197.95	2.14
		60	2003.4	203.94	9.82
	10/350	30	402.07	178.79	2.25
		60	1892.4	238.89	7.92
back striking	2.6/50	120	60.71	194.22	0.31
		150	190.43	225.59	0.84
	10/350	12	45.57	199.99	0.23
		150	89.56	217.12	0.41

TABLE.3 FEATURES OF SHORT-CIRCUIT FAULTS

Type	Transition resistance[Ω]	$E_{DJ}[10^6A^2]$	$E_{AJ}[10^6A^2]$	K
Single-phase ground	10	0.065	58.95	0.0011
	500	0.0084	3.21	0.0026
Two-phase short circuit	10	5.05	425.61	0.012
	500	0.43	51.96	0.0084
Two-phase ground	10	3.95	303.03	0.013
	500	0.11	13.91	0.0082
Three phase short circuit	10	0.42	137.34	0.0030
	500	0.018	7.27	0.0025

According to the data above, K in the shielding lightning fault is higher than that in the back striking lightning fault. While, the lightning current waveform did not play a major role. With the increase of the lightning current amplitude, K became bigger. In the short-circuit faults, various types had a small effect on K, meanwhile K decreased along with the transition resistance increasing.The smallest K in the lightning faults is 0.23 which is nearly twenty times larger than the biggest K in short-circuit faults, 0.012. Therefore the criterion can effectively identify lightning faults from short-circuit faults.

Summary

This paper proposes an integrated lightning identification method. Firstly, compare the integral of disturbed signal components in time domain to distinguish between lightning interference and faults. Then extract the energy ratio of fault signals by wavelet transformation to identify fault of lightning from short-circuit fault. A large number of simulations considering for numerous fault conditions have proved the synthesized method displayed in this paper is effective and reliable.

References

[1] Dommel H W．Michels J M．High speed relaying using traveling wave transient analysis[C]．IEEE PES Winter Meeting．New York:1978.

[2] SiMa Wenxia, Xie Bo, Yang Qing, Wang Jin．Identification of lightning over-voltage about UHV transmission line[J]．High Voltage Engineering, 2010, 36(2)：306-312．

[3] Leopoldo Angrisani, Pasquale Daponte, Mossimo D Apuzzo．Wavelet network-based detection and classification of transients[J]．IEEE transactions on instrumentation and measurement, 2001, 50(5):1425-1435．

[4] Si Dajun, Shu Hongchun, Chen Xueyun, et a1．Study on characteristics and identifications of transients on transmission lines caused by lightning strikes [J]．Proceedings of the CSEE, 2005, 25(7)：64-69．

[5] Li Haifeng, Wang Gang, Zhao Jiancang．Study on characteristics and identification of transient s on transmission lines caused by indirect lightning strikes [J]. Proceedings of the CSEE, 2004, 24(3):114-119．

[6] Shu Hongchun, Zhang Guangbin, Sun Shiyun, et al . Identification of shielding failure and back striking in UHVDC transmission lines [J]．Proceedings of the CSEE , 2009 , 29 (7) : 13219．

[7] Wu Hao, Xiao Xianyong, Deng Wujun．Identification of lightning and short-circuit faults in the traveling wave measuring device on transmission lines [J]．High Voltage Engineering, 2007, 33 (6)：63-67．

[8] [8] Zou Guibin, Gao Houlei, Zhu Feng, Wang Hao．The integral identification method of lightning and short-circuit faults on transmission lines [J]．Power System Protection and Control, 2012, 40(9)：44-48．

[9] He Zhengyou, Chen Xiaoqin．A study of electric power system transient signals identification method based on multi-scales energy statistic and wavelet energy entropy[J]．Proceeding of the CSEE, 2006, 26(10):33-38．

[10] Guo Ningming, Tan Jian, Chen Xiangxun．The effect and identification of lightning strikes on transmission lines[J]．Automation of Electric Power Systems．2008, 32(5)：76-79．

[11] Wang Gang, Li Haifeng, Zhao Jiancang, et．al．Identification of transients on transmission lines caused by direct lightning strokes based on multi-resolution signal decomposition [J]. Proceedings of the CSEE, 2004, 24 (4) :139－144．

[12] Zhan Huamao．Research on the over-voltage theory and experiment of lightning strikes on the ultra-high tower of transmission line[D]．Wu Han：Huazhong University of Science and Technology．

Advanced Materials Research Vol. 936 (2014) pp 2196-2200
© (2014) Trans Tech Publications, Switzerland
doi:10.4028/www.scientific.net/AMR.936.2196

Research of Power-on Detection in POE Topology

Zhao HAN[1,2 a], Jie WU[1,2 b], Qing-yun DONG[1,2], Ke REN[1,2], Juan DONG[1,2]

[1] Modern Physics Department of University of Science and Technology of China,

[2] State Key Laboratory of Particle Detection and Electronics, Hefei 230026

[a]anzhao7@mail.ustc.edu.cn, [b]wujie@ustc.edu.cn

Keywords: POE, connection detect, symmetrical architecture, signature resistance, step response

Abstract. POE (Power Over Ethernet) realizes the multiplexing of power transmission and data transmission. To ensure the safety of power supply process, PD (Powered Device), when connected, must be detected by PSE (Power Sourcing Equipment). This article describes the methods of PD detection especially in the symmetrical architecture. The symmetrical architecture means that PSE and PD are connected and either of them can play a role of PSE or PD. In our new approach, signature resistance is replaced by signature capacitance. The connection of PD changes the capacitance load of the system, so the step response can be used to detect the change of capacitance load. This method requires zero static current, which reduces the system power consumption. The theoretical analysis, PSPICE simulation and the experimental results are given.

Overview of POE (Power Over Ethernet)

POE is a power supply technology which transmits electric power via Ethernet cables such as class-5/class-6 unshielded twisted pair (UTP) or shielded twisted pair (STP) etc. POE satisfies the IEEE 802.3af-2003[1] standard. Some small network devices, such as IP phones, network cameras, wireless access points and data terminals, are capable of being powered via Ethernet connection instead of via AC outlet. Its prominent advantage is power transmission on the basis of existing network cables, which consequently simplifies cabling greatly, reduces the construction cost of network infrastructure and will expand the application of Ethernet technology. Its disadvantage is that the power supply to be transmitted should not be very large due to the restriction of the direct-current resistance of twisted pair.

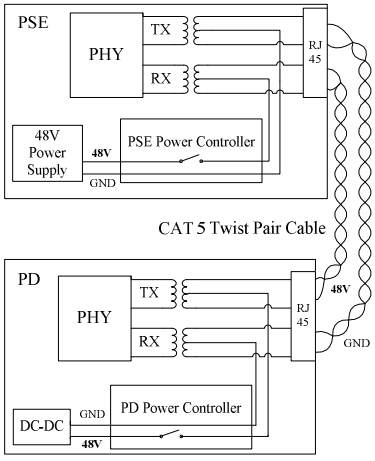


Fig. 1 A simple POE diagram

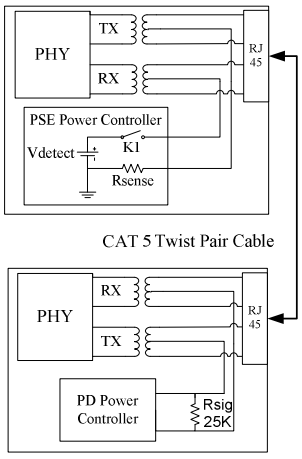


Fig. 2 A PD detection diagram

Fig. 1 shows a simple POE topology diagram. The upper half is PSE (Power Sourcing Equipment), and the lower half is PD (Powered Device). Ethernet data is transmitted differentially and coupled at both ends by high-frequency network adapters. Therefore, adding a 48v common mode voltage difference between transmit pair and receive pair does not affect the data transmission. The

reliability and effectiveness are guaranteed, and the multiplexing of data transmission and power transmission is realized.

PD detection of POE

When no PD is connected to PSE, PSE should not output the 48v power. This allows reducing unnecessary waste of power and prevents the 48v power supply of PSE from being damaged by accidental short circuit. When PD is connected to PSE via twisted pair, PSE should detect automatically that there is PD connected, and then it can output the power supply. In 820.3af, this process is achieved by detecting the signature resistance.

As Fig. 2 shows, PD has a signature resistance R_{sig}[2] of 25KΩ. PSE generates a 2.7v~10.1v voltage V_{detect}, then closes K1 to output the voltage to the twisted pair. It gets the current value by measuring the voltage drop across R_{sense}. When PD is not connected, PSE outputs V_{detect} and then detects that there is no voltage drop across R_{sense}. When PD is connected, as a result of the signature resistance, PSE detects that there is voltage drop across R_{sense}. As V_{detect} and the current value are given, if PSE calculates using volt ampere-characteristic that the signature resistance of the connected PD equals 25KΩ. PSE believes what is connected is a PD, which needs to be powered. Then it enters the next step and outputs 48v power supply. If PD is disconnected afterwards, PSE will detect that output current equals zero, then it will output V_{detect} again and detect continuously until PD is connected.

To detect R_{sig} by outputting V_{detect} of 2.7v～10.1v is safer and more easily controlled than detect R_{sig} by outputting 48v. Because 48v module is a power module, it may be easily burned by accidental short circuit. However, it's easier to limit the output power of V_{detect} when using only V_{detect} for detecting, so even short circuit won't damage the devices.

For R_{sense}, we generally select a resistance of a few tens of milliohms. In this way, when the module outputs 48v, it can monitor the current and at the same time consume less power. Because R_{sense} is several orders of magnitude smaller than R_{sig}, we don't take its impact into consideration when calculating the current.

Analysis under symmetric architecture using signature resistance method

We can notice that in standard POE, the architecture of PSE and PD connected through the network cable is asymmetrical. The power supply terminal PSE has no request of receiving power while PD has no request of supplying power. The two devices under POE topology in the project should be symmetrical architecture, which means that either device can be used as a power supply side or a power receiving side. The function of the two devices can change according to the actual situation. Under this architecture, if we use signature resistance detection method, the topology is shown in Fig. 3.

Two identical device structures both have V_{detect} output module and current detection module. The output has parallel signature resistance R_{sig}. Due to the presence of the signature resistance on both devices, V_{detect} output can be detected by current through local R_{sense} whether or not it is connected to a power receiving equipment. The difference is that twisted pair connects through a parallel signature resistor when there is no device connected. So the current is V_{detect} / R_{sig}. When there is a device connected, twisted pair connects through two parallel signature resistors. So the current is $2 \times V_{detect} / R_{sig}$. As a result, we cannot determine the connection by traditional method of detecting whether the current is zero or not. The final decision should be based on the magnitude of the current.

When the power supply outputs 48v, 48v power is applied to two R_{sig}. So it is inevitable that these two resistors have power consumption when applying signature resistance method. If R_{sig} is small, the current detection is simple because of large current flowing through R_{sense} at the expense of greater power consumption. We can reduce the power consumption by increasing the R_{sig}, which reduces the current, but makes it more difficult for detection.

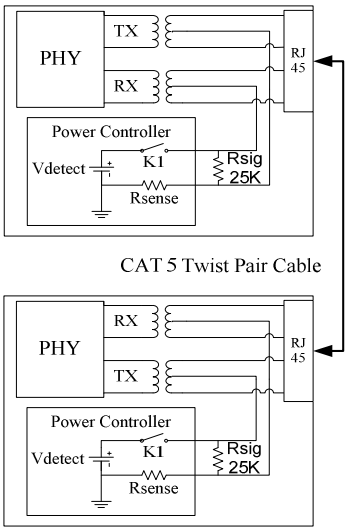


Fig.3 Using signature resistance method under symmetric architecture

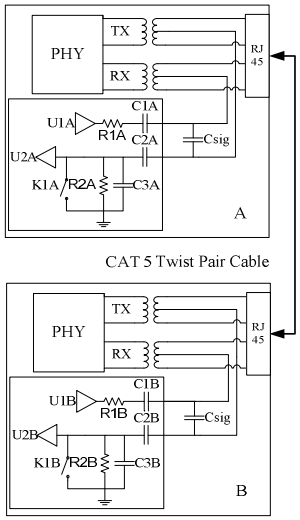


Fig. 4 Another method to detect PD under symmetric architecture

Analysis under symmetric architecture using step response method

We have designed another method to detect PD, which is used for symmetric architecture, as shown in Fig .4. The structures of the two devices are exactly the same. In Fig. 4, R1 is a series current-limiting resistor of 1KΩ, the value of R2 is 20KΩ, C1 and C2 are capacitors of 0.33uF, the value of C3 is 0.47uF, and the signature capacitance C_{sig} is 0.1uF. We assume that device A powers on first and then acts as PSE, device B acts as PD. When PD connects to PSE, PSE does not output 48v to external device, so the influence by PD on the system is only adding a C_{sig} between twisted pairs.

Principles calculation

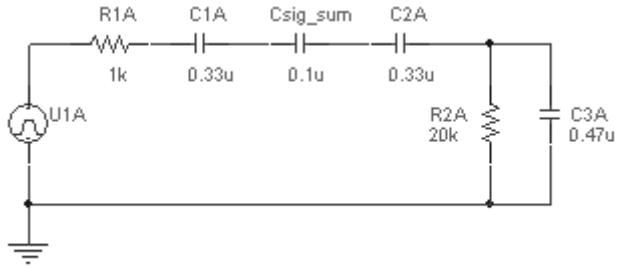


Fig. 5 Equivalent circuit

PSE A first switches on K1A until C3A completely discharges, then it switches off K1A. After K1A is switched off, U1A outputs a step signal. The voltage across C3A can be read via U2A. The equivalent circuit at the moment is shown as Fig. 5.

Whether B is connected with A will influence the value of C_{sig_sum} in Fig. 5. As can be seen in Fig. 4, we can easily find that C_{sig_sum} is 0.1uF when B is disconnected with A. When B is connected with A, C_{sig_sum} is 0.2uF (Because two C_{sig}s parallel connected).

At initial moment, the quantity of charge on C3A is 0 and U1A outputs a step signal. We need to know how the voltage across C3A changes when C3A in nought state is under the influence of step signal. At the beginning time, the voltage output by U1A leaps from 0v to 3.3v, so the influence caused by C1A, C2A, C3A, C_{sig_sum} on the circuit is almost like short circuit. The value of the current at this time is 3.3v/R1A, and this current charges the four capacitors. After a long enough time, the output of U1A is 3.3v, charging and discharging the four capacitors are completed, so the influence caused by C1A, C2A, C3A, C_{sig_sum} on the circuit equals the influence of open circuit, and the voltage across C3A is 0. Under the stimulus of step signal, C3A is first charged by U1A and then discharged through R2A, so the voltage across C3A performs as a waveform which first rises then falls. We analyze the time when the peak appears and the value of the peak in the following paragraphs.

Based on Fig. 5, we list the second order differential equations and substitute the initial conditions of nought state, and then we can get the voltage across C3A U(t) as:

$$U(t) = K_1 e^{-\frac{t}{\tau_1}} + K_2 e^{-\frac{t}{\tau_2}}$$

In this equation, τ_1 is electrical charge time constant. When the step signal appears, current charges the four capacitors through R1A, so we can get:

$$\tau_1 \approx R1A * (C1A // C2A // C3A // C_{sig_sum})$$

τ_2 is electrical discharge time constant. After the four capacitors are completely charged, C3A discharges mainly through R2A, so we can get:

$$\tau_2 \approx R2A * C3A$$

It can be easily seen that whether or not the powered device is connected, that is whether C_{sig_sum} is 0.1uF or 0.2uF, $\tau_1 << \tau_2$ because of $R2A >> R1A$. The electrical charge time constant is much smaller than the electrical discharge time constant, so the voltage across C3A increases first and then decreases. If the powered device is connected, C_{sig_sum} changes from 0.1uF to 0.2uF, but the change of τ_1 is not so large compared with τ_2, so the time when the voltage across C3A rises to peak has almost no change.

Whether or not the powered device is connected will influence the value of C_{sig_sum} (0.1uF or 0.2uF). During the process of charging, C1A, C2A, C3A, C_{sig_sum} are series connected, so it is easy to see that when C_{sig_sum} gets larger, the peak voltage across C3A rises.

Simulation result

A PSPICE simulation is done, and we get the waveforms as shown in Fig. 6 and Fig. 7.

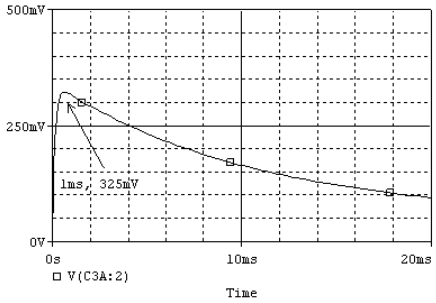


Fig. 6 Simulation waveform when powered device is disconnected

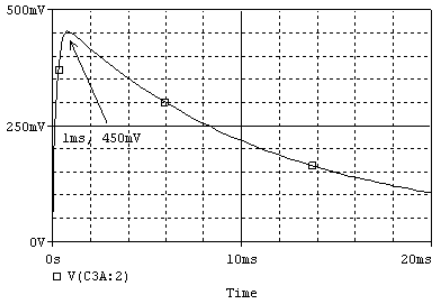


Fig. 7 Simulation waveform when powered device is connected

From Fig. 6 and Fig. 7, we can find the waveforms are consistent with our expectation. For the two cases, the time durations from the beginning to the time when peak appears are almost the same and they are all about 1ms, so we use 1ms as sampling time. However, for the two cases, the wave amplitude difference in the sampling time is obvious. So we can sample the voltage across C3 in 1ms after step signal effecting. By comparing this voltage with threshold voltage, we can know whether the powered device is connected or not.

Experimental results

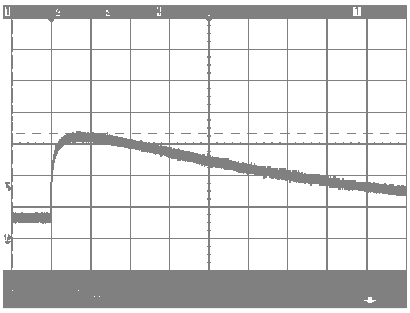


Fig. 8 Measured waveform when powered device is disconnected

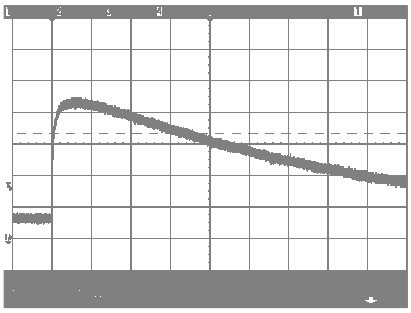


Fig. 9 Measured waveform when powered device is connected

Fig. 8 shows the measured waveform when powered device is disconnected and Fig. 9 shows the measured waveform when powered device is connected. The measured results match well with the simulation results. According to the experimental results, we can sample the voltage across C3 in 1ms after the step signal effecting, and we take the threshold for 400mv. When the voltage across C3 is larger than threshold, we believe that the powered device is connected.

When power sourcing equipment and powered device are connected using long twisted pair, we need to consider the influence of cable capacitance. Cable capacitor parallel connected with C_{sig} makes C_{sig_sum} larger, and then makes the peak voltage of C3 larger as well. So when we use this method in practical applications, revisions are needed for the detection threshold voltage according to the cable length.

Conclusions

When we use Power Over Ethernet technology, in order to ensure security, PSE will definitely detect the connection of powered devices during the working process.

When the device outputs 48v power supply, if using signature resistance method, R_{sig} will certainly consume energy. Static power consumption is about 180mW when 48v power is applied to two parallel 25KΩ resistors. If you select larger R_{sig} to reduce power consumption, it will increase the difficulty of the current detection. However if we use step response method which uses C_{sig} instead of R_{sig}, the static power consumption is zero. It is ideal for the use in low-power design.

Comparing the signature resistance method (Fig. 3) and the step response method(Fig. 4), the former requires a switch to control the excitation signal output, while the latter uses direct capacitive coupling, in which the implementation is relatively simple.

Our project has stringent power requirements, so step response method has been used to detect the connection of the powered devices and the system works well in the project.

This paper is Supported by (1) R&D of Key Instruments and Technologies for Deep Resources Prospecting (the National R&D Projects for Key Scientific Instruments), Grant No. ZDYZ2012-1-05-03 (2)Major National Science and Technology Special Program of China under Grant 2011ZX05008-005-61

References

[1] IEEE 802.3af Data Terminal Equipment (DTE) Power via Media Dependant Interface (MDI) [S]: IEEE Computer Society, 2003.
[2] Freescale Semiconductor Inc. MC34670 IEEE 802.3af PD With Current Mode Switching Regulator [R] USA: Freescale Semiconductor Inc. 2006
[3] Linear Technology Corporation LTC4259A Quad IEEE 802.3af Power over Ethernet Controller with AC Disconnect [R] USA: Linear Technology Corporation, 2004
[4] Power over Ethernet. IEEE 802.3af White Paper. http://belden.com/docs/upload/PoE_Basics_WP.pdf
[5] Anon. Power over Ethernet. Electronic Design, 2004(4): 9~17.
[6] Morrison, David G. Power-over-Ethernet chips give LANs a new outlet. Electronic Design, 2003(10): 51~62.

Advanced Materials Research Vol. 936 (2014) pp 2201-2206
© (2014) Trans Tech Publications, Switzerland
doi:10.4028/www.scientific.net/AMR.936.2201

The Research of Photovoltaic Array Intelligent Fault Diagnosis Based on the Bp Neural Network

Zhang Wen Jin[1, a], Ge Qiang[2,b], Huang ChenYang[3,c]

[1] 196 West Huayang YangZhou,Jiangsu,P.R.China

[a]971909298@qq.com, [b] yzgeq@yzu.edu.cn

Keywords: photovoltaic array; fault diagnosis; BP neural network; network training; Matlab simulation.

Abstract: In consideration of the photovoltaic arrays fault characteristics and the limitations of traditional fault diagnosis methods, a intelligent fault diagnosis system for photovoltaic arrays based on BP neural network is proposed.; The faults' consequences of battery cracking, short circuit and the shadow is analyzed. The neural network is trained by appropriate fault samples. The simulation and experimental research on online fault diagnosis of photovoltaic modules in the Matlab environment are performed，and results proved the accuracy,effectiveness and environmental adaptability of the proposed system.

Introduction

Photovoltaic (PV) power is probably the strongest-growing electricity generating technology because of its advantages of clean ,cheap and reproducible [1-2], photovoltaic power generation's application fields and expanding scale is constantly developing.But Photovoltaic array has some faults inevitably due to the natural environment and the influence of its aging problem in the process.If the fault is not found and eliminated in time, it will directly affect the normal operation of the photovoltaic power generation systems, even burn out the battery components when seriously [3].Therefore the fault diagnosis for photovoltaic system has very important significance to the power system's normal operation.At present the photovoltaic diagnostic methods are mainly:Infrared test [4],Earth capacitance measurement（ECM）[5-6],Time domain reflectometry（TDR）[7]. ECM and TCR need to stop the system when the system is testing;Infrared detection needs a lot of infrared cameras and sensors, increasing the operation cost of the system. This paper proposes a intelligent fault diagnosis system of photovoltaic array based on BP(back propagation) neural network, which can display the corresponding relationship between the photovoltaic array's fault and cause of the fault in the neural network structure,connection weights and threshold. The experiment's data will input into the trained neural network fault diagnosis, so as to realize the online fault diagnosis of PV arrays.

Analysis of PV common faults

Photovoltaic power generation system is hard to avoid some faults for long-term working in the outdoor environment[8-10]. Photovoltaic array's common faults are are shown in table 1.

Table 1. Analysis of PV faults

Fault type	Description	Consequences
Panels aging damage	The fault happens after long time running , Such as short circuit 、 open circuit fault, etc	Produce arc and have fault due to overheat and damage
Panels cracking	When Panels have cracks on the surface, Water and air will corrosion film	Battery life greatly reduced
Shading	Building 、 cloud or objects such as the tree shading	Battery local temperature will be too high

According to current situation,The third type fault is probability maximum damage.Therefore we will discuss the causes and consequences of photovoltaic array's hot spot phenomenon following.

The experiment select a matrix module in a three lines four columns from the photovoltaic array. As shown in figure 1，each row is a set，the voltage is U_1-U_3 and current is I. Assumes that the dotted line in the figure is the shade module，while the second group's output current is still I. The shade part become load，and the current direction is contrary to other modules. At this point the second set's current will be more than I/4.If it continues for a long time the solar panels' temperature will be too high, so that the whole system will not work normally.

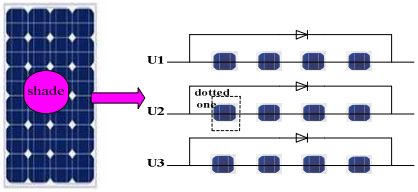


Fig.1 The principle diagram of the PV array hot spot phenomenon

At present,solutions of the phenomenon of hot spots are the bypass diode in parallel and infrared image analysis method basically，but these two methods have their limitations.The parallel diode itself will consume power then cause power loss,and its offset voltage will affect the photovoltaic array's normal work voltage;The infrared image analysis can't realize real-time control and can't estimate when temperature difference is not obvious. The BP neural network intelligent fault system in this paper will make up for the deficiencies of the above methods. The system with strong self-learning, adaptive, contact and nonlinear pattern recognition memory functions and especially suitable for very complex faults.

The application of BP neural network in PV fault diagnosis

The establishment of the BP neural network

Due to the highly nonlinear and strong coupling relationship between the photovoltaic modules'output characteristics and environmental factors,the fault diagnosis of photovoltaic arrays is essentially the input data samples connect with one or more fault state processes.In order to realize the online fault diagnosis of PV array, we introduces the BP neural network as the tool of fault diagnosis which can solve the nonlinear problem effectively [11].

In this paper,the BP neural network composed of input layer,hidden layer and output layer.Each input node corresponding to a fault input,and adjacent layer interconnect with each other.The sam layer neuron without any connection with each other,and input layer and output layer have no direct link .

Now we set up the network's fault input mode as $X=(T_c,I_m,U_m)^T$， the hidden layer's output as $y=(y_1,y_2.y_3)^T$,Build up the mapping relationship between the fault parameters and fault causes. The neural network basic structure is shown in figure 2.While T_c,I_m,U_m as the input signal stand for panel temperature,peak current and peak voltage respectively, y_1,y_2,y_3 corresponding to the various faults in table 1.

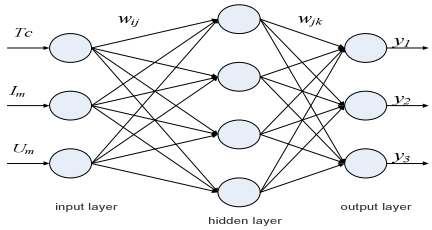


Fig.2 Basic structure of BP neural network

The transfer function of hidden layer adopts hyperbolic tangent tansig function，Now we set the input layer nodes as i（1-3），hidden layer nodes as j（1-4），output layer nodes as k（1-3），.For input layer nodes i，the output of the hidden layer and output layer $y_i(k)$ can be represented as [8-10]：

$$y_i(k) = \frac{e^{I_i(k)} - e^{-I_i(k)}}{e^{I_i(k)} + e^{-I_i(k)}} \tag{1}$$

$I_i(k)$ in the formula (1) is the input signal of node i in the k layer，it usually expressed as output's weighted sum of all node which can be shown as following formula:

$$I_i(k) = \sum_j w_{ij}(k) y_j(k) - \theta_j(k) \tag{2}$$

w_{ij} is node connection weights of the I node in k layer,$y_j(k)$ is output of the j node in the k layer, $\theta_j(k)$ is threshold of the neuron.

Therefore we can realize online fault diagnosis from the output data from the above formula, through extracting the connection weights and thresholds in the trained neural network.

The strategy of BP neural network fault diagnosis

Now establish a system that can fully display monitoring dynamic according to the characteristics of the PV array fault diagnosis, schematic diagram is shown in figure 3.The system is mainly composed of knowledge base, data base,neural network module,panels,interpretation mechanism,translation mechanism,monitoring center. When the fault occurs,it can be quickly located through the knowledge stored in base of diagnosis knowledge，which can help people in monitoring center diagnose and maintain the fault [11-12].

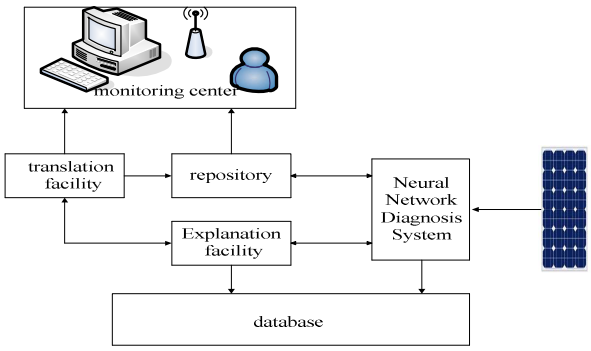


Fig.3 The principle diagram of the BP neural network fault diagnosis

The photovoltaic modules adopted in the experiment is Jiang Su Hosun solar power company's monocrystalline silicon series of JHX100M72.Under the condition of STC(1000W/m2,25℃) the output data is shown in table 2，the panel is made up of 72 series panels.

The experiments adopted increasing the external series resistance value method to simulate the cracking phenomenon,short circuit panels to simulate the phenomenon of short circuit,cardboard block was used to simulate shadow phenomenon.Through the simulation and experiment validation to prove the feasibility of the diagnosis system.

Assuming that solar panels' expected outputs of fault types are:normal（0,0,0）,Panels cracking（1,0,0）,Panels aging and short circuit（0,1,0）,Partial shadow（0,0,1）.

Table 2. PV module parameter

Parameters of the category	Data
maximum power Pm	55W
open-circuit voltage Uoc	21.7V
short-circuit current Isc	3.45A
The voltage of maximum power point Um	17.4V
The current of maximum power point Im	3.15A

The flow chart of neural network fault diagnosis when photovoltaic power generation system is running is shown in Figure 4.To judge whether a fault happens by detecting if the data exceed the normal parameters deviation of solar panels or not,then assess the type of failure,and finally inform people of monitoring center to maintain timely.

BP neural network model training and experimental

In order to verify the validity and the accuracy of the fault diagnosis system，This experiment collect 200 groups sample data of these faults under condition of different temperature, peak voltage, peak current for training network. Neural network training sample run in Matlab environment, training for 1000 times, the training error is 0.001, the training step length is 0.05, using tansig training function.

As shown here, neural network can meet the error requirements after 414 times training. The system has a good learning performance with control precision reaching 0.0009.The results are very accurate.

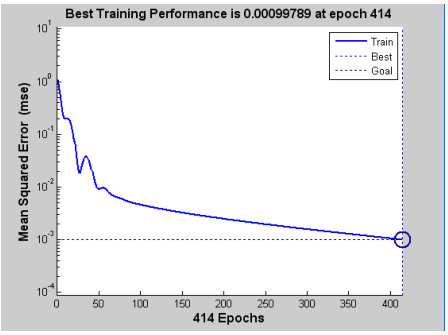


Fig.5 The curve of BP neural network training

After the network training is finished，four group actual measured data will be inputed into diagnosis system to observe its output whether in line with the expected results. The

input data and output results is shown in table 3. As shown in the table，faulty node value is close to 1，non-faulty node value is close to 0，the accuracy reach 90%. The network output and target output has reached preliminary requirements which can prove the feasibility and accuracy of the system.

Table 3. The predictions of the model

T_c/℃	I_m/A	U_m/V	y_1	y_2	y_3
43.21	4.05	24.2	0.000	0.001	0.002
42.95	3.59	18.5	0.968	0.001	0.000
43.15	3.85	22.6	0.001	0.994	0.001
50.12	4.01	23.5	0.001	0.002	0.987

Conclusion

Since the highly nonlinear of the photovoltaic cells , diversity of environmental conditions and various influencing factors making photovoltaic array fault diagnosis become a complex problem。This paper presents a kind of on-line fault diagnosis system based on BP neural network, input factors are battery temperature, maximum power voltage and maximum power current. The system can test four state as normal, cracking, short circuit and shadows. The simulation and experimental results prove the feasibility, accuracy and environmental adaptability of the proposed fault diagnosis system, it has good application prospect.

References

[1] LI Dan-ping, GE Qiang, TAN Lei. The experiment of max power point tracking based on DSP of PV system [J] Journal of Yangzhou University (Natural Science Edition), 2010, 13(3):58-60.

[2] WU Hao-Tian,Ge Qiang,Huang Cheng-Yang. The partial shading condition photovoltaic array maximum power tracking algorithm simulation[J] Journal of Yangzhou University (Natural Science Edition),2012,5(2):52-55

[3] WANG Yuanzhang, LI Zhihua, Wu Chunhua,. A Survey of Online Fault Diagnosis for PV Module Based on BP Neural Network [J]. Power System Technology, 2013.37(8)：2094-2101.

[4] Nian Bei，Fu Zhi zhong．Automatic detection of defects in solar modules：image processing in detecting[C].International Conference on Wireless Communications Networking and Mobile Computing．Chengdu，China：IEEE，2010：1-4．

[5] Takumi J，Kenji K．Experimental studies of failure detection methods in PV module strings[C].IEEE 4th World Conference on Photovoltaic Energy Conversion．Waikoloa，HI：IEEE，2006：2227-2230．

[6] Takumi J M．Fault detection by signal response in PV module strings[C].IEEE Photovoltaic Specialists on Industrial Electronics．San Diego，CA，USA：IEEE，2008：1-5．

[7] Takumi T，Junji Y，Masayoshi I．Disconnection detection using earth capacitance measurement in photovoltaic module string[J]．Progress in Photovoltaics，2008，16(8)：669-677．

[8] ZHONG Dan, Research on Fault Detection of PV Array Based on Composite Data Fusion [D]. Tianjin University, 2012. .

[9] DUAN Hou-feng, Fault Diagnosis for Power Transformer Based on Genetic Algorithm for optimization of neural network [D] Beijing jiaotong university, 2008.

[10] LIANG Xing-yan, ZHANG Wei. The research of maximum power point tacking in photovoltaic power system based on back propagation networks. [J] Manufacturing industrial, 2012.12: 112-116.

[11] Syafaruddin E, Karatepe T H. Controlling of artificial neural network for fault diagnosis of photovoltaic array[C].16th International Conference on Intelligent System Application to Power Systems. Hersonissos：IEEE，2011：1-6.

[12] HU Yihua, CHEN Hao, XU Ruidong. A Type of PV Array Fault Diagnosis Strategy Based on Voltage Scan [J]. Proceedings of the CSEE, 2010.12:185-191.

CHAPTER 21:

Electronic Engineering

Advanced Materials Research Vol. 936 (2014) pp 2209-2213
© (2014) Trans Tech Publications, Switzerland
doi:10.4028/www.scientific.net/AMR.936.2209

Application of AM-OLED Micro-display in Stereo Display system

Tai Yonghang[1,a], Shi Junsheng[1,b *], Chen Zaiqing[2,c], Li Qiong[3,d] and Zhuo Bin[1,e]

[1]Color & Image Vision Lab., Yunnan Normal University, Yunnan Kunming, China

[2]College of Information, Yunnan Normal University, Yunnan Kunming, China

[3]Solar Energy Research Institute, Yunnan Normal University, Yunnan Kunming, China

[a]taiyonghang@gmail.com, [b]shi-js@263.net, [c]391644326@qq.com, [d]liqiong.yn@gmail.com

Keywords: AM-OLED; Stereo Display; Dual Video; Interface Circuit

Abstract. OLED micro-display is applied widely in the HMD stereo display field. Based on dual 0.5 inch 800×600 high resolution AM-OLED displays, we proposed a 3D circuit design scheme which used PC's VGA interface as video input, PIC18LF2550 as the MCU. According to the principle of the human eye binocular disparity, PC stereo video sources achieved odd frames and even frames displaying simultaneous in two AM-OLED panels, which implemented the 3D function. Display system has been tested by playing the stereoscopic video source of the left and right sides format form the PC and the effect presented a good performance which verified the effectiveness of the proposed scheme.

Introduction

With the development of the dimensional technology, the core components of stereoscopic display developed from small CRT to LCD, and then to the current micro AM-OLED. Cause of low power consumption, high refresh rate, wide viewing angle, high contrast, high brightness and other characteristics, OLED is increasingly being applied to the near-eye stereoscopic display system [1]. Foreign stereoscopic display technology is relatively mature, the corresponding products are greater. eMagin developed the world's first 3D capabilities HMD "eMagin Z800 3D Visor" in 2006, this helmet is equipped with dual 0.5 inches 800×600 high resolution OLED micro-display chip [2] ; Sony launched HMZ-T1 head-mounted 3D display with a newly developed 0.7 inches 1280×720 resolution OLED panels in December 2011, which can achieve 20 meters watch 750 inches giant screen of 3D effects ; SMD company released a resolution of 1920×1080 Full HD 3D HMD ST1080 in January 2012, its headset weighs only 180 grams [3]. Some domestic universities are mainly on the helmet stereo display with more research. Southeast University designed and implemented a resolution of 1024×768, refresh rate of 180Hz sub-field of LCOS color helmet display, which is enable real-time color video image display; Beijing Institute of Technology Cheng Dewen, Wang Yongtian et al, whose used FFS prism new optical components, the new aberration theory and design optimization methods HMD visual optical system to optimize the design, the optical design can satisfy the system view and make its weight reduce greatly structure more compact at the same time [4]. This paper used dual VGA interface as the video input interface, AM-OLED as stereoscopic display panels, based on binocular parallax principle of the human eye and SVGA050 micro chip stereo display function, and definitively realize stereoscopic display through the computer graphics frame display technology. Our design is two-way video signals imaged in both eyes, which significantly reduces crosstalk between the eyes, provide the best stereo effect by adjusting the distance and the position between the dual AM-OLED and optical system.

Stereoscopic Display System Interface Circuit Design

Based on the structure and characteristics of the AM-OLED, the design of hardware interface circuit is shown in Fig.1. VGA Decoder module decodes external input for VGA video signal by using the AD's chip AD9883; MCU used the production of Microchip's high-performance, low-power control chip PIC18LF2550, mainly used for A/D and display module configuration register; power modules provided an external 5V power conversion by USB, respectively produce

3.3V, 5V, 1.8V power supply provides power for the various modules[5]; OLED used OLEiD Company's new high-resolution ,active 0.5 inches AM-OLED display module SVGA050. For a good solution to the product weight and wearing comfort, our system is divided into two parts: master-board and OLED panels. Each OLED panel retains only the display chip and A/D decoder; all other devices are designed on the master-board. Whole system consists of a master (80×80mm) and two OLED panels (40×40mm). Two OLED panels via a connector join to the master-board, which transmitting the video source, power supply and IIC (Inter IC Bus) control signals to the A/D and OLED chips. The following introduced the master-board and the OLED panel functions.

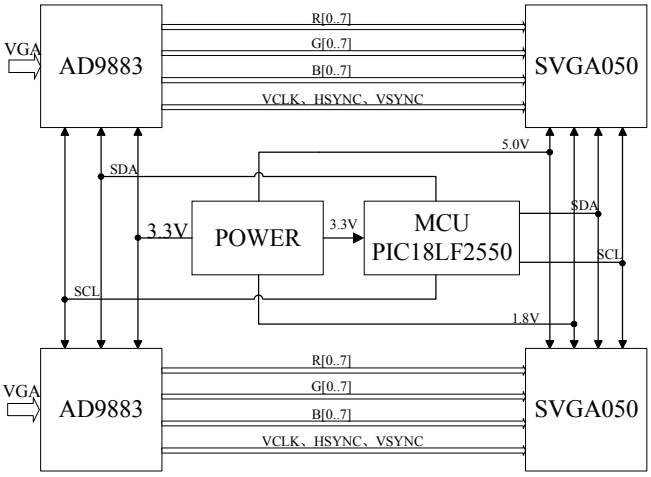


Fig.1 AM-OLED stereo video display system

Master-board Design

The master-board consists of MCU controller and power module. MCU used Microchip's low-power mainstream production control chip PIC18LF2550, the MCU is only 5.8μA in idle state consumes, even its power consumption is as low as 1.8μA in a low- power sleep state[6], Master Synchronous Serial Port module supports 3-wire SPI and IIC master-slave mode, this eliminates the use of general analog IO IIC bus inconvenience for programming provides a convenient. Its main role is set the AM-OLED display and AD9883 registers parameters through the IIC bus[7]. Through the control buttons on the system panel, you can adjust the display mode of the system, including switching OLED internal test pattern and selecting a different video sources as well as brightness, contrast adjustment. The system includes MODE, UP, DOWN three function keys, which MODE is the mode selection keys to cycle four kinds, such as functions brightness, contrast, display pattern, the input source; UP and DOWN for the upper and lower adjustment key, you can adjust specific parameters in different modes.

OLED Panel Design

OLED panels consists high-resolution, active 0.5 inches AM-OLED and AD9883. This system used SVGA050 is produced by OLEiD's latest development of active, high-resolution digital OLED micro-display chip. Fig. 2 shows the block diagram of the OLED panel, gives a signal interface micro-display chip, R, G, B video signals for the three input terminals, HS, VS, respectively horizontal sync and vertical sync signals, P_SDA, P_SCL were IIC serial bus data input and clock input. As can be seen from the figure, the user just need to give the micro-display chip to provide power, and through the IIC bus on the rational allocation of internal registers can be externally input analog video signal on the OLED panel display correctly.

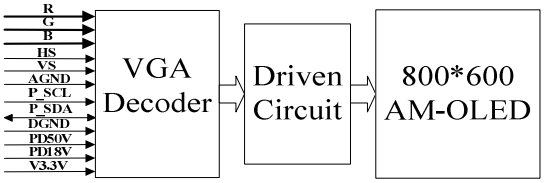


Fig.2 OLED panel structure diagram

Since VGA interface output is an analog signal, you need an analog to digital converter chip to decode the signal. The system chosen the AD decoder chip produced by a A/D conversion chip AD9883, capable graphics card on the PC analog RGB signal output speed 8-bit A/D conversion [8].

Power Modules Design

In this system, it is required to provide power modules are mainly Decoder AD9883 (3.3V) in VGA Decoder Module, PIC18LF2550 (3.3V) in MCU control module, SVGA050 micro-display chip (1.8V and 5.0V Dual) in the display module, and the USB input power is supplied 500mA 5V power, so the design chosen two DC-DC module voltage of 5V and 3.3V respectively convert 1.8V, respectively, as the AD9883, MCU, SVGA050 power. Meanwhile, in order to reduce power consumption and extend the service life, SVGA050 did not require work when the power is disconnected, so the design selected specially enable control terminal with DC-DC module, when it does not operate in a long time, the MCU can be cut off SVGA050 power supply.

IIC Module Registers Configuration

In this system, each module MCU register configuration is achieved through the IIC bus. For the IIC, only two bus lines: a serial data line (SDA) and a serial clock line (SCL). Obviously, OLED is a receiver. Display Address (Slave Addr) can be selected via SelAdr0 pin. Default SelAdr0 through an internal 10K resistor is pulled high (1.8V). Binocular application, which will be a display SelAdr0, grounded. Corresponding to the display read / writes address shown in Table 1. In this system, using the resolution is SVGA 800×600, field frequency is 60Hz, the line frequency is 37.9KHz, point frequency is 40MHz. AD9883 sampling clock by configuring the phase-locked loop (PLL) to generate, using the horizontal sync signal (HSYNC) as the reference clock, then frequency obtained by A / D converter sampling clock required. By decoding chip AD9883 internal 25 register settings, you can achieve the corresponding functions.

TABLE 1 SLAVE ADDRESS AND SELADR0 CONFIGURATION LIST

A7 (MSB)	A6	A5	A4	A3	A2	A1 (SelAdr0)	A0 (R/W)	Slave Addr (R/W)
0	0	0	1	1	1	0	1/0	1DH/1CH
0	0	0	1	1	1	1(default)	1/0	1FH/1EH

Dimensional Display Function Is Implemented

The three-dimensional display scheme based on the human visual design principles of binocular parallax. Binocular disparity is due to two positions in space and different perspectives of the same scene is formed on the retina of both eyes are very similar but slightly different images, which inconsistencies binocular retinal image [9]. The main advantage of the existing three-dimensional display of all of the human eye binocular parallax .As is shown in Table1, SVGA050 with 3D video display capability. SVGA050 display in progressive scan mode, 3D video signals using the frame sequential patterns, such as updating the left eye shows odd frames, even frames update right eye display. In interlaced mode, 3D video signal using a field sequential mode, as left-eye display updates the odd field, even field update right-eye display. Frame sequential or field sequential 3D video display through the 3D signal pin and SVGA050 display 02H register with the realization, 02H register the main function is to set the 3D features. As shown in Table 2, when the 3D pin 02H register 3D set level and consistent, SVGA050 valid input video signal data, the display is updated to the current input frame field data, otherwise, the data is invalid, the display to maintain a frame field data .In this system, OLED in the progressive scan mode, 3D video signal using the frame sequential output mode as the odd frame update left-eye display, even right-eye display frame update.

TABLE 2 3D FUNCTION CONTROL

3D pin	3D refresh	02H	Pattern	Display
0	X	X	2D	refresh
1	0	0	3D	refresh
		1		Keep the last show
	1	0		Keep the last show
		1		refresh

In order to achieve three-dimensional display requirements, according to binocular parallax, the monitor needs to use a 3D display function SVGA050 achieve stereoscopic display video source. SVGA050 display in progressive scan mode, 3D video signals using the frame sequential mode; in interlaced mode, 3D video signals using field sequential mode. Frame sequential or field sequential 3D video display through the 3D signal pin and SVGA050 02H register with the realization of the display, as shown in Table 2,02H register is used to set the 3D video display format, including 3D and 3D enabled refresh. When the 3D pin level status and 02H register 3D settings consistent, SVGA050 valid video signal data input, the display is updated to the current input frame field data, if inconsistent, displayed on a display to maintain field data. 3D pin signals the presence of synchronous edge is locked. 3D shows the timing diagram shown in Fig.3.

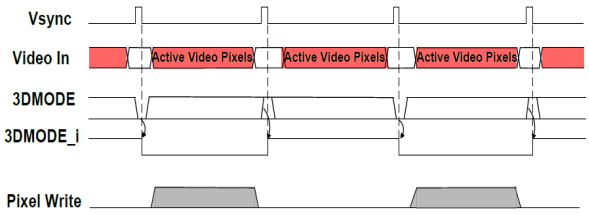


Fig.3 3D video display timing

Experimental Testing and Analysis

Fig.4 shows a stereoscopic video display system physical map. Binocular stereoscopic display system requires achieve a clear near-eye display when video via optical amplification system. In order to verify the feasibility of the program, we have designed an experimental platform. PC's VGA port via VGA converter convert dual VGA video signal to input master. PC's setup parameters are: screen resolution of 800×600, a refresh rate of 120Hz. Though the PC, so the format stereoscopic video source via the Stereoscopic Player playback software playback around two OLED panel displays the video source, respectively, odd and even-numbered frame image frame, and ultimately to achieve a 3D display.

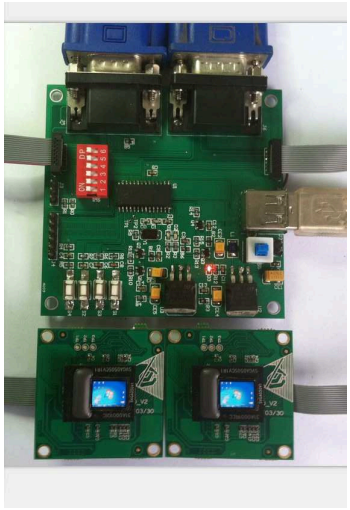


Fig.4 AM-OLED stereo video display system

Conclusions

Based on the 0.5-inch SVGA050 AM-OLED micro-display, we have designed and developed a set of stereoscopic display interface circuitry in this work. USB port provides 5V DC as the only input power, PC's VGA as the input video source, the parameters of each module registers are under control of the MCU (PIC18LF2550) through the IIC serial bus. According to the principle of the human eye binocular disparity, PC stereo video sources achieved odd frames and even frames

displaying simultaneous in two AM-OLED panels, which implemented the 3D function. This hardware design operated simply and low power consumption, which has a high practical value in the civilian HMD system and provide an experimental platform for the 3D visual characteristics of human eyes subsequent research.

Acknowledgments

Funding for the projects was provided by the National Natural Science Foundation (60963020), Major Research Project of Education Department in Yunnan Province (ZD2009006) and Science &Technology Projects of Yunnan Province (2013FD017).

References

[1] Ding Yuan-yuan, et al. Design of video display driving system for active matrix OLED [J]. Journal of Jilin University (Engineering and Technology Edition), 2009, 39(1):210-214.

[2] Tai Yong-hang, Yun Li-jun. A Method for AM-OLED Gamma Correction J. Opto-Electronic Engineering. 39(2012) 131-134.

[3] Lee JH, Nam WJ, Jung SH, et al. A new current scaling pixel circuit for AMOLED [J]. Electron Device Letters, IEEE, 2004, 25(5): 280-282.

[4] Lijun Yun, Yonghang Tai. Design and Implementation of Video Display System based on AM-OLED Microdisplay [M]. 2010 International Conference on Display and Photonics. Nanjing; IEEE. 2010.

[5] Microchip Technology Inc. PIC18F2550 Datasheet [J]. 2006.

[6] Tai Y, Yun L, Shi J, et al. Design of OLED gamma correction system based on the LUT [C]. 2011

[7] OLEiD. SinoPannel_preliminary datasheet V0.2. [J]. 2009,

[8] Chen Z, Shi J, Yun L, et al. A design of near-eye 3D display based on dual-OLED.[C]. ICDP, 2010.

[9] Rushton S, Mon-Williams M, Wann JP. Binocular vision in a bi-ocular world: new-generation head-mounted displays avoid causing visual deficit [J]. Displays, 1994, 15(4): 255-260.

Advanced Materials Research Vol. 936 (2014) pp 2214-2219
© (2014) Trans Tech Publications, Switzerland
doi:10.4028/www.scientific.net/AMR.936.2214

The Design of Wide-Stopband HTS Bandpass Filter

Hong YANG[1, a], Yan ZHOU [1,b]

[1]College of Electrical Engineering, Chongqing University of Posts and Telecommunications, Chongqing, China

Email：[a] yanghong@cqupt.edu.cn, [b]zhouxue198683@163.com

Keywords: Wide-stopband; HTS; bandpass filter; Stepped impedance comb line; insertion loss

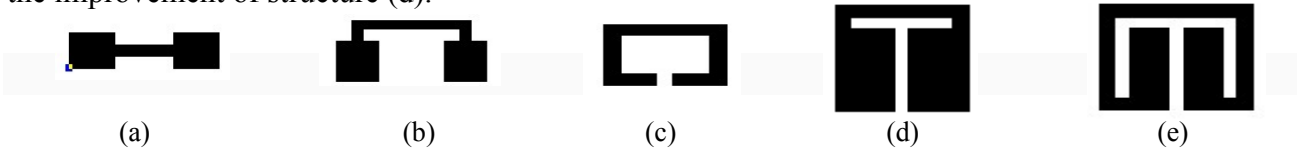
Abstract: This paper presents the design of a wide-stopband HTS bandpass filter(BPF). The 9-pole wide-stopband BPF has a center frequency 2.21GHz and bandwidth 100 MHz. Based on the step impedance resonator，this filter increase the harmonic frequency to more than 3 times of fundamental frequency. Optimization simulation results shows that insertion loss is less than 0.3 dB in the passband，and stopband suppression is greater than 80 dB within 0~f0-BW and greater than 60 db within the f0 + BW ~ 3 f0. Within the passband, dB (S (2, 1)) < -20. This design not only achieved a good wide stopband and solved the interference problem but also had a simple structure which is easy to implement.

Introduction

With the development of communication technology and the improvement of spectrum utilization, solving the interference problem is a major problem in today's communication. In order to inhibit harmonics and unwanted signals the wide stopband filter is essential[1,2]. Because of high temperature superconducting material has a very low microwave surface resistance, high temperature superconducting filter made of high temperature superconducting thin film has higher Q value and lower insertion loss than filter using conventional materials. HTS filter can effectively reduce the noise coefficient of the receiver system, and improve the sensitivity, and enhance its inhibition of jamming signal, etc. [3]. In this paper, a wide stopband HTS band-pass filter using stepped impedance comb line resonator structures[4] was designed. This filter has small insertion loss and good frequency selection characteristic, and parasitic passband can be moved to 3 times above of the center frequency. In addition, this filter meet the requirement of wide stop-band with a compact structure.

The Design Principle

In a microwave integrated circuit, a variety of resonator can be used in filter, but commonly used is the half-wavelength SIR type [5]. Several typical half wavelength SIR resonators structure are shown in figure 1. Structure (a), (b), (c) respectively on the geometric shape are called linear, u-shaped (pin) and ring. Structure (d) and (b) have similar u-shaped structure, and (d) has the internal coupling. Structure (d) use their open terminal to achieve miniaturization. Structure (e) is the improvement of structure (d).



(a) (b) (c) (d) (e)

Fig.1 Several typical half wavelength SIR resonators

In combination with the actual requirement of high performance (wide stopband, strong outside-band restraint and low insertion loss, etc)receiver, a wide stopband HTS band-pass filter was designed. Structure of resonator was shown in figure 1 (e) (stepped impedance comb line). As shown in figure 2, the LC equivalent circuit model of (e) is composed of long transmission lines and symmetric coupled line [6]. Capacitance Cg can extend certain stopband bandwidth, so filter can achieve certain wide stopband based on this structure.

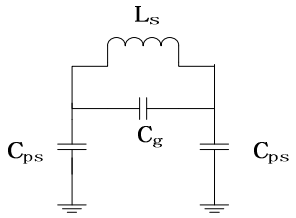


Fig. 2 The equivalent circuit of step impedance comb line resonator

There are many ways to design the filter but the commonly used are CAD method and synthetic method. Because of the CAD method is suitable for the simpler resonator structure or few grade filter, synthetic method is used to design the filter in this paper. Synthesis is use low-pass filter prototype (such as butterworth, chebyshev, or elliptic function) though frequency conversion to synthesize the coupling matrix and the external quality factor of filter based on the theory of coupling. Then through the deep optimization and simulation ,we can design the requirements filter.

Coupling theory of the resonator is very important in the filter design. The key of designing a filter using synthesis method is to derived coupling matrix of filter. After knowing the coupling matrix (internal coupling) and external quality factor (external coupling) of filter, initial value of the filter can be obtained.

The Design of fiLter

This wide stopband HTS filter use sided YBCO / MGO / YBCO high-temperature superconducting thin films. Designed structural parameters are shown as follows:

Permittivity:9.8 Substrate thickness:0.5mm

Conductor conductivity: 4.9e+12 Loss tangent: 1×10^{-5}

This BPF use nine-pole Chebyshev low-pass filter[7] prototype which has 0.01dB ripple. Through look-up the table, we can get the initial value of each element [8]:

g_0=1.0000，g_1=0.8144，g_2=1.4270，g_3=1.8043，g_4=1.7125，g_5=1.9057，g_6=1.7125，g_7=1.8043，g_8=0.4270，g_9=0.8144，g_{10}=1.0000。

Get these values into the equation of the external quality factor Qe and normalized coupling coefficient $k_{i,\,i+1}$. [8-10]

$$Q_{ei} = \frac{g_0 g_1}{BW} \tag{1}$$

$$Q_{eo} = \frac{g_9 g_{10}}{BW} \tag{2}$$

$$k_{i,i+1} = \frac{BW}{\sqrt{g_i g_{i+1}}} \tag{3}$$

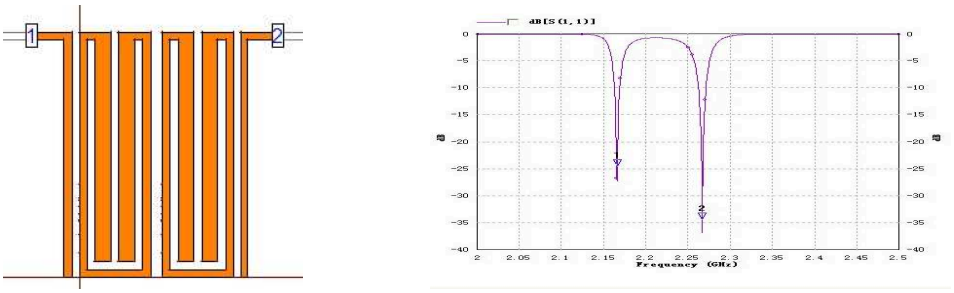
Here, BW = (w2-w1) / w0. By the equation (1) and (2) the external quality factor of the filter can be calculated , i.e. Qei = Qeo = 18.02. By the equation (3) the coupling coefficient between the

resonators at all levels can be calculated, the results are shown in Table 1. Get the external quality factor Qe and the filter center frequency f0 into the equation of the external quality factor $Q_e \approx f_0/\Delta f_{\pm 90^o}$, then obtain ±90º relative phase Bandwidth $\Delta f_{\pm 90^o}$=122.8MHz.

Table 1. Coupling coefficient of the nine grade filter

resonator	1,2	2,3	3,4	4,5	5,6	6,7	7,8	8,9
coupling coefficient	0.0419	0.0282	0.0257	0.025	0.025	0.0257	0.0282	0.0419
slit width [mm]	0.3394	0.5038	0.5382	0.5481	0.5481	0.5382	0.5038	0.3394

Using full-wave electromagnetic simulation software IE3D simulate two-pole resonator structure as shown in Fig 3 (a), then we can get two separated frequencies f_1, f_2 as shown in Fig 3 (b).



(a)The topological structure (b)The simulation results

Fig. 3 Coupling coefficient of the simulation

Corresponding coupling coefficient can be expressed as

$$k = \frac{f_1^2 - f_2^2}{f_1^2 + f_2^2} \quad (4)$$

Depending on the topology shown in Figure 3, we can change the slit width between two resonators as shown in Table 2 in turn, through a plurality of simulations, then can get the resonance frequency of different slit width s (unit: mm). As shown in Table 2, we can calculate the corresponding coupling coefficient k by formula (4).

Table 2. The simulation results of coupling coefficient

s [mm]	0.1	0.15	0.2	0.25	0.3	0.35	0.4	0.45	0.5
f_1 [GHz]	2.12848	2.14087	2.15093	2.15944	2.16641	2.17195	2.17647	2.18111	2.18421
f_2 [GHz]	2.30031	2.28947	2.28096	2.27322	2.26703	2.26169	2.25697	2.25232	2.24845
k	0.0775	0.0670	0.0586	0.0513	0.0454	0.0405	0.0363	0.0321	0.029

Curve between the slit width and the coupling coefficient was shown in Figure 4. The horizontal axis represents the coupling slit width, the vertical axis represents the coupling coefficient. Through the curve, the coupling slit width s of nine-pole filter corresponded by coupling coefficient k can be get. Then initial value of coupling slit width of HTS band-pass filter can be get, as shown in table 1.

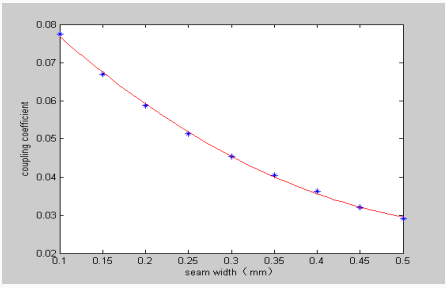


Fig.4 Fitting curve of the coupling coefficient and the seam width

The position relationship between the resonators determines the internal coupling of filter, but energy can not be delivered by the way which only has internal coupling. So appropriate external coupling is needed to get the best response of the filter. If Qe is known, according to the relationship between phase and frequency of S11, the tap position of the input and output of filter can be determined. It is important to note that in some cases the phase of S11 at the resonant frequency is not 0 but there are certain deviation. In this case, we should determine $\Delta f_{\pm 90}{}^{o}$[10] based on the offset point.Simulate the resonator, adjust the tap position,to make $\Delta f_{\pm 90}{}^{o}$ =122.8MHz. The tap distance from the bottom edge is 1.45 mm. As shown in Fig 5.

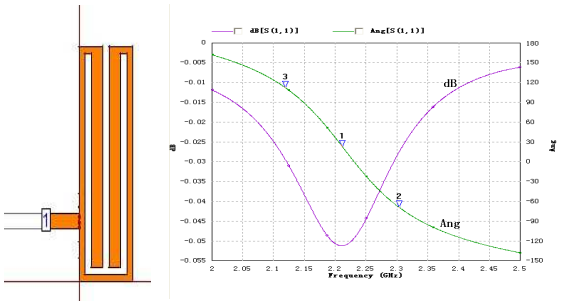


Fig. 5 Tap position simulation

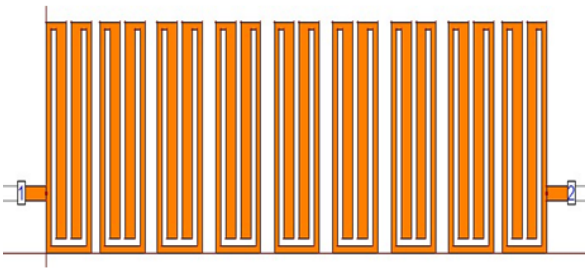
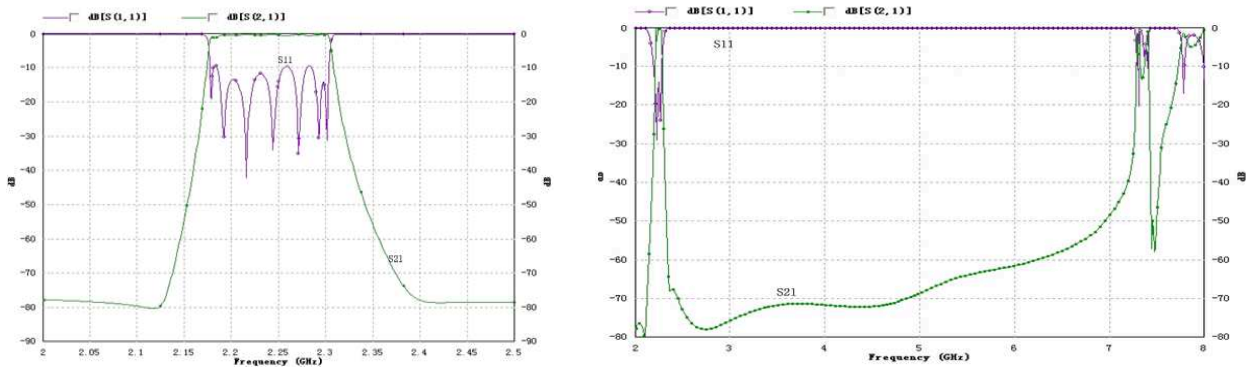


Fig.6 Topological structure

Simulation and Optimization of the Whole Filter Circuit

According to the tap position and Coupling slit width showing above, topology of nine-pole wide stopband HTS bandpass filter can be get. As shown in Figure 6. According to the topological structure of the figure 6, the passband and stopband simulation results are shown in figure 7.



(a)simulation results of passband (b)simulation results of stopband

Fig.7 The simulation results of filter

As shown in figure 7(b), the parasitic passband is moved to more than 3 times of the center frequency . Out-band rejection is greater than 70dB Within 0 ~ f0-BW and greater than 60dB within f0 + BW ~ 3 f0. As shown in figure 7(a), the frequency bandwidth of this broad stop-band filter is consistent with the design goals, but the inband reflection S11 is about -10dB having some gap with an ideal inband reflection (less than-20dB) , so further optimization of the filter is needed.

Because of taking approximate of the formulas and rounding in calculations caused inaccurate results further adjustments to the filter is needed. Adjusted by hand can be used, but debugging is difficult and should take a long time in the case of having too many grades. A feasible method is using the powerful computing ability of computer and the optimization function of IE3D software to optimize the filter.

Set the length of the resonator and the slit width between resonator and tap position as optimization variables, set up a appropriate scope of variables. Fine tune the topology of the filter

showing in figure 6 to reduce reflection coefficient S11. The results after optimization are shown in figure 8.

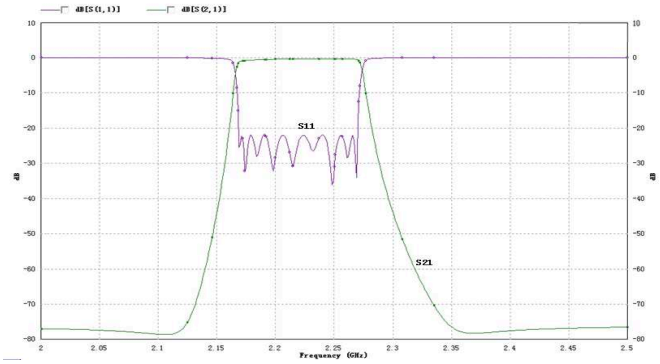


Fig. 8 Optimization results

As shown in optimization results, passband bandwidth of the filter is about 0.1GHz, the center frequency is 2.21GHz (s band), passband reflection S11 is less than-20dB, insertion loss is less than 0.3dB. Filter performance is ideal by achieving a low insertion loss and wide stopband result.

Conclusion

In this paper, wide stopband HTS bandpass filter is researched and designed. Choose stepped impedance comb line resonator and the synthetic method to design the filter. According to the low-pass filter prototype and coupling theory comprehense coupling coefficient and the external quality factor of filter. Then using optimization function of IE3D software to get good results. Using this method can reduce the design complexity and shorten the design cycle. In addition, this paper provided some reference for microwave workers in the actual work.

References

[1] Narayan Rana. Compact Wide Stopband SIR Filter for Radio Altimeter[C].Aerospace Conference,Big Sky,MT.2012IEEE, 2012.pp:1-5.

[2] Xingbing Ma, Hongxing Zheng, Chengguang Sun.Compact Lowpass Filter with Wide Stopband[C].ConsumerElectronics.2012IEEE.2012.PP:1720-1722.

[3] T. Zhang, J. Du, Y.J. Guo and X.-W. Sun. On-chip integration of HTS bandpass and lowpass filters with Josephson mixer[J]. ELECTRONICS LETTERS, 2012, 48 (12):729-731

[4] LIN Ya, GAO Mingwu, CAI Kai, HUANG Yipei. Design of microstrip bandpass filter with upper-skirt frequency suppression[J].Journal of Chongqing university of post and telecommunications, 23(1):61-64.

[5] HAN Hongshuo, CHEN Jie. 21st century foreign deep space exploration development plans and progress. Spacecraft Engineering, 2008 V01.17 No.3

[6] Lung-Hwa Hsieh and Kai Chang,Compact Elliptic-Function Low-pass Filters Using Microstrip Stepped Impedance Hairpin Resonators[J].IEEE Ttans.Microwave TheoryTech, January2003.51(1):193-199.

[7] LIU Yuan, QIAN Kewei. Nover optimization algorithms for cross-coupled filter[J]. Journal of Chongqing university of post and telecommunications,24(6):770-775.

[8] GAN Benba, WU Wanchun. The structure and design of modern filter [M].beijing: Science Press,1973

[9] LIU Guoying. Research of high sensitivity channelized superheterodyne receiver front-end system[D].chengdu: University of Electronic Science and Technology,2009

[10] HAN Fangmao. Research of high sensitivity channelized receiver front-end subsystem[D]. chengdu: University of Electronic Science and Technology,2008

Advanced Materials Research Vol. 936 (2014) pp 2220-2224
© (2014) Trans Tech Publications, Switzerland
doi:10.4028/www.scientific.net/AMR.936.2220

Design of a Reader Antenna for UHF RFID

Hong YANG[1, a], Li GUO [1,b]

[1]College of Electrical Engineering, Chongqing University of Posts and Telecommunications, Chongqing, China

Email：[a] yanghong@cqupt.edu.cn, [b]541862155@qq.com

Key words:RFID; reader antenna; miniaturization;circularly polarization; ultra high frequency; slit in the path

Abstract: A compact and circular polarized antenna for UHF band RFID handset reader was designed, and realized by cutting slits in the antenna patch and etching slots on the ground. Numerical simulation was performed for the characteristics of the antenna with the software HFSS 13.0.The simulation results show that when the size of antenna patch is 68mm×68mm, -10dB return loss impedance bandwidth is 49MHz,VSWR is less than 2 and the largest gain is -0.61dB for antenna in 907～931MHz. Compared with the traditional reader antenna with the same material of the substrate，the improved antenna has a much higher gain．and the size was reduced by 20% and the max gain is raised -0.11dB.

Introduction

Radio Frequency Identification (RFID) technology is a kind of using Radio Frequency communication to realize the non-contact automatic identification technology. In recent years, RFID has entered the stage of commercial application, such as large scale integrated circuit, network communication and information security[1]. The RFID system is consisted by the reader, reader antenna and tag.The reader sends continuous wave (CW) signal to the tag to activate its microchip and then commands that are modulated to the signal.The tag responds its identification code using backscattering of modulated electromagnetic wave.Circularly polarized antennas are widely adopted in RFID communications to ensure the reliability of communications between readers and tags[2],and this makes it convenient to read the label information.

In China, RFID system assigned frequency band 840 ~ 845MHz and 920 ~ 925MHz for RFID band. With the rapid development of RFID,designed a reader antenna which is suitable for Chinese UHF RFID system having an important significance to promote RFID application.Traditional forms antennas for handheld RFID reader is too large,while On the premise of keep the antenna performance,reduction the reader antenna size is more difficulty than reduction reader circuit. Therefore,the size of the antenna miniaturization has become the current trend of the RFID reader antenna research[3]-[5]. In this paper , We designed a new type of small antennas in order to improve the size and performance of the domestic reader antenna.

Antenna design

In order to realize the miniaturization of reader, it is necessary to design special miniaturization of microstrip antenna[6].According to the theory of microstrip antenna, we can achieve the purpose by improved the dielectric substrate`s relative dielectric constant, loaded the short circuit probe and slotted or slit in the radiation patch or other methods to reduce the size of the patch antenna.Slots

and slits` essence is by extending the microstrip antenna radiation patch`s excitation current on the surface, it`s Equivalent to prolong the equivalent current path to achieve the goal of reducing the antenna size. Based on the concept,designed a circularly polarized reader antenna which is suitable for handheld RFID reader working in 920MHz.

By transmission line theory, according to the working frequency, we can calculate the radiation patch antenna size By (1) - (4) :

$$W = \frac{c}{2f}\left(\frac{\varepsilon_r + 1}{2}\right)^{-1/2} \quad (1)$$

$$L = \frac{c}{2f\sqrt{\varepsilon_e}} - 2\Delta l \quad (2)$$

$$\varepsilon_e = \frac{\varepsilon_r + 1}{2} + \frac{\varepsilon_r - 1}{2}\left(1 + \frac{10h}{W}\right)^{-1/2} \quad (3)$$

$$\Delta l = 0.412h\frac{(\varepsilon_e + 0.3)(W/h + 0.264)}{(\varepsilon_e - 0.258)(W/h + 0.8)} \quad (4)$$

In formula : W and L are the the radiation patch`s width and length respectively; ε_e is the effective relative dielectric constant; Δl is equivalent radiation slits length; W have some effects on band width, input impedance and radiation efficiency, when elect a width greater than the above formula, the antenna's radiation efficiency become higher, so prone to distortion caused by the high-order mode field.

This article takes the form of a square patch antenna, so we choose W = L.Theoretically,the floor can be considered infinite, but in practical engineering design, taking into account many factors such as antenna installation size,quality and cost ,the floor size should be as small as possible. When the floor satisfied the formula $W_0 \geq W + 0.2\lambda_g$,the floor can be regarded as infinite[7].

In order to realize the miniaturization design of antenna,we Can change the microstrip patch antenna surface current path to achieve. In Literature[8], low cost FR-4 material is choose as the substrate,by cutting the triangle Angle on the patch to realize circular polarization and Opening square groove in the center of the patch to achieve miniaturization. Fig.1 shows the geometry of the proposed circularly polarized antenna.

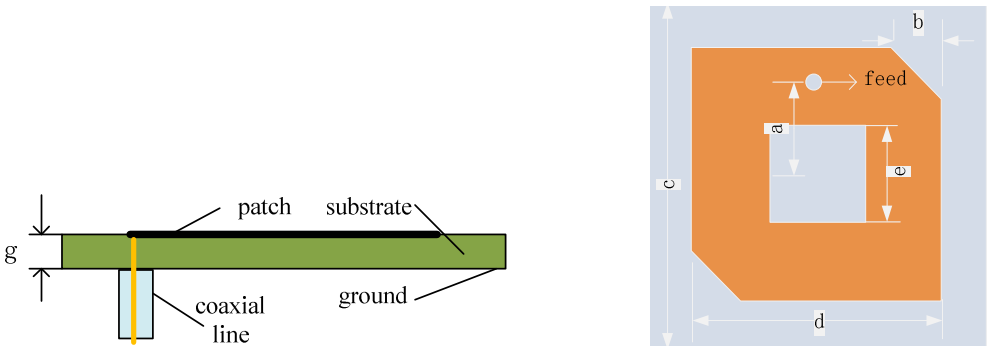
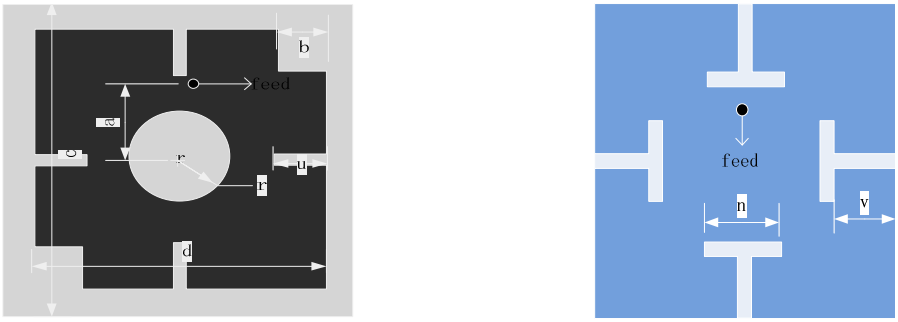


Fig.1 Side view and vertical view of the antenna

This antenna consists of three parts:the upper surface is d×d of square patch which is digging square holes and cutting triangle Angle on it,the middle is the substrate and the lower surface of the substrate is a c×c square floor. When the antenna size is 90mm × 90mm × 3mm, the antenna return loss and axial ratio bandwidth is covered China UHF RFID band 920 ~ 925MHz and the antenna gain is -1dB.

The author made some improvements based on consulting a large number of literature.A square side length b was chosen instead of cutting triangle which could help to increase bandwidth of the antenna;Open a circular hole in the middle,the length and the width of the slits were chosen as u and 1.5mm respectively. It will affect antenna`s size and resonant frequency.At the same time, open a "T" shape On the floor,the length is n and v, slits width is 1.5 mm .

The improved antenna is shown in fig.2:



(a) (b)

Fig.2 A side view (a)of the improved antenna and the front and back structure(b)

Simulation And Experimental Results

Ansoft High Frequency Structure Simulator (HFSS) was used to simulate and optimize the parameters of the proposed antenna.As can be seen from Fig.3, with the slits is deeper on the antenna patch ,the chip area become smaller ,the resonant frequency is decreases,The bandwidth of the antenna become narrow,Therefore increase the depth of slits blindly would cause sacrifice the bandwidth of the antenna.

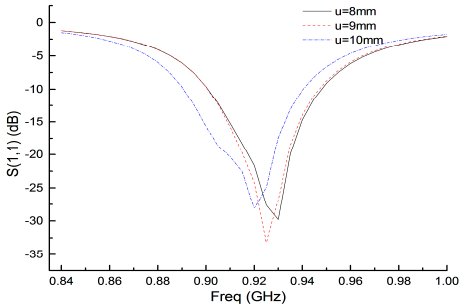


Fig.3 Effects of changing U on S11

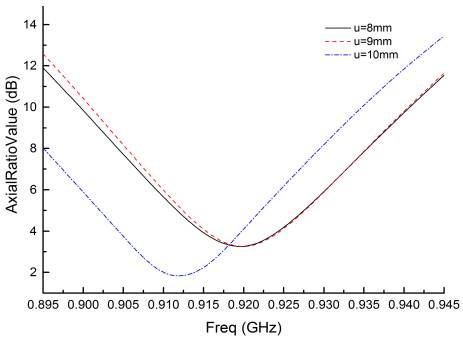


Fig.4 Change trends of antenna axial ratios with u

Fig.4 is the antenna axial ratio changed with u,from Fig.4 can see that axial ratio and the slits depth is irregular changing. When the slits length is increase the resonance frequency decreases .

The return loss and the axial ratio with the change of square cutting angle are shown in Fig.5 and Fig.6.As can be seen from Figure 5,when the length b increase,the S11 curve moves to the right. With the resonance frequency increases gradually , the bandwidth of the antenna becomes larger than before.But when the cutting angle size was chosen as 8mm,the return loss has a certain convex and it Shows that S11 index is deterioration.Thus curve analysis shows that within a certain

range,the patch`s cutting angle can not only produce circularly polarized but also be used to adjust the antenna bandwidth.

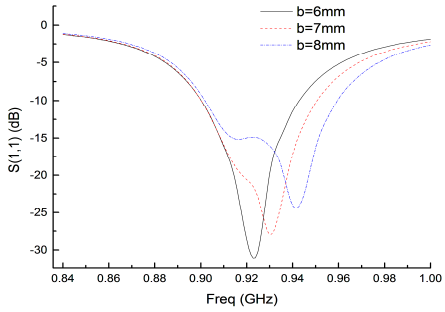


Fig.5 Effects of changing square cutaway b on

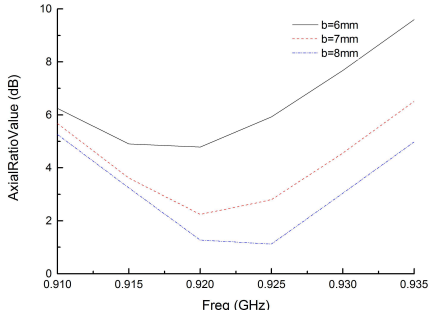


Fig.6 Changing trends of antenna axial ratios with b

simulate and optimize the parameters of the proposed antenna:when u=8.4mm,b=6.6mm,v=15.5mm,k=7.5mm,n=6.4mm,antenna performance is the best.Its return loss shown in Fig.7. Fig.7 shows the -10dB bandwidth is 45MHz (900~945MHz), and it covers the required bandwidth (920~925MHz).

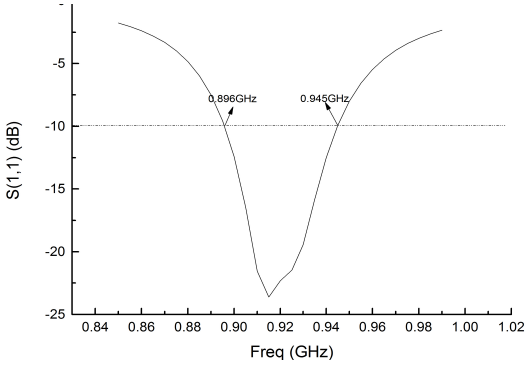


Fig.7 Graph of microstrip antenna return loss

Fig.8 and Fig.9 are the antenna radiation pattern.It can be seen that the antenna has good radiation performance.Compared with the traditional reader antenna ,the peak antenna gain is -0.61 dB at 920MHz and the size reduced by 20% accordingly.

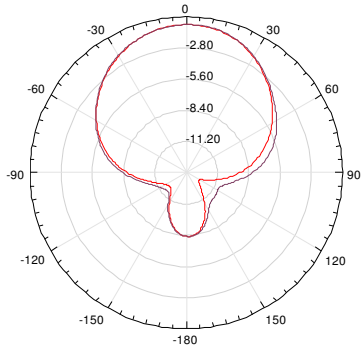


Fig.8 Planar antenna radiation pattern

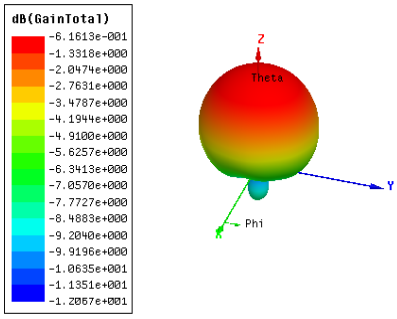


Fig.9 3D antenna radiation pattern

Fig.10 shows simulated axial ratio in the broadside of the antenna. The simulated 3 dB axial ratio bandwidth is about 12MHz from 914MHz to 926MHz around the center frequency 920MHz which reaches the requirement of the UHF RFID reader antenna.

The higher VSWR,the higher reflected power and the lower transmission efficiency. In the bandwidth of 907 ~ 931MHz simulated VSWR is less than 2 and in 920MHz VSWR = 1.3 indicates that the antenna has a good matching .

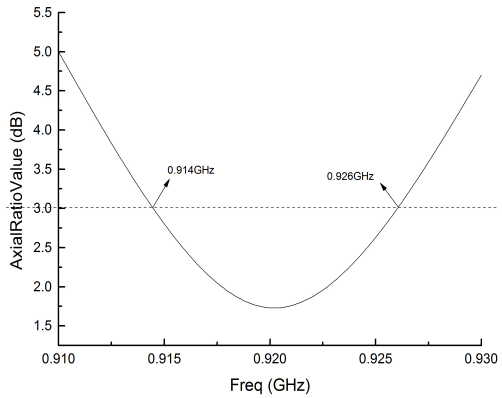


Fig.10 Antenna axial ratio changes graph

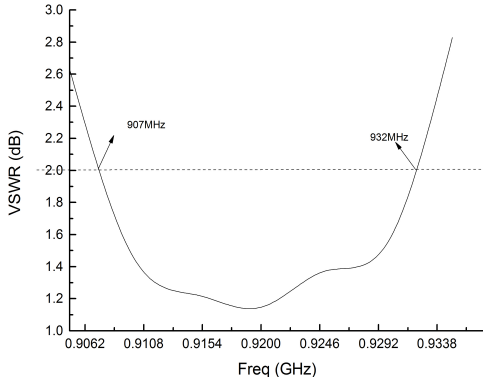


Fig.11 Antenna VSWR curve graph

Conclusion

This paper presents a read range performance study of compact reader antennas for a handheld UHF RFID reader.A novel design of circularly polarized RFID reader antenna with cutting slits in the antenna patch and opening round hole on the radiation patch to reduce the physical size;Through the square cutting angle to realize circular polarization;Through etching slots on the floor to improve antenna gain.Based on the above principles to design a handheld reader antenna which is suitable for china to use in UHF RFID band.The simulation optimization shows that antenna main performance index in volume, VSWR, bandwidth, gain and circularly polarized all satisfies the requirement of handheld RFID reader antenna.

References

[1] Wang shan,ding jun. The small antenna design based on RFID[J]，Electronic Design Engineering，2013，21(12）:184-186.

[2] LAU P Y, YUNG K K O, YUNG E K N.Alow-cost printed CP patch antenna for RFID smart bookshelf in library[J].IEEE Trans Ind Electron,2010, 57 (5) : 1583 -1589.

[3] UKKONEN L, SYDÄNHEIMO L,KIVIKOSKI. Read range performance comparison of compact reader antennas for a handheld UHF RFID reader[J].IEEE Appl Pract,2007，1(1)：24-31.

[4] Lai min-yin.Broadband UHF RFID tag antenna mountable on metallic objects[J],Journal of Chongqing University of Posts and Telecommunications(Natural Science Edition),2011,23(2)：198-201.

[5] LIN Ruo-bo.Optimizating micro-strip antenna based on photonic crystal PBG structure[J].Journal of Chongqing University of Posts and Telecommunications(Natural Science Edition),2012.24(4):431-436.

[6] Zhang li.The Miniaturization Design of an Antenna for Hand-Held RFID Reader[J].Chinese Journal of Electron Devices，2012，35（4）:379-382.

[7] Yang hong .Analysis and design of an Φ-shaped compact multi-frequency micro-strip antenna[J].Journal of Chongqing University of Posts and Telecommunications(Natural Science Edition),2011,23(3):315-319.

[8] Hu ru gang.Research on the antenna of UHF RFID system.beijing:Beijing jiaotong university,2008.

Advanced Materials Research Vol. 936 (2014) pp 2225-2229
© (2014) Trans Tech Publications, Switzerland
doi:10.4028/www.scientific.net/AMR.936.2225

An Effective Model for Wire Medium Based on the 4th Order Dispersion Equation

Zhun Yang, Wei Song [a] and Xin-Qing Sheng

School of Information and Electronics, Beijing Institute of Technology, 100081, China

[a]wsong@bit.edu.cn

Keywords: wire medium; 4th order dispersion equation; effective model.

Abstract: In this paper, the wire medium made of parallel thin wires is studied by using the FDTD method incorporating the sub-cell technique of thin wire. The conventional effective model for the wire medium is based on the 2th order dispersion equation; and it becomes inaccurate for EM behavior calculation of wire medium when the transversal spatial harmonics becomes high. A new effective model is proposed based on the 4th order dispersion equations and surface fitting, which guarantees the modeling accuracy for higher spatial harmonics.

Introduction

Wire medium (Fig. 1) is a type of periodic structure consisting of parallel metallic wire array with interesting EM properties and applications. It enables the realization of sub-wavelength imaging with literarily no limit of resolution [1,2]. This is verified both numerically [3,4] and experimentally [2,5]. In [6], the exact dispersion equation of the ideally conducting thin wire array is deduced under the only assumption that the radii of wires are much smaller than the lattice periods and the wavelength, and it can be written as follows:

$$\frac{1}{\pi}\ln\frac{b}{2\pi r}+\frac{1}{bp_y^{(0)}}\frac{\sin p_y^{(0)}a}{\cos p_y^{(0)}a-\cos q_y a}+\sum_{n\neq 0}\left(\frac{1}{bp_y^{(n)}}\frac{\sin p_y^{(n)}a}{\cos p_y^{(n)}a-\cos q_y a}-\frac{1}{2\pi|n|}\right)=0, \tag{1}$$

where $\mathbf{q}=(q_x,q_y,q_z)^T$ denotes the wave vector of an extraordinary mode. Parameters *a* and *b* denote the lattice periods in the y- and z-directions respectively, and *r* denotes the radius of the wire, as shown in Fig.1. $p_y^{(0)}$ is the y component of the n^{th} Floquet mode wave vector:

$$p_y^{(n)}=-j\sqrt{\left(q_z+\frac{2\pi n}{b}\right)^2+q_x^2-k^2},\quad \mathrm{Re}\left\{\sqrt{()}\right\}>0, \tag{2}$$

where $k=\omega\sqrt{\varepsilon_0\mu_0}$ denotes the wave number in the free space.

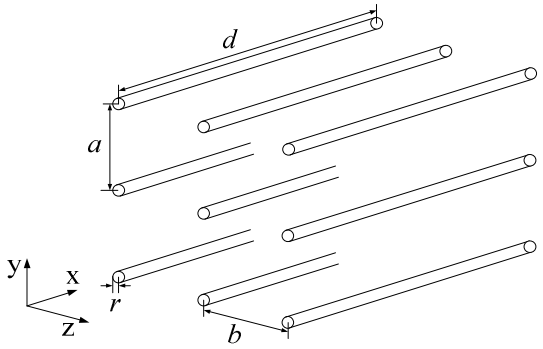


Fig. 1. The wire medium formed by an array of thin wires periodically arranged in rectangular lattice.

From Eq. 1 and Eq. 2, an approximated dispersion equation can be obtained by using the second-order Taylor expansion of sine and cosine functions of small arguments:

$$q_x^2 + q_y^2 + q_z^2 = k^2 - k_p^2 . \tag{3}$$

Based on Eq. 3, a uniaxial effective model was proposed to characterize the wire medium under a further assumption of $a, b << \lambda$ [7],

$$\overline{\overline{\varepsilon}} = \varepsilon\left(k, q_x\right)\mathbf{xx} + \mathbf{yy} + \mathbf{zz} \quad , \quad \varepsilon\left(k, q_x\right) = \varepsilon_0\left(1 - \frac{k_p^2}{k^2 - q_x^2}\right) , \tag{4}$$

where the notation k_p plays the role of an equivalent "plasma frequency" which depends on the geometrical parameters *a*, *b* and *r*

$$k_p^2 = \frac{2\pi/(ab)}{\log\frac{\sqrt{ab}}{2\pi r} + F(a/b)} \quad , F(\xi) = -\frac{1}{2}\log\xi + \sum_{n=1}^{+\infty}\left(\frac{\coth(\pi n\xi) - 1}{n}\right) + \frac{\pi}{6}\xi . \tag{5}$$

For the square grid ($a = b$), $F(1) = 0.5275$. Equation 4 indicates that this wire medium possesses not only plasma-like frequency dispersion, but also strong spatial dispersion.

By adopting an additional boundary condition [8], the transmission through an effective wire medium slab was theoretically studied [9]. The effective model of Eq. 4 is verified by the numerical results of the transmission- and reflection- coefficients [9].

The transmission coefficient *T* is an important parameter in studying the wire medium, especially for a sub-wavelength imaging device where *T* directly affects the quality of the image. However, it is noted that the above effective model becomes inaccurate as the transverse spatial harmonics increase. Therefore, discrepancy between the EM behaviors of the effective model and the physical structure occurs. In this study, we propose a new effective model to include higher order spatial dispersions by using higher (4^{th}) order expansion of the exact dispersion equation of the photonic states. Surface fitting is applied by using the data from a 3-D full wave simulation. Significant improvement in accuracy is demonstrated in numerical experiments.

The proposed 4 th order dispersion equation

In the following, we will first review the derivation of the transmission coefficient $T_{\text{effective}}$ in the conventional effective model [9]. Assume $q_z = k_z = 0$. Denoting $k_x = -j\gamma_x = -j\sqrt{k_y^2 - k^2}$, and the propagation constant of TM wave in the wire medium as γ_{TM}, we can obtain

$$\gamma_{TM} = \sqrt{k_p^2 + k_y^2 - k^2} \text{ , and } q_x = -j\gamma_{TM} . \tag{6}$$

By solving the system of equations for the total magnetic field, the expression of $T_{\text{effective}}$ can be obtained as follows:

$$T_{\text{effective}} = -\frac{1}{1 + \frac{\gamma_{TM} k_y^2}{\gamma_x\left(\gamma_{TM}^2 + k^2\right)}\operatorname{ctanh}\left(\gamma_{TM} d/2\right)} . \tag{7}$$

Next, we will evaluate the accuracy of the conventional effective model of Eq. 3 and Eq. 4 based on the full-wave simulation of the 3-dimensional PEC thin wire array. The FDTD method incorporating the sub-cell technique of thin wire [10] is adopted. The system is illuminated by a TM mode plane wave with an H_z excitation at operating frequency of $f_0 = 3GHz$. The corresponding wave number and wavelength in free space are denoted as k_0 and λ respectively. The length of the thin wires is $d = \lambda/2$. Wire medium with square lattice is considered in this paper. A fixed filling ratio $\pi r^2/a^2 = 0.001$ is adopted, indicating the physical thin wire array strictly meets the only assumption $r << a, b, \lambda$ in [7]. According to Eq. 5, with the increment of k_p, the lattice becomes denser roughly proportionally. For example, $a = b = \lambda/20$ corresponds to $k_p = 4.8415k_0$.

The transmission coefficient T_{FDTD} is obtained from the FDTD results with numerical error controlled under 0.05%. Based on T_{FDTD}, γ_{TM_FDTD} can be calculated accordingly. On the other hand, $T_{\text{effective}}$ and $\gamma_{TM_effective}$ are obtained analytically following Eq. 6 and Eq. 7. The comparison of γ and T for the case $k_p = 4.8415k_0$ are plotted in Fig. 2. It is obvious that with the increment of k_y, $\gamma_{TM_effective}$ and $T_{TM_effective}$ deviate from γ_{TM_FDTD} and T_{FDTD}.

In the conventional effective model, $\gamma_{TM_effective}$ corresponds to the second-order approximation of the dispersion equation Eq. 1. It increases monotonically with k_y, and the relation is linear for large k_y (ref Eq. 6). However, γ_{TM_FDTD} as a function of k_y is not a monotonic curve. That means a higher-order approximate dispersion equation is needed for describing this curve more accurately. In the following, a scheme to obtain a higher order dispersion equation corresponding to a more accurate effective model is proposed. Denote $\gamma'_{TM_effective}$ and $T'_{\text{effective}}$ as the propagation constant of TM wave and the transmission coefficient in the proposed effective model respectively. $\gamma'_{TM_effective}$ is expected to agree with γ_{TM_FDTD} better than the conventional one. Next the forth-order Taylor expansion of Eq. 1 is chosen. However, a complete solving of a fourth-order dispersion equation in obtaining $\gamma'_{TM_effective}$ is cumbersome, and the expression of $\gamma'_{TM_effective}$ is implicit. In order to express $\gamma'_{TM_effective}$ explicitly, we use the following approximations and proportional relationships

$$p_y^{(0)} = \sqrt{q_x^2 - k^2} \approx c_1 \cdot q_x + c_2 \cdot k + c_3, \quad a = c_4/k_p, \quad k_p = c_5 \cdot q_x, \quad k = c_6 \cdot q_x \tag{8}$$

where c1-c6 are the undetermined constants. Then an explicit expression of $\gamma'_{TM_effective}$ which consists of terms such as $k_y^4 k/k_p^3$, k_y^4/k_p^2, k_y^2, $k_y^2 k/k_p$ ..... k^4/k_p^2 ..... is obtained with the odd-order of k_y discarded due to the symmetry of q_x^2 on k_y. Through fitting the known surface of γ_{TM_FDTD} as a function of k_y and k_p, the dominant terms of $\gamma'_{TM_effective}$ are picked up and a neat expression of $\gamma'_{TM_effective}$ is obtained:

$$\gamma'_{TM_effective} = \sqrt{k_p^2 + k_y^2 - k^2 + \left(k_y^2 + k_p^2\right) \cdot \left(A\frac{k_y^2}{k_p^2} + B\frac{k_y^2}{k^2} \right)}, \tag{9}$$

where $A = -0.35112$ and $B = 5.22602e\text{-}4$ respectively. In the fitting process, the residual sum of squares is 4.75322 for 106 points and the Adjusted R-Square is 0.99893. The form of γ'_{TM} ensures that the TM and TEM (corresponding to $q_x = k$) modes exist in the wire medium (ref. [7] and [9]). Because of the symmetry of the structure in the y- and z- directions, a general form of the 4th order approximate dispersion equation can be written as:

$$q_x^2+\left(q_y^2+q_z^2+k_p^2\right)\left(A\frac{q_y^2+q_z^2}{k_p^2}+B\frac{q_y^2+q_z^2}{k^2}+1\right)=k^2\,. \tag{10}$$

The corresponding 4th order effective model is derived following the similar steps in [7]:

$$\varepsilon\left(k,q_x,q_y,q_z\right)=\varepsilon_0\left(\frac{1}{A\frac{q_y^2+q_z^2}{k_p^2}+B\frac{q_y^2+q_z^2}{k^2}+1}-\frac{k_p^2}{k^2-q_x^2}\right). \tag{11}$$

The fitting curve of $\gamma'_{TM_effective}$ with $k_p=4.8415k_0$ is shown in Fig.2. It can also be seen from Fig.2 that the calculated $T'_{effective}$ agrees with T_{FDTD} much better than $T_{effective}$. That shows the proposed 4th order effective model is more accurate than the conventional 2th order effective model.

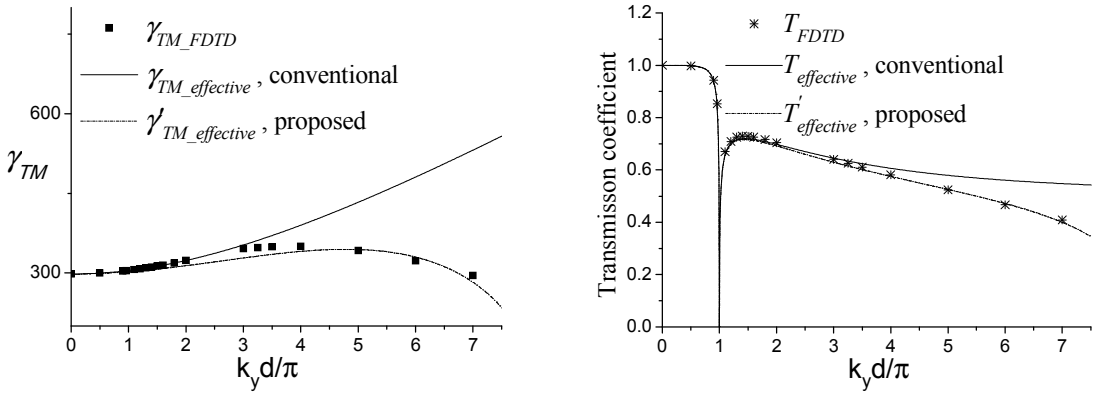


Fig. 2. Comparison of γ and T obtained by using different models as functions of the transverse wave component k_y.

Validation

The above numerical experiments are based on wire medium of square lattice. Next, the proposed 4th order effective model is applied to a different type of wire medium. This medium is based on a rectangular lattice (*b=1.5a*), and the rest parameters are the same with the above examples. The analytical results are compared with the FDTD results in Fig. 3. It is clearly shown that the proposed higher-order effective model can describe the characteristics of the wire medium with improved accuracy for different types of wire media compared with the conventional model.

Summary

In this paper, the wire medium which consists of parallel metallic thin wires is simulated by using the FDTD method incorporating the sub-cell technique of thin wire. The FDTD results show that the conventional effective model based on the 2nd order Taylor expansion of the exact dispersion equations fails to describe the EM behavior accurately for high spatial harmonics. Then a new effective model is proposed by using the surface fitting method based on the 4th order Taylor expansion of the exact dispersion equations. Compared with the conventional model, the proposed model improves the modeling accuracy for a higher spatial harmonics. Numerical experiments also shows that this model is general suited for various type of wire medium.

Acknowledgement

This work was supported by the National Natural Science Foundation of China (Grant no. 61102022) and by the Fundamental Research Foundation of Beijing Institute of Technology of China (Grant no. 20120542014).

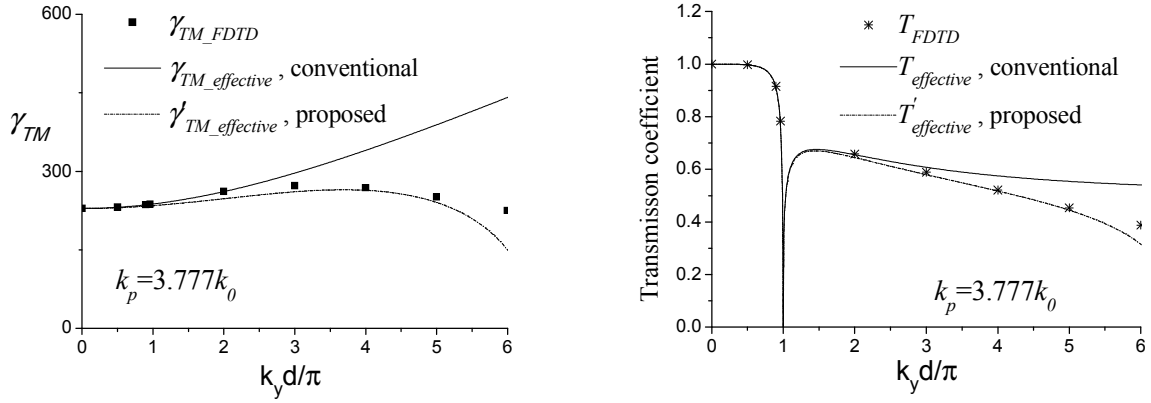


Fig. 3. Comparison of γ and T based on different models for a wire medium with rectangular lattice.

References

[1] Pavel A. Belov, Constantin R. Simovski, and Pekka Ikonen, Canalization of subwavelength images by electromagnetic crystals, Phys. Rev. B **71**(19), 193105(2005).

[2] Pavel A. Belov, Yang Hao, and Sunil Sudhakaran, Subwavelength microwave imaging using an array of parallel conducting wires as a lens, Phys. Rev. B **73**(3), 033108 (2006).

[3] Yan Zhao, Pavel A. Belov, and Yang Hao, Spatially dispersive finite-difference time-domain analysis of sub-wavelength imaging by the wire medium slabs, Opt. Express. **14**(12), 5154-5167 (2006).

[4] Yan Zhao, Pavel A. Belov, and Yang Hao, Modelling of wave propagation in wire media using spatially dispersive Finite-Difference Time-Domain method: numerical aspects, IEEE Trans. Antennas Propag. **55**(6), 1506-1513 (2007).

[5] Pavel A. Belov, Yan Zhao, Simon Tse, Pekka Ikonen, Mário G. Silveirinha, Constantin R. Simovski, Sergei Tretyakov, Yang Hao, and Clive Parini, Transmission of images with subwavelength resolution to distances of several wavelengths in the microwave range, Phys. Rev. B **77**(19), 193108 (2008).

[6] P. A. Belov, S. A. Tretyakov, and A. J. Viitanen, Dispersion and reflection properties of artificial media formed by regular lattices of ideally conducting wires, J. of Electromagn. Waves and Appl. **16**(8), 1153–1170 (2002).

[7] P. A. Belov, R. Marques, S. I. Maslovski, I. S. Nefedov, M. Silveirinha, C. R. Simovski, and S. A. Tretyakov, Strong spatial dispersion in wire media in the very large wavelength limit, Phys. Rev. B **67**(11), 113103 (2003).

[8] Mário G. Silveirinha, Additional boundary condition for the wire medium, IEEE Trans. Antennas Propag. **54**(6), 1766-1780 (2006).

[9] Pavel A. Belov, and Mário G. Silveirinha, Resolution of subwavelength transmission devices formed by a wire medium, Phys. Rev. E **73**(5), 056607 (2006).

[10] Riku M. Mäkinen, Jaakko S. Juntunen, and Markku A. Kivikoski, An improved thin-wire model for FDTD, IEEE Trans. Microw.Theory Tech. **50**(5), 1245-1255 (2002).

Advanced Materials Research Vol. 936 (2014) pp 2230-2234
© (2014) Trans Tech Publications, Switzerland
doi:10.4028/www.scientific.net/AMR.936.2230

Design of a Sine Sweeping Constant Current Source Based FPGA and DDS

Ya-ping YU [1,2,a], Hui ZHAO[1, b*], Yuan LIU [1,c], Ren-jie YANG [1,d],

Gui-mei DONG[1,e], Yuan-shuai XING [1,f]

[1] College of Engineering and Technology, Tianjin Agricultural University, Tianjin 300384, China

[2] School of Electrical &Automation, Tianjin University, Tianjin 300072, China

[a]email: yaping261@163.com, [b] email:zhaohui3379@126.com, [c]email: lywzwzly@126.com, [d]email: rjyang1978@163.com, [e]email: guimeidong@gmail.com, [f]email:164490281@qq.com

Keywords: FPGA; DDS; Howland current pump; sweeping constant current source

Abstract: This paper designed a range of 0.1 ~ 250 kHz sine wave sweeping constant current source, which sine wave generator based on FPGA chip and DDS technology, the desired sine wave frequency was obtained by controlling the frequency control words. Low-pass filter circuit was realized by using the LTC1560-1, conversion circuit from the voltage to the current was consisted of a Howland current pump. The constant current source shows a good spectral impedance purity and amplitude.

Introduction

The factors, such as fat, moisture, tenderness and freshness, are important performance indexes for evaluating meat quality. It is a new field of application of bio-impedance technology to analyze these quality factors by impedance spectroscopy in recent years. The experiment showed that: when the current frequency is less than 50 Hz, the current flows mainly through the extra cellular fluid, the extra cellular fluid resistance was measured; but at higher frequencies, such as 200 kHz or more, current can be through the cell membrane. Because of different tissues characteristics and composition of components, meat can show different impedance characteristics corresponding to different quality [1]. Meat impedance characteristics showed that poultry meat quality measurements can be achieved by bioelectrical impedance measurement and analysis.

There are many relevant reports for impedance spectroscopy analysis methods. Both the implementation of automatic sweep signal source and the separation of the real and imaginary parts of the impedance are key technology. Because of changes of the complex impedance of tissue from the body with time, activated signal (frequency range from low to high or from high to low in turn be loaded into the tested target) must be completed in short enough time, which required very short current source frequency switching time. Therefore, it is the first condition to provide a stable frequency drive current to ensure system accuracy and reliability [2].

Design of Sweep Constant Current Source

The Structure of Sweep Constant Current Source

The circuit structure of voltage-controlled current source is shown in Fig.1. signal generator generates a sinusoidal signal of different frequency and voltage amplitude; filter circuit can deal with the signal frequency beyond useful frequency range; the circuit of voltage followed is used to match impedance and enhance the driving capability of the voltage signal; the voltage-current conversion circuit can change the sinusoidal voltage signal into a current signal of the same frequency.

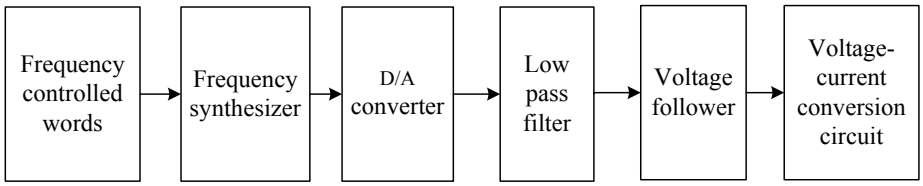


Fig.1 Sweep constant current source circuit block diagram

Voltage Source Signal Generated Circuit Based on DDS Technology

According to the measure system, sweep range is from 0.1 to 250 kHz, impedance values can show the different impedance characteristics of meat tissue from low frequency to high frequency and be able to more fully reflect the impedance characteristics, thereby these factors associated with meat quality. The frequency range of measurement system is 0.1Hz ~ 250 kHz, sweep step is variable, when the frequency is less than 1kHz sweep at the interval 100 Hz, at 1 ~ 10kHz, sweep interval is selected 1kHz, at more than 10 kHz sweep interval is selected 10 kHz. DDS technology is used to build a sine wave signal generator in this system [3], it is shown in Fig 2.

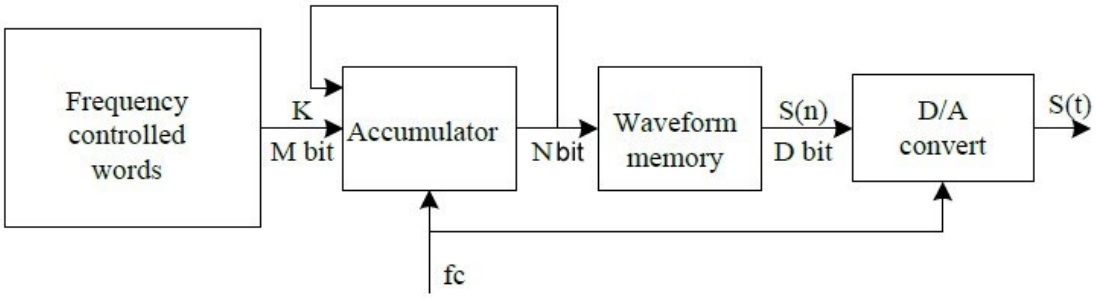


Fig.2 DDS sweep signal source block diagram

Where K is the frequency control word, M, 28 bit, is controlled word length to control the frequency, fC is the system clock frequency, N, 32 bit, is the word length of the phase accumulator, and ROM data bit has the same length with D / A converter word length, both are D. equation (1) is the output signal frequency fout.

$$f_{out} = \frac{K \times f_c}{2^N} \tag{1}$$

According to equation (1), when the reference clock is determined，according to the range of the output frequency, the frequency control word can be obtained:

$$K = \frac{f_{out} \times 2^N}{f_c} \tag{2}$$

Different frequency controlled word K is stored in the look-up table in sequence, the result needed in the look-up table can be obtained by the sweep controller to give the desired signal source frequency. System clock is 16MHz, frequency controlled word length is 28.

In this design, the length of D is 12 bit. the phase accumulator is incremented by step K , the accumulator outputs N-bit binary code in the system clock fC, the length of the data needed is intercepted to quantify ROM address bits as address of the waveform ROM, the output waveform amplitude of ROM code S (n) becomes ladder wave S (t) by the D / A converter, D/A converter adopts TI's high-speed digital to analog converter DAC2904, its switching frequency up to 125MHz, which can guarantee a constant current source for the design phase requirements [4], and then smoothed by the low-pass filter, a synthesis signal waveform can be obtained.

The Low Pass Filter

The design adopted LTC1560-1 of Linear Technology as the low pass filter which used 5th order, continuous-time, low-noise, low-pass elliptic filter. Without connecting external components it can constitute a high-performance LPF, which f_C, its cut-off frequency, is 500 kHz or 1MHz. When connected pin 5 to V+, f_C is 500 kHz. ± 5V power supply for LTC1560-1, and has a power-off mode (controlled by pin 7). The cut-off frequency 500kHz was designed by elliptical low-pass filter circuit in the system. Fig.3 VI is LTC1560-1 input signal that connected to the output of the signal generator, the filtered signal output from 8 feet to output buffer U3. In idle state, FPGA can control SHDN (Pin 7) to shut off power.

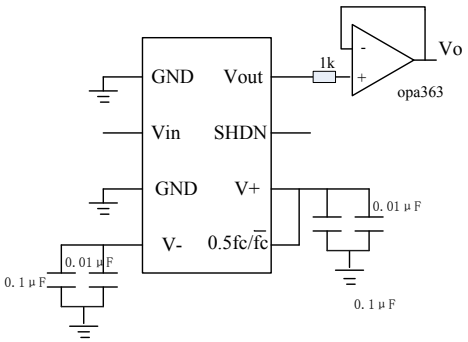


Fig.3 Low-pass filter circuit

The Voltage-Current Conversion Circuit Based on Howland Current Pump

Voltage current conversion circuit is shown in Fig.4.

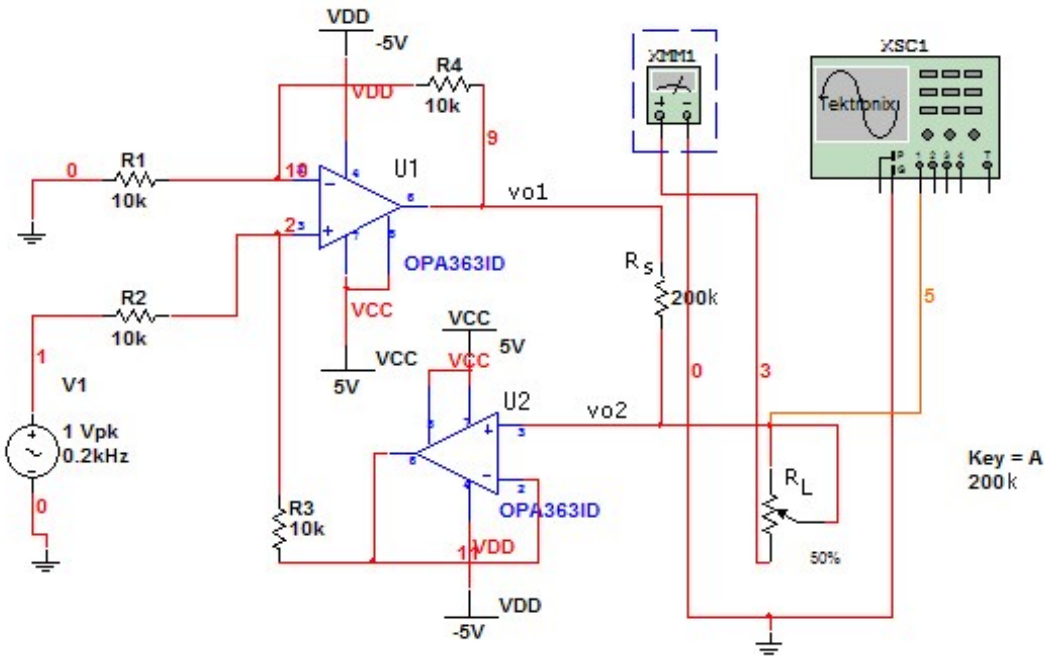


Fig.4 Voltage-current conversion circuit

When the operational amplifier operates in the linear region, the two input terminals of the amplifier is approximately short-circuited, the current through the conversion resistor R_S is equal to the current flowing through the load R_L, the potential of the inverting input terminal V- equals to that of the no-inverting input V+, so the following equations can be gotten[5]:

$$v_+ = \frac{R_4 v_i + R_3 v_{o2}}{R_3 + R_4} = \frac{R_1}{R_1 + R_2} v_{o1} = v_- \tag{3}$$

$$v_{o2} = i_s R_L \tag{4}$$

$$v_{o1} = i_s \left(R_s + R_L \right) \tag{5}$$

It can be obtained from the above equations:

$$i_s = \frac{R_1 R_4 + R_2 R_4}{(R_1 R_3 + R_1 R_4) R_s + \left(R_1 R_4 - R_2 R_3 \right) R_L} v_i \tag{6}$$

Assumed R1R4=R2R3, then equation (6) can be expressed:

$$i_s = \frac{R_1 R_4 + R_2 R_4}{R_1 R_3 + R_1 R_4} \frac{v_i}{R_s} \tag{7}$$

Equation (7) showed that the output current i_s is independent of the load resistance R_L in voltage-current conversion circuit, only which is proportional to the input signal voltage under ideal conditions, R_1~R_4 met the condition of $R_1R_4=R_2R_3$, so the suitable external resistors are the key of the stability and reliability of output current. In practice, Accuracy of resistor value chosen is 0.5% or even 0.1%, in this system, R_1~R_4 consisted of a fixed resistor and resistor trimming resistor in series, which adjusted the trim resistor to ensure resistor value matched. If further assume $R_1=R_2=R_3=R_4$, which the equation (7) can be simplified as:

$$i_s = \frac{v_i}{R_s} \tag{8}$$

As can be seen from the above equation, the output current i_s is completely determined by input voltage signal v_i and resistor Rs.

Simulation of Constant Current Circuit

With Multisim Software simulation, input sinusoidal voltage amplitude is 1 V, under changing the excitation signal (the range of 0.1-250kHz) and different load values, the simulation results are shown in table 1, current value measured is RMS value.

Table 1

I/mA f/kHz / R/Ω	0.1kHz	0.3kHz	0.5kHz	1kHz	10kHz	20kHz	50kHz	100kHz	200kHz	250kHz
R=10Ω	5.096	3.853	3.657	3.567	3.533	3.533	3.538	3.539	3.551	3.550
R=30Ω	4.899	3.825	3.647	3.564	3.532	3.533	3.537	3.543	3.546	3.544
R=50Ω	4.709	3.796	3.636	3.560	3.533	3.533	3.537	3.543	3.545	3.540
R=80Ω	4.436	3.749	3.619	3.555	3.532	3.534	3.537	3.542	3.537	3.531

R=100Ω	4.265	3.716	3.606	3.552	3.532	3.533	3.536	3.542	3.537	3.527
R=120Ω	4.108	3.682	3.593	3.549	3.532	3.534	3.537	3.541	3.532	3.519
R=150Ω	3.874	3.637	3.572	3.545	3.532	3.533	3.537	3.539	3.526	3.506
R=180Ω	3.664	3.572	3.550	3.537	3.533	3.533	3.536	3.538	3.516	3.496
R=200Ω	3.534	3.533	3.533	3.533	3.532	3.534	3.536	3.535	3.510	3.487

From the above table it can be obtained, when the frequency is from 0.3 kHz ~ 1kHz, the range of the impedance value from 100Ω~ 200Ω, the variation range of the output current varies with load is less than 0.11mA. When the frequency is greater than 1kHz, and the range of change of the current with the load change is smaller than 0.04mA, it achieved to the constant current standard.

Conclusions

This design of sine sweep constant current source adopted FPGA chip, it is easy to implement and to set fast frequency value; LTC15602-1 made the amplitude of the sinusoidal signal better stability and spectral purity; Howland current pump made the current source of stable output by voltage controlled; application of low-power chip and power-off mode deduced power consumption of the entire system.

Acknowledge

The design is supported by Development Foundation of Tianjin Agricultural University (Project no. 2011N04).

References

[1] Q.Ding, Z.Y. Wang, L. Huang, et al. Electrical bio-impedance measurement technology and its application in detection of mea t quality, Transducer and Microsystem Technologies, 28(2009) 4-7.

[2] A.S. Ross, G..J.Saulnier, J.C. Newell, et al. Current source design for electrical impedance tomography. Physiological Measurement, 24(2003)509.

[3] J. Kang, H. Wei, C. H. Hong, et al. Design of mixing frequency constant-current source based on direct digital synthesizer. Chinese Journal of Scientific Instrument, 2010, 9(2010)029.

[4] Y.X.Yang, J Wang, F.L. Niu, et al. Design of a sine sweeping current source, Chinese Journal of Scientific Instrument, 27 (2006) 162-164.

[5] H.C. Zhang, Z.S.Teng, H.J. Lin, et al. Design of precision voltage-controlled constant current source with low power dissipation single-supply, Chinese Journal of Scientific Instrument, 29 (2008) 2678 -2682.

CHAPTER 22:

Measurements, Data and Signal Processing, Computational Methods and Algorithms

Advanced Materials Research Vol. 936 (2014) pp 2237-2242
© (2014) Trans Tech Publications, Switzerland
doi:10.4028/www.scientific.net/AMR.936.2237

The Effect of Measurers' View Angle Deviation on Measurement Data

Shao-long JIA, Ya-nan TIAN, Jian-hang JI and Xiao-mei SHANG*

College of Textile and Clothing Engineering, Soochow University, No. 1, Shizi Street, Suzhou City, Jiangsu Province, 215006, China

*Corresponding author's email: shangxiaomei@suda.edu.cn

Keywords: manual anthropometry; view angle deviation; height data; circumference data

Abstract. In the actual work of manual anthropometry, there is a distance between the height of measurers' horizontal sight and the height of the measured body parts, the distance can result in a non-horizontal observation view angle. To explore the phenomenon, this study obtained a lot of manual anthropometric measurement data, on the basis of these data, screened some data influenced by the view angle deviation. Furthermore, using mathematical analysis software, make the data do packet sampling and ANOVA test. After these data analysis, we got the result that the view angle deviation could make influences on those height data and circumference data, but the potential influence degree was different among these data.

Introduction

At present, the forefront of anthropometry has focused on 3D anthropometric technology [2]. This technology has entered the stage of applications, with the purpose to realize the clothing size standardization, but also to promote the development of digital garment customization system [1,3]. However, due to many factors, such as the clothing industry lacking of computer technology application talents, and capital investment, the industry is still widely using manual anthropometric methods [5]. Therefore the content discussed in this paper is still mainly in the service of manual anthropometric. In the actual manual measurement, the measurers touch the body parts directly. According to the manual anthropometric principles and methods, the measurers try their best to control the accuracy of the measurement data, but it still can't avoid data deviation. The factors come from various aspects, but this study mainly focus on the effect of measurers' view angle deviation on the measurement data.

Scientific research proved that if you observe cylinder in a non-horizontal view angle, the data you read will exist deviation [7]. Similarly, looking down or looking up in the measurement process can also appear the same deviation. Therefore, utilizing measurers in different height measuring the same subject to simulate the phenomenon, it converted the view angle deviation to the distance between the height of the measurers' horizontal sight and the height of the measured body parts, so as to facilitating the experiment. Firstly, gained a large number of manual measurement data. Secondly, analyzed experimental data for the reasons of view angle deviation. Thirdly, using mathematical analysis software, make the data obtained do packet sampling and ANOVA test. Finally, analyzed and evaluated the mathematical results. This study can enrich the manual anthropometric experience, enhance the measurement accuracy, and will play a supporting role in improving the three-dimensional anthropometric technology.

Methodology

Previous Work

Selected fifteen measurers with certain measurement level randomly, six men as subjects, aged from 20 to 25 years old, height from 165 cm to 185 cm. Besides, the experimental equipment included Martin-type Authropolometer, tape, triangle, sitting ruler, record boards, etc. During each

experimental process, decorated the same environment, the measurers used the same manual techniques. At the same time, ensured the consistency of the equipment specifications.

Experimental Process

It is necessary to have a correct and objective understanding to the human body. Generally, the measurement data includes two aspects: height data and circumference data. This study selected four kinds of height data and three kinds of circumference data. The measurement methods just as follow.

Height Measurement Methods

Neck base height(lateral) (I): use Martin-type Authropolometer measure the vertical distance between the standing surface and the trapezius landmark on the right side of the neck. Waist height (II): use Martin-type Authropolometer measure the vertical distance between the standing surface and the waist line. Out seam (III): use tape measure the surface distance from waist to ankle. Crotch height (IV): use Martin-type Authropolometer measure the vertical distance between the standing surface and the crotch.

Circumference Measurement Methods

Chest circumference (V): use tape measure the maximum horizontal circumference of chest at the fullest part. Waist circumference (VI) : use tape measure the horizontal circumference of waist at the level of its nature indentation, passing over right and left waist (nature indentation) landmarks. Hip circumference (VII): use tape measure the horizontal circumference of the truck at the level of the maximum protrusion of the right buttock.

Data Collection

Standard Data Collection

Three skilled measurers acquired measurement data from the six subjects. Then the data analysis showed that the data was available. Finally, got the average of the three groups of human body size data as the standard data.

Experimental Data Collection

The fifteen measurers were trained the basic manual measurement technique by the three skilled measurers. After they met the basic technique requirement, then did manual measurement. The measurers in different height were in the same pose when they measured the same body part, so the view height was different, and the view angle was different. Specific view angle deviation phenomenon of measurement as shown in figure 1.

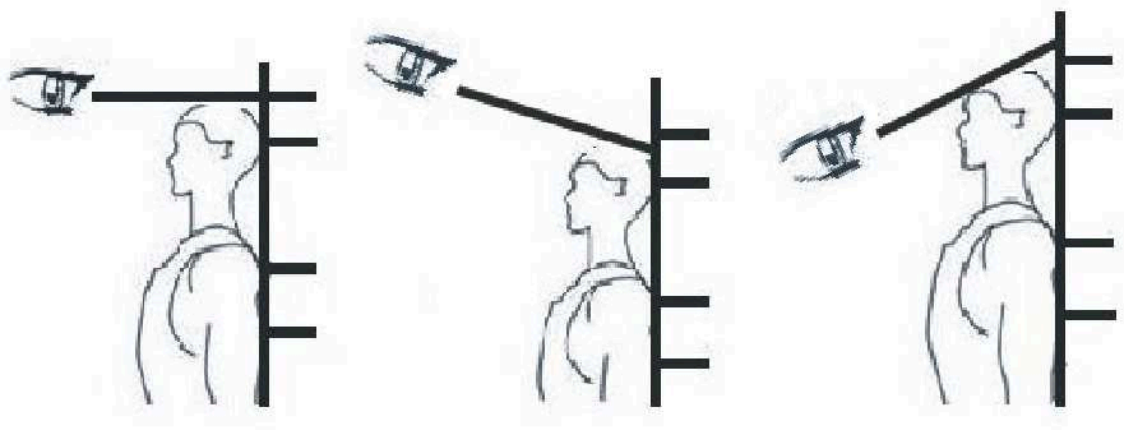


Figure 1 The View Angle Deviation Phenomenon

View Angle Deviation Degree Classification

The classification was based on the distance between the height of the measurers' horizontal sight and the height of the measured body parts. While measures stood vertically, the height of measured body parts was always lower than the height of the measurers' horizontal sight. So the measurers had to stoop or bend down. Therefore, the more higher was the measurer, the more lower would he bend down, then the view angle deviation degree would be greater. In order to make the influences more clearly, the data research chose the sample whose height is 181cm of a male body data, it made a significant height distance. As to the sample data, the view angle deviation degree classification as shown in table1. From the table1, we can see that the degree of the measurer' view angle deviation was in the tendency of uniform narrowed gradually, from A to B, to C, and to D.

TABLE1 THE VIEW ANGLE DEVIATION DEGREE CLASSIFICATION OF THE SAMPLE （WHOSE HEIGHT IS 181CM）

Measurers' height[cm]	View distance as to the sample[cm]	Number of view angle deviation degree classification
170	17	A
165	12	B
160	7	C
155	2	D

Data Analysis

Analysis Process Description

Firstly, compared the experimental data with the standard data, got the arithmetical average deviation, then preliminary analyze the numerical accuracy differences. Secondly, on the base of the preliminary analysis, used the method of mathematical statistics, made the data do packet sampling and ANOVA test. Then tested the numerical discrete significance and grouping with significant.(It indicated that the factor can make influences if any groups, otherwise no effect.) Finally, builded single-factor model to accurately explain the influences that the view angle deviation made on those measurement data. Furthermore, speculated the influences degree according to the numerical laws. The assumption for data samples with F is $H_o: \mu_1 = \mu_2 = \cdots \mu_K$, $H_A: u_i$ not all equal. If the calculated value is larger than $F_{\alpha(df1,df2)}$, then receive the hypothesis H_A, and it indicates that the factor can make significant effects. On the contrary, accept H_0, it illustrates the factor is not significant. At the same time, cooperated with Duncan statistics to compare the influence degree that different factors made on the data .

$$F = MS_t^2 / MS_e^2 \quad (1)$$

$$MS_t = SS_t / df_t \quad (2)$$

$$MS_e = SS_e / df_e \quad (3)$$

$$SS_t = \sum_{i=1}^{k} n_i \left(\overline{x_{i_n}} - \overline{x_{...}}\right)^2 \quad (4)$$

$$SS_e = \sum_{i=1}^{k} \sum_{j=1}^{n_i} \left(x_{ij} - \overline{x_{...}}\right)^2 \quad (5)$$

$$df_t = k - 1 \quad (6)$$

$$df_e = N - k \quad (7)$$

Preliminary Data Analysis

Compared the experimental data differences, preliminary analyzed whether the measurers' view angle deviation can make influences on those height data and circumference data. The changing tendency of the measurement data with different view angle deviation as shown in figure 2.

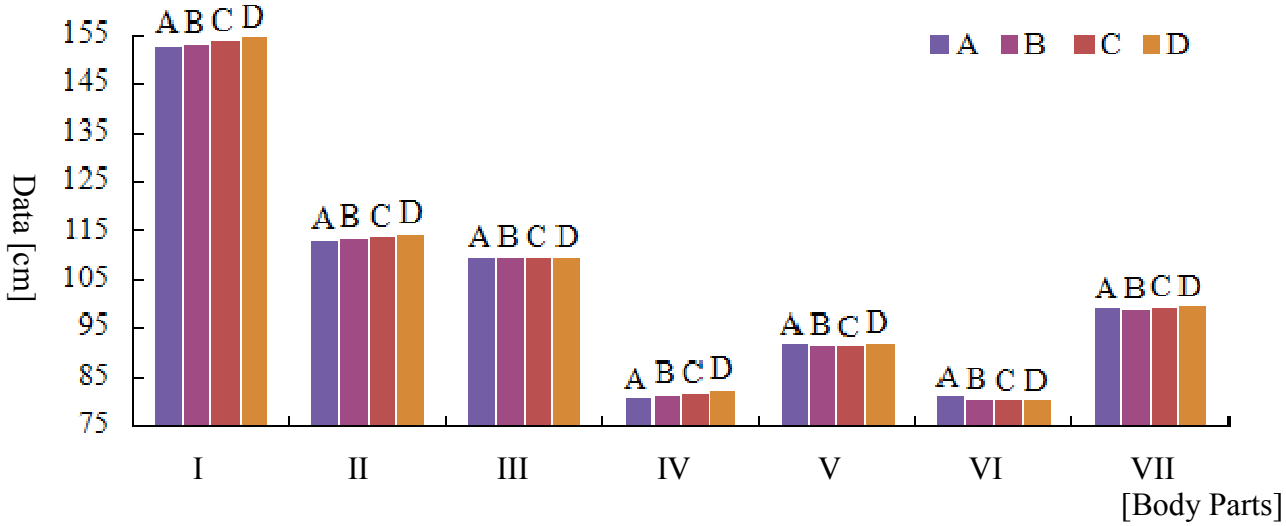


Figure 2 The measurement Data of Different View Angle Deviation

The figure 2 indicated: on the one hand, based on the standard height data, neck base height(lateral), waist height, and crotch height showed obvious changing trend, while out seam did not show any trend of change. The data phenomenon meaned the view angle deviation could make effects on the the three data accuracy, while the data of out seam did not show a significant change. On the other hand, chest circumference, waist circumference, and hip circumference were floating within the corresponding standard data scope, but did not present obviously changing tendency. This data phenomenon showed that the view angle deviation did not make a certain trend on the accuracy of the three circumference data.

Height Data Analysis

Using the mathematical analysis software, made the height data do packet sampling and ANOVA test. We got the result as shown in table2.

TABLE 2 DUNCAN ANALYSIS OF THE HEIGHT DATA(FOR THE SAMPLE 181CM)

The classification number/ Experimental times	The significance grouping of neck base height(lateral)		The significance grouping of waist height		The significance grouping of out seam	The significance grouping of crotch Height	
	1	2	1	2	1	1	2
A/6	148.83		110.67		106.33	78.15	
B/10	149.46		111.60	111.60	107.04	78.43	78.43
C/10	149.32		111.40	111.40	107.05	79.00	79.00
D/8		150.68		112.00	106.96		79.61
Significance	0.27	1.00	0.10	0.28	0.05	0.19	0.07

According to the table2, we found that, among the four height data involved in the analysis, in addition to out seam, all the other three data showed a significant phenomenon of grouping. Therefore, the view angle deviation did affect the accuracy of the three height data.

In addition, we also found the following data feature: First, the degree of the view angle deviation changed with the changing of the distance between the height of the measurers'

horizontal sight and the height of the measured body parts, then the data accuracy changed as well. Second, based on the comparison and analysis, the height data generated significant differences. The sight distance was bigger, the disparity between experimental data and standard data was bigger, the data accuracy was lower. For the out seam, whose data showed no significant differences, its measurement method was using tape measure the surface distance from waist to ankle. The method was different compared with the other three height data, and the view angle was different, as a result, it showed no same data appearance .

Circumference Data Analysis

Using the mathematical analysis software, made the circumference data do packet sampling and ANOVA test. We got the result as shown in table 3.

TABLE 3 DUNCAN ANALYSIS OF THE CIRCUMFERENCE DATA(FOR THE SAMPLE 181CM)

The classification number/ Experimental times	The significance grouping of chest circumference	The significance grouping of waist circumference	The significance grouping of hip circumference
	1	1	1
A/6	91.58	81.02	99.12
B/10	91.30	80.50	98.67
C/10	91.36	80.24	99.36
D/8	91.83	80.45	99.38
Significance	0.07	0.09	0.04

According to the table3, we found that, all the three circumference data showed no significant grouping. Therefore, the view angle deviation of measurers did not affect the accuracy of the three circumference data. The three circumference measurement method was using the tape measure the circle distance, this progress did not make large view angle deviation. Therefore, the related circumference data did not show obvious changing trend and significant grouping phenomenon.

Conclusions and Further Work

Through data collection and analysis got the following conclusions:

On the one hand, while did manual measuring, the view angle deviation of measurers made some influences on the three height data, whose measuring tool was Martin-type Authropolometer. The reason was that, the three height data appeared significant grouping. During the progress of using Martin-type Authropolometer, the height of measurers' horizontal sight and the measured body parts was different, this distance resulted in a non-horizontal observation view angle. Finally, the view angle deviation affected the three height data accuracy.

On the other hand, while did manual anthropometry, the view angle deviation of measurers made no obvious influences on the three circumference data, whose measuring tool was tape. The reason was that, the three circumference data did not appear significant grouping. During the progress of using tape, the height of measurers' horizontal sight and the measured body parts was different, the distance did not result in a significant non-horizontal observation view angle. Finally, the accuracy of the three circumference data appeared higher and more stable.

Due to the limited experimental content and data analysis, it is unable to show that, during the measurement progress of using Martin-type Authropolometer, the view angle deviation will make differences on all actual measurement data. So it is necessary to go deep into measurement study.

Acknowledge

The authors would like to thank all anonymous reviewers for constructive comments. The work described in this paper was partially funded by the Priority Academic Program Development of Jiangsu Higher Education Institutions.

References

[1] XU Jiayan, Young male body size measurement system research based on the classification and the surface morphology, Suzhou, Soochow university, 2009.

[2] KUANG Caiyuan, The digital image of young male body of research based on the non-contact measurement system, Suzhou, Soochow university, 2011.

[3] TAO Tieyuan. The difference analysis for young men in different bodily form feature, Modern silk science & technology, 2010 (3): 24-26.

[4] XIA Pengze, CENG Changsong, JIANG Zhihua, People physical characteristic and its change rule along with the age [J], Journal of textile, 2001 (3): 54-55.

[5] WANG Aihua, Based on the three areas in China clothing MTM research and male adult male body jacket specifications and the establishment of the database, Shanghai, Dong Hua university, 2004.

[6] WANG Qiming, ZHANG Wenbin, Men's size measurement and standard forms of research [J], Journal of DongHua university (natural science edition), 2003 (5): 54-58.

[7] J.E.L.Carter, R.L.Mirwald, B.H.Heath RoII, and D.A. Bailey, Somato types of 7 to 16-Year-Old Boys in Saskatchewan, Canada, American Journal of Human Biology, 1997(9): 257–272.

[8] Marina Alexander, Gina R.Pisut, Evanesce, Investigating women's plus-size body measurements and hip shape variation based on Size USA data, International Journal of Fashion Design, Technology and Education, 2012: 3–12.

[9] Jagir R.K., Wane P.E., Variation in measurements across different brands of same style ladies'pants in Swaziland, International Journal of Fashion Design, Technology, and Education, 2011: 51–57.

[10] Shang Xiaomei, LU Chen, WANG Hui, Human body circumference curve fitting model based on automatic measurement, Journal of Textile Research, 2010(4):128-131.

Advanced Materials Research Vol. 936 (2014) pp 2243-2246
© (2014) Trans Tech Publications, Switzerland
doi:10.4028/www.scientific.net/AMR.936.2243

The engine fault diagnosis based on time domain and frequency domain

Yao Zhuting[a] Pan Hongxia[b]

[1]College of Mechanical and Power Engineering, North University of China, 030051 Taiyuan, China

[a] email:ztyao713@163.com, [b] email: Panhx1015@163.com

Keywords: engine, fault diagnosis, time domain, frequency domain.

Abstract. Engine is as a power machine, the operating status is good or bad, directly affects the working status of equipment. The status monitoring and fault diagnosis is very necessary to ensure that the equipment runs in its best, and improves equipment maintenance quality and efficiency. The engine failure shows the complexity and diversity of the interaction and complex relationship between the various subsystems of the engine, that is the fault of complexity, ambiguity, correlation, relativity and multiple faults coexistence. The available information are much in the engine diagnosis, for example, the vibration signal from bearings, cylinder head or cylinder block surface; oil, cooling water, pressure of intake, exhaust and fuel; temperature signal; noise, speed or oil-sample signals. In this paper, an engine as an example, engine fault diagnosis experimental system is built, the normal state, left one and right six cylinders off the oil, air filter blockage (inlet wood blockage is 30%, the inlet has screen cloth.) in the load of 2565Nm, and the speeds of 1500r/min, 1800r/min, 2200r/min are studied. The experimental results analysis, feature extraction and fault diagnosis are finished based on the time domain and frequency domain.

Introduction

As a typically reciprocating engine power machine, complex structures of the engine determine its failures show the characteristics of complexity and diversity. The impacts of uncertainties, induced by such as operating environment, system noise and sensor accuracy, result in reducing the accuracy of engine fault diagnostic. There are many available diagnostic information in the engine, such as the vibration signal from the bearings, cylinder head or cylinder block surface; oil, cooling water; pressure of intake, exhaust and fuel, temperature signal; noise, speed or oil-sample signals, etc.. Each type signal contains a large amount of information, taking into account the complexity, nonlinearity and uncertainty of engine dynamic behavior, the function and structure, and rely only on a small amount of information or a single information diagnosis is obviously not comprehensive, it is difficult to make an accurate evaluation on the whole engine conditions. In this paper, an engine as an example, engine fault diagnosis experimental system, experimental results analysis, feature extraction and fault diagnosis are finished based on the time domain and frequency domain [1].

Engine Fault Diagnosis Experimental System

The acquisition and analysis of the experimental system based on the vibration signal and TDC signal are shown in Fig.1. Piezoelectric sensors collected vibration signal, TDC sensor samples TDC signal, amplification processing by the multi-charge amplifier, enters the DASP data acquisition system, and achieve the fault diagnosis of the engine by the computer signal analysis system and data analysis processing.

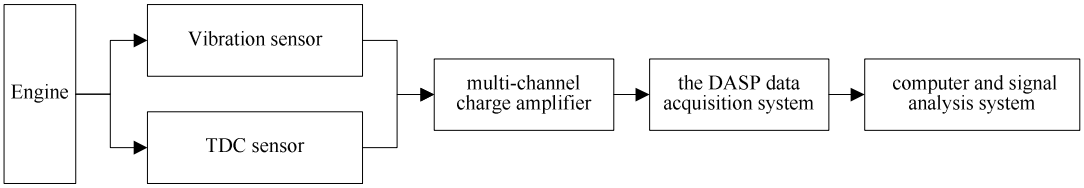


Fig.1 Signal acquisition and analysis works principles of engine system

Sample Types and Experimental Procedures

The vibration signal of the cylinder head, the cylinder block and a TDC signal of V12 cylinder diesel engine in different revolving speeds are collected when the throttle opening is controlled in 100% working conditions. Based on the possibility of failure in the diesel engine actually running process, the vibration signal of the cylinder head and cylinder body of the engine are measured by the signal acquisition system in the normal state, left one and right six cylinders off the oil, air filter blockage (inlet wood blockage is 30%, the inlet has screen cloth.) in the load of 2565Nm, and the speeds of 1500r/min, 1800r/min, 2200r/min.

Experimental Results Analysis and Feature Extraction

When the experimental requirements conditions are met, in order to improve the signal to noise ratio, the measured vibration signals are carried out pre-processing, they include filtering, mean, eliminating the trend, and then the required characteristic parameters of time domain and frequency domain are extracted. The fault-sensitive feature vectors are selected to be able to accurately identify the fault status of engine [2].

Time Domain Feature Extraction of Vibration Signals

Time domain analysis is the process to record the amplitude of measured signal and the law of energy distribution with changing over time, and analyzes the composition and characteristics of signal, and it includes time-domain waveform analysis and the amplitude domain parameter analysis.

The characteristic parameters of amplitude domain include the dimension characteristic parameters and the dimensionless characteristic parameters. Many sensitive failure characteristic parameters of engine are selected, the dimension parameters include RMS, skewness, kurtosis, variance; the dimensionless parameter include margin index, skewness index, kurtosis index, waveform indicators, peak indicators and pulse indicators.

Experiments analysis select three states of engine, they are the normal state F1, left one and right six cylinders off the oil F2, clogged air filter F3 in speed of 1500r/min, the sampling frequency is 40kHz, the vibration signals of three measurement points are dealt with in the different conditions, the original time-domain curves are shown from Fig.2 to Fig.3, the domain characteristic parameters of measuring point 2 in the F1 is shown in Table 1.

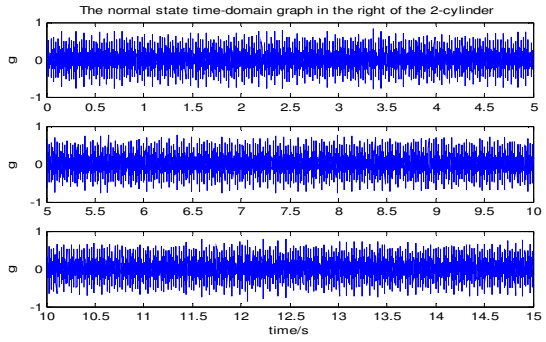


Fig.2 The Normal State

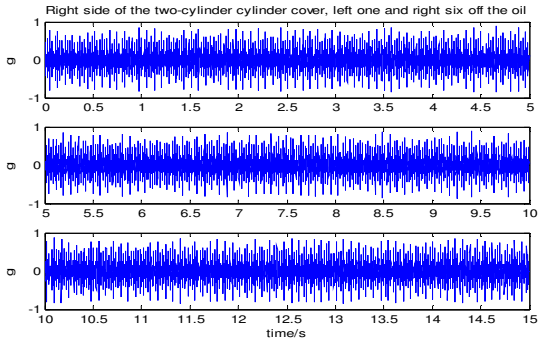


Fig.3 Left One And Right Six Off The Oil

Table 1 Time Domain Indexes In Test 2

Measured	RMS	Skewness	kurtosis	variance	margin index	skewness indicator	kurtosis indicators	waveform indicators	peak indicators	pulse indicators
Normal state	5.1647	2.1973	2143.2	26.686	5.4238	0.4225	3.0073	1.2582	3.6259	4.5744
Left 1, right 6 cylinder off oil	6.6330	-15.531	5386.9	44.046	5.2738	-2.3708	2.7834	1.2263	3.6977	4.5357
Filter clogging	4.9528	-0.2445	1886.8	24.551	5.4001	-0.0262	3.1245	1.2640	3.6031	4.5538

The contrast from Fig.2 and Fig.3 can be seen that peak and RMS of the normal state and fault condition are not same.

By contrasting the characteristic parameters of Table 1 in the normal state and fault conditions can be seen that RMS changes in the event of failure are not large; Skewness and skewness index decrease significantly, they indicate that the probability density curve gravity center of failure signal is very asymmetry; Kurtosis changes evidence, kurtosis indicators correspondingly increase or decrease, it indicates that the convex of the probability density curve peak has changed, and the occurrence of local or overall defects; variance significantly increase or decrease descript the fluctuation is relatively large of the signal vibration amplitude; margin index decreases when the left 1 and right 6 cylinders off the oil, it indicates the signal impacts weakened; waveform index changes a little, it indicates its stability is good[3].

The Characteristic Parameter Extraction of the Vibration Signal in the Frequency Domain

Time-domain analysis is generally used only for simple diagnosis, and frequency domain analysis can determine the failure position. It can reflect the change in signal frequency-domain characteristics by changing gravity center location and the dispersion degree of spectral energy distribution in the power spectral. The following frequency domain characteristic parameters reflect the power spectrum changes are selected, and they are power spectral gravity center indicator, mean square spectral variance, related factor, harmonic factor and spectral origin moment [4].

The spectrum of each measuring point in three states are shown from Fig.4 to Fig.7, the frequency-domain characteristic parameters are shown in Table 2.

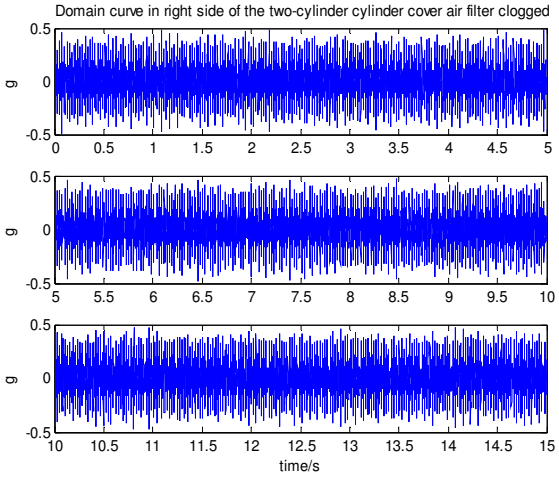


Fig.4 Cylinder Cover Air Filter Clogged

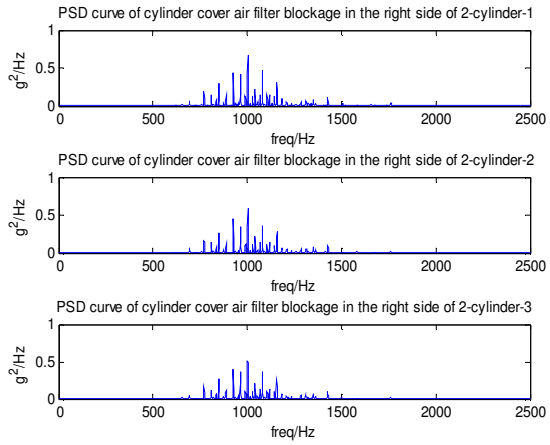


Fig.5 Psd Curve Of Cylinder Cover Air Filter Blockage

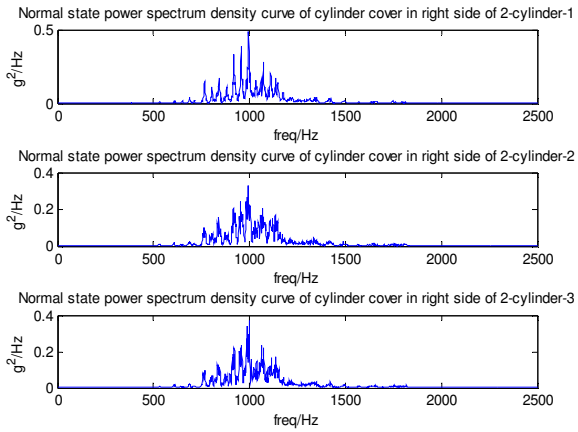


Fig.6 Psd Curve Of Normal State

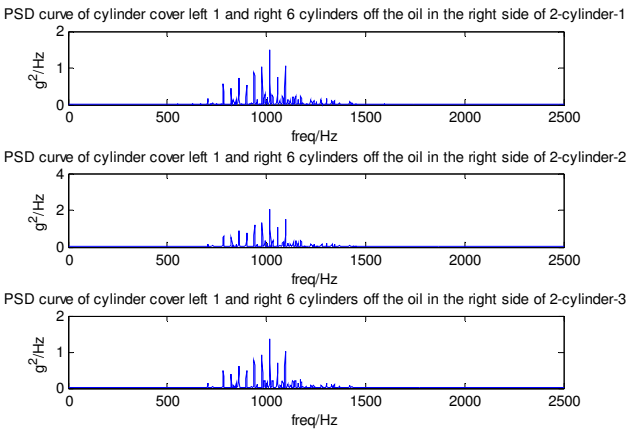


Fig.7 Psd Curve Of Left 1 And Right 6 Cylinders Off The Oil

TABLE 2 THE FREQUENCY DOMAIN CHARACTERISTIC PARAMETERS IN RIGHT SIDE OF 2-CYLINDER

Measuring point 2	power spectral center of gravity indicator	mean square spectral variance	related factor	harmonic factor	spectrum origin moment
Normal state	961.2321	739905	-0.0930	3.2701	9246098
Left 1 and right 6 cylinders off oil	1017.1340	314480	0.1420	2.0271	7858194
Air filter clogging	994.1660	665406	-0.0360	3.0281	8048218

Frequency domain characteristic parameters can be seen by contrasting the normal state and fault state in Table 2, the power spectral gravity center indicator increases in the left 1 and right 6 cylinders off the oil, the mean square spectral variance and spectral origin moment are significantly reduced. Because of reducing the amplitude of the vibration signal at this time, the position of power spectrum gravity center shifted to the right, while the related factor increases, it shows its energy is more dispersed, the harmonic factor decreased shows that the spectral width decreases [5].

Comparison Fig.5 and Fig.7 can be seen, the measured cylinder cover power spectrum gravity center of index increases in the right side two-cylinder when air filter is clogged, the rest of characteristic parameters change just opposite with the left 1 and right 6 cylinders off oil. By contrasting Fig.5 and Fig.7 can be seen, the frequency spectrum in different conditions and different measurement points are not the same, frequency-domain characteristic parameters will change.

Conclusions

It can be seen by analyzing the vibration signal of engine status and fault status, the extracted characteristic parameters of time domain and frequency domain can reflect the changes of the engine status. The vibration signal of the four points are collected in three conditions, and characteristic parameters of time domain and frequency domain are extracted, and the signs of engine failure are acquired, and fault diagnosis of diesel engines are finished.

Acknowledgements

This work was financially supported by Natural Science foundation of Shanxi, project No. 2010011031-1. The authors would like to thank all members of the research team.

References

[1] Jian-Da Wu, Chao-Qin Chuang, Fault diagnosis of internal combustion engines using visual dot patterns of acoustic and vibration signals, NDT & E International, Volume 38, (2005), p605–614

[2] Shiyuan Liu, Fengshou Gu, A Ball, Detection of engine valve faults by vibration signals measured on the cylinder head, Journal of Automobile Engineering, 2006 vol. 220, no. 3, p379-386

[3] Xu Dong Shi, Zhen Zhen Zhang, Xiao Lin Liu, Design and Realization of Aircraft Engine Wire Fault Detection Database, Advanced Materials Research, Vol.159, 2011, p274-278

[4] Peng Hengyi, Research on Fault Diagnosis of Internal Combustion Engine Based on Vibration Analysis [D], Huazhong University of Science and Technology, 2004

[5] Yan Li, Study on Engine Fault Diagnosis Based on Multi-Information Fusion [D], North University of China, 2010

Advanced Materials Research Vol. 936 (2014) pp 2247-2253
© (2014) Trans Tech Publications, Switzerland
doi:10.4028/www.scientific.net/AMR.936.2247

The Application Of Improved Dynamic Decision Tree Based On Particle Swarm Optimization During Transportation Process

LI Xin-hai [1, a *], LI Li [2,b] and FU Xing [3,c]

[1] Shijiazhuang University,Shijiazhuang, China

[2] Shijiazhuang University,Shijiazhuang, China

[3]Agricultural University of Hebei, Baoding,China

[a]1138908823@qq.com, [b]4256938@qq.com, [c]18032812689@126.com

Keywords: Data mining , Particle Swarm Optimization Algorithm , Decision tree, Transportation，ID3

Abstract： For the relationship of environmental parameters and variables in the each transport process, by using data mining, the system gets the corresponding decision tree. In a certain environment parameters conditions, the occurrence of the event is determined by the decision tree. Through the No Free Lunch Theorem (NFL) revelation, the original PSO algorithm is improved to enhance the validity of the original decision tree. To the final experiments results, once again demonstrate the improved algorithm is efficient.

Introduction

As we all know, incidents such as collision, falling during transportation will cause huge economic losses, therefore how to effectively control the occurrence of the incident has become a pressing issue. We found that the emergency is to some extent associated with the environmental parameters, through the measurement of the related hardware. If we can seize the potential relationship between the two, we will be able to effectively control the occurrence of unexpected events. We separate part of the data derived from the measured data to data mining .Successively, data cleaning, data integration, data loading change, data mining, pattern evaluation, knowledge representation, We can get the knowledge ,that transportation process parameter changing cause events. Analyse the present conditions through the knowledge, to make effective prevention and timely treatment to reduce the financial losses, which can be called as the Miracle Fighters of the new era.

ID3 Algorithm

Let S is a set containing s data samples, the set category attribute takes m different values, corresponding to m different categories C_i, $i \in \{1,2,3,\ldots,m\}$. S_i is assumed to be the number of the samples in the class C_i, then the amount of information needed to classify the given data set can be computed as Eq. 1,P_i is the probability that any data object belongs to the category C_i. Use S_i/S to calculate.Set an attribute A take v different values $\{a_1, a_2,\ldots,a_v\}$, the collection S is divided as attribute A

$$I(s_1, s_2, \ldots, s_m) = -\sum_{i=1}^{m} p_i \log(p_i) \tag{1}$$

The subsets $\{S_1, S_2, \ldots, S_v\}$, in which S_j contains the data samples with the attribute A getting the value of a_j, adenoted s_{ij} for the number of samples which the subset S_j belong to attribute C_i, then the information entropy required to classify the collection T in accordance with attribute A: Eq. 2

$$E(A) = \sum_{j=1}^{v} \frac{s_{1j} + s_{2j} + \ldots + s_{mj}}{s} I(s_{1j}, s_{2j}, \ldots, s_{mj}) \tag{2}$$

the smaller E (A) is, the more successful the set is divided, in which $I(s_{1j}, s_{2j}, \ldots s_{mj})$ represent the information entropy to divide the subset S_j,: Eq. 3

$$I(s_{1j}, s_{2j}, \ldots, s_{mj}) = -\sum_{i=1}^{m} p_{ij} \log(p_{ij}) \tag{3}$$

Wherein $P_{ij} = s_{ij}/S_j$,is the probability that any data sample of subset S_j, belongs to the class C_i, then the information gain dividing the current node as attribute A can be calculate as follows: Eq. 4

$$Gain(A) = I(s_1, s_2, \ldots, s_m) - E(A) \tag{4}$$

According to the ID3, we can easily achieve the corresponding decision tree based on the data of the transport process , code the VC++ program. The validity of the resulting decision tree is 0.682243. Classify and organize the same branch of the decision tree in Fig. 1, the original decision tree.

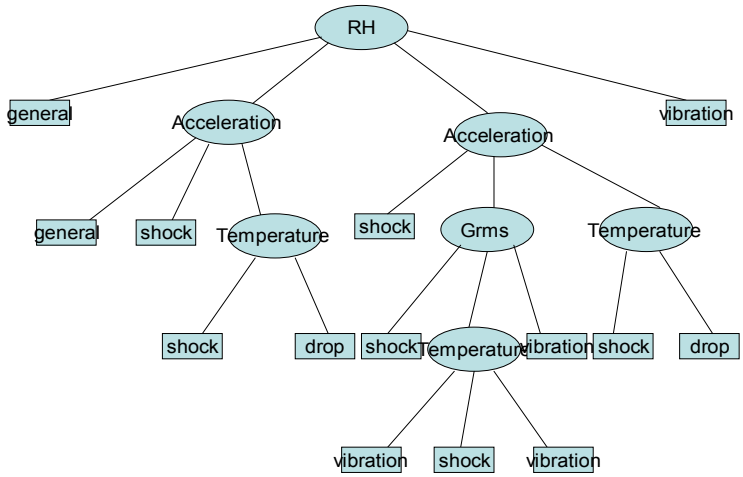


Fig. 1: The original decision tree

Lack of ID3 Algorithm

ID3 algorithm uses non-backtracking top-down strategy to search all of the attribute space. The algorithm establishing the decision tree with a fast classifying speed and a small depth, is simple to achieve. Traditional 1D3 algorithm select an attribute A as the classifying attribute, for it makes information gain Gain (A) maximum. Studies have shown that this approach has disadvantages: the algorithm often are in favor of the attributes with more values, because the weighted sum method makes the classification of instances tend to abandon data tuple with a small amount of data, however the attribute with more values may not be the optimal one, that means firstly selected attribute with the largest information gain according to ID3 algorithm is not so important in reality.

Dynamic Decision Tree

In view of the inadequacies of ID3 algorithm (the method introducing information gain tend to choose the attribute with more values), we adopt “actual information gain” , instead of the information gain. "Actual information gain" methods is to compute a intrinsic information value (Sinfo) to split the original set, considering the scale and quantity of the subset. we can get the "Actual information gain" through Eq. 5:

$$actualGain(A) = [I(s_1, s_2, ..., s_m) - E(A)] / S\inf o \tag{5}$$

Usual Sinfo is just the the number of the subsets, after dividing the original set. Although ,this kind of decision tree will to some extent reduce those situations where we choose the attribute as the splitting attribute just because it will produce more subsets , but this kind of solving methods will inevitably lower the information gain of this attribute. So a technique to balance this dilemma is to introduce a “related Factor” to multiple the number of the subsets ,as Eq.6 and we need Particle Swarm Optimization to get the “related Factor”.

$$S\inf o = v * r\text{elatedF}actor \tag{6}$$

A paper, “No free lunch therems for optimization” , makes a rigorous demonstration of the NFL theory. The theorem points out that, for any questions, any two given algorithms A, B, A, B share the same performance on the average of all problems. However, the main value of NFL theorems lies in its inspiration of research and application the optimization algorithms, it largely reflects the nature of the optimization algorithm. There is no universal algorithm that all the problems can be solved with the best efficiency. The NFL theorem argues that there is a good algorithm in this collection. So,we are able to find a better algorithm in a special field such as the data mining of unknown events during transportation process . Through Particle Swarm Optimization , get a set of related factor optimizing the decision tree at utmost ,and form a most suitable decision tree for this field.

Particle Swarm Optimization

Particle swarm optimization(PSO),a typical swarm intelligence algorithm, was proposed by James Kennedy and Russell Eberhart in 1995. PSO ,similar with genetic algorithm ,is a kind of optimization based on iteration. What is different from GA is PSO does not have crossover and mutation, it achieves one-way flow of information , by following its optimal particle ,thus having a faster convergence rate .

At first generate the initial population, that is produce a set of particle in the feasible solution space, and each particle represents a feasible solution of optimization problem, get a fitness value for each particle according to the corresponding objective function. Each particle motions in the solution space by a speed determining its direction and distance. Typically the particles will follow the current best one, and get the final optimal solution by the iterative search. In each generation, the particle will change following the two extremum, one is the optimal solution of the particle itself so far(pBest), the other the entire population(gBest). Suppose a n-dimensional space is made up of m particles. $X=\{x_1,\ldots,x_i,\ldots,x_m\}^T$, the i-th particle position $x_i=\{x_{i1},x_{i2},\ldots,x_{in}\}^T$, its speed $v_i=\{v_{i1},v_{i2},\ldots,v_{in}\}^T$, the individual extremum $p_{id}=\{p_{i1},p_{i2},\ldots,p_{in}\}^T$ the population extremum $p_{gd}=\{p_{g1},p_{g2},\ldots,p_{gn}\}^T$, in accordance with the principle of following the current optimum particles, the particle x_i will change its speed and position as the following Eq. 7 and Eq. 8.

$$v_{id}^{(t+1)} = v_{id}^{(t)} + c_1 r_1 (p_{id}^{(t)} - x_{id}^{(t)}) + c_2 r_2 (p_{gd}^{(t)} - x_{id}^{(t)}) \tag{7}$$

$$x_{id}^{(t+1)} = x_{id}^{(t)} + v_{id}^{(t+1)} \tag{8}$$

Where d=1，2,…,n，i=1,2,…,m，m is the population size, t is the current evolutionary generation, r1 and r2 are random numbers between 0 and 1, c1 and c2 are Learning Factor or Acceleration Constant. In addition, set V_{max} as speed upper limit to avoid the speed is too big, that is when $V_{id} > V_{max}$,set $V_{id} = V_{max}$, when $V_{id} < -V_{max}$, set $V_{id} = -V_{max}$,. In formula (7) , $v_{id}^{(t)}$is particle velocity previously, $c_1r_1(p_{id}^{(t)} - x_{id}^{(t)})$ is the cognitive section , $c_2r_2(p_{gd}^{(t)} - x_{id}^{(t)})$ is the social section ,representing information sharing and mutual cooperation between the particles.

Algorithm is mainly calculated as follows:

A. initialization , set the learning factor c_1,c_2, the maximum evolution generation T_{max}, the current evolution algebra t = l; generate m particle $x_1,x_2,\ldots,x_m$ randomly in definition space to get population matrix X(t), generate the displacement of each particle randomly $v_1,v_2,\ldots,v_m$ and get the displacement changing matrix V(t).

B. Evaluate the population and calculate the Fitness Value $F(x_i)$ of each particle.

C. Compare the current fitness value $F(x_i)$ of the particle and its history optimal value (pBest) , if $F(x_i)$ is better than pBest, set $F(x_i)$ as pBest , and the current position of the particle as the position pbestX in the space.

D. Compare the current fitness value $F(x_i)$ of the particle and the population optimal value (gBest) , if $F(x_i)$ is better than gBest, set $F(x_i)$ as gBest , and the current position of the particle as the position gbestX .

E. Update the velocity of the particle according to Eq. 8and Eq. 9 ,and generate a new population X(t+1).

F. Check up whether the fitness value has reached a given accuracy or not, If achieved or the number of evolution has reached T_{max} , then end the loop, otherwise t = t +1 , turn B.

What should be mentioned is that it can be classified as local model and global model according to search range of the population . global model means it need to traverse the entire population to get the gBest , otherwise, the local model search the surrounding particle . obviously the global model provide a faster rate of convergence as a sacrifice of robustness. As the local model,the formula changed as Eq. 9:

$$v_{id}^{(t+1)} = v_{id}^{(t)} + c_1r_1(p_{id}^{(t)} - x_{id}^{(t)}) + c_2r_2(p_{id}^{(t)} - x_{id}^{(t)}) \tag{9}$$

Shi et al introduced the inertia weight w into formula(7), then the formula becomes: Eq. 10

$$v_{id}^{(t+1)} = w^t v_{id}^{(t)} + c_1r_1(p_{id}^{(t)} - x_{id}^{(t)}) + c_2r_2(p_{gd}^{(t)} - x_{id}^{(t)}) \tag{10}$$

Obviously, inertia weight w describes the influence of last generation particle on the current. The bigger w is , the stronger the global optimization capability is ,the feebler the local optimization capability is . At the beginning , Shi et al set inertia weight as constant , but through later experiments , they found the dynamic inertia weight leads to better optimization results. At present , a widely used method is 1inearly decreasing weight(LDW) proposed by Shiet al. Eq. 11

$$w^{(t)} = (w_{ini} - w_{fin})(T_{max} - t) / T_{max} + w_{fin} \tag{11}$$

T_{max} represents the maximum number of evolution generation , w_{ini} is the initial inertia weight , w_{fin} inertia weight of maximum evolution generation.

Improved ID3 algorithm based on Particle Swarm Optimization

Get a set of random number within a certain range as the "related factor" ,calculate the "Actual information gain" of each attribute when creating a decision tree with the "related factor" , in the same way ,get n bunches of "related factor", and get n trees , which is used as n particles and the initial population , compute the validity of each decision tree ,which is used as the fitness value of the particle . Reproduce the population according to the fitness value and the Particle Swarm Optimization until the fitness value has reached a given accuracy, or the number of evolution has reached T_{max}.

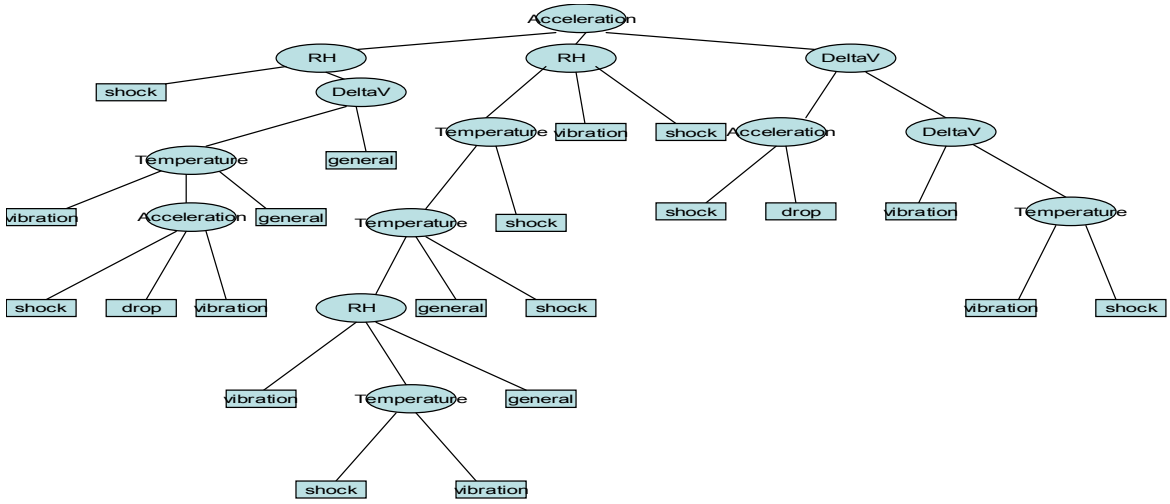


Fig. 3:Improved decision tree

Corresponding algorithm is described as follows:

Improved ID3 algorithm based on the Particle Swarm Optimization:

A . pretreat the original data set S as the root node S.

B. get a set of related factor relatedFactor[n][m] randomly as the n particles, $x_1,x_2,\ldots,x_n$ to generate the population matrix X(t), get a set of displacement randomly $v_1,v_2,\ldots,v_n$ to generate the displacement matrix V(t), set $c_1 = c_2 = 2$ and the current generation t=1 .

C. Calculate the information gain of the attribute C_i, i ∈ {1,2,3,…,m}Eq. 12

$$Gain(C_i) = [I(s_1, s_2, ..., s_m) - E(C_i)] / v * r\text{elatedF}actor \tag{12}$$

D. Repeat C operation, calculate the information gain of the m attributes Gain(C_1), Gain(C_2),…, Gain(C_m), divide the father node into several child nodes according to the attribute with the largest information.

E. duplicate B, C, D operation until all the nodes can not be subdivided so far to get the decision tree T.

F. duplicate, B, C, D, E operation to form N decision trees T_j, (j = 1,2, ..., N) , corresponding to n bunches of related factor relatedFactor[n][m].

G. test the validity (test data set is the same) of T_j decision trees with specified test data and get its validity V_j.

H. repeat B, C, D, F, G operation to obtain the validity of N decision trees, V_1 ,V_2 ,…,V_N,and set pBest[i]= V_i.

I. compare the value V_1 ,V_2 ,…,V_N, and select the maximum value V_m as the gBest.

J. Update the related factor according to equation (10) equation (8) ,and generate the second bunch of decision tree with it . For each tree (i) ,if V_i >pBest[i] , pBest[i]= V_i; select the maximum of the bunch (V_m), if V_m >gBest, gBest= V_m. Set w_{ini}=0.9, w_{fin}=0.4.
K. Repeat J operation until it is reached T_{max},and get the decision tree with gBest as final result.

The improved sample

Mend the formula in the above sample , revise the source code ,and get the following running result. Suppose the number of the particle is 20, that is there are 20 decision trees, and the size of loop is 20 ,so the validity of each decision tree in 20 loops are showed in the Table 1,and the related factor of the last loop are listed in the Fig. 2. Classify and organize the same branch of the decision tree in Fig. 3: improved decision tree

TABLE 1: THE VALIDITY OF EACH DECISION TREE IN 20 LOOPS

generation	pBest	gBest	20 fitness value(validity of the 20 decision tree)										20 fitness value(validity of the 20 decision tree)									
1	0.618979	0.618979	0.560748	0.584112	0.579439	0.577103	0.581308	0.579439	0.578104	0.577103	0.576324	0.604673	0.601529	0.612928	0.618979	0.615487	0.612461	0.609813	0.612974	0.610592	0.614855	0.612617
2	0.644237	0.644237	0.570093	0.585421	0.563863	0.563084	0.562617	0.582555	0.619493	0.612150	0.636552	0.628972	0.622770	0.617601	0.614666	0.628838	0.644237	0.641355	0.636614	0.632399	0.628628	0.625234
3	0.691589	0.691589	0.691589	0.630841	0.607477	0.600467	0.646729	0.649533	0.655541	0.644860	0.636552	0.641121	0.633815	0.636293	0.639827	0.634846	0.638629	0.634346	0.630566	0.627726	0.631087	0.641589
4	0.676012	0.691589	0.680143	0.570093	0.676012	0.647196	0.629907	0.619938	0.628838	0.633178	0.651090	0.642991	0.662702	0.660436	0.656362	0.650200	0.647352	0.649533	0.651457	0.663032	0.674865	0.675234
5	0.705607	0.705607	0.661323	0.705607	0.657321	0.633178	0.620561	0.612150	0.606142	0.615654	0.610592	0.609346	0.634664	0.653427	0.646298	0.644860	0.659190	0.653037	0.648158	0.643821	0.639941	0.650935
6	0.684112	0.705607	0.682243	0.690187	0.686822	0.665140	0.648131	0.613707	0.623498	0.648364	0.643821	0.653271	0.672048	0.671340	0.665708	0.658879	0.652960	0.667056	0.671248	0.680166	0.674865	0.684112
7	0.699065	0.705607	0.682243	0.696262	0.657321	0.663925	0.699065	0.696262	0.678238	0.665888	0.655244	0.656075	0.656754	0.657321	0.650611	0.644860	0.659190	0.661215	0.661352	0.670820	0.671913	0.668692
8	0.713915	0.713915	0.682243	0.696262	0.654206	0.661215	0.665421	0.649533	0.638184	0.669393	0.671859	0.693458	0.706032	0.702492	0.703810	0.702270	0.703427	0.695093	0.706432	0.713915	0.706345	0.707944
9	0.709112	0.713915	0.682243	0.640187	0.676012	0.647196	0.659813	0.688474	0.687583	0.709112	0.693666	0.698131	0.689040	0.703271	0.693027	0.688248	0.678505	0.691589	0.685542	0.679128	0.688637	0.682710
10	0.736449	0.736449	0.706275	0.696262	0.654206	0.705607	0.736449	0.724299	0.700935	0.685748	0.686397	0.674766	0.686491	0.700935	0.693027	0.684246	0.677259	0.677570	0.676745	0.685358	0.679292	0.673832
11	0.725857	0.736449	0.721581	0.672897	0.725857	0.686916	0.665421	0.647975	0.640854	0.647196	0.640706	0.642991	0.657604	0.650312	0.647017	0.652203	0.646106	0.640771	0.650907	0.652648	0.665027	0.675234
12	0.740187	0.740187	0.712992	0.696262	0.697321	0.710280	0.740187	0.714953	0.696929	0.696262	0.694704	0.682243	0.671198	0.668224	0.680805	0.672897	0.687227	0.691005	0.683892	0.693666	0.693556	0.695794
13	0.750779	0.750779	0.740924	0.696262	0.750779	0.747664	0.712150	0.736760	0.726302	0.742991	0.723780	0.708411	0.723025	0.710280	0.700216	0.698932	0.690343	0.682827	0.676745	0.676012	0.684211	0.684579
14	0.785047	0.785047	0.752147	0.785047	0.772586	0.721963	0.749533	0.719626	0.698264	0.697430	0.701973	0.688785	0.677995	0.676791	0.677211	0.672230	0.671651	0.672313	0.675096	0.686916	0.679784	0.676168
15	0.750779	0.785047	0.743752	0.696262	0.750779	0.747664	0.712150	0.704050	0.684913	0.704439	0.689512	0.680374	0.670348	0.683801	0.675054	0.667557	0.662305	0.664136	0.665750	0.674974	0.675357	0.670093
16	0.734579	0.785047	0.772507	0.696262	0.727321	0.710280	0.734579	0.711838	0.704940	0.688084	0.674974	0.673832	0.685641	0.678349	0.677211	0.677570	0.670405	0.671145	0.664651	0.659398	0.661092	0.656542
17	0.761682	0.785047	0.763271	0.761682	0.747819	0.692897	0.715888	0.731589	0.716903	0.675234	0.663551	0.666355	0.678845	0.672118	0.672897	0.686248	0.680374	0.681075	0.681693	0.676532	0.677324	0.677570
18	0.819315	0.819315	0.790832	0.785047	0.819315	0.757009	0.771963	0.757009	0.746328	0.724299	0.726895	0.734579	0.733220	0.728972	0.728972	0.726302	0.718380	0.714953	0.706982	0.713915	0.706345	0.711682
19	0.831776	0.831776	0.831776	0.700935	0.760436	0.737850	0.792336	0.768629	0.738838	0.773178	0.722513	0.714486	0.737145	0.714704	0.705119	0.694259	0.745981	0.718738	0.731039	0.785358	0.720767	0.793178
20	0.82243	0.831776	0.763687	0.785047	0.822430	0.757009	0.787664	0.761682	0.750334	0.764019	0.742471	0.742056	0.728972	0.715732	0.704529	0.694927	0.694704	0.702103	0.695437	0.726781	0.690113	0.700000

Summary

Through the experimental data, it is verified that the introduction of the dynamic decision tree based on Particle Swarm Optimization for the improvement of the validity of traditional ID3 decision tree algorithm is achieved .The validity of the new decision tree is 0.831776 ,which is improved by 21.918% than the old one created by the traditional ID3 algorithm , and we can get a better tree than before .We are able to control the environmental parameters during transportation using of the improved decision tree, in order to achieve the effect of controlling emergencies, prevention, and pretreatment. The only pity is that the robustness need to be enhanced, especially when some parameters was not that suitable, the validity of the decision tree would be badly influenced , and we expect it to be mended as soon as possible .

```
2.030891 0.779298 3.544115 1.247444 3.540757 2.762535 2.357402 2.599719 4.867092 1.354564
2.704855 1.671957 1.846980 4.201483 3.673513 2.631916 0.193182 2.018647 2.053743 0.793329
4.405499 2.482223 3.795740 3.875240 2.120884 2.798700 4.419996 1.393017 4.062319 0.490738
4.788659 2.968993 2.235786 4.425184 1.146428 3.836482 1.538438 0.616169 0.833460 3.325755
2.429579 4.836573 2.578661 4.607532 4.823298 1.565752 2.780084 1.478622 0.856655 1.307566
1.676992 0.469222 1.694082 0.807825 0.821711 4.054231 1.016572 3.203833 0.755486 3.248543
0.361492 2.637104 0.296640 0.369732 3.960540 0.359661 1.345561 0.246742 3.238014 1.866512
0.613575 0.657064 3.623310 2.083346 2.183142 0.274514 3.832972 3.143864 2.302316 4.908444
1.644642 0.963775 3.553270 1.592914 0.203406 3.222297 3.998840 0.517441
```

Fig. 2

Acknowledgment

This paper is sponsored by the Hebei Provincial Natural Science Foundation of China, Higher School Scientific Research Project of Hebei Province, Hebei Educational Programs, under the Grants No. 12210318, No. QN20132023 and No. 13041904.

References

[1] DUAN Rujiao, ZHAO Wei, HUANG Songling, CHEN Jianye, Method for high-speed corner detection based on the fuzzy ID3 decision tree, J Tsinghua Univ(Sei&Tech), 1000-0054(2011)12-1787-05.

[2] XUE Feng, WANG Ci-guang, MU Feng, Genetic and ant colony collaborative optimization algorithm based on information entropy and chaos theory, Control and Decision, 1001-0920(2011)01-0044-05.

[3] PEI Shengyu, ZHOU Yongquan, LUO Qifang, Co-evolutionary particle swarm algorithm based on information entropy, Computer Engineering and Applications, 2011,47(3):225-228.

[4] Zhu Haodong, Zhong Yong, Optimization of ID3 algorithm, J.Huazhong Univ.of Sci.& Tech.(Natural Science Edition), 1671-4512(2010)05-0009-04.

[5] ZHU Hao-dong, Research on Improvement and Simplification of ID3 Algorithm, JOURNAL OF SHANGHAI JlAOTONG UNIVERSITY, 1006-2467(2010)07-0883-04.

[6] HUANG Xin-jian, NIU Qian, Improved fuzzy clustering method based on swarm optimization algorithm, COMPUTER ENGINEERING AND DESIGN, 1000-7024(2012)03-1132-04.

[7] YANG Zhe, LI Ling-zhi, JI Qi-jin, ZHU Yan-qin,Network trafic classification using decision

[8] Tree based on minimum partition distance,Journal on Communications, 1000-436X(2012) 03-0090-13.

[9] HUANG Ying-jie, YAO Xi-fan, GU Yao-da, Hybrid Particle Swarm Optimization Based on Entropy for Flexible Job Shop Scheduling Problems, Journal of Hunan University(Natural Sciences), 1674-2974(2012)03-0048-05.

[10] QIAN Wang-wei, Research on ID3 Decision Tree Classification Algorithm Based on M apReduce, JISUANJI YU XIANDAIHUA, 1006-2475(2012)02-0026-05.

[11] WANG Cheng-chang, CHEN Hong-zhong, FANG Yu, DENG Rong, Task Scheduling in Grid Environment Based on Hybrid PSO Algorithm,Computer Science, (2012)Vol.39,No.2.

[12] GAO Hao-jiang, ZHANG Yi-sheng, XIAO Tian-yuan, Optimization 0f Stacking Method Based 0n Cluster Analysis and Decision Tree, Computer Engineering, l000-3428(20l1)12-0221-03.

[13] WANG Xiao-wei, JIANG Yu-ming, Analysis and improvement of lD3 decision tree algorithm, Computer Engineering and Design, 1000-7024(2011)09-3069-04.

[14] XIAO Di, GE Qi-cheng, LIN Jin-guo, CHENG Ming, Double Populations Genetic and Particle Swarm Algorithm and Its Application in SMB Optimization, 1005-9830(2012)0l-0031-06.

[15] ZHU Xiao-jian,SHEN Jun, Minimum energy consumption mulicast routing in ad hoc networks based 0n particle swarm optimization, Journal on Communications, 1000-436X(2012) 03-0052-07.

Advanced Materials Research Vol. 936 (2014) pp 2254-2258
© (2014) Trans Tech Publications, Switzerland
doi:10.4028/www.scientific.net/AMR.936.2254

Modeling and Simulation Method of Component Based Petri Net

Yaohong Zhang [1, a] , XianFeng Zhang [1,b]

[1] School of Information Systems and Management, National University of Defense Technology, Changsha, China

[a]yaohongzhang@nudt.edu.cn, [b]tianshanxuefeng@126.com

Keywords: modeling; simulation; component; Petri net.

Abstract: The structure of Petri net model is relative fixed after it is built, so it can't describe dynamic change behavior of real system structure easily. Description formalness, coupling mechanism and simulation method were presented, the dynamic change of Petri net structure in simulation run was realized based on the idea of software component design. The reuse capability of Petri net model is enhanced, integration with other models is convenience and hierarchical modeling mode is realized, and the capability of modeling and simulation of Petri net is improved.

Introduction

Petri net is a description and analysis tool for discrete event systems modeling and simulation, it can describe concurrency, synchronization, resource distribution and other issue easily, has been used in the modeling and simulation of complex systems widely. But Petri net has some shortcomings, for example, its structure is relatively fixed, makes it difficult to describe the dynamic structure changes of actual systems. The variable structure Petri net is introduced to solve this problem by adding dynamic change element such as place, transition and so on. [1, 2, 3]

Component based design method is a software develop method which uses reusable function modules and combines these modules to construct complex software systems. It has used in the field of modeling and simulation domain on account of its good scalability and flexibility. [4,5]We introduced the idea of component based design in Petri net modeling, and researched description formalness, coupling mechanism and simulation method, to realize changeable structure Petri net modeling and simulation.

Component Based Petri Net Model Description

Component based Petri net model is an extension of the basic Petri net model, its model is divided into atomic component Petri net model and composite component Petri net model, atomic component Petri net model is the basis of building simulation model, and it is a encapsulated Petri net, its internal structure shields the outside world, exchanging information through input and output ports with external environment, the composite component Petri net model is combination of atomic component Petri net model by port coupling way. Atomic component Petri net model is described as:

$$PNM=(P,T,I,M_0,Inports,Outports,Atts,Funcs)$$

P is a set of non-empty finite place, T is a set of non-empty finite transition, I is a limited non-empty input arc set which satisfies $I \subseteq P \times T$, O is a limited non-empty output arc set which satisfies $O \subseteq T \times P$, $M_0 : P \to Z^0$ is the initial marking, *Inports* is a input port set, *Outports* is a output port set, *Atts* is a set of attributes which are used to monitor states of model, *Funcs* is a set of interface functions which are used to control the states transition of model. For all $p \in P$, define ${}^*p = \{t \in T | (t,p) \in O\}$, and $p^* = \{t \in T | (p,t) \in I\}$.

Input ports and output ports are special kinds of place to provide information exchange interface, namely:

$$Inports \subseteq P, Outports \subseteq P$$

For the input ports, satisfies：

$\forall p \in Inports, {}^{*}p = \Phi, \quad and \quad p^{*} \neq \Phi$

For the output ports, satisfies：

$\forall p \in Outports, p^{*} = \Phi, \quad and \quad {}^{*}p \neq \Phi$

Two special types of graphics element are extended on the basis of basic Petri nets with graph format “◎", "○,△" , which represent input port and output port respectively, as shown in Figure 1.

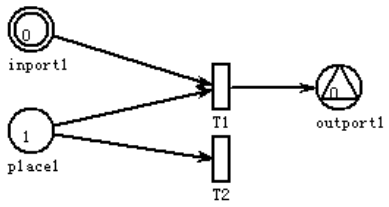


Figure 1 Component Petri net modeling elements

The composite component Petri net model is described as:

CPNM=(PNMS,Inports,Outports,Attr,Func,CR)

PNMS is a set of sub-models , *Inports,Outports,Attr,Func* is defined as the atomic component Petri net model. *CR* is defined the port coupling relationship between models, and satisfies:

$$CR : (M_1, I) \rightarrow (M_2, O) \text{ and}$$

$$I \in Inports(M_1), O \in Outports(M_2), M_1 \neq M_2$$

Port coupling relationship of the model can be divided into three types:

External input coupling: composite model input port is connected to the input port of one or more sub-model.

External output coupling: the sub-model output port connected to the composite model output ports.

The Internal Coupling: the sub-model output port is connected to the input port of the other sub-models.

Port coupling relationship describes token flow path between models, and simulation environment controls message dispatch by port coupling relationship table.

Simulation Method of the Model

Component Petri net model has a hierarchical tree structure and supports hierarchical modeling, as shown in Figure 2.

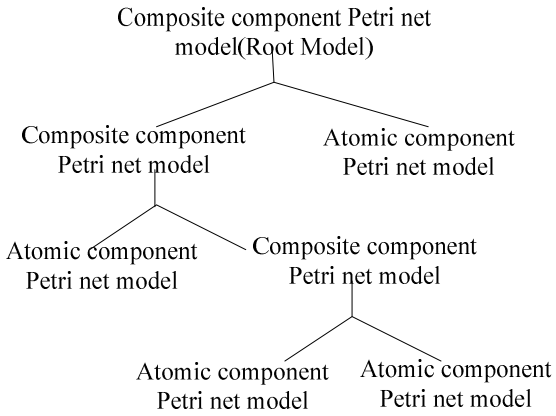


Figure 2 Component Petri net model structure

The operational mechanism of atomic component Petri net is similar to basic Petri net, which is realized by firing of transition, at first we must judge which transition is enabled. for $t \in T$, define ${}^{*}t = \{p \in P | (p,t) \in I\}$, and $t^{*} = \{p \in P | (t,p) \in O\}$. When rule (1) is satisfied, t is enabled.

$$\text{For all } p \in {}^{*}t, M(p) > 0. \qquad (1)$$

After transition is fired, the marking of Petri net will change as rule (2).

$$M'(p)=\begin{cases} M(p)-1, & p\in {}^{*}t \\ M(p)+1, & p\in t^{*} \\ M(p), & p\notin {}^{*}t\cup t^{*} \end{cases} \quad (2)$$

The entire component Petri net model simulation run starts from the top-level model:

Step 1: Scan the sub-model collection $PNMS$ of Root, for M$\in PNMS$, if it is atomic component model, go to step 2, otherwise go to step 3.

Step 2: According to rules (1) and (2), modifies the state of the model, scans its output ports set, removing token from output ports, insert corresponding token to input port of other models according to port coupling relationship table, return to step 1.

Step 3: Replace model Root by M, go to step 1.

Changeable Model Structure Control Mechanism

The design standards of the component Petri net model can be used Active X, CORBA or JavaBeans. We used Microsoft Active X component design specifications, the properties of the model correspond to the attributes of Active X components, the model interface functions correspond to Active X component interfaces.

Simulation environment uses model's interface function to control the dynamic changes of the model structure and model states. The generic interface functions are designed to realize these functions, for example:

- AddObject

Add a Petri net model in the current simulation environment.

- RemoveObject

Remove a Petri net model from the current simulation environment.

- AddPlace

Add a place in the current model.

- RemovePlace

Remove a place from current model.

- AddTransition

Add a transition in the current model.

- RemoveTransition

Remove a transition from the current model.

- AddArc

Add an arc in the current model.

- RemoveArc

Remove an arc from the current model.

The dynamic changes of the structure of Petri nets involves Petri net model dynamic join / leave, Petri network element changes, Petri net model coupling relationship changes. Meanwhile, in order to achieve the reuse of Petri net models, models library is established to provide effective management for model information, port information and attribute information and so on. User can modify the existing models in the model library, and combine them to create a new model, without having to be developed from scratch.

Example Description

Component based Petri net modeling Combines characteristics of basic Petri net modeling with object oriented modeling, and supports top-down or bottom-up analysis, so the establishment of a complex system modeling is rapid. Figure 3 give a sample of an air defense command information system's model architecture.

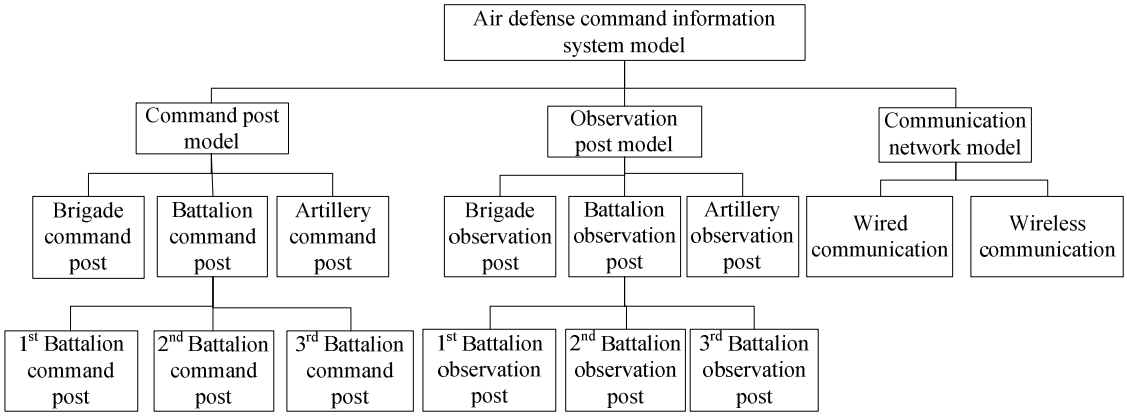


Figure 3 Air defense command information system model architecture

The bottom is atomic components Petri net model, can be constructed by basic Petri net modeling method. For example, atomic components Petri net model of 1st battalion command post is shown in Figure 4 below.

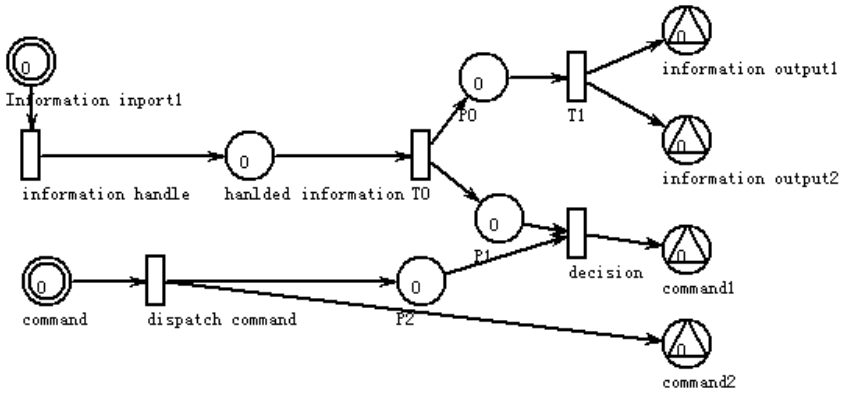


Figure 4 1st battalion command post Petri net model

The Battalion command post model consists of three subordinate battalion command post Petri net model combination(1st,2nd,3rd), port coupled relational table is shown in Table 1.

TABLE 1 BATTALION COMMAND POST MODEL PORT COUPLING RELATIONAL TABLE

Source model	port	Destination model	port	Couple style
1st battalion command post	Information Output 1	battalion command post	Information Output 2	external output coupling
2nd battalion command post	Information Output 1	battalion command post	Information Output 3	external output coupling
1st battalion command post	Information Input 1	battalion command post	Information Input 1	external input coupling
1st battalion command post	Information output 2	3rd battalion command post	Information Input 2	Internal Coupling
…	…	…	…	…

While simulation running, the simulation environment will dynamically create the model, and add it to simulation environment and interact with other models, it also can be removed from simulation environment to realize dynamic changes of model structure.

Summary

The combination of components based software design method with Petri net supports the hierarchical modeling of Petri net, facilitates reuse of Petri net. Component interface control mechanisms realizes dynamic changes of the structure of Petri net during simulation, Meanwhile, models can be embedded into other simulation environment by regulating the port coupling relationship table and interface functions to achieve interoperability with other kinds models.

References

[1] Michel Diaz, Petri Nets: fundamental models, verification, and applications, Wiley, 2009.

[2] Jiang Z B, Zuo M J and Richard Fung Y K, *Colored Petri Nets with Changeable Structure (CPN-CS) for their Applications in Modeling one-of-a-Kind Production(OKP) Systems*. Computer and Industry Engineering,2001,41(3):279-308.

[3] Xiangang Zhao, Bai Wang , Liutong Xu, Grid Application Scheduling Model Based on Petri Net with Changeable Structure. GCC '07 Proceedings of the Sixth International Conference on Grid and Cooperative Computing,733-736.

[4] Miller.J.A,Y. Ge, J. Tao, Component-based simulation environments: JSIM as a case study using Java Beans, Winter Simulation Conference Proceedings, 1998: 373 -381

[5] Buss, A, Component based simulation modeling with simkit, Winter Simulation Conference Proceedings, 2002: 243 -249

Advanced Materials Research Vol. 936 (2014) pp 2259-2262
© (2014) Trans Tech Publications, Switzerland
doi:10.4028/www.scientific.net/AMR.936.2259

ON THE HYBRID MEAN VALUE OF THE SQUARE RESIDUE

QI Lan

College of Mathematics and Statistics

Yulin University, Yulin

Shaanxi 719000

P.R.China

qilanmail@163.com

Keywords: square residue, the Mangoldt function,asymptotic formula.

Abstract: Let n be a positive integer, S(n) denote the square residue. This paper is mainly to study the hybrid mean value properties of the square residue S(n) and the Mangoldt function, and give an interesting asymptotic formula.

Introduction and result

For any positive integer n, let $n = p_1^{\alpha_1} p_2^{\alpha_2} \cdots p_r^{\alpha_r}$ is the factorization of n into prime powers, where $p_1, p_2, \cdots, p_r$ are distinct prime numbers and $\alpha_i \geq 1$. The square residue $S(n)$ is denoted as $S(n) = p_1 p_2 \cdots p_r$ .For example, $S(2) = 2, S(3) = 3, S(4) = 2, S(5) = 5, S(6) = 6, S(7) = 7, S(8) = 2, \cdots$.

In problem 63 of reference [1], Professor F.Smarandache suggested that we study the properties of the square residue $S(n)$, many scholars had studied before, and obtain some interesting results[2-6].For example, Gou Su[2] presented the asymptotic formula

$$\sum_{n \leq x} d(S(n)) = \frac{6}{\pi^2}[x \ln x + (2\gamma - 1)x] + O(x^{\frac{1}{2}} \ln^2 x),$$

where $d(n)$ is Dirichlet divisor function, γ is Euler constant.

Wang Ming-jun[3] proved the the asymptotic formula

$$\sum_{n \leq x} \sigma(S(n)) = \frac{3x^2}{\pi^2} \prod_p (1 + \frac{1}{p^2 - 1}) + O(x^{\frac{3}{2}+\varepsilon}).$$

Ge Dan and He Yan-feng[4] gived some mean value formulas by analytic method, the one of them is

$$\sum_{n\le x} d(k,S(n)) = x\prod_{p|k}(1+\frac{1}{p}) + O(x^{\frac{1}{2}+\varepsilon}),$$

where $k,n \in N$, $(k,S(n))$ denotes the common divisor of k and $S(n)$.

The Mangoldt function is the famous number theory function, it seems no one know the relation between the square residue and Mangold function before.

In the paper, we shall use the elementary method to study the hybrid mean value of the square residue $S(n)$ and the Mangoldt function , and give an interesting asymptotic formula. That is the following:

Theorem 1 Let $x \ge 2$, we have the asymptotic formula

$$\sum_{n\le x} \Lambda_1(n)S(n) = \frac{1}{2}x^2 + O(\frac{x^2}{\log x}),$$

where

$$\Lambda_1(\mathrm{n}) = \begin{cases} \log \mathrm{p}, & \text{if n is a prime p;} \\ 0, & \text{otherwise.} \end{cases}$$

Theorem 2 Let $x \ge 2$, we have the asymptotic formula

$$\sum_{n\le x} \Lambda(n)S(n) = \frac{1}{2}x^2 + O(\frac{x^2}{\log x}),$$

where $\Lambda(n)$ is the Mangoldt function.

The Proof of theorem

In this section, we will complete the proofs of the theorems. According the definition of the square residue $S(n)$, the function $S(n)$ is a multiplicative function, obviously we have $S(p^k) = p$.

Let

$$\mathrm{a(n)} = \begin{cases} 1, & \text{if n is a prime ;} \\ 0, & \text{otherwise,} \end{cases}$$

We have

$$a(n) = \pi(x) = \frac{x}{\log x} + O(\frac{x^2}{\log x}).$$

By Abel's identity[5], we have

$$\sum_{n\le x} \Lambda_1(n)S(n) = \sum_{p\le x} p\log p = \sum_{n\le x} a(n)n\log n$$

$$= \pi(x) \cdot x \log x - \int_2^x \pi(t)(\log t + 1)\,\mathrm{d}\,t$$

$$= x^2 + O(\frac{x^2}{\log x}) - \int_2^x (t + \frac{t}{\log t} + O(\frac{t \log t + t}{\log^2 t}))\,\mathrm{d}\,t$$

$$= \frac{1}{2}x^2 + O(\frac{x^2}{\log x}).$$

This proves Theorem 1.
Using the same method,we may immediately get:

$$\sum_{n \le x} \Lambda(n) S(n) = \sum_{p^k \le x} p \log p$$

$$= \sum_{p \le x} p \log p + \sum_{\substack{p^k \le x \\ k \ge 2}} p \log p,$$

noting that $p^k \le x$ and $k \ge 2$,we get $p \le \sqrt{x}$,

then

$$\sum_{\substack{p^k \le x \\ k \ge 2}} p \log p = \sum_{p \le \sqrt{x}} p \log p \sum_{k=2}^{[\frac{\log x}{\log p}]} 1 \le \sum_{p \le \sqrt{x}} p \log p \frac{\log x}{\log p} \le x^{\frac{3}{2}} \log x,$$

so we have

$$\sum_{n \le x} \Lambda(n) S(n) = \frac{1}{2}x^2 + O(\frac{x^2}{\log x}).$$

Thus we have complete the proof of theorem 2.

References

[1] F.Smarandache, Only problems, Not solutions, Xiquan Publ. House, Chicago,1993.

[2] G.Su,On the mean value of square residue, Journal of Yanan University. 21(4) (2002)8-9.

[3] W.Mingjun.On the mean value of square residue.Journal of Weinan Teachers University.24(2)(2009)18-19.

[4] G.Dan and H.Yanfeng. On some mean value formulas of the square residues, Basic Sciences Journal of Textile University.17(1)(2004)7-10.

[5] Z.Wenpeng,Research on Smarandache problems in Number Theory(collected papers), Hexis, Phoenix,2004.

[6] Z.Wenpeng,L.Junzhuang,L.Duansen,Research on Smarandache problems in Number Theory (collected papers) (Vol. 2),Hexis, Phoenix,2005.

[7] T.M.Apostol, Introduction to Analytic Number Theory,Springer-Verlag, New York,1976.

Advanced Materials Research Vol. 936 (2014) pp 2263-2266
© (2014) Trans Tech Publications, Switzerland
doi:10.4028/www.scientific.net/AMR.936.2263

Feature extraction method based on moment invariants

Wanbing Li[1] , Hongwei Quan[1, a] , Xiafei Huang[2]

[1]Department of Mechanical and Electrical Engineering, Xijing University, Xi'an, 710123, China

[2]Institute of Information and Control, College of Automation, Hangzhou Dianzi University, Hangzhou 310018, China

[a]quanhw@126.com (corresponding author)

Keywords: feature extraction, moment invariant, Harris corner, image registration

Abstract. To match two or more images originated from the same scenario, a new fast automatic registration algorithm based on sparse feature point extraction is proposed. At the first step, the improved Harris corner detection algorithm is used to get two sets of feature points from the reference image and registration image. Second, a group of sparse feature points are selected from the reference image set as initial control points. Then, the corresponding matching points in the registration image set are searched based on local moment invariant similarity detection. Experimental results demonstrate that this method is fast and efficient.

Introduction

For different sensors the physical characteristics or imaging mechanism widely varied. There may be a rotation, translation and scaling existed in two or more images originated from same scenario. So it is necessary for image registration before the pixel-level image fusion. Image registration is the process in which two or more images originated from same scenario collected by different sensors or in different times are matched or combined. During the last decades, image registration has undergone rapid development and growing amount and diversity of methods and techniques [1-6]. In 1992 Brown published his comprehensive survey of image registration methods in his work. In order to solve the problems discussed above, in this paper a new fast automatic registration algorithm based on sparse feature points is proposed.

Sparse Feature Point Extraction

How to accurately extract the feature points is a key issue to image fusion algorithms. In [7] Schmid et al. take repeatability rate and information degree as performance index to evaluate the point detection algorithm, where the results from evaluation showed that Harris corner extraction algorithm can achieve the optimal effects. Based on the analysis to traditional feature point extraction algorithms, Schmid proposed an improved Harris corner extraction algorithm in his paper. In our work this algorithm is used for extracting the Harris corner of the reference image and registration image as the initial matching set.

The traditional Harris corner extraction algorithms use the autocorrelation function to judge the signal changes in horizontal and vertical direction in image. If the obvious changes take place in two directions, this point will be considered as a feature corner. The autocorrelation function can be represented by following matrix:

$$A = e^{-\frac{x^2+y^2}{2\sigma^2}} \otimes \begin{bmatrix} J_x^2 & J_x J_y \\ J_x J_y & J_y^2 \end{bmatrix} \tag{1}$$

where J define a grey image; J_x and J_y designate differential capacity in two directions respectively. Differential matrix is weighted with standard Gaussian parameter $\sigma = 2$.

In typical methods the differential matrix in Eq.1 can be obtained by calculating the convolution of J and template $[-2,-1,0,1,2]$. According to autocorrelation function, if the eigenvalue of the matrix corresponding to current point is very large, we consider this point as a corner. In order to avoid extracting eigenvalue of each point from matrix A, the growth of information G is used to judge whether the change of current point signal in two directions is obvious or not. The variable G is defined by following equation:

$$G = \det(A) - \alpha[\text{trace}(A)]^2 \tag{2}$$

where det(·) denotes the determinant operation of a matrix and trace(·) denotes the trace of a matrix. In virtue of analysis to Harris corner in [7], for the images in same scenario, no matter how large the rotation angle is, the repeating extraction rate of corners can reach up to 90%. For a rich textured SAR image, the extracted feature corners with Harris algorithm can reach a large number, which make the computational cost is very large. In order to decrease the computational cost, we usually choose a group of separated points with a certain distance (i.e. $d = 30$ pixels) as initial points of interest in feature point set of reference image. By this way the Harris corner with the largest value in growth rate in image can be determined first; then the sparse feature point set is selected as initial control points by comparing distance d. The detailed selection process of sparse feature points is as follows:

Step 1: Filtering the reference image and registration image using GF (Gaussian filter) with parameter $\sigma = 0.85$;

Step 2: Calculating the growth of information with Eq.2;

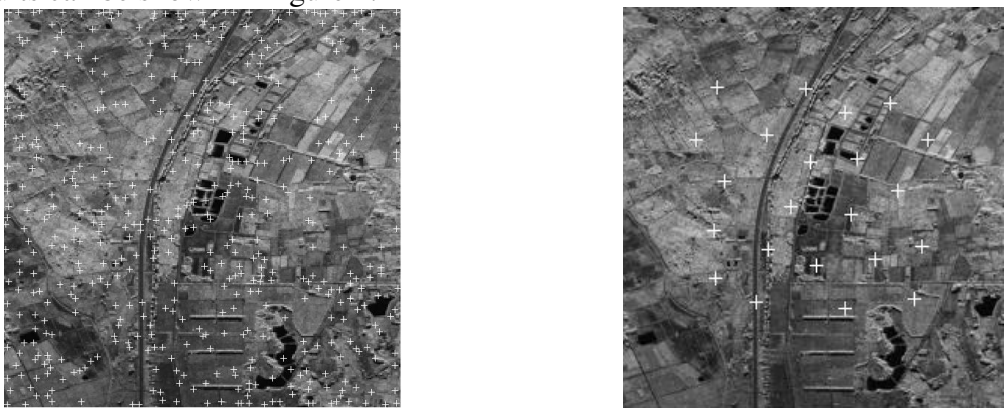
Step 3: Using template of 3×3 to suppress non-maximum points;

Step 4: Determining the feature corners using experimental threshold;

Step 5: Choosing the information growth maximum points in feature corner set;

Step 6: Selecting n initial feature points according to sparse distance d.

The results can be shown in Figure 1.



(a) (b)

Fig. 1 (a) Image with Harris corner extraction and (b) Image with sparse feature points selection

Bidirectional Moment Invariant Registration Algorithm (BMIRA)

After obtaining the sparse feature points, we use a similarity decision mechanism for searching the homonymous control points in registration image. Because there are a large amount problems existed in traditional template matching methods such as slow matching speed, noise sensitive, in our algorithm we choose the moment invariants for searching the homonymous control points, which can not be affected by rotation, translation, scaling.

Define the $p+q$ order moment of the image $f(x,y)$:

$$m_{pq} = \sum_{(x,y)} x^p y^q f(x,y) \tag{3}$$

and the $p+q$ order central moment of $f(x,y)$:

$$\mu_{pq}=\sum_{(x,y)}(x-x_t)^p(y-y_t)^q f(x,y) \tag{4}$$

where $x_t=\frac{m_{10}}{m_{00}}$ and $y_t=\frac{m_{01}}{m_{00}}$ is barycentric coordinate of $f(x,y)$. The normalized central moment of $f(x,y)$ can be represented by

$$v_{pq}=\frac{\mu_{pq}}{\mu_{00}^{\gamma}},\gamma=\frac{p+q}{2}+1,\ p+q=2,3,\cdots \tag{5}$$

Multiple moment invariants can be obtained by using normalized central moments. Through the experiment, the following group of moment invariants is selected with better effects as well as certain robustness in application of image recognition and registration:

$$\kappa_1=(v_{30}-3v_{12})^2+(3v_{21}-v_{03})^2 \tag{6}$$

$$\kappa_2=(v_{30}+v_{12})^2+(v_{21}+v_{03})^2 \tag{7}$$

$$\begin{aligned}\kappa_3=&(v_{30}-3v_{12})(v_{30}+v_{12})\left[(v_{30}+v_{12})^2-3(v_{21}+v_{03})^2\right]\\&+(3v_{21}-v_{03})(v_{21}+v_{03})\left[3(v_{30}+v_{12})^2-(v_{21}+v_{03})^2\right]\end{aligned} \tag{8}$$

$$\begin{aligned}\kappa_4=&(3v_{21}-v_{03})(v_{30}+v_{12})\left[(v_{30}+v_{12})^2-3(v_{21}+v_{03})^2\right]\\&-(v_{30}-3v_{12})(v_{21}+v_{03})\left[3(v_{30}+v_{12})^2-(v_{21}+v_{03})^2\right]\end{aligned} \tag{9}$$

$$\begin{aligned}\kappa_5=&\left[v_{50}-10v_{32}+5v_{14}-10(v_{20}v_{30}-v_{30}v_{02}-3v_{12}v_{20}+3v_{12}v_{02}-6v_{11}v_{21}+2v_{11}v_{03})\right]^2\\&+\left[v_{05}-10v_{23}+5v_{41}-10(v_{02}v_{03}-v_{03}v_{20}-3v_{21}v_{02}+3v_{21}v_{20}-6v_{11}v_{12}+2v_{11}v_{30})\right]^2\end{aligned} \tag{10}$$

For using Euclidean criterion to measure the similarity between points easily, we take the absolute value of the moment invariants $\kappa=(\kappa_1,\kappa_2,\cdots,\kappa_5)$ after logarithmic transformation, from which the local characteristic matrix $A(r)$ for current point is derived:

$$A(r)=\left(\mathrm{abs}\left(\log(\kappa_1)\right),...,\mathrm{abs}\left(\log(\kappa_5)\right)\right) \tag{11}$$

According to the description above, the time consumption mainly causes by comparing the similarity of feature points in reference image and registration image. The flow chart of the algorithm based on Bidirectional moment invariant of sparse feature points is demonstrated as Figure 2.

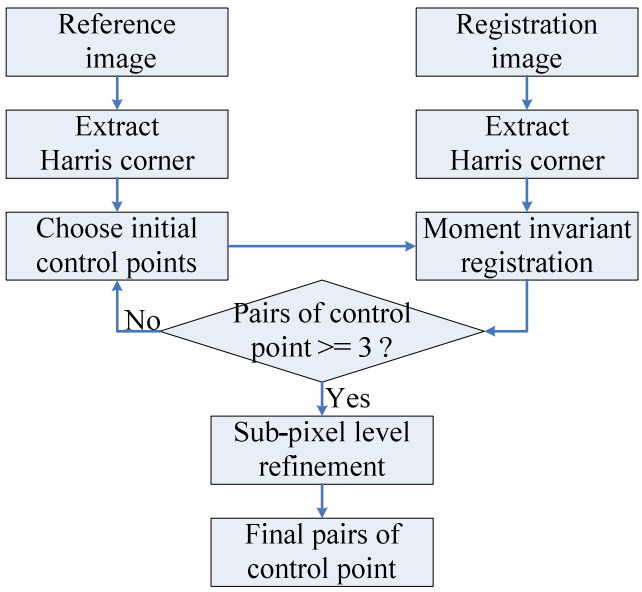


Fig. 2 Flow chart of the bidirectional moment invariant algorithm

Finally, we use the method in [63] to determine the position coordinates of the pair of control point in registration image. Given the matching template plane function $M(x, y)$, the registration image is located in (x_s, y_s), the coordinates of the peak can be calculated using following formula:

$$x = x_s - \frac{1}{2} + \frac{M(x_s, y_s) - M(x_s - 1, y_s)}{2M(x_s, y_s) - M(x_s - 1, y_s) - M(x_s + 1, y_s)} \tag{12}$$

$$y = y_s - \frac{1}{2} + \frac{M(x_s, y_s) - M(x_s, y_s - 1)}{2M(x_s, y_s) - M(x_s, y_s - 1) - M(x_s, y_s + 1)} \tag{13}$$

Experiment and Results Analysis

To demonstrate the operation of the feature extraction algorithm proposed here, and compare its performance with other classic algorithms, in this section we provide a simple registration example for SAR image in Fig.1. The computer configuration is as follows. Processor is Pentium IV 2GHz, Memory 512Mbit, and the operation system is Windows XP. The value of α is 0.06. Table 1 shows the performance evaluation for three algorithms.

Table 1 Performance evaluation for three algorithms

Registration Algorithm	Transform Parameters $(\Delta\theta, \Delta x, \Delta y)$	Time Consumption(s)
SIFT	(162.0124, 0.4516, -0.5731)	35
Manual	(172.1065, 1.2307, 1.2612)	16
BMIRA	(161.5479, -0.0342, 0.4098)	7

Summary

To match the similar band SAR images, a new fast automatic registration algorithm based on sparse feature points is proposed. At the first step, the improved Harris corner detector algorithm is used to get two sets of feature points from the reference and sensed images. At the second step, a group of sparse feature points are selected from the reference image set as initial control points. Then, the corresponding match points in the sensed image set are found based on local moment invariant similarity detection. Experimental results demonstrate that this method is fast and efficient.

Acknowledgments

This work was supported by Scientific Research Foundation of Xijing University [XJ120218, XJ130108].

References

[1] Flusser, J., Suk, T. Degraded image analysis: an invariant approach [J]. IEEE Transactions on Pattern Analysis and Machine Intelligence, 1998, 20(6): 590-603.

[2] Bentoutor, Y., Taleb, N., Kpalma, K. An automatic image registration for application in remote sensing [J]. IEEE Transactions on Geoscience and Remote sensing, 2005, 43(9): 2127-2137.

[3] Spall, J. C. Multivariate stochastic approximation using a simultaneous perturbation gradient approximation [J]. IEEE Transactions on Automation Control, 2002, 37(3): 332-341.

[4] Wells, W. M., Viola, P., Atsumi, H. Multi-modal volume registration by maximization of mutual information [J]. Medical Image Analysis, 1996, 1(1): 35-51.

[5] Walessa, M., Datcu, M. Model-based despeckling and information extraction from SAR images [J]. IEEE Transactions on Geoscience Remote Sensing, 2000, 38(5): 2258-2268.

[6] Schmid, C., Mohr, R., Bauckhage, C. Evaluation of interest point detectors [J]. International Journal of Computer Vision, 2000, 37(2): 151-172.

[7] Harris, C., Stephens, M. A combined corner and edge detector [C]. In Alvey Vision Conference, 1988, pp: 145-151.

Advanced Materials Research Vol. 936 (2014) pp 2267-2270
© (2014) Trans Tech Publications, Switzerland
doi:10.4028/www.scientific.net/AMR.936.2267

Numerical Movement Tracking of Mitral Valve Annulus

Wan Zhang[1,a *], Ran Yin[1], Yuxiao Deng[1], Junyi Zeng[1], Lu Ding[1] and Yipeng Li[2]

[1]The First Affiliated Hospital of Nanchang University, Nanchang, Jiangxi, 330006，China

[2]State grid Jiangxi electric power research institute, 330096, Nanchang, China

[a]wzhang21@163.com

Keywords: movement tracking, mitral valve, annulus

Abstract. Clinical diagnosis and therapy planning are increasingly often supported by 3D imaging modalities. Visual and quantitative evaluation of the valve is an important step in the clinical workflow according to experts as knowledge about mitral morphology and dynamics is crucial for interventional planning. We consider optimal matching of the annulus curves as sub-manifolds by a variational approach based on diffeomorphic transformations.The performance of the algorithm is illustrated by numerical results for examples from medical image analysis.

Introduction

The mitral valve is a dual-flap valve in the heart that lies between the left atrium (LA) and the left ventricle (LV)[1]. Disorders of the mitral valve are the second most frequent heart problems, cumulating 14 percent of total number of deaths caused by valvular heart disease each year in the United States and require elaborate clinical management. Visual and quantitative evaluation of the valve is an important step in the clinical workflow according to experts as knowledge about mitral morphology and dynamics is crucial for interventional planning .

We consider optimal matching of sub-manifolds (annulus curves in this paper) by a variational approach based on diffeomorphic transformations[2-6]. In an abstract setting, the optimal matching is formulated as a minimization problem involving actions of diffeomorphisms. The objective functional consists of two parts measuring the elastic energy of the dynamically deformed sub-manifolds and the quality of the matching.

Method

Cubic B-spline Function

As an important mathematical tool to be used in this paper, cubic B-spline function was introduced here firstly. For a spline of degree n, each one of these basic polynomials has degree n, which would suggest that we need n+1coefficients to describe each piece. However, there is an additional smoothness constraint that imposes the continuity of the spline and its derivatives up to order n-1 at the knots, so that, effectively, there is only one degree of freedom per basic polynomial. Here, we will only consider splines with uniform knots and unit spacing, which can be uniquely characterized in terms of a B-spline expansion

$$s(x) = \sum_{k \in Z} c(k) \beta^n (x - k) \tag{1}$$

which involves the integer shifts of the central B-plines of degree n denoted by $\beta^n(x)$; the parameters of the model are the B-spline coefficients c(k). B-splines, defined below, are symmetric, bell-shaped functions constructed from the (n+1)fold convolution of a rectangular pulse $\beta^0(x)$

$$\beta^0(x)=\begin{cases}1, & -1/2<x<1/2\\ 1/2, & |x|=1/2\\ 0, & otherwise\end{cases} \tag{2}$$

$$\beta^n(x)=\underbrace{\beta^0(x)*\beta^0(x)*\cdots\beta^0(x)}_{(n+1)times} \tag{3}$$

The family of B-splines of degree 3 (cubic B-splines) is shown in figure 1. Since the B-spline model is linear, studying the properties of the basic atoms can tell us a lot about splines in general. Thanks to this representation, each spline is unambiguously characterized by its sequence of B-spline coefficients c(k), which has the convenient structure of a discrete signal, even though the underlying model is continuous.

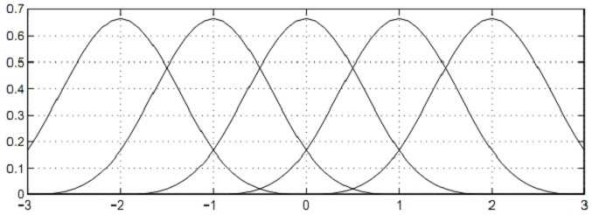


Fig. 1 Cubic B-splines

Shape Matching

The notion of matching requires definition of a good distance among 3D sub-manifolds in R^3. We also consider deformations of R^3, such deformations will form a group G of diffeomorphisms $F:R^3\to R^3$.

Let us consider a diffeomorphism $F:R^3\to R^3$, i.e. $x\in R^3$, $F(x)\in R^3$, reference and target curves are denoted by γ and φ respectively. The reference curve γ is deformed by F to F(γ). The goal is to find F such that φ and F(γ) be close, i.e. the distance between two curves, dist(φ, F ◦ γ), to be small. We also want the deformation to be small. The magnitude of a deformation is determined by the energy of corresponded diffeomorphism. The problem is to find a diffeomorphism F which minimizes the following objective functional

$$J=\lambda\cdot Energy(F)+dist^2(\phi,F\circ\gamma) \tag{4}$$

The first is the regularization term. The positive parameter λ is a measure of regularity of a minimizer. When $\lambda=0$ there a lot of solutions are expected. As λ is positive and approaches zero, the solution F becomes less smooth, but the distance decreases and the curves are better matching.

At point x_t an infinitesimal deformation $V_t(x_t)\in R^3$ is a rate of change of x_t with respect to t. Then the relation between the velocity V_t and the diffeomorphism F_t can be described by the following ODE equation system

$$\begin{cases}dF_t/dt=V_t(F_t(x))\\ F_0(x)=x, \quad \forall x\end{cases} \tag{5}$$

Initialization

Between consecutive instances, the computation was initialized by affine transform. Given B(i) as the set of selected key points at time t_i, where $t_1=0,\cdots,t_p=1$. We solve:

$$B(i+1)=T_i[B(i)], \quad i=1,\cdots,p-1 \tag{6}$$

Where T_i is affine transform, then the initial trajectory was generated by:

$$\begin{aligned} &S(1) = S_0 \\ &S(2) = T_1[S(1)] \\ &\cdots \\ &S(p) = T_{p-1}[S(p-1)] \end{aligned} \tag{7}$$

To solve (6), define

$$B(i) = [X_1 \cdots X_N], \quad X_i = [x_1^i x_2^i x_3^i]^T \tag{8}$$

$$B(i+1) = [Y_1 \cdots Y_N], \quad Y_i = [y_1^i y_2^i y_3^i]^T \tag{9}$$

Suppose

$$T_i(X) = AX + b = \begin{pmatrix} a_{11} & a_{12} & a_{13} \\ a_{21} & a_{22} & a_{23} \\ a_{31} & a_{32} & a_{33} \end{pmatrix} X + b \tag{10}$$

We solve it by minimization of least square error, in which the error is

$$E(A,b) = \sum_{i=1}^{N} \| Y_i - AX_i - b \|^2 = \sum_{i=1}^{N} \sum_{i=1}^{3} (y_j^i - a_{j1}x_1^i - a_{j2}x_2^i - a_{j3}x_3^i - b_j)^2 \tag{11}$$

Take derivative of it, we have

$$\begin{aligned} 0 = \frac{dE(A,b)}{da_{jk}} &= \sum_{i=1}^{N} x_k^i (y_j^i - a_{j1}x_1^i - a_{j2}x_2^i - a_{j3}x_3^i - b_j) \\ &= \alpha_k a_{j1} + \beta_k a_{j2} + \gamma_k a_{j3} + \varepsilon_k b_j + \delta_{jk} \\ 0 = \frac{dE(A,b)}{db_j} &= \sum_{i=1}^{N} (y_j^i - a_{j1}x_1^i - a_{j2}x_2^i - a_{j3}x_3^i - b_j) \\ &= \varepsilon_1 a_{j1} + \varepsilon_2 a_{j2} + \varepsilon_3 a_{j3} + \sum_{i=1}^{N} y_j^i - N b_j \end{aligned} \tag{12}$$

Where

$$\alpha_k = -\sum_{i=1}^{N} x_k^i x_1^i, \beta_k = -\sum_{i=1}^{N} x_k^i x_2^i, \gamma_k = -\sum_{i=1}^{N} x_k^i x_3^i, \varepsilon_k = -\sum_{i=1}^{N} x_k^i, \delta_{jk} = -\sum_{i=1}^{N} x_k^i y_j^i \tag{13}$$

After further derivation we can get

$$\begin{aligned} &A = \Delta * (M^{-1})^T \\ &b = \frac{1}{N} A\varepsilon - \frac{1}{N} \eta \end{aligned} \tag{14}$$

Where

$$\Delta = YX' + \frac{1}{N} \eta \varepsilon^T, \quad \eta = -\sum_{i=1}^{N} Y_i, \quad \varepsilon = -\sum_{i=1}^{N} X_i \tag{15}$$

Numerical Tracking

In the computation below, we use the previous techniques to numerically construct the diffeomorphic flows roughly approximating the dynamic deformations between multiple 3D-snapshots of the human mitral valve annulus. The given snapshots are modeled by parametrized closed curves in R^3 for the mitral annulus: firstly a few points on the mitral valve annulus were tagged by experienced physicians at different time instances, then the cubic B-spline functions were applied to perform the interpolation on these tagging points to generate continuous annulus curves. For the annulus, we have a series of given snapshots, and we focus on two annulus snapshots, we define the first annulus as the reference annulus (or the beginning moment, identified as red in figure 2), and the other as the target annulus (or the end moment, identified as blue in figure 2), the computed movement of the annulus at the three intermediate moments are plotted in figure 2 as yellow curves.

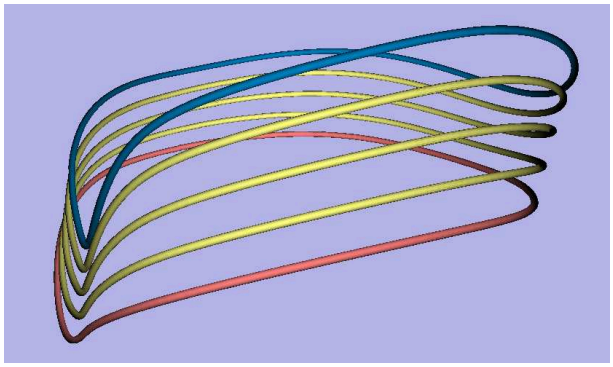


Fig. 2 Computed Mitral Valve Annulus Movement

Summary

Clinical diagnosis and therapy planning are increasingly often supported by 3D imaging modalities. Visual and quantitative evaluation of the mitral valve annulus is an important step in the clinical work. In this paper, we consider optimal matching of the annulus curves as sub-manifolds by a variational approach based on diffeomorphic transformations.The performance of the algorithm is illustrated by numerical results for examples from medical image analysis.

References

[1] R. Klabunde, Cardiovascular physiology concepts, Lippincott Williams and Wilkins, 2004.

[2] S. Joshi, M. Miller, Landmark matching via large deformation diffeomorphisms, IEEE Trans. Image Proc. 9 (2000)1357–1370.

[3] E. Klassen, A. Srivastava, W. Mio, and S. Joshi, Analysis of planar shapes using geodesic paths on shape spaces, IEEE Trans. Patt. Anal. and Mach. Intell. 26 (2004)372–383.

[4] A. Trouve, Diffeomorphisms groups and pattern matching in image analysis, Int. J. of Comp. Vis. 28 (1998) 213–221.

[5] E. Zuazua, Controllability and observability of partial differential equations, Elsevier, Amsterdam, 2007

[6] M. I. Miller, L. Younes, Group action, diffeomorphism and matching: A general framework, Int. J. Comp. Vis., 41 (2001)61–84.

Advanced Materials Research Vol. 936 (2014) pp 2271-2275
© (2014) Trans Tech Publications, Switzerland
doi:10.4028/www.scientific.net/AMR.936.2271

Simulation of Ising Model by Monte Carlo Method

SONG Cui-ying[1, a], LI Chuan-Dong[2]

[1]Department of Physics, Tianjin University of Commerce, Tianjin 300134, China

[2]Fujian electric power test and Research Institute, Fujian 350007, China

[a]lxyscy@tjcu.edu.cn

Keywords: Monte Carlo, Ising Model, magnetization intensity

Abstract: Simulating Ising model to calculate magnetization intensity by Monte Carlo method. The Ising model was introduced simply, sampled importantly, and calculated with programming. It shows the dependency relationship between the magnetization intensity and the size of dot-square line in different temperatures for Ising model. It cans edulcorate the approximation of analytic method by computer simulating. It obtains a method to appraise a model right or wrong by comparing the model and the experimental data.

Foreword

It is a usual tool to much science to computer simulation. It is for many reasons to simulate by computer to physical system. Computer simulation can edulcorate the approximation of analytic model[1]. A kind of simulation must be shown to resolve a problem by analytic method usually, such as approximation of mean field. It can study problems analytic method can not resolve by computer simulation.

It obtains the standard to compare all kinds of approximate theories for the complex system can be studied by computer simulation method. At the same time, it allows to compare the model and experimental data for computer simulation method, and it find a way to evaluate the model right or wrong[2,3]. The starting point to a computer simulation is a determinate model of a physical system, and calculate the properties of the physical system, those properties or observable values can get by averaging from someone sample space. It is calculated by Mote Carlo method to the magnetization intensity of Ising Model in this article.

Brief of Model

The system that shows order to disorder phase transition can be studied by equilibrium statistical mechanics. It is the simplest example that dot matrix constituted by two different matters, A and B (Fig.1) . It suppose that there is only interaction nearest, and uses V_{AB} to figure the interaction energy between A and B, V_{AA} and V_{BB} figure the interaction energy between A and A, B and B. First, it think the condition that the system is at T=0K.

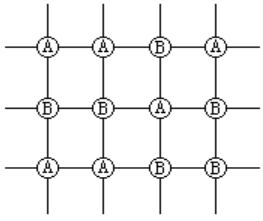


Fig.1 Every Square-dot Should be A or B in two Dimensions Matrix

①If $V_{AB} > 1/2 (V_{AA} + V_{BB})$, then all of A are adjacent to each other, and all of B are neighbor. It is beneficial to this combination form to energy. The whole dot matrix was separated into areas under this condition, some include A only, and the others include B only.

②If $V_{AB} > 1/2 (V_{AA} + V_{BB})$, then it is beneficial that A and B is nearest each other to energy. So A and B will be Alternating arrangement in dot matrix.

Both of above two conditions are ordered state. If temperature is raised, heat energy K_B will impel randomization of position of A and B. The system will *melt* at a special degree. The whole system will be out-of-order completely when temperature rising. The form of partition function to this kind of system should be as follows.

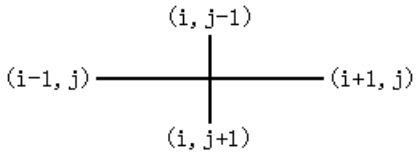
$$Z_N(T) = \sum \exp(-\beta \sum V_{ij})$$

It is called Ising model to the mathematical model of this kind of system. It defines as below. $G=L^d$ is a dot-square of d-dimension. There is a spinning S_i in every mount point i, it can be +1 or -1. Every spinning can interact by the exchange coupling energy J. And an external magnetic field H can be exist, Hamiltonian for the system be as follows.

$$\Re = -J \sum_{i,j} S_i S_j + \mu H \sum_i S_i$$

The Sample of Two Dimensions Ising Model

To study this problem in two dimensions, it should think about Hamiltonian of Ising Model $\Re = -J \sum_{(i,j)} S_i S_j$, J means exchange interaction for nearest neighbor mount point. It can be positive, ferromagnetism, and negative, antiferromagnetism. The variable S means a spinning, can be +1 or -1. The symbol <i,j> represent the four nearest neighbor mount point (i,j) for limitation of simple square.



The x represents a spinning. It produces a Markov chain $x_0, x_1, \ldots\ldots, x_n$ to make configuration $x_{(+)}$ only depend on its configuration $x_{(i)}$ ago. The probability from x_i to x_{i+1} can get by a transition probability $W(x_{i+1}|x_i)$.

The transition means that all state $x_0, x_1, \ldots\ldots, x_n$ should be Boltzmann distribution.

$$P(x) \propto \exp\left(-\frac{\Re(x)}{K_B T}\right)$$

How does it choose transition probability to ensure the state distribution following the Boltzmann law? If limitation to conduct the reverse single spinning S_i, it suppose that energy will lose when a spinning S_i reverse to $-S_i$. Because it always is ground state of model, or close to, so it should is accepted as probability is 1. In condition of energy exchange $\Delta\Re = \Re(X^{new}) - \Re(X^{old})$ is negative, $W(x_{new}|x_{old})=1$. But it must fall into a minimum energy in some areas. The change of

energy increasing can be accepted to avoid this thing. However the change of increasing much energy does not happen so much, so the probability is very low. On the contrary, the energy change is little, means the energy of new configuration is similar with the old configuration, then it is high probability to allow the change. The minimum energy in some areas can be broken away from to reach further.

How does it choose the transition in the condition of the energy change $\Delta\Re$ is positive? A choice looks reasonable and provable accurately is as follows.

$$W(X_{i+1}|X_i) = \min[1, \exp(-\frac{\Delta\Re}{K_B T})]$$

That is called Metropolis function. But it is not the only choice to transition probability. There are other choices, such as Glauber function$\{\frac{1}{2}[1-\tanh(\Delta \hat{A}/2K_B T)]\}$。

It built transition probability to single reverse spinning. All spin has only a chance of reversing direction at once, then a scanning is completed. A scanning is called spinning-Monte Carlo step. short for MCS.

There are several probable method to scan whole dot-square once. The scanning means that scan from the beginning to the end regularly. An other probable method is that the accessing mount points are sampled randomly. If the attempt times are equal to the count of mount point, it means a Monte Carlo step is complete. Some mount point maybe think about some times in a Mento Carlo step, and some others are not including. If the random numbers themselves have no problem in average, every mount point gets a reverse chance.

Someone initial configuration S_0 must be used in order to start important sample, and then new states are generated continuously. Which should initial spinning configuration be chosen? It supposes that the average properties of Ising model are studied in some temperature, such as magnetization and magnetic susceptibility. And it suppose that the spinning configuration start randomly, and not a complete order. Now the system is made evolutions in time by function, such as Metropolis function. The hardening is carried on indeed, it get into order area from out-of-order in phase diagram. It will take very long time to build up a balance state. The excess energy must be removed before the balance state established.

Now it is back to talk about transition probability. The configuration x_{i+1} is not different with x_i obviously. It allows single particle spinning but not many particles, because the last will cause two configurations further in phase space. The state order can be looked as the track in the phase space. It must be relative between the neighbor configurations from this point. The n_d states must be abandoned in two sample point in order to get a unbiased statistical sampling for state. It based on the temperature that how many stats must be abandon, and based on conservation law. See it in algorithm1.

Algorithm 1 Ising moel

```
                ( * dot-square initial*)
          DO    10    I=1，L
          DO     10    J=1，L
          LATTICE（I, J）=-1
10        CONTINUE
           COUNT=0
```

```
DO    20    MCS=1，MCSMAX
        GENERATE-ONE-STEP;          （Make a scanning）
        IF（MCS.GE.Nδ）THEN
        COUNT=COUNT+1
        END IF
        IF（COUNT=Nδ）THEN
       COUNT=0
        DO-ANALYSIS;                （Analyze）
        END IF
20      CONTINUE
        END
```

After preparation of the acknowledge, it need to talk about the core part of important sample algorithm of Ising model, GENERATE-ONE-STEP in algorithm 1 (make a scanning). Designing transition probability make attempt to reverse all spins always. It is a Monte Carlo step. A new configuration can be gotten from last configuration after a Monte Carlo step. So first step is algorithm 2, L is size of dot-square in it.

```
Algorithm 2     GENERATE-ONE-STEP
DO     10     I=1，L
    DO    10     J=1，L
      COMPUTE-THE-ENERGY-DIFFERENCE; (calculate energy difference)
          DECIDE-TO-FLIP-OR-NOT;          （decide reverse or not）
10  CONTINUE
```

It is nor necessary to calculate linear function with every reversing spin. There are five probable values for energy difference. The function can calculate in advance and deposit in a array to seek quickly. The energy difference is follows.

$$\Delta\Re = 2S_i \frac{J}{K_B T} \sum_{nn(j)} S_i$$

The symbol nn(j) means four nearest neighbors of central spin in function.

There is a problem only. The last title calculation of energy difference must be solved. It is a choice as same as decision of percolation, and must choose one from different border conditions. The key of every spin can not hang alone at the edge of square. The spins must interact with the nearest neighbor. The periodic edge condition is chosen here.

Using remainder function is a method to realize periodic edge condition. At the edge of square, i is 1 or L or j is 1 or L in central spin (I,j), the nearest neighbor can be calculated as follows.

```
ip1=i＋1   （mod L）          im1=i－1   （mod L）
jp1=j＋1     （mod L）          jm1=j－1   （mod L）
```

This algorithm spends very long time. Every calculation of remainder function has several math calculations, time is the key. The innermost layer of the circle must be made up of the less times of math calculation. A table is used to solve that. It need two tables in fact, one for “add” calculation, one for “subtract” calculation (algorithm 3).

Algorithm 3 The table instead of remainder function

```
REAL  IP（L），IM（L）
      DO    10    I=1，L
      IP（I）=I+1
      IM（I）=I+1
      IP（L）=1
      IM（1）=L
10    CONTINUE
```

The algorithm of important sample for two dimensions has finished. All most parts have designed. It should affirm the phase transition point in simple dot-square for two dimensions, J/K_BT_C. Of course, it has known accurately to the analytical result for the two dimensions Ising model. It is a chance to judge the job good or not to data analysis. The phase transition point for limited system will be dim. The effect of limited size is relative with the edge condition. It is different result between the order parameter and the magnetization to the simple sample for the percolation. Same to the phase transition causing by heating.

Conclusions

It shows the relationship between the magnetization and the size of dot-square line for two dimensions Ising model in fig.2. It obviously seen that the magnetization depends on the size of dot-square. The effect is most remarkable near the critical temperature. At the low temperature, T is more lower than T_c, the effect of the size of dot-square is not sensitive to the result. The magnetization there converge quickly to the true limitation of thermodynamics. Although it does not exist self magnetic in limitation of thermodynamics, the magnetization is not zero at high temperature.

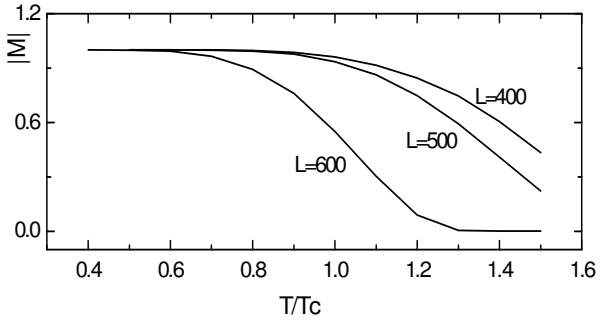


Fig.2 The Dependence Relationship between the Magnetization and the Size of Dot-square line. Data is about two Dimentions Ising Model.

References

[1] R Harris and Martin Grant. Monte Carlo simulation of a kinetic Ising model for Dendritic growth[J], J. Phys. A:Math. Gen.. 1990(23):L567-L571

[2] Henk W.J.Blöte and Youjin Deng. Cluster Monte Carlo simulation of the transverse Ising model[J],Phys.Rev.E, 2002(66):066110(1-8).

[3] George A. Baker Jr. A Markov-property Monte Carlo method: One-dimensional Ising model[J], Journal of Statistical Physics, 1993(72):621-641.

Advanced Materials Research Vol. 936 (2014) pp 2276-2280
© (2014) Trans Tech Publications, Switzerland
doi:10.4028/www.scientific.net/AMR.936.2276

On Infinite Lower Order of Vector Valued Dirichlet Series

Wanchun Lu

Department of Mathematics, Pingxiang University, Pingxiang ,337055, China

luwanchun540@163.com

Keywords: vector valued Dirichlet series, analysis functions, infinite order, growth.

Abstract: In this paper, the infinite lower order of vector valued Dirichlet series is investigated. By using a kind of new growth parameters of infinite lower order of analysis functions is introduced, the characterizations of coefficients of series are obtained.

Introduction

Let

$$f(s)=\sum_{n=0}^{+\infty}a_n e^{-\lambda_n s}\ , s=\sigma+it\ , (\sigma,t\ \text{ are real variables}), \tag{1}$$

where $a_n's$ belong to a complex commutative Banach algebra B with identity element ω with $\|\omega\|=1$ and $\lambda_n's\in\mathbb{R}$ satisfy the conditions $0=\lambda_0<\lambda_1<\lambda_2<\cdots<\lambda_n\uparrow+\infty$

$$\overline{\lim_{n\to+\infty}}\frac{\log\|a_n\|}{\lambda_n}=0\ ,\ \overline{\lim_{n\to+\infty}}\frac{n}{\lambda_n}=D<+\infty\ , \tag{2}$$

Then, the vector valued Dirichlet series in (1) represents an analytic function $f(s)$ in right plane(see [1]). In [1], B. L. Srivastava defined the growth parameters such as order, type, lower order, lower type of the vector valued analytic Dirichlet series. He also obtained the result for coefficient characterization of order and type. G.S. Srivastava [2] studied generalized order and generalized type of slow vector valued Dirichlet series. And he [3] studied relative type of this series also. In this paper we obtain infinite lower order of vector valued Dirichlet series.

For the vector valued analytic function $f(s)$ defined as above by (1) the maximum modulus, the maximum term and the index of maximum term are defined as

$$M(\sigma,f)=\sup_{-\infty<t<+\infty}\{\|f(\sigma+it)\|\}\ (\sigma>0)\ ,$$

$$m(\sigma,f)=\max_{n\in N}\{\|a_n\|e^{-\lambda_n\sigma}\}\ (\sigma>0)\ ;$$

$$N(\sigma)=\max_{n\in\mathbb{N}}\{n:m(\sigma,f)=\|a_n\|e^{-\lambda_n\sigma}\}\quad(\sigma>0)\ .$$

The order ρ and the lower order λ of $f(s)$ are defined as

$$\rho=\overline{\lim_{\sigma\to0}}\frac{\log^+\log^+M(\sigma,f)}{-\log\sigma}\ ,\quad\lambda=\underline{\lim_{\sigma\to0}}\frac{\log^+\log^+M(\sigma,f)}{-\log\sigma}\ .$$

We shall call the vector valued analytic function $f(s)$ to be of infinite order growth if $\rho=\infty$.

Let Δ_0 be the class of all functions β satisfying the following two conditions:

(i) $\beta(x)$ is defined on $[a,\infty)$, $a>0$, and is positive, strictly increasing, differentiable and tends to ∞ as $x\to\infty$;

(ii) $\dfrac{\mathrm{d}\beta(x)}{\mathrm{d}\log x}=o(1)$ as $x\to\infty$.

For a vector valued analytic function $f(s)$ given by (1) and $\beta(x)\in\Delta_0$, set

$$\lambda(\beta, f) = \varliminf_{\sigma \to 0} \frac{\beta(\log^+ M(\sigma, f))}{-\log \sigma}.$$

Then $\lambda(\beta, f)$ will be called, respectively, lower β-order of $f(s)$. To avoid some trivial cases we shall assume throughout that $M(\sigma, f) \to \infty$ as $\sigma \to 0$.

Main Results

Lemma 1

If the vector valued Dirichlet series given by (1) satisfies (2), then

$$m(\sigma, f) \le M(\sigma, f) \le K(\varepsilon) m(\sigma(1-\varepsilon), f) \frac{1}{\sigma},$$

where $K(\varepsilon)$ is a positive number of ε and $f(s)$.

Proof: From the second equation of (2), for given $\varepsilon > 0$, there exists an $n_0 = n_0(\varepsilon)$, such that for $n > n_0$, $n < (D+\varepsilon)\lambda_n$. Taken $\sigma > 0$, $\varepsilon \in (0, \sigma)$, we have

$$\begin{aligned} M(\sigma, f) &\le \sum_{n=1}^{n_0} \|a_n\| e^{-\lambda_n \sigma} + \sum_{n=n_0}^{\infty} \|a_n\| e^{-\lambda_n (1-\varepsilon)\sigma} e^{-\lambda_n \varepsilon \sigma} \\ &\le n_0 m(\sigma, f) + m((1-\varepsilon)\sigma, f) \sum_{n=n_0+1}^{\infty} e^{-n\varepsilon\sigma/(D+\varepsilon)} \\ &< n_0 m(\sigma, f) + \frac{m((1-\varepsilon)\sigma, f)}{1 - e^{-\varepsilon\sigma/(D+\varepsilon)}} \end{aligned} \tag{3}$$

The lemma now follows from (3) and the well known relation $m(\sigma, f) \le M(\sigma, f)$.

Lemma 2

If the vector valued Dirichlet series given by (1) satisfies (2), then

$$\lambda = \varliminf_{\sigma \to 0} \frac{\beta(\log^+ m(\sigma, f))}{-\log \sigma}.$$

Proof: By the first inequality of Lemma 2.1, this gives, since $\beta \in \Delta_0$, that

$$\varliminf_{\sigma \to 0+} \frac{\beta(\log^+ m(\sigma, f))}{-\log \sigma} \le \varliminf_{\sigma \to 0+} \frac{\beta(\log^+ M(\sigma, f))}{-\log \sigma}. \tag{4}$$

By the second inequality of Lemma 2.1, we have

$$\begin{aligned} \log^+ M(\sigma, f) &\le \log^+ m(\sigma(1-\varepsilon), f) - \log \sigma + O(1) \\ &\le C \log^+ m(\sigma(1-\varepsilon), f) \cdot (-\log \sigma) \end{aligned} \tag{5}$$

for all $\sigma (\sigma > 0)$ sufficiently close to 0. Here C is a constant. Now, (5) gives

$$\beta(\log^+ M(\sigma, f)) \le \beta(\log^+ m(\sigma(1-\varepsilon), f)) + \log((-\log \sigma)^C) \cdot \left. \frac{\mathrm{d}\beta(x)}{\mathrm{d} \log x} \right|_{x = x^*(\sigma)},$$

where $\log^+ m(\sigma(1-\varepsilon), f) < x^*(\sigma) < C \log^+ m(\sigma(1-\varepsilon), f)(-\log \sigma)$. This easily gives

$$\varliminf_{\sigma \to 0+} \frac{\beta(\log^+ M(\sigma, f))}{-\log \sigma} \le \varliminf_{\sigma \to 0+} \frac{\beta(\log^+ m(\sigma, f))}{-\log \sigma} \tag{6}$$

Theorem 1

If the vector valued Dirichlet series given by (1) satisfies (2) and is lower order $\lambda(\beta, F)$, then

$$\lambda(\beta,f)\geq\varliminf_{k\to\infty}\frac{\beta(\lambda_{n_{k-1}})}{\log\lambda_{n_k}-\log^+\log\|a_{n_k}\|}$$

for any increasing sequence $\{n_k\}$ of natural numbers.

Proof: Let $\theta=\varliminf_{k\to\infty}\frac{\beta(\lambda_{n_{k-1}})}{\log\lambda_{n_k}-\log^+\log\|a_{n_k}\|}$. First, let $0<\theta<\infty$. Then given $\varepsilon>0(\varepsilon<\theta)$, there exist $k_0=k_0(\varepsilon)$ such that for all $k>k_0$, we have

$$\log\|a_{n_k}\|>\lambda_{n_k}\exp\{-\frac{\beta(\lambda_{n_{k-1}})}{\theta-\varepsilon}\}.$$

Choose $\sigma_k=\frac{1}{2}\exp\{-\frac{\beta(\lambda_{n_{k-1}})}{\theta-\varepsilon}\}$, $k=k_0+1,k_0+2,\cdots$. Let $\sigma_{k+1}\leq\sigma\leq\sigma_k$, then, by Lemma 2.1, the above inequality gives

$$\begin{aligned}\log^+M(\sigma,f)&\geq\log\|a_{n_k}\|-\sigma\lambda_{n_k}\geq\log\|a_{n_k}\|-\sigma_k\lambda_{n_k}\\&\geq\lambda_{n_k}\exp\{-\frac{\beta(\lambda_{n_{k-1}})}{\theta-\varepsilon}\}-\sigma_k\lambda_{n_k}\geq\sigma\beta^{-1}(-(\theta-\varepsilon)\log(2\sigma)).\end{aligned}$$

So

$$\beta(\frac{1}{\sigma}\log^+M(\sigma,f))\geq(\theta-\varepsilon)\log(\frac{1}{2\sigma}),$$

or

$$\beta(\log^+M(\sigma,f))+\log(\frac{1}{\sigma})\cdot\frac{\mathrm{d}\beta(x)}{\mathrm{d}\log x}\bigg|x=x^*(\sigma)>(\theta-\varepsilon)\log(\frac{1}{2\sigma}),$$

where $\log M(\sigma,f)<x^*(\sigma)<\frac{1}{\sigma}\log M(\sigma,f)$. This easily gives, since $\beta\in\Delta_0$, that

$$\lambda(\beta,f)\geq\theta. \tag{7}$$

(7) is obvious for $\theta=0$. For $\theta=\infty$, the above arguments with an arbitrarily large number in place of $\theta-\varepsilon$ give $\lambda(\beta,f)=\infty$. This proved the lemma.

Theorem 2

If the vector valued Dirichlet series given by (1) satisfies (2) and β-order $\rho(\beta,F)$ of $f(s)$ is non-zero. Further, let $\varphi(n)=\frac{\log\|a_n\|-\log\|a_{n+1}\|}{\lambda_{n+1}-\lambda_n}$ be a non-decreasing function of n for $n>n_0$. Then

$$\lambda(\beta,f)=\varliminf_{n\to\infty}\frac{\beta(\lambda_{n-1})}{\log\lambda_n-\log^+\log\|a_n\|}.$$

Proof: As $\varphi(n)$ forms a non-decreasing function for $n>n_0$, it follows that $\varphi(n)>\varphi(n-1)$ for infinitely many values of n, since otherwise $\rho(\beta,f)=0$. Clearly $\varphi(n)\uparrow 0$ as $n\to\infty$. When $\varphi(n)>\varphi(n-1)$, the term $\|a_n\|\mathrm{e}^{-\lambda_n\sigma}$ becomes the maximum term and we have

$$m(\sigma,f)=\|a_n\|\mathrm{e}^{-\lambda_n\sigma}\quad\text{for}\quad\varphi(n)>-\sigma\geq\varphi(n-1).$$

By Lemma 2.2, we have

$$\lambda(\beta,f)=\varliminf_{\sigma\to0}\frac{\beta(\log^+m(\sigma,f))}{-\log\sigma}.$$

First, suppose that $0<\lambda(\beta,f)<\infty$, then given $\varepsilon>0$, there exists $\sigma_1=\sigma_1(\varepsilon)>0$ such that for $0<\sigma<\sigma_1$, we have

$$\beta(\log^+ m(\sigma,f))\geq\overline{\lambda}\log\frac{1}{\sigma},$$

where $\overline{\lambda}=\lambda(\beta,f)-\varepsilon$. Let $\|a_{n_1}\|e^{-\lambda_{n_1}\sigma}$ and $\|a_{n_2}\|e^{-\lambda_{n_2}\sigma}$ ($n_1>n_{0,}\varphi(n_1-1)>-\sigma_1$) be two consecutive maximum terms so that $n_1\leq n_2-1$. Let $n_1\leq n\leq n_2-1$. It is easily seen that $\varphi(n_1)=\varphi(n_1+1)=\cdots=\varphi(n)=\cdots=\varphi(n_2-1)$ and that

$$\|a_n\|e^{-\lambda_n\sigma}=\|a_{n_2}\|e^{-\lambda_{n_2}\sigma}\quad\text{for}\quad-\sigma=\varphi(n).$$

Hence,

$$\beta(\log\|a_n\|+\lambda_n\varphi(n))\geq\overline{\lambda}\log(-\frac{1}{\varphi(n)}). \tag{8}$$

By the first equation of (2) and $\varphi(n)\uparrow 0$ as $n\to\infty$, and notice that $\varphi(n)$ is non-decreasing, (8) gives

$$\beta(\lambda_n)\geq\overline{\lambda}\log(-\frac{1}{\varphi(n)}) \tag{9}$$

for all sufficiently large values of n.

Again, as $\varphi(n)$ forms a non-decreasing function of n for $n>n_0$, we have

$$\log\|a_{n+1}\|=\log\|a_{n_0}\|+\sum_{j=n_0}^{n}(\lambda_j-\lambda_{j+1})\varphi(j)\geq\log\|a_{n_0}\|+(\lambda_{n_0}-\lambda_{n+1})\varphi(n).$$

Therefore

$$\log^+\log\|a_{n+1}\|\geq\log^+(\log\|a_{n_0}\|+\lambda_{n_0}\varphi(n))+\log^+(-\lambda_{n+1}\varphi(n))+o(1),$$

or

$$\frac{\log\lambda_{n+1}-\log^+\log\|a_{n+1}\|}{\beta(\lambda_n)}\leq-\frac{\log^+(-\varphi(n))}{\beta(\lambda_n)}+o(1).$$

Using (9), we have

$$\lambda(\beta,f)\leq\varlimsup_{k\to\infty}\frac{\beta(\lambda_{n-1})}{\log\lambda_n-\log^+\log\|a_n\|}. \tag{10}$$

The above inequality is obvious for $\lambda(\beta,f)=0$. When $\lambda(\beta,f)=\infty$, the above arguments with an arbitrarily large number in place of $\overline{\lambda}$ give that

$$\varlimsup_{n\to\infty}\frac{\beta(\lambda_{n-1})}{\log\lambda_n-\log^+\log\|a_n\|}=\infty.$$

Finally, by Theorem 2.1 and (10) we can prove the theorem.

References

[1] B.L. Srivastava, A study of spaces of certain classes of Vector Valued Dirichlet Series, Ph. D. Thesis, I.I.T Kanpur, 1983.

[2] G.S.Srivastava, Archna Sharma, On generalized order and generalized type of vector valued Dirichlet series of slow growth. Internationa Journal of Mathematical Archive, 2(2011), 2652-2659.

[3] G.S. Srivastava, A note on relative type of entire functions represented by vector valued Dirichlet series. Journal of Classical Analysis, 2(2013), 61-72.

[4] W.Q. Liu, D.C. Sun, Growth of Dirichlet series of infinite order in the plane. Acta Mathematica Scientia, 32A(2012), 808-815.

[5] W.C. Lu, C.F. Yi, Y.H. He, On the zero order of Laplace-Stieltjes transforms in the whole plane. Mathematics in Practice and Theory, 43(2013), 222-227.

[6] G.S. Srivastava, S. Kumar, Uniform approximation of entire functions of slow growth on compact sets. Acta Mathematica Scientia, 32B(2012), 2401-2410.

[7] O.B. Skaskiv, O.Y. Zadorozhna, Two open problems for absolutely convergent Dirichlet series. Matematychni Studii, 38(2012), 106-112.

[8] J.R. Yu, Some properties of random Dirichlet series, Acta Math. Sinaca, 21(1978), 97-118.

[9] G.S. Srivastava, A. Sharma. On bases in the space of vector valued entire Dirichlet series of two complex variables. Bulletin of Mathematical Analysis and Applications, 4(2012), 83-90.

[10] J.R. Yu, D.C. Sun, On the distribution of values of random Dirichlet series (I), Lectures on Comp. Anal., World Scientific, Singapore, 1988.

[11] G.S. Srivastava, A. Sharma, Spaces of entire functions represented by vector valued Dirichlet series. Journal of Mathematics and Applications, 34(2011), 97-107.

[12] G.S. Srivastava, A. Sharma, Bases in the space of vector valued analytic Dirichlet series. International Journal of Pure and Applied Mathematics. 70(2011), 993-1000.

Advanced Materials Research Vol. 936 (2014) pp 2281-2285
© (2014) Trans Tech Publications, Switzerland
doi:10.4028/www.scientific.net/AMR.936.2281

An Improved Mean Filter Algorithm for Impulse Noise Elimination

Tang Wang[1, a],Tang Jin[1, b]

[1]School of Automation, Beijing University of Posts and Telecommunications, Beijing, China

[a]tangwang@bupt.edu.cn, [b]tangjin@bupt.edu.cn

Keywords: Standard Mean Filter, Threshold, Impulse Wave, Noise Detection

Abstract: Since the standard mean filter has some drawbacks, an improved mean filter is proposed in this paper to overcome them. In this improved algorithm, noise detection is used to find the noise which is caused by impulse wave in the image. Based on the result of noise detection, window size would be selected in the improved mean filter to minimize the influence of the noise. According to the result of computer simulation, it shows that the improved mean filter is much more efficient than the standard mean filter in eliminating the impulse noise as well as in protecting the details of the image. It also shows its advantage in filtering speed.

Introduction

When images are formed or delivered or processed, they are easily to be influenced by impulse noise, which would cause the loss of information on image details and result in blurred images [1]. So in order to minimize the impact of the impulse noise, many filtering methods are used to solve these problems. The standard mean filter is widely used in this kind of situation, for its simplicity and good results. It replaced each point with the average value of the points around. However the standard mean filter still has its own drawbacks: when the detect window is small, it can preserve the details of the image, but cannot remove the noise effectively; when selecting a big detect window, it can remove the noise more effectively, but would damage the details of the image while eliminating the impact of impulse noise, and make the image blurred [2]. In this case, an improved mean filter is proposed to solve the problem. It has two steps to fulfill its task: First, it detects the noise points and separates them with the image points; Second, it uses the standard mean filter to deal with those noise points and keep the image points unchanged. So, the improved mean filter would wipe out most influence caused by the noise and protect the details of the image at the same time.

The Improved Mean Filter

The improved mean filter has two steps: detect noise points and minimize the influence of those noise points.

Detect Noise Points

Detect noise points is an important step, it is the foundation of the improved algorithm. There are many ways to detect noise points. In reference [3], it finds out the maximum point and the minimum point of the image, and uses them to divide the image into several blocks. Then it regards the medium value of maximum point and minimum point as a threshold, and uses it to judge whether a point is image point or noise point [3]. But the method of detecting noise point in this paper is different. Since the most image points are far away from 0 or 255, but the most impulse noise points are gathered near 0 or 255[4]. So the noise points have a great chance to be the minimum points or the maximum ones of the image. Take a uncheck point P(i,j) for example, the value of this point is assumed to be V(i,j), the aggregate of the point and the other eight points around it is supposed to be:

$$A_{i,j} = \{v(i+a,j+b) \mid a,b \in [-1,1] \text{ and } a,b \in N\} \quad (1)$$

The maximum value and minimum value of Ai,j is remarked as Max(i,j) and Min(i,j). If V(i,j) happens to equal to either Max(i,j) or Min(i,j), then it would be treated as a suspicious point. If it is a medium point, then it would be treated as an image point and kept unchanged. The suspicious point could be either noise point or image point, so it is necessary to judge it one more time. The rest values of Ai,j, which are equal to neither Max(i,j) nor Min(i,j), are formed as another aggregate Ri,j. But, if the rest values are equal to either Max(i,j) or Min(i,j), then, they all would be in the aggregate Ri,j. Once the aggregate Ri,j is fixed, according to the number of the values in Ri,j, the mean value of Ri,j is known, and it is named M(i,j). If the difference between V(i,j) and M(i,j) is below the threshold T, then the point P(i,j) would be treated as a image point. Otherwise, the point P(i,j) would be treated as a noise point.

So, to judge whether a point is a noise point, it has two conditions to meet:

- V(i,j) = Max(i,j) or V(i,j)= Min(i,j)
- | V(i,j) - M(i,j) |> T.

Filter the Image

Once those noise points are set, the next step is to filter the image. Take a 3*3 window for example, when the point P(i,j) is regarded as a noise point, the filter method is to replace the point value V(i,j) with M(i,j), the mean value of the aggregate Ri,j **.**

Experiments and Analysis

In order to verify this theory, several experiments were taken to show the effect of this theory. The results of the experiments are displayed as follows.

In figure1, image(a) is the original image without any noise, image(a1) is the noise image with4% impulse noise points. Image(a2) and image(a4) wereboth filtered by standard mean filter.Image(a2)was filtered by a 3*3 filter window, but image(a4) was filtered by a 5*5 filter window. It can be seen that image(a2) still has some noise points left, but the details of the image are kept well. In image(a4), there are less noise points, but the image become a little fuzzy. Things are better in image(a3) and image(a5), which were filtered by the improved mean filter. Image(a3) was filtered by a 3*3 filter window and image(a5) was filtered by a 5*5 filter window. The image(a3) and image(a5) are more clear compared with image(a2) and image(a4), and have less noise points than image(a2) and image(a4).

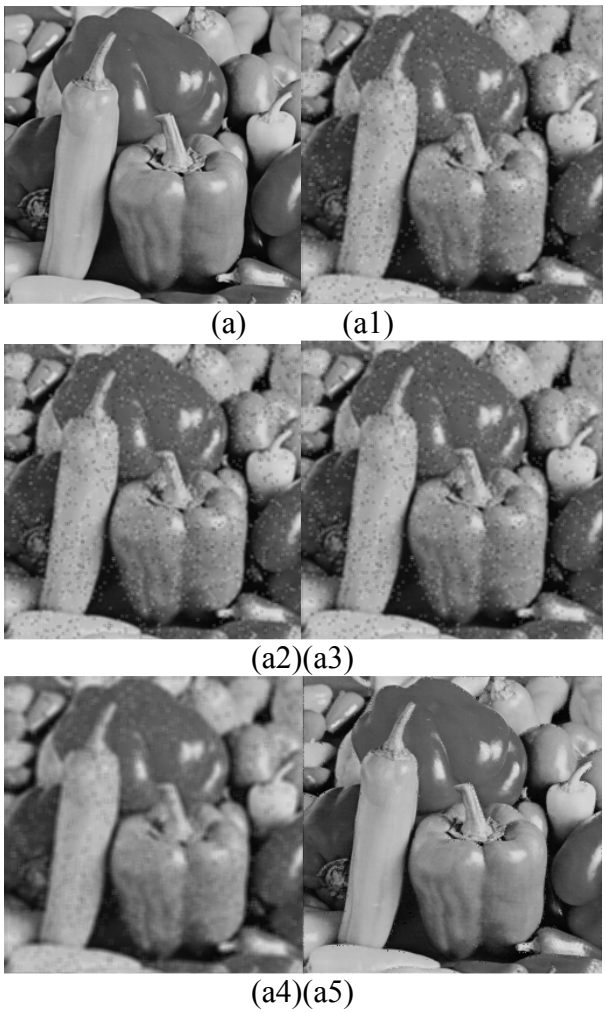
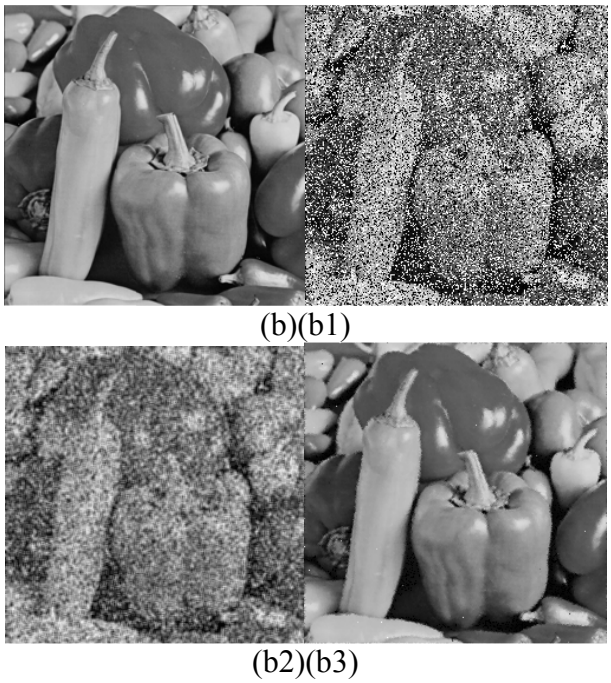
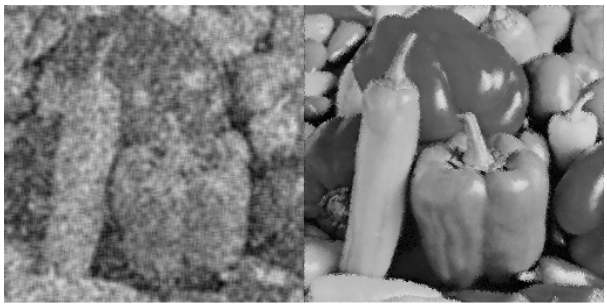


Fig. 1. Experiment images with 4% impulse noise: (a) original image;(a1) 4% impulse noise image;(a2) the 3*3 standard mean filter result;(a3) the 3*3 improved mean filter result; (a4) the 5*5 standard mean filter result; (a5) the 5*5 improved mean filter result





(b4) (b5)

Fig. 2. Experiment images with 40% impulse noise: (b) original image;(b1) 40% impulse noise image;(b2) the 3*3 standard mean filter result;(b3) the 3*3 improved mean filter result; (b4) the 5*5 standard mean filter result; (b5) the 5*5 improved mean filter result

To analyze the algorithm result in a quantitative way, signal to noise ratio (SNR) is chosen to be a standard in this paper. The function of SNR is:

$$\text{SNR}= 10\lg\left[\frac{\sum_{i,j} F_{i,j}^2}{\sum_{i,j}\left(F_{i,j}-V_{i,j}\right)^2}\right]. \quad (2)$$

In this function, V(i,j) is supposed to be the original point value of the point P(i,j), F(i,j) is supposed to be the final point value of P(i,j) after the filter part. The parameter i should be in the range of 0 – w, w is the width of the image, and the parameter j should be in the range of 0 – h, h is height of this image.

Judging from table 1, when the density of impulse noise is low, the improved mean filter has improved about 50% than the standard mean filter in signal to noise ratio, which means it does a better job than the standard mean filter. When impulse noise points are almost as many as image points, the improved mean filter has obvious superiority. It has almost twice the success rate than the standard mean filter, which may directly tell from image (b3) and image(b5). They are much clear than image (b2) and image (b4). According to table 1, it also indicates that improved mean filter has a better effect when uses a small filter window than a big one.

TABLE 1.SNR VALUES FOR EACH IMAGE

Noise / SNR / Method	4%	40%
Standard mean filter 3*3 window	20.6739	10.7870
Improved mean filter 3*3 window	32.4051	25.4450
Standard mean filter 5*5 window	19.5391	12.2100
Improved mean filter 5*5 window	28.6549	21.0664

Compared with those two mean filter, the advantage of the improved mean filter is obvious. It also shows that it is necessary to divide noise points from image ones, and to filter the noise points instead of the whole image.

Conclusion

Based on the standard method of mean filter, an improved method is proposed in this thesis to eliminate the impact of impulse noise. According to the property of impulse noise, and the

difference between impulse noise points and image points, two steps are taken to find noise points. First, find the suspicious points as much as possible, avoiding omissions. Second, use another function to ascertain the noise points among them. This method has solved the difficulty between minimizing the impact of those noise points and protecting the details of the image to a large extent.

References

[1] Gao Kefang, Guo Jiangang. An Adaptive Median Filtering Algorithm Based on Noise Detection[J]. Journal of Fujian Agriculture and Forestry University. 2009.5.

[2] Zhang Xuming, Xu Binshi, Dong Shiyun. Adaptive Median Filtering for Image Processing[J]. Journal of Computer-aided Design &Computer Graphics. 2005.2.

[3] Zhu Yuhong. An Improved Median Filter Algorithm in Digital Image[J]. Journal of Chang Chun Post and Telecommunication institute.2001.3.

[4] Zhao Chunjiang. Algorithm for Digital Image Processing[B].2009.3.

Advanced Materials Research Vol. 936 (2014) pp 2286-2290
© (2014) Trans Tech Publications, Switzerland
doi:10.4028/www.scientific.net/AMR.936.2286

Background Extraction by Fast Independent Component Analysis in Video Surveillance

Ding rui [1,a] Tang Jin [2,b], and Wang Wei[2,c]

[1] College of Information Engineering, Capital Normal University

Beijing, 100048, China

[2]School of Automation, Beijing University of Posts and Telecommunications,

Beijing, 100876, China

[a]dingrui1111@gmail.com [b]tangjin@bupt.edu.cn, [c]waweiy@qq.com

Keywords: Fast Independent Component Analysis (FastICA), dynamic background extraction

Abstract: To solve dynamic background extraction in complicated outdoor surveillance, a method of background extraction based on fast independent component analysis(FastICA) is presented. Since foreground regions and background in an image are considered to be independent, and background images in video show a high correlation coefficient, the method can directly recover the background signal without recover other source signals. In this paper, the principle of FastICA are introduced, and the detailed processes of the method and results are given, which show that the method can realize extracting background image .

Introduction

In recent years, Researchers at home and abroad has done a lot of research on the algorithm for background extraction, Summed up in two categories：The first category is traditionally built on the multi-frame method which is based on the statistical, statistical histogram method, statistical value method, The methods above are more suitable for the background of simple situation, It can get the better effect of the background image. The second category is as processor computing power increased, some more complex algorithm of background extraction, such as block method, selective updating method ,Single Gauss model method, Gaussian mixture distribution model method[1]. Block method is the research and analysis of adjacent pixels, more effective information can be used, reduce the calculation of s redundancy brought by background model of pixels forms and improve the speed of the system. Single Gauss model, Gauss mixture distribution model can correctly initialize model which in the scene contains no moving objects, there are some difficulties in practical application. Independent component analysis has find a linear transformation for non Gauss data, making signals between components are statistically independent or as independent as possible, if the image of the foreground and background images that are independent of each other ,It should use the independent component analysis method to extract background.

Independent Component Analysis is a method to extract independent source signals from mixed signals, It is a novel blind source separation technology to realize the enhancement and analysis of signal, which making the multi-channel signal accord to the principle of statistical independence and using the optimization algorithm to decompose the signal into several independent components[2,3], ICA is a statistical analysis method based on higher-order statistics characteristic of signal, Currently in speech recognition, communications, biomedical signal processing and other fields, It has been widely used. In image processing, mainly used in image denoising, face recognition, feature extraction of medical image[4,5], But the ICA used in study on background extraction is relatively less, is a relatively new field of study.

Background extraction

The modern monitoring technology is committed to establishing the mapping relation between image and the description of the event, making the computer filter out the useless or interference information from the video data which is massive dynamic, uncertain , automatic analysis, extracting the crucial and useful information from video source, and convert into knowledge and decision.

When the monitoring scene in a fixed light, fixed background environment, each background pixel enough to cope with the impact of image noise by modeling with Single Gauss model method; In light change with the time, adaptive single Gauss model can correctly model the background; however, when there are dynamic objects in the background scene, the single Gauss model is incapable to take action.

For the two kinds of model of dynamic background used most often is mixed Gauss model and non parametric model. Gauss mixture model and non parameter model can well model the dynamic scene, but the consumption of computation and memory is large, It is difficult to detect the moving targets on real-time.

In addition, when the background image which obtained by the above method having a motion detection by background subtraction method , also need to continuously update the background in order to adapt to the change of scene, and when updated needed to follow the FIFO rule, the earliest sample will be abandon when the latest sample is added in the model . But if the foreground image and background image in the image are recognized as two independent source, using independent component analysis method to realize background subtraction without updating the background[6]。

FastICA algorithm

The model based on ICA as shown in Figure 1. Assuming there are M unknown. The independent signals is:

$$s(t) = [s_1(t), s_2(t), s_3(t), \cdots s_m(t)]^T$$

The observation signal received which linear stacking on N sensors through the detection and analysis system of unknow. The signal is

$$x(t) = [x_1(t), x_2(t), x_3(t), \cdots x_n(t)]^T,$$

and X=AS,A is called hybrid systems (or matrix).

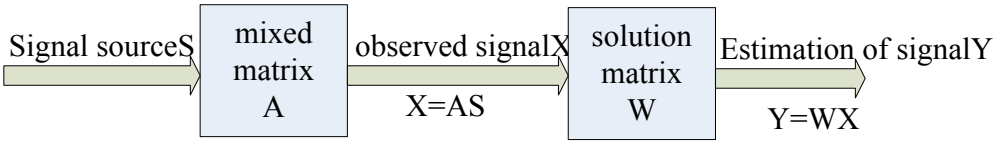


Fig. 1 The basic ICA model

W in Fig. 2 is a solution of mixed system (or matrix), Observations signals X get through the system and then obtained the output signal Y(t) which is close to S(t). This process can be expressed by Y(t)=WX(t). the basic idea of the ICA algorithm is to solve the separation system W, enable the output signal Y(t) statistical independence as possible, to approaching of the independence source signal S(t).

FastICA algorithm, or the fixed point algorithm, is that Hyvärinen and others are the first to propose and develop in 1997[7], FastICA algorithm according to the objective function can be divided into three algorithm: based on kurtosis, based on maximum likelihood, based on maximum entropy, The more commonly used is the FastICA algorithm based on the maximum entropy. Treat negative entropy maximum as each iteration of the data direction, Achieved that extracting the independent component in order, Fully reflects the projected track that is the traditional idea of linear transformations. In addition, the algorithm based on the maximizing principles of non-Gaussian, use the optimization algorithms of the fixed point, making the convergence more quickly and healthy.

When use the FastICA algorithm based on negative entropy maximum as a search direction, For the random variable Y whose probability density is P(y), The negative entropy is defined as:

$$J(y) = H(y_{gauss}) - H(y)$$

In the formula y_{gauss} is a Gaussian random variable and the random variables y have the same mean and covariance matrix.

$$H(y) = -\int P_y(\xi) \lg P_y(\xi) d\xi$$

It is the differential entropy of the random variable Y. When calculating in practical, Using the approximate calculation

$$J(y) \propto [E\{G(y_{gauss})\} - E\{G(y)\}]^2$$

Its extreme value of negative entropy corresponds to the extreme of G(y), After creating the negative entropy maximum goal function, To seek the extreme value based on Newton iteration method, get the independent component.

Background extraction in image sequences based on FastICA algorithm

Compared with the average of FastICA algorithm, the processing of independent component of the image has increased to three steps: the first is to put an image into a one-dimensional vector; the second is to handle with the independent components of the decomposition, the third is to use the reverse operation to process independent component which is processed, and then get the processed images.

The specific steps that the achivement of the background extraction method based on surveillance video image sequences are as follows:

1) Regard every frame of two-dimensional image sequence signals as a input observation source signal X;

2) Mean value for X, enable $E\{x_i\} = U$.

3) Albinism process for X, making the signal that albinism processed Z satisfied with $E\{zz^T\} = I$.

Albinism process: asking for the autocorrelation matrix transformation of the matrix of observational data source, asking for characteristic values, sort it and leaves the characteristic value which corresponds to the signal vector.

4) Initialize the random weight-vectorW_i of Z_i, Setting convergence errors $0 < \varepsilon << 1$;

5) Calculations $W_i(k)$ and $W_i(k+1)$ based on Newton iteration method, k is the number of iterations, until the D-value between $W_i(k)$ and $W_i(k+1)$ is less than the convergence error ε.

6) After extracting a component, remove the independent components from the observed signal, calculate the next separate component;

7) When a loop exceeds a preset value, stop the search.

8) To restore the Y_i to a two-dimensional image.

The experiment and analysis

The experimental data, the two section monitoring video are from the Front Gate of one scenic spot of Beijing, the frame rate of the video is 30fps, the size of image is 288 * 352, the environment of the Front Gate of attractions is complex, it is next to the parking lot, person flow is large, and there are many cars come and leave.。

Experiment first verify the text situation of the algorithm when there is only one individual object moving in a relatively simple environment, the experiment intercept 6 frames of images from the first videos, as shown in the Figure 2, a staff riding a bicycle crossing the road in the picture.

The detected background was shown in figure 3 (a), in order to show the effect, using the results to process the fourteenth images with background subtraction method, and the effect of binarizing as shown in figure(b).



(a)The 10th frame image (b)The 12th frame image (c)The 14th frame image



(d)The 16th frame image (e)The 16th frame image (f)The 20th frame image

Fig. 2 The simple case of original image



(a)The background (b)The 14th frame of removed background

Fig. 3 Detection results under simple conditions



(a)The 60th frame image (b)The 90th frame image (c)The 120th frame image



(d)The 150th frame image (e)The 180th frame image (f)The 250th frame image

Fig. 4 The original image under complex environment

By the test, choosing more than 3 frames of image at random, using the algorithm of FastICA could effectively extract the background. Because of the environment of the testing video is simple, the experimental results are not enough to display the advantages of the extraction by the FastICA algorithm in dynamic background, so the text intercept 6 frames of images from second videos, as shown in figure 4 the video has a lot of visitors and in complex environment, a car driving into the middle of the parking lot, and pedestrians walking cross from the upper right of the image to the parking lot。

The 6th images of the complex environment processed by FastICA processing, test results are shown in figure 5. A lot of crossing pedestrians in the original video are weakened as the faint shadow, If they are simple thresholding can obtain a clear background, at the same time the detection results is effectively remove the coming car from a distance, and the pedestrian walk in the parking lot.。



Fig. 5 Background detection results

Conclusion

The experimental results show that using the independence of foreground image and background image and the correlation of the background image in video image sequences, regarding the background image and foreground image (or moving object) as two independent signal source, Fast independent component analysis method described in this article can be effective for extracting the background of outdoor surveillance video . Because of the complexity and diversity of the outdoor environment, more testing is needed for this method in the case of other mutation.

Acknowledgments

The authors thank the financial support of Science and Technology Planning Project of Beijing Municipal Commission of, Education, grant KM201210028003.

Reference

[1] Wren, A. Azarbayejani, et al, “Pfinder: real time tracking of the human body” I EEE Transactions on Pattern Analysis and Machine Intelligence, 1997, 19 (7) : 780-785.

[2] P. Comon,“Independent component analysis—A new concept,” Signal Process, 1994, 36: 287-314.

[3] D. rui, S. caicheng, M.Eerk, et al “Method of infrared point target detection based on cICA ,”Transactions of beijing insititute of Technology, vol. 29, no.11, 2009 pp. 1001-1005.

[4] Kwak K C, Pedrycz W. Face recognition using an enhanced independent component analysis approach,” IEEE Trans. On Neural Networks, 2007, 18(2): 530-541.

[5] D. rui, S. caicheng, M.Eerk, et al, “Processing method of infrared line-scan image based on independent component analysis,”Optical Technique, vol. 35, February 2009, pp. 288-291.

[6] T. Duming and L. Shiachih, “Independent component cnalysis-based background subtraction for indoor surveillance,” IEEE Trans on image processing, vol. 18, no.1, January 2009, pp.158-167.

[7] Hyvarinen A, “Fast and robust fixed-point algorithms for independent component analysis,” IEEE Trans Neural Networks, 1999, 10(3).

CHAPTER 23:

Communication and Information Technologies

Advanced Materials Research Vol. 936 (2014) pp 2293-2297
© (2014) Trans Tech Publications, Switzerland
doi:10.4028/www.scientific.net/AMR.936.2293

The Design of Multi-Protocol Network Based on Point-to-Point Protocol and Frame Relay

Wentao Gong[1, a]

[1]Internet and Education Technology Center China University of Petroleum Qingdao, China

[a] gongwt@upc.edu.cn

Keywords: network; frame relay; multi-protocol

Abstract. Local area network and wide area network are different network protocols, small and medium enterprises due to the geographical distribution of discrete and interface diversity, leading to its needs to be compatible with different network protocols, it is difficult to use a single network protocol to realize network architecture, and due to the ipv4 address scarcity, making its application or maintenance cost greatly increased, based on this, this paper presents the design of multi-protocol network architecture based on point-to-point protocol and frame relay, and with the advantages of the router is compatible with a variety of interfaces and protocols to connect different network interfaces, the paper also gives the configuration of routing information protocol and static routing through local area network, the paper presents the core information of frame relay and point-to-point protocol among the routers, and the paper gives the realization of the network address translation in the end.

Introduction

With the rapid development of network technology [1], making the network devices becomes more and more. The IP address is known as the Internet Protocol address. The common IP address is divided into IPv4 and IPv6; the small and medium-sized enterprises in the application of Internet addresses are the IPV4.

With the rapid expansion of the network scale, the IPv4 address has been turned into a kind of scarce resources, the local small enterprises and small companies are unable to afford the high IP address of the application and maintenance costs. To solve this problem, the relevant experts and proposes the NAT (Network Address Translation) solution [2-3].

RIP (Routing Information Protocol) is a distance vector routing protocol based on DVRP (Distance Vector Routing Protocol) interior gateway protocol IGP (Interior Gateway Protocol). The RIP protocol was first introduced by Xerox Company in the late development of the last century, at present RIP is the routing protocol UNIX operating system to the various types of routers and layer three switches and other equipment support [4-5].

RIP routing protocol uses the hops in the network to compute the distance to the destination network, the default maximum hop count is 15, and set network unreachable when the hop is 16, there are many factors that make RIP protocol suitable for LAN (Local Area Network) [6-8].

Frame relay is an open system interconnection OSI (Open System Interconnect) data link layer in the model, by using a simplified method to realize the exchange and transmission of data units in the data link layer, and to the gradual development of the X.25 packet switching technology, and supports the statistical multiplexing protocol, can be a single link above transmission a plurality of the virtual circuit VC (Virtual Circuit), effectively reduces the network cost and effective utilization of the link bandwidth of backbone network [2-3].

The advantages of router support different interfaces can connect different networks, compatible with PPP (Point-to-Point Protocol) and RIP protocol, the different regions of the different types of interfaces LAN eventually get through, through the configuration of different routing protocols, RIP and static routing for each segment can be connected to the each other, in order to achieve local through objective, then the private network of its service network to NAT mode into the public network.

In this paper, the architecture of the kind of Multi-Protocol Network design based on PPP and Frame Relay is proposed in section 2, and the configuration process of the architecture is proposed in section 3, and the whole paper is summarized in section 4.

The Design of the Kind Of Multi-Protocol Network Based on PPP and Frame Relay

The Composition of Multi-Protocol Network Design Based on PPP and Frame Relay

In this framework, as shown in Fig.1, the total of five routers, four of which are inside the local area network, and one is outside the network. There are four switches, three in the LAN, and one is outside the network.

The switch SW1's network is connected to the server, using the public address.

The network architecture, the switch SW1 and the router RT2 are outside the local area network, and the router RT2 is the egress router, between the RT2 and the RT5 connection through the PPP link, and uses PPP authentication.

RT5 is connected with the switch SW2, and connects the internet user.

RT2 and RT3 are connected by the frame relay connection, uses Frame Relay authentication, and the SW3 connects the common user network.

RT2 and RT4 are common connection; and the switch SW4 connects the common user network.

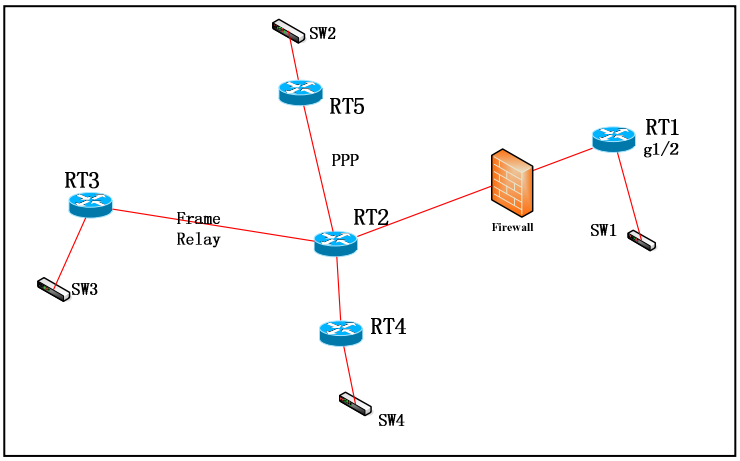


Figure 1. The Composition of the Multi-Protocol Network Based on PPP and Frame Relay

The Design of Multi-Protocol Routing

According to the planning, the network routing protocol is mainly used RIP and static route.

The RIP protocol through route poisoning routing information is used to guarantee the correctness and fault network directly connected routers.

Static routing is a routing protocol, its configuration is simple, and all the routers are required to configure a static route, so that it can reach all local area network. In the global network, all the routers and the switches should configure static routing table.

There are many routers have to open the RIP routing, such as RT2 and RT3, RT4, RT5 and other directly connected routers, all the other routers and switches need static routing.

The PPP Authentications

Specific certification process has the following three steps:

The first step: the main verification party sends a random number, and sends the main verification of the end users.The second step: the attested party receipts validation master validation request, check the local user password, if the configuration of the chap authentication password.The third step: the main verification party checks the information, and relies on MD5 algorithm to create an abstract for the message and the local password and authentication methods.

The Configuration Process of the Architecture

The Configuration of the Architecture

The configuration of the architecture comes as following: there are five routers and four switches in the architecture, as shown in Fig.2.

The router RT1 and the switch SW1 both locate outside the local area network and the router RT1 connect the switch SW1, and there is the virtual local network named vlan3 in the switch SW1, and the gateway is 100.1.3.1, and the net mask is 255.255.255.0.

The entire virtual local network is configured in the following picture.

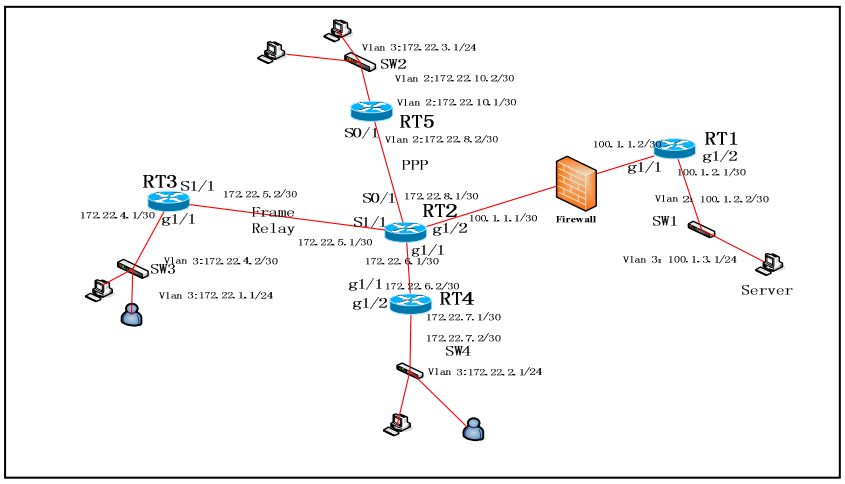


Figure 2. The Configuration of the Multi-Protocol Network Based on PPP and Frame Relay

The Configuration of the PPP Authentication

The PPP chap authentication set the RT2 as the server, and set RT5 as the client end, which is to be verified.

The system's interface on RTB, in the statement for the user and the key, and the password is set as the simple format

The configuration in the interface of the router RT2 comes as follows:

[RT2] local-user rt5
[RT2] password simple BBB
[RT2] service-type ppp
[RT2]Interface Serial0/1
[RT2- Serial0/1] Description link-to-rt5
[RT2- Serial0/1] Link-protocol PPP
[RT2- Serial0/1] PPP authentication-mode chap
[RT2- Serial0/1] PPP chap user RT5
[RT2- Serial0/1] PPP chap password simple BBB
[RT2- Serial0/1] IP address 172.22.8.1 255.255.255.252

The password must be the same in the router RT2 and in the router RT5.

The configuration in the interface of RT5 comes as follows:

[RT5] local-user rt2
[RT5] password simple BBB
[RT5] service-type ppp
[RT5] Interface Serial0/1
[RT5- Serial0/1] Description link-to-rt2
[RT5- Serial0/1] Link-protocol PPP
[RT5- Serial0/1] PPP authentication-mode chap
[RT5- Serial0/1] PPP chap user RT5
[RT5- Serial0/1] PPP chap password simple BBB
[RT5- Serial0/1] IP address 172.22.8.2 255.255.255.252

The Configuration of the Frame Relay

In order to configure the frame relay authentication, we need the corresponding port on the DCE (Data Communications Equipment) and DTE (Data Terminal Equipment) ends are respectively configured with an IP address.

The configuration in the router RT2 comes as follows:
[RT2] interface s1/1
[RT2-s1/1] description to RT3
[RT2-s1/1] link FR
[RT2-s1/1]FR interface-type DCE
[RT2-s1/1.0] interface s1/1.0 p2mp
[RT2-s1/1.0] FR DLCI 100
[RT2-s1/1.0] IP address 172.22.5.1 30
The configuration in the router RT3 comes as follows:
[RT3] interface s1/1
[RT3-s1/1] description to RT2
[RT3-s1/1] link FR
[RT3-s1/1] FR interface-type DTE
[RT3-s1/1.0] interface s1/1.0 p2mp
[RT3-s1/1.0] FR DLCI 100
[RT3-s1/1.0] IP address 172.22.5.2 30

The Configuration of the RIP

The router RT2 configures the RIP dynamic routing protocol comes as follows:
[RT2] rip 1
[RT2-rip1] version 2
[RT2-rip1] undo summary
[RT2-rip1] network 172.22.5.1
[RT2-rip1] network 172.22.6.1
[RT2-rip1] network 172.22.8.1
And the others routers are configured in the same way.

The Configuration of the Static Routing

All of the core equipments of RIP dynamic routing protocol configuration are completed, it's need to configure the default static routing.
The switch SW2 configures the static default route:
[SW2] ip route-static 0.0.0.0 0.0.0.0 172.22.10.1
The switch SW3 configures the static default route:
[SW3] ip route-static 0.0.0.0 0.0.0.0 172.22.4.1
The switch SW4 configures the static default route:
[SW4] ip route-static 0.0.0.0 0.0.0.0 172.22.7.1
The router RT5 configures the static default route:
[RT5] ip route-static 0.0.0.0 0.0.0.0 172.22.8.1
[RT5] ip route-static 172.22.3.1 24 172.22.10.2
The router RT2 configures the static default route:
[RT2] ip route-static 0.0.0.0 0.0.0.0 100.1.1.2
[RT2] ip route-static 172.22.10.1 30 172.22.8.2
[RT2] ip route-static 172.22.3.1 24 172.22.8.2
[RT2] ip route-static 172.22.4.1 30 172.22.5.2
[RT2] ip route-static 172.22.1.1 24 172.22.5.2
[RT2] ip route-static 172.22.7.1 30 172.22.6.2
[RT2] ip route-static 172.22.2.1 24 172.22.6.2

The Configuration of the NAT

The router RT2 uses the 100.1.4.1 to the 100.1.4.10 as the nat address-group, and the configures of the static default route in the router RT2 comes as follows:
[RT2] firewall enable
[RT2] nat address-group 1 100.1.4.1 100.1.4.10
[RT2] acl number 2001

[RT2-acl-basic-2001] rule 0 permit source 172.22.0.0 0.0.255.255
[RT2] interface GigabitEthernet1/2
[RT2- GigabitEthernet1/2] description link-to-rt1
[RT2-GigabitEthernet1/2] nat outbound 2000 address-group 1
[RT2-GigabitEthernet1/2] ip address 100.1.1.1 255.255.255.252

Conclusion

This paper discusses and summarizes the development of LAN point-to-point protocol, frame relay and RIP dynamic routing and static routing and other related areas, and sums up the characteristics of RIP and the configuration of the points, and gives the disposition of dynamic routing protocol RIP and frame relay implementation process, and finally completes the kind of multi-protocol network design based on point-to-point protocol and frame relay.

References

[1] China Education and Research Network [EB/OL]. 1993.

[2] Xinwen Zhang, Formal model and analysis of usage control, Ph.D. thesis, George Mason University, Fairfax, Virginia, (2006):3-15.

[3] Rosen E, Rekhter Y. BGP/MPLS IP Virtual Private Networks (VPNs)[S]. RFC 4364, 2006.

[4] Label Switching Networks[S]. RFC 3443, 2003.

[5] Colton A. Cisco IOS for IP Routing. 3rd ed., Rocket Science Press, Inc., 2003.

[6] Rekhter Y, Li T. RFC1771, ABorder Gateway Protocol 4 (BGP-4) [S], 1995.

[7] David C.Chou, and Kirill Yuro, “Security development in Web Services environment”, Computer Standards & Interfaces, (2005):233-240,.

[8] J.Park, R.Sandhu, “The UCONABC usage control model”, ACM Transactions on Information and System Security (TISSEC), Vol.7, No.1, (2004): 128-174.

Advanced Materials Research Vol. 936 (2014) pp 2298-2301
© (2014) Trans Tech Publications, Switzerland
doi:10.4028/www.scientific.net/AMR.936.2298

Construction and sharing of library digital resources in China and Southeast Asia

Do Thi Thanh Thuy [1,2]

[1] School of information management, Wuhan university, Wuhan 430072, China

[2] Library of Bacgiang province, Vietnam

thuytvbg@gmail.com

Keywords: Digital resources sharing, resources sharing, China, Southeast Asian, digital library.

Abstract. Resources development & sharing has become an important subject of widespread concern in the world and it is the inevitable demand of information society development. Sharing is not only a useful way to save money, reduce duplication of investment, improve resource utilization and realize resources complement, but also an important way to greatly improve the information flow and information services support capabilities, and promote society access to information in general. This paper introduces the importance of resources sharing between the libraries of China and Southeast Asian and it refers to the cooperation ways of digital resources sharing.

Introduction

As the core of building a digital library, the digital resources construction refers to the process in wich the information resources are selected, collected, organized and managed to form a usable digital resources system. The digital resource construction and sharing plays an important role in the implementation of the digital library extensive project.. With the development of China and southeast Asian free trade area, the cooperation is making big progresses between the countries. As a library based on social and economic service, we must sieze the opportunities to development in depth. Therefore, Digital resources sharing program becomes a current subject that is worth to be studied in depth.

Review of literature

Resource sharing has been the goal of libraries for many centuries. There is no one library that can afford to build a collection that is sufficiently comprehensive to satisfy all of its users' requests. By joining cooperative acquisition or collection development programs, libraries provide their users greater range of library materials or better depth of subject coverage [1].

Interlibrary loan (ILL)services facilitate the sharing of resources among libraries. As stated in ALA Interlibrary Loan code for the United States, “the purpose of interlibrary loan is to obtain, upon request of a library user, material not available in the user's local library” [2]. The increasing amount of electronic resources in libraries may have affected the use of ILL services. A study conducted by Egan [3] indicated that the requests for nonreturnable, photocopied materials decreased because there are more full-text e-journals available online now. Wiley and Chrzastowski found that the requests for periodical articles fell 26% between 1990 and 2003 because libraries started subscribing to more packaged periodical databases [4]. An investigation conducted by Beaubien (2007) [5] found that requests for nonreturnable materials decreased 4% while the requests for returnable materials (books, audio-visual materials, microfiches, etc.) increased 26% from 1998 to 2004. The statistical data on ILL in Taiwan from2001 to 2008 show similar trends. The number of requests for periodical article copies declined from168,620 items to 108,017 items, while the requests for monograph borrowing increased from 17,710 items to 38,322 items [6]. Walton (2008) [7] explained that the convenience of electronic resources did change the users' information behavior and that they prefer accessibility over

resource quality. Meanwhile, the growth of open access resources also reduces the number of requests for ILL.

The importance of Digital resources construction and sharing in libraries of China and Southeast Asian

The need to the free trade area development

The construction and development of China-Southeast Asian free trade area benefit the people in 11 countries of China-southeast Asian area. People in those countries are urgent to know the information about economy, society, civilization of those countries, so it offers a big chance to construct the digital resources system. It becomes an important project significantly. By construct the system, we could satisfy the need of people from these countries and improve the cross culture understanding and cooperation.

The need of library development

The world today has entered the time of globalization. In this time, library has been digitalizing, networking and media serving. Digital resource sharing project is a big advantage of library. So the digital resources sharing is the direction of library service in future.

The capacity of service improvement

Digital resources sharing and construction project could make the best of the resources and fund raising on one side, and on another side, it satisfies the need and want of readers and benefits the countries all involved into the work. So, the digitalizing resources construction project could improve the library service the best.

Resource Sharing is the key of library digital

Compared to other carriers in the form of resources, one of the biggest advantage of digital resources is the share ability. Under the principle of equality and mutual benefit between the Library and the libraries, even libraries and other relevant agencies to conduct resources sharing, complementary digital resources to expand the data sources, to improve the number of the library's digital resources. Special, enhance the overall competitiveness of the Library.

If the digital library are fragmented, the implementation of the principle not open shared, this will not only result in duplication of investment and low resource utilization of the phenomenon, the competitiveness of the digital library is a weakened.

Sharing of digital resources available from the following aspects:

Establish the concept of information resource sharing:

The digital technology allows a paper to this literature can easily become the electronic information, digital document delivery through the network a snap. However, some management concepts still remain only in the museum, can not think of the transfer of the Museum. Thus, even if the implementation of digital library information resources, information resources retrieval system is still closed, is still limited to the retrieval of the museum readers. In fact, the role of electronic library resources lies not only in terms of museum users, but also because the resources sharing. Thus, we must change management concepts, and establish the concept of resource sharing, and increase with the application in practice, so that in a networked environment to provide readers broader sources of information.

Increase efforts to share input into the construction

To establish a shared center, fully functional and running quickly shared network of information resources and reliable resources for the layout of the protection system is essential; other libraries to support each other, all library resources, special collection open to shared the harmonization and layout. Which need to invest greater human and material resources, digital resources shared building in the part of the library has some of the features, but in the current situation is far from enough, takes a great effort in the future for a long period of time need continuous attention is still the focus of digital library construction.

Formulate Sharing specification

Orderly operation of the shared resource good must Sharing of information resources, financial security, the rights and obligations of members, as well as information resources sharing system and operational mechanism, the overall layout to make clear. The introduction of punitive measures to destroy or hinder the behavior of Sharing and incentives contribute to the sharing of resources. Uniform operation of the standard specification starting point to develop a code of conduct, to create a favorable institutional environment for the library literature resources sharing.[8]

Cooperation ways to digital resources integration

Put the focus on the special digital documents

We could strengthen the communication among the libraries of China and Southeast Asian countries and integrate the digital resources of China and Southeast by the free trade area cooperation on culture. For example, the special documents. As we know, the cooperation focus mainly on economy. We could gather information related to economy cooperation of China and southeast Asian countries. By doing this, we could make a big progress on library service in the future.

Integrating the national digital documents with internet

With the development of the information, web, and other advanced technologies on information process, internet is a most important way to communicate. We could dive into a sea of knowledge with an easy searching engine. We could mal, a best of the internet to gather, chronicle, and download some knowledge and documents about Southeast Asian countries. One problem we will confront with is too many knowledge and resources. Sorting out the valuable information requires the wisdom and capacity of information collectors.

National digital document collection by official ways

First, cooperation on documents communication between government by visiting to Southeast Asian countries; Second, Actively contact with embassies and libraries to explore the future issues in details and practice that; Third, Siezing the opportunities of cooperation with free trace area and appeal the support of provincial governments and officials. Making best of document resources to gather, processing and indexing the related information for the further tmst and praise of official from other countries, then to sieze the opportunities to collect document resources of those countries.

Collecting the national digital documents resources from Southeast Asian countries by folk ways

With the trade cooperation with Southeast Asian countries, We will be happy to see more and more merchants entering the southeast Asian countries recently, and Southeast Asian merchants also look for opportunities on commercial development. Meanwhile, some big enterprises of China are standing on the southeast Asian countries, which bring more and more technicians and workers out of China. Library could sieze the good chance to employ the volunteers, merchants living in southeast Asian countries, workers, overseas and consultants to help collecting national digital resources.

Found the China and Southeast Asean digital document resources center

The center includes a platform of communication, information display platform and a library service website. Information resources sharing platform offers a media to exchange some selected document from neighbor provinces, and collect, process, and develop those information about southeast Asian countries. The main function of it is to collect information, check out and read, internet serve, information development and digital resources construction. Information service center divides into information searching reading rooms on a service platform. It becomes a largest scale information center in China. China and Southeast Asean library service web system mainly is an information base on construct, collect, intergrate, and develop the bilingual digital document resources system. After the establishment of the resource center, we will provide information checking service to southeast Asian countries with our human resource center and advanced internet technology, then we will build the close tie with southeast Asian libraries and copperate with Southeast Asian countries on document exchange, resource sharing and digital service.[9]

Conclusions

The benefits derives from resource sharing are increasing especially in this digital are. No one library in the world can have collection of everything and is not possible for a library to acquire every single item for its collection. With the advancement of latest technology, resource sharing is make easier to access any time, any where and by any one. Libraries must ensure that resource sharing must be carried out through cooperation and collaboration in order to fulfil the user needs and to stay relevant in this challenging era.

Construction and sharing of library digital resources in China and Southeast Asia is not only the need of library service but also the need of free trade development. Librarians in China and Southeast Asian countries should seize the opportunities to learn the significance of construction project, solve the problems and make the resource sharing project to be beneficial to economy and all people in China and Southeast Asian countries.

References

[1] 12G. E. Evans & M. Z. Saponaro (2005). Developing library and information center collections, 5th ed. Westport, Conn: Libraries Unlimited.

[2] 12American Library Association (2008). Interlibrary Loan Code for the United States Available at:http://www.ala.org/ala/mgrps/divs/rusa/resources/guidelines/interlibrary.cfm. Accessed December 12, 2009.

[3] 12N. Egan (2005). The Impact of electronic full-text resources on interlibrary loan: a ten-year study at John Jay College of Criminal Justice. Journal of Interlibrary Loan, Document Delivery and Electronic Reserves, 15 (3), 23–41.

[4] 12L. Wiley, T. Chrzastowski (2005). The impact of electronic journals on interlibrary lending: a longitudinal study of statewide interlibrary loan article sharing in Illinois. Library Collections, Acquisitions, and Technical Services, 29 (4), 364–381.

[5] 12A. Beaubien (2007). ARL white paper on interlibrary loan. Available at: http://www.arl.org/bm ~ doc/ARL_white_paper_ILL_june07.pdf. Accessed December 10, 2009.

[6] 12Science and Technology Policy Research and Information Center (2009). Yearbook of national document delivery service, 2008 Taipei: STIP (in Chinese).

[7] 12J. Walton (2008). The changing use of electronic document delivery in the inter-library loan service: a survey. Interlending and Document Supply, 36 (1), 43–56.

[8] 12Huang Kai (2012), “Digital Library Core Competitiveness Construct of Dilemma and Breakthrough”, Asian Libraries: Resource Sharing, Copperation and Development, 2012 China-ASEAN Cultural Forum. 190 - .

[9] W. Shuiqiao and Zh. Qingsong (2012), “Construction and Sharing of Library Digital Resources in China and Southeast Asia”, Asian Libraries: Resource Sharing, Copperation and Development, 2012 China- ASEAN Cultural Forum. 154-164.

Advanced Materials Research Vol. 936 (2014) pp 2302-2306
© (2014) Trans Tech Publications, Switzerland
doi:10.4028/www.scientific.net/AMR.936.2302

A Model Integration Framework based Portability for GNSS Simulation

Hongwei Zhou[1], Hongtao Hou[2], Wangxun Zhang[2] , Qun Li[2], Qiang Chang[2]

[1]Beijing Institute of Tracking and Telecommunication Technology， Beijing 100084, China

[2]College of Information Systems and Management, National University of Defense Technology, Changsha, HuNan 410073, China,

Email: hht07312@sina.com

Keywords: Navigation Satellite System Simulation, Simulation Model Portability Standard, Model Framework, Simulation Reuse

Abstract: Performance Simulation for Global Navigation Satellite System (GNSS) that be used for performance simulation and evaluation analysis of the GNSS, is a part of the critical algorithm test and system index analysis for GNSS. In this article, the requirements of GNSS are analyzed firstly, and the characteristic of model portability for GNSS is studied, then the model integration framework based on Simulation Model Portability is proposed. The system architecture consists of model design, development, integrating, executing and analysis. Lastly, the regional performance of GALILEO Navigation Satellite System in China is tested and analyzed based on the integration framework.

Introduction

Global Navigation Satellite System (GNSS) are playing an increasingly important role in human life following communications and network. It can provide all-weather positioning, velocity-measuring and timing for the surface of the Earth and near-earth space users, and be widely used in both military and civil field[1]. GNSS consists of satellite subsystem, rocket system, operation control system, users subsystem, launching site subsystem and TT&C subsystem, is a space engineering system with very large scale and complex structure. To support system integration, functional verification, performance validation and analysis of GNSS, it is necessary to build model and simulate the behavior and processes of GNSS with modern computer simulation techniques and methods.

At present, there are been built or building four GNSS around the world, which are GPS,GLONASS, COMPASS and GALILEO. It attaches great importance to Simulation for GNSS in the course of construction. As simulation for GNSS depends on integrating multi-domain model and building complete circuit of navigation satellite system, it makes much more difficult for the scale and integrating. By the late nineties, the U.S. military began to large-scale simulation by using distributed interactive simulation technology for GPS. The Simulation Model Portability Standard[2,3] (SMP) was developed by European Space Agency in 2003, which were faced with difficulties by multi-domain model integration and analyzing during designing GALILEO, and supports integrating models for GALILEO and a series of aeronautical engineering.

The Define and Characteristic of Portability

Good portability of the navigation simulation model is critical to rapidly and effectively integration for the performance simulation of GNSS[4,5]. The High Level Architecture (HLA) method is used to solve the interoperability problem among heterogeneous simulation system. And if the performance simulation of GNSS which coupling between models is very complex will use HLA to integrate models, the performance and efficiency of the simulation, it will be significantly reduced, and the problem of types, computational complexity of GNSS analysis will not be solved, simulation in mass will not be realistic. And description of simulation model will be more normalization and standardization, which is a basic requirement for the development of model integration and reuse.

Simulation Model Portability Standard[6,7,8] (SMP) is developed for improving the portability, maintainability and reusability of modeling and simulation specification by European Space Agency (ESA) since 2003. SMP specification absorbs many advanced approaches in the field of software engineering and simulation, and extracted metadata information from the simulation model, and represented the model with Platform Independent Model (PIM) base on meta model, and developed simulator components, service components, model components and interfaces between them.

The separation of the simulation engine and model is one of basic method for simplifying the modeling work, easy reuse and integration model during modeling. Based on this, The SMP2 has introduced three design ideas:

1) Separation simulator component and simulation service component.

2) Separation Platform Independent Model (PIM) and Platform Specific Model (PSM).

3) Separation Design-Time Component (DTC) and Run-Time Component (RTC).

There are four forms in SMP2 simulation model components: PIM-DTC component , PIM-RTC component , PSM-DTC component and PSM-RTC component. SMP2 standard consists of SMP2 component model, meta model, C++ mapping mechanism and user's manual[8,12]. Model development and integration method based on SMP2 specification can be used for the research of the performance simulation system of GNSS.

GNSS's Model Integration Framework based Portability

The performance simulation of GNSS simulates and evaluates the performance of the GNSS's services segment, support to evaluate the performance indexes of global or regional grid[9,10,11]. For the different type of analysis task, the tasks can be further subdivided into many subtasks, and the development, integration and analysis of GNSS's model put forward higher requirements: Reusability of simulation model, Scalability of integration framework, Efficiency of the model development, Usability of system configuration.

According to characteristics of the above requirements and SMP2's specification, model framework, execution framework and integration framework of GNSS should be reasonably establish, will support many performance simulations and analyses[13]. Figure 1 shows the structure of the model components of GNSS, which includes every key model and core algorithm of different segments. In developing these models and algorithms, different organizations and users may not be used the same tools and implementation methods, but the interface of models and algorithms can be consistent with SMP2 specification, so that it make possible for reuse and transplantation of the model and algorithm .

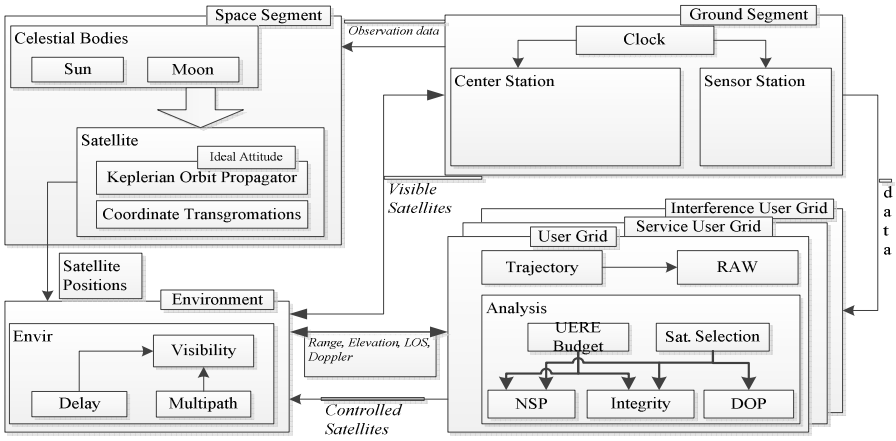


Fig. 1. The model components of GNSS simulation

Based on the navigation performance analysis, the model or algorithm required by different analyses is not the same, which requires the model framework has good reusability and integration. For example, during Visibility analysis, environmental segment model need to get positions of satellite and user in the current epoch, then calculate the observed elevation angle, in order to

determine the satellite's visibility; while analyzing Dilution of Precision (DOP), Navigation System Precision (NSP), user grid model need to obtain the visible satellites in the current epoch, then choose appropriate satellite selection algorithm, and calculate various types of DOP and NSP value by using the appropriate budget method of User Equivalent Range Error (UERE). In the above simulation, the basic models and algorithms is consistent and can be directly reused, while they also need to be quickly replaced for the validation and evaluation of key algorithms. So it is necessary to establish a unified simulation model integration framework to support reuse and integration of the various types of models and algorithms of navigation system. While Component-based and interface-based of SMP2 design method, a simplified portability navigation simulation model integration framework is showed in the fig. 2.

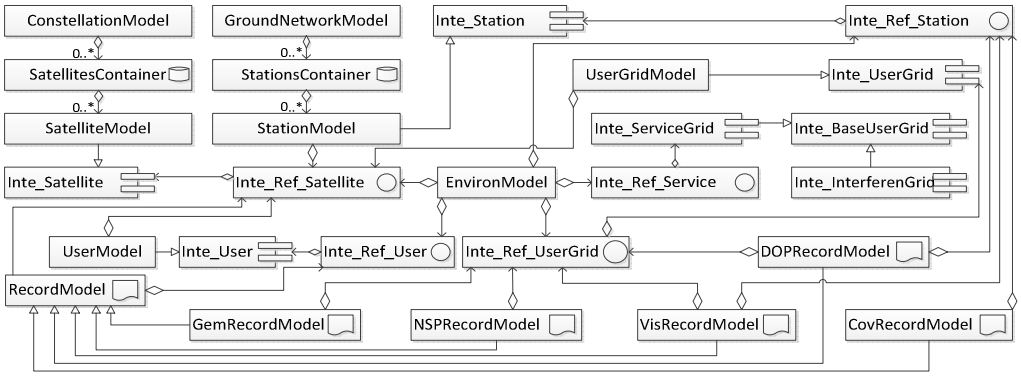


Fig. 2. Model integration framework based portability

In the figure, SatelliteModel, StationModel represent the domain model of the satellite model, station model, which models design algorithm interface by SMP2 specification, such as Inte_Satellite, Inte_Station, etc. The other models can be referenced these models by accessing these interfaces, such as Inte_Satellite provide the satellite's health status, the orbital elements, etc. Some domain model users can use some model or algorithm to replace some model, for example the environmental model can select different delay correction algorithm for Ionospheric and Tropospheric for simulation, which include Egnos algorithm, Hopfield algorithm, Saastmanion algorithm, etc. SatellitesContainer, StationsContainer are various types of containers based on SMP2 specifications, and support the other model entities to query and manage these entities. Inte_Ref_Satellite, Inte_Ref_UserGrid provide references of the interface for domain models, these references may be multi-reference, such as EnvironModel is an environment model, and Inte_Ref_UserGrid is a one-to-many reference from EnvironModel to UserGridModel. RecorderModel, DOPRecorderModel are functional models, and indicate different recording models. Oriented performance simulation analysis, these recording models needs to provide the interface to logging simulation data, in order to analysis.

The method of separation application model framework and simulation scenario framework will help the domain user more focusing on the familiar navigation domain problems, rather than the specific implementation details of the model framework. The simulation users more focus on the development of the application platform or framework, not the details of the model or algorithm.

Experiment for GNSS Simulation Based Portability

According to above integrated model framework, the simulation application development and test architecture based on SMP2 for GNSS can be divided into simulation model design, development, integration and execution of four stages.

The main task of the model design phase of Navigation simulation is that designing SMP2 Catalogue file based on SMDL, model design documents. Simulation users can design model with class-based, interface-based, component-based, event-based and dataflow-based design approaches of SMP2, then can get the model's information, including object structure, combination structure and interaction structure.

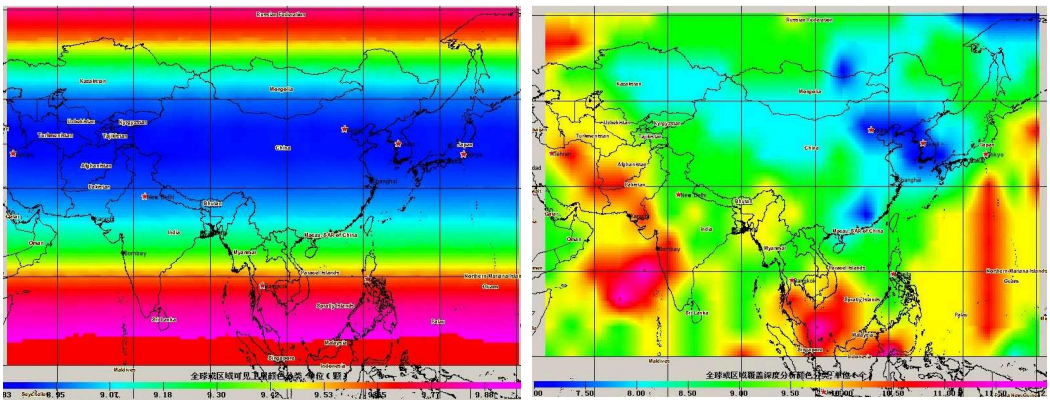
The main task of the model development phase of navigation simulation is that translates models from Catalogue file into a model framework code, that is to say that transforms PIM into PSM, then designs a specific algorithm in the framework, finally a compiler is needed to generate binary models form sources.

The main task of the model integration phase of navigation simulation is that generates the Assembly file, which contains the configuration information and assembly relationships of the model instances, by using instance generation, configuring and integration of the model under the constraints of Catalogue based on SMDL.

The main task of the model execution phase of GNSS simulation is that generates the Schedule file, which arranges the scheduling strategy of navigation model's instance based on the Assembly file and SMDL.

By using above method, we study the performance simulation of GALILEO system. Based on the navigation performance indexes, we define 50°E~150°E, 0°N~60°N as an analysis region, 5°×5° as grid resolution, analyses include visibility, geometry, coverage, DOP, NSP, etc. Satellite orbit determination algorithm is Keplerian two-body orbital model, simulation cycle is a constellation regression cycle, simulation step is 300 seconds, and algorithm involved in the model are such as GPS, GALILEO algorithms.

Based on SMP2 method, we design and develop a software which support model development and simulation SMP2-based. The result of the test shows in Fig.3. Fig.3 (a) is a distribution diagram of the number of visible satellite in this region of GALILEO, there are most about from 8 to 9; Fig.4 (b) is a distribution diagram of number of ground stations in view at each time step in this region, most of the distribution about from 7 to 9. These results are consistent with the data provided by ESA.



(a) Regional Visibility (b) Regional Coverage

Fig. 3. Experiment results of GNSS simulation based on SMP2

Conclusions

In this paper, based on SMP2 specification, we study the model framework of GNSS simulation, and proposed an SMP2-based model integration framework for GNSS, then develop and integrate the models, to support the performance analysis of GNSS. Performance analysis by using traditional methods are tightly coupled with the specific needs of domain or expertise, when the constellation configuration is changed, or accuracy and approach of algorithm is changed, we need to re-develop, and the algorithms and models are lack of reusability and portability. Using the proposed method, domain staff will focus on the development of the domain model ,do not care about the simulation platform, so that the developed model can not only support the demonstration program, but can verify the performance impact caused by the different algorithms or models. Navigation simulation model based SMP2 specification are more reusability and portability.

Software engineering oriented SMP2 and integrating various behavior modeling formalisms around SMP2 is our next work.

Acknowledgements

The authors wish to acknowledge the reviewers of this paper for their valuable comments and insistence on the example. This effort was partly supported by the National Science Foundation of China.

References

[1] Hou Hongtao,Li Qun Wang Chao. Appl. Math. Inf. Sci. 7, No. 6, 2095 -2102 (2013)

[2] European Space Agency. EGOS-SIM-GEN-TN-0099, 2005.10.

[3] Hou Hongtao, Zhou Hongwei, Li qun, et al. Journal of System Simulation, 2010, 22(6):1350-1354

[4] Lei Yonglin, Su Nianle, Li Jingjie, et al. System Engineering Theory & Practice, 2010, 30(5): 899-908.

[5] Wang Chao, Song Lili, Li Qun, et al. Proceedings of the International Conference on Computational Intelligence and Software Engineering (CISE 2010).Wuhan, 2010.

[6] Lei Yonglin, Wang Weiping, Li Qun, et al. Simulation Modelling Practice and Theory, 2009,17:1690-1709.

[7] Wang Chao, Li Qun, Wang Weiping. 2011 International Conference on Electric Information and Control Engineering, 2011:125-129.

[8] Zhang Wei, Yu Yongli, Zhao Xinhui, et al. Proceedings of 2011 9th International Conference on Reliability, Maintainability & Safety, 2011:774-778.

[9] Paul A. Fishwick. New Jersey: Prentice-Hall Inc, 1995:29-33.

[10] Su Nianle, Yu Wenguang, Hou Hongtao, et al..Proceedings of 7th IEEE East-West Design & Test Symposium, Moscow, 2009:501-506.

[11] Peter Fritzen. The Royal Aeronautical Society "RaeS Simulation of On-board Systems" Proceedings, London, 2004:134-139.

[12] Pidgeon A. 6th NASA/ESA Workshop on Product Data Exchange, Germany, Friedrich, 2004:145-153.

[13] GSSF Team. Paris: EUROPEAN SPACE AGENCY, 2007.

Advanced Materials Research Vol. 936 (2014) pp 2307-2312
© (2014) Trans Tech Publications, Switzerland
doi:10.4028/www.scientific.net/AMR.936.2307

A Fast Fault-identification Algorithm Tailored for Optical Interconnection Networks in high-performance computers

He Li*

College of Computer Science, Chongqing University of Posts and Telecommunications, Chongqing 400065, P.R.China

cquptheli@126.com

Keywords: optical interconnection; optical multi-mesh hypercube networks; diagnosability; pessimistic strategy; diagnosis algorithm

Abstract. Due to integrated positive features of both hypercube and tori, optical multi-mesh hypercube (OMMH) networks in high-performance computers are regarded as a class of promising optical inter- connection networks. This paper firstly derive that the diagnosability of OMMH under the pessimistic strategy is (2n+6)/(2n+6), which shows that the OMMH possesses strong self-diagnosingability. With the improved cycle decomposition method by Yang in *J. Parall. Distrib. Comput.* [10], a fast diagnosis algorithm to identify all faulty nodes *tailored for* OMMH, which runs in $O(N\log_2 N)$ time is also proposed, where N is the number of the processors of an OMMH.

Introduction

High-performance computers is based on high-performance processors, with hundreds of cores integrated onto a single die. Intra-chip and inter-chip communication networks are becoming critical components in such systems. Nanophotonics is a promising disruptive technology that can potentially achieve simultaneous improvements. Chip-level networks as opposed to cluster-level optical networks used in high-performance computing and data-centers have more challenges: the increasing size of multiprocessor systems makes the possibility that faulty processors present in such systems become large. *System-level diagnosis* [4] is an effective approach to identifying the faulty processors existing in the system and then isolating them or replacing them by fault-free processors. Among the different classes of diagnosis models to locate the faulty nodes, the PMC model [9] is possibly the most well studied one. This evaluation is reliable if and only if the testing processor is fault-free.

A scalable optical interconnection network called optical multi-mesh hypercube (OMMH) network[7, 8] which integrates positive features of both hypercube and mesh topologies is proposed. The OMMH network has been physically demonstrated using a combination of free-space and fiber optics technologies, and has shown good performance characteristics for a reasonable size network. Motivated by the graph decomposition techniques used in [5], this paper addresses the fault identification of OMMH under the PMC model. We will show that the (l,m, n)-OMMH is also (2n + 6)/(2n + 6)-diagnosable under the pessimistic diagnosis strategy. And then, a fast fault identification algorithm for optical multi-mesh hypercube networks using the PMC model is proposed,
which can run in $O(N\log_2 N)$ time, where N is the number of the processors of an OMMH.

This paper is organized as follows: In Section 2, we introduce the (l,m, n)-OMMH network and preliminaries. In Section 3, we prove the diagnosability of the (l,m, n)-OMMH under the pessimistic diagnosis strategy. A fast fault-identification algorithm for optical multi-mesh hypercube networks using the PMC model is proposed in Section 4. Finally, we give some concluding remarks in Section 5.

Preliminaries

A multicomputer system is modeled by the underlying graph G = (V (G),E(G)) of its interconnection network, with each node representing a processor and each edge representing a bidirectional communication link between two processors. More knowledge of graph theory, please reference[3] .

Definition 1 [7, 8]. *An* (l,m, n)*-OMMH network, denoted* $MH_n^{l\times m}$*, is defined as the Cartesian product graph* $T_{l\times m}\times Q_n$*, where* $T_{l\times m}$ *denotes an* $l\times m$ *Torus,* Q_n *denotes an* n*-cube.*

It is obvious from this definition that $l,m\geq 3$. Fig.1 present two small-sized OMMH networks with two methods.

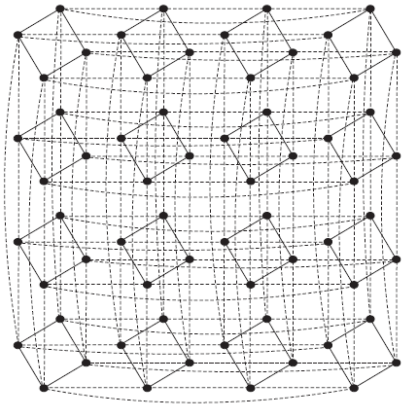


Fig.1 OMMH network $MH_2^{4\times 4}$

Remark 1. $MH_0^{l\times m} = T_{l\times m}$*, a torus with* l *rows and* m *columns.*

Theorem 1.[6] $(MH_n^{l\times m}) = n + 4.$

Lemma 1. *Assume* C *is a cycle within a graph* G*; and* σ *is a syndrome on* G*: (1) If* C *is* σ*-zero, then all nodes on* C *are of the same status, namely they are either all fault-free or all faulty.*
(2) If C *is* σ*-nonzero, then at least one node on* C *is faulty.*

Lemma 2. *An* (l, m, n)*-OMMH is Hamiltonian.*

Proof: We prove this lemma by induction on n. We first prove that the result holds for $n=0$, obviously, there is a Hamiltonian cycle within $MH_0^{l\times m}$ with $l,m\geq 3$. Assume there is a Hamiltonian cycle within $MH_k^{l\times m}$ with $l,m\geq 3$, $k\geq 1$. By Definition 1, $MH_{k+1}^{l\times m}$ can be partitioned into two $MH_k^{l\times m}$ notated $0MH_k^{l\times m}$ and $1MH_k^{l\times m}$, and each of them is adjacent to each other, without loss of generality, $v\in 0MH_k^{l\times m}$ and $u\in 1MH_k^{l\times m}$, and u differs from v in exactly one digit position, by the Definition of OMMH, v is adjacent to u. According to assumption, each $MH_k^{l\times m}$ contains a Hamiltonian cycle.

Then we can get a Hamiltonian cycle within $MH_{k+1}^{l\times m}$. The Lemma is true.

The diagnosability of the (l,m,n)-OMMH network under the pessimistic diagnosis strategy

For pessimistic diagnosis (t/t-diagnosable), Chwa and Hakimi provided a necessary and sufficient condition.

Lemma 3 [1]. *Let G = (V,E) the graph representation of a system* S*, with V representing* S*'s processors and* E *the interconnection among them. Then,* S *is* t1/t1*-diagnosable under the pessimistic strategy if and only if for any* $V'\subset V$ *, such that* $|V'|=2p$*, for any* $1\leq p\leq t_1$, $|N(G,V')|\geq t_1-p+1$.

Lemma 4. *For any* $V'\subset V(MH_n^{l\times m})$, $|V'|=2$, $|N(MH_n^{l\times m}),V'|\geq 2n+6$

Proof. We prove the lemma by induction n.For any $V^{'}\subset V(MH_{r+1}^{l+m})$, $\left|V^{'}\right|=2$,let $V^{'}=\{u,v\}$.The basic $n=0$,the claim can be checked by inspection. Assume that the lemma is true in $MH_n^{l\times m}$ for $n=r$,we will prove that the lemma is true for $n=r+1$.then u and v are adjacent or nonadjacent in $MH_{r+1}^{l\times m}$.

Case 1. If u and v are adjacent in $MH_n^{l\times m}$,by lemma 1,we have $N(MH_n^{l\times m},\{u\})\bigcap N(MH_n^{l\times m},\{v\})=\phi$. Then we further have $\left|N(MH_n^{l\times m},V^{'})\right|=\left|N(MH_n^{l\times m},\{u\})\right|+\left|N(MH_n^{l\times m},\{v\})\right|-2=2n+6$.

Case 2. If u and v are nonadjacent in $MH_n^{l\times m}$,then we further consider the following subcases. **Subcase 2.1.**If $u,v\in V(0MH_r^{l\times m})$,by the induction hypothesis, we have $\left|N(0MH_r^{l\times m},V^{'})\right|\geq 2r+6$.

By Definition 1,for $u,v\in MH_{r+1}^{l\times m}$,there exist only two corresponding vertices $u^{'},v^{'}\in V(1MH_r^{l\times m})$,such that $uu^{'},vv^{'}\in E(MH_{r+1}^{l\times m})$ and $u^{'}\neq v^{'}$.Thus.we have $\left|N(MH_{r+1}^{l\times m},V^{'})\right|=\left|N(0MH_r^{l\times m},V^{'})\right|+\left|\{u^{'},v^{'}\}\right|\geq 2(r+1)+6$.Analogously, if $u,v\in V(1MH_r^{l\times m})$,we easily obtain $\left|N(MH_{r+1}^{l\times m},V^{'})\right|\geq 2(r+1)+6$.

Subcase 2.2. If $u\in V(0MH_r^{l\times m})$ and $v\in V(1MH_r^{l\times m})$,then we have $\left|N\left(MH_{r+1}^{l\times m},V^{'}\right)\right|\geq\left|N\left(0MH_r^{l\times m},\{u\}\right)\right|+\left|N\left(1MH_r^{l\times m},\{v\}\right)\right|=2(r+1)+6$. Analogously, if $u\in V(1MH_r^{l\times m})$ and $v\in V(0MH_r^{l\times m})$,we easily obtain $\left|N\left(MH_{r+1}^{l\times m},V^{'}\right)\right|\geq 2(r+1)+6$ .Therefore, the lemma is true for $l,m\geq 3$ and $n\geq 0$.

Lemma 5 [2]. G is a connected graph, for any $V^{'}\subset V(G)$, let $V^{''}=V(G)-V^{'}$.

1) If $\left|V^{''}\right|\geq\kappa(G)$, then $\left|N(V(G)-V^{'},V^{'})\right|\geq\kappa(G)$;

2) If $\left|V^{''}\right|<\kappa(G)$, then $\left|N\left(V\left(G\right)-V^{'},V^{'}\right)\right|=\left|V^{''}\right|$.

Theorem 2. For any $V^{'}\subset V(MH_n^{l\times m})$, $\left|V^{'}\right|=2p$, $1\leq p\leq n+3$, $\left|N\left(MH_n^{l\times m},V^{'}\right)\right|\geq(2n+6)-p+1$ $(l,m\geq 3)$.

Proof. We first can sure that the preceding claim is true for $p=1$ by Lemma 6. Then, we will prove that the assertion is true for $2\leq p\leq n+3$ by induction on n. For $n=0$, we can directly inspect that the assertion is fulfilled. Now, assume the assertion is true for $n=r\geq 1$. Let us prove that the assertion is true for $n=r+1$. Let $V^{'}=V_0\bigcup V_1$, $V_0\subseteq V(0MH_r^{l\times m})$, $V_1\subseteq V(1MH_r^{l\times m})$. Then we can distinguish the following two cases.

Case 1. If $V_0=\phi$, $V_1\neq\phi$,then $\left|V_1\right|=2p\leq 2n+6$ .By the induction hypothesis, $\left|N\left(1MH_r^{l\times m},V_1\right)\right|\geq(2r+6)-p+1$ .Thus we have $\left|N\left(MH_{r+1}^{l\times m},V_1\right)\right|\geq\left|N\left(1MH_r^{l\times m},V_1\right)\right|+\left|N\left(0MH_r^{l\times m},V_1\right)\right|\geq(2r+6)-p+1+2p>(2(r+1)+6)-p+1$.

Analogously, if $V_0\neq\phi,V_1=\phi$,we can easily obtain $\left|N(MH_{r+1}^{l\times m},V_0)\right|\geq(2(r+1)+6)-p+1$.

Case 2. If $V_0\neq\phi$, $V_1\neq\phi$,then $1\leq\left|V_0\right|\leq 2r+5$, $1\leq\left|V_1\right|\leq 2r+5$ .For $0MH_r^{l\times m}$, $\left|0MH_r^{l\times m}-V_0\right|\geq l\times m2^r-(2r+6)>r+4$ .By Lemma 4, we have $\left|N(0MH_r^{l\times m},V_0)\right|=\left|N(V(0MH_r^{l\times m})-V_0,V_0)\right|\geq\kappa(0MH_r^{l\times m})=r+4$ .Analogously, for $1MH_r^{l\times m}$,we can obtain $\left|N(1MH_r^{l\times m},V_1)\right|=\left|N(V(1MH_r^{l\times m})-V_1,V_1)\right|\geq\kappa(1MH_r^{l\times m})=r+4$ .Thus we have $\left|N(MH_{r+1}^{l\times m},V^{'})\right|\geq\left|N(0MH_r^{l\times m},V_0)\right|+\left|N(1MH_r^{l\times m},V_1)\right|\geq 2(r+4)>(2(r+1)+6)-p+1$.

Therefore, the theorem is true for n ≥ 0.By Theorem 2 and Lemma 5, we have the following.

Theorem 2. $MH_n^{l\times m}(l,m\geq 3)$ is (2n + 6)/(2n + 6) -diagnosable under the pessimistic diagnosis strategy.

A fast pessimistic diagnosis algorithm for OMMH

For derivation of the pessimistic diagnosis algorithm of the OMMH, its decomposition property must be analyzed. To achieve the goal, first we decompose an OMMH into subcubes with the same structure. Second, a diagnosis algorithm is provided to adopt every σ-zero cycle conducted by all fault-free nodes to diagnose any σ-nonzero cycle which is adjacent to the σ-zero cycle. Eventually, each node in any undiagnosed σ-nonzero cycle, which is not adjacent to any σ-zero cycle, can be diagnosed in finite steps.

Since $MH_n^{l\times m}$ can be viewed as 2^n-cubes in which 2^n nodes having identical hypercube address form $l\times m$ torus, but the conventional the cycle decomposition method cannot be immediately applied to the $MH_n^{l\times m}$. Let MH^* represent a decomposed proper subcube of an $MH_n^{l\times m}$. A heuristic procedure is derived for decomposing a $MH_n^{l\times m}$ into MH^* for maximizing F, F is the number of faulty nodes. Let cn and N^* denote the order of an MH^* and the total number of MH^* s in the $MH_n^{l\times m}$, respectively. Let $MH^*\times 2^k$ indicate an $MH_n^{l\times m}$ with $|V(MH^*)|\times 2^k$ nodes constructed by 2^k MH^* s in an $MH_n^{l\times m}$, where $l,m\geq 3$, $n\geq 0$. Next algorithm **Procedure-Decom** is formally stated. Obviously, all MH^* s in $MH_n^{l\times m}$ are disjoint.

Procedure-Decom

Input: An $MH_n^{l\times m}$ with $l,m\geq 3$, $n\geq 0$

Output: An MH^*, cn and N^*

Initialization: $N^*\leftarrow 1$, $cn\leftarrow l\times m\times 2^n$, $k\leftarrow 0$, $t\leftarrow n$, $MH^*\leftarrow MH_0^{l\times m}$ (a torus)

Step 1: If $N^*<cn$ then $MH^*\leftarrow MH^*\times 2^k$, $N^*\leftarrow N^*\times 2^k$, $cn\leftarrow cn/2^k$ and $k\leftarrow k+1$ else go to Step 3.

Step 2: if $N^*<cn$ then $MH^*\leftarrow MH^*\times 2^t$, $t\leftarrow n-1$ and go to Step 1.

Step 3: if $cn<F$, then $cn\leftarrow F+1$ and go to Step 7.

Step 4: $cn\leftarrow 1$, $N^*\leftarrow l\times m\times 2^n$, $k\leftarrow 0$, $t\leftarrow n$, $MH^*\leftarrow MH_0^{l\times m}$ (a torus)

Step 5: If $cn\times 2^k<F$, then $MH^*\leftarrow MH^*\times 2^k$, $cn\leftarrow cn\times 2^k$, $N^*\leftarrow N^*/2^k$ and $k\leftarrow k+1$.

Step 6: If $cn\times 2^t\leq F$ then $MH^*\leftarrow MH^*\times 2^t, cn\leftarrow cn\times 2^t, N^*\leftarrow N^*/2^t, t\leftarrow n-1$ and go to Step 5.

Step 7: Output the N^*, MH^*, cn

Clearly, the induced subhypergraph $MH_{cn}^{l\times m}$ by Procedure-Decom is isomorphic to $MH_n^{l\times m}$. Let HC be a Hamiltonian cycle within $MH_n^{l\times m}$, HC can be mapped onto a Hamiltonian cycle within the subhypergraph $MH_{n-cn}^{l\times m}$, which is also a cycle within $MH_n^{l\times m}$. To describe the new diagnosis algorit- hm, we need the following notions.

Definition 2. *$CD(HC)=\{HC(x):l,m,x\in\{0,1\}^{n-cn}\}$, where $l\geq 3$, $m\geq 3$ called a cycle decomposition for $MH_n^{l\times m}$ induced by HC in* ***Procedure-Decom.***

Definition 3. *Let C be a cycle in a cycle decomposition* CD(HC) *of $MH_n^{l\times m}$ and σ is a syndrome on $MH_n^{l\times m}$, then:*

(i) *C is σ-guarded if C is σ-nonzero but is adjacent to some σ-zero cycle. All nodes on a σ-guarded cycle are s-guarded.*

(ii) *C is σ-unguarded if C is σ-nonzero and is not adjacent to any σ-zero cycle. All nodes on a σ-unguarded cycle are σ-unguarded.*

Based on the previous discussions, the pessimistic diagnosis algorithm for OMMH is sketchily described as follows.

Algorithm CD-DIAG-OMMH

Input: An $MH_n^{l\times m}$ with $l,m\geq 3$, $n\geq 6$ .A cycle decomposition CD(HC) for an $MH_n^{l\times m}$ and a syndrome σ on $MH_n^{l\times m}$.

Output:A set F of nodes that are diagnosed as faulty.

Step 1(Initialization): $F\leftarrow\phi, V^{'}\leftarrow\phi, V^{''}\leftarrow\phi$

Step 2: Get a cycle decomposition CD(HC) of $MH_n^{l\times m}$ by applying **Procedure-Decom** given above.

Step 3: For each cycle in $CD(HC)$, decide if it is σ-zero or σ-nonzero by checking all the test outcomes on the cycle. Diagnose all the σ-zero nodes as fault-free. Add all σ-nodes to $V^{'}$.

Step 4: For each σ-nonzero node u, if there is an σ-zero node which is adjacent to u; then diagnose u as fault-free or faulty according as $\sigma(v,u)=0 or 1$. then add u to $V^{'}$ or F according as $\sigma(v,u)=0 or 1$.

Step 5: For each σ-nonzero node u that was not diagnosed in the previous steps, if it has a neighbor v that was diagnosed to be fault-free (that is, u is σ-unguarded but is adjacent to a fault-free σ-guarded node) in the previous steps, then add u to $V^{'}$ or F according as $\sigma(v,u)=0 or 1$.

Step 6: For each remaining σ-nonzero node u, if there is a node v is adjacent to u and diagnosed as fault-free in step 4:(that is, u is σ-unguarded and is not adjacent to any fault-free σ-guarded node that is adjacent to a fault-free σ-guarded node, in turn), then add u to $V^{'}$ or F according as $\sigma(v,u)=0 or 1$

Step 7: Add all the nodes having been diagnosed as faulty to set F.

If $|F|=2n+6$,then return F;

else

$V^{''}=V(MH_n^{l\times m}-F-V^{'})$,then rerurn $(F,V^{'},V^{''})$.

To prove the correctness of this diagnosis algorithm, we need the following lemmas.

Lemma 6. *Let* $l,m\geq 3, n\geq 6$, *Assume* CD(HC) *is a cycle decomposition for* $MH_n^{l\times m}$, *and* σ *is a syndrome on* $MH_n^{l\times m}$ *produced by a set* F *of faults with* $|F|\leq 2n+6$, *Then the following results hold;*

(i) There exists a σ*-zero cycle in* CD(HC)*;*

(ii) All nodes on a σ*-zero cycle are fault-free;*

Proof. Note that $l,m\geq 3$, $n\geq 6$ implies

(i) Applying **Procedure-Decom** on $MH_n^{l\times m}$, $cn\leq N^{*}$, and cn ≤ F-1. Thus , there is at least one cycle that consists of fault-free nodes. By Lemma 1, this cycle is an σ-zero cycle.

(ii)There are totally 2^{cn} nodes on a σ-zero cycle. Note that $2^{cn}\geq 2^{F}\geq 2n+7\geq F+1$. The claim follows from Lemma 1.

Theorem 3. *Assume there are at most* $2n+6$ *faulty nodes in an* OMMH *with* $l,m\geq 3$, $n\geq 6$. *The algorithm can produce a fault set of size at most 2n+6 and containing at most one fault-free node.*

Proof. Lemma 6 (i) assures the existence of at least one σ-zero cycle. This is the start point of this algorithm. Lemma 6 (ii) and the assumptions of the PMC model assure that, upon completion of the algorithm, $S\subseteq V(MH_n^{l\times m})-F$. So all the faulty nodes have been isolated to within the set $V(MH_n^{l\times m})-S$. It remains yet to prove that

$$|V^{''}|\leq 1 \text{ and } |V^{'}|+|V^{''}|\leq 2n+6$$

Clearly, the two inequalities hold for the case where $|V^{'}|=2n+6$. So we assume $|V^{'}|\leq 2n+5$.

Let us have a look at what happens just after **Step 6** of the algorithm has been executed, one of the following three possibilities may take place.

Case 1: All nodes have been identified. Then $|V''|=0$ and hence $|V'|+|V''|\le 2n+6$.

Case 2: There is exactly one unidentified node, say v. Then $V''=\{v\}$. So $|V''|=1$ and $|V'|+|V''|\le 2n+6$.

Case 3: There were exactly two unidentified node, say u and v. Note that this would imply $F\supseteq N(\{u,v\})$ and $|N(\{u,v\})|\ge 2n+6$. Thereby we could conclude $|F|\ge 2n+6$. A contradiction.

Theorem 4. Algorithm CD-DIAG-OMMH runs in O(Nlog2N) time, where $N=l\times m\times 2^n$ is the total number of nodes in the $MH_n^{l\times m}$, where $l,m\ge 3$, $n\ge 6$.

Proof. We analyze the execution time for the algorithm statement by statement.

Step 1 takes O(n) time; **Step 2** takes O(1) time; **Step 3** takes O(N) time; **Steps 4 – 6** takes $O(N\log_2 N)$ time, and **Step 7** takes O(1) time. Therefore, the time complexity of the CD-DIAG is $O(N\log_2 N)$.

Conclusion

In this paper, the diagnosability of the OMMH networks $MH_n^{l\times m}$ under the pessimistic diagnosis strategy based on the PMC model were firstly studied, which was shown that $MH_n^{l\times m}$ is $(2n+6)/(2n+6)$- diagnosable under the pessimistic diagnosis strategy for $l,m\ge 3$, $n\ge 0$. Then, under the PMC model, we proposed an algorithm by exploiting its cycle decomposition properties to diagnose the n-dimensional OMMH. The algorithm runs in $O(N\log_2 N)$ time, where $N=l\times m\times 2^n$.

Acknowledgment

This work is supported by Research Project of Chongqing Education Commission(No.KJ120508).

References

[1] K.Y. Chwa, S.L. Hakimi, On fault identification in diagnosable systems, IEEE Trans. Computers,30 (6) (1981) 414-422.
[2] J. Fan, Diagnosability of the M¨obius cubes, IEEE Trans. Parallel and Distributed Systems, 9 (9)(1998) 923-928.
[3] J.A. Bondy, U.S.R. Murty, Graph Theory with Applications, North-Holland, New York, 1980.
[4] S.L. Hakimi, A.T. Amin, Characterization of the connection assignment of diagnosable systems, IEEE Trans. Comput. 23 (1) (1974) 86-88.
[5] E. Kranakis, A. Pelc, Better adaptive diagnosis of hypercubes, IEEE Trans. Comput. 49 (2000) 1013-1020.
[6] X. Li, X. Yang, L. He, Diagnosability of optical multi-mesh hypercube networks under the comparison diagnosis model, International Journal of Computer Mathematics. in press.
[7] A. Louri, H. Sung, An optical multi-mesh hypercube: a scalable optical interconnection network for massively parallel computing, J. Lightwave Technol. 12 (4) (1994) 704-716.
[8] A. Louri, H. Sung, Scalable optical hypercube-based interconnection network for massively-parallel computing, Appl. Opt. 33 (32) (1994) 7588-7598.
[9] F.P. Preparata, G. Metze, R.T. Chien, On the connection assignment problem of diagnosable systems, IEEE Trans. Electron. Comput. 16 (6) (1967) 848-854.
[10] X. Yang, A fast pessimistic one-step diagnosis algorithm for hypercube multicomputer systems, J. Parallel Distrib. Comput. 64 (2004) 546-553.

Advanced Materials Research Vol. 936 (2014) pp 2313-2317
© (2014) Trans Tech Publications, Switzerland
doi:10.4028/www.scientific.net/AMR.936.2313

Research on Agent-based Mobile Database Structure

Qiu-yan Tian[1, a], Long Fei[2, b] and Wei Tian[3, c]

[1,3]Electronic Engineering Department, Changchun Institute of Engineering Technology, Changchun, China

[2]Institute of Urban Environmental Sciences, Changchun Normal University, Changchun, China

[a]tqykali@163.com, [b] flyflylong@163.com, [c] tianweifeng@sohu.com

Keywords: Mobile database; Structure; Agent.

Abstract. With the transaction processing, data query, location query and other functions of mobile devices, the demand for mobile database has also increased. The analysis of the agent-based mobile database structure and the deficiencies of existing systems provide the basis for future research..

Introduction

In a network-centric computing era, it will become the universal demand that people can access information network to obtain the required information at any time and any place accompanied by the rapid development of mobile communication technology, and a large number of popular move equipment have been brought about by the development of economic more and more users are beginning to have a variety of portable computing devices such as laptops, PDAS, personal digital assistant and personal information manager and so on., we call them to mobile computers. Moreover, to support mobile users to access network data and achieve freedom without restraint communications and handling of kinds of business data. The future of mobile computers will be equipped with mobile networking equipment which is mainly based on the wireless network. Then, the concept of "mobile computing" and "mobile database" came into being.

The Mobile Database

User needs and the dual of technological progress make mobile computing as a major expansion of distributed computing. The computing environment which mobile devices via wireless or fixed network connecting with fixed or other mobile device is named mobile computing environments, mobile computing is a distributed computing in the expansion of mobile computing environment [1]. Because of the characteristics of the mobile computing environment, it makes the queries, transaction processing and other issues closely related to the physical location of querying customers, network connections and even the power supply up in the database field, so traditional distributed databases, client / server database can not or can not effectively support mobile computing environment It must be improved by re-design a new database technology, which can comprehensively support mobile computing environment- mobile database.

Mobile database is a distributed database in a mobile computing environment, which is an extension of traditional distributed database system [2]. It can be seen as distributed systems which client is dynamically connected with the fixed server nodes. An ideal mobile database should achieve the following objectives:

Availability and Scalability: to avoid system instability, while providing high availability and scalability;

Mobility: allows the mobile computer to access or update the database in the case of network disconnect;

Serializability: support to meet the serializable execution of concurrent transactions;

Convergence: the system always converges to a consistent state, and thus avoids confusion.

The Key Technologies Mobile Database

Mobile computing provides the research for researchers in the field of database and data management, and then the key technologies of mobile database include the following aspects:

Replication and Caching Techniques

The main purpose of data replication is to improve the distributed database system's availability, reliability, and access performance. Cache technology caches the part of the data through the client,, to achieve the purpose of reducing access to the database server to improve performance. The technology is the key technology to solve the disconnection of the mobile database to maintain the consistency of data. It is also used to patch to adapt the technology of mobile computing on the base of the existing DBMS

Data Broadcasting Techniques

Popularly speaking, data broadcasting is that using the asymmetry of client and server communication to sent data to the client in the form of a periodic broadcast in mobile computing environment. The biggest advantage is that the overhead of broadcast change if the number of mobile users change, with data broadcasting, you can solve the disconnected problem of database system in a cert extent.

The Technology of Mobile Query

In the mobile computing environment, the related updating and querying location information is an important application. Move query is all query technology of mobile database. In mobile database systems, location-based changes to provide the information of location related for the user is an important application.

The Mobile Transaction Processing

Transaction processing is a basic function of database management system. It is mainly used to maintain the consistency of data to support for multi-user concurrent access to make users enable reliably query and update the database. In general, users access the database system is accomplished through the transaction.

Agent Technology

Agent Concept

The research of Agent originated in the field of artificial intelligence. From a broad point of view, Agent shall includes: reactivity, autonomy, social and spontaneous; from the narrow point of view, agent should also have some of the usual human characteristics, such as knowledge, beliefs, intentions, commitments and other mental state[3]. From the above analysis of the agent feature that we can give a simple definition of Agent: Agent is a computer system which is in a specific environment and can sense the environment, enable achieve a goal of designers and users, and can flexibility and independently run computing entity or program in that environment.

Mobile Agent

Mobile agent is a program which can autonomously migrate from one host to another host in heterogeneous network, and can interact with other Agent or resources [4]. Mobile agent has the autonomy, mobility, collaboration, security, intelligence and other characteristics.

The traditional distributed computing is based on Client / Server architecture, its bandwidth cost serious, network load is not balanced, and the fault tolerance is poor. Mobile agent as a new distributed computing tools. Through sending their own code and the state to the remote host and the way of remote host performing overcomes the Client / Server program's shortcomings, is the expansion of traditional C / S model. It adds a new level of an agent between the client and the server. The model is shown in Figure 1.

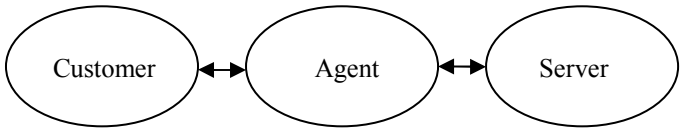


Figure 1: The model of agent-based mobile database

Thus, the agent-based mobile database has the following advantages:

The agent-based system is distributed and asynchronous, therefore, the entire computer environment is open, is extensible;

The agent-based system supports the disconnected operation of mobile clients;

The use of agent technology can significantly reduce traffic flow on the wireless communications network;

Agent resides in the high-speed and fixed network, on behalf of all mobile customers to retrieve every database;

Agent is able to combine the knowledge of client and server, and reasoning on the server, to determine their own work in the next step;

Multiple agents can dynamically adjust the distribution to maintain the optimal configuration;

Agent can reach the server directly to retrieve the final result, to avoid the delay of the middle data transmission.

Agent-based Classification of Mobile Database System Architecture

Agent-based database systems in the mobile location and function, we can be divided into the following categories:

Customer-Customer Agent-Server Structure

In this structure, Customer agent is equivalent to a local server proxy which resides on the local client. Work is: the cached client needs to access the data; the period of disconnection simulates the server's operations in the normal run-time; maintenance all of updates log; to integrate with the data when re-connecting to complete mobile customer's support. These operations are open to customers, so the above procedures do not need to change. Figure 2.



Figure 2: The customer agent-based mobile database structure

Customer- Server Agent-Server Structure

In the mobile environment, users may need server to complete compute-intensive operations. In this case, the limited resources of client can not meet the requirements of cache space, and then you need to set an Agent to collect client needs on the fixed network, summing up requests of multiple clients to submit requests to the server. Server Agent plays the role of a bridge, before disconnecting, the client passes request to the server Agent; after disconnected, the server Agent instead of the client hands request to the server, complete a series of operations; re-connecting, the server Agent will passed the final structure to the client which successfully complete the task. Although this structure can help clients reduce operating, but the user can't continuous access when it's disconnected. Figure 3.

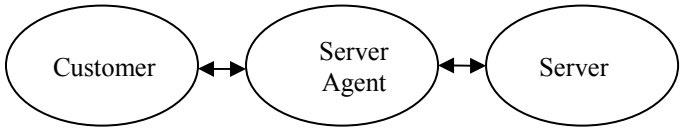


Figure 3: The server agent-based mobile database structure

Customer-Customer Agent-Server Structure

However, in practice, there is only an Agent having definite problems, and no matter which side of this Agent is located, for the optimization of communication is only in one direction, in order to solve this problem, combining the advantages and shortcomings of these two structures, it has developed a couple of application structure of the Agent and divided it into two parts: the client agent can collect user requests, and returns the results to the user, the server Agent is as customers which resides on the local. Thus, the relational task can be handed in both agents to complete. Figure 4.

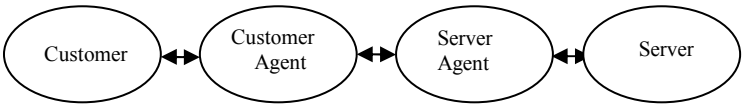


Figure 4: The customer/server agent-based mobile database structure

The structure of these systems, regardless of the location and role of Agent to the customer ,the relationship between client, Agent and server is a linear, and in practical applications, mobile systems are mostly comes from the expansion of distributed systems. The relationship of Server to server, server to client is the network, the server not only to support mobile customers, but also supports traditional fixed clients, multiple servers also need the replication and synchronization of data. In addition, a mobile host may be physically far away from the original host when reconnecting to the fixed network Therefore, these linear structures can't support each other enough for the mobile host moves across servers, autonomy, collaboration and other features We need to be extended to the Agent and the division of functions and further research.

Agent-based Database Architecture.

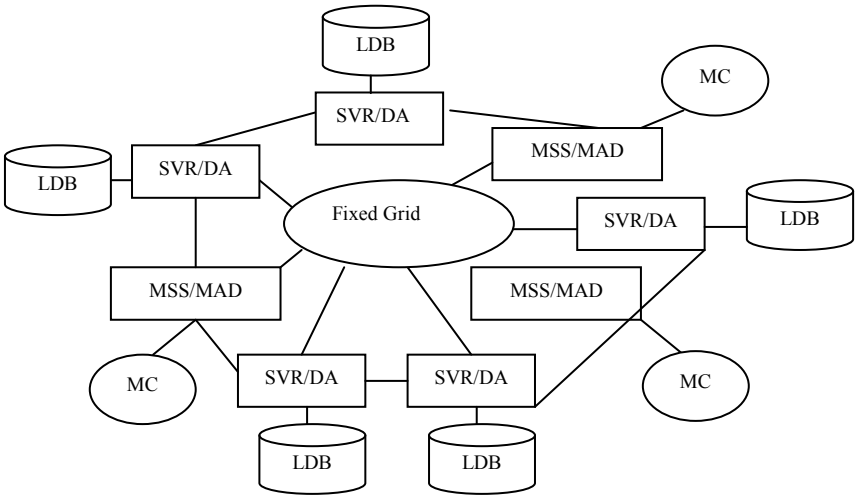


Figure 5 Agent-based mobile database structure

MC: Mobile Client mobile client
MSS: Mobile Support Station
MAD: Mobile Agent Dock
SVR: Server (fixed host to manage local database)
DA: Database Agent
LDB: Local Database

General mobile agent-based data system organization is shown like Figure 5, in this system, the server is generally seen as a fixed node, each server maintains a local database, to retain all requests history on the server; Database Agent is still located on the server Agent, responsible for handling the requests that client accesses to the database directly operate the database. To receive and return the

information of nodes to the client through communicating with mobile Agent; mobile support nodes are in a fixed high-speed network to support wireless network elements, it not only communicates with the mobile client through wireless network , but also communicates with the server through a fixed network; Mobile Agent Terminal is located on the Mobile Agent Management System of MSS. It is based on the client's request to create Mobile Agent, and sends Mobile Agent to the correct address, and receives the mobile Agent which returns from the server, to transfer the results to the appropriate client; mobile clients with mobility and frequent network disconnection.

Summary

With network technology and wireless communication technologies in depth and popularity, more and more users use mobile devices for transaction processing and data queries, location queries and so on. The demand for mobile database has also increased. However, mobile-database's mobility, disconnect, bandwidth limited, network communications of non-symmetry, and power consumption of the limited nature of such features, determine that mobile computing environment must be different from the traditional distributed computing. So, we will seek to solve these issues on the base of Agent study and have innovation on the base of the existing Agent-based.

Acknowledgment

The article gets Jilin province science and technology development projects support, Project Numbers: Ji Jiao Ke He Zi [2014] No 262; Chang Shi Yuan Zi Ke He Zi [2010] No 005.

References

[1] Ren Wei. "Research on the System Framework based on the Agent Mobile Database", Microcomputer Information, volume 15, pp. 158-159, (2007).

[2] Li Hui-fang. "Research on the Query of Mobile Database Based on Mobile Agent", Computer Knowledge and Technology, volume6, pp. 8166-8167, (2010).

[3] Wang Xiong-jie, Xiong Qian-xing. "Mobile Database Synchronization Model Based on Mobile Agent and Web Service", Computer & Digital Engineering, volume38, pp. 78-81, (2010).

[4] Zhao Yi-jiang, Shao Ding-hong. "Research on database transaction connection pool based on multi-agent tools", Computer Engineering and Design, volume 32, pp. 2031-2032, (2011).

Advanced Materials Research Vol. 936 (2014) pp 2318-2322
© (2014) Trans Tech Publications, Switzerland
doi:10.4028/www.scientific.net/AMR.936.2318

A New Cache-Based Network Coding Retransmission Scheme in Communication Wireless Networks

Lian Wang[1, a *], Min Liu[1,b *]

[1]Chongqing University of Posts and Telecommunications, China

[a]wanglian@cqupt.edu.cn, [b]380809958@qq.com

Keywords: wireless broadcast, cache-based retransmission, network coding, buffer list.

Abstract: Cache-based network coding has been proposed recently as an effective method to improve retransmission efficiency. In this way, the receiver will cache the encoded packets that cannot be decoded rather than delete. However, some cache-based methods neglect the overlap relationship among encoded packets or cached encoded packets. In this paper a new cache-based network coding retransmission scheme in wireless network (CNCR) has been proposed, in which the buffer list of failed encoded packets at the receiver will be updated by simplifying the cached encoded packets according to their overlap relationship. Furthermore the special case " the cross relation " has been introduced, the requested packet in this case will be retransmitted immediately, and the fast decoding of encoded packets cached in the buffer list can be realized. Finally the simulation results show that CNCR can improve the recovery efficiency , and have apparently superiority to previous works proposed.

Introduction

Wireless transmission is bandwidth-limited and high-loss due to the poor quality of the wireless channel. To address this problem, it is necessary to design more efficient retransmission schemes to increase the transmission efficiency . Network Coding [1] (NC) is a new coding technique that can encode the input data in the linear or nonlinear way at intermediate nodes. At present, the retransmission schemes based on network coding have been widely researched and applied [2-5].

That retransmission schemes based on network coding is obviously superior to the ARQ in transmission efficiency has been verified [6], therefore the further research is focused on reducing retransmissions. Xiao proposes a method that encodes the lost packets in their sending order, but the performance of this method becomes worse when a receiver lost more than one packet [7]; Fan introduces a method to reduce the decoding complexity, however, it also reduces the possibility of encoding and increases the retransmissions [8]. The above encoding strategies recover lost packets only through a single retransmitted packet without considering multiple retransmitted packets. Rozner [9] proposes the Efficient Retransmission (ER) algorithm, but it requires all encoded packets should be decoded by all receivers, which wastes a lot of encoding opportunities and leads to the poor performance. Zhan [10] proves that allowing the encoded packets to fail to be decoded at some receivers can effectively decrease the retransmissions, and proposes a Cache-based Multicast Retransmission Encoding algorithm (CMRE). CMRE allows receivers to cache the encoded packets, which cannot be decoded, to facilitate the subsequent decoding. Although cache-based retransmission schemes using network coding [10,11] can decrease the number of retransmissions, they may not be able to take full advantage of the cached and improve the retransmission performance.

In this paper, a new cache-based network coding retransmission scheme in wireless communication networks (CNCR) is proposed, CNCR allows the receivers to cache the encoded packets failed to be decoded, and updates the buffer list by simplifying the cached encoded packets, and requests the lost packets to realize the fast decoding of the encoded packets cached in the buffer list. CNCR can further reduce the number of retransmissions and overhead.

The rest of this paper is organized as follows. Section 1 illustrates the single-hop wireless broadcasting network model. Section 2 presents the details of our proposed CNCR scheme. Section 3 evaluates the performance of CNCR through simulation results.

Network Model

Our model consists of a source node and $N(N>2)$ receivers $R_i(1 \le i \le N)$. The communicating procedure is divided into two phases: the initial transmission phase and the recovery phase. In the initial transmission phase, the source node broadcasts a set $P=\{P_{i,\ldots,}P_K\}$ totally K packets. During this phase, each receiver listens to the requested packets as well as the other packets requested by other receivers. Corresponding to each requested packet, each receiver sends an *ACK/NAK* packet to the source node. At the end of initial transmission phase, the source node maintains a $N\times K$ receiving information matrix T in which each entry $T(i,j)(1 \le i \le N, 1 \le j \le K)$ indicates whether the receiver R_i has successfully received packet P_j or not. $T(i,j)=0$ if P_j is received correctly by R_i and $T(i,j)=1$ otherwise.

In the recovery phase, a packet retransmission scheme is employed to deliver the lost packets to the receivers that requested them until all receivers obtain their requested packets correctly. We define the probability that a receiver R_i loses a packet is P_i and assume that all packets have a fixed length during both initial transmission and recovery phases.

Cache-Based Network Coding Retransmission Scheme

A. p*roblem statement*

Cache-based network coding can be described as follows: during the recovery phase, the source node generates a encoded packet by XORing a set of the lost packets according to receiving information matrix T and retransmits it. Then the receivers recover their lost packets through the encoded packet or cache the encoded packet if the receivers fail to decode it. When the receivers recover lost packets through subsequent encoded packets, they can decode the cached encoded packets and then recover their lost packets.

	P_1	P_2	P_3	P_4	P_5	P_6	P_7	P_8	P_9	P_{10}
R_1	0	1	0	1	0	1	1	0	0	0
R_2	0	1	0	0	1	1	0	1	0	0
R_3	0	0	1	0	1	0	1	0	1	0
R_4	0	0	0	1	1	1	0	0	0	1
R_5	1	1	1	1	0	0	0	1	0	0

Fig. 1: Receiving Information Matrix

Fig. 1 illustrates an example of receiving information matrix with 4 receivers after 10 packets are broadcast. For example, according to a cache-based network coding retransmission scheme named Multi-packet Decoding and Network Coding based Broadcasting Retransmission (MDNCBR) [8], the source node generates four encoded packets :

$C_1=P_1\oplus P_2\oplus P_3\oplus P_4$, $C_2=P_2\oplus P_4\oplus P_5$, $C_3=P_3\oplus P_6\oplus P_7$, $C_4=P_4\oplus P_7\oplus P_8\oplus P_9\oplus P_{10}$, where R_2 , R_3 , R_4 can recover their corresponding lost packets from these encoded packets, R_1 and R_5 cannot decode these encoded packets but cache them. To illustrate the point, the decoding situation of R_1 can be denoted by $(P_2, P_4)|(P_2, P_4)|(P_6, P_7)|(P_4, P_7)$, where the first (P_2, P_4) represents R_1 cannot recover P_2 , P_4 from C_1 ; the second (P_2, P_4) represents R_1 cannot recover P_2 , P_4 from C_2 ; (P_6, P_7) represents R_1 cannot recover P_6 , P_7 from C_3 ; (P_4, P_7) represents R_1 cannot recover P_4 , P_7 from C_4 . Similarly, the decoding situation of R_5 can be denoted by $(P_1, P_2, P_3, P_4)|(P_2, P_4)|P_3|(P_4, P_8)$, where " P_3 " represents R_5 can recover P_3 from C_3 correctly.

As described above, the cached encoded packets in R_1 and R_5 cannot be decoded through the subsequent encoded packets, thus decreasing retransmission efficiency. By observing the above cached encoded packets , it is easy to find there is some overlap relationship among them, which may

lead to failure to decode the cached encoded packets and decreasing the decoding efficiency of the cached encoded packets. This problem raises an important question. How can we find the optimal way to achieve the higher retransmission efficiency by using the overlap relationship among the cached encoded packets.

To address this problem, this paper proposes a new cache-based retransmission scheme to achieve higher decoding efficiency of the encoded packets cached in the receivers.

B. a*ssumptions and definitions*

To describe CNCR scheme proposed in this paper, we make the following few assumptions:

1) The source node broadcasts packets in a time of fixed slots in the initial transmission phase.

2) Assume the packet loss rates of different receivers are irrelevant and follow the Bernoulli trial.

3) The source node can obtain the ID numbers of lost packets, network coding operates in the order of ID number.

4) A receiver keeps a buffer list to cache the encoded packets which cannot be decoded. Receivers recover the lost packets through dealing with the encoded packets cached in their buffer list.

5) The encoding and decoding operations for network coding are bitwise XOR.

Definition 1 If two neighboring encoded packets cached in the buffer list meet the condition, namely all the ID numbers of the lost packets in the former encoded packet are smaller than the latter's is called cross relation.

When the buffer list caches too many encoded packets, it not only increases storage overhead of receivers, but also increases the time consuming to decode these encoded packets, resulting in more transmission delay. For lost packets are encoded in the sequential order of ID number from the smallest to the largest, according to the principle of network coding, if two encoded packets cached in the buffer list meet the cross relation, the lost packet which has the maximum ID number in the former encoded packet cannot be recovered through the subsequent encoded packets. For example, as shown in Fig. 1, at the receiver R_1, the second (P_2, P_4) and (P_6, P_7) meet the cross relation, the lost packet P_4 cannot be recovered through subsequent encoded packets C_3, C_4.The receiver can ask the source node for the lost packet which has the maximum ID number in the former encoded packet so that it can realize the fast decoding of the cached encoded packets.

C. *CNCR scheme*

CNCR scheme allows the encoded packets to fail to be decoded at some receivers. When a receiver fails to decode the encoded packets due to losing more than one packet, the receiver caches these encoded packets, and updates the buffer list by simplifying the cached encoded packets according to their overlap relationship. If the subsequent encoded packets can be decoded to recover the lost packets correctly, put the recovered packets into the cached encoded packets in the buffer list to recover the before lost packets. At the same time, the receivers request the lost packets immediately when the cached encoded packets meet the cross relation, and put the retransmitted packets into the cached encoded packets in the buffer list to recover the before lost packets. In CNCR scheme, receivers recover the lost packets through the cached encoded packets which fail to be decoded, and take full advantage of the cached encoded packets. CNCR scheme effectively improves recovery efficiency and further reduces retransmissions.

The major process of the CNCR scheme is described as follows:

Step 1: The source node broadcasts packets in the initial transmission phase, after K slots, the source node obtains the receiving information matrix T;

Step 2: Search for the first "1" position in each row in matrix T in turn. Put these packets into the coding list, and reset these positions into "0" at the same time;

Step 3: Encode the packets in the coding list in the sequential order of ID number from the smallest to the largest, and broadcast these encoded packets;

Step 4: When the receivers fail to decode the encoded packets, if the buffer list is empty, the receivers cache the encoded packets directly; otherwise, update the buffer list by simplifying the encoded packets cached in the buffer list;

Step 5: If two neighboring encoded packets in the buffer list meet the cross relation, the receivers ask the source node for the lost packet which has the maximum ID number in the former encoded packet;

Step 6: Put the retransmitted packets or recovered packets into the relevant encoded packets in the buffer list, and recover corresponding lost packets.

As shown in Fig. 1, according to CNCR scheme, at the receiver R_5, after updating the buffer list by simplifying $C_1 \oplus C_2$ to $P_1 \oplus P_3 \oplus P_5$, R_5 recovers the lost packet P_1 through $C_3 \oplus P_1 \oplus P_3 \oplus P_5$; at the receiver R_1, the second (P_2, P_4) and (P_6, P_7) meet the cross relation, R_1 ask the source node for the packet P_4; in the end, put the packets P_1, P_4 respectively into the cached encoded packets in the buffer list of R_1 and R_5, recover the respective lost packets.

As described above, using CNCR scheme only needs 5 retransmissions to recover all lost packets, CNCR can effectively reduce retransmissions, and improve the efficiency of retransmission.

Simulation Results

In this section, we compare our CNCR scheme with the traditional retransmission (ARQ), NCWBR approach [8], and MDNCBR [12] algorithm. We evaluate the performance of retransmissions and network overhead, and analyze the experimental data.

The simulator of OPNET is used to simulate the wireless broadcasting network. The simulation scenario consists of a source node and five receivers in the topology structure of 500 m*500 m. The source node broadcasts size of 152bit packets by 1 packet/s to the receivers. In this paper, we design four groups of experiments with changing the number of sending packets with 100,200,300,400.

A. t*he number of retransmissions*

The number of retransmissions is the sum of retransmitting packets and encoded packets. The number of retransmissions is an important parameter of retransmission performance. The retransmissions are less, the packet recovering ability is stronger, and the network coding efficiency is higher. Fig. 2 shows the variation of the number of retransmissions that when the number of sending packets is changed, and the packet loss rates of all receivers are equal to 0.4. Fig. 3 shows the variation of the number of retransmissions, when the packet loss rate is changed, the packet loss rate in the figure ranges from 0.1 to 0.4 with step size of 0.1. As shown in Fig. 2and Fig. 3, the number of retransmissions of CNCR is significantly less than ARQ's and NCWBR's, and slightly higher than MDNCBR's. With the increase of the number of sending packets and the packet loss rate, the advantages are more obvious. Compared with ARQ and NCWBR, CNCR recovers lost packets by caching the encoded packets failed to be decoded, and the number of retransmissions greatly reduces. Compared with MDNCBR, CNCR simplifies and updates the buffer list, improving the decoding efficiency of the cached encoded packets, so the number of retransmissions is less.

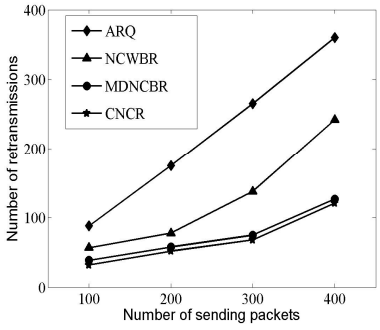


Fig. 2: Comparing of Retransmissions

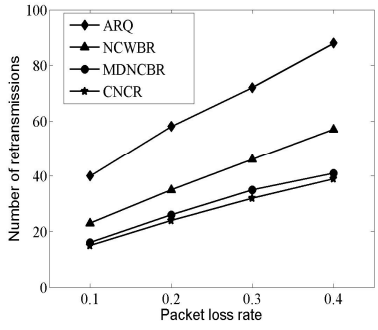


Fig. 3: Comparing of Retransmissions

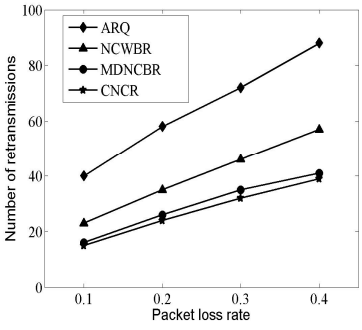


Fig. 4: Comparing of Network Overhead

B. n*etwork overhead*

Network overhead is the sum of the total bits of retransmitting packets, encoded packets and feedbacks. Network overhead is a very important parameter of the network quality. The network overhead is less, the bits used during data transmission in the network are less, thus reducing the link

congestion of transmission and improving the network throughput. As shown in Fig. 4, the network overhead of CNCR in each scenario is the least, due to the number of sending packets is the same, the number of retransmissions is less, the bits transmitted in the network are less. Moreover, MDNCBR and CNCR do not need to send NAK feedbacks in the recovery phase, thus the overhead is further reduced.

Conclusions

A new cache-based network coding retransmission scheme in wireless network has been proposed in this paper. The main contribution of this paper include (a) improving decoding efficiency by updating the buffer list according to the overlap relationship among the cached encoded packets and (b) defining the cross relation among the encoded packets cached in buffer for fast decoding the cached encoded packets. Simulation results show CNCR can effectively reduce the number of retransmissions and network overhead, and then improve the performance of retransmission compared with existing methods.

Acknowledgments

This research was supported in part by the Program for Innovation Team Building at Institutions of Higher Education in Chongqing (Grant No. KJTD201310).

References

[1] R. Ahlswede, N. Cai, S. Y. R. Li. Network information flow. *IEEE Trans. on Information Theory.* 2000, pp. 1204-1216.

[2] S. Katti, H. Rahul, W. Hu. Xors in the air: practical wireless network coding. *Proc. of ACM SIGCOMM.* 2006, pp. 243-254.

[3] Y. Wu, P. A. Chou, S. Y. Kung. Information exchange in wireless networks with network coding and physical-layer broadcast. *Proc. of 2005 Conf. Information Sciences and Systems.* 2005, pp. 78.

[4] B. Ni, N. Santhapuri, Z. Zhong. Routing with opportunistically coded exchanges in wireless mesh network. *Proc. of 2nd IEEE Workshop on Wireless Mesh Network.* 2006, pp. 157-159.

[5] R. Koetter, M. Medard. An algebraic approach to network coding. *IEEE/ACM Trans. on Networking. 2003,* pp. 782-795.

[6] D. Nguyen, T. Nguyen, B. Bose. Wireless broadcasting using network coding. *IEEE Trans. on Vehicular Technology.* 2009, pp. 914-925.

[7] X. Xiao, W. Wang, L. Yang. Wireless broadcasting retransmission approach based on network coding. *Journal on Communications.* 2009, 30(9): 69- 75.

[8] P. Fan, Z. Chen, W. Chen. Reliable relay assisted wireless multicast using network coding. *IEEE Journal on Selected Areas in Communications.* 2009, pp. 749- 762.

[9] E. Rozner, A. Iyer, P.Mehta. ER: efficient retransmission scheme for wireless lans. *Proc. of 7th International Conf.* on *Emerging Networking Experiments and Technologies.* 2007, pp. 1-12.

[10] C. Zhan, Y. Xu, J. Wang. Reliable multicast in wireless networks using network coding. *Proc. of IEEE International Conf. Mobile Ad-Hoc and Sensor Systems.* 2009, pp. 506-515.

[11] Y. Yao, J. Q. Yi, Z. Ren, Y. Wen. Efficient rapid multi-packet decoding and network coding based broadcasting retransmission. *Journal of Huazhong University of Science. 2013,* 41(6): 30-36.

CHAPTER 24:

Product Design and Engineering Management

Advanced Materials Research Vol. 936 (2014) pp 2325-2328
© (2014) Trans Tech Publications, Switzerland
doi:10.4028/www.scientific.net/AMR.936.2325

The Shapes of Products and the Lifestyle With Slow Rhythm

Linsen Guo

School of Art and Design, Nanchang Hangkong University

Nanchang Jiangxi Province China 330063

ncugls@163.com

Key Words: the shapes of products; slow rhythm; lifestyle

Abstract: The lifestyle with excessively quick steps can exert influence on health, and the excessive consumption and the essence of life run in the opposite direction. The lifestyle with "slow rhythm" objects against the excessive consumption and wasting, and advocates the simplified and humanized design, which has something in common with the appropriate "laying down" put forward in Chinese Buddhism. It's the highest wisdom to "lay down" the design with little improvement to the life quality and those unhealthy lifestyles.

Introduction

The shapes of products can exert influence on lifestyle. The current lifestyle is becoming speedier and speedier, but its rhythm with excessively quick steps can have influence on the health, and the excessive consumption and the essence of life run in the opposite direction. The wise man will go after the lifestyle with "slow rhythm" and really enjoy the life.

The Connotation of the Product Shapes

In reality, the product shapes are the transmission of a series of visual symbols. The core idea of the design of product shapes is the coding procession of various symbols, and to take a comprehensive consideration of the visual factors, such as the product shapes, colors and textures, etc. and transmit the product function and embody its features[1].

The shapes of products cover the following three categories: the entity shape, the space shape, and the detail shape. The entity shape is the common appearance possessed by all products and the most direct feeling owned by the observers. But the space shape largely embodies the spirit, especially in architecture. A few thousand years ago, the ancient men sensed the importance of space to the human being. The unreal and real rely on and oppose to each other, and the unreal possesses something real, and vise versa. The connation covered by the unreal and real is limitless, which is always the highest state pursued by the past literati and painters and the west aesthetics can never compare with. The detail shapes can best reveal whether the designer is mature or not. A mature product design usually possesses abundant details, such as the Japanese design, whose details embody the love towards human being; and the Denmark furniture has an extraordinary advantage in detail design, which brings a wonderful reputation throughout the world[2]. Although the excessive emphasis on the details will inevitably cause the complexity, the appropriate details surely can improve the design, which we need to learn from the west.

The Lifestyle

Confronting the various puzzles and crises in the current world, the people have gained a clearer and clearer awareness on the disadvantages present in the traditional developing view. It has been a common sense for the educated throughout the world to step on the way of sustainable development. However, a clear and deep understanding towards the born weak points of the non-sustainable lifestyle characterized by luxury and waste and conforming to the traditional developing viewpoint has not emerged among the people; enough importance has not been attached to and enough research has also not been conducted on the necessity and urgency to transform the traditional lifestyle and establish a sustainable one meeting the need of sustainable development. The sustainable lifestyle is the concrete revealing of the sustainable development in the social life. This lifestyle is the total of various ones not only satisfying the current people's requirements, but also not endangering the future generations to satisfy their needs. Examined from its essence, it involves two aspects of regulations: one is the fit for the material life, i.e. it requires that the material life should start from the human's basic needs, target their healthy living and be strictly confined within the capacity of the earth environment and the endurable scope of its resources. The other one is the consumption level of material, i.e. it not only demands that the persons belonging to the same generation possess the equality on consuming rights, but also every generation , especially the current generation, shouldn't consume the resources at the expense of harming the future ones' consuming rights and developing potentials, but ensure the offspring's sustainable living. At present, it's unavoidable to establish this new type of life concept and lifestyle.

The lifestyle is a culture, and the culture of appreciating beauty in essence is "a typical system of meaning symbols, and similar to a barometer, embodying the social varieties in great details." Thus, it can be seen that the lifestyle and the culture of appreciating beauty can be testified and manifested by each other. Confronting the diversified puzzles and crises in the current world, the human being own a clearer and clearer understanding towards the disadvantages of traditional developing viewpoint. Following the pathway of sustainable development is commonly accepted by the people of all walks. But the people don't have a clear understanding towards the disadvantage featured by luxury and squander and keeping accordance with the traditional developing viewpoint. The sustainable development has a lot in common with the "slow life rhythm" in essence advocated by current men: the "slow life rhythm" objects against excessive consumption and waste but advocates the simplified and humanized design and solving the various conflicts in life with the simplest methods.

The Relationship Between the Product Shapes and Lifestyles

The influence of design style on the lifestyle can best reveal the relationship between them. The industrial design is the focused reflection of economic foundation, social awareness, culture and art, the guiding direction of the trend and the symbol of scientific and technological development. "Being practical, economical, beautiful, appropriate to human being, satisfied with the demands and creative" are the targets and principles pursued by the industrial design. Whatever design methods and styles the designers employ to put their plans into practice, all of them will embody their pursuit for the new social lifestyle.

The Personalized and Diversified Design Style

The current society tends to be high-leveled and multicultural and people's value choice and demand have changed greatly. The changes of value viewpoint and demand desire a better lifestyle, a more comfortable living environment and a higher life quality than any past time provided by the society, which brings the fact that the market is determined by the buyer but not the seller, and the enterprises have to seek for the breakthrough in the design. The current society is "an era with personified products", and the people require that the products meet their personal pursuit and living attitude. So the personified and diversified design style is the best prescription satisfying different leveled lifestyles.

The Style of Conceptual Design

The style of conceptual design is categorized as a leading and fronting one and the imagination of the future. For instance, the conceptual automobile is the concept as "the transporting equipment of loading men" , but not that of " the automobile". And the design of the chair only centers around the concept of "sitting", and not every chair has its own backing cushion. While if it has its own supporting structure and can satisfy the need of "sitting", then it is a practical one. Here, the design functions as the way to improve the planning and guiding of people's lifestyle.

The Developing Trend of Future Product Shapes

Being humanized and multicultural is the main developing trend in the future society and the practice of emotional shape in the product design just follows the need of society development, especially the emphasis on being humanized will in turn help its quick rise in the product shaping and gradually grow up as the developing mode of the future product shaping.

The emotional shape which mainly follows the human being's visual feeling and meets their own entities' psychological and physiological desires can greatly express their emotion and harmonize all relationships[3]. Thus, the emotional shape will surely turn to be the developing trend of the product shaping and the mainstream direction of future industrial design.

The design of "slow rhythm" will become the future mainstream in the design. The original intention of designing is to offer a hand to the life and thus the consumer can leave more energy in the enjoyment of life. However, with the improvement of living standard, the people realize that "the hands" around them are more and more, and even turn to be the obstacles in the life, which is in conflict with the starting point of design. The lifestyle with excessively quick steps can exert influence on health, and the excessive consumption and the essence of life run in the opposite direction. The wise men of life begin to advocate "slowing down a little", which has something in common with the "laying down" put forward in Chinese Buddhism. It's the highest wisdom to "lay down" the design with little improvement to the life quality and those unhealthy lifestyles.

The lifestyle with excessively quick steps can exert influence on health, and the excessive consumption and the essence of life run in the opposite direction. The lifestyle with "slow rhythm" objects against the excessive consumption and wasting, and advocates the simplified and humanized design, which has something in common with the appropriate "laying down" put forward in Chinese Buddhism. It's the highest wisdom to "lay down" the design with little improvement to the life quality and those unhealthy lifestyles.

References

[1] Zhuchi,Wu, The Art Morphology, Publishing House of Shanghai Jiaotong University,Shanghai 2003.

[2] Shouzi,Wang,The Modern Design History Around the World, Hong Kong New Century Publishing House, Hong Kong,1995.

[3] (America) Donald A. Norman, translated by Qiufang Fu, Jinshan Chen, Emotional Design , Publishing House of Electronics Industry,Beijing, 2005.

Advanced Materials Research Vol. 936 (2014) pp 2329-2334
© (2014) Trans Tech Publications, Switzerland
doi:10.4028/www.scientific.net/AMR.936.2329

Application of Traditional Chinese Decorative Patterns in Ceramics Design

Chaoying Ouyang, Yajie Xiong, Lin Li

School Of Arts & Design.HuBei University Of Technology,China

oycyen001@126.com

Keywords: Traditional Chinese decorative patterns, ceramics

Abstract: As an important part of traditional Chinese culture, traditional Chinese decorative patterns, to a great extent, symbolise local customs as well as social, political and economic circumstances of China. Ceramics is of both use value and aesthetic value. Decorative patterns facilitate the latter of the two as a main means. Nowadays, designers are facing a great challenge of how to inherit the aesthetics and the spirit of traditional Chinese decorative patterns and how to apply modern design concepts to contemporary ceramics design. This paper investigates the origins, implications, categorizations and application examples of traditional Chinese decorative patterns in both ancient and modern ceramics designs. Based on the investigation, the paper strives to demonstrate the essence of traditional Chinese decorative patterns, enhance the charm of modern ceramics design, as well as to explore new cultural added value of traditional Chinese decorative patterns.

Introduction

Chinese invented ceramics as early as in the Neolithic Age, which was the product of the smart use of clay and fire. As an evidence of Chinese wisdom and an indispensible part of Chinese culture, ceramics has gone through vicissitudes of thousands of years. It has been a long time since its stories with traditional Chinese decorative patterns started. The connotation and spirit that it has embodied represents the wealth of Chinese national history. Thus conducting a study on traditional patterns is a way of reviving the soul of Chinese nation.

Traditional Chinese Decorative Patterns

Traditional Chinese decorative pattern is one of traditional Chinese arts. It is a form of fine arts that features figures, animals, plants, text, nature, methodology, folktale, proverbs and other topics, with a variety of techniques of expressions including metonymy, analogy, pun, symbolism, and homophone. Embodied with pursuit and best wishes for life, fortune, and well-being , it is closely associated with emotional appeal, cultural background, expression technique and social circumstances in terms of form and implications. Decorative patterns are materialised expressions of people's mind with certain principles of formal beauty.

Traditional Chinese decorative patterns originated from nature worship, worship for stars, sky and sea; totemism , regarding a certain animal or plant as the symbol of the clan; reproduction worship, praising and desiring for the fertility of the biosphere; myths and tales, Nuwa Creating Human, Jingwei Filling the Sea and Kua Fu Chasing the Sun. The evolution and development of traditional Chinese decorative patterns have undergone a very long history. They possess various styles and forms, while retaining to express entrepreneurial spirit and wishes of people.

Traditional patterns appeared as early as in the Neolithic Age. Coloured pottery, which is also called pottery painting, is the earliest example of the combination of pottery and patterns. The Main patterns of coloured pottery are: animal patterns, plant patterns, weaving patterns, and geometry patterns. Among animal patterns, mermaid, fish and fish-bird patterns are the most remarkable. Most plant patterns are revolving and leaf-shaped. As for weaving patterns, they are linear, mat-style, branch, and other kinds. Dots, triangle and abstract patterns drawn with curves are the main styles of geometry patterns . When conveying ideas, primitive humans utilised abstract geometric patterns to generalise with emphasis on emotion expression and the sensibility of the author, rather than for accuracy. After they experienced motion, balance, repetition, strength and weakness, primitive humans expressed them with drawings. There are various approaches of formal beauty applied in decorative patterns such as variation and unification, symmetry and balance, contrast and accordance, paces and rhythm, and others. Due to harsh living conditions, human reproduction was largely influenced by nature. Human beings worshiped reproduction by instinct. Consequently, productive animals like fish and frog became symbols of reproduction. They were presented by primitive humans on patterns to express their desire for fertility.

In the bronze ware age of Xia, Shang and Zhou dynasties, decorative patterns were no longer just simple, primitive, and joyful. Instead, they were used to symbolise the feudal monarchy, and became somewhat solemn and awesome for the reasons of religions and mythologies. Variations appeared like animal face patterns, Kui-shaped pattern, and phoenix-shaped pattern.

Qin and Han dynasties saw the first great unification period in Chinese history when productivity was greatly improved. In pre-Qin period, primitive totems, sorcery and religion were highlighted. While in Qin-Han period, patterns became finer and more colourful. Combination of animal images and co-existence of plants were often used. Lines became smooth, graceful, and dynamic.

"Of the four hundred and eighty temples from the Southern Dynasty, how many are showered in the mist and rain?" This is a line from a poem depicting the prosperity of Buddhism of the period of Wei, Jin, Southern and Northern Dynasties. A great number of Buddhism relief decorative patterns emerged at that time, including lotus pattern, honeysuckle pattern, dragon pattern, and bird pattern. Lotus stands for paradise, honeysuckle immortality, and samsara soul.

In Chinese history the Tang Dynasty was another period of great unification when decorative patterns turned to be a style of magnificence, saturation, sophistication, and heavy colours. Natural lives were often the topic of pattern depiction, for example, rolled grass pattern, Baoxiang flower pattern, pomegranate pattern, etc.

In the Song Dynasty patterns turned out to be more realistic style. Poses of animals in motion and shapes of plants were depicted with dots, lines, and facades. Those materials were flattened and structured in symmetry, making patterns dynamic and elegant.

The Yuan Dynasty was the first dynasty ruled by a minority nation when Mongolian culture, Islamic culture and Han culture co-existed. As a result, the patterns in the Yuan Dynasty manifested the contradiction and fusion, and represented aesthetics of complexity, but also magnificence. Later, the Ming Dynasty saw both existence of freehand and neat style with strong decorative beauty. Notable examples are cloud pattern, stem-twining flower pattern, dragon pattern, phoenix pattern, fish pattern, etc. Close to the end of feudal society, the Qing Dynasty failed to make enough innovation in decorative patterns although there was adequate exquisiteness, as they came in elegant colour and thick lines with strong sense of decoration.

In general, the development and evolution of traditional Chinese decorative patterns started from simple lines expressing human feelings in primitive age. It went on to vary and prosper due to the material and spiritual enjoyment of the court, nobility, and men of letters, and was influenced by

religion thus to evolve in new styles. Considered as an essential part of traditional Chinese culture, the wonderfulness of decoration patterns and their rich implications are beyond description.

Traditional Chinese Decorative Patterns and Ceramic Woks

Use Function and Aesthetic Function

Ceramics is an umbrella name for pottery and porcelain. Its raw material comes from tempered clay, which is abundant on the earth . During the early stages of ceramics, it was used only as convenient utensils until aesthetic function was added to it. Blue and white porcelain, Sancai, and coloured ceramics, with patterns of different periods of history, all imply wealth and power and have thus promoted their value through aesthetic function. Ceramics can be categorised by function as there are daily usage ceramics, art ceramics and industrial ceramics. They all own both materiality, which means the practicability and use value, and the spirituality that emphasises aesthetic value. Their colour, shape, patterns and other elements, are all symbols that brings both visual and psychological enjoyment. Decorative patterns, in particular as the main vehicle of expression of local customs and aesthetics, boost aesthetic value as well as the price of ceramics in a way of arousing resonance and acceptance of people.

Art of decorative patterns has a long history in China. As a symbol of social circumstances and daily life of different periods, it is an irreplaceable record of traditional Chinese culture. Accompanying China in her best and worst times, decorative patterns stemmed from simplicity of primitive ages, to rough style on bronze ware in slave society, and later to exquisiteness in feudal ages. It has evolved into main categories of the following: auspiciousness, geometry, animal, plant and figure, which are embodied with different art styles and aesthetic consciousness.

Pattern design is based on social and economic conditions of the time in question, and is genuine reflections of ancient economic, political and cultural life. For example, the mermaid patterns in primitive society implied an abundant life and reproductions. This is the consequence of harsh living conditions of that time, as daily life, and even reproduction were under constant threat. Later in the Shang Dynasty, class differentiation came into being and thus there were slaves and slave owners. Animal patterns, especially fierce animals, symbolised the awe of slave owner class. During the Southern and Northern Dynasties, people longed for peaceful life as the country suffered long-time chaos caused by wars. Subsequently, Buddhism became popular as people hinged their hopes on samsara. It was believed that sufferings before death result in entry to nirvana in afterlife. Lotus patterns were often seen at that time as the symbol of Buddhism, implying “Sukhavati”, “pureness” and “auspiciousness”.

With the society completing a transformation from one with an elitism culture to a popular one, handicrafts made in exquisite manner and small numbers were replaced by ones made with machines and large quantities. In this process, ceramics shifted from the treasure of the rich and noble to the daily product affordable for ordinary people. In the meantime, it has become a representative modern product, made with controlled cost and with a simple style, instead of the outcome of careful design and sheer workmanship. After the ceramics was commercialised, businesses have continually joined in this trade. The advance of technology and productivity made making it no longer a problem, but it is still a question for businesses that how to make their own product outstanding. On this occasion, traditional decorative pattern, with its unique attractiveness and culture connotation, can give ceramics the special cultural additional value as well as the aesthetic value. Nowadays, designers are facing a great challenge in inheriting the aesthetics and the spirit of these beautiful and meaningful patterns, and also in combining modern design concepts with contemporary ceramics design.



Figure 1, Deer and Crane Enjoying Spring Together on the first facade



Figure 2, Tiger and Mouse patterns on the second facade



Figure 3, Lotus and Shrimp patterns on the third facade



Figure 4, Magpies in a Plum Tree on the fourth facade

Application of Traditional Decorative Patterns Illustrated in a Folk Pottery Pot with Yellow Glaze

Patterns are drawn on the four facades of the pottery. The first facade is a transformed pattern of "Deer and Crane Enjoying Spring Together"; the second an animal pattern of the mouse and the tiger; the third the pattern of the lotus and the shrimp; the fourth the "Magpies in a Plum Tree" pattern which depicts a magpie resting in a plum tree.

On the first facade there is a pattern of the deer and the crane, implying "Deer and Crane Enjoying Spring Together". The phrase is intended to suggest that nature is thriving and flourishing in spring. In Chinese "deer" is homophonic to "land" and "crane" to "together". The images are combined to form the auspicious pattern of "Deer and Crane Enjoying Spring Together". In the way of exaggeration and simplification, the author combined the deer and crane into a pattern. To keep the crane standing higher than the deer in the pattern, the author positioned the crane in the branch and the deer under the tree.

On the second facade is a pattern of the tiger and the mouse. The worship for the tiger is believed to originate from the totem worship for the tiger in Chu culture. The tiger has been regarded as a protector by labouring people since the Han Dynasty as it symbolises bravery and firmness. The first symbolic meaning of the mouse is agility for its keen sense of smell, timidity and wariness. Thanks to its small size of the body, the mouse can always make a successful escape whenever in danger. As a result, the mouse was regarded as a symbol of agility. What's more, the mouse is believed to have foresight of future good and ill luck. The second symbolic meaning of the mouse is vitality. The author added trees to the image to keep its style coherent with those on the other three facades and to highlight the patterns of the tiger and the mouse. By doing this it also makes the whole picture more saturated.

On the third facade there are the patterns of the lotus and the shrimp. In a local slang, the shrimp stands for "smoothness and success" which means the ability to tackle problems and resourcefulness. The lotus has two implications. One is that "the lotus remains stainless after rising from the slimy bed and modest while standing over the clear water". The lotus is a symbol of honest and elegant gentleman. The other is the Sukhavati, which stands for pureness and auspiciousness.

On the fourth facade is a pattern named "Magpies in a Plum Tree". "Magpie" was regarded as a symbol of "happiness" in ancient times, as the two Chinese characters are homophonic. In addition, "plum" is homophonic to "eyebrow". Therefore, a magpie standing in a plum tree depicts the look that delighted people usually show. "Magpies in a Plum Tree" is one of the auspicious patterns frequently seen in Chinese folk arts.

The patterns on the body of the pot are presented on a basis of sections. On the top are the patterns of auspicious-wings and the patterns of transformed twining branch. In the middle are single patterns in detail: the pattern of “Deer and Crane Enjoying Spring Together”, the Pattern of the Tiger and the Mouse, the Pattern of the Shrimp, and the Pattern of Magpies in a Plum Tree. On the bottom is the Pattern of the Box. This pattern, together with the patterns of auspicious-wings and the patterns of transformed twining branches fully surrounds the pot body in two-sides continual and tape shape. Geometrical patterns and figure patterns form contrast and cooperation, making the patterns on the pot look lively and dynamic. The patterns are made both in main and secondary positions as well as in detail and general, thus to present the contrast of expression strength on the pot body and a sense of rhythm. The simple natural handling of the patterns serves as a good example of “great skills seem awkward and extreme sophistication leads to simplicity”. With the rough and simple lines in the patterns the author expressed his wish and love for life.

Conclusion

When applying traditional Chinese decorative patterns in modern ceramics design, modern designers cannot simply copy the originals. Instead, they should combine their works with current social circumstances, trend and aesthetics, as well as traditional Chinese culture, so as to create works in the modern style. Only in this way can the root-seeking complex of Chinese nation be fully expressed and traditional Chinese culture inherited.

References

[1] Ouyang Chaoying and Zhao Peng, Cultural Connotations and Expressive Characteristics of Visual Images of Chinese Religions, *Principles of Design,* (2005) 105.

[2] Information on http://baike.baidu.com/ link?url=sl0fFZ_j5aazqV_xp8KAQDJaMTRMekDszvDaRyHl8MQ1FAgsxb0rwcB4UsVUujVb

[3] Information on http://baike.baidu.com/ link?url=t8llNjFAJp5mV-hsa7qhDqJrLbvx CHJLOINto5KkV9 mv1vzuJ5MtZjuF275sNV4w

Advanced Materials Research Vol. 936 (2014) pp 2335-2338
© (2014) Trans Tech Publications, Switzerland
doi:10.4028/www.scientific.net/AMR.936.2335

Packaging Material Barriers Faced by Foods and Agricultural Products Export of China and Countermeasures

HongLing Shao[1,a], HaiXia Cui[1,b] and Jian Lu[1,c]

[1]College of Economics and Trade, Agricultural University of Hebei, No.2596 Lekai South Street, Baoding City, Hebei Province, China 071000

[a]shaohongling@126.com, [b]hx_cui79@126.com, [C]ndlujian@126.com

Keywords: food and agricultural product, packaging material, barriers

Abstract: Foods and agricultural products safety problems caused by the packaging materials have attracted extensive attention all over the world and some developed countries take it as a technical trade measure to increase the threshold of foods and agricultural products import, which brings about great negative impact to the export countries. Based on the analysis of the packaging material barriers faced by foods and agricultural products export in China, this paper will put forward some countermeasures to break through the packaging material barriers of foreign countries.

Introduction

With the global increasing emphasis on food safety problem, the safety problem caused by the food and agriculture product packaging has attracted extensive attention all over the world and some developed countries take it as a technical trade measure to increase the threshold of foods and agricultural products import, which bring about great negative impact to the export countries. As a large agricultural country, the agricultural product export occupies an important position in the foreign trade of China. Although the export scale of foods and agricultural products in China continues to expand, in recent years the foods and agricultural products export of China is frequently blocked by foreign countries for packaging quality problems, resulting in serious economic losses. Packaging material barriers caused more and more attention. Based on the analysis of the packaging material barriers faced by foods and agricultural products export in China, this paper will put forward some countermeasures to break through the packaging material barriers of foreign countries.

The Packaging Material Barriers Faced by Foods and Agricultural Products Export of China

The foods and agricultural products in China are mainly exported to the United States, Japan, the European Union and other countries. These countries not only put forward more and more strict hygiene requirements for foods and agricultural products themselves, but also put forward higher requirements for the chemical composition analysis of packaging materials and material selection. In order to strengthen the safety management of imported foods and agricultural products packaging, starting from safeguarding national interests, they issued a series of strict technical regulations and measures to become the trade barriers faced by exporters.

They Established the Relatively Perfect Law and Regulation System

The sanitary requirements on foods and agricultural products packaging containers and materials in the United States are embodied in "food, drug and cosmetic" of code of federal regulations, which points out that the foods must be packaged in the conditions of meeting sanitary requirements, the production of foods packaging materials must be based on good manufacturing practice, and the packaging materials contacting with foods and their components must conform to the requirements. In the United States the food packaging material is included in the management scope of food additives and according to the degree that some chemical substances in packaging materials endanger human body by foods, the management of packaging materials is divided into three modes that are free from management, foods additives examination and approval and foods contact substance notification.[1]

European Union established the safety regulations of food packaging materials and carried out the research for the packaging influence on food in the1950's, and so far, it has established a relatively perfect system of law and regulation on food packaging materials. Its food packaging materials management includes the framework regulations, special regulations and separate regulations. The framework regulations stapulate the general principles on the management of food packaging materials. The special regulations stapulate the special requirements of each kind of material listed in the framework regulations. The separate regulations are the special provisions for a certain substance alone.The requirements of European Union for food packaging materials usually include the substance list allowed to be used in the packaging materials, quality specification standard, exposed quantity data, migration quantity data, test and analysis method etc..[2]

"Food Sanitation Law" that was issued by Japan in 1947 mentioned food contact material issues and stipulated prohibiting to produce, sell and use the food containers and packaging materials containing harmful substances. Japan's Labor Ministry may formulate the standards and hygienic requirements of food packaging materials according to the need, and the standards of food packaging materials issued by it are divided into three categories. The first is the general standard that stapulates the content requirements of the heavy metals , especially the lead content requirement, in all food containers and packaging materials. The general standard also stipulates that the synthetic pigment used in packaging materials must be approved by Labor Ministry. The second is the category standard that formulates the category standards of metal cans, glass, ceramic, rubber and other substances and the standards of thirteen kinds of polymers. The third is the standard for specific purpose that is formulated for the materials with specific purposes.[3]

They Introduced the Risk Assessment to Evaluate the Safety of New Materials

In addition to considering the structure and properties of the packaging materials themselves, they make a migration simulation test with their contact products to evaluate the effect of packaging materials on agricultural products and foods safety. The code of federal regulations in America stipulates that the materials contacting foods must comform to the provisions of Food and Drug Administration and pass the chemical composition test and migration test. The migration test is used to evaluate the content level of food residue from packaging materials and is the required test of new packaging materials. According to the regulations of Food and Drug Administration, when the substances that can not be used as food ingredients and are harm on human health are used for food field, they must be proved to be no toxic through accurate chemical data and deduction. However, in Europe all materials must go through the very strict toxicity assessment no matter whether the number of migration or having the possibility of migration.[4]

They have Other Provisions of Foods and Agricultural Products Packaging Materials

European Union formulated the maximum migration value of food packaging printing ink and stipulated that the general migration limit of 4 - methyl diphenyl ketone and diphenyl ketone in the food packaging printing ink materials must be less than 0.6 milligrams per kilogram. "Food Sanitation Law" of Japan clearly demands that food packaging can not be too garish and the special ink that is stable and not easy volatile to generate harmful substances must be used to print food packaging.[5]

The United States demanded to evaluate the risk of bisphenol A and prohibited containing it in food and beverage containers through Food Safety Enhancement Act in 2009. France also has the same provisions. France announced that the non-biodegradable plastic packaging materials would be replaced by the environmental degradable materials to package the foods and the agricultural products since January 1, 2010.

In addition, most developed countries have higher standard on the tractability and the recyclable rate of agricultural products packaging materials in their environmental regulations. They require to use the green packaging material that can save energy, reduce waste, recycle or be easy to decompose naturally after being used and not pollute the environment. They carry on the quarantine of hygiene and animals and plants to the packaging produced with natural materials.

The Countermeasures to Break through the Packaging Material Barriers of Foods and Agricultural Products

Though the increasingly strict regulations and standards on the packaging materials of foods and agricultural products in foreign countries promote the foods, agricultural products and packaging industry in China to develope more healthily, safely and environmentally, they have the negative impact on the export of foods and agricultural products of China. In order to deal with increasingly strict packaging material barriers of foods and agricultural products in foreign countries and expand exports, we advise to take the following measures.

Exert the Macro-control Function of Government

Use the successful experience of developed countries in the foods and agricultural products packaging industry for reference, the government should do the following things. Firstly, establish and perfect the foods and agricultural products packaging regulations. China has not the packaging law. Secondly, constantly update and improve the foods and agricultural products packaging standard system so that the packaging materials of foods and agricultural products have the definite standard and speed up the packaging materials standardization. In the fields that the country has not yet established a unified standard, such as ink field of food packaging, establish the new standard and inspection method to be beneficial to supervise the ink market of food packaging.Thirdly, the relevant functional departments of government should strengthen cooperate to further explore and implement the long-term mechanism of food safety supervision, to intensify the supervision of all aspects of export foods and agricultural products and their packaging materials and to strengthen the traceability system construction of quality safty of export foods and agricultural products and their packaging to ensure quality safety of export foods and agricultural products and their packaging. Fourthly, establish and perfect the warning mechanism of the packaging material barriers of export foods and agricultural products as soon as possible, and strengthen the notification and consulting website construction to issue warning information timely for the enterprises.[5]

Strengthen the Guidance and Coordination Function of Industry Association

Firstly, strengthen the communication between the packaging industry and the food and agricultural product industry to combine packaging design, production and application organically. Secondly, through the establishment of integrity system, realize the self-supervision of industry to promote the sustained and healthy development of the whole food and agricultural product packaging industry. Thirdly, actively collect relevant information, timely update, and establish the perfect information disclosure channel. Through the internet and other means of information dissemination, make the domestic export enterprises understand packaging materials related information of other countries as soon as possible.

Improve the Enterprises' Awareness of Quality Safety of Foods and Agricultural Products Packaging

Export enterprises should improve the awareness of quality safety of foods and agricultural products packaging to ensure their own quality safety of foods and agricultural products and to ensure the quality safety of export foods and agricultural products packaging. Export enterprises may take the following measures. Firstly, pay close attention to and deeply understand the packaging materials regulations of foods and agricultural products of other countries and formulate corresponding measures according to the enterprises' situation. Secondly, strengthen the awareness of environmental protection, increase the investment of science and technology and develop non-toxic, harmless and biodegradable green packaging materials to insure the process from raw material purchase to product manufacturing to accord with the environmental protection requirements of import countries. Thirdly, actively develop new markets and implement the diversification strategy of export markets to avoid packaging material barriers of foods and agricultural products and strengthen enterprises ability to resist packaging risks.

Summary

In order to avoid the threat of packing materials to consumer health, Europe and the United States have enacted the strict laws and decrees of foods and agricultural products contact materials safety, which become the trade barriers faced by the export enterprises of foods and agricultural products and make the export enterprises suffer huge economic losses. The government of the export country, the industry association and the enterprises need to work together to cope with the packaging material barriers of developed countries and to guarantee the economic benefits of export enterprises and consumers' food safety.

This paper is supported by Hebei Science and Technology Department project (No.13457515D) and Hebei Education Department project (No.SQ123013) of China

References

[1] Yan-ming Zheng and Hui-yong Li: Safety Management of Food Packaging Materials[J]. China Standardization,8,(2008), 68-69.

[2] Jing Wang, Wen Liu and Yue Dai: Research on Food Packaging Container and Their Material Standard System[J]. Agriculture Products Processing,1,(2011), 6-78.

[3] Yong-xiang Fan and Zhu-tian Wang: Analysis on Safety Management Situation and Countermeasure of Food Packaging Materials at Home and Abroad[J]. Chinese Journal of Food Hygiene,4,(2006), 342-345.

[4] Cheng Ying: Analysis on Foreign Food Packaging Regulations[J].Shanghai Packaging, 2,(2013), 64-65.

[5] Fan-zhen Kong: New Change of Trade Barrier Abroad in Food Packaging and the Countermeasures[J]. Shanghai Packaging,4,(2010), 55-57.

Advanced Materials Research Vol. 936 (2014) pp 2339-2343
© (2014) Trans Tech Publications, Switzerland
doi:10.4028/www.scientific.net/AMR.936.2339

Safeguard System on the Quality of Excellent Engineers Training

Changming Liu

Yangtze University , Jingzhou, 434023, P.R. China

Keywords: Excellence Program; Excellent Engineers; Training; Quality; Safeguard System

Abstract. Based on literature research, this study proposed a topic on the safeguard system of quality of excellent engineers training. Four safeguard elements of training quality are elaborated, namely, faculty building(premise), collaboration with enterprises(key point), governmental support(guarantee) and the participation of students(basis). Likewise, basic knowledge structure, engineering capability training and engineering accomplishment cultivation are safeguard elements of training quality. Meanwhile, the construction of collaboration, control of practice, improvement of safeguard mechanism and the fulfillment of participating members are safeguard conditions of training quality. It is concluded that Excellence Program can be achieved and effective by constructing the safeguard system of training quality and serious process control.

Introduction

According to the Outline of Mid-long Term Educational Reform and Development, the Ministry of Education put up the Training Program of Excellent Engineers (Excellence Program for short). By 2012, 130241 students, from 824 undergraduate programs or pilot classes and 288 graduate programs in 194 universities, had participated in Excellence Program. The participating universities accounted for 19.1% of those universities with engineering courses. All universities with strong industry background were involved in Excellence Program. The promotion of Excellence Program facilitated the deep reform of university engineering education. It also attracted the attention of relevant ministries and local government to notice and support the educational reform of university. Excellence Program is just unfolding and plays an important role in this reform. However, it is a problem worth to be noticed and discussed on the smooth implementation of Excellence Program and guarantee of engineers cultivation quality.

Safeguard Basis on the Quality of Excellent Engineers Training

There are some elements that quality and effectiveness of Excellence Program largely rely on.

Premise—Faculty Building

Excellence Program aims at cultivating reserve talents of engineering with engineering knowledge, capability and achievement. To improve students' engineering capabilities and achievements, teachers with such talents come first. Therefore, the implementation of Excellence Program primarily requires a group of reasonable-structure, high-quality and good-capability teachers with rich engineering experiences. The group should consist of faculty with engineering practice and research capability. The members of this group can be further divided into two subgroups. One subgroup should have university teachers with good educational experiences and engineering background. The other subgroup should be made up of experienced engineering staff who can give educational instructions. Therefore, there are important tasks, such as electing,

cultivating and constructing a double-structure group of teachers, for universities to apply for Excellence Program.

Key Point—Collaboration with Enterprises

Cultivating reserve talents of engineering needs the participation and collaboration of enterprises, which is a key to the implementation and effectiveness of Excellence Program. Universities applying for Excellence Program should have deep cooperation with enterprises. In other words, those universities should have long-term cooperation with relevant enterprises, learning of their talents requirements and fully absorbing their advice of talents cultivation. Meanwhile, universities applying for Excellence Program are supposed to take advantage of human resource and material resource of enterprise to cultivate students' engineering awareness and capabilities. Under the instruction of the Ministry of Education, universities should maintain long-term cooperation with mutual benefits and correspondingly cultivate reserve talents of engineering. Without the participation and collaboration of enterprises, universities could not succeed in applying for Excellence Program.

Guarantee—Governmental Support

Excellence Program is an engineering talents cultivating program proposed by the Ministry of Education against the background of social development of economic construction. The promotion and implementation of this program involves in initiative of universities, full participation and cooperation of enterprises, as well as support and coordination of government. The local government should enact some policies and measures to encourage enterprises to participate in Excellence Program. Enterprises can be a bridge and band in the implementation of Excellence Program. They can also play a leading role in this program. The smooth implementation of Excellence Program can be achieved with effect only by creating conditions for the cooperation between universities and enterprises. Finally, large quantities of reserve talents can be cultivated and serve for the development of economy and society through this program.

Basis—Students' Participation

The premise of the implementation of Excellence Program is the warm participation of students, regardless of universities' emphasis, enterprises' input or governmental support. Universities should explain the original intention and spirit of Excellence Program to help their students learn the significance of this program and how enterprises can benefit from it. Then, students can be more confident and active to participate in this program. Only when students actively participate in this program as the program required can Experience Program be smoothly implemented. Therefore, it is a premise and basis of Excellence Program to change the program into students' self-requirements and fully motivate their subjective initiatives. Otherwise, the program is with no sense.

Safeguard Elements of the Training Quality of Excellent Engineers

The cultivation of reserve talents of engineering needs to clarify basic elements of talents quality—an important link to ensure the training quality of talents. Otherwise, Excellence Program can not be successful without clear goals and standards. So, what quantities an excellent reserve talent of engineering should have?

Basic Knowledge Structure

The talents-orientation of the Excellence Program needs to satisfy the reality and future demand of economic and social development, meeting the requirements of employers on the knowledge, capability and quality of talents. Due to the diversified types of disciplines and different industry backgrounds, universities applying for the Excellence Program can be different in talents cultivating levels, types and goals. Therefore, according to the service requirements of talents, each university should fully take advantage of talents cultivation to train high-quality excellent engineers by closely cooperating with relevant enterprises and industries. However, wherever the engineers are from, they all need some basic knowledge structures, such as humanistic knowledge, mathematical knowledge, economy knowledge, management knowledge and technological knowledge.

Engineering Capability Training

Engineering capability training is the most important task because the aim of Excellence Program is to cultivate reserve talents of engineering. So, what constitute the engineering capability? At least, it includes engineering design capability, engineering construction capability and engineering management capability. Engineering design capability refers to the combination of the overall conception capability, application capability of new technology, practice capability of new idea and design capability of new plan. Engineering construction capability can change design drawing into engineering entity, which includes the understanding of design thinking and design intention, revise of design alternative and realization of design drawing. When encountering practical engineering problems, engineering construction capability can be beneficial to the solutions of these problems. Engineering management capability consists of dispatch of constructors, control of construction schedule, check of construction quality, security of construction safety, choice of construction material, application of construction technology, optimization of construction process and control of construction cost.

The acquisition of all these mentioned capabilities is a process needing to be understood and accumulated in engineering practice. Therefore, it is the core of Excellence Program to strengthen engineering practice.

Engineering Accomplishment Cultivation

Engineering knowledge and engineering capability are basic tools for an excellent engineer. However, only knowledge and capability are not enough. An excellent engineer should also have good engineering accomplishment. It refers to the accomplishment of identification of engineering value, design of engineering proposal, innovation of engineering technology, management of engineering talents and exchange of international cooperation. The identification of engineering value requires acute identification and assessment of social value, ecological value, environmental value, energy value and development value. The identification process is supposed to provide assessment advice for engineering decision-making in order to guarantee the accuracy of feasibility study. Based on the identification process, the design of engineering proposal ought to make a plan for overall scheme, recruiting scheme-making staff and arranging the research and draft of scheme. Fast choice, revise and perfection of scheme can make high-quality engineering proposal. The innovation of engineering technology elaborates new ideas, technologies, material and equipment as many as possible in the process of engineering scheme and implementation. The management of engineering talents requires recognizing, choosing, cultivating and employing different kinds of

engineers. Discovering talents and putting them in place can enhance the efficiency of talents employment. The exchange of international cooperation means to have knowledge and skills of international shared as well as to understand international engineering discipline and regulations. Qualified engineers should have the ability to equally communicate and negotiate with their international counterparts. They even need to launch a lawsuit with necessary.

It needs practical foundation for the acquisition of knowledge, ability and accomplishment. Excellent engineering capability and accomplishment can not be formed without engineering practice and training. Therefore, engineering practice and training are key links during the cultivation of excellent engineers, guaranteeing the quality of excellent reserve talents of engineering.

Safeguard Conditions of Excellent Engineers Training

To insure the quality of excellent engineers training, the following conditions are needed:

Building Cooperation Mechanism

To build good cooperative relationship with enterprises, universities should ensure both sides benefiting from cooperation under the principal of reciprocity and mutual benefit. In other words, universities should actively take their interests into consideration as enterprises do. Meanwhile, universities should help enterprises overcome the technological problems in production process and provide technological innovation, reform and invention for them. Then, enterprises can get concrete benefits. Therefore, an interests-driven mechanism should be built in the course of cooperation. Full fusion of emotion and adjustment of economic leverage will promote further development and continuation of cooperation.

Controlling Practical Process

Practice training is key link during the cultivation of excellent engineers. Only by exercising engineering practice can Excellence Program be functional in cultivating reserve talents of engineering. Firstly, controlling process requires that practical training time needs to be more than one year. Secondly, controlling process allows students to be involved in engineering practice and to get introduction from engineers. Thirdly, in order to strengthen training effectiveness and training quality, an inspection mechanism should be built to check the time, place, tutor, content and skills of practice.

Perfecting Safeguard Mechanism

Excellence program, a national campaign, needs corresponding national safeguard mechanism, such as laws, policies and talents. China should enact educational regulations on rights and obligations of university and enterprise in the course of talents cultivation as soon as possible. Laws and policies should explicit the role set of both sides, especially for the role and responsibility of enterprise in the course of educational cooperation. Favorable treatment, such as tax allowance and exemption, technological support, patent application and staff training, are also supposed to be included in laws and policies. Then, the initiative of talents cultivation can be enhanced while the quality and effectiveness of Excellence Program can be ensured.

Participation of Relevant Parties

The smooth implementation of Excellence Program requires relevant parties to have mutual cooperation and down-to-earth working style. During each course, relevant parties should take the every session of program seriously and provide reserve talents of engineering best training on knowledge, capacity and achievement. Then, Excellence Program can be in practice with effect.

References

[1] Lin Jian, Analysis on Excellence Program (2010-2012) (Part 1), Researches in Higher Education of Engineering, 2013(4):1

[2] Lin Jian, Safeguard of Excellent Engineers Training Quality (Part 1), Researches in Higher Education of Engineering, 2013(1):23

[3] Liu Changming: Research of the Excellent Engineers' Quality Training. Materials Processing Technology Part3 TRANS TECHPUBLICATIONS ISSN:1022-6680.p1812-1815

[4] Liu Changming was born in 1955 in Tianmen, Hubei Province. He is currently a professor of Changjiang University. His main research interests include science of education and science of personnel.

[5] Phone Number: 13593851155 E-mail: jyylcm@163.com

Advanced Materials Research Vol. 936 (2014) pp 2344-2351
© (2014) Trans Tech Publications, Switzerland
doi:10.4028/www.scientific.net/AMR.936.2344

Design Methodologies of Ship General Arrangements-A Review

Duanfeng Han[1, a], Hany Abdelkhalek [1 ,b], Miao Chen[1, c]

[1] College of shipbuilding Engineering, Harbin Engineering University,

Harbin 150001, Heilongjiang, PR China.

[a]handuanfeng@hrbeu.edu.cn, [b]hany_abdelkhalek@hotmail.com, [c]chenmiao_1102@163.com

Keywords: General Arrangement, Methodologies, Layout Design, Early-Stage Design.

Abstract: This paper presents an overview of ship general arrangement design methodologies and philosophies and early-stage design capabilities, particularly during the last decade. The arrangement of a ship has a unique feature in that it can both enable successful shipboard operations and constrain the performance of all subsystems. Stable ship layout is critical to producible, and therefore cost effective, designs and time. This paper overviews the efforts made by the researchers in the last decade to improve generating the arrangement rapidly . Also, identify areas of the ship general arrangements process that are insufficiently addressed or not addressed at all in order to keep pushing the field of general arrangements forward.

Introduction

Over the past 60 years, the cost of new naval ships has outpaced consumer product inflation by a significant margin. Of the 7-11% growth in cost, about half has been attributed to customer-driver, rather than economy-driven, factors [1]. About one-quarter of the increase for surface combatants is due to complexity. The ship's mission requirements, its constituent systems, and the layout of those systems are key factors in the overall complexity of a vessel. From the naval architect's perspective, mission requirements and system selections may be non-negotiable. The remaining lever for managing a ship's complexity lies in the ship's arrangement. General arrangement design, as a system engineering process, is a unique blend of experience and judgment combined with the systematic evaluation of performance. Its objective is to optimize the ship as a total system. The product of the process not only is a representation of design decisions, it also serves as a focal point for establishing an effective dialogue within the design community and also with the operational community[2].

In the field of naval design, the study of concepts and theories in generating general arrangement of these complex engineered systems at an early stage of design (preliminary design) and factors affect decision makers has a serious attention. The need for the naval architect, at the formative preliminary design stages of a ship design, to have a clear understanding of the issues affecting configuration has become more important, because of the risk that the readily available design tools enable the novice ship designer at his/her personal computer all-to-readily to produce what appear to be worked up ship design solutions. In order to motivate the progress in this field we should begin to focus on the philosophy of different methodologies taken by last researchers, and on the points naval architects should keep in mind. This article will handle those two directions, the factors affect them, and the challenges facing each approach. to enrich advantage of the article ,four issues are considered to merit further attention in future considerations.

Design Considerations for the Naval Architect Affect the Early-Stage Design [3]

Vehicle type-Monohull superstructures are more constrained in volume and area than catamaran superstructures. Catamaran side hulls are normal quite cramped and demand a linear, fore-and-aft arrangement[4]. **Vehicle size-Generally**, larger vehicles provide more options arrangements. **Operational environment-Expected sea state**, temperatures and wind loading determine the need for items such as additional insulation, bulkhead strengthening, and viewing options, all of which impact the arrangements. **Operating requirements**-Considerations include operating speed, expected traffic conditions and whether the vehicle is expected to remain at sea during storms. Harbor tugs, for example, feature raised pilot houses with windows in three or four sides, and at times in their overhead, as a way to maximize visibility while ship handling at close quarters in a congested harbor. However, their freeboard (distance from the water to the deck) is low, because there are no storm waves in the harbor **.Type of cargo**-Containers dictate a cargo arrangement built up of rectangular elements ,petroleum dictates double hulls, vehicle ferries must have gently sloping ramps for driving on and off **.Physical security and control**-Security for combatants can include armor for critical compartments and the bridge, which constrains arrangements. Security for commercial ships can include ways to make boarding by pirates difficult. Ferry designs may include limited access openings to better control the entry and exit of passengers **.Type and quantity of personnel aboard the vehicle**- Arrangements vary from spacious, with gracious continuity in flow for luxury yachts and cruise liners, to compact and cluttered in combatants. Special arrangements are needed for handicapped persons, and for male/female crew members, as well as officer/enlisted [5].**Type and size of equipment, and requirements for its at-sea maintenance, access and disassembly**-Propulsion and cargo handling equipment often determine key aspects of arrangements, such as air intakes, exhausts and structural foundations. Extra volume is needed around equipment if at-sea repairs are envisioned **.Sources of noise and vibration**-Personnel living and working spaces are located as far as possible from sources noise and vibration in order to enhance operator performance and personnel comfort [6] **.**

Ship General Arrangement Methodologies and Generating Philosophies

Functional Arrangement Design [7],The philosophy of this method is juxtaposition of what were drafting tables, so that those designers working up the upper decks and superstructure could better interface with the outboard profile designer, while those responsible for the lower deck arrangements interfaced with the inboard profile design. In modern practice this approach translates to the necessity for the ship designer to ensure that 3-D models of compartment locations are considered not just in terms of a given deck arrangement but also of the relationships with adjacent decks and the topside.

Stylised Layout [8],design of specific functions of machinery, living, working, payload, services and liquids, with the object of avoiding excessive interaction between functional areas which could lead subsequently to loss of design control. Produced as a means of maintaining coherence in ship layout.

Outlining Ship Systems[9], a basis for “logical selection of design configurations within boundaries of the feasibility envelope”. Each arrangement was then individually evaluated for a range of parameters, such as ease of modernisation and conversion, modularity and minimisation of vulnerability and topside clutter. Its philosophy to outline the ship design to five systems ,that is containment, mobility, ship support, mission support and human support.

Arrangement Design Methodology, a sequential approach constrained by the initial concept design output and hull form plus subdivision of the decks and bulkheads. They [10]stated that architectural layout programs were examined for their potential for application to ship layout, but could not deal with ship shape and space limitations; also, optimisation techniques were infeasible because of the large number of independent variables involved in ship layout. They provided an update of General Arrangement CAD system.

Creative Ship Design , using the disposition of the principal spaces in the ship to determine both the initial sizing of the ship and the selection of hull dimensions and form parameters[11]. its philosophy, establish a method of using damage stability and structural continuity considerations to determine main transverse bulkhead disposition and thereby controlling the evolution of the general arrangement, within a previously determined envelope of the hull form.

Integrated Synthesis [12],allocating the various compartments of the ship sequentially. The philosophy point to this sequence was not suggested as the recommended way of obtaining the layout, but rather as a suitable start point for an integrated synthesis to take and to utilise the ship arrangement, produced by such a sequence, to size, dimensionalise and select form parameters. It was also argued that with integration of the ship architecture with weight, space and form parameters, a better initial design solution could be achieved, since a more comprehensive initial design description: [13] a) Would provide a better basis for initial cost tradeoffs and parametric selection; b) Could be used to explore alternative layouts, while the hull form and dimensions were still fluid;. c) Could be readily altered, both as regards layout disposition and the consequent hull dimensions and form impact.

Circle of influences [14], classifying the compartment relationships and thereby yield a 3-D block layout, around which a hull form could be “wrapped”.

Intelligent Ship Arrangement (ISA)[15,16,17], focuses on arranging spaces into pre-defined structural zones. its philosophy “to provide an optimization technology and design tool to assist the arrangements designer to create effective, rationally based surface ship arrangements with the maximum amount of intelligent decision making support”. Secondary goals relate to the capture and application of Navy requirements and best practices and to the objective comparison of alternative layout configurations. ISA was developed to assist designers in creating layouts at the end of the conceptual design phase (Analysis of Alternatives, AoA) and at the beginning of preliminary ship design phase[18].

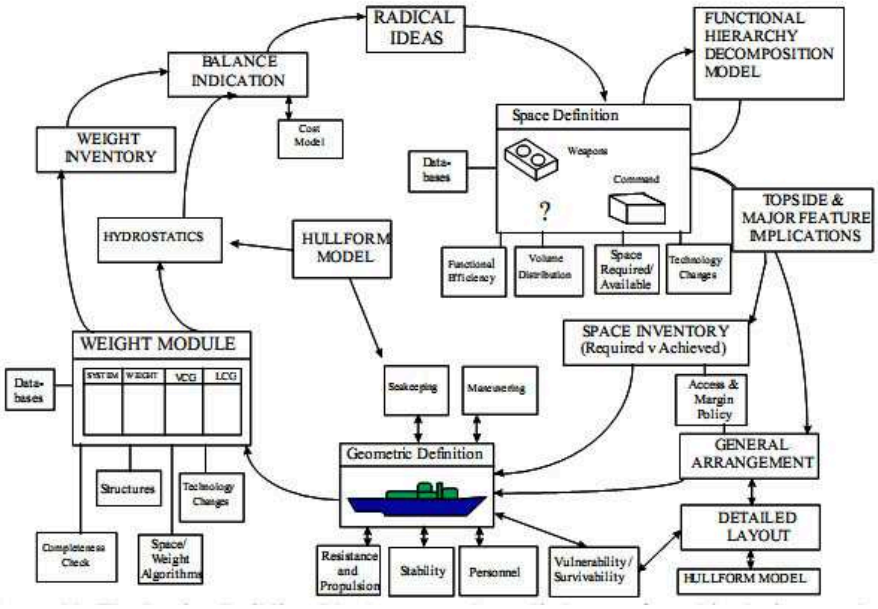


Fig 1: The Design Building Block approach applied to surface ship design synthesis.[22]

Design Building Block(DBB) [19,20,21],its philosophy in combining three systems of computer graphics that incorporation within an existing and established computer aided ship design system will integrate ship architecture into the initial ship synthesis. the system (PARAMARINE) took the essential naval architectural capabilities of the (GODDESS) system and reconfigured them into an object-oriented configuration, executable on modern personal computers [20]. This system was then able to accept a new module, known as (SURFCON), which implemented the Design Building Block approach in a fully integrated manner. The DBB approach has been applied on a surface ship, Fig 1.

The facility of an information rich three dimensional representation of a new ship concept, when integrated with a proper naval architectural numerical description, means the ship designer is able to explore many issues that traditionally were difficult to consider with a purely numerical description and, possibly, a separate sketch or profile. With this integrated representation, the concept designer is able to undertake a greater range of studies, better address innovative and novel options and investigate issues previously left until later in the design process. With such a tool the designer can produce concept descriptions that are able to move more smoothly into the later design phases when much more detailed graphical representations [23].

Packing Ship Systems [24,25], developed a design tool that automatically generates a large number of feasible designs by packing systems into a positioning space. The intention of the tool is to increase the detail of a design in the conceptual design phase whilst maintaining a high level of design flexibility. This allows for more prediction tools to be used in this early stage increasing the knowledge about the concept designs. In the tool objects and clusters of objects (systems, spaces, and components) are defined as building blocks which can be placed into a positioning space. By using different object types (i.e. envelope, subdivision, hard, soft, and logical) the designer of this method is able to make a detailed parametric description of the vessel which a search algorithm can alter. The parametric model allows for large changes to the entire design (e.g. hull, superstructure, decks, bulkheads, etc.) thus maintaining the desired flexibility within the design [26].

Network Science Approach [27] , developing a method to generate and analyze 3-D distributed system and compartment arrangements without designing a ship. Its philosophy shows in the following steps, First, network concepts of centrality and hierarchy are used to highlight and rank the

embedded drivers of an early-stage arrangement prior to developing spatial layouts by directly analyzing the relationship network in a methodical and holistic manner. Second, a network partitioning method is used to cluster shipboard elements into communities of mutually-compatible elements to minimize the degradation of other items located in the same region of the ship. These communities can form the basis of functional zone definitions. Varying the number of partitions reveals a multi-scale depiction of the relationship network. Third, the communities are assigned to structural zones based on cumulative zone preference values. Finally, two new visualization techniques help designers establish connections between the network of inter-element relationships and spatial ship arrangements.

The integration of personal movement [28]**,** an innovative approach to ship design for operation which integrates human factors, operability and personnel movement simulation into the design process. Its philosophy concentrates on integrating operational issues in preliminary ship design and on the implications on the design process undertaken using the Design Building Block approach [29] to preliminary ship design, using the software tools (PARAMARINE) and (maritime-EXODUS) together with a set of software tools called (Demonstrator) a rapid trial and error technique.

The Development of Ship Arrangement Methodologies

The development path, which consist of three methodologies: manual design "optimization," computer-based optimization, and post-processing sets of feasible solutions.

Manual optimization, The traditional approach to ship arrangements includes drawing deck plans by hand, either on paper or within a generic computer aided design tool [30,22]. The hierarchical procedure of defining main compartments, followed by more refined functional compartment definitions, and lastly systems, as the only practical approach to the complex layout problem.

Computer-based optimization, With the development of more powerful computers, semi-automated approaches were developed to increase the number of designs that could be generated and evaluated. The premise is that computers can generate and grade layouts faster than a human can. Elemental information and basic thought processes utilized in the manual approach were captured in database format, and rational evaluation mechanisms were developed [31,23,24]

Post-processing the "best" designs, An experienced naval architect is assumed capable of identifying a quality layout upon seeing it, and therefore, different mechanisms have been developed to keep the designer involved. Rather than simply accepting the single highest-scoring solution from an optimization, a set of high-quality solutions are retained to be analyzed by human designers. [25,32] have developed post-processing tools that allow designers to infer relationships and understand compromise decisions through rapid comparison of the set of potential solutions Fig2 .

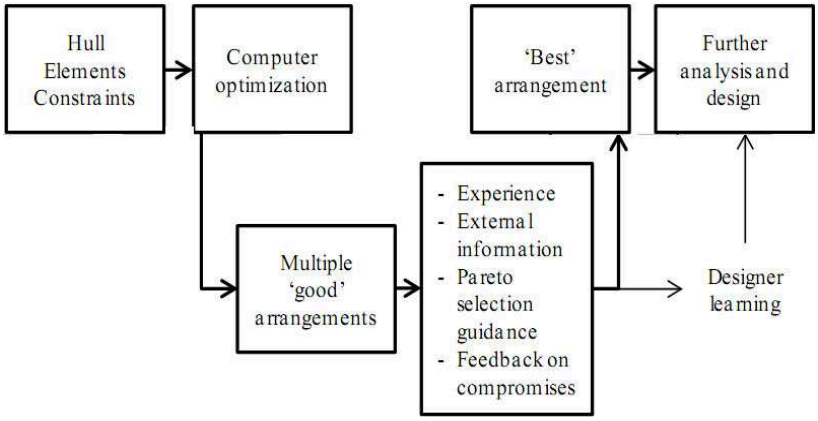


Fig 2: Computer-based optimization with designer selection (right). [26]

Discussion

The following issues are considered to merit further attention in future considerations:

Issue1: Arrangements are the heart of the human factor program of marine vehicles, at every stage of the design, naval architect is involved. because of the preliminary ship design is a multi-criteria process, The architect should consider some of the criteria that can be considered as being part of the important issues driving the design evolution (human factors , user behavior and layout style...) and integrate it into early design. This allows him relative to his expert, to perform a considerable design drivers and solutions when the design is still evolving and opens up the possibility of changing the way in which the designer progresses a design .

Issue2: the previous methods, each one has its own unique way of tackling the ship system arrangement and configuration problem. some deal with the area and others with volume, not all handled a full ship arrangement and analysis. the combination and interaction of those methods and philosophies, developing of a new arrangement tools, design a new optimization algorithms, will lead to create new approaches to general arrangement.

Issue3: advancements are needed in the following areas of the ship general arrangements process: The ability to capture knowledge in an natural manner to facilitate maintenance and reuse of that information. The ability to understand the nature of ship arrangements on a macro-scale and to define appropriate metrics to provide insight into non-dominated solution sets and guidance for down-selecting designs. The ability to view the requirements elucidation process, and the role of ship layouts in that process, as an overlay of multiple data types in order to preserve the richness of information that is lost when mapped in the domain of traditional general arrangements drawings. The ability to provide users with efficient, natural tools for generating and evaluating general arrangements to promote designer exploration and learning and to reduce modeling demands on the designer.

Issue4: The general focus is on surface warships, although the need to approach could be applicable to preliminary design of any other type of ship and of other enclosed environments where complex personnel operations take place (The integration of personal movement method could be applicable to other limited type of ship).

Summary and Conclusions

The ship arrangements methodologies has been steadily increasing during the past 30 years. navies around the world are interested in performing analyses that rely on system layouts during preliminary design in order to build confidence in the ultimate feasibility of candidate designs. The coupling between requirements and ship size, cost, and performance is due in large part to the arrangement of the vessel. The earliest stages of ship design is considered the most crucial design stages in terms of the consequences of any decision taken. Flexibility of early stages design, as well as that of a design process in general, is the characteristic that allows design solutions to be readily adapted to changing conditions and meet a ranged set of design requirements. Developing the three-dimensional compartment and component arrangements for these ships is a challenging and time-consuming task partially because each layout includes hundreds or thousands of elements with interconnecting and sometimes conflicting relationships. Deep understanding of the relationships and circulation among ship spaces with keep in mind the previous aspects, in the same time, developing the design methodologies and creating new approaches will rabidly generate a stable arrangements that reduce time it is then cost.

References

[1] Arena, Mark V., Irv Blickstein, Obaid Younossi, and Clifford A. Grammich. 2006. Why Has the Cost of Navy Ships Risen?: A Macroscopic Examination of the Trends in U.S. Naval Ship Costs Over the Past Several Decades. MG-484-NAVY. RAND Corporation.

[2] Hope, Jan Paul. 1981. "The process of naval ship general arrangement design and analysis." Naval Engineers Journal 93 (4): 29-38.

[3] Jonathan M,Ross (2009), "Human Factors for Naval Marine Vehicle Design and Operation-human factors in defence ", Ashgate publishing company.

[4] ABS (2007), American Bureau of shipping homepage, http://www.eagle.org/,downloaded September.

[5] ABS (2001), Guide for crew habitability on ships, American Bureau of shipping, Houston, TX, December.

[6] ABS (2001), Guide for passenger comfort ships, American Bureau of shipping, Houston, TX, December.

[7] Barry, D J, (1961), "Management Approach to Functional Arrangement Design", Trans SNAME 1961.

[8] Baker, R, (1956), "Habitability in Ships of the Royal Canadian Navy", Trans SNAME 1956.

[9] Leopold, R & Reuter, W, (1971), "Three Winning Designs – FDL, LHA, DD963 Methods and Selected Features", Trans SNAME 1971.

[10] Carlson, C M & Fireman, H, (1987), "General Arrangement Design Computer System and Methodology", U S Naval Engineers Journal, May 1987.

[11] Andrews, D,J, (1981),"Creative Ship Design", Trans RINA 1981.

[12] Andrews, D,J, (1984), "Synthesis in Ship Design" PhD , University of London, 1984.

[13] Singer, David J., Justin W. Gillespie, Hans Hopman, Etienne Duchateau, David Andrews, and Richard Pawling. 2012. Preliminary Ship Design General Arrangements Naval International Cooperative Opportunities in Science & Technology Program (NICOP) Project.

[14] Andrews, D,J, (1986), "An Integrated Approach to Ship Synthesis", Trans RINA 1986.

[15] Daniels, A.S. & Parsons, M.G., "Development of a Hybrid Agent-genetic Algorithm Approach to Ship Arrangements". Ship Technology Research, 2008. 55(2): p. 78-86.

[16] Nick, E.K. & Parsons, M.G. "Fuzzy Optimal Allocation of Spaces to Zone-decks in General Arrangements", Proceedings of the Practical Design of Ship and Offshore Structures Conference. 2007. Houston, United States.

[17] Daniels, A.S., Tahmasbi, F., & Singer, D.J. "Intelligent Ship Arrangement (ISA): Methodology - Improvements and Capability Enhancements", Proceedings of the 10th International Marine Design Conference. 2009. Trondheim, Norway.

[18] Nick, E.K., Parsons, M.G., & Nehrling, B. "Fuzzy Optimal Allocation and Arrangement of Spaces in Naval Surface Ship Design", Proceedings of the 9th International Marine Design Conference. 2006. Ann Arbor, United States.

[19] Andrews, D .J. & Diks, C, "The Building Block Design Methodology Applied to Advanced Naval Ship Design", Proceedings of the 6th International Marine Design Conference. 1997. Newcastle, UK.

[20] MUNOZ, J A & FORREST, C J M: - "Advantages of Software Integration from Initial Design through to Production Design" ICCAS 2002, Malmo, Sept 2002.

[21] PAWLING, R, "The Application of the Design Buidling Block Approach to Innovative Ship Design", PhD thesis, University College London, 2007.

[22] Andrews, D J & Pawling, R, "SURFCON –A21st Century Ship Design Tool", IMDC 03, Athens, 2003.
[23] Andrews, D.J, (1998), 'A comprehensive methodology for the design of ships (and other complex systems)', Proc. R. Soc. Lond. A. 1998.
[24] Van Oers, B.J. "A Packing Approach for the Early Stage Design of Service Vessels." PhD Thesis. Delft University of Technology, 2011.
[25] Van Oers, B.J., et al. "Issues when Selecting Naval Ship Configurations from a Pareto-optimal Set." Proceedings of the 12th AIAA/ISSMO Multidisciplinary Analysis and Optimization Conference. Victoria, British Columbia, Canada: 2008.
[26] Van Oers, B.J., et al. "A 3D Packing Approach for the Early Stage Configuration Design of Ships." Proceedings of the 10th International Naval Engineering Conference. Portsmouth, United Kingdom: 2010.
[27] Justin, W, Gillespie, "A Network Science Approach to Understanding and Generating Ship Arrangements in Early-Stage Design", PhD thesis, University of Michigan, 2012.
[28] Lorenzo Casarosa, The integration of human factors, operability and personnel movement simulation into the preliminary design of ships utilising the Design Building Block approach.
[29] Andrews, D. J. and Pawling, R. G., 2004 "Fast Mothership – A Design Challenge", RINA International.
[30] Cort, A., and W. Hills. 1987. "Space layout design using computer assisted methods." Naval Engineers Journal 99 (3): 249–260.
[31] Nick, Eleanor. 2008. Fuzzy Optimal Allocation and Arrangement of Spaces in NavalSurface Ship Design. Doctoral Dissertation. University of Michigan..
[32] Wagner, Karel, Alain Wassink, Bart van Oers, and Hans Hopman. 2010. Modeling Complex Vessels for Use in a 3D Packing Approach: An Application to Deepwater Drilling Vessel Design. In Proceedings of the 9th International Conference on Computer and IT Applications in the Maritime Industries (COMPIT'10), 259-272. Gubbio, Italy.

Advanced Materials Research Vol. 936 (2014) pp 2352-2357
© (2014) Trans Tech Publications, Switzerland
doi:10.4028/www.scientific.net/AMR.936.2352

The Design and Simulation of Collision Avoidance System Based on Dual-Mode Collaborative

Chen Shuo[1, a], Yu JiMing[1,b] and Liu Yan[1,c]

[1]No99 Hongjing Road, Jiangning District, Nanjing, China

[a]337195553@qq.com, [b]yujm@jit.edu.cn, [c]liuyan@jit.edu.cn

Keywords: vehicle collision avoidance, obstacle, BP artificial neural network, driving path planning, simulation

Abstract: This article establish a model to give a detailed analysis of road vehicle collision avoidance systems according to the angle between vehicle and obstacle, and raise a vehicle collision avoidance detecting mechanism based on location mapping and distance detecting; furthermore, The authors combined this mechanism and BP artificial neural network to establish a new vehicle collision avoidance systems which is based on the collaboration between precise distance angle model and BP artificial neural network. We called this mechanism as BP artificial neural network vehicle collision avoidance model, the abbreviation is BP collision model. The convergence simulation of such model present that this model can resolve problem of collision avoidance and plan driving Path very well.

Introduction

The purpose of vehicle collision avoidance systems is to alarm the driver at dangerous moment, or directly control the car to avoid collision. ACC,adaptive cruise control, system is a kind of Collision avoidance function control system. however, this system need to consider lots of complex factors, such as the basic characteristics of the vehicle location and speed, and the traffic road congestion level, as well as the road situation (e.g. directly road, T-junction, Crossroads).those complex factors bring lots of difficulty to the construction of collision model by using Classical mathematical method, and cause ACC model only can be used on simple road situation. recently, many researcher try to use fuzzy mathematics , artificial neural network ,or together of them to establish predict model to analyse collision problem. they have achieved some results, but there are still some difficulty needed to be resolved, e.g although fuzzy mathematics is better able to adapt to human perception and behavior as well as some of the difficult to accurately quantify the working conditions quantified using fuzzy approach, however, due to limitations of its own characteristics, it is difficult to characterize better on complex road situation. Although artificial neural network model has good self-learning features to suit the driver driving habits, but such mode required some learning and training must be carried out in advance, and there is relatively slow convergence problems in this model, additionally, traditional artificial neural network model is also difficult to characterize better on complex road situation same with fuzzy mathematics model.

In this paper, we try to raise a new collision avoidance systems which combine traditional accurately mathematical model and BP artificial neural network. New model combined two traditional models each other, they learn from each other; new model has a self-adaptive inferential control system in terms of artificial neural networks, and train neural network to achieve a better convergence effect by using additional momentum term learning algorithm, the success of the convergence of the neural network also confirmed the proposed model is reasonable and reliability.

Model Construction

Accurately Mathematical Model Based On Road Obstacle

The main factors that affect driving action include the vehicle speed, nearby vehicle speed, as well as the distance with nearby vehicles as so on. However, in complex cases, the environment traffic of local vehicle, road width, road sections are all able to determine the degree of risk.

Firstly, let's describe the environment of vehicles running, as we see from figure1, the vehicle is running on the road, we assume the scanning angle scope of vehicle is $[-\sigma,\sigma]$, negative number represent vehicle turn to left. We assume the scanning angle of vehicle is 2σ, and 2σ is divided into n blocks, we denote the angle of block i as θ_i ($\theta_1 = 0$), Each direction obstacle distance which is measured by using microwave radar or machine vision approach is l_i.

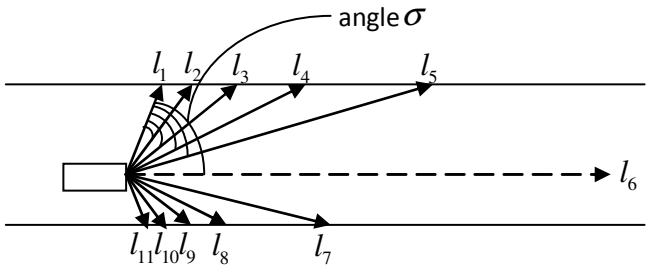


Fig. 1 Schematic diagram of environment of vehicles running

This method uses multiple parameters to characterize the road situation, this model take lots of factors into consideration, such as the distance to nearby vehicle and nearby obstacle, the location of local vehicle, as well as the distance to road marginal. Those factors all can be presented in $\vec{l} = (l_1, l_2, ..., l_n)$, the precise degree is decided by n.

On the basis of road model, we analyse the vehicle collision avoidance procedure

Let's assume the speed of local vehicle is $v_c (\geq 0)$, brake acceleration is a_c, the minimum safety distance is d_s which is the minimum distance between local vehicle and obstacle keeping for avoid collision. Driver reaction time is T_r. Subsequently, we construct a accurately model with output of turning angle $\varphi_r \in [-\sigma,\sigma]$ and acceleration a_r.

Firstly, we try to find a safety zones, the every safety distance of every direction should be more than a safety threshold; this threshold should be decided by vehicle speed v_c and reaction time T_r.

Make safety running distance as $c_s = \frac{v_c^2}{2a_c} + v_c T_r$ (formula 1)

Make safety running angle as $\theta_s = \frac{d_s}{c_s}$ (formula 2)

The sense of c_s is minimum safety distance between local vehicle and obstacle (different with d_s), based on this model , we get a conclusion that vehicle must find a forwarding angle which there is a accessibility region with radius equal or bigger than c_s, at the same time d_s should be out of the scope of this region(e.g figure 2). To simplify the calculations, we make fan arc length equal to d_s ,so we got a safety running angle θ_s.

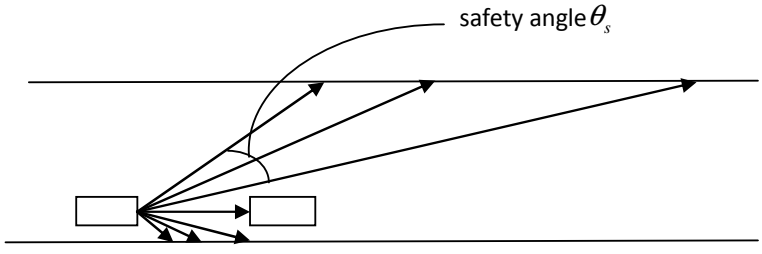


Fig. 2 Schematic diagram of safety zones

With this safety running angle θ_s ,the task of vehicle collision avoidance systems will become to find a safety running angle region θ_s in the scope of the scanning angle $[-\sigma,\sigma]$, the all l_i of this safety running angle region should ensure equal or bigger than c_s ,the formula is $l_i \geq c_s$, then we translate this region to $\varphi_r \in [-\sigma,\sigma]$ as a output;

The algorithm of finding safety running angle region is described as below:

Step1: set a initial value $k=\frac{n}{2}+1$ (the index of the initial angle block), $n_s=\frac{\theta_s n}{2\sigma}$ （the block amount of safety running angle region ）, $\mu=\frac{2\sigma}{n}$ （the angle scope of every block）, $i=j=k$, the binary function of this model is $f(x,y)=\min\{l_{x+j}\mid\ 0\leq|j|\leq y\}$

Step2: if $i\in[1,n]$ and $f(i,\frac{n_s}{2})\geq c_s$ then $\varphi_r=i\mu$ go to Step6,otherwise to Step3;

Step3:if $j\in[1,n]$ and $f(j,\frac{n_s}{2})\geq c_s$ then $\varphi_r=j\mu$ go to Step6,otherwise to Step4;

Step4:if $i\notin(1,n)$ and $j\notin(1,n)$ then go to Step5,otherwise if $i\in(1,n)$,then $i=i+1$, if $j\in(1,n)$ then $j=j-1$, go to Step2.

Step5:can not find safety running angle region, output $a_r=a_c$.

Step6:find a safety running angle region, output φ_r value.

The essence of the above algorithm is to looking for a safe running area in the area closest current direction.

Bp Artificial Neural Network Model Based On Self-Learn Mode

Above collision avoidance model has real-time, accurate calculation and other characteristics, but does not have the learning function and adapt to the driver's characteristics; but BP artificial neural network has good classification, prediction, reasoning characteristics for input mode. Then, we will establish a BP artificial neural network model to analyse collision avoidance problem.

We take the vector of 2.1 $\vec{l}=(l_1,l_2,.....,l_n)$ as input parameters of BP artificial neural network, we make turning angle φ as output parameters by using turning angle mapping algorithm , $\vec{y}=(y_1,y_2,.....,y_n)$ （$y_i\in\{0,1\}\ \&\sum_{i=1}^{n}y_i=1$） , the BP artificial neural network model is as below figure 3;

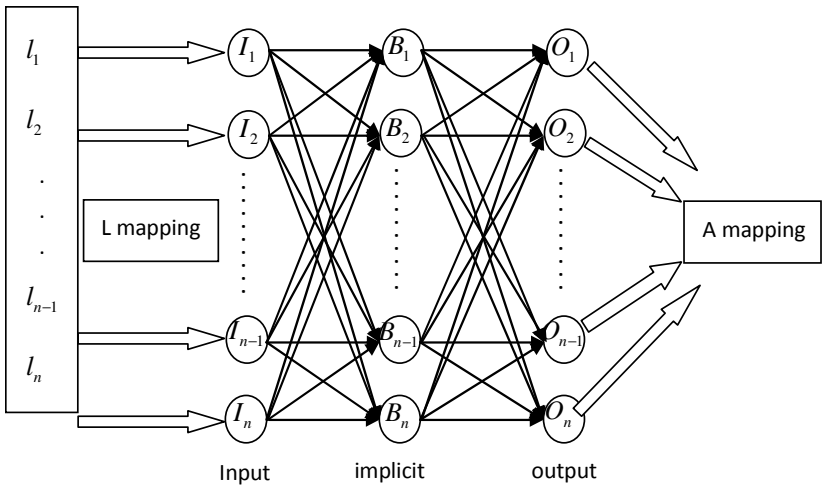


Fig. 3 The BP artificial neural network model

The input parameters is $\vec{I}=(I_1,I_2,.....,I_n)$,connection weight matrix is W^i （$i=1,2$） ,output parameters is $\vec{O}=(O_1,O_2,.....,O_n)$, implicit layer is $\vec{B}=(B_1,B_2,.....,B_n)$, the threshold between implicit layer and output layer is $\vec{\gamma^i}=(\gamma_1^i,\gamma_2^i,.....,\gamma_n^i)$ ($i=1,2$),we set Sigmoid as transfer function $y=f(x)=\frac{1}{1+e^{-x}}$.

The calculate procedure for input parameters is below:

Input layer: finish vector location mapping and normalized processing, the node value of this layer is $I_i=\frac{l_i}{\sum_{j=1}^{n}l_j}$.

Implicit layer and out layer: the input of every node $s_j=\sum_{i=1}^{n}X_iW_{ij}^k-\gamma_j^k$,the output of every node $Y_j=f(s_j)$.

A Mapping: this mechanism complete the mapping between turning angle and output parameters, And vice versa; because only one turning angle value is not good to the calculation of BP artificial neural network, so we construct two function between turning angle φ and output parameters $\vec{O}=(O_1,O_2,.....,O_n)$, the functions is below:

$\varphi(O)=\mu\prod_{i=1}^{n}iO_i-\sigma$, $O_i(\varphi)=\begin{cases}1 & (i=\left[\frac{(\varphi+\sigma)}{\mu}\right])\\ 0 & (else)\end{cases}$, （the define of μ and σ refer to 2.1）

The Combination And Collaboration Between Two Model

BP artificial neural network can better adapt the human behavior, the driving characteristics of the human , the training and learning of the neural network based on the driving characteristics of the human is more helpful for the neural network to avoid collision in the same driving conditions, the characteristics that artificial neural network present similar behavior according to a similar input parameter achieve the good approach to purpose of collision avoidance.but the problem is we must provide training sample in advance, so the sample can't cover all traffic and road scenarios, then in loss scenario, BP artificial neural network will not output reasonable reaction;

Due to above question, we should provide a low level 'intelligent' for BP artificial neural network, to improve the behavior of our model, so that the program can output a basic reaction for any scenario.

As a compensation, the accurately mathematical model based on road obstacle of 2.1 combine with BP artificial neural network of 2.2, firstly, the filter or alarm mechanism judge the dangerous status , and reload the environment parameters $\vec{l} = (l_1, l_2, ..., l_n)$ into collaboration system; secondly, BP artificial neural network model calculate out the turning angle of collision avoiding; thirdly, the verification mechanism will verify whether the output of BP collision model is correctly or not, the verification is based on the comparison with accurately mathematical model; if BP artificial neural network model result is not correct, the correct result of accurately mathematical model will feed back to BP artificial neural network, BP artificial neural network will learn the correct result, and adjust the network parameter; the whole BP collision model is described as figure4;

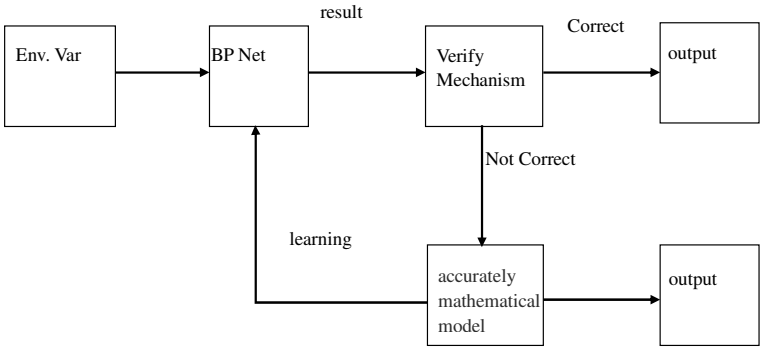


Fig. 4 The learning model for the BP artificial neural network

The verification mechanism is mainly to calculate whether the vehicle can avoid collision in current speed and turning angle, so the verification only need to calculate whether result φ comply the formula $f(i, n_s) \geq c_s$ (refer 2.1).

While the BP artificial neural network has no any training and learning (initial situation, random weight value), if above collaboration system is directly used to collision avoiding control, at the beginning, the result of BP artificial neural network is always wrong; after BP artificial neural network learned lots of traffic scenario and know what is correct output for this scenario, then BP artificial neural network will response all similar scenario correctly, the accuracy of BP artificial neural network will become more and more higher. Further, the reaction of driver for the emergency case should be as the main source of neural network learning, otherwise the collaboration system degenerates to accurately mathematical model; on the contrary, if BP artificial neural network mainly depend on learning driving reaction, and ignore the result of accurately mathematical model, then whole BP collision model will become a pure artificial neural network.

Model Simulation (Convergence Test)

Firstly, we set the connection weight value of BP artificial neural network as a random value, then we collect some traffic environment parameter to simulate the procedure of figure4, and test the system convergence of such artificial neural network. The learning algorithm of BP artificial neural network is standard error correction method, also collaborate with adaptive learning rate adjustment algorithm.

Base on model one, We construct some learning sample as below table 1 to test the system convergence.

TABLE 1 LEARNING SAMPLE BASE ON MODEL ONE

Input parameters	Output parameters
1.2,3.4,2.4,4.5,3,6,7,8,9	0,0,0,0,0,0,0,1,0
7,8,9,6,3,4.5,2.4,3.4,1.2	0,1,0,0,0,0,0,0,0
6,6,7,8,9,8,6,7,6	0,0,0,0,1,0,0,0,0
1,1,5,6,7,5,3,2,1	0,0,0,1,0,0,0,0,0
……	……
8,8,9,1,1,1,1,1,1	1,0,0,0,0,0,0,0,0

Learning algorithm uses the steepest descent learning algorithm, collaborate with momentum $W(n+1)=\alpha\frac{\partial E}{\partial W}+\beta W(n)$ to train BP artificial neural network, convergence test result is below.

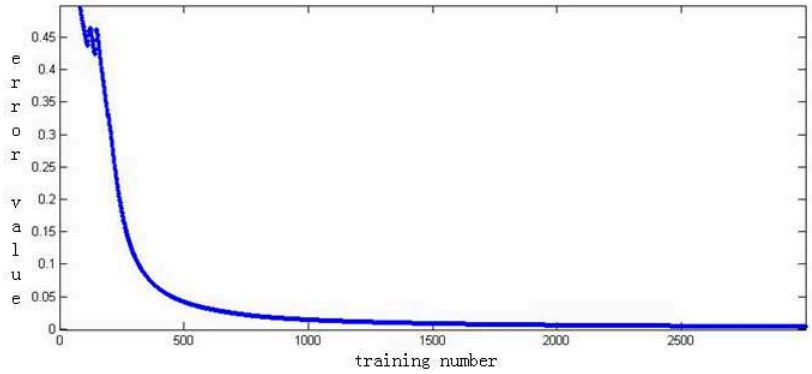


Fig. 5 Module simulation

Conclusion

This article is mainly from accurate detect obstacle perspective, to establish a collision avoiding algorithm which combine BP artificial neural network and accurately mathematical model, and then specify the specific calculation step and procedure. The convergence test of BP collision model present a good collaboration effect, the simulation result also prove that this model is reasonable and reliable.

The next important research point is about the collaboration system adaptive with neural network model, and the problem of error concussion and slow convergence of BP artificial neural network. So a successful convergence decide the whole effect of BP collision system, we plan to improve the initial value of BP network and introduce a Simulated annealing algorithm to collaborate with BP network, those further job will improve the performance of BP artificial neural network more deeply.

Acknowledgement

This work was supported by college students practice and innovation training project in Jiangsu province in 2012, Metal mine intelligent production control of IOT application demonstration project, The underground metal mine ramp intelligent traffic signal control and simulation(11KJD510002), Engineering laboratory analysis of Jiangsu Province, Engineering Research Center For Analysis an Control of Mine IOT. The authors would like to thank them for the help.

References

[1] SOTELO M, Van LINT J W C. NUNES U, et al. Introduction to the special issue on emergent cooperative technologies in intelligent transportation systems [J]. IEEE Trans on Intell Transport Sys , 2012, 13(1) :1-4.

[2] Carolina García-Costa, Esteban Egea-López, Joan García-Haro. A stochastic model for design and evaluation of chain collision avoidance applications. Transportation Research. Volume 30,May 2013,Pages 126-142.

[3] CHEN L, PENG Y, TSENG Y. An infrastructure-less framework for preventing rear-end collisions by vehicular sensor networks [J].Communications Letters, 2011, 15(3): 358-360.

[4] Jeich Mar. The car-following and lane-changing collision prevention system based on the cascaded fuzzy inference system [J].IEEE Transaction on Vehicular Technology 2005, 54(3): 910-911.

[5] Xu AiGuo. Research and experiment of intelligent decision methods of car based on soft computing [D].Beijing:BUAA,2004.

[6] Yuan CengRen. Artificial neural network and application [M]. Beijing; Tsinghua University Press, 2000:301-319.

Advanced Materials Research Vol. 936 (2014) pp 2358-2363
© (2014) Trans Tech Publications, Switzerland
doi:10.4028/www.scientific.net/AMR.936.2358

Quantitative Risk Assessment and Early Warning for PH Value of Disqualified Imported Textile

Wei Mengyuan[1,2] , Hu Xiangyuan[1], Jiang Chun[3], Zang Jiaxin[1],

Xue Wenliang[1,a]

[1] Key Laboratory of Textile Science & Technology, Ministry of Education, Donghua University, Shanghai 201620, China

[2] Shanghai Entry-Exit Inspection and Quarantine Bureau, Shanghai 200135, China

[3] Shanghai Textile Holdings (group) Corp. Shanghai 200336, China

[a]xwl@dhu.edu.cn

[1] Corresponding to xwl@dhu.edu.cn.

Keywords: quantitative risk assessment, PH value, disqualified textiles

Abstract. The assessment of potential risks posed by PH value in clothing to consumers is of increasing concern worldwide. If the PH value is too high, it is harmful to skin. Some papers focus on hazard assessment and exposure assessment, using quantitative and semi-quantitative method, rather than assessment for the factors related to the PH value. In order to perform early-warning research and risk management, the quantitative risk assessment is used in this paper to analyze the imported textile testing data and find the factors related to the PH value. The data mining technique and K-means algorithm is the core of the method. It can be concluded that the disqualified textiles have relations with main fiber components and fabric color. Then cluster the data by K-means algorithm for every factor, define the different class as related danger level, respectively severe, moderate, light.

Introduction

In recent years, the demand for imported textile products has increased prominently. But there are some security issues in these products. According to statistics of the General Administration of Quality Supervision [1], only in 2011, the failure rate is as high as 10.17 percent. Although these disqualified textiles may not threaten life directly as disqualified food, they have a great harm to health and can't be discounted [2].For example, if PH value of clothing is too high, it will stimulate the skin, and even lead to skin infections [3]. Therefore, risk management[4] is used to find the factors related to the PH value and take some measures to reduce risk. The European chemicals agency performs hazard and exposure assessment [5]. However these assessments define the dangerousness rather than the related factors for risk management. Usually, the quantitative risk assessment uses the Bayesian algorithm [6]. It calculates the probability of the factors, add or multiply the value to get the probability under certain condition [7], but it is not good at internal analysis. Some quantitative risk assessment uses Rough sets based algorithm [8], classifying the data according to the constructed function. But this algorithm is not well in non-numerical analysis. Some data in this paper is not numerical. So the paper uses the K-Means algorithm to classify the factors into

different levels [9] according to their percentage in the same attribute. By this way, the related attributes for risk management and the most relevant factors can be found to perform the early warning research and risk management.

Methodology

Data Collection and Sorting

SPSS Clementine [10] is data mining software and can import SPSS files, SAS files, Excel and so on. In order to input the data and establish the model conveniently, the data in the imported textiles test report (provided by the Shanghai Entry-Exit Inspection and Quarantine Bureau) is processed to Excel format. Excel is convenient to convert the data after collecting them. The layout is shown in Table1.

TABLE 1 DATA SAMPLE

Register Number	PH value	Main components	Color
911852**	6.4	Wool	Black
911852**	6.5	Mulberry Silk	Green

Cluster Analysis

The data collection is divided into many classes composed by many similar objects. The process is called clustering. These objects in the same class are similar to each other, different from other classes'. Cluster analysis originates from taxonomy, but it is not classification. The difference between them is that the type of required classes in clustering is unknown.

K-means clustering algorithm [11] is commonly used and also used in this paper to calculate the K-means node. It is a typical distance-based clustering algorithm, using distance as the similarity evaluation indicator. It means that the shorter the distance of the two objects is, the greater the similarity is. We herein show the definition of the K-means algorithm as follows:

(1) Select a set of K randomly from the collection, number of which is N, as initial cluster centers;

(2) Measure the distance between each residual data and each centroid. Classify the residual data to the nearest centroid's class;

(3) Recalculate the centroid of each class;

(4) Iterate 2-3 steps until the new centroid equal to the original centroid or the distance between them is less than the specified threshold, the algorithm terminates.

Data Analysis

As for PH value issue, this paper will analyze its relationship with fiber components, and fabric color.

PH Value and Main Fiber Components

Excel spreadsheet is imported as source node. Then select the node and pick out the data that the PH value is not within the standard range. The structure of model is shown in Fig. 1 and the percentage distribution graph of main fiber components is shown in Table 2.

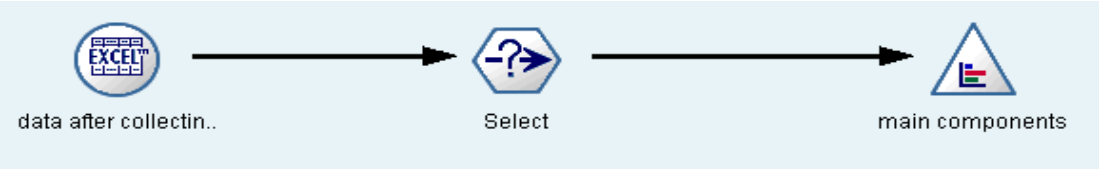


Fig. 1 Disqualified Textiles and Main Fiber Components Model

TABLE 2 PERCENTAGE DISTRIBUTION OF MAIN FIBER COMPONENTS

Number	Main fiber components	Percentage
1	Polyester	3.3
2	Cotton	56.67
3	Mulberry silk	4.17
4	Rabbit hair	0.83
5	Linen	3.33
6	Wool	22.5
7	Cashmere	7.5
8	Rayon	1.67
	Total	100

It is obvious to be seen from Table 2 that the percentage of cotton textiles is highest, accounting for 56.67%. It is because that the dye process for cotton must be in the alkaline environment [12]. After dyeing, acid should be used to neutralize the alkali, so the PH value can be within the standard range. If acid is not enough, the PH value will be high. So it is necessary to classify the data to monitor the safety of the products. K-means algorithm is used .Set K = 3, the structure of model is shown in Fig. 2 and the results are shown in Table 3.

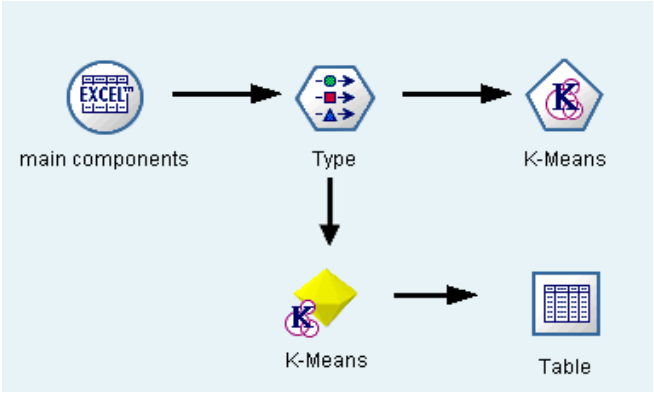


Fig. 2 Main fiber components cluster analysis model

TABLE 3 CLUSTER ANALYSIS RESULTS OF MAIN FIBER COMPONENTS IN DISQUALIFIED TEXTILES

Number	Main components	Percentage	Class	K-means
1	Polyester	3.3	Class 1	0.003
2	Cotton	56.67	Class 2	0
3	Mulberry silk	4.17	Class 1	0.013
4	Rabbit hair	0.83	Class 1	0.047
5	Linen	3.33	Class 1	0.002
6	Wool	22.5	Class 3	0
7	Cashmere	7.5	Class 1	0.072
8	Rayon	1.67	Class 1	0.032

It can be concluded from Table 3 that class 2, cotton textiles, has highest proportion, classified as severe warning. The class 3, wool textiles, is moderate warning. The class 1, other kinds of textiles, is light warning. So textiles safety supervision department should focus on textiles belonging to the severe, moderate warning and make great efforts in test, especially for cotton, wool textiles.

PH Value and Fabric Color

PH value is different for different color textiles in the dyeing process. Just as main fiber component, the percentage distribution graph of fabric color is shown in Table 4:

TABLE 4 PERCENTAGE DISTRIBUTION OF COLOR IN DISQUALIFIED TEXTILES

Number	Color	Percentage
1	White	12.05
2	Navy blue	10.84
3	Black	15.66
4	Red	13.25
5	Yellow	8.43
6	Grey	15.66
7	Blue	8.43
8	Green	7.23
9	Purple	1.20
10	Brown	7.23
	Total	100

Judging from the Table 4, the number of white and grey is large, accounting for 37.71%, although the percentage of the disqualified white and grey textiles in the total textiles is not high. In general, these disqualified problems occur to the dark color textiles. But for PH value, it is potential for the light color textiles to be disqualified.

Cluster the data in Table 4 by K-means. The results are shown in Table 5.

TABLE 5 CLUSTER ANALYSIS RESULTS OF COLOR IN DISQUALIFIED TEXTILES

Number	Color	Percentage	Class	K-means
1	White	12.05	Class 1	0.1
2	Navy blue	10.84	Class1	0.183
3	Black	15.66	Class1	0.15
4	Red	13.25	Class1	0.017
5	Yellow	8.43	Class3	0.041
6	Grey	15.66	Class1	0.15
7	Blue	8.43	Class3	0.041
8	Green	7.23	Class3	0.041
9	Purple	1.20	Class2	0
10	Brown	7.23	Class3	0.041

The class 1 in the above table, namely white, navy blue, black, red and brown, has higher percentage, is classified as serve warning. Yellow, blue, green and brown, is moderate warning. Purple, class1, is light warning. The departments should take reasonable arrangements of detection in textiles according to the danger level during safety supervision.

Conclusion

In this paper, the data mining technique is used to analyze the imported textile testing data to find the factors related to the disqualified textiles. It can be concluded that disqualified textiles have relations with main fiber components, fabric color. Cluster the data in the same attribute by K-means algorithm and define the different danger level, respectively severe warning, moderate warning and light warning.

Supported by AQSIQ Science and Technology Projects (No. 2013IK116).

References

[1] General Administration of Quality Supervision, Inspection and Quarantine of the People's Republic of China. The report of National quality status for imported apparel products [R]. China: AQSIQ, 2011.

[2] P. G. Zweers, S. Gunnarsdóttir, T.G. Vermeire, T.P. Traas, M. Koers-Jacquemijns and D. T. Sijm, Verification of a REACH Environmental Prioritization System Against Regulatory Risk Indices, Hum Ecol Risk Assess,19,4(2013) 1049-1066.

[3] M. H. Schmid-Wendtner and H. C. Korting, The PH of the skin surface and its impact on the barrier function, Skin Pharmacol Physiol,19,6(2006) 296–302.

[4] F.C Daia, C.F Lee and Y.Y Ngai, Landslide risk assessment and management: an overview, Eng Geol, 64,1(2002) 65–87.

[5] Information on http://echa.europa.eu/

[6] T. Aven, Quantitative risk assessment: the scientific platform, CU Press, New York, 2011.

[7] H.H. Einstein, R. L. Sousa, K. Karam, I. Manzella and V. Kveldsvik, Rock slopes from mechanics to decision making, CRC Press, London, 2010.

[8] T. J. Crowe, P. M. Fong, T.A. Bauman and J. L. Zayas-Castro, Quantitative risk level estimation of business process reengineering efforts, J. Bus. Process. Manag. 8, 5(2001) 490-511.

[9] H.S. Phillips, S. Kharbanda, R. Chen, W. F. Forrest, R.H. Soriano, T.D. Wu, A. Misra, J.M.Nigro, H.Colman, L.Soroceanu, P.M.Williams, Z.Modrusan,B.G. Feuerstein and K.Aldape, Molecular subclasses of high-grade glioma predict prognosis, delineate a pattern of disease progression, and resemble stages in neurogenesis, Cancer Cell, 9,3(2006) 157–173.

[10] W. Xue and H. G. Chen, Data mining based on Clementine, RUC Press, Beijing, 2012.

[11] A.K.Jain, Data clustering: 50 years beyond K-means, Pattern Recogn Lett, 31, 8(2010) 651–666.

[12] B. R. Babu, A.K. Parande, S. Raghu and T. P. Kumar, Cotton textile processing: waste generation and effluent treatment, J. Cot. Sci, 11(2007) 141–153.

Advanced Materials Research Vol. 936 (2014) pp 2364-2367
© (2014) Trans Tech Publications, Switzerland
doi:10.4028/www.scientific.net/AMR.936.2364

Discussions of Resource Utilization of Coal Gangue

Huamin Li

Planning and Design Research Institute of Coal Industry, Beijing, 100120, China

Keywords: coal gangue, utilization, electricity generation, chemical utilization, building materials

Abstract: The ways of using coal gangue in electricity generation, chemical utilization and building-material production are introduced and national coal gangue utilization status and development trend is analyzed in this paper. Pointing out the main problems in present utilization of coal gangues, suggestions on coal gangue resource utilization are given that provide reference for eliminating coal gangue pollution, enhancing environmental protection and saving up energy.

Foreword

Coal gangue is a kind of rock that comes with coal during coal forming. It is the solid waste in the process of coal producing and processing，and was regarded as “industrial waste” and “public nuisance”. China is one of the main countries that produce and consume coal; coal gangue takes up the most part of industrial solid waste. To now, there be more than 5000Mt of coal gangues in China, and coal gangues are increasing by the speed of more than 100Mt per year. There are more than 1500 coal gangue maintains，taking of more than 100km^2 lands. Those coal gangues not only increased the contradiction between human and land, but also changed the structure and function of the land, and damaged the plant ecosystems. Coal gangues will spontaneously combust when exposing to the sun, and release harmful gases, polluting the air, causing fire disaster, subsidence damage and explosion. Waste dumps also cause soil pollution. The harmful elements in coal gangues will get into water and soil with the rain, influencing the quality of water and soil.

According to coal gangue’s different calorific value and chemical component, it can be used in many resource assimilation ways, including the use of the coal gangues’ heat (ashes can be reused), producing building materials, recycling useful mineral, making chemical products etc.

The approaches and status of resource utilization

The heat usage of the coal gangues

The heat usages of coal gangues include fuel utilization and electricity generation. Fuel utilization requires relatively high heat value, only a few coal gangues can meet this criterion. However, most of the coal gangues can be used to generate electricity. In our country heat value of the coal gangues are mostly under 6.3MJ/kg，in which 3.3~6.3MJ/kg, 1.3~3.3MJ/kg and lower than 1.3MJ/kg each takes up 30%. The coal gangues, which heat value is higher than 6.3MJ/k, take up about 10%. Those coal gangues that heat productivity is higher than 7.5MJ/kg can be used as the fuels of boiling furnace and circulating fluidized bed boiler directly. Slime can be added into coal gangues that produce heat in the range of 5.02～7.5MJ/kg，and used this mixture for generating of electricity. After mixed with coal slime and washing middlings can be used as circulating fluidized bed electric generation.

In our country, coal gangue electric generation has a twenty-year history. In early times, boiling stove burning technology is the main method, which causes problems of serious pollution and low combustion efficiency. In the 1990s, the circulating fluidized bed combustion technology began to

employ. This small-sized industry gradually changed into 135MW, 300M and 600MW sets，making the utilization of the coal gangue, along with the slime electric generation a world-class technology. Up to now, national utilization of coal gangue electricity plant's total installation scale has reached 26000MW. Generating electricity by coal gangues has become a vital part of large-scale use of coal gangues. This can not only save up good-quality coals, reducing the coal and electricity shortage, but also be recycled as building materials in some electric plants, realizing environmental friendly.

The building materials utilization of coal gangues

Another way of large-scale use of coal gangue is to produce building materials, including coal gangue brick-making, cement and lightweight aggregates.

Coal gangue brick making: Coal gangue bricks include sintered bricks and pastes. Sintered bricks are mainly made from coal gangue, taking up 80% weight of the ingot, and some are made just by coal gangues. In the sintering process, by using coal gangue's own calorific value, using as less coal as possible, can save up soil taken from farmlands and save up energy. Coal gangues using for pastes require a thermal value between 2.10 and 3.30MJ/kg. Coal gangue pastes are usually made from burned coal gangues (such as Spontaneous combustion coal gangues) mixed with certain percentage of cement, lime (or limestone), enhancers, and water, through the process of crushing, batching, mixing high-pressure molding and curing processes, without the use of high-temperature sintering. Nowadays, there are thousands enterprises devote coal gangue brickmaking, annually using 16Mt of coal gangues, annually save up farmlands about 7km^2，and save up coals about 0.6Mt per year.

Producing cement by coal gangues: Mainly used as cement's adjuvant. In some areas that lack of clay silicon and aluminum raw materials, there is a long history for using coal gangue instead of some part of silicon and aluminum raw materials with mature production technology, but due to unstableness of the presence of components and high application cost and other factors, it is now commonly used at present. Coal gangue used as cement admixture is affected by factors such as loss on ignition, therefore in less use. Utilization of coal gangues as aggregate has stableness problems, is also not widely used.

Producing lightweight aggregates by coal gangues: 40 percent of China's stockpiling of coal gangue is suitable for firing lightweight aggregate. About 10% of the burned coal gangues after crushing and selecting can make directly into lightweight aggregates. Carbonaceous shale and coal washing waste rocks are usually used for firing lightweight aggregates. Coal gangues that contain 13% or less carbon are best suited for this process.

Extract Usable Components and Make Chemical Products

Coal gangues that contains high portion of Aluminum can be used to extract Al_2O_3, produce Aluminum chloride and crystalline aluminum chloride. Coal gangues contain high portion of Silicon can be used to produce Sodium silicate, alum and Sodium metasilicatenonahydrate. Coal gangues can also be used to produce calcined kaolin. Up to now, the industrial utilization of coal gangues is still at experimental stage. However, there are projects on extract Al_2O_3 from fly-ash has industrial demonstration running. Also, there are also progresses on researches of extracting germanium, gallium, vanadium and other useful components from coal gangues.

The Main Problems in Coal gangue Utilization

Low Utilization Rate of Coal gangue Resource

Up to now, the coal gangues and other forms of solid waste, which used for power generation as a low calorific value fuel and the production of building materials, are about 300Mt in China. In 2010, 770Mt coal gangue is discharged national wide; electricity generating and building material

utility is less than 40%. To the 180Mt coal gangues that can be used as electric generation, the efficiency is only about 30%. This is far from the requirement of utilize coal gangues properly, causing the amount of stored up coal gangues to increase. As we can see, there is a huge gap between newly produced coal gangue and the limited amount of coal gangue of present coal gangue utilization takes up. The problems of resource wasting and environmental issues are severe.

According to prediction, the year 2015, 2020 our country's coal production will reach about 3800Mt, 4200Mt. The production of coal gangue will reach 950Mt, 1050Mt，among which the low-calorific level coal gangue that can be used to generate electricity will reach 620Mt, 680Mt. Therefore, properly dealing with and utilizing coal gangue is under great pressure. The coal gangue utilization can be strengthened.

Present coal gangue Integrated Utilization Do Not Deliver the Circular Economy Mode

Due to historical reasons, present coal gangue integrated utilization electricity plant did not consider including mines' circular economic logistics chain when established, and locate coal gangue integrated utilization electric plants as mines' plants that provide their own electric. As the development of mines and coal-energy, present coal gangue electricity generation enterprises cannot satisfy the need in unit efficiency, level of environmental protection, economy aspect, coal gangue assimilative capacity and contribution to circular economy to the mines. By improving technology, operational management level, industrial level and scientifically establish new project to turn the tide is the main task in present.

Coal gangue is Located at the Lower End in the Utilization Value Chain

Coal gangue is widely used in electricity generation and brickmaking. However, due to low added value, most of them are at the end of the value chain. Especially in the coal gangue building materials aspect, which mainly used in wall materials, have low prices therefore most industries are worse off. Reuse of useful component in coal gangues and make high added value is still in the research and demonstration process, not ready for implement. Therefore, the efficient way to search for high-level utilization of coal gangue is in need.

Lack of Research on Coal gangue Composition and Basic Feature

Up to now, the lack of research on coal gangue composition and basic feature is obvious, especially on beneficial component, acidity, heavy metal pollution and other problems are vital. The amount and distribution of acidic spontaneous combustion coal gangues is not clear, which affects the development of environmental protection technology and high-level utilization of coal gangues.

Suggestions

Value Planning and Developing Circular Economy

Value the planning of coal gangue utilization as well as the planning of coal and electricity and other related aspect. Consider coal gangue utilization distribution as a whole, according to the conception of circular economy and local coal industry distribution. In area with sufficient coal gangue resources, plan coal gangue utilization program according to local coal gangue quality and characteristics to improve the utilization rate.

Speed up the Pace of Industry, Academia, and Research Joint

Set up research group to develop coal gangue utilization important project and key-technology. Focus on the vital problems such as big set of coal gangue electricity generation, producing Alumina and Silicon aluminum alloy, organize specific research and establish national research center to perfect the technology support system, speed up the pace of industry, academia, and research joint to provide guaranteed coal gangue utilization and cutting-edge scientific development.

Doing Well On Basic Data Research and Evaluation

Do well on coal gangue on the basic data researches and evaluation on coal gangue's distribution, amount, type, and specialty. Establish database, method base, decision base of coal gangue utilization can provide detailed and reliable information for efficiently develop and utilize the coal gangue.

Supporting Coal gangue Resource Utilization Project on Environmental Capability Aspect

Tons of coal gangue production has brought severe environmental pollution to local areas. Coal gangues emit lots of pollutants, but show no quantitative reflection. After the resource utilization of coal gangue, pollutants are organized emitted. The amount of pollutant emission is in fact reduced, but the net increase amount in accounting basis is raised. Therefore suggest the nation to consider resource output regions' actual situation, and support coal gangue resource utilization on environmental capability aspect， improving integrated environmental benefits.

Reference

[1] Changsen Zhang. New technology of the Coal gangue Integrate Utilization [M]. Beijing:Chemical Industry Press, 2008.

[2] Guoneng Electricity [2011] No. 396. About Promoting Healthy Development of Electric Generation of Low-calorific Value Coal [S].

[3] Huamin Li, Problems and Suggestions on Coal gangue Utilization [J]. Coal Engineering, 2011, (5): 89~:93.

Advanced Materials Research Vol. 936 (2014) pp 2368-2373
© (2014) Trans Tech Publications, Switzerland
doi:10.4028/www.scientific.net/AMR.936.2368

Research on Modes of Recycling and Remanufacturing with Considering the Carbon Footprint

Yue Jiang [1,a *]

[1] Department of Management Science, School of Management, Xiamen University, Xiamen 361005
[a]jiangyuehxg@126.com

Key words: carbon tax, mode of recycling and remanufacturing, remanufacture

Abstract: Three modes of recycling and remanufacturing are discussed when the carbon tax is imposed, the impact of carbon emissions on the mode of recycling and remanufacturing is further analyzed. The results show that the optimal price and sales of the new product and remanufactured product in the second stage are relevant with the carbon emissions in their manufacturing and selling process, not relevant with the carbon emissions in their recycling process. OEM will be more inclined to remanufacture themselves with the increasing environment awareness of consumers.

Introduction

With the introduction of relevant laws and policies, the increasing of customer environment awareness, and the business opportunities arising in the remanufacturing and recycling process, more and more companies begin to get involved in the recovery and remanufacturing activities. The value of the product has not been completely consumed when it is in the use of termination, there is also surplus value can be reused, so recycling and remanufacturing in more and more important, on one hand, it can improve the efficiency of resource, on the other hand, it can reduce the pollution, so how to recycle and remanufacture is a problem that the government and the enterprise must consider. During the past decades, society at large has awakened to the issue of climate change. Climate changing and global warming are higher on the minds of consumers around the world than ever before. IPCC 2009 indicated that the carbon emissions are the main factor, a carbon tax on enterprises will be imposed in the future according to the report about the design about carbon tax in China. So the cost of carbon is a factor that must be considered in choosing the mode of recycling and remanufacturing. The paper is organized as follows: After this introductory section, the relevant literature is reviewed. Section 3 is about the modes of recycling and remanufacturing with considering the carbon footprint. The analysis of three modes of recycling and remanufacturing is described in Section 4. Our conclusions are given in the final section.

Literature Review

Our paper is positioned among two main streams of literature. The first is related to the carbon emissions, the second relates to recycling and remanufacturing. Regarding the first stream, Benjaafar(2009) is the first who consider carbon emissions in supply chain, he establishes a model of carbon emission allowances, model of carbon tax allowances and model of carbon trading. HonLoongLam(2009) designs a supply chain network considering carbon footprint, the performance of supply chain about the carbon is aslo discussed in this paper. FlavioManenti(2010) constructs a index system about environmental development and carbon footprint. Xianyuan(2012) Chang builds a production decision model using the method of decision optimization considering both the cost and the carbon emissions. For the second stream, Yi Wang(2009) studies the impact on manufacturers and distributors with the law system of manufacturer responsibility and distributor responsibility. Savaskan(2007) and Shunli Xue(2007) consider optimal decision in three recycling channels, which

are manufacturer responsible for recycling, distributor responsible for recycling and the third party responsible for recycling. Webster (2007) researched the impact on recycling rate of government compensation. In summary, existing papers have made some achievements in Carbon footprint aspect and recycling and remanufacturing aspect, but only recovery cost is considered in recycling and remanufacturing, the cost of carbon emission is not considered, so this paper introduces the cost of carbon emissions into the recycling and remanufacturing process, the modes of recycling and remanufacturing are analyzed with considering carbon emission using a combination methods of qualitative and quantitative.

Model

Our paper considers a two-stage game model which only an original equipment manufacturer (OEM) and a remanufacturer are considered when carbon tax is imposed by government according to the emissions of carbon. In the first stage only new products are sold, in the second stage, there is competition between new product and remanufactured product, and the supply of the remanufactured products are decided by the first stage.

The First Stage

We assume that the standardization of market size is 1, the evaluation of the customer about the product is uniform distribution on [0,1] ,and we also assume that cumulative distribution function is F(v)=v, the willingness to pay of the customer is decided by the quality of the product, if the willingness of the new product is v, then the willingness of the remanufactured product is βv，$0 \le \beta \le 1$。 p_1 is the price of the new product in the first stage, q_1 is the demand of the new product in the first stage, in this time there ares only new product in the market, so when the utility of customer $v - p_1 \ge 0$, then consumers will purchase products, so the demand of the new product in the first stage is $q_1 = \int_{p_1}^{1} dF(v) = 1 - P_1$ (1). The raw materials and manufacturing process of each product are the same as each other, so the carbon emissions of each product in the manufacturing process are the same as each other, we assume that is Ω_n. Due to the locations of customers, sales channels are different, so the carbon emissions of product are different, but in order to simplify the model, we assume that the average carbon emissions of the product in selling process is Ω_s, we also assume the tax of the carbon is t yuan each tone, c_n is unit production cost of new product, then profit function of OEM in the first stage is

$$\Pi_{OEM}^{1} = (p_1 - c_n - \Omega_n t - \Omega_s t) q_1 \quad (2)$$

According to equation (1) and (2), We can get that $\Pi_{OEM}^{1} = (P_1 - c_n - \Omega_n t - \Omega_s t)(1 - P_1)$ In order to maximize the profit, we can get

$$p_1^* = \frac{1}{2} + \frac{c_n}{2} + \frac{\Omega_n t}{2} + \frac{\Omega_s t}{2}, \quad q_1^* = \frac{1}{2} - \frac{c_n}{2} - \frac{\Omega_n t}{2} - \frac{\Omega_s t}{2} \quad \Pi_{OEM}^{1*} = \frac{1}{4} - \frac{1}{4}(c_n + \Omega_n t + \Omega_s t)^2 \quad (3)$$

The Second Stage

In the second stage, there are both new product and remanufactured product in the market, consumers buy new products or remanufactured product is mainly based on self-selection, which is determined by comparing the utility surplus, utility surplus is equal to utility minus price. p_n is the price of new product in the second stage, q_n is the demand of new product in the second stage, p_r is the price of the remanufactured product in the second stage, q_r is the demand of the remanufactured in the second stage. In the second stage the customers will buy new product if the utility of the new product is greater than zero and the utility of new product is greater than the utility of remanufactured product, that is $v - p_n \ge 0$ and $v - p_n \ge \beta v - p_r$, so we can get $\begin{cases} v \ge p_n \\ v \ge \frac{p_n - p_r}{1 - \beta} \end{cases}$ (4)

The customers will buy the remanufactured product if utility of the remanufactured product is greater than zero and the utility of the remanufactured product is greater than then new product, that is $\beta v - p_r \geq 0$ and $\beta v - p_r > v - p_n$, so we can get $\begin{cases} v \geq \frac{p_r}{\beta} \\ v < \frac{p_n - p_r}{1-\beta} \end{cases}$ (5).When $p_r \geq \beta p_n$, only inequalities(4) are solvable, at this time, only new product in needed; $p_r \leq p_n - (1-\beta)$ time, only inequalities(5) are solvable, at this time, only remanufactured product is needed; $p_n - (1-\beta) < p_r < \beta p_n$ is considered in our paper, at this time the solution of (4) is $\frac{p_n - p_r}{1-\beta} < \beta < 1$， the solution of (5) is $\frac{p_r}{\beta} < v < \frac{p_n - p_r}{1-\beta}$, both new product and remanufactured product are needed in the market, the demands of new product and remanufactured product are $q_n = \int_{\frac{p_n - p_r}{1-\beta}}^{1} dF(v) = 1 - \frac{p_n - p_r}{1-\beta}$

$q_r = \int_{\frac{p_r}{\beta}}^{\frac{p_n - p_r}{1-\beta}} dF(v) = \frac{p_n - p_r}{1-\beta} - \frac{p_r}{\beta}$ (6). So we can get $p_n = 1 - q_n - \beta q_r$ $p_r = \beta - \beta q_r - \beta q_n$ (7)

Recycle and Remanufacture

According to recycling rules in our nations, in the second stage, OEM must recycle their waste products which are generated in the first stage, if individual responsibility for recycling is used, OEM can control waste products completely. OEM can choose remanufacturing and also choose not remanufacturing, if OEM chooses remanufacturing, then there is no remanufacturer in the second stage, OEM can control the new product and manufactured product completely, this is a monopoly model of new product and remanufactured product, which is denoted as mode A. If OEM do not want to remanufacture, OEM can sell the waste products to the remanufacturer, OEM can control the price and the quantity of the waste product which have impacts on the price of the remanufactured product, this is a Stackbelberg model between OEM and remanufacturer which is denoted as mode B, OEM is a leader, and remanufacturer is a follower. If collective recycling obligation is used, OEM need give some recycling fee, so OEM do not care the recycling problem, the third party which is authorized by the government do the work about recycling, and sell the waste product to the remanufacturer, at this time there is no direct relationship between OEM and remanufacturer, this is a Cournot model which is denoted as mode C.

Analysis of Three Modes of Recycling and Remanufacturing

Ω_r is the carbon emissions of each remanufactured product in the manufacturing process. Ω_h is the unit carbon emissions of the waste product in the recycling process. c_r is the unit cost of production of remanufactured product; d is the recycling fee of waste product; ρ is the recycling rate; γ is the remanufacturing rate; Π_i^j is the profit in the second stage, $i \in (OEM, R)$, $j \in (A, B, C)$. We have the following assumptions: (1) The process of selling new product is the same as the process of selling remanufactured product, so the carbon emissions of selling the remanufactured product Ω_s which is equal to the new product. (2) OEM and third-party recycler sell the waste product to remanufacturer at recycling cost. We also give the constraint which is used in the following part, $\gamma\rho q_1^* \geq q_r$ is the condition which is must be satisfied in the second stage. It ensures that the need of the remanufactured product is less the supply.

Mode A

If Mode A is used, OEM sells new product to customers, and at the same time recycles the waste product which is generated in the first stage, then remanufacturing is continuing, and sell the re-manufactured product. In this process the carbon tax is imposed by the government according to the emissions of carbon. The process of Mode A is shown in figure 1.

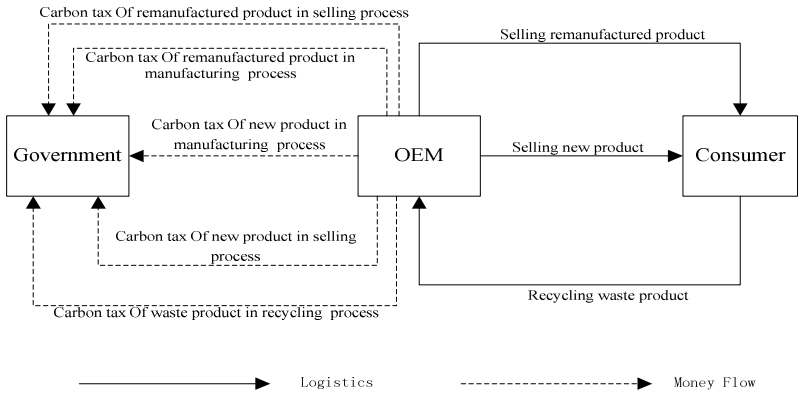


Figure1.Schematic diagram of Mode A

OEM profit function can be expressed as

$$\Pi_{OEM}^{A} = (p_n - c_n)q_n + (p_r - c_r - d)q_r - d(\rho q_1^* - q_r) - \Omega_n q_n t - \Omega_r q_r t - \Omega_s q_n t - \Omega_s q_r t - \rho q_1^* \Omega_h t \quad \text{s.t.} \quad \gamma\rho q_1^* \geq q_r \tag{8}$$

The optimal solution can be obtained using Lagrange multiplier method

$$q_r^{A*} = \gamma\rho q_1^* \qquad q_n^{A*} = \frac{1}{2} - \frac{1}{2}c_n - \beta\gamma\rho q_1^* - \frac{1}{2}\Omega_n t - \frac{1}{2}\Omega_s t$$

$$p_n^{A*} = \frac{1}{2} + \frac{1}{2}c_n + \frac{1}{2}\Omega_n t + \frac{1}{2}\Omega_s t \quad p_r^{A*} = \frac{1}{2}\beta(1 - 2\gamma\rho q_1^* + 2\beta\gamma\rho q_1^* + c_n + \Omega_n t + \Omega_s t) \tag{9}$$

Theorem 1: Equation (9) is the optimal price and sales of the new product and remanufactured product in Mode A. Theorem 1 shows that: (1) The price of new products is related to the manufacturing cost of new product c_n, the carbon emissions of new product in manufacturing process Ω_n, the carbon emissions of new product in selling process Ω_s and the carbon tax t, but not related to the carbon emissions of waste product in recycling process Ω_h. (2) The price of remanufactured product is related to manufacturing cost of new product c_n, the carbon emissions of new product in manufacturing process Ω_n, the carbon emissions of new product and remanufactured product in selling process Ω_s, the carbon tax t, the evaluation index of customers about remanufactured product β, recovery rate ρ and remanufacturing rate γ, but not related to remanufacturing cost c_r, the carbon emissions of remanufactured product in remanufacturing process Ω_r and the carbon emissions of waste product in recycling process Ω_h. (3)$q_n^{A*} \leq q_1^*$ shows that remanufactured product make a cannibalization of the new products in the market share, but $q_n^{A*} + q_r^{A*} > q_1^*$ shows that remanufacturing which mixing market strategy with new product and remanufactured product can expand market share.

Mode B

If Mode B is used, OEM sells new products to customers, and at the same time recycles the waste product which is generated in the first stage, but OEM do not choose remanufacturing, OEM sells the waste product to remanufacturer, remanufacturing is done by the remanufacturer, and then remanufacturer sells the remanufactured product to customers. In this process, OEM and remanufacturer need pay carbon tax according to the carbon emissions. The process of Mode B is shown in figure 2.The profit functions of OEM and can be remanufacturer expressed as

$$\Pi_{OEM}^{B} = (p_n - c_n)q_n - d(\rho q_1^* - q_r) - \Omega_n q_n t - \Omega_S q_n t - \Omega_h \rho q_1^* t - \Omega_s \gamma \rho q_1^* t$$
$$\Pi_{R}^{B} = (p_r - c_r - d)q_r - \Omega_r q_r t - \Omega_s q_r t \quad \text{s.t. } \gamma\rho q_1^* \geq q_r \tag{10}$$

The optimal solution can be obtained using Stackbelberg method

$$q_n^{B*} = \frac{1}{2} - \frac{1}{2}\beta\gamma\rho q_1^* - \frac{1}{2}c_n - \frac{1}{2}\Omega_n t - \frac{1}{2}\Omega_s t \quad q_r^{B*} = \gamma\rho q_1^*$$

$$p_n^{B*} = \frac{1}{2} + \frac{1}{2}c_n - \frac{1}{2}\beta\gamma\rho q_1^* + \frac{1}{2}\Omega_n t + \frac{1}{2}\Omega_s t \quad p_r^{B*} = \frac{1}{2}\beta(1 - 2\gamma\rho q_1^* + \beta\gamma\rho q_1^* + c_n + \Omega_n t + \Omega_s t) \tag{11}$$

Theorem 2: Equation (11) is the optimal price and sales of the new product and remanufactured product in Mode B. We can get the followings by comparing Theorem 1 and Theorem 2: (1) $p_n^{A*} > p_n^{B*}$ shows that the optimal price of new product if remanufactured by OEM is more than by remanufacturer. (2)$q_n^{A*} < q_n^{B*}$ shows that the sales of new product if remanufactured by OEM is less than by remanufacturers.(3)$p_r^{A*} > p_r^{B*}$ $q_r^{A*} = q_r^{B*}$ show that the price of remanufactured product if remanufactured by OEM is more than by remanufacturers, and the sales of remanufactured product if remanufactured by OEM is equal to by remanufacturers.

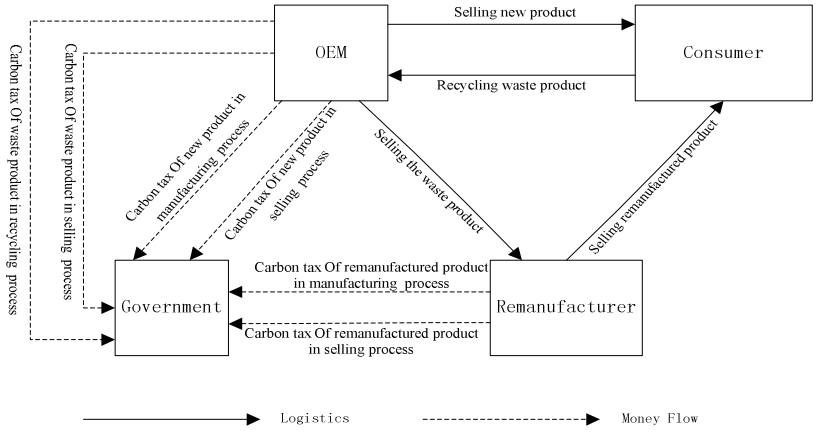


Figure2.Schematic diagram of Mode B

Mode C

If Mode C is used, OEM is not responsible for recycling, the recycling work is done by the third party who is assigned by the government, OEM do not care the recycling work after recycling fee is paid for. The third party sells the waste product to the remanufacturer. In this process, OEM, remanufacturer and the third party need pay carbon tax according to the carbon emissions. The process of Mode C is shown in figure 3.

The profit functions of OEM and can be remanufacturer expressed as

$$\Pi_{OEM}^{C} = (p_n - c_n)q_n - d\rho q_1^* - \Omega_n q_n t - \Omega_s q_n t \quad \Pi_R^C = (p_r - c_r - d)q_r - \Omega_h \rho q_1^* t - \Omega_s \rho q_1^* t$$
$$\text{s.t.}\gamma\rho q_1^* \geq q_r \tag{12}$$

The optimal solution can be obtained using Cournot method

$$q_n^{C*} = \frac{1 - \beta\gamma\rho q_1^* - \Omega_n t - \Omega_s t - c_n}{2 - \beta} \quad q_r^{C*} = \gamma\rho q_1^*$$

$$p_n^{C*} = \frac{1 - \beta + \Omega_n t + \Omega_s t + c_n + \beta^2\gamma\rho q_1^* - \beta\gamma\rho q_1^*}{2 - \beta} \quad p_r^{C*} = \frac{\beta(1 - \beta + \Omega_n t + \Omega_s t + c_n + 2\beta\gamma\rho q_1^* - 2\gamma\rho q_1^*)}{2 - \beta} \tag{13}$$

Theorem 3: Equation (13) is the optimal price and sales of the new product and remanufactured product in Mode C. We can get the followings by comparing Theorem 1, Theorem 2 and Theorem 3:(1)$p_n^{A*} > p_n^{B*} > p_n^{C*}$ $q_n^{A*} < q_n^{B*} < q_n^{C*}$ show that the impact about market share of remanufactured product on new product in Mode A is the largest, in Mode C is the least.(2)$p_r^{A*} > p_r^{B*} > p_r^{C*}$ $q_r^{A*} = q_r^{B*} = q_r^{C*}$ show that the remanufactured profit of OEM in Mode A is more than the profit of remanufacturer in Mode B and Mode C. (3) In the three modes, environment awareness β

has impact on the new product and remanufactured product. With the increasing of environmental awareness, then the competitiveness of remanufactured product will increased gradually, the profit of remanufactured product will also increase, this be a huge opportunity for OEM, so OEM will more be inclined to recycle and remanufacture by themselves.

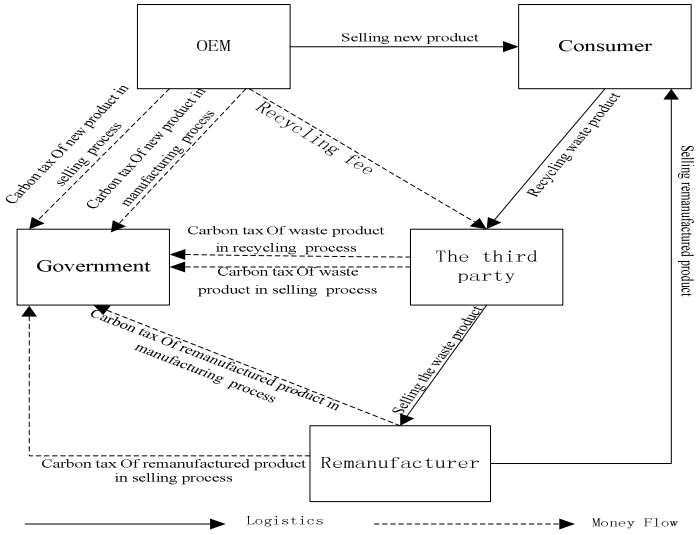


Figure3.Schematic diagram of Mode C

Conclusions

It is very important to design motivating policy about carbon emissions for OEM, remanufacturers and government. The impact of carbon tax on three modes is considered and three modes are analyzed in our paper. Our research shows that the carbon emissions of new product in manufacturing and selling process have impact on the optimal price and sales of the new product in the second stage, but is not related to the carbon emissions in recycling process. Second, with the increasing of environment awareness, OEM will be more inclined to recycle and remanufacture by themselves.

References

[1] Benjaafar S, Li Y Z, Daskin M. Carbon footprint and the management of supply chains: Insights from simple models. Minneapolis: University of Minnesota,2009.

[2] Lam H L, Varbanov P S, Klemes J J. Optimization of regional energy supply chains utilizing renew ables: P-graph approach. Computer and Chemical Engineering, 2009, 34(5):782-789.

[3] Manenti F, Lime N, Linan L Z, Cuoci A, Frassoldati A. Generalized classes for lower levels of supply chain management: Object-oriented approach. Computer Aided Chemical Engineering, 2010, (28):139-144.

[4] Xiangyun Chang, Huiyun Zhu. Production decisions of manufacturing / remanufacturing with the carbon constraints. Technology Progress and Policy, 2012, (29):75-78.

[5] Yi Wang, Linyan Sun, Hongjiao Yang, Gang Li. Decisions of remanufacturing supply chain in different laws and cooperative research. Journal of management science, 2009, 22(1):2-8.

[6] Webster S,Mitra S. Competitive strategy in remanufacturing and the impact of take-back laws. Journal of Operations Management,2007, 25: 1123-1140.

[7] Shunli Xue, Yu Xu, Tao Jia. Optimization model of green remanufacturing system and optimal design on contract. Science and science management, 2007(6):23-27.

[8] Webster S, S Mitra. Competitive Strategy in Remanufacturing and the Impact of Take-back Laws. Journal of Operations Management, 2007, 25(6):1123-1140.

CHAPTER 25:

Geophysical Research and Resources

Advanced Materials Research Vol. 936 (2014) pp 2377-2382
© (2014) Trans Tech Publications, Switzerland
doi:10.4028/www.scientific.net/AMR.936.2377

Spatiotemporal Distribution of Rainfall Erosivity in the Bailong River Basin, Gansu Province

Peng Zhang[1,a], Gang Wang[2,b], Liming Tian[1], Yali Zhang[1]

[1]Key Laboratory of Western China's Environmental Systems (Ministry of Education), Lanzhou University, 222 South Tianshui Road, Lanzhou 730000, China

[2] Lanzhou Meteorological Bureau of Gansu Province, 74 North Jiayuguan Road, Lanzhou 730020, China

[a]pzhang2011@lzu.edu.cn, [b]gangwang323@163.com

Keywords: Rainfall erosivity; soil erosion; Bailong River Basin; spatial and temporal distribution.

Abstract: Rainfall erosivity is one of the key parameters that determine soil erosion, sediment yield, and water quality, thus its importance has grown in modeling of the environmental effects of climate change. The spatial and temporal distribution of rainfall erosivity in the Bailong River Basin in China's Gansu Province were analyzed. We derived a rainfall erosivity map based on data from 18 meteorological stations in and around the basin using the inverse distance weighting interpolation approach. The annual mean rainfall erosivity within the Bailong River Basin was 798.8 MJ mm ha^{-1} h^{-1} yr^{-1}. The mean annual amount of erosive rainfall accounts for 36.0 to 47.1% of annual precipitation, depending on the station. Rainfall erosivity was greatest from June to September, and rainfall during this period accounts for 77.7% to 84.8% of the total annual rainfall erosivity.

Introduction

Soil erosion has become increasingly strong in response to global climate warming and associated changes in rainfall regimes, and this problem has been exacerbated by human activities that expose soil to erosion by damaging the natural ecological balance. Currently, soil erosion by water is one of several major environmental problems around the world, and especially in China. Soil erosion is particularly severe in western China, where it affected 2.97×10^6 km^2, accounting for 83.1% of the total area of erosion in China. Rainfall is one of the main factors that drive soil erosion, leading to problems such as decreased agricultural productivity, increased frequency and severity of debris flows, and ecosystem damage. Rainfall erosivity represents the potential of rainfall to cause soil erosion, and is determined by a combination of rainfall intensity, rainfall duration, and other parameters (Zhang et al. 2002a). Rainfall erosivity comprehensively reflects the effects of splash erosion by raindrops and the effects of runoff on the soil. Raindrops induce a lower or greater degree of downslope transport of soil particles, depending on their energy and the intensity of the rain, and runoff can also scour the surface; the combination can cause large losses of soil (Silva 2004). At present, rainfall erosivity is the most common quantitative index used to estimate soil erosion, including in prominent and widely used models such as the Universal Soil Loss Equation.

Sukhanovski et al. (2002) proposed a new index to estimate rainfall erosivity based on a physically based description of the erosional characteristics of an artificial rain, the A index, which was developed with the use of methods of continuum media mechanics. Although many models have been proposed around the world to estimate rainfall erosivity using various precipitation parameters, each model was adapted to a specific region. It is clear that many factors that vary among regions can affect the calculation of rainfall erosivity, including climatic conditions. The objectives of the present study were to evaluate the spatial and temporal distribution of rainfall erosivity in the study area, using the Bailong River Basin as a case study, and to analyze the relationship between rainfall erosivity and debris flow activity from a semi-quantitative perspective.

Methods

There are many models for calculating *R* in different regions based on annual, monthly, or daily rainfall data. In this study, we computed the annual *R* using the daily precipitation model proposed by Zhang et al. (2002b), as data with the required temporal resolution was available and the method has been widely applied to estimate rainfall erosivity in China (Cheng et al. 2009). The formula is as follows:

$$R_i = \alpha \sum_{j=1}^{k} \left(P_j\right)^{\beta} \tag{1}$$

$$\alpha = 21.586\beta^{-7.1891} \tag{2}$$

$$\beta = 0.8363 + \frac{18.144}{P_{d12}} + \frac{24.455}{P_{y12}} \tag{3}$$

Where R_i is the rainfall erosivity value in half-month i (MJ mm ha^{-1} h^{-1} yr^{-1}), k is the number of days in half-month i, and P_j is the rainfall on the jth day in half-month i. P_j equals the actual rainfall if the rainfall is greater than the threshold value of 12.0 mm; otherwise, P_j equals zero. The terms α and β are parameters of the model. P_{d12} is the mean daily precipitation for all rainfalls greater than 12.0 mm and P_{y12} is the yearly mean precipitation for days with precipitation greater than 12.0 mm. Table 2 shows the values of α and β parameters for the 5 stations in the Bailong River Basin and the 13 stations surrounding the basin.

The point estimates of rainfall erosivity generated using data from the 18 meteorological stations were interpolated by means of inverse distance weighting to produce a map of erosivity for the basin. Angulo-Martinez et al. (2009b) and Xin et al. (2011) had used the inverse distance weighting interpolation method to obtain the rainfall erosivity map, and this approach performed best for their study area.

Results and Discussion

Daily Rainfall Data

The rainfall database consists of data provided by the National Meteorological Information Center of China from 5 meteorological stations within the Bailong River Basin and 13 meteorological stations around the study area. Each station provided continuous daily precipitation records that we used to compute the rainfall erosivity (*R*), which we used to analyze the spatial and temporal distribution of rainfall erosivity in the Bailong River Basin. The stations have continuous rainfall records ranging from 32 to 55 years. Daily rainfall data provide more detailed information on precipitation variations than yearly or monthly data, and are therefore more useful for computing rainfall erosivity (Xin et al. 2011). We chose 12.0 mm of daily rainfall as the threshold for erosive rainfall in our study area. Although these authors did not test whether this threshold varied from slope classes.

Spatial Distribution

Figure 1 shows the spatial distribution of the average rainfall erosivity in the Bailong River Basin calculated using inverse distance weighting interpolation method and the *R* values based on periods of 32 to 55 years. *R* decreases gradually from the southeast towards the northwest, in accordance with the rainfall distribution along this direction. Moreover, the value of *R* increases moving downstream, with the exception of an area surrounding Zhouqu. The rainfall erosivity for most of the areas within the basin ranged between 800 and 1100 MJ mm ha^{-1} h^{-1} yr^{-1}, including the areas around Diebu and Dangchang, and some parts of Wudu and Wenxian, which together account for about 70% of the total area of the basin. The rainfall erosivity for the areas around Zhouqu and Wenxian ranged between 500 and 800 MJ mm ha^{-1} h^{-1} yr^{-1}. Zhouqu had the lowest value within the basin (504.5 MJ mm ha^{-1} h^{-1} yr^{-1}). However, Zhouqu is one of the areas within the basin that is at highest risk of geological disasters such as debris flows and landslides and the soil losses in this area are serious. These results suggest that the rainfall erosivity and the rate of debris flows and other disasters are inversely correlated. The rainfall erosivity was significantly negatively correlated

with the occurrence of debris flows (R^2 = 0.15, P<0.05). There are several possible explanations for this seeming contradiction. First, the climate in the Zhouqu area differs greatly from that of other areas. The ability of rainfall to cause erosion is calculated based on the average annual precipitation and does not account for extreme precipitation events. Therefore, the results in Figure 1 differ somewhat from the actual status. In addition, the lithology of the Zhouqu area is relatively stable compared with that of other areas in the basin. The vegetation cover is also higher than that in any other areas, and the rock strata are less broken than in any other areas. Furthermore, rainfall of 12 mm at a site with a coarse sandy soil and gentle slopes may not cause any erosion; whereas the same rainfall at a site with a compact clay soil and steep slopes may cause severe erosion.

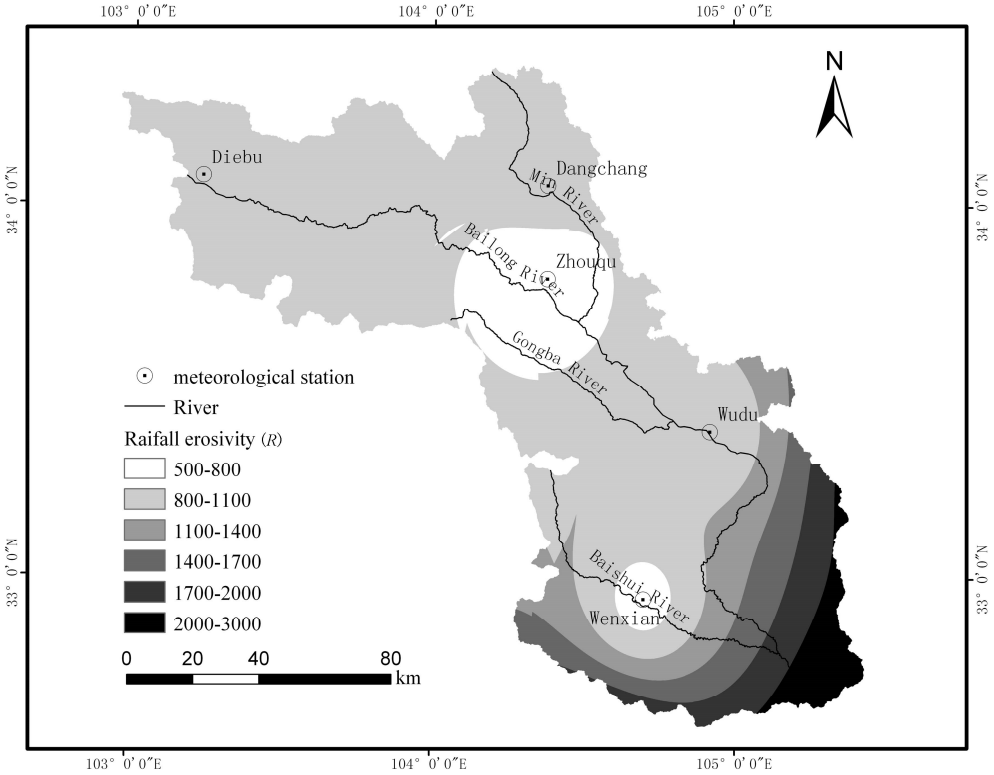


Figure 1 Rainfall erosivity map of the Bailong River Basin based on inverse distance weighting interpolation of the *R* values from the 18 meteorological stations.

The reasons for the low occurrence of debris flows in the Wenxian area are because of the low degree of fracturing of the rock, the high vegetation cover, and appropriate weather conditions. The reasons why the Bailong River Basin is one of the four areas with the highest occurrence of geological disasters in China include the high mountains, steep slopes, relatively low degree of vegetation cover, deep valleys, high frequency of extreme rainstorms, and the serious soil loss due to the fragile ecological environment. Soil loss can exacerbate the frequency of debris flows in our study area because it reduces the amount of soil available to absorb rainfall, leading to increased surface flows and the concentration of these flows in low-lying areas. Another possibility is that the areas with the highest risk of debris flows due to steep slope, low vegetation cover, and other factors may have lost all or most of their erodible material in previous debris flows. Thus, insufficient debris remains to be carried along by flowing water.

It is important to note that rainfall erosivity only represents the potential for erosion. Whether erosion and debris flows actually occurs depends on whether erodible material is present, and whether other factors such as slope allow the falling water to transport this material. However, the spatial distribution of rainfall erosivity is not consistent with the actual status of soil loss. The differences between the spatial distribution of rainfall erosivity and the spatial distribution of soil erosion demonstrate that the rainfall erosivity can only explain some of the variations in soil erosion caused by rainfall. This conclusion agrees with the results of Silva (2004), who reported that rainfall erosivity accounted for about 80% of the variation in soil loss in Brazil. However, some areas within the basin exhibit a stronger correlation between rainfall erosivity and the actual status of soil

erosion. For example, the red area in Figure 1 that stretches from north of Wudu to south of Wenxian (with a rainfall erosivity ranging from 1100 to 1400 MJ mm ha^{-1} h^{-1} yr^{-1}) in Beiyu River district in Wudu has a complicated geological structure and highly fractured rock. Local records indicate that geological disasters such as debris flows have occurred annually in this area, and that the soil loss in this area is serious.

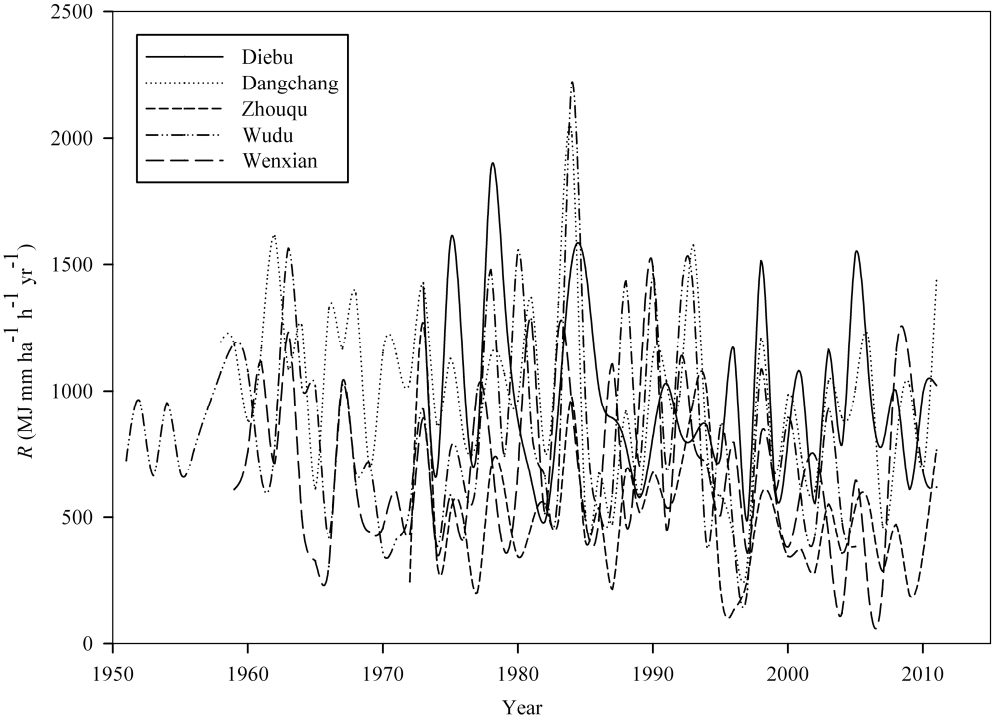


Figure 2 Annual variability in rainfall erosivity (*R*) in the Bailong River Basin.

Temporal Variation of Rainfall Erosivity

Annual rainfall erosivity changes dramatically over time, with high inter-annual variability at all five stations within the basin (Fig. 2). The differences between the stations are large and the ratio between the maximum and minimum *R* values at a given station ranged between 3.88 and 12.54, with coefficients of variation (CV) ranging between 1.10 and 1.21 (Table 1). This degree of variation is higher than in previous research, which reported coefficients of variation of about 0.5 in a typical small basin in the Three Gorges Reservoir area of China (Sun et al. 2011) and at some stations in Switzerland (Meusburger et al. 2012). This difference probably resulted from differences in the rainfall and other climate factors between study areas. The values of rainfall erosivity at different stations changed significantly over time. The values at all five stations have shown a downward trend during the study period. Within the basin, the decrease in rainfall erosivity ranged from 6.65 MJ mm ha^{-1} h^{-1} yr^{-1} at Danchang to 1.32 MJ mm hm^{-2} h^{-1} yr^{-1} at Wenxian. This trend is similar to the trend for annual rainfall volume. These parallel trends explain why the rainfall erosivity in the Bailong River Basin appears to have been decreasing during the study period.

TABLE 1 VARIATIONS IN ANNUAL RAINFALL AND ANNUAL RAINFALL EROSIVITY IN THE BASIN

Station	Length of record (yr)	Annual rainfall (mm)			Erosive rainfall (mm)[a]	Annual rainfall erosivity (MJ mm ha^{-1} h^{-1} yr^{-1})			
		Average	Max.	Min.		Average	Max.	Min.	Cv[b]
Dangchang	54	580.4	775.7	388.3	263.7	987.3	2011.9	319.8	1.10
Diebu	39	572.1	762.0	416.5	269.3	980.3	1874.9	482.7	1.18
Wenxian	53	442.3	671.9	290.9	184.9	684.8	1491.9	119.8	1.16
Wudu	55	468.6	689.3	270.5	215.5	837.3	2219.9	216.6	1.21
Zhouqu	40	424.4	561.5	303.4	152.8	504.5	1267.7	133.7	1.18

[a] Erosive rainfall was defined as total rainfall greater than 12.0 mm in a single event.
[b] CV, coefficient of variation.

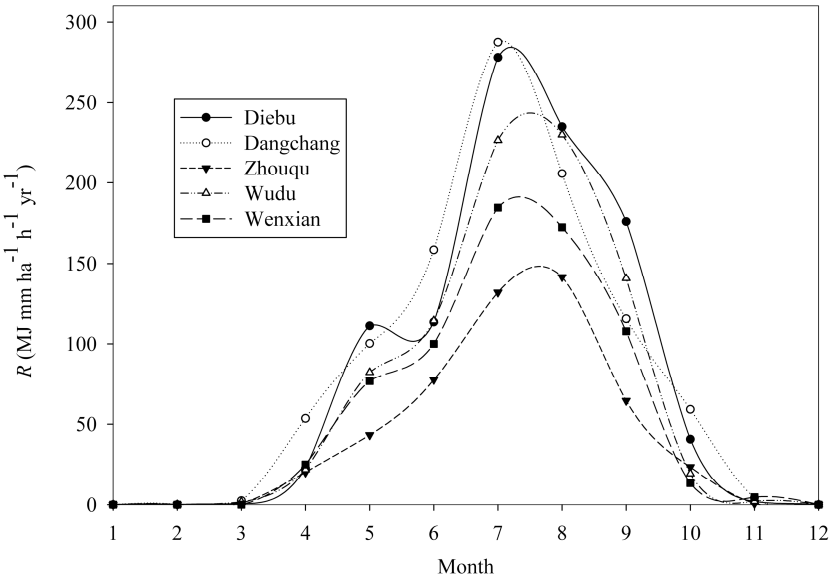


Figure 3 The distribution of rainfall erosivity (*R*) throughout the year at the five meteorological stations in the Bailong River Basin.

Figure 3 shows the distribution of rainfall erosivity throughout the year based on the proportion of the total annual value in each month. The erosivity reached its highest values during the summer, and showed a monomodal distribution. The rainfall erosivity between June and September accounted for 77.7 to 84.8% of the total annual value. Including the May value increases this proportion to 87.9 to 94.6% of the annual total. The peak values generally occurred in July and August, and these two months accounted for 50.0 to 54.4% of the annual total. The distribution of *R* values follows the overall distribution of precipitation during the year. The distinct increasing trend for rainfall erosivity between May to September agrees with climate change predictions, which forecast reductions in average summer rainfall but increases in high-intensity rainfall events for many parts of Central Europe and the Alps (Frei et al. 2006; Meusburger et al. 2012). The rainfall erosivity values are low in January, February, March, November, and December and because these values account for only 0.3 to 0.7% of the annual total, they can essentially be ignored. The values are low because there is hardly any rainfall or snow in the winter and spring in these areas.

Conclusions

We mapped rainfall erosivity in the Bailong River Basin using the inverse distance weighting interpolation method based on data from 18 meteorological stations in and around the basin. Rainfall erosivity is one of the key input parameters that determines soil erosion, sediment yield, and water quality modeling, but in our study area, it is particularly important as a potential predictor of the occurrence of debris flows, which occur frequently and pose a serious risk to human life and infrastructure such as roads and electrical power lines.

Rainfall erosivity increases gradually from the northwest to the southeast, in parallel with changes in the rainfall distribution. The rainfall erosivity in most areas of the basin (about 70% of its area) is between 800 and 1100 MJ mm ha^{-1} h^{-1} yr^{-1}. The rainfall erosivity was highly variable both between stations and over time. However, all stations showed a trend of decreasing erosivity in recent years as a result of decreasing annual rainfall. Rainfall with erosive potential accounted for 36.0% to 47.1% of the annual total. All stations demonstrated a positive correlation between annual precipitation and annual rainfall erosivity. The results suggest that in complex terrain like that of our study area, *R* is not an adequate predictor of the probability of erosion. To determine that probability, it will be necessary to include the values of other parameters such as vegetation cover, slope, and soil texture in a predictive equation. We hope to perform these calculations in our future research.

Acknowledgments

This study was funded by the National Key Technology R&D Program (No. 2011BAK12B05).

References

[1] M. Angulo-Martinez, M. Lopez-Vicente, S.M. Vicente-Serrano and S. Begueria. Mapping Rainfall Erosivity at A Regional Scale: A Comparison of Interpolation Methods in the Ebro Basin (NE Spain). Hydrology and Earth System Scences (2009b)13, 1907-1920.

[2] L.L. Cheng, W.W. Zhao, Y.H. Zhang and H.Y. Xu. Effect of Spatial Distribution of Rainfall Erosivity on Soil Loss at Catchment Scale (in Chinese). Trans. *CSAE* (2009)25(12), 69-73.

[3] C. Frei, R. Scholl, S. Fukutome, J. Schmidli and P.L.Vidale. Future Change of Precipitation Extremes in Europe: Intercomparison of Scenarios from Regional Climate Models. Journal of Geophysical Research, (2006)111, D06105, doi: 10.1029/2005jd005965.

[4] K. Meusburger, A. Steel, P. Panagos, L. Montanarella and C. Alewell. Spatial and Temporal Variability of Rainfall Erosivity Factor for Switzerland. Hydrology and Earth System Scences, (2012)16, 167-177.

[5] A.M. Silva. Rainfall Erosivity Map for Brazil. Catena, (2004)57, 251-259.

[6] Y.P. Sukhanovski, G. Ollesch, K.Y. Khan and R. Meibner. A New Index for Rainfall Erosivity on A Physical Basis. Journal of Plant Nutrition and Soil Science, (2002)165(1), 51-57.

[7] H.Y. Sun, X.Y. Liao, Z.J. Chen and H.M. Wang. Study on Rainfall Erosivity in Typically Small Basin of Three Gorges Reservoir Area. In International Symposium on Water Resource and Environmental Protection (ISWREP), (2011), 886-890.

[8] Z.B. Xin, X.X. Yu, Q.Y. Li and X.X. Lu. Spatiotemporal Variation in Rainfall Erosivity on the Chinese Loess Plateau during the Period 1956-2008. Regional Environmental Change, (2011)11, 149-159.

[9] W.B. Zhang, Y. Xie and B.Y. Liu. Research Evolution of Rainfall Erosivity (in Chinese). Journal of Soil Water conservation, (2002a)16(2), 43-46.

[10] W.B. Zhang, Y. Xie and B.Y. Liu. Rainfall erosivity estimation using daily rainfall amounts (in Chinese). Scientia Geographica Sinica, (2002b)22(6), 705-711.

Advanced Materials Research Vol. 936 (2014) pp 2383-2388
© (2014) Trans Tech Publications, Switzerland
doi:10.4028/www.scientific.net/AMR.936.2383

The Mineral Characteristics and Occurrence of Gold in Nali Gold Deposit, Guangxi

LI Zhiwen[1, a], LIU Chengdong[1, b*], ZHAO Xuanqing[2, c], LU Jianhui[2]
GUO Guolin[1]

[1.] State Key Laboratory Breeding Base of Nuclear Resources and Environment East China Institute of Technology, Nanchang, 330013, China

[2]. Guangxi zhuang autonomous region, the fourth geological team, Nanning, 530031, China

[a]lzw0706@163.com, [b]chdliu@ecit.cn, [c] 526772154@qq.com

[*]Corresponding author. Liu Cheng-dong, E-mail: chdliu@ecit.cn.

Keywords: Gold deposit, characteristics of process mineralogy, occurrence of Au, Nali, Guangxi.

Abstract. Using the analysis techniques of polarizing optical microscope and electron probe, mineral composition, ore texture and structure and the occurrence of Au in the primary ore are studied. The research shows that the main ore minerals in the ore include realgar, pyrite and arsenopyrite etc. Sulfur-stibarsen is the main carrier of Au, and is the major associated mineral of realgar, surrounded mainly by realgar, and partly is the associated mineral of arsenopyrite. The existence of visible gold and microscopic gold in the ore of this mining area can be excluded, and the gold might exist mainly in the form of inclusion gold, which is the so-called "nano-Au".

Introduction

Nali gold deposit is located at Yanjiang, Long'an County, northwest 120km of the capital of Guangxi Zhuang Autonomous Region, Nanning, belonging to the extension of the ore bodies in Leiyaoling orefield. After a comprehensive study of the characteristics of process mineralogy, the mineral composition, texture, structure of the primary deposit and the main occurrence state of the useful associated elements are revealed, which provide scientific basis for the selection of the metallurgical program.

Geological Background

Tectonically, the study area is in the gold mineralization belt of southwest Guangxi, well developed with numerous faults. NE trending faults are the major structures in the Nali gold region. Since Triassic, the sedimentary stratum of the upper crust of the Youjiang rift basin and its expansion zone is very thick, which is made up of the upper structural layer of the Youjiang basin and the lower structural layer of the platform. The thick sedimentary stratum leads to the mineralization products covered or deeply buried so that there are a lot of tectonic magmatic belts. These factors provide favorable conditions for the formation of gold deposits, showing a large ore prospect in the deep part of Nali gold deposit, while the prospecting task is rather tough [1].

The orefield, with several fold structures and fault structures, is located in the area of the south China paraplatform, which is in the Youjiang regenerated geosynline. The fault structures developed in Neilu syncline axis is interlayer fracture zone. There are some small folded rock formations, small scale lenticular ore bodies and few magmatic activities. The Triassic formations are well-exposed in this area but the Tertiary strata is just exposed in the southwest of the orefield.

The wall rock alterations closely associated with gold mineralization are silicification, pyritization, kaolin, fade, sericitization and carbonatization. The certain size and occurrence of the ore body provide favorable conditions for the prospecting.

Ore Characteristics

The gold orebody and occurrence of the research area mainly occur in the sand mudstone interlayer fracture zone of the middle Triassic series Lanmu group. Surrounding rocks of ore body composed of cataclastic rock, tectonic breccia and so on. The original rocks are powder sandstone, mudstone and silty mudstone shale. The main ore-bearing rocks are cracked rock, muddy siltstone and silty mudstone, along with middle-weak silicification and limonite. The colors of the original rocks are brown yellow, gray, light gray, experienced intense metamorphism.

Ore Mineral Characteristics

Realgar, pyrite and other metal minerals are quite visible in hand specimen. Microscope shows that the major ore minerals in the rock are realgar, arsenopyrite, pyrite, chalcopyrite and so on, accounting for about 15%-35%, some samples are about 10%, while the main ore mineral of the rock is realgar.

Realgar fills the rocks as veins, granular aggregates form, whose content accounts for roughly 50%-75% of the total amount of ore minerals, due to affecting by the pyrite alteration, the edge and internal of realgar have significantly grown limonite alteration, and the iron are enriched. Parts of realgar intersperses in the late quartz veins, then the late quartz veins are separated by realgar. There are also a small amount of realgar ore veins covering the surface of the late quartz veins, indicating that the area has undergone multi-stage tectonic movements. After the formation of hydrothermal quartz veins, ore contained fluids added in, resulting in the ore enrichment in this area. Pyrite is mainly subhedral and anhedral, and sometimes hexagonal, hexagonal granulars can be seen, very few are irregular cataclastic or disseminated, particle sizes are quite different, the maximum can reach to 0.2mm, whereas some particles are difficult to detect under the powerful microscope, only can be observed in the high magnification image of electron microprobe, but the vast majority of particles concentrates mainly in 0.05-0.15mm, the average particle size is less than 0.10mm, accounting for 20%-45% of the total content of the ore. Arsenopyrite are unevenly distributed in the ore, a small portion is surrounded by realgar, particles are generally smaller and the content is less, most of them are crushed in cataclastic structure, accounting for about 5% of the total content of ore, crystal has been basically destroyed, basic illegible, a few short columnar grain crystal fragmentation filled with clay minerals, and the arsenopyrite and pyrite can be seen co-existed.

Characteristics of the Gangue Minerals

The main gangue minerals are quartz, feldspar, mica, clay minerals and carbonate minerals, in which sericite is mainly in the mica mineral, with a certain amount of hydromica, and a little biotile and muscovite; clay minerals and carbonates are even less.

There are two types of quartz: firstly, quartz in the terrigenous detrital with relatively small particles; secondly, debris filled the late hydrothermal fluids, along the fractures filled with quartz veins, due to the late hydrothermal filling then partly detrital quartz grains regrowth makes the crystal become larger, so that the particle diameter is relatively coarse. The content of quartz can be accounted for roughly 40%-60% of the total rock, particle sizes vary largely, the maximum can reach about 0.7mm, and the smallest are the quartz particles in the debris. The vast majority of feldspar are already developed more intense alteration, transformed into sericite, clay and other minerals, the place of the local alteration can see the feldspar alteration residual particles, approximately accounting for 10%-30% of the total rocks; due to the alteration, mineral boundaries blur, particle sizes are generally about 0.1-0.2mm. Sericite, hydromica clay minerals particles are a major component of the matrix and in the samples we can see the mica clay minerals and small amounts of carbonate minerals.

Texture and Structure of the Ore

Ore has cracked, silty, clay, fine and brecciated textures; and has massive and disseminated structures, rocks show certain directional texture. Ore minerals are mainly distributed in the intense

alteration beddings, less developed in quartz veins. The ore minerals are roughly even distributed in the ore, relatively enriched locally, and in the enriched area, pyrite distributes micro-bedding with clay and other darkcoloured minerals.

Based on the electron microprobe (EPMA) and spectroscopy (EDS) analysis of the ore, inside the realgar contains a certain amount of arsenic ,antimony sulfide ore, a small amount of arsenopyrite and chalcopyrite ore minerals, and occasionally accompanied by pyrite. The vast majority of arsenic, antimony sulfide ore is the associated minerals of realgar, basically surrounded by realgar, a small part of what is the associated minerals of arsenopyrite. Due to the extremely low content, chalcopyrite ore and other minerals, accounting for about 1% of the ore minerals, have no substantive effect on the mineralization. In addition, in a few samples we found that pyrite grains contain or semi-contain the smaller arsenopyrite particles, this situation may produce intergrowth when the ore is crushed, but the total quantity is not large, and it has sample inclusion relation with few mineral types, the majority of the mineral particles distributed in the form of monomers ore.

The ore minerals and gangue minerals in the ore are closely. After crushed, due to the particle size becoming smaller, the former connected minerals, split at the interface between the different minerals, then separated to a certain extent. From the mineral texture, except for a few coarse-grained disseminated ore after crushing to get quite a few monomer dissociation tablets, the vast majority of the ore must undergo grinding in order to get a higher degree of dissociation. Since the main mineral ore exists substantially in the form of a monomer, although there are interludes and inclusion relations but few total amount, simple structure, and interspersed with each other and contained the size of the particle aggregates is less different with the particle size of the ore mineral monomer. In addition, due to the gangue minerals contain more hydromica, sericite and other clay minerals, they have high degree of alteration, while its hardness are quite different with ore minerals. The above factors suggest that dissociation of ore minerals is better.

Gold Occurrence and Metallurgical Processes Suggestions

Occurrence

According to the classification of gold mineral granularity, the gold can be divided into visible gold (> 0.2mm), microscopic gold (0.2μm-0.2mm), submicroscopic gold (<0.2μm). And generally consider the submicroscopic gold with size less than 0.1μm (scanning electron microscope can not be detected) as “invisible gold” [2]. The visible gold has not be found through the visual inspection in hand specimen. In addition, the existence of microscopic gold has also not been detected by careful observation of ten specimens under microscope. Therefore, the inexistence of visible gold can be confirmed, and the gold should be existed by the way of “invisible gold”, which is submicroscopic gold and ultramicro gold.

Gold-bearing minerals are found to be metal sulfide by using electron probe analysis. They are realgar, pyrite, arsenopyrite, sulfur-stibarsen and chalcopyrite, and the low content of arsenopyrite and chalcopyrite has little effect on gold mineralization. By analyzing components of ten samples, 47 efficient measuring points are gotten, and 17 points of them contain gold. These 17 points account for about 36% of the total amount of gold. There are 3 gold-bearing measuring points exist in realgar with the gold content of 0.36%-0.61%, averaging at 0.46%. Pyrite has 3 gold-bearing measuring points and the gold content is 0.22%-0.36%, with an average of 0.27%. Sulfur-stibarsen has 11 gold-bearing measuring points and the gold content is 0.08%-1.81%, with an average of 0.54%. The test results can be seen in table 1, showing the highest gold content is 1.81%, and the lowest is 0.08%, averaging at 0.48%, and from which we can find that the content of gold value differs by one order of magnitude, indicating the enrichment in the distribution of gold.

From the result of eleven point in sulfur-stibarsen, the average content of gold is 0.54%, far more higher than the average of the total gold samples, which indicated that the sulfur-stibarsen is the main carrier of Au, occupying 5%-10% of the sulfide and the gold content occupying 80% of the

total; in addition, it's content level differ by one order of magnitude, indicating that the Au in the sulfur-stibarsen also exists a certain enrichment. On the other hand, the sulfur-stibarsen mainly exist in realgar veins and the realgar veins include a certain amount of Au (0.36%-0.61%), thus, the gold mineralization is closely related to the forming of realgar veins.

In order to further identify the occurrence of the Au in these gold-bearing sulfide, electron probe are applied to do lot of line scanning on the thin section, and find that only few gold grains exist, and the gold kurtos is widespread in realgar on mapping of the electron probe X ray; the white dots on the map display the existence of the specified Au and the dots evenly distributed along the realgar position, and cannot find enrichment in other sulfides. It shows that the particle sizes of gold are smiler than the zone of resolution in scanning micro zone of electron probe ($1\mu m^2$). From the results of phase analysis in single mineral, the occurrence of Au is inclusion gold, and the main gold-bearing minerals are sulfur-stibarsen and realgar. From the scattering mapping of electron probe in ore, we can see that the sulfur-stibarsen exist in realgar as inclusions, thus, the comprehensive utilization of the Au and Sb can be considered.

In addition, the gold mainly exists in the form of lattice gold when the content of Au/As less than 0.02; when the content of Au/As is more than 0.02, inclusion gold are produced[2]. In table 1, the content of arsenic in pyrite is 0.13%-0.50% and the average is 0.31%, showing the mineral is arsenic pyrite; the average ratio of Au/As in the pyrite (arsenic pyrite) is fifteen times of cardinal number (0.02), indicating that the occurrence of gold in pyrite (arsenic pyrite) are inclusion gold.

Study on Technological of Gold Bearing Sulfides

Through the above study on occurrence state of gold, gold in the Nali gold deposit mainly exists in the form of inclusion gold, and occur in the carrier of arsenic, antimony sulfide ore, realgar and pyrite (containing arsenic pyrite). Gold particle sizes are micro, dominated by <0.1μm sub-microscopic gold, and a small number is ultra-microscopic gold. The form of gold is mainly irregular and sub-round granular.

Arsenic and antimony sulfide ore, mostly unevenly polyhedral, distributes in realgar edges and interior, whereas realgar fills among the rocks as veins. Late hydrothermal quartz are common interspersed by realgar. Arsenic and antimony sulfide ore and realgar have smooth edges, disseminated with small particles, mainly dominated by fine particles, partly medium grain and particulate, and uniformity is over 90%, belonging to fine-micro particle uniformly disseminated type.

The particle sizes of pyrite (containing arsenic pyrite) is unequal, irregular cataclastic and disseminated distributed between gangue ore in disseminated structures. Gangue minerals are in cubic and polytropic along the distribution of micro-bedding such as clay minerals. Parts of pyrite (containing arsenic pyrite) coexist with arsenopyrite, and barely included in the realgar, the crystals are complete, containing impurities on the surface, disseminated particles are micro, uniformity is below 10%, belonging to fine-medium particle uniformly disseminated type.

Metallurgical Processes Recommended

In view of occurrence and content of gold, and fine gold bearing sulfide dissemination size, C, As, S and other harmful elements are extremely unfavorable to smeltingare, so the conventional cyanideleaching, leaching, amalgamation method can not be applied [3]. This deposit belongs to metamorphic hydrothermal gold deposit, sulfur and arsenic antimony ore are the main carrier minerals of gold with highest gold distribution rate, followed by realgar; therefore, in the gold deposit which sulfide is the main gold bearing minerals, the key factor deciding the recovery rate of Au is the recovery of gold carrier sulfide minerals [4].

Gold in the mining area is in the form of inclusion gold hosted in sulfide, belongs to the refractory gold ores, gold bearing minerals should be fine ground before the flotation, for the micro gold, the size of gold-carry minerals need to be considered, so as to determine the appropriate grinding fineness [5]; to crush the ore, extract realgar and sulfur arsenic and antimony ore, eliminating the gangue minerals as much as possible. These sulfides are usually undissolved in

cyanide solution, nor penetration, making gold uneasy to leaching directly, and the ores must undergo roasting pretreatment before the leaching. Then use the cyanide leaching method to extract, meanwhile, a certain amount of mixed oxidant (H_2O_2 + $KMnO_4$) and mixed additives ($Pb(Ac)_2$ + A) should be added in the process of cyanide leaching.

Roasting pretreatment method is suggested to use microwave roasting, which has the feature of selective heating to useful minerals, different minerals have different absorption and thermal expansion to microwaves, when heating microwaves, some mineral would expand, forming cracks useful for leaching [6]; using microwaves to treat the refractory gold ores, making them decomposed, the included gold would separate from C, As, S minerals, changing the refractory ore to easy to leach. Therefore, microwave roasting can be used as one of the pretreatment methods in this area [7].

As to the above discussion, the following points should also pay attention to: Firstly, although the gangue minerals and metal sulfide intergrowth simply with small total amount, the two dissemination relations still need to pay attention to; Secondly, in order not to affect the gold leaching, clay minerals, dark minerals, water soluble minerals are generally difficult to fine grinding, filtration and sedimentation, dissemination and cleavage characteristics should be considered [8]; Thirdly, carbonate minerals altered from mica minerals exist in this area, with small content, the individual samples accounted for about 5%-8% of the total, the CO_3^{2-} ions consume lots of acid, which will also affect the cyanide leaching of gold [5].

TAB.1 ELECTRONIC PROBE ANALYSIS RESULTS OF AURIFEROUS MINERALS (W/%)

Sample	Se	Bi	S	As	Fe	Mo	Co	Pb	Ni	Ag	Cu	Cd	Zn	Sb	Te	Au	Total	Mineral
N9.3	1.82	0.00	26.23	4.75	0.04	0.33	0.00	0.11	0.00	0.00	0.00	0.00	0.19	65.78	0.00	0.08	99.32	
N9.4	3.19	0.14	26.71	8.73	0.00	0.23	0.00	0.08	0.00	0.00	0.05	0.08	0.21	60.81	0.00	0.74	100.96	
N9.6	2.76	0.00	27.01	7.39	0.00	0.32	0.00	0.00	0.00	0.00	0.00	0.00	0.11	64.09	0.00	0.08	101.76	
N9.7	3.01	0.02	26.05	5.73	0.08	0.26	0.02	0.11	0.00	0.06	0.04	0.00	0.27	64.21	0.00	0.17	100.02	
N8.3	3.71	0.00	25.50	4.70	0.01	0.33	0.04	0.13	0.00	0.00	0.00	0.00	0.05	64.97	0.00	0.24	99.68	
N8.7	2.82	0.00	25.41	1.51	0.09	0.32	0.00	0.15	0.00	0.04	0.00	0.01	0.09	68.77	0.00	0.76	99.96	
N7.8	0.89	0.00	26.92	6.16	0.04	0.25	0.00	0.14	0.06	0.03	0.00	0.03	0.07	65.82	0.00	0.57	100.97	$AsSbS_3$
N1.3	3.61	0.00	26.21	6.52	0.01	0.33	0.00	0.15	0.01	0.02	0.01	0.00	0.13	61.21	0.00	1.81	100.40	
N3.6	3.41	0.00	25.84	3.39	0.00	0.24	0.00	0.02	0.00	0.00	0.03	0.00	0.14	67.13	0.00	0.21	100.41	
N3.18	2.86	0.00	26.48	3.52	0.00	0.37	0.00	0.14	0.00	0.00	0.02	0.01	0.12	66.34	0.00	0.72	100.59	
N3.19	3.02	0.00	25.42	3.82	0.01	0.28	0.00	0.05	0.00	0.03	0.06	0.05	0.05	65.18	0.00	0.57	98.52	
Average	2.83	0.01	26.16	5.11	0.03	0.30	0.01	0.10	0.01	0.02	0.02	0.02	0.13	64.94	0.00	0.54	100.24	
N1.1	0.00	0.01	30.22	68.65	0.07	0.37	0.00	0.13	0.00	0.00	0.06	0.00	0.03	0.05	0.01	0.61	100.21	
N3.17	0.00	0.00	29.25	68.77	0.02	0.43	0.00	0.05	0.00	0.02	0.00	0.00	0.07	0.03	0.00	0.41	99.07	
N2.7	0.00	0.00	30.08	67.65	0.07	0.37	0.00	0.09	0.00	0.00	0.02	0.00	0.13	0.05	0.00	0.36	98.82	As_4S_4
Average	0.00	0.00	29.85	68.36	0.05	0.39	0.00	0.09	0.00	0.01	0.03	0.00	0.08	0.04	0.00	0.46	99.37	
N8.5	0.00	0.00	50.51	0.50	46.70	0.49	0.17	0.10	0.05	0.01	0.00	0.03	0.01	0.00	0.00	0.22	98.80	
M-G6.1	0.00	0.00	50.81	0.13	46.87	0.56	0.15	0.19	0.01	0.03	0.00	0.03	0.02	0.02	0.00	0.22	99.04	
M-G6.8	0.00	0.03	50.70	0.31	46.41	0.57	0.13	0.29	0.16	0.00	0.00	0.01	0.00	0.00	0.02	0.36	98.98	FeS_2
Average	0.00	0.01	50.67	0.31	46.66	0.54	0.15	0.19	0.07	0.01	0.00	0.02	0.01	0.01	0.01	0.27	98.94	

Conclusion

Based on the process mineralogy studies in the primary ore in Nali gold deposit, Guangxi, several main research results are as follows:

(1) Mineral assemblage: the main ore minerals related closely to gold mineralization as follows: sulfur-stibarsen, realgar, and pyrite. Most sulfur-allemontite occurs in inner realgar but few in the edge of realgar, the two minerals are co-occurred. In addition, there is a small amount of pyrite coexistent with arsenopyrite.

(2) Texture and structure: the ore minerals like realgar, pyrite and arsenopyrite distribute evenly in the ore, and enriches locally. Realgar occurs as veinlet, filling the rock fractures; pyrite occurs as disseminated structure and distributes in the ore irregularly; Most of arsenopyrite occurs as xenomorphic monomer in the ore with small particle sizes, and partly are altered, being difficult to identify. Due to the reasons of few interpenetrations and inclusion relationship of minerals, simple structures, high alteration and so on, the degree of separation is good.

(3) Occurrence: Synthesizing former work, all the ore in this area are oxidized ore, and the main useful components are Au with low grade, but locally enriched. Through detailed study of 10 samples, the existence of visible gold and microscopic gold in ore of this area can be excluded. The gold is mainly the submicroscopic gold and little ultramicro gold, and occurs as inclusion gold.

Acknowledgments: the field work of this article accomplished in the help of Guangxi No.4 geological brigade, and the indoor work gets strong support from Fundamental Science on Radioactive Geology and Exploration Technology Laboratory (ECIT).

References

[1] WU Ronghua, PANG Baocheng, TAN Jie, ect. Preliminary analysis of distribution regularity and prospecting direction of gold deposits in Guangxi [J].Mineral Resources and Geology, 2012, 26(4): 291-298.

[2] LI Zengsheng, ZHU Xiaoqing, HAN Tao. Current problems in the study of the occurrence of “invisible gold” in sulfides [J]. Acta Mineralogica Sinica, 2011, Suppl: 209-210.

[3] WU Xiuqun. Study on the oeeurrenee of gold and its speeifie technologica Property in Lan-Ni-Gou Gold Mine [J]. GOLD, 1992, 13 (6): 11-16.

[4] AI Guodong, DAI Tagen, CHEN Minghui. typomorphic characteristics of pyrite-arsenopyrite-antimonite and occurrence of gold in gold deposit: A case study of the gold deposits in Hunan Province [J]. Geology and Resources, 2010, 19 (2): 157-163.

[5] MA Chi, BIAN Xiaodong, WANG Shoujing. Influence factors of refractory gold ore dressing and smelting in the process mineralogy [J].Morden Ming, 2012, No.5: 17-20.

[6] LI junmeng. The current status and dvelopment tendency of pretreation process for refactory gold ores [J]. Hydrom etallurgy of China, 2003, 22 (1): 1-8.

[7] WEI Mingan, ZHANG Ruimin. Study on microwave pretreatment of refractory microdimensional gold packaged by pyrite in gold ores [J]. Ming Metallurgy, 2001, 10(1): 74-77.

[8] YANG Hongying, GONG Enpu, YANG Li. Process mineralogy of low-grade double refractory gold ore and influencing factor on gold leaching [J]. Journal of Northeastern University (Natural Science), 2008, 29 (12): 1742-1745.

Advanced Materials Research Vol. 936 (2014) pp 2389-2395
© (2014) Trans Tech Publications, Switzerland
doi:10.4028/www.scientific.net/AMR.936.2389

Effect of Deficit Irrigation on Root-shoot Development and Grain Yield of Winter Wheat

HU Bin[1,2], ZHANG Min[1],

[1] National Engineering Laboratory for Efficient Utilization of Soil and Fertilizer Resources, College of Resources and Environment, Shandong Agricultural University, Tai'an, Shandong 271018, China;

[2] Soil and Fertilizer Station of Shandong Province, Ji'nan, Shandong 250100

Keywords: deficit irrigation; winter wheat; root; canopy; grain yield

Abstract: In order to investigate the optimal water-saving and high-efficient irrigation patterns of winter wheat in North China Plain, during 2010—2011 and 2011—2012 winter wheat growing seasons, 3 irrigation treatments were conducted, i.e., irrigated 120 mm only at jointing stage (T1), irrigated 120 mm only at heading stages (T2), and irrigated 60 mm each at jointing and heading stages (T3), respectively, to study the effect of deficit irrigation on root-shoot development and grain yield of winter wheat in North China Plain. The results showed that under the condition of irrigated 120 mm during the winter wheat growing season, the treatment which irrigated 60 mm each at jointing and heading stages, the leaf area index significantly (LSD, $P<0.05$) increased at milky stage, which was mainly due to increase the leaf area index at 0—20 and more than 60 cm above the ground surface. The 2 growing season results revealed that dry matter accumulation at maturity stage in T3 was significantly (LSD, $P<0.05$) higher than those in T1 and T2. Compared with T2, the root length density in T1 and T3 were significantly (LSD, $P<0.05$) higher below the ground surface 50 cm. The results indicated that irrigated 60 mm each at jointing and heading stages during the winter wheat growing seasons, grain yield was the highest, which could be attributed to significantly (LSD, $P<0.05$) increase the spike numbers. Under the condition of irrigated 120 mm during the winter wheat growing seasons in North China Plain, it is suggests that winter wheat should be irrigated 60 mm each at jointing and heading stages, to achieve reasonable water use efficiency and grain yield.

Introduction

The North China Plain is one of the most important grain production areas of China; high and stable grain yield of winter wheat is very important to ensure food security of China. However, water resources are limited in this region [19]. Water resource of per capita is only 790 m^3. Hence, how to improve water use efficiency of winter wheat in this region is the key of stable and high grain yield.

The crop's reasonable canopy structure is the important factors for ensuring high and stable crop production [18]. Canopy has the important influence on crop dry matter accumulation above the ground surface and economic output [3]. Li et al. [10] showed that planting patterns could change in the vertical distributions of leaf area index; hence, the canopy structure was improved. Under filed conditions, crop growth is dependent on the ability of the canopy to intercept incoming radiation, which is function of leaf area index and canopy structure, and convert it into biomass. The difference of winter wheat canopy structure influence the light distribution in crop colony, as a result, leading to difference of the grain production[5,9] .

Root system is the absorption organs of moisture and nutrient for the plant in agricultural production, its research increasingly brought to the attention of the agricultural scientific research workers. Studies have shown that the different water conditions have significant influence on the spatial and temporal distribution of winter wheat root system, soil water utilization, and grain yield[13,17] . Therefore, maintaining rational canopy and enhancing root system absorbing power are the premise of ensuring crops grain yield.

For the importance of food production in North China Plain and the shortage of water resources, the amount of research about deficit irrigation in this region is growing [6,11,15] , but the research on root-shoot development of winter wheat is few.

This study aims to determine the effect of deficit irrigation on the canopy structure and grain yield of winter wheat, which could provide the theory basis and technical support for stable and high grain yield of winter wheat under the condition of deficit irrigation.

MATERIAL AND METHODS

A. Experimental site

The study area was located at Dong lufang village, Anzhan town, Feicheng City, (36°43′48″N,116° 45′ 32″E). The plot areas were warm temperature semi-humid and semi-arid climate zones, where the mean precipitation is 697 mm, approximately 70% of which is received from June to September, that is, the summer maize growing season. During the growing season of winter wheat, precipitation amount is only 30% of the mean annual precipitation. The precipitation under natural conditions for the winter wheat growing seasons in 2010 and 2011 were 172.2 and 208.4 mm, respectively. The concentrations of nitrogen, rapidly available potassium, and phosphorus at a depth of 0－20 cm below the ground surface were 80, 15 and 15 mg/kg, respectively.

Winter wheat cultivar “Jimai 20” was manually planted on October 12 in 2010 and on October 17 in 2011, respectively.

B. Experiment Design

In this area, previous studies have shown that winter wheat could get the best grain yield, water use efficiency, and economic benefits under the condition of irrigated 120 mm[10,11] . Therefore, in this study, total irrigation amount was controlled at 120 mm was applied to the treatments as follow: irrigated 120 mm only at jointing stage (T1), irrigated 120 mm only at heading stage (T2), and irrigated 60mm each at jointing and heading stages (T3), respectively. In 2011, the jointing and heading stages were April 7 and May 1; in 2012, were April 9 and April 29, respectively. Water was supplied to the plots from a pump outlet using plastic pipes, and a flow meter was used to measure the amount of water applied.

During the both growing seasons, before sowing, 150 kg hm^{-2} of urea, 300 kg hm^{-2} of Calcium superphosphate (P_2O_5 15%), and 75 kg hm^{-2} of potassium chloride(K_2O 60%) were applied. At jointing stage, 150 kg hm^{-2} of urea was applied.

The area of each plot was 16 m^2, the treatments were randomized using a complete factorial design and were applied in 3 replications. A 1.5-m-wide zone with no irrigation was positioned between the 2 irrigation plots to minimize the effects of the 2 adjacent plots.

C. Measurements

Leaf area index (LAI)

At filling satge, the LAI was determined by sampling small plots consisting of 20 consecutive plants from the central rows, and the LAI above the ground surface of 0–20, 20–40, 40–60, and above the ground surface 60 cm were separated, respectively. Leaf area was calculated by the following equation:

$$\text{Leaf area} = \text{leaf length} \times \text{leaf width} \times 0.78. \quad (1)$$

In the above equation, the leaf length was the distance from leaf pillow to leaf finial, and the leaf width was measured at the widest part of the leaf. The sampling areas were spaced to avoid the effect of previous samplings.

Dry matter accumulation above the ground surface and plant height

From jointing to maturity stage, dry matter accumulation and plant height were measured every 7 days, 20 consecutive plants were sampled. After the plant height was measured, which was placed in the drying owen at 105℃ for 20 minutes. Then, dry matter above the ground surface was determined after drying at 80 ℃ for 72 h.

Root length density

Roots were sampled at maturity stage from soil cores. The diameter of the corer was 10 cm. From each treatments, soil cores were obtained at 10-cm increments down to 180 cm. The cores were then taken to the laboratory, and the soil was manually removed in washing cans. After separating the roots from the debris, root length was measured by using a 1.27-cm grid. The roots were oven dried at 80 ℃ to determine the dry weight.

Grain yield and yield components

Grain yield was measured at maturity by sampling 2 m^2 of each plot. Spike number per m^2, kernel numbers per spike, and thousand kernel weights were determined.

Statistical analysis

Analysis of variance (ANOVA) was used to analyze the effects of the different treatments. ANOVA was performed at a 0.05 level of significance to determine whether the treatments were different. Multiple comparisons were made between the significant effects using the least significant difference (LSD) test at $\alpha = 0.05$.

RESULTS AND DISCUSSION

A. The vertical distribution of LAI

Fig. 1 shows the vertical distribution of LAI on May 2nd in 2011. T3 resulted in the highest LAI, followed by T1, and the lowest LAI was observed in T2.When irrigated only once during the growing season of winter wheat, the LAI over 60 cm above the ground surface were significantly increased at jointing stage in T1 treatment. When irrigated 2 times during the growing season of winter wheat, compared with T1 and T2 treatment, the LAI both at 0–20 cm and over 60 cm above the ground surface were increased significantly in T3 treatment; however, there were not significant effects observed in the LAI at 20–40 and 40–60 cm above the ground surface.

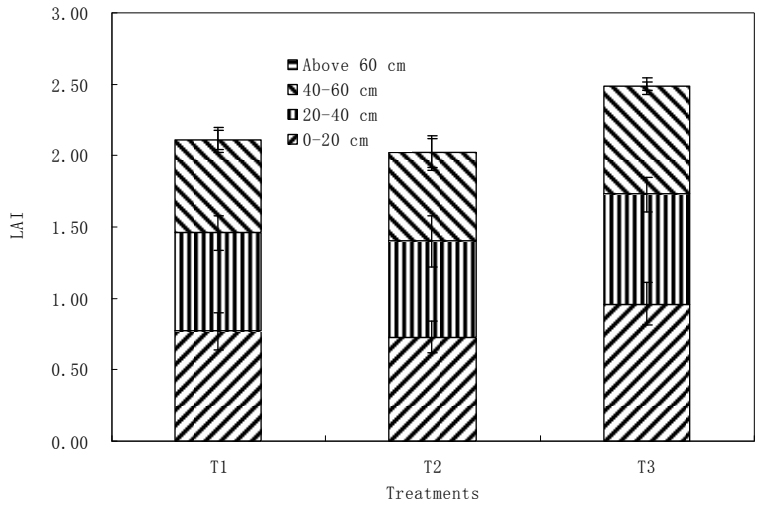


Figure.1 Vertical distributions of LAI in winter wheat canopy

B. Plant height and above ground dry matter

Under the condition of irrigated 120 mm, the plant height and aboveground dry matter were significantly affected by irrigation times and period (Table 1). At jointing stage, in the both growing seasons, the plant height and aboveground dry matter were not significant differences among any treatments. At maturity stage, in 2010–2011, T1 treatment significantly promote the growth of winter wheat; hence, significantly increased plant height. However, the above ground dry matter variation trend was different from that in plant height, the highest aboveground dry matter was found in T3, followed by T1, and the lowest was observed in T2; in 2011–2012, the plant height of T1 and T2 were significantly higher than T2, the variation trend of above ground dry matter in 2011–2012 was similar to that in 2010–2011.

TABLE 1 PLANT HEIGHT AND ABOVEGROUND DRY MATTER AT JOINTING AND MATURITY STAGES DURING WINTER WHEAT GROWING SEASONS IN 2010－2011 AND 2011－2012

Treatments	Jointing stage		Maturity stage	
	Plant Height / (cm)	Aboveground dry matter / (g/cm^2)	Plant Height / (cm)	Aboveground dry matter / (g/cm^2)
2010－2011				
T1	31.72 a	351.47 a	71.15 a	1211.23 b
T2	31.59 a	350.83 a	58.33 c	1050.12 c
T3	31.47 a	347.45 a	69.67 b	1395.03 a
2011-2012				
T1	35.26 a	362.83 a	69.67 a	1220.89 b
T2	32.69 a	362.77 a	61.99 b	1080.92 c
T3	32.63 a	367.25 a	69.76 a	1422.71 a

C. The root length density

Under the condition of irrigated 120 mm during the winter wheat growing season, irrigation frequency and stages had significant effect on the vertical distribution of root length density (Fig.

2).Under the condition of irrigated only once, compared with T2, the root length density in T1 below the ground surface 20 cm and 50 cm were both significantly increased. Under the condition of irrigated 2 times, the root length density below the ground surface 30 cm in T3 was not significant difference from that in T1; however, below the ground surface 50 cm, the root length density both in T3 and T1 were significantly higher than that in T2. Thus, it was apparent that under the condition of irrigated 120 mm, irrigated at jointing stage resulted in a significant increase in root length density.

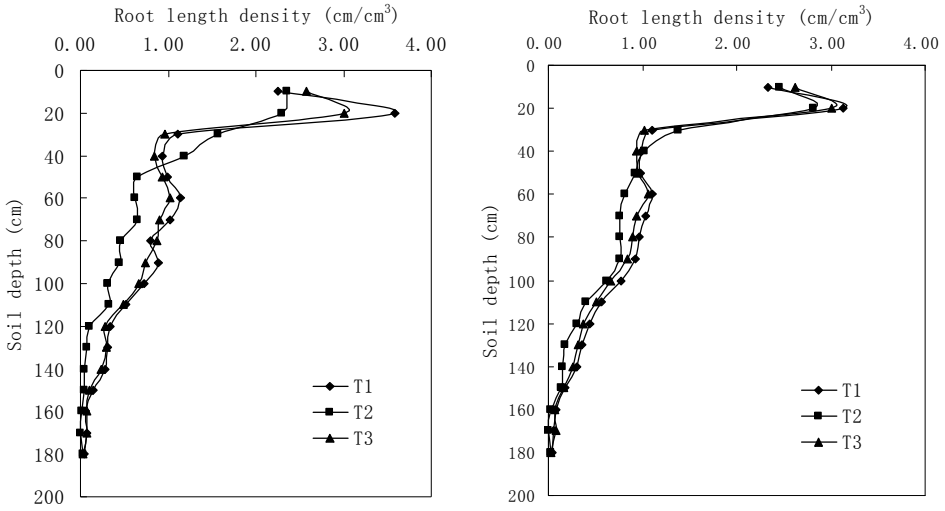


Figure.2 Effect of deficit irrigation on root length density at maturity in 2010－2011 and 2011－2012

D. Grain yield and yield components

Table 2 indicates that the grain yield and yield components were significantly affected by different irrigation regime in the both growing seasons. In 2010–2011, the grain yield in T3 was significantly higher than those in T1 and T2.The grain yield in T1 was not significant higher than that in T2. T3 resulted in the highest grain yield, which contributed to the spike numbers were significantly increased. Every treatment had not significant effect on kernel numbers and thousand kernel weight. In 2011–2012, the grain yield in T3 was significantly higher than those in T1 and T2. In yield components, the results showed that every irrigation treatment had significant effect on spike numbers. T3 resulted in the highest spike number, followed by T1, and the lowest was found in T2. Kernel numbers were not significantly different among any treatments. Compared with T1 and T3, thousand kernels weight in T2 was significantly increased. Hence, under the condition of irrigated 120 mm during the winter wheat growing season, irrigated 60 mm each at jointing and heading stages could improve spike number; hence, the grain yield could significantly increased.

TABLE 2 YIELD AND YIELD COMPOSITION OF WINTER WHETHER IN 2010－2011AND 2011－2012

Treatments	Spike numbers/ （Spikes/m^2）	Kernel numbers / (kernels/Spike)	1000 kernels weight/ （g）	Grain yield （g/m^2）
2010－2011				
T1	556.25 b	30.71 a	39.09 a	557.92 b
T2	551.67 b	31.19 a	36.23 a	550.25 b
T3	580.42 a	29.41 a	37.90 a	678.29 a

2011－2012				
T1	556.27 b	29.2 ab	40.16 b	699.14 b
T2	477.93 c	31.5 a	46.13 a	691.40 b
T3	658.05 a	30.0 a	39.32 b	769.16 a

DISCUSSION

The result indicated that, in North China Plain, irrigated 120 mm during the growing season of winter wheat, irrigation frequency and stages could significantly alter the LAI above the ground surface, plant height, and dry matter accumulation; and that, the root length density under the ground surface could also alter significantly. The result showed that irrigated 60 mm each at jointing and heading stages of winter wheat significantly increase spike number, hence, the grain yield significantly enhanced.

Under field condition, the crops grain yield is determined by the ability of the canopy to intercept incoming radiation and radiation use efficiency [1]. As for crops grain yield, approximately 70–80% was the product of the photosynthetic matter of green organ produced after heading stage in the late growing season; this was approximately 60% more than that produced by the flag leaves and spikes. Hence, how to optimize canopy structure is a most important measure to increase crop community photosynthetic productivity [12]. Zhou et al.[20] found that the maize root characteristics were significantly corrected with photosynthetic ratio in ear leaves; moreover, the drought resistance in coeno-species was result from the coefficient of root and shoot. Hence, improving the root and shoot characteristic is very important to increase crops grain yield and drought resistance.

In North China Plain, water is limited. However, irrigation is mostly required during the growing season of winter wheat [7]. Hence, how to improve water use efficiency is the key to carry out agricultural sustainable development. Researches showed that irrigation patterns could significantly affect canopy structure of crops [8,16]. Through irrigation regulation and control, both the root systems of maize [14] and tomato [2] could be improved, as a result, the relationship between yield and water use efficiency was harmonized [4]. Therefore, maintaining reasonable canopy structure and increasing root absorbing ability is the central premise of guarantee crops grain yield. Crops water use efficiency is mainly determined by transpiration rate of leaves and water absorbing ability of roots; hence, the essence of high efficient water use in crops is the structure and function of root and canopy achieve optimum balance. Therefore, exploring the action mechanism of root and shoot equilibrium in assimilate distribution and water use, could provide theoretical basis and technical support for the development of saving water agriculture in North China Plain.

References

[1] Acreche MM, Briceno-Felix G and Martin SJA. Radiation Interception and Use Efficiency as Affected by Breeding in Mediterranean Wheat. *Field Crops Research*, 2009, **110**: 91–97

[2] Chen X-M, Cai H-J and Shan Z-J. Regulating Effect of Non-pressure Subirrigation on Distribution Characteristics of Tomato Root. *Transactions of the CSAE*, 2009, **25**(3): 10–15

[3] Fan Z-X, Wang P and Liang Z-X. Effects of Optimized Irrigation and Nitrogen Fertilization on the Canopy Structure of Winter Wheat. *Chinese Journal of Eco-Agriculture*, 2005, **13**(3): 79–81

[4] Gao Z-H, Chen X-Y and Luo Y-P. Winter Wheat Root and Shoot: Equilibrium and Growth Stability Under Different Soil and Water Conditions. *Scientia Agricultura Sinica*, 2007, **40**(3): 540–548

[5] Gu Q-R, Zhang Y-W and Xiong S-P. Effects of Eifferent Density Treatments on Canopy Architecture and Grain Yield of High Gluten of Wheat. *Journal of Henan Agricultural Sciences*, 2010, **9**: 42–45

[6] Hu M-Y, Zhang Z-B and Xu P. Relationship of Water Use Efficiency with Photoassimilate Accumulation and Transport in Wheat Under Deficit Irrigation. *Acta Agronomica Sinica*, 2007, **33**(11): 1884–1891

[7] Jiang J and Zhang Y-Q. Soil-water Balance and Water Use Efficiency on Irrigated Farmland in the North China Plain. *Journal of Soil and Water Conservation*, 2004, **18**(3)：61–65

[8] Jin YH, Zhou DW and Jiang SC. Comparison of Soil Water Content and Corn Yield in Furrow and Conventional Ridge Sown Systems in a Semiarid Region of China. *Agricultural Water Management*, 2010, **97**: 326–332

[9] Li C-M, Xiong S-P and Zhao Q-M. Effects of Organic Manure and Urea Mixture on Canopy Architecture, Gain Yield and Protein Content of Wheat. *Scientia Agricultura Sinica*, 2008, **41**(12): 4287–4293

[10] Li QQ, Chen YH and Liu MY. Effects of Irrigation and Planting Patterns on Radiation Use Efficiency and Yield of Winter Wheat in North China. *Agricultural Water Management*, 2008, **95**: 469–476.

[11] Li QQ, Zhou XB and Chen YH. Water Consumption Characteristics of Winter Wheat Grown Using Different Planting Patterns and Deficit Irrigation Regime. *Agricultural Water Management*, 2012, **105**: 8–12

[12] Li Y-D, Tang L and Zhang Y-P. Relationship of PAR Interception of Canopy to Leaf Area and Yield in Rice. *Scientia Agricultura Sinica*, 2010, **43**(16): 3296–3305

[13] Li Y-S, Wang L and Liu S-P. The Influence of Different Amounts of Water Supplied at Different Depths in Soil-root Interface on Root Distribution and Yield of Winter Wheat. *Acta Ecologica Sinica*, 2002, **22**(10): 1680–1687

[14] Shao G-Q, Li Z-J and Ning T-Y. Effects of Normal Urea and Release-controlled Urea on Root and Shoot Growth and Yield of Maize in Different Water Conditions. *Acta Agronomica Sinica*, 2009, **35**(1): 118–123

[15] Sun H Y, Shao L W and Liu X W. Determination of Water Consumption and the Water-saving Potential of Three Mulching Methods in a Jujube Orchard. European Journal of Agronomy, 2012, **43**: 87–95

[16] Wang P-J, Xie D-H and Zhang J-H. Inversion of Winter Wheat Water Content with the Relationship between Canopy Parameters and Spectra Based on Different Irrigations. Spectroscopy and Spectral Analysis, 2012, 32(1): 209–213

[17] Xue L-H, Duan J-J and Wang J-M. Effects of Different Irrigation Regimes on Spatial-temporal Distribution of Roots, Soil Water Use and Yield of Winter Wheat. *Acta Ecologica Sinica*, 2010, **30**(19): 5296–5305

[18] Zhang L, van der Werf W and Bastiaans L. Light Interception and Utilization in Relay Intercrops of Wheat and Cotton. Field Crops Research, 2008, **107**: 29–42

[19] Zhou X-B, Sun S-J and Chen Y-H. Relationship between Water Character and Yield Component under Defferent Distribution Patterns of Winter Wheat Population. *Journal of Soil and Water Conservation*, 2007， **21**（1）：119–122

[20] Zhou X-P, Zhang S-Q and Yang X-Q. Heterosis of Maize Root Activity and Its Relationship with Photosynthetic Characteristics. *Acta Agriculturae Boreali-Occidentalis Sinica*, 2008, **17**(4): 84–90

Keywords Index

(LiFeO$_4$+AC)/Li$_4$Ti$_5$O$_{12}$ 496
[Piperazine-1,4-Diyldi(Methylene)]Bis(Phosphonic Acid) 915
2,2,6,6-Tetramethylpiperidin (TEMPO) 447
22MnB5 Steel 1830
2A12 Aluminum Alloy 1071
3-D Finite Element 2017
316 Stainless Steel 1694
4th Order Dispersion Equation 2225
5-Sulfosalicylic Acid 864
6Cr6W2MoV Steel 1267
7XXX Aluminum Alloys 1754
9%Ni Steel 1953
9,9-Bis(4-Hydroxyphenyl)Fluorene 28

A

α-Alumina 145
A5083-H111 Al Alloy 1701
AA2024 1735
AA6061/SiC/55p Composite 1735
Absorption Coefficient 1994
Acid Effect 1989
Acid Etching 1106
Acoustics Radiation 2071
ACPTFM 1730
Acrylic Acid 89
Acrylonitrile Content 1942
Action Mechanism 1404
Activated Carbon 881, 1809
Active Phase Loading 981
Active Reflector 1351
Adhesive 1816
Adiabatic Coating 1035
Adjustable Porous Properties 942
Admixture 1428
Adsorption 789, 829, 834, 850, 854, 859, 875, 1404
AE 1518
Aerogel 374
Afterglow 552
Ag/SnO$_2$/TiO$_2$ 486
AgCu28 1671
AgCuTi Brazing Filler Metal 1239
Age 1485
Agent 2313
Agglutinating Reagent 1035
Aging 1184, 1647
Aging Oil 1553
Agricultural Product 2335
Al-Cu-Mg-Si Alloy 1247
Al-Mg-Si-Zn Alloy 1224
Al/Mg$_2$Si Composites 23
Alginate 300
Alkali-Aggregate Reaction (AAR) 1428
Alligator Weed 868
Alloy 1234
Alumina 1239
Aluminosilicates 822
Aluminum 1047
Aluminum Alloy 1791, 1963
Aluminum Alloy Bellows 1742
Aluminum Titanate 238
AM-OLED 2209
Ammonia Gas 919
Amphiphilic Copolymer 776
Amphiphilic Diblock Polymer 95
Analysis Functions 2276
Analysis of Influence 1433
Aniline 1007
Annealing 140
Annealing Oxygen Flow Rate 651
Annulus 2267
Anode 1112
Anodic Oxidation 965
ANSYS 1414
Anti-Aging 39
Anti-Bacterial Property 394
Anti-Crease Finish 1605
Anti-Tumor Activity 728
Antibacterial 780
Antibacterial Activity 784
Antimicrobial Activity 669
Antimicrobial Properties 681
Appearance Design 1882
Ar-Dilution 264
Arc Welding 2011
Arrhenius Model 1985
Artificial Liver 789
Asphalt Pavement 1527

ASTM A743 CA6NM 1303
Asymptotic Formula 2259
Atom Transfer Radical Polymerization 12
Atomic Mobility 545, 1201
Atomic Transfer Radical Polymerization 95
AuCu20 1671
Austenite Catalytic 1173
Austenitic Stainless Steel 1298
Automotive Exhaust Clean-Up 352
Automotive Panels 1224
AWS 410 NiMo 1303
AZO Glass 439
Azoxybenzene 343
Azoxystrobin 859

B

β-Cyclodextrin 784
Back Analysis 1463
Back-Filling Method 1624
Bailong River Basin 2377
Bainite 1312
Band Gap Grading 633
Bandpass Filter 2214
Barkhausen Noise 1576
Barriers 2335
Basalt Fiber Reinforced Polymer (BFRP) 1331
Bauxite 1153
Bearing Capacity 1438
Beeswax-Chitosan Latex 1077
BEI 1485
Bellows Shape 1742
Belt Grinding 1252
Bending Properties 1451
Bending Stress 1373
Bending Vibration 1840
Bentonite 136
BGA Packages 628
Bifurcation 2120
Bilayered Perovskites 571
Bimodal Nanocrystalline Materials 400
Binding Systems 1816
Biocements 712
Bioceramics 687
Biodesulfurization 740
Biomaterial 695, 701
Biomedical Application 734
Biosurfacant 669
Biphenyldiol 3
Bipolar Membranes 248
Bis(*p*-Aminophenoxy)dimethylsilane(*p*-APDS) 67
Bittern 986
Blasting Vibration 1490
Bone Substitute 695
Botrytis Cinerea 674
BP Artificial Neural Network 2352
BP Neural Network (BPNN) 1614, 2201
Brake-by-Wire 2087
Brake Disc 2035
Brazing 1620
Break Drafting Ratio 1825
Bridge 2094
Brush Plating 1025
BSA 751
Buffer List 2318
Building Materials 2364

C

C@$ZrSiO_4$ Inclusion Pigment 170
C70250 Alloy 1168
Cable Net Structure 1351
Cache-Based Retransmission 2318
Caged Bicyclic Phosphate 17
Calcareous Shell 701
Calcium Phosphate 695, 701
Calcium Treatment 1323
CALPHAD 545, 1201, 1209
Canopy 2389
Capillary Porosity 1485
Carbide Composing 1267
Carbon-Carbon Composites 1801
Carbon Dioxide 624
Carbon Nanotube (CN) 12
Carbon Tax 2368
Carbonization 181
Carboxyl 674
Carboxymethyl Chitosan Magnetic Nanoparticles 304
Cardanol 39
Case-Based Reasoning (CBR) 1560
Cast Iron 1851, 2063
Casting 23
Casting Defect 1791
Casting Process Optimization 1845
Catalyst 145, 881

Catalytic Temperature 1173
Catalyze 1012
Cathode 447
Cathode Material 491
Cathodic Protection 1112
Cause 1851
Cavity 1666
Cavity Effects 639
$CaZrO_3$ 149
CCT 1312
CdMnTe 613
CdS 136
Ce/N Co-Doped TiO_2 529
Cellulose Diacetate 1002
Cellulose Fibers 784
Cement 1378
Cement Particles 1404
Cement Paste 1409
Cement Stabilized Gravel 1446
Cementitious Materials 1624
Center Combination Design 2135
Centrifugal Separation 1553
CeO_2 352
Ceramic 2329
Ceramic Head 770
CFD Simulation 1662
CFRC 1801
Chaotic Behavior 2120
Characteristics of Process Mineralogy 2383
Characterization 82, 687, 701, 712
Chemical Activation 868, 1624
Chemical Degradation 1556
Chemical Duplex Plating 1676
Chemical Reductive Precipitation 459
Chemical Utilization 2364
Chlorpyrifos 843
Chromium 892
Chromium Nitrite 1047
Circularly Polarization 2220
Circumference Data 2237
Cladding 1273
Clay Dosage 1433
Cleaning Machine 2094
Closed Explosion 2130
Co-Continuity 74
Co-Doped 315
Coagulation Bath 226
Coal Gangue 2364
Coarse-Grained Soil 1387
Coarsening 1184
Coated Fabric 1031
Coating 176, 1047
Coating-Substrate Structure 1999
Cobalt-Nickel 981
Coercivity 315
Cohesive Zone 400
Coiling Torque 1614
Cold Drawn 1948
Cold Metal Transfer 1769
Color Design 1882
Combined Process “Rolling-Pressing” 1918
Compabilization 39
Compacted Loess 1511
Compaction Zone Stree 1862
Comparison 1836
Compatibility 212
Component 2254
Component Analysis 1878
Components Separation 304
Composite 424, 1816, 1821, 1973
Composite Cylinder 2041
Composite Film 419, 1066
Composite Laminates 43
Composite Material 82, 154
Composite Particles 734
Composite Tubular Membrane 212
Compostie 359
Compound Chelating Agent 238
Compound Colorants 170
Compression 1742
Compressive Mechanics Properties 429
Compressive Residual Strength 43
Compressive Strength 89, 1356, 1456
Compressive Stress 255
Computational Fluid Dynamic (CFD) 1933, 2114
Concept Design Phase 2140
Concrete 1342, 1463
Concrete Beams 1468
Concrete Failure 1518
Concrete Structure 1438
Conductive Polymer 955
Conductivity 911
Cone Contact Areas 770
Conformal Mapping 127

Conformal Mapping Method 127
Conjugated Polymer 53
Connection Detect 2196
Contact Angle 233, 1077
Contact Material 486
Conversion Coatings 1082
Cooling Intensity 1720
Cooperative Energy Transfer 585
Copper 1125
Copper Alloy Strip 1168
Copper Oxygen 233
Copper Source 618
Copper Substrate 276
Core @ Shell Composite Particles 34
Core-Shell Microspheres 929
Core-Shell Polymerization 337
Core/Shell 359
Corrosion 1112, 1120, 1125
Corrosion Behavior 1102
Corrosion Inhibitor 1091
Corrosion Mechanism 1091
Corrosion Protection 1071
Corrosion Rate 1158
Corrosion Resistance 1082, 1097, 1106, 1132
Corrosion Resistant 1796
CP-MAS NMR 784
Crack 127, 1641
CrN 1047
Crosslinker Type 89
Crosslinkers 1549
Crumb Rubber Concrete 1442
Cryogenic Steels 1953
Cryogenic Treatment 1047, 1173
Crystal Growth 975
Crystal Violet 1989
Crystallization 164
CTOD 1146
Cu-Doped ZnO Film 618
Cu-Ni-Si Alloy 1102
$Cu(In,Ga)Se_2$ 197, 633
Curing Agent Content 63
Curing Kinetics 28
Curing Time 63
Cutting Parameters 1687
Cyclic Voltammetry 960
Cyclone Dust Removal 2094
Cytotoxicity Assay 757

D

Damage 1373
Damage Efficiency 2082
Damage Model 1342
Damage Tolerance Analysis 2017
Damping Effect 1490
Data Mining (DM) 2247
DDS 2230
De-Noising 2179
Decision Tree 2247
Defect 1851
Defect Analysis 1681
Deficit Irrigation 2389
Deformation 1247, 1886
Degradation 746, 1373
Degree of Substitution 992
Dehydration 1553
Depleted Uranium 509
Deposition 1066
Design of Experiment (DoE) 1801
DeST-C 1522
DEST-H 1496, 1502
Development 763
Dewatered Sludge 887
DHDPS 643
Diagnosability 2307
Diagnosis Algorithm 2307
Diamond 1676
Diamond Films 276
DICTRA 545
Die-Attach Process 1900
Dielectric 115, 119
Dielectric Property 101
Dielectric Spectroscopy 105
Diesel Engine 1857
Diesel Particulate Filter 2050
Different Drugs 746
Differential Scanning Calorimetry (DSC) 2030
Diffusion 1189
Digital Library 2298
Digital Resources Sharing 2298
Dimethyldichlorosilane 67
Dislocation 986
Dispersant 850
Dispersion 394, 1404
Disqualified Textiles 2358
Dissimilar Barrier Butt Joints 1735

Dissimilar Welded Joint 1780
Dissolution 1571
Dissolution of Graphite 1158
Distribution 613
DNA Biosensors 415
Doping 814
Down Coiler 1614
Doxorubicin 723
Drilling Parameter 1560
Drilling Speed 1560
Drive Systems 2120
Driving Path Planning 2352
Drop Test 628
Drug Delivery 322, 723
Drug Delivery System 717
Drug Release 322
Dry-Jet Wet Spinning 997
Dry Shrinkage Performance 1446
Dryer 1851
Dual Video 2209
Ductility 1414, 1456
Durability 1531
Dye 875
Dynamic Background Extraction 2286
Dynamic Bayesian 2149
Dynamic Mechanical Behavior 63
Dynamic Propertry 591
Dynamic Recrystallization (DRX) 1179

E

Early-Stage Design 2344
Economical Insulation Layer 1496
ECR-PECVD 264
Edible Mushroom 707
EDIFs 127
Effective Model 2225
Effective Power 2109
Efficiency 2160
EGR 1097
EIS 1102
Elastic Modulus 1910
Elastic Strain Behavior 115
Electorless Plating 1676
Electrical Conductivity 459
Electrical Contact Materials 459
Electrical Properties 486
Electrical Property 571
Electrical Stress 1900
Electricity Generation 2364
Electro-Spinning 123, 439
Electrocatalytic Hydrogenation 965
Electrochemical 1125
Electrochemical Activity 471
Electrochemical Characteristics 1963
Electrochemical Performances 491
Electrochemical Polymerization 955
Electrochemical Properties 364
Electrochemical Property 607
Electrode Potential 1116
Electrodeposition 960
Electrolysis 464
Electromagnetic Flowmeter 1587
Electron Back Scattered Diffraction (EBSD) 1910
Electron Beam Welding 1910
Electron Withdrawing Groups 950
Electronic Properties 529
Electronic Property 591
Electrophoretic Deposition 259
Electrostrictive 110
Elliptical Hole 127
Emissivity 2075
Empty Holes 1490
Emulsion Polymerization 734
Emulsion Stabilization 1592
Encapsulant 643
Energy Consumption (EC) 1496, 1502, 1522, 1775
Energy Control 2155
Energy Efficient Building 1423
Energy Harvesting 2160
Energy-Saving Standard 1502
Energy Transfer 207
Engine 2243
Engineering Characteristics 1387
Enrichment 864
Environment Welding 1701
Epitaxial Growth 282
EPMA 1201
Epoxy Resin (ER) 3, 63, 390, 429, 643
EPS Mixed Lightweight Soil 1382
Equal-Channel Step Matrix 1918
Equilibrium Isotherm 789
Equilibrium Separation Distance 624
Equivalent Damp Ratio 1506
Er^{3+} 585
Eriochrome Black T 834
Error Backpropagation Algorithm 1759

Error Correction 1587
Essential Oil 780
Ethanol 419
Eu 207
Eugenol 780
EVA 17
Evaluative Requirement 1973
Evodia Rutaecarpa 304
Excellence Program 2339
Excellent Engineers 2339
Expanded Graphite 424
Expansion Joint 2094
Experiment Research 1707
Explosion 2024
Extinction Coefficient 950

F

Fabrication Technique 82
Failure Analysis 628
Failure Mode 82
Failure Probability 770
FAST Engineering 1351
Fast Independent Component Analysis (FastICA) 2286
Fatigue Test 1361
Fault Diagnosis 2201, 2243
fcc Fe 545
fcc Phase 1201, 1209
Fe-Co Alloy 1201
Feature Extraction 2263
Ferric Oxide 1153
Ferro-Matrix Friction Material 1262
Ferro-Titanium 1195
Ferroelectric 110, 115, 119
Ferroelectric Properties 101
Ferroelectric Thin Film 269
Fiber Concrete 1456
Fiber Precursor 905
Fiber Reinforced Ceramic 154
Fibrillation 327
Field Emission 379
Film 238
Filtration 327
Fine Grained 1420 Al-Li Alloy 1647
Fine Layer Formation 259
Finite Element (FE) 43, 1317, 1890
Finite Element Analysis (FEA) 1511, 2125
Finite Element Method (FEM) 1331, 1653, 1836, 1886, 2041
First-Principle 529
First-Principles Calculations 591, 1209
Fixed Interference Method 136
Flame Retardant Magnesium Hydroxide 919
Flameproof Enclosure 2125
Flexural Toughness 1442
Flouride 822
Flow 2103
Flow Stress 1141
Fluorapatite 164
Fluorescence Property 901
Fluorescence Quantum Yield 950
Fluoroalkylsilane 540
Fly Ash 1428
FNR 795
Foam 1994
Food 2335
Forecast 1614
Forging 1641
Forging Technology 1179
Formation Mechanism 1086
Formation Process 187
Formic Acid Oxidation 332
Forming Accuracy 1725
Forming Limited Diagram 1609
Four Point Bending Fatigue 1290
FPGA 2230
Fracture 2054
Fracture Morphology 1163
Fracture Toughness 400
Fragility Analysis 1473
Fragments 2082
Frame Relay 2293
Free Calcium Oxide 1399
Free-Drop 628
Free Magnesium Oxide 1399
Frequency Constraint 1479
Frequency Domain 2243
Frequency Domain Spectroscopy 1958
Friction 2063
Friction Coefficient 1273
Friction Stir Welding (FSW) 1735
Frost Resistance 1419
FTIR 784
Function Fitting 1485

Functionally Graded Orthotropic Material 1999
Furnace Refining Process 1258
Fuzzy Control Strategy 2155
Fuzzy-PI 1730
Fuzzy Theory 2165

G

γ-Alumina Washcoat 981
Ga-Graded 633
GaAs 577
Gamma-Irradiation 707
GaN 656
Gas Chromatography 1567
Gas Explosion 2130
Gas Metal Arc (GMA) Welding 1873
Gas Sensor 310, 419
GCrl5 Bearing Steel 1229
Ge Film 480
Gear Steel 1323
Gel 1549
Gelatin Methacrylate Hydrogel 663
Gemini Surfactant 1125
General Arrangement 2344
Genetic Algorithm (GA) 415
Geopolymer 434, 892
Geopolymerization 892
GFRP Bars 1468
Ghana 822
Girth Welds 1747
Glass-Ceramic 164
GMA Welding Multiple Steps 1303
GMA Welding Process 1759
Gold Catalyst 343
Gold Deposit 2383
GRA 1801
Graft 12
Grain Boundary Premelting 523
Grain Size 400
Grain Yield 2389
Graphene 369
Graphene Nanosheets 364
Graphene Oxide-MnO_2 Composites 607
Graphite Felt 471
Grashof Number 409
Gray Cast Iron 1158
Green Materials 1969
Grinding 1404, 1707
Grinding Aids 1404
Grinding Ratio 1252
Grinding Roller 1868
Grooved Rolls 1918
Growth 2276
Growth Morphology 1086

H

Hand-Made Craft 1973
Hardness 459, 1229
Harris Corner 2263
Heat Loss 2075
Heat Power 509
Heat Transfer 2103
Heat Transfer Coefficient 1720
Heat Treatment 933, 1158, 1216, 1676, 1720
Heating Behavior 1694
Heating Rate 523
Heavy Forging 1641
Height Data 2237
Heteroepitaxy 656
Heterogeneous-Reinforced 218
HH-PDI 295
High Alloy Medium-Upper Carbon Steel 1173
High Capacity 496
High Entropy Alloy 1635
High Frequency Cladding 1657, 1878
High Power LED PKG 1900
High-Pressure 624
High Rate 496
High Saturation Magnetization 734
High Slurry Concentration 919
High-Speed Dry Sliding 2063
High-Speed Switching Valve 2171
Highstrength Steel 1146
Hip Joint Endoprosthesis 770
Historical Data 2179
Holding Time at Elevated Temperature 1780
Hollow Fiber Membrane 218, 226
Hollow Tiny Bead 1035
Homogeneous-Reinforced 226
Homology Modelling 795
Hot Filament Chemical Vapor Deposition (HFCVD) 276
Hot Rolling Simulation 1141
Hot Stamping 1830

Howland Current Pump 2230
HPWM 2171
HTS 2214
Hull Line 2109
Humidifier 1882
Hyaluronic Acid 322
Hybrid Battery-Supercapacitor 496
Hybrid Electrical Vehicle (HEV) 2155
Hybrid Fiber 1937
Hydration 1336
Hydraulic Control Unit 2171
Hydraulic Prop 1657, 1878
Hydrogel Microspheres 751
Hydrogen 515, 1120, 1298
Hydrogen Dilution Ratio 202
Hydrogen Flow Rate 603
Hydrogen Sulfide 310
Hydrogenation 1012
Hydrophilicity 801, 1630
Hydrothermal Crystallization 259
Hydrothermal Method 1676
Hydrothermal Modification 919
Hydrothermal Stripping 491, 1153
Hydrothermal Synthesis 347, 352, 901
Hydroxyapatite (HA) 695

I

ID3 2247
IDA 1473
Ilmenite Concentrate 1195
Image Registration 2263
Imidacloprid 850, 854
Immobilisation 892
Immobilized Cells 740
Immobilized Enzyme 674
Impedance Tube 1994
Impulse Wave 2281
Impurity Diffusion 545
In Vitro Release 746
INA-V Drafting 1825
Inclusion Chemistry 8, 243
Incoloy 800 1620
Indium Oxide 123
Indium Phosphate-Phosphite 901
Infiltration 1511
Infinite Order 2276
Influencing Factor 1017, 1490
Infrared Emissivity 1031
Infrared Microscopic 613
Infrared Stealth 1031
Initial Pressure 2130
Insertion Loss 2214
Insulation 1958
Insulator-Metal Transition 651
Insulators Detection 2184
Integral 2190
Interface Circuit 2209
Interface Reaction 1239
Interlayer 276
Intermetallics 1273
Intumescent Flame Retardant 17
Ion Implantation 1132
Ionic Liquid 997, 1002
Iron 1120
Iron Ion 1556
Iron Ladle 1886
iSIGHT 1845
Ising Model 2271
Isolated Continuous Girder Bridge 1473
Isophthalonitrile (IPN) 1012

J

Jack-Up 1112
Janus 929
Jute Fiber 1356

K

$K_2GdZr(PO_4)_3:Tb^{3+}$ 585
Kaolin 822
KAZE Algorithm 2184
Kinetic 854, 859
Kinetic Adsorption 789
Kinetics of Polymerization 1393
KNN 149

L

La 809
Laser-Induced Fluorescence 2007
Laser Shock Peening 1653
Laser Surface Carburizing 1086
Laser Welded 1451
Lateral Damage Effect 1927
Lateral Structures 599
Lattice Parameter 149
Layer-by-Layer 243
Layout Design 2344

Lead 864
LED 1985
Levenberg–Marquardt Algorithm 1873
LF 1258
Li-Ion Battery 447, 480
Life Prediction 1361
$LiFePO_4$ 480
Lifestyle 2325
Lifetime 1985
Light Transparency 639
Lightning Strike 2190
$LiMn_2O_4$ 452
Linked Vessels 2130
Lipopeptide 669
Liquid Film Width 523
Liquid-Liquid 1662
Lithium-Sulfur Batteries 369
Load Distribution 1868
Local Heating Technique 1742
Long Afterglow Phosphor 562
Long Life 496
Lost Carbonate Sintering 2054
Lost Foam Casting (LFC) 1681
Low-Cycle Fatigue 1361
Low Molecular Polyamide 651 (PA651) 63
Low-Pressure Die Casting (LPDC) 1791
LS-DYNA 2082
Luminescence 207
Luminescent Mechanism 562
Luminescent Properties 562
Lumped-Parameter Model 2140
LYTAG Concrete 1414, 1419

M

m-Xylylenediamine (MXDA) 1007
M_7C_3 Carbide 1184
M50NiL 1132
Macro Strain 1298
Macromolecular Polymer 1597
Magnesium 1666
Magnesium Alloy 1082
Magnesium Oxide 374
Magnesium Oxysulfate Hydrate 986
Magnetic 359
Magnetic Chitosan Resin 829
Magnetic Circuit Structure 1716
Magnetic Domain 1576
Magnetic Exchange Bias 315
Magnetic Field 1716
Magnetic Nanoparticles 674, 723, 734
Magnetic Properties 1234
Magnetic Property 571
Magnetization Intensity 2271
Magnetoelectric 105
Magnetron Sputtering 287
Mahalanobis Distance 1759, 1873
Mangoldt Function 2259
Manual Anthropometry 2237
Manufacturing 1937
Marine Engineering Concrete 1373
Marsh Cone Method 1409
Martensite 1312
Masonry Structure 1331
Material Parameters 1927
Material Science 1423
Material Selection 2125
Material Structure 1882
MATLAB Simulation 2201
Matrix Microstructure 2063
Matter-Element Model 1905
Mechanical Analysis 1342, 1351
Mechanical Design Parameters 887
Mechanical Press 1730
Mechanical Property 3, 74, 486, 933, 1442, 1635, 1671, 1701, 1735, 1796, 1942
Mechanical Response 1582
Mechanical Tests 1953
Mechanicl Stability 1283
Mechanism 1549, 1556
Medicinal Mushroom 707
Melt-Blown Nonwoven Fabric 1630
Melt Spinning 1163
Mesoporous Activated Carbon 868
Mesoporous Alumina Sphere 834
Mesoporous Carbon 476
Mesoporous Zirconia 343
Meta-Xylenediamine (MXDA) 1012
Metakaolin 434
Metal Foam 2054
Metal Liner 2041
Metallurgy's Effect 1258
Methacrylic Acid-Styrene-Acrylic Polyether Copolymer 854
Methacrylic Acid-Styrene Copolymer 859
Methodologies 2344

Methyl Methacrylate 776
Metrology 1567
MgO 1336
Mica 164
Micro-Channel 1662
Micro-Electroforming 1716
Micro-Genetic Algorithm 1463
Micro-Scale Abrasion 1047
Micro Strain 1298
Microalloyed Steel 1141, 1786
Microcrystalline Silicon Film 264
Microporosity 687
Microsphere 53, 145
Microstructural Changes 1303
Microstructure 23, 164, 202, 282, 379, 434, 687, 1312, 1620, 1635, 1671, 1701, 1735, 1769, 1796, 1963, 2011
Microstructure Evolution 1141
Microstructure Refinement 1641
Microtubes 123
Microwave-Assisted Synthesis 607
Microwave Heating 452, 1694, 1809
Microwave Reaction 304
Microwave Regeneration 2050
Migration 74
Mine Exploration Robot 2125
Mineral Admixture 1409, 1419
Miniaturization 2220
Minority Carrier Lifetime 603
Mitral Valve 2267
Mix Design 1527
Mn 1229
Mn^{2+} 552
Mo Content 1267
Mobile Database 2313
Mode I Crack Problem 1999
Mode of Recycling 2368
Mode of Remanufacturing 2368
Model 1840
Model Framework 2302
Modeling 1775, 1918, 2254
Modelling Method 2030
Modification 248, 643, 1017
Moisture Content 1511
Molar Volume 1201, 1209
Molecular Imprinted Film 843
Molecular Weight 1597
Molecular Weight Distribution 1597
Molten Salt Electrolysis 1189, 1195
Molten Salt Method 970, 975
Moment Invariant 2263
Monolith 981
Monolithic Column 942
Monte Carlo 2271
Montmorillonite 1017
Morphology Control 986
Morpholoy 911, 960
Movement Tracking 2267
MR Brake 2087
Mullite Whisker 975
Multi-Carboxylic Metallophthalocyanine 248
Multi-Protocol 2293
Multi-Walled Carbon Nanotubues 176
Multidisciplinary Design Optimization 1845
Multiferroic 105
Multilayer 243
Multilayer Fabric 1821
Multilayer Structure 1066
Multilevel Storage 599
Multiple Factors 1342
Multiple Principal Elements 1635
Multiwalled Carbon Nanotubes (MWCNTs) 390, 419
MWNTs 310
MWNTs-$HAuCl_4$ 310

N

Na_2SO_4 Solution 1373
NaCl Solution 1373
$NaGdF_4:Eu^{3+}$ 359
Naïve Bayesian Classifier 1857
Nali 2383
Nano-SiO₂ 434
Nano-β-$Ni(OH)_2$ 491
Nanocatalysts 352
Nanocomposite 295, 300, 337, 369, 384, 390, 394, 476
Nanofiber 327
Nanofluid 409
Nanoindentation 1910

Nanomaterial 379, 415
Nanoparticle 717, 1153, 1764
Nanorod 452
Nanostructure 695
Nanotube TiO_2 384
Nanowhisker 452
Natural 1969
Natural Frequency 1890
Natural Rubber 394
Navigation Satellite System Simulation 2302
Near-Neutral pH Stress Corrosion Cracking 1116
Net Adhesion Force 624
Net-Zero Building 1423
Network 2293
Network Coding 2318
Network Training 2201
Neural Network 1759
Ni-Cr-Mo 1209
Nickel (II) 829
Nickel Acetylacetonate 905
Nickel Base Filler 1620
Nickel-Based Superalloy 1252
NiTi 1216
Nitrile Rubber 1942
NNO 850
NO_x 1857
Nodular Cast Iron 1158
Noise Detection 2281
Non-Asbestos 1937
Non-Ballast Ship 2109
Non-Crimp 1821
Non Crimp Fabric (NCF) 1816
Non-Hydrolytic Sol-Gel Process 170, 970, 975
Non-Ideal Behavior 2160
Non-Isothermal Crystallization Kinetics 933
Non-Quenched 1179
Nontraditional Machining 1764
Nonwoven 1994
NSGA-II 1687
Nuclear Field 534
Numerical Analysis 509
Numerical Simulation 409, 1317, 1666, 1681, 1840, 2024, 2082

O

Obstacle 2352
Occurrence of Au 2383
Office Building 1522
Offshore Infrastructure 1146
Offshore Steel 1312
Oil-Gas Separator 1933
Okra Polysaccharide 757
Oleoylchitosan 717
Oligomer 955
On-Line Control 1873
On-Line Monitoring 1567
One-Dependence Classifier 1857
One-Dimensional Hexagonal Piezoelectric Quasicrystals 127
Ontology 1894
Operating Condition 1775
Optical 359
Optical Interconnection 2307
Optical Interferometry 110
Optical Multi-Mesh Hypercube Networks 2307
Optical Properties 618
Optimization 763, 1560, 1687, 2094, 2140
Optimization Design 1479, 2135
Optimum Condition 868
Optimum Proportion 1382
Optimum Synthesis Process 67
Optoelectronic Properties 950
Organic Silicon-Modified Epoxy Resin 28
Oriented Growth 505
Orthogonal Array 1801
Oxidation 875
Oxidation Desulfurization 881
Oxide Skin Defects 1168
Oxygen-Free Copper 1671

P

P-Aminodiphenylamine 955
p-Aminophenol 67
Packaging Material 2335
Paint Baking Response 1224
Paper 1851
Parabolic Trough Receiver 2075
Partially-Filled Pipes Flow Measurement 1587

Particle Size 459
Particle Size Distribution 1404
Particle Swarm Optimization (PSO) 415, 2155
Particle Swarm Optimization Algorithm 2247
Pd-Based Nanoclusters Catalysis 332
Peak Pressure 2130
Peak Temperature 1780
Pearlitic Wire 1948
PECH 419
PECVD 255
PELE 1927
Penetrating Performance 1927
Perera Approach 74
Performance 1025
Performance Deterioration 1366
Permanent Magnet Generator 1716
Perovskite 282
Perylene Dicarboximide 950
Perylenetetracarboxy Diimides 911
Pessimistic Strategy 2307
Petri Net 2254
PGLA 801
pH-Sensitive 723, 751
pH Value 2358
Phase Change Memory 599
Phase Field Crystal 523
Phase Separation 74
Phase Structure 181
Phase Transformation 1216, 1298
Phase Transition 149
Phellinus pini 728
Phenol 300
Phosphoric Acid 868
Photocatalyst 384
Photocatalytic Activity 300, 347, 529
Photocatalytic Degradation 819
Photocatalytic Properties 809, 814
Photovoltaic Array 2201
Photovoltaic Power Generation 2179
Physical Vapor Deposition 332
Physiologically Active Component 707
PID 2165
Piezoelectric 110
Piezoelectric Constant 149
Piezoelectric Properties 101
Pipeline 1747
Pipeline Steel 1116
PLA 681, 801
Plane Woven-Reinforced Laminates 2017
Plant-Mixed Hot Regeneration 1527
Plasma 1630
Plasma-Atomic Emission Spectrometer 1571
Plasmon Resonance 639
Plastic Concrete 1433
Plasticization 1002
PLGA Microspheres 746
Plugging 1549
PLZT 115, 119
POE 2196
Polar Fraction 929
Polarization Reversal 269
Poly(lactic-Co-Glycolic Acid) 717
Poly(propylene) (PP) 39
Poly(ε-caprolactone) 95
Polyacetylene 424
Polyacrylamide 1556
Polyacrylate 337, 942
Polyacrylonitrile 905, 997
Polyaniline 364
Polyaniline Fibres 960
Polyanilne Fibres 955
Polycarboxylate Superplasticizer 1393
Polycarboxylic Acid 1605
Polycrystalline Aluminium 505
Polyethylene-1,4-Buthylene Adipate Glyco 58
Polyethylenglycol Allylether 1393
Polymer 1378, 1541
Polymer Blend 8
Polymerization 776
Polypropylene (PP) 1630
Polypropylene Carbonate Polyols 58
Polypyrrole 447
Polysaccharide 728
Polystyrene 34, 95
Polytetramethyleneether Glycol 58
Polyurethane 212
Polyvinyl Alcohol 740
Polyvinyl Chloride 226
Polyvinyl Pyrrolidone 905
Polyvinylidene Difluorid 212
Porcelain 1775
Pore Structure 1366
Porogenic System 942
Porous Ceramics 822
Porous Composite 2050

Porous Defects 1754
Porous Silica Nanoparticle 322
Potassium Dichromate ($K_2Cr_2O_7$) 801
Potentiometric Electrode 136
Powder Metallurgy 1290
Power Predication 2179
Power Spectrum 1576
PP 17
Pr Addition 23
Pre-Aging 1224
Precious Metal 282
Precipitation 145, 1184, 1247
Precipitation Hardening 1173
Prediction 1468
Prediction Model 154
Preparation 728
Prepreg 1973
Pressure 1666
Pressure Bar 1825
ProCAST 1845
Process Optimization 1681
Process Parameters Optimization 1707
Product Packaging Design 1969
Profile Control Agent 1549
Progressive Damage Analysis 43
Property 997, 1229, 1747
Proportion of Mixture 1433
Protein Adsorption 663
Protein·Dimerization Interface 795
Pseudo Ductile Cementitious Composites 1456
Pseudoelasticity 1216
Pt/TiO_2 300
PTFE 1025
PTS 643
PU Composite Board 1994
Pull-Out Force 1356
PVC Geomembrane 1582
PVD 1047
Pvd Thin Films 1056
PVDF 218
PZN–PZT 101

Q

Quality 2339
Quantitative Risk Assessment 2358
Quantum Chemical DFT Methods 540
Quantum Well 534
Quicklime Treatment 887

R

R-Phase 1216
R60702 1796
Radial Basis Function Method 2098
Radius Filler 1973
RAFT 776
Rainfall 1511
Rainfall Erosivity 2377
Raman Spectroscopy 1120
Random Vibration 2160
Rare Earth Compounds 207
Rate Capability 480
RBFNN 1473
Re 1262
Reaction Bonded Silicon Carbide 176
Reactive Extrusion 39
Reader Antenna 2220
Rearrangement Mechanism 540
Recombinant Chitinase 674
Recombinant Material 1423
Recrystallization Modeling 505
Recycled Cellulose Aerogel 938
Regeneration 875
Reinforcement Technology 1438
Relaxation Function 1958
Remanufacture 2368
Renewable Resources 34, 39
Residential Building 1496, 1502
Residual Stress 1576, 1653
Resistance 2114
Resistance Heating 1830
Resources Sharing 2298
Response Surface Method 2135
Response Surface Method (RSM) 1933
Resveratrol 763
Retained Austenite 1283
RFID 2220
RhB 347
Rheological Properties 1409
Ride Comfort 2098
RIH 2075
Rise Angle 2109
Robust Design 1479
Roller Force 1862
Rolling Mill 1890
Root 2389
Root Mean Square (RMS) 1576, 1873

Rotary Viscosimeter 1409
Rotational Shell 2071
Roving Twist Factor 1825
Rubber Particles 1446, 1456
Runge Kutta Neural Network 415

S

σ Phase 1247
S' Phase 1247
Sacrificial Anode 1963
Safeguard System 2339
Safety Parameter 2030
Salt Sensitivity 89
Sand Blasting 1106
Sandwich Structure 2054
SAPO-34 Zeotype 259
Saturated Alkali Treatment 1356
Sea-Battlefield 2149
Seawater 1102
SEC-MALLS 1597
Second Phase Particle 1786
Secondary Hardening 1267
Sedimentation Behavior 1592
Seismic 1414
Selecting Models 1506
Selenization 197
Self-Assembly 53, 476, 911, 1066
Self-Energizing 2087
Self-Organized 965
SEM 276
SEM Test 1382
Semi-Analytical Method 2071
Semi-Aromatic Polyamide 933
Semi-Dieless Metal Bellows Forming Process 1742
Semi-Solid 1791
Semiconducting Property 295
Semiconductor 577
Sensor 843
Separation Efficiency 1933
Sequential Coupling Methods 2035
Service Life 1531
Servo Control System 1730
Shale Gas 1541
Shape Deviations 770
Shape Memory Alloy 1216
Shape Memory Effect 140
Shape Memory Polyurethane 140
Shapes of Products 2325
Shear Strength 1620
Sheet Cooling 1720
Sheet Metal Forming 1609, 1836
Shock Absorber 1361
Shock Wave 1653
Shock Wave Metal Foam Material 2024
Shot Coke 1809
Shrinkage 1456
Si 1229
SiC 656
Side Impact 2140
SIFs 127
Signature Resistance 2196
Silane Coating 1531
Silane Film 1071
Silica Aerogel 1042
Silica Gel 864, 875
Silicon 1764
Silicon Nitride 255
Silicon Rich Oxide 207
Silicon Thin Film 202
Silicone-Containing Diamine 67
Silk 1605
Siloxane 3
Silsesquioxanes 337
Silver Colloid 1989
Silver Nanorods 681
Simulated Seawater 1373
Simulated Seawater Environment 1366
Simulating Calculation 1463
Simulation 577, 1836, 2103, 2254, 2352
Simulation Model Portability Standard 2302
Simulation Reuse 2302
Singular Integral Equation 1999
Sintering 701
SiO_2 429
SiO_2/Na_2O Molar Ratio 434
Situation Assessment 2149
Slag 1428, 1553
Sliding Wear 1273
Slit in the Path 2220
Slow Rhythm 2325
Sludge Semi-Dry 887
Slug Flow 1662
Small Molecular 1541
SmCo Film 315

SMEDDS 763
SO_4^{2-}/ZrO_2 881
Sodium Alginate 740
Soil Erosion 2377
Soil Type 1116
Sol-Gel 374, 384
Sol-Gel Method 238, 809, 814, 819
Solar Cell 633
Solder-Bonded Interfaces 1900
Solid Oxide Electrolyzer 464
Solid-Plastic State 187
Solidification 187
Solidification Process 1666
Solubility Parameter 929
Solution Method 1468
Solvent Effect 2007
Solvothermal Synthesis 915
Sound Pressure 2071
Southeast Asian 2298
Spark Erosion 1764
Spatial 2377
Specific Wear Rate 1273
Spectral Characteristics 585
Spin Dephasing 534
Spiral Bevel Gears 1707
Spray 1720
Spray Formed 1754
Sputtering 197
Square Residue 2259
Squeeze Casting 1666
$Sr_4Al_{14}O_{25}:Eu^{2+}$ 562
SSOS 992
Stainless Steel (SS) 1097, 1720
Stainless Steel Sheet 1769
Standard Mean Filter 2281
Starch 74
Steam 464
Stearic Acid 233
Steel 2011
Steel Adding Storey 1506
Steel Plate 1146
Steel Slag 1399
Step Response 2196
Stepped Impedance Comb Line 2214
Stereo Display 2209
Stiffness Degradation 43
Stitch-Free Fabric 1821
Strain 1342
Strain Analysis 1609
Strained Silicon 255
Strength 1433
Strength and Deformat 1387
Strengthening 1331
Strengthening Mechanism 1647
Stress 1886, 2011
Stress Field 2035
Stress-Strain Relationship 1582
Stress-Strain State 1918
Strip Cooling 1720
Strontium Titanate 464
Structural Studies 1953
Structure 287, 315, 577, 757, 997, 1025, 1336, 2313
Structure Directing Agent 901
Structures 1747
Student Consumer Group 1882
Submerged Arc Welding Filled with Ni Wire 1780
Submersible Screw Pump 1942
Substrate Effect 264
Substrate Roughness 202
Substrate Temperature 287
Sulfide Inclusions 1323
Sulfide Ion 136
Sulfur 369
Super-Capacitor (SC) 607
Super-Hard Cutting Tools 1894, 1905
Superabsorbent 89
Supercapacitors 364
Supercharged Boiler 2165
Superconducting 1234
Supercritical CO_2 1541
Superheater 2103
Superhydrophobic Surface 233
Superhydrophobicity 1042
Superplastic Forming 1647
Surface-Enhanced Raman Scattering 1989
Surface Integrity 1252
Surface Layer Behavior 1707
Surface Metallization 1676
Surface Modification 801, 1816
Surface Morphology 452
Surface Passivation 603
Surface Roughness 1252
Surface Sizing 992
Surface Transition Layer 269
Surface Treatment 1071

Surfactant 624, 1541
Surrogate Model Method 2098
Suspension System Parameters Optimization 2098
Sweeping Constant Current Source 2230
Swelling 929
Swelling Behaviour 751
Swelling Properties 1942
Symmetrical Architecture 2196
Synergetic Effect 1518
Synthesis 712

T

Taguchi Method 1801
Tailored Properties 1830
Taylor's Series 1479
Te Inclusions 613
TEM 656
Temperature 1189, 1701, 1985
Temperature Decentralization 1267
Temperature Effect 2007
Temperature Field 1317, 1657, 2035
Tempered Steel 1179
Tempering 1146
Tempering Hardness 1173, 1267
Tempering Treatment 1830
Temporal Distribution 2377
Tensile Curve 1163
Tensile Properties Simulation 2017
Tensile Property 23, 1456
Tensile Strength 1468
Tensile Stress 255, 770
Tensile Test 1283
Test 1851
Tetragonality 119
Textile Reinforcement 1816
Texture 505, 1910, 1948
Thermal Conductivity 154
Thermal Degradation 3, 17
Thermal Fatigue Cracks 1905
Thermal Fatigue Knowledge 1894
Thermal Fatigue Life 2035
Thermal Mechanical Coupling Mechanism 2041
Thermal Parameter 1463
Thermal Reactive Material 2030
Thermodynamic Property 591
Thermodynamics 854, 859, 1239
Thermodynamics Calculation 1323
Thermographic Analysis 1303
Thermoplastic Slurry 187
Thickener 1035
Thickening Agents 1541
Thickness Reduction Rate 1609
Thin Film 282, 651
Thin-Film Solar Cells 197
THPC 1017
Threshold 2281
TI-35Nb-7Zr-5Ta 1290
Ti-Ni-Cu Alloy 1163
TiC 1262
TiFe 1189, 1195
$TiFe_2$ 1189, 1195
Time Domain 2243
Time-History Analysis 1331
Time-Resolved Kerr Rotation 534
TiN 1056
TiO₂ 819
TiO_2 Nanotube 965
Titanium 476, 1086
Titanium Alloy 1086, 1106, 1910
Titanium Concentrate 1189
Titanium Dioxide 809, 814
Titanium Surface Modification 663
TMCP 1146
Tool-Path 1725
Torque Analysis 2087
Total Resistance 2109
Toughness Strengthen 181
Toxin 789
Traditional Chinese Decorative Patterns 2329
Training 2339
Transformation 1173, 1267
Transformer 1567, 1958
Transition Width 1780
Transmission 639
Transmission Electron Microscopy (TEM) 12, 352
Transmission Line 2184, 2190
Transparency 1042
Transportation 2247
Transverse Flux Permanent Generator 2135

Trap 552
Traveling Heater Method 613
Triaxial Test 1387
Tribological Property 1066
Tricalcium Silicate 1336
TRIP Effect 1283
Tungsten Fiber Composite Jacket 1927
TURBISCAN 1592
Turning Depth 1840
Turning Work-Piece 1840
Two-Dimensional Braid 218
Two-Layer Film 419
Two Point Incremental Forming 1725

U

ULTP 1047
Ultra-Fine Carbide 1267
Ultra High Frequency 2220
Uncertain Parameters 1479
Uncertainty 1567
Unconfined Compressive Strength 1382
Uniaxial Tension Test 1582
Unidirectional Solidification 1317
Urea 145
Urushiol 34
Utilization 2364
UV Light Sensing 123

V

V Contents 1267
Vacuum Annealing 1796
Vanadium-Bearing Titanomagnetite 1262
Vanadium Oxide 651
Vanadium Redox Flow Battery 471
Vapor-Liquid Equilibrium 1007
Vector Valued Dirichlet Series 2276
Vehicle Collision Avoidance 2352
Vehicle Lateral Stability 2171
Vented Explosion 2130
Vertical Roller Mill 1862, 1868
View Angle Deviation 2237
Viscous-Plastic State 187
Visible Quantum Cutting 585
Void 1900
Volume Fraction 1283
Volume Stability 1399

W

W/C 1485
Warp Knit Fabric 1821
Water 843
Water Absorption 938
Water Contamination 822
Water-Cooled Stool 1317
Water Cooling 1720
Water Flux 212
Water-Granulated Nickel Slag 1624
Water Level Controller 2165
Water Permeability 1456
Water Vapour Transmission Rate 1077
Waterborne Polyurethane 58
Waterproof 1531
Waterproof Coating 1378
Wave Glider 2114
Wavelet Transformation 2190
Waviness 82
Weapon-Grade Uranium 509
Wear 1056, 2063
Web-Core Steel Sandwich Plate 1451
Wedge Mechanism 2087
Weibull Distribution 1862
Weld Thermal Cycle 1786
Weld Width 1451
Welding 1146
Welding Parameters 1769
Welding Procedures 1747
Wet-Dry Cycle 1366
Wheel 1791
Whiskers 970
Wide-Stopband 2214
Wigley Hull 2114
Wilson Equation 1007
Winter Wheat 2389
Wire Medium 2225
Wireless Network 2318
WO_3 809
WO_3 Nanoplates 347

X

X-Ray Diffraction (XRD) 2011
X60 1116
X80 1747
XPS 1125
XRD 1120

Y

Y_2O_3 Doping 181
Yarn Quality 1825
Yb 207

Z

Zinc Organophosphonate 915
Zinc Oxide 394
Zircon 970
Zirconium Content 1571
Zirconium Powder 1571
Zn_2GeO_4 552
ZnO Nanofibers 439
ZnO Thin Films 287
ZnO: (Al, In) 1031
ZnS 295, 379
ZrN 1056
ZrO_2 181

Authors Index

A

Aad, E.A. 1953
Abbaspour, M. 409
Abdelkhalek, H. 2344
Adachi, S. 534
Adeborna, S. 822
Akhmaltdinov, R. 577
Aldlemey, M.S. 1158
Amaonova, A. 577
An, L.Q. 486
An, N.S. 295
An, T.B. 1273
An, Y.H. 1234
Araújo, J.A. 1047, 1056, 1290
Ashiuchi, E.S. 1047

B

Bai, J. 164
Bai, J.Q. 681
Bai, K. 2179
Bai, W. 843
Bai, W.B. 53
Bao, L.F. 1189, 1195
Bao, S.G. 2063
Bao, X.H. 1716
Bao, Y. 238
Bao, Y.Z. 1179
Bao, Z.R.G.T. 343
Barbosa, T.D. 1047
Bardl, G. 1816
Bi, X.Y. 1716
Bi, Z.C. 1146
Bian, K.F. 1490
Boumerzoug, Z. 2011
Bouquerel, J. 1953
Bu, S.F. 429
Bychkov, E. 1953

C

Cai, C.B. 1576
Cai, J. 1442
Cai, Y. 1502
Cai, Z.S. 58, 1042
Camargo, N.H.A. 687, 695, 701, 712
Cantwell, W. 2054
Cao, G.Y. 1035
Cao, J. 1725
Cao, K. 1125
Cao, W.Q. 1283
Cao, Y. 1342
Cao, Y.F. 992
Chabicovsky, M. 1720
Chandraraj, N. 656
Chang, J.J. 681
Chang, L. 1560
Chang, Q. 2302
Chang, W.H. 434
Chang, Y.Y. 439
Chatraphorn, S. 633
Chavarette, F.R. 2160
Chayasuwan, D. 164
Che, J.X. 269
Chen, B.L. 34, 929, 1473
Chen, B.Y. 780
Chen, C.Z. 1086
Chen, G. 74, 1845
Chen, G.R. 1463
Chen, G.S. 2041
Chen, H. 233, 529, 1701
Chen, H.W. 780
Chen, H.Z. 1681
Chen, J. 819
Chen, J.B. 1378
Chen, J.H. 1451
Chen, J.J. 1120
Chen, J.L. 459, 887
Chen, J.M. 255
Chen, J.Y. 892, 1479
Chen, L. 491, 1153, 1336, 1653, 1836
Chen, L.C. 618
Chen, L.X. 67, 643
Chen, M. 2344
Chen, M.A. 1786
Chen, P. 1017
Chen, Q.H. 34, 39, 929
Chen, R.L. 1323

Chen, R.Y. 248
Chen, S. 123, 2352
Chen, S.H. 3, 1071
Chen, T. 170, 746, 751, 975
Chen, W. 571
Chen, W.L. 197
Chen, W.S. 1620
Chen, W.T. 859
Chen, X. 628
Chen, Y. 332, 728
Chen, Y.B. 1132
Chen, Y.H. 639
Chen, Y.J. 933, 1630
Chen, Y.L. 295
Chen, Z.J. 233
Chen, Z.P. 1168
Chen, Z.Q. 515, 2209
Cheng, H. 264, 434
Cheng, H.M. 997
Cheng, N.P. 515
Cheng, S.L. 1258
Cheng, T.C. 1312
Cheng, X.F. 2094
Cherif, C. 1816, 1821
Chirapatpimol, K. 110, 119
Chokethawai, K. 110, 119, 2007
Chu, F.Y. 1387
Chu, H.Z. 1687
Chu, I.T. 2030
Chu, Y.Q. 471
Chuang, Y.C. 1994
Chumprasert, L. 101, 115, 119
Code, F. 1720
Cui, F. 1735
Cui, H.X. 2335
Cui, L. 269, 1635
Cui, L.Y. 322
Cui, R. 434
Cui, X.F. 1025
Cui, X.Z. 1527
Cui, Y.H. 2130
Cui, Y.Q. 751, 1780

D

da Costa Ferreira, D. 2160
da Costa, B.D. 687
da Silva, D.F. 712
da Silva, E.P. 1216
Dai, C. 834
Dai, J.J. 1086
Dai, L. 1468
Dai, M.J. 276
Dalmônico, G.M.L. 695
Dang, P. 1796
Dangerfield, R. 352
Davarani, S.M.H. 259
de Carvalho, G.C. 1303
de Moraes, A.N. 687
Deng, J.J. 1373
Deng, L.Y. 233
Deng, R. 2114
Deng, W.L. 1262
Deng, W.X. 28
Deng, Y.T. 1393
Deng, Y.X. 2267
Deng, Z. 887
Deng, Z.Q. 379
Dewael, D. 1953
Diao, X.Z. 809, 814
Dias, F.C. 1056
Digheche, K. 2011
Ding, H.X. 359
Ding, J.D. 95
Ding, L. 986, 2267
Ding, W.P. 789
Ding, W.W. 887
Ding, Y. 2149
Ding, Y.H. 304, 429
Döbrich, O. 1821
Dong, C. 784
Dong, C.W. 1890
Dong, G.M. 2230
Dong, G.X. 12
Dong, H. 1283
Dong, H.Z. 1681
Dong, J. 2196
Dong, L.H. 1102
Dong, L.L. 1989
Dong, Q.Y. 2196
Dong, S.Q. 509
Dong, W.G. 1485
Dong, Y. 669
Dong, Z. 1894, 1905
Du, P. 1342
Du, Q. 1851
Duan, M.X. 763

Duan, Q. 322, 681
Duan, W.F. 950
Duan, W.Y. 2114
Duan, Y.W. 282, 607
Duan, Y.X. 1973
Duong, H.M. 938
Duponchel, B. 1953

E

Efavi, J.K. 822
Ejaz, A. 1120
El Kady, H. 2109
Elhadad, A. 2114
Elmi, N. 1423

F

Fan, G.C. 2190
Fan, L.Y. 643
Fan, T.F. 854
Fan, Y.H. 233
Fan, Z. 1541, 1927
Fan, Z.L. 226
Fang, F. 1948
Fang, F.R. 669
Fang, J.Z. 176
Fang, L. 394
Fang, M.H. 801
Fang, Q.Q. 315
Farooq, A. 1764
Fatemi, S. 259, 384
Fei, H.M. 1560
Fei, L. 2313
Feng, G. 238, 970, 975
Feng, J.D. 938
Feng, J.G. 850, 854, 859
Feng, K.Q. 1262
Feng, L. 1624
Feng, M.J. 343
Feng, Q.G. 1825
Feng, S.Q. 1635
Feng, X.S. 1735
Feng, Y.N. 1071
Ferreira, J.L.A. 1290
Finstad, T.G. 207
Fobil, J. 822
Franco, A.H. 1290
Franczak, P.F. 687, 695, 701, 712
Frangis, N. 656
Fu, J.W. 390
Fu, K.L. 975
Fu, X. 2247
Fuis, V. 770
Furushima, T. 1742

G

Gan, H.L. 212
Gan, W.J. 95
Gao, A.L. 1730
Gao, B. 1927, 2024
Gao, B.X. 950
Gao, C.H. 986
Gao, D.Y. 789, 1433
Gao, G.M. 1082
Gao, H.T. 347
Gao, J.G. 3, 337
Gao, K. 434
Gao, K.W. 1132
Gao, L.G. 2109
Gao, L.S. 643
Gao, P. 1179
Gao, R. 1361
Gao, Z.J. 1527
Gao, Z.Y. 1730, 2135
Ge, J.J. 1042
Ge, Q. 2201
Gebril, M.A. 1158
Gemelli, E. 687
Ghanavati, S. 1423
Gishin, M.J. 409
Gkanatsiou, A. 656
Gong, K.R. 1273
Gong, L.J. 669
Gong, W.T. 2293
Gong, X.M. 1201
Gou, G.Q. 1701
Gu, G.R. 287
Gu, J.Y. 255
Gu, Y.Y. 740, 1809
Guan, W.Q. 674
Guo, A.R. 603
Guo, C.F. 1894, 1905, 1933
Guo, G.L. 2383
Guo, H.J. 1035
Guo, J.J. 1091
Guo, L. 2220
Guo, L.F. 1999

Guo, L.J. 1735
Guo, L.S. 2325
Guo, N. 740, 881
Guo, W. 154
Guo, X.Y. 850
Guo, Y.Q. 181

H

Haider, F.I. 1158
Han, C.H. 63
Han, D.F. 2109, 2344
Han, H.Z. 3
Han, X.L. 1522
Han, Z. 2196
Han, Z.R. 1609
Han, Z.Y. 269
Hany, S. 1953
Hao, A.M. 591
Hao, H. 850, 854, 859
Hariri, S. 1953
He, B.H. 784
He, G.F. 868
He, J. 603
He, J.H. 929
He, M. 1446
He, S.X. 310
He, W.J. 1163
He, X.D. 1747
He, X.J. 1468
He, Y.G. 1179
He, Y.L. 545, 1184, 1201, 1209
Heng, C.L. 207
Henrique Cerqueira Costa Basquerotto, C. 2160
Henriques, V.A.R. 1056
Herrera, P. 1216
Hnizdil, M. 1720
Hojo, M. 140
Hong, W. 1112
Hosaka, S. 599
Hou, B.R. 1125
Hou, H.J. 276
Hou, H.L. 1647
Hou, H.T. 2302
Hou, Y.F. 740, 881, 1809
Hou, Y.K. 1373
Houfek, L. 2120
Houfek, M. 2120
Hu, B. 2389
Hu, C.Y. 1091
Hu, H. 1666
Hu, H.H. 1725
Hu, H.Y. 255
Hu, J. 327, 1283
Hu, L.M. 1433
Hu, M.M. 424
Hu, Q.Q. 1378
Hu, S.B. 1910
Hu, T.T. 523
Hu, X.B. 496
Hu, X.X. 545
Hu, X.Y. 218, 226, 2358
Hu, Y.Y. 248
Hu, Z.F. 552
Huan, G.L. 218, 226
Huang, C.H. 1994
Huang, C.Y. 1312, 2201
Huang, D.Y. 434
Huang, H.B. 34
Huang, J. 613
Huang, J.H. 1994
Huang, L.P. 304
Huang, N.B. 1963
Huang, Q.L. 226
Huang, S.H. 1224, 1247
Huang, S.J. 707
Huang, W.T. 2030
Huang, X.B. 28
Huang, X.F. 2263
Huang, X.l. 1132
Huang, X.Z. 304
Huang, Y. 1252
Huang, Y.D. 480
Huang, Y.T. 1234
Huang, Y.Y. 2063
Huang, Z.G. 480
Hui, Q. 515
Huo, D. 452, 459

I

Iskakova, K. 577

J

Jabbari, Z. 259
Janicek, P. 770
Ji, J.H. 2237

Ji, V. 2011
Ji, Z.G. 562
Jia, L.Q. 1676
Jia, M.L. 343
Jia, Q. 1258
Jia, R.Q. 2125
Jia, S.L. 2237
Jia, X. 1989
Jiang, C. 2358
Jiang, J.C. 2130
Jiang, J.P. 2094
Jiang, K.Y. 1694
Jiang, N. 950
Jiang, P. 1351
Jiang, Q.Q. 1153
Jiang, T.Q. 95
Jiang, T.T. 202
Jiang, W. 723, 734
Jiang, W.H. 170, 238, 970, 975
Jiang, X.H. 1862
Jiang, X.X. 1451
Jiang, Y. 429, 2368
Jiang, Y.B. 327
Jiang, Y.D. 310, 419, 603, 651
Jin, G. 1025
Jin, J. 1132
Jin, P. 1900
Jin, Q. 1527
Jin, T. 2286
Jin, X.D. 2103, 2165
Jin, Z.Q. 1531
Jing, M.X. 145

K

Kacem, H. 1953
Kais, A.A. 1953
Kaji, R. 534
Käppler, I. 1816
Kim, I.S. 1759, 1873
Kim, Y.S. 1759, 1873
Kong, X.H. 43
Kong, Z. 562
Kotra, M. 505
Kou, S.W. 1091
Krishna Sastry, K.V. 1801
Kuo, D.H. 197

L

Lan, L.F. 1239
Lan, L.L. 287
Lan, Q. 2259
Larki, A.N. 1423
Larwongsa, P. 115
Lee, C.C. 2050
Lee, J.H. 1759, 1873
Lee, J.P. 1759, 1873
Lee, K.L. 618
Lei, C.X. 332
Lei, M. 332
Lei, Q. 1102
Lei, X.R. 892
Lei, Z. 1331
Leszczynski, M. 656
Leung, C.K.Y. 1456
Levandowski, N. 695, 701, 712
Lezhnev, S. 1918
Li, A.L. 1361
Li, B.S. 955, 960
Li, C.D. 2271
Li, C.H. 740, 1273
Li, C.L. 1796
Li, C.M. 942
Li, C.N. 1496, 1502, 1522
Li, D. 2184
Li, D.S. 1985
Li, D.Y. 2075
Li, F.F. 347
Li, F.P. 864
Li, G.C. 843
Li, G.F. 1116
Li, G.H. 1428
Li, H. 2307
Li, H.B. 1490
Li, H.D. 901, 915
Li, H.J. 212, 1716
Li, H.M. 2364
Li, H.P. 1025
Li, H.Q. 1168
Li, H.T. 1671
Li, J.C. 1209
Li, J.G. 315, 459
Li, J.J. 1473
Li, J.S. 2030
Li, K.Q. 1624

Li, L. 1035, 1184, 1969, 2247, 2329
Li, L.H. 1234
Li, L.J. 919
Li, M.L. 2035
Li, M.X. 1106
Li, P.G. 1234, 1399
Li, P.W. 394
Li, Q. 2209, 2302
Li, R.Y. 269
Li, S. 1560
Li, S.C. 1531, 1840
Li, S.K. 1933
Li, S.Y. 1086
Li, T.Y. 1071
Li, W. 603
Li, W.B. 2263
Li, W.W. 471, 1851
Li, W.X. 776
Li, W.Z. 95, 1851
Li, X. 17, 127, 343, 795, 1999
Li, X.D. 459, 1317
Li, X.H. 2247
Li, X.W. 1224, 1247, 1754
Li, X.Y. 911
Li, X.Z. 1910
Li, Y. 992, 1262, 1485, 1886, 2054
Li, Y.G. 1012
Li, Y.H. 322, 681
Li, Y.J. 1234
Li, Y.P. 2267
Li, Y.Q. 1035
Li, Y.X. 1937
Li, Y.Y. 717
Li, Z. 1102, 2179
Li, Z.G. 1451, 1707
Li, Z.H. 1224, 1247, 1754
Li, Z.K. 1862
Li, Z.W. 1694, 2383
Liang, C.H. 1963
Liang, M.H. 1747
Liang, W. 585
Liang, X.Y. 613
Liang, X.Z. 1687
Liang, Y.F. 1173, 1267
Liang, Y.Y. 746, 751
Liao, M. 359
Liao, S.C. 1404
Limpichaipanit, A. 105, 110, 115, 119
Lin, C.P. 2030
Lin, G.F. 843
Lin, H. 1404
Lin, H.M. 905
Lin, J.H. 34, 39, 53, 929
Lin, K.L. 434
Lin, Q.Q. 1106
Lin, W.I. 8, 243
Lin, W.P. 1747
Lin, Y.B. 480
Lin, Z. 1857
Lin, Z.J. 459, 496
Lioutas, C.B. 656
Liu, A.J. 728
Liu, B. 1106, 1657
Liu, C.D. 2383
Liu, C.H. 728
Liu, C.M. 1614, 2339
Liu, C.Y. 8, 243
Liu, D.H. 1479
Liu, F.S. 717
Liu, G.F. 1173, 1267
Liu, G.G. 1366
Liu, G.J. 347
Liu, G.Q. 639, 763
Liu, G.X. 123
Liu, H. 176, 834
Liu, H.L. 218, 226
Liu, H.W. 1224, 1247, 1754
Liu, H.X. 1571
Liu, H.Y. 58
Liu, J. 491, 1153, 1878
Liu, J.M. 170, 238, 970, 975
Liu, K.G. 1676
Liu, L.Z. 123
Liu, M. 881, 2318
Liu, M.H. 1937
Liu, M.Z. 89
Liu, N. 1002
Liu, P.F. 1511
Liu, Q.Y. 1438, 1446
Liu, R.W. 1549, 1556

Liu, S.H. 459
Liu, S.L. 123, 202
Liu, T. 1102
Liu, T.C. 1428
Liu, W. 868, 1900
Liu, W.J. 850, 854, 859
Liu, X.H. 2087
Liu, X.L. 332
Liu, X.M. 1438
Liu, X.W. 202
Liu, Y. 1701, 2230, 2352
Liu, Y.C. 1994
Liu, Y.G. 400
Liu, Y.H. 12
Liu, Y.J. 476
Liu, Y.L. 707
Liu, Y.Q. 1490
Liu, Z.B. 607
Liu, Z.L. 992, 2035
Liu, Z.Q. 639, 919, 1592, 1597
Long, X.H. 1473
Long, Y.F. 763
Long, Y.Z. 123
Lou, D.C. 154
Lou, J.J. 1527
Lu, B. 1120
Lu, J. 2071, 2335
Lu, J.H. 2383
Lu, J.S. 1097
Lu, M. 248
Lu, Q.S. 1097
Lu, W.C. 2276
Lu, X.G. 545, 1184, 1201, 1209
Lu, X.Z. 439
Lu, Y.L. 523
Lu, Z.P. 1120
Luo, H.Y. 1567, 1958
Luo, K.W. 434
Luo, L.L. 864
Luo, N.H. 1428
Luo, Y. 1479
Luo, Z. 145
Lv, M.Z. 394
Lv, Q.F. 1511
Lv, X. 2171
Lv, X.L. 1433
Lv, X.R. 1942

M

Ma, A.B. 1366
Ma, B. 1635
Ma, C.A. 471, 965
Ma, C.F. 2075
Ma, C.M. 780
Ma, J. 2041
Ma, J.S. 1239
Ma, L.X. 2087
Ma, Q.X. 1641
Ma, Q.Y. 540
Ma, S.H. 1336
Ma, S.W. 369
Ma, W.B. 2098
Ma, Y.Q. 1173, 1267
Ma, Z. 1399
Magadoux, E. 1720
Mahdavinejad, M. 1423
Man, T.H. 1179
Manabe, K. 1742
Mano, Y. 1298
Mao, J.K. 154
Mao, Z.P. 1031
Matthäi, P. 1821
Mau, J.L. 707
Meesuk, L. 136
Melo, T.F.O. 1047
Meng, J. 864
Meng, Q.L. 1769
Meng, X. 1361
Mi, X.D. 400
Miao, L.F. 170, 970, 975
Miao, Z. 1082
Milochova, M. 1953
Min, G.H. 1163
Min, J.H. 613
Min, L.J. 757
Ming, P.M. 1716
Ming, X.Z. 1707
Mirzaei, M. 409
Mou, Q.P. 1809
Mouftiez, A. 1953
Mu, H. 523
Mu, Y. 1378
Muterlle, P.V. 1056, 1216, 1290, 1303
Myoung, P.C. 149

N

Ngamjarurojana, A. 101, 105, 110, 115, 119, 2007
Nguyen, S.T. 938
Nie, X.L. 1882, 1969
Ning, C.Y. 663
Ning, H.L. 1239
Ning, H.X. 1894
Ning, L. 1882
Nishikawa, M. 140
Niu, L.F. 585
Niu, L.Y. 1769

O

Ou, Y.X. 17
Ouyang, C.Y. 1882, 1969, 2329

P

Pakdehi, S.G. 981
Pan, H. 1066
Pan, H.P. 207
Pan, H.X. 2243
Pang, C.M. 1366, 1373, 1456
Panin, E. 1918
Park, M.H. 1759, 1873
Pei, Y.Y. 789
Peng, B. 439
Peng, D.L. 332
Peng, J. 1035
Peng, J.B. 1239
Peng, J.W. 28
Peng, L.J. 1071
Peng, Z.J. 1239
Peruzzi, N.J. 2160
Polychroniadis, E.K. 656
Popov, V. 415
Poupin, C. 1953
Promjun, T. 101, 105, 2007
Prystawko, P. 656
Pu, M.L. 723, 734
Pu, R. 819

Q

Qi, J.J. 379
Qi, T.S. 746, 751
Qi, X.X. 1258
Qi, Z. 1857
Qian, L.Y. 784, 1077
Qian, Y. 965
Qian, Y.C. 264
Qiao, J.S. 1451
Qin, H.G. 1366, 1373
Qin, J. 28
Qiu, H. 1356
Qiu, Q.Q. 965
Qiu, T. 562
Qiu, W.Q. 276
Qiu, Z.Y. 269
Qu, H.D. 2179
Qu, J.T. 1331
Qu, W.Q. 1671
Quan, H.W. 2263
Quan, P.L. 255
Quan, Q. 218

R

Ramazanova, G.I. 187
Rao, V.S. 1801
Rasoolzadeh, M. 981
Raudensky, M. 1720
Ren, J.Z. 1825
Ren, K. 2196
Ren, X.Q. 207
Ren, Y. 58
Rong, H.Q. 905
Rui, D. 2286
Rui, Q. 2098

S

Sakdanuphab, R. 633
Salimi, M. 981
Salminen, P. 74
Santos, M.T. 1303
Sasaki, O. 1742
Sattinova, Z.K. 187
Schneider, M.S. 701
Sha, L. 1382
Shan, F.K. 123
Shan, Z.D. 1681
Shang, Q. 746, 751
Shang, X.M. 2237
Shao, H.L. 2335
Sharp, S. 352

Shen, B. 1141
Shen, F. 1468
Shen, H. 2024
Shen, H.L. 1567, 1958
Shen, J. 374
Shen, M. 613
Shen, M.G. 1317
Shen, P. 613
Shen, X.D. 1336
Shen, X.Q. 145
Shen, Y. 2054
Shen, Y.Q. 723, 734
Shen, Y.Y. 1102
Sheng, X.Q. 2225
Shi, J. 1283
Shi, J.S. 2209
Shi, M.T. 868
Shi, R.M. 1189, 1195
Shi, Y. 911
Shiao, C.C. 780
Shiue, R.K. 1312, 1620
Shu, B. 255
Shu, G.P. 1506
Shu, W. 226
Shu, X.F. 628
Shu, Y.M. 1582
Silva, C.R.M. 1047, 1056, 1290
Silva, D.F. 695, 701
Somwan, S. 110
Song, C.Y. 2271
Song, H. 829
Song, J.G. 295
Song, J.J. 255
Song, L.H. 424
Song, N. 176
Song, S.Q. 1433
Song, W. 2225
Song, X.C. 1735
Song, X.X. 919
Song, Z.Y. 2125
Soroodan Miandoab, E. 384
Soyama, H. 1298
Steier, V.F. 1047
Su, C. 447
Su, W.Y. 207
Sui, W. 1527
Sukprasong, S. 101, 2007
Sun, B.J. 1541
Sun, C.L. 1234
Sun, C.N. 1830
Sun, H.C. 728
Sun, H.Y. 1125
Sun, M.D. 1361
Sun, N. 1506
Sun, Q.R. 1549
Sun, S.J. 789
Sun, W. 1456
Sun, W.C. 1541
Sun, W.H. 1146
Sun, X. 607
Sun, X.D. 459
Sun, Y.P. 1886, 1890
Sztwiertnia, K. 505

T

Tada, K. 1742
Tai, H.L. 419
Tai, Y.H. 2209
Takakuwa, O. 1298
Tan, D. 276
Tan, F.Z. 992
Tan, G.X. 663
Tan, L. 1179
Tan, Y. 663
Tang, C.W. 992
Tang, J. 2281
Tang, K. 613
Tang, W. 2281
Tang, W.H. 1234
Tang, W.Z. 1527
Taniguchi, S. 2050
Tao, B.L. 424
Tao, C. 2140
Tao, S. 892
Teng, S.H. 1066
Thuy, D.T.T. 2298
Tian, B.J. 337
Tian, C.C. 58
Tian, H. 476
Tian, L.H. 287
Tian, L.M. 2377
Tian, N. 834
Tian, Q.Y. 2313
Tian, R.Q. 751
Tian, S.F. 400
Tian, W. 2313
Tian, Y.F. 1393
Tian, Y.N. 2237

Tian, Y.Y. 834
Tian, Z.L. 1273
Toivakka, M. 74
Tolochko, O. 1163
Tong, H. 1485
Tong, K. 1747
Tong, Z.B. 2184
Tsai, M.H. 1994
Tsai, S.Y. 707, 2030
Tseng, J.M. 2030
Tu, J. 868
Tu, Y.C. 197

U

Udomphan, K. 136

V

Villamarin, E.B. 1216
Vogt, J.B. 1953

W

Wan, C.D. 1894, 1905, 1933
Wan, M.H. 552
Wang, B.Q. 801
Wang, C. 3, 315, 337, 552
Wang, C.G. 1701
Wang, C.X. 986
Wang, D. 933, 1630
Wang, D.D. 315
Wang, D.M. 1404
Wang, D.Y. 434
Wang, F. 374, 1224, 1247, 1694, 1754
Wang, F.P. 776
Wang, G. 1496, 2377
Wang, G.C. 1382
Wang, G.F. 1234
Wang, H. 663
Wang, H.B. 562
Wang, H.D. 970, 975
Wang, H.L. 1973
Wang, H.M. 1522, 1942
Wang, H.P. 997, 1002
Wang, H.T. 486
Wang, H.Y. 295, 2098
Wang, J. 1153, 1446
Wang, J.B. 8, 332, 2094
Wang, J.C. 1017
Wang, J.H. 82
Wang, J.J. 1184
Wang, J.Q. 486, 1106
Wang, K. 1393
Wang, L. 63, 613, 1239, 1342, 1366, 2094, 2318
Wang, L.J. 613
Wang, L.S. 332
Wang, M. 1229
Wang, M.Y. 1184
Wang, M.Z. 1845
Wang, N.Q. 591
Wang, Q.C. 1725
Wang, Q.L. 2098
Wang, Q.Z. 776
Wang, R. 1791
Wang, R.G. 352
Wang, S.C. 843
Wang, S.J. 1942
Wang, S.M. 2135
Wang, S.S. 1963
Wang, T. 509
Wang, W. 1764
Wang, W.H. 728
Wang, W.Q. 1769
Wang, X. 1336
Wang, X.G. 1404
Wang, X.H. 819, 1007
Wang, X.L. 1635
Wang, X.M. 1701
Wang, X.S. 552
Wang, X.Y. 491, 1153
Wang, Y. 603, 1025, 1331, 1662, 1796
Wang, Y.H. 552, 585, 843
Wang, Y.J. 1496, 1502
Wang, Y.L. 509
Wang, Y.M. 491, 728, 933, 1630
Wang, Y.P. 933, 1630
Wang, Y.Q. 1647
Wang, Y.R. 300, 624
Wang, Y.X. 834
Wang, Z. 145
Wang, Z.G. 1614
Wang, Z.H. 905
Wang, Z.J. 43

Wang, Z.M. 1506
Wang, Z.S. 1576
Wei, C.B. 276
Wei, H.M. 950
Wei, K.X. 1587
Wei, L.H. 1518
Wei, M.Y. 2358
Wei, S. 1985
Wei, W. 2286
Wei, W.G. 2017
Wierzbanowski, K. 505
Wongchaisuwat, A. 136
Wroński, M. 505
Wu, B.J. 287
Wu, C. 1317
Wu, C.G. 2094
Wu, C.S. 1786
Wu, C.Z. 585
Wu, G.J. 464
Wu, H.M. 1582
Wu, J. 2196
Wu, J.H. 1725
Wu, J.W. 374
Wu, M.M. 1840
Wu, P.T. 933
Wu, Q. 238, 970, 975
Wu, Q.Q. 1759, 1873
Wu, X.D. 1323
Wu, X.F. 651
Wu, X.M. 850, 854, 859
Wu, X.R. 1671
Wu, X.Z. 864
Wu, Y.C. 464
Wu, Y.L. 359
Wu, Y.M. 986
Wu, Y.T. 2075
Wu, Y.X. 1451, 1730
Wu, Z. 379
Wu, Z.M. 651
Wu, Z.P. 1234

X

Xia, Q. 763
Xia, X.F. 1120
Xia, Y.B. 613
Xia, Z.L. 95
Xiang, C.J. 1168
Xiang, D. 1676
Xiang, W.N. 868
Xiao, B. 1428
Xiao, C.F. 218, 226
Xiao, G.J. 1252
Xiao, H.N. 784, 1077
Xiao, Q. 359, 1120
Xiao, X.Q. 53
Xie, G.Z. 310, 419
Xie, H.T. 2103, 2165
Xie, J. 1730, 2135
Xie, K. 464
Xie, M. 459
Xie, Y.H. 304
Xin, W. 1857
Xing, J.W. 58
Xing, Y.S. 2230
Xiong, B.Q. 1224, 1247, 1754
Xiong, D.D. 359
Xiong, M.R. 1973
Xiong, Q.Y. 875
Xiong, T. 1229
Xiong, X. 2190
Xiong, X.W. 1707
Xiong, Y. 89
Xiong, Y.J. 1969, 2329
Xiong, Y.X. 2075
Xu, A.Y. 905
Xu, B. 1042
Xu, C.S. 58
Xu, G. 1229
Xu, H. 1031
Xu, H.J. 933, 1630
Xu, H.M. 868
Xu, J. 986
Xu, L. 364, 369, 1605
Xu, L.H. 447
Xu, M.T. 439
Xu, P. 2075
Xu, Q. 1609
Xu, Q.Y. 1630
Xu, R. 154, 332
Xu, S.C. 1973
Xu, W.Z. 58
Xu, X.Y. 170
Xu, Y.D. 2041
Xu, Y.H. 2171
Xuan, R.X. 255
Xue, J. 264, 1097
Xue, W.L. 2358

Xue, Z.L. 1229
Xue, Z.Q. 181

Y

Yan, B.J. 202
Yan, D.F. 1116
Yan, D.X. 1973
Yan, F. 390
Yan, G.F. 829
Yan, G.R. 1687
Yan, H.W. 2190
Yan, K.B. 1433, 2024
Yan, L. 145
Yan, L.P. 534
Yan, L.Z. 1224
Yan, R.X. 674
Yan, T. 1560
Yan, T.T. 1356
Yan, Z.M. 763
Yang, B. 1463
Yang, C. 881
Yang, C.L. 394
Yang, F. 67, 447
Yang, H. 2214, 2220
Yang, J. 127, 1973
Yang, J.B. 1485
Yang, J.J. 315
Yang, M. 1886, 1890
Yang, R.C. 359
Yang, R.J. 2230
Yang, R.M. 12
Yang, S.Y. 529
Yang, T.C. 1312
Yang, X. 1592, 1597
Yang, Y.H. 1252
Yang, Y.Z. 1999
Yang, Z. 2225
Yao, G. 1809
Yao, L.F. 374, 529
Yao, N.N. 364, 369
Yao, R.R. 364
Yao, S.D. 207
Yao, W. 419, 1378
Yao, Y. 1342
Yao, Z.T. 2243
Yaya, A. 822
Ye, P. 1862, 1868
Ye, S. 1868
Ye, Y. 784
Yi, C.H. 212
Yi, H. 1252
Yi, J.K. 2024
Yi, S. 23
Yin, H.C. 1576
Yin, J.F. 1356
Yin, J.R. 429
Yin, P.G. 207
Yin, R. 2267
Yin, X.M. 997
Yin, Y. 599
Yin, Y.B. 1754
Yin, Y.H. 1735
Ying, J. 140
Yoodee, K. 633
Yoshikawa, N. 2050
Younes, A. 1816
Yu, A. 1666
Yu, C. 1312
Yu, F. 603
Yu, J.L. 1775
Yu, J.M. 2352
Yu, L.C. 1382
Yu, L.Y. 2087
Yu, T. 327
Yu, W.L. 509
Yu, X.H. 829
Yu, X.L. 1031
Yu, Y. 955, 960, 2130
Yu, Y.P. 2230
Yu, Y.T. 2149
Yuan, G.Z. 628
Yuan, T. 776
Yuan, Y.T. 176
Yuan, Z.B. 1609
Yue, C. 2063
Yue, G.H. 332
Yun, J. 67
Yun, P. 2140

Z

Zang, J.X. 2358
Zeng, J.Y. 2267
Zeng, W.F. 429
Zeng, Y.Q. 1247
Zha, J.R. 975
Zhai, H.X. 2179
Zhan, Z.L. 1179

Zhang, A.J. 2171
Zhang, A.L. 1409, 1419
Zhang, B. 1189, 1195
Zhang, B.L. 942
Zhang, B.X. 2094
Zhang, C. 447
Zhang, D.C. 1886, 1890
Zhang, D.X. 1323
Zhang, D.Y. 2094
Zhang, E.J. 997
Zhang, E.P. 562
Zhang, G.D. 310
Zhang, G.M. 1262
Zhang, H. 515, 843
Zhang, H.D. 123
Zhang, H.F. 651
Zhang, H.H. 1141, 1791, 1830
Zhang, H.M. 255
Zhang, H.T. 942
Zhang, H.Y. 2103, 2165
Zhang, J. 562, 763, 1106
Zhang, J.C. 123
Zhang, J.H. 881, 1809
Zhang, J.J. 613
Zhang, J.L. 1694
Zhang, J.P. 322
Zhang, J.W. 1002
Zhang, J.Y. 154, 776
Zhang, L. 663, 955, 960, 1102
Zhang, L.C. 1409, 1414, 1419
Zhang, L.P. 1031
Zhang, L.S. 1428
Zhang, M. 459, 1937, 2184, 2389
Zhang, N. 674
Zhang, N.N. 2155
Zhang, P. 1366, 1373, 2377
Zhang, P.F. 2082
Zhang, P.H. 801
Zhang, P.X. 1780
Zhang, Q. 975, 1592, 1597, 1796, 1840
Zhang, Q.R. 795
Zhang, Q.W. 207, 2130
Zhang, Q.Y. 942
Zhang, R.L. 887
Zhang, S.Y. 1106
Zhang, W. 322, 2267
Zhang, W.D. 58
Zhang, W.J. 2201
Zhang, W.W. 955, 960, 1077
Zhang, W.X. 2302
Zhang, X. 89
Zhang, X.D. 1716
Zhang, X.F. 2254
Zhang, X.J. 170, 1173, 1267
Zhang, X.L. 814, 1571
Zhang, X.M. 1025
Zhang, X.N. 639
Zhang, X.Q. 829
Zhang, X.W. 1796
Zhang, X.Y. 618, 746, 1531
Zhang, X.Z. 1666
Zhang, Y. 379, 476, 1356
Zhang, Y.A. 1224, 1247, 1754
Zhang, Y.C. 1985
Zhang, Y.F. 1825
Zhang, Y.H. 2254
Zhang, Y.K. 1905
Zhang, Y.L. 496, 1647, 2377
Zhang, Y.M. 997
Zhang, Y.T. 304
Zhang, Y.Y. 1624
Zhang, Z.C. 1742
Zhao, D.J. 12
Zhao, D.L. 364, 369
Zhao, D.Y. 63, 390
Zhao, F.M. 965
Zhao, F.Q. 1378, 1399
Zhao, H. 552, 2230
Zhao, H.Y. 607
Zhao, J.H. 1404
Zhao, J.Y. 2125
Zhao, K. 1614
Zhao, L.Y. 2155
Zhao, M.M. 2035
Zhao, N. 950
Zhao, P. 1624, 1780
Zhao, Q. 276
Zhao, S.H. 905

Zhao, T.J. 1531
Zhao, W. 218
Zhao, W.L. 1641
Zhao, X. 571
Zhao, X.Q. 2383
Zhao, Y.F. 1948
Zhao, Y.G. 746
Zhao, Y.X. 1511
Zhao, Y.Y. 2054
Zhao, Z. 2179
Zhapbasbayev, U.K. 187
Zhen, Y.Z. 829
Zheng, L.H. 34, 929
Zheng, M. 1553
Zheng, W. 1025
Zheng, X. 1571
Zhi, X. 1112
Zhong, S. 669
Zhong, Y. 1031
Zhong, Y.W. 28
Zhou, D. 287, 809
Zhou, H.F. 763
Zhou, H.W. 2302
Zhou, J. 1707
Zhou, J.P. 2082
Zhou, L. 663, 1576
Zhou, L.C. 1948
Zhou, M.X. 1229
Zhou, W.Q. 1336
Zhou, Y. 310, 419, 1262, 2214
Zhou, Y.F. 540
Zhou, Y.H. 819
Zhou, Z. 1845
Zhou, Z.F. 1273
Zhu, B.Y. 1657, 1878
Zhu, F. 255
Zhu, F.D. 1657, 1878
Zhu, H. 1791
Zhu, J. 82
Zhu, J.S. 1927
Zhu, L. 1451
Zhu, L.X. 1747
Zhu, P.L. 887
Zhu, Q. 459
Zhu, R.X. 1082
Zhu, S.H. 1141
Zhu, W.H. 1571
Zhu, X.P. 1393
Zhu, Y.C. 486
Zhu, Y.L. 2190
Zhu, Z.J. 74
Zhuang, L. 1086
Zhuo, B. 2209
Zia, A. 1423
Zong, J. 2179
Zong, Y. 571
Zou, L.L. 789
Zou, N.Y. 1985
Zu, G.Q. 374
Zuo, D.Y. 212